European Community on Computational Methods in Applied Sciences

ECCOMAS Thematic Conference

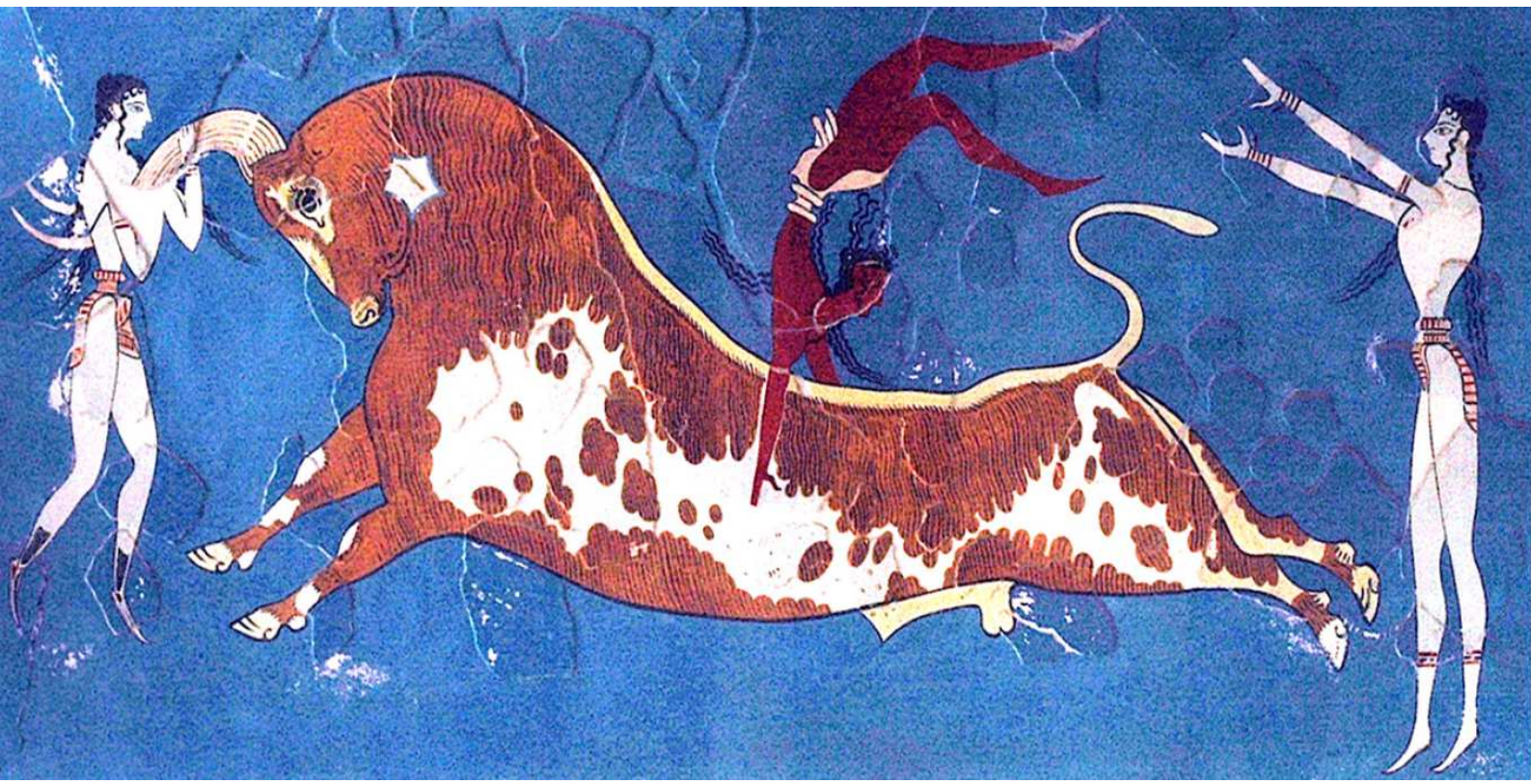
COMPDYN 2015

5th International Conference on
Computational Methods in Structural Dynamics and Earthquake Engineering

PROCEEDINGS

Volume II

M. Papadrakakis, V. Papadopoulos, V. Plevris (Eds)



An IACM Special Interest Conference

COMPDYN 2015

Computational Methods in Structural Dynamics and Earthquake Engineering

Proceedings of the 5th International Conference on Computational
Methods in Structural Dynamics and Earthquake Engineering
Held in Crete, Greece
25-27 May 2015

Edited by:

M. Papadrakakis
National Technical University of Athens, Greece

V. Papadopoulos
National Technical University of Athens, Greece

V. Plevris
School of Pedagogical and Technological Education, Athens, Greece

A publication of:

Institute of Structural Analysis and Antiseismic Research
School of Civil Engineering
National Technical University of Athens (NTUA)
Greece

COMPDYN 2015
Computational Methods in Structural Dynamics and Earthquake Engineering
M. Papadrakakis, V. Papadopoulos, V. Plevris (Eds)

First Edition, September 2015

© The authors

ISBN: **978-960-99994-7-2**

PREFACE

This volume contains the full-length papers presented in the 5th International Conference on Computational Methods in Structural Dynamics and Earthquake Engineering (COMPDYN 2015) that was held on May 25-27, 2015 on the Crete Island, Greece.

COMPDYN 2015, one of the thematic Conferences of the European Community on Computational Methods in Applied Sciences (ECCOMAS), is a Special Interest Conference of the International Association for Computational Mechanics (IACM) and has been promoted by the European Committee on Computational Solid and Structural Mechanics (ECCSM) of ECCOMAS. The purpose of the Conference is to bring together the scientific communities of Computational Mechanics, Structural Dynamics and Earthquake Engineering in an effort to facilitate the exchange of ideas in topics of mutual interests and to serve as a platform for establishing links between research groups with complementary activities. The communities of Structural Dynamics and Earthquake Engineering will benefit from this interaction, acquainting them with advanced computational methods and software tools which can highly assist in tackling complex problems in dynamic/seismic analysis and design, while also giving the Computational Mechanics community the opportunity to become more familiar with very important application areas of great social interest. The COMPDYN 2015 Conference is supported by the National Technical University of Athens (NTUA), the European Association for Structural Dynamics (EASD), the European Association for Earthquake Engineering (EAEE), the Greek Association for Computational Mechanics (GRACM) and the John Argyris Foundation.

The editors of this volume would like to thank all authors for their contributions. Special thanks go to the colleagues who contributed to the organization of the Minisymposia and to the reviewers who, with their work, contributed to the scientific quality of this e-book.

M. Papadrakakis
National Technical University of Athens, Greece

V. Papadopoulos
National Technical University of Athens, Greece

V. Plevris
School of Pedagogical and Technological Education, Athens, Greece

ACKNOWLEDGEMENTS

The conference organizers acknowledge the support towards the organization of the "5th International Conference on Computational Methods in Structural Dynamics and Earthquake Engineering", to the following organizations:

- European Community on Computational Methods in Applied Sciences (ECCOMAS)
- International Association for Computational Mechanics (IACM)
- School of Civil Engineering, National University of Athens (NTUA)
- Greek Association for Computational Mechanics (GRACM)
- European Association for Structural Dynamics (EASD)
- European Association for Earthquake Engineering (EAEE)
- John Argyris Foundation
- Hellenic Republic – Region of Crete

Plenary Speakers and Invited Session Organizers

We would also like to thank the Plenary and Semi-Plenary Speakers and the Minisymposia Organizers for their help in the setting up of a high standard Scientific Programme.

Plenary Speakers: Alain Combescure, C. Farhat, James Ricles, Shinobu Yoshimura

Semi-Plenary Speakers: Domniki Asimaki, Dimitri Beskos, Alexander Idesman, H. A. Jensen, Boris Jeremić, Andreas J. Kappos, Steen Krenk, Daniel Rixen, Y. B. Yang, Yong Yuan

MS Organizers: Pedro Costa Alves, António Arêde, Mitsuteru Asai, Panagiotis Asteris, Alessandro Baratta, Rui Barros, Elsa Caetano, Rui Calcada, Álvaro Cunha, Guido De Roeck, Raimundo Delgado, Pedro Delgado, Raimundo Delgado, Ioannis Dikaros, Dan Givoli, Jose Maria Goicolea, Muneo Hori, Mohammed Hussein, Alexander Idesman, Andreas Kappos, Spyros A. Karamanos, Radek Kolman, Dimitris Lignos, George Manos, Hermann Matthies, Mikayel Melkumyan, Jiri Naprstek, Roger Ohayon, Stavroula Pantazopoulou, Anthoula Panteli, Vissarion Papadopoulos, K-C. Park, Vagelis Plevris, Goran Sandberg, Evangelos Sapountzakis, Geza Seriani, Tasos Sextos, Sergey Sorokin, Aram Soroushian, Constantine Spyrakos, John Tsompanakis, Dimitris Vamvatsikos, Peter Van den Broeck, Katrien Van Nimmen, Ioannis Vayas, Castorina Vieira, Shinobu Yoshimura

SUMMARY

Preface..... iii

Acknowledgements..... iv

Contents..... viii

Volume I

Semi-plenary Lectures 1

Minisymposia

MS 1: Vibrations Induced By Rail And Road Traffic 26
Organized by Pedro Costa Alves and Mohammed Hussein

MS 2: Advances In Computational Structural Vibrations 146
Evangelos Sapountzakis and Ioannis Dikaros

MS 3: Progress And Challenges In Geotechnical Earthquake Engineering 218
Organized by Castorina Vieira and John Tsompanakis

MS 4: Innovative Systems For Seismic Resistant Steel Buildings 299
Organized by Ioannis Vayas

MS 5: Modern Methods In Creation Of Seismic Isolation Systems 349
Organized by Mikayel Melkumyan

MS 6: Numerical Simulation And Experimental Verification On Problems In The Field Of Earthquake Engineering And Structural Dynamics 388
Organized by George Manos

MS 7: Seismic Safety Assessment Of Structures 721
Organized by Raimundo Delgado, António Arêde and Pedro Delgado

MS 8: Periodicity-Induced Effects And Methods In Structural Dynamics 922
Organized by Sergey Sorokin

MS 9: Advances In Modeling Of Wave Propagation And Applications 946
Organized by Dan Givoli and Geza Seriani

MS 10: Control Of Vibrations In Civil Engineering By Passive, Active And Semi-Active Devices 972
Organized by Rui Barros and Alessandro Baratta

MS 11: Software Development In The Field Of Earthquake Engineering And Structural Dynamics 1011
Organized by Tasos Sextos

MS 12: Advances In Numerical Methods For Linear And Non-Linear Dynamics 1054
Organized by Alexander Idesman

MS 13: Renewable Energy Structures (Wind Turbines, Solar Irradiation, Hydropower) 1236
Organized by Álvaro Cunha and Elsa Caetano

MS 15: Reduced-Order Modeling Of Aero, Civil And Mechanical Dynamical Systems 1342
Organized by K-C. Park, Roger Ohayon, Hermann Matthies and Goran Sandberg

MS 16: Loss, Risk, Uncertainty And Modeling For Seismic Performance Assessment Of Structures 1379
Organized by Dimitris Vamvatsikos and Dimitris Lignos

MS 17: Dynamic Effects On Railway Bridges 1637
Organized by Rui Calcada, Raimundo Delgado and Jose Maria Goicolea

MS 18: Seismic Analysis Methods For Existing Bridges Prior To And After Retrofitting 1731
Organized by Andreas Kappos

MS 19: High-Performance Computing For Structural Mechanics And Earthquake / Tsunami Engineering 1824
Organized by Shinobu Yoshimura, Muneo Hori and Mitsuteru Asai

MS 20: New Technologies And Methods For Damage Control And Seismic Retrofit Of Heritage Structures In Earthquakes: Simulation, Devices And Digital Technologies 1838
Organized by Stavroula Pantazopoulou

MS 22: Accuracy And Computational Efficiency Of Structures Dynamic/Seismic Analyses 1899
Organized by Aram Soroushian and Anthoula Panteli

MS 23: Non-Linear Dynamics And Wave Propagation 1941
Organized by Jiri Naprstek, Radek Kolman and K-C. Park

MS 24: Seismic Behavior Of Industrial Facilities And Pipelines 2004
Organized by Spyros A. Karamanos and Vissarion Papadopoulos

MS 25: Modeling And Vulnerability Assessment Of Masonry Structures 2105
Organized by Vagelis Plevris and Panagiotis Asteris

MS 27: Condition Assessment And Intervention On Monuments And Historic Structures 2273
Organized by Constantine Spyrakos

MS 28: Human Induced Vibrations 2440
Organized by Guido De Roeck, Peter Van Den Broeck and Katrien Van Nimmen

Volume II

Regular Sessions

RS 1: Algorithms For Structural Health Monitoring 2536

RS 2: Constitutive Modelling Under Earthquake Loading 2611

RS 3: Dynamics Of Coupled Problems And Micro 2659

RS 4: Geotechnical Earthquake Engineering 2728

RS 5: Impact Dynamics 2865

RS 6: Inverse Problems In Structural Dynamics 2961

RS 7: Structural Dynamics 2995

RS 8: Numerical Simulation Methods For Dynamic Problems 3151

RS 9: Optimum Design In Structural Dynamics And Earthquake Engineering 3274

RS 10: Steel And Composite Structures 3610

RS 11: Performance-Based Earthquake Engineering 3675

RS 12: Repair And Retrofit Of Structures 3861

RS 13: Seismic Isolation 4011

RS 14: Seismic Risk And Reliability Analysis 4114

RS 15: Soft Computing Applications 4223

RS 16: Soil-Structure Interaction 4268

RS 17: Sound And Vibration 4364

RS 18: Concrete Structures 4528

RS 19: Wave Propagation And Soil Dynamics 4584

CONTENTS

Semi-plenary Lectures

THE USE OF MODEL REDUCTION TECHNIQUES IN COMPLEX SIMULATION-BASED PROBLEMS INVOLVING FINITE ELEMENT MODELS……1
H.A. Jensen, A. Muñoz, E. Millas

SEISMIC ANALYSIS OF LONG TUNNEL: SIMPLIFIED OR UNIFIED……16
Yong Yuan, Haitao Yu

Minisymposia

MS 1: VIBRATIONS INDUCED BY RAIL AND ROAD TRAFFIC

RAILWAY-INDUCED GROUND VIBRATIONS IN THE PRESENCE OF LOCAL TRACK IRREGULARITIES AND WHEEL FLATS……26
Georges Kouroussis, Georgios Alexandrou, David Connolly, Konstantinos Vogiatzis, Olivier Verlinden

IMPACT RESPONSES OF PRESTRESSING TENDONS IN RAILWAY CONCRETE SLEEPERS IN HIGH SPEED RAIL ENVIRONMENTS……38
Sakdirat Kaewunruen, Alex Remennikov

EXPERIMENTAL AND NUMERICAL EVALUATION OF THE EFFICIENCY OF A STIFF WAVE BARRIER IN THE SOIL……49
Pieter Coulier, Vicente Cúellar, Geert Degrande, Geert Lombaert

FAST COMPUTATION OF TRAIN-INDUCED VIBRATIONS IN HOMOGENEOUS AND LAYERED SOILS……66
Lutz Auersch

THE INFLUENCE OF DEGRADATION OF SHEAR MODULUS OF SOIL ON PREDICTED RAILWAY VIBRATIONS IN TUNNELS EXCAVATED WITH TBM: A NUMERICAL ANALYSIS……83
J. Fernández Ruiz, P. Alves Costa, P. Lopes, L. Medina Rodríguez

A MIXED SPACE-TIME AND WAVENUMBER DOMAIN MODEL FOR PREDICTING GROUND VIBRATION FROM RAILWAY TRACKS……96
Samuel Koroma, David Thompson, Mohammed Hussein, Evangelos Ntotsios

VIBRATIONS IN BUILDINGS DUE TO RAILWAY TRAFFIC IN TUNNELS: MODELLING STRATEGIES AND INFLUENCE OF SOIL STIFFNESS……108
P. Lopes, P. Alves Costa, R. Calçada, A. Cardoso

THE DYNAMIC INTERACTION OF TWIN TUNNELS EMBEDDED IN A HOMOGENEOUS HALF-SPACE……120
Waleed I. Hamad, Hugh E.M. Hunt, James P. Talbot, Mohammed F.M. Hussein, David J. Thompson

PREDICTIONS OF THE DYNAMIC RESPONSE OF PILED FOUNDATIONS IN A MULTI-LAYERED HALF-SPACE DUE TO INERTIAL AND RAILWAY INDUCED LOADINGS……133
Evangelos Ntotsios, Waleed Hamad, David Thompson, Mohammed Hussein, Hugh Hunt, James Talbot

MS 2: ADVANCES IN COMPUTATIONAL STRUCTURAL VIBRATIONS

MODELLING OF WARPING EIGENVIBRATION BY NON-UNIFORM TORSION……146
Justín Murín, Mehdi Aminbaghai, Juraj Hrabovský, Herbert Mang

GENERALIZED WARPING EFFECT IN THE DYNAMIC ANALYSIS OF BEAMS OF ARBITRARY CROSS SECTION……..165
Ioannis Dikaros, Evangelos Sapountzakis, Amalia Argyridi, Dimitrios Papadopoulos

MODAL AND FREQUENCY DOMAIN BASED TECHNIQUES FOR FINITE ELEMENT MODEL CORRELATION……..191
Judith Mercer, Guglielmo Aglietti, Andrew Kiley

ON THE FORCED VIBRATION TEST BY VIBRODYNE……209
Mariano Modano, Francesco Fabbrocino, Antonio Gesualdo, Giovanni Matrone, Ilenia Farina, Fernando Fraternali

MS 3: PROGRESS AND CHALLENGES IN GEOTECHNICAL EARTHQUAKE ENGINEERING

SOIL STRUCTURE INTERACTION ASSESSMENT WITH ADVANCED NUMERICAL SIMULATIONS……218
Davide Forcellini, Stefania Gobbi

UNDERSTANDING SHEAR WAVE VELOCITIES CORRELATIONS WITH N-SPT AND QC-CPT VALUES……230
Muhsin Elie Rahhal, Farah Harake

NUMERICAL SIMULATIONS OF LIQUEFACTION PHENOMENA AFTER EMILIA ROMAGNA (20 MAY 2012) EARTHQUAKE……242
Davide Forcellini, Laura Tonni, Cristina Osti, Guido Gottardi

SEISMIC EVALUATION OF EMBANKMENT-TYPE STRUCTURES WITH COUPLED HYDRO-MECHANICAL MODEL……251
Ioanna Rapti, Fernando Lopez-Caballero, Arezou Modaressi-Farahmand-Razavi, Alexandre Foucault, Francois Voldoire

SEISMIC RESPONSE ANALYSIS OF A GEOGRID REINFORCED WALL CONSTRUCTED WITH RECYCLED CONSTRUCTION AND DEMOLITION WASTE……262
Castorina Silva Vieira

SEISMIC GROUND RESPONSE AT LOTUNG (TAIWAN)……277
Dimitrios Karofyllakis, Gaetano Elia, Mohamed Rouainia

THREE DIMENSIONAL ANALYSIS OF A CFRD DAM USING THE MATERIAL POINT METHOD……287
F. Zabala, R. D. Rodari, L. O. Oldecop

MS 4: INNOVATIVE SYSTEMS FOR SEISMIC RESISTANT STEEL BUILDINGS

COLLAPSE RISK EVALUATION OF SELF-CENTERING STEEL MRFS WITH VISCOUS DAMPERS IN NEAR-FAULT REGIONS……299
George Kamaris, Angelos Tzimas, Theodore Karavasilis, Carmine Galasso

BEHAVIOR OF HIGH STRENGTH STEEL FUSEIS SEISMIC RESISTANT SYSTEMS……318
Stella Avgerinou, Ioannis Vayas

PERFORMANCE OF MULTI-STOREY COMPOSITE STEEL-CONCRETE FRAMES WITH DISSIPATIVE FUSE DEVICES……334
Alper Kanyilmaz, Carlo Andrea Castiglioni

MS 5: MODERN METHODS IN CREATION OF SEISMIC ISOLATION SYSTEMS

ON THE USE OF MECHANICAL METAMATERIALS FOR INNOVATIVE SEISMIC ISOLATIONS SYSTEMS……349
F. Fraternali, G. Carpentieri, R. Montuori, A. Amendola, G. Benzoni

METHODS OF CREATION OF BASE ISOLATION SYSTEMS FOR RETROFITTING OF EXISTING REINFORCED CONCRETE FRAME BUILDINGS……359
Mikayel Melkumyan

INNOVATIVE TECHNIQUE FOR THE BASE ISOLATION OF EXISTING BUILDINGS……377
Alessandro De Stefano, Paolo Clemente, Stefano Invernizzi, Emiliano Matta, Antonino Quattrone

MS 6: NUMERICAL SIMULATION AND EXPERIMENTAL VERIFICATION ON PROBLEMS IN THE FIELD OF EARTHQUAKE ENGINEERING AND STRUCTURAL

A NOVEL MECHANISM FOR RESTRAINING SEISMIC ACTIONS IN DUCTILE BRIDGES: ANALYTICAL MODELING AND EXPERIMENTAL VERIFICATION……388
Vasileios Pilitsis, Vassilis K. Papanikolaou, Ioannis Tegos, Kosmas-Athanasios Stylianidis

EXPERIMENTAL AND ANALYTICAL INVESTIGATION OF AN UNCONVENTIONAL, ROCKING TYPE RESPONSE MECHANISM FOR EARTHQUAKE-RESISTANT BRIDGES……402
Vasileios Pilitsis, Ioannis Tegos, Vassilis K. Papanikolaou, Kosmas-Athanasios Stylianidis

IN-SITU MEASURED DYNAMIC RESPONSE OF THE BELL TOWER OF AGIOS GERASIMOS IN LIXOURI-KEFALONIA, GREECE AND ITS UTILIZATION IN THE NUMERICAL PREDICTIONS OF ITS EARTHQUAKE RESPONSE……417
G.C. Manos, E. Kozikopoulos

THE DYNAMIC AND EARTHQUAKE RESPONSE OF A TWO STORY OLD R/C BUILDING WITH MASONRY INFILLS IN LIXOURI-KEFALONIA, GREECE INCLUDING SOIL-FOUNDATION DEFORMABILITY……435
George Manos, Dionisios Naxakis, Vasilios Soulis

THE DYNAMIC AND EARTHQUAKE RESPONSE OF BASILICA CHURCHES IN KEFALONIA, GREECE INCLUDING SOIL FOUNDATION DEFORMABILITY AND WALL DETACHMENT……460
George Manos, Evaggelos Kozikopoulos

NUMERICAL SIMULATION OF THE LIMIT NON-LINEAR BEHAVIOUR OF UNREINFORCED STONE MASONRY UNDER IN-PLANE STATE OF STRESS FROM GRAVITATIONAL AND SEISMIC ACTIONS……487
G.C. Manos, L. Kotoulas, V. Soulis, O. Felekidou

EXPERIMENTAL INVESTIGATION AND NUMERICAL SIMULATION OF SHEAR BEHAVIOUR OF RC T-BEAM SPECIMENS WITH OR WITHOUT SFRP-STRIPS UNDER CYCLIC LOADING……505
George Manos, Konstantinos Katakalos, Marios Theofanous

CYCLIC RESPONSE OF A STEEL BEAM-TO-COLUMN CONNECTIONS – AN EXPERIMENTAL AND NUMERICAL STUDY……519
G.C. Manos, A. Nalmpantidou, V. Kourtides, A. Anastasiadis,

THE DYNAMIC RESPONSE OF A MOCK-UP OF THE RESTORED ANCIENT NORTH WALL SCHEME FOR THE MACEDONIAN PALACE AT VERGINA - GREECE……537
George Manos, Konstantinos Katakalos, Lambros Kotoula, Olympia Felekidou

STUDY OF THE LOADING ARRANGEMENT FOR THE STIFFNESS TESTS OF THE COLUMN HEAD ASSEMBLY AND ITS SPRINGS UTILIZED AT THE NIARCHOS CULTURAL CENTER AT ATHENS - GREECE……551
G.C. Manos, V. Kourtides, K. Katakalos, L. Kotoulas, A. Nalmpantidou

ANALYTICAL AND EXPERIMENTAL STUDY ON THE RESPONSE OF A SEISMIC RESTRAINER SYSTEM FOR BRIDGES……568
Olga Markogiannaki, Ioannis Tegos

ANALYTICAL AND EXPERIMENTAL INVESTIGATION ON EXPLOITING PREFABRICATION IN PIER CONSTRUCTION OF PRECAST BRIDGES……583
Nikolaos G. Orologopoulos, Vasileios G. Pilitsis, Konstantinos Katirtzoglou, Ioannis A. Tegos, Kosmas-Athanasios Stylianidis

MODELING AND IDENTIFICATION OF THE DYNAMIC RESPONSE OF AN EXISTING THREE-STORY STEEL STAIRWAY……595
Triantafyllos Makarios, George Manolis, Ioanna Karetsou, Michael Papanicolaou, Vasiliki Terzi

INVESTIGATION OF NOVEL ANCHORING DEVICES FOR OPEN HOOP CFRP STRIPS BONDED ON R/C ELEMENTS UNDER MONOTONIC AND CYCLIC LOADING-UNLOADING CONDITIONS……607
Konstantinos B. Katakalos, George C. Manos

SEISMIC FRAGILITY ASSESSMENT OF MEDICAL COMPONENTS……628
Luigi Di Sarno, Fabio Gustuti, Gennaro Magliulo, Crescenzo Petrone

MULTIPLE SUPPORT EXCITATION OF A BRIDGE BASED ON BEM ANALYSIS OF THE SUBSOIL-STRUCTURE-INTERACTION PHENOMENON……639
Ioanna-Kleoniki Fontara, Magdalini Titirla, Frank Wuttke, Asimina Athanatopoulou, George Manolis, Anastasios Sextos

SLENDER PROFILES FOR MOMENT RESISTING FRAMES IN MODERATE SEISMICITY REGIONS - NUMERICAL AND EXPERIMENTAL INVESTIGATIONS……653
Matthias Wieschollek, Benno Hoffmeister And Markus Feldmann

CONCRETE-TO-CONCRETE INTERFACES UNDER CYCLIC LOADING: FINITE ELEMENT ANALYSIS TOWARDS EXPERIMENTAL VERIFICATION……666
Vassilis Papanikolaou, Georgia Thermou

DEFORMATION CAPACITY OF NON-CONFORMING RC SHEAR WALLS: ANALYTICAL AND NUMERICAL ESTIMATION - TEST VERIFICATION……680
Konstantinos Christidis, Vasiliki Anagnostopoulou, Konstantinos Trezos, Christos Zeris

SEISMIC ANALYSIS OF PRESTRESSED STADIUM ROOF……696
P. Rosko, A. Bekö

THE USE OF ELASTIC OSCILLATIONS OF DIFFERENT WAVELENGTHS TO EVALUATE THE DYNAMIC PARAMETERS OF BUILDINGS AND STRUCTURES AND ASSESS THE STRENGTH OF MATERIALS OF THE BUILDING CONSTRUCTION……706
Sergey Savin, Valerios Tsakalidis

MS 7: SEISMIC SAFETY ASSESSMENT OF STRUCTURES

SEISMIC PERFORMANCE OF HIGH-RISE STEEL MRFS WITH OUTRIGGER AND BELT TRUSSES THROUGH NONLINEAR DYNAMIC FE SIMULATIONS……721
Emanuele Brunesi, Roberto Nascimbene, Gian Andrea Rassati, Lorenzo Casagrande

EFFECT OF OPENINGS ON NONLINEAR DYNAMIC RESPONSES OF MASONRY INFILLED RC FRAMES……736
Y. P. Yuen, J. S. Kuang

A DESIGN PROCEDURE FOR SEISMIC RETROFITTING OF REINFORCED CONCRETE FRAME AND CONCENTRIC BRACED STEEL BUILDINGS WITH DISSIPATIVE BRACINGS……746
Alessandro Vittorio Bergami, Camillo Nuti

ROCKING BEHAVIOUR OF SIMPLE UNREINFORCED LOAD-BEARING MASONRY WALLS INCLUDING SOUNDPROOFING RUBBER LAYERS……759
C. Mordant, V. Denoël, H. Degée

NUMERICAL MODELLING, ANALYSIS AND RETROFIT OF THE HISTORICAL MASONRY BUILDING “LA SAPIENZA”……772
Silvia Caprili, Federico Mangini, Walter Salvatore

INFLUENCE OF MODELLING PARAMETERS ON THE FRAGILITY ASSESSMENT OF PRE-1970 ITALIAN RC STRUCTURES……788
Gerard O'Reilly, Timothy Sullivan

DEVELOPMENT OF A SIMPLIFIED DISPLACEMENT-BASED PROCEDURE FOR THE SEISMIC ASSESSMENT OF RC WALL BUILDINGS……810
Timothy Sullivan, Matthew Fox

STRENGTH AND STABILITY ASSESSMENT OF EXISTING BUILDINGS IN ISRAEL……825
Nicolae Gluck, Rina Farhat, Rami Eid, Uri Tzadka

PROBABILISTIC EVALUATION OF DAM BASE SLIDING……836
Gabriele Fiorentino, Luca Furgani, Simone Magliano, Camillo Nuti

NUMERICAL SEISMIC SAFETY ASSESSMENT OF RC BRIDGES WITH HOLLOW PIERS ……845
Pedro Delgado, António Arêde, Nelson Vila Pouca, Aníbal Costa

EFFICIENCY OF DIFFERENT RETROFITTING TECHNICHS FOR RC COLUMNS UNDER BIAXIAL LOADING: EXPERIMENTAL STUDY……865
H. Rodrigues, A. Furtado, P. Rocha, A. Arêde

A MODEL FOR CARBON AND STAINLESS STEEL REINFORCING BARS INCLUDING INELASTIC BUCKLING FOR EVALUATION OF CAPACITY OF EXISTING STRUCTURES……876
Zhihao Zhou, Davide Lavorato, Camillo Nuti, Giuseppe Carlo Marano

USING DIFFERENT UNCERTAINTY MODELS FOR SEISMIC ASSESSMENT OF RC BRIDGES……887
Ricardo Monteiro, Raimundo Delgado, Rui Pinho

PERFORMANCE BASED EARTHQUAKE ENGINEERING APPROACH APPLIED TO BRIDGES IN A ROAD NETWORK……900
C. Zelaschi, G. De Angelis, F. Giardi, D. Forcellini, R. Monteiro

DEMAND HAZARD ANALYSIS: A TOOL FOR ASSESSING THE ADEQUACY OF CAPACITY DESIGN APPROACH FOR DEFINITION OF THE DESIGN SHEAR FORCES IN THE FRAME BUILDINGS……911
Jure Žižmond, Matjaž Dolšek

MS 8: PERIODICITY-INDUCED EFFECTS AND METHODS IN STRUCTURAL DYNAMICS

USING PERIODICITY TO MITIGATE GROUND VIBRATION……922
Lars Vabbersgaard Andersen

TWO-DIMENSIONAL LINEAR MODEL OF ELASTIC SHELL MADE OF ANISOTROPIC HETEROGENEOUS MATERIAL……933
Petr Tovstik, Tatiana P. Tovstik, Daniil Al'chibaev

MS 9: ADVANCES IN MODELING OF WAVE PROPAGATION AND APPLICATIONS

MULTI-SCALE/MULTI-DATA INVERSION FOR ELASTIC EARTH STRUCTURE - A CONCEPT……946
Andreas Fichtner, Michael Afanasiev, Korbinian Sager, Laura Ermert

A FICTITIOUS DOMAIN APPROACH FOR WAVE PROPAGATION PROBLEMS IN UNBOUNDED DOMAINS……959
Silvia Falletta, Giovanni Monegato

MS 10: CONTROL OF VIBRATIONS IN CIVIL ENGINEERING BY PASSIVE, ACTIVE AND SEMI-ACTIVE DEVICES

EFFECTIVENESS OF TUNED MASS DAMPER IN DAMAGE REDUCTION OF BUILDING UNDER FAR-FIELD GROUND MOTIONS……..…….…….972
Chayut Ngamkhanong, Tospol Pinkaew

NEURO-FUZZY MODELING OF A SPONGE-TYPE MR DAMPER……..……..984
Manuel T. Braz-César, Rui C. Barros

SEISMIC RESPONSE REDUCTION OF BUILDING STRUCTURES USING A SEMI-ACTIVE CONTROL SYSTEM BASED ON A BRAIN EMOTIONAL LEARNING CONTROLLER……..……998
Manuel T. Braz-César, Rui C. Barros

MS 11: SOFTWARE DEVELOPMENT IN THE FIELD OF EARTHQUAKE ENGINEERING AND STRUCTURAL DYNAMICS

AN INTEGRATED FRAMEWORK FOR THE ANALYSIS OF MIXED-TYPE REINFORCED CONCRETE STRUCTURES……..…..1011
Vahid Sadeghian, Oh-Sung Kwon, Frank Vecchio

NUMERICAL SEISMIC ASSESSMENT OF AN EXISTING BRIDGE WITH DIFFERENT SUPPORT CONFIGURATIONS……..……1024
Ciro Del Vecchio, Maria C. Caruso, Luigi Di Sarno, Oh-Sung Kwon, Andrea Prota

OBJECTIVE EVALUATION OF THE Q FACTOR OF IRREGULAR RC BUILDINGS DESIGNED ACCORDING TO EC8 – DESIGN AND ANALYSES PROCEDURES……..1040
Vasiliki Anagnostopoulou, Stratis Volakos, Christos Zeris

MS 12: ADVANCES IN NUMERICAL METHODS FOR LINEAR AND NON-LINEAR DYNAMICS

CRACKING AND FRACTURE OF HSS BRACES UNDER CYCLIC LOADING……..1054
Madhar Haddad, Robert Tremblay, Liang Chen, Lucea Tirca

CALCULATING THE FREQUENCY OF AN ACTUAL STRUCTURE USING THE RAYLEIGH TECHNIQUE……..……1070
Alexandre De M. Wahrhaftig, Reyolando M. L. R. F. Brasil

EFFICIENT NONLINEAR DYNAMIC ANALYSIS OF FRAME STRUCTURES……..1080
Johannes Burtscher

A NEW 3D CO-ROTATIONAL BEAM ELEMENT FOR NONLINEAR DYNAMIC ANALYSIS……..1087
Thanh-Nam Le, Jean-Marc Battini, Mohammed Hjiaj

ENERGY METHOD FOR COUPLING NEWMARK AND ALPHA-SCHEMES TIME INTEGRATORS WITH DIFFERENT TIME STEPS……..1111
Michael Brun, Anthony Gravouil, Alain Combescure

MULTIGRID SOLVER WITH DOMAIN DECOMPOSITION SMOOTHING FOR STEADY-STATE INCOMPRESSIBLE FSI PROBLEMS……..1128
Eugenio Aulisa, Simone Bná, Giorgio Bornia

OPTIMAL DESIGN FOR HIGH RESISTANT ROCKFALL BARRIERS……1145
Juan Escallon, Perry Bartelt, Eleni Chatzi

SMOOTH AND NON-SMOOTH SOLUTIONS FOR GEOMETRICALLY EXACT BEAMS SUBJECTED TO IMPACT……1169
Tien Long Nguyen, Mohammed Hjiaj, Carlo Sansour

A VARIATIONAL FORMULATION OF DISCONTINUOUS-GALERKIN TIME INTEGRATORS……1178
Pablo Mata Almonacid, Yongxing Shen, Vahid Ziaei-Rad

SVD FAMILY FOR ANALYZING CAR CRASH BEHAVIOR……1188
Thi-Thanh-Thuy Vuong, Louis Jezequel, Yves Tourbier

COMPARISON OF INTEGRATION ALGORITHMS FOR REAL-TIME HYBRID SIMULATION USING FREQUENCY DOMAIN-BASED ERROR INDICATORS……1208
Reza Mirza Hessabi, Ali Ashasi-Sorkhabi, Yanhui Liu, Oya Mercan

DE3: YET ANOTHER HIGH-ORDER INTEGRATION SCHEME FOR LINEAR STRUCTURAL DYNAMICS……1216
Alexandre Depouhon, Emmanuel Detournay, Vincent Denoël

A MESHLESS NEURAL NETWORK APPROACH FOR THE DYNAMIC ANALYSIS OF ELASTIC SYSTEMS……1224
Luca Facchini, Michele Betti

MS 13: RENEWABLE ENERGY STRUCTURES (WIND TURBINES, SOLAR IRRADIATION, HYDROPOWER)

GENETIC OPTIMIZATION OF TOWER VIBRATIONS WITH PENDULUM TMD UNDER THE INFLUENCE OF SEVERAL WIND SPECTRUMS……1236
Gino B. Colherinhas, Maura A. M. Shzu, Suzana M. Avila, Marcus V. G. De Morais

SLENDER LARGE-SCALE PARABOLIC TROUGHS USING SHAPE-OPTIMIZED HOLLOW STRUCTURES MADE OF HIGH-STRENGTH CONCRETE……1249
Christoph Kämper, Janna Krummenacker, Patrick Forman, Peter Mark, Jürgen Schnell

PROPABILISTIC FATIGUE ANALYSIS OF OFFSHORE WIND TURBINES……1257
Dimitrios V. Bilionis, Dimitrios Vamvatsikos

ONE YEAR OF CONTINUOUS DYNAMIC MONITORING OF A WIND TURBINE. STRUCTURAL INTEGRITY AND FATIGUE ASSESSMENT……1274
Gustavo Oliveira, Filipe Magalhães, Álvaro Cunha, Elsa Caetano

A CLOSED-FORM APPROACH TO PREDICT GUST INDUCED FATIGUE DAMAGES……1288
Frank H. Kemper

MULTIVARIATE STOCHASTIC METHODS FOR THE STRUCTURAL DESIGN OF WIND TURBINES……1306
Frank H. Kemper, Juan Jose Calle Escribano

SEMI-ACTIVE PENDULUM TO CONTROL OFFSHORE WIND TURBINE VIBRATIONS……1317
Suzana Moreira Avila, Pedro Varella Barca Guimarães

ANALYSIS OF COUPLED SYSTEMS CONSISTING OF SUPPORT STRUCTURE AND HIGH VOLTAGE SUBSTATION EQUIPMENT WITH VERIFICATION VIA FULL-SCALE SHAKING TABLE TESTS……1330
Shakhzod M. Takhirov, Amir S.J. Gilani, Frank Blalock, Cary Ahrano

MS 15: REDUCED-ORDER MODELING OF AERO, CIVIL AND MECHANICAL DYNAMICAL SYSTEMS

STOCHASTIC REDUCED-ORDER MODELS FOR CALCULATING RESPONSE STATISTICS OF STRUCTURAL SYSTEMS SUBJECTED TO RANDOM INPUT……1342
Alin Radu, Mircea Grigoriu

SEMI-ANALYTICAL REDUCED-ORDER MODELS FOR THE UNSTEADY AERODYNAMIC LOADS OF SUBSONIC WINGS……1353
Marco Berci

MS 16: LOSS, RISK, UNCERTAINTY AND MODELING FOR SEISMIC PERFORMANCE ASSESSMENT OF STRUCTURES

VERTICAL ACCELERATION DEMANDS ON NONSTRUCTURAL COMPONENTS IN BUILDINGS……1379
Lukas Moschen, Ricardo A. Medina, Christoph Adam

INFLUENCE OF ROTATED GROUND MOTION COMPONENTS ON THE RESPONSE DISTRIBUTION OF INELASTIC OSCILLATORS……1400
Dimitrios Giannopoulos, Dimitrios Vamvatsikos

A NEXT GENERATION SCALAR INTENSITY MEASURE FOR ANALYTICAL VULNERABILITY STUDIES……1410
Athanasia Kazantzi, Dimitrios Vamvatsikos

NEAR -SOURCE PULSE-LIKE SEISMIC DEMAND FOR MULTI-LINEAR BACKBONE OSCILLATORS……1421
Georgios Baltzopoulos, Dimitrios Vamvatsikos, Iunio Iervolino

SEISMIC RELIABILITY ASSESSMENT OF ROCKING BEHAVIOUR UNDER NEAR-FAULT EXCITATIONS……1435
Elias Dimitrakopoulos, Themelina Paraskeva

POST-EARTHQUAKE RECOVERY OF A COMMUNITY AND ITS ELECTRICAL POWER SUPPLY SYSTEM……1451
Max Didier, Li Sun, Siddhartha Ghosh, Bozidar Stojadinovic

ESTIMATION OF CUMULATIVE SEISMIC DAMAGE TO URM BUILDINGS DURING EARTHQUAKE SEQUENCES……1462
Amaryllis Mouyiannou, Maria Rota, Andrea Penna

RELATIONSHIP BETWEEN THE VARIATION OF SEISMIC CAPACITY AFTER DAMAGING EARTHQUAKES, COLLAPSE PROBABILITY AND REPAIR COSTS: DETAILED EVALUATION FOR A NON-DUCTILE BUILDING……1478
M. Gaetani D'Aragona, M. Polese, A. Prota

EARTHQUAKE LOSS ASSESSMENT OF STEEL FRAME BUILDINGS DESIGNED IN HIGHLY SEISMIC REGIONS……1496
Seong-Hoon Hwang, Ahmed Elkady, Samy Al.Bardaweel, Dimitrios G. Lignos

CATASTROPHE RESILIENCE RELATED TO URBAN NETWORK SHAPE: PRELIMINARY ANALYSIS……1513
Anna Bozza, Domenico Asprone, Alessandro Fiasconaro, Vito Latora, Gaetano Manfredi

APPLICATION OF A DAMAGE STATE METHOD BASED ON PERIOD ELONGATION FOR TIME VARIANT VULNERABILITY OF DEGRADING REINFORCED CONCRETE BUILDINGS……1532
Konstantinos Trevlopoulos, Philippe Guéguen

RECORD-TO-RECORD VARIABILITY IN THE SEISMIC RESPONSE OF RC WALLS BUILDINGS SUBJECTED TO GROUND MOTIONS MATCHED TO THE CONDITIONAL SPECTRUM……1548
Matthew Fox, Timothy Sullivan

INFLUENCE OF JOINT RESPONSE IN THE ASSESSMENT OF SEISMIC PERFORMANCE OF EXISTING REINFORCED CONCRETE FRAMES……1560
Maria Teresa De Risi, Paolo Ricci, Gerardo Mario Verderame

ASSESSMENT OF MULTISTORY RC BUILDINGS SUFFERING INTER-STORY POUNDING……1580
Maria Favvata, Sofia Mochla, Maria Naoum, Chris Karayannis

SEISMIC RETROFIT DECISION-MAKING OF BRIDGES BASED ON LIFE-CYCLE COST CRITERIA……1591
Hossein Ebrahimian, Fatemeh Jalayer, Gaetano Manfredi

RISK-BASED DESIGN CHECK FOR COLLAPSE SAFETY USING FEW GROUND MOTIONS……1628
Marko Brozovič, Matjaž Dolšek

MS 17: DYNAMIC EFFECTS ON RAILWAY BRIDGES

DYNAMIC ANALYSIS OF TRAIN-BRIDGE SYSTEM SUBJECTED TO EARTHQUAKE ACTION CONSIDERING TOPOGRAPHIC EFFECTS……1637
Hong Qiao, He Xia, Xianting Du, Yong Nan

DRIVE-BY STRUCTURAL HEALTH MONITORING OF RAILWAY BRIDGES USING TRAIN-MOUNTED ACCELEROMETERS……1652
Cathal Bowe, Paraic Quirke, Daniel Cantero, Eugene J. Obrien

TEMPERATURE WARPING AND TRAIN-TRACK DYNAMIC ANALYSIS OF CRTS II SLAB BALLASTLESS TRACK……1664
Jingjing Yang, Nan Zhang

PARAMETRIC EVALUATION OF VISCOUS DAMPER RETROFIT FOR HIGH-SPEED RAILWAY BRIDGES……..1672
Sarah Rådeström, Viktor Tell, Mahir Ülker-Kaustell, Raid Karoumi

TRANSVERSAL VIBRATION CONTROL FOR CATENARY POLES ON A HIGH SPEED RAILWAY BRIDGE……..1682
Celine Anicotte, Dominique Botton

SEISMIC RESPONSE OF CABLE-STAYED BRIDGE STEEL TOWER PROVIDED WITH BRACING SYSTEM……..1700
Mohamed Omar

MODAL PROPERTIES OF SIMPLY SUPPORTED RAILWAY BRIDGES DUE TO SOIL-STRUCTURE INTERACTION……..1709
Christoffer Svedholm, Costin Pacoste, Raid Karoumi

SAFETY ASSESSMENT OF A SMALL SPAN HIGH-SPEED RAILWAY BRIDGE USING AN EFFICIENT PROBABILISTIC METHODOLOGY……..1720
João M. Rocha, António A. Henriques, Rui Calçada

MS 18: SEISMIC ANALYSIS METHODS FOR EXISTING BRIDGES PRIOR TO AND AFTER RETROFITTING

OPTIMAL DESIGN AND DYNAMICS OF TRUSS BRIDGES……..1731
G. Carpentieri, M. Modano, F. Fabbrocino, F. Fraternali

SEISMIC RESPONSE ANALYSIS OF A COUPLED VEHICLE- BRIDGE SYSTEM……..1741
Qing Zeng, Elias Dimitrakopoulos, Themelina Paraskeva

A STRUCTURAL HEALTH MONITORING DATA MANAGING SCHEME WITH RESILIENCY TO SEISMIC EVENTS: IMPLEMENTATION ON A ROAD NETWORK BRIDGE……..1757
George Sergiadis, Stelios Hadjidimitriou, Vasileios Charisis, Panagiotis Panetsos, Theodoros Chrysanidis

EVALUATION OF THE STIFFNESS AND DAMPING OF ABUTMENTS TO EXTEND DIRECT DISPLACEMENT-BASED DESIGN TO THE DESIGN OF INTEGRAL BRIDGES……..1767
Stergios Mitoulis, Sotiris Argyroudis, Mervyn Kowalsky

METHODOLOGY FOR THE DEVELOPMENT OF STRUCTURE SPECIFIC FRAGILITY CURVES FOR BRIDGES IN A ROADWAY NETWORK……..1780
Sotiria Stefanidou, Andreas Kappos

SEISMIC RETROFITTING OF R/C BRIDGES WITH THE USE OF UNBONDED TENDONS……..1799
Olga Markogiannaki, Ioannis Tegos

EXPERIMENTAL AND NUMERICAL ANALYSIS ON THE CYCLIC BEHAVIOR OF BRIDGE PIERS WITH AND WITHOUT CFRP RETROFIT……..1812
Pedro Delgado, Frutuoso Sousa, Patrício Rocha, António Arêde, Nelson Vila Pouca, Aníbal Costa, Raimundo Delgado

MS 19: HIGH-PERFORMANCE COMPUTING FOR STRUCTURAL MECHANICS AND EARTHQUAKE / TSUNAMI ENGINEERING

META-MODELING FOR CONSISTENT SEISMIC RESPONSE ANALYSIS……1824
Muneo Hori, Seizo Tanaka, Tsuyoshi Ichimura, W.L.L.Wijerathne, J.A.S.C. Jayasinghe

MS 20: NEW TECHNOLOGIES AND METHODS FOR DAMAGE CONTROL AND SEISMIC RETROFIT OF HERITAGE STRUCTURES IN EARTHQUAKES: SIMULATION, DEVICES AND DIGITAL TECHNOLOGIES

PARAMETRIC NUMERICAL STUDY OF THE SEISMIC RESPONSE OF CLASSICAL COLUMNS……1838
Ioannis Kavvadias, Lazaros Vasiliadis

ASSESSMENT OF SEISMIC VULNERABILITY OF HISTORICAL DEFENSIVE WALLS……1850
Graziano Leoni, Alessandro Zona, Quintilio Piattoni, Alessandra Meschini, Enrica Petrucci, Andrea Dall'Asta, Luigino Dezi

VULNERABILITY OF TORSIONALLY SENSITIVE HISTORICAL BUILDINGS UNDER SEISMIC LOADS……1865
Stylianos Pardalopoulos, Stavroula Pantazopoulou

ASSESSMENT OF STONE MASONRY WALLS WITH DETERIORATION AT THEIR BASE USING NON-LINEAR FINITE ELEMENT ANALYSES……1885
Georgios Papadopoulos, Dimos Charmpis, Rogiros Illampas

MS 22: ACCURACY AND COMPUTATIONAL EFFICIENCY OF STRUCTURES DYNAMIC/SEISMIC ANALYSES

FROM THE NOTIONS OF NONLINEARITY TOLERANCES TOWARDS A DEFICIENCY IN COMMERCIAL TRANSIENT ANALYSIS SOFTWARES AND ITS SOLUTION……1899
Aram Soroushian, Peter Wriggers, Jamshid Farjoodi

ON THE CONVENTIONAL FINITE ELEMENT SIZES IN PSEUDOSTATIC SEISMIC ANALYSES OF 2D FRAMES……1908
Amir Hossein Pariz, Bahram Kordbagh, Kiyanoush Ghazvini, Seyed Mohsen Borghei Razavi, Abbas Ali Jalalabadi

ON THE PERFORMANCE OF A TECHNIQUE TO ACCELERATE TIME INTEGRATION WHEN APPLIED TO SPACE STRUCTURES ANALYSES……1914
Alireza Garakaninezhad, Reza Kamyab Moghadas

USING ENERGY - BASED PUSHOVER METHODS IN SEISMIC EVALUATION OF STEEL BRACING STRUCTURES…..1921
Kaveh Nezamisavojbolaghi

MS 23: NON-LINEAR DYNAMICS AND WAVE PROPAGATION

ANALYSIS OF INFLUENCE OF SHORT MAGNETORHEOLOGICAL DAMPING ELEMENTS ON VIBRATIONS ATTENUATION OF RIGID ROTORS……1941
Jaroslav Zapomel, Petr Ferfecki

DESTRUCTION OF THIN FILMS WITH A DAMAGED SUBSTRATE AS A RESULT OF WAVES LOCALIZATION CAUSED BY PERIODIC IMPACT……1949
Andrei Abramian, Sergey Vakulenko

PRESTRESS TUNING OF THE NONLINEAR DYNAMICS OF TENSEGRITY METAMATERIALS……1960
F. Fraternali, A. Amendola, E. Hernández-Nava, R. Goodall, R.E. Skelton, V.F. Nesterenko

COMPARISON OF NUMERICAL AND SEMI-ANALYTICAL SOLUTION OF A SIMPLE NON-LINEAR SYSTEM IN STATE OF THE STOCHASTIC RESONANCE……1971
Jiří Náprstek, Cyril Fischer, Radomil Král, Stanislav Pospíšil

TIME DOMAIN SIMULATION OF VORTEX-INDUCED VIBRATION OF A CURVED BEAM USING A WAKE OSCILLATOR MODEL……1983
Yang Qu, Andrei Metrikine

PROBLEM OF NON-STATIONARY WAVES IN VISCOELASTIC ORTHOTROPIC STRIP SOLVED USING ANALYTICAL METHOD……1995
Vítězslav Adámek, František Valeš, Jan Červ

MS 24: SEISMIC BEHAVIOR OF INDUSTRIAL FACILITIES AND PIPELINES

PROBABILISTIC ASSESSMENT OF PIPELINE - FAULT CROSSING……2004
Vasileios Melissianos, Dimitrios Vamvatsikos, Charis Gantes

SEISMIC PERFORMANCE OF INDUSTRIAL PRESSURE VESSELS: PARAMETRIC INVESTIGATIONS OF SIMPLIFIED MODELING APPROACHES FOR VULNERABILITY ASSESSMENT……2021
Christos Z. Karakostas, Ioannis F. Moschonas, Vassilios A. Lekidis, Savvas P. Papadopoulos

SEISMIC PERFORMANCE ASSESSMENT OF OIL & GAS PIPING SYSTEMS THROUGH NONLINEAR ANALYSIS……2038
Oreste S. Bursi, Fabrizio Paolacci, Md Shahin Reza

SEISMIC FRAGILITY ANALYSIS OF STEEL STORAGE TANKS……2054
Fabrizio Paolacci, Hoang N. Phan, Daniele Corritore, Silvia Alessandri, Oreste S.Bursi, M. Shahin Reza

SURROGATE MODELLING OF LIQUID STORAGE TANKS FOR SEISMIC PERFORMANCE DESIGN AND ASSESSMENT……2066
Konstantinos Bakalis, Michalis Fragiadakis, Dimitrios Vamvatsikos

BURIED PIPELINES SUBJECTED TO GROUND DEFORMATION CAUSED BY LANDSLIDE TRIGGERING……2081
Angelos Tsatsis, Rallis Kourkoulis, George Gazetas

PERFORMANCE EVALUATION OF BURIED STEEL PIPES SUBJECT TO STRIKE SLIP FAULT OFFSETS……2093
E. Uckan, B. Akbas, F. Cakir, J. Shen, M. O'Rourke, M. Caglar, F. Paolacci

MS 25: MODELING AND VULNERABILITY ASSESSMENT OF MASONRY STRUCTURES

SHEAR STRENGTH AND DEFORMATION MECHANISMS OF COMBINED AND CONFINED MASONRY WALLS SUBJECTED TO CYCLIC LOADING……..2105
Arturo Tena-Colunga, Artemio Juárez-Ángeles, Víctor Hugo Salinas-Vallejo

ASSESSMENT OF THE LATERAL STIFFNESS OF WALLS WITH OPENINGS……..2123
Arturo Tena-Colunga, Germán Rivera-Hernández

DEM & FEM/DEM MODELS FOR LATERALLY LOADED MASONRY WALLS……..2144
Daniele Baraldi, Emanuele Reccia, Antonella Cecchi

3D FE PUSHOVER AND NON-LINEAR DYNAMIC ANALYSES OF A MASONRY CHIMNEY BEFORE AND AFTER SHORTENING……..2158
Elisa Bertolesi, Antonio Del Grosso, Gabriele Milani, Fabio Minghini, Antonio Tralli

SEISMIC PERFORMANCE OF HOLLOW BRICK INTERNAL PARTITIONS……..2167
Crescenzo Petrone, Gennaro Magliulo, Marco Russo, Gaetano Manfredi

DEFINITION OF MECHANICAL PROPERTIES OF EXISTING MASONRY ACCOUNTING FOR EXPERIMENTAL NOWLEDGE BY BAYESIAN UPDATING……..2177
Stefano Bracchi, Maria Rota, Andrea Penna, Guido Magenes

EVALUATION OF SEISMIC VULNERABILITY ASSESSMENT PARAMETERS FOR PORTUGUESE VERNACULAR CONSTRUCTIONS WITH NONLINEAR NUMERICAL ANALYSIS……..2191
Javier Ortega, Graça Vasconcelos, Mariana Correia, Hugo Rodrigues, Paulo B. Lourenço, Humberto Varum

MODELLING OF DIAGONAL COMPRESSION MASONRY WALLETS BY FINITE ELEMENTS WITH EMBEDDED DISCONTINUITIES……..2206
Gelacio Juárez-Luna, Arturo Tena-Colunga

ON THE SEISMIC RISK OF MEDIEVAL ITALIAN MASONRY TOWERS……..2216
Gianni Bartoli, Michele Betti, Silvia Monchetti

SEISMIC VULNERABILITY OF THE PIERO DELLA FRANCESCA'S FRESCO CALLED "RESURRECTION"……..2236
Giulio Castori, Antonio Borri, Romina Sisti, Alessandro De Maria, Marco Corradi

SENSITIVITY ANALYSIS OF THE SEISMIC RESPONSE OF BRITTLE STRUCTURAL ELEMENTS UNDER NEAR-FIELD SEISMIC INPUT EFFECTS……..2248
Paloma Pineda, Jorge D Navarro-Rubio, Miguel Ángel Gil-Martí

ANISOTROPIC FAILURE CRITERION FOR BRITLE MATERIALS USING ARTIFICIAL NEURAL NETWORKS……..2259
Vagelis Plevris, Panagiotis Asteris

MS 27: CONDITION ASSESSMENT AND INTERVENTION ON MONUMENTS AND HISTORIC STRUCTURES

EVALUATION OF THE SEISMIC VULNERABILITY OF THE "ANCIEN HÔPITAL DE SION" USING APPLIED ELEMENT MODELLING (AEM) AND LOCAL MECHANISM ANALYSIS.....2273
Angelo Garofano, Pierino Lestuzzi

NONLINEAR ANALYSIS AND SEISMIC STRENGTHENING OF MASONRY ARCHES: THE BLOCK-JOINT AND BLOCK-BLOCK FEM MODELS.....2287
Francesco Pugi, Alessio Francioso

SEISMIC PROTECTION OF HEAVY NON-STRUCTURAL MONOLITHIC OBJECTS AT THE TOP OF A HISTORICAL MASONRY CONSTRUCTION THROUGH BASE ISOLATION.....2300
Andrea Chiozzi, Michele Simoni, Antonio Tralli

THE COMBINATION OF NDTS FOR THE DIAGNOSTIC STUDY OF HISTORICAL BUILDINGS: THE CASE OF KAISARIANI MONASTERY.....2321
Antonia Moropoulou, Maria Apostolopoulou, Petros Moundoulas, Maria Karoglou, Ekaterini Delegou, Kyriakos Lampropoulos, Margarita Gritsopoulou, Asterios Bakolas

EXPERIMENTAL AND NUMERICAL INVESTIGATIONS FOR THE STRUCTURAL CHARACTERIZATION OF A HISTORIC RC ARCH BRIDGE.....2337
R. Ferrari, D. Froio, E. Chatzi, C. Gentile, F. Pioldi, E. Rizzi

EVALUATION OF THE DYNAMIC RESPONSE FOR A HISTORIC BYZANTINE CROSSED-DOME CHURCH THROUGH BLOCK-JOINT AND KINEMATIC ANALYSIS.....2354
Constantine C. Spyrakos, Francesco Pugi, Charilaos A. Maniatakis, Alessio Francioso

NUMERICAL INVESTIGATION OF THE SEISMIC RESPONSE OF HEPHAESTUS TEMPLE IN ATHENS, GREECE.....2366
Maria-Eleni Dasiou, Ioannis Psycharis

LASER SCANNING, MODELING, AND ANALYSIS FOR DAMAGE ASSESSMENT AND RESTORATION OF HISTORICAL STRUCTURES.....2375
Shakhzod Takhirov, Khalid M. Mosalam, Mohamed A. Moustafa, Liliya Myagkova, Brian Quigley

STRUCTURAL HEALTH MONITORING AND DIAGNOSTIC INVESTIGATIONS OF THE SCROVEGNI CHAPEL, ITALY.....2396
Claudio Modena, Filippo Lorenzoni, Mauro Caldon, Maria Rosa Valluzzi

STRUCTURAL MONITORING OF MONUMENTAL BUILDINGS: THE BASILICA OF SANTA MARIA DEGLI ANGELI IN ASSISI (ITALY).....2410
Nicola Cavalagli, Massimiliano Gioffrè, Vittorio Gusella

SEISMIC RISK OF HISTORIC STRUCTURES AND MONUMENTS: A NEED FOR A UNIFIED POLICY.....2423
Constantine C. Spyrakos

MS 28: HUMAN INDUCED VIBRATIONS

THE IMPACT OF VERTICAL HUMAN-STRUCTURE INTERACTION FOR FOOTBRIDGES.....2440
Katrien Van Nimmen, Kristof Maes, Geert Lombaert, Guido De Roeck, Peter Van Den Broeck

INFLUENCE OF HUMAN INDUCED FLOOR VIBRATIONS ON THE MEASUREMENT PRECISION OF FORCE PLATES IN A BIOMECHANICS LABORATORY.....2457
Horst Werkle, Wolfgang Francke, Andrei Firus

EQUIVALENT SPECTRAL MODEL FOR PEDESTRIAN-INDUCED FORCES ON FOOTBRIDGES: A GENERALIZED FORMULATION.....2469
Alberto Ferrarotti, Federica Tubino

EXPERIMENTAL INVESTIGATINO ON COHERENCY FACTOR OF RHYTHMIC JUNMPING AND ITS APPLICATION FOR SIMULATION OF CROWD JUMPING LOAD.....2484
Ziye Pan, Yonglei Zhao, Jun Chen

DYNAMIC ANALYSES OF A CURVED CABLE-STAYED FOOTBRIDGE UNDER HUMAN INDUCED VIBRATIONS: NUMERICAL MODELS AND EXPERIMENTAL TESTS.....2495
Elisa Bassoli, Paola Gambarelli, Laura Simonini, Loris Vincenzi

ROBUST VIBRATION SERVICEABILITY DESIGN OF A TUNED MASS DAMPER FOR THE PHÉNIX FOOTBRIDGE.....2512
Klaus Lievens, Peter Van Den Broeck, Guido De Roeck, Geert Lombaert

WALKING-INDUCED VIBRATION OF A FOOTBRIDGE.....2525
Eleonora Lai, Maria Gabriella Mulas

Regular Sessions

RS 1 : ALGORITHMS FOR STRUCTURAL HEALTH MONITORING

APPLICATION OF LASER MEASUREMENT TO THE DRIVE-BY INSPECTION OF BRIDGES.....2536
Abdollah Malekjafarian, Eugene J Obrien

UNCERTAINTY OF BRIDGE VIBRATION PROPERTIES AND ITS CONSEQUENCE FOR DAMAGE IDENTIFICATION.....2545
Marian Ralbovsky, Maciej Kwapisz, Alois Vorwagner

VIBRATION MEASUREMENT-BASED SIMPLE TECHNIQUE FOR STRUCTURAL APPRAISAL OF STEEL BRIDGES.....2558
W.A.Indika Priya Wijesooriya, Sudath C. Siriwardane, P.B. Ranjith Dissanayake

STRUCTURAL HEALTH MONITORING USING TIME-DELAY EMBEDDING AND PHASE-SPACE WARPING.....2568
Mohammad H. Alhamaydeh, Kenneth Wong, Ralston Fernandes, Jeongcheol Seok, Eihab M. Abdel-Rahman, Sami El-Borgi

SYSTEM IDENTIFICATION AND DAMAGE DETECTION OF R.C. STRUCTURE.....2576
Prodip K. Paul, Anjan Dutta, Sajal K. Deb

EXPERIMENTAL VERIFICATION OF DAMAGE LOCATION TECHNIQUES FOR FRAME STRUCTURES ASSEMBLED USING BOLTED CONNECTIONS.....2588
Bartlomiej Blachowski, Andrzej Swiercz, Nikos Pnevmatikos

ANALYSIS OF THE VIBRATION LEVELS OF A SLENDER FOOTBRIDGE MEASURED BY A CONTINUOUS DYNAMIC MONITORING SYSTEM.....2600
Carlos Moutinho, Filipe Magalhães, Elsa Caetano

RS 2 : CONSTITUTIVE MODELLING UNDER EARTHQUAKE LOADING

A MULTISCALE APPROACH FOR MODELING OF INFILLED FRAMES.....2611
Andrea Fiore, Francesco Porco

MACRO-MODEL CALIBRATION OF A STRONG CLAY MASONRY INFILL TO IN-PLANE CYCLIC TESTS.....2623
Milad Oliaee, Paolo Morandi, Guido Magenes

SHEAR HYSTERESIS MODEL FOR REINFORCED CONCRETE ELEMENTS INCLUDING THE POST-PEAK RANGE.....2640
Dimitrios K. Zimos, Panagiotis E. Mergos, Andreas J. Kappos

RS 3 : DYNAMICS OF COUPLED PROBLEMS AND MICRO-MACRO SYSTEMS

DYNAMIC ANALYSIS OF GRADIENT ELASTIC BEAMS BY FINITE ELEMENTS.....2659
Ioannis Pegios, Ioannis Dinopoulos, Sofia Papargyri-Beskou

VIBRATIONS OF SPORTS STADIUM GRANDSTAND STRUCTURE DUE TO CROWD-JUMPING LOADS.....2674
Tadeusz Tatara, Bartosz Ptasznik

NATURAL FREQUENCY OF TRAFFIC FLOW-BRIDGE SYSTEM BASED ON CELLULAR AUTOMATON TECHNIQUE.....2690
Mao Ye, Shifan Huang, Baoxing Cao, Min Ren

INFLUENCE OF FLOATER RESPONSE ON WIND TURBINE TOWER MOMENTS IN FLOATING WIND TURBINE SYSTEM.....2700
Muhammad Bilal Waris, Takeshi Ishihara

A NEW APPROACH ON THE CALCULATION OF DYNAMIC LOAD FACTORS OF HUMAN INDUNCED LOAD.....2711
Lu Dai, Na Yang

COMPUTATIONAL MODELING OF MULTI-SCALE FEATURES IN CEMENTITIOUS MATERIALS.....2722
Ram Mohan, Arunachalam Rajendran, Wayne Hodo

RS 4 : GEOTECHNICAL EARTHQUAKE ENGINEERING

SOFT COMPUTING APPLICATION IN SOIL CLASSIFICATION ANALYSIS.....2728
Saman Yaghmaei-Sabegh

NONLINEAR ANALYSIS ON SEISMIC RESPONSE OF A MULTI-GEOMORPHIC COMPOSITE SITE.....2735
Chen Guoxing, Jin Dandan, Gao Hongmei, Zhu Jiao

FINITE ELEMENT ANALYSIS OF AN EARTH DAM SUBJECTED TO BLAST-INDUCED LOADING USING A HIGH STRAIN-RATE BOUNDING SURFACE MODEL.....2743
Tianhua Xu, Limin Zhang

3D FAILURE ENVELOPE OF A SINGLE PILE IN SAND.....2752
Zheng Li, Panagiotis Kotronis, Sandra Escoffier

SOME EXPERIMETNAL EVIDENCES ON DYNAMIC SOIL-STRUCTURE INTERACTION.....2761
Maria Rossella Massimino, Giovanni Biondi

COUPLING BETWEEN STRATIGRAPHIC AND TOPOGRAPHIC EFFECTS ON SLOPES.....2775
S. Rizzitano, E. Cascone, G. Biondi

CLASS A PREDICTION FOR SEISMIC CENTRIFUGE MODELING OF MULTI-BLOCK QUAY-WALL: UNDRAINED (PLAXIS) VERSUS COUPLED (FLAC) EFFECTIVE STRESS ANALYSIS.....2787
Panagiota Tasiopoulou, Nikos Gerolymos, George Gazetas

STATIC AND DYNAMIC ANALYSES OF DAHR EL BAIDAR SLOPE.....2802
T. Matar, F. Hage Chehade, J. Harb, M. Rahhal, D. Youssef Abdel Massih, C. Abdallah, E. Ibrahim, L. Khalaf-Keyrouz, G. Nasr, G. Abou-Jaoude, A. Sursock

A SEISMIC PERFORMANCE-BASED DESIGN APPROACH FOR SLOPE STABILIZING PILES.....2815
Marianna Adinolfi, Raffaele Di Laora, Rosa Maria Stefania Maiorano, Stefano Aversa

THREE-DIMENSIONAL NUMERICAL MODELLING OF CIRCULAR TUNNELS UNDER SEISMIC ACTIONS.....2828
E. Bilotta, R.M.S. Maiorano, A. Viglione, S. Aversa

NONLINEAR DYNAMIC RESPONSE OF HARDENING, SOFTENING AND ELASTOPLASTIC SDOF SYSTEMS USING GENERALIZED SINGLE STEP ALGORITHMS WITH NEWTON-RAPHSON ITERATIONS.....2838
George Papazafeiropoulos, Vagelis Plevris, Manolis Papadrakakis

RS 5 : IMPACT DYNAMICS

CREATION OF A NEW EQUATION OF MOTION TO CALCULATE DISSIPATED ENERGY BETWEEN TWO ADJACENT BUILDINGS.....2865
Hosein Naderpour, Seyed Mohammad Khatami, Rui Carneiro Barros

PRELIMINARY INVESTIGATIONS OF THE LOW-VELOCITY IMPACT RESPONSE OF A SMART TRIMORPH PLATE FOR ACTIVE DAMAGE MITIGATION.....2876
Akuro Big-Alabo, Philip Harrison, Matthew Cartmell

POUNDING BETWEEN BRIDGE DECKS: COMPUTATIONAL DETAILS AND RESULTS……2890
Bharat Mandal, Vincenzo Bianco, Giorgio Monti

NUMERICAL INVESTIGATION OF THE BEHAVIOUR OF RC WIDE BEAMS UNDER IMPACT LOADS……2904
Ali Abbas, Demetris Cotsovos

STRUCTURE RESPONSE UNDER BLAST WAVE LOAD……2915
D. Makovička, D. Makovička, Jr.

PERFORMANCE OF STEEL COLUMNS SUBJECTED TO VEHICLE IMPACT – EXPERIMENTAL AND NUMERICAL STUDIES……2926
J. Korndörfer, B. Hoffmeister, M. Feldmann

VALIDATION OF A NUMERICAL AND ANALYTICAL MODEL OF IMPACTED COLUMNS BY MEANS OF SMALL-SCALE DROP WEIGHT EXPERIMENTS……2937
Carles Colomer Segura, Nils Horbach, Markus Feldmann

VIBRATION ANALYSIS OF HIGH-SPEED RAIL SYSTEM USING THE MOVING ELEMENT METHOD……2951
Reda Mezeh, Marwan Sadek, Fadi Hage Chehade, Dalia Abdelmassih, Nisrinemakhoul, Ahmad Younes

RS 6 : INVERSE PROBLEMS IN STRUCTURAL DYNAMICS

TIME REVERSAL IN ELASTODYNAMICS AND APPLICATIONS TO STRUCTURAL HEALTH MONITORING……2961
Christos Panagiotopoulos, Yiannis Petromichelakis, Chrysoula Tsogka

MODEL-BASED JOINT INPUT-STATE ESTIMATION ON A THIN-WALLED CANTILEVER BEAM……2971
Øyvind W. Petersen, Ole Øiseth, Torodd S. Nord

SENSITIVITY ANALYSIS OF DISCRETE-FORCE IDENTIFICATION ALGORITHMS TO MEASUREMENT NOISE……2983
A. Rezayat, V. Nassiri, K. Maes, G. Lombaert, S. Vanlanduit, P. Guillaume

RS 7 : STRUCTURAL DYNAMICS

ELASTIC INVERTED PENDULUM UNDER HYSTERETIC NONLINEARITY IN SUSPENSION: STABILIZATION AND OPTIMAL CONTROL……2995
Mikhail E. Semenov, Andrey M. Solovyov, Andrey M. Semenov, Vladimir A. Gorlov, Peter A. Meleshenko

SEISMIC ENERGY RESPONSE OF TEN-STORY STEEL ROCKING FRAMES WITH COLUMN MID-HEIGHT UPLIFT AT FIRST STORY……3004
Mitsumasa Midorikawa, Naoto Kotani, Taichiro Okazaki, Tetsuhiro Asari, Tadashi Ishihara, Tatsuya Azuhata

NONLINEARITY DETECTION AND IDENTIFICATION USING DISCRETE-TIME VOLTERRA SERIES: APPLICATION TO A SOLAR ARRAY STRUCTURE……3014
Cristian Hansen, Samuel Da Silva, Emmanuel Foltête, Scott Cogan

FREQUENCY DETUNING EFFECTS FOR PARAMETRICALLY AND DIRECTLY EXCITED ELASTIC STRUCTURES……..3029
Stefan Neumeyer, Matthijs H. M. Van Gastel, Vladislav S. Sorokin, Jon Juel Thomsen

A FAST SEMI-ANALYTICAL METHOD FOR COMPUTING THE RESPONSE OF RAILWAY TRACKS ON NONLINEAR FOUNDATIONS……3036
T. Hoang, D. Duhamel, G. Foret, H. Yin, G. Cumunel, P. Joyez, R. Caby

VALIDITY DOMAIN OF AN ENERGETIC METHOD FOR THE ESTIMATION OF MODAL DAMPING IN THE CASE OF NON LINEAR LOCALIZED DISSIPATION……3048
M. Krifa, N. Bouhaddi, G. Chevallier, And S. Cogan

NONLINEAR DYNAMICS OF A 2D ARRAY OF COUPLED PENDULUMS UNDER PARAMETRIC EXCITATION……3057
Aymen Jallouli, Najib Kacem, Noureddine Bouhaddi

FINITE ELEMENT SIMULATION OF A STEEL BRACED FRAME STRUCTURE DAMAGED BY THE 2011 TOHOKU EARTHQUAKE……3065
Taichiro Okazaki, Yuriko Kato, Naoto Kotani, Mitsumasa Midorikawa, Tetsuhiro Asari

NUMERICAL INVESTIGATION OF THE SEISMIC RESPONSE OF PRECAST BUILDINGS WITH INTEGRATED RC CLADDING WALLS……3072
Ioannis Kalyviotis, Ioannis Psycharis

EVALUATION OF THE APPLICABILITY OF THE LUGRE MODEL FOR MODELLING THE DYNAMIC BEHAVIOUR OF BOLT CONNECTED FRAMES……3084
Sergio Sánchez Gómez, Mihai I.Badila, Andrei Metrikine

NONLINEAR DYNAMICS OF PARAMETRICALLY EXCITED CARBON NANOTUBES FOR MASS SENSING APPLICATIONS……3096
S. Souayeh, N. Kacem, F. Naja, E. Foltête

A COMPUTATIONAL MODEL FOR LARGE-AMPLITUDE NONLINEAR VIBRATION OF CIRCULAR CMUTS UNDER PRIMARY RESONANCE……3107
Aymen Jallouli, Najib Kacem, Patrice Lemoal, Gilles Bourbon, Joseph Lardies

SEISMIC ASSESSMENT OF THE FULL SCALE FOUR STOREY E-DEFENSE ROCKING SHEAR WALL SHAKE TABLE TEST……3117
Giorgio T. Proestos, Hossein Aghabeigi, Paolo M. Calvi

OUT-OF-PLANE BEHAVIOUR OF SINGLE-BODY UNREINFORCED-MASONRY WALL RESTRAINED BY A FLEXIBLE DIAPHRAGM……3127
Sanjeev Prajapati, Omar Alshawa, Luigi Sorrentino

INVESTIGATION OF DYNAMIC RESPONSE OF ROCKING WALL STRUCTURES USING INELASTIC MODAL DECOMPOSITION TECHNIQUE……3139
Irshad M. Qureshi, Pennung Warnitchai, Tahir Mehmood

RS 8 : NUMERICAL SIMULATION METHODS FOR DYNAMIC PROBLEMS

EVALUATION OF THE DYNAMIC AMPLIFICATION FACTOR FOR RAILWAY BRIDGES SUBJECTED TO A SERIES OF MOVING MASS……3151
Mehrdad Bisadi, Quincy Tsun Ming Ma, Sherif Beskhyroun

A MODE SELECTION ALGORITHM FOR THE FLEXIBILITY-BASED COMPONENT MODE SYNTHESIS……3162
Jin-Gyun Kim, Phill-Seung Lee, Kwang-Chun Park

BEHAVIOUR OF REINFORCED CONCRETE KNEE BEAM-COLUMN JOINT IN CASE OF GROUND CORNER COLUMN LOSS-NUMERICAL ANALYSIS……3172
B. Abdelwahed, B. Belkassem, L. Pyl, J. Vantomme

3-D DYNAMIC ANALYSIS OF BRIDGES WITH ROCKING ISOLATION UNDER EXTREME EARTHQUAKES……3184
Tzu-Ying Lee, Kun-Jun Chung, Hung-Yuan Lee

STRUCTURAL INTEGRITY ANALYSIS AND OPTIMIZATION OF AN ELEVATOR FRAME, THROUGH FE MODELING AND EXPERIMENTAL TESTS……3194
Dimitrios Giagopoulos, Iraklis Chatziparasidis, Nikolas Sapidis

SEISMIC ANALYSIS OF COUPLED BUILDINGS WITH MR DAMPER……3205
Fangshu Lin, Xilin Lu

NUMERICAL ASSESSMENT ON THE SEISMIC RESPONSE OF A BASE-ISOLATED BUILDING UNDER BI-DIRECTIONAL MOTION……3216
Marco Furinghetti, Alberto Pavese

DYNAMIC SENSITIVITY OF MULTI-BLOCK STACKS SUBJECTED TO BASE PULSE EXCITATION – EXPERIMENTAL EVIDENCE AND NON SMOOTH CONTACT DYNAMIC SIMULATIONS……3234
Nina Čeh, Antonio Pellegrino, Jean-Francois Camenen, Nik Petrinić, Gordan Jelenić, Tomasz Koziara, Nenad Bićanić

ADAPTIVE CONTROL OF THE ROCKING MOTION OF ART OBJECTS……3248
Rosario Ceravolo, Marica Leonarda Pecorelli, Luca Zanotti Fragonara

REDUCED ORDER MODEL OF CIRCULAR FLANGE-BOLTED CONNECTION AND ITS APPLICATION TO DYNAMIC SUBSTRUCTURING OF TELECOMMUNICATION TOWERS……3262
Bartlomiej D. Blachowski, Witold Gutkowski, Piotr Wisniewski

RS 9 : OPTIMUM DESIGN IN STRUCTURAL DYNAMICS AND EARTHQUAKE ENGINEERING

COMPARATIVE STUDY OF THE WIND AND EARTHQUAKE DYNAMIC RESPONSES OF FIRE EXPOSED STEEL FRAMED BUILDINGS……3274
Fabio Mazza, Marco Fiore

ESTIMATING OF OVERSTRENGTH FACTOR OF CONCENTRICALLY X-BRACED STEEL FRAMES……3288
T. Branci, D. Yahmi

SENSOR PLACEMENT OPTIMIZATION USING ENSEMBLE KALMAN FILTER AND GENETIC ALGORITHM……..3296
Dana Nasr, George Saad

TOPOLOGY OPTIMIZATION OF TWO-DIMENSIONAL WAVE BARRIERS FOR THE REDUCTION OF GROUND VIBRATION TRANSMISSION……..3309
Cédric Van Hoorickx, Ole Sigmund, Mattias Schevenels, Boyan S. Lazarov, Geert Lombaert

MULTI-OBJECTIVE OPTIMIZATION UNDER UNCERTAINTY WITH REAL-TIME INTEGRATED DECISION MAKING APPLIED TO STRUCTURAL ENGINEERING……..3320
Mariapia Marchi, Mauro Munerato, Luca Rizzian, Stefano Costanzo

A CODE COMPATIBLE APPROACH TO JUSTIFY THE SEISMIC DESIGN OF SIMPLIFIED STRUCTURES……..3344
H.F. Karadogan, Y. Durgun, I.E. Bal, S. Z. Yuce, E. Yuksel, C. Soydan

DESIGN OF "DOG-BONE" CONNECTION: THE ROLE OF VERTICAL LOADS……..3368
Rosario Montuori

NON-LINEAR ANALYSES OF SEISMIC RESISTANT CONCRETE FRAME FOR THE VALIDATION OF A FAILURE MODE CONTROL METHODOLOGY……..3388
Roberta Muscati

FEASIBILITY STUDY ON OFFSHORE SOLAR UPDRAFT TOWER POWER PLANT……..3412
Hayami Sato, Yasuo Suzuki, Kunitomo Sugiura

IMPLEMENTATION OF ROBUST CONTROL THEORY IN SMART STRUCTURE DESIGN USING FREQUENCY DOMAIN DATA……..3419
A. J. Moutsopoulou, A. D. Pouliezos, G. E. Stavroulakis

AN ENHANCED COMPONENT BASED MODEL FOR STEEL LINKS IN HYBRID STRUCTURES: DEVELOPMENT, CALIBRATION AND EXPERIMENTAL VALIDATION……..3435
M. Manfredi, F. Morelli, W. Salvatore

ROBUST CONTROL OF SMART STRUCTURES WITH OPTIMALLY PLACED ACTUATORS AND SENSORS……..3451
Amalia Moutsopoulou, Georgia Foutsitzi, Christos Gogos, Georgios Stavroulakis

OPTIMAL DESIGN OF STRUCTURAL INTERFACES BY A POWER FLOW MODE APPROACH……..3461
Thomas Weisser, Noureddine Bouhaddi

CONTROL METHOD FOR ADJACENT BUILDINGS CONSIDERING SOIL-STRUCTURE INTERACTION……..3472
Luis Pérez, Suzana Avila, Graciela Doz

HOW TO ACHIEVE REGULAR SEISMIC BEHAVIOR OF IRREGULAR BRIDGES WITH UNEQUAL HEIGHT PIERS?……..3485
Mena Ishak, Sameh Mehanny

OPTIMIZATION OF QUATROPOD JACKET SUPPORT STRUCTURES FOR OFFSHORE WIND TURBINES SUBJECT TO SEISMIC LOADS USING GENETIC ALGORITHMS……..3505
Mohammad Alhamaydeh, Samer Barakat, Omar Nassif

EVALUATION OF SEISMIC RESPONSE OF BUILDINGS USING DYNAMIC ANALYSIS ON STICK MODELS……..3514
Marco Bovo, Marco Savoia

A PROCEDURE FOR THE DETAILING DESIGN OF SIMPLY SUPPORTED R.C. BRIDGE DECKS SUBJECTED TO IN-PLANE ACTIONS……3530
Fabrizio Palmisano, Angelo Elia

MULTI-OBJECTIVE STRUCTURAL OPTIMIZATION UNDER STRESS CRITERIA BASED ON MIXED PLATE FEM AND GENETIC ALGORITHMS……..3545
Pierre Garambois, Sebastien Besset, Louis Jézéquel

THE STUDY OF X-BRACING ON LIMIT STATE BEHAVIOR OF BUCKLING RESTRAINED BRACE (BRB) IN STEEL FRAMES USING PUSHOVER ANALYSIS……3559
Peyman Shadman Heidari, Ali Golara, Pouya Shadman Heidari, Roohollah Ahmady Jazany

OPTIMIZED RETROFIT OF SEISMICALLY DESIGNED STRUCTURES TO WITHSTAND PROGRESSIVE COLLAPSE……3568
Georgios S. Papavasileiou, Dimos C. Charmpis

ASSESMENT OF OPTIMUM STRENGTHENING DESIGN OF A REINFORCED CONCRETE BUILDING WITH VULNERABILITY CRITERIA……..3580
Evangelia Skoulikari, Vissarion Papadopoulos, Nikos Lagaros

ENERGY BASED OPTIMUM DESIGN OF TUNED MASS DAMPERS……3593
Giuseppe Carlo Marano

A PRELIMINARY ASSESSMENT OF SLENDERNESS AND OVERSTRENGTH HOMOGENEITY CRITERIA USED IN THE DESIGN OF CONCENTRICALLY BRACED STEEL FRAMES IN MODERATE SEISMICITY……3599
Alper Kanyilmaz, C.A Castiglioni, Hervè Degèe, Pierre-Olivier Martin

RS 10 : STEEL AND COMPOSITE STRUCTURES

SIMPLE FORMULAE FOR DAMAGE ESTIMATION OF COMPOSITE STEEL/CONCRETE MOMENT RESISTING FRAMES……3610
George Kamaris, Konstantinos Skalomenos, George Hatzigeorgiou, Dimitri Beskos

RENEWABLE ENERGY TENSEGRITY STRUCTURES……3621
F. Fraternali, E. De Chiara, A. Fortunato, E. Sicignano, R. E. Skelton

SEISMIC PERFORMANCE OF INNOVATIVE STEEL AND CONCRETE HYBRID COUPLED SHEAR WALLS……..3629
Luca Tassotti, Alessandro Zona, Graziano Leoni, Andrea Dall'Asta

DAMAGE DETECTION AND MONITORING OF COMPOSITE STRUCTURES WITH THE USE OF PIEZOELECTRIC SENSORS……..3638
Piotr Kêdziora, Adam Stawiarski, Marek Barski

INFLUENCE OF CONNECTIONS MODELING ON THE SEISMIC BEHAVIOUR OF INDUSTRIAL BUILDINGS……..3652
Luca Tassotti, Mohammed Radi, Fabrizio Gara, Laura Ragni

INELASTIC CYCLIC NUMERICAL ANALYSIS OF STEEL STRUTS USING DISTRIBUTED PLASTICITY APPROACH……3663
Alper Kanyilmaz

RS 11 : PERFORMANCE-BASED EARTHQUAKE ENGINEERING

SIMPLIFIED SEISMIC COLLAPSE ASSESSMENT OF GENERIC FRAME STRUCTURES SUBJECTED TO PDELTA AND MATERIAL DETERIORATION……3675
David Kampenhuber, Christoph Adam

DISTRIBUTED AND CONCENTRATED INELASTICITY BEAM-COLUMN ELEMENTS: APPLICATION TO REINFORCED CONCRETE FRAMES AND VERIFICATION……3694
Armin Gharakhanloo, Amir M. Kaynia, Gergios Tsionis

A GROUPED MAXIMAL CONDITIONED SPECTRAL ORDINATE METHOD (MCSO) FOR GROUND MOTION SELECTION……3704
Ahmad Nicknam, Ehsan Yousefi Dadras, Mohammad Javad Asgari

ADVANCED MODELS FOR THE LIMIT ANALYSIS OF MASONRY STRUCTURES……3716
A. Fortunato, E. De Chiara, F. Fraternali, M. Angelillo

DYNAMIC RESPONSE OF A GOTHIC CATHEDRAL IN CYPRUS……3726
Zehra Cagnan, Christis Chrysostomou, Nicholas Kyriakides, Renos Votsis

APPLICATION OF THE PUSHOVER-BASED PROCEDURE TO PREDICT THE LARGEST PEAK RESPONSE OF ASYMMETRIC BUILDINGS WITH BUCKLING-RESTRAINED BRACES……3739
Kenji Fujii

SEISMIC LOSS OPTIMIZATION OF FRAME BUILDINGS USING VISCOUS DAMPERS……3767
Arun M. Puthanpurayil, Oren Lavan, Rajesh Dhakal

HOW CAN INSURERS GET PREPARED TO CATASTROPHES? ASSESSING EARTHQUAKE EXPECTED LOSSES FROM HISTORICAL CATALOGUE……3778
Anna Bozza, Domenico Asprone, Fatemeh Jalayer, Gaetano Manfredi

APPLICATION OF INCREMENTAL DYNAMIC ANALYSIS TO SEISMIC EVALUATION OF UNDERGROUND STRUCTURE……3793
Tong Liu, Yong Yuan, Zhiyi Chen

GRAPHICAL DYNAMIC TRENDS FOR EARTHQUAKE INCIDENCE RESPONSE OF PLAN-ASYMMETRIC SYSTEMS……3801
M. Faggella, R. Gigliotti, G. Mezzacapo, E. Spacone

SIGNIFICANCE OF EARTHQUAKE INCIDENCE ON RESPONSE OF PLAN-IRREGULAR INFILLED R/C BUILDINGS……3809
M. Faggella, G. Mezzacapo, R. Gigliotti, E. Spacone

BEHAVIOR OF NON-CONFORMING R.C. MEMBERS UNDER COMPRESSIVE AXIAL LOAD AND BIAXIAL BENDING……3816
Marta Del Zoppo, Marco Di Ludovico, Aurelio Ghersi

STIFFNESS MODELING OF RC COLUMNS REINFORCED WITH PLAIN REBARS……3830
Okan Ozcan

CORRELATION BETWEEN THE PROBABILISTIC SEISMIC ASSESSMENT OF FRAME STRUCTURES WITHOUT AND WITH ADDED DAMPERS……3841
Luca Landi, Cristina Vorabbi, Pier Paolo Diotallevi

RS 12 : REPAIR AND RETROFIT OF STRUCTURES

NUMERICAL MODELING OF FRP - RETROFITTED CIRCULAR RC COLUMNS INCLUDING SHEAR……3861
Konstantinos G. Megalooikonomou, Giorgio Monti

SEISMIC VULNERABILITY IN CASE OF FIRE OF EXISTING R.C. FRAMED BUILDINGS: MODELLING AND NONLINEAR DYNAMIC ANALYSIS……3875
Fabio Mazza, Antonio De Luca

THE EFFECT OF STEEL SLIT PANELS IN RETROFITTING WEAK BUILDINGS……3889
Fatemeh Jamshidzadeh, Benyamin Mohebi

REHABILITATION OF AN EDIFIED BUILDING IN A SEISMIC ZONE IN ALGERIA ACCORDING TO THE EUROCODE 8-3……3896
Amar Kassoul, Abdelkader Zerrouk, Imane Djafar Henni

SEISMIC ANALYSIS AND RETROFIT OF A MID-RISE BUILDING……3909
Fernando Saitta, Paolo Clemente, Giacomo Buffarini, Giovanni Bongiovanni

ADVANCED NUMERICAL MODELLING FOR DAMAGE ANALYSIS OF RC STRUCTURES: A CASE STUDY ON BEAM-COLUMN JOINTS……3919
C. Del Vecchio, M. Di Ludovico, A. Prota, G. Manfredi

SEISMIC RETROFITTING EFFECT OF 10-STORY RESIDENTIAL BUILDING RETROFITTED USING PASSIVE SEISMIC CONTROL SYSTEM WITH AMPLIFIER MECHANISM……3934
Y. Takase, T. Ikeda, T. Suzumura

VERIFICATION OF THE TOGGLE DAMPING SYSTEM FOR THE SRC BUILDING DURING THE 2011 OFF THE PACIFIC COAST OF TOHOKU EARTHQUAKE……3946
Takaaki Ikeda, Yuya Takase, Yoshiaki Senoo

SEISMIC RESPONSE VERIFICATION AND RETROFITTING OF RC BUILDING SUBJECTED TO 2014, CEPHALONIA EARTHQUAKES……3953
Ioannis Kavvadias, Ifigeneia Litina, Varvara Kyriakidou, Fani Mamatsopoulou, Lazaros Vasiliadis

DESIGN METHODOLOGY FOR SEISMIC UPGRADING OF TORSIONALLY UNBALANCED EXISTING R.C. BUILDINGS……3972
Georgia Thermou, Manousos Psaltakis

A COMPUTATIONAL INVESTIGATION FOR THE SEISMIC RESPONSE OF RC STRUCTURES STRENGTHENED BY CABLE ELEMENTS……3997
Angelos A. Liolios

RS 13 : SEISMIC ISOLATION

INCREMENTAL DYNAMIC ANALYSIS OF FIRE-EXPOSED BASE-ISOLATED R.C. FRAMED BUILDINGS SUBJECTED TO NEAR-FAULT GROUND MOTIONS……4011
Fabio Mazza, Fabio Alesina

ROLLING-BALL RUBBER-LAYER ISOLATION SYSTEM: STATE OF THE ART, PERFORMANCE AND DESIGN PROCEDURE……4025
Marco Donà, Giovanni Tecchio, Claudio Modena, Alan H. Muhr

THE EFFECT OF MODIFIED LINEAR VISCOELASTIC IMPACT MODELS ON THE POUNDING RESPONSE OF A BASE-ISOLATED BUILDING WITH ADJACENT STRUCTURES……4038
Eftychia A. Mavronicola, Panayiotis C. Polycarpou, Petros Komodromos

ANALYSIS AND EXPERIMENT OF ISOLATED BRIDGES USING POLYNOMIAL ROCKING BEARINGS……4056
Tzu-Ying Lee, Lyan-Ywan Lu, Jing-Hung Tzeng, Kun-Jun Chung

FINITE ELEMENT INVESTIGATION OF A NEW SEISMIC ENERGY ABSORPTION DEVICE THROUGH SIMOULTANEOUSLY YIELD AND FRICTION……4065
Magdalini Titirla, Panikos Papadopoulos

SEISMIC ANALYSIS OF BASE-ISOLATED CYLINDRICAL LIQUID STORAGE TANK USING COUPLED ACOUSTIC-STRUCTURAL INTERACTION……4078
Aruna Rawat, Vasant Matsagar, A.K. Nagpal

OPTIMIZATION OF SEISMIC ISOLATION SYSTEMS WITH VISCOUS FLUID DAMPERS USING GENETIC ALGORITHMS……4086
Samer Barakat, Mohammad Alhamaydeh, Omar Nassif

IN PLAN DISTRIBUTION OF ISOLATORS EFFECTIVE STIFFNESS FOR MINIMIZING THE TORSIONAL RESPONSE OF BASE ISOLATED BUILDINGS……4096
Konstantinos Kostinakis, Asimina Athanatopoulou, Dimitra Arampatzi, Athanasios Atsalos

RS 14 : SEISMIC RISK AND RELIABILITY ANALYSIS

THE EFFECTS OF THE SEISMIC INPUT ON THE SEISMIC RESPONSE OF RC BUILDINGS……4114
Maria Pianigiani, Valentina Mariani, Marco Tanganelli, Stefania Viti

BIDIRECTIONAL ANALYSIS OF A REAL RC BUILDING ACCORDING TO THE ITALIAN CODE PROVISIONS……4126
Stefania Viti, Valentina Mariani, Marco Tanganelli, Mario De Stefano

THE EFFECTS OF THE AXIAL LOAD VARIATION ON THE SEISMIC PERFORMANCE OF EXISTING RC BUILDINGS……..4136
Valentina Mariani, Marco Tanganelli, Stefania Viti, Mario De Stefano

IMPROVED FRAGILITY FUNCTIONS FOR RC BRIDGE POPULATIONS……..4147
C. Zelaschi, R. Monteiro, R. Pinho

SIMPLIFIED CLOSED-FORM SOLUTION FOR THE DETERMINATION OF THE MOMENT-CURVATURE RESPONSE OF A CIRCULAR RC SECTION……..4160
Domenico Raffaele, Roberto Gentile, Mauro Mezzina

ENERGY DISSIPATION CHARACTERISTICS OF SLAB TYPE BUILDINGS WITH SPECIAL CONNECTORS……4171
Erkan Şenol, Ahmet Anıl Dindar, Ercan Yüksel, Faruk Karadoğan

SEISMIC FRAGILITY ANALYSIS OF EXISTING URM BUILDINGS: A STUDY ON KATHMANDU VALLEY……..4182
Sujan Shrestha, Lorenzo Colarusso, Domenico Liberatore, Daniela Addessi

MAPPING HAZARD POTENTIALS IN SEISMIC ZONES BASED ON GEOTECHNICAL DATA FOR DESIGNING TRANSPORTATION NETWORKS INFRASTRUCTURE……..4196
Mohamed Elmasry, Tarek Abdelaziz, Amr Wagdy

RELIABILITY-BASED METHOD FOR ASSESSING LIQUEFACTION POTENTIAL OF SOILS……..4214
M.Naghizaderokni, Dr.A.Janalizade, M.Naghizaderokni

RS 15 : SOFT COMPUTING APPLICATIONS

SEISMIC RESILIENCE OF A BRIDGE BASED ON FUZZY-PROBABILISTIC APPROACH……..4223
J. Andrić And D.G. Lü

NEURAL NETWORKS FOR THE PREDICTION OF MINE-INDUCED VIBRATIONS TRANSMISSION FROM THE GROUND TO BUILDING FOUNDATION……..4235
Krystyna Kuzniar

BAYESIAN IDENTIFICATION OF ELASTIC PARAMETERS IN COMPOSITE LAMINATES APPLYING LAMB WAVES MONITORING……..4246
Marek Slonski

DEVELOPMENT OF A HYBRID SYSTEM FOR IDENTIFICATION OF ELASTIC MATERIAL IN COMPOSITE LAMINA: APPLICATION OF LAMB WAVES AND NEURAL NETWORKS……..4254
Zenon Waszczyszyn, Piotr Nazarko, Pawel Packo, Lukasz Ambrozinski, Tadeusz Uhl

RS 16 : SOIL-STRUCTURE INTERACTION

SIMPLIFIED MODEL FOR COUPLED VIBRATION OF ADJACENT STRIP FOOTINGS……..4268
Jue Wang, Ding Zhou, Weiqing Liu

CALIBRATION AND VALIDATION OF A SIMPLIFIED MODEL OF NONLINEAR SOIL-STRUCTURE INTERACTION FOR SHALLOW FOUNDATIONS……..4277
Simon Lambert, Charisis Chatzigogos, Andrea Godoy

OPTIMIZATION OF WIND TURBINE FOUNDATIONS FOR POOR SOIL……..4292
Wael Mohamed, Per-Erik Austrell

A SSI NUMERICAL MODEL FOR LAYERED SOILS USING A BEM-FEM FORMULATION IN TIME DOMAIN……..4305
A. Romero, P. Galvín

THE ROLE OF SOIL-STRUCTURE INTERACTION IN THE REDISTRIBUTION OF INTERNAL FORCES IN CONCRETE BUILDINGS DUE TO SEISMIC EXCITATION……..4324
Giorgos Mantzaras, Dimitris Karabalis

SOIL-PILE-STRUCTURE-INTERACTION: EXPERIMENTAL RESULTS AND NUMERICAL SIMULATIONS……..4339
Maria Giovanna Durante, Luigi Di Sarno, Colin A Taylor, George Mylonakis, Armando Lucio Simonelli

A NEW SEISMIC DESIGN METHOD FOR DEEPLY EMBEDDED FOUNDATIONS ACCOUNTING FOR SSI EFFECTS……..4350
Nikos Gerolymos, Athanasios Zafeirakos

RS 17 : SOUND AND VIBRATION

DISPERSION ANALYSIS OF ACOUSTIC WAVES IN FLUID MEDIA DISCRETIZED BY ENERGY-ORTHOGONAL FINITE ELEMENTS……..4364
Francisco José Brito Castro

WAVE BASED DESIGN OPTIMISATION OF COMPOSITE STRUCTURES OPERATING IN DYNAMIC ENVIRONMENTS……..4390
Dimitrios Chronopoulos, Manuel Collet, Mohamed Ichchou, Ioannis Antoniadis

NEW REDUCED ORDER FINITE ELEMENT FORMULATIONS FOR VIBRATION ATTENUATION USING PIEZOELECTRIC SHUNT DAMPING……..4409
Walid Larbi, Luciano Pereira Da Silva, Jean-François Deü

SYSTEM IDENTIFICATION AND ACTIVE MODAL CONTROL OF A FLEXIBLE TRUSS STRUCTURE……..4425
Carlos Joventino, Gustavo Abreu, Vicente Lopes Jr.

A 2D WAVE FINITE ELEMENT-BASED SUPERELEMENT FORMULATION FOR ACOUSTIC ANALYSIS OF CAVITIES OF ARBITRARY SHAPES……..4439
Jean-Mathieu Mencik, Denis Duhamel, Marie-Laure Gobert

ON THE IMPLEMENTATION OF BOUNDARY CONDITIONS IN RBF-PS METHOD APPLIED TO VIBRATION ANALYSIS OF KIRCHHOFF PLATES……..4455
Artur Krowiak

MODELLING OF THE VIBRO-ACOUSTIC TRANSMISSION ON MULTI-PLATE PERFORATED PANELS USING TWO-SCALE HOMOGENIZATION……..4468
Eduard Rohan, Vladimír Lukeš

DRY FRICTION INFLUENCE ON STRUCTURE DYNAMICS……..4483
Marco Claudio De Simone, Domenico Guida

ANALYSIS OF VIBRO-ACOUSTIC PROPAGATION IN A MOBILE SCREW COMPRESSOR FOR THE DETERMINATION OF EMITTED ACOUSTIC POWER RADIATED OUTSIDE ITS HOUSING……..4492
Jan Dupal, Jan Vimmr, Vítězslav Adámek, Ondřej Bublík

INTERNAL PARAMETRIC RESONANCE AND AEROELASTIC EFFECTS FOR LONG-SPAN SUSPENSION BRIDGES……..4508
Raffaele Ardito, Antonio Capsoni, Andrea Guerrieri

RS 18 : CONCRETE STRUCTURES

FEM SIMULATION OF THE EXPERIMENTAL RESPONSE OF AAC MASONRY INFILLS IN RC FRAMES……..4528
Riccardo Raimondo Milanesi, Paolo Morandi, Guido Magenes, Baris Binici

DOUBLE-LAYER PLATFORM OF HIGH PERFORMANCE COMPUTING FOR DAMAGE PREDICTION OF RC BUILDINGS SUBJECT TO EARTHQUAKE AND SUBSEQUENT TSUNAMI IN A TARGET AREA……..4548
Panon Latcharote, Yoshiro Kai

DETERMINATION OF THE PERIODS OF COUPLED SHEAR WALLS BY RECURSIVE DIFFERENTIATION METHOD……..4571
Duygu Ozturk, Kanat Burak Bozdogan

SEISMIC BEHAVIOUR OF BRIDGE STRUCTURES MADE OF NATURAL FIBRE REINFORCED POLYMER-CONCRETE COMPOSITE……..4577
Jiaxin Chen, Nawawi Chouw

RS 19 : WAVE PROPAGATION AND SOIL DYNAMICS

FINITE ELEMENT ELASTIC ANALYSIS OF 3-D FLEXIBLE PAVEMENTS UNDER MOVING LOADS……..4584
Niki Beskou, Stefanos Tsinopoulos, Dimitrios Theodorakopoulos

NUMERICAL ANALYSIS OF THE PLANE WAVES SCATTERING BY SEMI-SPHERICAL ALLUVIAL VALLEY……..4596
S L. Chen, X J. Zhu

PLANE WAVE AT THE INTERFACE BETWEEN WATER AND A GASSY POROELASTIC LAYER WITH UNDERLYING ELASTIC SEABED……..4604
Weiyun Chen, Guoxing Chen

A WAVE-BASED REDUCTION TECHNIQUE FOR THE DYNAMIC BEHAVIOR OF PERIODIC STRUCTURES……..4621
Denis Duhamel, Jean-Mathieu Mencik

ANALYSIS OF GROUND MOTION ALONG A TOPOGRAPHIC RELIEF: THE CERRETO DI SPOLETO CASE-HISTORY (CENTRAL ITALY)…….4635
Dario Rinaldis, Salomon Hailemikael, Antonella Paciello, Guido Martini

A PERFECTLY MATCHED LAYER FOR SEISMIC WAVE PROPAGATION IN UNBOUNDED DOMAIN BY USING HETEROGENEOUS MULTI-TIME STEP SUBDOMAIN METHODS…….4645
Eliass Zafati, Michaêl Brun, Irini Djeran-Maigre

LONGITUDINAL SEISMIC VIBRATIONS OF A SEGMENTED PIPELINE CONSIDERED AS THE PERIODICALLY INHOMOGENEOUS ROD…….4663
Mukhady Israilov

EXAMINING THE INITIATION MECHANISMS OF STATIC AND DYNAMIC LIQUEFACTION USING THREE DIMENSIONAL DEM SIMULATIONS…….4672
Zitao Zhang, Yu-Hsing Wang

DAMAGE CHARACTERIZATION IN WAVEGUIDES WITH ULTRASONIC SHEAR WAVES…….4682
Dimitra Achillopoulou, Annamaria Pau, Fabrizio Vestroni

APPLICATION OF NEW DAMAGE INDICATOR-BASED SEQUENTIAL LAW TO ESTIMATE FATIGUE LIFE OF OFFSHORE JACKET STRUCTURES…….4690
Redion Kajolli, Sudath C. Siriwardane, Ove T. Gudmestad

COMPDYN 2015
5th ECCOMAS Thematic Conference on
Computational Methods in Structural Dynamics and Earthquake Engineering
M. Papadrakakis, V. Papadopoulos, V. Plevris (eds.)
Crete Island, Greece, 25–27 May 2015

APPLICATION OF LASER MEASUREMENT TO THE DRIVE-BY INSPECTION OF BRIDGES

Abdollah Malekjafarian[1], **and Eugene J. OBrien**[1,2]

[1] School of Civil, Structural and Environmental Engineering, University College Dublin
Newstead Building, Belfield, Dublin 4, Ireland
e-mail: abdollah.malekjafarian@ucdconnect.ie

[2] UCD Earth Institute, University College Dublin
Belfield, Dublin 4, Ireland
euegene.obrien@ucd.ie

Keywords: Bridge, Inspection, Drive-by, Indirect, Laser Vibrometer.

Abstract. *This paper introduces the application of laser vibrometer measurements to the drive-by inspection of bridges. Drive-by methods usually process the acceleration response measured from an accelerometer installed on a vehicle passing over a bridge. In this paper, two laser vibrometers and two accelerometers are installed on the vehicle to measure a relative velocity between the bridge and vehicle and the vehicle acceleration. The vehicle velocity is removed from the relative velocity by subtracting the time integration of the vehicle acceleration. It is shown by subtracting two following bridge spatial velocities at moving coordinates, that the spatial velocity of the road roughness can be removed. As a result, the bridge velocity at the moving coordinate is obtained. By applying the FFT to the bridge velocity, the fundamental frequency of the bridge is visible in the spectrum.*

1 INTRODUCTION

In recent years, in monitoring transport infrastructures, Structural Health Monitoring (SHM) is becoming more prevalent. Vibration-based methods are among the most significant methods within the field of SHM of bridges. Generally, these methods are based on changes in modal parameters (natural frequencies, damping ratios and mode shapes) of the structure, due to the occurrence of damage in the bridge [1]. Traditionally, in what are called direct methods, many sensors are installed on the bridge to detect changes in the bridge modal parameters. Providing such equipment for all bridges is a financial challenge, particularly for small bridges where a mains power supply may not be available and the cost of installation is considerable.

In recent years, a number of researchers have sought to overcome the difficulties of direct methods by introducing a new concept of bridge monitoring called indirect methods or drive-by methods using sensors installed on a specialist vehicle passing over the bridge. Drive-by approaches have many advantages in terms of simplicity, economy, efficiency and mobility. The idea was first proposed by Yang et al. [2] in which the fundamental frequency of the bridge is estimated from the acceleration response measured on a passing vehicle. Several researchers have now developed methods to identify the bridge fundamental frequency from the acceleration signal measured on a passing vehicle [3-6] and to prove the idea in an experimental case study [7-9]. In addition, several studies have been carried out to identify the bridge damping using the signal measured on a passing vehicle [10, 11]. In most the recent studies, the possibility of estimating the bridge mode shapes from indirect measurement has been investigated [12-14]. Consideration of the road surface profile in indirect methods is a critical issue as it can excite vehicle-related frequencies to a much higher amplitude level than bridge-related ones, making it difficult to identify the bridge frequencies. Some authors have developed methods to overcome this challenge, such as; (1) using the excitation due to ongoing traffic to increase the relative influence of the bridge in the vehicle response [9, 15] and (2) subtracting the signals from successive trailer axles – provided those axles have identical properties [16, 17]. In the view of all that has been mentioned so far, there is a great potential for drive-by methods for the purpose of bridge inspection [18].

In this paper, the idea of using a laser vibrometer on the vehicle is proposed to overcome the issues associated with road profile. It is suggested that by mounting a laser vibrometer beside the accelerometer on the vehicle, the relative velocity between the axle and the bridge can be measured. By integrating the acceleration signal, the axle velocity can be obtained. Subtraction these two velocity signals, the bridge velocity at the moving coordinate (at the point of vehicle bridge interaction) can be calculated with high accuracy. A numerical case study is investigated using Finite Element (FE) models of vehicle bridge interaction (VBI) and is used to validate the effectiveness and performance of the concept. The simulations confirm the capability of the proposed approach to remove the vehicle frequency from the response measured on the vehicle.

2 FINITE ELEMENT OF VBI

González [19] describes coupled and uncoupled vehicle bridge interaction (VBI). A coupled Finite Element (FE) model similar to that used by [14] is employed for the numerical analysis. The half-car system shown in Fig. 1 is used here to represent the vehicle. The vehicle body and axle component masses are represented by m_s and m_u (sprung and unsprung). The axle mass connects to the road surface via a spring with linear stiffness k_t which represents the tyre. By imposing equilibrium of all forces and moments acting on the masses and

expressing them in terms of the degrees of freedom, the equations of motion of the vehicle model are obtained:

$$\mathrm{M_v}\,\ddot{y}_v + \mathrm{C_v}\,\dot{y}_v + \mathrm{K_v}\,y_v = f_{int} \tag{1}$$

where $\mathrm{M_v}$, $\mathrm{C_v}$ and $\mathrm{K_v}$ are the respective mass, damping and stiffness matrices of the vehicle and $\ddot{y}_v$, $\dot{y}_v$ and y_v are the respective vectors of nodal acceleration, velocity and displacement. f_{int} is the time-varying dynamic interaction force vector applied to the vehicle degrees of freedom.

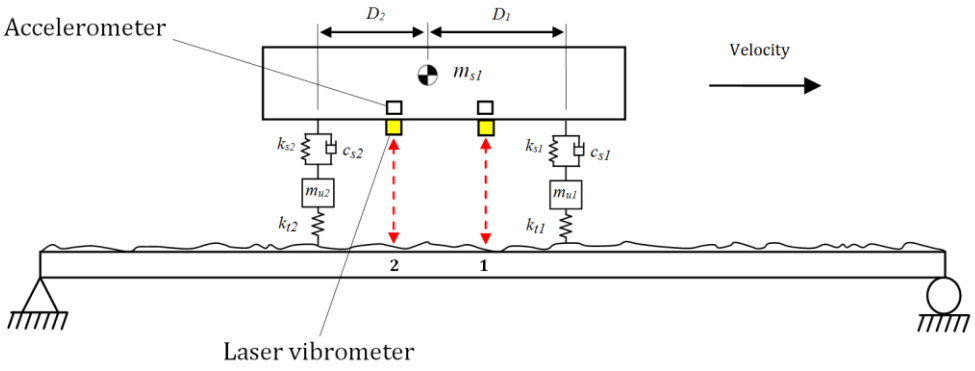


Figure 1: The half-car model on the bridge.

The bridge is represented by a simply supported beam of total span length L, flexural rigidity EI and mass per unit length m^*, using the finite element method. The model consists of 20 discrete beam elements, each with 4 degrees of freedom (2 per node). The response of the beam model to a series of moving time-varying forces is given by the system of equations:

$$\mathrm{M_b}\,\ddot{y}_b + \mathrm{C_b}\,\dot{y}_b + \mathrm{K_b}\,y_b = f_{int} \tag{2}$$

where $\mathrm{M_b}$, $\mathrm{C_b}$ and $\mathrm{K_b}$ are global mass, damping and stiffness matrices of the beam model, respectively and $\ddot{y}_b$, $\dot{y}_b$ and y_b are the vectors of nodal bridge accelerations, velocities and displacements, respectively.

The dynamic interaction between the vehicle and the bridge is implemented in MATLAB. The vehicle and the bridge are coupled at the tyre contact points via the interaction force vector. Combining equations (1) and (2), the coupled equation of motion is formed as:

$$\mathrm{M_g}\ddot{u} + \mathrm{C_g}\dot{u} + \mathrm{K_g}u = F \tag{3}$$

where $\mathrm{M_g}$ and $\mathrm{C_g}$ are the combined system mass and damping matrices, respectively, $\mathrm{K_g}$ is the coupled time-varying system stiffness matrix and F is the system force vector. The equations for the coupled system are solved using the Wilson-Theta integration scheme [20]. The optimal value of the parameter θ =1.420815 is used for unconditional stability in the integration scheme. The initial condition of the solution is considered to be zero displacement, velocity and acceleration in all simulations.

3 DRIVE-BY BRIDGE INSPECTION

3.1 Numerical case study

A bridge is modelled using the FE method with the properties given in Table 1. The first two natural frequencies of the bridge are 4.97 and 19.88 Hz. A half-car model (Fig. 1) with the properties given in Table 2 is investigated travelling over a bridge at a speed of 4 m/s.

Properties	Unit	Symbol	value
Length	m	L	16
Mass per unit	kg/m	m	28125
Modulus of elasticity	MPa	E	35000
Second moment of area	m^4	J	0.5273

Table 1: Properties of the bridge.

Property	Unit	Symbol	Value
Body mass	kg	m_{s1}	16200
Axle mass	kg	m_{u1}	700
		m_{u2}	1100
Suspension stiffness	N/m	k_{s1}	4×10^5
		k_{s2}	1×10^6
Suspension damping	Ns/m	c_{s1}	10×10^3
		c_{s2}	20×10^3
Tyre stiffness	N/m	k_{t1}	1.75×10^6
		k_{t2}	3.5×10^6
Moment of inertia	kg m^2	I_{s1}	1.56×10^5
Distance of axle to centre of gravity	m	D_1	2.5
		D_2	2.5
Body mass frequency	Hz	$f_{body,1}$	1.58
Axle mass frequency	Hz	$f_{axle,1}$	8.83
		$f_{axle,2}$	10.21

Table 2: Properties of the half-car.

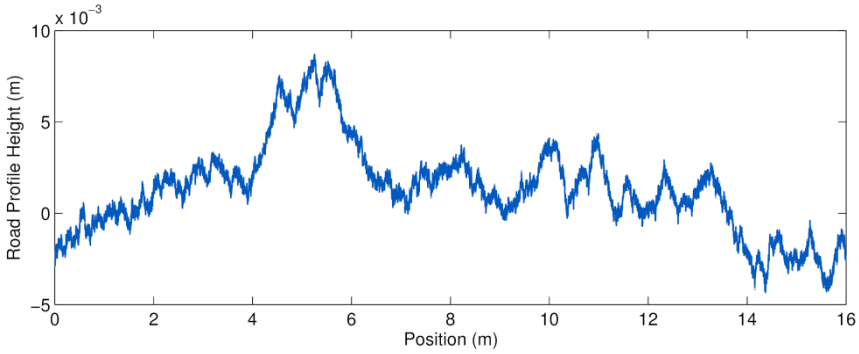


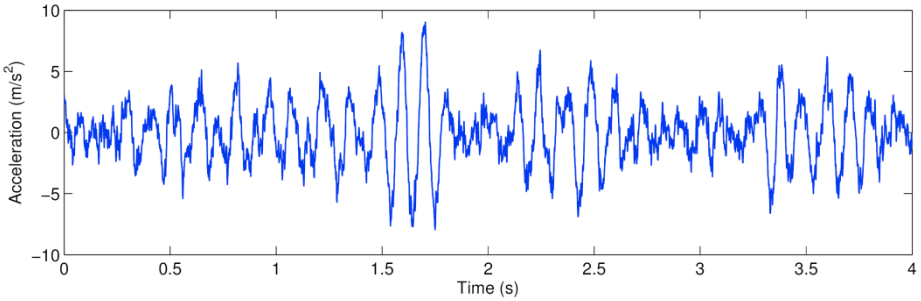
Figure 2: Class "A" road profile.

A road profile (shown in Fig. 2) is included in the simulations. The irregularities of this profile are randomly generated according to the ISO standard [21] for a road class 'A' (very good profile, as expected in a well maintained highway). The simulation is carried out using the FE method programmed in the MATLAB software environment. The sampling time in-

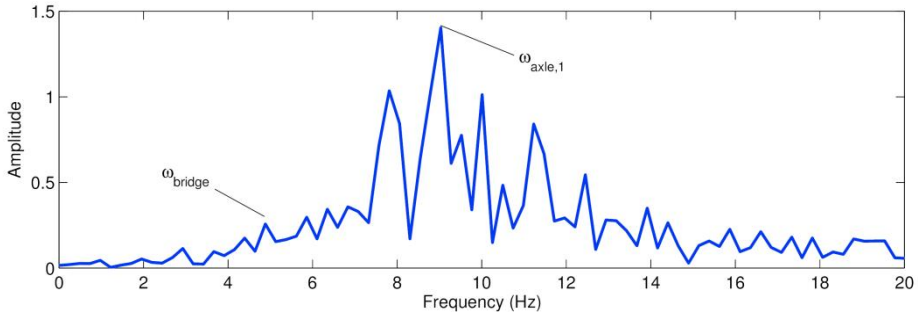
terval is selected to be 0.001 s. The total length of the acceleration response of the vehicle is 4 s.

3.2 Drive-by inspection using acceleration measured on the vehicle axle

Drive-by bridge monitoring is usually based on the acceleration response measured on the axle of the vehicle passing over the bridge. The acceleration response measured at the first axle of the vehicle is shown in Fig. 3(a). In order to analyse the axle response, a Fast Fourier Transform (FFT) is performed on the simulated vehicle response. The obtained FFT spectrum of the vehicle response is shown in Fig. 3(b). As expected, there is a small peak due to the fundamental frequency of the bridge and there is a dominant peak related to the axle frequency.



(a)



(b)

Figure 3: Response measured at the first axle; (a) acceleration, (b) FFT spectrum.

3.3 Drive-by inspection using laser measurement on the vehicle

In this section the concept of using laser vibrometer measurement on the vehicle to remove the vehicle frequency from the spectrum is introduced. A vehicle instrumented with two laser vibrometers and two accelerometers (Fig. 1) is used. Relative velocities among the bridge surface and the vehicle body are measured using two measurement points:

$$\dot{y}_{relative,i}(t) = \dot{y}_{body,i}(t) - \dot{y}_{bridge,i}(t),\ i = 1,2 \tag{4}$$

The body acceleration is measured using the accelerometer installed at exactly the same location as the laser vibrometer. The velocity of the bridge is calculated by integration of the body acceleration (Fig. 4). Therefore, the bridge spatial velocity $\dot{y}^{i}_{bridge}(t)$ can be obtained by subtracting the body velocity from the relative velocity.

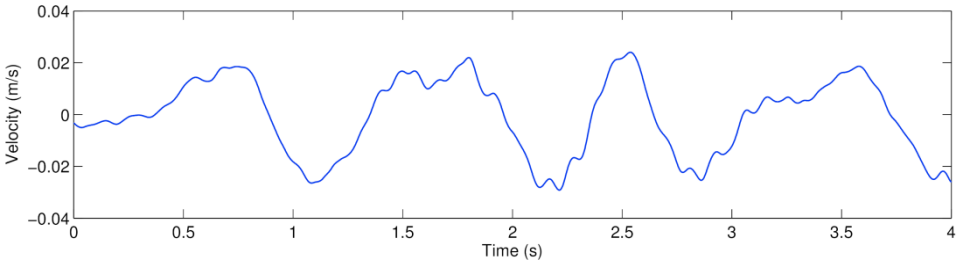


Figure 4: Body velocity measured at the first accelerometer ($\dot{y}_{body,1}(t)$).

The spatial velocity includes two parts. The first part is the bridge response relative to the moving reference and the second part is the spatial velocity of the road profile (Fig. 5), i.e., the road profile converted to velocity relative to the moving reference:

$$\dot{y}_{bridge,i}(t) = \dot{u}_i'(t) + \dot{r}_i(t), \quad i = 1,2 \tag{5}$$

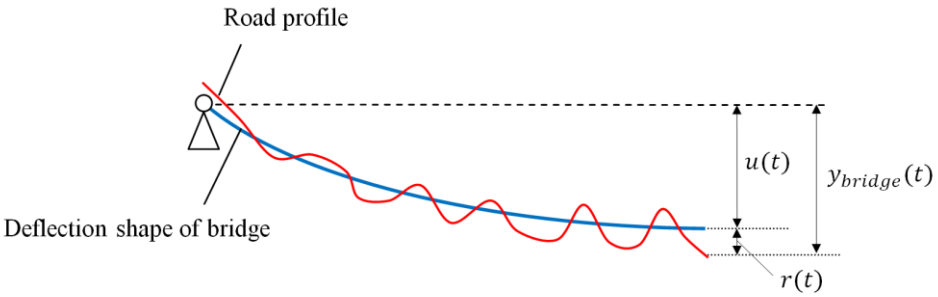


Figure 5: Bridge vibration under the laser vibrometer.

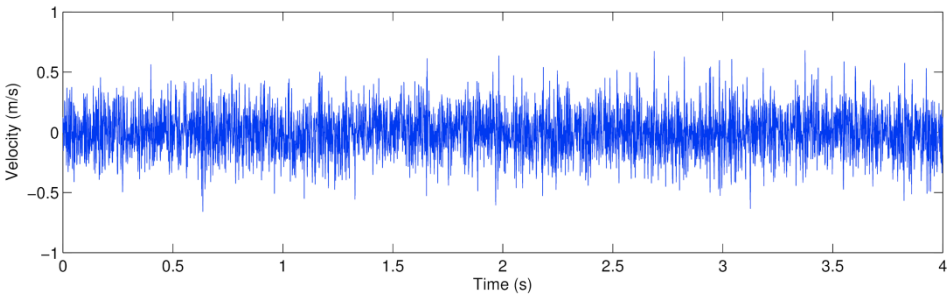


Figure 6: Relative velocity measured at the first laser ($\dot{y}_{relative,1}(t)$).

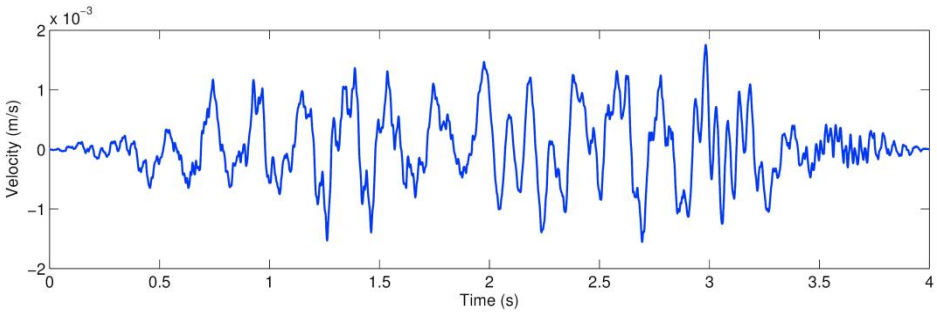


Figure 7: Velocity difference ($\Delta\dot{y}$).

The spatial velocities at two following points on the vehicle are measured (Fig. 6). In order to remove the spatial velocity of the road profile from the response, the second response is subtracted from the first with a time shift to allow for their relative positions.

$$\Delta\dot{y} = \dot{y}_{bridge,2}(t+\Delta t) - \dot{y}_{bridge,1}(t)$$
$$= \dot{u}_2(t+\Delta t) + \dot{r}_2(t+\Delta t) - \dot{u}_1(t) - \dot{r}_1(t) \quad (6)$$

where Δt is the time interval between two measurement points. If Δt is selected to that $r_2(t+\Delta t) = r_1(t)$, the road profile is removed from the response and a time shifted difference of the bridge response is obtained:

$$\Delta\dot{y} = \dot{u}_2(t+\Delta t) - \dot{u}_1(t) \quad (7)$$

The velocity differences obtained from Eq. 7 are shown in Fig. 7. As a result, a bridge response at the moving coordinate is obtained which can show the most important characteristics of the bridge dynamics. The frequency spectrum of the obtained bridge response is shown in Fig. 8. A dominant peak is observable in the spectrum which is related to the bridge fundamental frequency. This can be expected to be damage sensitive.

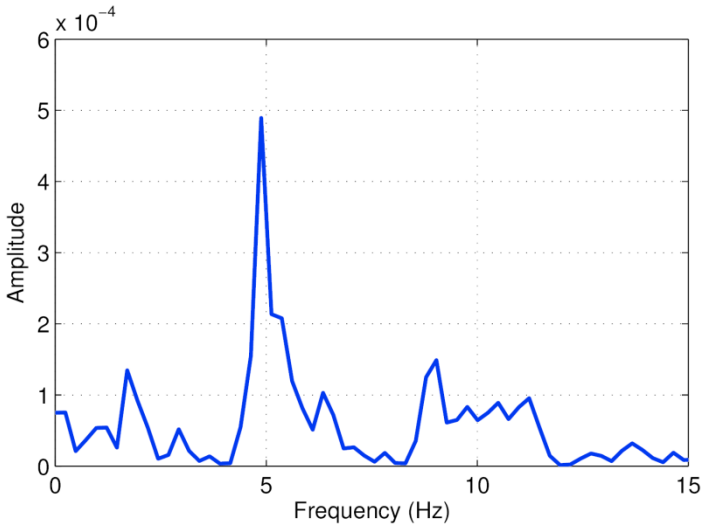


Figure 8: Frequency spectrum of the bridge response.

4 CONCLUSIONS

This paper describes the application of laser measurement to the drive-by bridge inspection problem. Subtraction of responses measured using laser vibrometers and accelerometers is used to obtain the bridge spatial velocity. Finally, spatial velocity of road roughness is removed by subtraction of the bridge spatial velocities measured at two following laser vibrometers. It is shown that the FFT spectrum of the differences response shows a dominant frequency which is corresponds to the bridge fundamental frequency.

5 ACKNOWLEDGMENT

The authors wish to express their gratitude for the financial support received from the Irish Research Council's *PhD in Sustainable Development* Graduate Research Education Programme.

REFERENCES

[1] W. Fan, P.Z. Qiao, Vibration-based Damage Identification Methods: A Review and Comparative Study. *Structural Health Monitoring-an International Journal*, **10**(1), 83-111, 2011.

[2] Y.B. Yang, C.W. Lin, J.D. Yau, Extracting bridge frequencies from the dynamic response of a passing vehicle. *Journal of Sound and Vibration*, **272**(3-5), 471-493, 2004.

[3] Y.B. Yang, C.W. Lin, Vehicle-bridge interaction dynamics and potential applications. *Journal of Sound and Vibration*, **284**(1-2), 205-226, 2005.

[4] Y.B. Yang, K.C. Chang, Extracting the bridge frequencies indirectly from a passing vehicle: Parametric study. *Engineering Structures*, **31**(10), 2448-2459, 2009.

[5] A. González, E.J. OBrien, P.J. McGetrick,Detection of Bridge Dynamic Parameters Using an Instrumented Vehicle, in *Proceedings of the Fifth World Conference on Structural Control and Monitoring*. 2010: Tokyo, Japan.

[6] A. Malekjafarian, E.J. OBrien. Application of output-only modal method to the monitoring of bridges using an instrumented vehicle. S. Nanukuttan and J. Goggins, eds. *Civil Engineering Research in Ireland*. Belfast, Northern Ireland, 2014.

[7] C.W. Lin, Y.B. Yang, Use of a passing vehicle to scan the fundamental bridge frequencies: An experimental verification. *Engineering Structures*, **27**(13), 1865-1878, 2005.

[8] P. McGetrick, C.W. Kim, E.J. OBrien. Experimental Investigation of the Detection of Bridge Dynamic Parameters Using a Moiving Vehicle. *The Twenty-Third KKCNN Symposium on Civil Engineering*. Taipei, Taiwan, 2010.

[9] Y.B. Yang, et al., Experimental study of a hand-drawn cart for measuring the bridge frequencies. *Engineering Structures*, **57**, 222-231, 2013.

[10] P.J. McGetrick, A. Gonzalez, E.J. OBrien, Theoretical investigation of the use of a moving vehicle to identify bridge dynamic parameters. *Insight*, **51**(8), 433-438, 2009.

[11] A. Gonzalez, E.J. OBrien, P.J. McGetrick, Identification of damping in a bridge using a moving instrumented vehicle. *Journal of Sound and Vibration*, **331**(18), 4115-4131, 2012.

[12] Y. Oshima, K. Yamamoto, K. Sugiura, Damage assessment of a bridge based on mode shapes estimated by responses of passing vehicles. *Smart Structures and Systems*, **13**(5), 731-753, 2014.

[13] Y.B. Yang, Y.C. Li, K. Chang, Constructing the mode shapes of a bridge from a passing vehicles: a theoretical study. *Smart Structures and Systems*, **13**(5), 797-819, 2014.

[14] A. Malekjafarian, E.J. Obrien, Identification of bridge mode shapes using Short Time Frequency Domain Decomposition of the responses measured in a passing vehicle. *Engineering Structures*, **81**, 386-397, 2014.

[15] Y.B. Yang, Y.C. Li, K.C. Chang, Effect of road surface roughness on the response of a moving vehicle for identification of bridge frequencies. *Interaction and multiscale mechanics*, **5**(4), 347-368, 2012.

[16] Y.B. Yang, Y.C. Li, K.C. Chang, Using two connected vehicles to measure the frequencies of bridges with rough surface: a theoretical study. *Acta Mechanica*, **223**(8), 1851-1861, 2012.

[17] J. Keenahan, et al., The use of a dynamic truck-trailer drive-by system to monitor bridge damping. *Structural Health Monitoring*, **13**(2), 143-157, 2014.

[18] A. Malekjafarian, P. McGetrick, E.J. OBrien, A review of indirect bridge monitoring using passing vehicles. *Shock and Vibration*, Article ID 286139, 2015.

[19] A. González, *Vehicle-bridge dynamic interaction using finite element modelling*, in *Finite element analysis*, Sciyo: Rijeka, Croatia. p. 637–662. 2010

[20] J.W. Tedesco, W.G. McDougal, C.A. Ross, *Structural dynamics: theory and applications*. California, USA: Addison- Wesley Longman,1999.

[21] ISO 8608:1995, Mechanical Vibration-road Surface Profiles-reporting of Measured Data', International Standards Organisation. 1995.

COMPDYN 2015
5th ECCOMAS Thematic Conference on
Computational Methods in Structural Dynamics and Earthquake Engineering
M. Papadrakakis, V. Papadopoulos, V. Plevris (eds.)
Crete Island, Greece, 25–27 May 2015

UNCERTAINTY OF BRIDGE VIBRATION PROPERTIES AND ITS CONSEQUENCE FOR DAMAGE IDENTIFICATION

Marian Ralbovsky[1], Maciej Kwapisz[1], and Alois Vorwagner[1]

[1] AIT Austrian Institute of Technology GmbH
Giefinggasse 2, 1210 Vienna, Austria
e-mail: marian.ralbovsky@ait.ac.at
e-mail: maciej.kwapisz@ait.ac.at
e-mail: alois.vorwagner@ait.ac.at

Keywords: Uncertainty, Modal properties, Damage Detection, Clustering, Monte-Carlo Simulation.

Abstract. *This study deals with the topic of bridge health monitoring based on identification of bridge vibration properties, which are influenced by uncertainties. Focus is laid on quantification of the uncertainties from continuous monitoring data. The determined uncertainties are then used in probabilistic evaluation of structural state. The purpose is to acquire besides the "best-match" structural state also the reliability of identification. A method for automated extraction of modal parameters and evaluation of their uncertainties is presented. It comprises clustering and statistical evaluation of Stochastic Subspace Identification system poles. The statistical properties of modal parameters are used to build a set of probabilistic variables sampled using Monte-Carlo Simulation. The generated sets are used for probabilistic damage detection, which uses a forward approach of finding the best match within a database of precalculated structural states. The presented study was performed using monitoring data acquired on a prestressed concrete box-girder bridge in course of 9 months of continuous data recording.*

1 INTRODUCTION

Vibration-based damage detection on bridges is being applied since decades and it was the topic of research published in many articles and dissertations. The amount of published literature indicates that most researchers prefer data-only based approaches for damage detection. Maeck [1] described and applied in his dissertation different data-only detection algorithms, as well as some mixed approaches. Peeters [2] presented in his dissertation the advances in damage detection methods that are based on bridge modal properties (data-only), determined using Stochastic Subspace Identification (SSI) from continuous ambient vibration monitoring. The SSI-method represents a robust tool for system identification, which was later further improved [3]. The SSI-method was used also in this paper to extract bridge model properties. Santos [4] focused in his dissertation on novelty-detection and classification methods for damage detection purposes. Novelty detection aims to detect changed structural behavior from the measured data, and it represents level-1 damage identification. When combined with classification techniques [5] and a database of pre-calculated structural states, the measured structural parameters can be used for level-2 and level-3 identification. This approach was also applied in the work presented here. The model updating techniques aim at level-3 identification and solve the damage detection problem using an inverse approach that optimizes computational model [6]. The task of optimization of the bridge model puts high demands on computational effort. Therefore, the model should be small – built preferably using beam elements, particularly if the monitoring is continuous and the optimization must be performed repetitively.

The damage detection based on bridge vibration properties is affected by their accuracy and by the ability of post-processing techniques to compensate effects other than structural damages, which also influence vibration properties. Inaccurately determined vibration properties may cause that the wrong structural state will be matched with the measurements. The aim of the presented work was to evaluate accuracy of acquired vibration properties in one case study and to evaluate the effect that it had on selection of corresponding structural state (damage scenario). The presented approach uses the Monte-Carlo Simulation. Mares et.al. [7] used the approach of Monte-Carlo Simulation to investigate influence of modelling uncertainties on results of model updating (i.e. in the inverse problem). In the work presented here, the approach of Monte-Carlo Simulation is used in the forward problem.

The presented paper contains two technical chapters. Chapter 2 deals with uncertainty of modal parameters, and describes the sources of uncertainty and how the evaluation of uncertainties was implemented in an automated algorithm. Also, the measurement results and their statistical evaluation (uncertainty) are presented using data acquired on a prestressed concrete bridge in course of 9 months of continuous monitoring.

Chapter 3 intends to present the whole process of damage detection, starting with description of the tested bridge and installed monitoring system, further proceeding to creation of database of structural states, process of Monte-Carlo Simulation and results of probabilistic damage detection including simulated damage scenarios.

2 UNCERTAINTY OF MODAL PROPERTIES

The modal parameters of the bridge (eigenfrequencies, mode shapes, and damping ratios) are not only affected by structural damage, but vary also due to environmental influences and traffic intensity. Another source of uncertainty is the algorithm of modal parameter extraction. The process of dealing with measurement variations and uncertainties has two stages:

1. Compensation of known effects
2. Evaluation of remaining uncertainties

In the first stage, known effects can be compensated, if the relation between the influencing parameters and their effects is known. The purpose of the compensation is to reduce the magnitude of measurement variations. Typical example is the influence of temperature on bridge eigenfrequencies. Figure 1 shows the relation between measured eigenfrequencies and structural temperature acquired in presented case study.

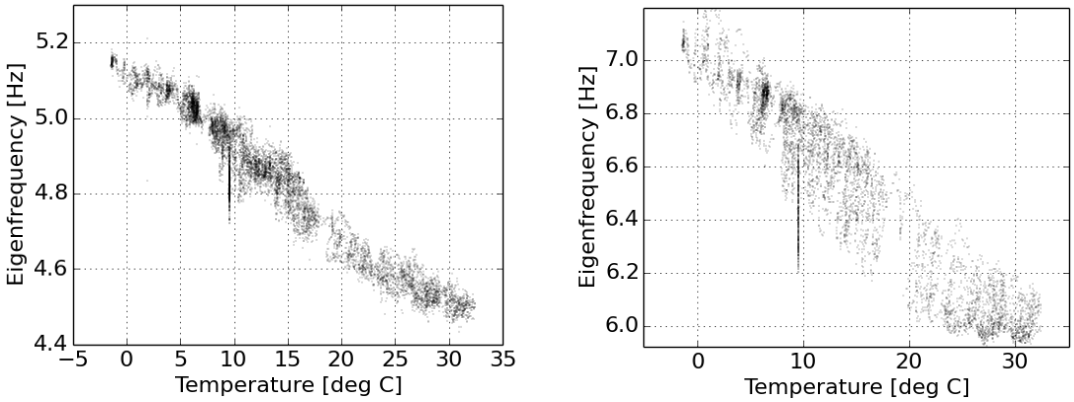


Figure 1: Relation between measured eigenfrequencies and structural temperature.

In the second stage, the remaining uncertainties are evaluated and form a basis for definition of input probabilistic variables for the Monte-Carlo Simulation. The evaluation of the uncertainties should be done using a scheme that can capture all expected sources of uncertainty that are still present in the compensated data. In the presented example, the expected sources of uncertainty after compensation of temperature effects were the following:

- Influence of traffic loads, including both changes of modal properties due to vehicle-bridge interaction, as well as due to the unknown excitation properties of dynamic axle forces. The extraction of modal parameters works well if the excitation source has properties of white noise. The actual excitation by traffic loads is not white noise, and it varies in time.
- Residual errors in temperature-compensation due to incomplete temperature information. The temperature is measured on few points in the structure and the distribution of temperature fields in the whole structure is not fully known.
- Other environmental influences, for example moisture and wind.
- Accuracy of the algorithm used for extraction of modal parameters, including both algorithm-inherent errors, as well as errors that originate from user interaction.

2.1 Automated extraction of system poles

To extract modal properties from measured accelerations, the Stochastic Subspace Identification (SSI) technique was used, which was well described by Peeters [2]. This chapter describes the procedure used for automated extraction of modal parameters and evaluation of short-term uncertainties. These include uncertainties related to traffic loads and to the extraction algorithm.

The variation of traffic loads was considered by application of overlapping time windows in the evaluation (Figure 2). As the traffic load varies in time, the dynamic excitation is dif-

ferent in each of the evaluated time windows. Data from each time window was processed by SSI separately. The identified system poles from 6 time windows were then grouped together and processed by clustering.

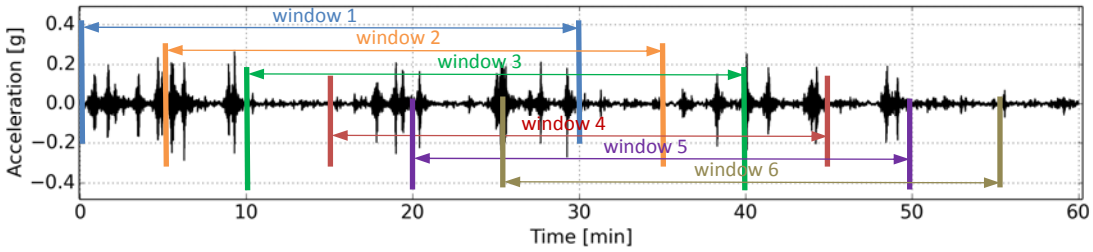


Figure 2: Overlapping time windows in data processing.

The SSI-method requires certain decisions to be made by the user. For example the user is expected to state the expected system order prior to the calculation and also to select the "correct" solution poles from among the many poles that were identified as possible solutions. The requirement of user interaction is not only impractical for processing of continuous monitoring data, but it is also the source of possible errors. Automated procedures that do not require user interaction were developed in the past for methods in frequency domain [8] as well as in time domain [3]. To evaluate the variation of solutions that could be selected from the SSI stabilization plot, the following procedure was applied. A relatively broad range of feasible model orders (Figure 3) was defined and all stable poles in this range were selected. Then, a clustering technique was applied to arrange the solutions into different groups. Each group of solutions contains stable poles of one mode. From each group, statistical moments of all variables could then be evaluated.

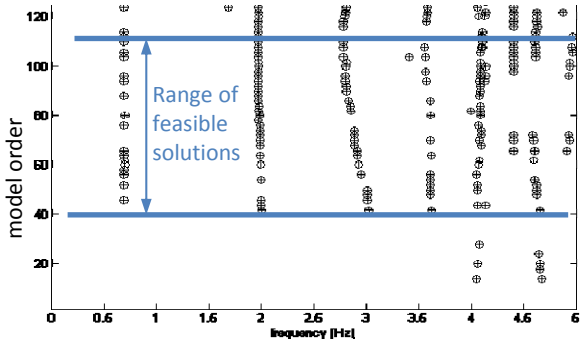


Figure 3: SSI stabilization plot showing identified stable poles.

2.2 Clustering of solutions

The purpose of clustering technique is to divide all feasible poles into groups, each representing one mode shape. A simple grouping of poles by range of frequencies is possible only in case of well separated modes. This was not the case at the given bridge, which has 8 spans with equal length, resulting in closely spaced modes. Therefore, a clustering technique had to be applied to sort the poles. The basis for application of clustering technique is calculation of a distance matrix, which defines the similarity between each pair of poles. The typical number of poles processed within one clustering run was around 1500, which resulted in a distance matrix with dimensions of 1500x1500. The distance between each pair of poles was calculated using similarity of frequencies (ratio f_i / f_j) and similarity of mode shapes (MAC value). The exact expression of distance between poles i and j is given in Equations 1 and 2.

$$D_{i,j} = 1 - MAC_{i,j} \cdot \left[r_{ij}\xi_j \left(\left(1 - r_{ij}^2\right)^2 + \left(2\xi_j r_{ij}\right)^2 \right)^{-0.5} + r_{ij}^{-1}\xi_i \left(\left(1 - r_{ij}^{-2}\right)^2 + \left(2\xi_i r_{ij}^{-1}\right)^2 \right)^{-0.5} \right] \quad (1)$$

$$r_{ij} = \frac{f_i}{f_j} \quad (2)$$

where f and ξ are identified frequency and damping ratio, respectively
$MAC_{i,j}$ is value of Modal Assurance Criterion
r_{ij} is the ratio of the frequencies.

The clustering algorithm groups together poles that have maximum distance between any two poles in the group smaller than a specified threshold. A small threshold produces many small groups, while a high threshold produces few large groups. This relation is displayed in Figure 4. The threshold needs to be specified by the analyst only once and is used for processing of all data from continuous monitoring. The threshold value used for the evaluation was in this case specified at 0.049.

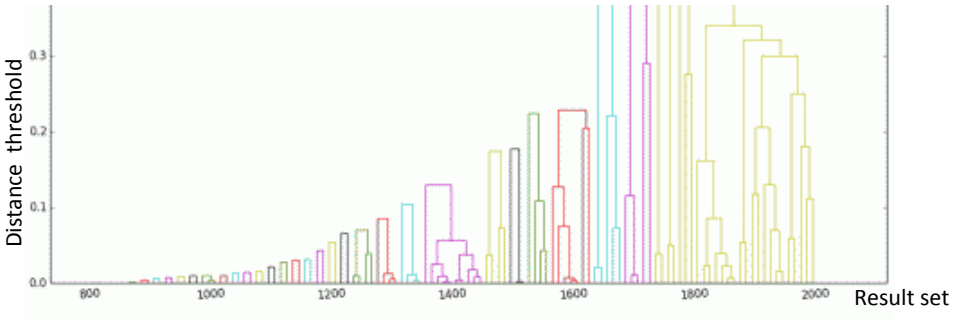


Figure 4: Clustering dendrogram.

The clustering algorithm tends to form large groups for poles with good stability. Therefore, small groups of poles can be sorted out as not relevant. In the presented case, any group containing less than 30 poles was not considered in following evaluations.

2.3 Statistical evaluation

Following the sorting of poles into groups by clustering, values in each group were statistically evaluated. The mean and the standard deviation were calculated for all modal parameters. Prior to this calculation, the modes were scaled to unity length and reversed if necessary to align the signs of mode shape values. As result, mean and standard deviation of frequency, damping, and all mode shape values were determined. Figure 5 shows the time history of one identified eigenfrequency. Displayed are the mean and the standard deviation, each evaluated using 1 hour of recorded data.

Figure 6 shows the variation of identified mode shape values in course of the whole monitoring period of 9 months. The presented histograms were calculated from mean mode shapes, whereas each mean mode was evaluated from one cluster, which contains identified poles using 1 hour of recorded vibration data.

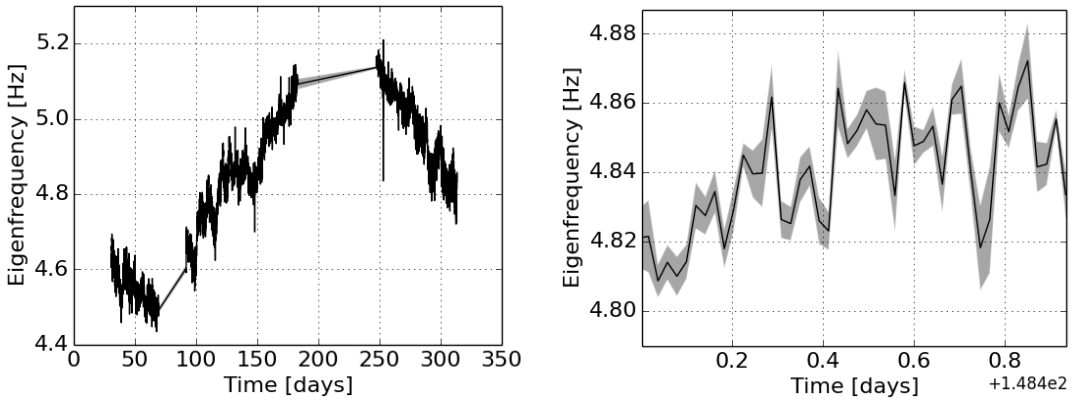


Figure 5: Eigenfrequency mean (black) and $\pm 1\sigma$ (grey) from all data (left) and in detail (right).

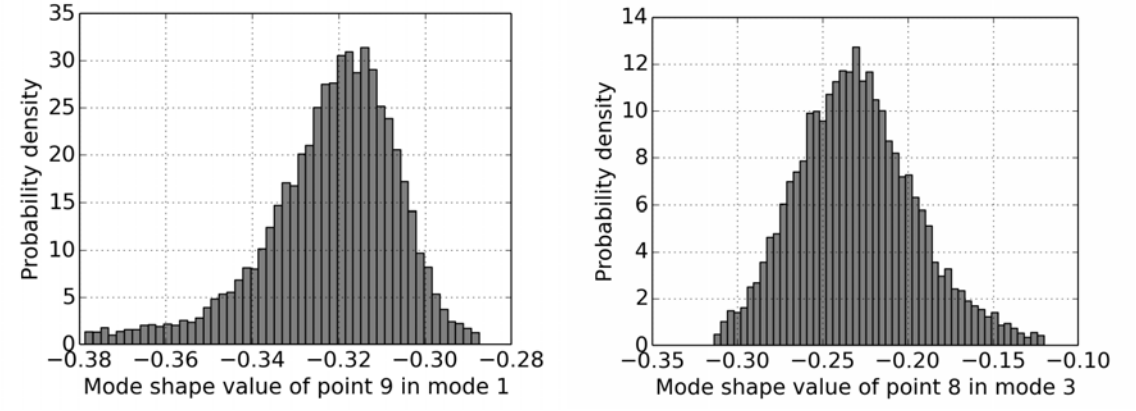


Figure 6: Two histograms that show variation of mode shape values, evaluated using data from 9 months.

The mode shape values at different measurement points show generally a good correlation. A strong correlation is advantageous for damage detection capability, since it narrows the space of random variations. Figure 7 shows the evaluated correlation matrix between mode shape values of all measurement points in two different mode shapes.

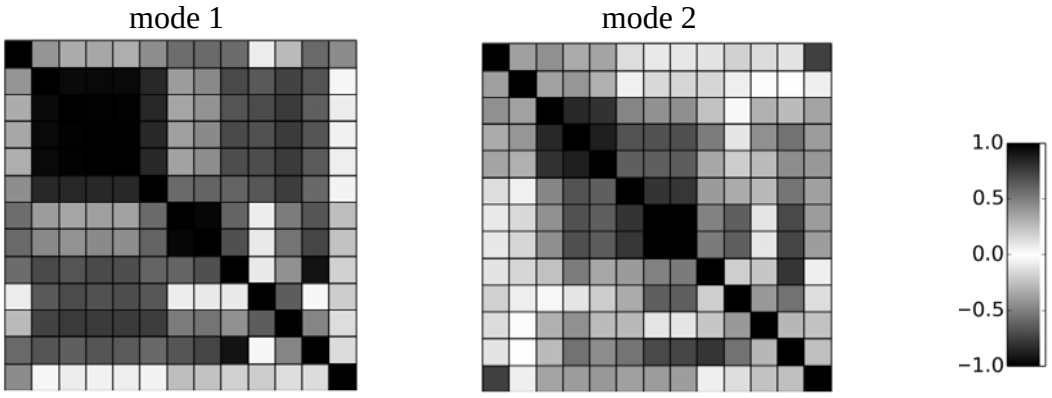


Figure 7: Matrix of correlation coefficients between mode shape values of all measurement points.

3 DAMAGE DETECTION

3.1 Test structure and monitoring system

The test structure is a prestressed concrete bridge with 10 spans. Its cross-section is a box-girder that is constant along whole length of the bridge. The cross-section has height of 3.2 m and the total length of the bridge is 327 m. Monitoring system was installed in the bridge, where different sensor types were used. For purposes of this study only data from the acceleration sensors were used. The position of the acceleration sensors is displayed in Figure 8. Sensors were placed in midspan of 9 spans, and few additional sensors at quarter-span positions were installed.

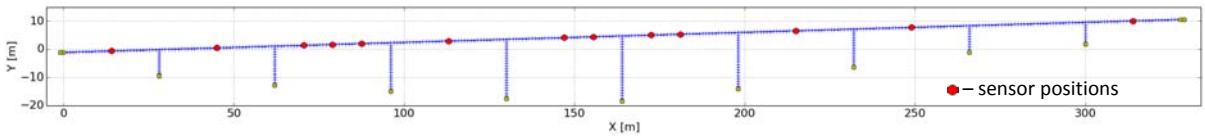


Figure 8: 2D-Finite Element model of the bridge and position of sensors

The acquired data used in this paper encompasses recordings from 9 months of data acquisition, containing both summer and winter periods.

3.2 Damage scenarios

Aim of this study was to investigate damage detection capability for the case of reduction of prestressing force in specific regions of the bridge. The reduction of prestressing force produces cracking in concrete and thus reduction of cross-sectional bending stiffness. A small reduction of prestressing force does not yet result in stiffness reduction because the whole cross-section is initially under compression. But after the tensile strength of concrete is reached and cracks occur, cross-sectional stiffness drops rapidly. Therefore, damage detection methods based on stiffness identification are most effective when detecting occurrence of first cracking.

A set of damage scenarios was calculated using the 2D Finite-Element model shown above. The damages scenarios were described by 3 parameters: position in the bridge, spatial extent (affected bridge length), and magnitude of bending stiffness reduction. Table 1 summarizes all damage scenario parameters.

Position	Affected bridge length [m]	Bending stiffness reduction [%]
Middle of span 1	2.8	2.2
Middle of span 2	4.7	11.5
Middle of span 3	8.5	20.8
Middle of span 4	10.4	30.1
Middle of span 5	12.3	39.3
Middle of span 6		48.3
Middle of span 7		57.3
Middle of span 8		66.3
Middle of span 9		…
Middle of span 10		86.6

Table 1: Properties of modeled damage scenarios.

There were 10 different damage positions, in each of them 5 different spatial extents (affected bridge length) were modeled, and in each of them 27 different stiffness reductions were modeled. This resulted in a total of 1350 damage scenarios that form a database. Modal parameters were calculated for each of the prepared damage scenarios. This database of model parameters in different damage scenarios serves for damage detection purposes. Using the measured modal parameters, one particular damage scenario can be found that shows the closest match with the measurements.

3.3 Monte-Carlo Simulation

Analysis of the forward propagation of measurement uncertainty was performed on the basis of Monte-Carlo Simulation. In the publication of Doebling [10], similar procedure to the approach used here is described. Doebling used definition of probabilistic input variables using normal distributions, and assumed that the variables are independent. Then, a set of input parameter samples was generated by application of appropriate sampling techniques. The work presented here uses similar approach. The main difference is that correlation of input variables was taken into account.

In chapter 2, the evaluation of uncertainty of measured modal parameters was described. The evaluated means, standard deviations and correlation coefficients were used to define a set of probabilistic variables. Each modal parameter (eigenfrequencies and mode shape values) was modeled as probabilistic variable with a normal distribution. The first two measured modes were used for damage detection. For each mode, 14 probabilistic variables were defined, which are the eigenfrequency and the mode shape values at 13 measurement points.

Matrix of correlation coefficients was defined according to results presented in chapter 2. In here, only the correlation coefficients of mode shape values within one mode have nonzero elements. The eigenfrequencies are considered as independent variables. Also, the correlation between values of two different modes was assumed to be zero.

The Latin Hypercube Sampling technique was used for generation of the sample set, which had the size of 1000 samples for each variable. Figure 9 shows an example of values generated by Latin Hypercube Sampling for two probabilistic variables with strong correlation. Displayed are values of mode shape 2 at point 4 vs. at point 3, which have a correlation coefficient of 0.86.

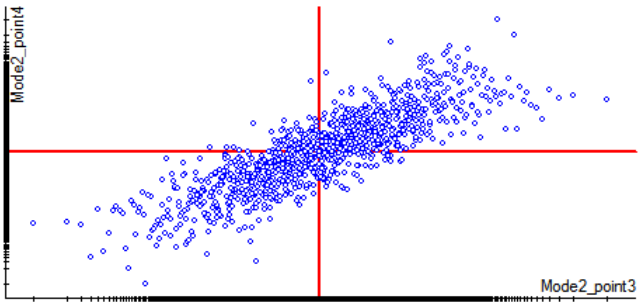


Figure 9: Generated samples of two mode shape values with strong correlation.

3.4 Probabilistic damage detection

To investigate the influence of modal parameter uncertainties on damage detection results, damage detection was performed for each sample of modal parameters generated by Latin Hypercube Sampling. In here, all generated samples represent healthy structural state. Ideally, the damage detection would result in 100% of the generated samples assigned to healthy structural state.

The damage detection for each sample of modal properties was done by comparing it to the database of pre-calculated damage scenarios. The damage scenario that matches best the sample of modal properties is selected as the identified damage case. Measure of match similarity was calculated according to Equation 3. In here, the frequency differences are normalized by standard deviation of measured frequencies and summed up. Then, measure of similarity of mode shapes is added, again normalized by standard deviation of MAC-values.

$$J_{i,d} = \sum_m \frac{\left| f_{i,m} - f_{d,m} \right|}{\sigma\left(f_m\right)} + \sum_m \frac{1 - MAC\left(\phi_{i,m}, \phi_{d,m}\right)}{\sigma\left(MAC\left(\phi_m\right)\right)} \tag{3}$$

where $J_{i,d}$ is objective function for matching modal parameter set i with damage scenario d,

$f_{i,m}$ is eigenfrequency of modal parameter set i of mode m,

$f_{d,m}$ is eigenfrequency of mode m in damage scenario d,

$\sigma(f_m)$ is standard deviation of eigenfrequency of mode m,

$MAC(\phi_{i,m}, \phi_{d,m})$ is Modal Assurance Criteria between modal parameter set i and damage scenario d of mode m,

$\sigma(MAC(\phi_m))$ is standard deviation of MAC-value between generated modal parameter sets and mean mode shape of mode m.

The standard deviation of MAC-values was evaluated by calculating MAC-values between all generated mode shapes and the mean mode shape. Histogram of these MAC-values is shown in Figure 10 for two modes. Table 2 lists standard deviations of frequency and MAC-value for the first two measured modes.

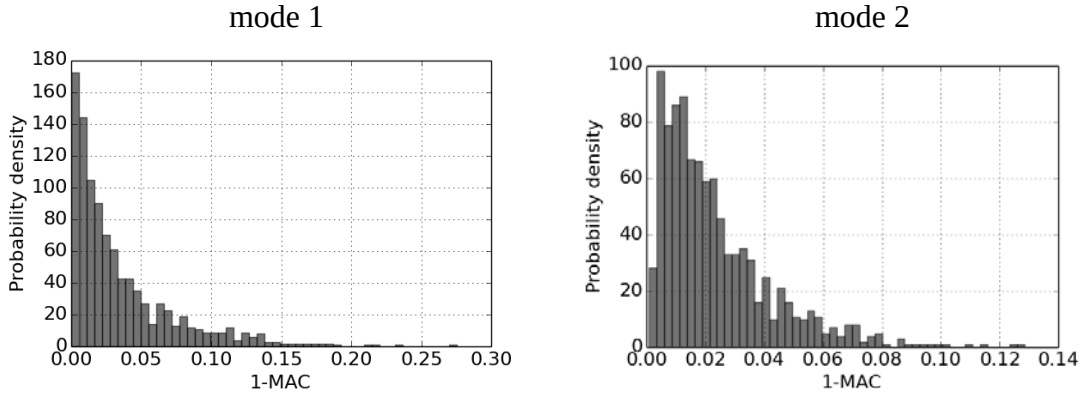


Figure 10: Histogram of MAC-values between generated mode-shape sets and the mean mode shape.

Mode	σ (f) [Hz]	σ(1-MAC) [-]
1	0.025	0.038
2	0.032	0.019

Table 2: Standard deviations of measured frequencies and MAC-values.

For each generated set of modal parameters i, the objective function $J_{i,d}$ is evaluated for all damage scenarios d. Then, the damage scenario with lowest objective function is picked. The procedure is repeated for all generated sets and thus a set of matching damage scenarios is acquired. The last step in this probabilistic damage detection is evaluation of occurrence frequency of particular damage scenarios. Results of this evaluation of occurrence frequency are visualized in the following figures.

The visualization contains quite complex information that has to be displayed together in one picture. Therefore, the following visualization rules were adopted:

- Each of the displayed vertical bars shows 4 properties: position of damage, spatial extent of damage, stiffness reduction E_{red}, and the probability that the stiffness reduction (E_k) is larger than E_{red}.
- The position and spatial extent of damage is displayed by position and width of the vertical bars on the axis called “Bridge coordinate”.
- The stiffness reduction E_{red} is displayed using the color code.
- The height of the bar defines the probability that the stiffness reduction is larger than E_{red} at the given position and spatial extent of the damage scenario.
- Vertical position of the blue rectangle defines the probability of healthy structural state (no damage)

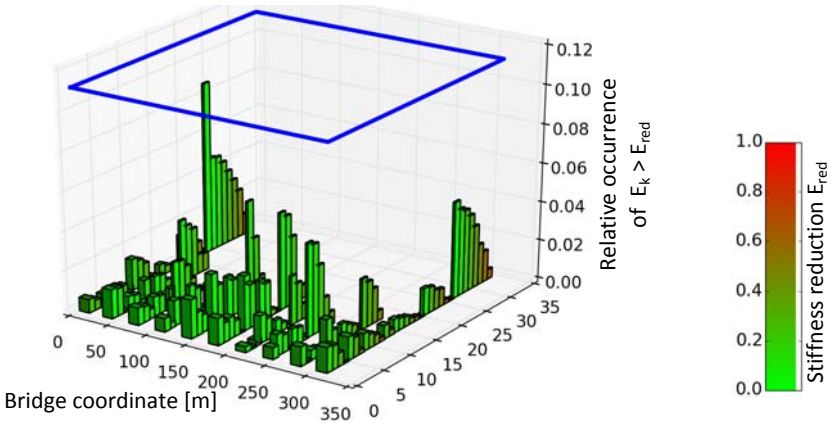


Figure 11: Relative occurrence of matching damage scenarios in healthy structural state.

From the figure above it can be seen that the healthy structural state (blue rectangle) has higher probability than any other damage scenario, therefore the structure is most likely undamaged.

In this type of visualization, the bars that would indicate high probability of damage would be red and high. On the other hand, a high green bar would represent a high probability of small stiffness reduction. Additionally, width of the bar indicates how localized the damage is.

Further, in this type of visualization it can be seen how good the localization of the damage is. In the figure above, different damage scenarios have small probabilities of occurrence. However, these damage scenarios are spread across the whole bridge length and do not concentrate on one region. This fact reinforces the conclusion that the structure is in healthy state.

In order to demonstrate results of probabilistic damage detection at occurrence of damage, the measured modal parameters were modified using simulated damage scenarios and the probabilistic damage detection was repeated. Figure 12 shows results of damage identification for simulated damage of stiffness reduction at bridge coordinate X=113.8m, affected bridge length was L=4.7m and magnitude of stiffness reduction was E_k=11.5% and E_k=30%, respectively. The displayed results show that the blue rectangle has a low position, which means the structure is not likely in healthy state. The matching damage scenarios concentrate more in one region, which indicates the likely position of damage. It can be observed that certain wide green bars have similar height as other narrow orange bars, which means that the probability of small stiffness reduction on a larger area is approximately equal to probability of higher stiffness reduction on a more localized area.

Simulated damage: X=113.8m, L=4.7m, E_k=11.5 % X=113.8m, L=4.7m, E_k=30 %

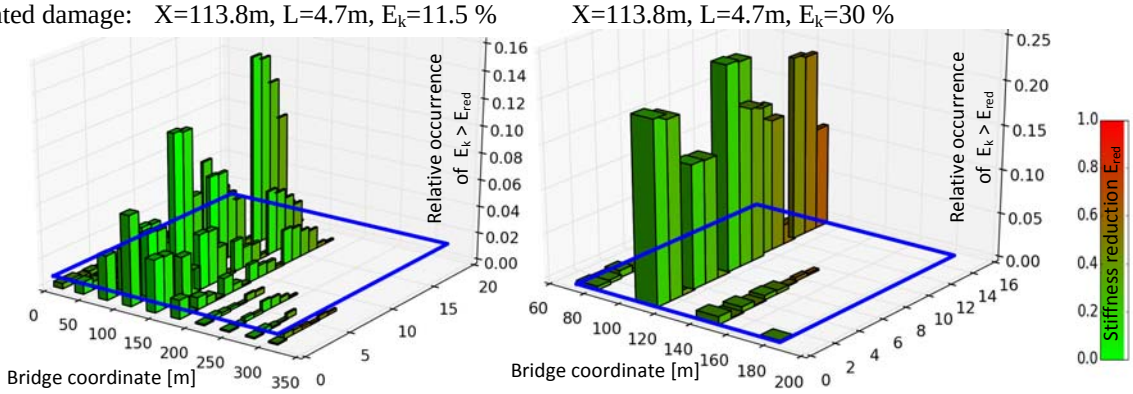


Figure 12: Relative occurrence of matching damage scenarios in two simulated damage cases.

Figure 13 shows a similar evaluation for a different position of simulated damage (X=181.5m) and larger affected bridge length (L=12.3m). In both simulated damage scenarios, the damage can be quite well localized at a stiffness reduction of 30%.

Simulated damage: X=181.5m, L=12.3m, E_k=11.5 % X=181.5m, L=12.3m, E_k=30 %

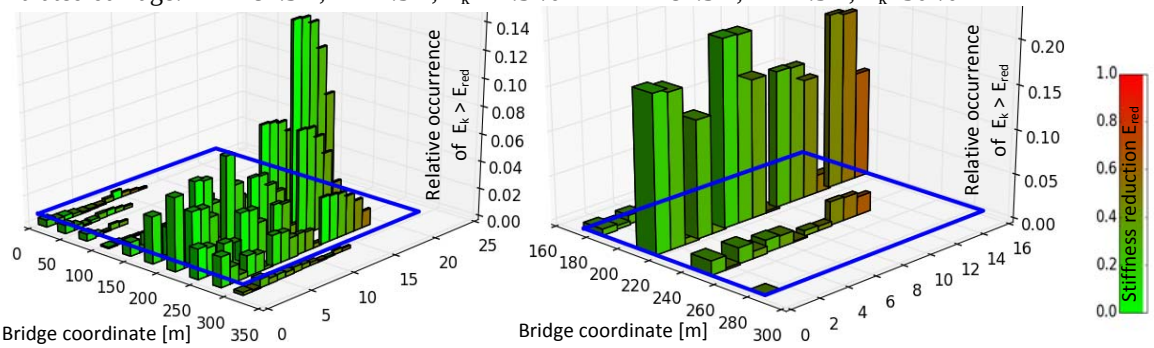


Figure 13: Relative occurrence of matching damage scenarios in other two simulated damage cases.

Figure 14 shows results for a simulated damage with a high stiffness reduction (E_k=57.3 %). The high probability of identified damage is indicated by presence of high red bars. The damage localization is unambiguous.

Simulated damage: X=113.8m, L=4.7m, E_k=57.3 %

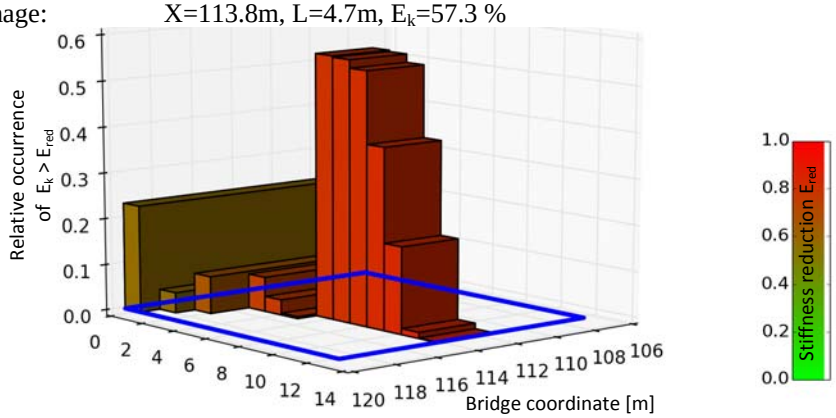


Figure 14: Relative occurrence of matching damage scenarios in a simulated damage case with high stiffness reduction.

4 CONCLUSIONS

- Procedure for evaluation of modal parameter uncertainties was presented. It is recommended to consider besides uncertainties caused by environmental influences also the uncertainties of the automated extraction of modal parameters.
- Damage detection was performed using the forward approach by matching of modal parameters to database of pre-calculated damage states.
- Effect of modal parameter uncertainty on damage detection results was evaluated using Monte-Carlo Simulation.
- Healthy structural state was clearly identified by relatively high probability of undamaged state and smaller probabilities of weak damage scenarios spread across the whole bridge (not localized in any specific area).
- In the simulated damage scenarios, the localization became clearer if the introduced stiffness reduction was higher. Already at level of 30 % stiffness reduction the localization was very good.
- The presented probabilistic process of damage detection seems to be a practicable method for damage detection that considers uncertainties of input parameters.

ACKNOWLEDGEMENTS

Part of the presented work was accomplished within the research project TRIMM (Tomorrow's Road Infrastructure Monitoring and Management), which was part of FP7 research programme funded by the European Commission.

REFERENCES

[1] J. Maeck, *Damage Assessment of Civil Engineering Structures by Vibration Monitoring*, PhD thesis, Katholieke Universiteit Leuven, 2003.

[2] B. Peeters, *System identification and Damage Detection in Civil Engineering*, PhD thesis, Katholieke Universiteit Leuven, 2000.

[3] J. Lau, J. Lanslots, B. Peeters, H. Van der Auweraer, *Automatic modal analysis: reality or myth?*, 25th International Modal Analysis Conference, Orlando, USA, February 2007.

[4] J. P. Santos, *Smart Structural Health Monitoring Techniques for Novelty Identification in Civil Engineering Structures*, PhD thesis, Universidade de Lisboa, Instituto Superior technico, 2014.

[5] Ch. Efstathiades, C.C. Baniotopoulos, P. Nazarko, L. Ziemianski, G.E. Stavroulakis, *Application of neural networks for the structural health monitoring in curtain-wall systems*, Engineering Structures vol. 29, pp.3475–3484, 2007.

[6] J.M.W. Brownjohn, P.-Q. Xia, H. Hao, Y. Xia, *Civil structure condition assessment by FE model updating: Methodology and case studies*. Finite Elements in Analysis and Design vol. 37, pp. 761-775, 2001.

[7] C. Mares, J.E. Mottershead, M.I. Friswell, *Stochastic model updating: Part 1- theory and simulated example*, Mechanical Systems and Signal Processing vol. 20, pp. 1674–1695, 2006.

[8] P. Verboven, E. Parloo, P. Guillaume, M. Van Overmeire, *Autonomous Structural Health Monitoring – Part 1: Modal Parameter Estimation and Tracking*, Mechanical Systems and Signal Processing vol. 16, pp. 637–657, 2002.

[9] M. Döhler, L. Mevel, P. Andersen, *Efficient uncertainty computation for modal parameters in stochastic subspace identification*. 4th International Conference on Uncertainty in Structural Dynamics, Leuven, Belgium, 2012.

[10] S. W. Doebling, F. M. Hemez, *Overview of Uncertainty Assessment for Structural Health Monitoring*, 3rd International Workshop on Structural Health Monitoring, Stanford, USA, September 2001.

COMPDYN 2015
5th ECCOMAS Thematic Conference on
Computational Methods in Structural Dynamics and Earthquake Engineering
M. Papadrakakis, V. Papadopoulos, V. Plevris (eds.)
Crete Island, Greece, 25–27 May 2015

VIBRATION MEASUREMENT-BASED SIMPLE TECHNIQUE FOR STRUCTURAL APPRAISAL OF STEEL BRIDGES

W.A. Indika Priya Wijesooriya[1], Sudath C.Siriwardane[2], and P.B.R. Dissanayake [3]

[1] Department of Civil Engineering, University of Peradeniya, Sri Lanka.
waipwijesooriya@yahoo.com

[2] Department of Structural, Mechanical Engineering and Material Science, University of Stavanger, Norway.
sasc.siriwardane@uis.no

[3] Department of Civil Engineering, University of Peradeniya, Sri Lanka.
ranjith@fulbrightmail.org

Keywords: Structural Health Monitoring, Vibration Measurement, Model Parameters, Finite Element Method.

Abstract. *The structures experience increasing traffic volume and weight, deteriorating of components and large number of stress cycles. Therefore, assessment of the current condition (i.e. Structural Health Monitoring) of steel railway bridges becomes necessary. Most of the commonly available approaches for Structural Health Monitoring are based visual inspection and non-destructive testing methods. The visual inspection is unreliable as those depend on uncertainty behind inspectors and their experience. Also, the non-destructive testing methods are found to be expensive. Therefore, recent researches noticed that dynamic modal parameters or vibration measurements-based Structural Health Monitoring Methods are economical and may also provide more realistic predictions to damage state of civil infrastructure. Therefore this paper proposes a simple technique to locate the damage region of railway truss bridges based on measured modal parameters. The technique is discussed with a case study. Initially paper describes the details of considered railway bridge. Then methods and observations of visual inspection, material testing and in-situ load testing are discussed under separate sections. Then the development of validated FE model of the considered bridge is comprehensively discussed. Hence, variations of modal parameters versus position of the damage were plotted. These plots are considered as the main reference for locating the damage of the railway bridge in future periodical inspection by comparing the measured corresponding modal parameters. Finally the procedure of periodical vibration measurement and damage locating technique were clearly illustrated.*

1 INTRODUCTION

A most of railway bridges in the world (i.e. mainly in UK, parts of Europe and North America) are near the end of their design lives and many of them exceeds 100 years of age [1, 2]. Replacement of all these at once will be extremely expensive and practically impossible as there are large number of old bridges (e.g. it is estimated that there is more than 6000 in UK). As a result, in the past two decades, a significant amount of effort has been directed towards the development of structural health monitoring and non-destructive assessment methods to maintain these bridges more efficiently [2-12].

Structural appraisal has been received more attention from bridge engineers due to recent failures in bridges in both developed and developing countries such as collapse of the Interstate 35W bridge in Minneapolis, Minnesota in July 2007; the Hoan bridge failure in Milwaukee, Wisconsin in 2000;partially collapse of Cosen bridge in Latchford, Canada in 2003 and etc. The detailed inspections of steel truss bridges in the word revealed cracks and fractures, severe deterioration due to corrosion of members, some of which already reached a complete loss of the cross section of the member [13-16]. Some of these damages are located in the regions, where it is difficult to access for visual inspections.

In health monitoring of bridges, visual inspections are widely used. However, uncertainties of skills of inspectors and above mentioned accessibility issues finally hindered the visual inspection based health monitoring of bridges for part of the structure. Even though the nondestructive testing-based damage detection approaches are more accurate, those approaches are highly expensive and time consuming. Recently researches noticed that dynamic model parameters or vibration measurements-based structural health monitoring techniques may provide more realistic predictions to damage state of steel structures [13,17]. This approach is mainly based on variation of model parameters (i.e. i.e. natural frequency, mode shapes and model damping) with structural integrity. Therefore, periodical model parameter measurements can be used to monitor structural condition. Since model parameter measurements can be cheaply acquired, the approach could provide an inexpensive structural assessment technique [17,18]. Even though large number of studies have been done on this area, vibration measurement-based detection of damage or deterioration due to more or equal to the complete loss of cross section has not been properly discussed for railway bridges.

To overcome the above problem to some extent, this paper discusses a vibration measurement based simple technique to locate the damaged or deteriorated region for detailed inspection and quantification of damage. The scope of study is limited to the steel truss bridges. The concept of this damage locating technique is change of model parameters (i.e. natural frequency and mode shapes) due to presence of damage or deterioration. The damages or deterioration due to fully section loss of members, which are difficult to access for visual inspections, are more precisely locate by this proposed technique and it is the one of the main limitations of this approach. This approach provides a warning of damage or deterioration before it is too late to attend for necessary detailed inspection or maintenance. The paper describes the proposed technique with a comprehensive case study as bellow.

2 CONSIDERED BRIDGE

The selected bridge is one of the major railway bridges in Sri Lanka spanning 160 m (Figure 1). It is a six span-riveted bridge with double lane rail tracks having warren type semi through trusses, supported on cylindrical piers. The bridge deck is made of wrought iron and the piers are made of cast iron casings with infilled concrete. The bridge was constructed in 1885. Details of trains carried by the bridge and their frequencies illustrate that the bridge is suffered from variable amplitude loading.



Figure 1: General views of the riveted railway bridge

3 VISUAL INSPECTION

The condition survey revealed that some places of the bridge have been subjected to mild corrosion due to the absence of anti corrosive coating (see Figure 1). No visual cracks were observed in any component of the super structure. In situ measurements of member sizes, connections and support bearings verified the fact that the existing drawings were applicable and only few significant variations were observed.

4 MATERIAL TESTING

The sampling of materials, specimen preparation and testing were carried out according to the ASTM standards. The chemical analyses as well as microscopic examinations lead to the conclusion that the bridge super structure material is wrought iron. The obtained values for elastic modulus, yield strength, ultimate strength in tension, fatigue strength and density are 195 GPa, 240 MPa, 383 MPa, 155 MPa and 7600 kg/m^3 respectively.

5 STATIC AND DYNAMIC LOAD TESTING

Static and dynamic load tests were performed to study the real behavior of the bridge under various load combinations. The in-situ measurements were performed using two M8 engines, each weighting 1120 kN, which is the heaviest rail traffic in current operation. The bridge was instrumented with strain gauges placed at selected locations to measure normal strains. In addition, the tri-axial vibrations were recorded at several locations using accelerometers. Displacement transducers were used to measures vertical deflection at three places around the mid-span area of the bridge. The measured locations are shown in Figure 2.

To obtain the different type of load combinations, which are critical to the bridge, the two test-engines were placed together as well as moved under different speeds. The considered three static load combinations are defined as static load case (SLC) 1,2 and 3 by considering criteria of maximum shear effect, maximum bending effect (maximum deflection) and maximum torsion effect to the bridge deck respectively. The loading positions corresponding to the mentioned three load cases are shown in Figure 3. The criteria, which were considered for dynamic load combinations, basically illustrate that impact effect to the bridge with different levels of speed and traction force effect. Apart from the above mentioned formal field load testing, the bridge was subjected to a two days continuous field measurement program under present day actual traffic. When the bridge is affected by maximum load due to the present day heaviest train passage, the obtained sample measurements are shown in Figure 4. Finally the dynamic factors were obtained as 1.3, 1.4 and 1.4 for main truss girders, secondary cross girders and stringers respectively.

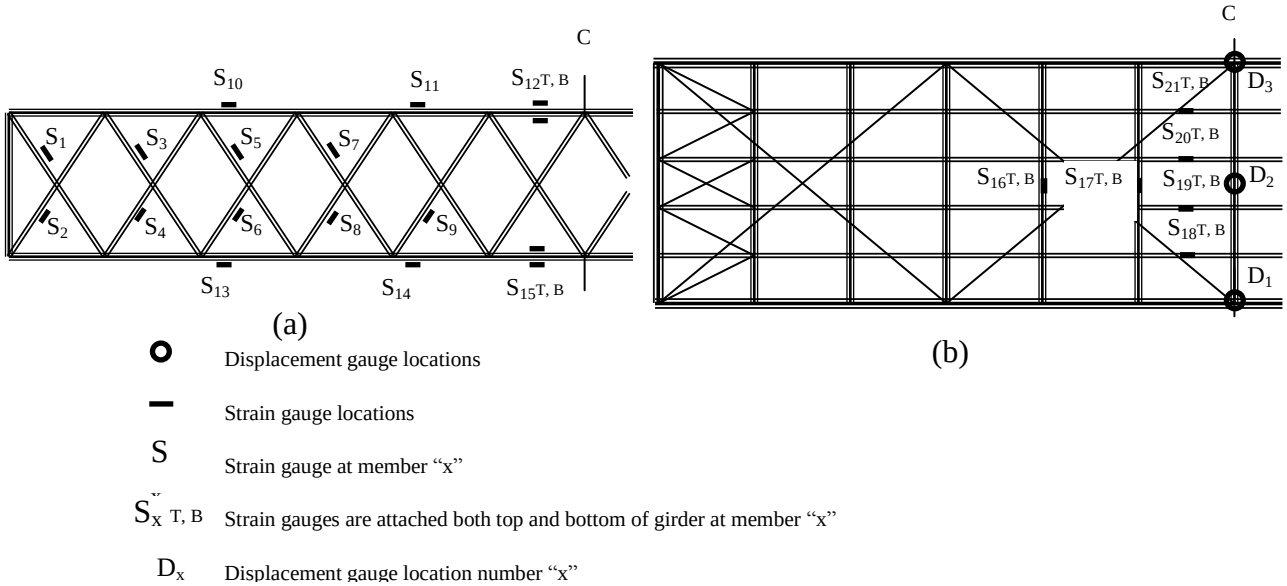


Figure 2. Locations of the strain gauges and displacement gauges (a) Main truss girder (b) Horizontal bridge deck

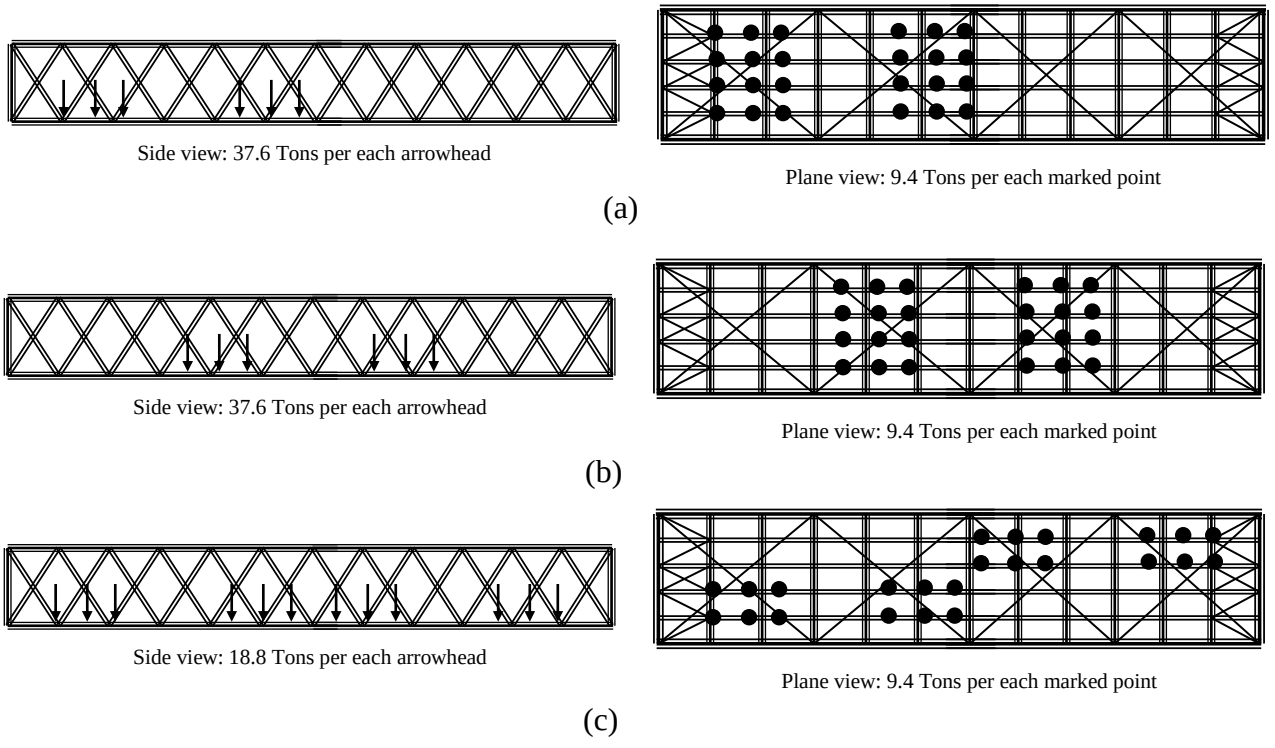


Figure 3. Loading positions corresponding to three static load cases (a) SLC 1 (b) SLC 2 (c) SLC 3

6 DEVELOPMENT OF VALIDATED FINITE ELEMENT MODEL

Then the bridge deck was analyzed using the finite element (FE) method employed general- purpose package SAP 2000. A three-dimensional (3D) model (Figure 5) of one complete middle span of the bridge was analysed under actual loading to determine stresses in members and deflections, as well as variations of stresses under moving loads. The material properties recorded in section 4 and section properties calculated above were utilized for this FE analysis. The bridge deck was modelled with 3D frame elements and the riveted connections were assumed to be fully-fixed [4]. Moving load employed time history dynamic analysis was con-

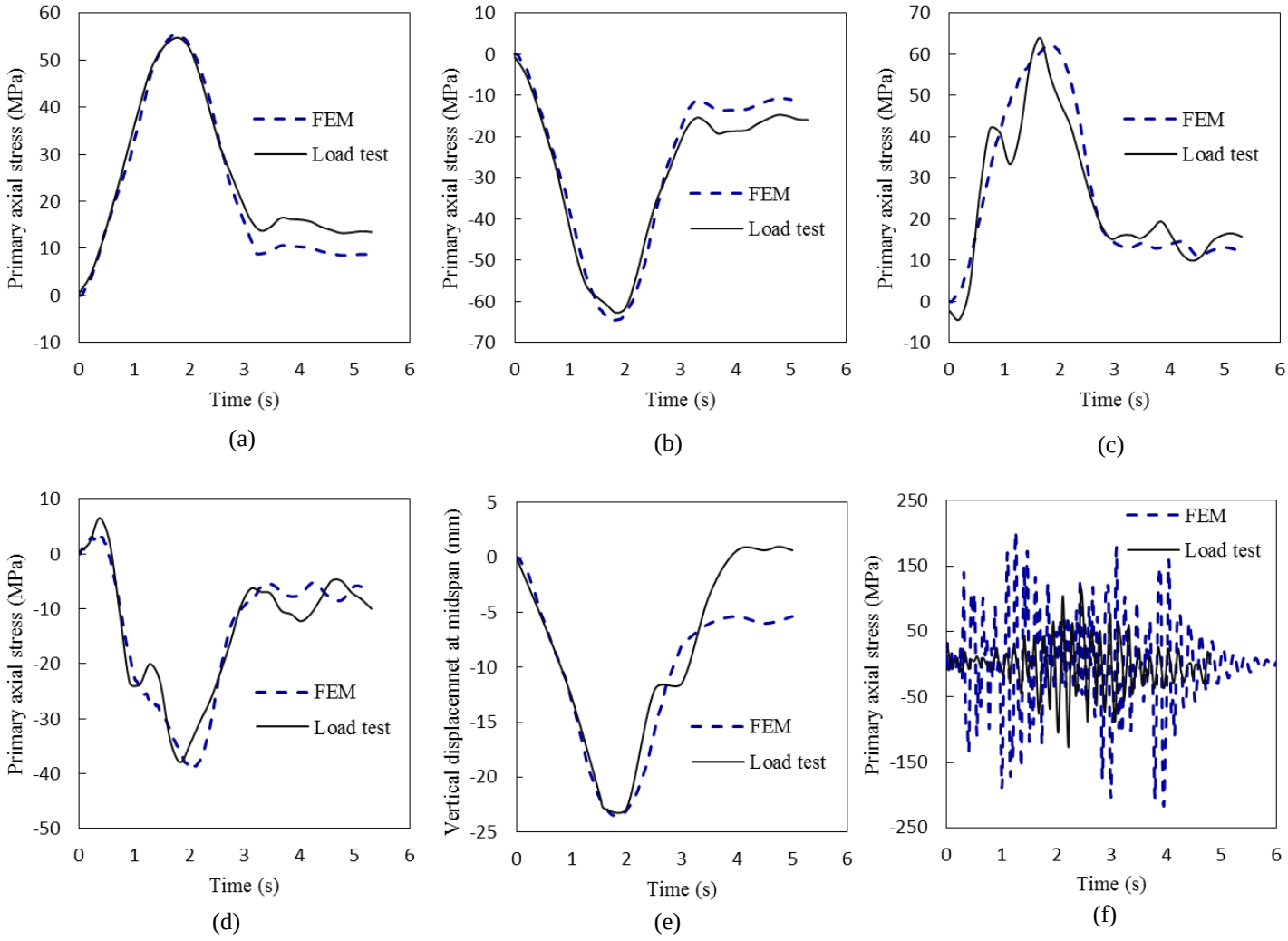


Figure 4. Comparison of FEM time history analysis results with field measurements: (a) Stresses at MT3,2 bottom chord of the main girder, (b) Stresses at MC3,2 top chord of the main girder, (c) Stresses at DT3 diagonal tension members, (d) Stresses at DC3 diagonal compression members, (e) Vertical displacemnt at midspan, (f) Vertical acceleration at midspan

ducted for each different load cases discussed in section 5. After appearing the general corrosion sign of each member of each location, the input values of sectional parameters were changed by calculated values of corroded section to obtain the load histories of the members.

The validation of FE model was done by comparing the results from analysis with those from field-tests as shown in Table 1. In this paper, further validation of the FE model is done by comparing the results of time history dynamic analysis with those from measured time histories during appraisal in year 2001 as shown in Figure 4. These figures show that there is a good agreement among analytical results of the FE model and the measurement of the actual bridge. Therefore, the considered 3D frame element model was defined as "validated FE model" which can reasonably represent the actual static and dynamic behavior of the bridge at 2001.

7 MODEL PARAMETER VARIATION WITH RESPECT TO DAMAGE

In this study, it is assumed that damage of the member represent fully section loss or through thickness crack of inaccessible members (i.e. difficult to access for visual inspections) such as main girder bottom chord and cross girders. It was also assumed that probability is

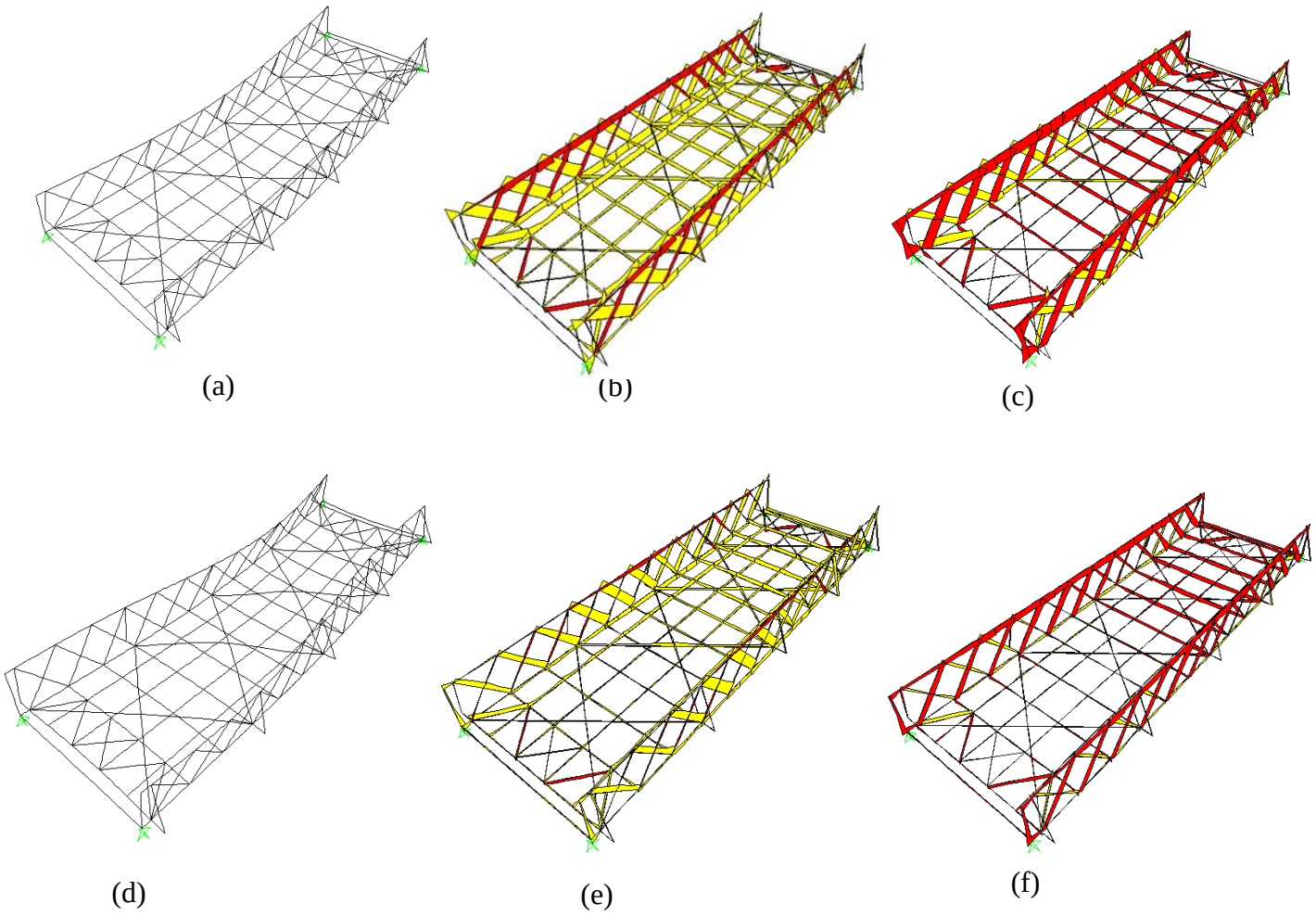


Figure 5. The FE analysis results for moving train load: (a) Vertical displacement when the train is in the middle of the bridge (b) Maximum stress taken over all stress points at each cross sections when train is in the middle of the bridge (c) Minimum stress taken over all stress points at each cross sections when train is in the middle of the bridge (d) Vertical displacement when the train just before leave the bridge (e) Maximum stress taken over all stress points at each cross sections when the train just before leave the bridge (f) Minimum stress taken over all stress points at each cross sections when the train just before leave the bridge
Yellow color: Tensile stress
Red color: compressive stress

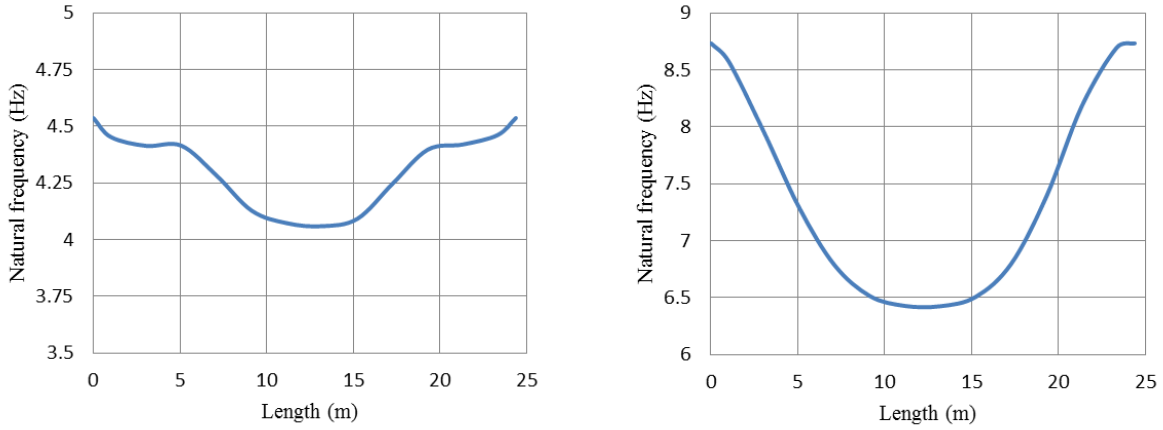
Table 1. Comparison of FE analytical results with load test results

Static load case	Displacement (mm)			Stress (MPa)		
	Location of measurement	Load test	FEM	Location of measurement	Load test	FEM
SLC 1	D_1	19.4	21.0	S_6	-40.2	-40.6
				S_5	51.4	57.3
				$S_{15,}$T,B	47.3	48.2
SLC 2	D_1	21.3	22.5	S_6	-37.8	-37.7
				S_5	44.5	43.6
				$S_{15,}$T,B	53.5	53.9
SLC 3	D_1	-	19.1	S_6	-39.5	-39.9
				S_5	35.2	41.5
				$S_{15,}$T,B	39.0	44.7

very low to damage or deteriorate two or more members until complete loss of cross section in an interval of two periodical inspections. Thus validated FE model obtained in section 6

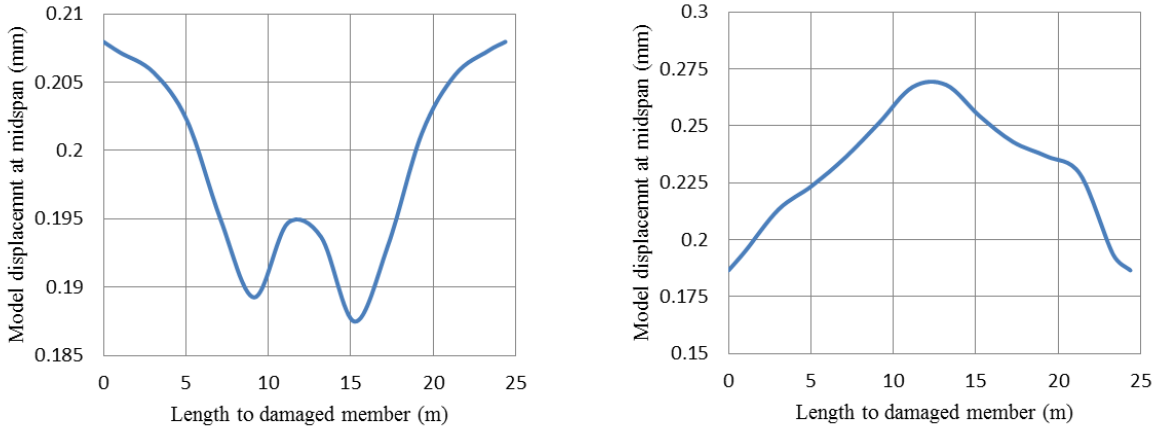
was used to simply remove one member at a time and re-analyze to get the modal parameters of each mode of free vibration. Hence, the location, type of member and observed values of modal parameters are recorded and plot variations of modal parameters versus position of the damage as shown in Figure 6 -9.

At modal nodes (points of zero modal displacements), the stress is minimum for the particular mode of vibration. Hence, it can be seen that less change in a particular modal parameter when damage is located in members which are close to the modal node. However, the parameters in other modes of vibration can still be used to locate this damage of member [16]. Therefore, it is important to plot the variation of model parameters for few modes of vibrations. Finally, these plots were used as main reference for locating the damage of the railway bridge in future periodical inspection by comparing the measured corresponding model parameter.



(a) (b)

Figure 6: Variation of natural frequency versus length to damaged member of main girder bottom chord: (a) mode 1, (b) mode 2

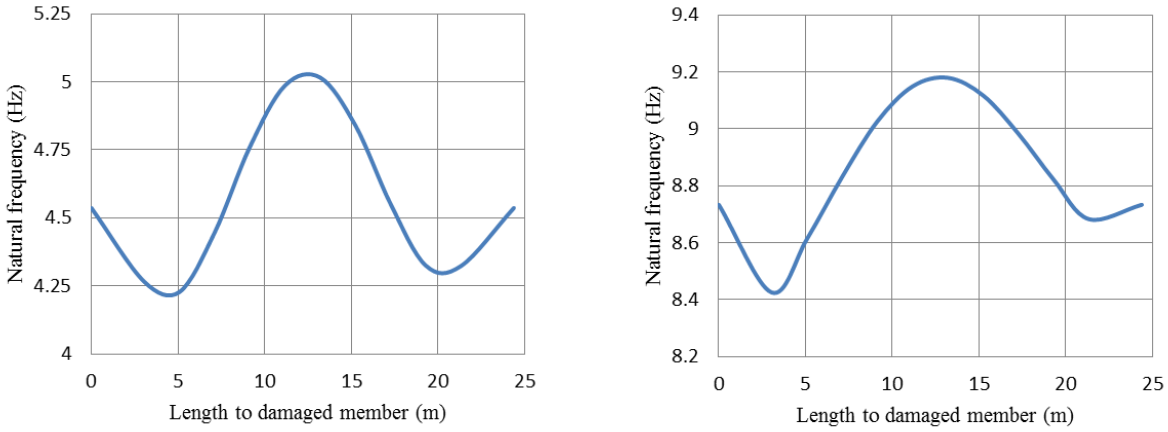


(a) (b)

Figure 7: Variation of mid span modal displacement versus length to damaged member of main girder bottom chord: (a) mode 1, (b) mode 2

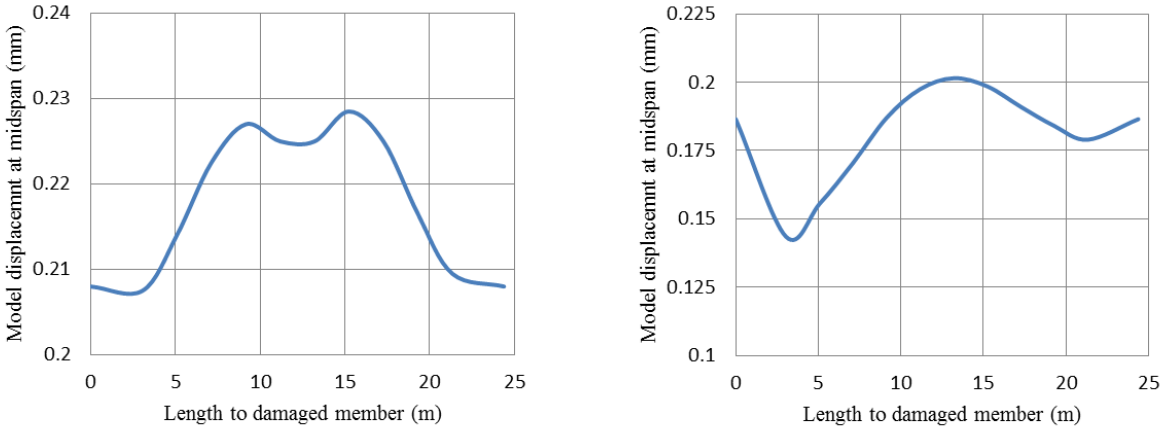
8 PERIODICAL VIBRATION MEASUREMENT AND LOCATING DAMAGES

After ten years later of previous inspection (i.e. 2011), bridge was instrumented with accelerometers placed at selected locations to measure all three directions accelerations. In order to



(a) (b)

Figure 8: Variation of natural frequency versus length to damaged member of cross girder: (a) mode 1, (b) mode 2



(a) (b)

Figure 9: Variation of mid span modal displacement versus length to damaged member of cross girder: (a) mode 1, (b) mode 2

measure free vibration, accelerations were recorded after the train had crossed the bridge. Hence natural periods of each mode were determined and corresponding natural frequencies were predicted as 4.72 Hz and 9.1Hz respectively for mode 1 and 2. The mode displacements were obtained by FFT transformation of measured accelerations. The predicted mode displacements at mid-span are 0.212mm and 0.191mm respectively for mode 1 and 2. Then these values compared with plots obtained in section 7. Hence, the suspected region of damage has been located in cross girders as circled in Figure 2(b).Then bridge inspectors stops the train operation for one night and detailed inspection was conducted. Finally its revealed that loosening of many of rivets finally hindered the contribution of cross girder number 16th to the stiffness of the bridge. Suspected reason for these loosing might be the fatigue.

9 CONCLUSIONS

A simple technique was proposed to locate the damage region of railway bridges based on measured model parameters. The case study shows the applicability of the introduced technique. The technique mainly depends on plots of variation of model parameter respect to the position of damage which was obtained by validated FE model. The validated FE model, which represents more reasonably the actual static and dynamic behavior of the railway

bridge at the time of validated, was obtained by comparing the measured responses with FE model given responses. The periodical model parameter measurement has to be conducted and obtained measurement should be compared with above plots to locate the region of damage. As this periodical model parameter measurement is based only on acceleration under usual moving train loads, it can be concluded that this measurement can be cheaply acquired and the proposed method provides an inexpensive structural appraisal technique. Influence of partially loss of member cross section for change of model parameters are recommended for future studies.

ACKNOWLEDGMENT

The authors wish to express their sincere gratitude to Emeritus Professor M.P Ranaweera and the team of experts who worked in the Sri Lankan Railway Bridge project, for their great advice, which laid the foundation for this research. The kind support given by the Sri Lanka Railways (SLR) is also appreciated. Authors wish to convey their gratitude to Mr. Øyvind Olav Olsen for given assistance for this project.

REFERENCES

[1] B.M. Imam, T.D. Righiniotis, Fatigue evaluation of riveted railway bridges through global and local analysis. *J. Constr. Steel. Res.* 66, 1411–1421, 2011.

[2] H. Rosemarie, K. Bertram, N. Alain, Assessment of existing steel structures: A guideline for estimation of the remaining fatigue life, *Structure and Infrastructure Engineering*,3, 245-255, 2007.

[3] B. Sherif, M. Shuichi, O.Toshiyuki, Nondestructive damage detection scheme for steel bridges, *J App. Mech*., 9, 63-74, 2006.

[4] B. Imam, T.D. Righiniotis, M.K. Chryssanthopoulos, Fatigue assessment of riveted railway bridges, *Int. J. Steel Struct*., 5, 485-494, 2005.

[5] L. Köröndi, A. Szittner, M. Kálló, L. Krisróf, Determination of fatigue safety and remaining fatigue life on a riveted railway bridge by measurement, *J. Constr. Steel. Res*., 46, 430, paper number 327, 1998.

[6] Z.X. Li, T.H.T. Chan, J.M. Ko, Fatigue analysis and life prediction of bridges with structural health monitoring data- Part 1: methodology and strategy, *Int. J Fatigue.*, 23,45-53, 2011.

[7] Z.X. Li, T.H.T. Chan, J.M. Ko, Fatigue analysis and life prediction of bridges with structural health monitoring data- Part II: application, *Int. J Fatigue.*, 23, 55-64, 2011.

[8] Z.X. Li, T.H.T. Chan, J.M. Ko, Fatigue damage model for bridge under traffic loading: application made to Tsing Ma Bridge, *Theo. & App. Fracture Mechanics,* 35 , 81-91, 2011.

[9] Z.X. Li, T.H.T. Chan, J.M. Ko, Determination of effective stress range and its application on fatigue stress assessment of existing bridges, *Int. J Solid & Struct.*,39, 2401-2417, 2002.

[10] Z.X. Li, T.H.T. Chan, R. Zheng, Statistical analysis of online strain response and its application in fatigue assessment of a long span steel bridge, *Eng. Struct*., 25: 1731-1741, 2003.

[11] Z.X. Li, T.H.T. Chan, Fatigue criteria for integrity assessment of long span steel bridge health monitoring, *Theo. & App. Fracture Mechanics*., 46, 114-127, 2006.

[12] S. Siriwardane, M. Ohga, R. Dissanayake, K. Taniwaki, Application of new damage indicator-based sequential law for remaining fatigue life estimation of railway bridges, *J. Constr. Steel. Res*., 64, 228-237, 2008.

[13] Y. Matsumoto, H. Yamaguchi, T. Yoshioka, A field investigation of vibration-based structural health monitoring in a steel truss bridge, *IABSE-JSCE Joint Conference on Advances in Bridge Engineering-II*, Dhaka, Bangladesh, August 8-10, 2010.

[14] J. Beisswenger, M.J. Cramer, T.P. Murphy, *Old Cedar Avenue Bridge over Long Meadow Lake*, Rehabilitation Report, SRE Consulting Group, July 2014.

[15] K. Lima, N. Robson, S. Oosterhof, S. Kanji, J. DiBattista, C.J. Montgomery, Rehabilitation of a 100-year-old steel truss bridge, *CSCE 2008 Annual Conference*, June 10-13, 2008.

[16] M. Mohammed, Ettouney, S. Alampalli, *Infrastructure Health in Civil Engineering: Theory and Components*, CRC press, 2012.

[17] O.S. Salawu, Detection of damage through changes in frequency: a review, *Engineering Structures*, 19(6), 718-723, 1997.

[18] O.S. Salawu, C. Williams, A review of full-scale dynamic testing of bridge structures, *Engineering Structures*, 17 (2), 113-121, 1995.

COMPDYN 2015
5th ECCOMAS Thematic Conference on
Computational Methods in Structural Dynamics and Earthquake Engineering
M. Papadrakakis, V. Papadopoulos, V. Plevris (eds.)
Crete Island, Greece, 25–27 May 2015

STRUCTURAL HEALTH MONITORING USING TIME-DELAY EMBEDDING AND PHASE-SPACE WARPING

Mohammad H. AlHamaydeh[1], Kenneth Wong[2], Ralston Fernandes[3], Jeongcheol Seok[2], Eihab M. Abdel-Rahman[2], and Sami El-Borgi[3]

[1] Department of Civil Engineering
American University of Sharjah
P.O. Box 26666, Sharjah
United Arab Emirates
e-mail: malhamaydeh@aus.edu

[2] Systems Design Engineering
University of Waterloo
200 University Avenue West
Waterloo, Ontario, N2L 3G1 Canada
{k6wong,jseok,eihab}@uwaterloo.ca

[3] Department of Mechanical Engineering
Texas A&M University at Qatar
3123 TAMU, Doha, Qatar
{ralston.fernandes,sami.el_borgi}@qatar.tamu.edu

Keywords: Damage, Time-Delay Embedding, Phase-Space Warping, Fill Factor.

Abstract. *This paper presents a method to utilize Time-Delay Embedding (TDE) to perform structural health monitoring and obtain a damage metric that tracks deterioration in structural health over time. Proof-of-concept is demonstrated through an experimental investigation. The experimental setup consisted of high-rise building model, made of aluminium, mounted on a digitally-controlled shaker table. Floor accelerations are recorded using accelerometers on each elevation to capture the dynamic response during the base excitation. Natural modes of vibration and their corresponding frequencies were determined experimentally using a frequency sweep of low-amplitude sinusoidal support excitations. The model building was excited at its natural frequency with moderate-amplitude sinusoidal base excitation to establish its "pristine" condition baseline. Subsequently, damage is introduced to columns on the first floor by cutting two notches at mid-height, significantly reducing their cross-sectional areas. The same base motion protocol was re-applied and acceleration data was collected and processed to detect the pre-known damage patterns as well as the total failure using changes in the oscillation orbits. The damage metric is shown to adequately detect structural damage.*

1 INTRODUCTION AND BACKGROUND

With the observed increase in frequency and intensity of seismic activity, there is a need to detect damage in important structures such as bridges and high-rise buildings. This can be done through continuous monitoring for structural integrity purposes. Further, ongoing Structural Health Monitoring (SHM) is not limited to seismic activity but can also be used to maintain long-term safety, viability and value of structures.

SHM is the non-intrusive collection and analysis methods for damage detection and diagnosis. The goal of SHM is to characterize the structure's performance and to help maintain the structural performance over its service life. Vibration-based SHM assumes that the structural dynamic response will depart from a baseline healthy performance pattern(s) when damage occurs in the structure. Thus, damage detection is contingent upon successfully extracting sensitive damage feature(s), patterning such feature(s) and realizing changes in these patterns as damage progresses. To achieve that, a SHM system incorporates four components: data acquisition, damage feature extraction, damage pattern recognition (diagnosis) and damage prognosis. These components relate to the collection of data from sensors or sensor networks, the identification of a critical feature that is sensitive to the damage state in the structure, the use of the damage feature(s) to quantify damage, and the estimating of the remaining service life using system prognosis methods [1]. Over the past three decades, numerous methods with the objective of extracting sensitive damage feature(s) have been tested on several structures [2]–[6]. Tools for damage detection using structural dynamics analysis, such as modal update and Fourier and wavelet transforms, have been examined over a large span of structures ranging from simple cantilevers to large bridges and multi-story buildings [7], [8]. By nature, tall buildings are particularly susceptible to strong ground motions propagating from long distances with ample energy levels at low predominant frequencies [9]. Moreover, tremors can cause low level damage that might not be apparent initially but will lead to damage accumulation and long-term impact on the structural integrity of the building.

Time-Delay Embedding (TDE) was introduced in the 1980s as a method to reconstruct inaccessible states of dynamic systems [10]–[12]. The method uses the time-history of a single accessible state in a coupled dynamic system to reconstruct the full system states. To reconstruct the other states, the time-history of the available state is delayed by a *'proper'* time step. For example, when using TDE one can measure the acceleration of one floor in a building to estimate the states of the key parts in the coupled dynamic system, such as other floors accelerations. The reconstructed phase-space can then be used to track damage evolution. One approach to achieve this is the so-called Phase-Space Warping (PSW) [13]–[15]. PSW uses the healthy system response to construct local linear maps in phase-space that describe the characteristics of the healthy system response. It then compares evolution of the actual system response in phase-space to the healthy system local maps to extract a damage tracking metric.

In this paper, a novel method is developed to detect structural damage in high-rise buildings using TDE and PSW.

2 TIME-DELAY EMBEDDING AND PHASE-SPACE WARPING

A simple representation of an n-story frame is a coupled MDOF oscillator:

$$\begin{aligned} &m_1\,\ddot{x}_1 + c_1\,\dot{x}_1 + k_1\,x_1 - k_2\,x_2 = f_1(x_1,\dot{x}_1,x_2,\dot{x}_2,t)\\ &m_2\,\ddot{x}_2 + c_2\,\dot{x}_2 - k_2\,x_1 + k_3\,x_2 = f_2(x_1,\dot{x}_1,x_2,\dot{x}_2,t)\\ &m_n\,\ddot{x}_n + c_n\,\dot{x}_n - k_n\,x_{n-1} + k_{n+1}\,x_n = f_n(x_{n-1},\dot{x}_{n-1},x_n,\dot{x}_n,t) \end{aligned} \qquad (1)$$

where x_1 to x_n are the horizontal displacements of the lumped mass of the n-floors, c_1 to c_n are the damping coefficients, k_1 to k_n are the stiffness of the floors, and the functions f_1 to f_2

contain nonlinear coupling terms between the n-floors motions and external forces. The vibration of this system is excited due to external loads such as ground excitations. Typically, the system periodic motions are on the order of 0.1 to 1 second. On the other hand, the damage processes we are concerned with are slow, leading over long-time, to performance degradation. The typical half-life for these processes is on the order of thousands of hours (10^6 seconds). As far as the dynamic system in n-equations is concerned, this is a slow-variation in the system parameters that modulates the dynamic response. Conversely, damage is also driven by the system fast dynamics (oscillations). Assuming, for simplicity, that a single-damage process appears in the system, we can represent it by the state variable y. As a result, the system evolution is now composed of fast observable dynamics, the native states, and a very slow unobservable dynamic process, the damage state $\dot{y}$; an additional equation can be added as:

$$\dot{y} = \varepsilon g(x_{n-1}, \dot{x}_{n-1}, x_n, \dot{x}_n, y) \tag{2}$$

where ε is a small non-dimensional parameter describing the slow evolution of the damage process compared to the fast oscillations of the system and the function g describes the evolution of the damage mechanism over time. The goal is to use the observable part of the dynamics $(x_{n-1}, \dot{x}_{n-1}, x_n, \dot{x}_n)$ to reconstruct the unobservable part of the dynamics, y. Therefore, damage detection over time can be paused as a system identification problem for a hierarchal dynamic system containing fast-time and slow-time scales. Since the system response is coupled, the observable fast-time dynamics is interrogated to identify the slow-time dynamics (damage) of the oscillator.

To achieve this goal, the method of Phase-Space Warping (PSW) is employed which tracks the orbits of the system in phase space as they evolve over time. The orbits are constructed using the observable states $(x_{n-1}, \dot{x}_{n-1}, x_n, \dot{x}_n)$. Degradation is a process that drives the orbits progressively away, in shape and/or location in the phase space, from the healthy (baseline) orbit of the system. This 'drift' (distance between the current orbit and the baseline orbit) is measured as the orbit evolves over time and quantified as the scalar tracking metric ε(t). It has been demonstrated [13], [14] that a one-to-one relationship exists between ε(t) and y(t). The difference between the time scales of the oscillator's native fast dynamics and the damage process's slow dynamics is proven to be useful through periodic sampling the system dynamics. Each sample (snapshot) can then be used to construct an 'averaged' orbit, assuming that the damage process is stationary (y(t) = constant) over the medium time-scale (100s of periods). Finally, the average orbits are compared to the baseline orbit over the long time-scale (10,000s of periods) and the difference is quantified as the tracking metric ε(t). This approach has the advantages of reducing data collection and computational costs by periodic sampling over the long time-scale and improving the signal-to-noise ratio by averaging over the medium time-scale, thereby facilitating low-cost early detection of damage or degradation. As the drift and the tracking metric ε(t) grow to exceed the signal noise level, given a pre-set confidence level, damage detection is declared. For brevity, the intricate mathematical details of the procedure are not presented herein. However, the reader is referred to the aforementioned references for further details.

3 EXPERIMENTAL INVESTIGATION

The experimental setup consisted of model 4-story building made of aluminium mounted on a digitally-controlled shaking table as can be seen in Figure 1. Floor accelerations are rec-

orded using accelerometers on each elevation to fully capture the dynamic response during the base shaking. Natural modes of vibration and their corresponding frequencies are determined experimentally using a frequency sweep of low-amplitude sinusoidal support excitations. The model building is excited at its fundamental frequency (4.37Hz) with moderate-amplitude sinusoidal base excitation to establish its "healthy" or "pristine" condition baseline using the collected and processed data.

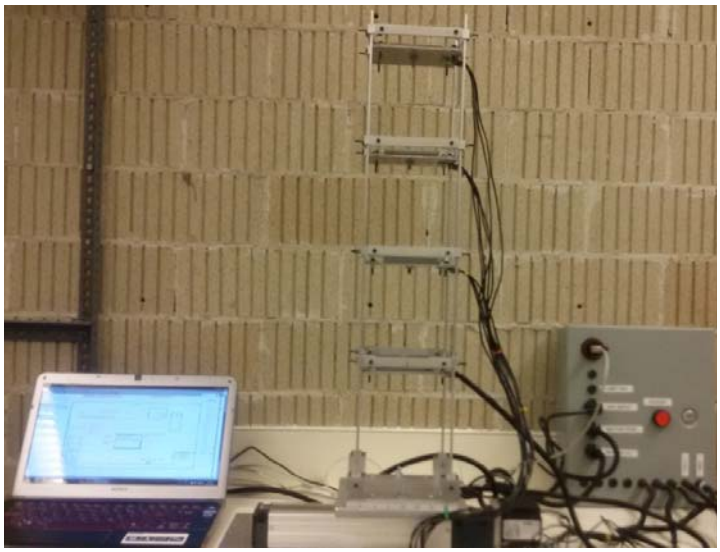


Figure 1: 4-story model building mounted to the shaker table and controller setup.

Subsequently, damage is introduced to columns on the first floor by cutting two notches at the mid-height, significantly reducing their cross-sectional areas (Figure 2). The same base motion protocol is re-applied and acceleration data is collected and processed to detect the pre-known damage patterns as well as the total failure using changes in the oscillation orbits.



Figure 2: Column damage introduced by notched cross-section (cut-out).

4 RESULTS AND DISCUSSION

The healthy or pristine baseline state of the structure is captured through its frequency signature (Fast Fourier Transform, FFT), which is presented in Figure 3. It can be seen that FFT

amplitude is highest for the first harmonic and exhibiting descending peaks for the higher harmonics except for the third harmonic. The dominance of a third harmonic among the higher harmonics indicates that the building is symmetric along the direction of oscillations.

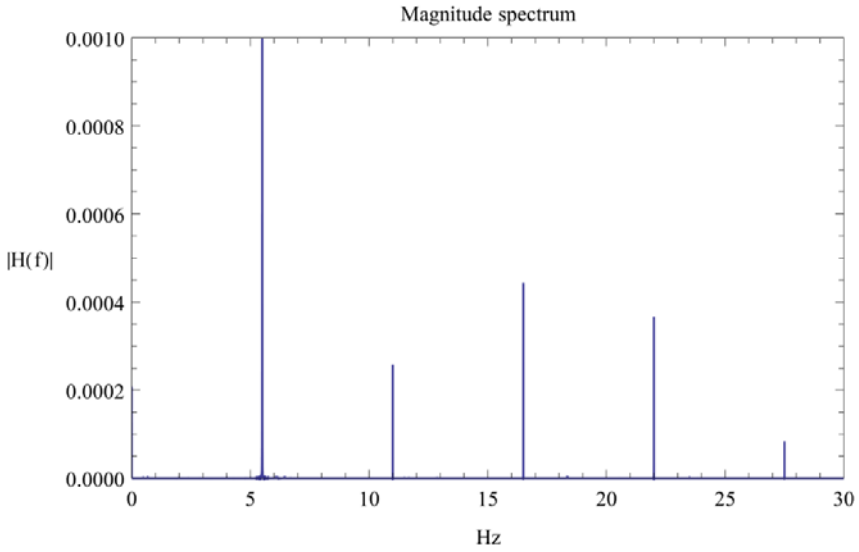


Figure 3: FFT for the model building healthy state.

Figure 4 illustrates the effect of the inflected damage to the columns at the first floor by notching their cross-sections. Inspection of the FFT signature, in comparison to the healthy state, it can be readily appreciated that the harmonics have wider bases. i.e. the damage-induced nonlinearities blur the otherwise narrow-banded peaks at the structure's harmonics. This is most evident in the first harmonic. This indicates that the introduced nonlinearities are in fact significant and relevant to the building response as the system has suffered noticeable change in characteristics (reduced stiffness). It is also seen that the damage is manifested through the re-ordered amplitudes of higher harmonics (the fourth harmonic is more dominant than the third). This is in agreement with the loss of symmetry that the building model underwent physically.

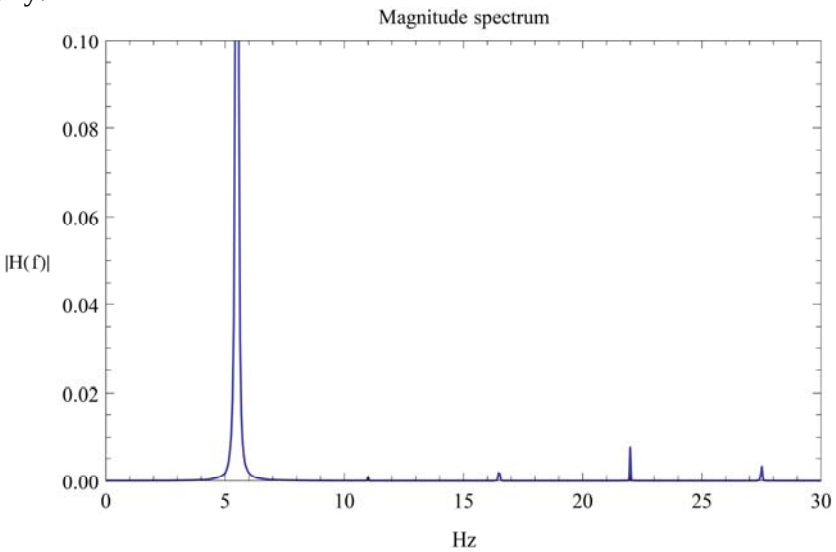


Figure 4: FFT for the model building state with notched columns.

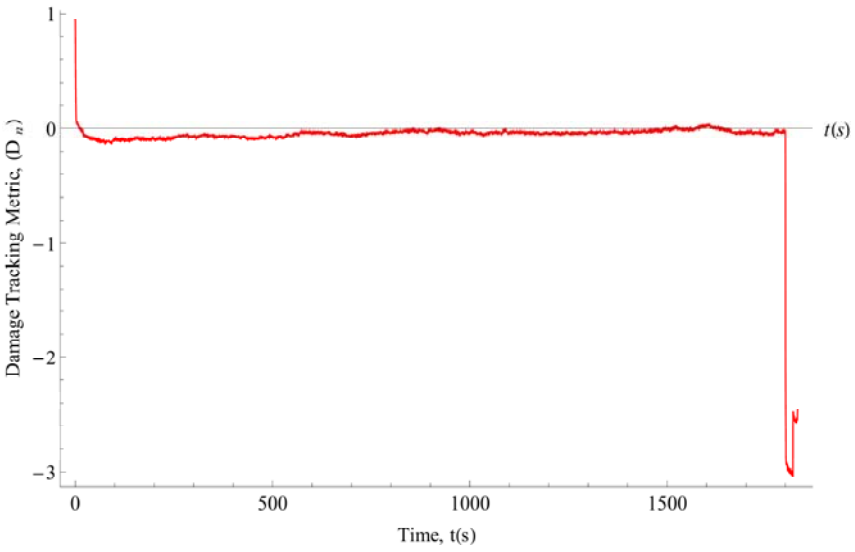


Figure 5: PSW damage metric

The PSW damage metric depicts the evolution and time-history of structural damage as demonstrated in Figure 5. The damage metric has very small values throughout the ground excitation application all the way till the introduction of the notches to the first story columns. At which point, the damage metric drops abruptly to -2.8, clearly indicating a significant abrupt damage. Increasing levels of damage induced by fatigue in the notched column cross-sections are also apparent from the increasing negative slope the fill factor assumes as it approaches -3. After many oscillations with increasing damage, one of the notched columns broke. This was immediately identified by the damage metric changing abruptly again to approximately -2.1. The severe inflected damage through the loss of one of the two notched columns magnified the horizontal irregularity (lack of symmetry) in the model. Subsequent oscillations exerted higher demands on the remaining column and in turn inflected increasingly higher rate of damage. This higher rate is demonstrated through the steeper negative slope in the damage metric which ultimately results in accelerated failure in the remaining notched column. The final collapse of the building is signified by a third abrupt jump in the fatigue metric.

5 CONCLUSIONS

A novel method to track structural damage in MDOF systems is presented. The method assumes that damage is a slowly changing variable in the measured floor acceleration signal. A damage metric is estimated from the slowly varying in the shape and position of phase space orbits as time passes. As a first step, the method of Time-Delay Embedding (TDE) is used to reconstruct the pseudo phase-space from acceleration measurements. Then, the tracking procedure is carried out using the method of Phase-Space Warping (PSW). Results show that the methods used are capable of identifying slowly changing damage using acceleration signals. The damage index revealed information about the health state of the overall coupled dynamic system under test, a 4-story model building in this case.

It is shown that TDE and PSW methods can provide an accurate overall ‘big picture’ estimator of structural damage. Unlike conventional vibration-based damage detection techniques described in the current literature (such as comparisons of FFT signatures only), this method can supply information about damage evolution in an insightful and unique manner. Another major strength to the presented SHM approach is that it provides an ongoing estimate of the

current health of the structure and with slight modifications, can also provide structural damage prognosis in the form of an estimated time to failure. This opens doors to real-time SHM encompassing diagnosis, monitoring and prognosis of important structures such as bridges and high-rise buildings.

6 ACKNOWLEDGMENT

This research project received financial support from the American University of Sharjah (AUS), through grant FRG14-2-15. The expressed or implied findings, views and conclusions in this document are those of the authors and should not be interpreted as those of the sponsors.

REFERENCES

[1] C. R. Farrar and D. A. Jauregui, "Comparative study of damage identification algorithms applied to a bridge: I. Experiment," *Smart Materials and Structures*, vol. 7, no. 5, pp. 704–719, Oct. 1998.

[2] F.-K. Chang, *Structural Health Monitoring 2000*. CRC Press, 1999, p. 1062.

[3] D. L. Balageas, Ed., "Structural Health Monitoring 2002," in *Proceedings of the 1st International European Workshop on Structural Health Monitoring*, 2002.

[4] C. Boller and W. J. Staszewski, Eds., "Structural Health Monitoring 2004," in *Proceedings of the 2nd International European Workshop on Structural Health Monitoring*, 2004.

[5] A. Güemes, Ed., "Structural Health Monitoring 2006," in *Proceedings of the 2nd International European Workshop on Structural Health Monitoring*, 2006.

[6] F. K. Chang, Ed., "Structural Health Monitoring 2007: Quantification, Validation, and Implementation," in *Proceedings of the 6th International Workshop on Structural Health Monitoring*, 2007.

[7] L. A. N. Laboratory, "A Review of Structural Health Monitoring Literature: 1996-2001 (LA-13976-MS)," 2004.

[8] M. Taha and A. Noureldin, "Wavelet transform for structural health monitoring: a compendium of uses and features," *Journal of Structural Health Monitoring*, 2006.

[9] M. AlHamaydeh, K. Galal, and S. Yehia, "Impact of lateral force-resisting system and design/construction practices on seismic performance and cost of tall buildings in Dubai, UAE," *Earthquake Engineering and Engineering Vibration Journal*, 2013.

[10] A. Fraser and H. Swinney, "Independent coordinates for strange attractors from mutual information," *Physical review A*, 1986.

[11] T. Buzug and G. Pfister, "Optimal delay time and embedding dimension for delay-time coordinates by analysis of the global static and local dynamical behavior of strange attractors," *Physical review A*, 1992.

[12] M. Kennel, R. Brown, and H. Abarbanel, "Determining embedding dimension for phase-space reconstruction using a geometrical construction," *Physical review A*, 1992.

[13] D. Chelidze, J. Cusumano, and A. Chatterjee, "A dynamical systems approach to damage evolution tracking, part 1: description and experimental application," *Journal of Vibration and Acoustics*, 2002.

[14] J. Cusumano, D. Chelidze, and A. Chatterjee, "A dynamical systems approach to damage evolution tracking, part 2: model-based validation and physical interpretation," *Journal of Vibration and Acoustics*, 2002.

[15] D. Chelidze and M. Liu, "Multidimensional Damage Identification Based on Phase Space Warping: An Experimental Study," *Nonlinear Dynamics*, vol. 46, no. 1–2, pp. 61–72, Aug. 2006.

COMPDYN 2015
5th ECCOMAS Thematic Conference on
Computational Methods in Structural Dynamics and Earthquake Engineering
M. Papadrakakis, V. Papadopoulos, V. Plevris (eds.)
Crete Island, Greece, 25–27 May 2015

SYSTEM IDENTIFICATION AND DAMAGE DETECTION OF R.C. STRUCTURE.

Prodip K. Paul[1], Anjan Dutta[2], and Sajal K. Deb[3]

[1] PhD Student, Dept. of Civil Engineering, Indian Institute of Technology,
Guwahati, India.
e-mail: paulprodip@gmail.com

[2] Corresponding author, Professor, Dept. of Civil Engineering, Indian Institute of Technology,
Guwahati, India.
e-mail: adutta@iitg.ernet.in

[3] Professor, Dept. of Civil Engineering, Indian Institute of Technology,
Guwahati, India.
e-mail: skdeb@iitg.ernet.in

Keywords: Nonlinear system identification, instantaneous modal parameters, N4SID, Sequential nonlinear least square estimation, damage detection.

Abstract. *Evaluation of system parameters of civil engineering structures using system identification techniques has attracted considerable attention in recent years. Recorded dynamic responses of the structures due to ambient or earthquake excitations are utilized for identification of system parameters of the structures. Huge amount of works have been carried out in the field of linear time invariant system identification; but the application in time varying system identification is very limited. In the present study, three numbers of numerically simulated models of 1/5th scaled bare frame two storey R.C. buildings have been considered. Nonlinear time history analyses are carried out to detect the changes of modal parameters of the deteriorating structure. Further, acceleration responses are collected from different floors during base excitation of models. Linear Deterministic-Stochastic Identification (DSI) technique (e.g. N4SID) is then used for the identification of modal parameters (natural frequency). Since, a linear DSI algorithm would not be applicable for structures excited to nonlinear range, hence modal parameters are obtained for short data time windows. These instantaneous modal parameters are found to represent the deterioration of the structure reasonably well. Further, an approach referred to as the sequential non-linear least-square estimation (SNLSE) is used to compare the identified result obtained from N4SID algorithm using short time data window. In this approach, acceleration responses and external excitations are measured, whereas the structural parameters and response state vector are estimated similar to the Extended Kalman Filter (EKF) approach. It is superior to EKF in terms of stability and convergence.*

1 INTRODUCTION

In developing and developed countries, where exists a lot of aged important and costly structures exists has survived various intensities of earthquakes throughout its life span. A concern is raised in the minds civil engineering community about the health of such structures. Whether, any major internal externally invisible damage has occurred or estimating the life of such structures or whether it can survive any other major earthquake or whether it can carry any further load as in the case of bridges. Traditional damage detection techniques for identifying local damages referred to as non-destructive testing (NDT) such as CT scanning and ultrasonic, etc., are taboo these days with the advent of system identification techniques based on vibration data.

But most of the theories upon which structural dynamic analysis is founded rely heavily on the assumption that the dynamic behavior of the structure is linear. Failure to obey the superposition principle implies that the structure is nonlinear. In fact, most practical engineering structures have a certain degree of nonlinearity due to nonlinear dynamic characteristics of structural joints, boundary conditions and material properties. For practical purposes, in many cases, they are regarded as linear structures, whenever the degree of nonlinearity is small and therefore insignificant in the response range of interest, whereby linear model analysis methods can be applied to analyze their dynamic characteristics. Civil structures are designed and exhibit highly non-linear characteristics under severe loads such as strong seismic excitation. Thus, non-linear structural identification (SI) is necessary for civil infrastructure if health monitoring or accurate simulation of response is needed. As per Ewins 0,the identification process for linear multi-degree of freedom (DOF) systems is now mature and the methods, whilst operating in the time or frequency domains and using a variety of intermediate models, almost all yield a final model based upon modal parameters, viz. natural frequency, mode shape, modal damping and modal mass. Earlier attempts for identification of nonlinear systems can be found in the works of Masri and Caughey [2], Zhang et al. [3] based on curve fitting methods, with little success. Kerschen et al.[4] classified the nonlinear system identification in the literature into the following seven categories: time-domain methods, frequency-domain methods, time-frequency methods, methods that by-pass nonlinearity is using linearization, modal methods, black box methods and structural model updating methods.

Overschee and Moor [5] proposed subspace identification approach for linear system and implemented the same in practical application. A combined deterministic-stochastic algorithm namely Numerical Algorithm for Subspace State Space System Identification (N4SID) is a popular algorithm in research community as well as for practicing civil engineers for linear system identification of civil structures. It uses acceleration inputs at various DOF's and ground excitation to identify the modal parameters like eigenvalues, eigenvectors, damping etc.

Deterministic-stochastic subspace identification (DSI) technique was utilized successfully by Moaveni and Asgarieh [6]0 an input-output parametric linear system identification method, for characterization of nonlinear dynamic structural system based on time varying amplitude-dependent instantaneous (i.e. based on short-time window) modal parameters. They applied the technique both on analytical and physical hysteretic models and claimed that it performs much better than wavelet based analysis. As N4SID is also a deterministic-stochastic subspace identification method, this is applied in this present work to verify its applicability and feasibility to analytical nonlinear models.

N4SID suffers drawback as it is purely a black-box system identification tool and the results are difficult to interpret by engineers until recently Kim and Lynch [7] in their paper on black-box system identification attempted to provide a detailed explanation on geometrical interpre-

tation of N4SID algorithm to provide civil engineers a deeper appreciation with the algorithm. N4SID is quite robust tool for linear system, few researchers Paulo et al. 08] tried to modify the linear N4SID to bilinear systems by playing with the system matrix. Our civil structures which are nonlinear cannot be generalized to behave in bilinear manner. Still it needs to be explored more.

Since the development of Kalman Filter in 1960 by Rudolf E. Kalman, extensive use of kalman filter for estimate of state variables has been found in literature. The Kalman filter estimate is sometimes denoted the "least mean-square estimate". The kalman filter algorithm was originally developed for systems assumed to be represented with a linear state-space model. The kalman filter for nonlinear models is denoted the Extended Kalman Filter (EKF). Many researchers used EKF for nonlinear structural system identification with various modifications. Hoshiya and Saito [9]0 applied EKF to the system identification problem of seismic structural systems. A weighted global iteration procedure with an objective function was proposed for stable and convergent estimation, which was incorporated in EKF. Investigation was carried out for MDOF, bilinear hysteretic systems. Yang and Lin [10] carried out on-line identification of non-linear hysteretic structures using an adaptive tracking technique. The hysteretic model was modeled using Bouc-Wen model which was incorporated in the nonlinear term of the EKF. The main drawback was that generalized nonlinearity could not be handled.

In order to remove all the drawbacks of LSE and EKF approaches for the on-line system identification, a new approach referred to as the sequential non-linear least-square estimation (SNLSE) was proposed by Yang and Lin [11]0. Simulation results for both linear and nonlinear structures will be presented to demonstrate the efficiency of the proposed adapted SNLSE in tracking the structural damage. In this approach, acceleration responses and external excitations are measured, whereas the structural parameters and response state vector are estimated similar to the EKF approach. It is superior to EKF in terms of stability and convergence.

With the advent of the recently developed SNLSE technique, an attempt was made in this paper to identify the modal parameters of degrading RCC structure excited to nonlinear range (material nonlinearity) using the SNLSE technique and N4SID technique with short time data window and compare the result with that obtained from exact analysis using "OpenSees" software.

2 DESCRIPTION OF THE LABORATORY SCALED MODELS

Three bare frame models are considered and designated them by Model-1, Model-2 & Model-3. These Models were developed considering a RC prototype with a scale factor of 1/5. Nonlinear dynamic analysis was performed using OpenSees Software.

2.1 Similitude & Scaling

The laws of similitude are followed to arrive at appropriate input motion, dimensions of test models as well as for finalization of additional mass requirement for gravity load simulation. The similitude requirements are derived from dimensional analysis which depends on physical characteristics like length, force, time. Table 1 shows derived scaling relationship of the parameters relevant to the present study.

Parameters	Scale	Prototype
		1/5-scale model
Length	S	5
Mass	S^2	25
Displacement	S	5
Time	$\sqrt{S}$	2.236
Acceleration	S	5

Table 1: Similitude Requirement.

2.2 Geometrical and material properties of the models

The test models have been designated as Model I, Model II and Model III. The descriptions of various geometrical properties of all the test models are furnished in Table 2 and the various material properties are shown in Table 3.

Particulars	Model I	Model II	Model III
Floor Panel Size (mm)	1000 x 1000	1000 x 1000	1000 x 1000
Slab Thickness (mm)	40	40	40
Column Height (mm) at GS	660	490	660
Column Height (mm) at FS	660	660	660
Column size (mm) at GS	75 x 75	75 x 75	100 x 100
Column size (mm)at FS	75 x 75	75 x 75	75 x 75
Beam size (mm)	60 x 90	60 x 90	60 x 90

GS: Ground Storey; FS: First Storey

Table 2:Geometrical Properties

2.3 Compensating Mass for Scale Test Models

The case of scale test model, the geometry of the structure is decided in accordance to the scale factor. However, the mass of the prototype structure does not get proportionately reduced as per similitude requirement. Hence, additional masses need to be added to maintain requirement of scaling relationship for gravity load similitude as mentioned in Table 1.The mass of the prototype building have been determined as 75088 kg considering unit weight of concrete as 2435 kg/m3. The total mass of the test model is 600 kg. The mass required for fulfilling similitude requirement is3000 kg. Hence, an additional mass of 2400 (=3000-600) kg is required to be uniformly distributed over two floors of the model.

Particulars	Model 1	Model 2	Model 3
Concrete			
Density (Kg/m^3)	2435	2435	2435
Compressive Strength(N/mm^2)	15	15	15
Reinforcing Steel : Longitudinal Bars			
Type of Steel	Fe 250	Fe 250	Fe 250
Diameter of bars (mm)	6	6	6
Number of bars	4	4	4
Young's Modulus (N/mm^2)	2.00E+005	2.00E+005	2.00E+005
Reinforcing Steel : Stirrups			
Spacing of stirrups (mm)	45	45	45
Diameter of bars (mm)	3	3	3
Clear cover			
Beams (mm)	15	15	15
First storey columns (mm)	15	15	15
Ground storey columns (mm)	15	15	20

Table 3: Material Properties

2.4 Details of Ground Motion

Two different earthquake ground motions have been considered for subjecting excitation to the analytical test models. Earthquake records with different peak accelerations, displacements and durations have been selected for use in analytical experiment. These were recorded during El Centro (1940): Comp – 180 & Victoria (1980): Comp - CPE045 earthquakes. The descriptions of relevant characteristics of the earthquake records are presented in Table 4. For nonlinear identification, spectrum compatible time histories are used.

Earthquake components	Peak ground acceleration (g)	Frequency Range (rad/sec)
El Centro (1940): Comp - 180	0.32	0-65
Victoria (1980): Comp - CPE045	0.62	0-160

Table 4: Characteristics of the selected Earthquake records.

2.5 Scaled time Histories

As mentioned in the Section-2.1, the sampling rate of earthquake records used for shake table excitation need to be scaled through a factor $1/\sqrt{S}$, where S denotes scale factor. The

Table 5 represents original and scaled sampling rate of earthquake records used for Time History Analysis.

Earthquake components	Original Time Interval (Sec)	Scaled Time Interval (Sec)
El Centro (1940): Comp - 180	0.02	0.008944
Victoria (1980): Comp - CPE045	0.01	0.004472

Table 5: Time interval of earthquake records used for Time History analysis.

3 MODELLING CONSIDERATION

3.1 The Analytical Model

The System for Earthquake Engineering Simulation (OpenSees) software Mazzoni et al. [12]0 was used to make an analytical model of the structure for performing nonlinear dynamic analysis. The numerical model is shown in Figure 1.

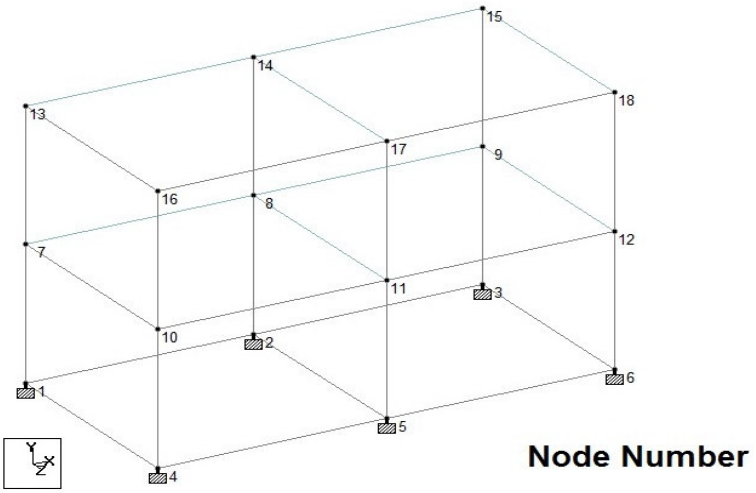


Figure 1: The Analytical Model

All the 6 numbers of support nodes are constrained in all DOF i.e. fixed support. Concentrated plasticity with elastic interior (beam with hinges) elements has been considered for beam and column elements. Plastic hinge length for column considered as 0.113m from beam column joint and for beam it is 0.130m.

3.2 Element Section Type

Fiber Section has been considered. Reinforcement detail of column section has been shown in Figure 2.

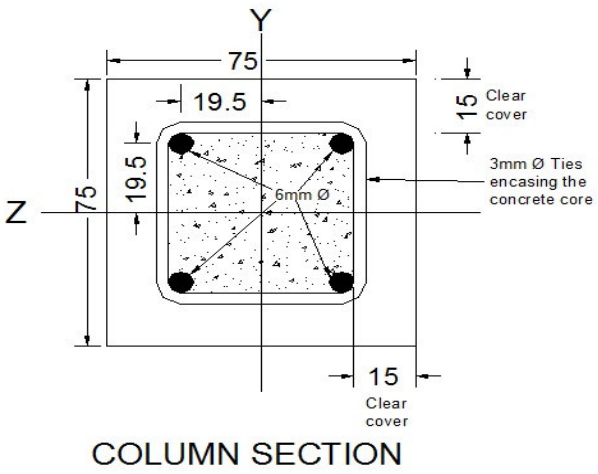


Figure 2: Typical Reinforcement Details of Column Section.

3.3 Material behavior for concrete or the concrete model for concrete fibers.

OpenSees " Concrete02" material –Linear Tension softening is used here. This is an uniaxial concrete material object with tensile strength and linear tension softening. It uses mander model Mander et al. [13]0 for confined inner core strength and unconfined strength for cover.

3.4 Material behaviour for Steel or the Steel model for Reinforcement fibers.

OpenSees "Steel02" material, Giuffre-Menegotto-Pinto Model with Isotropic Strain Hardening has been considered. This is an uni-axial Steel material object. Isotropic hardening has been ignored in the present case.

4 COMPARATIVE STUDY OF THE CHANGE OF MODAL PARAMETERS OF PROGRESSIVELY DETERIOTING STRUCTURE.

4.1 RCC Prototype Model-1

Total of 15 data window taken with each data window containing 100 points i.e. 15x100=1500 time step x 0.00447=9.387sec of Victoria (1980): Comp - CPE045 (Spectrum Compatible) time-history for lab-scaled analytical model no-1. The scale factor for amplitude of excitation was selected such that the structure is taken into nonlinear range. The scale factor selected was 0.204g. It is expected that the modal frequencies of the structure should degrade as the behavior of the structure changes from linear to nonlinear. This is evident from the results as obtained in Table 6. The results of System Identification using N4SID, SNLSE and exact analysis by OpenSees software are presented in Figure 3.

Data window	Time (sec)		Frequency (Rad/Sec)					
			N4SID		SNLSE		OpenSees (Exact)	
	From	To	Mode-I	Mode-2	Mode-I	Mode-2	Mode-I	Mode-2
1	0.00	0.45	54.92	134.59	53.69	143.34	44.62	117.54
2	0.45	0.89	54.60	120.24	43.20	113.71	42.35	108.48
3	0.90	1.34	42.63	101.77	46.00	118.34	43.58	113.70
4	1.35	1.79	45.54	109.61	44.76	114.67	43.96	115.43
5	1.79	2.24	40.61	98.23	44.74	114.51	39.67	104.36
6	2.24	2.68	39.54	100.37	42.84	110.03	36.86	100.16
7	2.69	3.13	45.21	107.61	40.26	104.47	37.00	102.26
8	3.13	3.58	42.29	105.07	39.54	102.66	35.87	95.59
9	3.58	4.02	41.31	106.47	38.62	101.05	36.86	95.92
10	4.03	4.47	40.63	113.68	38.36	100.46	36.23	97.35
11	4.47	4.92	39.22	102.23	37.95	99.62	37.01	97.86
12	4.92	5.36	38.28	105.07	37.85	99.28	35.70	99.33
13	5.37	5.81	39.23	110.46	37.77	99.03	36.06	100.07
14	5.82	6.26	40.37	105.67	37.72	98.84	37.01	96.76
15	6.26	6.71	42.96	105.07	37.68	98.70	37.47	96.53
16	6.71	7.15	43.76	104.50	37.66	98.65	38.22	97.27
17	7.16	7.60	41.43	97.85	37.65	98.61	37.73	98.20
18	7.60	8.05	38.78	88.29	37.64	98.56	37.95	96.84
19	8.05	8.49	42.47	96.93	37.63	98.50	38.03	96.77
20	8.50	8.94	40.61	108.05	37.62	98.48	38.22	97.06
21	8.94	9.39	40.47	101.23	37.62	98.47	38.20	97.16
22	9.39	9.83	39.77	92.24	37.62	98.46	37.85	97.01
23	9.84	10.28	41.09	95.45	37.62	98.46	38.59	97.51
24	10.29	10.73	37.77	79.12	37.62	98.44	38.40	97.17

Table 6: Comparative study of N4SID, SNLSE output with that of exact modal parameters given by OpenSees software (base excitation scale factor 2). (Model-1)

Figure 4 shows the variation of natural frequencies of first and second mode of vibration of Model-1 subjected to Victoria (1980): Comp - CPE045 (Spectrum Compatible) time-history but with magnified base excitation factor=4. To study the performance of SNLSE algorithm in comparison to short time data window technique of N4SID, all the three models were also subjected to a different base excitation El Centro (1940): Comp – 180 (Spectrum compatible) earthquakes and the results obtained are shown in Figure 5.

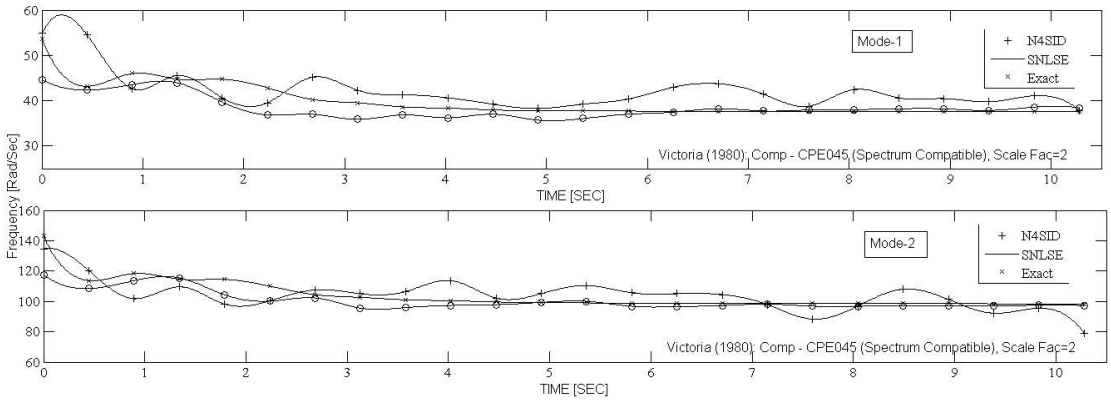


Figure 3: Instantaneous natural frequencies of first two vibration modes of prototype RCC model-1 with scale factor for base excitation=2 of Victoria(1980) Comp-CPE045(Spectrum Compatible), identified using N4SID, SNLSE.

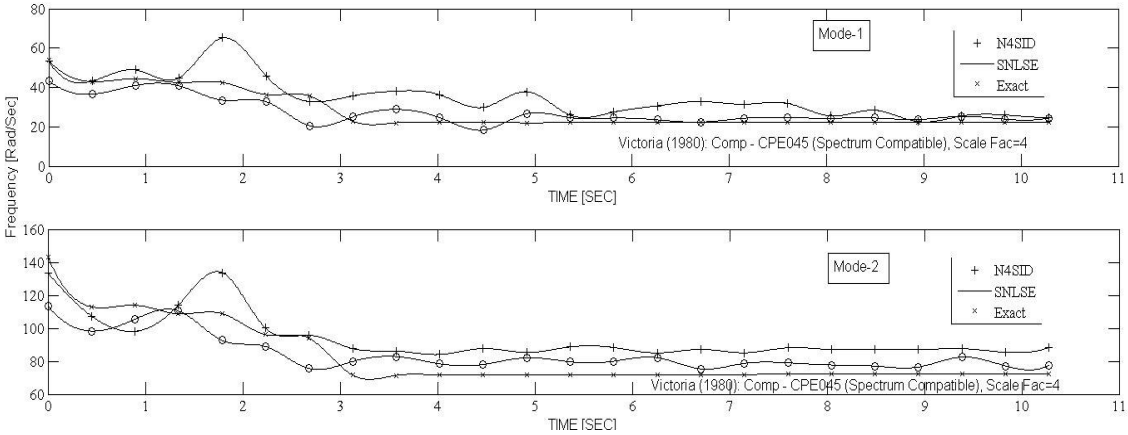


Figure 4: Instantaneous natural frequencies of first two vibration modes of prototype RCC model-1 with scale factor for base excitation=2 of Victoria(1980) Comp-CPE045(Spectrum Compatible), identified using N4SID, SNLSE

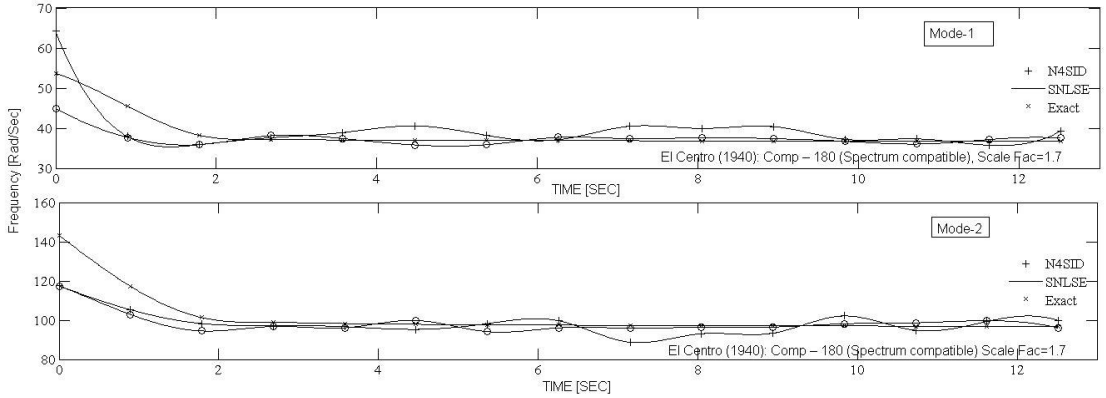


Figure 5: Instantaneous natural frequencies of first two vibration modes of prototype RCC model-1 with scale factor for base excitation=1.7 El Centro (1940): Comp – 180 (Spectrum compatible), identified using N4SID, SNLSE

4.2 RCC Prototype Model-2

Similar to Model-1, Model 2 is also subjected to Victoria (1980): Comp - CPE045 (Spectrum Compatible) with Scale Factor=2 i.e.0.204g and also El Centro (1940): Comp – 180 (Spectrum compatible) Scale Factor=1.7, earthquakes and the results obtained are shown in Figure 6 and Figure 7 respectively.

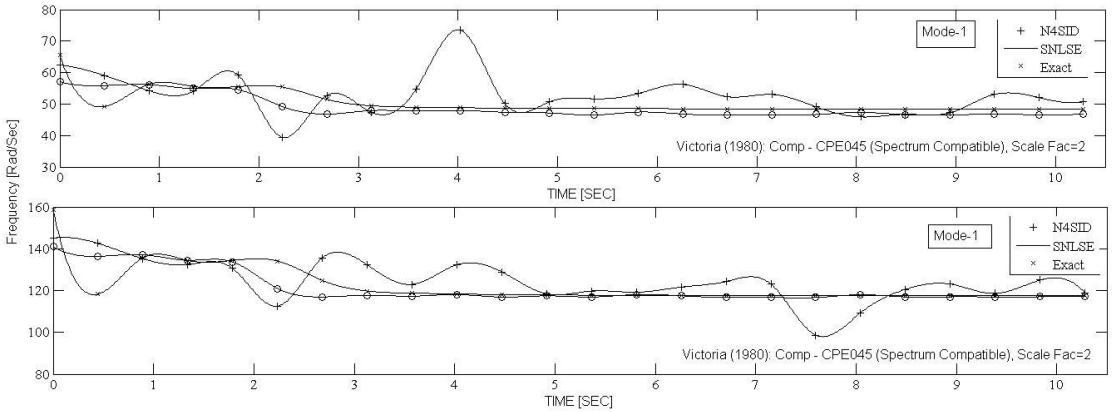


Figure 6: Instantaneous natural frequencies of first two vibration modes of prototype RCC model-2 with scale factor for base excitation=2 of Victoria(1980) Comp-CPE045(Spectrum Compatible), identified using N4SID, SNLSE

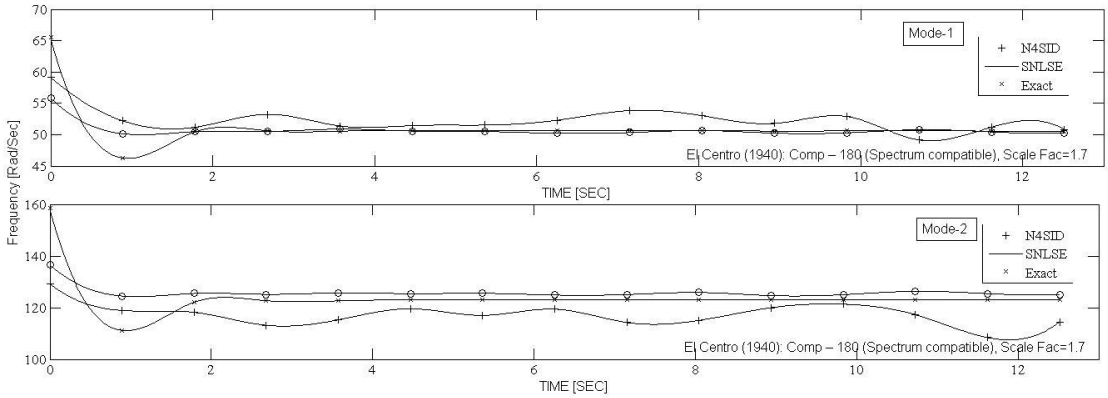


Figure 7: Instantaneous natural frequencies of first two vibration modes of prototype RCC model-2 with scale factor for base excitation=1.7 El Centro (1940): Comp – 180 (Spectrum compatible), identified using N4SID, SNLSE.

4.3 RCC Prototype Model-3

Model-3 is also treated in the same way as model-2 and the results as obtained are shown in Figure 8 & Figure 9.

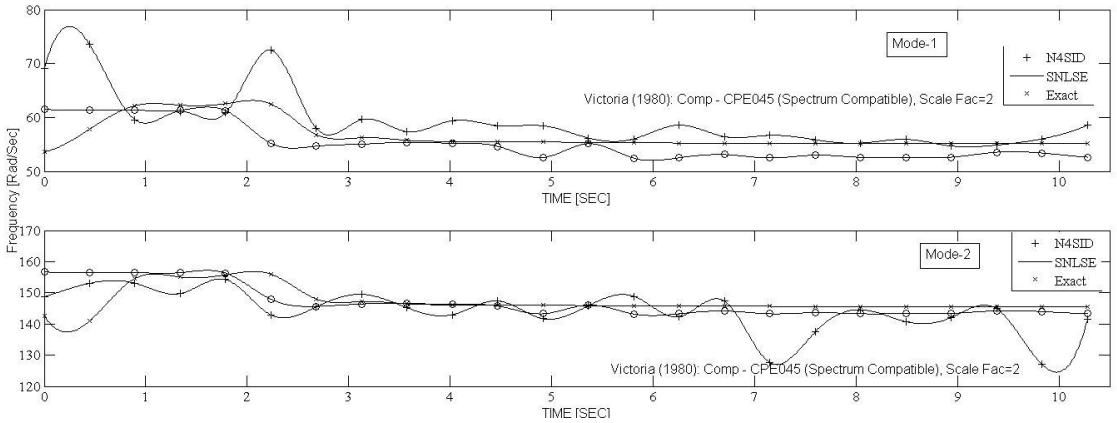


Figure 8: Instantaneous natural frequencies of first two vibration modes of prototype RCC model-3 with scale factor for base excitation=2 of Victoria(1980) Comp-CPE045(Spectrum Compatible), identified using N4SID, SNLSE

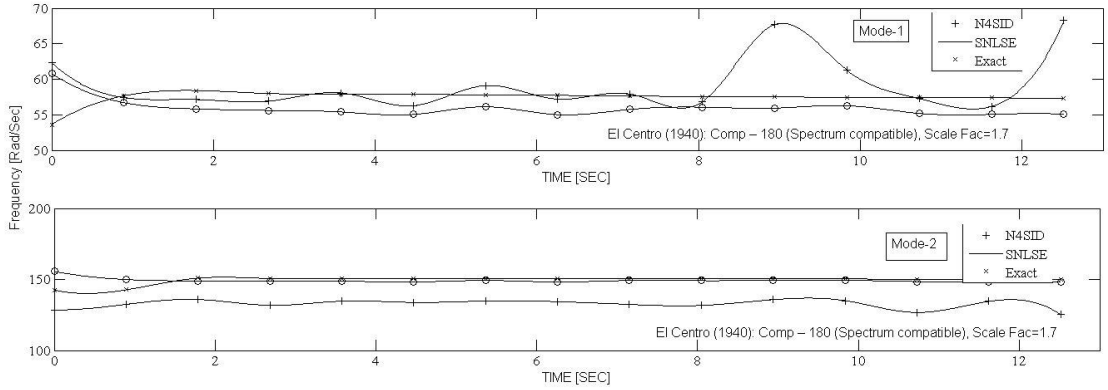


Figure 9: Instantaneous natural frequencies of first two vibration modes of prototype RCC model-3 with scale factor for base excitation=1.7 El Centro (1940): Comp – 180 (Spectrum compatible), identified using N4SID, SNLSE.

5 CONCLUSIONS

In this study, performance of the deterministic-stochastic subspace identification (N4SID) method for instantaneous modal analysis of nonlinear dynamic systems is evaluated based on numerical data. In the numerical study, system identification results of nonlinear MDOF with 2-DOF systems obtained from N4SID are compared to those from Sequential Nonlinear least square estimate (SNLSE) method and the exact values from finite element analysis using "OpenSees" software. Accuracy of system identification results are investigated due to variability of two input factors: input excitation, level of input excitation and structural geometry used in the identification.

- The response nonlinearity and its intensity can be tracked through identified instantaneous natural frequencies as well as SNLSE technique.
- Modal parameters obtained using SNLSE are consistently more accurate than those obtained using N4SID using short time data window.

- The results obtained from N4SID are more sensitive to type of structure; deviation from exact value depends from structure to structure.
- Instantaneous damage tracking using SNLSE is more accurate than N4SID.

REFERENCES

[1] D.J. Ewins, *Modal Testing: Theory, Practice and Application*, 2nd *Edition.* Research Studies Press Ltd., Hertfordshire, 1999.

[2] S.F. Masri, H. Sassi, T.K. Caughey, Nonparametric identification of nearly arbitrary nonlinear systems. *Journal of applied mechanics*, **49,** 619-628, 1982.

[3] Zhang Jian, Sato Tadanobu, Iai Susumu, Hutchinson Tara, A pattern recognition technique for structural identification using observed vibration signals: Nonlinear case studies. *Engineering Structures*, **30**, 1417-1423, 2008.

[4] G. Kerschen, K. Worden, A.F. Vakakis, J.C. Golinvala, Past, present and future of nonlinear system identification in structural dynamics. *Mech system signal processing*, **20,** 505-592, 2006.

[5] P. Van Overschee, B De Moore, *Subspace identification for linear systems*. Kluwer Academic Publishers, Norwell M.A., USA, 1996.

[6] Babak Moaveni, Eliyar Asgarieh, Deterministic-stochastic subspace identification method for identification of nonlinear structures as time-varying linear systems. *Mechanical Systems and Signal Processing*, **31**, 40-55, 2012.

[7] Junhee Kim and P. Lynch, Subspace system identification of support-excited structures part-I: Theory and Black box system identification. *Earthquake engineering and structural dynamics*, **41**, 2235-2251, 2012.

[8] Paulo Lopes dos Santos, Jose A. Ramos and Jorge L. Martins de Carvalho, Identification of Bilinear Systems with White Noise Input: An Iterative Deterministic-Stochastic Subspace Approach. *IEEE Transaction on control systems technology*, **17**, 1145-1153 2009.

[9] Hoshiya Masaru and Saito Etsuro, Structural Identification by Extended Kalman Filter. *Journal of Engineering Mechanics*, **110**, 1757-1770, 1984.

[10] Jann N. Yang and Lin Silian, On-line identification of non-linear hysteretic structures using an adapted tracking technique. *International Journal of Non-linear Mechanic,* **39**, 1481-1491, 2004.

[11] Jann N.Yang, Hongwei Huang, Silian Lin, Sequential non-linear least-square estimation for damage identification of structures. *International Journal of Non-Linear Mechanics,* **41**,124–140, 2006.

[12] S. Mazzoni, M.H.Scott, F.Mc Kenna, G.L.Fenves, *Open System for Earthquake Engineering Simulation –user manual* (version 2.4.2 rev 5540). Pacific Earthquake Engineering Research Center, University of California, Berkeley, California, 2006.

[13] J.B. Mander, M.J.N. Priestley, R. Park , Theoretical Stress-Strain Model for confined concrete, *ASCE,***114**, 1804-1825, 1988.

COMPDYN 2015
5th ECCOMAS Thematic Conference on
Computational Methods in Structural Dynamics and Earthquake Engineering
M. Papadrakakis, V. Papadopoulos, V. Plevris (eds.)
Crete Island, Greece, 25–27 May 2015

EXPERIMENTAL VERIFICATION OF DAMAGE LOCATION TECHNIQUES FOR FRAME STRUCTURES ASSEMBLED USING BOLTED CONNECTIONS

Bartlomiej Blachowski[1], Andrzej Swiercz[1], and Nikos Pnevmatikos[2]

[1] Institute of Fundamental Technological Research
Polish Academy of Sciences
Warsaw, Poland
bblach@ippt.pan.pl, aswiercz@ippt.pan.pl

[2] Technological Educational Institution of Athens
Department of Civil Engineering, Surveying and Geoinformatics
Athens, Greece
pnevma@teiath.gr

Keywords: bolted lap connection, frame structure, experimental modal analysis, damage location.

Abstract. *This work is focused on experimental verification of existing techniques for localization of a loosened bolted connection. To this end, a laboratory-scale 2-meter-long steel frame is used. The structure consists of 11 steel beams forming a four-bay frame, which is subjected to impact loads using a modal hammer. The accelerations are measured at 20 different locations on the frame, including joints and beam elements. Two states of the structure are considered: a healthy and a damaged one. The damage is introduced by means of loosening two out of three bolts at one of the frame connections. Experimental modal analysis reveals that the loosened bolts in the connection cause a shift only in some of the frame's natural frequencies, while the others remain insensitive to the damage.*

1 INTRODUCTION

Many papers devoted to damage localization methods deal with damage scenarios in the form of reduced beam cross sections [1,2], cracks [3,4], reduced plate thickness or plate cracks [5,6]. In reality, however, many structural failures start from damages which occur at connections. One of examples is the loosening of one or more bolts in bolted lap joints. The work on damage identification of bolted connections in a steel frame by Yang et al. [7] is a representative study. The method of artificial neural networks was adopted for damage detection in truss bridge joints, Mehrjoo et al. [8]. The influence of joint stiffness on global modes of structures was presented in the work of Blachowski and Gutkowski [9]. A damage detection approach to bolted flange joints in pipelines was presented by Razi et al. [10].

Another tool for damage detection is the wavelet-based method, as shown in the works of Staszewski, [11] and Newland, [12]. An exemplary application of the wavelet transform in to damage detection in a steel frame with plastic hinges has been presented by Pnevmatikos [13].

This work is focused on experimental verification of existing techniques for localization of a loosened bolted connection. To this end, a laboratory-scale steel frame is used. The work is divided into two parts: the first one is related to the performed experimental study and the second one to the computational techniques for damage localization. The computational techniques includes: modal assurance criterion, frequency response function (FRF), and wavelets transformation. In order to localize a damaged bolted connection a new measure is introduced called Damage Connection Index. This is essentially the sum of absolute values of the difference in angles of rotation at the given bolted connection.

2 TESTED STRUCTURE

2.1 Overview of the experimental stand

For the purpose of experimental verification of damage locating methods, a simple frame structure shown in Figure 1(a) is used. The structure is modular and consists of four square bays, each 0.51m high and wide. Each bay is composed of steel elements of equal length with a rectangular cross-section of 8 by 80 mm. The total number of elements is 11 and the total length of the structure is 2.04 m. The structure is supported at the outermost nodes, preventing both translational and rotational displacements. The connections between elements are realized by means of rigid connector elements (nodes) and allen bolts (6mm diameter), which are shown in Figure 1(c) and 1(b), respectively. Each such connection is designed to use 3 bolts screwed into threaded holes in the elements. The original structure (without modification) is referred here as the *reference structure* and the responses (accelerations) collected in the test I are called the *reference responses*.

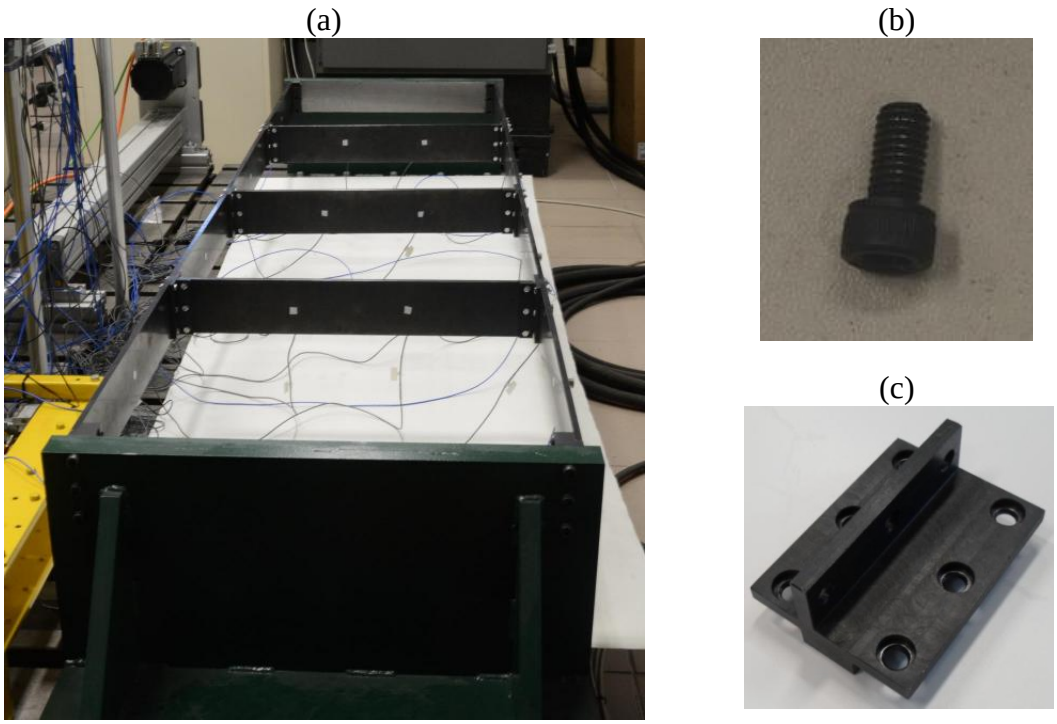


Figure 1: (a) The examined frame structure, (b) an allen bolt used for the element-node connections, (c) a connector element (node).

A modification is introduced to node 5 and element 10 (see Figure 2). The modification of the connection consists in removing 2 bolts (bottom and upper), leaving the middle one. In contrast to the reference structure and the reference responses, we will use here the notions of *modified structure* and *modified responses*, respectively. The modified responses gathered during the measurement session are denoted as test II.

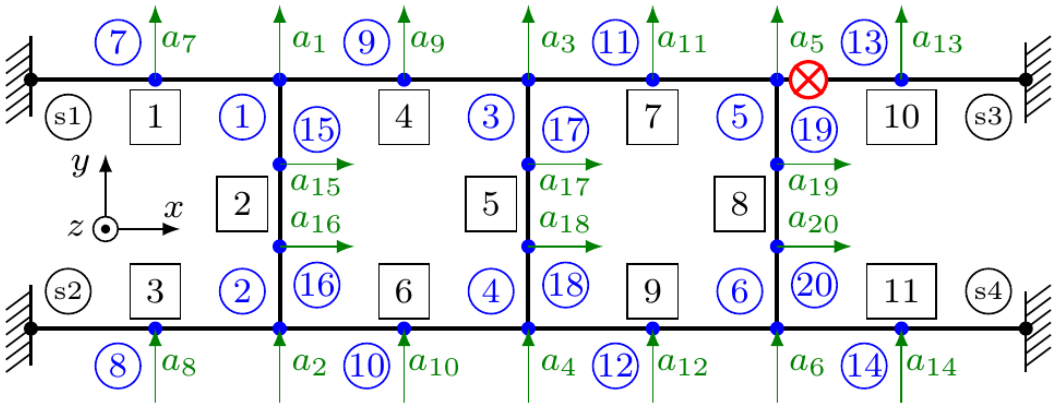


Figure 2: Scheme of the tested frame structure. Notation: *s1-s4* fixed nodal points, 1-20 (in circles) nodal points, 1-11 (in boxes) element numbers, a_1-a_{20} measured accelerations at nodal points. The location of the loosened bolted connection in shown in red.

2.2 Instrumentation & measurement procedure

Vibrations of the reference and modified structures were measured using 20 single axis accelerometers arranged as presented in Figure 2. All transducers were located in the mid-plane of the structure: at the centers of elements (the main axis parallel to the X-axis), one-third and two-thirds of the elements' lengths (the main axis parallel to the Y-axis). The structural vibrations were induced using a modal hammer with an embedded force sensor. The applied plastic tip allowed for covering the excitation frequency range of up to 1 kHz. The measurements were divided into two scenarios: for test I (for the reference structure) and test II (for the modified structure). For each scenario, two trial series were performed. The single trial serie consisted of tests with the impact loading applied at the selected set of nodes: 2, 5, 8, 10, 11, 13, 16, 17, 19 (cf. Figure 2). For every single test, 20 acceleration responses and one impulse force from the modal hammer were collected.

In all, 21 signals in the time domain (recording time 40 s) with a sampling rate of 32 kHz were collected during the single trial serie. For the collected signals, the Frequency Response Functions (FRF's) were computed. Finally, based on FRF's, a classical modal analysis was conducted leading to the estimation of modal parameters for the reference and modified structures. The measurement data were collected using the PULSE system (*Bruel&Kjaer*) and the modal analysis was performed utilizing the PolyMAX method implemented in the commercial software LMS Test.Lab (*Siemens PLM Software*).

3 ANALYSIS OF MODE SHAPES AND FREQUENCIES

For the collected data, the classical modal analysis was performed aimed at determination of modal parameters of the above-mentioned two states (reference and modified) of the structure. Further considerations are focused on resonant frequencies and modal shapes, since damping ratios are generally very low (do not exceed 0.3%) with very little variations.

The identified frequencies for the reference and modified structures are presented in Table 1. Moreover, Table 1 contains absolute and relative frequency differences and modal assurance criterion (MAC) values computed for each corresponding pair of frequencies. At first glance, the corresponding resonant frequencies are close to each other; however, modes 11 and 12 vary from Test I to Test II (cf. Figure 3). This presents the sensitivity of the modal frequencies to the introduced nodal modification. As presented in Figure 3, the absolute difference for the 13^{th} modal frequency is very low, but the corresponding MAC value presented in Table 1 is also relatively low. This means, that the 13^{th} modal shape is sensitive to the structural modification, while the corresponding modal frequencies obtained for the reference and modified structures are similar. Only the 12^{th} mode is sensitive with respect to both the modal shape and the modal frequency.

Mode no.	Test I (intact structure) frequency [Hz]	Test II (modified structure) frequency [Hz]	Absolute difference [Hz]	Relative difference [100%]	MAC value [100%]
	f_i^I	f_i^{II}	$f_i^I - f_i^{II}$	$\frac{f_i^I - f_i^{II}}{f_i^I}$	$\frac{((\Phi_i^I)^T \Phi_i^{II})^2}{\lvert\Phi_i^I\rvert^2 \lvert\Phi_i^{II}\rvert^2}$
1	12.33	12.29	0.04	0.34	77.6
2	26.65	26.58	0.07	0.27	98.8
3	40.53	40.35	0.18	0.45	98.8
4	78.38	78.23	0.15	0.19	100.0
5	97.14	97.06	0.09	0.09	100.0
6	109.50	109.44	0.06	0.05	100.0
7	115.14	115.13	0.01	0.01	100.0
8	138.32	138.20	0.12	0.09	100.0
9	161.37	161.37	−0.01	−0.00	97.8
10	162.30	162.30	0.00	0.00	98.6
11	169.00	166.44	2.57	1.52	98.1
12	173.24	170.23	3.01	1.74	89.1
13	173.81	173.68	0.13	0.08	76.6
14	207.08	206.25	0.83	0.40	99.8
15	305.37	304.80	0.56	0.19	99.9
16	346.09	345.59	0.50	0.15	99.9
17	373.81	373.65	0.16	0.04	100.0

Table 1: Resonant frequencies, their differences and MAC values of the (reference and modified) structure obtained from experimental tests.

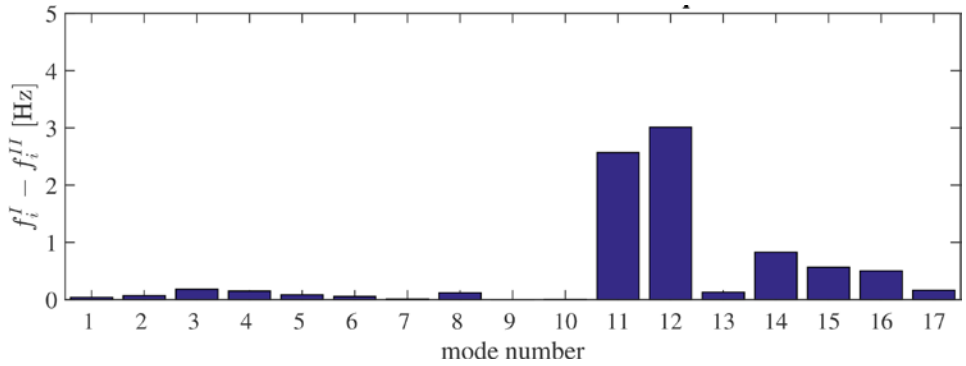


Figure 3: Absolute differences between the modal frequencies of the reference and modified structure.

In Figures 4 and 5 are shown the frequency response functions (FRFs) for the frequency band 100-200 Hz obtained for two states of the structure. In the first case, the collected response (output) at node 8 is referred to the excitation force applied at the same nodal point (cf. Figure 2). For tests I and II, two trials were executed revealing frequency shifting. A similar effect was observed for the 13th nodal point, presented in Figure 5.

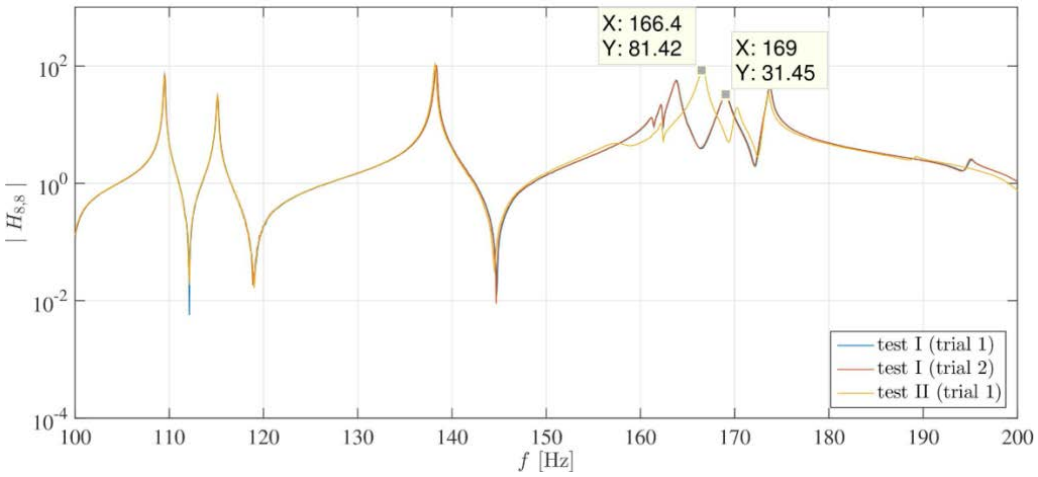


Figure 4: Comparison of frequency response functions (FRFs) of the reference (test I) and modified (test II) structures obtained for the excitation at nodal point no. 8.

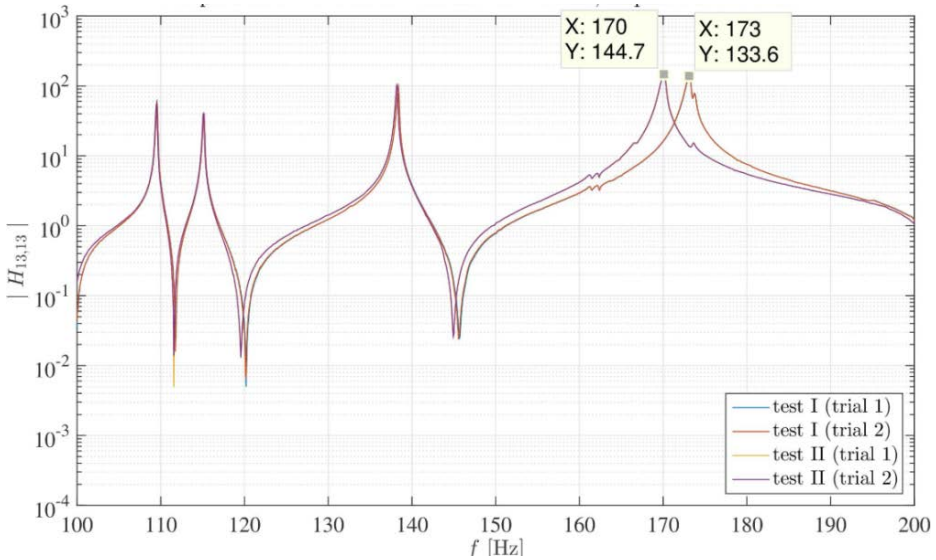


Figure 5: Comparison of frequency response functions (FRFs) of the reference (test I) and modified (test II) structures obtained for the excitation at nodal point no. 13.

A comparison of selected modal shapes of the two states of the structure is presented in Figure 6. Figure 6(a) shows using the example of the 8th mode that most identified modal shapes do not exhibit any substantial changes. Only for three modes, 11th, 12th and 13th the differences are significant (cf. Figures 6(b), 6(c), 6(d)).

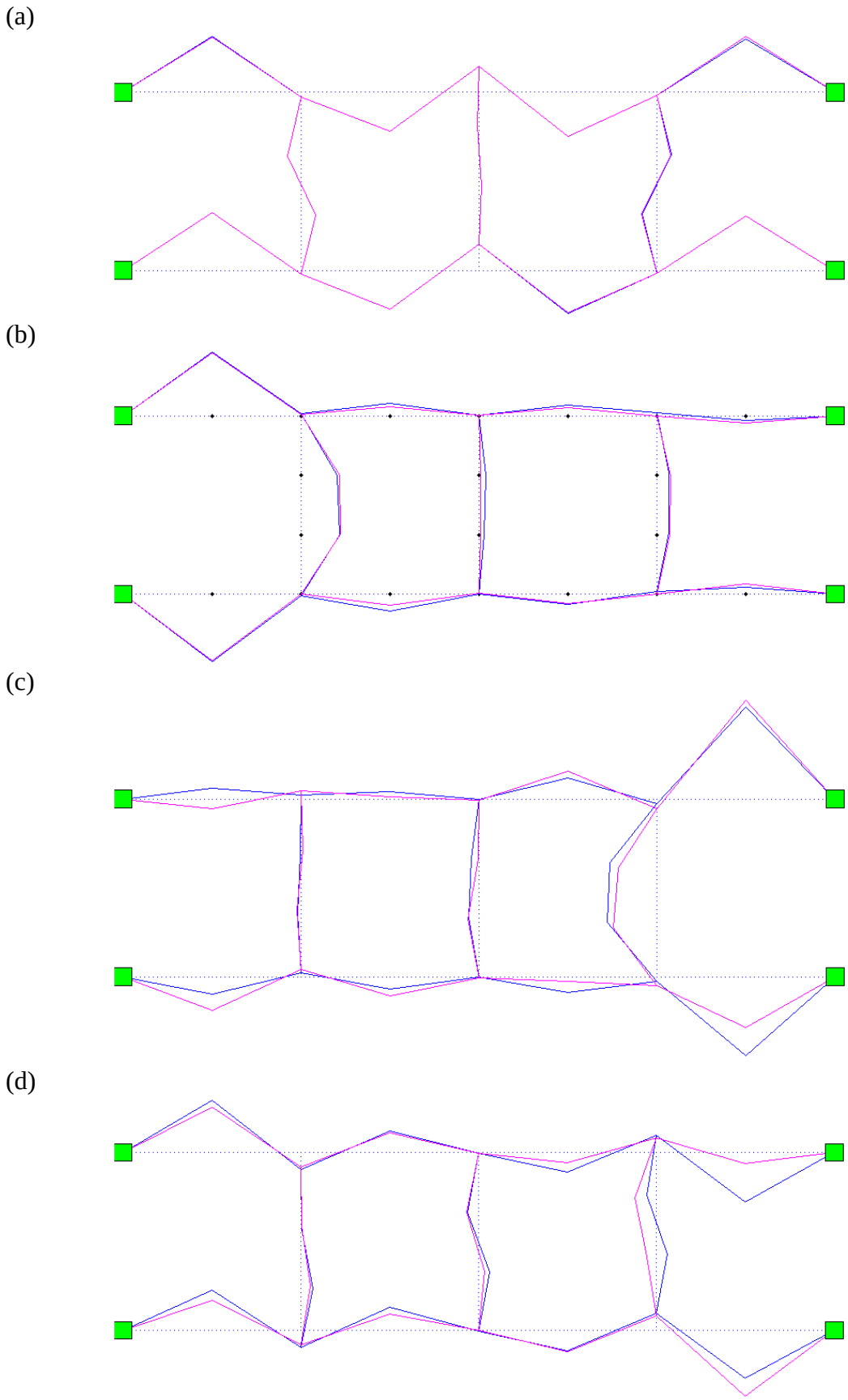


Figure 6: Comparison of modal shapes obtained for the reference (red lines) and modified (blue lines) structures: (a) mode shape no. 8, (b) mode shape no. 11, (c) mode shape no. 12, (d) mode shape no. 13.

The loosened bolted connection causes changes to the *i*-th modal vector of the frame. Let us define the difference in the angles of rotation $\Delta\alpha_j^{(i)}$ for *i*-th modal shape and *j*-th connection:

$$\Delta\alpha_j^{(i)} = \sum_{k=1}^{m}\left[T_{j,k}(\Phi_{i,k} - \widehat{\Phi}_{i,k})\right] \tag{1a}$$

or in matrix notation

$$\Delta\boldsymbol{\alpha}^{(i)} = \boldsymbol{T}\left(\boldsymbol{\Phi}_i - \widehat{\boldsymbol{\Phi}}_i\right) \tag{1b}$$

where m is the number of measured DOFs, $\boldsymbol{\Phi}_i$ and $\widehat{\boldsymbol{\Phi}}_i$ are the *i*-th modal vectors of the healthy and damaged structures, $\boldsymbol{T}$ is a matrix transforming modal displacements into angles of rotation. For each mode shape, the dimension of the vector $\Delta\boldsymbol{\alpha}^{(i)}$ is equal to 18, since we consider 18 connections located as shown in Figure 7. For example, the computation of the angle of rotation $\Delta\alpha_2^{(i)}$ (for connection no. 2) is performed based on the first and ninth (cf. Figure 2) components of modal vectors $\boldsymbol{\Phi}_i$ and $\widehat{\boldsymbol{\Phi}}_i$ as follows:

$$\Delta\alpha_2^{(i)} = \frac{2}{L_4}\left(\Phi_{i,9} - \Phi_{i,1}\right) - \frac{2}{L_4}\left(\widehat{\Phi}_{i,9} - \widehat{\Phi}_{i,1}\right) \tag{2}$$

In the above equation, L_4 denotes the length of the element no. 4, and $\Phi_{i,1}$, $\Phi_{i,9}$ and $\widehat{\Phi}_{i,1}$, $\widehat{\Phi}_{i,9}$ are the first and ninth components of the *i*-th modal vectors $\boldsymbol{\Phi}_i, \widehat{\boldsymbol{\Phi}}_i$, respectively.
Thus, in the second row of the transformation matrix $\boldsymbol{T}$ only two components are non-zero, i.e.

$$T_{2,1} = -\frac{2}{L_4}, \quad T_{2,9} = \frac{2}{L_4}$$

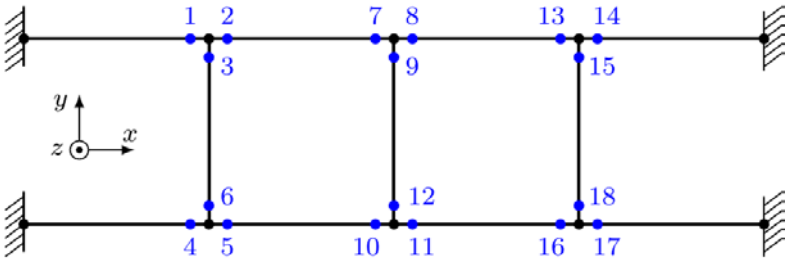


Figure 7: Localization of the considered nodal connections.

Carrying out calculations for all identified modal vectors we get the rectangular-shaped matrix $\Delta\boldsymbol{\alpha}$ with the dimensions 18x17. For the assessment of the severity of damage in an individual connection, the Damage Connection Index (DCI) is proposed:

$$a_j = \sum_i |\Delta\boldsymbol{\alpha}^{(i)}|^n \tag{2}$$

where a_j is the sum of the differences in angles of rotation over all identified modes, and n is a parameter. Figure 8 presents the a_j values for each bolted connection as marked in Figure 7.

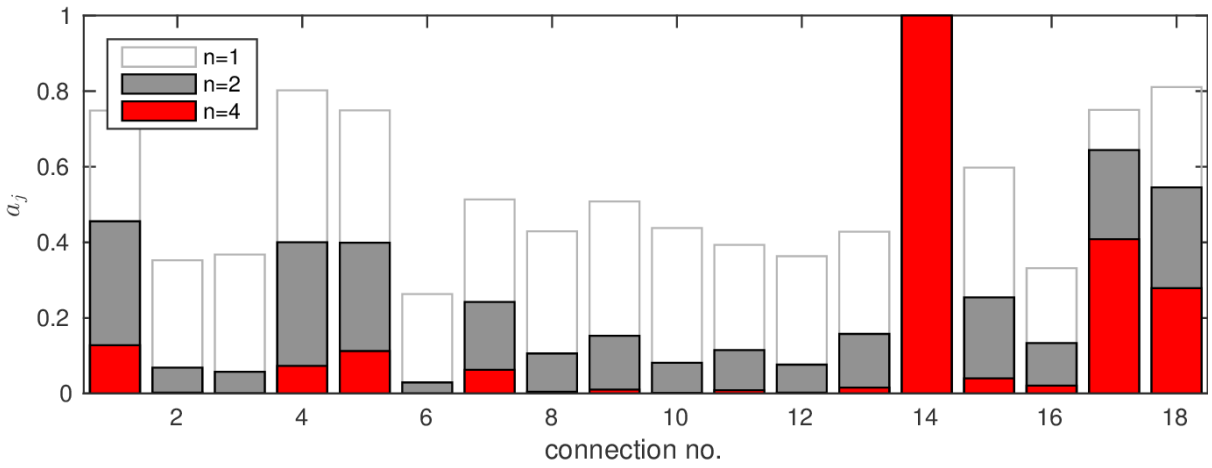


Figure 8: Values of the DCI for different values of the exponent *n*.

Depending on the assumed parameter *n*, the values of the DCI differ significantly. For *n=1* the DCI values are comparable; however, an extreme value is obtained for the connection no.14. When increasing the parameter *n*, the observed differences between the DCI values became more substantial. For *n=2* and *n=4*, the highest value of the vector $\boldsymbol{a}$ is reached for *j=14* and this clearly indicates the localization of the introduced modification.

4 WAVELET TRANSFOM ANALYSIS

Wavelet analysis provides a powerful tool to characterize local features of a signal. Unlike the Fourier transform, where the function used as the basis of decomposition is always a sinusoidal wave, other basis functions can be selected for the wavelet shape according to the features of the signal. The basis function in wavelet analysis is defined by two parameters: scale and translation. These properties lead to a multi-resolution representation for non-stationary signals.

The continuous wavelet transform of a signal $f(t)$ is defined as:

$$f(a,b) = \frac{1}{\sqrt{a}} \int_{-\infty}^{\infty} f(t) \overline{\Psi}\left(\frac{t-b}{a}\right) dt \tag{3}$$

where *a*, *b* are the scale and translation parameters respectively and $\overline{\Psi}$ denotes the complex conjugate of Ψ. The functions $\Psi(t,a,b)$ are called wavelets. They are dilated and translated versions of the mother wavelet $\Psi(t)$. There are a lot of types of wavelet functions $\Psi(t)$; Figure 9 shows the Haar wavelet function which was used in the analysis in this paper. The Haar wavelet's mother wavelet function $\Psi(t)$ can be described as:

$$\Psi(t) = \begin{cases} 1 & 0 \le t < \frac{1}{2} \\ -1 & \frac{1}{2} \le t < 1 \\ 0 & \text{otherwise} \end{cases} \tag{4}$$

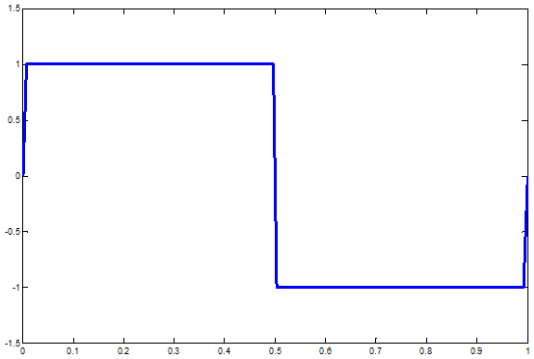
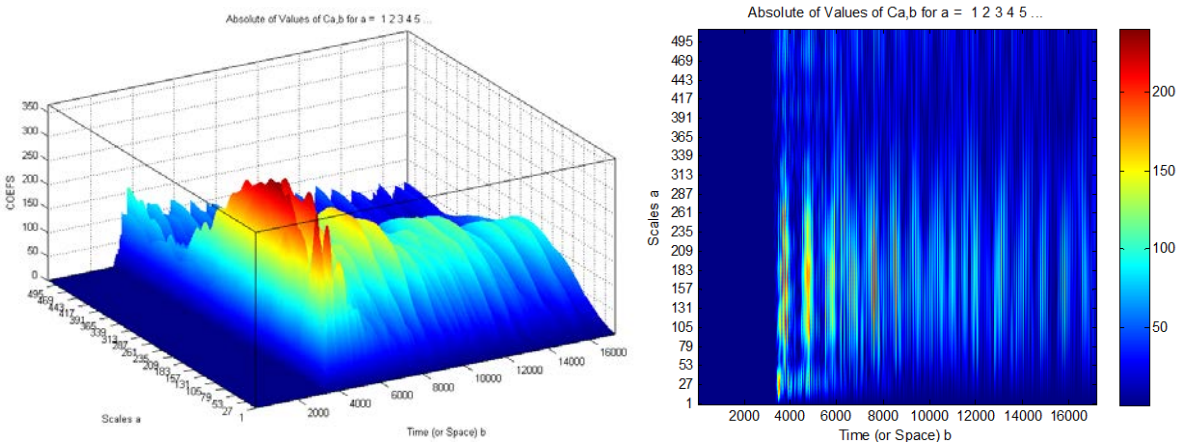
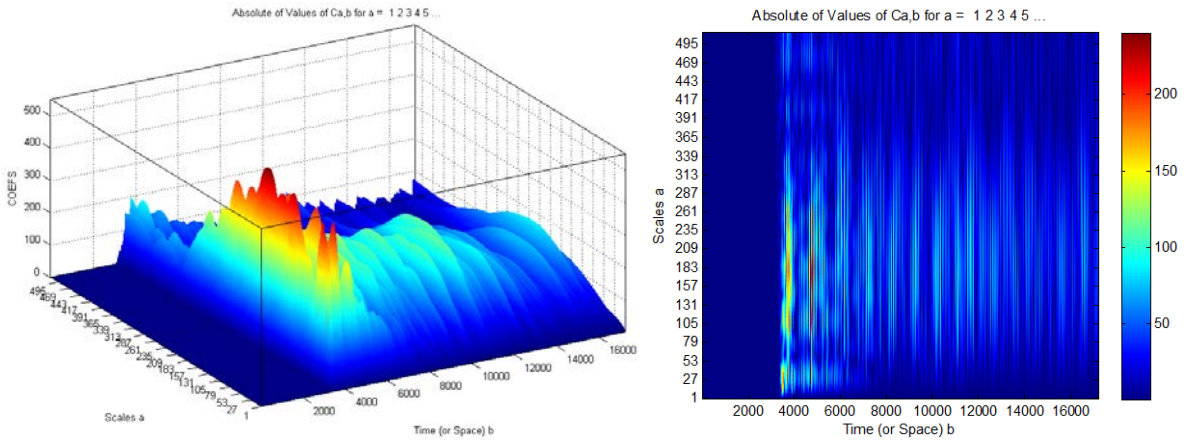


Figure 9: Continuous wavelet Haar function $\Psi(t)$.

An application of continuous wavelet analysis to damage detection in a frame structure subjected to impact loading was also performed. Wavelet analysis was made of the obtained response acceleration data collected in the test I, corresponding to the reference structure, and those collected in the test II, corresponding to the modified structure. The Haar wavelet function was used in the analysis of the output signals. The results of the wavelet analysis of the reference and modified structures are shown in Figure 10. In this figure, the magnitude versus scale (frequency) and time is presented for the reference, Figure 10 (a), and the modified structure Figure 10 (b).



(a)



(b)

Figure 10: Continuous wavelet analysis results of (a) the reference and (b) the modified structure. (Remark: time labels do not represent physical unit, but the number of samples)

It should be noted that there is a difference in the magnitude of scales for the reference and the modified structure. In the modified structure, the frequencies are more clearly separated from each other. Another observation is that the magnitude of the frequencies is higher for the modified structure than for the reference one.

5 CONCLUSIONS

This work presents an experimental case study of a frame structure, aimed at diagnosis of the state of its bolted connection. To this end, classical experimental modal analyses were performed for the reference (Test I) and modified (Test II) structures. All bolted connections of the reference structure are rigid, whereas in the modified structure two of two bolts from a selected connection are removed. Modal parameters were determined using 20 uniformly distributed accelerometers collecting signals induced by a modal hammer.

The localization of the damaged bolted connection is performed using perturbation of the modal shapes, obtained experimentally for the reference and modified structure. The procedure is based on the Damage Connection Index, which utilizes the differences in rotation angles calculated at the bolted connections for an individual mode shape.

Generally, one can conclude that the FRFs determined for the reference and modified structures overlap in the frequency range from 0 to 400 Hz. The introduced structural modification produces some perturbations in the narrow band of the frequency. The final observation is that only 3 out of 17 mode shapes and corresponding frequencies reveal measurable differences.

A wavelet analysis of the output signal of both structures shows that there is some difference between those two signals. The wavelet representation gives a qualitative index which helps to conclude the damage. As a next step, a procedure for quantifying the damage should be developed.

ACKNOWLEDGEMENTS

The two first authors are grateful for financial support from the National Science Centre of Poland (grant N N501 0494 40).

REFERENCES

[1] A. Świercz, P. Kołakowski, J. Holnicki-Szulc, Structural damage identification using low frequency non-resonance harmonic excitation, *Key Engineering Materials*, **347**, 427-432, 2007.

[2] A. Świercz, P. Kołakowski, J. Holnicki-Szulc, Impulse Virtual Distortion Method for Single Damage Identification in Structures, *Proc. of the 16th International Conference on Computer Methods in Mechanics - CMM'05*, 2005.

[3] S. Caddemi, A. Morassi, Multi-cracked Euler-Bernoulli beams: Mathematical modeling and exact solutions, *International journal of solids and structures*, **50(6)**, 944-956, 2013.

[4] S. Caddemi, A. Morassi, Crack detection in elastic beams by static measurements, *International journal of solids and structures*, **44(16)**, 5301-5315, 2007.

[5] A. Zak, M. Krawczuk, W. Ostachowicz, Elastic wave propagation in a cracked isotropic plate, *Proceedings of the 3rd European Workshop Structural Health Monitoring*, 316-323, 2006.

[6] M. Krawczuk, M Palacz, W Ostachowicz, Wave propagation in plate structures for crack detection, *Finite elements in analysis and design*, **40(9-10)**, 991-1004, 2004.

[7] J. Yang, Y. Xia, and C. Loh, Damage Identification of Bolt Connections in a Steel Frame. *Journal of Structural Engineering*, **140(3)**, 2014.

[8] M. Mehrjoo, N. Khaji, H. Moharrami, A. Bahreininejad, Damage detection of truss bridge joints using Artificial Neural Networks, *Expert Systems with Applications*, **35(3)**, 1122-1131, 2008.

[9] B. Blachowski, W. Gutkowski, Revised assumptions for monitoring and control of 3D lattice structures, *Proceedings of the 11th Pan-American Congress of Applied Mechanics PACAM XI*, Foz do Iguassu, Brasil, 4-8 January 2010.

[10] P. Razi, R.A. Esmaeel, F. Taheri, Improvement of a vibration-based damage detection approach for health monitoring of bolted flange joints in pipelines, *Structural Health Monitoring*, **12 (3)**, 207-224, 2013.

[11] W.J. Staszewski, Structural and mechanical damage detection using wavelets, *Shock Vibration Digest*, **30(6)**, 457–472, 1998.

[12] D.E. Newland, *An introduction to random vibrations, spectral and wavelet analysis.* Longman Singapore Publishers (Pte) Ltd, 1993.

[13] N.G. Pnevmatikos, Damage detection of structures using discrete wavelet transform, *Fifth World Conference on Structural Control and Monitoring (5WCSCM)*, Tokyo, Japan, 12-14 July 2010.

COMPDYN 2015
5th ECCOMAS Thematic Conference on
Computational Methods in Structural Dynamics and Earthquake Engineering
M. Papadrakakis, V. Papadopoulos, V. Plevris (eds.)
Crete Island, Greece, 25–27 May 2015

ANALYSIS OF THE VIBRATION LEVELS OF A SLENDER FOOTBRIDGE MEASURED BY A CONTINUOUS DYNAMIC MONITORING SYSTEM

C. Moutinho[1], F. Magalhães[1] and E. Caetano[1]

[1] Vibest, Department of Civil Engineering, Faculty of Engineering, University of Porto
R. Dr. Roberto Frias, 4200-465 Porto, Portugal
e-mail: {moutinho, ecaetano, filipema}@fe.up.pt

Keywords: Pedestrian Bridges, Vibration Problems, Vibration Analysis, Experimental Testing, Numerical Models, Dynamic Monitoring, Modal Identification.

Abstract. *This paper is related to the work involving the numerical and experimental dynamic analysis of a very flexible pedestrian bridge located in Porto. Given the high level of vibrations reported by the users of that structure, the Laboratory of Vibrations and Structural Monitoring (www.fe.up.pt/vibest) from Faculty of Engineering of University of Porto (FEUP) became interested in this case, following the previous work of this research group in this area of Civil Engineering. In a first stage, the structure is described and the identified dynamic properties are listed. Then, experimental and numerical simulations of several scenarios of pedestrian loads exciting the bridge are presented. Given the "lively" behavior of the structure, it was decided to install a dynamic monitoring system in order to characterize the effective levels of vibration experienced by that structure during long periods of time. The results of the dynamic monitoring are exposed in this paper, which gives reason to the actual existence of complaints from pedestrians.*

1 INTRODUCTION

Many Civil Engineering structures have vibration problems in terms of serviceability limit states due to several transient or periodic dynamic loads, e.g., footbridges subjected to pedestrian actions, road and railway bridges excited by traffic loads and tall buildings exposed to wind forces. Generally, the safety of the structure is not compromised, affecting only its proper in-service functioning.

In the case of pedestrian bridges, the excessive vibrations are often attributed to the existence of resonance phenomena arising from the proximity of step frequency of pedestrians relative to the natural frequencies of the structure. This problem may assume particular relevance in very flexible structures often characterized by having low inherent damping, in line with the current trends of footbridge conception and design. For new structures, the use of recent guidelines in this area, for instance Sétra [1] or Hivoss [2] guidelines, may serve to prevent the occurrence of these problems. However, in existing footbridges the situation is

already installed, which often requires the adoption of corrective measures such as the use of vibration control devices.

In these cases, and before any rehabilitation, the implementation of continuous dynamic monitoring systems is useful for making a very realistic assessment of the vibration levels, thus enabling a subsequent rigorous study of the intervention in the structure. This is the context of this paper, where a specific case of a footbridge located in Porto was instrumented with one accelerometer at a critical section, with the data being collected during the last months crucial to the evaluation of the situation and to study a possible implementation of a control system.

2 CHARACTERIZATION OF THE STRUCTURE

2.1 General description

The footbridge under analysis is a structure that connects a commercial infrastructure located by the sea, known as Transparent Building, with the Porto City Green Park (see Figure 1). It comprises two spans of 30m each, simply supported at the ends with hinges and at mid-length by means of a concrete column. The deck is 3.5 m wide and has an inclination of 6% starting with a lower elevation at the green park and ending in the Transparent Building at a higher level. The cross-section is composed of two lateral steel girders type IPE600, 600 mm high, connected by a secondary steel structure which, in turn, gives support to a wood floor. The mass of the structure, including all structural and non-structural elements, was estimated at 380kg/m.



Figure 1: General view of the footbridge.

2.2 Identification of modal properties

The identification of the modal properties of the structure in terms of natural frequencies, damping ratios and modal shapes, was performed in the context of the research work developed by Abreu [3] and Antão [4]. For this purpose, two ambient vibration tests were performed. Aiming at a preliminary evaluation of the natural frequencies of the structure, a first test was conducted using a single seismograph including force-balance accelerometers positioned in several sections of the deck, namely, at mid-span and at 1/3rd span sections of one side of the footbridge in order to capture symmetrical and anti-symmetrical vibration modes (see Figure 2a)). For each measurement point, acceleration-time series lasting 9 minutes were acquired and subsequently processed in order to obtain estimates of Power Spectral Density

functions (PSD). The Average Normalized Power Spectral Densities (ANPSD), including all measurements, is shown in Figure 2b) which allows identifying the natural frequencies of the structure associated with the peaks of the graph. Second column of Table 1 summarizes the results obtained in this test regarding the first four natural frequencies, allowing to conclude that the first two frequencies are 1.85 and 2.02 Hz, critical in terms of resonance with pedestrians walking along the bridge, and two other higher frequencies of 3.03 and 3.56 Hz, which may be excited by pedestrians in running or jogging activities. Frequencies above the 4th mode were not considered because they are not relevant in terms of resonance phenomena involving pedestrians.

The second test consisted of using 3 accelerometers (see Figure 3a)) distributed along the deck according to Figure 3b). In this case, the total length of the footbridge was divided into 8 equal spaced intervals. The reference accelerometer was positioned in one side of section 3 and the other two units were used to measure the other points, one on each side of the deck in order to capture torsion effects. By calculating each Frequency Response Function (FRFs) from the reference accelerometer to the non-reference accelerometers the modal shapes associated with each natural frequency were identified. The modal shape of the first 2 bending modes is represented in Figure 4a) and 4b), with the description of the first 4 modes indicated in Table 1.

Damping properties of the footbridge were also evaluated by using an expedite method consisting of exciting the structure with a frequency close to each natural frequency using a pedestrian skipping at a fixed position. After achieving a resonant response, the excitation stops suddenly and the free motion of the structure is recorded. By analyzing the free decay curve, the respective damping factor can be estimated using the logarithmic decrement method. This process was repeated by adopting different levels of excitation intensity, because damping ratios are known to increase with the increase of the vibration amplitude. Table 2 summarizes the estimates obtained for the first 2 vibration modes of the structure.

a) 

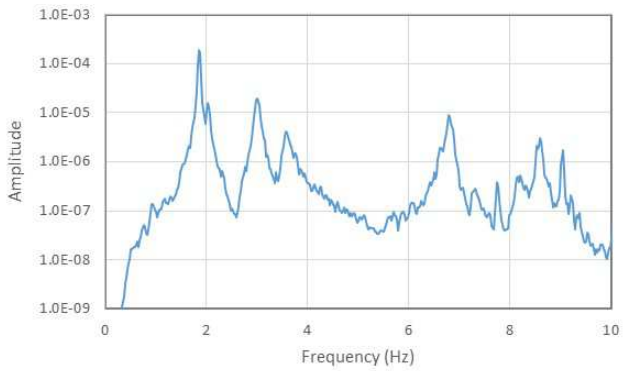
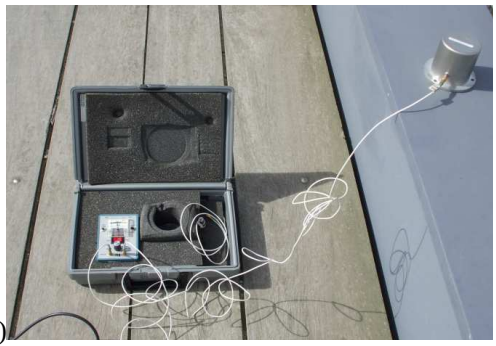
b) 

Figure 2: a) Seismograph measuring ambient vibrations; b) ANPSD including all measurements.

a) 

b) 

Figure 3: a) Accelerometer installed in one section; b) Numbering of the measurement sections.

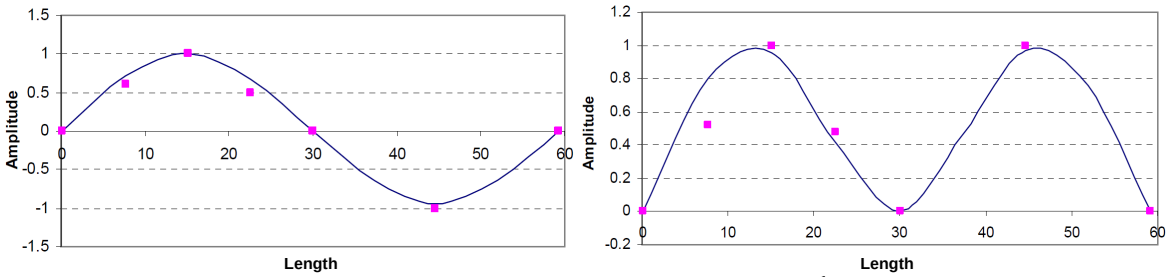


Figure 4: a) Identified 1st bending mode; b) Identified 2nd bending mode

Order	Measured Frequency (Hz)	Calculated Frequency (Hz)	Type of Vibration Mode
1	1.85	1.82	1st bending
2	2.02	2.06	1st torsion
3	3.03	3.09	2nd bending
4	3.56	3.38	2nd torsion

Table 1: Identified and calculated natural frequencies.

Vibration Mode	Damping ratio Low vibrations (%)	Damping ratio High vibrations (%)
1	1.28	1.88
2	1.35	1.67

Table 2: Identified damping ratios.

2.3 Tests with pedestrians

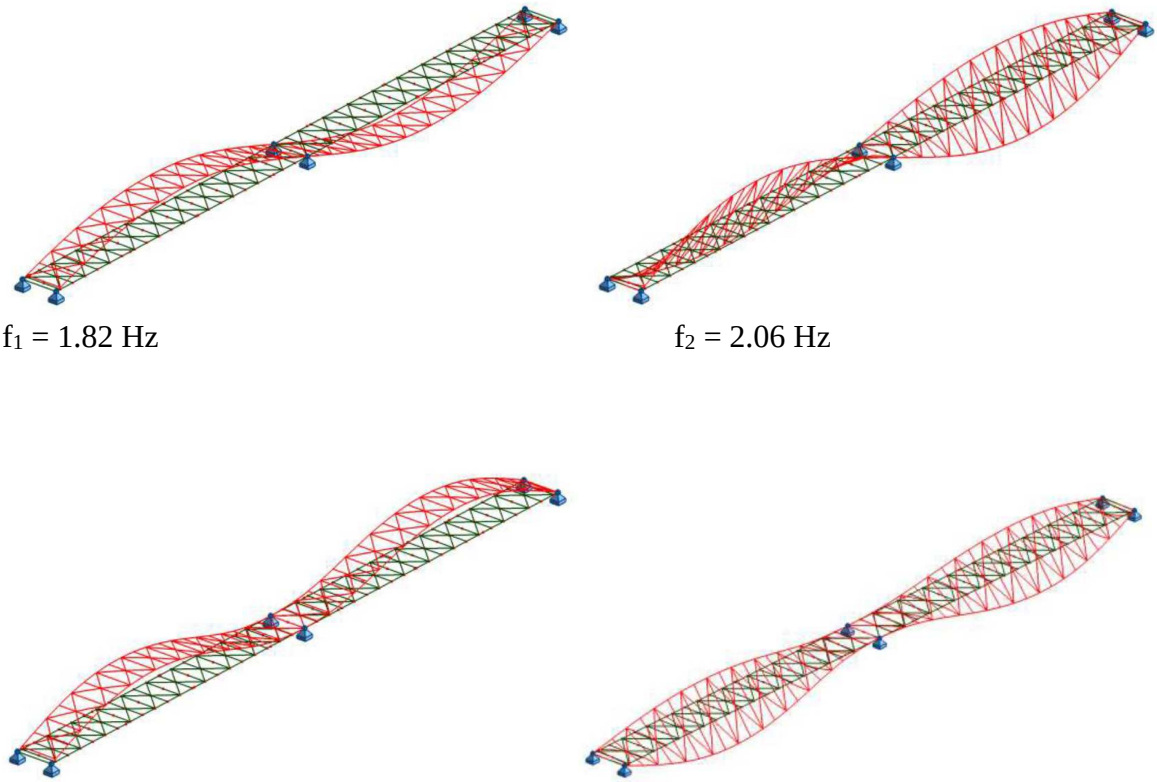
In order to have an estimate of the vibration levels of the structure caused by pedestrians walking along the deck, a simple test was conducted, consisting of using either single or group of young students. In a first stage, the pedestrians passed through the structure at a time with a step frequency close to the 1st vibration mode. The maximum response obtained in the middle of one of the two main spans of the structure was 0.56 m/s^2. Then, the pedestrians crossed the footbridge together two times, synchronizing the step frequency between them and make it coincide with that of the 1st vibration mode, as well. In that case, the maximum response was very close to 2 m/s^2. These values should be seen as indicative of the structure response to such actions.

3 NUMERICAL MODELING

3.1 Numerical model of the structure

Based on the geometrical and material characteristics of the footbridge and given the identified dynamic properties, a numerical model of the structure was developed using Robot software. The accuracy of the numerical model was improved by slightly adjusting the characteristics of the structural sections and element masses, until a good approximation between experimental and numerical natural frequencies and mode shapes is achieved. This was not a difficult task, given the simple structural functioning of the system under analysis. Table 1 contains the numerical natural frequencies of this model, which can be compared with the ex-

perimental data, and Figure 5 shows the 3-dimensional representation of the first 4 mode shapes obtained numerically, which are in very good agreement with the experimental estimates.



f_1 = 1.82 Hz f_2 = 2.06 Hz

f_3 = 3.09 Hz f_4 = 3.38 Hz

Figure 5: First 4 vibration modes obtained numerically.

3.2 Simulation of the structural response to pedestrians actions

This numerical model was used to simulate the structural response to several scenarios of most probable pedestrian loads. It was considered that only the first 4 vibration modes are critical in terms of occurrence of resonance phenomena. Other higher modes are difficult to excite by regular activities of pedestrians, even considering the higher harmonic components of the dynamic load. Scenarios involving crowds crossing the bridge were also assumed to be non-realistic, mainly because the structure serves as an entrance to a building with limited access. Therefore, only single and groups of pedestrians were considered, consisting of the following idealized situations: Single or 3 synchronized pedestrians walking in the center of the deck in resonance with the 1st vibration mode; Single or 2 synchronized pedestrians walking laterally to the deck in resonance with the 2st vibration mode (torsion); Single pedestrian running in the center of the deck in resonance with the 3rd vibration mode; and a single pedestrian running laterally to the deck in resonance with the 4th vibration mode.

The loads corresponding to these scenarios were modeled according to reference [5] and the damping ratios of all vibration modes assumed a conservative value of 1%. The maximum vibration levels achieved in each situation were evaluated at critical sections, as summarized in Table 3. In that table, a classification of vibrations according to Sétra and Hivoss guidelines in this area is also indicated (see Table 4 for proposed classification).

Scenario	Maximum Acceleration (m/s^2)	Comfort Class
1 pedestrian walking (f=1.82 Hz)	0.80	Medium
1 pedestrian walking (f=2.06 Hz)	0.97	Medium
3 pedestrians walking (f=1.82 Hz)	2.40	Minimum
2 pedestrian walking (f=2.06 Hz)	1.94	Minimum
1 pedestrian running (f=3.09 Hz)	2.18	Minimum
1 pedestrian running (f=3.38 Hz)	0.70	Medium

Table 3: Structure response to several idealized scenarios.

Comfort classes	Maximum Acceleration Limits (m/s^2)
Maximum comfort	< 0.5
Medium comfort	0.5 – 1.0
Minimum comfort	1.0 – 2.5
Intolerable vibrations	> 2.5

Table 4: Comfort classes for vertical accelerations according to Sétra and Hivoss guidelines.

4 CONTINUOUS DYNAMIC MONITORING SYSTEM

4.1 Description of the system

Given the symmetry of the structure and shape of the first vibration modes, the evaluation of the maximum vibration levels can be performed at mid-span in one of the two spans at any side of the deck. As a result, only one sensor was adopted and positioned at the mid-span close to the green park at the south-west side. This way, it was possible to install a solar-powered acquisition system by means of a solar panel installed on the outside of the lateral girder (see Figure 6a)). The acquisition system is composed of a microcontroller able to perform Analog-to-Digital Conversion (ADC) of 16-Bit resolution, which saves data in a local micro SD-card. Inside the box that is used to keep this electronic device, there also exits a battery to guarantee the functioning of the system during night periods and a solar controller (see Figure 6b)). The accelerometer is of MEM type and measures acceleration in the vertical direction. The acquisition system produces data files lasting 10 minutes, which results in 144 files or 16.1 MB per day of information, considering a sampling frequency of 40 Hz.

a)  b) 

Figure 6: Data acquisition system: a) Solar panel; b) Box with microcontroller, battery and solar controller.

4.2 Evaluation of autonomy and robustness

Unlike many applications installed in structures by Vibest, this particular one was developed specifically for this application, which means that the autonomy and robustness of the system are variables that were not completely known initially. The solar system was designed for relatively sunny days, which means that the autonomy was not assured for cloudy days. At the same time, because of the continuous functioning of the system during many months, the robustness for faults in the acquisition was not proven.

After 6 months of operation, these aspects could be evaluated. For this purpose, the graph of Figure 7 shows the periods where valid data exist or do not exist. The horizontal axis represents the total period of 178 days from 5th October 2014 to 31st March 2015, and the vertical axis represents one day divided into 144 intervals of 10 minutes. The failures (dark spots) occurred exclusively due to power issues, especially during the night or on dark days. No problems were detected in the acquisition system itself. This shows that the system worked 90.5% of the time, corresponding to a very good performance of hardware solution, specially taking into account that the acquisition included the winter period.

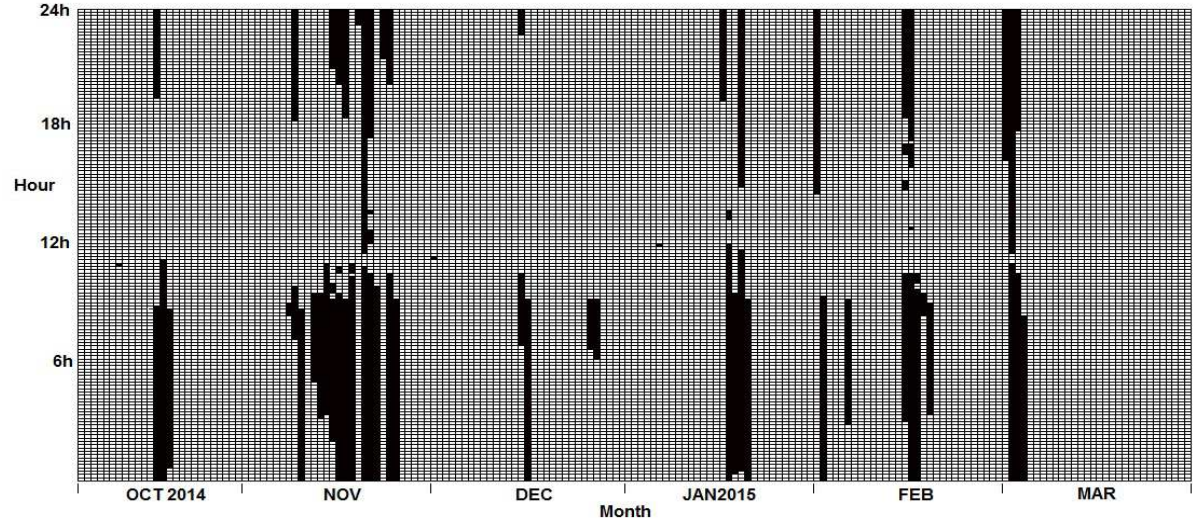


Figure 7: Failures on the signal acquisition detected for 6 months.

5 ANALYSIS OF MEASURED VIBRATIONS OVER TIME

5.1 Maximum vibration levels

The maximum levels of vibrations in the considered period are showed in Figure 8, where the horizontal and vertical axes have the same meaning as the previous Figure 7. The dark areas correspond to periods of low levels of vibrations, which occur essentially in night periods. In an opposite situation, in lighter areas the levels of vibration are higher. The colored bar on the right side establishes a correspondence between color and maximum acceleration values (in m/s^2). Analyzing this graph, several interesting conclusions can be drawn just by observing the vibration levels of the structure. For instance, it is clear that pedestrians use the footbridge mainly in the afternoon, which is also evident in the representation of the daily vibration amplitudes shown in Figure 9. In addition, the time shift of 1 hour occurred in the end of October is visible in Figure 8, by changing the people's schedules at lunch time.

In any event, Figures 8 and 9 show that the maximum vibration levels induced be pedestrians often reach values between 0.5 and 1.5 m/s^2 approximately, which highlights the “lively” behavior of the structure. In fact, by framing these vibration levels in the comfort classes suggested by Sétra or Hivoss guidelines, indicated in Table 4, it can be concluded that the foot-

bridge provides only minimum comfort in many practical situations. In more specific cases, the structure may experience vibration levels higher than 2.5 m/s^2 attributed to intentional resonant loads, inducing intolerable vibrations from the human comfort point of view.

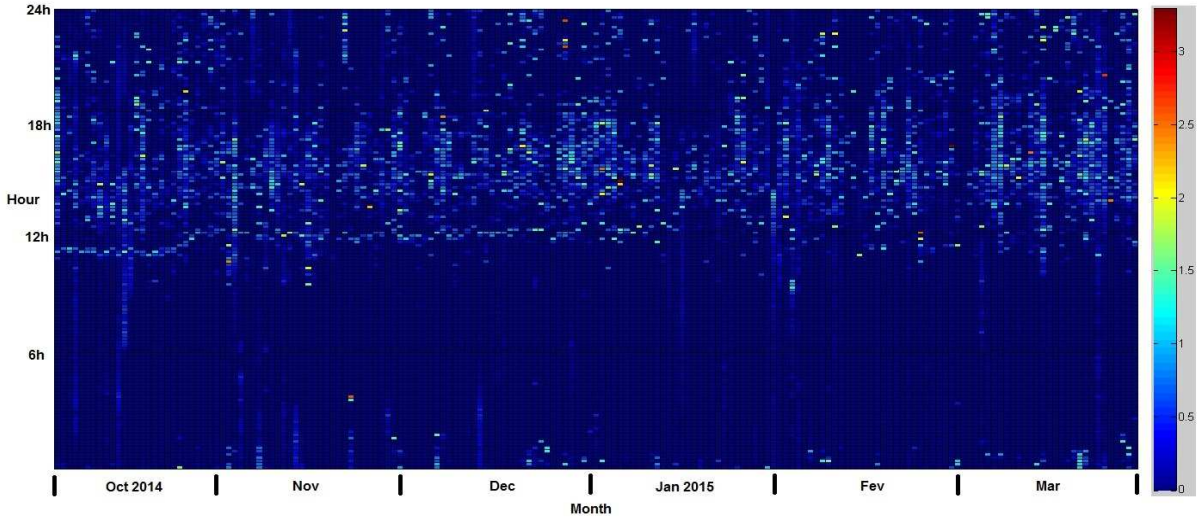


Figure 8: Maximum vibration levels during 6 months.

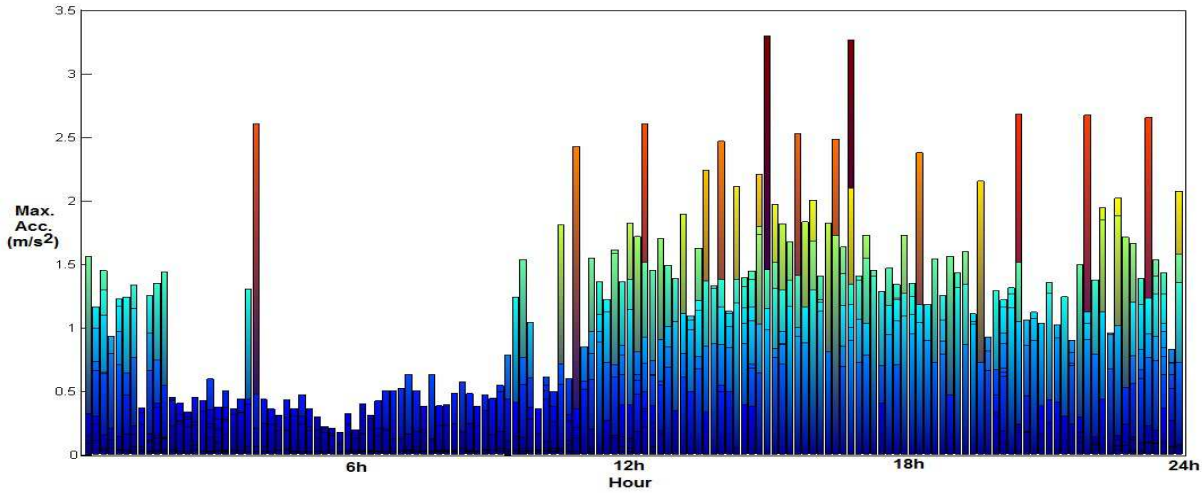


Figure 9: Daily maximum vibration.

5.2 Frequency distribution of vibrations

There is often interest not only in identifying the maximum vibration levels, but also in characterizing the correspondent vibrating frequency. This allows finding out which vibration modes are more active in the dynamics of the structure, which can be useful for some applications, such as vibration control. That analysis was performed for the same period of 6 months, with the main results shown in Figure 10a). In this case, each dot represents an occurrence of a maximum in the acceleration records which was selected according to some criteria. In particular, vibrations should be characterized by very stable and clean pseudo-sinusoidal signals dominated by a single frequency after being filtered by a low pass filter at 6 Hz. This means that only vibrations arising from the dynamics of the first vibration modes are considered. This procedure rules out situations of peaks conditioned by punctual spikes in signals, and cases where the response has contributions of several frequencies in order to facilitate the construction of graphs with the frequency in one axis.

The analysis of Figure 10a) shows that there are 2 dominant vibration modes, namely, the 1st mode of 1.85 Hz and the 3rd mode of 2.90 Hz approximate frequency, which corresponds to the first pure bending modes of the footbridge. This means that, generally, pedestrians walk near the center of the deck and don't excite torsion vibration modes, which seems an obvious situation. Considering that Figure 10a) represents more than 13,000 occurrences, and selecting the critical ones above 0.50 m/s^2, figure 10b) establishes the histogram of the significant events associated with each vibration mode. More than 80% of significant vibration levels are due to dynamics of the 1st vibration mode and about 15% are due to the 3rd mode.

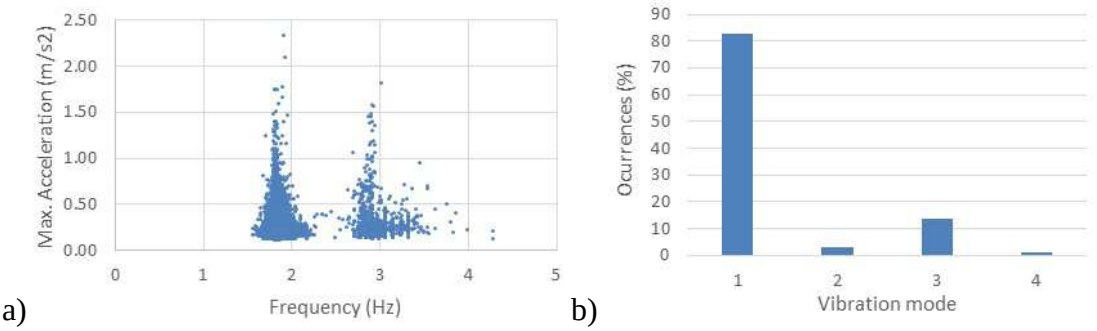


Figure 10: a) Frequency vs amplitude of vibrations; b) Histogram of significant levels of vibration.

5.3 Identification of natural frequencies

Beyond the evaluation of the vibration levels, the data collected over time can also be used to identify modal properties of the structure. The practical interest of this information in the context of this research work is related to a possible implementation of control devices to reduce vibrations in this footbridge, especially if it involves inertial vibration absorbers (also known as Tuned Mass Dampers). It is well established that these devices are very sensitive to frequency tuning, which may consist of a major problem in their use.

The identification of modal properties of dynamic systems can be achieved using several methods. A preliminary view about how natural frequencies distribute over time can be obtained by calculating the Power Spectral Densities of time signals of a previously defined length, windowing and overlapping, and then averaging them over a certain period of time in a process known as the Welch method [6]. Figure 11 illustrates the 3D graph that can be obtained using a daily averaging over a total period of 178 days, where the natural frequencies of the structure are shown as elevations in a frequency ranging from 0 to 10 Hz.

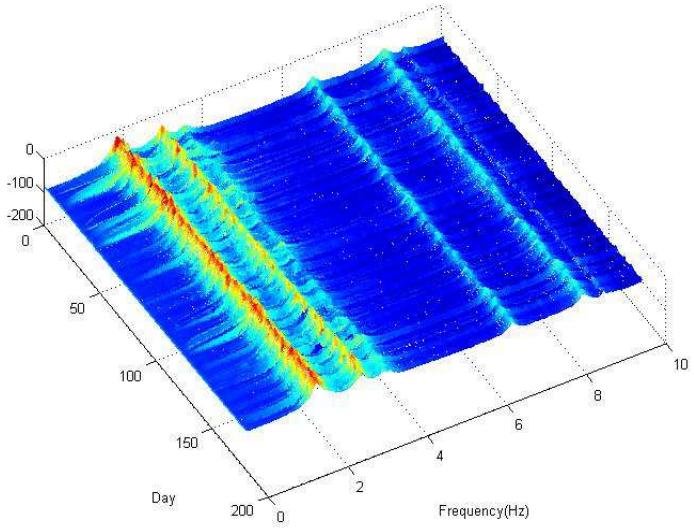


Figure 11: Daily averaged Power Spectral Densities for a period of approximately 6 months.

Nevertheless, the natural frequencies of the structure were identified over that period using the p-LSCF method [6]. In this case, it is necessary to consider that the existence of only one sensor limits the identification of the natural frequencies associated with each vibration mode because only one modal component is available. In addition, the existence of pedestrians on the bridge disturbs the modal identification, especially during the afternoon periods. Despite this, it was possible to make a clear identification of the first 4 natural frequencies according to Figure12. The representation of 6 days of results in Figure 13 allows concluding that the natural frequencies have a significant daily variation probability due to temperature effects, which should be considered in future analyses involving this structure.

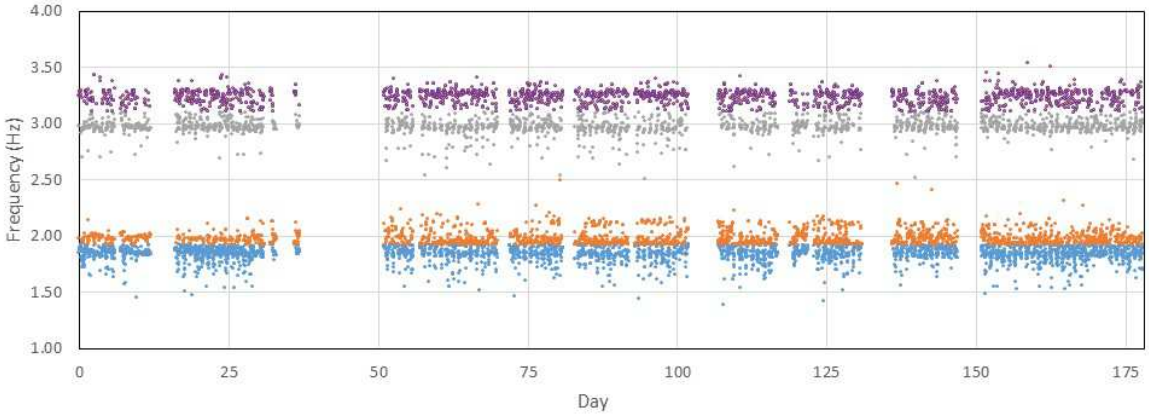


Figure 12: Identified natural frequencies in a period of 6 months approximately.

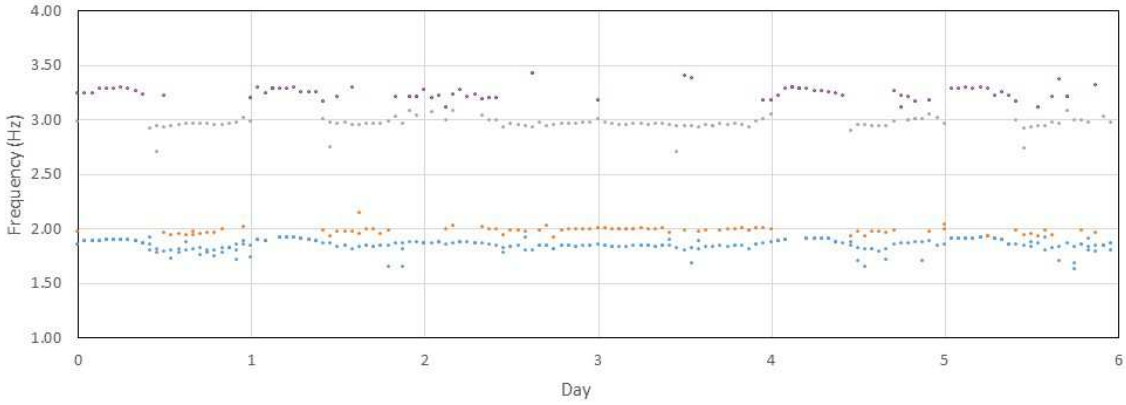


Figure 13: Detail representing 6 days.

6 CONCLUSIONS

This paper allows attesting the vulnerability of the footbridge under analysis to relatively high levels of vibrations. This was concluded by performing initial tests with pedestrians followed by numerical simulations using a calibrated numerical model of the structure. It was found out that a single pedestrian walking in resonance conditions induces maximum accelerations on the footbridge higher than 0.5 m/s^2, which is the limit indicated by several codes as providing high level of comfort to its users. If 3 pedestrians walk synchronously in the same conditions, the vibrations almost reach the intolerable limit.

On the other hand, the implementation of a continuous dynamic system composed of one accelerometer installed at mid-span of one of the two main spans of the bridge allowed recording the effective levels of vibrations for several months. It could be observed that very often the vibrations reach accelerations between 0.5 and 1.5 m/s^2 approximately, correspond-

ing to a range of medium to minimum comfort level. More than 80% of high vibration levels are associated with the dynamics of the 1st vibration mode, meaning that any possible installation of a vibration control device should be mainly directed at this frequency.

However, in this case, it is necessary to consider the relatively high variation of the natural frequencies of the system over time, possibly due to temperature effects or even to the humidity of the wood deck.

ACKNOWLEDGMENTS

The author acknowledges the support provided by the Portuguese Foundation for Science and Technology (FCT) in the context of the research project "Development of a smart damping system for reducing vibrations in Civil Engineering structures" (PTDC/ECM-EST/0535/2012).

REFERENCES

[1] SÉTRA, *Guide méthodologique – Passerelles piétonnes – Évaluation du comportement vibratoire sous l'action des piétons*, 2006.

[2] Hivoss, *Design of Footbridges – Guideline*, 2008.

[3] B. Abreu, *Study of the dynamic behavior of footbridges* (in Portuguese), MSc Thesis, FEUP, 2008.

[4] R. Antão, *Analysis of vibrations of Transparent Building Footbridge and proposal of a control system* (in Portuguese), FEUP, 2013.

[5] H. Bachmann, W. Ammann, *Vibrations in Structures Induced by Man and Machines*, Structural Engineering Documents, IABSE, 1987.

[6] F. Magalhães, *Operational Modal Analysis for testing and monitoring of bridges and special structure*, PhD thesis, FEUP, 2008.

COMPDYN 2015
5th ECCOMAS Thematic Conference on
Computational Methods in Structural Dynamics and Earthquake Engineering
M. Papadrakakis, V. Papadopoulos, V. Plevris (eds.)
Crete Island, Greece, 25–27 May 2015

A *MULTISCALE* APPROACH FOR MODELING OF INFILLED FRAMES

Andrea Fiore[1], **Francesco Porco**[1]

[1] Politecnico di Bari, Dicatech
Via Orabona, 4 - 70126 Bari, Italy
andrea.fiore@poliba.it

Keywords: Existing Building, Seismic Assessment, Reinforced Concrete, Infilled Frame, Equivalent Strut, Meso-scale, RBSM model.

Abstract. *The behavior of existing reinforced concrete buildings towards to the seismic actions is strongly affected by the infill walls. Although they assume an important role in the global response of the buildings, modeling of infilled frames is quite complex as a result of the many variables involved. These factors (such as the various constructive solutions; the non-homogeneous and anisotropic mechanical behavior of the masonry texture; the interaction between masonry panel and surrounding frame; the in-plane and out-of-plane behavior) make uncertain the structural response.*
The technical literature on the issue suggests approaches that ranging from the macro-scale analysis to micro-scale analysis. The different proposals confirm the complexity to simulate the kinematic mechanism between elements of the panel (mortar and bricks) and between infill panel and surrounding frame. Furthermore, these different models cannot be applied in general. They are most of the times calibrated on experimental tests carried out on samples packaged with materials and executive methods that are specific of the test place. Therefore, there is the need to define simplified models that take into account the geometry, mechanical properties of the masonry walls and elements of the surrounding frame.
The present study proposes a meso-scale approach (a "Rigid Blocks Method") for simulating of the infilled frames in order to define the main parameters that characterize the simplified "Equivalent Strut model" (i.e. the macro-modelling of the infill walls). With the meso-scale model the infill wall is supposed as a mechanism consisting of rigid blocks connected by axial and shear elastic-plastic springs. The model is usually used for in-plane dynamical analysis of masonry structures. The use of an equivalent rod for modeling the infill panels is a simplified approach purely numeric. It is simple and reduces the computational costs when it is need to evaluate the global behaviour on building scale. The results achieved with the proposed approach are as result of extensive numerical tests on samples of infilled frames, with or without openings, which have geometries and material properties within significant ranges.

1 INTRODUCTION

Over the years, the variability exhibited by the infilled frames (in particular for buildings designed under vertical loads only) has strongly stimulated researchers to investigate the interaction between masonry panels and reinforced concrete elements [1,2]. These studies are important in order to establish the retrofit interventions needed to ensure the seismic safety to the deficient buildings [3,4]. The role of the experimental tests is undoubtedly fundamental for the knowledge of the actual response. However, the great variability of the significant parameters involved in the interaction frame-infill does not allow to carry out tests whenever they are needed because the tests are expensive and usually limited to few cases. A valid alternative for the knowledge is provided by research study based on numerical modelling of infilled frame. The several studies available, however, present a great degree of uncertainty due to the high variability of the significant involved parameters. Among these, the mechanical properties of the constitutive materials (mortar and bricks) and of the global masonry texture (intended as a continuous material) are crucial. In addition, another fundamental aspect is represented by the model adopted for simulating the infills within the computational model of the building [5,6,7,8].

Consequently, on the basis of the framework above outlined, the present thesis has the aim to reduce the influence of some variables by proposing a simplified procedure for the calibration of the *Equivalent Strut* model. In the field of the approaches of macro-modelling, this model is the most used to evaluate and simulate the effects of the infills in the global response of the frame. It describes the response of infilled frame under a horizontal load observed from the experimental test. In particular, by increasing of the thrust action, it is observed the detachment of the masonry from the boundary reinforced concrete frame, and the panel exhibits a behaviour no more in line with a two-dimensional element (that it resists to shear stress) but as an "*one-dimensional equivalent rod*". The rod follows the distribution of the compression forces along the diagonal of the panel acting as a *strut* in opposition to the horizontal action. The equivalent strut is defined once known the geometrical and mechanical characteristics and the constitutive law (force-displacement) that regulates its behaviour during the nonlinear phase (post-elastic). The above parameters are dependent by experimental results, therefore, especially in the case of existing structures, they can not be generalized to all possible cases and are reliable only in some cases that are comparable with the characteristics of the test from which derive.

The aim of the present work is to define the Force-Displacement constitutive law of the *equivalent strut*. The law is obtained by a simplified procedure that use the results of a simplified discrete model implemented within common finite element software (*SAP2000*). In order to define the model into software are needed few input data as the geometry of the infilled frame and mechanical parameters of the masonry panel. The model numerically simulates an experimental test by which to evaluate the actual variations in stiffness and strength of the infill-frame system. The purely numerical findings allow to define the characteristic branches of the law, which is the force-displacement relationship (F_w - d_w) that regulates the elastic and plastic behaviour of the strut. Although the transition from *meso-scale* to *macro-scale* analysis could seem a loss in the description of the global response of the infilled frame, it is actually offset by the possibility to study three-dimensional structures, which usually become, with a *meso-scale* approach, more computationally burdensome. Moreover, the simplification to insert simple beam elements for simulating the infill panel, involves a low degree of uncertainty. This advantage is due to use of constitutive laws that are defined on the actual masonry texture and not based on the experimental tests from the literature conducted on panels mechanically different. In conclusion, the procedure is proposed with the aim to improve the

equivalent strut method which is able to assess the effects of interaction between the infills and primary RC elements on building-scale analysis.

2 A SIMPLIFIED PROCEDURE TO ASSESSING THE EFFECTS OF INFILL PANELS

2.1 The *meso*-modelling

The "*meso-scale*" models are usually referred to as "*discrete models*". If they are applied to structural systems that require a limited number of elements, they allow to reduce the computational burden required by the continuous or discontinuous approaches. The *Rigid Body Spring Model* (RBSM), used in the proposed procedure, belongs to this type of models.

The basic idea of the method (Figure 1) consists in describing the masonry (intended as a composite periodic material denominate RVE - *Representative Volume Element*) as a mechanism composed of the unitary cells constituted by of rigid blocks and elasto-plastic springs [9,10,11] The elastic features of the springs are defined by means of a specific identification procedure with the objective of transferring the information about the main characteristics of the masonry texture from the "*meso-scale*" to "*macro-scale*".

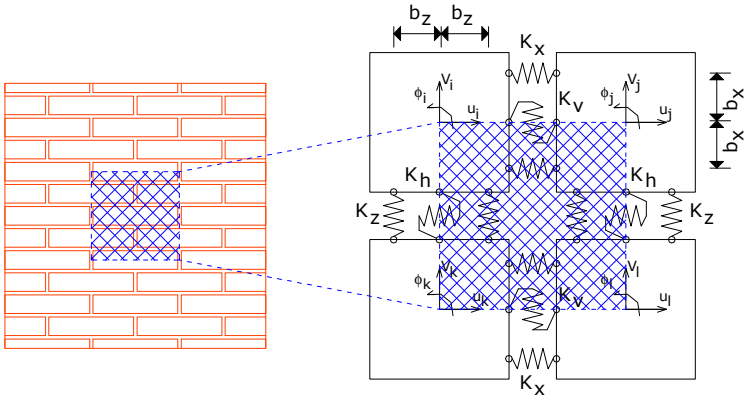


Figure 1: Scheme of a regular masonry texture and an example of the unit cell consists of four rigid blocks connected by elasto-plastic springs.

The connection between the rigid blocks occurs by means of two axial springs (indicated with K_x or K_z, depending on the direction) and a shear spring (K_h, K_v , depending on configuration) arranged along each of the common sides between the blocks at a distance equal, respectively, to b_x and b_z. The hysteretic behaviour of the springs is obtained on the basis of the mechanical parameters of the constitutive elements of the panel (mortar and blocks) and takes account of the mechanical degradation of mortar joints in the cycles of loading and unloading.

2.2 Constitutive law of the springs

In the original version of the model, the stiffness of the springs and the distance between the connection points are assigned with the criterion to approximate the average strain energy in correspondence of the reference volume of each spring. Assigning to the shear springs different stiffness in horizontal and vertical direction, together with a calibration of the distances between the connections, it is possible to model the effects of some masonry texture (for example, stone blocks interlocking often present in the case of significant degradation of the masonry that significantly changes the resistance of the panel). The constitutive laws for elas-

tic-plastic behaviour are assigned using a phenomenological approach [12], based on the results of cyclic tests available in the technical literature [13,14,15].

For the purposes of this thesis, the use of a *meso-scale* modelling is an easy and quick step within the proposed procedure, aimed at defining some characteristic features of the global response of the infilled frame. For these reasons the properties of the springs are defined according to a simplified approach. The elastic stiffness of each spring is estimated through the geometrical and mechanical properties of the infill (Figure 2), such as the *modulus of elasticity* of the masonry panel in horizontal direction (E_{wh}), *modulus of elasticity* of the masonry panel in vertical direction (E_{wv}), *shear modulus* (G), areas of influence of the axial spring (A), areas of influence of the shear spring (A_T), thickness of the head joint (g_t), thickness of the bed joint (g_l) and thickness of the masonry panel (t_w)

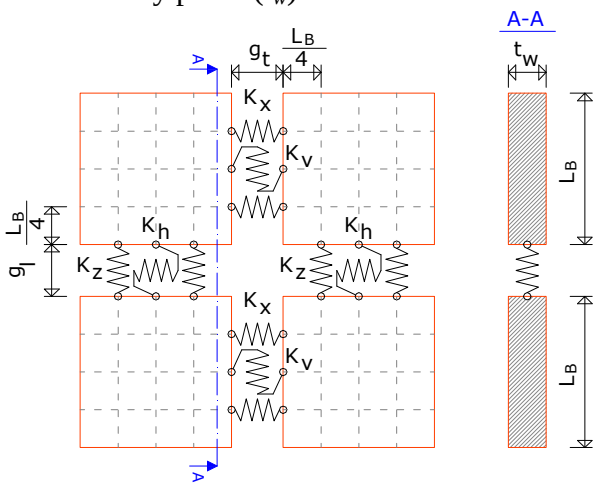


Figure 2: Simplified periodical cell describing the masonry texture.

When the kinematic of the model is such as to engage the springs over the elastic response, force-displacement laws regulate the plastic behaviour of the system. As with the elastic behaviour, also for the decreasing behaviour of the stiffness has been adopted a simplified approach. Figure 3 shows the constitutive laws of the springs, respectively, axial and shear, used in the present work.

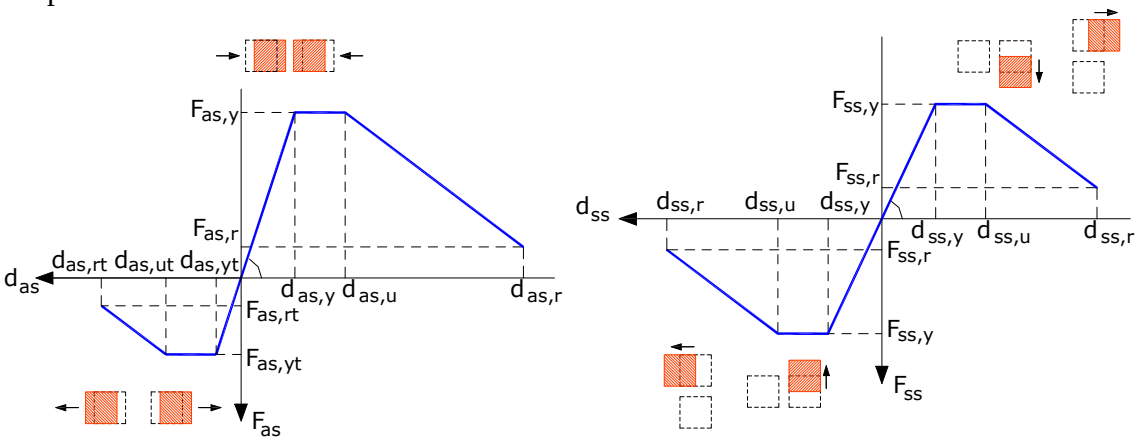


Figure 3: Constitutive laws of the axial and shear springs.

For both, the force-displacement law is constituted by *3* branches. In the figures, the subscript "*as*" indicates the axial spring, while "*ss*" the shear spring. The fundamental variables of the laws are calibrated with an approach depending on the material strengths: compression strength of the masonry in horizontal direction (σ_{wh}), compression strength of the masonry in

vertical direction (σ_{wv}), tensile strength of the masonry (σ_{wt}), shear strength of the masonry along the bed joints (τ_{wh}), shear strength of the masonry along the head joints (τ_{wv}).

2.3 Description of the simplified procedure

First step: *"meso-analysis of the infilled frame"*

The first step of the procedure is to assess the response of the infilled frame by a nonlinear static analysis (pushover). The behaviour of the masonry panel is simulated by the model described in the previous section. The reinforced concrete frame is instead modelled with *beam* elements whose response is described by a *lumped-plasticity model*. According to this, the post-elastic behaviour is modelled by introducing plastic hinges, in which all non-linearity is localized at the ends of the elastic beams. The non-linearity of the plastic hinge is defined by a M-ϕ or M-θ relationship, depending on the shear span L_V, which identifies the distance between the end section of the element and the inflection point of the deformed shape (which varies during the incremental pushover loading). The relation adopted in the present work is contained within US standards FEMA 273 [16] which defines a relationship between the dimensionless strength (Q / Q_{CE}) and rotation θ (or displacement Δ) for respectively beams and columns. In the case of existing structures, the evaluation of plastic hinges have to take into account the effective strength values of materials in according to numerical approaches (in this context interesting are the research developed by authors [17,18]. Assuming as a *control point* of the pushover analysis the application point of the F_h load, the two main results at this *step* are, respectively, the *capacity curve* of the configuration with infill (indicated hereinafter with the acronym "INF") and the response of the springs in terms of forces and displacements.

Second step: *"evaluation of the infill conribution without RC frame"*

The F_h-d_h curve of the INF configuration is intended as the "*sum*" of two distinct contributions, respectively, due to the bare frame (B) and the masonry panel (MP). The first contribution is evaluated using a nonlinear static analysis on the model without infill panel. The second, however, is obtained by subtracting (in correspondence with each displacement value) from the response of the INF configuration, the share due to the bare frame B (Figure 4).

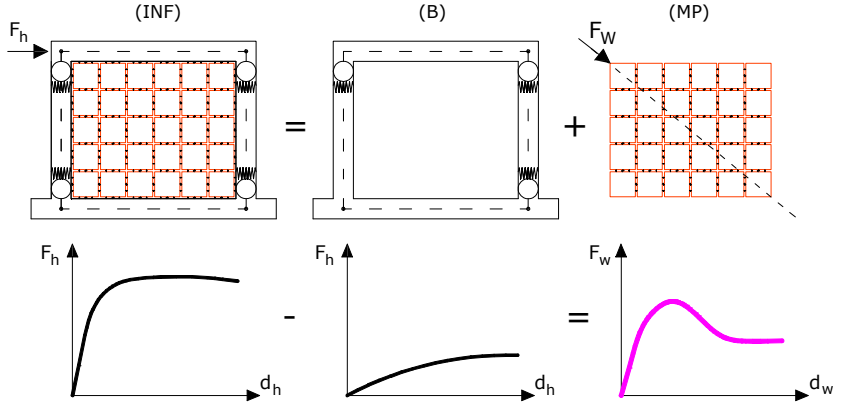


Figure 4 - Graphical description of the simplified evaluation of the masonry panel response.

With the above assumption is obtained the relationship between the horizontal thrust load ΔF_h^{MP} (equal to F_h^{INF} - F_h^{B}) and the horizontal displacement d_h of the wall panel only. The ΔF_h^{MP} - d_h curve is successively expressed according to F_w^{MP} and d_w^{MP} components along the d diagonal of the panel, by means of numerical expressions based on the geometry of the infilled frames.

Third step: *"Evaluation of the constitutive law of the Equivalent Strut"*

Once obtained the response F_w^{MP}- d_w^{MP} for masonry panel, it's possible to evaluate the constitutive law of the equivalent strut on the backbone of MP curve in order to define the ESM model. The law that will be defined consists of four branches delimited by four characteristic points identified on the MP curve. The first branch describes the elastic response up to the yield point "*S*". The second branch describes the behaviour of the equivalent strut from when begins the plastic deformation up to achieve the point of maximum strength capacity "*M*". This is followed by the descending branch due to the propagation of crack in the panel such that induce a significant decrease of resistance until to the point "*D*". Finally, the fourth branch describes the force-displacement relation until the failure (point "*R*") with a residual resistance maintained in order to ensure stability and convergence to the numerical solution (Figure 5).

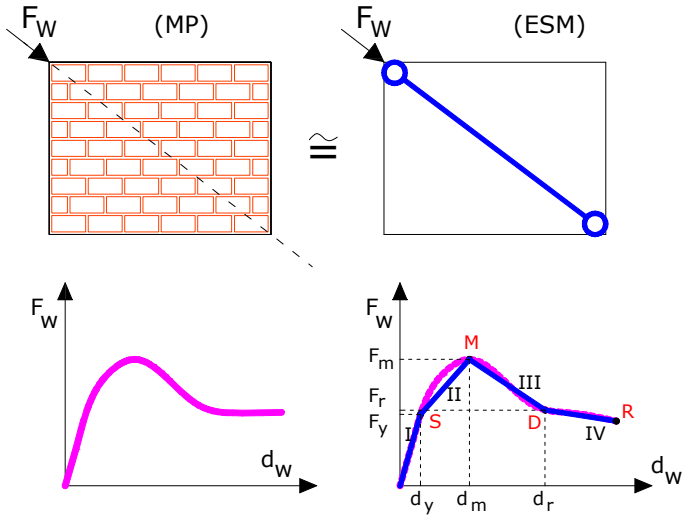


Figure 5: Graphical equivalence between MP and ESM models for the evaluation of F_w-d_w law.

The *M* and *R* points are preliminarily identified and coincide, respectively, with the maximum point and last point of the MP curve. While, *S* and *D* points are directly evaluated by an iterative approach that minimizes the difference between the subtended areas of the MP curve and the defined constitutive law.

The width (*w)* of the *equivalent strut* is evaluated neglecting the degradation of stiffness and the uncracked panel. The used equation derives from a purely linear elastic relation considering the yield point *S* on the MP curves. The width *w* is obtained by the following balance equation:

$$\frac{F_y}{d_y} = \frac{E_{w\theta} t_w W}{d} \tag{1}$$

where $E_{w\theta}$ is the modulus of elasticity of the masonry in the diagonal direction [19].

$$E_{w\theta} = \left[\frac{\cos^4\theta}{E_{wh}} + \frac{\sin^4\vartheta}{E_{wv}} + \cos^2\theta \sin^2\theta \left(\frac{1}{G} - 2\frac{\nu}{E_{wv}}\right)\right]^{-1} \tag{2}$$

3 CASE STUDY

3.1 Characteristic of the sample and set-up of experimental test

The case study of the present work, indicated by the abbreviation "SIB", is part of a broad experimental campaign conducted by Cavaleri and Di Trapani at the laboratory of the University Palermo, Italy [20]. The experimentation involved eight infilled frames (S1 series) with slenderness $L_w/h_w = 1$ designed to represent a typical configuration recognizable in existing buildings designed for gravity loads and without any seismic detail. Two specimens identical of the S1B sample, respectively, S1B-1 and S1B-2, were packed. The Figure 6 reports the geometrical details of the sample.

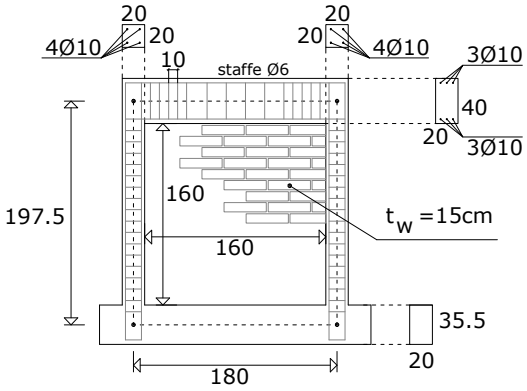


Figure 6: Geometry and reinforcement of the sample.

The mean concrete strength, measured after *28* days, was *25MPa*, while the elastic Young modulus was about *25500MPa*. The reinforcement steel bars had a medium strength of *450MPa*. The mechanical characteristics of the infill is defined on the basis of compression tests, lateral and diagonal preliminarily performed, while further loading tests were performed on bricks and mortar. The results of this preliminary experimental campaign are widely discussed in Cavaleri *et al.* (2012) [21]. The infill panel were constructed by placing the bricks with vertical holes and parallel to the direction of the static loads acting on the columns. The thickness of the mortar joints is equal to *15mm*. Significant data for implementation of the meso-model of the sample are listed in Table 1.

E_{wv}	6401	MPa
E_{wh}	5038	MPa
G	2560	MPa
σ_{wv}	8.66	MPa
σ_{wh}	4.18	MPa
τ_{wv}	0.30	MPa
τ_{wh}	0.31	MPa

Table 1: Mechanical properties of masonry employed for S1B-1 specimen.

3.2 Experimental results

The specimens of infilled frames were tested by increasing the displacement at each cycle up to a drift about *2.5 % - 3.0 %*. Damage mechanisms were monitored during the tests in order to detect propagation of cracks on infills and frames. Stiffness, strength, and ductility evaluations were carried out by observation of force-displacement cycles. A low strength degrading after peak reaching was observed for all specimens, demonstrating an efficient con-

finement effect produced by the frames on the infill panels. The first cracking, which have involved both frames and infills of both specimens, have arisen from a displacement of *10 mm* (drift of about *0.63%*), in particular, diagonal cracks occurred at the beam-column joints, while along the mortar joints the cracks are distributed according a typical propagation "*stair-step*". For larger displacements, over *20 mm* (drift of about 1.25%), more evident cracking propagation, corresponding to the beginning of strength decay was observed accompanied by the formation of sub-horizontal cracks in the middle of columns and more severe damage at beam column joints. However, both specimens exhibited a significant stiffness degradation at each cycle, especially after the peak strength was reached. On the other hand the peak strength (in particular for S1B-1 specimen) did not significantly decrease until large displacements occurred. By ideally enveloping the force-displacement cycles measured by the tests with a monotonic curve (in red) global ductile behaviour was observed (Figure 7).

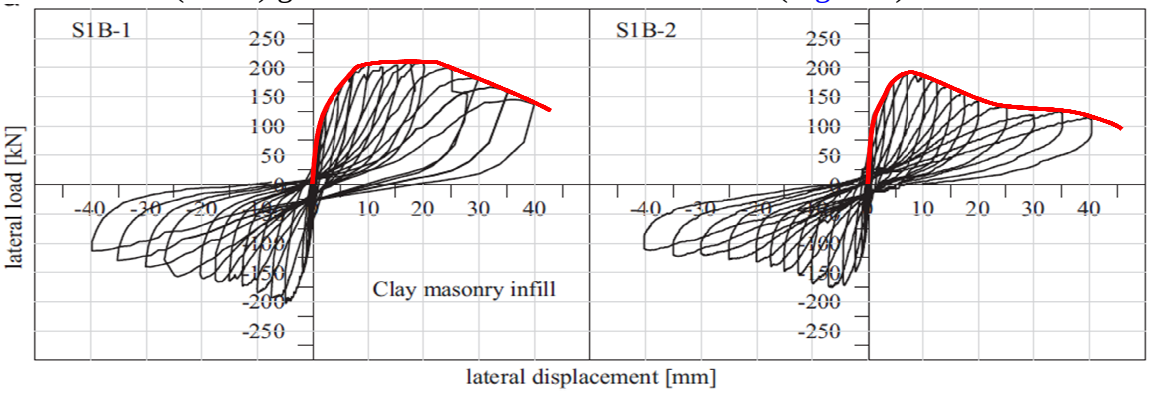


Figure 7: Force–displacement cyclic test results for specimens of S1B series.

3.3 Numerical Modeling

In order to simulate the experimental tests, has been implemented in *SAP2000 software* a finite element model of the S1B sample. The numerical model is constituted by a set of discrete elements (blocks and spring) enclosed by a contour of the beam elements having the function of describing the behaviour of the reinforced concrete frame. The rigid blocks spring model (RBSM) is constituted by a regular discretization of 6 x 6 two-dimensional plane elements (*4*-nodes *shell* elements). The total degrees of freedom are 108. The behaviour perfectly rigid of blocks is guaranteed by assigning to *4*-nodes of each *shell* a "*Diaphragm*" internal constraint with Y rotational axis perpendicular to the OXZ reference system. The internal constraint connects the nodes of the shell element by means of ideal rigid rods devoid of mass and stiffness. The connections between rigid blocks is with "*NLlink*" elements of "*multilinear plastic*" typology, i.e. nonlinear springs (on the right of the Figure 8 are highlighted, respectively, the axial spring - in red- and the shear spring - in blue). At the interface between frame and masonry panel (i.e. between beam and *NLink* elements along the sides of the rigid blocks adjacent to the frame), are arranged *Rigid* typology. The *rigid NLink* maintain unchanged the relative distances between the nodes on axis line of the reinforced concrete element and the boundary line of the concrete, in order to simulate the material between them. The model is constrained to the ground by means of interlocking constraints at the base columns, while for simulating the position of specimen in the test device, the hinge constraints at the end nodes of the *rigid NLink* elements were arranged.

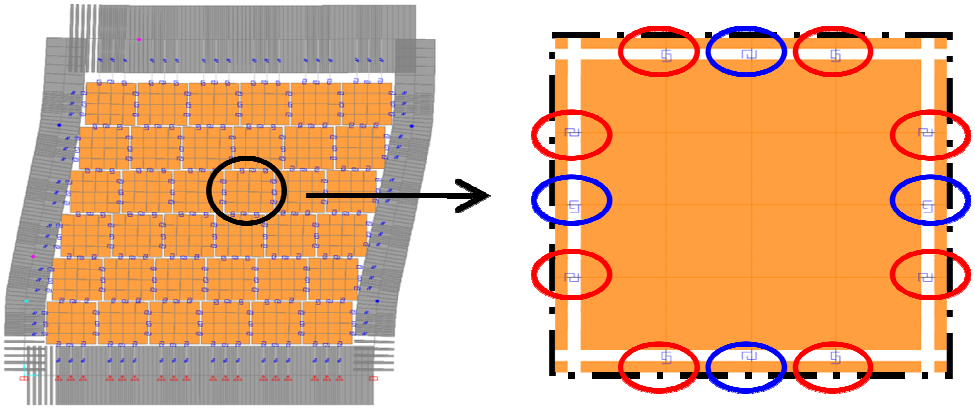


Figure 8: Response of the Finite Element Method (left); extrude view of the single rigid bloc and his connections.

4 RESULTS

The simplified procedure described in *§ 2* is applied to the S1B sample. By assuming the application point of the horizontal load as the *control point*, nonlinear static analysis (push-over) on the discrete model with blocks and springs and the frame model without infills were performed. The capacity curves of two configurations are indicated hereinafter with the abbreviations, respectively, INF and B. Applying the first two steps of the procedure is obtained the relationship between the horizontal thrust load ΔF_h^{MP} and the horizontal displacement dh for the building panel MP only (Figure 9). In particular, ΔF_h^{MP} was evaluated with a simplified approach by the followed numerical difference: $F_h^{INF} - F_h^{B}$. The F_h^{MP} - $d_h^{M}P$ relation is then expressed according to the F_w^{MP} and d_w^{MP} components along the *d* diagonal of the panel.

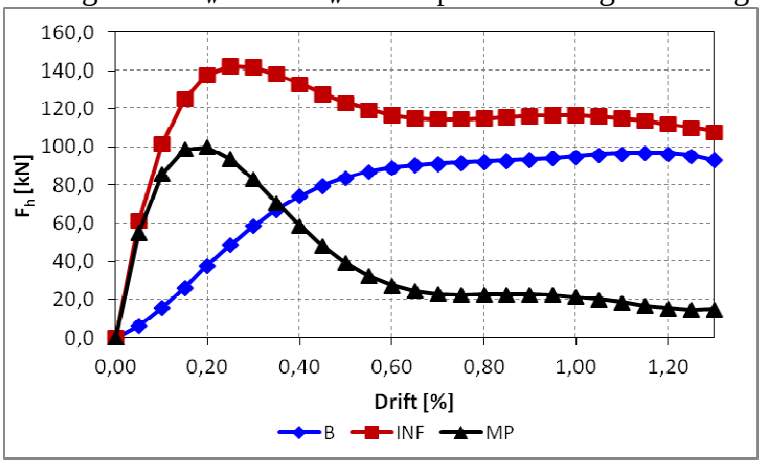


Figure 9: The assessment of the Force-Displacement Capacity Curve of the Masonry Panel (MP) - first and second step of the proposed procedure.

The *4* branches of the constitutive law of the equivalent strut are directly built on the backbone of the MP curve (Figure 10). In order to determine the law more easily two points are directly fixed on the MP curve. In particular, M and R points are, respectively, equal to the maximum point and last point of the MP curve. The yield strength (S point) and the end point of the first degrading branch (D point) are defined by iteration by minimizing the difference between the areas subtended by the MP curve and the constitutive law. The length of the strut is evaluated by Eq. 1 and is equal to *245mm*.

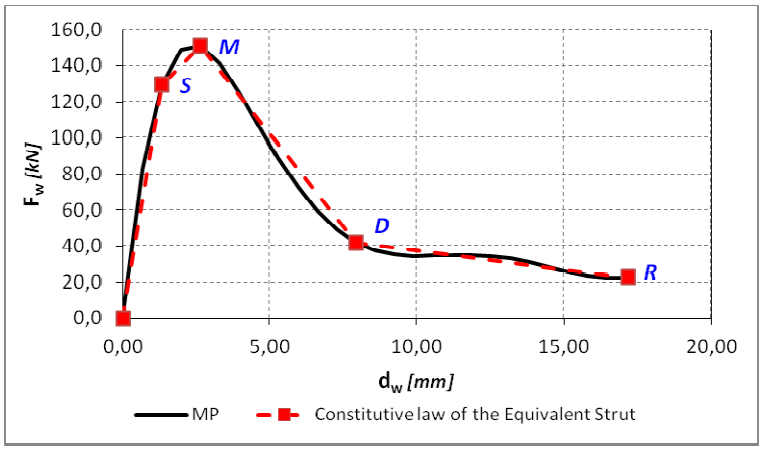


Figure 10 - Graphical definition of the Constitutive Law on the MP curve.

Figure 11 shows the force-displacement curves of the B and EMS configuration (respectively without infill and with equivalent strut), together with the monotonic envelopes of the cyclic responses obtained by tests carried out on both specimens of the S1B sample.

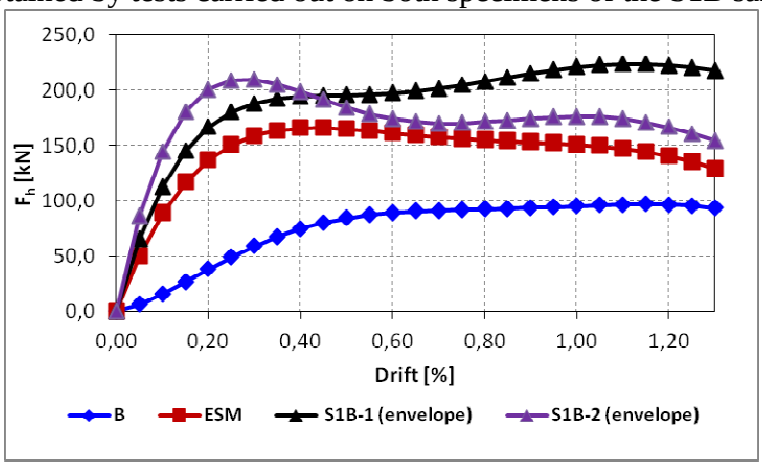


Figure 11 - Comparison between numerical and experimental capacity curves

The comparison shows the expected increases in resistance due to the contribution of the infill. In order to quantify this increase, the following *incremental factor* is defined:

$$\delta_S{}^{(i)} = \frac{F_h^{(i)}}{F_h^{(B)}} \tag{3}$$

with the *i* apix for indicating the *i*-th curve reported in the comparison.

The function $\delta_S = \delta_S(drift)$ for the S1B sample (intended as the function of the average between the increments of both specimens) and for the *Equivalent Strut Model* (EMS) are inversely proportional to the increase of drift. Specifically, starting from a drift about of *0.4%*, i.e. when the specimens still show an elastic behaviour, the increases of the strength than the bare frame, are constant and tend to value equal to 2. The average percentage error in assessing the response of the S1B sample with the ESM model is above 21%

5 CONCLUSIONS

It should be highlighted some aspects which characterize the whole conceptual framework of the proposed procedure.

- The definition of the constitutive laws of the springs is essential to achieve similar results to those observed experimentally. The use of the simplified modelling RBSM, and of the entire procedure proposed, is more reliable if the initial data relating to the mechanical parameters of the materials are sufficiently detailed (elastic modulus, compressive strength ...). The degree of reliability increases further when the above parameters are derived directly from experimental laboratory tests on specimens preliminarily packaged for the purpose (tests on walls), as well as observed in the case study.
- The calibration of the simplified model RBSM becomes less "reliable" when are little the information about the mechanical properties and resistance parameters of the infill walls. In particular, it is more difficult to define the laws of the springs. The springs greatly influence the results obtained by the procedure, therefore, if the information required for their definition are few and uncertain, definitely has an impact on the model.
- The results obtained, both preliminarily on the RBSM in its simplified form, both on the model with equivalent strut, show the significant contribution in strength provided by infills.

ACKNOWLEDGEMENTS

The research presented in this article was partially funded by the Department of Civil Protection, Project ReLUIS-DPC 2014-2018

REFERENCES

[1] P.G. Asteris, S.T. Antoniou, D.S. Sophianopoulos, C.Z. Chrysostomou, Mathematical macromodelling of infilled frames: state of the art. *Journal of Structural Engineering*, **137**(12), 1508–1517, 2011.

[2] P.G. Asteris, D.M. Cotsovos, C.Z. Chrysostomou, A. Mohebkhah, G.K. Al-Chaar, Mathematical micromodeling of infilled frames: state of the art. *Engineering Structures*, **56**, 1905–1921, 2013.

[3] F. Porco, A. Fiore, S. Casolo. Comparison between seismic retrofitting solutions for existing reinforced concrete buildings: a case study. *International Journal of Structural Engineering*, **5**(3),242-261, 2014.

[4] F. Porco, A. Fiore, G. Uva, D. Raffaele. The influence of infilled panels in retrofitting interventions of existing reinforced concrete buildings: a case study. *Structure and Infrastructure Engineering*, **11**(2), 162-175, 2015.

[5] G. Uva, F. Porco, A. Fiore, Appraisal of masonry infill walls effect in the seismic response of RC framed buildings: a case study. *Engeneering Structures*, **34**(1),514–26, 2012.

[6] A. Fiore, F. Porco, D. Raffaele, G. Uva, About the influence of the infill panels over the collapse mechanisms actived under pushover analyses: two case studies. *Soil Dynamics and Earthquake Engineering*, **39**,11-22, 2012.

[7] G. Uva, F. Porco, D. Raffaele, A. Fiore, On the role of equivalent strut models in the seismic assessment of infilled RC buildings. *Engineering Structures*, **42**:83-94, 2012.

[8] A. Fiore, F. Porco, G. Uva, M. Sangirardi. The influence of uncertainties of infill panels relative to the seismic response of RC existing buildings, *Structures Under Shock and Impact*, **13**, 479–490, 2014.

[9] S. Casolo, Modelling in-plane micro-structure of masonry walls by rigid elements. *International Journal of Solids and Structures*, **41**, 3625-3641, 2004.

[10] S. Casolo, Macroscopic modeling of structured materials: Relationship between orthotropic Cosserat continuum and Rigid elements. *International Journal of Solids and Structures*, **43**, 475-496, 2006.

[11] S. Casolo, F. Peña, Rigid element model for in-plane dynamics of masonry walls considering hysteretic behaviour and damage. *Earthquake Engineering & Structural Dynamics*, **36**(8), 1029-1048, 2007.

[12] G. Boffi, S. Casolo, Non-linear dynamic analysis, in Monument 98 - Workshop on Seismic Performance of Monuments, Lisbon: LNEC, 99-108, 1998.

[13] K. Naraine, S. Sinha, Cyclic behavior of brick masonry under biaxial compression. *Journal of Structural Engineering* ASCE 117:5, 1336–1355, 1991.

[14] L. Binda, G. Gatti, G. Mangano, C. Poggi, G. Sacchi Landriani, The collapse of the civic tower of Pavia: a survey of the materials and structure. *Masonry International* **6**:1, 11–20, 1992.

[15] A. Anthoine, G. Magenes, G. Magonette, Shear compression testing and analysis of brick masonry walls, pp. 1657–1662 in Proceeding of the *10th European Conference on Earthquake Engineering*, edited by G. Duma, A. A. Balkema, Rotterdam, 1995.

[16] FEMA. (1997). "Nerph guidelines for the seismic rehabilitation of buildings." FEMA-273, Washington, DC.

[17] G. Uva, F. Porco, A. Fiore, M. Mezzina, The assessment of structural concretes during construction phases", *Structural Survey*, **32**(3), 189-208, 2014.

[18] F. Porco, G. Uva, A. Fiore, M. Mezzina, Assessment of concrete degradation in existing structures: a practical procedure, *Structural Engineering and Mechanics*, 52(4), 701-721, 2014.

[19] P. Morandi, S. Hak, G. Magenes, Comportamento sismico delle tamponature in laterizio in telai in c.a.: definizione dei livelli prestazionali e calibrazione di un modello numerico (in Italian). In Proceeding of *XIV Convegno ANIDIS, L'Ingegneria Sismica in Italia*. Bari, 18-22 Settembre 2011, digilabs di Fiore G. & C. s.a.s., Bari. ISBN/ISSN: 978-88-7522-040-2.

[20] L. Cavaleri, F. Di Trapani. Cyclic response of masonry infilled RC frames: Experimental results and simplified modeling. *Soil Dynamics and Earthquake Engineering* **65**, 224–242, 2014.

[21] L. Cavaleri, F. Di Trapani, G. Macaluso, M. Papia, Attendibilità dei modelli per la valutazione dei moduli elastici delle murature suggeriti dalle norme tecniche (in Italian). Ingegneria Sismica **1**-2012.

COMPDYN 2015
5th ECCOMAS Thematic Conference on
Computational Methods in Structural Dynamics and Earthquake Engineering
M. Papadrakakis, V. Papadopoulos, V. Plevris (eds.)
Crete Island, Greece, 25–27 May 2015

MACRO-MODEL CALIBRATION OF A STRONG CLAY MASONRY INFILL TO IN-PLANE CYCLIC TESTS

Milad A. Oliaee[1], Paolo Morandi[2], and Guido Magenes[2]

[1] ROSE School, IUSS
EUCENTRE, Pavia, Italy
e-mail: milad.oliaee@gmail.com

[2] Department of Civil Engineering and Architecture
University of Pavia, Italy

Keywords: Infills, Seismic Performance, Structural Dynamics, Earthquake Engineering, Macro Model, Calibration, Nonlinear Dynamic Analysis, Nonstructural Components

Abstract. Poor performance of reinforced concrete infilled frame buildings observed in recent post-earthquake reconnaissance may underline a deficiency in our knowledge on the seismic behavior of RC buildings with masonry infills. Past experiments have lacked tests on strong infills recently introduced in modern construction practices in Europe. As the strong typology significantly influences global building behavior, a comprehensive appraisal of the seismic performance for both full and open infill panels will improve our assessment of building performance. A recent experimental campaign on single-story RC frames infilled with a strong masonry typology has been carried out to evaluate and identify drift indices at the damage and ultimate limit state. Calibration of a macro model to the data has improved the accuracy of a macro model for nonlinear dynamic analysis of infilled RC frame buildings. Specific focus on the hysteretic properties of the frame and infill elements in the numerical model has brought significant improvement in accuracy. The need to model local effects has been circumvented by special interpretation of the experimental data. In particular, the infill's effect on the global behavior of the infilled frame subassembly has been extracted by taking comparing the hysteresis of the infilled frame and the bare frame at matching target drifts. The macro model's hysteresis rules are specifically intended for infill struts and have been adjusted for the strong infill typology. A smooth hysteresis closely mimics the tangent stiffness of the reloading and unloading branches to better match energy dissipation, strength, and stiffness. The strength envelope has been modified to account for a post-peak strength plateau exhibited by the strong infill. The results from the parametric optimization may be implemented in nonlinear dynamic analyses with adjustment to existing empirical equations that estimate the strut properties per the masonry characterization.

1 INTRODUCTION

Macro models capture the global response of masonry infills by reducing the number and complexity of finite elements required to obtain accurate numerical results, particularly for nonlinear dynamic modeling. The infill strut calibration serves as an opportunity to best match the experiment subassembly and extrapolate the results to other geometries in a real building model. Because the strong masonry infill overwhelmingly participates in the building response, special attention has been given to strength properties and hysteretic parameters to capture the net effect of the infill on the global seismic performance. For that purpose, the macro model has been optimized to determine the characteristics of the strong infill to be included in the performance-based design and assessment of buildings.

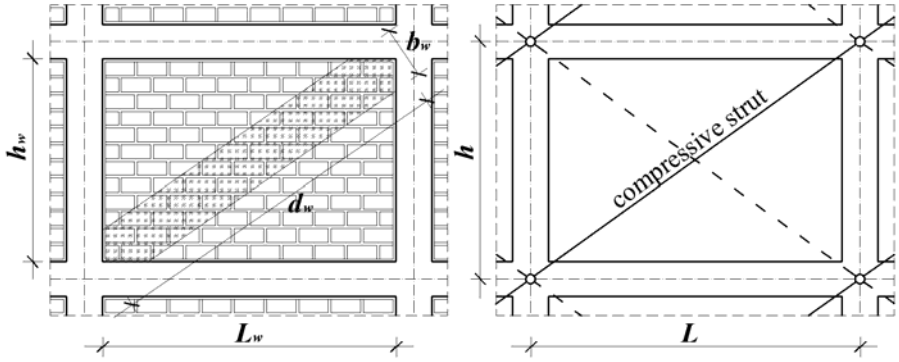


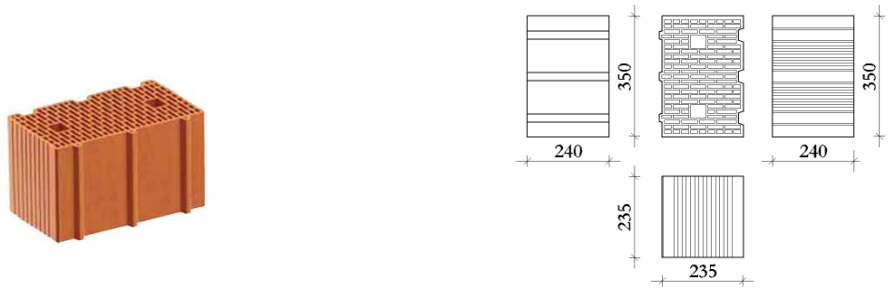
Figure 1: Equivalent diagonal single-strut model.

In general, the strength, energy dissipation and stiffness of the response represent important criteria for making modeling decisions. Due to the complexity of the hysteresis rules, the parameters cannot be independently calibrated, and the resulting optimization problem is rendered multivariate and nonlinear. A preliminary trial and error approach was unsatisfactory as the results failed to meet all the objectives of the calibration. Instead numerous combinations of the parameters are evaluated to obtain the best solution by locating the global minimum for an array of error surfaces. That is, the combination of relative error per specific strength, energy dissipation and stiffness criteria.

To reduce the size of the problem, the initial set-up procedure helps to eliminate all but three parameters from the optimization process. During the process, each error criterion is given equal weight. The best combination of parameters with the least error is chosen as the final solution. The error criteria focus on the post-peak region of the cyclic tests where the strong infill typology has demonstrated significant displacement capacity in recent tests [1].

1.1 Experimental Campaign

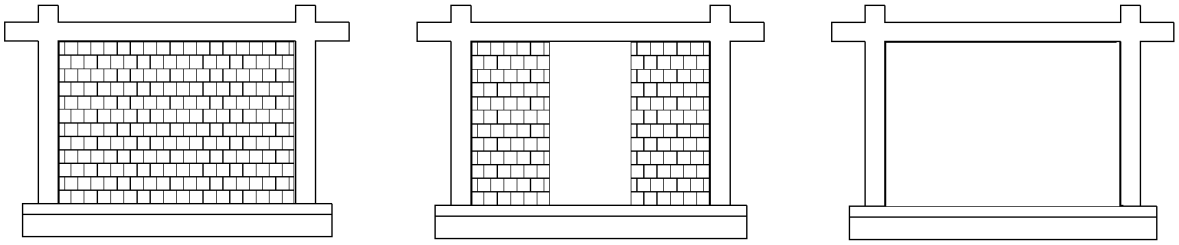
The strong masonry infill typology considered here represents an upper bound of the possible strength & stiffness properties a masonry infill can exhibit. The typology represents a single-leaf unreinforced masonry infill of 35 cm thickness, consisting of vertically hollowed lightweight tongue and groove clay block units, having nominal dimensions of 235 x 350 x 235 mm with a nominal volumetric percentage of holes near 50%. The mortar bed-joints consist of a general purpose mortar type M5 whereas the interlocking head-joints are without mortar. The perimeter of the infill panel has been set in complete contact with the surrounding frame.



(a) (b)

Figure 2: Masonry unit (a) isometric view & (b) profile views with dimensions (mm).

A series of in-plane quasi-static cyclic tests have been carried out on a single-story, single-bay RC frames with a full infill panel, open infill panel, and no infill panel. The freames have been designed according to modern European (and Italian) code provisions.



(a) (b) (c)

Figure 3: Schematic of the a) full infill panel, b) open infill panel and c) bare frame.

Prior to the cyclic tests, a detailed characterization of all material components (i.e., concrete, reinforcing steel, mortar, masonry units and masonry) has been performed [1]. An extensive numerical study on a wide range of infill typologies had hypothesized that a thicker, stronger & stiffer masonry unit could control damage at lower ground motion intensity [2]. The dry tongue and groove joints dry head joints have been known to have significant strength benefits [3].

		Reference Typology	Selected Typology
Masonry unit properties			DANESI Poroton Plan 700 TS
Nominal vertical resistance	[*MPa*]	8.0	8.0
Vertical resistance[1]	[*MPa*]	-	12.9
Horizontal resistance[1]	[*MPa*]	-	2.2
Thickness	[*mm*]	350	350
Height	[*mm*]	230 - 250	235
Percentage of holes	[%]	50 - 55	50
Minimum shell thickness	[*mm*]	4.5 - 5.0	4.8

[1]Preliminary characterization

Table 1: Strong infill masonry unit properties.

Table 1 lists the characterization of the masonry infill typology prior to full scale cyclic tests. During the cyclic tests, a single actuator applies lateral load quasi-statically along the

beam centerline (Figure 4). The end plate remains in contact with the beam cap by the fastening of steel rods to the opposing beam end. The post-tensioning force imparted to the beam varies during each half cycle of loading due to tightening and relaxation of the tendons.

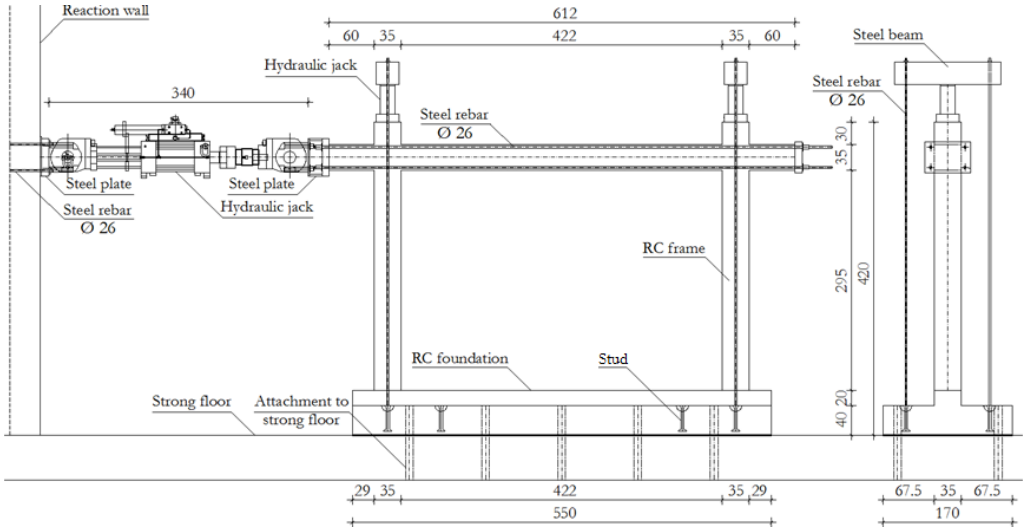


Figure 4: Front & side view of the experiment apparatus mounted on the bare frame specimen.

A comparison of the hysteresis and the average peak envelopes are shown for the fully infilled frame and infilled frame with a one-third bay length opening in Figure 5. The drift indices indicating limit states have been defined according to EC8 and NT8 [4, 5].

Taking into account the infill damage propagation observed during the test, performance levels for a single strong masonry infill with and without the opening have been defined as illustrated in Figure 5. For the infill without an opening, a 0.50% drift index has been assigned for the damage limit state and 1.75% drift index for the ultimate limit state. For the case of the infill with the opening, drift values of 0.35% and 1.0% denote the damage and ultimate limit states, respectively. In both the cases, an operational limit state, equal to 2/3 the damage drift index has been selected in accordance with seismic design provisions but not indicated on the plots.

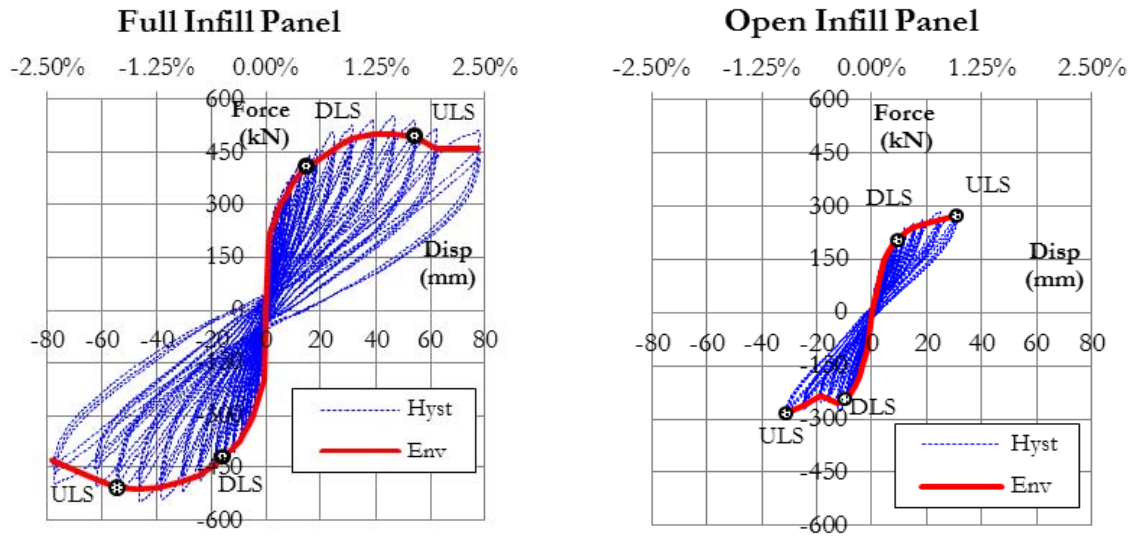


Figure 5: Hysteresis and envelope of the RC frame response with the full infill panel and open infill panel.

1.2 Interpretation of the Experimental Data

With the incentive to reduce the number of parameters during the optimization process, the infill effect's on the bare frame response is extracted by taking the difference between the response of the bare frame and the infilled frame at equal target drifts during the initial calibration procedure. The resulting hysteretic response is not just the shear contribution of the confined infill panel but also the change in the bare frame's response due to the presence of the infill panel.

The single bay specimen has the condition in which the frame members drag strut forces induced by the infill panel at low drift. Likewise for frame members without infills in adjacent bays, the effect of the strut action becomes unbalanced due to the infill bearing load onto the column faces below the joint. These forces offset the neutral axis of the concrete section and alter the plastic moment resisting capacity of the flexural hinges. For this reason, the calibration procedure for the strong infill uses the combined response of the infilled frame in relation to the bare frame response. That way the infill strut doubles to capture the shear contribution of the infill and the change in response from the bare frame as well.

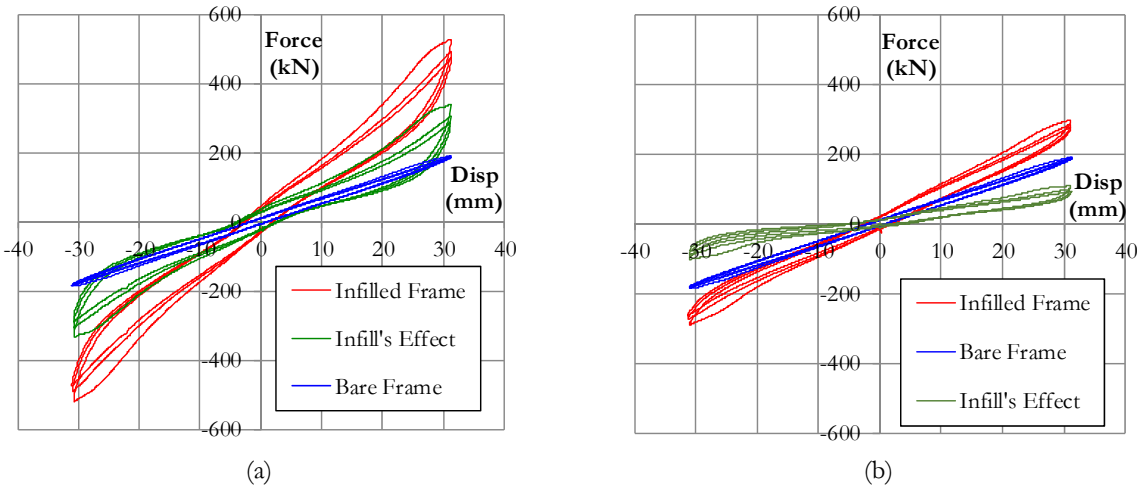


Figure 6: A portion of the hysteretic response of a) the fully infilled frame and b) infilled frame with opening.

Repeated cycles corresponding to one percent drift are shown above in Figure 6 for the two different infill configurations. The net effect of the infill is shown in green. For the fully infilled frame, the infill's effect exceeds the bare frame response and thus dominates resistance to lateral load. The infill with the opening shows less resistance than that of the bare frame.

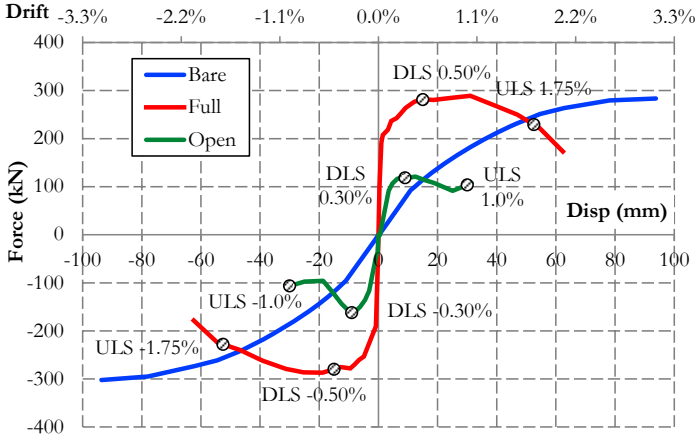
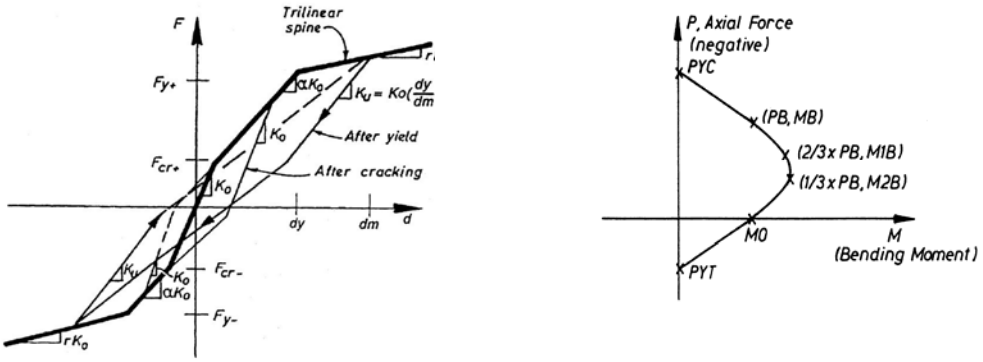


Figure 7: The envelope curves averaging the cyclic peaks of net infill's effect on story shear.

The strength and stiffness of the infill strut ultimately influence the amount of interaction between the bare frame plastic hinges and the strut action of the infill in the numerical model. The envelope of the average peaks for the full and open infill panels with respect to the bare frame are shown above in Figure 7.

1.3 Bare Frame Model Parameters

Before the infill strut parameters are chosen, the beam-column element properties are calibrated to the bare frame response. Because closely spaced stirrups provide confinement along the entire length of the column, the plastic hinge curvature ductility is left unchanged. Perhaps the most important parameters for modeling the RC frame are the axial-moment yield surface and the reduced unloading/reloading rotational stiffness of the hysteretic rules. These parameters dictate the cyclic development of shear resistance by the bare frame in combination with the infill strut.



(a) (b)

Figure 8: The rotational spring hysteresis (a) and the axial force-bending moment interaction surface (b).

The beam-column elements have lumped plasticity offset from each end [6]. The inelastic rotational springs have a trilinear moment-curvature spline. The beam-column yield interaction surface for the concrete connects intermediate points via a cubic spline (see Figure 8). The smooth spline interpolation is advantageous over a straight line interpolation for condition in which the axial force varies widely. The reduced reloading stiffness factor have been set higher than the beams, such the order of hinge formation is not altered.

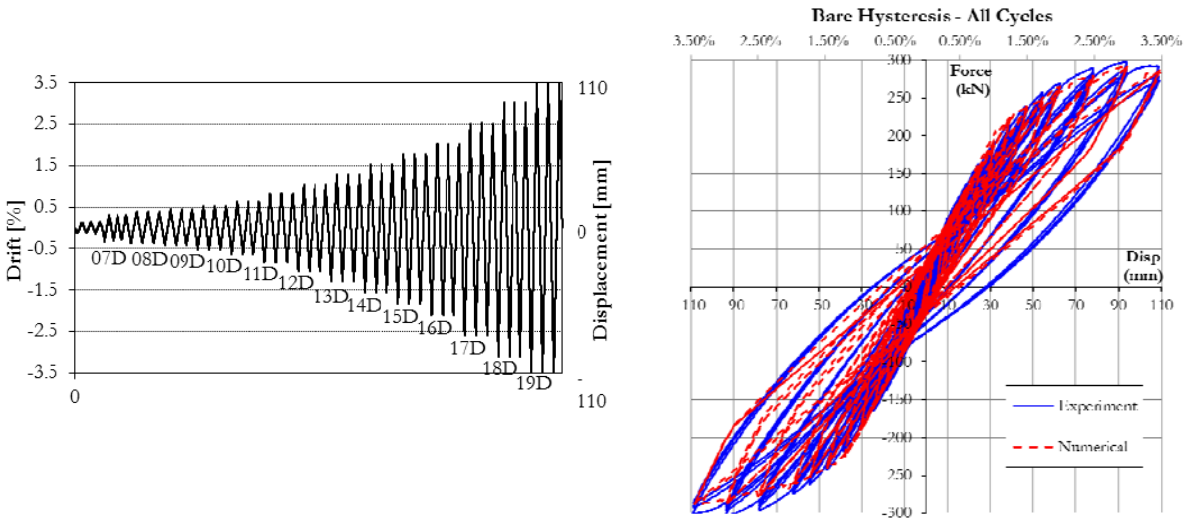


Figure 9: Displacement load history and force-displacement hysteresis of the bare frame test in comparison to the numerical model.

The bare frame model has an elastic prestressed element collinear to the beam element so when the specimen is pushed, the axial compressive force in the beam relaxes. The unloading and reloading stiffness parameters of the modified Takeda hysteresis rules influence the development of shear resistance of the frame [7].

The final values for the reloading parameter, α, are 0.17 for the beam and 0.35 for the column. The values for the unloading parameter, β, are 0.05 for the beam and 0.07 for the column. The values show a good match with the hysteresis backbone and the unloading curves at large deformations (see Figure 9). The target drift labels are shown in the displacement load history plot and they serve as a reference for the drift targets of infilled frame tests also.

1.4 Masonry Infill Model Parameters

The Decanini equations are used to estimate the strength of the infill struts depending on masonry characterization, the infill panel aspect ratio and the beam/column widths [8]. The equations adopt the strut elastic modulus $E_{w\theta}$ and stiffness parameter λ proposed by Stafford Smith [9] but also consider the mode of failures depicted in Figure 10.

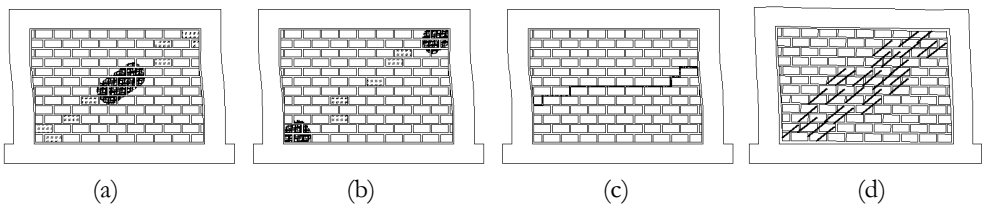


Figure 10: Diagrams for the four failure modes considered by the empirical equations: (a) Compression at the infill panel center, (b) Compression at the infill corners, (c) Sliding shear failure; (d) Diagonal tension failure.

The governing failure mode for the test subassembly is shear sliding failure, presented by Equation 1 below. The strut width for the open infill panel has been reduced according to Seah and Dawe's empirical parameter r_b that reduces the strut area based on the width of the opening [10]. r_b for an opening a third length of the bay reduces the strength to roughly half.

$$\sigma_{w_1} = \frac{(1.2 \cdot sin(\theta) + 0.45 \cdot cos(\theta)) \cdot f_{wu} + 0.3 \cdot \sigma_v}{\frac{b_w}{d_w}} \quad \text{(Shear Sliding)} \tag{1}$$

θ is the inclined angle of the strut, f_{wu} is the strength in shear sliding on a prism test, σ_v is the vertical bearing stress on the panel, b_w is the width of the strut, and d_w is the length of the diagonal. Following the model calibration to the bare frame cyclic tests, the properties of the single-strut macro model are adjusted within the user domain of Ruaumoko with the original Crisafulli hysteresis rules [11, 12]. They are tuned to best match the extracted hysteresis representing the infill shear contribution and the change in the bare frame response due to local effects. Note that during the calibration of the infilled frame, the bare frame parameters remain unchanged.

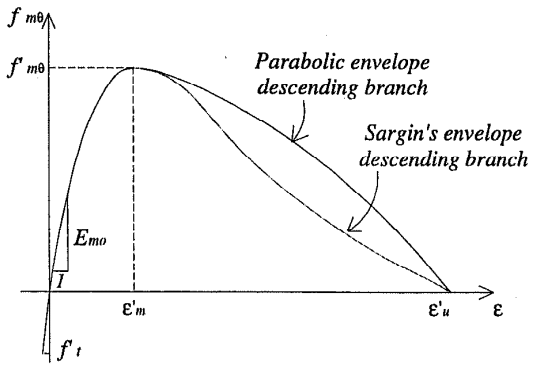


Figure 11: Comparison of the parabolic curve and Sargin's envelope.

The stress-strain constitutive model outlines the backbone that the loading and unloading paths achieve by the hysteresis rules. The original strength envelope is defined by a parabolic common for modeling cementitious materials in uniaxial compression (see Equation 2). Because the strong infill has significant post-peak strength, the alternative strength envelope, Sargin's envelope, is not ideal for the descending branch [13] but instead adopted for the ascending branch. For the descending branch, the parabolic curve is implemented but broadened a large ultimate strain such that a plastic plateau continues beyond peak resistance. For the strong masonry infill, the ultimate strain is set equal to 20 times the peak strength strain.

$$\sigma(\varepsilon) = f_m \left[1 - \left[\frac{(\varepsilon - \varepsilon_m)}{(\varepsilon_u - \varepsilon_m)} \right]^2 \right] \tag{2}$$

f_m is the maximum compressive strength, ε_m is the strain at peak strength, and ε_u is the ultimate strain at no strength. The fully infilled frame has a second plateau in the infill response beyond two percent drift and continuing to the end of the cyclic tests. The most effective way to model such behavior with the current model's platform is to decrease the strut's cross-sectional area via a piece-wise function. The starting and ending strut areas provide for the first and second strength plateaus. In between the plateuas, the intermediate softening branch is linearly interpolated. Figure 12 shows the strut area, material strength, and strut strength.

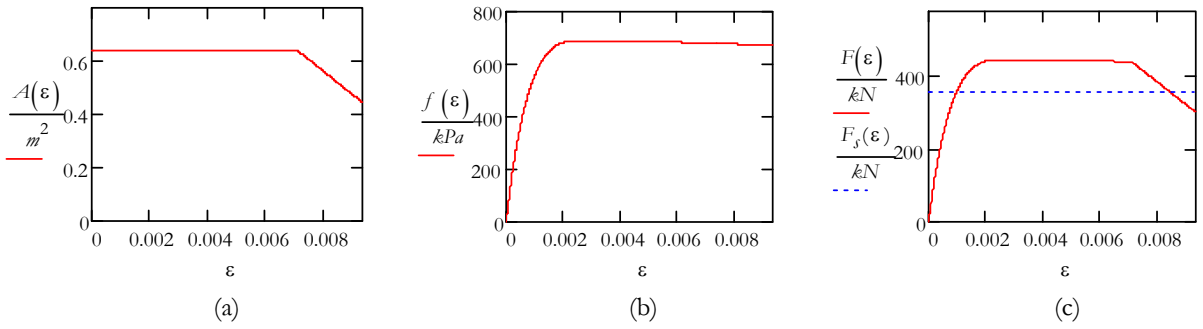


Figure 12: The strut cross-sectional area (a), axial stress (b), and axial force (c) strain relations. The dotted blue line, F_s, marks 80% force degradation.

Before the hysteresis rules are outlined, the function that provides the smooth, curved path for unloading and reloading must be presented. For every change in loading direction of the

strut, a hysteretic rule determines the starting point, ending point, initial tangent modulus, and the final tangent modulus. The values are passed to a smoothening function in the normalized strain domain to interpolate a curve between the two points with matching tangent slopes.

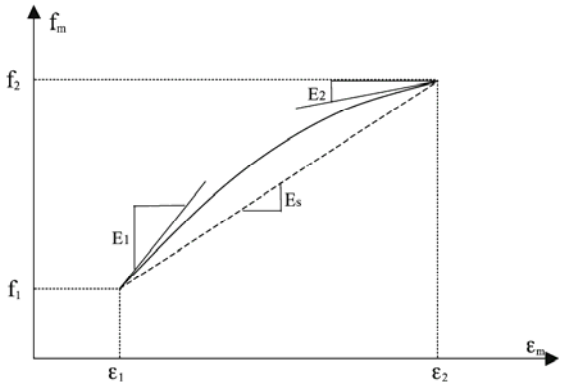


Figure 13: Conceptual plot of the interpolating curve function in the Crisafulli rules.

1.5 Hysteretic Rules

To determine the path dependent unloading and reloading points, there are four basic rules: 1) loading, 2) unloading, 3) reloading before the change point and 4) reloading after the change point. The intermediate change point separates the reloading path. It forecasts reentry to the backbone curve and transforms a convex pre-change point curve at a post-change point concave curve.

The unloading path effectively influences energy dissipation, as it provides the lower bounding edge for the hysteresis loop area. The secant modulus during unloading dictates the reduced stiffness of the strut and, in turn, elongates the transitory period of the structure. The secant unloading stiffness is used to define this effect for large displacements.

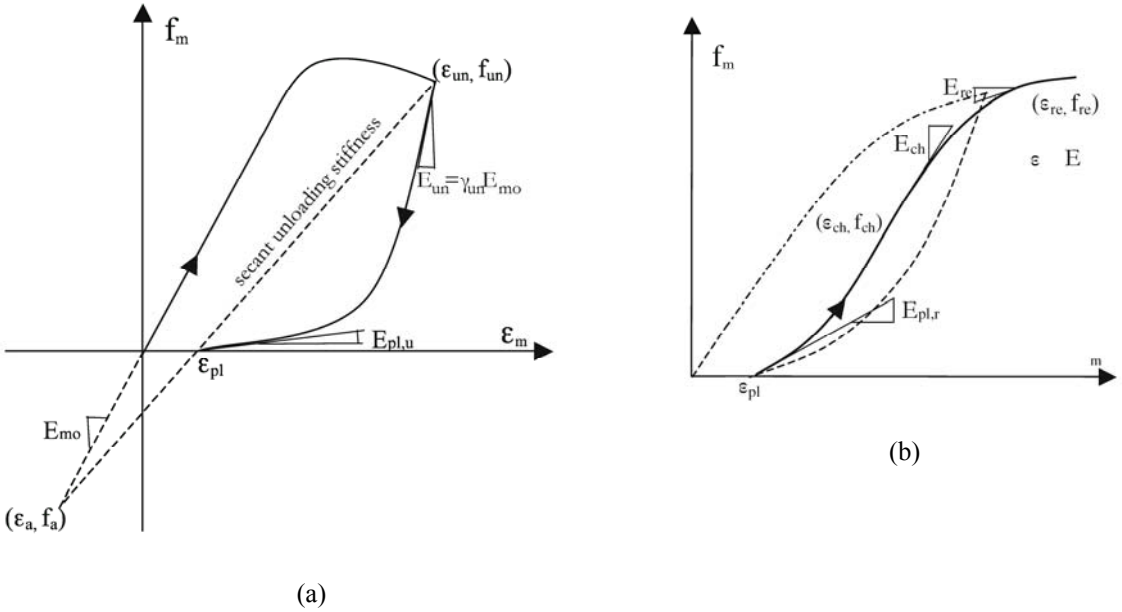


Figure 14: Conceptual plot of the unloading and reloading Crisafulli hysteretic rules.

During reloading, if α_{re} is greater than zero, the cyclic response of the infill strut falls below the virgin envelope by overshooting a reentry strain beyond the original unloading strain.

Thus α_{re} reduces the strength by calculating the strength at a larger strain on the descending branch. Thus the hysteretic loops stagger as cycles undergo increasing strain.

In addition to strength degradation at increasing strain, an empirical counter is implemented to account for in-cycle strength degradation. The repeated cycle counter is raised to a fraction of a power and reduces α_{re} in the denominator such that the cycles with repeated maximum strain have strength degradation also. In summary, the hysteretic rules capture the three basic modes of cyclic deterioration: (1) post-peak strength degradation, (2) reduced reloading stiffness, and (3) deteriorating unloading stiffness.

2 CALIBRATION PROCEDURE

Before optimization, the shape of strength envelope must be identified. The compressive strength of the strut f'_c is set to directly match the Decanini equations while the strut area A_1 is initially set to the maximum shear strength during the cyclic tests. The strain ε'_m is chosen to best represent the knee of the average envelope for the full infill panel, and the strain at peak strength for the open infill panel. The tensile strength of the strut, f_t, may be assumed to be zero. Third, for the strong infill the ultimate strain ε_u should be set to 20 times the strain ε'_m.

For the fully infilled configuration, the drop in strength to the second plateau is estimated by the average envelopes, but anchored by the initial strut area A_1 such that the drop from A_1 to A_2 at axial displacement intervals d_1 and d_2 are fixed and determined before optimization begins. For the open infilled frame, d_2 is taken as the maximum displacement during the cyclic tests. Thus the shape of the backbone remains the same during optimization.

The final parameter set before optimization is the strut elastic modulus E_{mo}. It effects the loading and unloading stiffness in the rules. Optimizing the unloading stiffness for energy dissipation in the post-peak range impedes upon the accuracy of the backbone's initial stiffness, so to compromise the elastic modulus is reduced and unloading stiffness is fine-tuned by the parameter γ_{un} during optimization (see Figure 14a).

The last remaining parameters to be determined during optimization are α_{re}, γ_{un}, and A_1. The initial strut area is included because the numerical average cyclic envelope depend on the combination of α_{re} and A_1. That is, the virgin envelope according to A_1 is reduced by α_{re}, even for the first cycle of each post-peak target drift. A strategy to identify specific attributes of the combined cyclic response has been followed to determine the best combination of parameters according to a set criteria.

2.1 Optimization Criteria

Because the model behavior varies heavily with the hysteresis path, the cyclic response renders typical optimization algorithms impractical. Instead a strategy to target specific attributes of the cyclic response has been created, and criteria help to identify the best combination of parameters. The criteria have a profound effect on the optimization process and should be defined carefully before making decisive modeling decisions.

Force To best quantify the extent to which the model of matches the peak cycles, the peak forces of the response history between the damage and ultimate state drift indices are compared.

$$Env_{err} = \frac{\sum_{i=9D}^{14D} \left(max\left(F_{exp_i}\right) - max\left(F_{num\ i}\right) \right)}{\sum_{i=9D}^{14D} max\left(F_{exp_i}\right)} \tag{3}$$

Energy The sum of the normalized energy dissipation for cycles at matching target drifts of the bare and infilled frames are compared. For the fully infilled frame, there are ten possible target drifts in which the three cycles, positive and negative can be compared. For the open infilled frame, only five. The drift target indices in Equation 4 are specifically for the fully infilled frame.

$$E_{err} = \sum_{i=8D}^{17D} \left[\frac{\sum_{j=1}^{nj-1} \left[\frac{\left(F_{exp\,i,j} - F_{exp\,i,j+1}\right)}{2} \left(d_{i,j} - d_{i,j+1}\right) \right]}{\sum_{i=8D}^{17D} \left[\sum_{j=1}^{rows\left(F_{exp\,i}\right)-1} \left(d_{i,j+1}\right) \right]} - \frac{\sum_{j=1}^{nj-1} \left[\frac{\left(F_{num\,i,j} - F_{num\,i,j+1}\right)}{2} \left(d_{i,j} - d_{i,j+1}\right) \right]}{\sum_{i=8D}^{17D} \left[\sum_{j=1}^{rows\left(F_{num\,i}\right)-1} \left(d_{i,j+1}\right) \right]} \right] \tag{4}$$

Stiffness Finally, the average secant unloading stiffness for each matching cycle of the bare and infilled frames are compared. The secant loading stiffness is defined by a segment between initial unloading and the onset of reloading shown previously in Figure 14. The values of stiffness are compared to the experiment by Equation 5.

$$Stiff_{err} = \frac{\sum_{i=8D}^{17D} \left[\left(K_{exp\,i}\right) - \left(K_{num\,i}\right) \right]}{\sum_{i=8D}^{17D} max\left(K_{exp\,i}\right)} \tag{5}$$

3 RESULTS

The final surfaces for $\gamma_{un} = 7$ with the lowest global minimum error are shown in Figure 15 for the full infill and open infill configurations.

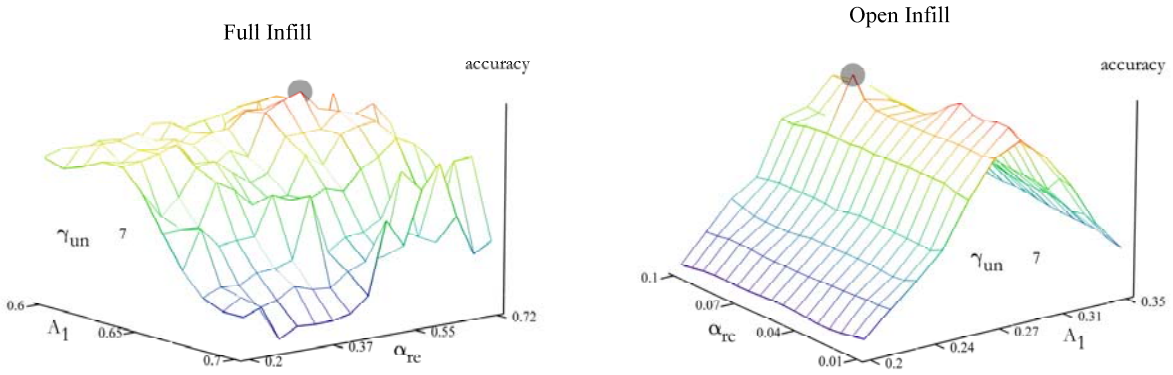


Figure 15: Final inverted error surfaces for the full infill and open infill calibrations.

Each surface represents the combined relative error based on the energy, force and stiffness criteria mentioned. Thus the point indicating the global maximum having the highest accuracy is the best solution. Accuracy is computed as the negative value of the absolute error. The final values for the fully infilled specimen and the infilled frame with opening are shown in Table 2. The results of the optimization concerning γ_{un} match for both the calibrated infill configurations. They indicate the unloading stiffness is controlled by the characteristics of the masonry and not the infill configuration.

Config	Full	Open
f'_c *(kPa)*	688	688
f_t	0	0
ε'_m	$2.10 \cdot 10^{-3}$	$1.63 \cdot 10^{-3}$
ε_u	$44.2 \cdot 10^{-3}$	$32.6 \cdot 10^{-3}$
ε_{cl}	0	0
E_{mo}	97929	97929
γ_{un}	**7**	**7**
α_{re}	**0.55**	**0.09**
A_1 *(m²)*	**0.64**	**0.294**
A_2 *(m²)*	0.4	0.221
d_1 *(mm)*	39.2	22.1
d_2 *(mm)*	52	27

Table 2: Final selection of parameters of the macro models for each configuration with values in bold found by optimization.

Also, the final value A_1 is larger than the original value of A_1 before optimization because α_{re} has reduced the cyclic response. The final parameters chosen following optimization are listed in Table 2 below. For the full infill panel, the optimized strut width complements the "one-third" rule originally proposed by Holmes in 1961 [14].

3.1 Post-Peak Envelope

The numerical and experiment envelopes match well for the fully infilled frame. Figure 16 shows the first cycle and the average peaks for the three cycles. The numerical model slightly overestimates the initial peak strength and underestimates the plateau in the post-peak region. However, the difference is relatively small and the shape of the softening branch is preserved with the exception of the first push cycle, in which there is a small drop in the strength beyond the ultimate limit state. As predicted, the numerical model underestimates the initial stiffness, analogous to the cracked stiffness in the beam-column elements.

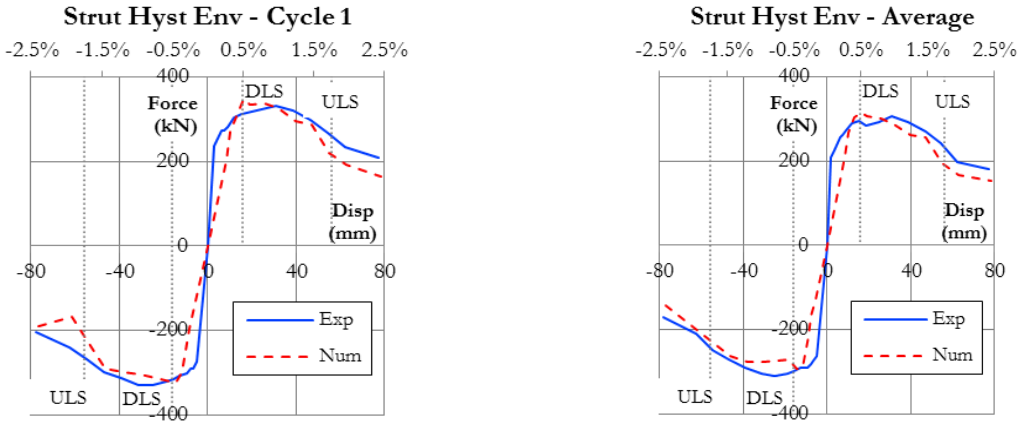


Figure 16: Envelopes of the first cycle and average of the cyclic tests for the full infill configuration.

Matching the envelope for the open infill configuration has been more challenging given the asymmetric response and the short range of experimental data viable for optimization. As seen in Figure 17, a good match has been found for the first cycle, however, the comparison to the experiment average cycles reveals a reduction in strength not captured well by the numerical model for the pull cycles. Although optimization is implemented for the push cycles

only, the pull cycles also agree with the experimental results. This result is coincidental and perhaps explained by the effect of the shape of the hysteretic loops on the energy criteria.

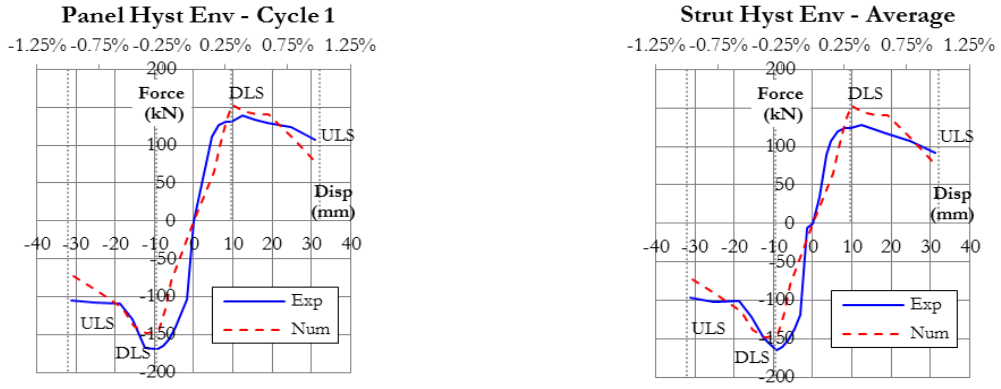


Figure 17: First cycle and average envelope comparison for the open infill configuration.

3.2 In-Cycle Effects at Repeated Drift

An interesting prospect arises when investigating the change in the hysteretic loops across sequential cycles at repetitive matching target drifts. For the fully infilled frame, the approach to the backbone curve changes from a rounded to pointed edge, which would indicate material degradation within the panel occurs only at incremental target drifts. For the cycles within a single target drift, the width of the loops decrease steadily in succession both in the experiment and in the numerical model. Also, by inferring that the unloading stiffness remains unchanged, most of the energy dissipation capacity loss arises from reloading branch cutting into the original loop profile. Because the peak force recedes with every repetition, the length of the loop also decreases, further impacting the net energy dissipation.

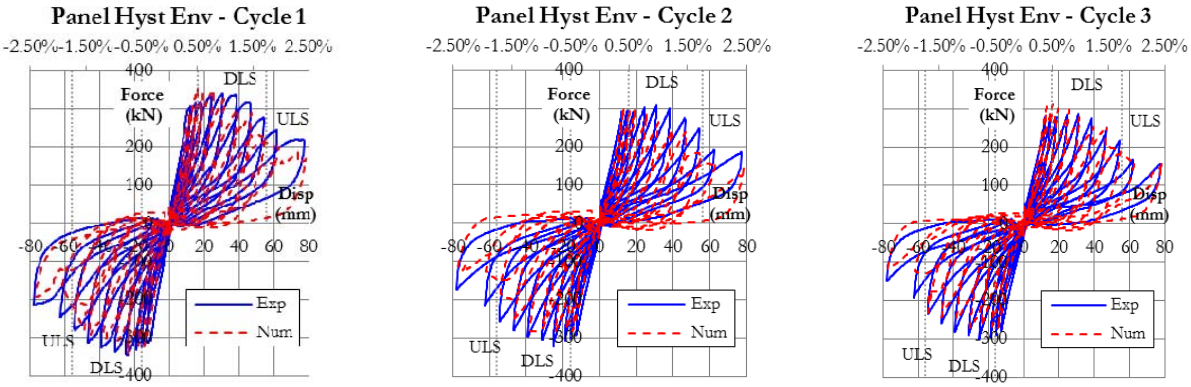


Figure 18: Effect of repeated cycles on the shape of the hysteresis for the full infill configuration.

For the open infill, the bare frame energy dissipation dominates the response following the first cycle, visible by the extreme thinning of hysteresis loops in Figure 19 below for the second and third cycle. The thickness of the loops also thin, denoting a decrease in energy dissipating capacity. There is no criteria set indicating the shape of the loops, but rather only the total area, or the net energy dissipation per cycle.

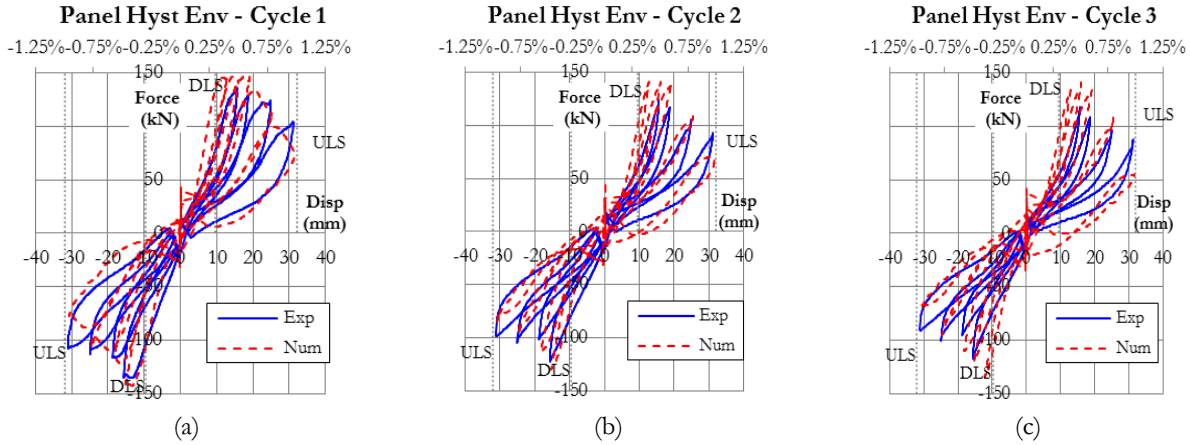


Figure 19: Effect of repeated cycles on the shape of the hysteresis for the open infill configuration.

3.3 Energy Dissipation

The normalized energy dissipation considers the accumulated displacement path during a half cycle. In contrast to viscous damping, hysteretic damping has a maximum effect at maximum deformation.

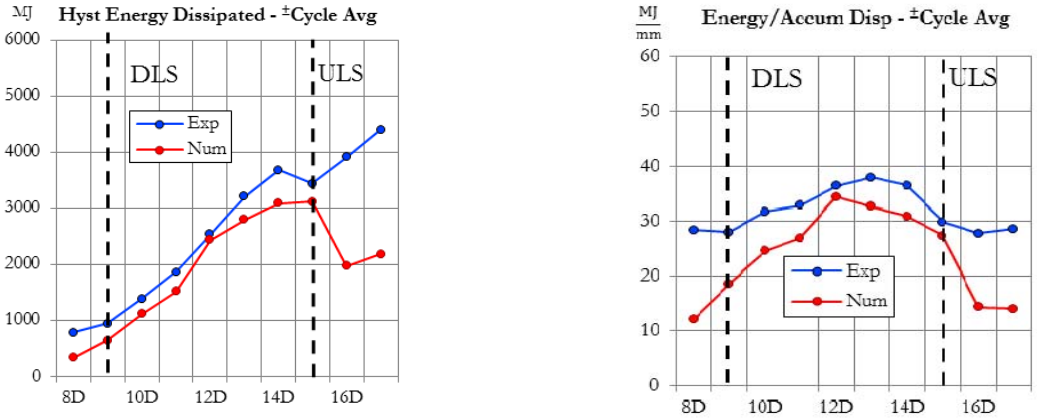


Figure 20: Total (left) and normalized (right) hysteretic energy model comparison, full infill.

The averaged energy dissipation for the full infill configuration shows a good match between the damage and ultimate limit state, although the numerical model consistently underestimates energy dissipation because the reloading branch cannot be adjusted. Consequentially, a compromise is found between the unloading stiffness and the energy dissipated per cycle.

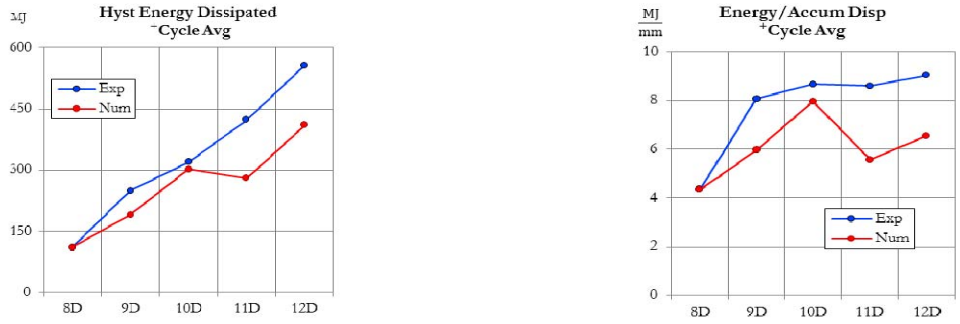


Figure 21: Total (left) and normalized (right) hysteretic energy model comparison, open infill.

Note the drop below the original normalized energy dissipation at the ultimate limit state in Figure 20. The visual damage and initiation of expulsions from the panel observed during testing correlate quantitatively the hysteretic properties of the infill's effect. The open infill hysteretic energy is constantly increasing with target drift for the experiment on the infilled frame with the opening. Unfortunately, the numerical model is unable to capture that behavior well, as a sudden drop occurs at target 11D in Figure 21.

3.4 Stiffness Reduction

The secant unloading stiffness is important and may be indirectly controlled by changing γ_{un}, which effects the sudden drop immediately at the onset of unloading. Figure 22 indicates that γ_{un} should increase with drift, as the numerical model is overestimating the unloading stiffness at smaller displacement cycles.

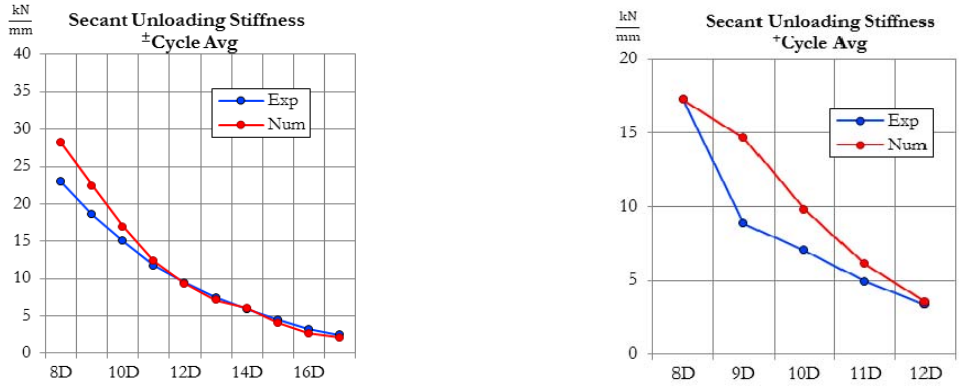


Figure 22: Secant unloading stiffness per cycle for the full and open infill configuration.

3.5 Overview

Figure 23 and 24 convey the sequence of the calibration procedure, from the bare frame model to the strut calibration and finally to the final combined infilled frame response.

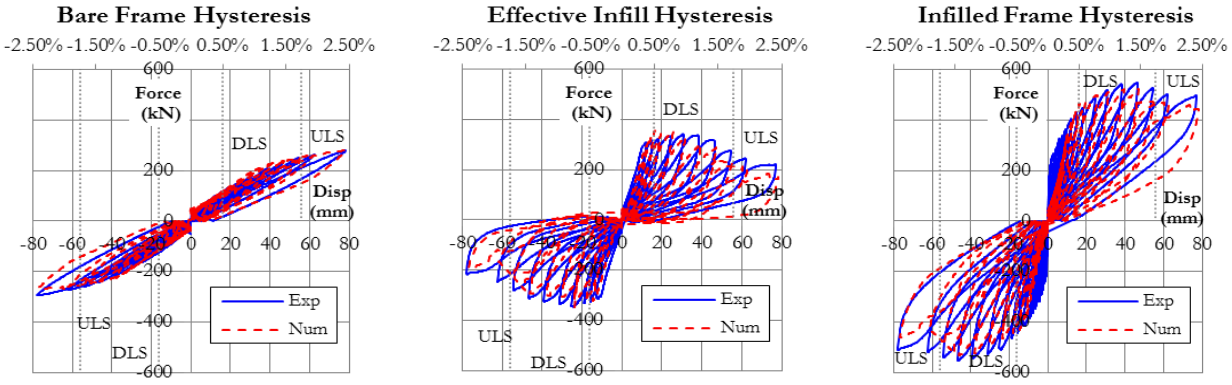


Figure 23: The bare frame, infilled frame and infill hysteresis for the full infill configuration.

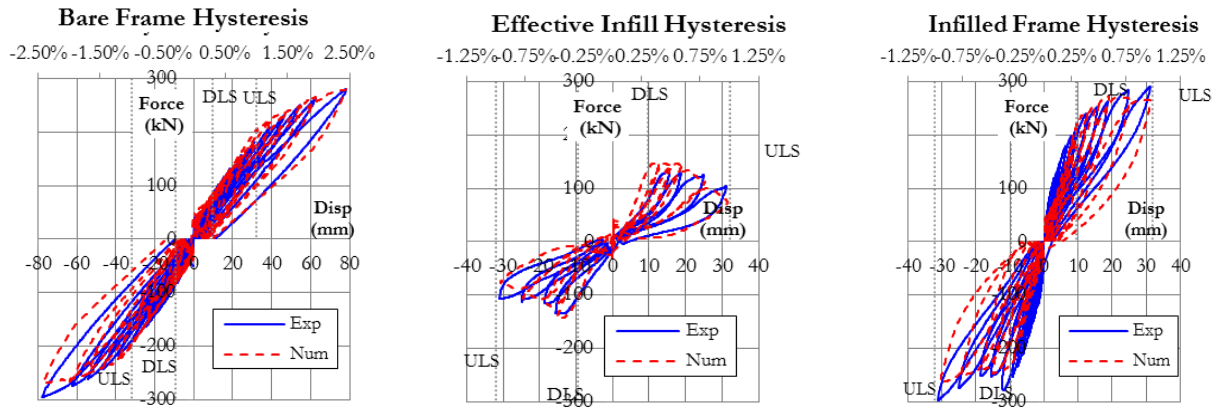


Figure 24: The bare frame, infilled frame, and infill hysteresis for the first cycles of the full and open infill configurations.

4 CONCLUSIONS

The calibration procedure presented focuses on accurately modeling the seismic performance of RC frame buildings infilled with a strong masonry typology. A series of cyclic tests on an RC frame subassembly with a full infill panel, an open infill panel and the infill panel omitted have taken place after a detailed characterization of the masonry. The cyclic testing of the bare and infilled frames at matching target drifts have allowed a unique interpretation of the data to which the single strut has been calibrated. The extracted hysteresis from the data represents the infill shear contribution in addition to changes in the RC frame response. The modeling of local effects has been circumvented by also considering the change in the frame response during the calibration of the strut. The strong masonry infill typology exhibits significant post-peak displacement capacity. The shape of the backbone curve of the uniaxial stress-strain constitutive model has two strength plateaus for the full infill panel.

The shape of the envelopes have been set prior to the optimization of hysteretic and strength parameters. The method uses a set of error criteria to help identify the best combination of parameters without particular bias. The generated error surfaces have been inverted to show the global maximum corresponding to the best accuracy. The final parameters show a good comparison to the full scale tests and can be applied to other frame geometries by extrapolating the parameters with adjustment to the empirical equations for consideration of the strong infill typology.

REFERENCES

[1] Morandi, P., Hak, S., and Magenes, G. (2014). In-plane experimental response of strong masonry infills. *International Masonry Conference.* Guimaraes: International Masonry Society.

[2] Hak, S., Morandi, P., Magenes, G., Sullivan, T. (2012). "Damage control for clay masonry infills in the design of RC frame structures," Journal of Earthquake Engineering, Vol. 16, S1, pp. 1-35.

[3] Maheri, M. R., Najafgholipour, M. Q., and Rajabi, R. (2011). The influece of mortar head joints on the in-plane and out-of-plane seismic strength of brick masonry walls. *Transactions of Civil and Environmental Engineering*, *35*, pp. 63-79.

[4] CEN (2004a). *Eurocode 8.* Brussels, Belgium: EN 1998-1, European Committee for Standardisation, ENV 1996-1-1.

[5] NTC08 (2008). *Norme tecniche per le costuzioni.* Rome, Italy: Ministero delle Infrastrutture.

[6] Giberson, M.F. (1967) "The response of nonlinear multi-story structures subjected to earthquake excitation," *EERL Report*, California Institute of Technology, Pasadena, California.

[7] Fukada, Y. (1969). Study on the restoring force characteristics of reinforced concrete buildings (in Japanese), Proceedings, Kanto District Symposium, Architectural Institute of Japan, Tokyo, Japan, No. 40.

[8] Stafford Smith, B. "Behavior of square infilled frames", ASCE Proceedings, February 1966, pg. 381-403.

[9] Dawe, J. L., and Seah, C. K. (1988). Lateral load resistance of masonry panels in flexible steel frames. *Proc. 8th International Brick and Block Masonry Conference.* Dublin, Ireland.

[10] Carr, A. J. (2007). *Ruamoko Manual.* University of Cantebury, Christchurch, New Zealand.

[11] Crisafulli, F. J. (1997). Seismic Behavior of Reinforced Concrete Structures with Masonry Infills. PhD Thesis. University of Cantebury, Christchurch, New Zealand.

[12] Sargin M., Ghosh S.K., Handa V.K. (1971) Effects of lateral reinforcement upon the strength and deformation properties of concrete. Mag Concr Res 23(75–76):99–110

[13] Holmes, M. (1961). Steel frames with brickwork and concrete filling. *Proceedings of the Institute of Civil Engineers*, pp. 473-478.

COMPDYN 2015
5th ECCOMAS Thematic Conference on
Computational Methods in Structural Dynamics and Earthquake Engineering
M. Papadrakakis, V. Papadopoulos, V. Plevris (eds.)
Crete Island, Greece, 25–27 May 2015

SHEAR HYSTERESIS MODEL FOR REINFORCED CONCRETE ELEMENTS INCLUDING THE POST-PEAK RANGE

Dimitrios K. Zimos[1], **Panagiotis E. Mergos**[1], **and Andreas J. Kappos**[1]

[1] Research Centre for Civil Engineering Structures, City University London
Northampton Square, London EC1V 0HB
e-mail: { Dimitrios.Zimos.1, Panagiotis.Mergos.1, Andreas.Kappos.1 }@city.ac.uk

Keywords: Earthquake Engineering, Non-ductile Reinforced Concrete Elements, Shear Hysteretic Behaviour, Post-Peak Response, Shear Failure, Loss of Axial Load Bearing Capacity.

Abstract. *Reinforced concrete (R/C) buildings designed according to older seismic codes represent a large part of the total building stock; hence, it is important to accurately and efficiently assess their response to actions induced by natural hazards, such as earthquake. Substandard R/C structural elements are prone to shear failure subsequent, or even prior, to yielding of their longitudinal reinforcement. This can potentially lead to loss of axial load bearing capacity of vertical elements and initiate progressive collapse of the building.*

So far, there have been efforts to model the full-range behaviour of such elements following a macro-modelling approach, usually based on quite a limited amount of experimental results, especially with respect to the post-peak part of their response, and adopting assumptions that are not entirely appropriate.

In the present study, an extensive database of shear and flexure-shear critical rectangular R/C columns has been compiled, to the purpose of investigating R/C member post-peak response and calibrating the models mentioned below. It includes both monotonic and cyclic tests, the latter constituting the majority, it spans a broad range of design, material and loading parameters and the majority of the specimens have been tested up to axial failure.

A shear macro-model is developed, which is able to capture the full hysteretic behaviour of R/C elements. In addition to the behaviour up to peak shear resistance, an effort is made to properly capture the post-peak response, calibrating an empirical model for the descending branch directly, instead of indirectly defining it through shear and axial failure that has traditionally been the case. The angle of the shear failure plane is an important parameter of this model, hence an empirical relationship has been developed for it, as well. The onset of axial failure constitutes a vital aspect of post-peak response, since it signals the initiation of a process of loss of an individual R/C element's axial load-bearing capacity simultaneously with the redistribution of vertical loads to neighbouring ones; thus, it was also closely examined and empirical models were derived.

1 INTRODUCTION

Reinforced concrete frame buildings designed according to older seismic codes (or even without adhering to any code) represent a large part of the total building stock. Transverse reinforcement in their structural elements is typically inadequate, widely spaced or poorly detailed, rendering them vulnerable to shear failure subsequent, or even prior, to yielding of their longitudinal reinforcement. This can eventually lead to loss of axial load capacity of vertical elements, through disintegration of the poorly confined concrete core and consequent axial load capacity decrease [1], and initiate vertical progressive collapse of a building. This collapse type has been shown through post-earthquake reconnaissance to be the most common reason of R/C frame building collapse, primarily due to failure of columns or beam-column joints [2]. Thus, it would be useful to be able to accurately and efficiently assess their response to earthquake-induced actions. Naturally, in such complex and computationally demanding analyses, especially when an attempt to model progressive collapse is made, the need for a macro-modelling approach of element behaviour arises.

2 CRITICAL REVIEW OF EXISTING MODELS

There have been several studies, especially in the recent years, attempting to model the full-range cyclic behaviour of shear-deficient elements. Some of the best-known models offer reasonable predictions of member response, but this is often not true in the post-peak range. In some cases, the post-peak descending branch is not explicitly considered, i.e. shear failure and axial failure models are calibrated and the descending branch is assumed to be the "connecting line" between these two, falling short of predicting the response measured experimentally (e.g. [3], [4]). Moreover, the shear strength is typically considered zero at the onset of axial failure - although this is not always the case, as will be shown later on, resulting in higher potential deviations. Another model [5] explicitly accounts for the post-peak descending branch, but is not calibrated against experimental results at all, thus being less accurate, as shown through the model verification against experimentally obtained results and noted by the authors; those that consider it directly and are indeed calibrated, are either associated with substantial scatter [6] or they neglect the effect of some critical parameters, such as transverse reinforcement [7]; furthermore, the datasets on which their empirical models were based are quite limited ([6], [7]), largely due to the scarcity of experimental tests of specimens up to the onset of axial failure until recently. Most of these constitutive models are based on inter-storey drift ratio (e.g. [3], [4], [7]), although it has been pointed out that a localised drift ratio (at the shear-damaged region) might be more appropriate, since deformations tend to concentrate at that region after shear failure [8]. Another shortcoming of some models is the consideration of a horizontal residual strength branch without solid experimental basis [6], [9], [10].

One of the most recent and comprehensive member-type models, which however does not cover the behaviour of R/C elements subsequent to the onset of shear failure, is the phenomenological, force-based, spread inelasticity model by Mergos & Kappos [11]–[13]. It is composed of 3 sub-elements, accounting for flexural, shear and anchorage-slip deformations (Figure 1). The shear sub-element primary V-γ curve includes the shear cracking point, the onset of yielding of the transverse reinforcement, where the maximum shear strength is attained, and a horizontal branch, where shear strains increase with constant force up to the onset of shear failure. The curve can be altered according to the flexural deformations in the plastic hinge zones, thus accounting for shear-flexure interaction.

The model was tested against different column specimens, which had failed in flexure, shear or flexure-shear, and adequate correlation was found. A specimen of interest for this

study in particular, i.e. a column specimen typical of buildings with inadequate transverse reinforcement [1], has been analysed using this model [14] and is presented herein. The analytical predictions are shown in Figure 2 along with the experimental results. The comparison with the experimentally observed behaviour up to the point of the onset of shear failure yields good accuracy.

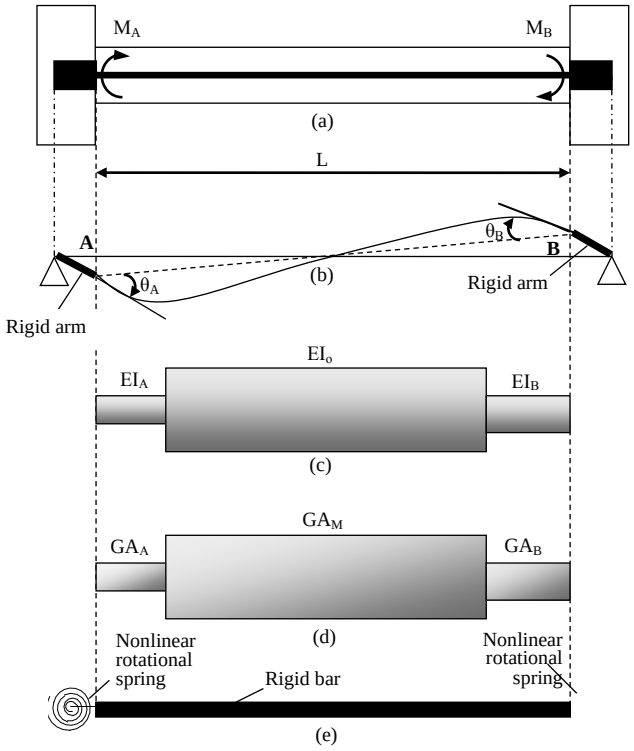


Figure 1: Finite element model: (a) geometry of R/C member; (b) beam–column finite element with rigid offsets; (c) flexural sub-element; (d) shear sub-element; (e) anchorage slip sub-element. [12]

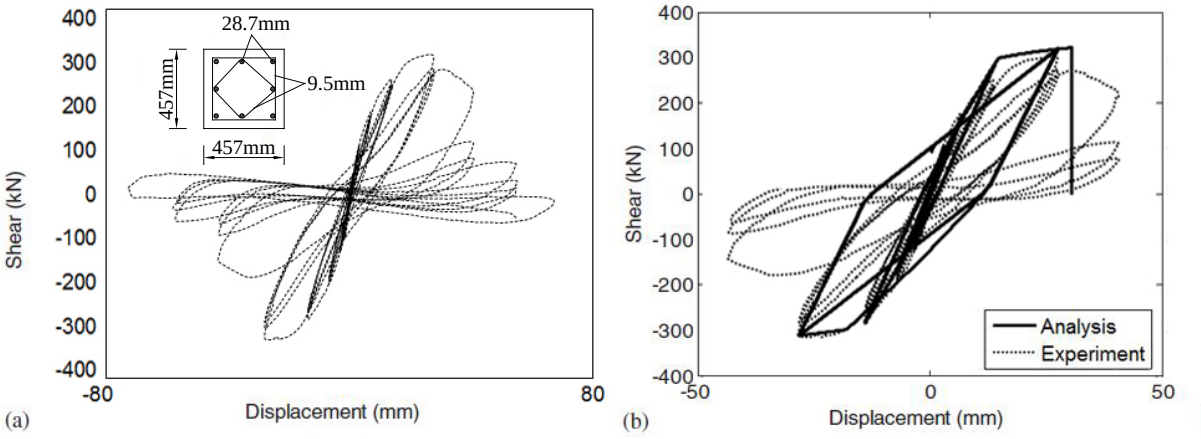


Figure 2: Sezen & Moehle [1] Specimen-1: (a) full lateral load vs total displacement hysteretic behaviour, as obtained from the experimental test; (b) lateral load vs total displacement hysteretic response resulting from analysis compared with the corresponding part of the experimental response [14].

Subsequent to the initiation of shear failure, the model is incapable of capturing the substantial strength degradation and follow the descending part of the response, which extends up to axial failure of the column. However, this part is critical in assessing the behaviour of an existing structure, even more so when it comes to predicting the initiation and cascade of pro-

gressive collapse in a building. Therefore, the primary aim of the present study is to incorporate post-peak shear strength degradation mechanisms to the existing member-type model, with a view to accurately capturing the response of shear-deficient elements up to the onset of axial failure.

3 POST-PEAK RESPONSE MODELLING

3.1 Database compiled

For the investigation of RC element post-peak response and the calibration of subsequent sub-models, a large database of shear and flexure-shear critical elements, which were cycled beyond the onset of shear failure, was compiled. It comprises 150 rectangular R/C columns, 67 of which have sustained flexure-shear failure and 83 failed in shear. Their main characteristics are summarised in Table 1.

	Min	Mean	Max
ρ_l (%)	0.16	2.25	4.76
ρ_w (%)	0.08	0.38	1.59
s/d	0.11	0.44	2.52
L_s/d	0.88	1.94	4.00
$\tau_{ave,max} / \sqrt{f_c}$	0.22	0.57	1.23
v	-0.26	0.26	0.80

Table 1: Main specimen characteristics of the database.

3.2 Modelling approach

The basic assumption adopted is that after the onset of shear or flexure-shear failure, the flexural and slip-induced deformations do not increase further than their values at failure, i.e. all post-peak deformations are localised in the shear sub-element. This assumption has been adopted in similar models (e.g. [4]) and is also experimentally validated through deformation decomposition (e.g. [15], [16]).

Furthermore, it has been observed that after the onset of shear failure, shear deformations tend to concentrate in a specific member region, the 'critical length' [8], [17]; this length is defined by the critical shear crack angle.

Based on the aforementioned assumptions, shear deformations are expressed as:

$$\gamma = \gamma_{sh,f} + \frac{\delta_{pp}}{L_{cr}} = \gamma_{sh,f} + \frac{\delta_{pp}}{h \cot \theta_{sh}} \quad (1)$$

where γ is the average shear strain in the critical zone, $\gamma_{sh,f}$ is the shear strain at the onset of shear failure, δ_{pp} is the post-peak total lateral displacement, L_{cr} is the critical length, h is the height of the section and θ_{sh} is the angle of the critical shear crack (with respect to the member axis).

The axial load capacity degrades with lateral displacement reversals, due to the disintegration of the confined concrete core [1]; the onset of axial failure is defined at the point where capacity and axial load demand become equal. It has long been claimed (e.g. [18]), based on limited amount of experimental data (e.g. [19], [20]), that axial failure occurs when shear

strength degrades to zero (or is at least negligible); many post-peak models have been based on this assumption (e.g. [3], [4]). Nonetheless, this can certainly not be assumed for all specimens. In fact, for some of them it's completely misleading and this can be readily shown in Figure 3, where the lateral strength at the onset of axial failure of the 88 specimens that have sustained axial failure in the database, is shown (normalised to the respective strength at shear failure, to get the residual lateral strength). Apparently, the shear strength of only a fraction of the specimens has degraded below 10% of the maximum strength.

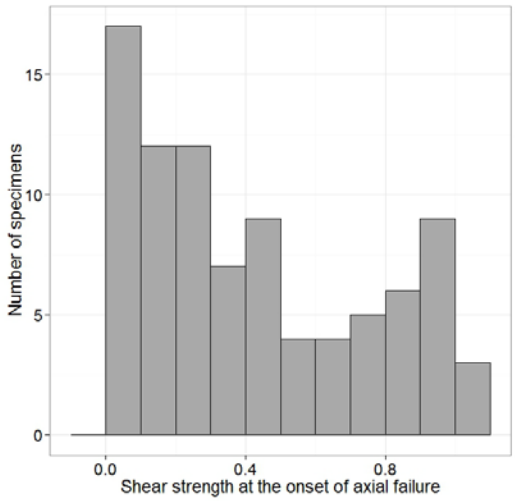


Figure 3: Distribution of the remaining shear strength (normalised by the maximum shear strength) at the onset of axial failure. The ostensibly extraordinary values near 1.00 are due to the inclusion of specimens having undergone simultaneous shear and axial failure.

Consequently, the assumption of zero strength at the onset of axial failure is not verified experimentally and will not be adopted in this model; instead, a displacement-based criterion will be sought. Simultaneously, of course, if the shear strength does indeed degrade to zero before this critical deformation is reached, that point will be considered the onset of axial failure, i.e. shear strength will not be allowed to assume negative values.

3.3 Critical crack angle

The critical shear crack angle has often been assumed independent of column properties (e.g. 45^o) in the process of developing a shear strength or an axial failure displacement model. As this angle affects (through L_{cr}) the modelling of the post-peak part of the shear force vs deformation curve, a realistic estimate of its value would be more appropriate; hence an appropriate model for this angle was sought.

It is first noted that this angle is not the angle of the first shear crack(s) that appear on a specimen along the principal compressive stress trajectories, when the tensile strength of concrete is reached. These can be readily calculated according to structural mechanics principles and result in steeper angles than the experimentally observed ones [8]. The critical shear crack angle corresponds to an idealised failure plane, which forms at or before shear failure and is different to the initial crack inclination.

Statistical analysis was performed on a subset of the database with either a given value of angle, or adequate photographic evidence to measure it directly; the crack angle was measured with respect to the longitudinal axis of the member. In the case of flexure-shear critical members with a fan-shaped crack pattern at the end-region, the steepest one was taken into account - being considered equivalent to the inclination of the crack that would form in the intermediate region without prior development of flexural hinges [21] -, disregarding potential

horizontal parts due to flexural cracking. Furthermore, cracks parallel to the longitudinal axis - usually caused by bond-split of the longitudinal reinforcement - were disregarded. Only double-curvature experiments were taken into account, since the few cantilever ones were observed to develop higher angle values which might not be representative of an actual building column. There were 51 shear critical (S) and 32 flexure-shear critical (FS) specimens satisfying the aforementioned criteria. Based on this dataset, the following patterns emerge (Figure 4):

- In line with structural mechanics principles, increasing axial load ratio (ν) tends to decrease the shear crack angle, since the trajectories of the principal compressive stresses - along which the first shear cracks will form – are oriented closer to the longitudinal axis of the member. The inclination of the shear failure plane, which is investigated herein, seems to have a similar correlation with the axial load ratio, being of course partly dependent on the initial shear cracks' inclination (it is emphasised again, though, that it forms generally at a different angle).
- Transverse reinforcement ratio (ρ_w) has a strong positive correlation with the angle. It is recalled that transverse reinforcement has hardly any influence on the principal stress trajectories prior to shear cracking, hence on the initial crack inclination. However, the angle of interest in the present model apparently includes the propagation of shear crack at varying angles, the angle change being significantly affected by the yielding transverse reinforcement.

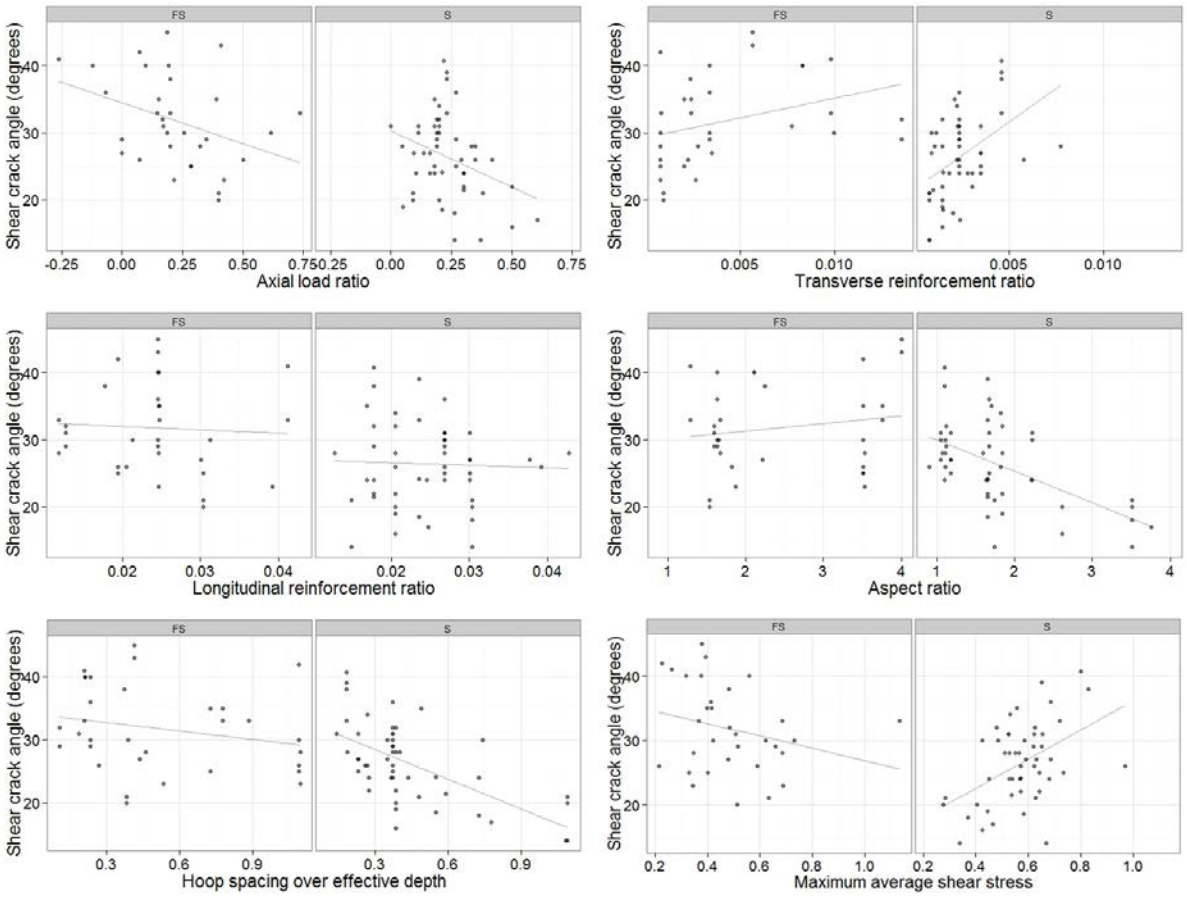


Figure 4: Correlation of the measured angle (in degrees) with axial load ratio (top left), transverse reinforcement ratio (top right), longitudinal reinforcement ratio (centre left), aspect ratio (centre right), hoop spacing over effective depth (bottom left) and maximum average shear stress (bottom right), divided into shear (S) and flexure-shear (FS) critical specimens.

- Longitudinal reinforcement ratio (ρ_l) seems to play no role whatsoever in either case (S or FS). This is consistent with the mechanics of shear cracking and contradicts previous studies (e.g. [21]) that have considered it as one of the main parameters.
- Aspect ratio (L_s/d) has a negative correlation in the case of shear critical elements, as expected, because of the influence on the trajectories of the principal compressive stresses. However, no definite trend was observed in flexure-shear critical elements, so no clear conclusions could be drawn.
- The normalised maximum average shear stress ($\tau_{ave,max} / \sqrt{f_c} = V_{max} / bd\sqrt{f_c}$) in S elements has the expected correlation according to the mechanics of cracking initiation, i.e. the higher the shear stress, the higher the angle. However, in FS specimens, the inverse seems to be the case.
- Hoop spacing over effective depth (s/d) has the inverse correlation of transverse reinforcement ratio, as expected, since the two parameters are highly correlated.
- In general, FS members seem to have higher shear crack angle values, the crack being confined in the end-region of the member that has yielded.
- Other important parameters that influence the shear crack angle, like cross-section shape and loading conditions, were beyond the scope of the current investigation, which was based on a database of only rectangular specimens - mainly square - and included only a double-curvature loading condition with forces acting at the ends of the members.

Existing shear crack angle models were tested against the experimentally measured values (Figure 5), to select an appropriate one to use in the context of the current model. Moharrami et al.'s model [22] is based on structural mechanics principles, hence the resulting angles are much steeper, in line with Elwood & Moehle's remarks [8]; this model was part of the development of a shear strength model, not a shear crack model per se. Chang's model [23] seems to heavily underestimate the angle, as well; probably because it's theoretically derived and not calibrated against experimental results, albeit not predicting the first shear cracks like the previous model. Ousalem et al.'s model [24] produces substantial scatter, largely attributed to the axial load ratio; both low and high values lead to great over- or underestimation, as it was developed based on specimens roughly in the range (0.05, 0.35). The only model which could decently represent the observed angles, is Kim & Mander's [21]. Still, it produces considerable scatter with a mean experimental-to-predicted value of 1.07 and a *CoV* of 23.9%, while it takes into account the longitudinal reinforcement ratio and disregards the effect of the axial load ratio.

Based on the aforementioned trends and significance tests of the predictor variables at a significance level of 5%, various empirical relationships were explored, since no existing model was deemed adequate. The best model developed is the following:

$$\theta_{\min} = \tan^{-1}\frac{h}{2L_s} < \theta_{sh} = \beta\frac{\rho_w^{0.14}}{\sqrt{\nu + 0.9}} < \theta_{\max} = 45^o \quad (2)$$

where β is a parameter that differentiates between shear and flexure-shear critical elements and is equal to 66 for S and 75 for FS elements and ρ_w is introduced with its actual value (not in %). The minimum value is a geometrical limitation of the shear crack applying to columns with a very low aspect ratio, as also explained by Elwood & Moehle [8]. Were this limit not imposed, the angle could be lower than the angle of the diagonal connecting the two ends of the column, essentially leading to an L_{cr} higher than the length of the column itself.

The model (Eq. 2) yields a mean experimental-to-predicted value of 1.00, a median of 0.97 and a Coefficient of Variation (*CoV*) of 19.6% (Figure 6). It applies to specimens in the fol-

lowing range of parameters: $-0.26 \leq v < 0.75$, $0.00 < \rho_w < 1.35$ (%), $1.18 \leq \rho_l \leq 4.28$ (%), $330 \leq f_{yl} \leq 700$ (MPa), $270 \leq f_{yw} \leq 587$ (MPa), $13.5 \leq f_c \leq 86$ (MPa), $0.9 \leq L_s/d \leq 4.0$.

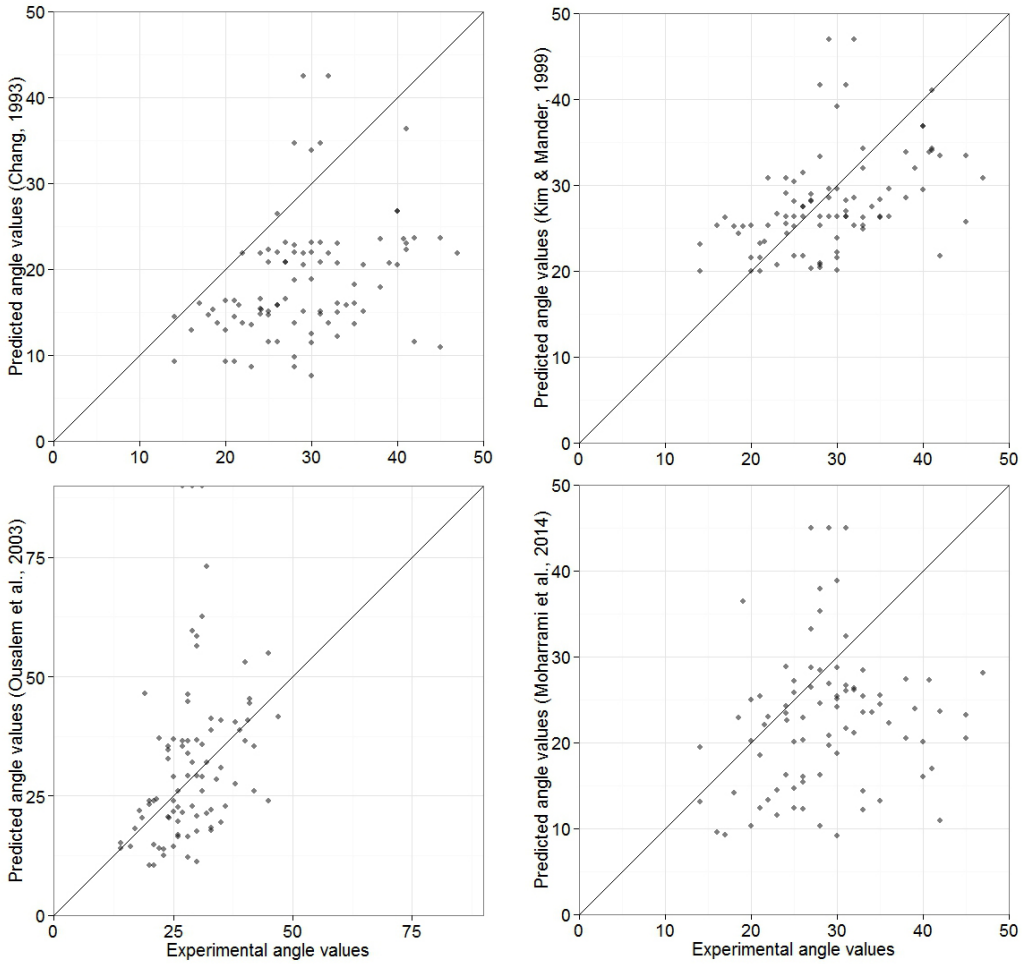


Figure 5: Shear crack angles (in degrees) measured experimentally against the ones calculated according to the predictive models of Chang [23] (top left), Kim & Mander [21] (top right), Ousalem et al. [24] (bottom left) and Moharrami et al. [22] (bottom right).

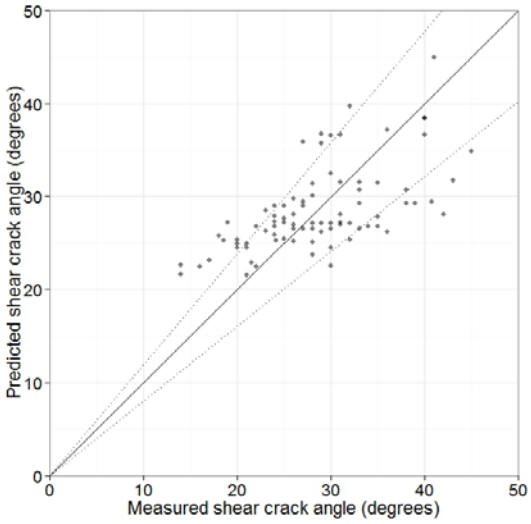


Figure 6: Shear crack angles (in degrees) measured experimentally against the ones calculated by the predictive model (Eq. 2).

3.4 Descending branch

With a view to developing a shear strength degradation model, the appropriate shape of the post-peak branch of the shear force vs deformation curve was investigated. From an observation-based classification, a bi-linear curve with a horizontal branch representing residual strength was a viable option for less than 10% of all specimens. This suggests either that practically no residual strength is developed in R/C members with the characteristics of this database, or that axial failure occurs in most specimens before they reach their residual capacity. Another option could be a non-linear branch, which would have to encompass both concave and convex degradation curves. However, a linear post-peak branch model was pursued, taking into account its simplicity, its compatibility with existing shear behaviour macro-models and its match with the experimental results, with the Coefficient of Determination (R^2) of fitting a linear least-squares line to the experimental post-peak response of each individual specimen of the database having an average value of 0.95 and a Coefficient of Variation (*CoV*) of 7.43%. Thus, the proposed strength degradation model is the following:

$$\frac{V}{V_{\max}} = 1 - S_{pp}(\gamma - \gamma_{sh,f}) \tag{3}$$

where V_{max} is the maximum shear strength that occurs at the onset of shear failure, $\gamma_{sh,f}$ the corresponding shear strain, $\gamma \geq \gamma_{sh,f}$ and $V \leq V_{max}$ the shear strain and strength at any loading level after shear failure and S_{pp} the slope of the post-peak curve, i.e. the rate of shear strength degradation (see Figure 7).

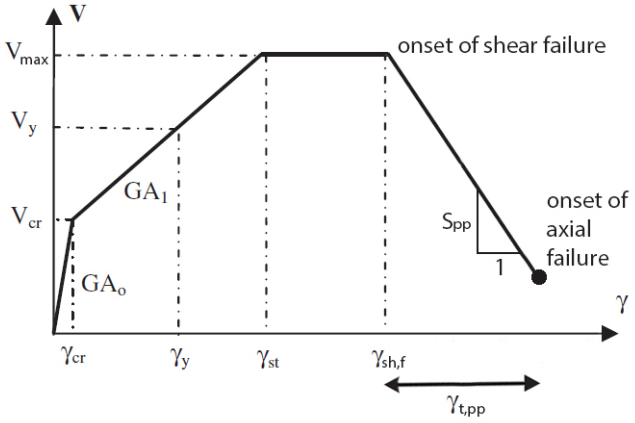


Figure 7: V-γ primary curve including the post-peak range (without shear-flexure interaction).

The post-peak behaviour of specimens with a degradation of at least 30% of V_{max} was considered, in order to obtain a genuine descending branch in the response. Thus, experiments that were conducted up to 85% or 80% of V_{max}, which constituted the overwhelming majority until recently, were excluded. The critical crack angle - for the calculation of the critical length and the normalisation of the lateral displacements - was calculated according to the aforementioned predictive model (Eq. 2). The principal direction, i.e. the direction of shear failure occurrence, was considered only, since the other one is influenced by the preceding shear failure, so it is not necessarily identical to the principal one.

Considering the slope of monotonic and cyclic specimens with various lateral displacement protocols (47 flexure-shear and 71 shear critical specimens) led to excessive scatter; for example, the best models would hardly amount to an R^2 of 0.45 and a *CoV* less than 60%. Furthermore, lumping them all together would lead to confusion between the capacity boundary of monotonic specimens as well as those with large displacement reversals and the cyclic en-

velopes of cyclic specimens with smaller reversals, hence confounding in-cycle with cyclic degradation. It has been pointed out theoretically that these degradation types should be separated (e.g. in FEMA P440A [25]); it was also proven experimentally, for example by observing the apparent difference in the descending branch slope of the identical specimens D13 and D14, which were cycled following different loading protocols [26]. Therefore, it was decided to treat them separately. A fraction of the specimens was selected, which were either monotonic or cyclic with very large lateral displacement reversals (exhibiting apparent in-cycle degradation). These amounted to a total of 28, 18 of which were shear critical and 10 flexure-shear.

Examining the correlation of the descending branch slope (in a curve depicting V/V_{max} vs γ) with design and loading parameters (Figure 8), the following are observed:

- Higher axial load ratio increases the post-peak slope, as has been often noted in similar studies (e.g. [7]). Naturally, it leads to higher stresses along the inclined crack interface, causing faster deterioration of shear resisting mechanisms, albeit increasing shear friction at the same time.
- Higher longitudinal reinforcement is beneficial, decreasing the degradation rate, mainly through the dowel action of the longitudinal bars as well as carrying a - potentially significant - part of the vertical load, hence reducing the damage inflicted on the crack interface during each reversal. Interestingly, the longitudinal reinforcement area normalised by the confined section area gives a better prediction than when normalised by the entire section area, the latter being the usual variable of preference in pre-peak models. This is possibly due to the fact that after the critical shear crack has formed at the onset of shear degradation, the effective area is the confined one, as the unconfined cover concrete either has already failed due to spalling of the section at the member critical length or it does not actively contribute as resistance mechanism, due to substantial reduction in its strength.
- Higher transverse reinforcement is beneficial, as expected, as the transverse steel bars crossing the critical crack are one of the main resistance mechanisms.
- The average diameter of longitudinal bars (normalised by the effective depth, to avoid scaling issues), $\Phi_{l,ave}/d$, seems to play an important role, too. The same longitudinal reinforcement ratio realised through less bars of larger diameter will increase the shear resisted by dowel action.
- Aspect ratio is an important parameter of a member's shear behaviour, but was found not to hold high predictive strength herein. This is due to the fact that shear strains concentrated in the critical length were considered, therefore eliminating the effect of aspect ratio, which is pronounced when taking into account the inter-storey drift ratio (e.g. in [7]).

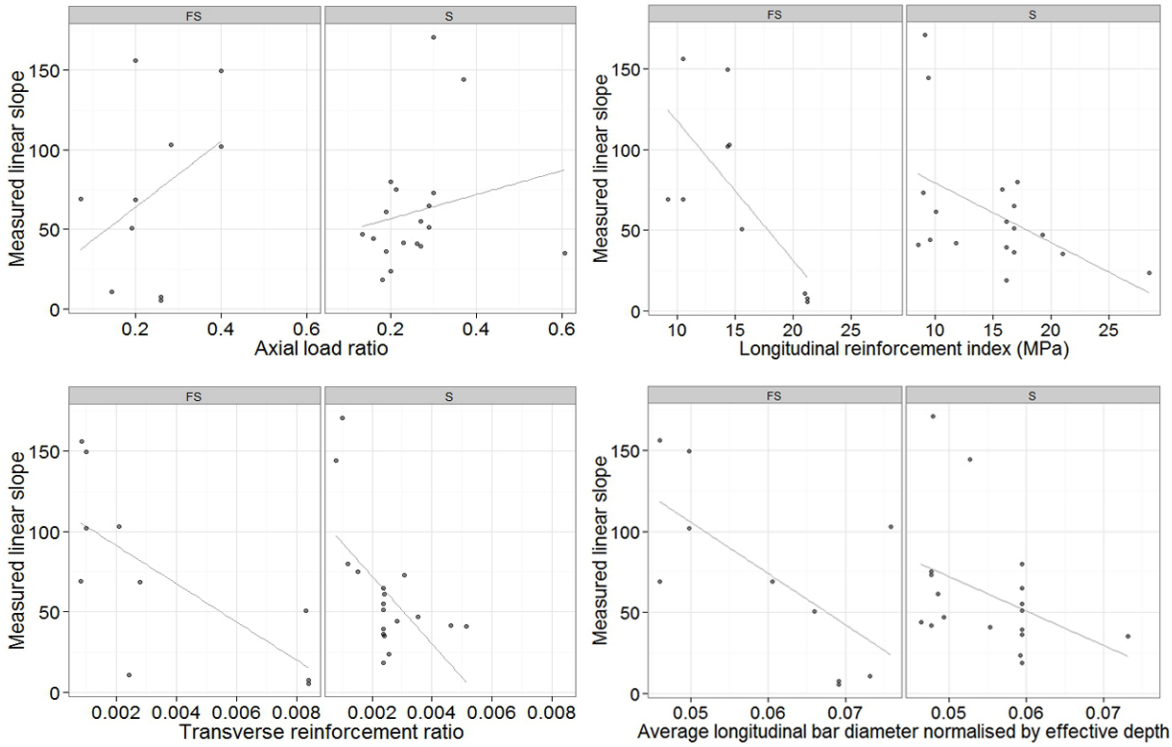


Figure 8: Correlation of the measured slope of the linear post-peak branch with axial load ratio (top left), longitudinal reinforcement index (top right), transverse reinforcement ratio (bottom left), average longitudinal bar diameter normalised to the effective depth (bottom right), for shear (S) and flexure-shear (FS) critical specimens.

Based on these trends and significance tests of the predictor variables at a significance level of 5%, various empirical models were explored. The best predictive model was the following:

$$S_{pp} = 7.36 + \frac{0.28\sqrt{\nu + 0.02}}{\left(\rho_w + 0.0011\right)\left[\frac{\rho_l f_{yl}}{A_{conf,\%}}\left(\frac{\Phi_{l,ave}}{d}\right) + 0.06\right]} \quad (4)$$

where ρ_w and ρ_l are introduced with their actual value (not in %) and f_{yl} in MPa. This model yields an R^2 of 0.82, which is considered quite high, taking into account the high uncertainty inherent in post-peak phenomena (for instance, the effect of experimental set-up and the randomness of the succession of degrading phenomena taking place at a lower level) as well as comparing it with existing models (e.g. R^2 of 0.6 in [6]). The mean experimental-to-predicted value is 1.00 and the median 0.87 (Figure 9). It can be applied to specimens in the ranges: $0.05 \leq \nu \leq 0.60$, $0.00 < \rho_w < 0.85$ (%), $0.045 \leq \Phi_{l,ave}/d \leq 0.075$, $1.50 \leq \rho_l/A_{conf,\%} \leq 4.30$ (%), $330 \leq f_{yl} \leq 700$ (MPa), $270 \leq f_{yw} \leq 587$ (MPa), $13.5 \leq f_c \leq 86$ (MPa), $1.1 \leq L_s/d \leq 3.8$.

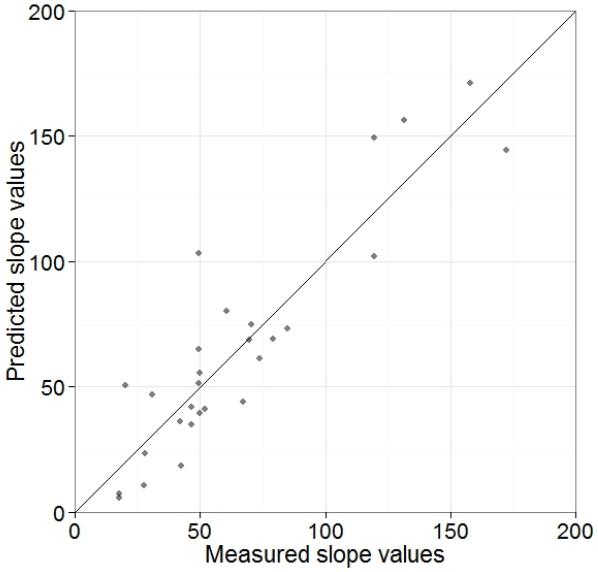


Figure 9: Values of the post-peak descending branch slope (dimensionless) measured experimentally against the ones calculated using the predictive model (Eq. 4).

3.5 Axial failure

Existing models predicting the lateral displacement at the onset of axial failure were applied in this extensive dataset of 88 specimens having sustained axial failure, to find the most accurate one to employ. Nonetheless, their predictive ability was not adequate (Figure 10). Ousalem et al. and Yoshimura models [26], [27] seem to systematically overestimate the lateral displacement. Matamoros & Von Ramin model [28], on the other hand, seems to systematically underestimate it. Elwood & Moehle, Zhu et al., and Wibowo et al. models [7], [8], [29] seem to capture the displacements on average, albeit exhibiting very high scatter. Most of these models ([8], [26], [28], [29]) apply only to flexure-shear critical specimens. Furthermore, all of them but one [7] are based on a rather limited dataset.

Consequently, it was decided to develop a new empirical model that would accurately capture the trends observed in this dataset and would fit with the shear model of this study.The variable chosen to fit the shear model - and because it correlates better with predictive variables - was the following:

$$\gamma_{t,pp} = \frac{\delta_{ax,f} - \delta_{sh,f}}{L_{cr}} \tag{5}$$

where $\gamma_{t,pp}$ is the total post-peak shear strain (see Figure 6), $\delta_{ax,f}$ is the lateral displacement at the onset of axial failure, $\delta_{sh,f}$ is the lateral displacement at the onset of shear failure and L_{cr} is the already mentioned critical length, where shear strains concentrate after the onset of shear failure.

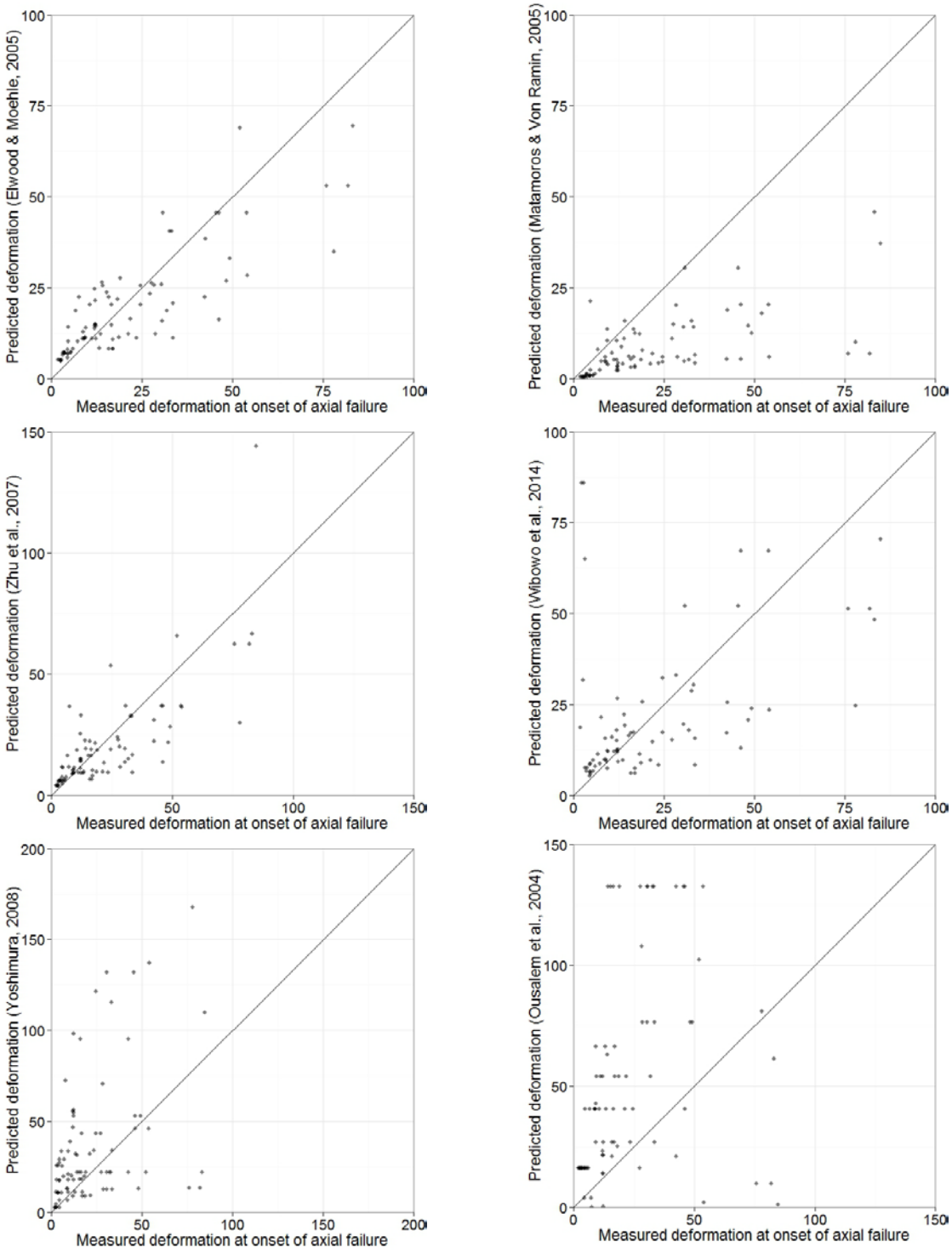


Figure 10: Existing models of lateral displacement at the onset of axial failure applied in the specific database. The measured displacements lie on the horizontal axis, while the predicted ones on the vertical. The plotted line is the "identity" line, i.e. where these two would be exactly equal. The models depicted are: Elwood & Moehle [8] (top left), Matamoros & Von Ramin [28] (top right), Zhu et al. [29] (centre left), Wibowo et al. [7] (centre right), Yoshimura [27] (bottom left) and Ousalem et al. [26] (bottom right).

Examining the correlation of the total post-peak shear strain with design and loading parameters (Figure 11), the following are observed:

- Axial load ratio is a pivotal parameter, decreasing the member's deformability, as has been noted time and time again in similar studies (e.g. [1], [7], [8], [30]). Interestingly enough, the axial load ratio was found much less significant than the longitudinal reinforcement axial load ratio ($\nu_l = P / (A_{sl} f_{yl})$), which was proposed as a predictor in a previous study [19], so the latter was used in model development herein.

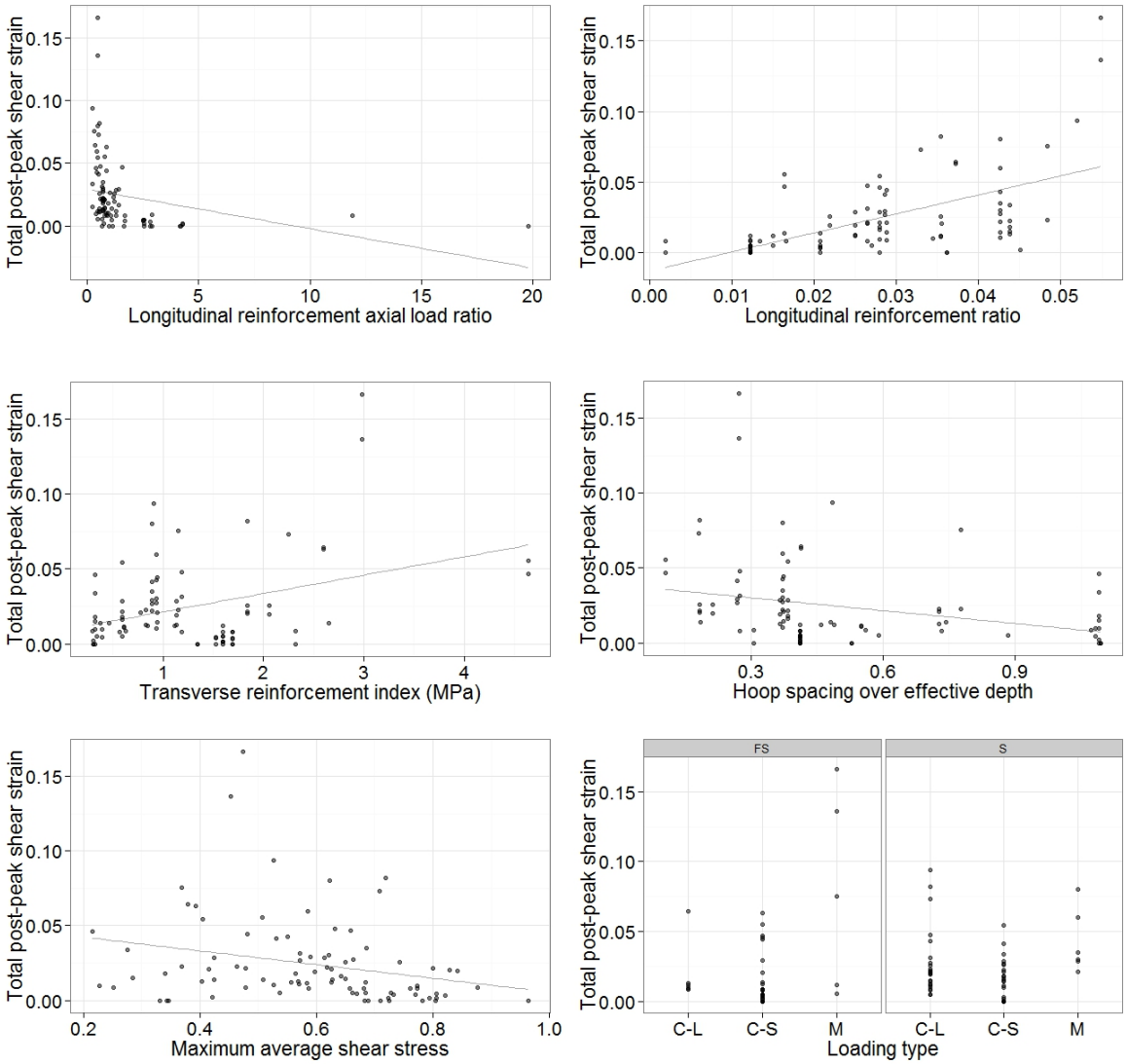


Figure 11: Correlation of the total post-peak shear strain at the onset of axial failure (derived from the experimentally measured values and based on the abovementioned angle model, Eq. 2) with axial load ratio based on the capacity of the longitudinal reinforcement (top left), longitudinal reinforcement ratio divided by the percentage of confined area (top right), transverse reinforcement ratio multiplied by its yield strength (centre left), hoop spacing over effective depth (centre right), maximum average shear stress (bottom left) and the loading type, divided into shear (S) and flexure-shear (FS) critical specimens (bottom right).

- According to these data, it seems that simultaneous shear and axial failure does not necessarily occur when the aforementioned ratio is higher than unity, some of these specimens reaching a total post-peak shear strain of 0.047; however, in specimens with a ratio higher than two, it was in every case less than 0.01 and mostly zero, indicating that this could be an appropriate threshold for certain simultaneous shear and axial failure. However, this should not be the only criterion, since there are even specimens with a ratio

lower than unity, which have experienced such failure. Each of these specimens, though, had a ratio higher than 0.65, in line with observations of a previous study [31].

- Higher longitudinal reinforcement is beneficial, increasing the post-peak deformability, as observed in previous studies [19], [31]. Longitudinal bars take up part of the axial load, partially relieving the confined concrete core from damage inflicted by the displacement reversals. Also, it allows for redistribution of a higher percentage of the axial load from the concrete in later stages.
- Naturally, transverse reinforcement is beneficial, as underlined repeatedly in the past (e.g. [8], [17], [27], [30]). It confines the concrete core, allowing for higher load capacity and takes up a significant part of the shear demand, decreasing the shear strength degradation of the member and the damage inflicted to the core along the shear failure plane.
- Lower hoop spacing decreases the buckling potential of longitudinal bars and increases the confinement of the core, even with constant transverse reinforcement ratio, hence increasing deformability. This has led to appreciating that larger ties at larger spacing lead to lower deformability (e.g. [17]).
- The higher the average shear stress at the point of maximum lateral loading - causing more damage, hence higher degradation -, the lower the achieved deformation at the onset of axial failure, as expected.
- It has been noted several times that monotonic response (M) leads to higher deformability than the cyclic one (e.g. [1], [19]). From the correlations, it seems that also the cyclic specimens with large displacement reversals (C-L), so large that in-cycle degradation is obvious, have also higher deformation capacity, as compared with the ones with small reversals and no in-cycle degradation (C-S). A simplified parameter is introduced herein to account for this effect, in lack of series of experimental tests with various displacement protocols, so as to investigate this issue in depth.
- Flexure-shear critical specimens (FS) seem to exhibit higher deformability on average, when contrasted to shear-critical ones (S).

Based on these trends and significance tests of the predictor variables at a significance level of 5%, various empirical relationships were explored. The best models developed are the following two:

$$\gamma_{t,pp} = 2.2 F_t L_t \frac{\rho_l}{\sqrt{\nu_l A_{conf,\%}}} \sqrt[3]{\frac{\rho_w f_{yw}}{s/d \; f_c}} - 0.005 \geq 0 \tag{6}$$

$$\gamma_{t,pp} = 0.65 \left(\frac{\rho_l}{A_{conf,\%}} \right)^{1.2} \sqrt{\frac{\rho_w f_{yw}}{\nu_l \, s/d \; \tau_{ave,max} / \sqrt{f_c}}} \geq 0 \tag{7}$$

where F_t is a parameter that differentiates between shear and flexure-shear critical elements and is equal to 1 for S and 1.07 for FS elements, L_t is equal to 1 for cyclic displacement protocols and 1.35 for monotonic response and ρ_l, ρ_w are introduced with their actual value (not in %). The first model (Eq. 6) yields a mean experimental-to-predicted value of 1.04, a median of 0.94 and an R^2 of 0.84, while the second one (Eq. 7) 1.02, 1.02 and 0.83 (Figure 12).Both models apply to specimens in the following range of parameters: $0.07 < \nu < 0.66$, $0.00 < \rho_w \leq 1.35$ (%), $0.15 < \rho_l \leq 3.8$ (%), $331 \leq f_{yl} \leq 700$ (MPa), $303 \leq f_{yw} \leq 587$ (MPa), $13.5 \leq f_c \leq 33.6$ (MPa), $1 < L_s/d \leq 4.25$.

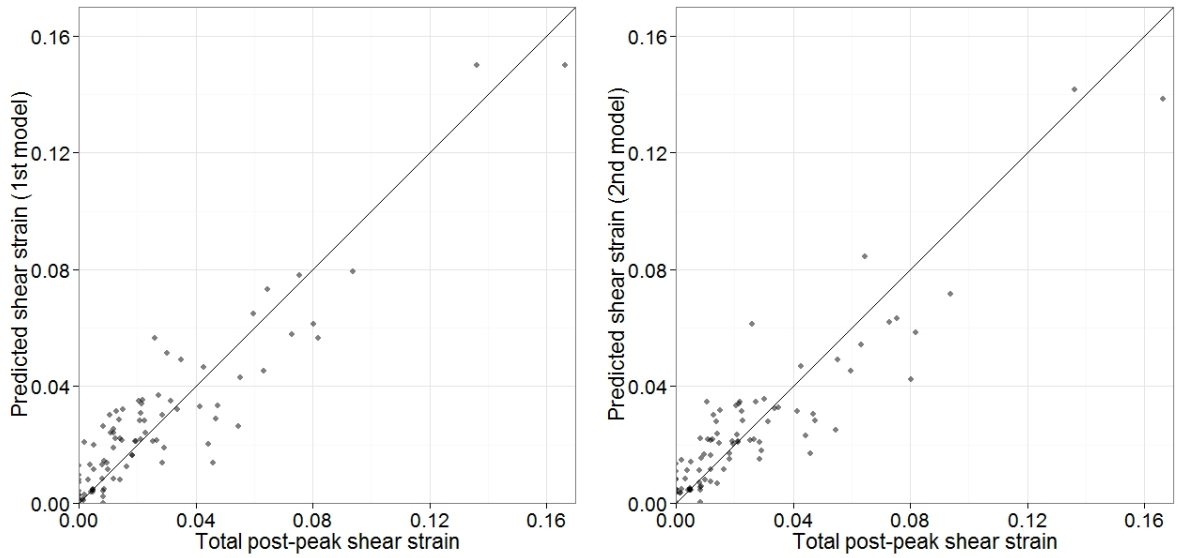


Figure 12: Values of the total post-peak shear strain at the onset of axial failure (derived from the experimentally measured values and based on the abovementioned angle model, Eq. 2) against the ones calculated using the 1st predictive model (Eq. 6) (left) and the 2nd one (Eq. 7) (right).

4 CONCLUSIONS

The post-peak response of shear-deficient members was the focus of this study. This is the core of the effort to extend the capabilities of an existing efficient member-type model [12], with a view to reliably capturing the full-range response of such members. From a rather large database of rectangular shear and flexure-shear critical specimens that was compiled, it was found that the best modelling approach for the post-peak descending branch of the shear force vs deformation curve is a straight line, due to its simplicity, compatibility with other existing models and matching the experimentally determined response.

A predictive model for the critical shear crack angle of an R/C member, which differentiates between shear and flexure-shear critical elements, is put forward. It was found to yield rather accurate predictions and it was used for the development of the subsequent models. Decreasing axial load ratio, as well as increasing transverse reinforcement ratio, lead to an increase in the critical angle, influencing the initiation and propagation of shear cracks, respectively. The longitudinal reinforcement ratio was found to have no effect, despite having been considered influential in previous studies. The change in shear crack propagation as the failure type changes from shear to flexure-shear leads to larger angles in the latter case, as well as inverse correlation of the angle with the aspect ratio and the maximum average shear stress.

A model for the linear degradation rate of shear strength as deformation increases was also developed. It was found to be very accurate, considering monotonic and cyclic specimens with large displacement reversals. Higher transverse and longitudinal reinforcement ratios, longitudinal reinforcement yield strength, and average diameter of longitudinal bars have a beneficial effect, reducing the shear strength degradation rate. On the other hand, increasing axial load ratio leads to more pronounced strength degradation. The aspect ratio does not have a significant effect in this model, largely due to the assumption that post-peak shear strains are concentrated within a critical length, rather than being evenly distributed along the R/C member.

Shear strength has been typically considered zero at the onset of axial failure, due to extensive degradation, based on a limited pool of experimental results. It was demonstrated herein

that this is usually not the case, thus it cannot always be considered a valid assumption. This, of course, does not imply a residual lateral strength during (or after) axial failure; that is a separate matter to be further investigated.

Two alternative predictive models are put forward among those developed for the total post-peak shear strain of an R/C member. They are considered accurate in the context of the phenomenon under study, the latter model being more parsimonious. This strain is found to positively correlate with transverse and longitudinal reinforcement, smaller hoops spaced more closely and lower axial and shear loads. Moreover, members that fail in shear after prior yielding of longitudinal reinforcement, as well as members loaded monotonically or undergoing larger - and fewer - displacement cycles seem to reach higher deformation.

Simultaneous shear and axial failure, a daunting phenomenon in the context of vertical progressive collapse of R/C frame structures, was briefly examined herein. It seems that a longitudinal reinforcement axial load ratio (axial load over longitudinal reinforcement axial capacity) of 0.65 can be considered an appropriate threshold for its occurrence. Conversely, a ratio equal or higher than 2.00 is associated with such failure. The "grey area" in-between should be further investigated for additional appropriate classification criteria.

Accounting for the effect of different cyclic loading protocols on the post-peak degradation of shear strength is a necessary future step, with a view to properly capturing the effect of cyclic (as opposed to in-cycle) degradation of the shear mechanism. Furthermore, considering a potential non-linear post-peak branch of the shear response curve is deemed a worthwhile effort, which might increase the accuracy in the prediction of this phase of the response. A recommended future endeavour would be to conduct a series of experimental tests with various displacement protocols and put forward a parameter to capture properly the damage caused by continuous displacement reversals, including large displacement reversals as well as low-cycle fatigue.

REFERENCES

[1] H. Sezen, J. P. Moehle, Seismic tests of concrete columns with light transverse reinforcement. *ACI Structural Journal*, **103(6)**, 842–849, 2006.

[2] W. M. Ghannoum, J. P. Moehle, Y. Bozorgnia, Analytical Collapse Study of Lightly Confined Reinforced Concrete Frames Subjected to Northridge Earthquake Ground Motions. *Journal of Earthquake Engineering*, **12(7)**, 1105–1119, 2008.

[3] K. J. Elwood, Modelling failures in existing reinforced concrete columns. *Canadian Journal of Civil Engineering*, **31(5)**, 846–859, 2004.

[4] H. Sezen, Shear deformation model for reinforced concrete columns. *Structural Engineering and Mechanics*, **28(1)**, 39–52, 2008.

[5] M. Baradaran-Shoraka, K. J. Elwood, Mechanical Model for Non Ductile Reinforced Concrete Columns. *Journal of Earthquake Engineering*, **17(7)**, 937–957, 2013.

[6] M. R. Leborgne, W. M. Ghannoum, Calibrated analytical element for lateral-strength degradation of reinforced concrete columns. *Engineering Structures*, **81**, 35–48, 2014.

[7] A. Wibowo, J. L. Wilson, N. T. K. Lam, E. F. Gad, Drift performance of lightly reinforced concrete columns. *Engineering Structures*, **59**, 522–535, 2014.

[8] K. J. Elwood, J. P. Moehle, Axial capacity model for shear-damaged columns. *ACI Structural Journal*, **102(4)**, 578–587, 2005.

[9] J. M. Ricles, Y. S. Yang, M. J. N. Priestley, Modeling nonductile R/C columns for seismic analysis of bridges. *Journal of structural engineering*, **124(4)**, 415–425, 1998.

[10] J. A. Pincheira, F. S. Dotiwala, J. T. D'Souza, Seismic analysis of older reinforced concrete columns. *Earthquake Spectra*, **15(2)**, 245–272, 1999.

[11] P. E. Mergos, A. J. Kappos, A distributed shear and flexural flexibility model with shear–flexure interaction for R/C members subjected to seismic loading. *Earthquake Engineering & Structural Dynamics*, **37(12)**, 1349–1370, 2008.

[12] P. E. Mergos, A. J. Kappos, A gradual spread inelasticity model for R/C beam–columns, accounting for flexure, shear and anchorage slip. *Engineering Structures*, **44**, 94–106, 2012.

[13] P. E. Mergos, A. J. Kappos, Damage Analysis of Reinforced Concrete Structures with Substandard Detailing. *Computational Methods in Earthquake Engineering*, **30**, 149–176, 2013.

[14] P. E. Mergos, Assessment of the Seismic Behaviour of Existing Reinforced Concrete Structures. *PhD Thesis*, Aristotle University of Thessaloniki, Thessaloniki, Greece, 2010. (in Greek)

[15] N. Shirai, B. A. Lejano, H. Adachi, M. Nakanishi, Flexure And Shear Behavior Of High Strength Reinforced Concrete Column Subjected To High And Fluctuating Axial Load. *11th World Conference on Earthquake Engineering*, Acapulco, Mexico, 23-28 June, 1996.

[16] M.R. Leborgne, Modeling the Post Shear Failure Behavior of Reinforced Concrete Columns. *PhD Thesis*, The University of Texas at Austin, Austin, Texas, US, 2012.

[17] K. Henkhaus, S. Pujol, J. Ramirez, Axial Failure of Reinforced Concrete Columns Damaged by Shear Reversals. *Journal of structural engineering*, **139(7)**, 1172–1180, 2013.

[18] K. J. Elwood, J. P. Moehle, Shake table tests and analytical studies on the gravity load collapse of reinforced concrete frames. *PEER Report 2003/01*, University of California, Berkeley, US, November, 2003.

[19] M. Yoshimura, T. Nakamura, Axial collapse of reinforced concrete short columns. *The 4th US-Japan Workshop on Performance-Based Earthquake Engineering Methodology for Reinforced Concrete Building Structures, PEER Report 2002/21*, Toba, Japan, 22–24 October, 187–198, 2002.

[20] A. C. Lynn, J. P. Moehle, S. A. Mahin, W. T. Holmes, Seismic Evaluation of Existing Reinforced Concrete Building Columns. *Earthquake Spectra*, **12(4)**, 715–739, 1996.

[21] H. Ousalem, T. Kabeyasawa, A. Tasai, Evaluation of ultimate deformation capacity at axial load collapse of reinforced concrete columns. *13th World Conference on Earthquake Engineering*, Vancouver, British Columbia, Canada, 2004.

[22] J. Kim, J. Mander, Truss modeling of reinforced concrete shear-flexure behavior. *Technical Report MCEER-99-0005*, Buffalo, New York, US, March 8, 1999.

[23] M. Moharrami, I. Koutromanos, M. Panagiotou, Analysis of shear-dominated RC columns using the nonlinear truss analogy. *Earthquake Engineering & Structural Dynamics*, **44(5)**, 677–694, 2014.

[24] G. A. Chang, Seismic Energy Based Damage Analysis of Bridge Columns. *PhD Thesis*, State University of New York, July, 1993.

[25] H. Ousalem, T. Kabeyasawa, A. Tasai, Effect of hysteretic reversals on lateral and axial capacities of reinforced concrete columns. *5th US-Japan Workshop on Performance-Based Earthquake Engineering Methodology for Reinforced Concrete Building Structures, PEER Report 2003/11*, Hakone, Japan, 10–11 September, 211–221, 2003.

[26] Applied Technology Council, Effects of Strength and Stiffness Degradation on Seismic Response. *FEMA P440A*, Washington, D.C, US, June, 2009.

[27] M. Yoshimura, Formulation of Post-Peak Behavior of old Reinforced Concrete Columns until Collpase. *14th World Conference Earthquake Engineering,* Beijing, China, 2008.

[28] A. B. Matamoros, M. Von Ramin, Estimating the Drift Ratio at Axial Load Failure of Reinforced Concrete Columns on the Basis of a Model to Calculate Shear Strength. *1st NEES/E-Defense Workshop on Collapse Simulation of Reinforced Concrete Building Structures, PEER Report 2005/10*, September, 261–274, 2005.

[29] L. Zhu, K. J. Elwood, T. Haukaas, Classification and seismic safety evaluation of existing reinforced concrete columns. *Journal of structural engineering*, **133(9)**, 1316–1330, 2007.

[30] H. Ousalem, T. Kabeyasawa, A. Tasai, Y. Ohsugi, Experimental study on seismic behavior of reinforced concrete columns under constant and variable axial loadings. *Proceedings of the Japan Concrete Institute*, **24(2)**, 229–234, 2002.

[31] A. B. Matamoros, C. Woods, Drift at Axial Failure of R/C Columns Most Vulnerable to Collapse. *Structures Congress 2010*, Orlando, Florida, US, May 12-15, 2010.

COMPDYN 2015
5th ECCOMAS Thematic Conference on
Computational Methods in Structural Dynamics and Earthquake Engineering
M. Papadrakakis, V. Papadopoulos, V. Plevris (eds.)
Crete Island, Greece, 25-27 May 2015

DYNAMIC ANALYSIS OF GRADIENT ELASTIC BEAMS BY FINITE ELEMENTS

Ioannis Pegios[1], Ioannis Dinopoulos[1], Sofia Papargyri-Beskou[1]

[1]Department of Civil Engineering, Aristotle University of Thessaloniki, Thessaloniki GR-54124, Greece

ipegios@civil.auth.gr, intinop@civil.auth.gr, spapargy@civil.auth.gr

Keywords: Gradient Elasic Beams, Finite Element Method, Dynamic Stiffness Matrix, Free Vibrations, Forced Vibrations

Abstract. *The dynamic stiffness matrix of a gradient elastic flexural Bernoulli-Euler beam finite element is analytically constructed with the aid of the basic and governing equations of motion in the frequency domain. The flexural element has one node at every end with three degrees of freedom per node, i.e., the displacement, the slope and the curvature. Use of this dynamic stiffness matrix for a plane system of beams enables one through a finite element analysis to determine its dynamic response to harmonically varying with time external load or the natural frequencies and modal shapes of that system. The response to transient loading is obtained with the aid of Laplace transform with respect to time and the numerical inversion of the transformed solution. Because the exact solution of the governing equation of motion in the frequency domain is used as the displacement function, the resulting dynamic stiffness matrices and the obtained structural responses or natural frequencies and modal shapes are also exact. Two examples are presented to illustrate the method.*

1. INTRODUCTION

Micro-electromechanical systems (MEMS) and nano-electromechanical systems (NEMS), usually modeled by liner elastic bars, beams, plates and shells, have extremely small dimensions and hence their mechanical behavior is significantly affected by their microstructure. Microstructural effects cannot be taken into account by the classical theory of elasticity and one should use generalized or higher-order elasticity theories. These theories are characterized by non-locality of stress and internal length parameters and can take into account microstructural effects in a macroscopic manner.

Among those theories, Mindlin's [1] general theory of elasticity with microstructure and in particular his form II theory associated with the second gradient of strain and consisting of just one constant (internal length) in addition to the other two classical elastic constants, has found many applications in structural analysis of microstructures. This simple theory, usually known as the gradient theory of elasticity, has been successfully used during the last 15 years or so to solve a variety of static and dynamic problem by analytical and numerical methods, as described, e.g., in the recent review article of Tsinoloulos et al [2].

Most of the works on static and dynamic analysis of gradient elastic structures have been devoted to beams. One can mention here the works of Chang Gao [3], Papargyri-Beskou et al [4, 5], Lam et al [6], Giannakopoulos and Stamoulis [7], Kong et al [8] and Papargyri-Beskou and Beskos [9] on gradient elastic Bernoulli- Euler beams and Papargyri- Beskou et al [10], Wang et al [11] Akgoz and Civalek [12], and Triantafyllou and Giannakopoulos [13] on gradient elastic Timoshenko beams. In all these works, the analysis was done by analytic methods and the beams were simple, statically determinate and under simple type of loading.

Problems of static and dynamic analysis of gradient elastic beams and beam structures involving statical indeterminancy, complex type of loading and variable beam cross-sections, cannot be practically solved by analytical methods. Only numerical methods of solution, such as the finite element method (FEM), can be efficiently used for the above type of problems.

Pegios et al [14] have very recently developed a FEM for the static and stability analyses of gradient elastic beams and beam structures by analytically constructing exact element stiffness matrices on the basis of displacement functions, which are the exact solutions of the governing equations of the static and stability problems, as described in Papargyri-Beskou et al [4]. Because use is made of exact stiffness matrices, the structural response is also exact and one can model every beam member by only one finite element, Asiminas and Koumousis [15] have recently constructed stiffness and consistent mass matrices for Bernoulli- Euler beam elements on the basis of the gradient elastic theory of Papargyri-Beskou et al [4] to study static and free vibration problems of simple beams. Their displacement function was the cubic polynomial solution of the classical theory and as a result of that their stiffness and mass matrices are approximate. Kahrobaiyan et al [16] and Zhang et al [17] have also recently constructed stiffness and consistent mass matrices for Bernoulli-Euler and

Timoshenko beam elements, respectively, on the basis of the gradient elastic theory of Lam et al [6]. The displacement function used by Kahrobaiyan et al [16] is the exact solution of the governing equation of equilibrium, while that by Zang et al [17] the classical cube polynomial. As a result of the above, Kahrobaiyan et al [16] have exact stiffness and approximate mass matrices, while Zang et al [17] have both approximate stiffness and mass matrices. Approximate stiffness and/or mass matrices in FEM imply discretization of every member of the structure into 2-4 finite elements for acceptable accuracy.

In this work, the dynamic stiffness matrix of a gradient elastic Bernoulli-Euler beam finite element is analytically / numerically constructed with the aid of the basic and governing equation of flexural motion of that element and its associated boundary conditions as described in Papargyri-Beskou et al [5] in frequency domain. Because the exact solution of the governing equation of motion in the frequency domain is used as the displacement function, the resulting dynamic stiffness matrices and hence the dynamic response to zero or harmonically varying with time forces is the exact one. When the external forces are general transient, the element dynamic stiffness is defined in the transformed with respect to time domain. The problem is then formulated and solved in the transformed domain and the time domain response is finally obtained by a numerical inversion of the transformed solution as described for classical beam structures in Beskos and Narayanam [18]. Thus, the present method is capable of providing the exact solution for both free and forced vibration problems involving gradient elastic beams, in contrast to all the existing methods, which can only provide approximate solutions. Of course, the expressions used in deriving dynamic stiffness matrices are more complicated here than in the other works. However, the discretization here involves only one finite element per physical member instead of 2-4 elements per physical member in all the other methods.

Two examples are presented to illustrate the method and demonstrate its advantages. These examples deal with free and forced vibrations of a gradient elastic cantilever beam.

2. GRADIENT ELASTIC BEAM THEORY

The basic and governing equations of a gradient elastic Bernoulli-Euler beam in bending under dynamic lateral loading as well as the associated classical and nonclassical boundary conditions derived in Papargyri-Beskou et al [5] are reproduced in this section for reasons of completeness and easy reference.

Consider a straight prismatic beam under a dynamic lateral load q(x,t) distributed along the longitudinal axis of the beam, as shown in Fig. 1, where t denotes time. Thus, the loading plane is x-y and the cross-section A of the beam is characterized by the two axes y and z with the former one being its axis of symmetry. Under the lateral load q(x,t), the beam experiences bending vibrations in the x-y plane measured by its lateral deflection u(x,t) along the x axis. Assuming gradient elastic material behavior, one has that the normal to the cross-section

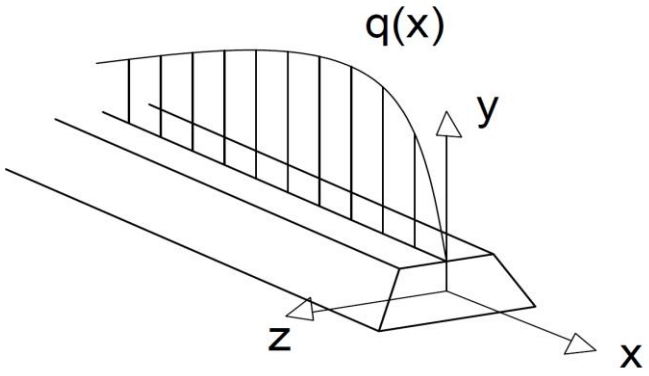


Fig. 1 Geometry and loading of a prismatic beam in bending

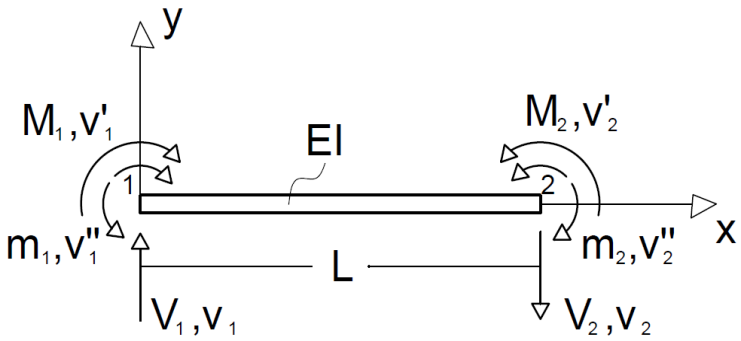


Fig. 2 Mechanics convention for generalized nodal forces and displacements of a gradient elastic flexural beam element in frequency domain.

bending stress σ_x has the form

$$\sigma_x = E\left(\varepsilon_x - g^2 \frac{\partial^2 \varepsilon_x}{\partial x^2}\right) \tag{1}$$

where E is the modulus of elasticity, g is the gradient coefficient with dimensions of length (internal length representing the microstructural effects macroscopically) and ε_x is the normal bending strain expressed as

$$\varepsilon_x = -y \frac{\partial^2 v}{\partial x^2} \tag{2}$$

Utilizing the kinematics of the Bernoulli-Euler theory, the constitutive relation (1) and the dynamic equilibrium of axial forces and bending moments, one can finally

obtain the governing equations of dynamic equilibrium for the gradient elastic beam in terms of the lateral deflection u(x) as [5]

$$EI\left(\frac{\partial^4 v}{\partial x^4} - g^2\frac{\partial^6 v}{\partial x^6}\right) + \mu\frac{\partial^2 v}{\partial t^2} = -q(x,t) \tag{3}$$

where I is the cross-sectional moment of inertia about the z axis and μ the mass per unit length of the beam. The above equation, which is of the sixth degree with respect to x, reduces to the classical one of the fourth degree for g=0.

Assuming that the lateral load q(x,t) varies harmonically with time in the form

$$q(\mathrm{x},\mathrm{t}) = \tilde{q}(\mathrm{x})\,\mathrm{e}^{i\omega t} \tag{4}$$

one has that the deflection $\upsilon(\mathrm{x},\mathrm{t})$ also varies harmonically with time in the form

$$\upsilon(\mathrm{x},\mathrm{t}) = v(\mathrm{x})\,\mathrm{e}^{i\omega t} \tag{5}$$

where $\tilde{q}(\mathrm{x})$ and v(x) represent amplitudes, ω is the circular vibration frequency and $i=\sqrt{-1}$. On account of Eqs (4) and (5), Eq.(3) takes the form

$$v^{IV} - g^2 v^{VI} - a^2 v = \tilde{q}/EI \tag{6}$$

Where primes and overdots indicate differentiation with respect to x and t, respectively and

$$a^2 = \mu\omega^2/EI \tag{7}$$

Equation (6) represents the governing equation of lateral motion in the frequency domain.

If one considers a beam element of length L with its two ends defined by x=0 and x=L, as shown in Fig.2, and makes use of a variational statement, he can recover the governing equation (6) and all possible classical and non-classical boundary conditions so as to satisfy the following equations [5]:

$$[V(L)-EI[v'''(L)-g^2v^V(L)]]\delta v(L)-[V(0)-EI[v'''(0)-g^2v^V(0)]]\delta v(0)=0$$

$$[M(L)-EI[v''(L)-g^2v^{IV}(L)]]\delta v'(L)-[M(0)-EI[v''(0)-g^2v^{IV}(0)]]\delta v'(0)=0$$

$$[m(L)-EIv'''(L)]\delta v''(L)-[m(0)-EIg^2v'''(0)]\delta v''(0)=0 \quad (8)$$

In the above, V is the shear force, M is the bending moment and m is the double moment due to the microstructure, while primes denote derivatives with respect to x. The forces and moments are considered positive as shown in Fig. 2. It is observed that for g=0 Eqs (8) reduce to the corresponding ones for the classical case.

In view of Eqs (8) one can observe that, when dealing with the classical boundary conditions, either the deflection v or the shear forces $V=EI(v'''-g^2v^v)$ and the strain (slope) v' or the bending moments $M=EI(v''-g^2v^{IV})$ at the boundary of the beam have to be specified. For the case of the non-classical boundary conditions, one has to specify either the boundary strain gradient (curvature) v'' or the boundary double moments $m=EIg^2v'''$.

2. GRADIENT ELASTIC DYNAMIC STIFFNESS MATRIX

This section deals with the development of the dynamic stiffness matrix in the frequency domain of a gradient elastic flexural beam element with two nodes 1 and 2 at its two ends, as shown in Fig.3. On the basis of Eqs (8) describing the boundary conditions of the problem, one concludes that there are three nodal generalized displacements (v=displacement, v'=slope, v''=curvature) and three nodal generalized forces (V, M, m) associated with those displacements at every node, as shown in Fig. 3 (matrix convention).

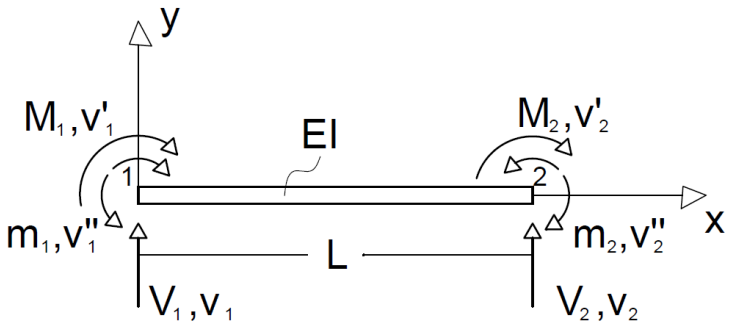


Fig. 3 Matrix convention for generalized nodal forces and displacements of a gradient elastic flexural beam element in frequency domain.

For the construction of the stiffness matrix of the finite element of Fig.3 one needs to select a displacement function and adopt a definition of that matrix. In this work, the displacement function is selected to be the exact solution of the homogeneous part of Eq. (6), which has the form [5]

$$v(x) = \sum_{i=1}^{6} C_i e^{\lambda_i x} \tag{9}$$

where the, in general complex, exponents λ_i are the 6 roots of the algebraic equation

$$\lambda^4 - g^2 \lambda^6 - a^2 = 0 \tag{10}$$

and C_i are constants of integration to be determined. Because use is made of the exact solution of the governing equation of the problem as the displacement function, it is expected that the stiffness matrix to be constructed will be exact and hence the response of a beam structure to a harmonically varying with time loading analyzed on the basis of the finite element method with that element stiffness matrix for every physical member will be also exact.

The dynamic stiffness matrix of the finite element of Fig. 3 will be constructed here on the basis of the displacement function (9) and the basic definition of any coefficient of that matrix. Thus, for the dynamic stiffness matrix [k] connecting the vector of the amplitudes of the generalized nodal forces {f} with the vector of the amplitudes of the corresponding nodal displacements {u} as

$$\{f\} = [k] \{u\} \tag{11}$$

The stiffness coefficient k_{ij} in the frequency domain is defined as the nodal generalized force at the degree of freedom i due to unit nodal generalized displacement of the degree of freedom j, while all the other displacements are zero. It is obvious that since v(x) depends on the frequency ω, so does the dynamic stiffness matrix [k]. In this work, since every node has 3 dof, the finite element of Fig. 3 has 2x3=6 of and hence the size of the stiffness matrix [k] will be 6x6, while the indices i, j will take the values 1, 2, …, 6. Thus, the dynamic stiffness matrix will be constructed here column by column on the basis of six generalized displacements states, the displacement function (9) and the expressions for *V*, *M*, *m* in terms of that displacement and its derivatives as defined in Eqs (8).

Thus the derivatives of v=v(x) of Eq. (9) are evaluated and listed as

$$v^{(n)}(x) = \sum_{i=1}^{6} C_i \lambda_i^n e^{\lambda_i x} \tag{12}$$

where the superscript (n) indicates the n^{th} (n=1,2,..,5) order derivative with respect to x, while the generalized forces V, M and m are expressed in terms of the above derivatives with the aid of Eqs (8) as

$$V(x) = EI(v''' - g^2 v^V)$$

$$M(x) = EI(v'' - g^2 v^{IV})$$

$$m(x) = EIg^2 v''' \tag{13}$$

Consider the first displacement state defined as

$$v(0) = v_1 = 1, \quad v'(0) = v_1' = 0, \quad v''(0) = v_1'' = 0.$$

$$v(L) = v_2 = 0, \quad v'(L) = v_2' = 0, \quad v''(L) = v_2'' = 0. \tag{14}$$

where $v_1, v_2', v_1'', v_2, v_2', v_2''$ are the generalized nodal displacements of the finite element of Fig. 3. The above Eqs (14) in view of the expressions (9) and (12) can be written in the form

$$\sum_{i=1}^{6} C_i = 1, \quad \sum_{i=1}^{6} C_i \lambda_i = 0, \quad \sum_{i=1}^{6} C_i \lambda_i^2 = 0,$$

$$\sum_{i=1}^{6} C_i e^{\lambda_i L} = 0, \quad \sum_{i=1}^{6} C_i \lambda_i e^{\lambda_i L} = 0, \quad \sum_{i=1}^{6} C_i \lambda_i^2 e^{\lambda_i L} = 0, \tag{15}$$

The above Eqs (15) can be thought of as a linear system of six equations with six unknowns, the constants C_i (i=1,2,…,6) and easily solved. Using the definition of the dynamic stiffness coefficients k_{ij} and the different sign convention of Fig.2 (mechanics convention) and Fig.3 (matrix convention), one can obtain the dynamic stiffness coefficients for the first column of [k] corresponding to the displacement state (14) in the form)

$$k_{11} = V(0), \quad k_{21} = M(0), \quad k_{31} = m(0)$$

$$k_{41} = -V(L), \quad k_{51} = -M(L), \quad k_{61} = -m(L) \tag{16}$$

where the right-hand sides of Eqs (16) can be computed by using Eqs (13), (9) and (12) with values of the constants C_i (i=1,2,…,6) those obtained from the solution of Eqs (15).

Because Eq. (10) has to be solved numerically, the whole abovementioned procedure for the computation of the k_{ij} of Eq. (16) is done numerically with the aid of Mathematica [19].

After repeating the above procedure five more times, the remaining four columns of the matrix [k] can be also determined. Due to the symmetry of the matrix [k], the satisfaction of the relation $k_{ij} = k_{ji}$ with the aid of Mathematica [19] serves as a verification of the exactness of these expressions for k_{ij} . Thus, the stiffness equation (11) connecting the vectors {f} and {u} through the dynamic stiffness matrix [k] for the finite element of Fig.3 can be explicitly written down with

$$\{f\}=\{V_1, M_1, m_1, V_2, M_2, m_2\}^T$$

$$\{u\}=\}=\{v_1, v_1^{'}, v_1^{''}, v_2, v_2^{'}, v_2^{''}\}^T \tag{17}$$

and the various elements k_{ij} of the dynamic matrix [k] determined with the aid of Mathematica [19] and not shown explicitly fere due to their complexity.

4. FREE AND FORCED FLEXURAL VIBRATIONS

Consider a beam structure experiencing flexural vibrations under dynamic loading varying harmonically with time. Following standard procedures (e.g., Martin [20]), one is able to formulate this problem into a FEM form in the frequency domain reading as

$$\{F\}=[K(\omega)]\{U\} \tag{18}$$

In the above, [K(ω)] is the total structural dynamic stiffness matrix depending on frequency ω and obtained as an appropriate superposition of the dynamic stiffness matrices [k] of the various finite elements comprising the structure as given by (11) and {U} and {F} are the vectors of the amplitudes of the generalized nodal

displacements and external forces of the whole structure, respectively. After application of the boundary conditions of the problem in terms of the generalized nodal displacements, one can solve Eq. (18) for the known operational frequency ω and determine the unknown amplitudes of the generalized nodal displacements.

In case of free vibrations, one has {F}={0} and in order for the resulting equation in (18) after application of the boundary conditions to have non-zero solutions for {U}, the condition

$$\mathrm{Det}[K(\omega)]=0 \tag{19}$$

Should be satisfied. Equation (19) is the frequency equation with roots ω_i (i=1,2,...∞) the natural frequencies of the beam structure. Once the natural frequencies have been obtained, the modal shapes {U} can be also determined from (18) with {F}={0} in the standard way. Because Eq.(19) is too complicated, it can only be solved numerically by determining the value of the det[K(ω)] for a sequence of values of ω and recording those values for which (19) is satisfied. However, since the whole procedure involves complex arithmetic, one computes the real valued function D(ω)=ln|det[K(ω)]| versus ω and identifies the natural frequencies as the local minima of D(ω) by following Kitahara [21].

When the external loading is transient, the whole problem is solved in the Laplace transformed with respect to the time domain and the time domain response is obtained by a numerical inversion of the transformed solution (Beskos and Narayanan [18]). Consider the Laplace transform defined for a function Φ(x,t) given by

$$\bar{\Phi}(x,s) = L\{\Phi(\mathrm{x},\mathrm{t})\} = \int_0^\infty \Phi(x,t)e^{-st}dt \tag{20}$$

where s is the, in general complex, Laplace transformed parameter. Application of the above Laplace transform onto Eq. (3) under zero initial conditions results in

$$\bar{\upsilon}^{IV} - g^2\bar{\upsilon}^{VI} + a^2\bar{\upsilon} = \bar{q}/EI \tag{21}$$

where

$$a^2 = \mu s^2/EI \tag{22}$$

and indicates that one can go from the frequency into the Laplace transform domain by simply replaced ω by -is. Hence, Eq. (18) can also be used in the Laplace transform domain in the form

$$\{\bar{F}\} = [K(s)]\{\bar{U}\} \tag{23}$$

where [K(s)] is [K(ω)] with ω=-is and overbars in vectors $\{\bar{U}\}$ and $\{\bar{F}\}$ indicate transformed quantities. Equation (23) is solved numerically for $\{\bar{U}\}$ for a sequence of values of s and the transformed solution is inverted numerically to obtain the time domain response. This inversion is done with the highly accurate algorithm of Durbin [22] as explained in Beskos and Narayanan [18].

5. NUMERICAL EXAMPLES

Consider a gradient elastic cantilever beam of length L and flexural rigidity EI subjected to a vertical lateral concentrated load P_0 suddenly applied at its free end, as shown in Fig.4. For this structure the first five natural frequencies and its dynamic response to the load P_0 are determined by the FEM.

The whole beam is considered to be a single finite element with nodes 1 and 2 at the fixed and free ends, respectively, as shown in Fig.4. The dynamic behavior of that beam element 1-2 is described by the stiffness equation (11) in the frequency domain with [k] being of the order of 6X6. Application of the boundary conditions

$$v_1, = v_1^{'} = v_1^{''} = 0 \tag{24}$$

with the first two conditions in (24) being the classical and the third condition the non-classical one, reduces Eq.(11) to the form

$$\begin{Bmatrix} P \\ 0 \\ 0 \end{Bmatrix} = \begin{bmatrix} K_{44} & K_{45} & K_{46} \\ K_{54} & K_{55} & K_{56} \\ K_{64} & K_{65} & K_{66} \end{bmatrix} \begin{Bmatrix} v_2 \\ v_2^{'} \\ v_2^{''} \end{Bmatrix} \tag{25}$$

where $K_{ij} = K_{ij}(\omega)$ and P_0, v_2, v_2' and v_2" stand for amplitudes. The frequency equation (19) with [K(ω)] being explicitly given in (25), is solved as described in section 4 and the first five normalized natural frequencies $\omega_n/\omega_n^{\,c}$ (n=1,2,…,5) are shown in

Table 1 for various values of the normalized gradient coefficient g/L. The normalizing factors ω_n^c are the classical natural frequencies $\omega_n^c = [(2n-1)^2\pi^2/4L^2)]\sqrt{EI/\mu}$ [23].

One can observe from Table 1 that frequencies increase for increasing values of the gradient coefficient g, as expected due to the stiffening effect of gradient elasticity. Furthermore, one can observe from Table 1 that for g/L=0.0001→0, one recovers the values of the natural frequencies of the classical case.

The forced vibration problem is described by Eq.(25) considered to be in the Laplace transformed domain. In that case P is replaced by P_0/s , $K_{ij}(\omega)$ become $K_{ij}(s)$ by simply replacing ω by –is and v_2, v_2' and v_2'' become $\bar{v}_2$, $\bar{v}_2'$ and $\bar{v}_2''$,respectively. Thus, according to Section 4, Eq.(25) in the Laplace transformed domain is solved for a sequence of values of s and the time domain response is obtained by a numerical inversion of the transformed solution using the algorithm of Durbin [22]. Figure 5 provides the free end deflection of the cantilever beam versus time for various values of g/L on the basis of the data in Papargyri-Beskou et al [5] reading as L=1.219m, I=5993.73 cm^4 , E=20.685X10^4MPa, μ=60.709 Kg/m and P_0 =35584N. The present results are identical with those in [5] obtained by an analytic method. One can observe from Fig.5 that increasing values of g/L decrease the maximum values of the deflection and shift them to smaller time values of occurrence. Furthermore, one can observe that for g→0 , one can recover the response of the classical case [24], as expected.

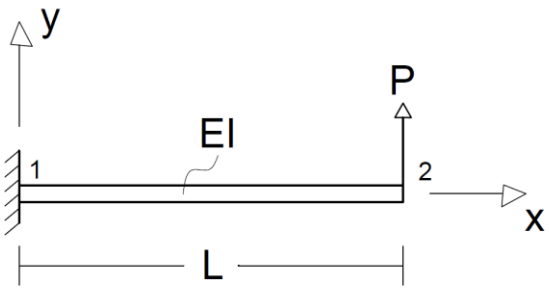


Fig.4. Geometry and loading of a cantilever gradient elastic flexural beam.

Table 1. First five normalized natural frequencies of gradient elastic cantilever beam for various values of g/L.

g/L	0.0001	0.005	0.01	0.050	0.100
$\omega_1^g/\ \omega_1^c$	1.0000	1.01018	1.02037	1.10658	1.22523
$\omega_2^g/\ \omega_2^c$	1.0000	1.01028	1.02102	1.12476	1.29145
$\omega_3^g/\ \omega_3^c$	1.0000	1.01059	1.02258	1.16470	1.42304
$\omega_4^g/\ \omega_4^c$	1.0000	1.01124	1.02525	1.22553	1.60883
$\omega_5^g/\ \omega_5^c$	1.0000	1.01227	1.02903	1.30263	1.82896

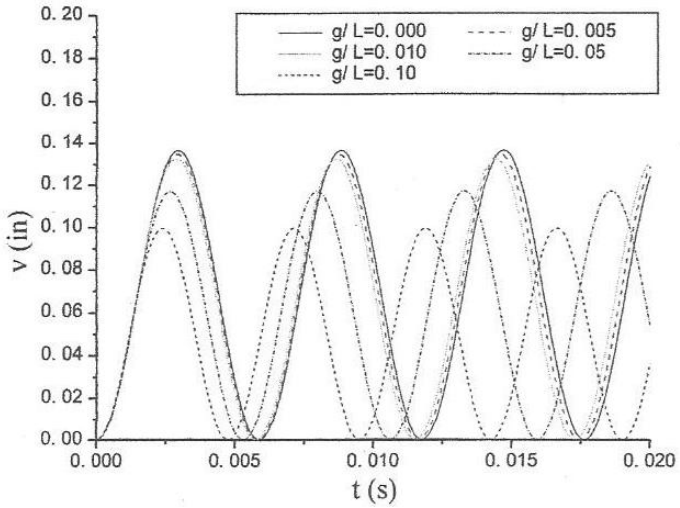


Fig. 5 Free end deflection of gradient elastic cantilever beam versus time for various values of g/L

6. CONCLUSIONS

One the basis of the previous developments, the following conclusions can be stated:

1) The dynamic stiffness matrix for a gradient elastic Bernoulli-Euler finite beam element has been constructed in the frequency domain. The displacement function used is the exact solution of the governing equation of motion in the frequency domain and this results to an exact dynamic stiffness matrix, exact dynamic response to harmonically varying with time load and exact natural frequencies.

2) When the external loading is transient, the response is obtained with the aid of the Laplace transform with respect to time and a numerical inversion of the transformed solution. The Laplace transformed domain formulation is obtained from the frequency domain one by simply replacing the frequency ω by -is, where s is the Laplace transform parameter .

3) The proposed FEM formulates the problem in a static –like form in the frequency or the Laplace transform domain with obvious conceptual and computational gains. Since the present FEM is associated with exact stiffness matrices, the discretization is restricted to one finite element per physical member,

which leads to matrices of much smaller size. Of course, the stiffness coefficients are more complicated than in the conventional FEM that employs approximate displacement functions in polynomial form. The advantages of the proposed FEM over analytic methods for dynamic analysis of gradient elastic beam structures are generality, versatility and efficiency, especially for complicated geometries and loading.

4) It was observed, at least in the examples considered here, a decrease of deflections and an increase of the natural frequencies with increasing values of the gradient coefficient as a result of the stiffening effect of gradient elasticity theory.

REFERENCES

[1] RD Mindlin, Microstructure in linear elasticity, Archive of Rational Mechanics and Analysis, 16: 51-78, 1964.

[2] SV Tsinopoulos, D Polyzos, DE Beskos, Static and dynamic BEM analysis of strain gradient elastic solids and structures, Computer Modeling in Engineering and Sciences (CMES), 86: 113-144, 2012.

[3] CS Chang, J Gao, Wave propagation in granular rod using high-gradient theory, Journal of Engineering Mechanics of ASCE, 123: 52-59, 1997.

[4] S Papargyri-Beskou, K.G. Tsepoura, D Polyzos, D.E. Beskos, Bending and stability analysis of gradient elastic beams, International Journal of Solids and Structures, 40: 385-400, 2003.

[5] S. Papargyri-Beskou, D. Polyzos, D.E. Beskos Dynamic analysis of gradient elastic flexural beams, Structural Engineering and Mechanics, 15: 705-716, 2003.

[6] DCC Lam, F. Yang, ACM Chong, J. Wang, P. Tong, Experiments and theory in strain gradient elasticity, Journal of the Mechanics and Physics of Solids, 51: 1477-1508, 2003.

[7] A.E. Giannakopoulos, K. Stamoulis, Structural analysis of gradient elastic components, International Journal of Solids and Structures, 44: 3440-3451,2007.

[8] S. Kong, S. Zhou, Z. Nie, K. Wang, Static and dynamic analysis of micro beams based on strain gradient elasticity theory, International Journal of Engineering Science, 47: 487-498, 2009.

[9] S. Papargyri-Beskou, D.E. Beskos, Static analysis of gradient elastic bars, beams, plates and shells, The Open Mechanics Journal, 4: 65-73, 2010.

[10] S. Papargyri-Beskou, D. Polyzos, D.E. Beskos, Wave dispersion in gradient elastic solids and structures: a unified treatment, International Journal of Solids and Structures, 46: 3751-3759, 2009.

[11] B. Wang, J. Zhao, S. Zhou, A microscale Timoshenko beam model based on strain gradient elasticity theory, European Journal of Mechanics, A/ Solids, 29: 591-599, 2010.

[12] B. Akgoz, O. Civalek, A size-dependent shear deformation beam model based on the strain gradient elasticity theory, International Journal of Engineering Science, 70: 1-14, 2013.

[13] A. Triantafyllou, A.E. Giannakopoulos, Structural analysis using a dipolar elastic Timoshenko beam, European Journal of Mechanics, A/Solids, 39: 218-228,2013.

[14] I.P. Pegios, S. Papargyri-Beskou, D.E. Beskos, Finite element static and stability analysis of gradient elastic beam structures, Acta Mechanica, in press.

[15] E.L. Asiminas, V.K. Koumousis, A beam finite element based on gradient elasticity, Proceedings of 10th HSTAM International Congress on Mechanics, D.E. Beskos and G.E. Stavroulakis (Editors), Technical University of Crete Press, May 25-27, 2013, Chania, Crete, Greece, Paper No 123.

[16] MH Kahrobaiyan, M Asghari, MT Ahmadian, Strain gradient beam element, Finite Elements in Analysis and Design, 68: 63-75, 2013.

[17] B. He Y Zhang, D. Liu, Z. Gan, L. Shen, Non-classical Timoshenko beam element based on the strain gradient elasticity theory, Finite Elements in Analysis and Design, 79: 22-39, 2014.

[18] D.E. Beskos, GV Narayanan, Dynamic response of framework by numerical Laplace transform, Computer Methods in Applied Mechanics and Engineering, 37: 289-307, 1983.

[20] HC Martin, Introduction to Matrix Methods of Structural Analysis, Mc Graw-Hill, New York, 1966.

[19] Mathematica, Version 4.1, Wolfram ResearchInc., Champaign, Illinois, USA, 2004.

[21] M. Kitahara, Boundary Integral Equation Methods in Eigenvalue Problems of Elastodynamics and Thin Plates, Elsevier, Amsterdam, 1985.

[22] F. Durbin, Numerical inversion of Laplace transform: an efficient improvement of Dubner and Abate's method, The Computer Journal 17:371-376, 1974.

[23] SS Rao, Vibration of Continuous Systems, John Wley & Sons, Inc., Hoboken, N.J., USA, 2007.

[24] DE Beskos, AY Michael, Solution of plane transient elasto-dynamic problems by finite elements and Laplace transform, Computers and Structures 18, 695-701, 1984.

COMPDYN 2015
5th ECCOMAS Thematic Conference on
Computational Methods in Structural Dynamics and Earthquake Engineering
M. Papadrakakis, V. Papadopoulos, V. Plevris (eds.)
Crete Island, Greece, 25–27 May 2015

VIBRATIONS OF SPORTS STADIUM GRANDSTAND STRUCTURE DUE TO CROWD-JUMPING LOADS

Tadeusz Tatara[1], **Bartosz Ptasznik**[2]

[1] Cracow University of Technology
31-155 Kraków, ul. Warszawska 24, Poland
e-mail: ttatara@pk.edu.pl

[2] Graduate of Cracow University of Technology
31-155 Kraków, ul. Warszawska 24, Poland
e-mail: bart.pta@gmail.com

Keywords: grandstand, natural frequency, crowd-jumping load, dynamic stresses, limit state, safety of the structure.

Abstract. *In recent years the destiny of stadiums has much changed. Formerly the stadiums were used occasionally. The present stadiums are much more versatile; take place in them may concerts and a variety of sporting events, while inside grandstands are located commercial units. As a result, the requirements for the design of these structures are more rigorous, in particular for dynamic loads. The design of grandstands has also evolved. This is due to the requirements of spectators who wish to have a perfect, direct and unobstructed view of anything, and be as close as possible playing action. In parallel, economic considerations limit grandstands supporting structure while maximizing sitting places. This combination leads to longer and more flexible brackets which in combination of spontaneous human behavior raises problems of vibration of the structure. A crowd of people can generate significant dynamic loads especially when it involves rhythmic jumping. Such situations occur during sporting events or concerts. The rhythm of music leads to synchronization behavior of people gathered in the grandstands. Such harmonic force may raise the issue of a resonant vibration, resulting in exceeding the limit states. The paper refers to computational examination of theoretical model of one grandstand in stadium in Krakow. The dynamic interaction function is applied as the dynamic loading reflects to actual behavior of the fans in the grandstands. The calculation of the dynamic response is carried out in the Abaqus 6.12 code. To best replicate reality, a numerical model was built based on a construction project taking into account the actual properties of the structural materials. The study analyzed the convergence of solutions determining the first three natural frequencies of the structure. The first calculated natural frequency (f = 3.24Hz) is close to frequency (f = 2.8Hz) which can generate fans crowd. On the other hand the second natural frequency of the structure (f=4.5Hz) is almost twice of frequency of "Labado" dance. The applied dynamic force cause increasing of stresses in structural elements about 40 - 60%. The level of calculated stresses as well as displacements of grandstand is safe for the structure.*

1 INTRODUCTION

In recent years the destiny of stadiums has much changed. Formerly the stadiums were used occasionally, once every two weeks, when the local team played their matches. The present stadiums are much more versatile; take place in them may concerts and a variety of sporting events, while inside grandstands are located commercial units. As a result, the requirements for the design of these structures are more rigorous, in particular for dynamic loads.

The design of grandstands has also evolved. This is due to the requirements of spectators who wish to have a perfect, direct and unobstructed view of anything, and be as close as possible playing action. In parallel, economic considerations limit grandstands supporting structure while maximizing sitting places. This combination leads to longer and more flexible brackets which in combination of spontaneous human behavior raises problems of vibration of the structure. A crowd of people can generate significant dynamic loads especially when it involves rhythmic jumping. Such situations occur during sporting events or concerts. The rhythm of music leads to synchronization behavior of people gathered in the stands. Such harmonic force may raise the issue of a resonant vibration, resulting in exceeding the limit states.

There are known examples of sports stadiums stands disasters that took place virtually anywhere in the world. These disasters have caused the death and injury of many spectators. There were various reasons for those disasters. Analysis of the causes of grandstands stadium disasters have also contributed to their design changes and reducing capacity of stadium. As example the findings of the report from the Hillsborough disaster occurred on 15 April 1989 at the Hillsborough Stadium in Sheffield, England resulted in the elimination of standing terraces at all major football stadiums in England, Wales and Scotland. Collapse of wooden terrace of Ibrox Stadium (Glasgow – 1902) resulting in the death of 26 people led to the prohibition of wooden scaffold type terraces in favour of terraces with a base of earth banking. The collapse of upper part of the makeshift scaffold-type stand in Bastia Stadium in 1992 were caused by lack of time, failing safety procedures, and fraudulent actions what resulted in critical construction errors. It led to the death of 18 fans and injuring over 2,000 more. In 26 November 2007 eight people were killed and about 150 were injured as a result of the collapse of the stands on one of the sectors of the stadium in the city of Salvador in the Brazilian state of Bahia.

The paper refers to computational examination of theoretical model of one grandstand in stadium "Vistula" in Krakow. The dynamic interaction function is applied as the dynamic loading. The loading reflects the actual behavior of the fans in the grandstands. This forcing corresponds to a dance called "Labado". The calculation of the dynamic response is carried out in the Abaqus 6.12 code. To best replicate reality, a numerical model was built based on a construction project taking into account the actual properties of the structural materials. The first calculated natural frequency (f = 3.24Hz) is close to frequency (f = 2.8Hz) which can generate fans crowd. On the other hand the second natural frequency of the structure (f=4.5Hz) is almost twice of frequency of "Labado" dance. The applied dynamic force cause increasing of stresses in structural elements about 40 - 60%. The level of calculated stresses as well as displacements of grandstand is safe for the structure.

2 CHARACTERISTICS OF DYNAMIC LOAD GENERATED BY THE CROWD

The main issue the analysis is to define the dynamic structural loads. In humans, it is highly dynamic nature. The study loads and impacts caused by man engaged in medical science, in particular, orthopedics and biomechanics. As a result of studies of people received load model

delivered by the man on the ground. As the first results of the vertical component of the pressure that causes pedestrian, Skorecki published in 1966 [1]. Since then began to construct test platform for testing load that causes a man on the move. The main reason for conducting this study was progression in the sport. Data from measurements performed on the most popular Kistler platforms enable to assume the dynamic load induced by man in motion – comp. Fig.1.

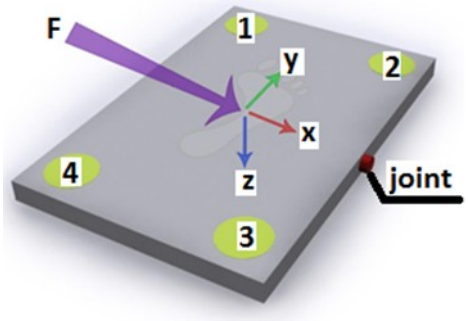


Figure 1: Distribution of sensors and forces on the Kistler's platform [2].

The basic element of the platform is a rigid, rectangular plate supported at four corners of the piezoelectric gauges providing information about the vertical and horizontal load. These professional made measuring devices are now standard in research of forces transmitted by the man on the ground during normal operation and sport activities. Knowledge of the impact on the ground in time and space used in sports to evaluate the forces resulting in human osteomuscular system, sport techniques, sports footwear type assessment, and many other biomechanical factors [1]. Biomechanics research results made it possible to determine the load that transfers to the structure by a man on the move. The vertical component of the load has a decisive influence on the induced deformations and vibrations of structures. Basic human physical activity is cyclical, and on this basis, a classification of human physical activity of the corresponding frequency range is introduced in Table 1 [1].

Type of activity	Full range Hz	Slow, Hz	Average, Hz	Fast, Hz
Marching	1,4-2,4	1,4-1,7	1,7-2,2	2,2-2,4
Run	1,9-3,3	1,9-2,2	2,2-2,7	2,7-3,3
Jumps	1,3-3,4	1,3-1,9	1,9-3,0	3,0-3,4

Table 1: Classification of human physical activity [1].

2.1 Human impact – jumps

Jumps (jumping in place) are physical activity, which is characterized by four phases: preparation (lowering), reflection (climb), flight and landing – cf. Fig. 2.

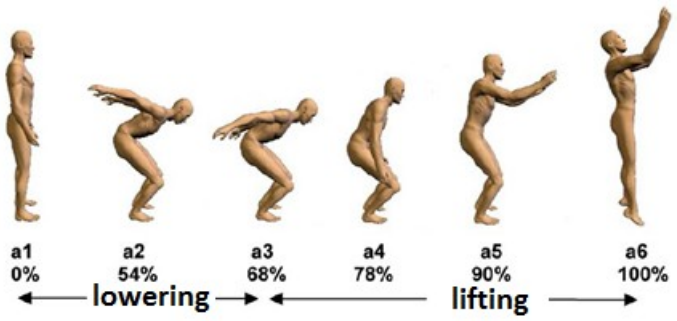


Figure 2: Phase of human movement during jump [1].

The main parameters characterizing the rhythmic leaps and jumps are frequency as a function of time and time of the dynamic interaction. Depending on the type of jumps, the frequency is typically in the range of 1.8 to 3.4 Hz. Vertical dynamic effects are mainly generated while jumping. The time of this interaction depends primarily on: frequency, bounce height, weight of person, gender, type of footwear, the conditions of the substrate surface (soft surface) and its movements – cf. Fig. 3. Jumping's in place simultaneously on both feet at the same time is the most dangerous for the constructions [3].

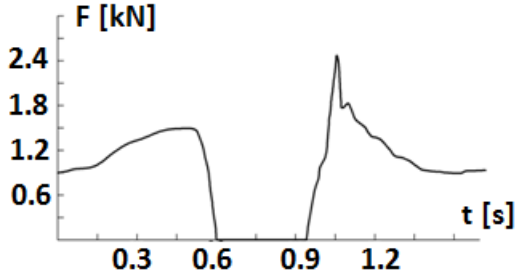


Figure 3: The dependence of the impact F of vertical jump vs time [1].

Jumping is physical activity that, unlike the gait is practically not sensitive to vibrations of the substrate (in the sense of the generated load). This is due to the fact that the vertical movement of the body can achieve the displacement amplitude times greater than the displacement of the substrate. Displacement of basic components of human body due to typical jump amounts to approx. 0.5 m.

2.2 Dynamic loads for dancing and jumping - standard recommendations

In dynamic analysis it is often convenient to express the applied loading as a Fourier series representing the variation of load with time as a series of sine functions. Any periodic loading can be decomposed in to a combination of a constant load and several harmonics. Synchronized dynamic loading [4] caused by activities such as jumping and dancing are periodic and mainly depend upon:

a) the static weight of the jumper(s)/dancer(s) (G);
b) the period of the jumping/dancing load(s) (T_p);

c) the contact ratio (a), i.e. the ratio of the duration within each cycle when the load is in contact with the floor and the period of the jumping/dancing.

Mathematically the load at any instant (t) may be expressed as:

$$F(t) = G\left[1 + \sum_{n=1}^{\infty} r_{\mathrm{n}} \sin\left(\frac{2\pi n}{T_{\mathrm{p}}} t + \varphi_{\mathrm{n}}\right)\right] \tag{1}$$

where:

n - the number of the harmonic being considered 1, 2, 3, ...;
r_{n} - the dynamic load factor for the n^{th} harmonic;
φ_{n} - the phase lag of n^{th} harmonic;
T_{p} – jump period.

The values of r_{n} and φ_{n} are functions of the value of the contact ratio α. In practice for the evaluation of displacement and stresses, only the first few harmonics need be considered as the structural response at higher values is generally not significant. It is generally sufficient to consider the first three harmonics for vertical loads and the first harmonic for horizontal loads. For the calculation of acceleration, additional harmonics will need consideration. Table 2 gives typical values for four various activities [5, 6].

Activity	Contact ratio α
Pedestrian movement	⅔
Low impact aerobics	
Rhythmic exercises	½
High impact aerobics	
Normal jumping	⅓
High jumping	¼

Table 2: Typical values of the contact ratio α for various activities [5].

The resultant values of r_{n} and f_{n} for a given period of dancing Tp or a jumping frequency (1/Tp) may be obtained from literature (e.g. [4]). For individual loads the frequency range that should be considered is 1.5 Hz to 3.5 Hz and for larger groups 1.5 Hz to 2.8 Hz as coordinated movement at the higher frequencies is impractical. For a large group the load $F(t)$ calculated from equation (1) may be multiplied by 0.67 to allow for lack of perfect synchronization. Vertical jumping also generates a horizontal load which may be critical for some structures, e.g. temporary grandstands. A horizontal load of 10 % of the vertical load should be considered.

Equation (1) represents the vertical action of one person performing any rhythmic movement. At the time of its cessation, the load is reduced to a static load. The values of coefficients r_{n} and φ_{n} of the formula (1) can be determined using functions (2) and (3) developed by Ji, Ellis and Wang [5, 7]. These functions, however, only apply to the division of activities described in Table 2.

$$r_n = \begin{cases} \frac{\pi}{2} & if \quad 2n\alpha = 1 \\ \left|\frac{2\cos(n\pi\alpha)}{1-(2n\alpha)^2}\right| & if \quad 2n\alpha \neq 1 \end{cases} \tag{2}$$

$$\varphi_n = 0 \quad if \qquad 2n\alpha = 1$$

or

$$\varphi_n = \begin{cases} tan^{-1}\left(\frac{1+\cos(2n\pi\alpha)}{\sin(2n\pi\alpha)}\right) - \pi, & \frac{\sin(2n\pi\alpha)}{1-(2n\alpha)^2} < 0 \\ -\frac{\pi}{2}, & sin(2n\pi\alpha) = 0 \\ tan^{-1}\left(\frac{1+\cos(2n\pi\alpha)}{\sin(2n\pi\alpha)}\right), & \frac{\sin(2n\pi\alpha)}{1-(2n\alpha)^2} > 0 \end{cases} \quad if\ 2n\alpha \neq 1 \tag{3}$$

Values of the first six Fourier coefficients series, which can be regarded as sufficient for its implementation are contained in Table 3.

		n=1	n=2	n=3	n=4	n=5	n=6
α=2/3	r_n	9/7	9/55	2/15	9/247	9/391	2/63
	φ_n	-π/6	-5π/6	-π/82	-π/6	-5π/6	-π/2
α=1/2	r_n	π/2	2/3	0	2/15	0	2/35
	φ_n	0	π/2	0	-π/2	0	-π/2
α=1/3	r_n	9/5	9/7	2/3	9/55	9/91	2/15
	φ_n	π/6	-π/6	-π/2	-5π/6	-π/6	-π/2

Table 3: Fourier coefficients and phase lags for the different contact ratios [8].

Figure 4 shows the course of the function (3.4) at time applying 3 and 12 coefficients of a Fourier series. The diagram illustrates two cycles of "normal jumping" with frequency equals 2 Hz and the contact ratio α = 1/3. Contact ratio α = 1/3 is equivalent to that two-thirds of each cycle of the body has no contact with the ground. For the calculations it was assumed normalized load of 1.0 corresponding to the static weight of the jumper (G_s = 1). It is easy to note that the higher coefficients of the Fourier series (n > 3), are not critical to this maximum. However, it can affect the response of construction, in particular at the critical value of the frequency ratio to the natural frequency of the structure.

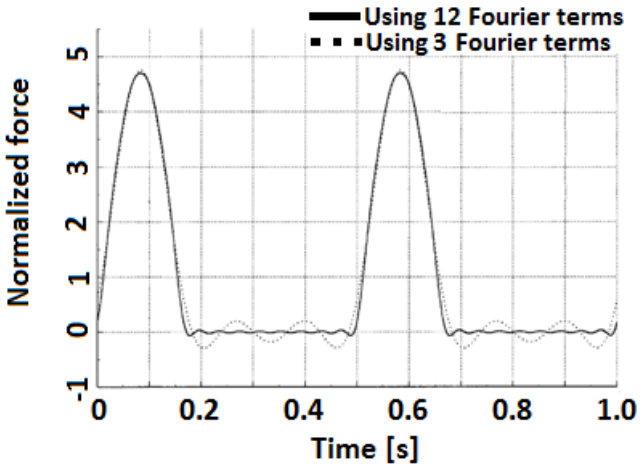


Figure 4: Load-time history for two jumps with frequency equals 2 Hz [8].

Equation (1) describes the dynamic load derived from one person. This can be extended to the case of the populated grandstand. Multiplying the static effects in this case will be lower than in the case of one person. This is due to imperfect coordination in jumping group of spectators in relation to the one person. Therefore, the load equation for a crowd jumping will be as follows:

$$F(f,x,y,t) = G(x,y)\left(1 + C_e \sum_{n=1}^{\infty} r_n \, sin\left(\frac{2n\pi}{T_p}t + \varphi_n\right)\right) \quad (4)$$

where:

F(f, x, y, t) – distributed force which varies with time at a comfortable frequency,
G(x,y) – density and distribution of static loads from spectators,
C_e – crowd dynamic coefficient, $C_e \in (0,1)$

The C_e coefficient depends on the coordination of people in the group, the type of jumps (dance) and the frequency of the rhythm of the music. Numerical simulations in which the phase lag of each person treated as a random variable normally distributed subordinate, shows a reduction of C_e coefficient of one-third in the case of large groups [9]. On the basis of the results shown in [9], the C_e coefficient can be described as function of number of people (υ) in form:

$$C_e(\upsilon) = -0.0799 \ln(\upsilon) + 0.9797 \quad (5)$$

Another way to cover a greater number of people is correction of the Fourier series. These values were determined experimentally by Ji and Ellis [5], but only for the first three terms of the series - cf. Equation (6).

$$F(f,x,y,t) = G(x,y)\left(1 + \sum_{n=1}^{\infty} r_{n,\upsilon} \, sin\left(\frac{2n\pi}{T_p}t + \varphi_n\right)\right) \quad (6)$$

where:

$r_{1,\upsilon} = 1.61\upsilon^{-0.082}$
$r_{2,\upsilon} = 0.94\upsilon^{-0.24}$
$r_{3,\upsilon} = 0.44\upsilon^{-0.31}$

3 ANALYZED STRUCTURE AND ITS NUMERICAL MODEL

3.1 Characteristics of the structure

Analyzed the northern grandstand is single level and is part of the municipal stadium in Krakow - cf. Fig. 5. Grandstand, consists of five sectors and allows the presence of 5806 spectators. The main structural element of the grandstand is RC frame. The frame consists of six columns with cross section 1.4 x 2.2 m, connected in two rows of girders, the lower section 1.6 x 0.96 and the upper 2.0 x 2.2 m - cf. Figure 4.8. The frame is the base for steel sloping beams (IKS 1000-3) supporting prefabricated concrete slabs with a thickness of 9cm. In the mid-span beams are based on the columns (HEB 550), which, by means of girders (HKS 550x5) are connected with a RC frame.

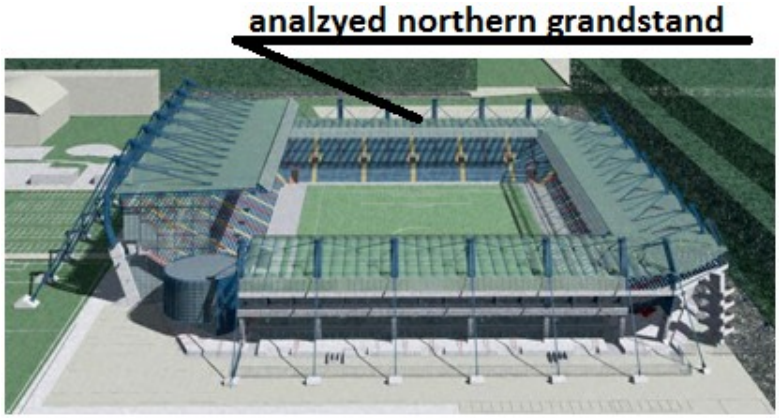


Figure 5: Visualization of the municipal stadium in Krakow and analyzed grandstand [10].

Cores of the main roof superstructure are designed with a tubular cross-sections of diameter D = 1040 mm and a thickness of 80 mm. Pylons support the truss girders at the distances of 9.9 m. Truss girders are braced by means of trusses at a spacing of 3.3 m. They support structure under purlins – comp. Figs. 6, 7. Roof's covering is made of polycarbonate cellular structure.



Figure 6: North grandstand view of the stadium [11].



Figure 7: Construction of the roof of the north grandstand [11].

Tables 4 and 5 present the basic geometrical and structural data of the analyzed grandstand.

Building area		2937.66 m^2
The total area of closed spaces		3588.88 m^2
Cubature of closed spacer		17233.85 m^3
The dimensions of the stands with peripheral structural elements	length	103.00 m
	width	50.86 m
	height	28.83 m
Number of seats		5806

Table 4: Basic technical data of the analyzed grandstand.

Concrete	B30 (C25/30)
Reinforcing steel	A-III 34GS
Structural steel	St3S, 18G2A

Table 5: The used materials.

3.2 Numerical model of the grandstand

3D numerical model of the grandstands is made in the Abaqus 6.12 code - cf. Fig. 8. The beam - shell model is adopted considering the geometry of the object. The model assumes simplification. At the support points full restraint were used (u_x, u_y, u_z, r_x, r_y, $r_z = 0$), what means that modeling of piles and flexibility of the substrate were neglected. Stairs of the grandstand are modeled using shell elements. Double span panels are connected to the main structure by means of joints. Joints also used in the connections between columns and sloping girders as well as in nodes connecting roof and pylons. Other connections are defined as rigid as they are welded or monolithic (RC). Due to the low stiffness roof cover with polycarbonate its modeling was neglected. The model uses linear elements of "B31" and the shell "S4R". Selection of an appropriate finite element mesh density was adopted on the basis of the convergence of the natural frequency (see Section 4). The material characteristics of the structure are listed in table 6.

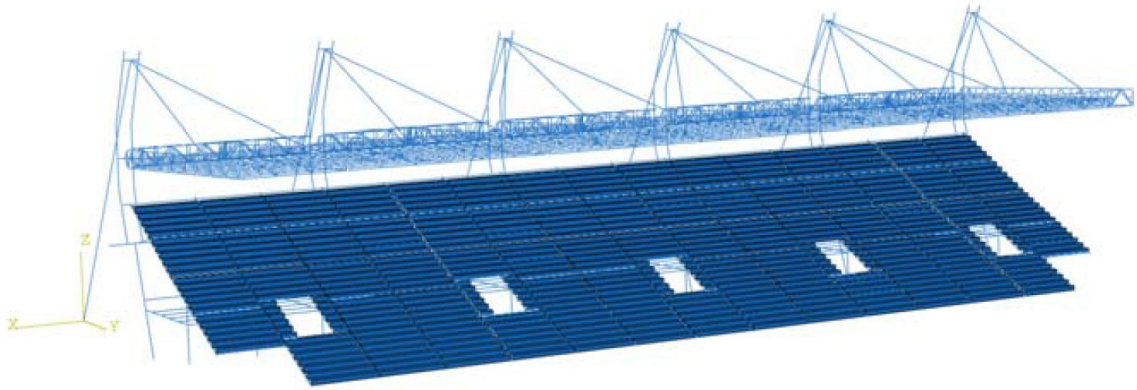


Figure 8: Numerical model of the analyzed grandstand.

Concrete	density	2600 kg/m^3
	Young's modulus	37 GPa
	Poisson ratio	0.15
Steel	density	7850 kg/m^3
	Young's modulus	210 GPa
	Poisson ratio	0.33

Table 6: Material characteristics of the structure.

4 RESULTS OF THE NUMERICAL ANALYSIS

4.1 Sensivity analysis

Several different grid mesh were analyzed and their influence on the convergence of the value of the first three natural frequencies of the model. Three finite element meshes for preliminary analysis were adopted. Data concerning number of elements and values of natural frequencies are summarized in Table 7. Several different grid mesh were analyzed and their influence on the convergence of the value of the first three natural frequencies of the model. Three finite element meshes for preliminary analysis were adopted. Data concerning number of elements and values of natural frequencies are summarized in Table 7.

Number of elements	f_1 [Hz]	f_2 [Hz]	f_3 [Hz]
14910	3,18	4,40	5,33
47854	3,24	4,50	5,40
160936	3,24	4,49	5,41

Table 7: The sensitivity of frequency on the number of elements.

4.2 Calculated natural frequencies and assumed dumping

The first stage of dynamic analysis concerned the calculation of the natural frequency of the structure to the value of 8.4 Hz according to [6]. The calculated values are summarized in the table 8.

No. of frequency	Value of the natural frequency [Hz]
1	3.24
2	4.50
3	5.40
4	6.70
5	7.50
6	>8.40

Table 8: The calculated natural frequencies of the analyzed grandstand.

In this paper Rayleigh damping was adopted (proportional to mass and stiffness) and the coefficients of proportionality were determined from equation (7):

$$\xi_i = \frac{\alpha}{2\omega_i} + \frac{\beta\omega_i}{2} \tag{7}$$

using the following data:

- $f_1 = 3.24$ Hz, $f_2 = 4.50$ Hz,
- damping coefficients ξ_1 and ξ_2 corresponding to f_1 and f_2 are equal 1.3% and 1.5% respectively.

For the above data, the proportionality coefficient values are equal to $\alpha = 0.186$ and $\beta = 0.00083$.

4.3 Applied dynamic loads

The weight of one person was assumed equal to 0.78kN, which, with a capacity of 5806 people on the grandstand gives the average load equal to 3 kN/m^2. Two functions of dynamic load (jumping) were used in further analysis. The first one refers to dance "Labado" which describe the actual behavior of the spectators in the grandstand. Jump function during one period T_p describes equation (8):

$$F_s(t) = \begin{cases} K_p G_s \sin\dfrac{\pi}{t_p}, & if \quad 0 < t < t_p \\ 0, & if \quad t_p < t < T_p \end{cases} \tag{8}$$

where:

G_s – static action,
t_p – contact time,
K_p - coefficient determining the growth of the dynamic interaction calculated from eq. (9):

$$K_p = \frac{\pi}{2\alpha} \tag{9}$$

This function, excluding the impact of static influence is shown in fig. 9.

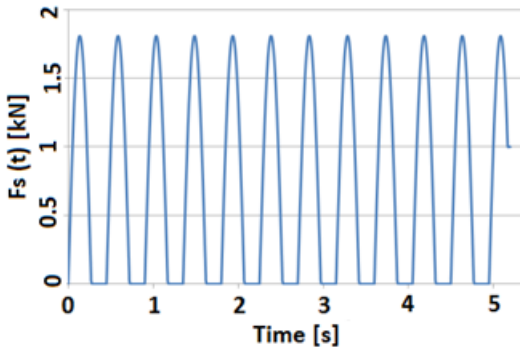


Figure 9: A function of load (dance "Labado") vs. time, at frequency of 2.2 Hz.

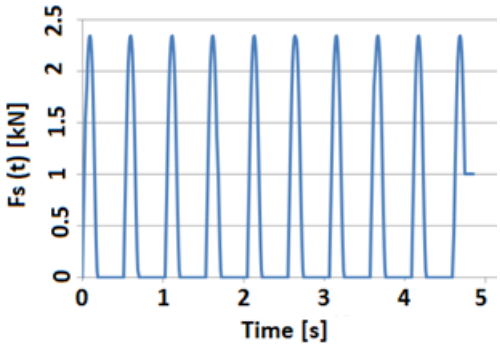


Figure 10: A function of load vs. time, at a frequency of 1.9 Hz.

The second function was obtained from equation (1) for jumps frequency equal 1,9Hz using data from table 3 and assuming value of C_e equal 0.5 - cf. Fig. 10.

4.4 Selected elements and values to be analyzed

Dynamic response analysis was performed for the 3D adopted model of grandstand and two assumed loads. This chapter presents the results of analyzes for a few selected elements of the grandstand - cf. Fig. 11. Highlighted items are:

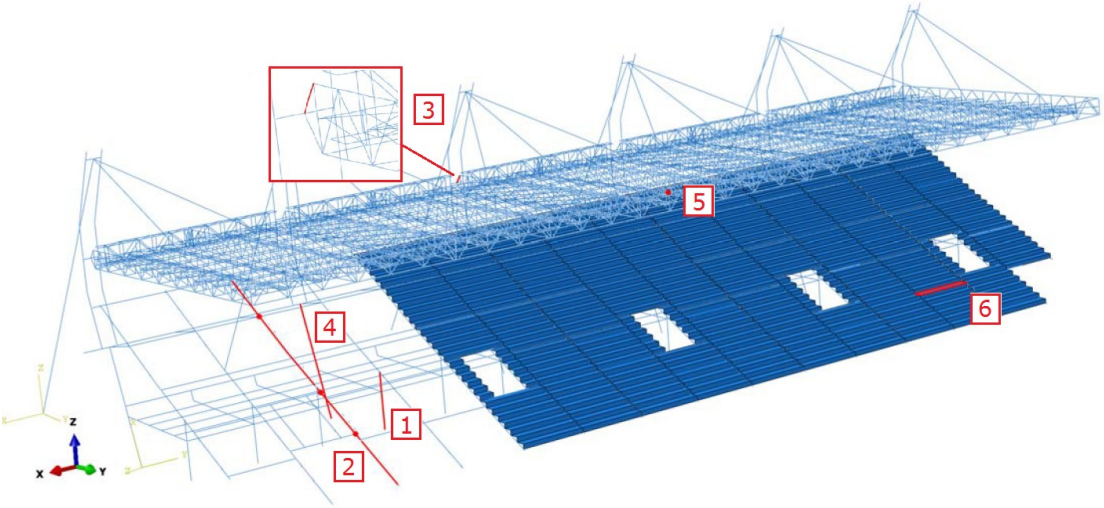


Figure 11: Analyzed elements.

- 1 – HEB 550 steel column; HMH stress,
- 2 –IKS 1000-3 sloping girder; HMH stress, displacement u_z,
- 3 – RK 200x6.3 cross brace; HMH stress,
- 4 – RC column 1.4 x 2 m; principal stress,
- 5 – free end of the roof girder; displacement u_z;
- 6 – plate of audience; displacement u_z.

In order to obtain the maximum output value (from the weight and dynamic loads) it has been examined several locations of people hopping on grandstand. These situations illustrate the figures 12 - 16.

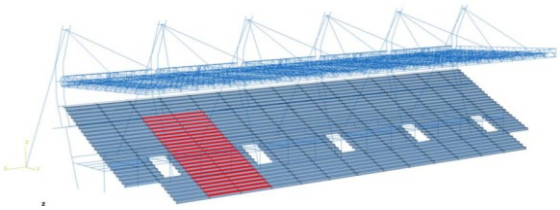


Figure 12: Location of fans no. 1.

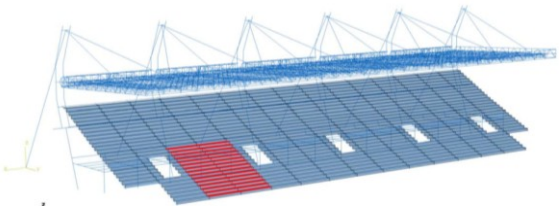


Figure 13: Location of fans no. 2.

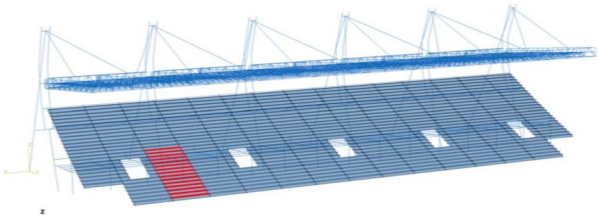


Figure 14: Location of fans no. 3.

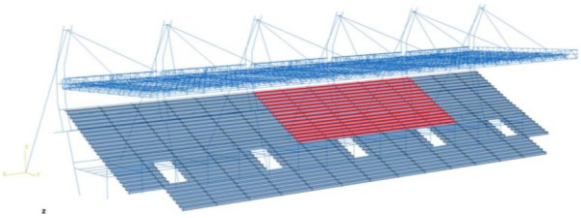


Figure 15: Location of fans no. 4.

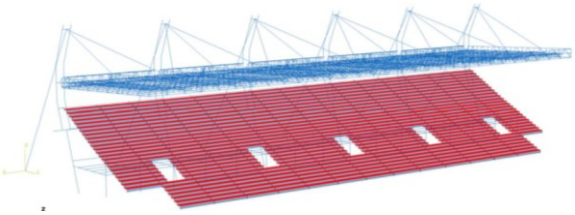


Figure 16: Location of fans no. 5.

4.5 The dynamic response of the grandstand

The response of the grandstand due tu applied loads was calculated by integrating the equations of motion using the module Abaqus / Implicit. The resulting maximum stress values (HMH - for steel parts, the principal - for RC elements) and vertical displacements were compared with static and the codes' values. Table 9 summarizes the results of stress HMH for steel elements. Changes of the values of these stresses over time are shown in Fig. 17 - 19. The response of the grandstand due to applied loads was calculated by integrating the equations of motion using the module Abaqus / Implicit. The resulting maximum stress values (HMH - for steel parts, the principal - for RC elements) and vertical displacements were compared with static and the codes' values. Table 9 summarizes the results of stress HMH for steel elements. Changes of the values of these stresses over time are shown in Fig. 17 - 19.

Element number	Static value	Dynamic value for excitation with 1.9 Hz	Dynamic value for excitation with 2.2 Hz
1	25.5 MPa	44.2 MPa	39.0 MPa
2	104.2 MPa	172.9 MPa	169.6 MPa
3	46.0 MPa	66.6 MPa	55.1 MPa

Table 9: Values of HMH stress in the steel elements.

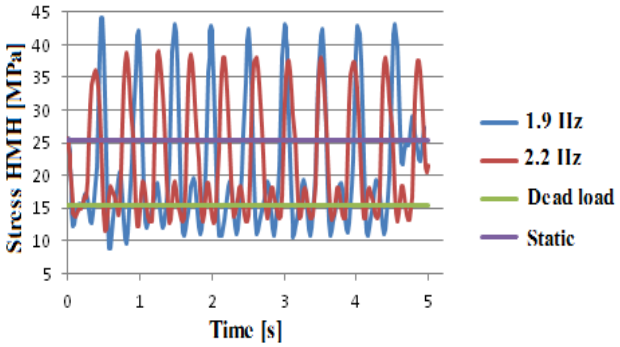


Figure 17: Stress HMH in element no. 1.

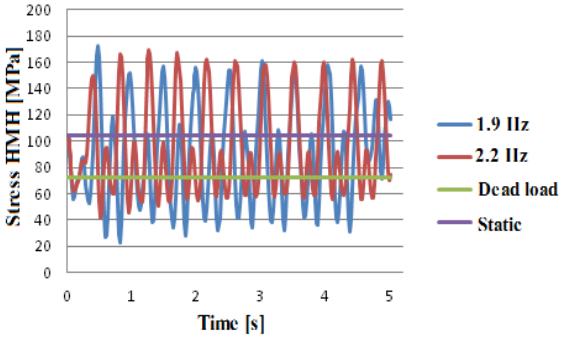


Figure 18: Stress HMH in element no. 2.

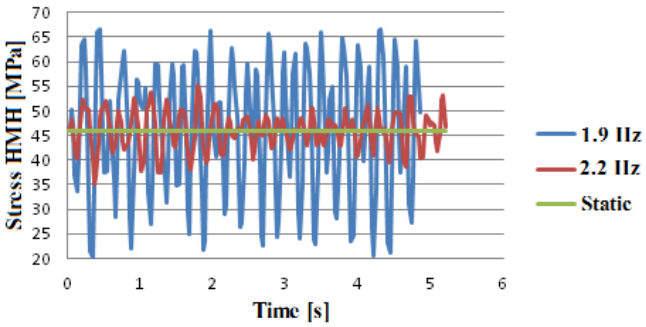


Figure 19: Stress HMH in element no. 3.

Table 10 presents the results of principal stresses for one of RC column in support cross-section - element no. 4. The graphs in Figures 20 and 21 illustrate the change of these values over time.

Part of the column	Static value	Dynamic value for excitation with 1.9 Hz	Dynamic value for excitation with 2.2 Hz
Tension	5.4 MPa	8.5 MPa	8.4 MPa
Compression	-9.3 MPa	-12.9 MPa	-12.8 MPa

Table 10: Values of principal stresses in element no. 4.

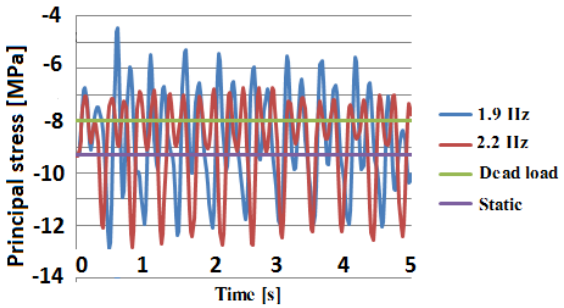


Figure 20: Stress σ_x in element no. 4 - compression.

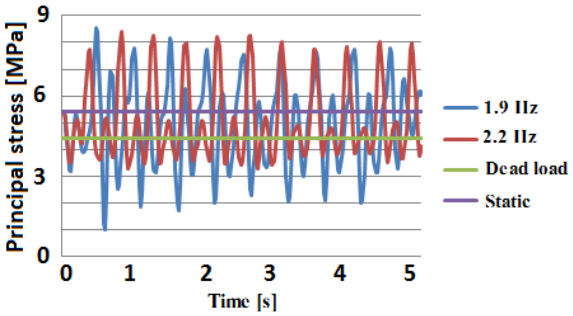


Figure 21: Stress σ_x in element no. 4 - tension.

The limit values according to the EN 1992-1 and EN 1993-1 are equal:

- for conrete C25/30:

(10)

where:

– characteristic value of compressive strength of concrete,
– partial factor of concrete,
– design value of compressive strength of concrete,
– the average value of the axial tensile strength of concrete.

- for steel S235:

(11)

where:

– yield strength - the characteristic value,
– material factor,
– yield strength - the design value.

Table 11 shows the vertical component of displacements for elements no. 2, 5 and 6. Changes of vertical displacements for elements no. 2 and 5 vs. time are shown in Figure 22 and 23.

Element number	Static value	Dynamic value for excitation with 1.9 Hz	Dynamic value for excitation with 2.2 Hz
2	1.6 cm	3.89 cm	4.12 cm
5	3.80 cm	5.46 cm	4.40 cm
6	0.02 cm	0.25cm	0.52cm

Table 11: Displacement values for the elements no. 2, 5, and 6.

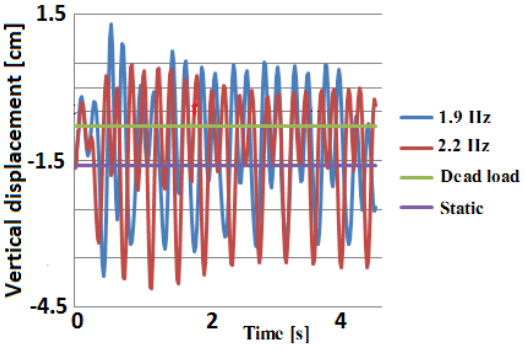


Figure 22: Vertical displacement of the element no. 2 in the middle of the span vs. time.

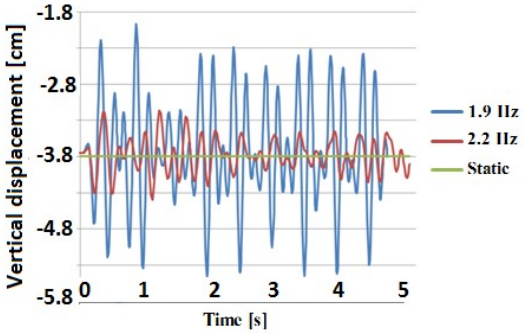


Figure 23: Vertical displacement of the end of the roof girder vs. time (element no. 5).

Span of the roof girder between supports is 1418cm. So the allowable deflection according to polish standard is equal 1/200 of the span, ie. 7.1cm. Maximal vertical displacement of the free end of the roof beam is 3.48 cm - cf. Fig. 23.

5 CONCLUSIONS

The study deals with the problem of vibration of the grandstand the municipal stadium in Krakow caused by spontaneous behavior of spectators. Calculations were carried out in the ABAQUS 6.12. Dynamic load was applied with characteristics that led one of the speedway stadiums in Poland to the state of emergency. Analysis of the results of calculation adopted structural model allowed us to formulate the following conclusions:

I. The first natural frequency of the structure (f_1 = 3.24 Hz) is close to maximal frequency of dynamic load which can be generated by crowd (f = 2.8 Hz).
II. The second natural frequency of the structure (f_2 = 4.5 Hz) is almost twice greater than frequency of excitation by dance called „Labado" (f = 2.2 Hz). It results increasing level of vibrations of construction elements.
III. Dynamic excitation causes an increase in stress in the elements of a 40% - 66%. Excitation also has an impact on the rooftop structures and increases the effort of some elements.
IV. Neglect of dynamic effects in the design of the grandstand entertainment facilities can be fatal. In order to prevent potential excessive vibrations of the structure should ensure a sufficiently high first natural frequency.
V. In the absence of resonance assuming dynamic load with a lower frequency it results in an increased dynamic effects for the system. The higher the frequency the lower the spikes and hence a greater dynamic load.
VI. The level of calculated stresses and displacements does not endanger the safety of use of the grandstand.

REFERENCES

[1] K. Żółtowski, *Pedestrian on footbridges, load and response of structure* (in Polish), Gdańsk University of Technology Publishing House, 2007.

[2] http://hm.pjwstk.edu.pl/raporty/%2810.2%29UruchomienieIEksploatacjaLaboratorium%20%2 81%29.pdf

[3] A. Flaga, *Pedestrian bridges* (in Polish), WKiŁ, 2011.

[4] T. Ji, B. R. Ellis, Floor vibration induced by dance type loads - Theory. *Structural Engineer*, vol. 72, No. 3, 37-44, 1994.

[5] B. R. Ellis, T. Ji, The response of structures to dynamic crowd loads, *Digest 426*, 2004.

[6] BS 6399: Part 1: 1996 Loading for buildings. Part 1. Code of practice for dead and imposed loads.

[7] Ellis B. R., Ji T., Loads generated by jumping crowds: numerical modelling, *The Structural Engineer*, 35-40, 2004.

[8] B. R. Ellis, T. Ji, J. D. Littler, The response of grandstands to dynamic crowd loads, *Proc. Instn Civ. Engrs Structs & Bldgs*, 355-365, 2000.

[9] G. G. Browning, Human Perception of Vibrations due to Synchronised Crowd Loading in Grandstands, *Doctoral thesis*, University of Bath 2011.

[10] http://stadiony.net

[11] http://wisla.krakow.pl

COMPDYN 2015
5th ECCOMAS Thematic Conference on
Computational Methods in Structural Dynamics and Earthquake Engineering
M. Papadrakakis, V. Papadopoulos, V. Plevris (eds.)
Crete Island, Greece, 25–27 May 2015

NATURAL FREQUENCY OF TRAFFIC FLOW-BRIDGE SYSTEM BASED ON CELLULAR AUTOMATON TECHNIQUE

Mao Ye[1], Shifan Huang[2], Baoxing Cao[3] and Min Ren[4]

[1, 2,3,4]Tamkang University- Guangzhou University Joint Research Center for Engineering Structure Disaster Prevention and Control, Guangzhou University, Guangzhou, China
e-mail: [1] dr.maoye@gmail.com; [2]617647493@qq.com; [3]1136580450qq.com; [4]rm_58@163.com

Keywords: Traffic flow, Roadway bridge, Finite element, Natural frequency, Cellular automation.

Abstract. *Based on Cellular automation (CA) traffic flow simulation technology widely used in the transportation field, a general framework of investigating the variation of natural frequencies of a roadway bridge under vehicle flow was developed. The results revealed that the values of the frequencies decrease as the traffic density increases and the effect on high modes of the bridge under vehicle flow is more significant.*

1 INTRODUCTION

Research on the dynamic behavior of bridges under moving vehicle loads can be dated back to many years ago, especially for railway bridges [1-8]. There are numerous publications regarding the dynamic analysis of train-bridge interactions [1-5]. Some of them focused on the effect of trains on the natural frequencies of bridges due to the effects of carriage masses coupled with the bridges through suspension systems, namely railway bridge on-load natural frequency. Ren et al. [7] focused on continuous bridges and some results showed that the vertical train-bridge natural frequency periodically varied when the trains were distributing on the whole bridge. Recently, the significance and the variation trend of driving frequencies and dominant frequencies in the response arising from the trainload was examined by Lu et al [6].

In recently year, there have been an increasing number of problems related to highway bridges. One of the problems is that the natural frequencies of the bridges decrease. As a result, it was desirable that the frequencies variation of bridge under traffic flow should be considered. Based on traffic-induced vibration tests on three bridges, the measured natural frequencies can change up to 5.4% for the short span bridges whose mass is relatively small [9]. The interaction between vehicular traffic and bridge vibration for a short span bridge was studied experimentally and analytically by Kwon et al [10]. The relative and absolute frequency changes of damaged reinforced concrete bridge structures under moving vehicular loads are sensitive to the weight of the moving vehicle, and the frequency ratio between the vehicle and bridge has some effect on them [11]. A theoretical framework is presented for the variation in frequencies of vibration of the VBI system by Yang et al [12-14], which indicated that the effect will be crucial when the vehicle mass is not negligible compared with the bridge mass or when the resonance condition is approached.

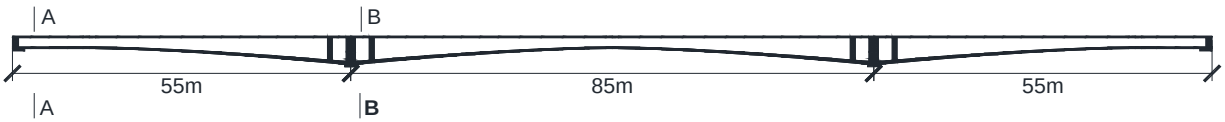
Some theoretical studies above are related to bridge on-load natural frequencies. For a train-bridge system [6-8], the train is modelled as multiple carriages and the bridge is modeled as a beam. For studying a vehicle-bridge system, similar to that of a train-bridge system, the vehicle is modeled as a moving mass [14] or a several degrees-of-freedom system [10-13] and the bridge is modeled as a beam. However, the vehicle-bridge system is much different from the train-bridges system such as load distribution and mechanical characteristics. Therefore, the model of vehicle-bridge system mentioned above can capture the physical essence of roadway bridge on-load natural frequencies. It is impossible to be applied to the real bridge.

This study aims to present a method to investigate the variation of natural frequencies of a roadway bridge under vehicle flow and various tasks are provide in several sections.

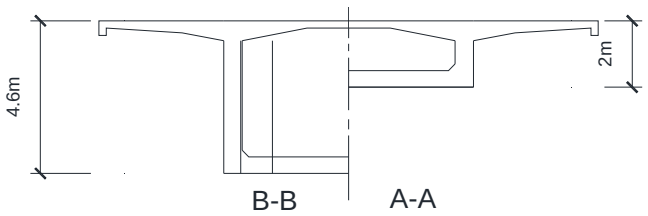
2 FEM BRIDGE MODEL

The case study is a continue box-girder bridge. The bridge has three spans, namely 55m+85m+55m, with a total length of 195 m. The width of the bridge is 15m. A scheme of the bridge is shown in Fig. 1. ANSYS was used to construct a full 3-D FEM of the bridge.

The bridge has been considered composed by three different materials for different structural elements: the box-girder (steel reinforced concrete), the pavement of the bridge (bituminous concrete), bridge supports (rubber bearing), with the characteristics reported in Table 1. The damping and nonlinear properties of the bridge are not considered in this study.



(a) Elevation



(b) Typical cross sections
Fig. 1. A scheme of the bridge (units: m).

Solid elements are used to build the model as shown in Fig.2. There are a total of 26,296 elements and 50,459 nodes. The first four natural frequencies of the bridge were determined using Block Lanczos method and presented in Table 2 respectively.

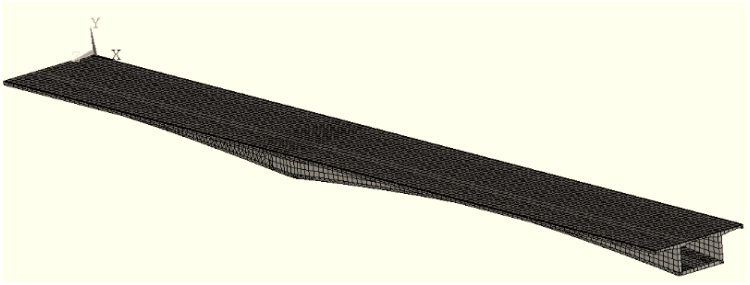


Fig. 2. A FE model of the bridge (a half)

Table 1. Mechanical Characteristics

Material	Steel reinforced concrete	Bituminous concrete	Rubber bearing
Young Modulus (N/m^2)	3.7e10	4.5e9	3.7e8
Density (kg/m^3)	2500	2440	2150
Poisson ratio	0.2	0.4	0.4

Table 2. Natural frequency for the first six modes

Mode No.	1	2	3	4
Natural frequency (Hz)	1.069	1.862	2.245	2.638

3 STOCHASTIC TRAFFIC FLOW ON A ROADWAY BRIDGE

Cellular automaton (CA) traffic flow simulation technology [16-18] is adopted to develop the stochastic traffic flow. The method is able to provide detailed instantaneous information of each vehicle through replicating major traffic phenomena on roadways. Thus it is an ideal technology to be integrated into the advanced bridge analysis considering traffic flow in a more realistic manner.

3.1 Theoretical basis

CA traffic model is to simulate the stochastic traffic flow through discrete time and space and each lane is divided into cells with an equal length. Each cell can be either empty or occupied by one vehicle at a time. At each time step, a vehicle moves, accelerates, decelerates or changes lanes based on some predefined rules [16-18]. The rules of a typical CA traffic model

include: (1) the rules of the single-lane CA model; and (2) the conditions for lane changing. Vehicle i is taken as an example to introduce the CA traffic model rules. $v_i(t)$ and $v_i(t+1)$ are the velocities at time t and $t+1$ respectively. $L_i(t)$ and $L_{i+1}(t)$ denote the locations of vehicle i and the vehicle immediately ahead of vehicle i. $v_{\max}$ represents the maximum velocity. $\mathbf{gap}_i(t)$ is the distance between vehicle i and vehicle $i+1$. ρb denotes the randomization probability.

The rules for the single-lane CA model are shown as follows:

Rule 1: acceleration, $v_i(t+1) = v_i(t)+1$ if $v_i(t) < v_{\max}$ and $\mathbf{gap}_i(t) > v_i(t)+1$.

Rule 2: deceleration, $v_i(t+1) = \mathbf{gap}_i(t)-1$ if $\mathbf{gap}_i(t) <= v_i(t)+1$.

Rule 3: randomization, $P(v_i(t+1) = v_i(t)-1 \mid v_i(t) > 0) = \rho b$.

Rule 4: vehicle motion. If the three conditions above are not satisfied, then $v_i(t+1) = v_i(t)$.

Vehicle i will change to the target lane with the probability of ρch if all the three following criteria are satisfied:

Rule 5: $\mathbf{gap}_i(t) <= v_i(t)+1$.

Rule 6: $\mathbf{gapo}_i(t) > v_i(t)+1$, $\mathbf{gapo}_i(t) = L_{f,i}(t) - L_i(t)$, $L_{f,i}(t)$ denote the location of the nearest vehicle on the target lane moving ahead of vehicle i.

Rule 7: $\mathbf{gapoback}_i(t) > v_{\max}$, $\mathbf{gapoback}_i(t) = L_i(t) - L_{b,i}(t)$, $L_{b,i}(t)$ is the location of the nearest vehicle on the target lane moving behind vehicle i.

To complete a lane-changing simulation, the location and the velocity of vehicle i will be updated through two sub-steps:

Step 1: vehicle i moves to the target lane transversely without moving forward.

Step 2: vehicle i moves forward obeying the single lane rule as illustrated above after moving into the target lane.

3.2 Traffic flow simulation on the bridge

In the present study, the bridge is a two-lane one-way bridge and a steel reinforced concrete bridge. Actually, frequencies variation of the bridge under vehicle flow is not obviously, because the vehicle mass is small compared with the bridge mass. Even though, it is sufficient to interpret the method suggested in the paper to analysis the natural frequencies of a roadway bridge under vehicle flow.

The total length of the bridge is 195 m (L_b). Chen et al.[18] suggested that approaching roadways on both sides of the bridge should be considered, because the actual traffic flow through a bridge is also affected by the traffic on the approaching roadways. The approaching roadway has the length of 975 m (L_r) at each end of the bridge in the present study [18]. The length of 'roadway-bridge-roadway' system is 2145m. The bridge and the approaching roadways have the same number of available lanes. All the lanes on the bridge and the connecting roadways share the same width and each lane is divided into equally-spaced cells. The rules of the bridge and the approaching roadways are the same. The length of each cell (L_c) is set to be 7.5 m [18], which is the typical distance between the centers of two vehicles when the road is in a complete congestion. Then, the number of all cells in one lane is 286 (N).The velocity limit $V_{\max}$ is assumed to be 120 km/h, which is the typical speed limit on highways in China. The period of each time step is 1s. So $v_{\max}$ in the CA model can be computed accordingly:

$$v_{\max} = \frac{V_{\max}}{L_c} = \frac{120(\mathbf{km/h})}{7.5(\mathbf{m/cell})} = 4.44(\mathbf{cell/s}) \approx 4(\mathbf{cell/s}) \quad (1)$$

In the following CA-based traffic flow simulation, the periodic boundary condition is adopted. The initial velocities of all the vehicles are randomly set among $0 \sim 4$(**cell/s)**. The CA traffic simulation rules will decide the velocity of each individual vehicle according to the speed limit adaptively. The probability of braking (ρb) is 0.5. The probability of changing lane (ρch) is 0.8. Various vehicles on highways are grouped into eight categories, the weights of various vehicles are summarized in Table 2. The proportions of the vehicles in each category are assumed to be 0.125 equally.

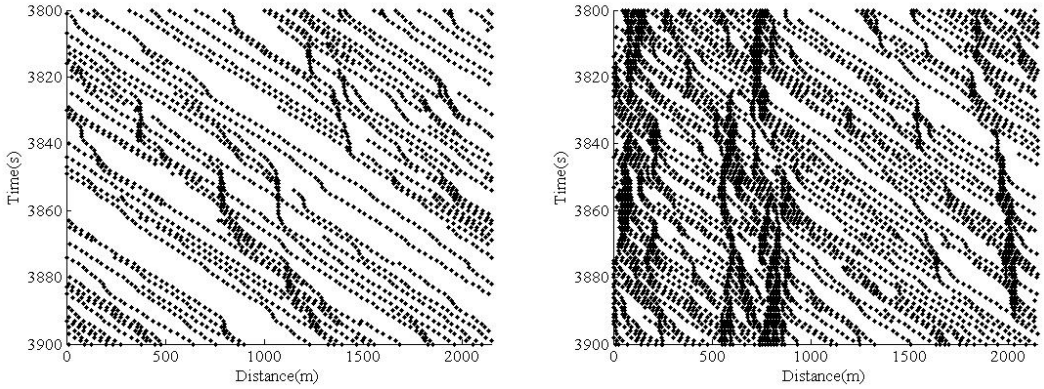
Table 2. The weight of various vehicles

Categories	car	Mini bus	Light bus	bus	Mini truck	Light truck	Truck	Heavy truck
Weight (kg)	2000	7220	10000	20000	10000	15000	25000	32000

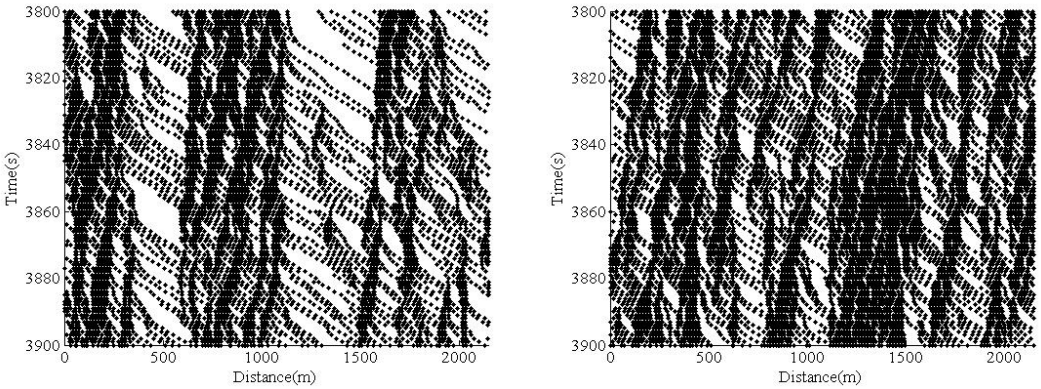
With the adoption of the periodic boundary condition, the traffic occupancy in the whole system keeps constant for each simulation. Four densities (ρ) are considered in the present study: (1) $\rho = 0.08$ (11 veh/km/lane), (2) $\rho = 0.16$ (22 veh/km/lane), (3) $\rho = 0.24$ (32 veh/km/lane), (4) $\rho = 0.36$ (50 veh/km/lane). The first three densities (1), (2), (3) correspond to Level of service of B, D, F respectively. The last density (4) are proposed for this research. The observation of the traffic flow will start after $t_0 = 10C$ (C is the number of all cells in one lane, here $C = 286$) when the traffic flow is typically believed to become steady [18]. Thus, the traffic flow starting from 3000 s in this study will be presented in the following sections.

The typical two-lane traffic simulation of a 'roadway-bridge-roadway' system is conducted and the results are shown in Fig. 3. As presented in Fig. 3, the time versus space information of the simulated traffic flow on one lane is given. The x-axis shows the physical location of each vehicle on the 'roadway-bridge-roadway'. The y-axis shows the time range after 3000 s of simulation elapsed. At any time instant on the y-axis, the information of the physical distribution of each vehicle along the spatial simulation region (x-axis) can be found by drawing a line horizontally. Similarly, at any spatial location on the x-axis, the time-variant information of vehicles at one particular location can also be retrieved by drawing a line vertically.

In Fig. 4, we show four different situations at four different densities. Operational condition of the bridge is free flow at $\rho = 0.08$. As the density increase, traffic congestion appears. The ability to maneuver is severely restricted due to traffic congestion at $\rho = 0.16$. At $\rho = 0.24$ and $\rho = 0.36$, the traffic flow breakdown. Vehicles arrive at a rate greater than the rate at which they are discharged. Operations within queues are highly unstable, vehicles experiencing brief periods of movement followed by stoppages.



(a) $\rho = 0.08$ (b) $\rho = 0.16$



(c) $\rho = 0.24$ (d) $\rho = 0.36$

Fig. 3. Traffic flow simulation result

4 TIME-VARIANT NATURAL FREQUENCIES OF BRIDGE

The FE model of the bridge and traffic flow on the bridge have been obtained above. Each vehicle in the stochastic traffic flow is modeled as a mass, it is convenient to determine time variant natural frequencies of bridge under traffic flow. The weights of various vehicles are presented in Table 2. The following is the procedure used to determine time variant natural frequencies of bridge under vehicle flow.

Step 1: Establish FE model of the bridge in ANSYS.

Step 2: Simulate traffic flow cross the bridge based on Cellular automaton (CA) traffic flow simulation technology.

Step 3: Obtain positions of all vehicles distributed on the bridge at time step t from traffic flow simulation result.

Step4: Establish the FE models of all vehicles on the FEmodel of bridge according to the position of vehicle and vehicle type. MASS 21 is adopted to simulate the vehicle.

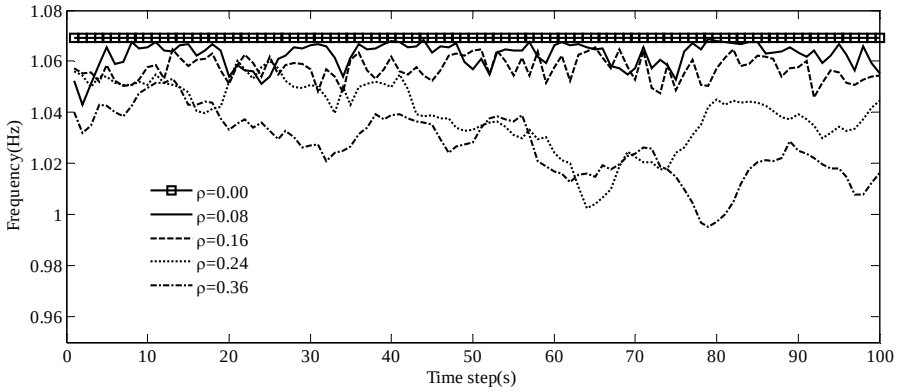
Step5: Calculate the frequency of traffic flow-bridge system at time step t.

Step6: Check the traffic flow. If the traffic flow has crossed the bridge, the time variant natural frequencies of bridge under traffic flow is finish.

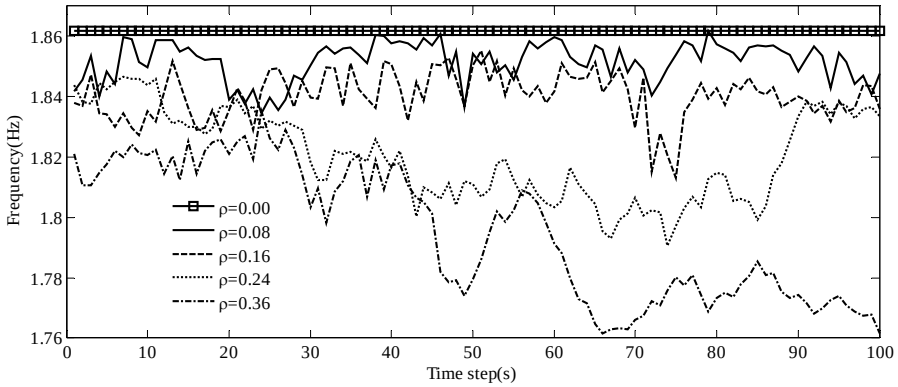
Step7: At time step $t+1$, go to step 3 and repeat the procedure until the traffic flow has crossed the bridge.

Due to the traffic flow through the bridge, the natural frequencies of the bridge at any one moment is usually different from that at the next moment. The variations of the first four frequencies with time as the vehicles pass over bridge are shown in Fig.4. Legend $\rho = 0.00$ represents that there are no vehicles on the bridge. Compared to the natural frequencies of bridge ($\rho = 0.00$), the frequencies of bridge under vehicle flow decrease at any time instant. From Fig. 4, as the traffic density increase, the natural frequencies decrease in general. Larger fluctuations of the natural frequencies under traffic flow over time are observed in Fig.5 when the traffic density is high.

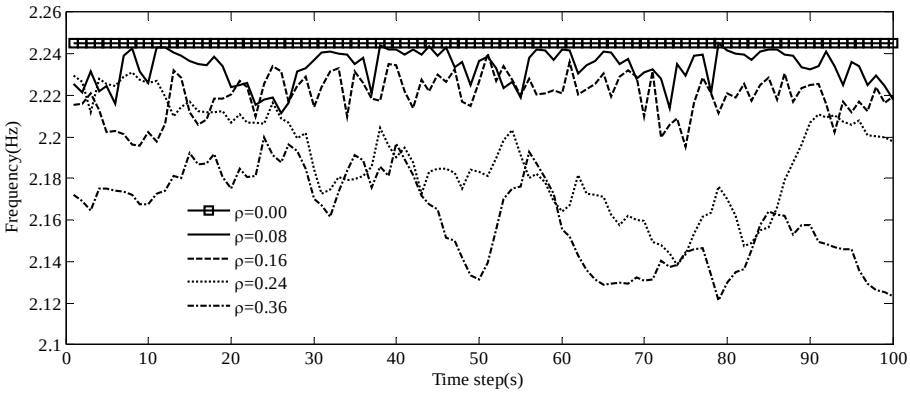
In order to investigate the effect of the vehicles on different mode of bridge under vehicle flow, the time-history of difference between natural frequencies of the bridge and the bridge with vehicle for the four traffic densities are shown in Fig.5 (a)-(d), respectively. From Fig.6, it can be concluded that the effect of the vehicles on the higher modes of the bridge under vehicle flow are more significant than on the lower modes in general.



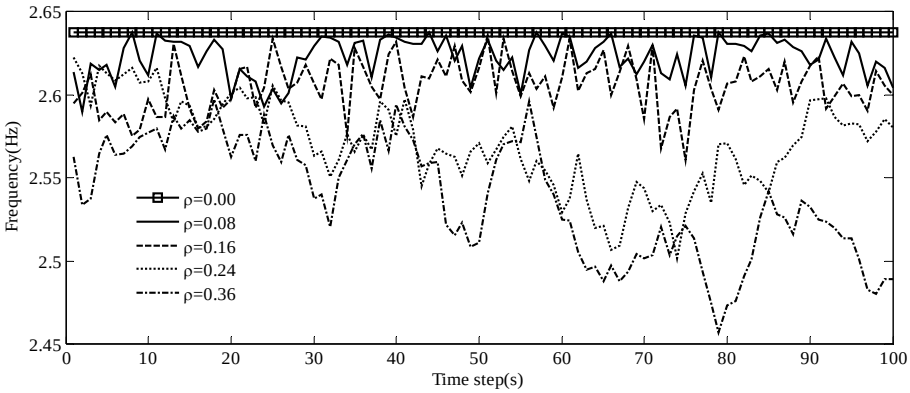
(a) 1st natural frequency



(b) 2nd natural frequency

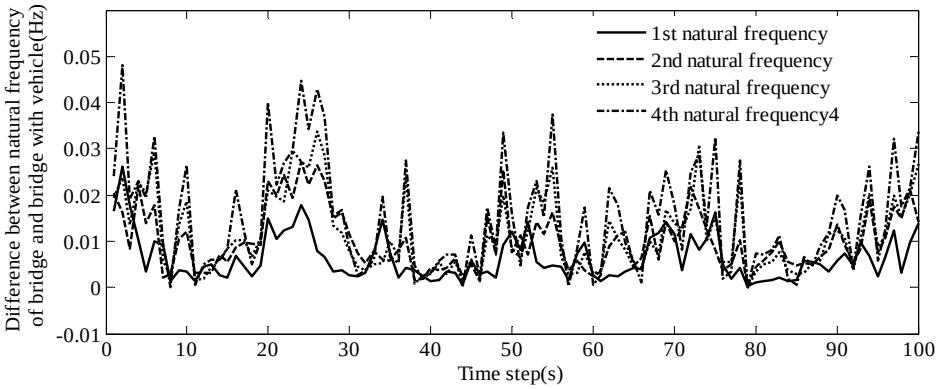


(c) 3rd natural frequency

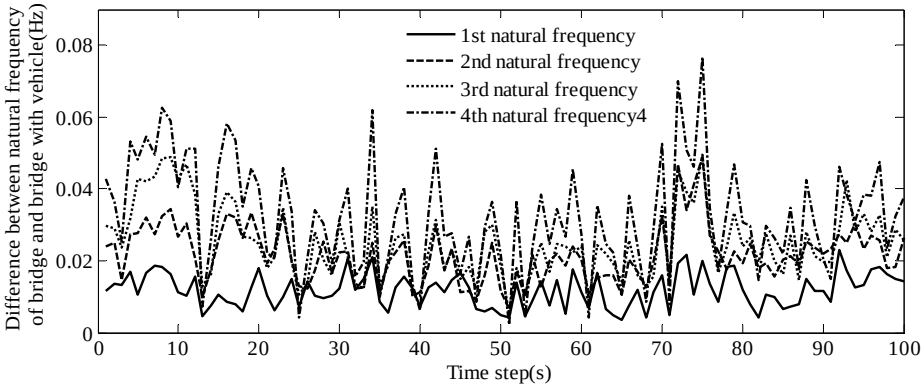


(d) 4th natural frequency

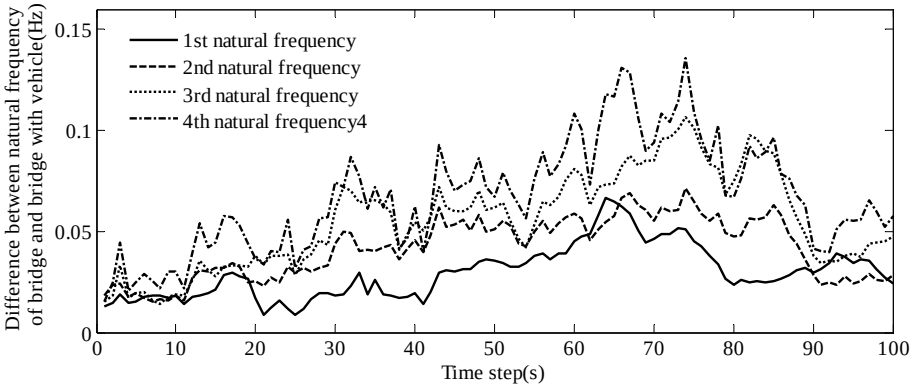
Fig. 4. The variations of the first four frequencies with time as the vehicles pass over bridge



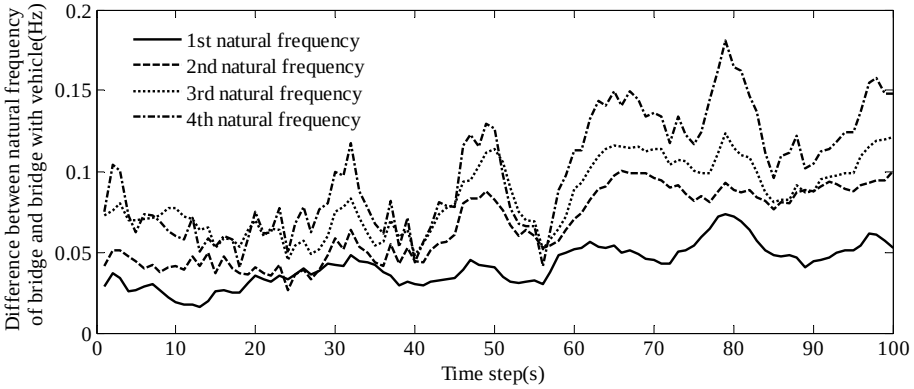
(a) $\rho = 0.08$



(b) $\rho = 0.16$



(c) $\rho = 0.24$



(d) $\rho = 0.36$

Fig. 5. Effect of the vehicles on different mode of bridge under vehicle flow

5 CONCLUTION

Based on traffic flow simulation technology, a general framework of investigating the variation of natural frequencies of a roadway bridge under vehicle flow was developed. The obtained results revealed that the natural frequencies decrease in general as the value of the traffic density increase. Compared to the natural frequencies of the empty bridge, the natural frequencies of bridge under vehicle flow decrease at any time instant. Moreover, it was shown that the effect of the vehicles on high modes of the bridge under vehicle flow is more significant. The method presented can be used in practical engineering.

ACKNOWLEDGEMENTS

This work is supported by China National Natural Fund (Project No. 51178126, 51208125), Science and Technology Program of Guangzhou (Project No. 2013J2200074), Guangdong Province of high level talents in Higher School project, Guangdong Natural Fund (Project No. s2011030002800) and China Scholarship Council, and the financial supports were gratefully acknowledged.

REFERENCES

[1] Elias G. Dimitrakopoulos, Qing Zeng,three-dimensional dynamic analysis scheme for the interaction between trains and curved railway bridges. *Computers and Structures*, 149,43-60, 2015.

[2] Peyman Mellat, Andreas Andersson, Lars Pettersson, Raid Karoumi, Dynamic behavior of a short span soil–steel composite bridge for high-speed railways-Field measurements and FE-analysis. Engineering Structures, 69, 49–61, 2014.

[3] K. Liu, H. Zhou, G. Shi, Y.Q. Wang, Y.J. Shi and G. De Roeck, Fatigue assessment of a composite railway bridge for high speed trains. Part II: Conditions for which a dynamic analysis is needed. Journal of Constructional Steel Research, 82, 246-254, .2013.

[4] Alessandra Zambrano, Determination of the critical loading conditions for bridges under crossing trains. Engineering Structures, 33,320–32, 2011.

[5] Nan Zhang, He Xia, Guido De Roeck, Dynamic analysis of a train-bridge system under multi-support seismic excitations. Journal of Mechanical Science and Technology, 24, 2181-2188, 2010.

[6] Yong Lu a,c, Lei Mao, Peter Woodward, Frequency characteristics of railway bridge response to moving trains with consideration of train mass. Engineering Structures, 42, 9-22, 2012.

[7] Jianying Ren, Mubiao Su and Qingyuan Zeng, Vertical load-carrying natural frequency of railway continuous steel truss bridges. Traffic and Transportation Studies, 1387-1398, 2010.

[8] Jianzhong Li, Mubiao Su, and Lichu Fan, Natural Frequency of railway girder bridges under vehicle loads. Journal of Bridge Engineering, 8, 199-203, 2003.

[9] Chul-Young Kim, Dae-Sung Jung, Nam-Sik Kim, Soon-Duck Kwon and Maria Q. Feng, Effect of vehicle weight on natural frequencies of bridges measured from traffic-induced vibration. Earthquake Engineering and Engineering Vibration, 2, 109-115, 3003

[10] S.D.Kwon,C.Y.Kim, and S.P.Chang, Change of modal parameters of bridge due to vehicle pass, IMAC-XXIII: Conference & Exposition on Structural Dynamic, 2015

[11] S.S. Law, X.Q. Zhu, Dynamic behaviour of damaged concrete bridge structures under moving vehicular loads, Engineering Structures, 26, 1279-1293, 2004.

[12] Y. B. Yang, M. C. Cheng and K. C. Chang, Frequency variation in vehicle bridge interaction systems. International Journal of Structural Stability and Dynamics, 13, 350019-1-1350019-22, 2013.

[13] Guojin Tan, Yongchun Cheng, Hong Zhao and Fushou LIU, Research on the influence law of vehicles to the natural frequency of highway simply supported girder bridges. ICCTP-Integrated Transportation Systems- Green Intelligent Reliable ASCE, 3201-3208, 2010.

[14] Raham Zarfam, Ali Reza Khaloo, Ali Nikkhoo, On the response spectrum of Euler–Bernoulli beams with a moving mass and horizontal support excitation, Mechanics Research Communications, 47, 77-83, 2013.

[15] ANSYS Modeling and Meshing Guide: ANSYS Release 11.0[M/CD]. ANSYS Inc.,2008.

[16] Nagel K, Schreckenberg M, A cellular automaton model for freeway traffic. J Phys I France, 2, 2221-9, 1992.

[17] Xin-Gang Lia, Bin Jiaa, , Zi-You Gaoa, Rui Jiang, A realistic two-lane cellular automata traffic model considering aggressive lane-changing behaviour of fast vehicle. Physica A, 367, 479-486, 2006.

[18] S.R. Chen, J. Wu, Modeling stochastic live load for long-span bridge based on microscopic traffic flow simulation. Computers and Structures, 89, 813-824, 2011.

COMPDYN 2015
5th ECCOMAS Thematic Conference on
Computational Methods in Structural Dynamics and Earthquake Engineering
M. Papadrakakis, V. Papadopoulos, V. Plevris (eds.)
Crete Island, Greece, 25–27 May 2015

INFLUENCE OF FLOATER RESPONSE ON WIND TURBINE TOWER MOMENTS IN FLOATING WIND TURBINE SYSTEM

Muhammad Bilal Waris[1] **and Takeshi Ishihara**[2]

[1]Department of Civil and Architectural Engineering, Sultan Qaboos University
P.O. Box: 33, Muscat 123, Sultanate of Oman.
waris@squ.edu.om

[2]Department of Civil Engineering, University of Tokyo,
7-3-1, Hongo, Bunkyo-ku, Tokyo 113-8656, Japan.
ishihara@t.u-tokyo.ac.jp

Keywords: Floating Wind Turbine, FEM, Tower moment, Coupled system.

Abstract. *The study uses finite element modeling to discuss the effect of floater response on tower moments in a floating offshore wind turbine system. A semi-submersible floating platform supporting a single NREL-5MW wind turbine was investigated. In order to understand the contribution of different modes of floater motion to tower load, tension leg mooring and catenary mooring were used. The mooring systems were designed to provide similar dynamic response amplitude in surge, while the pitch response was inherently different. Wind and wave loads were considered separately and then together to identify their respective contribution to response and tower loads. Both wind and wave loads were found to be critical for tower base moment while wind loads govern the tower top moments. In comparison with catenary mooring, the tension leg mooring was found to reduce the tower base moment by up to 50 % at higher wind speeds due to restraint to pitch motion. The two types of mooring provided a similar tower top moment which indicates it is independent of pitch motion.*

1 INTRODUCTION

Wind is one of the most consistent and global form of renewable energy. Due to rapid depletion of natural resources, there is an increase in trend towards use of wind energy as an alternate and sustainable source of power generation. In the last couple of decades, there has been a rapid increase in wind farm installations. In the last five years, there was an average annual increase of almost 27.6 % in global wind power generation. Wind turbines installed worldwide till end of 2011 contribute 430 TWH of power, which is 2.5 % of global demand. Denmark has the highest national contribution from wind energy at 21%. [1, 2]

The widespread application of wind energy has some practical limitation. Rural areas with steady wind and large space for wind farms have low energy demand while urban areas with high energy demand lack the space and steady wind resource. Most of the metropolis of the world are situated near shorelines and have a huge offshore wind and space resource at hand. This potential was first recognized in early 1970's and lead to the rapid development of offshore wind farms. However, all such farms have been made in shallow water, where the water depth is less than 30 m and bottom mounted setup is possible. This constraint significantly reduces the ability to fully harness the offshore wind potential and has limited application to regions with adequate wind resource in shallow water. To exploit the rich deep offshore wind resource, floating support systems have to be developed. Marine and offshore oil industries have successfully established technical viability of floating structures but their design is safety oriented and expensive. In their design, mooring system is taken in linear range while hydrodynamic and aerodynamic dampings are ignored. In contrast, for wind energy applications, the design of the floating systems should be based on economy and needs to be optimized to achieve the lowest life cycle cost for the entire structure. Hence the purpose of this research is to investigate the effect of floater displacement on wind turbine.

Several concepts [3, 4, 5, 6, 7, 8, 9, 10, 11] were proposed for using multiple wind turbines on a single floater. Such floaters have the advantage of using a single mooring and power supply system thus reducing the cost. Owing to their large size, they are more stable but have to carry large wave current loads, while the wind turbines suffer wake effect due to close proximity to other wind turbines on the floater. Over the last decade several concepts [12, 13, 14, 15, 16] of single wind turbine floaters have been investigated, these systems would resolve issues involved in the multi-turbine system but they suffer from stronger wave induced loads. The wave loads influence the wind turbine through six degrees of freedom of the supporting floater system as shown in figure 1. Three modes are translational (surge, sway and heave) and three are rotational (roll, pitch and yaw). Out of the six surge, heave and pitch are the major modes of oscillation and are expected to contribute heavily to wind turbine tower moment. The extent of restraint in these modes depends upon the type of mooring system used for station keeping and stability of the floater in open water. The different types of mooring are catenary, taut and tension leg mooring. Catenary system provides the least restraint while the tension leg system has the highest restraint to floater response. The first is cheaper and stable in case of its partial failure while the latter is expensive and unstable in case of its partial damage.

In this paper, a previously developed numerical tool [2, 14] is used to investigate the effect of floater response modes on the wind turbine tower moments over the range of operational wind speed for wind turbine. The catenary and tension leg type mooring system are considered to account for the level of restraint to floater response. The study also investigates the influence of individual wind and wave loads on the floater response and wind turbine tower moments.

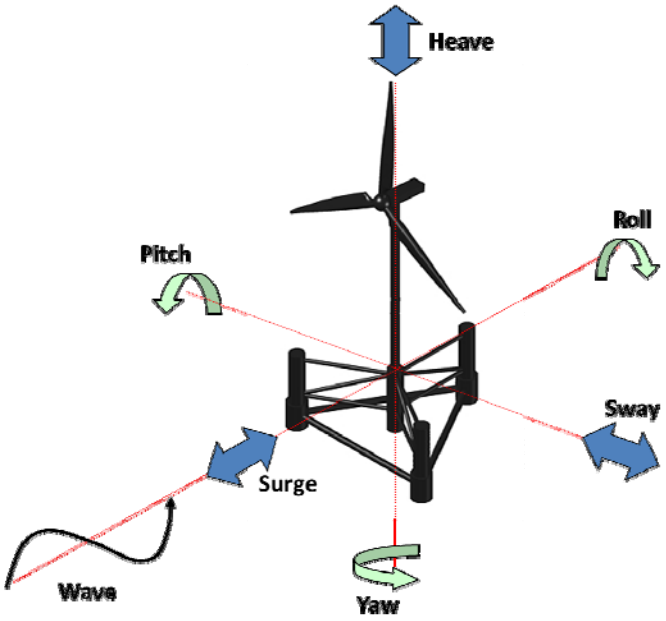


Figure 1 Degree of Freedom of a floating wind turbine

2 FLOATER WIND TURBINE SYSTEM

2.1 Wind Turbine

A modified National Renewable Energy Laboratory's (NREL) offshore 5-MW baseline wind turbine developed by Jonkman [12] was used in this study. The basic properties of the wind turbine are outlined here (table 1) with respect to some modifications that are essential for input in the numerical program. As the used scheme [2] cannot consider pitch control, wind turbine was considered as stall regulated. The aerodynamic and geometric details of the rotor blades and tower provided in Jonkman [12] were used.

Rated Power	5 MW
Rotor Orientation, Configuration	Upwind, 3-blades
Drivetrain	High Speed, Multi-stage gearbox
Rotor, Hub diameter	126, 3 m
Hub Height	90 m
Cut-In, Rated, Cut-Out wind speed	5.0, 11.4, 25 m/sec
Cut-In, Rated Rotor Speed	6.9 rpm, 12.1 rpm
Rated tip speed	80.0 m/sec
Overhang, Tilt	5.0 m, 5.0°
Rotor Mass	110,000 Kg
Tower Mass	240,000 Kg

Table 1 Details of NREL 5MW wind turbine [12]

2.2 Semi-Submersible Floater System

A triangular tri-pontoon semi-submersible floater was considered to support the NREL 5 MW wind turbine as shown in figure 1. The span in all three directions was 60.0 m. The pontoons had an overall depth of 30.0 m with a draft of 20.0 m. The floater had a mass of

5,638,760 kg for the catenary mooring system which was reduced to 75 % for tension leg mooring system to account for tether pre-tension. The details of the floater are listed in table 2.

Span		60.0 m
Draft		20.0 m
Overall Height		30.0 m
Peripheral Bracing		Φ 2.50 m
Inner Bracing		Φ 1.80 m
Corner pontoon	Top (20 m)	Φ 9.0 m
	Bottom (10 m)	Φ 10.0 m
Central pontoon		Φ 9.0 m

Table 2 Dimensions of the semi-submersible floater

2.3 Mooring System

The floater was assumed to be situated in deep water with seabed 100 m below water level. The catenary mooring system with three mooring lines each having span of 400 m was considered. The length of each line was 417.84 m. The mooring lines were separated at 120°, with front two lines having an angle of 120° and -120° with the incident wave and the third aligned in the wave direction. All the three lines had a common fairlead at the base of the central pontoon of the floater that supports the wind turbine. In tension leg mooring arrangement, three tethers are considered connected to each of the corner pontoons having length of 80 m. A buoyancy force of 25 % of the original weight of floater was considered that provided a pre-tension of 4950 KN in each tether. These values are selected to obtain similar dynamic surge response for two types of mooring systems. The mooring arrangement for tension leg is considered to eliminate pitch motion of the floater, while the arrangement for catenary magnified the pitch motion. It is essential to indicate here that the current study, does not present a comparison of the two types of mooring system but has used these systems to investigate influence of response modes on wind turbine loads.

3 NUMERICAL MODEL

3.1 Numerical Scheme

A finite element scheme [2, 14] that can use beam, pre-stressed beam and truss type elements and considers coupled interaction between floater, wind turbine and mooring system was used. The scheme uses Morison equation [17] with Srinivasan's Model [6] for estimation of hydrodynamic force, non-hydrostatic model [14] for restoring force and penalty method [18] for contact of mooring with seabed. The equation of motion can be written as

$$[M]\{\ddot{X}\}+[C]\{\dot{X}\}+[K]\{X\}=\{F\} \tag{1}$$

Where

$$[M]=\begin{bmatrix} M_T & 0 & 0 \\ 0 & M_F & 0 \\ 0 & 0 & M_M \end{bmatrix},[C]=\begin{bmatrix} C_{TT} & C_{TF} & 0 \\ C_{FT} & C_{FF} & C_{FM} \\ 0 & C_{MF} & C_{MM} \end{bmatrix},[K]=\begin{bmatrix} K_{TT} & K_{TF} & 0 \\ K_{FT} & K_{FF} & K_{FM} \\ 0 & K_{MF} & K_{MM} \end{bmatrix},$$

$$\{X\}=\begin{Bmatrix} X_T \\ X_F \\ X_M \end{Bmatrix} \quad ;\{F\}=\begin{Bmatrix} F_T \\ F_F \\ F_M \end{Bmatrix}=\begin{Bmatrix} F_\gamma \\ F_\gamma \\ F_\gamma \end{Bmatrix}+\begin{Bmatrix} 0 \\ F_\beta \\ F_\beta \end{Bmatrix}+\begin{Bmatrix} 0 \\ F_H \\ F_H \end{Bmatrix}+\begin{Bmatrix} 0 \\ F_R \\ F_R \end{Bmatrix}+\begin{Bmatrix} 0 \\ 0 \\ F_C \end{Bmatrix}+\begin{Bmatrix} F_W \\ F_W \\ 0 \end{Bmatrix}+\begin{Bmatrix} F_B \\ F_B \\ 0 \end{Bmatrix}$$

"T", "F" and "M" refer to turbine, floater and mooring system respectively. [X] represents the unknown displacements in six degree of freedom. [M], [C] and [K] are the mass, damping and stiffness matrices of the system respectively. {F} is total external force vector changing with time. $\{F_\gamma\}$ is gravitational force, $\{F_\beta\}$ is buoyancy force, $\{F_H\}$ is hydrodynamic force, $\{F_R\}$ is restoring force, $\{F_C\}$ is seabed contact force, $\{F_W\}$ is aerodynamic force acting on wind turbine and floater system above sea level and $\{F_B\}$ is blade element momentum force on the wind turbine rotor during operation.

3.2 Finite Element Model

The finite element model for the floating offshore wind turbine system was prepared using beam, pre-stress beam and truss elements [2]. The NREL 5 MW wind turbine was modeled using 85 beam elements, with 10 elements for the tower and 24 elements in each blade. The floater was modeled using 109 beam elements. For catenary system, each mooring line was modeled using 30 truss elements and for tension leg system each tether was modeled using 10 pre-stressed beam elements.

3.3 Environmental Conditions

In this study, wind turbulence conditions specific to offshore (Type-I) were considered. The method developed by Phuc [19] was used for the generation three dimensional wind time histories at several points considering auto spectral and cross-spectral functions. For the wind turbine tower, the wind histories were generated at nodes of the tower, while for the rotor a 7x7 square grid of points was considered that encompassed the rotor area. The sea-state was modeled using JONSWAP spectrum [20], which gives the wind-wave height and wind-wave period relationships as:

$$H_S = \frac{0.0094 \times 0.16^{-\frac{5}{3}}}{g} U^2_{1Hr|h=10m} \approx \frac{0.20}{g} U^2_{1Hr|h=10m} \tag{2}$$

$$T_P = \frac{25/4}{g} U_{1hr|h=10m} \tag{3}$$

Where 'g' is the acceleration due to gravity and '$U_{1hr|h=10\,m}$' is the hourly mean wind speed at 10 m height above the mean sea surface. Since in wind turbine analysis, the wind speed is usually considered as 10 min mean and at the hub height, equations (2) and (3) need to be modified to use this definition. The relationship between mean wind speeds for different averaging durations can be estimated based on ASCE 7-02 [21]. The wind speed at different heights is related by the normal wind speed profile with exponent value of 0.14 defined in IEC-61400-3 [22].

$$U_{1Hour|h=10m} = \frac{U_{10\min|h=10m}}{1.08} \tag{4}$$

$$U_{10\min|h=10m} = U_{hub}\left(\frac{h}{H_{hub}}\right)^{0.14} = U_{hub}\left(\frac{10}{H_{hub}}\right)^{0.14} \tag{5}$$

'U_{hub}' represents the 10 minute mean wind speed at the hub height 'H_{hub}' above the sea level. Using these relationships (equation 2-5), the significant wave height 'H_S' and peak wave period 'T_P' were estimated using the 10 minute mean wind speed at hub height 'U_{hub}'

over a range of 5 ~ 25 m/sec as shown in figure 2. The wave time history was generated using JONSWAP spectrum [20] for the respective value of significant wave height and peak wave period. A wave current velocity of 2.0 m/sec was considered to account for the effect of current.

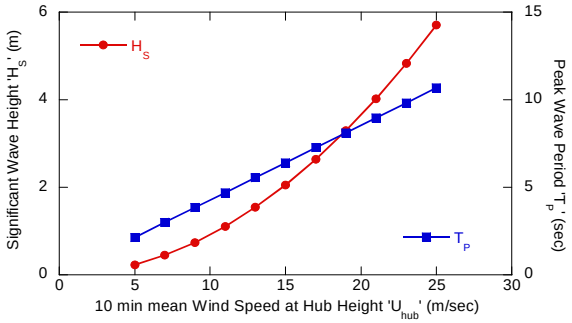


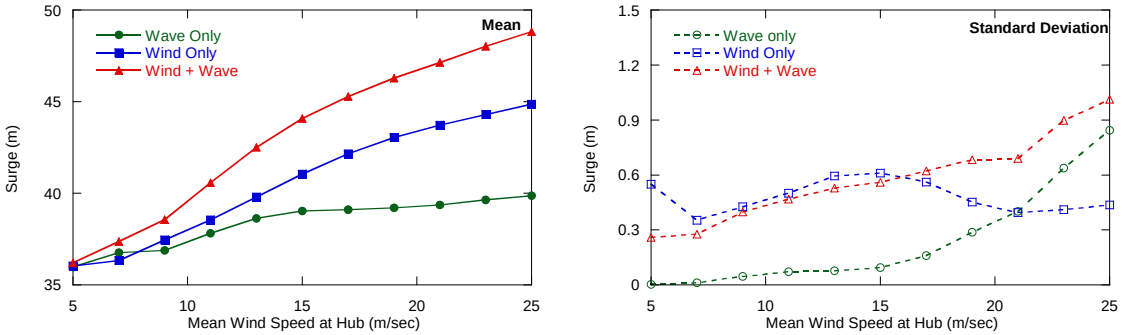
Figure 2 Relationship of wind speed at hub height with significant wave height and peak wave period

4 RESULTS AND DISCUSSION

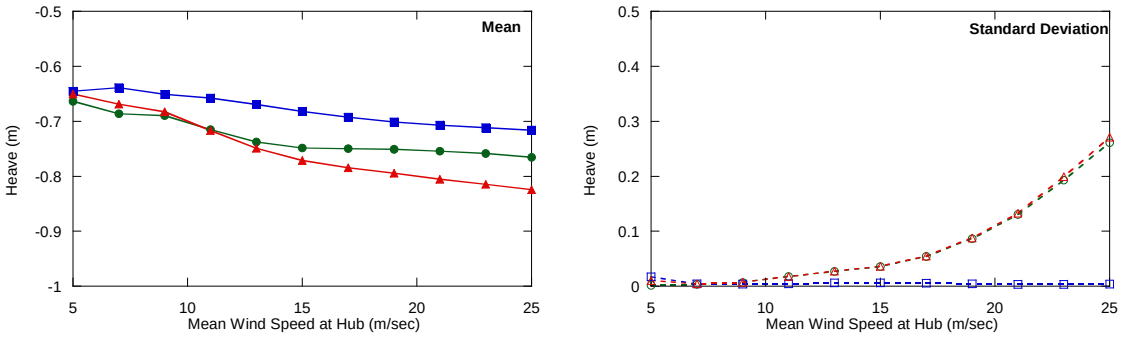
Three types of loading scenarios were considered; wave only, wind only and wind and wave combined. The effect of wave current was considered in all cases. For each load scenario, 11 simulations of 20 min duration were run for wind speed from 5 to 25 m/sec. For the wave only cases, the waves were modeled using the respective wind speed but the wind was ignored. To account for the drift due to currents, initial 600 seconds of the simulation have been removed for statistical estimation. The results are presented as the mean and standard deviation of surge, heave and pitch response of the floating wind turbine system for respective mean wind velocity. The wind turbine loads are presented as the tower base and tower top moments.

4.1 Response of the floating wind turbine system

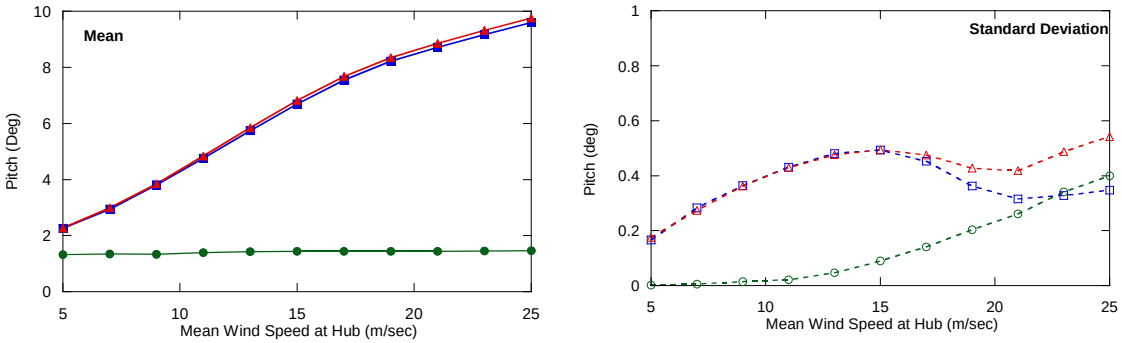
The response of the two types of mooring systems are discussed separately and observed for similarity. Mean and standard deviation of surge, heave and pitch response at the tower base for catenary and tension leg mooring are shown in figures 3 and 4 respectively. For the catenary mooring in figure3(a), mean surge indicates that the wave current results in a mean drift of nearly 35 m. The response had a monotonic increase with wind speed and wave height. The wind loads had stronger effect on mean surge relative to wave loads this is be because of large aerodynamic load on the wind turbine. The mean surge for wind + wave load is almost the arithmetic sum of the individual response for wind and wave that indicates the floater system behaves like a linear spring. The standard deviation of surge shows that the dynamic behaviour is more sensitive to wave load showing monotonic increase, while the wind load shows no clear relationship. In figure3(b), the mean heave response is not sensitive to wind load while the wave load has an overall sinking effect on the floater. The negative values indicate increase in draft. The standard deviation shows that the dynamic component of heave is sensitive to wave load only with negligible contribution from wind. The system again shows a linear behavior when the two loads are combined. The mean pitch response in figure 3(c) is sensitive to wind load only, due to the thrust on the wind turbine rotor while the dynamic part is sensitive to the both the wind and wave load. The pitch response does not show a linear behavior, the values for the wind only and combined cases were the same till 15 m/sec while the latter gets larger afterwards and contribution from wave loads increased.



(a) Surge



(b) Heave

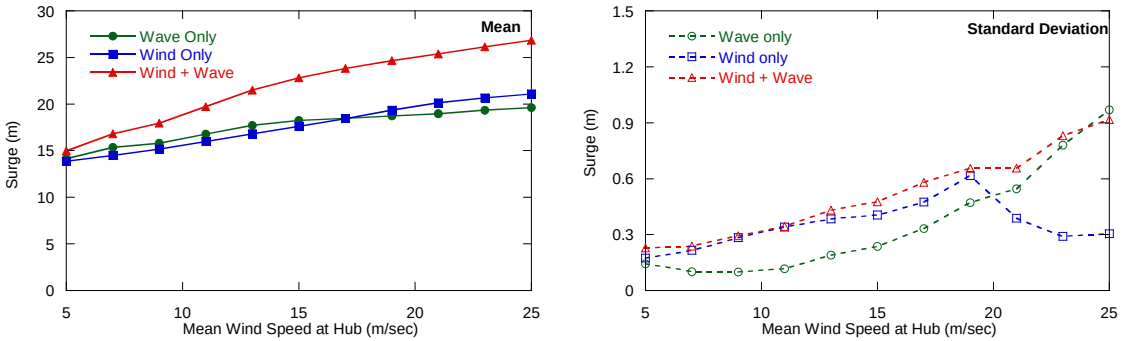


(c) Pitch

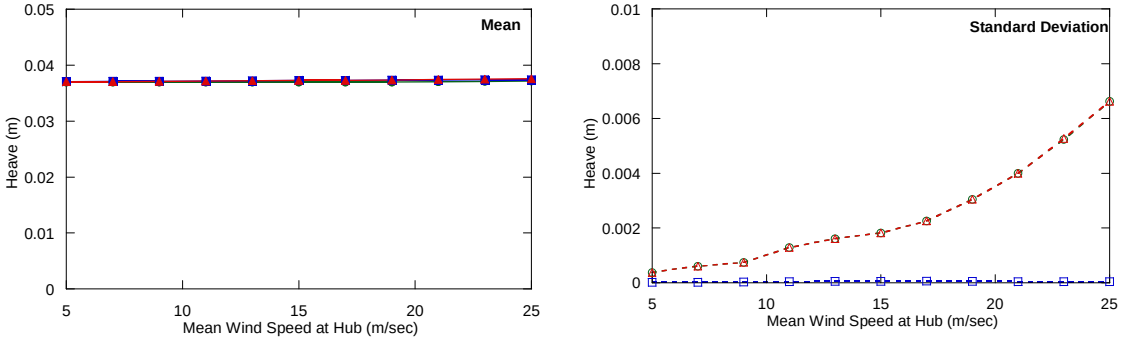
Figure 3 Response of floater with catenary mooring

For tension leg mooring in figure 4(a), the mean surge drift under currents is nearly 14 m that is around 40 % of that catenary mooring. The wind and wave loads have similar effects on mean surge response as seen in case of catenary mooring. However, comparative effect of the two is almost similar. The mean heave response is independent of the environmental load because of the strong restraint. The mean pitch though infinitesimal is more affected by wind load as observed in case of catenary mooring. For dynamic component (standard deviation), the wind and wave again showed similar contribution to surge response, the heave response was dependent on wave loads while contribution from wind loads was very small. The pitch response had monotonic increase with wave loads. Comparing the two types of mooring system, it can be observed that because of the pitch and heave restraint the floater response be-

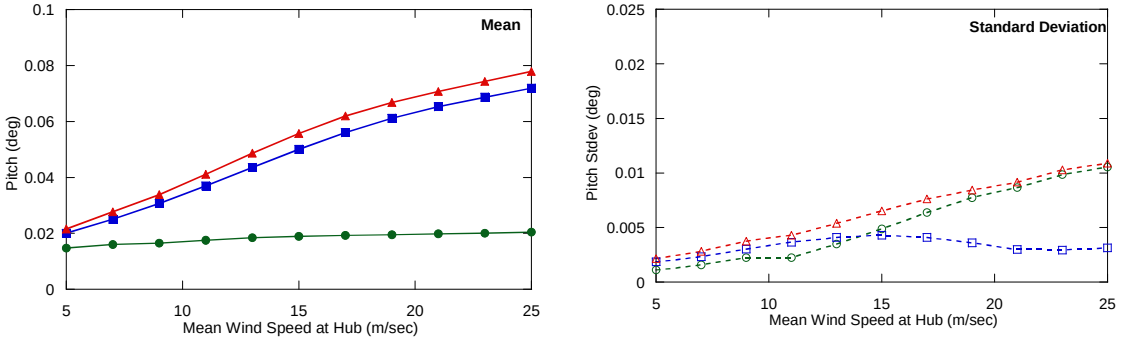
comes less sensitive to load from the wind turbine. Though the mean responses for the two types are very different, the standard deviation of surge is quite similar as was intended. Considering this similarity of dynamic surge, it can be said that contribution of surge to wind turbine loads for the two types of mooring would be nearly similar and the difference in loads would be because of the pitch response of the floater in case of catenary mooring system.



(a) Surge



(b) Heave



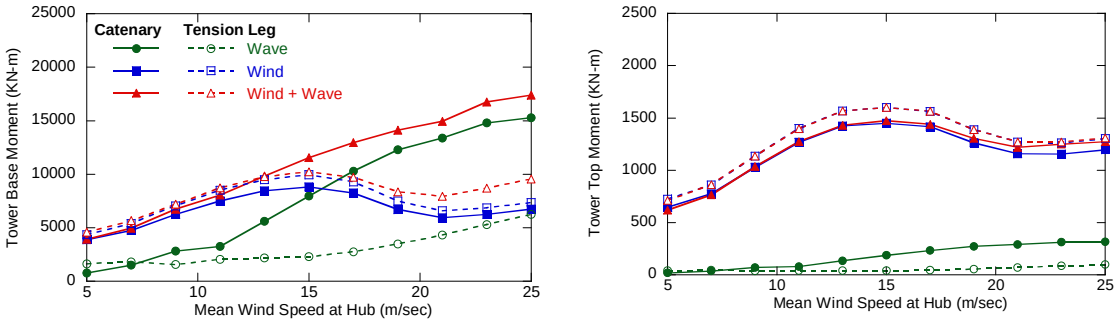
(c) Pitch

Figure 4 Response of floater with tension leg mooring

4.2 Wind turbine tower loads

In the previous section, the response for the two types of mooring systems has been discussed and contributions of wind and wave loads to the significant modes of response (surge, heave and pitch) were identified. To discuss the contribution of the these loads and effect of

pitch motion the wind turbine loads, two critical points for design of wind turbine are considered i.e. tower base moment for support structure and tower top moment for the yaw system. Figure 5 shows these two loads for the two types of mooring systems. The results show that both the wind and wave loads are critical for tower base (support system), while wind loads govern the tower top (yaw system) for both types of mooring system. Further, the combined wind and wave loads do not result in much larger loads and a simple summation of loads due to wind only and wave only will give conservative results. Considering the comparison of the tension leg mooring and Catenary Mooring system, it can be observed that tension leg mooring results in reduction of tower base moment due to wave loads at higher wind velocities. Since the two types have dynamic surge component of the same order, this difference can be only attributed to pitching motion in case of catenary mooring system. The tower base moment due to wind load only is slightly smaller in catenary mooring, because of increased aerodynamic damping arising from the pitching motion that aggravate the rotor disc displacement. Finally, both types of mooring systems have similar tower top loads which indicate that the top load is not sensitive to pitching motion but depend on the surge displacement of the floater which is similar for the two types of mooring systems.



(a) Tower Base Moment (b) Tower Top Moment

Figure 5Wind turbine moments in a floating wind turbine system

5 CONCLUSIONS

A numerical study was carried out to investigate contribution of environmental loads and floater response mode on wind turbine loads. Catenary and tension leg mooring system with similar surge component were used. It is observed that the contribution of environmental loads to modes of motion is independent of mooring system. The mean and dynamic surge response is more sensitive to wave loads, while the mean pitch response is sensitive to wind loads and dynamic pitch is influenced by wave loads. Both wind and wave loads are found to be critical for support system (tower base) and wind loads are critical for yaw system (tower top). Comparison of wind turbine loads for tension leg and Catenary mooring systems show that tension leg mooring results in reduction of wave loads at tower base because of the pitch restraint. The yaw system load (tower top moment) is of the same order for the two types of mooring system, which indicates that this load is independent of floater pitching motion, and depend upon the surge displacement similar for the two types of mooring systems.

REFERENCES

1. *World Wind Energy Report*, World Wind Energy Association, 2012.
2. M.B. Waris, *Dynamic response prediction of floating offshore wind turbine system using fully nonlinear model*, Ph.D. Dissertation, The University of Tokyo, Tokyo, 2010.
3. T. Utsunomiya, E. Nishida, On sea experiment of a hybrid SPAR for floating offshore wind turbine 1/10 scale model, *Proceedings of the ASME 29th International Conference on Ocean*, Offshore and Arctic Engineering, Shanghai, 2010.
4. B. Skaare, T.D. Hanson, F.G. Nielsen, R. Yttervik, A.M. Hansen, K. Thomsen, T.J. Larsen, Integrated dynamic analysis of floating offshore wind turbines, *Proceedings of European wind energy Conference and Exhibition*, Milan, 2007.
5. T.P. Fuglseth, M. Undeland, Modelling of floating wind turbines for simulation and design of axial thrust and power control strategies, *Renewable Energy*, Chiba, 2006.
6. N. Srinivasan, S. Chakrabarti, R. Radha, Damping controlled response of a truss pontoon semi-submersible with heave plates, *Proceedings of the 24th International Conference of OMAE*, Halkidiki, Greece, 2005.
7. M. Murakami, M. Takada, M. Fujiyoshi, T. Katada, S. Nagata, T. Fujita, The Hitz concept of an offshore floating-type wind turbine generation system, *Offshore Wind Energy Forum*, Tokyo, 2004.
8. K. Yago, Y. Ohkawa, H. Suzuki, T. Sawai, A basic study on the floating wind power system, *17th Ocean Engineering symposium – The society of Naval Architects of Japan*, Yokohama, 2003.
9. B. Skaare, T.D. Hanson, F.G. Nielsen, Integrated dynamic analysis of floating offshore wind turbines, *Wind energy Conference and Exhibition*, Athens, 2006.
10. P.V. Phuc, *Dynamic Response Analysis of Floating Offshore Wind Turbine System in the Parked Condition*, Ph.D. Dissertation, The University of Tokyo, Tokyo, 2008.
11. D. Roddier, C. Cermelli, A. Weinstein, Wind Float: A Floating Foundation for Offshore Wind Turbines, *Journal of Renewable and Sustainable Energy*, **2(3)**, 1-34, 2010.
12. J.M. Jonkman, *Dynamic Modeling and Load Analysis of an Offshore Floating Wind Turbine*, Ph.D. Dissertation, University of Colorado, Colorado, 2007.
13. S.H. Jeon, M.W. Seo, Y.U. Cho, W.G. Park, W.B. Jeong, Sloshing Characteristics of an Annular Cylindrical Tuned Liquid Damper for Spar-type Floating Offshore Wind Turbine, *Journal of Structural Engineering and Mechanics*, **47(3)**, 331-343, 2013.
14. M.B. Waris, T. Ishihara, Dynamic response analysis of floating offshore wind turbine with different types of heave plates and mooring systems by using a fully nonlinear model, *Coupled Systems Mechanics*, **1(3)**,247-268, 2012.
15. B. Wang, S. Rahmdel, C. Han, S. Jung, S. Park, Hydrodynamic Response of Alternative Floating Substructures for Spar-type Offshore Wind Turbines, *Journal of Wind and Structures*, **18 (3)**, 267-279, 2014.
16. N. Alati, V. Nava, G. Failla, F. Arena, A. Santini, On the Fatigue Behavior of Support Structures for Offshore Wind Turbines, *Journal of Wind and Structures*, **18 (2)**, 117-134, 2014.

17. J. R. Morison, M. P. O'Brien, J.W. Johnson, S.A. Schaaf, The force exerted by surface waves on piles, *Petroleum Transactions*, AIME, **189**, 149-154, 1950.

18. S.H. Ju, J.J. Stone, R.E. Rowlands, A new symmetric contact element stiffness matrix for frictional contact problems, *Computers and Structures*, **54(2)**, 289 – 301, 1995.

19. P.V. Phuc, *Numerical and Theoretical Study on the Wind Response of Wind Turbine in the Strong Wind Condition*, M.Sc. Thesis, Department of Civil Engineering, The University of Tokyo, Japan , 2005.

20. S.K. Chakrabarti, *Hydrodynamics of offshore structures*, Computational Mechanics Publications, Southampton, 1987.

21. ASCE 7-02, *Minimum Design Loads for Buildings and Other Structures*, Revision of ASCE 7-98, 2002.

22. IEC 61400-3, *Wind turbines – Part 3: Design requirements for offshore wind turbines, 1st Edition*, IEC, 2007.

COMPDYN 2015
5th ECCOMAS Thematic Conference on
Computational Methods in Structural Dynamics and Earthquake Engineering
M. Papadrakakis, V. Papadopoulos, V. Plevris (eds.)
Crete Island, Greece, 25–27 May 2015

A NEW APPROACH ON THE CALCULATION OF DYNAMIC LOAD FACTORS OF HUMAN INDUNCED LOAD

Lu Dai, Na Yang

School of Civil Engineering, Beijing Jiaotong University, Beijing 100044, China

E-mail: 12115272@bjtu.edu.cn, nyang@bjtu.edu.cn

Keywords: dynamic load factor, human induced load, single foot force model, numerical calculation.

Abstract: *An appreciation of the nature of the force induced by walking is essential in order to predict the structural response from pedestrians. The typical walking model applied on structures is the Fourier series force model, the most important parameter in the model is the dynamic load factor (DLF) which is the basis for this most common model of perfectly periodic human-induced force. Based on Fourier decomposition, many researchers have tried to quantify DLFs, but the existing factors are not suitable for low or high walking frequency, as the more and more load need to be considered in the structural calculation nowadays, the application range of DLFs need to be extended. Based on the single foot force model, this study recalculated the dynamic load factors and expanded the applied frequency range to both low and high frequencies using numerical simulation method, compared the human induced load force model of different walking frequencies. The calculated DLFs in low and high frequency obtained from this study are useful for the following analysis of structural response under more kinds of pedestrian load.*

1 INTRODUCTION

In recent decades, the human induced load by walking person has become an extremely popular topic in structural engineering area, especially for the light and slender footbridges of low modal frequencies. The walking load induced structural vibration not only is a serviceability problem, but also affects the structural safety.

The excessive footbridge vibration due to the pedestrian passage is a major consideration in the footbridge design. To understand the complicated mechanical mechanism of pedestrian-footbridge vibration, a number of numerical and experimental investigations have been performed over the past decades. Li et al [1] investigates vibration characteristics of footbridge induced by crowd random walking, developed a single foot force model for the vertical component of walking-induced force avoiding the phase angle inaccessibility of the continuous walking force. S. Zˇivanovic´ et al. [2] gave a literature review on vibration serviceability of footbridges under human-induced excitation, identified humans as the most important source of vibration for footbridges. M.J. Hudson et al [3] provided a comprehensive state-of-the-art review of AVC for human-induced vibrations in floor structures, discussed a range of active control laws are also discussed and the suitability of these for the mitigation of human-induced vibrations in floors, providing the basis for future research in this area so that the benefits of AVC may be fully realized. V. Racic et al [4] reviewed the experimental identification and analytical models of human walking forces, the review is therefore an interdisciplinary article that bridges the gaps between biomechanics of human gait and civil engineering dynamics. S.C. Kerr [5] investigated the differences between human induced loading on a floor with that generated whilst ascending or descending a staircase, the data obtained from numerous force plate experiments have been compared to existing experimental data and conclusions have been drawn as to what differences between the two should warrant concern by the staircase designers. Luca Bruno [6] based on the mathematical and numerical decomposition of the coupled multiphysical nonlinear system into two interacting subsystems, proposed a mathematical and computational model used to simulate crowd–structure interaction in lively footbridges. Tianjian Ji et al [7] investigated the action of an individual bouncing on a structure, and conducted an individual bouncing test and its responses to bouncing was recorded, then proposed a load model based on the measurements and the concept that dynamic responses induced by the sum of harmonic functions are at discrete loading frequencies. Aikaterini Pachi [8] based on a field test in shopping mall and footbridges, summarized people's walking frequency and walking velocity, compared the difference of different walking purpose.

This paper focus on the human load induced by walking pedestrian, based on the Fourier series model and the simplified single foot force model, adopting numerical simulation methods, recalculated the dynamic load factors (DLFs), which is essential for the walking model. The DLFs calculation results show a relatively larger frequency range compared to the traditional DLFs, so that the high and low frequency pedestrian can be considered in the following calculation and simulation, providing a more accurate analysis results by taking more kinds of load into consideration.

2 THE LOAD MODEL FOR WALKING PEDESTRIAN

To analyze the structural response under walking load, the reasonable simulation model for pedestrian induced force is necessary. There are many kinds of force model of walking person, among which, the most common used is the Fourier series model, and it is also the simplest model. The studies in the following parts of this paper are all based on the Fourier series force model.

2.1 The traditional walking model

Accurate evaluation of vertical force induced by one walking pedestrian is crucial to estimate the vibration of footbridge. The typical Fourier series time-domain model for walking is based on the assumption that both human feet produce exactly the same force and that the force is periodic. It is well known that the continuous walking force can be considered as a sum of a statistic and a dynamic component, and it can be represented by a Fourier series (eq.1):

$$F_p(t) = G + \sum_{i=1}^{n} G\alpha_i \sin\left(2\pi i f_p t - \phi_i\right) \tag{1}$$

Where G: the weight of walking person, α_i: the Fourier's coefficient of the ith order, f_p: the walking frequency (Hz), ϕ_i: the phase angle of the ith order, i: the order number, n: the total number of the harmonic order.

Based on the above Fourier series model, the walking pattern is shown as the following figure.

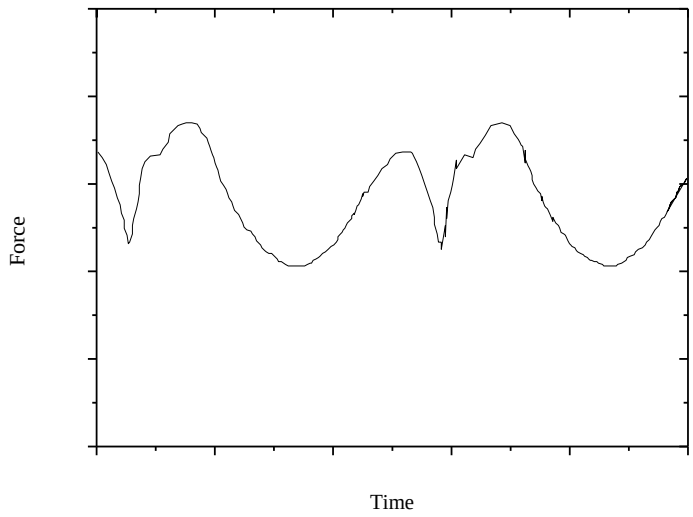


Figure 1: The traditional Fourier series walking load model

2.2 The single foot force model

In the traditional walking force model, the phase angle is an important factor, while it is also the most difficult parameter to obtain, and in the previous study, there still not clear instructions for the phase angle. So based on the Fourier series model, Li (2010) [1] proposed a single foot force model to describe the dynamic loading of pedestrian walking, not only avoiding the inaccessibility of phase angle and also accounting for subsequent random vibration modeling of footbridge. Generally, the common single foot load–time force curve, illustrated in figure 2, is characterized with two peaks, and the first one is higher than the second one.

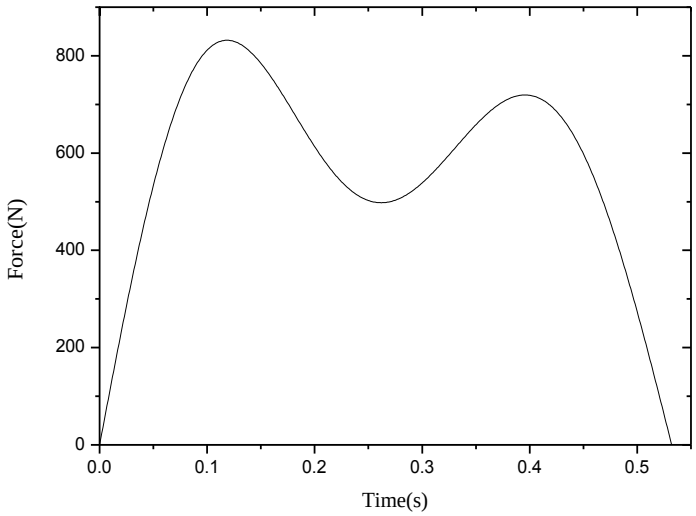


Figure 2: The single foot force model

The single foot force is assumed to be formulated also by Fourier series as:

$$F_e(t) = G\sum_{n=1}^{+\infty} A_n \sin\left(\frac{\pi n}{T_e}t\right), 0 \le t \le T_e \tag{2}$$

Where A_n and T_e is the Fourier coefficient and constant cycle.

3 THE CALCULATION FOR DYNAMIC LOAD FACTORS

It can be seen from the above analysis that the dynamic load factors (DLFs) is the essential parameter in the walking load simulation, and in the previous study there are many calculation and test results for such DLFs values.

3.1 The existing DLFs

Based on Fourier decomposition, many researchers have tried to quantify DLFs which are the basis for this most common model of perfectly periodic human-induced force. S.

Z˘ivanovic´ [2] summarized the DLFs calculation results in the previous study, shown in table 1.

Author	DLFs	Frequency Range
Blanchard	α_1=0.257	4-5Hz
Bachmann and Ammann	α_1=0.4-0.5, $\alpha_2=\alpha_3$=0.1	2.0-2.4Hz
Schulze	α_1=0.37, α_2=0.10, α_3=0.12, α_4=0.04, α_5=0.08	2.0Hz
Bachmann	α_1=0.4/0.5, $\alpha_2=\alpha_3$=0.1/-	2.0/2.4Hz
	$\alpha_1=\alpha_3$=0.1	2.0Hz
Kerr	α_1=1.6, α_2=0.7, α_3=0.2	2.0-3.0Hz
Young	α_1=0.37$(f-0.95)\le 0.5$, $\alpha_2=0.054+0.0044f$, $\alpha_3=0.026+0.005f$, $\alpha_4=0.01+0.0051f$.	1-2.8Hz
Yao	α_1=0.1, α_2=0.25	2.0Hz(bouncing)

Table 1: The DLFs results from the previous study

Despite the DLFs results from traditional Fourier series model, Li's single foot force model also has its own dynamic load factors, shown in equation 3.

$$
\begin{aligned}
A_1 &= \begin{cases} -0.0698 f_s + 1.211, 1.6Hz \le f_s \le 2.32Hz \\ -0.1784 f_s + 1.463, 2.32Hz < f_s \le 2.4Hz \end{cases} \\
A_2 &= \begin{cases} 0.1052 f_s - 0.1284, 1.6Hz \le f_s \le 2.32Hz \\ -0.4716 f_s + 1.210, 2.32Hz < f_s \le 2.4Hz \end{cases} \\
A_3 &= \begin{cases} 0.3002 f_s - 0.1534, 1.6Hz \le f_s \le 2.32Hz \\ -0.0118 f_s + 0.5703, 2.32Hz < f_s \le 2.4Hz \end{cases} \\
A_4 &= \begin{cases} 0.0416 f_s - 0.0288, 1.6Hz \le f_s \le 2.32Hz \\ -0.2600 f_s + 0.6711, 2.32Hz < f_s \le 2.4Hz \end{cases} \\
A_5 &= \begin{cases} -0.0275 f_s + 0.0608, 1.6Hz \le f_s \le 2.32Hz \\ 0.0906 f_s - 0.2132, 2.32Hz < f_s \le 2.4Hz \end{cases}
\end{aligned}
\tag{3}
$$

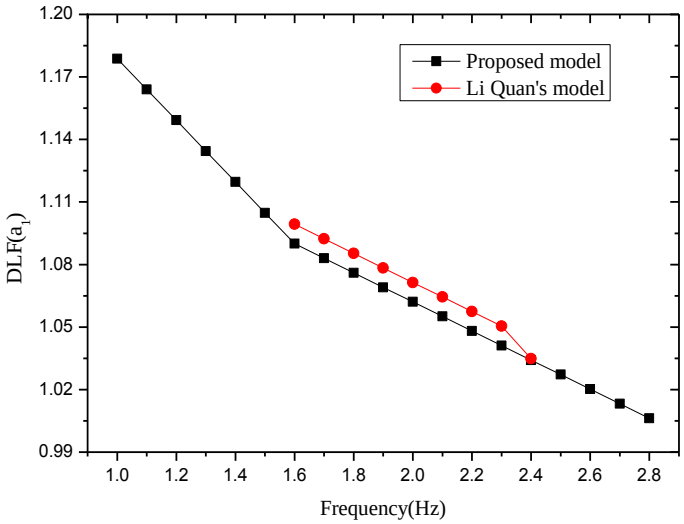
From the above analysis, it can be seen that although there are a variety of dynamic load

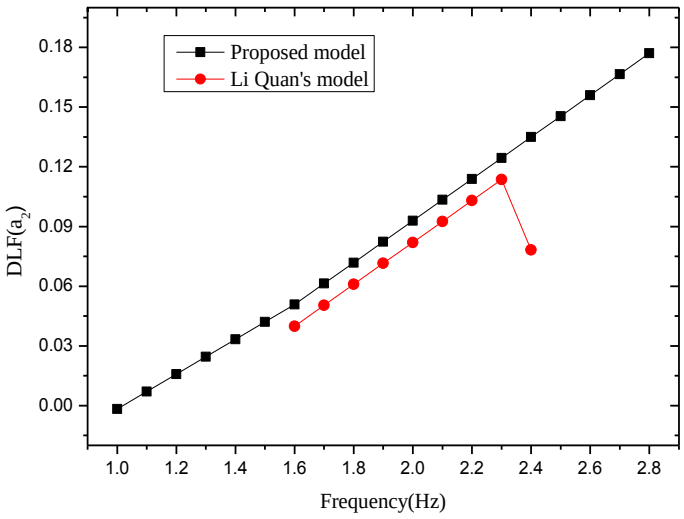
factors calculation results, the frequency range for applied computation is still narrow. For the single foot force model, the frequency range is 1.6-2.4Hz, which could not cover the load forms, so it is necessary to enlarge the DLFs frequency range for following applying analysis.

3.2 The DLFs for enlarged walking frequency

It is known that the single foot force model is more convenient without the phase angle value, so adopt the model to conduct the following study. The basis DLFs values come from Young's model, because the frequency range is relatively large in his model.

According to the equal relationship of the corresponding coefficients in the above mentioned two models, recalculate the dynamic load factors in the single foot force model. In order to have a more efficient calculation, only adopt the first three dynamic harmonic orders. Compared to the original DLFs proposed by Li, the results are shown in figure 3.





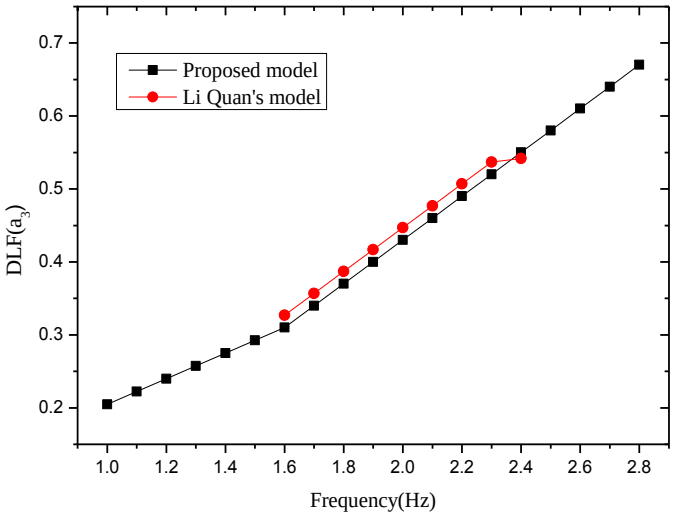


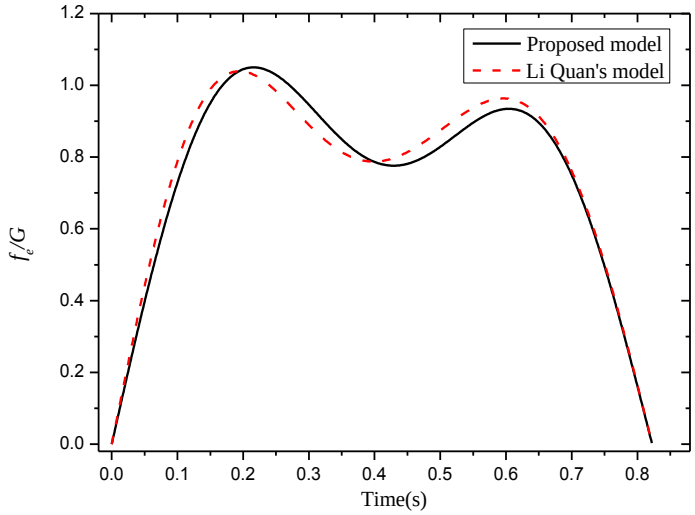
Figure 3: The DLFs calculation results for enlarged frequency

It can be seen by recalculation the coefficients, the DLFs range enlarged from 1.6-2.41Hz to 1.0-2.8Hz, and the numerical values for these factors can be calculated by equation 4.

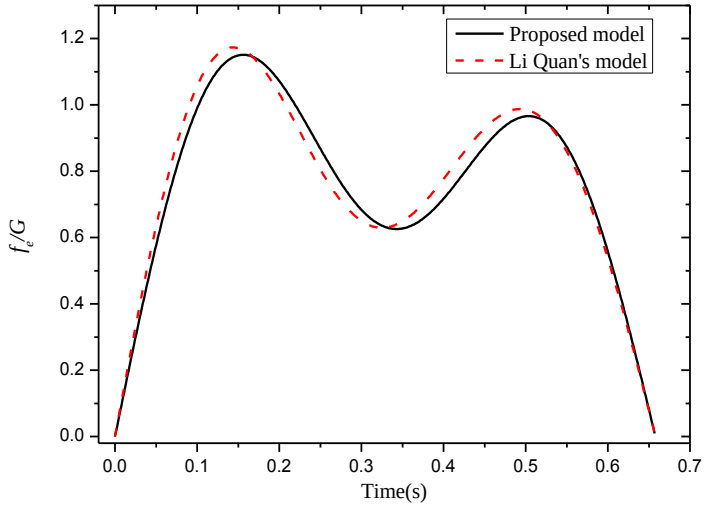
$$
\begin{aligned}
A_1 &= \begin{cases} -0.1480\, f_s + 1.3268, 1Hz \le f_s \le 1.6Hz \\ -0.0698\, f_s + 1.2017, 1.6Hz < f_s \le 2.8Hz \end{cases} \\
A_2 &= \begin{cases} 0.0875\, f_s - 0.0892, 1Hz \le f_s \le 1.6Hz \\ 0.1052\, f_s - 0.1175, 1.6Hz < f_s \le 2.8Hz \end{cases} \\
A_3 &= \begin{cases} 0.1752\, f_s + 0.0297, 1Hz \le f_s \le 1.6Hz \\ 0.3002\, f_s - 0.1703, 1.6Hz < f_s \le 2.8Hz \end{cases}
\end{aligned} \tag{4}
$$

4 THE APPLICATION OF CALCULATED DLFS

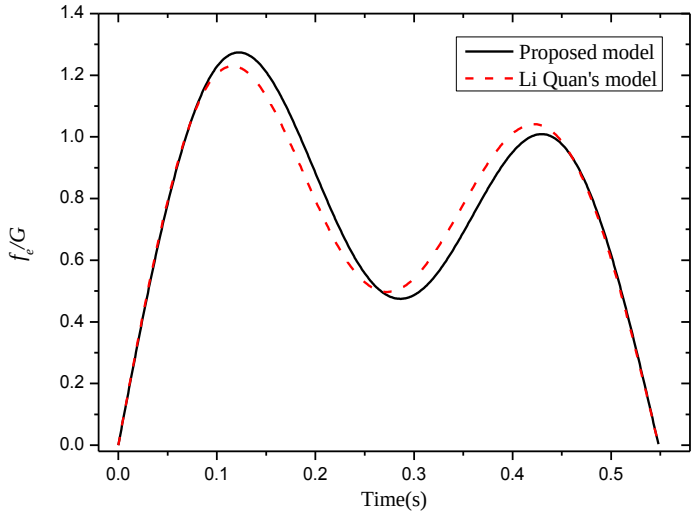
Based on the DLFs calculation results, the pattern of single foot walking force can be obtained, the pedestrian induced load is shown in figure 4 compared to Li's model.



(a) Walking frequency: 1.6Hz



(b) Walking frequency: 2.0Hz



(c) Walking frequency: 2.4Hz

Figure 4: The walking pattern of adopting the recalculated DLFs

It should be noted that by recalculating, the DLFs frequency range has been enlarged, figure 5 shows the human induced load of different walking frequencies using the recalculated DLFs.

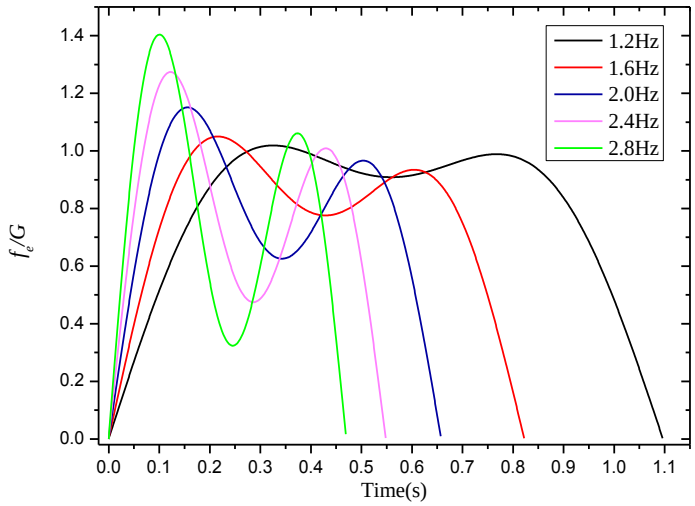


Figure 5: The pedestrian induced load under different walking frequencies

From the above analysis, it can be seen that single foot force model can be applied in a larger frequency range due to the calculation of DLFs.

5 CONCLUSIONS

Based on the study on pedestrian induced load model, this paper summarized the previous study on dynamic load factors and enlarged the DLFs frequency range based on the single foot force model. The main conclusions are as follows:

- The dynamic load factors for the Fourier series walking load model in previous study are summarized.
- Based on the single foot force model, recalculated the DLFs to enlarge the application frequency range for walking load model.
- By adopting the recalculated DLFs, it is feasible that the pedestrian induced single foot force model can be applied in larger frequency range. The more complex load forms can be considered in the structural response analysis.

Acknowledgements

The work described in this paper was supported by National Natural Science Foundation of China (NSFC: 51178028), the National Natural Science Foundation of China for Excellent Young Scholars (NSFC: 51422801), National Natural Science Foundation of China (Key Program) (NSFC: 51338001) and Program for New Century Excellent Talents in University (NCET-11-0571).

REFERENCES

[1] Quan Li, Jiansheng Fan, Jianguo Nie, Quanwang Li, Yu Chen, Crowd-induced random vibration of footbridge and vibration control using multiple tuned mass dampers. *Journal of Sound and Vibration*, **329**, 4068–4092, 2010.

[2] S. Živanović, A. Pavic, P. Reynolds, Vibration serviceability of footbridges under human-induced excitation: a literature review. *Journal of Sound and Vibration*, **279**, 1–74, 2005.

[3] M.J. Hudson, P. Reynolds, Implementation considerations for active vibration control in the design of floor structures. *Engineering Structures*, **44,** 334–358, 2012.

[4] V. Racic, A. Pavic, J.M.W. Experimental identification and analytical modelling of human walking forces : Literature review. *Journal of Sound and Vibration*, **326,** 1–49, 2006.

[5] S.C. Kerr, N.W.M. Bishop. Human induced loading on flexible staircases. *Engineering Structures*, **23,** 37–45, 2001.

[6] Luca Bruno, Fiammetta Venuti. Crowd–structure interaction in footbridges: Modelling, application to a real case-study and sensitivity analyses. *Journal of Sound and Vibration*, **323,** 475–493, 2009.

[7] Ernesto Duarte, Tianjian Ji. Action of Individual Bouncing on Structures. *Journal of Structural Engineering*, **135:7,** 818-827, 2009.

[8] Aikaterini Pachi, Tianjian Ji. Frequency and velocity of people walking. *The Structural Engineer*, **2:1,** 36-40, 2005.

COMPDYN 2015
5th ECCOMAS Thematic Conference on
Computational Methods in Structural Dynamics and Earthquake Engineering
M. Papadrakakis, V. Papadopoulos, V. Plevris (eds.)
Crete Island, Greece, 25–27 May 2015

COMPUTATIONAL MODELING OF MULTI-SCALE MATERIAL FEATURES IN CEMENT PASTE – AN OVERVIEW

Ram V. Mohan[1], Wayne D. Hodo[2], and A. Rajendran[3]

[1] Department of Nanoengineering
North Carolina A&T State University, 2907 E Lee Street, Greensboro, NC
e-mail: rvmohan@ncat.edu

[2] Engineering Research and Development Center
Vicksburg, MS
e-mail: wayne.d.hodo@usace.army.mil

[3] Department of Mechanical Engineering
Oxford, MS
e-mail: raj@olemiss.edu

Keywords: Multi-Scale Modeling, Molecular Dynamics, Cement Paste, Calcium Silicate Hydrate, Repeated Volume Element

Abstract. *Computational modeling of complex, heterogeneous, multi-scale features of cement paste requires starting from their fundamental building blocks that includes material chemistry, microstructural morphology. This would enable capturing scale relevant features that influence the properties and behavior of materials through associated computational, material and mechanistic models. Such modeling starting from nanoscale material features through material chemistry modeling via molecular dynamics (MD); modeling of complete three-dimensional virtual microstructure including the evolution of microstructure due to hydration of cementitious materials are briefly highlighted. Material chemistry modeling discussions from our recent work on nanoscale shear deformation to obtain the stress-strain behavior solely based on the material chemistry structure of hydrated cementitious material constituent CSH Jennite is summarized. Micro-scale modeling involving finite element based repeated volume element (RVE) modeling applied to the virtual three-dimensional complex microstructures at different degrees of hydration of the cement paste is also summarized. Complete details are presented in our other current and future publications in the literature. Multi-scale modeling that links across various length scales and material features in complex heterogeneous material systems provides an effective way of coupling material science and engineering features for their better understanding and tailored material design. These approaches present a new future direction for integrated material science and engineering of materials and structures.*

1 INTRODUCTION

Cementitious materials, an excellent example of highly complex, heterogeneous material systems, are cement-based systems that include cement paste, mortar, and concrete; though commonly used are one of the most complex in terms of material morphology and structure than most materials, for example, crystalline metals. Processes and features occurring at nanometer sized morphological structures affect the performance, deformation/failure behavior at larger, engineering length scales. In addition, cementitious materials undergo chemical and morphological changes gaining strength during the transient hydration process. Hydration in cement is a very complex process creating complex microstructures and the associated molecular structures that vary with hydration. Multi-scale modeling of such material systems requires starting from fundamental building blocks for the analysis and understanding at each of the disparate length scales capturing the scale relevant features through associated computational models. In conjunction, techniques to correlate and transcend across the morphological features at each of the length scales, and associated computational coupling techniques across the multiple scales are required. In this paper, recent work from our research group on the nano to continuum level modeling of cementitious materials is highlighted.

This paper discussions are with an emphasis on the computational modeling at different length scales building the foundations of our research work consisting of,

- Molecular Dynamics (MD) modeling for the nano scale features of the cementitious material chemistry.
- Micro-mechanics modeling employing the cement microstructure morphology that takes into account the variations in the morphological features.

Brief discussions of our on-going work on the scale relevant modeling of the multi-scale heterogeneous cementitious materials are presented in this paper to provide a forum for technical interactions and collaborations on the current state of the art, technology and research coupling material science and engineering.

2 NANOSCALE MATERIAL CHEMISTRY LEVEL MODELING

Portland cement in the powder form consists of four different major constituents: Tri-Calcium silicate (C_3S), Di-Calcium silicate (C_2S), Tri-Calcium aluminate (C_3A), and Tetra calcium aluminoferrite (C_4AF) [1]. Hydration of cement is the chemical reaction between cement compounds and water, which cause hardening of cement forming the heterogeneous composite material. The most important hydrated cement product is Calcium Silicate Hydrate (CSH). Due to the complexity of CSH, molecular structure of CSH has not been fully resolved yet. Other naturally occurring minerals Jennite [2] and Tobermorite14 [3] molecular structures are the closest representation of CSH crystal that are accepted in the field. In these chemical formula representations, the notation common in the cementitious material community is followed: C refers to CaO; S refers to SiO_2, A refers to Al_2O_3, F refers to Fe_2O_3, and H refers to H_2O.

MD is employed in modeling materials science and biomolecules to study and investigate structure and behavior of the interacting atoms of any molecular system. The methodology is based on transient dynamics analysis of atoms represented by system of particles based on classical Newtonian mechanics. The transient dynamic atomistic configurations under varying thermodynamic state conditions is coupled with statistical mechanics to obtain the predicted, thermo-physical properties as well as molecular level behavior of material systems based on their atomistic positions and velocities.

The total potential energy for the material system varies for different molecular types based on associated molecular parameters and atoms. The potential energy of the CSH Jennite mo-

lecular structure in our research is determined using a COMPASS force field in the present work. The functional form of the COMPASS (condensed-phase optimized molecular potentials for atomistic simulation studies) contains three major terms, which are bond terms, non-bond terms, and cross terms [4]. Bond terms include bond stretch, angle bending, angle rotation, and out of plane angle terms, associated with molecular, material chemistry level configuration of hydrated cement paste CSH Jennite structure.

3 MICRO SCALE MODELING

The advent of scalable computing capabilities makes it possible to model large molecular and representative volume element (RVE) based material systems. Individual elastic properties and density for clinkers, unhydrated and hydrated products are usually and can be further estimated through molecular dynamics simulations. These properties could then be utilized in the microscopic level RVE simulations. The representative volume element (RVE) is defined as the smallest volume of material that captures the global characteristics of the material. Random results for overall properties of the material will be obtained if the tested volumes are smaller than this statistically representative sub-domain of the microscopic geometry. Such a volume must be sufficiently large to allow a meaningful sampling of the micro-scale stress and strain fields as well as sufficiently small for the influence of macroscopic gradients to be negligible, and for an analysis of these micro fields to be possible.

CEMHYD3D Ver. 3, developed by NIST (National Institute of Standards and Technology, USA), was used to simulate the hydration process and formation of the digitally generated virtual microstructure for a typical Type-I general purpose cement [5]. CEMHYD3D allows creation of a starting three-dimensional microstructure based on a measured geometrical particle size distribution (PSD), volume fractions and surface area fractions of the constituent phases for the cement powder, extracted from 2D composite SEM (scanning electron microscope) images of cement at various degrees of hydration and modeling the hydration kinetics [5].

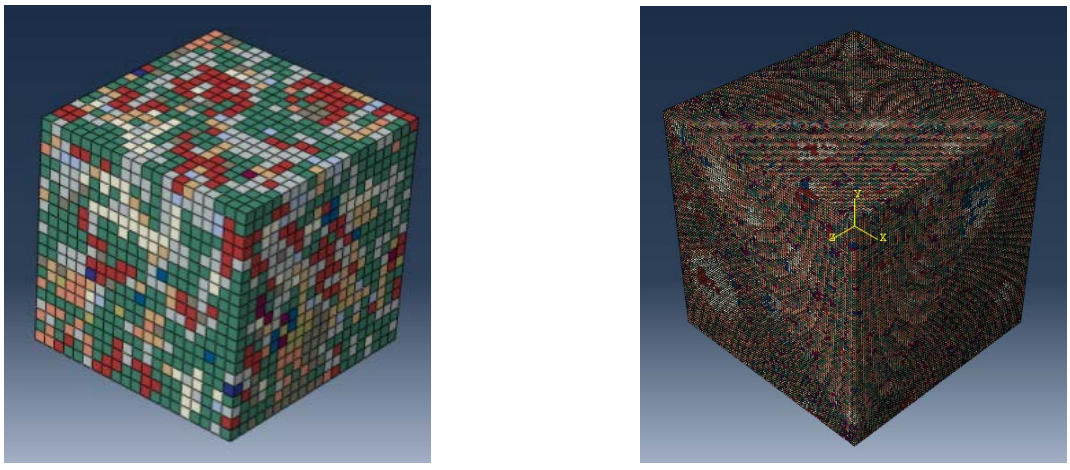


Figure 1: 100x100x100 micron finite element model (left) and hydrated cement microstructure (right) [7].

The three-dimensional virtual microstructure is modeled as a micro-scale representative volume element (RVE) in a finite element analysis code to generate cubes of several microns in dimension and subjected to various prescribed deformation modes to obtain the effective elastic tensor of the material. The micro-structure voxel information generated by CEMHYD3D is imported into the general purpose ABAQUS® finite element code using an

in-house developed Matlab® code and meshed using continuum hexahedral (C3D8) elements to generate RVE domains of various dimensions (Fig. 1). Microstructure analysis based on cement RVE considered both periodic boundary condition (PBC) and kinematic boundary conditions (KBC). RVE calculated elastic properties such as moduli are compared with the values obtained for this complex material microstructure configuration via asymptotic expansion homogenization (AEH), originally developed for woven fabric composites [6]. Complete details are available in reference [7].

4 RESULTS AND DISCUSSIONS

Brief discussions of key results from shear deformation and failure of nanoscale CSH Jennite are presented next. Complete details are available in reference [8].

4.1 Nanoscale shear deformation of CSH Jennite

The molecular/chemistry level structure of CSH Jennite is defined by a triclinic unit cell of dimensions a=10.6 Å, b=7.3 Å, c=10.9 Å, and angles α=101.3°, β=97.0°, γ=109.7°. In Figure 2 a crystal of CSH Jennite, consisting of 64 unit cells in a 4x4x4 arrangement, is illustrated. The molecular structure of jennite is layered, formed by sheets of calcium oxide connected to short silica chains, three silica monomers long, that are not connected to each other. The calcium oxide sheets are linked to each other by additional calcium octahedral sites. The layers containing the calcium octahedral sites connecting the calcium oxide sheets also contain most of the free water molecules in the structure.

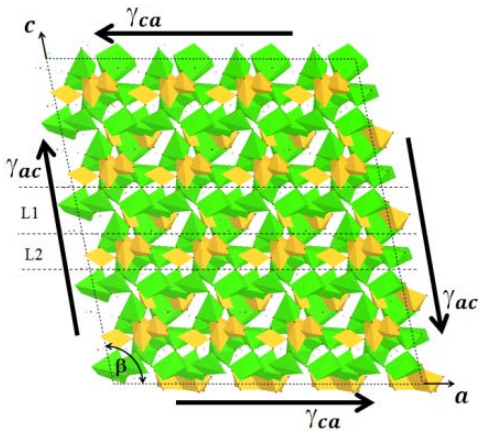


Figure 2: Molecular structure of nanoscale CSH Jennite viewed across the (ac) crystallographic plane. Arrows indicate the direction of the shear stress simulated [8].

As a load-bearing system, nanoscale CSH Jennite can be considered as a structure in which interconnected layers of calcium oxide are responsible for the structural integrity of the system. The short silica chains distributed on calcium oxide layers can be considered to act as nanoscale reinforcements. These short silica chains are not bonded to each other but only to the calcium oxide layers; hence they cannot be considered as the load-bearing skeleton of the structure. Based on the structural characteristics of nanoscale CSH Jennite illustrated above, results from mechanical behavior of the material under shear deformation and the changes produced by the deformation applied on the calcium oxide layers are briefly illustrated. Complete details of MD modeling methodology and shear deformation of nanoscale CSH Jennite are available in reference [8].

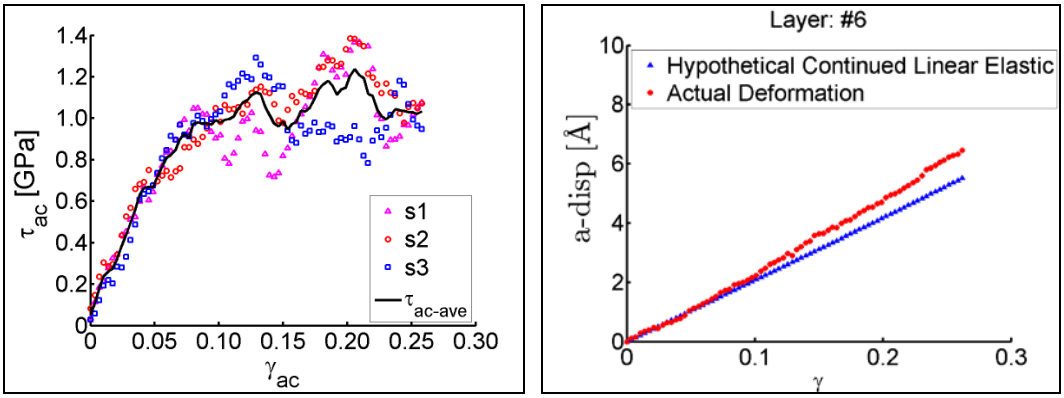


Figure 3: Shear stress-strain behavior of nanoscale CSH Jennite from MD (left); center of mass displacement (continued linear elastic vs. actual) [ ].

Figure 3 presents the shear stress-shear strain behavior obtained from shear deformation of nanoscale CSH Jennite built upon 64 unit cells. MD computational analysis experiments were repeated using three different initial configurations of the material chemistry structure and show a good, repeatability of the linear and non-linear transition. The shear deformation is characterized by a linear region followed by a non-linear transition at a strain of about 0.08. Shear modulus obtained from the chemistry level modeling is 11.2±0.7 GPa. Layered structure of the predominant calcium oxide in the molecular structure indicates that shear deformation is primarily due to sliding of calcium oxide layers. The computed displacement after the onset of non-linear region is larger than the displacement with a continued elastic deformation. This is further indicated by a change in slope of the computed displacement curve as seen in Figure 3 (right). This correlates well with the transition from linear to non-linear behavior of the stress-strain plot shown in Figure 3 (left). Complete discussions are presented in reference [8].

4.2 Microstructural orthotropic elastic matric predictive modeling of cement paste

RVE analysis of cement microstructure involved six axial and 6 shear deformation cases resulting in the orthotropic elastic matrix. The corresponding effective engineering constants of the bulk properties are obtained. Table 1 presents the effective properties obtained from elastic tensors based on kinematic boundary conditions (KBC), periodic boundary conditions (PBC) applied to 3D cement virtual microstructure, as well as the results from asymptotic expansion homogenization (AEH). CSH gel formation in the cementitious materials increasingly support the mechanical stresses in the microstructure as the hydration proceeds, and is noted in the corresponding increase in the elastic modulus (E) and shear modulus (G) values. Also, due to the increase in CSH gel volume fraction and reduction in other unhydrated component fractions, microstructure also tends to become nearly isotropic with higher degree of hydration. The difference between the PBC and KBC conditions is found to be smaller (< 4%). Elastic modulus and shear modulus values obtained from AEH estimates are slightly higher than the KBC and PBC estimates. Complete details are presented in reference [7].

5 CONCLUDING REMARKS

Complex heterogeneous material systems with material features ranging from nano to macro scales require multi-scale modeling analysis for their understanding at each of the disparate length scales capturing the scale relevant features through associated computational models. Such computational models for complex heterogeneous material systems should not only be limited to homogenized engineering scales, but also need to include and emulate the

effects of the morphological variations and material chemistry changes that impact the material properties and behavior at engineering length scale as discussed for cementitious materials.

Method	Domain Size (microns)	DOH	G (GPa)	E (GPa)
KBC	100x100x100	0.8	9.08	24.20
		0.3	5.71	16.39
PBC	100x100x100	0.8	9.35	24.69
		0.3	6.39	17.65
AEH	100x100x100	0.8	9.15	24.05
		0.3	5.88	15.79

Table 1: Mechanical properties of cement paste from microstructure RVE analysis.

ACKNOWLEDGMENTS

The authors from North Carolina A&T State University and University of Mississippi acknowledge the support by the U.S. Army Research Office under a cooperative agreement award contract No. W911NF-11-2-0043 (Program Manager: Dr. Joseph Myers), and the U.S. Army Engineering Research and Development Center's Military Engineering Basic/Applied "MMFP" Research Program. Special thanks to contributions of all graduate students, and post-docs performing the modeling analysis. Complete list of authors are in the detailed current and future publications cited.

REFERENCES

[1] AIC C01, *Standard specification for Portland cement*, ASTM C150, April 15, 2012.

[2] E. Bonaccorsi, S. Merlino, H. Taylor, The crystal structure of jennite, $Ca_9Si_6O_{18}(OH)_6 8H_2O$, *Cement and Concrete Research*, **34**, 1481-1488, 2004.

[3] E. Bonaccorasi, S. Merlino, A. R. Kampf, The crystal structure of Tobermorite 14Å (Plombierite), a C-S-H phase, *Journal of the American Ceramic Society*, **88**, 505-512, 2005.

[4] H. Sun, COMPASS: An ab initio force-field optimized for condensed phase applications – Overview with details on alkane and benzene, *Journal of Physical Chemistry B*, **102**, 7338-7364, 1998.

[5] D.P. Bentz, *CEMHYD3D: A three-dimensional cement hydration and microstructure development modeling package, ver. 3*, National Institute of Standards and Technology, NISTIR 7232, 2005.

[6] P. Chung, K. Tamma, R. Namburu, Asymptotic expansion homogenization for heterogeneous media: computational issues and applications, *Composites-Part A: Applied Science and Manufacturing*, **32**, 1921-1301, 2001.

[7] M. M. Shahzamaian, T. Tadepalli, A. Rajendran, W. Hodo, R. Mohan, R. Valisetty, P. Chung, Representative volume element based modeling of cementitious materials, *Journal of Engineering Materials and Technology-Transactions of ASME*, **136**, 2014.

[8] J. Rivas-Murillo, A. Mohamed, W. Hodo, R. Mohan, A. Rajendran, R. Valisetty, Computational modeling of shear deformation and failure of nanoscale hydrated calcium silicate hydrate in cement paste: Calcium silicate hydrate Jennite, *Int. J. Damage Mechanics*, In Print, 2015.

COMPDYN 2015
5th ECCOMAS Thematic Conference on
Computational Methods in Structural Dynamics and Earthquake Engineering
M. Papadrakakis, V. Papadopoulos, V. Plevris (eds.)
Crete Island, Greece, 25–27 May 2015

SOFT COMPUTING APPLICATION IN SOIL CLASSIFICATION ANALYSIS

S. Yaghmaei-Sabegh[1]

[1] Department of Civil Engineering, University of Tabriz, Tabriz, Iran
e-mail: s_yaghmaei@tabrizu.ac.ir

Keywords: Soft computing, Soil classification, Ground motion records, Neural networks.

Abstract. *This paper deals with a new application of soft computing methods in soil classification procedure that is technically easy to use and does not require complex mathematical definitions for the model components. Two types of radial-basis neural networks, namely, probabilistic neural networks and generalized regression neural networks were used in this study. The proposed quick-automatic soil classification methods are implemented to analysis number of ground-motion stations located at North-West of Iran. The efficiency of proposed methodologies is compared with soil classification results based on measurement of the average shear wave velocity at a subsurface depth of 30 m. In addition, the results from neural network-based soil classification system were evaluated and compared with two empirical schemes which are based on the spectral shape of normalized response spectra and the average horizontal to vertical spectral rations of ground motions. The results revealed the acceptable ability of proposed methods to predict the soil class in the study area.*

1 INTRODUCTION

The previous destructive earthquakes experiences indicated that the local subsoil conditions can extensively influence the seismic demands and structural damages pattern which should be considered properly in seismic performance evaluation of the structures. The amplitude and frequency content of seismic motions could significantly be influenced by the soil response which is controlled by the mechanical properties of the soil. In fact, reliable design of the structures due to earthquakes will not be possible without considering local site effects.

In many countries like Iran, Turkey and Mexico, there is a lack of detailed information of the site conditions at most of the existing strong motion stations. Site classification based on borehole data or interpretation of geologic maps and geomorphologic data could not be done. For this reason, empirical methods have been developed by various researchers for site classification based on analysis of recorded strong ground motion data. These methods are generally quick and inexpensive in comparison with other schemes which are based on measurement of shear wave velocity. Standard Spectral Ratio, SSR, [1] and the horizontal-to-vertical spectral ratio technique, H/V or HVSR, [2] are most popular and widely used techniques for estimating site conditions. SSR is defined as the ratio between the Fourier spectrum calculated on the horizontal (or vertical) component recorded at a site of interest and the Fourier spectrum of the same component recorded at the outcropping rock. H/V technique is another simple and effective tool used widely for site effect analyses which does not require the presence of a reference rock station. The basic assumption of this method is that the vertical component of the ground motions is almost free from the amplification effects of soil. Applications of H/V method in soil response evaluation have been extensive [3-8].

The feasibility of using of two effective type of radial basis function neural networks named probabilistic neural networks (PNN) and generalized regression neural networks (GRNN) is examined in this paper for soil classification purpose. The efficiency of proposed soft computing methodologies is compared with soil classification results based on measurement of shear wave velocity. In addition, the results from neural network-based soil classification system was evaluated and compared with two other schemes which are based on the spectral shape of normalized response spectra and the average horizontal to vertical spectral rations of ground motions.

2 IMPLEMENTATION OF NEURAL NETWORK CAPABILITY IN SITE CLASSIFICATION

Soft computing techniques have been successfully used for solving pattern recognition and classification problems in the past. Artificial neural networks (ANNs) as one of widely used computational models consist of an assembling of connected processing units called neurons. The nonlinear nature of artificial neural network and their ability to learn in a complex environment while different factors influence the results of prediction, render it the capability of site classification. The theory, design and application of artificial neural networks as a powerful tool have been advancing broadly during the past decade for solving complicated problems in different fields including seismology, earthquake engineering, construction engineering, geotechnical engineering and geosciences. The use of two types of radial basis function (RBF) neural networks, namely, probabilistic neural networks (PNN) and generalized regression neural networks (GRNN) were proposed by Yaghmaei-Sabegh and Tsang [7]. The following features of PNN and GRNN rendering them the suitable tools in classification analysis:

i) no learning rule is required
ii) no pre-defined convergence criterion is needed

iii) removes design-decisions about the number of layers and also the number of neurons in hidden layer

iv) the simplicity in design

A typical structure of PNN consists of four layers, namely, input, pattern (first hidden layer), summation (second hidden layer), and output layers. Fig 1 shows structure of a typical PNN. The input variables X are each assigned to a node in the input layer and then conveyed directly to the hidden layer without weights. Each unit in the pattern layer implements a RBF by computing the Gaussian kernel of the Euclidean distance between the existing input vector and the training pattern. It is generally expressed in an exponential form as Equation (1):

$$\phi(X) = \exp\left[-\frac{(X - Y_i)^T (X - Y_i)}{2\sigma^2}\right] \tag{1}$$

where X is the input set to be classified; σ is the smoothing parameter or bandwidth; Y_i is the i^{th} training pattern and the superscript T denotes the transpose of a vector.

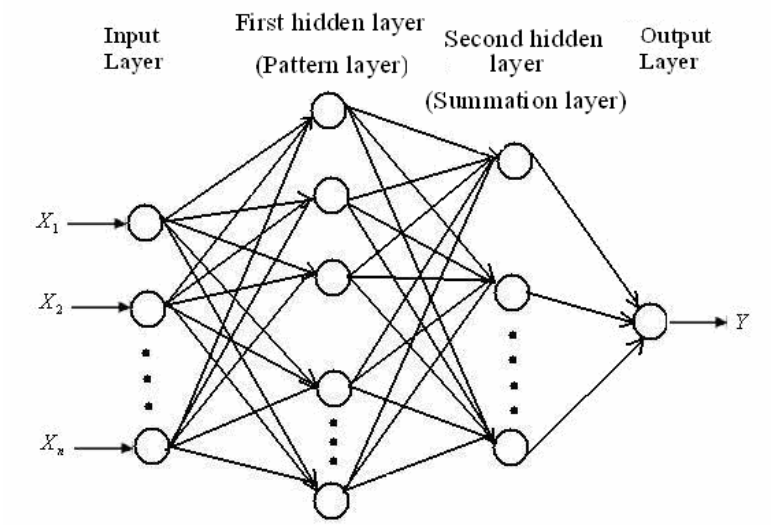


Figure 1: A typical structure of probabilistic neural network (PNN).

The GRNN, which is an alternative type of RBF neural network, approximates a function between input and output vectors based on a standard statistical technique called kernel regression. GRNN consists of four layers as of PNN. The pattern layer as the first hidden layer has one neuron for each case of the training data set and computes the Euclidean distance of the test case from the center point of a neuron and then applies the RBF kernel function. The next hidden layer in the network is the summation layer that represents the major difference between PNN and GRNN. The summation layer consists of two neurons only, namely, S-summation neuron and D-summation neuron. The S-summation neuron computes the sum of the weighted outputs from the pattern layer, while the D-summation neuron calculates the unweighted outputs from the pattern layer. The summation layer and output layer together produce a normalization of output set.

3 RESULTS AND DISCUSSIONS

Among 73 stations which have been triggered in 2012 Ahar-Varzaghan doublet events at North-West of Iran, 44 station with known Vs30 measures have been used in the analysis.

The uncorrected accelerometer records were corrected for the instrument response and baseline. Then a high-pass 4'th order Butterworth filtering was used as a conventional filtering method to remove noise from all raw time series. Finally, the average spectral values of horizontal components have been considered in evaluation process.

PNN and GRNN models have been processed for each station and a continuous value ranging from 1 to 4 is assigned to each station. The basic procedure starts with a selected set of representative horizontal to vertical spectral ratio (HVSR) curves for four site classes. A set of four reference HVSR curves has been collected according to Yaghmaei-Sabegh and Tsang [7].

Finally, the reference patterns and the input data are compared through the pattern recognize analysis with designed PNN and GRNN. The prediction results of two empirical methods proposed by Phung et al., [9] and Zhao et al. [8] are used in comparisons as well. Phung et al., [9] have proposed a technique for site condition using strong-motion dataset in Taiwan based on the spectral shape of normalized response spectra. In 2006, an empirical site-classification method was proposed by Zhao et al. [8] for strong-motion stations in Japan using H/V response spectral ratio. In fact, they have designed a classification scheme based on new site classification index (*SI*) as follow:

$$SI_k = \frac{2}{n}\sum_{i=1}^{n} F(-abs[\ln(\mu_i) - \ln(\overline{\mu}_{ki})]) \qquad (2)$$

where k and n are the site class number and the total number of periods, respectively. As well, F( ) is the normal cumulative distribution function, μ_i is the mean response spectral ratios of the horizontal and vertical components (H/V) for the site of interest in the *i*th period, and $\overline{\mu}_{ki}$ is the mean H/V ratio for the *k*th site class averaged over all sites of the database for the *i*th period.

The results of classification based on PNN and GRNN neural networks along with Phuang et al. [9] and Zhao et al. [8] sites class have been presented in Table 1. Vs30-based site classes have been superimposed into Table 1 to give a clear image about different empirical methods used in the analysis.

The site classification criteria in Iranian seismic design code [10] are based on average shear wave velocity in the top 30 m soil layers. Four different site classes are defined in this code as a rock site, very dense soil and soft rock site, stiff soil site, and soft soil site (named as soil type 1 to 4). Shear wave velocity (Vs30) values have been adopted from Mousavi et al [11] for selected sites of current study. As seen in Table 1, the classification results of GRNN are consistence with those obtained based on the averaged shear-wave velocity (Vs30) as a widely used site description variable. It is worth nothing that, the classification method of Phung et al. [9] could be used for classifying a site into either rock (R) or soil (S).

4 CONCLUSIONS

Nowadays, soft-computing based methods have been developed increasingly in engineering fields by the growth of computer processors. In this regards, the high capability of PNN and GRNN models for soil classification has been validated in this paper using the dataset of 2012 Varzaghna-Ahar earthquake ground motions records. Unlike of multi-layer feed-forward networks that commonly take a large number of iteration to converge to the preferred values, the time process of designed GRNN and PNN is very short. GRNN gives a continuous (more precise) output value as a site class. Analysis showed the consistency of site classification of GRNN with VS30 measurements. The proposed proce-

dure is considered particularly useful for regions where geotechnical, geologic and geomorphologic data are not available, which indeed represent the majority of areas in the world.

Station	Phung et al. (2006) Site Class	Zhao et al. (2006) Site Class	Yaghmaei-Sabegh and Tsang (2011) Site Class		Measured Vs30 (m/s)	Vs30-based Site Class
			PNN	GRNN		
Varzeghan	R	4	4	*2.75*	275	3
Khajeh	R	2	*2*	*1.75*	450	2
Kalaybar	R	1	*1*	*1.62*	850	1
Haris	R	2	*3*	*2.04*	530	2
Damirchi	R	1	*2*	*1.59*	1241	1
Hoorand	R	1	*1*	*1.4*	500	2
Meshkin Shahr	R	4	*1*	*2.34*	500	2
Hadi Shahr	R	2	*2*	*1.79*	475	2
Basmanj	S	4	*4*	*3.57*	564	2
Soofiyan	R	2	*3*	*2.27*	707	2
Khomarloo	R	1	*1*	*1.44*	921	1
Zanjireh	R	1	*2*	*1.7*	919	1
Shabestar	R	2	*2*	*1.55*	922	1
Ziveh	R	2	*2*	*1.8*	304	3
Amand	R	1	*2*	*1.78*	743	1
Sharabiyan	R	2	*2*	*2.2*	484	2
Lahrood	R	1	*2*	*1.6*	981	1
Tasooj	R	1	*3*	*2*	709	2
Marand	R	1	*2*	*1.65*	546	2
Sarab	R	2	2	*2.07*	406	2
Ajab Shir	R	2	*3*	*2.4*	657	2
Naghadeh	S	4	*3*	*3.12*	275	3
Torkmanchay	R	3	*2*	*1.67*	542	2
Avin	R	4	*3*	*2.46*		
Yekan Kahriz	R	1	*1*	*1.26*	738	1
Qara geshlakh	S	2	*3*	*2.89*	275	3
Hashrood	S	3	*3*	*2.58*	681	2
Band	R	4	*3*	*3*	275	3

Sharafkhaneh	R	4	*3*	*3*	466	2
Karigh	R	1	*1*	*1.28*	589	2
Germi	S	3	*4*	*3.8*	712	2
Nir	S	2	*3*	*1.89*	541	2
Oldoo	R	2	*2*	*1.79*	445	2
Taleb Qeshlaghi	R	1	*1*	*1.75*	978	1
Azarshahr	R	4	*4*	*2.85*	660	2
Kooraeim	R	2	*1*	*1.74*	787	1
Rashkan	R	3	*2*	*1.814*	275	3
Astara	S	3	*3*	*2.8*	189	3
Helabad	R	3	*4*	*3*	387	2
Namin	R	2	*1*	*1.6*	1236	1
Ardebil 2	S	3	*3*	*2.84*	275	3
Talesh	S	2	*1*	*1.45*	559	2

Table 1: Site classification results based on different empirical methods; PNN, GRNN, Phung et al. (2006) and Zhao et al. (2006) methods

REFERENCES

[1] R.D. Borcherdt, Effects of local geology on ground motion near San Francisco Bay, *Bulletin of the Seismological Society of America,* **60**, 29–61, 1970.

[2] Y. Nakamura, A method for dynamic characteristics estimation of subsurface using micro-tremor on the ground surface," Quarterly Report of RTRI 30, 25–33, Railway Technical Research Institute, Tokyo, Japan, 1989.

[3] P. Triantafyllidis, P.M. Hatzidimitriou, N. Theodulidis, P. Suhadolc, C. Papazachos, D. Raptakis, K. Lontzetidis, Site Effects in the City of Thessaloniki (Greece) Estimated from Acceleration Data and 1D Local Soil Profiles, *Bulletin of the Seismological Society of America* **89**(2), 521-537, 1999.

[4] V. Amico, D. Albarello, M. Mucciarelli, Validation through HVSR measurements of a method for the quick detection of site amplification effects from intensity data: An application to a seismic area in Northern Italy, *Soil Dynamic and Earthquake Engineering* **22**(6), 475–83, 2002.

[5] V.Y. Sokolov, C. Loh, W.Y. Jean, Application of horizontal-to-vertical (H/V) Fourier spectral ratio for analysis of site effect on rock (NEHRP-class B) sites in Taiwan, *Soil Dynamic and Earthquake Engineering* **27**, 314-323, 2007.

[6] K. Sivaram, P. Mahesh, S.S. Rai, Stability Assessment and Quantitative Evaluation of H/V Spectral Ratios for Site Response Studies in Kumaon Himalaya, India Using Ambient Noise Recorded by a Broadband Seismograph Network, *Pure Appl. Geophys*. **169**, 1801–1820, 2012.

[7] S. Yaghmaei-Sabegh, S. H.-H. Tsang, A New Site Classification Approach based on Neural Networks, *Soil Dynamic and Earthquake Engineering* **31**: 974-981, 2011.

[8] J.X. Zhao, K. Irikura, J., Zhang, Y. Fukushima, P.G. Somerville, A. Asano, Y. Ohno, T. Takahashi, H. Ogawa, An Empirical Site-Classification Method for Strong-Motion Stations in Japan Using H/V Response Spectral Ratio, *Bulletin of the Seismological Society of America* **96**, 914-925, 2006.

[9] V. Phung, G.M. Atkinson, D.T. Lau, Methodology for site classification estimation using strong ground motion data from the Chi-Chi, Taiwan, Earthquake, *Earthquake Spectra* **22**(2),511-31, 2006.

[10] Iranian code of practice for seismic resistant design of buildings, Standard No.2800, 3rd edition, Building and housing research center (BHRC), (2005).

[11] M. Mousavi, H. Zafarani, S. Rahpeyma, A. Azarbakht, Test of Goodness of the NGA Ground-Motion Equations to Predict the Strong Motions of the 2012 Ahar–Varzaghan Dual Earthquakes in Northwestern Iran, *Bulletin of the Seismological Society of America*104(5),2512-2528, 2014.

Nonlinear analysis on seismic response of a multi-geomorphic composite site

CHEN Guoxing JIN Dandan GAO Hongmei ZHU Jiao
Institute of Geotechnical Engineering, Nanjing Tech University, 21009, China

Abstract: Based on the explicit FE method and parallel computing cluster platform of ABAQUS, a large-scale two-dimensional (2D) nonlinear analytical model for a multi-geomorphic composite site consisting of valley flat, terraces, undulating hilly terrain was established by considering the inhomogeneity of ground soils and influence of terrain change. Nonlinear seismic effect characteristics of the composite site were analyzed, including the peak ground acceleration (PGA), spectral acceleration, duration and acceleration transfer functions. The main results demonstrated that: (1) the PGA of different observation points on the ground surface vary with each other, which was caused by the terrain differences. For the same input motions, the ground surface PGA of valley flat area show obviously larger than that of the first terrace area. (2) the horizontal spectral acceleration of ground surface appears a double-peak or multi-peak phenomena, the spectra shape peak moves to a larger period in the floodplain area compared with that in first terrace area and the period difference comes to be from 0.05s to 0.25s. (3) the sensitive frequency band of seismic site response was 0.5Hz to 1.75Hz, when the frequency is lower than 0.2Hz or higher than 2Hz, the seismic amplification characteristics is not apparent.（4）PGA exhibits spatial variation characteristics which varies in both lateral and depth directions, and there is a non-monotonic decreasing characteristic with soil depth, greater motion amplification and focusing effect of some shallow soil layers were found. In some degree, the 2D results can reflect nonlinear site effect and the influence of lateral heterogeneity of soils on seismic wave propagation.

Key words: seismic site effect; multi-geomorphic units; soil nonlinear characteristics; focusing effect in soil amplification; PGA

1 INTRODUCTION

Seismic damage investigation and theoretical study has shown that the spread of seismic wave would be influenced by the change of geographic and geomorphic conditions, which may cause difference of seismic spatial distribution characteristics. It was found in seismic damage investigation of Tonghai earthquake in 1970, Yongshan-Daguan earthquake of Yunnan province in 1974 and Haicheng earthquake in 1975 that the top and its neighboring positions of low hill site or isolated mounds have a larger seismic response [1,2]. Previous literatures [3-6] had studied the effects of terrain conditions on the seismic ground motion, analytical solutions of different terrain problems such as arc mounds, depressed river alluvial, and side slope had been given. Wei Rulong et.al [7] had studied the seismic response of bank slope surface in the transition region between rivers and terraces, and it was found that there existed amplification phenomenon of surface ground acceleration. Also some literatures [8,9] had indicated that the seismic response differences caused by the difference of terrain should not be ignored.

As linear structures such as long-span bridge, pipeline projects and transmission tower (line) engineering have emerged in a large amount, the effect of topographical change on the seismic responses has been obtained more and more attentions[10-12], there is firm rules in the "code of seismic design of buildings" (GB50011-2001) that tell us we should pay high attention to the amplification effect on the design ground motion parameters caused by unfavorable location such as complicated terrain or obvious terrain changes.

The seismic response analysis results of site may provide scientific basis for the engineering seismic design, the ground seismic amplification coefficient should be evaluated in the seismic zoning work, it aims at selecting favorable locations in the seismic design of civil engineering. So far, the seismic zoning and seismic safety evaluation of engineering sites for key projects are always conducted by one dimensional (1D) site analysis method. However, it is unreasonable when it comes to large-scale complex site, in this case, it is necessary to use two or three dimensional (2D or 3D) models to analyze the seismic site effect. In addition, analysis assuming that the soil is linear or equivalent linear, homogeneous and elastic in engineering applications, may not reflect the real nonlinear of soils under great ground

motion according to the propagation mechanism of seismic wave, besides, the homogeneous and elastic models may not indicate the influence of inhomogeneity of ground soils and fluctuation of topography to the seismic wave propagation. In previous studies, the site model was always greatly simplified, and the results are far from the truth.

Based on the explicit FE method and parallel computing cluster platform of ABAQUS[13], considering the nonlinearity and consumption characteristics of damping energy of soil, according to a actual site in Chuzhou city of Anhui province, China, the nonlinear scattering problem of valley flat and terraces under S wave is analyzed. Also nonlinear seismic effect characteristics of multi-geomorphic composite site are studied.

2 THE SITE MODEL AND INPUT SEISMIC WAVE

The Chuzhou city of Anhui province, China, which is located in the east of Langya Mountain was taken as the site prototype. The site area is about 95km^2, see in Fig.1. In the north of the site, there is a branching river from the west to the east, from which we can find that there are obvious landforms of valley flat; in the south, there are first terrace and undulating hilly terrain. The spatial distribution of soil presents obvious nonlinearity.

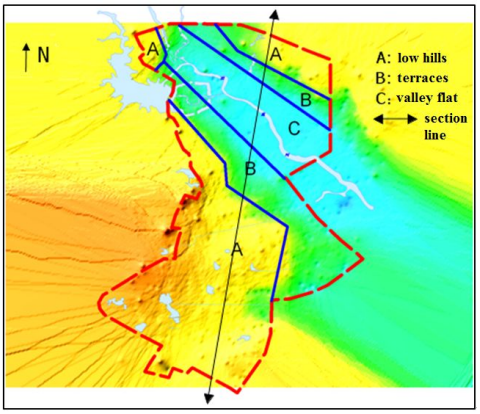


Fig.1 Topography and section location

According to the geotechnical engineering investigation materials and wave velocity data, a large –scale section across valley flat, terrace and undulating hilly terrain is selected, and the corresponding section model is established for the 2D analysis of nonlinear seismic effect characteristics of multi-geomorphic composite site. See in Fig.2, in which, the serial numbers on the ground surface represent the positions of observation points. And the elevation of terrace and low hills come to be 30-50m, the upper portion of the site is clayey soil and the lower portion is gravel soil. The exposed elevation of the valley flat is about 10m, and the upper portion is silty clay, the middle portion is sludge and mucky soil, also, the lower portion is gravel layer.

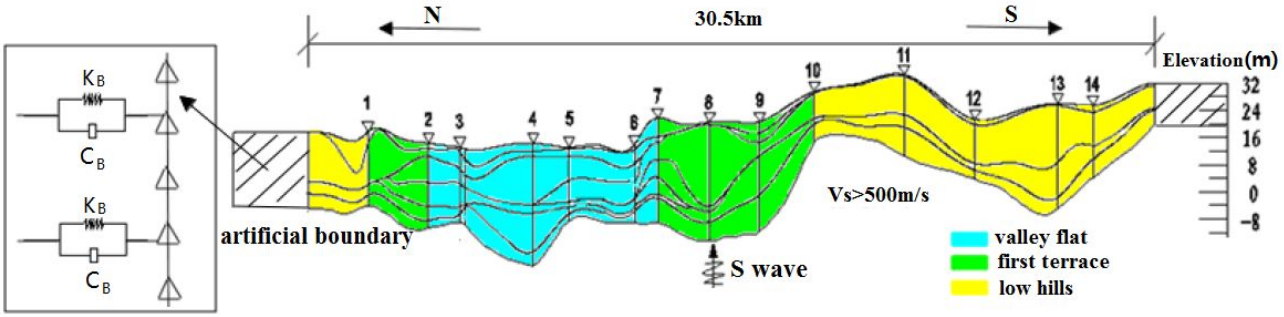


Fig.2 The profile and calculation area

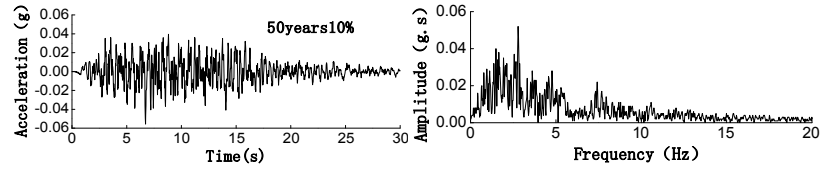
Form the ground surface to the bedrock, the site soil distribution comes to be: filling soil, clay, mucky silty clay, fine sand, medium-coarse sand and gravel, the same kind of soil in different geomorphic unit have different soil property. Table 1 shows the dynamic triaxial test results of the typical site.

Table 1 Dynamic triaxial test results of the typical site

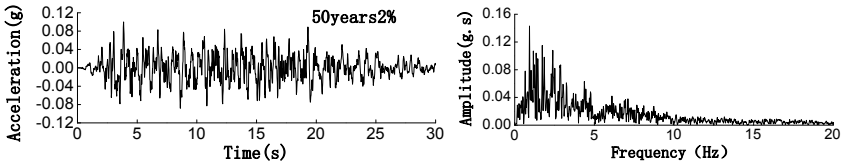
Soil type	Density kg/m^3	Parameter	Shear strain (10^{-4})							
			0.05	0.1	0.5	1	5	10	50	100
fine sand	1960	G/Gmax	0.9933	0.9851	0.9241	0.8576	0.5444	0.3738	0.1066	0.0563
		λ d	0.0040	0.0050	0.0213	0.0306	0.0741	0.0944	0.1238	0.1291
clay	1990	G/Gmax	0.9975	0.9951	0.9760	0.9531	0.8025	0.6702	0.2890	0.1689
		λ d	0.0303	0.0373	0.0602	0.0736	0.1135	0.1325	0.1670	0.1751
silty clay	1950	G/Gmax	0.9983	0.9966	0.9831	0.9668	0.8533	0.7441	0.3677	0.2253
		λ d	0.0329	0.0402	0.0638	0.0776	0.1193	0.1402	0.1821	0.1932

The modified Davidenkov dynamic viscoelastic constitutive model [14] is taken to simulate the dynamic characteristics of the site soil and subroutines of soil dynamic nonlinear constitutive relationship are compiled using the FORTRAN language, besides, the UMAT/VUMAT connector of ABAQUS is used in the integration of the subroutines of dynamic constitutive relationship model into the ABAQUS software. Seismic wave energy would transmit toward into the far-field sites, thus it requires that there are no reflections on the truncated boundary or at least the boundary is close to non-reflective. In Fig.2, vertical constraints are set also horizontal viscous dampers and linear springs on the both sides of the soil calculation region are adopted. And the reference [15] is useful for the values range of spring rate KB and damping coefficient CB. The calculation cut-off frequency is selected as 20Hz, considering the wavelength varies with depth which is related to the cut-off frequency， the vertical grid size is selected as 1/8~1/10 of the wavelength, that is 0.5~1.2m， besides， according to the horizontal heterogeneity, the horizontal grid size is selected as 5~8m.To ensure accuracy and reduce calculating time, we adopt mainly quadrilateral finite elements in meshing the model, and also use few triangular elements for assistance. The total number of the elements of the site model is 95414, and the corresponding degrees of freedom are 190818. The parallel computing and dynamic explicit algorithm are adopted to analyze the nonlinear seismic effect characteristics of the large-scale composite site.

Based on the seismic hazard analysis of this site, two seismic wave respectively in two intensity levels （with exceeding probability of 10% and 2% in 50 years）are selected as the input ground motions, the corresponding PGA of the input ground motion is 55cm/s^2 and 100 cm/s^2， for convenience sake， the seismic waves are named W1-55， W1-100，W2-55and W2-100，The acceleration time course of the input waves and the corresponding Fourier spectra are shown in Fig.3 and Fig4.

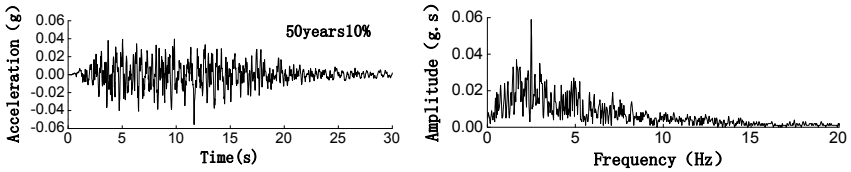


（a）W1-55

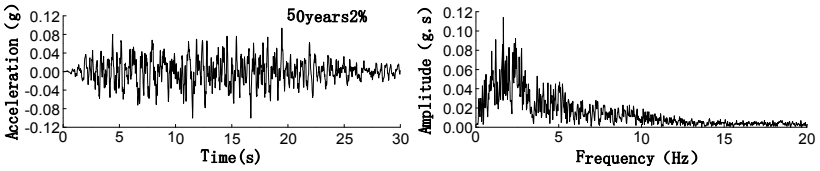


（b）W1-100

Fig 3 The acceleration time course of the input wave W1 and the corresponding Fourier spectrums



（a）W2-55



（b）W2-100

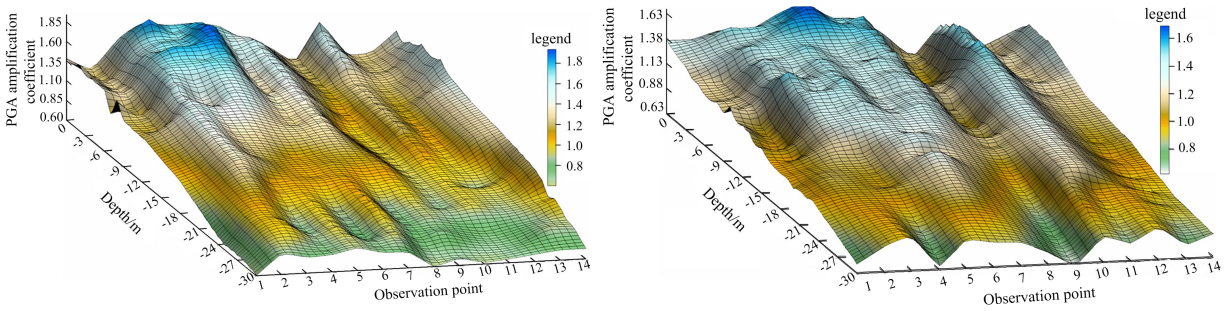
Fig 4 The acceleration time course of the input wave W2 and the corresponding Fourier spectrums

3 NUMERICAL CALCULATION RESULTS

When analyzing the seismic response characteristics of the site, it is not comprehensive to evaluate only using single index. In this paper，comprehensive analysis of seismic amplitudes，spectra and ground motion duration were conducted to study the seismic response characteristics of the site.

3.1 Variation characteristics of PGA

Based on the above calculation model, the PGA characteristics with depth were obtained, and Fig.5 gives the PGA amplification coefficient of different observation points, from which we can find that: (1) Compared with the input ground motion， the peak acceleration of soils near the ground surface show an obvious amplification phenomenon , the seismic amplification effect of soils deeper than 15m seem weakened with the growth of depth, and gradually the amplification factor of PGA become smaller than 1.0. (2) The PGA display a non-monotonic decreasing characteristic with depth and a greater focusing effect of some particular soil layers, and this is more common in valley flat area, such as the observation points No.3 to 7. (3) As it's a multi-geomorphic composite site, the PGA amplification coefficient of each observation point varies from each other for the reason of topographic change. For example, the PGA of observation points No.3 to 7 in valley flat （slope toe, the corresponding bedrock is flat）is larger than that of observation points No.8,9,11,12 and 13, which may be caused by the geological differences and terrain fluctuation.



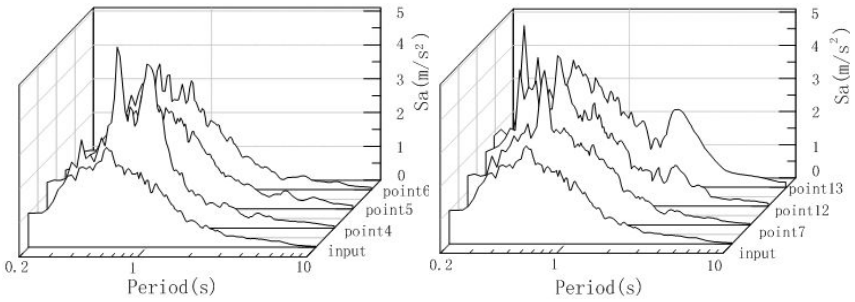
（a）average value of different conditions (50 years 10%) （b）average value of different conditions (50 years 2%)

Fig.5 The profile of PGA with depth

3.2 Seismic spectra

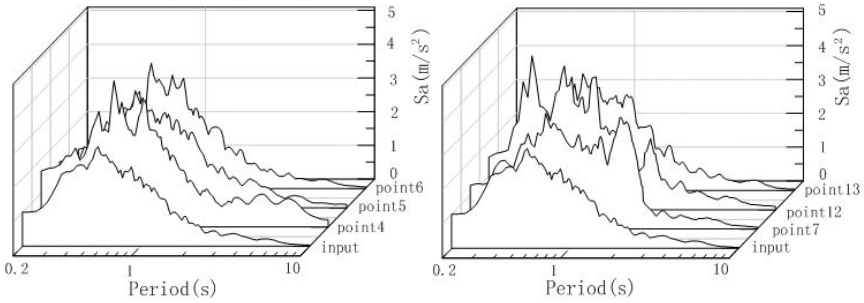
Fig.6 and Fig.7 give the acceleration response spectra of observation points under different seismic excitation. From which, we can find that the horizontal acceleration response spectra present a double- or multi- peak phenomenon under different seismic wave. No matter in which geomorphic unit, the horizontal acceleration is largely amplified in period of 0.4s-1.2s. Parts of the observation points (No.7-10 in terrace) present another peak of acceleration response spectra in period of 1.2s-1.5s. from the comparison between Fig.6 (under seismic wave W1) and Fig.7 (under seismic wave W2), we fan find that the acceleration response spectra characteristics have something to do with the characteristics of input

ground motions, in this paper, the seismic wave W1 is relatively more abundant in low-frequency component than seismic wave W2, and the ground motion amplification effect under W1 seem larger than that under W2.



（a）valley flat （b）terrace

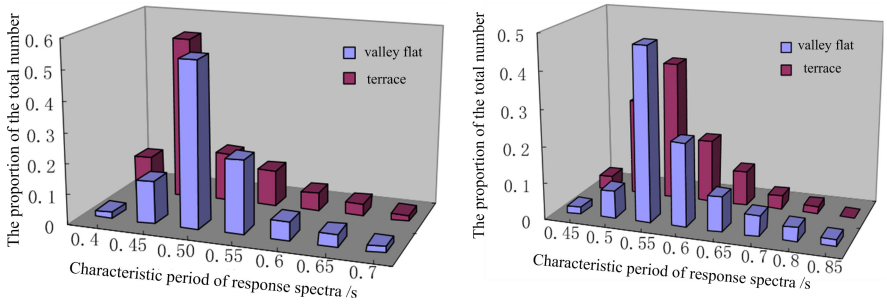
Fig.6 Acceleration response spectra of observation points(under W1)



（a）valley flat （b）terrace

Fig.7 Acceleration response spectra of observation points(under W2)

Fig.8 shows characteristic periods of ground surface acceleration response spectra, and it can be found that characteristic periods of valley flat are on the whole larger than that of terrace, the characteristic period of valley flat ranges from 0.50 to 0.55s under input motion with peak acceleration of 55cm/s^2 , and under the same condition, the correspondingly ranges from 0.45 to 0.50s in terrace. the period difference between terrace area and valley flat area comes to be from 0.05s to 0.25s.



（a）50 years 10% （b） 50 years 2%

Fig.8 The characteristic periods of response spectra

Fig.9 shows Fourier spectrum ratio (the ratio of acceleration response Fourier spectrum value of each observation point to the acceleration Fourier spectrum value of input ground motion) under different frequency. The results show that the acceleration response Fourier spectrum of each observation point is amplified in different degree compared with the acceleration Fourier spectrum value of input ground motion. the Fourier spectrum ratio curve is steady under frequency of 0.2Hz and 0.25Hz, that is the acceleration response Fourier spectrum value of each observation point has little difference with that of input ground motion. When it comes to the frequency range of 0.5Hz-1.75Hz， the Fourier spectrum ratio curve present multi-peak phenomenon, which indicates that the seismic site effect is significant. However, when the frequency is larger than 2Hz, the site amplification effect seems weakened, and the Fourier spectrum ratio curve

becomes more and gentler with the increasing of frequency. The site effect of observation points（No.2-7）in valley flat become obvious when the frequency is larger than 0.75Hz. and when it is in the frequency range of 0.75Hz-1.50Hz， the seismic amplification effect comes to be the most obvious. However, the observation points(No.10-14) in low hills present a noticeable seismic response when the frequency is relative small（about 0.25Hz），and the seismic amplification effect comes to be the most obvious. In the frequency range of 0.2Hz-1.7Hz.thus, we can find that the low hills area has a lower sensitive frequency than that of the valley flat area.

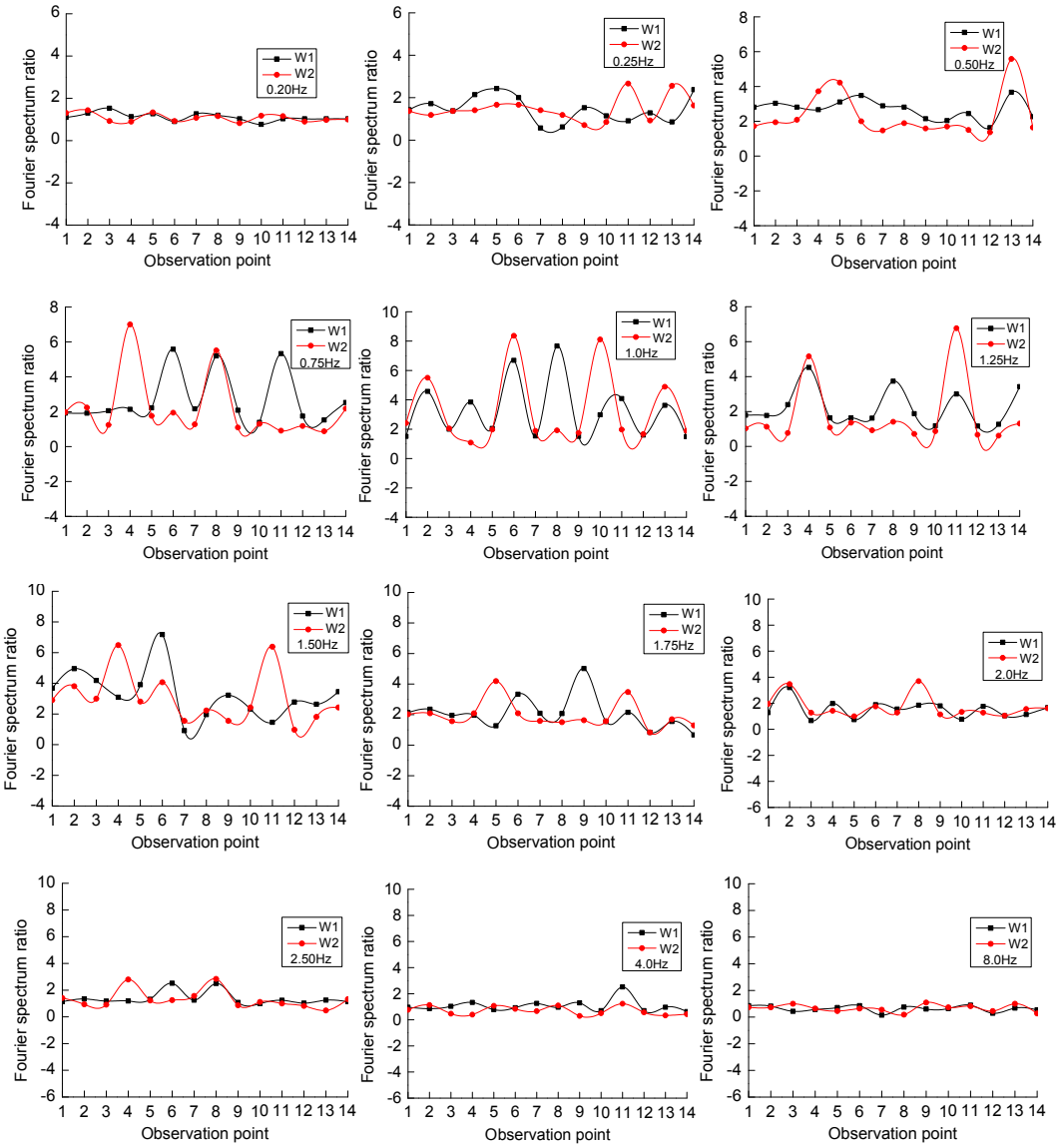


Fig.9 Acceleration Fourier spectrum ratio under different frequency

3.3 Seismic duration

The seismic disasters caused by earthquake motion is relative to both the seismic motion intensity and seismic duration, thus, it is necessary to consider the influence of the seismic duration besides the seismic response strength. However, so far， the definition of seismic duration is not unified.

there are three major categories of standards: the first standard is based on the absolute value of ground motion acceleration; the second one is based on the relative value of ground motion acceleration, the third one is based on the seismic accumulated energy, in this paper, the second standard is adopted, that is the duration time in the acceleration time history curve from the first time to the last time that the acceleration comes to be 1/5 of PGA.

Fig.10 gives the duration time of ground surface acceleration in different positions in the site under different seismic

waves. The position of observation point has an important effect on the duration time， which may also indicate that the local terrain changes have influence on the seismic site response. The acceleration duration time is significantly prolonged in some positions. For example, the acceleration duration time of observation points 8-9（in the transition region between valley flat and low hills）are obviously longer than that of the other positions. Besides, the input ground motion characteristics has something to do with the acceleration duration time. In general, the acceleration duration of each observation point seems in uniform distribution under seismic wave W1, and the amplitude of fluctuation is small, however, when under seismic wave W2, the acceleration duration time distribution seems fluctuated.

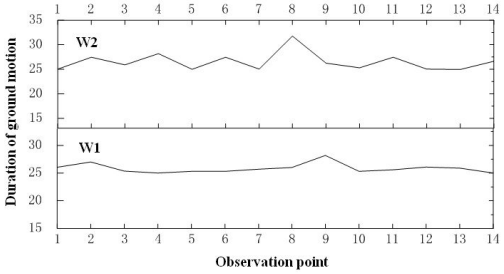


Fig.10 Duration time of ground motion

4 CONCLUSIONS

Taking the seismic microzonation site in Chuzhou city of Anhui province as the prototype, based on the explicit FE method and 32 CPU parallel computing cluster platform of ABAQUS, considering the inhomogeneity of ground soils，a large-scale refined two-dimensional(2D) FE nonlinear analytical model for a multi-geomorphic Composite site that consists of valley flat，terraces，undulating hilly terrain and monadnock was established. The SH wave is taken as the bedrock earthquake motion and nonlinear seismic effect characteristics of the composite site were analyzed, which may provide some scientific basis for engineering practice. The main conclusions are as follows:

(1) The PGA of different observation points on the ground surface vary with each other, which is caused by the terrain differences. When it's under the same input ground motion, the ground surface PGA of valley flat show obviously larger than that of the first terrace.

(2) The horizontal acceleration response spectrum of ground surface appears a double-peak or multi-peak phenomenon, the spectra shape peak moves to a larger period in the floodplain area compared with that in first terrace area and the period difference comes to be from 0.05s to 0.25s.Moreover, the acceleration response spectrum is related with the input ground motion.

(3) The amplification effect and focusing effect of seismic motion are more obvious in specific frequency band(0.5Hz-1.75Hz), when the frequency is lower than 0.2Hz or higher than 2Hz, the seismic amplification characteristics is not apparent；to the valley flat ，the sensitive frequency comes to be 0.75Hz-1.50Hz. while the sensitive frequency of low hills is 0.25Hz-1.75Hz.

（4）The location of observation point has influence on the acceleration duration， the changing terrain may cause difference of seismic motion duration， besides， the motion duration, in some way, is dependent on the input ground motion characteristics.

The large-scale two dimensional nonlinear analysis models, in a sense, may reflect the propagation characteristic of seismic wave, which may also indicate the amplification effect and focusing effect of seismic motion in specific frequency. To the multi-geomorphic composite site which is with nonlinear soil distribution and changing terrain, the one-dimensional equivalent linearization model is not suitable.

The above conclusions are obtained by the given model condition, and the seismic site response is relative with many factors such as geographic and geomorphic conditions, soil properties, input ground motion and so on. It is a complex process to study the ground motion distribution of a composite site. Further research should be conducted to improve the

understanding of the seismic site effect, which may provide a basis for the seismic design of major construction project in composite site.

REFERENCES

[1] Qian Peifeng, Shen Yunfen, Guo Daiyu, et al. Parts of seismic hazard in the Tonghai earthquake and their analysis [J]. Journal of Seismological Research, 1984,7(3): 357-363.

[2] Liu Zhengrong, Lei Suhua, Hu Suhua. The Yongshan-daguan earthquake (M=7.1) on may 11, 1974. [J]. Chinese Journal of Sinica, 1977, 20(2): 110-114.

[3] Liang Jianwen, Zhang Yushan, Gu Xiaolu, et al. Surface motion of circular-arc layered alluvial valleys for incident plane SH waves[J]. Chinese Jounal of Geotechnical Engineering, 2000, 22(4): 396-401.

[4] Recep Iyisan. A numerical study on the basin edge effect on soil amplification [J]. Bull Earthquake Eng, 2013, 11:1305–1323.

[5] Gelagoti F, Kourkoulis R, Anastasopoulos I, Tazoh T, Gazetas G. Seismic wave propagation in a very soft alluvial valley: sensitivity to ground-motion details and soil nonlinearity, and generation of a parasitic vertical component[J]. Bull Seismol Soc Am, 2010, 100(6):3035–3054.

[6] STEWART J P, SHOLTIS S E. Case study of strong ground motion variations across cut slope[J].Soil Dynamics and Earthquake Engineering,2005, 25: 539－545.

[7] WEI Yunjie, BAO Yan, LI Zhanlu. Genetic analysis of earthquake-induced geologic hazards in Ganxigou drainage basin of Pengzhou[J]. Journal of Engineering Geology, 2011, 19(4): 582-587.

[8] Lee Shiann-Jong, Komatitsch Dimitri,Huang Bor-Shouh et al. Effects of topography on seismic-wave propagation: an example from Northern Taiwan[J]. Bulletin of the Seismological Society of America, 2009, 99(1): 314－325.

[9] ZHOU Guoliang, LI Xiaojun, HOU Chunlin et al.Characteristic analysis of ground motions of canyon topography under incident SV seismic waves[J]. Rock and Soil Mechanics, 2012, 33(4): 1161-1166.

[10]Vincenzo Di Fiore. Seismic site amplification induced by topographic irregularity: results of a numerical analysis on 2D synthetic models[J].Review on Engineering Geology, 2010,114(3–4):109-115.

[11]Mohammad Khandan Bakavoli, Ebrahim Haghshenas, Mohsen Kamalian.Experimental study of seismic behavior of two hilly sites in Tehran and comparison with 2D and 3D numerical modeling[J].Soil Dynamics and Earthquake Engineering, 2011,31(5-6): 737-756.

[12] Limin Wang, Yinhe Luo, Yixian Xu.Numerical investigation of Rayleigh-wave propagation on topography surface [J].Journal of Applied Geophysics, 2012, 86:88-97.

[13] MAO Kunming, CHEN Guoxing. Construction of parallel computing heterogeneous cluster platform based on Abaqus software[J]. Journal of Earthquake Engineering and Engineering Vibration, 2011, 31(5): 184-189.

[14] CHEN Guoxing. Geotechnical earthquake engineering[M]. Beijing: Science Press, 2007.

[15] LIU Jingbo, GU Yin, DU Yixin. Consistent viscous-spring artificial boundaries and viscous-spring boundary elements[J]. Chinese Journal of Geotechnical Engineering, 2006, 28(9): 1070-1075.

COMPDYN 2015
5th ECCOMAS Thematic Conference on
Computational Methods in Structural Dynamics and Earthquake Engineering
M. Papadrakakis, V. Papadopoulos, V. Plevris (eds.)
Crete Island, Greece, 25–27 May 2015

FINITE ELEMENT ANALYSIS OF AN EARTH DAM SUBJECTED TO BLAST-INDUCED LOADING USING A HIGH STRAIN-RATE BOUNDING SURFACE MODEL

Tianhua Xu[1] **and Limin Zhang**[2]

[1] PhD student, Department of Civil and Environmental Engineering
The Hong Kong University of Science and Technology, Clear Water Bay, Kowloon, Hong Kong
e-mail: txuaa@ust.hk

[2] Professor, Department of Civil and Environmental Engineering
The Hong Kong University of Science and Technology, Clear Water Bay, Kowloon, Hong Kong
e-mail: cezhangl@ust.hk

Keywords: Earth dam, Blasting, Seismic loading, Bounding surface model, Strain rate.

Abstract. *When soil or rock excavations near an earth dam are assisted with blasting, the dam may be damaged by the blast-induced loading. In order to investigate the response of an earth dam under blast-induced seismic loading, an artificial blast test on a 15 m-height earth dam is simulated. A recently proposed high strain-rate bounding surface model is adopted to model the stress-strain behavior of the dam materials. The detonation process of explosives is modeled by applying a pressure loading on the side wall of the borehole. Simulation results show that at a given elevation, the peak ground acceleration decreases with the distance to the blast hole. The peak horizontal acceleration on the upper parts of the dam is smaller than that at the dam bottom, which is different from responses to a tectonic earthquake. The maximum values of permanent and peak dynamic displacement occur near the upstream and downstream surfaces.*

1 INTRODUCTION

Although the design of earth dams against seismic loading still relies on empirical or semi-empirical methods, nonlinear finite element analysis has gained more attention, because it provides details about the performance of an earth dam under seismic loading conditions. Recently, Dakoulas [1] investigated the influence of canyon geometry on the seismic response of an earth dam; Elia and Rouainia [2] used a multi-surface kinematic hardening model to analyze the performance of a 42 m-height homogeneous earth dam under seismic loading; Zou et al. [3] and Liu et al. [4] reproduced the response of the 156 m-height Zipingpu Dam to the 2008 Wenchuan Earthquake. These are good examples that provide information on the seismic acceleration and deformation of various kinds of earth dams under earthquakes.

In addition to tectonic earthquakes, seismic loading can be induced by blasting operations for soil and rock excavation. Damage on earth dams caused by blast-induced seismic loading has been observed. For example, the upstream sand shell of the Swir II dam was reported liquefied by blasting operations 200 m upstream of the dam, and the upstream slope was reduced as a result [5]. When compared with a tectonic earthquake, the location of energy release in a blast-induced earthquake is much closer to the ground surface. The P- and S-wave cannot separate from each other within such a short distance, thus the responses to both waves are important. High frequency components of the seismic wave can also be reserved in a blast-induced earthquake. However, research on the response of an earth dam to blast-induced seismic loading is still rather limited.

In this research, finite element simulations are carried out to investigate the response of an earth dam to a blast-induced earthquake. The numerical model is developed following the set-up of an artificial blasting test on a 15 m-height earth dam. The earthquake is generated by applying a blast pressure loading in a borehole in the model such that the characteristics of blast-induced seismic waves can be captured. A recently proposed rate-dependent bounding surface model is used to model the dam materials, which is able to reproduce the soil behavior under high strain-rate cyclic loadings. The simulation results offer insight into the response of an earth dam under blast-induced seismic loadings.

2 FINITE ELEMENT MODEL

2.1 Test site

In order to investigate the feasibility of estimating the shear wave velocity of dam materials using artificial blast tests, Ha et al. [6] performed a series of borehole blasting tests near the Seongdeok dam, which is a 15 m-height core wall dam located near Choungsong, Korea. The geometry of the dam is shown in Figure 1. The width of the dam crest is 5 m. The upstream and downstream slopes are 1:2.0 and 1:1.8, respectively.

As reported by Ha et al. [6], four tests with weights of charge varying from 5 to 19 kg were performed. The explosives were detonated within boreholes at depths of 6 – 25 m. Before

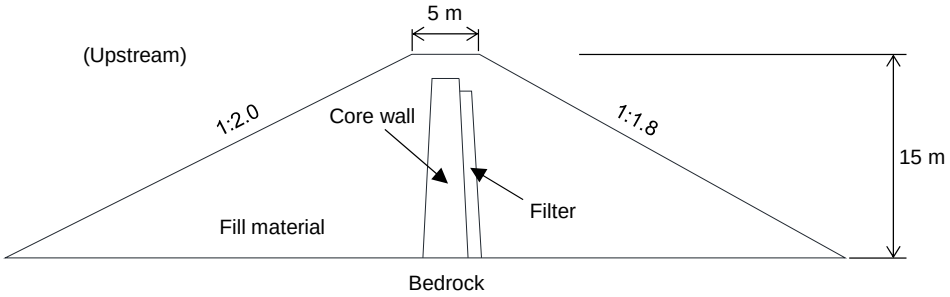


Figure 1: Profile of the Seongdeok dam.

detonation, the required amount of explosive was placed at the bottom of the borehole. Subsequently the borehole was backfilled with crushed rock. The boreholes were about 60 m from the dam axis downstream. Accelerometers were installed on the dam crest and the rock outcrop near the boreholes. The measured time histories of ground horizontal acceleration are used to verify the simulation results in this research.

2.2 Finite element model

Figure 2 shows the finite element model used in the simulations. The model was developed in LS-DYNA [7]. The *x* and *y* directions of the model are indicated in the figure, and the *z* direction is perpendicular to the *x*-*y* plane pointing to the reader. The model is developed by extruding a 2D model from the plane $z = 0$ to the plane $z = 1$ m. The dam is modeled according to the actual dimensions. Two zones, the fill material and the core wall, are considered. The bedrock in the finite element model extends to a depth of 80 m below the bottom of the dam. The blast hole is located 60 m away from the dam axis. The bottom of the blast hole is 25 m below the ground surface. The diameter and length of the hole are 5 cm and 9.1 m, respectively.

The domain is discretized using 8-noded hexahedral Lagrangian elements. Each element uses one single Gaussian integration point. As the model is a pseudo-3D model, the *z* displacements of all nodes are constrained. The bottom of the finite element model, *BC* in Figure 2, is taken as a fixed boundary. Both the *x* and *y* displacements are set to 0 at this boundary. A silent boundary is adopted for the two sides of the model, *AB* and *CD*. These silent boundaries absorb the stress wave by applying a counter stress calculated according to the elastic wave velocity [6]. Before the dynamic simulation, gravitational force was applied to the whole model to reproduce the initial stress state. The gravitational force is retained during the entire dynamic simulation process.

In this research, the blast loading is simulated by applying a pressure loading with a time history suggested for borehole blasting [8, 9, 10], which can be represented by

$$p(t) = p_0\left(\exp(-\alpha t) - \exp(-\beta t)\right) \tag{1}$$

where $p(t)$ is the blast pressure acting on the side wall of the blast hole at time t; p_0, α and β are model parameters. Equation (1) can be written as

$$p(t) = \frac{p_{peak}}{k^{1/(1-k)}\left(1-k^{-1}\right)} k^{\frac{1}{1-k}\frac{t}{t_0}}\left(1-k^{-\frac{t}{t_0}}\right) \tag{2}$$

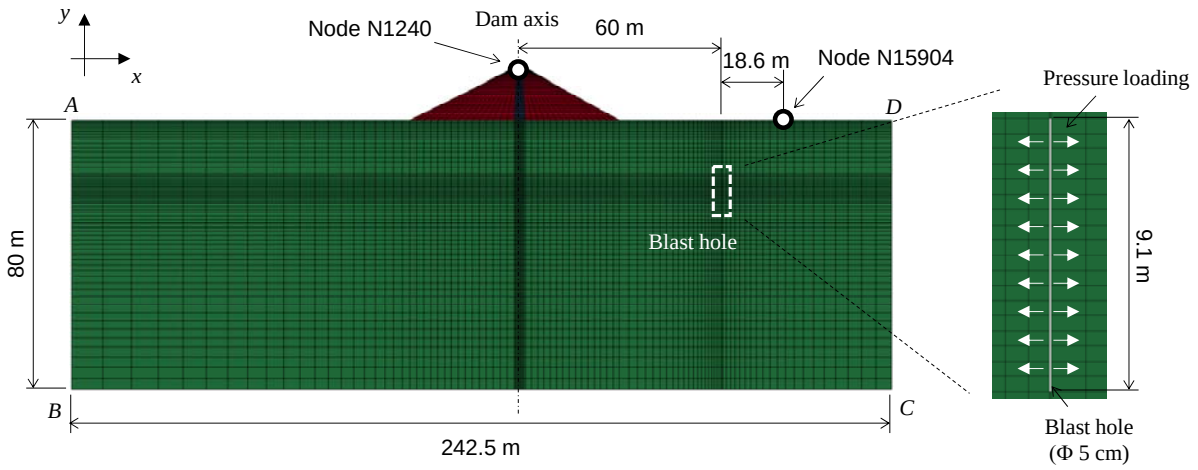


Figure 2: Finite element model used in the simulation.

where p_{peak} is the peak pressure, which is equal to $p_0[(k^{(1/(1-k))}-k^{(k/(1-k))})]$; $k = \beta/\alpha$; t_0 is the occurrence time of the peak pressure, which can be calculated by $t_0 = \ln(k)/(\beta-\alpha)$. According to Equation (2), the time history of the blast pressure can be determined by specifying three parameters: p_{peak}, k and t_0. Figure 3 shows the time histories of the normalized pressure, $p(t)/p_{peak}$, with different parameters. In the simulation, the adopted parameters are p_{peak} = 1 MPa, k = 1.5 and t_0 = 20 ms. These parameters are selected to reproduce the time history of ground acceleration measured at the rock outcrop and the dam crest to the greatest extend. The adopted time history of blast pressure is shown by the black curve in Figure 3.

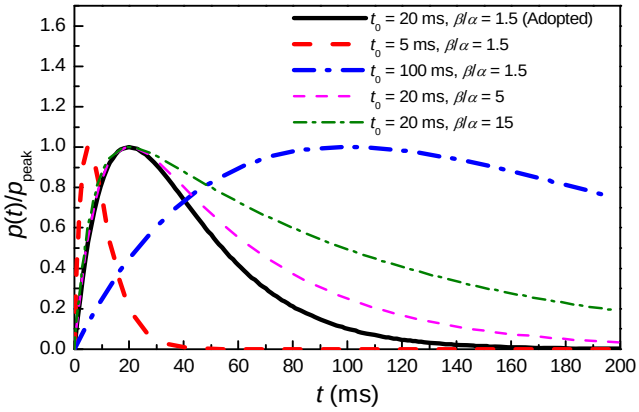
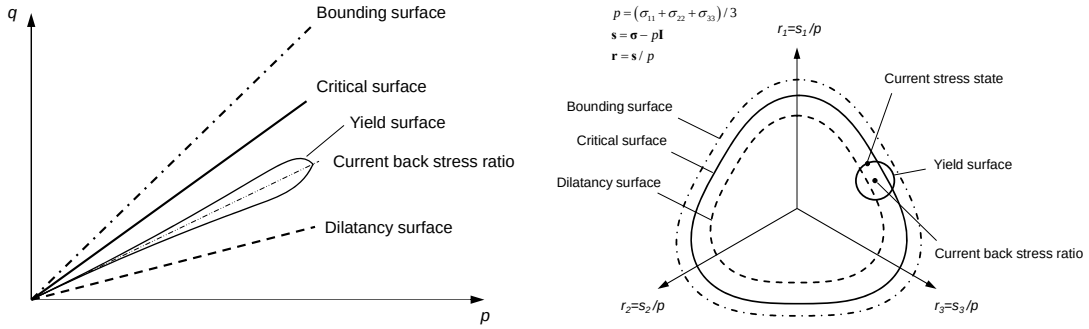


Figure 3: Time histories of normalized pressure loading with different parameters.

3 MATERIAL MODELS

3.1 Dam materials

A recently proposed high strain-rate bounding surface model is utilized in this research to model the behavior of dam materials [11]. The model was proposed on the basis of the bounding surface framework. As shown in Figure 4, a spindle-like yield surface is used in the model. Both isotropic and kinematic hardening conditions are defined, so both the shape and location of the yield surface evolve during a loading process. In the general stress space, the critical stress states are represented using a critical surface. A dilatancy surface is introduced as the boundary of shear-induced contractive and dilative behavior. Moreover, a bounding surface is used to enclose all the possible stress states. These model surfaces reproduce the plastic behavior of soil. The sizes of these model surfaces depend on the strain rate, thus the influence of strain rate on the mechanical behavior can be considered. The model formulations have been presented by Xu and Zhang [11].



(a) (b)

Figure 4: Model surfaces in the high strain-rate bounding surface model: (a) on the p-q plane; (b) in the general stress ratio space.

Soil behavior	Parameters	Fill	Core wall
Soil property	ρ (g/cm^3)	2.00	1.80
Rate-dependent elasticity	$G_{0,ref}$	45.00	35.00
	$K_{0,ref}$	71.30	57.55
	k_G	0.10	0.10
	k_K	0.10	0.10
Critical state	$\alpha^c_{c,ref}$	1.70	1.25
	k_c	0.01	0.005
	c	0.75	0.75
	e_0	0.3634	0.3387
	λ	0.0069	0.0044
	ξ	0.70	0.70
Dilatancy	n^d	2.29	1.50
	A_d	1.68	1.91
	k_d	-0.15	-0.50
Kinematic hardening	n^b	2.26	2.87
	k_b	0.20	0.10
	h_0	30.00	50.00
	c_h	0.50	0.50
Limit compression line	p_r	5500	5500
	ρ_c	0.374	0.374
	θ	0.20	0.20
	X	0.80	0.80

Table 1: Model parameters for dam materials.

Comprehensive element test data are not available for the materials in the Seongdeok dam. Considering that this research is to provide a general understanding of the response of an earth dam under blast-induced seismic loading, the model parameters for the dam fill and core wall material of the Nuozhadu dam in China are adopted in the simulation. The model parameters adopted in this research are listed in Table 1. Moreover, the Rayleigh damping is applied to dam materials to provide basic damping at low strain levels [12]. The Rayleigh damping coefficients are determined so that the damping ratio is 10% for the motions at the frequencies of 10 and 200 Hz.

3.2 Bedrock

The bedrock in the finite element model is modeled using the Mohr-Coulomb model. According to the site investigation [6], the bedrock at the test site is hard rock with an RQD (Rock Quality Designation) value of 90%. The shear modulus of the bedrock is 5.05 GPa, and the Poisson's ratio is assumed to be 0.20. The friction angle and cohesion are 40° and 3.5 MPa, respectively. The Rayleigh damping is also applied to the bedrock with the same damping coefficients as the dam materials to consider the attenuation of blast wave in the bedrock.

4 RESPONSE OF THE DAM SUBJECTED TO BLAST-INDUCED LOADING

4.1 Ground acceleration

Figure 5 shows the time histories of horizontal acceleration at two typical nodes shown in Figure: N15904 and N1240. N15904 is located on the surface of bedrock. The distance be-

tween N15904 and the blast hole in the model is the same as that between the accelerometer at the rock outcrop and the blast hole in the tests. N1240 is at the same location with the accelerometer at the dam crest. The measured data at these two locations are also shown in Figure 5. For comparison, the time shown in the *x*-axis has been translated so that the peaks of the curves match each other. The peak values of the simulated horizontal acceleration at the rock outcrop and the dam crest are 0.36 g and 0.04 g, respectively, which are of the same magnitude with the measured data. The measured and simulated duration of the blast-induced seismic vibration are both within 600 ms. The comparison between the measured and simulated data shows that the artificial blasting test at the Seongdeok dam is well simulated.

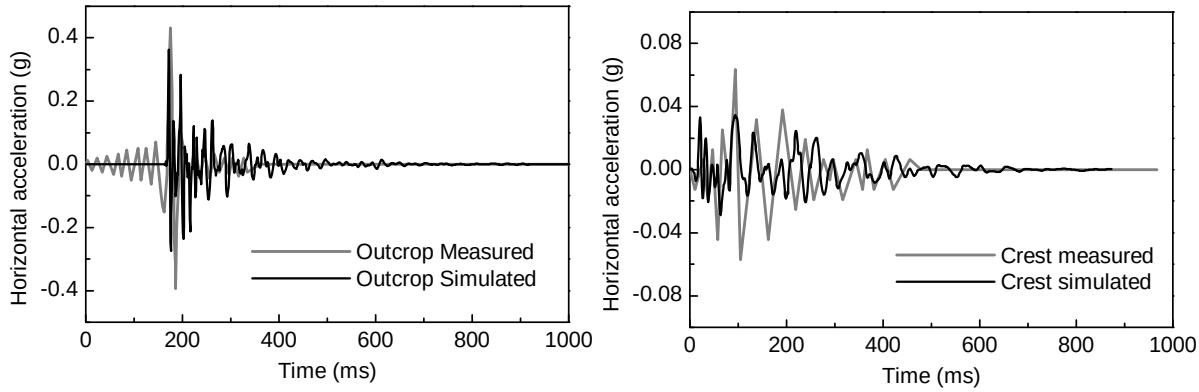


Figure 5: Time histories of ground acceleration of typical nodes.

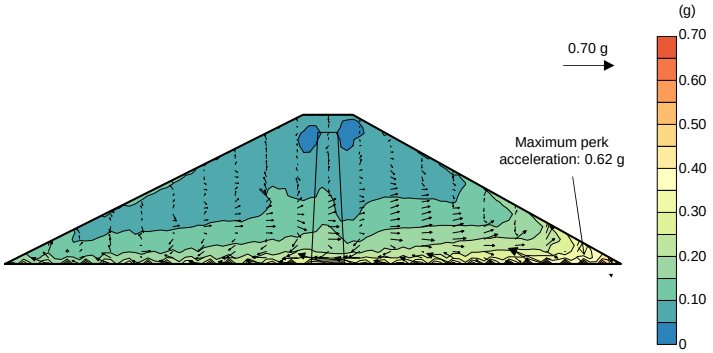


Figure 6: Distribution of peak resultant acceleration in the dam body.

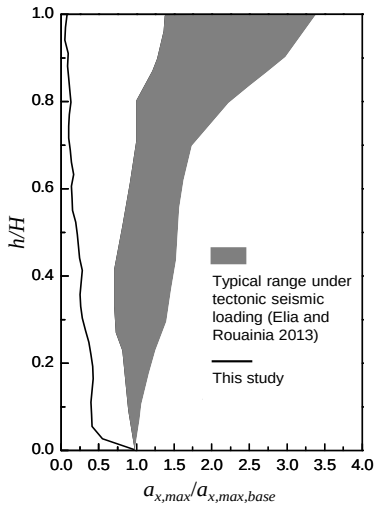


Figure 7: Amplification of horizontal acceleration along dam axis.

The distribution of peak resultant acceleration is shown in Figure 6. At the same elevation, the peak resultant acceleration is larger near the blast hole. The maximum value of the peak resultant acceleration, 0.62 g, occurs near the bottom right corner of the dam body. Figure 7 shows the distribution of the amplification factor of horizontal acceleration along the dam axis. In the figure, $a_{x,max}$ is the peak horizontal acceleration, $a_{x,max,base}$ is the peak horizontal acceleration at the bottom of the dam, h is the height over the dam bottom of a location, and H = 15 m is the height of the dam. Based on the simulation result, the peak horizontal acceleration occurs at the bottom of the dam. Generally, the peak horizontal acceleration decreases with increasing elevation. The typical range of the distribution of $a_{x,max}$ / $a_{x,max,base}$ along the dam axis for an earth dam under a tectonic earthquake is also shown in the figure. When subjected to tectonic seismic loading, the peak horizontal acceleration at the dam crest is larger than that at the dam bottom, which differs greatly from the observation in this study.

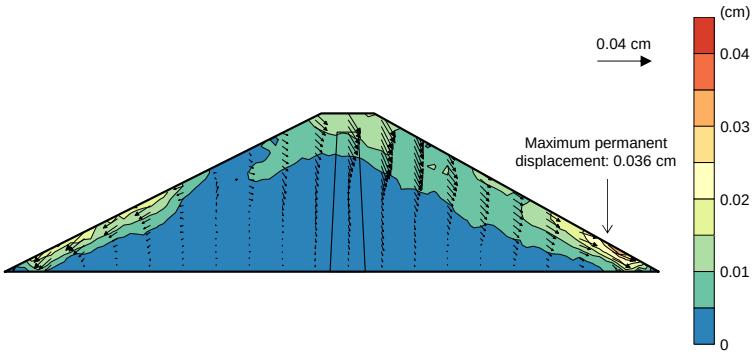


Figure 8: Contour of permanent resultant displacement.

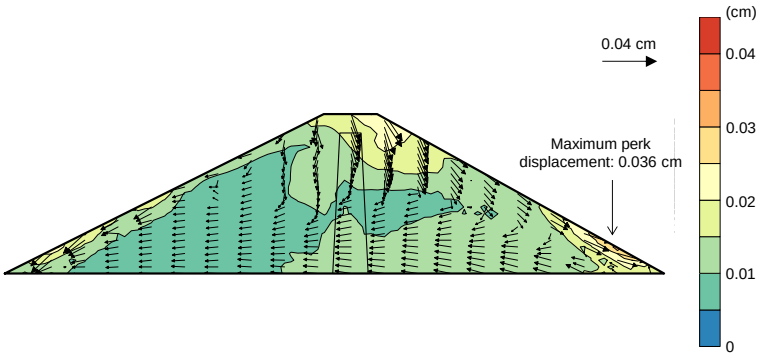


Figure 9: Contour of peak permanent displacement.

4.2 Ground displacement

As the artificial blasting test is performed solely for the measurement of the shear wave velocity of dam materials, the deformation of the dam body should be small. However, the characteristics of the dam deformation under blast-induced seismic loading can still be captured by the numerical simulation in this research. Figure 8 shows the permanent resultant displacement within the dam body. According to the figure, the deformation zone appears mainly on the dam surfaces near the bottom of the dam. The peak permanent displacement is 0.04 cm in this artificial blasting test and occurs at the bottom right of the dam body. The deformation zone is larger at the downstream part than that at the upstream part. The maximum dynamic displacement is shown in Figure 4.2.2. The maximum dynamic displacement in a large part of the dam body is along the direction of the blast wave propagation and larger than the permanent displacement.

5 SUMMARY

In this research, the response of an earth dam subjected to the seismic loading induced by nearby borehole blasting was investigated with the aid of finite element simulation. The blasting was simulated by applying a pressure loading on the side wall of the borehole. A rate-dependent bounding surface model was adopted to model the mechanical behavior of dam materials. According to the simulation result, the peak resultant acceleration will be larger near the blast hole at a given elevation. For locations along the dam axis, the peak horizontal acceleration decreases as the elevation increases. The permanent deformations of the dam body are the largest near the upstream and downstream surfaces.

ACKNOWLEDGMENT

This research was substantially supported by the National Science Foundation of China (No. 51129902) and the National Basic Research Program (No. 2011CB013506).

REFERENCES

[1] P. Dakoulas, Nonlinear seismic response of tall concrete-faced rockfill dams in narrow canyons. *Soil Dynamics and Earthquake Engineering*, **34**(1), 11-24, 2012.

[2] G. Elia, M. Rouainia, Seismic performance of earth embankment using simple and advanced numerical approaches. *Journal of Geotechnical and Geoenvironmental Engineering*, **139**(7), 1115-1129, 2013.

[3] D. Zou, B. Xu, X. Kong, H. Liu, Y. Zhou, Numerical simulation of the seismic response of the Zipingpu concrete face rockfill dam during the Wenchuan earthquake based on a generalized plasticity model. *Computers and Geotechnics*, **49**, 111-122, 2013.

[4] H. Liu, Y. Chen, T. Yu, G. Yang, Seismic Analysis of the Zipingpu Concrete-Faced Rockfill Dam Response to the 2008 Wenchuan, China, Earthquake. *Journal of Performance of Constructed Facilities*, 04014129, 2013.

[5] W.A. Charlie, Discussion of "War Damages and Reconstruction of Peruca Dam" by Ervin Nonveiller, Josip Rupcic, and Zvonimir Sever. *Journal of Geotechnical and Geoenvironmental Engineering*, **126**(9), 854-855, 2000.

[6] I.S. Ha, Estimation of shear wave velocity of earth dam materials using artificial blasting test. *Soil Dynamics and Earthquake Engineering*, **55**, 120-129, 2013.

[7] J.O. Hallquist, *LS-DYNA theory manual*. Livermore Software Technology Corporation, Livermore, California, 2006.

[8] W.I. Duvall, Strain-wave shapes in rock near explosions. *Geophysics*, **18**(2), 310-32, 1953.

[9] S.H. Cho, K. Kaneko, Influence of the applied pressure waveform on the dynamic fracture processes in rock. *International Journal of Rock Mechanics and Mining Sciences*, **41**(5), 771-784, 2004.

[10] G.W. Ma, X.M. An, Numerical simulation of blasting-induced rock fractures. *International Journal of Rock Mechanics and Mining Sciences*, **45**(6), 966-975, 2008.

[11] T.H. Xu, L.M. Zhang, Numerical implementation of a bounding surface plasticity model for sand under high-strain-rate loadings in LS-DYNA. *Computers and Geotechnics*, **66**, 203-218, 2015.

[12] R.W. Clough, J. Penzien, *Dynamics of Structures*. McGraw Hill, New York, 1993.

COMPDYN 2015
5th ECCOMAS Thematic Conference on
Computational Methods in Structural Dynamics and Earthquake Engineering
M. Papadrakakis, V. Papadopoulos, V. Plevris (eds.)
Crete Island, Greece, 25–27 May 2015

3D FAILURE ENVELOPE OF A SINGLE PILE IN SAND

Zheng Li[1,2], Panagiotis KOTRONIS[1] and Sandra ESCOFFIER[2]

[1]LUNAM Université, Ecole Centrale de Nantes, Université de Nantes, CNRS
Institut de Recherche en Génie Civil et Mécanique (GeM)
1 Rue de la Noë, F-44321 Nantes, France
e-mail: {zheng.li,Panagiotis.Kotronis}@ec-nantes.fr

[2] LUNAM Université, IFSTTAR, GERS, SV
F-44341 Bouguenais, France
e-mail: sandra.escoffier@ifsttar.fr

Keywords: Pile, Foundation, Capacity diagram, Sand, Failure envelope.

Abstract. *Pile foundations are widely used in geotechnical and offshore engineering. When subjected to a combination of horizontal, vertical forces and bending moments, a 3D failure envelope is necessary in order to evaluate the safety of the pile-soil system. We present a study on the failure envelope of a single elastic pile in sand. In order to find it in the three-dimensional space (i.e. horizontal force H, bending moment M and vertical force V), the radial displacement method and swipe tests are numerically performed. An analytical equation providing good agreement with the 3D numerical results is finally proposed.*

1 INTRODUCTION

The failure envelope of a single elastic vertical pile in sand is numerically investigated via swipe tests and a large number of radial displacement controlled tests. The analytical equation proposed by Meyerhof [1] is validated and adopted in the H-V plane. For the H-M-V space however, a new 3D analytical failure envelope is introduced. The proposed failure envelope is useful for the development of new simplified modelling strategies for soil-structure interaction problems (e.g. macro-elements [2]) that can be applied in design engineering offices [3].

2 NUMERICAL MODEL

2.1 SOIL CONSTITUTIVE LAW

A hypoplastic constitutive law, similar to an elastic perfectly plastic Drucker-Prager model, is used to numerically reproduce the behaviour of a single pile in sand. The basic framework of the hypoplastic formulation is provided with the following equations (bold letters define hereafter tensors and vectors, the dot"˙" symbol is the derivative with respect to time and $\|\|$ the norm of a tensor):

$$\dot{\mathbf{T}} = \mathcal{L}\mathbf{D} + \mathbf{N}\|\mathbf{D}\| \tag{1}$$

where $\dot{\mathbf{T}}$ and $\mathbf{D}$ are the stress rate and stretching rate tensors. The stiffness matrix $\mathcal{L}$ depends on the bulk modulus K and the shear modulus in the elastic range $G_{\max}$ and has the following form (the Lamé coefficient $\mu = G_{\max}$ according to Hooke's law):

$$\mathcal{L} = K\mathbf{1}\otimes\mathbf{1} + 2\mu\left[\mathbf{I} - \frac{1}{3}\mathbf{1}\otimes\mathbf{1}\right] \tag{2}$$

The constitutive tensor $\mathbf{N}$ is defined following the approach proposed by Niemunis [4]:

$$\mathbf{N}(\mathbf{T}) = -y(\mathbf{T})\mathcal{L}\mathbf{m}(\mathbf{T}) \tag{3}$$

where $y(\mathbf{T})$ is a scalar function that controls the variation of the nonlinear term and $\mathbf{m}(\mathbf{T})$ defines the plastic flow direction. The scalar function $0 \leq y(\mathbf{T}) \leq 1$ is chosen as a function of the current stress $q(\mathbf{T}) = \sqrt{3J_2}$ and a predefined limit stress $\sigma_{\mathrm{y}}(\mathbf{T})$ as follows:

$$y(\mathbf{T}) = \left(\frac{q(\mathbf{T})}{\sigma_{\mathrm{y}}(\mathbf{T})}\right)^{n_c} \tag{4}$$

with n_c is a constant that controls the isotropic evolution of $y(\mathbf{T})$ and J_2 the second invariant of the deviatoric stress tensor. Assuming a dry sand and thus a zero cohesive strength ($c = 0$), $k_c = 0$ and the yield function reads:

$$F = q(\mathbf{T}) - M_c\, p(\mathbf{T}) = 0 \tag{5}$$

The plastic flow direction $\mathbf{m}(\mathbf{T})$ is defined according to the bounding surface model [5, 6, 7] and it is given by Eq. 6:

$$\mathbf{m}(\mathbf{T}) = \frac{\partial G/\partial \mathbf{T}}{\|\partial G/\partial \mathbf{T}\|} \tag{6}$$

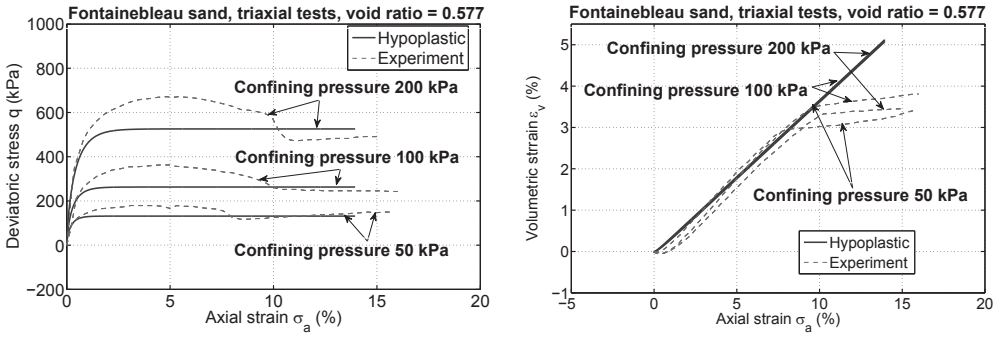
2.2 CALIBRATION AND VALIDATION OF THE SOIL CONSTITUTIVE LAW FOR FONTAINEBLEAU SAND

The soil constitutive law is calibrated and validated using experimental data on dry Fontainebleau sand. The homogeneous sand has a mid-particle diameter D_{50} around 0.206 mm, a density, $\rho_s = 2.65$ g/cm^3 and a minimum and maximum void ratio $e_{min} = 0.510$ and $e_{max} = 0.882$, respectively [8]. The main parameters of the soil model are summarized in Table. 1.

	e	n_c	ϕ_c	ψ
Dense sand	0.577	0.4	33°	9°

Table 1: Model parameters used in the simulation of drained triaxial tests

Comparisons with triaxial tests for dense are shown in Fig. 1. Different confining pressures are considered (50 kPa, 100 kPa and 200 kPa).



(a) (b)

Figure 1: Triaxial compression tests on dense Fontainebleau sand, simulation vs. experiments, [9]

2.3 FINITE ELEMENT MESH AND BOUNDARY CONDITIONS

A numerical model of a single vertical pile in soil is carried out using the finite element code ABAQUS standard [10]. The contact behavior between the pile and the soil is considered using a friction coefficient $\mu = tan(\phi_c) = 0.65$ related to the critical friction angle $\phi_c = 33°$ of the soil. Nodal displacements are fixed in the X, Y and Z directions at the base of the finite element mesh. The displacements at the other lateral boundaries are blocked in the normal directions (see Fig. 2).

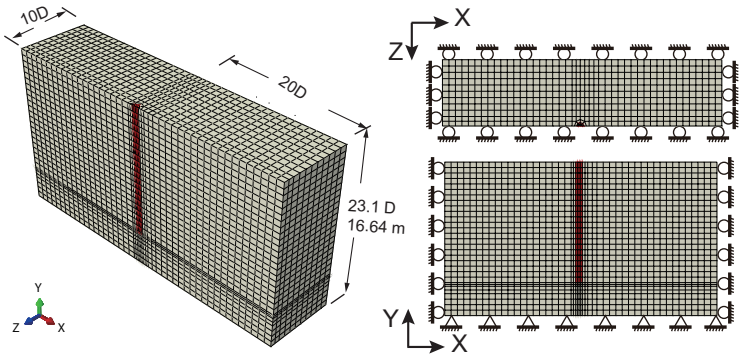


Figure 2: Finite element model for a single vertical pile in soil

3 NUMERICAL STUDY OF THE 3D FAILURE ENVELOPE

3.1 PARAMETERS OF THE FINITE ELEMENT MODEL

In the finite element model, the pile has a length of 13 m, a diameter of 0.72 m, a slenderness ratio of 18 and the pile head is considered on the ground surface level. Poulos and Davis [11] proposed a method to classify piles in different categories based on a flexibility factor. According to this method, the pile is classified as flexible.

3.2 3D NUMERICAL FAILURE ENVELOPE

In order to numerically reproduce the 3D failure envelope, the radial displacement test proposed by Gottardi et al. [12] is adopted. The sign conventions for the pile head loads (horizontal force, vertical force and bending moment) are presented in Fig. 3.

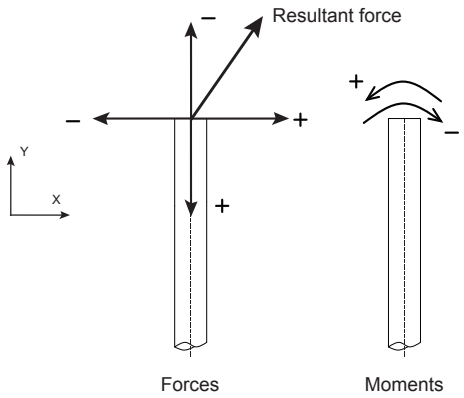


Figure 3: Sign conventions for the pile head loadings

3.2.1 NUMERICAL FAILURE ENVELOPE IN THE H-V PLANE

To investigate the form of the failure surface in the H-V plane, free pile head conditions (M=0) are considered. A displacement is applied on the top of the pile head (that can rotate freely) in a certain direction δ. The angle of the displacement δ varies from $0 \sim 360^\circ$ to scan the failure surface in all directions. The final strength is chosen as the point where numerical calculation diverges. By connecting the values at the ends of the different load paths the complete failure surface is thus obtained. Examples of load paths in the H-V plane from the numerical

radial displacement tests are shown in Fig. 5(a). Numerical swipe tests are also performed in H-V plane, Fig. 5(b) and for more complex loads in Fig. 5(c). A large number (around 500) of numerical radial displacement tests are performed and the ultimate strength (or failure locus) of each test is plotted in Fig. 5(d).

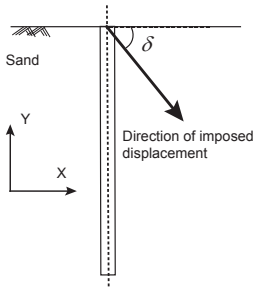


Figure 4: Radial displacements tests in the H-V plane

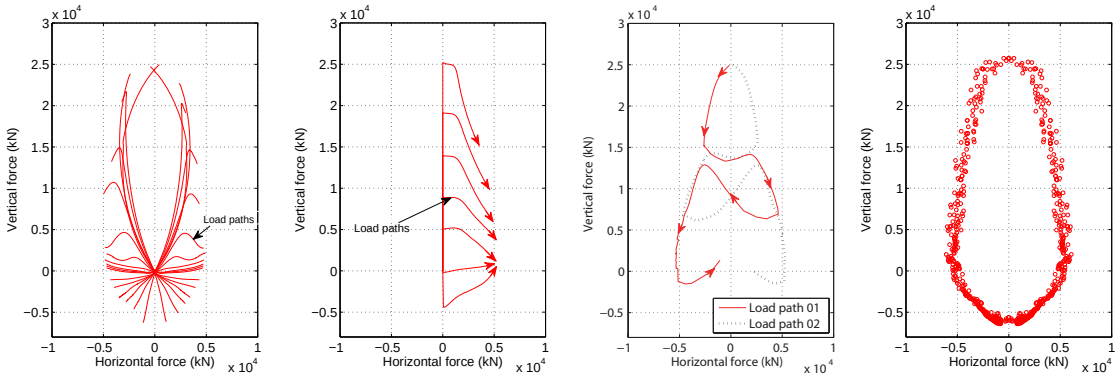
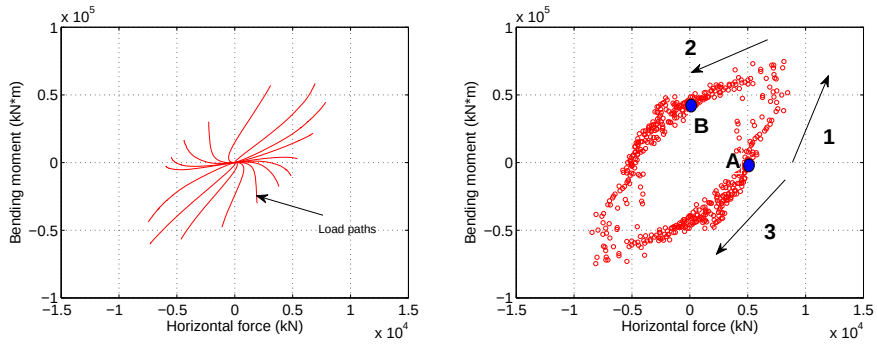


Figure 5: Selected load paths from numerical radial displacement tests (a), load paths from numerical swipe tests (b), numerical swipe tests with more complex load paths (c) and complete results from numerical radial displacement test (d), in H-V plane (M=0), [9].

3.2.2 NUMERICAL FAILURE ENVELOPE IN THE H-M PLANE

The failure envelope is hereafter investigated in the H-M plane and for different vertical loading levels. First, the pile is loaded until a certain vertical force. Then, radial displacement loadings are applied considering a constant ratio between the combined rotation-displacements increments. Similar to the H-V plane, load paths in the H-M plane start from the origin and stop at the failure envelope, see Fig. 6(a). Results of the numerical radial displacement tests are provided in Fig. 6(b).



(a) (b)

Figure 6: (a) Load paths (b) numerical radial displacement tests in the H-M plane corresponding to V=0, [9]

3.2.3 NUMERICAL FAILURE ENVELOPE IN THE H-M-V 3D SPACE

By combining the results in the H-V plane and in the H-M plane for different vertical load levels, the complete failure envelope is plotted in Fig. 7.

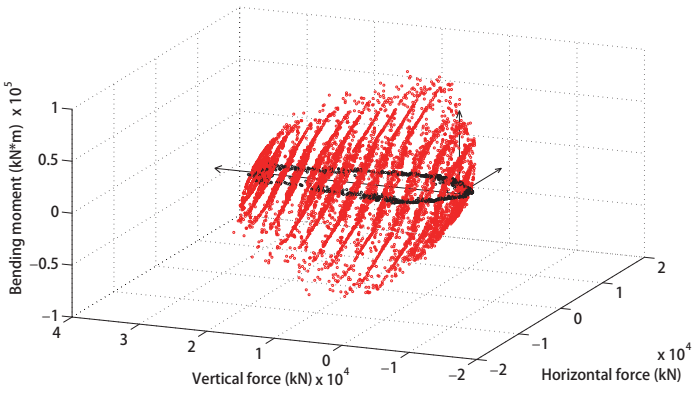


Figure 7: Numerical failure envelope in the H-M-V 3D space, [9]

From the numerical radial tests in Fig. 7 the horizontal bearing capacity (V=0 and M=0) is estimated at H_0 =5000 kN, the vertical compression bearing capacity (H=0 and M=0) V_{c0} =25000 kN, the vertical tension bearing capacity (H=0 and M=0) V_{t0} = 5100 kN and the ultimate bending resistance (H=0 and V=0) $M_0 = 0.42 \times 10^5$ kN·m.

3.3 ANALYTICAL EQUATIONS

3.3.1 ANALYTICAL EQUATION FOR THE FAILURE ENVELOPE IN THE H-V PLANE

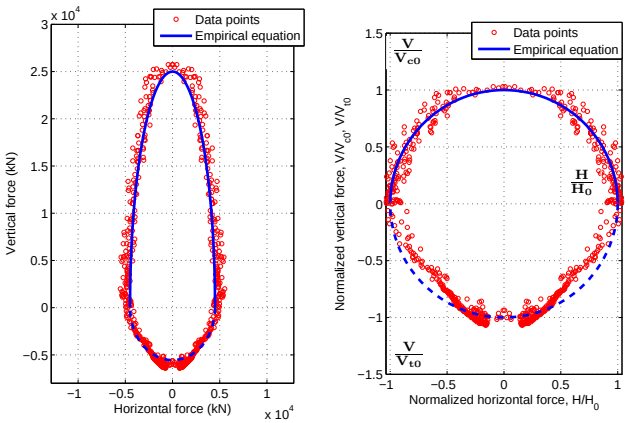
Meyerhof and Ranjan [1] proposed a semi-empirical formula to evaluate the interaction between the horizontal and vertical forces that reads:

$$\left(\frac{H}{H_0}\right)^2 + \left(\frac{V}{V_0}\right)^2 = 1 \tag{7}$$

where H_0 and V_0 are the horizontal and vertical bearing capacities of the pile. Eq. (7) can be written in a normalized form as follows:

$$f = m^2 + v^2 - 1 \tag{8}$$

where $m = H/H_0$ and $\upsilon = V/V_{c0}$ in compression or $\upsilon = V/V_{t0}$ in tension. m and υ are dimensionless quantities. The comparison of the semi-empirical Eq. (8) with the numerical results is shown in Fig. 8 (a) and (b). The agreement is satisfactory although some discrepancies are identified in the tension part (dash line).



(a) (b)

Figure 8: Comparison of Eq. (8) with the numerical results (a) in the H-V plane and (b) in the normalized $\frac{H}{H_0}$ - $\frac{V}{V_{c0}}$ - $\frac{V}{V_{t0}}$ space, [9]

3.3.2 ANALYTICAL EQUATION FOR THE FAILURE ENVELOPE IN THE H-M-V 3D SPACE

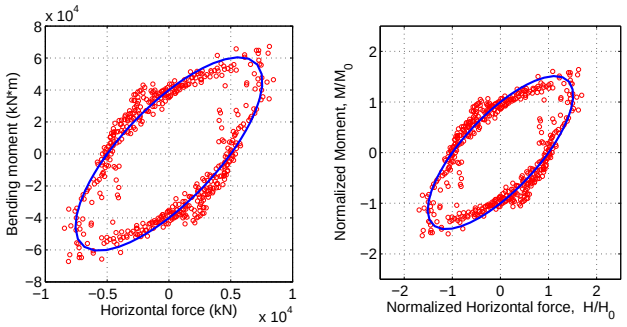
As shown in section 3.2.2, the failure envelope in the H-M plane has an inclined elliptical shape. Inspired from the work of Gottardi et al. [12], a similar equation is proposed hereafter for a single pile in sand:

$$f = \alpha m^2 + \xi n^2 - \beta mn - \rho(\upsilon) = 0 \tag{9}$$

where $m = H/H_0$ the normalized horizontal force, $n = M/M_0$ the normalized bending moment and $\upsilon = V/V_{c0}$ or $\upsilon = V/V_{t0}$ the normalized vertical force (dependent on the sign of the vertical load). α, ξ, β and ρ are constants that control the shape of the ellipse. The parameters are first fitted using the normalized numerical data in the H-M plane at zero vertical force. They are found equal to $\alpha = 1.0$, $\xi = 1.0$, $\beta = 1.5$ and $\rho = 1.0$, Eq. (9) thus becomes:

$$f = 1.0m^2 + 1.0n^2 - 1.5mn - 1.0 = 0 \tag{10}$$

The fitted curves are plotted in Fig. 9 (a) and (b) and show a good agreement with the numerical data both in the H-M and in the normalized H/H_0 - M/M_0 plane.



(a) (b)

Figure 9: Comparison of Eq. (10) with the numerical results (a) in the H-M plane and (b) in the normalized $\frac{H}{H_0}$ - $\frac{M}{M_0}$ plane, [9]

The vertical load influences the size of the elliptical cross-sections but not their inclinations. In order to introduce this behaviour, it is proposed hereafter to link the parameter ρ in Eq. (9) and Eq. (10) with the vertical load as follows:

$$f = 1.0m^2 + 1.0n^2 - 1.5mn - (1 - \upsilon^2) = 0 \tag{11}$$

The 3D failure envelope for a single vertical pile in sand defined by Eq. (11) is plotted in Fig. 10 together with all the numerical data points.

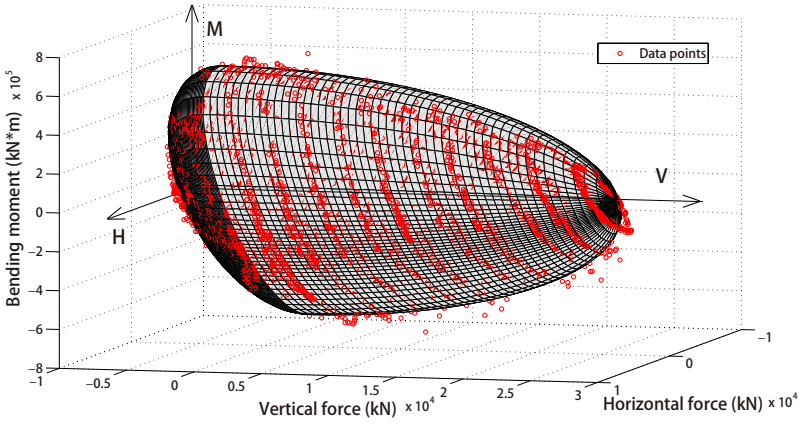


Figure 10: 3D failure envelope for a single vertical pile in sand: yield surface provided by Eq. (11) Vs. numerical data points, [9]

4 CONCLUSIONS

This paper presents a numerical study on the 3D failure envelope of a single elastic pile in sand and analytical equations are proposed. The key parameters for the analytical equations are relatively easy to determine either experimentally or numerically making the above equations useful for engineering design offices. More details on this work can be found in [9], [13] and [14].

REFERENCES

[1] G. G. Meyerhof and G. Ranjan. The bearing capacity of rigid piles under inclined loads in sand. I: Vertical piles. *Canadian Geotechnical Journal*, 9(4):430–446., 1972.

[2] S. Grange, P. Kotronis, and J. Mazars. A macro-element to simulate 3D soil-structure interaction considering plasticity and uplift. *International Journal of Solids and Structures*, 46(20):3651 – 3663, 2009.

[3] S. Grange, L. Botrugno, P. Kotronis, and C. Tamagnini. The effects of soil-structure interaction on a reinforced concrete viaduct. *Earthquake Engineering and Structural Dynamics*, 40(1):93–105, 2011.

[4] Andrzej Niemunis. *Extended hypoplastic models Dissertation submitted for habilitation*. Habilitation thesis, Ruhr-University, Bochum, 2002.

[5] Y. F. Dafalias. Bounding surface plasticity. I: Mathematical foundation and hypoplasticity. *Journal of Engineering Mechanics*, 112(9):966–987, 1986.

[6] Y.F. Dafalias and L.R. Herrmann. *Bounding surface formulation of plasticity*. John Wiley and Sons, Ltd., 1982.

[7] J. P. Bardet. Bounding surface plasticity model for sands. *Journal of engineering mechanics*, 112(11):1198–1217., 1986.

[8] I. Andria-Ntoanina, J. Canou, and J. C. Dupla. Caractérisation mécanique du sable de Fontainebleau NE34 à lappareil triaxial sous cisaillement monotone. Technical report, Laboratoire Navier - Géotechnique (CERMES, ENPC/LCPC), 2010.

[9] Z. Li, P. Kotronis, and S. Escoffier. Numerical study of the 3D failure envelope of a single pile in sand. *Computers and Geotechnics*, 62:11–26, 2014.

[10] Abaqus/Standard. *Abaqus 6.10 Documentation (SIMULIA Abaqus 6.10)*. Dassault Systèmes, 2010.

[11] H. G. Poulos and E. H. Davis. *Pile foundation analysis and design*. John Wiley and Sons, Inc., New York, 1980.

[12] G Gottardi, G.T. Houlsby, and R. Butterfield. Plastic response of circular footings on sand under general planar loading. *Géotechnique*, 49(4):453–469, 1999.

[13] Z. Li, S. Escoffier, and P. Kotronis. Using centrifuge tests data to identify the dynamic soil properties: application to Fontainebleau sand. *Soil Dynamics and Earthquake Engineering*, 52:77–87, September 2013.

[14] Z. Li, P. Kotronis, S. Escoffier, and C. Tamagnini. A hypoplastic macroelement for single vertical piles in sand subject to threedimensional loading conditions. *Earthquake Engineering and Structural Dynamics (submitted)*, 2015.

COMPDYN 2015
5th ECCOMAS Thematic Conference on
Computational Methods in Structural Dynamics and Earthquake Engineering
M. Papadrakakis, V. Papadopoulos, V. Plevris (eds.)
Crete Island, Greece, 25–27 May 2015

SOME EXPERIMETNAL EVIDENCES ON DYNAMIC SOIL-STRUCTURE INTERACTION

M.R. Massimino[1], **G. Biondi**[2]

[1] University of Catania, Viale A. Doria 6, 95125 Catania, Italy
e-mail: mmassimi@dica.unict.it

[2] University of Messina, Contrada di Dio, S. Agata, Messina, Italy
gbiondi@unime.its

Keywords: Dynamic soil-structure interaction, shaking table tests, laminar box, input motion characteristics

Abstract. *Due to dynamic soil-structure interaction (DSSI), the foundation soil experiences an additional motion which is added to its free-field response and DSSI is ruled by the soil compliance and by the vibration of the structure. In this framework soil non-linear behavior, as well as soil-foundation interface non-linearity, can represent crucial aspects and may govern the seismic response of the overall soil-structure system. Experimental tests on physical models allow identifying the interaction mechanism and also provide a benchmark for theoretical and/or numerical analyses. The present paper describes some experimental evidences concerning dynamic soil-structure interaction. Specifically, the paper deals with the results of two shaking table tests performed on a physical model consisting of a one-storey steel frame and a sand deposit. The steel frame (1.3 x 0.95 x 1.3 m) represents a 1:6 scaled model of a one-storey reinforced concrete building prototype. To reproduce the effects of the foundation soil on DSSI, a special laminar box (5m x 1m x 1.2m) was placed over the table, fixed to it and then filled with dry Leighton Buzzard sand up to a depth of 90 cm. During the tests sine-dwell excitations, with different acceleration amplitudes and frequencies, were applied as input motions and the overall model response was monitored through a large set of accelerometers and displacement transducers. Selected experimental results are presented and discussed in the paper using both time- and frequency-domain representations of the acceleration responses. The obtained results highlight the influence of the frequency and of amplitude of the input motion on the coupled and/or uncoupled response of the considered soil-structure system. In some cases an uplifting of the foundation was clearly observed during the tests and represented a natural isolation for the system; accordingly, the accelerations recorded in the soil underneath the foundation are not completely transmitted.*

1 INTRODUCTION

Seismic response of structures depends on many factors related to both structural and geotechnical issues. Among the latter, the local site effects and the dynamic interaction between the foundation soils and the structure are the more relevant. The cyclic non-linear behavior of the foundation soil affects the soil-structure interaction under seismic condition, produces absorption of the incident wave energy and, generally, leads to a reduction in the energy of the waves which are transferred to the structure. This complex interaction mechanism, generally denoted as dynamic soil-structure interaction (*DSSI*), can be studied through different approaches. Theoretical or numerical approaches (e.g. [1-10]) are powerful tools even if the obtained results are affected by the reliability of the data and by the analysis assumptions. Monitoring of full-scale structures is frequently characterized by unknown boundary conditions and requires a large monitoring period which is a rare occurrence (e.g. [11-15]). Thus, experimental tests on laboratory physical models allow the main aspects of the dynamic soil-structure interaction mechanism to be identified, are useful to calibrate and to validate theoretical and or numerical models and, finally, provide a benchmark for theoretical and or numerical analyses (e.g. [16-23]).

The present paper deals with two shaking table tests performed on a physical model consisting of a one-storey steel frame (hereafter referred to as the "*model structure*") and a Leighton Buzzard sand deposit pluviated into a special laminar box (hereafter referred to as the "*shear stack*") consisting in a large flexible soil container, designed to reproduce, as far as possible, the kinematic response of the soil system. Some of the test results are presented in terms of acceleration responses and are discussed highlighting the influence of the frequency and amplitude of the input motion on the coupled and/or uncoupled response of the soil-structure system.

2 FACILITIES, MODEL SET-UP AND INSTRUMENTATIONS

The adopted shaking table consist of a six-degree-of-freedom shaking table (3x3 m) belonging to the old *Earthquake Engineering Research Centre* (*EERC*) at the University of Bristol. In order to reproduce the effect of the foundation soil the *shear stack* (5x1x2 m) was placed over the table, fixed to it and filled with soil using a special deposition procedure. Figure 1a shows a 3D view of the adopted facilities; further details can be found in [20,24].

The formation of a soil deposit with a controlled uniform relative density is a crucial aspect of the physical modeling since it significantly affects the response of the whole soil-structure system. For the experimental tests described herein the shear stack was filled with dry Leighton Buzzard sand using a special sieve designed for soil pluviation. A relative density D_r of about 50% and a low-strain shear modulus G_o of about 25 MPa can be estimated for the sand pluviated into the shear stack [24]; the reduction of the shear modulus and the increase in the damping ratio with shear strain level γ can be described using the relationships plotted in Figure 2.

The model structure consists of a one-storey steel frame characterized by a longitudinal frame span equal to 111 cm, a transverse span equal to 76 cm and a storey height equal to 130 cm. Figure 1b shows the main geometrical properties of the model structure. The model was designed using appropriate scaling factors [27-28]. A steel roof plate was located on the top of the structure and, to simulate a centered uniformly distributed surcharge, a number of lead blocks were placed and fixed on the roof plate. The significant difference between the weight of the steel roof plate surcharged with the lead blocks and the weight of the model allowed us to schematize the model structure as a single degree of freedom (*SDOF*) system of

mass *m* having a natural frequency equal to 5.5 Hz and a flexural stiffness equal to about 555 kN/m. A detailed description of the dimensions and mechanical properties of the prototype can be found in [29].

Once the sand has been completely pluviated into the shear stack, the upper 10 cm were removed from the central area. This allowed us to locate the model structure, ensuring an embedment of about 10 cm to the foundation beams.

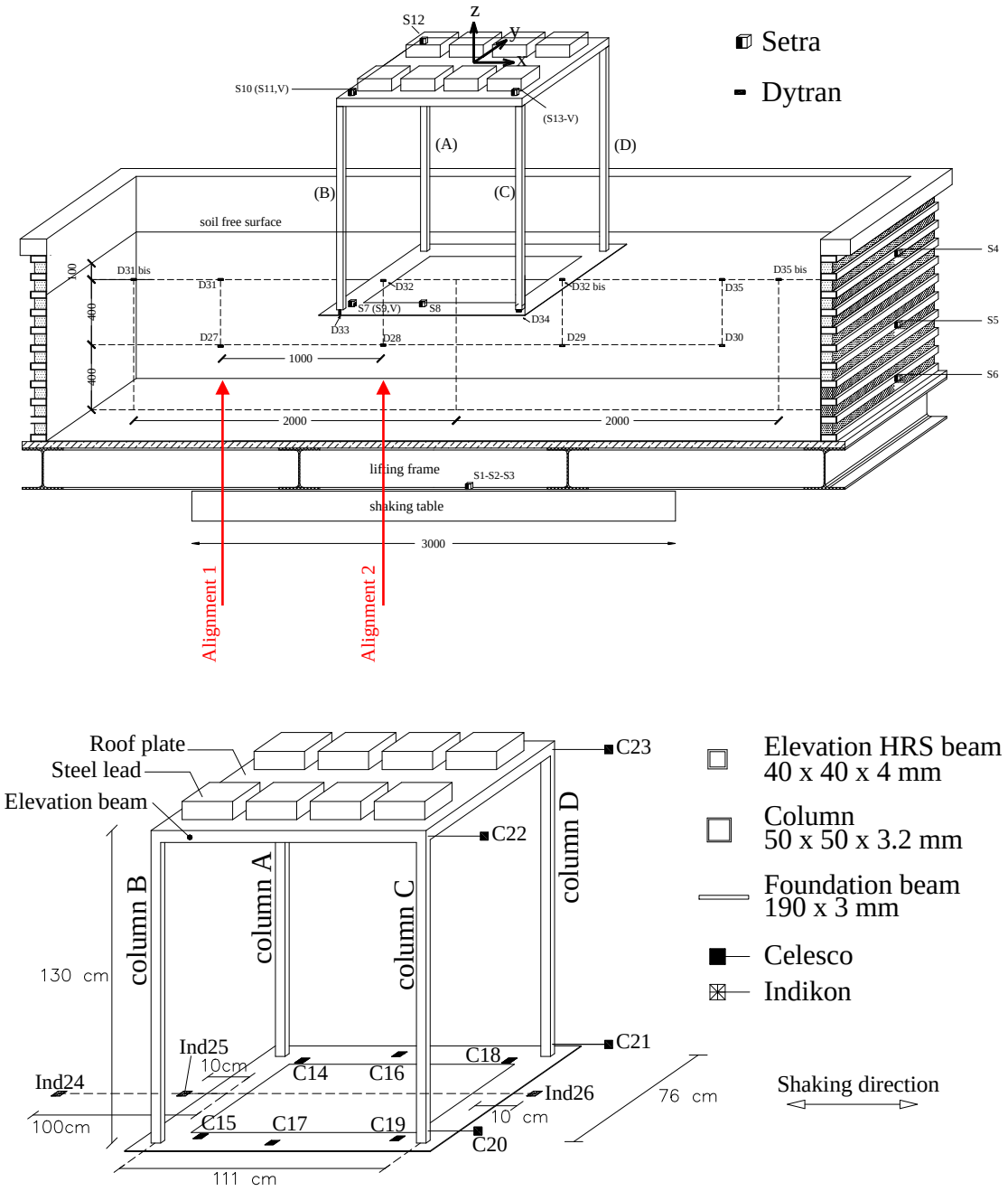


Figure 1: a) 3D schematic view of the physical model and of the adopted facilities and location of the accelerometers; b) schematic of the model structure: geometrical properties and location of displacement transducers.

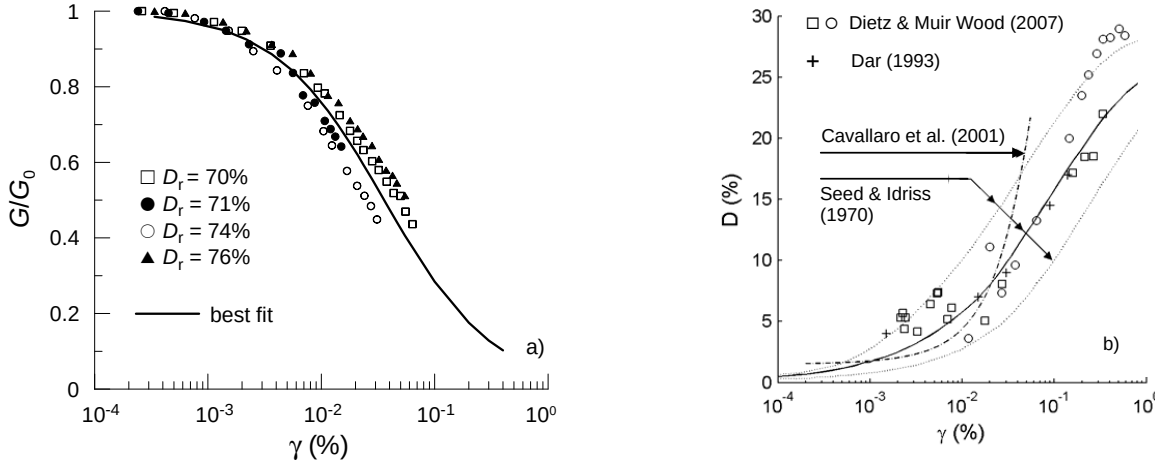


Figure 2: Leighton Buzzard sand: a) reduction of normalized shear modulus with shear strain [24]; b) damping ratio versus shear strain [25].

During the tests the dynamic response of the models was monitored through 10 Dytran accelerometers, 13 Setra piezoelectric-unidirectional accelerometers, 12 Celesco displacement transducers and 3 Indikon no-contact magnetic displacement transducers. The distribution of accelerometers (Fig. 1a) allows detecting the acceleration variation within the depth of the soil deposits. Celesco displacement transducers (Fig. 1b) were used to record the horizontal displacements imposed to the shaking table, the horizontal response of the shear stack and of the columns of the model structure and the vertical displacement of the foundations. Finally, Indikon displacement transducers (Fig. 1b) were used to record the "*free-field*" settlements of the sand deposit due to the densification induced by the motion.

3 EXPERIMENTAL ACTIVITIES

Two physical models (i.e. two soil-structure systems) were prepared and the experimental activities, hereafter identified as *Test 1* and *Test 2*, were carried out on both models.

Bothe tests consisted of two main phases: *i*) a preliminary white-noise excitation; *ii*) a sequence of sine-dwell excitations with a constant frequency f_i (f_i = 2 and 4 Hz in *Test 1* and *Test 2*, respectively) and peak acceleration amplitude A_i which increased run by run, from 0.08g to 0.53g in *Test 1* and from 0.04g to 0.68g in *Test 2*. A conclusive white-noise excitation was also applied at the end of *Test 2*.

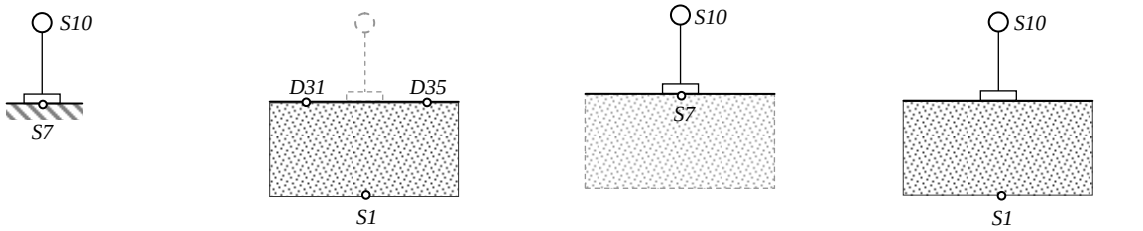
The white-noise consisted of random very low-level excitations having a very large frequency range (0 ÷ 100 Hz) and root mean square acceleration equal to 0.02 g, applied to the table in the direction of the main side of the shear stack. This test was performed in order to investigate the natural frequencies of vibration and the damping ratio of the soil deposit, of the model structure and of the whole soil-structure system. This test

For both *Test 1* and *Test 2* the dynamic excitation consisted of sine-dwell acceleration time-histories with an amplitude which increased from zero to the peak value A_i, during the first five cycles, remained constant in the following 20 cycles and then decreased down to zero in the last 5 cycles. *Test 1* was characterized by an input motion frequency lower than the natural frequency (f_{sf} = 3.5 Hz) of the whole soil-structure system (f_i/f_{sf} = 0.57); conversely for *Test 2* it was f_i/f_{sf} = 1.14.

During the sine-dwell excitation tests several shakes (named *runs*), characterized by different peak amplitudes A_i, were applied to the system. In the present paper, to focus on the effect of the frequency of the input motion on the observed responses, only the results obtained during the runs of *Test 1* (f_i = 2 Hz) and *Test 2* (f_i = 4 Hz) characterized by the same amplitudes A_i will be described and discussed. Table 1 shows the pairs of runs for which the comparison will be presented. Further details on the whole experimental activities can be found in [24].

Test 1 (f_i = 2 Hz)	run	*II*	*VI*	*VII*	*VIII*	*XI*
	A_i (*g*)	0.11	0.31	0.35	0.40	0.53
Test 2 (f_i = 4 Hz)	run	*II*	*IV*	*V*	*VI*	*VIII*
	A_i (*g*)	0.12	0.32	0.36	0.40	0.53

Table 1: Selected runs for the comparison between the responses recorded during the sine-dwell sequences of *Test 1* and *Test 2*.



Model structure "fixed" to the table		*Soil deposit*		*Model structure over the soil deposit*		*Soil-structure system*	
f_{ff} (Hz)	D_{ff} (%)	f_s (Hz)	D_s (%)	f_f (Hz)	D_f (%)	f_{sf} (Hz)	D_{sf} (%)
5.1	1.36	12.6	11.12	3.4	3.62	3.5	3.29

Table 2: Fundamental frequencies and damping ratios evaluated through the white-noise excitation tests before the sine-dwell excitation sequence.

4 DYNAMIC IDENTIFICATION OF THE SOIL-STRUCTURE SYSTEM

The main results of the white-noise excitation tests are shown in Table 2 in terms of values of the first natural frequency and of the damping ratio. The data listed in Table 2 refer to the model structure placed on the sand deposit (f_f, D_f), only to the soil deposit (f_s, D_s) and, finally, to the whole soil-structure system (f_{sf}, D_{sf}); for comparison, the values of the first natural frequency (f_{ff}) and of the damping ratio (D_{ff}) computed for the model structure "fixed" to the table, are also listed in the table.

It is apparent that the computed natural frequency for the model structure placed on the sand deposit (f_f = 3.4 Hz) is lower than that computed for the model structure "fixed" to the shaking table (f_{ff} = 5.1 Hz) and is very similar to that corresponding to the whole soil-structure system (f_{sf} = 3.5 Hz). Similarly, the damping ratio D_f = 3.62 % is higher than that estimated for the model structure "fixed" to the table (D_{ff} = 1.36 %) and is very similar to that of the whole soil-structure system (D_{sf} = 3.29 %).

It is worth nothing that the experimental values of the damping ratio obtained through the white noise excitation tests for the model structure fixed to the table (D_{ff} = 1.36 %) and for the whole soil-structure model (D_{sf} = 3.29 %) are lower than conventional values of modal damping ratio usually adopted in dynamic analysis of structures ([24]). However, the obtained value D_{ff} is consistent with the values of structural damping suggested by several authors (e.g.

[30-32]) for very low stress levels, as those imposed during the white noise excitation test. As expected, due to the effect of soil-structure dynamic interaction, the experimental damping ratio D_{sf} (soil-structure model) resultes greater than D_{ff}.

Also the drop in the natural frequency, from f_{ff} = 5.1 Hz to f_f = 3.4 Hz, clearly represents a consequence of dynamic soil-structure interaction. The value f_{ff} = 5.1 Hz is very close to that (f_{ff} = 5.5 Hz) estimated, analytically, with reference to the theoretical scheme of a fixed-base model structure. The difference could be ascribed to the actual constraint conditions of the steel model, which was fixed to the shaking table using bolts.

For the soil deposit, the white-noise excitation tests provide a value of the natural frequency (f_s = 12.6 Hz) greater than those of the frame and of the whole soil-structure system; the latter is essentially governed by the frame natural frequency.

5 TEST RESULTS AND DISCUSSION

During the sine-dwell excitations the behavior of the soil-structure system was investigated in terms of accelerations and displacements responses. Herein, the acceleration responses recorded during the selected runs (Table 1) will be presented, using both time- and frequency-domain representations, and analyzed to detect amplification and de-amplification phenomena inside the soil deposit and along the model structure. To this purpose, the *alignments 1* and *2*, indicated in Figure 1b, were considered.

Figures 3 and 4 show a comparison between the acceleration time-histories recorded during *Test 1* and *Test 2* for *alignment 1* and *alignment 2*, respectively. For each pair of runs having the same input acceleration amplitude A_i, the plots in Figures 3 and 4 clearly show that the accelerations recorded during *Test 1* (f_i = 2 Hz) are always larger than those recorded during *Test 2* (f_i = 4 Hz). Since each pair of runs differs only in the input frequency f_i, the influence of this parameter, on both the free-field soil response (*alignment 1* – Fig. 3) and on the coupled soil-structure response (*alignment 2* – Fig. 4), is clearly evident.

For both *alignment 1* (Fig. 3) and *alignment 2* (Fig. 4), at a distance of 40 cm from the table (*D27* and *D28*), lower acceleration values can be observed for all the runs of both tests. This de-amplification, which significantly influenced the response of the whole soil-structure system, is typical in presence of a rigid base (as in the case of a shaking table experiment).

As it moves towards the soil surface, the acceleration starts to grow. Along *alignment 1* (free-field conditions) the acceleration at the soil surface (*D31*) reaches approximately the value A_i of the input motion only for the runs of *Test 1* with A_i = 0.11g and 0.31g; for the other runs of *Test 1* and for the all the runs of *Test 2* the acceleration recorded at the soil surface are lower than A_i. Along *alignment 2* it is possible to identify a clear amplification at the foundation level for all the runs of *Test 1*; however, for input motions with lower amplitudes (A_i = 0.11g and 0.31g) the acceleration recorded in the soil (*D32*) was not completely transmitted to the foundation. Actually, an up-lifting of the foundation occurred during all the runs of *Test 1*; this influenced the time-histories recorded by *D32* and *S7*, which appear clearly different from those recorded by both *D28* and *S10*. Along *alignment 2*, the time-histories recorded during *Test 2* at the foundation level (*S7*) show acceleration amplitudes approximately equal to the peak input value; conversely, lower values were recorded by *D32*. Finally, moving from the foundation of the model structure to its roof, the acceleration increases in the case A_i = 0.11*g*, is approximately constant in the case A_i = 0.31 g and decreases for all the remaining runs.

The acceleration responses recorded during the selected runs (Table 1) were also analyzed in the frequency-domain. The amplification functions (*AFs*) were computed from the Fourier amplitude spectrum (*FAS*) evaluated for each of the recorded acceleration responses.

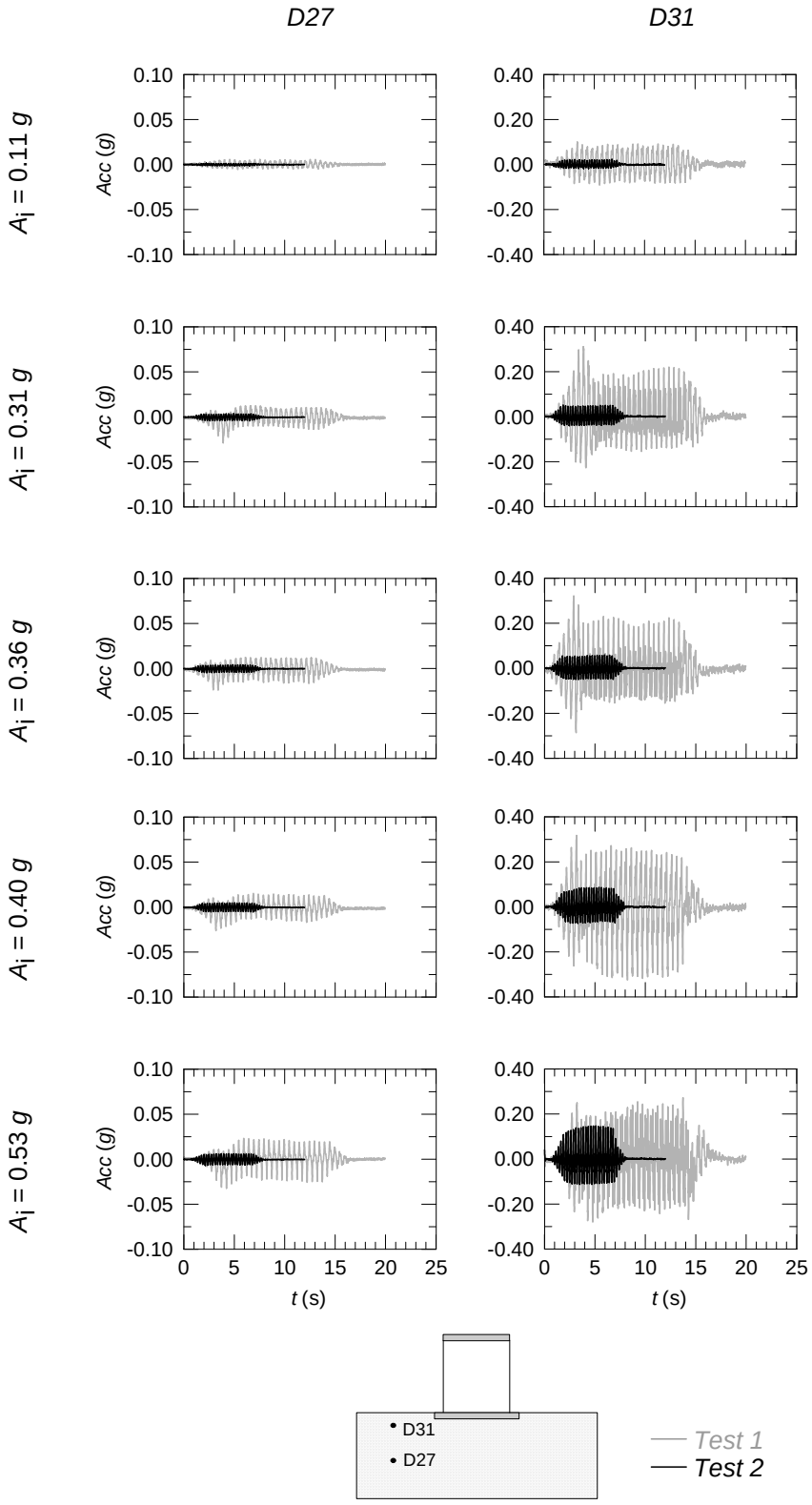


Figure 3: Horizontal accelerations recorded during *Test 1* and *Test 2* by the accelerometers *D27* and *D31* along *alignment 1* (free-field condition).

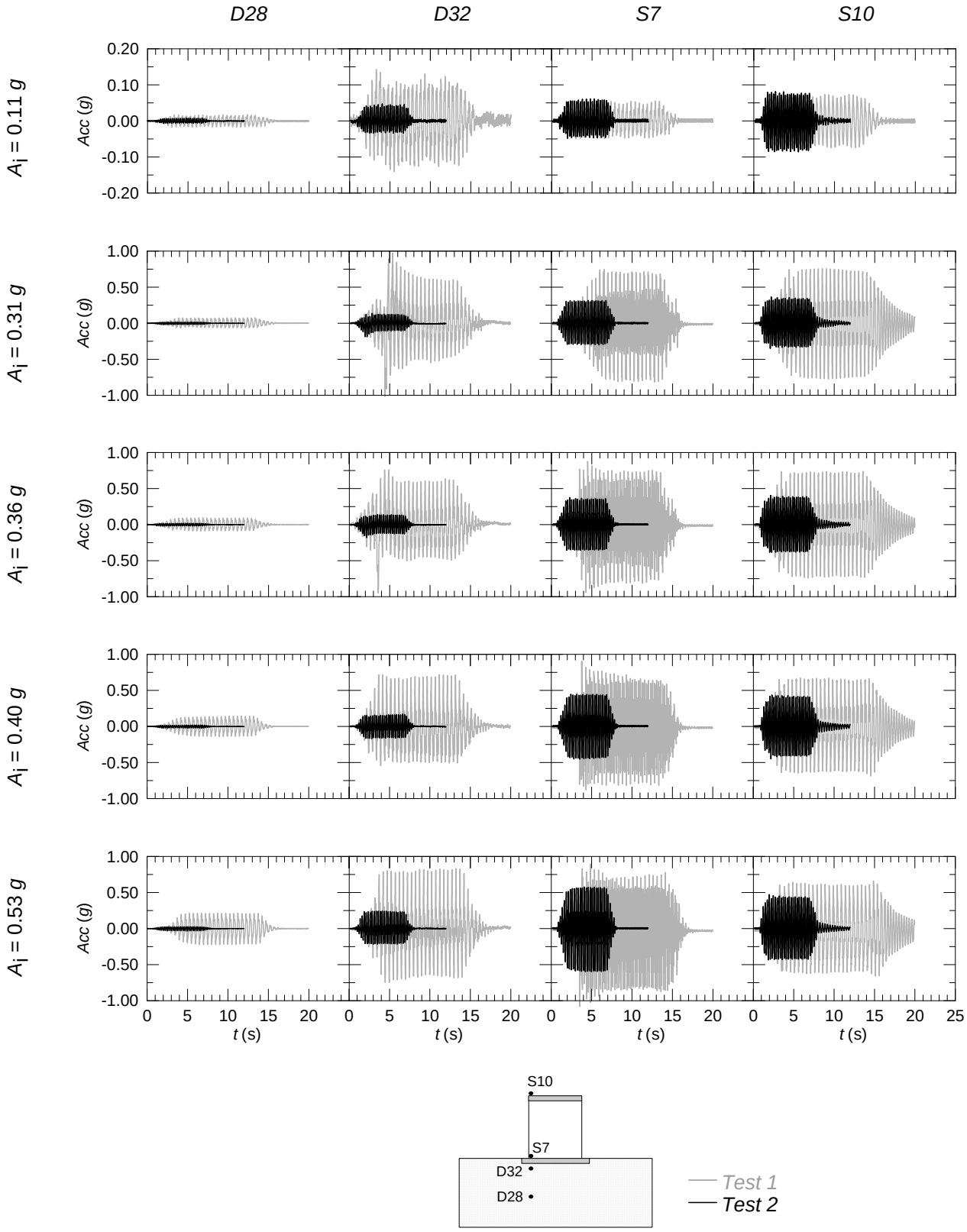


Figure 4: Horizontal accelerations recorded during *Test 1* and *Test 2* by the accelerometers *D28* and *D32* along *alignment 2* (involving the soil and the model structure).

The results are presented in Figures 5 and 6 for some of the runs listed in Table 1. Details on the procedure adopted to estimate the *AFs* can be found in [24]. During the runs characterized by low input motion amplitudes (A_i = 0.11 *g*; Figs. 5a and 6a), the *AF*s computed for both tests clearly show a narrow band of amplification at frequencies very close to the natural frequency of the model structure (f_f = 3.4 Hz; Tab. 3). As the amplitude of the motion increases (Figs. 5 b,c and 6 b,c) the bandwidth of the computed amplification functions increases and the frequency corresponding to the peak of *AFs* decreases.

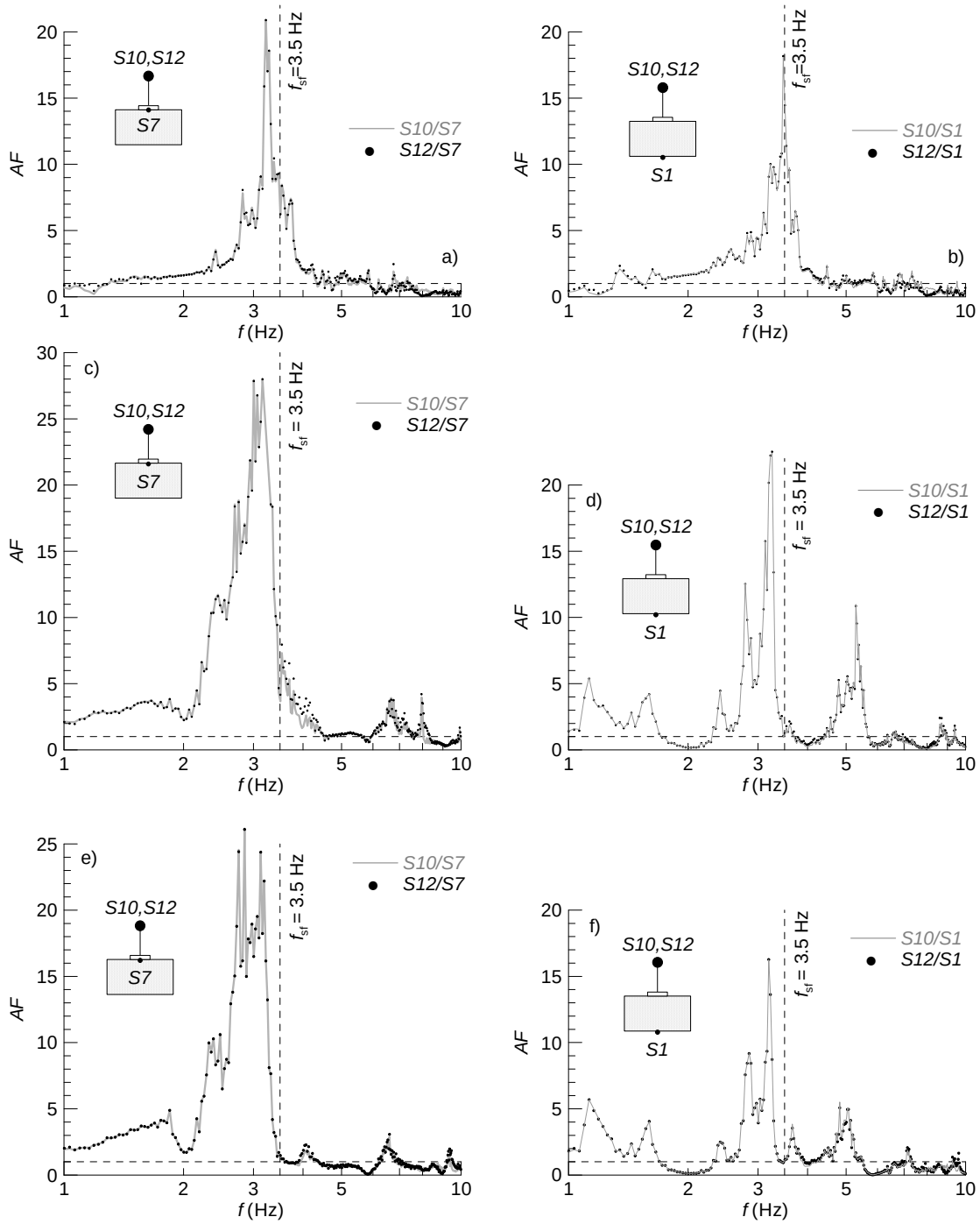


Figure 5: Amplification functions computed for some of the acceleration time-histories recorded during some selected runs of *Test 1*: a,b) A_i = 0.11 *g*; c,d) A_i = 0.36 *g*; e,f) A_i = 0.53 *g*.

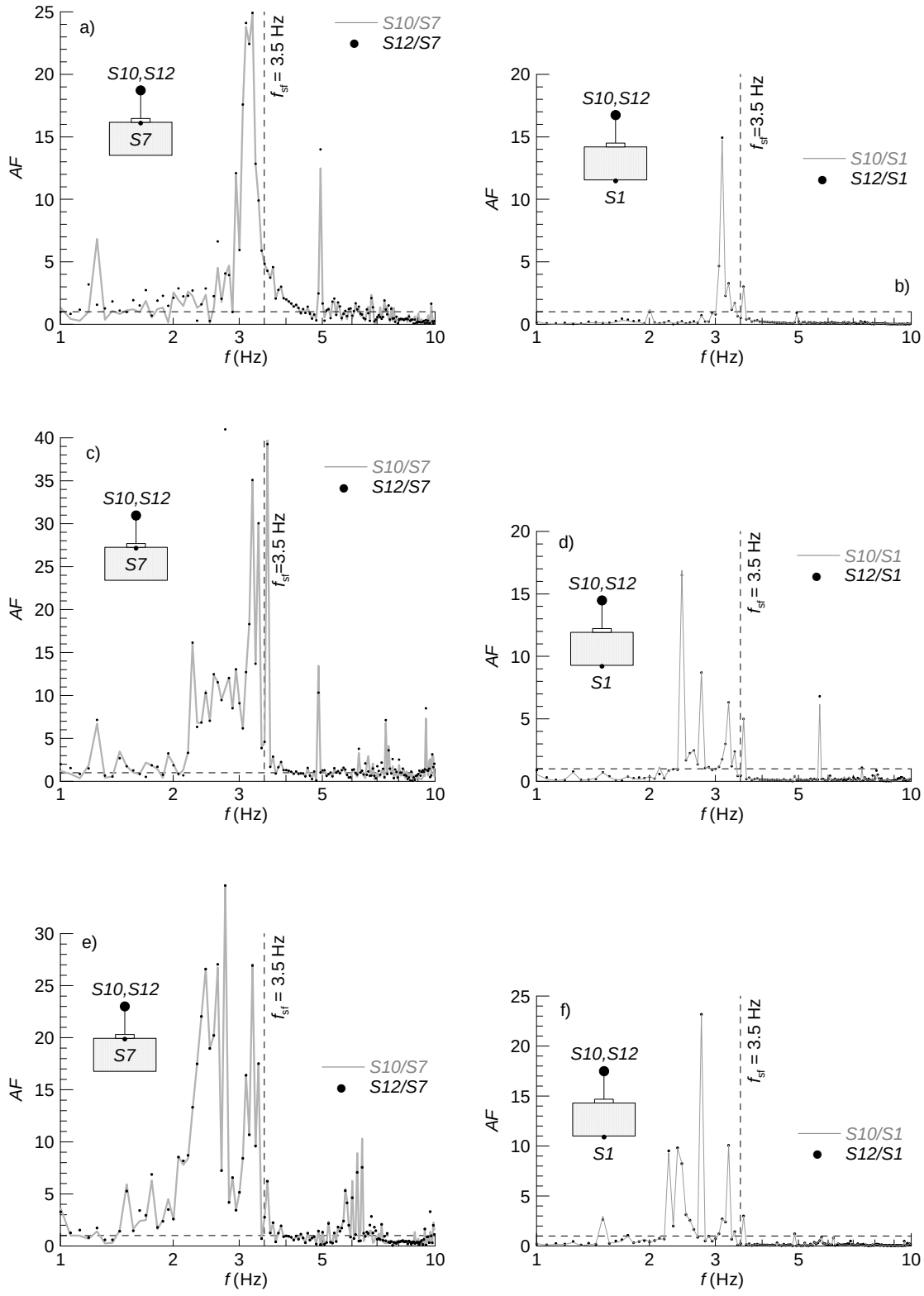


Figure 6: Amplification functions computed for the acceleration time-histories recorded during some selected runs of *Test 2*: a, b) A_i = 0.11 *g*; c,d) A_i = 0.36 *g*; e,f) A_i = 0.53 *g*.

Since the response of the steel model was elastic, this shifting of the amplification band can be attributed only to the tilting motion which was observed during those runs characterized by larger amplitude of the input motion.

As regards the coupled soil-frame system, during *Test 1* (Figs. 5 b,d,f) a narrow amplification band can again be observed whatever is the amplitude of the input motion. In the case $A_i = 0.11g$ (Fig.5b) the peak of the *AF* occurs at about 3.5 Hz, which coincides with the natural frequency of the soil-frame system (Tab. 2). Moreover, as the amplitude of the input motion increases, the frequency corresponding to the peak of the *AF*s reduces (Figs. 5 d,f), i.e. it becomes closer to the input frequency $f_i = 2$ Hz in *Test 1* and farther from $f_i = 4$ Hz in *Test 2*. This shifting of the amplification band could be attributed to the effect of the non-linear soil behavior. In fact, as the amplitude of the imposed motion increases, larger strains arise in the soil deposit leading to a reduction of the soil shear modulus. Accordingly, the natural frequencies of the soil deposit reduce. Similar conclusions can be drawn with reference to the amplification functions computed for the selected runs of *Test 2* (Figs. 6 b,d,f); in this case the shifting of the amplification band is more evident.

Due to the shifting of the natural frequency of the coupled soil-structure system toward the value $f_i = 2$ Hz, the *AF* amplitudes computed for *Test 1* are generally higher than those evaluated for *Test 2* (Figs. 5 and 6). This result is consistent with those obtained analyzing the acceleration response in the time domain (Figs. 3 and 4).

6 CONCLUDING REMARKS

The paper describes the results of two sets of shaking table experiments (*Test 1* and *Test 2*) performed on a physical model consisting of a Leighton Buzzard sand deposit and a model structure consisting of a one-storey steel frame. Both tests included preliminary white-noise excitations and sine-dwell excitations having a constant input frequency ($f_i = 2$ Hz in *Test 1*; $f_i = 4$ Hz in *Test 2*) and input acceleration amplitude A_i ranging in the intervals 0.08-0.53 *g* during *Test 1* and 0.04-0.68 *g* during *Test 2*.

The white noise excitation tests allowed us estimating the natural frequency of the soil deposit ($f_s = 12.6$ Hz) and the natural frequency for the model structure placed on the sand deposit ($f_f = 3.4$ Hz); this is lower than the natural frequency of the model structure "*fixed*" to the shaking table ($f_{ff} = 5.1$ Hz) and is very similar to that of the coupled sand-frame system ($f_{sf} = 3.5$ Hz). The input frequencies of the two sets of sine-dwell excitations were selected to be somewhat lower and somewhat higher than f_{sf}.

The results obtained during some selected runs of *Test 1* and *Test 2* were analyzed using both time- and frequency-domain representations of the acceleration responses.

Due to non-linear effects of soil cyclic behaviour a failure was observed at a depth of about 40 cm from the shaking table, producing a natural isolation for both the soil deposit and the model structure. Moving towards the soil surface the acceleration starts to grow, even if the de-amplification observed at a depth of 40 cm influences the response of the whole soil-structure system. In some cases the accelerations recorded in the soil underneath the foundation were not completely transmitted to it as a result of uplifting phenomena, which were clearly observed.

Horizontal accelerations recorded during *Test 1* ($f_i = 2$ Hz) are definitely higher than those recorded during *Test 2* ($f_i = 4$ Hz) even if the input acceleration amplitudes are the same for each pair of the selected runs (Table 1). This confirms the significant influence of the frequency of the input motion and highlights the importance of the coupling with the natural frequency of the system.

ACKNOWLEDGEMENTS

This study was carried out under the supervision of Prof. Michele Maugeri to whose memory is dedicated.

REFERENCES

[1] J.P. Stewart, G.L. Fenves, R.B. Seed, Seismic soil-structure interaction in buildings. I: analytical methods. *J. Geotechnical and Geoenvironmental Engineering*, **125** (1), 26-37, 1999.

[2] J.P. Stewart, G.L. Fenves, R.B. Seed, Seismic soil-structure interaction in buildings. II: empirical findings. *J. Geotechnical and Geoenvironmental Engineering*, **125** (1), 38-48, 1999.

[3] M.R. Massimino, Experimental and numerical modelling of a scaled soil-structure system. Maugeri M. Editor. *Seismic Prevention of Damage for Mediterranean Cities, a case History: the City of Catania (Italy)*, Wit Press, 2005.

[4] G. Abate, M.R. Massimino, M. Maugeri, Finite element modeling of a shaking table test to evaluate the dynamic behaviour of a soil-foundation system. *AIP Conference Proceedings*, **1020**, 569-576, 2008.

[5] R. Paolucci, M. Shirato, M.T. Yilmaz, Seismic behaviour of shallow foundations: shaking table experiments vs numerical modelling. *Earthquake Engineering and Structural Dynamics*, **37**, 577-595, 2008.

[6] A. Cavallaro, M.R. Massimino, M. Maugeri, Noto Cathedral: soil and foundation investigation. *Construction and Building Materials Journal*. **17**, 533-541.

[7] G. Abate, C. Caruso, M.R. Massimino, M. Maugeri, Evaluation of shallow foundation settlements by an elasto-plastic kinematic-isotropic hardening numerical model for granular soil. *Geomechanics and Geoengineering Journal*. **3**(1), 27-40, 2008.

[8] M. Maugeri, G. Abate, M.R. Massimino, Soil-structure interaction for seismic improvement of Noto Cathedral (Italy). Sakr M.A., Ansal A. Eds. *Special Topics in Earthquake Geotechnical Engineering in Geotechnical, Geological and Earthquake Engineering*. Springer, 2012.

[9] G. Abate, M.R. Massimino, M. Maugeri, Numerical modelling of centrifuge tests on tunnel-soil systems. *Bulletin of Earthquake Engineering*, 2014.

[10] F. Grassi, M.R. Massimino, The evaluation of kinematic bending moments in a pile foundation using complete 3D finite element modelling. S. Syngellakis Editor. *Earthquake ground motion: Input Definition for Aseismic Design.* Wit Press, 147-161.

[11] D.E. Hudson, Dynamic tests of full-scale structures.Wiegel, R.L. Editor. *Earthquake engineering*, Prentice Hall, 127-149, 1970.

[12] M.D. Trifunac, M.I. Todorovska, Recording and interpreting earthquake response of full-scale structures. *NATO Workshop on Strong Motion Instrumentation for Civil Engineering Structures*, Istanbul, June 2-5, 1999.

[13] E. Cascone, G. Biondi, A case study on soil settlements induced by preloading and vertical drains. Geotextiles and Geomembranes, **38**, 51–67, 2013.

[14] E. Cascone, V. Bandini, A. Galletta, G. Biondi. Acceleration of the consolidation process of a clay soil by preloading and vertical drains: field measurements and numerical predictions. Karstunen & Leoni Ed.s, *2nd International Workshop on Geotechnics of Soft Soils - Focus on Ground Improvement*. Glasgow, September 3-5, 2008.

[15] M. Maugeri, F.Castelli, M.R. Massimino, G. Verona, Observed and computed settlements of two shallow foundations on sand. *Journal of Geotechnical and Geoenvironmental Engineering, ASCE,* **124 (**7), 1998.

[16] A.W. Crewe, M.L. Lings, C.A. Taylor, A.K. Yeung, R. Andrighetto, Development of a large shear-stack for resting dry sand and simple direct foundations on a shaking table. Proc. *5th SECED Conference on European seismic design practice*, Balkema, 1995.

[17] M. Maugeri, G. Musumeci, D. Novità, C.A. Taylor, Shaking table test of failure of a shallow foundation subjected to an eccentric load. *Soil dynamic and Earthquake Engineering*, **20**, 435-444, 2000.

[18] G. Biondi, P. Capilleri, M. Maugeri, Dynamic response analysis of earth-retaining walls by means of shaking table tests. *8th U.S. National Conference on Earthquake Engineering*, San Francisco, April 18-22, 2006.

[19] I. Anastasopoulos, V. Drosos, N. Antonaki, A. Rontogianni, The role of soil-foundation-structure interaction on the performance of an existing 3-storey building: shaking table testing. *15 WCEE*, Lisboa, 2013.

[20] G. Biondi, M.R. Massimino, M. Maugeri, C. Taylor. Influence of the input motion characteristics on the dynamic soil-structure interaction by shaking table tests. Fourth International Conference on Earthquake Resistant Engineering Structures, ERES IV, Ancona, Italy, September 22, 2003.

[21] G. Abate, M.R. Massimino, M. Maugeri, Finite element modelling of a shaking table test to evaluate the dynamic behaviour of a soil-foundation system. Proc. Seismic Engineering International Conference Commemorating the 1908 Messina and Reggio Calabria Earthquake, MERCEA 2008, Reggio Calabria, Italy, July 8-11, 2008.

[22] G. Abate, M.R. Massimino, M. Maugeri, D. Muir Wood, Numerical modelling of a shaking table test for soil-foundation-superstructure interaction by means of a soil constitutive model implemented in a FEM code. *Geotechnical and geological engineering*, **28**, 37-59, 2010.

[23] M.R. Massimino, M. Maugeri, Physical modelling of shaking table tests on dynamic soil-foundation interaction and numerical and analytical simulation. *Soil Dynamic and Earthquake Engineering Journal*. **49**,1–18, 2013.

[24] G. Biondi, M.R. Massimino, M. Maugeri, Influence of frequency content and amplitude of input motion in DSSI investigated by shaking table tests. *Bulletin of Earthquake Engineering*, 1-35, 2014.

[25] A. Cavallaro, M. Maugeri, R. Mazzarella, Static and dynamic properties of Leighton Buzzard sand from laboratory tests. *4th International Conference on Recent Advances in Geotechnical Earthquake Engineering and Soil Dynamic and Symposium in honour of Prof. WD Liam Finn*, San Diego, March 26–31, 2001.

[26] M. Dietz, D. Muir Wood, Shaking table evaluation of dynamic soil properties. *4th International conference on earthquake geotechnical engineering*, June 25–28, 2007.

[27] S. Iai, Similitude for shaking table tests on soil-structure-fluid model in 1g gravitational field. *Soils and Foundations*, **29**(1), 105-118, 1989.

[28] S. Iai, T. Sugano, Soil-structure interaction studies through shaking table tests. *Earthquake Geotechnical Engineering*, Balkema, 927-940, 1999.

[29] M. Maugeri, D. Novità, C. Taylor, Unidirectional shaking table tests of 1:6 reduced scale steel model. *12th European Conference on Earthquake Engineering*, London, 2002.

[30] G.W. Housner, R.R. Martel, J.L. Alford, Spectrum analysis of strong-motion earthquakes. *Bulletin of Seismological Society of America*, **43**: 97-119, 1953.

[31] N.M. Newmark, W.J. Hall, Seismic design criteria for nuclear reactor facilities. *4th World Conference on Earthquake Engineering*, Santiago, Chile, 1969.

[32] J.D. Stevenson, Structural damping values as a function of dynamic response stress and deformation levels. *Nuclear Engineering and Design*, **60**: 211-237, 1980.

COMPDYN 2015
5th ECCOMAS Thematic Conference on
Computational Methods in Structural Dynamics and Earthquake Engineering
M. Papadrakakis, V. Papadopoulos, V. Plevris (eds.)
Crete Island, Greece, 25–27 May 2015

COUPLING BETWEEN STRATIGRAPHIC AND TOPOGRAPHIC EFFECTS ON SLOPES

S. Rizzitano[1], E. Cascone[2] and G. Biondi[2]

[1] University of Enna "Kore"
Via delle Olimpiadi, 94100 Enna, Italy
samuela.rizzitano@unikore.it

[2] University of Messina
Contrada di Dio, 98166 Messina, Italy
{ecascone, gbiondi}@unime.it

Keywords: Topographic effects, 2D Seismic response analysis, Slopes, Equivalent-linear approach.

Abstract. *In this paper the seismic response of simple slope geometries under vertically propagating in-plane shear waves is assessed through two-dimensional finite element analyses to investigate the amplification of the ground motion induced by soil topography. Topographic horizontal and vertical amplification factors were evaluated through different sets of analyses of slopes overlying a compliant bedrock. The effect of soil non-linear behavior was accounted for through equivalent-linear approximation, varying the range of shear strains in which soil responds linearly; to this purposes several relationships describing the variation of normalized shear modulus and damping ratio with induced shear strain were adopted. Finally, the influence of the amplitude and of the frequency of the input motion was also analyzed.*

The results of the analyses confirmed that a complex interaction exists between stratigraphic and topographic effects and that the two effects can be neither evaluated independently nor easily uncoupled.

Specifically, horizontal and vertical topographic amplification factors were found to depend on the tendency of soil to exhibit a non-linear behavior and on the degree of non-linearity arising in its seismic response. These, on turn, are related to all the factors affecting non-linear dynamic response: soil stiffness and damping ratio at small strain, characteristics of the input motion and non-linear stress-strain relationship. Finally, the comparison with the results of linear visco-elastic analysis showed that without accounting for soil non-linear behavior, topographic amplification factors may result underestimated.

1 INTRODUCTION

Studies on seismic response of slopes, generally, deal with case-studies (e.g. [1-6]) or are systematic parametric studies carried out to evaluate inertial and/or weakening effects (e.g. 7-10) or to assess topographic amplification [11-16]. In the latter cases seismic response analyses were carried out and soil behavior was assumed either linear visco-elastic (*LVE*) [11, 13-15] or non-linear through the equivalent-linear (*EL*) approximation [1, 2, 12]. Generally, the case of incoming in-plane shear waves (SV waves) was considered.

In this framework the numerical evaluation of topographic effects is usually performed decoupling the topographic effects and the effects due to heterogeneities in soil profile (hereafter referred to as stratigraphic effects) from the computed site response. To this purpose the results of *2D* seismic response analyses, accounting for both stratigraphic and topographic amplification, are generally compared with *1D* analysis results reflecting only stratigraphic effects.

Some studies investigated topographic effects by considering the case of a slope in a homogeneous half-space [15, 17, 18], other studies included the stratigraphic amplification by introducing a rigid [1, 12-14] or a compliant bedrock [2, 19].

Generally, few are the systematic parametric analyses which account for both non-linear soil behaviour and for the presence of a compliant bedrock.

The present paper describes the results of *2D* seismic response analyses of slopes subjected to vertically propagating *SV* waves using the finite element (*FE*) code *QUAKE*/*W* [20]. The analyses were carried out: *a*) varying the slope angle, the frequency and the amplitude of the input motion; *b*) considering the case of slopes over a compliant bedrock; *c*) assuming. that soil behaves as an equivalent-linear (*EL*) visco-elastic material. Table 1 provides an overview of the cases and parameters considered in the analyses.

***2D* ANALYSIS (*H* = 50 m, *D* = 250 m, *L*/*H* = 30)**

Effect	Model	Soil properties	Bedrock properties	i (°)	a_o (g)	f (Hz)	Figure
Coupling, Plasticity index *PI*	Homogeneous soil layer (*PI* = 30, 50, 100, 200 %) over compliant bedrock (I_R = 0.2)	γ = 20 kN/m^3 ν = 1/3 V_s = 500 m/s	γ_b = 20 kN/m^3 ν_b = 1/3 $V_{s,b}$ = 2500 m/s	30 45 60	0.1	2 , 3, 4.5	2
Soil non-linear behavior	Homogeneous soil layer (*PI* = 30 %) over compliant bedrock (I_R = 0.2)	γ = 20 kN/m^3 ν = 1/3 V_s = 500 m/s	γ_b = 20 kN/m^3 ν_b = 1/3 $V_{s,b}$ = 2500 m/s	45	0.1 0.2 0.3	3	3
	Homogeneous soil layer (*PI* = 30, 50, 100 %) over compliant bedrock (I_R = 0.2)			45	0.1	0.5	4
	Homogeneous soil layer (*PI* = 30, 50, 100, 200 %) over compliant bedrock (I_R = 0.2)			45	0.1	0.5, 2	5
Frequency *f*	Homogeneous soil layer (*PI* = 30 %) over compliant bedrock (I_R = 0.2)	γ = 20 kN/m^3 ν = 1/3 V_s = 500 m/s	γ_b = 20 kN/m^3 ν_b = 1/3 $V_{s,b}$ = 2500 m/s	45	0.1	0.5, 1.25, 2, 4.5,10	6

Table 1: Summary of the numerical analyses.

Figure 1 shows the scheme of the *FE* model adopted in the analyses together with the conditions imposed to the height *h* and to the width *l* of the elements of the mesh (Figure 1c) to avoid that the high frequency components of the input seismic motion are filtered out during the propagation process and to ensure the accuracy of the numerical solution.

In the analyses H = 50 m, D = 250 m and L/H = 30 (Figure 1a) were considered. A viscous Lysmer and Kuhlemeyer boundary was applied to the bottom of the mesh of the *FE* model (Figure 1b) to absorb scattered energy and mitigate the effect of wave reflections. Finally, in all the cases zero vertical displacement condition was applied along lateral vertical boundaries (Figure 1b).

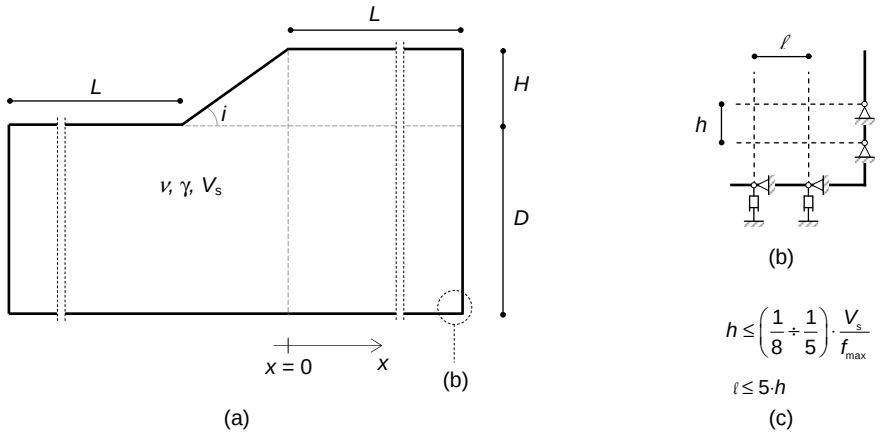


Figure 1: 2*D* FE model scheme and boundary conditions.

In all the analyses unit weight γ = 20 kN/m^3, constant shear-wave velocity V_s = 500 m/s and Poisson's ratio ν= 1/3 were assumed for the soil. For the compliant bedrock a unit weight γ_b = 20 kN/m^3 and a value of the shear wave velocity $V_{s,b}$ = 2500 m/s were assumed; thus, the considered impedance ratio is I_R = 0.2. The bedrock depth was fixed at z_b = 250 m.

Dissipation of energy was introduced in the system through the Rayleigh damping matrix defined as a combination of the mass and stiffness matrices through the coefficients α and β which depend on the modal damping ratio. Further detail on the numerical modelling can be found in [19].

In the *EL* analyses (Table 1) the reduction of the normalised shear modulus G/G_0 and the increment of the damping ratio ξ with the strain level γ were described using the relationship proposed by Vucetic and Dobry [21] for different values of the plasticity index *PI*.

The effects of soil non-linear behaviour were investigated considering different values of the amplitude (a_0 = 0.1, 0.2 and 0.3 *g*) and of the frequency (f = 0.1, 1.25, 2, 3, 4.5 and 10 Hz) of the input motion and a wide range of values of plasticity index (*PI* = 30 %, 50 %, 100 % and 200 %) for which the corresponding $G/G_0 - \gamma$ and $\xi - \gamma$ curves are characterized by linear thresholds of shear strain γ_l varying from 0.001 % to 0.01 % [22].

Coupling between stratigraphic and topographic effects was examined and the obtained results are presented in terms of horizontal and vertical topographic amplification factors A_h and A_v

$$A_h = \frac{a_{h,max}}{a_{h,ff}} \qquad A_v = \frac{a_{v,max}}{a_{h,ff}} \tag{1}$$

where $a_{h,max}$ and $a_{v,max}$ are the peak horizontal (*h*) and vertical (*v*) acceleration computed at the ground surface and a_{ff} is the peak acceleration of the *free-field* (*ff*) response. The values of *a*ff were detected through supplementary *1D* analyses carried out with reference to soil columns of height *D* and *H* + *D* (Figure 1a) adopted to simulate the *1D free-field* response in front of the toe and behind the crest of the slope, respectively. Specifically, the profiles of the horizontal and vertical maximum acceleration obtained at the ground surface behind the crest and in front of the slope were normalized respect to the corresponding *free-field* values, obtaining the topographic amplification factors.

The results obtained in the analyses are discussed separately; in particular, the coupling between stratigraphic and topographic effects is discussed in section 2, the influence of non-linear behaviour is discussed in the section 3, finally, the influence of input motion frequency is discussed in the section 4.

2 COUPLING BETWEEN STRATIGRAPHIC AND TOPOGRAPHIC EFFECTS

Figure 2a-f shows the results in terms of A_h and A_v obtained for f = 2 Hz and $a_0 = 0.1g$: it can be noted that the horizontal topographic amplification factor is significantly affected by *PI* on all over the ground surface. A_h increases for decreasing *PI*, attaining its peak close to the toe of the slope. For increasing values of the slope angle the maximum values of A_h close to the toe increase, whereas maximum values close to the crest reduce. The vertical topographic amplification factor increases for increasing *PI* and reaches its maximum values, in turn increasing with the slope angle, at or close to the toe of the slope.

Also in the case f = 3 Hz and $a_0 = 0.1g$ (Figure 2g-l), horizontal and vertical topographic amplification factors are affected by *PI*: the seismic motion is slightly amplified in front of the toe and is moderately amplified behind the crest. The already observed trend of A_h is confirmed: it increases for increasing values of the angle of the slope in front of the toe and decreases for increasing *i* behind the crest.

For f = 4.5 Hz and $a_0 = 0.1g$ (Figure 2m-r) a noticeable influence of *PI* on A_h can be observed at and behind the crest of the slope where the profile of the horizontal topographic amplification factor is characterized by sharp peaks; the effect of *PI* on the vertical topographic aggravation factor is rather negligible in front of the toe of the slope while it is relevant at and behind the crest.

As expected, independently of the input frequency, the effect of soil non-linearity on the topographic amplification factors fades away as the lateral boundaries ($x = \pm 1500$ m, not shown in Figure 2) are approached, since there the system seismic response coincides with the *1D* free field response ($A_h = 1$ and $A_v = 0$).

The influence of the non-linear behaviour of the soil on topographic amplification factors depends on the values of *free-field* accelerations of the soil deposits behind the crest and in front of the toe of the slope. For smaller values of *PI*, that is for smaller values of linear threshold shear strain γ_l, soil behaves elastically in a narrow range of shear strains and earthquake induced strains lead to a greater reduction of the shear modulus (implying a reduction of the system natural frequencies and an increase in the impedance ratio) and to larger values of the mobilized damping ratio (implying a reduction of the amplitudes of the amplification peaks).

The combination of these two counteracting effects depends on the soil stiffness at small shear strain (which influences the system natural frequencies) and on the amplitude of the induced strain levels, affected by the amplitude of the seismic acceleration arising in the system.

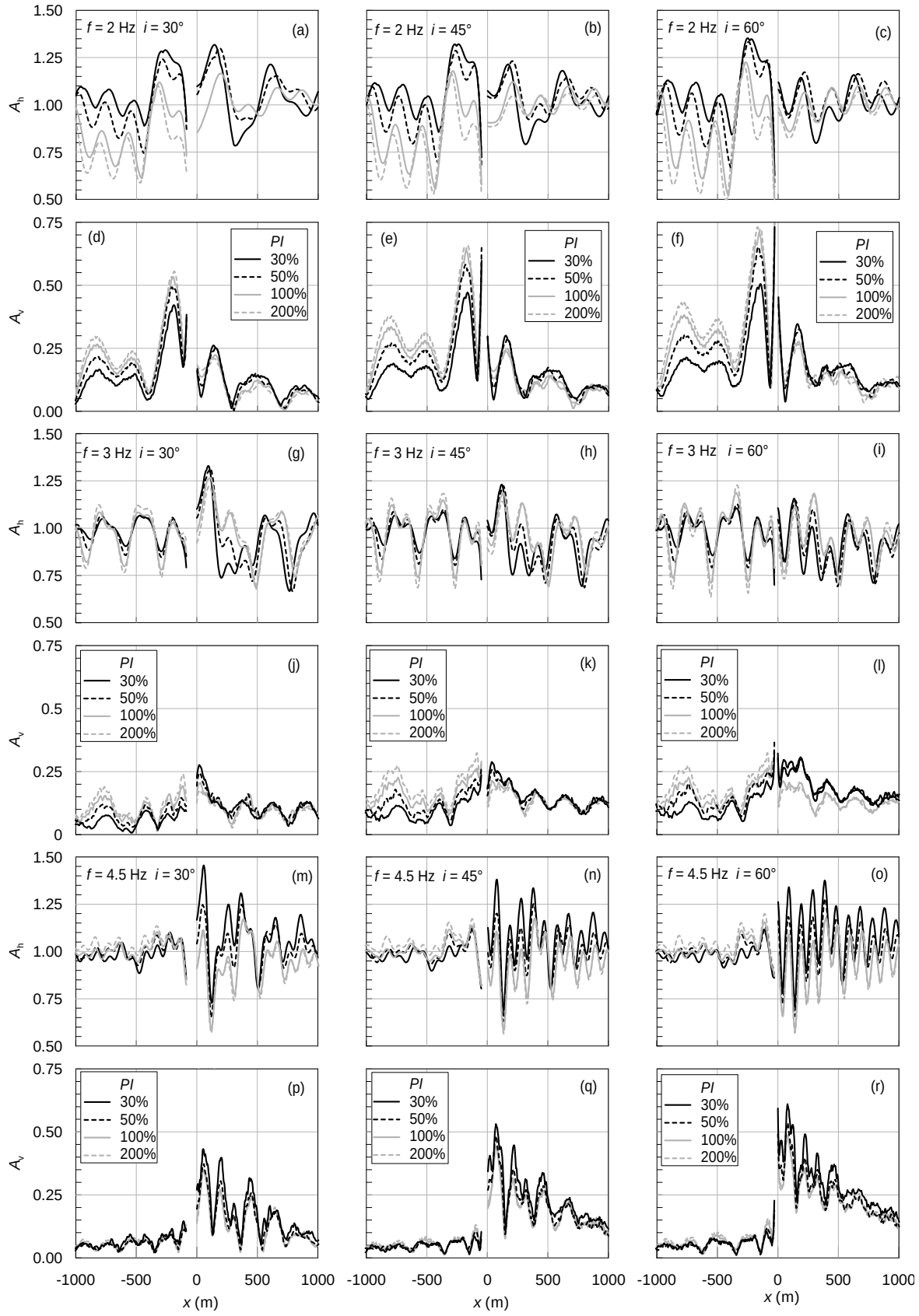


Figure 2: Horizontal and vertical topographic amplification factors computed at the ground surface for $a_0 = 0.1g$, for different values of slope angle (i = 30°, 45°, 60°), plasticity index (PI = 30, 50, 100, 200%) and input frequency (f = 2, 3, 4.5 Hz).

These results confirm that the stratigraphic and the topographic effects cannot be investigated separately since they are coupled in a complex interaction. As it could be expected for non-linear systems this interaction is governed by the system mechanical and geometrical properties and by the characteristics of the input motion.

3 INFLUENCE OF SOIL NON-LINEAR BEHAVIOUR

To point out the influence of the non-linear soil behaviour on the seismic response of the slope, different values of a_o and *PI* were considered (Table 1).

The results relevant for the case $i = 45°$, $PI = 30\%$ and $f = 3$ Hz are shown in Figure 3. It can be observed that the profiles of both horizontal and vertical topographic amplification factors along the ground surface are remarkably affected by the amplitude of the input motion. The influence of soil non-linear behaviour is also apparent: in fact, for increasing values of a_o, A_h is approximately increasing close to the toe of the slope, where absolute maximum amplification is attained, and is heavily decreasing close to the crest, while the profiles variously intertwine for increasing distance from the slope crest (Figure 3a). A similar trend is observed also for A_v (Figure 3b).

Figure 3 also shows the results of the *LVEB* analyses, carried out by [19] considering a slope in a homogeneous soil deposit overlying a compliant bedrock and assuming a constant value of shear modulus *G* and a damping ratio $\xi = 5\%$. In this case the results are independent of the amplitude of the input motion when expressed in a normalized form through A_h and A_v. The differences in the profiles of A_h and A_v obtained in the *EL* analyses with respect to the profile evaluated in the *LVEB* analyses confirm the influence of the non-linear soil behaviour.

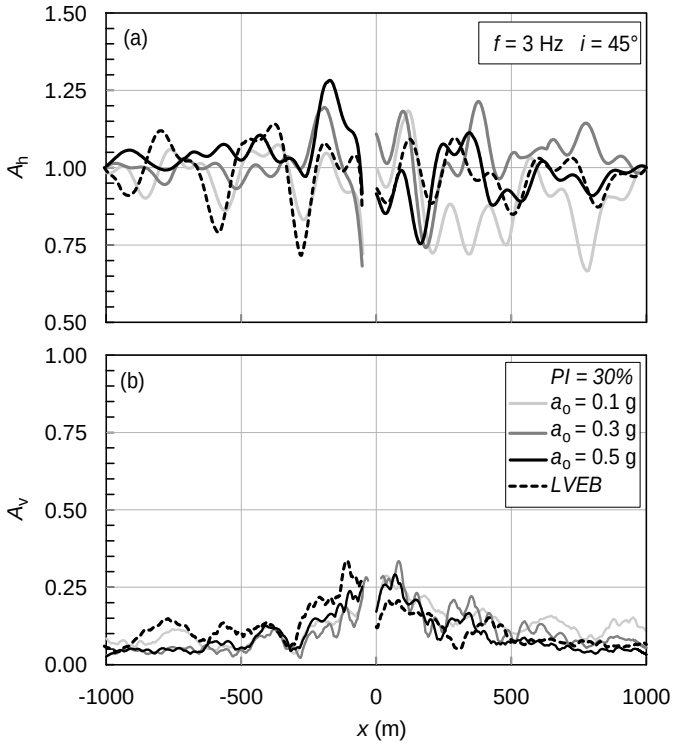


Figure 3: Horizontal (a) and vertical (b) topographic amplification factors computed at the ground surface for $PI = 30\%$, $i = 45°$, $f = 3$ Hz and different input motion amplitudes a_0.

The degree of nonlinearity introduced for each analysis can be represented through the profiles of the mobilized values of the normalized shear modulus G/G_o and damping ratio ξ.

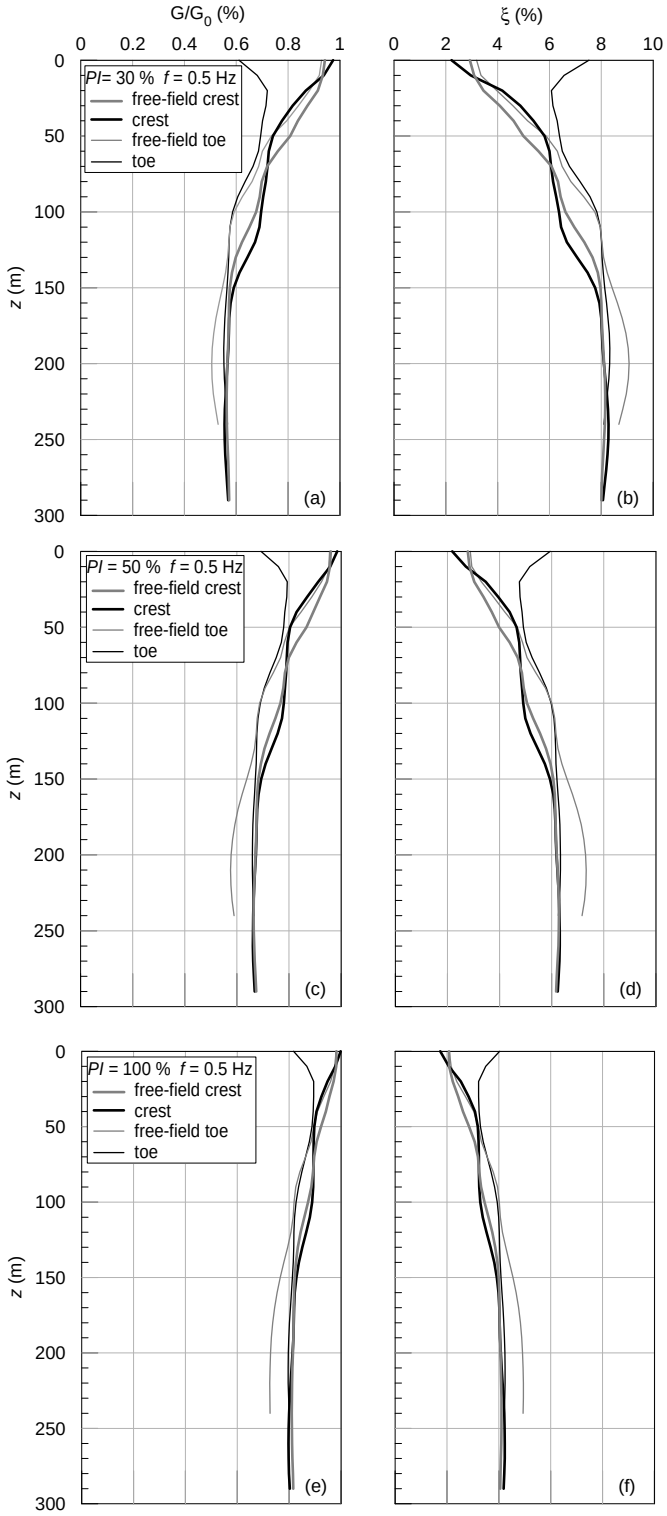


Figure 4: Profiles of the mobilized normalized shear modulus and damping ratio ($i = 45°$, $a_0 = 0.1\ g$).

In Figure 4 the profiles relevant to the cases $i = 45°$, $a_0 = 0.1g$, $f = 0.5$ Hz and $PI = 30$, 50 and 100 % are plotted for the two vertical boundaries of the *FE* model (*free-field* condition) and for the verticals through the crest and the toe of the slope. From all the plots the effect of soil non-linear behaviour is apparent, being more relevant when $PI = 30$ and 50 % are assumed, corresponding to smaller values of the linear threshold shear strain γ_l. As an

example, for PI = 30%, values of G/G_0 as small as 0.6 in the lower 100 m of the soil profile and in the range 0.6-1 in the upper portion of the profile are attained; the corresponding mobilized damping ratio, from the initial value $\xi_0 \cong 2\%$ increases with depth up to about ξ = 9 %. In all the cases of Figure 4 non-linear effects are more relevant for profiles through the toe of the slope.

Finally, the degree of nonlinearity introduced in the analysis, adopting different values of the plasticity index can be observed in the profiles of Figure 5 showing the results obtained for the case i = 45° and input frequency f equal to 0.5 Hz (Figures 5a,b) and 2 Hz (Figures 5c,d). For decreasing value of PI the effects of soil nonlinearity become more relevant and profiles of the mobilized G/G_0 and ξ typical of inhomogeneous soil deposits are obtained.

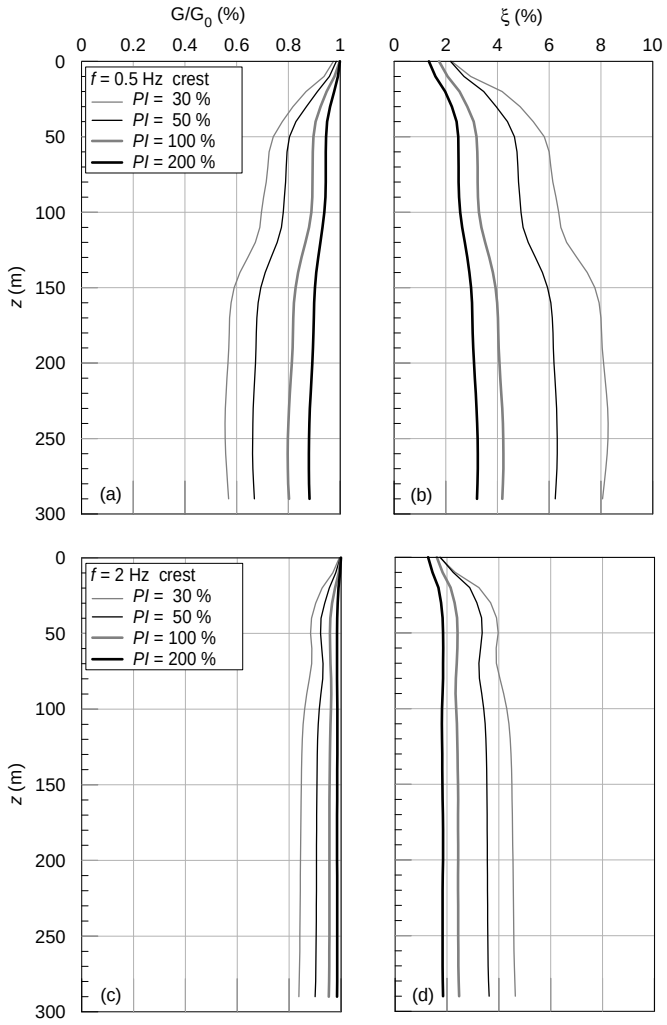


Figure 5: Profiles of the mobilized normalized shear modulus and damping ratio obtained for the vertical through the crest of the slope (i = 45°, a_0 = 0.1 g).

4 INFLUENCE OF INPUT MOTION FREQUENCY

To investigate the influence of the frequency of the input motion on the slope response, *EL* analyses were carried out assuming a_0 = 0.1g and f in the range 0.5-10 Hz; moreover, to fully capture the effect of frequency, the plasticity index PI was varied in the range 30-200% (Table 1).

The results obtained for the whole range of the considered input frequencies (0.1÷10 Hz) and for all the considered values of *PI* (30÷200 %) are synthetically shown in Figure 6 where the horizontal and the vertical topographic amplification factors are plotted against the normalized frequency H/λ. For $PI = 100$ and 200 % the response of the system is approximately linear regardless the values of f (Figures 4e,f and Figure 5). In these cases, such as for the linear system, the stratigraphic effects prevail on the computed response because the input frequencies are practically coincident with the natural frequencies estimated for the linear system; with the only exception of $f = 0.5$ Hz ($H/\lambda = 0.05$), for which the curves of A_h (Figure 6a) exhibit a peak, the horizontal topographic amplification factor A_h is close to or below unity for both values of *PI*.

For lower values of plasticity index (PI = 30%, 50%) the effect of soil non linear behaviour is not negligible (Figure 4a-d, Figure 5) and the values of A_h increase especially for the case PI = 30%.

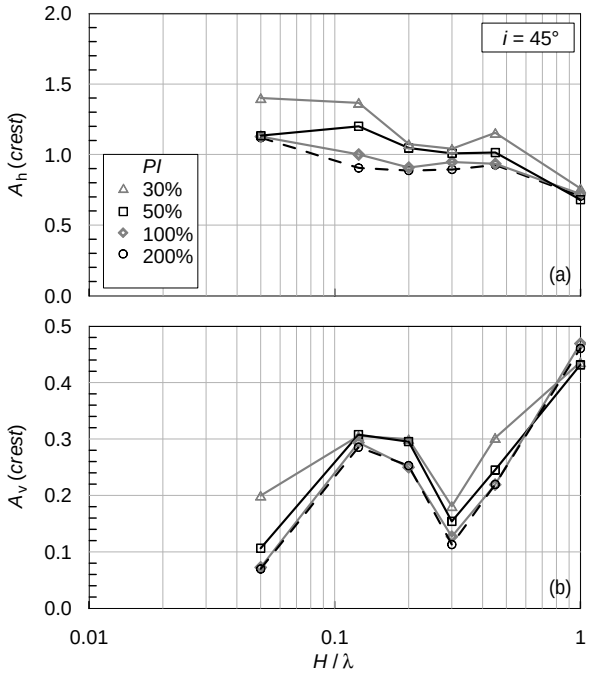


Figure 6: Horizontal (a) and vertical (b) topographic amplification factors at the crest of the slope (i = 45°, $a_0 = 0.1\ g$).

Concerning the vertical topographic amplification factor, the plots of Figure 6b show that A_v varies significantly with the normalized frequency H/λ but it is not appreciably affected by the plasticity index (with the only exception of the case PI = 30%).

Moreover, it is worth noting that the results commented above were obtained in the case $a_0 = 0.1$ g, however, as a consequence of non-linear soil behaviour, different results would possibly be obtained for different amplitudes of the input motion.

As it is usual for non-linear systems [23, 24, 25], the actual slope response cannot be predicted *a priori* since it depends on all the factors (a_0, f, G_0, ξ_0, PI) affecting soil non-linear behaviour.

Once more, it is confirmed that due to coupling between stratigraphic and topographic effects a proper evaluation of topographic amplification should, in principle, require specific non-linear *2D* analyses.

5 CONCLUDING REMARKS

This paper describes the results of *2D* numerical *FE* seismic response analyses carried out to investigate, under different assumptions, the seismic response of slopes subjected to vertically propagating *SV* waves.

Different sets of analyses were carried out focusing on slopes overlying a compliant bedrock, assuming that soil behaves as an equivalent-linear visco-elastic material. The amplification of the ground motion was evaluated in terms of topographic amplification factors.

The effect of soil non-linear behaviour was investigated varying the range of shear strains in which soil responds linearly by changing the relationship adopted to describe the variation of normalized shear modulus and damping ratio with induced shear strain; the influence of the amplitude and of the frequency of the input motion was also analyzed.

The results demonstrate that topographic amplification is affected by the non-linear behaviour of the soil. Specifically, horizontal and vertical topographic amplification factors were found to depend on the tendency of soil to exhibit a non-linear behaviour and on the degree of non-linearity arising in its seismic response. These, on turn, are related to all the factors affecting non-linear dynamic response: soil stiffness and damping ratio at small strain, characteristics of the input motion and non-linear stress-strain relationship.

The results also confirmed the expected complex interaction between topographic and stratigraphic effects and highlighted that their reliable evaluation cannot be performed through a decoupled approach and require a non-linear *2D* seismic response analyses.

REFERENCES

[1] G.A. Athanasopoulos, P.C. Pelikis, E.A. Leonidou, Effects of surface topography on seismic ground response in the Egion (Greece) 15-6-1995 earthquake. *Soil Dynamics and Earthquake Engineering*,**18**,135-149, 1999.

[2] G. Gazetas, P.V. Kallou, P.N. Psarropoulos, Topography and soil effects in the MS 5.9 Parnitha (Athens) earthquake: the case of Adámes. *Natural Hazards*, **27(1-2)**, 133-169, 2002.

[3] D. Assimaki, E. Kausel, G. Gazetas, Wave propagation and soil–structure interaction on a cliff crest during the 1999 Athens earthquake. *Soil Dynamics and Earthquake Engineering*, **25**, 513–527, 2005.

[4] G. Biondi, M. Maugeri, Seismic response analysis of Monte Po hill (Catania). *Seismic Prevention of Damage. A Case Study in a Mediterranean City*', *Wit Press, Southampton, UK*, **Chapter 10**,177-195, 2005.

[5] D. Assimaki, G. Gazetas, E. Kausel, Effects of local soil conditions on the topographic aggravation of seismic motion: parametric investigation and recorded field evidence from the 1999 Athens Earthquake. *Bulletin of the Seismological Society of America*, **95(3)**, 1059-1089, 2005.

[6] G.D. Bouckovalas, G. Gazetas, A.G. Papadimitriou, Geotechnical aspects of the Aegion (Greece) earthquake. *Proc. 2nd Int. Conf. on Geotechnical Earthquake Engineering.* Lisbon, 739–748, June 1999.

[7] G. Biondi, E. Cascone, M. Maugeri, E. Motta, Seismic response of saturated cohesionless slopes. *Soil Dynamics and Earthquake Engineering*, **20(1-4)**, 209-215, 2000.

[8] G. Biondi, E. Cascone, M. Maugeri, Flow and deformation failure of sandy slopes. *Soil Dynamics and Earthquake Engineering*, **22 (9-12)**, 1104-1014, 2002.

[9] V. Bandini, E. Cascone, G. Biondi, A GLE multi-block model for the evaluation of seismic displacements of slopes. *Proc. Seismic Eng. Int. Conf. commemorating the 1908 Messina and Reggio Calabria Earthquak*, **1**, 485-492, Reggio Calabria,2008.

[10] V. Bandini, G. Biondi, E. Cascone, S. Rampello, A GLE-based model for seismic displacement analysis of slopes including strength degradation and geometry rearrangement. *Soil Dynamics and Earthquake Engineering,* **71**, 128-142, 2015.

[11] S.A. Ashford, N. Sitar, J. Lysmer, N. Deng, Topographic Effects on the Seismic Response of Steep Slopes. *Bulletin of the Seismological Society of America*, **87**, 701-709, 1997.

[12] N. Sitar, G.W. Clough, Seismic response of steep slopes in cemented soils. *Journal of Geotechnical Engineering, ASCE,* **109**, 210-227, 1983.

[13] R. Tripe, S. Kontoe, T.K.C. Wong. Slope topography effects on ground motion in the presence of deep soil layers. *Soil Dynamics and Earthquake Engineering*, **50**, 72-84, 2013.

[14] I.M. Idriss, H.B. Seed, Response of earth banks during earthquakes. *Journal of the Soil Mechanics and Foundations Division, ASCE*, **93(SM 3),** 61-82, 1967.

[15] G.D. Bouckovalas, A.G. Papadimitriou, Numerical evaluation of slope topography effects on seismic ground motion. *Soil Dynamics and Earthquake Engineering*, **25(7)**, 547-558, 2005.

[16] A.G. Papadimitriou, Topographic aggravation of the peak seismic acceleration near two dimensional hills and slopes. *Proc. 5th International Conf. on Earthquake Geotechnical Engineering,* Santiago, Chile, 2011.

[17] K.V. Nguyen, B. Gatmiri, Evaluation of seismic ground motion induced by topographic irregularity. *Soil Dynamics and Earthquake Engineering*, **27(2)**,183-188, 2007.

[18] A.G. Papadimitriou, Y. Chaloulos, Aggravation of the peak seismic acceleration in the vicinity of 2D hills, canyons and slopes. *5th International Conference on Recent Advances in Geotechnical Earthquake Engineering and Soil Dynamics*, San Diego, California, 2010.

[19] S. Rizzitano, E. Cascone, G. Biondi, Coupling of topographic and stratigraphic effects on seismic response of slopes through 2D linear and equivalent linear analyses. *Soil Dynamics and Earthquake Engineering*, **67**, 66-84, 2014.

[20] J. Krahn, Dynamic modeling with QUAKE/W: an engineering methodology. *GEO-SLOPE International Ltd*. Calgary, Alberta, Canada, 2004.

[21] M. Vucetic, M, R. Dobry, Effect of soil plasticity on cyclic response. *Journal of Geotechnical Engineering, ASCE,* **117(1)**, 89-107, 1991.

[22] M. Vucetic, Cyclic threshold shear strains in soils. *Journal of Geotechnical Engineering, ASCE*, **120(12)**, 2208 – 2228, 1994.

[23] S. Hartzell, L.F. Bonilla, R.A. Williams, Prediction of nonlinear soil effects. *Bulletin of the Seismological Society of America*, **94(5)**, 1609-1629, 2004.

[24] G. Biondi, M.R. Massimino, M. Maugeri, Influence of frequency content and amplitude of input motion in DSSI investigated by shaking table tests. *Bulletin of Earthquake Engineering*, 1-35, 2014.

[25] M. R. Massimino, G. Biondi, Some experimental evidences on dynamic soil structure interaction. *Proc. 5th ECCOMAS Thematic Conference on Computational Methods in Structural Dynamics and Earthquake Engineering*, Crete Island, Greece, 2015 (this conference).

COMPDYN 2015
5th ECCOMAS Thematic Conference on
Computational Methods in Structural Dynamics and Earthquake Engineering
M. Papadrakakis, V. Papadopoulos, V. Plevris (eds.)
Crete Island, Greece, 25–27 May 2015

CLASS A PREDICTION FOR SEISMIC CENTRIFUGE MODELING OF MULTI-BLOCK QUAY-WALL: UNDRAINED (PLAXIS) VERSUS COUPLED (FLAC) EFFECTIVE STRESS ANALYSIS

Panagiota Tasiopoulou[1], Nikos Gerolymos[2], and George Gazetas[3]

[1] National Technical University of Athens, Greece
9, Iroon Polytechniou Str., Polytechnic Campus. Zografos P.C 15780
e-mail: ptasiopoulou@gmail.com

[2] National Technical University of Athens, Greece
9, Iroon Polytechniou Str., Polytechnic Campus. Zografos P.C 15780
gerolymos@gmail.com

[3] National Technical University of Athens, Greece
9, Iroon Polytechniou Str., Polytechnic Campus. Zografos P.C 15780
gazetas@ath.forthnet.gr

Keywords: quay-wall, seismic effective stress analysis, coupled flow dynamic response, FLAC, PLAXIS.

Abstract. *Effective stress analyses are conducted aiming to provide Class A predictions for a seismic centrifuge test of a multi-block gravity quay-wall. Two different codes are used: i) the finite difference code FLAC 2D (coupled effective- stress analysis) and ii) the finite element code, PLAXIS 2D (undrained effective-stress analysis). Two versions of the original UBCSAND constitutive model, implemented in each code, are used after meticulous calibration in order to reproduce equivalent liquefaction resistance curves. Apart from predicting the experimental response, the study aims at performing a comparison between the two codes widely-used in practice.*

1 INTRODUCTION

The latest advances in port and maritime industry have redefined the role of harbor facilities in the economy. Ports are nowadays multipurpose lifeline facilities that function as embarkation, storage and maintenance facilities for the transportation of cargo and passengers. Waterfront structures form the core of nearly all harbor facilities (be it commercial, industrial, or simply passenger terminals). Therefore maintaining their integrity (as well as a minimum serviceability threshold) during seismic events, constitutes a necessity for the sustainability pf the facility as a whole, since most of the components comprising any waterfront plant (e.g. pipelines, cranes, storage tanks etc.) are either founded, or directly dependent, upon them.

Gravity quay wall structures have repeatedly suffered substantial outward displacement and rotation even when subjected to moderate earthquake shaking. (e.g. [1]-[7]). The most astonishing case study comes from the port of Kobe, where during the 1995 earthquake, wall displacements reached as much as 5 m [8]. Yet, even during the mild Lefkada (Greece) earthquake of 2003 (Ms = 6.4) most of the coastal structures sustained relatively large displacements up to 25 cm. An even more recent example is the damage of the Lixouri harbour quay wall in the two 2014 Cephalonia (Greece) earthquakes, despite the relatively small magnitude (Ms ≈ 6) of the events.

The dynamic response of gravity quay walls is strongly affected by non-linear soil behaviour. Development of excess pore pressures and accumulation of shear and volumetric strains both at the retained and the foundation soil, produces shear strength degradation which may be accompanied by liquefaction. The above phenomena are further complicated when accounting for soil-structure interaction. The strong rocking of quay walls (due only to their inertial forces), when founded on a compliant foundation soil in combination with the one-sided action of earth pressures leads to the accumulation of horizontal displacement and rotation towards the seaside. Evidently, the deformation modes that synthesize the response of the quay wall at large displacements and near failure conditions cannot be realistically assessed by conventional design procedures. The use of suitable constitutive soil models [22] that balance simplicity and effectiveness in conjunction with powerful numerical techniques is a key-step for a successful prediction.

In this paper, effective stress numerical analyses are conducted aiming to provide Class A predictions for a seismic centrifuge test of a multi-block gravity quay-wall, replica of a typical wall at Piraeus port in Greece. The centrifuge testing was conducted at University of Dundee and the experimental measurements will be published by [9]. Two different codes are used: i) finite difference code, FLAC 2D [10] and ii) finite element code, PLAXIS 2D. Two different versions of the original elasto-plastic effective stress constitutive model [11]-[12], UBCSAND, have been implemented in each code: i) UBCSAND-904aR for FLAC [13] and ii) UBC3D-PLM for PLAXIS [14]. These versions are calibrated appropriately in an attempt to achieve equivalence in their predictions of liquefaction resistance stress ratios for the same number of loading cycles under undrained conditions. The goal of this study is twofold: a) to predict of the experimental response and b) to compare the computed response by two codes widely-used in practice, FLAC (coupled effective- stress analysis) and PLAXIS (undrained effective-stress analysis).

2 SEISMIC CENTRIFUGE MODELING

A dynamic centrifuge model test was conducted at the University of Dundee centrifuge facility is examined. The model used a fine quartz based silica sand (HST95) and simulated the response of a multi-block gravity quay wall made of aluminium alloy, as a replica of a typical

wall at Piraeus port in Greece. The sand bed was formed into an ESB (equivalent shear beam) model container by carrying out air pluviation at a relative density of D_r = 80%. It was then saturated with water and subjected to an acceleration field of 60g. A sketch of the experimental setup (including the instrumentation layout) is illustrated in figure 1. While in flight, a sequence of actual ground-acceleration records were applied at the base of the model as input motion. However, only numerical results for the first acceleration time history (a record from the M_L = 5.9 L' Aquila 2009 earthquake, shown in Figure 2) are presented as class A predictions. Details on the experimental procedure and measurements will be published by [9].

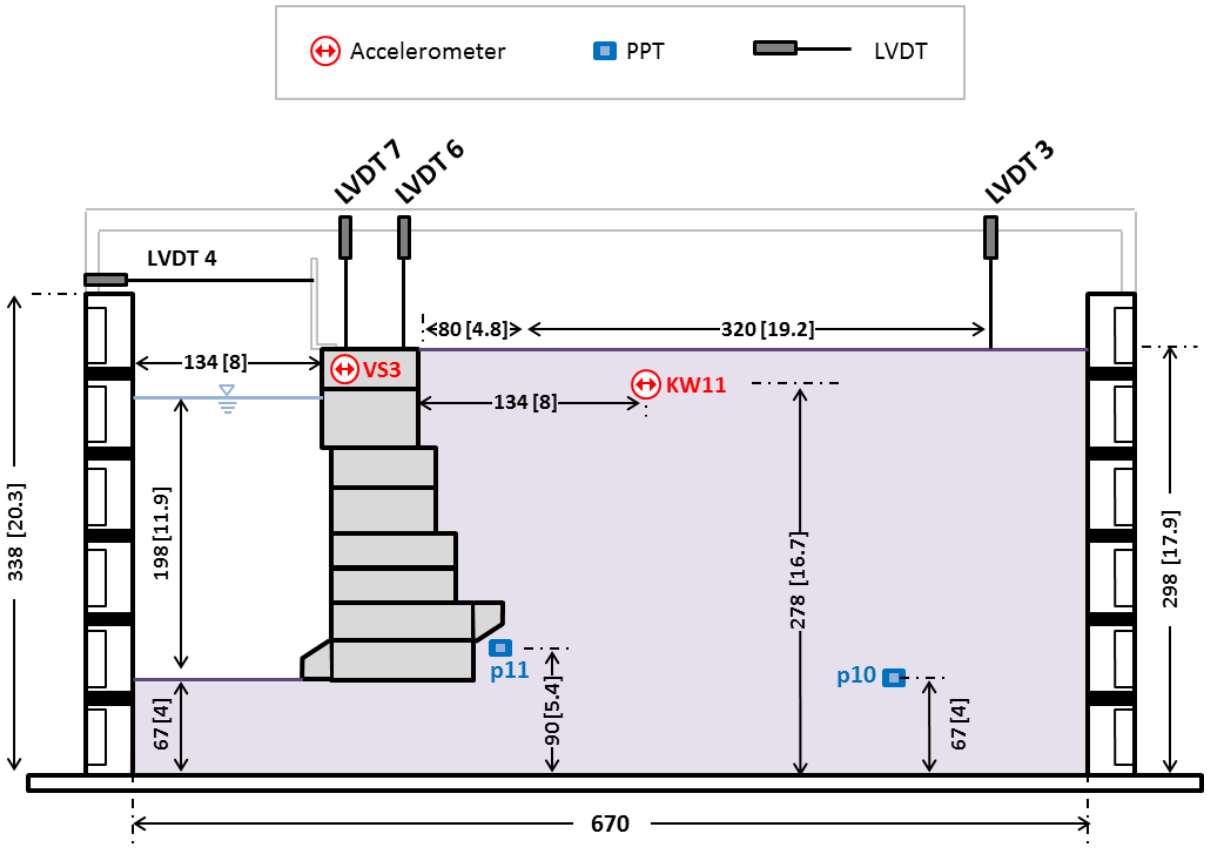


Figure 1. Centrifuge model setup and instrument locations for Class A prediction.

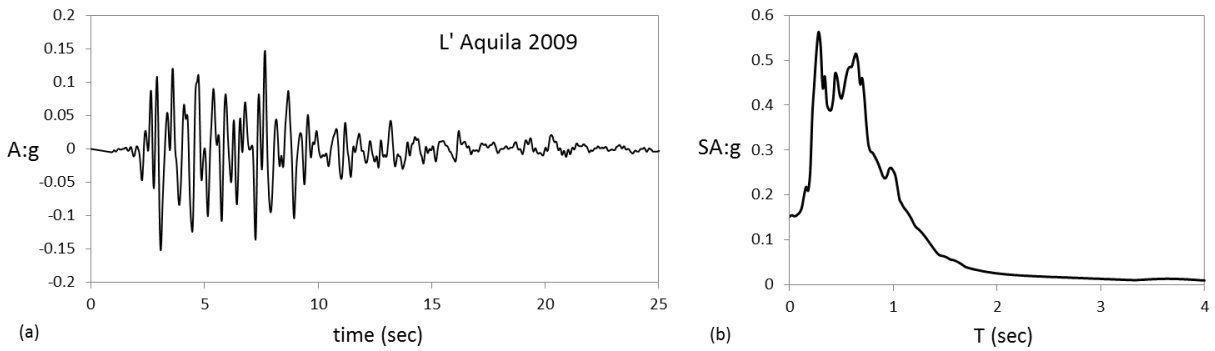


Figure 2. Base input motion: Acceleration time history and corresponding spectrum

3 NUMERICAL MODELING

Numerical effective stress analysis of a section of the centrifuge model is performed in prototype scale with both finite difference code FLAC and finite element code PLAXIS. The analysis is conducted taking into account for material (in the soil) and geometric (interface) nonlinearities. The aluminium alloy frames and rubber spacing layers of the ESB model container were also modelled in detail, assuming elastic behaviour. Prescribed displacements were imposed on the horizontal boundaries of each frame prohibiting their movement in the vertical direction, and kinematic constraints were assigned to the external and internal vertical edges of the model allowing it to move as a laminar box ([14]- [17]).

The contact conditions between the blocks of the quay wall as well as between the quay wall and the adjacent soil were modelled with special interface elements allowing for slippage and gapping via a Coulomb frictional law. Special interface elements were also placed along the inner edges of the ESB model container. The friction interface angles were assumed equal to 18^o between the blocks of the quay wall, 10^o and 14^o at the back and at the base of the wall, respectively, and 10^o for the inner vertical edges of the container. The waterfront was simulated through hydrostatic pressures applied to the front side of the wall, as well as the seabed. To avoid spurious oscillations at very small deformations and for high frequency components of motion, Rayleigh damping was also introduced into the model, accounting for equivalent hysteretic damping values between 1.5% and 3% in the range of 0.2 Hz and 2 Hz. The initial horizontal effective stresses were set to 0.5 times the vertical effective stresses. The input motion in prototype scale, in Figure 2, was applied to the base of the numerical models.

3.1 COUPLED ANALYSIS - FLAC

The finite difference mesh of the model, portrayed in Figure 3, involves a grid spacing of 0.5 m x 0.5 m. FLAC allows for coupled flow dynamic analysis, accounting for interaction of the poro mechanical soil properties. The coefficient of hydraulic permeability was estimated to $k = 3 \times 10^{-4}$ m/s (in prototype scale) and assumed to be constant throughout the analysis.

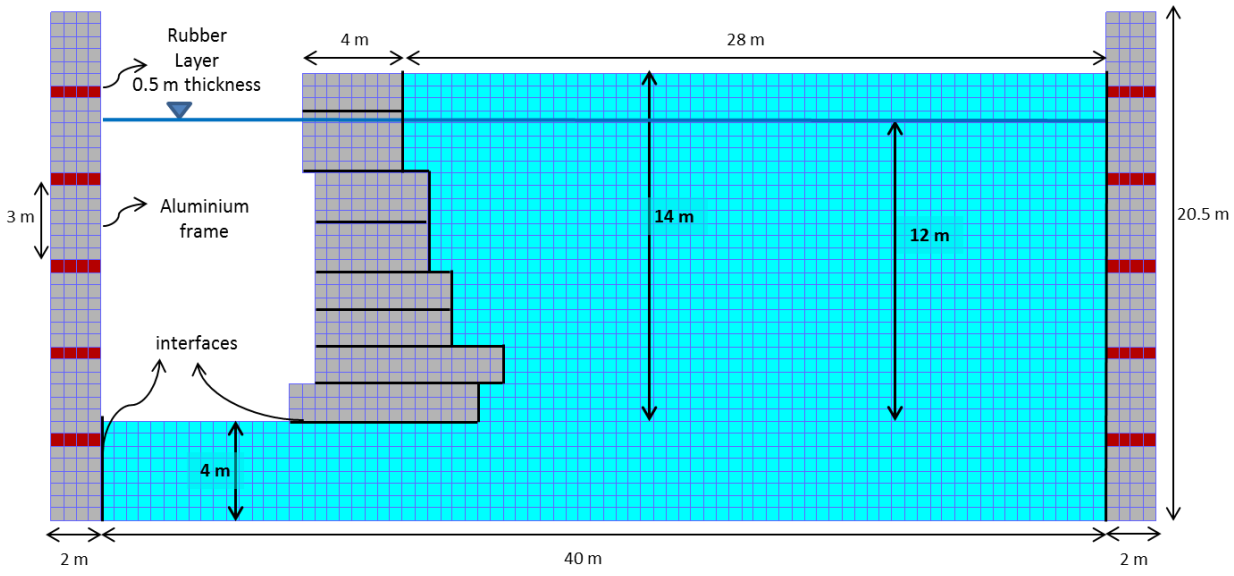


Figure 3. Numerical model in FLAC.

3.2 UNDRAINED ANALYSIS - PLAXIS

Undrained effective stress analysis was conducted with finite element code PLAXIS 2D AE. Both the quay wall and the soil are modelled with 15-node triangular plane strain elements, elastic for the former and nonlinear for the latter (3130 elements in total). The finite element mesh is shown in Figure 4.

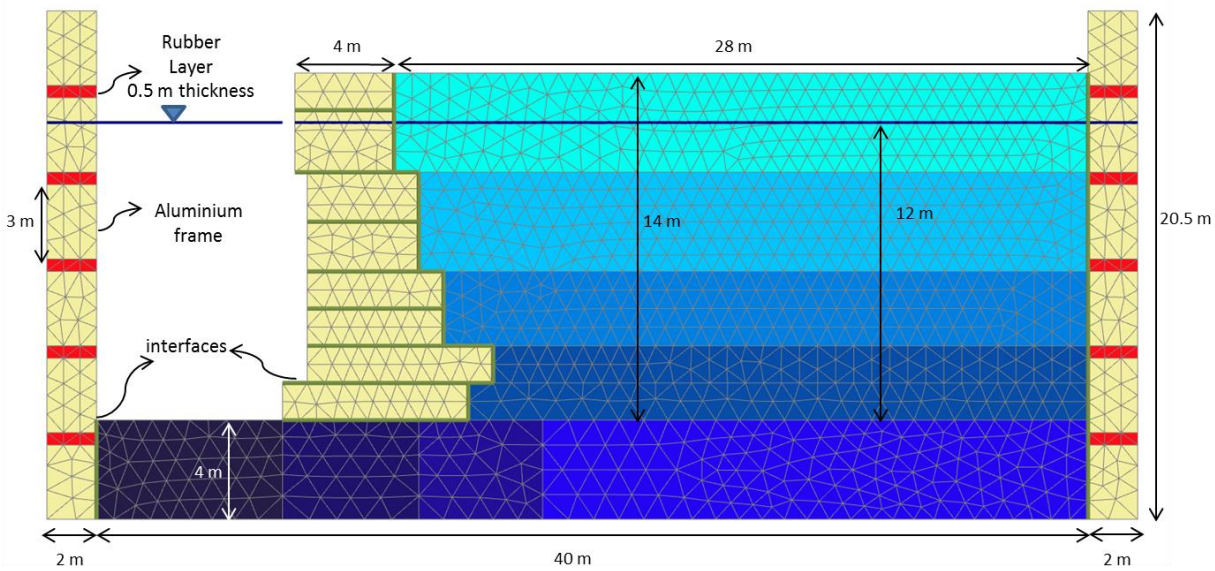


Figure 4. The finite element model (PLAXIS)

4 CONSTITUTIVE MODEL

Cyclic soil behaviour is described through an elasto-plastic effective stress constitutive model, UBCSAND, originally developed at University of British Columbia by [11] and [12]. It involves two yield surfaces (a primary and a secondary one) of the Mohr-Coulomb type. The primary surface evolves according to an isotropic hardening law while a simplified kinematic hardening rule is used for the second yield surface. The elastic response is described by the elastic shear and bulk moduli given by:

$$G^e = k_G^e \cdot p_a \cdot \left(p \,/\, p_a \right)^{ne} \tag{1}$$

$$B^e = k_B^e \cdot p_a \cdot \left(p \,/\, p_a \right)^{me} \tag{2}$$

in which k_G^e and k_B^e are the elastic shear and bulk numbers in respect, p_a is the reference stress, p is the mean effective stress and ne, me are exponents for stress dependency. The plastic shear modulus is given by:

$$G^p = G_i^p \left(1 - \frac{\eta}{\eta_f} R_f \right)^2 \tag{3}$$

in which G_i^p component variates for primary, secondary and post-dilation loading, η is the current stress ratio, η_f is the stress ratio at failure, equal to $sin\left(\varphi_p\right)$, φ_p being the peak friction angle and R_f is a failure ratio that truncates hyperbolic curve. The plastic flow rule is non-associated and is based on the Drucker-Prager's law and Rowe's stress dilatancy hypothesis:

$$d\varepsilon_v^p = \left(sin\left(\varphi_{cv}\right) - \eta\right) d\gamma^p \tag{4}$$

where φ_{cv} is the phase transformation friction angle.

Different versions and extensions of the model, based on the above-described framework, have been developed by various researchers. The most widely-used ones, are those implemented in finite difference code, FLAC and finite element code, PLAXIS, such as UBCSAND-904aR [13] and UBC3D-PLM [14], respectively. One of the most significant divergences of the two versions, when performing seismic effective stress analysis, lies on their approach on the stiffness degradation of the secondary plastic shear modulus, which practically controls the number of loading cycles to cause liquefaction.

4.1 UBCSAND 904aR in FLAC

In this version of the model, G_i^p component has the following form:

$$G_i^p = k_G^p \cdot \frac{p_a}{p} \cdot \left(\frac{p}{p_a}\right)^{np} \cdot f\left(hfac_1, hfac_2, n_{cyc} \ldots\right) \tag{5}$$

where k_G^p is the plastic shear modulus number, np is a constant, $hfac_1$ is a factor controlling the number of cycles to trigger liquefaction and $hfac_2$ is a factor refining the shape of pore water pressure rise with cycles, n_{cyc} is the number of loading cycles etc. Obviously, the decisive parameter to define the liquefaction resistance versus number of loading cycles is $hfac_1$. The smaller the value of $hfac_1$, the greater the excess pore water pressure development and the lesser the liquefaction resistance.

4.2 UBC3D-PLM in PLAXIS

In this version, G_i^p component is described as:

$$G_i^p = k_G^p \cdot \frac{p_a}{p} \cdot \left(\frac{p}{p_a}\right)^{np} \cdot f\left(fac_{hard}, n_{cyc,\ldots}\right) \tag{6}$$

in whih fac_{hard} affects the number of cycles for liquefaction occurrence. This parameter has the same trend as $hfac_1$, in the previous version; thus, lower values lead to lesser number of cycles required to cause liquefaction.

4.3 Calibration Methodology

[13] proposed a set of equations for the calibration of the UBCSAND model parameters, with the corrected SPT value $(N_1)_{60}$ being the sole variable. The calibration procedure aimed

at matching the cyclic resistance ratio indicated by the NCEER/NSF curve for a given corrected SPT blow count to induce liquefaction at 15 uniform loading cycles. In order to apply this methodology to our study, the empirical correlation between $(N_1)_{60}$ and relative density, D_r , proposed by [18] was used:

$$(N_1)_{60} \simeq 46 (D_r)^2 \tag{7}$$

Thus, applying the methodology by Beaty and Byrne (2011) for both versions of UBCSAND , while assuming that φ_p = 42°, as indicated by experiments of HST95 Silica sand for $D_r = 80\%$, the values of the common model parameters were derived, as shown in Table 1. Then, the different parameters of the two versions, $hfac_1$ for UBCSAND-904aR and fac_{hard} for UBC3D-PLM, were calibrated based on experimental liquefaction resistance curves for various sands with $D_r = 80\%$ ([19]-[21]), as shown in Figure 5. The goal of this calibration process was to achieve equivalence of the two versions in predicting the number of loading cycles to cause liquefaction under specific cyclic stress ratios. Finally, in order to incorporate stress dependency, or the so-called Kσ effects, the model parameters, $hfac_1$ and fac_{hard}, are given as functions of the vertical effective stress, as illustrated in Figures 6 and 7. Representative results of computed response for both versions are shown in figure 8, for CSR = 0.3, initial effective stress σ'_{v0} = 100 kPa and lateral earth pressure coefficient at rest K_0 = 0.5.

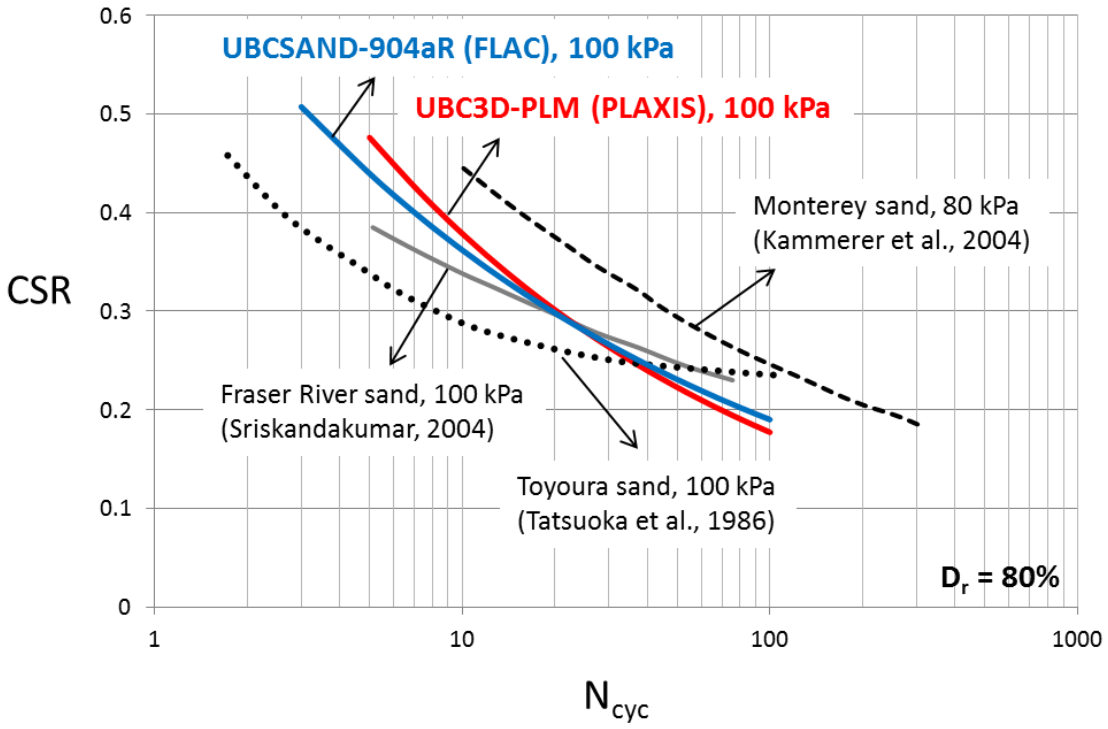


Figure 5. Comparison between predicted and experimental liquefaction resistance curves in undrained cyclic simple shear testing for D_r = 80%.

Parameters	Unit	Description	UBC3D-PLM (PLAXIS)	UBCSAND-904aR (FLAC)
φ_p	(deg)	Peak friction angle	42	42
φ_{cv}	(deg)	Phase transformation friction angle	36.1	36.1
k^e_B	-	Elastic bulk modulus number	937	937
K^e_G	-	Elastic shear modulus number	1338.6	1338.6
k^p_G	-	Plastic shear modulus number	3580.5	3580.5
me	-	Exponent for stress dependency of elastic bulk modulus	0.5	0.5
ne	-	Exponent for stress dependency of elastic shear modulus	0.5	0.5
np	-	Power for stress dependency of plastic shear modulus	0.4	0.4
R_f	-	Failure ratio	0.662	0.662
p_a	(kPa)	Reference stress	100	100
fac_{hard}	-	Fitting parameter to adjust number of cycles to liquefaction	see Fig. 7	N/A
fac_{post}	-	Fitting parameter to adjust post- dilation behaviour	0.01	N/A
$hfac_1$	-	Fitting parameter to adjust number of cycles to liquefaction	N/A	see Fig. 6
$hfac_2$	-	Fitting parameter to refine shape of pore pressure rise with cycles	N/A	1
$(N_1)_{60}$	-	Corrected SPT blow counts	29.4	29.4

Table 1. Constitutive model parameters for UBC3D-PML (PLAXIS) and UBCSAND-904aR (FLAC).

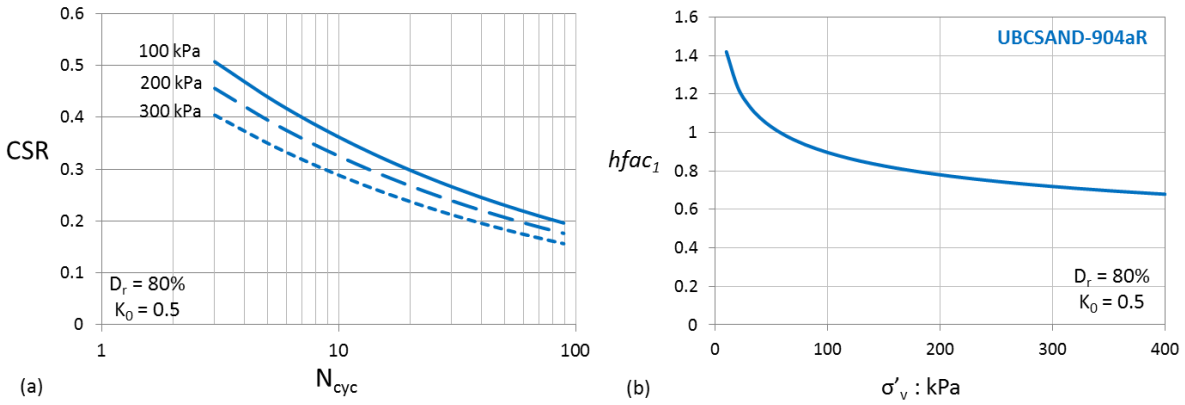


Figure 6. (a) Cyclic stress ratios versus number of equivalent uniform loading cycles in undrained direct simple shear loading to cause r_u=98% for D_r = 80% and varying vertical effective stress. (b) Corresponding values of $hfac_1$ parameter of UBCSAND-904aR (in FLAC).

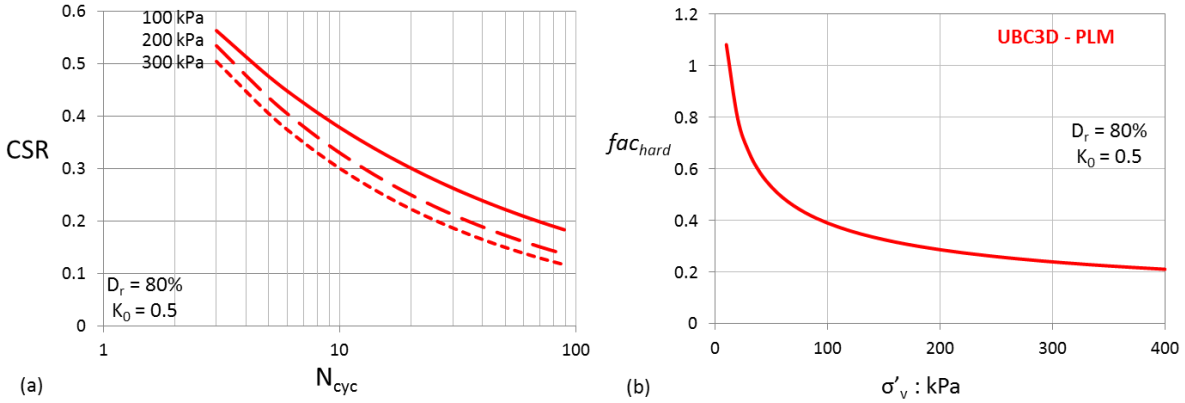


Figure 7. (a) Cyclic stress ratios versus number of equivalent uniform loading cycles in undrained direct simple shear loading to cause ru=98% for Dr = 80% and varying vertical effective stress. (b) Corresponding values of fac_{hard} parameter of UBC3D-PLM (in PLAXIS).

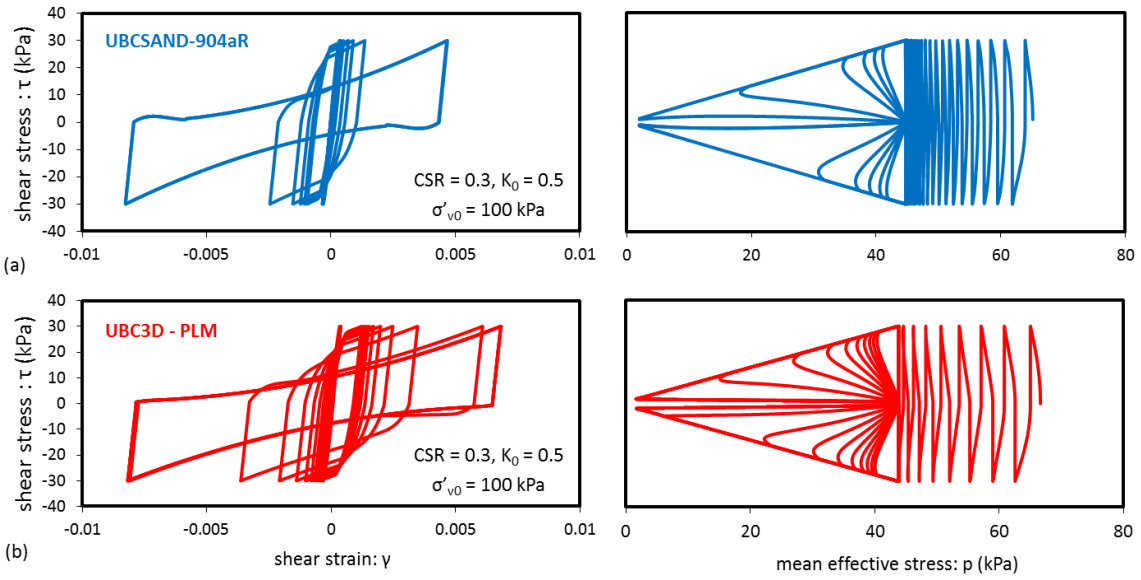


Figure 8. Simulated cyclic direct simple shear tests with (a) UBCSAND-904aR (in FLAC) and (b) UBC3D-PLM (in PLAXIS) for D_r = 80%.

5 CLASS A PREDICTION: FLAC AND PLAXIS

Numerical predictions obtained from both FLAC and PLAXIS are shown in terms of time histories at the measurement locations shown in Figure 1. Initially, comparison of the developed deformation mechanism of the quay-wall-soil-container system is held in order to ensure that both models can successfully reproduce the outward quay-wall displacement and rotation, as has been observed in various case histories. Figure 9 confirms that both models produce similar deformed meshes after the end of shaking. The contours of horizontal displacements obtained from both models, illustrated in Figure 10, indicate that sliding at the base of the quay-wall prevailed against bearing capacity failure.

The numerical analyses provide similar results in terms of the quay-wall outward displacement and rotation, as well as the settlement at the backfill (see Figures 11 and 12). Both models predict a residual horizontal displacement of the quay-wall in the order of 22 cm and a residual rotation of 0.24 deg.

Acceleration time histories, shown in Figure 13, also compare well, apart from some high-frequency spikes in case of FLAC analysis. The inward accelerations are systematically larger than their outward (seaward) counterparts which appear to have been curtailed due to excessive sliding at the base of the wall. The absence of long period pulses in the accelerogram obtained at the backfill is a sign of either no or limited soil liquefaction occurrence.

However, both analyses predict positive excess pore pressure development at the backfill away from the quay-wall, close to the base of the model (see Figure 14). In particular, in case of PLAXIS, where totally undrained conditions apply and no flow (dissipation) is accounted for, there is a pore pressure build up close to liquefaction. On the other hand, analysis in FLAC allows for concurrent generation and dissipation of pore water pressure leading thus, to less positive excess pore water pressure development. In contrast to what happens in the backfill away from the quay-wall, negative excess pore pressures develop close to the wall-soil interface (point 11 in Figure 1) due to the outward displacement of the quay-wall, in agreement with previous studies ([6], [7]).

6 CONCLUSIONS

Class A predictions were presented for seismic centrifuge modeling of a multi-block gravity quay-wall supporting a dense backfill of D_r=*80%*. Numerical analyses were performed with two different codes: i) finite difference code FLAC (coupled flow effective stress analysis) and ii) finite element code PLAXIS (undrained effective stress analysis). The constitutive models used for soil behavior are extensions of the original elasto-plastic model, UBCSAND. The two versions were extensively calibrated in order to render them equivalent in terms of cyclic liquefaction resistance. The analyses provided results in remarkable agreement, especially for the quay-wall performance. In detail, both analyses predicted that the quay-wall moved seawards by 22 cm at the top and rotated 0.24 deg. Sliding at the base of the quay-wall was the predominant mechanism to induce outward quay-wall displacement.

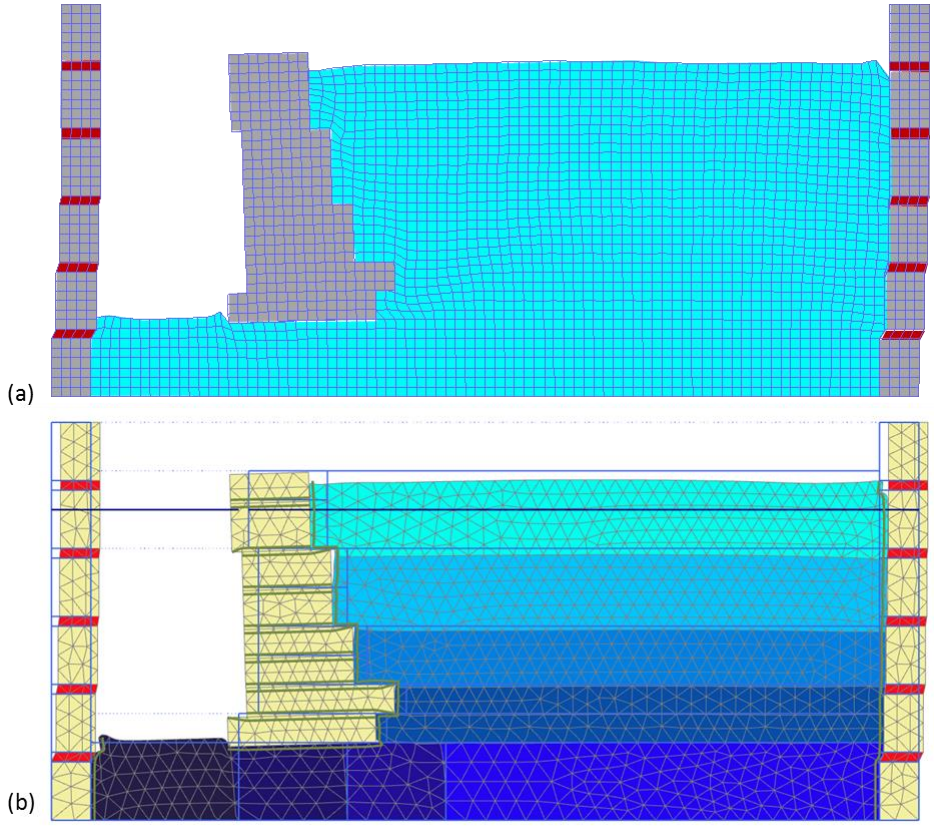


Figure 9. Deformed meshes after the end of shaking magnified 7 times: (a) FLAC and (b) PLAXIS.

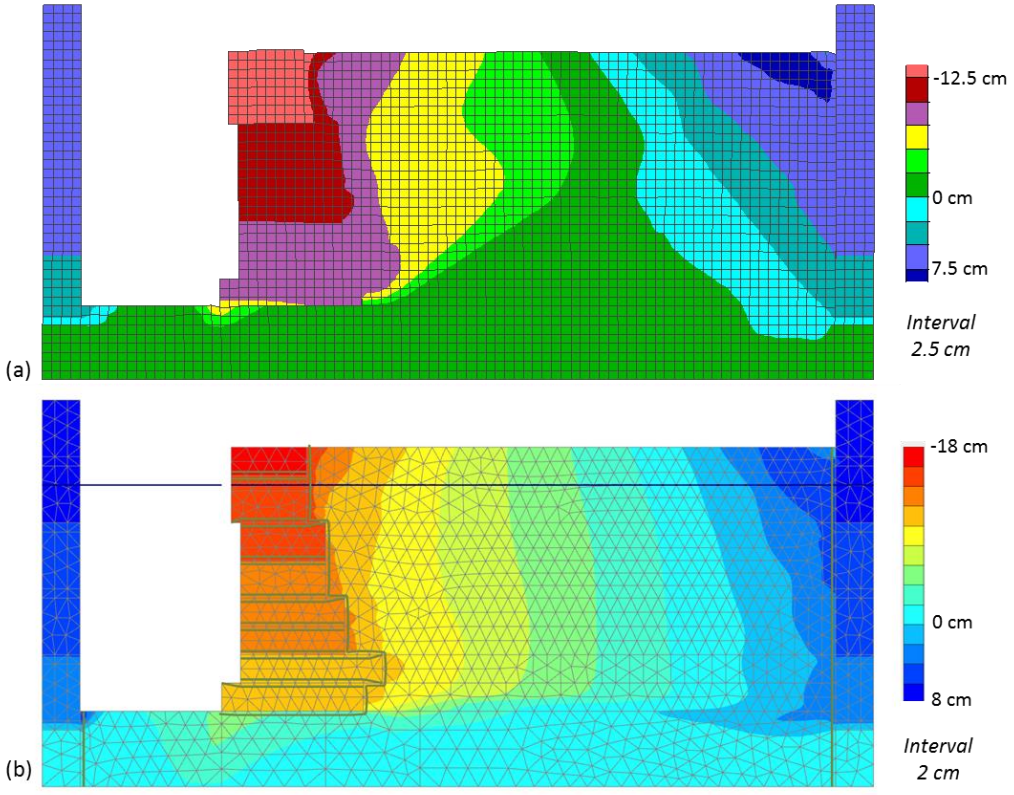


Figure 10. Contours of horizontal displacements after the end of shaking: (a) FLAC and (b) PLAXIS.

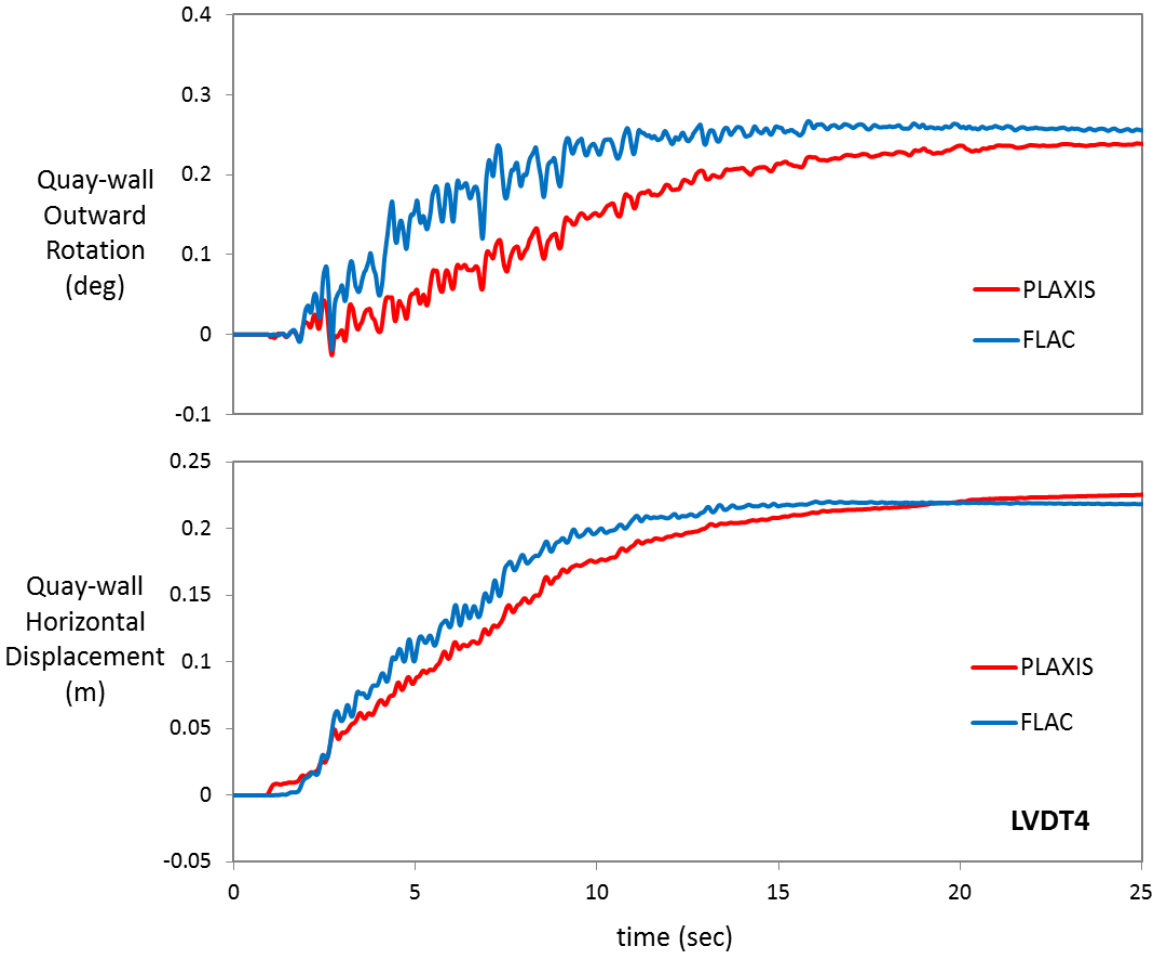


Figure 11. Predicted quay-wall rotation (top) and horizontal displacement at top (bottom).

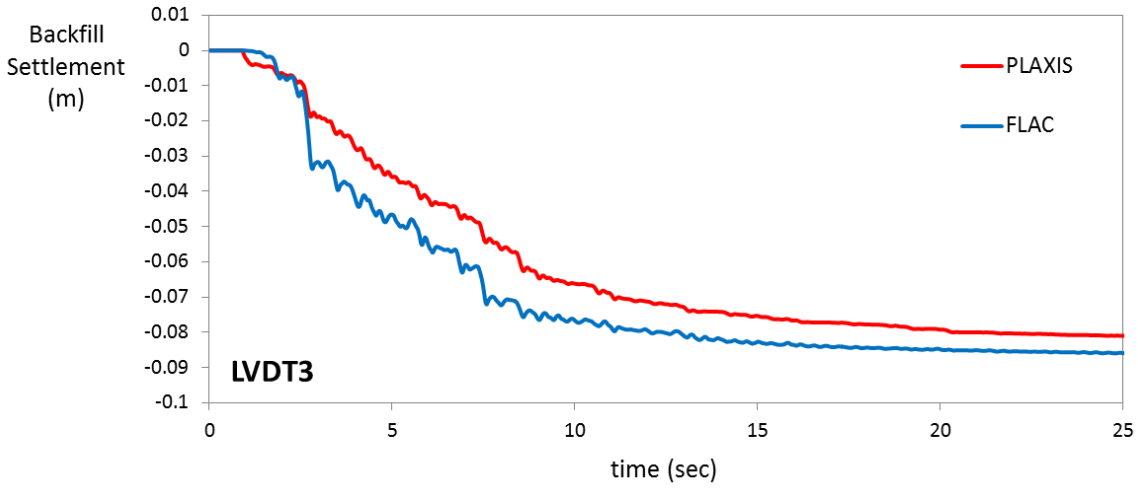


Figure 12. Predicted settlement of the backfill at location LVDT3 in Figure 1.

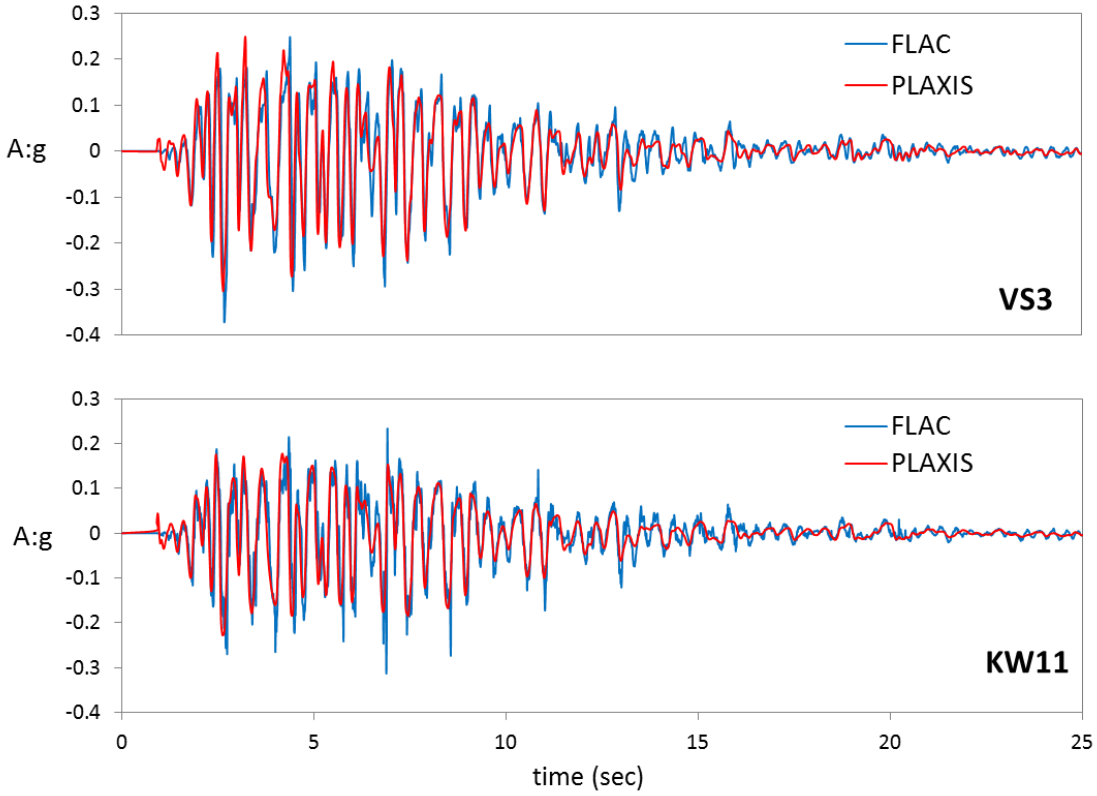


Figure 13. Predicted acceleration time histories at the top block of the quay-wall (top) and at the backfill 2m below to surface (bottom).

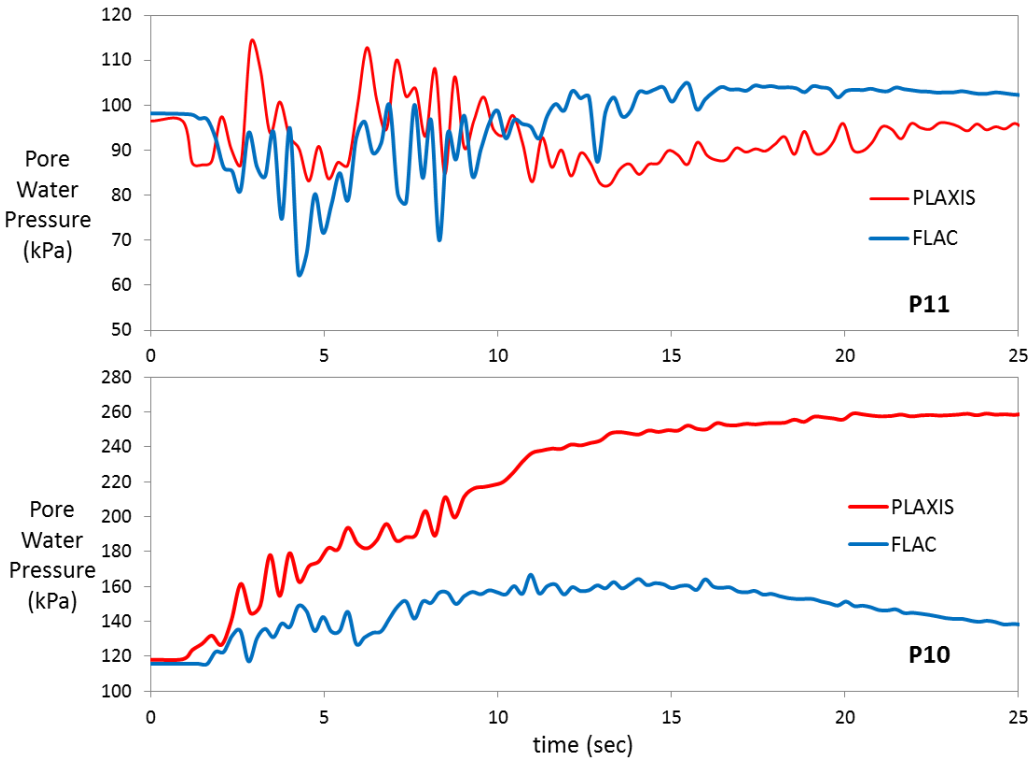


Figure 14. Predicted pore water pressures at locations shown in Figure 1.

ACKNOWLEDGEMENT

This research has been co-financed by the European Union (European Social Fund – ESF) and Greek national funds through the Operational Program "Education and Lifelong Learning" of the National Strategic Reference Framework (NSRF) - Research Funding Program: Thales. Investing in knowledge society through the European Social Fund, Project ID "UPGRADE".

REFERENCES

[1] Pitilakis K. and Moutsakis A., Seismic analysis and behaviour of gravity retaining walls – the case of Kalamata harbour quaywall. *Soil and Foundations*, **29**(1), 1-17, 1989.

[2] Egan J.A., Hayden R.F., Scheibel. L.L., Otus M., Serventi G.M., Seismic repair at Seventh Street Marine Terminal. *Grouting Soil Improvement and Geosynthetics, Geotechnical Special Publication, ASCE*, **30**, 867-878, 1992.

[3] Iai S., Matsunaga Y., Morita T., Miyata M., Sakurai H., Oishi H., Ogura H., Ando Y., Tanaka Y., Kato M., Effects of remedial measures against liquefaction at 1993 Kushiro – Oki earthquake. *Proc. Fifth U.S. – Japan Workshop on Earthquake resistant design of Lifeline Facilities and Countermeasures against Soil Liquefaction*, National Center for Earthquake Engineering Research, NCEER-94-0026, 135-152, 1994.

[4] Sugano T., and Iai S., *Damage to port facilities*. The 1999 Kocaeli Earthquake Turkey – Investigation into Damage to Civil Engineering Structures, Earthquake Engineering Committee, Japan Society of Civil Engineers, 6-1 – 6-14, 1999.

[5] Zarzouras O., Gerolymos N., Gazetas G., Seismic Response of Caisson Quay-Wall in a Liquefied Environment. Analysis of a Case History. *Proc. of the 6th Hellenic Conference on Geotechnical and Geoenvironmental Engineering*, Vol. 1, 549–556, Volos, Greece, September 29–October 1, 2010.

[6] Tasiopoulou P., Gerolymos N., Tazoh T. and Gazetas G., Pile-Group Response to Large Soil Displacements and Liquefaction: Centrifuge Experiments Versus a Physically Simplified Analysis. *Journal of Geotechnical and Geoenvironmental Engineering, ASCE* , **139**(2), 223-233, 2013.

[7] Tasiopoulou P., Gerolymos N, Gazetas G., Seismic Effective Stress Analysis of Gravity Block-Type Quay Walls: Application to Piraeus Port. *2nd European Conference on Earthquake Engineering and Seismology*, Istanbul, Turkey, 24-29 August, 2014.

[8] Inagaki H., Iai S., Sugano T., Yamazaki H. and Inatomi T., Performance of caisson type quay walls at Kobe port. *Soils and Foundations*, Special Issue on Geotechnical Aspects of the January 17 1995 Hyogoken-Nambu Earthquake, 119-136, 1996.

[9] Anastasopoulos I., Loli M., Antoniou M., Knappet J., Brennan A., Centrifuge testing of multi-block quay walls. *SECED 2015 Conference: Earthquake Risk and Engineering towards a Resilient World*, Cambridge UK, 9-10 July 2015.

[10] Itasca, *Fast Lagrangian Analysis of Continua*, Itasca Consulting Group Inc., Minneapolis, Minnesota, 2005.

[11] Puebla H., Byrne P.M. and Phillips R. Analysis of CANLEX Liquefaction Embankments: Prototype and Centrifuge Models. *Canadian Geotechnical Journal*, **34**(5), 641-657, 1997.

[12] Beaty M. and Byrne P., An effective stress model for predicting liquefaction behaviour of sand. *Geotechnical Earthquake Engineering and Soil Dynamics III, ASCE Geotechnical Special Publication*, **75**, 766-777, 1998

[13] Beaty M. and Byrne P., *UBCSAND constitutive model, Version 904aR*. Documentation Report: UBCSAND constitutive model on Itasca UDM Web Site, 2011.

[14] Galavi V., Petalas A. and Brinkgreve R.B.J, Finite element modeling of seismic liquefaction in soils. *Geotechnical Engineering Journal of the SEAGS & AGSSEA*, **44**(3), 55-64, 2013.

[15] Zienkiewicz, O.C., Bicanic N. and Shen F.Q., Earthquake input definition and the transmitting boundary conditions. *Proceedings of Advances in Computational Nonlinear Mechanics I*, Doltsinis (eds), Springer-Verlag, 109-138, 1988.

[16] Gerolymos N., Giannakou A., Anastasopoulos I., Gazetas G., Evidence of Beneficial Role of Inclined Piles: Observations and Summary of Numerical Analyses. *Bulletin of Earthquake Engineering*, **6**(4), 705-722, 2008.

[17] Zafeirakos A. and Gerolymos N., On the Seismic Response of Under-Designed Caisson Foundations. *Bulletin of Earthquake Engineering*, **11**(5), 1337-1372, 2013.

[18] Idriss, I. M. and Boulanger, R. W., *Soil liquefaction during earthquakes*, Monograph MNO-12, Earthquake Engineering Research Institute, Oakland, CA, 2008.

[19] Kammerer J W., Riemer M., Pestana J. and Seed R., A new mult-directional direct simple shear testing database. *13th World Conference on Earthquake Engineering*, Vancouver, B.C., Canada, Paper No. 2083, August 1-6, 2004.

[20] Sriskandakumar, S., *Cyclic loading response of fraser sand for validation of numerical models simulating centrifuge tests*. Master's thesis. The University of British Columbia, Department of Civil Engineering, 2004.

[21] Tatsuoka F., Ochi K., Fujii, S. and Okamoto, M., Cyclic triaxial and torsional strength of sands for different preparation methods. *Soils and Foundations*, **26**(3), 23-41, 1986.

[22] Tasiopoulou, P. and Gerolymos, N., Development of a modified elastoplasticity model for sand. *Proceedings of the Second International Conference on Performance–Based Design in Earthquake Geotechnical Engineering*, Taormina (Italy), 28-30 May, 2012.

COMPDYN 2015
5th ECCOMAS Thematic Conference on
Computational Methods in Structural Dynamics and Earthquake Engineering
M. Papadrakakis, V. Papadopoulos, V. Plevris (eds.)
Crete Island, Greece, 25–27 May 2015

Static and Dynamic Analyses of Dahr El Baidar Slope

T. Matar[1], F. Hage Chehade[2], J. Harb[3], M. Rahhal[4], D. Youssef Abdel Massih[5], C. Abdallah[6], E. Ibrahim[7], L. Khalaf-Keyrouz[8], G. Nasr[9], G. Abou-Jaoude[10], and A. Sursock[11]

[1]Lebanese U., F. of Eng., Modeling Center, Doctoral School of S. and T., Lebanon, therese.matar@gmail.com
[2]Lebanese University, Modeling Center, Doctoral School of S. and T., Lebanon, fchehade@ul.edu.lb
[3]Notre Dame University Louaize, Lebanon, jharb@ndu.edu.lb
[4]Saint Joseph University, ESIB, Lebanon, muhsin.rahal@usj.edu.lb
[5]Lebanese University, Faculty of Engineering II, Roumieh, Lebanon, dalia.abdelmassih@ul.edu.lb
[6]Lebanese National Council For Scientific Research, Remote Sensing Center, Lebanon , chadi@cnrs.edu.lb
[7]Notre Dame University Louaize, Lebanon, eibrahim@ndu.edu.lb
[8]Notre Dame University Louaize, Lebanon, lkhalaf@ndu.edu.lb
[9]Lebanese University, Faculty of Engineering II, Roumieh, Lebanon, george.j.nasr@gmail.com
[10]Lebanese American University, Beirut, Lebanon. grace.aboujaoude@lau.edu.lb
[11]Lebanese National Council For Scientific Research, Geophsyical Center, Lebanon, asursock@cnrs.edu.lb

Keywords: slope stability, seismic movement, failure, geotechnical investigation, geophysical tests, correlation, soil properties, dynamic response.

Abstract. *The slope of Dahr El Baidar located on the central mountain of Lebanon hosts a section of the Arab Highway that is under construction to connect Beirut to neighboring Arab countries. This slope has experienced several failures; yet most involved geotechnical companies have investigated the slope with classical geotechnical procedures. In this paper, the analysis of the slope is performed using an integrated geo-assessment approach to identify the principal causes of failure and understand its dynamic behavior. The study includes geological, geophysical and geotechnical soil characterization of the designated area. The geological analysis reveals the presence of faults in the vicinity, in addition to a layer of weak clay at the surface. The geotechnical investigation is based on the interpretation of several boreholes. Geophysical tests are performed using ambient noise vibration technique in order to reveal the resonant frequency and thickness of the soil deposit material. A correlation between geotechnical and geophysical tests was used to establish soil properties in the studies. The above data is used towards a better understanding of the cause and occurrence of the failing zone. A dynamic analysis is conducted to determine the slope amplification and compare the simulated frequencies with the measured ones.*

T. Matar[1], F. Hage Chehade[2], Jacques Harb[3], M. Rahhal[4], D. Youssef Abdel Massih[5], C. Abdallah[6], E. Ibrahim[7], L. Khalaf-Keyrouz[8], G. Nasr[9], G. Abou-Jaoude[10], and A. Sursock[11]

1 INTRODUCTION

Estimations over the last 40 years indicate that mass movements cost each year 10-15 millions of US dollars in this small country (Lebanon) with numerous fatalities and injuries (Khawlie, 2000). Cracks in houses and roads, destruction of agricultural terraces, and scarps of different sizes are very common. Minor movements occurred in other years. Climatic and geological parameters combined with human modifications of land act simultaneously towards increasing mass movements in Lebanon.

As geological parameters have major influence in land movements, some of these large movements in Lebanon have been correlated with major earthquakes. On the other hand, climatic conditions also play an important role whereas, for example, periods of heavy precipitation in the mid to late winter season trigger landslides. Another major parameter affecting land movement is extensive man-induced activities and land alterations such as road and residential construction, deforestation, quarrying, or changing the water regime in irrigation and drainage diversion. Chaotic and rapid urban growth, which is spread throughout the country, is one of the principal causes of natural resource depletion that induces natural hazards such as desertification, mass movement, flash floods, etc. Studies dealing with mass movements (MM) in Lebanon seem to be few and mostly descriptive, yet a few cited works tackled the problem. The first to talk about landslides in Lebanon was Dubertret (1945). He included some description on landslides in the various texts "Notice de la Carte Géologique". He delineated different types of landslides, rock falls and mudflows. Tavitian (1974) studied the Aquoura earthflow giving the engineering properties of the materials and slope stability. Khawlie and Hassanain (1984) studied the phenomenon over several areas in Lebanon giving the types and distinctive features of various occurrences. They related it to different natural and human causes, interpreting both its geological and engineering dimensions. Other studies have dealt indirectly with the subject focusing on instability of surficial materials, e.g. the engineering geological evaluation of marls (Khawlie and Ghalayini, 1985), or the analysis of the terrain and materials in assessing stability of highways (Khawlie and A'war, 1992), or the inherent lithological and geotechnical variability of the basal Cretaceous sandstone (Khawlie and Touma, 1993). The majority of previously mentioned studies treated mass movement phenomenon depending on field work purposes. Sadek, et al., (1999) has started with preliminary and simple modeling for assessing road instability in their studies related to mass movement hazards and slope stability. Rahhal et al. (2003) and Rahhal (2014) discussed the factors triggering slope instabilities in Lebanese mountains, as well as the determination of factors of safety for slopes under earthquake loading. Abdallah et al, (2005) used univariate statistical correlations to determine simple relations between classes of terrain parameters and mass movement occurrence. Youssef Abdel Massih et al. (2007), (2010) have used finite element and finite difference methods for evaluating the stability of some slopes. Several other techniques based on satellite images (Abdallah et al. 2007) were used for assessing mass movement hazard in Lebanon.

In the continuity with the geo-assessment of Dahr el Baidar slope made by Rahhal et al. (2014),, this paper presents static and dynamic stability analyses of Dahr El Baidar slope in Lebanon. The first objective of this research is to understand the causes that lead to slope failure using geotechnical and geophysical investigations. Then, 2D and 3D finite element and finite difference models are used to check the behavior of the slope under earthquake conditions.

2 SITE LOCATION

Dahr El Baidar is located at 33º48'18"N 35º45'42"E on the slope of a mountainous area in the center of Lebanon. The site is hosting a portion of the "Pan Arab Highway", a main road connecting the coastal zone to the Bekaa valley reaching east the Lebanese Syrian border. It is a vital infrastructure project that has been delayed at several instances due to slope stability problems. In-spite of the numerous geotechnical investigations, this particular site still presents a challenge to designers and contractors as a result of its complexity.

3 SOIL INVESTIGATION

3.1 Geology and tectonic of the region

The major tectonic features in Lebanon surrounding Dahr El-Baidar are (i) the Yammouneh Fault which is part of the Levantine fault extending from the Aquaba golf, passing by the Jordan valley and Dead Sea, Bekaa valley and north to the Taurus Zaghros Mountains of Turkey; (ii) the Roum Fault which is a branching of the Levantine Yammouneh fault starting from Roum village South, and extending North-West up to the capital Beirut and (iii) the Occidental flexures parallel to the Yammouneh fault regrouping a multitude of minor faults with variable activities. The Dahr el-Baydar slope is located on the center of Mount Lebanon, in a zone distanced around 5 kilometers from the Yammouneh fault, 31 km from the coastal line and 26 km from the Roum fault. The area is characterized by a significant tectonic activity. The plateau of Dahr El Baidar is a rock formation ranging from the lower to middle cretaceous (C_1 to C_3 respectively); around 6 km west of the Yammouneh fault (Dubertret, 1945). This area is positioned in a subducted zone, bounded by two minor East-West faults and highly scattered by other minor faults connected to the Yammoueh fault. The predominant ones are (i) The Kab-EliasWadi El-Delm fault, 3.5 km south in the East-West direction, limiting the Jurassic plateau of Jabal El Barouk against the depression of Dahr El Baidar, (ii) a portion of the Yammouneh fault extending around 6 km oriented NNE-SSW to the East, and (iii) a 2km stretch of Jabal El Roueiss fault in the E-W orientation. The system of faults is active however, their individual activity is difficult to trace due to the lack of instrumentation on site and close vicinity.

3.2 Geotechnical and Geophysical investigation

Aiming to study the most probable cause of the slopes failure in this region, an experimental campaign was carried out. Eight geotechnical boreholes were drilled in the area (Noted AB in Figure 1).

Table 1 shows the location (coordinates, and altitude) of the different boreholes, as well as the depth reached.

Twelve HVSR (or H/V) ambient vibration tests (Nogoshi and Igarashi (1971), Nakamura (1989)) were conducted on Dahr El Baidar site (Noted by a pin in Figure 1) using Lennartz-5s velocimeters (cut-off period of 5 seconds) connected to a CityShark^{TM} acquisition unit (Chatelain et al., 2000) with a 200 Hz sampling rate.

Geopsy software (http://www.geopsy.org; Wathelet et al. 2008) is used to compute the H/V spectral ratios of the registered ambient noise at several locations. A b-value of 40 was used in the smoothing procedure of Konno & Ohmachi (1998) for the computed Fourier amplitude spectra. The two horizontal components (North-South and East-West) are then combined by computing the quadratic mean and H/V ratios calculated by averaging the H/V ratios obtained

on individual 10s windows. The peak observed at the H/V spectrum will be considered as the natural frequency of the soil at the location of the test.

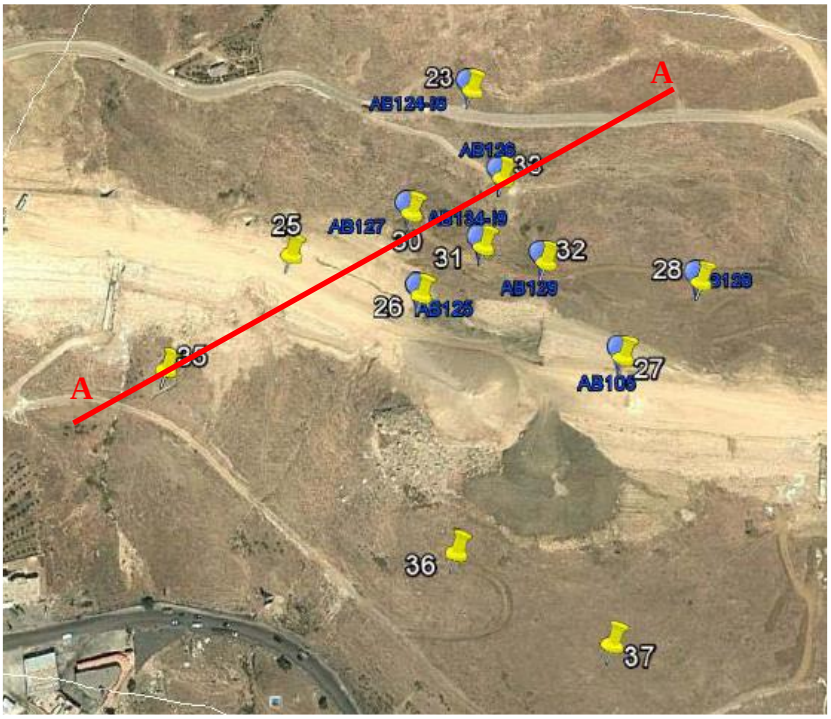


Figure 1: Site Location (from Google earth) including the location of the Pan Arab Highway, HVSR tests and Boreholes.

Table 1: Borehole Local Coordinates, Altitude, Depth reached and date realized.

Borehole	Local X	Local Y	Altitude above sea level (m)	Depth (m)
AB 105	-310399.52	-38422.13	1313.83	16
AB 125	-310528.57	-38393.22	1322.18	20
AB 126	-310482.90	-38314.05	1350.21	35
AB 127	-310539.69	-38340.86	1338.52	30
AB 128	-310352.51	-38369.13	1321.38	30
AB 129	-310452.10	-38366.86	1333.07	30
AB 134	-310491.86	-38360.21	1337.96	20

4 GEOTECHNICAL AND GEOPHYSICAL DATA ANALYSIS

4.1 Geotechnical Results

In section A-A (Figure 2), the water table is deep and the following soil layers and properties are considered: At the surface, a marly fill is found next to the crack line. Then, cemented brown sand with presence of clay of low plasticity (CL) is identified with the following shear strength properties (an effective cohesion c’ = 44kPa and an effective friction angle ϕ' = 17°, a plasticity

index of PI=18%, and a Standard Penetration Test number SPT N =11). Below, a clayey sand is found (c' = 26kPa and ϕ' = 25.8°, PI=14%, and SPT N =21). A greyish marl and limestone (with pressumeter results giving Limit Pressure P_l = 2.7 MPa and Menard elastic modulus E_m = 43.5 MPa) is interbedded between two clay layers with different properties: the upper clay has a P_l = 420 kPa, and E_m = 3.3MPa, while the lower clay has a P_l = 2.8 MPa and E_m = 163 MPa. In depth, marl with different colors (brown, grey and beige) is found with P_l = 3.9 MPa and E_m = 121 MPa. Below, Marly Sandstone is identified

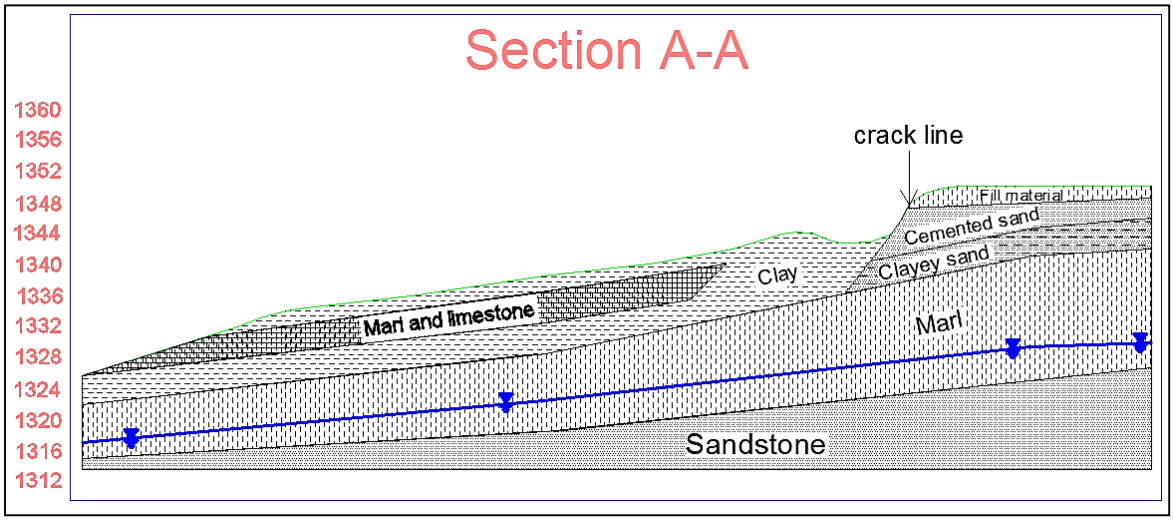


Figure 2: Soil Layers in section A – A

4.2 HVSR Geophysical Results

Due to the site heterogeneity, no clear H/V peak frequency is observed at some points. However, a dominant frequency f_0 between 3 and 5.5Hz is noticed on most of the H/V measurements. The estimated f_0 from the HVSR measurements at the borehole locations with the corresponding depth D of soft soil to the stiffer layer are reported on Table 2. Equation 1 is used:

$$f_0 = \frac{V_S}{4H} \qquad \text{Eq.1}$$

Where
f_0 is the fundamental soil frequency
H is the depth of the soft layer to the bedrock
V_s is shear wave velocity of the softer layer

For values of Table 2, the shear wave velocity will range from 100m/s to 300m/s.

5 STATIC ANALYSIS ON THE SITE

A static analysis of Dahr El Baidar slope is performed using Plaxis software (Vermeer & Brinkgreve, 1998) based on the Mohr-Coulomb model material for soil behavior. Section A (Figure 2) with same coordinates presented in the geotechnical study is modeled hereafter. Soil properties shown in table 3 based on available soil data are used in the model.

Table 2: f_0 and shear wave velocity

HVSR tests	**Bore-hole**	**f_0 (Hz)**	**D (m)**	**V (m/s)**
Pt 23	AB 124	3.2	12.5	160
Pt 25		3.2		
Pt 26	AB 125	3.5	11	154
Pt 27	AB 105	5.5	4	88
Pt 28	AB 128	3.1	8	100
Pt 30	AB 127	3.8	20	304
Pt 31	AB 134	3.4	13	177
Pt 32	AB 129	No clear Peak		
Pt 33	AB 126	2.9	15	174
Pt 35		No clear Peak		
Pt 36		No clear Peak		
Pt 37		No clear Peak		

Table 3: Soil properties used in Plaxis model.

Soil Layer	Cohesion (MPa)	Friction Angle (degrees)	Dilancy Angle (degrees)	Young Modulus (MPa)	Poisson Ratio
Cemented Sand	44	17	9	23	0.2
Clayey Sand	26	25.8	13	25.6	0.2
Marl &lime-stone	28	24	12	43.5	0.2
Clay	41	12.4	7	16	0.2
Marlstone	33	24	12	62	0.2
Clayey Marl	32	18	9	10	0.2
Sandy Clay	41	12	6	25.6	0.2
Marl	24	26	13	28	0.2
Sandstone	5	30	15	24	0.3

As a result, the most probable failure surface appears at the interface Clay/Marl. The top layer of clay is sliding as shown in figure 3 below.

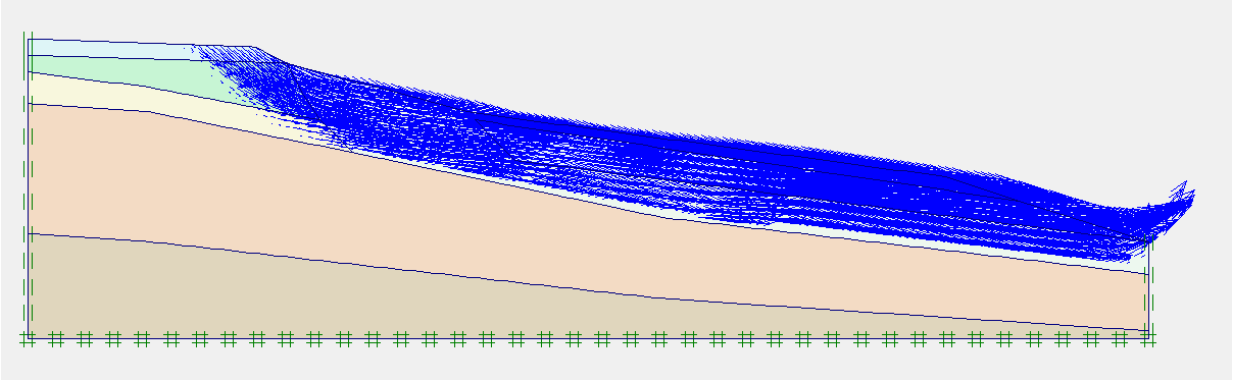


Figure 3: Failure surface of section A – at the interface Marl and clay

The initial conditions determined above reveal the state of the site at the time of soil investigation, where the slope is stable with a factor of safety of 2.9
In order to illustrate the state of the site where failure occurred, an interface is set at the top layer of Marl. This interface element will allow decreasing the mechanical properties of Marl at its interface with clay by choosing a suitable value for the strength reduction factor (R_{inter}). This factor relates the interface strength to the soil strength (c_i and φ_i , friction angle and cohesion) by:

$$c_i = R_{inter} x c_{soil} \quad \text{Eq.2}$$

$$\tan\varphi_i = R_{inter} \tan\varphi_{soil} \leq \tan\varphi_{soil} \quad \text{Eq.3}$$

where c_{soil} and φ_{soil} are respectively the cohesion and friction angle of the soil.
A total collapse of soil is seen once Marl properties decreases 1/3 as summarized in the following table:

Table 4: Mechanical properties of Marl interface.

	Initial conditions	At Total failure
Cohesion (kPa)	28	10
Friction Angle (degrees)	24	10
R_{inter}	1	0.3
F.S.	2.9	Close to 1 (i.e. Collapse)

As the soil properties at the time of slide triggering are unknown and after obtaining such results in the models, it is suspected that the main triggering factor is water. As we know, soils properties are affected by the presence of water especially the soils with very high fine contents (marl and clay). These soils lose an important part of their cohesion in the presence of water, reducing at the same time their shear strength.

Knowing that a 2D model do not represent accurately the failure shape and the complete behavior and heterogeneity of the site, a 3D model was conducted using FLAC^{3D} software. The soil is assumed to be composed by 3 layers: Clay, Marl and Sandstone in a Mohr Coulomb model with average values of soil properties obtained by geotechnical tests as shows the following figure.

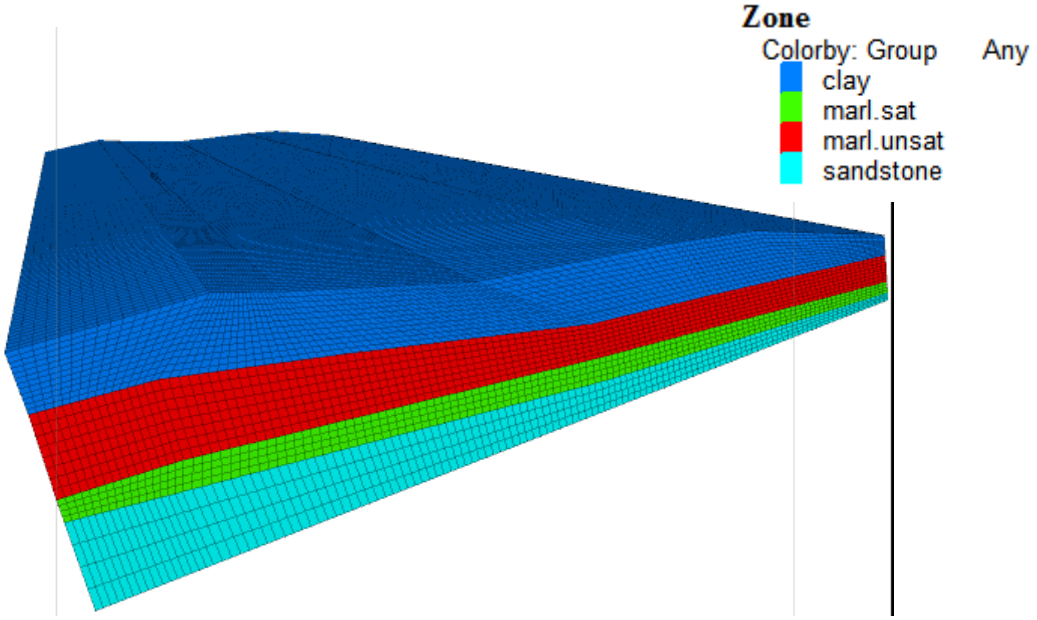


Figure 4: FLAC^{3D} static model

After using the shear strength reduction technique to determine the 3D slope safety factor, the failure surface obtained is the same as the one in the 2D section A, at the interface of Marl and Clay as shown in figure 5.

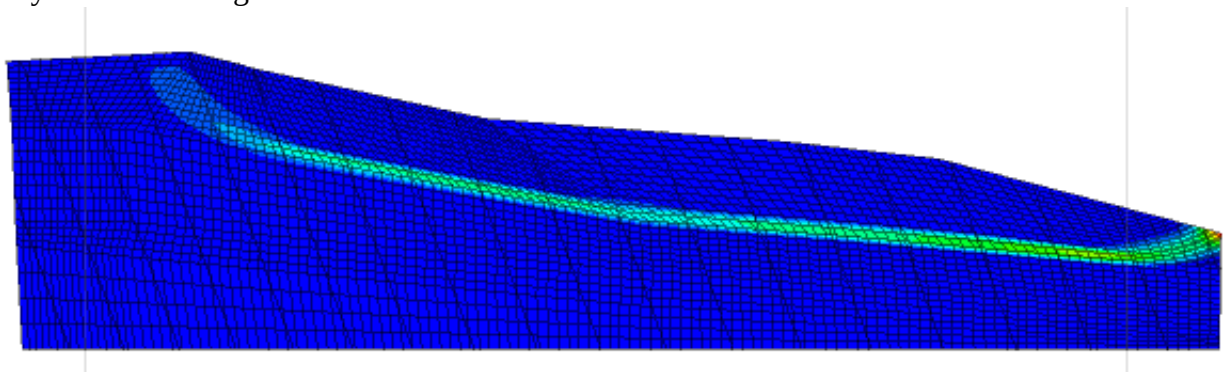


Figure 5: Section showing Failure surface of the 3D model

The safety factor of the slope in 3D model is 3.25 which is close to the one obtained by the 2D model (equal to2.9). So it can be concluded that the 3D model confirmed the results already found in the 2D model.

6 DYNAMIC ANALYSIS ON THE SITE

For the dynamic model, the same soil properties, water table level, boundary conditions and initial stresses are considered.
A mesh of 0.5m*0.5m*0.5m is used, satisfying the condition that the dimension of an element should not exceed λ/10, where λ is the minimal wavelength. $\lambda = Vs_{min}/f_{max}$ where Vs_{min}, the smallest shear wave velocity is 88m/s and f_{max} the maximum signal frequency is 20Hz.

As for dynamic boundaries, free field conditions are applied to lateral boundaries and quiet boundaries at the base in order to reduce wave reflections and model a half space at the base. Dynamic input is applied to the model using a table signal with a time step of 0.01s and a frequency varying from 1 to 20Hz. This table is converted in stresses to apply a velocity wave in the horizontal plane according to the following equation:

$$\sigma_s = 2(\rho V_s)\, v_s \qquad \text{Eq.4}$$

where: σ_s= applied shear stress
ρ= mass density of the bedrock
V_s= speed of s-wave propagation of the bedrock
v_s = input shear particle velocity
and V_s is given by:

$$V_s = \sqrt{(G/\rho)} \qquad \text{Eq.5}$$

where G is the shear modulus of bedrock.
Note that the input signal is a delta like signal of flat spectrum as shown in figure 6, in order to be able to observe clearly the amplification response for all frequencies ranging between 1 and 20 Hz.

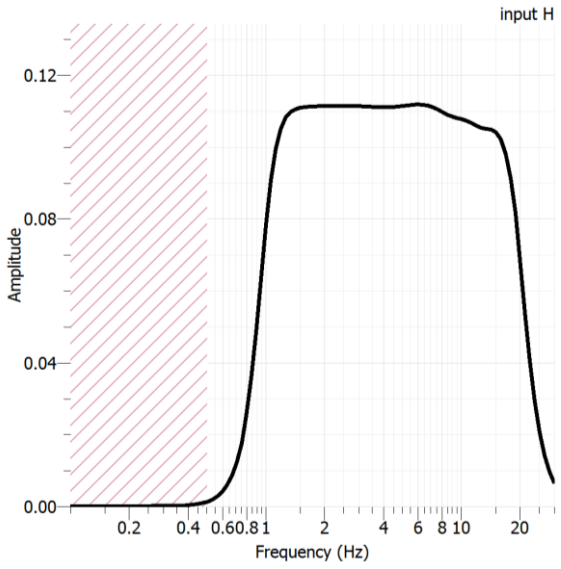


Figure 6: input spectrum

The shear wave velocity is plotted for 7 selected points. The time step of the dynamic output is 0.00172s as calculated by FLAC^{3D}. The output velocity is re-sampled in order to obtain the response with the same time step as the input signal. The figures below show the velocity spectrum of points A, B, C, D, E, F and G (cf. Figure 7) in X, Y and Z directions.

T. Matar[1], F. Hage Chehade[2], Jacques Harb[3], M. Rahhal[4], D. Youssef Abdel Massih[5], C. Abdallah[6], E. Ibrahim[7], L. Khalaf-Keyrouz[8], G. Nasr[9], G. Abou-Jaoude[10], and A. Sursock[11]

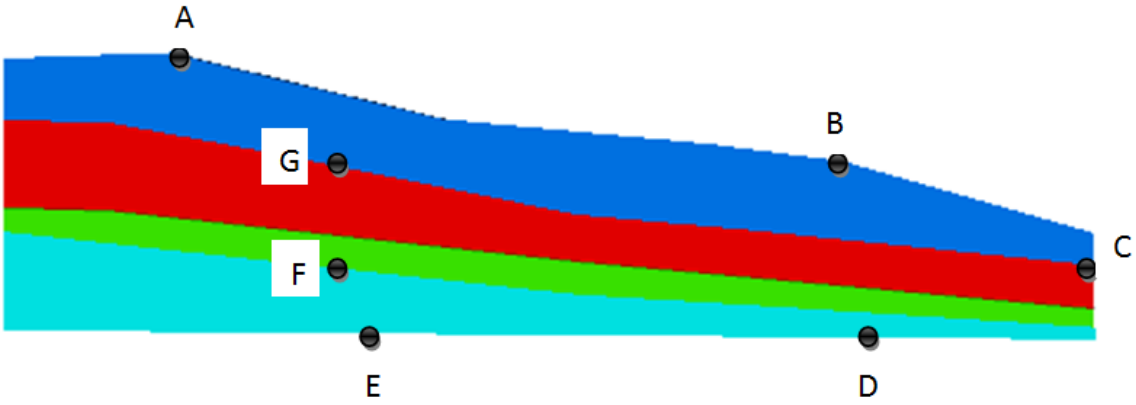


Figure 7: Selected points

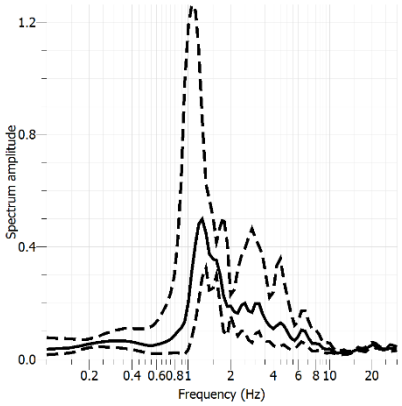


Figure 8: point A spectrum

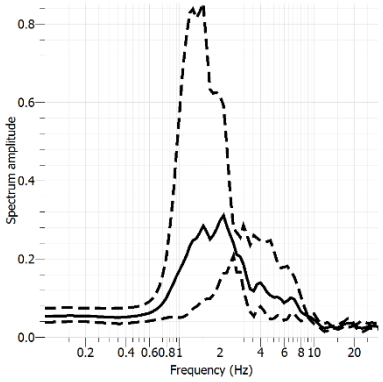


Figure 9: Point B spectrum

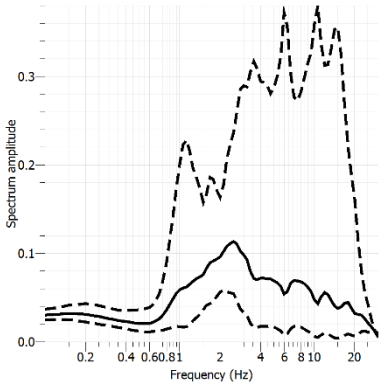


Figure 10: Point D spectrum

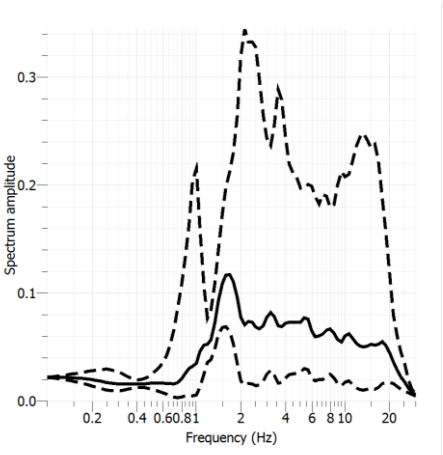


Figure 11: Point E spectrum

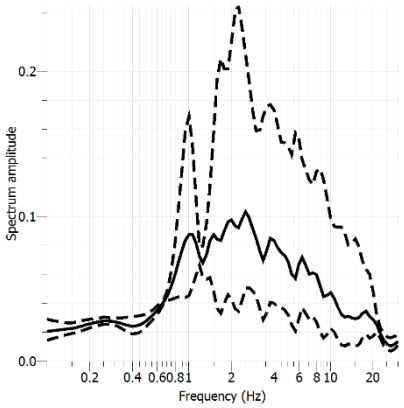


Figure 12: Point F spectrum

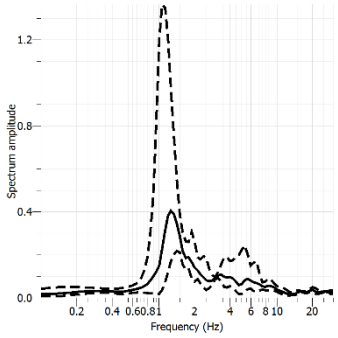


Figure 13: Point G spectrum

One can notice that at points A, B and G (Figures 8, 9 and 13), a first amplification between 1 and 2 Hz and a second amplification between 3 and 4 Hz. The first amplification may be caused by an industrial activity (confirmed by the H/V tests) and the second amplification matches well with the natural frequency found in the geophysical test. The results indicate the importance of understanding the role of soft material, especially clayey soils, in amplifying soil movements whenever this type of soils is found on top of a more rigid formation which is in our case sandstone. For points D, E and F (Figures 10, 11 and 12) at proximity of sandstone, no clear peak is observed.
After comparing the spectrums of points A and B in horizontal direction with the input signal spectrum, it is found that an important amplification is obtained between 0.1 and 8 Hz.

As a conclusion, the results of the dynamic analysis were in good agreement with the frequencies obtained by the H/V tests and have shown high amplification for a wide frequency range.

7 CONCLUSIONS

In this paper, an integrated geo-assessment is conducted on Dahr El Baidar slope – Lebanon that hosts a section of the Arab Highway under construction. The geological analysis shows the presence of faults in the vicinity as well as a layer of weak clay at the surface. The geotechnical investigation is based on the interpretation of 7 boreholes. Geophysical tests are performed using ambient noise vibration technique based on the HVSR method. The analysis of soil data based on the cross sections reveals a high fine percent, and fine soils loose an important part of their cohesion in the presence of water, due to the reduction of their shear strength. It is suspected that the failure is probably induced at the interface of two materials with different rigidities or within a soft material itself. Similarly, the dynamic analysis reveals that the natural frequency found by the geophysical tests is accurate and there is an important amplification at the surface once a dynamic wave is applied.

Further analysis is needed to evaluate the slope failure under earthquake loading and additional geophysical tests are also necessary to better estimate the dynamic properties of the soil. Scenarios of the different cross sections will be examined later to determine the static and dynamic failure surfaces and examine the triggering factors behind the slope instabilities.

ACKNOLEDGMENT

This work is part of the assessment and prediction of the behavior of various critical slopes in Lebanon carried by RUMMARE, a Research Unit on Mass Movement hazard Assessment and Risk Evaluation grouping researchers from major universities and research centers in Lebanon. The contributions of graduate students Akram Ghsossoub and Anthony Fayad should be acknowledged. The RUMMARE researchers would like to thank the Lebanese National Council for Scientific Research for funding this unit.

REFERENCES

[1] Abdallah, C., Chorowicz, J., Bou Kheir, R., Khawlie, M., 2005. "Detecting major terrain parameters relating to mass movements' occurrence using GIS, remote sensing and statistical correlations, case study Lebanon." *Remote Sensing of Environment*, 99, 448-461.

[2] Abdallah, C., Chorowicz, J., Bou Kheir, R., Dhont, D., 2007. "Comparative use of processed satellite images in remote sensing of mass movements: Lebanon as a case study." *International Journal for Remote Sensing*, 28:19, 1 - 20.

[3] Dubertret, L., (1945). "Geological Map of Zahlé, 1/50,000. " Ministry of National Defence-Geography Department, Lebanon.

[4] Dubertret, L. (1960). "Carte Géologique au 50000 Feuilles de Hermon." Institut Geographique National, Beirut, Lebanon

[5] Khawlie, M. (2000). "L'environnement du Liban : une ressource perdue (en arabe)." Menrikh publisher, 372p.

[6] Khawlie, M., and Hassanain, H. (1984). "Failure phenomena and environmental control of the relatively unstable Hammana area, Lebanon." Engineering Geology, 20, 253-264.

[7] Khawlie, M., Ghalayini, I., (1985). "Geological evaluation of marls in relation to their mass behavior, Achrafieh area, Beirut." *The Lebanese Science Bulletin*, 1(1), 83-98.

[8] Khawlie, M., A'war, R., (1992). "Terrain evaluation for assessment of highways in the mountainous eastern Mediterranean of Lebanon." *Bulletin of the international association of engineering geology*, 46, 71-78.

[9] Khawlie, M., Touma, G., (1993). "Determining the behavior of the highly variable basal cretaceous sandstone (Nubian Facies) in Brummana Lebanon." *Lebanese Science Bulletin*, 6(1), 33-45.

[10] Konno, K. and T. Ohmachi, (1998). "Ground-motion characteristics estimated from spectral ratio between horizontal and vertical components of microtremor." Bulletin of the Seismological Society of America, 88(1), 228-241.

[11] Nakamura,Y., (1989). "A method for dynamic characteristics estimation of subsurface using microtremors on the ground surface." *Quarterly reports of the Railway*, Technical Research Institute, Tokyo, 30, 25–33.

[12] Nogoshi M. and Igarashi T. (1971). "On the amplitude characteristics of microtremor." *Journal of seismological Society of Japan*, 24, 26-40.

[13] Rahhal, M.E., Nini, R., Favre, J.L. (2003) *Analysis of Factors Causing Slope Instabilities,* Proceedings 56th Canadian Geotechnical Conference, Winnipeg, Manitoba, CANADA, Volume 2: pages 368-375.

[14] Rahhal, M.E. (2014) *The Factor of Safety in Slopes under Earthquake loading*, Geo Congress 2014- Atlanta USA, ASCE Geotechnical special Publication No 234: pages 1274-1283.http://dx.doi.org/10.1061/9780784413272.124

[15] Rahhal, M., Youssef Abdel-Massih, D., Harb, J., Hage-Chehade, F., Abdallah, C., Khalaf-Keyrouz, L., Abou Jaoude, G., Ibrahim, E., Nasr, G., Sursock, A. (2014). *Modelling Dahr El Baidar Slope with integrated geo-assessment*, Proceedings, Second European Conference on Earthquake Engineering and Seismology, Istanbul, TURKEY, August 25-29, 2014.

[16] Sadek S., M. Bedran, and I. Kaysi (1999) "A GIS Platform for Multi-Criteria Evaluation of Route Alignments," *Journal of Transportation Engineering*, Vol. 125 No.2, pp. 44-152.

[17] Tavitian, C. (1974). "Clay mineralogy and geotechnical properties of cretaceous clay-shales in Lebanon." Ph.D. thesis, University of Salford, 247p.

[18] Vermeer P.A. & Brinkgreve R.B.J. ″PLAXIS Finite element code for soil and rock analyses″, version 7, Rotterdam : Balkema (1998).

[19] Wathelet, M., D. Jongmans, M. Ohrnberger, and S. Bonnefoy-Claudet (2008). "Array performances for ambient vibrations on a shallow structure and consequences over Vs inversion." *Journal of Seismology*, **12**, 1-19.

[20] Youssef Abdel Massih D., Soubra, A.H., Harb J. & Rouania, M. (2010). "Dynamic slope stability analysis by a reliability-based approach." *Fifth International Conference on Recent Advances on Geotechnical Earthquake Engineering and Soil Dynamics*, San Diego, California, May 24-29 2010,10p.

[21] Youssef Abdel Massih D., Soubra A.-H. and El-Hachem E. (2007). "Slope stability analysis in seismic areas by a reliability approach". *4th International Conference on Earthquake Geotechnical Engineering (4ICEGE)*, Thessaloniki, Greece, 25-28 June, 12p.

COMPDYN 2015
5th ECCOMAS Thematic Conference on
Computational Methods in Structural Dynamics and Earthquake Engineering
M. Papadrakakis, V. Papadopoulos, V. Plevris (eds.)
Crete Island, Greece, 25–27 May 2015

A SEISMIC PERFORMANCE-BASED DESIGN APPROACH FOR SLOPE STABILIZING PILES

M. Adinolfi[1], R. Di Laora[1], R.M.S. Maiorano[1], S. Aversa[1]

[1] Università degli Studi di Napoli Parthenope, Napoli, Italy
e-mail: marianna.adinolfi@uniparthenope.it, raffaele.dilaora@uniparthenope.it, rossella.maiorano@uniparthenope.it, stefano.aversa@uniparthenope.it

Keywords: slope stability, slope stabilizing piles, seismic factor of safety, performance based design.

Abstract. *Piles have been used to increase the stability of landslides in static regime for many decades, as they provide resistance against a laterally moving soil mass by transferring the loads into more stable underlying ground.*
Nevertheless, the presence of such a reinforcement has beneficial effects even under seismic shaking. The paper aims at proposing a simple procedure for the estimation of permanent displacements of slopes stabilized with piles. The method is made up of 3 different stages: (a) evaluation of stability conditions of the natural slope and the ultimate load offered by the piles; (b) combination of the two ingredients above, through limit equilibrium considerations, to assess the critical acceleration of the reinforced slope; (c) use of the classical Newmark method to calculate the permanent displacement under specified input motions. A parametric study is also performed to quantify the beneficial effect of piles under earthquake shaking.

1 INTRODUCTION

In the last decades, permanent displacement analysis of slopes in earthquake-prone areas has gained popularity in current engineering practice. This is mainly due to the fact that the traditional capacity-based seismic design of a geotechnical structure (i.e., a pseudo-static analysis with a factor of safety larger than unity) appears to be quite over-conservative, as does not take into account that the seismic action lasts for a short period of time. In reality, a factor of safety temporarily lower than one may lead to acceptable permanent displacement. On the other hand, the use of piles to stabilize active landslides or as a preventive measure in safe slopes has become one of the most common slope reinforcement techniques and, accordingly, numerous methods have been developed for the analysis of piled slopes in static regime by means of analytical [1-6] and numerical [7-9] approaches.

Few contributions [10] investigated the behaviour of reinforced slopes under seismic shaking and, thus, the present paper tries to outline a simple procedure for estimating permanent displacements of the combined pile-slope system. The method involves three steps:

(a) evaluation of stability conditions of the natural slope and the ultimate load offered by the piles in static regime;

(b) combination of the two ingredients above, through limit equilibrium considerations, to assess the critical acceleration of the reinforced slope;

(c) employment of the Newmark method [11] to calculate the permanent displacement under a specified time-history. In addition, the paper presents a parametric study to assess the beneficial effect, in terms of reduction of permanent seismic displacements, offered by statically-designed piles.

2 STABILITY ANALYSIS OF UNREINFORCED SLOPES

Slope stability analysis is generally formulated in terms of the safety factor with respect to soil shearing strength parameters: it is defined as the factor by which the soil shearing strength parameters should be divided to give the condition of incipient failure.

The critical slip surface is the surface that produces the minimum factor of safety in static analysis or the minimum critical acceleration in pseudo-static analysis.

Several methods, based on the principle of limiting equilibrium and the method of slices, are available to find the factor of safety in a rigorous way given a possible failure surface [12-16] and all of these methods require a predefined possible slip surface.

In the method of Sarma [15], used and modified in the following paragraphs, the process of finding the critical slip surface is linked to the technique for finding the minimum factor of safety (or critical acceleration). It was developed as a means of computing the critical horizontal acceleration that is required to bring the mass of soil upon slip surface to a state of limiting equilibrium.

3 ULTIMATE LATERAL LOADS ON SLOPE STABILIZING PILES IN STATIC REGIME

The increase of the safety margin in slope stability depends on the amount of resisting force which can be developed by the pile at the level of the sliding plan and the mechanism of interaction between the sliding soil mass and the pile.

Viggiani [4] proposed analytical expressions for a single rigid pile of length L, crossing an unstable horizontal layer of thickness l_1 and penetrating the underlying stable soil for a length

$l_2 = \lambda\, l_1$. Both layers are modeled as purely cohesive materials and thereby such a formulation is suitable for treating undrained conditions in fined grained soils, where upper and lower layers have undrained shear strength equal to s_{u1} and s_{u2}, respectively. The Author, following an approach derived from that proposed by Broms [17] for piles loaded by transverse loads applied at their upper end, identified 6 possible failure mechanisms, corresponding to a stiff pile having infinite (mechanisms A, B, C) and finite (mechanisms B_1, B_Y, B_2) cross-section yielding moment M_y (Figure 1). Defining the dimensionless quantities:

$$\chi = \frac{k_{u1}\, s_{u1}}{k_{u2}\, s_{u2}} \qquad \lambda = \frac{l_2}{l_1} \qquad m = \frac{M_y}{k_{u1}\, s_{u1}\, d\, l_1^2} \tag{1a,b,c}$$

where k_{u1} and k_{u2} are bearing capacity factors whose values can be taken as 4 and 8 respectively, the shear force offered by the pile for the six mechanisms are found to be[1]:

Mode A

$$\frac{T_A}{k_{u1}\, s_{u1}\, d\, l_1} = \frac{k_{u2}\, s_{u2}\, d}{k_{u1}\, s_{u1}\, d}\frac{l_2}{l_1} = \frac{\lambda}{\chi} \tag{2}$$

Mode B

$$\frac{T_B}{k_{u1}\, s_{u1}\, d\, l_1} = \sqrt{\frac{(1+\lambda)^2}{(1+\chi)^2} + \frac{(\chi+\lambda^2)}{\chi(1+\chi)}} - \frac{(1+\lambda)}{(1+\chi)} \tag{3}$$

Mode C

$$\frac{T_C}{k_{u1}\, s_{u1}\, d\, l_1} = 1 \tag{4}$$

Mode B_1

$$\frac{T_{B1}}{k_{u1}\, s_{u1}\, d\, l_1} = \frac{\lambda}{\chi+2}\left[\sqrt{\frac{2\chi+2}{\chi} + 4\frac{\chi+2}{\lambda^2}m} - 1\right] \tag{5}$$

Mode B_Y

$$\frac{T_{BY}}{k_{u1}\, s_{u1}\, d\, l_1} = 2\sqrt{\frac{m}{(1+\chi)}} \tag{6}$$

Mode B_2

$$\frac{T_{B2}}{k_{u1}\, s_{u1}\, d\, l_1} = \frac{1}{2\,\chi+1}\left[\sqrt{1+(2\,\chi+1)(1+4m)} - 1\right] \tag{7}$$

[1] Expression (5) contains a typographical error in the original work.

For a homogeneous soil ($\chi = 0.5$), the stabilizing shear force corresponding to the minimum value among the above mechanisms are depicted in Figure 2 as function of λ and m. For further details, the reader can refer to the original work.

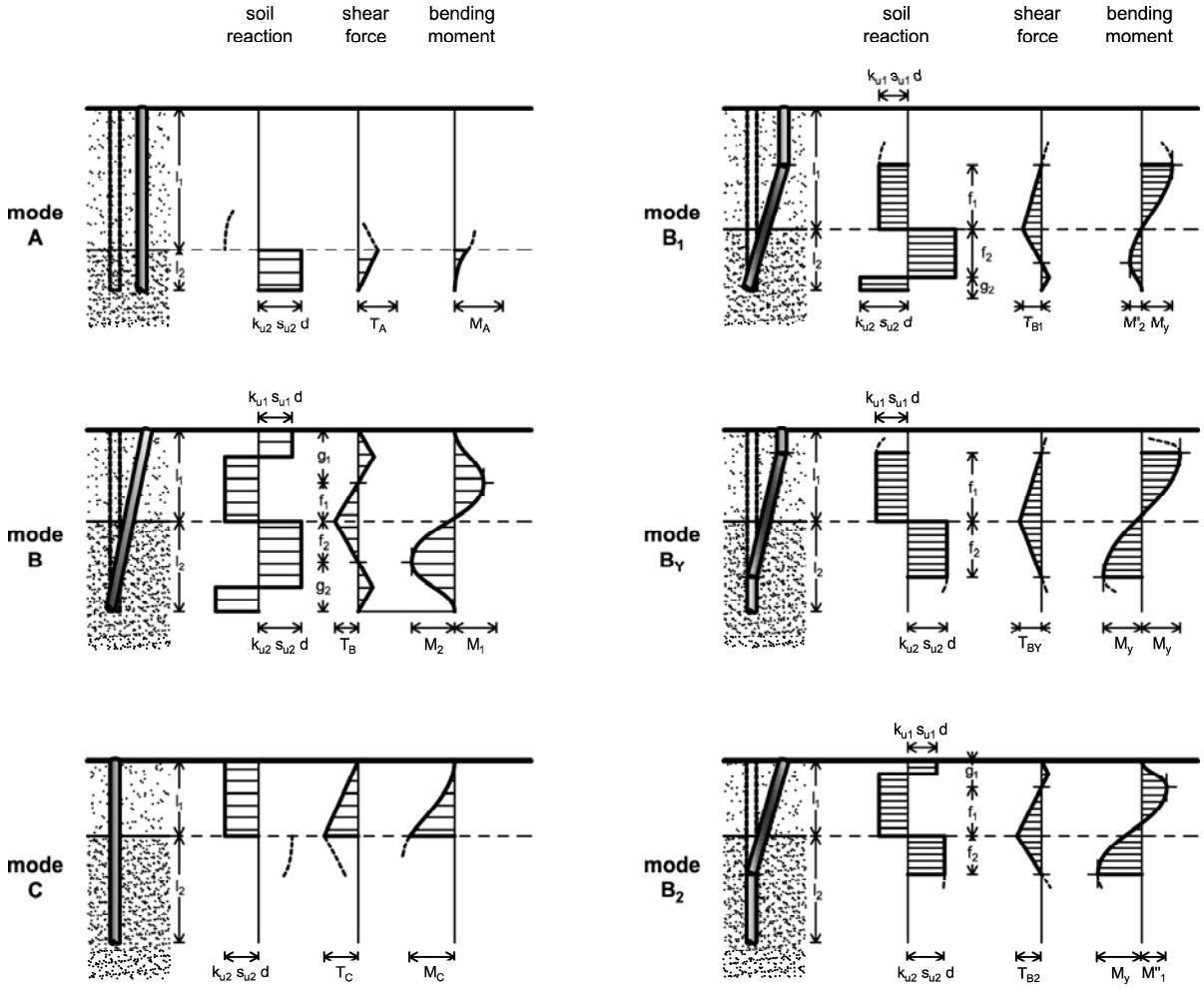


Figure 1: Failure modes for a pile with infinite cross section capacity (left column) and with plastic hinges (right column), modified from Viggiani, 1981.

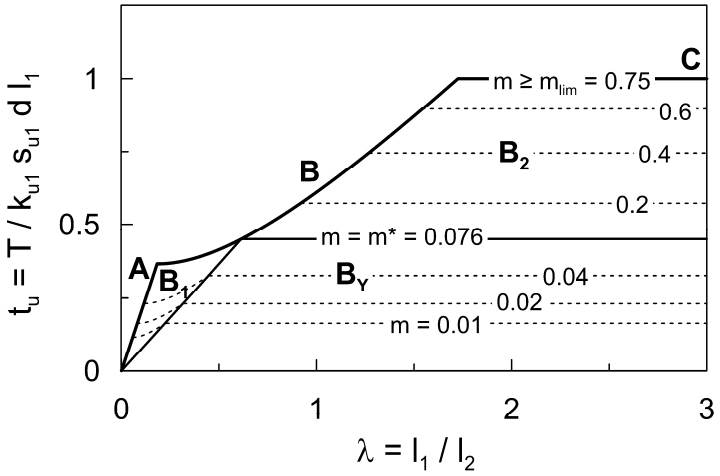


Figure 2: Stabilizing shear force as function of geometrical and mechanical problem parameters (modified from Viggiani 1981 for χ =0.5).

4 ANALYSIS OF REINFORCED SLOPES

Stabilizing piles are often utilized in slopes as a remedial measure to increase safety margin against collapse under static actions (i.e., in absence of any seismic loading). It is indeed evident that an additional resisting force provided by the presence of a structural element crossing the unstable soil mass and penetrating the stable soil will increase safety against a collapse mechanism. The amount of such resisting contribution depends on geometrical and mechanical features of the specific slope-pile system. In reinforced slopes, landslide body is subjected to a constant driving force due to body forces (self-weight and seismic body forces), while the resisting forces are due to the shear strength along the failure surface and to the lateral shear strength produced by pile contributions to stability (Figure 3). The sliding mass is divided in n slices and the forces acting on ith slice are shown in the following figure.
As in the original work, geometric quantities:

- E_i and E_{i+1}: lateral thrust on vertical side of section i and i+1 in terms of total stresses;
- X_i and X_{i+1}: shear forces on vertical side of section i and i+1;
- W_i: weight of ith slice;
- $k_h W_i$: horizontal force on ith slice acting at center of gravity slice;
- N_i: normal force at base of slice in terms of total stresses;
- T_i: shear force at base of slice;
- z_i: height of point of application of E_i above slip line;
- c_i' and ϕ_i': effective shear strength parameters of material at base of slice;
- H_i: height of sliding mass at section i;
- b_i: breadth of slice;
- α_i: angle made by slip line mid point and the horizontal;
- x_i and y_i: coordinate of mid point of base of slice with respect to the axes;
- x_g and y_g: coordinate of centre of gravity of sliding mass with respect to the axes

were calculated for each slice.
It is assumed that slices are of thickness sufficiently small to consider that normal force N_i acts at the mid point of the slice and, since there are no other external forces on the free surface, $\Sigma\Delta E_i = 0$ and $\Sigma\Delta X_i = 0$.

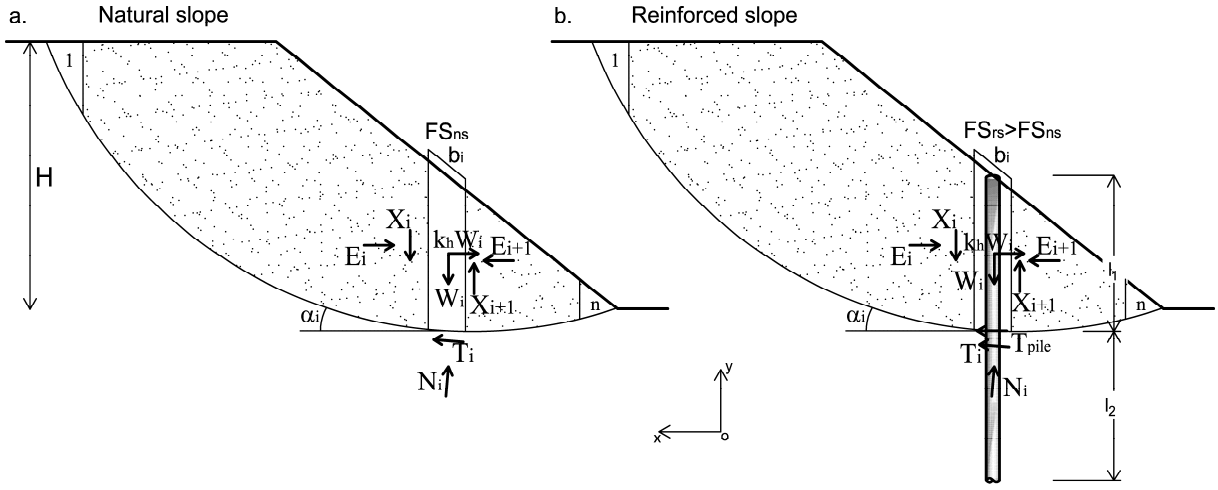


Figure 3: Critical slip surface (a) and reinforced slope with piles (b).

From the vertical and horizontal equilibrium of the slice, considering an additional resisting force due to piles and assuming that, under the action of the seismic force $k_h W$, the complete shear strength of the surface is mobilized, the following system may be considered:

$$N_i \cdot \cos\alpha_i + T_i \cdot \text{sen}\alpha_i + T_{pile} \cdot \text{sen}\alpha_i = W_i - \Delta X_i \tag{8}$$

$$T_i \cdot \cos\alpha_i - N_i \cdot \text{sen}\alpha_i + T_{pile} \cdot \cos\alpha_i = k_h \cdot W_i - \Delta E_i \tag{9}$$

$$T_i = N_i \cdot \tan\varphi_i' + c_i' \cdot b_i \cdot \sec\alpha_i \tag{10}$$

where, using equations (8), (9) and (10), are obtained:

$$Ti = \left[c_i' \cdot b_i + Wi \cdot \tan\varphi_i' \right] \cdot \frac{\cos\varphi_i'}{\cos(\varphi_i' - \alpha_i)} - \left[\Delta X_i \cdot \frac{\text{sen}\varphi_i'}{\text{sen}(\varphi_i' - \alpha_i)} \right] - \left[T_{pile} \cdot \frac{\text{sen}\alpha_i \cdot \text{sen}\varphi_i'}{\cos(\varphi_i' - \alpha_i)} \right] \tag{11}$$

$$Ni = \left[W_i - c_i' \cdot b_i \cdot \tan\alpha_i \right] \cdot \frac{\cos\varphi_i'}{\cos(\varphi_i' - \alpha_i)} - \left[\Delta X_i \cdot \frac{\cos\varphi_i'}{\cos(\varphi_i' - \alpha_i)} \right] - \left[T_{pile} \cdot \frac{\text{sen}\alpha_i \cdot \cos\varphi_i'}{\cos(\varphi_i' - \alpha_i)} \right] \tag{12}$$

$$Di = \left[W_i \cdot \tan(\varphi_i' - \alpha_i) \right] + \left[c_i' \cdot b_i \cdot \frac{\cos\varphi_i' \cdot \sec\alpha_i}{\cos(\varphi_i' - \alpha_i)} \right] + \left[T_{pile} \cdot \frac{\cos\varphi_i'}{\cos(\varphi_i' - \alpha_i)} \right] \tag{13}$$

Following the appendix of the original work [15] for derivation of the formula for X_i for homogeneous slope and neglecting the contribution of pore pressure, the quantities are given for each slices:

$$\beta_i = 2 \cdot \alpha_i - \varphi_i' \tag{14}$$

$$E_i = \frac{\gamma \cdot H^2}{2} \cdot \left\{ \frac{1 - \text{sen}\beta \cdot \left[\text{sen}\varphi' + \left(4 \cdot c'/\gamma \cdot H \right) \cdot \cos\varphi' \right]}{1 + \text{sen}\beta \cdot \text{sen}\varphi'} \right\} \tag{15}$$

$$X_i = E_i \cdot \tan\varphi' + c' \cdot H_i \tag{16}$$

$$F_i = X_{i+1} - X_i \tag{17}$$

The X_i values that were obtained from this solution were used to determine the F_i (the factor of safety on the vertical sections of the slices i.e. local safety factor) values which were subsequently used in equations (20) and (21). These quantities are implemented in the well-known parameters of the original method:

$$S_1 = \sum D_i \tag{18}$$

$$S_2 = \sum W_i (x_i - x_g) + \sum D_i (y_i - y_g) \tag{19}$$

$$S_3 = \sum F_i \cdot [(y_i - y_g) \cdot \tan(\varphi_i' - \alpha_i) + (x_i - x_g)] \tag{20}$$

$$S_4 = \sum F_i \cdot \tan(\varphi_i' - \alpha_i) \tag{21}$$

Since F_i is assumed to be known, equations (18), (19), (20) and (21) can be solved simultaneously to obtain λ and k:

$$\lambda = S_2 / S_3 \tag{22}$$

$$k = (S_1 - \lambda \cdot S_4) / \sum W_i \tag{23}$$

In order to obtain the static factor of safety, the strength parameters of the material along the slip surface must be reduced by a known factor of safety, and the critical acceleration computed. The value of the factor which gives zero critical acceleration is the factor of safety which obtains without the earthquake forces.
For further details the reader can refer to the original work [15].

5 PERMANENT DISPLACEMENTS OF REINFORCED SLOPES UNDER EARTHQUAKE SHAKING

In order to reduce damages, due to activation of landslides during seismic events, a performance based design approach is proposed, by applying Newmark's sliding block method [11]. The model involves critical accelerations related to the unreinforced and stabilized slopes computed through limit equilibrium analysis proposed in the previous paragraphs. This procedure is able to estimate how the increase in global resisting force due to slope stabilizing piles can increase the seismic performance of the slope in terms of cumulative displacements.

5.1 Parametric study

Slope stability analyses in plane strain conditions through conventional methods, as the global limit equilibrium, have been performed for three homogeneous slopes in fined grained soils and undrained conditions (cohesive soils). This hypothesis is certainly acceptable when dealing with the seismic performance of slopes in fined grained soils, as done in the present paper. It follows that safety is increased by considering the presence of different pile layouts for each critical sliding surface. In addition, the increase in global resisting force is beneficial under seismic shaking, as a higher magnitude of driving force (that is, a larger value of acceleration) is required to generate displacements.
The Sarma's limit equilibrium method [15], as upon modified for piled slopes, has been implemented in Matlab code and used for direct calculation of critical seismic coefficient (k_c) and to determine the factor of safety (FS): the soil is assumed to follow the Tresca failure criterion and slice interfaces are vertical. Assuming undrained shear strength s_u=36, 42, 50 kPa, slope height H=10, 12.5, 15 m and slope angle α= 63°, 55°, 50° (respectively slope n°1, slope n°2 and slope n°3), critical slip surfaces for each slope are reported in Figure 4. These critical slip surfaces are characterized by the minimum safety of factor (FS=1.02, 1.04, 1.05), associated with the minimum critical acceleration (k_c=0.020, 0.017, 0.035).

In order to improve the stability of such precarious slopes, a row of stabilizing piles is embedded within landslides body. Following the general procedure suggested by Kourkoulis [8], the total shear force needed to increase stability is evaluated by imposing desired value of safety factors. Figure 5 shows the optimum pile configurations providing the required resisting force for each slopes: different layouts are obtained varying pile-to-pile distance (s).

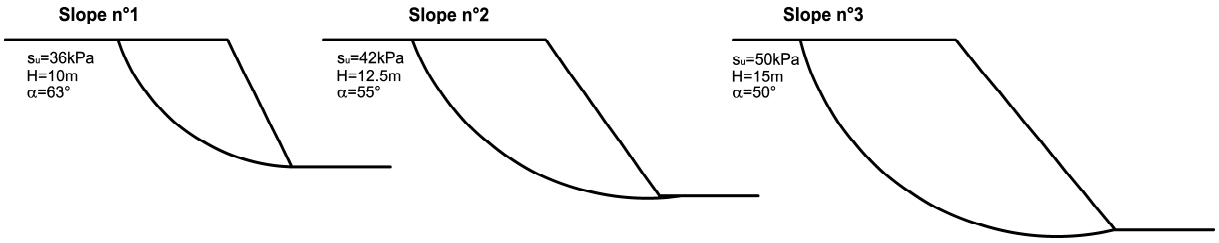


Figure 4: Case studies: unreinforced slopes

Table 1: Slopes features

		s/d	d (m)	s (m)	FS	k_c	T_{pile}(kN/m)	M_y(kNm)
SLOPE 1	*CONF. 1*	3	0.8	2.4	1.304	0.1835	134.8	577.2
	CONF. 2	4	0.8	3.2	1.248	0.1563	112.3	769.0
	CONF. 3	5	0.8	4	1.197	0.1291	89.9	769.0
	UNREINFORCED	0	0	0	1.027	0.0204	0.0	0.0
SLOPE 2	*CONF. 1*	2.5	0.8	2	1.302	0.1641	212.2	749.0
	CONF. 2	3	0.8	2.4	1.252	0.1423	180.7	805. 8
	CONF. 3	4	0.8	3.2	1.203	0.1195	147.6	1049.0
	UNREINFORCED	0	0	0	1.040	0.0179	0.0	0.0
SLOPE 3	*CONF. 1*	2.5	0.8	2	1.301	0.1598	288.0	518.8
	CONF. 2	3	0.8	2.4	1.250	0.1382	238.0	769.0
	CONF. 3	4	0.8	3.2	1.200	0.1151	184.4	913.8
	UNREINFORCED	0	0	0	1.054	0.0356	0.0	0.0

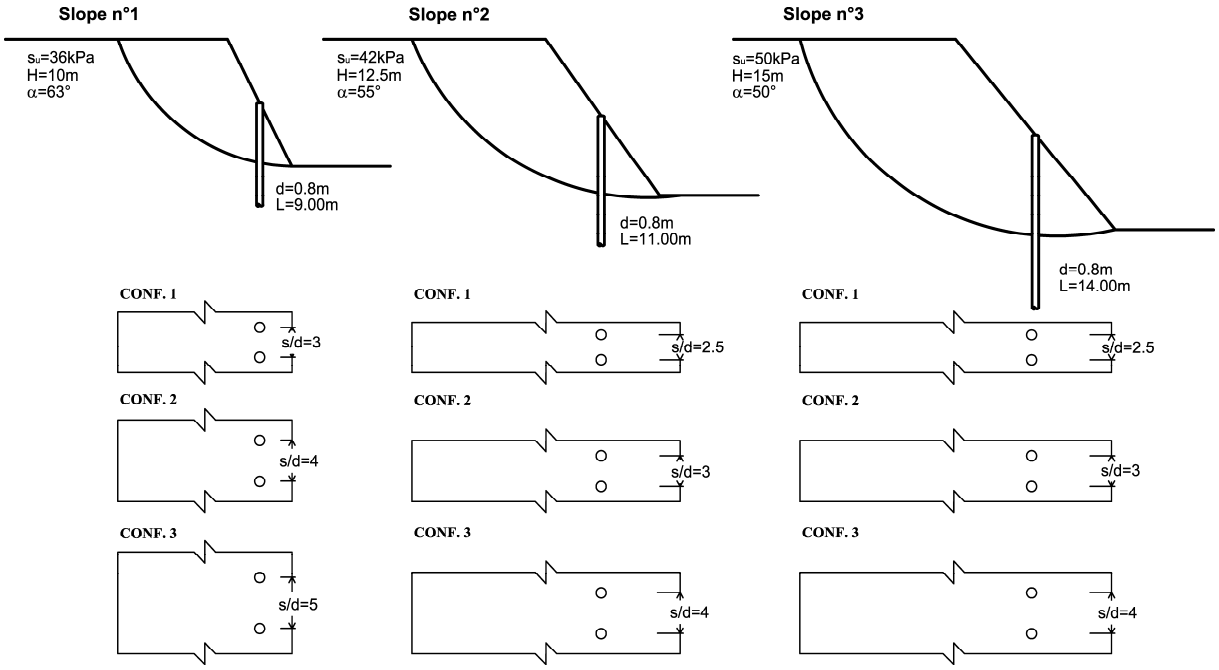


Figure 5: Case studies: piled slopes

In Table 1 the yield moment M_y is defined by conventional formulae for cylindrical concrete piles whereas shear forces of each pile (T_{pile}) referring to the above pile modes of failure in order to verify desired value of safety factors (FS= 1.20, 1.25, 1.30). The Sarma method, modified adding the resisting force due to piles, leads to evaluation of k_c and FS on piled slopes related to the previous critical slip surfaces of Figure 4.

5.2 Results

A total of 30 earthquake strong-motion records selected from different databases [18-20] are plotted in Figure 6: the parts of the record exceeding the critical acceleration are integrated to obtain the relative velocity-time history of the block and then cumulative relative displacements of the landslide block. Peak accelerations were scaled to values of a_{max}=0.25g.

Table 2: Seismic database.

N°	Event	Station	PGA (g)	N°	Event	Station	PGA (g)
1	Chi Chi, 1999	TCU045	0.361	16	Bingol, 2003	007142xa	0.515
2	Friuli, 1976	ATMZ270	0.315	17	Avej, 2002	007718xa	0.446
3	Irpinia, 1980	ASTU270	0.320	18	South Iceland, 2000	006349xa	0.744
4	Irpinia, 1980	ABAG 270	0.189	19	South Iceland, 2000	004674xa	0.318
5	Izmit, 1999	001231xa	0.161	20	Duzce, 1999	006500xa	0.496
6	Izmit, 1999	GBZ000	0.244	21	Oelfus, 1998	004992xa	0.145
7	Loma Prieta, 1989	CYC285	0.484	22	Mt. Hengill area, 1998	005079XA	0.173
8	Tabas, 1978	000182xa	0.338	23	Kozani, 1995	006115xa	0.208
9	Ardal, 1977	000158xa	0.908	24	Firuzabad, 1994	007156xa	0.310
10	Montenegro, 1979	000198xa	0.181	25	Spitak, 1988	000465xa	0.202
11	Hollister,1961	USGS 1028	0.484	26	Etolia, 1988	000428xa	0.166
12	Montenegro, 1979	000200xa	0.224	27	SE_Tirana, 1988	003802xa	0.113
13	Northridge, 1994	24278 090	0.568	28	Umbria Marche, 1997	ENCB090	0.383
14	Olfus, 2008	013006xa	0.665	29	Umbria Marche, 1997	IBCT090	0.162
15	Olfus, 2008	013010xa	0.536	30	Trinidad, 1983	CDMG 1498	0.194

Critical accelerations (k_c), reported in Table1, have been estimated by iteratively performing a pseudo-static analysis to determine the yield factor of safety in slope equilibrium Sarma method. The significant reduction of displacements due to piles used to stabilize landslides can be judged in Figure 7, where the permanent displacements evaluated with the Newmark analyses using the Tolmezzo earthquake (ATMZ270) are reported for three unreinforced slopes (red lines) and for the same piled slopes.

It is worth to note that displacements in the piled slopes are significantly lower, than the ones in the unreinforced slopes. The reductions is ranging between 99 to 93% in the first slope (subjected to maximum displacement of 40cm in unreinforced slope), a reduction of 98 to 91% in the second slope (subjected to maximum displacement of 43cm in unreinforced slope) and a reduction of 97 to 83% in the third slope (subjected to maximum displacement of 27cm in unreinforced slope).

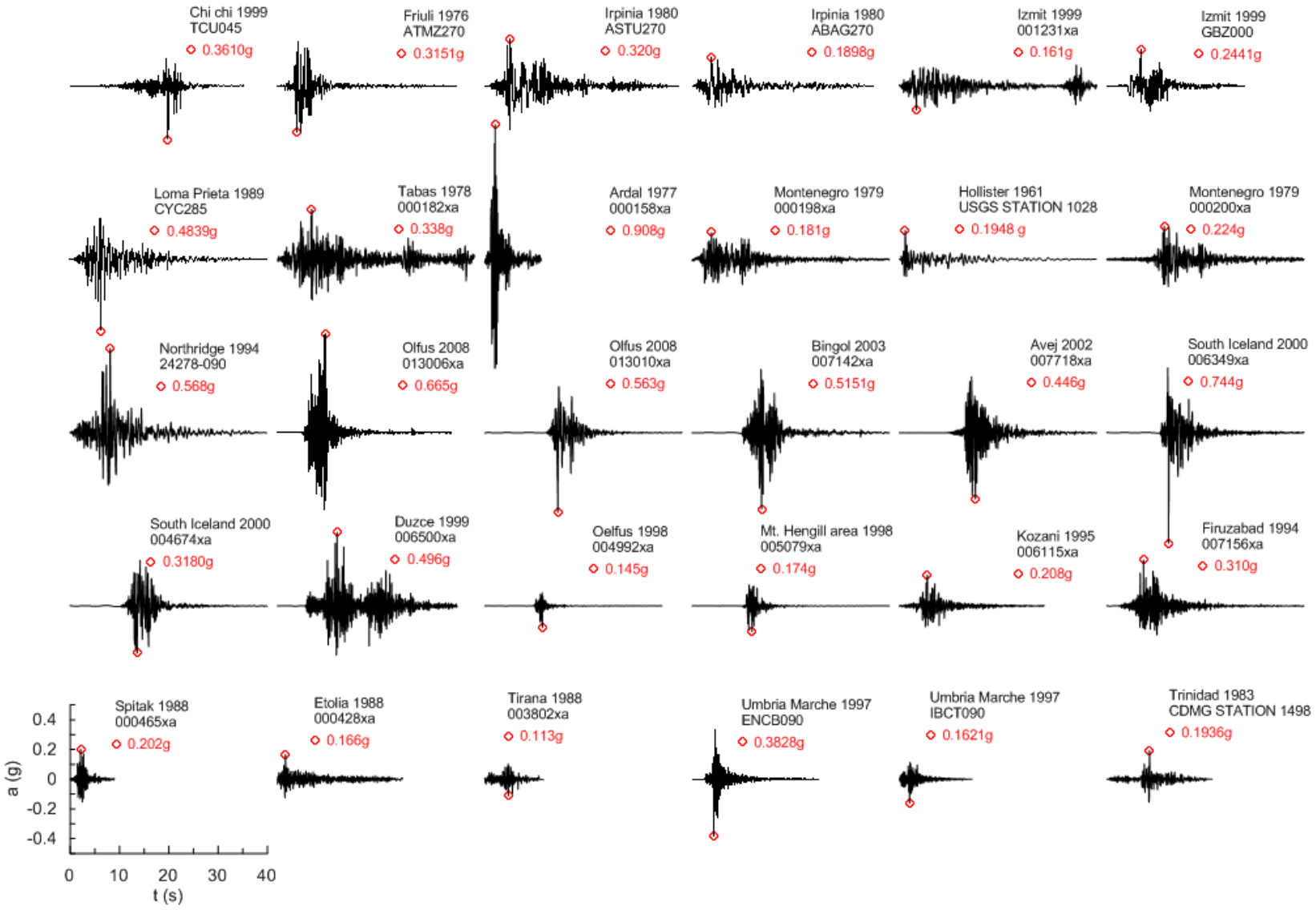


Figure 6: Time histories used in the analyses

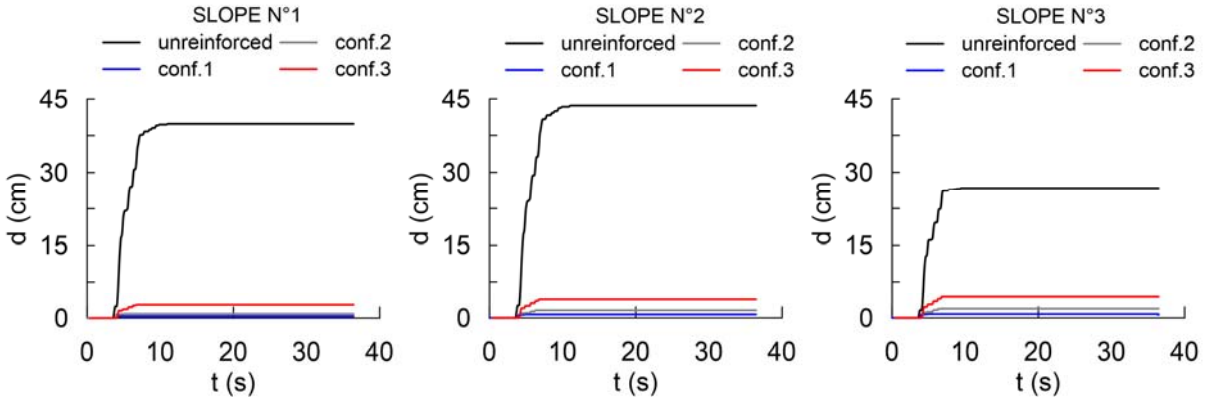


Figure 7: Newmark analyses (ATMZ270 earthquake)

Newmark analyses were carried out for the whole database of Figure 6 in order to evaluate the reduction of dynamic displacements on unreinforced and stabilized slopes.
The results are shown in Figure 8 where seismic permanent displacements are plotted in function of the static safety factors (FS): on the left hand displacements of unreinforced precarious slopes whereas, on the right, displacements of piled slopes.
It is evident that the effect of piles stabilization can be evaluated in terms of reduction of seismic induced displacements more than in terms of increment of a conventional seismic safety factor.

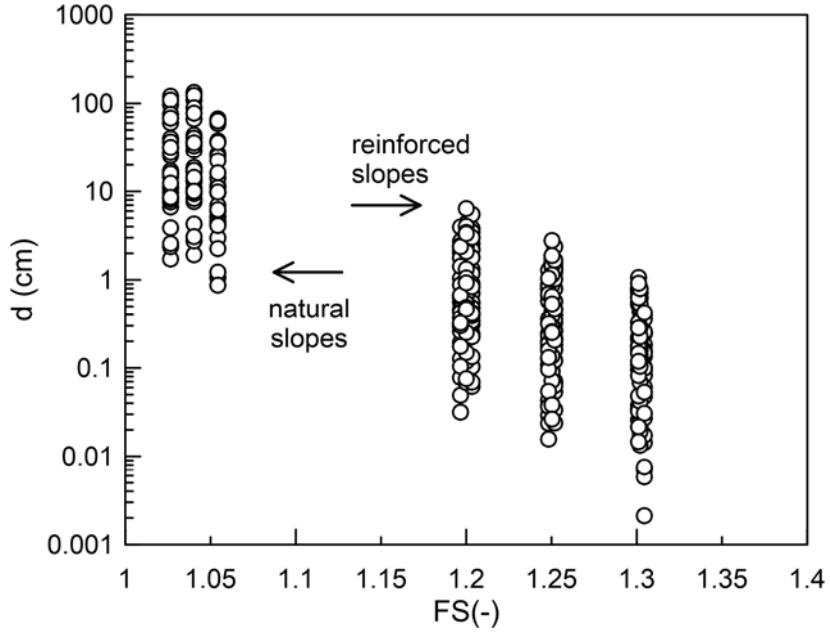


Figure 8: Effects of stabilization by piles in terms of seismic displacements and safety factors

6 CONCLUSIONS

In the present work a simple methodology has been proposed for evaluating the permanent displacements of slopes reinforced by piles under earthquake shaking. After evaluating the ultimate load of pile stabilizing slope under static regime (in the application this was done by means of Viggiani [4] method in undrained conditions), the procedure extends the well-known Sarma [15] method, by adding in the equilibrium equations the contribution of the pile,

to obtain the critical acceleration. A classical Newmark method was then employed for the estimation of permanent displacements under different earthquake time-histories. By making use of this procedure, a parametric study has been conducted to evaluate the ability of statically-designed piles in reducing earthquake-induced permanent displacement of slopes. The study shows that when piles are designed to increase the safety factor in static regime up to typical values (i.e., designed according to classical capacity-based concepts) they can reduce drastically the seismic displacements. It is fair to mention that this study presents different limitations due to the simplifying hypotheses adopted. Therefore, while the work highlights interesting trends, the generalization of these results requires caution and will be investigated in future research.

ACKNOWLEDGEMENTS

This research was supported by National relevant Interest Research Program (PRIN 2010-2011). The Authors would like to express their gratitude to the responsible of the research project, Prof. Leonardo Cascini.

REFERENCES

[1] Ito T, Matsui T, Hong PW. Design method for stabilizing piles against landslide – one row of piles. Soils Found 1981;21(1):21–37.

[2] Chen LT, Poulos HG. Piles subjected to lateral soil movements. J Geotech Geoenviron Eng ASCE 1997;123(9):802–811.

[3] Zeng S, Liang R. Stability analysis of drilled shafts reinforced slope. Soils Found 2002; 42(2):93–102.

[4] Viggiani C. Ultimate Lateral Load on Piles Used to Stabilize Landslides. Proc. 10th Int. Conf. Soil Mech. Found. Engng. Stockholm, 1981; 3: 555-560.

[5] Poulos HG. Design of reinforcing piles to increase slope stability. Can Geotech J 1995; 32:808–818.

[6] Ausilio E, Conte E, Dente G. Stability analysis of slopes reinforced with piles. Comp and Geotec 2001; 28(8): 591-611.

[7] Won J, You K, Jeong S, Kim S. Coupled effects in stability analysis of pile-slope systems. Comp and Geotech 2005; 32:304-315.

[8] Kourkoulis R, Gelagoti F, Anastasopoulos I, Gazetas G. Slope stabilizing piles and pile-groups: parametric study and design insights. J Geotech Geoenviron Eng ASCE 2011;137(7):663–678.

[9] Kourkoulis R, Gelagoti F, Anastasopoulos I, Gazetas G. Hybrid method for analysis and design of slope stabilizing piles. J Geotech Geoenviron Eng ASCE 2012;138(1):1–14.

[10] Li X, He S, Wu Y. Seismic Displacement of Slopes Reinforced with Piles. J. Geotech. Geoenviron. Eng. ASCE 2010.136:880-884.

[11] Newmark N.W. Effects of earthquakes on dam and embankments. The Fifth Rankine lecture of the British Geotecnical Society, Geotecnique, 1965, vol. 15, n° 2.

[12] Janbu N. Stability analysis of slopes with dimensionless parameters. Harvard Soil Mechanics Series no. 46, 1954.

[13] Bishop, A. W. & Morgenstern, N. R. Stability coefficients for earth slopes. Geotechnique 1960: 10, No. 4, 129-150.

[14] Morgenstern, N. R. & Price, V. E. The analysis of the stability of general slip surfaces. Geotechnique 1965: 15, No. 1, 79-93.

[15] Sarma S K. Stability analysis of embankments and slopes. Geotechnique 1973; 23(3):423-433.

[16] Sarma, S K, Stability analysis of embankments and slopes. Journal of the Geotechnical Engineering Division, ASCE 1979: 105, 1511-1524.

[17] Broms B. Lateral resistance of piles in choesionless soils. J soil Mech Found Div 1964; 90(SM3): 123-156.

[18] Scasserra G, Lanzo G, Stewart J P, D'Elia B. SISMA (Site of Italian Strong Motion Accelerograms): a web-database of ground motion recordings for engineering applications. Seismic Engineering Conference commemorating the 1908 Messina and Reggio Calabria Earthquake, Reggio Calabria, Italy 2008: 2:1649-56.

[19] Chiou B, Darragh R, Gregor N, Silva W. NGA Project Strong-Motion Database. Earthquake Spectra 2008; 24(1): 23-44. Pacific Earthquake Engineering Research Center PEER Ground Motion Database Beta Version 2010; Available online from URL: http://peer.berkeley.edu/

[20] Seismosoft, Earthquake Engineering Software Solutions. Seismosignal and Seismospectra - computer programs for signal processing of strong-motion data 2013; available online from URL: http://www.seismosoft.com

COMPDYN 2015
5th ECCOMAS Thematic Conference on
Computational Methods in Structural Dynamics and Earthquake Engineering
M. Papadrakakis, V. Papadopoulos, V. Plevris (eds.)
Crete Island, Greece, 25–27 May 2015

THREE-DIMENSIONAL NUMERICAL MODELLING OF CIRCULAR TUNNELS UNDER SEISMIC ACTIONS

E. Bilotta[1], R.M.S. Maiorano[2], A. Viglione[2], S. Aversa[2]

1

[1] Università degli Studi di Napoli Federico II, Napoli, Italy
e-mail: emilio.bilotta@unina.it

[2]Università degli Studi di Napoli Parthenope, Napoli, Italy
e-mail:stefano.aversa@uniparthenope.it, rossella.maiorano@uniparthenope.it, ag.viglione@gmail.com

Keywords three-dimensional modelling, tunnels, seismic actions..

Abstract. *Dynamic effects on shallow circular tunnels in soft ground have often been neglected based on the assumption that their response to earthquakes loading is relatively safe as compared to that of surface structures. Nevertheless, several example of recorded damage to underground structures for which seismic forces were not considered in the design can be quoted. In some cases, damage was associated with strong ground shaking and site amplification, which increased the stress level in the tunnel lining. Ovaling or racking deformations are mostly due to shear waves propagating perpendicularly to the tunnel axis, resulting in a distortion of the cross-section of the structure, while axial compression and extension, or longitudinal bending are due to shear waves propagating parallel or obliquely to the tunnel axis. Pseudo-static and simplified dynamic analyses enable to assess transient changes in internal forces during shaking. In the simplified methods, a tunnel structure is generally designed by imposing a displacement field to its boundary, as obtained from a site seismic response under free field conditions, and calculating the forces in the lining in an uncoupled manner. Axial and bending deformations are generated by the components of the seismic waves producing particle motion parallel or perpendicular to the longitudinal axis of the tunnel, respectively. Nevertheless, experimental evidences of permanent changes in internal loads in the tunnel lining would suggest that a full three-dimensional dynamic analysis including plastic soil behavior should be performed when modelling the dynamic interaction between the tunnel and the ground. In the paper three-dimensional numerical analyses were performed to simulate the response of circular tunnels subjected to different seismic loads acting in the transversal and in the longitudinal direction of the tunnel axis. The main purpose of this study was to provide a three-dimensional numerical model, which would allow the tunnel lining behavior and the displacement field surrounding the tunnel to be evaluated for different directions of seismic wave propagation.*

1 INTRODUCTION

Tunnels and underground structures are fully embedded in the ground, hence during earthquake they usually tend to move following the surrounding ground, without experiencing strong inertial loading, due to their limited mass. For such a reason the seismic design of tunnels generally does not create much concern, in comparison to that of the aboveground structures.

Despite this fact, some tunnels suffered severe damage in past and recent earthquakes [1, 2]. In most cases damages were caused by ground failure or liquefaction, but sometimes damage has occurred also associated with strong ground shaking, possibly amplified by local site conditions: when the stress level exceeded the concrete tensile strength, the tunnel lining cracked locally [2, 3, 4].

The change of internal forces in a tunnel lining during earthquakes can be calculated following several approaches [e.g. 3, 5]. As a general rule, the level of complexity of calculation must be consistent with the level of detail of the ground investigations and definition of seismic actions. Existing guidelines suggest pseudo-static or uncoupled dynamic analyses for preliminary design stages [e.g. 6, 7], to assess transient changes of internal forces during shaking. It is worth noticing that both experimental and numerical evidences of permanent changes of internal loads in the tunnel lining [8, 4] suggest a full dynamic analysis to be performed to achieve the most reliable seismic design of such underground structures, including soil-structure interaction and plastic soil behaviour.

In addition, full dynamic analyses can be carried out to model the complete three-dimensional geometry of the tunnel undergoing seismic waves of any direction. The existing works that analyze the soil-structure interaction of tunnels in 3D conditions and considering the inelastic behavior of soil are very few [9, 10].

In this paper three-dimensional Finite Element analyses were performed to simulate the response of a circular tunnel both in the transversal section and along the tunnel axis. The non-linear and irreversible soil behavior was modelled through an elasto-plastic strain hardening model with small strain overlay [11]. The effect of a stratigraphic discontinuity, simulated through a sudden change of ground stiffness, was also taken into account.

The purpose of the study is that of providing an insight on the three-dimensional interaction between the tunnel lining behavior and ground surrounding the tunnel, when subjected to different directions of seismic wave propagation and in presence of a singularity in the ground layering, as often occur in practice.

2 NUMERICAL ANALYSES

2.1 3D Models

To study the tunnel behavior under the effect of seismic shaking in transversal and longitudinal directions, different 3D geometrical configurations have been analyzed in this work through Plaxis 3D ([12]). For all of them a tunnel with a 6.0 m internal diameter of and lining thickness of 0.30 m has been modelled at a depth of 12.0 m (crown level) in a homogenous sand layer of 23.2 m (Figure 1). A 3D model (T in Figure 1) was made to be shaken in the transversal direction (x-axis), two models (Model L1 and Model L2 in Figure 1) were shaken in longitudinal direction (y-axis). Model sizes are shown in the figure.

The tunnel lining is modelled with volume elements ($E = 36.6*10^6$ kN/m) with a normally rough interface ($R_{INT} = 0.7$); moreover to reduce boundary effects, two rings 1.5 m long with lower stiffness ($E = 36.6*10^5$ kN/m) are placed at the tunnel ends. A Rayleigh damping has

been assigned to the lining ($\alpha_{Rayleigh}$ = 0.4245, $\beta_{Rayleigh}$ = 2.448*10^{-3}). This corresponds to an average damping ratio of 5% in the range of frequency of interest.

To reduce the boundary effects in the dynamic analysis, in the model T viscous dashpots were applied on the (y – z) vertical sides, while normal displacements were restrained to zero on the (x – z) vertical sides and the (x – y) bottom. Conversely, the longitudinal models have viscous boundaries on the (x – z) vertical sides and restrained displacements on the (y – z) vertical sides and the (x – y) bottom.

Model L2 is characterized by the presence of a sudden change of ground conditions along the tunnel aimed to model the effect of a large contrast of soil dynamic impedance on the lining forces.

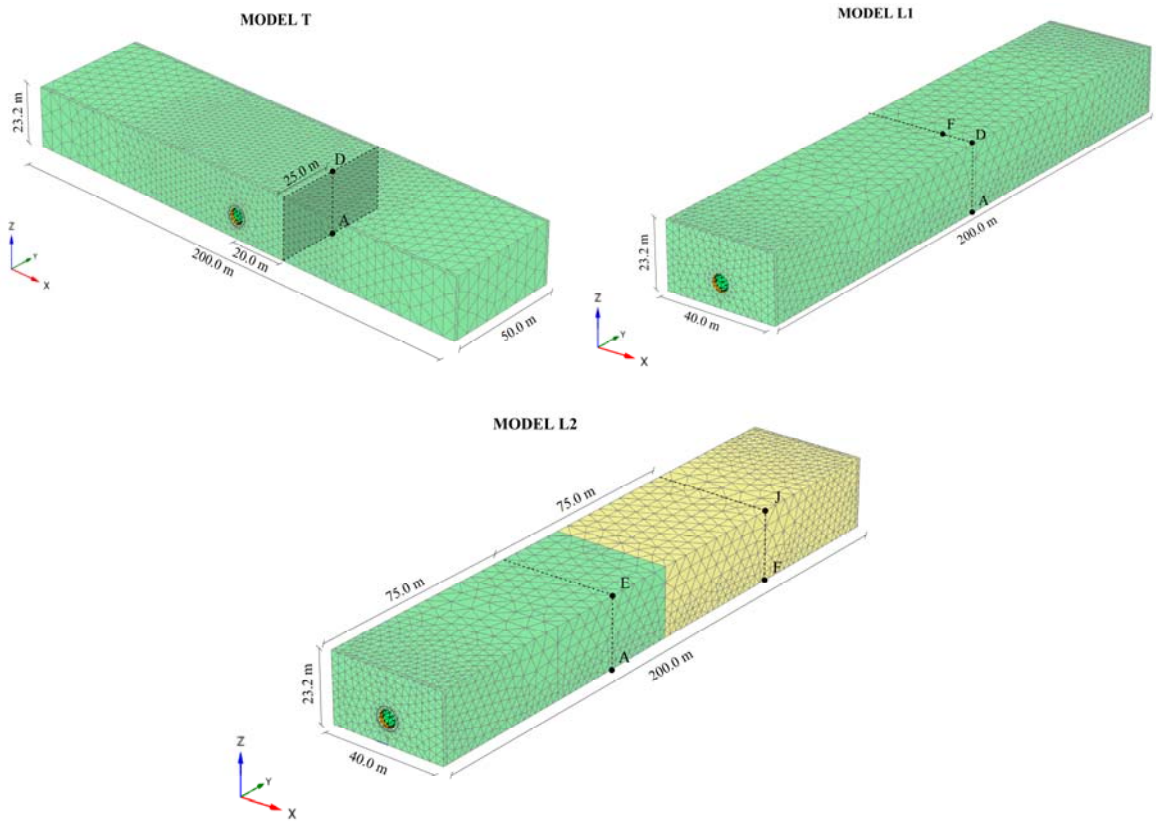


Figure 1: Models T, L1 and L2

2.2 Materials

The sand was modeled using the Hardening Soil small strain model ([11]). The calibration of the model mechanical parameters was performed by using the results of laboratory volume element tests (triaxial and torsional shear tests, [13]) and by back analyzing the available centrifuge tests, as discussed in [14]. The stiff ground was modeled by simply amplifying 10 times sand stiffness without changing the other parameters. In Table 1, the main significant model parameters are shown.

Table 1: Soil parameters.

HS-ss parameters	**dense sand**	**stiff ground**
γ_d (kN/m^3)	15.2	15.2
$E_{50,ref}$ (MPa)	18.6	186
$E_{oed,ref}$ (MPa)	20.5	205
$E_{ur,ref}$ (MPa)	62.16	621.6
ν_{ur} (-)	0.2	0.2
m (-)	0.4	0.4
$G_{0,ref}$ (MPa)	72.7	727
$\gamma_{0.7}$ (10^{-4})	$5.8*10^{-4}$	$5.8*10^{-4}$
$\gamma_{cut-off}$ (10^{-4})	$10.1*10^{-5}$	$10.1*10^{-5}$
ϕ_{PK} (°)	38.6	38.6
ψ_{PK} (°)	8.2	8.2
c' (kPa)	0.01	0.01
$\alpha_{Rayleigh}$	0.2010	0.2010
$\beta_{Rayleigh}$	$0.4547*10^{-3}$	$0.4547*10^{-3}$

2.3 Input

Input signals are applied as acceleration time histories at the bottom of the model, in x- and y-direction respectively in the transversal (T) and longitudinal (L1, L2) models.

Several natural input signals extracted from the Italian database SISMA ([15]), with different frequency content, each scaled to different values of a_{max} were used in the analyses. In this paper only the results for the input signal ENCB090 are reported. In Figure 2 the acceleration time histories and Fourier spectra of this signal, scaled to 0.13g, are shown.

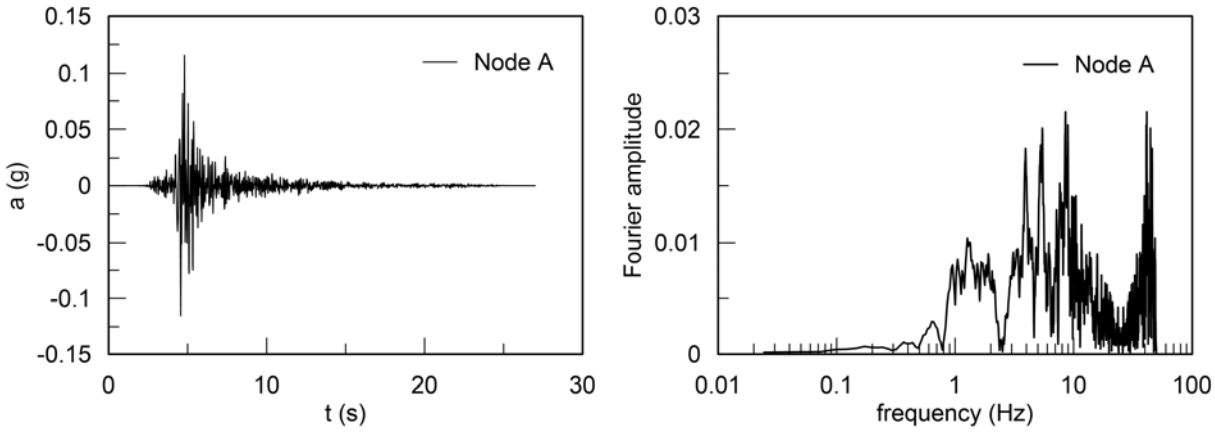


Figure 2: Input ENCB090 (scaled to 0.13 g)

3 RESULTS

In Figure 3 the acceleration time histories calculated at the ground surface in the three models are shown (a_x for model T and a_y for model L1 and L2). The comparison between the models T and L1 in the same node D (see Figure 1) is good, indicating that the free-field response was well achieved. In model L2, the response of the same node (named E in Figure 1) is slightly different, possibly indicating the effect of reflected waves due to the presence of the abrupt change of stiffness in the vicinity.

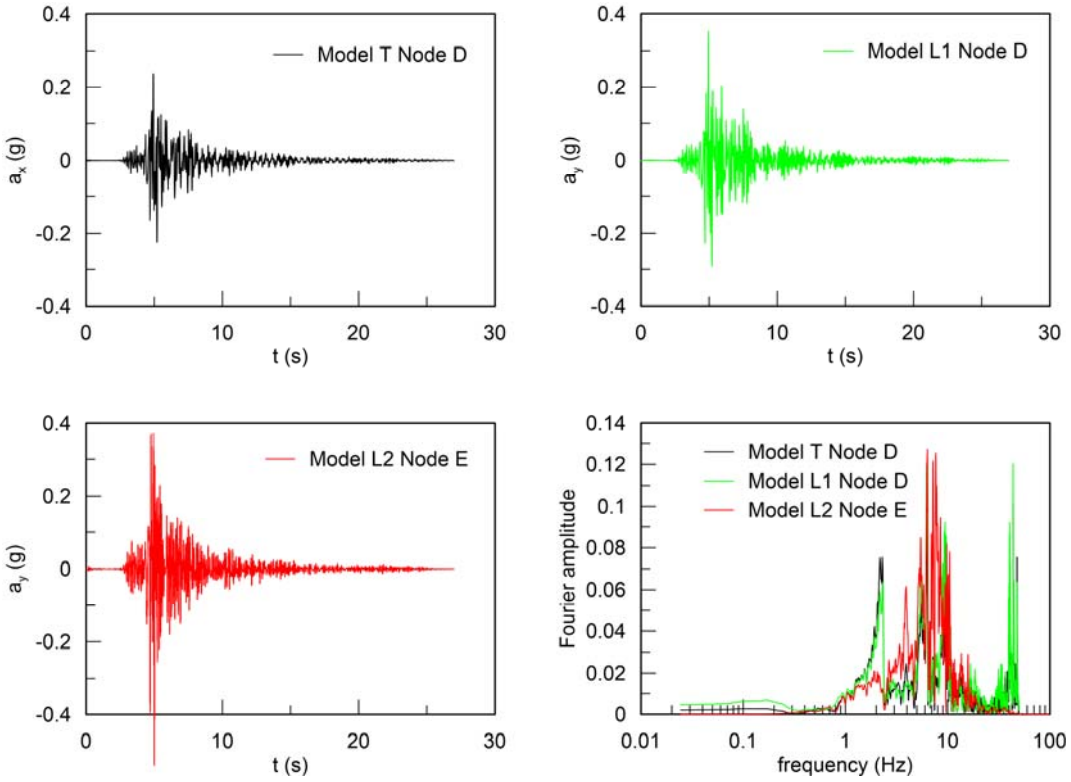


Figure 3: Acceleration at ground surface (ENCB090 scaled to 0.13 g)

The changes of hoop forces and bending moments in the transverse section of the model T shown in Figure 1 (N_2 and M_{22} respectively) are plotted along the angle θ at 5s and 10s during the earthquake in Figure 4. Similar plot are shown for the same section of model L1 in Figure 5. Although in the latter case the input signal is applied in longitudinal direction, the change of internal forces in the transverse section, although small, is comparable to the corresponding change calculated for model T, where the input signal is applied in the transverse direction.

In Figure 6 and 7 the change of axial force N_1 and longitudinal bending moment M_{11} along the crown and the invert generatrix of the tunnel lining are shown (at 5s and 10s) for the two model L1 and L2.

An important boundary effect can be observed in the results up to about 50 m from the boundary. Therefore the calculated forces are realistic only in the central part of the mesh, that is between 50m and 150m, where the results at the crown and at the invert are quite similar.

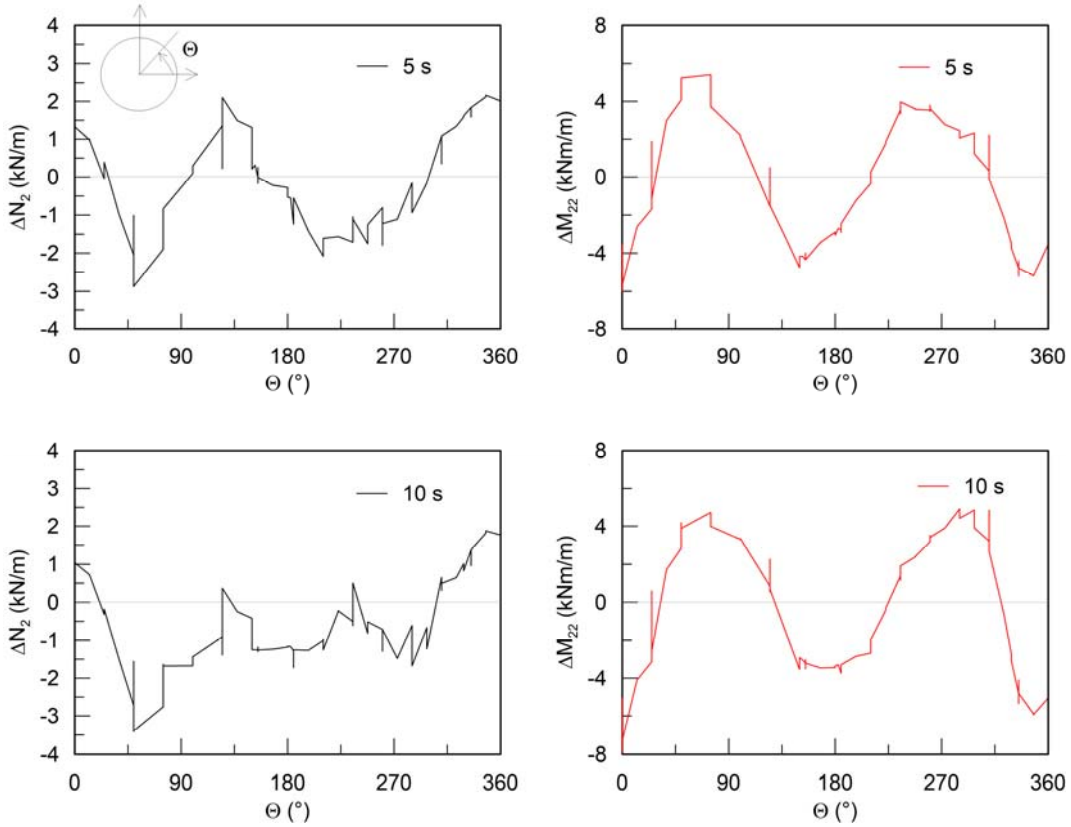


Figure 4: Model T: forces in the lining due to ENCB090 scaled to 0.13 g

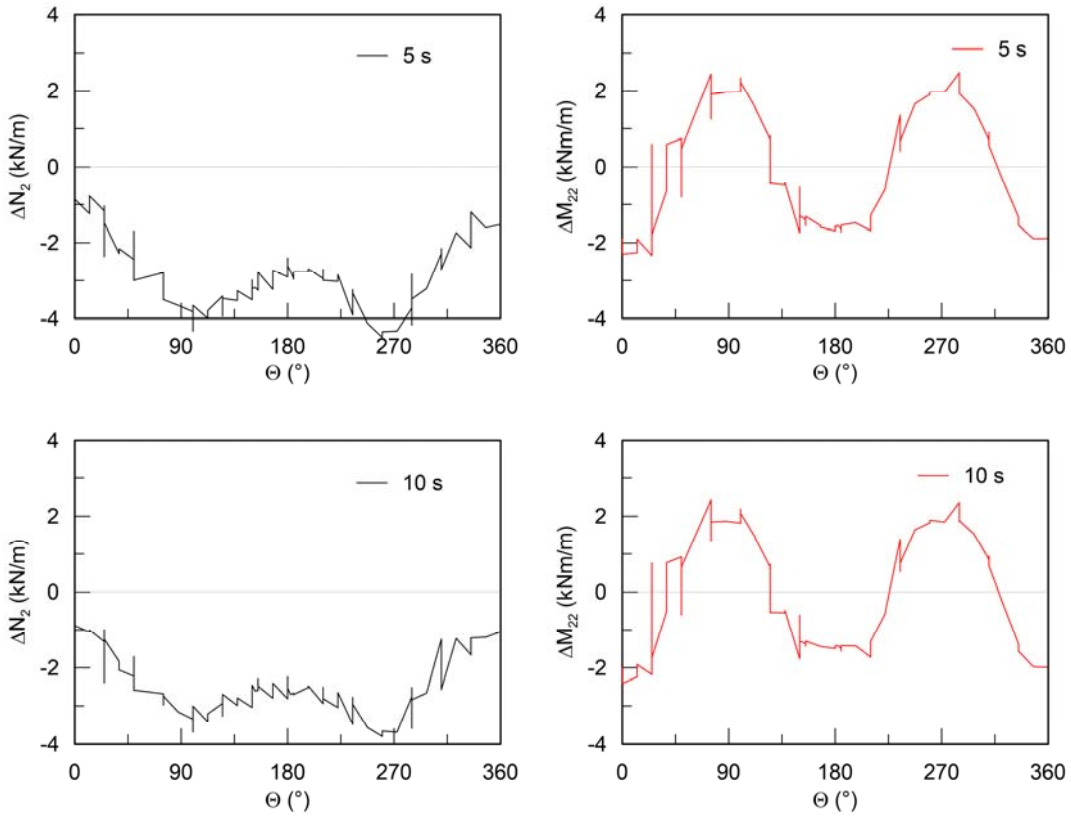


Figure 5: Model L1: forces in the lining due to ENCB090 scaled to 0.13 g

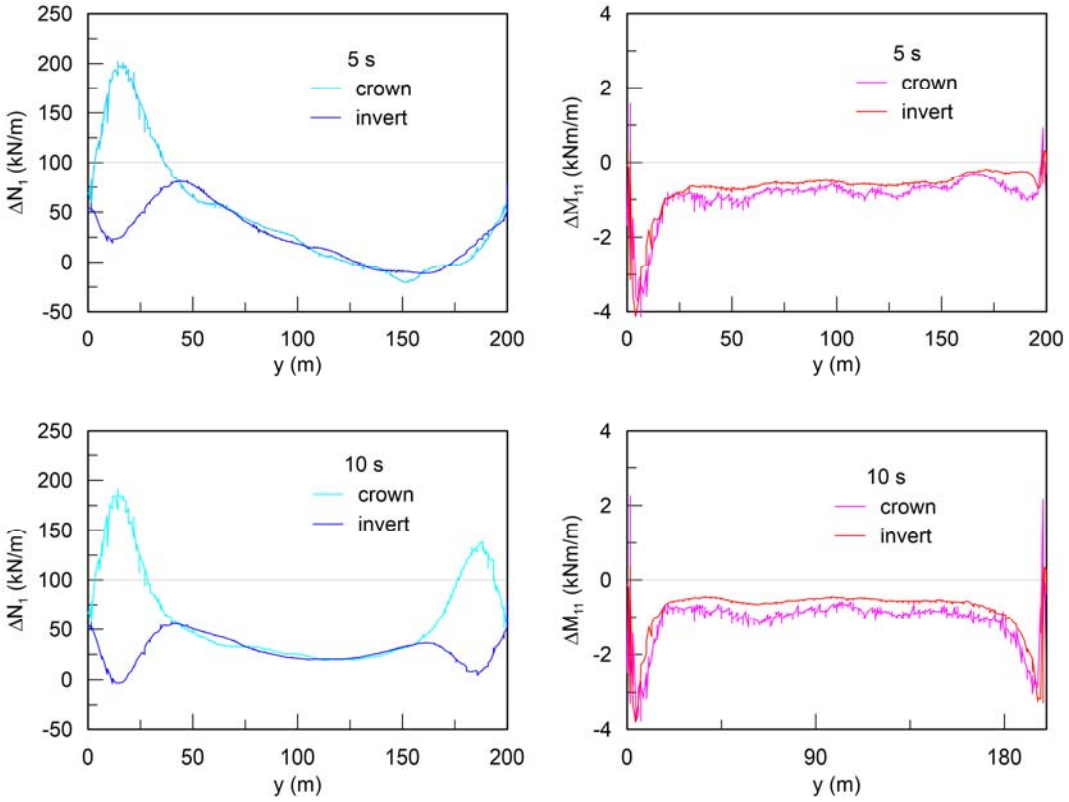


Figure 6: Model L1: forces in the longitudinal direction of lining due to ENCB090 scaled to 0.13 g

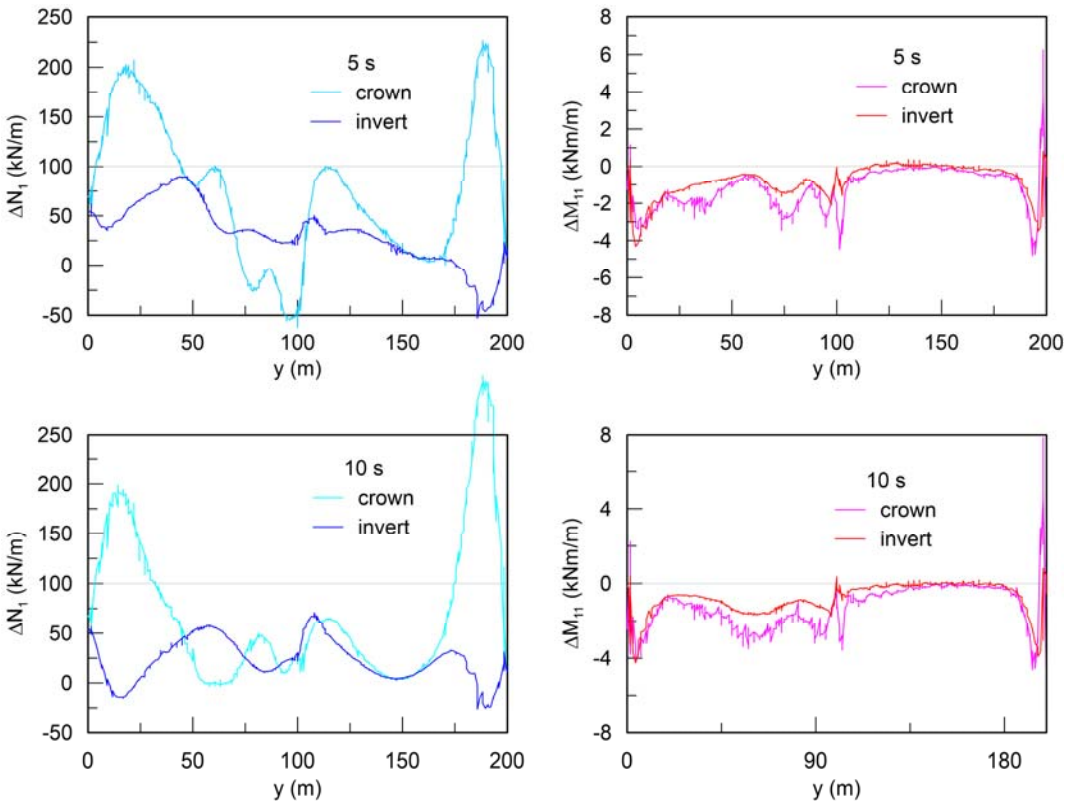


Figure 7: Model L2: forces in the longitudinal direction of lining due to ENCB090 scaled to 0.13 g

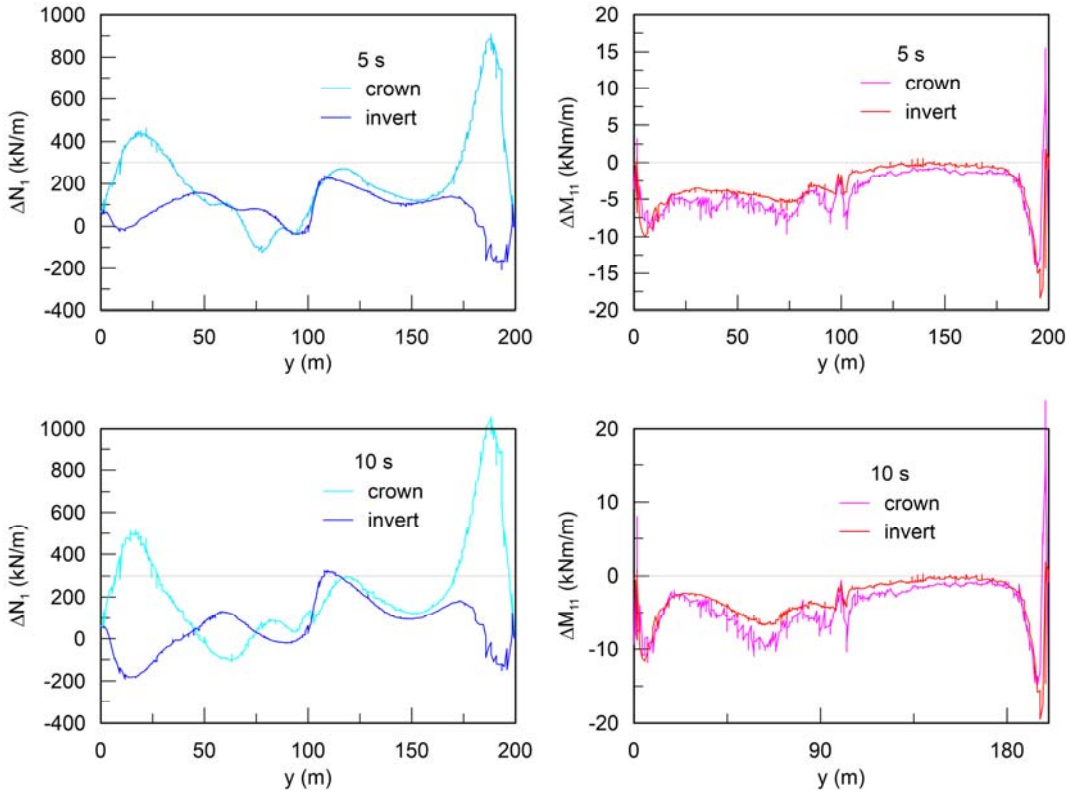


Figure 8: Model L2: forces in the longitudinal direction of lining due to ENCB090 scaled to 0.35 g

In Figure 7 an effect of the change of stiffness is evident both in the distribution of axial forces and of bending moments. Bending moments are smaller within the stiff ground and larger in the sand. Change of axial forces produce locally both compression (negative values) and extension (positive values) in the lining. Large extension may develop in a critical section. This is close to the section of discontinuity of the ground stiffness, but does not coincide necessarily with it.

In Figure 8 similar distribution of axial forces and bending moments for the model L2 are shown for an acceleration time history scaled to 0.35g. The same effects observed in Figure 7 are here enhanced by the larger amplitude of ground motion.

4 CONCLUSIONS

In the paper the results of a series of finite element numerical analyses performed in 3D conditions are shown, aimed at modelling the seismic behavior of tunnel when subjected to different directions of seismic wave propagation. An elasto-plastic strain hardening model accounting for small strain stiffness was used to investigate the effects of the non-linear and irreversible behavior of ground. The ground conditions were also changed to include a discontinuity of ground stiffness, thus investigating the local effects on the internal forces arising in the tunnel lining.

The following remarks can be drawn:

- the larger change of internal forces, both in longitudinal and transverse direction occurs during the initial part of the seismic event;

- both compression and extension develop along the tunnel lining due to the longitudinal component of the seismic waves;
- plastic deformations develop during shaking: these are associated with irreversible accumulation of forces in the tunnel lining; they cannot be evaluated by using the simplified formulations that account only for transient effects due to wave passage;
- due to a stratigraphic discontinuity involving a high contrast of ground stiffness the seismic change of internal forces in the tunnel lining tend to concentrate locally; hence, large extension may develop in a critical section, which does not coincide necessarily with the section of discontinuity of the ground stiffness.

The obtained results are affected by a few simplifications. Among them it is worth noticing that: i) the primary stress state around the tunnel does not take into account the stress modification due to tunnel construction; ii) the influence on the results of the behavior at the interface between the lining and the ground has been not completely investigated. Further analyses are currently ongoing to overcome such limitations.

ACKNOWLEDGEMENTS

The activity was carried out as part of WP 3 ‘Tunnels’ of the sub-project on ‘Earthquake Geotechnical Engineering’, in the framework of the research programme funded by Italian Civil Protection through the ReLUIS Consortium.

REFERENCES

[1] N.Yoshida, Damage to subway station during the 1995 Hyogoken-Nambu (Kobe) earthquake. *Earthquake geotechnical case histories for performance-based design*, Kokusho Ed., 373-389, 2009.

[2] W.L. Wang, T.T. Wang, J.J. Su, C.H. Lin, C.R. Seng, T.H. Huang, Assessment of damage in mountain tunnels due to the Taiwan Chi-Chi earthquake. *Tunn and Undergr Space Technol* **16**, 133-150, 2001.

[3] Y.M.A. Hashash, J.J. Hook, B. Schmidt, J.I.-C. Yao, Seismic design and analysis of underground structures. *Tunn and Undergr Space Technol* **16**, 247–293, 2001.

[4] T.D. O’Rourke, S.H. Goh, C.O. Menkiti, R.J. Mair, Highway Tunnel Performance during the 1999 Duzce Earthquake. *Proc 15th Int Conf on Soil Mech and Geotech Eng, Istanbul, Turkey*, 1365–1368, 2001.

[5] K. Pitilakis, G. Tsinidis, Performance and seismic design of underground structures, State-of-Art, Earthquake Geotechnical Engineering Design. *Geotech Geol and Earthq Eng* **28**, 279-340, 2014.

[6] ISO TC 98/SC 3 N229, *Bases for design of structures – Seismic actions for designing geotechnical works*, 2003.

[7] NCHRP, *Seismic analysis and design of retaining wall, buried structures, slopes and embankments*. Transportation Research Board, Washington DC, 2008.

[8] S. Kontoe, L. Zdravkovic, D.M. Potts, C.O. Menkiti, Case study on seismic tunnel response. *Can. Geotech. J*. **45**, 1743-1764, 2008.

[9] S.H. Kim, K.J. Kim, Two-phase finite element procedures for dynamic analysis of saturate porous media. *Engineering Computations*, **17**, 758-774, 2000.

[10] G.D. Hatzigeorgiou, D.E. Beskos, Soil-structure interaction effects on seismic inelastic analysis of 3-D tunnels. *Soil Dynamics and Earthquake Engineering*, **30**, 851-861, 2010.

[11] T. Benz, P.A. Vermeer, R. Schwab, A small-strain overlay model. *Int. J. Numer. Anal. Meth. Geomech*., **33**, 25–4, 2009.

[12] R.B.J. Brinkgreve, E. Engin, W.M. Swolfs. *Plaxis 3D*. 2013

[13] C. Visone, F. Santucci de Magistris. Mechanical behavior of the Leighton Buzzard Sand 100/170 under monotonic, cyclic and dynamic loading conditions. In: *Proceedings of XIII ANIDIS Conference, Bologna Italy*, 2009.

[14] G. Lanzano, F. Santucci de Magistris, E. Bilotta, Calibration of the mechanical parameters for the numerical simulations of dynamic centrifuge experiments, in *Numerical Methods in Geotechnical Engineering - Proceedings of the 8th European Conference on Numerical Methods in Geotechnical Engineering, NUMGE 2014*, 1, 169-174, 2014.

[15] G. Scasserra, G. Lanzo, J.P. Stewart, B. D'Elia, SISMA (Site of Italian Strong-Motion Accelerograms): a web-database of ground motion recordings for engineering applications. In: *Proc. of the seismic engineering conference commemorating the 1908 Messina and Reggio Calabria Earthquake, Reggio Calabria*, vol. 2. Melville, New York: AIP; 1649–56, 2008.

COMPDYN 2015
5th ECCOMAS Thematic Conference on
Computational Methods in Structural Dynamics and Earthquake Engineering
M. Papadrakakis, V. Papadopoulos, V. Plevris (eds.)
Crete Island, Greece, 25–27 May 2015

NONLINEAR DYNAMIC RESPONSE OF HARDENING, SOFTENING AND ELASTOPLASTIC SDOF SYSTEMS USING GENERALIZED SINGLE STEP ALGORITHMS WITH NEWTON – RAPHSON ITERATIONS

George Papazafeiropoulos[1], Vagelis Plevris[2], and Manolis Papadrakakis[1]

[1] National Technical University of Athens
Institute of Structural Analysis and Antiseismic Research
Zografou Campus, Athens 15780, Greece
gpapazafeiropoulos@yahoo.gr, mpapadra@central.ntua.gr

[2] Computational Mechanics Laboratory, Department of Civil Engineering
School of Pedagogical & Technological Education
Heraklion, Athens, 141 21, Greece
vplevris@aspete.gr

Keywords: Nonlinear dynamic response, Newton-Raphson, stability, elastic, plastic, hardening, softening, elastoplastic, single step time integration algorithm.

Abstract. *The dynamic equation of motion of a SDOF system with a nonlinear elastic hardening spring, a SDOF system with a nonlinear elastic softening spring and a SDOF system with a nonlinear elastic-plastic spring is integrated numerically using a family of linear generalized single step-single solve algorithms. For this purpose, these algorithms are extended by using a Newton-Raphson type iterative procedure in each time step to ensure dynamic equilibrium. After a literature review of the available time integration schemes used for nonlinear problems, the linear family of algorithms is presented along with several common time integration algorithms as special cases of the generalized algorithm. An explicit flowchart is given showing the integration procedure used in the present study. The modified algorithm is applied to the aforementioned three types of SDOF systems and results concerning phase portraits, (relative) energy decrease, iterations needed for equilibrium and internal force - displacement curves are presented. It is shown that the algorithms with optimal numerical dissipation and dispersion perform in general better than others, and that from the algorithms with optimal numerical dissipation and dispersion, only the one with zero-displacement and zero-velocity overshooting behavior can capture efficiently the elastoplastic dynamic response.*

1 INTRODUCTION

The dynamic analysis of engineering structures under dynamic loading (earthquake, impact, etc.) with the finite element method results in a set of ordinary differential equations as follows:

$$M\ddot{u} + p\left(u,\dot{u}\right) = f\left(t\right) \tag{1}$$

where M is the mass matrix, p is the internal force vector, which is in general a nonlinear function of the displacements u and velocities $\dot{u}$ and is equal to the sum of the forces in the structure due to stiffness and damping, and f is the external force vector which is a function of time t. In the case of a linear elastic structure with viscous damping $p\left(u,\dot{u}\right)$ is equal to:

$$p\left(u,\dot{u}\right) = \bar{K}u + \bar{C}\dot{u} \tag{2}$$

where $\bar{K}$ is the stiffness matrix and $\bar{C}$ is the damping matrix, both of them independent of the displacement and velocity. Linear equations of dynamic equilibrium of the form of (1) in which $p\left(u,\dot{u}\right)$ is given by (2) can be solved using various superposition methods in the time or frequency domain, which greatly simplify the problem. However, in dynamic analysis of nonlinear response, superposition cannot be used and one has to resort to step-by-step methods.

Direct time integration (or time stepping, or step by step) methods are a widely used approach to solve dynamic linear or nonlinear response analysis problems. In these methods the equilibrium relations are satisfied at discrete time points (or steps) of the loading and the response history. The response during each step is calculated from the displacement and velocity at the beginning of the step and from the history of loading during the step. Thus the response for each step is an independent analysis problem.

The most common characteristics of integration schemes are the following:

- Stability. An integration scheme is said to be stable if the numerical solution, under any initial conditions, does not grow without bound. An algorithm is unconditionally stable for linear problems if the convergence of the solution is independent of the size of the time step.
- Convergence. An integration scheme is convergent if the numerical solution approaches the exact solution as the size of the time step tends to zero.
- Accuracy. Two numerical errors are associated with the accuracy of any algorithm: (a) numerical dispersion (often expressed in terms of period elongation) and (b) numerical dissipation (often expressed in terms of either the amplitude decay or the algorithmic damping ratio).
- Algorithmic dissipation. It is a kind of filtering of the higher frequency oscillations, necessary to eliminate the spurious high frequency modes inherent in a finite element mesh.
- Self-starting. This type of algorithms requires data from two time steps to proceed the solution. If data from more than two time steps are needed, the algorithm must be implemented with a starting procedure.
- Overshooting. It is the tendency of an algorithm to exceed heavily the exact solution in the first few time steps, but eventually to converge to the exact solution.

Taking into account the above characteristics, a time integration scheme should have the following desirable features [1]:

- Unconditional stability.
- At least second-order accuracy in time.
- No more than zero-order displacement and velocity overshooting behavior with minimal numerical dissipation and dispersion.
- Self-starting features with no more than one set of single-field system of implicit equations to be solved at each time step to include ease of implementation and computational simplicity.

Regarding linear dynamic response, accuracy is the main concern, since many time integration algorithms are unconditionally stable. However, algorithms which are unconditionally stable for linear dynamics, often lose this stability for nonlinear dynamics, and therefore numerical stability is of primary interest in such cases.

In this study, after a concise literature review about the numerical direct time integration algorithms applicable to the dynamic equilibrium equations of structural analysis of the form (1), a general single step linear integration group of algorithms is presented, which incorporates many well-known algorithms, and which is modified to account for nonlinear response, by introducing a Newton-Raphson iterative procedure at each time step. Afterwards, the modified algorithm is applied to known nonlinear dynamic analysis example problems and the results are studied. Apart from its robustness in solving nonlinear problems, it is proved that the algorithm can be designed to cope with cases with any degree of nonlinearity.

2 LITERATURE REVIEW

The simplest direct time integration method for dynamic analysis is the piecewise exact method in which the equation of motion is solved exactly for linear loading during each time step, in which it is assumed that the actual loading history has constant slope [2]. Although the equation of motion is solved rigorously during each time step, the linear interpolation of the excitation function introduces some error into the calculated response; this can be eliminated either by reducing the length of the time step, or adjusting the latter so that the introduced loading history fits best the actual one.

The numerical direct time integration methods can be classified as either explicit or implicit. An explicit scheme is one in which the response values for the next step are calculated only from quantities belonging to the current step. On the other hand, an implicit scheme is one in which the expressions giving the values for the next step include one or more values of the next step, and therefore successive iterations are needed to arrive to the solution for the next step. Implicit methods lead in general to increased computational effort, although it is possible for some of them to be converted into an explicit formulation. Algorithms that require two or more implicit systems to be solved at each time step have improved properties [3], but they require twice or more the computational effort of simpler methods.

Another classification that can be made is according to the formulation used to ensure conservation (or decay) of energy within a time step which is a sufficient condition for algorithmic stability [4]. This energy criterion is summarized in the following inequality:

$$\left(U_{n+1}+K_{n+1}\right)-\left(U_{n}+K_{n}\right)\leq W_{ext} \tag{3}$$

where U_{n+1} and U_n represent the strain energy at the end and at the beginning of the time step respectively, K_{n+1} and K_n are the corresponding kinetic energies and W_{ext} represents the work

done by external forces within the time step. This classification results in the following three categories of algorithms which satisfy inequality (3):

- Algorithms which employ numerical dissipation.
- Algorithms extending others by using constraints of energy conservation imposed via Lagrange multipliers (Constraint Energy Method), the first of which was presented in [5].
- Algorithms which enforce energy conservation algorithmically such as the energy-momentum method presented in [6]. In the absence of external loading these algorithms are designed to obey the following laws:

$$\frac{dL_t}{dt} = 0, \quad \frac{dJ_t}{dt} = 0, \quad \frac{dE_t^{tot}}{dt} \leq 0 \tag{4}$$

where L_t is the linear momentum, J_t is the angular momentum and E_t^{tot} is the total energy. Combinations of algorithms of different categories from the above have also been made. The Constraint Energy Momentum Algorithm developed in [7] combines numerical dissipation algorithms and enforced energy conservation algorithms, whereas combinations of numerical dissipation algorithms and algorithms which ensure energy conservation algorithmically are presented in [4,11].

Another alternative for more accurate and stable time integration algorithms is the concept of composition, namely the combination of two or more algorithms which gives other composite algorithms which are more efficient. Each time step is divided into two or more substeps, at which different independent integration schemes are applied. Equilibrium is satisfied at each time substep. The final solution depends on the algorithms used as well as on the way of partition of the time steps. The most representative method is presented in [8], whereas a classification of these methods is presented in [9].

An additional method to solve time dependent problems is the Whole Element Method (WEM) in which time is incorporated along with the other spatial variables into a direct variational method. Therefore, the initial condition problem can be converted into a boundary value problem, containing both spatial and temporal variables. This method is outlined in [10].

3 MODIFIED NONLINEAR TIME INTEGRATION ALGORITHM

3.1 The linear generalized single step single solve algorithm

The equation of motion of a Single Degree of Freedom (SDOF) linear structure is given by the combination of the SDOF counterparts of (1) and (2):

$$M\ddot{u}(t) + C\dot{u}(t) + Ku(t) = f(t) \tag{5}$$

with initial conditions:

$$u(0) = u_0, \quad \dot{u}(0) = \dot{u}_0 \tag{6}$$

Equation (5) can be applied to MDOF structures, given that the latter can be decomposed into a finite number of SDOF structures using various superposition methods. In [1] it is shown that the Dahlquist theorem holds not only for the linear multistep methods (LMS), but also for the general single step single solve (GSSSS) time integration algorithms, which are spectrally identical to the former. This theorem states that a GSSSS algorithm which is unconditionally stable, can be at most second order accurate.

Equation (5) can be represented as a time weighted residual as follows:

$$\int_0^{\Delta t} W^T \left(M\ddot{u} + C\dot{u} + Ku - f \right) dt \tag{7}$$

where the weighted time field is assumed to be of the form

$$W = 1 + w_1\Gamma + w_2\Gamma^2 + w_3\Gamma^3 \tag{8}$$

and:

$$\Gamma = \overline{\tau} / \Delta t, \quad \overline{\tau} = t - t_n, \quad \Delta t = t_{n+1} - t_n \tag{9}$$

The dependent field variables (u, $\dot{u}$, $\ddot{u}$) can be approximated by the following asymptotic series expansions:

$$u = u_n + \Lambda_1 \dot{u}_n \tau + \Lambda_2 \ddot{u}_n \tau^2 + \Lambda_3 \frac{\ddot{u}_{n+1} - \ddot{u}_n}{\Delta t} \tau^3 \tag{10}$$

$$\dot{u} = \dot{u}_n + \Lambda_4 \ddot{u}_n \tau + \Lambda_5 \frac{\ddot{u}_{n+1} - \ddot{u}_n}{\Delta t} \tau^2 \tag{11}$$

$$\ddot{u} = \ddot{u}_n + \Lambda_6 \frac{\ddot{u}_{n+1} - \ddot{u}_n}{\Delta t} \tau \tag{12}$$

and the load vector is expanded to first order via a Taylor series:

$$f = f_n + \frac{f_{n+1} - f_n}{\Delta t} \tau \tag{13}$$

The updates of displacement and velocity are given by the relations:

$$u_{n+1} = u_n + \lambda_1 \dot{u}_n \Delta t + \lambda_2 \ddot{u}_n \Delta t^2 + \lambda_3 \left(\ddot{u}_{n+1} - \ddot{u}_n \right) \Delta t^2 \tag{14}$$

$$\dot{u}_{n+1} = \dot{u}_n + \lambda_4 \ddot{u}_n \Delta t + \lambda_5 \left(\ddot{u}_{n+1} - \ddot{u}_n \right) \Delta t \tag{15}$$

The update of acceleration is given by substitution of equations (8) to (15) into (7) as follows:

$$\begin{aligned} &\left(W_1\Lambda_6 M + W_2\Lambda_5 C\Delta t + W_3\Lambda_3 K\Delta t^2 \right) \ddot{u}_{n+1} = \\ &-M\left(\ddot{u}_n - W_1\Lambda_6 \ddot{u}_n \right) \\ &-C\left(\dot{u}_n + W_1\Lambda_4 \ddot{u}_n \Delta t - W_2\Lambda_5 \ddot{u}_n \Delta t \right) \\ &-K\left(u_n + W_1\Lambda_1 \dot{u}_n \Delta t + W_2\Lambda_2 \ddot{u}_n \Delta t^2 - W_3\Lambda_3 \ddot{u}_n \Delta t^2 \right) \\ &+\left(1 - W_1 \right) f_n + W_1 f_{n+1} \end{aligned} \tag{16}$$

where the constants W_i are given by:

$$W_i = \frac{\sum_{j=0}^{3} \frac{w_j}{1+i+j}}{\sum_{j=0}^{3} \frac{w_j}{1+j}}, \quad i = 1,2,3 \tag{17}$$

There are 12 independent integration constants that are needed in order to apply the equations (16), (14) and (15) to proceed to the next step: W_1, $W_1\Lambda_1$, $W_2\Lambda_2$, $W_3\Lambda_3$, $W_1\Lambda_4$, $W_2\Lambda_5$, $W_1\Lambda_6$, λ_1, λ_2, λ_3, λ_4, λ_5. Each set of these parameters defines the algorithm uniquely, and can be considered in some way as the algorithm's signature. Many known time integration algorithms,

which will be presented later, result from suitable selection of these parameters. In [1], the integration parameters are calculated by imposing several different constraints to the algorithm, regarding order of accuracy, overshooting behavior (in terms of displacement and velocity orders), spurious roots at the high and low frequency limits, dissipation and dispersion properties, bifurcation of the principal roots, etc, which results in the derivation of 9 different algorithms belonging to the above family. In this study, W_1 is calculated directly from (17), after specifying the parameters w_1, w_2, w_3.

3.2 Design of the linear generalized single step single solve algorithm – special cases

An algorithm is termed to have the property of continuous acceleration, if the acceleration $\ddot{u}_{n+1}$ calculated at $t=t_n$ satisfies the equation of motion (strong form) at $t=t_n$. Otherwise, the algorithm is termed to have the property of discontinuous acceleration [1].

The procedure for designing the algorithm presented in the previous section to apply it to time integration problems (i.e. setting its 12 integration constants), is presented in [1]. The algorithms of the generalized single step family are the following:

- Zero-order displacement, zero-order velocity, optimal numerical dissipation and dispersion (U0-V0-Opt)
- Zero-order displacement, zero-order velocity, continuous acceleration (U0-V0-CA)
- Zero-order displacement, zero-order velocity, discontinuous acceleration (U0-V0-DA)
- Zero-order displacement, first-order velocity, optimal numerical dissipation and dispersion (U0-V1-Opt)
- Zero-order displacement, first-order velocity, continuous acceleration (U0-V1-CA)
- Zero-order displacement, first-order velocity, discontinuous acceleration (U0-V1-DA)
- First-order displacement, zero-order velocity, optimal numerical dissipation and dispersion (U1-V0-Opt)
- First-order displacement, zero-order velocity, continuous acceleration (U1-V0-CA)
- First-order displacement, zero-order velocity, discontinuous acceleration (U1-V0-DA)

The values of the parameters are shown for various well-known integration schemes in tables. In Table 1 the parameters of the central difference method, the average constant acceleration method [12], the linear acceleration method [12], the Fox-Goodwin formula [14], the backward acceleration method [13] and the general family of Newmark methods [12]. In Table 2 the parameters of the zero-order displacement and zero-order velocity overshooting algorithms are presented [1]. In order to evaluate the integration constants, the quantity $\rho_{\inf}$, which is the minimum absolute value of the principal roots of the amplification matrix at the high-frequency limit, has to be first assigned a desired value, which must lie in the range given at the appropriate row of the table. If $\rho_{\inf}=1$, the resulting algorithm is non-dissipative. In Table 3 the parameters are given for the zero-order displacement, first-order velocity overshooting algorithms, presented in [1]. It has to be mentioned that the formulas presented in Table 3 correspond to three special cases of these zero-order displacement, first-order velocity overshooting algorithms, namely the generalized a-method, the HHT-a method and the WBZ a-method, presented in [15,16,17] respectively. Table 4 shows the parameters of the first-order displacement and zero-order velocity overshooting algorithms. If $\rho_{\inf}=1$, the first-order displacement, zero-order velocity, optimal numerical dissipation and dispersion, the first-

	Central Difference Method	Average constant acceleration [12]	Linear Acceleration Method [12]	Fox-Goodwin formula [14]	Backward acceleration method [13]	Family of Newmark Methods [12]
w_1	-15	-15	-15	-15	-15	-15
w_2	45	45	45	45	45	45
w_3	-35	-35	-35	-35	-35	-35
$W_1\Lambda_1$	1	1	1	1	1	1
$W_2\Lambda_2$	0	0.25	1/6	1/12	0.5	β
$W_3\Lambda_3$	0	0.25	1/6	1/12	0.5	β
$W_1\Lambda_4$	0.5	0.5	0.5	0.5	0.5	γ
$W_2\Lambda_5$	0.5	0.5	0.5	0.5	0.5	γ
$W_1\Lambda_6$	1	1	1	1	1	1
λ_1	1	1	1	1	1	1
λ_2	0.5	0.5	0.5	0.5	0.5	0.5
λ_3	0	0.25	1/6	1/12	0.5	β
λ_4	1	1	1	1	1	1
λ_5	0.5	0.5	0.5	0.5	0.5	γ

Table 1: Integration parameters for various known time integration schemes.

	U0-V0-Opt	U0-V0-CA	U0-V0-DA
ρinf	[0 1]	[1/3 1]	[0 1]
w_1	-15(1-2ρinf)/(1-4ρinf)	-15(1-5ρinf)/(3-7ρinf)	-15
w_2	15(3-4ρinf)/(1-4ρinf)	15(1-13ρinf)/(3-7ρinf)	45
w_3	-35(1-ρinf)/(1-4ρinf)	140ρinf/(3-7ρinf)	-35
$W_1\Lambda_1$	1/(1+ρinf)	(1+3ρinf)/2/(1+ρinf)	1
$W_2\Lambda_2$	1/2/(1+ρinf)	(1+3ρinf)/4/(1+ρinf)	1/2
$W_3\Lambda_3$	1/2/(1+ρinf)^2	(1+3ρinf)/4/(1+ρinf)^2	1/2/(1+ρinf)
$W_1\Lambda_4$	1/(1+ρinf)	(1+3ρinf)/2/(1+ρinf)	1
$W_2\Lambda_5$	1/(1+ρinf)^2	(1+3ρinf)/2/(1+ρinf)^2	1/(1+ρinf)
$W_1\Lambda_6$	(3-ρinf)/2/(1+ρinf)	1	(3+ρinf)/2/(1+ρinf)
λ_1	1	1	1
λ_2	1/2	1/2	1/2
λ_3	1/2/(1+ρinf)	1/2/(1+ρinf)	1/2/(1+ρinf)
λ_4	1	1	1
λ_5	1/(1+ρinf);	1/(1+ρinf)	1/(1+ρinf)

Table 2: Integration parameters for zero-order displacement, zero order velocity overshooting algorithms.

	U0-V1-Opt [15]	U0-V1-CA [16]	U0-V1-DA [17]
ρinf	[0 1]	[1/2 1]	[0 1]
w_1	-15(1-2ρinf)/(1-4ρinf)	-15(1-2ρinf)/(2-3ρinf)	-15
w_2	15(3-4ρinf)/(1-4ρinf)	15(2-5ρinf)/(2-3ρinf)	45
w_3	-35(1-ρinf)/(1-4ρinf)	-35(1-3ρinf)/2/(2-3ρinf)	-35
$W_1\Lambda_1$	1/(1+ρinf)	2ρinf/(1+ρinf)	1
$W_2\Lambda_2$	1/2/(1+ρinf)	ρinf/(1+ρinf)	1/2
$W_3\Lambda_3$	1/(1+ρinf)^3	2ρinf/(1+ρinf)^3	1/(1+ρinf)^2
$W_1\Lambda_4$	1/(1+ρinf)	2ρinf/(1+ρinf)	1
$W_2\Lambda_5$	(3-ρinf)/2/(1+ρinf)^2	ρinf(3-ρinf)/(1+ρinf)^2	(3-ρinf)/2/(1+ρinf)
$W_1\Lambda_6$	(2-ρinf)/(1+ρinf)	1	2/(1+ρinf)
λ_1	1	1	1
λ_2	1/2	1/2	1/2
λ_3	1/(1+ρinf)^2	1/(1+ρinf)^2	1/(1+ρinf)^2
λ_4	1	1	1
λ_5	(3-ρinf)/2/(1+ρinf)	(3-ρinf)/2/(1+ρinf)	(3-ρinf)/2/(1+ρinf)

Table 3: Integration parameters for zero-order displacement, first order velocity overshooting algorithms.

	U1-V0-Opt	U1-V0-CA	U1-V0-DA
ρinf	[0 1]	[1/2 1]	[0 1]
w_1	-30(3-8ρinf+6ρinf^2) / (9-22ρinf+19ρinf^2)	-60(2-8ρinf+7ρinf^2) / (11-48ρinf+41ρinf^2)	-30(3-4ρinf)/(9-11ρinf)
w_2	15(25-74ρinf+53ρinf^2) / 2 / (9-22ρinf+19ρinf^2)	15(37-140ρinf+127ρinf^2) / 2 / (11-48ρinf+41ρinf^2)	15(25-37ρinf)/2/(9-11ρinf)
w_3	-35(3-10ρinf+7ρinf^2) / (9-22ρinf+19ρinf^2)	-35(5-18ρinf+17ρinf^2) / (11-48ρinf+41ρinf^2)	-35(3-5ρinf) / (9-11ρinf)
$W_1\Lambda_1$	(3-ρinf)/2/(1+ρinf)	(1+3ρinf)/2/(1+ρinf)	(3+ρinf)/2/(1+ρinf)
$W_2\Lambda_2$	1/(1+ρinf)^2	2ρinf/(1+ρinf)^2	1/(1+ρinf)
$W_3\Lambda_3$	1/(1+ρinf)^3	2ρinf/(1+ρinf)^3	1/(1+ρinf)^2
$W_1\Lambda_4$	(3-ρinf)/2/(1+ρinf)	(1+3ρinf)/2/(1+ρinf)	(3+ρinf)/2/(1+ρinf)
$W_2\Lambda_5$	2/(1+ρinf)^3	4ρinf/(1+ρinf)^3	2/(1+ρinf)^2
$W_1\Lambda_6$	(2-ρinf)/(1+ρinf)	1	2/(1+ρinf)
λ_1	1	1	1
λ_2	1/2	1/2	1/2
λ_3	1/2/(1+ρinf)	1/2/(1+ρinf)	1/(1+ρinf)^2
λ_4	1	1	1
λ_5	1/(1+ρinf)	1/(1+ρinf)	(3-ρinf)/2/(1+ρinf)

Table 4: Integration parameters for first-order displacement, zero order velocity overshooting algorithms.

order displacement, zero-order velocity, continuous acceleration and the first-order displacement, zero-order velocity, discontinuous acceleration algorithms recover, the first the midpoint rule a-form algorithm, and the two last the Newmark average acceleration a-form algorithm.

3.3 Modification of the linear algorithm for nonlinear dynamic response

In this section the generalized linear family of algorithms presented above is modified to account for materially nonlinear dynamic response. To proceed from the current step $(u_n, \dot{u}_n, \ddot{u}_n)$ to the next time step $(u_{n+1}, \dot{u}_{n+1}, \ddot{u}_{n+1})$, the secant stiffness and damping matrices are needed, which in general depend on u_{n+1} and $\dot{u}_{n+1}$. Since the latter are unknown, the tangent stiffness and damping matrices are calculated and iterations are performed to arrive to a converged solution. Convergence is attained via a Newton-Raphson iterative procedure. In some time integration algorithms, this iteration is avoided by using the initial tangent matrices instead of updating them, even though this approximation is not correct in principle.

The outline of the modified nonlinear time integration algorithm used in this study is shown in Figure 1. The given data are the mass, stiffness and damping properties of the SDOF oscillator and the imposed external force, denoted by $M, \bar{K}, \bar{C}, f$ respectively.

Before application of the algorithm, the necessary integration constants are calculated, as well as the maximum tolerance $tol_{\max}$ and the maximum number of iterations until convergence $k_{\max}$.

4 BENCHMARK PROBLEMS STUDIED

4.1 Comparison of the different time integration schemes used

In this section, 13 different time integration schemes presented in the Tables 1-4 are compared through their application for solving a number of benchmark problems. The schemes compared are the average constant acceleration method [12], the linear acceleration method [12], the Fox-Goodwin formula [14], the backward acceleration method [13], the U0-V0-Opt, the U0-V0-CA, the U0-V0-DA, the U0-V1-Opt, the U0-V1-CA, the U0-V1-DA, the U1-V0-Opt, the U1-V0-CA, and the U1-V0-DA algorithms. The last 9 integration schemes are presented in [1] and details about their notation can be seen in Tables 2-4. Two of the benchmark problems involve the time integration of the equation of motion of nonlinear SDOF dynamic systems which are unforced and undamped (no external excitation is applied to them and no damping forces exist during their oscillation respectively), and at the third benchmark problem a SDOF oscillator is harmonically excited by imposing an external force with a sinusoidal time history. The response of the SDOF spring in the last case is elastoplastic, with a linear elastic and a perfectly plastic branches, exhibiting an identical yield limit in both tension and compression. An efficient nonlinear time integration scheme should conserve total energy in the first two cases, since in the last case the energy is dissipated through hysteretic response of the oscillator spring (its force-displacement diagram forms a closed loop). Thus an appropriate measure of the inaccuracy of the various time integration schemes employed can be the deviation of the total energy from its initial value:

$$e = \left| \frac{E - E_0}{E_0} \right| \tag{18}$$

in which E and E_0 are the current and initial total energy, respectively.

Three benchmark problems are solved with the various integration schemes developed in this study: the SDOF oscillator with hardening spring, the SDOF oscillator with softening spring and the elastoplastic oscillator. The two first of these examples were also studied in [18] for an assessment of the performance of various time integration schemes and in [19] for testing the differential quadrature time integration scheme, which performed successfully.

Initialize $u_n = u_0, \dot{u}_n = \dot{u}_0$

Find $K_0 = \bar{K}\left(u_0, \dot{u}_0\right)$, $C_0 = \bar{C}\left(u_0, \dot{u}_0\right)$ and $p_0 = p\left(u_0, \dot{u}_0\right)$ from (2)

Find $\ddot{u}_0 = \left(f_0 - p_0\right)/M$ from (1)

Set $K_n = K_0$, $C_n = C_0$, $p_n = p_0$, $u_n = u_0$, $\dot{u}_n = \dot{u}_0$, $\ddot{u}_n = \ddot{u}_0$

for $n = 1 : length(f) - 1$

Initialize iteration counter $k = 1$

Initialize convergence tolerance $tol = tol_{\max}$

Initial estimate of $\ddot{u}_{n+1}^1$ at next time step ($n+1$) and first iteration ($k = 1$), from (16)

Update u_{n+1}^1 and $\dot{u}_{n+1}^1$ according to (14) and (15) respectively.

Find $K_{n+1}^1 = \bar{K}\left(u_{n+1}^1, \dot{u}_{n+1}^1\right)$, $C_{n+1}^1 = \bar{C}\left(u_{n+1}^1, \dot{u}_{n+1}^1\right)$ and $p_{n+1}^1 = p\left(u_{n+1}^1, \dot{u}_{n+1}^1\right)$ from (2)

while $tol \geq tol_{\max}$ & $k \leq k_{\max}$

Set $K_{n+1}^{k+1} = K_{n+1}^k$, $C_{n+1}^{k+1} = C_{n+1}^k$, $p_{n+1}^{k+1} = p_{n+1}^k$, $u_{n+1}^{k+1} = u_{n+1}^k$, $\dot{u}_{n+1}^{k+1} = \dot{u}_{n+1}^k$, for the next iteration

Find $\ddot{u}_{n+1}^{k+1}$ from (16)

Find the residual $R_{n+1}^{k+1} = \ddot{u}_{n+1}^{k+1} - \ddot{u}_{n+1}^1$

Set da equal to a very small quantity (infinitesimal variation of acceleration)

Find $d\ddot{u}_{n+1}^{k+1} = \ddot{u}_{n+1}^{k+1} + da$

Find $du_{n+1}^{k+1}, d\dot{u}_{n+1}^{k+1}$ from (14) and (15) respectively, using $u_{n+1}^1, \dot{u}_{n+1}^1, d\ddot{u}_{n+1}^{k+1}$

Find $dK_{n+1}^{k+1} = \bar{K}\left(du_{n+1}^{k+1}, d\dot{u}_{n+1}^{k+1}\right)$, $dC_{n+1}^{k+1} = \bar{C}\left(du_{n+1}^{k+1}, d\dot{u}_{n+1}^{k+1}\right)$ and $dp_{n+1}^{k+1} = p\left(du_{n+1}^{k+1}, d\dot{u}_{n+1}^{k+1}\right)$ from (2)

Update $d\ddot{u}_{n+1}^{k+1}$ according to (16)

Find the residual $dR_{n+1}^{k+1} = d\ddot{u}_{n+1}^{k+1} - \ddot{u}_{n+1}^1$

Find $tol = \dfrac{da}{\ddot{u}_{n+1}^1 - \ddot{u}_n} \Big/ \dfrac{dR_{n+1}^{k+1} - R_{n+1}^{k+1}}{R_{n+1}^{k+1}}$

Update $\ddot{u}_{n+1}^{k+1} = \ddot{u}_{n+1}^{k+1} - tol\left(\ddot{u}_{n+1}^{k+1} - \ddot{u}_n\right)$

Update u_{n+1}^{k+1} and $\dot{u}_{n+1}^{k+1}$ according to (14) and (15) respectively

Find $K_{n+1}^{k+1} = \bar{K}\left(u_{n+1}^{k+1}, \dot{u}_{n+1}^{k+1}\right)$, $C_{n+1}^{k+1} = \bar{C}\left(u_{n+1}^{k+1}, \dot{u}_{n+1}^{k+1}\right)$ and $p_{n+1}^{k+1} = p\left(u_{n+1}^{k+1}, \dot{u}_{n+1}^{k+1}\right)$ from (2)

Update iteration counter $k = k + 1$

end

Update $K_n = K_{n+1}^{k+1}$, $C_n = C_{n+1}^{k+1}$, $p_n = p_{n+1}^{k+1}$, $u_n = u_{n+1}^{k+1}$, $\dot{u}_n = \dot{u}_{n+1}^{k+1}$, $\ddot{u}_n = \ddot{u}_{n+1}^{k+1}$

end

Figure 1: Flowchart of the modified algorithm used in this study.

4.2 SDOF oscillator with hardening spring

The first benchmark problem studied is the SDOF oscillator with hardening spring, for which the equation of motion is:

$$\ddot{u} + S_1 u\left(1 + S_2 u^2\right) = 0 \tag{19}$$

This type of oscillator represents the well-known unforced and undamped Duffing oscillator. The system is conservative and its total energy is constant and given by analytical integration of (19):

$$E = \frac{1}{2}\dot{u}^2 + \frac{1}{2}S_1 u^2 + \frac{1}{4}S_1 S_2 u^4 \tag{20}$$

In this example S_1=100, S_2=10 and the initial conditions are $u_0 = 1.5$ and $\dot{u}_0 = 0$. The time step used is Δt=0.005 and the duration of the dynamic analysis is equal to 200 time steps. The $\rho_{\inf}$ parameter is selected to be equal to unity for all integration algorithms used. Concerning the Newton-Raphson iterative procedure used, the maximum convergence tolerance and the maximum number of iterations are $tol_{\max} = 0.01$ and $k_{\max} = 200$ respectively.

4.3 SDOF oscillator with softening spring

The second benchmark problem studied is the unforced and undamped SDOF oscillator with softening spring, for which the nonlinear dynamic equation of motion is:

$$\ddot{u} + S\tanh\left(u\right) = 0 \tag{21}$$

The system is conservative and its total energy is constant and given by analytical integration of (21):

$$E = \frac{1}{2}\dot{u}^2 + S\ln\left(\cosh\left(u\right)\right) \tag{22}$$

In this example S=100 and the initial conditions are $u_0 = 4$ and $\dot{u}_0 = 0$. The time step used is Δt=0.05 and the duration of the dynamic analysis is equal to 200 time steps. The $\rho_{\inf}$ parameter is selected to be equal to unity for all integration algorithms used. Concerning the Newton-Raphson iterative procedure used, the maximum convergence tolerance and the maximum number of iterations are $tol_{\max} = 0.01$ and $k_{\max} = 200$ respectively.

4.4 SDOF oscillator with elastoplastic spring

The third benchmark problem studied is the harmonically forced SDOF oscillator with elastoplastic spring, for which the initial conditions are $u_0 = 0$ and $\dot{u}_0 = 0$. The time step used is Δt=0.005 and the duration of the dynamic analysis is equal to 800 time steps. The $\rho_{\inf}$ parameter is selected to be equal to unity for all integration algorithms used. Concerning the Newton-Raphson iterative procedure used, the maximum convergence tolerance and the maximum number of iterations are $tol_{\max} = 0.01$ and $k_{\max} = 200$ respectively. As regards the elastoplastic behavior of the spring, the yield limit is assumed equal to 100 for both tension and compression and the modulus of elasticity in the linear elastic range is assumed to be equal to 50.

5 TIME INTEGRATION RESULTS

5.1 Phase portraits

The time integration results are presented in terms of phase portraits, which provide an overview of the evolution of the total energy of the oscillator. In each phase portrait, the oscillation begins from the rightmost border of each diagram, and rotates clockwise around the maxima and minima of the displacement and velocity, thus inscribing an ellipse. Maximum kinetic energy in each cycle occurs at the upper and lower extrema, whereas maximum potential occurs at the left and right extrema. If the total energy of the oscillator remains constant, the ellipse is supposed to have a single line along its thickness. In the cases studied here, the total energy decreases gradually as the oscillation proceeds, resulting in decreasing kinetic and potential energy maxima and minima (in terms of absolute values), thus leading to ellipses of lower area being inscribed into the initial one. The main reason for the energy decrease is that the convergence of the Newton-Raphson iterations occurs within a specified tolerance, if the solution is not accepted when maximum number of iterations is reached, and this error accumulates along time steps, leading eventually in large errors in the final response. Exception is the elastoplastic oscillator, in which energy is supposed to be dissipated due to the fact that its force – displacement diagram forms a closed loop as will be shown in later sections. The energy dissipation in each cycle is equal to the area of this loop.

In Figure 2, phase portraits of the response of the SDOF oscillator with hardening spring are shown with the 13 different integration methods mentioned above. It is noted that in the cases of the U0-V1-Opt, the U0-V1-CA and the U0-V1-DA algorithms, their integration parameters have been selected so that they actually correspond to the generalized a-method (denoted by CH-a in the appropriate subplot title and referred in [15]), the HHT-a method (denoted by HHT-a in the appropriate subplot title and referred in [16]) and the Wood-Bossak-Zienkiewicz method (denoted by WBZ-a in the appropriate subplot title and referred in [17]) respectively. It is clearly seen that the optimal numerical dissipation and dispersion methods (…-Opt) preserve the total energy much better that their corresponding continuous acceleration (…-CA) and discontinuous acceleration (…-DA) methods.

In Figure 3, phase portraits of the response of the SDOF oscillator with softening spring are shown with the 13 different integration methods. Observations analogous to those of Figure 2 can be made, since the optimal numerical dissipation and dispersion methods (…-Opt) lead to a much lower total energy decrease compared to the other methods. The decrease of total energy is more pronounced for all the time integrators except for the optimal ones, in the case of the softening spring, for which it has to be mentioned that the time step is 10 times higher than the one used for the hardening spring.

Finally, in Figure 4 the corresponding phase portraits are shown for the elastoplastic SDOF system. It is observed that except for the optimal numerical dissipation and dispersion algorithm with zero displacement and velocity overshooting (U0-V0-Opt), the phase portrait of which can be easily observable, all the other algorithms exhibit numerical instabilities. This is clear in the cases of U0-V1-Opt (CH-a) and U1-V0-Opt algorithms. Furthermore, apart from the three aforementioned algorithms, in all the other cases the solution is observed to be in error from the start of the dynamic analysis; as the displacement increases towards the positive direction, the velocity becomes negative and decreases. Taking into account the initial conditions of the elastoplastic oscillator, where the initial displacement and the initial velocity are both zero, this is not possible. Therefore, it is actually shown that the U0-V0-Opt algorithm performs best, compared to the others.

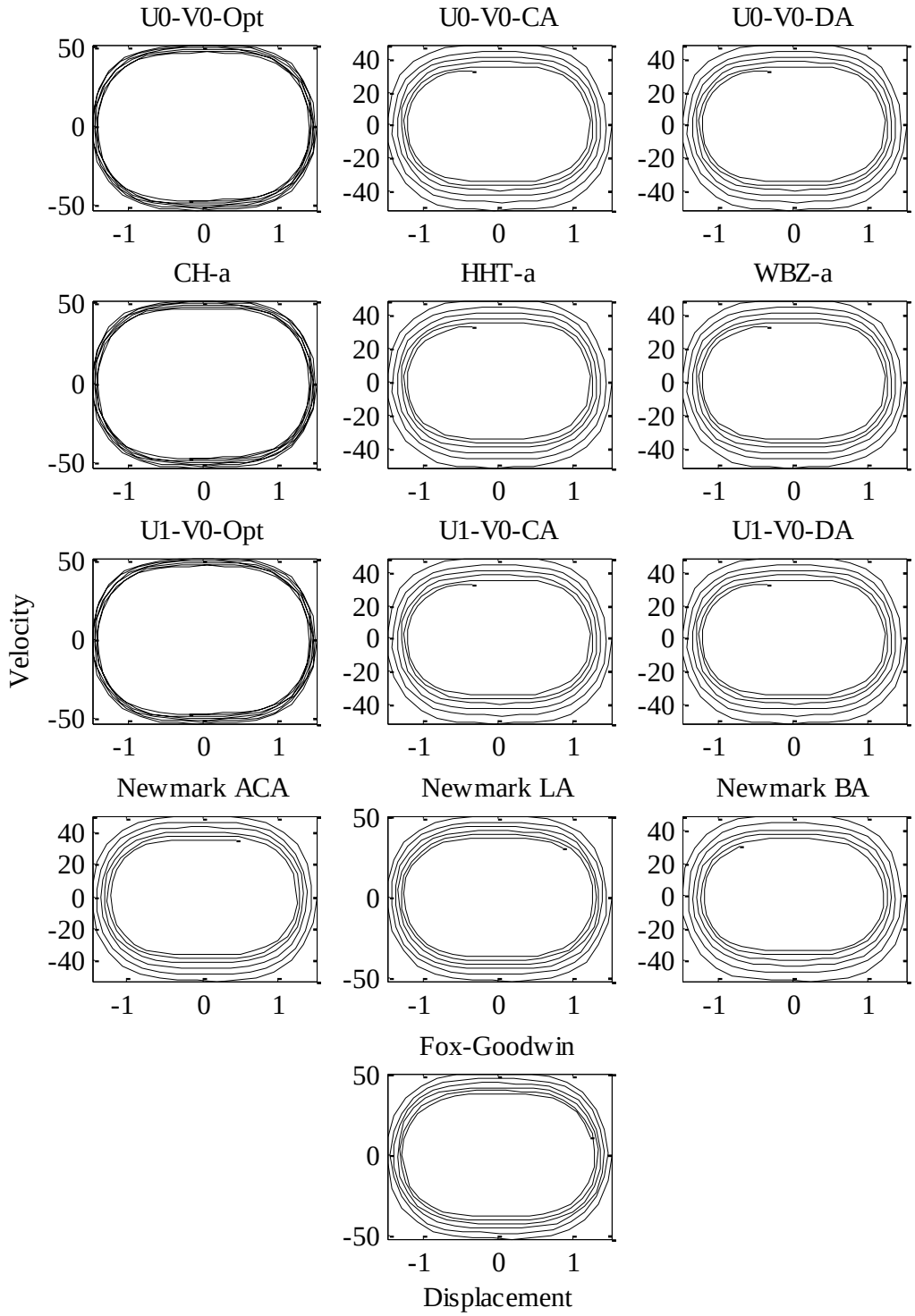


Figure 2: Phase portraits of the hardening spring $d^2u/dt^2+100u(1+10u^2)=0$, $(u)_0=1.5$, $(du/dt)_0=0$, $\Delta t=0.005$, $t=200\Delta t$, $\rho_{inf}=1$, $tol_{max}=0.01$, $k_{max}=200$.

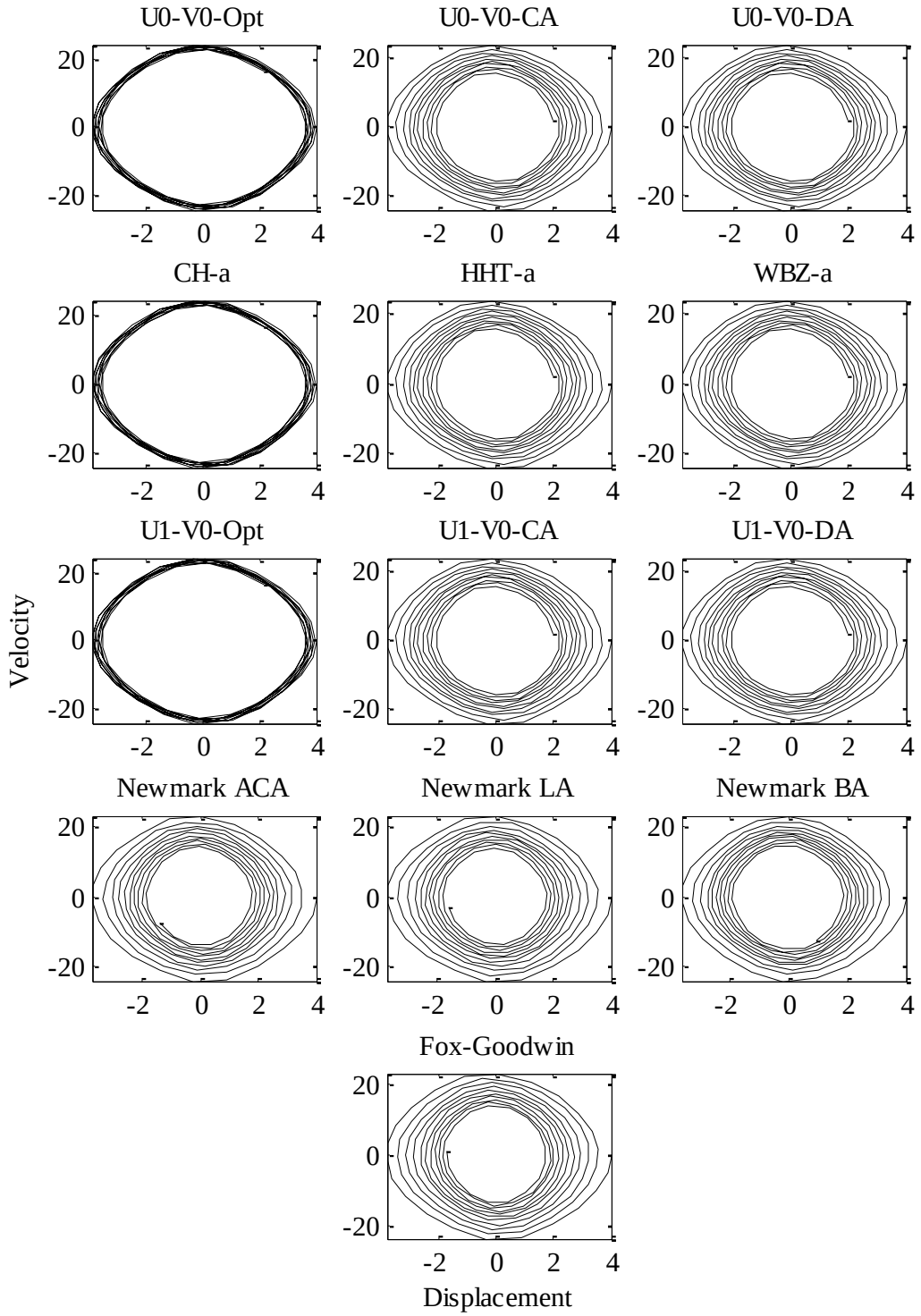


Figure 3: Phase portraits of the softening spring $d^2u/dt^2+100\tanh(u)=0$, $(u)_0=4$, $(du/dt)_0=0$, $\Delta t=0.05$, $t=200\Delta t$, $\rho_{inf}=1$, $tol_{max}=0.01$, $k_{max}=200$.

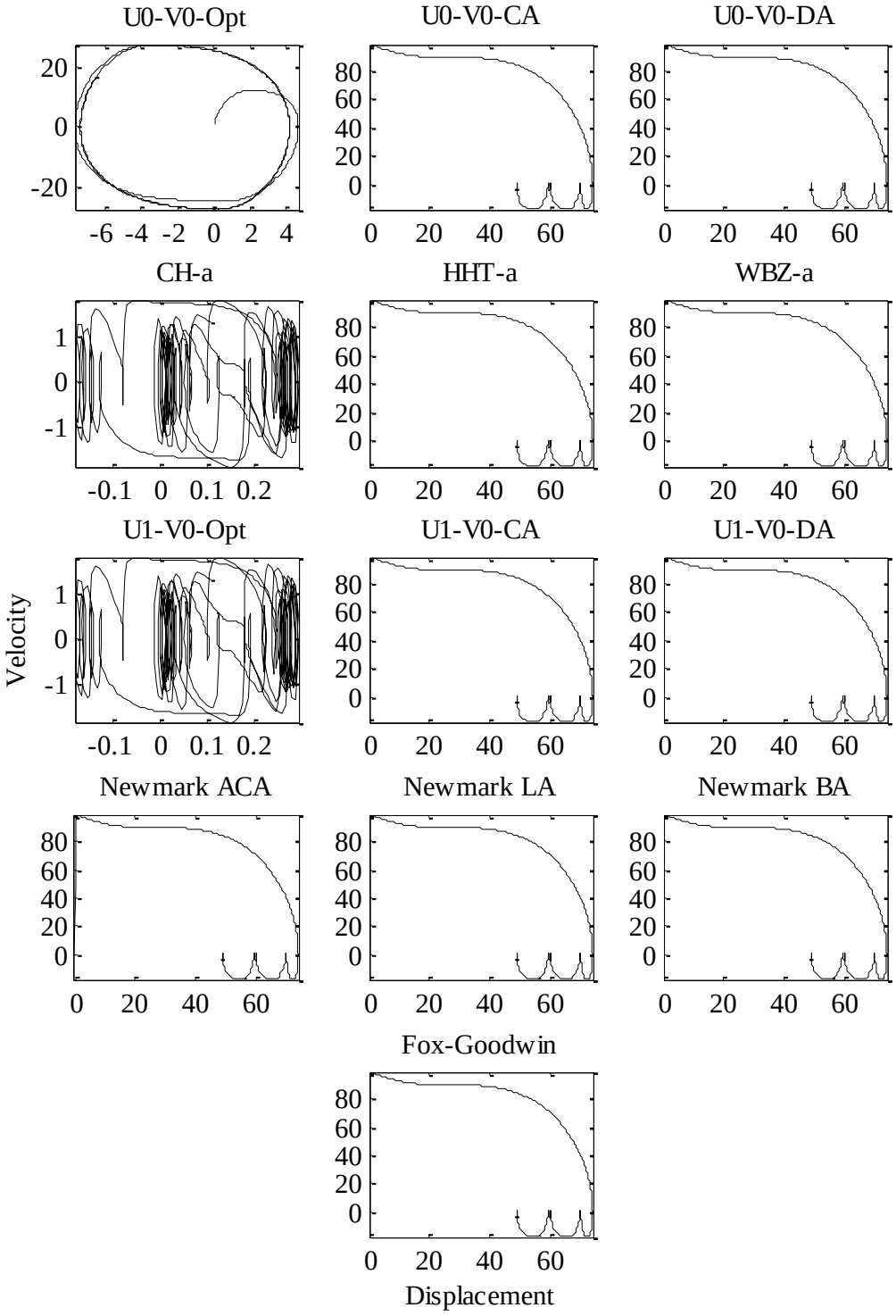


Figure 4: Phase portraits of the harmonically excited elastoplastic SDOF system, $(u)_0=0$, $(du/dt)_0=0$, $\Delta t= 0.005$, $t= 800\Delta t$, $\rho_{inf}=1$, $tol_{max}=0.01$, $k_{max}=200$.

5.2 Energy variation

The energy variation for the various numerical integrators is shown in Figure 5 for the oscillator with the hardening spring, in Figure 6 for the oscillator with the softening spring and in Figure 7 for the oscillator with the elastoplastic spring. In each of these figures, the numerical integrators used are grouped into three categories, which are the optimal numerical dissipation and dispersion methods (represented with the continuous bold line), the continuous acceleration and discontinuous acceleration methods (represented with the dashed bold line) and finally the family of Newmark methods and the Fox-Goodwin method (represented with the continuous thin lines). The integration constants and other parameters are the same with those used for the results shown in Figures 1 to 3 respectively. The ideal time integration scheme would conserve energy in the first two oscillators, namely the energy deviation shown in Figures 4 and 5 would be zero. Among the algorithms studied here, energy reduction is present to a higher or lower extent. The lowest energy deviation is observed for the optimal numerical dissipation and dispersion algorithms. For the last, the energy reduction is about one third of that observed for continuous/discontinuous acceleration algorithms and the other common integration methods, in the case of the SDOF system with hardening spring (Figure 5). The reduced energy deviation for optimal numerical dissipation and dispersion algorithms is more pronounced in the case of the SDOF system with softening spring, where it is approximately one fourth of that observed for the remaining integration algorithms, as seen in Figure 6. In both Figures, the rate of decrease of total energy becomes maximum at the first few cycles of dynamic response for all the time integrators used.

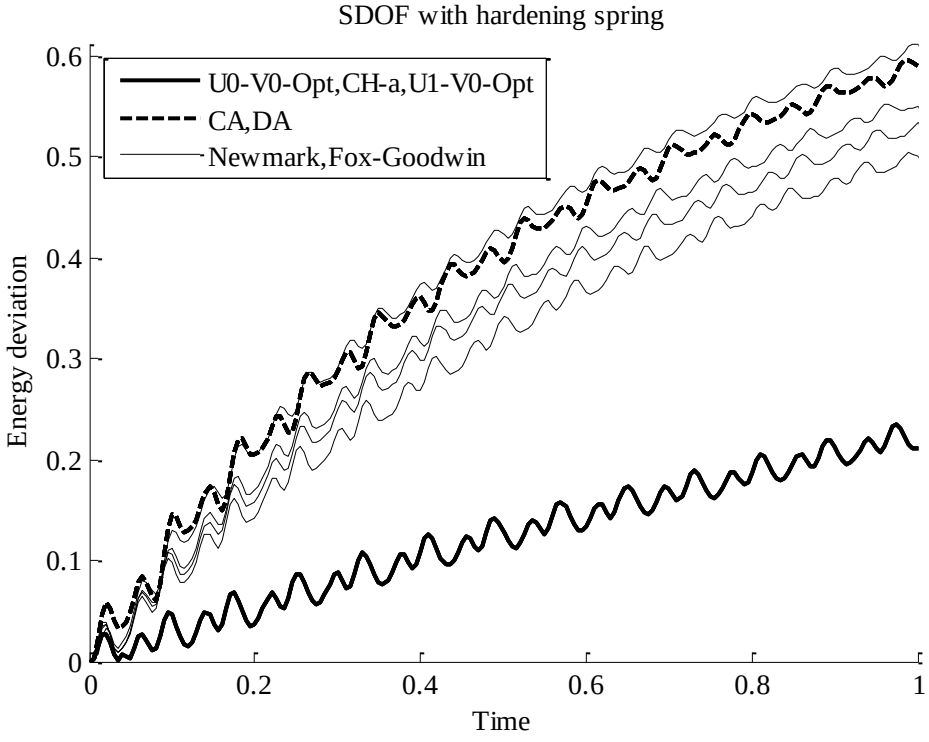


Figure 5: Total energy relative error of the SDOF oscillator with hardening spring $d^2u/dt^2+100u(1+10u^2)=0$, $(u)_0=1.5$, $(du/dt)_0=0$, $\Delta t=0.005$, $t=200\Delta t$, $\rho_{inf}=1$, $tol_{max}=0.01$, $k_{max}=200$.

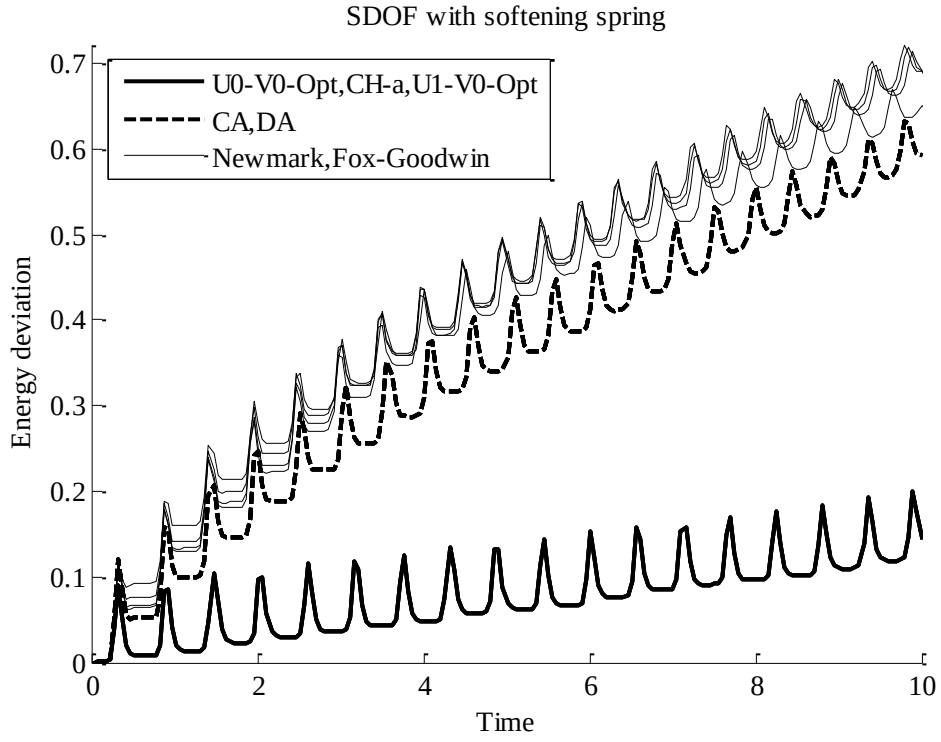


Figure 6: Total energy relative error of the SDOF oscillator with softening spring $d^2u/dt^2+100\tanh(u)=0$, $(u)_0=4$, $(du/dt)_0=0$, $\Delta t=0.05$, $t=200\Delta t$, $\rho_{inf}=1$, $tol_{max}=0.01$, $k_{max}=200$.

In the case of the elastoplastic SDOF system, instead of the relative energy error, the value of the energy decay is plotted in Figure 7, since this system is not supposed to be conservative and its total energy variation cannot be analytically calculated. It is seen that the energy decay for the U0-V0-Opt algorithm is initially zero and gradually increases, with periodic undulations but with constant average slope. For the other two optimal numerical dissipation and dispersion methods (CH-a and U1-V0-Opt), there is a steep decrease of the energy decay from zero towards a large negative value, which means that at the initial time steps the spring does not dissipate energy as it should, but it increases the internal energy of the system, a fact that is clearly impossible. The same holds for the other algorithms used; this is a clear indication that these algorithms fail to simulate the dynamic response of the system, at least with the selected time step, while the U0-V0-Opt algorithm can efficiently integrate the differential equation of motion with increased accuracy and stability.

5.3 Number of iterations needed

The robustness of the U0-V0-Opt algorithm can be also deduced by comparison of the iterations needed by each time integration scheme to achieve convergence for the three types of oscillators used in this study. In Figure 8 the number of iterations for each of the 13 different time integration algorithms used in this study versus time is presented, for the SDOF system with the hardening spring. The corresponding results for the SDOF system with the softening spring and the SDOF system with the elastoplastic spring are presented in Figure 9 and Figure 10 respectively. The maximum number of iterations is equal to $k_{\max} = 200$. The integration constants and other parameters are identical to those used for the results presented in Figures 1-6 respectively for hardening, softening and elastoplastic SDOF systems. It is apparent that the optimal numerical dissipation and dispersion algorithms need an average of 10 iterations and a maximum of roughly 15 iterations to converge to the nonlinear solution at each time

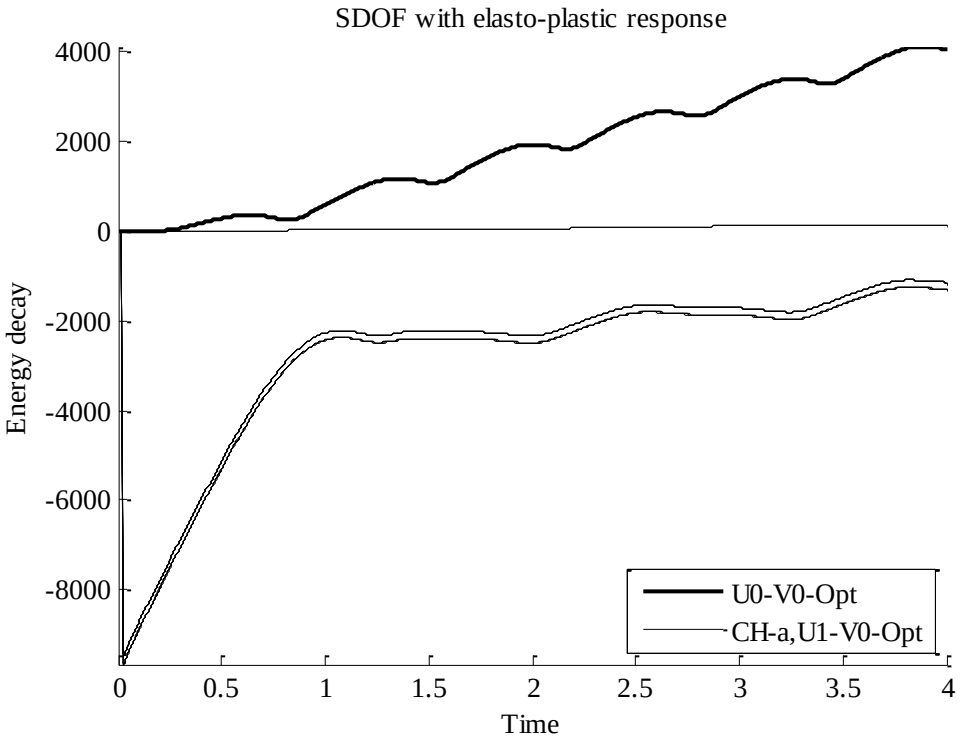


Figure 7: Total energy error of the harmonically excited elastoplastic SDOF system, $(u)_0=0$, $(du/dt)_0=0$, $\Delta t=0.005$, $t=800\Delta t$, $\rho_{inf}=1$, $tol_{max}=0.01$, $k_{max}=200$.

step for the two first types of oscillators considered, whereas for the third type of oscillator only the U0-V0-Opt algorithm achieves convergence with a maximum of 20 iterations throughout the duration of the analysis. In contrast, the remaining algorithms are shown to reach the maximum iteration limit repetitively, at which time steps the solution is accepted without further check for equilibrium in terms of the dynamic equation of motion. This implies that for those algorithms much more error is accumulated to the calculated dynamic response of the oscillator, and consequently the numerical total energy decrease is higher. This error can be of course reduced by decreasing the time step; from another point of view this means that given an acceptable level of accuracy and stability, the U0-V0-Opt algorithm can be used with a larger time step than that used by the other integration algorithms, and therefore it is more numerically efficient, since it requires less computational effort for a given time span.

5.4 Internal force vs displacement diagrams

The computational energy loss during the dynamic analysis can be explained if the internal force – displacement diagram of the two types of oscillators studied here is plotted for the various time integration algorithms used. Such plots are shown in Figure 11 for the SDOF system with hardening spring, in Figure 12 for the SDOF system with softening spring and in Figure 13 for the SDOF system with the elastoplastic spring. It is obvious that the energy loss occurs due to the fact that in the internal force – displacement graphs a loop is formed between loading and unloading branches. The area inside the loop is equal to the amount of energy lost during an oscillation cycle. For the first and second oscillator types considered here, the loop is formed probably because of the numerical singularities existing at the maximum and minimum displacements from the equilibrium position. At these points the equilibrium path is totally reversed. On the other hand, the convergence tolerance and/or the maximum unsuccess

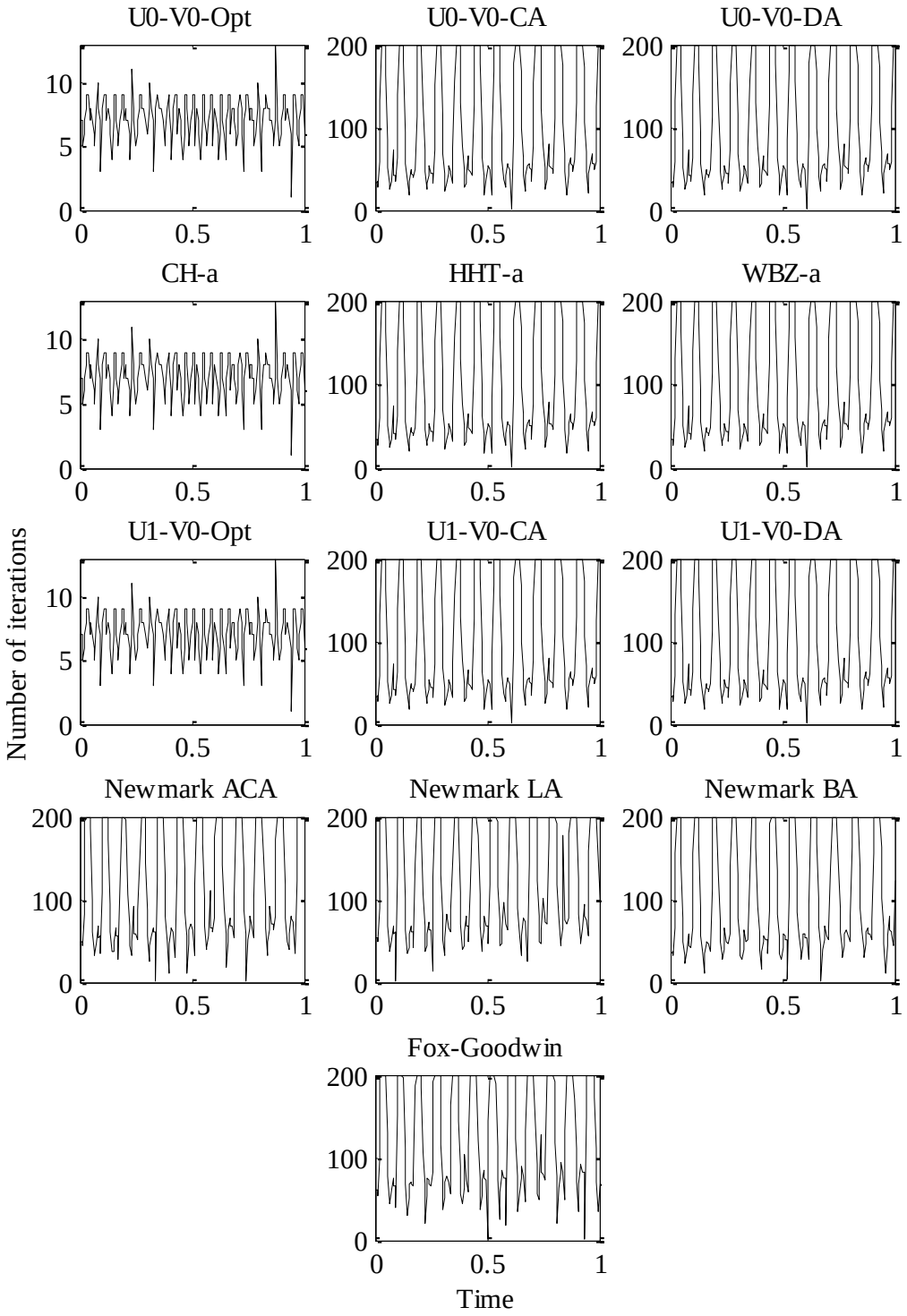


Figure 8: Number of iterations needed for the SDOF oscillator with hardening spring $d^2u/dt^2+100u(1+10u^2)=0$, $(u)_0=1.5$, $(du/dt)_0=0$, $\Delta t=0.005$, $t=200\Delta t$, $\rho_{inf}=1$, $tol_{max}=0.01$, $k_{max}=200$.

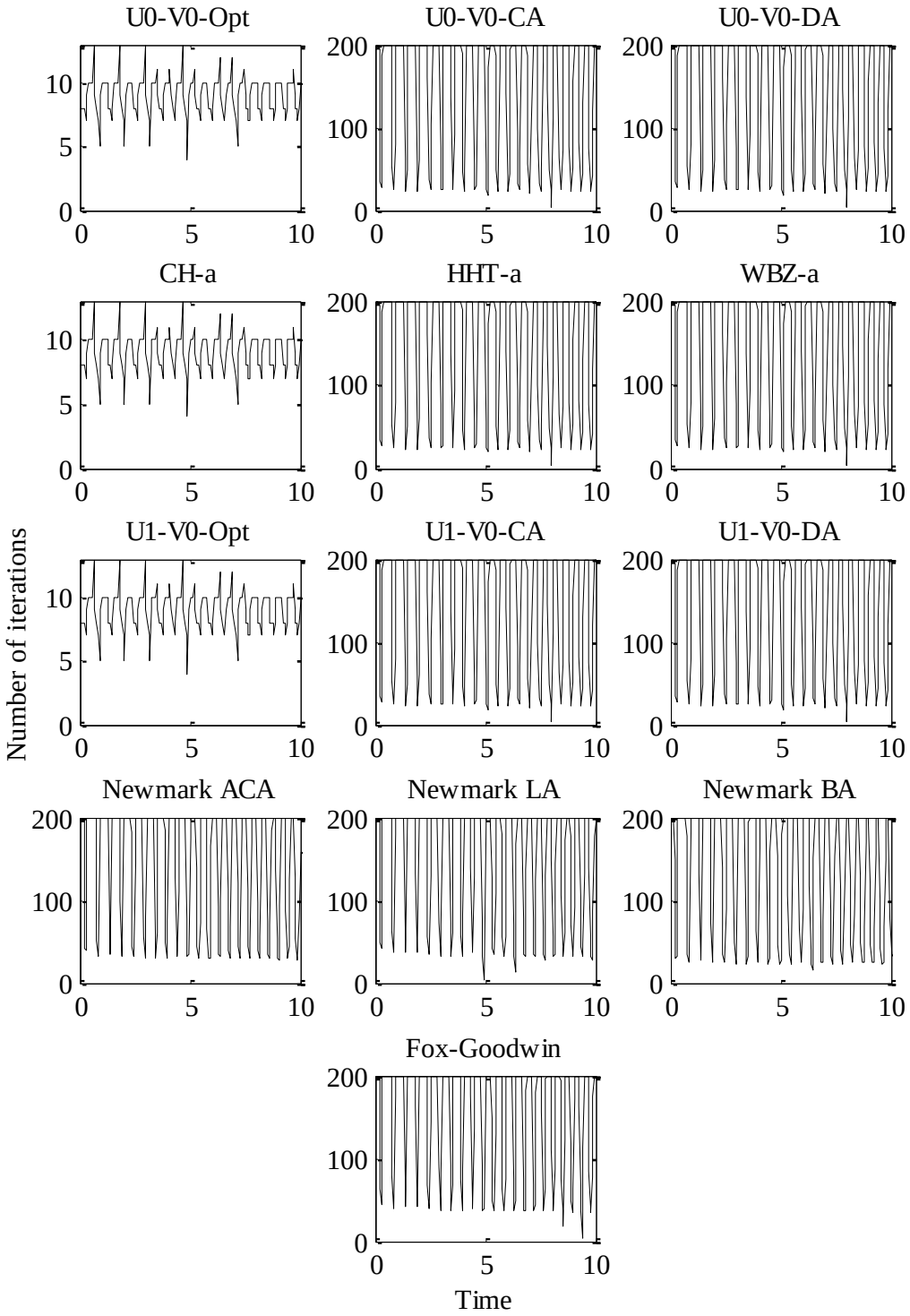


Figure 9: Number of iterations needed for the SDOF oscillator with softening spring $d^2u/dt^2+100\tanh(u)=0$, $(u)_0=4$, $(du/dt)_0=0$, $\Delta t=0.05$, $t=200\Delta t$, $\rho_{inf}=1$, $tol_{max}=0.01$, $k_{max}=200$.

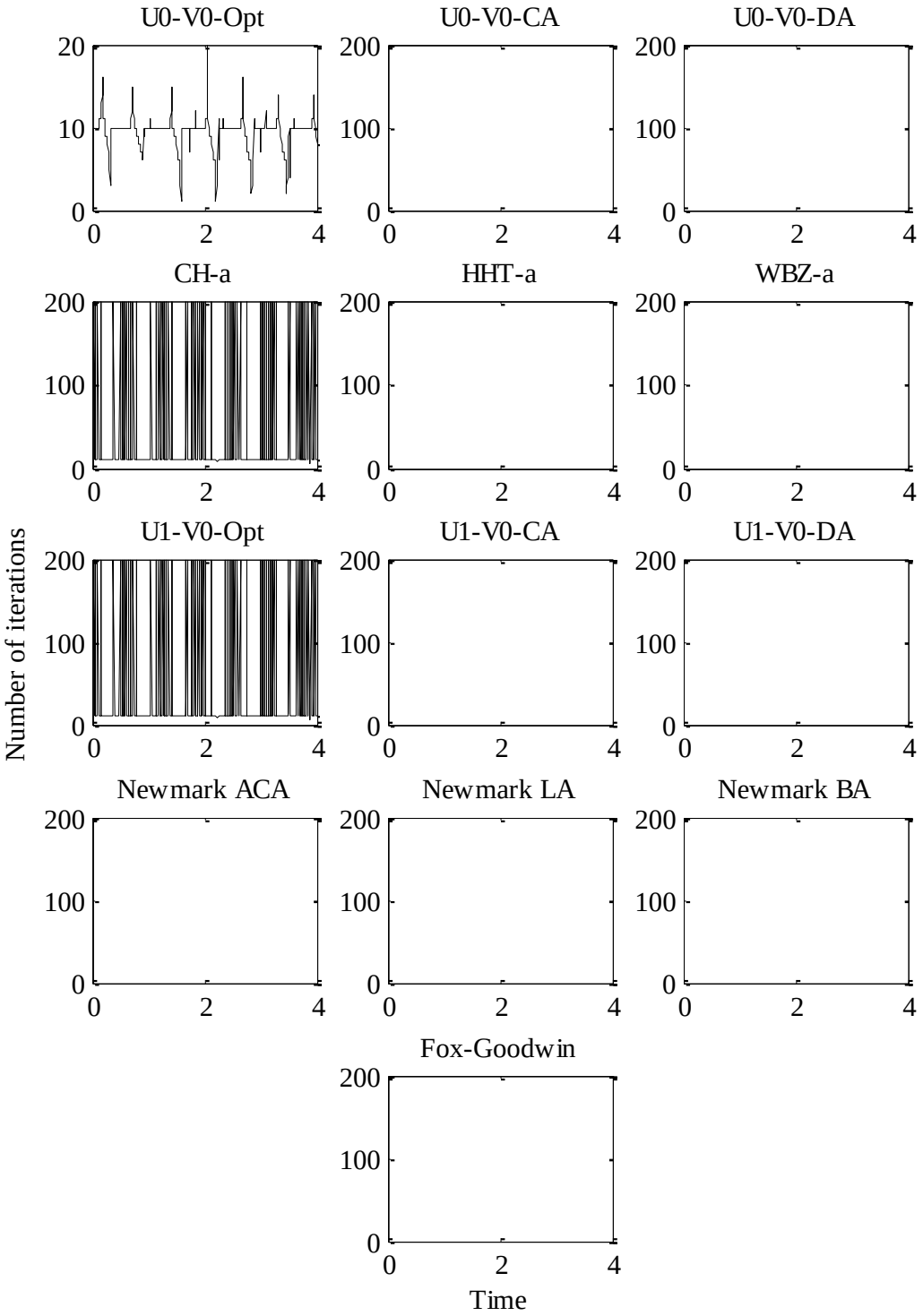


Figure 10: Number of iterations needed for the harmonically excited elastoplastic SDOF system, $(u)_0=0$, $(du/dt)_0=0$, $\Delta t= 0.005$, $t= 800\Delta t$, $\rho_{inf}=1$, $tol_{max}=0.01$, $k_{max}=200$.

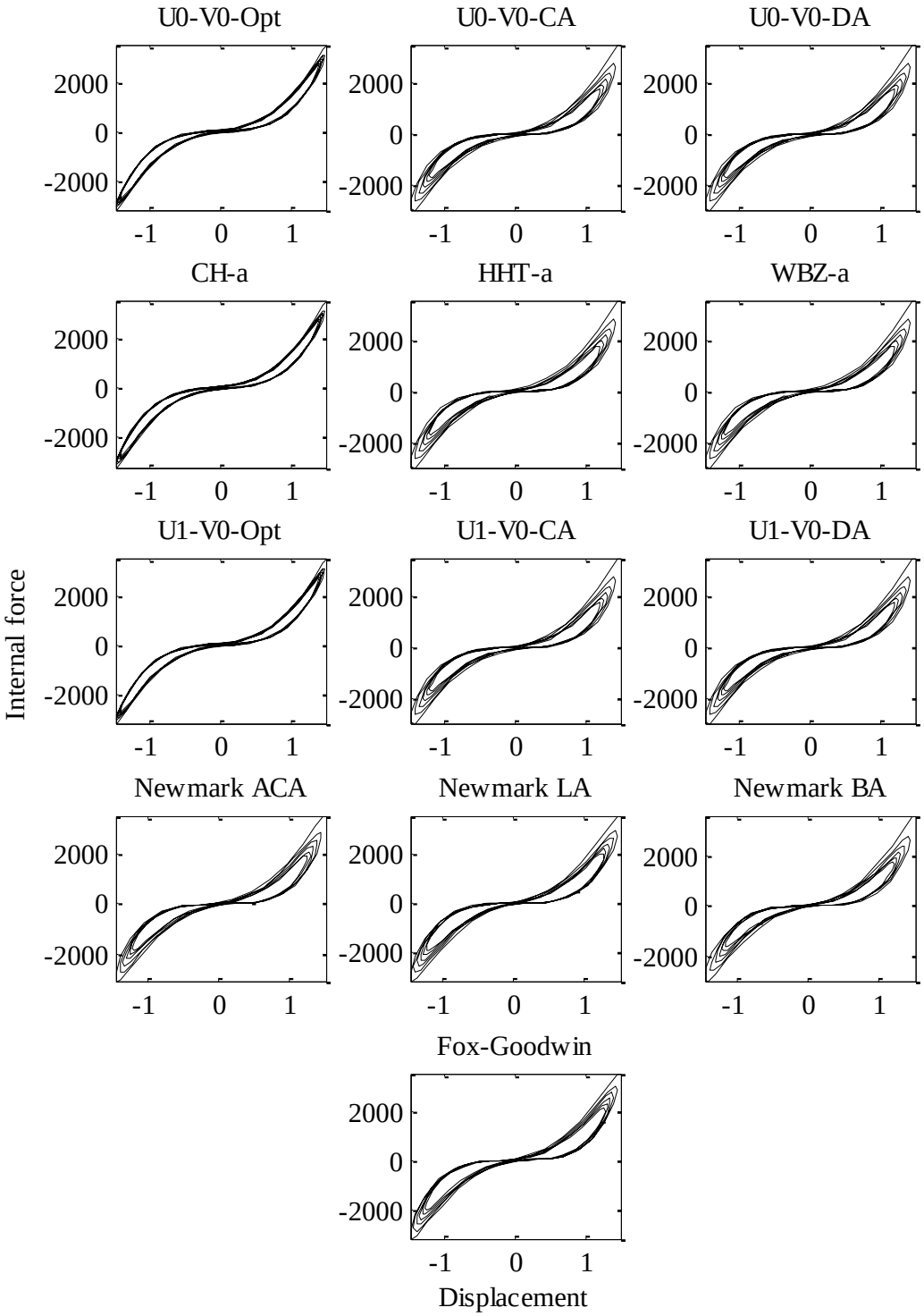


Figure 11: Internal force vs displacement curves for the hardening spring $d^2u/dt^2+100u(1+10u^2)=0$, $(u)_0=1.5$, $(du/dt)_0=0$, $\Delta t=0.005$, $t=200\Delta t$, $\rho_{inf}=1$, $tol_{max}=0.01$, $k_{max}=200$.

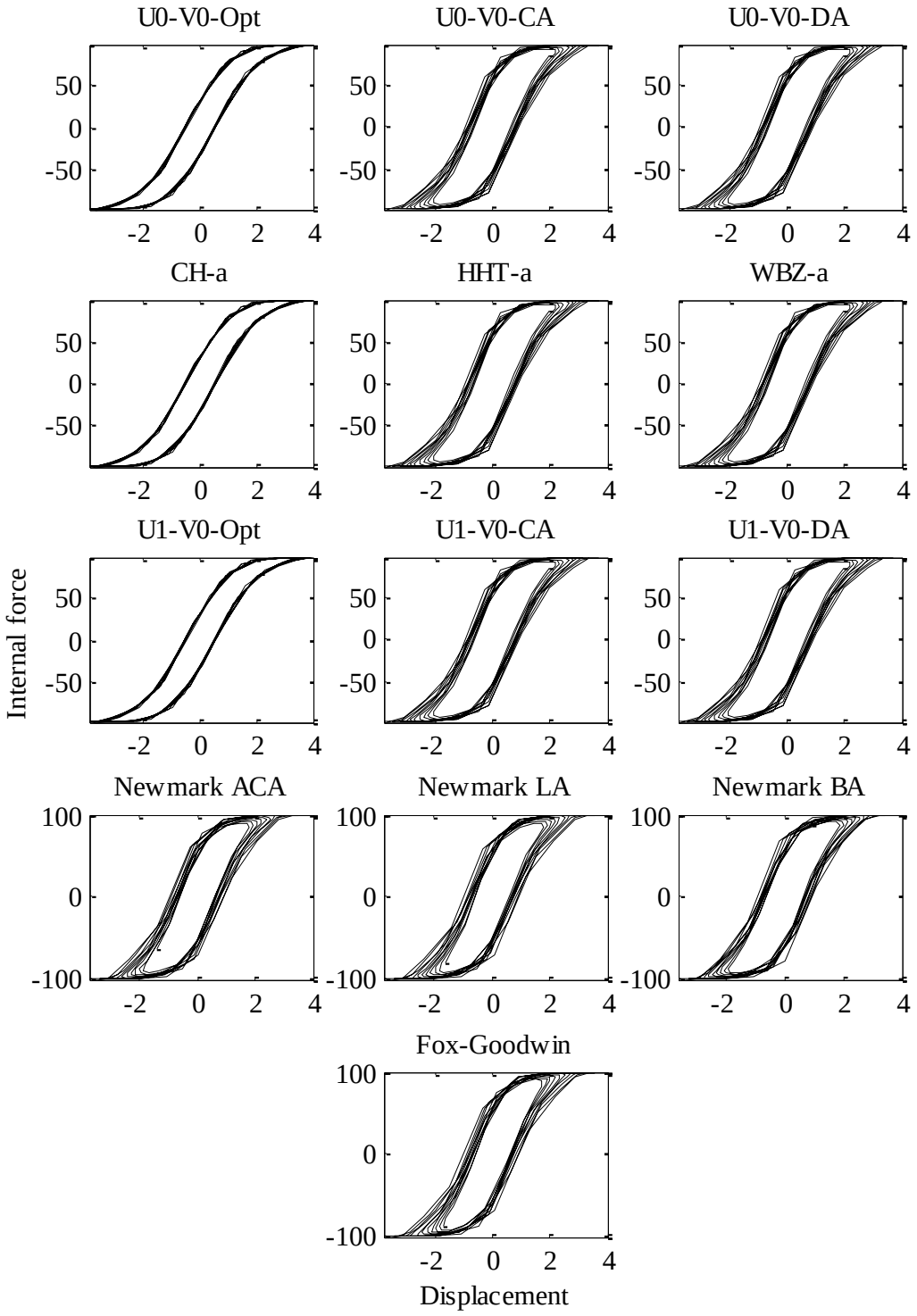


Figure 12: Internal force vs displacement curves for the softening spring $d^2u/dt^2+100\tanh(u)=0$, $(u)_0=4$, $(du/dt)_0=0$, $\Delta t=0.05$, $t=200\Delta t$, $\rho_{inf}=1$, $tol_{max}=0.01$, $k_{max}=200$.

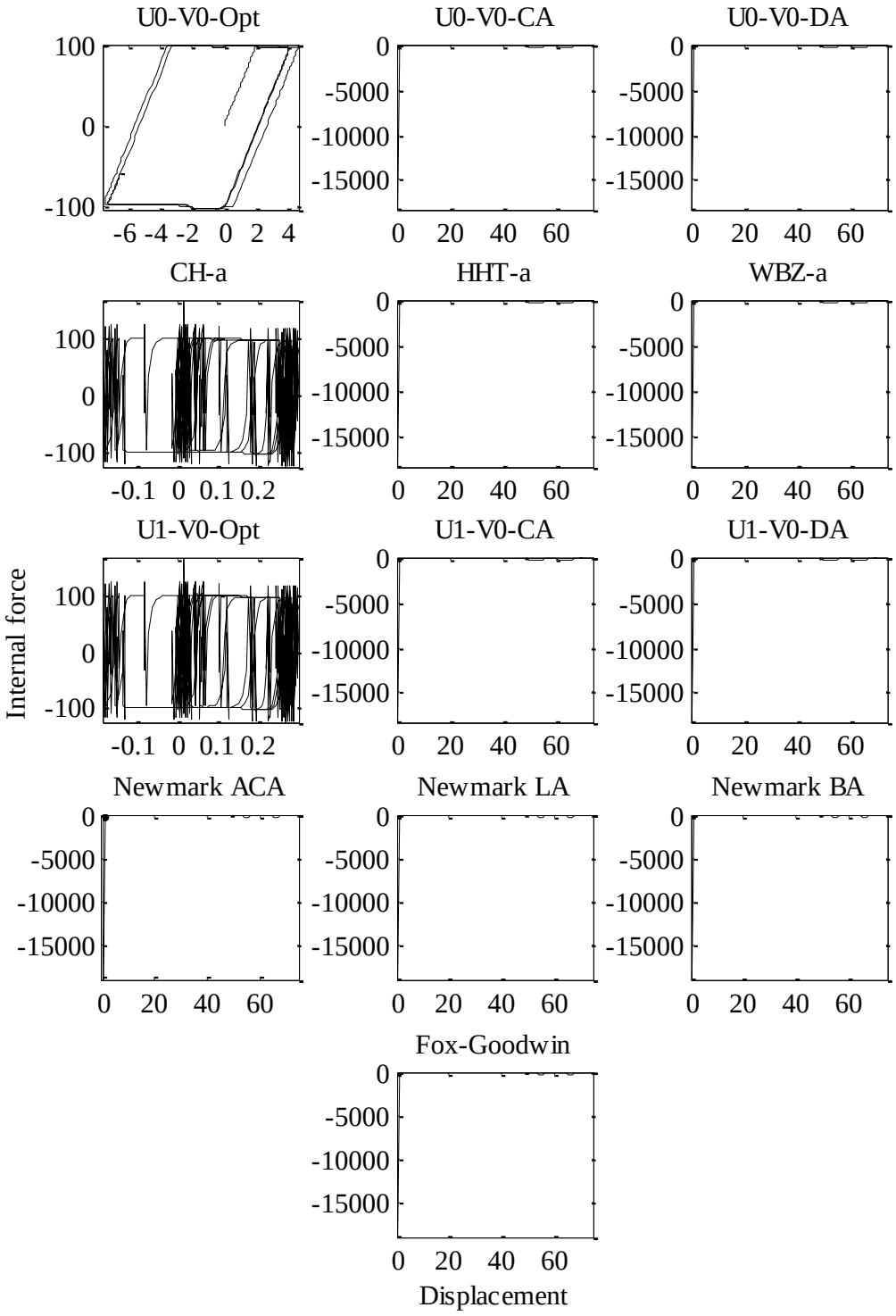


Figure 13: Internal force vs displacement curves for the harmonically excited elastoplastic SDOF system, $(u)_0=0$, $(du/dt)_0=0$, $\Delta t= 0.005$, $t= 800\Delta t$, $\rho_{inf}=1$, $tol_{max}=0.01$, $k_{max}=200$.

ful iterations reached, lead to errors in the calculation of the tangent stiffness, which are responsible for the different slopes between loading and unloading branches. For the third oscillator type the existence of the loop results from the elastoplastic behavior of the spring and is physically correct.

In addition, the area inside the loops is minimum for the optimal numerical dissipation and dispersion algorithms, compared to the remaining ones for the two first types of oscillators. Apart from this, the loop areas are generally larger for the SDOF system with softening spring, which means that the algorithmic energy dissipation will be higher for this type of oscillator. This is mainly due to the higher initial total energy in the SDOF system with softening spring compared to that of the SDOF system with hardening spring, since the relative energy loss observed in Figures 4 and 5 is roughly the same for the two oscillators.

The closed force – displacement loop for the elastoplastic behavior can be clearly seen in Figure 13 in the case of U0-V0-Opt algorithm. It is verified that the yield limit is equal to its assumed value for both tension and compression, and that the modulus of elasticity in the linear elastic range is equal to 50. Apparent instabilities exist for the remaining algorithms, which corroborate the superiority of U0-V0-Opt algorithm.

6 CONCLUSIONS

- The family of linear generalized single step single solve algorithms, of which most common time integration algorithms are special cases, can be extended to solve materially nonlinear dynamic response via a Newton-Raphson iterative procedure.
- In the nonlinear regime, the extended generalized algorithms perform satisfactorily, with acceptable accuracy and stability, in cases where the remaining common algorithms fail to trace the dynamic response.
- The algorithm which has zero-order displacement overshooting behavior, zero-order velocity overshooting behavior and optimal numerical dissipation and dispersion (U0-V0-Opt) can deal with nonlinear elastic as well as nonlinear elastic-plastic response with a relatively large time step.
- Time integration algorithms for which convergence or equilibrium is not ensured at time steps can lead to large errors in the calculated response. The relative energy decrease for conservative systems can be as much as 60% of its initial value.
- Algorithms that are unconditionally stable for linear problems, may lose their stability in nonlinear dynamic simulations.
- Further research has to be made to investigate the relation between the stable time increment of generalized single step single solve algorithms applied in nonlinear problems and various other input data.

REFERENCES

[1] X. Zhou, K.K. Tamma, Design, analysis, and synthesis of generalized single step single solve and optimal algorithms for structural dynamics. *Int. J. Numer. Meth. Engng*, **59**, 597–668, 2004.

[2] R.W. Clough, J. Penzien, *Dynamics of structures, 3th Edition*. Computers & Structures, Inc, 2003.

[3] J.H. Argyris, P.C. Dunne, T. Angelopoulos, Dynamic response by large step integration. *Earthquake Engineering & Structural Dynamics*, **2**, 185-203, 1973.

[4] D. Kuhl, M.A. Crisfield, Energy-conserving and decaying algorithms in non-linear structural dynamics. *Int. J. Numer. Meth. Engng*, **45**, 569-599, 1999.

[5] T.J.R. Hughes, T.K. Caughey, W.K. Liu, Finite-element methods for nonlinear elastodynamics which conserve energy. *Journal of Applied Mechanics, Transactions of the ASME*, **45**, 366-370, 1978.

[6] D. Kuhl, E. Ramm, Constraint energy momentum algorithm and its application to nonlinear dynamics of shells. *Computer Methods in Applied Mechanics and Engineering*, **136**, 293–315, 1996.

[7] J.C. Simo, N. Tarnow, The discrete energy-momentum method. Conserving algorithms for nonlinear elastodynamics. *Journal of Applied Mathematics and Physics*, **43**(5), 757–792, 1992.

[8] K.J. Bathe, Conserving energy and momentum in nonlinear dynamics: a simple implicit time integration scheme. *Computers and Structures*, **85**(7-8), 437–445, 2007.

[9] L. Zhang, T. Liu, Q. Li, A robust and efficient composite time integration algorithm for nonlinear structural dynamic analysis. *Mathematical Problems in Enginnering*, *Hindawi Publishing Corporation*, 2014.

[10] M.B. Rosales, C.P. Filipich, Time integration of non-linear dynamic equations by means of a direct variational method. *Journal of Sound and Vibration*, **254**(4), 763–775, 2002.

[11] F. Armero, E. Petöcz, A new class of conserving algorithms for dynamic contact problems. J.A. Désidéri, P. LeTallec, E. Oñate, J. Périaux, E. Stein eds. *2nd ECCOMAS Conf. on Numerical Methods in Engineering*, Paris, France, September 9-13, 1996.

[12] N.M. Newmark, A method of computation for structural dynamics. *Journal of Engineering Mechanics*, **85**(EM3), 67–94, 1959.

[13] U.M. Ascher, L.R. Petzold, *Computer methods for ordinary differential equations and differential-algebraic equations*, SIAM, 1998.

[14] L. Fox, E.T. Goodwin, Some new methods for the numerical integration of ordinary differential equations. *Mathematical Proceedings of the Cambridge Philosophical Society*, **45**, 373–388, 1949.

[15] J. Chung, G.M. Hulbert, A time integration method for structural dynamics with improved numerical dissipation: the generalized a-method. *Journal of Applied Mechanics*, **60**(2), 371-375, 1993.

[16] H.M. Hilber, T.J.R. Hughes, R.L. Taylor, Improved numerical dissipation for time integration algorithms in structural dynamics. *Earthquake Engineering & Structural Dynamics*, **5**, 283-292, 1977.

[17] W.L. Wood, M. Bossak, O.C. Zienkiewicz, An alpha modification of Newmark's method. *International Journal for Numerical Methods in Engineering*, **15**(10), 1562-1566, 1980.

[18] Y.M. Xie, An assessment of time integration schemes for non-linear dynamic equations. *Journal of Sound and Vibration*, **192**(1), 321-331, 1996.

[19] J. Liu, X. Wang, An assessment of the differential quadrature time integration scheme for nonlinear dynamic equations. *Journal of Sound and Vibration*, **314**, 246-253, 2008.

COMPDYN 2015
5th ECCOMAS Thematic Conference on
Computational Methods in Structural Dynamics and Earthquake Engineering
M. Papadrakakis, V. Papadopoulos, V. Plevris (eds.)
Crete Island, Greece, 25–27 May 2015

CREATION OF A NEW EQUATION OF MOTION TO CALCULATE DISSIPATED ENERGY BETWEEN TWO ADJACENT BUILDINGS (COMPDYN 2015)

Hosein Naderpour1, Seyed M.Khatami1 and Rui C.Barros2

1 Faculty of Engineering, Semnan University, Semnan, Iran
address
naderpour@semnan.ac.ir

2 Faculty of Engineering, University of Porto (FEUP), Porto, Portughal

Keywords: Impact, Velocity, Coefficient of restitution, Dissipated energy, Damping

. Building pounding has been recently studied by different researchers around the world to evaluate impact between two adjacent buildings. Numerical studies are an important part of impact, in which several researchers have tried to simulate the impact by using different formulas. Estimation of the impact force and the dissipated energy depends significantly on some parameters of impact. Mass of bodies, stiffness of spring, coefficient of restitution, damping ratio of dashpot and impact velocity are some known and unknown parameters to simulate the impact and to measure dissipated energy during collision.

In this paper, a mathematic part of steady state response of single degree of freedom system due to the external force has been evaluated. Impact damping ratio due to viscose damping was calculated to simulate nonlinear viscoelastic model and the results of impact were compared with other similar impact damping ratios, suggested in previous studies. Here, a new equation of motion is presented to get the best available estimation of impact damping ratio and is also simulated to compute impact force during seismic excitation.

[1] Assistant Professor, Faculty of Engineering, Semnan University, Semnan, Iran mail:naderpour@semnan.ac.ir

INTRODUCTION

In the introduction to the paper, the author(s) will specify the present stage of the branch researches (by quoting the adequate bibliography) and will specify the purpose of the paper. Building pounding has been a stimulating research topic during the last few decades in earthquake engineering. This phenomenon describes impacts under two adjacent buildings under seismic excitations. If adjacent buildings were not separated suitably from each other, impact forces could cause damage to buildings even if structures were well designed. Unfortunately, enough attention is not being paid to the building pounding effects in the codes. However, several researchers have tried to investigate the effects of such collisions worldwide. Anagnostopolos [1] was among the first researchers, who explained the possible dangers due to building pounding. The 1985 Mexico City earthquake was one of the source of excitation which caused severe damages to the buildings. Several reports showed that in at least 15% of buildings damages were due to impact of adjacent buildings [2]. Investigation of the building pounding has been divided into two parts, experimental tests and numerical analyses. In this regard, Papadrakakis and Mouzakis [3] conducted shaking table experiments on pounding between two-story reinforced concrete buildings without separation distance under the earthquake records. Two steel buildings, having three and eight stories have been tested by shaking table (Filiatrault [4]). The tests were carried out with two different gaps, zero and 15 mm. The experimental results were compared with analytical predictions based on linear elastic spring theory. The comparisons showed that acceleration at the contact level was not well predicted. Watanaba and Kawashima [5] have investigated pounding of distributed masses to model colliding bridge decks. They showed that five elements were used per deck; the collision element stiffness would be five times greater than that of the diagram stiffness. Cole et al. [6] have indicated that building pounding and its impact would depend upon the structural properties and collision velocity of both buildings. A theoretical maximum collision force has been determined by them, for a system with two distributed masses. Velocity, mass and stiffness at the time of impact have an equation, and the number and magnitude of the impacts depend on these three options mentioned. Barros and Khatami [7] addressed some common misrepresentations in building codes on the issue of separation distance required between two adjacent concrete buildings under near-fault ground motions. In numerical analyses, link elements are located between two buildings investigated. Komodromos et al also took advantage of link elements extensively in his research [8]. Barros and Vasconcelos [9] investigated building pounding between two adjacent concrete buildings by numerical analyses. They presented the results of analyses using different stiffness and damping ratios. Two concrete buildings with 8 and 10 stories have been modeled by Raj Pant and Wijeyewickrema [10]. Different types of springs with different stiffness or various dampers with different damping ratio have also been used in recent numerical studies at FEUP by Cordeiro [11] and by Vasconcelos [12], in their parametric studies of pounding between adjacent buildings. Barros and Khatami [13] estimate the effect of damping ratio on the numerical study of impact forces between two adjacent concrete buildings subjected to pounding. In yet another study, Barros and Khatami [14] compare results of two SDOF frames with different link elements based on mathematic equations. In some of their analyses, structures were modeled as single degree freedom systems and collision was simulated using linear viscoelastic models of impact force.

In this study, a new equation of motion is suggested to calculate the impact force in the nonlinear viscoelastic model. By using a mathematic equation and developing the men-

tioned equation, damping impact ratio is simulated and the behavior of nonlinear viscoelastic model is compared with other suggested formula.

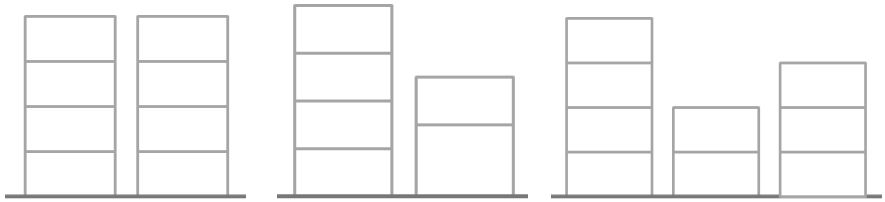
Building Pounding

Investigation of previous earthquake around the world shows specific characteristics related to building pounding. Pounding is one of the primary reasons of many building damages in earthquake. This phenomenon has been reported in many earthquakes between two adjacent buildings. Seismic pounding occurs during earthquake, in building with different dynamic characteristics, adjacent buildings vibrating out of phase and in buildings by having insufficient separation. Past studies and reports about building pounding have shown three cases of impact between adjacent buildings. The classification mentioned collisions are:

2,A- Adjacent buildings with the same heights and the same floor levels.

2,B- Adjacent buildings with different total height and with different levels.

2,C- Row of buildings.



2,A 2,B 2,C

Fig 1. Different types of pounding between buildings

Previous investigations have shown that the pounding hazard depends significantly upon four factors:

-building construction type based on relative height, period and story mass;

-ground acceleration;

-soil condition;

-distance between buildings.

The most important parameters are buildings height and distance between buildings. Since different buildings have various behaviors during seismic excitation, insufficient gap size between structures can provide damages for collided buildings. In order to evaluate pounding between two buildings and measure impact force and dissipated energy, an un-real link element between two bodies is assumed. Mentioned link element is included spring and dashpot, which are located parallel to each other. Dashpot is used to calculate the value of dissipated energy during impact.

Dissipated Energy in Viscous Damping and Rate Independent Damping

Pounding occurs when buildings have different dynamic characteristics, height, mass, number of stories and buildings materials. This phenomenon between adjacent buildings could cause severe damage and even collapse during seismic excitation.

To measure energy absorption due to impact, an un-real link element is assumed between adjacent structures. This link element can be obtained by spring and dashpot, which are located parallel with each other. Dashpot absorbs energy when the relative displacements exceed the available seismic gap. So, determination of impact force depends upon two different terms, which are mentioned as:

$$E_D = \int f_D d\delta = \int (c\dot{\delta})\dot{\delta}dt = \int c\dot{\delta}^2 dt \quad (1)$$

$$E_S = \int f_S d\delta = \int (k\delta)\dot{\delta}dt \quad (2)$$

It means, Impact force is calculated by stiffness of spring and damping of dashpot. It is simplified to be:

$$f_S = k.\delta \text{ and } f_D = c.\dot{\delta}. \quad (3)$$

Where k is stiffness of spring and c denotes damping coefficient. δ and $\dot{\delta}$ are lateral displacement and velocity, respectively.

When there is collision, both terms should be added with each other to measure the impact force. The impact force is considered to be:

$$f = f_S + f_D \quad (4)$$

It means, the impact force could be written as:

$$f = k\delta + c\dot{\delta} \quad (5)$$

It is assumed that the lateral displacement becomes $\delta = \delta_0 \sin(wt - \phi)$, then impact force by using dashpot would be defined as:

$$f_D = c\dot{\delta}(t) = cw\delta_0 \cos(wt - \phi) \quad (6)$$

$$f_D = cw\sqrt{\delta_0^2 - \delta_0^2 \sin^2(wt - \phi)} \quad (7)$$

$$f_D = cw\sqrt{\delta_0^2 - [\delta(t)]^2} \quad (8)$$

It could be an estimation that new equation would be represented as:

$$\left(\frac{\delta}{\delta_0}\right)^2 + \left(\frac{f_D}{cw\delta_0}\right)^2 = 1 \quad (9)$$

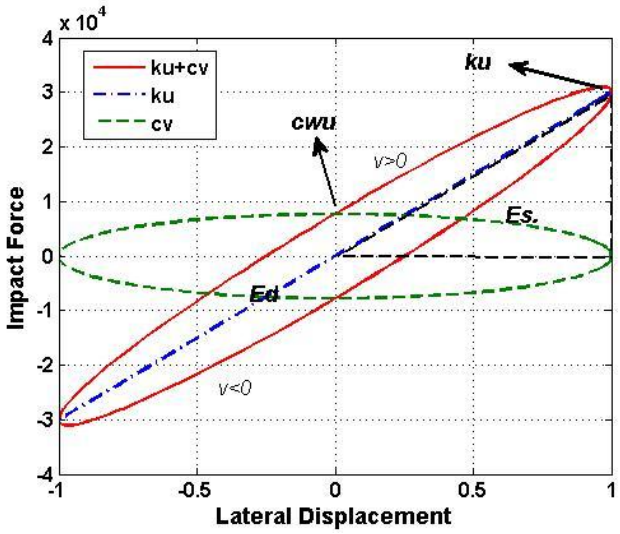


Fig 2. Hystresis loop by spring and dashpot

Three available terms of impact are depicted. Blue line shows a linear behavior by f_S, which is included a spring. It is obviously shown that impact force by using spring is $f_s = k\delta$, and dissipated energy is zero. Green line is an important curve in this figure. In fact, the curve is an ellipse, where energy is dissipated in this area and the value of dissipated energy is $\pi cw\delta_0^2$. When two different terms of impact joint with each other, ellipse rotates and red line is provided and is demonstrated a complete impact. Red ellipse is divided by two parts, E_{s0} and E_D.

Two different damping coefficients are explained by viscous damping and rate independent damping. Both mentioned damping are developed as:

$$E_D = \pi cw\delta_0^2 \tag{10}$$

$$\pi cw\delta_0^2 = 2\pi\zeta \frac{w}{w_n} k\delta_0^2 \tag{11}$$

In terms of viscose damping, it is recommended to use c for impact damping factor as:

$$c = \frac{2k\zeta}{w_n} \tag{12}$$

This equation of motion shows that impact damping coefficient depends significantly on damping ratio, frequency and stiffness of system.

In order to solve equation (12) to get impact damping coefficient with rate independent damping, it could be written as:

$$w_n = w\sqrt{1-\zeta} \tag{13}$$

$$c = \frac{2k\zeta}{w\sqrt{1-\zeta}} \tag{14}$$

Defining c from equation (14)

$$c = \frac{2\zeta\sqrt{km}}{\sqrt{1-\zeta}} \tag{15}$$

The calculated equation shows a relation between damping coefficient system and rate independent damping.

Nonlinear Impact Models

Impact model between two bodies during earthquake has been shown by a spring and damper, which are located parallel with each other. The explanation of the impact model focuses on two structures next to each other when they collide during seismic excitation.

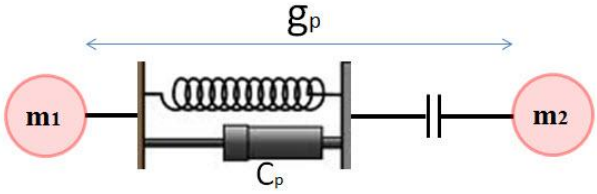


Fig 3. Hertz Damped Model

The impact force between two bodies depends significantly on collided masses, velocity and acceleration. In this part, some available models are demonstrated to get better image from contact.

In order to calculate value of the energy dissipation, some researchers have suggested different equations to simulate the damping ratio. They have tried to get the most appropriate assumption for evaluating dissipated energy during collisions. A summary of previous studies about impact damping ratio of pounding shows that the suggested formula by Anagnostopolus [1], and two represented formulas by Jankowski [15] are based on coefficient of restitution (CR) and calculate the impact damping ratio by mathematic equations. Coefficient of restitution is a factor, which simulate an equation between velocity before and after collision. This equation could be written as:

$$0 < CR = \frac{v_{before}}{v_{after}} < 1 \tag{16}$$

As it is shown, coefficient of restitution is calculated to be in the range of 0 and 1. If CR becomes equal to 0, collision is perfectly plastic and if CR becomes equal to 1, collision shows an elastic behavior.

Non-Linear Viscoelastic Model

In order to improve the impact model, Jankowski [15] presented an idea that a nonlinear viscose damper located parallel to the spring for absorbing the energy. The equation of nonlinear viscoelastic model can be written as:

$$F_c(t) = k_h.\delta(t)^{1.5} + c_h\dot{\delta}(t) \tag{17}$$

$$c_h = 2\zeta\sqrt{k_h\sqrt{\delta(t)}\frac{m_1 m_2}{m_1 + m_2}} \tag{18}$$

$$\zeta = \frac{9\sqrt{5}}{2}\frac{1-CR^2}{CR(CR(9\pi-16)+16)} \tag{19}$$

Another formula in terms of non-linear viscoelastic model was developed by Seyed Mahmoud [16]. He suggested a new equation to determine impact damping ratio, which absorbs the energy less than that simulated by Jankowski model. The equation could be written as:

$$\zeta = \frac{1-CR^2}{CR(CR(\pi-2)+2)} \tag{20}$$

Proposed Non-Linear Viscoelastic Model

To calculate impact damping ratio and develop the linear and nonlinear viscoelastic model using a mathematic process [15], a steady state response of single degree of freedom system due to the external force, $p(t) = p_0\sin(wt)$, was evaluated. Based on mentioned force, dissipated energy due to viscose damper in a harmonic excitation can be written by the following the equation:

$$\Delta E = \int f_D d\delta = \int_0^{2\pi/w}(c_k\dot{\delta})\dot{\delta}dt \tag{21}$$

And also by focusing strongly on damping term of equation of motion:

$$\Delta E = \int_0^{\delta_{\max}} c_k\dot{\delta}d\delta \tag{22}$$

Based on equations on dynamics of structure [17]:

$$\Delta E = 2\pi\zeta\frac{w}{w_n}k\delta^2 \tag{23}$$

The equation between w and w_n could be assumed to be 1. Considering final velocity and masses, it could be written as:

$$\int f_D d\delta = \int_0^{2\pi/w} (c_k \dot{\delta})\dot{\delta} dt = 0.5 m \dot{\delta}_{final}^2 \tag{24}$$

Where $\dot{\delta}_{final}$ denotes the final velocity and m is an equivalent of two masses ($m = \frac{m_1 m_2}{m_1 + m_2}$)

Solving the equation of 24 for δ:

$$\delta_{\max} = \sqrt{\frac{m}{4\pi\zeta k}} . \dot{\delta}_{final} \tag{25}$$

For each value of deformation during impact, as the energy transfers from elastic strain energy to kinetic energy, the relative velocity can be calculated as follows:

$$2\pi\zeta k\delta^2 + 0.5 m \dot{\delta}^2 = 0.5 m \dot{\delta}_{final}^2 \tag{26}$$

Solving equation 26,

$$0.5 m \dot{\delta}^2 = 0.5 m \dot{\delta}_{final}^2 - 2\pi\zeta k\delta^2 \tag{27}$$

Consequently, velocity would be:

$$\dot{\delta} = \sqrt{\dot{\delta}_{final}^2 - \frac{4k\xi\pi\delta^2}{m}} \tag{28}$$

Defining the equation 17 and considering displacement of zero ($\delta = 0$), it is an assumption that equation 28 can be changed increasing velocity to determine the velocity during collision for $\dot{\delta} > 0$ and $\dot{\delta} < 0$.

$$\dot{\delta} = -\sqrt{\dot{\delta}_{final}^2 - \frac{4k\xi\pi\delta^2}{m}} \quad \text{for } \dot{\delta} < 0$$

$$\dot{\delta} = \sqrt{\dot{\delta}_{final}^2 - \frac{4k\xi\pi\delta^2}{m}} + \frac{(\dot{\delta}_0 - |\dot{\delta}_{final}|)(\delta_{\max} - \delta)}{\delta_{\max}} \quad \text{for } \dot{\delta} > 0 \tag{29}$$

By using dissipated energy from damper and using equation 22, it could be calculated by:

$$\Delta E = 2\zeta\sqrt{k.m}\int \dot{\delta} d\delta \tag{30}$$

Considering above equations and substituting the equation 29 into equation 30:

$$\Delta E = 2\zeta\sqrt{k.m}(\int\sqrt{\dot{\delta}_{final}^2 - \frac{4\zeta\pi k\delta^2}{m}}d\delta + \frac{(\dot{\delta}_0 - |\dot{\delta}_{final}|)}{\delta_{\max}}\int_0^{\delta_{\max}}(\delta_{\max} - \delta)d\delta) \tag{31}$$

Considering the equation 25 into equation 31:

$$\Delta E = 2\zeta\sqrt{k.m}(\int_0^{\delta_{\max}}\sqrt{\frac{4\pi\zeta k\delta_{\max}^2}{m} - \frac{4\zeta\pi k\delta^2}{m}}d\delta) + \frac{\dot{\delta}_0 - |\dot{\delta}_{final}|}{2}.\delta_{\max} \tag{32}$$

The equation is simplified to equation 32:

$$\Delta E = 2\zeta\sqrt{k.m}[(\sqrt{\frac{4\zeta\pi k}{m}})\int_0^{\delta_{\max}}\sqrt{\delta_{\max}^2 - \delta^2}d\delta + \frac{\dot{\delta}_0 - |\dot{\delta}_{final}|}{2}.\delta_{\max}] \tag{33}$$

$$\Delta E = 4k\sqrt{\pi}\zeta^{1.5}\int_0^{\delta_{\max}}\sqrt{\delta_{\max}^2 - \delta^2}d\delta + 2\zeta\sqrt{k.m}\frac{\dot{\delta}_0 - |\dot{\delta}_{final}|}{2}.\delta_{\max} \tag{34}$$

Solving the equation 34, it can be concluded that dissipated energy will be:

$$\Delta E = 4k\sqrt{\pi}\zeta^{1.5}(0.25\pi\delta_{\max}^2) + 2\zeta\sqrt{k.m}\frac{\dot{\delta}_0 - |\dot{\delta}_{final}|}{2}.\delta_{\max} \tag{35}$$

As kinetic energy loss was noted in equation 32, it can be equal to dissipated energy from damper during impact as:

$$\frac{1}{2}\frac{m_1m_2}{m_1+m_2}(1-CR^2)(\dot{\delta}_{imp})^2 = (4k\sqrt{\pi}\zeta^{1.5}(0.25\pi\delta_{\max}^2)) + (2\zeta\sqrt{k.m}\frac{\dot{\delta}_0 - |\dot{\delta}_{final}|}{2}.\sqrt{\frac{m}{4\pi\zeta k}}.\dot{\delta}_{final}) \tag{36}$$

Modifying $\delta_{\max}^2$ from equation 25 into equation 36:

$$\frac{1}{2}\frac{m_1m_2}{m_1+m_2}(1-CR^2)(\dot{\delta}_{imp})^2 = (4k\sqrt{\pi}\zeta^{1.5}(0.25\pi\frac{m}{4\pi\zeta k}.\dot{\delta}_{final}^2) + (\zeta\sqrt{k.m}(\dot{\delta}_0 - |\dot{\delta}_{final}|)\sqrt{\frac{m}{4\pi\zeta k}}.\dot{\delta}_{final}) \tag{37}$$

The equation 38 could be written as:

$$\frac{1}{2}(1-CR^2)(\dot{\delta}_{imp})^2 = 0.25\sqrt{\pi}\zeta^{0.5}\dot{\delta}_{final}^2 + \zeta^{0.5}\frac{\sqrt{\pi}}{\pi}(\dot{\delta}_0 - |\dot{\delta}_{final}|).\dot{\delta}_{final}) \tag{38}$$

And finally, the equation for giving ζ :

$$\zeta = \left(\frac{(1-CR^2)}{CR(\sqrt{\pi}(0.5CR+\frac{1}{\pi})-CR)}\right)^2 \quad (39)$$

Proposed non-linear impact model is considered based on coefficient of restitution, (CR). Selecting different CRs and calculating various results in terms of impact damping ratio, impact forces and dissipated energies is changed. Proposed impact damping ratio shows a curve based on different CRs, from zero to 320 using CR=0.9 and CR=0.1, respectively.

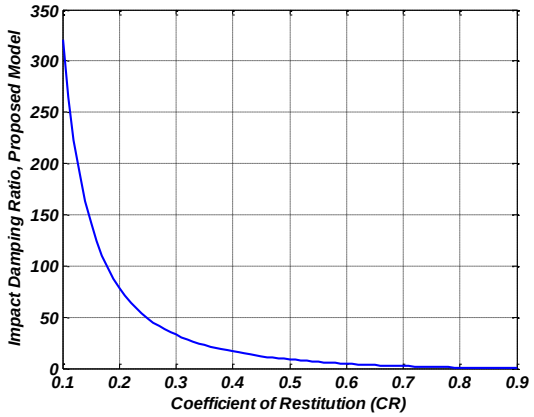


Fig 4. Comparison of different coefficient of restitution to calculate impact damping ratio

The value of ζ , calculated by coefficient of restitution is listed in the Table 1, as:

CR	0.1	0.2	0.3	0.4	0.5	0.6	0.7	0.8	0.9
ζ	320.71	78.59	32.74	16.39	8.74	4.62	2.26	0.90	0.21

Table 1: Value of impact damping ratio using different coefficient of restitution

Conclusion

In this paper, building pounding between two adjacent structures was discussed and effect of pounding was studied. During earthquake, two buildings collide with each other and it could provide damage for structural elements. To investigate the pounding and impact between buildings, a non-real element is considered to calculate the value of impact and energy absorption. Mathematic equation of motion of impact force needs to define some parameters such as stiffness of spring, damping of dashpot, lateral displacement and velocity of bodies. Impact damping coefficient of dashpot is determined by using coefficient of restitution. Three previous models of this equation were evaluated by using linear viscoelastic model of impact and a new equation was suggested to calculate the damping of dashpot. A steady state response of single degree of freedom system due to the external force was considered and a new equation of motion was presented. To investigate the ac-

curacy of suggested formula, the results of an experiential analysis were used and the results of formula were calibrated. Comparison of results showed good accuracy between experimental and numerical results. Finally, by using a SDOF system and an earthquake record and considering the proposed equation of motion, impact force of three investigated models were calculated. By focusing on suggested formula, impact force could be determined and dissipated energy shown by hysteresis loop.

REFERENCES

Anagnostopouls, S.A. "*Pounding of Building in Series during Earthquakes*". Earthquake Engineering and Structural Dynamic. 16(3).443-456.1998.

Bertero, V. "*Observation of Structural Pounding, Proc. ASCE International Conference on the 1985 Mexico City Earthquake*". 264-278.ASCE, NY, NY, USA.1986.

Papadrakakis, M and Mouzakis, H. "*A Lagrange multiplier solution method for pounding of building during earthquakes* ". Journal of Earthquake Engineering and Structural Dynamic, 20, 981-998.1991.

Filiatrault, A and Wagner, P. "*Analytical Prediction of Experimental Building Pounding*". Journal of Earthquake Engineering and Structural Dynamic, 24, 1131-1154.1995.

Kavashima C.G and Watanaba, K. "*Earthquake Induced Interaction between Adjacent Reinforced Concrete Structural with Non Equal Heights*" Earthquake Engineering and Structural Dynamics. 34(1).1-20. 2005.

Cole.G,L and Dhakal, R.P. " *The Effect of Diaphragm Wave Propagation on the Analysis of Pounding Structures*". Proc. 2 nd Int. Conference on computational method in structural dynamic an earthquake engineering (COMPADYN) Paper CD 200.Rhodes. Greece.2009.

Barros, R and Khatami, S.M. "*Importance of Separation Distance on Building Pounding under Near-Fault Ground Motion, using the Iranian Earthquake Code*" 9th International Congress on Civil Engineering, Isfahan University of Technology (IUT), Isfahan, Iran. 2012.

Komodromos, P and Polycarpou, P. "*On the Numerical Simulation of Impact for the Investigation of Earthquake-Induced Pounding of Building*". Tenth International Conference on Computational Structures Technology, Civil-Comp Press, Stirlingshire, Scotland.2010.

Vasconcelos, H. "*Study about Collision between Reinforced Concrete Building and Comparison of Their Resistance Envelope by Push over Analysis*" MS.c Thesis, FEUP. Portugal. 2011.

Raj, P and Wijeyewickrema, C. " *Seismic Pounding between Reinforced Concrete Buildings: A Study using two recently proposed Contact Element Models*". 14ECEE, Ohrid, Macedonia. 2010.

COMPDYN 2015
5th ECCOMAS Thematic Conference on
Computational Methods in Structural Dynamics and Earthquake Engineering
M. Papadrakakis, V. Papadopoulos, V. Plevris (eds.)
Crete Island, Greece, 25–27 May 2015

PRELIMINARY INVESTIGATIONS OF THE LOW-VELOCITY IMPACT RESPONSE OF A SMART TRIMORPH PLATE FOR ACTIVE DAMAGE MITIGATION

Akuro Big-Alabo[1], Philip Harrison[2], and Matthew P. Cartmell[3]

[1] University of Glasgow
Systems, Power and Energy Research Division, School of Engineering, G12 8QQ, Scotland, UK
e-mail: a.big-alabo.1@research.gla.ac.uk

[2] University of Glasgow
Systems, Power and Energy Research Division, School of Engineering, G12 8QQ, Scotland, UK
e-mail: Philip.Harrison@glasgow.ac.uk

[3] University of Sheffield
Department of Mechanical Engineering, Mappin Street, Sheffield, S1 3JD, England, UK
e-mail: m.cartmell@sheffield.ac.uk

Keywords: Trimorph plate, Low-velocity impact, Elastoplastic contact model, Impact damage, Active damage mitigation.

Abstract. *The elastoplastic impact response of a trimorph plate subjected to low-velocity large mass impact has been investigated using analytical models. In formulating the impact model, the displacement of the impactor, vibration of the plate and local contact mechanics were accounted for. The vibration of the trimorph plate was modelled using the classical laminate plate theory, while the local contact mechanics was modelled using a Meyer-type compliance model that accounts for post-yield effects in the loading and unloading stages of the impact. The impact model is a set of coupled nonlinear differential equations and was solved using the NDSolve function in Mathematica™. Both the modelling and solution approach were validated using a benchmark case study. Investigations were carried out for an Al/PVDF/PZT trimorph plate configuration. Contrary to the general position in the literature that the response of a large mass impact is insensitive to the compliance model used to estimate the impact force [1], the simulations of the present impact model show that the indentation history was sensitive to the compliance model used. Also, the elastoplastic compliance model predicted a permanent indentation which the elastic compliance model cannot estimate. Therefore, the use of elastoplastic compliance models in large mass impact analysis is imperative. Finally, the application of a smart trimorph plate with piezoelectric actuator layer for active mitigation of impact damage was discussed.*

1 INTRODUCTION

Transversely flexible plates (i.e. plates that could bend in the direction perpendicular to their plane) are used in many structural applications (e.g. building panels, car and airplane bodies, ceilings and floorings) in environments where they can be exposed to damage due to impact by blunt projectiles. Therefore, a good understanding of the response of transversely flexible plates to blunt object impact is necessary for design decision-making, damage diagnosis, and active control of impact response. The response of a transversely flexible plate to a blunt object impact is governed by the interaction between flexural oscillations and local indentation of the plate [2]. The simplest analytical cases of transversely flexible plate impacts are the asymptotic cases of the infinite plate response and the quasi-static bending response. Each of these asymptotic cases is modelled by a single differential equation [3]. In general, the model for the impact response of a transversely flexible plate is a set of coupled differential equations that accounts for the flexural oscillations of the plate, the displacement of the impactor and the local indentation. This model has been referred to as the complete model [3] and is applied in the present study to investigate the impact response of a transversely flexible laminated plate structure.

Analytical studies of the normal impact of rigid spheres on transversely flexible monolithic and laminated rectangular plates abound in the literature. Most of these studies deal with elastic impact [1, 2, 4, 5] and those that deal with elastoplastic impact use simplified models for the elastoplastic indentation [6 – 9] that may introduce significant errors in the prediction of the impact response of the plate [6]. The use of well validated elastoplastic contact models in the complete modelling approach is quite challenging computationally, but has the advantage of producing more reliable results and providing details of the impact response that would not have been obtained otherwise. Hence, analytical models that are capable of predicting the elastoplastic response of a transversely flexible plate exposed to impact of a blunt projectile are desirable.

In this paper, analytical models have been derived to investigate the elastoplastic response a transversely flexible trimorph plate subjected to low-velocity, large mass impact. A trimorph plate is defined as a general three-layer laminated plate in which each layer is made of a different material [10]. An example of the application of the trimorph plate configuration is the integration of sensor and actuator layers to a host layer for the purpose of active sensing and control of the plate response. The analytical models for the impact response of the trimorph plate are formulated using the classical laminate plate theory (CLPT) and an elastoplastic contact model that accounts for post-yield effects in the loading and unloading stages. The impact models are used to study the impact response of an Al/PVDF/PZT trimorph plate configuration. The rest of the paper is structured as follows: first, the analytical models for analysis of the impact response of the trimorph plate are formulated; secondly, the expressions for determination of the material properties of the trimorph plate are presented and discussed; thirdly, results from simulations of the analytical models are discussed; fourthly, the feasibility of active damage mitigation using a smart trimorph plate is discussed; and finally, the conclusions of the present study are discussed.

2 IMPACT MODEL OF TRIMORPH PLATE

The impact system studied is a rectangular trimorph plate that is simply supported on all sides and subjected to the transverse elastoplastic impact of a rigid mass with spherical contact surface. The point of impact is at the centre of the plate. It is assumed that the layers of the trimorph plate are perfectly bonded and each layer is made up of an isotropic material. Figure 1 shows a sketch of the impact system with the layers of the trimorph plate having

different shading patterns to indicate different material make-up. This section presents the formulation of the analytical models used for investigation of the trimorph plate. First, the model for transverse vibration of the trimorph plate is derived based on the CLPT. Next, the elastoplastic contact model used to estimate the impact force and account for the local deformation is presented. The section concludes with a combination of the vibration and contact models to formulate an elastoplastic impact model for the trimorph plate.

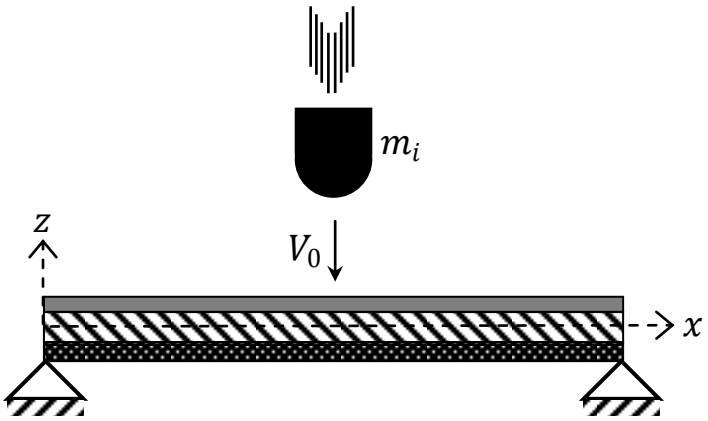


Figure 1: Impact of a trimorph plate by a spherical projectile.

2.1 Vibration model for thin rectangular trimorph plate

The transverse oscillations or vibrations of a thin rectangular plate can be accurately modelled using the classical plate theory (CPT). A thin plate is one in which the thickness to length ratio is less than or equal to 0.1 [11]. When the amplitude of the transverse vibration of the plate is small in comparison to the thickness of the plate, the effect of in-plane forces arising from membrane stretching can be neglected, and the equation for transverse vibration of the plate according to the CPT is given as [1]:

$$\frac{\partial^2 M_x}{\partial x^2} + 2\frac{\partial^2 M_{xy}}{\partial x \partial y} + \frac{\partial^2 M_y}{\partial y^2} = \rho h \frac{\partial^2 w}{\partial t^2} - q(x, y, t) \tag{1}$$

where M_x, M_{xy}, and M_y are moment resultants, $w = w(x, y, t)$ is the transverse displacement, and $q(x, y, t)$ is the transverse excitation. The moment resultants can be determined from the constitutive equations derived using the classical laminated theory (CLT). The constitutive equations for a thin trimorph plate with isotropic layers have been derived based on the CLT in reference [10], and from these equations the moment resultants are given as:

$$\begin{matrix} M_x \\ M_y \\ M_{xy} \end{matrix} = \begin{bmatrix} B_{11} & B_{12} & 0 \\ B_{12} & B_{11} & 0 \\ 0 & 0 & B_{66} \end{bmatrix} \begin{matrix} \varepsilon_x^0 \\ \varepsilon_y^0 \\ \varepsilon_{xy}^0 \end{matrix} + \begin{bmatrix} D_{11} & D_{12} & 0 \\ D_{12} & D_{11} & 0 \\ 0 & 0 & D_{66} \end{bmatrix} \begin{matrix} k_x^0 \\ k_y^0 \\ k_{xy}^0 \end{matrix} \tag{2}$$

where $[B_{ij}]$ and $[D_{ij}]$ are the extension-bending and pure bending stiffness matrices respectively, $\{\varepsilon_x^0 \;\; \varepsilon_y^0 \;\; \varepsilon_{xy}^0\}^T$ is the strain vector, and $\{k_x^0 \;\; k_y^0 \;\; k_{xy}^0\}^T$ is the curvature vector. The subscript '0' indicates mid-plane strains and curvatures. The expressions for determination of the elements of the stiffness matrices are discussed in Section 3. The elements of both the strain and curvature vectors can be expressed in terms of the displacements of the mid-plane as shown.

$$\varepsilon_x^0 = \frac{\partial u^0}{\partial x}; \quad \varepsilon_y^0 = \frac{\partial v^0}{\partial y}; \quad \varepsilon_{xy}^0 = \frac{\partial u^0}{\partial y} + \frac{\partial v^0}{\partial x}$$
$$k_x^0 = -\frac{\partial^2 w}{\partial x^2}; \quad k_y^0 = -\frac{\partial^2 w}{\partial y^2}; \quad k_{xy}^0 = -2\frac{\partial^2 w}{\partial x \partial y} \tag{3}$$

The combination of the constitutive equations derived using the CLT and the equations of motion derived using the CPT is called the classical laminate plate theory. Substituting equations (2) and (3) in equation (1) and neglecting in-plane displacements, the governing equation for the transverse vibration of the trimorph plate is derived thus:

$$\rho h \frac{\partial^2 w}{\partial t^2} + D_{11} \left(\frac{\partial^4 w}{\partial x^4} + \frac{\partial^4 w}{\partial y^4} \right) + 2(D_{12} + 2D_{66}) \frac{\partial^4 w}{\partial x^2 \partial y^2} = q(x, y, t) \tag{4}$$

The transverse displacement and excitation can be expressed in series form as:

$$w(x, y, t) = \sum_{m=1}^{\infty} \sum_{n=1}^{\infty} W_{mn}(t) X_m Y_n \tag{5a}$$

$$q(x, y, t) = \sum_{m=1}^{\infty} \sum_{n=1}^{\infty} Q_{mn}(t) \sin\left(\frac{m\pi x}{a}\right) \sin\left(\frac{n\pi y}{b}\right) \tag{5b}$$

In equation (5b), $Q_{mn}(t)$ is the load coefficient determined as:

$$Q_{mn}(t) = \frac{4}{ab} \int_0^a \int_0^b q(x, y, t) \sin\left(\frac{m\pi x}{a}\right) \sin\left(\frac{n\pi y}{b}\right) dx dy \tag{6}$$

X_m and Y_n are admissible shape functions that satisfy the boundary conditions but not necessarily the PDE. Equation (4) can be reduced to an ODE using the Galerkin variation approach [11]. The vibration model (equation (4)) has been presented in such a way that the LHS of the equation is a partial differential expression (*PDEx*) in terms of the transverse displacement and the RHS is the external excitation. Thus the Galerkin variation formula for derivation of the reduced model can be expressed as:

$$\int_0^b \int_0^a \left(PDEx - q(x, y, t) \right) X_m Y_n dx dy = 0 \tag{7}$$

Equation (7) can be evaluated for any boundary condition but the present analysis has been limited to simply-supported boundary conditions on all edges of the rectangular plate (SSSS) for mathematical convenience, and without loss of generality. For SSSS, the shape functions can be expressed as $X_m = \sin(m\pi x/a)$ and $Y_n = \sin(n\pi y/b)$. Substituting equations (4), (5a) and (5b) in equation (7) and evaluating the resulting double integral for SSSS, the reduced model for small transverse oscillations of the trimorph plate is:

$$\ddot{W}_{mn}\} + K\{W_{mn}\} = F(t)\{\gamma_{mn} \tag{8}$$

where $W_{mn}(t)$ is the time-domain transverse displacement of the (m, n) vibration mode;

$K = \frac{\pi^4}{\rho h}\left[D_{11} \left(\frac{m^4}{a^4} + \frac{n^4}{b^4} \right) + \frac{2m^2 n^2 (D_{12} + 2D_{66})}{a^2 b^2} \right]$ is the mechanical bending stiffness per unit mass;

$F(t)$ is the transverse excitation; and γ_{mn} is a constant derived from the evaluation of equation (6). Considering an excitation that is applied at a point (x_0, y_0) then,

$$\gamma_{mn} = \frac{4}{\rho hab} \mathrm{Sin}\left(\frac{m\pi x_0}{a}\right) \mathrm{Sin}\left(\frac{n\pi y_0}{b}\right. \tag{9}$$

where ρ is the density of the plate; h is the total thickness of the plate; a and b are the planar dimensions of the plate.

2.2 Elastoplastic contact model

Static contact models can be used to estimate the impact force during low-velocity impact of a transversely flexible plate [1, 2]. The low-velocity impact of a transversely flexible plate often results in elastoplastic indentation at the point of impact. In such cases, the use of Hertz contact model or linearised elastoplastic contact models to estimate the impact force introduces significant errors in the predicted impact response [6, 9]. Recently, Big-Alabo et al [12, 13] developed an elastoplastic contact model in which all of the loading and unloading stages are modelled using Meyer-type compliance models. The main advantages of the elastoplastic model are its simplicity and computational tractability when used for impact analysis [12]. Details of the formulation of the elastoplastic model can be found in [12, 13]. This elastoplastic contact model has been used in the present impact analysis with a slight modification in the expression for the unloading stage as explained below. The contact model has four loading stages consisting of one elastic loading stage, two elastoplastic loading stages and one fully plastic loading stage. Also, there is a single unloading (restitution) stage. The elastoplastic contact model is given as follows.

Elastic loading stage

$$F_e = K_h \delta^{3/2} \qquad 0 \le \delta \le \delta_y \tag{10}$$

where F_e is the elastic loading force, and K_h is the Hertzian contact stiffness calculated as $K_h = (4/3)ER^{1/2}$. The constants E and R are the effective modulus and radius respectively, and are calculated as: $E = [(1-\upsilon_i^2)/E_i + (1-\upsilon_t^2)/E_t]^{-1}$ and $R = [1/R_i + 1/R_t]^{-1}$. The subscripts i and t stand for indenter and target respectively, and υ is the Poisson's ratio.

Elastoplastic loading stages

- Region I: Nonlinear elastoplastic loading

$$F_{ep}^{I} = K_h\left(\delta - \delta_y\right)^{3/2} + K_h\delta_y^{3/2} \qquad \delta_y \le \delta \le \delta_{tep} \tag{11}$$

where F_{ep}^{I} is the nonlinear elastoplastic loading force, and δ_y is the indentation at yield. The expression for calculating δ_y is given as: $\delta_y = \left(1.1\pi RS_y/K_h\right)^2$ where S_y is the yield stress of the target.

- Region II: Linear elastoplastic loading

$$F_{ep}^{II} = K_l\left(\delta - \delta_{tep}\right) + K_h\left[\left(\delta_{tep} - \delta_y\right)^{3/2} + \delta_y^{3/2}\right. \qquad \delta_{tep} \le \delta \le \delta_p \tag{12}$$

where F_{ep}^{II} is the linear elastoplastic loading force, K_l is the linear contact stiffness in Region II, δ_{tep} is the indentation at the transition between Regions I and II. The constants in equation (12) are determined as: $K_l = 5.40K_h\delta_y^{1/2}$ and $\delta_{tep} = 13.93\delta_y$.

Fully plastic loading stage

$$F_{fp} = K_p\left(\delta - \delta_p\right) + F_{\delta=\delta_p} \qquad \delta_p \le \delta \le \delta_m \tag{13}$$

where F_{fp} is the fully plastic loading force, K_p is the linear contact stiffness during the fully plastic loading stage, δ_p is the indentation at the onset of fully plastic loading and $F_{\delta=\delta_p}$ is the

value of the contact force at δ_p. The constants in equation (13) are determined as: $K_p = 4.6\pi RS_y$; $\delta_p = 82.5\delta_y$; and $F_{\delta=\delta_p} = 70.0K_l\delta_y + 47.6K_h\delta_y^{3/2}$.

Unloading (restitution) stage

$$F_u = K_u\left(\delta - \delta_f\right)^{3/2} \qquad \delta_f \le \delta \le \delta_m \tag{14}$$

where F_u is the elastic unloading force, K_u is the nonlinear contact stiffness during unloading, and δ_f is the fixed or permanent indentation at the end of the unloading. The constants in equation (14) are determined as: $K_u = (4/3)ER_d^{1/2}$ and $\delta_f = \delta_m - \left(3F_m/4ER_d^{1/2}\right)^{2/3}$ where R_d is the deformed effective radius, and $R_d \ge R$; δ_m and F_m are the indentation and force at the end of the loading. For a half-space impact the end of the loading response coincides with the point when the maximum indentation occurs, but this is not necessarily so for transversely flexible plate impact [1]. Nevertheless, the impact loading ends when the velocity of the impactor is zero for both half-space impact and transversely flexible plate impact.

Whereas the Hertz stiffness is related to the effective radius, the unloading stiffness is related to a deformed effective radius due to plastic deformation effects [13]. In references [12, 13] R_d was determined as: $R_d \cong R$ when the maximum penetration is in the elastoplastic loading regime or the initial phase of the fully plastic loading regime; and $R_d \cong R + \delta_m/2$ when the maximum penetration is well into the fully plastic loading regime e.g. $\delta_m/\delta_p \ge 2$. The approximations used in [12] could lead to an underestimation of the permanent indentation at the end of the unloading. Based on published observations of the unloading response during elastoplastic indentation [14 – 16], the expressions in equation (15) are proposed here to calculate R_d. A comparison of the unloading response predicted using equation (15) and the expressions in [12] against published experimental data [17] is shown in Figure 2, and equation (15) is seen to give a better prediction of the experimental data.

$$\begin{aligned}
R_d &= R && 0 \le \delta_m \le \delta_y \\
R_d &= \left[\left(\frac{\delta_m - \delta_y}{\delta_{tep} - \delta_y}\right)^{3/2} + 1\right]R && \delta_y \le \delta_m \le \delta_{tep} \\
R_d &= \left[0.8\left(\frac{\delta_m - \delta_{tep}}{\delta_p - \delta_{tep}}\right) + 2\right]R && \delta_{tep} \le \delta_m \le \delta_p \\
R_d &= 2.8R && \delta_m > \delta_p
\end{aligned} \tag{15}$$

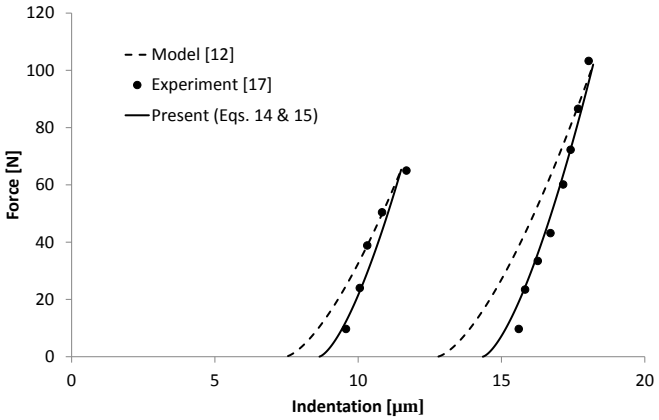


Figure 2: Unloading response during static indentation of AISI steel by a spherical tungsten carbide indenter.

2.3 Impact model for thin rectangular trimorph plate

During transversely flexible plate impact the local indentation of the plate is defined as the difference between the displacements of the impactor and plate [1], with the former being larger. When the displacement of the plate is equal to or higher than that of the impactor, contact between the plate and the impactor ceases. Assuming the displacement of the impactor is designated as $w_i(t)$ then, the local indentation can be expressed as:

$$\delta(t) = w_i(t) - w(t) \tag{16}$$

The equation of motion for the impactor can be expressed as:

$$\ddot{w}_i = -F(t)/m_i \tag{17}$$

where m_i is the mass of the impactor and $F(t)$ is the impact force, which is estimated using the elastoplastic contact model presented in sub-section 2.2. Equations (8), (10) – (14), and (17) form the complete impact model for analysis of the trimorph plate. These equations produce a set of P + 1 coupled ODEs in each impact stage that must be solved simultaneously; P represents the number of vibration modes used in the solution. For impact at the centre of the plate (i.e. $x_0 = a/2$ and $y_0 = b/2$), $P = (m+1)(n+1)/4$ where $m, n = 1, 3, 5, \ldots$ are odd integers.

3 DETERMINATION OF MATERIAL PROPERTIES OF TRIMORPH PLATE

The trimorph plate is a composite laminate in which each layer has different material properties. To solve the impact model formulated in Section 2 the material properties of the trimorph plate must be determined. In this section, the material properties of the trimorph plate are obtained using analytical techniques.

3.1 Stiffness of the trimorph plate

The bending-extension and bending stiffness elements are determined from the CLT as:

$$B_{ij} = \frac{1}{2}\sum_{k=1}^{L} \bar{Q}_{ijk}\,(z_k^2 - z_{k-1}^2 \quad ; \; D_{ij} = \frac{1}{3}\sum_{k=1}^{L} \bar{Q}_{ijk}\,(z_k^3 - z_{k-1}^3 \tag{18}$$

where L is the total number of layers; $\bar{Q}_{ijk}$ is the transformed reduced stiffness of the kth layer of the laminate, and is obtained from the material properties of the kth layer as shown in [10]. Staab [18] presented alternative expressions to equations (18), and the stiffness coefficients were expressed in terms of lamina thickness and the distance of the lamina centroid measured from the mid-plane. Here, simpler expressions are derived to express the stiffness coefficients in terms of lamina thickness and the total thickness of the laminate.

From Figure 3, the following can be deduced geometrically: $z_k - z_{k-1} = h_k$; $z_k = \sum_{i=1}^{k} h_i - h/2$ for $k > 0$ or $z_{k-1} = \sum_{i=1}^{k-1} h_i - h/2$ for $k > 1$; where h_k is the thickness of the kth layer. If the conditions stated are not satisfied then, $z_k = 0$ or $z_{k-1} = 0$ respectively. The quadratic expression of the B_{ij} elements can be expanded as:

$z_k^2 - z_{k-1}^2 = (z_k + z_{k-1})(z_k - z_{k-1}) = (z_k - z_{k-1} + 2z_{k-1})(z_k - z_{k-1}$

Therefore, $z_k^2 - z_{k-1}^2 = (h_k + 2z_{k-1})h_k = h_k\left(h_k + 2\sum_{i=1}^{k-1} h_i - h\right)$.

Also, $z_k^3 - z_{k-1}^3 = (z_k - z_{k-1})^3 + 3(z_k - z_{k-1})z_k z_{k-1}$.

Therefore, $z_k^3 - z_{k-1}^3 = h_k^3 + 3h_k \quad \sum_{i=1}^{k} h_i - h/2\big) \quad \sum_{i=1}^{k-1} h_i - h/2\big)$.

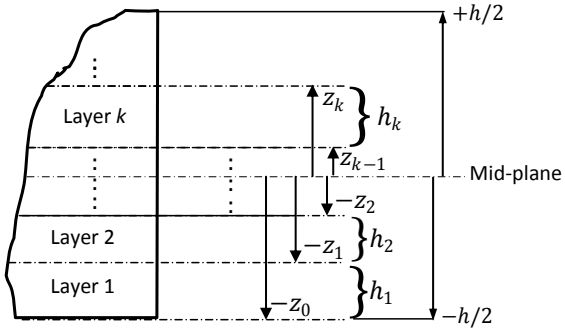


Figure 3: Sketch illustrating vertical geometry of a general laminate.
Figure 2.6 *Sketch illustrating vertical geometry of a general laminate*

Consequently, the bending-extension and bending stiffness coefficients can be determined as:

$$B_{ij} = \frac{1}{2}\sum_{k=1}^{L} \bar{Q}_{ijk}\, h_k \left(h_k + 2\sum_{i=1}^{k-1} h_i - h \right)$$
$$D_{ij} = \frac{1}{3}\sum_{k=1}^{L} \bar{Q}_{ijk} \left[h_k^3 + 3h_k \left(\sum_{i=1}^{k} h_i - h/2 \right) \sum_{i=1}^{k-1} h_i - h/2 \right) \tag{19}$$

The validity of equation (19) was confirmed by comparing with results obtained using equation (18) and Staab's expressions [18]. All three expressions produced exactly the same results for the Al/PVDF/PZT laminate used in the present impact analysis (see Table 1 for material properties).

3.2 Effective transverse properties of the trimorph plate

To calculate the constants of the contact model in Section 2.2, the Young's modulus, Poisson ratio and yield stress of the target in the transverse direction must be known. Since the trimorph plate is made up three different isotropic materials laminated together, effective properties are needed and cannot be obtained from available material properties data. An approximate analytical solution to the problem is the 'strength of materials' approach which has been applied in studying the low-velocity impact response of sandwich laminates [19] and functionally graded laminates [20], and verified experimentally for impact analysis [21]. The strength of materials approach is suitable for use under plane stress conditions, quasi-static loading and when the effect of the in-plane material properties of the target on the transverse deformation can be neglected [19]. These conditions apply to the impact of the trimorph plate; hence, strength of materials approach is considered to be appropriate for the present investigation. The effective transverse properties of the trimorph plate can be estimated as:

$$\begin{aligned} E_t &= h/(h_1/E_1 + h_2/E_2 + h_3/E_3) \\ v_t &= (v_1h_1 + v_2h_2 + v_3h_3)/h \\ \rho_t &= (\rho_1h_1 + \rho_2h_2 + \rho_3h_3)/h \\ S_y &= h/\left(h_1/S_{y1} + h_2/S_{y2} + h_3/S_{y3}\right) \end{aligned} \tag{20}$$

where $h = h_1 + h_2 + h_3$ is the total thickness of the plate; the subscript, t, represents the target which here is the plate; the subscripts 1, 2, and 3 represent the layers of the plate from bottom to top; h_k, E_k, v_k, ρ_k, and S_{yk} are the thickness, Young's modulus, Poisson's ratio, density and yield stress of the *k*th layer of the trimorph plate, respectively.

4 DISCUSSIONS OF RESULTS

4.1 Validation of modelling and solution approach

The impact model derived above have been solved by direct numerical integration using the NDSolve function in *Mathematica*™. To validate the modelling and solution approach used in the present analysis, a well-known impact problem first studied by Karas [22] is re-examined. This problem has been studied by many others including Goldsmith [2] and Abrate [1], and can be considered as a benchmark case. The impact event involves the elastic impact of a simply-supported square steel plate struck by a steel ball. The material and geometrical properties of the impact system are: properties of steel – ρ = 7806 [kg/m^3], E = 206.8 [GPa] and υ = 0.3 [-]; Plate dimensions = 0.2 × 0.2 × 0.008 [m^3]; Impactor diameter = 0.02 [m]; velocity = 1.0 [m/s]. The impactor mass was calculated to be 0.0327 [kg]. Since the impact is assumed to be elastic the Hertz contact model is used to estimate the impact force.

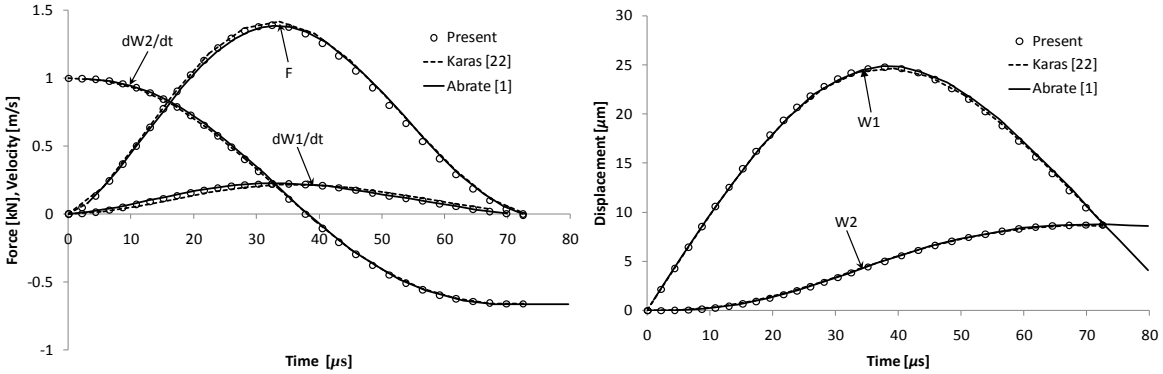


Figure 4: Impact response of a transversely flexible steel plate struck by a steel ball. F – force, dW1/dt – plate velocity, dW2/dt – impactor velocity, W1 – plate displacement, W2 – impactor displacement.

Karas [22] and Abrate [1] both used the complete modelling approach, but while the former solved the reduced models using small-increment integration scheme the latter employed the Newmark time integration scheme. The results obtained by Karas [22] and Abrate [1] and that of the present approach are compared in Figure 4, and all three methods are in good agreement. This shows that results obtained using the NDSolve function are reliable. Hence, the NDSolve function has been used to solve the elastoplastic impact models of the trimorph plate.

4.2 Elastoplastic impact analysis of Al/PVDF/PZT trimorph plate

A study of the elastoplastic impact response of a trimorph plate with layers arranged as Al/PVDF/PZT from top to bottom was carried out. The spherical surface of the impactor is in contact with the aluminium layer. The material and geometrical properties of the plate layers are shown in Table 1.

Material	ν [-]	E [GPa]	ρ [kg/m^3]	S_y [MPa]	h [mm]
Al	0.33	70	2700	320	3.0
PVDF	0.44	1.1	1770	50	1.0
PZT	0.3	64	7600	250	1.0

Table 1: Material and geometrical properties of the layers of the trimorph plate.

The other material and geometrical properties of the impact system are: $a = 100\ [mm]$; $b = 100\ [mm]$; $m_i = 1\ [kg]$; $V_0 = 0.30\ [m/s]$; $E_i = 210\ [MPa]$; $E_i = 7800\ [kg/m^3]$; $\nu_i = 0.30\ [-]$; $R_i = 10\ [mm]$. Impactor material: steel.

Effect of number of vibration modes used in the solution

The accuracy of the solution of the impact models depends on the number of vibration modes used in the solution. The impact force history was determined for different numbers of vibration modes as shown in Figure 5. The figure shows that nine vibration modes (i.e. $m = n = 5$) are sufficient to guarantee accurate results. Hence, the results presented and discussed in this section have been obtained using a nine mode approximation. In Figure 5, the blue lines represent the elastic loading response, the red lines represent the elastoplastic loading response, and the black lines represent the response when unloading from an elastoplastic loading stage. This colour definition has also been used in later figures.

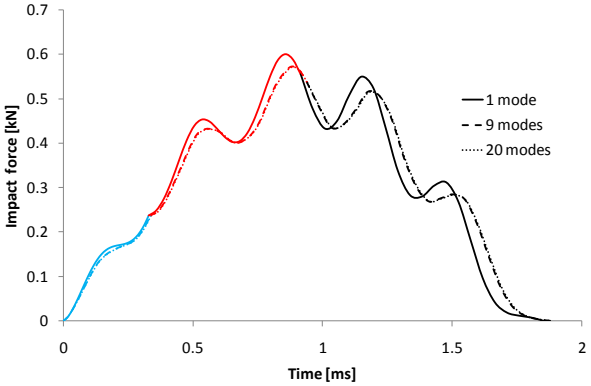


Figure 5: Effect of the number of vibration modes used in the solution of the impact model on the accuracy of the results obtained for the Al/PVDF/PZT plate.

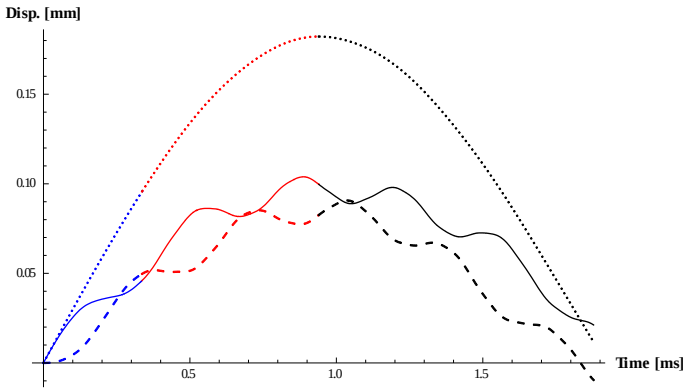


Figure 6: Displacement histories of Al/PVDF/PZT plate struck by steel impactor. Dotted line – impactor displacement, short-dash line – plate displacement, solid line – indentation.

Figure 6 shows the displacement histories during the elastoplastic impact response of the Al/PVDF/PZT plate. The displacement of the impactor is smooth whereas there are oscillations in the displacement of the plate giving rise to oscillations in the indentation. The response has a maximum indentation of 103.95 [μm], which occurs in the nonlinear elastoplastic loading stage, and a permanent indentation of 21.16 [μm]. The maximum contact force is 573.95 [N] and the impact duration is 1.88 [ms]. The loading ends when the velocity of the impactor is zero and this occurs when the time is 0.94 [ms] (see Figure 7). The results of the simulation shows that the point of maximum indentation (0.89 [ms], 103.95 [μm]) is

different from the end point of the impact loading (0.94 [ms], 99.7 [μm]), and this observation has also been reported previously by Abrate [1].

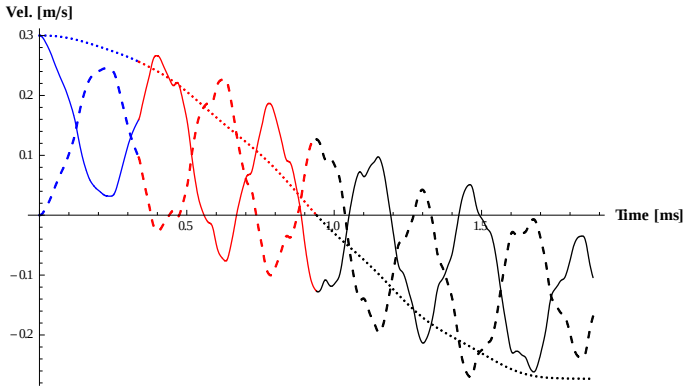


Figure 7: Velocity histories of Al/PVDF/PZT plate struck by steel impactor. Dotted line – impactor velocity, short-dash line – plate velocity, solid line – relative velocity.

Effect of contact model used to estimate the impact force

To investigate the effect of the contact model used to estimate the impact force on the response predicted, the results of three contact models (i.e. the present contact model, the contact model of Majeed et al [23] and the Hertz contact model) were compared. An initial impact velocity of 2.0 [m/s] was used in the simulations to ensure that the indentation response is well into the elastoplastic stage. The impact responses predicted by the three contact models are compared in Figure 8. The force histories predicted by all three contact models are in good agreement, demonstrating that the force history is not quite sensitive to the contact model used. However, the indentation history predicted by the Hertz contact model is different from that predicted by the elastoplastic contact models. The latter predict significant elastoplastic deformation with a permanent indentation at the end of the impact. The present contact model predicts a maximum indentation of 0.37 [mm] and a permanent indentation of 59.8 [μm], the contact model of Majeed et al [23] predicts 0.38 [mm] and 65.7 [μm] respectively, while the Hertz contact model predicts a maximum indentation of 0.34 [mm] and no permanent indentation. This shows that the contact model used for estimating the impact force of a large-mass impact can significantly affect the accuracy of the predictions and limit the information that can be obtained. This observation differs from the position taken by most investigators that the predicted response during large mass impact is insensitive to the contact model used to estimate the impact force [1]. Hence, the choice of contact model used to study large mass impact events is an important consideration.

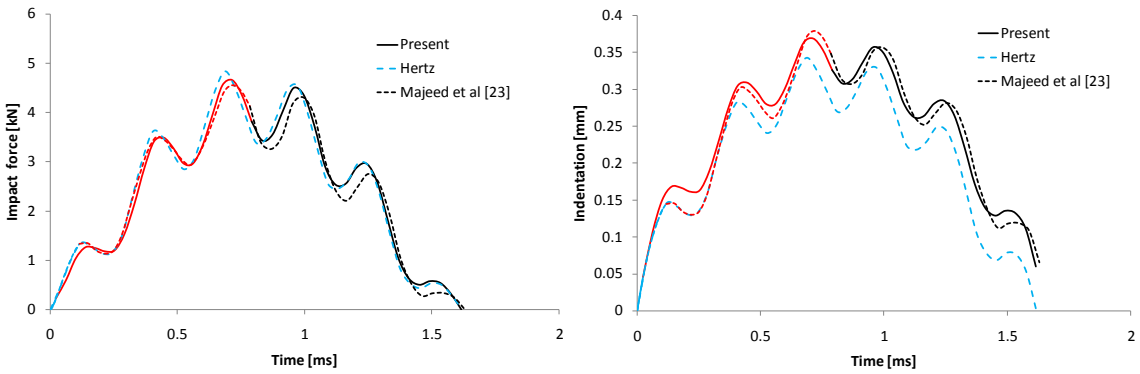


Figure 8: Impact response of Al/PVDF/PZT plate struck by steel impactor at an initial impact speed of 2.0 [m/s].

5 ACTIVE IMPACT DAMAGE MITIGATION

Piezoelectric actuation can be used to alter the effective transverse stiffness (flexibility) of a structure by creating a pre-stress to make it apparently stiffer or more compliant [24]. The effective transverse stiffness of a plate with piezoelectric layer actuation is the sum of the mechanical bending stiffness and the induced piezoelectric stiffness. The latter may be positive or negative, depending on whether the induced in-plane piezoelectric stress is tensile or compressive. Studies [6] on the effect of flexibility on the impact response of a plate showed that the impact response of the plate is significantly influenced by altering its flexibility. This means that a plate with piezo-actuator layers can be used to influence its impact response to a rigid blunt projectile by actively inducing a state of pre-stress in the plate. This idea can be exploited to actively mitigate blunt object impact damage.

A few studies have attempted to investigate the application of piezo-actuation during impact [7, 8], but these studies applied active bending and damping induced by piezo-actuation to investigate the control of low-velocity impact response. In this section, a parametric study is carried out to demonstrate that the flexibility of a trimorph plate, which can be altered using active pre-stressing induced by piezo-actuation, could be exploited to mitigate impact damage effects. To achieve this, a parameter, α, used to alter the effective transverse stiffness of the trimorph plate without changing the dimensions or material properties of the plate (as would be expected during active pre-stressing induced by piezo-actuation) is introduced into the transverse vibration model as shown in equation (21). The parameter, α, represents the percentage change in the effective transverse stiffness of the plate. When $\alpha < 0$, the plate is apparently less flexible and when $\alpha > 0$, the plate is apparently more flexible. The normal case is represented by $\alpha = 0$ when the effective transverse stiffness is determined by the mechanical bending stiffness only.

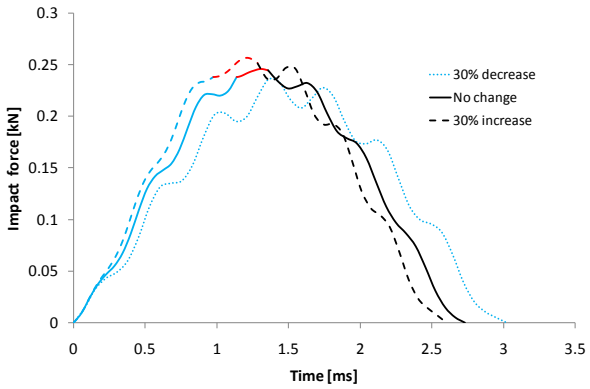


Figure 9: Influence of transverse flexibility on the elastoplastic impact response of Al/PVDF/PZT plate.

$$\ddot{W}_{mn}\} + K(1-\alpha)\{W_{mn}\} = F(t)\{\gamma_{mn} \tag{21}$$

Figure 9 shows the effect of α on the impact response of the Al/PVDF/PZT plate. In this figure, the mass of the impactor is 2.0 [kg] and the impact velocity is 0.10 [m/s]. Three cases are considered i.e. $\alpha = 0$, $\alpha = -0.3$, and $\alpha = 0.3$. The reference point is taken when the effective stiffness is equal to the mechanical stiffness, i.e. $\alpha = 0$. For $\alpha = 0$, the maximum impact force is 246.15 [N], the impact duration is 2.73 [ms] and the permanent indentation is 3.36 [μm]. When $\alpha = -0.3$, the effective stiffness is 30% higher than normal ($\alpha = 0$) and the impact response, which is more localised, is characterised by a higher maximum impact force (263.45 [N]), shorter impact duration (2.60 [ms]) and larger permanent indentation (5.10 [μm]). For $\alpha = 0.3$, the effective stiffness is 30% lower than normal and the response has become purely elastic with no permanent indentation. The maximum impact force is about

4.0% lower than for $\alpha = 0$ and the impact duration is longer (3.02 [ms]). The implication is that an impact, which should ordinarily result in a permanent indentation, can be converted to one with no permanent indentation. This result is significant because it demonstrates that alteration of the effective stiffness of the plate could be exploited to either reduce or completely eliminate elastoplastic impact effects.

6 CONCLUSIONS

The elastoplastic impact response of a transversely flexible trimorph plate struck by a spherical impactor has been investigated analytically. The investigations reveal that the contact model used to predict the impact force of a large mass impact event can significantly affect the resulting predictions, and also limit detailed description of the impact response. Also, investigations on the effect of transverse flexibility on the impact response of the trimorph plate showed that elastoplastic impact effects could be reduced significantly or eliminated by altering the effective transverse stiffness of the plate; an observation that could be exploited for active impact control to mitigate impact damage.

ACKNOWLEGDEMENT

The first author is grateful to the Commonwealth Scholarship Commission (CSC), UK for funding his PhD research (CSC Award Ref: NGCA-2011-60), of which this work is a part.

REFERENCES

[1] S. Abrate, *Impact on composite structures*. Cambridge University Press, 1998.

[2] W. Goldsmith, *Impact: The theory and physical behaviour of colliding solids*. Dover Publications, 2001.

[3] S. Abrate, Modeling of impacts on composite structures. *Computers and Structures*, **51**, 129 – 138, 2001.

[4] C. Zener, The intrinsic inelasticity of large plates. *Physical Review*, **59**, 669 – 673, 1941.

[5] A.P. Christoforou, S.R. Swanson, Analysis of impact response in composite plates. International Journal of Solids and Structures, **27 (2)**, 161 – 170, 1991.

[6] A.P. Christoforou, A.S. Yigit, Effect of flexibility on low velocity impact response. *Journal of Sound and Vibration*, **217 (3)**, 563 – 578, 1998.

[7] A.S. Yigit, A.P. Christoforou, Control of low-velocity impact response on composite plates. *Journal of Vibration and Control*, **6**, 429 – 447, 2000.

[8] D.A. Saravanos, A.P. Christoforou, Impact response of adaptive piezoelectric laminated plates. *AIAA Journal*, **40(10)**, 2087 – 2095, 2002.

[9] D. Zheng, W.K. Binienda, Effect of permanent indentation on the delamination threshold for small mass impact on plates. *International Journal of Solids and Structures*, **44**, 8143 – 8158, 2007.

[10] A. Big-Alabo, M.P. Cartmell, Vibration analysis of a trimorph plate for optimised damage mitigation. *Journal of Theoretical and Applied Mechanics*, **49 (3)**, 641 – 664, 2011.

[11] R. Szilard, *Theory and Applications of Plate Analysis: Classical, Numerical and Engineering Methods*. John Wiley & Sons Inc., 2004.

[12] A. Big-Alabo, P. Harrison, M.P. Cartmell, Elastoplastic half-space impact analysis using a novel contact model that accounts for post-yield effects. A. Cunha, E. Caetano, P. Ribeiro, G. Müller (eds.). *9th International Conference on Structural Dynamics (EURODYN 2014)*, Porto, Portugal, 30 June - 2 July, 2014.

[13] A. Big-Alabo, P. Harrison, M.P. Cartmell, Contact model for elastoplastic analysis of half-space indentation by a spherical impactor. *Computers and Structures*, **151**, 20 – 29, 2015.

[14] K.L. Johnson, *Contact mechanics*. Cambridge University Press, 1995.

[15] L.Y. Li, C.Y. Wu, C. Thornton, A theoretical model for the contact of elastoplastic bodies. *Proc. IMechE, Part C: Journal of Mechanical Engineering Science*, **216**, 421 – 431, 2002.

[16] R. Hill, B. Storakers, A.B. Zdunek, A theoretical study of Brinell hardness test. *Proceedings of Royal Society London A*, **423**, 301 – 330, 1989.

[17] O. Bartier, X. Hernot, G. Mauvoisin, Theoretical and experimental analysis of contact radius for spherical indentation. *Mechanics of Materials*, **42**, 640–656, 2010.

[18] G.H. Staab, *Laminar composites*. Butterworth Heinemann, 1999.

[19] M.R. Khalili, K. Malekzadeh, R.K. Mittal, Effect of physical and geometrical parameters on the transverse low-velocity impact response of sandwich panels with a transversely flexible core. *Composite Structures*, **77**, 430 – 443, 2007.

[20] M. Shariyat, F. Farzan, Nonlinear eccentric low-velocity impact analysis of highly prestressed FGM rectangular plate, using a refined contact law. *Archive of Applied Mechanics*, **83**, pp 623–64, 2013.

[21] R.A. Larson, A.N. Palazotto, Property estimation in FGM plates subject to low-velocity impact loading. *Journal of Mechanics of Materials and Structures*, **4 (7-8)**, 1429 – 1451, 2009.

[22] K. Karas,: Platten unter seitchem stoss. *Ingenieur Archiv*, **10**, 237-250, 1939.

[23] M.A. Majeed, A.S. Yigit, A.P. Christoforou, Elastoplastic contact/impact of rigidly supported composites. *Composites: Part B*, **43**, 1244 – 1251, 2012.

[24] H. Waisman, H. Abramovich, Active stiffening of laminated composite beams using piezoelectric actuators. *Composites Structures*, **58**, 109 – 120, 2002.

COMPDYN 2015
5th ECCOMAS Thematic Conference on
Computational Methods in Structural Dynamics and Earthquake Engineering
M. Papadrakakis, V. Papadopoulos, V. Plevris (eds.)
Crete Island, Greece, 25–27 May 2015

POUNDING BETWEEN BRIDGE DECKS: COMPUTATIONAL DETAILS AND RESULTS

Bharat Mandal[1*], Vincenzo Bianco[1], and Giorgio Monti[1]

[1] Sapienza University of Rome
Department of Structural Engineering and Geotechnics
Via Antonio Gramsci 53 – 00197 – Rome - Italy
*bharatmandal@yahoo.com

Keywords: Pounding, bridge decks, numerical modelling, response spectrum.

Abstract. *The observation of damage to structures, either buildings or bridges, due to earthquake induced pounding, dates back to early San Fernando (1971) and Mexico City (1985) post-earthquake reconnaissance reports. Recent ground shakings that have struck Italian territories have renewed the awareness of the necessity to clarify some aspects related to the pounding-induced forces acting on the bridge and viaduct piers. Historically pounding has been studied by either of two approaches, that are: 1) the stereo-mechanical approach, based on the physical laws of the impact phenomenon and the definition of a restitution factor, and 2) the force-based approach, based on the definition of the local force due to impact. Moreover, impact can be either soft or hard, depending on the amount of earthquake-induced energy dissipated locally through the damage of the colliding bodies. In this study, pounding response of two linear SDOF (Single Degree Of Freedom) systems has been studied through different models, namely: 1) Linear Spring, 2) Kelvin-Voigt, 3)Hertz, 4) Hertz-damp and 5) Stereo-mechanical model. Those models have been applied using both backward and forward spectrum-compatible and artificially generated ground motions. After introducing 1) the details of each of those models, 2) the main differences among them, and 3) the numerical computational strategy implemented, the main results are presented. Among these latter, being the early results of an exploratory and propaedeutic work for a Doctoral Thesis, the pounding-inducted response spectra, either in terms of peak displacement or pounding force, are developed.*

1 INTRODUCTION

Pounding is the cyclic hammering that can occur, during a seismic event, between close structures oscillating out-of-phase when the gap between these latter is not large enough to accommodate their earthquake-induced horizontal displacements.

It is a phenomenon that has been largely documented in the past, as a major cause of both buildings and bridges collapses during earthquakes (*e.g.* [1-8]). In particular, as to the bridges, impact between decks and abutments had already been observed in the 1971 San Fernando earthquake [1]. In the 1994 Northridge earthquake, at a location approximately 12 km far from the epicenter, significant pounding damage was observed at the expansion hinges and abutments of the still standing portions of a number of bridges [4]. During the 1995 Hyogo-Ken Nanbu earthquake in Kobe, Japan, several pounding-related failures had occurred: 1) longitudinal movements of the elements of the Hanshin Expressway superstructure reached almost 30 cm and caused considerable pounding damage at the expansion joints, 2) span collapse due to restrainer failure, and 3) fracture of the bearing supports causing the collapse of several decks [5]. Reconnaissance visits after the 1999 Sep 21 Chi-Chi earthquake in Taiwan revealed hammering at the expansion joints in some bridges which resulted in damage to shear keys, bearings and anchor bolts [6]. During the 2001 Bhuj earthquake, in India, a large number of railway and highway bridges were damaged. A number of reinforced concrete slab culverts on stone masonry abutments sustained damage at the seating of the span. Adjacent spans having girder/slab with different depths, were severely damaged. The large movement of the girders along either the longitudinal or the transversal direction imposed severe strains on the neoprene bearings [7].

From these field observations some general conclusions can be drawn about the typical pounding damages induced to bridges, which can comprehend (Fig. 1): 1) bearing damage, for either longitudinal or transversal earthquake, with consequent unseating and bridge collapse; 2) amplification of longitudinal displacements with consequent unseating; 3) damage to both the abutment and piers transversal retainers; 4) local damage to the impacting decks surfaces, typically summarized as concrete spalling, in its lightest form; 5) shear failure at the abutment beneath the fixed supports; 6) damage to the piers due to excessive displacements imposed.

The kind of damage undergone by a case-study bridge can depend on a number of parameters, both geometrical and mechanical. Moreover, based on these latter, impact between colliding parts can be classified as *soft* impact or *hard* impact. Where the former refers to the case in which most of the energy is dissipated locally, through local damage, while the latter refers to the case in which, due to the high stiffness of the colliding bodies, energy lost locally is negligible with respect to the amount of energy transferred to the impacting bodies in terms of momentum, which results in this way predominant. In this latter case, more likely for the longitudinal impact, the large horizontal force transferred from one deck to the adjacent one, can result in a significant change in the dynamic behavior of the entire bridge.

In this work attention is focused on the case of Reinforced Concrete (RC) viaducts composed of simply supported girders in series (Fig. 2). In this case the two adjacent spans, each with its restrained pier, in correspondence of the beam hinge extremity, can be modelled by two adjacent SDOF systems connected by an impact element.

Attention is first focused on the numerical modelling strategies available in the literature and, in the second part of the paper, the early results of a propaedeutic work for a Doctoral thesis are presented. Attention is dedicated to the possibility to produce spectra, either providing the maximum displacement or force, induced by pounding, during an earthquake. In fact,

spectra can be a very useful analytical tool for practicing engineers committed with the design or rehabilitation of bridges in seismic-prone areas [9].

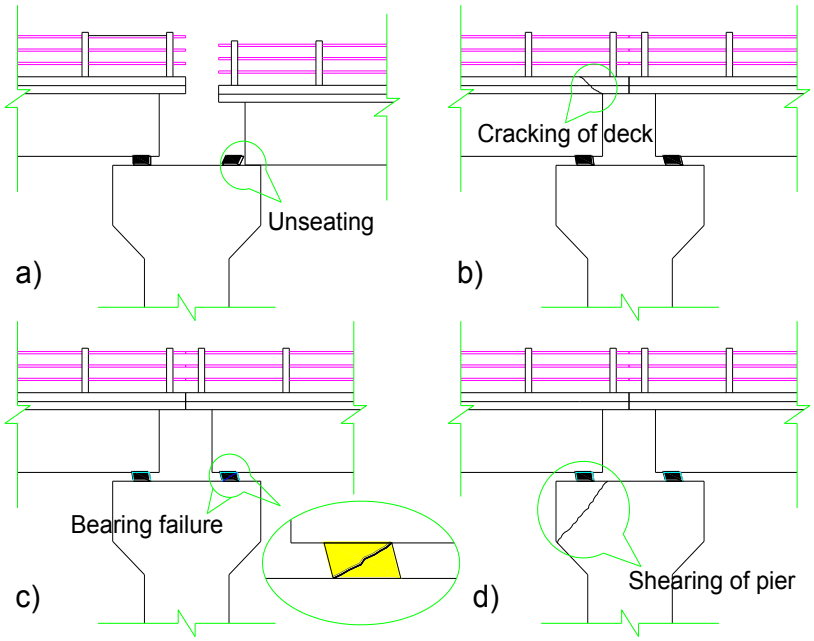


Figure 1: Examples of damage due to earthquake-induced pounding: a) unseating of girder, b) shear cracking of deck, c) bearing shear failure and d) shearing of pier/abutment.

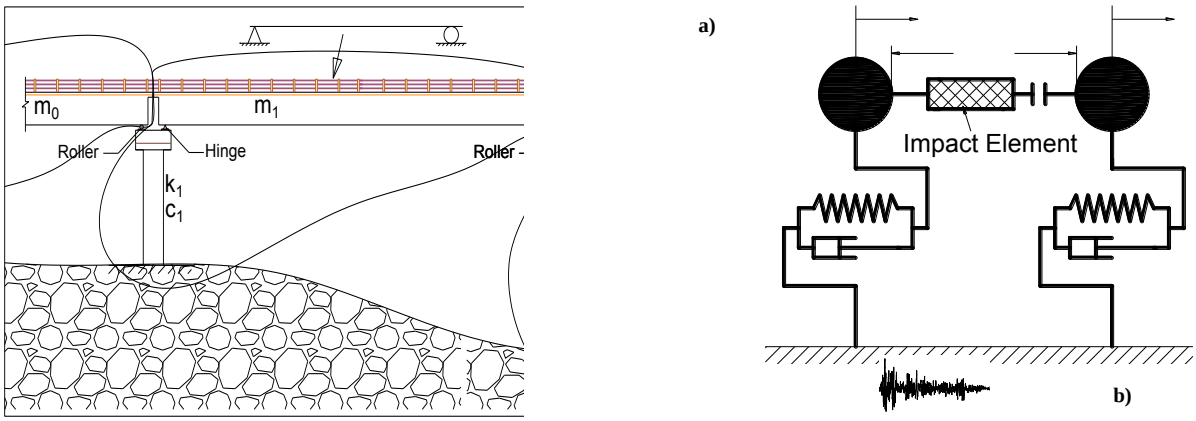


Fig. 2. Idealized Model of bridge: a) adjacent bridge segments, and b) two SDOF model with impact element.

2 POUNDING MODELS AVAILABLE IN THE LITERATURE

Pounding phenomenon has attracted the attention of academic community in the last decades and a relatively large amount of specific scientific literature has already been produced (*e.g.* [10-21]).

The equations of motion representing the dynamic equilibrium of the two colliding masses subject to earthquake can be written as follows:

(1)

where: m_1 and m_2 are the mass of first and second colliding bodies, respectively; and are the relevant damping values; k_1 and are the horizontal displacement stiffness of the vertical structures supporting the first and second mass, respectively; is the ground acceleration and is the pounding force arising locally in the instant of impact; $x_1(t)$ and (t) are the time step-dependent values the two masses displacements while the first derivatives $(\dot{x}_1, \dot{x}_2)$ and the second derivatives $(\ddot{x}_1, \ddot{x}_2)$ are the velocities and accelerations respectively. In a time step-wise implementation, impact occurs at each time instant t in which the following inequality is fulfilled (Fig. 2):

(2)

where: δ is the measure of the penetration, g_p is the gap among the two colliding masses.

From a numerical point of view, pounding has been traditionally studied by either one of two models, that are: a) stereo-mechanical, or b) force-based.

2.1 Stereo-Mechanical Model (SMM)

The Stereo-mechanical model is based on the use of: a) the momentum conservation principle and b) the coefficient of restitution, e. The former can be written as:

(3)

where: $(\dot{x}_1', \dot{x}_2')$ and $(\dot{x}_1, \dot{x}_2)$ are the velocity values after and before impact, respectively. This principle means that the momentum after impact is equal to the momentum before impact. The coefficient of restitution, which is the ratio of the relative velocity after impact to the relative velocity before impact, is given by:

(4)

and gives a measure of the energy loss during impact. In fact it varies between 0, meaning perfectly plastic impact occurred, and 1.0, which means that impact was perfectly elastic. In the former case, the two masses get stuck during impact and move together afterwards while, in the latter, the two masses undergo maximum rebound with no energy loss during impact. With this approach, the impact duration time is neglected and impact is considered central and without any transient stresses and deformations in the impacting bodies.

At each time step in which Eq. (2) is fulfilled, the two bodies velocities are modified according to the following expressions:

(5)

2.2 Force-based models

In the force-based models, the local impact force F_p of Eq. (1) is different than zero and evaluated as function of the penetration value $\delta(t)$. Different models simply differ by the way its dependence on the gap value is defined. Some of the alternatives adopted by so far by other researchers are reported hereinafter.

2.2.1. Linear Spring Model (LSM)

This model is the simplest since it assumes a linear dependence of on δ. The impact force is evaluated by:

$$\text{for} \qquad \text{for} \tag{6}$$

where the linear spring stiffness k_L is proportional to the axial stiffness of the colliding bodies. Typical values of k_L range from $8.76x10^8\ N/m$ to $5.25x10^9\ N/m$ for bridge decks [18]. This model cannot account for the energy loss during impact so that it is more indicated for analyzing the *hard impact*.

2.2.2. Linear viscous-elastic model or Kelvin-Voigt Model (KM)

The linear viscous elastic model, also known as Kelvin–Voigt model [18-19], consist in modelling the impact element by a rheological model comprehending a linear spring in parallel with a viscous damper. The linear spring has stiffness k_k and the viscous damper is characterized by the damping coefficient c_k that accounts for the local energy dissipation during impact. The impact force is given by:

$$\text{for} \qquad \text{for} \tag{7}$$

where $(\dot{x_1} - \dot{x_2})$ is the relative velocity. The value of can be evaluated as function of the coefficient of restitution e of Eq. (4), by the following expression:

$$\xi \cdot \tag{8}$$

where the coefficient ξ is given by:

$$\xi = \tag{9}$$

Provided that it depends on both geometry and mechanical properties of the impacting bodies, some authors [19,20] suggest the value of $k_k = 9.35x10^7\ N/m$ for $e = 0.65$ and $/m$, for $e = 0.64$. With respect to the linear model it offers the advantage of allowing the local energy loss to be accounted for even if, in some cases, it generates tensile forces acting on the bodies just before separation [18,19].

2.2.3. Non Linear model or Hertz Model (HM)

According to this model, also known as Hertz model, the impact element is composed of a non-linear spring with stiffness k_h, so that the impact force is evaluated by:

$$\text{for} \qquad \text{for} \qquad \text{for} \qquad \text{for} \tag{10}$$

where n is the Hertz coefficient, which is typically assumed as equal to $3/2$, since previous studies showed that the system displacement is relatively insensitive to it [21]. The impact stiffness k_h depends on both the geometrical and mechanical properties of the colliding masses. The value of k_h, suggested by some authors and based on small scale experiments [22], typically ranges from ¯ to ¯. Other authors [20] identified, through an optimization technique, a value of ¯ with $e = 0.64$.

This model allows, with respect to the Linear model, a more faithful representation of the impact force, but has the disadvantage of neglecting the local energy loss due to plastic deformation, local cracking and friction during impact.

2.2.4. Non Linear viscous-elastic model or Hertz-Damp Model (HDM)

According to this model, the impact element is composed of a non-linear spring, following the Hertz Law of contact [19] and characterized by stiffness k_{hd}, in parallel with a viscous non-linear damper, with viscous coefficient c_{hd}. The viscous damper is activated only during the approaching phase of the collision, when the colliding bodies are actually approaching each other ($(\dot{x_1} - \dot{x_2}) > 0$), in order to simulate the energy loss typically occurring during this phase [19]. On the contrary, it is deactivated during the contact restitution phase, when the colliding bodies are moving away from each other ($(\dot{x_1} - \dot{x_2}) \leq 0$). The impact force can be evaluated by the following expression:

for

for (11)

for

where the Hertz coefficient is assumed equal to $n = 3/2$; the stiffness coefficient k_{hd} depends on both mechanical and geometrical properties of the colliding bodies. The damping coefficient $c_{hd}(t)$ can be evaluated by:

(12)

where the damping ratio ξ can be evaluated, as function of e that accounts for the energy dissipation during collision, by the following approximate expression:

$$\xi = \frac{\bar{}}{} \quad (13)$$

Some author [19] suggests the value of impact stiffness $k_{hd} = 2.75 \times 10^9\ N/m^{\bar{2}}$, obtained by experimental data fitting of the maximum recorded impact force and for a value of .65. Other authors [22] suggest, for RC impacting structures, a value ranging from ¯ to ¯.

Even though more computationally demanding than the models presented in previous sections, this is expected to be the more accurate modelling strategy, as confirmed by works based on experimental and numerical comparisons [19].

3 ADOPTED BRIDGE MODEL

For the studies herein presented, a viaduct made by a series of simply supported prestressed RC girders with $50\ m$ span length and simply supported was taken into consideration (Fig. 2a). Attention was focused on the longitudinal pounding between two adjacent decks, each hinged to the relevant pier cap. Pounding between these latter was studied by the simple model (Fig. 2a) composed of two SDOF systems placed at a distance equal to the longitudinal gap between decks across the pier cap. The mass of each SDOF comprehending the deck only, was assumed equal to $2.04 \times 10^6\ kg$. The horizontal flexibility of the hinged pier was modelled, for each SDOF, by a horizontal elastic spring characterized by stiffness k_{SDOF}. The damping capability of each SDOF was modelled by a dashpot, characterized by a damping ratio, $\zeta = 5\%$. A parametric study was carried out in order to figure out the typical range of variation of the lateral stiffness of RC piers [23]. From these latter results it arose that the natural vibration period of piers typically ranges from $T = 0.2\ sec$ to $T = 4.0\ sec$.

In this section the results of some preliminary analyses, which were carried out in order to compare the results obtainable by the various pounding models presented above, are presented (Fig. 3). Vibration periods of the two SDOFs were assumed equal to $T_1 = 2\ sec$ and T sec, for the first and second mass, respectively. The recorded *El Centro* earthquake accelerogram was assumed to simulate the ground shaking (Fig. 3a). The gap was assumed equal to $g_p = 5\ cm$.

3.1 Numerical implementation

Due to the presence of earthquake-induced instantaneous pulse values of force, pounding phenomenon is governed by highly non-linear equations, so that it can only be solved by numerical methods. Herein, a stepwise numerical solving algorithm, which combines a fourth order Runge-Kutta Method (*RK4*) with a Predictor-Corrector Method, was employed. Where the *RK4* (*e.g.* [24-25]) is a a) one-step and b) explicit, numerical method. In fact, a) at current time step , *RK4* uses derivative information concerning only the beginning of the step, and b) the solving expression is explicit since it only depends on the value assumed by the variable at the beginning of the time step $x(t_i)$ so as not to necessitate iteration.

First of all, by means of the so-called State Space Formulation, Eq. (1) can be transformed into a system of four first order Ordinary Differential Equations (*ODEs*). In fact, for the *j*-th mass ($j = 1,2$), by the following positions:

(14)

the relevant 2nd order ordinary equation of Eq. (1), can be transformed in the following system of two 1st order ODEs:

(15)

At the generic time step t_{i+1}, the incremental value of displacement and velocity are obtained by the *RK4* expression, herein reported for the displacement only, for the sake of brevity:

(16)

where h is the incremental time step (single valued), and k^1 to k^4 are the *RK4* incremental coefficients, evaluated a) once on the initial instant of the time step (k^1), b) twice on the middle instant of the time step (k^2, and k^3), and c) once on the final instant of the time step (k^4), as indicated by the following expressions:

(17)

Within the generic incremental time step, after having evaluated the current value of displacements $x_1(t_{i+1})$ and $x_2(t_{i+1})$ initially assuming $F_p = 0$ in Eq. (15) (*predictor phase*), the check for pounding occurrence is carried out by Eq. (2) and, if pounding actually occurs, the actual values of displacements are re-calculated by the above numerical strategy substituting the current value of $F_p \neq 0$ into Eq. (15) (*corrector phase*). When the Stereo-mechanical method was implemented, the corrector phase was implemented by updating the current value of the velocities by Eq. (5).

3.2 Differences among pounding models

A parametric study was carried out in order to assess the variation of the peak displacement of each mass as function of a) the adopted pounding model, and b) the relevant value of the stiffness coefficient (Fig. 3). In particular: Figs. 3b and 3e represent the peak displacements, for the 1st and 2nd SDOF respectively, for each of the four force-based models and for increasing values of the impact stiffness, while Figs. 3c and 3f plot the variation of the peak displacement, for the 1st and 2nd SDOF respectively, obtained for varying values of the restitution coefficient. The results obtained by the force-based models assuming singular values of impact stiffness, suggested by other authors [19,20] are also plotted (markers in Figs. 3b, e). From the obtained results it arises that, for each force-based model, the peak displacement response is almost independent of the value assumed for the relevant impact stiffness. Overall, independently of the force-based model, the peak displacement of the 1st SDOF (stiffer) is smaller than that of the 2nd SDOF. Variation of the peak response obtained by varying the value of the restitution coefficient, in the ambit of the Stereo-mechanical model, is larger with respect to the force-based models. Anyway, it has to be pointed out that the same response as that obtained by either of the force-based models can be obtained by the Stereo-mechanical model assuming a suitably calibrated value of e. Note also that 1) the largest peak displace-

ment response is obtained by the linear model, for either SDOF, with respect to the more complicated models, and 2) the smallest peak displacement is obtained by the Hertz-damp model. This is due to the fact that the linear force-based model completely neglects local energy losses, resulting in this way more indicated for hard impact. The opposite happens for the Hertz-damp model that ends up providing the smallest peak displacement, since it allows the local energy loss to be accounted for by the impact damping coefficient. Provided that the correct value of the pounding damping is assumed, the Hertz-damp model allows also to model the case of soft impact yielding, in this way, the most correct results.

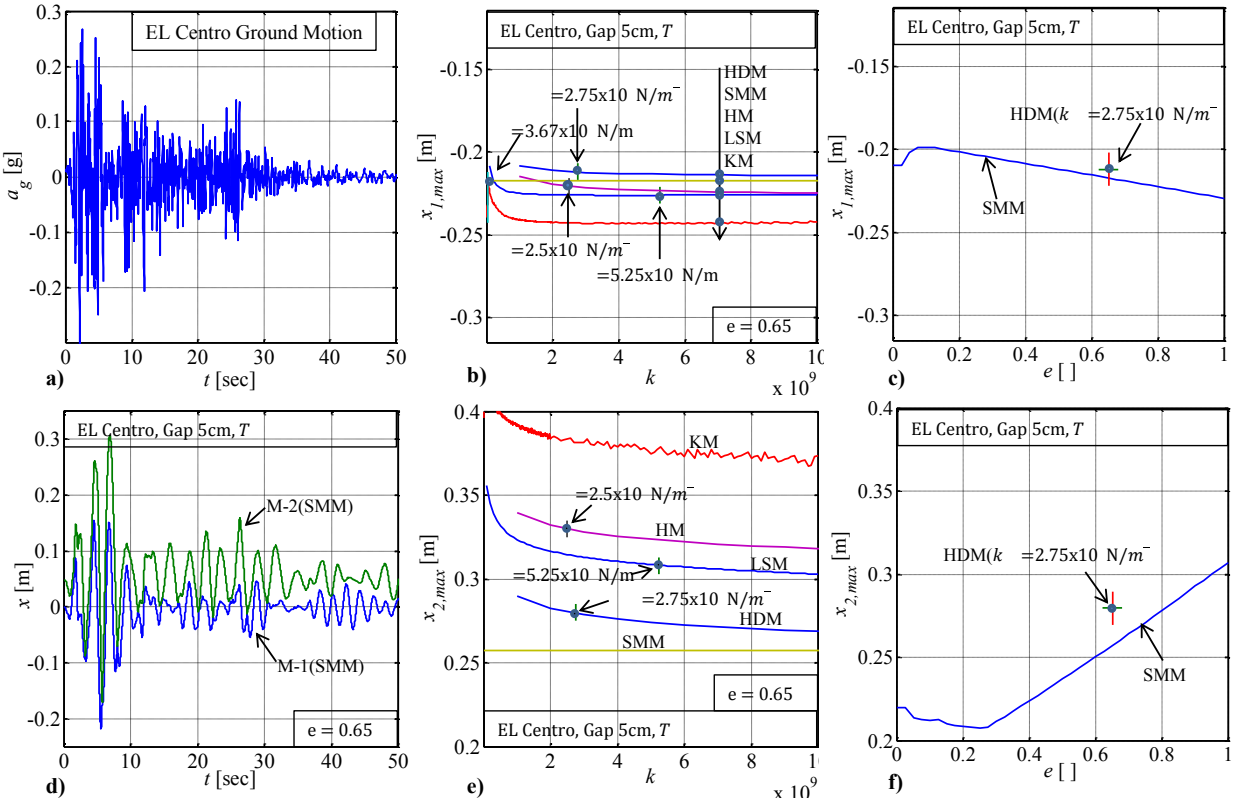


Figure 3: Comparison of Pounding Models: a) *El Centro* recorded ground motion; d) displacement response time-history for the two SDOFs for SMM with $e = 0.65$; maximum displacement response of the 1st SDOF and the 2nd SDOF obtained for (b,e) the various force-based models and for (c,f) the various values of the restitution coefficient by means of the Stereo-mechanical model.

4 RESULTS

In this section the results obtained applying the Hertz-damp model with impact stiffness value , and damping coefficient evaluated on the basis of 65 [19] are presented. Twenty spectrum compatible accelerograms were generated by SIMQKE software [26]. These latter were generated for the three soil type (A, B and D) and for three seismic zones (1, 2 and 3) contemplated by one of the more recent Italian Codes [27]. The so obtained ground motions were characterized by 25 sec overall duration, with 3 rising part and 20 sec of stationary duration. Since it was observed that earthquake direction can affect the maximum response [23], both forward and backward seismic attacks were considered. The results of the numerous analyses carried out were plotted in the form of spectra, both in terms of peak displacement (Figs. 4,5) and in terms of peak pounding force (Figs. 6,7).

In Fig. 4 the peak displacement spectrum of the 1st SDOF is plotted for different values of T_2, for Zone 1 and Soil A, and compared with the equivalent spectrum in the absence of pounding. As can be gathered, in general terms, pounding can yield either an amplification or a de-amplification with respect to the case of absence of pounding. Moreover, it can be noticed that peak displacement undergoes amplification for values of $T_1 > T_2$ which means that pounding induced amplification of the seismic response, in terms of displacements, mainly concerns the more flexible out of the two colliding bodies. This means that the tallest pier will be subjected to the largest pounding induced displacement amplification. On the contrary, the stiffer, among the two colliding SDOFs, always undergoes displacement reduction with respect to the case of absence of pounding.

The peak displacement spectrum $x_{1,max}(T_1)$ is plotted in Fig. 5 for different seismic zones (rows) and soil types (columns) and for increasing values of T_2. As can be gathered, given a seismic zone, the displacement amplification increases for decreasing mechanical characteristics of the foundation soil. In fact, for zone 1, changing the soil type from a bedrock (A) to a softer soil (D), the average spectrum of the band composed of the spectra for decreasing values of T_2, almost quadruples.

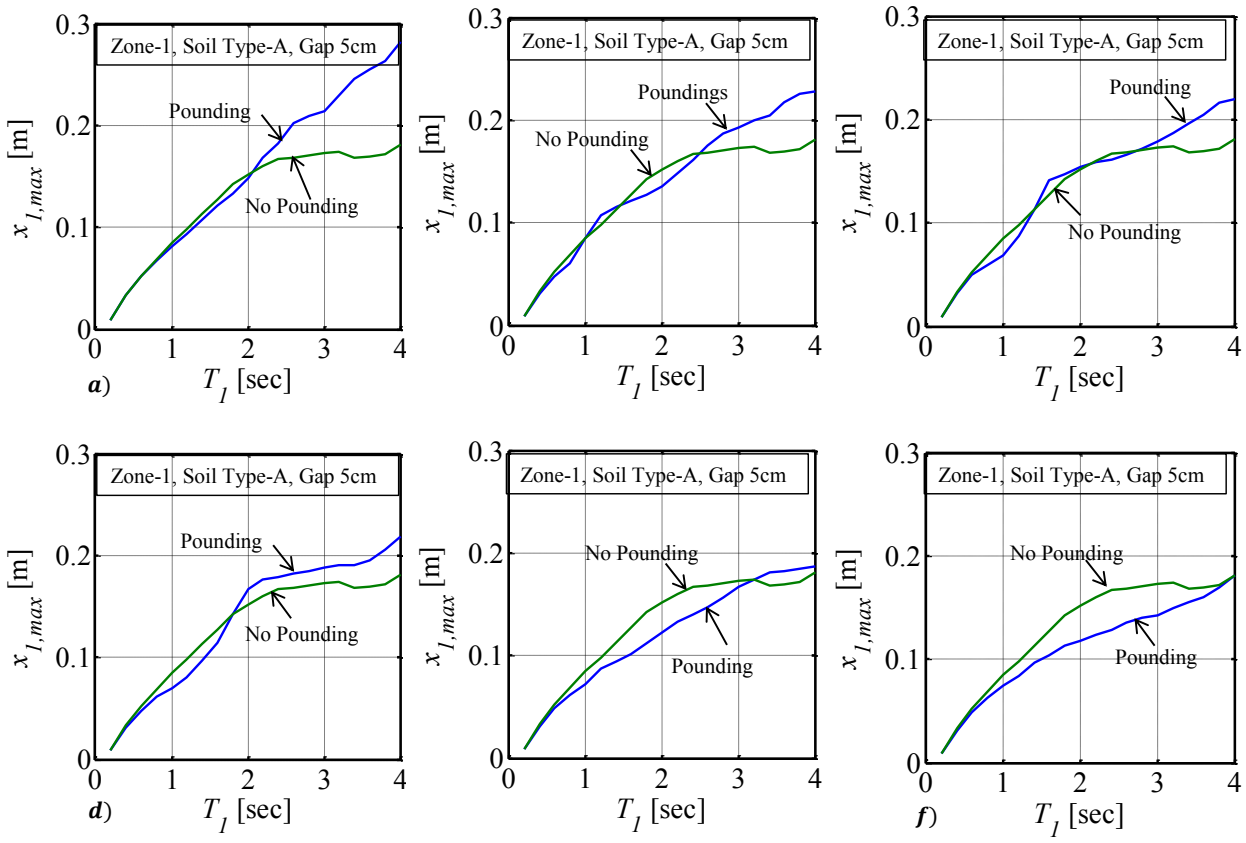


Figure 4: Non-pounding (red line) and pounding (blue line) displacement response spectra for Zone-1 and Soil Type-A for Gap size = 5cm and for different values of T_2: a)$T_2 = 0.2sec$; b) $T_2 = 1.0sec$; c) $T_2 = 1.4sec$; d) ec; e)$T_2 = 3.2sec$; f) $T_2 = 4.0sec$.

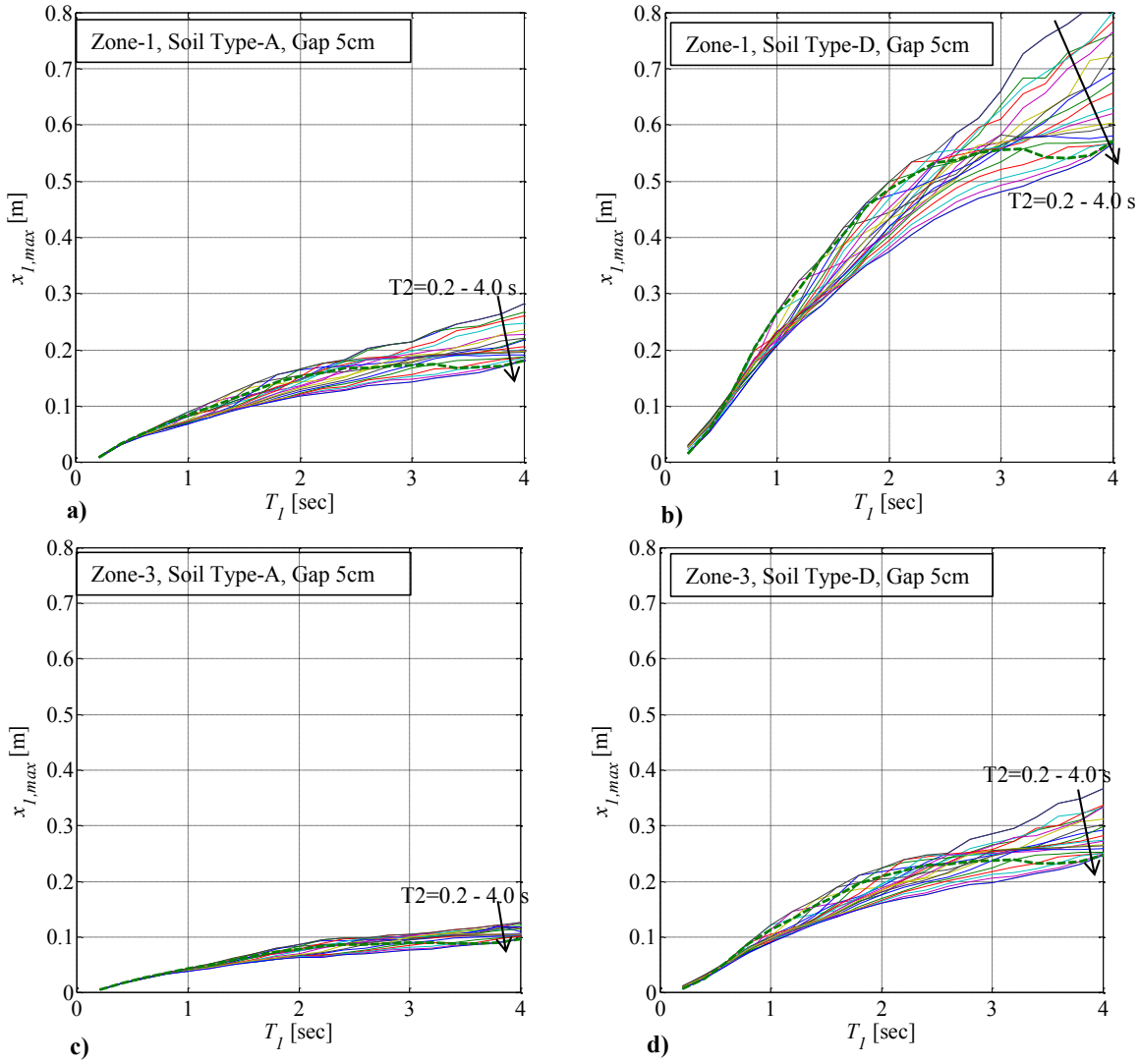


Figure 5: Non-pounding (red dotted line) and pounding displacement response spectra for T2=0.2:0.2:4.0 sec; a) Zone-1, Soil Type-A; b) Zone-1, Soil Type-D; c) Zone-3, Soil Type-A; d) Zone-3, Soil Type-D

In Fig. 6 the pounding force spectrum $F_p(T_1)$, which actually gives also the value of the pounding force affecting the 2nd SDOF in absolute value, is plotted for different values of T_2, for Zone 1 and Soil A. As can be gathered, for values of $T_1 = T_2$, since the two SDOF are actually oscillating on phase, pounding does not occur. Note that, for increasing values of the T the inclination of the increasing branches of the spectrum decreases.

The pounding force spectrum $F_p(T_1)$ is plotted in Fig. 7 for different seismic zones (rows) and soil types (columns) and for increasing values of T_2. The maximum value of the pounding force increases for increasing values of peak ground acceleration, going from zone 1 to zone 3, and for softening mechanical characteristics of the foundation soil (going from class A to D).

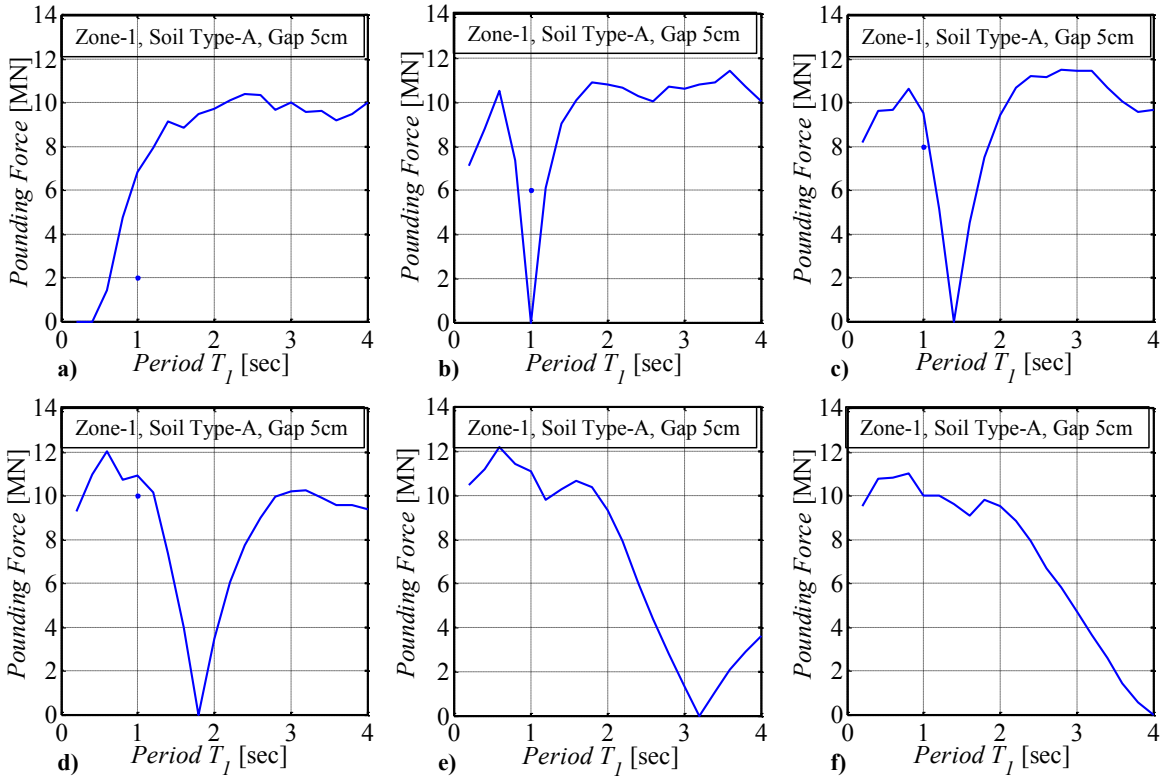


Figure 6: Pounding force response spectrum for Zone-1, Soil Type-A and for different values of T_2: a) $T_2 = 0.2\ sec$; b) $T_2 = 1.0\ sec$; c) $T_2 = 1.8\ sec$; d) $T_2 = 3.2\ sec$; e) $T_2 = 4.0\ sec$.

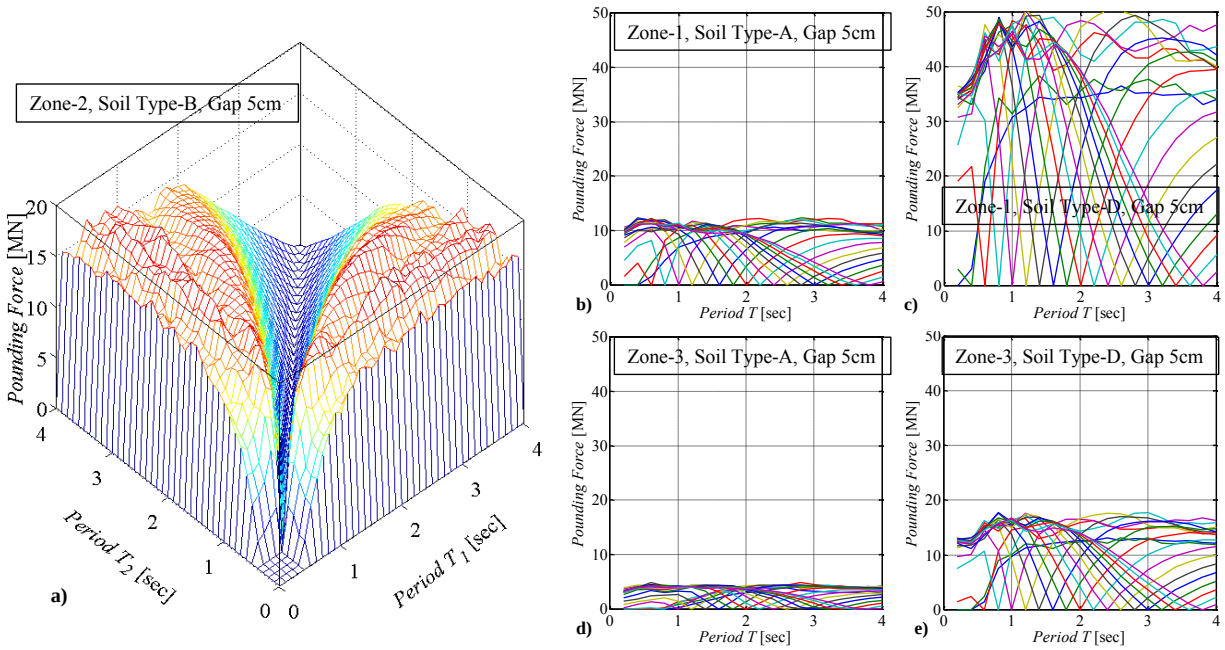


Figure 7: Pounding force response spectra for T2=0.2:0.2:4.0 sec; a) Zone-2, Soil Type-B; b) Zone-1, Soil Type-A; c) Zone-1, Soil Type-D; d) Zone-3, Soil Type-A; e) Zone-3, Soil Type-D.

5 CONCLUSIONS

This paper presented the early results obtained within the work for a Doctoral Thesis concerned with pounding between adjacent bridge structures. In the first part the pounding models available in the literature were analyzed in detail and their differences were highlighted. In the second part of the paper the adopted numerical strategy is described in detail.

In the third and last part of the paper the results obtained by numerical analyses are plotted in terms of both peak displacement spectra and pounding force. It arose that, as expected, spectra are a very effective and slender analytical tool to be used by practitioners concerned with the design of RC bridges in seismic-prone areas. Further developments include the development of equations to correctly predict the above spectra.

REFERENCES

[1] Bertero, V.V., and Collins, R.Cl., (1973), "Investigation of the failures of the Olive View stairtowers during the San Fernando earthquake and their implications on seismic design", Report no. EERC 73-26, Earthquake Engineering Research Center, University of California, Berkeley, CA, 1973.

[2] Earthquake Engineering Research Institute, (1982), "The Central Greece earthquakes of February-March 1981. Reconnaissance and Engineering Report", Report JP-05, Oakland, CA, 1982.

[3] Bertero, V. V., (1987), "Observations on structural pounding", Proc. Int. Conf. Mexico Earthquakes, ASCE, 1987, pp. 264-278.

[4] Hall, J.F., (1995), "Northridge Earthquake of January 17, 1994 - Reconnaissance Report", Vol. 1., Earthquake Spectra; 95-03, Oakland, CA, 1995.

[5] Comartin, C.D., Greene, M., and Tubessing, S.K., (1995), "The Hyogo-Ken Nonbu Earthquake of January 17, 1995- Preliminary Reconnaissance Report", Earthquake Engineering Research Institute, 95-04, Oakland, CA, 1995.

[6] Earthquake Engineering Research Institute. 1999 Chi-Chi, Taiwan, Earthquake Reconnaissance Report, Supplement A to vol. 17. April 2001.

[7] Earthquake Engineering Research Institute. 2001 Bhuj, India Earthquake Reconnaissance Report, Supplement A to vol. 18. July 2002.

[8] C.V.R. Murty, Umesh Dayal, Jaswant N. Arlekar, Sailender K. Chaubey and Sudhir K. Jain; A National Technological Crisis: Structural and Geotechnical damages sustained during M7.9 Bhuj earthquake force. Department of Civil Engineering, IIT Kanpur.

[9] Ruangrassarnee, A., Kawashima, K., (2001), "Relative displacement response spectra with pounding effect", Earthquake Engineering and Structural Dynamics, 2001; 30:1511-38.

[10] C.P. Pantelidis, X. Ma, (1998), "Linear and nonlinear pounding of structural systems", *Computers & Structures*, Vol. 66, No. 1, pp. 79-92, 1998.

[11] Shehata E. Abdel Raheem; Pounding mitigation and unseating prevention at expansion joints of isolated multi-span bridges. *Engineering Structures 31 (2009) 2345-2356.*

[12] S.L. Dimova, Numerical Problems in modeling of collision in sliding systems subjected to seismic excitations. *Advances in Engineering Software*, 31, 2000.

[13] K.T. Chau, X.X. Wei, X. Guo and C.Y. Shen, Experimental and Theoretical simulations of seismic poundings between two adjacent structures. *Earthquake Engineering and Structural Dynamics*, 32(4), 537-554, 2003.

[14] R. Jankowski, Pounding Force response spectrum under earthquake excitation. *Engineering Structures*, 28(8), 1149-1161, 2006.

[15] Kaiming Bi, Hong Hao and Nawawi Chouw. Required separation distance between decks and abutments of a bridge crossing a canyon site to avoid seismic pounding. *Earthquake Engineering and Structural Dynamics*, 39(3), 303-323, 07/2009.

[16] C.J. Athanassiadou, G.G. Penelis, and A.J. Kappos. Seismic response of adjacent buildings with similar or different dynamic characteristics. *Earthquake Spectra*, 10(2), 1994, 293-317.

[17] B. Li, K. Bi, N. Chouw, J.W. Butterworth, and H. Hao. Experimental investigation of spatially varying effect of ground motions on bridge pounding. *Earthquake Engineering and Structural Dynamics*, 2012, 41(14): 1959-1976.

[18] S. Muthukumar, R. DesRoches, (2006), "A Hertz contact model with non-linear damping for pounding simulation", *Earthquake Engineering and Structural Dynamics,* 35(7), 811-828, 2006.

[19] Jankowski, R., (2005), "Non-linear visco-elastic modeling of earthquake-induced structural pounding", *Earthquake Engng Struct. Dyn*., 2005, 34:595–611.

[20] Guo, A., Li, Z., Li H., and Ou, J., (2009) "Experimental and analytical study on pounding reduction of base-isolated highway bridges using MR dampers", Earthquake Engng Struct. Dyn. 2009, 38:1307–1333.

[21] K.T. Chau, and X.X. Wei, "Pounding of structures modelled as non-linear impacts of two oscillators", Earthquake Engineering and Structural Dynamics, 2001; 30:633-651.

[22] Van Mier, J.G., Pruijssers A., Reinhardt, H.W. and Monnier, T., (1991). "Load Time Response of Colliding Concrete Bodies", *Journal of Structural Engineering*, 117(2):354-374.

[23] Mandal, B., "Development of Seismic Response Spectra for bridges including deck hammering", PhD Thesis (in preparation), Department of Structural Engineering and Geotechnics, Sapienza University of Rome, Italy.

[24] Rice, J.R., (1983), Numerical Methods, Software, and Analysis (New York: McGraw-Hill), § 9.2.

[25] Shampine, L.F., Watts, H.A., (1977), "The art of writing a Ringe-Kutta Code, part I", Math. Software III, (J.R. Rice ed.), New York: Academic Press.

[26] SIMQKE_GR.zip, Programmi Gratuiti per Ingegneria Civile (Civil Engineering Free Software) sviluppati con la collaborazione degli studenti Da Piero e Gelfi.

[27] OPCM3274, (2003) "Ordinance of the President of the Council of Ministers", 20 march 2003.

COMPDYN 2015
5th ECCOMAS Thematic Conference on
Computational Methods in Structural Dynamics and Earthquake Engineering
M. Papadrakakis, V. Papadopoulos, V. Plevris (eds.)
Crete Island, Greece, 25–27 May 2015

NUMERICAL INVESTIGATION OF THE BEHAVIOUR OF RC WIDE BEAMS UNDER IMPACT LOADS

Ali A. Abbas[1] **and Demetris M. Cotsovos**[2]
[1] Senior Lecturer in Structural Engineering, School of Architecture, Computing and Engineering, University of East London, London, UK
e-mail: abbas@uel.ac.uk
[2] Lecturer in Structural Engineering, Institute of Infrastructure and Environment, School of the Built Environment, Heriot-Watt University, Edinburgh, UK

Keywords: Reinforced concrete, finite elements, dynamic analysis, wide beams, impact.

Abstract. *The present work sets out to investigate numerically the dynamic responses of simply-supported reinforced concrete (RC) beams under impact loading. The beams comprise wide sections and thus can be also considered as one-way slab panels often used in pre-cast concrete floor construction. The study was carried out using dynamic Non-linear Finite-Element Analysis (NLFEA) and was validated using published experiential data on RC wide beams tested using a drop-weight at high rate. The numerical predictions obtained show that that the response of the RC wide beams under impact loading differs significantly from that established under equivalent static loading. This change predominantly takes the form of an increase in the maximum sustained load which is primarily attributed to (i) the response of a part of, rather than the whole, structural element and (ii) the development of inertia forces rather than material strain-rate sensitivity. The numerical study is based on the assumption that the effect of high loading rates on the behaviour of structural concrete is mainly linked to the development of inertia forces and not the strain-rate sensitivity of its material properties. Thus, the emphasis is on investigating the effect of loading rate on important aspects of structural response (e.g load-deflection curves, deformation profiles, load-carrying capacity, reaction forces, crack patterns and modes of failure) in an attempt to provide insight into the effect of loading-rate on the mechanics underlying RC structural dynamic response. It is also important to consider that during drop-weight testing it is not easy to correlate the measured response to the actual physical state of the specimens as the maximum value of the contact force generated during impact frequently corresponds to a specimen physical state characterized by high concrete disintegration and low residual strength and stiffness. Therefore, the true load-carrying capacity is likely to be significantly lower than the maximum value of the measured applied load. As a result the validated numerical models developed are employed for conducting a parametric investigation in order to determine the true load-bearing capacity of the examined structural forms under different intensities and loading rates characterising the applied load.*

1 INTRODUCTION

The need to address the growing demands for improving a variety of services (e.g. faster transportations, higher energy production, manufacturing and housing) has led to the construction of increasingly intricate structures. High-rise buildings, tunnels, bridges, slab-track for high-speed railways, off-shore and marine structures, storage and industrial facilities as well as nuclear power-plants are just some examples of such structures, the majority of which is fully or partially constructed from reinforced concrete (RC). Considering the high construction costs associated with such structures and their importance to the economy and society, it is essential that they achieve an elevated level of resilience and safety in order to sustain the action of loads (such as, for example, those generated by production activities, high-speed trains, accidents due to collisions or explosions, natural disasters or even acts of terrorism) induced at rates and intensities significantly higher than those of the dynamic loads considered by current design codes.

It has been established both experimentally [1-5] and numerically [6-9] that RC structural response exhibits significant departures from that observed under equivalent static (low-rate) loading once certain thresholds of applied loading rate are surpassed. Such changes become more pronounced with increasing loading rates and primarily take the form of an increase in the maximum sustained load and stiffness. Impact loading is a characteristic example of high-rate loading and is generated during the collision of an object onto a certain area of a structure. Such loads are applied locally and their form (i.e. intensity, duration, loading-rate and time-history) depends on the mass, velocity and shape of the object, the dynamic characteristics of the structural element (i.e. mass and stiffness) and the properties of the contact area. The application of such loads on RC structures results in the generation of stress waves, the propagation of which, within a heterogeneous material such as concrete results in the development of a complex triaxial stress field [10-12]. This field is further accentuated by the cracking processes of concrete and the deflection of the waves on the developing cracks and on the boundaries of the structure. Hence, defining the response of RC structures under high rate loading is a complex wave-propagation problem within a highly nonlinear medium. The available numerical and test data reveals that, with increasing loading rates, RC structural response such as deflection and cracking profiles becomes more localised. This is because the portion of the RC element reacting to the external load reduces in length as failure occurs prior to the generated waves reaching the supports [7, 8]. This phenomenon, combined with the inertia forces developing along the element span in the transverse directions, underlie the mechanisms governing RC structural responses [7, 8]. The observed change in these responses is attributed by many researchers to the strain-rate sensitivity that is assumed to characterize the *material* properties of concrete and steel. Many constitutive models used to describe the behaviour of concrete subjected to high loading rates assume that the concrete material properties are dependent on strain-rate. In contrast with this view, recent work investigating the fundamental behaviour of concrete by modelling small cylinder specimens [10, 11] found that concrete material properties are essentially independent of stain rate and that the effect of loading rate on the specimen behaviour is primarily attributed to the inertia forces which develop within a specimen and the effect is at the *structural* rather than the *material* level.

The strain-rate independent assumption has been also employed in the present work in order to ascertain the significance of the role that inertia plays in the beam's dynamic response when subjected to high loading rates. Thus, the presently-examined wide RC wide beam specimens were modelled by means of static material properties of concrete coupled with the dynamic characteristics of the system at a structural level. The numerical study uses published experimental data on wide RC beams [1] and aims at studying the mechanics underlying RC

structural response under high rate loading conditions through the use of a commercial non-linear finite-element (NLFEA) analysis package ANSYS [13]. After validating the finite-element (FE) predictions obtained against their experimental counterparts, emphasis was focused on investigating the effect of loading rate on important aspects of RC structural responses such as load-deflection curves, deformation profiles, load-carrying capacity, reactions, crack patterns and modes of failure. During drop-weight testing it is difficult to correlate the measured responses to the actual physical state of the specimens as the measured maximum value of imposed load frequently corresponds to a specimen that is already disintegrated and exhibiting low residual load-bearing capacity and stiffness. This stage of structural response has little practical significance as it depends heavily on *post*-failure mechanisms for transferring the applied loads to the specimen supports. Therefore, the true load-carrying capacity is likely to be significantly lower than the maximum value of measured applied load. To address this, a parametric study was carried out to determine the true load-bearing capacity under different intensities and loading-rates of the imposed impact load.

2 EXPERIMENTAL BACKGROUND

A large number of experiments has been carried out to date to investigate the responses of RC beams under impact loading [1-5]. In the majority of these cases, the load is applied by means of a steel mass (impactor) allowed to fall onto the mid-span region of the specimen from a predefined height depending on the desired rate of loading. The ratio of the mass of the steel impactor to the mass of the RC beam specimen used in the various case studies vary significantly, ranging from low values of 17% (the steel impactor being much lighter than the RC specimen) to large values such as 150% (the steel impactor being heavier than the RC specimen). The load is usually applied through the use of pads or platens (made of steel, ply or rubber) in order to moderate the damage in the area of contact between the steel impactor and the RC specimen. The duration of loads generated during drop-weight tests is usually extremely short (i.e. a few milliseconds) and the intensity of the applied load increases rapidly from zero to a maximum value. Typically, the variation of strain and displacement at various points along the specimen length, the velocity and acceleration of the steel impactor, as well as measurements of the support reactions are recorded. In addition, crack formation and propagation up to failure, is closely monitored as it provides an indication of the corresponding internal stress state of the beam at every stage of the loading process. However, it should be noted, that the latter information is not usually available in literature. Information concerning crack patterns and deformation profiles is usually recorded *after* (and not throughout) the application of the impact load. Therefore, as explained earlier, this usually relates to a specimen of little practical use as it is heavily degraded and is dependent on *post*-failure mechanisms for transferring the applied loads to the supports. This is often achieved through the use of a high-speed video camera. Similar RC beams to those tested under impact loading are usually also tested under static loading, for purposes of comparison.

Typical load deflection curves are shown in Figure1a describing the responses of RC beams under impact and equivalent static load exerted at mid-span, which reveal that an increase in loading-rate leads to an increase in the maximum sustained load and to a stiffer response. The corresponding deflected shapes indicate that, as the rate of the applied load increases, the portion of the RC beam mostly affected by the application of the external load tends to concentrate at the mid-span region of the specimen, where the load is exerted and as a result cracking tends to concentrate in a region of the RC beam around the point at which the external load is applied. This localised response increases with increasing loading rates. The variation in the recorded peak value of the applied load, i.e. contact force generated dur-

ing impact, (maxPd) expressed as a ratio of its maximum static counterpart (maxPs) is shown in Figure 1b. The data indicates that an increase in the rate of applied loading results in the RC beam being able to sustain higher levels of loading. Data obtained from such tests is characterised by a large scatter partly due to a wide range of parameters (associated with the experimental setup and the specimen) which differ from test to test. This scatter predominantly reflects the difficulty in correlating the measured responses under impact load to the actual physical state of the specimens discussed earlier. This is different to the way the load carrying capacity term is usually defined and understood under static loading. So in design terms, one has to be careful in estimating the maximum impact load that can be sustained by a given beam as this will depend on the level of damage that can be tolerated and the residual strength required following impact.

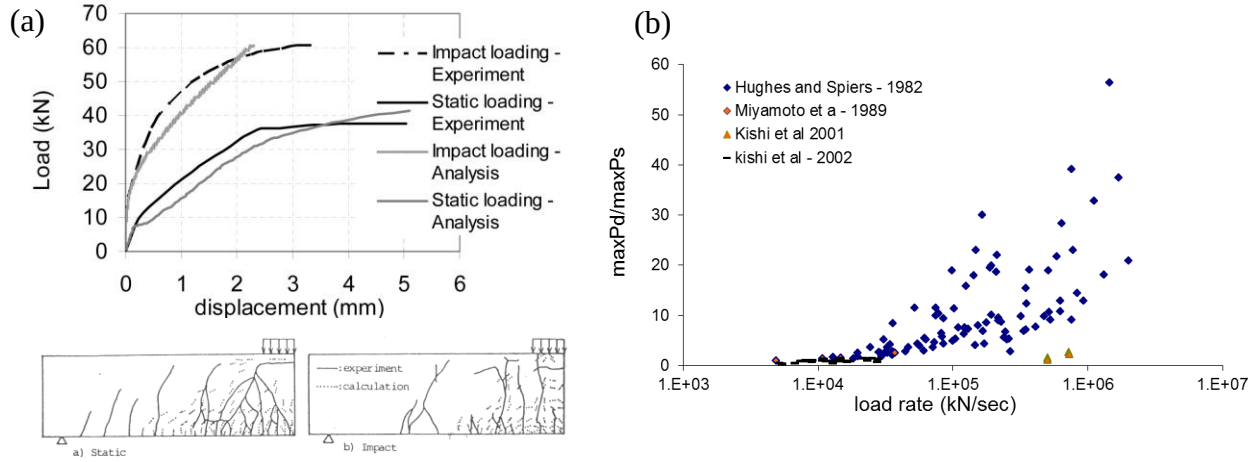


Figure 1: Experimental background on (a) static and impact tests [9] along with numerical counterparts and (b) scatter in impact test data

2.1 Specimens considered

Published experimental data on RC wide beams [1] forms the basis of the present numerical study and the salient features of the specimens are depicted in Figure 2. Each specimen was 1800 mm in length, 360 mm in width and 125 mm in thickness and was simply supported on rollers near the ends of its span in the longitudinal direction, forming a clear span of 1600 mm. The static responses were initially established under monotonic loading applied until failure and then under impact loading via drop-weight testing, which was achieved by dropping a 38 kg steel impactor with a flat contact face from a height of 5m (thus achieving a velocity of 10 m/sec on impact). The ratio of the mass of the steel impactor to that of the beam is approximately 13% which is towards the lower end of corresponding values in the majority of experimental investigations. This is considered advantageous to using heavy drop weights which usually result in a complete disintegration of the test specimen thus making it more difficult to derive meaningful conclusions regarding the specimens' response. Both static and impact loads were applied through a steel cross-beam placed on top of the RC beam extending along the full width of the RC beam, in order to better distribute the applied load on the concrete surface and avoid the development of local stress consecrations which can in turn cause cracking in the region of the beam were the external load is exerted. The mean cube compressive strength of the concrete was found to be 64.30 MPa, while the mean tensile splitting strength was found to be 3.94 MPa. The mean ultimate strength and strain was found to be 670 MPa and 0.067, respectfully.

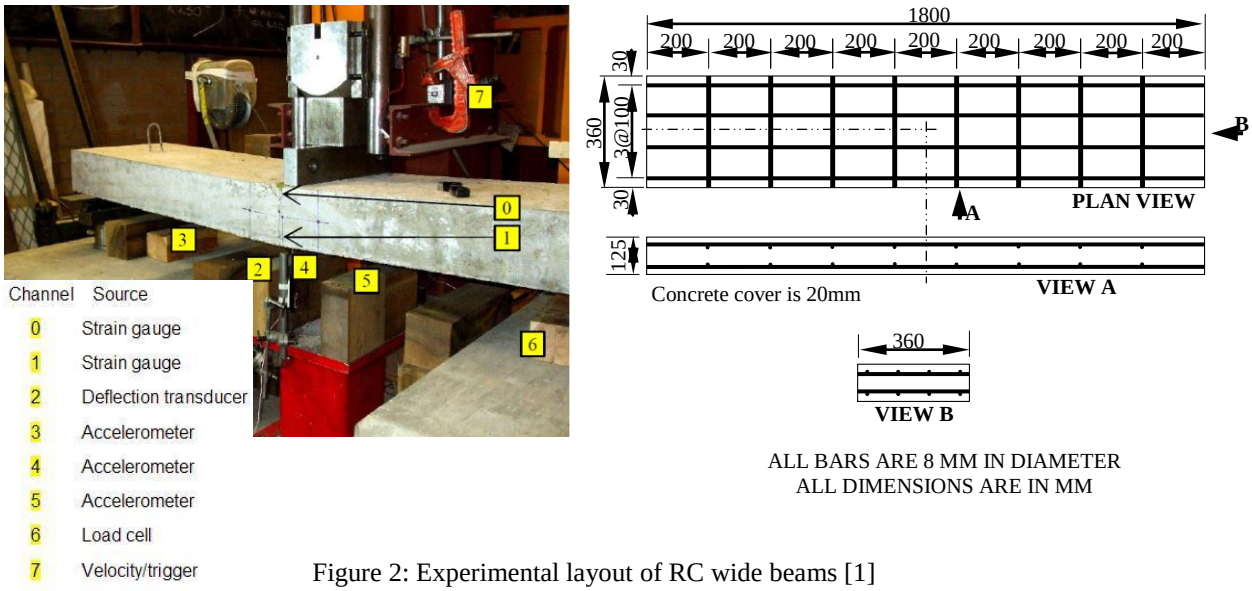


Figure 2: Experimental layout of RC wide beams [1]

2.2 Response under static loading

The load-deflection curves describing the response of the RC beam under static load is presented in Figure 3. The specimen initially behaved elastically up to around 12 kN and cracking started forming at mid-span at the lower face of the beam. As the loading was increased, cracking extended upwards resulting in a gradual reduction in the stiffness of the beam. The maximum load carrying capacity was found to be 32kN beyond which the load decreased gradually followed by an abrupt reduction in the load carrying capacity due to failure in the compressive zone of the beam at mid-span. The FE-based load-deflection curve is also depicted on Figure 3 which shows good agreement with corresponding experimental data.

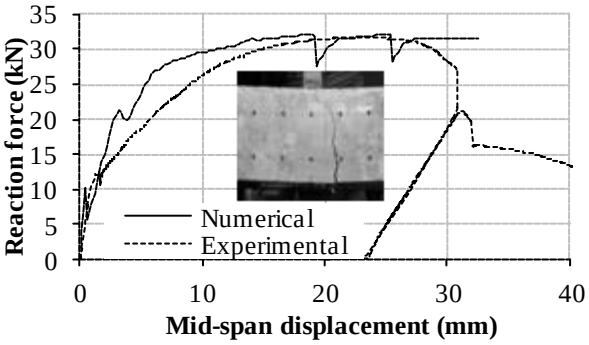


Figure 3: Experimental [1] and numerical results under static loading

2.3 Response under impact loading

Figure 4a shows the load generated during impact whereas the load deflection curves in Figure 4b indicates that under high-rate loading conditions, the response of the RC wide beam becomes stiffer while allowing the beam to attain higher levels of loading. Furthermore, under impact loading cracking initiates at a much earlier stage in the loading process compared to that observed under static loading while at the same time these cracks propagate much faster extending rapidly towards the upper face of the beam. The photographic record confirms that cracking initiates at the lower surface of the mid-span region of the beam and almost immediately extends upwards. The crack pattern indicates that the beam exhibits a localised response confined to its middle portion during the first stages of the experiment. The crack has a vertical flexural form that penetrates deeply into the compressive zone. This is a typical mode of failure which corresponds to the specimen's true load-carrying capacity (i.e. relating to the specimen still acting as a continuum). This appears to occur within a very short period of time

that is much less than the duration of the whole test, beyond which the experimentally established behaviour is likely to describe post-failure phenomena of little practical significance.

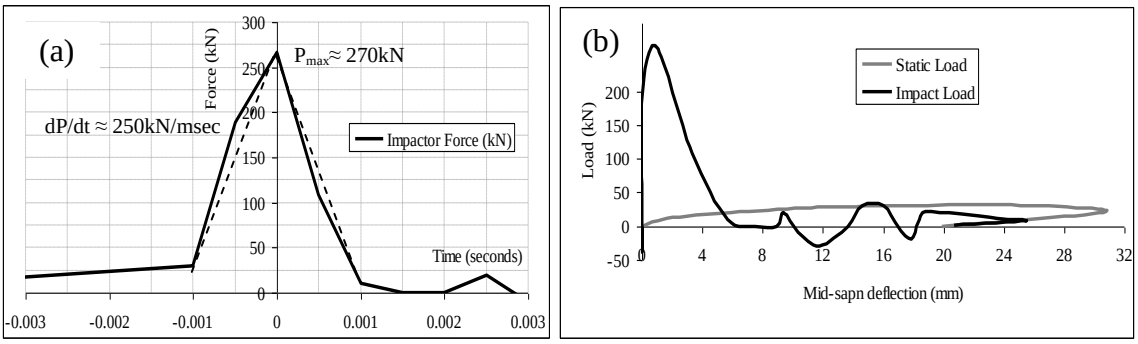


Figure 4: Experimental data [1] showing (a) impact load history and (b) static and impact load-deflection curves

3 FE MODELING STRATEGY

Due to the difficulties and limitations associated with RC element tests under high-rate loading, resort has been made to the use of nonlinear FE analysis. Use of the FE method can provide a more detailed description of the structural response and also allows the investigation to be extended to structural forms more complex than the simple RC structural elements that can be studied experimentally. Another advantage of the numerical investigation is that, unlike testing, which relies on measuring and recording the effect of the rate of loading on structural behaviour, it allows a more comprehensive study of the causes of change in the behaviour exhibited by the RC structural elements. In order to accurately model the problem at hand, it is necessary to fully identify the complexities that characterise it. The FE analysis code adopted for the current investigation (ANSYS) is capable of carrying out 3D non-linear static and dynamic analyses, employing appropriate material models capable of accounting for the non-linear behaviours of concrete and steel. Due to the non-linear behaviour of concrete, the governing equation of motion is solved numerically through the implicit Newmark integration scheme [8, 14]. Provided that the stability criteria are observed, the method yields comparable results with explicit FE formulations in RC element analysis. A brief description of the model parameters is provided herein for completeness.

3.1 Concrete material modelling

ANSYS is a well-known commercial FEA package that is widely used in a variety of complex structural problems. The present study uses a concrete model derived based on regression analysis of test data on concrete cylinders and cubes subjected to uniaxial compression and tension under quasi-static load rates. The ensuing stress-strain curves are depicted in Figures 5a and 5b, respectively.

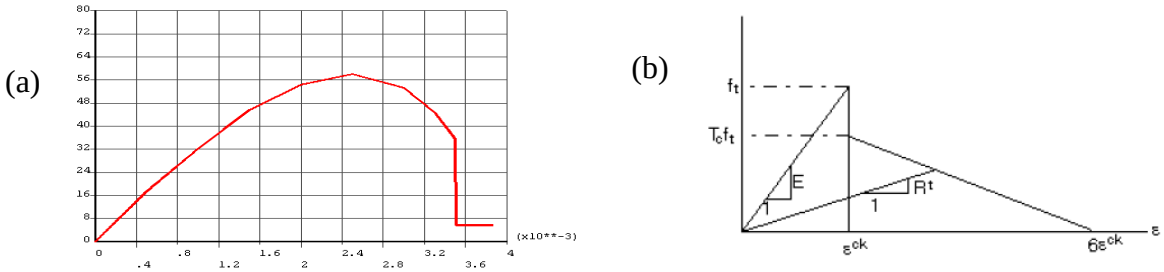


Figure 5: Uniaxial stress-strain relations adopted in ANSYS for concrete under (a) compression and (b) tension

By assuming that concrete is an orthotropic material, the uniaxial stress-strain curves described above are applied to each principal-stress axis, thus leading to a formulation of a general constitutive model describing the behaviour of concrete under triaxial loading conditions. The analytical formulation in ANSYS also defines the slope of the descending softening branch of the tensile stress-strain curve. The default value is 0.6, the effect of the variation of this parameter was not investigated in the present study.

3.2 Reinforcement modelling

Steel reinforcement is explicitly included in the FE model using one-dimensional bars under uniaxial tension and compression only. Full bond is assumed between steel and concrete, with local bond transfer bounded by the tensile capacity of the concrete at the Gauss points near the reinforcement. Steel constitutive behaviour follows a simple bi-linear hardening model accounting for the initial elastic and an averaged post-yield behaviour of the bars (see Figure 6). Similarly to the concrete case, the effect of the loading-rate on steel behaviour is discounted at the material level.

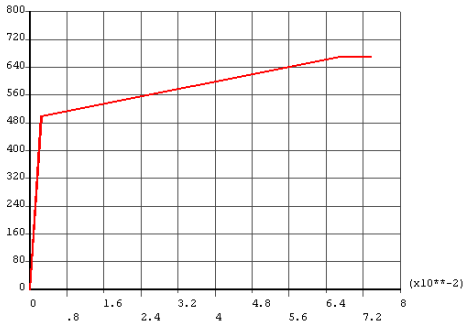


Figure 6: Uniaxial stress-strain relations for steel bars

3.3 Crack modelling

Following the modelling capabilities of the adopted FE analysis program (ANSYS), cracking is modelled using the smeared-cracking approach. Following this modelling convention, cracks are allowed to form at the integration points where stress evaluation takes place and their effect is spread within a region associated with a particular Gauss point.

3.4 FE mesh and loading

The concrete medium is modelled by using a dense mesh of 8-noded brick elements with an edge size of between 20 mm to 30 mm and the FE mesh is depicted in Figure 7. The element formulation adopts a reduced integration scheme to avoid numerical problems due to locking. Reinforcement bars are modelled by 2-noded single Gauss point truss elements with cross-sectional areas distributed to the relevant nodes of the beam's cross-section so as to be equivalent, in terms of both cross-sectional area and location, to the actual reinforcement of the beams. Because of the double symmetry of the problem at hand, a 100mm strip of the concrete slab was modelled with suitable boundary conditions. As in the case of the experimental investigation, the external load is applied at mid-span of the RC beam through a rigid element. The value of the applied load increases linearly at a constant rate until the load-carrying capacity of the RC beam is reached and failure occurs. Initially the static problem is investigated in order to effectively calibrate the model followed by the investigation of the dynamic problem. Various rates of loading are investigated herein ranging from 250 kN/sec to 250,000 kN/sec. the latter being equivalent to the loading rate applied during the drop-weight discussed earlier.

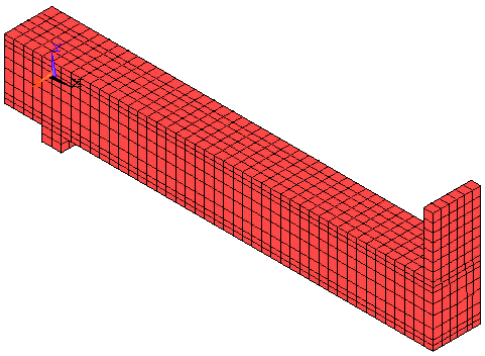


Figure 7: FE mesh adopted

4 PREDICTED FE RESPONESES UNDER STATIC LOADING

In the FE modelling of the static test, the external load is applied in the form of displacement increments at mid-span and the load-deflection results obtained are presented in Figure 3 which, as pointed out earlier, compares well with experimental data. Overall, the numerical investigation predicts a response similar to that established experimentally, yielding very similar values of load-carrying capacity and maximum deflection (30kN and 30mm, respectively). Figure 8a shows the deformed shape of the beam in the case of static loading, whilst the cracking pattern presented in Figure 8b, which shows that flexural cracks begin to appear in the mid-span region of the specimen and gradually extend towards the supports as the load increases. The cracking pattern correlates closely with its experimental counterpart.

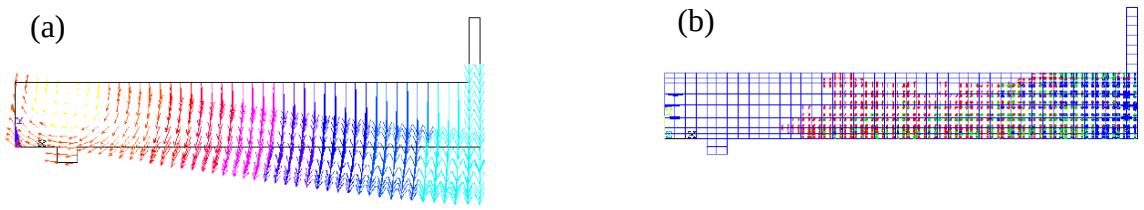


Figure 8: Static-load FE results showing (a) deflected shape and (b) cracking pattern

5 PREDICTED FE RESPONESES UNDER HIGH RATE LOADING

In the dynamic case studies, the effect of a number of different rates of loading on the dynamic responses of the RC wide beam was investigated numerically. The loading rates considered were 2.5, 25 and 250nkN/msec (the latter being equal to the loading rate applied during the drop-weight test [1] discussed earlier). The load is applied monotonically up to failure at a constant rate in order to study the dynamic responses of the subject specimens. The numerical predictions obtained are presented in Figure 9a in the form of applied load versus mid-span deflection curves, which reveal a considerable increase in stiffness and maximum sustained load with higher values of applied loading rate and at the same time, a decrease in the maximum deflection at mid-span. However, it is also evident that the level of loading applied during testing (approximately 270kN at a rate of 250kN/msec) is considerably lower than the maximum value of imposed load obtained numerically for the case of monotonic loading applied with the same loading rate. Nevertheless, the numerically predicted value of the mid-span deflection at 270 kN is similar to that established experimentally thus providing evidence concerning the validity of the numerical model presently employed.

The deformation profiles prior to failure, shown in Figure9b, suggest that as the rate of loading increases the response of the beam tends to become more localised resulting in the reduction of the portion of the element affected by the application of the external load which tends to concentrate at the mid-span region of the beam. In particular, as the rate of loading increases, the deflected shape of the beams progressively attains a narrowing bell-shaped form in the vicinity of the loading point (with its convex portions near the supports gradually increasing at the expense of the middle concave portion, which deflection becomes disproportionally large). The predicted crack patterns exhibited under different rates of loading prior to failure (see Figure 9c) are consistent with the deformed profiles of the beam, indicating that as the rate of loading increases, cracking becomes more localized primarily around the point at which the load is exerted.

Strain rates exhibited in the region adjacent to the point of application of the external load were calculated for the maximum loading rate presently considered as depicted in Figure 10.

The strain rate is found to reach values in the range of ±10 sec^{-1} for the larger part of the duration of the loading process and only towards the final part do they become greater than 200 sec^{-1}. Considering available tests data describing the effect of increasing loading rates on the behaviour of plain concrete under high rates of uniaxial compressive and tensile loading [10-12] – see Figure 11 – it is shown that the loading rate corresponding to the above range of values of calculated strain rates (i.e. ±10sec-1) may, at best, result only in a small increase in concrete strength. Even during the latter stages of the loading process the crack patterns presented earlier show that the specimen has suffered considerable cracking and therefore the calculated strain rates do not correspond to the beam acting as a *continuum* but to one that has disintegrated considerably.

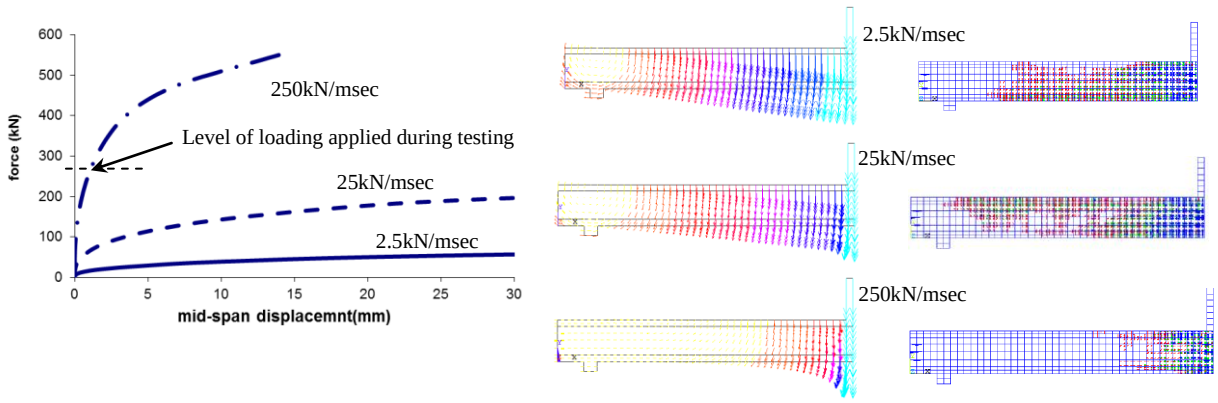
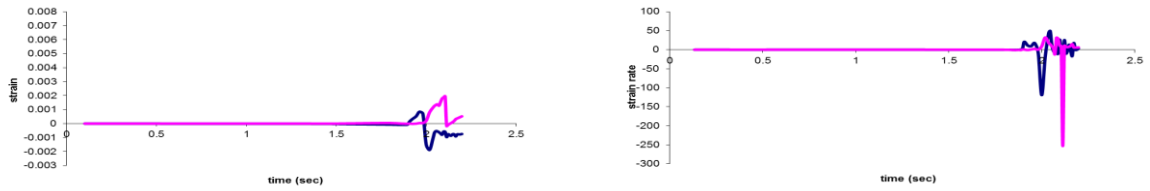


Figure 9: Predicted response of RC Beam showing (a) load-deflection curves, (b) deflected shapes and (c) crack patterns exhibited prior to failure



(a) (b)

Figure 10: Predicted values of (a) strains and (b) strain rate in the region adjacent to the point of application of the external load

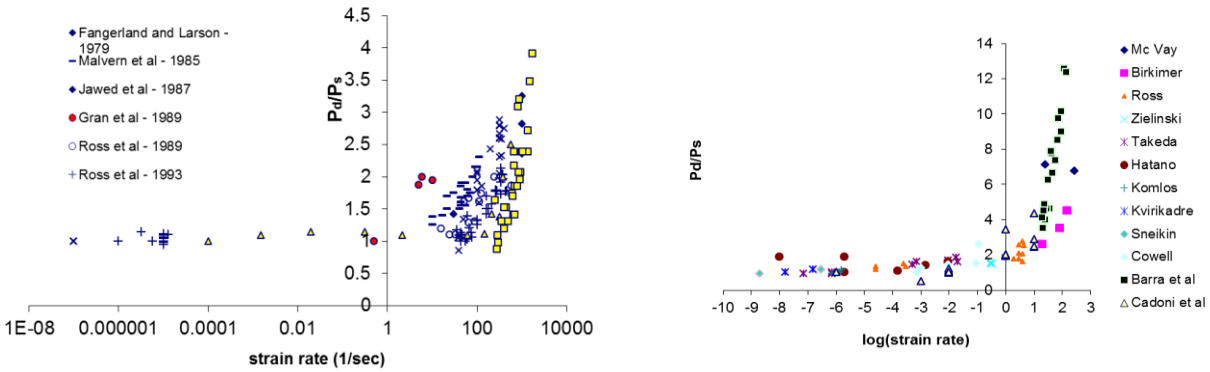


Figure 11: The effect of increasing loading rates on the behaviour of plain concrete specimens under high rates of uniaxial (a) compressive [10,11] and (b) tensile loading [12]

6 CONCLUSIONS

Comparing the numerical predictions with their experimentally established counterparts describing the responses of the RC wide beams (or one-way slabs) under static and impact loading, it can be concluded that both sets of data show good agreement. In particular, both experimental and numerical investigations clearly demonstrate that during high-rate loading (i.e. impact) the specimen is capable of undertaking higher levels of loading. Nevertheless it is clearly demonstrated that the experimental investigation is unable to correlate the measured responses to the actual physical state of the specimens as the measured maximum value of imposed load corresponds to a specimen well below its load-bearing capacity established experimentally.

A comparison of the load-deflection curves under static and impact loads shows that under high-rate loading conditions, the response of the RC beam becomes stiffer and allows the beam to attain higher levels of loading. This change in structural response is essentially linked to the deformation profile exhibit by the beams with increasing loading rates which becomes more localised and confined to the mid-span loading region (i.e. the area at which the load is exerted) as the loading rate increases. Nevertheless the mode of failure appears to remain unaffected by loading rate.

Form the preceding analysis, it can be concluded that the numerical investigation of RC wide beams under high-rate loading yield similar results to that established experimentally using drop-weight testing. In particular, it can be suggested that the agreement observed between numerical and experimental data validates the initial assumption that the effect of loading rates on the specimen behaviour can be attributed – at least for the rates considered – to the inertia effect of the RC beam mass (which results in a reduction in the length of the beam which responds to the applied load) and not to the loading-rate sensitivity of the material properties of concrete and steel. However, more research is required in order to correlate the measured responses to the actual physical state of the specimens considered in order to accurately determine certain important aspects of RC structural response (i.e. load-carrying capacity) under increasing rates of impact load. Such information is essential in order to develop advanced analysis methodology which in turn can facilitate the development of efficient design solutions (in terms of both safety and economy) capable of safeguarding the structural integrity, resilience and performance requirements. To this end, further experimental and numerical studies are currently being conducted by the authors on a variety of structural configuration subjected to various types of high-rate loading.

REFERENCES

[1] A.A. Abbas, A.D. Pullen, D.M. Cotsovos, Structural response of RC wide beams under low-rate and impact loading. *Magazine of Concrete Research*, **62**, 723-740, 2010.

[2] Y. Chen, I. May, Reinforced Concrete members under drop-weight impact. *ICE Proceedings, Structures & Buildings*, **162**, 1, 45-56, 2009.

[3] G. Hughes and D. Spiers, *An investigation on the beam impact problem*. Cement and Concrete Association, Technical Report 546, 1982.

[4] N. Kishi, H. Mikami, K.G. Matsuoka, T. Ando, Impact behaviour of shear- failure-type RC beams without shear rebar. *International Journal of Impact Engineering*, **27**, 955-968, 2002.

[5] S. Saatci, F.Vecchio, Effects of shear mechanisms on impact behavior of reinforced concrete beams. *ACI Structural Journal,* **106**, 1, 78-86, 2009.

[6] A.Q. Bhutti, N. Kishi, H. Mikani, T.Ando, Elasto-plastic impact analysis of shear-failure-type RC beams with shear rebars'. *Materials & Design,* **30**, 502-10, 2009.

[7] D.M. Cotsovos, M.N. Pavlovic, Modelling of RC Beams under Impact Loading. *ICE Proceedings, Structures & Buildings,***165**, 2, 77-94,2012.

[8] D.M. Cotsovos, N.D. Stathopoulos, C. Zeris, Fundamental behaviour of RC beams subjected to high rates of concentrated loading. *ASCE Journal of Structural Engineering,* **134**, 1839-1851, 2008.

[9] A. Miyamoto, M. King, M. Fujii, Non-linear dynamic analysis and design concepts for RC beams under impulsive loads. *Bulletin of the New Zealand National Society for Earthquake Engineering,* **22**, 98-111, 1989.

[10] D.M. Cotsovos, M.N. Pavlovic, Numerical investigation of concrete subjected to compressive impact loading. Part 1: A fundamental explanation for the apparent strength gain at high loading rates. *Computers & Structures,* **86**,145-163, 2008.

[11] D.M. Cotsovos, M.N. Pavlovic, Numerical investigation of concrete subjected to compressive impact loading. Part 2: Parametric investigation of factors affecting behaviour at high loading rates. *Computers & Structures,* **86**,164-180, 2008.

[12] D.M. Cotsovos and M.N. Pavlovic, Numerical investigation of concrete subjected to high rates of uniaxial tensile loading. *International Journal of Impact Engineering,* **35**, 319-335, 2008.

[13] ANSYS, Version 13.0, Swanson Analysis Systems Inc., Houston, PA, 2004.

[14] T. Belytschko, A survey of numerical methods and computer programs for dynamic structural analysis. *Nuclear Engineering and Design*, **37**, 23-34, 1976.

COMPDYN 2015
5th ECCOMAS Thematic Conference on
Computational Methods in Structural Dynamics and Earthquake Engineering
M. Papadrakakis, V. Papadopoulos, V. Plevris (eds.)
Crete Island, Greece, 25–27 May 2015

STRUCTURE RESPONSE UNDER BLAST WAVE LOAD

D. Makovička[1] and D. Makovička, Jr.[2]

[1] Czech Technical University in Prague, Klokner Institute
CZ-166 08 Prague 6, Šolínova 7, Czech Republic
daniel.makovicka@klok.cvut.cz

[2] Static and Dynamic Consulting
CZ-284 01 Kutná Hora, Šultysova 170/8, Czech Republic
d.makovicka@makovicka.cz

Keywords: Explosion, Blast Wave, Dynamic Load, Response, Assumption, Bridge Structure.

Abstract. *The paper follows from the theory of explosion and interaction of an impact wave formed by the explosion and a structure. This is a complex mechanism depending on the geometry and composition of the structure, the magnitude and the angle of the blast wave, and relative distance of the blast. Firstly, the paper determines the parameters of the blast wave excited by a small charge explosion. The empirical formulas on the basis of our own experimental results are shown and used for the structure analysis. Evaluations of structures loaded by an explosion based on dynamic response in rotations round the central line of plate or beam systems during the dynamic load of this type is in the paper discussed and comparison of own limit values and published ones is presented. Blast loads typically produce very high strain rates in the range of 10^{-2} to10^{-4} s^{-1}. This high straining rate would significantly increase the stress and strain capacities of concrete and steel reinforcement, and accordingly affects the dynamic performance of the target structure. The effect of strain rate for concrete material is discussed. The formulas for increased compressive strength of concrete and steel reinforcement are presented. The ductility of structural members is influenced by the corresponding values under high strain rate of reinforcement. Damage to the structure is assessed accordingly, firstly by the angle of rotation of the middle axis/surface, and secondly by the limit internal forces of the selected structure. The extreme nature of blast resistance makes it necessary to accept that structural members have some degree of inelastic response in most cases. This enables the application of structure dissipation using the ductility factor and increased of concrete strength. The limits are correlated with qualitative damage expectations. The methodology of dynamic response assessment and its application to the simple bridge structure is discussed.*

1 INTRODUCTION

The explosion of a gaseous or solid explosive medium generates a pressure wave in the centre of the explosion. Its intensity and history are determined by the chemical properties of the explosive and its reaction with ambient environment. The pressure wave begins propagating from the explosion centre in approximately spherical wave fronts which reflect from and are modified by their impact on the surface of building structures or the ground. The effect of pressure in the propagating wave, together with the wave reflected from the surface of the building or the ground, form the magnitude of the load applied to the structure and its history.

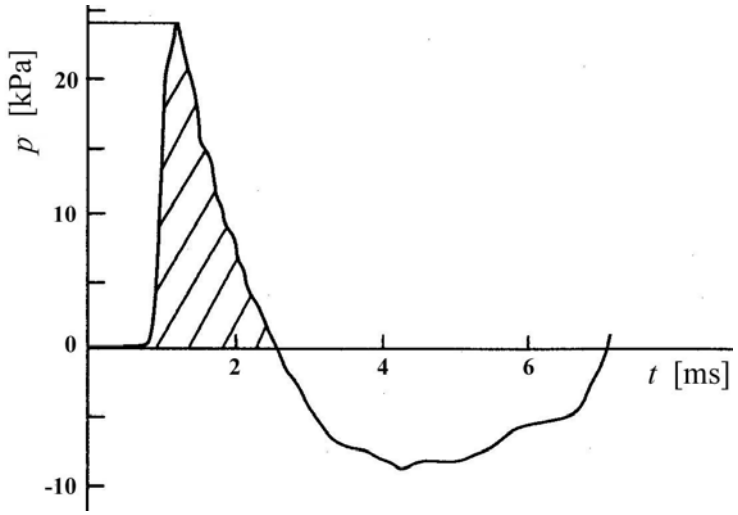


Figure 1: Loading blast wave (explosion in the open air space)

2 LOAD

When a charge explodes in an open space, the pressure effect of the impact wave on an obstacle (the load of the structure) depends on the situation of the structure with respect to the focus of the explosion, the impact wave parameters, etc. The entire phenomenon of the impact wave effect on the structure is then usually simplified for calculation purposes, using numerous assumptions, especially as regards the intensity and the time course of the impact wave effect and its distribution in contact with the given object [1]:

a) Triangle-shaped development of the load in time with the maximum intensity corresponding to the sum of the pressures of the impacting (Fig. 1) and reflected wave and the duration of the action, usually corresponding only to the duration of the action of the overpressure phase of the shock wave;

b) The shock wave can be considered as having a flat front, meaning that the rise time to maximum intensity is neglected, and additionally that the load starts to act on the entire structure at one moment; the phase shift of the start of the action of the load at individual structure points is thus neglected;

c) It is usually assumed that the load acts on the building structure in a continuous and uniform manner (any local effect of the focused load is neglected);

d) The response of the structure is usually considered on the basis of the superimposition of two triangular loads, which correspond to the overpressure phase and subsequently the underpressure phase of the shock wave.

In case of explosions of gaseous mixtures (in contradiction to the explosions of charges of solid or liquid explosives) apart from the triangular overpressure phase also the underpressure phase is significant, the effect of which can be repeatedly considered as fast triangular loads,

but with the opposite sign and a phase shift; both phases (overpressure and underpressure) may be considered separately in such a way as would enable the superposition of obtained results of both phases to obtain total effects.

When an actual event takes place, the specific course of the load action depends on the swirl flow bypassing the structure surface, the atmospheric pressure, the temperature conditions and other factors that are usually neglected in a simplified analysis. The parameters of the explosive, too, are determined on the basis of average values; empirical formulas are used, and operate with mean (probable) coefficient levels. Thus the structure calculations concerning the impact wave effects are significantly burdened by these inaccuracies in the input quantities of the entire phenomenon.

Empirical formulas created by various authors [1, 2, 3, 4] are usually used for the time course of the pressure wave and subsequently the structure load. The structure of the formulas according to various authors is very similar, and they usually differ only in the magnitudes of the coefficients. Due to the variability of these coefficients, the uncertainty of the formulas is usually found to be in the range of ±20%, and possibly even more. The reliability of individual formulas improves with increasing distance of the pressure wave from the focus of the explosion.

The overpressure determined at the face of the air impact wave that spreads from the explosion site to the surroundings stems from the reduced distance [1, 3] is:

$$\overline{R} = \frac{R}{\sqrt[3]{C_w}} \tag{1}$$

where $\overline{R}$ is the reduced separation distance from the epicentre of the explosion [m/kg$^{1/3}$], R is the distance from the explosion epicentre [m], and C_W is the equivalent mass of the charge [kg TNT].

It is assumed that the energy released by the explosion is proportional to the mass of the explosive, and the solution consists in introducing a reference charge chosen to be represented by tritol (trinitrotoluene, TNT). Therefore the mass of various explosives is expressed in terms of the so-called tritol equivalent (k_{TNT}). If this equivalent cannot be found in the specialized literature, it can be calculated with sufficient accuracy using the relationship

$$k_{TNT\text{-}p} = 0.3\ Q_v - 0.2 \quad (\text{for } 2\ \text{MJ/kg} \le Q_v \le 5\ \text{MJ/kg}) \tag{2}$$

where $k_{TNT\text{-}p}$ is the pressure tritol equivalent of the explosive (equal to 1 for TNT), Q_v is the calculated explosion heat [MJ/kg] and Q_v = 4.2 MJ/kg for TNT.

Then the total equivalent mass C_W can be determined using the relationship [3]

$$C_w = C_N \cdot k_{TNT\text{-}p} \cdot k_E \cdot k_G \tag{3}$$

where C_w is the mass of the equivalent charge [kg TNT], C_N is the mass of the used charge of the (actual) explosive [kg], $k_{TNT\text{-}p}$ is the pressure tritol equivalent, k_E is the charge seal coefficient, and k_G is the geometry coefficient of the impact wave spreading in the space.

The seal coefficient can be determined using the relationship

$$k_E = 0.2 + 0.8 / (1 + k_B) \tag{4}$$

where k_B is the cover mass [kg] divided by the explosive mass [kg], and expresses the ballistic ratio. The following applies to the geometry coefficient k_G, 1 for detonation in an open air space, 2 for ground explosion.

The explosion wave spreads in spherical wave fronts from the focus point of the explosion. When the explosion is on the ground, the explosion energy is roughly double because, after complete reflection from the surface of the terrain, the pressure wave spreads in hemispherical

wave fronts. The spreading geometry coefficient k_G is not stated by some authors in the formulas for determining the total equivalent mass; in such cases, and in the case of a ground explosion, the equivalent charge mass C_w is as a rule substituted by twice its value in empirical formulas.

In the simplified calculation [3], a ground explosion is represented by a situation when the explosive is located directly on the surface of the terrain (h = 0 m thus k_G = 2). An explosion in an open air space is a situation when the delay of the reflected wave from the surface of the terrain to the pressure wave front is higher than the duration of the overpressure phase of the pressure wave (k_G = 1). A linear interpolation is made between the both values of k_G.

On the basis of comparing various resources in the literature (namely [1, 3, 4]) and our own results of tests of masonry [5] and window glass structures during explosions of small charges, the authors of this paper proposed the application of realistic formulas. The empirical formulas below were verified in experiments using small charges (Semtex) in the vicinity of the loaded structure. Their resulting form then corresponds to the impact wave effects from a small solid charge in an open air during this explosion. Maximum overpressure p_+ and underpressure p_- at the face of the air impact wave, velocity v of the wave face propagation and its durations τ_+ and τ_- are applicable both to ground and above-ground explosions:

$$p_+ = \frac{1.07}{\overline{R}^3} - 0.1 \quad \text{[MPa]} \quad \text{for } \overline{R} \le 1 \text{ m/kg}^{1/3} \tag{5}$$

$$p_+ = \frac{0.0932}{\overline{R}} + \frac{0.383}{\overline{R}^2} + \frac{1.275}{\overline{R}^3} \quad \text{[MPa]} \quad \text{for } 1 < \overline{R} \le 15 \text{ m/kg}^{1/3} \tag{6}$$

$$p_- = \frac{0.035}{\overline{R}} \quad \text{[MPa]} \tag{7}$$

$$\tau_+ = 1.6 \cdot 10^{-3} \cdot \sqrt[6]{C_\mathrm{w}} \cdot \sqrt{R} \quad \text{[s]} \tag{8}$$

$$\tau_- = 1.6 \cdot 10^{-2} \cdot \sqrt[3]{C_\mathrm{w}} \quad \text{[s]} \tag{9}$$

$$v = 340 \cdot \sqrt{1 + 8.3 \cdot p_+} \quad \text{[m/s]} \tag{10}$$

After a normal (perpendicular) impact of the explosion wave on a solid obstacle, a reflected wave is formed with the reflection overpressure p_{ref} that loads the building structure from the front side. The overpressure value in the reflected wave corresponds to approximately twice the value of the overpressure for low overpressure values p_+ of approximately up to 5 MPa (up to eight times the value for high overpressures of the order of several MPa) in the incident wave for the given distance R [3].

$$p_{ref+} \approx 2\, p_+ \tag{11}$$

$$p_{ref-} \approx 2\, p_- \tag{12}$$

The duration of the action of the pressure t_D is about the same as the duration of blast wave τ_+ or τ_-.

3 STRUCTURE RESPONSE

3.1 Load combination

The structure should be analysed using the following load combinations simplified as an equivalent static analysis (13) or as a dynamic analysis (14, 15):

$$\delta\,(1.2D + 0.25L) \tag{13}$$

$$D + (0.25 \text{ or } 0.50)L \tag{14}$$

or for alternate load path method (checking if residual load-carrying capacity upon notional removal of a selected load-bearing element)

$$(0.9 \text{ or } 1.2)D + (0.5L \text{ or } 0.2S) + 0.2W_n \tag{15}$$

where D is dead load ($1.2D$ or $1.0D$ is usually recommended), L is live load, S is snow load for roof, W_n is wind load for periphery structure elements, $\delta \approx 1 \sim 2$ is dynamic load factor (DOD UFC [6] recommends $\delta = 2.0$; other publications conclude that the use of a fixed dynamic load factor of 2.0 is highly conservative).

3.2 Structure ductility and material strengthening

When a structure is loaded by an explosion, the formation of cracks not leading to a collapse is as a rule permitted. Thus ductility factor q may be used to reduce the magnitude of the explosion load. This is a highly efficient way of taking inelastic manifestations of the dynamic load into account.

$$q = x_m / x_{el} \tag{16}$$

where x_m is the maximum elastic plastic displacement of the structure, and x_{el} is the elastic part of the displacement.

The applicable ductility factor is usually $q < 3$ for reinforced concrete structures. (On the basis of a more detailed analysis of the structure, higher ductility factor values may be used, for example, on the basis of seismic standard EN 1998-1)

The strength characteristics of the structure material may also be increased in the calculation of the structure response. An estimate of this increase (minimum material strengthening factor k_1) is shown in Table 1 [7], in dependence on the duration of the explosion load t_D.

t_D [s]	≥1.0	10^{-1}	10^{-2}	10^{-3}
k_1	1.0	1.05	1.10	1.20

Table 1: Estimation of factor k_1 in dependence on load duration t_D for concrete.

Blast loads usually produce very high strain rates in the range of 10^{-2} to 10^{-4} s. In comparison with Table 1 this strain rate would increases the stress and strain capacities of concrete and its steel reinforcement [8]. The increased compressive strength $f_{cd}^{'}$ of concrete under dynamic loading can be calculated as:

$$f_{cd}^{'} = f_c^{'} K_d \tag{17}$$

$$K_d(\varepsilon) = \left(\frac{\dot{\varepsilon}}{\dot{\varepsilon}_s}\right)^{1,026\alpha} \text{ for } \dot{\varepsilon} \le 30s^{-1} \tag{18}$$

$$K_d(\varepsilon) = \gamma \left(\frac{\dot{\varepsilon}}{\dot{\varepsilon}_s}\right)^{1/3} \text{ for } \dot{\varepsilon} > 30s^{-1} \tag{19}$$

$$\log\gamma = 6.156\alpha - 2 \tag{20}$$

$$\alpha = 1/(5 + 9 f_c^{'} / f_{co}^{'}) \tag{21}$$

where $\dot{\varepsilon}$ is the strain rate, $\dot{\varepsilon}_s$ (quasi-static strain rate) is 30×10^{-6} s^{-1}, $f_{co}^{'}$ is the reference strength set as 10 MPa and $f_c^{'}$ is 28-day compressive strength of concrete at static strain rate.

Steel reinforcement also shows higher strength and ductility under high strain rate. Soroushian and Choi [9] proposed a model for stress-strain response of steel under various loading rates. They reported that the increase in steel yielding stress, ultimate strength, and ultimate strain are proportional to the logarithmic function of the strain rate, as follows:

$$\frac{f_y^{'}}{f_y} = (-0.451\times10^{-6} f_y + 1.46) + (-9.20\times10^{-7} f_y + 0.093)\log_{10}\dot{\varepsilon} \tag{22}$$

$$\frac{f_p^{'}}{f_p} = (-6.83\times10^{-6} f_y + 1.72) + (-1.37\times10^{-6} f_y + 0.144)\log_{10}\dot{\varepsilon} \tag{23}$$

$$\frac{\varepsilon_u^{'}}{\varepsilon_u} = (-8.93\times10^{-6} f_y + 1.4) + (-1.79\times10^{-6} f_y + 0.0834)\log_{10}\dot{\varepsilon} \tag{24}$$

where f_y, f_p and ε_u are the yielding strength, ultimate strength, and ultimate strain of steel reinforcement under static loading, respectively; and $f_y^{'}$, $f_p^{'}$ and $\varepsilon_u^{'}$ are their corresponding values under high strain rate of $\dot{\varepsilon}$.

For example for concrete C35/45 and for t_D = 0,002 s are Standard recommendations for concrete: Czech: strengthening factor k_1 = 1.20 [7] and U.S.: over-strength factor Ω = 1.25 [6]. According to CEB-FIB 1990 [8] is K_d = 1.29 (the stress $f_c^{'}$ = 40 MPa increases to $f_{cd}^{'}$ = 51,2 MPa) and for reinforcement 10505 (f_y = 490 MPa, f_p = 550 MPa):

$$f_y^{'}/f_y = 1.44 \qquad f_p^{'}/f_p = 1.68 \qquad \varepsilon_u^{'}/\varepsilon_u = 1.38$$

It means that the approximation of strain rate by factors k_1 and Ω for concrete stress characteristics is relatively convenient and safety enough.

3.3 Response assumption

The magnitudes of the internal forces in the analysed structure are considered as a part of the evaluation of the limit bearing capacity conditions, based on load combinations when they are reduced using ductility factor q. The resulting internal forces are then evaluated on the basis of design standards for the appropriate structure material type, or as a variant, also according to its increased strength using factor k_1. However, this procedure entails two important uncertainties in the case of bent structures, i.e. a suitable choice of the ductility factor, on the one hand, and the material strengthening factor, on the other. During very rapid reshaping of the structure, which is typical for explosion loads, both factors may achieve numeric values of the order of tens, and not only of units, as mentioned above. Thus they may lead to considerable overdesigning of the structure.

Evaluations of structures loaded by an explosion based on dynamic displacements and rotations round the central line of plate, wall or beam systems during the action of a dynamic load of this type have been of very topical interest in recent times, as regards the process of evaluating the effects of an explosion on a structure. The dynamic rotation round the central line of an appropriate structure element is therefore the criterion used to evaluate the response occurring at the following angle:

$$\psi = \text{arctg}\,(x_m / (0.5\, h_{span})) \tag{25}$$

where x_m is the maximum achieved dynamic displacement caused by the explosion load and h_{span} is the span of the plate ceiling structure or the height of the wall structure within one storey, or the span of any beam, the height of a column, etc.

The authors applied this procedure to various types of materials and structure systems, and on the basis of an experimental comparison they determined the failure angle ψ_{max}, i.e. the angle where damage is caused to the structure by breaking (Table 2).

Type	Structure material	ψ_{max} [°]
1	Concrete C16/20 to C40/50	6.5
2	Masonry, full bricks 10, mortar 4 or mortar 10	5.0
3	Masonry, cement bricks, mortar 4	4.5
4	Masonry, cellular concrete or perforated precise blocks, mortar 4	4.0
5	Steel S235	10.5
6	Wood, hard and soft	12
7	Window glass, thickness 3 mm	6

Table 2: Limit failure angle ψ_{max} [°] upon breaking of the material.

4 RESPONSE OF BRIDGE STRUCTURE

As an example the reinforced concrete bridge structure was used. The bridge includes four long spans (30 m, 2×45 m, 30 m) with intermediate piers (12.25 m, 17.25 m, 15.25 m) and was made of concrete C 30/37. The computational model and its cross sections in the middle of spans and in supports are illustrated in Fig. 2. The bridge was analyzed under blast load of the explosion 100 kg TNT above the mid span above the bridge floor in high 2 m. The dimensions and distribution of structure parts were modelled while respecting the structure geometry and its dimensions, in order to obtain the most precise model of the bridge's mass and stiffness. Besides bridge dead load, the mass of asphalt part of the roadway were included in the bridge mass.

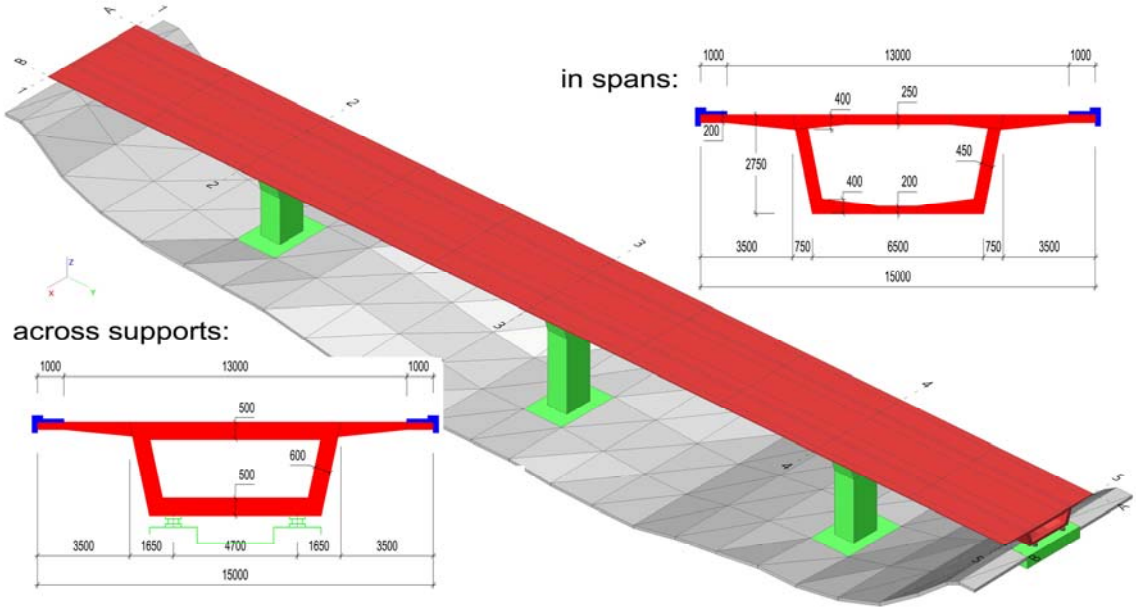


Figure 2: Bridge structure.

The blast load exerted on bridge floor surface was considered as series of blast histories (by equations 5 to 10) acting in the selected points of central part of the floor span (Fig. 3) and graduated in ten zones in terms of intensity as well as the whole history action on the basis of the real overpressure and underpressure phase of blast wave – dynamic load histories, as a function of the impact wave velocity of propagation (10).

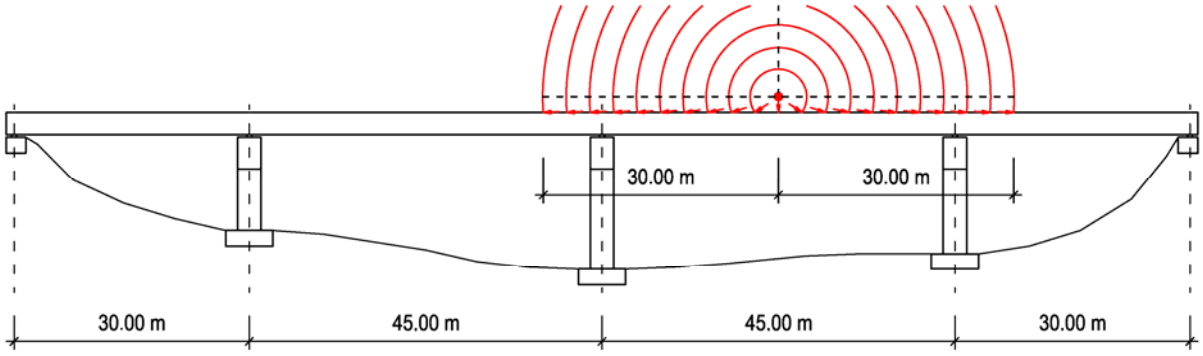


Figure 3: Location of explosion.

100 lowest natural modes and frequencies of vibration in the interval 1.9 Hz to 21.6 Hz were considered in the computation.

The decomposition of dynamic load history to the natural modes of vibration is used for the forced vibration analysis by means of Scia Engineer program.

The damping of the structure of the building has been set as a damping ratio of 4 %. For higher natural frequencies the damping is usually higher, but the computer program does not allow setting a different damping for these higher frequencies.

The calculation of forced vibration has been made with 1000 time steps of 0.0005 s. The dynamic response is calculated respectively for each time step. The dynamic analysis was made for linear elastic behaviour of the structure material.

As an example of the bridge deformation, isolines of vertical displacements of the bridge floor are shown in Fig. 3, Fig. 4 presents angle of rotations in the bridge floor and Fig. 5 indicates time histories in displacements at selected points in the middle of span (in the central part of the roadway and on the boundaries of payments).

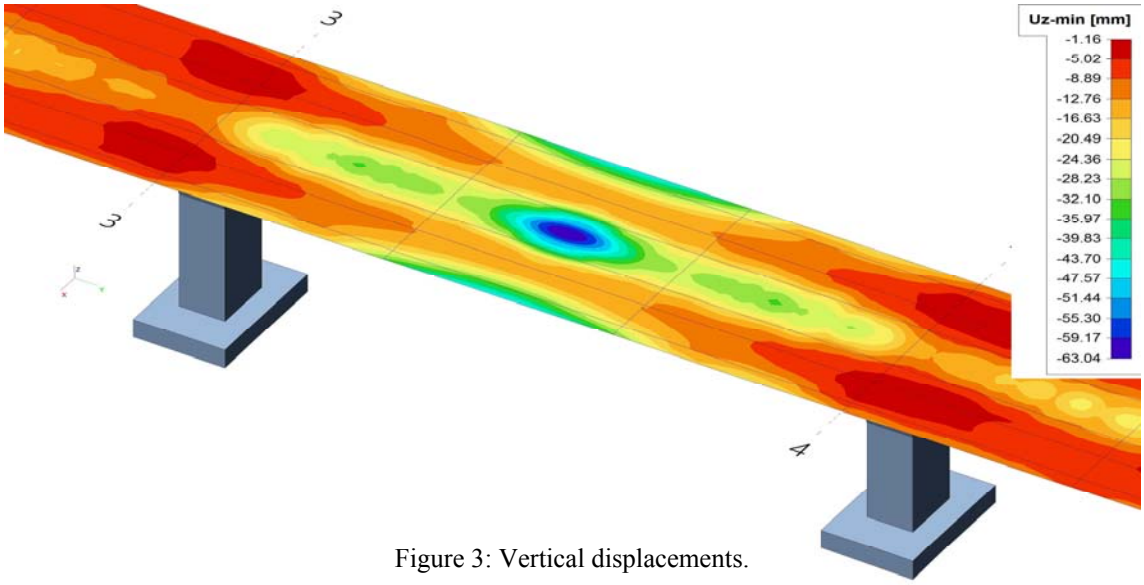


Figure 3: Vertical displacements.

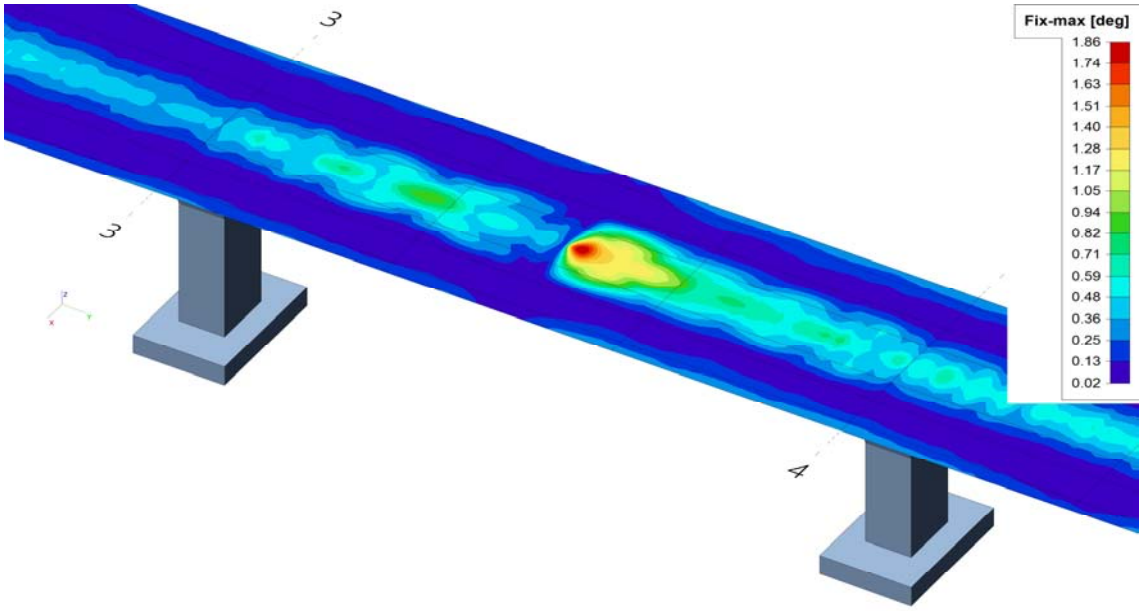


Figure 4: Angle of rotations round axis *x*.

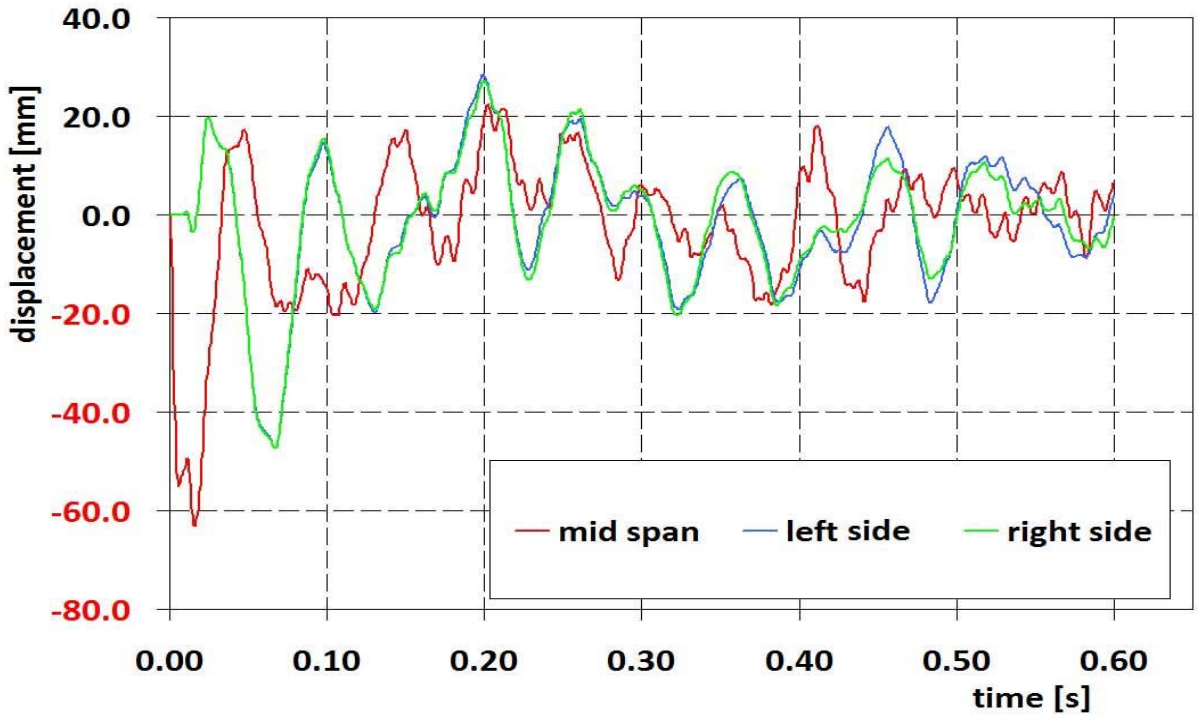


Figure 5: Time history in selected points of bridge floor.

The calculated rotations (angle ψ) of the middle surface of structural parts are used for structure assessment. The maximal angle of the rotation is 1.9 degrees round the both horizontal axes.

From all the rotations it is clear that in the concrete part of the bridge cross section the failures may occur. The concrete bridge structure responds to the medium structure hazard (the supposed angle of failure is fast one third of limit value), but due to the local damage of the central part of the bridge cross section, the bearing capacity of the whole bridge structure may be serious threatened under imposed vehicle load.

5 CONCLUSIONS

Paper is determined to the problem of an explosion and the threat to the safety of the structure due to the explosion of a explosive charge installed in a car and initiated for example on the bridge.

The explosion load is usually burdened with a number of uncertainties, related to determining the amount of explosive medium, its location in relation to the loaded structure, and the conditions in the surroundings. These load effects were derived by the authors based on the experimental results of small charge explosions. They may be used for an engineering estimation of the probable blast loads. This methodology enables us to determine with sufficient accuracy the time course of the impacting shock wave and its interaction with the structure itself.

The effect of ductility factor of structure and strain rate of concrete material on the analysis methodology is discussed. The approximation of strain rate by various strengthening factors is calculation friendly and usually safety enough with regard to uncertainties of input data, especially to location and parameters of blast wave.

The authors have used limit rotation values (angle of failure) determined experimentally on the basis of the explosion load of masonry, reinforced concrete and window glass plates, as a efficient method for response assumption. Evaluating a structure on the basis of the limit rotation is a methodology under development at present, and is in accordance with recent research trends for structure loaded by blast wave of explosion.

A reinforced concrete bridge structure has been used as an example for determining and documenting the load due to a blast effect. The bridge response is assessed on the basis of the results of a 3D dynamic calculation using displacements and rotation of the cross section parts of this structure.

The results for the response of the bridge to this load are presented in parts, together with the principles for evaluating the structure according to the displacements and to the angle of failure corresponding to the given explosion load.

REFERENCES

[1] D. Makovička, B. Janovský, *Handbook of Explosion Protection for Buildings (in Czech)*, Prague, CTU Publishing House, 2008.

[2] R. Zheng, P. Zohrevand, H. Erdogan, A. Mirmiran, Performance of FRP-retrofitted concrete bridge columns under blast loading, *CMEM*, **2**, 346-361, 2014.

[3] D. Makovička, D. Makovička, Blast resistant design and limits of the response of a structure to an external explosion, G. Schleyer, C.A. Brebbia eds. *Structures Under Shock and Impact XII*, WIT Press, Southampton, 229-239, 2012.

[4] D. Makovička, D. Makovička, Blast resistant design of structure to terrorist explosion, A. Cunha, E. Caetano, P. Ribeiro, G. Müller eds. *Proceeding of 9th International Conference EURODYN 2014*, June 30-July 2, Porto, 3519-3524, 2014.

[5] D. Makovička, Failure of masonry under impact load generated by an explosion, *Acta Polytechnica*, **39** (1), 63–91, 1999.

[6] UFC 4-023-03, *Design of buildings to resist progressive collapse*, U.S. Dept. of Defense, Washington, 2005.

[7] ČSN 73 0032 (Czech Standard), *Calculation of building structures loaded by dynamic effect of machines (in Czech)*, Prague, Czech Standard Institute, 1977.

[8] CEB-FIP, *Design of concrete structures*, *CEB-FIP Model-Code*. British Standard Institution, London, UK, 1990.

[9] Soroushian, P., Choi, K., Steel mechanical properties at different strain rates. *Journal of Structural Engineering*, **113** (4), 663-672, 1987.

[10] D. M. McCann, S. J. Smith, Blast resistant design of reinforced concrete structures, *STRUCTURE magazine*, 22-26, April, 2007.

ACKNOWLEDGMENT

The study is based on outcomes of the research project VG20122015089 supported by the Ministry of the Interior of the Czech Republic, for which the authors would like to thank the Ministry.

COMPDYN 2015
5th ECCOMAS Thematic Conference on
Computational Methods in Structural Dynamics and Earthquake Engineering
M. Papadrakakis, V. Papadopoulos, V. Plevris (eds.)
Crete Island, Greece, 25–27 May 2015

PERFORMANCE OF STEEL COLUMNS SUBJECTED TO VEHICLE IMPACT – EXPERIMENTAL AND NUMERICAL STUDIES

J. Korndörfer, B. Hoffmeister and M. Feldmann

Institute for Steel Structures, RWTH Aachen
Mies-van-der-Rohe-Str. 1, 52074 Aachen, Germany
e-mail: korndoerfer@stb.rwth-aachen.de

Keywords: Impact tests, steel columns, member-structure interaction, LS-Dyna.

Abstract. *Hazard scenarios regarding exceptional actions often include the possibility of a vehicle impact against a building. Here the impact against columns is of particular interest as they are the most exposed members. At the same time consequences are vast, since their failure can result in the collapse of the building.*

To evaluate the dynamic response of an impacted member, six slightly downscaled vehicle impact tests have been performed at RWTH Aachen University. Three different boundary conditions for the column have been examined, including a simply supported column (ideally pinned) with and without a concentrated mass attached to the column head as well as a column with realistic boundary conditions and connections at column base and column head. By varying the boundary conditions and the attached mass the influence of various types of interaction between the column and the surrounding structure has been assessed experimentally. Also the velocity of the impact body has been varied to achieve different degrees of impairment and residual strengths of the column.

In a second step state of the art commercial software (LS-Dyna) has been used to perform impact simulations with refined finite element models to augment the experimental results. Different member configurations have been investigated to further evaluate the influence of several parameters like impact velocity, mass and stiffness distribution of the member. The numerical models together with the implemented fundamental physical laws were validated by recalculations of the experimental tests.

1 INTRODUCTION

The European project ‘Robustimpact’ aims at the development of an innovative design concept that helps to properly assess and improve the resistance of steel structures subjected to impact loads. One of the design concepts followed within this project is the residual strength method which aims for high energy dissipation through plastic deformation of the impacted member, exploiting the extremely ductile behaviour of steel, while keeping sufficient residual strength for global structural stability after the impact.

The level of residual strength of an impacted steel column highly depends on the deformation caused by the impact since lateral deflections of the member imply additional bending moments due to axial loading. Steel columns are typically characterised by a high slenderness ratio which means that not only bending, but also stability failure must be considered as a possible ultimate limit state. In general, the level of deformation caused by impact loading cannot be assessed properly without taking the correct boundary conditions as well as the stiffness and mass of the surrounding structure into account. Earlier studies [1] have shown, that the inertia of the connected mass is able to provide significant axial restraint during the first phase of the impact, resulting in reduced deflections at the point of impact.

2 EXPERIMENTAL INVESTIGATIONS

To investigate the response of an impacted member, six slightly downscaled vehicle impact tests (2:3) were performed at RWTH Aachen University. Three different support conditions for the column were examined, including a simply supported column (ideally pinned) with and without a concentrated mass attached to the column head as well as a column with realistic boundary conditions and connections at column base and column head. By varying the boundary conditions and attached mass the influence of various types of interaction between the column and the surrounding structure was assessed experimentally. For the columns a HEB 140 steel section was selected; the nominal yield strength of the material was 355 MPa (coupon tests indicated 6% overstrength). Also the velocity of the impact body varied to achieve different degrees of impairment and residual strengths of the column. Table 1 summarizes the test program and the varied parameters.

For testing, the columns were arranged horizontally in front of a retaining wall with the strong axis of the steel section orthogonal to the impact direction. The dimensions of the column and the distance of the point of impact to the column base were selected within the limitations of the testing facility and can be found in Table 1. For test #2-1 & #2-2 a seven ton mass was connected to the pin joint at the column head. For test #3-1 & #3-2 the total length of the column was increased to 3.0 m with a realistic column to beam connection at a ‘height’ of 2.5 m and

Table 1: Overview of the test program.

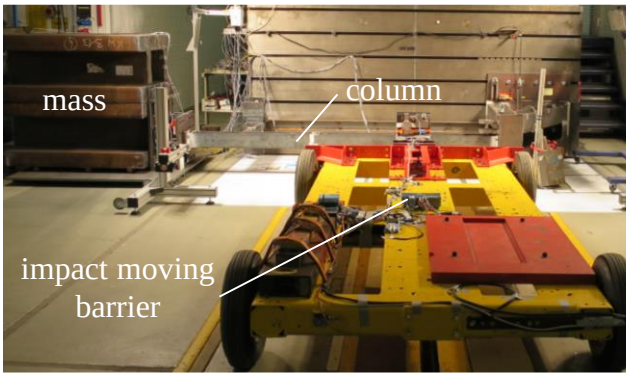


Figure 1: Photo of test setup for impact test 3-1/2.

the mass rigidly connected at 3.0 m (see Figure 1). In all tests the mass was supported by round steel bars to allow for free movement in axial direction of the column.

As an impactor, a very stiff impact moving barrier was used which was adjusted to a weight m_0 of 1500 kg. For the impact tests it was accelerated to a final impact velocity v_0 of 8 resp. 10 m/s. The kinetic energy stored in the impact vehicle at the time of the impact amounted to 48 or 75 kJ, respectively. The kinetic energy can be calculated with the well-known formula:

$$E_{kin,veh} = 0.5 \cdot m_0 \cdot {v_0}^2 \quad (1)$$

A block of aluminium honeycombs was mounted in front of the impact moving barrier to account for an idealized elasto-plastic force-displacement behaviour, which corresponds to the crashworthiness of a standard passenger vehicle. The plastic strength of the crush-area was determined to 300 kN under loading in axial direction by preliminary tests. With a crushable length of 320 mm, a total plastic energy of around 96 kJ could be absorbed by one honeycomb block. A steel plate was placed in front of the block to cater for a uniform load distribution in the honeycombs.

The columns were equipped with strain gauges in three different beam sections. Additionally optical marks were glued along the beam axis to allow for the extraction of displacement information from video footage, which was captured with a high speed camera (2000 fps). Acceleration sensors were placed at the point of impact on the column, at the centre of gravity of the impact vehicle and at the head mass. Draw wire sensors were connected to the supporting structure and to the head mass to track displacements of the supports and of the head mass. Force transducers were used to measure the force between the block of honeycombs and the impact vehicle (which corresponds to the contact force at the impacted section). For tests #2-1/2 and #3-1/2, additional force transducers were deployed to gauge the forces transferred between the head mass and the column head. Results of the experimental tests are presented together with the outcome of the numerical recalculations in chapter 3.2.

3 NUMERICAL RECALCULATIONS

Detailed Finite-Element models were deployed to perform numerical verification of the impact tests described in Section 2. For this purpose, the software LS-Dyna was used which is a powerful and proven tool for highly nonlinear problems in the short-term dynamic regime.

3.1 Model description

For the modelling of the steel column, endplates and the beam, connected to the column in test #3-1 and #3-2, shell elements (Belytschko-Tsay formulation) with a linear shape function and 5 integration points through shell thickness were used. Belytschenko-Wong-Chiang warping stiffness was added to increase the accuracy of the elements. The shells were discretised with a quadrilateral mesh, with an average element edge length of 10 mm. The impact moving barrier, including the block of honeycombs and the steel plate, used for load introduction, were modelled with hexahedral solid elements (single point integration formulation, type 1). Element edge lengths of 10 to 25 mm were applied for the deformable parts. In preliminary studies, a

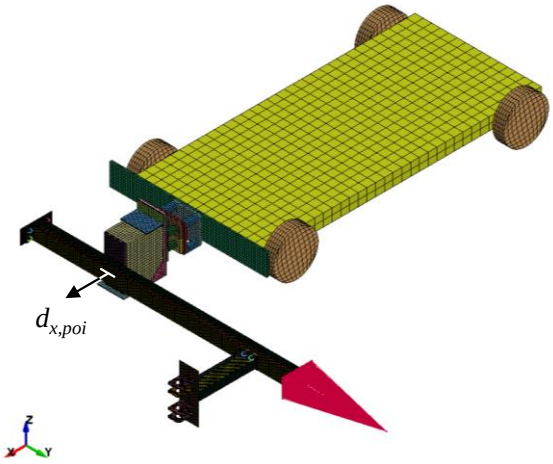


Figure 2: Model for recalculation of test 3-1/2

finer discretisation did not increase the quality of the results significantly. Proper hourglass control settings were applied for each element type to minimize the impact of zero energy hourglass modes.

An isotropic, multilinear material law was used to describe the stress-strain relationship of the S355 mild steel. The multilinear curve was adjusted to fit to the stress-strain curve obtained from tensile tests on the base material. LS-Dyna offers two material models for the description of honeycomb material which were investigated in preliminary studies. Although recommended element formulations and hourglass control preferences were set, the usage of Mat_126_MODIFIED_HONEYCOMB resulted in an emergence of significant hourglass energy in the honeycomb block (50% of the internal energy stored in the honeycomb after impact). Mat_26_HONEYCOMB was found to give much better results in this respect (with hourglass energies around 5% of the internal energy). The axial behaviour of the honeycomb was determined in static and dynamic (droptower) compression tests at RWTH Aachen and could be described as a bilinear function until fully compressed (at a total compression of 80%). However, the behaviour under off-axis loading was not assessed experimentally. Instead, assumptions for off-axis behaviour of the honeycombs have been met, based on current literature, e.g. [2]. All other parts of the impact moving barrier were modelled as non-deformable (rigid) bodies.

The hinges as well as the connection of the head mass were idealised as nodal rigid bodies with certain boundary conditions at their centre of gravity. To capture the effects of the impact load on the bolted, semi-strength connection, used in the experimental tests #3-1/2, a more detailed, realistic approach was followed. The shank of each bolt was modelled as an elastic spotweld beam and connected to circular shell plates at both ends, which represent the bolt head and the nut. Contact between the bolt shank and the bolt hole was established with the use of several elastic springs that behave very stiff under compression and soft in tension. An initial axial force was applied to the spotweld beams whereby the connected plates were compressed between the bolt head and the nut. The preload in the bolts and gravity load was initialised in a separate dynamic relaxation phase before the impact phase.

3.2 Results

Within this paper, selected examples of results are shown and discussed for brevity. The contact forces between the impact moving barrier and the column as well as the lateral displacements of the column at the point of impact are shown in Figure 3. Results of the experimental tests are represented as solid lines, whereby the numerical results are plotted in dashed lines. In the first phase of the impact, the contact force oscillates at an almost constant level. It can be observed, that the peak contact force varies only slightly in all tests, despite the differences in the test configurations (it is always limited by the plastic resistance of the honeycombs or the impacted column). However, there is a big difference in the column displacement at the point of impact. As can be expected, the simple supported setup without head mass and an impact speed of 10 m/s shows the highest deflections (300 mm plastic deformation) while the setup with the semi-strength connections and the connected head mass undergoes the lowest deflections (50 mm permanent deformation). The measured deflections in Test #2-1 and #2-2, which

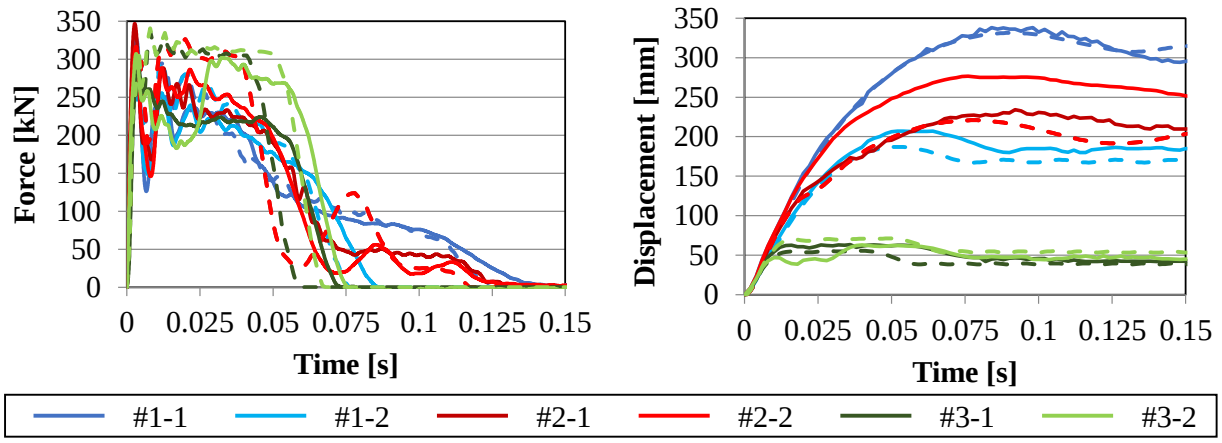


Figure 3: Contact Force between column and IMB (left), column displacement at the point of impact (right)

basically had identical test parameters (simply supported; with head mass; same impact velocity) differ significantly from each other (25% lower deflections at test #2-1 compared to #2-2). In both tests not negligible deformations of the support structure were observed, which could be the reason for the notable difference.

The energy stored in the column can be determined by integrating the force-displacement data shown in Figure 3.

$$E_{int,col} = \int F_{x,poi} \cdot dd_{x,poi} \tag{2}$$

Furthermore, the deformation energy of the aluminium honeycombs can be evaluated by integrating the force over the relative displacement between the impact moving barrier and the displacement of the column at the point of impact.

$$E_{int,veh} = \int F_{x,poi} \cdot d(d_{x,veh} - d_{x,poi}) \tag{3}$$

Finally, the kinetic energy of the impact moving barrier and the head mass, considered in test #2-1/2 and #3-1/2, can be calculated as a function of their velocity (adopting equation (3)). The total energy is obtained by summing up the separate values. The energetic (re-)distribution during the tests is shown in Figure 4.

Although the energy balance is not perfectly constant (e.g. friction work is neglected) it can be stated, that all relevant work portions are considered. The maximum deviation between input and output energy (10%) can be noticed in test #2-1. During this test, the head mass moved more than 60 mm in axial direction and strongly oscillated after the impact. Additionally, parts of the supporting structure slipped at the retaining wall. This resulted in additional energy dissipation through friction, which is not accounted for in the energy balance.

The kinetic energy is converted mainly into deformation energy in the steel member and the block of aluminium honeycombs. Since the plastic resistance of the honeycombs is slightly higher than the load that causes the formation of a plastic hinge in the simply supported case but lower than the one that is needed to initiate yielding in the realistically supported member, the ratio of the energy stored in the column and the energy in the aluminium honeycombs differs strongly from one test setup to another. This fits to the finding that the contact force seems to be roughly the same for all test setups, although the lateral displacements of the column at the point of impact differ significantly. The kinetic work, done by the head could not be calculated for test #2-1, since no acceleration signal was measured during that test.

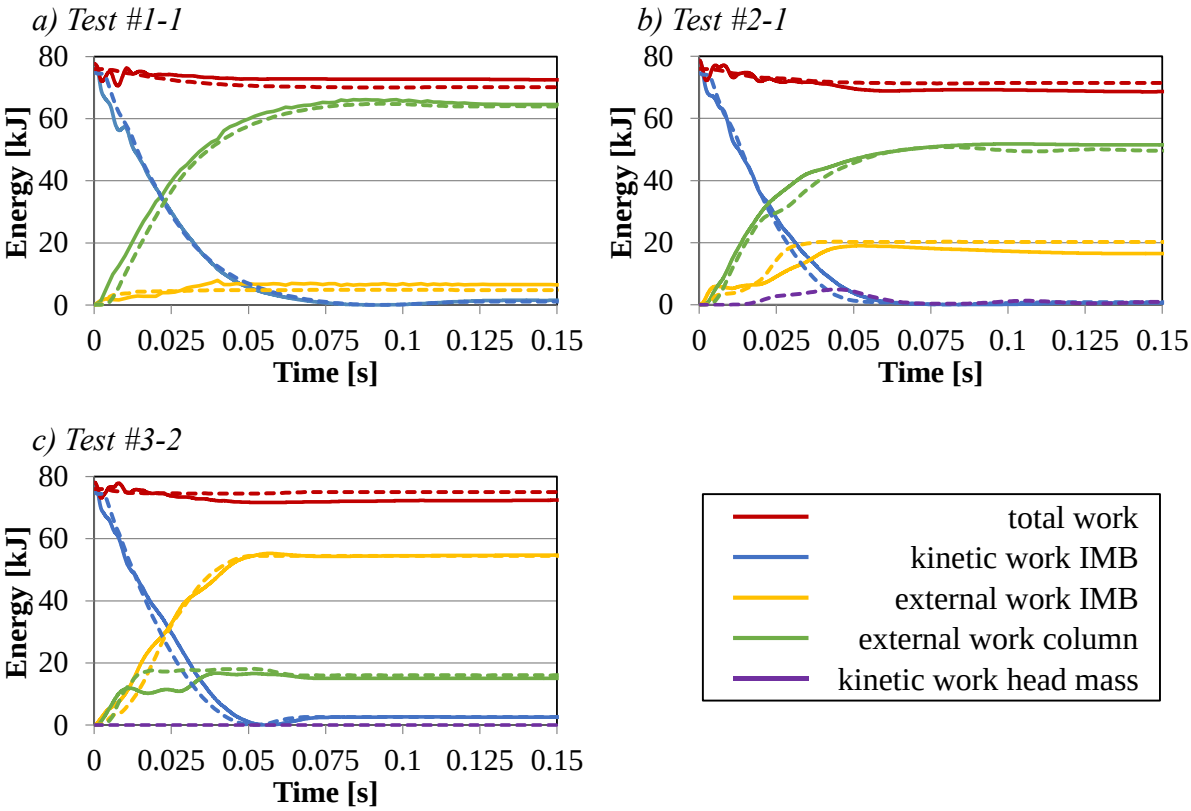


Figure 4: Energy (re-)distribution during tests with different setups.

4 PARAMETRIC STUDY

In addition to the numerical recalculations, a parametric study was performed to further investigate the influence of relevant parameters on the dynamic response of an impacted steel column. As for the numerical recalculations, LS-Dyna was used as a simulation tool. Material parameters, modelling techniques and control settings that proved successful for the recalculation were adopted for the parametric study as well.

4.1 Model description

For the parametric study, a HEB 220 column with a height of 3.6 meters was modelled using shell elements. All nodes at the column base and column head were coupled and the boundary conditions were applied to the master node in the centre of gravity of the section. Discrete spring elements were used to account for partially stiff joint rotation behaviour at the column base and the column head. The head mass was described as a discrete translational point mass and was rigidly connected to the column head.
The impactor was simplified as a solid block with a height of 0.25 meters and a width greater than the width of the impacted column. The weight of the impacting body was adjusted to 1.5 tons. For the parametric study, the impactor was considered to behave very stiff and purely elastic which implicates that the kinetic energy stored in the impactor is completely transformed into strain work in the impacted column and not in the impactor. This allows for better comparison of the column response at a certain level of kinetic energy input into the system. In all tests the point of impact was chosen to 0.625 m above the column base. The general model for the

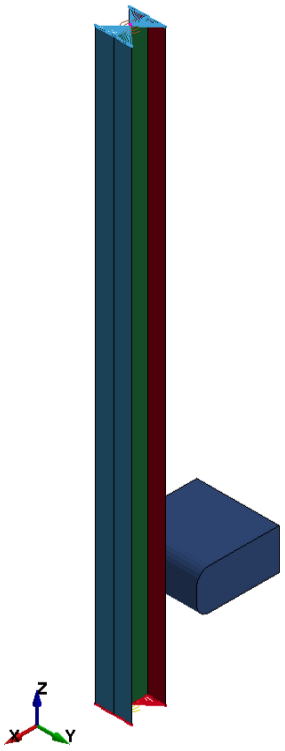


Figure 5: Model for the parametric study.

parametric study is shown in Figure 5. For the study the following parameters have been selected for further investigation:

- Boundary conditions at the column base and column head to represent different joint configurations
- Mass and weight of the head mass to account for various utilization levels of the column by gravity loads
- Impact velocity to simulate different impact scenarios

More than 40 simulations have been performed and evaluated. The most important findings are discussed within the next section.

4.2 Results

The two diagrams in Figure 6 show the maximum lateral deflection of columns with different rotational boundary conditions at the point of impact. Three different rotational stiffness variations – 0 kNm/rad (pinned support), 10.000 kNm/rad and ∞ kNm/rad (rigid support) – have been applied. Furthermore, the weight of the head mass varied from 0 to 200 tons. For comparison, a fully axially restraint column (res) was also included in the numerical study. The results shown in the left diagram correspond to an impact velocity of 60 km/h whereas the lateral deformations shown in the right diagram were obtained with an impact velocity of 80 km/h. The red columns indicate a collapse of the impacted member due to global buckling accompanied by local bucking of the web at the point of impact. The maximum lateral displacements, obtained at the end of the simulations with column collapse are higher than 350 mm in most cases but trimmed in the diagrams to allow for a better visibility of other values.

By comparing the maximum lateral deflections of the impacted column, several conclusions can be drawn. Not surprisingly, the boundary conditions have a significant influence on the deformation behaviour of the impacted column. The lateral deformations in the column decrease with increasing rotational stiffness at the column base and the column head. The rotational stiffness at the column base has a higher influence on the global stiffness of the impacted system than the rotational stiffness at the column head resulting from higher rotational demands. The hinged columns without axial restraint suffer severe local deformations and buckling of the web at the height of impact which results in a noticeably reduced axial load bearing capacity and a subsequent collapse of the column. The systems with a rotational stiffness of 10000 kNm/rad at the column base and column head ($v_0 = 80$ *km/h*) yield almost identical results compared to the rigidly connected system with the same impact velocity.

Obviously, different impact velocities lead to different degrees of lateral deformation in the column. The higher the impact velocity, the higher the lateral displacements for a given system configuration as can be recognized comparing both diagrams shown in Figure 6. In average, the lateral deflection increase by 50% due to the higher impact velocity. This is considerably less than one could expect following simplified energy based approaches to determine the lateral deflection (e.g. [3] or [4]). Here the lateral deflections are more or less proportional to the kinetic energy of the impactor which increases with the square of the impact velocity. However, these approaches assume an idealized plastic mechanism neglecting local distortions at the point

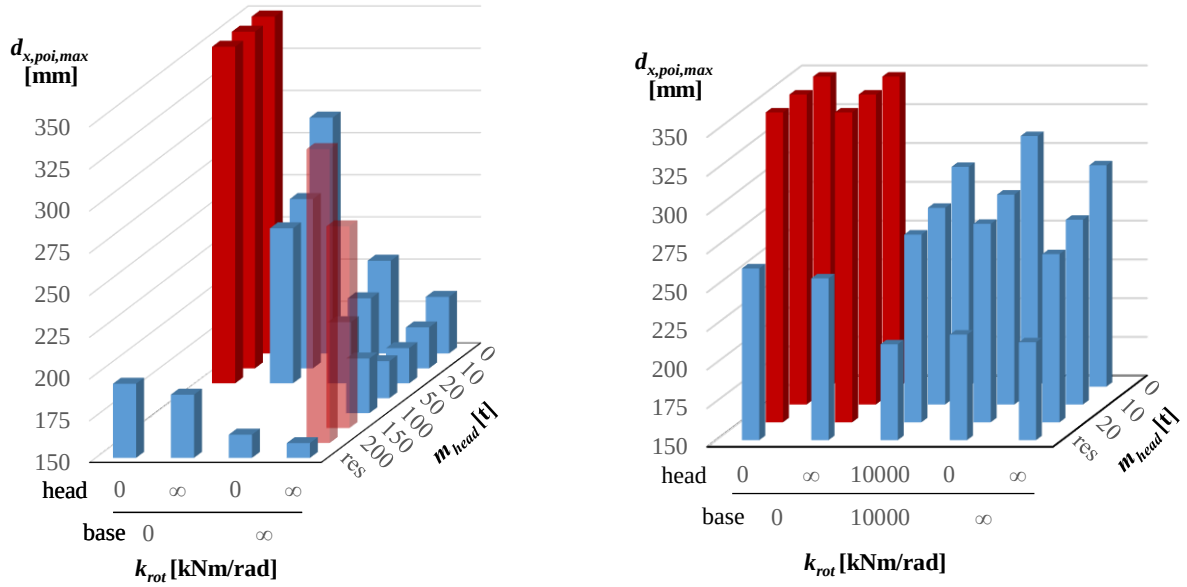


Figure 6: Maximum lateral deflections of the column at the point of impact.
(m_0=1.5 t, v_0=60 km/h (left), v_0=80 km/h (right))

of impact as well as the effect of an attached head mass. Moreover, strain rate and strain hardening effects are mostly disregarded in these simplified approaches.

Considering the influence of the head mass two opposite effects can be observed on the maximum lateral displacement at the point of impact. In the first phase of the impact, the inertia of the head mass adds a short term axial restraint to the system. In consequence, considerable axial tensile forces develop in the column. In the second phase of the impact, the head mass accelerates and starts moving towards the column base. This causes the development of dynamic compression forces which can lead to further plastification in the impacted zone or in combination with the gravity load to complete collapse of the column due to P-Δ effects. As can be seen in Figure 6 even small head masses provide enough inertia to generate an initial axial restraint resulting in decreasing maximum lateral displacements at the point of impact. However for heavier head masses the resulting maximum lateral displacements can increase until collapse due to the latter effect.

Figure 7 shows axial forces at the top of the column as well as the lateral deflections at the point of impact for the column configuration with infinite rotational stiffness and different head masses at an impact speed of 60 km/h (which corresponds to the results shown on the rightmost row of the left diagram in Figure 6). At time $t = 0$, the gravity load acts on the column resulting from the head mass and the initial lateral deflections at the point of impact are zero. During the impact, the lateral deflections at the point of impact rapidly increase. As described before, noticeable tensile forces develop at the column head, since the shortening of the column is impeded by the inertia of the head mass. Subsequently, the head mass accelerates and pushes at the column head. The compressive forces reach maximum values of 2200-2300 kN and cause further deformations in the plastic hinge at the point of impact. In case the deflected column has sufficient resistance to withstand and to absorb the compressive impulse, the axial force in the column oscillates around the static force value until the head mass comes to rest (0-100 tons). For the head masses with a weight 150 and 200 tons, a complete collapse of the column can be observed. Further investigations have been performed to study the collapse mechanism in these cases.

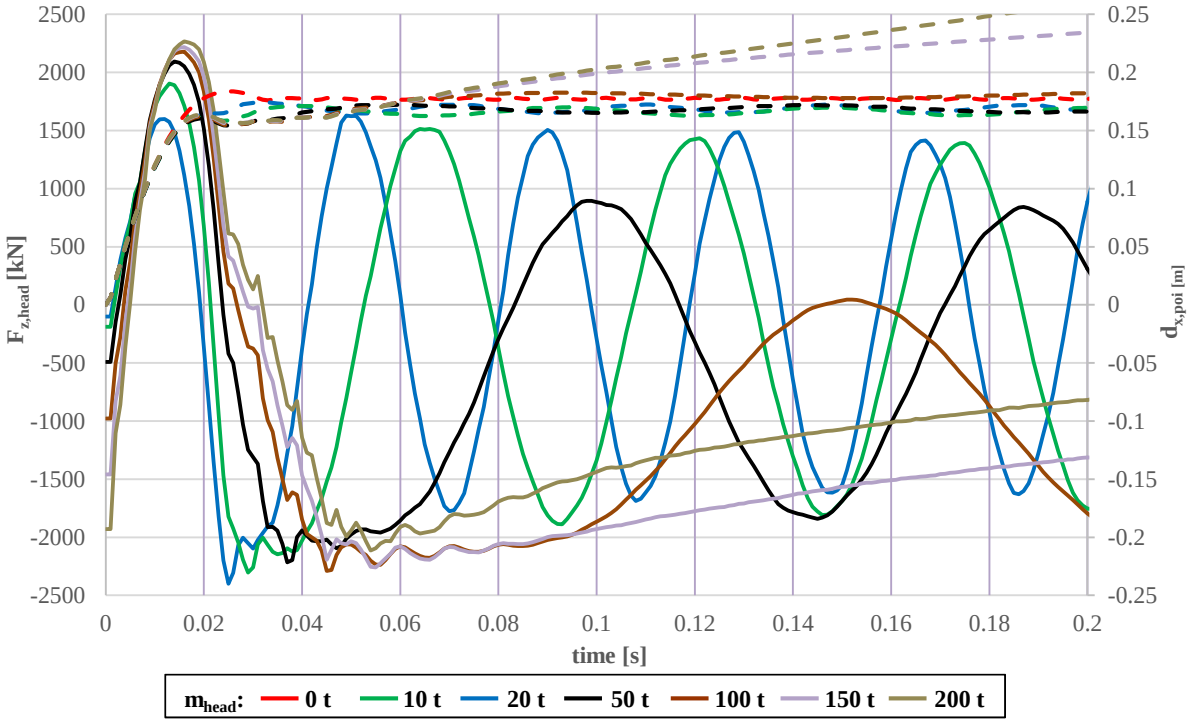


Figure 7: Axial Forces (solid lines) at the column head and lateral displacements (dashed lines) at the point of impact over time. (m_0 = 1.5 t, v_0 = 60 km/h, $k_{rot,base} = k_{rot,head} = \infty$)

In a first step, the chronology of the collapse progress is assessed. Based on the history of contact forces at the point of impact and axial forces at the column head it can be assumed that the impact event and the subsequent increase in lateral deflections caused by the head mass can be considered as two separate events. Thus, the compression of the column caused by the accelerated head mass can be described as a secondary impact at the column head in axial direction. However, the lateral deformation of the column resulting from the initial, lateral impact event must be incorporated. In contrast to the simply supported systems that collapse (see Figure 6) no significant local deformations can be noticed for the clamped columns ($k_{rot,base} = k_{rot,head} = \infty$) as a consequence of the initial, lateral impact.

A common approach to assess the axial residual strength of the deformed system is to perform a pushover analysis applying an increasing axial load at the head of the pre-damaged column. Under quasi static load conditions the column could be considered beyond its ultimate limit state if the maximum force, resulting from the pushover analysis is lower than the static gravity load of the head mass. However the calculated dynamic axial forces significantly exceed the static gravity forces as can be seen in Figure 7. As a consequence the dynamic load component of the head mass can't be neglected in this contemplation.

To account for the dynamic component of the head mass, an energy based approach is proposed. If the static gravity load is below the maximum force resulting from the pushover analysis it can be taken as an offset for the calculation of the residual external work that the column can absorb until it collapses. Additional energy input (e.g. in the form of kinetic energy of the head mass) leads to increasing elastic or plastic deformations in the column. The maximum residual work that can be done until collapse corresponds to the area under the pushover curve with a lower limit given by the quasi-static gravity load ($F_{z,head,qs}$).

$$E_{int,col,res} = \int \left(F_{z,head} - F_{z,head,qs}\right) \cdot du_{z,head} \qquad \text{for } F_{z,head} > F_{z,head,qs} \qquad (4)$$

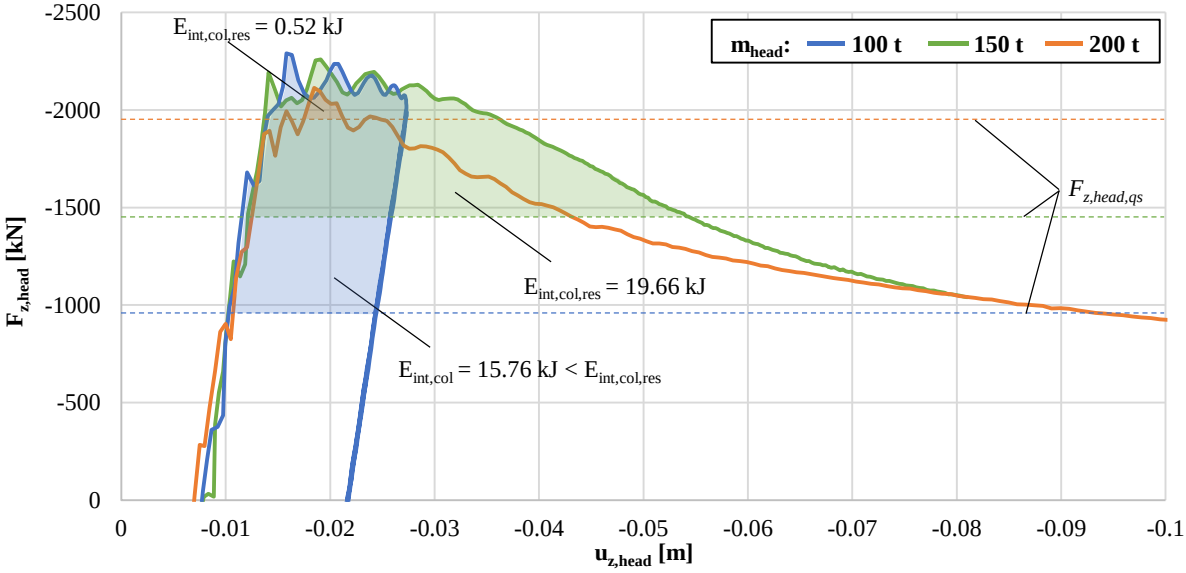


Figure 8: Axial compressive forces at the column head and corresponding axial displacements.
(m_0 = 1.5 t, v_0 = 60 km/h, $k_{rot,base}$ = $k_{rot,head}$ = ∞)

If the kinetic energy of the accelerated head mass is higher than the residual external work, the column fails. This assumption can be assessed by reviewing Figure 8. Here, the compressive axial forces are plotted dependent on the axial displacement at the column head (shortening of the column) for selected setups. The highlighted areas under the curves correspond to the kinetic energy of the head mass that is transformed into strain energy in the column as a result of the secondary impact. The two curves for the setups with 150 (green) and 200 (orange) tons head mass can be seen as pushover curves, since the impact of the accelerated head mass causes a complete collapse of the column. In these cases the kinetic energy which amounts to 21.7 kJ for the 150 ton head mass and 28.8 kJ for the 200 ton head mass exceed the respective residual capacity of the deformed column. The blue curve corresponds to the setup with 100 tons head mass which does not collapse. Here the blue area is equal to the kinetic energy that is converted into plastic strain energy in the column. The maximum kinetic energy of the head mass before the first compressive cycle amounts to 17.69 kJ and decreases to 2 kJ in subsequent oscillation cycles. The difference between the kinetic energy before and after the first compressive cycle is almost equal to 15.76 kJ which corroborates the assumptions made before. The remaining energy of 2 kJ is shifting its form from kinetic energy to elastic strain energy in the column in each cycle.

5 SUMMARY AND CONCLUSIONS DRAWN

The work presented within this paper covers the description of full scale impact tests performed at the University of Aachen. In addition, numerical recalculations have been performed using refined LS-Dyna models. Subsequent to the calibration of the finite element models, numerical investigations have been extended to a parametric study on isolated columns under impact loading to assess the influence of different boundary conditions, the weight of the connected head mass as well as varying impact velocities.

The impact tests were conducted with an impactor with elastic, perfectly plastic behaviour. Depending on the boundary conditions of the impacted column, different shares of the input energy were transformed into plastic strain energy in the column and the impacting vehicle. If no head mass was considered, the energy redistribution was found to mostly depend on the plastic capacity of the impact vehicle and the impacted member. By adding a head mass to the

column head, the lateral displacements at the point of impact were reduced noticeably in the test.

These observations were confirmed in the numerical simulations. However, when gravity loading was considered, the head mass imposed additional lateral displacements in a *secondary* impact event. While already small head masses provided a certain axial restraint and in fact decreased the lateral deflections during vehicle impact, heavier head masses led to increasing total lateral deflections as a result of the aforementioned *secondary* impact. In this respect it is important to notice that the impacted member must not only be able to carry the static component of the head mass (gravity load) but also needs to be able to absorb the kinetic energy imposed by the accelerated head mass without collapse.

The investigations on isolated columns, presented within this paper, will be complimented by impact simulations at the global structural level, considering the stiffness of the surrounding structure, realistic mass distribution and catenary effects of connected beams.

6 ACKNOWLEDGEMENT

The work presented here is carried out as a research project by different European partners with a financial grant from the Research Fund for Coal and Steel (RFCS) of the European Community. The authors gratefully acknowledge the financial support.

REFERENCES

[1] HAUKE B. et al., "Composite Column and Wall System for Impact and Blast Resistance – Final report RFS-CR-04047", RFCS publications, European Commission, Brussels, 2008

[2] JACKSON K. et al., "Material Model Evaluation of a Composite Honeycomb Energy Absorber", Proceedings of the 12th international LS-DYNA Users Conference, Detroit, June 3-5, 2012

[3] M. Gündel, B. Hoffmeister und B. Hauke, „Bemessung von Baustrukturen in Stahl- und Verbundbauweise für Anprall- und Explosionslasten", >>bauforumstahl e.V., Düsseldorf, 2010.

[4] N-004: Norsok Standard: Design of steel structures, 2004.

COMPDYN 2015
5th ECCOMAS Thematic Conference on
Computational Methods in Structural Dynamics and Earthquake Engineering
M. Papadrakakis, V. Papadopoulos, V. Plevris (eds.)
Crete Island, Greece, 25–27 May 2015

VALIDATION OF A NUMERICAL AND ANALYTICAL MODEL OF IMPACTED COLUMNS BY MEANS OF SMALL-SCALE DROP WEIGHT EXPERIMENTS

Carles Colomer Segura[1], Nils Horbach[1] and Prof. Dr.-Ing Markus Feldmann[1]

[1]Institute of Steel Construction and Lightweight Construction
RWTH Aachen University
Mies-van-der-Rohe-Str. 1, 52074 Aachen, Germany
e-mail: carles.colomer@rwth-live.de

Keywords: Impact of Columns, Simplified Model, Membrane Effects, Structural Dynamics, Drop Weight, Experiment, Validation

Abstract. *The analysis of structures under extreme accidental actions such as explosion or impact has been an ongoing topic of research since the 50's. Especially regarding the dynamic behaviour of impulsively loaded columns, many analytical and numerical models have been developed, which aim at predicting the ultimate load bearing capacity of the column and its residual level of deformation, which is directly linked to the residual capacity of the column after the impact.*

Nevertheless most of the existing approaches lack an appropriate consideration of membrane related resisting mechanisms, either by completely neglecting the presence of any longitudinal restraints or by assuming them as perfectly rigid. A realistic evaluation of the dynamic behaviour of the column requires therefore a more exact approach in order to consider arbitrary longitudinal connector stiffnesses. This paper presents a new analytical approach to the deformational and energetic behaviour of impacted column elements, which allows for an closed form solution of the maximum displacements under arbitrary longitudinal boundary conditions.

On the other hand, a small-scale drop weigth tower has been constructed in order to validate the results of the analytical model and compare them to predictions of other numerical approaches. The test rig has been conceived to allow for longitudinal displacements of the specimen, thus allowing to measure the motion of the column both in transversal and longitudinal direction.

1 INTRODUCTION

The ability to predict the real damage of impulsively loaded columns is of major importance, as their failure might affect the structural integrity of the whole building. While at the early stages all investigations were based on analytical models [1, 2] (mostly consisting of the reduction of the column to a single degree of freedom system), the advent of the finite element method and the great increase in computer power of the latest decades has allowed engineers to simulate complex loading scenarios of columns in more and more realistic building environments. Nowadays, many investigations [3, 4, 5] focusing on detailed aspects of the behaviour are based on complex FEM. Nevertheless, for general design recommendations, the interest remains on the global behaviour of the column (Will it fail or not? How much will it deform?), where simplified design methods are still a very useful tool [6, 7].

Most of these simplified design methods are based on energetic considerations, where the bearing capacity of the column is limited by the amount of strain energy that can be absorbed by the column undergoing deformation due to the impact. At small displacements, the absorbed strain energy is purely related to the bending resistance of the column. Nevertheless, at higher displacement levels (to be expected in accidental events) the energy absorption capability of the column is dominated by its membrane behaviour and the absorbed longitudinal strain energy. Very often, this latter term is simplified or even neglected in most analytical formulations, because of its complexity due to the nonlinear dependence on the displacements, thus leading to analytical models that underestimate the true energy absorbing capabilities of the column.

At the Institute of Steel Structures of the RWTH Aachen, exact analytical models have been developed, which can exactly assess the energy absorption capabilities of columns both due to bending and membrane effects under consideration of arbitrary longitudinal boundary conditions [8, 9].

In a first stage (Chapter 2), the longitudinal deformation behaviour of a beam undergoing arbitrary transversal deformation will be investigated. This will allow to describe the coupled (transversal-longitudinal) behaviour of the beam with increasing transversal deformation and thus understand the combined energy absorption mechanisms (bending-membrane) happening during the deformation process. In Chapter 3, an analytical solution of the energy absorption capability of the beam due to bending and membrane at any level of deformation will be given.

In order to validate this model, a small-scale experimental weight drop set-up (Chapter 4) has been constructed and used to impact small beam elements under variation of mechanical boundary conditions.

Using imaging measuring techniques, as well as optical laser displacement transducers and accelerometers, the experimental set-up allows for very detailed investigations of the applied impact energy and the deformational response of the specimen. These results are used in Chapter 5 to validate the analytical model in two experiments with free and fixed longitudinal boundary conditions.

2 CONSIDERATION OF GEOMETRIC NONLINEAR EFFECTS IN AN ARBITRARILY DEFORMED BEAM

Under consideration of geometric nonlinearities, transversal displacements lead to longitudinal displacements and/or activation of membrane forces along the beam. A proper

analysis of the energetic behaviour of the beam including geometric nonlinear effects requires the analytical determination of the longitudinal deformation function $\Upsilon_2(s,t)$, related to an arbitrary deflection function $\Psi(s,t)$ and arbitrary boundary conditions in longitudinal direction as in figure 1.

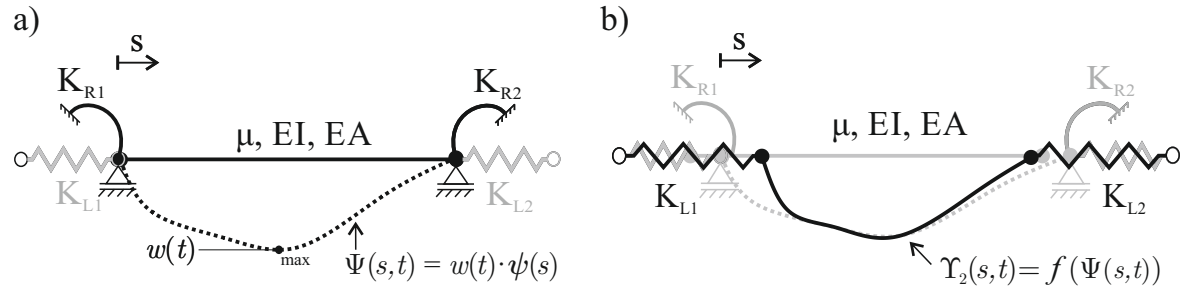


Figure 1: Arbitrary deformation of a beam in transversal direction (a) and associated deformation in longitudinal direction due to geometric nonlinear effects (b)

For the consideration of geometric nonlinear effects along the beam, the following geometric nonlinear strain definition is used:

$$\varepsilon_2 = \frac{\partial \Upsilon_2}{\partial s} + \frac{1}{2}\left(\frac{\partial \Psi}{\partial s}\right)^2 \tag{1}$$

where ε_2 represents the axial stretching of the beam due to a transversal deflection $\Psi(s,t)$, which is calculated as the difference between the shortening under no axial restrainment $\frac{1}{2}\left(\frac{\partial \Psi}{\partial s}\right)^2$ and the actual shortening including the spring stiffnesses of the longitudinal supports (k_{L1}, k_{L2}) and axial beam stiffness ($k_{EA} = EA/L$). For the upcoming analysis, it is useful to define the non-dimensional spring stiffnesses:

$$k^*_{\mathrm{L1}} = k_{\mathrm{L1}}/k_{\mathrm{EA}} \qquad \text{and} \qquad k^*_{\mathrm{L2}} = k_{\mathrm{L2}}/k_{\mathrm{EA}} \quad .$$

Assuming that the axial force remains constant along the entire length of the beam, the

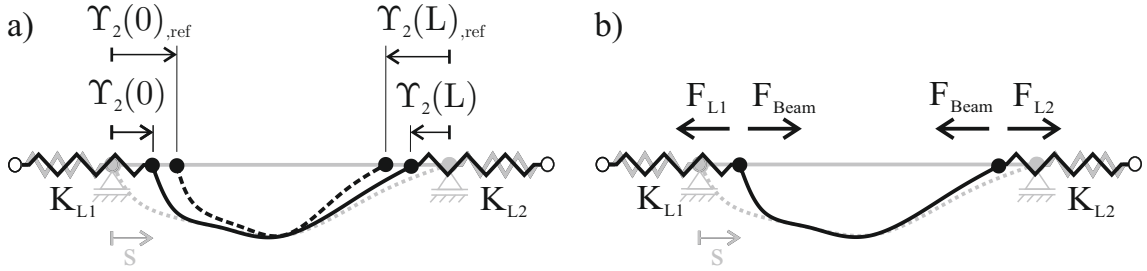


Figure 2: Longitudinal deformation of a beam due to geometrical nonlinear effects (a) and equilibrium of longitudinal forces (b)

axial stretching of the beam can be easily calculated by integrating eq. (1) over the beam length:

$$\varepsilon_2 = \frac{\Upsilon_2(\mathrm{L}) - \Upsilon_2(0)}{\mathrm{L}} + \frac{1}{2\mathrm{L}}\int_0^{\mathrm{L}} \left(\frac{\partial \Psi}{\partial s}\right)^2 \tag{2}$$

In order to determine the longitudinal displacement of the left and right supports ($\Upsilon_2(0)$ and $\Upsilon_2(\mathrm{L})$ respectively), the equilibrium of axial forces in the system depicted in figure 2 b) is imposed, leading to the following linear system of equations:

$$\left.\begin{aligned} F_{L1} = F_{Beam} \rightarrow k_{L1}\Upsilon_2(0) &= \frac{EA\left(\Upsilon_2(L) - \Upsilon_2(0)\right)}{L} + \frac{EA}{2L}\int_0^L \left(\frac{\partial \Psi}{\partial s}\right)^2 \mathrm{d}s \\ -F_{L2} = F_{Beam} \rightarrow -k_{L2}\Upsilon_2(L) &= \frac{EA\left(\Upsilon_2(L) - \Upsilon_2(0)\right)}{L} + \frac{EA}{2L}\int_0^L \left(\frac{\partial \Psi}{\partial s}\right)^2 \mathrm{d}s \end{aligned}\right\} \tag{3}$$

The solution for $\Upsilon_2(0)$ and $\Upsilon_2(L)$ from eq. (3) can be found to:

$$\left.\begin{aligned} \Upsilon_2(0) &= \frac{k_{1eq}}{2}\int_0^{\mathrm{L}} \left(\frac{\partial \Psi}{\partial s}\right)^2 \mathrm{d}s \\ \Upsilon_2(\mathrm{L}) &= \frac{-k_{2eq}}{2}\int_0^{\mathrm{L}} \left(\frac{\partial \Psi}{\partial s}\right)^2 \mathrm{d}s \end{aligned}\right\} \tag{4}$$

with

$$k_{1\mathrm{eq}} = k^*_{\mathrm{L2}} / \left(k^*_{\mathrm{L1}} \cdot k^*_{\mathrm{L2}} + k^*_{\mathrm{L1}} + k^*_{\mathrm{L2}}\right) \tag{5}$$

$$k_{2\mathrm{eq}} = k^*_{\mathrm{L1}} / \left(k^*_{\mathrm{L1}} \cdot k^*_{\mathrm{L2}} + k^*_{\mathrm{L1}} + k^*_{\mathrm{L2}}\right) \tag{6}$$

From here, the overall shortening of the beam $\Delta\Upsilon_{2,1\rightarrow\mathrm{L}}$ can be defined as:

$$\Delta\Upsilon_{2,0\rightarrow\mathrm{L}} = \Upsilon_2(0) - \Upsilon_2(\mathrm{L}) = \frac{k_{1,eq} + k_{2,eq}}{2}\int_0^{\mathrm{L}} \left(\frac{\partial \Psi}{\partial s}\right)^2 \mathrm{d}s \tag{7}$$

The non-dimensional spring stiffnesses ($k_{1,\mathrm{eq}}$, $k_{2,\mathrm{eq}}$) range from (0,0) for a fixed-fixed restraint to (0,1) for a fixed-free situation. In case of no longitudinal restraint ($k_{L1} = 0$ and $k_{L2} = 0$), the values of ($k_{1,\mathrm{eq}}$, $k_{2,\mathrm{eq}}$) are equal to (0.5,0.5) and lead to a symmetrical shortening of the beam. The values of ($k_{1,\mathrm{eq}}$, $k_{2,\mathrm{eq}}$) can be determined according to figure 3.

From a mechanical point of view, the axial force in the beam for any longitudinal boundary condition where $k_{1,eq} + k_{2,eq} = 1$ (either free-fixed, fixed-free or free-free conditions for the springs K_{L1} and K_{L2}) must be equal to 0 due to force equilibrium along the beam axis. In this situations, eq. (7) yields:

$$\Delta\Upsilon_{2,0\rightarrow\mathrm{L},ref} = \frac{1}{2}\int_0^{\mathrm{L}} \left(\frac{\partial \Psi}{\partial s}\right)^2 \mathrm{d}s \tag{8}$$

which is defined as the reference overall shortening for which no axial forces are developed and hence, no strain membrane energy is absorbed by the system.

In the general case of a horizontally restrained beam, the overall shortening of the beam $\Delta\Upsilon_{2,0\rightarrow\mathrm{L}}$ is always smaller than $\Delta\Upsilon_{2,0\rightarrow\mathrm{L,ref}}$, leading to the development of membrane forces. In this state, the axial stretching of the beam is calculated from eq. (2) to:

$$\varepsilon_2 = \frac{\left(\Delta\Upsilon_{2,0\rightarrow\mathrm{L},ref} - \Delta\Upsilon_{2,0\rightarrow\mathrm{L}}\right)}{\mathrm{L}} = \frac{1 - k_{1,eq} - k_{2,eq}}{2\mathrm{L}}\int_0^{\mathrm{L}} \left(\frac{\partial \Psi}{\partial s}\right)^2 \mathrm{d}s \tag{9}$$

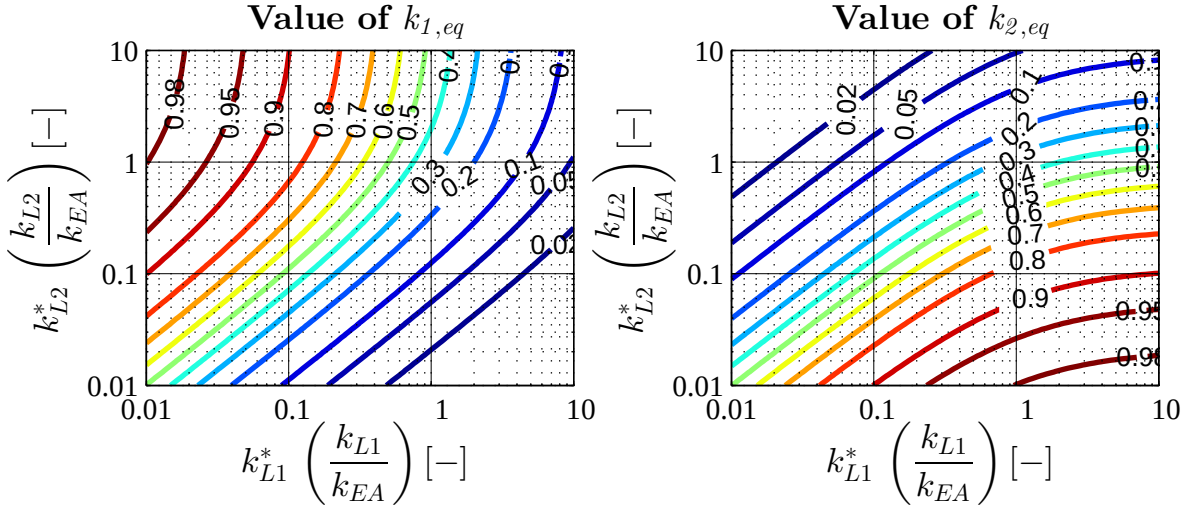


Figure 3: Non-dimensional spring stiffnesses for arbitrary longitudinal boundary conditions

which is always positive as membrane forces can only be positive.

In this state, the deformations of the beam in longitudinal direction can be calculated from eqs. (1) and (9) to:

$$\frac{\partial \Upsilon_2}{\partial s} = \varepsilon_2 - \frac{1}{2}\left(\frac{\partial \Psi}{\partial s}\right)^2 = \frac{1 - k_{1,eq} - k_{2,eq}}{2\mathrm{L}} \int_0^{\mathrm{L}} \left(\frac{\partial \Psi}{\partial s}\right)^2 \mathrm{d}s - \frac{1}{2}\left(\frac{\partial \Psi}{\partial s}\right)^2 \tag{10}$$

which integrated along the beam axis and imposing the boundary conditions in (4) yields:

$$\begin{aligned} \Upsilon_2(s,t) &= \frac{s - k_{1,eq}(s - \mathrm{L}) - k_{2,eq} \cdot s}{2\mathrm{L}} \int_0^{\mathrm{L}} \left(\frac{\partial \Psi}{\partial s}\right)^2 \mathrm{d}s - \frac{1}{2}\int_0^{s} \left(\frac{\partial \Psi}{\partial s}\right)^2 \mathrm{d}s = \\ &= \left(\frac{s - k_{1,eq}(s - \mathrm{L}) - k_{2,eq} \cdot s}{2\mathrm{L}} \int_0^{\mathrm{L}} \left(\frac{\partial \psi}{\partial s}\right)^2 \mathrm{d}s - \frac{1}{2}\int_0^{s} \left(\frac{\partial \psi}{\partial s}\right)^2 \mathrm{d}s\right) \cdot w(t)^2 \end{aligned} \tag{11}$$

This expression describes the longitudinal displacements of a beam due to an arbitrary transversal deformation under consideration of geometric nonlinear effects and arbitrary longitudinal support stiffnesses.

By defining the following functional:

$$f_{\Upsilon_2}(s) = \left(\frac{s - k_{1,eq}(s - \mathrm{L}) - k_{2,eq} \cdot s}{2\mathrm{L}} \int_0^{\mathrm{L}} \left(\frac{\partial \psi}{\partial s}\right)^2 \mathrm{d}s - \frac{1}{2}\int_0^{s} \left(\frac{\partial \psi}{\partial s}\right)^2 \mathrm{d}s\right) \tag{12}$$

eq. 11 can be rewritten as:

$$\Upsilon_2(s,t) = f_{\Upsilon_2}(s) \cdot w(t)^2 \tag{13}$$

3 ENERGY ABSORPTION CAPABILITY OF A COLUMN UNDER CONSIDERATION OF MEMBRANE ACTION

The strain energy absorbed by a beam undergoing a deformation as defined in figure 1 can be calculated by integral calculation over the length of the beam as:

$$E_{\varepsilon^*,S} = E_{\varepsilon,S} + E_{\kappa,S} = \frac{1}{2}\int EA \cdot \varepsilon^2 \cdot \mathrm{d}s + \frac{1}{2}\int EI \cdot \kappa^2 \cdot \mathrm{d}s \tag{14}$$

where the terms $E_{\varepsilon,S}$ and $E_{\kappa,S}$ correspond to the absorbed energy components due to membrane and bending action respectively. For a correct evaluation of the absorbed energy, the boundary conditions need to be considered in the evaluation of these integrals. Thus, the general expression for the calculation of the absorbed strain energy due to bending and membrane action become respectively:

$$E_{\kappa,S} = \frac{1}{2}\left[\int EI\left(\frac{\partial^2\psi(s)}{\partial s^2}\right)^2 \mathrm{d}s + k_{R1}\cdot\left(\frac{\partial\psi}{\partial s}(0)\right)^2 + k_{R2}\cdot\left(\frac{\partial\psi}{\partial s}(L)\right)^2\right]\cdot w(t)^2 \tag{15}$$

$$E_{\varepsilon,S} = \frac{1}{2}\left[\int EA\cdot\varepsilon^2\cdot\mathrm{d}s + k_{L1}\cdot\Upsilon(0)^2 + k_{L2}\cdot\Upsilon(\mathrm{L})^2\right] \tag{16}$$

with the help of the eqs. (9) and (4) as well as the definitions of $k_{1,eq}$ and $k_{2,eq}$ from eqs. (5) and (6), eq. (16) can be rewritten as:

$$E_{\varepsilon,S} = \frac{k_{\mathrm{EA}}k^*_{\mathrm{L1}}k^*_{\mathrm{L2}}}{8\left(k^*_{\mathrm{L1}}+k^*_{\mathrm{L2}}+k^*_{\mathrm{L1}}\cdot k^*_{\mathrm{L2}}\right)}\left(\int_0^L\left(\frac{\partial\psi}{\partial s}\right)^2\mathrm{d}s\right)^2\cdot w(t)^4 \tag{17}$$

This last expression shows the nonlinear dependency of the absorbed membrane energy as a function of the transversal deformation $w(t)$.

Fur the upcoming analysis, eq. (14) will be rewritten as

$$E_{\varepsilon^*,S} = C_{\kappa,w^2}\cdot w^2 + C_{\varepsilon,w^4}\cdot w^4 \tag{18}$$

with

$$C_{\kappa,w^2} = \frac{1}{2}\left[\int EI\left(\frac{\partial^2\psi(s)}{\partial s^2}\right)^2\mathrm{d}s + k_{R1}\cdot\left(\frac{\partial\psi}{\partial s}(0)\right)^2 + k_{R2}\cdot\left(\frac{\partial\psi}{\partial s}(L)\right)^2\right] \tag{19}$$

$$C_{\varepsilon,w^4} = \frac{k_{\mathrm{EA}}k^*_{\mathrm{L1}}k^*_{\mathrm{L2}}}{8\left(k^*_{\mathrm{L1}}+k^*_{\mathrm{L2}}+k^*_{\mathrm{L1}}\cdot k^*_{\mathrm{L2}}\right)}\left(\int_0^L\left(\frac{\partial\psi}{\partial s}\right)^2\mathrm{d}s\right)^2 \tag{20}$$

where C_{κ,w^2} and C_{ε,w^4} are coeficients purely dependent on the deformation shape and boundary conditions and w is the amplitude of the transversal deformation.

3.1 Consideration of the plastic development in the column

In problems where large deformation levels are expected, it is important to take into account the development of plastic hinges during the deformation of the column (as in figure 4). With increasing transversal deformation w new plastic hinges appear, which lead to changes in the deformation shape $\psi(s)$. This means that the eq. (18) is only valid for a given deformation interval, in which the deformation shape ψ remains constant. Therefore, this equation should be more correctly be written in its incremental form for a given stage i in the plastic evolution of the beam:

$$\Delta E_{\varepsilon^*,S,w_i\to w} = C_{\kappa,w^2,i}\cdot(w-w_i)^2 + C_{\varepsilon,w^4,i}\cdot\left(w^2-w_i^2\right)^2 \tag{21}$$

It is important to note, that the expression (21) does not consider the energy contribution due to the remaining plastic resistance from the previous stages of the plastic evolution of

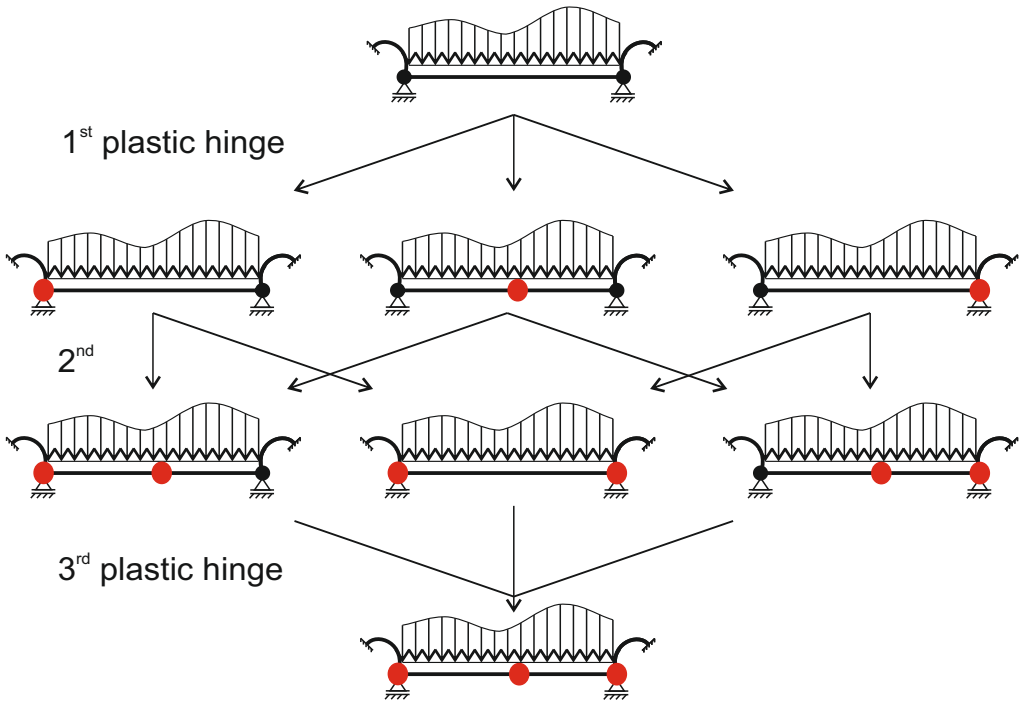


Figure 4: Plastic evolution of an arbitrarily supported beam

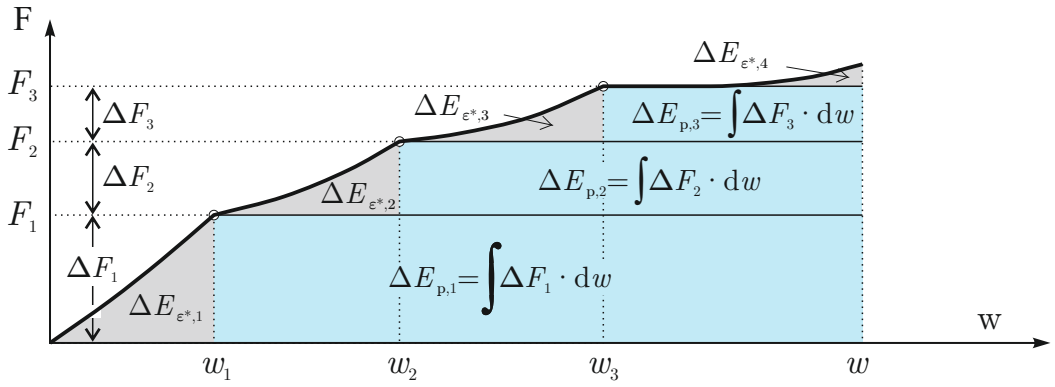


Figure 5: Generalized Force-Displacement diagram of a plastic beam and integration areas for the determination of the totally absorbed energy

the beam. In order to account for this components, additional integral terms $\Delta E_{p,i}$ need to be considered in the calculation of the total energy, as illustrated in figure 5. If the deflections w_i are known from the plastic analysis, the only remaining unknown terms are the force increments between plastic stages ΔF_i, which can be calculated derivating eq. (21):

$$\Delta F_i = \frac{\partial \Delta E_{\varepsilon^*,S,w_{i-1}\to w_i}}{\partial w} = 2 \cdot C_{\kappa,w^2,i} \cdot (w_i - w_{i-1}) + 4 \cdot C_{\varepsilon,w^4,i} \cdot \left(w_i^2 - w_{i-1}^2\right) \cdot w \qquad (22)$$

The plastic energy components $\Delta E_{p,i}$ can be calculated using eq. (22) to:

$$\Delta E_{p,i} = \int_{w_i}^{w} \Delta F_i \cdot \mathrm{d}w = 2 \cdot C_{\kappa,w^2,i} \cdot (w_i - w_{i-1}) \cdot (w - w_i) + 4 \cdot C_{\varepsilon,w^4,i} \cdot \left(w_i^2 - w_{i-1}^2\right) \cdot \left(w^2 - w_i^2\right) \qquad (23)$$

4 EXPERIMENTAL INVESTIGATIONS

4.1 Testing set-up

In order to perform impact experiments, a small-scale impact test facility has been constructed at the Institute of Steel Construction of the RWTH Aachen (see figure 6). Using the inner flange of a building column as a support for the guide-rails of the drop tower. The maximum drop height is limited to 2.5 metres, with a weight of the impact console of 2.8 kg, which can be increased modularly upto 10 kg. The applicable impact energy can reach upto $\sim$ 250 J with a maximum impact speed of 7.0 m/s.

As illustrated in figure 6, the test rig for impacting steel plates has been designed to allow for adjusting the rotatory and longitudinal boundary conditions arbitrarily. Directly attached to a 20mm thick steel base plate, there is a guiding rail with a length of $\sim$ 1840 mm supporting two runner blocks. In order to allow for high levels of deformation in the test specimen, a stiff support structure has been constructed to elevate the impact point of the specimen from the longitudinal rail, thus allowing for a free transverse deformation of max. 20 cm.

Two roll bearings bolted to the support structure hold an 30 x 30 mm square axle with a 10 mm wide mill-cut slot where the test specimen is introduced and fixed by clamping. The maximum size of the test specimen is limited to 1650 x 200 x 10 mm. The measuring

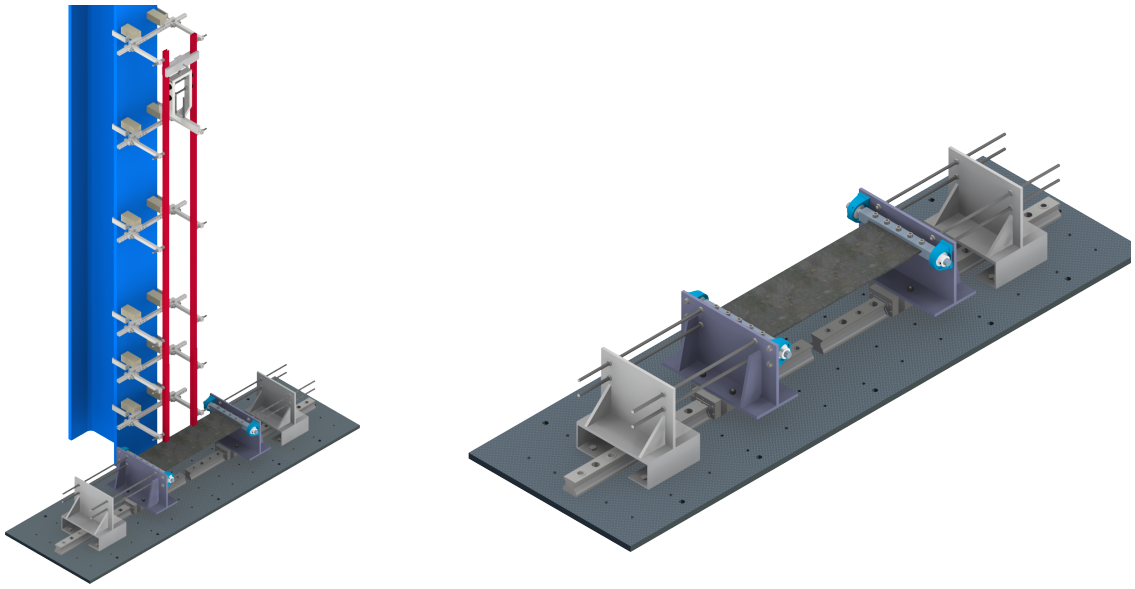


Figure 6: Overview of the small-scale drop weight tower (a) and detail of the test rig for impacting small scale specimens (b)

system for the experimental set-up is composed by:

1. An accelerometer attached to the impact console for measuring the impact force.
2. Two high-speed cameras with a resolution of 1024 x 512 pixel at 923 fps, in combination with Tracker software [10], a free video analysis tool built on the Open Source Physics Java framework.

4.2 Planned experiments

The goal of the experiments described in figure 7 is to validate the analytical approaches presented in the Chapters 2 and 3 regarding the geometrical nonlinear behaviour and the associated energy absorbing mechanisms of impacted columns by means of small scale experiments.

In the test configuration (a), a simply supported plate with the dimensions 500 x 110x 3 mm was tested under free-free rotationary and free-free longitudinal boundary conditions. In the test configuration (b), the longitudinal boundary conditions have been set to fixed-fixed, in order to activate membrane effects. In both experiments, an impact mass of 2.8 kg has been raised to a height of 1.82 m and let fall freely against the middle of the specimen, thus applying an impact energy of ~ 50 J.

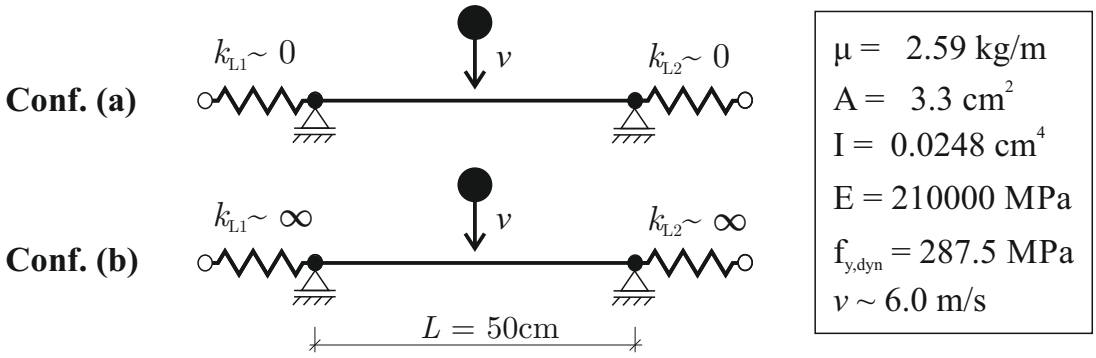
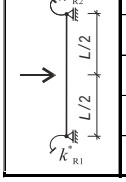


Figure 7: Boundary conditions for the performed experiments

5 EXPERIMENTAL RESULTS AND VALIDATION OF THE MODEL

In this chapter the results of the experimental tests are compared to the results of the analytical approach described in chapter 3 and also compared to the results of a numerical approach based on the model reduction concept specially designed for accounting for membrane effects [9]. The analytical approach allows for the estimation of the maximum

Load



Stage	BC's	C_{κ,w^2}	BC's	C_{ε,w^4}	BC's	C_{ε,w^4}	Limits	w^*_i
1	k^*_{R1}	9979	k^*_{L1}	0	k^*_{L1}	1.71e7		0
2	∞	0	0	0	∞	1.19e7		0.0285
3	k^*_{R2}	-	k^*_{L2}	-	k^*_{L2}	-		-
4	∞	-	0	-	∞	-		-

Figure 8: Values of the coefficients of the coefficients $C_{\kappa,w^2,i}$ and $C_{\varepsilon,w^4,i}$ for the boundary conditions in the experiments

deflections of the beam based on the determination of the coefficients $C_{\kappa,w^2,i}$ and $C_{\varepsilon,w^4,i}$ for each stage of the plastic evolution of the beam as described in figure 4. Since there are

no rotational supports at both ends, only the elastic (1) and perfectly plastic (2) stages are considered (see figure 8).

5.1 Experiment 1: Conf. (a)

The goal of this experiment was to investigate the behaviour of the beam under free-free longitudinal and rotationary boundary conditions. The measured deformational behaviour is shown in figure 12. In this situation, the only resistance mechanisms initially considered to absorb the impact energy are due to the bending deformation of the beam.

Using the analytical approach from chapter 3, it is possible to estimate the necessary deformation to absorb the impacting energy (50J) to 0.101 m. This result contradicts apparently the measurements and can only be explained if further attention is paid to secondary effects that might contribute to the absorption of the impact energy. As it can be observed in figure 12, the lateral supports undergo a significant longitudinal displacement within a short a time. This effect, combined to the fact that the lateral supports have a mass of $\sim$ 20 kg each, lead to an unexpected absorption of part the impact energy through the lateral supports in form of kinetic energy (see figure 9) that was later dissipated by friction and thus, did not cause any additional transverse deflection.

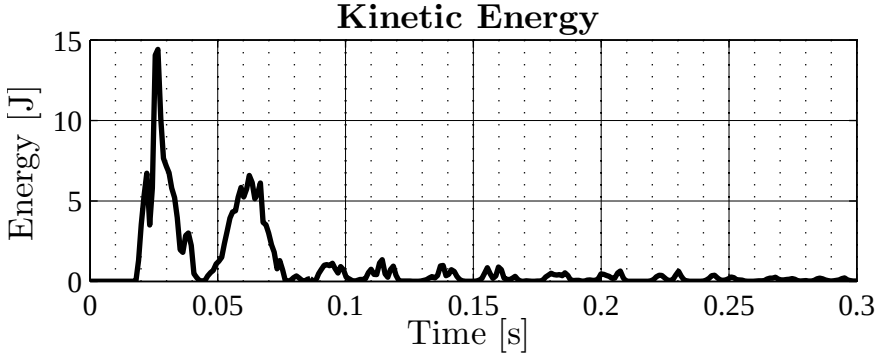


Figure 9: Evolution of the kinetic energy absorbed by the support construction due to its movement in longitudinal direction, Test Conf. (a)

Hence, the impact energy applied to the specimen is distributed into $\sim$ 15 J into the supports (and then dissipated by friction) and $\sim$ 35 J into the bending of the beam. In fact, figure 10 shows the energy absorption curve calculated for the system tested in Conf. (a). Here it is evident that the assumption of all impact energy being absorbed by the specimen leads to overestimating the transverse deflections, while the consideration of the kinetic lateral components leads to a much more accurate estimation of the maximum achieved deformation with a value of $w_{\max} = 0.076$m.

5.2 Experiment 2: Conf. (b)

The goal of this experiment was to investigate the behaviour of the beam under fixed-fixed longitudinal boundary conditions in order to validate the ability of the proposed analytical model to describe the energy absorbing mechanisms due to membrane action. The measured deformational behaviour is shown in figure 13. On the contrary to the tests in the Conf. (a), the only resistance mechanisms that can absorb the impact energy are related to the bending and longitudinal deformation of the beam. Here the lateral

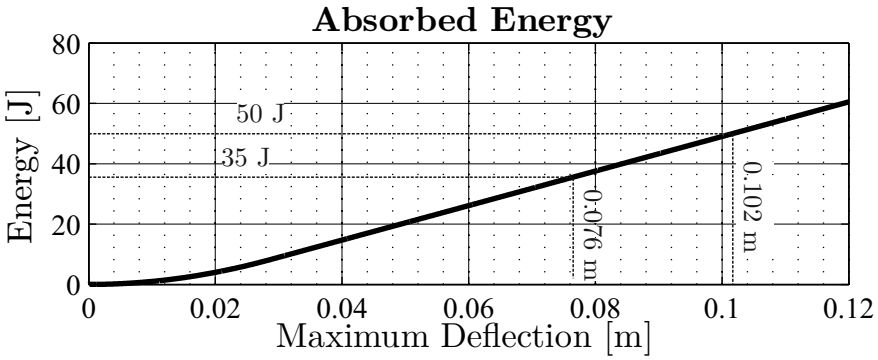


Figure 10: Energy absorption curve acc. to chapter 3 for Test Conf. (a)

supports are fixed and do not displace, thus they cannot absorb any kinetic energy.

Using the analytical approach explained in chapter 3, it is possible to estimate the necessary deformation to absorb the impacting energy (50J) to 0.036 m. This result agrees very well with the measurements shown in figure 13. As it can be observed in figure 11, the effects of the longitudinal restrain on the energy absorption capability of the specimen are of great importance and can be analytically described by the proposed model.

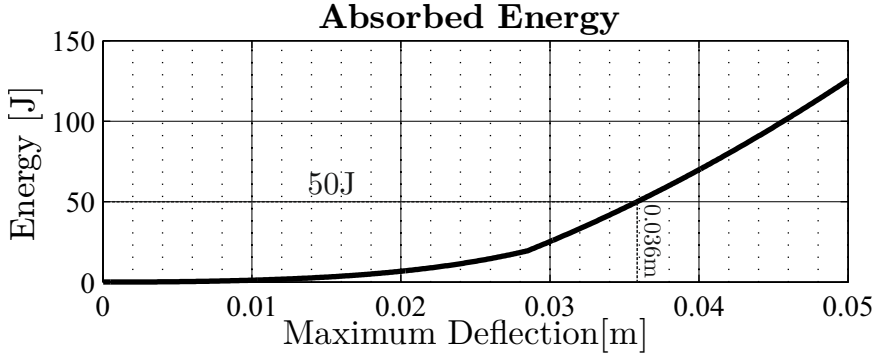
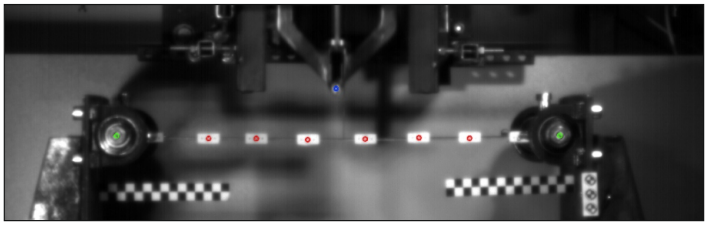
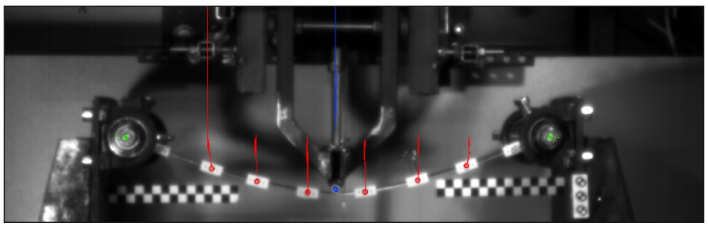


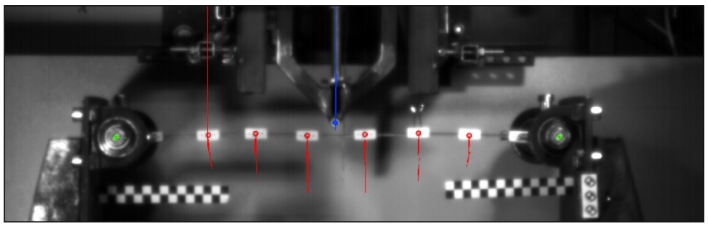
Figure 11: Energy absorption curve acc. to chapter 3 for Test Conf. (b)



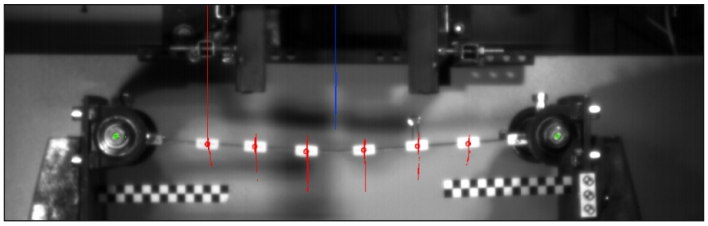
a) Prior to impact



b) At maximum Deflection



c) Bouncing back



d) Remaining plastic deformation

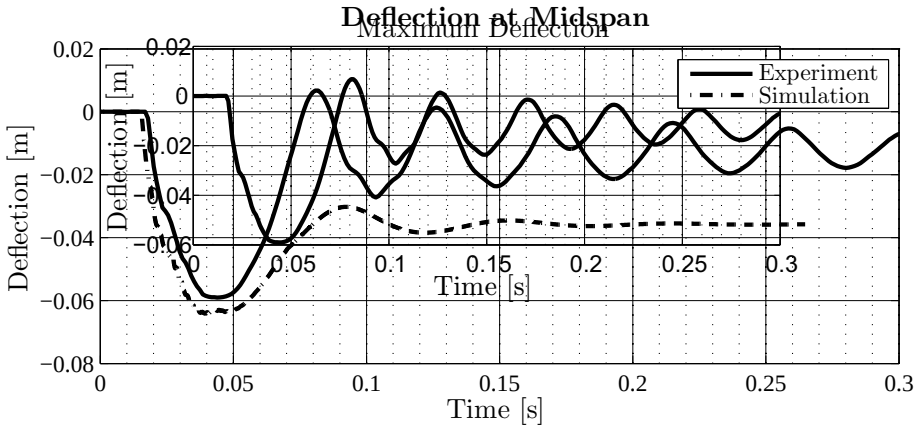
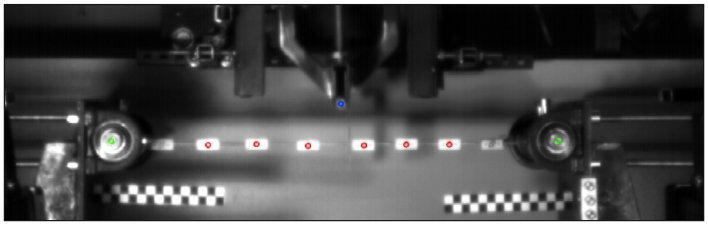
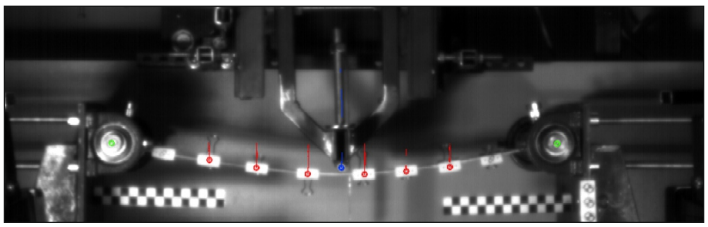


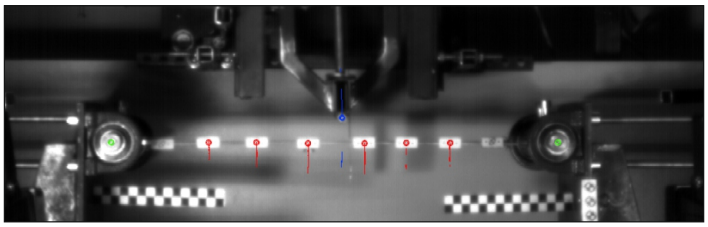
Figure 12: Evolution of the deformation during the impact test, Experiment and numerical Simulation, Test Conf. (a)



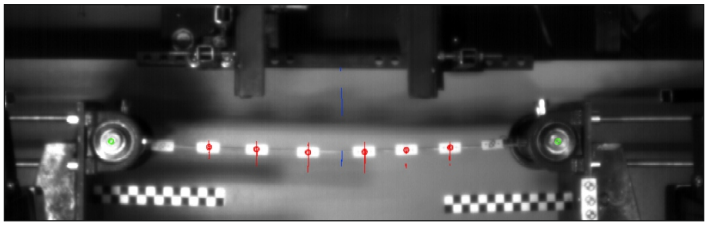
a) Prior to impact



b) At maximum Deflection



c) Bouncing back



d) Remaining plastic deformation

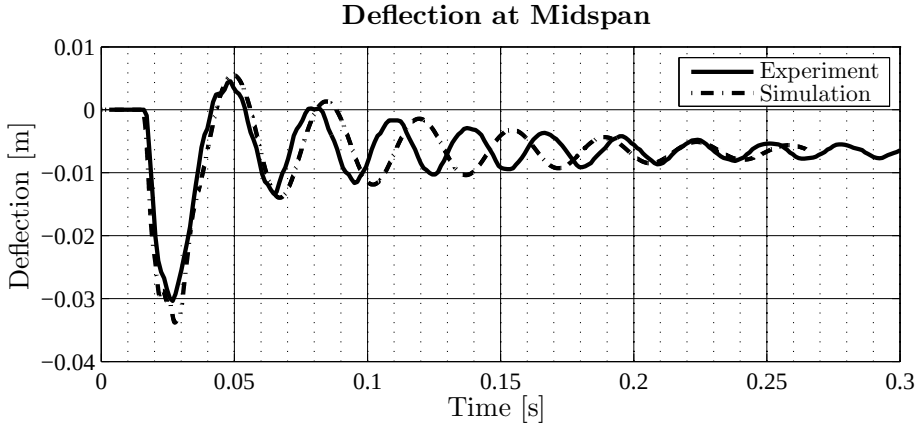


Figure 13: Evolution of the deformation during the impact test, Experiment and numerical Simulation, Test Conf. (b)

6 CONCLUSIONS

In this work, a new approach to the analytical determination of deformations of impacted columns has been presented and validated by means of experiments on a small-scale drop weight test rig.

The resistance behaviour of a column is dramatically increased if the membrane behaviour is taken into account in the energetic analysis of the column. This has been performed by considering a non-linear strain hypothesis, which lead to an additional energy absorption term dependent on the fourth power of the transversal displacement and the coefficient C_{ε,w^4}. Since the new analytical approach aims at describing the energy behaviour at large deformation levels, the evolution of the plastic stages has been included in the model, leading to a cumulative integration of the energy absorption function as described in chapter 3.1. This approach has been succesfully validated by means of the experiment Conf. (b).

Another interesting fact could be observed during the performance of test Conf. (a). In a longitudinal unrestrained situation, the impact energy is partially transformed into kinetic energy by a longitudinal movement of the lateral supports. Real columns tend to have large head masses and thus, this becomes an interesting effect that should not remained unconsidered.

REFERENCES

[1] C.H. Norris, R.J. Hansen, M.J. Holley, J.M. Biggs, S. Namyet and J.K. Minami,*Structural Design for Dynamic Loads*, McGraw-Hill, New York, 1959.

[2] J.M. Biggs, *Introduction to structural dynamics*, McGraw-Hill, New York, 1964.

[3] M. Feyerabend, *Der harte Querstoß auf Stützen aus Stahl und Stahlbeton*, Univ. Karlsruhe, PhD, 1988.

[4] , Klaus Willnow, *Stahlstützen unter räumlicher dynamischer Beanspruchung durch Anprall: Dissertation*, Ruhr-Universität Bochum, 1996.

[5] H.A.B. Al-Thairy, Haitham Ali Bady, *Behaviour and design of steel columns subjected to vehicle impact*, University of Manchester, 2012.

[6] Fire and Blast Information Group (FABIG), *Simplified methods for analysis of response to dynamic loading*, Steel Construction Institute, Technical Note, 2002.

[7] *NORSOK standard N-004: Design of Steel Structures*, NORSOK, 2013

[8] C. Colomer Segura and M. Feldmann,*A New Simplified Design Method for Steel Structures under Impulsive Loading*, WIT Transactions on the Built Environment, WIT-Press, Vol. 141, 2014.

[9] C. Colomer Segura and M. Feldmann,*A New Model Reduction Technique to Predict the Effects of Blast Loading on Structures*, EURODYN'2014 - 9th European Conference on Structural Dynamics, 2014.

[10] D. Brown, Tracker Software, Open Source Physics (OSP) Project, www.cabrillo.edu/∼dbrown/tracker/

COMPDYN 2015
5th ECCOMAS Thematic Conference on
Computational Methods in Structural Dynamics and Earthquake Engineering
M. Papadrakakis, V. Papadopoulos, V. Plevris (eds.)
Crete Island, Greece, 25–27May 2015

VIBRATION ANALYSIS OF HIGH-SPEED RAIL SYSTEM USING THE MOVING ELEMENT METHOD

Reda Mezeh[1,a], Marwan Sadek[1,b], Fadi Hage Chehade[2], Dalia ABDELMASSIH[3], Nisrine MAKHOUL[4] and Ahmad YOUNES[5]

[1] Laboratory of Civil Engineering and geoEnvironment (LGCgE), University of Lille 1- Polytech Lille, Villeneuve d'Ascq 59655, France.
[a] reda.mezeh@ed.univ-lille1.fr
[b] marwan.sadek@polytech-lille.fr

[2]Lebanese University, Doctoral School of Science & Technology- PRASE, Beirut, Lebanon.
fchehade@ul.edu.lb

[3]Lebanese University, Doctoral School of Science & Technology- PRASE, Beirut, Lebanon.
daliaabdelmassih@ul.edu.lb

[4]University of Balamand, PO Box 10, Triploi Lebanon
Nisrine.Makhoul@balamand.edu.lb

[5]Lebanese University, University Institute of Technology, Saida, Lebanon.
ayounes@ul.edu.lb

Keywords: Impact Vibration, Time Domain, Wheel / Rail contact, Moving Element Method, High Speed.

Abstract. *The paper proposes to extend the modeling of the rolling vibration to that of the impact vibration caused by discrete irregularities on wheels and / or rail. It presents a time domain formulation of the vertical interaction between the wheel and the rail, for the prediction of the impact vibrations.*

The problem of interaction wheel / rail is solved by the moving element method. The input data of the interaction model, the contact model wheel / rail and vibrational pattern of the wheel are firstly formulated. It allows the definition of a relative vertical movement between the wheel and the rail, called relative roughness.

The proposed computational scheme is applied to investigate the dynamic response of high-speed rail system. A parametric study is carried out function of the main influential parameters mainly the traveling train speed and the severity of track irregularity. The results of numerical simulations show the efficiency of the proposed method and its main advantage for the analysis of the generated vibrations.

1 INTRODUCTION

Railway noise and the induced vibrations transmitted into the ground are considered a major problem, in view of their influence on the conformity of the neighboring population. Several authors have been interested in dealing with a problem of interaction between train and track to quantify the induced noise level and then compare it with the acceptable level that is mentioned in the technical regulation. In this context, in France the Noise Act 1992 imposes the acceptable noise level limits for residents; at the European scale, the maximum noise levels are limited at source by the SPI.

The finite element method FEM is a well-established numerical method for solving complex problems including the case of moving loads. For example, Thambiratnam et al. [1] presented a simple finite element method for the dynamic analysis of beams on elastic foundation subjected to a concentrated moving load.

In dealing with moving load problems, the classical FEM encounters difficulty when the moving load travels in high speed or/and the dynamic excitation has a small wavelength, these difficulties can be overcome by refinement of the mesh size, but at the expense of significant increase in computational time. Another problem will be encountered, when the moving load approaches the boundary of the finite domain.

In an attempt to overcome the complication encountered by FEM, Krenk et al. [2] proposed the use of the FEM in convected coordinates to obtain the response of an elastic half-space subject to a moving load. Koh et al. [14] adopted the idea of convected coordinates for solving train-track problems, and named the numerical algorithm as moving element method (MEM). This method was subsequently applied to the analysis of moving loads on a viscoelastic half-space [3, 4, 5]. Anderson [5] dealt with the problem of a beam loaded by a variable harmonic loading, adopting an analytical formulation.

In this paper, the particular convection problem of a moving load in infinite Euler beam resting on a Kelvin foundation which simulates a train-track interaction problem, has been treated in a new way. The main idea of this approach is to use the classic formulation of the FEM in a fixed reference. By adopting a suitable temporal mesh, the numerical system that results has been solved by an adaptive algorithm, ie the geometric configuration of the dynamic system at the beginning of a time step was found using the system configuration in the step which proceeds, by using a suitable interpolation functions. The disturbing effect of the negative numerical damping resulting from the use of the Galerkin formulation in the MEM which may be in the case of high velocity the cause of a numerical divergence will be treated by this approach, without the need to introducing an amount of physical damping. The performance and the tolerance of this method have been tested for the excitation in the form of relative roughness between rail and wheel.

2 FORMULATION AND METHODOLOGY

The High speed rail-HSR- system is comprised of a train traversing over a rail beam in the positive x- direction. The origin of the fixed axis x is located on the centre of the beam such that the train is at x=0 when t=0. The constant passing velocity of the train is denoted by V. The rolling surface of the rail is considered to have some imperfections due to rail irregularity. For simplicity, we assume no interaction between the two rails of the railway track, then the half of the lower structure subjected to half weight of the train was studied. In a typical analysis, the two parts are connected as a coupled system that accounts for interaction between the wheel and the rail.

2.1. Train model

The train is modeled as a moving spring-mass model, which is a system of three rigid components, namely the car body, bogie and wheel-set; as shown in figure 1. The car body and the bogie of mass m_1 and m_2 respectively, are connected through the secondary suspension system which is modeled as a spring-damper unit. The inter-connection between the bogie and the wheel set of mass m_3 occurs through the primary suspension system. The three vertical degrees of freedom of the car body, bogie and wheel set are denoted by u_1, u_2 and u_3 respectively. The contact between the wheel and the rail beam is modeled by the contact force F_c.

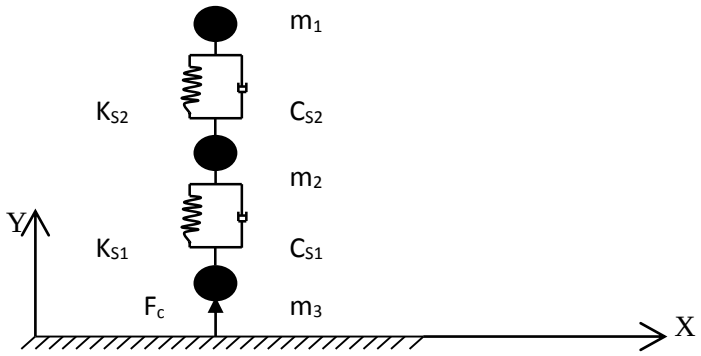


Figure 1 Moving sprung mass model

The governing equations for the train model may be written as:

$$\begin{aligned} &m_1\ddot{u}_1 + K_{s2}(u_1 - u_2) + C_{s2}(\dot{u}_1 - \dot{u}_2) = -m_1 g \\ &m_2\ddot{u}_2 + K_{s1}(u_2 - u_3) + C_{s1}(\dot{u}_2 - \dot{u}_3) - K_{s2}(u_1 - u_2) - C_{s2}(\dot{u}_1 - \dot{u}_2) = -m_2 g \\ &m_3\ddot{u}_3 - K_{s1}(u_2 - u_3) - C_{s1}(\dot{u}_2 - \dot{u}_3) = -m_3 g + F_c \end{aligned} \quad (1)$$

2.2. Equation of motion in the fixed co-ordinates

In this study we assume the Winkler hypothesis in which the foundation's reactive pressure is proportional to the deflection of the rail beam [6].

The railway track is modeled as an Euler-Bernoulli beam with constant bending stiffness EI and mass per unit length $\overline{m}$ supported by a viscoelastic layer comprising of vertical springs $\overline{K}$ and dashpots $\overline{C}$. The vertical displacement and rotation of the track are denoted by y and θ respectively. The governing equation of the rail beam subjected to a moving train load in the fixed co-ordinates system (x,y) is given by:

$$EI\frac{\partial^4 y}{\partial x^4} + \overline{K}y + \overline{C}\frac{\partial y}{\partial t} + \overline{m}\frac{\partial^2 y}{\partial t^2} = -F_c\delta(x - s) \quad (2)$$

Where t is the time, s is the distance traveled by the train at instant t; δ is the Dirac-delta function.

The railway beam is now truncated and discretized into so-called moving elements as shown in figure 2. For a typical moving element, the governing differential equation is multiplied by an arbitrary weighting function and integrated over the element length. By adopting Galerkin's approach, the element mass, damping and stiffness matrices can be obtain as given below

$$M_e = \overline{m}\int_0^L N^T N dr$$

$$C_e = \overline{C}\int_0^L N^T N dr \tag{3}$$

$$K_e = EI\int_0^L N^T{}_{,rr} N_{,rr} dr + \overline{K}\int_0^L N^T N dr$$

Where N refers to the vector of shape functions, which are represented by Hermitian cubic polynomials and r, is the local element reference. The subscript r denotes partial derivative with respect to r.

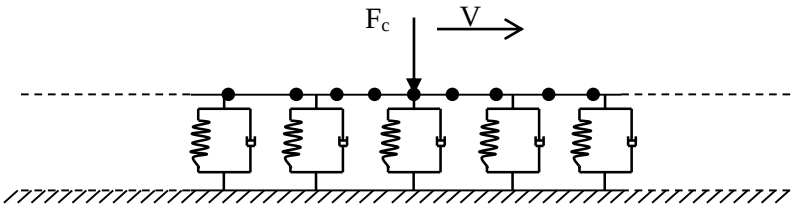


Figure 2 Discretization of the railway beam into moving elements

After assembling the individual element matrices with respect to their positions in the railway track and considering the train model as well as the wheel-rail interaction, the equation of motion for the combined train-track system can be written as

$$M\ddot{Z} + C\dot{Z} + KZ = P \tag{4}$$

Where Z is the global displacement vector of the train-track system; M, C, and K the global mass, damping and stiffness matrices, respectively; and P the global external load vector.

2.3. Wheel-rail contact model

In this study, we use the simplified approach based on a linearized Hertz contact model [4], in which it is assumed that the pseudo-static reaction force at the contact point equals the self-weight of the upper structure W [9]. This model allows us to study the phenomenon of wheel jumping, which takes place in the case of the absence of contact between wheel and rail.
The linearized contact force F_c is given by:

$$F_c = \begin{cases} K_L(y_{rc} + y_t - u_w), (y_{rc} + y_t - u_w) \geq 0 \\ 0, \qquad\qquad\quad , (y_{rc} + y_t - u_w) < 0 \end{cases} \tag{5}$$

Where K_L is the linearized Hertzian spring constant [4] computed as follows:

$$K_L = \sqrt[3]{\frac{3E^2 W\sqrt{R_w R_r}}{2(1-\nu^2)^2}} \tag{6}$$

Where y_{rc}, y_t and u_w denote respectively, the displacement of the track at contact point, track surface irregularity and the displacement of the wheel in contact with the track; R_w and R_r denote the radii of the wheel and railhead, respectively; E denotes the elastic modulus of the material; and ν the Poisson's ratio. Track irregularity is the major cause of dynamic loads generated by a moving train. In this paper, the vertical track irregularity profile y_t is assumed as a sinusoidal function [4, 7, 10] which can be written as:

$$y_t = a_t \sin(\frac{2\pi x}{\chi_t}) \quad (7)$$

Where a_t represent the amplitude and λ_t the wave length of the track irregularity.

2.4. Moving element method

A new approach of the moving element method MEM is proposed for solving this dynamic problem; the principle of this method is to solve the problem of a moving load, on a small time step by considering the problem as a problem with concentrated fixed load with variable amplitude over the studied time interval. Using the proposed interpolation functions, the initial condition of the next time step is deduced. The formulation of this numerical method is based on that of the finite element method, where the matrices are provided in the paragraph 2.2.This method is efficient since we can find the dynamic response of the system when moving a small distance, saying up to a portion of a millimeter; which is very expensive and sometimes can't be solved by the classical FEM, which requires the creation of a node in every point of application of a moving charge. In our model, we adopted a time-space coupled mesh chosen precisely to minimize on the one hand the boundary effect, and the disruption of the dynamic response due to a possible reflection of the induced waves and in the other hand the mesh size effect which is found to have a significant influence on the system dynamic response. Figure 3 shows a schematic drawing explaining briefly the proposed MEM algorithm.

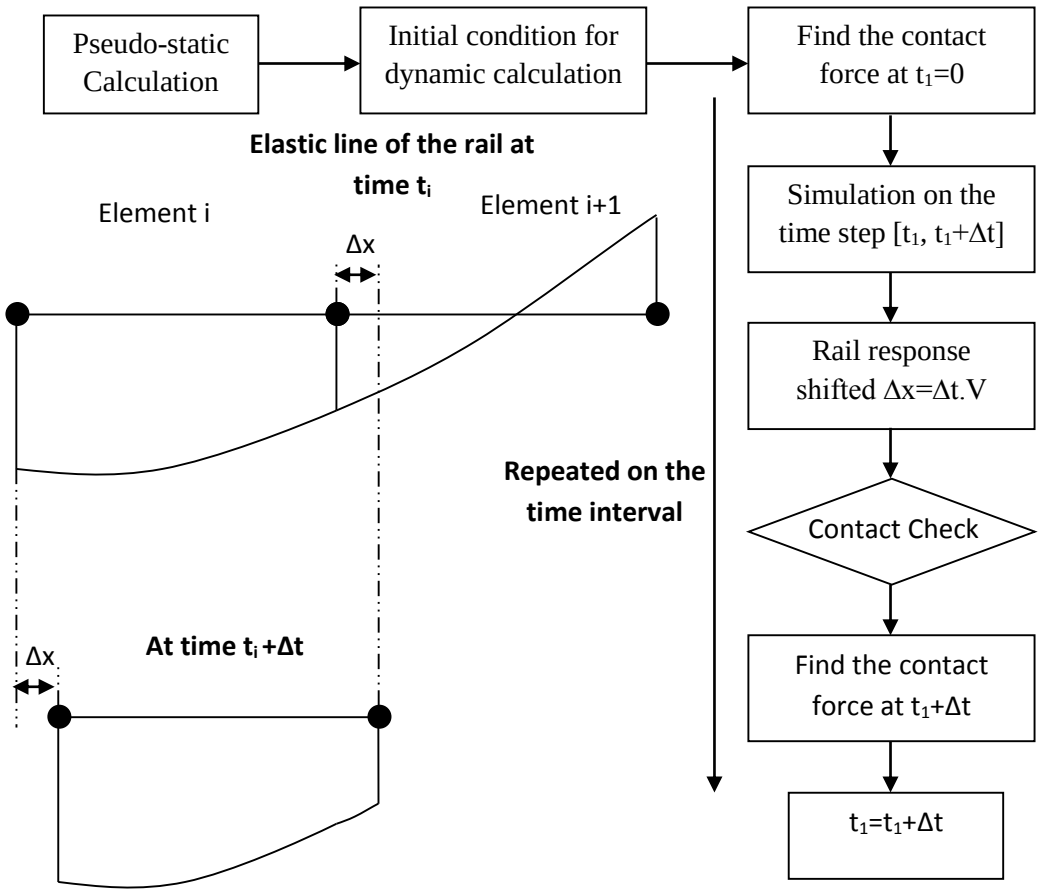


Figure 3 Schematic algorithm of the MEM

3 VALIDATION OF THE MEM

To investigate the usefulness and the tolerance of the proposed method, we will compare in this part the dynamic response of a beam resting on a viscoelastic foundation which is subjected to a concentrated moving harmonic force, which travels at velocity V as illustrated in figure 4, found analytically to the results provided by the numerical method.

Based on the analytical method adopted by Anderson et al. [5], the displacement field can be written in the moving coordinates (X,Y), where the origin is attached to the point of application of load; as follow:

$$U(X,t)=\begin{cases} Ae^{-\beta_1 X+i(\alpha_1 X-\omega t)}+Be^{-\beta_2 X+i(\alpha_2 X-\omega t)}, & X\geq 0 \\ Ce^{-\beta_3 X+i(\alpha_3 X-\omega t)}+De^{-\beta_4 X+i(\alpha_4 X-\omega t)}, & X<0 \end{cases} \tag{8}$$

Where A, B, C, and D are constants to be determined using continuity conditions of displacement field and solicitations, α_j and β_j are the real part and the imaginary part of the wavenumbers; α_j represents propagation and β_j represents attenuation of the jth wave component.

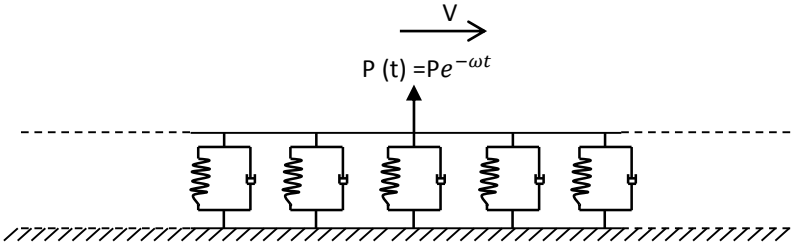


Figure 4 Rail-beam subjected to harmonic excitation

The validations are realized on linear structures for which the analytical solution may be found for all velocities and frequencies of load. We use here in the analysis a European high-speed rail which has the following properties: S=76.86 cm^2, I=3060 cm^4, ρ=7850 Kg/m^3, E=2×10^{11} N/m^2, m=60.34 Kg/m, EI=6.12×10^6 $N.m^2$, the stiffness of the Winkler foundation used is 1.6×10^7 N/m [16].

In order to choice the reasonable parameters in analysis; we define the critical values of velocity, of frequency and of viscous damping [16] which depends only on the structural characters:

$$\begin{aligned} V_0 &= \sqrt[4]{\frac{EI\bar{K}}{\bar{m}^2}} \\ \omega_0 &= \sqrt{\frac{\bar{K}}{\bar{m}}} \\ C_0 &= 2\sqrt{\bar{m}\bar{K}} \end{aligned} \tag{9}$$

To test the capability of the proposed approach of the MEM to solve a problem where the load exciting the beam is variable in both time and space, a finite beam section of the length L is modeled, and numerical integration is performed over the time interval T_I. The analysis is carried for single-frequency harmonic excitation at various combinations of loading frequency and convection velocity. The displacement time series on the central node and the beam displacement field after 15 periods are displayed. The numerical results (the dotted line) are plotted against the corresponding analytical solution (the continuous line) as shown in figures 5 and 6. Note that the analytical solution are stationary, whereas the response provided by the MEM gives rise to a transitional part, which will end when the loading excite the firsts eigen

frequencies of the beam. In all cases, the numerical results after several periods are seen to be nearly identical to the analytical results. Note that the proposed method has no limitation on the convection velocity and load pulsation, in other words there is no negative numerical damping disrupting the dynamic response. Then a difference with the classical MEM appears that there is no need to insert an additional physical damping to compensate the negative numerical damping.

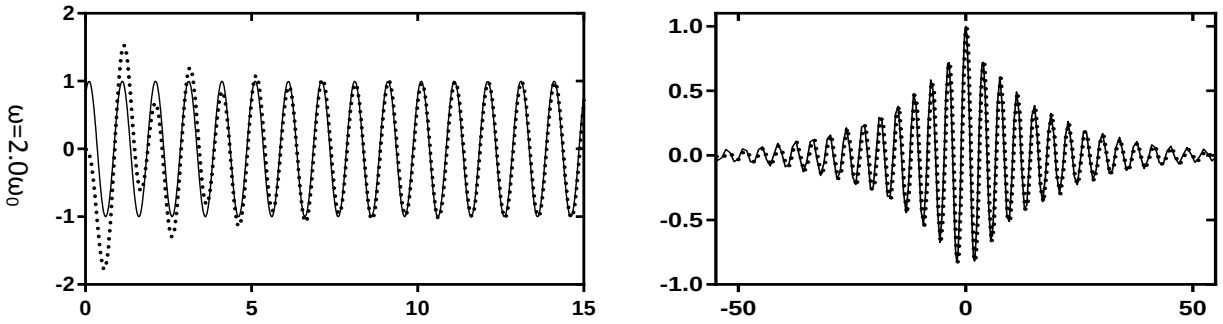


Figure 5 Numerical (dotted) versus analytical (continuous) results, V=0

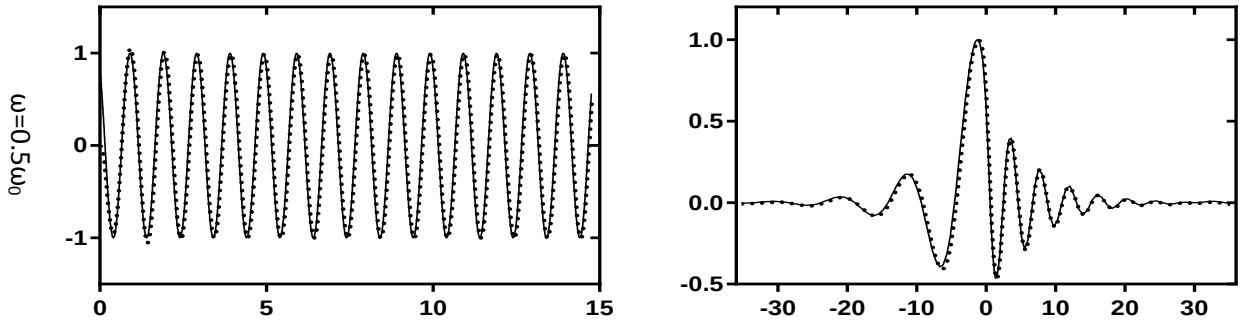


Figure 6 Numerical (dotted) versus analytical (continuous) results, $V=V_0$

m_1	3500 Kg	m_2	250 Kg	m_3	350 Kg
K_{s1}	$1.26*10^6$ Nm^{-1}	K_{s2}	$1.41*10^5$ Nm^{-1}		
C_{s1}	$7.1*10^3$ Nsm^{-1}	C_{s2}	$8.87*10^3$ Nsm^{-1}		

Table 1 Parameters for train model

4 NUMERICAL RESULTS

In this section, the dynamic behavior of a train traveling along a railway track is simulated using the moving sprung-mass model. The MEM model adopted in the study comprises of a truncated railway track of 70 m length discretized non-uniformly with elements ranging from a coarse 1 m to a more refined 0.2 m size. The equations of motion are solved using Runge-Kutta method employing a variable time step. Values of parameters related to the properties of train are summarized in table 1.

4.1. Effect of passing speed

As the response of high-speed rails system strongly depends on the severity of track irregularity, it would be useful to investigate the effects of irregularity wavelengths and train speeds on the response of the HSRs. The amplitude of all track irregularities considered in this

investigation is taken to be 0.5 mm. Figure 7 shows the variation of dynamic amplification factor DAF in wheel-rail contact force against train-speed for various track irregularity wavelength.

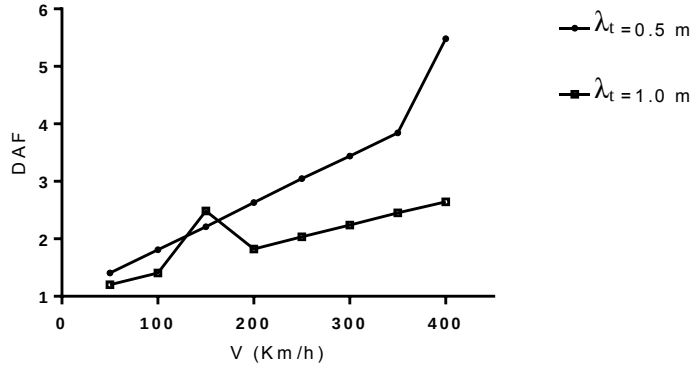


Figure 7 DAF against train speed V for various track irregularity wavelength

The general trend of the curves is increasing with respect to the passing speed, it can be seen that the DAF is generally close to 1.0 for small values of V. Conversely, when the wavelength is small resulting in a more severe track irregularity condition.

4.2. Effect of track irregularity amplitude

The effects of train speed and track irregularity amplitude are investigated in this part. The wavelength of all track irregularity is taken to be 0.5 m. Figure 8 shows the variation of dynamic amplification factor (DAF) in wheel-rail contact force against track irregularity amplitude for various train speeds.

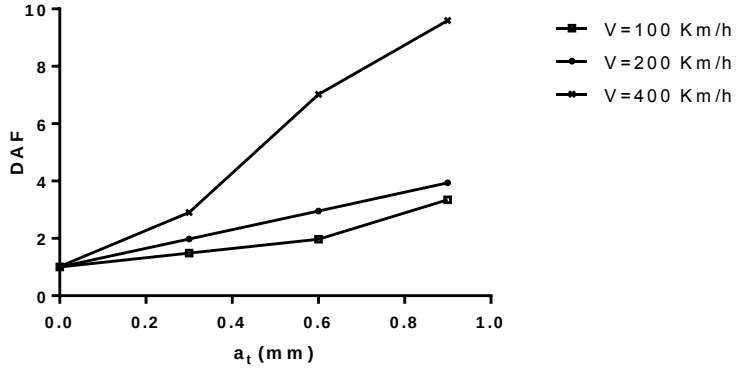


Figure 8 DAF against train irregularity amplitude for various passing speed

For the perfectly smooth (a_t=0 mm) track, the DAF is found be 1 as to be expected in view that there is no dynamic load. The results in Fig. 8 also show that when the amplitude of track irregularity and/or train speed increase, the DAF is increased.

5 CONCLUSION

The paper has presented a numerical model for the simulation of dynamic train and track interactions at the wheel/rail interface based on adaptive form of the FEM. The computational

model adopts the linearized contact theory of Hertz to account for the contact between the wheel and rail. Wheel/rail irregularities are the common source that creates dynamic disturbances to both the vehicle and the track system. It has been demonstrated that the model proposed in the paper is an efficient research tool to investigate the dynamic effects caused by rail defect, which are damaging to the vehicle and track components. The results obtained using the MEM with the proposed computational procedure to account for moving harmonic load are found to compare well with available analytical solutions in the literature.
In particular, the dynamic response of the track/train system has been shown to dramatically increase with an increase in the train speed. The relationship between the vehicle components, namely the unsprung mass and the dynamic wheel/rail load, can be quantified using the established model.

ACKNOLEDGMENT

This work is sponsored by a franco-lebanse project CEDRE and performed by a collaboration between Lebanese University and University of Sciences and Technologies of Lille. The research team thanks the CEDRE for funding this work.

REFERENCES

[1] D. Thambiratnam, Y. Zhuge, Dynamic analysis of beams on an elastic foundation subjected to moving loads, Journal of Sound and Vibration 198, 149-169, 1996.

[2] S. Krenk, L. Kellezi, S.R.K. Nielson, P.H. Kirkegaard, Finite elements and transmitting boundary conditions for moving loads, Proceedings of the 4th European conference on structural dynamics- EURODYN'99, 447-452, 1999.

[3] C.G. Koh, G.H. Chiew, C.C. Lim, A numerical method for moving load on continuum, Journal of Sound and Vibration **300**, 126-138, 2007.

[4] M.T. Tran, K.K. Ang, V.H. Luong, Vertical dynamic response of non-uniform motion of high-speed rails. Journal of Sound and Vibration **333**, 5427-5442, 2014.

[5] L. Andersen, S.R.K. Nielsen, P.H. Kirkegaard, Finite element modeling of infinite Euler beams on Kelvin foundations exposed to moving loads in convected co-ordinates. Journal of Sound and Vibration **241**, 587-604, 2001.

[6] M. Saitoh, Lumped parameter models representing impedance functions at the end of a finite beam on a viscoelastic medium. Computers and Structures **92-93**, 317-327, 2012.

[7] K.K. Ang, J. Dai, Response analysis of high-speed rail system accounting for abrupt change of foundation stiffness. Journal of Sound and Vibration **332**, 2954-2970, 2013.

[8] Z. Dimitrovova, A general procedure for the dynamic analysis of finite and infinite beams on piece-wise homogeneous foundation under moving loads. Journal of Sound and Vibration **329**, 2635-2653, 2010.

[9] C. Esveld, Modern Railway Tack , 2nd edition, MRT Productions. Duisburg, 2001.

[10] C.G. Koh, J.S.Y. Ong,D.K.K. Chua, J. Feng, Moving element method for train-track dynamics. International Journal for Numerical Methods in Engineering **56**, 1549-1567, 2003.

[11] G. Kouroussis et al., Discrete modeling of vertical track-soil coupling for vehicle-track dynamics. Soil Dynamics and Earthquake Engineering **31**, 1711-1723, 2011.

[12] Jens C.O. Nielsen, High frequency vertical wheel –rail contact forces- Validation of a prediction model by field testing. Wear **265**, 1465-1471, 2008.

[13] V. Delavaud, Modélisation temporelle de l'interaction roue/rail, pour une application au bruit de roulement ferroviaire. Thèse de doctorat de l'ENSTA PARIS TECH, 2011.

[14] D. Connolly, A. Giannopoulos, M.C. Forde, Numerical modeling of ground borne vibrations from high speed rail lines on embankments. Soil Dynamics and Earthquake Engineering **46**, 13-19, 2013.

[15] C.G. Koh, J.S.Y. Ong, D.K.H. Chua, J. Feng, Moving element method for train-track dynamics, International Journal for Numerical Methods in Engineering **56**, 1549-1567, 2003.

[16] V.H. Nguyen, D. Duhamel, A new numerical approach for infinite Euler Bernouilli beam on a Winkler foundation under high-velocity moving loads, Structural Dynamics, EURODYN2002, Grundmann & Shueller (eds.), 2002.

COMPDYN 2015
5th ECCOMAS Thematic Conference on
Computational Methods in Structural Dynamics and Earthquake Engineering
M. Papadrakakis, V. Papadopoulos, V. Plevris (eds.)
Crete Island, Greece, 25–27 May 2015

TIME REVERSAL IN ELASTODYNAMICS AND APPLICATIONS TO STRUCTURAL HEALTH MONITORING

Christos G. Panagiotopoulos [1], **Yiannis Petromichelakis**[1] **and Chrysoula Tsogka**[1,2]

[1]Institute of Applied & Computational Mathematics
Foundation for Research and Technology Hellas, Heraklion, Greece

[2] Department of Mathematics and Applied Mathematics
University of Crete, Heraklion, Greece
e-mail: tsogka@uoc.gr

Keywords: Elastic wave propagation, time reversal, source localization, damage detection, structural health monitoring, finite element method.

Abstract. *In structural health monitoring, detection of localized damage can be achieved by exploiting recorded signals at a limited number of sensors within the structure. Here we propose the localization of damage using an array of sensors as a computational time-reversal mirror (TRM). Time reversal (TR) is a physical process that exploits the time reversibility of wave equations and achieves re-focusing of the wave on the source of its origin by sending back, reversed in time, the signals recorded on an array of transducers. TR was originally introduced by Mathias Fink and his group and has several applications ranging from medical imaging to telecommunications [14].*

In the present work, we perform time reversal numerically in order to effectively detect and localize defects in a bounded two-dimensional elastic domain. This is a generalization of a respective time-reversal implementation in an acoustic medium [12]. The solid contains a number of N_r sensors which can act as sources as well. Our data is the response matrix of the scattered field, that is, the difference between the total field obtained in the damaged structure and the incident field corresponding to the response in the healthy structure.

Numerical solution of the wave propagation problem is performed using a mixed finite element formulation in terms of the velocity and stress fields [6]. In order to dissociate the response caused by N_d different defects, we apply the singular value decomposition (SVD) of the response matrix, while back-propagation of the projection of each singular vector corresponding to a non-zero singular value is performed in order to highlight each defect separately.

1 Introduction

An important component of several approaches in the design and construction of structural health monitoring systems are methods to efficiently identify and localize damage. Response recordings by sensors placed on a structure are often used to monitor the structure's integrity and to detect the appearance of damage [23]. Detection of damage can be done by comparing the response of the structure in its reference state with that recorded in the damaged state. Imaging of the damage, however, needs more sophisticated procedures. In this paper, we consider this query using time reversal imaging procedures of elastic waves propagating in bounded domains. Numerical back propagation of the recorded response will focus on defects' locations, since a defect behaves as a secondary source. The difficulty is that we do not know the time at which this secondary source will be activated. This time corresponds to the time that is needed for the incident wave to propagate from the source to the defect. An indication of the refocusing time can be obtained by the bounded variation norm of the TR field as in [12]. Here we propose to monitor the energy density function instead of the norm of the displacement, since it is a natural physical quantity and seems to give better numerical results.

Time reversal consists of two steps: a forward and a backward propagation one. In the forward propagation step, waves are emitted from some source and travel through the medium. During this step the wave-field is being recorded by one or more receivers. In the backward step, the previously recorded signals are reversed in time and they are rebroadcasted from their respective receiver positions. Wave paths that were traversed in the forward propagation step are now reproduced in the backward one [3]. Ideal conditions for the time reversal process would be those corresponding to the case where receivers fill the whole medium (or its entire boundary), recording the field and its derivatives [15], without any noise [16]. The time *reversibility* is based on the spatial *reciprocity* (symmetry in engineering) and the time reversal *invariance* (under the transformation $t \rightarrow -t$) of linear wave equations.

The time reversal technique has been recognized in recent years, because of its robustness and simplicity, as a quite appealing approach to resolve source localization problems. This branch of inverse problems finds numerous applications in several fields, e.g., medicine, telecommunications, underwater acoustics, seismology and engineering structures. Time reversal, with full or partial information, has been mathematically justified considering energy estimates for the wave equation [5], utilizing the Green's function properties [9] or modal analysis [17].

Numerical time reversal for elastic media has been considered in [11, 25] while experimental results are reported in[24, 21, 20]. The DORT (french acronym for decomposition of the time reversal operator) method applied to elastic wave scattering can be found in [4]. It has been shown that time reversal imaging can be also used in dissipative elastic media [2], which is important since any real structural system exhibits some damping.

In this paper we describe the numerical implementation of time reversal in elastic media and carry out simulations in order to assess the effectiveness of this process in damage identification problems. In general, we assume that response is recorded on N_r sensors, belonging in $\Omega_r \in \Omega$, while excitation is assumed to be produced by N_s source points forming $\Omega_s \in \Omega$. These two subspaces may be totally separated, coincide or just have an overlap. The described methodology can be applied to sensors that form an array, as well as to a distributed sensor configuration. For simplicity of presentation, we focus our attention on an array configuration where sources and receivers are collocated.

2 The time reversal process

Time reversal forward step In structural health monitoring (SHM) the forward step of TR corresponds to a physical process where the data response matrix is collected on a set of sensors located at $\boldsymbol{x}_r$, $r = 1, \ldots, N_r$. Each column of the response matrix corresponds to the response received at all sensors $\boldsymbol{x}_r$ and in all directions $i = x, y$ when a source point emits a pulse from the location $\boldsymbol{x}_s$ in a specific direction. In our case, the forward step is numerically simulated. A source located at $\boldsymbol{x}_s$ emits a pulse in the direction $\boldsymbol{e}_i$ and the response is recorded at the receiver locations $\boldsymbol{x}_r$. We consider a linear elastic material filling a bounded domain Ω with Dirichlet boundary conditions on its boundary $\partial\Omega$,

$$\begin{aligned}
&\rho\frac{\partial^2\boldsymbol{u}}{\partial t^2}(\boldsymbol{x},t) - \operatorname{div}\sigma\left(\boldsymbol{u}(\boldsymbol{x},t)\right) = \delta(\boldsymbol{x}-\boldsymbol{x}_s)\boldsymbol{e}_i f(t), (x,t)\in\Omega\times(0,T],\\
&\boldsymbol{u}(\boldsymbol{x},t) = 0, \qquad (\boldsymbol{x},t)\in\partial\Omega\times(0,T]\\
&\boldsymbol{u}(\boldsymbol{x},0) = 0, \qquad \boldsymbol{x}\in\Omega\\
&\frac{\partial\boldsymbol{u}}{\partial t}(\boldsymbol{x},0) = 0, \qquad \boldsymbol{x}\in\Omega
\end{aligned} \tag{1}$$

The displacement vector $\boldsymbol{u}$ is associated with the strain tensor by

$$\varepsilon_{ij}(\boldsymbol{u}) = \frac{1}{2}\left(\frac{\partial u_i}{\partial x_j} + \frac{\partial u_j}{\partial x_i}\right).$$

The stress tensor is given by Hooke's law

$$\sigma(\boldsymbol{u}) = C : \varepsilon(\boldsymbol{u}),$$

which connects stress to strains via the fourth order tensor of elastic moduli C (stiffness tensor). The inverse constitutive equation considering $A = C^{-1}$, the flexibility or compliance tensor, can be written as $\varepsilon = A\sigma$. Our numerical implementation is based on an equivalent formulation which consists in writing the elastodynamic problem as a first order hyperbolic system, the velocity-stress system,

$$\begin{aligned}
&\rho\frac{\partial\boldsymbol{v}}{\partial t} - \operatorname{div}\sigma = \delta(\boldsymbol{x}-\boldsymbol{x}_s)f(t)\boldsymbol{e}_i,\\
&A\frac{\partial\sigma}{\partial t} - \dot{\varepsilon} = 0,
\end{aligned} \tag{2}$$

for $(\boldsymbol{x},t)\in\partial\Omega\times(0,T]$ with $\dot{\varepsilon} = \frac{1}{2}\left(\frac{\partial v_i}{\partial x_j} + \frac{\partial v_j}{\partial x_i}\right)$. Here we omitted the dependence of the unknowns $\boldsymbol{v} = \partial\boldsymbol{u}/\partial t$ (the velocity vector) and the stress tensor σ on $(\boldsymbol{x},t)$. We should also add to our system, initial conditions $\boldsymbol{v}(t=0)=0$, $\sigma(t=0)=0$ and the boundary condition $\boldsymbol{v}=0$ on $\partial\Omega$. We solve the elastodynamic problem for all source locations $\boldsymbol{x}_s$, $s = 1, \ldots, N_s$ and the two directions $i = x, y$ and record the velocity $\boldsymbol{v}$ at all receiver locations $\boldsymbol{x}_r$, $r = 1, \ldots, N_r$. At the end of the forward step we have collected the response matrix $P(t)$ whose dimension at each time step is $2N_s \times 2N_r$.

Time reversal backward step The backward step of the time reversal process in the context of SHM applications is always performed numerically. However, it may be found in several alternative forms. For example, in [15] it is stated that one may force either just the field variable or the field variable and its first derivative recorded in the forward process. In the case of elastic wave propagation, a similar formulation is found in [25] where displacements' reversed time

history is imposed on points of sensors that record the response. Under this assumption the backward step would be given by the following initial-boundary value problem:

$$\begin{aligned}
&\rho\frac{\partial\tilde{\boldsymbol{v}}}{\partial t} - \operatorname{div}\tilde{\sigma} = 0, && (\boldsymbol{x},t)\in\partial\Omega\times(0,T],\\
&\tilde{\boldsymbol{v}}(\boldsymbol{x},t) = 0, && (\boldsymbol{x},t)\in\partial\Omega\times(0,T],\\
&\tilde{\boldsymbol{v}}(\boldsymbol{x},t) = \boldsymbol{v}(\boldsymbol{x},T-t), && (\boldsymbol{x},t)\in\Omega_r\times[0,T],\\
&\tilde{\boldsymbol{v}}(\boldsymbol{x},0) = 0, && \boldsymbol{x}\in\Omega,\\
&\sigma(\boldsymbol{x},0) = 0, && \boldsymbol{x}\in\Omega.
\end{aligned} \tag{3}$$

In [16], and some references therein, the wave is rebroadcasted through appropriate initial conditions. Alternatively, one can follow the approach used in [13] or [12] for acoustic waves, and adapt it to the case of linear elasticity that consists in solving the problem,

$$\begin{aligned}
&\rho\frac{\partial\tilde{\boldsymbol{v}}}{\partial t}(\boldsymbol{x},t) - \operatorname{div}\tilde{\sigma} = \sum_{q=1}^{N_r}\delta(\boldsymbol{x}-\boldsymbol{x}_q)\boldsymbol{v}(T-t), && (\boldsymbol{x},t)\in\Omega\times(0,T],\\
&A\frac{\partial\tilde{\sigma}}{\partial t} - \dot{\tilde{\varepsilon}} = 0, && (\boldsymbol{x},t)\in\Omega\times(0,T],\\
&\tilde{\boldsymbol{v}}(\boldsymbol{x},t) = 0, && (\boldsymbol{x},t)\in\partial\Omega\times(0,T],\\
&\tilde{\boldsymbol{v}}(\boldsymbol{x},0) = 0, && \boldsymbol{x}\in\Omega,\\
&\sigma(\boldsymbol{x},0) = 0, && \boldsymbol{x}\in\Omega.
\end{aligned} \tag{4}$$

In this case we set the reversed time recorded values of the field variable, as sources introducing right hand side loading terms on respective directions and spatial locations.

3 Damage identification

Several procedures for damage identification and localization, based on time reversal, have been proposed in the literature. In [1] an approach is considered for 2D scalar wave propagation problems, both forward and backward steps are assumed to take place in the cracked configuration of the medium. While for the forward step it is assumed that solution is obtained, or measured, for the correct cracked configuration, for the backward step a variety of cracked patterns is assumed, for each of them a wave propagation simulation is necessary, while the estimated cracked configuration is the one which gives the best refocusing on the source point. This procedure has been also extended to the case of elastic waves [18]. In [25] a technique similar with the methodology presented here has been proposed, however, in [25] there is no selectivity in the refocusing since the DORT method is not considered.

In our approach, we consider as data the impulse response matrix (IRM) of the scattered field, due to the damaged areas. This means that we assume that measurements of the response matrix in the healthy structure are available, and by subtracting them from the measured response in the damaged structure we obtain the scattered field.

3.1 Stopping criterion

During the backward step we expect the time reversed field to focus on the damaged area at some particular time, but this time is not known a priori. Based on the fact that we seek for a time at which the field is focused in space, stoping criteria based on the minimisation of appropriate norms of the field (e.g., Shannon entropy, bounded variation norm) have been proposed and successfully used in [12]. Another measure called “mathematical energy” has

been adopted in [18]. In the current work we choose to track the total energy defined by

$$\mathcal{E}(t) = \frac{1}{2}(A\sigma, \sigma) + \frac{1}{2}(\rho v, v), \tag{5}$$

or it's discrete analogue as presented in [7]. More precisely, we first define the discrete energy density and normalise it by its maximal value at each time step before computing its L^1 norm in space.

3.2 Multiple damaged areas

The DORT method [22] was developed as an imaging procedure capable to refocus selectively the field on different targets (defects). An extension of DORT for the detection of multiple linear and nonlinear scatterers has been presented recently in [4].

In this work, following the methodology developed in [8, 12], we propose to compute the singular value decomposition of the response matrix frequency by frequency, and then, by projecting the response matrix on the singular vectors that correspond to the largest singular values, we can selectively refocus the elastic field on different defects.

The IRM $P(t)$, is a $N_S \times N_R = (2N_s) \times (2N_r)$ matrix. In order to proceed, we first compute its Fourier transform and obtain $\widehat{P}(\omega)$. For each ω in the available bandwidth, we compute the singular value decomposition of $\widehat{P}(\omega)$ as,

$$\widehat{P}(\omega) = U(\omega)S(\omega)V^*(\omega) \tag{6}$$

where $U(\omega)$ is an $N_S \times N_S$ and $V(\omega)$ an $N_R \times N_R$ unitary matrix, while $V^*(\omega)$ is the conjugate transpose and $S(\omega)$ the $N_S \times N_R$ rectangular diagonal matrix with the non-negative real singular values on the diagonal. The N_S columns of $U(\omega)$ and the N_R columns of $V(\omega)$ are called the left and right singular vectors of $\tilde{P}(\omega)$ respectively. We can also write,

$$\widehat{P}(\omega) = \sum_{j=1}^{N_\sigma} \sigma_j(\omega) U_j(\omega) V^*(\omega), \tag{7}$$

where N_σ is the number of non-zero singular values. In the acoustic case and for small size scatterers there is an one-to-one correspondence between the scatterers and the significant singular values and vectors of the IRM. In the elastodynamic case, and even for small scatterers, each scatterer has two or more associated singular values (and vectors) [10]. For well separated defects, each singular value is associated with a specific damage, and the corresponding singular vector has the ability to re-focus the field on the specific defect allowing for distinguishing and illuminating even the weaker damaged areas.

To focus on different defects we compute the projection of each column $\widehat{P}^{(l)}$ of the response matrix on the k-th singular vector as

$$\widehat{P}_k^{(p)}(\omega) = \left(U_k^*(\omega) \widehat{P}^{(l)}(\omega) \right) V_k(\omega) \tag{8}$$

which is a column vector associated with the k-th singular value of the matrix . We may reconstruct by inverse Fourier transform the column vector $P_k^{(l)}(t)$, reverse it in time, and then send it back in the elastic medium. We expect this procedure to focus the energy of the elastic field on the defected areas of our domain.

4 NUMERICAL IMPLEMENTATION

The elastic wave propagation in two dimensions is solved with a mixed finite element formulation based on the discretization of the stress-velocity fields, expressed by the system of equations in eq.(2). Details of this mixed formulation may be found in [6]. The spatial discretization is compatible with mass-lumping, which leads to diagonal mass matrices, so that explicit time discretization schemes are obtained. For this specific formulation a rectangular spatial grid is necessary. Our methodology has been also implemented and tested using a finite element discretization of the displacement formulation [19], however, results are not presented here.

A specific distribution of sensors, spread over a line, that constitutes both sources and receivers is considered and called an array of sensors. The material of the rectangular domain is assumed to be that of steel with Lame's coefficients λ=$96.95GPa$ and μ=76.17GPa, while the mass density is ρ=7700kg/m^3. The pressure waves velocity is c_p=5689.9m/s and that of shear waves c_s=3145.2m/s. The size of the domain equals to L_x=62.747mm and L_y=69.037mm. The FEM mesh consists of 400×400 elements, while the array of the 21 equidistant sensors lies on a line of length 31.452mm, as shown in Figure 1. Damage is considered in the material as two distinct small areas of softer material given by a 10% degradation of both Lame's coefficients. The first of them is at location $(0.6L_x, 0.25L_y)$ and its area is equal to 0.1mm^2 while the latter one is located at $(0.6L_x, 0.75L_y)$ and its area is 0.4mm^2. In order to construct the response matrix for the scattered field, each dof, corresponding to a spatial location of a sensor and a specific direction x_1 or x_2, is excited, and response is computed and stored for all sensors and both directions. The function of excitation in time is that of a ricker-pulse with a central frequency of 1MHz. This corresponds to a wavelength for the shear waves of 3mm and a pressure wave wavelength of 5.7mm.

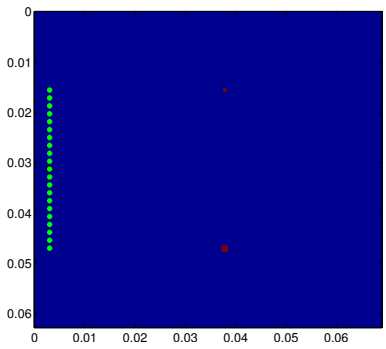


Figure 1: Geometry of elastic domain under consideration. Horizontal $y-$axis from left to right and vertical $x-$axis from top to bottom. Sensor array elements are shown with green dots and areas of damage are shown as red squares in the domain.

Plots in Figures 2 to 5, show results for the backpropagation steps using the field as recorded on the array, or after projecting it on the singular vectors corresponding to the first three singular values of the IRM. In all these figures we back propagate the column of the IRM that is obtained when the source is assumed to be on the central array element and exciting in the x-direction.

The left plot in each figure refers to the functional described by the integral,

$$\mathcal{I}(\mathbf{y}) = \int_0^T \mathcal{E}(\mathbf{y}, t)\, dt, \qquad \mathbf{y} \in \Omega, \tag{9}$$

where $\mathcal{E}(\mathbf{y}, t)$ is the energy density of the field on the spatial point $\mathbf{y}$ at time t, and T is the total duration time of the experiment. This functional is able to show the trajectories that the energy follows during the backward step of time reversal. As it can be seen these trajectories include the damaged areas. The plot in the middle is the time evolution of the energy criterion which may be used as an indicator for choosing the time instant at which the field focuses on the defects. The energy density of the time-reversed field at selected minima indicated by our criterion is shown on the right plot of each figure. We observe that by using the SVD we are able to detect and locate both damaged areas included in our domain.

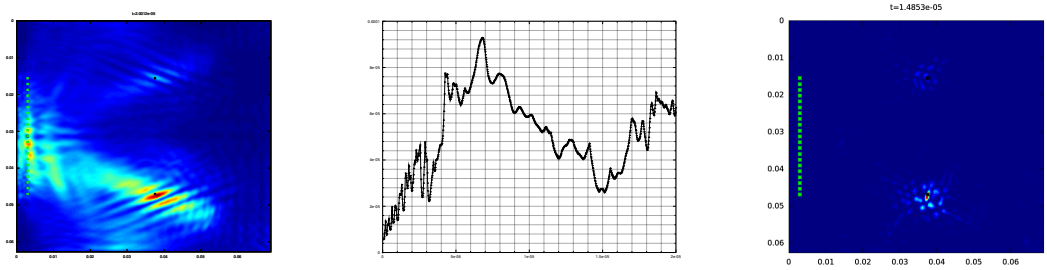


Figure 2: Backpropagation of the field recorded when the source is assumed to be on the central array element exciting in the x-direction.

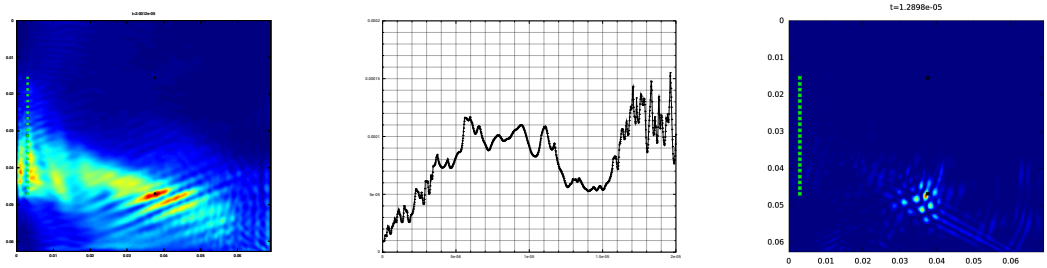


Figure 3: Backpropagating the same column of the response matrix as in Figure 2, but after projection on the singular vector corresponding to the first singular value.

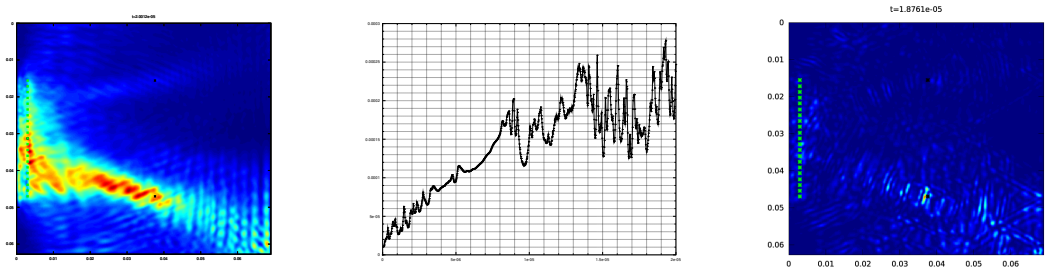


Figure 4: Backpropagating the same column of the response matrix as in Figure 2, but after projection on the singular vector corresponding to the second singular value.

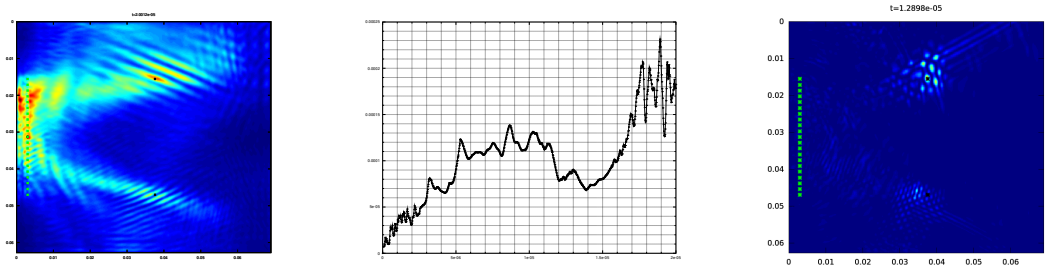


Figure 5: Backpropagating the same column of the response matrix as in Figure 2, but after projection on the singular vector corresponding to the third singular value.

5 CONCLUSIONS

We presented in this paper a computational methodology that uses the singular value decomposition of the array impulse response matrix in order to detect and localize defects in elastic materials. The energy density of the of the field seems a natural quantity to follow and a time-stopping criterion based on the L_1 norm of the normalized energy is proposed. The relevance of our methodology to SHM has been illustrated with numerical simulations.

REFERENCES

[1] Eyal Amitt, Dan Givoli, and Eli Turkel. Time reversal for crack identification. *Computational Mechanics*, 54(2):443–459, 2014.

[2] Habib Ammari, Elie Bretin, Josselin Garnier, and Abdul Wahab. Time-reversal algorithms in viscoelastic media. *European Journal of Applied Mathematics*, 24(04):565–600, 2013.

[3] Brian E Anderson, Michele Griffa, Carene Larmat, Timothy J Ulrich, and Paul A Johnson. Time reversal. *Acoustics Today*, 4(1):5–16, 2008.

[4] Ettore Barbieri and Michele Meo. Time reversal DORT method applied to nonlinear elastic wave scattering. *Wave Motion*, 47(7):452–467, 2010.

[5] Claude Bardos and Mathias Fink. Mathematical foundations of the time reversal mirror. *Asymptotic Analysis*, 29(2):157–182, 2002.

[6] E. Bécache, P. Joly, and C. Tsogka. A new family of mixed finite elements for the linear elastodynamic problem. *SIAM Journal of Numerical Analysis*, 39:2109–2132, 2002.

[7] Eliane Becache, Patrick Joly, and Chrysoula Tsogka. Fictitious domains, mixed finite elements and perfectly matched layers for 2-d elastic wave propagation. *Journal of Computational Acoustics*, 9(03):1175–1201, 2001.

[8] Liliana Borcea, George Papanicolaou, Chrysoula Tsogka, and James Berryman. Imaging and time reversal in random media. *Inverse Problems*, 18(5):1247, 2002.

[9] Hernán L Calvo, Rodolfo A Jalabert, and Horacio M Pastawski. Semiclassical theory of time-reversal focusing. *Physical review letters*, 101(24):240403, 2008.

[10] David H Chambers and James G Berryman. Time-reversal analysis for scatterer characterization. *Physical review letters*, 92(2):023902, 2004.

[11] Pier Paolo Delsanto, PA Johnson, Marco Scalerandi, and JA TenCate. Lisa simulations of time-reversed acoustic and elastic wave experiments. *Journal of Physics D: Applied Physics*, 35(23):3145, 2002.

[12] Gregoire Derveaux, George Papanicolaou, and Chrysoula Tsogka. Time reversal imaging for sensor networks with optimal compensation in time. *The Journal of the Acoustical Society of America*, 121(4):2071–2085, 2007.

[13] Oliver Dorn. Time-reversal and the adjoint method with an application in telecommunication. *arXiv preprint math/0412379*, 2004.

[14] Mathias Fink, Didier Cassereau, Arnaud Derode, Claire Prada, Philippe Roux, Mickael Tanter, Jean-Louis Thomas, and François Wu. Time-reversed acoustics. *Reports on progress in Physics*, 63(12):1933, 2000.

[15] Mathias Fink and Claire Prada. Acoustic time-reversal mirrors. *Inverse problems*, 17(1):R1, 2001.

[16] Dan Givoli. Time reversal as a computational tool in acoustics and elastodynamics. *Journal of Computational Acoustics*, 22(03), 2014.

[17] Dan Givoli and Eli Turkel. Time reversal with partial information for wave refocusing and scatterer identification. *Computer Methods in Applied Mechanics and Engineering*, 213:223–242, 2012.

[18] Izhak Levi, Eli Turkel, and Dan Givoli. Time reversal for elastic wave refocusing and scatterer location recovery. *Journal of Computational Acoustics*, 2014.

[19] Christos G Panagiotopoulos, Elias A Paraskevopoulos, and George D Manolis. Critical assessment of penalty-type methods for imposition of time-dependent boundary conditions in FEM formulations for elastodynamics. In *Computational Methods in Earthquake Engineering*, pages 357–375. Springer, 2011.

[20] Hyun Woo Park, Seung Bum Kim, and Hoon Sohn. Understanding a time reversal process in lamb wave propagation. *Wave Motion*, 46(7):451–467, 2009.

[21] Hyun Woo Park, Hoon Sohn, Kincho H Law, and Charles R Farrar. Time reversal active sensing for health monitoring of a composite plate. *Journal of Sound and Vibration*, 302(1):50–66, 2007.

[22] Claire Prada, Jean-Louis Thomas, and Mathias Fink. The iterative time reversal process: Analysis of the convergence. *The Journal of the Acoustical Society of America*, 97(1):62–71, 1995.

[23] Georgios E Stavroulakis. *Inverse and crack identification problems in engineering mechanics*, volume 46. Springer Science & Business Media, 2000.

[24] Chun H Wang, James T Rose, and Fu-Kuo Chang. A synthetic time-reversal imaging method for structural health monitoring. *Smart materials and structures*, 13(2):415, 2004.

[25] Xiao Dong Wang and GL Huang. Identification of embedded cracks using back-propagating elastic waves. *Inverse Problems*, 20(5):1393, 2004.

COMPDYN 2015
5th ECCOMAS Thematic Conference on
Computational Methods in Structural Dynamics and Earthquake Engineering
M. Papadrakakis, V. Papadopoulos, V. Plevris (eds.)
Crete Island, Greece, 25–27 May 2015

MODEL-BASED JOINT INPUT-STATE ESTIMATION ON A THIN-WALLED CANTILEVER BEAM

Øyvind W. Petersen[1], Ole Øiseth[1] and Torodd S. Nord[2,3]

[1]Norwegian University of Science and Technology
7491 Trondheim, Norway
oyvind.w.petersen@ntnu.no, ole.oiseth@ntnu.no

[2] Centre for Sustainable Arctic Marine and Coastal Technology, Norwegian University of Science and Technology
7491 Trondheim, Norway
torodd.nord@ntnu.no

[3] The University Centre in Svalbard (UNIS)
Longyearbyen, Spitsbergen

Keywords: Force identification, response estimation, sensor network

Abstract. *In the field of structural dynamics, measuring external forces directly is often not feasible, whereas structural response data is far more accessible. Force identification is an inverse problem concerned with estimating forces using measured dynamic response. This paper presents a practical application of a joint input-state estimation algorithm. The algorithm gives minimum-variance unbiased estimates of states and input forces in a discrete-time linear system, where stochastic noise in the measurement data and model description are accommodated for. An experimental study of a thin-walled cantilever beam is presented to demonstrate joint input-state estimation. The finite element modelling is done in the software ABAQUS with shell elements. A modally reduced order model is created, containing 13 selected modes. We introduce the general approach of obtaining strain measurements in a modal format. A sensor network is designed from a discussion on optimal placement of accelerometers and strain gauges. It is also shown that the sensor network constitute a sufficient observational ensemble for estimation of states and forces. The studies demonstrate successful identification of forces generated by a simple mass-spring system. In addition, the strain is predicted at a location not co-located with the sensor network. The predicted strain agrees well with a reference strain measured at the same location. Lastly, we address some of the practical problems encountered and recommendations for further experiments.*

1 INTRODUCTION

1.1 Problem background

Force identification is a problem within structural dynamics concerned with estimation of external forces using measured dynamic response. Structural design and reliability assessment are areas where knowledge of model uncertainties of the forces to which the structure is exposed to is important. A better understanding of the true ambient forces could also be used to compare or update existing load models. In many cases, it is impractical to measure the forces directly, leading to the use of inverse identification methods. Herein, the inverse problem is solved to find the system inputs using the dynamic response together with an established system model. Often it is also desired to use the response data, sampled at a few locations, to estimate the complete structural response. If the true response is known, the information can be valuable for applications such as structural health monitoring, response to secondary installations or fatigue prediction.

In this paper we apply an established algorithm and show its feasibility for force identification and response estimation in a laboratory experiment on a thin-walled cantilever beam. Included is also a discussion on optimal placement of measurement sensors in light of recent advances on sensor networks.

1.2 Inverse force identification

Most practical cases of inverse identification are usually prone to ill-posedness since all state variables and initial conditions rarely are known [1]. The problem therefore has to be treated with special methods. Popular solution methods in the time domain feature Kalman filters [2, 3], occasionally in conjunction with least squares optimizers [4, 5]. We here present an application of the joint input-state estimation algorithm [6], which has a structure closely related to the Kalman filter. The algorithm was first introduced to structural dynamics by Lourens [7], who modified it to apply for modally reduced order models. The method has also has been verified experimentally by Lourens et al. [8] and Niu et al. [9]. Recently, it has also been applied by Nord et al. [10] to identify ice forces in a laboratory setting, giving input estimates in agreement with a reference solution by frequency domain deconvolution.

The framework for model-based force identification is often by means of finite element (FE) modelling and user-supplied parameters. Nord et al. [10] used a strain-displacement relation suitable for force identification using a model based on Timoshenko beam elements. We here aim to skip this step and let FE software directly provide all necessary parameters. The intent is to render an approach where the user does not have to supply strain-displacement relations manually.

2 FORCE IDENTIFICATION BY JOINT INPUT-STATE ESTIMATION

2.1 Stochastic state-space model

In applications of joint input-state estimation, the system is first transformed into state-space form. The basis is a time-invariant linear dynamic system with n_{DOF} degrees of freedom (DOFs) $\mathbf{u} \in \mathbb{R}^{\mathrm{n}_{DOF}}$:

$$\mathbf{M}\ddot{\mathbf{u}}(t) + \mathbf{C}\dot{\mathbf{u}}(t) + \mathbf{K}\mathbf{u}(t) = \mathbf{S}_{\mathbf{p}}\mathbf{p}(t) \tag{1}$$

Here, $\mathbf{M}$, $\mathbf{C}$ and $\mathbf{K}$ represents the mass, damping and stiffness matrix respectively, $\mathbf{S}_{\mathbf{p}} \in \mathbb{R}^{\mathrm{n}_{DOF} \times \mathrm{n}_p}$ is the force application matrix assigning the histories of the n_p external forces con-

tained in $\mathbf{p} \in \mathbb{R}^{\mathrm{n}_p}$ to the designated DOFs. When the damping is assumed proportional, the corresponding modally reduced order equation reads:

$$\ddot{\mathbf{z}}(t) + \mathbf{\Gamma}\dot{\mathbf{z}}(t) + \mathbf{\Omega}^2\mathbf{z}(t) = \mathbf{\Phi}^T\mathbf{S}_\mathbf{p}\mathbf{p}(t) \tag{2}$$

Here, $\mathbf{z} \in \mathbb{R}^{\mathrm{n}_m}$ is the vector with n_m selected modal coordinates and $\mathbf{\Phi} \in \mathbb{R}^{\mathrm{n}_{DOF} \times \mathrm{n}_m}$ is the corresponding mass-normalized mode shape matrix. $\mathbf{\Omega} \in \mathbb{R}^{\mathrm{n}_m \times \mathrm{n}_m}$ and $\mathbf{\Gamma} \in \mathbb{R}^{\mathrm{n}_m \times \mathrm{n}_m}$ are diagonal matrices collecting the natural frequencies ω_i and damping ratios ξ_i for every mode:

$$\mathbf{\Omega} = \mathrm{diag}(\omega_1, \ldots, \omega_{\mathrm{n}_m}), \quad \mathbf{\Gamma} = \mathrm{diag}(2\omega_1\xi_1, \ldots, 2\omega_{\mathrm{n}_m}\xi_{\mathrm{n}_m}) \tag{3}$$

The state-space transform is completed by rewriting Eq. 2 and defining the state vector $\mathbf{x} \in \mathbb{R}^{\mathrm{n}_s}$ ($\mathrm{n}_s = 2 \times \mathrm{n}_m$) and the system matrices $\mathbf{A}_c \in \mathbb{R}^{\mathrm{n}_s \times \mathrm{n}_s}$ and $\mathbf{B}_c \in \mathbb{R}^{\mathrm{n}_s \times \mathrm{n}_p}$ according to Eq. 5:

$$\dot{\mathbf{x}}(t) = \mathbf{A}_c\mathbf{x}(t) + \mathbf{B}_c\mathbf{p}(t) \tag{4}$$

$$\mathbf{x}(t) = \begin{pmatrix}\mathbf{z}(t)\\ \dot{\mathbf{z}}(t)\end{pmatrix}, \quad \mathbf{A}_c = \begin{bmatrix}\mathbf{0} & \mathbf{I}\\ -\mathbf{\Omega}^2 & -\mathbf{\Gamma}\end{bmatrix}, \quad \mathbf{B}_c = \begin{bmatrix}\mathbf{0}\\ \mathbf{\Phi}^T\mathbf{S}_p\end{bmatrix} \tag{5}$$

The discrete-time equivalent is found by introducing a sampling rate of $\frac{1}{\Delta t}$ together with a zero-order hold assumption on the force. An explicit solution to Eq. 4 then reads

$$\mathbf{x}_{k+1} = \mathbf{A}\mathbf{x}_k + \mathbf{B}\mathbf{p}_k \tag{6}$$

where $k \in \mathbb{N}$ is the time index and $t_k = k\Delta t$, $\mathbf{x}_k = \mathbf{x}(t_k)$, $\mathbf{p}_k = \mathbf{p}(t_k)$. The discrete system matrices $\mathbf{A} \in \mathbb{R}^{\mathrm{n}_s \times \mathrm{n}_s}$ and $\mathbf{B} \in \mathbb{R}^{\mathrm{n}_s \times \mathrm{n}_p}$ are defined as:

$$\mathbf{A} = e^{\mathbf{A}_c\Delta t}, \quad \mathbf{B} = (\mathbf{A} - \mathbf{I})\mathbf{A}_c^{-1}\mathbf{B}_c \tag{7}$$

The response measurements, n_d in total, are collected in the vector $\mathbf{y} \in \mathbb{R}^{\mathrm{n}_d}$ and related to the physical coordinates through selection matrices $\mathbf{S}_a, \mathbf{S}_v$ and $\mathbf{S}_d \in \mathbb{R}^{\mathrm{n}_d \times \mathrm{n}_{DOF}}$:

$$\mathbf{y}(t) = \mathbf{S}_a\ddot{\mathbf{u}}(t) + \mathbf{S}_v\dot{\mathbf{u}}(t) + \mathbf{S}_d\mathbf{u}(t) \tag{8}$$

Hence the measurements can be displacements, velocities and accelerations (or linear combinations of these). Rewritten on state-space form and subjected to the same discretization format as above, the measurement equation yields:

$$\mathbf{y}_k = \mathbf{G}\mathbf{x}_k + \mathbf{J}\mathbf{p}_k \tag{9}$$

Here $\mathbf{G} \in \mathbb{R}^{\mathrm{n}_d \times \mathrm{n}_s}$ and $\mathbf{J} \in \mathbb{R}^{\mathrm{n}_d \times \mathrm{n}_p}$ symbolizes the output influence matrix and direct transmission matrix, respectively:

$$\mathbf{G} = \begin{bmatrix}\mathbf{S}_d\mathbf{\Phi} - \mathbf{S}_a\mathbf{\Phi}\mathbf{\Omega}^2 & \mathbf{S}_v\mathbf{\Phi} - \mathbf{S}_a\mathbf{\Phi}\mathbf{\Gamma}\end{bmatrix}, \quad \mathbf{J} = \begin{bmatrix}\mathbf{S}_a\mathbf{\Phi}\mathbf{\Phi}^T\mathbf{S}_p\end{bmatrix} \tag{10}$$

Finally, the stochastic aspect is introduced by adding the model noise $\mathbf{w}_k \in \mathbb{R}^{\mathrm{n}_s}$ and the measurement noise $\mathbf{v}_k \in \mathbb{R}^{\mathrm{n}_d}$ to the state-space equations:

$$\mathbf{x}_{k+1} = \mathbf{A}\mathbf{x}_k + \mathbf{B}\mathbf{p}_k + \mathbf{w}_k \tag{11}$$

$$\mathbf{y}_k = \mathbf{G}\mathbf{x}_k + \mathbf{J}\mathbf{p}_k + \mathbf{v}_k \tag{12}$$

The former accounts for errors in the model description and the latter allow for inaccuracies in the measurement signals. Both are taken as zero mean white noise vectors and assumed mutally uncorrelated. The noise covariance, here assumed time invariant, is collected in the matrices $\mathbf{E}[\mathbf{w}_k\mathbf{w}_k^T] = \mathbf{Q}$ and $\mathbf{E}[\mathbf{v}_k\mathbf{v}_k^T] = \mathbf{R}$.

2.2 Joint input-state estimation

The joint input-estimation algorithm, originally developed by Gillijns [6], was further adapted to structural dynamics by Lourens et al. [8]. The algorithm is similar to the Kalman filter, except the true input is replaced by an optimal estimate [11]. It operates as follows:

- Estimate input forces by a minimum variance unbiased criteria (Eq. 13 - 16)
- Update state estimate with receiving measurement (Eq. 17 - 20)
- Estimate state ahead in time (Eq. 21 - 22)

$$\tilde{\mathbf{R}}_k = \mathbf{G}\mathbf{P}_{k|k-1}\mathbf{G}^T + \mathbf{R} \tag{13}$$
$$\mathbf{M}_k = (\mathbf{J}^T\tilde{\mathbf{R}}_k^{-1}\mathbf{J})^{-1}\mathbf{J}^T\tilde{\mathbf{R}}_k^{-1} \tag{14}$$
$$\hat{\mathbf{p}}_{k|k} = \mathbf{M}_k(\mathbf{y}_k - \mathbf{G}\hat{\mathbf{x}}_{k|k-1}) \tag{15}$$
$$\mathbf{P}_{\mathbf{p}[k|k]} = (\mathbf{J}^T\tilde{\mathbf{R}}_k^{-1}\mathbf{J})^{-1} \tag{16}$$

$$\mathbf{L}_k = \mathbf{P}_{k|k-1}\mathbf{G}^T\tilde{\mathbf{R}}_k^{-1} \tag{17}$$
$$\hat{\mathbf{x}}_{k|k} = \hat{\mathbf{x}}_{k|k-1} + \mathbf{L}_k(\mathbf{y}_k - \mathbf{G}\hat{\mathbf{x}}_{k|k-1} - \mathbf{J}\hat{\mathbf{p}}_{k|k}) \tag{18}$$
$$\mathbf{P}_{k|k} = \mathbf{P}_{k|k-1} - \mathbf{L}_k(\tilde{\mathbf{R}}_k - \mathbf{J}\mathbf{P}_{\mathbf{p}[k|k]}\mathbf{J}^T)\mathbf{L}_k^T \tag{19}$$
$$\mathbf{P}_{\mathbf{xp}[k|k]} = \mathbf{P}_{\mathbf{px}[k|k]}^T = -\mathbf{L}_k\mathbf{J}\mathbf{P}_{\mathbf{p}[k|k]} \tag{20}$$

$$\hat{\mathbf{x}}_{k+1|k} = \mathbf{A}\hat{\mathbf{x}}_{k|k} + \mathbf{B}\hat{\mathbf{p}}_{k|k} \tag{21}$$
$$\mathbf{P}_{k+1|k} = \begin{bmatrix}\mathbf{A} & \mathbf{B}\end{bmatrix}\begin{bmatrix}\mathbf{P}_{k|k} & \mathbf{P}_{\mathbf{xp}[k|k]} \\ \mathbf{P}_{\mathbf{px}[k|k]} & \mathbf{P}_{\mathbf{p}[k|k]}\end{bmatrix}\begin{bmatrix}\mathbf{A}^T \\ \mathbf{B}^T\end{bmatrix} + \mathbf{Q} \tag{22}$$

To initiate the estimation process, an initial state $\hat{\mathbf{x}}_{0|-1}$ with error covariance $\mathbf{P}_{0|-1}$ must be supplied. For an explanation of the covariance matrices (denoted $\mathbf{P}$ with varying subindex), refer to works by Gillijns and De Moor [11]. When the system and noise covariance matrices are time invariant, the filter often quickly reach a steady state. In this event the optimal weighing matrices for the state and the input, $\mathbf{L}_k$ and $\mathbf{M}_k$, remain unchanged in every step. The same holds for the error covariance.

2.3 Requirements for identification

Maes et al. [12] derived a set of criteria to be fulfilled in order to perform a successful identification of forces using joint input-state estimation in conjunction with a reduced order model. The design of a sensor network, i.e. determining types of measurements and sensor locations, plays a significant role in obtaining fair results. In addition to satisfying the criteria presented in Sec. 2.3.1 – 2.3.3, one must also recognize practical issues, such that the number of available sensors often is limited and the possible sensor locations restricted.

2.3.1 Observability

Observability concerns whether one is able to uniquely determine an initial state $\mathbf{x}_0$ from finite time series of known input forces and measurements. If this is true, the entire state history can be reconstructed from Eq. 6. In the case of the reduced order model, with none of the natural frequencies identical, the observability is fulfilled if and only if the matrix

$$(\mathbf{S}_d + \mathbf{S}_v + \mathbf{S}_a)\mathbf{\Phi} \tag{23}$$

does not contain any zero columns [12]. This can often intuitively be evaluated by interpreting the vectors of $\mathbf{\Phi}$ as modal configurations and the selection matrices as on-off buttons in each DOF. E.g. if a sensor is placed close to an inflection point of a mode, the mode will not be captured and and consequently its contribution to the total response cannot be judged. The observability criterion need only be fulfilled if state estimates are of interest, and not only the input.

2.3.2 Direct invertability

For system inversion without time delay, a direct invertability criterion must be met. $\mathbf{J}$, referred to as the direct transmission matrix, is important since it represents the direct influence from the input to the measurements, see Eq. 9. Direct invertability is fulfilled if and only if $\text{rank}(\mathbf{J}) = \text{rank}(\mathbf{S}_a\mathbf{\Phi}\mathbf{\Phi}^T\mathbf{S}_p) = \text{n}_p$ [12]. This is only ensured if the number of accelerometers is greater or equal to to n_p. In addition the forces must excite at least n_p modes distinguishable in the acceleration signals.

2.3.3 Stability

The stability in inversion of the state-space system depends on the transmission zeros λ_j [12], satisfying the relation:

$$\begin{bmatrix} \mathbf{A} - \lambda_j\mathbf{I} & \mathbf{B} \\ \mathbf{G} & \mathbf{J} \end{bmatrix} \begin{bmatrix} \mathbf{x}_0 \\ \mathbf{p}_0 \end{bmatrix} = \begin{bmatrix} \mathbf{0} \\ \mathbf{0} \end{bmatrix} \tag{24}$$

Under this condition, a force on the form $\mathbf{p}_k = \mathbf{p}_0\lambda_j^k$ will give a non-zero response while the observed measurements are identical to zero. Since the presence of such a force cannot be told, uniqueness in inversion is not achieved. Any $|\lambda_j| > 1$ is called an unstable transmission zero, however any $|\lambda_j| < 1$ is called stable since the undetectable force component converges towards zero when k increases. If $|\lambda_j| = 1$, marginal stability is obtained, signalling no data on static response is present. When strains or displacements are included to the sensor network, detection of static components corresponding to the 0 Hz frequency is restored. The matrix $\mathbf{J} - \mathbf{G}(\mathbf{A} - \mathbf{I})^{-1}\mathbf{B}$ should then be non-singular. Transmission zeros must be checked for all sensor configurations.

3 LABORATORY EXPERIMENT

3.1 Laboratory setup

Vibrations of a 3 m long cantilever beam are studied in the laboratory experiment. Notably, the extruded aluminium section has an unusual cross (+) shape, see Fig. 1. A 10 mm thick plate is welded to the beam end and bolted to a rigid wall. As shown in Fig. 1, washers separates the

end plate from the wall, allowing free movement in the end plate. The beam is free to bend both vertically and laterally. As a consequence of low torsional stiffness, torsional vibrations also composes an important component of motion. A brief list of the equipment used for acquiring data during the tests is listed in Table 1.

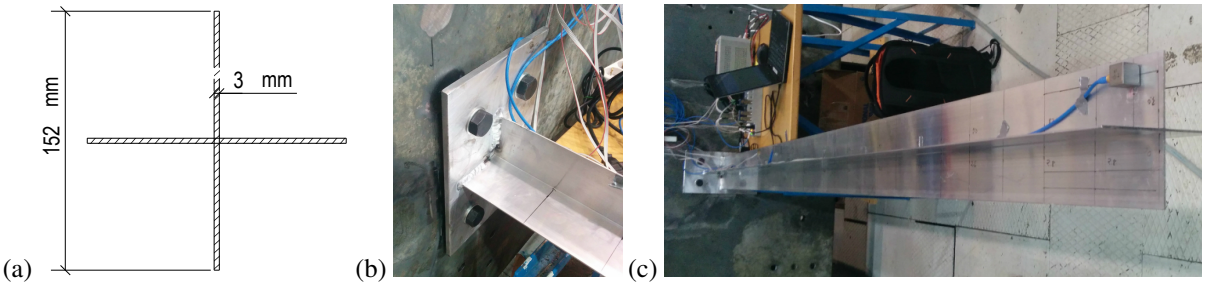


Figure 1: Left: cross section geometry; middle: bolted support and end plate-beam connection; right: beam mounted to wall (rotated).

Function	Model
Accelerometer	Kistler K-Beam 8395A, range $\pm$2g, sensitivity 2000 mV/g
Strain gauge	HBM 1-LV41-3/120 Ohm, Wheatstone quarter bridge
Accelerometer module	NI 9234
Strain module	NI 9235
Data acquisition system	NI cDAQ-9178

Table 1: List of equipment used for acquiring measurement data.

3.2 Finite element model

A FE model of the thin-walled section was created using 8-node quadrilateral shell elements (S8R) in the software ABAQUS. Translational DOFs in the end plate at the location of the bolts were pinned. The mesh was generated using an average element width of 20 mm. It is evident that the support and its rotational stiffness would be more difficult to model using beam elements. In addition, conventional beam elements could have problems describing the torsional behaviour of the section, advocating the choice of shell elements. Mode shapes, natural frequencies as well as the modal strain parameter $\mathbf{S}_d\mathbf{\Phi}$ were extracted from the FE model. Exact shape functions of the element are therefore not explicitly needed by the user to relate strains and displacements. The reduced order model is here comprised of the 13 modes with lowest natural frequencies, which of 6 are bending modes and 7 are torsional, see Table 2. The damping ratio is taken as 0.3% for all modes. Some of the modes relevant for vertical eccentric loading is displayed in Fig. 2.

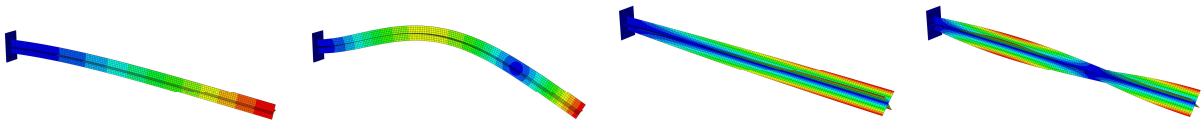


Figure 2: Mode 2, 7 (vertical bending), 3 and 4 (torsion).

n	f_n [Hz]	Type
1	7.8	Lateral bending
2	9.2	Vertical bending
3	10.5	Torsion
4	31.4	Torsion
5	51.7	Lateral bending
6	52.5	Torsion
7	57.3	Vertical bending
8	73.8	Torsion
9	95.4	Torsion
10	117.4	Torsion
11	139.9	Torsion
12	146.0	Lateral bending
13	156.2	Vertical bending

Table 2: Natural frequencies of FE-model.

3.3 Optimal sensor placement

In this section we study positioning of sensors in relation to the criteria described in Sec. 2.3. Two triaxial accelerometers and three uniaxial strain gauges are disposable for the sensor network. First, the accelerometer locations are determined. The objective is to ensure the direct transmission matrix $\mathbf{J} = \mathbf{S}_a\mathbf{\Phi}\mathbf{\Phi}^T\mathbf{S}_p$ has full rank. $\mathbf{S}_p$ is determined by setting the force action point eccentrically at the cantilever end, 40 mm from the centroid, see Fig. 3. It is seen from the quantity $\mathbf{\Phi}^T\mathbf{S}_p$ in Fig. 4 that a vertical force component (316y) induces vertical bending and torsion in the beam, while the lateral component (316z) excites lateral bending modes only.

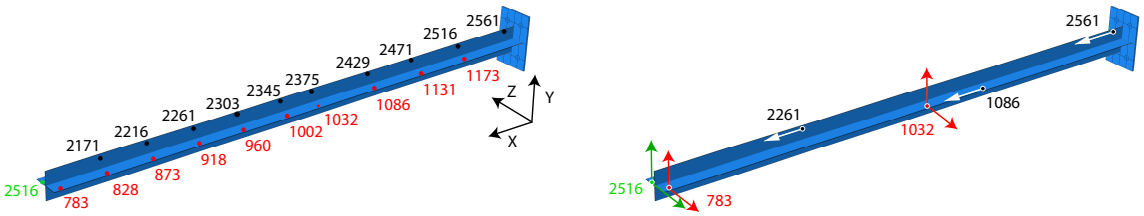


Figure 3: Geometry and sensors: accelerometers (red), strain gauges (black) and force (green): Left: possible sensor nodal positions; right: final sensor network denoted with measuring directions.

In the following, accelerometer locations approximately 60 mm from the centroid as shown in Fig. 3 are considered. $\mathbf{S}_a\mathbf{\Phi}$, interpreted the modal projections on accelerometer locations, are sought to be maximized for the modes to have good influence on the sensors. In Fig. 4 we promptly identify the cantilever tip location (783y) to be suitable for capturing bending (modes 2, 7, 13) as well as torsion (modes 3, 4, 6, 8-11). For the second accelerometer, 1032y seems as a feasible choice with good modal influence for all modes except lateral bending. For reasons of symmetry in geometry, similar results are obtained when repeating the procedure for lateral accelerations in the same nodes, but are left out here. Acceleration data for the x-direction is discarded since none of the incluced modes exhibit axial motion. When $\mathbf{S}_a$ is determined from accelerometers measuring in node 783 and 1032 in both y-direction and z-direction, $\text{rank}(\mathbf{J}) = \text{n}_p = 2$ and direct invertability is ensured.

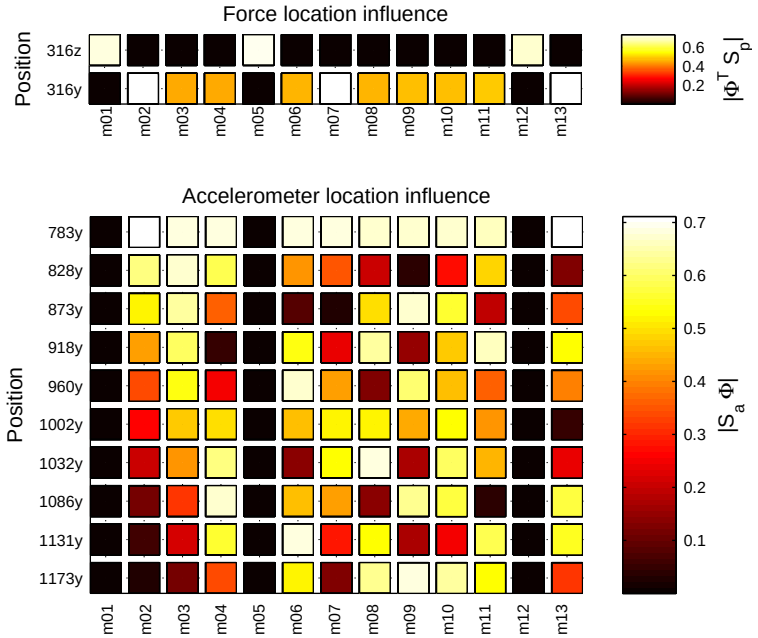


Figure 4: Top: Force influence for lateral (z) and vertical (y) component. Bottom: Accelerometer influence in vertical direction (y) for a variety of locations.

No unstable transmission zeros exist for this network of accelerometers. However, the system is marginally stable without measurement data sensitive to static loading. In a similar manner as above, we look at possible strain gauge locations through $\mathbf{S}_d\mathbf{\Phi}$ in Fig. 5 with the goal to maximize modal influence. For the lowest vertical bending mode (m02) the influence is limited for all positions, but highest close to the support (2561x, value 0.014). This location is therefore included. 2261x appear as the best choice for a second sensor. Again, similar results are obtained when considering the location of a third strain to capture lateral bending modes. For this specific problem, shear strain could also be measured to increase the influence from torsion modes. The total network ($\mathrm{n}_d = 7$) including the third strain gauge is shown in Fig. 3. The marginal transmission zeros are now eliminated for this sensor configuration. We further check this from $\mathbf{J} - \mathbf{G}(\mathbf{A} - \mathbf{I})^{-1}\mathbf{B}$, whose singular values are 0.189×10^{-5} and 0.314×10^{-5}, concluding the matrix has full rank.

For the observability criteria, the single accelerometer at the end suffices since this is a non-zero point for all modes. The states should therefore be estimated adequately with the entire sensor network. We readily confirm $(\mathbf{S}_d + \mathbf{S}_a)\mathbf{\Phi}$ has no zero columns.

3.4 Data acquisition and noise parameters

The load, applied eccentrically at the free end of the beam, was induced by attaching a spring supported mass ($k \approx 180$ N/m, $m = 0.78$ kg). The spring was given an initial displacement, and upon release the free vibrations of the combined beam spring-mass system were sampled at a rate of 2048 Hz. In addition to the described sensor network, the strain in node 2429 (cf. Fig 3) was measured to later serve as a reference in response prediction. The acceleration data series was detrended and low-pass filtered (6. order Butterworth filter, cutoff frequency 350 Hz) to hinder the filter receiving data in the frequency range above the includes modes, which could lead to difficulties when compensating for unexpected behaviour. The same was done for the

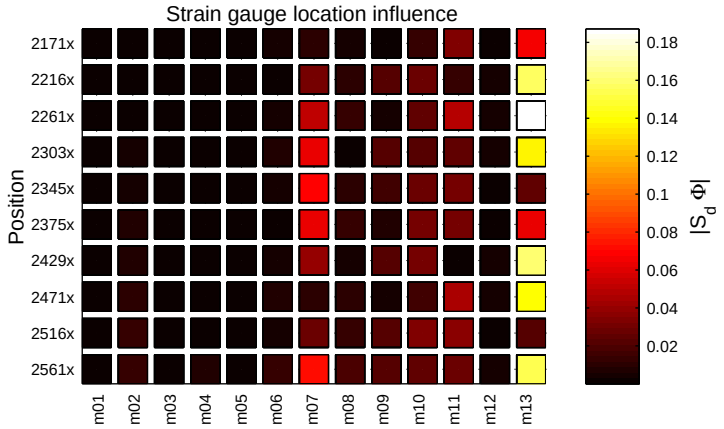


Figure 5: Influence for strain gauges measuring in beam longitudinal direction (x).

strain data, but with a cutoff frequency of 50 Hz since the data was severely contaminated with colored noise from the AC power supply.

When determining the noise covariance matrix ($\mathbf{R}$), not only the latent white noise in the sensor signals must be included, but also disturbances originating from second order effects, deviation in sensor locations and sensor accuracy in the prevailing frequency range. In view of this, the noise magnitude can be challenging to quantify. In addition, the correlation is usually unknown and is therefore often assumed as zero. Similar difficulties are encountered when deciding the model noise ($\mathbf{Q}$). Model errors in natural frequencies and damping ratios, system non-linearities, and the accuracy of the discretization in Eq. 6 will contribute to the noise. A common solution is to choose the noise magnitudes as a small percentage of the variables they represent [7]. The diagonal elements of $\mathbf{R}$ corresponding to accelerations were set to 10^{-4} and for strains to 10^{-14}. Likewise for $\mathbf{Q}$, diagonal elements were fixed as 10^{-12} and 10^{-10} for the modal displacements and velocities, respectively.

4 RESULTS AND DISCUSSION

4.1 Force identification

The forces identified with the joint input-state estimator are shown in Fig. 6. The total force magnitude is approximately 6 N, corresponding to 30 mm elongation of the spring. The frequency content in Fig. 7 shows the forces are dominant at 2.4 Hz, a feature of the spring-mass. Since the spring elongation also depends on the cantilever deflection at the force action point, a peak is seen at 9 Hz for the y-component. This originates from the lowest vertical bending and torsion mode, which for the real structure has very close natural frequencies. Although there are some discrepancy between the modelled and true natural frequencies, the filter fairly adjusts the results in favor of the true behaviour. The same is observed at 9 Hz (torsion) for the lateral component.

However, the result should be interpreted with caution. The results are dependent on the prescribed model noise. In particular, spurious compensating forces can occur if the system model differs too much from the real behaviour. Similarly, the measurement noise covariance affects the weighting between acceleration signals, dominant at the natural frequencies, and strain signals, dominant at the forcing frequency.

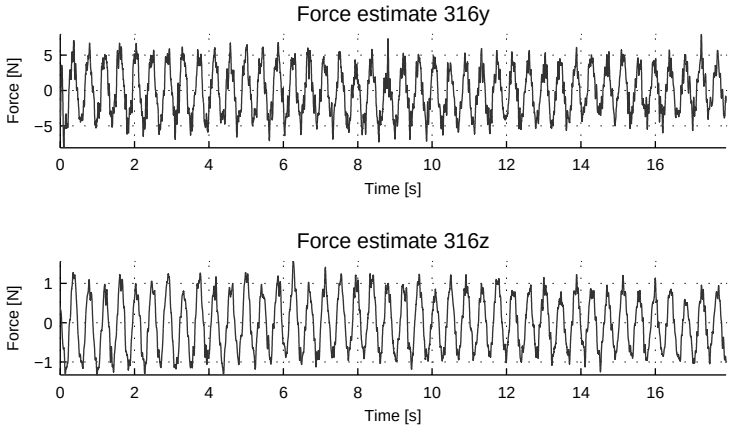


Figure 6: Time series for the identified vertical (316y) and lateral (316z) force component.

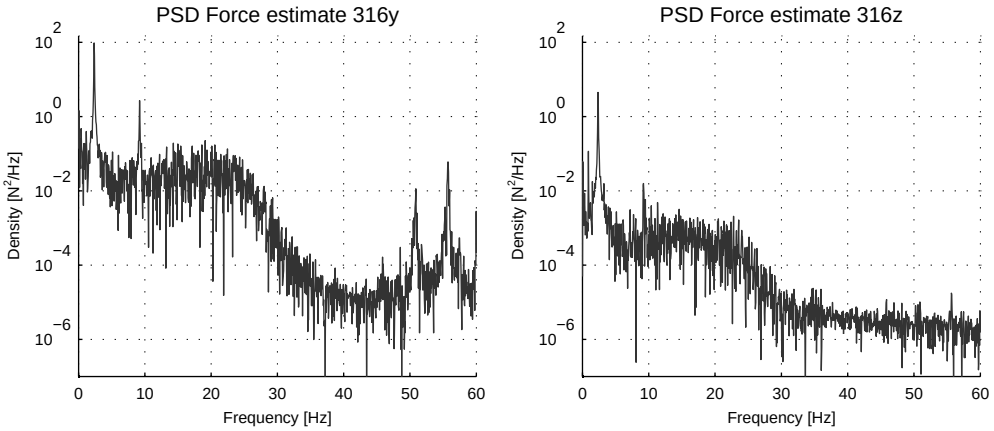


Figure 7: Power spectral density of the vertical (316y) and lateral (316z) force component.

4.2 Response estimate

To check the quality of the response estimate, the reference strain measured in node 2429 (cf. Fig 3) is studied. A prediction of the strain in the same node, collected in $\hat{\mathbf{y}}_k$, can be generated from the set of state estimates, $\hat{\mathbf{x}}$, obtained simultaneously with the force estimates. Furthermore, new selection matrices ($\mathbf{S}_a = \mathbf{S}_v = \mathbf{0}$, $\mathbf{S}_d \neq \mathbf{0}$) are created and $\hat{\mathbf{x}}$ is inserted in Eq. 9, yielding:

$$\hat{\mathbf{y}}_k = \begin{bmatrix} \mathbf{S}_d\boldsymbol{\Phi} & \mathbf{0} \end{bmatrix} \hat{\mathbf{x}}_k \tag{25}$$

A comparison of the predicted and measured strain is plotted in Fig. 8. The frequency and amplitude coincides remarkably well. The result suggests the states are estimated accurately.

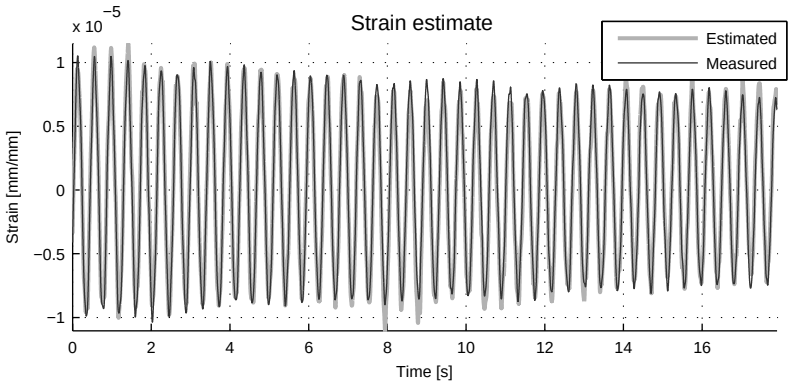


Figure 8: Comparison of predicted and measured strain in node 2429.

5 CONCLUDING REMARKS

The forces on a structure that cannot be measured directly can instead found by using measured dynamic response. We have in this paper applied a joint input-state estimation algorithm to estimate the forces and response for a cantilever beam. The FE model was established using shell elements, which for the thin-walled section has been shown as a viable approach. The designed sensor network, consisting of accelerometers and strain gauges, meets the criteria for joint input-state estimation with reduced order models. The force estimates obtained by the algorithm are reasonable. In addition the response at an unmeasured point of the structure has been successfully predicted.

To properly verify the identified force is correct, the true force can be measured directly to serve as a reference solution. In addition, system identification techniques could be applied to make the model a closer resemblance of the real structure. This would be even more important if identification of a more broad banded force were performed. A hammer impact, for example, would also involve the higher modes to a larger extent, which could give interesting results. For the presented study, the accelerometers had a measuring range of only $\pm$2g, meaning the motion had to be limited. As a consequence, very low bending strains are observed, causing a critical low signal to noise ratio. An other problem encountered the tests is the high flexibility of the section, which for even moderate movements gives rise to second order effects (i.e. displaced geometry axes), affecting the sensor signals. A set of simulated measurement data can also be generated if the force are measured directly. A comparison of the real and simulated data could then be used to better quantify the measurement noise.

REFERENCES

[1] T. Uhl. The inverse identification problem and its technical application. *Archive of Applied Mechanics*, 77(5):325–337, 2007.

[2] E.-M. Lourens, E. Reynders, G. De Roeck, G. Degrande, and G. Lombaert. An augmented Kalman filter for force identification in structural dynamics. *Mechanical Systems and Signal Processing*, 27:446–460, 2012.

[3] J.-S. Hwang, S.-G. Lee, P. Ji-hoon, and Y. Eun-Jong. Force identification from structural responses using Kalman filter. In *Materials Forum*, volume 33, 2009.

[4] C. K. Ma, J. M. Chang, and D. C. Lin. Input forces estimation of beam structures by an inverse method. *Journal of sound and vibration*, 259(2):387–407, 2003.

[5] J.-J. Liu, C.-K. Ma, I.-C. Kung, and D.-C. Lin. Input force estimation of a cantilever plate by using a system identification technique. *Computer Methods in Applied Mechanics and Engineering*, 190(11):1309–1322, 2000.

[6] S. Gillijns. *Kalman Filtering Techniques for System Inversion and Data Assimilation*. PhD thesis, Katholieke Universiteit Leuven - Faculty of Engineering Technology, Leuven (Belgium), 2007.

[7] E.-M. Lourens. *Force identification in structural dynamics*. PhD thesis, Katholieke Universiteit Leuven - Faculty of Engineering, Leuven (Belgium), 2012.

[8] E.-M. Lourens, C. Papadimitriou, S. Gillijns, E. Reynders, G. De Roeck, and G. Lombaert. Joint input-response estimation for structural systems based on reduced-order models and vibration data from a limited number of sensors. *Mechanical Systems and Signal Processing*, 29:310–327, 2012.

[9] Y. Niu, M. Klinkov, and C.-P. Fritzen. Online force reconstruction using an unknown-input Kalman filter approach. In *Proceedings of the 8th International Conference on Structural Dynamics,*, pages 2569–2576, EURODYN 2011.

[10] T. S. Nord, E.-M. Lourens, O. Øiseth, and A. Metrikine. Model-based force and state estimation in experimental ice-induced vibrations by means of Kalman filtering. *Cold Regions Science and Technology*, 111:13–26, 2015.

[11] S. Gillijns and B. De Moor. Unbiased minimum-variance input and state estimation for linear discrete-time systems with direct feedthrough. *Automatica*, 43(5):934–937, 2007.

[12] K. Maes, E.-M. Lourens, K. Van Nimmen, E. Reynders, G. De Roeck, and G. Lombaert. Design of sensor networks for instantaneous inversion of modally reduced order models in structural dynamics. *Mechanical Systems and Signal Processing*, 2014.

COMPDYN 2015
5th ECCOMAS Thematic Conference on
Computational Methods in Structural Dynamics and Earthquake Engineering
M. Papadrakakis, V. Papadopoulos, V. Plevris (eds.)
Crete Island, Greece, 25–27 May 2015

SENSITIVITY ANALYSIS OF DISCRETE-FORCE IDENTIFICATION ALGORITHMS TO MEASUREMENT NOISE

A. Rezayat [1], V. Nassiri [2], K. Maes [3], G. Lombaert [3], S. Vanlanduit [1,4], P. Guillaume [1]

[1] Acoustics & Vibrations Research Group (AVRG), Vrije Universiteit Brussel (VUB)
Pleinlaan 2, 1050 Brussels, Belgium
e-mail: arezayat@vub.ac.be

[2] University of Leuven (KUL) & Universiteit Hasselt, I-BioStat, Leuven, Belgium

[3] Department of Civil Engineering, KU Leuven, Belgium

[4] Op3Mech Research Group, University of Antwerp, Belgium

Keywords: Load identification, Modal analysis, Structured sparsity, ℓ_p-norm, Sensitivity to noise.

Abstract. *The increasing complexity of mechanical structures makes the measurement of dynamic loadings on the structure non practical, since the applied forces can not be measured in a direct way. Recently, a vast category of inverse algorithms have been developed in order to solve the load identification problems. In contrast with forward methods that compute the output (effect) of a system subject to inputs (cause), inverse methods offer the possibility to compute the input parameters of a system with known output data and the system model. Inverse problems suffer in general from instability problems due to high condition number. They are almost always under-determined and highly sensitive to measurement errors. Optimization techniques based on regularized cost functions are the most popular remedies to this problem. This paper deals with a sensitivity analysis of the classical regularization techniques, compared to a newly developed method (G-FISTA). The aim is to reconstruct applied loads on structures in noisy environments. Multiple simulation studies are done considering several situations of noise level, point force locations and sensor configurations. This study shows that the location and time history of discrete forces on structures can be better estimated using structured-sparse penalty functions techniques. A detailed noise study is done using the pseudo-inverse, Tikhonov and G-FISTA methods in frequency domain, and their performances are evaluated.*

1 Introduction

The direct measurement of parameters such as the applied forces on a structure is not always practical. In this case, another set of (more accessible) parameters are often measured, such as accelerations or strains. The force identification using structural vibration data has attracted a lot of interest. The inverse load identification using system responses is especially of interest in civil engineering and structural mechanics. This importance is more pronounced at the design stage of structures. For structures such as tall buildings, wind turbines and aircrafts, the knowledge of the active dynamic loads may be useful for structural health monitoring, i.e. fatigue assessment. In almost all cases, these loads cannot be measured directly, or the direct measurement is not practical and cost-effective. Many attempts were made to solve this problem by using indirect measurement techniques. The inverse approach consists of computing the input parameters of a system, with known output data and the structure model.

The great challenge with inverse problems is that they are not mathematically well-posed in almost all cases. A problem is called well-posed in the sense of *Hadamard*, if there exists a unique solution to the problem, which continuously depends on its data. As soon as the number of equations becomes smaller than the amount of unknowns, the problem becomes under-determined. When this condition satisfied, a high condition number makes the problem ill-conditioned. The strong sensitivity of the system to measurement errors causes instability in the calculation of the solution. This lack of stability is related to the fact that the behavior of the structure with respect to a specific excitation force (e.g. impact) can be exactly reproduced using another force configuration, with different force location and amplitude. The mathematical challenge will be to find the most realistic and physical force combination among all the infinite amount of possibilities. This is usually done by performing optimizations. In the particular case of mechanical structures, the inverse load identification aims to estimate force locations and reconstruct their time history on the basis of measured structural response and the dynamic model of the structure.

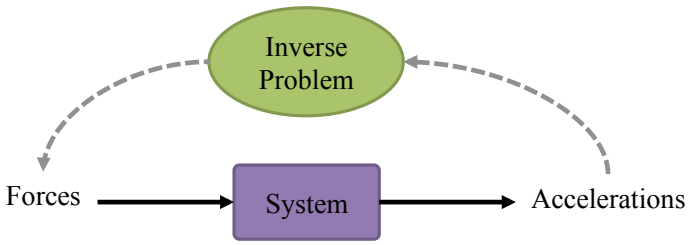


Figure 1: The inverse problem consists of reconstructing input excitations, based on a model and the vibration data.

In the literature, the load identification problems are treated differently depending on the choice of working domain. In some studies such as in [1–5], time domain techniques are used to solve the problem. Recently, there have been great advances in the development of new time domain techniques, especially in the joint input and state identification [6]. The joint input-state estimation algorithm is introduced in structural dynamics as an extension of the joint input-state estimation algorithm proposed in [7], including the correlation between process noise and measurement noise. This correlation is inherently present for civil engineering applications when

accelerations are measured in presence of ambient excitation [9]. The conditions for system inversion on structural dynamics were recently derived in [8]. The algorithm is used for the identification of hammer and artificial muscle forces applied to the bridge deck.

In the frequency domain, a classical solution for this problem is using the pseudo-inverse of the system model, [10, 11, 13, 15]. Although the pseudo-inverse approach can be computed easily, the outcome of this method is not satisfying in most cases, due to poor localization capability of the pseudo-inverse operator. In optimization based techniques, the cost function can include a penalization term or not (regularization). In the study of Bond and Adams [14], the force identification is done after an external study on the signal entropy. Among the non-penalized methods, Parloo et al. [15] has suggested a technique that is based on ℓ_p-norm cost functions for localized forces. The value of p tends to zero in an iterative manner until convergence is achieved (non-convex problem). On the other hand, the cost function can contain a penalization term to stabilise the solution. The most common way of regularization is the addition of the ℓ_2-norm to the cost function, such as in the study of Tikhonov and Arsenin [16]. The problem appears when the excitations are applied only on a few locations. There is a clear need for an adequate cost function that can ensure both localization and amplitude reconstruction for point forces. Recently, new techniques have been suggested to solve the ill-conditioned problem in frequency domain [17]. The proposed algorithm (G-FISTA) appears to have good localization capabilities. This method is based on the minimization of a cost function containing a mixed penalty function. The optimization algorithm used in this study is based on the work of Beck et al. [18]. Making use of grouped or structured sparsity, G-FISTA promotes solutions with a sparse pattern over the force point locations, and continuity in the frequency content of the force vector.

In the scope of this paper, we focus our main interest on discrete dynamic forces, acting at multiple point locations. Several methods are used to reconstruct the forces applied on a beam structure. The sensitivity of these algorithms to noise is evaluated using the simulation data of a cantilever beam. Different force/sensor configurations and noise levels are investigated in this work. In the following sections, the load reconstruction problem will be reformulated for penalized least squares optimization. The solution method will be explained and simulation results will be discussed in details.

2 Problem statement

While the forward problem consists of calculating the vibration response of structures to input forces, the inverse force identification problem deals with the reconstruction of unknown dynamic forces acting on a structure, using the output responses. More particularly, the impact force identification consists of estimating the impact force locations and their time evolution as a set of two unknown parameters. A special case of dynamic loading is the impact force produced by a hammer.

In this case study, the structure consists of a cantilever beam of rectangular section in laboratory conditions. By means of system identification techniques, a linear system model describing the beam behaviour is obtained from the roving hammer experiment. This model is then used together with some simulated acceleration data in order to reconstruct impact loads on the beam. The acceleration data is then polluted with a zero-mean Gaussian noise $N_x(f)$ in different signal to noise ratios.

The problem will be solved by pseudo-inverse (Moore-Pnrose), Tikhonov and G-FISTA

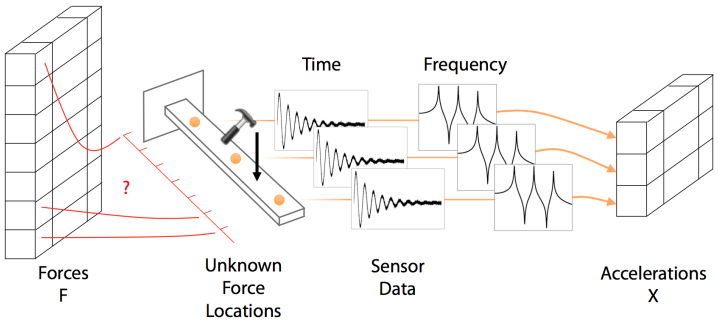


Figure 2: While the number of of unknown candidate force locations is big, only a few vibration sensor data is used for the localization process.

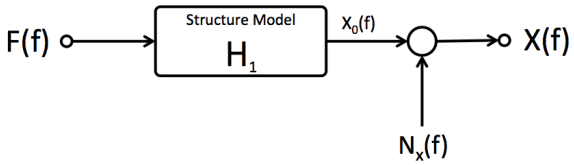


Figure 3: Gaussian white noise with different SNR is added to the simulated accelerations.

methods. Different sensor configurations are examined in this study. A comparative study is done on the effect of the number of point forces. Each sensor configuration is tested using acceleration data containing noise.

3 Solution methods

The inverse force reconstruction problem described in the previous section is solved by an optimization technique in frequency domain, as presented in [17]. Equation 1 represents the linear governing equations of the problem. The matrices $\bar{F}$ and $\bar{X}$ are created by concatenating respectively the force and accelerations of each frequency f into a column vector. The $\bar{H}$ matrix is a block diagonal matrix obtained by placing all the system (FRF) matrices on the diagonal.

$$\bar{X}(f) = \bar{H}(f)\bar{F}(f) \ , \ f \in \{f_1, \ldots, f_N\} \tag{1}$$

3.1 Direct inversion

The most classic solution to this problem is the Pseudo-inverse or the Moore-Penrose inversion. This method is very fast, but it fails to localize the loads in case of discreet forces. Although this problem is almost always ill-posed, there are some situations where the direct inversion of the transfer function can produce results, such as for Uslu et al. [13]. Despite the uniqueness property of the estimated solution, the obtained results are not fully satisfying, because the estimated forces are smeared out over all candidate force locations (poor localization). This is not an unusual result, because the pseudo-inverse does not produce a sparse solution.

$$\bar{F}(f) = \bar{H}^{\dagger}(f)\bar{X}(f) \ , \ f \in \{f_1, \ldots, f_N\} \tag{2}$$

3.2 Regularization

The solution of this problem can be estimated using least squares as in equation 3.

$$\hat{F} = \text{argmin}_{\bar{F}} \left\{ \frac{1}{2} \|\bar{H}\bar{F} - \bar{X}\|_2^2 \right\} \tag{3}$$

Since the number of rows in $\bar{H}$ is smaller than the number of columns, the problem in (3) is ill-posed. One promising method to overcome the ill-posedness of this problem is to penalize the least squares, as follows:

$$\hat{F} = \text{argmin}_{\bar{F}} \left\{ \frac{1}{2} \|\bar{H}\bar{F} - \bar{X}\|_2^2 + \lambda g(\bar{F}) \right\} \ , \ \lambda \geq 0 \tag{4}$$

This expression is known regularized least squares problem, and the function g represents the penalty term. Penalized least-squares is an effective and popular method proposed to solve ill-posed systems of linear equations. Different choices of penalty functions lead to different solutions, therefore the selection of penalty function g should be made in an efficient way [19–21].

3.2.1 Tikhonov

Tikhonov method consists of regularizing the cost function by an ℓ_2-norm as penalty function [2, 3, 16]. The solution is described as the following:

$$\hat{F} = \text{argmin}_{\bar{F}} \left\{ \frac{1}{2} \|\bar{H}\bar{F} - \bar{X}\|_2^2 + \lambda \|\bar{F}\|_2^2 \right\} \ , \ \lambda \geq 0 \tag{5}$$

3.2.2 G-FISTA

As described in [17], the use of l_2-norm in the first argument of the cost function is motivated by the effectiveness of least-squares in dealing with Gaussian noises on smooth data. While the data fidelity is evaluated by an l_2-norm, an l_1-norm can promote sparsity in the solution, which is more convenient in case of discrete (or localized source) problems.

Considering the physics of the problem, we suggest that an adequate penalty function should possess at least the following three properties:

1. **Sparsity constraint:**
   Since the external forces are usually applied only at a few unknown (discrete) locations on the structure, the force vector is assumed to be zero on most of the candidate force locations. In this sense, the force vector is expected to resemble a high contrast pattern. In other words, along the force locations, a sparse solution is desirable for each frequency. Therefore, using an ℓ_1-penalized model (over the candidate locations) seems to be more suitable (sparsity).

2. **Continuity constraint:**
   As the structure is excited with localized external forces (such as hammer or shaker), the force vector should retain its continuity over the frequency axis. In case of an impulse excitation (ex. hammer), the force will appear in almost every frequency due to the broad-band frequency content of the impact force. To ensure the continuity of the force vector in the frequency axis, we suggest the use of the ℓ_2-norm penalty. This means that at a given location on the structure, the probability for an element in the frequency axis to be non-zero depends on other elements of that particular location in the frequency axis. In other words, for each force location, the estimated force vector should be zero or non-zero along the frequencies (non-sparsity). Therefore, the use of ℓ_2-norm is promoted along the frequencies.

3. **Convex cost function:**
   The convexity of the problem in equation (4) will guarantee a unique solution. For $\lambda \geq 1$, the cost function $g(\lambda)$ is convex.

The continuity constraint (ℓ_2-norm penalty) is applied within each group elements, and the sparsity constraint (ℓ_1-norm penalty) is applied between the groups. Therefore, the new penalty function becomes a hybrid $\ell_{1\&2}$-norm, as described in equation 6, where k is the number of unknown force locations. As this penalty function is convex, it contains all the desirable properties mentioned in previous sections. The new penalized least squares problem is defined in equation 7.

$$\|\bar{F}\|_{1\&2} = \sum_{i=1}^{k} \|\bar{F}_{G_i}\|_2 \tag{6}$$

$$\hat{F} = \text{argmin}_{\bar{F}} \left\{ \frac{1}{2} \|\bar{H}\bar{F} - \bar{X}\|_2^2 + \lambda \|\bar{F}\|_{1\&2} \right\}. \tag{7}$$

The FISTA optimization algorithm proposed by [18] solves an ℓ_1-norm penalized least squares problem for real parameters. In summary, the algorithm can be interpreted as a special case of Majorize-Minimization algorithm (MM) that tries to find the minimum of a surrogate cost function instead of the actual cost function [22]. The detailed algorithm is presented in [19].

4 Validation strategy

The numerical validation process consists of simulating a cantilever beam subject to point forces, i.e. hammer impacts. This steel beam has the following dimensions: $100 \times 1 \times 3$ cm. The structural model has been obtained experimentally in lab conditions, using the roving-hammer test. The system contains 7 degrees of freedom. A force vector is applied numerically to this model and the accelerations are recorded. The number of applied impact points, their amplitudes and the noise contamination levels can be controlled in the simulations.

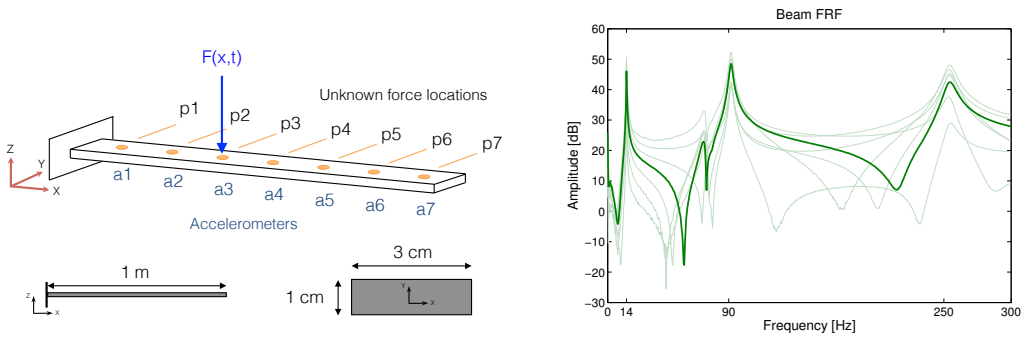


Figure 4: The simulated cantilever beam contains 7 unknown force locations. Some FRF curves corresponding to locations 1 till 7 are presented in the right side figure as examples.

The first step of the validation process is to estimate the location of the applied loads on the beam. In this step only a limited range of frequencies around the resonances are used to decrease the computation time. As a second step, a reduced system of equations is created, taking into account only the force locations estimated in the previous step. Then, the new system is solved using classical methods such as pseudo-inverse over the complete frequency range to reconstruct the complete force time history.

In a general case when there is no prior information on the applied forces, model selection techniques should be used in order to find the best regularization parameter. In this paper though, in order to have a fair comparison between all the techniques, we evaluate the force estimations over a wide range of λ (regularization parameter) and choose the solution corresponding to the best match between imposed and estimated force indexes. In such a way, the λ_{opt} for each method is defined as $argmin_\lambda \left\{ \|\hat{\beta} - \beta_0\|_2^2 \right\}$, where $\hat{\beta}$ and β_0 are the estimated and exact force indexes respectively (see β definition in [15]).

5 Results and discussions

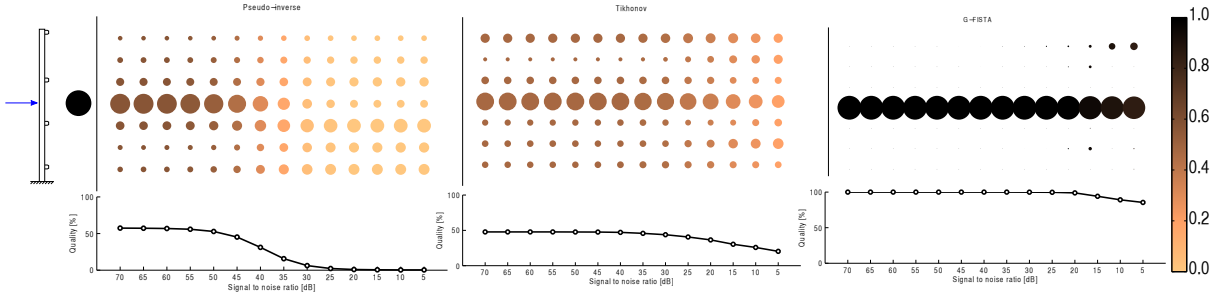
The simulation results are illustrated in this section. The size of the circles in the figures correspond to the $\hat{\beta}$ value, and the color represents the difference between the imposed and estimated force index. These results clearly show that the classical inversion methods such as pseudo-inverse does not produce satisfying force estimations, as predicted from the theory. The resultant force indexes are more distributed than localized. The G-FISTA method is stronger in localizing forces on the beam, even if multiple impact forces are applied. The effectiveness of G-FISTA in localizing forces from noisy data is well pronounced in the simulations. The misfit of the estimated and the exact force vector is represented by a parameter called $Quality$, which is calculated for each SNR values as $Quality = \|\hat{\beta} - \beta_0\|_2 \times 100$. This parameter emphasises on the localization of forces.

The simulation studies indicate that the consideration of a structured sparse penalty in the cost function (as in G-FISTA) highly improves the force estimations accuracy. The strength of G-FISTA in localizing point forces relies on the fact that this algorithm constitutes a general case with a mixed penalty function that can be simplified in either ℓ_1 or ℓ_2-norms as special cases. In other words, if only one big group (consisting of all components of F together) is defined, then the structured sparsity will act the same as usual ℓ_2 regularization (i.e. Tikhonov). However, if each frequency component of the force vector F is allocated to a separate group, (i.e. one element per group) the structured sparsity will become equivalent to the ℓ_1 penalised case. Therefore, G-FISTA is a general algorithm that can deal with all cases of point force identification problems. This makes G-FISTA a strong toolbox to deal with different force configurations without the need for prior knowledge on the type of the applied force.

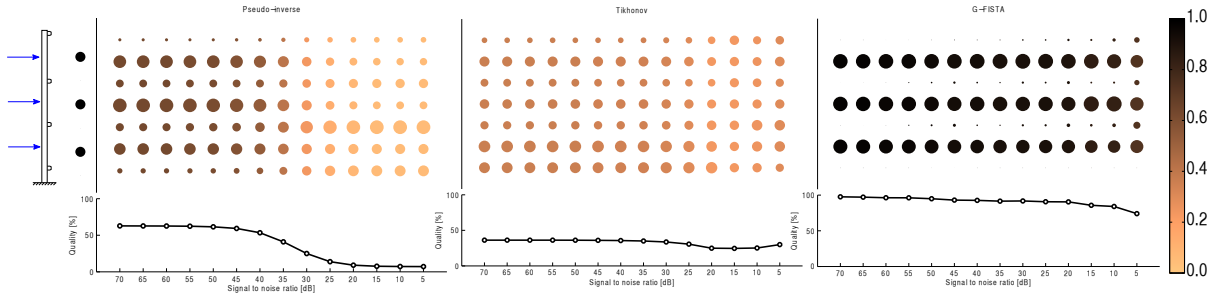
Another aspect of this works concerns the investigation of the number of used sensors. Two types of force/sensor configurations are investigated. In the first case, one point force is applied at location 4 on the beam, and the result qualities are compared in different noisy simulations. For all the evaluated methods except the pseudo-inverse, the localization quality increases with the number of considered sensors (see figure 8). The results illustrate that the G-FISTA method delivers more accurate force localization estimations among all tested methods. The latter assumption is true in case of high amount of noise SNR.

In another study, the number of sensors is fixed to four, and different amount of point forces are applied to the beam. Figures 5a till 7 show that the pseudo-inverse and Tikhonov have already a poor force localization for the least noisy data set. In the other hand, G-FISTA appears to be more robust in terms of data noise contamination. For all of the tested algorithms, the estimation quality decreases when more forces are applied on the structure. This can be explained in the case of sparsity based methods: these algorithms generally promote sparse pattern in the force vector. The more non-zero elements are present in the force vector, the more difficult would be for the algorithm to converge. The overall characteristics of G-FISTA still shows that this method can produce better localization estimations, compared to other evaluated

techniques. For cases where the number of applied point forces is bigger than the amount of sensors, all methods fail.

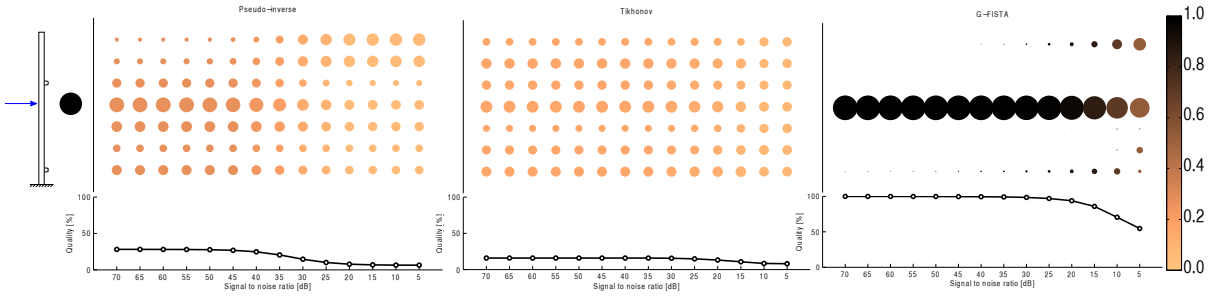


(a) Force at point $\{4\}$ and accelerometers at $\{1, 3, 5, 7\}$.

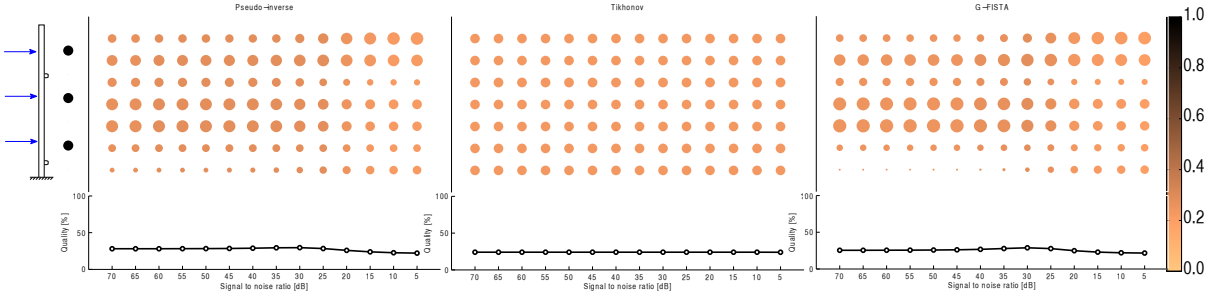


(b) Forces at points $\{2, 4, 6\}$ and accelerometers at $\{1, 3, 5, 7\}$.

Figure 5: Simulation results show that the unknown point forces are better estimated using G-FISTA method. The size and color of the bubbles represent respectively the estimated force index $\hat{\beta}$ and fitting quality. Four sensors are considered.



(a) Force at point $\{4\}$ and accelerometers at $\{1, 5\}$.



(b) Forces at points $\{2, 4, 6\}$ and accelerometers at $\{1, 5\}$.

Figure 6: Simulation results show that the estimation quality decreases with noise level. In this configuration all methods fail to localize forces. The size and color of the bubbles represent respectively the estimated force index $\hat{\beta}$ and fitting quality. Only two sensors are considered.

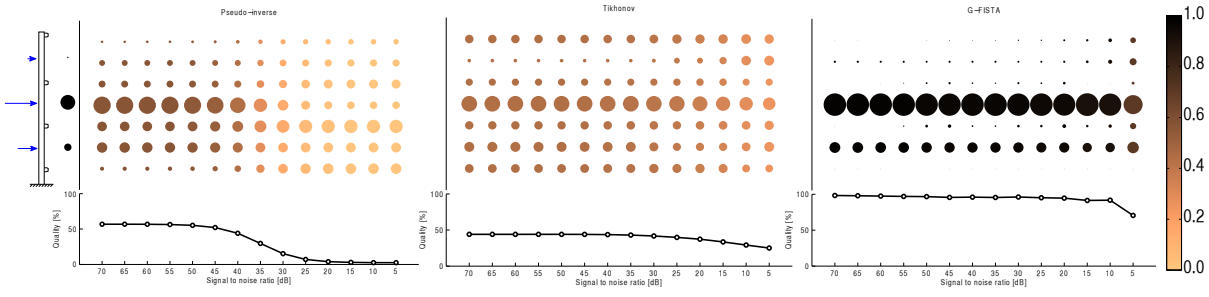
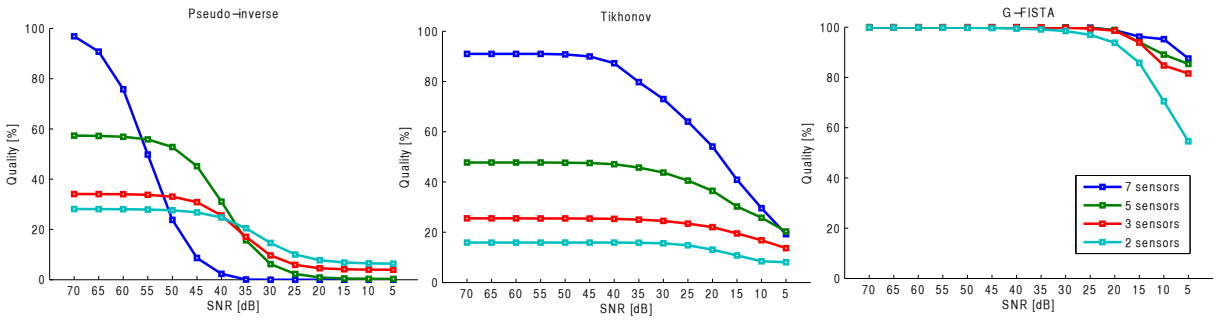
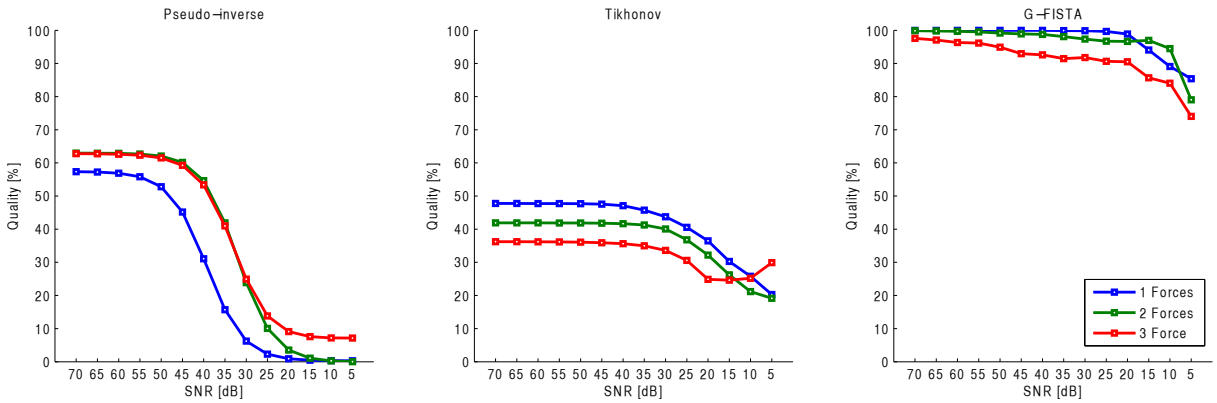


Figure 7: The simulation of multiple forces with different amplitudes show that G-FISTA method produces better estimation quality. Forces are applied at points $\{2, 4, 6\}$ with amplitudes $(50N, 100N, 10N)$, and accelerometers placed at $\{1, 3, 5, 7\}$.



(a) Force at point $\{4\}$ and different sensor settings: $\{1-7\}$, $\{1,3,5,7\}$, $\{1,4,7\}$ and $\{2,5\}$.



(b) Sensors placed at $\{1,3,5,7\}$ and different active force locations: $\{4\}$, $\{3,5\}$ and $\{2,4,6\}$.

Figure 8: The influence of number of sensors and forces is investigated using simulations. The results show that G-FISTA is less sensitive to the number of used sensors, even at high noise levels. The quality decreases when number of active forces increase.

6 Conclusion

In this paper, multiple numerical studies are conducted, aiming at localization and reconstruction of dynamic loads on a cantilever beam structure. The sensitivity of several algorithms to measurement noise is investigated. The influence of number of forces/sensors is also studied in this paper. The ill-conditioned load identification problem is reformulated as a new mathematical problem. The problem is then solved by means of pseudo-inverse, Tikhonov regularization and G-FISTA. The latter method is based on a particular mixed cost function taking advantage of structured sparsity.

The results show generally that the classical methods such as the pseudo-inverse and Tikhonov fail to localise the loads correctly. It is shown that the amount of considered sensors will generally increase the force localization quality. In all simulations, G-FISTA seems to be more accurate and it estimates the correct force locations, even in situations where the number of installed sensors is low. It can be concluded that the amount of sensors needed for an accurate estimation is at least equal to the number of force points applied to the structure. In terms of sensitivity to noise, the simulations illustrate the robustness of G-FISTA approach in localizing impact forces on a beam structure.

In the present study, the G-FISTA delivers the best overall force estimations in comparison to pseudo-inverse and Tikhonov regularization. Although the computation cost of this method is relatively higher than other force identification techniques, it still remains the best choice for point force reconstruction for off-line data processing.

Acknowledgements

The research presented in this paper has been performed within the framework of the project G.0738.11 “Inverse identification of wind loads on structures”, funded by the Research Foundation Flanders (FWO), Belgium. Their financial support is gratefully acknowledged.

REFERENCES

[1] D. Ginsberg, C.P. Fritzen, New approach for impact detection by finding sparse solution. *In Proceedings of ISMA*, pages 2051-2064, 2014.

[2] E. Jacquelin, A. Bennani, P. Hamelin, Force reconstruction: analysis and regularization of a deconvolution problem. *Journal of Sound and Vibration*, 265(1):81-107, July 2003.

[3] T.S. Jang, H. Baek, S.L. Han, T. Kinoshita, Indirect measurement of the impulsive load to a nonlinear system from dynamic responses: inverse problem formulation. *Journal of Mechanical Systems and Signal Processing*, 24(6):1665-1681, 2010.

[4] M. Klinkov, C.P. Fritzen, Online estimation of external loads from dynamic measurements. *Proceedings of ISMA*, pages 3957-3968, 2006.

[5] Y.M. Mao, X.L. Guo, Y. Zhao, Experimental study of hammer impact identification on a steel cantilever beam. *journal of Experimental Techniques*, 34(3):82-85, May 2009.

[6] E. Lourens, C. Papadimitriou, S. Gillijns, E. Reynders, G. De Roeck, G. Lombaert, Joint input-response estimation for structural systems based on reduced-order models and vibration data from a limited number of sensors. *Journal of Mechanical Systems and Signal Processing*, 29:310-327, 2012.

[7] S. Gillijns, B. De Moor, Unbiased minimum-variance input and state estimation for linear discrete-time systems with direct feedthrough. *Journal of Automatica* , 43, 934–937, 2007.

[8] K. Maes, E. Lourens, K. Van Nimmen, E. Reynders, G. De Roeck, G. Lombaert, Design of sensor networks for instantaneous inversion of modally reduced order models in structural dynamics. *Journal of Mechanical Systems and Signal Processing* , 5253:628-644, (2015).

[9] Y. Niu, M. Klinkov, C.P. Fritzen, Online force reconstruction using an unknown-input Kalman filter approach. *In Proceedings of the 8th International Conference on Structural Dynamics, EURODYN* , pages 2569–2576, 2011.

[10] M. Aucejo, Structural source identification using a generalized Tikhonov regularization. *Journal of Sound and Vibration* , 333(22):5693-5707, 2014.

[11] R. Hashemi, M.H. Kargarnovin, Vibration base identification of impact force using genetic algorithm. *Journal of Mechanical Systems Science and Engineering* , 1(4):204-210, 2008.

[12] E. Parloo, P. Verboven, P. Guillaume, M. Van Overmeire, Force identification by means of in-operation modal models. *Journal of Sound and Vibration*, 262(1):161-173, 2003.

[13] A.A. Uslu, K.Y. Sanliturk, M. Gul. Force estimation using vibration data. *In INTER-NOISE and NOISE-CON Congress and Conference Proceedings* , pages 2961-2969. Institute of Noise Control Engineering, 2007.

[14] R. Bond, D.E. Adams, Entropy-based impact load identification. *US Patent* , App. 13/882,891, 2011.

[15] E. Parloo, P. Verboven, P. Guillaume, M. Van Overmeire, Force identification by means of in-operation modal models. *Journal of Sound and Vibration* , 262(1):161-173, 2003.

[16] AN. Tikhonov, VY. Arsenin, Solution of ill-posed problems, 1977.

[17] A. Rezayat, V. Nassiri, S. Vanlanduit, P. Guillaume, Force identification using mixed and penalized optimization techniques. *International Conference on Noise and Vibration Engineering (ISMA)*, page 2095, 2014.

[18] A. Beck, M. Teboulle, A fast iterative shrinkage-thresholding algorithm for linear inverse problems. *SIAM Journal on Imaging Sciences* , 2(1):183-202, 2009.

[19] A. Rezayat, V. Nassiri, S. Vanlanduit, P. Guillaume, Force identification using mixed and penalized optimization techniques. *Proceedings of the 9th International Conference on Structural Dynamics, EURODYN* , pages 3957-3968, 2014.

[20] L. Boyd, S. Vandenberghe, Convex optimization. *Cambridge university press* , 2009.

[21] P.C. Hansen, Discrete inverse problems: insight and algorithms. *SIAM* , vol 7, 2010.

[22] V. Nassiri, Robust alternatives to least squares for sparse estimation with applications. *PhD thesis* , Vrije Universiteit Brussel (VUB), 2013.

COMPDYN 2015
5th ECCOMAS Thematic Conference on
Computational Methods in Structural Dynamics and Earthquake Engineering
M. Papadrakakis, V. Papadopoulos, V. Plevris (eds.)
Crete Island, Greece, 25–27 May 2015

ELASTIC INVERTED PENDULUM UNDER HYSTERETIC NONLINEARITY IN SUSPENSION: STABILIZATION AND OPTIMAL CONTROL

Mikhail E. Semenov[1,2,3], Andrey M. Solovyov[2], Andrey M. Semenov[2], Vladimir A. Gorlov[1], and Peter A. Meleshenko[1,2]

[1]Zhukovsky–Gagarin Air Force Academy
Starykh Bolshevikov st. 54 "A", 394064, Voronezh, Russia
e-mail: mkl150@mail.ru

[2]Voronezh State University
Universitetskaya sq. 1, 394006, Voronezh, Russia

[3]Voronezh State University of Architecture and Civil Engineering
XX-letiya Oktyabrya st. 84, 394006 Voronezh, Russia

Keywords: Elastic inverted pendulum, Hysteretic nonlinearity, Stabilization, Bionic algorithm, Difference scheme

Abstract. *This paper is dedicated to investigation of the elastic inverted pendulum with hysteretic nonlinearity in the suspension point. We consider the problem of stabilization and optimal control of such a system. In the frame of the bionic model we present an algorithm which provides an effective procedure for finding of optimal control parameters together with application of this algorithm to the system under consideration. The results of numerical simulations, namely, the phase portraits and the dynamics of Lyapunov function are presented and discussed.*

1 INTRODUCTION

The problem of inverted pendulum plays a central role in the control theory [1, 2, 3, 4]. The model of inverted pendulum provides many challenging problems to control design. Because of their nonlinear nature pendulums have maintained their usefulness and they are now used to illustrate many of the ideas emerging in the field of nonlinear control [5].

Such a mechanical system can be found in various field of technical sciences, from robotics to cosmic technologies. The stabilization of inverted pendulum is considered in the problem of missile pointing because the engine of missile is placed lower than the center of mass and such a fact leads to aerodynamical unstability. Similar problem is solved in the self-balancing transport device (the so-called segway). Moreover, such a mechanical system can be be applied in various fields such as physics, applied mathematics, engineer sciences, neuroscience, economics etc.

First theoretical description of the inverted pendulum was carried out by Stephenson [6] and the first experimental investigation of the stabilization process for such a system (using oscillations of the suspension point) was considered in the works of Kapitza [7]. In general, the problem of inverted pendulum is of more than one hundred years history and it still relevant even in the present days (see, e.g., [8, 9, 10, 11] and related references).

Backlash in the suspension point is a kind of hysteretic nonlinearity. It should be pointed out that the hysteretic phenomenons are insufficiently known in our days. This fact leads to an interesting problem on the presence of a backlash in the suspension point of a pendulum. In this paper we consider an elastic inverted pendulum using the operator technique for hysteretic nonlinearities. Namely, we obtain the equation of motion of the elastic pendulum with a hysteretic nonlinearity in the suspension point. The numerical solution of the equations of motion can be obtained using the difference scheme. We analyze the problem of optimization for the system under consideration. The numerical realization of optimization procedure is made using the so-called bionic algorithm. Also we obtain the numerical results for such a system in the form of a phase portrait and dynamics of Lyapunov function.

2 ELASTIC INVERTED PENDULUM WITH BACKLASH IN SUSPENSION

Let us consider the model of stabilization of inverted pendulum in the vicinity of vertical position. The pendulum is considered as an elastic rod which is hingedly fixed on the cylinder. Motion of cylinder is excited by the horizontal motion of a piston (see the Fig. 1) Mathematical

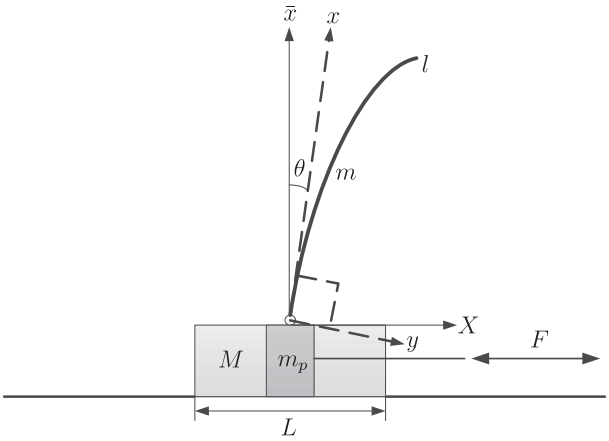


Figure 1: Model of elastic inverted pendulum: geometry of the problem.

model of a similar mechanical system (however without the hysteretic nonlinearity) was considered in [13].

Here (x, y) is a base of an elastic rod with mass m and density ρ; the Ox axis coincides with a tangent to rod's profile in the suspension point; θ is an angle of slope for the co-ordinates of a rod, I is a centroidal moment of inertia of the rod's section; $(X, \bar{x})$ is a co-ordinates of a considered mechanical system, M is a mass of a cylinder with length L, F is a force joined to a piston with mass m_p (such a force is treated as control).

The purpose of this paper is investigation of the possible stabilization (in a vicinity of vertical position) of elastic inverted pendulum in the presence of backlash in a suspension point together with investigation of various aspect of such a dynamical system.

In the following consideration we use the operator technique for hysteretic nonlinearities following the ideas of Krasnosel'skii and Pokrovskii [12]. Output of the backlash-inverter on the monotonic inputs can be described by the following expression:

$$X(t) = \Gamma[X_0, L]Y(t) = \begin{cases} 0, & |Y(t) - X_0| \leqslant \frac{L}{2}; \\ Y(t) - \frac{L}{2}, & Y(t) - X_0 > \frac{L}{2}; \\ Y(t) + \frac{L}{2}, & Y(t) - X_0 < -\frac{L}{2}; \end{cases}$$

Here $X(t)$ is a displacement of the cylinder's center, $Y(t)$ is a displacement of the piston in a horizontal plane.

It should be pointed out one more time that such a converter is considered on the monotonic inputs. On the piece-wise monotonic inputs this operator can be determined using the semigroup identity [12]

$$\Gamma[X(t_1), L]Y(t) = \Gamma\left[\Gamma[X_0, L]Y(t_1), L\right]Y(t).$$

And then, using the special limit construction such an operator can be redefined on all continuous functions.

2.1 Physical model

Let us assume that the deviation y and angle θ are small, i.e., $x \approx \bar{x}$ and the boundary conditions that determine the curvature of the pendulum are[1]:

$$\begin{cases} y(0,t) = y_{xx}(0,t) = 0, \\ y_{xx}(l,t) = y_{xxx}(l,t) = 0. \end{cases} \tag{1}$$

The function $X(\bar{x}, t)$ describes behavior of the pendulum's profile in time and shows deviation of the pendulum's points relative to vertical axis, $(X, \bar{x})$ are coordinates of the pendulum's profile, $X(0,t) = s(t)$ is a displacement of the suspension point in horizontal plane.

Coordinate system transformation in the matrix form is given by

$$\begin{pmatrix} X \\ \bar{x} \end{pmatrix} = \begin{pmatrix} \cos\theta & \sin\theta \\ -\sin\theta & \cos\theta \end{pmatrix} \begin{pmatrix} y \\ x \end{pmatrix} + \begin{pmatrix} X(0,t) \\ 0 \end{pmatrix}. \tag{2}$$

Let us construct the physical model of the considered mechanical system taking into account the backlash in the suspension point of an elastic rod. In order to do this we use the Lagrange formalism.

[1] In this paper we use the following notations: $a_x = \frac{\partial a}{\partial x}$, $a_t = \frac{\partial a}{\partial t}$.

Taking into account that y and θ are small the Lagrange function can be written as:

$$L(t) = \frac{Ms_t^2}{2} + \frac{1}{2}\int\limits_0^l \left[\rho s_t^2 + \rho y_t^2 + \rho(x\theta_t)^2 + \rho(2s_t x\theta_t + 2x\theta_t y_t + 2s_t y_t) + 2\rho g y\theta - EIy_{xx}^2\right] \mathrm{d}x. \tag{3}$$

Taking s as the generalized coordinate in the Lagrange function we have:

$$\frac{\mathrm{d}}{\mathrm{d}t}\frac{\partial L}{\partial s_t} - \frac{\partial L}{\partial s} = f(t). \tag{4}$$

Here $f(t)$ is a force joined to the suspension point of a rod.

General peculiarity of the system under consideration is the presence of backlash in the suspension point. Due to the fact that the backlash can be considered as a hysteretic nonlinearity we can use the technique of hysteretic converters. According to classical patterns of Krasnosel'skii and Pokrovskii [12], the hysteretic operators are treated as converters in an appropriate function spaces. The dynamics of such converters are described by the relation of "input-state" and "state-output".

Thus, the force joined to suspension point, can be found from the relation:

$$f(t) = \Gamma\left[X(0,t), Y(t), L, F_0\right] F = \begin{cases} 0, & |X(0,t) - Y(t)| \leqslant L; \\ F, & |X(0,t) - Y(t)| > L, \end{cases} \tag{5}$$

where L is the length of a cylinder, F is a force (this force affects the piston) which can be treated as a control.

The equation of motion of a piston is:

$$m_p Y_{tt}(t) = F. \tag{6}$$

Here Y is a displacement of the piston in a horizontal plane.

Passing to coordinate system $(X, \bar{x})$ the system of equations which describes the physical model of the considered mechanical system has the following form[2]:

$$\begin{cases} X_{tt} + \dfrac{EI}{\rho} X_{xxxx} = gX_x(0,t), \\ MX_{tt}(0,t) + mgX_x(0,t) + EIX_{xxx}(0,t) = f(t), \\ (M+m)X_{tt}(0,t) + ml(X_{tt})_x(0,t) = f(t), \\ g(M+m)X(0,t) - \dfrac{MEI}{\rho} X_{xxx} = lf(t), \\ f(t) = \Gamma\left[X(0,t), Y(t), L, F_0\right] F, \\ m_p Y_{tt}(t) = F. \end{cases} \tag{7}$$

2.2 Stabilization

Let us consider the problem of control of the pendulum using the feedback principles, i.e., the force which affects the piston can be presented by the following equality:

$$F = k\,\mathrm{sign}(\alpha e_1 + e_2), \tag{8}$$

[2]In order to reduce the description we do not present all the steps of transformations because of their obviousness

where $\alpha > 0,\ k > 0$ and

$$e_1 = \int_0^l X_x \mathrm{d}l, \tag{9}$$

$$e_2 = \int_0^l (X_t)_x \mathrm{d}l. \tag{10}$$

Here e_1 is an average angle of rod's deviation, e_2 is an average angular velocity of the rod.

Thus, in order to solve the stabilization problem for the elastic inverted pendulum we should use the system of equation (7) together with the equalities (8)-(10):

$$\begin{cases} X_{tt} + \dfrac{EI}{\rho} X_{xxxx} = g X_x(0,t), \\ M X_{tt}(0,t) + mg X_x(0,t) + EI X_{xxx}(0,t) = f(t), \\ (M+m) X_{tt}(0,t) + ml (X_{tt})_x(0,t) = f(t), \\ g(M+m) X(0,t) - \dfrac{MEI}{\rho} X_{xxx} = l f(t), \\ f(t) = \Gamma \left[X(0,t), Y(t), L, F_0 \right] F, \\ m_p Y_{tt}(t) = F, \\ F = k \operatorname{sign}(\alpha e_1 + e_2), \\ e_1 = \displaystyle\int_0^l X_x \mathrm{d}l, \\ e_2 = \displaystyle\int_0^l (X_t)_x \mathrm{d}l. \end{cases} \tag{11}$$

The solution of the posed problem on stabilization of elastic inverted pendulum in the vicinity of the upper position is consisted in search of the optimal values for coefficients α and k. Let us note that the numerical realization of the presented problem can be made using difference scheme.

3 OPTIMIZATION PROBLEM

As was mentioned above the solution of the problem on stabilization of elastic inverted pendulum in the vicinity of the upper position is consisted in search of the optimal values for coefficients α and k from the equality (8).

In many technical problems the question on stabilization has a general interest. However, together with the stabilization of the system there is the problem of optimization (this problem corresponds to asymptotically optimal characteristics of the system). In the system under consideration the problem of optimization corresponds to minimizing of the functional which determines the deviation of the pendulum from the vertical position. Let us consider a functional (the so-called objective functional) as follows:

$$\mathfrak{J} = \frac{1}{T} \int_0^T \left\{ \int_0^l (X_x)^2 \mathrm{d}l + \int_0^l [(X_t)_x]^2 \mathrm{d}l \right\} \mathrm{d}t. \tag{12}$$

Here T is the time interval in which we find an optimal control.

Solution of the equations (11) that describe the dynamics of the system under consideration should be obtained under conditions that provide the minimization of functional (12). Physically this means that the problem is equivalent to minimization of mean-square deviation of the pendulum relative to vertical position.

In order to solve the optimization problem in the system under consideration we use the bionic algorithms of adaptation because the hysteretic peculiarities in the considered pendulum's model lead to some difficulties in use of the classical optimization algorithms due to non-differentiability of the functions in the system of equations.

Such algorithms are a part of the line of investigation which can be called as "adaptive behavior". Main method of this line consists in the investigation of artificial organisms (in the form of computer program or a robot) that are called as animats (these animats can be adapted to environment). The behavior of animats emulates the behavior of animals.

One of the actual line of investigation in the frame of animat-approach is an emulation of searching behavior of animals. Let us consider the bionic model of adaptive searching behavior on the example of caddis flies larvae or *Chaetopteryx villosa*. Main schema of searching behavior can be characterized by two stages:

- Motion in a chosen direction (conservative tactics);
- Random change of the motion direction (stochastic searching tactics).

We consider this model for the simple case of maximum search for the function of two variables. Let we describe main stage of the considered model:

1. We consider an animat which is moved in the two-dimensional space x, y. Main purpose of animat is maximum search for the function $f(x, y)$.
2. Animat is functioned in discrete time $t = 0, 1, 2, \ldots$. Animat estimates the change of current value of $f(x, y)$ in comparison with the previous time $\Delta f(t) = f(t) - f(t-1)$.
3. Every time animat moves so its coordinates x and y change by $\Delta x(t)$ and $\Delta y(t)$ respectively.
4. Animat has two tactics of behavior: a) conservative tactics; b) stochastic searching tactics.

Displacement of animat in the next time $\Delta x(t+1)$, $\Delta y(t+1)$ for these tactics determines in a different ways. Switching between the cycles drives by $M(t)$. Time dependence of $M(t)$ can be determined using the equation:

$$M(t) = k_1 M(t-1) + \xi(t) + I(t), \tag{13}$$

where k_1 is a parameter which determines the switching persistence of tactics $(0 < k_1 < 1)$, $\xi(t)$ is a normal distributed variate with an average value equal to zero and mean-square deviation equal to σ, $I(t)$ is an intensity of irritant. For the value of $I(t)$ there are two possibilities:

$$I(t) = k_2 \Delta f(t) \tag{14}$$

and

$$I(t) = k_2 \frac{\Delta f(t)}{f(t-1)}, \tag{15}$$

where $k_2 > 0$. As follows from (14) and (15) the intensity is positive when the step leads to increasing of function, otherwise the intensity is negative. It should be noted also that the equation (15) can be applied in the case $f(t) > 0$.

We assume that at $M(t) > 0$ animat follows the tactics a) and at $M(t) < 0$ it follows tactics b). So, the value of $M(t)$ can be considered as a motivation to selection of tactics a).

Thus, the algorithm of maximum search can be considered as follows:

Tactics a): Animat moves in the chosen direction. The displacement of animat is determined by R_0

$$\Delta x(t+1) = R_0 \cos\varphi_0, \tag{16}$$

$$\Delta y(t+1) = R_0 \sin\varphi_0, \tag{17}$$

where the angle φ_0 defines the constant direction of motion of animat:

$$\cos\varphi_0 = \frac{\Delta x(t)}{\sqrt{\Delta x^2 + \Delta y^2}}, \tag{18}$$

$$\sin\varphi_0 = \frac{\Delta y(t)}{\sqrt{\Delta x^2 + \Delta y^2}}. \tag{19}$$

Tactics b): Animat makes an accidental turn. The displacement of animat is determined by r_0 but the direction of motion is accidentally varied

$$\Delta x(t+1) = r_0 \cos\varphi, \tag{20}$$

$$\Delta y(t+1) = r_0 \sin\varphi, \tag{21}$$

where $\varphi = \varphi_0 + w$, φ_0 is an angle which characterizes the direction of motion at current time t, w is a normal distributed variate (average value of w equal to zero and mean-square deviation equal to w_0), φ is an angle which characterizes the direction of motion at time $t+1$.

In that way we can use the proposed algorithm for searching the optimal control in the problem of stabilization of elastic inverted pendulum. Taking into account the reasoning presented above we can apply the presented algorithm to functional $\mathfrak{J}(\alpha, k)$ where the coefficients α and k determine the character of control of the mechanical system under consideration following the equation (8). Due to the fact that the presented bionic algorithm is used to maximum search of the function of two variables we will consider minimization of functional (12) as a procedure for finding the coefficients α and k that lead to realization of the condition

$$-\mathfrak{J}(\alpha, k) \to \max. \tag{22}$$

4 SIMULATION RESULTS

In this section we present a simulation of the behavior of elastic inverted pendulum with the backlash in suspension. We use the corresponding difference scheme and the bionic algorithm for finding of the optimal values of coefficients α and k.

The characteristics and initial conditions for the mechanical system under consideration are:

$$m = 1\,\text{kg},\ M = 10\,\text{kg},\ m_p = 1\,\text{kg}\, l = 1\,\text{m},\ \rho = 0.5,\ E = 10,\ I = 4,\ \theta_0 = 0.06^\circ.$$

In order to estimate the stability of the system under consideration we also use the Lyapunov criterion. Namely, we use the following Lyapunov function:

$$V = e_1^2 + e_2^2.$$

Using the bionic algorithm we have obtained the following optimal values of coefficients: $\alpha = 9$ and $k = 2$. The phase trajectory of such a system together with the dynamics of Lyapunov function in time (namely, in discrete time which corresponds to difference scheme) for different values of a control coefficients are presented in the Fig. 2. In this figure the integral angle e_1 and integral angular velocity e_2 correspond to equations (9) and (10) respectively. As we can see from presented figures the Lyapunov function satisfies the following condition

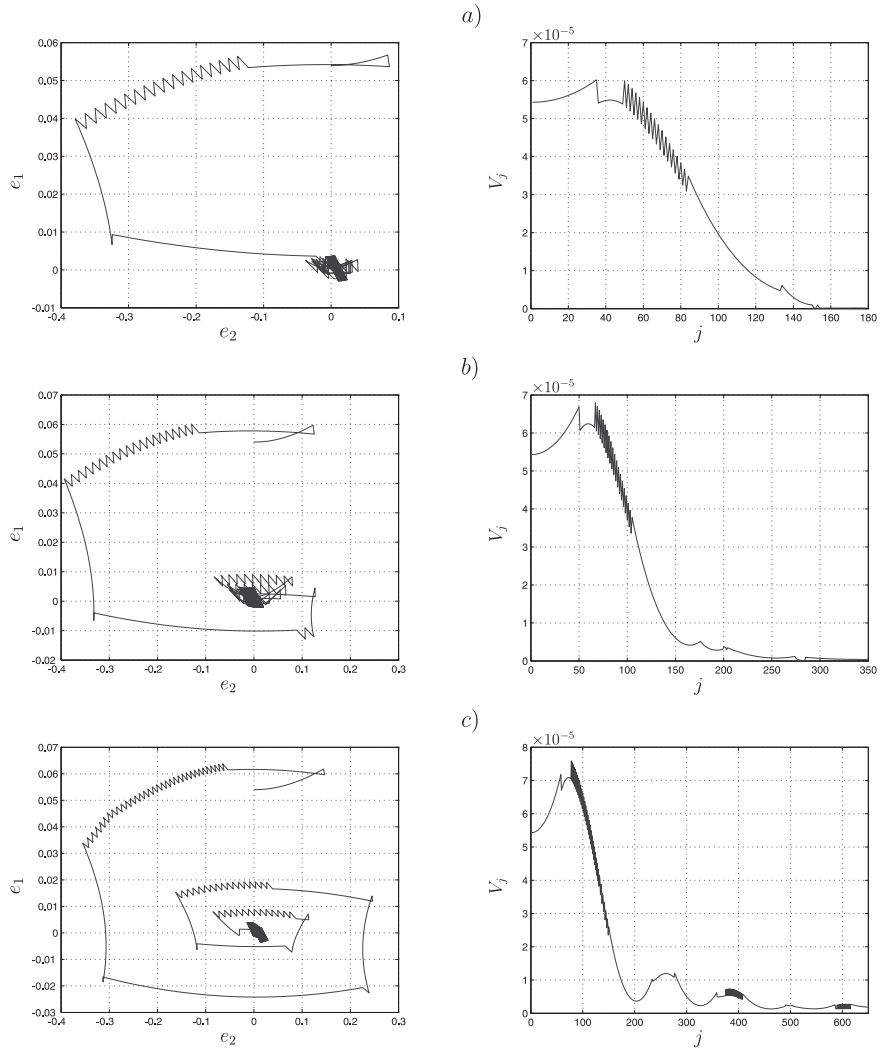


Figure 2: Phase trajectories (left panels) and dynamics of Lyapunov function (right panels) in the presence of a backlash in suspension point. Parameters of a backlash and control coefficients are: a) – $L = 0.01\,\text{m}$, $\alpha = 9$, $k = 2$; b) – $L = 0.02\,\text{m}$, $\alpha = 9$, $k = 2$; c) – $L = 0.02\,\text{m}$, $\alpha = 10.5$, $k = 1.5$.

(during all the considered time interval):

$$V_t(t) \leqslant 0.$$

This means that the considered inverted pendulum eventually tends to stable vertical position.

5 CONCLUSIONS

In this paper we have considered the stabilization problem of elastic inverted pendulum under hysteretic control in the form of backlash in suspension point. Also the problem of optimization

for the system under consideration is analyzed. Main coefficients, namely α and k that provide the solution of optimization problem for the considered system are obtained using the so-called bionic algorithm. All the numerical results on stabilization of the system under consideration have obtained using the numerical method based on the difference scheme. The results of numerical simulations show that the considered system eventually tends to stable state. This fact is presented in the form of corresponding phase portraits for the considered system. Moreover, in order to estimate the stability of the elastic pendulum with the backlash in the suspension point we have used the Lyapunov criterion and the dynamics of corresponding Lyapunov function has also been presented.

REFERENCES

[1] E.I. Butikov, Subharmonic resonances of the parametrically driven pendulum. *J. Phys. A: Math. Theor.*, **35**, 6209, 2002.

[2] F.L. Chernous'ko, S.A. Reshmin, Time-optimal swing-up feedback control of a pendulum. *Nonlinear Dynam.*, **47**, 65–73, 2007.

[3] S. Sazhin, T. Shakked, D. Katoshevski, V. Sobolev, Particle grouping in oscillating flows. *Eur. J. Mech. B-Fluid.*, **27**, 131–149, 2008.

[4] J. Huang, F. Ding, T. Fukuda, T. Matsuno, Modeling and velocity control for a novel narrow vehicle based on mobile wheeled inverted pendulum. *IEEE Transactions on Control Systems Technology*, **21**, 1607–1617, 2013.

[5] K.J. Åström, K. Furuta, Swinging up a pendulum by energy control. *Automatica*, **36**, 287–295, 2000.

[6] A. Stephenson, On an induced stability. *Phil. Mag.*, **15**, 233, 1908.

[7] P.L. Kapitza, Pendulum with a vibrating suspension. *Usp. Fiz. Nauk* (in Russian), **44**, 7–15, 1951.

[8] E.I. Butikov, An improved criterion for Kapitza's pendulum stability. *J. Phys. A: Math. Theor.*, **44**, 295202, 2011.

[9] J.J. Wang, Simulation studies of inverted pendulum based on PID controllers. *Simul. Model. Pract. Th.*, **19**, 440–449, 2011.

[10] E.I. Butikov, Oscillations of a simple pendulum with extremely large amplitudes. *Eur. J. Phys.*, **33**, 1555–1563, 2012.

[11] M.E. Semenov, D.V. Shevlyakova, P.A. Meleshenko, Inverted pendulum under hysteretic control: stability zones and periodic solutions. *Nonlinear Dynam.*, **75**, 247–256, 2014.

[12] M.A. Krasnosel'skii, A.V. Pokrovskii, *Systems with Hysteresis*. Springer Verlag, 1989.

[13] C. Xu, X. Yu, Mathematical model of elastic inverted pendulum control system. *Control Theory and Technology*, **2**, 281–282, 2004.

COMPDYN 2015
5th ECCOMAS Thematic Conference on
Computational Methods in Structural Dynamics and Earthquake Engineering
M. Papadrakakis, V. Papadopoulos, V. Plevris (eds.)
Crete Island, Greece, 25–27 May 2015

SEISMIC ENERGY RESPONSE OF TEN-STORY STEEL ROCKING FRAMES WITH COLUMN MID-HEIGHT UPLIFT AT FIRST STORY

Mitsumasa MIDORIKAWA[1], Naoto KOTANI[2], Taichiro OKAZAKI[3], Tetsuhiro ASARI[4], Tadashi ISHIHARA[5], Tatsuya AZUHATA[6]

[1] Prof., Faculty of Eng., Hokkaido Univ., Dr. Eng.
Kita 13, Nishi 8, Kita-ku, Sapporo, 060-8628 Japan
midorim@eng.hokudai.ac.jp

[2] Graduate Student of Hokkaido Univ.
Kita 13, Nishi 8, Kita-ku, Sapporo, 060-8628 Japan
kotani.naoto@frontier.hokudai.ac.jp

[3] Assoc. Prof., Faculty of Eng., Hokkaido Univ., Ph. D.
Kita 13, Nishi 8, Kita-ku, Sapporo, 060-8628 Japan
tokazaki@eng.hokudai.ac.jp

[4] Asst. Prof., Faculty of Eng., Hokkaido Univ., Dr. Eng.
Kita 13, Nishi 8, Kita-ku, Sapporo, 060-8628 Japan
asari@eng.hokudai.ac.jp

[5] Senior Research Engineer, Building Research Institute, Dr. Eng..
1, Tachihara, Tsukuba, Ibaraki, 305-0802 Japan
tishihar@kenken.go.jp

[6] Chief Research Engineer, Building Research Institute, Ph. D.
1, Tachihara, Tsukuba, Ibaraki, 305-0802 Japan
azuhata@kenken.go.jp

Keywords: Rocking frame, Colum mid-height uplift, Steel damper, Earthquake energy response

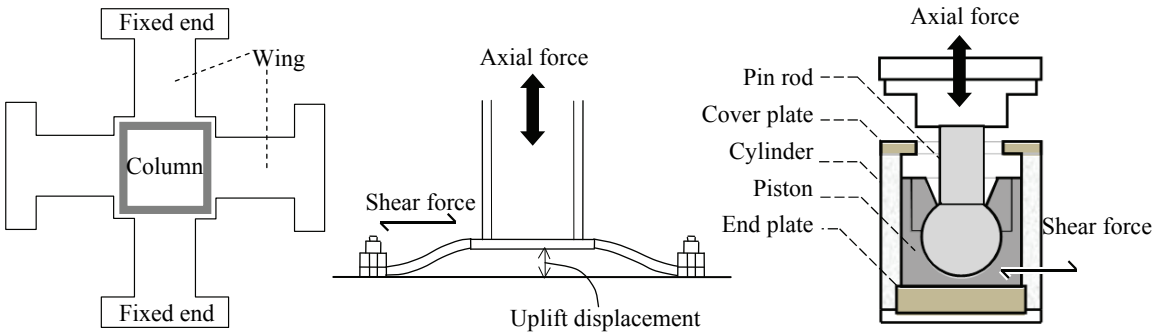
Abstract. *Lessons learned from past earthquake damage suggest the potential benefit of rocking systems that reduce earthquake damage. This paper evaluates a structural system that achieves a rocking mechanism by permitting uplift at the mid-height of the first-story columns (CMU system). Steel dampers installed in these columns dissipate the seismic energy and reduce deformation. Suggested system is compared with corresponding ordinary frame without rocking mechanism (Fixed system) in the view of energy response. For the ground motions examined in this study, the seismic energy input to the CMU system was 0.6 to 2.2 times that to the Fixed system, while the energy dissipated by the steel system was significantly smaller (0 to 57%) in the CMU system than in the Fixed system.*

1 INTRODUCTION

Observations from past earthquakes suggest that some buildings survived severe ground motion because of accidental uplift at their foundation [1, 2]. Motivated by such notion [3], the writers initially developed rocking systems that are provided with a mechanism that permit column-base uplift (CBU) [4]. The CBU system was achieved by placing the devices shown in Fig. 1a-b at the base of the columns. In this system, the column base is connected to the foundation through wing plates. The wing plates are designed to yield and dissipate energy when the column uplifts, while fully transferring the shear forces. The stable and reliable performance of this system has been demonstrated by large-scale shake table tests [4].

While CBU rocking systems can reduce seismic damage, the systems increase the likelyhood of damage in second-floor beams compared to fixed-base systems. Consequently, the writers propose an alternative rocking frame that allows uplift at the middle of the columns instead of the column bases. The column mid-height uplift (CMU) mechanism fully resists shear forces and is generally accompanied by steel dampers. Fig. 1(c) shows a CMU system accompanied with steel dampers that has been validated by cyclic loading tests [5]. The ball in the piston is free to rotate, and the piston can slide upwards. Shear forces are transferred fully by the piston bearing against the cylinder. Conceptually, the CMU rocking system can reduce story drift of the first story compared to the CBU system because the CMU system forces double-curvature bending of the first-story columns while the CBU system forces single-curvature bending [6]. In fact, an earlier study by the authors [5] suggests that the first-story drift will not be increased by the addition of CMU systems.

This paper describes a computational study of the CMU system. The potential benefit of the CMU system is examined through seismic input energy and energy dissipation. A series of nonlinear time history analyses was conducted on a ten-story steel building equipped with a CMU system [7]. For comparison, the analyses were repeated for cases where (a) steel damper was removed (denoted as CMU-ND) and where (b) the first-story columns were continuous and fixed to the foundation (denoted as Fixed).



(a) CBU mechanism (Plan) (b) CBU mechanism (Elevation) (c) CMU mechanism

Figure. 1 Uplift mechanism

2 ANALYSIS PROCEDURE

The seismic performance of buildings equipped with CMU systems is examined by nonlinear time history analysis. A commercial software [8] was used for the study. As shown in Fig. 2, the model was a single bay, ten-story frame representing the Y-3 elevation of a prototype steel building. A concentrated mass of 288 kN was placed at each beam-column node.

Concentrated plastic hinges were placed at both ends of each beam or column. The moment versus rotation relationship of the plastic hinge was defined by a trilinear curve capturing the yield moment and plastic moment. The steel system was proportioned according to the seismic code of Japan and the weak beam-strong column rule. The section, yield moment and plastic moment of each beam and column is shown in Table 1. The yield strength of steel is assumed to be 294 N/mm^2.

The CMU system was modeled using (a) a contact element that permits elongation but is does not contract, (b) a linear shear element, and (c) a bilinear element that models the steel dampers (see Fig. 3). The shear element had the same shear stiffness as the column over a length of 50 mm. In compression, the contact element had 10 times the axial stiffness of the column over the entire length. The bilinear element was fitted to experimental data: The initial stiffness was 10% the axial stiffness of the column (= 2.2×10^5 kN/m), the yield strength was 30% of the gravity load in the column (= 431 kN), and the post-yield stiffness was 3 and 1%,

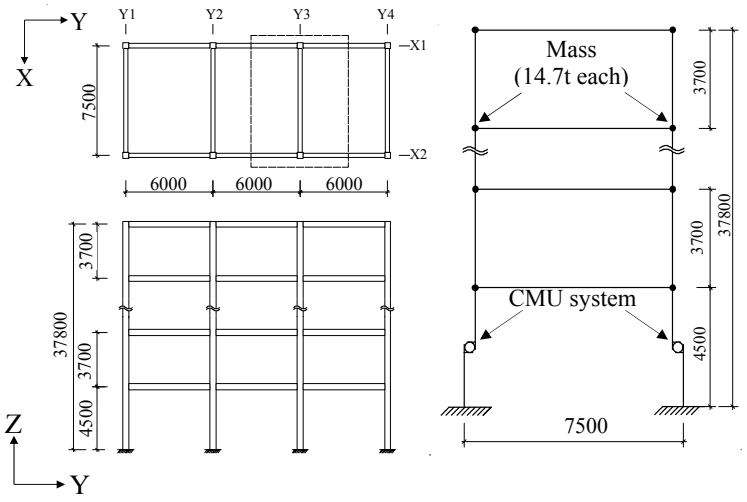
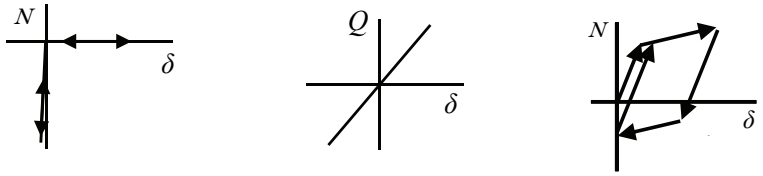


Figure 2 Analytical model

Table 1 Member sections

	Member section	Yield moment	Plastic moment
1-7F Column	□-500 × 500 × 25	2110 kN.m	2490 kN.m
8-10F Column	□-500 × 500 × 19	1660 kN.m	1940 kN.m
2-6F Beam	H-700×300×13×24	1630 kN.m	1840 kN.m
7-RF Beam	H-588×300×12×20	1130 kN.m	1270 kN.m



(a) Contact element (b) Shear element (c) Bilinear element

Figure 3. Elements comprising the CMU system

respectively, of the initial stiffness in the tension side and compression side. The building model equipped with this CMU system is referred to as the CMU model.

For comparison, analysis was repeated for two other cases: the bilinear element removed (CMU-ND model); and the first-story columns modeled with a continuous element with no CMU system (Fixed model). The first natural vibration period of the Fixed model (T_l) and CMU model (T_u) was computed as 1.34 s and 2.47 s, respectively. The first natural period of the CMU model was estimated using a model where, in one column, the CMU is replaced by a hinge and in the other column, the bilinear element is replaced by a linear element whose stiffness equaled the secant stiffness of the steel damper at an uplift rotation angle of 1/200.

Damping was proportional to the initial stiffness of the Fixed model with a damping ratio h=0.02. Viscous damping of the contact element and bilinear element were set to zero.

The model was subjected to four recorded ground motions listed in Table 2, each scaled to a peak ground velocity (PGV) of 0.5, 0.75, 1.0, and 1.25 m/s, resulting in a total of 16 analysis cases. Fig. 4 shows the energy spectrum for the four motions computed for damping ratio h = 0.1, while Fig. 5 shows the pseudo-velocity spectrum for damping ratio h = 0.05. A previous study by the authors [7] indicate that the vertical ground motion has minimal effect on the lateral response of structures with CBU systems. The same is believed to apply to CMU systems.

Table 2 Unscaled ground motions

Earthquake	Station	Analysis time	Direction	PGA (m/s^2)	PGV (m/s)
1994, Northridge	Tarzana	15 s	EW	17.4	1.14
1995, Hyogo-Ken Nanbu	JMA-Kobe	15 s	NS	8.18	0.91
2000, Tottori-Ken Seibu	Hino	21 s	NS	9.18	1.28
2004, Nigata-Ken Chuetsu	Yamakoshi	31 s	EW	7.22	0.87

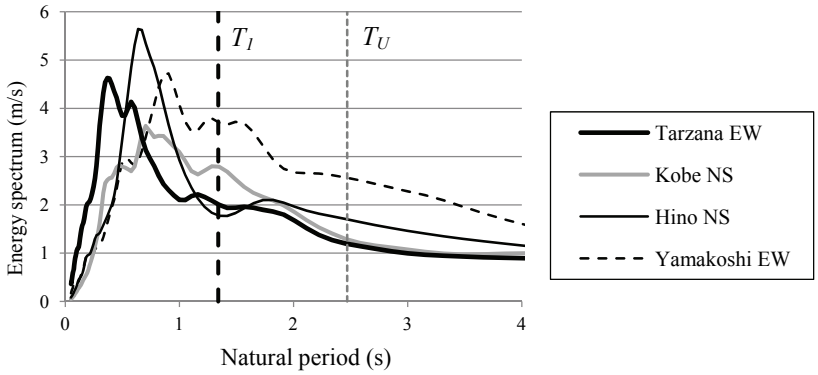


Figure.4: Energy spectra (h = 0.1)

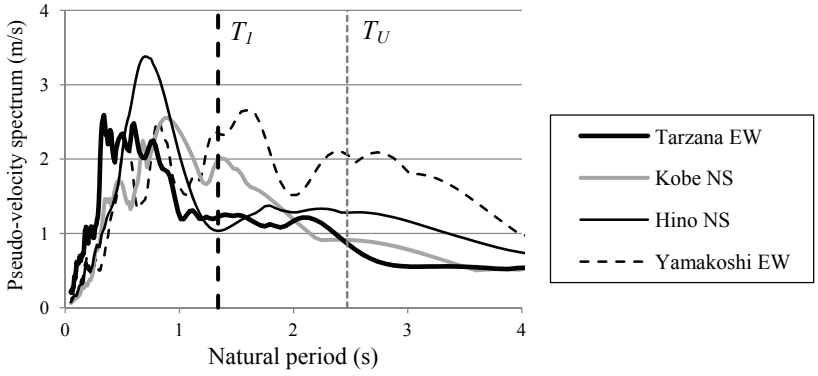


Figure 5: Pseudo-velocity spectra (h = 0.05)

3 ANALYSIS RESULTS

Fig. 6 shows the time history of the relative roof drift computed for ground motions scaled to a PGV of 1.0 m/s. In this paper, the relative roof drift refers to the roof drift minus the drift caused by rocking, i.e., the rigid body component associated with column uplift. The figure suggests that permission of column uplift resulted in reduction in shear deformation and elongation in response period. The response period was longer in the CMU-ND model than the CMU model. Fig. 7 plots the maximum roof drift and maximum relative roof drift obtained from each ground motion and for each PGV. The CMU and CMU-ND model recorded a larger roof drift than the Fixed model in 14 out of the 16 analysis cases. The maximum roof drift tended to be somewhat smaller in the CMU model than in the CMU-ND system: the presence of dampers reduced the maximum roof drift in 12 out of the 16 analysis cases. On the other hand, for all analysis cases, the CMU and CMU-ND models recorded a 1 to 60% reduction in relative roof drift compared to the Fixed model. The CMU system, with or without dampers, was more effective for ground motions Yamakoshi and Kobe, whose predominant period was close to the natural period of the structure, T_1 = 1.34 s, than for the other two motions.

Fig. 8 and 9 show the time history of column uplift displacement of the CMU and CMU-ND models, respectively, computed for ground motions scaled to a PGV of 1.0 m/s. The figures indicate that the presence of steel dampers reduced uplift displacement and mitigated high vibration modes. The ratio of maximum uplift displacement between the CMU model and CMU-ND model was 65, 60, 49 and 37%, respectively, for the Tarzana, Kobe, Hino and Yamakoshi record.

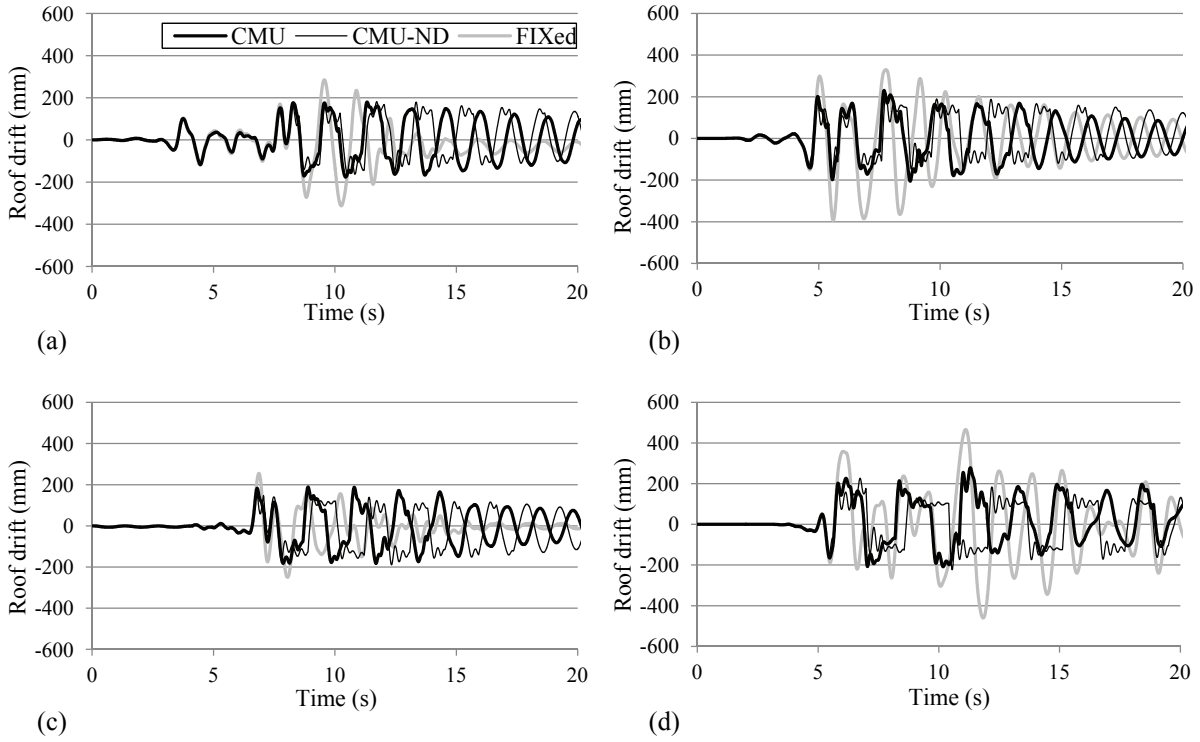


Figure 6: Time histories of relative roof drift: (a) Tarzana; (b) Kobe; (c) Hino; and (d) Yamakoshi record

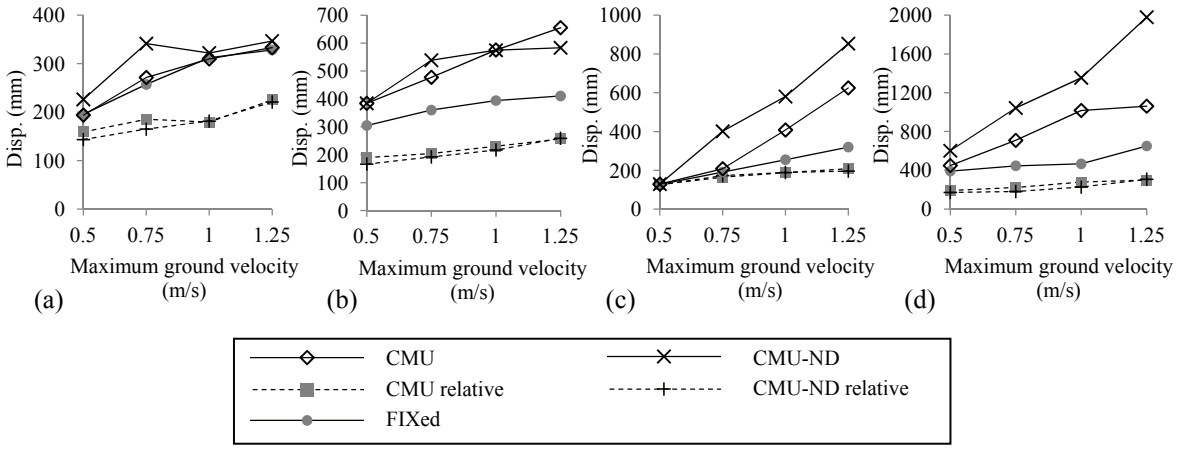


Figure 7: Maximum roof drift and relative roof drift:
(a) Tarzana; (b) Kobe; (c) Hino; and (d) Yamakoshi record;

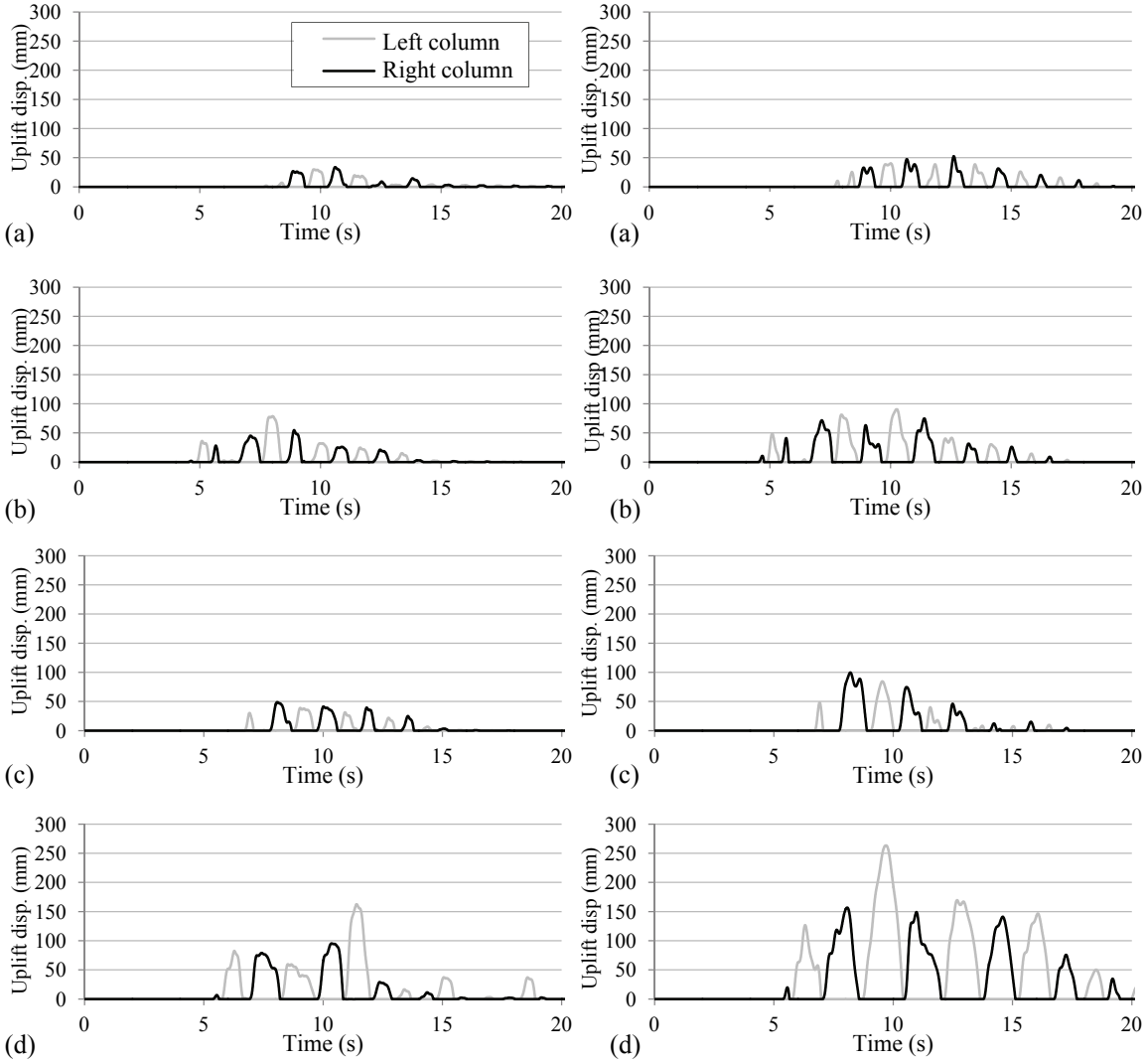


Figure 8: Time histories of column uplift displacement in CMU model: (a) Tarzana; (b) Kobe; (c) Hino; and Yamakoshi record.

Figure 9: Time histories of column uplift displacement in CMU-ND model: (a) Tarzana; (b) Kobe; (c) Hino; and (d) Yamakoshi record.

4 DISCUSSION BASED ON ENERGY

The dynamic motion of a building structure subject to horizontal earthquake ground motion satisfies the balance of energy expressed by Eq. (1).

$$\sum \int_0^t F_e \dot{x} dt = \left(\sum \frac{1}{2} M \dot{y}^2 + \sum \frac{1}{2} M \dot{x}^2\right) + \sum C \int_0^t \dot{x}^2 dt + \sum Mgy + \sum \int_0^t F(x') \dot{x}' dt + \sum \int_0^t D(y') \dot{y}' dt \quad (1)$$

Where, x: horizontal displacement of the mass relative to the ground, y: vertical displacement of the mass relative to the ground, F_e:seismic load ($= -M\ddot{z}_0$), $\ddot{z}_0$: horizontal ground acceleration, M: mass, C: damping coefficient, g: gravitational acceleration, $F(x')$: restoring force of a member, x': deformation of a member, $D(y')$: restoring force of a steel damper, and y': deformation of a steel damper. Summation is performed over all masses and all elements that comprise the structure.

Eq. (1) may be expressed in a compacted form as Eq. (2).

$$E_I = (E_{LK} + E_{VK}) + E_d + E_p + (E_s + E_h) \quad (2)$$

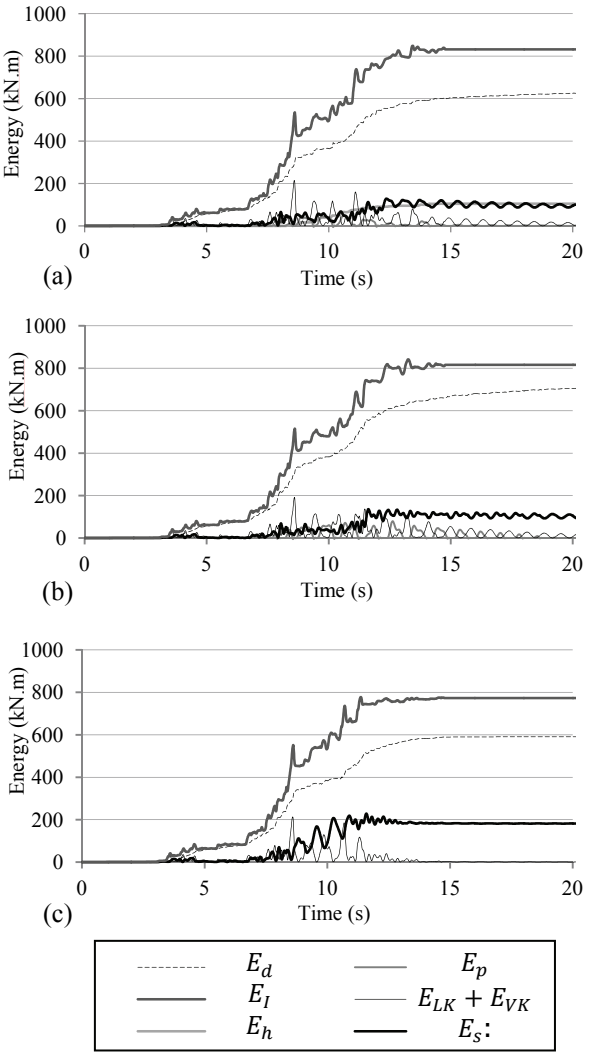


Figure 10: Energy response computed for Tarzana record; (a) CMU; (b) CMU-ND; and (c) Fixed model.

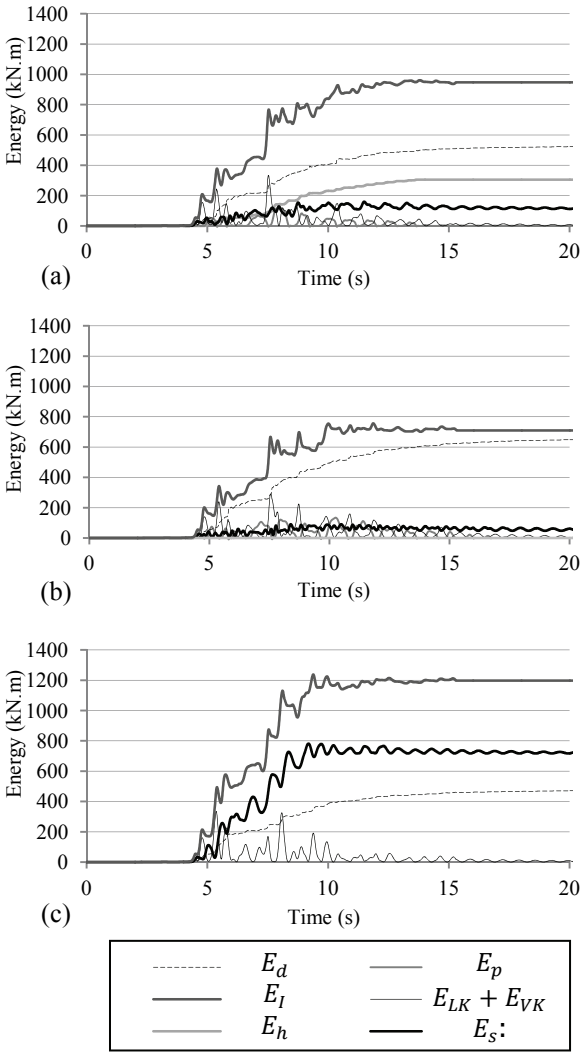


Figure 11: Energy response computed for Kobe record; (a) CMU; (b) CMU-ND; and (c) Fixed model.

Where, E_I: lateral input energy, E_{LK}: kinetic energy due to horizontal vibration, E_{VK}: kinetic energy due to uplift motion, E_d: energy dissipated by damping, E_p: potential energy associated with uplift, E_s: energy dissipated by the structure, and E_h: energy dissipated by the steel dampers.

Figs. 10 to 13 show the time history of energy response of the CMU, CMU-ND, and Fixed model, respectively, computed for ground motions scaled to a PGV of 1.0 m/s. For the Kobe and Yamakoshi records, the energy dissipated in the structure was one-fifth in the CMU and CMU-ND models compared to the Fixed model. These are the two records for which the CMU system effectively reduced the relative roof drift (see Fig. 6 and 7). For the Tarzana record, the energy dissipated in the structure was one-half in the CMU and CMU-ND models compared to the Fixed model. On the other hand, for the Hino record, the CMU-ND model dissipated double the energy in the structure compared to the Fixed model. These results suggest that, while the CMU system can be beneficial against many ground motions, there is a range of ground motions against which there may be no benefit.

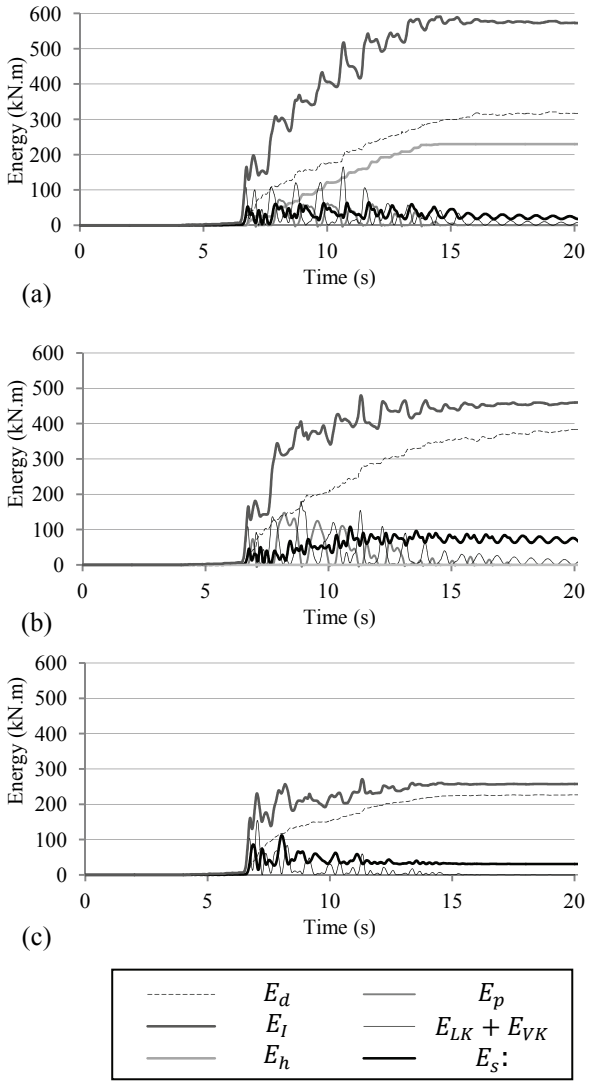


Figure 12: Energy response computed for Hino record; (a) CMU; (b) CMU-ND; and (c) Fixed model.

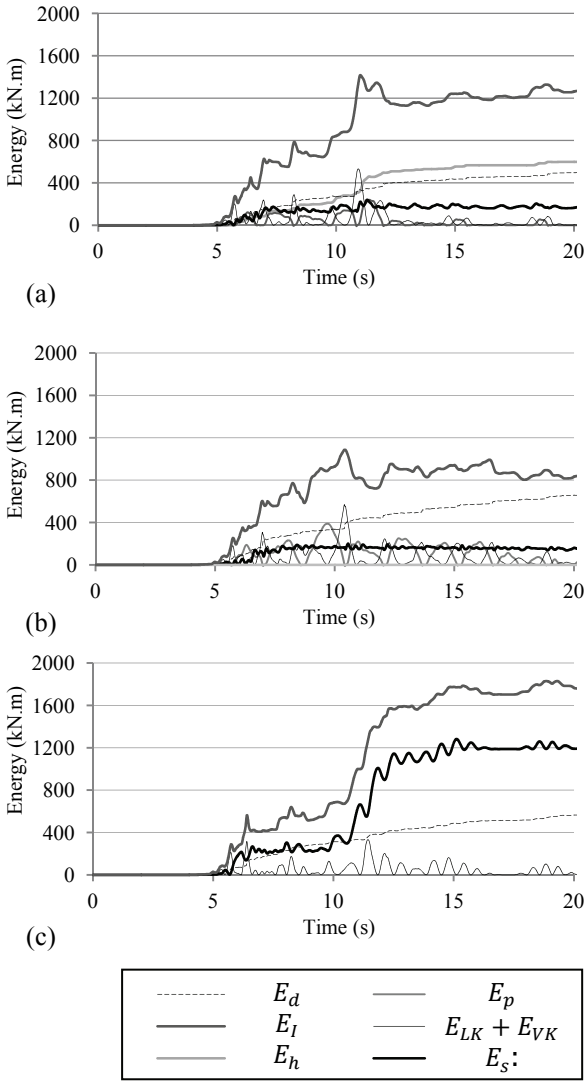


Figure 13: Energy response computed for Yamakoshi record; (a) CMU; (b) CMU-ND; and (c) Fixed model.

Table 3 lists the ratio E_h/E_I, the proportion of input energy that was dissipated by the steel dampers in the CMU model. The steel damper dissipated a substantial portion, up to 47%, of the input energy.

Tables 4 and 5 show the proportion of CMU system to CMU-ND in the input energy and the value of energy dissipated by the steel system of CMU system divided by that of CMU system respectively. For the same ground motion, the seismic energy input to the CMU system was 0.6 to 2.2 times that to the Fixed system. Nonetheless, as shown in Table 5, for the ground motions examined in this study, the energy dissipated by the steel system was significantly smaller (0 to 57 %) in the CMU system than in the Fixed system.

5 CONCLUSIONS

A series of nonlinear time history analyses was conducted on models of a ten-story steel building. One model had column mid-height-uplift (CMU) systems, equipped with dampers, placed in the first-story columns (CMU model). The second model had CMU systems with no dampers (CMU-ND model). The third model was an ordinal frame with no CMU system (Fixed model). The models were subjected to four recorded ground motions, each scaled to a maximum ground velocity of 0.5, 0.75, 1.0, and 1.25 m/s. The following are the findings from the analysis results:

- For the same ground motion, the seismic energy input to the CMU system was 0.6 to 2.2 times that to the FIX system. Nonetheless, for the ground motions examined in this study, the energy dissipated by the steel system was significantly smaller (0 to 57 %) in the CMU system than in the FIX system.
- Little difference was observed between the CMU system and CMU-ND system in terms of energy dissipation. However, the maximum roof drift in the CMU system was 50 to 110 % that in the CMU-ND system. The damper reduced the maximum roof drift in 12 out of the 16 analysis cases.

Table 3: E_h/E_I, the proportion of energy dissipated by steel dampers

maximum ground velocity	Tarzana	Kobe	Hino	Yamakoshi
0.5m/s	5%	30%	0%	34%
0.75m/s	16%	31%	11%	38%
1.0m/s	13%	32%	40%	47%
1.25m/s	13%	37%	45%	41%

Table 4: E_I computed for the CMU model divided by E_I computed for the CMU-ND model.

maximum ground velocity	Tarzana	Kobe	Hino	Yamakoshi
0.5 m/s	93 %	73 %	104 %	78 %
0.75 m/s	115 %	76 %	133 %	78 %
1.0 m/s	108 %	79 %	224 %	78 %
1.25 m/s	81 %	61 %	131 %	71 %

Table 5: E_S computed for the CMU model divided by E_S computed for the CMU-ND model.

maximum ground velocity	Tarzana	Kobe	Hino	Yamakoshi
0.5 m/s	3 %	14 %	100 %	2 %
0.75 m/s	32 %	13 %	35 %	8 %
1.0 m/s	48 %	16 %	57 %	14 %
1.25 m/s	56 %	19 %	47 %	17 %

ACKNOWLEDGEMENT

A part of this work was supported by Japan Society for the Promotion of Science (JSPS) Grant-in-Aid for Scientific Research: Grant Number 25289177 and 24560707.

REFERENCES

[1] Y. Hayashi, Damage reduction effect due to basemat uplift of buildings, *Journal of Structural and Construction Engineering*, Architectural Institute of Japan, **485**, 53-62, 1996, (in Japanese).

[2] A. Rutenberg, P.C. Jennings, G.W. Housner, The response of Veterans Hospital Building 41 in the San Fernando Earthquake, *Earthquake Engineering and Structural Dynamics*, **10**(3), 359-379,1982.

[3] K. Iwashita, H. Kimura, Y. Kasuga, N. Suzuki, Shaking table test of a steel frame allowing uplift, *Journal of Structural and Construction Engineering*, Architectural Institute of Japan, **561**, 47-54, 2002, (in Japanese).

[4] M. Midorikawa, T. Azuhata, T. Ishihara, A. Wada, Dynamic behavior of steel frames with yielding base plates in uplift motion for seismic response reduction, *Journal of Structural and Construction Engineering*, Architectural Institute of Japan, **572**, 97-104, 2013, (in Japanese).

[5] Y. Kato, M. Midorikawa, Y. Kawai T. Ishihara, H. Matsumoto, Static loading tests of column mid-height uplift mechanism with steel dampers, *Proceedings of Constructional Steel*, **22**, 399-404, 2014, (in Japanese).

[6] H. Matsumoto, W. Naruo, M. Midorikawa, T. Asari, T. Ishihara, Seismic response of steel frames that permit column mid-height uplift in the first story, *Proceedings of Constructional Steel* **21**, 685-692, 2013, (in Japanese).

[7] M. Midorikawa, T. Sudo, T. Asari, T. Azuhata, T. Ishihara, Three-dimensional seismic response of ten-story steel frames with yielding base plates allowed to uplift, *Journal of Structural and Construction Engineering*, Architectural Institute of Japan,**637**, 495-502, 2009, (in Japanese).

[8] MIDAS IT Co., Ltd., *Analysis & Design, MIDAS/Gen ver.761*, 2009

[9] K. Iwashita, H. Taniguchi, T. Ishihara, Energy approach to the earthquake response of building allowing uplift at pile head, *Journal of Structural and Construction Engineering*, Architectural Institute of Japan, **637**, 495-502, 2009, (in Japanese).

[10] M. Midorikawa, T. Azuhata, T. Ishihara and A. Wada, Shaking Table Tests on Seismic Response of Steel Braced Frames with Column Uplift, *Earthquake Engineering and Structural Dynamics*, **35(14)**, 1767-1785, 2006.

COMPDYN 2015
5th ECCOMAS Thematic Conference on
Computational Methods in Structural Dynamics and Earthquake Engineering
M. Papadrakakis, V. Papadopoulos, V. Plevris (eds.)
Crete Island, Greece, 25–27 May 2015

NONLINEARITY DETECTION AND IDENTIFICATION USING DISCRETE-TIME VOLTERRA SERIES: APPLICATION TO A SOLAR ARRAY STRUCTURE

Cristian Hansen[1,a], **Samuel da Silva**[1,b], **Emmanuel Foltête**[2,c] **and Scott Cogan**[2,d]

[1]UNESP - Univ Estadual Paulista, Faculdade de Engenharia de Ilha Solteira, Departamento de Engenharia Mecânica
Av. Brasil 56, 15385-000, Ilha Solteira, SP, Brasil
e-mail: [a]engcristianhansen@gmail.com, [b]samuel@dem.feis.unesp.br

[2] Université de Franche-Comté, Institut FEMTO-ST, Département Mécanique Appliquée
26, rue de l'Epitaphe - 25000 Besançon, France
e-mail: [c]emmanuel.foltete@femto-st.fr, [d]scott.cogan@univ-fcomte.fr

Keywords: nonlinearity detection, nonlinear system identification, Volterra series, panel structures

Abstract. *The aim of this paper is to identify a nonlinear model using time responses obtained from a sine sweep excitation applied to a simplified solar array structure. The nonlinearity is mainly caused by impacts, gaps and friction between the clamped interfaces of adjacent panels. A nonparametric model is identified using Volterra series, where the kernels are expanded with Kautz functions in order to decrease the problems associated with convergence and number of samples. The multiple convolutions provided by the Volterra kernels are used to propose a decision criterion based on a threshold limit to detect the level of linear or nonlinear behavior. The approach is also able to separate the linear and nonlinear contributions of the measured total response. The application performed in the experimental setup demostrates that the proposed method is successful in identifying the main nonlinear mechanism involved, despite of the complicated nature of the nonlinear system investigated.*

1 INTRODUCTION

Nonlinearities in healthy conditions is common in practice due to inherent nonlinear effects such as jumps, gaps, super harmonics, cycle limits, discontinuities, as well as others that appear frequently in the responses of structures [1]. This behavior is mainly due to excitation conditions, large displacements, geometric effects, nonlinear constitutive equations of the stress-strain etc [1–3]. Thus, the conventional linear procedures for structural analysis can fail when the system monitored is highly nonlinear in the healthy state [4, 5].

To illustrate these results, an experimental application is performed in a simplified test rig to simulate the complex dynamics of folded solar panels. The benchmark contains a snubber mounted with a small gap, that provides impacts under large displacements. The spatial mass distribution of the panels results in complex dynamics with many modal shapes in a small frequency bandwidth. The application of an excitation signal with energy in a small frequency bandwidth around the first resonance mode is expected to yield a single mode contribution in the response. However, impacts excite a large frequency bandwidth similar to an impact hammer test. Hence, several harmonics are excited due to coupling with high order modes. The biggest challenge is to separate the natural modal contribution from the contribution of the nonlinear behavior caused by the impacts. Several recent papers have investigated techniques to identify and to detect these effects [6, 7].

The Volterra series can be applied to solve this problem using its capability to decompose the response of a nonlinear system in linear and nonlinear contributions [8–12]. The contribution of the present paper is to propose a nonlinear indicator based on Volterra kernels to the detect the contribution of the linear and nonlinear kernels computed from the total experimental response measured directly on the solar array structure.

2 DISCRETE-TIME VOLTERRA SERIES

The response $y(k)$ of a nonlinear system is described by a discrete-time Volterra series using multiple convolutions [13]:

$$y(k) = \sum_{\eta=1}^{+\infty} \mathscr{H}_\eta(k) = y_1(k) + y_2(k) + y_3(k) + \cdots \tag{1}$$

where $y_1(k)$, $y_2(k)$, $y_3(k)$, $\cdots$ are the linear, quadratic, cubic and so on contributions of the output $y(k)$ in $k = 1, \cdots, K$ (K is the number of time samples) and $\mathscr{H}_\eta(k)$ is the Volterra functional given by multidimensional convolutions:

$$\mathscr{H}_\eta(k) = \sum_{n_1=0}^{N_1} \cdots \sum_{n_\eta=0}^{N_\eta} \mathcal{H}_\eta(n_1, \ldots, n_\eta) \prod_{i=1}^{\eta} u(k - n_i)$$

where $u(k)$ is the input signal and $\mathcal{H}_\eta(n_1, \ldots, n_\eta)$ are the η *th*-order Volterra kernels considering the truncated values $N_1, \ldots, N_\eta$ for each kernel.

However, the number of samples $N_1, \ldots, N_\eta$ is high because the practical systems have large memories and the identification of the kernels $\mathcal{H}_\eta(n_1, \ldots, n_\eta)$ is ill-posed with serious convergence problems. Fortunately, the Volterra kernels can be expanded using Kautz functions to overcome these drawbacks:

$$\mathcal{H}_\eta(n_1, \ldots, n_\eta) \approx \sum_{i_1=1}^{J_1} \cdots \sum_{i_\eta=1}^{J_\eta} \mathcal{B}_\eta\left(i_1, \ldots, i_\eta\right) \prod_{j=1}^{\eta} \psi_{i_j}(n_j) \tag{2}$$

where $J_1, \cdots, J_\eta$ are the number of samples in each orthonormal projections of the Volterra kernels $\mathcal{B}_\eta(i_1, \ldots, i_\eta)$ and and $\psi_{i_j}(n_i)$ are the Kautz functions that are appropriate for the representation of underdamped oscillatory systems.

If the Kautz basis is chosen adequately the order of projection $\mathcal{B}_\eta(i_1, \ldots, i_\eta)$ is drastically reduced [10]. Details about the Kautz functions and how to use it for nonlinear mechanical systems identification can be found in [14] and [9].

Equation (1) can be rewritten based on the orthonormal Kautz basis:

$$y(k) \approx \sum_{\eta=1}^{+\infty} \mathscr{B}_\eta(k) \tag{3}$$

where $\mathscr{B}_\eta(k)$ is the $\eta-th$ orthonormal Volterra functional operator:

$$\mathscr{B}_\eta(k) \approx \sum_{i_1=1}^{J_1} \cdots \sum_{i_\eta=1}^{J_\eta} \mathcal{B}_\eta(i_1, \ldots, i_\eta) \prod_{j=1}^{\eta} l_{i_j}(k)$$

that is a multiple convolution between the orthonormal kernel given by $\mathcal{B}_\eta(i_1, \ldots, i_\eta)$ and $l_{i_j}(k)$, that is a simple filtering of input signal $u(k)$ by the Kautz function $\psi_{i_j}(n_i)$:

$$l_{i_j}(k) = \sum_{n_i=0}^{V-1} \psi_{i_j}(n_i) u(k - n_i) \tag{4}$$

where $V = \max\{J_1, \ldots, J_\eta\}$ and $\psi_{i_j}(n_i)$ are the Kautz functions described by complex-conjugate parameters $s_{1,2} = -\xi_\eta \omega_\eta \pm j\omega_\eta \sqrt{1 - \xi_\eta^2}$. Normally, an optimization procedure is used to obtain the parameters ω_η, ξ_η.

The values of the orthonormal Volterra kernel $\mathcal{B}_\eta(i_1, \ldots, i_\eta)$ can be grouped in a vector $\mathbf{\Phi}$ and can be found by solving:

$$\mathbf{\Phi} = (\mathbf{\Gamma}^T \mathbf{\Gamma})^{-1} \mathbf{\Gamma}^T \mathbf{y} \tag{5}$$

where the matrix $\mathbf{\Gamma}$ contains $l_{i_j}(k)$ and $\mathbf{y} = [y(1) \cdots y(K)]$. It is worth noting that η can usually be truncated in 3 kernels to represent most of the structural nonlinearities with a smooth behavior.

The prediction error can be computed by:

$$e(k) = y(k) - y_{exp}(k) \tag{6}$$

where $y_{exp}(k)$ is the experimental output and $y(k)$ is the output estimated by Volterra model.

The complex-conjugate parameters of the Kautz functions are obtained by minimizing the normalized mean square error-prediction (NMSE):

$$\min \quad F = \frac{||e(k)||_2}{||y_{exp}(k)||_2} \tag{7}$$

subject to $\boldsymbol{\rho}_{low} \leq \boldsymbol{\rho} \leq \boldsymbol{\rho}_{up}$, where the Kautz filters parameters (using $\eta = 3$) grouped in the vector $\boldsymbol{\rho} = [\omega_1 \ \xi_1 \ \omega_2 \ \xi_2 \ \omega_3 \ \xi_3]^T = [\omega_{lin} \ \xi_{lin} \ \omega_{quad} \ \xi_{quad} \ \omega_{cub} \ \xi_{cub}]^T$ and $||\ ||_2$ is the Frobenius norm, also called the Euclidean norm.

The vectors $\boldsymbol{\rho}_{low}$ and $\boldsymbol{\rho}_{up}$ are composed by the lower and upper boundary values of search. This work adopted a sequential quadratic programming (SQP) approach to seek the vector $\boldsymbol{\rho}$ using an initial condition vector $\boldsymbol{\rho}_0$.

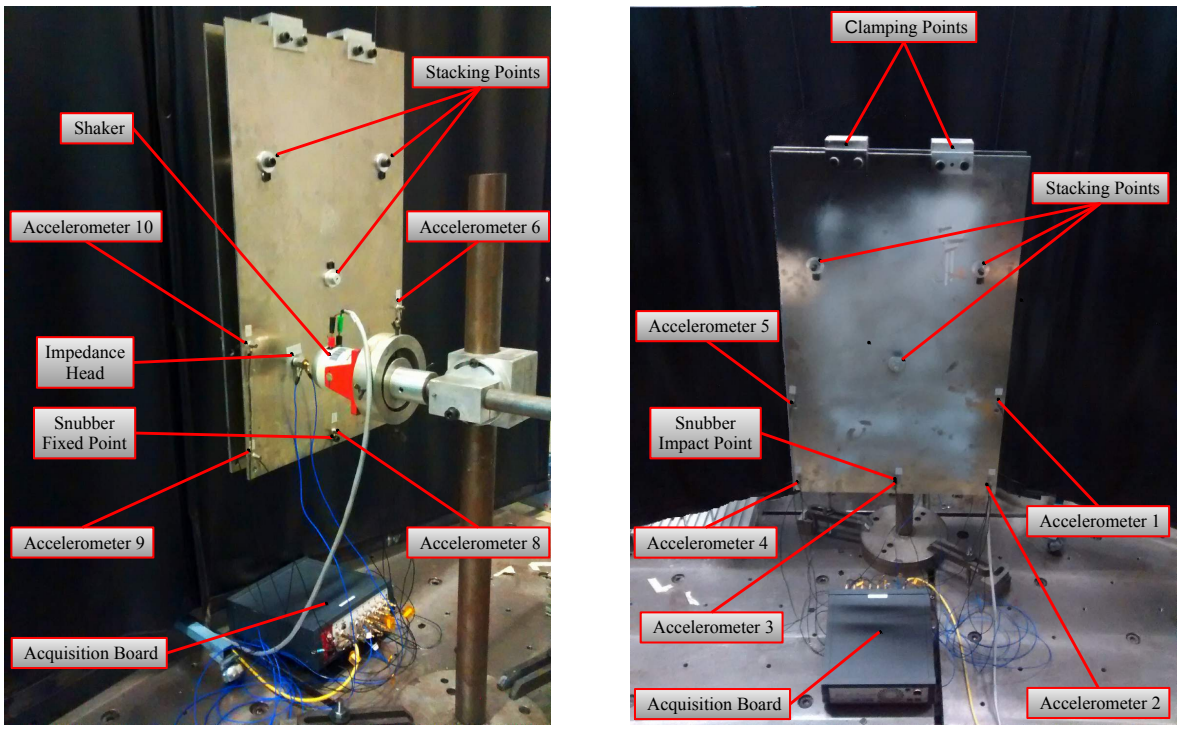
3 APPLICATION IN A SOLAR ARRAY STRUCTURE

This section shows an experimental application of the methodology using a simplified solar array structure [6, 7].

3.1 Description of the experimental setup

The benchmark consists of two parallel aluminium plates mounted in a free-free configuration, as seen in Figures 1(a) and 1(b). They are clamped together at the top edge and connected at three stacking points. The geometrical properties of the plates are $770 \times 440 \times 5$ mm of, length, width and thickness, respectively, and the distance between plates is fixed at 40 mm.

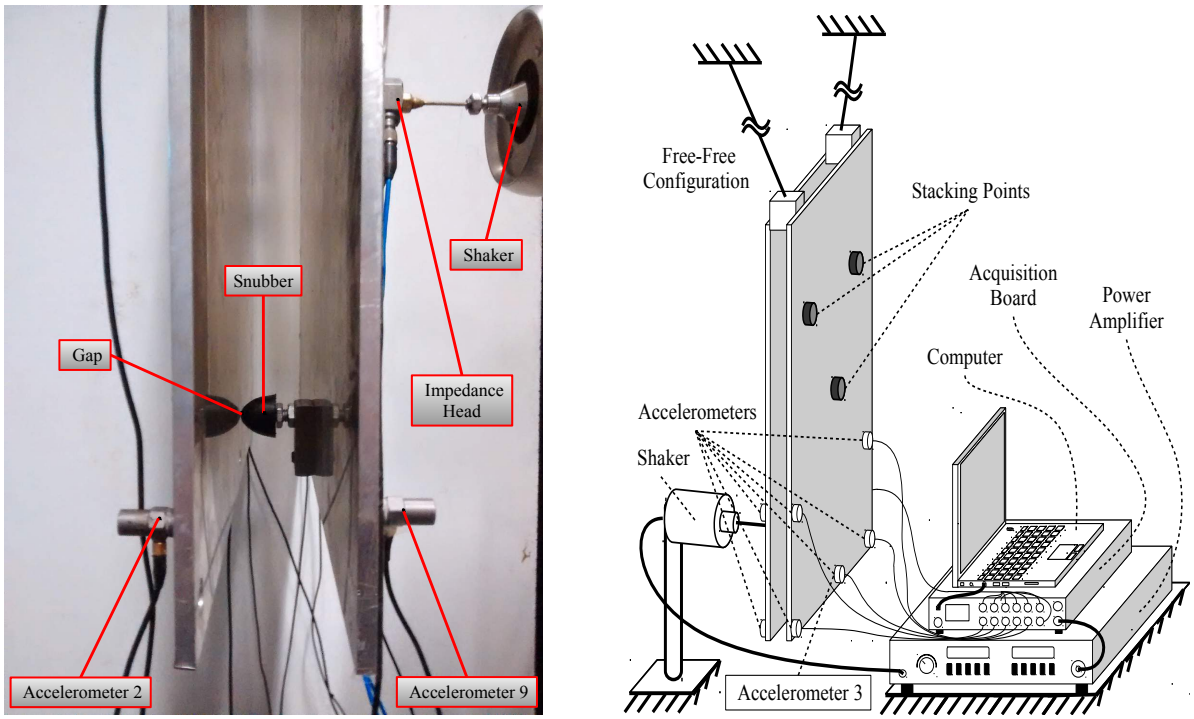
A snubber was also mounted on a steel support glued at the middle length of the bottom free edge, as shown in Figures 1(a), 1(b) and 2(a). When the level of excitation amplitude applied in the shaker is high, the rubber exhibits nonlinear behavior and impacts between the adjacent panels. As pointed out in Ref. [6], the small contact areas between the stacking points and the plates are an additional possible source of non-linear behavior, as they may induce large, localized bending deformations. In this study, a gap of less than one millimeter (≈ 0.2 mm) is introduced such that there is no contact when the level of force is low in order to insure a linear regime of vibration (see Figure 2(a)).



(a) Experimental setup. (b) Detail of the experimental setup.

Figure 1: Test rig setup.

The structure was monitored using 10 accelerometers, 5 on each plate at the same positions. In this work, only the measurements at accelerometer 3, mounted in the impact region of the target plate, were used. An impedance head was also employed to measure the drivepoint accelerations and the excitation force. All signals measured were sampled at 1280 Hz, 6400 samples for tests with short duration (to identification and analysis) and 256000 samples for tests with long duration (to characterize the nonlinear behavior). In order to remove the contribution from the high order modes and DC component, a bandpass filter was applied from 5 to 120 Hz.



(a) Zoom in the impact region, showing the snubber.

(b) Schematic representation.

Figure 2: Description of the experimental setup.

3.2 Detection of nonlinearities using classical methods

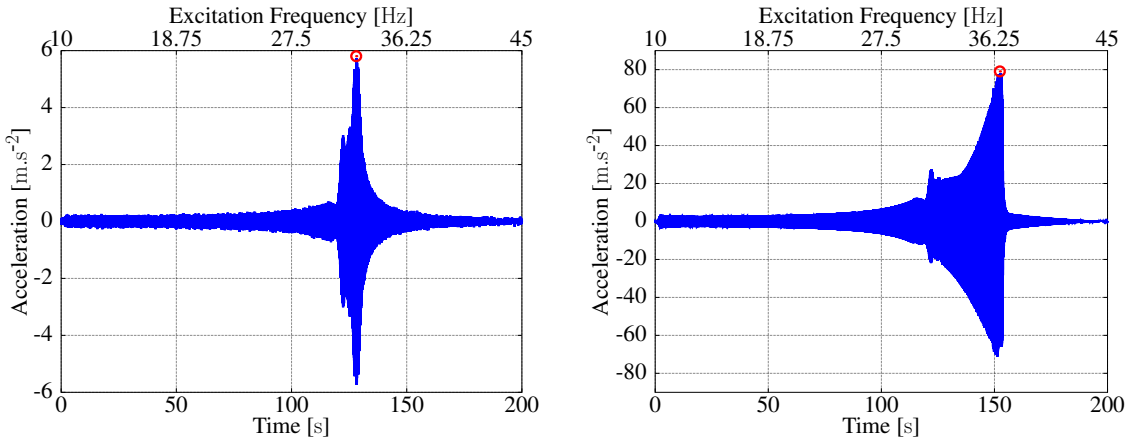
The stepped sine test is an effective tool to detect nonlinear behavior. But an alternative and easier test is to excite the system with a long duration sweep sine. Figure 3 shows the acceleration considering low (fig. 3(a)) and high (fig. 3(b)) voltage amplitude supplied to the shaker. In all cases the sine sweep is applied ranging the frequency from 10 to 45 Hz during 200 seconds. Figure 3(a) shows a smooth decay after resonance (linear vibration). However, fig. 3(b) presents two differences: a jump is observed close to the frequency of 36.25 Hz and the resonance frequency is changed.

Figures 3(a) and 3(b) show the maximum amplitude of the time of flight (TOF). Figure 4(a) presents the ratio between the time and excitation frequency to estimate the output frequency of TOF. When the energy[1] of the force excitation is low, the TOF occurs at the same frequency, both in upward and downward sine sweep tests. However, when the force is increased, the resonance frequency is bigger following a sigmoid ratio as a function of the applied energy. Another important issue is that this behavior is different depending the type of sweep test. This is a clear indication of the existence of nonlinearities.

Figure 4(b) shows the frequency response function (FRF) plots. The FRFs show some distortions caused by nonlinear effects as a function of force level applied by the shaker. By analyzing Figure 4(b) it is possible to confirm that the solar array structure presents a strong nonlinear regime of motion associated with stiffness hardening that cause a jump on the right side.

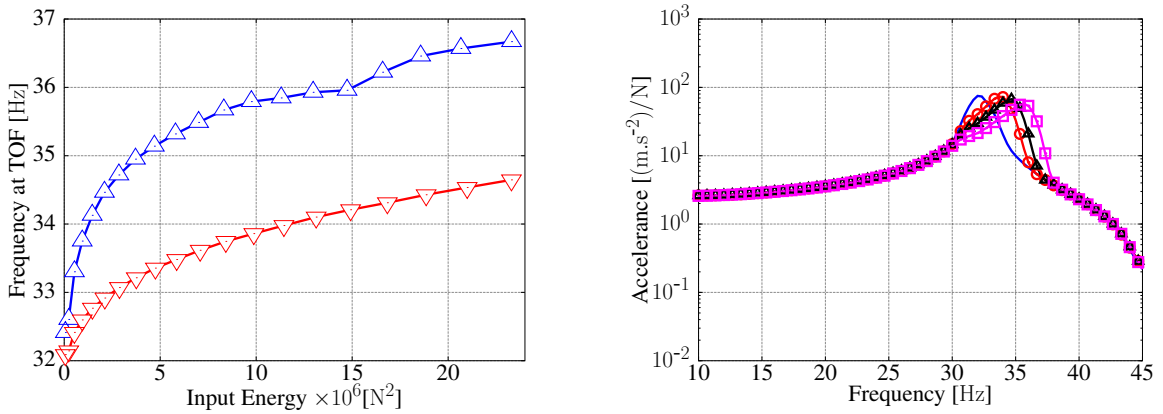
Figures 5(a) and 5(b) show the time-frequency distribution considering the acceleration signal in the upward and downward sweep tests, respectively. One can observe the first three harmonics caused by impacts and large displacements, mainly in the resonance range.

[1]Computed by $L2$ norm.



(a) Low excitation amplitude level (0.01 V). (b) High excitation amplitude level (0.20 V).

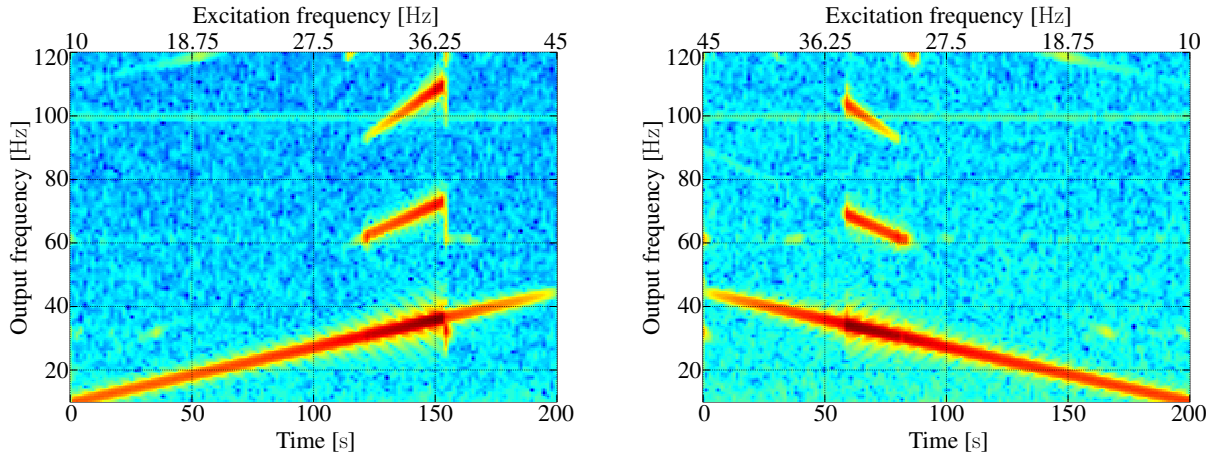
Figure 3: Output to sine sweep with frequency from 10 to 45 Hz considering different voltage amplitudes applied in the shaker. The maximum amplitude of the time of flight is represented by ○.



(a) Frequency at TOF, the marker △ represents the sine sweep up (10→45 [Hz]) and the marker ▽ represents the sine sweep down (45→10 [Hz]).

(b) Accelerance, in continous line — for (0.03 V), ○ for (0.08 V), △ for (0.12 V) and □ for (0.20 V).

Figure 4: Frequency at TOF and FRF estimated using the sine sweep test with long duration.



(a) Sine sweep up test, 10→45 Hz. (b) Sine sweep down test, 45→10 Hz.

Figure 5: Time-frequency distribution of the acceleration signal considering the high level of amplitude excitation, 0.20 V.

3.3 Identification of the Volterra model

The identification of the Volterra kernels is performed using the sine sweep signal in two steps [11]. Firstly, the kernel $\mathcal{H}_1(n_1)$ is identified to describe the linear contribution. Secondly, the high order kernels $\mathcal{H}_2(n_1, n_2)$ and $\mathcal{H}_3(n_1, n_2, n_3)$ are identified using the response signal filtered by $\mathcal{H}_1(n_1)$ estimated previously. All parameters in the Kautz functions are used based on the optimization procedure described in [9, 15].

A total of 30 blocks were measured with 6400 samples each for 20 different levels of voltage amplitude applied in the shaker. Disturbances are included in the excitation signal by changing 12^{o} in each block (360^{o} total).

The choice of the number of Kautz functions can be complicated for structures with strong nonlinear effects and in this work with high order modes excitated by impacts. For the first kernel, a couple of Kautz functions is enough to adequately describe the linear behavior of a single degree-of-freedom system, based on previous experience using the Volterra series [12, 16–26]. The second kernel is related essentially to asymmetries in the response appearing as second harmonics in the time-frequency distribution. However, shaker-structure interaction can result mainly in a second harmonic excitation.

For the third kernel an optimization procedure can show the best number of Kautz functions to use, but the choice here was limited to 6 Kautz functions because of convergence problems trying solve a high order equation using more functions. So, the Volterra model was estimated for each test, using 2, 4 and 6 Kautz functions for $\mathcal{H}_1(n_1)$, $\mathcal{H}_2(n_1, n_2)$ and $\mathcal{H}_3(n_1, n_2, n_3)$, respectively.

The Kautz filter parameters used to build the orthonormal kernels were found with a sequential quadratic programming (SQP) algorithm minimizing the objective function F in Eq. (7) with the stopping criterion based on a step size less than 10^{-8}.

The initial condition vector $\boldsymbol{\rho_0}$ for the low excitation amplitudes applied on the shaker (0.01 V) was defined as $\boldsymbol{\rho_0} = [\omega_0 \;\; \xi_0 \;\; \omega_0 \;\; \xi_0 \;\; \omega_0 \;\; \xi_0]$, where ω_0 is the resonant frequency computed by the fast Fourier transform of $y_{exp}(k)$ for the low amplitude level (0.01 V) and $\xi_0 = 10^{-3}$. For the all other amplitudes levels, the initial condition vector is computed by:

$$\boldsymbol{\rho}_0 = \frac{1}{N} \sum_{i=1}^{N} {}_i\boldsymbol{\rho}^* \tag{8}$$

where N is the number of blocks for each level of amplitude applied in the shaker ($N = 30$) and ${}_i\boldsymbol{\rho}^*$, $i = 1, 2, 3, \ldots N$, is the optimum value vector for each block of the immediately lower amplitude level.

The lower and upper boundary values of the search was defined by:

$$\boldsymbol{\rho}_{low} = \left[\begin{array}{cccccc} 0.8\boldsymbol{\rho}_0(1) & 0 & 0.8\boldsymbol{\rho}_0(3) & 0 & 0.8\boldsymbol{\rho}_0(5) & 0 \end{array} \right] \tag{9}$$

$$\boldsymbol{\rho}_{up} = \left[\begin{array}{cccccc} 1.2\boldsymbol{\rho}_0(1) & 1 & 1.2\boldsymbol{\rho}_0(3) & 1 & 1.2\boldsymbol{\rho}_0(5) & 1 \end{array} \right] \tag{10}$$

The fitness (FIT $= F^{-1} \times 100$ [%]) of the optimization procedure is shown in Figure 6. A bigger fit is reached when the vibration is linear (amplitudes from 0.02 to 0.06 V). When the level of force increases, the fit is poor (amplitudes from 0.08 to 0.20 V) because the model is insufficent to detect the large nonlinear behavior caused by coupling with the high order modes.

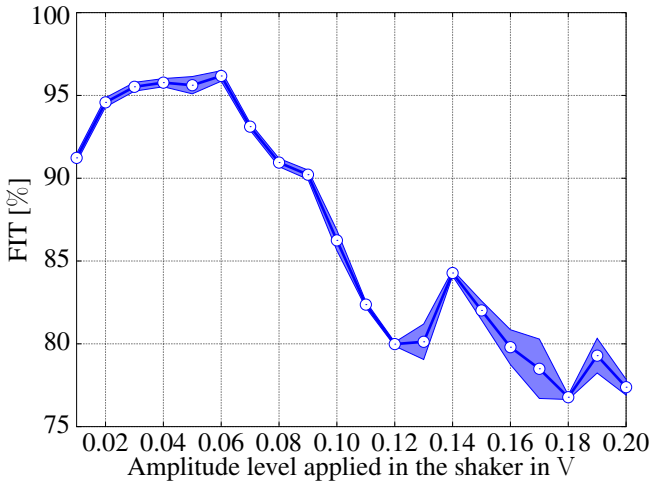
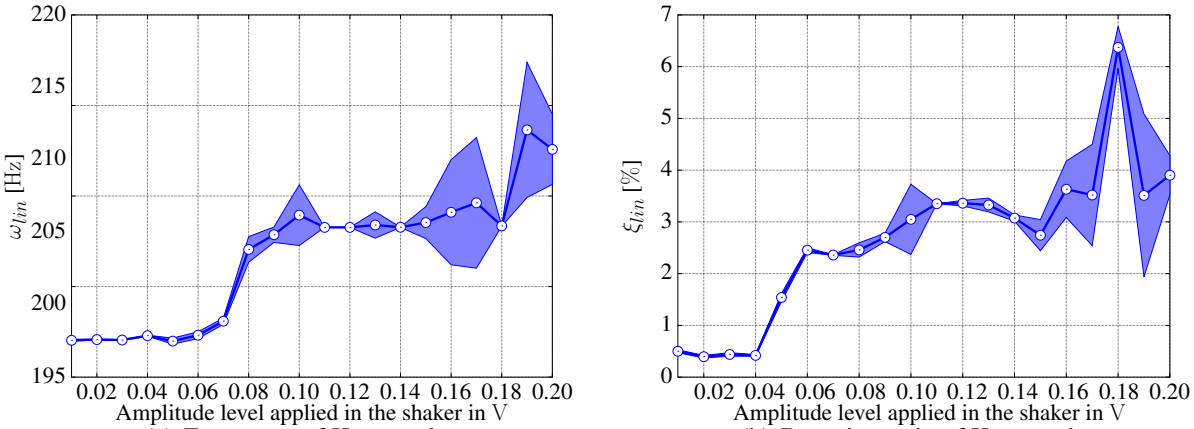


Figure 6: Fitness values lie within one standard deviation of the mean for each test.

The parameters, frequency and damping ratio, of Kautz poles related with each Volterra kernel are shown in Figures 7, 8 and 9. The values are seen to lie within one standard deviation of the mean. In a broader view, all parameters, with the exception of ξ_{quad}, are increasing with the levels of amplitude applied to the shaker, showing that the impacts are changing the structural behavior constantly following the excitation levels.

Figure 7(a) presents the same frequency, ω_{lin}, for low levels of amplitude applied in the shaker (up to level 0.07 V). The damping ratio, ξ_{lin}, of the Kautz poles are increased by the impacts that occur with the levels up to 0.05 V, as shown in Figure 7(b).

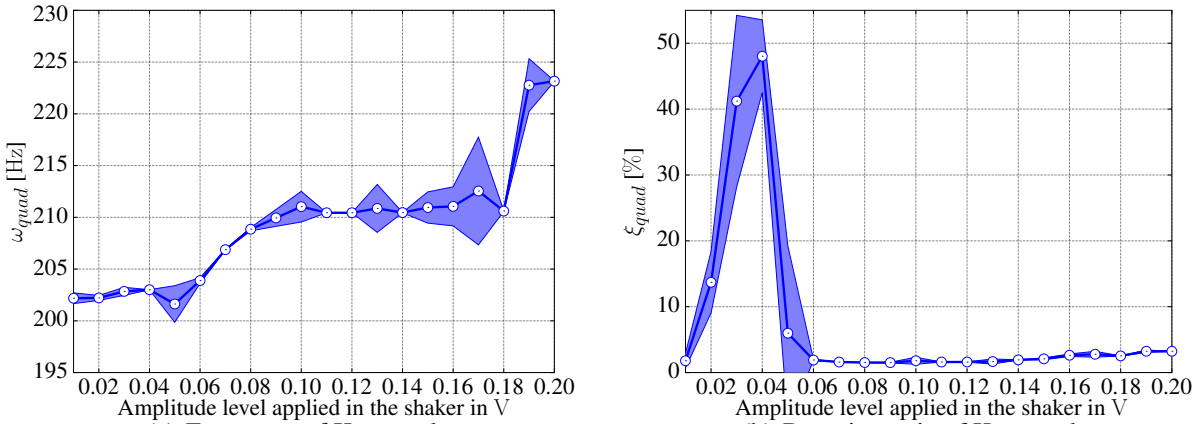


(a) Frequency of Kautz poles.

(b) Damping ratio of Kautz poles.

Figure 7: Kautz poles of $\mathcal{H}_1(n_1)$, values lie within one standard deviation of the mean for each test.

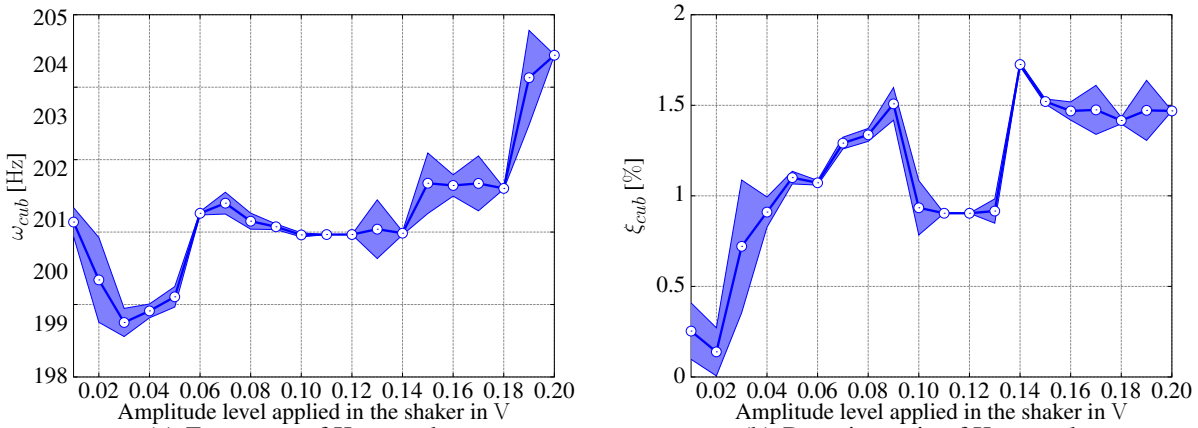
The high order kernels do not have significant contributions at low levels of excitation since the behavior is linear. Hence, if the second and third kernels are included in the identification process at low amplitudes then the results are not consistent because the system is essentially linear. Figure 8(b) confirms that for the levels up to 0.05 V the poles are highly damped with null contributions in the high order kernels. The frequency of the Kautz poles in the second kernel increases with the level of excitation, as shown in Figure 8(a). This effect is caused by the shaker-structure interaction in the resonance range of the system.



(a) Frequency of Kautz poles. (b) Damping ratio of Kautz poles.

Figure 8: Kautz poles of $\mathcal{H}_2(n_1, n_2)$, values lie within one standard deviation of the mean for each test.

Figure 9(a) and 9(b) show the evolution of the Kautz pole parameters, frequency and damping ratio, for the third kernel. Similar behavior is found, except in the range from 0.10 to 0.13 V in the damping ratio.



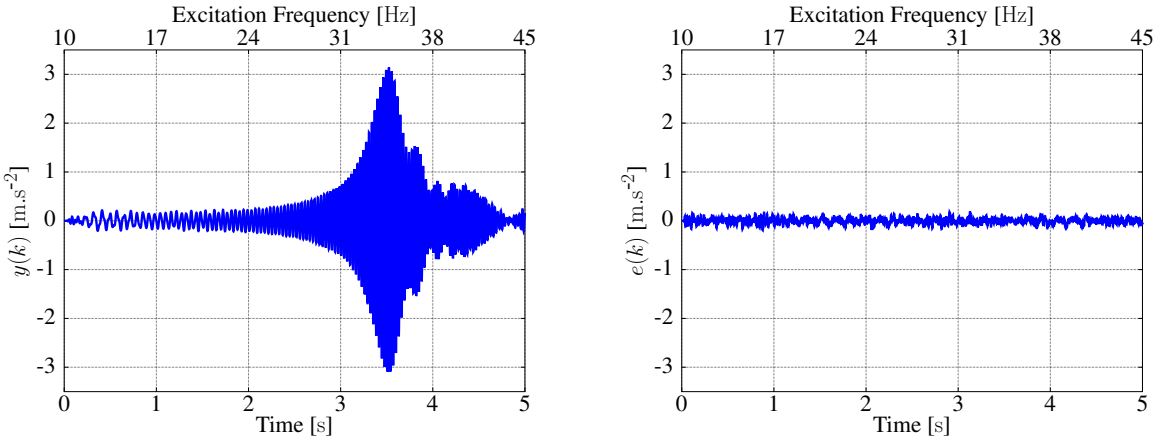
(a) Frequency of Kautz poles. (b) Damping ratio of Kautz poles.

Figure 9: Kautz poles of $\mathcal{H}_3(n_1, n_2, n_3)$, values lie within one standard deviation of the mean for each test.

Figure 10(a) shows the estimated output obtained by the multiple convolution computed using the Volterra kernels $\mathcal{H}_1(n_1)$, $\mathcal{H}_2(n_1, n_2)$ and $\mathcal{H}_3(n_1, n_2, n_3)$ for the excitation level 0.01 V applied in the shaker. The prediction error computed by Eq. (6) is shown in Figure 10(b). The second and third kernels, $\mathcal{H}_2(n_1, n_2)$ and $\mathcal{H}_3(n_1, n_2, n_3)$, respectively, do not have a significant contribution to the linear behavior and the response of the Volterra model, $y(k)$, for this case (linear behavior) can be approximated using only the linear contribution, $y_1(k)$.

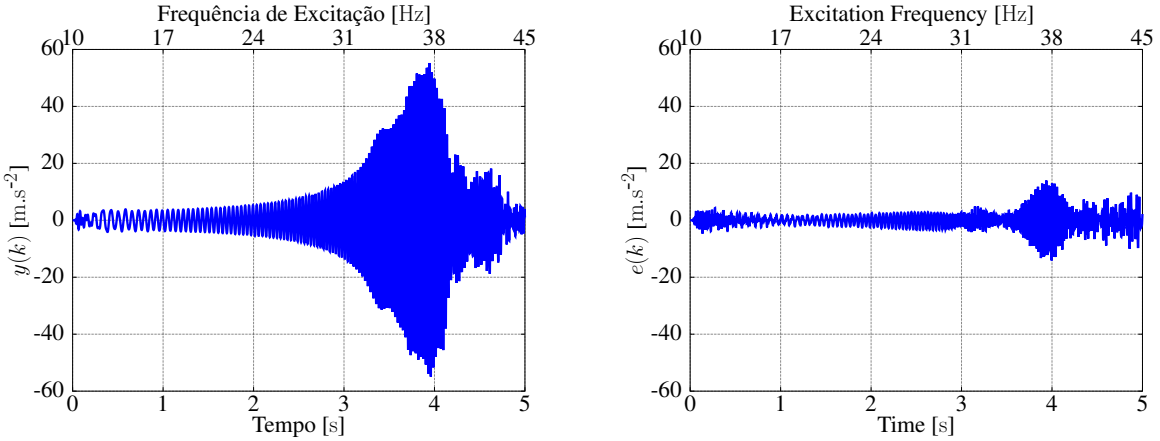
When the amplitude level applied in the shaker is high, the nonlinear vibrating regime is reached and the nonlinear contributions, $y_2(k)$ and $y_3(k)$ have importance in the total response, $y(k)$. Figure 11(a) shows the output identified by the Volterra model for high amplitude level applied in the shaker and Figure 11(b) the prediction error to this condition.

Figures 12, 13 and 14 present the linear, quadratic and cubic contributions of the total response when the amplitude level is 0.20 V. It is worth noting that the quadratic contribution is lower than the linear contribution because the symmetry of the output signal, as shown in Figure 13. On the other hand, when the level excitation is high, the cubic contribution is significant in comparison to the linear response, as shown in Figure 14.



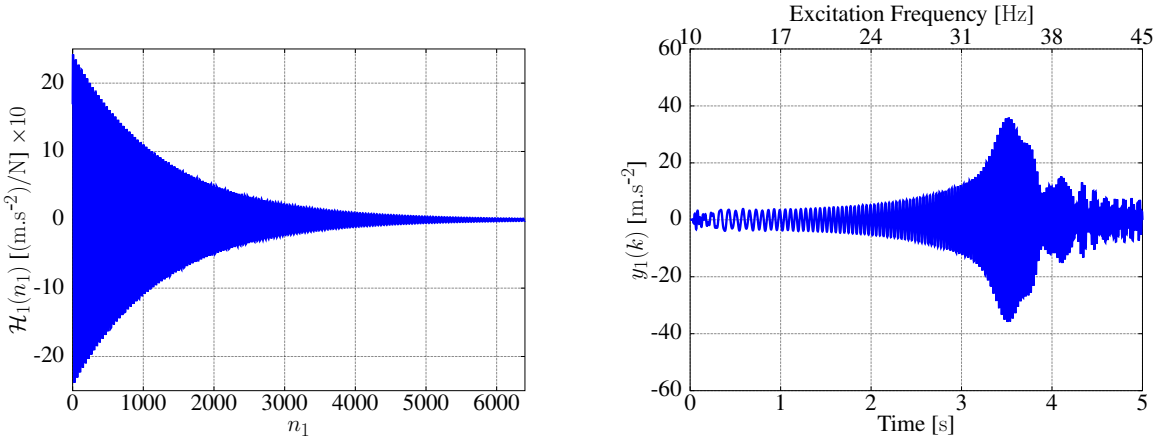
(a) Estimated output by the Volterra model. (b) Prediction error.

Figure 10: Output for the low level amplitude (0.01 V).



(a) Estimated output by the Volterra model. (b) Prediction error.

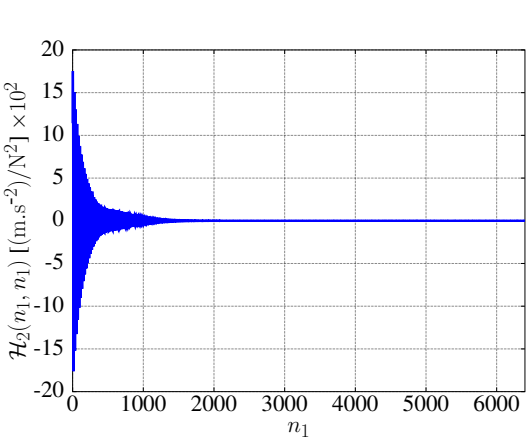
Figure 11: Output for the high level amplitude (0.20 V).



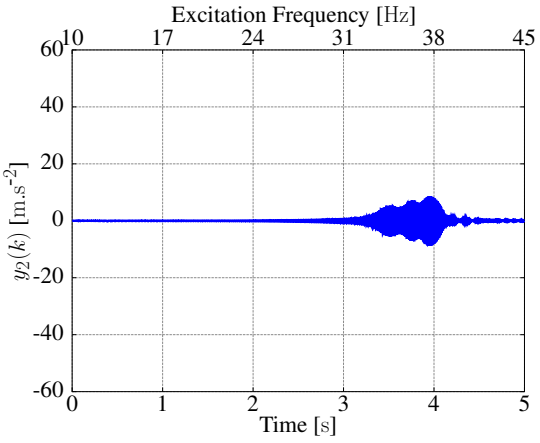
(a) Volterra kernel $\mathcal{H}_1(n_1)$. (b) $y_1(k)$ estimated by $\mathcal{H}_1(n_1)$.

Figure 12: Linear contribution considering 0.20 V of amplitude applied in the shaker.

The diagonal of the second kernel, $\mathcal{H}_2(n_1, n_1)$, is show in Figure 13(a) and its contribution, $y_2(k)$, was estimated by quadratic convolution, as shown in Figure 13(b). We note that the quadratic contribution is smaller than the linear contribution because of the symmetry in the response.



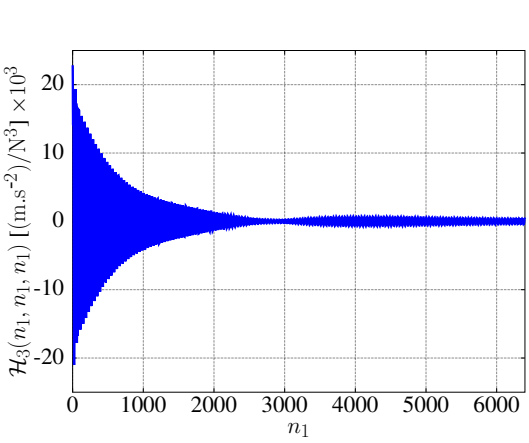
(a) Diagonal of Volterra Kernel $\mathcal{H}_2(n_1, n_2)$.



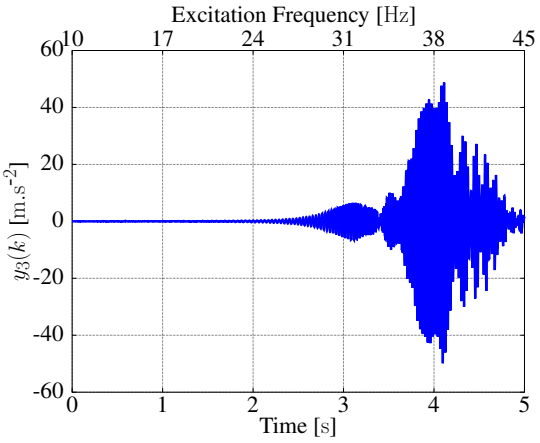
(b) $y_2(k)$ estimated by $\mathcal{H}_2(n_1, n_2)$.

Figure 13: Quadratic contribution considering 0.20 V of amplitude applied in the shaker.

The diagonal of the third kernel, $\mathcal{H}_3(n_1, n_1, n_1)$, is shown in Figure 14(a) and its contribution, $y_3(k)$, was computed by cubic convolution, as shown in Figure 14(b). The cubic contribution have the same level of significance in the total response when compared with the linear contribution.



(a) Diagonal of Volterra kernel $\mathcal{H}_3(n_1, n_2, n_3)$.



(b) $y_3(k)$ estimated by $\mathcal{H}_3(n_1, n_2, n_3)$.

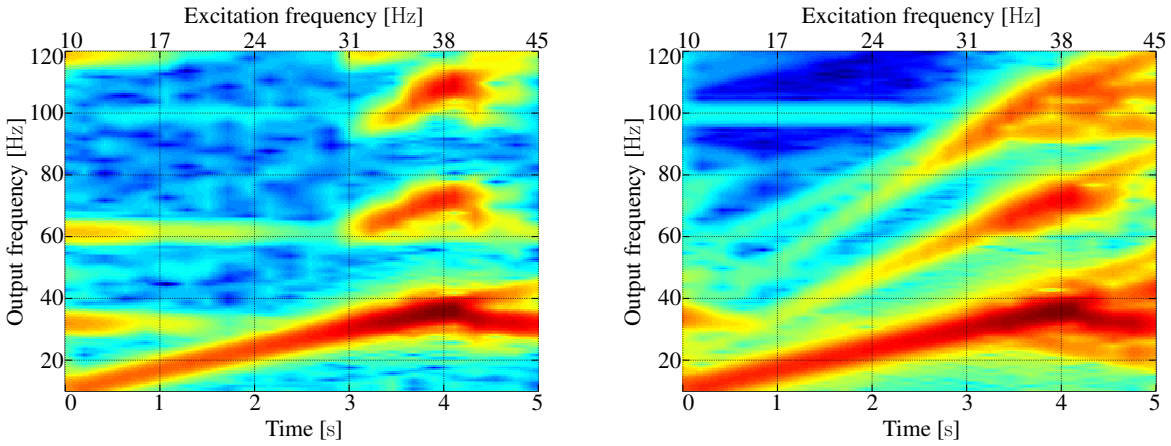
Figure 14: Cubic contribution considering 0.20 V of amplitude applied in the shaker.

For high levels of amplitude applied in the shaker, the nonlinear contributions, $y_2(k)$ and $y_3(k)$, are relevant comparing with the total response, $y(k)$. So, compute the nonlinear contributions is necessary to obtain a representative model of a structure with nonlinear behavior.

3.4 Model Validation

The Volterra model identified was validated through the qualitative analysis of the time-frequency distribution of the acceleration signal considering the high level of amplitude excitation applied in the shaker, 0.20 V, as shown Figures 15(a) and 15(b).

Figure 16 also presents the validation of the FRF computed using the output estimated by Volterra model comparing with experimental FRF. It is possible to observe a good fit in the resonance range for the different levels of amplitude applied in the shaker.



(a) Experimental. (b) Volterra model.

Figure 15: Time-frequency of the accelaration signal for the level of 0.2 V.

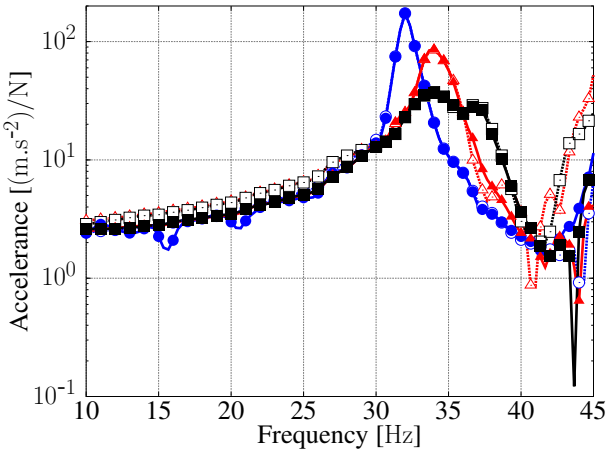


Figure 16: Frequency response function computed for a Volterra model response and experimental data. ● for the experimental and ○ for the model considering 0.01 V, ▲ for the experimental and △ for the model considering 0.10 V, ■ for the experimental and □ for the model considering 0.20 V.

3.5 Nonlinear index based in Volterra model

The output energy ratio κ can be described by using each contribution of the Volterra model:

$$\kappa = \frac{E_\alpha}{E_1 + E_2 + E_3};\ \alpha = 1, 2, 3 \tag{11}$$

where, E_1, E_2 and E_3 are the energy of linear, quadratic and cubic contributions, respectively, computed by $L2$ norm.

Figure 17, shows the κ for each Volterra contribution for all excitation amplitudes tested.The indicator shows that until the level of 0.04 V the linear contribution is dominant. After 0.04 V the energy contribution of the cubic stiffness caused by the third Volterra kernel starts to dominate. It is worth noting that the quadratic contribution is null for all levels.

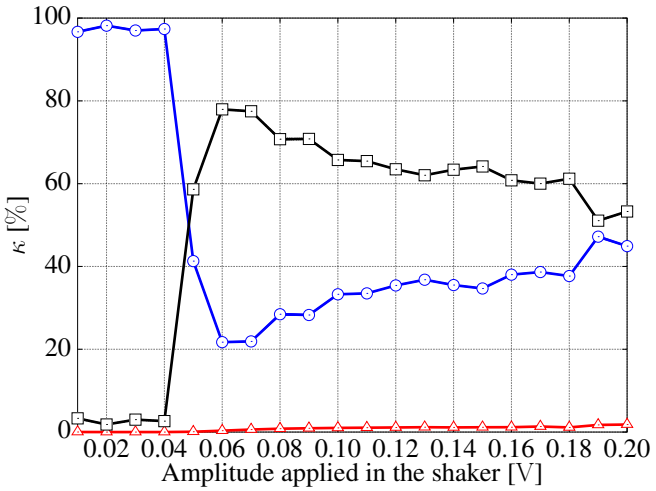


Figure 17: Indicator to detect nonlinearities based on the Volterra kernel contributions. ○ is the linear ratio, △ is the quadratic and □ is the cubic contribution.

4 FINAL REMARKS

The results of this study show that the use of Volterra series can identify a nonparametric model capable of describing the complex dynamic behavior of a solar array structure using directly the time domain data obtained for different excitation amplitudes and vibration regimes. The kernels identified can be used to filter the linear and nonlinear contributions and to compute an indicator for detecting nonlinearity. Future studies will consider a larger range of modal contributions with more kernels for each mode. The multiple inputs and multiple output cases can also be investigated using the Volterra cross-kernels.

5 ACKNOWLEDGMENTS

The authors acknowledge the financial support provided by Research Foundation of São Paulo (FAPESP, Brasil) through the grant number 12/09135-3 and the National Council for Scientific and Technological Development (CNPq, Brasil) through the grant number 470582/2012-0. The first author is thankful to FAPESP for his scholarship grants 13/09008-4 and 14/02431-1. The first and the second authors would like to thank the kind hospitality of Prof. Emmanuel Foltête and Scott Cogan during their stay in Besançon in 2014.

REFERENCES

[1] Gaëtan Kerschen, Keith Worden, Alexander F. Vakakis, and Jean-Claude Golinval. Past, present and future of nonlinear system identification in structural dynamics. *Mechanical Systems and Signal Processing*, 20(3):505 – 592, 2006.

[2] Keith Worden and G. R. Tomlinson. *Nonlinearity in Structural Dynamics - Detection, Identification and Modelling*. Institute of Physics Publishing, London, United Kingdom, 1 edition, 2001.

[3] L.N. Virgin. *Introduction to Experimental Nonlinear Dynamics: A Case Study in Mechanical Vibration*. Cambridge University Press, Cambridge, United Kingdom, 1 edition, 2000.

[4] C. R. Farrar, K. Worden, M. D. Todd, G. Park, J. Nichols, D. E. Adams, M. T. Bement, and K. Farinholt. Nonlinear system identification for damage detection. Technical Report LA-14353, Los Alamos National Laboratory (LANL), 2007.

[5] Keith Worden, Charles R. Farrar, Jonathan Haywood, and Michael Todd. A review of nonlinear dynamics applications to structural health monitoring. *Structural Control and Health Monitoring*, 15(4):540–567, 2008.

[6] A. Hot, G. Kerschen, E. Foltête, and S. Cogan. Detection and quantification of non-linear structural behavior using principal component analysis. *Mechanical Systems and Signal Processing*, 26(0):104 – 116, 2012.

[7] J.P. Noël and G. Kerschen. Frequency-domain subspace identification for nonlinear mechanical systems. *Mechanical Systems and Signal Processing*, (0):91–102, 2013.

[8] W. J. Rugh. *Nonlinear System Theory - The Volterra/Wiener Approach*. The Johns Hopkins University Press, 1991.

[9] Samuel da Silva, Scott Cogan, and Emmanuel Foltête. Nonlinear identification in structural dynamics based on Wiener series and Kautz filters. *Mechanical Systems and Signal Processing*, 24(1):52 – 58, 2010.

[10] Samuel da Silva. Non-linear model updating of a three-dimensional portal frame based on Wiener series. *International Journal of Non-Linear Mechanics*, 46(1):312 – 320, 2011.

[11] W. Silva. Identification of nonlinear aeroelastic systems based on the Volterra theory: Progress and opportunities. *Nonlinear Dynamics*, 39(1-2):25–62, 2005.

[12] Sidney Bruce Shiki, V. Lopes Jr, and S. da Silva. Damage detection in nonlinear structures using discrete-time Volterra series. *Key Engineering Materials*, 569-570:876–883, 2013.

[13] M. Schetzen. *The Volterra and Wiener theories of nonlinear systems*. New York: Wiley, 1980.

[14] Samuel da Silva. Non-parametric identification of mechanical systems by Kautz filter with multiple poles. *Mechanical Systems and Signal Processing*, 25(4):1103 – 1111, 2011.

[15] Sidney Bruce Shiki, V. Lopes Jr, and Samuel da Silva. Identification of nonlinear structures using discrete-time Volterra series. *Journal of the Brazilian Society of Mechanical Sciences and Engineering*, pages 1–10, 2013.

[16] S. B. Shiki, Jean-Philippe Noël, Gaëtan Kerschen, V. Lopes Jr, and S. da Silva. Identification of mechanical systems with local nonlinearities through discrete-time Volterra series and Kautz functions. In *11th International Conference on Recent Advances in Structural Dynamics - RASD 2013*, Pisa, Italy, 2013.

[17] Cristian Hansen, Luís Gustavo G. Villani, and S. da Silva. Aplicação de séries de Volterra na detecção de danos em uma viga com comportamento não-linear. In *VIII Congresso Nacional de Engenharia Mecânica - CONEM 2014*, Uberlândia, Brasil, August 2014.

[18] Cristian Hansen, Sidney Bruce Shiki, and S. da Silva. Non-parametric identification of a non-linear buckled beam using discrete-time Volterra series. In *9th International Conference on Structural Dynamics - Eurodyn 2014*, pages 2013–2018, Porto, Portugal, June-July 2014.

[19] Cristian Hansen, Sidney Bruce Shiki, and Samuel da Silva. Structural health monitoring in a buckled beam using volterra serie. In Vincent Le Cam, Laurent Mevel, and Franck Schoefs, editors, *7th European Workshop on Structural Health Monitoring (EWSHM 2014)*, Nantes, France, July 2014. IFFSTTAR, Inria, Université de Nantes.

[20] O. Scussel, G. J. Q. Vasconcelos, S. B. Shiki, and S. da Silva. Identification of mechanical systems through Volterra series - study of benchmark cases. In *Conferência Brasileira de Dinâmica, Controle e Aplicações (DINCON 2013)*, Fortaleza, CE, October 2013.

[21] S. da Silva. Damage detection in a 2 dof nonlinear mechanical systems using Volterra series and Kautz filter. In *20th International Congress of Mechanical Engineering (COBEM 2009)*, Gramado, Brasil, 2009. ABCM, UFRGS.

[22] S. B. Shiki, V. Lopes Jr, and S. da Silva. Identification of parameters in nonlinear structures using discrete Volterra series. In *IV Symposium on Intelligent Materials and Control*, 2012.

[23] Sidney Bruce Shiki, S. da Silva, and V. Lopes JR. Nonlinear mechanical systems identification through Wiener/Volterra series. In *22nd International Congress of Mechanical Engineering (COBEM 2013)*, 2013.

[24] S. B. Shiki, S. da Silva, J.P. Noël, and G. Kerschen. Identification of a geometrically nonlinear beam using Volterra series. *Mechanics Research Communications*, Submetido para avaliação, 2013.

[25] Sidney Bruce Shiki, Cristian Hansen, and S. da Silva. Nonlinear features identified by Volterra series for damage detection in a buckled beam. In *International Conference on Structural Nonlinear Dynamics and Diagnosis - CSNDD 2014*, volume 16, Agadir, Morocco, May 2014.

[26] S. B. Shiki, Cristian Hansen, and S. da Silva. Parameter identification of a nonlinear beam with hardening behavior using Volterra series. In *5th Conference on Nonlinear Vibrations, Localization and Energy Transfer - NV2014*, Istanbul, Turkey, July 2014.

COMPDYN 2015
5th ECCOMAS Thematic Conference on
Computational Methods in Structural Dynamics and Earthquake Engineering
M. Papadrakakis, V. Papadopoulos, V. Plevris (eds.)
Crete Island, Greece, 25–27 May 2015

FREQUENCY DETUNING EFFECTS FOR PARAMETRICALLY AND DIRECTLY EXCITED ELASTIC STRUCTURES

S. Neumeyer[1], M. H. M. van Gastel[2], V. S. Sorokin[1], and J. J. Thomsen[1]

[1]Department of Mechanical Engineering, Technical University of Denmark
Kgs. Lyngby, Denmark
stene@mek.dtu.dk

[2] Department of Mechanical Engineering, Eindhoven University of Technology
Eindhoven, The Netherlands

Keywords: parametric and direct excitation, frequency detuning, nonlinear vibrations.

Abstract. *This study investigates the frequency detuning effects of parametric and direct excitation for near-resonant nonlinear structural vibrations. Specifically, the detuning effects of a two-to-one frequency ratio between the parametric and direct excitation, and of a drift in natural frequency, are studied. These effects are investigated theoretically using a Duffing-Mathieu equation as the model system, and experimentally using a cantilever beam as the model object. The approximate analytical responses are derived using the method of varying amplitudes, and compared with results of direct numerical integration and experiments showing good agreement. For frequency detuned superthreshold parametric excitation some of the theoretical frequency-amplitude solution branches appear to merge. For some ranges of parametric excitation frequency a drop in experimental steady-state vibration amplitude was found, indicating performance degradation whereas for other frequency ranges, frequency detuning may yield an increased steady-state vibration amplitude. This makes frequency detuning a feature which can purposefully be avoided or utilized, dependent on the application.*

1 INTRODUCTION

Structures subjected to combined parametric and direct excitation may experience frequency detuning between the parametric and direct excitation, e.g. caused by uncertainties with respect to physically adding the parametric component. Another cause of frequency detuning could be that the systems natural frequencies drift during operation due to, e.g. wear, damage, or varying mass loading. The effect of adding a superthreshold parametric excitation, where the response is dominated by the parametric component [1], to a directly excited system with perfect tuning, i.e. a two-to-one frequency ratio between the parametric and direct excitation, has recently been given some attention [2]. This was done because utilization of combined parametric and direct excitation may be useful for structural and mechanical vibrations [3, 4]. However frequency detuning has not been investigated for a system subjected to combined parametric and direct excitation, in particular not with superthreshold parametric excitation.

2 MODEL SYSTEM

As a model system relevant for elastic structures, a Duffing-Mathieu equation with independent parametric Ω_p and direct Ω_d excitation frequencies, is considered:

$$\ddot{x} + \beta\dot{x} + \omega_0^2\Big(1 + p\cos\left(\Omega_p t\right)\Big)x + \gamma x^3 = d\cos\left(\Omega_d t + \phi\right), \tag{1}$$

where $\dot{(\,)}$ denotes temporal derivatives, $\beta = 2\omega_0\zeta$ where ω_0 is the linear natural frequency and ζ is the damping ratio, $(\ldots)\omega_0^2 x$ describes the linear elastic restoring force and γx^3 describes the third-order nonlinear elastic restoring force, p is a parametric excitation amplitude, d is a direct excitation amplitude, t is time, and ϕ is the phase between the parametric and direct excitation.

3 THEORETICAL PREDICTIONS

In applications involving imposed combined parametric and direct excitation, the frequencies Ω_p and Ω_d are typically tuned to be commensurate, e.g. with parametric amplifiers $\Omega_p/\Omega_d = 2$, which provides a periodic steady-state response. Frequency detuning, by contrast, generally yields quasi-periodic steady-state responses. To solve (1) for the quasi-periodic response, we use the method of varying amplitudes (MVA) [5], and compare quantitatively with results of direct numerical integration and qualitatively with experimental observations. First a frequency detuning σ_{pd} between the parametric and direct excitation is introduced, defined by:

$$\Omega_d = \tfrac{1}{2}\Omega_p + \sigma_{pd}. \tag{2}$$

The MVA assumes a solution form consisting of a series of harmonics with time-varying amplitudes X_{m1} and X_{m2}:

$$x(t) = \sum_{m=1}^{n} X_{m1}(t)\cos\left(\tfrac{1}{2}m\Omega_p t\right) + X_{m2}(t)\sin\left(\tfrac{1}{2}m\Omega_p t\right), \tag{3}$$

which by contrast to perturbation methods such as multiple scales or averaging is without restrictions such as slowly varying amplitudes, or the presence of small parameters [5, 6]. Also, by contrast to the method of harmonic balance, where the coefficients X_{m1} and X_{m2} would be constants and (3) an approximation, the allowed time dependency of X_{m1} and X_{m2} means that (3) merely represents a shift of variables, which is exact for all values of n. The shift from the original dependent variable x to $2n$ new variables, X_{m1} and X_{m2}, implies that $2n$ equations are

needed. This can be accomplished by introducing constraints in the form of $2n-1$ additional equations. The constraints are introduced by substituting (3) into (1), and requiring $2n-1$ groups of terms to equal zero. The $2n^{\text{th}}$ equation includes all the remaining terms of the original equation, and the $2n-1$ groups of terms are proposed to be the coefficients of the involved harmonic terms. Considering only the first two terms in (3), i.e. $n=1$, one obtains two equations for the amplitudes X_{11} and X_{12}:

$$\ddot{X}_{11}+\beta\dot{X}_{11}+\Omega_p\dot{X}_{12}+\tfrac{1}{2}\beta\Omega_pX_{12}+\left(\omega^2\left(1+\tfrac{1}{2}p\right)-\tfrac{1}{4}\Omega_p^2\right)X_{11} + \tfrac{3}{4}\gamma\left(X_{11}^2+X_{12}^2\right)X_{11}=d\cos\left(\sigma_{pd}t+\phi\right), \quad (4)$$

$$\ddot{X}_{12}+\beta\dot{X}_{12}-\Omega_p\dot{X}_{11}-\tfrac{1}{2}\beta\Omega_pX_{11}+\left(\omega^2\left(1-\tfrac{1}{2}p\right)-\tfrac{1}{4}\Omega_p^2\right)X_{12} + \tfrac{3}{4}\gamma\left(X_{11}^2+X_{12}^2\right)X_{12}=-d\sin\left(\sigma_{pd}t+\phi\right)+H., \quad (5)$$

where $H.$ denote higher harmonics. Until now approximations are not involved. Approximations are introduced by neglecting higher harmonics subsequently, which is adequate at small values of the nonlinearity term γx^3 and parametric excitation term $p\omega_0^2x$, i.e. small compared to the linear stiffness term ω_0^2x. Thus (1) is restated by (4) and (5), with X_{11} and X_{12} as the dependent variables instead of x. To solve (4) and (5), one employs the MVA again, ending up with four equations and four time dependent amplitudes, Y_{111}, Y_{112}, Y_{121}, and Y_{122}, to solve for. Solutions for these four amplitudes are lengthy and omitted here, but one ends up with a steady-state solution to (1):

$$x(t)=\Big(X_{110}+Y_{111}\cos\left(\sigma_{pd}t+\phi\right)+Y_{112}\sin\left(\sigma_{pd}t+\phi\right)\Big)\cos\left(\tfrac{1}{2}\Omega_pt\right) +\Big(X_{120}+Y_{121}\cos\left(\sigma_{pd}t+\phi\right)+Y_{122}\sin\left(\sigma_{pd}t+\phi\right)\Big)\sin\left(\tfrac{1}{2}\Omega_pt\right). \quad (6)$$

Figs. 1(a,b) present, respectively, sub- and superthreshold steady-state vibration amplitudes, i.e. the maximum absolute values of (6), as a function of direct excitation frequency for the perfectly tuned case ($\sigma_{pd}=0$). Fig. 1(a) shows that for subthreshold parametric excitation a response which qualitatively resembles a nonlinear hardening Duffing oscillator frequency response is obtained. Fig. 1(b) shows that adding superthreshold parametric excitation to a directly excited system yields a bistable amplified steady-state peak. The solid line denote stable solution branches and the dashed line denote unstable solution branches. Each solution branch has an unbounded response maximum, contrary to the bounded subthreshold steady-state vibration amplitude. Good agreement between the theoretical predictions and results of direct numerical integration is noted. A distinct feature of the superthreshold parametric near-resonant steady-state vibration amplitude compared to the subthreshold parametric near-resonant steady-state vibration amplitude is, that for a certain frequency range it increases significantly. This might be useful for sensor applications because the transition from a small amplitude to a large amplitude becomes more pronounced, and it might also be useful for energy harvesters since more energy can be harvested.

Figs. 2(a,b) show two detuned ($\sigma_{pd}\neq 0$) superthreshold steady-state vibration amplitudes with, respectively, a frequency ratio $\Omega_p/\Omega_d=2.05$ and 1.95 between the parametric and direct excitation. The somewhat larger deviation between the approximate analytical solution and results of direct numerical integration around the intersection between the lower and upper solution branches can be reduced by introducing higher harmonics, though omitted here since the calculations become more lengthy with only minor increase in accuracy. For some frequencies

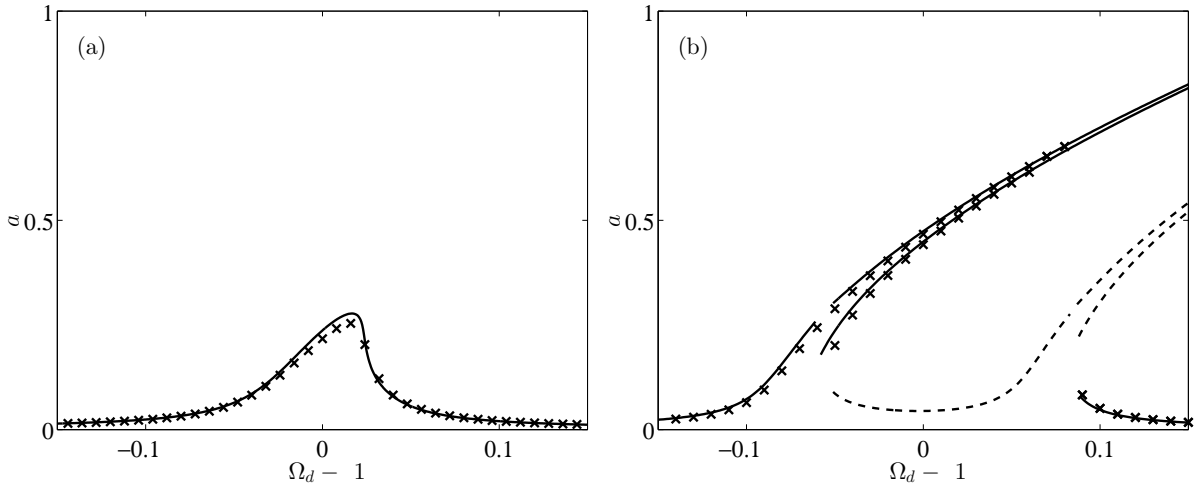


Figure 1: Theoretical steady-state vibration amplitude as a function of direct excitation frequency $\Omega - 1$ for (a) subthreshold parametric excitation ($p = 0.15$), and (b) superthreshold parametric excitation ($p = 0.35$). Solid and dashed lines denote, respectively, approximate analytical stable and unstable responses, symbols denote direct numerical integration. ($\gamma = 0.1$, $d = 0.01$, $\beta = 0.1$, $\phi = -\pi/4$, $\Omega_p/\Omega_d = 2$, $\sigma_{pd} = 0$).

up to five solution branches coexist. Two of these are duplicates in the frequency-amplitude relation except for a difference in phase, i.e. with frequency detuning between the parametric and direct excitation, the bistable amplified peak of fig. 1(b) appears to merge into one line. Jumps are observed, not only during a downsweep, but also during an upsweep. The upsweep jump is, for the chosen parameters, considerably smaller than for the downsweep, but this might be otherwise for other parameter values. Also, the frequency distance between the two peaks changes as function of frequency detuning between the parametric and direct excitation. For a negative nonlinear coefficient γ the steady-state vibration amplitude bends to the left instead of to the right, and the upper parts of the stable and unstable solution branches interchange stability.

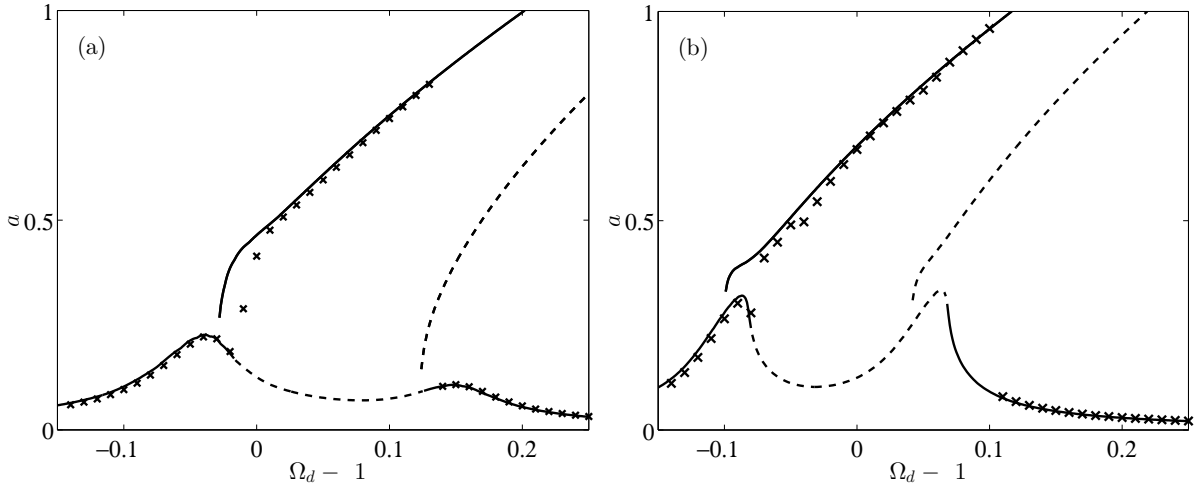


Figure 2: Theoretical superthreshold steady-state vibration amplitude as a function of direct excitation frequency $\Omega - 1$ for (a) $\Omega_p/\Omega_d = 2.05$ ($\sigma_{pd} = -0.025$), and (b) $\Omega_p/\Omega_d = 1.95$ ($\sigma_{pd} = 0.025$). ($p = 0.35$).

Compared to the perfectly tuned case, confer fig. 1(b), an upsweep jump emerges, and both peaks appear to shift to either the left or right of zero direct excitation frequency. Furthermore, superthreshold parametric excitation increases the near-resonant steady-state vibration amplitude as compared to employing subthreshold parametric excitation, and a slight frequency detuning of superthreshold parametric excitation can result in a further increase in steady-state vibration amplitude.

The theoretical part showed good agreement between approximate analytical responses and results of direct numerical integration, both in the perfectly tuned and detuned cases. For detuned superthreshold parametric excitation some of the frequency-amplitude solution branches appear to merge, and the frequency distance between the two peaks changes.

4 EXPERIMENTAL OBSERVATIONS

Fig. 3 shows the experimental setup. A cantilever beam is fixed in a shaker with an angle between the imposed base-excitation and the axial direction of the cantilever beam, such that the transverse displacement of the cantilever beams free end is affected by both the parametric and direct excitation. The dual frequency (Ω_d, Ω_p) signal to the shaker is produced by a waveform generator and amplified by a power amplifier. The transverse deflection of the cantilever beam is measured by a laser displacement sensor at the beam end and normalized with the beam length. For each excitation frequency detuning experiment both up- and downsweeps are conducted for the parametric and direct excitation frequencies. The direct excitation frequency is altered in an inner sweep, and the parametric excitation frequency in an outer sweep.

Figs. 4(a,b) show results for variation in direct and *subthreshold* parametric excitation frequencies. Fig. 4(a) provides an isometric view and fig. 4(b) the corresponding top view. As appears the maximum steady-state vibration amplitude is mostly sensitive to direct excitation frequency detuning (variations in $\tilde{\Omega}_d$), and much less to parametric excitation frequency detuning (variations in $\tilde{\Omega}_p$). One response notch, entangled by a red circle, is observed alongside jumps occurring due to a nonlinear hardening response. Slight variations in the parametric and direct excitation frequencies around the notch can result in a significantly lower response.

Figs. 4(c,d) show results for variation in direct and *superthreshold* parametric excitation frequencies. As compared to the case with subthreshold parametric excitation, another notch appears making the frequency range with a higher steady-state vibration amplitude significantly smaller, albeit the maximum steady-state vibration amplitude increases. These notches are also considerably larger in the case of superthreshold parametric excitation, as compared to the subthreshold case. With superthreshold parametric excitation the steady-state vibration amplitude increases for a part of the frequency range, but another part of the frequency range, i.e. the

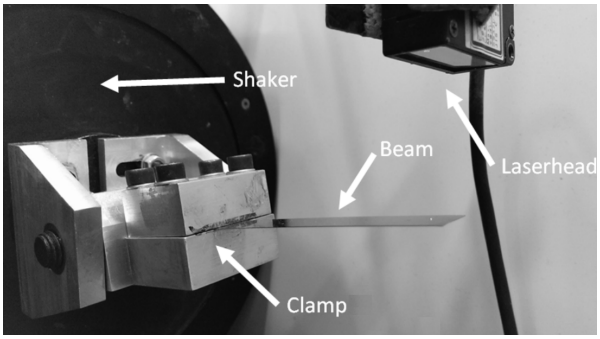


Figure 3: Experimental setup.

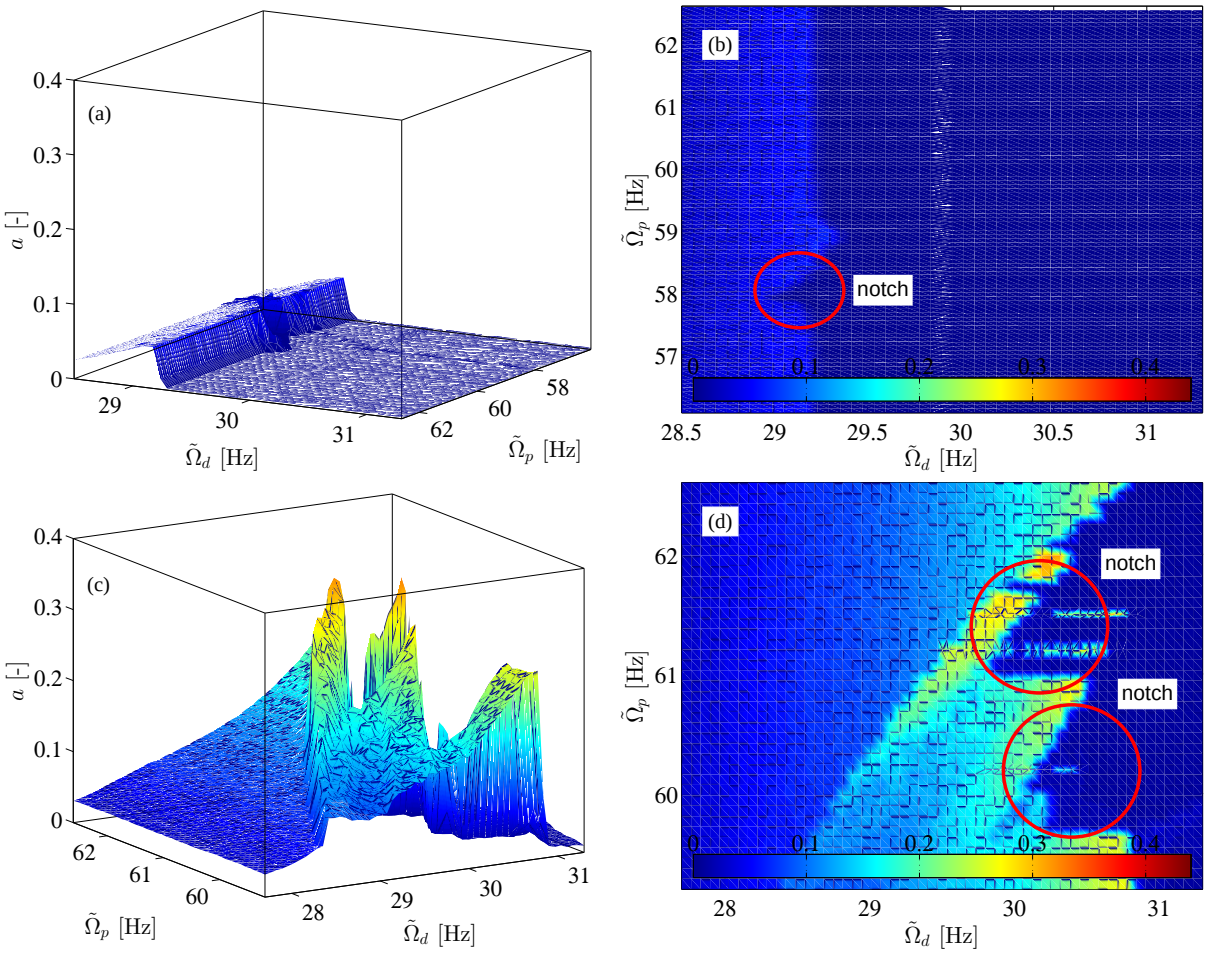


Figure 4: Experimental results: Isometric and top view of subthreshold (a,b) and superthreshold (c,d) steady-state vibration amplitude a as a function of direct and parametric excitation frequencies using a downsweep with $\tilde{\Omega}_d$ fixed while $\tilde{\Omega}_p$ is varied.

area entangled by the extra notch, indicates that there exist additional frequency ranges where a smaller steady-state vibration amplitude is obtained. Outside the frequency region of the notches, detuning of both the direct and parametric excitation frequencies has a small influence on the response.

The theoretical predictions presented in figs. 2(a,b) depict two special cases of the experimental observations presented in figs. 4(c,d); the two frequency ratios $\Omega_p/\Omega_d = 2.05$ and 1.95 correspond to two distinct lines in figs. 4(c,d). Good agreement is noted: jumps and the overall qualitative behaviour appears similar, and the change in frequency distance between the two peaks as predicted theoretically, confer figs. 2(a,b), is also observed experimentally. Also, in both cases frequency detuning between parametric and direct excitation can increase the response. Thus, frequency detuning can result in both decreased and increased steady-state vibration amplitudes, making it an effect which should either be avoided or utilized dependent on the applications.

5 CONCLUSIONS

Frequency detuning effects for combined parametric and direct near-resonant excitations of nonlinear structural vibrations were investigated. This is relevant for applications where frequency detuning can be expected between the parametric and direct excitation, or between the

parametric and direct excitation and the systems natural frequency during system operation. The studies were conducted theoretically using a Duffing-Mathieu equation as the model system, and experimentally using a cantilever beam as the model object. The approximate analytical responses were derived using the method of varying amplitudes, and compared with results of direct numerical integration, showing good agreement both in the perfectly tuned and detuned case. Good qualitative agreement also with experiments were noted. For detuned superthreshold parametric excitation some of the theoretical frequency-amplitude solution branches appear to merge. For some frequency detuning ranges a drop in experimental steady-state vibration amplitude was found, indicating performance degradation whereas for other frequency ranges, frequency detuning may yield an increased steady-state vibration amplitude. This makes frequency detuning a feature which can purposefully be avoided or utilized, dependent on the application, e.g. sensors and energy harvesters.

REFERENCES

[1] J.F. Rhoads, S.W. Shaw, The impact of nonlinearity on degenerate parametric amplifiers, *Applied Physics Letters*, **23**, 234101.1–3, 2010.

[2] S. Neumeyer, J.J. Thomsen, Macroscale mechanical domain parametric amplification: superthreshold pumping and optimal excitation parameters, *1st International Colloquium on Time-Periodic Systems: Current trends in theory and application (Euromech 532)*, Darmstadt, Germany, 2012.

[3] D. Rugar, P. Grütter, Mechanical parametric amplification and thermomechanical noise squeezing, *Physical Review Letters*, **67**, 699–702, 1991

[4] M. Cartmell, *Introduction to Linear, Parametric, and Nonlinear Vibrations*, Chapman and Hall, 1990.

[5] V.S. Sorokin, J.J. Thomsen, Vibration suppression for strings with distributed loading using spatial cross-section modulation, *Journal of Sound and Vibration*, **335**, 66–77, 2015

[6] A.H. Nayfeh, D.T. Mook, *Nonlinear oscillations*, Wiley, 1979.

COMPDYN 2015
5th ECCOMAS Thematic Conference on
Computational Methods in Structural Dynamics and Earthquake Engineering
M. Papadrakakis, V. Papadopoulos, V. Plevris (eds.)
Crete Island, Greece, 25–27 May 2015

A FAST SEMI-ANALYTICAL METHOD FOR COMPUTING THE RESPONSE OF RAILWAY TRACKS ON NONLINEAR FOUNDATIONS

T. Hoang[1], D. Duhamel[1], G. Foret[1], H. Yin[1], G. Cumunel[1], P. Joyez[2] and R. Caby[2]

[1]Université Paris-Est, Navier (UMR 8205 ENPC-IFSTTAR-CNRS)
Ecole Nationale des Ponts et Chaussées
6 et 8 Avenue Blaise Pascal, Cité Descartes, Champs-sur-Marne
77455 Marne-la-Vallée Cedex 2, France
e-mail: {tien.hoang, denis.duhamel, gilles.foret, hai-ping.yin, gwendal.cumunel}@enpc.fr

[2]Eurotunnel Group
BP no. 69, 62904 Coquelles Cedex, France
e-mail: {patrick.joyez, raphael.caby}@eurotunnel.com

Keywords: Railway, Nonlinear Foundation, Dynamics, Iteration Procedure

Abstract. *The nonlinear vibration of railway tracks is a subject of some recent investigations. A main source of non-linearity comes from the railway foundations. For example, ballast and its lower layers or support systems of non-ballasted railway could have nonlinear behaviors. Models of beam under moving forces are often used for this dynamic system, and then the models are solved by numerical method or perturbation technique for some special nonlinear cases. This communication present a new method for calculating the response of railway tracks under moving trains loads. Based an analytical model of periodically supported beam, this model holds for all kinds of nonlinear foundations. Then, by using harmonic balance techniques and iteration procedures, a new method is developed to calculate the response of the model provided that the loading forces form a periodic impulse series. This kind of loading force represents charges of moving trains with equal mass wagons. This method is demonstrated to converge to the analytic solution of the model in case of linear foundation. Then, it is applied to bilinear and nonlinear foundation as examples. The results show that the nonlinear parameters of foundation have a strong influence on the railways track responses. This semi-analytical method is simple and could be efficient to compute the nonlinear vibrations of railway tracks.*

1 INTRODUCTION

The nonlinear vibration of railway tracks is a subject of many investigations [2–9]. A main source of non-linearity comes from the railway foundations. For example, ballast and its lower layers or support systems of non-ballasted railway could have nonlinear behaviours. Models of beam on continuous or periodical supports under moving forces are often used for this dynamic system.

The first model was developed by Fryba [10] by considering beams on an elastic foundation. Then this model has been developed for other linear foundations [11–14]. In order to take into account the discrete supports, Mead [15, 16] presented periodically supported beams for railway tracks. This model is also developed by other authors for different kind of linear supports and moving forces [17–21]. Although the analytical methods are well developed for linear cases, these methods can not be easily applied to nonlinear foundations. An alternative is to use numerical methods [2–7] or perturbation techniques [8, 9]. However, the perturbation techniques have some limitations when applied to general cases.

We propose here a semi-analytical method for solving the problem of the dynamics of railway tracks on nonlinear foundations. Based on the model of periodically supported beam by Hoang et al. [1], a numerical method is developed for nonlinear behaviours. This method approaches Fourier series of the response by using harmonic balance techniques and an iteration procedure [22, 23]. The method is then compared to analytical solutions for linear foundation situations. The bilinear and nonlinear constitutive laws are considered as examples for the method. These examples show that this is a simple way to approach the responses of the system.

2 MODEL OF RAILWAY ON NONLINEAR FOUNDATION

2.1 Reduced relation between force and displacement of railway sleepers

Here we consider a railway track with sleepers distributed periodically in a nonlinear foundation whose reaction force is characterized by a function $f(w, w')$, $w(t)$ is the displacement of the sleeper as shown in figure 1. The rail is subjected to moving forces Q_j characterized by the distance to the first moving force D_j ($j = 1..K$ with K is the number of moving forces).

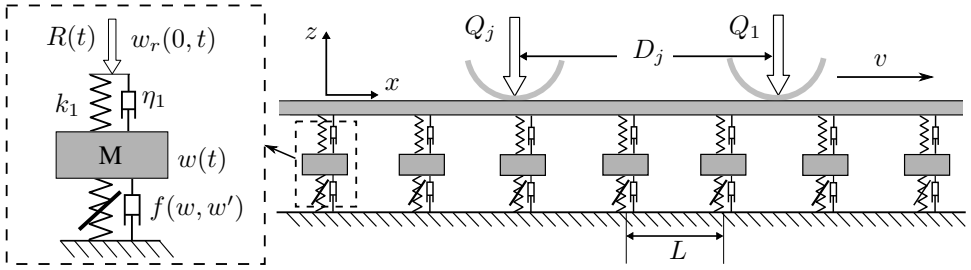


Figure 1: Periodically supported beam subjected to moving forces

When the rail is modelled by a Euler-Bernoulli beam, the response of railway tracks is governed by the following dynamical equation:

$$EI\frac{\partial^4 w_r(x,t)}{\partial x^4} + \rho S\frac{\partial^2 w_r(x,t)}{\partial t^2} - F(x,t) = 0 \tag{1}$$

where $F(x,t)$ is the total force (moving forces and reaction forces) acting on the beam, ρ, E are the density, the Young's modulus and S, I are the section and the longitudinal inertia of the rail.

Only the stationary response of the system is considered and the reaction forces of all sleepers are described by a same function but with a delay equal to the time for a load moving from a support to an other (so-called "periodic condition"). This condition leads to a description of the total force as the following:

$$F(x,t) = \sum_{n=-\infty}^{\infty} R(t - \frac{x}{v})\delta(x - nL) - \sum_{j=1}^{K} Q_j \delta(x + D_j - vt) \tag{2}$$

From equation (1) and (2), by using the Fourier transform and Dirac comb propriety (see [1]), we deduce a general relation between the Fourier transform of the vertical displacement $\hat{w}_r(0,\omega)$ and of the reaction forces $\hat{R}(\omega)$ of the rail at the sleeper position as the following:

$$\hat{w}_r(0,\omega) = \hat{R}(\omega)\eta_E(\omega) - \sum_{j=1}^{K} \frac{Q_j e^{-i\omega\frac{D_j}{v}}}{vEI\left[\left(\frac{\omega}{v}\right)^4 - k_b^4\right]} \tag{3}$$

with $k_b = \sqrt[4]{\frac{\rho S\omega^2}{EI}}$ and $\eta_E(\omega)$ given by:

$$\eta_E(\omega) = \frac{1}{4k_b^3 EI}\left[\frac{\sin(Lk_b)}{\cos(Lk_b) - \cos(L\frac{\omega}{v})} - \frac{\sinh(Lk_b)}{\cosh(Lk_b) - \cos(L\frac{\omega}{v})}\right]$$

For a linear foundation, an analytic solution could be deduced from this equation and the constitutive law of the foundation. In other cases, we can not solve analytically this system. The next section will introduce a model developed from equation (3) for the dynamics of sleepers on a nonlinear foundation. Then, a new numerical method based on harmonic balance techniques and iteration procedures will be used to solve the dynamic equation. Finally, the method is applied to the foundations with linear and nonlinear behaviours. The comparison shows that the numerical method agrees with the analytical results in case of linear behaviour. For other cases, the numerical method shows well the effects of nonlinearities on the response.

2.2 Dynamical equation of railway sleepers on nonlinear foundation

Consider the system of sleepers and foundation as shown in figure 1. This system contains a linear part corresponding to the rail pad (upper the sleeper) and a nonlinear part corresponding to the foundation (under the sleeper). Here η_1, k_1 are the damping and spring coefficients of rail pad; w, w' are the vertical displacement and the velocity of the sleeper and $f(w,w')$ is the force acting on the foundation.

The displacement of the sleeper is governed by the following equation:

$$Mw''(t) + \eta_1 w'(t) + k_1 w + f(w,w') = \eta_1 w_r'(0,t) + k_1 w_r(0,t) \tag{4}$$

where prime stands for the derivation in time t and M is the mass of the railway sleeper. In addition, the reaction force of the sleeper on the rail is given by:

$$R(t) = -\eta_1\left[w_r(0,t) - w(t)\right]' - k_1(w_r(0,t) - w(t)) \tag{5}$$

By taking the Fourier transform of (5), we obtain:

$$\hat{R}(\omega) = -A(\omega)\left[\hat{w}_r(0,\omega) - \hat{w}(\omega)\right]$$

where $A(\omega) = i\omega\eta_1 + k_1$ (this is the frequency stiffness of the rail pad). By injecting the last equation into equation (3), we have:

$$\hat{w}_r(0,\omega) = \frac{A(\omega)\eta_E(\omega)}{1 + A(\omega)\eta_E(\omega)}\hat{w}(\omega) - \frac{\Gamma(\omega)}{vEI}\sum_{j=1}^{K} Q_j e^{-i\omega\frac{D_j}{v}} \tag{6}$$

with $\Gamma(\omega) = \left\{(1 + A(\omega)\eta_E(\omega))\left[\left(\frac{\omega}{v}\right)^4 - k_b^4\right]\right\}^{-1}$.

Making the Fourier transform and then the inverse Fourier transform of the right term of equation (4) leads to the following result:

$$\eta_1 w_r'(0,t) + k_1 w_r(0,t) = \frac{1}{2\pi}\int_{-\infty}^{\infty} A(\omega)\hat{w}_r(0,\omega)e^{i\omega t}d\omega \tag{7}$$

By injecting $\hat{w}_r(0,\omega)$ in equation (6) into the last equation and then the obtained expression into equation (4), one can write:

$$\begin{aligned} w'' + \beta w' + \omega_0^2 w + g(w,w') = {} & \frac{1}{2\pi M}\int_{-\infty}^{\infty} \frac{A^2(\omega)\eta_E(\omega)e^{i\omega t}}{1 + A(\omega)\eta_E(\omega)}\hat{w}(\omega)d\omega \\ & -\frac{1}{2\pi M}\int_{-\infty}^{\infty} \frac{A(\omega)\Gamma_E(\omega)}{vEI}\sum_{j=1}^{K} Q_j e^{-i\omega\frac{D_j}{v}} e^{i\omega t}d\omega \end{aligned} \tag{8}$$

where $g(w,w') = \dfrac{f(w,w')}{M}$, $\omega_0^2 = \dfrac{k_1}{M}$ and $\beta = \dfrac{\eta_1}{M}$.

Equation (8) is the dynamical equation of the sleeper. This equation is similar to that of nonlinear oscillators but contains terms of the interaction between the rail and the sleepers on the right of the equation. In order to simplify this coupling terms but only periodical solution of $w(t)$ is considered but the general nonlinear function $f(w,w')$ is kept. This response occurs when the moving forces Q_j are a periodic series of forces (see [1]) which is presented in next section.

2.3 Loads of a train as an impulse train

When the charges of each wagon of the train equal a given load ($Q_j = Q$) and there is a great number of wagons so that the periodical solution could be considered, the load of a train can be approximated by an impulse train with a distance from a reference impulse given by:

$$D_j = \begin{cases} jH & \text{for front wheels} \\ jH + D & \text{for back wheels} \end{cases} \tag{9}$$

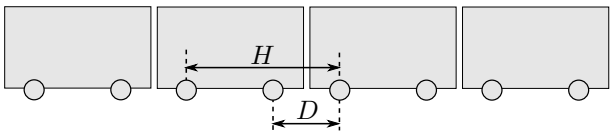


Figure 2: Charge of a train as a periodical series of loads

where H and D are the length of each wagon and distance between the font and the back wheel of a boogie. Using the propriety of Dirac comb, one can write:

$$\sum_{j=-\infty}^{\infty} Q_j e^{-i\omega\frac{D_j}{v}} = \frac{2\pi v Q}{H}(1+e^{-i\omega\frac{D}{v}}) \sum_{n=-\infty}^{\infty} \delta\left(\omega + \frac{2\pi v}{H}n\right) \tag{10}$$

By injecting the last equation into the last term of equation (8), we obtain:

$$\frac{1}{2\pi M}\int_{-\infty}^{\infty} \frac{A(\omega)\Gamma}{vEI}\sum_j Q_j e^{-i\omega\frac{D_j}{v}} e^{i\omega t} d\omega = \sum_n \frac{Q(1+e^{-i\frac{D}{v}\omega_n})A(\omega_n)\Gamma(\omega_n)e^{i\omega_n t}}{MHEI} \tag{11}$$

with $\omega_n = 2\pi n\dfrac{v}{H}$.

The last equation describes a periodic function of harmonics ω_n. Thus, we can find a periodical solution of $w(t)$ in Fourier series form:

$$w(t) = \sum_n c_n e^{i\omega_n t} \tag{12}$$

where $\{c_n\}$ are Fourier coefficients of $w(t)$ given by:

$$c_n = \frac{1}{T}\int_{-T/2}^{T/2} w(t)e^{-i\omega_n t}dt \quad \text{with} \quad T = \frac{H}{v} \tag{13}$$

Thus, we have:

$$\hat{w}(\omega) = 2\pi\sum_n c_n \delta(\omega - \omega_n)$$

By injecting the last equation into the first term on the right side of (8), we get:

$$\frac{1}{2\pi M}\int_{-\infty}^{\infty} \frac{A^2(\omega)\eta_E(\omega)e^{i\omega t}}{1+A(\omega)\eta_E(\omega)}\hat{w}(\omega)d\omega = \frac{1}{M}\sum_n \frac{A^2(\omega_n)\eta_E(\omega_n)}{1+A(\omega_n)\eta_E(\omega_n)}c_n e^{i\omega_n t} \tag{14}$$

Thus, equation (8) becomes:

$$w'' + \beta w' + \omega_0^2 w + g(w,w') = \sum_n c_n P_n e^{i\omega_n t} - \sum_n F_n e^{i\omega_n t} \tag{15}$$

where:

$$P_n = \frac{A^2(\omega_n)\eta_E(\omega_n)}{M\left[1+A(\omega_n)\eta_E(\omega_n)\right]} \quad \text{and} \quad F_n = \frac{Q(1+e^{-i\omega_n\frac{D}{v}})}{MHEI}A(\omega_n)\Gamma(\omega_n) \tag{16}$$

Particularly, we have: $P_0 = \frac{k_1}{M} = \omega_0^2$ and $F_0 = \frac{2QL}{MH}$.

Thus, we reduce (8) which is a general dynamical equation of the railway sleeper to a simple equation with characteristic parameters P_n, F_n. In fact, we see that F_n corresponds to the charges of the train affecting on the sleeper and P_n corresponds to the coupling of the sleeper with the rail and other sleepers. In the next section, we will present a numerical method for this equation and then consider some examples of foundations.

3 SEMI-ANALYTICAL METHOD

Taking Fourier coefficients of equation (15) leads to the following result:

$$\frac{1}{T}\int_{-T/2}^{T/2}(w''+\beta w'+\omega_0^2 w)e^{-i\omega_n t}dt+\frac{1}{T}\int_{-T/2}^{T/2}g(w,w')e^{-i\omega_n t}dt=c_nP_n-F_n$$

By injection of equation (12) to the last equation, we obtain:

$$-\omega_n^2 c_n+i\beta\omega_n c_n+\omega_0^2 c_n+\frac{1}{T}\int_{-T/2}^{T/2}g(w,w')e^{-i\omega_n t}dt=c_nP_n-F_n \tag{17}$$

where $g(w,w')=f(w,w')/M$ with w,w' given by equation (12):

$$w(t)=\sum_n c_n e^{i\omega_n t},\quad w'(t)=\sum_n i\omega_n c_n e^{i\omega_n t} \tag{18}$$

Hence, equation (17) forms a system of nonlinear equations of variable $\{c_n\}$. In general, we can not find the analytical solution of this equation. By using harmonic balance techniques and iteration procedure, we will look at an approximation of the solution $w(t)$ for the m first harmonics in the following form:

$$w_{mk}(t)=\sum_{n=-m}^{m}c_{nk}e^{i\omega_n t}\quad\forall k\geq 1 \tag{19}$$

Here we take $\forall n,\ c_{n1}=0$. We built series $\{c_{nk}\}$ such that $c_{nk}\to c_n$ when $k,m\to\infty$ by inserting an evolution index k in equation (17). Such a series $\{c_{nk}\}$ is given by the following equations:

$$\begin{cases}-\omega_n^2 c_{nk}+(i\beta\omega_n+\omega_0^2)c_{n(k+1)}+\mathcal{F}_{nk}=P_n c_{nk}-F_n & \text{if } 0\leq|n|\leq N_0\\ -\omega_n^2 c_{n(k+1)}+(i\beta\omega_n+\omega_0^2)c_{nk}+\mathcal{F}_{nk}=P_n c_{n(k+1)}-F_n & \text{if } N_0<|n|\leq m\end{cases}$$

where N_0 is defined for the convergence of the solution (it normally depends on force $f(w,w')$) and $\mathcal{F}_{nk}$ is calculated by:

$$\mathcal{F}_{nk}=\frac{1}{T}\int_{-T/2}^{T/2}g(w_{mk},w'_{mk})e^{-i\omega_n t}dt \tag{20}$$

Finally, we get the series $\{c_{nk}\}$ as the following:

$$c_{n(k+1)}=\begin{cases}\dfrac{(\omega_n^2+P_n)c_{nk}-F_n-\mathcal{F}_{nk}}{\omega_0^2+i\beta\omega_n} & \text{if } 0\leq|n|\leq N_0\\ \dfrac{(\omega_0^2+i\beta\omega_n)c_{nk}+F_n+\mathcal{F}_{nk}}{\omega_n^2+P_n} & \text{if } N_0<|n|\leq m\end{cases} \tag{21}$$

The last equation defines a recurrent sequence $\{c_{nk}\}$ in k. If this sequence $\{c_{nk}\}$ converges to $\{c_n\}\forall n$ when $k\to\infty$, by replacing this series $c_{nk}, c_{n(k+1)}$ by its limit c_n, we find once again equation (17). Hence, this sequence converges to the solution of (17). By consequence, we can rebuild approximations of the response from (19) by using the sequence $\{c_{nk}\}$ when the value of k is large enough. In the next section, we will use this formulation to calculate the response of the sleeper on different foundations.

4 EXAMPLES

4.1 Linear foundation

Let's consider a foundation with a linear constitution law given by:

$$f(w) = k_2 w + \eta_2 w' \tag{22}$$

In this case, the integral in equation (17) can be calculated analytically as following:

$$\frac{1}{T}\int_{-T/2}^{T/2} g(w,w')e^{-i\omega_n t}dt = \int_{-T/2}^{T/2} \frac{k_2 w + \eta_2 w'}{TM} e^{-i\omega_n t}dt = \left(\frac{k_2}{M} + \frac{i\eta_2\omega_n}{M}\right) c_n$$

Thus, equation (17) has an analytic solution given by:

$$c_n = \frac{F_n}{\omega_n^2 + P_n - \omega_0^2 - i\beta\omega_n - (k_2 + i\eta_2\omega_n)/M} \tag{23}$$

Now we calculate the solution of (17) by the numerical method. We need to verify that series $\{c_{nk}\}$ defined by (21) converges also to the analytic solution. By injecting function $f(w,w')$ in equation (22) into equation (20), we get:

$$\mathcal{F}_{nk} = \left(\frac{k_2}{M} + \frac{i\eta_2\omega_n}{M}\right) c_{nk}$$

Thus, equation (21) becomes:

$$c_{n(k+1)} = \begin{cases} \dfrac{\left[\omega_n^2 + P_n - (k_2 + i\eta_2\omega_n)/M\right] c_{nk} - F_n}{\omega_0^2 + i\beta\omega_n} & \text{if } 0 \le |n| \le N_0 \\ \dfrac{\left[\omega_0^2 + i\beta\omega_n + (k_2 + i\eta_2\omega_n)/M\right] c_{nk} + F_n}{\omega_n^2 + P_n} & \text{if } N_0 < |n| \le m \end{cases}$$

We see that:

$$c_{n(k+1)} - c_n = \begin{cases} \dfrac{\omega_n^2 + P_n - (k_2 + i\eta_2\omega_n)/M}{\omega_0^2 + i\beta\omega_n}\left(c_{nk} - c_n\right) & \text{if } 0 \le |n| \le N_0 \\ \dfrac{\omega_0^2 + i\beta\omega_n + (k_2 + i\eta_2\omega_n)/M}{\omega_n^2 + P_n}\left(c_{nk} - c_n\right) & \text{if } N_0 < |n| \le m \end{cases}$$

Here c_n is the analytical solution in (23). The last equations are geometric sequences which converge to c_n if and only if:

$$\begin{cases} \left|\dfrac{\omega_n^2 + P_n - (k_2 + i\eta_2\omega_n)/M}{\omega_0^2 + i\beta\omega_n}\right| < 1 & \text{if } 0 \le |n| \le N_0 \\ \left|\dfrac{\omega_0^2 + i\beta\omega_n + (k_2 + i\eta_2\omega_n)/M}{\omega_n^2 + P_n}\right| < 1 & \text{if } N_0 < |n| \le m \end{cases}$$

Therefore, if N_0 is chosen such that the last inequalities are satisfied, we have proved that the numerical method converges to the analytic solution.

Figure 3 shows the results of the analytical and numerical methods for a railway track (type UIC60) with parameters given in table 1. The numerical method gives a good approximation of the analytical solution after 15 iterations. In fact the response corresponding to a linear foundation (22) with parameters $k_2 = 20\text{MNm}^{-1}$ and $\eta_2 = 0.2\text{MNsm}^{-1}$.

Content	Notation	Value	Unite
Rail mass	ρS	60	kgm^{-1}
Rail stiffness	EI	6.3	MNm^2
Train speed	v	45	ms^{-1}
Charge of a wheel	Q	75	kN
Block mass	M	100	kg
Sleeper length	L	0.6	m
Length of boogie	D	3	m
Length of wagon	H	18	m
Stiffness	k_1	220	MNm^{-1}
Damping coefficient	$\eta 1$	1.0	MNsm^{-1}

Table 1: Parameters of a linear railway track

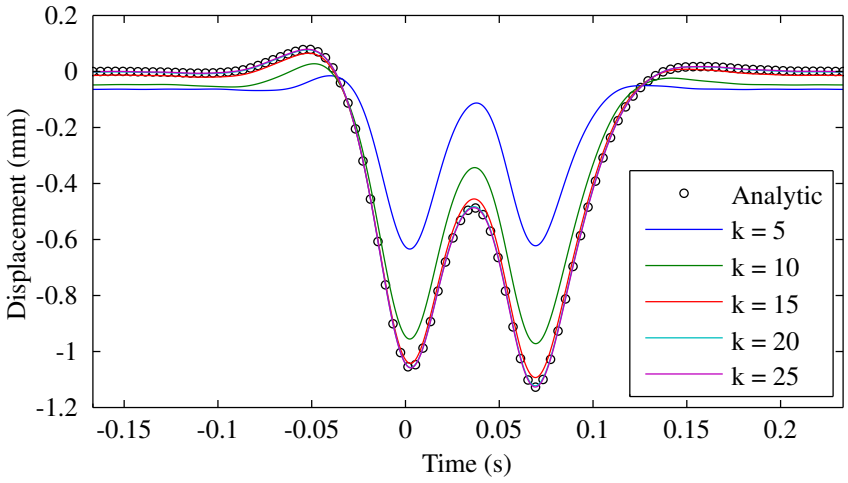


Figure 3: Displacement of a sleeper on a linear foundation by analytical and numerical method

4.2 Bilinear foundation

Now a bilinear foundation is considered with two different stiffness for compression and tension. Such a constitutive law can be described by the following function:

$$f(w, w') = \begin{cases} k_2^+ w + \eta_2 w' & \text{if } w < 0 \\ k_2^- w + \eta_2 w' & \text{if } w \geq 0 \end{cases} \tag{24}$$

Here we compute the response of the railway sleeper by the numerical method and we investigate the convergence of this response when increasing the number of iterations and harmonics. The upper graph in figure 4 shows the results of the numerical method with different number of harmonics (while the number of iterations $k = 100$ remains the same). We see that when the number of harmonics is bigger than 10, the response converges well (the variation is very small). We find again the convergence of the response with different numbers of iteration with $m = 15$ (see the bottom graph in figure 4). Here, the calculation is taken with a railway track given by table 1 and the foundation parameters $k_2^+ = 20, k_2^- = 10$ MKm^{-1}.

For $m = 15, k = 100$, we now calculate the response for different tension stiffness in order to study the effect of this nonlinear parameter. Figure 5 shows these responses for different

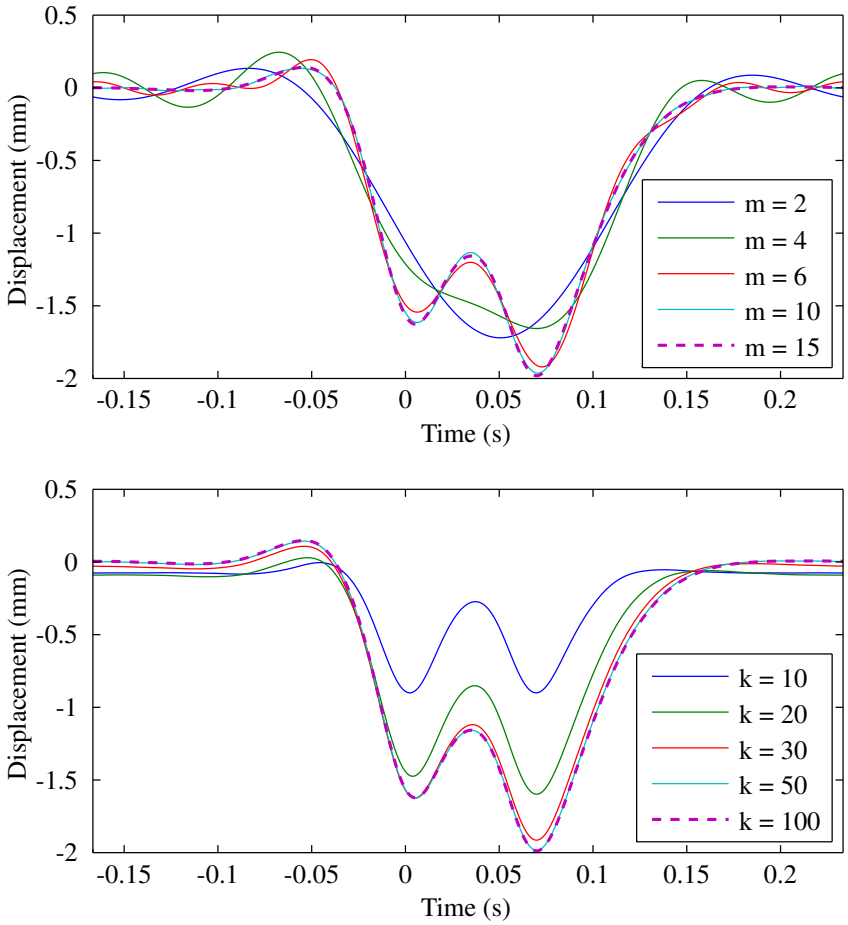


Figure 4: Displacement of a sleeper on a bilinear foundation by numerical method with different numbers of harmonics m (upper figure) and iterations k (lower figure)

ratios $e = k_2^-/k_2^+$.

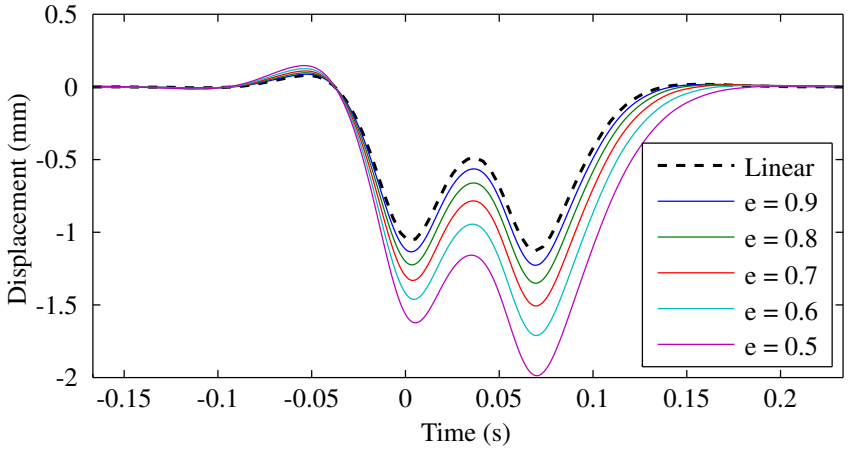


Figure 5: Displacement of a sleeper on bilinear foundations

4.3 Nonlinear foundation

In this section, a nonlinear foundation with a cubic term in the stiffness is considered:

$$f(w, w') = \eta_2 w' + k_2 w + \varepsilon k_3 w^3 \tag{25}$$

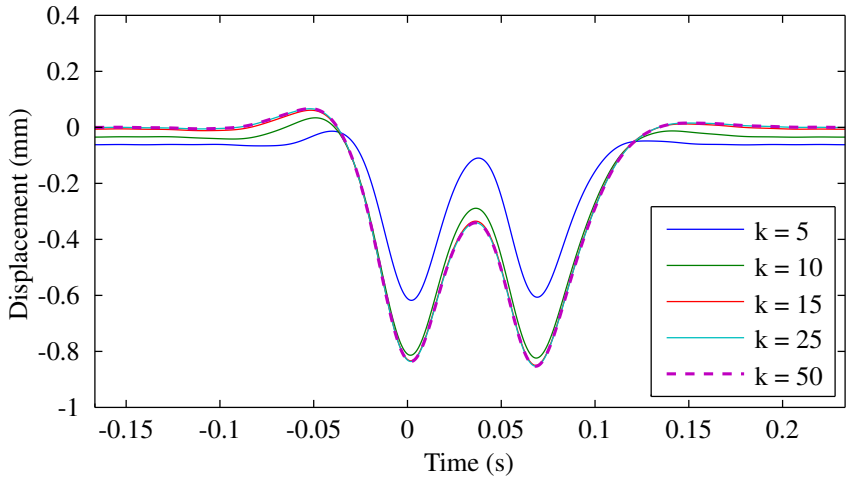


Figure 6: Displacement of a sleeper on a nonlinear elastic foundation by numerical method with different numbers of iterations

The response is calculated for different numbers of iterations k with $m = 15$ in order to study the convergence of the method. Figure 6 shows the convergence for $k \geq 15$. Here we take $k_2 = 20$ MNm^{-1}, $k_3 = 20$ kNmm^{-3} and $\varepsilon = 0.8$. The effect of the nonlinear parameter ε is also investigated in figure 7 where the amplitude of the displacement decreases when the nonlinear force increases.

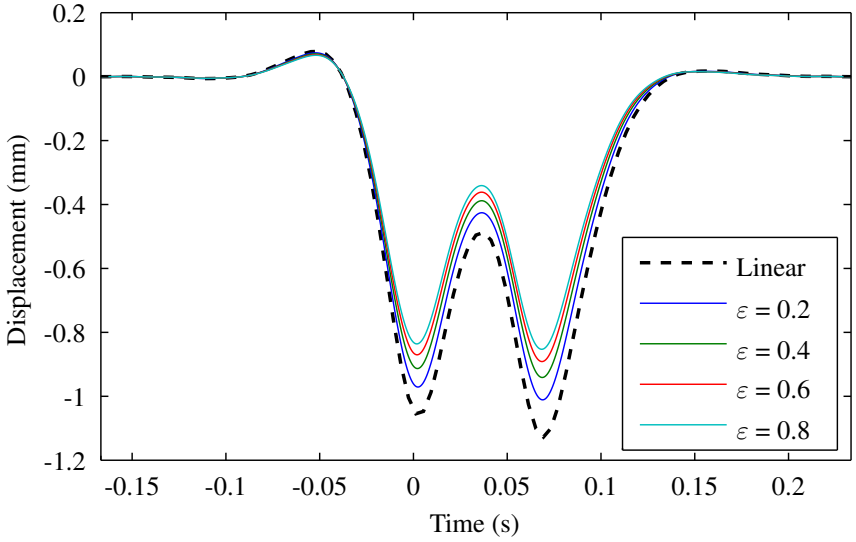


Figure 7: Displacement of a sleeper on nonlinear foundations

5 CONCLUSION

A semi-analytic model for periodically supported beams has been developed and applied for the response of railway sleepers on different kinds of foundations. In linear cases, this method is proved to converge to the analytical solution. For other cases, this method is a simple way to approximate the response of railway tracks on complex foundations.

References

[1] T. Hoang, D. Duhamel, G. Foret, H. Yin, P. Joyez, R. Caby, Dynamical response of railway tracks in tunnel, *11th World Congress on Computational Mechanics (WCCM XI - ECCM V - ECFD VI)*, Barcelona, Spain, 20-25 July 2014.

[2] V. H. Nguyen, D. Duhamel, Finite element procedures for nonlinear structures in moving coordinates. part ii: Infinite beam under moving harmonic loads, *Computers and Structures*, **86**, 2056–2063, 2008.

[3] J.-S. Chen, Y.-K. Chen, Steady state and stability of a beam on a damped tensionless foundation under a moving load, I*nternational Journal of Non-Linear Mechanics*, **46**(1), 180–185, 2011.

[4] H. Ding, L.-Q. Chen, S.-P. Yang, Convergence of Galerkin truncation for dynamic response of finite beams on nonlinear foundations under a moving load, *Journal of Sound and Vibration*, **331** (10), 2426–2442, 2012.

[5] E. Sapountzakis, A. Kampitsis, Nonlinear response of shear deformable beams on tensionless nonlinear viscoelastic foundation under moving loads, *Journal of Sound and Vibration*, **330** (22) 5410–5426, 2011.

[6] P. C. Jorge, F. Simoes, A. P. da Costa, Finite element dynamics analysis of beams on non-uniform nonlinear viscoelastic foundations under moving loads, *9th Intenational Conference on Structural Dynamics (EURODYN2014)*, 2014.

[7] Y. Dugush, M. Eisenberger, Vibrations of non-uniform continuous beams under moving loads, *Journal of Sound and Vibration*, **254** (5), 911–926, 2002.

[8] M. Ansari, E. Esmailzadeh, D. Younesian, Frequency analysis of finite beams on nonlinear KelvinVoight foundation under moving loads, *Journal of Sound and Vibration*, **330** (7), 1455–1471, 2011.

[9] M. Kargarnovin, D. Younesian, D. Thompson, C. Jones, Response of beams on nonlinear viscoelastic foundations to harmonic moving loads, *Computers & Structures*, **83** (23-24), 1865–1877, 2005.

[10] L. Fryba, Vibration of solids and structures under moving loads, *Noordhoff International Publishing*, 1972.

[11] L. Andersen, S. Nielsen, P. Kirkergaard, Finite element modelling of a infinite Euler beams on Kelvin foundations exposed to moving loads in convected co-ordinates, *Journal of Sound and Vibration*, **241** (4), 587–604, 2001.

[12] X. Sheng, M. Li, C. J. C. Jones, D. J. Thompson, Vibration analysis of the continuous beam subjected to a moving mass, *Journal of Sound and Vibration*, **303**, 873–894, 2007.

[13] M. Ichikawa, Y. Miyakawa, A. Matsuda, Vibration analysis of the continuous beam subjected to a moving mass, *Journal of Sound and Vibration*, **230** (3), 493–506, 2000.

[14] F. F. Calm, Dynamic analysis of beams on viscoelastic foundation, *European Journal of Mechanics - A/Solids*, **28** (3), 469–476, 2009.

[15] D. J. Mead, Free wave propagation in periodically supported, infinite beams, *Journal of Sound and Vibration*, **11** (2), 181–197, 1970.

[16] D. J. Mead, Wave propagation in continuous periodic structures: research contributions from southampton, *Journal of Sound and Vibration*, **190** (3), 495–524, 1996.

[17] X. Sheng, C. Jones, D. Thompson, Response of infinite periodic structure to moving or stationary harmonic loads, *Journal of Sound and Vibration*, **282**, 125–149, 2005.

[18] P. M. Belotserkovskiy, On the oscillation of infinite periodic beams subjected to a moving concentrated force, *Journal of Sound and Vibration*, **193** (3), 705–712, 1996.

[19] A. V. Metrikine, K. Popp, Vibration of a periodically supported beam on an elastic half-space, *European Journal of Mechanics A/Solid*, **18**, 679–701, 1999.

[20] M. A. Foda, Z. Abduljabbar, A dynamic green fuction formulation for the response of a beam structure to a moving mass, *Journal of Sound and Vibration*, **210** (2), 295–306, 1998.

[21] A. V. Vostroukhov, A. Metrikine, Periodically supported beam on a visco-elastic layer as a model for dynamic analysis of a high-speed railway track, *International Journal of Solids and Structures*, **40**, 5723–5752, 2003.

[22] A. H. Nayfeh, Introduction to perturbation techniques, *Wiley Classics Library Edition*, 1993.

[23] A. H. Nayfeh, D. T. Mook, Nonlinear oscillations, *Wiley Classics Library Edition*, 1995.

COMPDYN 2015
5th ECCOMAS Thematic Conference on
Computational Methods in Structural Dynamics and Earthquake Engineering
M. Papadrakakis, V. Papadopoulos, V. Plevris (eds.)
Crete Island, Greece, 25–27 May 2015

VALIDITY DOMAIN OF AN ENERGETIC METHOD FOR THE ESTIMATION OF MODAL DAMPING IN THE CASE OF NON LINEAR LOCALIZED DISSIPATION

M. Krifa, N. Bouhaddi, G. Chevallier, and S. Cogan

FEMTO-ST Institute - Applied Mechanics department
24 chemin de l'Epitaphe, 25000 Besançon, France
{mohamed.krifa,noureddine.bouhaddi,gael.chevallier,scott.cogan}@univ-fcomte.fr

Keywords: Bolted joints, modal damping, localized dissipation, nonlinear dissipation, energetic method.

Abstract. *Modal damping estimation errors can be introduced when using assumptions such as proportional damping or a diagonal generalized matrix of localized dissipation at interfaces [1]. Previous work has studied the estimation of modal damping in bolted joints using many methods [2, 3]. One such method, used in this work, is the iterative energetic method (EM), developed in [4]. The present study investigates the EM for calculating the modal damping associated with localized nonlinear dissipative interfaces of a global linear structure. This method has limitations in two cases: localized linear damping [5] and localized nonlinear damping. The validity domain of the EM in the linear case was studied previously in [5]. The main conclusions were that EM is not valid in the following conditions : when eigenfrequencies are closely spaced, when localized dissipation exceeds a specific damping level, and if the response is not projected on a single mode of vibration. To the best of our knowledge, the nonlinear limitations of the EM are still unknown and have yet to be identified in the literature. The main goal of this paper is to investigate the iterative EM and define its validity domain for harmonic excitations as a function of the level of external structural loads and the level of nonlinear damping. We propose to investigate these parameters and their influence for the prediction of equivalent modal damping in a simple beam structure with a bolted nonlinear interface. Through use of an academic example with exact solutions, we will be able to quantify the error of our predictions, and thus provide accurate validity domains for the method.*

1 INTRODUCTION

The problem of damping remains an important challenge when computing the vibration levels of assembled structures. Virtual tools, Computer Aided Design and Finite Element Simulations are used to predict both mass and stiffness matrices with good accuracy, but damping is often badly estimated. This leads to an erroneous estimation of vibration levels. Generally the localized dissipation in the interfaces presents nonlinear effects. These nonlinear effects must be taken into account when modeling damping locally. It is assumed here that the structure has a globally linear behavior. The main interest of this study is to investigate the iterative EM and define its validity domain for harmonic excitation as a function of the level of external loads and the level of nonlinear localized damping. An exact method is used as reference to investigate the influence of these two parameters and compare the resulting error in the modal damping estimation.

2 Estimation of modal damping

To estimate modal damping in assembled structures with localized nonlinearities two computational methods will be considered herein. The first method uses a time integration solver of a globally nonlinear system and will be considered as the reference method. The second method is the *Iterative Energetic Method* (IEM), which is based on the estimation of the modal damping by the ratio between the dissipated energy and the maximal potential energy, over a cycle of stationary vibration. Localized damping can be induced in several manners, for example, by viscoelastic materials, pressure loss in fluids and solid friction. In this work, in order to model bolted joints a nonlinear viscoelastic damping model is used to represent a bolted interface.

2.1 Reference Method

In the reference method, the system will be considered as a globally nonlinear system :

$$M\ddot{u} + Ku + C\dot{u} + f_{nl}(t, \dot{u}) = f_{ext}(t) \tag{1}$$

where

- M, K et C are respectively mass, stiffness and damping matrices
- $f_{ext}(t) = F\cos(\omega t)$ Harmonic excitation
- $u(t) = \{u_1, u_2, u_3, ..., u_n\}^T$ Displacement vector
- $\dot{u}(t) = \{\dot{u}_1, \dot{u}_2, \dot{u}_3, ..., \dot{u}_n\}^T$ Velocity vector
- $f_{nl}(t, \dot{u})$ Nonlinear dissipation force

The nonlinear dissipated force describes the friction in the bolted interfaces. The i^{th} interface is expressed by the following expression :

$$f_{nl}^i(t, \dot{u}) = (c_0^i + c_1^i \left|\Delta\dot{u}_i\right|)\Delta\dot{u}_i \tag{2}$$

where $c_0^i[N/(m/s)]$ and $c_1^i\left[N/(m/s)^2\right]$ are two coefficients of the nonlinear viscous damping, $\Delta\dot{u}_i = u_j - u_k$ is the relative velocity, and j, k are the nodes of the i^{th} interface.

The calculation of the modal damping is performed into two steps : The first step is to evaluate the response of the system using a time integration solver, for example the Runge-Kutta method [6]. This step requires the transformation of the second-order equation (1)

$$\ddot{u} = M^{-1}(f_{ext}(t) - f_{nl}(t, \dot{u}) - Ku - C\dot{u}) \tag{3}$$

and by applying a change of variable $y_1(t) = u(t)$ and $y_2(t) = \dot{u}(t)$ on the equation (3) we obtain the following first-order system

$$\begin{cases} \dot{y}_1 = y_2 \\ \dot{y}_2 = M^{-1}(f_{ext}(t) - f_{nl}(t, y_2) - Ky_1 - Cy_2) \end{cases} \tag{4}$$

The second step consists in the calculation of the modal damping with the following expression

$$\xi_\nu = \frac{1}{4\pi} \frac{E_\nu^{diss}}{E_\nu^{pot}} \tag{5}$$

Dissipated energy is calculated by the following expression :

$$E_\nu^{diss} = \int_0^T \dot{u}(t)^T f_c(t) dt + \sum_{i=1}^{n_inter} \int_0^T \Delta\dot{u}_i(t)^T f_{nl}^i(t) dt \tag{6}$$

where

- $T = \frac{2\pi}{\omega_\nu}$ Cycle of periodic vibration of mode ν
- $f_c(t) = C\dot{u}(t)$ Dissipated force due to the material
- n_inter Number of interfaces in the system

Potential energy is calculated as follow :

$$E_\nu^{pot} = \frac{1}{2} u(\omega_\nu)^T K u(\omega_\nu) \tag{7}$$

where

- $u(\omega_\nu) = \|u_{\max}\| e^{j\varphi}$ Frequency response deduced from the temporal response
- $\|u_{\max}\|$ Maximum amplitude of the time response in a vibration cycle of the established regime when the structure is excited at the resonance frequency ω_ν
- φ Dephasing angle between the Dofs and the external load

The above method was implemented in Matlab and will be considered as the reference method when comparing damping results with the iterative energetic method IEM.

2.2 Iterative Energetic Method IEM

The Iterative Energetic Method consists in calculating modal damping using a multiscale approach which is divided in two main steps : step (1) local nonlinear contact analysis to estimate energy dissipation and step (2) estimate modal damping for the globally linear elastodynamic structure.

The present method is based on the ideas presented in earlier work [4, 5]. The main advantage of the IEM method is to avoid the high computational burden associated with to reference approach. It is based on calculating the modal damping by the ratio between dissipated energy and maximal potential energy, over a cycle of periodic vibration, as described in the equation (5). Meanwhile the estimation of both dissipated and potential energies requires an accurate characterization of the response levels of the system and the latter remains an approximation since they depend a priori on a knowledge of the different dissipation mechanisms. An iterative approach, as described by figure(1), is thus needed to converge when estimating the modal damping for the global system.

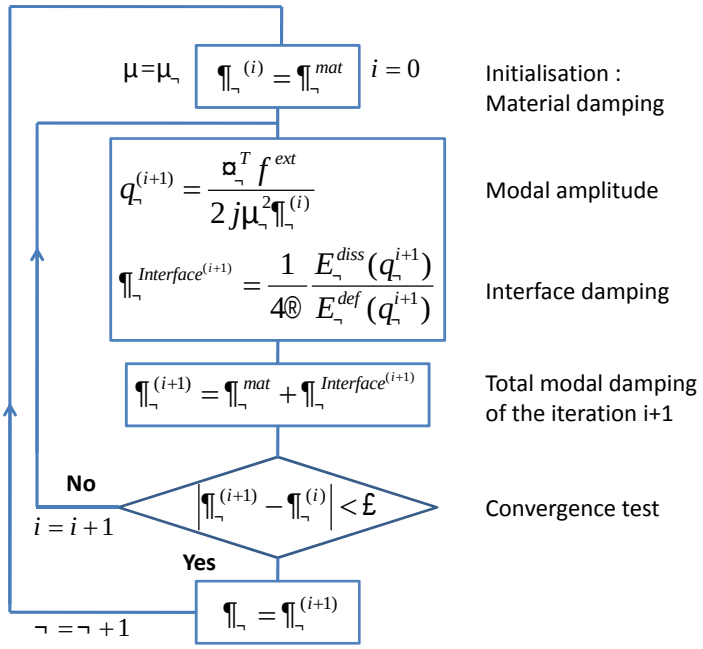


Figure 1: Flowchart of iterative process

The Flowchart of figure (1) presents the iterative process of the IEM. To calculate the ν^{th} total modal damping ξ_ν, we assume damping is equal to material damping ($\xi_\nu^0 = \xi_\nu^{mat}$) in the iteration 0. The modal amplitude q_ν is then calculated using this incorrect material damping. Next the interface damping $\xi_\nu^{Interface}$ is calculated. The sum of these two sources of modal dissipation due to material and interface effects provides the estimation of the total modal damping in the iteration 1. If the difference between the successive damping is more than the convergence coefficient ε, the process continues to the next iteration to correct consecutively the modal amplitude $q_\nu^{(i+1)}$, the energies and the next modal damping estimation. These steps are repeated iteratively until convergence. Once the convergence obtained the eigenmode is actualized ($\omega_\nu = \omega_{\nu+1}$) to calculate the next modal damping of the structure.

3 Simulations

In this section the system and design parameters will be presented first followed by an investigation of the validity domain of the IEM.

3.1 System description

The system studied is composed of a beam clamped on one end and connected to a localized nonlinear dissipative interface on the other end. The system is discretized into ten 2D beam finite elements (2 DOFs per node). The full model has 20 DOFs. The excitation force is applied to node number 1 of the beam.

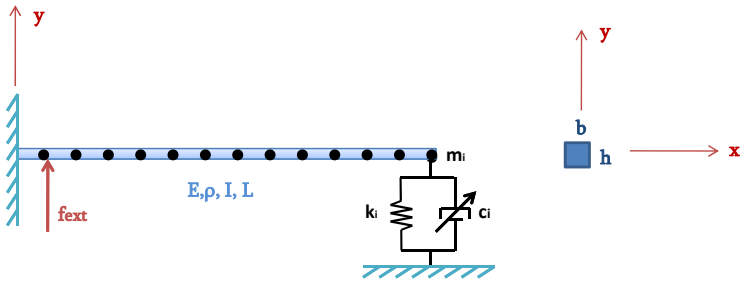


Figure 2: Simple beam with localized nonlinear dissipative interface

The dissipation force is expressed in terms of the velocity by the equation :

$$f_c(t, \dot{u}) = c_i \times \dot{u}_i \tag{8}$$

and the nonlinear viscous model is expressed by the following expression

$$c_i = c_0 + c_1 \left|\dot{u}_i\right| \tag{9}$$

where c_0 and c_1 are two damper coefficients of the nonlinear viscous damping. The used parameters are performed in table (1).

Beam properties			Interface properties		
E	Steel Young modulus (GPa)	210	k_i	Linear stiffness (N/m)	10^6
ρ_s	Steel density (kg/m^3)	7800	c_0	Viscous damper (N/(m/s))	20
h	Beam thikness (m)	$2\ 10^{-2}$	c_1	Viscous damper $(N/(m/s)^2)$	[0,..,400]
b	Beam width (m)	$2\ 10^{-2}$	m_i	Mass (Kg)	$2\ 10^{-4}$
L	Beam length (m)	0.6			

Table 1: Physical and geometric properties of the system.

The first three modes of the associated conservative system are $f_1 = 214.31Hz$, $f_2 = 505.50Hz$ and $f_3 = 1205.85Hz$.

3.2 Validity domain of IEM

The proposed IEM has been implemented on an academic example in MATLAB. Two numerical simulations have been performed in order to highlight its domain of validity. The goal of this section consists in studying the influence of the following parameters on the accuracy of this method: external structural loads level and nonlinear localized damping level.

3.2.1 Level of external structural loads

To investigate the effect of high levels of external structural loads a series of simulations have been performed by changing the load amplitudes while keeping the damping parameters constant. In this section, the studied parameters are performed in table (2).

Case	Force (N)	Case	Force (N)
1	F = 1 N	6	F = 80 N
2	F = 5 N	7	F = 100 N
3	F = 10 N	8	F = 120 N
4	F = 25 N	9	F = 150 N
5	F = 50 N		

Table 2: Load amplitude simulation parameters.

Figures (3) and (4) show the comparison of modal damping between the IEM and the reference method respectively for the cases F = 10 N and F = 150 N. The error of estimating damping is greater for the case of high loads (F = 150 N) than the case of low loads (F = 10 N).

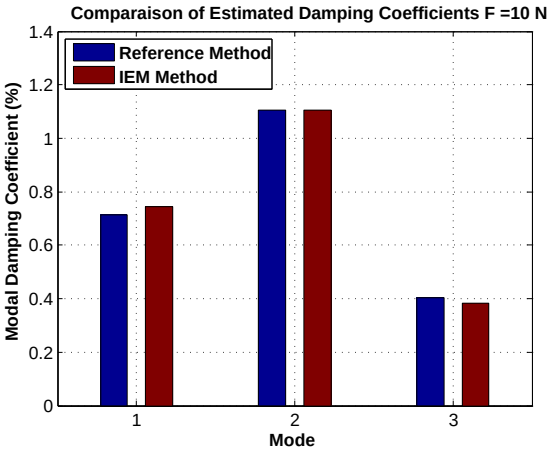


Figure 3: IEM vs. Reference $F = 10N$

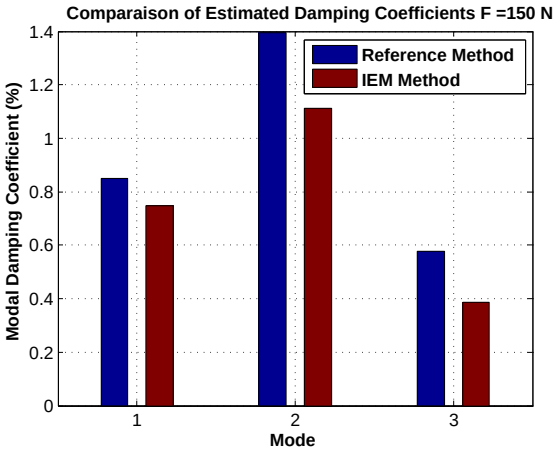


Figure 4: IEM vs. Reference $F = 150N$

The evolution of the reference modal damping estimation with the increase of the external load is given in Figure (5). Here we are interested in the first three modes because in this case others modes give a few modal damping coefficients ($\xi_\nu \ll 1\%$). Figure (6) presents the error of damping estimation committed by the IEM. The estimated error increases with increasing external load level as described in the curves of the figure (6). Figure (6) shows that the error is minimal for the first three modes when F = 10 N. In the following we will take this value to excite the system when studying the influence of nonlinear localized damping.

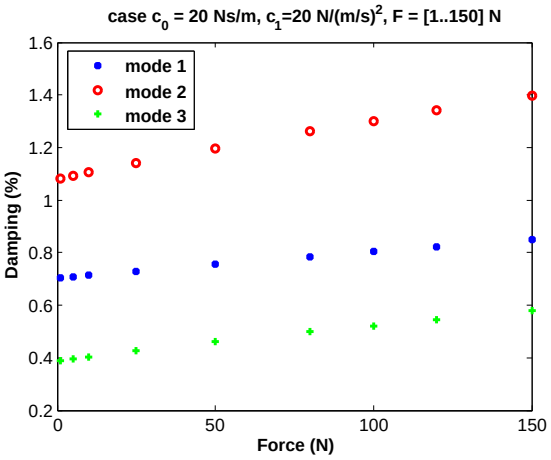


Figure 5: Modal damping estimated by Ref method (%)

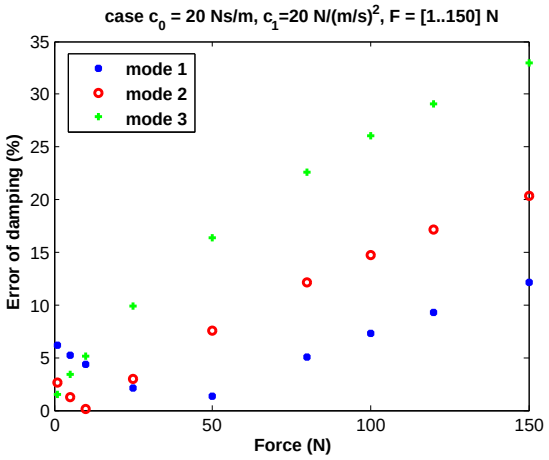


Figure 6: Error of damping by IEM method (%)

3.2.2 Level of nonlinear localized damping

To investigate the effect of high level of nonlinear localized damping a series of simulations have been performed by changing the damping amplitudes while keeping the loads amplitude parameter constant. In this section, the parameter values used are indicated in table (3).

Case	Damping c_1	Case	Damping c_1
1	0	5	150
2	20	6	200
3	50	7	300
4	100	8	400

Table 3: Nonlinear localized damping simulation parameters

To have an idea of the level of the localized nonlinear damping we compare the restoring force versus velocity between two cases : Figure (7) shows a nonlinear localised damper level with a nearly linear behavior and Figure (8) shows a high nonlinear localised damper level.

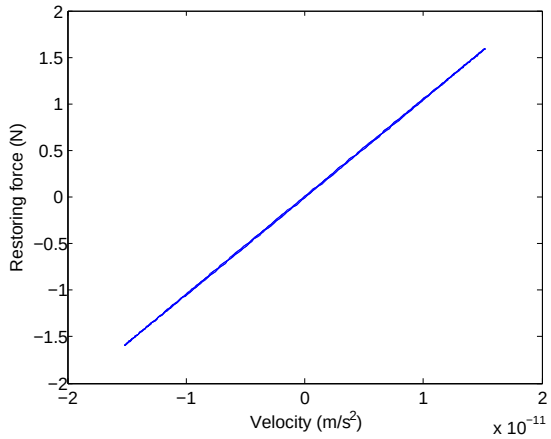


Figure 7: Few nonlinear localised damper level

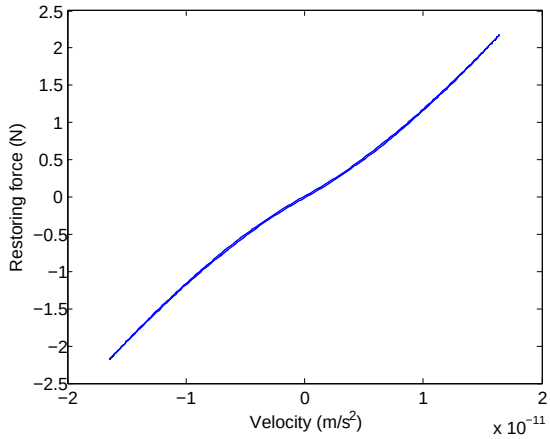


Figure 8: High nonlinear localised damper level

The evolution of the reference modal damping estimation with the increase of the localized nonlinear damper level is given in Figure (9). Figure (10) presents the evolution of the estimation error for the three first modes of the system. When the nonlinear damper level increases the error of damping estimation by IEM increases too.

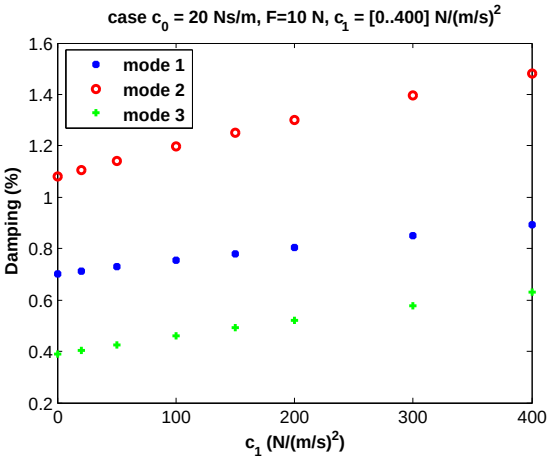


Figure 9: Modal damping estimated by Ref method (%)

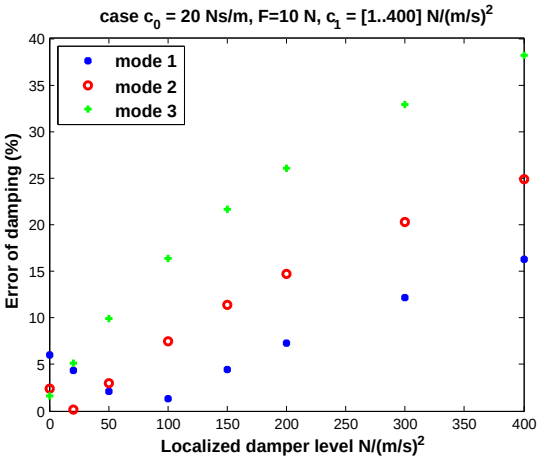


Figure 10: Error of damping by IEM method (%)

4 CONCLUSIONS

In this paper, the iterative energetic method is presented and investigated for specific conditions in nonlinear interface joints in order to study its limitations. The method is based on the ratio between the dissipated energy in the interfaces and potential energy of the global structure. Firstly, the authors compared the modal damping calculated by two methods with the aim of demonstrating the effects of the external structural loads. Secondly, the effects of the localized damping level when nonlinear localized viscous damping increases was investigated. Finally, when dealing with nonlinear systems, the IEM method is computentially faster than the reference method but it is less accurate for estimating precise results of modal damping in these both cases of high level of external structural loads and high nonlinear localized damper level.

ACKNOWLEDGMENTS

The financial support of the "Agence Nationale de la Recherche ANR" (ANR-12-MONU-00016-01) is acknowledged.

REFERENCES

[1] S. Adhikari, Rates of change of eigenvalues and eigenvectors in damped dynamic systems. *AIAA Journal*, 37 (11), pp. 11521158, 1999.

[2] R. A. Ibrahim and C. L. Petit. Uncertainties and dynamic problems of bolted joints and other fasteners. *Journal of Sound and Vibration*, **279** :857936, 2005.

[3] S.Bograd, P. Reuss, A. Schmidt, L. Gaul and M. Mayer, Modeling the dynamics of mechanical joints. *Mechanical Systems and Signal Processing*, Volume 25, Issue 8, p. 2801-2826, 2011.

[4] A.Caignot, P.Ladevze and D. Nron J.-F. Durand, Virtual testing for the prediction of damping in joints. *Engineering Computations*, 5, 621-644.15, 2010.

[5] M. Krifa, N. Bouhaddi and S. Cogan, Estimation of modal damping for structures with localized dissipation. *International Modal Analysis Conferences (IMAC)*, February 2-5, Orlando, Florida, USA.

[6] A. Fortin, Analyse numérique pour ingénieurs, *Presses internationales Polytechnique*, 2008.

COMPDYN 2015
5th ECCOMAS Thematic Conference on
Computational Methods in Structural Dynamics and Earthquake Engineering
M. Papadrakakis, V. Papadopoulos, V. Plevris (eds.)
Crete Island, Greece, 25–27 May 2015

NONLINEAR DYNAMICS OF A 2D ARRAY OF COUPLED PENDULUMS UNDER PARAMETRIC EXCITATION

Aymen Jallouli, Najib Kacem* and Noureddine Bouhaddi

FEMTO-ST Institute - UMR 6174, Applied Mechanics Department
24, chemin de l'Épitaphe, F-25000 Besançon, France

*najib.kacem@femto-st.fr

Keywords: Array of Pendulums, Parametric Excitation, Nonlinear Dynamics, HBM, ANM.

Abstract. *In this paper, we investigate the frequency response of a 2D array of coupled pendulums under parametric excitation. We developed a computational model while considering the main source of nonlinearities. The nonlinear equations of motion are derived and solved using the Harmonic Balance Method (HBM) coupled with the Asymptotic Numerical Method (ANM). Numerical simulation are performed in the case of 3X3 array to investigate the effect of changing the coupling coefficients in the 2D direction and adding an imperfection on the collective dynamics of the array.*

1 INTRODUCTION

The sine-Gordon model and its discrete analog are ubiquitous models in mathematical physics with a wide range of applications extending from chains of coupled pendulums [1] and Josephson junction arrays [2] to gravitational and high-energy physics models [3, 4]. For instance, Ikeda et al. investigated the behavior of intrinsic localized modes (ILMs) for an array of coupled pendulums subjected to horizontal [5] and verical [6] sinusoidal excitation. Thakur et al. [7] analyzed the collective dynamical behavior of an array of coupled pendulums with a small fraction of random long-range connection under parametric excitation. Moreover Alexeeva et al. [8] demonstrated the stabilizing effect of adding length impurities on a chain of pendulums parametrically excited. The collective dynamics has been studied for several one-dimensional discrete systems. However, to our knowledge, few analyses were devoted to bidimensional systems like Josephson junction oscillator arrays [9]. In this context, a computational model for the nonlinear dynamics of a 2D array of coupled pendulums under parametric excitation is proposed. The principal goal is to track the frequency responses of the considered system in terms of bifurcation topologies and energy transfer with respect to the excitation amplitude and to investigate the effects of adding an impurity to the system.

The coupled nonlinear equations of motion have been solved using the harmonic balance method coupled with the asymptotic numerical continuation technique [10]. Several numerical simulations have been performed for a particular set of design parameters and two configurations with respect to the coupling coefficients in both directions have been considered. It is shown that the number of branches, their stability and the bifurcation topology of the frequency response of each pendulum can be tuned with respect to an added impurity.

2 PROBLEM FORMULATION

The discreet system, depicted in Figures 1 and 2, is composed of n equidistant horizontal axle A_i. Along these axles, at equally spaced intervals, there are p similar pendulums. Each pendulum consists of a rigid rod, with a mass m attached at the end. At rest, all the pendulums point down the vertical. $\theta_{i,j}$ the angle between the (i,j) pendulum and the downward vertical, k_x and k_y are the linear torque constant respectively in x and y axis. By neglecting the mass of the rigid rods, all the pendulums have the same moment of inertia $I = ml^2$, where l is the length of the pendulum. The considered periodic structure is excited by vibrating the support that holds the system. The driven frequency of the parametric force is equal to 2ω and with amplitude A_e. The boundary conditions are $\theta_{0,j} = \theta_{i,0} = \theta_{n+1,j} = \theta_{i,n+1} = 0$. The potential and kinetic energy of the system can be written as:

$$V = \sum_{i,j} \tfrac{1}{2}k_x(\theta_{i,j} - \theta_{i-1,j})^2 + \tfrac{1}{2}k_x(\theta_{i,j} - \theta_{i+1,j})^2 + \tfrac{1}{2}k_y(\Delta_{i,j-1} - d)^2 + \tfrac{1}{2}k_y(\Delta_{i,j+1} - d)^2 \\ mg\left(l - l\cos\left(\theta_{i,j}\right) - A_e\cos\left(2\omega t\right)\right) \tag{1}$$

$$T = \sum_{i,j} \frac{1}{2}mv_{i,j}^2 \tag{2}$$

Where $\Delta_{i,j+1}$ is defined as the distance between the mass attached to the pendulum (i,j) and (i,j+1) and can be written as:

$$\Delta_{i,j+1} = d + lsin\left(\theta_{i,j+1}\right) - lsin\left(\theta_{i,j}\right) \approx d + l\theta_{i,j+1} - l\theta_{i,j} \tag{3}$$

and $v_{i,j}$ is the velocity of the moving mass of (i,j) pendulum,

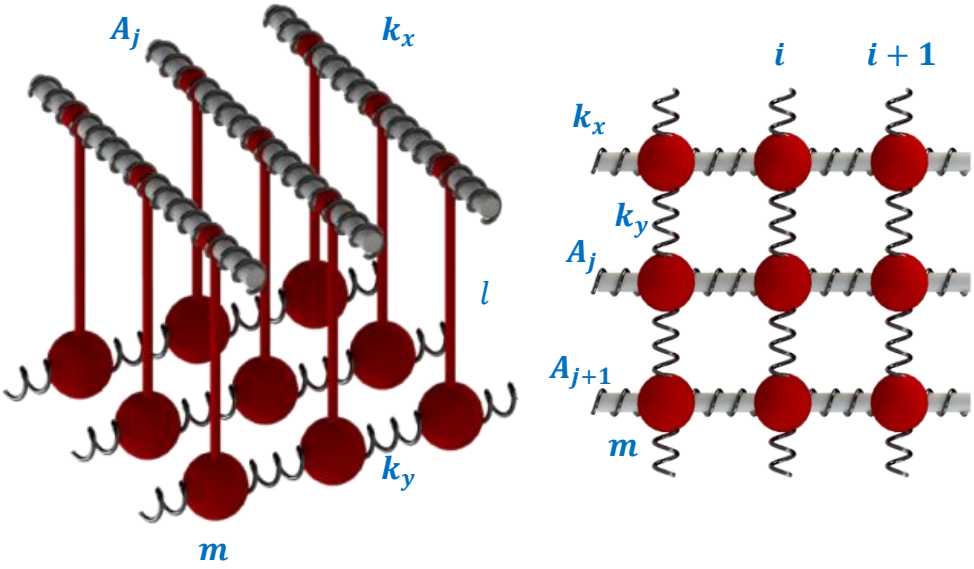


Figure 1: Schematic of the 2D array of coupled pendulums

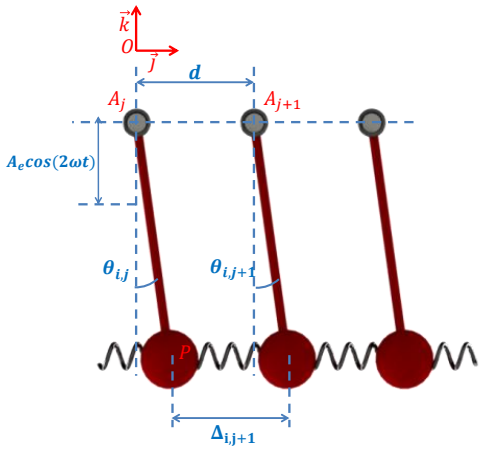


Figure 2: Front view of the system

$$\overrightarrow{v_{i,j}} = \overrightarrow{\dot{r}_{OA}} + \vec{\omega} \times \overrightarrow{r_{AP}} \tag{4}$$

where

$$\overrightarrow{\dot{r}_{OA}} = 2A_e\omega\sin(2\omega t)\vec{k} \qquad \vec{\omega} = \dot{\theta}_{i,j}\vec{i} \qquad \overrightarrow{r_{AP}} = l\left(\sin\left(\theta_{i,j}\right)\overrightarrow{j} - \cos\left(\theta_{i,j}\right)\overrightarrow{k}\right)$$

The Lagrange equations are:

$$\frac{d}{dt}\left(\frac{\partial L}{\partial \dot{\theta}_{i,j}}\right) - \frac{\partial L}{\partial \theta_{i,j}} = Q_{i,j} \tag{5}$$

where $L = T - V$ and $Q_{i,j} = \alpha l\dot{\theta}_{i,j}$ is the generalized forces applied to the (i,j) pendulum and α is the damping coefficient.

The resulting equation of motion of the (i,j) pendulum is obtained as:

$$\begin{array}{l} ml^2\ddot{\theta}_{i,j} + \alpha l\dot{\theta}_{i,j} + k_x\left(2\theta_{i,j} - \theta_{i+1,j} - \theta_{i-1,j}\right) + l^2k_y\left(2\theta_{i,j} - \theta_{i,j+1} - \theta_{i,j-1}\right) \\ +ml\left[g + 4A_e\omega^2\cos\left(2\omega t\right)\right]\sin(\theta_{i,j}) = 0 \end{array} \tag{6}$$

By expanding $\sin(\theta_{i,j})$ in Taylor series up to the third order, the equation (6) can be written as:

$$\begin{array}{l} ml^2\ddot{\theta}_{i,j} + \alpha l\dot{\theta}_{i,j} + k_x\left(2\theta_{i,j} - \theta_{i+1,j} - \theta_{i-1,j}\right) + l^2k_y\left(2\theta_{i,j} - \theta_{i,j+1} - \theta_{i,j-1}\right) \\ +ml\left[g + 4A_e\omega^2\cos\left(2\omega t\right)\right]\left(\theta_{i,j} - \frac{1}{6}\theta_{i,j}^3\right) = 0 \end{array} \tag{7}$$

Equation (7) describes a system of Duffing oscillators coupled by linear springs k_x and k_y in the x and y directions and subjected to parametric excitation ($4mlA_e\omega^2\cos(2\omega t)$). To determine the natural frequencies and their eigenvectors, Equation (7) can be written as:

$$M\ddot{\theta} + B\dot{\theta} + K\theta + G\left(\theta, t\right) = 0 \tag{8}$$

with

$$M = \begin{bmatrix} ml^2 & & 0 \\ & \ddots & \\ 0 & & ml^2 \end{bmatrix}; B = \begin{bmatrix} \alpha l & & 0 \\ & \ddots & \\ 0 & & \alpha l \end{bmatrix};$$

$$K = \begin{bmatrix} mgl + 2k_x + 2l_0^2k_y & -k_x & 0 & -l_0^2k_y & 0 & \cdots & 0 \\ \vdots & \vdots & \vdots & \vdots & \vdots & \vdots & \vdots \\ 0 & \cdots & 0 & -l_0^2k_y & 0 & -k_x & mgl + 2k_x + 2l_0^2k_y \end{bmatrix}$$

Where M denotes the mass matrix, B the damping matrix, K the stiffness matrix with dimension $N_{pen} \times N_{pen}$ and G contains the nonlinear terms with dimension N_{pen}, where N_{pen} is the number of pendulums in the array. The natural frequencies ω_ν and the eigenvectors θ_ν of the corresponding linear system can be computed by solving the following eigenvalue problem

$$\left(K - \omega_\nu^2 M\right)\theta_\nu = 0 \tag{9}$$

3 SOLVING PROCEDURE

The goal of this section is to determine numerically the periodic solutions of the 2D periodic system. Therefore, we use the harmonic balance method and the asymptotic numerical method (HBM and ANM). But first, we rewrite the nonlinearity of the system (7) in a quadratic form. This technique is not applicable for any equation of motion, because some nonlinearity cannot

be transformed into quadratic terms [10]. Consequently, we transformed the equation (6) into equation (7) by developing the sin term to the third order Taylor series expansion. Let us consider an autonomous system of differential equations:

$$\dot{Y} = f(Y, \lambda, t) \tag{10}$$

where Y is a vector of unknowns, f is a smooth nonlinear vector valued function and λ is a real parameter. The dot represents the derivative with respect to time t. First, we transform the system (10) into a new system where the nonlinearities are quadratic, which can be written as follows:

$$m\left(\dot{Y}\right) = c\left(\lambda, t\right) + l\left(Y\right) + q(Y, Y) \tag{11}$$

where $c\left(\lambda, t\right)$ is a constant vector with respect to Y, $l(Y)$ is the linear vector and $q(Z, Z)$ is the quadratic vector. After writing the system in a quadratic form, we decompose the solution into Fourier series:

$$Y\left(t\right) = Y_0 + \sum_{k=1}^{H} Y_{c,k} \cos\left(k\omega t\right) + Y_{s,k} \sin\left(k\omega t\right) \tag{12}$$

By replacing this solution in Equation (10) and expanding $f(Y, \lambda)$ into Fourier series, we obtain an algebraic system with $2H + 1$ vector of unknowns Y_i the unknown pulsation ω, and the parameter λ. The components of the Fourier series are collected into column vector U that contains all the unknowns Y_i with a size $(2H + 1)N_e q$; $U = [Y_0^T, Y_{c,1}^T, Y_{s,1}^T, \ldots, Y_{c,H}^T, Y_{c,H}^T]$ where N_{eq} is the number of equation in (10). The system (12) is transformed into a quadratic one with $(2H + 1)N_{eq}$ and can be written as:

$$\omega M\left(U\right) = C + L\left(U\right) + Q(U, U) \tag{13}$$

where $M(.)$, C, $L(.)$ and $Q(.,.)$ are operators depending on $m(.)$, c, $l(.)$ and $q(.,.)$. Once the algebraic system is obtained, we use the asymptotic numerical method (ANM) to solve it. In order to apply the ANM, Equation (12) is reformed into:

$$R\left(U, \omega\right) = C + L\left(U\right) + Q\left(U, U\right) - \omega M\left(U\right) = 0 \tag{14}$$

4 RESULTS AND DISCUSSION

In this section, we consider a small array of 3×3 coupled oscillators where the extreme pendulums are coupled to the frame.

$$\theta_{0,j} = \theta_{i,0} = \theta_{3,j} = \theta_{i,3} = 0, i, j \in \{1, 2, 3\} \tag{15}$$

Figure 3 displays the frequency responses of 3×3 arrays of pendulums parametrically excited and having the same coupling springs in the x and y direction ($k_x = l^2 k_y$. The physical parameters are listed in Table 1. The dotted and the solid lines denote the unstable and the

configuration	mass	length	excitation	damping	k_x	k_y	Impurity
1	$0.1kg$	$0.2m$	$0.01m$	$0.01Ns/m$	0.5	$0.5/{l_0}^2$	0%
2	$0.1kg$	$0.3m$	$0.0075m$	$0.01Ns/m$	0.15	$0.5/{l_0}^2$	0%
3	$0.1kg$	$0.3m$	$0.0075m$	$0.01Ns/m$	0.15	$0.5/{l_0}^2$	5%

Table 1: Design parameters of the array configurations

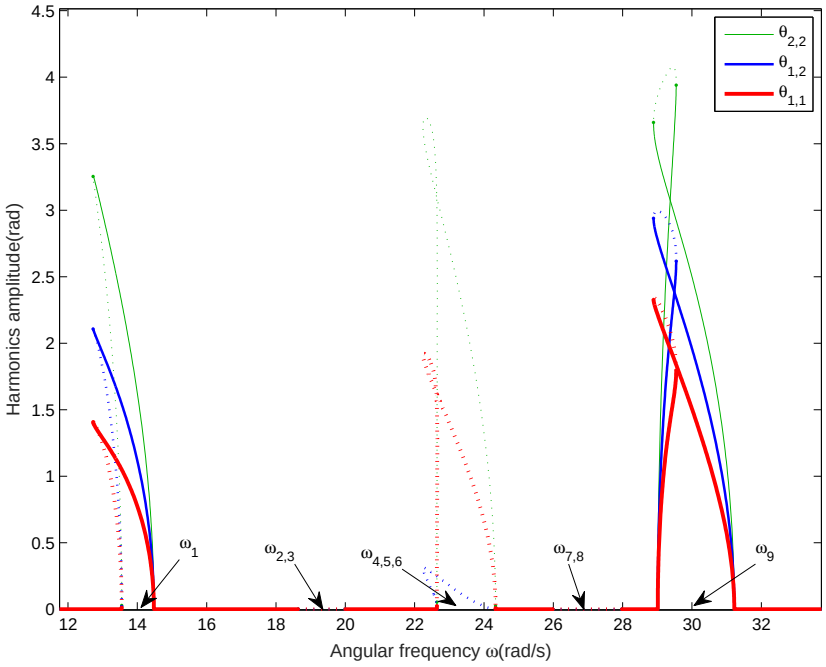


Figure 3: Frequency responses of the 2D array of pendulums for the first configuration listed in Table 1

stable steady state solutions, respectively. The equidistant pendulums with respect to the center of the array have the same response which is illustrated by the three resonance regions. As we can notice the curves bend to the left and exhibit softening characteristics due to the negative sign of the cubic nonlinearity ($-\frac{mgl}{6}\theta_{i,j}^3$). For this configuration, we notice that there are triple and double resonant frequency and the apparent modes are equal to three because the other eigen-modes are perpendicular to the excitation vector.

The second configuration of Table 1 considers two different coupling springs in the x and y directions. In this case, the system becomes symmetric with respect to the central pendulum. Therefore, the number of stable regions increases as shown in Figure 4,. By solving the system (8), no triple or double eigen-frequencies are found and the number of excited modes is equal to four.

To create the disorder in the array, we introduce an impurity in the system. We change the length of one pendulum in the array. To do so, we choose to increase the length of the pendulum located in the position (1,2) by 5%. By comparing this configuration to the pervious one, we remark that the system loses its symmetry and each pendulum has a specific frequency response. In this case, the number of resonant regions increases, which leads to the augmentation of the stable solutions (Figure 5).

5 CONCLUSION

In this paper, the nonlinear dynamics of a small 2D array of pendulums was modeled by determining the equation of motion of each pendulum using the Lagrange equations. The obtained system has been solved using the Harmonic Balance Method (HBM) coupled with the Asymptotic Numerical Method (ANM). The collective dynamic was investigated by plotting the frequency responses for several configurations. We demonstrated that for an axisymmetric

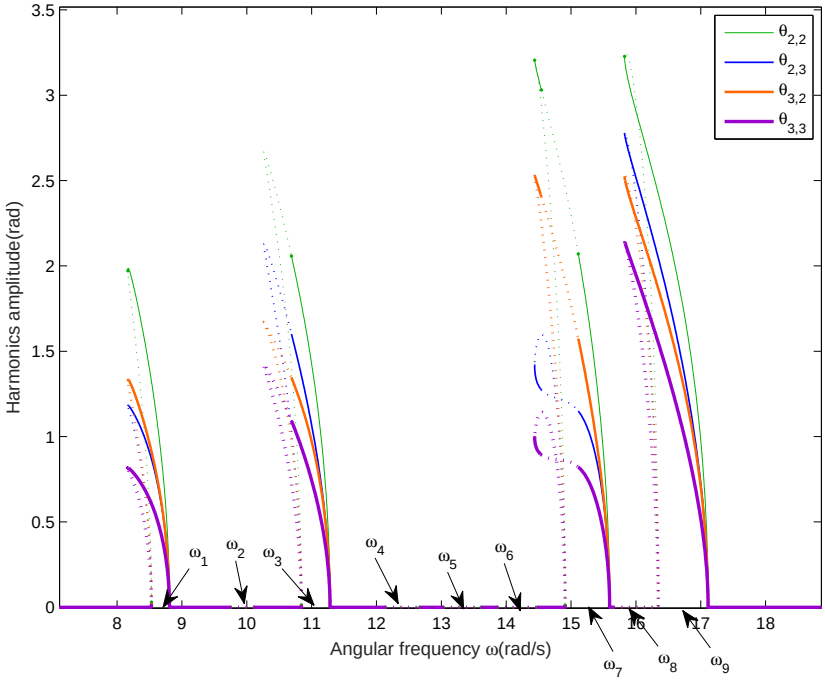


Figure 4: Frequency responses of the 2D array of pendulums for the second configuration listed in Table 1

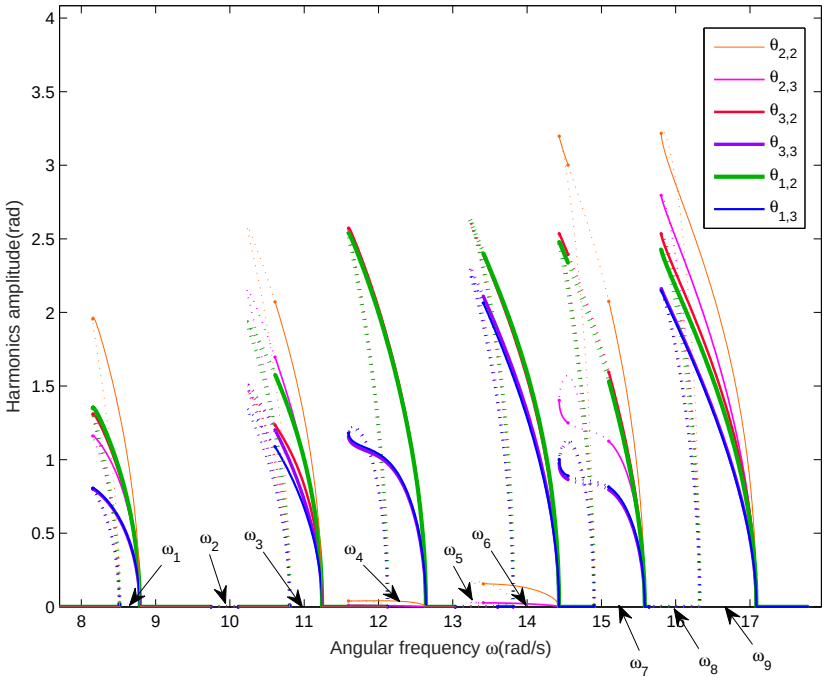


Figure 5: Frequency responses of the 2D array of pendulums for the third configuration listed in Table 1

array, where the coupling coefficient are equal ($k_x = l^2 k_y$), the pendulums that are equidistant with respect to the center of the array has the same frequency response. However, by changing the coupling coefficients, the system becomes symmetric and this leads to an augmentation of the number of the steady state solutions which can be tuned with respect to an added impurity. In a future work, the intrinsic localized modes of the proposed system will be analyzed in terms of existence and stability in presence of impurities.

REFERENCES

[1] A. C. Scott. A nonlinear klein-gordon equation. *American Journal of Physics*, **37**(1):52–61, 1969.

[2] A. V. Ustinov, T. Doderer, R. P. Huebener, N. F. Pedersen, B. Mayer, and V. A. Oboznov. Dynamics of sine-gordon solitons in the annular josephson junction. *Phys. Rev. Lett.*, **69**:1815–1818, Sep 1992.

[3] R. Khomeriki. Nonlinear band gap transmission in optical waveguide arrays. *Phys. Rev. Lett.*, **92**:063905, Feb 2004.

[4] E. Kenig, B. A. Malomed, M. C. Cross, and R. Lifshitz. Intrinsic localized modes in parametrically driven arrays of nonlinear resonators. *Phys. Rev. E*, **80**:046202, Oct 2009.

[5] T. Ikeda, Y. Harata, K. Nishimura. Intrinsic localized modes of harmonic oscillations in pendulum arrays subjected to horizontal excitation. *Journal of Computational and Nonlinear Dynamics*, **10**(2):021007, 2015.

[6] T. Ikeda, Y. Harata, C. Shi, K. Nishimura. Localization phenomena in pendulum arrays subjected to vertical excitation. In *ASME 2014 International Design Engineering Technical Conferences and Computers and Information in Engineering Conference*, pages V006T10A054–V006T10A054. American Society of Mechanical Engineers, 2014.

[7] R. B. Thakur, L. English, A. Sievers. Driven intrinsic localized modes in a coupled pendulum array. *Journal of Physics D: Applied Physics*, **41**(1):015503, 2008.

[8] N. Alexeeva, I. Barashenkov, G. Tsironis. Impurity-induced stabilization of solitons in arrays of parametrically driven nonlinear oscillators. *Physical review letters*, **84**(14):3053, 2000.

[9] J. E. Macías-Díaz. Numerical study of the transmission of energy in discrete arrays of sine-gordon equations in two space dimensions. *Physical Review E*, **77**(1):016602, 2008.

[10] B. Cochelin, C. Vergez. A high order purely frequency-based harmonic balance formulation for continuation of periodic solutions. *Journal of sound and vibration*, **324**(1):243–262, 2009.

COMPDYN 2015
5th ECCOMAS Thematic Conference on
Computational Methods in Structural Dynamics and Earthquake Engineering
M. Papadrakakis, V. Papadopoulos, V. Plevris (eds.)
Crete Island, Greece, 25–27 May 2015

FINITE ELEMENT SIMULATION OF A STEEL BRACED FRAME STRUCTURE DAMAGED BY THE 2011 TOHOKU EARTHQUAKE

Taichiro Okazaki[1], Yuriko Kato[2], Naoto Kotani[2], Mitsumasa Midorikawa[1], and Tetsuhiro Asari[1]

[1] Hokkaido University
Kita 13, Nishi 8, Kita-ku, Sapporo, 060-8628 Japan
{tokazaki, midorim, asari}@ eng.hokudai.ac.jp

[2] Hokkaido University
Kita 13, Nishi 8, Kita-ku, Sapporo, 060-8628 Japan
{y.kato0715, kotani.naoto}@frontier.hokudai.ac.jp

Keywords: Steel Structures, Seismic Design, Earthquake Damage, Finite Element Analysis, Braced Frames.

Abstract. *During post-earthquake reconnaissance after the March 11, 2011 Tohoku Earthquake, the writers examined a damaged parking ramp structure. The structure was a two-story steel structure with a 52.5 by 48.5-m floor plan which relied on chevron braces for lateral load resistance. The earthquake damaged nearly all first-story braces in their connection to the beam. The majority of bracing connections had fractured in the east-west frame while many bracing connections were distorted, but none of them fractured, in the north-south frame. The cause of the observed damage was examined by detailed finite element simulations. Planar models of the structure, one extracted from the east-west frame and another extracted from the north-south frame, were subjected to static cyclic loading and to a ground motion record obtained within 800 meters from the structure. The simulation captured the main features of the observed damage. The results suggest that the bracing connections in the east-west frame failed under a compressive force much smaller than the buckling load of the brace. Although they failed similarly, the bracing connections in the north-south frame were almost strong enough to develop the compressive strength of the brace. This difference may explain the reason why the damage differed in severity between the two loading directions. While fracture was not explicitly modeled in the simulation, the computed plastic strain indicated that the observed fracture in the bracing connections was due to severe cyclic deformation produced while the brace was in compression.*

1 INTRODUCTION

Steel concentrically braced frames have been used widely in high-seismic regions due to their efficiency in meeting lateral-load resisting requirements. Based on extensive research since the 1970's, it is well known that the cyclic loading performance of steel braces depend on their slenderness ratio and on the width-to-thickness ratio of their cross sectional elements, and that adequate detailing of the bracing connection is critical to avoid premature fracture at the end of the brace. These findings have been reflected in design codes around the world [1, 2]. In terms of analysis capabilities, researchers have proposed methodologies to predict the occurrence of fracture from cumulative damage and capture the structural response following brace fracture [3, 4]. Despite the substantial advances in research, many steel braced frames performed poorly in recent earthquakes [5, 6]. This paper examines a parking ramp structure damaged by the March 11, 2011 Tohoku earthquake. The member proportion and connection details of this structure represented common practice in Japan. Results from detailed finite element simulation are used to discuss the possible causes of the damage and means to improve the seismic performance of steel braced frames.

2 THE DAMAGED STRUCTURE

During post-earthquake reconnaissance after the 2011 Tohoku Earthquake, the writers examined a damaged parking ramp structure. The structure was a two-story steel structure with a 52.5 by 48.5-m, 9 by 7-span floor plan, comprising square-hollow structural section (HSS) columns, I-section beams, and round-HSS braces, all of galvanized steel. The beams were simply connected to the columns, and single-lap bolted connections were used for the bracing connections. Although not confirmed, it is believed that the base of the column base (which was covered in asphalt and hence not visible) was connected to a foundation through a base plate and anchor rods. Fig. 1 shows the primary dimensions and sections in the east-west and north-south braced bays. The slenderness ratio of the braces based on the diagonal, face-to-face distance between the beam and column, was 54 in the east-west bay and 69 in the north-south bay. The residual story drift ratio was 0.01 rad. in the east-west direction but minimal in the north-south direction. As indicated in Fig. 2, nearly all first-story braces were damaged in their connection to the beam. The majority of bracing connections had fractured in the east-west frames while many bracing connections were distorted, but none of them fractured, in the north-south frames. The damage is extremely concerning because this structure relied solely on the braces for lateral-load resistance. The structure was sealed from entry when the writers visited, and demolished shortly afterwards.

The use of single-lap bolted connections in the bracing connections seemed to be a primary cause of the extensive damage. The difference in out-of-plane flexibility was believed to have caused the fracture to occur only in the upper-end gusset plate and not in the lower-end gusset plate. Fig. 3 shows bracing connections at different stages of failure, from (a) out-of-plane

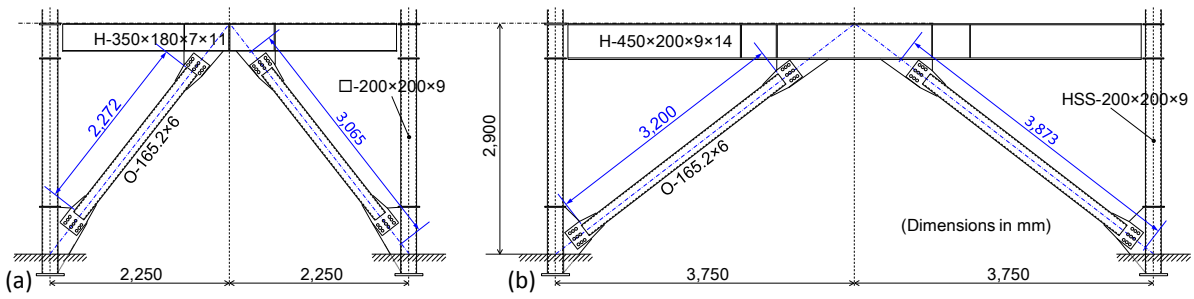


Figure 1. Primary dimensions of braced bay in: (a) east-west frame; and (b) north-south frame.

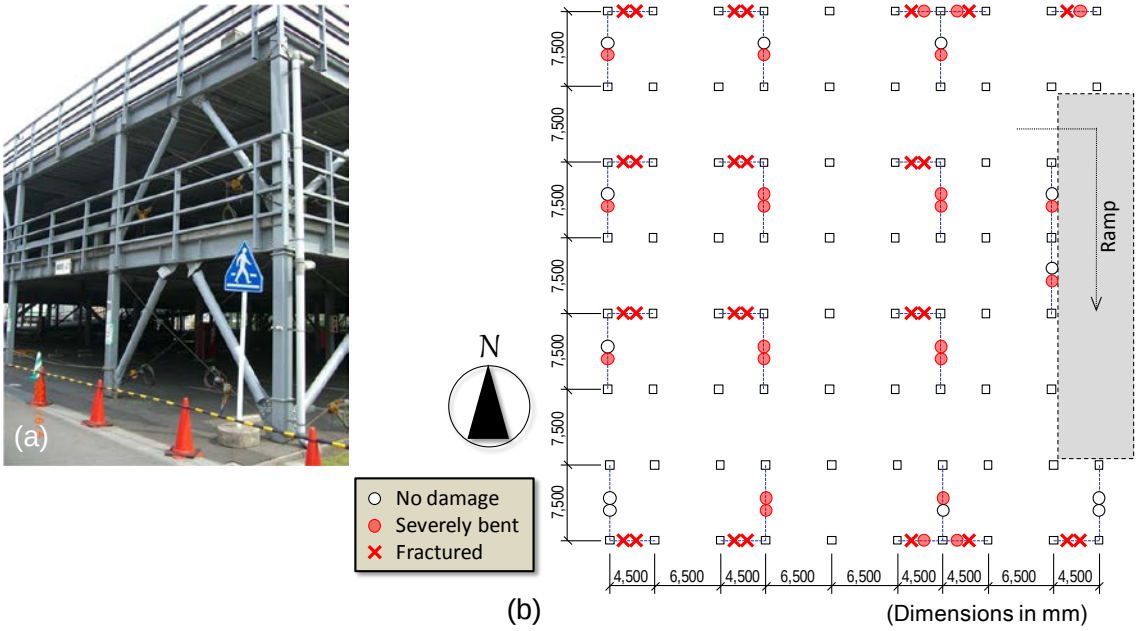


Figure 2. Damaged parking ramp: (a) photo; and (b) floor plan indicating damage location in the first story.



Figure 3. Connection damage: (a)bent out of plane; (b) fracture initiation; and (c) complete fracture.

distortion, (b) fracture initiation near the termination of the welds connecting the brace to the gusset plate, to (c) complete fracture. Although the cause of damage seemed to be straight-forward, a number of questions remained after the field study. Most notably, why was the damage clearly more severe in the east-west frames than in the north-south frames, and what was the actual lateral strength of the structure?

3 FINITE EEMENT MODELS

In order to seek answers to the questions, detailed numerical simulations were conducted using the finite element analysis software ADINA [7]. Separate planar, single-bay chevron braced frame models were constructed to represent the east-west frame and north-south frame. The columns were pinned at the base and the beams were simply connected to the columns. As shown in Fig. 4, the planar models were laterally braced at locations where orthogonal beams framed into the column or beam. The finite element models used isoparametric solid elements at regions where plastic deformation was expected. The regions expected to remain elastic were modeled by a beam element with 7 degrees of freedom at each end node. Two solid elements were used across the material thickness to capture local deformation and local buckling. At the bracing connection, the spliced material was merged at the faying surface and the bolts were not explicitly modeled. Material nonlinearilty was modeled based on the von Mises yield criteria and combined hardening rule assigning a 1:19 ratio between kinemat-

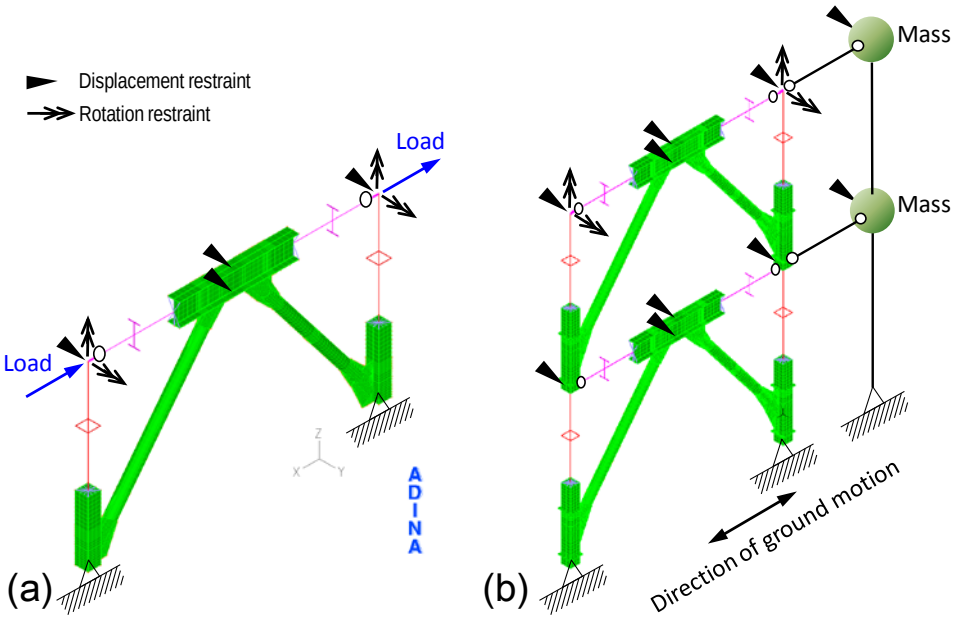


Figure 4. Finite element models: (a) statically loaded, single-story; and (b) dynamically loaded, two-story model.

ic and isotropic hardening. Geometric nonlinearity was modeled using a large displacement-small strain formulation. Unless stated otherwise, the brace was assigned a yield strength of 295 N/mm^2 and all other material was assigned a yield strength of 235 N/mm^2. The material strength values represented the specified minimum strength of structural steel in Japan.

The single-story model shown in Fig. 4a was subjected to static cyclic loading. Load was applied in displacement control, equal at both ends of the beam, increasing the story drift ratio from elastic cycles up to ±0.018 rad., and repeating each cycle twice.

The two-story model shown in Fig. 4b was connected to an elastic gravity column and concentrated mass that represented the system mass divided by the number of braced bays in the loading direction (16 in the east-west direction, 15 in the north-south direction). This model was subjected to a ground motion record obtained at a station within 800 meters from the structure. Raleigh damping was employed by assigning a damping ratio of 0.02 to the first two vibration modes.

4 ANSLYSIS RESULTS

4.1 Static Analysis

Fig. 5 plots the relationship between story shear and story drift ratio obtained from the static, cyclic loading analysis. Fig. 6 plots the relationship between axial force and elongation of one of the two braces (the brace that is first compressed), obtained from the same analysis. Each figure shows results obtained from the single-story, east-west and north-south model. Fig. 6 indicates the tensile yield strength 885 kN, and maximum compressive strength 689 and 621, respectively, for the east-west and north-south frame, computed according to the Japanese provisions [1] and based on the yield strength 295 N/mm^2.

Fig. 5 shows that both models exceeded the elastic limit at a story drift ratio of 0.003 rad., and subsequently experienced a drop in strength. The response gradually stabilized as the deformation amplitude increased, although, as described later, the apparently stable response relied on unrealistic deformation in the bracing connections. It is also noted that the stiffness of the system degraded to 30% of the initial value as the deformation increased. Fig. 6 shows

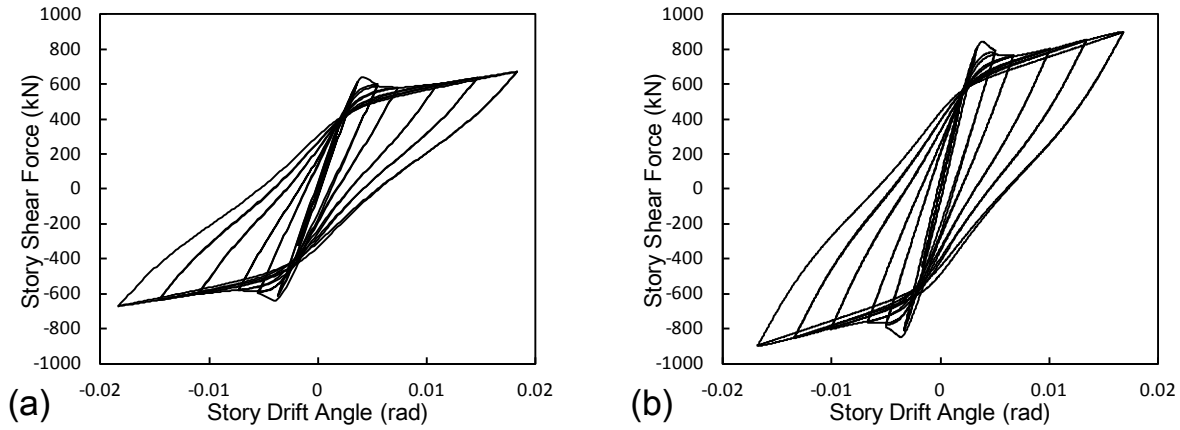


Figure 5. Static, cyclic loading response: (a) east-west model; and (b) north-south model.

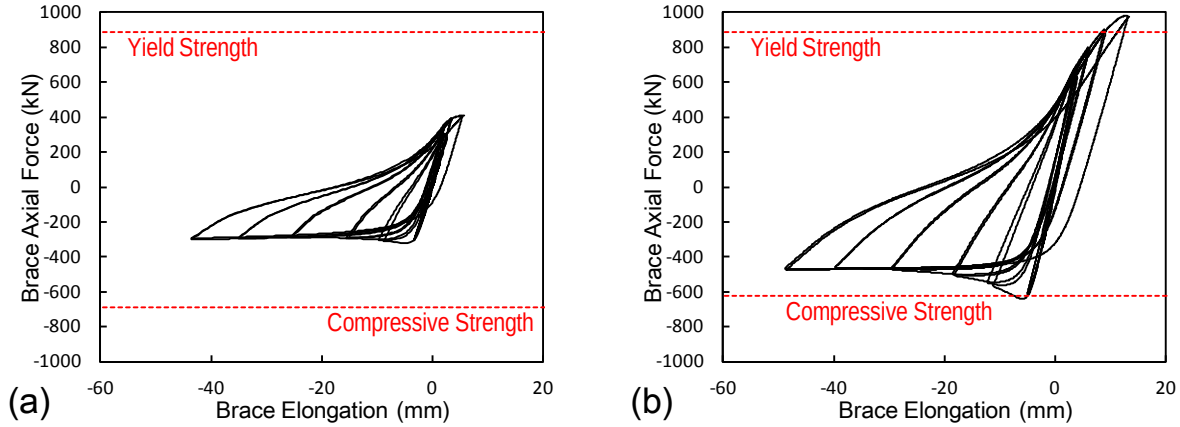


Figure 6. Hysteresis of brace in: (a) east-west model; and (b) north-south model.

that deformation of the brace progressed primarily in the shortening direction. This is a common feature of braces placed in a chevron arrangement: Due to the force unbalance following buckling of the compressed brace, the beam deflects downwards, and therefore, further elongation of the brace is prevented while contraction is promoted. A striking difference is noted between the strength of the two braces. While the north-south brace developed the yield strength in tension and the buckling strength in compression, the east-west brace developed less than half the design strength in tension or compression.

Fig. 7 shows the deformation of the model at the end of the analysis where the model was deformed to a story drift of -0.018 rad. In both models, deformation concentrated in the upper-end bracing connection. The beam is deflected downwards, as described above, due to the force unbalance between the two braces. In fact, throughout the analysis, all other members remained elastic while the upper-end bracing connection folded and straightened, and the beam deflected downwards twice within each loading cycle. The deformed shape suggests that, due to the intrinsic eccentricity in the single-lap connection and lack of edge support, the gusset plate deformed out of plane when compressed. The computed deformation coincides with the damage of the original structure described previously.

Out-of-plane deformation of the gusset plate started at a compressive force merely half of the buckling load of the brace in the east-west model, and near the buckling load of the brace in the north-south model. Analysis of the north-south model was repeated by reducing the yield strength of the brace from 295 to 235 N/mm^2. In this analysis, the brace buckled prior to failure of the gusset plate, and subsequently, inelastic action concentrated in the braces rather

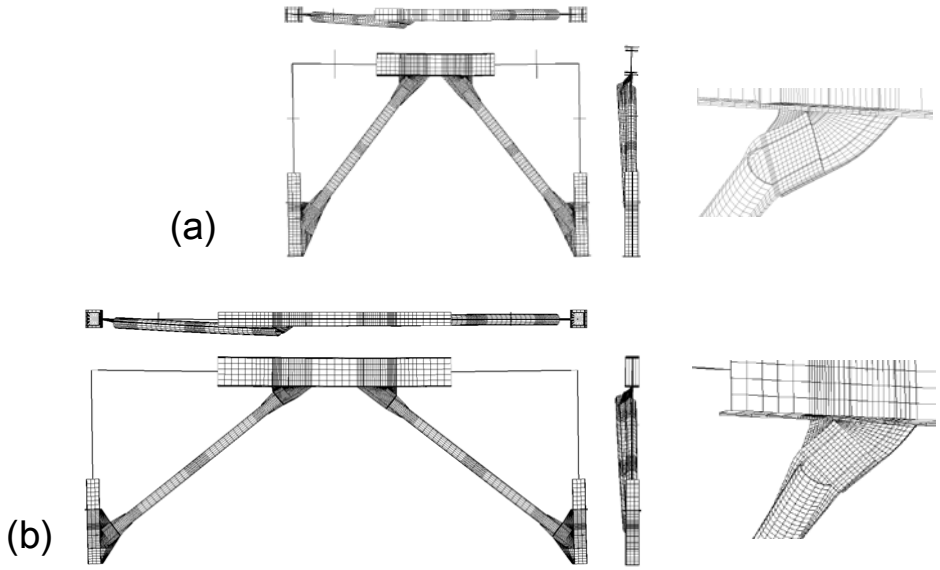


Figure 7. Deformed model at end of analysis: (a) east-west model; and (b) north-south model.

than in the gusset plates. Consequently, in compression, the gusset plate was substantially weaker than the brace in the east-west model, but the gusset plate and brace were similar in strength in the north-south model. While fracture was not explicitly modeled in the simulation, the computed plastic strain indicated that the observed fracture in the bracing connection (see Fig. 3) was due to severe cyclic deformation produced while the brace was in compression.

4.2 Dynamic Analysis

The same modeling scheme was used to construct a two-story model representing the east-west frame (see Fig. 4b). Concentrated floor mass was assigned to a continuous gravity column whose elastic properties equaled that of three columns independent from the lateral-load resisting system in the east-west direction. Although not shown in this paper, the simulated damage was similar to that obtained in the static analysis, and resembled the actual damage.

Fig. 8 shows the relationship between axial force and elongation obtained for one brace each from the first and second stories. As in Fig. 6, the design strength in tension and compression are indicated in the figure. Despite the presence of an elastic gravity column, damage concentrated in the first-story braces while the second-story braces remained elastic. This is contrary to the actual damage where the same failure in the bracing connection was found in a

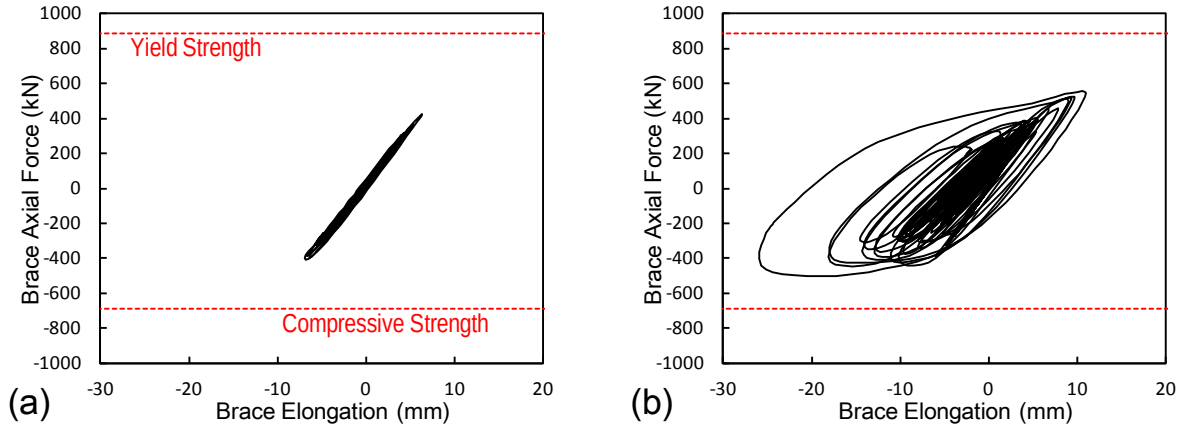


Figure 8. Hysteresis of braces in: (a) second story; and (b) first story.

large number of second-story braces as well as first-story braces. This discrepancy may be due to the fact that, while the first-story stiffness must have degraded gradually in the original structure, buckling of a brace caused a drastic loss of stiffness in the single-bay model. Fig. 8b indicates that the braces failed to develop their strength expected in design. The axial deformation was smaller than the imposed deformation in the static analysis. The residual deformation was minimal at the end of analysis. Work is ongoing to improve the model such that the results better match the observed damage.

5 CONCLUSIONS

Detailed finite element simulations were conducted to examine a parking ramp structure that was damaged by the 2011 Tohoku earthquake. The following are the primary findings obtained from the simulation results.

- The finite element analyses were able to reproduce the damage observed in the original structure. The results suggest that fracture of the gusset plate was due to the deformation concentration when the brace was in compression.
- The finite element analyses indicated that the gusset plate was significantly weaker in the east-west frame than in the north-south frame. This result may explain the substantial difference in damage between the two frames.

REFERENCES

[1] Architectural Institute of Japan (AIJ), *Recommendations for limit state design of steel structures*, AIJ, Tokyo, Japan, 2002. (in Japanese).

[2] American Institute of Steel Construction (AISC), *Seismic provisions for structural steel buildings*. ANSI/AISC Standard 341-05, Chicago, U.S.A.

[3] R. Matsui, T. Takeuchi, Energy dissipation performance of brace moment frames focusing on brace fracture, *Journal of Structural Engineering*, Architectural Institute of Japan, 665, 1337-1345, 2011. (in Japanese).

[4] T. Okazaki, D.G. Lignos, T. Hikino, K. Kajiwara, Dynamic response of a chevron concentrically braced frame. *Journal of Structural Engineering*, American Society of Civil Engineers, 139(4), 2013.

[5] T. Okazaki, D.G. Lignos, M. Midorikawa, J.M. Ricles, J. Love, Damage to steel buildings observed after the 2011 Tohoku-oki earthquake. *Earthquake Spectra*, Earthquake Engineering Research Institute, 29(S1), S219-S243, 2013.

[6] Architectural Institute of Japan (AIJ), Report on the Hanshin-Awaji Earthquake Disaster, Building Series - Volume 3 (Structural damage to steel buildings / shell and space structures, storage tanks and their supports), AIJ, Tokyo, Japan, 1997. (in Japanese).

[7] ADINA R&D, Inc., Theory and Modeling Guide. ARD 12-9, 2012.

COMPDYN 2015
5th ECCOMAS Thematic Conference on
Computational Methods in Structural Dynamics and Earthquake Engineering
M. Papadrakakis, V. Papadopoulos, V. Plevris (eds.)
Crete Island, Greece, 25–27 May 2015

NUMERICAL INVESTIGATION OF THE SEISMIC RESPONSE OF PRECAST BUILDINGS WITH INTEGRATED RC CLADDING WALLS

Ioannis Kalyviotis[1], **Ioannis Psycharis**[2]

[1] National Technical University of Athens
9 Heroon Polytechniou str., Zografou, Greece
e-mail: ikalyvio@central.ntua.gr

[2] National Technical University of Athens
9 Heroon Polytechniou str., Zografou, Greece
e-mail: ipsych@central.ntua.gr

Keywords: Precast buildings; Cladding walls; Fixed connections; Inelastic response; Precast walls.

Abstract. *Recent earthquakes have dramatically shown the importance of cladding connections on the seismic response of precast buildings. In the present work, a numerical investigation on the behaviour of precast structures with RC panel walls with 'fixed' connections is reported. Simplified structural calculations and numerical analyses show that the seismic forces induced to the connections of the panels can be quite large. An extensive numerical and experimental program has been performed at the Laboratory for Earthquake Engineering of the National Technical University of Athens, Greece, within the framework of the FP7 European project SAFECLADDING, for the investigation of the behaviour of integrated connections and their effect on the overall structural response. In the numerical analyses presented herein, the behaviour of the panel-beam connections was modeled with inelastic rotational springs which were calibrated against the experimental data. The results show that the roof diaphragm has a profound effect on the way the forces are transmitted to the structural members and on the forces induced to the connections. For typical ground motions compatible with the code requirements, the inelastic response is generally restricted to the columns, while the panels behave practically elastically.*

1 INTRODUCTION

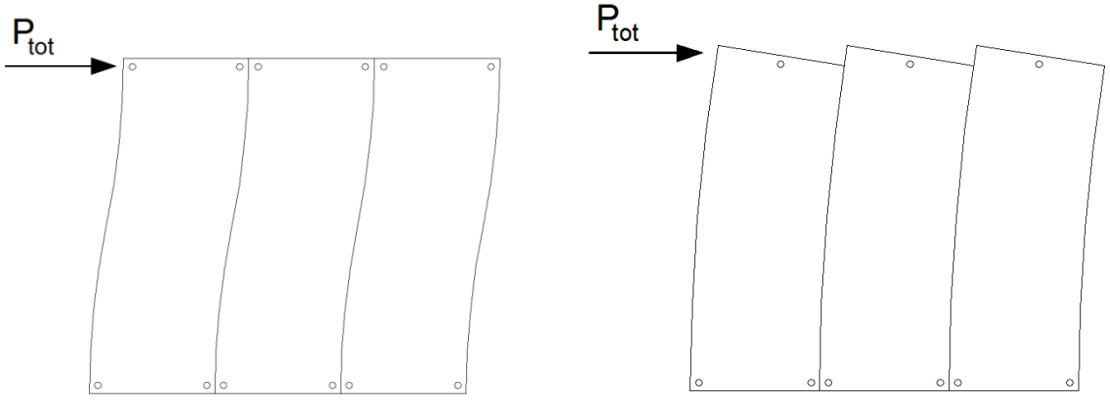
In common design practice of precast structures, RC cladding panels are not designed to contribute to the structure's lateral stiffness but are connected to the structure with fastening devices dimensioned to bear the panels' self-weight, wind loads and seismic loads corresponding to the panels' mass only. However, the behaviour of cladding wall systems in recent strong earthquakes, v.i.z. Gölcük, Turkey (1999); Düzce, Turkey (1999); L'Aquila, Italy (2009); Lorca, Spain (2010); Emilia, Italy (2012), dramatically showed that simple connections typically applied in practice are insufficient to resist the large forces induced to them during strong ground shaking, resulting to severe damage to the connections and collapse of the panels.

New innovative panel-to-structure connections and novel design approaches for a correct conception and dimensioning of the fastening system to guarantee good seismic performance of the structure have been investigated within the FP7 European project "SAFECLADDING: Improved fastening systems of cladding wall panels of precast buildings in seismic zones", GA No. 314122. Part of this investigation concerned fixed panel connections, referred as "integrated", which are designed to resist the large seismic forces that develop in them since the panels contribute to the lateral load resisting system of the structure. To this end, experimental and analytical investigations on the behavior of fixed connections and their effect on the overall response of the structure were performed at the Laboratory for Earthquake Engineering of the National Technical University of Athens (NTUA), Greece [10].

In the integrated systems, the panel connections are based on a hyperstatic arrangement of the fixed supports of each panel. Typically, vertical panels are used connected to the beams at four points (Figure 1a) or at three points (Figure 1b). Horizontal panel arrangements could also be used, however they are not recommended as they transfer large forces to the columns to which they are connected. For this reason, horizontal panels are not examined in this paper.

Several mechanisms can be used to materialize fixed panel-to-beam connections, as simple connections made of protruding bars ('rebar' connections – Figure 2) or more sophisticated connections made of industrially produced bolted shoes. The analyses presented herein are based on connections of the first type.

Figure 2 shows a panel of height up to the zero-moment point (shear length, ℓ_s), which is equal to one half of the total height in case of Figure 1a, and equal to the full height in case of Figure 1b. The connecting bars provide the tensile strength in the tension zone, while concrete provides the resistance in the compression zone.



(a) (b)

Figure 1. Arrangement of vertical panels with: (a) four connections; (b) three connections.

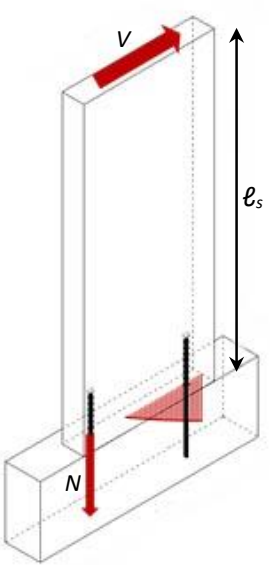


Figure 2. 'Rebar' connections: resisting mechanism at the panel-to-beam joint under seismic loading.

2 NUMERICAL MODELLING OF PANELS

2.1 General considerations

The overall lateral response of precast panels with integrated connections to lateral loading consists of the deformation of the panel itself and the response of the connection under tension. It is not easy to model this response numerically, since the latter involves tensile yielding of the bars and local debonding. For this reason, a simplified model is proposed, consisting of linear elements and nonlinear springs, capable to capture the overall response of the panel and the connections. In this model (Figure 3), the panel is modelled with 5 elastic beam elements while the panel-to-beam connections are modelled with hinges.

The panel behaviour is captured by the vertical beam element placed at the centerline of the panel and four horizontal elements are used to materialize the width of the panel and the eccentric connections with the beams. The inelastic response of the connections is modelled with inelastic rotational springs placed at the ends of the vertical beam element, the properties of which (moment – rotation law) are determined from an independent finite element analysis, as explained in the ensuing. Due to the opening of the panel-beam joint, zero-length nonlinear springs are used, since the overall nonlinear behaviour at the joint corresponds to a plastic hinge of zero length. In the out-of-plane direction, these springs behave elastically.

In Figure 3, the modelling of panels with four connections is shown. In case of panels with three connections, the same model can be used but with zero stiffness assigned to the top 'zero-length spring', in order to take under consideration that the panels are free to rotate at their top.

2.2 Moment – rotation law of the panel connections

As mentioned above, the Lumped Plasticity model is considered at the ends of the panels, where the overall inelastic behaviour at the panel-beam joint is modelled with zero-length springs. For the determination of the moment – rotation law that governs the behaviour of these springs, a special finite element analysis was performed using SAP 2000 [2].

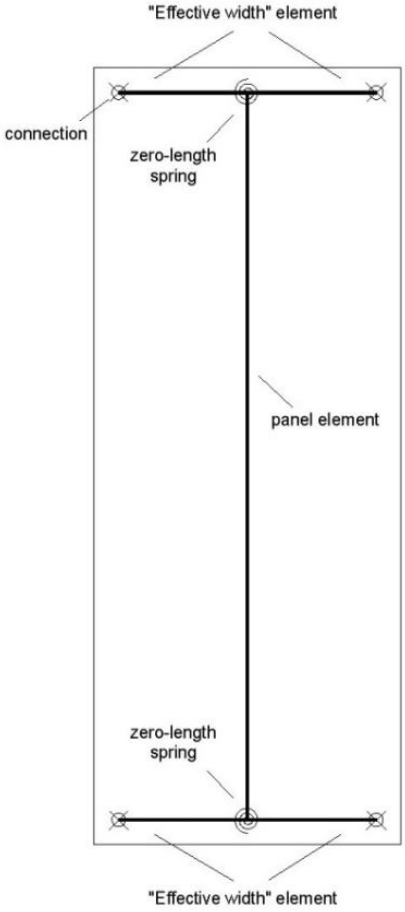


Figure 3. Numerical model of panel with four connections. In case of panel with three connections, the stiffness of the top 'zero-length spring' is set to zero.

Analyses were performed for panels with four and three connections. In the former case, the top beam was also included in the model (Figure 4a); in the latter, the panel was free at its top (Figure 4b). Both the panel and the beams were modelled with shell elements, while the connection bars were modelled with beam elements. In order to account for the possible debonding of the connection bars from the surrounding concrete, the nodes of the rebars were not connected directly to the corresponding nodes of the shell elements (modelling the panel or the beam), but through nonlinear springs, the behaviour of which was elastic – perfectly plastic. Thus, the 'bond' springs were yielding when the bond strength was reached, allowing local loss of the bonding along the bars. In order to capture well the local debonding, a quite dense mesh was applied around the rebars (max node distance was 20 mm). The joint between the panel and the beam was modelled with tensionless springs (gap elements). Representative results are shown in Figure 5.

The behaviour of the connections predicted by the numerical model was calibrated against the results of experiments conducted at NTUA concerning this type of connection. To this end, numerical models representing the test specimens (panels of height 2.65 m and length 1.50 m connected to the beam at their base and free at their top – Figure 2) were used and the derived capacity curves were compared with the experimental results for monotonic and cyclic loading. In this way, the appropriate properties of the springs modelling the bond between the connection bars and the concrete and the parameters of the contact springs were determined.

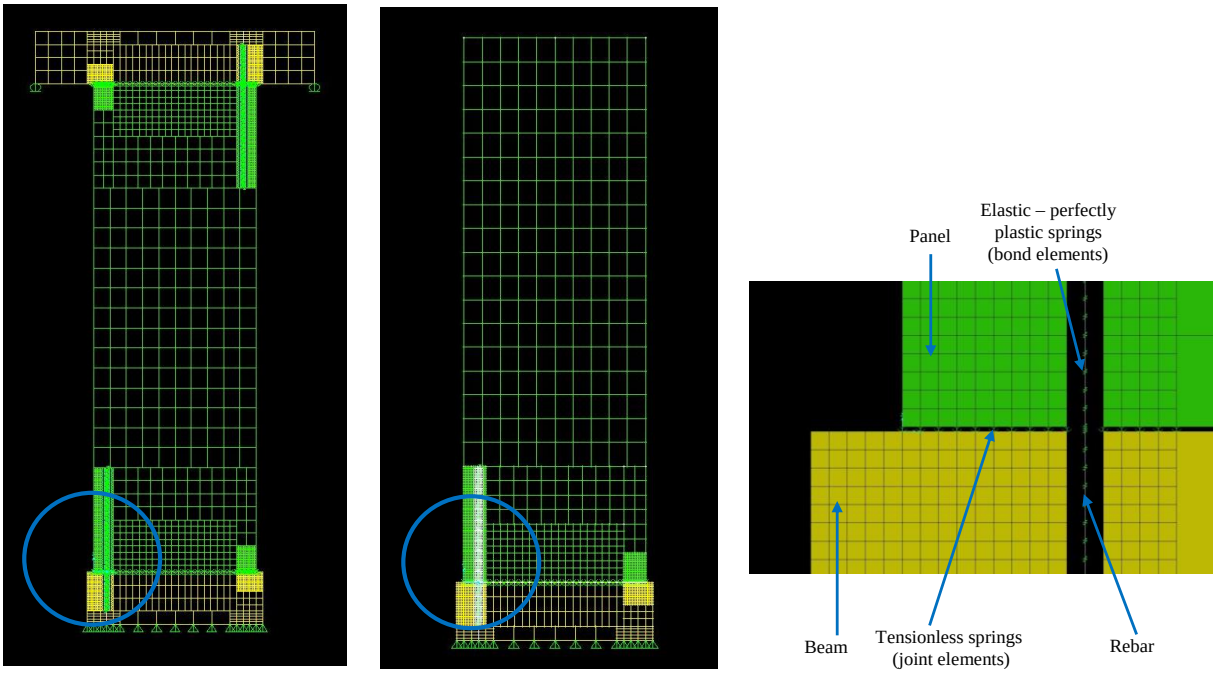


Figure 4. Model used for the analysis of the inelastic behaviour of panel-beam connections: (a) panels with four-point connections; (b) panels with three-point connections; (c) detail of connection.

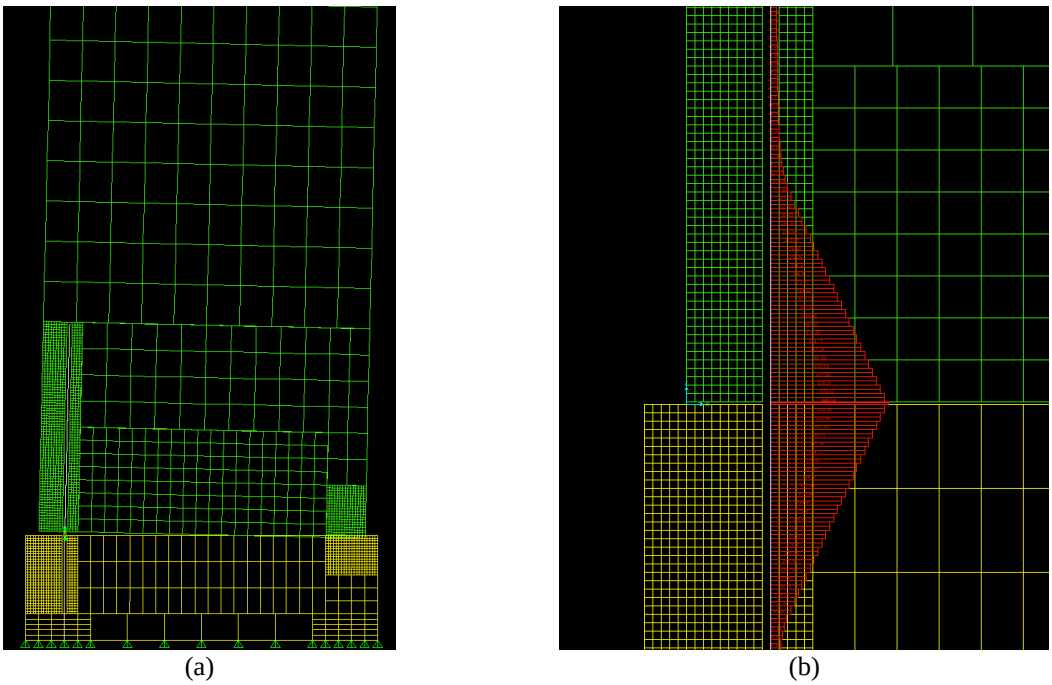


Figure 5. Representative numerical results: (a) deformed shape; (b) axial force induced to the connection bar at the final step of the analysis.

A comparison of the numerical results with the experimental data for the finally selected parameters is shown in Figure 6 for connections made of 1∅25 rebars, in which the horizontal force at the top of the panel versus the top displacement of the panel is plotted. It can be observed that the numerical behaviour captures accurately the initial stiffness and the post yield response, but the yield force is somehow overestimated.

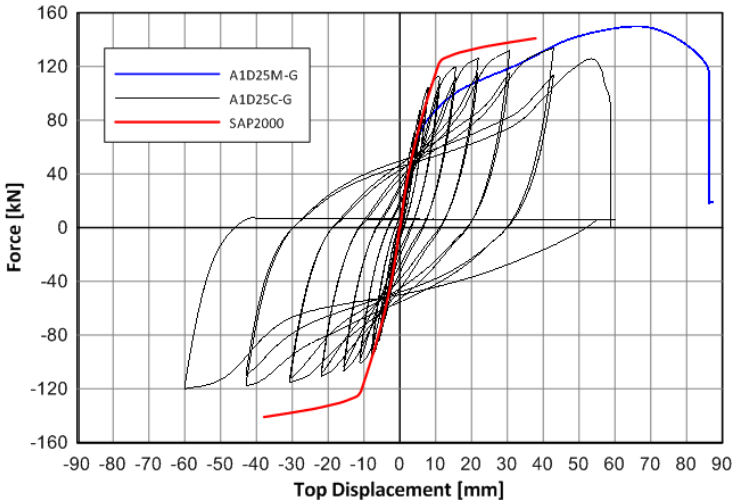


Figure 6. Comparison of the numerically predicted overall response (red line) of a panel with two bottom connections made of 1∅25 bars with experimental data for monotonic (blue line) and cyclic (black line) excitation.

3 CASE STUDY

As a case study, a single-storey industrial building of dimensions: length 60 m, width 40 m and height 7.5 m (Figure 7) was considered. The roof consisted either of Y shape precast elements or double-tee elements. In the former case, the roof elements were connected at a single point with the beams (Figure 8a) and were not connected to each other; thus, there was small diaphragmatic action in the roof (denoted as 'null diaphragm'). In the latter case, two configurations were examined: double-tee's not connected to each other (denoted as 'deformable diaphragm' – Figure 8b) or double-tee's connected to each other (denoted as 'rigid diaphragm' – Figure 8c).

The columns and the beams were of orthogonal cross section of dimensions 600 mm × 600 mm and 800 mm × 800 mm, respectively. Vertical panels of cross section 2500 mm × 200 mm were placed at all external sides, covering the full perimeter and the full height of the building. Analyses were performed for panels with three connections and for panels with four connections. The connections were made of vertical rebars of grade B500C and varying diameter (Table 1) and concrete grade C45/55. The building was designed according to EC2 [3] and EC8 [4].

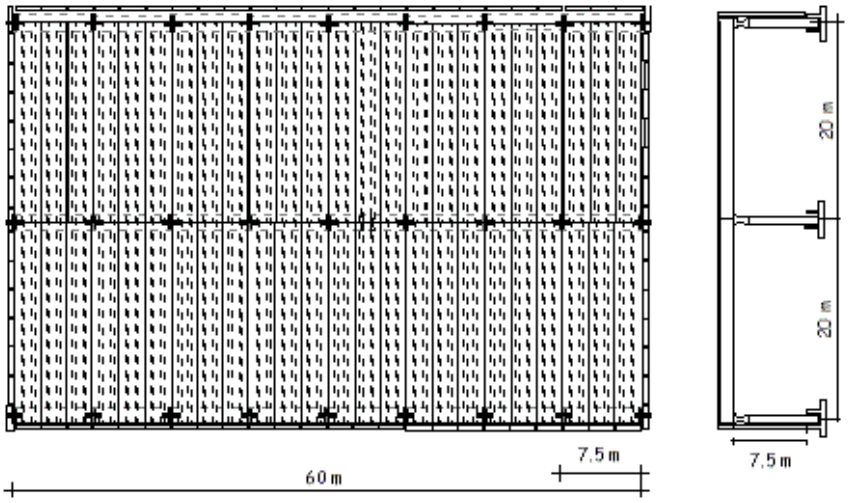
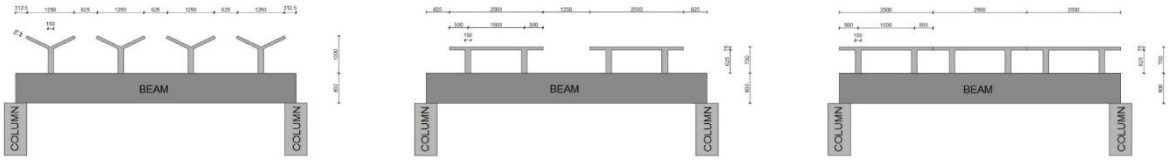


Figure 7. Plan view and cross section of the building considered.



(a) (b) (c)

Figure 8. Roof Configurations: (a) null diaphragm; (b) deformable diaphragm; (c) rigid diaphragm.

Panel in X direction		Panel in Y direction	
4-point	3-point	4-point	3-point
1∅25	2∅25	1∅28	2∅28

Table 1. Rebars of the connections considered.

Property	**Beam**	**Roof**	**Panel**
Young's modulus [GPa]	36.0	36.0	36.0
Shear modulus [GPa]	14.4	14.4	14.4
Cross section's area [m^2]	0.640	0.375	0.500
Torsional moment of inertia [m^4]	0.0577	0.0017	0.0063
Second moment of inertia about local z axis [m^4]	0.0341	0.2035	0.0017
Second moment of inertia about local y axis [m^4]	0.0341	0.0177	0.2604

Table 2. Element properties.

The analyses were performed using OpenSees [8]. The numerical model consisted of beam elements representing the columns, the beams, the roof elements and the panels (their properties are shown in Table 2). In all analyses, the mean strength of steel and concrete was taken into account ([3], [5], [9]). In order to deal with the numerical inconsistencies that derive from localization problems of reinforced concrete frame elements appropriate regularization techniques were applied ([1], [6], [7]).

Following the precast concrete practice, pinned connections between beams and columns were adopted. Therefore, beams were simply supported and were modelled with elastic elements. For the columns, distributed plasticity model with 5 integration points was used for the plastic hinges and the moment-curvature relationship was idealized with a tri-linear curve connecting the points corresponding to the concrete cracking, the yield of the reinforcement and the concrete spalling. Plastic hinges could also form at the connections of the panels, which were modelled with the zero-length rotational spring mentioned above (Figure 3).

The roof elements were considered to behave elastically and were connected to the top of the beams with hinged connections (Figure 9a), either at a single point (Y-shape elements) or at two points (double-tee elements – Figure 9b).

Analyses were performed for two different behaviour laws concerning the roof-to-beam connections, namely: (a) fully elastic connections (non-yielding); (b) elastic – plastic connections (yielding). In the first case, forces of unrealistically large magnitude can develop in the roof-to-roof, roof-to-beam and beam-to-column connections for rigid diaphragms and strong ground motions, due to the kinematic constraints imposed to the deformation of the beams by the double-tee elements. For this reason, yielding roof-to-beam connections were considered in case (b), representing a "more realistic" situation. In this case, the resistance of the connections was determined taking under consideration the friction and the dowel action of the steel angle bolts, which was calculated according to Vintzeleou & Tassios formula ([11], [12]).

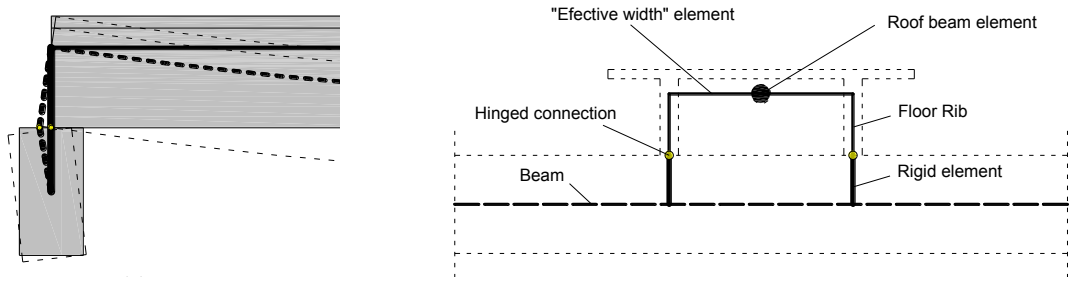


Figure 9. Roof-beam connections: (a) Schematic representation of the kinematic constraints; (b) Modelling of double-tee elements.

As mentioned above, the panels were modelled with five elastic beam elements and nonlinear zero-length rotational springs accounting for the overall nonlinear behaviour of the connections. For the determination of the moment – rotation constitutive law of these springs, pushover analyses were performed for the considered connections (Table 1) using the models of Figure 4. The derived capacity curves were transformed to bilinear curves, while sudden loss of strength was considered after the breakage of the bars. In order to capture the behaviour of the connection under cyclic loading, a hysteresis law was added. In Figure 10 such a hysteretic law for an indicative connection is depicted, while in Figure 11 the final idealised moment – rotation curves for the connections considered are shown.

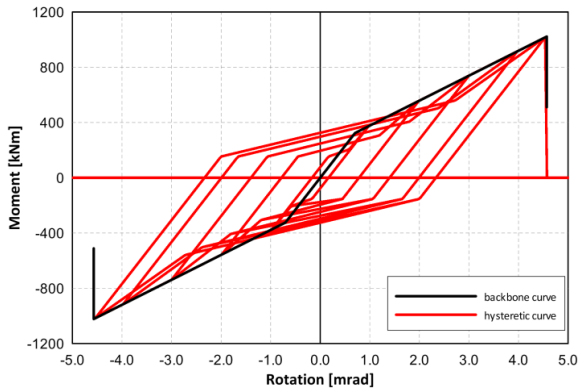


Figure 10. Hysteretic Moment – Rotation model of panel – beam connections made of 1∅20 rebar and panels with four connections.

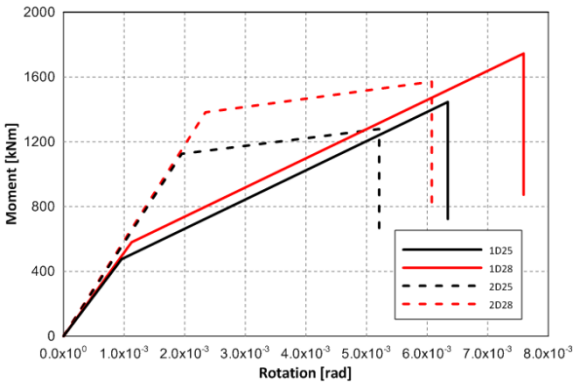


Figure 11. Idealised Moment – Rotation capacity curves of various panel – beam connections.

4 RESULTS OF THE NUMERICAL ANALYSES

4.1 Modal Analyses

Modal analyses were performed for buildings with integrated panels connected at three and four points and for buildings without panels; in the latter case, the panels contributed only with their mass (un-connected panels) while the structural system consisted of the bare frame only. Due to the large in-plane stiffness of the panels, the expected displacements of the buildings with panels were small and, for this reason, the columns were considered with their uncracked stiffness. Although this does not hold for the buildings without panels, the uncracked stiffness of the columns was also considered in that case in order to get comparable results.

As expected, the modes of vibration of the buildings with and without panels differ significantly. When the stiffness of the panels was neglected, the fundamental modes in both horizontal directions were translational with periods ranging from 0.90 to 1.19 sec for all types of

roof diaphragm. For the buildings with integrated panels, there were not clearly translational modes, while the effect of the diaphragmatic action was of major importance. The periods of the most important modes in each direction are given in Table 3. Indicative graphical representations of the most important mode are shown in Figure 12 for the building with deformable diaphragm.

No. of connections per panel	Diaphragm rigidity	Long direction		Short direction	
		Mode No.	Period [sec]	Mode No.	Period [sec]
4-point connections	Null	3	1.03	1	1.17
	Deformable	7	0.41	1	0.66
	Rigid	8	0.34	1	0.60
3-point connections	Null	3	1.03	1	1.17
	Deformable	7	0.43	1	0.68
	Rigid	6	0.40	1	0.64
Without panels	Null	3	1.13	1	1.19
	Deformable	2	0.90	1	0.93
	Rigid	2	0.99	1	1.03

Table 3. Periods of the important modes.

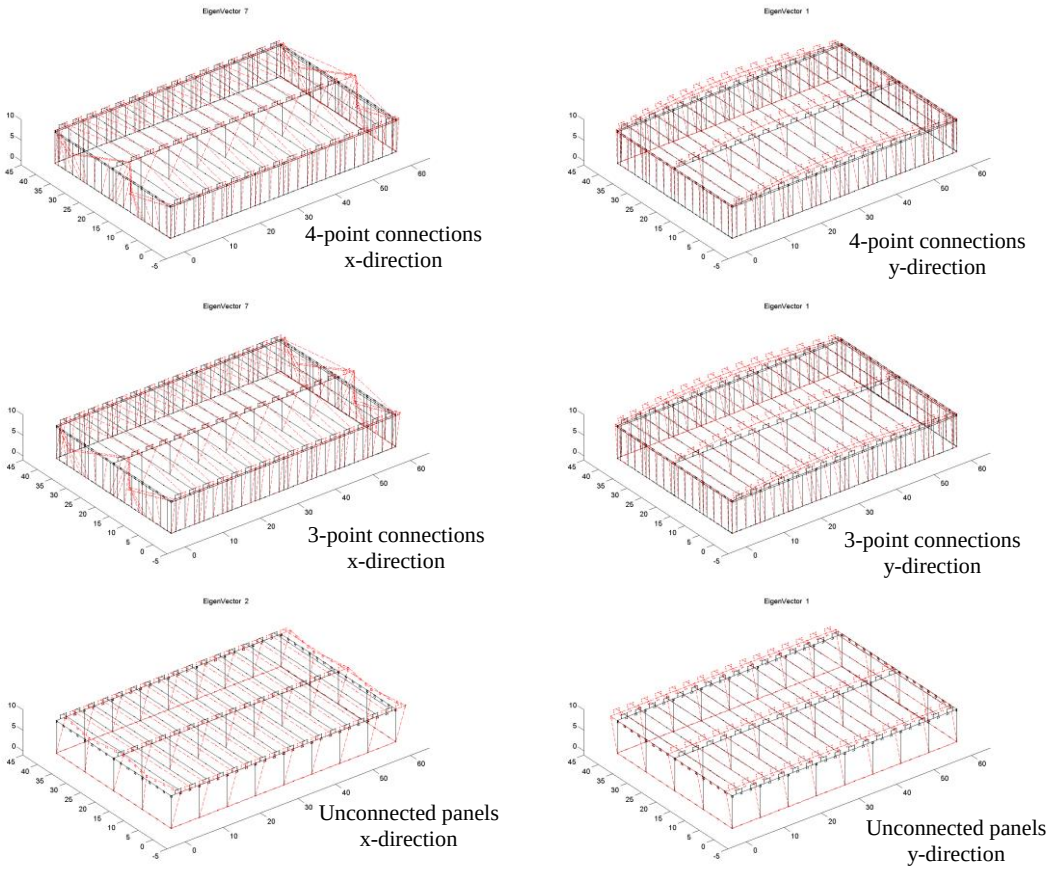
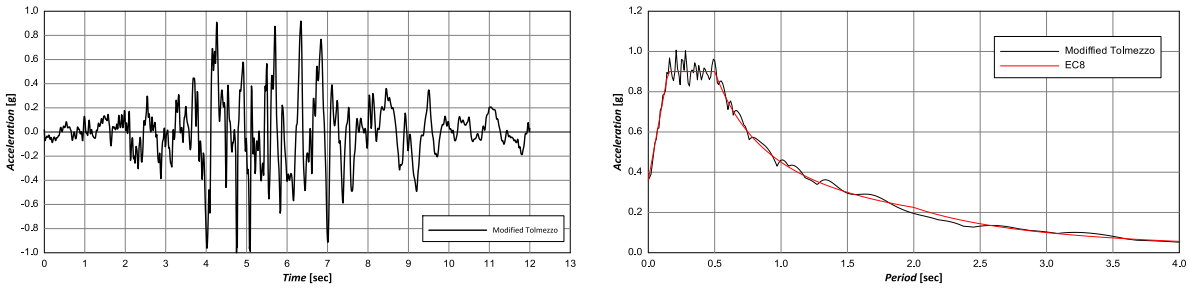


Figure 12. Most important mode of vibration for the building with deformable diaphragm.

4.2 Nonlinear Response History Analyses

For the nonlinear response history analyses (NLRHA), the modified Tolmezzo accelerogram (Figure 13a) was used. The record was modified to fit the EC8, type A response spec-

trum for soil category B (Figure 13b). Runs were performed for three levels of the peak ground acceleration (*pga*), namely: *pga* = 0.18 g (corresponding to 0.15 g for soil type A), *pga* = 0.36 g (corresponding to 0.30 g for soil type A) and *pga* = 0.60 g (corresponding to 0.50 g for soil type A).



(a) (b)

Figure 13. Modified Tolmezzo Accelerogram record used in the NLRHA: (a) Acceleration time history; (b) Response spectrum for *pga*=0.36 g and comparison with the EC8 spectrum.

The results show that the inelastic response observed in the structures was mainly due to the inelastic response of the columns and not of the panels, which behaved almost elastically. It is noted that, even for the rigid roof diaphragm, the drift of the internal columns and the columns located around the middle of the sides normal to the loading direction was considerably larger than the drift of the columns located at the external sides parallel to the loading direction (Table 4), which shows that there is significant in-plane deformation of the roof diaphragm leading to the yielding of the columns.

In general, it can be said that the response of structures with panels connected at four points showed similar characteristics with the response of structures with panels connected at three points.

Max drift [%]	**Long direction**			**Short direction**		
	0.18 g	**0.36 g**	**0.60 g**	**0.18 g**	**0.36 g**	**0.60 g**
External column in the side aligned with the direction of loading	0.09	0.16	0.33	0.10	0.30	0.56
External column in the side normal to the direction of loading	0.18	0.29	0.46	0.43	0.81	1.27
Internal column	0.18	0.29	0.46	0.31	0.64	1.06

Table 4. Maximum column drifts for the building with non-yielding roof-to-beam connections, rigid diaphragm and panels connected at four points.

When non-yielding roof-to-beam connections were considered, large forces developed in the roof-to-roof, roof-to-beam and beam-to-column connections, which in many cases exceeded their resistance. This phenomenon is attributed to the horizontal deflection of the longitudinal roof beams, which is restricted by the in-plane large stiffness of the double-tee elements. This is shown schematically in Figure 14: due to the deformation of the longitudinal beams, the displacements d_1 and d_2 at the two points where the double-tee roof elements are connected to the beams (at the bottom of their vertical ribs) are different from each other resulting in the distortion of the roof elements. It is evident that such large forces cannot develop in reality, as the roof-to-beam connections would yield or break leading to the relaxation of the internal forces induced to the structure.

Indeed, when yielding roof-to-beam connections were considered, the forces induced to beam-to-column connections were significantly reduced. However, large relative displace-

ments of the roof occurred in this case, which were affected by the diaphragmatic action of the roof and the intensity of the ground motion. The largest displacements were recorded for the flexible roof configuration and *pga* = 0.60 g, whereas no relative displacements generally occurred for *pga* = 0.18 g.

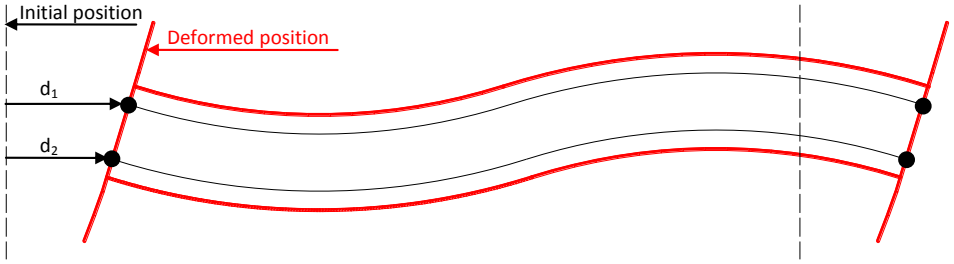


Figure 14. Deformation of roof double-tee elements during seismic loading.

5 CONCLUSIONS

The following conclusions can be drawn from the performed analyses:

- Buildings with integrated panel connections, resulting in the participation of the panels to the main structural system, are considerably stiffer than similar buildings with isostatic connections.
- The response of the structure with panels connected at four points shows in general similar characteristics with the one with panels connected at three points. However, there are differences in the values of the base shear and the top displacement.
- In systems with panels with integrated connections, the roof diaphragm has a profound effect on the way the forces are transmitted to the panels and the columns and, thus, affects significantly the overall seismic response. On the contrary, in buildings with panels free to move, the roof diaphragm rigidity does not affect the response of the structure.
- The nonlinear time history analyses performed for the modified Tolmezzo record show that much larger forces and displacements are induced to the internal columns than the external (façade) columns. The former behaved inelastically even for weak base excitations (*pga* = 0.18 g).
- The observed inelastic response is generally due to the inelastic response of the columns and not of the panels.
- In some connections, such as the roof-to-roof, roof-to-beam and beam-to-column, significant variation of the forces between connections located at different positions was observed. The larger forces developed at the roof-to-beam connections located close to the four corners of the building due to the horizontal deflection of the longitudinal beams during the seismic response, which cannot be easily accommodated by the double-tee roof elements due to their large in-plane stiffness. This phenomenon was significantly relaxed when yielding roof-to-beam connections were considered, but large relative roof displacements were observed in this case.

6 AKNOWLEDGEMENTS

The research presented herein was conducted within the project “SAFECLADDING: Improved fastening systems of cladding wall panels of precast buildings in seismic zones”,

which was financed by the European Commission in the framework of the Seventh Framework Programme (FP7) under Grant Agreement number 314122. The first author wants to thank the Onassis Foundation for the financial support of his postgraduate studies at NTUA through Scholarship number GZI015.

REFERENCES

[1] J. Coleman, E. Spacone, Localization issues in force-based frame elements. *Journal of Structural Engineering*, ASCE, **127**(11): 1257-1265, 2001.

[2] Computers & Structures, Inc., *SAP2000 – Integrated Software for Structural Analysis & Design, Technical Reference Manual*

[3] European Committee for Standardization (CEN), *Design of concrete structures – Part 1-1: General rules and rules for buildings*. Eurocode 2, EN 1992-1-1, 2004.

[4] European Committee for Standardization (CEN), Design of structures for earthquake resistance – Part 1: General rules, seismic actions and rules for buildings. Eurocode 8, EN 1998-1, 2004.

[5] European Committee for Standardization (CEN), *Design of structures for earthquake resistance – Part2: Bridges*. Eurocode 8, EN 1998-2, 2004.

[6] International Federation for Structural Concrete (fib). *Practitioners' guide to finite element modelling of reinforced concrete structures.* Fib Bulletin 45, State-of-art report prepared by Task Group 4.4.

[7] D.C. Kent, R. Park, Flexural Members with Confined Concrete. *Journal of the Structural Division, ASCE*, **97**(ST7): 1969-1990, 1971.

[8] F. McKenna, G.L. Fenves, M. H. Scott, B. Jeremic, *Open System for Earthquake Engineering Simulation (OpenSees)*, Pacific Earthquake Engineering Research Center, University of California, Berkeley, CA., 2000.

[9] T. Paulay, M.J.N. Priestley, *Seismic Design of Reinforced Concrete and Masonry Buildings*, John Wiley & Sons, New York, 1992.

[10] SAFECLADDING, *Deliverable 3.3: Updates on numerical and experimental analyses of typical integrated arrangements*, FP7 GA No. 314122, 2015.

[11] E.N. Vintzeleou, T.P. Tassios, Mechanics of load transfer along interfaces in reinforced concrete, prediction of shear force vs. shear displacement curves. *Studie de Reserche*, No. 7, Corpo di Perfezionamento per le Construzioni in Cemento Amato, Italcementi Societa per Azioni (S. p:A), Bergamo, Italy, pp. 121-161, 1985.

[12] E.N. Vintzeleou, T.P. Tassios, Behavior of dowels under cyclic deformations. *American Concrete Institute (ACI)*, **84** (1): 18-30, 1987.

COMPDYN 2015
5th ECCOMAS Thematic Conference on
Computational Methods in Structural Dynamics and Earthquake Engineering
M. Papadrakakis, V. Papadopoulos, V. Plevris (eds.)
Crete Island, Greece, 25–27 May 2015

EVALUATION OF THE APPLICABILITY OF THE LUGRE MODEL FOR MODELLING THE DYNAMIC BEHAVIOUR OF BOLT CONNECTED FRAMES

Sergio Sánchez Gómez[1], **Mihai I.Badila**[2], **Andrei Metrikine**[2]

[1]TU Delft
Faculty of Civil Engineering and Geosciences
Stevinweg1, 2628CNDelft, The Netherlands
e-mail: s.sanchezgomez, M.I.Badila, A.Metrikine@tudelft.nl

Keywords: Nonlinear dynamics, friction damping, LuGre model, Galerkin method.

Abstract. *In this paper the dynamics of a frame with bolted connections is studied both theoretically and experimentally. The connections are described using the Lund-Grenoble(LuGre) model. The problem of the dynamic response of the frame to a pulse load is studied using the Galerkin approach that reduces the governing equations to a set of nonlinear ODE's. They are latter solved numerically. It is shown that the theoretical predictions match the experimental observations well.*

1 Introduction

Nowadays buildings are becoming taller but also lighter and more slender. Those characteristics make buildings more sensitive to dynamic loads. Damping is an important but most uncertain parameter in the dynamic response of buildings under wind excitations. As a consequence, several researchers attempted to study it. Davenport [1] defined the main sources of energy dissipation in a tall building. Jeary [2] showed the relevance of the friction due to crack formation during high amplitude vibration and established a relation between damping and amplitude of vibration. Tamura [3] made significant improvements in damping prediction by developing practical models and applying data analysis methods [4], such as the random decrement technique to building measurements. Lagomarsino [5] developed a theoretical model to predict the friction damping in a building. However, he concluded that the model was not directly applicable. Because of the large amount of uncertainties in the damping prediction, developing a theoretical model to assess damping in buildings becomes very difficult. Only empirical formulas based on building measurements are available. All the mentioned researchers stated the importance of friction damping during high amplitude vibration scenarios in the damping prediction. The friction effects in a building can be very complex because they involve different phenomena that occur randomly such as the stribeck effect [6] and stiction effect [6] among others. The occurrence of these phenomena depends on many factors such as the construction material, the number of connected walls, the structural design of the building etc. The principal idea of this study is to find a general damping mechanism which captures the most important friction phenomena occurring in a building in high amplitude vibration scenarios. To this end, a friction damping mechanism called Lund-Grenoble(LuGre) model [7] is implemented. The details of this model are described in the following section. In order to get a better understanding of the LuGre mechanism a simple lab scale experiment has been carried out. In this paper an analytical approach to solve a case study applying the LuGre damping mechanism is presented. Moreover, the solutions of the model are compared with the lab scale experiment.

2 Model approach and governing equations

2.1 Model approach

Several damping mechanisms, ranging from linear viscous ones to complex combined mechanisms, are well described in literature [8, 9, 10]. Linear damping mechanisms are unlikely to predict damping in a high amplitude vibrations of buildings. This is because at high amplitudes the rubbing between contact surfaces produce friction. The friction damping has a nonlinear behaviour based on different phenomena (stribeck and stiction among others) that occur in an irregular manner. These phenomena make the magnitude of the friction change depending on the amplitude of vibration. Therefore, the focus on nonlinear mechanisms is necessary. Based on the goal of this study, the implementation of a single damping model to capture all the most important phenomena happening in a large amplitude vibration of buildings is needed. In consequence, the decision of using the LuGre model in this particular study was made. This decision is based on the fact that this is a general model that tackles the most relevant phenomena occurring when friction is present. The LuGre model was designed to deal with the friction between the surfaces of machine components. However, for this work an adaptation of this model in order to deal with friction in structural engineering problems is made. In this paper the LuGre model is applied to describe the dynamics of a frame structure. The results of the conducted study are compared with the data obtained from a lab scale experiment.

2.2 The LuGre model

In this section the LuGre model is presented in Eq. (1) and Figure (1). This model is an extension of the Dahl's model [6]. The Dahl's model, is a combination of the viscous model [11], Coulomb model [6] and the stiction model. However, the LuGre model, incorporates the bristle interpretation. The bristles represent the asperities at the microscopic level of the surfaces. This can be seen in Figure (1).

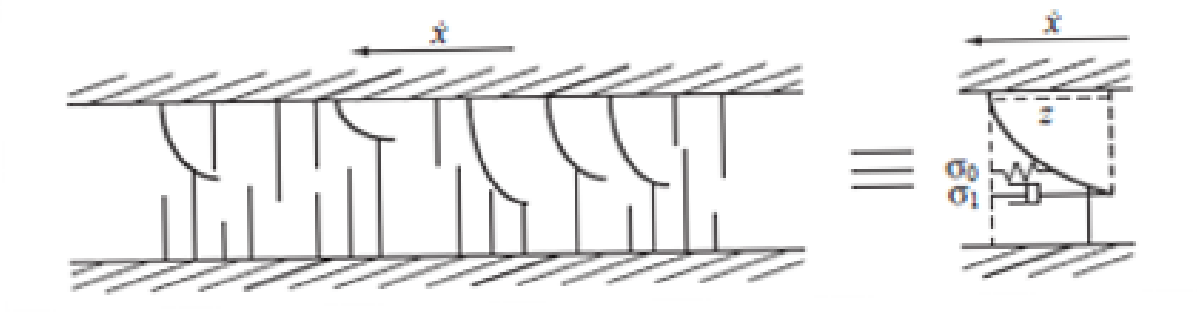


Figure 1: Bristle interpretation of the LuGre model

The LuGre model, is a combination of more simple damping models. This, also gives a very interesting point of view because with the simplification of the LuGre model, several other models are implicitly implemented.

$$
\begin{aligned}
F_L(v,z) &= \sigma_0 z + \sigma_1 \dot{z} + \sigma_2 \dot{x} \\
\dot{z} &= \dot{x} - \frac{\dot{x}}{g(\dot{x})} z \\
g(v) &= \frac{1}{\sigma_0}\Big(F_c + (F_s - F_c) e^{-\left(\frac{\dot{x}}{v_s}\right)^2}\Big)
\end{aligned} \tag{1}
$$

The LuGre model contains different parameters. Where F_L is the friction force, $\dot{x}$ is the relative sliding velocity at the friction interfaces, σ_0 is the bristle stiffness, σ_1 is the nonlinear damping coefficient, F_c is the Coulomb friction force, F_s is the stiction force, σ_2 is the linear viscous coefficient, and v_s is the stribeck velocity.

2.3 Case study

In this paragraph the application of the LuGre model in a case study is formulated and described below. The study consists in modeling a lab scale bolt connected steel frame. However, for simplification only one connection is taken into account. The model consists in a continuous Euler-Bernoulli beam [12] with a discrete element in its boundary as shown in Figure (2). The discrete element is composed by a translational spring and a friction mechanism. The friction damping mechanism is implemented using the LuGre model. In order to carry out the analytical nonlinear problem the Galerkin approach is employed.

2.3.1 Governing equations

The equation of motion and the boundary conditions for the model under consideration can be written in the following form(note that the LuGre element is accounted in the equation of motion):

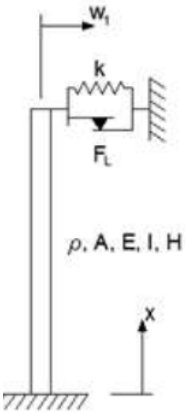


Figure 2: Physical interpretation of the model

$$
\begin{aligned}
EI\frac{\partial^4 w(x,t)}{\partial x^4} + \rho A\frac{\partial^2 w(x,t)}{\partial t^2} &= \delta(x-L)F(t) - \delta(x-L)F_L(\dot{w},\dot{z},z) \\
w(0,t) &= 0 \\
\frac{\partial w(0,t)}{\partial x} &= 0 \\
-EI\frac{\partial^2 w(H,t)}{\partial x^2} &= 0 \\
-EI\frac{\partial^3 w(H,t)}{\partial x^3} &= -kw(H,t)
\end{aligned} \tag{2}
$$

Where $w(x,t)$ is the beam deflection, E is the Youngs modulus, I is the moment of inertia of the cross sectional area, ρA is the inertial mass per unit of length, $\delta(x-L)$ is the Dirac delta function [13], $F(t)$ is the external load and $F_L(w,z,z)$ is the friction force.

The solution is assumed to be in the following form:

$$
w(x,t) = \sum_{n=1}^{\infty} W_n(x)q_n(t) \tag{3}
$$

Where $W_n(x)$ are the eigenfunctions that satisfy the boundary conditions and $q_n(t)$ are the unknown time dependent functions. Substituting Eq. (3) into the equation of motion and making use of the orthogonality condition, the Galerkin projection is formulated.

$$
\begin{aligned}
&\int_0^H \Big(EI\sum_{n=1}^{\infty} W_n''''(x)q_n(t) + \rho A\sum_{n=1}^{\infty} W_n(x)\ddot{q}_n(t)\Big)W_n(x)dx = \\
&\int_0^H \Big(\delta(x-L)F(t) - \delta(x-L)F_L(\sum_{n=1}^{\infty} W_m(x)\dot{q}_m(t),\dot{z},z)\Big)W_n(x)dx
\end{aligned} \tag{4}
$$

2.3.2 Evaluation of the natural frequencies and eigenfucntions

First, the eigenfunctions $W_n(x)$ should be determined before the solution can be carried out. The modes are calculated using the following equation of motion

$$EI\frac{\partial^4 w(x,t)}{\partial x^4} + \rho A\frac{\partial^2 w(x,t)}{\partial t^2} = 0 \tag{5}$$

and the boundary conditions given in Eq. (2). The physical representation of such a system is as shown in Figure (3).

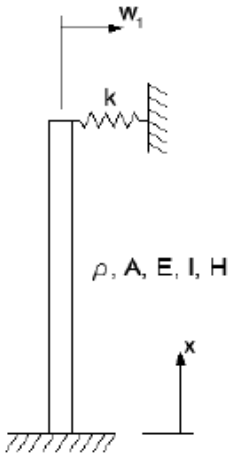


Figure 3: Model without the non-linear components

Note that the friction damping mechanism and the input force are not included in the Eq. (5), but they are accounted as a part of the equation of motion in Eq. (2). This enables to use the Galerkin approach. The solution of Eq. (5) is assumed as:

$$w(x,t) = W(x)cos(wt + \phi) \tag{6}$$

Substituting Eq. (6) into Eq. (5) the eigenvalue problem can be formulated.

$$W''''(x) - \beta^4 W(x) = 0 \tag{7}$$

where $\beta^4 = \frac{\lambda^2 \rho A}{EI}$ and the general solution for $W(x)$ is:

$$W(x) = C_1 e^{\beta x} + C_2 e^{-\beta x} + C_3 e^{i\beta x} + C_4 e^{-i\beta x} \tag{8}$$

inserting the general solution into the boundary conditions of Eq. (2), the natural frequencies and the mode shapes can be obtained:

$$\begin{pmatrix} 1 & 0 & 1 & 0 \\ 0 & 1 & 0 & 1 \\ cosh(\beta H) & sinh(\beta H) & -cos(\beta H) & -sin(\beta H) \\ (H\beta)^3 sinh\beta H - \frac{H^3 k}{EI} cosh(\beta H) & (H\beta)^3 cosh\beta H - \frac{H^3 k}{EI} sinh(\beta H) & (H\beta)^3 sin\beta H - \frac{H^3 k}{EI} cos(\beta H) & -(H\beta)^3 cos\beta H + \frac{H^3 k}{EI} sin(\beta H) \end{pmatrix} \begin{pmatrix} C_1 \\ C_2 \\ C_3 \\ C_4 \end{pmatrix} = 0$$

Now, by setting to zero the determinant the natural frequencies can be determined.

$$\mathbf{det}(\beta) = 0 \tag{9}$$

The eigenfunciton of the system can be obtained after the determination of the coefficients C_i.

$$W(x) = cosh(\beta_n x) - cos(\beta_n x) - \frac{cosh(\beta_n H) + cos(\beta_n H)}{sinh(\beta_n H) + sin(\beta_n H)}(sinh(\beta_n x) - sin(\beta_n x)) \tag{10}$$

2.3.3 Application of the Galerkin method

Once the natural frequencies and eigenfunctions are determined, the solution of the complete system can be carried out. Note that on the right hand side of Eq. (2) the Dirac delta function is presented. Therefore, in order to work out the right hand side of the equation a property of the Dirac delta function is applied [13].

$$\int_{-\infty}^{\infty} \Big(\delta(x-L)F_L(\sum_{m=1}^{\infty} W_m(x)\dot{q}_m(t), \dot{z}_n, z_n)\Big)W_n(x)dx = F_L(\sum_{m=1}^{\infty} W_m(H)\dot{q}_m(t), \dot{z}_n, z_n)\Big)W_n(H) \tag{11}$$

this leads to:

$$(\lambda_n^2 q_n(t) + \ddot{q}_n(t)\Big)\rho A\int_0^H W_n^2(x)dx = F(t)W_n(H) - F_L(\sum_{m=1}^{\infty} W_m(H)\dot{q}_m(t), \dot{z}_n, z_n)\Big)W_n(H) \tag{12}$$

Finally a set of equation can be formulated as.

$$\begin{aligned} \dot{q}_n &= v_n \\ \dot{v}_n &= \frac{F(t)W_n(H) - F_L(\sum_{m=1}^{\infty} W_m(H)\dot{q}_m(t), \dot{z}_n, z_n\Big)W_n(H)}{A_n} - \lambda_n^2 q_n(t) \\ \dot{z}_n &= \dot{v}_n - \frac{\dot{v}_n}{g(\dot{v}_n)}z_n \end{aligned} \tag{13}$$

where:

$$A_n = \rho A\int_0^H W_n^2(x)dx \tag{14}$$

A numerical method is used in order to solve this system of ordinary differential equations. The procedure is repeated adding modes until the system converges in order to find a sufficiently accurate solution.

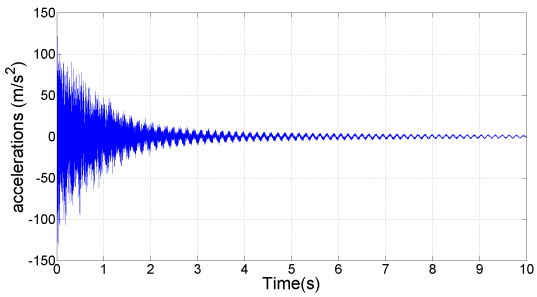
3 Experimental set up

In this section the experimental set up is presented. It consists of three steel beams with the following dimensions 1x0.1x0.01m. The beams are connected forming a frame shape; the vertical beams are assumed to be fully clamped. The horizontal beam is bolted through a square connection to the vertical beams (Figure (4)). Therefore, we force the system to generate more friction due to a larger friction surface. In this experiment several tests were performed. In order to excite the structure a hammer with a force transmitter was used to introduce an impulse signal to the structure.

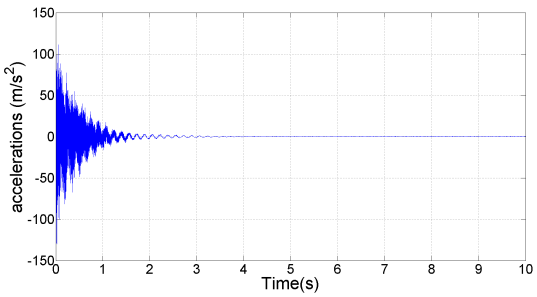


Figure 4: Experiment set up

First, the response of the structure was measured using a fully tight connection. The response of the system, measured from the accelerometer closer to the connection can be noted from Figure (5a). Second, the influence of the loosen connection was tested. Therefore, the lower bolts of the connection were loose and subsequently hand tightened. In consequence, higher friction and hence, higher damping was measured with the same accelerometer. This can be noted comparing the decay signal of Figure (5a) with Figure (5b).



(a) Response signal of the structure with the fully tight connection



(b) Response signal of the structure with loosen bolts

Figure 5: Measured signals

Finally, filtering the signal of test with the loosen connection it can be noted how nonlinearities appear in the system (Figure (6)).

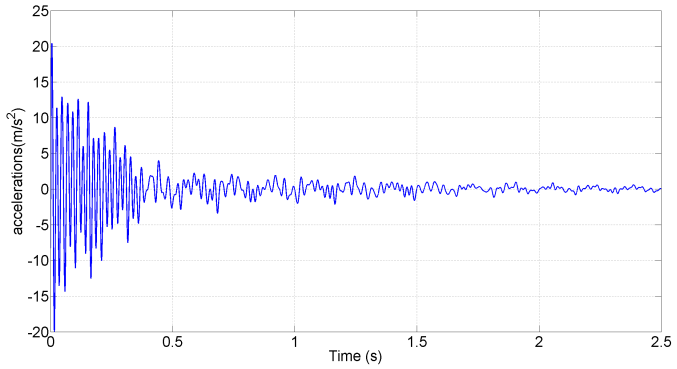


Figure 6: Filtered signal of the loosen bolts test

4 Results

The procedure proposed above (section 2) is used in this section to present the results of the study. The natural frequencies and the responses of the model are compared with the measurements from the experiment. Moreover, the sensibility study of the model parameters is presented. Although this is not a comprehensive analysis, several conclusions can be elucidated from studying how the parameters of the model influence the dynamic behaviour of the system. The properties of the system are described in Table (1).

Material properties		
Young modulus (E)	200e9	$\frac{N}{m^2}$
Density (ρ)	7850	$\frac{kg}{m^3}$
Geomerty		
Lenght (L)	1	m
Width (b)	0.1	m
Thickness (t)	0.01	m

Table 1: Material properties and geomerty

4.1 Natural frequencies and mode shapes

According to the procedure described in section 2.3.2. The modes are approximated by setting the non-linear parts to zero. This means that the natural frequencies and the mode shapes are determined using Eq. (5) and the boundary conditions described in Eq. (2). The experimental data obtained in the test with the fully tight connection (Figure (5a)) is used to compare it with the approximated natural frequencies obtained with the model(Figure (7a)).

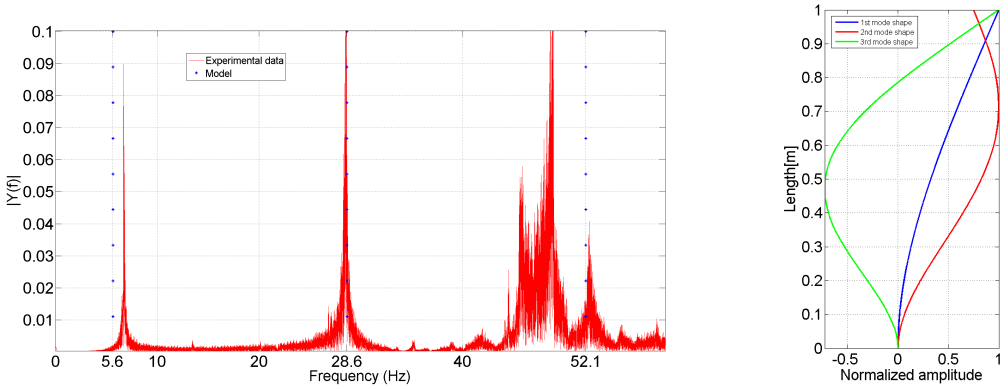


Figure 7: a) Modes of the model and the measurement; b) Model mode shapes

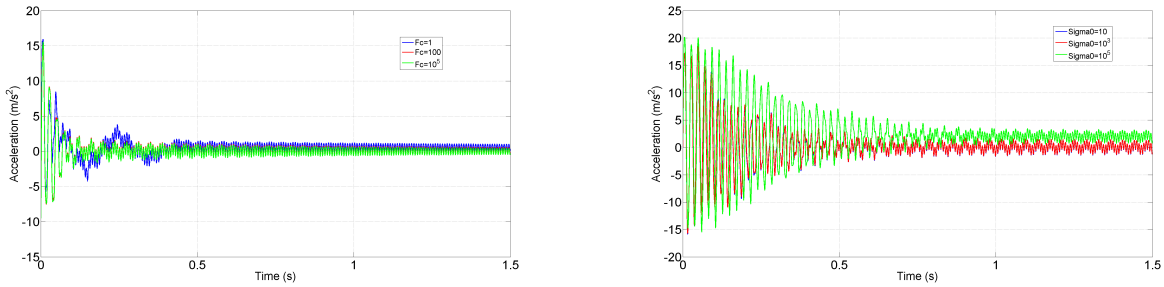
The stiffness of the attached spring is very difficult to determine experimentally. Therefore, it is tuned in order to match the natural frequencies of the experimental result of the fully tight connection test. As a result can be seen how the natural frequencies of the model match the results obtained from the experimental data.

4.2 The system response

Once the modes are found the system can be evaluated by using Eq. (2). Therefore the friction element and the input force are taken into account. The LuGre mechanism contains several parameters as described in section 2.2. This means that the influence of these parameters can be determined.

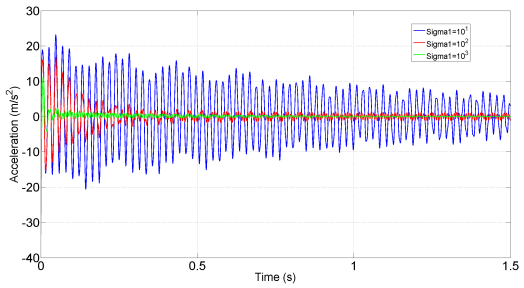
4.2.1 The influence of the LuGre parameters

The influence of the LuGre parameters is examined in the following figures.

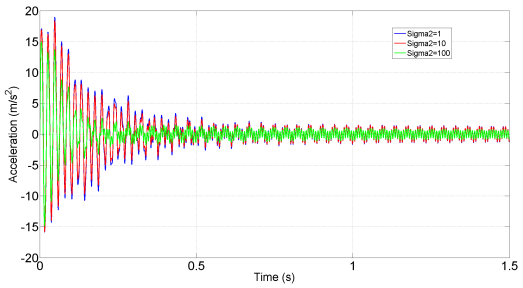


(a) Coulomb friction

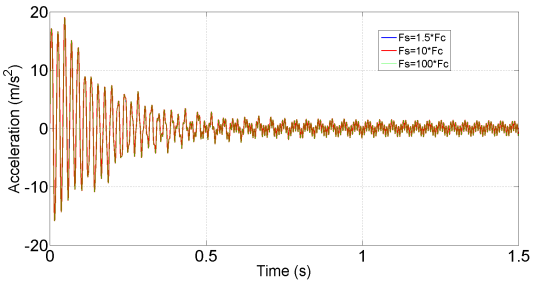
(b) Bristles stiffness



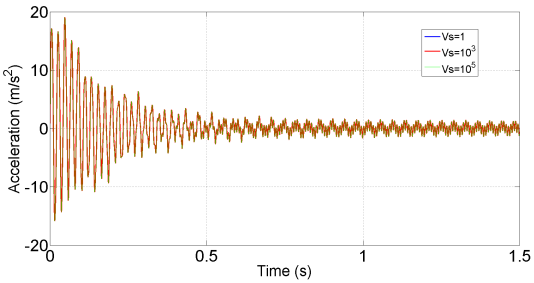
(c) Bristles damping



(d) Overall viscous damping



(e) Stiction force



(f) Stribeck velocity

Figure 10: LuGre parameters interpretation

From Figure (10a) it can be seen that the Coulomb friction is a parameter with a high influence on the performance of the friction damping. As occurred with the Coulomb friction the stiffness of the bristles σ_0 has a high influence on the total damping of the system(Figure (10b)). Moreover, the damping coefficient of the bristles σ_1 has a very important influence on the decay (Figure (10c)). The damping of the overall system has a large influence in the decay of the system as can be noted from Figure (10d). The effects of the stiction force are shown in Figure (10e). It can be noted that the influence of the stiction force is negligible. The final examined parameter is the stribeck velocity. This parameter has a little influence on the performance of the system as can be noted from Figure (10f).

As a consequence of the parameters examination, the parametrization of the model can be performed. Therefore, the following table contains a range of values suitable to match the case study.

σ_0	σ_1	σ_2	F_c	F_s	v_s
$10^{1.8}$	$10^{1.8}$	0.001	1	1.5	0.001

Table 2: LuGre parameters

A value for the different parameters has been selected in order to reproduce the output obtained from the lab scale experiment. The model results in comparison with the experimental data can be noted in Figure (11).

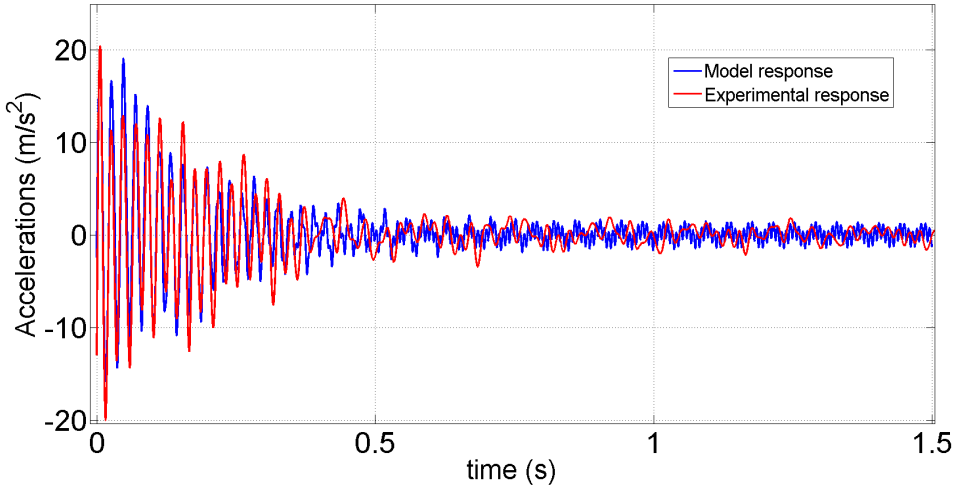


Figure 11: Comparison of the time domain response of the model and the experiment

From Figure (12), it can be seen that the results of the model match relatively well with the results obtained in the experiment.

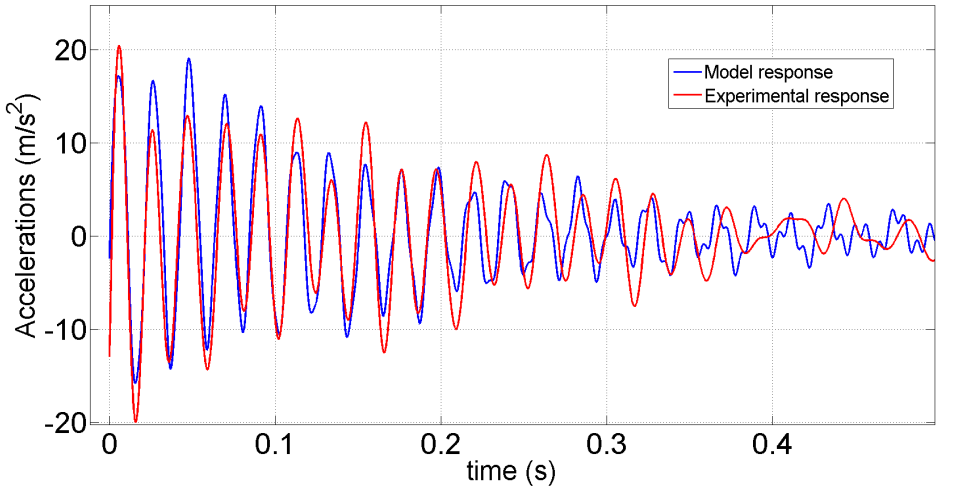


Figure 12: Detailed observation of the time domain response of the model and the experiment

5 Conclusions

In this paper, an analysis of the implementation and parameterization of the LuGre model has been accomplished. For this purpose, a case study which reproduces as accurately as possible, the response of a lab scale bolt structure has been performed. The reproduction of this experiment is performed using the LuGre model included as a boundary condition of an Euler-Bernoulli beam. In further research this model will be used in order to capture the response of another type of connections. The purpose is to use a single model, in this case the LuGre model in order to capture the friction-associated dissipation in a wide spectrum of conditions.

REFERENCES

[1] A.G. Davenport and P. Hill Caroll, Damping in tall buildings: its variability and treatment in design; *American Society of Civil Engineers (ASCE) (*1986*).*

[2] A.P. Jeary, Damping in tall buildings. A mechanism and a predictor; *Earth. Eng. Struct. Dyn, (*1986*)* $733 - 750$.

[3] Y. Tamura, N. Satake, T. Arakawa, A. Sasaki, Damping evaluation using full-scale data of buildings in Japan; *Journal of structural engineering.*

[4] J.C. Asmussen, Modal analysis based on the Randon Decrement technique-Applications to civil engineering structures; *Aalborg University, Denmark (*1997*).*

[5] S. Lagomarsino, Forecast models for damping and vibration poriods of buildings; *Wind Engineering and Industrial Aerodynamics, (*1993*).*

[6] V. van Geffen, A study of friction models and friction compensation; *Technische Universiteit Eindhoven (*2009*).*

[7] C. Canudas de Wit, H. Olsson, J.Åström, A new model for control of system with friciton; *IEEE transactions on automatic control. VOL* 40*. No* 3*, march* 1995.

[8] W.W. Soroka, Note on the relations between viscous and structural damping coefficients; *J. aeronaut. sci.* 16*,* $409 - 410$ *and* 448 *(*1949*).*

[9] D.E. Hudson, Equivalent viscous friction for hysteretic systems with earthquake-like excitations; *Proc. 3rd world conf earthquake* 12 *eng. Auckland and Wellington,* 11*,* 185-201 *(*1965*).*

[10] L.S. Jacobsen, Damping in composite structures; *Proc.* 2*nd world conf earthquake eng. Tokyo and Kyoto,* 1029-1044 *(*1965*).*

[11] S. adhikari AND J. Woodhouse, Identification of damping:Part 1, viscous damping; *Journal of Sound and vibration (*2001*)* 243*(*1*),* 43-61.

[12] J.M.J. Spijkers, A.W.C.M. Vrouwenvelder, E.C. Klaver, Dynamics of StructuresCT4140-Part 1-Vibrations of Structures; *Faculty of Civil Engineering and Geosciences Section of Structural Mechanics, Delft University of Technology.*

[13] J. Sethuraman, Dirac delta function and some of its applications; *Vinayaka Missions Kirupananda Variyar Engineering college.*

COMPDYN 2015
5th ECCOMAS Thematic Conference on
Computational Methods in Structural Dynamics and Earthquake Engineering
M. Papadrakakis, V. Papadopoulos, V. Plevris (eds.)
Crete Island, Greece, 25–27 May 2015

NONLINEAR DYNAMICS OF PARAMETRICALLY EXCITED CARBON NANOTUBES FOR MASS SENSING APPLICATIONS

S. Souayeh[1,2], N. Kacem[1,*], F. Najar[2] and E. Foltête[1]

[1]FEMTO-ST Institute, UMR 6174, Applied Mechanics Department, 24 chemin de l'Epitaphe, F-25000 Besançon, France

[2] Applied Mechanics and Systems Research Laboratory, Tunisia Polytechnic School BP 743, 2078 La Marsa, Tunisia address

*najib.kacem@femto-st.fr

Keywords: CNT, Parametric resonance, Nonlinear Dynamics, Mass detection, HBM, ANM.

Abstract. *In this paper, a computational model for large amplitude vibrations of a parametrically excited carbon nanotube (CNT) is developed. The continuous model includes geometric and electrostatic nonlinearities. The Galerkin discretization is used to transform the nonlinear partial differential equation to a finite degrees of freedom system which is numerically solved using the harmonic balance method (HBM) coupled with the asymptotic numerical method (ANM). The influence of higher modes on the nonlinear dynamics of the considered resonator is investigated in order to retain the number of modes which will be used by the HBM+ANM procedure. It is shown that at least two modes are required in order to predict accurately the CNT frequency responses.*

1 INTRODUCTION

Nano electromechanical systems (NEMS) have an important impact in a variety of domains such as the mass detection. Several types of NEMS resonators have been developed like cantilevered sensors, clamped-clamped beams and arrays of beams. Due to their reduced size, NEMS have high frequencies (1 GHz), low power consumption and quality factor in the range of 10^2-10^4. These tiny devices permit the investigations of nonlinear properties such as bifurcation topology, bistability and periodic attractors.

The mass spectrometry is the detection of tiny amounts of mass [1] and it is used for highly sensitive tasks. It provides quantitative identification of individual protein species in real time [2]. A Mass spectrometer is composed essentially by three parts: analyte ionization, analyte separation and detection [3]. It allows to achieve femtogram ($1\ fg = 10^{-15}\ g$), attogram ($1\ ag = 10^{-18}\ g$) and zeptogram ($1\ zg = 10^{-21}\ g$) resolutions. Recently, some devices can reach the mass sensitivity of the range of dalton ($1\ Da = 1\ AMU$) [4].

When attaching a mass to a resonator, the particle will change the mass response of the sensor. Therefore, the frequency shifts in the fundamental mode of vibration [5]. For an efficient detection of this particle, we should have an accurate method that allows the simultaneous detection of the mass and position. In addition, if we want to reach ultrasensitive sensing, the material composing the sensor plays an important role for precision. Due to the low mass of the nanotube (few attograms), a tiny amount of atoms deposited onto it represents a significant fraction of the total mass. Furthermore, nanotubes are mechanically ultra-rigid permitting the increase of the resonance frequency. Hence, the carbon nanotube (CNT) is the most appropriate device for mass detection applications [6]. Several investigations were done in order to develop a technique allowing the simultaneous position and mass detection. But, such algorithms are very complicated and demand a sophisticated mathematical methods to be solved. The alternative to avoid this problem is to find relations between mass and position of the added particles and the resonant frequencies of the cantilever by measuring the resonant frequencies of the beam without and with added mass for several vibrational modes. In [6], the design of a cantilevered CNT with modeled in the case of the primary resonance.

In this paper, the nonlinear dynamics of a carbon nanotube (CNT) is investigated. To this end, a multiphysics model of a clamped-clamped carbon naotube parametrically excited and including the main sources of nonlinearities is developed. An efficient numerical procedure has been used to investigate the responses of a CNT oscillator for the detection of the mass and the position of an added particle. The main idea is to provide numerical tools for NEMS designers in order to enhance the performances of resonant mass sensors.

Firstly, a design of an electrostatically actuated CNT is proposed and modeled. Then, the system of equations is specifically normalized the electrostatic nonlinearities are expanded up to the fifth order Taylor series in order to take into account all relevant nonlinear terms for NEMS [7, 8, 9, 10]. The Galerkin discretization procedure is used in order to transform the multiphysics continuum problem into a finite system of nonlinear ordinary differential equations in time. The reduced-order model is solved numerically using the harmonic balance method coupled with the asymptotic numerical continuation technique. Based on these numerical methods, the frequency responses of the CNT for a specific set of design parameters are derived and investigated in the nonlinear configurations, so that, we can retain the number of modes which gives the most accurate results. Finally, the frequency shifts of the resonance peaks are numerically tracked on the first mode for a particular CNT design and several added masses in different positions along the NEMS length.

2 DESIGN AND MODEL

We consider a carbon nanotube (CNT) resonator depicted in Figure 1. It consists of a single nanobeam with an annular cross section initially straight and clamped at its two ends. It is actuated by two symmetric electrodes providing an electrostatic force $v(\tilde{t}) = V_{dc} + V_{ac}\ \cos(\tilde{\Omega}\tilde{t})$, where V_{dc} is the dc polarization voltage, V_{ac} is the amplitude of the applied ac voltage, $\tilde{t}$ is the time and $\tilde{\Omega}$ is the excitation frequency.The two electrodes are positioned at a distance d_1 from the fixed end in order to place a piezoelectric or piezoresistive transduction [11] and at a distance d_2 from the free extremity.

The CNT is modeled as an Euler-Bernoulli beam of length L and with a quality factor Q. It has an internal radius $\tilde{R}_1$, an external one $\tilde{R}_2$.

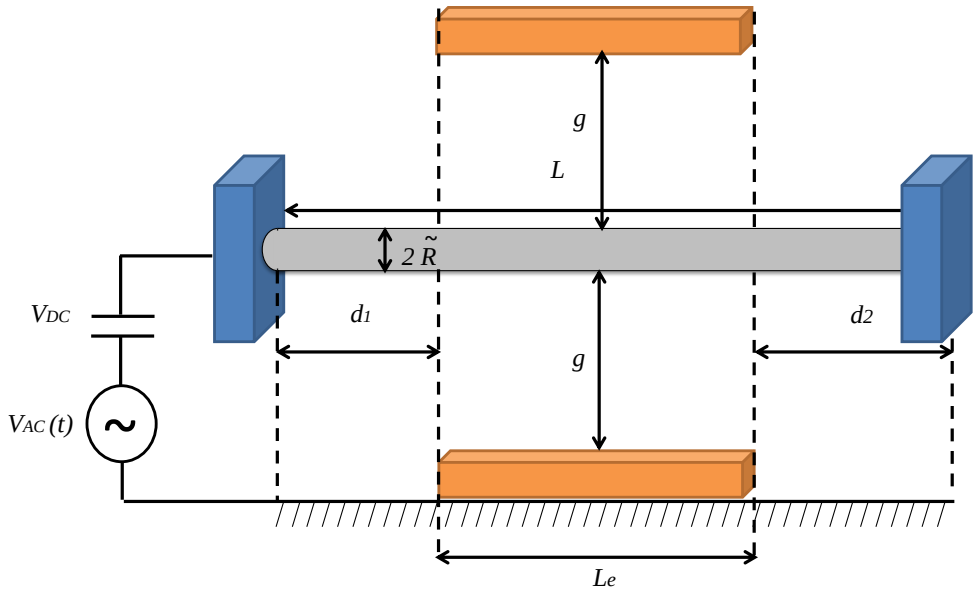


Figure 1: Schematic of a clamped-clamped carbon nanotube electrostatically actuated under parametric resonance.

3 ANALYTICAL SOLVING

Let the small and lumped added mass of mass m_p and of tiny size fall onto the CNTs surface. The CNT and the added mass constitute a continuum whose bending behavior is governed by the following equation applied to an infinitesimal volume $d\tilde{x}$, with $\delta_{\tilde{x}_0}(\tilde{x})$ the Dirac function. The equations of motion of the CNT can be written as [13]:

$$E\ I\ \partial_{\tilde{x},\tilde{x},\tilde{x},\tilde{x}}\tilde{w} + \rho\ A\ \partial_{\tilde{t},\tilde{t}}\tilde{w} + \tilde{c}\ \partial_{\tilde{t}}\tilde{w} + \delta_{\tilde{x}_0}(\tilde{x}) m_p \partial_{\tilde{t},\tilde{t}}\tilde{w} = \frac{E\ A}{2\ L}\left(\int_0^L \left(\partial_{\tilde{x}}\tilde{w}\right)^2\ d\tilde{x}\right)\partial_{\tilde{x},\tilde{x}}\tilde{w} + \mathcal{H}(\tilde{x})\ \tilde{F}$$
$$\mathcal{H}(\tilde{x}) = H\left(\tilde{x} - d_1\right) - H\left(\tilde{x} - L + d_2\right) \tag{1}$$

where $\partial_{\tilde{x}}$ denotes the partial differentiation with respect to $\tilde{x}$ which is the coordinate along the nanotube length L, $\partial_{\tilde{t}}$ is the partial differentiation with respect to the time $\tilde{t}$, $\tilde{w}(\tilde{x},\tilde{t})$ is

the in-plane bending deflection, E is the effective Young's modulus, $I = \frac{\pi}{4}\left(\tilde{R_2}^4 - \tilde{R_1}^4\right)$ is the moment of inertia of the circular cross-section, ρ is the density of the nanotube material, $A = \pi\left(\tilde{R_2}^2 - \tilde{R_1}^2\right)$ is the cross-section area and $\tilde{c}$ is the coefficient of the viscous damping per unit length and m_p is the mass of the added particle.

The carbon nanotube is subject to the electrostatic actuation $\mathcal{H}(\tilde{x})\ \tilde{F}$, where $\mathcal{H}(\tilde{x})$ includes Heaviside functions H in order to indicate the position of the electrodes with respect to the oscillator, wherein $d_1 + d_2 < L$, and $\tilde{F}$ is the electrostatic force expressed as

$$\tilde{F} = \frac{\pi\ \epsilon_0\left(V_{dc}+V_{ac}\ \cos\left(\tilde{\Omega}\ \tilde{t}\right)\right)^2}{\sqrt{(g-\tilde{w})\ \left(g-\tilde{w}+2\tilde{R}\right)}\ \left(\cosh^{-1}\left(1+\frac{g-\tilde{w}}{\tilde{R}}\right)\right)^2} - \frac{\pi\ \epsilon_0\left(V_{dc}+V_{ac}\ \cos\left(\tilde{\Omega}\ \tilde{t}\right)\right)^2}{\sqrt{(g+\tilde{w})\ \left(g+\tilde{w}+2\tilde{R}\right)}\ \left(\cosh^{-1}\left(1+\frac{g+\tilde{w}}{\tilde{R}}\right)\right)^2} \tag{2}$$

where ϵ_0 is the dielectric constant of the gap medium. The boundary conditions are:

$$\tilde{w}(0,\tilde{t}) = 0,\ \partial_{\tilde{x}}\tilde{w}(0,\tilde{t}) = 0,\ \tilde{w}(L,\tilde{t}) = 0,\ \partial_{\tilde{x}}\tilde{w}(L,\tilde{t}) = 0 \tag{3}$$

3.1 Normalization

For convenience, Equation (1) is normalized. This normalization is particular for our case because the time constant τ depends on V_{dc} and $_k$ (which we represent later). So, we have τ_k corresponding to each mode. The first step is to introduce the following nondimensional variables into Equation (2):

$$w = \frac{\tilde{w}}{g},\ x = \frac{\tilde{x}}{L},\ t = \frac{\tilde{t}}{\tau_k} \tag{4}$$

with k the mode number.

Then, Equation (1) is divided by the coefficient of $\partial_{t,t}w$ ($\frac{\rho\ A\ g}{\tau^2}$) and the electrostatic force is expanded up to the fifth order Taylor series. The Galerkin decomposition method is applied to the obtained equation. To this end, the beam deflection $w(x,t)$ can be written in this form

$$w(x,t) \ = \ \sum_{k=1}^{N_m} a_k(t)\ \phi_k(x) \tag{5}$$

where N_m is the number of modes retained in the solution, $a_k(t)$ is the k^{th} nondimensional modal coordinate and $\phi_k(x)$ is the k^{th} normalized linear undamped mode shape of a straight beam which is the eigenmode solution of

$$\frac{d^4\phi_k(x)}{dx^4} = \lambda_k^4\ \phi_k(x) \tag{6}$$

where λ_k is the solution of the transcendental equation

$$1 - \cos(\lambda_k)\ \cosh(\lambda_k) = 0 \tag{7}$$

The modal projection consists in substituting Equation (5) into the equation obtained after the normalization and the division by the coefficient of $\partial_{t,t}w$, multiplying the result by $\phi_k\,(x)$,

using Equation (6) to eliminate $\frac{d^4\phi_k(x)}{dx^4}$ and integrating the outcome from $x=0$ to 1. Doing so, we obtain the following equation of motion for the first mode

$$
\begin{aligned}
&a_i'' + c_i\, a_i' + a_i - 2\sum_{j=1}^{N_m}\sum_{k=1}^{N_m}\left(\int_0^1 \phi_k\phi_j\phi_i\, dx\right) a_k a_j'' + \sum_{j=1}^{N_m}\sum_{k=1}^{N_m}\sum_{l=1}^{N_m}\left(\int_0^1 \phi_l\phi_k\phi_j\phi_i\, dx\right) a_l a_k a_j'' \\
&-2\sum_{j=1}^{N_m}\sum_{k=1}^{N_m}\left(\int_0^1 \phi_k\phi_j\phi_i\, dx\right) c_j a_k a_j' + \sum_{j=1}^{N_m}\sum_{k=1}^{N_m}\sum_{l=1}^{N_m}\left(\int_0^1 \phi_l\phi_k\phi_j\phi_i\, dx\right) c_j a_l a_k a_j' \\
&-2\sum_{j=1}^{N_m}\sum_{k=1}^{N_m}\left(\int_0^1 \phi_k\phi_j\phi_i\, dx\right) a_k a_j + \sum_{j=1}^{N_m}\sum_{k=1}^{N_m}\sum_{l=1}^{N_m}\left(\int_0^1 \phi_l\phi_k\phi_j\phi_i\, dx\right) a_l a_k a_j \\
&-\left(N_0 + \alpha_1\left(\sum_{s=1}^{N_m}\sum_{p=1}^{N_m}\left(\int_0^1 \phi_s'\phi_p'\, dx\right) a_s a_p\right)\right) \\
&\left(\sum_{j=1}^{N_m}\left(\int_0^1 \phi_j''\phi_i\, dx\right) a_j - 2\sum_{j=1}^{N_m}\sum_{k=1}^{N_m}\left(\int_0^1 \phi_k\phi_j''\phi_i\, dx\right) a_k a_j + \sum_{j=1}^{N_m}\sum_{k=1}^{N_m}\sum_{l=1}^{N_m}\left(\int_0^1 \phi_l\phi_k\phi_j''\phi_i\, dx\right) a_l a_k a_j\right) \\
&= \alpha_2\, \mathcal{H}(x)\, F_i\left(\int_0^1 \phi_i\, dx\right)
\end{aligned}
\tag{8}
$$

$$
\mathcal{H}(x) = H\left(x - \tfrac{d_1}{L}\right) - H\left(x - 1 + \tfrac{d_2}{L}\right)
$$

where $\frac{d_1+d_2}{L} < 1$ and the expressions of the nondimensional parameters introduced in Equation (8) are

$$
\begin{aligned}
&\alpha_1 = \frac{E\, g^2\, \tau_k^2}{2\, L^4\, \rho\left(1+\delta_{x_0}(x)m\right)},\ \alpha_2 = \frac{\tau_k^2}{\rho\, A\, g^2\left(1+\delta_{x_0}(x)m\right)} V_{ac}\, V_{dc},\ c = \tilde{c}\frac{\tau_k}{\rho\, A\left(1+\delta_{x_0}(x)m\right)}, \\
&\Omega = \tilde{\Omega}\, \tau_k,\ R_2 = \frac{\tilde{R}_2}{g}
\end{aligned}
\tag{9}
$$

with $m = \frac{m_p}{\rho\, A\, L}$ the mass ratio. The electrostatic force F_i is written as

$$
F_i = \frac{\pi\, \epsilon_0 (V_{dc}+V_{ac}\, \cos(\Omega\, t))^2}{\sqrt{(1-a_i)\,(1-a_i+2\, R)}\left(\cosh^{-1}\left(1+\frac{1-a_i}{R}\right)\right)^2} - \frac{\pi\, \epsilon_0 (V_{dc}+V_{ac}\, \cos(\Omega\, t))^2}{\sqrt{(1+a_i)\,(1+a_i+2\, R)}\left(\cosh^{-1}\left(1+\frac{1+a_i}{R}\right)\right)^2} \tag{10}
$$

Equation (8) can be written in matrix-vector form as

$$
\begin{aligned}
&[M_0 + M_1(a) + M_2(a)]a'' + [C_0 + C_1(a) + C_2(a)]a' + [K_0 + K_1(a) + K_2(a)]a \\
&-[N_0 + \alpha_1\, T_2(a)][K_T(a) + K_{T1}(a) + K_{T2}(a)]a = \alpha_2\, \mathcal{H}(x)\, F1
\end{aligned}
\tag{11}
$$

where $a(t) = [a_1(t), a_2(t), a_3(t), ..., a_{N_m}(t)]^T$. The components of matrices M_0, M_1, M_2, C_0, C_1, C_2, K_0, K_1, K_2, $K_T(a)$, $K_{T1}(a)$ and $K_{T2}(a)$ are respectively M_{0ij}, M_{1ij}, M_{2ij}, C_{0ij}, C_{1ij}, C_{2ij}, K_{0ij}, K_{1ij}, K_{2ij}, K_{Tij}, K_{T1ij} and K_{T2ij}:

$$
\begin{aligned}
&M_{0ij} = \delta_{ij} \\
&M_{1ij} = -2 \sum_{j=1}^{N_m} \sum_{k=1}^{N_m} \left(\int_0^1 \phi_k \phi_j \phi_i \, dx \right) a_k \\
&M_{2ij} = \sum_{j=1}^{N_m} \sum_{k=1}^{N_m} \sum_{l=1}^{N_m} \left(\int_0^1 \phi_l \phi_k \phi_j \phi_i \, dx \right) a_l a_k \\
&C_{0ij} = c_i \, \delta_{ij} \\
&C_{1ij} = c_j \, M_{1ij} \\
&C_{2ij} = c_j \, M_{2ij} \\
&K_{0ij} = \delta_{ij} \\
&K_{1ij} = M_{1ij} \\
&K_{2ij} = M_{2ij} \\
&K_{Tij} = \int_0^1 \phi_j'' \phi_i \, dx \\
&K_{T1ij} = -2 \sum_{k=1}^{N_m} \left(\int_0^1 \phi_k \phi_j'' \phi_i \, dx \right) a_k \\
&K_{T2ij} = \sum_{k=1}^{N_m} \sum_{l=1}^{N_m} \left(\int_0^1 \phi_l \phi_k \phi_j'' \phi_i \, dx \right) a_l a_k
\end{aligned}
\tag{12}
$$

The scalar $T_2(a)$ and the entries of $F1$ are

$$
\begin{aligned}
&T_2(a) = \sum_{s=1}^{N_m} \sum_{p=1}^{N_m} \left(\int_0^1 \phi_s \phi_p \, dx \right) a_s a_p \\
&F1_i = F_i \int_0^1 \phi_i(x) \, dx
\end{aligned}
\tag{13}
$$

In the following section, the system of equations (11) is solved numerically in order to obtain the frequency responses of the nanotube.

4 NUMERICAL SIMULATIONS

In order to compute the periodic solutions of nonlinear differential equations, for nonlinear oscillators, three major steps are followed: the first one consists in transforming the nonlinearities of the original system into quadratic terms. The second one is the decomposition of the quadratic recast equations into truncated Fourier series by means of the harmonic balance method (HBM). The third one is the application of the continuation method (ANM) on the resulting system. At the end, the numerical results are derived. This method [14] is applied on system (11). Thereafter, a detailed description of the quadratic recast and of the combined technique HBM+ANM is given.

4.1 Quadratic recast

A periodically forced system has this form:

$$
\dot{w} = f(t, w, \Omega) \tag{14}
$$

where w is a vector of unknowns, f is periodic in t and Ω is a real parameter. To simplify the application of HBM method, the first step is to transform Equation (14) into a new system where the nonlinearities are at most quadratic polynomials as

$$m(\dot{Z}) = c(t,\Omega) + l(Z) + q(Z,Z) \tag{15}$$

where c is a constant vector with respect to the unknown Z, $l(.)$ is a linear vector with respect to the vector entry and $q(.,.)$ is a quadratic vector linear with respect to both entries.

The following variables are introduced in order to transform Equation (11) into a quadratic system, as described previously.

$$\begin{array}{l} v = \dot{a}\ (size\ N_m) \\ y = \dot{v}\ (size\ N_m) \\ x = \cos(2\,\Omega\,t)(size\ N_m) \\ M_{tot} = M_1(a) + M_2(a)(size\ N_m^2) \\ K_{tot} = K_{T1}(a) + K_{T2}(a)(size\ N_m^2) \\ S = K_{Ttot}a(size\ N_m) \\ T = T_2(a)\ (size\ 1) \\ F1 = FF1_1(a) + FF1_2(a)\ (size\ N_m^2) \end{array} \tag{16}$$

System (11) can be rewritten as

$$\underbrace{\left|\begin{array}{lcl|c|l|c|l} \dot{a} & = & 0 & + & v & + & 0 \\ \dot{v} & = & 0 & + & y & + & 0 \\ 0 & = & \cos(2\,\Omega\,t) & + & -x & + & 0 \\ 0 & = & 0 & + & M_{tot} - M_1(a) & + & -M_2(a) \\ 0 & = & 0 & + & K_{tot} - K_{T1}(a) & + & -K_{T2}(a) \\ 0 & = & 0 & + & S & + & -K_{Ttot}\,a \\ 0 & = & 0 & + & T & + & -T_2(a) \\ 0 & = & 0 & + & K_0\ \ a\ \ + & + & -N\ \ K_{Ttot}\ \ a\ - \\ & & & & M_0\ y\ +\ C_0\ v\ - & & \alpha_1\,T\,a - \alpha_1\,T\,S - \\ & & & & N_0\,K_T\,a - N_0\,S\text{-} & & \alpha_2\,\mathcal{H}(x)\,FF1_2(a)\,x \\ & & & & \alpha_2\,\mathcal{H}(x)\,FF1_1(a) & & \end{array}\right|}_{m(\dot{Z}) = c(t,\Omega) \quad + \ l(Z) \quad + \ q(Z,Z)} \tag{17}$$

where $Z = (a, v, y, M_{tot}, S, T, F1)^T$ is the unknown vector of size $N_{eq} = 4\ N_m + 3\ N_m^2 + 1$, c is a constant vector with respect to Z, $l(.)$ and $m(.)$ are linear vectors valued operators with respect to Z, and $q(.,.)$ is a quadratic vector. In our case, for two modes, $N_{eq} = 21$ corresponding to the number of equations of system (17).

4.2 The harmonic balance method (HBM)

The harmonic balance method is now applied to the system of Equations (17). The unkown vector Z is decomposed into Fourier series with H harmonics

$$Z(t) = Z_0 + \sum_{k=1}^{H} Z_{c,k}\cos(k\omega t) + \sum_{k=1}^{H} Z_{s,k}\sin(k\omega t) \tag{18}$$

Then, column vector U, with size $(2H+1) \times Neq$, where Neq is the number of equations in Equation (17), collects the components of the Fourier series as

$$U = [Z_0^t + Z_{c,1}^t + Z_{s,1}^t + Z_{c,2}^t + ... + Z_{c,H}^t + Z_{s,H}^t]^t \tag{19}$$

Substituting Equation (19) into Equation (17), collecting the terms of the same harmonic index and neglecting the higher order harmonics, we obtain this set of equations

$$\omega M(U) = C + L(U) + Q(U, U) \tag{20}$$

It contains $(2H+1) \times Neq$ equations for the $(2H+1) \times Neq$ unknowns U. Operators $M(.)$, C, $L(.)$, and $Q(.,.)$ depend only on the operators $m(.)$, c, $l(.)$ and $q(.,.)$ of Equation (17) and on the number of harmonics H.

4.3 The continuation procedure

From Equation (20), an algebraic system is obtained

$$R(U) = 0 \tag{21}$$

where $R \in R^{N+1}$ and $U = [U^t, \Omega, \omega] \in R^{N+1}$. The Asymptotic numerical method (ANM), which is based on the quadratic recasting, is applied to Equation (20) to obtain

$$R(U) = L0 + L(U) + Q(U, U) \tag{22}$$

where $L0$, $L(.)$ and $Q(.,.)$ are respectively constant, linear and bilinear vectors. Then, the solutions are obtained by considering the branches of solution as power series. Indeed, if U_0 is a point solution, the branch passing by U_0 is a power series expansion of the path parameter $a = (U-U_0)^t U_1$, where U_1 is the tangent vector at U_0 and $U(a) = U_0 + aU_1 + a^2U_2 + a^3U_3 + ... + a^nU_n$. This serie is replaced in Equation (21) where the powers of a are equated to zero providing a set of linear systems.

5 RESULTS AND DISSCUSSIONS

Due to the symmetry of the problem, the odd modes are retained. Due to the kind of the dominant nonlinearities, the even harmonics have no influence. In addition and after verifications, the first harmonic gives the most important informations. So, in our case, we have plotted the amplitudes W_{max-i}, $i \in \{1, 3\}$, of the first, the third and the fifth modes normalized by the gap g at $x = L$ and corresponding to the first harmonic.

The frequency responses of the first mode of the carbon nanotube's configuration of table 1, without added mass, are represented in Figure 2 when using one or two modes, in order to show the impact of each mode on the frequency responses and to retain the most appropriate number of used modes.

The amplitudes of the two frequency responses are remarkably different. Indeed, for a single mode the amplitude is equal to 0.27% of the gap, however, with two modes the amplitude is equal to 0.17% of the gap. Hence, we have to use at least two modes in order to obtain the most accurate results.

Now, we track the frequency response of the first mode when adding a mass at different positions on the CNT. The two frequencies have a hardening behavior when using a single or

Table 1: Design parameters of investigated carbon nanotube resonator.

Resonator	$L(\mu m)$	$R_1(nm)$	$R_2(nm)$	$g(nm)$	$V_{ac}(V)$	$V_{dc}(V)$	Q
1	40	350	500	200	3	15	900

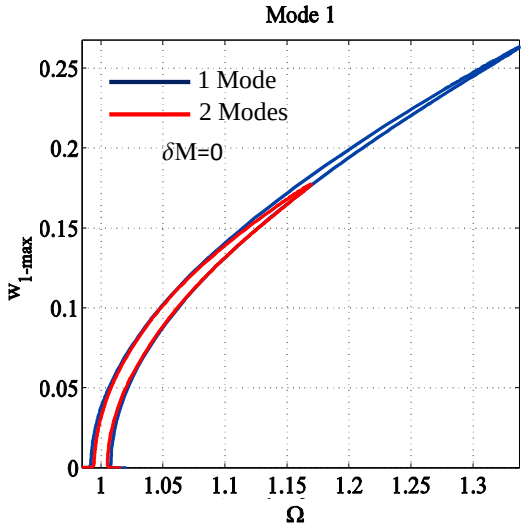


Figure 2: Frequency responses of the first mode when using one and two modes without added mass.

several modes. For our case, the positions can be limited between a clamped end and the middle of the clamped-clamped nanotube because the two halves of the resonator are symmetric as shown in Figure 1. In Figure 3, we represent the frequency responses of the first mode of the CNT (table 1) when adding a mass $m = 0.02$ at two different positions ($\delta_x = 0.5$ and $\delta_x = 0.1$) for several modes.

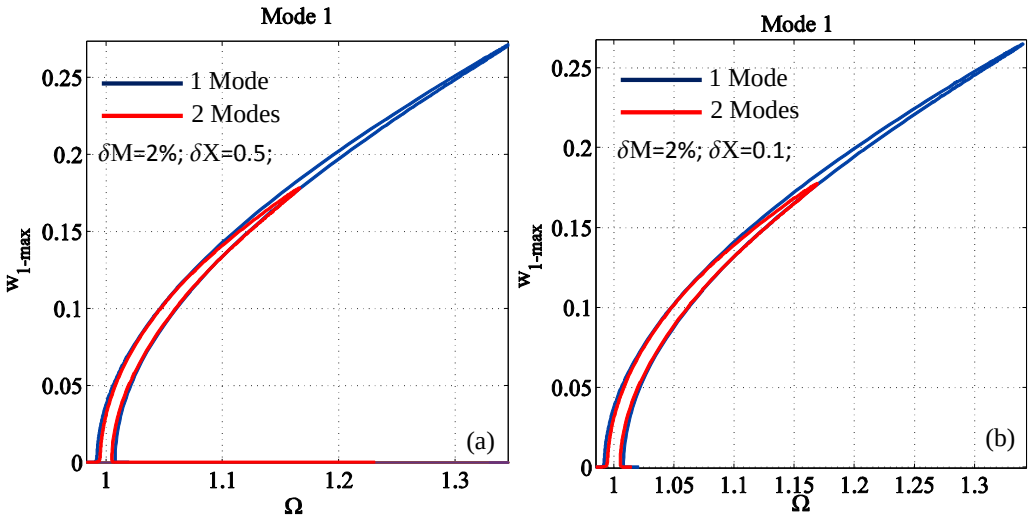


Figure 3: Frequency responses of the first mode when using one and two modes with (a) $\delta_M = 2\%$, $\delta_x = 0.5$ and (b) $\delta_M = 2\%$, $\delta_x = 0.1$.

The amplitudes of the two curves increase for the two cases (Figures 3 (a) and (b)). Indeed, when a particle is placed at a specific position along the neutral axis of the nanotube, the natural

frequencies decrease producing an increase on the amplitudes of the frequency responses.

6 CONCLUSION

In this paper, we modeled the nonlinear dynamics of a clamped-clamped carbon nanotube excited under parametric resonance and including geometric and electrostatic nonlinearities. Using the Galerkin discretization method, the Euler-Bernoulli partial differential equation describing the nonlinear motion of the resonator is transformed into a system of coupled nonlinear ordinary differential equations.

Firstly, we developed a numerical multimodal approach based on the harmonic balance method (HBM) and the asymptotic numerical method (ANM). It was demonstrated, for several design parameters, that the use of a single mode is not sufficient to capture the main nonlinear phenomena of the considered device and for mass detection, at least two modes are required.

REFERENCES

[1] J. Verd, A. Uranga, G. Abadal, J. Teva, F. Torres, M. F. Perez, J. Fraxedas, J. Esteve, N. Barniol, Monolithic mass sensor fabricated using a conventional technology with attogram resolution in air conditions, *Applied Physics Letters*, **91**, 013501, 2007.

[2] M. S. Hanay, S. Kelber, A. K. Naik, D. Chi, S. Hentz, E. C. Bullard, E. Colinet, L. Duraffourg, M. L. Roukes, Single-protein nanomechanical mass spectrometry in real time, *Nature nanotechnology*, 2012.

[3] A. K. Naik, M. S. Hanay, W. K. Hiebert, X. L. Feng, M. L. Roukes, Towards single-molecule nanomechanical mass spectrometry, *Nature nanotechnology*, **4**, 445–450, 2009.

[4] H. Chiu, P. Hung, H. W. C.Postma, M. Bockrath, Atomic-scale mass sensing using carbon nanotube resonators, *Nano Letters*, **8**, 533–537, 2008.

[5] K. L. Ekinci, Y. T. Yang, M. L. Roukes, Ultimate limits to inertial mass sensing based upon nanoelectromechanical systems, *Journal of Applied Physics*, **95**, 2682–2689, 2004.

[6] S. Souayeh, N. Kacem, Computational models for large amplitude nonlinear vibrations of electrostatically actuated carbon nanotube-based mass sensors, *Sensors and Actuators A: Physical*, **208**, 10–20, 2014.

[7] N. Kacem, S. Hentz, D. Pinto, B. Reig, V. Nguyen, Nonlinear dynamics of nanomechanical beam resonators: improving the performance of NEMS-based sensors. *Nanotechnology*, **20**(27), 275501, 2009.

[8] N. Kacem, S. Hentz, Bifurcation topology tuning of a mixed behavior in nonlinear micromechanical resonators. *Applied Physics Letters*, **95**(18), 183104, 2009.

[9] N. Kacem, J. Arcamone, F. Perez-Murano, S. Hentz, Dynamic range enhancement of nonlinear nanomechanical resonant cantilevers for high sensitive NEMS gas/mass sensors applications. *Journal of Micromechanics and Microengineering*, **20**(4), 045023, 2010.

[10] N. Kacem, S. Baguet, R. Dufour, S. Hentz, Stability control of nonlinear micromechanical resonators under simultaneous primary and superharmonic resonances. *Applied Physics Letters*, **98**(19), 193507, 2011.

[11] E. Mile, G. Jourdan, I. Bargatin, C. Marcoux, P. Andreucci, S. Hentz, C. Kharrat, E. Colinet, L. Duraffourg, In-plane nanoelectromechanical resonators based on silicon nanowire piezoresistive detection, *Nanotechnology*, **21**, 165504, 2010.

[12] A. Nayfeh, M. Younis, E. Abdel Rahman, Dynamic pull-in phenomenon in MEMS resonators, *Nonlinear Dynamics*, **48**, 153–163, 2007.

[13] H. M. Ouakad, M.I. Younis, Nonlinear dynamics of electrically actuated carbonnanotube resonators. *ASME Journal of Computational and Nonlinear Dynamics*, **5**, 1–13, 2010.

[14] B. Cochelin, C. Vergez, A high order purely frequency-based harmonic balance formulation for continuation of periodic solutions, *Journal of sound and vibration* **324**, 243–262, 2009.

COMPDYN 2015
5th ECCOMAS Thematic Conference on
Computational Methods in Structural Dynamics and Earthquake Engineering
M. Papadrakakis, V. Papadopoulos, V. Plevris (eds.)
Crete Island, Greece, 25–27 May 2015

A COMPUTATIONAL MODEL FOR LARGE-AMPLITUDE NONLINEAR VIBRATION OF CIRCULAR CMUTS UNDER PRIMARY RESONANCE

Aymen Jallouli, Najib Kacem*, Patrice Lemoal, Gilles Bourbon and Joseph Lardies

FEMTO-ST Institute - UMR 6174, Applied Mechanics Department
24, chemin de l'Épitaphe, F-25000 Besançon, France

*najib.kacem@femto-st.fr

Keywords: capacitive micromachined ultrasonic transducer (CMUT), nonlinear dynamics, harmonic blance method, asymptotic numerical method.

Abstract. *A computational multiphysics model for an electrically actuated clamped circular plate is developed. The Galerkin approach is used in order to transform the continuous model into a system having finite degrees of freedom. The discretized system is solved using the harmonic balance method (HBM) coupled with the asymptotic numerical method (ANM). The effects of the electrostatic excitation on the CMUT frequency responses are investigated for two set of design parameters. This model is an effective tool for MEMS designers to enhance the performances of CMUTs in term of generated acoustic power.*

1 INTRODUCTION

Recently, Capacitive Micromachined Ultrasonic Transducers (CMUTs) have attracted the attention of scientists and engineers and they are used in many applications such as generating 2D and 3D ultrasound images [1, 2], nondestructive evaluation [3] and developing capacitive pressure sensors [4]. Capacitive actuators have been used more extensively than piezoelectric ones due to their low mechanical impedance. Moreover, CMUTs can be produced with semiconductor fabrication techniques and they can be built on an Integrated Circuit (IC) while, for piezoelectric transducers, direct integration to IC is generally difficult. Another important benefit of CMUTs is the possibility to sustain to high temperatures which makes them suitable for high temperature applications such as automobile exhaust gas monitoring.

CMUTs are composed of two micro plates where the bottom electrode is fixed while the top electrode is vibrating. The distance between the two electrodes is called cavity. The vibration of the top electrode is due to the combination of the two electrostatic forces: a DC voltage deflects the microplate downward, and an AC voltage added to the bias voltage causing the vibration of the membrane which produces ultrasound waves. Several CMUT geometries have been proposed in the literature and Mendoza-Lopez et al. [5] proved that a circular CMUT has the highest displacement for the same voltage excitation.

Precise modeling of CMUTs is very important to build an optimized design and to understand its behavior. Among several modeling techniques, the Finite Element Method (FEM) is the most used one for CMUTs dynamics investigations [6, 7] or mathematical model validation [8]. Mason [9] suggested an equation of motion that describes the CMUT model assuming that the deflections at the operating point are small. Based on these equations, Ahrens et al. [10] used an equivalent electrical circuit for model simulations. Vogl et al. [11] developed an analytical reduced-order model for an electrically actuated clamped circular plate, taking into account the external forces and the residual stress. After determining the equation governing the plate, they studied the frequency response of the CMUT using the multiple scale method on the discretized model.

In this paper, a computational model for the nonlinear oscillations of circular CMUTs under primary resonance is developed. The continuous model includes Von Karman and electrostatic nonlinearities. The modal decomposition is used to transform the nonlinear partial differential equation into a finite degrees of freedom system which is numerically solved using the harmonic balance method (HBM) coupled with the asymptotic numerical method (ANM). Several numerical simulations have been performed in order to investigate the influence of design parameters on the frequency response of the considered MEMS. It is shown that the model enables the capture of all the nonlinear phenomena of the CMUT dynamics and describes the competition between the hardening and the softening behaviors. In practice, the proposed model can be used by CMUT designers in order to tune the impact of nonlinearities on the device performances.

2 PROBLEM FORMULATION

2.1 equations of motion

We consider a clamped circular microplate depicted in Figure 1, actuated by a static electric force $\tilde{V}_{dc}$ and an harmonic one $\tilde{V}_{ac}cos(\Omega\tilde{t})$. In this section, the model developed by Vogl and Nayfeh [11] is used. It describes the nonlinear dynamics of a circular, homogeneous and isotropic plate, using the following coupled partial differential equations:

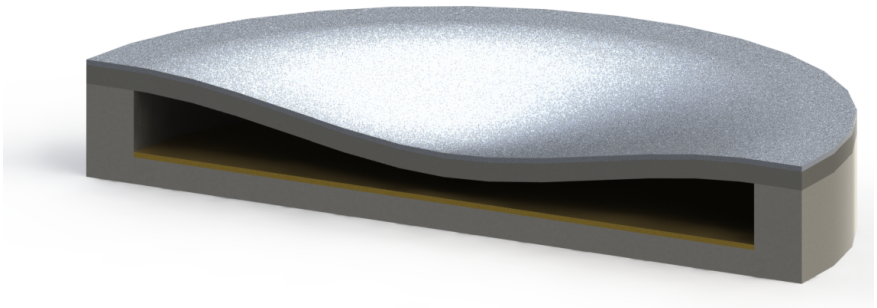


Figure 1: A schematic of a clamped circular plate electrostatically actuated.

$$\rho h\frac{\partial^2\tilde{w}}{\partial\tilde{t}^2}+2\tilde{c}\frac{\partial\tilde{w}}{\partial\tilde{t}}+D\tilde{\nabla}^4\tilde{w}=\frac{1}{\tilde{r}}\frac{\partial}{\partial\tilde{r}}\left(\frac{\partial\tilde{w}}{\partial\tilde{r}}\frac{\partial\tilde{\Phi}}{\partial\tilde{r}}\right)+\tilde{\tau}h\nabla^2\tilde{w}+\tilde{F}+\frac{\varepsilon_0\tilde{v}^2\left(\tilde{t}\right)}{2(d-\tilde{w})^2} \tag{1}$$

$$\tilde{\nabla}^4\tilde{\Phi}=-Eh\frac{\partial^2\tilde{w}}{\partial\tilde{r}^2}\left(\frac{1}{\tilde{r}}\frac{\partial\tilde{w}}{\partial\tilde{r}}\right) \tag{2}$$

where

$$\tilde{\nabla}^4=\left(\frac{\partial^2}{\partial\tilde{r}^2}+\frac{1}{\tilde{r}}\frac{\partial}{\partial\tilde{r}}\right)^2 \tag{3}$$

the tilde denotes a dimensional quantity, $\tilde{w}$ is the downward deflection, $\tilde{c}$ is a damping coefficient, ρ is the material mass density, h is the microplate thickness, $\tilde{\Phi}$ is the stress function, E is Young's modulus, D is the plate flexural rigidity defined as $D=\frac{Eh^3}{12(1-\nu^2)}$, ν is the Poisson's ratio, d is the effective gap distance between the top and bottom electrodes, ε_0 is the electric permittivity of the gap medium between the plate and electrode, $\tilde{\tau}$ is the residual stress, $\tilde{F}$ is an additional downward pressure, and $\tilde{v}\left(\tilde{t}\right)$ is the applied voltage. The boundary conditions of the vibrating circular plate are:

$$\begin{array}{l}\tilde{w}\left(R,\tilde{t}\right)=0,\frac{\partial\tilde{w}\left(R,\tilde{t}\right)}{\partial\tilde{r}}=0,\tilde{w}\left(0,\tilde{t}\right)\ is\ bounded\\ \frac{\partial^2\tilde{\Phi}\left(R,\tilde{t}\right)}{\partial\tilde{r}^2}-\frac{\nu}{R}\frac{\partial\tilde{\Phi}\left(R,\tilde{t}\right)}{\partial\tilde{r}}=0,\tilde{\Phi}\left(0,\tilde{t}\right)\ is\ bounded\end{array} \tag{4}$$

2.2 Normalization

We nondimensionalize the general equations according to:

$$\tilde{r}=Rr \qquad \tilde{t}=R^2\left(\frac{\rho h}{D}\right)^{1/2}t \qquad \tilde{w}=dw \qquad \tilde{c}=\frac{(D\rho h)^{1/2}}{R^2}c$$

$$\tilde{F}=\frac{Dd}{R^4}F \qquad \tilde{v}^2\left(\tilde{t}\right)=\frac{2Dd^3}{\varepsilon_0R^4}v^2(t) \qquad \tilde{\tau}=\frac{D}{R^2h}\tau \qquad \tilde{\Phi}=Ehd^2\Phi$$

The resulting dimensionless equation can be written as:

$$\frac{\partial^2w}{\partial t^2}+2c\frac{\partial w}{\partial t}+\nabla^4w=\frac{\beta}{r}\frac{\partial}{\partial r}\left(\frac{\partial w}{\partial r}\frac{\partial\Phi}{\partial r}\right)+\frac{\tau}{r}\frac{\partial}{\partial r}\left(r\frac{\partial w}{\partial r}\right)+F(r,t)+\frac{v^2(t)}{(1-w)^2} \tag{5}$$

$$\nabla^4 \Phi = -\frac{1}{r}\frac{\partial^2 w}{\partial r^2}\left(\frac{\partial w}{\partial r}\right) \tag{6}$$

where β is a nondimensional parameter defined as:

$$\beta = 12\left(1-\nu^2\right)d^2/h^2 \tag{7}$$

The nondimensional boundary conditions of the system are:

$$\begin{array}{l} w\left(1,t\right)=0, \frac{\partial w(1,t)}{\partial r}=0, w\left(0,t\right)\ is\ bounded \\ \frac{\partial^2 \Phi(1,t)}{\partial r^2}-\nu\frac{\partial \Phi(1,t)}{\partial r}=0, \Phi\left(0,t\right)\ is\ bounded \end{array} \tag{8}$$

2.3 Reduced order model

The Galerkin procedure is used in order to transform Equations (5) and (6) into a system of finite number of ordinary-differential equations by letting

$$w\left(r,t\right)=\sum_{m=1}^{N}\eta_m\left(t\right)\phi_m(r) \tag{9}$$

where $\phi_m(r)$ is the m^{th} shape function, $\eta_m\left(t\right)$ is the m^{th} generalized coordinate, and N is the number of retained modes. Due to the symmetry of the problem, only the symmetric modes are considered. Following Nayfeh [12], the shape functions for a clamped circular plate actuated by symmetric forces can be written as:

$$\phi_m\left(r\right)=\frac{J_0(r\sqrt{\Omega_{\mathrm{m}}})}{J_0(\sqrt{\Omega_{\mathrm{m}}})}-\frac{I_0(r\sqrt{\Omega_{\mathrm{m}}})}{I_0(\sqrt{\Omega_{\mathrm{m}}})} \tag{10}$$

where J_0 and I_0 are respectively the first kind Bessel function and the modified Bessel function. The mode shapes are chosen orthonormal:

$$\int_0^1 r\phi_m(r)\phi_n(r)dr=\delta_{mn} \tag{11}$$

Substituting Equation (9) into Equations (5) and (6), multiplying by $\left(1-w\right)^2 r\phi_q(r)$ and integrating the resulting equation over $r\in[0,1]$, we obtain the following nonlinear system which is defined in the appendix.

$$M\left(\eta\right)\ddot{\eta}+2cM\left(\eta\right)\dot{\eta}+N\left(\eta\right)\eta=P\left(\eta\right)+v^2(t)L \tag{12}$$

where $M\left(\eta\right)$ and $N\left(\eta\right)$ are $N\times N$ nonlinear matrices and $P\left(\eta\right)$ is $N\times 1$ nonlinear vector defined in the appendix, $\eta\left(t\right)=\left\{\eta_1\left(t\right),\eta_2\left(t\right),\ldots,\eta_N\left(t\right)\right\}$ is a $N\times 1$ vector containing the generalized coordinates.

3 SOLVING PROCEDURE

Vogl and Nayfeh [11] used the multiple scale method to analyze the CMUT primary resonance associated to the first bending mode. Nevertheless, the obtained solutions are only valid for a low level of nonlinearity. Therefore, we propose a computational solving procedure based on the harmonic balance method (HBM) coupled with the asymptotic numerical method

(ANM), for which the solutions are valid up to very large displacement compared to the gap. This technique, proposed by Cochelin and Vergez [13], gives the periodic solutions of a dynamical system when a control parameter is varied. A periodic forced system could be written in the following form:

$$\dot{Y} = f(Y, \lambda) \tag{13}$$

where Y is a vector of unknowns, f a smooth vector valued function and λ a real parameter. The over-dot denotes differentiation with respect to time variable t. We applied the harmonic balance method on the system to decompose the solution $Y(t)$ into a truncated Fourier series.

$$Y(t) = Y_0 + \sum_{k=1}^{H} Y_{c,k} \cos(k\omega t) + Y_{s,k} \sin(k\omega t) \tag{14}$$

Substituting Equation (14) into Equation (13), we obtain an algebraic system with $2H+1$ vector of unknowns Y_i, the unknown pulsation ω, and the parameter λ. The components of the Fourier series are collected into column vector U that contains all the unknowns Y_i with a size $(2H+1)N_{eq}$; $U = [Y_0^T, Y_{c,1}^T, Y_{s,1}^T, \ldots, Y_{c,H}^T, Y_{c,H}^T]$ where N_{eq} is the number of equations in Equation (13). The latter is transformed into a quadratic one with $(2H+1)N_{eq}$ and can be written as:

$$\omega M(U) = C + L(U) + Q(U, U) \tag{15}$$

where $M(.), C, L(.)$ and $Q(.,.)$ are operators which depend on $m(.), c, l(.)$ and $q(.,.)$. Once the algebraic system is obtained, we solve it using the asymptotic numerical method (ANM). To do so, Equation (15) is reformulated as:

$$R(U, \omega) = C + L(U) + Q(U, U) - \omega M(U) = 0 \tag{16}$$

As a first step, only the first bending mode is considered ($N = 1$). Equation (12) is reduced to:

$$\begin{array}{l} (\ddot{\eta} + 2c\dot{\eta} + \Omega^2\eta) - 2(\ddot{\eta} + 2c\dot{\eta} + \Omega^2\eta)\eta A + (\ddot{\eta} + 2c\dot{\eta} + \Omega^2\eta)\eta^2 B \\ = \beta\left[-\eta^3\left(C_1 + \frac{1+\nu}{1-\nu}C_2\right) + 2\eta^4\left(D_1 + \frac{1+\nu}{1-\nu}D_2\right) - \eta^5\left(E_1 + \frac{1+\nu}{1-\nu}E_2\right)\right] \\ -\tau\eta F + 2\tau\eta^2 G - \tau\eta^3 H + I - 2\eta J + \eta^2 K + v^2(t)L \end{array} \tag{17}$$

Equation (17) describes the dynamic behavior of the CMUT when considering only the first bending mode. In its quadratic form, Equation (17) can be written as:

$$\begin{array}{l} \dot{a} = y \\ \dot{y} = z \\ 0 = (\dot{z} + 2cy + \Omega^2 a) - 2(\dot{z} + 2cy + \Omega^2 a)aA + (\dot{z} + 2cy + \Omega^2 a)mB \\ -\beta\left[-n\left(C_1 + \frac{1+\nu}{1-\nu}C_2\right) + 2an\left(D_1 + \frac{1+\nu}{1-\nu}D_2\right) - mn\left(E_1 + \frac{1+\nu}{1-\nu}E_2\right)\right] \\ +\tau aF - 2\tau mG + \tau nH - I + 2aJ - mK - VVL \\ 0 = -m + aa \\ 0 = -n + ma \\ 0 = -V + V_{dc} + V_{ac}\cos(\omega t) \end{array} \tag{18}$$

$$m\left(\dot{X}\right) = l_0(\omega) + l(X) + q(X, X) \tag{19}$$

where $X = (a, y, z, m, n, V)$ is the unknown vector of size $N_eq = 6$. Equation (19) is then implemented in MANLAB, an object-oriented MATLAB program which solves a quadratic system using the ANM [13].

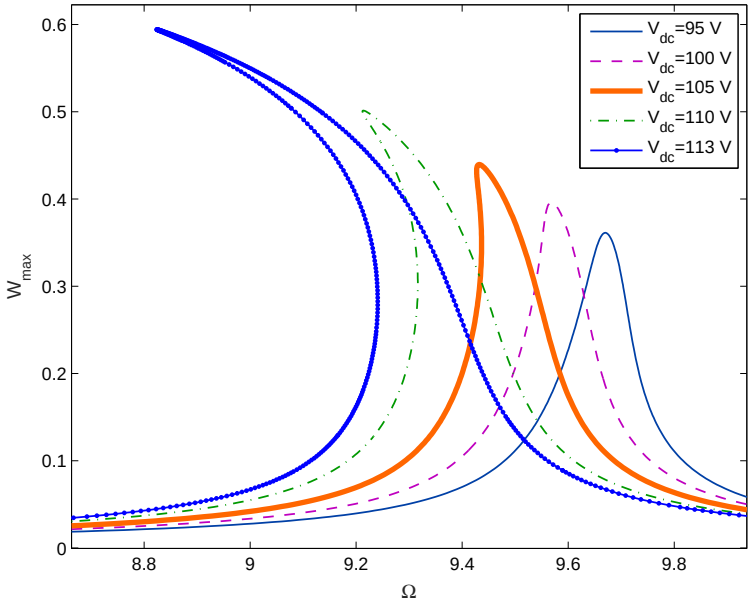


Figure 2: Forced frequency responses of the first CMUT design for $V_{ac} = 2V$ and several DC voltages. W_{max} is the out-of-plane normalized displacement of the membrane at its central point.

4 RESULTS AND DISCUSSION

In this section, several numerical simulations have been performed for two set of design parameters listed in Table 1 in order to investigate the effects of DC and AC voltages on the CMUT frequency responses under primary resonance.

For the first design, the ratio between the gap and the plate thickness is $d/h = 2$. Consequently, high DC voltages are needed to reach softening nonlinear behaviors. This is illustrated by Figure 2 which displays the evolution of the CMUT frequency response with respect to V_{dc} for $V_{ac} = 2V$. Since the excitation term is proportional to V_{dc}, increasing the DC voltage leads to an augmentation of the out-of plane displacement of the micro-plate $w(r, t)$. Moreover, the resonance frequency decreases due to the negative stiffness term which is proportional to V_{dc}^2. Remarkably, at a critical V_{dc}, the CMUT frequency response becomes nonlinear and the curve bends to the left (softening) due to the amplification of the electrostatic nonlinear terms.

Unlike the effect of V_{dc} on the CMUT frequency response, the variation of the AC voltage has a significant impact on the excitation amplitude and a negligible one on the negative electrostatic stiffness. Consequently, the resonance curves become more nonlinear when increasing V_{ac} without any remarkable frequency shift. This phenomena is displayed in Figure 3 for $V_{dc} = 50V$ where the frequency response exhibits a hardening behavior for $3V \leq V_{ac} \leq 6V$, since the geometric nonlinearities dominate the CMUT dynamics. Interestingly, for $V_{ac} = 7V$, the com-

Design	effective gap distance	plate thickness	plate radius	quality factor
1	$1\mu m$	$2\mu m$	$60\mu m$	50
2	$2\mu m$	$1\mu m$	$60\mu m$	50

Table 1: Design parameters of considered CMUTs

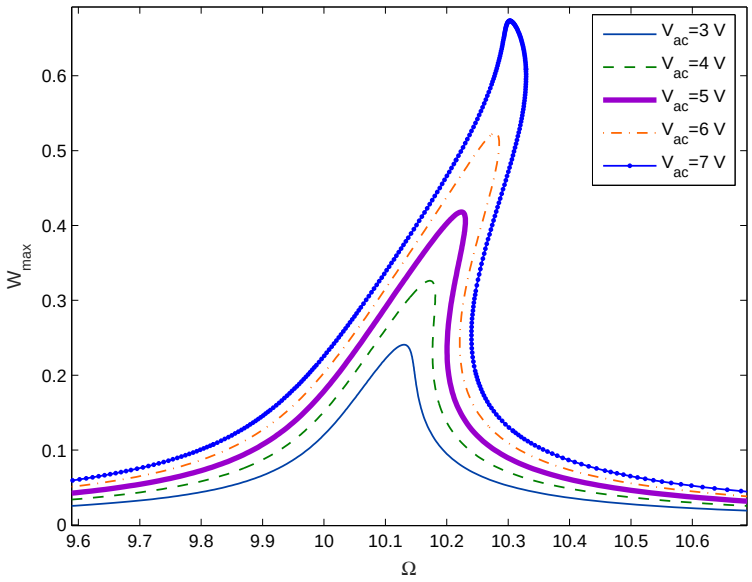


Figure 3: Forced frequency responses of the first CMUT design for $V_{dc} = 50V$ and several AC voltages.

petition between mechanical and electrostatic nonlinearities gives rise to a mixed hardening-softening behavior [14, 15, 16, 17] for which the displacement at the membrane center exceeded 60% of the gap.

The second design in Table 1 presents a larger gap with respect to the membrane thickness. Since the excitation amplitude is proportional to g^{-2} and compared to the first CMUT design, high DC voltages are needed in order to reach the softening behavior for $V_{ac} = 3V$ as shown in Figure 4. Moreover, the variation of the spring softening effect with respect to V_{dc} is slightly remarkable. Finally, Figure 5 displays the same phenomena described for the first design when V_{ac} is increased from $3V$ up to $11V$ and $V_{dc} = 100V$ for which the displacement at the membrane center is below 45% of the gap.

5 CONCLUSION

In this paper the nonlinear dynamics of circular CMUTs under primary resonance was investigated. The mathematical model, that takes into account the electrostatic and mechanical nonlinearities, is transformed into a set of coupled nonlinear ordinary differential equations using the Galerkin procedure. The harmonic balance method was then used to decompose the obtained system into a quadratic one which has been solved using the asymptotic numerical method. It has been shown that the DC voltage has a direct impact on the resonance frequency and the hardening or softening nonlinear effects while V_{ac} affects mostly the shape of the resonance curves. Moreover, depending on the chosen actuation voltages and the design parameters, the frequency response can switch between hardening, softening and mixed behaviors. In practice, the developed computational model can be used by MEMS designers to improve the performances of CMUTs in several applications such as High Intensity Focused Ultrasound (HIFU) in cancer therapy.

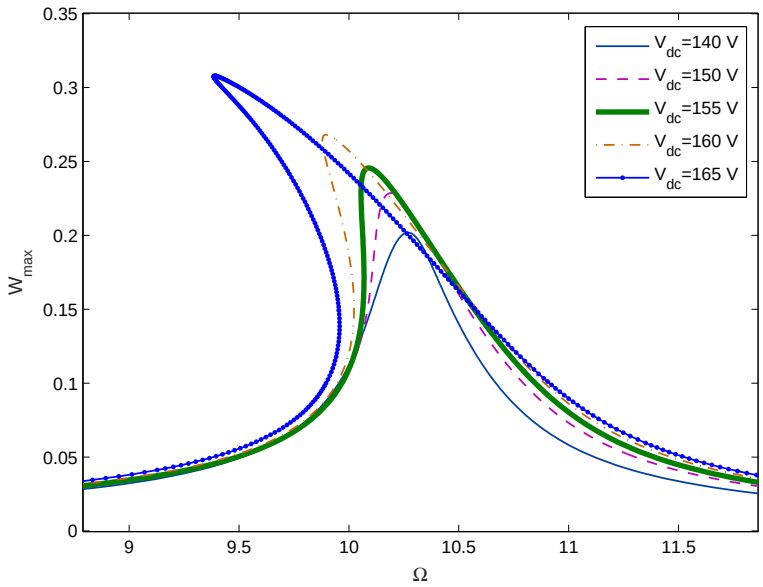


Figure 4: Forced frequency responses of the second CMUT design for $V_{ac} = 3V$ and several DC voltages.

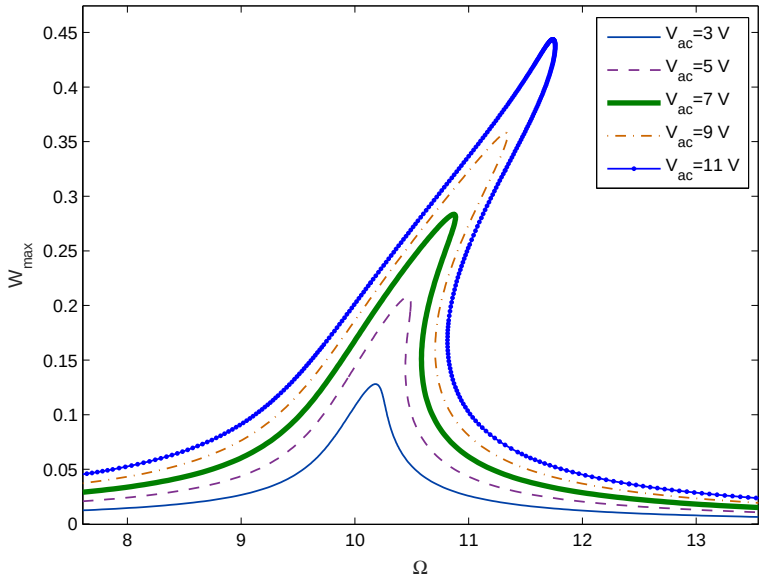


Figure 5: Forced frequency responses of the second CMUT design for $V_{dc} = 100V$ and several AC voltages.

REFERENCES

[1] T.G. Fisher, T.J. Hall, S. Panda, M.S. Richards, P.E. Barbone, J. Jiang, J. Resnick, S. Barnes, Volumetric elasticity imaging with a 2-d cmut array. *Ultrasound in medicine & biology*, **36**(6), 978–990, 2010.

[2] J. Song, S. Jung, Y. Kim, K. Cho, B. Kim, S. Lee, J. Na, I. Yang, O.-k. Kwon, D. Kim, Reconfigurable 2d cmut-asic arrays for 3d ultrasound image. In *SPIE Medical Imaging*, pages 83201A–83201A, International Society for Optics and Photonics, 2012.

[3] X. Wang, Y. Fan, W.-C. Tian, H.-J. Kwon, S. Kennerly, G. Claydon, A. May, An air-coupled capacitive micromachined ultrasound transducer for noncontact nondestructive evaluation. In *Sensors, 2007 IEEE*, pages 1464–1467, IEEE, 2007.

[4] H. Dudaicevs, M. Kandler, Y. Manoli, W. Mokwa, E. Spiegel, Surface micromachined pressure sensors with integrated cmos read-out electronics. *Sensors and Actuators A: Physical*, **43**(1), 157–163, 1994.

[5] J. Mendoza-López, C. Sánchez-López, Electromechanical performance comparison for different cmut element geometries. In *Synthesis, Modeling, Analysis and Simulation Methods and Applications to Circuit Design (SMACD), 2012 International Conference on*, pages 109–112, IEEE, 2012.

[6] B. Bayram, G.G. Yaralioglu, A.S. Ergun, B. Khuri-Yakub, Influence of the electrode size and location on the performance of a cmut [us transducer]. In *Ultrasonics Symposium, 2001 IEEE*, volume **2**, 949–952. IEEE, 2001.

[7] B. Bayram, E. Hæggstrom, G.G. Yaralioglu, B.T. Khuri-Yakub, A new regime for operating capacitive micromachined ultrasonic transducers. *Ultrasonics, Ferroelectrics, and Frequency Control, IEEE Transactions on*, **50**(9), 1184–1190, 2003.

[8] A. Lohfink, P.-C. Eccardt, Linear and nonlinear equivalent circuit modeling of cmuts. *Ultrasonics, Ferroelectrics, and Frequency Control, IEEE Transactions on*, **52**(12), 2163–2172, 2005.

[9] W.P. Mason, *Electromechanical transducers and wave filters*. D. Van Nostrand Co., 1948.

[10] O. Ahrens, A. Buhrdorf, D. Hohlfeld, L. Tebje, J. Binder, Fabrication of gap-optimized cmut. *Ultrasonics, Ferroelectrics, and Frequency Control, IEEE Transactions on*, **49**(9), 1321–1329, 2002.

[11] G.W. Vogl, A.H. Nayfeh, Primary resonance excitation of electrically actuated clamped circular plates. *Nonlinear Dynamics*, **47**(1-3), 181–192, 2007.

[12] A.H. Nayfeh, P.F. Pai, *Linear and nonlinear structural mechanics*. John Wiley & Sons, 2008.

[13] B. Cochelin, C. Vergez, A high order purely frequency-based harmonic balance formulation for continuation of periodic solutions. *Journal of sound and vibration*, **324**(1), 243–262, 2009.

[14] N. Kacem, S. Hentz, D. Pinto, B. Reig, V. Nguyen, Nonlinear dynamics of nanomechanical beam resonators: improving the performance of NEMS-based sensors. *Nanotechnology*, **20**(27), 275501, 2009.

[15] N. Kacem, S. Hentz, Bifurcation topology tuning of a mixed behavior in nonlinear micromechanical resonators. *Applied Physics Letters*, **95**(18), 183104, 2009.

[16] N. Kacem, J. Arcamone, F. Perez-Murano, S. Hentz, Dynamic range enhancement of nonlinear nanomechanical resonant cantilevers for high sensitive NEMS gas/mass sensors applications. *Journal of Micromechanics and Microengineering*, **20**(4), 045023, 2010.

[17] N. Kacem, S. Baguet, R. Dufour, S. Hentz, Stability control of nonlinear micromechanical resonators under simultaneous primary and superharmonic resonances. *Applied Physics Letters*, **98**(19), 193507, 2011.

APPENDIX

The reduced order model presented in this paper is defined as:

$$M(\eta)\ddot{\eta} + 2cM(\eta)\dot{\eta} + N(\eta)\eta = P(\eta) + v^2(t)L$$

$$M(\eta) = [M_{qs}(\eta)] = [\delta_{qs} - 2\eta_i A_{isq} + \eta_i\eta_j B_{ijsq}]$$
$$N(\eta) = [N_{qs}(\eta)] = [\Omega_q^2\delta_{qs} - 2\Omega_q^2\eta_i A_{isq} + \Omega_q^2\eta_i\eta_j B_{ijsq}]$$
$$P(\eta) = [P_q(\eta)] = \{\beta[\eta_m\eta_n\eta_p\left(C_{1mnpq} + \tfrac{1+\nu}{1-\nu}C_{2mnpq}\right) + 2\eta_i\eta_m\eta_n\eta_p\left(D_{1mnpq} + \tfrac{1+\nu}{1-\nu}D_{2mnpq}\right)$$
$$-\eta_i\eta_j\eta_m\eta_n\eta_p\left(E_{1mnpq} + \tfrac{1+\nu}{1-\nu}E_{2mnpq}\right)] - \tau\eta_m F_{mq} + 2\tau\eta_i\eta_m G_{imq} - \tau\eta_i\eta_j\eta_m H_{ijmq}$$
$$+I_q - 2\eta_i J_{iq} + \eta_i\eta_i K_{ijq}\}$$
$$L = \{L_q\}$$

where

$$A_{imq} = \int_0^1 r\phi_i\phi_m\phi_q dr \qquad B_{ijmq} = \int_0^1 r\phi_i\phi_j\phi_m\phi_q dr \qquad C_{1mnpq} = \int_0^1 \phi'_q\phi'_m\varphi_{1np}dr$$
$$C_{2mnpq} = \int_0^1 \phi'_q\phi'_m\varphi_{2np}dr \qquad D_{1imnpq} = \int_0^1 (\phi_i\phi_q)'\phi'_m\varphi_{1np}dr \qquad D_{2imnpq} = \int_0^1 (\phi_i\phi_q)'\phi'_m\varphi_{2np}dr$$
$$E_{1ijmnpq} = \int_0^1 (\phi_i\phi_j\phi_q)'\phi'_m\varphi_{2np}dr \qquad E_{2ijmnpq} = \int_0^1 (\phi_i\phi_j\phi_q)'\phi'_m\varphi_{2np}dr \qquad F_{mq} = \int_0^1 r\phi'_m\phi'_q dr$$
$$H_{ijmq} = \int_0^1 r\phi'_m(\phi_i\phi_j\phi_q)'dr \qquad I_q = \int_0^1 Fr\phi_q dr \qquad J_{iq} = \int_0^1 Fr\phi_i\phi_q dr$$
$$K_{ijq} = \int_0^1 Fr\phi_i\phi_j\phi_q dr \qquad L_q = \int_0^1 r\phi_q dr$$

with

$$\varphi_{1mn}(r) = \frac{1}{4r}\int_0^r \xi\phi'_m\phi'_n d\xi + \frac{r}{4}\int_r^1 \frac{\phi'_m\phi'_n}{\xi}d\xi \qquad \varphi_{2mn}(r) = \frac{r}{4}\int_0^1 \xi\phi'_m\phi'_n d\xi$$

COMPDYN 2015
5th ECCOMAS Thematic Conference on
Computational Methods in Structural Dynamics and Earthquake Engineering
M. Papadrakakis, V. Papadopoulos, V. Plevris (eds.)
Crete Island, Greece, 25–27 May 2015

SEISMIC ASSESSMENT OF THE FULL SCALE FOUR STOREY E-DEFENSE ROCKING SHEAR WALL SHAKE TABLE TEST

Giorgio T. Proestos[1], Hossein Aghabeigi[1], and Paolo M. Calvi[1, 2]

[1] University of Toronto
35 Saint George Street, Toronto, ON M5S 1A4
e-mail: {giorgio.proestos, hossein.aghabeigi}@mail.utoronto.ca

[2] University at Buffalo, The State University of New York
Ketter Hall, 212, Buffalo, NY 14228, United States
paolo.calvi@mail.utoronto.ca

Keywords: seismic assessment, reinforced concrete, prestressed rocking shear wall, nonlinear time history, nonlinear finite element.

Abstract. *An assessment of a four storey prestressed reinforced concrete structure is compared to existing results for a full scale shake table test. The E-Defense structure, which was tested in 2010 and was subjected to the Kobe earthquake record, is a complex concrete structure with prestressed rocking shear walls in one direction and a moment frame in the other. This work focusses on the seismic performance assessment of the rocking shear wall system subjected to the 1990 Kobe earthquake record at three intensity levels (25%, 50% and 100%), as was done in the shake table test. The purpose of this study is to assess if, rather than using heuristic approaches or experimental data to calibrate the nonlinear elements of a lumped plasticity model, a more advanced static nonlinear finite element procedure that can accurately capture the complexity of these elements could be used to calibrate the hysteresis of the plastic elements. In this study, the hysteretic response of the critical members, namely the rocking shear wall and the columns, were obtained through modelling in VecTor2, a two dimensional nonlinear finite element tool for reinforced and prestressed concrete structures. These hysteresis were then used to calibrate a nonlinear spring at the base of the shear wall in Ruaumoko and a full nonlinear time history analysis was conducted. The peak base shear and drift ratio at the peak were predicted well. Furthermore, the individual member responses, modeled in VecTor2, accurately captured the crack patterns and failure modes observed in the experiment. To mimic situations practitioners would encounter, the results were not adjusted after the analysis was conducted, the predictions were conducted in a blind prediction process.*

1 INTRODUCTION AND MODELLING APPROACH

Current techniques and modelling tools to assess the seismic performance of reinforced and prestressed concrete structures are vast. When engineers are faced with assessing the seismic performance of a large structure, decisions need to be made as to how complex and detailed the model will be. The analysis techniques under consideration may include simplified single degree of freedom models, linear modal analysis, linear fiber models, or more advanced lumped plasticity models, nonlinear fiber models, or full nonlinear finite element approaches. Contributing factors in deciding which approach to use involve with the tradeoff between the time required to implement the model, the complexity of the failure modes and the desired performance parameters to be assessed.

In 2010 Nagae *et. al.* [1] conducted a shake table test of a full scale four storey structure. The structure had a prestressed concrete rocking shear wall in one direction and a moment frame in the other. This paper outlines a blended approach to model the lateral load resisting system in the shear wall direction. The goal of the modelling was to conduct a seismic performance assessment that could be compared to experimental results. It was of particular interest to accurately estimate the peak base shear, the peak drifts, and the residual drifts and then to compare these results with the experimental values reported in the literature. To mimic conditions faced by practitioners, the results were not reviewed until after the full assessment was complete. Therefore, no aspects of the model were modified after the initial assessment was conducted.

One modelling approach to achieve this level of assessment for rocking shear wall systems, though not common in practice, is to use solid finite elements. Developing a full nonlinear finite element model of the entire structure is time consuming and computationally expensive [2]. The computational time for such a model may be on the order of hours or days. A common alternative is to use fiber models with zero tension capacity elements at the base of the shear wall [3, 4] so that the rocking mechanism can be captured. Similarly, lumped plasticity models can be implemented to establish predictions [2, 5]. Although fiber models and lumped plasticity models are significantly less time consuming to develop and run, establishing reliable hysteretic rules for the nonlinear elements becomes a critical part of the analysis. In situations where experimental results are not available or there is uncertainty surrounding the heuristic approaches used to estimate the hysteresis of the nonlinear elements, an issue commonly faced by practitioners, other procedures are needed to establish those parameters.

It was the intent of the authors to investigate the quality of an analysis that could be conducted with a lumped plasticity model but using a more advanced approach to estimate the hysteretic behaviour of the nonlinear elements. This blended approach has the advantage of being much less computationally expensive, the run time being several minutes rather than hours or days, and it provides a rational basis to develop the hysteretic rules. Specifically, the hysteretic behaviour of the rocking shear wall and the column elements were individually modelled using VecTor2 [6], a two dimensional nonlinear finite element model based on the Modified Compression Field Theory and the Disturbed Stress Field Theory [7, 8 and 9]. This blended modelling approach has the advantage that the VecTor2 modelling can accurately capture the full reverse cyclic load deformation responses of the elements, rocking mechanism, crack widths, prestressing, element stresses, crushing failure modes, shear failure modes and yielding failure modes. These elemental hysteresis were then used in a lumped plasticity model programmed in Ruaumoko [10] to conduct a nonlinear time history analysis. The global structure was subjected to the 1990 Kobe earthquake ground motion at 25%, 50% and 100% intensities, cumulatively, as was done in the 2010 E-Defense shake table tests [1]. Since the structure

was subjected to progressively larger ground motions the cumulative damage needed to be accounted for in the modelling. As was previously mentioned the results were assessed in a blind manner to simulate conditions typical in industry.

2 STRUCTURE DETAILS

In the test conducted by Nagae *et. al.* [1] two structures were tested, a prestressed structure and a conventional reinforced concrete structure. Each test specimen had a shear wall in one direction and a moment frame in the other. This study is focused on the prestressed structure in the shear wall direction. Some details of particular interest include the detailing at the shear wall and corresponding prestressing. For instance, although the wall is a rocking system, some partially bonded mild steel bars were included at the base of the wall that were intended to yield and provide hysteretic energy dissipation. The prestressing tendons, which promote the self-centering properties of the wall, were unbonded.

The following details in Table 1, Figure 1 and Figure 2 were used to develop the VecTor2 and Ruaumoko models, further details can be found in the publication by Nagae *et. al.* [1].

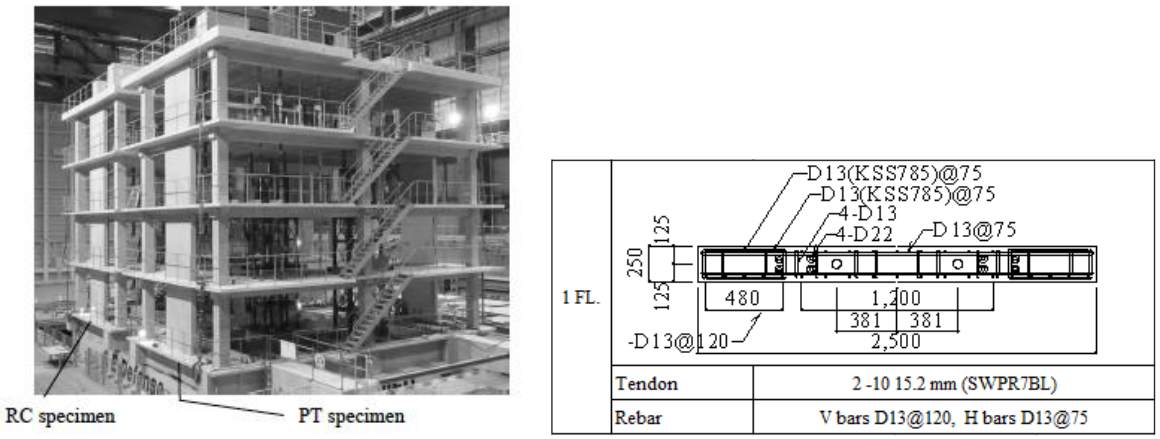


Figure 1: Photograph of experimental setup (left) and cross section of shear wall at the first floor (right), reproduced from [1]

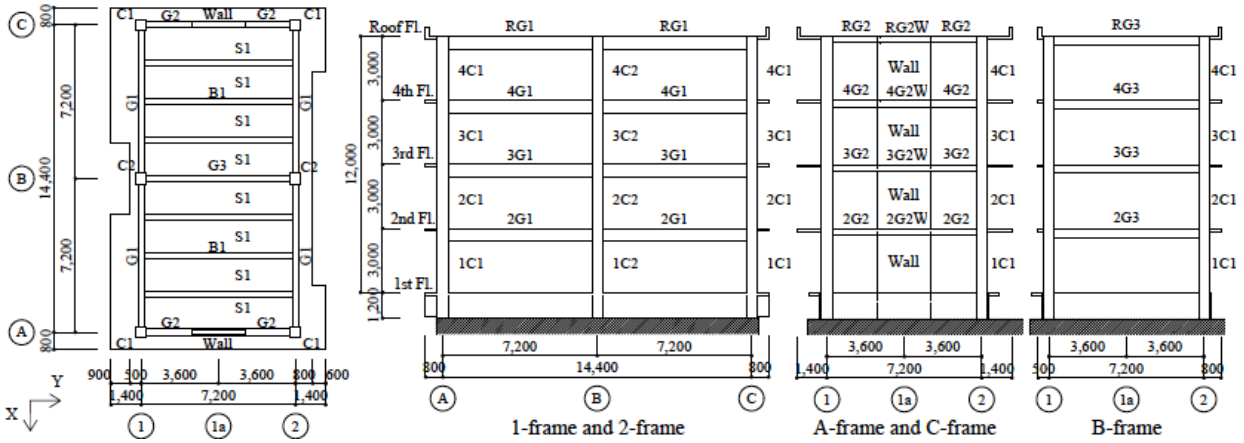


Figure 2: Elevation and plan of experimental setup, reproduced from [1].

	A_s (mm^2)	f_y (MPa)	f_u (MPa)
D22 Mild Steel	387	385	563
21 mm diam. PT Bar (column)	346	1198	1281
15 mm diam. PT Wire (wall)	140	1777	1969

Table 1: Steel material properties, reproduced from [1].

As was reported in the literature a concrete strength of 60 MPa was used.

3 VECTOR2 MODELLING

VecTor2 is a two dimensional nonlinear finite element tool capable of capturing the nonlinear behaviour of the cracked prestressed concrete rocking shear wall and the prestressed columns. Figure 3 shows the models used to develop the hysteretic responses.

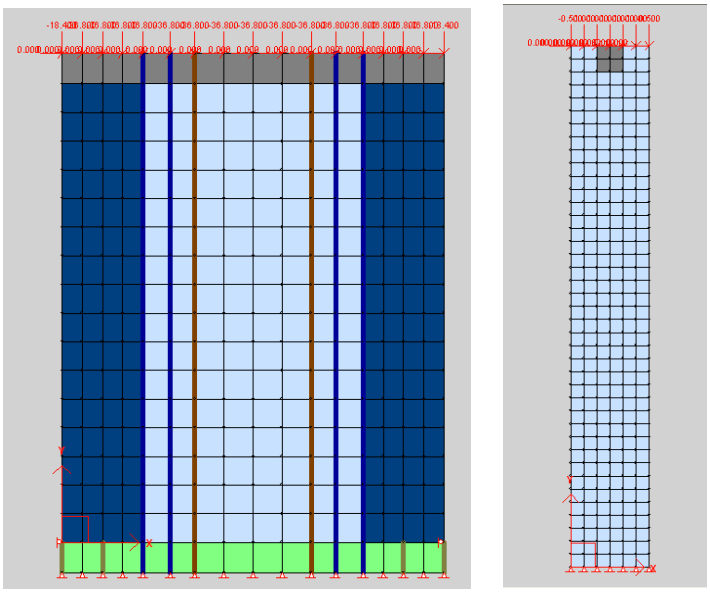


Figure 3: Finite element models for first storey rocking shear wall (left) and column (right).

In Figure 3, the dark blue regions in the model represent the interior columns of the shear wall with higher amounts of reinforcement (see Figure 1). The lighter blue regions represent the web region of the shear wall. The dark blue lines represent the partially bonded mild steel bars used by the designers as a means to increase the hysteretic damping. The brown lines are the unbounded prestressing strands, modelled as truss elements with the appropriate prestressing. The prestressing was implemented with a strain offset in the steel. Except the partially unbonded bars and the prestressing strands, the steel is modelled as smeared reinforcement. In this 3000 mm tall model of the first storey, the tendons are bonded to the top of the storey when in reality the tendons would be anchored to the top of the wall. Therefore, to ensure a uniform stress is introduced by the prestressing at the first floor, a row of stiff elements is used, they are shown in grey. The rocking is captured using a row of zero strength elements (green) and compression only truss elements (light brown). The stiffness of the compression only elements were set to approximate the stiffness of the foundation that was built using high strength concrete. The base of the structure was restrained from translating in the horizontal direction. The gravity load was imposed at the top of the wall. A simple pushover analysis was used to qualitatively verify the modelling assumptions, including mesh refinement. It was determined that a mesh

made from approximately 200 mm x 200 mm elements yielded similar results to finer mesh sizes and therefore would be less computationally demanding when conducting the full static reverse cyclic analysis.

The gravity load was applied in the VecTor2 model and the model was loaded in a reverse cyclic manner with displacement control of the top node. Figure 5 in the following section shows the hysteretic response of the shear wall. This response was used to calibrate the rotational spring used in the Ruaumoko modelling. As can be seen the self-centering property of the shear wall is accurately captured.

Figure 4, obtained using the program Augustus [11], shows the magnified deformed shape and crack pattern as well as a map of the principal compressive stresses and the principal compressive stress directions (white lines) at the maximum predicted drift. The maximum crack widths are approximately 1 to 2 mm. It is also interesting to note that there are clear diagonal shear cracks in the wall. This is significant because using simpler modelling techniques would omit this significant phenomena. The blue elements in the figure showing the compressive stresses in the concrete indicate that crushing is occurring at the toe of the shear wall. This failure mode is typical for these systems and, in this case, did govern the failure. The dark blue elements have a compressive stress in the concrete of nearly 60 MPa and the light green elements have roughly 0 MPa.

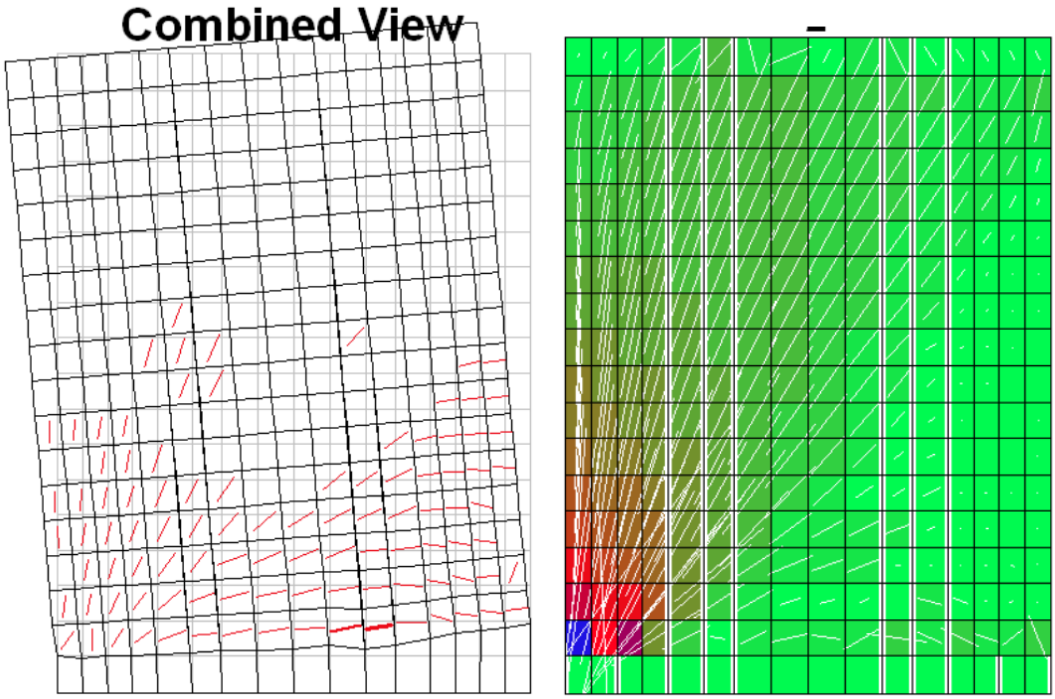


Figure 4: VecTor2 crack pattern and deformed shape (left) and principal compressive stress and principal compressive stress direction (right).

The columns were also modelled to account for prestressing; in this model all the reinforcement, including prestressing bars, were modelled as smeared, as can be seen in Figure 3. As with the shear wall, the prestressing was imposed with a strain offset in the steel, however, for the columns, the steel was bonded to the concrete since, in the experiment, the ducts were grouted. The rotation at the base was fixed and the top node was cycled in displacement control. The elements surrounding the node used for displacement control were strengthened to ensure a local failure did not govern the response (shown in grey). The gravity load appropriate to that

floor was applied in the VecTor2 model. Figure 5 shows a typical hysteretic response of the column elements. Unlike the wall the hysteresis loops, the columns absorb less energy and although at large displacements the columns exhibit significant nonlinearity, at small displacements the response remains fairly linear.

4 NONLINEAR TIME HISTORY ANALYSIS AND THE RUAUMOKO MODEL

In 2010 the E-Defense structure that was tested by Nagae *et. al.* [1], the structure was consecutively subjected to three horizontal instances of the 1990 Kobe earthquake record with progressively larger intensities (25% PGA, 50% PGA and 100% PGA). The results of this experimental work is documented elsewhere [1, 12]. To model the global structural behaviour a two dimensional lumped plasticity model was developed in Ruaumoko. The rocking at the base of the shear wall was modeled with a rotational spring and the columns with plastic hinges that could develop at either end of the elements. The calibration of the nonlinear hysteretic rules for the rocking at the base of the shear wall and the columns were fit to the VecTor2 results. It was determined that since an estimate of the residual drift was an important part of the seismic performance assessment, a flag-shape hysteretic model best fit the results as it would ensure the 'snap through the origin' behaviour of the rocking system, see Figure 5.

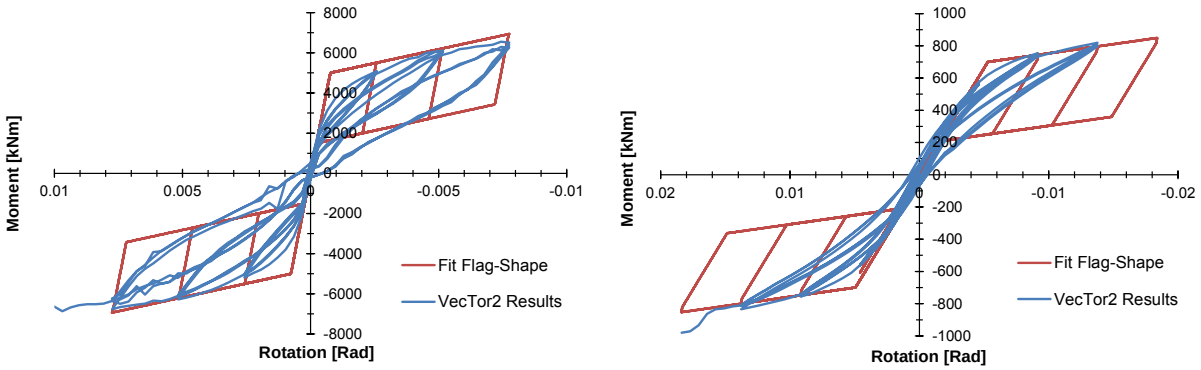


Figure 5: Shear wall (left) and column (right) hysteresis results from VecTor2 and element calibration.

For the shear wall, Taylor [13] beam-column elements that account for shear deformations were used. These elements use a Newton-Raphson iteration scheme to continually update the neutral axis based on the equilibrium requirements at every time step in the model. It was assumed the shear wall remained elastic above the base. Giberson beam-column elements [10] were used to model the columns. Similarly, the floor slabs were modeled as linear elastic and it was assumed that the connections remained rigid. The floor slabs were modeled with a thickness of 130 mm and with a width of half of the out-of-plane span. The elements were connected from the corner columns to the middle of the shear wall at each floor. Within the width of the shear wall (2500 mm) the elements are forced to rigidly deform with the wall, thereby capturing the correct shear span of the floor slabs. The damping was modeled by imposing a 5% damping ratio on all modes [14].

To account for possible P-Delta effects a set of dummy columns were used and slaved to the structural system. These column elements are pinned at both ends at every storey and the full gravity load of the structure is applied. Since these elements have no lateral resistance, as the structure deforms the main lateral load resisting system is needed to resist the P-Delta effects that develop. Figure 6 (left) shows a drawing of the Ruaumoko model for the structure. The hatched areas are the rigid links used to account for the effect of shear wall width. The red

elements are the floor slabs, the peripheral blue elements are the columns and the blue elements in the center, are the shear wall elements. A depiction of the system modelling is shown in Figure 6 (right). Here, the column to the right of the graphic represents the dummy columns used to capture the P-Delta effects.

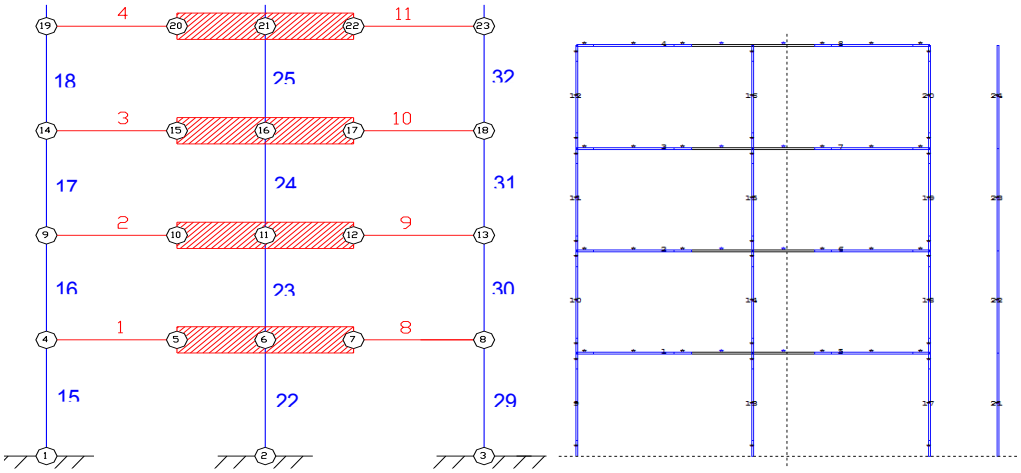


Figure 6: Ruaumoko model.

5 RESULTS OF NONLINEAR TIME HISTORY

The results of the nonlinear time history analysis from the blind Ruaumoko seismic assessment were compared to experimental results from the literature. Table 2 summarizes some of the key parameters.

	T_n (s)	V_{max} positive (kN)	V_{max} negative (kN)	Δ_{max} roof (mm)	$\Delta_{residual}$ roof (mm)
Experiment	0.29	3000	2950	204	80
Prediction	0.31	3274	3823	125	11

Table 2: Summary of analysis results.

As shown in Table 2, the prediction of the period was excellent. The prediction of the maximum positive peak was also good with a test to predicted ratio for the base shear of 0.92. The base shear for the maximum negative peak is somewhat over predicted. Although the overall shape of the column and shear wall hysteresis are captured with a flag-shape, not enough energy is dissipated at lower loads. Since the structure underwent two lower intensity earthquakes prior to the 100% record, additional damage would have occurred and lowered the stiffness of the structure for the final record. Although these records were applied in the model, the flag-shape hysteresis provides no dissipation and would remain completely undamaged before the yield point. Furthermore, it is possible that the hysteretic damping used in the Ruaumoko model is underestimated. Together, these differences resulted in an over prediction of the maximum base shear on the negative peak. The prediction of the maximum roof drift and residual drifts are also underestimated. This is likely caused by the fact the flag-shape hysteresis that always passes through the origin. Once the partially bonded, mild steel bars yield and shear cracks

develop the hysteresis does not pass directly through the origin, as is predicted in the VecTor2 models but unlike the assumed hysteresis.

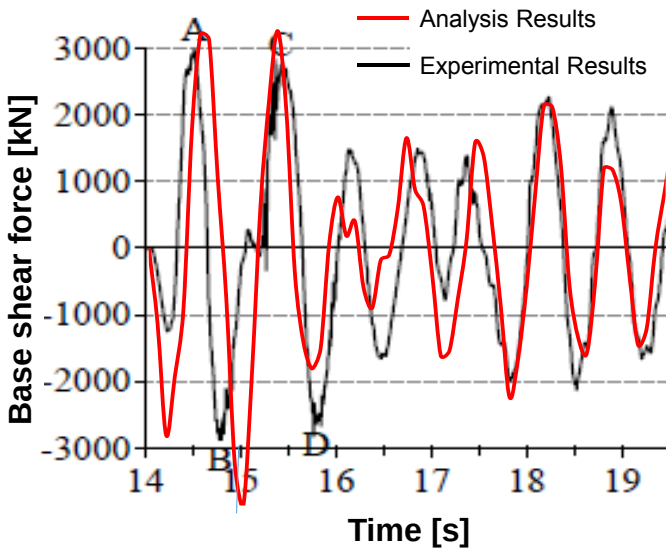


Figure 7: Comparison of the observed and predicted behaviour near the peak response, reproduced in part from [1].

The overall trends for the dynamic response near the peak, shown in Figure 7 and Figure 8 are good considering these results were established in a blind prediction manner.

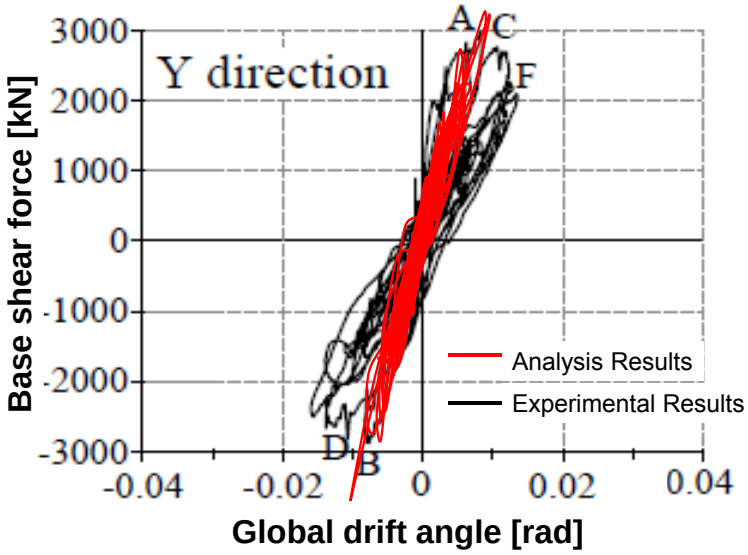


Figure 8: Global hysteretic behaviour, reproduced in part from [1].

Figure 8 shows the structural response in comparison with the experimental results. This plot corroborates the conclusions that the model did not undergo sufficient damage, for the reasons discussed previously. Specifically, unless the yield point of the flag hysteresis is reached no energy dissipation or damage occurs, which results in the discrepancy between the predicted and observed behaviour. This suggests that although the overall appearance of the flag-shape hysteresis used to model the nonlinear elements was reasonable, it is important that: the amount of energy dissipation is closely matched for all load levels, the gradual stiffness degradation is

captured and the damage caused by unloading at all load levels can be captured [15]. This is particularly important in this analysis since prior to the 100% intensity Kobe record was applied two other lower intensity records, the 25% Kobe and 50% Kobe were applied.

6 CONCLUSIONS

In modelling the seismic performance of a complex prestressed concrete structure there are benefits to using advanced nonlinear finite element techniques to calibrate the plastic elements in the global model. Using this approach, a relatively simple and computationally inexpensive lumped plasticity model can be used to conduct the nonlinear time history analysis. Although a nonlinear finite element model is required for the element calibration, it avoids the necessity of using generic heuristic methodologies or experimental results based on element categories. In using the VecTor2 model, the peak capacity, ductility and an estimate of the hysteretic dissipation can be rationally estimated. It also ensures that complex failure modes, such as shear failures, crushing failures and the rocking mechanism are accurately captured.

The estimate of the first positive peak shear force was captured with good accuracy with a test to predicted ratio for the base shear of 0.92. The peak base shear at the first negative peak was somewhat over estimated. This is likely a result of the flag-shape hysteresis used. In particular, in the linear portion for the hysteresis before yielding, when the structure unloads, no energy is dissipated. Since the actual hysteresis determined from VecTor2 is highly nonlinear throughout the loading and unloaded phases it is difficult to capture using piecewise linear relationships. For similar reasons, the peak roof displacement and residual displacements are somewhat under predicted by this model. It should be further investigated if a rational unloading rule can be programmed into the Ruaumoko model to better capture: the amount of energy dissipation at all load levels, the gradual stiffness degradation and the damage caused by unloading at all load levels. It appears that these aspects are significant. It should be noted that to objectively evaluate this modelling approach a ‘blind prediction’ methodology was employed and therefore, the results were reasonable. That is, the VecTor2 model, Ruaumoko model and hysteretic behaviours were not adjusted based on experimental data whatsoever before comparing the results to those in the literature. This methodology should be employed in assessing new modelling techniques as it provides a realistic basis of how the approach would perform in a practical environment.

7 REFERENCES

[1] T. Nagae, K. Tahara, K. Fukuyama, T. Matsumori, H. Shiohara, T. Kabeyasawa, S. Kono, M. Nishiyama, J. Moehle, J. Wallace, R. Sause, W. Ghannoum, Test Results of Four-Story Reinforced Concrete and Post-Tensioned Concrete Buildings: The 2010 E-Defense Shaking Table Test. Proceedings of the 15th World Conference on Earthquake Engineering, 24/28 Sept. 2012.

[2] L. Wiebe, C. Christopoulos, Mitigation of Higher Mode Effects in Base-Rocking Systems by Using Multiple Rocking Sections, Journal of Earthquake Engineering, 13:S1, 83-108, 2009.

[3] Y. C. Kurama, R. Sause, S. Pessiki, L. W. Lu, Lateral load behavior and seismic design of unbonded post-tensioned precast concrete walls. ACI Structural Journal, **96**(4):625–632, 1999.

[4] J. M. Ricles, R. Sause, M. M. Garlock, C. Zhao, Post-tensioned seismic-resistant connections for steel frames. Journal of Structural Engineering 2001; 127(2):113–121, 2001.

[5] D. Pennucci, G. M. Calvi, T. J. Sullivan, Displacement-based design of precast walls with additional dampers, Journal of Earthquake Engineering, 13(S1):40–65, 2009.

[6] F. J. Vecchio, VecTor2 nonlinear finite element analysis. Copyright 1990-2013 F.J. Vecchio, 1990.

[7] F. J. Vecchio, M. P. Collins, The modified compression field theory for reinforced concrete elements subjected to shear, J. Am. Concr. Inst., 83-2 219–231, 1986.

[8] F. J. Vecchio, Disturbed stress field model for reinforced concrete: formulation, J. Struct. Eng., 1070–1077, 2000.

[9] F. J. Vecchio, Disturbed stress field model for reinforced concrete: implementation, J. Struct. Eng., 12–20, 2001.

[10] A. J. Carr, Ruaumoko2D—a program for inelastic time-history analysis. University of Canterbury, Christchurch, 2008.

[11] E. C. Bentz, Augustus: Post Processor for VecTor2 - Version 5.6.5. Copyright 1996-2010 E. Bentz.

[12] Z. Tuns, J. Gavridou, W. Wallace, T. Nagae, T. Matsumori, 2010 E-Defense Four-Story Reinforced Concrete and Post-Tensioned Buildings – Preliminary Comparative Study of Experimental and Analytical Results, Proceedings of the 15th World Conference on Earthquake Engineering, 24/28 Sept. 2012

[13] R. G. Taylor, The nonlinear seismic response of tall shear wall structures, PhD Thesis, Department of Civil Engineering, University of Canterbury, New Zealand, 1977.

[14] E. Smyrou, N. M. J. Priestley, A. J. Carr, Modelling of elastic damping in nonlinear time-history analyses of cantilever RC walls, Bull Earthquake Eng DOI 10.1007/s10518-011-9286-y, 2011.

[15] H. Aghabeighi, G. T. Proestos, Investigating the behviour of a four storey prestressed rocking shear wall and gravity columns, Internal University of Toronto Report, O. S. Kwon, Dec. 2012.

COMPDYN 2015
5th ECCOMAS Thematic Conference on
Computational Methods in Structural Dynamics and Earthquake Engineering
M. Papadrakakis, V. Papadopoulos, V. Plevris (eds.)
Crete Island, Greece, 25–27 May 2015

OUT-OF-PLANE BEHAVIOUR OF SINGLE-BODY UNREINFORCED-MASONRY WALL RESTRAINED BY A FLEXIBLE DIAPHRAGM

Sanjeev Prajapati[1], **Omar AlShawa**[1], **and Luigi Sorrentino**[1]

[1]Department of Structural and Geotechnics Engineering, Sapienza University of Rome
e-mail: {sanjeev.prajapati, omar.alshawa, luigi.sorrentino } @uniroma1.it

Keywords: : Masonry, out-of-plane, flexible diaphragm, rocking motion.

Abstract. *Past earthquakes have shown the high vulnerability of existing masonry buildings, particularly to out-of-plane local collapse mechanisms. Out-of-plane response is one of the most debated topics in the last decades, because of its complex nature as for geometrical non-linearity, energy damping, record sensitivity. In this work is considered a monolithic wall, resting on a foundation, restrained by a flexible diaphragm. The wall rocks around two base pivots and has one degree of freedom. Its thickness is explicitly accounted for, and the diaphragm is modelled as a linear-elastic spring and a concentrated mass. The non-linear equation of motion is presented, within a lagrangian approach. The energy dissipation is associated to the impact of the wall against the foundation. The effect of size of the wall, diaphragm stiffness and mass are evaluated through parametric analyses. Neglecting the diaphragm mass, the results can be interpreted also as related to a wall restrained at the top by tie-rods.*

1 INTRODUCTION

Earthquakes of the past have shown the great vulnerability of unreinforced-masonry (URM) structures to out-of-plane (OOP) loading (e.g.,[1, 2, 3], and references therein). URM buildings are particularly vulnerable if connections to transversal structures are non-existent or inadequate (e.g., [4], and references therein). However, even if such connections are robust, flexible diaphragms can limit their effectiveness (Fig. 1).

The OOP response of URM connected to a flexible diaphragm has received a comparatively little attention in the past. ABK [5] performed tests on walls acted by two (top and bottom) independent actuators, in order to simulate a possible filter effect of a diaphragm. They suggested stability charts for a mechanism having a base pivot, a top roller and an intermediate hinge. Simsir et al. [6] performed shaking-table tests on a single-storey, single-cell house having a flexible top floor. The authors proposed a single-bar and a two-bars models for replicating the laboratory time histories. Derakhshan [7] proposed an analytical model of a single-storey or a two-storey wall connected to flexible diaphragms. The equations of motion are obtained after a series expansion of trigonometric terms up to second order, with equivalent linear rotational springs simulating the wall-segments response. Penner [8] performed experimental tests on walls having a flexible top restraint and simulated them by means of a commercially-available rigid-body software.

In this paper a wall connected to a flexible restraint will be considered. The restraint can be at any height of the wall, and the thickness of the latter is accounted for. The wall cannot crack along its height, so only a base pivot will be considered. Friction is assumed to be large enough to prevent sliding both at the base and at connection with the diaphragm. A parametric analyses investigates the sensitivity to wall geometry, diaphragm features, ground motion intensity measures.



Figure 1: Out-of-plane damage of a facade segment, L'Aquila (central Italy) 2009.

2 ANALYTICAL MODEL

In the technical literature most of the interest has been so far concentrated on a single rocking body, resting on a foundation, without any top restraint (e.g., [9], and references therein). However, in several cases a masonry wall supports a top horizontal structure. If a tie-rod or a connection to the floor is present, a top restraint can be introduced in the model. Due to this topology, the wall may rotate as a single body or crack along its height. The latter case is typical of slender walls [10], but will not be discussed here. The former case is typical of squatter walls or walls with comparatively small mass with respect to the diaphragm and to the masonry bonding strength [6]. In the following a model of a rocking body, having finite thickness and an horizontal flexible restraint, modelled as a spring, is developed (refer to Fig. 2a). The spring can be in a generic vertical position, not necessarily at the top, but at the centre of the wall thickness in order to preserve vertical symmetry.

2.1 Equation of motion

The analytical equation of motion is derived within a lagrangian approach [11]:

$$\frac{d}{dt}\left(\frac{\partial L}{\partial \dot{\theta}}\right) - \frac{\partial L}{\partial \theta} = Q \tag{1}$$

where:
$L = T - V$; T is the kinetic energy, V is the potential energy, t is the time, $\dot{\theta}$ is the angular velocity, θ is the angular displacement, Q is the non-conservative force.
In the case at hand, the kinetic energy is equal to:

$$T = \frac{1}{2} I_G \dot{\theta}^2 + \frac{1}{2} m \left(\mathbf{v}_{G,A}^2 + \chi \mathbf{v}_{D,A}^2\right)$$

where:
I_G is the moment of inertia of the body about its centre of mass, G (refer to Fig. 2a); m is the mass of the wall; $\chi = m_d/m$; m_d is the mass of the diaphragm; $\mathbf{v}_{G,A}$, $\mathbf{v}_{D,A}$ are the velocity vectors (refer to Fig. 2c).
Assuming a flat base and neglecting any indentation of the pivot with respect to the geometrical corner of the wall, the potential energy is equal to:

$$V = mg(P_{G,A,y} + \chi P_{D,A,y}) + \frac{1}{2} k_d S_{D,A,x}^2$$

where:
g is the gravity acceleration; $P_{G,A,y}$, $P_{D,A,y}$ are the y-component of position vectors; k_d is the stiffness of the spring; $S_{D,A,x}$ is the x-component of displacement vector (refer to Fig. 2c).
The non-conservative force Q is obtained after derivation of the virtual work W:

$$Q = \frac{dW}{d\theta}$$

The virtual work is obtained as:

$$W = -m\ddot{x}_g \left(S_{G,A,x} + \chi S_{D,A,x}\right) - m\ddot{y}_g \left(S_{G,A,y} + \chi S_{D,A,y}\right)$$

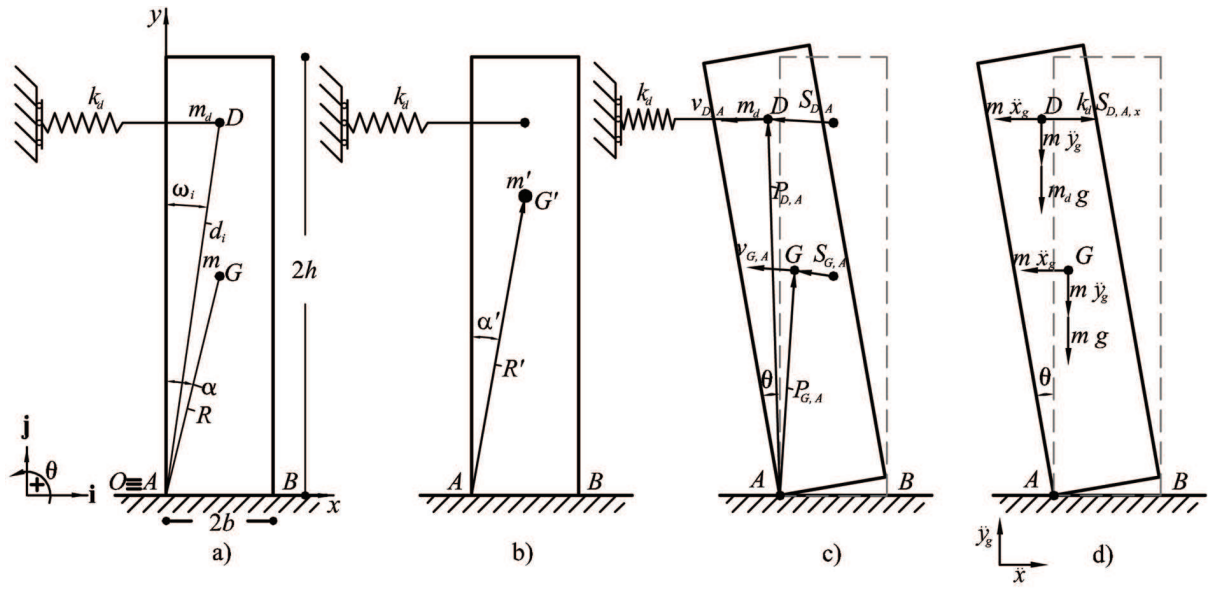


Figure 2: Proposed model: a) Geometric parameters; b) Centre of mass of wall mass + diaphragm mass; c) Position, displacement, and velocity vectors; and d) Conservative and non-conservative forces

where:
$\ddot{x}_g$, $\ddot{y}_g$ are the ground accelerations in x-direction and y-direction, respectively; $S_{D,A,y}$, $S_{G,A,y}$ are the y-component of displacement vectors (refer to Fig. 2c); $S_{G,A,x}$ is the x-component of the displacement vector.

By substituting all the terms in Eq. (1), one can find the following second order non-linear differential equation:

$$\ddot{\theta} \;=\; -p'^2 \left[\frac{\ddot{x}_g}{g} N_1(\alpha', \theta) + \frac{g + \ddot{y}_g}{g} N_2(\alpha', \theta) + \lambda N_3(R', d_i, \omega_i, \theta) \gamma(\theta) \right] \tag{2}$$

where:

$\ddot{\theta} =$ angular acceleration of the body;

$p' = \sqrt{\dfrac{m'R'g}{I'_O}}$, (frequency parameter of the wall [12]);

$m' = m + m_d$;

$R', \alpha' =$ polar coordinates of the centre of mass G' of the system, wall + diaphragm (refer to Fig. 2b);

$d_i, \omega_i =$ polar coordinates of diaphragm connection point D (refer to Fig. 2a);

$I'_O = I_G + m'R'^2$;

$\lambda = \dfrac{k_d R'}{m'g}$;

$\gamma(\theta) =$ fracture function; $\theta_u =$ fracture rotation (refer to Fig.3).

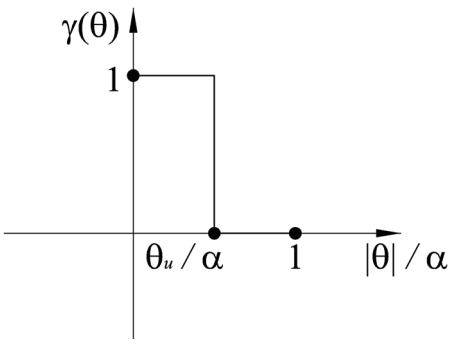


Figure 3: Fracture function of spring

The restraint is assumed as a linear-elastic spring, effective up to a limit displacement related to a limit rotation θ_u. Hence, the spring is active only if the fracture function $\gamma(\theta)$ = 1 (refer to Fig. 3). A qualitatively similar restraint has been considered in [13], where it anchored a block to its foundation. In some of the following analyses an additional condition will be set on the rotation causing the failure of the wall-spring connection. Once this connection has failed the wall will still carry the additional mass but will lose the contribution N_3 in Eq. (2). This condition can be considered representative of a facade losing the contribution of tie-rods. If the failure of the spring is considered as the ultimate limit state, the following plots shall be considered as meaningful up to the limit rotation θ_u/α.

It is possible to emphasise that if m_d = 0 the results can be interpreted as related to a wall restrained by tie-rods. If, additionally, χ = 0, the equation of motion reduces to that by Housner [14].

The condition of minimum ground acceleration for the initiation of motion from rest, when subjected to a base excitation, is given by: $\ddot{x}_g \geqslant \tan\alpha'(g+\ddot{y}_g)$. The condition for overturning is $\theta = \pi/2$. In case of overturning, for the sake of simplification of the following plots, normalised maximum rotation will be set equal to unity.

2.2 Dissipation of energy

Eq. (2) has no damping term. During the rocking motion the block impacts the base and a change of hinge from one corner to the other takes place. A loss of energy is associated to this switch of hinge, through a reduction of velocity after impact. This velocity is derived by assuming the conservation of angular momentum at the instant of impact [14], considering the position of the centre of mass G'. Experimentation on free rocking walls has shown that the analytical coefficient of restitution must be reduced by approximately 5 $\%$ [15]. Although this value was obtained for free-standing walls, it will be assumed also for the case at hand.

The solution of Eq. (2) is obtained through a state-space formulation and a Runge-Kutta method with variable time step in a Matlab environment. The impacts, spring fracture, and overturning are detected through an event strategy.

3 PARAMETRIC ANALYSIS

The derived equation of motion is used to evaluate the effect of wall aspect ratio and size, diaphragm mass, diaphragm stiffness, spring displacement capacity, ground excitation. Based on [10], twelve different aspect ratios are considered, taking $\alpha = [0.025 : 0.025 : 0.300]$ rad. Four values are selected for the size of the wall: $R = [1.5, 3.0, 4.5, 6.0]$ m. Five values of the diaphragm mass / wall mass ratio have been considered: $\chi = [0.00 : 0.05 : 0.20]$. Minimum

No.	Event	Year	Station	Component	PGA	PGV
					g	cm/s
1	Imperial Valley CA, USA,	1940	El Centro Array	40ELC180	0.31	29.80
2	Kern County, CA, USA	1952	Talf Lincoln School	TAFT111	0.18	17.61
3	San Fernando, CA, USA	1971	Pacoima Dam, abutment	PAC164	1.17	114.40
4	Friuli, Italy	1976	Tolmezzo	TOLMEZWE	0.35	32.11
5	Imperial Valley, CA, USA	1979	Site 1	IVC230	0.46	109.26
6	Imperial Valley, CA, USA	1979	Bonds Corner	BCR230	0.78	45.90
7	Irpinia, Italy	1980	Sturno	STURWE	0.31	70.00
8	Irpinia, Italy	1980	Bagnoli Irpino	BAGNIRWE	0.17	37.70
9	Irpinia, Italy	1980	Calitri	CALITWE	0.18	31.72
10	Nahanni, Canada	1985	Site 1	1ST280	1.10	46.10
11	Michoacan,Mexico	1985	Secretaria comunication zone and tran. Texcoco lake bed	SECREN27	0.17	59.81
12	Chile	1985	Llolleo	LLOLLN10	0.71	41.76
13	Landers, CA, USA	1992	Joshua Tree Fire	JOSHUA90	0.28	42.68
14	Northridge, CA, USA	1994	Rinaldi Receiving Station	RRS228	0.84	166.10
15	Northridge, CA, USA	1994	Sylmar-Olive View Med Parking Lot Free Field	SYL360	0.84	129.37
16	Kobe, Japan	1995	KJMA	KJM000	0.82	81.30
17	Kobe, Japan	1995	Takatori	TAK000	0.61	127.10
18	Umbria-Marche	1997	Colfiorito	R1139EW	0.44	24.60
19	ChiChi, Taiwan	1999	TCU129	TCU129W	1.01	59.62
20	Kocaeli, Turkey	1999	Yarimca Petrokimya Tesisleri	YPT330	0.35	62.18
21	L′Aquila, Italy	2009	Val Aterno, Fiume Aterno	AQAX	0.39	30.53
22	L′Aquila, Italy	2009	Val Aterno, Colle Grilli	AQGX	0.42	33.57
23	L′Aquila, Italy	2009	Val Aterno, Aquilparking	AQKY	0.34	38.53
24	L′Aquila, Italy	2009	Val Aterno, Castello	AQUX	0.28	20.91
25	L′Aquila, Italy	2009	Val Aterno, Centro Valle	AQVX	0.63	32.67

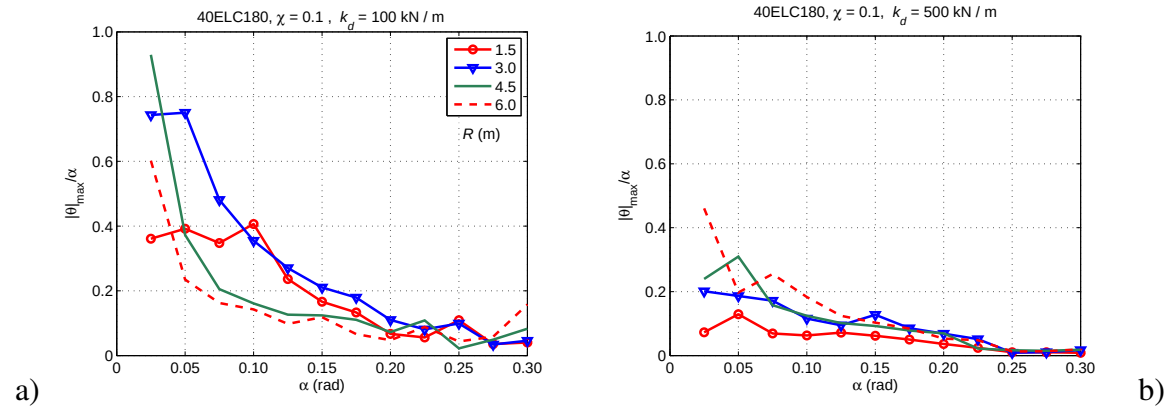
Table 1: Acceleration time history records considered. PGA (PGV) = Peak Ground Acceleration (Velocity).

and maximum values of the geometric parameters of the combined system result α' = 0.03, 0.26 rad and R' = 1.50, 6.92 m.

As for diaphragm stiffness, Derakhshan [7] suggested as minimum and maximum values approximately 100 and 5000 kN/m. These values are considered relevant for New Zealand and North American buildings. Consequently, five values of diaphragm stiffness are chosen: $k_d = [0, 100, 500, 1000, 5000]$ kN/m. Displacement capacity of diaphragms is simply varied parametrically, θ_u/α = [0.2 : 0.2 : 1.0]. A much larger maximum value, 10, has been also considered but is not plotted in the following, because delivers results rather similar to θ_u/α = 1.0. It is worth mentioning that Wilson [16] suggested a diaphragm limit displacement equal to 70% of the wall thickness.

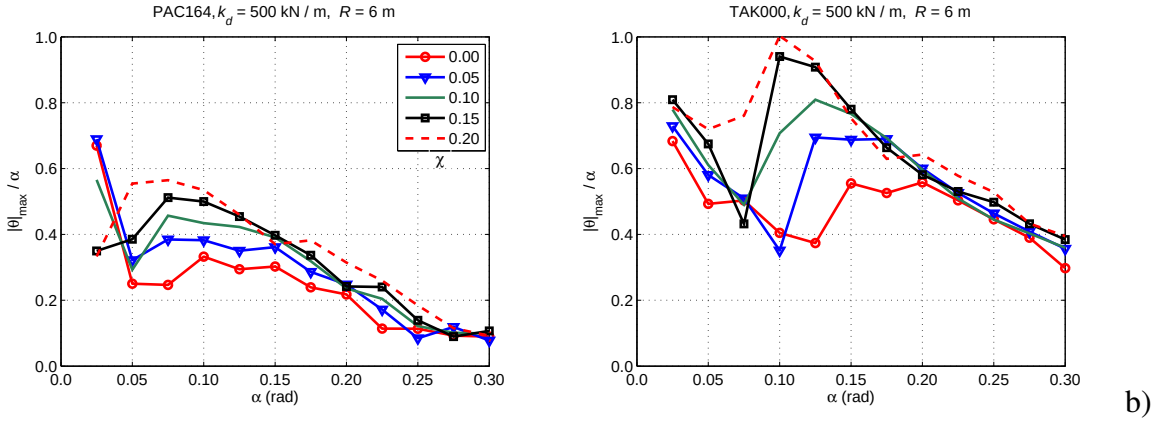
Twenty five acceleration natural records have been selected in order to cover a wide range of amplitude, frequency content, distance from the source, magnitude, source mechanism. The accelerograms are mostly the same in [17], with the addition of a few records related to more recent seismic events [18]. Only horizontal components of ground motion are considered. Some basic details of the accelerograms are shown in Table 1.

The total number of analyses computed is equal to 30 000. The response of the wall is plotted as normalised maximum rotation (y-axis), and as a function of α (x-axis) plus one of the parameters previously mentioned.



a) b)

Figure 4: Normalised maximum rotation for varying aspect ratio, angle α, and wall size R. Non dimensional diaphragm mass $\chi = 0.10$, Fracture rotation θ_u/α = 1.0, record 40ELC180 (Table 1). Diaphragm stiffness: a) $k_d = 100$ kN/m; b) $k_d = 500$ kN/m.



a) b)

Figure 5: Normalised maximum rotation for varying aspect ratio, angle α, and non dimensional diaphragm mass, χ. Size of the wall, R = 6.0 m, Diaphragm stiffness $k_d = 500$ kN/m, Fracture rotation θ_u/α = 1.0. Record: a) PAC164; b) TAK000 (Table 1).

3.1 Effect of wall size

It is well known in the literature that, other things being equal, rocking systems benefit from a larger size [14, 17]. This is the case also here, if the stiffness of the spring is comparatively small (refer to Fig. 4a). However, if the stiffness is increased the role of this so-called "scale effect" becomes less significant, and actually a "reversed scale effect" can be observed (refer to Fig. 4b). This appears to be so because the stability of the wall relies more and more on the spring. Nonetheless, the same spring, having constant stiffness, is used for walls of different size and, thus, weight. Consequently, the spring is more effective for small (lighter walls), than for large (heavier) walls.

3.2 Effect of diaphragm mass

The effect of non-dimensional diaphragm mass is investigated in Fig. 5. There it is possible to notice that increasing the floor mass, the response increases. This behaviour can be linked to the increase of the height of the centre of mass of the combined system, making the system more slender through a smaller angle α' (refer to Fig. 2b). This effect, detrimental on stability, is not compensated by the beneficial increase of size, R', associated to the additional floor mass.

3.3 Effect of diaphragm stiffness

In Fig. 6 the stiffness of the diaphragm is varied parametrically. The relevance of this parameter is dramatic, with large values of k_d significantly reducing the maximum rotation. Of course this depends on the assumption of a single-body mechanism. If the spring is that stiff and the connection is adequately robust, a different mechanism (with an intermediate hinge [10]), can be triggered and needs to be assessed. Low values of the stiffness show a less predictable behaviour, and the scattered response typical of rocking systems prevails.

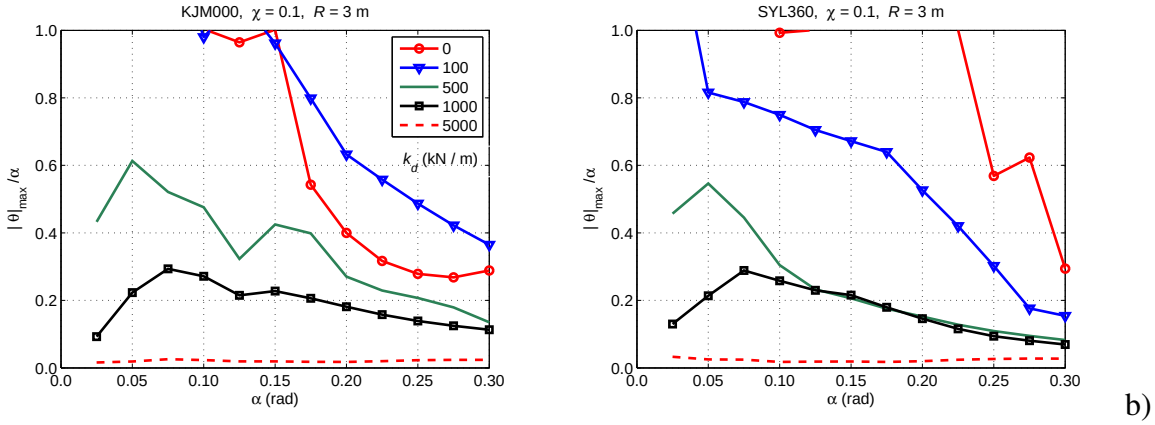


Figure 6: Normalised maximum rotation for varying aspect ratio, angle α, and diaphragm stiffness, k_d. Wall size R = 3.0 m, Non dimensional diaphragm mass $\chi = 0.10$, Fracture rotation θ_u/α = 1.0. Record: a) KJM000; b) SYL360 (Table 1).

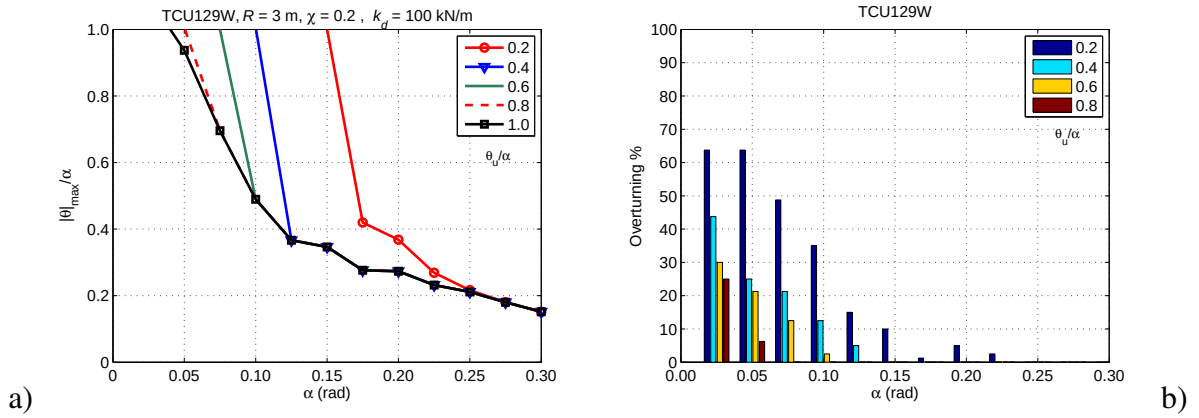


Figure 7: a) Normalised maximum rotation for varying aspect ratio, angle α, and non-dimensional rotation inducing the failure of the spring, θ_u/α. Size of the wall, R = 3.0 m, Non dimensional diaphragm mass χ = 0.2, Diaphragm stiffness $k_d = 500$ kN/m, Record: TCU129 (Table 1). b) Occurrence of overturning, varying non-dimensional fracture rotation, over the entire range of parametric analyses. For θ_y/α = 1.0, no overturning occurs. Record TCU129 (Table 1).

3.4 Effect of displacement capacity of the spring

The role of the displacement capacity of the spring is investigated in Fig. 7. Reducing the fracture rotation will cause an increase in the wall response, because the contribution N_3 in Eq. (2) will be lost. This is evident both in terms of maximum rotation (refer to Fig. 7a) and in

terms of occurrence of overturning (refer to Fig. 7b). The effect is less relevant for large values of α because, in this case, the wall is stable in itself.

3.5 Effect of ground acceleration record

The record-to-record sensitivity is investigated in Fig. 8. There the accelerograms are sorted for descending PGV (Peak Ground Velocity). The response shows an increasing trend for increasing PGV, as already observed in the literature for rocking systems ([19]), but this intensity measure is not sufficient to explain the observed behaviour. Some records (e.g., STURWE,

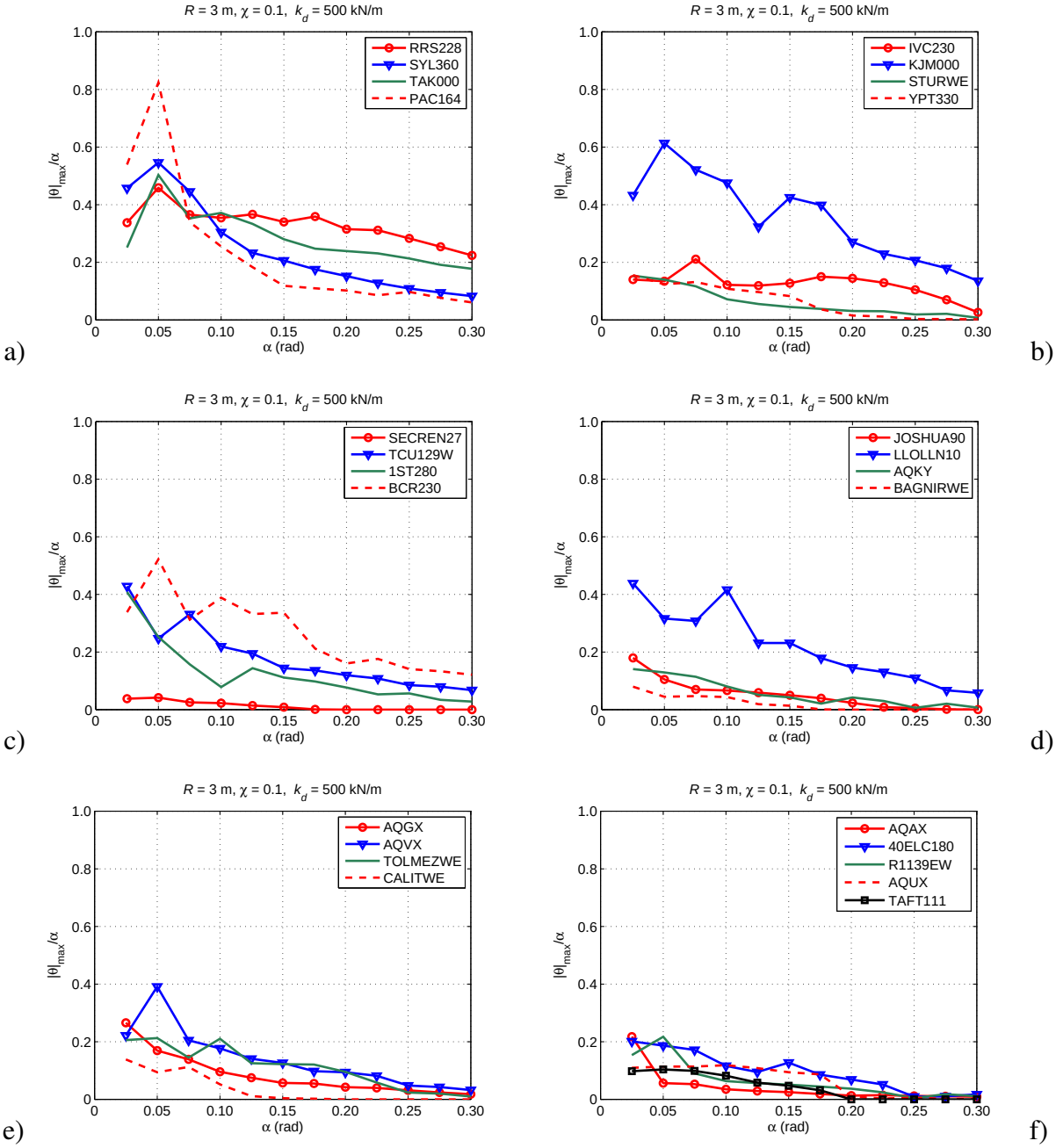


Figure 8: Normalised maximum rotation for varying aspect ratio, angle α, and Record (Table 1). Accelerograms sorted, a)-f), for descending Peak Ground Velocity. Size of the wall R = 3.0 m, Non-dimensional diaphragm mass χ = 0.10, Diaphragm stiffness k_d = 500 kN/m, Fracture rotation θ_u/α = 1.0.

YPT330, SECREN27) show a comparatively low maximum amplitude, despite the rather high PGV. In such cases the motion is not activated, or is barely activated, because the minimum acceleration is comparable with the PGA (Peak Ground Acceleration) of the record. The opposite takes place when, for similar PGV, the PGA is rather large (e.g., KJM000, LLOLLN10). Finally, it is possible to notice that an increasing stiffness of the restraint makes the response less scattered.

4 CONCLUSIONS

In this paper the non-linear equation of motion of a single-body wall supporting an additional mass and restrained by an elastic spring has been derived. The wall has a flat base and no indentation at the pivot corners. The spring may represent both a flexible diaphragm and a strengthening intervention through tie-rods.

The equation is used to investigate the sensitivity to a number of parameters. Some of these are related to the wall geometry. The response decreases with a decreasing aspect ratio (height/thickness ratio). Similarly it decreases with an increasing size of the wall. This latter effect is evident if the stiffness of the diaphragm is comparatively low. However, if the stiffness becomes substantial, a ”reversed scale effect” can be observed: the larger the wall the larger the response because the wall is heavier and the spring becomes less effective.

Other parameters are related to the diaphragm. Increasing its mass, compared to the wall, will cause an increase in the maximum rotation, because the centre of mass of the combined system is shifted to the top. The stiffness of the diaphragm is a parameter that dramatically influences the results. High, but still reasonable, values of the stiffness can substantially limit the response. However, in such case, it is necessary to check the robustness of the connections and the activation of a different mechanism, displaying an intermediate hinge. The displacement capacity of the restraint is also significant, because after the premature failure of the spring the stability of the system will rely on its geometry alone.

Record sensitivity is reduced by an increasing spring stiffness. Moreover, the system displays a sensitivity to Peak Ground Velocity, as observed in the literature for other rocking systems. However, this intensity measure is not sufficient to explain completely the observed response. In fact, due to the assumed flat base, sometimes the motion is not activated or it is barely activated.

The study needs to be completed investigating both ground motion characteristics (especially the role of the vertical component), wall characteristics (imperfections and indentations at the base), diaphragm characteristics (position with respect to wall height, displacement capacity and asymmetric - internal-external - behaviour), characteristics of the connection between wall and diaphragm (in order to establish possible dynamic amplifications and the role of an elasto-plastic response), and to consider this mechanism within a wider framework where other mechanisms are also accounted for.

ACKNOWLEDGEMENTS

The authors acknowledge the contribution of the European Commission through a PhD fellowship to the first author within the EU-NICE Erasmus Mundus project [20]. This work has been partially carried out under the program ”Dipartimento della Protezione Civile - Consorzio ReLUIS”, signed on 2013-12-27, Research line Masonry structures. The opinions expressed in this publication are those of the authors and are not necessarily endorsed by the Dipartimento della Protezione Civile.

REFERENCES

[1] M. Bruneau, State-of-the-art report on seismic performance of unreinforced masonry buildings. *Journal of Structural Engineering*, **120**, 230-251, 1994.

[2] L. Sorrentino, L. Liberatore, D. Liberatore, R. Masiani, The behaviour of vernacular buildings in the 2012 Emilia earthquakes. *Bulletin of Earthquake Engineering*, **12**, 2367-2382, 2014. DOI: 10.1007/s10518-013-9455-2.

[3] L. Sorrentino, L. Liberatore, L. D. Decanini, D. Liberatore, The performance of churches in the 2012 Emilia earthquakes. *Bulletin of Earthquake Engineering*, **12**, 2299-2331, 2014. DOI: 10.1007/s10518-013-9519-3.

[4] O. A. Shawa, G. Felice, A. Mauro, L. Sorrentino, Out-of-plane seismic behaviour of rocking masonry walls. *Earthquake Engineering and Structural Dynamics*, **41**, 949-968, 2012. DOI: 10.1002/eqe.1168.

[5] ABK, Joint Venture, *Methodology for mitigation of seismic hazards in existing unreinforced masonry buildings: wall testing, out of plane*. Agbabian Associates:El Segundo, CA, 1981.

[6] C. C. Simsir, M. A. Aschheim, D. P. Abrams, Out-of-plane dynamic response of unreinforced masonry bearing walls attached to flexible diaphragms. *In Proceedings of the 13ˆth World Conference on Earthquake Engineering*, Vancouver, B.C., Canada, August 1-6, 2004.

[7] H. Derakhshan, *Seismic assessment of out of plane loaded unreinforced masonry walls*. ResearchSpace@ Auckland, 2011.

[8] O. Penner, *Out-of-plane dynamic stability of unreinforced masonry walls connected to flexible diaphragms*. The University of British Columbia, Faculty of Graduate and Postdoctoral Studies, 2014.

[9] T. M. Ferreira, A. A. Costa, A. Costa, Analysis of the out-of-plane seismic behaviour of unreinforced masonry: A literature review. *International Journal of Architectural Heritage*, 2014. DOI: 10.1080/15583058.2014.885996.

[10] L. Sorrentino, R. Masiani, M. Griffith, The vertical spanning strip wall as a coupled rocking rigid body assembly. *Structural Engineering and Mechanics*, **29**, 433-453, 2008.

[11] L. Meirovitch, *Elements of vibration analysis, Vol. 2*. New York: McGraw-Hill, 1986.

[12] A. Mauro, G. de Felice, M. J. DeJong, The relative dynamic resilience of masonry collapse mechanisms. *Engineering Structures*, **85**, 182-194, 2015. DOI: 10.1016/j.engstruct.2014.11.021.

[13] N. Makris, J. Zhang, Rocking response of anchored blocks under pulse-type motions. *Journal of Engineering Mechanics*, **127**, 484-493, 2001. DOI: 10.1061/(ASCE)0733-9399(2001)127:5(484).

[14] G. W. Housner, The behavior of inverted pendulum structures during earthquakes. *Bulletin of the seismological society of America*, **53**, 403-417, 1963.

[15] L. Sorrentino, O. AlShawa, L. D. Decanini, The relevance of energy damping in unreinforced masonry rocking mechanisms. Experimental and analytic investigations. *Bulletin of Earthquake Engineering*, **9**, 1617-1642, 2011. DOI: 10.1007/s10518-011-9291-1.

[16] A. W. Wilson, *Seismic assessment of timber floor diaphragms in unreinforced masonry buildings*. Doctoral dissertation, ResearchSpace@ Auckland, 2012.

[17] L. Sorrentino, R. Masiani, L. D. Decanini, Overturning of rocking rigid bodies under transient ground motions. *Structural Engineering and Mechanics*, **22**, 293-310, 2006.

[18] L. Sorrentino, O. Alshawa, D. Liberatore, Observations of Out-of-Plane Rocking in the Oratory of San Giuseppe Dei Minimi during the 2009 L'Aquila Earthquake. *Applied Mechanics and Materials*, London; United Kingdom, June 21-22, 2014. Code 107472. DOI: 10.4028/www.scientific.net/AMM.621.101.

[19] L. Sorrentino, D. DAyala, G. de Felice, M. Griffith, S. Lagomarsino, G. Magenes, Review of out-of-plane seismic assessment techniques applied to existing masonry buildings. *International Journal of Architectural Heritage*, submitted 2015.

[20] M. Faggella, G. Monti, F. Braga, R. Gigliotti, M. Capelli, E. Spacone, M. Laterza, T. Triantafillou, H. Varum, M. Dost Safi, J. Subedi, A. Dixit, S. Lodi, Z. Rahman, S. Limkatanyu, Y. Xiao, L. Yingmin, H. Kumar, W. Salvatore, A. Cecchini, P. Lukkunaprasit, EUNICE, Eurasian University Network for International Cooperation in Earthquakes. *15ˆth World Conference of Earthquake Engineering,(15WCEE)*, Lisboa, Portugal, September 24-28, 2012.

COMPDYN 2015
5th ECCOMAS Thematic Conference on
Computational Methods in Structural Dynamics and Earthquake Engineering
M. Papadrakakis, V. Papadopoulos, V. Plevris (eds.)
Crete Island, Greece, 25–27 May 2015

INVESTIGATION OF DYNAMIC RESPONSE OF ROCKING WALL STRUCTURES USING INELASTIC MODAL DECOMPOSITION TECHNIQUE

Irshad M. Qureshi[1], **Pennung Warnitchai**[1,] **Tahir Mehmood**[1]

[1] School of Civil Engineering, Asian Institute of Technology, Thailand
e-mail: st107392@ait.asia, pennung@ait.asia

Keywords: Rocking wall structures, acceleration spikes, inelastic modal decomposition

Abstract. *Precast post-tensioned concrete rocking wall structures have been developed in the recent past as innovative damage avoidance structural systems. Recent experimental tests have identified the presence of large-amplitude high-frequency acceleration spikes in the dynamic response of rocking wall structures. The current study is focused on the investigation of the effects of these acceleration spikes on the dynamic performance of rocking wall structures. For this purpose, a 4 story rocking wall structure is designed and the response history analysis is performed. The results show a significant contribution of higher modes in the acceleration response which can increase the shear demand considerably. To further investigate these higher mode accelerations, inelastic modal decomposition of dynamic response is performed. Results show that the inelastic modal decomposition technique can be effectively used to understand and quantify the effects of these acceleration spikes and it can also be employed to check the effectiveness of different mitigation strategies for acceleration spikes.*

1 INTRODUCTION

Typically, seismic codes allow the structures to undergo large non-linear deformations against the rare seismic events while avoiding a total collapse of the structure. Although it ensures the life safety of occupants, excessive damage to the structures leads to a costly retrofitting and becomes a hindrance to the immediate serviceability of the structure after a major seismic event. In the recent past, extensive research work has been carried out to develop structural systems that are capable of resisting large seismic actions without inducing any significant damage to the structural members. Precast Seismic Structural Systems (PRESSS) technology [1] represents such a solution that relies on a nonlinear elastic behavior of gap opening and closing at the connection to accommodate the lateral demand without incurring any damage to the precast members. Such a connection is called as a rocking connection, developed essentially for beam column joints, but later on extended to the precast shear walls [1, 2]. A shear wall with a rocking connection is called as a rocking wall. A rocking wall consists of vertically stacked precast concrete panels clamped by unbonded Post-Tensioning (PT) from the top of the wall to the foundation. Initial post-tensioning in the PT tendons along with the self-weight resist the lateral force demand and once the lateral actions overcome the vertical forces, the wall starts to rock about its toes, commonly referred as Gap opening. The gap opening and closing phenomenon in a dynamic environment cause a high velocity contact simply called as impact between the wall base and the foundation. Recent experimental work on the dynamic performance of rocking walls have shown that the impact of wall base with the foundation can cause short-duration large-amplitude acceleration spikes in lateral direction called as Horizontal Acceleration Spikes (HAS). HAS phenomenon is not unique to the dynamic response of rocking wall structures only, but are also found in the systems whose dynamic response shows a sudden change in force values or direction such as self-centering and friction-damped base isolation systems [3, 4]. Wiebe and Christopoulos [5] analyzed the source of HAS in rocking wall structures and identified that a sharp change in the rate of change of elastic force during gap opening and closure at rocking wall-foundation interface creates an imbalance of forces in the system. To maintain the dynamic equilibrium, seismic masses accelerate and thus create an acceleration spike in lateral direction. In a low rise rocking wall where the gap would open in the first mode response, acceleration spikes can be described as an excitation of higher modes due to a change of force in first mode implying an interaction of different modes. HAS cannot only increase the inertial forces at different floor levels, but can also cause damage to the acceleration-sensitive non-structural elements like fire suppression systems, suspended ceilings, emergency power generators and computer systems [6]. Hence, there is need to identify, quantify and reduce these acceleration spikes. This work aims to quantify the effects of lateral acceleration spikes on the seismic demands of the rocking walls. For this purpose, a 4 story rocking wall is selected to investigate and quantify the effects of acceleration spikes on the dynamic performance of rocking wall structures.

2 CASE STUDY STRUCTURE

Previous experimental works have shown that the lateral acceleration spikes are more visible in low-rise rocking walls. Also, the presence of a dedicated Energy Dissipation (ED) mechanism for rocking walls is found to decrease the intensity of these effects. To investigate the phenomenon of HAS, a low-rise 4 story rocking wall with no external energy dissipation mechanism is selected. This will ensure that the acceleration spikes are more visible in the system response, making it easier to study in detail. Figure 1 and Table 1 shows the dimensions and different properties of the case study rocking wall. The case study rocking wall is part of a

complete structural system and is assumed to take all the lateral load of the structure. The connection between floor and the rocking wall is assumed to be similar to the one being used in Diaphragm Seismic Design Methodology (DSDM) project [7]. This vertically sleeved connection allows the lateral forces to be transmitted from the floor to the wall while prohibiting any vertical action to be transmitted from the rocking wall to flooring units. A constant story height of 3m is used for all floor levels. The lumped mass in lateral direction represents the floor load while the vertical seismic mass is the mass of the rocking wall only.

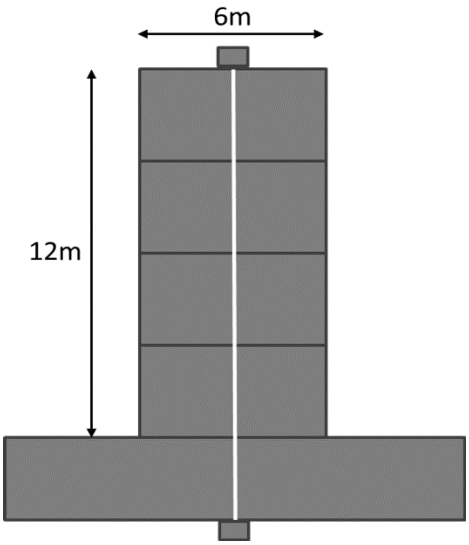


Figure 1: Case study rocking wall.

Table 1: Properties of case study rocking wall.

Thickness of wall (mm)		300
Comp. strength of wall concrete (MPa)		45
Ultimate strength of PT steel (MPa)		1860
Initial post-tensioning (MPa)		651
Area of Post-tensioning (mm^2)	No ED	15300
	With ED	7595
Total area of ED bars (mm^2)		11187
Lateral seismic mass for each floor (Ton)		350
Modal periods (sec)	1st Mode	0.395
	2nd Mode	0.073
	3rd Mode	0.035

The case study building is assumed to be located at a California site (Postal code 91495) with a soil type S_D. A suite of 5 pairs of 10 ground motions is selected such that the scaled spectra of the selected ground motions resemble the target spectrum. Furthermore, RSPmatch2005b software [8] is used for the time domain spectral matching of the ground motions spectrums with the target spectrum. Figure 2 shows the design spectra for the site along with the matched spectrums of different ground motions. Design forces for the case study rocking wall are calculated by using force based design procedure in accordance with the earlier works on the design of rocking wall structures [9].

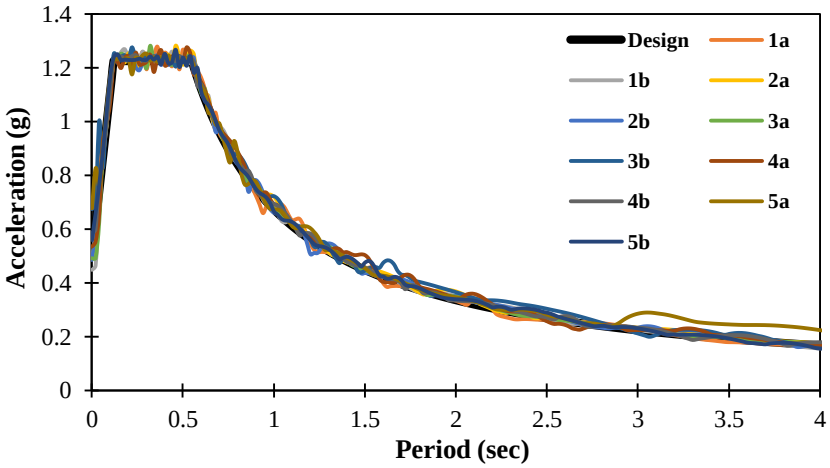


Figure 2: Matched ground motions spectra for 5% damping.

3 DYNAMIC MODELING OF ROCKING WALL

Different modeling techniques like lumped plasticity model, multi-spring fiber model and finite element models have been used in the past for the modeling of rocking wall structures. Lumped plasticity model is the simplest one but the input behavior of the bilinear elastic / flag shaped hysteresis for rocking/hybrid walls with sharp edged corners at gap opening and closure are found to increase the HAS unjustifiably [10]. 2D Multi-spring fiber model has been found efficient in predicting the neutral axis migration with significant accuracy and also gives relatively round corners at the gap opening and closure, provided that enough base springs are used. 3D finite element models are quite efficient in predicting the overall dynamic response as well as the local behavior due to impact at the wall-foundation connection. However, finite element models are computationally expensive, especially for the dynamic analyses. For the current study, multi-spring fiber model is selected as it is robust and computationally economical.

3.1 Multi-spring Fiber Model

Ruaumoko 2D [11] is used for the multi-spring fiber modeling of rocking wall. The model is shown in Figure 3. Modeling of different materials and members have been done based on the recommendations proposed by Smith and Kurama [12]. Elastic beam-column element is used to represent the rocking wall. PT steel is modeled by using a truss member with a pre stressing force and an elasto-plastic hysteresis behavior. Gap opening at the wall base is modeled by using a number of compression only contact springs connecting the wall base with the foundation through a rigid member to simulate plane section remain plane behavior. Contact spring stiffness basically comes from the axial stiffness of rocking wall and foundation and can be idealized as two axial springs acting in series. Assuming that the foundation is near rigid, rocking wall axial stiffness can be used as contact stiffness by using the relationship for axial stiffness as E_cA_c/H_c, where E_c, A_c and H_c are the modulus of elasticity of wall concrete, area of concrete that a particular spring is representing and the height of rocking wall contributing to the axial stiffness of rocking wall. Previous studies [13, 14] have found that a value of H_c equal to $0.5L_w$ gives reasonably accurate results and this value is used in the current study. 25 contact springs are used in this study to accurately predict the migration of neutral axis. Wilson-Penzien damping model which allows the users to provide constant modal damping for different modes have been used in this study. A constant 3% damping for all the modes have been used which is consistent with the findings of the previous experimental works [15, 16]. Nonlinear Response History Analysis (NLRHA) is conducted for the case study rocking wall for the selected ground motions. The selected ground motions are scaled up 1.5 times to represent a Maximum Considered Earthquake (MCE) level hazard.

4 NLRHA RESULTS

Figure 4 shows the envelope results for the time history analysis along with the design values. Lateral drift values for the rocking wall is found to be higher than the design value because of the lack of energy dissipation mechanism for rocking wall. The envelope results of lateral acceleration show the average value to be equal to 2g at the top floor. Furthermore, a bulge in the acceleration envelope at around first story shows the presence of higher mode effects in the acceleration response. Similar trend can be seen in the shear envelope where the average base shear value is 3.25 times the design value which is quite high for a 4 story structure.

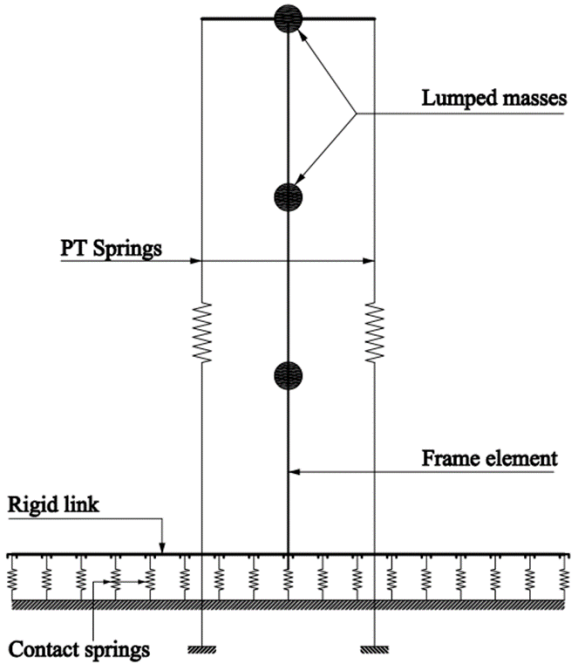


Figure 3: 2D Multi-spring fiber model.

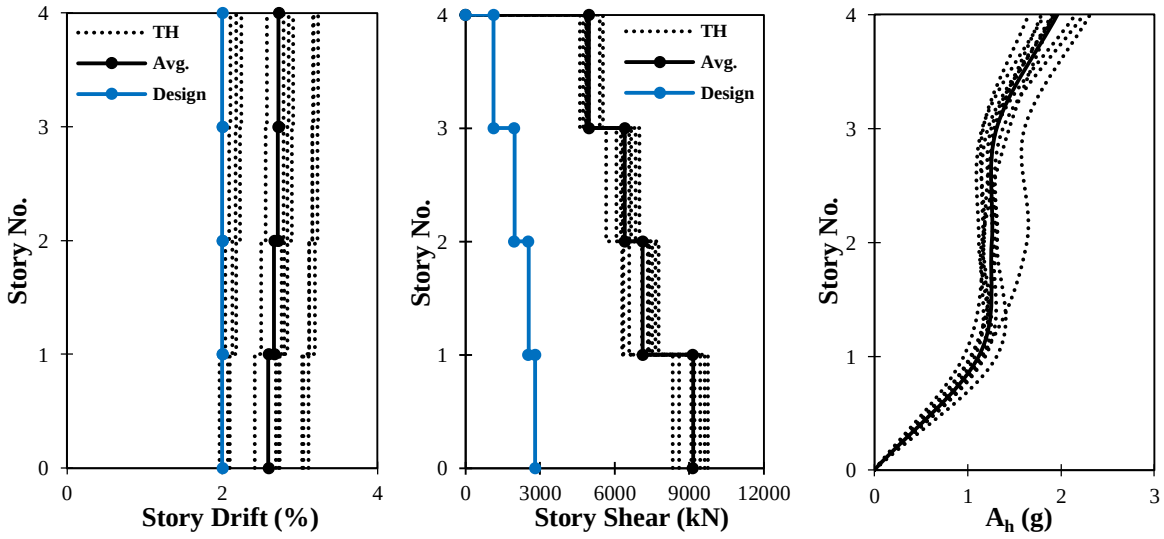


Figure 4: Comparison of envelope results.

To further study these higher mode effects, Figure 5 shows the time history of lateral accelerations at different floor levels for a particular ground motion. Lateral acceleration spikes have been recognized in the past experimental works as a peak in the acceleration values right after the gap opening and closure. Similar trend is obvious in the lateral acceleration histories where the acceleration values peaks during the start of a vibration cycle. Figure 6 shows the histories of story shear forces. The top story shear is found to be affected most by these acceleration spikes.

As explained earlier, the HAS phenomenon is a manifestation of the excitation of higher modes due to a sudden change of force in the first mode response implying a strong coupling of the modes. To further understand this phenomenon, different modal responses are separated to see their contribution to the total response. Modal decomposition techniques have been developed in the past to separate the total responses into modal responses [17-19]. Uncoupled

Modal Response History Analysis (UMRHA) procedure is one such technique that is based on the decomposition of total responses into uncoupled modal responses.

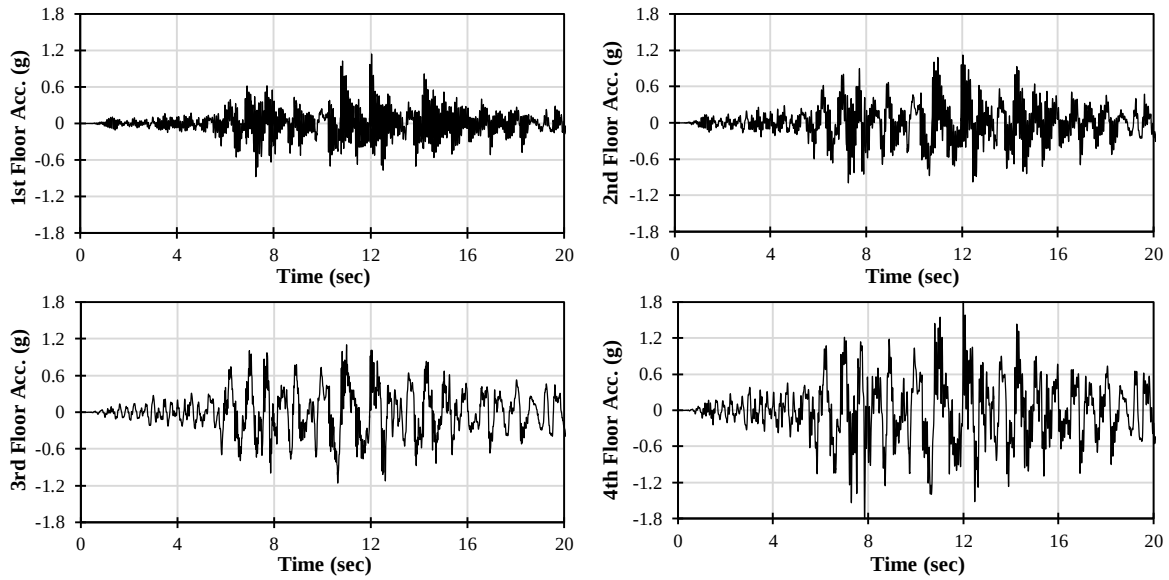


Figure 5: Time history of floor accelerations.

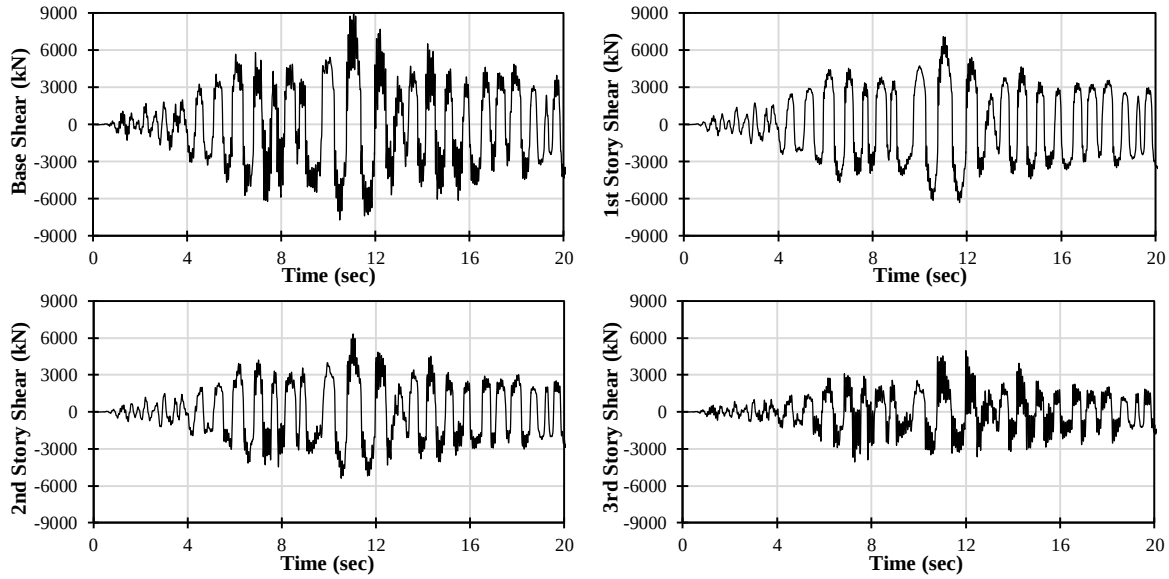


Figure 6: Time history of story shears.

5 UMRHA PROCEDURE

The UMRHA procedure [17] can be viewed as an extended version of the classical modal analysis procedure. In the latter, the complex dynamic responses of a linear Multi-Degree-of-Freedom (MDOF) structure are considered as a sum of many independent vibration modes. The response behavior of each mode is essentially similar to that of a Single-Degree-of-Freedom (SDOF) system which is governed by a few modal properties, making it easier to understand. Furthermore, only a few vibration modes can accurately describe the complex structural responses in most practical cases. This classical modal analysis procedure is applicable to any linear elastic structure. However, when the responses exceed the elastic limits, the governing

equations of motion become nonlinear and, consequentially, the theoretical basis for modal analysis becomes invalid. Despite this, the UMRHA procedure assumes that, even for inelastic responses, the vibration modes still exist, and the complex inelastic responses can be approximately expressed as a sum of these modal responses. By following this presumption, governing equation of motion of SDOF to a horizontal ground motion $\ddot{x}_g(t)$ can be written as:

$$\ddot{D}_i + 2\xi_i\omega_i\dot{D}_i + F_{si}(D_i, \dot{D}_i)/L_i = -\ddot{x}_g(t) \quad (1)$$

Where $L_i = M_i\Gamma_i$ and $M_i = \boldsymbol{\phi}_i^T\mathbf{M}\boldsymbol{\phi}_i$, ω_i and ξ_i are the natural vibration frequency and the damping ratio of the i[th] mode, respectively. Equation (1) is a standard governing equation of motion for inelastic SDOF systems. To compute the response time history of $D_i(t)$ from this equation, one needs to know the nonlinear function $F_{si}(D_i, \dot{D}_i)$. A cyclic pushover analysis is performed for each important mode to identify the nonlinear function $F_{si}(D_i, \dot{D}_i)$. The cyclic pushover analysis for the i[th] mode can be carried out by applying a force vector with the i[th] modal inertia force pattern $\boldsymbol{s}_i^* = \mathbf{M}\boldsymbol{\phi}_i$ (where M is the mass matrix of the building and $\boldsymbol{\phi}_i$ is the i[th] natural vibration mode of the building in its linear range. The relationship between roof displacement, obtained from the cyclic pushover (denoted by x_i^r), and Di is approximately given by

$$D_i = x_i^r/(\Gamma_i\phi_i^r) \quad (2)$$

where ϕ_i^r is the value of $\boldsymbol{\phi}_i$ at the roof level. The relationship between the base shear V_{bi} and F_{si} under this modal inertia force distribution pattern is given by

$$F_{si}/L_i = V_{bi}/\Gamma_i L_i \quad (3)$$

By this way, the results from the cyclic pushover analysis are first computed in the form of cyclic base shear (V_{bi})—roof displacement (x_i^r) relationship, and then transformed into the required F_{si}— D_i relationship. At this stage, a suitable nonlinear hysteretic model can be selected, and its parameters can be tuned to match with this F_{si}— D_i relationship. The response time history of $D_i(t)$ as well as $F_{si}(t)$ can then be calculated from the nonlinear governing Equation (1). The response of each mode belongs to the i[th] vibration mode and can be generally represented by $r_i(t)$. By summing the responses of all significant modes, the total response $r(t)$ is obtained:

$$r(t) = \sum_{i=1}^{m} r_i(t) \quad (4)$$

The force-related story response can be obtained by using their relationship with F_{si}, obtained from the modal pushover analysis in the linear response range. Similarly the deformation-related story responses can be obtained by using their relationship with D_i, obtained from the modal pushover analysis in the linear response range.

6 COMPARISON OF NLRHA AND UMRHA RESULTS

Different assumptions of UMRHA procedure include the use of an approximate hysteresis behavior for SDOF system, the use of elastic inertial force pattern to obtain the nonlinear modal responses, the linear summation of modal responses and the absence of interaction between different vibration modes. In the current study, it is made sure that the behavior of the selected hysteretic model, used for each SDOF system, matches perfectly with the hysteretic behavior of the structure under each modal inertial force pattern. Figure 7 shows the comparison of hysteresis behavior for the first mode. The cyclic modal pushover analysis is carried out for each vibration mode by applying the force vector with the i[th] mode inertial force pattern $\boldsymbol{s}_i^*$. The magnitude of the inertial force is reversed and increased gradually to push the structure into the

nonlinear range (i.e., gap opening). The results in the nonlinear range show that the pattern of story forces of the rocking wall is almost similar to the story forces pattern in the linear elastic range. Therefore, the assumption of using elastic inertial force distribution pattern for the estimation of nonlinear story force distribution is justifiable. Another assumption used in the formulation of the UMRHA procedure is the linear summation of modal responses, which is strictly speaking only valid for linear elastic responses. Since the shear response is modeled as linear elastic in this study, the linear summation of modal shear responses can be used to get the total shear response. The only assumption left in the UMRHA procedure is that there is no interaction among different modal responses. However, this limitation of the UMRHA procedure can be beneficial for the current study where the difference between the responses obtained from the NLRHA and the UMRHA procedure would represent the effect of acceleration spikes, a manifestation of modal interaction.

Figure 8 shows the comparison of envelope results of story forces, story shears and floor accelerations. Results show a significant difference in the results of NLRHA and UMRHA showing a presence of coupling of modes. Figure 9 and 10 show the histories of lateral floor accelerations and story shears. Comparison of histories shows that the UMRHA procedure is not able to predict the high frequency acceleration spikes observed in NLRHA during the start

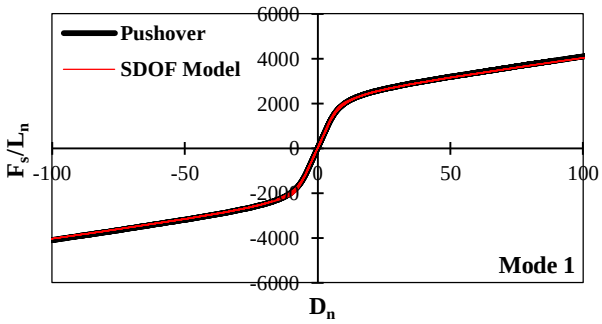


Figure 7: Comparison of hysteresis behavior for first mode

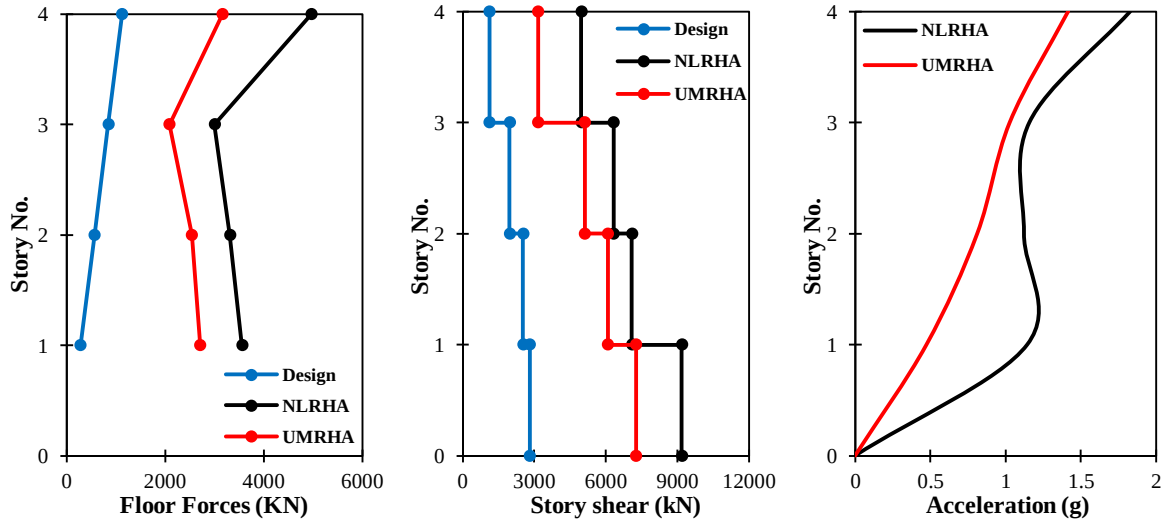


Figure 8: Comparison of envelope results.

of a vibration cycle. It is quite clear from the results that without the modal coupling the higher mode effects are quite low which is normally expected for a low-rise structure. Also, the bulge in the acceleration envelope as observed in the NLRHA results is not present in the UMRHA

acceleration envelope. This implies that if the acceleration spikes are removed from the acceleration response then the UMRHA procedure, with the removal of different assumptions, should be able to predict the acceleration response accurately. To check this, the rocking wall structure is redesigned with a dedicated energy dissipation mechanism and a reduced contact stiffness to keep the acceleration spikes to a minimum value. Energy dissipation bars at the wall-foundation joint are designed to take 45% of the moment demand with the other 55% being resisted by a combination of post-tensioning force and the self-weight of the rocking wall. Also,

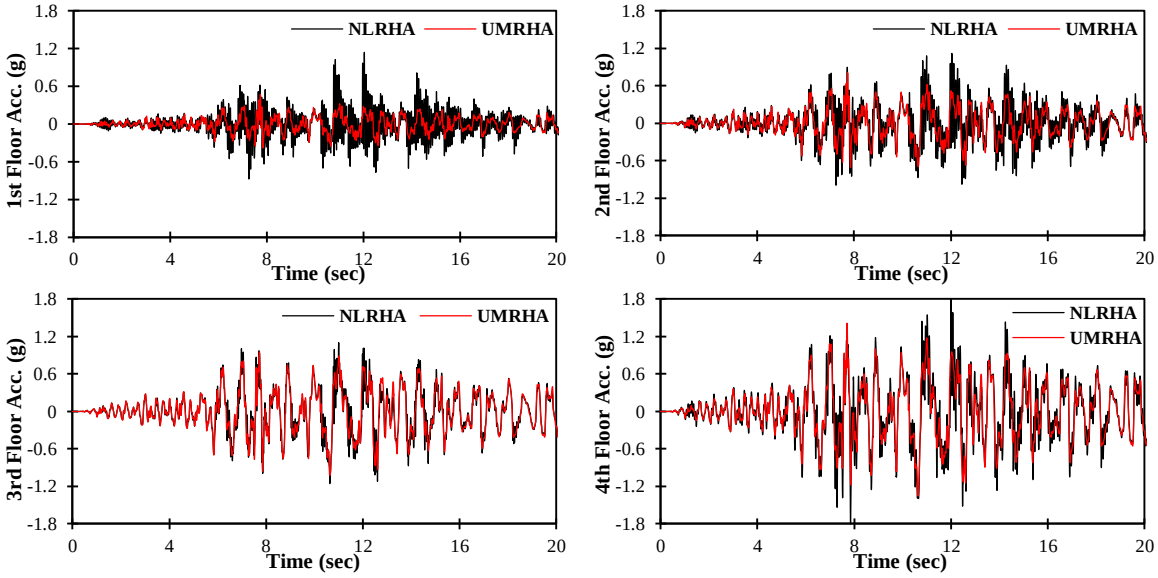


Figure 9: Comparison of floor acceleration histories.

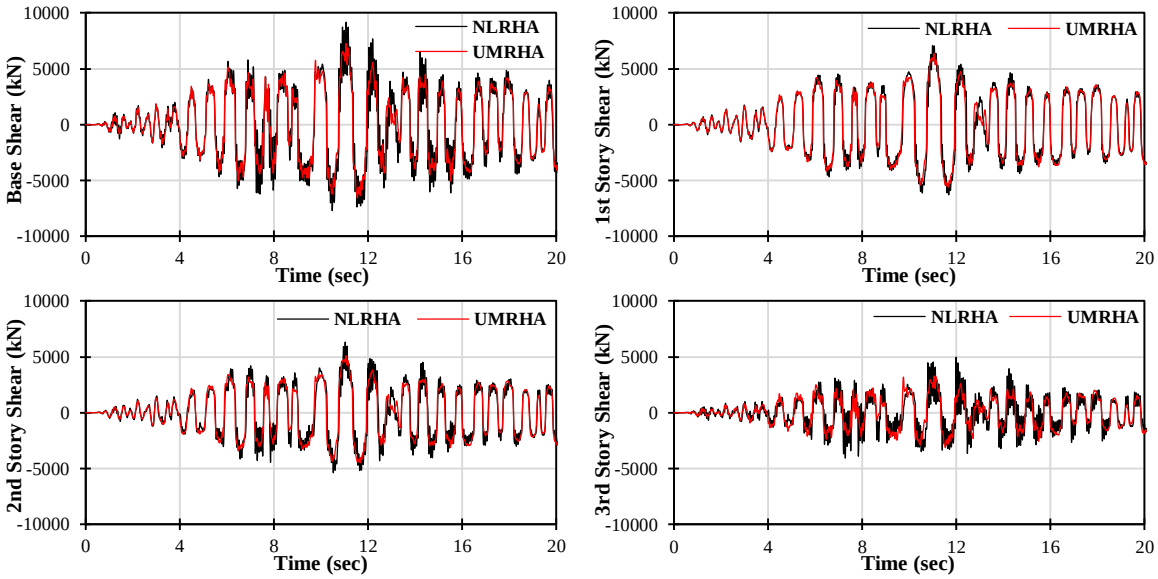


Figure 10: Comparison of story shear histories.

the contact stiffness is reduced by a factor of 4 to reduce the impact related acceleration spikes. The NLRHA and UMRHA procedures are employed for the same ground motion and the results are compared. Figure 11 shows the comparison of envelope results which are matching quite well. Histories of floor accelerations (Figure 12) further show that the UMRHA procedure is able to predict the response with much accuracy in the absence of acceleration spikes. The

comparison of results obtained from the UMRHA procedure and the NLRHA procedure for two different cases, without dedicated ED mechanism and with ED mechanism, shows that the UMRHA procedure works reasonably accurate when the acceleration spikes phenomenon is not present while for the cases where dynamic response is significantly affected by the acceleration spikes the UMRHA procedure failed to predict dynamic response accurately. Furthermore, the energy dissipation mechanism and the reduction in contact stiffness is found to reduce the acceleration response significantly, especially for the first floor level. Also, the shear demand for the rocking wall is also reduced significantly highlighting the effectiveness of the proposed strategies to reduce the acceleration spikes. This implies that the UMRHA procedure can be used effectively as a tool to differentiate the dynamic response that arises from the normal higher mode effects and the one that stems from the complex impact problem in the form of acceleration spikes. Furthermore, the effectiveness of different mitigation techniques for acceleration spikes can also be validated by using this method.

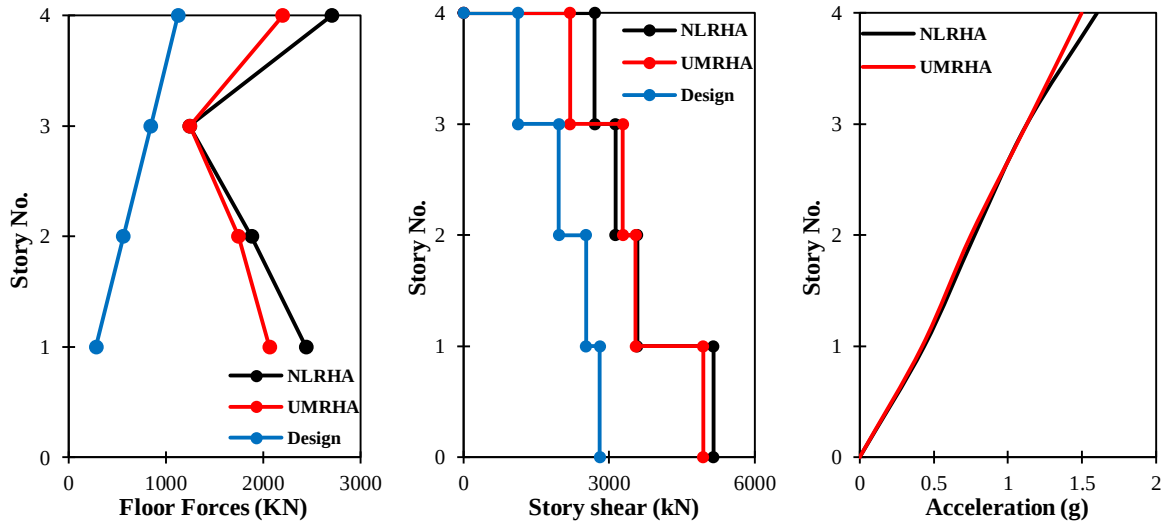


Figure 11: Comparison of envelope results with modified design.

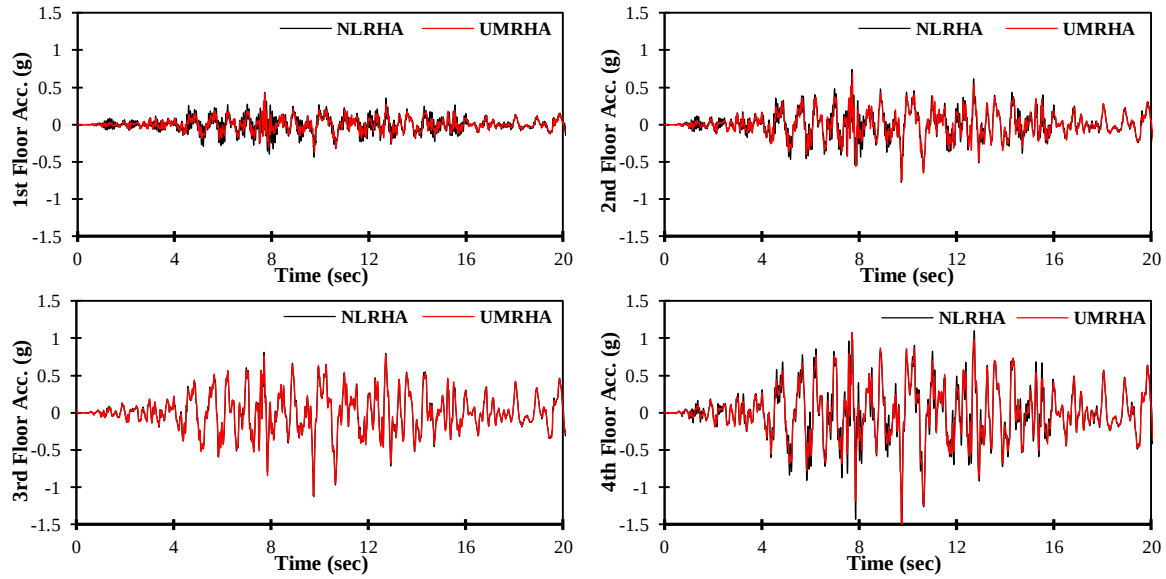


Figure 12: Comparison of floor acceleration histories with modified design.

7 CONCLUSIONS

The current study focuses on the phenomenon of lateral acceleration spikes in the dynamic response of rocking wall structures. A rocking wall structure is designed and a suite of ground motions is applied. Furthermore, inelastic modal decomposition of dynamic response is performed to investigate the higher mode effects. Based on the results, following conclusions are drawn.

- NLRHA results for 4 story rocking wall structure show a significant presence of high frequency accelerations in the dynamic response. Floor acceleration histories show that these high frequency accelerations are similar to the impact related acceleration spikes observed in the past experimental works and are also found to be responsible for a high shear amplification of 3.25 for the case study rocking wall.
- An innovative modal decomposition technique is used to investigate the higher mode effects. Different assumptions of the UMRHA procedure are removed except that the UMRHA procedure considers the modal responses as uncoupled. This modified UMRHA procedure allows to separate the impact related acceleration spikes from the total acceleration response and to quantify their effects on the shear response.
- The presence of energy dissipation mechanism and the reduction of contact stiffness at wall-foundation interface are found to be effective strategies for the reduction of these acceleration spikes. Furthermore, both of these strategies are found to reduce the acceleration and shear demand considerably ensuring a safety factor against any shear slip failure.

REFERENCES

[1] M.J.N. Priestley, S. Sritharan, J.R. Conley, S. Pampanin, Preliminary results and conclusions from the PRESSS five-story precast concrete test-building. *PCI Journal*, **44**:6, 42-67, 1999.

[2] Y.C. Kurama, Hybrid post-tensioned precast concrete walls for use in seismic regions. *PCI Journal*, **47**:5, 36-59, 2002.

[3] J.M. Kelly, The influence of base isolation on the seismic response of light secondary equipment. Research Report UCB/EERC-81/17, University of California, Berkeley, U.S.A., 1982.

[4] M. Dolce, D. Cardone, Seismic protection of light secondary systems through different base isolation systems. *Journal of Earthquake Engineering*, **7**:2, 223–250, 2003.

[5] L. Wiebe, C. Christopoulos, Characterizing acceleration spikes due to stiffness changes in nonlinear systems. *Earthquake Engineering & Structural Dynamics*, **39**:14, 1653-1670, 2010.

[6] E. Miranda, S. Taghavi, Approximate floor acceleration demands in multistory buildings. I: Formulation. *Journal of Structural Engineering* **131**:2, 203–211, 2005.

[7] M.J. Schoettler, A. Belleri, D. Zhang, J.I. Restrepo, R.B. Fleischman, Preliminary results of the shake-table testing for the development of a diaphragm seismic design methodology. *PCI Journal*, **54**:1, 100-124, 2009.

[8] J. Hancock, J. Watson-Lamprey, A.N. Abrahamson, J.J. Bommer, A. Markatis, E. McCory, R. Mendis, An improved method of matching response spectra of recorded

earthquake ground motion using wavelet. *Journal of Earthquake Engineering* **10**:SP1, 1-23, 2006.

[9] M.A. Rahman, S. Sritharan, An evaluation of force-based design vs. direct displacement-based design of jointed precast post-tensioned wall systems. *Earthquake Engineering and Engineering Vibration*, **5**:2, 285-296, 2006.

[10] L. Wiebe, C. Christopoulos, Mitigation of higher mode effects in base-rocking systems by using multiple rocking sections. Research Report ROSE-2009/01, IUSS Press, Pavia, Italy.

[11] A.J. Carr, Ruaumoko, *Volume 2: User manual for the 2-dimensional version, Ruaumoko2D*. Department of Civil Engineering, University of Canterbury, Christchurch, New Zealand, 2004.

[12] B.J. Smith, Y.C. Kurama. Seismic design guidelines for special hybrid precast concrete shear walls. Department of Civil engineering and geological sciences, University of Notre Dame, Report No. NDSE-2012-02.

[13] H.A. Spieth, A.J. Carr, A.G. Murahidy, D. Arnolds, M. Davies, J.B. Mander, Modeling of post-tensioned precast reinforced concrete frame structures with rocking beam-column connections. Research Report No. 2004-X, Dept. of Civil Engineering, Univ. of Canterbury, Christchurch, New Zealand.

[14] D. Pennucci, G.M. Calvi, T.J. Sullivan, Displacement-based design of precast walls with additional dampers. *Journal of Earthquake Engineering* **13**:S1, 40-65, 2009.

[15] L.A. Toranzo, The use of rocking walls in confined masonry structures: a performance-based approach. PhD thesis, University of Canterbury, New Zealand, 2002.

[16] M.J. Schoettler, Seismic demands in precast concrete diaphragms. Ph.D. thesis, Department of Structural Engineering, University of California - San Diego, La Jolla, California, USA, 2010.

[17] A.K. Chopra, R.K. Goel, A modal pushover procedure for estimating seismic demands for buildings. *Earthquake Engineering and Structural Dynamics* **31**:3, 561-582, 2002.

[18] A. Munir, P. Warnitchai, The cause of unproportionately large higher mode contributions in the inelastic seismic responses of high-rise core-wall buildings. *Earthquake Engineering and Structural Dynamics*, **41**:15, 2195-2214, 2012.

[19] C. Sangarayakul, P. Warnitchai, Approximate modal decomposition of inelastic dynamic responses of wall buildings. *Earthquake Engineering and Structural Dynamics*. **33**:9, 999-1022, 2004.

COMPDYN 2015
5th ECCOMAS Thematic Conference on
Computational Methods in Structural Dynamics and Earthquake Engineering
M. Papadrakakis, V. Papadopoulos, V. Plevris (eds.)
Crete Island, Greece, 25–27 May 2015

EVALUATION OF THE DYNAMIC AMPLIFICATION FACTOR FOR RAILWAY BRIDGES SUBJECTED TO A SERIES OF MOVING MASS

Mehrdad Bisadi[1], **Q.T. Ma**[1] **and S. Beskhyroun**[1]

[1] Department of Civil and Environmental Engineering, The University of Auckland
20 Symonds Street, Auckland 1010, New Zealand
mbis086@aucklanduni.ac.nz
{q.ma, s.beskhyroun}@auckland.ac.nz

Keywords: Railway Bridge, Finite Element, Dynamic Amplification Factor, Moving Mass Analysis.

Abstract. *This paper investigates the vertical dynamic behavior of steel rail viaducts subjected to train passage. The analyses in this study take into account the dynamics of the vehicle suspension systems, the mass of bogies and car bodies, and the dynamic properties of the viaduct as emulated by idealized mass and stiffness values. The rail vehicles are simulated as a series of moving mass with various wheel distances traversing over simply supported girders. Using finite element software, LUSAS, the dynamic amplification factors are evaluated and the results are compared with standard design practice for a wide range of speeds and a range of viaduct spans. The results show that the impact factors proposed by design codes are unconservative in many cases especially for high speed trains traversing the short span viaducts.*

1 INTRODUCTION

Research has shown modern high speed trains have the potential to induce resonance on railway bridges [1]. This phenomenon takes place when the frequency of excitation associated with moving train coincides with the natural frequencies of the bridge. Under such condition, the response of rail bridges is continuously amplified, as axle loads traverse over the bridge [2]. Excessive bridge response increases the likelihood of derailment, increase wheel and rail wear and may lead to the structural instability.

There exist two commonly used loading strategies to evaluate the dynamic response of the bridge-train system. These are known as the moving load and moving mass models. In a moving load model, the train is considered as a series of moving static axle loads and the inertial and dynamic effects of the suspension system are ignored. In a moving mass model, the train is simulated as a series of moving mass sprung systems that represents the wheels, bogies and coaches. This method is considered more realistic and leads to more accurate results when interactions are considered important [2,3]. Figure 1 shows a representative schematic of the models.

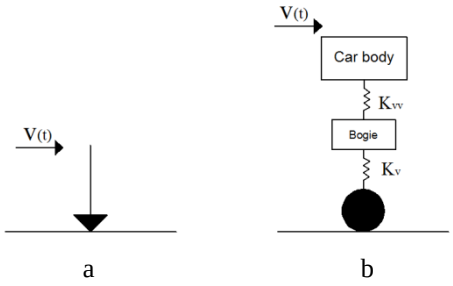


Figure 1: a) Moving load model b) Moving mass model

A number of researchers have developed sophisticated train models for evaluating the accurate dynamic response of railway bridges. Liu et al. developed a simple 3 degrees of freedom (DOF) train model to approximately investigate the properties of the train-bridge system [4]. While Xia et al. developed a 27 DOF train model to examine human comfort when a train traverse over a long suspension rail bridge [5]. In another study, Xia et al. developed an articulated train model to study the difference in bridge response from an articulated train compared to a non-articulated train passage [6]. Zhai et al. developed computer simulation software to predict vertical and lateral dynamic response of a train traversing a bridge and the results were validated by onsite experimental tests on two high speed railway bridges [7].

As far as rail bridge design is concerned, as opposed to pure analysis studies, most rail bridges worldwide are designed without a specific dynamic analysis. In this approach, a bridge system is analysed with a combination of axle loads in a static analysis. Then, the response is multiplied by a dynamic amplification factor, also known as an impact factor. This factor attempts to represent the increase in displacements and loadings due to dynamic effects [8,9]. However, as there is little known about the development of such factors, presumably they are based on limited empirical studies or moving loads approach, it is unsure whether it would accurately predict the dynamic effects of high speed moving loads.

The aim of this paper is to evaluate the vertical midspan dynamic amplification factor of steel railway bridges including the influences of varying axle distances, train suspension system, viaduct vertical natural frequencies and span lengths. The results are then compared with American railway bridges manual, AREMA, and Eurocode standard practice code [10,11].

2 RESONANCE ON RAILWAY BRIDGES

Dynamics of train-bridge systems are unique in that when trains traverse across a bridge, it increases the mass of the system significantly, trains represent a large portion of the mass in the system and make contact with bridges via a suspension system with individual dynamic characteristics. In simplistic terms, during train passage, the train bridge system can be approximately considered as a single system with the mass of the bridge and trains, resting on a structure with the stiffness of the bridge and is subjected to a dynamic load in accordance with the speed of the trains. The effect of the moving load can be considered as a single dynamic load with a forcing frequency depending upon train speeds, the axle wheel distances and span length of rail bridges. Higher train speed increases the forcing frequency and similarly shorter axle distance over spans also increase the effective forcing frequency. This frequency is expressed in equation 1, where (f_c), (V) and (L_b) are the forcing frequency, train speed and the bridge span length respectively [2].

$$f_c = \frac{V}{L_b} \tag{1}$$

In moving load analyses, the dynamics of the train system are typically ignored. In moving mass analysis, an attempt is made to incorporate this effect by modelling the train as a dynamic system of the car bodies and bogies (train suspensions). This leads to a two DOF system and consequently the train is defined by two natural frequencies. Equation 2 and 3 estimate these two natural frequencies as a function of the primary and secondary suspension system spring stiffness (k_v, k_{vv}) and mass of the bogie and car body (m_1 and m_2) [4].

$$f_{vc} = \frac{1}{2\pi}\sqrt{\frac{2}{\frac{1}{k_{vv}} + \frac{1}{2k_v}}}{m_2} \tag{2}$$

$$f_{vb} = \frac{1}{2\pi}\sqrt{\frac{2k_v + k_{vv}}{m_1}} \tag{3}$$

Dynamic characteristics of railway bridges also play a key role in train-bridge interaction problem. For this study, this is represented by the bending of a single simply supported bridge span. This leads to natural frequencies that are functions of bending stiffness (EI), span length (L_b) and mass of the bridge (m per unit length). Equation 4 shows the first vertical natural frequency of such a simply supported beam [12].

$$\omega_b = \frac{\pi}{2}\sqrt{\frac{EI}{mL_b^4}} \tag{4}$$

Research shows that amplified train-bridge response can be expected when the forcing frequency (f_c) coincides with any of the natural frequencies mentioned above. The most critical of these pairing is when the forcing frequency coincides with a natural frequency of the bridge. Equation 5 estimates the train speeds when this occurs. As the bridge is in fact a continuous system, other critical speeds occur at integer multiple of Equation 5 corresponding to a compatible vertical bridge mode shape. (L_c) denotes the carriage length. [2,13].

$$V = \frac{\omega_b L_c}{2i}, \quad \text{i} = 1,2,3,\ldots \tag{5}$$

3 IMPACT FACTOR AND RELATED ISSUE

Impact factors (I) or dynamic amplification factors simplify the rail bridge design process by approximately accounting for the train-bridge dynamic interaction by upscaling the results of a static analysis. Equation 6 presents the common definition for impact factor.

$$I = \frac{\text{max dynamic response}}{\text{max static response}} \tag{6}$$

Various equations exist in different bridge design standards for dynamic amplification factors as a function of span lengths and different traffic load models [8]. For instance, AREMA assumes two traffic load models, cooper E80 and alternative loads on four axles with a value of 100,000 lb force per axle, leading to equation 7 for an expression for the dynamic amplification factor. It can be observed from this equation, AREMA considers span length as the only parameter affecting the dynamic interaction [10].

$$I = 1.4 - \frac{3L_b^2}{14860} \qquad \text{L}_\text{b} < 24 \text{ feet}$$

$$I = 1.16 + \frac{1.829}{L_b - 9.1} \qquad \text{L}_\text{b} \geq 24 \text{ feet} \tag{7}$$

Eurocode EN1991-2 assumes different loading models for their rail bridges design guidance. Naturally, the formulas for impact factors are different, but notably, the Eurocode formulas are functions of train speed, bridge natural frequency for the existing bridges and span length for new bridges. Equations 8 and 9 present the dynamic impact factor formulas for carefully and normally maintained tracks as they appear in the Eurocode. EN1991-2 also prescribes a more detailed dynamic analysis if the train speed is expected to exceed 200 km/hr [11].

$$I = \frac{1.44}{\sqrt{L_b} - 0.2} + 0.82 \tag{8}$$

$$1.00 \leq I \leq 1.67$$

$$I = \frac{2.16}{\sqrt{L_b} - 0.2} + 0.73 \tag{9}$$

$$1.00 \leq I \leq 2.00$$

Equations 7 to 9 are plotted together in Figure 2. It highlights that AREMA is generally more conservative than the Eurocode particularly in longer span bridges.

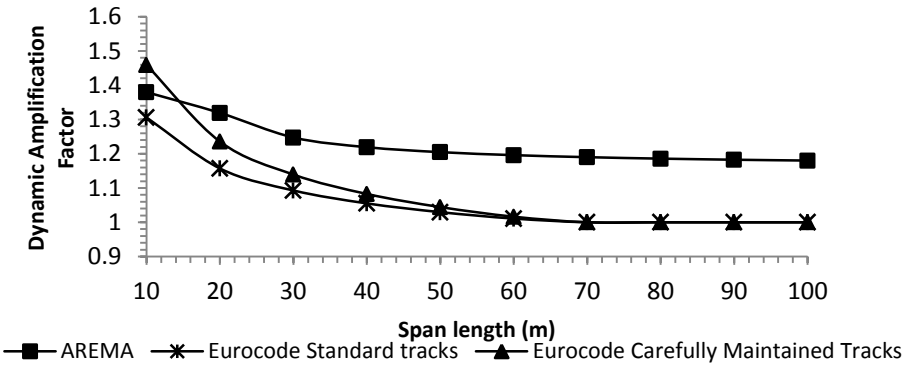


Figure 2: Comparison of dynamic amplification factor suggested by AREMA and Eurocod

4 FINITE ELEMENT ANALYSIS

4.1 Finite element model

Research has shown the vertical vibration and deflection are the most critical in studying the train bridge interaction and that a two dimensional model is sufficient in simulating study the vertical dynamic response [13]. This study employs a commercial finite element (FE) software, LUSAS (version 15.0.5) to create and analyse a two dimensional FE model of a train bridge system. The bridge is modelled as a linear elastic simply supported steel beam. The study considers a series of bridge span from 10 to 60 m and the mass of the bridge is set as 15 ton/m.

The train is simulated as a sequence of rigid sprung masses traversing over the beam. Figure 3 shows a schematic of the FE model. Each sprung mass represents a quarter of the car body mass and half of the bogie mass for one train wagon.



Figure 3: FE model of the interaction system

The simulated train consists of eight passenger cars and the length of each car is 25.5 m. Table 1 shows the train parameters for this study. These parameters have been taken from a real train with minor modifications [14].

Item	Unit	Value
Mass of car body	Ton	42
Mass of bogie	Ton	3
Mass of wheel	Ton	1.8
Vertical stiffness of primary suspension system	kN/m	210552
Vertical stiffness of secondary suspension system	kN/m	26319
Vertical damping of primary suspension system	kN s/m	15250
Vertical damping of secondary suspension system	kN s/m	18125

Table 1: Train dynamic characteristics.

4.2 Dynamic analysis

Modal superposition method is employed to analyse the FE model. The following assumptions are adopted:

- The materials behave linearly;
- Train moves with constant speeds;
- The spring and dashpots behave linearly.
- Modal damping coefficient is assumed to be 5%, and
- There is no separation between the wheels and the bridge.

A unit load is defined to produce small discrete locations over the path of train, by setting up a number of load cases. An eigenvalue analysis is carried out to compute the natural frequencies and eigenvectors of the bridge. Using the discrete unit load and the eigenvectors, modal forces are computed and then modal superposition method is applied to solve the interaction problem. Newmark time integration method is used and the dynamic responses of the train and the bridge are computed. To increase the accuracy of results, mass participation factors are considered over 90%, the discrete locations (δ) produced by the unit load is considered sufficient small and a proper time incerment (Δ_t) is used for the time integration method. The time step is computed according to equation 10 proposed by Clough and Penzien [15]. The distance incerment value is calculated by equation 11 suggested by LUSAS user manual [16].

$$\Delta_t = \frac{\omega_{\max}}{10} \tag{10}$$

$$\delta = 10 \times \frac{1}{2 \times \omega_{\max}} \tag{11}$$

4.3 Verification of the finite element model

Yang et al [2] has considered a bridge as a beam and train as a moving mass and used the analytical method, mentioned in section 4, to calculate the bridge dynamic response. The specifications of the system are as follows; Span length L_b = 25 m, Train speed V = 27.78 m/s, Young's module E = 2.87 kN/m^2, Poisson's ratio υ = 0.2, moment inertia I = 2.9 m^4, mass of the bridge m = 2.303 ton/m, mass of the bogie M_1 = 5.75 ton and spring rate K_v = 1595 kN/m. Mass of the wheel and the damping rate are neglected.

For verification of the FE model, dynamic analysis for the bridge has been carried out in LUSAS environment. Figure 5 and 6 show that there is a good agreement between the LUSAS results and the results from reference [2].

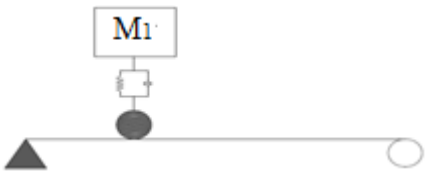
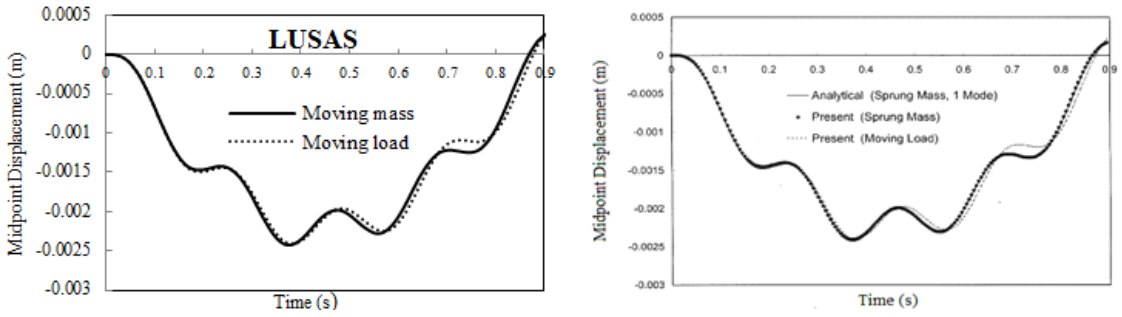
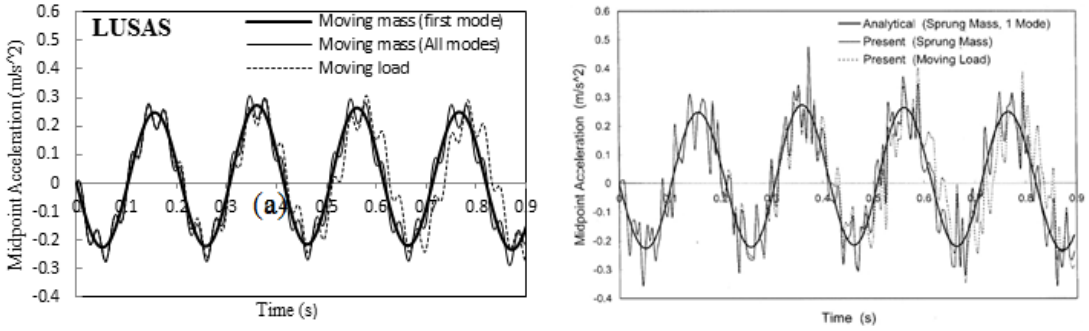


Figure 4: Simply supported beam subjected to a moving mass (Source: Reference [2])



(a) (b)

Figure 5: Beam midpoint vertical displacement a) FE model b) Numerical analysis (Source: Reference [2])



(a) (b)

Figure 6: Beam midpoint vertical acceleration a) FE model b) Numerical analysis (Source: Reference [2])

5 PARAMETRIC STUDY

5.1 Effect of rail vehicle suspension system

To evaluate the effect of the vehicle suspension system on the interaction model, three different stiffness values for the suspension are assumed. Table 2 shows the spring rates. Each of the vehicles in the table 2 crosses the bridge with speed range from 50 to 300 km/h. To take the dynamic bridge properties into the account, a non-dimensional parameter (S) as a function of Train speed (V), the bridge natural frequency (ω_b) and the span length (L_b) is defined. Equation 12 shows the non-dimensional parameter. The bridge dynamic amplification factors and bogie accelerations are computed and illustrated in figures 7 and 8.

Train	Spring rate (kN/m)		Damping rate (kN s/m)	
Type	Primary	Secondary	Primary	Secondary
Vehicle1	1177	132.5	511	606.5
Vehicle2	11800	2650	511	606.5
Vehicle3	30000	6000	511	606.5

Table 2: Characteristics of train suspension system

$$S = \frac{V}{\omega_b L_b} \tag{12}$$

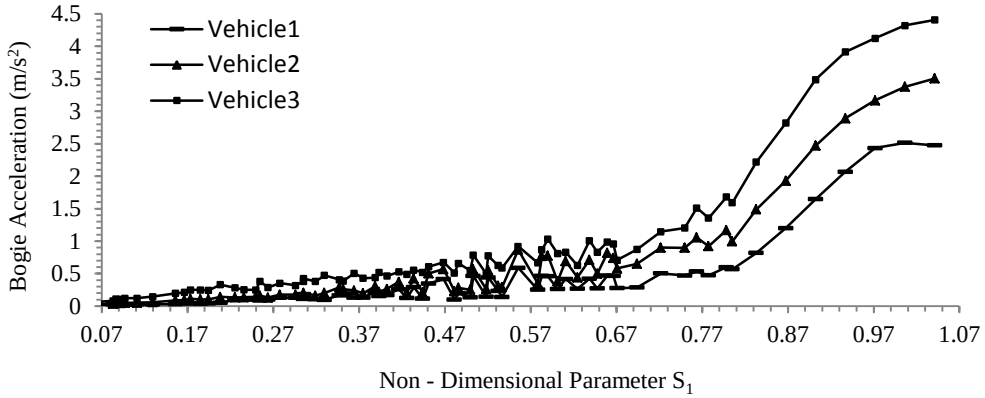


Figure 7: Vertical train bogie acceleration

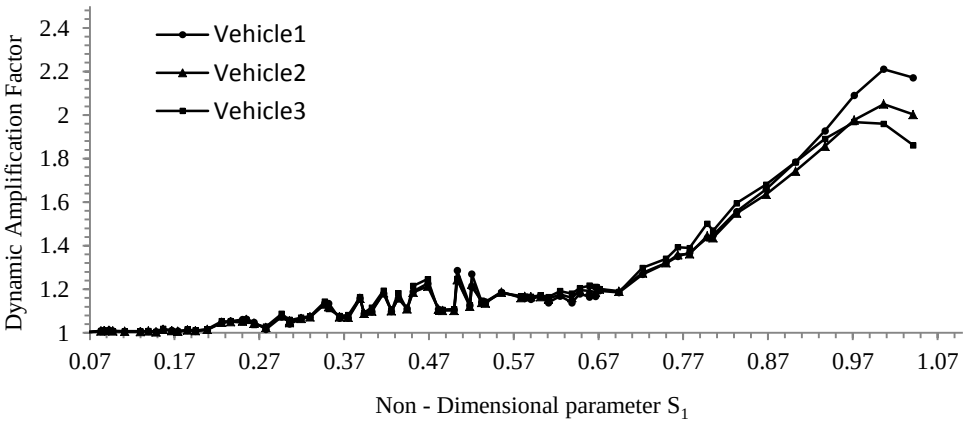


Figure 8: Vertical midpoint bridge dynamic amplification factor

It can be seen that the stiffer springs increase the vertical bogie accelerations. The main reason is that the higher spring rates increase the frequency of the sprung mass which may approach to that of the bridge and increase the risk of resonance. The high train frequency assuredly leads to passenger discomfort. On the other hand, the stiffer springs slightly reduce the response of the beam. As the reduction is small, the effect of that is negligible in the bridge design procedure. Some of the standard design codes propose stability indices for maximum train acceleration. This value in China standard code is 1.3 m/s^2 [14].

5.2 Effect of rail bridge characteristics

To evaluate the bridge dynamic amplification factor, various span lengths are considered for the bridge and four different values of the frequency are allocated to each span length. Table 3 shows the bridge specifications. The train with axle distances 14 m, 18 m and 21 m crosses each of the bridges. In total 72 analyses are carried out for the train speed range from 50 to 300 km/h. The dynamic amplification factors at the midpoint of the bridge are computed and illustrated in figure 9.

Span length (m)	First vertical natural frequency (Hz)	Damping ratio
10-20-30-40-50-60	3-4-5-6	5%

Table 3: Physical parameters of beam.

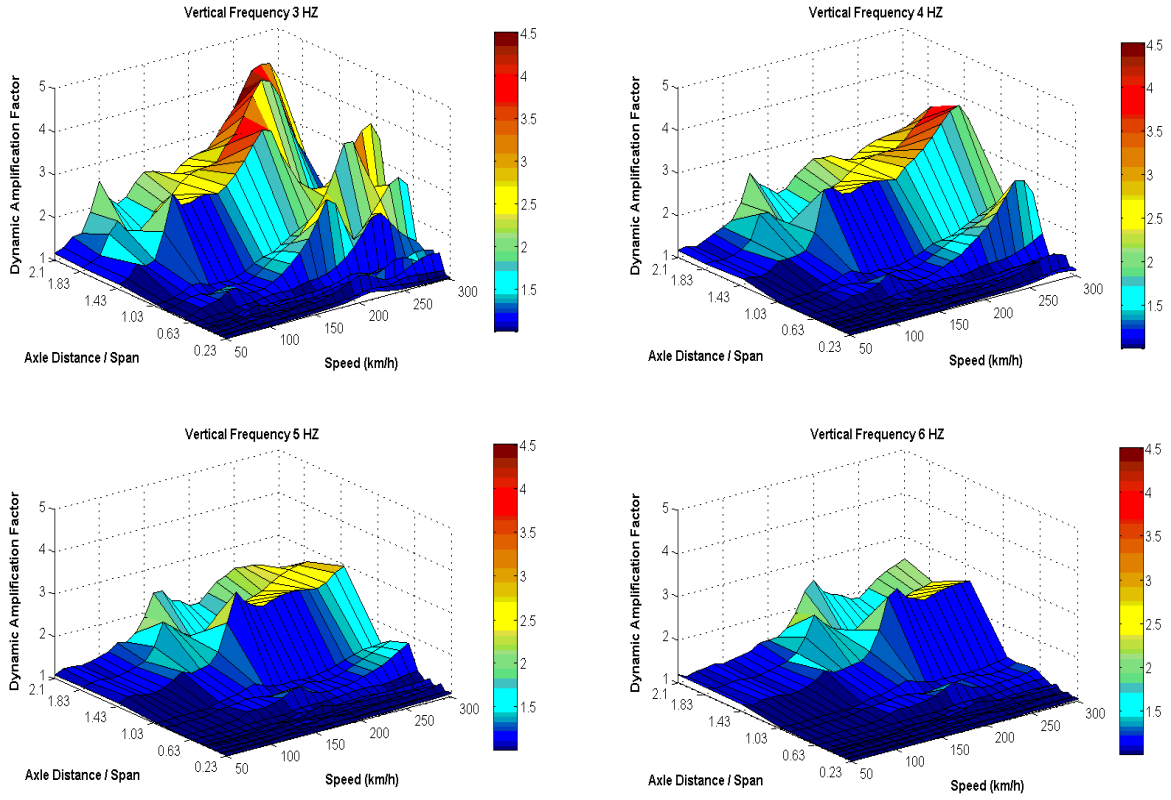


Figure 9: Midpoint vertical dynamic amplification factor of the bridges

Figure 9 shows the effects of train speeds, axle distances, bridges frequencies and span lengths on the dynamic amplification factor. Due to the resonance phenomenon, the dynamic amplification factors shift to larger values in response to higher train speeds, shorter span lengths and larger axle distances. The bridges with lower frequencies also experience higher dynamic responses. In comparison with the design codes, AREMA and Eurocode respectively suggest 1.4 and 2 as the maximum values for the dynamic amplification factors. However, the obtained values are much larger when the train with higher speeds traverses over the bridge with shorter span length.

6 CONCLUSION

A parametric study was carried out to investigate the effect of various parameters on the dynamic response of a train bridge system. The parameters include train speed, bridge natural frequency, span length, axle distance and train suspension system. The following conclusion has been drawn from this study:

- Stiffer suspension system results in larger values of bogie acceleration. However, it has a negligibale influence on the bridge response.
- The bridge dynamic amplification factors increase when train crosses the bridge with higher speeds. This response is more apparent in short span lengths, larger axle distances and lower bridge natural frequencies.
- Comparing the results with AREMA and Eurocode, it can be seen that the proposed impact factors are underestimate.

REFERENCES

[1] R. Delgado, R. Calçada, D. Riberio, J.R. Pinto, H. Figueiredo, Assessment of the dynamic response of high speed railway bridges in interoperable lines. R. Delgado, R. Calçada Boca, J.M. Goicolea, F. Gabaldon. *Dynamics of High-Speed Railway Bridges*, London, 2009.

[2] Y.B. Yang, J.D. Yau, Y.S. Wu, *Vehicle-bridge interaction dynamics with applications to high-speed railways*. World Scientific 2004.

[3] C. Rigueiro, C. Rebelo, L.S.d. Silva, Influence of ballast models in the dynamic response of railway viaducts. *Journal of Sound and Vibration*, 329, 3030-3040, 2010.

[4] K. Liu, G.D. Roeck, G. Lombaert, The effect of dynamic train–bridge interaction on the bridge response during a train passage. *Journal of Sound and Vibration*. 325, 240-251, 2009.

[5] H. Xia, Y.L. Xu, T.H.T. Chan. Dynamic interaction of long suspension bridges with running trains. *Journal of Sound and Vibration*, 237, 263-280, 2000.

[6] H. Xia, N. Zhang, G. D. Roeck, Dynamic analysis of high speed railway bridge under articulated trains. *Computer and Structures*. 81, 2467-2478, 2003.

[7] W. Zhaia, S. Wanga, N. Zhang, M. Gao, H. Xia, C. Cai, C. Zhao, High-speed train–track–bridge dynamic interactions – Part II: experimental validation and engineering application. *International Journal of Rail Transportation*.1, 25-41, 2013.

[8] S.A Hamidi, F. Danshjoo, Determination of impact factor for steel railway bridges considering simultaneous effects of vehicle speed and axle distance to span length ratio, *Engineering Structures*. 32, 1369-1376, 2010.

[9] J.F. Unsworth, *Design of modern steel railway bridges*. Taylor and Francis, 2010.

[10] *American Railway Engineering and Maintenance-of-Way Association Manual*. 2014.

[11] Designer's guide to Eurocode 1: actions on bridges, EN 1991-2, EN 1991-1-1, -1-3 to -1-7 and EN 1990 Annex A2. Thomas Telford 2010.

[12] A.K. Chopra, *Dynamics of structures: theory and applications to earthquake engineering, 4th Edition*. Prentice Hall, 2012.

[13] M. Sogabe, N. Matsumoto, M. Kanamori, T. Sato, H. Wakui. Impact factors of concrete girders coping with train speed-up. *Quarterly Report of Rail Technical Research Institute*. 1, 46-52, 2005.

[14] N. Zhang, H. Xia, W. Guo, Vehicle–bridge interaction analysis under high-speed trains. *Journal of Sound and Vibration*. 309,407-425, 2008.

[15] R. Clough, J. Penzien. *Dynamic of structures*. McGraw Hill, New York 1975.

[16] *Lusas finite element user manual*, Version 15-0-5, finite element analysis Ltd, UK.

COMPDYN 2015
5th ECCOMAS Thematic Conference on
Computational Methods in Structural Dynamics and Earthquake Engineering
M. Papadrakakis, V. Papadopoulos, V. Plevris (eds.)
Crete Island, Greece, 25–27 May 2015

A MODE SELECTION ALGORITHM FOR THE FLEXIBILITY-BASED COMPONENT MODE SYNTHESIS

Jin-Gyun Kim[1], Phill-Seung Lee[2], and Kwang-Chun Park[3]

[1] Korea Institute of Machinery and Materials

156, Gajeongbuk-ro, Yuseong-gu, Daejeon 305-343, Republic of Korea

jingyun@kimm.re.kr

[2] Division of Ocean Systems Engineering, Korea Advanced Institute of Science and Technology

291, Daehak-ro, Yuseong-gu, Daejeon 305-701, Republic of Korea

phillseung@kaist.edu

[3] Department of Aerospace Engineering Sciences and Center for Aerospace Structures, University of Colorado Boulder

Campus Box 429, Boulder, CO 80309, U.S.A

kcpark@colorado.edu

Keywords: Component mode synthesis; Mode selection; Error estimation; Computational dynamics; Finite element method

Abstract. *A major challenge in component mode synthesis (CMS) remains the absence of a robust mode selection algorithm which can provide a measure of accuracy of the reduced model compared to the full model. In order to address this challenge, two concepts have been proposed in tandem: mode selection and error estimation methods. In this paper, we reassess performance of a recently proposed mode selection method and an a posteriori error estimation method, and propose an efficient iterative algorithm that combines these two methods. The flexibility-based component mode synthesis (F-CMS) is used to demonstrate the performance of the above methods. Numerical examples illustrate the effectiveness of the present algorithm.*

1 INTRODUCTION

Component mode synthesis (CMS) is a popular reduced-order modeling technique of the large finite element model in computational dynamics. After introducing the first approach of the CMS method in 1960s, various methods have been proposed [1-12]. In particular, the flexibility based CMS (F-CMS) method was developed using localized Lagrange multipliers [13], and its extended works have been performed [14,15].

In CMS methods, since the reduced order model is constructed by assembling substructural modes, its accuracy depends on the selection of dominant substructural modes. Generally, the frequency cut-off rule has been used to select the substructural modes [15-17], and it relies on the basic assumption of the mode superposition which the lower substructural modes contribute more to the lower global modes. While the frequency cut-off rule is simple and easy to use, this assumption is not always true in the CMS methods. For the reason, Park and Park developed a new mode selection method using residual interface flexibility in the F-CMS method [12]. Also, Kim et al. [17] have developed another mode selection method based on the eigenvector relation between substructural and global modes, and it shows better performance than previous ones but also is applicable to various CMS methods such as Craig-Bampton (CB) and Automated multi-level substructuring (AMLS) methods. In addition, Kim and Lee recently developed new error estimation methods to directly estimate the relative eigenvalue error [18-20] unlike the previous methods [9, 21, 22]. In this paper, we propose an iterative mode selection algorithm that combines the mode selection and error estimation methods developed by Kim et al. [17, 20], and its feasibility is studied using the F-CMS method.

First, we introduce the F-CMS method in Section 2. The mode selection and error estimation methods are presented in Section 3. A new mode selection algorithm and its performances are presented in Sections 4 and 5, respectively. The conclusions are given in Section 6.

2 FLEXIBILITY BASED CMS (F-CMS) METHOD

The displacement-based discrete energy functional $\Pi(\mathbf{u}_g)$ of the global structure is

$$\Pi(\mathbf{u}_g) = \mathbf{u}_g^T\left(\frac{1}{2}\mathbf{K}_g\mathbf{u}_g - \mathbf{f}_g + \mathbf{M}_g\ddot{\mathbf{u}}_g\right),\ \mathbf{M}_g = \mathbf{L}^T\mathbf{M}_s\mathbf{L},\ \mathbf{K}_g = \mathbf{L}^T\mathbf{K}_s\mathbf{L}, \tag{1}$$

where $\mathbf{M}_g$ and $\mathbf{K}_g$ are global mass and stiffness matrices, respectively, and $\mathbf{u}_g$ and $\mathbf{f}_g$ are global displacement and force vectors. $\mathbf{M}_s$ and $\mathbf{K}_s$ are block diagonal mass and stiffness matrices of substructures. The substructures and global structure are related with an assembly Boolean matrix $\mathbf{L}$. Using $\delta\Pi(\mathbf{u}_g)$, the eigenvalue problem is obtained

$$\mathbf{K}_g(\boldsymbol{\varphi}_g)_i = \lambda_i\mathbf{M}_g(\boldsymbol{\varphi}_g)_i,\ i = 1, 2, ..., N_g,\ \mathbf{u}_g = \boldsymbol{\Phi}_g\mathbf{q}_g, \tag{2}$$

where λ_i and $(\boldsymbol{\varphi}_g)_i$ are the eigenvalue and eigenvector, respectively. N_g is the number of DOFs in the global model. $\boldsymbol{\Phi}_g$ and $\mathbf{q}_g$ are the global eigenvector matrix and generalized coordinate vector, respectively. Using the localized Lagrange multipliers $\boldsymbol{\lambda}_\ell$, Equation (1) can be redefined as the sum of the substructural and constraint energy functionals

$$\Pi(\mathbf{u}_s,\ \boldsymbol{\lambda}_\ell, \mathbf{u}_b) = \mathbf{u}_s^T\left(\frac{1}{2}\mathbf{K}_s\mathbf{u}_s - \mathbf{f}_s + \mathbf{M}_s\ddot{\mathbf{u}}_s\right) + \boldsymbol{\lambda}_\ell\left(\mathbf{B}^T\mathbf{u}_s - \mathbf{L}_b\mathbf{u}_b\right), \tag{3}$$

in which $\mathbf{u}_s$ and $\mathbf{f}_s$ are the displacement and force vectors of the substructures, respectively, $\mathbf{u}_b$ is the interface displacement vectors, and $\mathbf{B}$ denotes the interface Boolean matrix. $\mathbf{L}_b$ is

obtained by yanking out the rows with zero entries of $\mathbf{B}^T\mathbf{L}$. When $\mathbf{u}_s$ is decomposed by deformable and rigid body modes, Equation (1) can be expressed by $\Pi(\mathbf{q}_s, \boldsymbol{\alpha}_s, \boldsymbol{\lambda}_\ell, \mathbf{u}_b)$, which yields

$$\begin{bmatrix} \boldsymbol{\Phi}_s^T\mathbf{K}_s\boldsymbol{\Phi}_s + \boldsymbol{\Phi}_s^T\mathbf{M}_s\boldsymbol{\Phi}_s\dfrac{d^2}{dt^2} & \mathbf{0} & \boldsymbol{\Phi}_s^T\mathbf{B} & \mathbf{0} \\ \mathbf{0} & \mathbf{R}_s^T\mathbf{M}_s\mathbf{R}_s\dfrac{d^2}{dt^2} & \mathbf{R}_s{}^T\mathbf{B} & \mathbf{0} \\ \mathbf{B}^T\boldsymbol{\Phi}_s & \mathbf{B}^T\mathbf{R}_s & \mathbf{0} & -\mathbf{L}_b \\ \mathbf{0} & \mathbf{0} & -\mathbf{L}_b^T & \mathbf{0} \end{bmatrix} \begin{bmatrix} \mathbf{q}_s \\ \boldsymbol{\alpha}_s \\ \boldsymbol{\lambda}_\ell \\ \mathbf{u}_b \end{bmatrix} = \begin{bmatrix} \boldsymbol{\Phi}_s^T\mathbf{f}_s \\ \mathbf{R}_s^T\mathbf{f}_s \\ \mathbf{0} \\ \mathbf{0} \end{bmatrix}, \tag{4}$$

where $\boldsymbol{\Phi}_s$ and $\mathbf{R}_s$ are the eigenvector matrices of the deformable and rigid body modes of substructures, and the corresponding generalized coordinate vectors are denoted by $\mathbf{q}_s$ and $\boldsymbol{\alpha}_s$. It should be noted that $\boldsymbol{\Phi}_s$ and $\mathbf{R}_s$ are calculated from the substructural eigenvalue problem using $\mathbf{M}_s^{(k)}$ and $\mathbf{K}_s^{(k)}$ ($k = 1,2,...,N_s$). Here, N_s denotes the number of substructures. Then, $\boldsymbol{\Phi}_s$ can be divided as

$$\boldsymbol{\Phi}_s\,\mathbf{q}_s = \boldsymbol{\Phi}_d\,\mathbf{q}_d + \boldsymbol{\Phi}_r\,\mathbf{q}_r, \tag{5}$$

where subscripts d and r denote the dominant and residual terms, respectively. To construct the effective reduced model, only dominant substructural modes are retained. Substituting Equation (5) into Equation (4) and performing the Gauss elimination on $\mathbf{q}_r$, the condensed equations are obtained. Finally, we have the final reduced eigenvalue problem

$$\overline{\mathbf{K}}_p(\overline{\boldsymbol{\varphi}}_p)_i = \overline{\lambda}_i\overline{\mathbf{M}}_p(\overline{\boldsymbol{\varphi}}_p)_i,\ i = 1,2,...,\overline{N}_p,\ \overline{\mathbf{u}}_p = \overline{\boldsymbol{\Phi}}_p\overline{\mathbf{q}}_p, \tag{6}$$

$$\overline{\mathbf{K}}_p = \begin{bmatrix} \boldsymbol{\Phi}_d^T\mathbf{K}_s\boldsymbol{\Phi}_d & \mathbf{0} & \boldsymbol{\Phi}_d^T\mathbf{B} & \mathbf{0} \\ \mathbf{0} & \mathbf{0} & \mathbf{R}_s{}^T\mathbf{B} & \mathbf{0} \\ \mathbf{B}^T\boldsymbol{\Phi}_d & \mathbf{B}^T\mathbf{R}_s & -\mathbf{F}_{rbs} & -\mathbf{L}_b \\ \mathbf{0} & \mathbf{0} & -\mathbf{L}_b^T & \mathbf{0} \end{bmatrix},\ \overline{\mathbf{M}}_p = \begin{bmatrix} \boldsymbol{\Phi}_d^T\mathbf{M}_s\boldsymbol{\Phi}_d & \mathbf{0} & \mathbf{0} & \mathbf{0} \\ \mathbf{0} & \mathbf{R}_s^T\mathbf{M}_s\mathbf{R}_s & \mathbf{0} & \mathbf{0} \\ \mathbf{0} & \mathbf{0} & \mathbf{F}_{rbm} & \mathbf{0} \\ \mathbf{0} & \mathbf{0} & \mathbf{0} & \mathbf{0} \end{bmatrix},$$

$$\overline{\boldsymbol{\Phi}}_p = \left[\overline{\boldsymbol{\Phi}}_{q_d}{}^T \quad \overline{\boldsymbol{\Phi}}_{\alpha_s}{}^T \quad \overline{\boldsymbol{\Phi}}_{\lambda_\ell}{}^T \quad \overline{\boldsymbol{\Phi}}_{u_b}{}^T\right]^T, \tag{7a}$$

$$\mathbf{F}_{rbs} = \mathbf{B}^T\mathbf{M}_s^{-1/2}[\mathbf{M}_s^{-1/2}\mathbf{K}_s\mathbf{M}_s^{-1/2}]^+\mathbf{M}_s^{-1/2}\mathbf{B} - \boldsymbol{\Phi}_{db}\boldsymbol{\Lambda}_d^{-1}\boldsymbol{\Phi}_{db}^T, \tag{7b}$$

$$\mathbf{F}_{rbm} = \mathbf{B}^T\mathbf{M}_s^{-1/2}[\mathbf{M}_s^{-1/2}\mathbf{K}_s\mathbf{M}_s^{-1/2}]^{+2}\mathbf{M}_s^{-1/2}\mathbf{B} - \boldsymbol{\Phi}_{db}\boldsymbol{\Lambda}_d^{-2}\boldsymbol{\Phi}_{db}^T, \tag{7c}$$

where $\overline{\mathbf{M}}_p$ and $\overline{\mathbf{K}}_p$ are the reduced partitioned mass and stiffness matrices, respectively, and $\overline{\lambda}_i$ and $(\overline{\boldsymbol{\varphi}}_p)_i$ are the approximated global eigenvalue and eigenvector, respectively. $\mathbf{F}_{rbs}$ and $\mathbf{F}_{rbm}$ are the static and dynamic parts of residual flexibility. Here, $\overline{N}_p$ is the number of DOFs in the reduced model ($\overline{N}_p << N_g$).From the third row in Equation (7a), $\overline{\boldsymbol{\Phi}}_g$ is computed by

$$\boldsymbol{\Phi}_g \approx \overline{\boldsymbol{\Phi}}_g = \mathbf{L}\overline{\boldsymbol{\Phi}}_{u_b} = \boldsymbol{\Phi}_d\overline{\boldsymbol{\Phi}}_{q_d} + \mathbf{R}_s\overline{\boldsymbol{\Phi}}_{\alpha_s} - \hat{\mathbf{F}}_r\mathbf{B}\overline{\boldsymbol{\Phi}}_{\lambda_\ell}. \tag{8}$$

3 PREREQUISITES FOR THE MODE SELECTION ALGORITHMS

3.1 Mode selection method

The mode selection method developed by Kim et al. [17] is based on the relation between the substructural and global eigenvectors. $\boldsymbol{\Phi}_d\overline{\boldsymbol{\Phi}}_{q_d}$ in Equation (8) means a direct link between

the substructural and the global eigenvectors. Therefore, $\overline{\mathbf{\Phi}}_{q_d}$ is regarded as a relation matrix between the approximate global eigenvector matrix $\overline{\mathbf{\Phi}}_g$ and the dominant substructural eigenvector matrix $\mathbf{\Phi}_d$. Consequently, $\overline{\mathbf{\Phi}}_{q_d}$ can be utilized as an indicator of the contributions of the dominant substructural modes to the global modes.

In order to calculate the substructural modal contribution, we first construct a trial intermediate reduced model denoted by a tilde $(\tilde{\cdot})$, and it contains more substructural modes than the final reduced model. The numbers of the selected substructural modes for the intermediate and final reduced models are defined by $\tilde{N}_d$ and $\overline{N}_d$ ($\overline{N}_d < \tilde{N}_d$), respectively. Then, a relation matrix $\tilde{\mathbf{\Phi}}_{q_d}$ could be calculated solving the eigenvalue problem of the intermediate reduced model. $\left(\tilde{\phi}_{q_d}^{(k)}\right)_{ij}$ is a component of $\tilde{\mathbf{\Phi}}_{q_d}$ corresponding to the contribution of the ith substructural mode in the kth substructure to the jth global mode, and then the magnitude of each row of $\tilde{\mathbf{\Phi}}_{q_d}$ for a substructure implies the contribution level of the corresponding substructural mode to the global modes in $\overline{\mathbf{\Phi}}_g$. Then, the substructural modal contributions can be calculated as

$$C_i^{(k)} = \sqrt{\sum_{j=1}^{\tilde{N}_p} \left[\kappa_j \left(\tilde{\phi}_{q_d}^{(k)}\right)_{ij}\right]^2}, \tag{9}$$

where $C_i^{(k)}$ is an indicator of the contribution of the ith substructural mode of the kth substructure, and here κ_j denotes the weighting factor with the following rule

$$\kappa_j = 1 \text{ for } N_t^L \le j \le N_t^U, \text{ otherwise } \kappa_j = 0, \tag{10}$$

in which N_t^L and N_t^U denote the lower and upper limits of the target global modes, respectively. Both mode numbers are used to define the range of the target global modes.

3.2 Error estimation method

We here introduce the recently proposed error estimation method [20] that is another priority of the mode selection algorithm. Since λ_i and $(\boldsymbol{\varphi}_g)_i$ are the exact eigensolutions of the global eigenvalue problem in Equation (2), the following equations should be satisfied

$$\frac{1}{\lambda_i}(\boldsymbol{\varphi}_g)_i^T \mathbf{K}_g (\boldsymbol{\varphi}_g)_i = (\boldsymbol{\varphi}_g)_i^T \mathbf{M}_g (\boldsymbol{\varphi}_g)_i. \tag{11}$$

Here, the exact global eigensolutions are expressed by the approximated terms and the error terms $\delta\lambda_i$ and $(\delta\boldsymbol{\varphi}_g)_i$

$$\lambda_i = \overline{\lambda}_i + \delta\lambda_i, \ (\boldsymbol{\varphi}_g)_i = (\overline{\boldsymbol{\varphi}}_g)_i + (\delta\boldsymbol{\varphi}_g)_i, \tag{12}$$

and also, we assume that $\mathbf{K}_g$ can be divided as the approximated and its error matrices as

$$\mathbf{K}_g = \overline{\mathbf{K}}_g + \delta\mathbf{K}_g \ \text{ with } (\overline{\boldsymbol{\varphi}}_g)_k^T \overline{\mathbf{K}}_g (\overline{\boldsymbol{\varphi}}_g)_k = \overline{\lambda}_k, \tag{13}$$

in which $\delta\mathbf{K}_g$ is error in the global stiffness matrix. Using Equations (12) and (13) in Equation (11), we have

$$\frac{\overline{\lambda}_i}{\lambda_i} - (\overline{\boldsymbol{\varphi}}_g)_i^T \mathbf{M}_g (\overline{\boldsymbol{\varphi}}_g)_i = \frac{1}{\lambda_i}(\delta\boldsymbol{\varphi}_g)_i^T \left[\mathbf{K}_g - \lambda_i \mathbf{M}_g\right](\delta\boldsymbol{\varphi}_g)_i - \frac{1}{\lambda_i}(\overline{\boldsymbol{\varphi}}_g)_i^T \delta\mathbf{K}_g (\overline{\boldsymbol{\varphi}}_g)_i. \tag{14}$$

If the approximated global eigenvector $(\overline{\boldsymbol{\varphi}}_g)_i$ is close enough to the exact global eigenvector $(\boldsymbol{\varphi}_g)_i$, the right-hand side in Equation (14) that are much smaller than the terms in the left-hand side can be negligible. Consequently, Equation (14) can be rewritten by

$$\frac{\overline{\lambda}_i}{\lambda_i} - 1 \approx (\overline{\boldsymbol{\varphi}}_g)_i^T \mathbf{M}_g (\overline{\boldsymbol{\varphi}}_g)_i - 1, \tag{15}$$

where the left-hand side in Equation (15) is the relative eigenvalue error, and the right-hand side is the mass-orthonormality error of the approximated global eigenvector $(\overline{\boldsymbol{\varphi}}_g)_i$. This derivation procedure shows that the mass-orthonormality error is a direct approximation of the relative eigenvalue error. Then, we define the error estimation parameter η_i as

$$\eta_i = (\overline{\boldsymbol{\varphi}}_g)_i^T \mathbf{M}_g (\overline{\boldsymbol{\varphi}}_g)_i - 1. \tag{16}$$

4 MODE SELECTION ALGORITHM

We here propose a new mode selection algorithm combining the recently develop mode selection and error estimation methods [17, 20]. The proposed new mode selection algorithm will be compared with another mode selection algorithm using frequency cut-off rule. To distinguish those two algorithms, we here use "eigenvector based mode selection algorithm (E-MSA)" and "frequency cut-off mode selection algorithm (F-MSA)". The sequential procedures of these mode selection algorithms are summarized in Tables 1 and 2.

Step 1. Initial preparation

(a) $\mathbf{M}_g$ and $\mathbf{K}_g$ are given.

(b) The range of the target global modes is determined: N_t^L and N_t^U.

(c) Error tolerance ε is assigned.

(d) $\overline{N}_d$ is determined for the reduced models.

Step 2. Construction of the reduce model

(a) The substructural eigenvalue problem are solved: $[\mathbf{K}_s^{(k)} - \lambda_i^{(k)} \mathbf{M}_s^{(k)}](\boldsymbol{\varphi}_s^{(k)})_i = \mathbf{0}$, for $k = 1,2,...,N_s$.

(b) The dominant substructural modes are selected by the frequency cut-off rule.

(c) The reduced model is constructed and solved: $\overline{\mathbf{K}}_p (\overline{\boldsymbol{\varphi}}_p)_i = \overline{\lambda}_i \overline{\mathbf{M}}_p (\overline{\boldsymbol{\varphi}}_p)_i$.

Step 3. Convergence check

(a) Relative eigenvalue error is estimated using Equation (16).

(b) Convergence is check in target range: $\eta_i \le \varepsilon$ $(N_t^L \le i \le N_t^U)$.

If the target eigenvalues have converged, stop.

Otherwise, continue.

(c) Increase the number of retained modes:

$\overline{N}_d = \overline{N}_d + 1$.

(d) Go to step 2(b).

Table 1: Frequency cut-off mode selection algorithm.

Step 1. Initial preparation

(a) $\mathbf{M}_g$ and $\mathbf{K}_g$ are given.

(b) The range of the target global modes is determined: N_t^L and N_t^U.

(c) Error tolerance ε is assigned.

(d) $\tilde{N}_d$ and $\overline{N}_d$ are determined for the intermediate and final reduced models, respectively.

Step 2. Construction of the intermediate reduced model

(a) The substructural eigenvalue problem are solved: $[\mathbf{K}_s^{(k)} - \lambda_i^{(k)}\mathbf{M}_s^{(k)}](\boldsymbol{\varphi}_s^{(k)})_i = \mathbf{0}$, for $k = 1,2,...,N_s$.

(b) The dominant substructural modes are selected by the frequency cut-off rule for the intermediate reduced model.

(c) The intermediate reduced model is constructed $\tilde{\mathbf{M}}_p$ and $\tilde{\mathbf{K}}_p$.

Step 3. Construction of the final reduce model

(a) The intermediate eigenvalue problem is solved and $\tilde{\boldsymbol{\Phi}}_{q_d}$ is found: $\tilde{\mathbf{K}}_p(\tilde{\boldsymbol{\varphi}}_p)_i = \tilde{\lambda}_i\tilde{\mathbf{M}}_p(\tilde{\boldsymbol{\varphi}}_p)_i$.

(b) The substructural modal contributions $C_i^{(k)}$ are calculated using Equation (9) in the target range $N_t^L \sim N_t^U$.

(c) The dominant modes are selected using $C_i^{(k)}$ for the final reduced model.

(d) Final reduced model is constructed and solved: $\overline{\mathbf{K}}_p(\overline{\boldsymbol{\varphi}}_p)_i = \overline{\lambda}_i\overline{\mathbf{M}}_p(\overline{\boldsymbol{\varphi}}_p)_i$.

Step 4. Convergence check

(a) Relative eigenvalue error is estimated using Equation (16).

(b) Convergence is check in target range: $\eta_i \le \varepsilon$ $(N_t^L \le i \le N_t^U)$.

If the target eigenvalues have converged, stop.

Otherwise, continue.

(c) Increase the number of retained modes: $\overline{N}_d = \overline{N}_d + 1$.

(d) Go to step 3(c).

Table 2: Eigenvector based mode selection algorithm.

5 NUMERICAL EXAMPLES

We consider a cylindrical shell problem modeled by 24×24 MITC4 shell finite elements [23-25], and the free boundary condition is imposed. Length L is 12m, radius R is 0.5m, and thickness h is 0.005m. Young modulus is 69GPa, Poisson's ratio is 0.35, and structural density is $2700\,kg/m^3$. The cylindrical shell is partitioned into two substructures ($N_s = 2$), see Figure 1.

Performances of the mode selection and error estimation methods are tested in the target global range with $N_t^L = 5$ and $N_t^U = 15$. 70 substructural modes are retained for the intermediate reduced model ($\tilde{N}_d = 200$). Figures 2 and 3 show the performance of the mode selection and error estimation methods employed in this work. Also, we test the performance of E-MSA compared with F-MSA. 20 substructural modes are initially retained ($\overline{N}_d = 15$), and error tolerance ε is assigned by 10^{-3}. Using E-MSA, total modes in the target range converge much faster than F-MSA, see Table 3 and Figure 4.

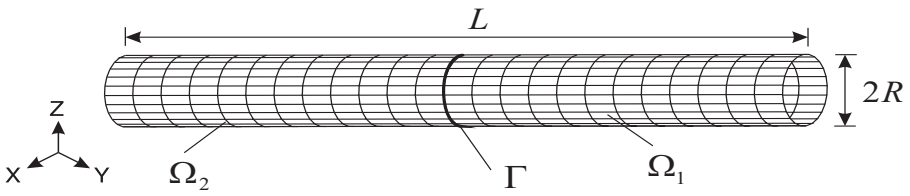


Figure 1: Cylindrical shell problem.

	Total number of iteration	Final number of retained substructural mode
E-MSA	8	28
F-MSA	52	72

Table 3: Numbers of iteration and retained mode.

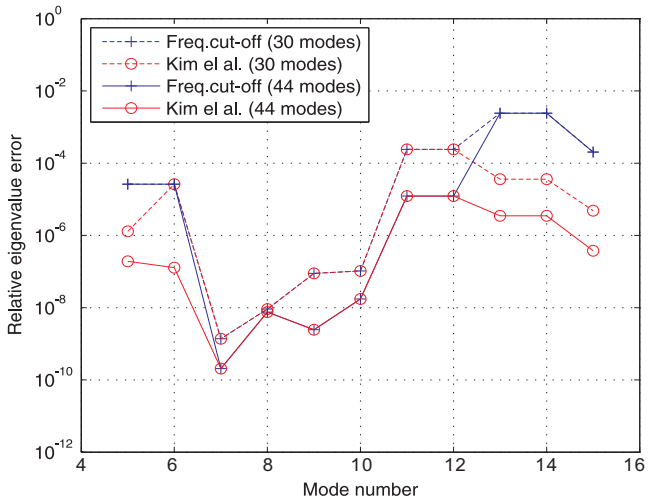


Figure 2: Relative eigenvalue error.

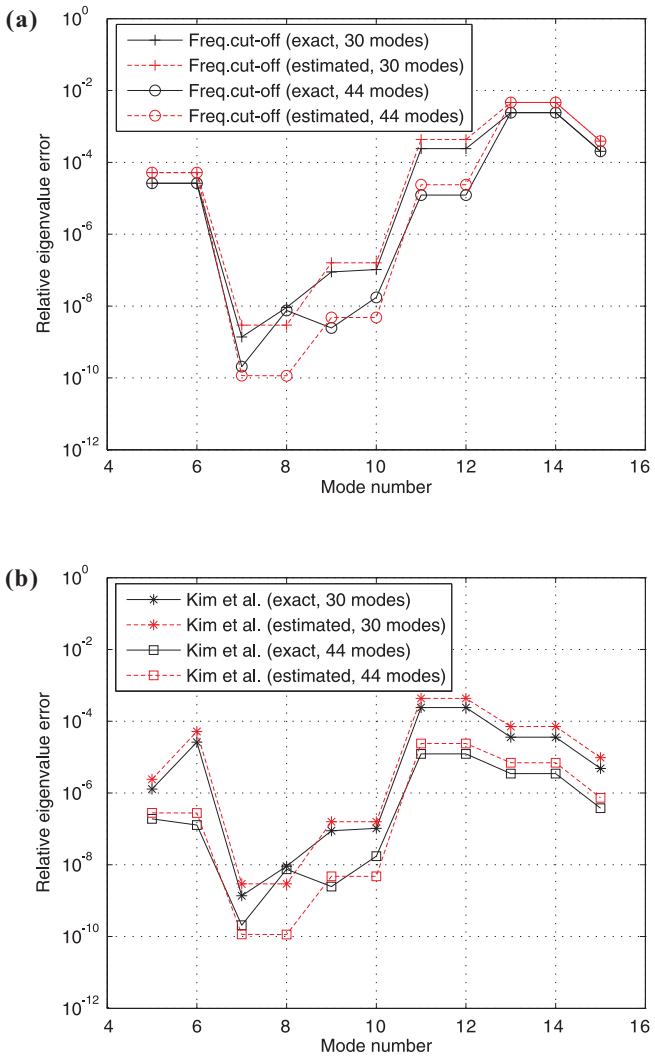


Figure 3: Exact and estimated relative eigenvalue errors. (a) Frequency cut-off rule, and (b) Kim et al. [17].

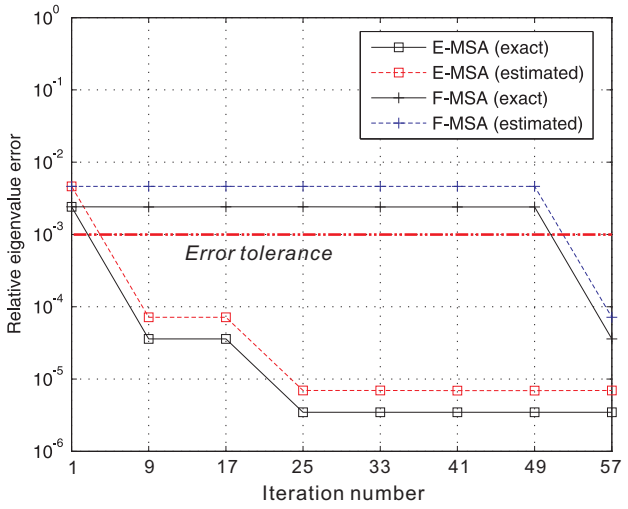


Figure 4: Convergence curve of the 14th mode.

6 CONCLUSIONS

We here propose a new mode selection algorithm in the F-CMS method, and then recently developed robust mode selection and error estimation methods are employed [17, 20]. The proposed mode selection algorithm was compared with the conventional mode selection algorithm using the frequency cut-off rule. We first reassessed the mode selection and error estimation methods, and then tested performance and features of the proposed mode selection algorithm using cylindrical shell problem. Those results show the excellent performance of the proposed mode selection algorithm. Although it is only studied in the F-CMS method here, this idea could be applicable to other CMS methods.

ACKNOWLEDGMENTS

This research was supported by Basic Science Research Program through the National Research Foundation of Korea (NRF) funded by the Ministry of Science, ICT & Future Planning (No. 2014R1A1A1A05007219).

REFERENCES

[1] W. Hurty, Dynamic analysis of structural systems using component modes. *AIAA Journal*, **3**(4), 678-685, 1965.

[2] R. Guyan, Reduction of stiffness and mass matrices. *AIAA Journal*, **3**(2), 380, 1965.

[3] R.R. Craig, B.C.C. Bampton, Coupling of substructures for dynamic analysis. *AIAA Journal*, **6**(7), 1313-1319, 1968.

[4] R.H. MacNeal, Hybrid method of component mode synthesis. *Computers & Structures*, **1**(4), 581-601, 1971.

[5] W.A. Benfield, R.F. Hruda, Vibration analysis of structures by component mode substitution. *AIAA Journal*, **9**, 1255-1261, 1971.

[6] S. Rubin, Improved component-mode representation for structural dynamic analysis. *AIAA Journal*, **13**(8), 995-1006, 1975.

[7] J.K. Bennighof, R.B. Lehoucq, An automated multilevel substructuring method for eigenspace computation in linear elastodynamics. *SIAM Journal on Scientific Computing*, **25**(6), 2084-2106, 2004.

[8] D.J. Rixen, A dual Craig-Bampton method for dynamic substructuring. *Journal of Computational and Applied Mathematics*, **168**(1-2), 383-391, 2004.

[9] D.D. Klerk, D.J. Rixen, S.N. Voormeeren, General framework for dynamic substructuring: history, review, and classification of techniques. *AIAA Journal*, **46**(5), 1169-1181, 2008.

[10] J.G. Kim, S.H. Boo, P.S. Lee, An enhanced AMLS method and its performance. *Computer Methods in Applied Mechanics and Engineering*, **287**, 90-111, 2015.

[11] J.G. Kim, P.S. Lee, An enhanced Craig-Bampton method, *International Journal for Numerical Methods in Engineering*, 03/2015; DOI: 10.1002/nme.4880.

[12] K.C. Park, Y.H. Park, Partitioned component mode synthesis via a flexibility approach. *AIAA Journal*, **42**(6), 1236-1245, 2004.

[13] D. Markovic, K.C. Park, A. Ibrahimbegovic, Reduction of substructural interface degrees of freedom in flexibility-based component mode synthesis. *International Journal of Numerical Methods in Engineering*, **70**, 163-180, 2007.

[14] K.C. Park, J.G. Kim, P.S. Lee, A mode selection criterion based on flexibility approach in component mode synthesis. *53th AIAA/ASME/ASCE/AHS/ASC Structures, Structural Dynamics, and Materials Conference*, Hawaii, USA, 2012.

[15] W.C. Hurty, A criterion for selecting realistic natural modes of a structure. *Technical Memorandum*, Jet Propulsion Laboratory, Pasadena, CA, 33-364, 1967.

[16] J.D. Collins, G.C. Hart, W.C. Hurty, B. Kennedy, Review and development of modal synthesis techniques. *Technical Report*, J. H. Wiggins, May 1972.

[17] J.G. Kim, P.S. Lee, K.C. Park, A mode selection method for accurate reduction of FE models in component mode synthesis. *Submitted to Computer Methods in Applied Mechanics and Engineering.*

[18] J.G. Kim, K.H. Lee, P.S. Lee, Estimating relative eigenvalue errors in the Craig‐Bampton method, *Computers & Structures*, **139**, 54-64, 2014.

[19] J.G. Kim, P.S. Lee, An accurate error estimator for Guyan reduction, *Computer Methods in Applied Mechanics and Engineering*, **278**, 1-19, 2014.

[20] J.G. Kim, P.S. Lee, A posteriori error estimation method for the flexibility-based component mode synthesis. *Submitted to AIAA Journal.*

[21] K. Elssel, H. Voss, An a priori bound for automated multilevel substructuring. *SIAM Journal on Matrix Analysis and Applications*, **28**(2), 386-397, 2007.

[22] H. Jakobsson, M.G. Larson, A posteriori error analysis of component mode synthesis for the elliptic eigenvalue problem. *Computer Methods in Applied Mechanics and Engineering*, **200**, 2840–2847, 2011.

[23] E.N. Dvorkin, K.J. Bathe, A continuum mechanics based four-node shell element for general nonlinear analysis. *Engineering Computations*, **1**(1), 77-88, 1984.

[24] H.M. Jeon, P.S. Lee, K.J. Bathe, The MITC3 shell finite element enriched by interpolation covers, *Computers and Structures*, **134**, 128-142, 2014

[25] Y. Lee, P.S. Lee, K.J. Bathe, The MITC3+ shell element and its performance, Computers and Structures, **131**(1), 12-23, 2014.

COMPDYN 2015
5th ECCOMAS Thematic Conference on
Computational Methods in Structural Dynamics and Earthquake Engineering
M. Papadrakakis, V. Papadopoulos, V. Plevris (eds.)
Crete Island, Greece, 25ï 27 May 2015

BEHAVIOUR OF REINFORCED CONCRETE KNEE BEAM-COLUMN JOINT IN CASE OF GROUND CORNER COLUMN LOSS-NUMERICAL ANALYSIS

B. Abdelwahed[1], B. Belkassem[1], L. Pyl[2], J. Vantomme[1]

[1] Polytechnic Faculty, Department of civil and materials engineering, Royal Military Academy
30 av. de la Renaissance, B-1000 Brussels, Belgium
e-mail: basem_salah79@yahoo.com
bachir.belkassem@rma.ac.be
john.vantomme@rma.ac.be
[2] Faculty of Engineering, Mechanics of materials and constructions department,
Free University of Brussels, Pleinlaan 2 - building Kb
1050 Brussels, Belgium
e-mail: lincy.pyl@vub.ac.be

Keywords: Progressive Collapse, RC joint, Structural Dynamics, Numerical Simulation, Reinforcement Anchorage.

Abstract. *Prevention of a progressive collapse event of a reinforced concrete structure is a key design consideration. Commonly a sudden column loss scenario is analyzed to ensure the structure has suitable robustness; however, there is still a lack of numerical information regarding the influence of the dynamic effects involved. Beam-column joints are a critical part in reinforced concrete frames designed for inelastic response to severe external loads. Structural response for an inverted knee beam-column joint which results from the loss of a ground corner column are performed in this study using LS-DYNA. The sudden failure of the ground corner column may turn the exterior beam-column joint into an inverted knee beam-column joint with some reinforcement requirements deficiencies. Three-dimensional finite element (FE) models of a knee beam-column joint are described and verified with experimental results available in literature; this is followed by a parametric study to investigate the influence of different types of anchorage for beam longitudinal bars. In addition to that, the effect of using additional joint vertical stirrups is examined numerically. It is shown that the various types of reinforcement anchorage in beams have significant effects on shear capacity, load-deflection characteristics and failure modes of knee beam-column joints. Anchorage beam bars with U shape produces better inelastic behaviour than 90° standard hooks and headed bars. Contribution of additional joint vertical stirrups is more influential with headed bars anchorage than with the other two anchorage types.*

1 INTRODUCTION

Reinforced concrete is the principal material used for structures engineering. From a safety point of view it is important that a concrete structure especially its connections, should have an adequate amount of continuity, integrity and high load carrying capacity, in order to exhibit ductile behavior that allows redistribution of forces after events, such as the loss of a ground column. Local failure shouldn't lead to total collapse of the structure.

The response of a structure after an initial damaging event is a critical consideration. This is reflected in the Eurocodes basic requirements that:
"A structure shall be designed and executed in such a way that it will not be damaged by events such as explosion, impact, and the consequences of human errors, to an extent disproportionate to the original cause." [1] This has led to the use of the sudden column loss scenario in which a key vertical element is removed and the structure analyzed to predict if further failure is likely. This situation has been investigated by a number of authors to determine the failure mechanisms and ultimate capacity of a damaged structure both steel [2] and Reinforced Concrete (RC) [3-6].
Progressive collapse experimental simulation after a sudden damaging event is time consuming, expensive and requires experience in order to achieve accurate results. Alternatively, the finite element method is a powerful tool for structural analysis. The majority of numerical investigations of the behavior of reinforced concrete members under a column removal scenario involve two-dimensional idealizations. This simplification provides good results with Dirk et al. [7] for a slab membrane tensile action investigated numerically with DIANA, but in case of beam-column joints, the results may be of questionable accuracy; how to consider joint stirrups confinement effect. Three- dimensional modeling has many advantages over the two-dimensional idealizations, in terms of applying load and specifying boundary conditions close to the real structure; also dilation of concrete and confinement effects may be taken into account. Yi et al, [3] conducted in-depth studies on the reinforced concrete assemblies under a column removal scenario using LS-DYNA simulating the improvement of its behavior by catenary action mechanism.

Corner ground column disappearing turns an exterior beam-column joint into an inverted knee joint; this may lead to some reinforcement deficiencies, such as the absence of joint vertical stirrups and column longitudinal bars with poor anchorage conditions. LS-DYNA program proposes several advanced constitutive models to simulate concrete material; most of them have the option of automatic generation of parameters to help users during the input phase. However, these sets of automatically generated parameters are based on reference experimental data that could not match very precisely with concrete properties in some cases. Therefore, one has to be careful about this point and must investigate these models with sensitivity analysis and optimizations to be sure that the modeled behavior is as close as possible to the real one. The general approach for reinforced concrete modeling; which is proposed in this paper, contains several important steps. The first one includes boundary conditions, hourglass treatment, mesh size, proper coupling algorithm for connecting both concrete solid element and reinforcement beam elements, also for reducing required CPU time, selective mass scaling technique will be implemented to achieve larger explicit time step. The second step is to get results for real case using different concrete material models with automatic parameters generation, followed by fitting and optimization of material parameters to match as possible the available experimental results in literature. The third step is a parametric study to investigate the influence of different beam bar anchorage types and the effect of joint vertical stirrups absence.

2 DESCRIPTION OF THE REFERENCE SELECTED EXPERIMENTAL TESTS

A series of well monitored experiments on RC beam-column knee joints were performed at Clarkson University by Wallace et al. [8] and at Chongqing Jiaotong University by Peng et al. [9]. The present paper offers the numerical simulation of these tests using LS_DYNA. The purpose of this study is to evaluate the efficiency of the numerical model and the used material models to predict the structural response for further parametric analysis.

2.1 Wallace specimen

The knee beam-column joint studied by Wallace et al., consists of a beam portion and column portion. The column has a cross section of 400 mm x 400 mm with an overall length of 1100 mm and the beam has a cross section of 280 mm x 400 mm and the length of the clear portion is 1100 mm. The beam-column joints are designed assuming that points of contra-flexure occur at the mid-height of columns and at the mid-span of beams. The top and bottom longitudinal reinforcements in the beam are bent down and up into the column. The beam is reinforced using 5è 18 mm as top and 3è 18 mm bottom longitudinal bars and è 10 mm as transverse steel repeated each 90mm. The column is reinforced with 8è 20 mm as longitudinal bars and è 10 mm ties spaced 90 mm. The dimensions and reinforcement details of the specimen is shown in Figure 1. Detailed design details of the specimen can be found in [8].

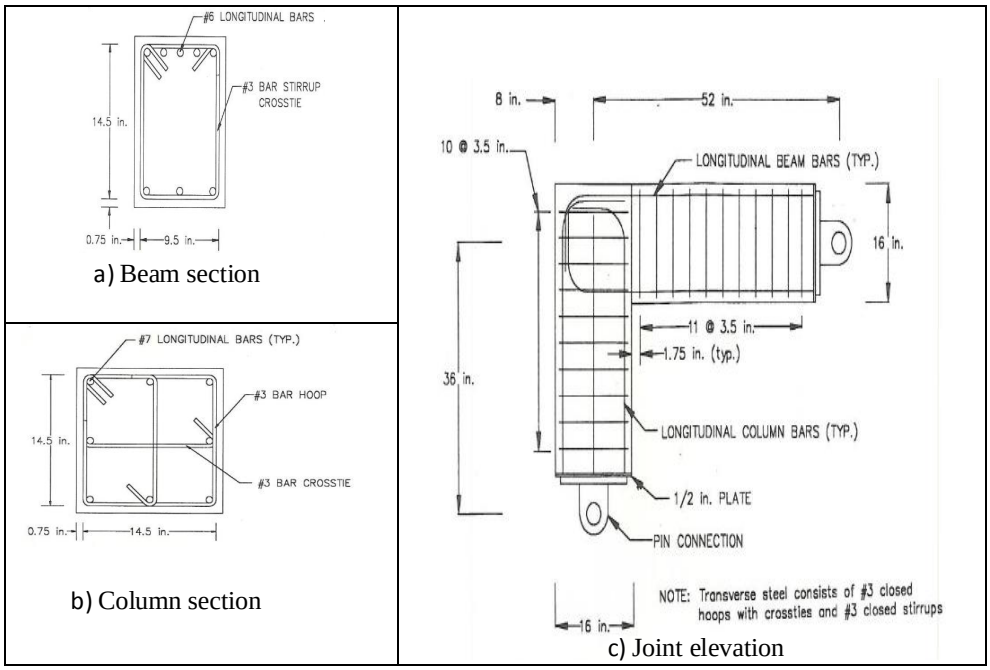
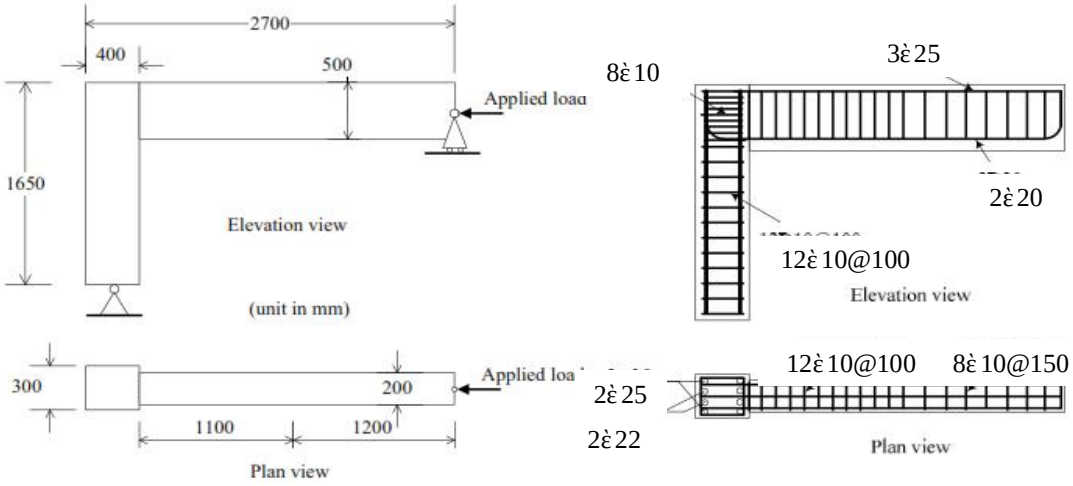


Figure 1 : Dimension and details of knee joint [8] (all dimension in inch).

2.2 Peng specimen

Peng and Wang [9] evaluated a series of non seismically detailed knee beam-column joints subjected to monotonic horizontal loading. The specimen represents an ñas-builtò corner beam-column joint subassemblage consisting of a column and beam; the lengths of the column and beams are chosen to correspond to the contra þexural points under lateral load, assumed to occur at the mid-height and mid-span of the frame. The dimensions and reinforcing details of the specimen is shown in Figure 2. The joint core contains no vertical transverse reinforcement. Beam longitudinal bars are anchored in the joint with 90° standard hooks. The column has a

300x 400 mm cross section, and the beam is 200 mm wide x 500 mm deep. The beam is reinforced using 3è25mm as top and 2è20mm bottom longitudinal bars and è10 mm as transverse steel repeated each 100mm. The column is reinforced with 4è22 and 4è25 mm as longitudinal bars and è10 mm ties spaced 100 mm. More details about the specimen can be found in [9].



a) Dimension and boundary condition

b) Steel reinforcement details

Figure 2 : Dimension and steel reinforcement details of knee joint [9] (all dimension in mm).

3 FINITE ELEMENT MODEL DEVELOPMENT

The first step, the description of the model includes structural geometry and element type, modeling of materials, boundary conditions and simulation time.

3.1 Structural geometry and element type

Figure 3 shows the three-dimensional FE model of the RC beam-column knee joint tested by Wallace et al., with two different mesh sizes. In order to improve the accuracy of the results while reducing computational cost, a mesh sensitivity analysis was carried out. Eight node solid elements with a single integration point were used to represent concrete; one disadvantage with one-point integration is the need to control the zero energy modes that arise, called hourglassing modes. In order to control these modes, LS-DYNA has several hourglass control types. Beam elements (2-node Hughes-Liu beam element) were used to model steel reinforcing bars.

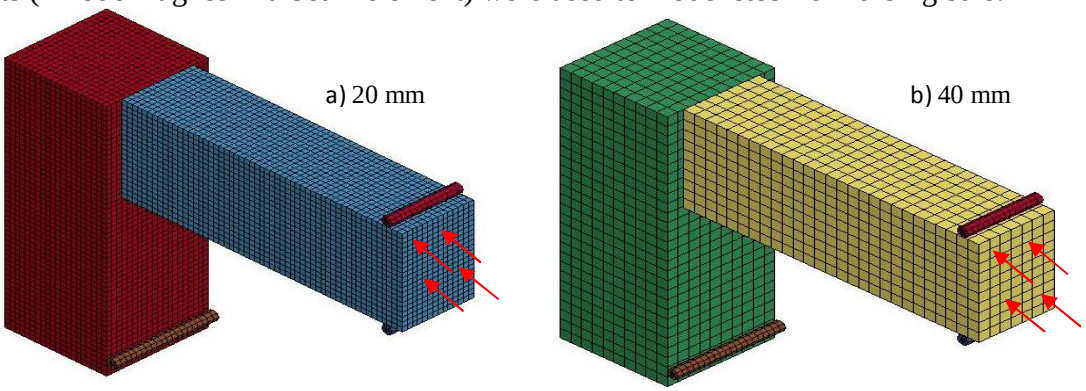


Figure 3 : Finite element meshes sizes for mesh sensitivity analysis.

3.2 Modeling of materials

Concrete

A good concrete model must consider the elasticity of concrete prior to cracking and the subsequent plastic states on the onset of cracking and beyond [10].
LS-DYNA has several material models to model concrete behaviour such as:

- Plasticity based Karagozian and Case concrete damage model designated as MAT_72_R3 in LS-DYNA [11];
- Continuous Surface Cap Model designated as MAT_CSCM_159, which is a visco-elastic-plastic concrete model [10].

These two materials models were used in this study to check which one is most suitable for this case study and able to give close results to the experimental ones. Table 1 presents properties of the used concrete material models.

Material ID in LS_DYNA	Material title in LS_DYNA	Supported element types	Strain rate sensitivity	Failure criteria	Equation of state requirement
72	Concrete damage	Solid	Yes	Yes	Yes
159	CSCM	Solid, shell	Yes	Yes	No

Table 1: Concrete material models in LS-DYNA [12].

Steel reinforcement

The steel reinforcement bars (longitudinal and shear reinforcements) were modeled as a strain sensitive uniaxial elastic-plastic material. The material model PIECEWISE_LINEAR_ PLASTICITY (MAT_024) from LS-DYNA was used in this study.

The concrete and steel elements require a good coupling mechanism in order to achieve interaction between the two parts; this analysis uses the CONSTRAINED_ LAGRANGE_ IN_SOLID formulation to achieve a proper interaction.

3.3 Boundary Conditions

Modeling of boundary conditions is often the most critical aspect in achieving sensible, reliable data from a finite element model [13]. The load on the beam-column joint is applied by specifying a prescribed horizontal displacement to the nodes of the beam end as shown in Figure 3. To simulate simply supported conditions, a selection of beam end nodes were prevented from vertical movement and a selection of column end nodes were prevented from both vertical and horizontal movement as shown in Figure 3.

3.4 Event Simulation Time

The flexural frequency of vibration was computed analytically for the two beam-column joints using conventional formulas of vibration theory [14]. Table 2 shows the computed flexural frequency of vibration for the two beam-column joints and the corresponding period of vibration. The event simulation time was chosen to be 1.5 sec which is approximately more than 100 times the period of flexural vibration for the Wallace specimen. Consequently, inertial effects are assumed to be negligible and the model can be used to represent a quasi-static experiment.

Knee joint ID	Flexural frequency of vibration	Flexural period of vibration
Wallace	543.19 rad/sec	0.01157 sec
Peng	276.104 rad/sec	0.0227 sec

Table 2: Analytical flexural period of vibration for reinforced concrete beam-column joints.

3.5 Run Time

A shortcoming in using an explicit code to simulate a quasi-static experiment is the fact that it can result in excessive run times which may limit mesh refinement trials. In order to control run time, a selective mass scaling card is implemented in this study, to increase the critical time-step for explicit time integration without adulterate the global solution; it is applied to limited regions with very small critical time steps [15]. For the finite element simulations presented in this study, the cost in CPU run time varied approximately from half hour to 11 hours (depending on the dimension of model and element size) for 1.5 sec. of event simulation time, on a Pentium III PC 600 MHz dual processor with 512 MB of RAM with LS-PrePost processor software version 4.1 with Finite element software LS_DYNA solver version ls-dyna_smp_d_R700_winx64 _ifort 101.exe. It should be recognized that for quasi-static structural problems, implicit methods are usually more effective than explicit methods; however, this depends on severity of non-linearities, which are present in the current study. It is very difficult to model the non-linearities and progressive damage/failure using an implicit code.

4 COMPARISON OF EXPERIMENTAL AND NUMERICAL RESULTS

A number of models were created with varying mesh sizes using different concrete material models for knee beam-column joints. In this paper, the results are presented for four simulations of the knee joint tested by Wallace et al, using Concrete Damage and CSCM concrete models, followed by simulation using selective mass scaling to determine how it affects the solution speed and added mass percentage as well.

4.1 Load vs. horizontal deflection of the knee joint

In order to simulate the experimental conditions, the models were analyzed in displacement control in LS-DYNA. Figures 4-6 show the numerical results in comparison with the experimental curve of the load vs. the horizontal joint displacement. Table 3 shows the maximum lateral load carrying capacity for the different mesh sizes with different concrete material models and the approximate run times associated with each of the mesh sizes. Table 3 also shows the number of elements associated with each mesh size and the corresponding disk space requirements.

From Figures 4-5, lateral load carrying capacity increases with decreasing mesh size, converging to the experimental at a mesh size of 20 mm. Figure 4 shows that the primary stiffness of the model was over estimated in the numerical analysis. The simulation was able to reproduce the main features of the joint behaviour such as the joint ultimate capacity, the resulting cracking pattern and the displacement capacity. Figure 6 shows agreement between the numerical results for the Peng specimen with available experimental and Abaqus results by Peng.

4.2 Crack profiles for different simulations

The damage in the RC model is shown by plotting the fringes of effective plastic strain. These effective plastic strain contours reveal the strain localization where failure propagates. The first

experimental flexural crack appeared at the beam-column interface at the displacement of 2.2 mm which is relatively close to the first numerical crack which appeared at 3 mm displacement; the cracks in the beam and column were attributed to bending at low displacement level, but appeared to be a result of combination of shear and bending in advanced loading stages. At higher loading level, cracks continued to form, usually where stirrups or hoops were located. Figure 7 shows the cracking pattern of the RC knee joint in the numerical simulation. From these comparisons, it can be observed that the damage plot in the numerical simulation can capture the typical crack profiles of the RC knee joint under closing moment. Closer examination of results for the two mesh sizes with different concrete material models show a small variation in the damage profile. The finer mesh size of 20mm with the CSCM model seems to show, a more accurate pattern of cracks damage profile as compared to other trials.

Mat ID , mesh size		No. of elements	Load carrying capacity [kN]	Approximate Run Time[sec]	Disk space used [B]
Wallace	CSCM, 20 mm	39208	274	20580	10259865
	CSCM, 40 mm	5504	194	1920	2863466
	KC3, 20 mm	39208	116	18341	9816368
	KC3, 40 mm	5504	105	1385	2788226
	CSCM, 20 mm, SMS	39208	291	8634	2883213
	Experimental= 264 kN			Analytical= 275.3 kN	
Peng	CSCM, 25 mm	64500	200	38650	10352654
	Experimental= 200 kN			Analytical= 192.7 kN	

Table 3: Mesh and concrete material models sensitivity analysis.

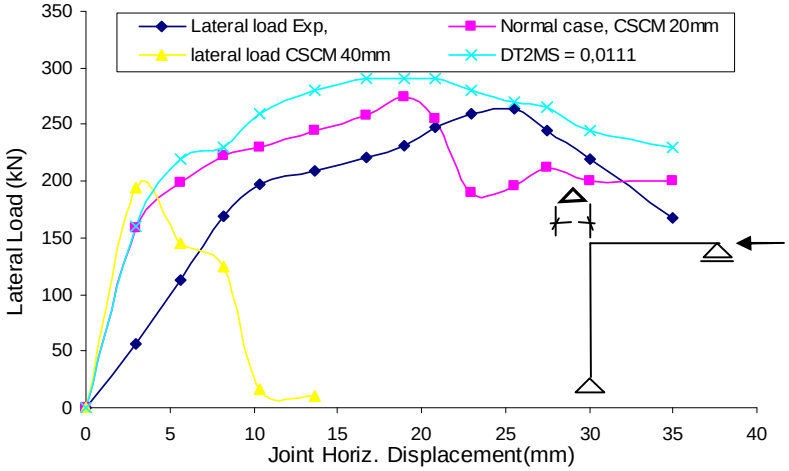


Figure 4 : Lateral Load versus Joint Displacement for Wallace specimen and different simulations.

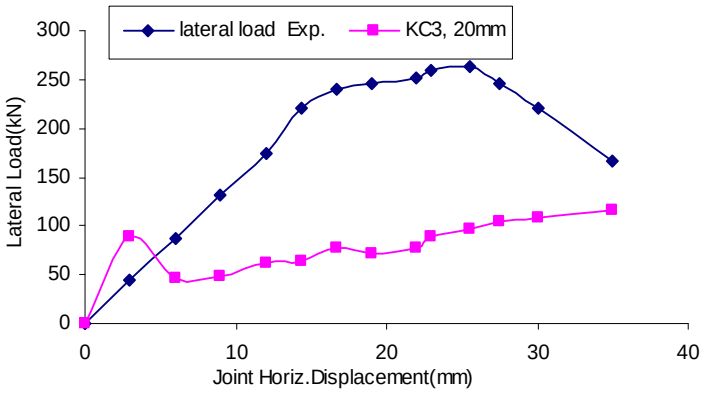


Figure 5 : Lateral Load versus Joint Displacement for Wallace specimen and concrete damage model KC3.

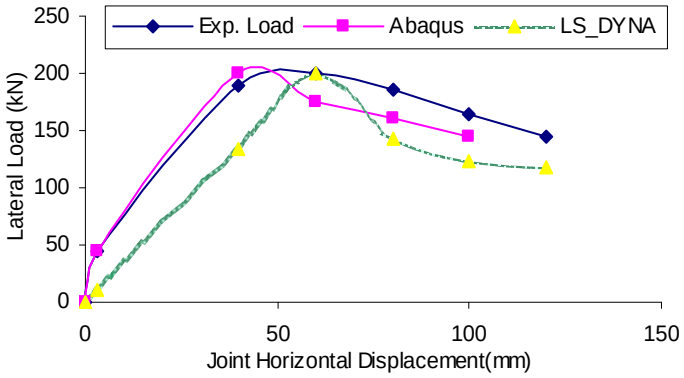
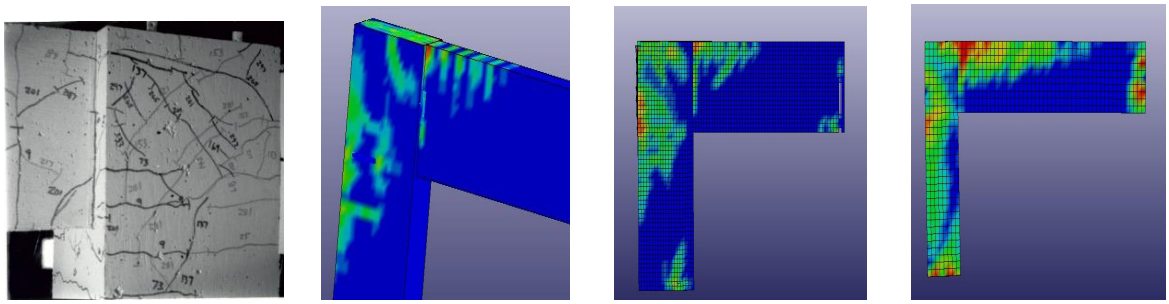


Figure 6 : Lateral Load versus Joint Displacement for Peng specimen and different simulation tools .



a) Typical crack pattern b) First flexural crack c) Final cracks, CSCM, 20 d) Final cracks, CSCM, 40

Figure 7 : Comparison of cracking pattern of RC joint with different element sizes for mesh sensitivity analysis.

In one of simulations, selective mass scaling (SMS) was used in order to increase the critical time step to reduce the overall computation time; the change in mass is tracked and observed in order to check if it is acceptable. Figure 8 shows that this simulation with SMS has a trivial increase for model kinetic energy (less than 1% internal energy); SMS significantly decreases computation time with trivial effect on results. In the further sections, the ýnite element models are used to investigate the inþuence of various parameters on the load carrying capacity of knee beam-column joints.

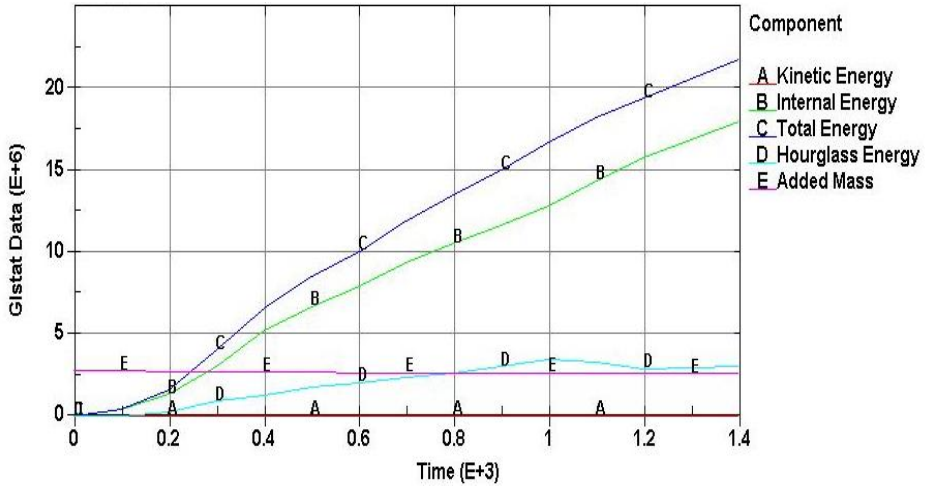


Figure 8 : Model energy balance with selective mass scaling.

5 PARAMETRIC STUDY

After verification of the FE model with respect to the experimental results, this section presents a parametric investigation to find more information about the behavior of RC knee joints with different reinforcement details. The response of the RC knee joints was studied by varying some key parameters such as joint vertical stirrups absence and using column longitudinal bars with poor anchorage condition simulating the case after ground column loss. Next, beam longitudinal bars may be anchored by 90° standard hook, headed end and U shape end. Figure 9 presents schematic drawings for the beamôs different anchorage ends.

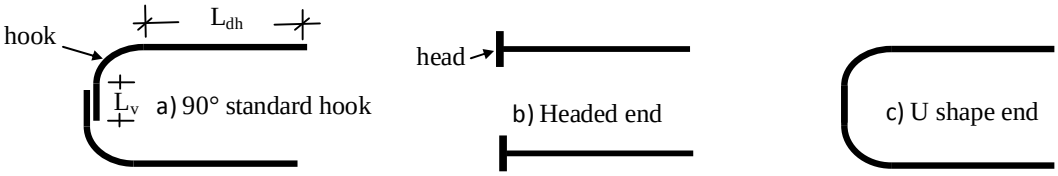


Figure 9 : Different alternatives for beam bars end anchorage.

The anchorage conýgurations in Fig. 9-a encompasses the following details: (1) horizontal anchorage (L_{dh}), (2) hook and (3) extension of the hook (L_v). The minimum horizontal anchorage (L_{dh}) is necessary to transfer the tensile stress in the þexural reinforcement in to the joint. The hook is responsible for the formation of the compression strut which in the case of knee joints is one of the major load transfer mechanisms from beam to column through the joint core. Sufficient extension (L_v) tail of the hook is necessary to prevent the pullout of þexural reinforcement. Figure 9-b presents headed bar ends by mounting a steel plate at the bar end instead of the hook portion and itôs vertical tail, in order to decrease steel congestion and ease concrete placement. Figure 9-c presents a U shaped bar by adjoining both top and bottom reinforcement in one in order to improve bond resistance between concrete and the beam main rebar.

The monotonic load displacement behaviour of these anchorage conýgurations with and without joint vertical stirrups are compared in Figures 10 to 13. Slippage of column longitudinal bars and joint shear failure observed in all the modeled joints is a direct consequence of the absence of good anchorage condition for column longitudinal bars. Among the considered anchorage conýgurations, the headed end without joint vertical stirrups exhibited the weakest

behavior when compared to other conýgurations; this explained by the fast rotation of the beam top bars at the beam-column interface, which goes together with accelerated bond deterioration. This may be observed in figure 13, in the elastic part of the curve. Figure 11 shows that a U shaped bar is observed to have better performance when compared to the other anchorage conýgurations. This can be attributed to the better conýnement of the joint core concrete. It can also be observed from figure 12, that the strength enhancement is more evident in the case of headed bars with additional joint vertical stirrups when compared to the other anchorage cases; this can be attributed to the better conýnement of joint core concrete and the avoiding of rotation of the beam top bars.

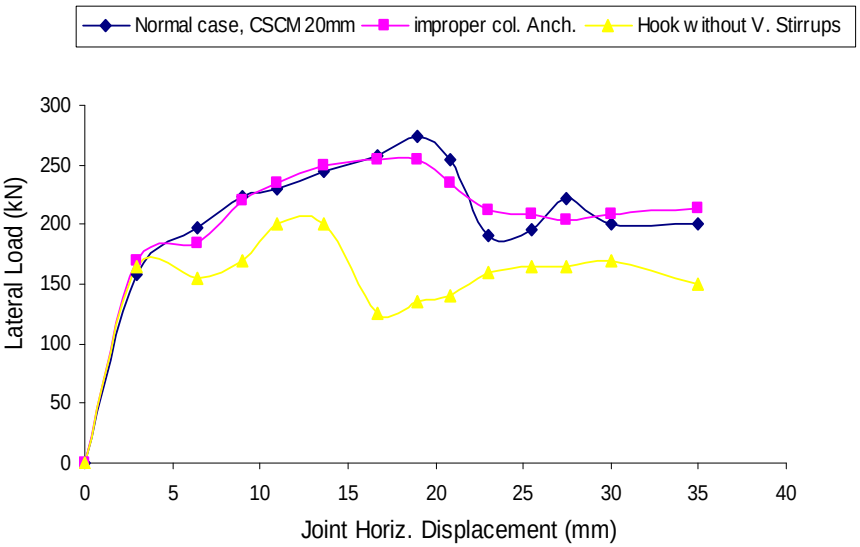


Figure 10 : Stirrups effect on RC joint with improper column bars anchorage and hooked beam bars anchorage.

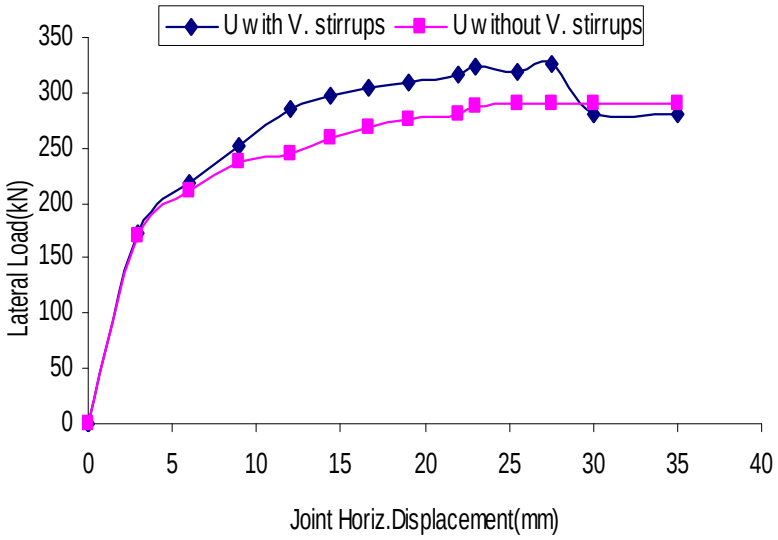


Figure 11 : Stirrups effect on RC joint with improper column bars anchorage and U shaped beam bars.

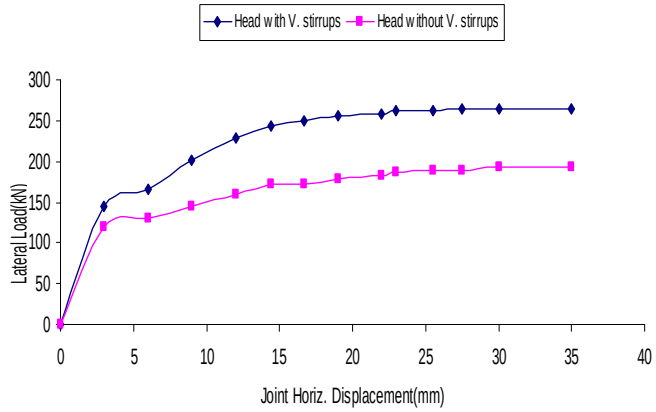


Figure 12 : Stirrups effect on RC joint with improper column bars anchorage and headed beam bars anchorage.

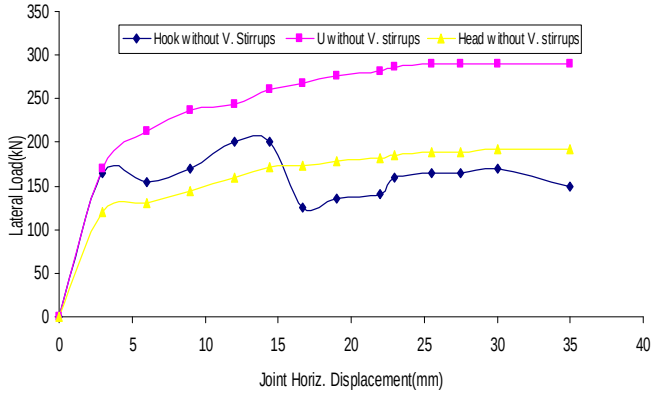


Figure 13 : Beam anchorage type effect on RC joint without vertical stirrups and improper column bars anchorage.

6 CONCLUSIONS

In this paper, the nonlinear ýnite element analysis software LS-DYNA is used to discuss the response of a RC inverted knee beam-column joint caused by event of a corner ground column loss. The results are summarized as follows:

- the concrete material model CSCM provides a proper material model for the complex behavior of concrete when only the most minimal information about the concrete, i.e. its unconfined compression strength, is known;
- selective mass scaling with some adjusted parameters is effective in reducing CPU required time with a small effect on model energy balance;
- U shaped beam bars end anchorage is better for progressive collapse resistance in terms of reducing joint rotation at beam joint interface and joint cracks; ductility was also improved by providing reinforcement continuity;
- adding joint vertical stirrups is more efficient with using headed end anchorage rather than the other two anchorage types.

In order to conduct a more accurate finite element analysis and to have a better representation of the physical problem, more research is needed on:

- more concrete material with easy input cards,
- the inþuence of selective mass scaling in increasing model resistance capacity and changing model energy balance as well.

Acknowledgments

The author would like to express his thanks to Dr. Leonard Schwer for assistance in numerical simulations and guidance in the use of LS-DYNA, also for his kind answer to many questions by adding helpful comments with valuable data.

REFERENCES

[1] EN 1990: Eurocode. Basis of structural design, 2002.

[2] J. L. Chen, Experimental Study on the Progressive Collapse Resistance of a Two-Story Steel Moment Frame. *Journal of Performance of Constructed Facilities, Vol.* 26, *No*. 5: 567-575, 2012.

[3] W. J. Yi, Experimental study on progressive collapse-resistant behavior of reinforced concrete frame structures. *ACI Structural Journal, Vol.* 105, *No*. 4: 433-439, 2008.

[4] M. Sasani, M. Bazan, S. Sagiroglu, Experimental and analytical progressive collapse evaluation of actual RC structure. *ACI Structural Journal, Vol.* 104, *No*. 6: 731-739, 2007.

[5] S.L. Yap, B. Li, Experimental Investigation of RC Exterior Beam-Column Subassemblages for Progressive Collapse. *ACI Structural Journal, Vol. 108, No*. 5: 542-552, 2011.

[6] K. Qian, B. Li, Performance of Three-Dimensional Reinforced Concrete Beam-Column Substructures under Loss of a Corner Column Concrete Scenario. *Journal of Structural Engineering-ASCE, Vol.*139, *No*. 4: 584-594, 2013.

[7] D. Gouverneur, Experimental and Numerical Analysis of Tensile Membrane Action in Reinforced Concrete Slabs in the Framework of Structural Robustness. PhD thesis, Ghent University, 2014.

[8] J. W. Wallace, S. W. McConnell, P. Gupta, P. A. Cote, Use of Headed reinforcement in Beam-Column Joints Subjected to Earthquake Loads. *ACI Structural Journal, Vol. 95, No. 5*, 590-606, Sept.-Oct., 1998.

[9] Z. Z. Peng, Z. Q. Wang, Abaqus FEM analysis on knee joints in reinforced concrete frames. *Journal of Chongqing Jiaotong University,Natural Science. Vol.* 29 No. 5: 677-790, 2010.

[10] Y.D. Murray, A. Abu-Odeh, R. Bligh, Evaluation of Concrete Material Model 159, *FHWA-HRT-05-063*, June, 2006.

[11] L. Malvar, J. Crawford, J. Wesevich, D. Simon, A plasticity concrete material model for DYNA3D. *International Journal of Impact Engineering Vol.* 19, 847-873, 1997.

[12] LSTC. *Keyword User's Manual: Material Models*. Livermore Software Technology Corporation, Livermore Carlifornia, 2013.

[13] P.S. Baglin, R.H. Scott, Finite Element Modeling of Reinforced Concrete Beam-Column Connections. *ACI Structural Journal, Vol. 97,* No. 6: 886-894. Nov.-Dec., 2000.

[14] W.T. Thompson, M.D. Dahleh, Theory of Vibration with Applications, 5th Edition, Prentice Hall, New Jersey, 1998.

[15] T. Borrval, Selective mass scaling in LS-DYNA to reduce non-physical inertia effects. *In Developers' forum, DYNAMORE*, Stuttgart, Germany, 2011.

COMPDYN 2015
5th ECCOMAS Thematic Conference on
Computational Methods in Structural Dynamics and Earthquake Engineering
M. Papadrakakis, V. Papadopoulos, V. Plevris (eds.)
Crete Island, Greece, 25–27 May 2015

3-D DYNAMIC ANALYSIS OF BRIDGES WITH ROCKING ISOLATION UNDER EXTREME EARTHQUAKES

T.Y. Lee[1], K.J. Chung[2], and H.Y. Lee[2]

[1] National Central University
Taoyuan County, Taiwan 32001, R.O.C.
tylee@ncu.edu.tw

[2] National Central University
Taoyuan County, Taiwan 32001, R.O.C.
{100322016,102322028}@cc.ncu.edu.com.tw

Keywords: Dynamic Analysis, Ultimate State, Bridge, Spread Foundation, Rocking Mechanism, Soil Spring.

Abstract. *Rocking response of spread foundation has been found to be a unique isolation system in bridge structures. Through the extension of structural periods due to rocking mechanism, the induced seismic force can be decreased. In addition, the underlying soil may go through plastic behavior and dissipate more energy under extreme earthquakes. However, the stability of the bridges with rocking response is generally concerned by practical engineers. This study is aimed to analyze the ultimate state of bridges with rocking response subjected to extreme ground motions by using 3D Vector Form Intrinsic Finite Element (VFIFE). The VFIFE, a new computational method, is adopted in this study because it has the superior in managing the engineering problems with material nonlinearity, discontinuity, large deformation and arbitrary rigid body motions of deformable bodies. Nonlinear behavior of soil is taken account in the interaction between soil and foundation. Nonlinear soil springs are developed in the VFIFE including vertical soil springs, lateral passive soil springs and friction force soil springs. All developed soil springs are verified to be feasible and accurate through numerical simulation. Finally, a five-span continuous bridge is analyzed to investigate the effectiveness of rocking isolation of bridges with spread foundation. The simulation results show that the induced seismic force decreases as the rocking response increases. Also the unstable response of the whole bridge does not occur under the extreme earthquakes.*

1 INTRODUCTION

Spread foundations are widely used in the substructure of bridges which are located in soil conditions with high bearing capacity. From the post-earthquake investigation, it is often observed that cracks occurred along the sides of spread foundations on the ground surface after strong earthquakes. Such cracks imply that the rocking response occurred in spread foundations during earthquakes. In the past studies, rocking response can be regarded as an isolation effect on bridge response. Since the natural periods of bridges elongate due to the rocking of foundations, the induced-seismic forces decrease. However, bridges are generally designed based on design codes with the regulations which restrain the sliding, overturning and settlement of foundations. Since bridge engineers concern the issue of overturning instability, the rocking isolation of spread foundations has not been popular in practical implementation. Therefore, this research is aimed to clarify the overturning instability and the isolation effect through ultimate numerical simulation when rocking response occurs in spread foundations.

Lately, modern bridge seismic design has been developed toward the seismic performance-based design on whole bridges as well as their elements. Understanding of the performance of the components of bridges, such as bearings, unseating prevention devices, columns, and the effect of soil-structure interaction under extreme condition shall be favorable to determine the goal of performance. The Vector Form Intrinsic Finite Element method (VFIFE), a new computational method developed by Ting et al. [1], is superior in managing highly nonlinear engineering problems even with fracture and collapse. Thus the VFIFE is used to simulate the dynamic behavior of the bridges with spread foundations under extreme earthquakes in this study.

Soil-structure interaction has been investigated for several decades. The superstructures and substructures of bridges may exhibit nonlinear behavior simultaneously under extreme earthquakes. In this paper, Winkler-based models proposed by Boulanger et al. [2] are adopted to develop nonlinear soil elements in the VFIFE for the analytical study on the ultimate state of bridges with soil-structure interaction.

A practical five-span bridge with spread foundations is analyzed in this study to predict the failure process. The bridge is subjected to near-field ground motions recorded at JMA Kobe in the 1995 Japan Kobe earthquake in simulation. The ground acceleration is amplified from 100% to 300% at an increment of 10%. The simulation results clarify the seismic performance for each structural element under extreme earthquakes. Besides, the optimum design parameters of bridges with spread foundations can be obtained to increase the seismic capacity of bridges under extreme earthquakes.

2 VECTOR FORM INTRINSIC FINITE ELEMENT

The Vector Form Intrinsic Finite Element (VFIFE) is developed based on theory of physics to mainly simulate failure responses of structural systems subjected to extreme loads. To analyze a continuous structural system by using the VFIFE, a lumped-mass idealization is first performed to construct a discrete model. All lumped masses are then connected by deformable elements which are massless and exhibit resisting forces during deformation. Applying Newton's Second Law of Motion, the equations of motion are assembled at each mass for all degrees of freedoms. Assume that a structural system consists of a finite number of particles. The equations of motion for a particle are written as

$$\mathbf{M}^{\alpha}\ddot{\mathbf{d}}^{\alpha}(t) = \mathbf{P}^{\alpha}(t) - \mathbf{f}^{\alpha}(t) \tag{1}$$

where $\mathbf{M}^{\alpha}$ is the diagonal mass matrix of the particle α and $\mathbf{d}^{\alpha}(t)$ is the displacement vector

when the particle α is at time t ; $\mathbf{P}^{\alpha}$ is the vector of applied forces or equivalent forces acting on the particle; $\mathbf{f}^{\alpha}$ is the vector of the total resistance forces or internal resultant forces exerted by all the elements connecting with this particle.

It is noted that each massless element is assumed to be in static equilibrium. Observed from Eq. (1), the VFIFE analysis is exempted from the assemblage of the global stiffness matrix for structures consisting of elements with multiple degrees of freedom. Therefore, a matrix algebraic operation for the entire system is not required. Instead, each equation of motion for each particle, Eq. (1), can be individually solved. Since the failure of structures involves changes in material properties and structural configuration, it is necessary to use discrete time domain analysis to solve the equations of motion. The central difference method, an explicit time integration method, is thus selected in the VFIFE to solve the equations of motion, Eq. (1).

Compared to the traditional finite element method, the unique of the VFIFE is that the element internal forces are calculated by using the element deformations obtained through subtracting rigid body displacements from total displacements. A set of deformation coordinates is defined for each element in each time increment to calculate the element deformations. Therefore, the VFIFE is capable of dealing with structural dynamic problems with large displacements, deformations and rigid body motion simultaneously.

When subjected to extreme earthquakes, bridges may undergo highly nonlinear behavior even structural failure. In the past large earthquakes, some bridges suffered deck unseating. Generally, deck unseating follows high material nonlinearity, geometric nonlinearity as well as rigid body motion. To simulate the ultimate states of bridges, the failure mechanism of major bridge components should be taken into account.

The studied failure components are isolators, unseating prevention devices and plastic hinges of decks and columns. Firstly, isolators are idealized as a bilinear model. Once the resistance force of an isolator reaches the designated rupture strength, the isolator fractures and then no longer exerts resistance shear force. Assume that the isolator becomes a sliding-like bearing and friction force exists on the fractured surface. When the relative displacement between superstructure and column exceeds the unseating prevention length, the superstructure will lose the supporting force provided by the column and then fall down from the cap beam due to the gravity force. The failure of isolators represents a typical failure mechanism completing material linear and nonlinear behavior, fracture, and sliding of structures. Such elements in the VFIFE have been developed in the previous studies. [3]

After an isolator ruptures, the interface between the superstructure and the column turns to a sliding surface if the relative displacement between the superstructure and the column is less than the unseating prevention length. The motion on the sliding surface can be separated into stick and slip phases. When the friction force is smaller than the maximum static friction force, there is no relative motion in the interface, namely in stick phase. Once the friction force overcomes the maximum static friction force, relative movement starts in the interface and the friction force converts to dynamic friction force, namely in slip phase. In this study, assume that the maximum static friction force is equal to the dynamic friction force, and the dynamic friction coefficient remains constant during sliding.

In the calculation process of the VFIFE, the material properties and structural configuration are assumed to be unchanged in each time increment. Therefore, the interface should be in either stick phase or slip phase during each incremental time. Before solving the response at the next time step $i+1$, the condition at the interface must be determined. In this study shear-balance procedure, which was proposed by Wang et al. [4] for analyzing sliding structures by state-space approach, is used to determine the phase of the interface.

The bilinear model is also used to idealize reinforced concrete columns and steel columns. No matter how the elements may change properties and configuration, even fracture in each time step, they are assumed to be unchanged in each time interval $t_i \le t \le t_{i+1}$. Thus, the internal forces are calculated based on the element properties and configuration at the initial time t_i. The deformation coordinates of elements are redefined at the beginning of each time step. In other words, once an element undergoes nonlinear or discontinuous behavior, all changes are reflected only at the beginning of next time step.

3 WINKLER-BASED MODEL

Generally the soil-structure interaction behavior is idealized by using a linear elastic model with an infinite capacity. However, the linear behavior between soil and foundations may be not realistic under extreme earthquakes. This study thus adopts the concept of a Beam-on-Nonlinear-Winkler-Foundation, a nonlinear model and called Winkler-Based Model, to model the soil-structure interaction behavior under large seismic loading.

The foundation is herein idealized as a linear elastic beam supported by a number of discrete. Each beam element has six degrees of freedom at both end nodes to consider nodal external loads and deformations. All Winkler springs are independent and considered as one-dimensional zero length elements [5]. Nonlinear Winkler springs can be used to simulate the soil vertical bearing forces, horizontal passive forces to the side of foundations, and vertical shear friction on the sides of foundations in the soil-structure interaction, as described below.

3.1 q-z Model

The q-z model consisting of elastic and plastic parts simulates an unsymmetrical hysteretic response as in Fig. 1. The elastic part captures the far-structure response while the plastic part captures the near-structure permanent displacement as in Fig. 2. A gap model consisting of a drag and a closure spring in parallel is inserted in series with the plastic spring. Soil radiation damping can be evaluated by using a dashpot on the far-structure elastic part.

The equations used to represent the q-z model are similar to those used for the p-y model described in Boulanger et al. [2]. In the elastic portion, the spring stress q is calculated as:

$$q = k_{in}\ z \tag{2}$$

where k_{in} = initial elastic stiffness; z = instantaneous displacement. The range of the elastic region is by the following relation:

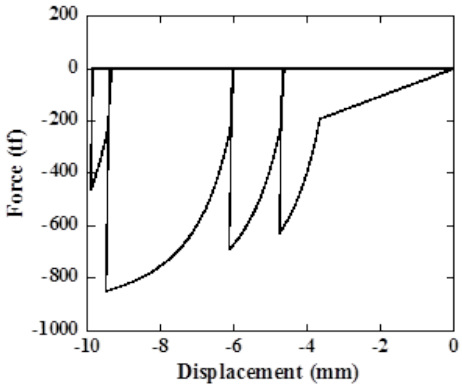


Figure 1: Hysteretic loop of q-z model

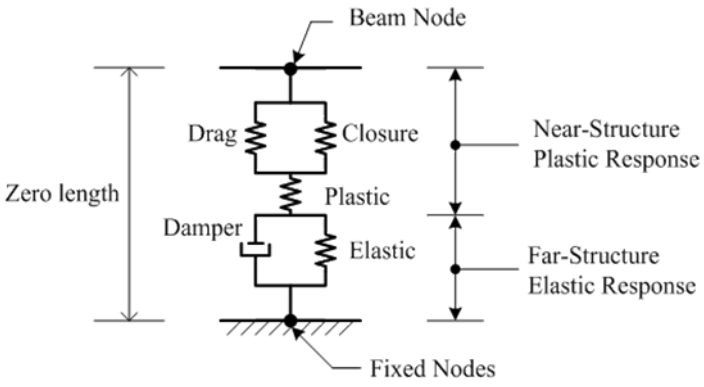


Figure 2: Conceptual construction of the springs (by Raychowdhury [5])

$$q_o = C_r q_{ult} \tag{3}$$

where q_0 = yield stress; C_r = parameter controlling the range of the elastic portion; q_{ult} = ultimate stress.

In the plastic portion, the spring q stress is calculated by

$$q = q_{ult} - (q_{ult} - q_o^p)\left[\frac{cz_{50}}{cz_{50} + \left|z^p - z_o^p\right|}\right]^n \tag{4}$$

where q_0^p = stress at the yield point; c and n = the constitutive parameters controlling the shape of the post-yield portion of the backbone curve ; z_{50} = the displacement at which 50% of the ultimate stress is mobilized ; z^p = the displacement at any point in the post-yield region ; z_0^p = the displacement at the yield point.

3.2 p-x Model

The p-x model is developed to simulate passive horizontal soil resistance against footing. The p-x model is characterized by a pinched hysteretic behavior as shown in Fig. 3. The p-x springs are generally placed at the side of foundation to consider the passive horizontal soil force.

3.3 t-x Model

The t-x model is aimed to simulate the frictional resistance between the soil and footing. The t-x model is characterized by a large initial stiffness and a hysteresis loop as shown in Fig. 4. The expressions governing the p-x model and t-x model are similar to Eqs. (2)-(4) but with different constants of C_r , n and c, which control the general shape of the hysteretic curve.

In this study, the above soil spring models are developed in the VFIFE to simulate the nonlinear soil-structure interaction behavior in the failure process of bridges under extreme earthquakes. The analysis model of spread foundation is depicted in Fig.5.

4 NUMERICAL SIMULATION

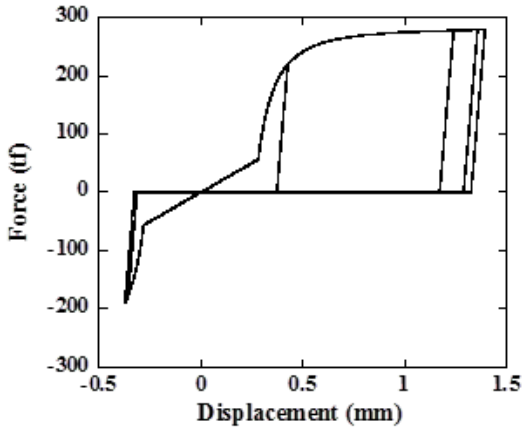


Figure 3: Hysteretic loop of p-x model

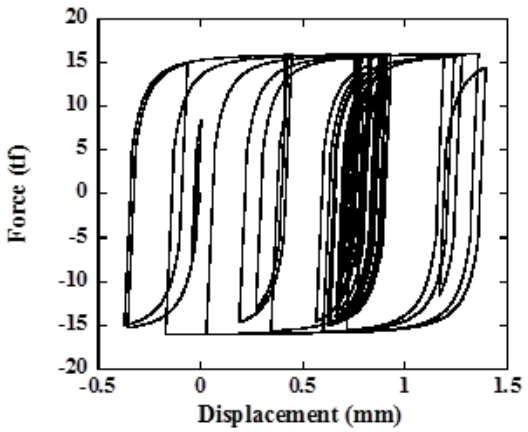


Figure 4: Hysteretic loop of t-x model

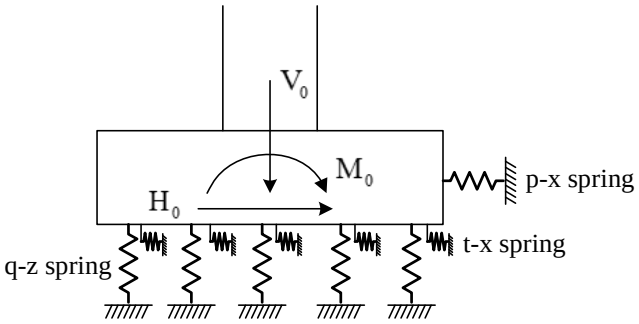


Figure 5: Analysis model of spread foundation

4.1 Target Bridge

A continuous bridge based on Japan highway design codes [6] is analyzed under near-field ground motions to predict the collapse mechanism while considering pounding effect of superstructures. Hinge and roller bearings are installed between the superstructures and the columns or abutments. This bridge consists of a five-span deck with a total length of 5@40 m = 200 m and a width of 12 m, which is supported by four reinforced concrete columns with a height of 12 m in each and two abutments as shown in Fig.6. Spread foundation is designed to consider the rocking isolation effect. The 3-D analysis model is depicted in Fig. 7. The bottoms of columns are idealized as a perfect elastoplastic model with a fracture ductility of 21.5 as shown in Fig. 8. After hinge bearings are damaged by the shearing forces, they are assumed to behave as roller bearings whose dynamic friction coefficient on the fracture interface is 0.15.

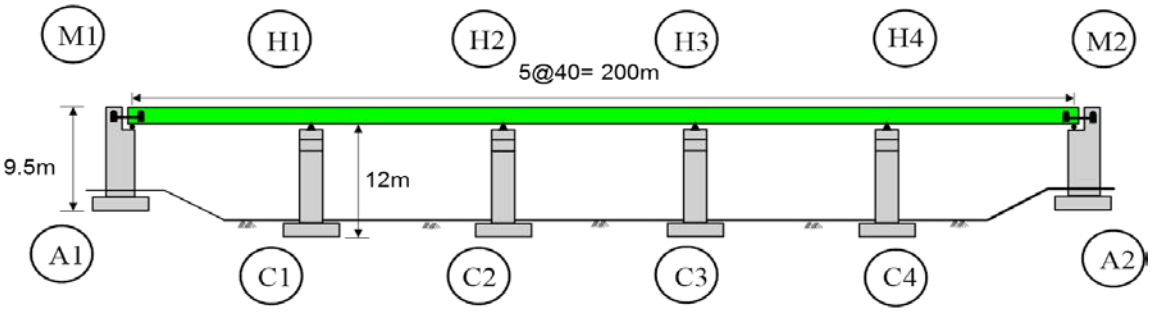


Figure 6: Target bridge

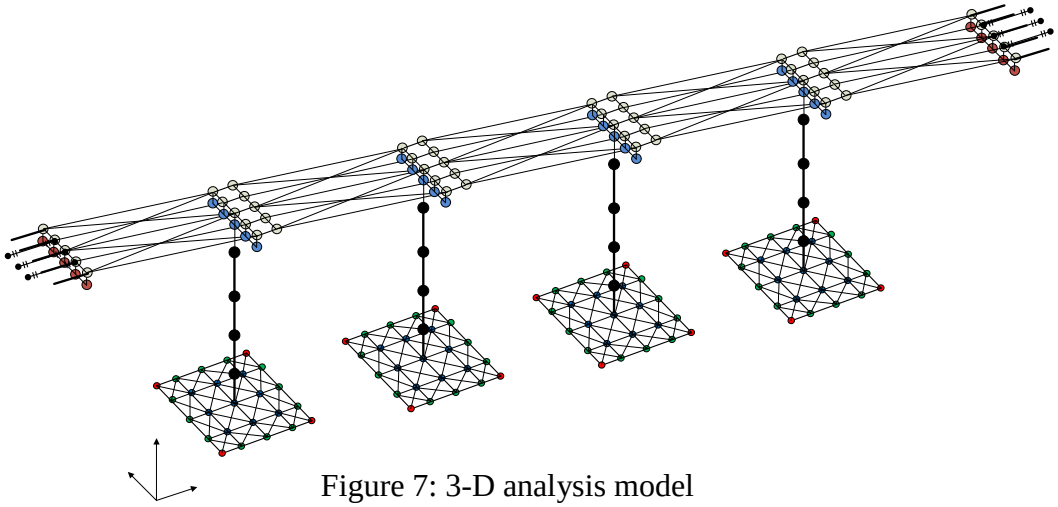


Figure 7: 3-D analysis model

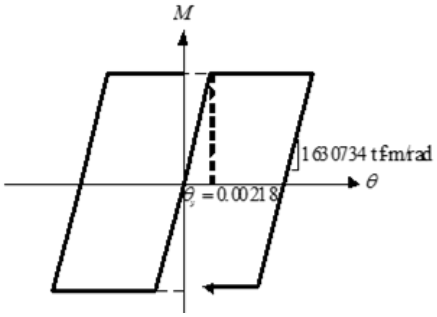


Figure 8: The hysteresis of the column

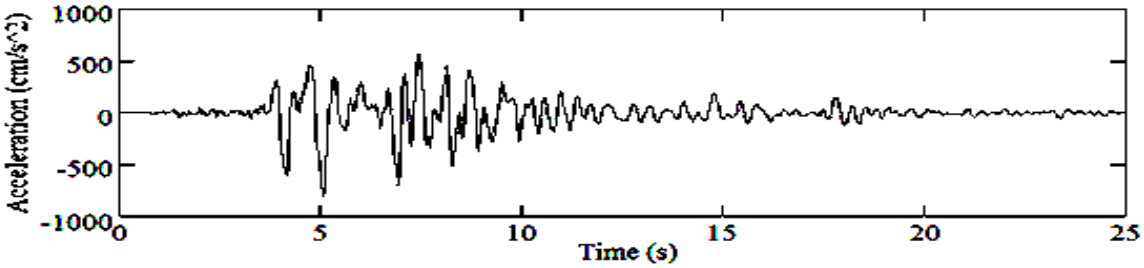


Figure 9: Ground motion recorded at Japan Meteorological agency in the 1995 Kobe earthquake

The pounding effect between the deck and abutment is considered by using an element with a gap of 28 cm. The unseating prevention length at each abutment is 96 cm. In simulations, the bridge is subjected to the near-field ground motions recorded at Japan Meteorological agency, in the 1995 Kobe, Japan earthquake, as in Fig. 9. The ground acceleration is amplified from 100% to 300% at an increment of 10% to result in member failure and the collapse of whole bridge.

4.2 Simulation Results

Figure 10 compares the seismic responses obtained by numerical simulations with linear soil springs and nonlinear Winkler soil springs under JMA Kobe earthquake. Figures 10(a), 10(b) and 10(c) represent the deck displacement, column rotation and vertical displacement at the edge of the foundation, respectively. Figure 10(d) indicates the soil compression force under the edge of the foundation. Observed from the results, the analysis model with linear soil springs overestimates the seismic responses of the target bridge under large earthquakes.

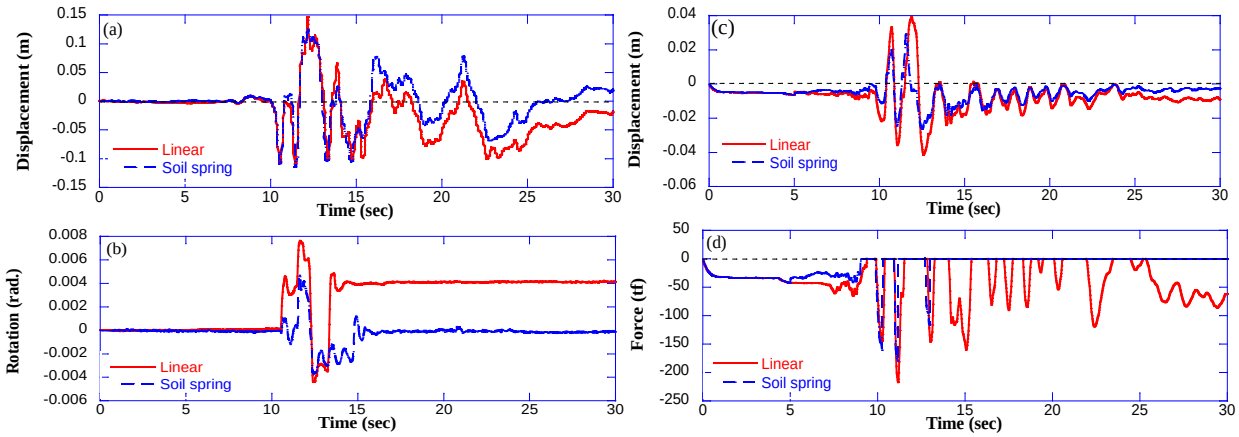


Figure 10: (a) deck displacement (b) column-rotation (c) vertical displacement at edge of foundation (d) soil compression at edge of foundation.

Figure 11 depicts the failure procedure of the target bridge under 250% of the JMA Kobe records. The first characters M, H, C, D and R of the notations in figures denote the roller bearing, hinge bearing, column, deck and tendon, respectively. In the beginning, all the hinge bearings in x-direction first fracture due to excessive shearing forces. Then all the columns gradually reach the ultimate ductility and finally collapse, which results in the falling of all the decks; meanwhile, all the tendons fracture as a result of the excessive tensile forces much larger than the ultimate strength of the tendons.

5 CONCLUSIONS

- The nonlinear soil springs, Winkler-based springs, are developed in the 3-D VFIFE to simulate the nonlinear soil-structure interaction behavior. Therefore, the VFIFE is capable of simulating the failure process of bridges with rocking isolation under extreme earthquakes. The dynamic behavior of all structural members in the extreme situation can be realized through numerical analysis.
- The simulation results confirm the effectiveness of rocking isolation on mitigation of seismic induced forces of bridges with spread foundations. Since the soil may undergo hysteretic behavior under strong earthquakes, such hysteretic behavior can dissipate much more energy to decrease the structural dynamic responses. Observed from the simulation results under large earthquakes, the analysis results with linear soil springs overestimate the seismic responses as compared with those with nonlinear soil springs.

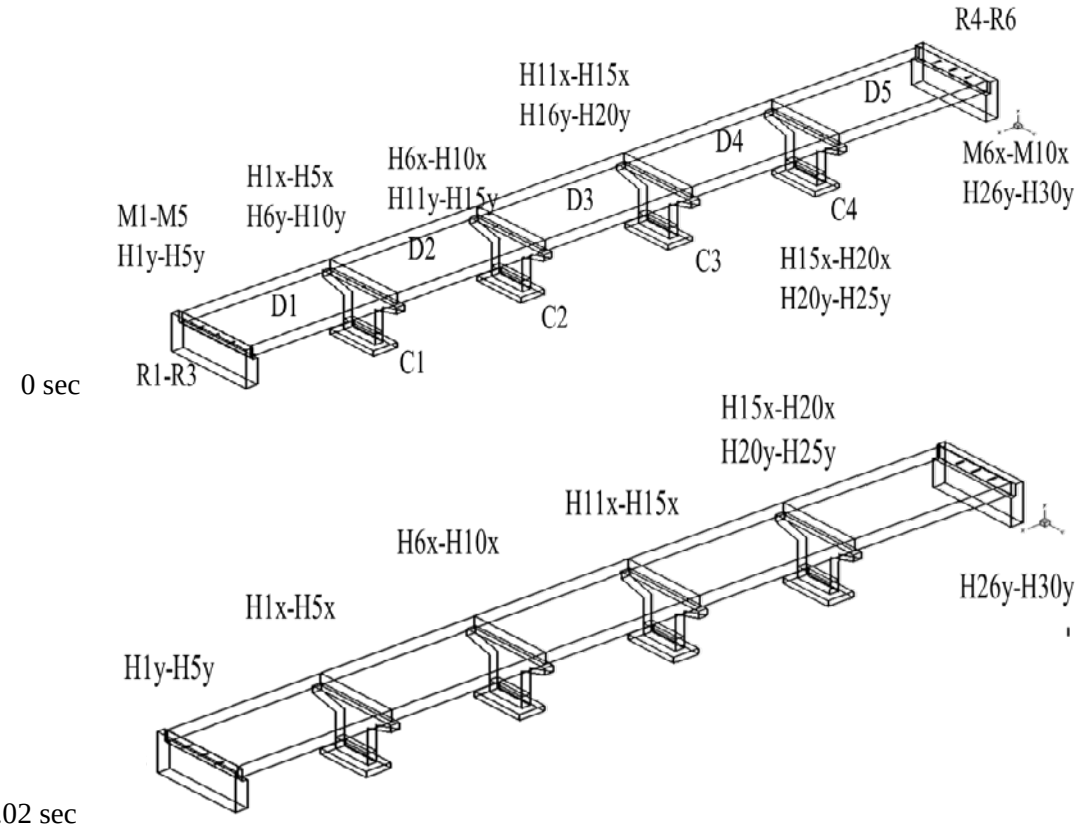


Figure 11: Failure process of the bridge with spread foundations under 250% of JMA Kobe records.

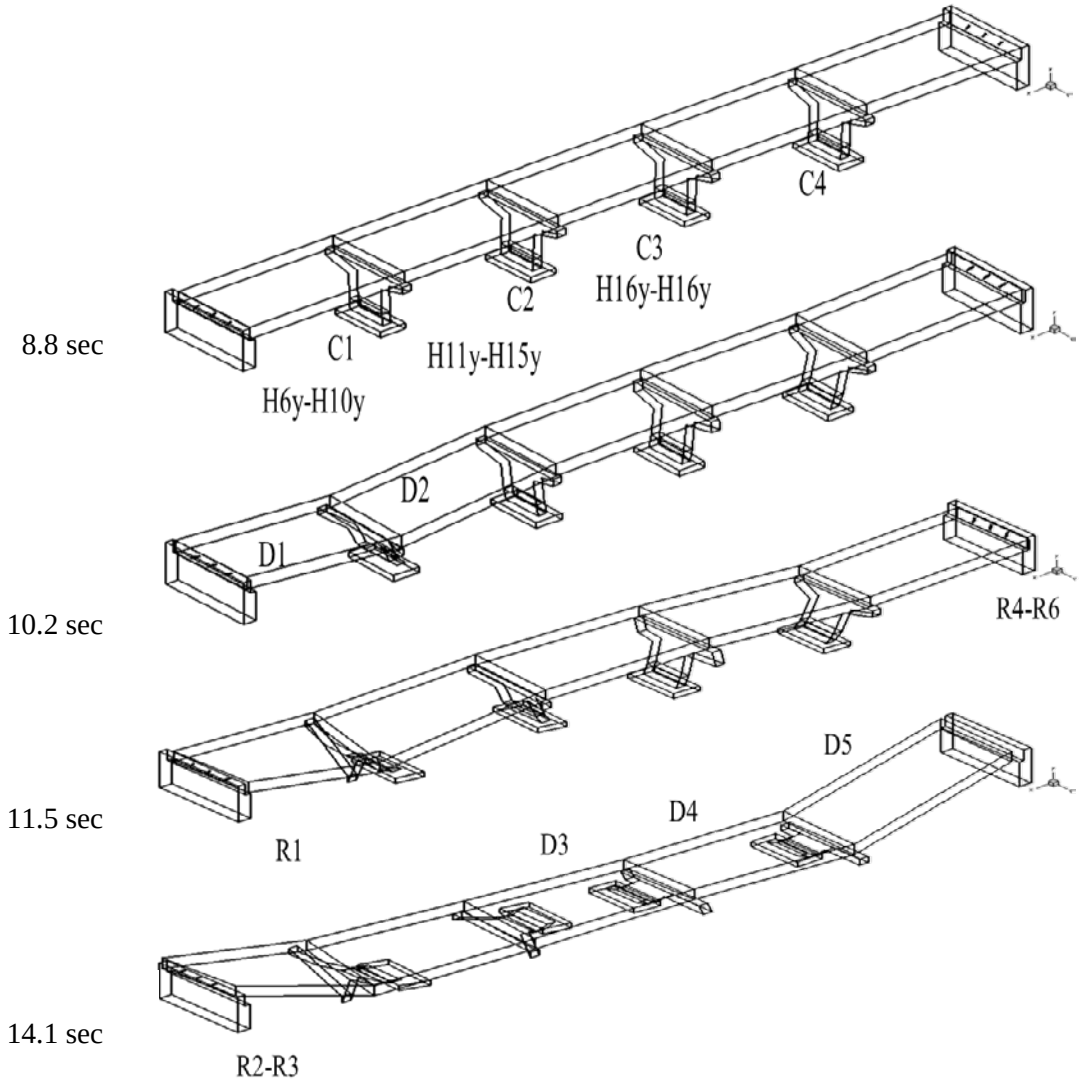


Figure 11(cont.) : Failure process of the bridge with spread foundations under 250% of JMA Kobe records.

- The simulation results show that the induced seismic force decreases as the rocking response increases. The collapse of the bridge is attributed to the failure of the columns, namely the unstable response of the whole bridge due to overturning of the footings does not occur under the extreme earthquakes.

REFERENCES

[1] E.C. Ting, C. Shih, Y.K. Wang, Fundamentals of a vector form intrinsic finite element: Part I. basic procedure and a plane frame element. *Journal of Mechanics*, **20**, 113-122, 2004.

[2] R.W. Boulanger, C.J. Curras, B.L. Kutter, D.W. Wilson, A. Abghari, Seismic soil-pile-structure interaction experiments and analysis. *Journal of Geotechnical and Geoenvironmental Engineering*, **125**, 750-759, 1999.

[3] T.Y. Lee, P.H. Chen, R.Z. Wang, Dynamic analysis of bridges in the ultimate state under earthquakes. *Sixth International Conference on Urban Earthquake Engineering,* Tokyo, Japan, March 3-4, 2009.

[4] Y.P. Wang, W.H. Liao, C.L. Lee, A state-space approach for dynamic analysis of sliding structures. *Engineering Structures,* **23**, 790-801, 2001.

[5] P. Raychowdhury, T.C. Hutchinson, Performance evaluation of a nonlinear Winkler-based shallow foundation model using centrifuge test results. *Earthquake Engng Struct Dyn,* **38**, 679-698, 2009.

[6] Japan Road Association 2002. Specifications for Highway Bridges, Part IV Substructures, Tokyo, Japan.

COMPDYN 2015
5th ECCOMAS Thematic Conference on
Computational Methods in Structural Dynamics and Earthquake Engineering
M. Papadrakakis, V. Papadopoulos, V. Plevris (eds.)
Crete Island, Greece, 25–27 May 2015

STRUCTURAL INTEGRITY ANALYSIS AND OPTIMIZATION OF AN ELEVATOR FRAME, THROUGH FE MODELING AND EXPERIMENTAL TESTS

Dimitrios Giagopoulos[1], **Iraklis Chatziparasidis**[1], **Nickolas S. Sapidis**[1]

[1] Department of Mechanical Engineering, University of Western Macedonia
Kozani 50100, Greece
e-mail: dgiagopoulos@uowm.gr, ihatz@kleemann.gr, nsapidis@uowm.gr

Keywords: *FE modeling, Large scale structures, Model updating, Stress evaluation, Structural Dynamics.*

Abstract. *A systematic structural integrity analysis and optimization of an elevator chassis under real dynamic load conditions are presented in this work. The special feature of this paper is that the study was performed on industrial an elevator system (produced by Kleemann Hellas S.A.), including all details/complexities of a commercial system. The procedure proposed for solving and analysing this specific problem includes the following steps. First, the frame and the cabin of the elevator are modeled numerically by discretizing them geometrically according to the FE method. FE modeling of this structure is not straightforward because of these two aspects of the analysis. (a) When safety gear is activated and the elevator stops, braking forces act on the system, whose dynamic response must be accurately simulated. (b) An efficient modeling method is required for the various elevator parts which are in contact with each other and are connected together by screws through "oval type" holes. The initial FE model is updated and validated through an experimental investigation of its dynamic response when the elevator stops using instantaneous or progressive safety gear. These experimental tests were performed under real operating conditions, using an experimental device that was designed exactly for this purpose and aimed at recording the acceleration time histories at the connection points of the frame with the safety gear and at other locations used as reference points. The acceleration time histories at the connection points are subsequently used as base excitation for the FE model of the frame and the corresponding stresses developed are evaluated. On the basis of these numerical results, the critical points of the frame are selected, as corresponding to larger stresses. Finally, to test the reliability of the proposed method, strain gauges are placed at the critical points of the frame and measurements are carried out, under similar dynamic load conditions, in order to experimentally verify the stresses calculated above. Comparison of the numerical and experimental data verifies that the proposed "mixed computational-experimental" analysis method is quite reliable.*

1 INTRODUCTION

Ever evolving elevator design requirements frequently require improvements/modifications of either specific mechanical components or even of entire structures. FE modeling of elevator systems is not straightforward because of these two aspects of the analysis. (a) When safety gear is activated and the elevator stops, braking forces act on the system, whose dynamic response must be accurately simulated. (b) An efficient modeling method is required for the various elevator parts which are in contact with each other. To achieve these modeling issues, it is important to develop an accurate Finite Element Analysis procedure, in order to simulate the dynamic behavior of these systems. This is the main technical issue addressed by the present work.

The equations of motion of mechanical systems with complex geometry are first set up by applying classical finite element techniques. As the order of these models increases, existing numerical and experimental methodologies for a systematic determination of their dynamic response become inefficient. Therefore, there is a need for the development and application of new appropriate methodologies for investigating the dynamics of large scale mechanical models in a systematic and efficient way. Traditionally, in the area of structural dynamics this is done by first employing methodologies that reduce the dimensions of the original system. This paper applies a time domain reduction method [1-5].

The main objective of the present work is to demonstrate the advantages of applying appropriate numerical and experimental methodologies in order to accurately predict the dynamic response and the identification of the critical points in an elevator system. This is done by applying a numerical method for determining the equations of motion for the main elevator parts, while the dynamic behavior of the remaining components are taken into account through the application of appropriate experimental measurements. The special feature of this paper is that the study was performed on industrial an elevator system including all details/complexities of a commercial system.

The organization of this paper is as follows. In the following section, a brief but complete outline of the methodology that reduce the dimensions of the original system is presented. Then, in the third section, the effectiveness and accuracy of the Finite Element Analysis procedure is demonstrated, by presenting numerical and experimental results obtained for the real elevator system. Here, the reliability of the methodology was tested first analytically in the elevator chassis with the platform of the cabin and next in the full elevator system (chassis and cabin). The study concludes by presenting a summary of the results obtained.

2 CLASS OF MECHANICAL SYSTEMS EXAMINED – EQUATIONS OF MOTION

The equations of motion of mechanical systems with complex geometry are commonly set up by applying finite element techniques. Quite frequently, a systematic investigation of the dynamics of large scale mechanical structures leads to models involving an excessive number of degrees of freedom. Therefore, a computationally efficient solution requires application of methodologies reducing the numerical dimension of the original model [1-6, 8, 9]. Next, the basic steps of a time domain reduction method is presented briefly.

For simplicity, consider a mechanical system consisting of two subsystems, say A and B. Moreover, let the equations of motion for subsystem A be derived from the following classical form

$$\hat{M}_A \underline{\ddot{x}}_A + \hat{C}_A \underline{\dot{x}}_A + \hat{K}_A \underline{x}_A = \underline{\hat{f}}_A(t) \tag{1}$$

where $\hat{M}_A$, $\hat{C}_A$ and $\hat{K}_A$ are, respectively, the mass, damping and stiffness matrix of the subsystem A, with the vector $\underline{\hat{f}}_A(t)$ representing the external forcing. For a typical model, the number of these equations may be quite large. However, for a given level of forcing frequencies, it is possible to reduce significantly the number of the original degrees of freedom, without sacrificing the accuracy in the numerical results, by applying standard component mode synthesis methods [1, 6]. This can be achieved through an approximate coordinate transformation of the form

$$\underline{x}_A = \Psi_A \underline{q}_A \tag{2}$$

The transformation matrix Ψ_A includes an appropriately chosen set of the lowest frequency normal modes of component A, corresponding to support-free conditions [1]. The number of these modes depends on the accuracy required in the response frequency range examined. Consequently, matrix Ψ_A is completed by a set of static correction modes of component A [3, 4]. Employing this transformation, the original set of equations (1) can be replaced by a considerably smaller set of equations, expressed in terms of the new generalized coordinates $\underline{q}_A$. More specifically, application of the Ritz transformation (2) onto the original set of equations (1) yields the much smaller dimension set

$$M_A \underline{\ddot{q}}_A + C_A \underline{\dot{q}}_A + K_A \underline{q}_A = \underline{f}_A(t) \tag{3}$$

where

$$M_A = \Psi_A^T \hat{M}_A \Psi_A,\ C_A = \Psi_A^T \hat{C}_A \Psi_A,\ K_A = \Psi_A^T \hat{K}_A \Psi_A \text{ and } \underline{f}_A = \Psi_A^T \underline{\hat{f}}_A.$$

Moreover, the set of unknowns can be split in the form

$$\underline{q}_A = (\underline{p}_A^T \quad \underline{x}_b^T)^T$$

where $\underline{p}_A$ includes coordinates related to the response of internal degrees of freedom of component A, while $\underline{x}_B$ includes the boundary points of component A with component B. Next, similar sets of equations of motion are obtained for component B. Namely, the equations of motion are first set up in the form

$$M_B \underline{\ddot{q}}_B + C_B \underline{\dot{q}}_B + K_B \underline{q}_B = \underline{f}_B(t) \tag{4}$$

with coordinates

$$\underline{q}_B = (\underline{p}_B^T \quad \underline{x}_b^T)^T$$

Then, a proper combination of equations (3) and (4) leads to the equations of motion of the composite system in the classical form

$$M \underline{\ddot{q}} + C \underline{\dot{q}} + K \underline{q} = \underline{f}(t) \tag{5}$$

with coordinates

$$\underline{q} = (\underline{p}_A^T \quad \underline{p}_B^T \quad \underline{x}_b^T)^T.$$

The stiffness matrix of the composite system can be obtained by considering the total potential energy of the system. Likewise, the mass matrix of the composite system is obtained by considering the corresponding kinetic energy, while the forcing vector is determined by considering the virtual work.

3 EXPERIMENTAL APPLICATION TO AN ELEVATOR SYSTEM

In this section, the emphasis is placed on applying the methodology proposed to a real elevator system. The ultimate goal was to develop an accurately Finite Element Analysis procedure, in order to simulate the dynamic behavior of this system. The proposed procedure is presented in detail in the following sections.

3.1 Finite Element Model

The experimental system examined addresses a real elevator system which is shown in Figure 1. In this example, the system consists of two main substructures. The first part is the chassis of the elevator, while the second part is the cabin. The geometry of these structures was discretized using mainly rectangular and triangular shell finite elements. Additionaly, some other elements like solid (hexahedral) and rigid body elements were also used. The total number of degrees of freedom of the resulting model (chassis and cabin) was about 4,500,000. Due to the large size of this model, the solution of the finite element model was completed by using appropriate commercial software [13, 14]. The FE models of these two parts are presented in Figures 2a and 2b, respectively.



Figure 1. ELEVATOR SYSTEM.

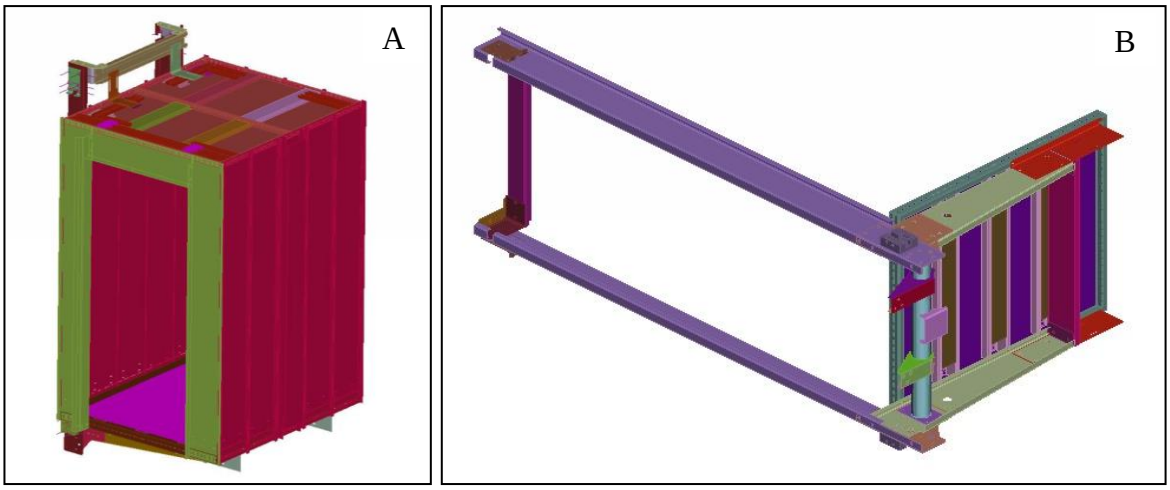


Figure 2. FINITE ELEMENT MODEL OF (A) THE CABIN AND (B) THE CHASSIS.

After development of the overall finite element model, including the coordinate reduction and synthesis part, the next step was to examine the dynamic response of system when safety gear is activated and the elevator stops. In order to accurately simulate this procedure, it's necessary first to verify the accuracy of the developed FE model and also identify the braking forces that acting on the system. To achieve this a combination of numerical and experimental methods was applied [9].

3.2 Determination of Acceleration Levels Under Real Dynamic Load Conditions

In order to verify the accuracy of the FE model of the system and also identify the braking forces acting on the system, we select, to examine only the elevator chassis including the platform of the cabin with full load. On this system, triaxial accelerometers are placed at (6) selected positions. These positions along with the measurement directions are presented in Figure 3: the two connection points of the frame with the safety gear (A1, A2) are included along with four other locations (A3-A6) which are used as reference points. A series of experimental trials were performed under real operating conditions (free fall of the elevator frame), using an experimental device designed and constructed exactly for this purpose (by Kleemann Hellas S.A), aimed at recording the acceleration time histories at the selected six points.

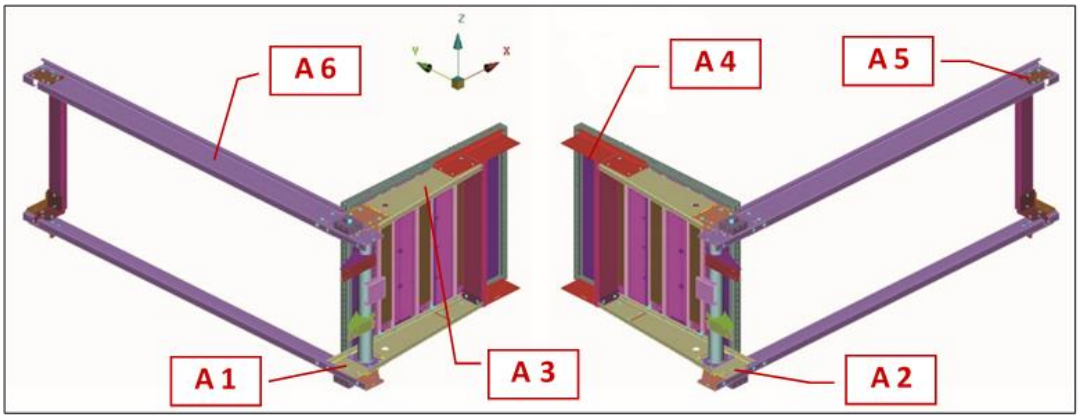


Figure 3. MEASUREMENT LOCATIONS OF ACCELERATION TIME HISTORIES.

These measurements were performed using a data acquisition system (CDAQ) by National Instruments, with the related software which was made at NI Labview environment. The measured frequency range for the tests conducted was selected to be 0-1024 Hz. Figure 4a depicts the data acquisition system, while Figure 4b presents a picture of the load (weight) placed on the elevator platform.

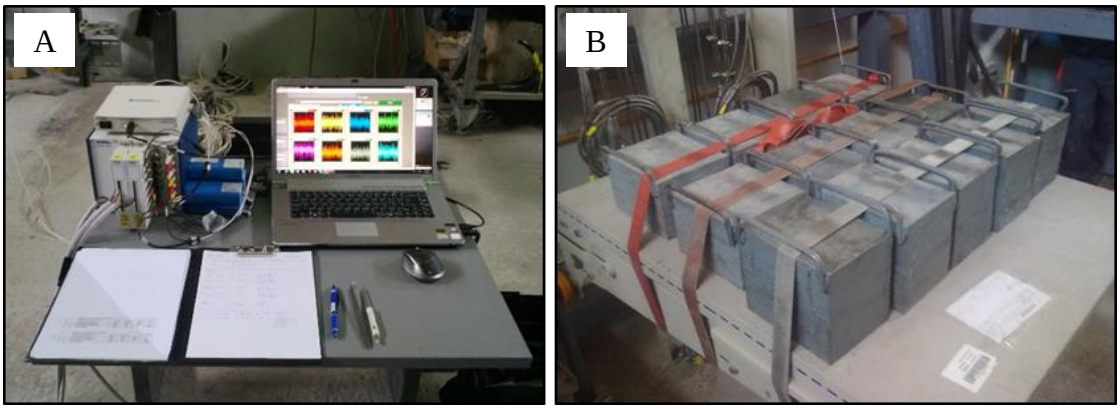


Figure 4. (A) DATA ACQUISITION SYSTEM and (B) ELEVATOR PLATFORM WITH LOAD.

Also, Figure 5 presents indicative photos of a two measurement positions.

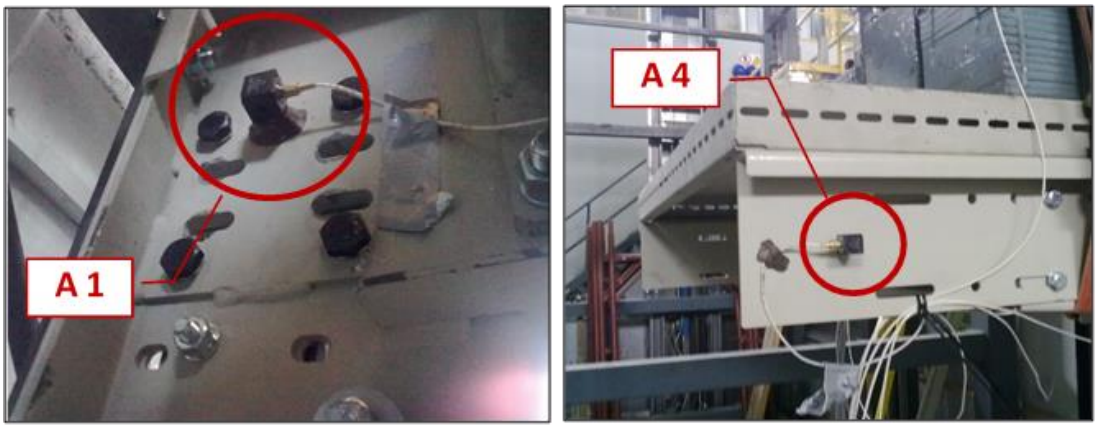


Figure 5. ACCELERATION MEASUREMENT LOCATIONS AT A CONNECTION POINT (A1) AND AT A REFERENCE POINT (A4).

Next, Figures 6a, 6b and 6c present typical acceleration time histories in the three directions (X-longitudinal, Y-vertical, Z-transverse), at the connection point A2 of the chassis with the safety gear. These time histories were measured during one of the tests performed by using a progressive safety gear. Also, each figure presents the corresponding peak-to-peak and GRMS values.

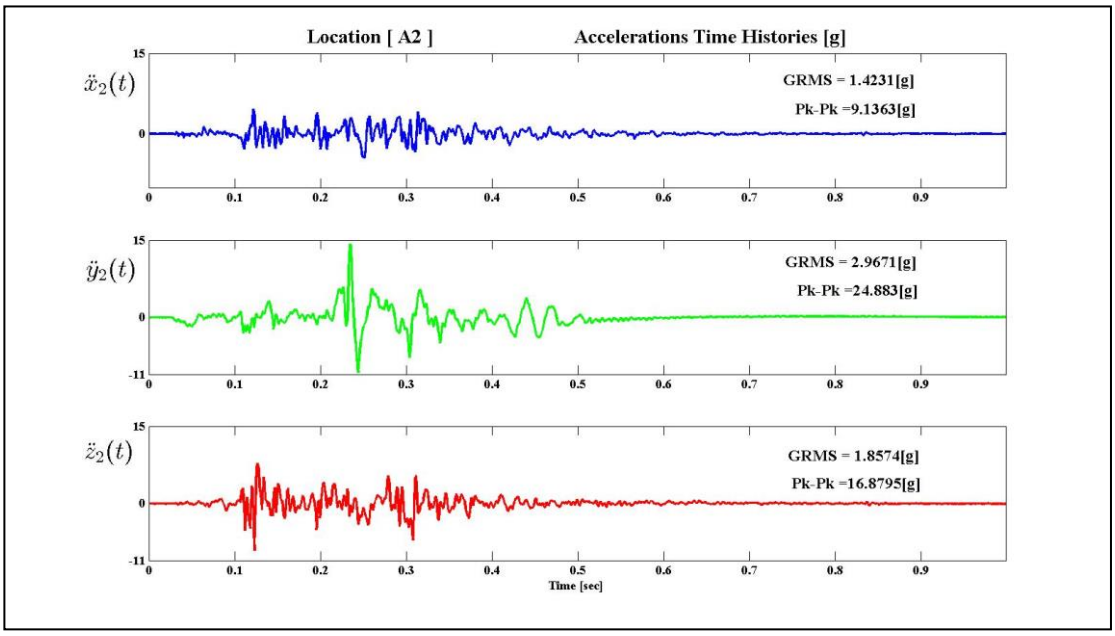


Figure 6. ACCELERATION HISTORIES IN THE: (A) X-LONGITUDINAL DIRECTION, (B) Y-VERTICAL DIRECTION AND (C) Z- TRANSVERSE DIRECTION, WITH PEAK TO PEAK AND GRMS VALUES.

3.3 Results of FE Model Analysis – Identification of Critical Points

Next, the measured acceleration time histories were used to determine the braking force that acting on the system. After several experimental trials, the form of the corresponding time-varying braking forces, in each progressive safety gear, were calculated. Then, these force time histories were imported as base excitation in the finite element model of the system. Also, in order to solve this transient response analysis problem in a computationally

effective way, a reduction in the dimensions of the original system is performed, so that the results are accurate in the frequency range 0-500 Hz. The total number of degrees of freedom in the reduced model was about 3,500, which is much smaller than the number of degrees of freedom in the original model (1,200,000). The reduced model was solved numerically in order to calculate the maximum stresses developed for the given loading. The identified critical points of the structure include mainly areas of the chassis arms on which the platform is based. Figure 7 shows selected results, in which some indicative points of the superstructure with maximum stresses are presented.

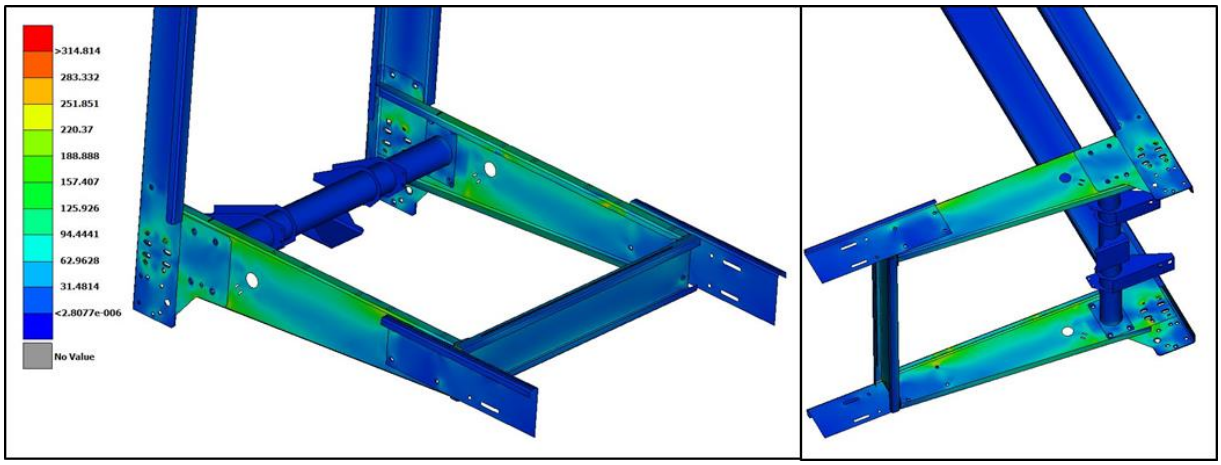


Figure 7. LOCATIONS OF THE CHASSIS WHERE MAXIMUM STRESSES APPEAR.

3.4 Validation of the Applied Methodology

In order to test the reliability of the method applied, strain gauges were placed at (5) selected critical points of the chassis and a new set of measurements was carried out under similar dynamic loading conditions, to experimentally verify the stress levels developed. These positions are presented in Figure 8 and include locations on the right side of the chassis arms (SG1, SG2 and SG3) and on the left side (SG4 and SG5).

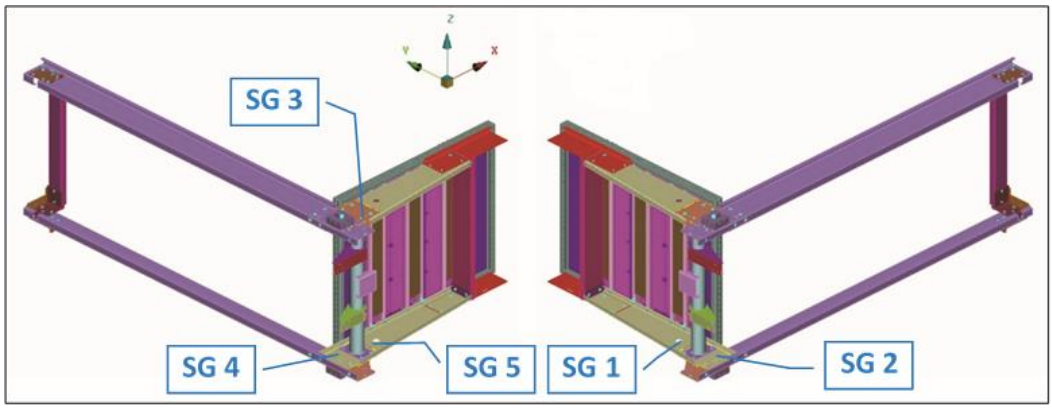


Figure 8. MEASUREMENT LOCATIONS WHERE MAXIMUM STRESS APPEARS.

For a complete monitoring of the stress state, three bridges with a 120^{o} angle rosette were placed at each of the selected points. Figure 9 presents photographs of the strain gauges at the measurement locations.

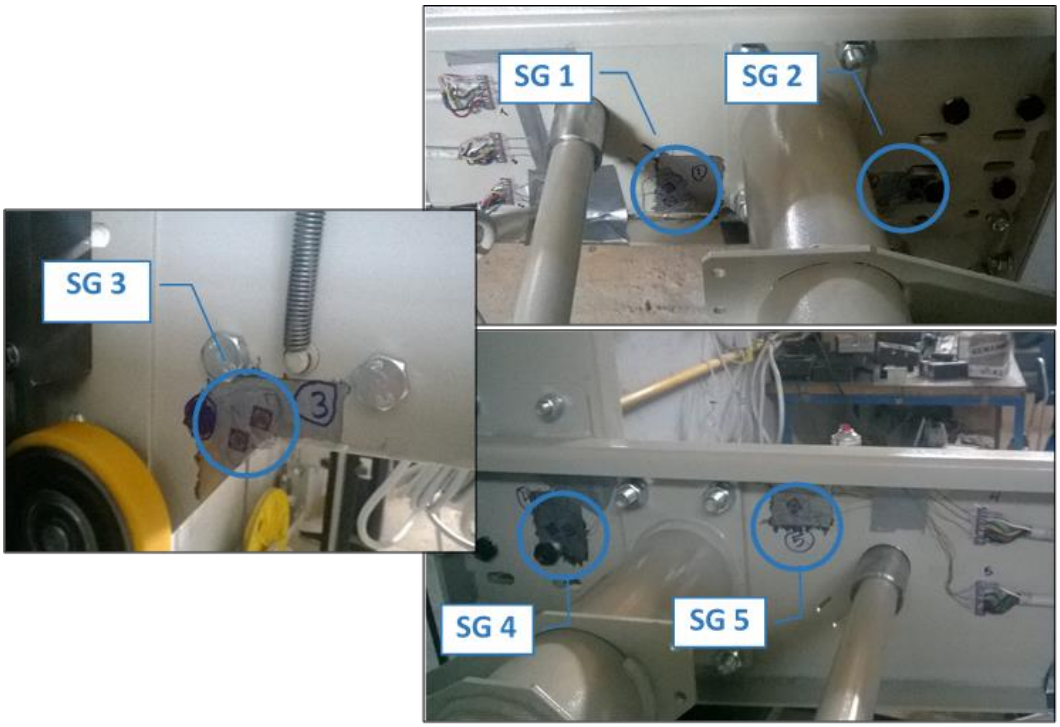


Figure 9. STRAIN GAUGES MEASUREMENT LOCATIONS.

At each measurement point, the stresses calculated are the normal stresses σ_x and σ_y, the shear stress τ_{xy} and the maximum equivalent von Mises stress. Figure 10 presents a typical part of the stress histories measured during one of the tests at the location (SG3). The first three figures show the histories of σ_x, σ_y and τ_{xy}, with the corresponding maximum positive and max mum negative values of these stresses. The last figure shows the history of the equivalent (von Mises) stress, together with the maximum value of this stress.

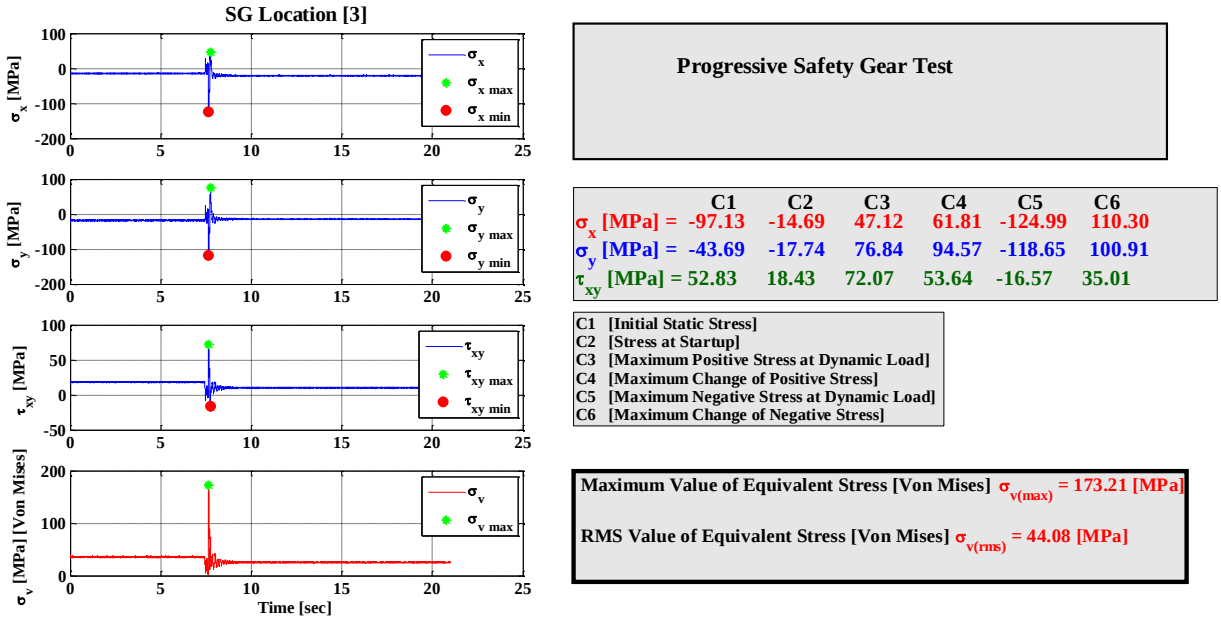


Figure 10. STRESS HISTORIES RECORDED DURING A TEST AT A MEASUREMENT LOCATION.

Some of the experimental and numerical results are summarized in Table 1. This table are presents the maximum values of the von Mises stress obtained in four tests (indicated by PG1-PG4) and for all the points where measurements were taken (denoted by SG1-SG5). More specifically, the third from the end column presents the maximum values for all tests, for each measurement location, the penultimate column presents the corresponding maximum values obtained by the finite element model and the last column presents their percentage difference. A comparison of the numerical and experimental data presented in Tables 1 verify that the proposed method is reliable.

	Maximum Value (peak) of Equivalent Stress Von Mises [MPa]				Maximum Value of all Structural Tests	Maximum Value of FEM Solution	Error (%)
Structural Tests	PG1	PG2	PG3	PG4			
Strain Gage Positions							
SG1	90.47	85.48	97.22	92.56	**97.22**	105.37	**7.73**
SG2	198.64	193.72	201.14	196.35	**201.14**	209.82	**4.14**
SG3	168.61	165.40	170.85	173.21	**173.21**	170.53	**1.57**
SG4	160.49	148.25	154.71	152.16	**160.49**	155.61	**3.14**
SG5	253.75	246.53	263.22	255.91	**263.22**	278.24	**5.40**

Table 1. MAXIMUM VALUE OF EQUIVALENT VON MISES STRESS [MPA].

3.5 Analysis of the FE Model of Full Elevator System (Chassis and Cabin)

Finally, in an effort to further illustrate the accuracy of the applied method, a similar analysis was applied on the finite element model of the full elevator system (chassis and cabin). More specifically, the model was solved numerically in order to calculate the maximum stresses developed for similar loading conditions, which were applied in the paragraph 3.3. Also, the corresponding experiment was set up. Figure 10, presents a comparison between the numerical and experimental results.

More specifically from the FE model analysis, arises that in some locations of the cabin the stresses developed exceeds the limits of the material yield strength. The most important of these locations are on the upper corners of the door, as shown in the Figure 11. The results of numerical analysis were confirmed from the experimental test. More specifically, the photo in figure 11, presents the deformation of the cabin at the top of the door, exactly in the same location where the FE model analysis results shows.

Comparison of numerical and experimental results indicated that the methodology applied gives accurate results and provides a useful tool in predicting the critical stress levels developed in the elevator systems under given loading conditions.



Figure 11. LOCATIONS OF THE ELEVATOR SYSTEM WHERE MAXIMUM STRESSES APPEAR AND COMPARISSON WITH EXPERIMENTAL RESULTS

4 SUMMARY

A systematic method was presented for determining the dynamic response and identifying the critical points of an elevator system when subjected to dynamic load conditions. The basic idea was to start the solution process by first discretizing geometrically the system with the finite element method. In order to verify the accuracy of the FE model of the system and also identify the braking forces acting on the system, examined only the elevator chassis including the platform of the cabin with full load. In this system, a series of experiments was performed in real operating conditions (free fall of the elevator frame), aimed at recording the acceleration time histories at selected locations. Next, a component mode synthesis method was applied in order to eliminate a substantial number of degrees of freedom of the original model. The measured acceleration histories were subsequently used in order to determine the braking force that acting on the system. Then, these force time histories were imported as a base excitation in the reduced finite element model of the system and the stresses developed under specific loading conditions were evaluated. From these numerical results, the critical points of the superstructure were selected, based on the level of the largest stresses. Finally, a new set of measurements was carried out in order to experimentally verify the stress levels developed. In an effort to further illustrate the accuracy of the applied method, a similar analysis applied in the finite element model of the full elevator system (chassis and cabin). Comparison of nu-

merical and experimental results indicated that the methodology applied gives accurate results and provides a useful tool in predicting the critical stress levels developed in the elevator.

ACKNOWLEDGEMENTS

This research was supported by Kleemann Hellas S.A. (http://www.kleemannlifts.com.)

5 REFERENCES

[1] Craig, Jr., R.R., 1981, Structural Dynamics - An Introduction to Computer Methods, J. Wiley & Sons, New York.

[2] Craig, Jr., R.R., A review of time-domain and frequency domain component mode synthesis methods, International Journal Analytical and Experimental Modal Analysis, Vol. 2, pp. 59–72, 1987.

[3] Vermot des Roches, G., Bianchi, J.P., Balmes, E., Lemaire, R. and Pasquet, T., Using component mode in a system design process, Proceedings of the IMAC-XXVIII 2010, Jacksonville, Florida, USA, 2010.

[4] Craig, Jr., R.R., Methods of component mode synthesis, Shock and Vibration Digest Journal, Vol. 9, pp. 3–10, 1977.

[5] Farhat, C. and Geradin, M., On a component mode synthesis method and its application to incompatible structures, Computers and Structures, Vol. 51, pp. 459–473, 1994.

[6] Bennighof, J.K. and Kaplan, M.F., Frequency window implementation of adaptive multi-level substructuring, *ASME Journal of Vibration and Acoustics*, Vol. 120, pp. 409-418, 1998.

[7] MacNeal, R.H., A hybrid method of component mode synthesis, *Journal of Computers and Structures*, Vol. 1, pp. 581–601, 1971.

[8] Giagopoulos, D. and Natsiavas, S., Hybrid (numerical-experimental) modeling of complex structures with linear and nonlinear components, Nonlinear Dynamics, Vol. 47, pp. 193-217, 2007.

[9] Giagopoulos, D. and Natsiavas, S., Dynamic Response and Identification of Critical Points in the Superstructure of a Vehicle using a Combination of Numerical and Experimental Methods, Experimental Mechanics, Vol. 55, pp. 529-542, 2015.

[10] Ewins, D.J., 1984, Modal Testing: Theory and Practice, Research Studies Press, Somerset, England.

[11] Mottershead, J.E. and Friswell, M.I., Model updating in structural dynamics: A survey, *Journal of Sound and Vibration*, Vol. 167, pp. 347-375, 1997.

[12] Papadimitriou, C., Ntotsios, E., Giagopoulos, D. and Natsiavas, S., Variability of updated finite element models and their predictions consistent with vibration measurements, Structural Control and Health Monitoring, Vol. 19, pp. 630-654, 2012.

[13] DYNAMIS 3.1.1, Solver Reference Guide, DTECH, Thessaloniki, Greece, 2013.

[14] ANSA and META-Post, BETA CAE Systems S.A., Thessaloniki, Greece.

COMPDYN 2015
5th ECCOMAS Thematic Conference on
Computational Methods in Structural Dynamics and Earthquake Engineering
M. Papadrakakis, V. Papadopoulos, V. Plevris (eds.)
Crete Island, Greece, 25–27 May 2015

SEISMIC ANALYSIS OF COUPLED BUILDINGS WITH MR DAMPER

Fangshu Lin[1], **Xilin Lu**[1]

[1] College of Civil Engineering, Tongji University
1239 Siping Road, Shanghai 200092, China
e-mail: fangshulin16@gmail.com, lxlst@tongji.edu.cn

Keywords: Coupled Building System, MR Damper, Structural Control Strategy, Seismic analysis.

Abstract. *The coupled building system has shown to be a viable approach to mitigate dynamic responses. In the system two adjacent buildings are connected together using coupling links such as magnetorheological (MR) dampers to work as a group. Therefore the forces can be transferred upon one another and eventually reduce critical responses. The coupled building systems have been successfully implemented for newly built buildings and used as a solution to retrofit existing buildings.*

The focus of this study is to comprehensively investigate the effectiveness of coupled building system interconnected by a MR damper considering both linear and nonlinear cases. The multistory benchmark SAC structures are selected as the adjacent buildings. Through numerical study, the control performance of different semi-active control strategies for MR damper are compared and evaluated. Furthermore, the robustness of different control strategies for pre-earthquake and post-earthquake cases is discussed. Finally, the cases of nonlinear adjacent buildings represented by hysteretic Bouc Wen models connected by MR damper are examined. The results show that using MR damper as the coupling link is an effective way to reduce the responses of both of the adjacent buildings under earthquake input. Some general conclusions and recommendations are also given for further research.

1 INTRODUCTION

The interconnecting of two adjacent buildings with dampers is an effective method to reduce dynamic responses. In recent years, various approaches of the coupled building system have been examined and applied to civil engineering structures [1-3]. In coupled building system, it is promising to use semi-active control device such as the magnetorheological (MR) damper as the coupled link. MR damper offers the adaptability similar to active control device with very small power sources. When utilizing the MR damper with complex nonlinear behavior in structural control, one of the challenges to achieve high levels performance is the selection and design of appropriate control algorithms based on the available feedback measurements.

The focus of this study is to comprehensively examine the efficacy of coupled building system interconnected by a MR damper under different control algorithms for both linear and nonlinear cases. Several control methods are implemented here including passive control and three semi-active controllers, i.e. clipped optimal controller, Lyapunov controller and pseudo-negative stiffness (PNS) controller. Through numerical study, the pros and cons of each control strategy for MR damper are discussed and evaluated. Furthermore the robustness of different control strategies for pre-earthquake and post-earthquake cases is discussed. The effectiveness of the coupled building system for seismic response mitigation is demonstrated in this study.

2 COUPLED BUILDING SYSTEM

2.1 Coupled building model

The adjacent buildings of 3 and 9 stories used in this study were designed based on the benchmark SAC structures which meet the seismic code and may represent typical low- and medium-rise buildings in Los Angeles, California region. Here the structures are simplified as two shear buildings. The two buildings are connected at the 3rd story with a MR damper. The story height of both building is 3.96 m. The mass and stiffness of each floor for building 1 are 4.945×10^5 kg and 1.72×10^8 N/m. For building 2, the mass and stiffness are 4.785×10^5 kg and 1.16×10^8 N/m. Damping in each mode is assumed to be 2% for both buildings. The first natural frequencies of two buildings are 0.49 Hz and 1.10 Hz.

The equation of motion of the coupled building system is

$$\mathbf{M}\ddot{\mathbf{x}} + \mathbf{C}\dot{\mathbf{x}} + \mathbf{K}\mathbf{x} = -\mathbf{M}\boldsymbol{\Gamma}\ddot{x}_g + \boldsymbol{\Lambda}f \tag{1}$$

where **M**, **C** and **K** are the mass, damping and stiffness matrices of the coupled system. $\boldsymbol{\Gamma}$ and $\boldsymbol{\Lambda}$ are the influence vectors considering ground motion and damper location, respectively. f is the feedback force of MR damper. **x** is the relative displacement vector. $\ddot{x}_g$ is the ground acceleration. The **M**, **C** and **K** matrices are defined as

$$\mathbf{M} = \begin{bmatrix} [\mathbf{M_1}]_{9\times9} & [\mathbf{0}]_{9\times3} \\ [\mathbf{0}]_{3\times9} & [\mathbf{M_2}]_{3\times3} \end{bmatrix}; \mathbf{C} = \begin{bmatrix} [\mathbf{C_1}]_{9\times9} & [\mathbf{0}]_{9\times3} \\ [\mathbf{0}]_{3\times9} & [\mathbf{C_2}]_{3\times3} \end{bmatrix}; \mathbf{K} = \begin{bmatrix} [\mathbf{K_1}]_{9\times9} & [\mathbf{0}]_{9\times3} \\ [\mathbf{0}]_{3\times9} & [\mathbf{K_2}]_{3\times3} \end{bmatrix} \tag{2}$$

The state-space expression of the equation of motion is

$$\dot{\mathbf{z}} = \mathbf{A}\mathbf{z} + \mathbf{B}\mathbf{u} \tag{3}$$

$$\mathbf{z} = \begin{bmatrix} \mathbf{x} \\ \dot{\mathbf{x}} \end{bmatrix}; \mathbf{u} = \begin{bmatrix} \ddot{x}_g \\ f \end{bmatrix} \tag{4}$$

$$\mathbf{A} = \begin{bmatrix} \mathbf{0} & \mathbf{I} \\ -\mathbf{M}^{-1}\mathbf{K} & -\mathbf{M}^{-1}\mathbf{C} \end{bmatrix}; \mathbf{B} = \begin{bmatrix} \mathbf{0} & \mathbf{0} \\ -\boldsymbol{\Gamma} & \mathbf{M}^{-1}\boldsymbol{\Lambda} \end{bmatrix} \tag{5}$$

where **z** is the state vector defined as displacement and velocity at lumped mass locations.

In this study, in order to illustrate the performance of nonlinear multi-story adjacent buildings connected by a MR damper, additional analyses are conducted. Here the hysteretic Bouc Wen models are selected to represent the nonlinearity of the structure in each floor. In this model, the ratio of the post yielding stiffness and elastic stiffness is selected to be 0.035.

2.2 MR damper model

In this study, a phenomenological Bouc-Wen model developed by Spencer et al. [4] is used to simulate the MR damper. The parameters of the Bouc-Wen model are given in Table 1 which is physically identified to represent a RD-8041-1 MR damper (LORD Corporation). The damper can generate specified peak to peak force higher than 550 lb (2447 N) due to a velocity input of 1.97 in/sec (5 cm/sec) with 1 Amp current level.

α_a	13.71 lb/in	α_b	41.99 lb/in-V	c_{0a}	3.72 lb-s/in
c_{0b}	5.96 lb-s/in-V	c_{1a}	14.91 lb-s/in	c_{1b}	102.68 lb-s/in-V
k_0	11.08 lb/in	k_1	0.01 lb/in	γ	23.44 in^{-2}
β	23.44 in^{-2}	A	155.32	x_0	0.00 in
n	2	η	60.00 s^{-1}		

Table 1: Parameters for the MR damper model.

2.3 Semi-active control strategies

One of the advantages of MR damper is that by semi-active control, the damper can effectively mitigate the responses as active control device while requiring very small power sources. Here in this study, five control strategies are implemented and evaluated. Note that in the implementation of all the algorithms, the available feedback measurements are the absolute acceleration of both buildings and control force. The other states are estimated using Kalman filter.

Passive on control (PON)

The first control method considered is passive on control, where the command voltage to the MR damper is held at a constant level of 2.8 V.

Clipped optimal control (COC1 and COC2)

The second and third are clipped optimal control, proposed by Dyke et al. [5]. First the LQG/H2 strategy is applied in calculating the optimal control force. The voltage input of MR damper is then determined using the following control law.

$$v = V_{max} H\{(f_d - f_m) f_m\} \tag{6}$$

where H{·} is the Heaviside step function, V_{max} is the maximum voltage to the current driver considering the saturation of the magnetic field in the MR damper.

Here two clipped optimal controllers COC1 and COC2 are designed which focus on minimizing the displacements and accelerations of both buildings, respectively. The maximum voltage applied is set to 2.8 V. For the design of COC1 and COC2, equal weight is selected for every floor and **R** is selected to be an identity matrix of proper order. A family of controllers can be designed by varying the weighting matrix **Q**. Here the **Q** matrix is determined based on the performance of these controllers in simulations by trial and error. For COC1 and COC2, the **Q** matrix weights are chosen to be 1.61×10^{15} and 1.78×10^{12} respectively.

Lyapunov stability-based control

Leitmann [6] applied Lyapunov's direct approach for the design of a semi-active controller. In this approach, Lyapunov fuction is selected as

$$V(\mathbf{z}) = \frac{1}{2}\|\mathbf{z}\|_P{}^2 \tag{7}$$

where $\|\mathbf{z}\|_P$ is defined by

$$\|\mathbf{z}\|_P = [\mathbf{z}^T\mathbf{P}\mathbf{z}]^{1/2} \tag{8}$$

and **P** is a real, symmetric, positive definite matrix. For a linear system, to ensure $\dot{V}$ is negative definite, the matrix **P** is determined using the Lyapunov equation below for a positive definite matrix $\mathbf{Q}_P$.

$$\mathbf{A}^T\mathbf{P} + \mathbf{P}\mathbf{A} = -\mathbf{Q}_P \tag{9}$$

The derivative of the Lyapunov fuction is

$$\dot{V} = -\frac{1}{2}\mathbf{z}^T\mathbf{Q}_P\mathbf{z} + \mathbf{z}^T\mathbf{P}\mathbf{B}\mathbf{f} + \mathbf{z}^T\mathbf{P}\mathbf{E}\ddot{x}_g \tag{10}$$

The only term that can be directly affected by a change in the control current is the middle term that contains the force vector **f**. Thus, the input to the damper which will minimize $\dot{V}$ is

$$v_i = V_{max}H((-\mathbf{z})^T\mathbf{P}\mathbf{B}_i f_i) \tag{11}$$

where H{·} is the Heaviside step function and f_i is the measured force of the *i*th damper.

In the controller design for this study, the positive definite matrix $\mathbf{Q}_P$ are selected arbitrarily based on the simulation results by trial and error.

Pseudo-negative stiffness (PNS) control

The PNS control method was first proposed by Iemura et al. [7, 8]. Here in this study, the PNS method is applied to MR damper with the input voltage changes depending on the movement direction [9]. The input voltage follows the solid line when the direction of motion is positive (from left to right) and follows the dashed line when the direction is negative (from right to left), shown in Figure 1. The control law expression is given by

$$v(x, \dot{x}) = -\text{sgn}(\dot{x}) \times S \times x + v_m \tag{12}$$

where *S* is the slope of the line, v_m is the input voltage at the central position, and *x* is the stroke of the damper. In this study, *S* and v_m are selected to be 4 V/in and 1.4 V respectively.

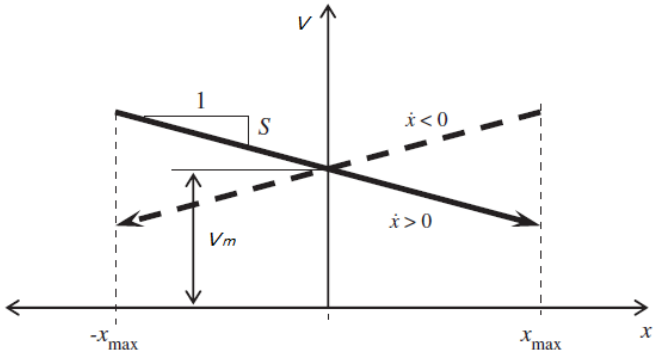


Figure 1: input voltage of PNS controller.

3 SIMULATION RESULTS

To evaluate the control performance of coupled building system with MR damper, numerical simulation is performed using different control strategies under El Centro earthquake input

in MATLAB/SIMULINK environment for both linear and nonlinear cases. PGA of the earthquake record is scaled to DBE (design basis earthquake) level for linear cases and MCE (maximum considered earthquake) level for nonlinear cases using the methods provided by relevant provisions with regards to the recommendations for earthquakes in California area [10]. Since the MR damper model used in this study is of lab scale, to achieve the required control capacity, the output force of the MR damper is multiplied by 4800 and the displacement is scaled such that 1 mm in the MR damper corresponds to 20 mm in the coupled building system. The sampling frequency is 4096 Hz.

The responses of both buildings and the control forces are selected as the evaluation criteria as shown in Table 2.

Peak Floor Displacement $J_1 = \max_{EQ}\left\{\frac{\max_{t,i}\lvert x_i(t)\rvert}{x^{max}}\right\}$	Normed Floor Displacement $J_5 = \max_{EQ}\left\{\frac{\max_{i}\lVert x_i(t)\rVert}{\lVert x^{max}\rVert}\right\}$	Control Force $J_9 = max_{EQ}\left\{\frac{\max_{t}\lvert f(t)\rvert}{W}\right\}$
Peak Interstory Drift $J_2 = \max_{EQ}\left\{\frac{\max_{t,i}\left(\frac{\lvert d_i(t)\rvert}{h_i}\right)}{d_n^{max}}\right\}$	Normed Interstory Drift $J_6 = max_{EQ}\left\{\frac{\max_{i}\left(\frac{\lVert d_i(t)\rVert}{h_i}\right)}{\lVert d_n^{max}\rVert}\right\}$	Peak Control Force $J_{10} = max_{EQ}\left\{\max_{t}\lvert f(t)\rvert\right\}$
Peak Floor Acceleration $J_3 = \max_{EQ}\left\{\frac{\max_{t,i}\lvert \ddot{x}_{ai}(t)\rvert}{\ddot{x}_a^{max}}\right\}$	Normed Floor Acceleration $J_7 = \max_{EQ}\left\{\frac{\max_{i}\lVert \ddot{x}_{ai}(t)\rVert}{\lVert \ddot{x}_a^{max}\rVert}\right\}$	RMS Control Force $J_{11} = max_{EQ}\{\lvert f_{RMS}(t)\rvert\}$
Peak Base Shear $J_4 = \max_{EQ}\left\{\frac{\max_{t}\lvert\sum_{i=1}^{\eta} m_i \ddot{x}_{a\eta_i}(t)\rvert}{F_b^{max}}\right\}$	Normed Base Shear $J_8 = \max_{EQ}\left\{\frac{\lVert\sum_{i=1}^{\eta} m_i \ddot{x}_{a\eta_i}(t)\rVert}{\lVert F_b^{max}\rVert}\right\}$	

Table 2: Summary of evaluation criteria.

3.1 Control performance assessment (linear)

First, the numerical simulation is conducted using a linear model of coupled building system interconnected by a MR damper. The evaluation results of the control performance under El Centro earthquake using the proposed criteria are listed and compared in Tables 3 and 4. As an example, the uncontrolled and COC2 controlled time histories of the top floor responses for both buildings are given in Figure 2. The performance of different control strategies considering the RMS responses over the height of the adjacent buildings is compared in Figure 3.

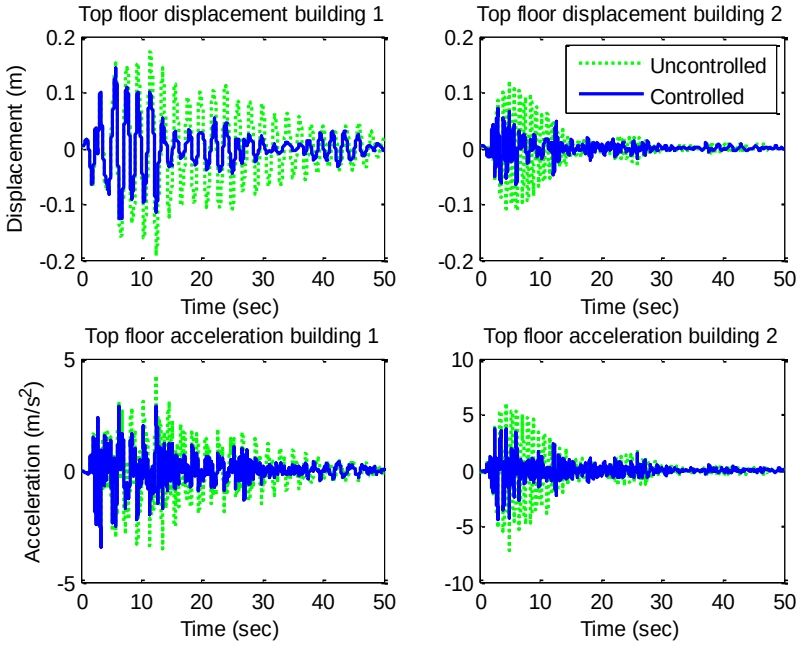
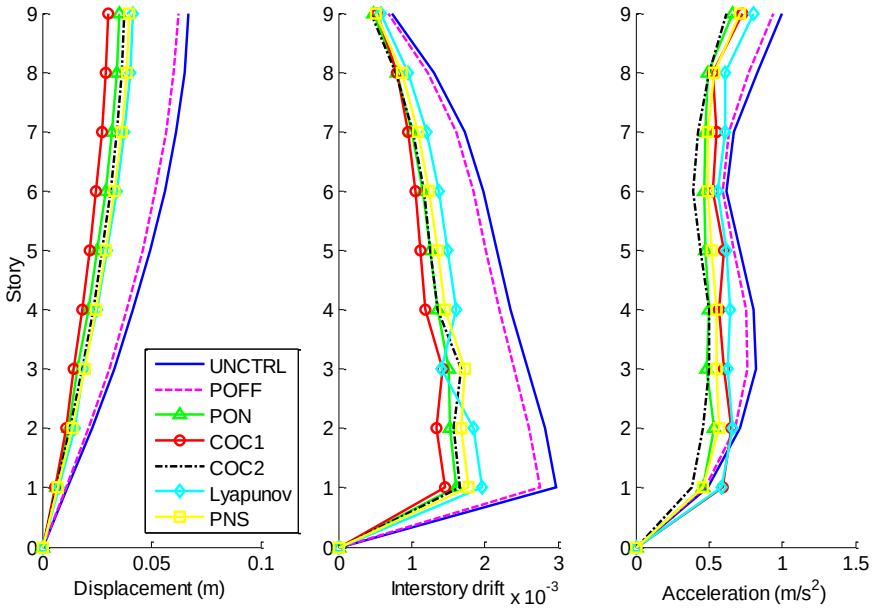
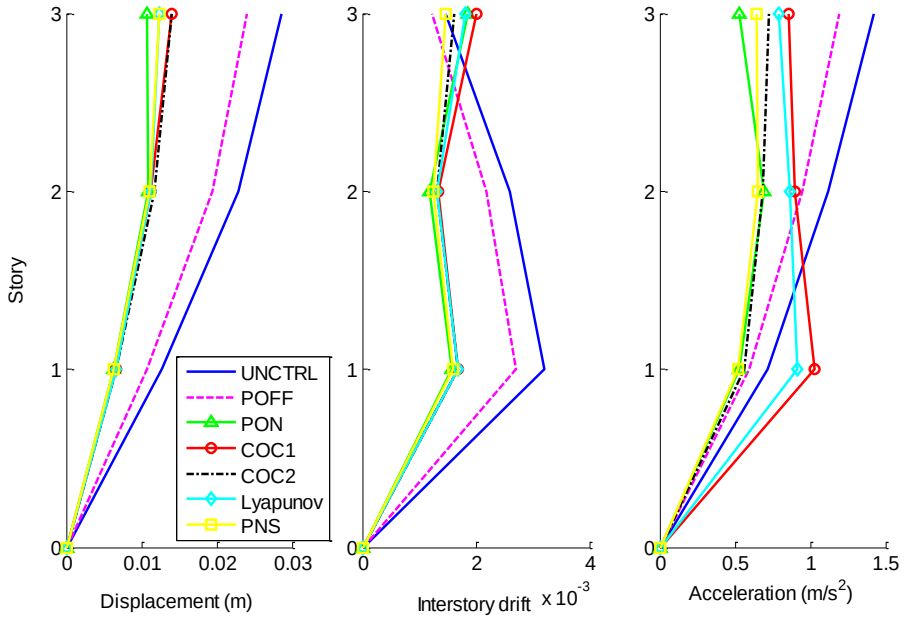


Figure 2: Time histories of top floor responses under COC2 control.



(a)



(b)

Figure 3: Uncontrolled and controlled responses under El Centro earthquake over the height of the adjacent buildings.
(a) RMS responses of building 1 (b) RMS responses of building 2

Controller	Evaluation Criteria										
	J1	J2	J3	J4	J5	J6	J7	J8	J9	J10	J11
PON	0.694	0.757	0.926	0.757	0.524	0.542	0.659	0.544	0.107	4778	908
COC1	0.648	0.788	0.932	0.799	0.451	0.490	0.725	0.493	0.117	5202	847
COC2	0.741	0.815	0.839	0.753	0.560	0.564	0.620	0.562	0.089	3945	684
Laypunov	0.812	0.722	0.895	0.726	0.622	0.664	0.807	0.665	0.110	4882	808
PNS	0.751	0.861	0.876	0.832	0.595	0.599	0.710	0.601	0.068	3035	668

Table 3: Comparison results under different control strategies for building 1 (9 stories).

Controller	Evaluation Criteria										
	J1	J2	J3	J4	J5	J6	J7	J8	J9	J10	J11
PON	0.475	0.773	0.519	0.588	0.379	0.581	0.489	0.493	0.333	4778	908
COC1	0.658	0.908	0.914	0.624	0.493	0.629	0.725	0.526	0.362	5202	847
COC2	0.588	0.686	0.617	0.573	0.492	0.526	0.512	0.528	0.275	3945	684
Laypunov	0.604	0.811	0.751	0.649	0.433	0.564	0.642	0.524	0.340	4882	808
PNS	0.497	0.604	0.501	0.604	0.435	0.497	0.457	0.499	0.211	3035	668

Table 4: Comparison results under different control strategies for building 2 (3 stories).

The results demonstrate that using MR damper as the coupling link is an effective way to reduce the responses of the adjacent buildings under earthquake input. Several observations are made. (i) The response mitigation is more obvious for shorter building. (ii) For taller building, COC1 provided the best control performance considering displacement, interstory drift and base shear. COC2 have the best performance in terms of acceleration. For shorter building, PON, COC2 and PNS control give similar results. Generally speaking, PON usually has slightly better control of peak displacement, while PNS performs slightly better in miti-

gating interstory drift and acceleration. (iii) In terms of the control force, the semi-active controllers always outperform the passive on case, especially for COC2 and PNS, with reduction around 25%.

3.2 Control performance assessment (nonlinear)

In this section, numerical simulation is conducted to evaluate the controller performance on a nonlinear model of the multi-story adjacent buildings system represented by hysteretic Bouc Wen model. The evaluation results of the control performance under El Centro earthquake using the proposed criteria are listed and compared in Tables 5 and 6. The uncontrolled and COC2 controlled time histories of the top floor responses for both buildings are given in Figure 4.

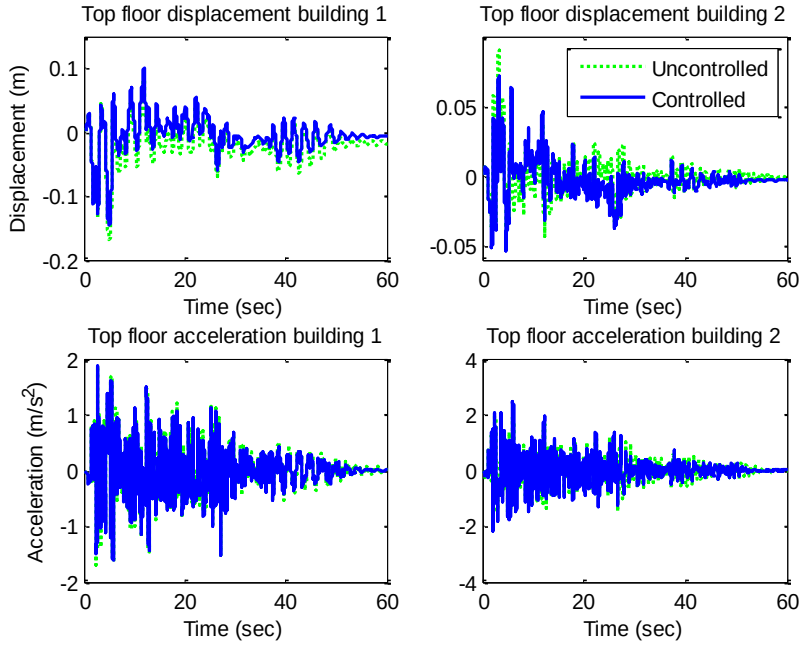


Figure 4: Time histories of top floor responses under COC2 control (nonlinear).

Controller	Evaluation Criteria										
	J1	J2	J3	J4	J5	J6	J7	J8	J9	J10	J11
PON	0.889	0.958	1.085	0.965	0.835	0.996	1.082	0.963	0.035	1559	399
COC1	0.773	0.902	1.095	0.978	0.805	0.921	1.074	0.932	0.027	1218	311
COC2	0.869	0.954	0.981	0.992	0.855	1.014	1.048	0.953	0.025	1100	231
Laypunov	0.882	1.023	0.953	1.002	0.840	1.015	1.087	0.978	0.037	1656	364
PNS	0.925	1.004	0.966	1.003	0.879	0.993	1.031	0.966	0.022	980	279

Table 5: Comparison results under different control strategies for building 1 (9 stories).

Controller	Evaluation Criteria										
	J1	J2	J3	J4	J5	J6	J7	J8	J9	J10	J11
PON	0.749	0.864	0.981	0.977	0.976	0.915	0.889	0.935	0.109	1559	399
COC1	0.806	0.792	1.178	0.964	1.136	0.951	1.005	0.899	0.085	1218	311
COC2	0.808	0.778	1.135	0.959	0.989	1.007	0.961	0.915	0.077	1100	231
Laypunov	0.888	0.949	1.318	1.012	1.042	0.932	0.953	0.924	0.115	1656	364

PNS	0.868	0.918	0.944	0.991	0.965	0.904	0.823	0.928	0.068	980	279

Table 6: Comparison results under different control strategies for building 2 (3 stories).

In general, the response reduction achieved in nonlinear cases is limited compare to the linear cases. The results follow the similar trends as the linear cases. Semi-active controller COC2 and PNS achieve the similar results using much less energy when comparing with PON. In Figure 4, it is observed that the residual displacements of both the buildings decrease compare to the uncontrolled case. The effectiveness of using MR damper as the coupling link to nonlinear adjacent structures is shown here.

3.3 Robustness analysis

The change of the dynamic properties of a building after strong earthquake due to the damage can be substantial. In order to include the stiffness degradation effects, a post-earthquake model (case 1) and a pre-earthquake model (case 3) are developed with 10% changes of the natural frequency from the nominal structural model (case 2). The robustness of different control algorithms are examined by the simulation using these models. The variation of control performance evaluated using index J5-J8 of the three cases are compared in Figures 5 and 6.

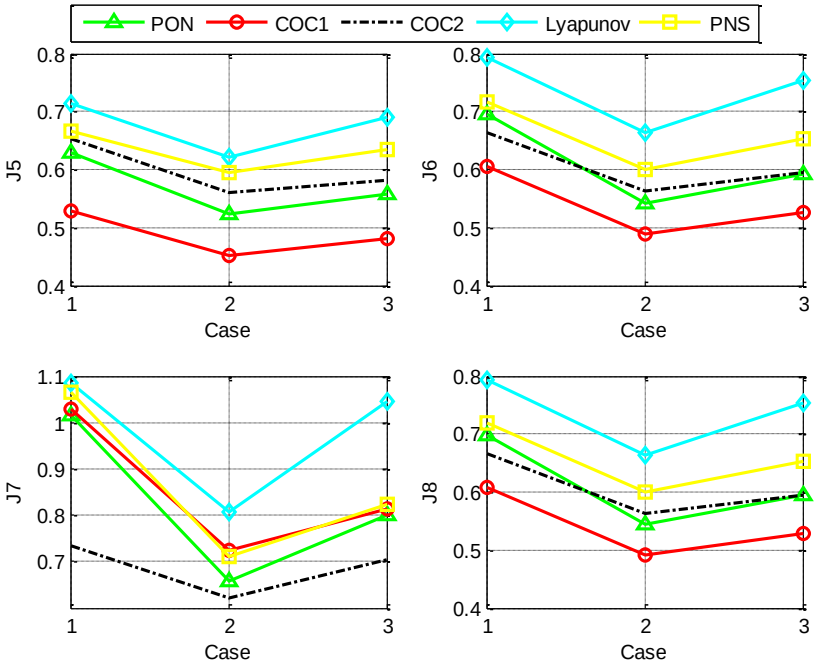


Figure 5: Variation of evaluation criteria indicators for building 1.

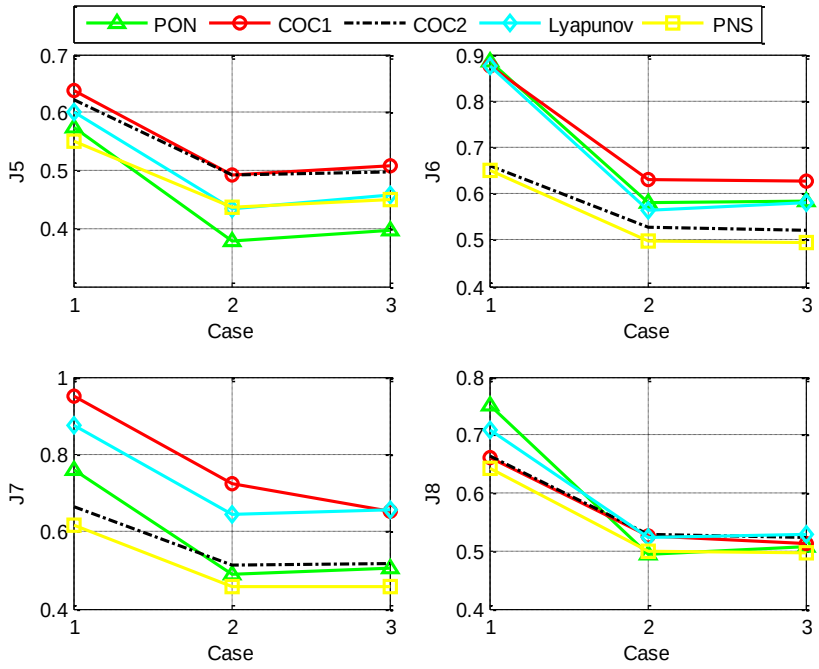


Figure 6: Variation of evaluation criteria indicators for building 2.

It is observed that, although the controllers are designed based on the nominal model, significant response mitigation is achieved for the post-earthquake and pre-earthquake cases as well, which confirms that the MR damper can provide reliable and robust control when the structure property changes. It is found that COC1 has better control considering displacement, interstory drift and base shear for building 1. PON provides a better control of displacement for building 2. COC2 and PNS are the most effective controllers in reducing interstory drift and acceleration of building 2.

The variation in the response using three models is less severe for COC2 in comparison to the other controllers of both buildings. Generally speaking, semi-active controller COC2 provides a more robust control. When facing changing conditions, the semi-active control system can still perform adequately and provide consistent levels of reduction.

4 CONCLUSIONS

The effectiveness in seismic response reduction of coupled building system interconnected by a MR damper is investigated for both linear and nonlinear cases. Different control strategies, including passive on, clipped optimal control, Lyapunov control and pseudo-negative stiffness (PNS) control are designed and evaluated. Some further robustness analyses are also performed. The following general conclusions can be drawn based on the simulation results:

- Using MR damper as the coupling link is effective in mitigating the dynamic responses of both of the adjacent buildings under earthquake input.
- For taller building, controller COC1 results in lower responses in terms of displacement, interstory drift and base shear. COC2 performs better in acceleration control. For shorter building, PON, COC2 and PNS control give very similar results. The response mitigation is relatively more obvious for shorter building.

- Semi-active controllers COC2 and PNS are superior at utilizing smaller damper force to achieve good control performance. 25% of energy can be saved compare to passive control.
- The residual displacements of both the buildings decrease in the nonlinear coupled building system with proper control.
- The robustness of semi-active controller COC2 is demonstrated through comparing the simulation results using pre-earthquake, nominal and post-earthquake models. Stable and robust control is still guaranteed by semi-active vibration control when the properties of the building changes.
- Generally speaking, semi-active controllers COC2 and PNS achieve better performance considering response reduction, robustness and energy saving. Moreover, semi-active controllers are more flexible compare to passive control, as the controller can be designed optimizing different control objectives.

REFERENCES

[1] R.E. Christenson, B.F. Spencer, E.A. Johnson, K. Seto, Coupled Building Control Considering the Effects of Building/Connector Configuration. *Journal of structural engineering ASCE*, **132**(6), 853-863, 2006.

[2] R.E. Christenson, B.F. Spencer, E.A. Johnson, Semiactive Connected Control Method for Adjacent Multidegree-of-Freedom Buildings. *Journal of Engineering Mechanics*, **133**, 290-298, 2007.

[3] HP. Zhu, H. Iemura, A study of response control on the passive coupling element between two parallel structures. *Structural Engineering and Mechanics*, **9**(4), 383-396, 2000.

[4] B.F. Spencer, S.J. Dyke, M.K. Sain, J.D. Carlson, Phenomenological model for magnetorheological dampers. *Journal of Engineering Mechanics,* **123**(3), 230-238, 1997.

[5] S.J. Dyke, B.F. Spencer, M.K. Sain, J.D. Carlson, Modeling and control of magnetorheological dampers for seismic response reduction. *Smart Materials & Structures*, **5**(5), 565-575, 1996.

[6] G. Leitmann, Semiactive Control for Vibration Attenuation. *Journal of Intelligent Material Systems and Structures*, **5**(6), 841-846, 1994.

[7] H. Iemura, A. Igarashi, N. Nakata, Semi-active control of full-scale structures using variable joint damper system. *Proceedings of the KKNN Symposium on Civil Engineering*, Kyoto, November 5-7, 41-46, 2001.

[8] H. Iemura, MH. Pradono, Passive and semi-active response control of a cable-stayed bridge. *Journal of Structural Control*, **9**, 189-204, 2002.

[9] H. Iemura, A. Igarashi, MH. Pradono, A. Kalantari, Negative stiffness friction damping for seismically isolated structures. *Journal of Structural Control and Health Monitoring*, **13**, 775-791, 2006.

[10] NEHRP Recommended Provisions for Seismic Regulations for New Buildings and Other Structures, *Report No. FEMA 450*, Washington, DC. , 2003.

COMPDYN 2015
5th ECCOMAS Thematic Conference on
Computational Methods in Structural Dynamics and Earthquake Engineering
M. Papadrakakis, V. Papadopoulos, V. Plevris (eds.)
Crete Island, Greece, 25–27 May 2015

NUMERICAL ASSESSMENT ON THE SEISMIC RESPONSE OF A BASE-ISOLATED BUILDING UNDER BI-DIRECTIONAL MOTION

M. Furinghetti[1], **A. Pavese**[2]

[1] UME School - Pavia
via Ferrata 1, 27100 Pavia - Italy
e-mail: marco.furinghetti@umeschool.it

[2] University of Pavia
via Ferrata 3, 27100 Pavia - Italy
e-mail: a.pavese@unipv.it

Keywords: Concave Sliding Surface device, Bi-Directional motion, cycling effect, friction coefficient, heating phenomena.

Abstract. *Experimental and analytical studies on Concave Sliding Surface devices have underlined that the hysteretic characteristics under bi-directional input motion are highly non-linear, in comparison with the uni-directional case. The force response of the device along both directions of motion strongly depend on the shape of the trajectory, because of the step-wise changing of direction of the frictional force, rather than in a uni-directional motion in which all forces have the same direction. Together with these aspects, also the variation of the frictional properties with respect to sliding velocity (Velocity Effect), vertical load (Vertical Load Effect) and heating phenomena originated at the sliding interfaces (Cycling Effect) increase the non-linearity of the behavior of such kind of isolators, leading to dispersions of the peak quantities when time history analyses are performed: such dispersions can not be neglected a priori, but they have to be accurately evaluated. In addition, experimental tests have shown widely sparse frictional properties of the sliding materials commonly used for CSS devices, even when the same conditions of loading are considered. Moreover, in real applications, the spatial distribution of both the devices and the isolated building affect the overall response, especially when irregularities in the installation of the isolators are considered, which results into uneven inclinations of the sliding surfaces with respect to the horizontal plane. In this endeavor a wide numerical campaign has been carried out on a case study, considering several layout conditions, the actual dispersion of the frictional characteristics of the device, and different models of the friction coefficient for all the isolators. The results of all the numerical simulations, performed by means of time history analyses, have allowed to underline some important aspects which must be accounted for when designing a structural system, isolated using a grid of CSS devices, under bi-directional seismic excitations.*

1 INTRODUCTION

A growing interest toward the response assessment of friction based devices has been observed during the last years both using numerical and experimental approaches [6, 7, 10, 13]. In the experimental field both Single and Double Curved Surface Slider devices (SCSS and DCSS) have been investigated in some details, in order to evaluate the overall features giving important indications on how such devices have to be modeled. In a previous study Lomiento et al. analyzed the frictional behavior of CSS devices subjected to bidirectional motions, in terms of dependency of the friction coefficient with respect to the sliding velocity (velocity effect) and to the applied vertical load (load effect) [4]. Moreover, due to the heating phenomena occurring at the sliding interfaces, it has been observed that the friction coefficient decreases under long lasting cyclic motions [4, 5] (cycling effect). A wide testing campaign was carried out on a DCSS device by Furinghetti et al.: results showed that the friction decay caused by the cycling effect assumes a decreasing exponential trend with respect to the dissipated energy, regardless the shape of the trajectory that the device is subjected to (Figure 1) [3]. A number of different trajectories were considered, among which the bidirectional cloverleaf ruled by the standard code UNI:EN15129:2009 [7].

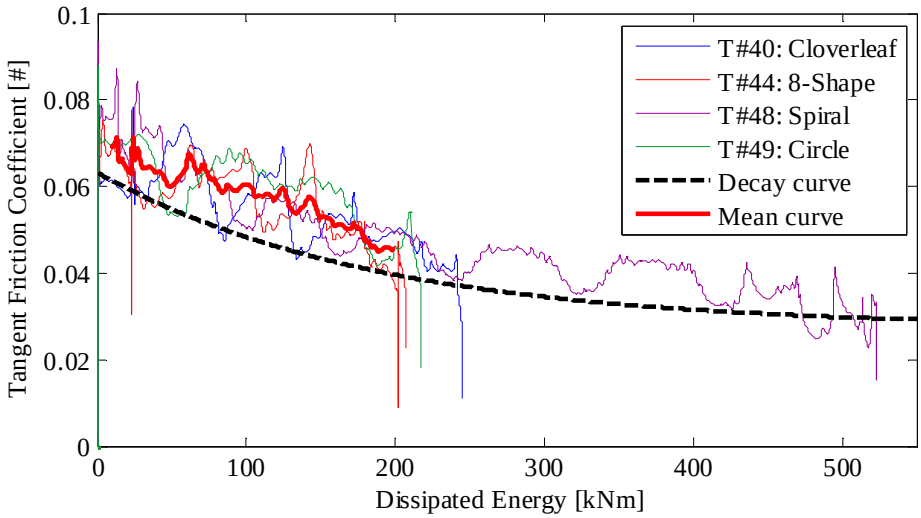


Figure 1: Frictional decay due to cyclic bidirectional loading [3].

Additional fluctuations were found, which could be originated by uneven rotations of the internal non-articulated slider, rather than oscillation of the vertical load. This behavior is supposed to significantly influence the overall response of a structural system isolated by means of CSS devices.

In the present study a wide numerical assessment is presented, aiming at evaluating the direct effects of the cycling loading on the response of a multy-storey building isolated with DCSS devices. An ad hoc mass-independent dynamic system has been directly defined, which allows to carry out parametric studies, considering an actual non-linear constitutive law for the isolation system, accounting for bi-axial interaction of the frictional force along the main directions of motion. The scope of this work is to highlight the influence of the cycling effect on the main response quantities, in terms of peak displacements, absolute accelerations and interstorey shears. Results show that accounting for the cycling effect leads to non-negligible variation of all the response parameters with respect to the reference case, in which no friction coefficient decay is considered.

2 MECHANICAL MODEL OF THE DEVICES

The structural system has been seismically isolated using Double Concave Sliding Surface devices (DCSS) with a non-articulated slider: such devices, shown in Figure 2, have the same characteristics as the one described in a previous work [3].

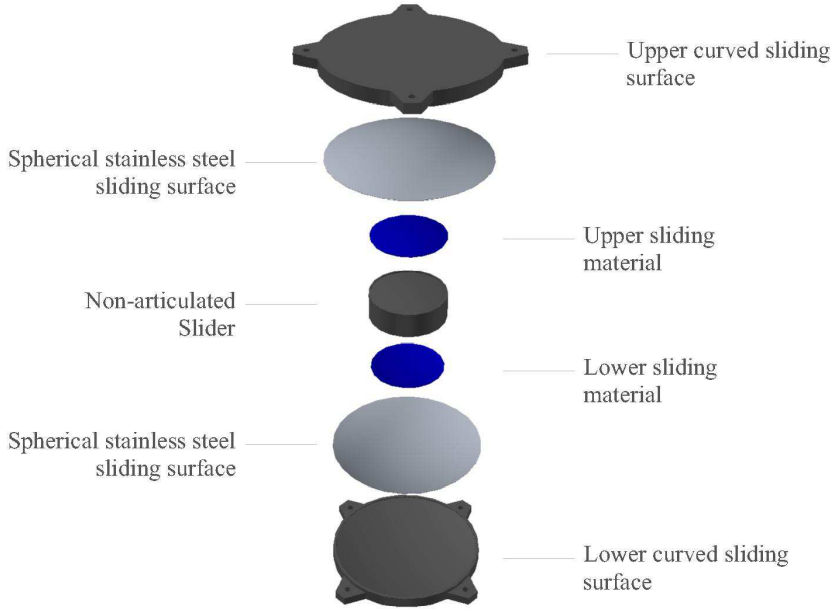


Figure 2: Components of the device.

The curvature radius for both the sliding surfaces is equal to 1,6 m and the height of the internal slider is 0,1m: these geometric quantities imply that the equivalent radius of curvature of the whole device is equal to 3,1m [10].

The mechanical model of the device has been considered as the summation of two contributions (eq.(1)).

$$F_{device} = F_r + F_f \tag{1}$$

The former is represented by the restoring force F_r (eq.(2)) caused by the projection of the vertical load applied to the device along the curved sliding surfaces [2]: the restoring behavior can be modeled using a linear spring with respect to the displacements along both x and y directions, with a stiffness coefficient given by the ratio between the vertical load W and the equivalent radius of curvature R_{eq} [2].

$$F_r = \frac{W}{R_{eq}} \cdot \begin{bmatrix} u_{0,x} \\ u_{0,y} \end{bmatrix} \tag{2}$$

The latter contribution consists of the frictional force F_f due to the sliding movements at both the upper and the lower curved surfaces (eq.(3)). The same model presented in a previous study has been used, thus assuming the total frictional force, returned by the product between the friction coefficient and the vertical load, aligned with respect to the tangent line to the trajectory of the device: hence, such a force has been stepwise projected along the main directions of motion x and y. The friction coefficient can be considered as a function of vertical load (load effect), sliding velocity (velocity effect) and the dissipated energy (cycling effect) [5, 8].

$$F_f = \mu(W,v,E)\cdot W\cdot \tanh\left(\frac{v}{v_s}\right)\cdot\left[\begin{array}{c}\dfrac{\dot{u}_{0,x}}{\sqrt{(\dot{u}_{0,x})^2+(\dot{u}_{0,y})^2}}\\ \dfrac{\dot{u}_{0,y}}{\sqrt{(\dot{u}_{0,x})^2+(\dot{u}_{0,y})^2}}\end{array}\right] \tag{3}$$

The parameter which rules the transition through the "zero velocity point" v_s has been assumed equal to 0,0075 m/s.

In this endeavor the friction coefficient has been assumed as a function of the dissipated energy only, in order to underline the direct consequences of the cycling effect on the main response quantities of the whole structural system. In a previous experimental campaign carried out on a full scale device at EUCENTRE TREES Lab in Pavia [3, 12] results have shown that the friction coefficient decreases with respect to the dissipated energy with an exponential trend, considering both unidirectional and bidirectional motions. According to the aforementioned evidence, in this work the same multiplication factor which rules the exponential decay of the friction coefficient caused by the cycling effect has been implemented, as shown in eq.(4).

$$\mu(W,v,E) = \mu(W,v)\cdot k_E = \overline{\mu}\cdot\left[a\cdot e^{-b\cdot E} + c\right] \tag{4}$$

The numerical values of the parameters of the exponential curve a, b and c are the same returned by the non-linear fitting procedure reported in Furinghetti et al. 2014 [3]; moreover the b value, the parameter which affects the hardness of the friction coefficient decay, has been assumed as uniformly distributed in a range between ±100% of the mean value: all the parameters of the device are listed in Table 1.

Parameter	Value
$\overline{\mu}$	0,0500
a	0,5675
b	0,0050 (±100%)
c	0,4325
R_{eq}	3,1 m

Table 1: Parameters of the mechanical model.

In Figure 3 some decay curves randomly extracted by the uniform numerical simulator are shown.

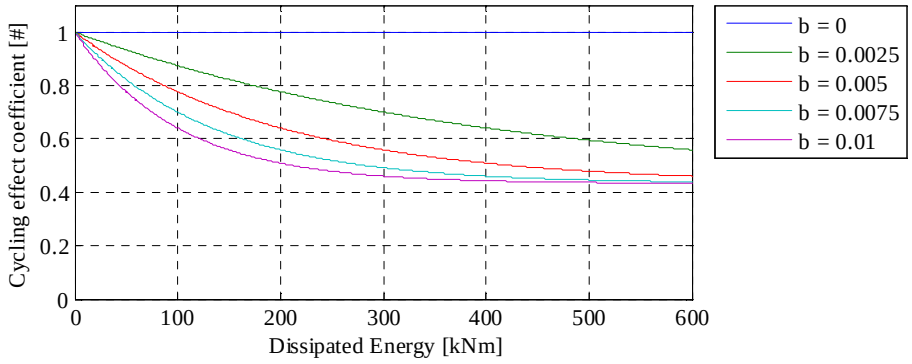


Figure 3: Friction Coefficient decay curves.

3 NUMERICAL MODEL OF THE DYNAMIC SYSTEM

In this paper a new formulation of the dynamic system of a building seismically isolated by means of DCSS devices is presented.

3.1 Modeling of the building

The building has been modeled as a shear type MDOF system, having the same period in both x and y directions; actually, the same mass and the same translational stiffness has been considered for each floor [11]. Moreover, no torsional stiffness has been assumed for all floors. Thus, given the total number of stories N_F:

$$\begin{aligned} m_1 &= m_2 = m_3 = \ldots = m_{N_F} = m \\ k_1 &= k_2 = k_3 = \ldots = k_{N_F} = k \end{aligned} \tag{5}$$

According to this assumption (eq.(5)), it is possible to introduce a "fictitious period" value (eq.(6)) which refers to the values of mass and stiffness of a single storey of the building, as follows:

$$T_s^* = \frac{2\pi}{\omega_s^*} = 2\pi\sqrt{\frac{m}{k}} \tag{6}$$

This definition is very useful, since the final scope is to define the dynamic system of the building, normalized with respect to the mass of a single storey. Moreover, for a given number of stories, a linear relationship between the period of the first mode of the building (considered fixed at the base) and the just defined fictitious period has been detected, as shown in Figure 4: it can be noted that as the number of floors increases, the proportional coefficient between the fictitious period and the 1st mode period increases.

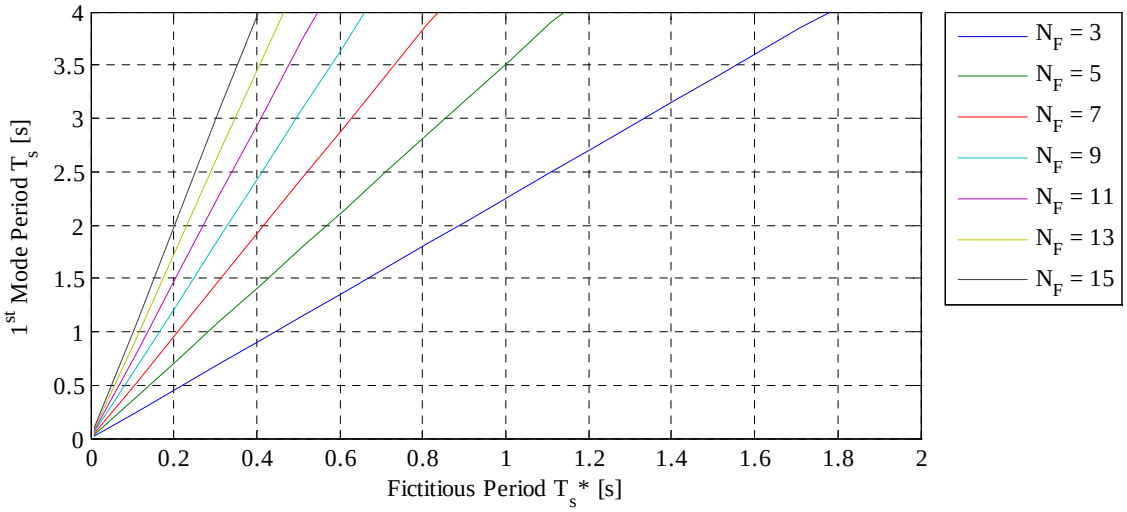


Figure 4: Linear relationship between the 1st mode period and the fictitious period.

Hence, considering the building "fixed at the base", the normalized mass and stiffness matrices for both x and y directions are an identity matrix and a shear-type stiffness matrix respectively (eq.(7)).

$$\frac{M_B}{m} = \begin{bmatrix} 1 & 0 & \cdots & 0 \\ 0 & 1 & \ddots & \vdots \\ \vdots & \ddots & \ddots & 0 \\ 0 & \dots & 0 & 1 \end{bmatrix}$$
$$\frac{K_B}{m} = \begin{bmatrix} 2 & -1 & & 0 \\ -1 & \ddots & \ddots & \\ & \ddots & 2 & -1 \\ 0 & & -1 & 1 \end{bmatrix} \cdot \omega_s^{*2} \tag{7}$$

For such a system, Rayleigh damping has been considered only for the building [11] (eq.(8)). Considering the fixed periods of all the unidirectional modes of the building, and according to the common definition of the damping matrix of the system, the proportional coefficients have been computed using a least-squares procedure and considering 5% of damping ratio for all the modes.

$$\frac{C_B}{m} = a_0 \frac{M_B}{m} + a_1 \frac{K_B}{m} \tag{8}$$

In Figure 5 results of an example for a five storey building having the 1st mode "fixed" period equal to 1,0sec are reported.

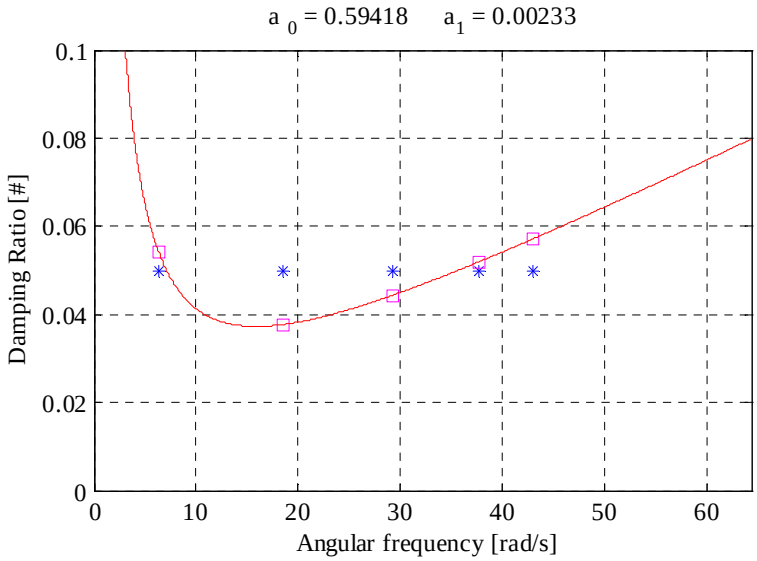


Figure 5: Least-squares procedure to determine Rayleigh Damping parameters.

In order to check the efficiency of such a model for the damping, a fixed-base building has been analyzed, when subjected to a double-impulsive acceleration time-history, which corresponds to a displacement step function (Figure 6) aiming at analyzing the response of the building under free-damped oscillations.

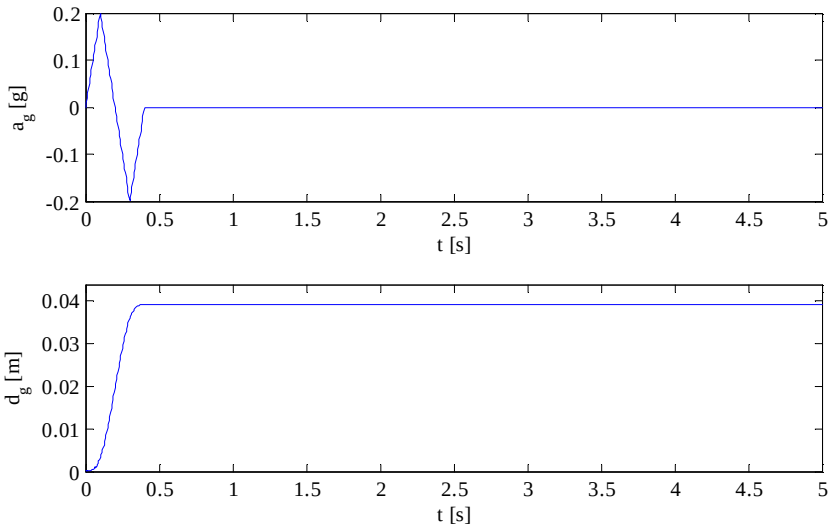
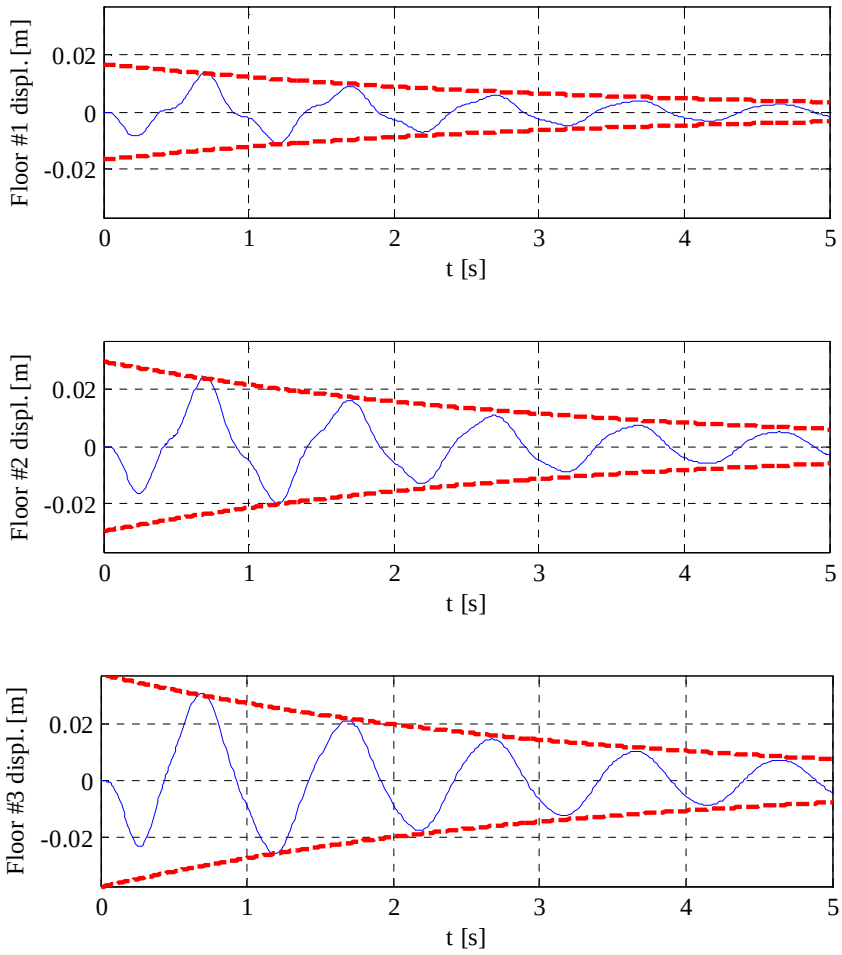


Figure 6: Input signal for the damping ratio check.

For all the stories, the exponential decay of the displacement due to damping has been checked, according to the assumed damping ratio (5%). In Figure 7 results are shown.



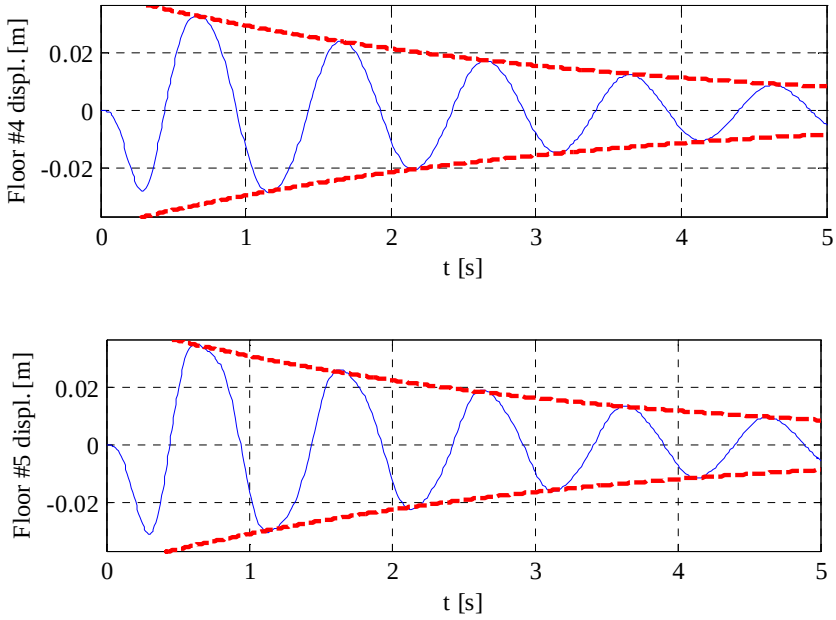


Figure 7: Displacement decay check under free-damped vibrations.

It can be noted that the theoretical exponential decay reflects the actual response of the building at each floor.

3.2 Modeling of the base-isolated system

The full model of the isolated structure consists of a MDOF model for both x and y directions: the first mass represents the isolated plate laid on the isolation system, whereas the others are the masses of each floor of the building. In Figure 8 all the considered degrees of freedom are shown.

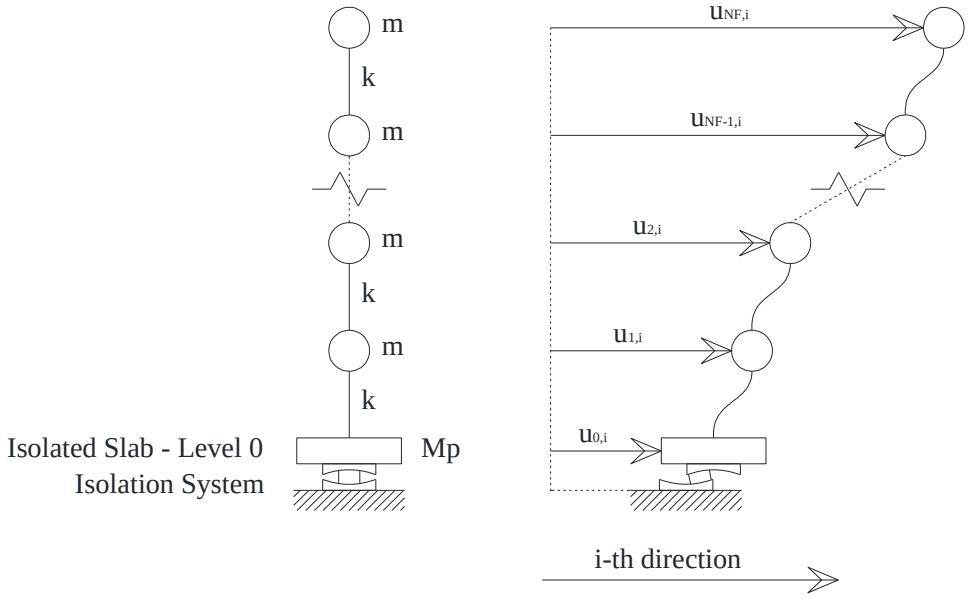


Figure 8: Dynamic model of the isolated structure.

Thus, according to Figure 8, the normalized mass and stiffness matrices can be written as shown in eq.(9):

$$\frac{M_{tot}}{m} = \frac{1}{m} \cdot \left[\begin{array}{c|cccc} M_p & 0 & 0 & \cdots & 0 \\ \hline 0 & m & 0 & \cdots & 0 \\ 0 & 0 & m & \ddots & \vdots \\ \vdots & \vdots & \ddots & \ddots & 0 \\ 0 & 0 & \cdots & 0 & m \end{array}\right] = \left[\begin{array}{c|cccc} N_F/r & 0 & 0 & \cdots & 0 \\ \hline 0 & 1 & 0 & \cdots & 0 \\ 0 & 0 & 1 & \ddots & \vdots \\ \vdots & \vdots & \ddots & \ddots & 0 \\ 0 & 0 & \cdots & 0 & 1 \end{array}\right]$$

$$\frac{K_{tot}}{m} = \left[\begin{array}{c|cccc} 1 & -1 & 0 & \cdots & 0 \\ \hline -1 & 2 & -1 & & 0 \\ 0 & -1 & \ddots & \ddots & \\ \vdots & & \ddots & 2 & -1 \\ 0 & 0 & & -1 & 1 \end{array}\right] \cdot \frac{k}{m} = \left[\begin{array}{c|cccc} 1 & -1 & 0 & \cdots & 0 \\ \hline -1 & 2 & -1 & & 0 \\ 0 & -1 & \ddots & \ddots & \\ \vdots & & \ddots & 2 & -1 \\ 0 & 0 & & -1 & 1 \end{array}\right] \cdot \omega_s^{*2} \tag{9}$$

Where r is the ratio between the mass of the whole building and the mass of the isolated slab. The normalized damping matrix is obtained in eq.(10) using the Rayleigh formulation, assuming the coefficients a_0 and a_1 previously described, considering the building fixed at the base.

$$\frac{C_{tot}}{m} = a_0 \frac{M_{tot}}{m} + a_1 \frac{K_{tot}}{m} \tag{10}$$

Concerning the isolation system, when a building with a large plan development is considered, it is possible to consider one equivalent device, having a constitutive law which is representative for the entire isolation system. Thus, according to this assumption, all the isolators have averagely the same vertical load, directly equal to the total weight of the isolated structure divided by the number of devices; the value of vertical load of the single device has been fundamental for the computation of the dissipated energy and, consequently, to account for the friction coefficient decay due to the cycling effect, since the calibrated model refers to a single full scale device [3]. Hence, the horizontal force along both x and y directions of the isolation system can be computed as shown in eq.(11):

$$\frac{F_{is}}{m} = g \cdot N_F \cdot \left(1 + \frac{1}{r}\right) \cdot \left\{ \frac{1}{R_{eq}} \begin{bmatrix} u_{0,x} \\ u_{0,y} \end{bmatrix} + \mu(W, v, E) \cdot \tanh\left(\frac{v}{v_s}\right) \cdot \begin{bmatrix} \dfrac{\dot{u}_{0,x}}{\sqrt{(\dot{u}_{0,x})^2 + (\dot{u}_{0,y})^2}} \\ \dfrac{\dot{u}_{0,y}}{\sqrt{(\dot{u}_{0,x})^2 + (\dot{u}_{0,y})^2}} \end{bmatrix} \right\}$$

being (11)

$$\frac{W_{tot}}{m} = \frac{g}{m} \cdot (M_B + M_P) = \frac{g}{m} \cdot M_B \cdot \left(1 + \frac{M_P}{M_B}\right) = \frac{g}{m} \cdot M_B \cdot \left(1 + \frac{1}{r}\right) = g \cdot N_F \cdot \left(1 + \frac{1}{r}\right)$$

Finally, the normalized dynamic system of the isolated structure can be defined for direction i = x, y (eq.(12)). The contribution of the isolation system has to be added only in the first equation for both directions, that is the translational dynamic equilibrium of the isolated slab.

$$\left[\frac{M_{tot}}{m}\right]\begin{pmatrix}\ddot{u}_{0,i}\\ \hline \ddot{u}_{1,i}\\ \ddot{u}_{2,i}\\ \vdots\\ \ddot{u}_{N_F,i}\end{pmatrix}+\left[\frac{C_{tot}}{m}\right]\begin{pmatrix}0\\ \hline \dot{u}_{1,i}-\dot{u}_{0,i}\\ \dot{u}_{2,i}-\dot{u}_{0,i}\\ \vdots\\ \dot{u}_{N_F,i}-\dot{u}_{0,i}\end{pmatrix}+\left[\frac{K_{tot}}{m}\right]\begin{pmatrix}u_{0,i}\\ \hline u_{1,i}\\ u_{2,i}\\ \vdots\\ u_{N_F,i}\end{pmatrix}+\frac{F_{is,i}}{m}\begin{pmatrix}1\\ \hline 0\\ 0\\ \vdots\\ 0\end{pmatrix}=-\left[\frac{M_{tot}}{m}\right]\cdot\ddot{u}_{g,i} \qquad (12)$$

It can be noted that the normalized damping matrix has been multiplied by the vector of relative velocities with respect to the isolated slab: in fact, the damping has to influence the response of the building relatively to its base, that is the isolated slab; whereas the isolated slab response is affected by the hysteretic damping due to the non-linear behavior of the DCSS devices. The coupling of motion along x and y directions is given by the bi-axial interaction modeling of the force response of the isolation system [1].

4 CASE STUDY

Given the parametric formulation of the dynamic system shown above, it is possible to analyze different structural layouts under a selected bidirectional seismic event, accounting for randomly distributed curves for the cycling effect.

In the present work, the Irpinia earthquake November 23rd 1980 has been considered, with both the x and y components acting simultaneously. In addition, both the x and y recordings have been scaled with a scale factor equal to 1,4 in order to achieve a displacement demand more comparable to the design displacement of the modeled device (0,2m). A relatively small scaling factor has been chosen in order not to obtain unrealistic ground acceleration time histories.

In Figure 9 the both the x and y components of the chosen seismic event are reported.

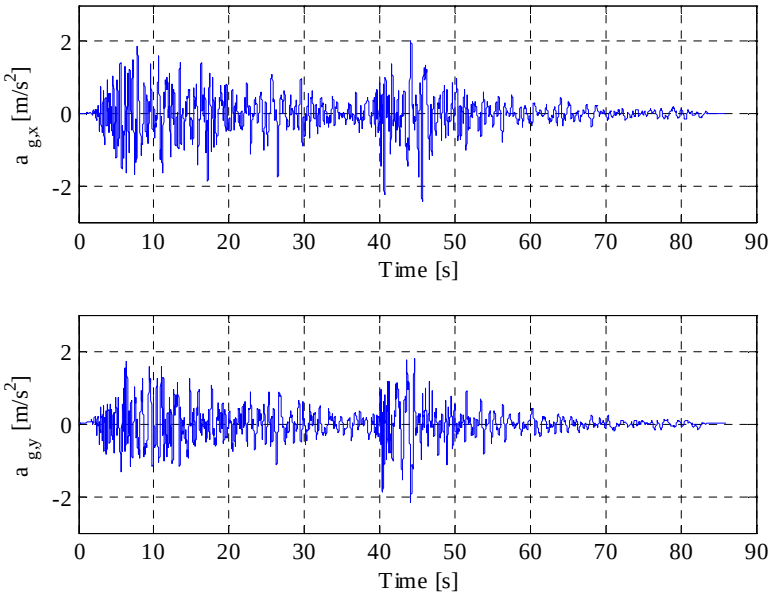


Figure 9: Irpinia earthquake: scaled x and y components.

Hence, buildings with five and seven floors have been considered, and for both of these typologies, three different fundamental periods have been assumed, as summarized in Table 2. Since the isolation system is modeled by means of an equivalent device, which implies that

each isolator is averagely loaded with the same vertical load, eq.(13) can be obtained. Given the number of isolators N_I and the single average vertical load W:

$$W = \frac{W_{tot}}{N_I} = \frac{g(M_P + M_B)}{N_I} = \frac{gM_P\left(1 + M_B / M_P\right)}{N_I} = \frac{gM_P(1+r)}{N_I} \tag{13}$$

Thus, the single average vertical load W of the devices is a function of the mass of the isolated slab M_P, the mass ratio r and the number of devices N_I.

Concerning the mass ratio r, it can be seen as a direct function of the number of floors N_F (eq.(14)):

$$r = \frac{M_B}{M_P} = \frac{m \cdot N_F}{M_P} = \left(\frac{m}{M_P}\right) \cdot N_F \tag{14}$$

In real applications the seismic mass per unit area of one floor is averagely equal to 1,0 ton/m^2, considering a concrete frame structure, external and internal masonry infills, a common structural technology of concrete and hollow-clay-tile floor system and 30% of the live load relative to residential buildings [9]. Whereas, concerning the isolated slab, a previous work has shown that a typical thickness of the reinforced concrete slab laid on the isolation level is equal to 0,5m [1], with a consequent value of mass per unit area equal to 1,25 ton/m^2. According to these mass density values for both the building floor and the isolated mass, the mass ratio r can be considered as 80% of the number of floors of the building. The value of the single average vertical load of the device for each case has been computed simulating a real case study: considering a grid of isolators made up of 10x5 DCSS devices (50 isolators), with 6m span along both directions and assuming the thickness of the isolated slab equal to 0,5m the values listed in Table 2 have been obtained: it can be noted that such values are comparable to the design vertical load values of the chosen isolator technology (about 2500 kN).

N_F [#]	T_s [s]	r [#]	W [kN]
5	0,50	4,0	1500
5	0,75	4,0	1500
5	1,00	4,0	1500
7	0,50	5,6	2000
7	0,75	5,6	2000
7	1,00	5,6	2000

Table 2: Parameters of the considered structural layouts.

For all the structural layouts listed above, 500 values of the parameter b have been randomly extracted using a numerical simulator which has a uniform distribution, given a variation range within ±100% of the mean value of the parameter; thus the total number of performed analyses is equal to 3000.

5 ANALYSES RESULTS

In the followings results are shown for all the structural layouts, as a comparison between neglecting rather than accounting for the cycling effect: precisely, since a bidirectional seismic event has been considered, all the peak vectorial response quantities of the structural sys-

tem have been computed, that is displacements, absolute accelerations and interstorey shear forces. In all the next figures all the response curves of all the performed analyses are reported, together with the reference case curve, that is without accounting for the cycling effect, and with the mean plus and minus the standard deviation curves. Moreover, for each storey the ratio between the mean, maximum and minimum response parameter with respect to the reference case has been evaluated and shown in the graphs.

In Figure 10 and Figure 11 the results in terms of maximum vectorial displacement for all levels are reported, considering five and seven floors respectively.

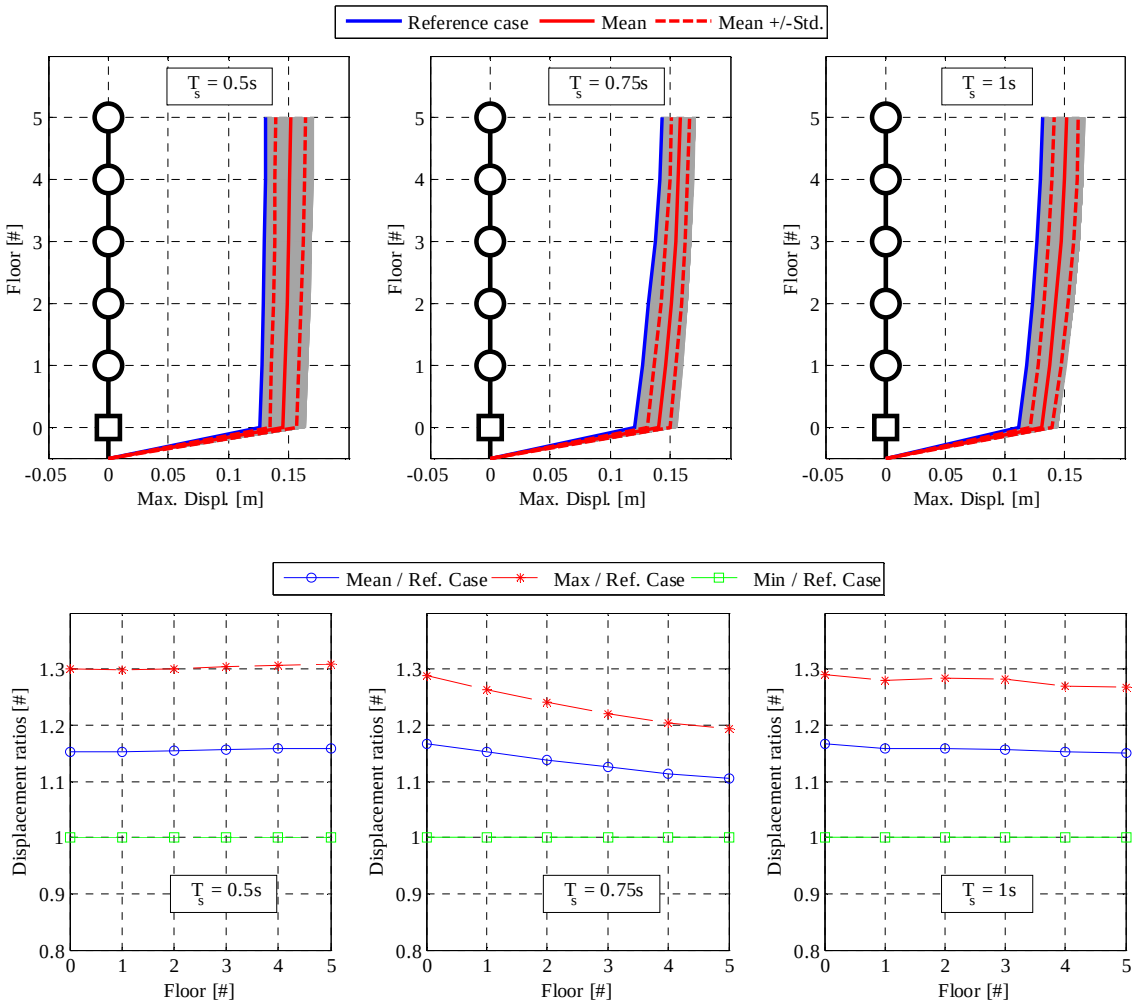


Figure 10: Displacement response: deformed shapes (up) and displacement ratios (down) for 5 storey building.

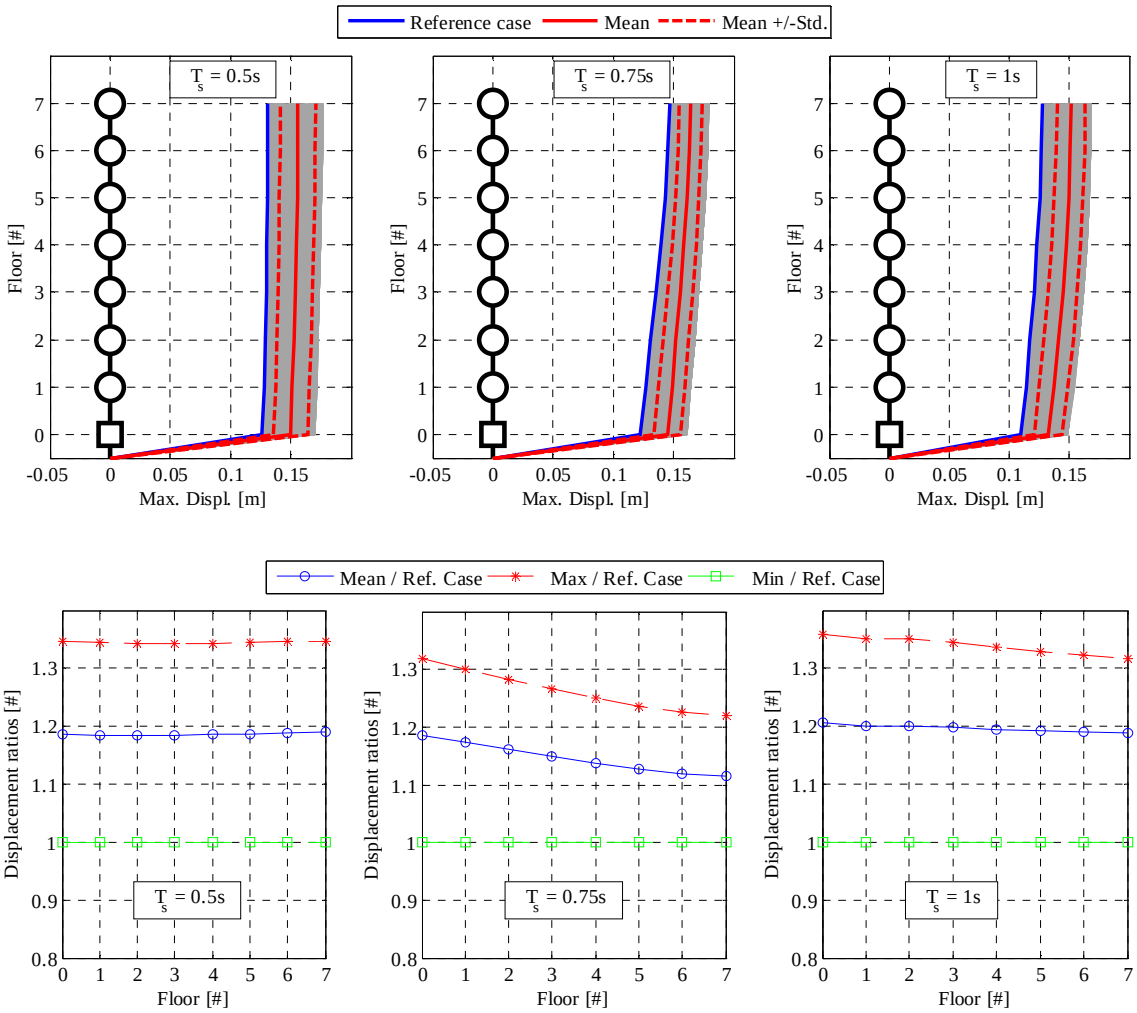


Figure 11: Displacement response: deformed shapes (up) and displacement ratios (down) for 7 storey building.

Results show that, for both the building typologies (5 and 7 stories) the presented model of the cycling effect of DCSS devices strongly influences the displacement response of an isolated system: it can be noted that the displacement demand at the isolation level increases up to 35% more than the reference case in the worst cases and the mean value is averagely 20% more; the graphs showing the displacement ratios underline that accounting for the cycling effect, the displacement demand is always higher with respect to the reference case for all the floors (the minimum ratio is equal to 1); for 0,75s period, considering both 5 and 7 storey buildings, the displacement ratios slightly decrease at the highest levels, whereas in the other cases they are rather constant.

Then, in Figure 12 and Figure 13 the results in terms of maximum vectorial absolute acceleration at all levels are reported for both the five and seven floors layouts.

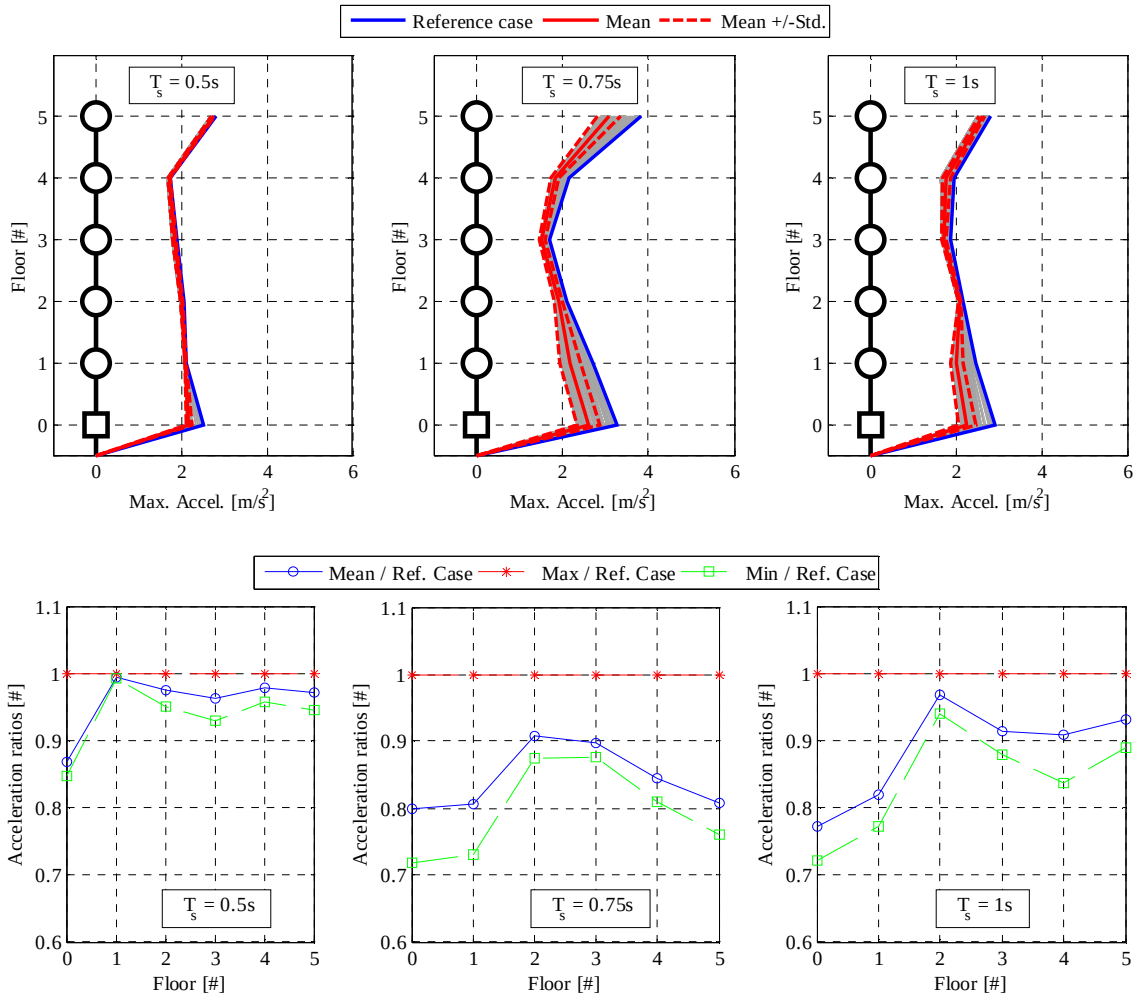
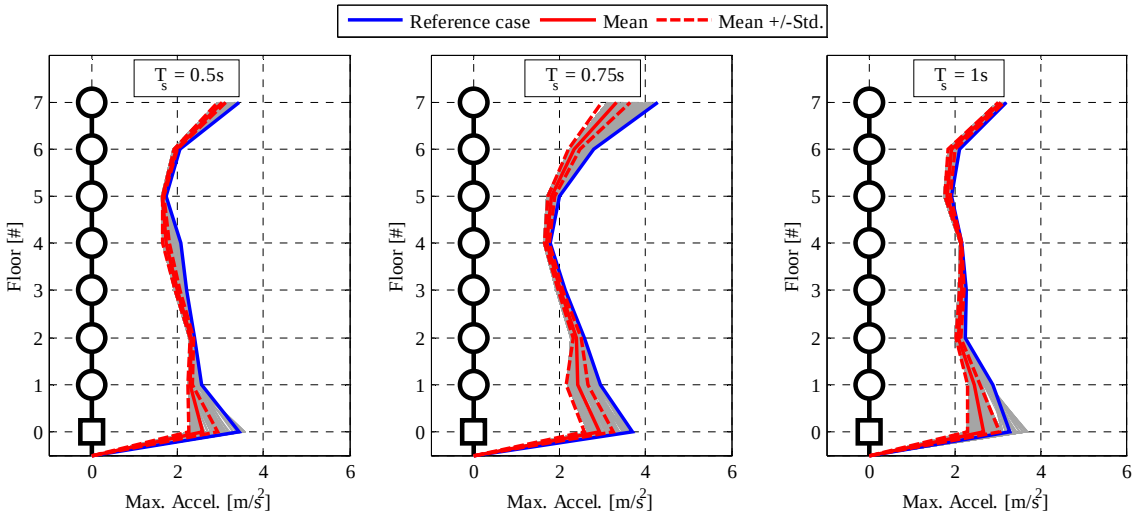


Figure 12: Acceleration response: acceleration profiles (up) and acceleration ratios (down) for 5 storey building.



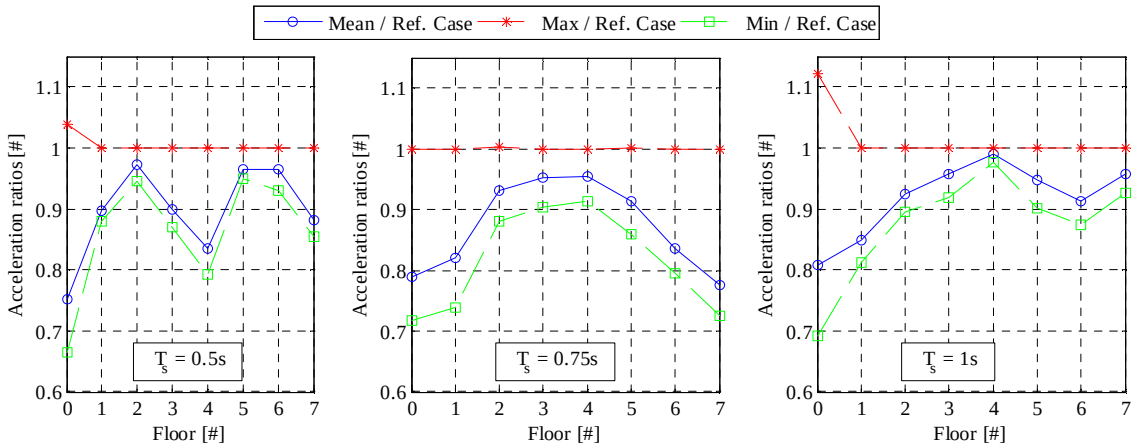


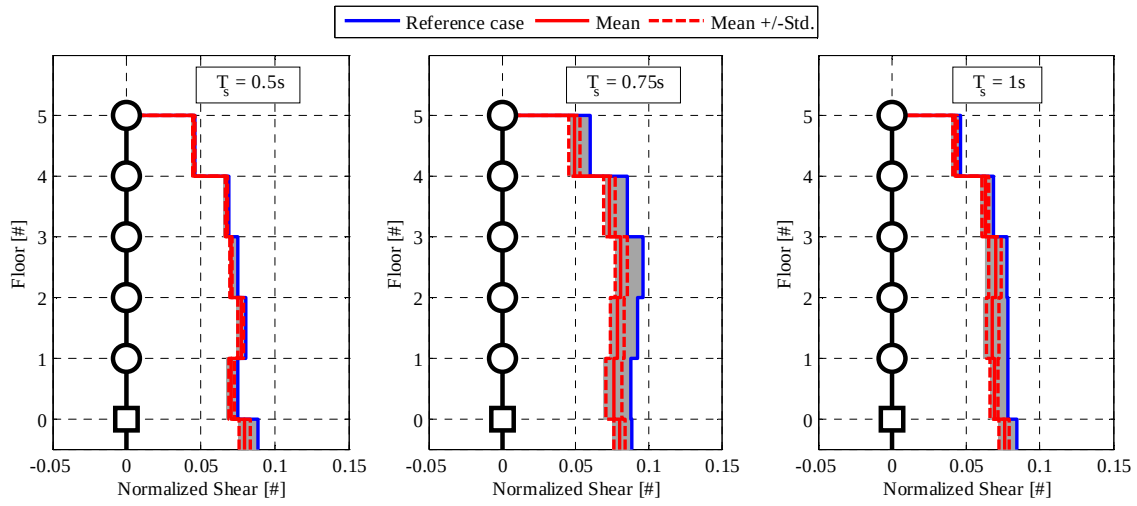
Figure 13: Acceleration response: acceleration profiles (up) and acceleration ratios (down) for 7 storey building.

For the 5 storey building the acceleration ratios of the maximum values are equal to 1 in all cases: this means that the cycling effect always reduces the absolute acceleration at all levels; nevertheless, for the 7 storey building the maximum value at the isolation level (level 0) is higher compared to the reference case, for structural periods equal to 0,5s and 1,0s. Generally, the acceleration response significantly decreases just above the isolation level and at the last floors of the structure, assuming in the middle more comparable values to the reference case.

Finally, in Figure 14 and Figure 15 the results in terms maximum vectorial interstorey shear, normalized with respect to the total weight of the isolated structure, at all levels are reported for both the five and seven floors layouts. To compute the normalized shears for the building $V_{B,i}$, at each storey the maximum vectorial drift $D_{B,i}$ has been computed, computing thus the shear according to eq.(15); for the i-th floor:

$$V_{B,i} = \frac{kD_{B,i}}{W_{tot}} = \frac{kD_{B,i}}{mgN_F\left(1+\frac{1}{r}\right)} = \frac{\omega_s^{*2} \cdot D_{B,i}}{gN_F\left(1+\frac{1}{r}\right)} \tag{15}$$

Whereas for the isolation level, the normalized shear is given by eq.(11), divided by the expression of the total weight.



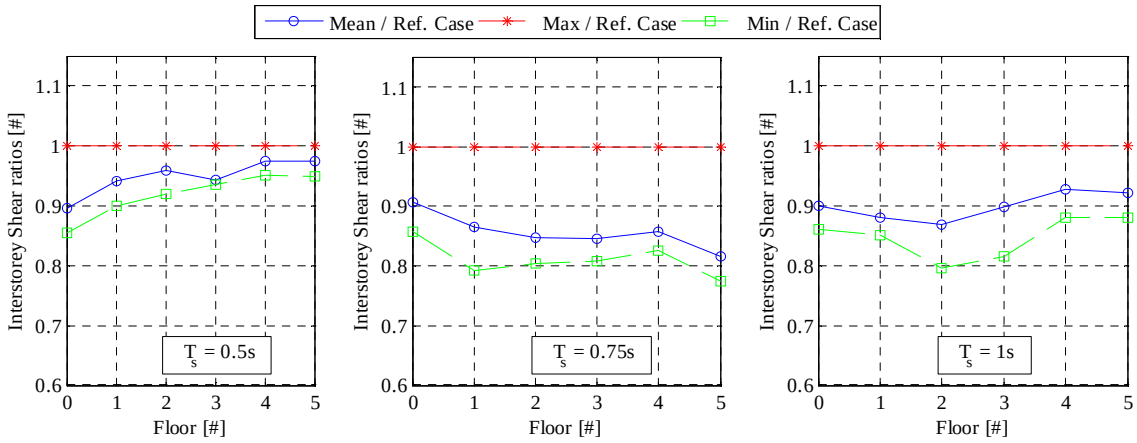


Figure 14: Shear response: Shear profiles (up) and shear ratios (down) for 5 storey building.

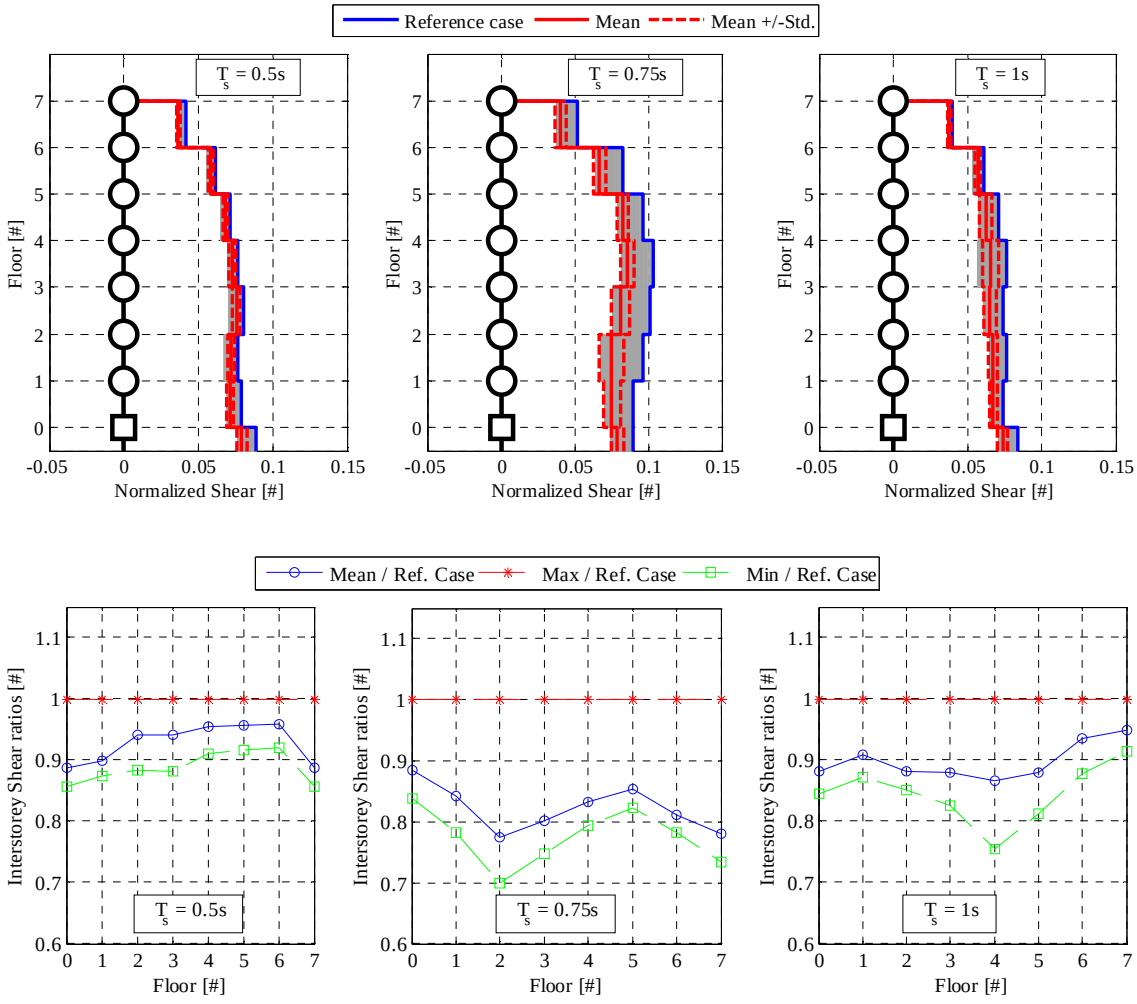


Figure 15: Shear response: Shear profiles (up) and shear ratios (down) for 7 storey building.

Also for the shear response, the reference case represents the upper bound of all the analyses performed accounting for the cycling effect. It can be noted that the mean and minimum values for all the stories are very close: this implies that also with a slight decreasing behavior

of the friction coefficient due to the cycling effect, the shear response for each level significantly decreases. The highest variation for the 5 storey building reaches -20% for both structural periods of 0,75s and 1,0s, and -30% for the structural period 0,75s.

6 CONCLUSIONS AND FUTURE DEVELOPMENTS

In the present endeavor a wide numerical campaign has been carried out in order to evaluate the variation of the peak response quantities of a structural system seismically isolated with DCSS devices due to the friction coefficient decay, caused by the cycling effect. Particularly, a new dynamic model for a MDOF system is presented, which does not depend on the mass of the structure. The considered structures consist of multy-storey buildings (5 and 7 stories) with different fundamental periods (0,5s – 0,75s – 1,0s), isolated by means of a reinforced concrete slab, laid on a grid of DCSS isolators. Since all the structural layout are supposed to correspond to large plan development buildings, it has been possible to model the isolation system using an equivalent DCSS device: this implies that all the isolators can be considered with the same average vertical load, directly equal to the total weight of the whole isolated structure divided by the number of installed devices. The constitutive law of the isolation system has been returned by the summation of the recentering and the frictional forces: the former is modeled with a linear spring with a stiffness coefficient given by the ratio between the applied vertical load and the equivalent radius of curvature, whereas the latter is returned by a frictional model which accounts for bi-axial interaction of the directions of motion. Concerning the friction coefficient, it has been assumed as a constant function with respect to both sliding velocity and vertical load, in order to evaluate the influences of the cycling effect only: this has been modeled by means of randomly extracted decay curves, which expresses a decay multiplication factor as a function of the dissipated energy of a single isolator. In order to compute the dissipated energy for a single device, in terms of the integral of the force-displacement law, it has been necessary to define the single average vertical load, simulating a real case: thus, two different values have been considered, for 5 and 7 storey buildings respectively (1500kN and 2000kN).

Results have been computed in terms of maximum vectorial displacements, absolute accelerations and interstorey shears for all levels; moreover, a comparison to the reference case (no cycling effect) has been provided. Concerning the displacement response, the reference case is the lower bound of all the analyses in which the cycling effect is considered. At each storey, the friction coefficient decay leads to higher displacement demands, up to 35% more than the reference case in the worst condition. Such variability looks more significant at the isolation level and at the lower stories of the building, slightly decreasing for the higher floors. The opposite behavior has been found for both absolute acceleration and interstorey shears: in fact for such response parameters the reference case becomes the upper bound. Thus, the friction coefficient decay reduces the absolute acceleration values at all levels (particularly at the highest stories and just above the isolation system) and the shear profile (averagely the same variation along the building height).

This work has underlined that the cycling effect, in terms of friction coefficient decay, leads to non-negligible variations of the main response parameters. Thus a future development will be the definition and the calibration of a sophisticated model of the cycling effect, as a function of dissipated energy, sliding velocity and vertical load, thanks to the results of several unidirectional and bidirectional tests of full scale DCSS devices.

AKNOLEDGEMENTS

Part of the current work has been carried out under the financial support Italian Civil Protection, within the framework of the Executive Project 2014–2016 (Project S2.0 – Seismic isolation and supplemental damping systems: evaluation of the seismic response of devices and structures).

REFERENCES

[1] M. Furinghetti, C. Casarotti, A. Pavese, Effects of bi-directional motion on a structural system isolated with DCSS devices with laying defects. *15th WCEE, World Conference on Earthquake Engineering*, Lisbon, Portugal, September 24-28, 2012.

[2] C. Casarotti, M. Furinghetti, A. Pavese, Evaluation of response of an isolated system based on Double Curved Surface Slider. *Computational method in Earthquake Engineering*, **30**, pp 397-416, 2013.

[3] M. Furinghetti, C. Casarotti, A. Pavese, Bi-directional experimental response of full scale dcss devices. *2ECEES, Second European Conference on Earthquake Engineering and Seismology*, Istanbul, Turkey, August 25-29, 2014.

[4] G. Lomiento, N. Bonessio, G. Benzoni, Concave sliding isolator's performance under multi-directional excitation. *Ingegneria Sismica*, **30:3**,17-32, 2013.

[5] G. Lomiento, N. Bonessio, G. Benzoni, Friction Model for Sliding Bearings under Seismic Excitation. *Journal of Earthquake Engineering*, **17**, 1162-1191, 2013.

[6] G. Mosqueda, A.S. Whittaker, G.L. Fenves, Characterization and modeling of friction pendulum bearings subjected to multiple components of excitation. *Journal of Structural Engineering*, **130**, 433-442, 2004.

[7] CEN, Comité Européen de Normalisation TC 340, *European Code UNI EN 15129:2009 Anti-seismic devices*. Brussels, 2009.

[8] F. Khoshnoudian, V.R. Hagdoust, Response of pure-friction sliding structures to three components of earthquake excitation considering variations in the coefficient of friction. *Scientia Iranica*, **16**, 429-442, 2009.

[9] M. Dolce, D. Cardone, F. C. Ponzo, A. Di Cesare, *Progetto di edifici con isolamento sismico, Seconda Edizione*. IUSS Press, 2010.

[10] D. Fenz, M. C. Constantinou, Behaviour of the double concave friction pendulum bearing. *Earthquake Engineering And Structural Dynamics*, **35**,1403–1424, 2006.

[11] A. K. Chopra, *Dynamics of Structures Theory and Applications to Earthquake Engineering*. Prentice Hall, Upper Saddle River, NJ, 1995.

[12] S. Peloso, A. Pavese, C. Casarotti, Eucentre trees lab: Laboratory for training and research in earthquake engineering and seismology. *Geotechnical, Geological and Earthquake Engineering*, **20**, 65-81, 2012.

[13] G.M. Calvi, A. Pavese, Conceptual design of isolation systems for bridge structures. *Journal of Earthquake Engineering*, **1**, 193-218, 1997.

COMPDYN 2015
5th ECCOMAS Thematic Conference on
Computational Methods in Structural Dynamics and Earthquake Engineering
M. Papadrakakis, V. Papadopoulos, V. Plevris (eds.)
Crete Island, Greece, 25–27 May 2015

DYNAMIC SENSITIVITY OF MULTI-BLOCK STACKS SUBJECTED TO PULSE BASE EXCITATION – EXPERIMENTAL EVIDENCE AND NON SMOOTH CONTACT DYNAMICS SIMULATIONS

Nina Čeh[1], Antonio Pellegrino[2], Jean-Francois Camenen[1], Nik Petrinić[2], Gordan Jelenić[1], Tomasz Koziara[3], Nenad Bićanić[1]

[1] Faculty of Civil Engineering, University of Rijeka
Radmile Matejčić 3, 51000 Rijeka, Croatia
e-mail: {nina.ceh,jfcamenen,gordan.jelenic,nenad.bicanic}@uniri.hr

[2] Impact Engineering Laboratory, Department of Engineering Science, University of Oxford
Begbroke Hill, Woodstock Road, Begbroke, Oxfordshire OX5 1PF, UK
{antonio.pellegrino,nik.petrinic}@eng.ox.ac.uk

[3] School of Computing and Engineering Sciences, University of Durham
Lower Mountjoy, South Road, Durham, DH1 3LE, UK
{tomasz.koziara}@durham.ac.uk

Keywords: Block Dynamics, Pulse Base Excitation, Simulations, Experimental Validation, Block Overturning, Non Smooth Contact Dynamics.

Abstract. *Experimental and computational dynamic sensitivity study of Multi-Block Stacks subjected to Pulse Base Excitation is considered. Advanced non contact optical measuring technique based on the GOM Aramis and Pontos systems, as well as the corresponding processing software (displacement history of control sensor points, with a high resolution high speed cameras) have been applied to replace conventional displacement measuring systems and accelerometers. The Non Smooth Contact Dynamics (NSCD) time integration simulation framework SOLFEC http://code.google.com/p/solfec/ is adopted here for comparative NSCD analyses, including a sensitivity study on interface characteristics, as a validation process. Series of test experiments were conducted and recorded on a bespoke platform with and without lateral constraints in the Oxford Impact Engineering Laboratory and Rijeka University Structural Dynamics Laboratory for an extensive series of controlled pulse base excitation tests of multi block stacks configurations. Impact is generated by a pin-ball mechanism with spring and a wooden projectile, attached to an optical bench. For the NSCD simulations the base was subjected to a constant acceleration over a finite time, thereby facilitating the characterisation of multi block stacks tumbling modes of failures (global or partial), as a function of stop gap distance. Creation of well documented benchmarks for the validation of simulation paradigms for discontinuous media will be extremely valuable for researchers and code developers (non smooth contact dynamics, discrete elements, discontinuous deformation analysis), as well as for safety case engineers and industry regulators.*

1 INTRODUCTION

In order to understand as well as to predict the highly nonlinear mechanical response of natural and/or engineered discontinuous, blocky systems, comprising changing and evolving contact conditions and friction between their components or constituent parts, it is important to develop reliable analytical capabilities for simulations of such systems. In spite of extraordinary advances in nonlinear computational mechanics and simulations paradigms, the validation and verification of their predictive powers remains one of the main challenges in the field for their incorporation into industry relevant procedures. It can be safely argued that a major research attention in nonlinear structural dynamics today has noticeably moved from a reliable response of a specific structural system to a specific excitation towards a generic predictive capability for a class of structural configurations.

There are a number of structures that are inherently discontinuous, either as a matter of convenience (e.g. ease of construction in structural masonry or dry stone walling) or as a deliberate strategy to avoid extensive thermal stresses (e.g. graphite cores in Advanced Gas Cooled Reactors, AGR, in nuclear power plants). Often these structures are deliberately discontinuous, organised as stacked and/or interlocked assemblies with a regular pattern and technologically intended gaps and clearances, allowing for limited sliding and rocking in between contacts during their dynamic response. Frequently, these structural assemblies are by themselves a vital safety critical component of an entire structural system (or form a crucial part of) and there is a growing need to be capable of predicting their behaviour under both static and dynamic (impact, seismic) conditions. This is particularly true with ageing and degradation of such systems (e.g. AGR cores), where the safety considerations with respect to their life extension may be paramount for the integrity assessment process of the entire plant operation. Moreover, some of the safety critical 'non structural' components (e.g. large control cabinets) need to be treated as un-anchored blocky structures in their seismic assessment.

Structural reliability and integrity assessment procedures are largely formulated for continuum structures and their extension to consider discontinuous structural assemblies or configurations is not adequate. Computational simulation frameworks for the analysis of blocky systems therefore often rely on some form of a homogenisation technique (simplified or complex), leading to a whole series of equivalent nonlinear continuum models [2-5]. Such idealisations then allow for the structural integrity and reliability assessment procedures to follow well established routes, developed for continuum structures and supported by a series of well recognised benchmarks, both computational and experimental. In particular, the homogenisation process allows for a reasonably straightforward dynamic characterisation (e.g. spectral signature, eigen frequencies and mode shapes for response spectrum techniques in earthquake considerations are easily evaluated) of what are in reality discontinuous, 'blocky' structures, for which no eigen problem can be formulated.

This contribution comprises preliminary results of both experimental and computational dynamic sensitivity study of Multi-Block Stacks subjected to Pulse Base Excitation. Advanced non contact optical measuring technique based on the GOM Aramis system [1] and the corresponding processing software (displacement history of control sensor points, with high resolution high speed cameras) have been applied to replace conventional displacement measuring systems and accelerometers. The Non Smooth Contact Dynamics (NSCD) [2] time integration methodology SOLFEC http://code.google.com/p/solfec/ [3] is adopted here, which effectively ignores the high frequency content of the contact interactions. Instead of a specified interpenetration-force relation, this paradigm employs the complementarity relation between the relative velocity and the contact force at an existing contact point: either the velocity is such that the bodies separate and the contact force is zero, or the force is such that

interpenetration is prevented and in consequence the relative velocity is zero. This velocity-force complementarity relation is added as an algebraic constraint to the implicitly integrated momentum balance and the ensuing nonlinear contact problem is therefore solved implicitly at every time step in order to find the contact forces and the velocities of contacting blocks.

2 CONTROLLED PULSE BASE EXCITATION EXPERIMENTS

A comprehensive series of experiments was conducted at the Oxford Impact Engineering Laboratory on a bespoke platform for a controlled double pulse base excitation, inspired by the classic ingenious simple test device at Roorkee University, Fig 1. [4].

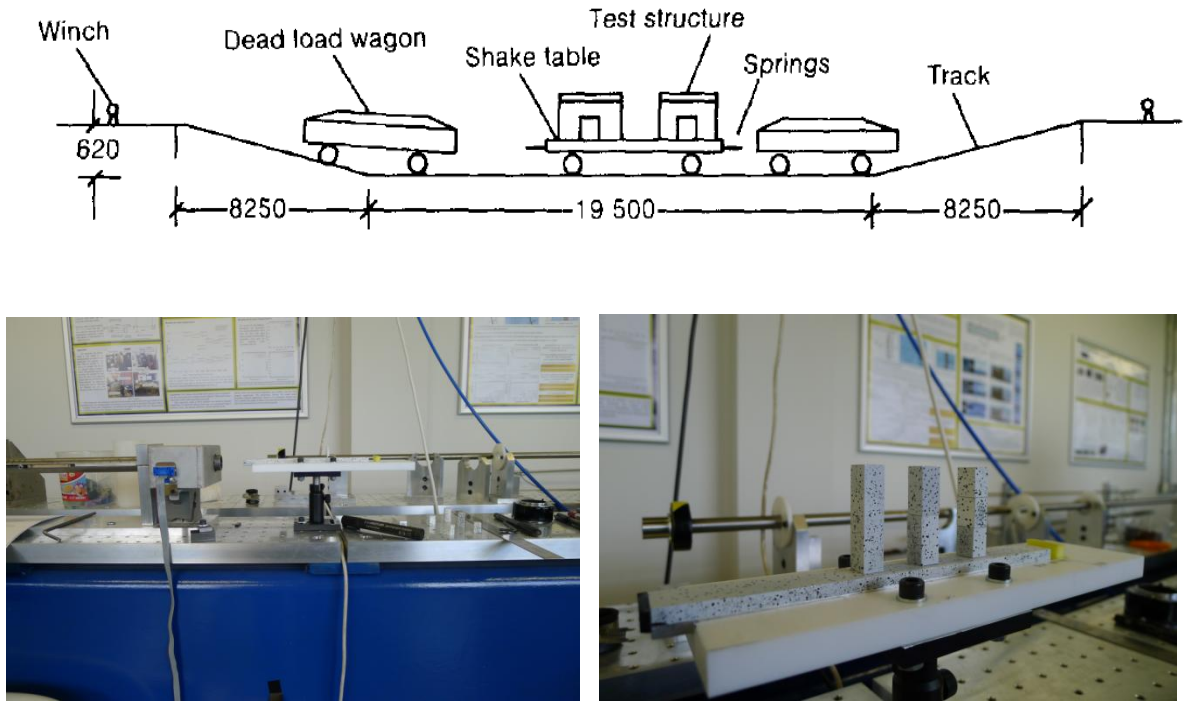


Figure 1: Original Roorke University Platform and its conceptual small scale counterpart ROORI-1 at Oxford

2.1 Block stack experiments with no lateral constraints

The experimental setup (named ROORI-1 as an homage to Roorke and Rijeka Universities) comprised an impact device, Fig 2 (a pin-ball mechanism with spring which was used to launch the wooden projectile) attached to an optical bench, with a teflon base and stopper aligned to the impact device and attached to the optical bench as well. A foam cushion was glued to the stopper, whereas a rubber cushion was glued to the front face of the aluminum base. Aluminum base was positioned at a predefined distance from the stopper (BD). The base excitation scenario implies an initial impulse (different intensities controlled by different pin-ball spring positions, denoted IM) followed by a reverse impulse (provided by the base hitting a stopper), after a given time delay (controlled by the block stopper distance BD).The shapes of the initial and reverse impulse are controlled by rubber cushions.

On top of aluminum base a single block or a stack of two or three blocks was positioned (and aligned to the impact device and teflon base). Every experiment was recorded with the Phantom video camera with a resolution of 800x600 pixels and the frame rate of 2000 fps.

The camera was triggered by a laser-beam curtain. Figure 1 illustrates the experimental setup of the bespoke platform.

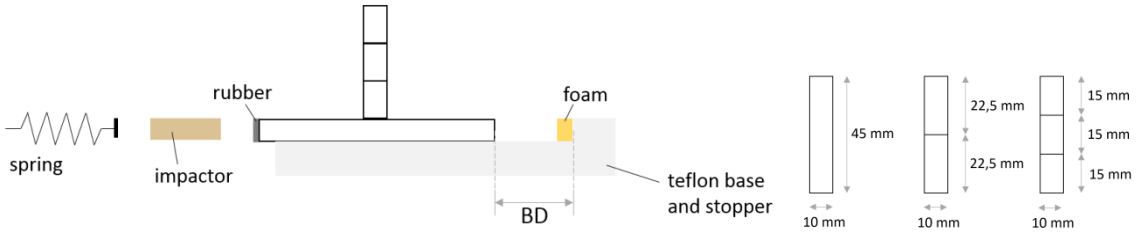


Figure 2: Scheme of series of experiments of dynamic sensitivity of multiblock structures

Initially, all the contact surfaces between each of the blocks and the bottom block and the base were kept smooth. Subsequently, the contact surfaces were made non smooth by the sand paper using a standard procedure of scraping aluminium surface along the sandpaper surface. Each set of experiments was repeated three times. A comparison between three repetitions shows repeatability of initial conditions as well as the repeatability of dynamic behaviour of the blocks. All the experiments were triggered manually and a good repeatability was achieved, especially for non smooth inter block contact surfaces, however for some scenarios with smooth contact surfaces, the responses appeared quite sensitive to small changes in initial conditions (Fig 3).

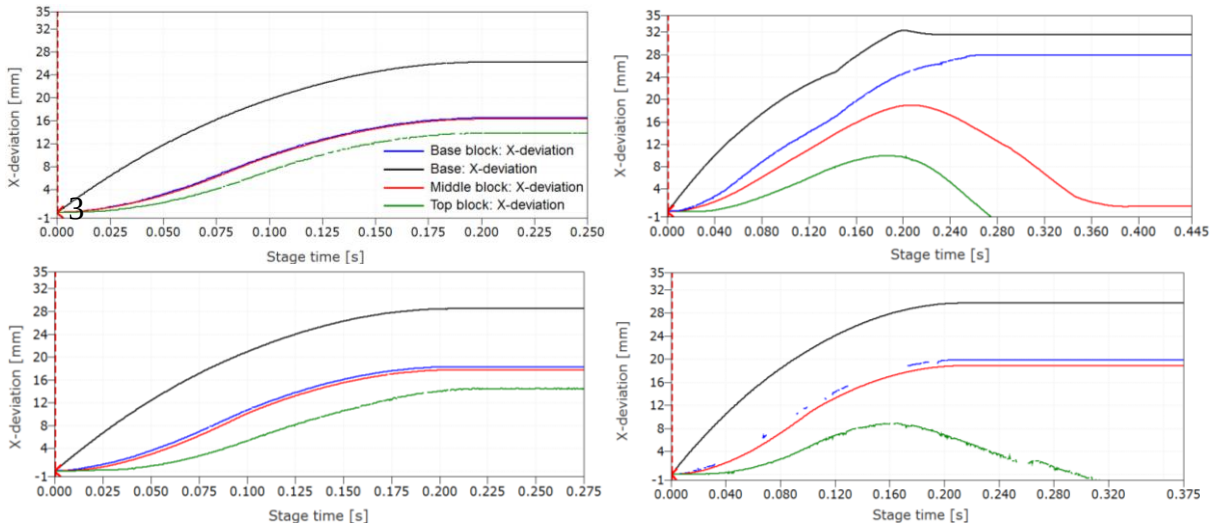


Figure 3: Displacement of base, bottom, middle and top block from four repetitions of experiment B3_IM10_BD4 (3 blocks, spring trigger position 10, distance to stopper 4 cm) – smooth contact surfaces. Note that the base history is repeated well from one test to another, whereas the horizontal displacements of the upper blocks can be quite different

Every video was converted into a series of images (in .jpg format). Each series of images was post processed using Aramis v6.3.1-0 software for optical deformation and displacement analysis. Since the resolution of the images was 800x600 pixels, each pixel represents approximately 0.18 mm. Choice for the facet size needs to be optimised, as it depends on speckle pattern, pixel size and scale in which a behaviour is observed. Velocities obtained us-

ing the facet size 10x10 pixels show largest scatter of results, while velocity obtained using the facet size 30x30 pixels converge to a distinct smooth trend (Fig 4).

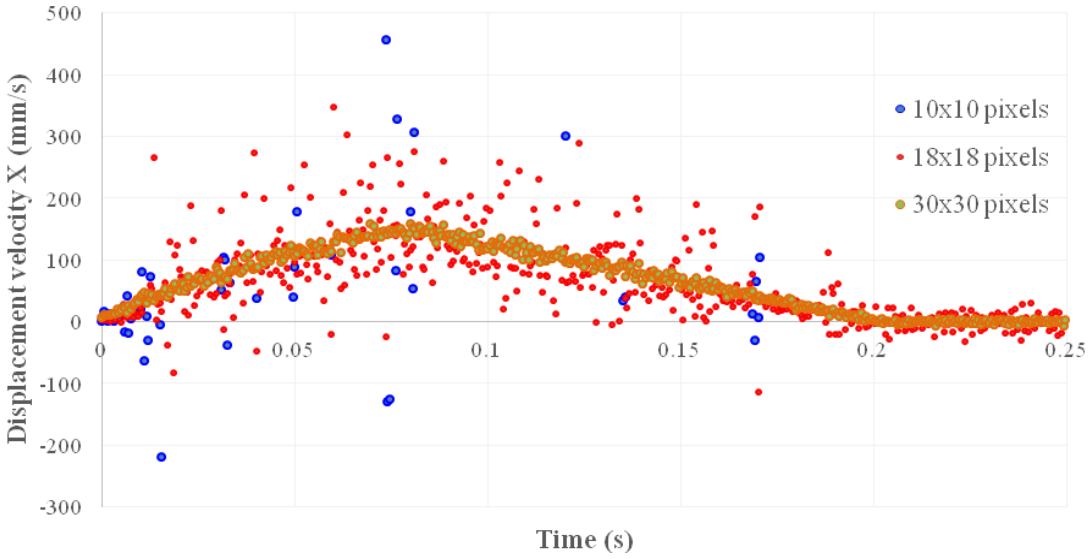


Figure 4: Velocity of the bottom block for a three blocks stack using different Aramis facet resolutions

The overturning conditions for a slender block subject to a single shock of constant base acceleration of a finite duration can be analytically established [7]. However, when the block of the same overall geometry is considered as a stack composed of three blocks, it is easy to conclude that for a single impulse an overtopping as the entire stack should always prevail over any partial overtopping (overtopping of a top block, or overtopping of two upper blocks). The existence of a second, reverse impulse and the time delay between the two impulses may affect the mode of overturning, depending on the timing of the second impulse. Within this study, a preliminary attempt has been made to provide a simple dynamic characterisation of discontinuous blocky stacks, through qualitative synthesis of experimental results, where only the eventual outcome (or mode of overturning) of each experiment carried out is recorded. The final configuration of the stack of three blocks (Fig 5) is used to classify each experimental result into one of four possible overturning modes

- Mode A – a stack of three blocks remains stable,
- Mode B – top block from the stack of three blocks overturns as a result of either rocking, sliding or combined motion,
- Mode C – top and middle blocks from stack of three blocks overturn as a result of either rocking, sliding or combined motion,
- Mode D – entire stack of three blocks collapses as a result of either rocking, sliding or combined motion.

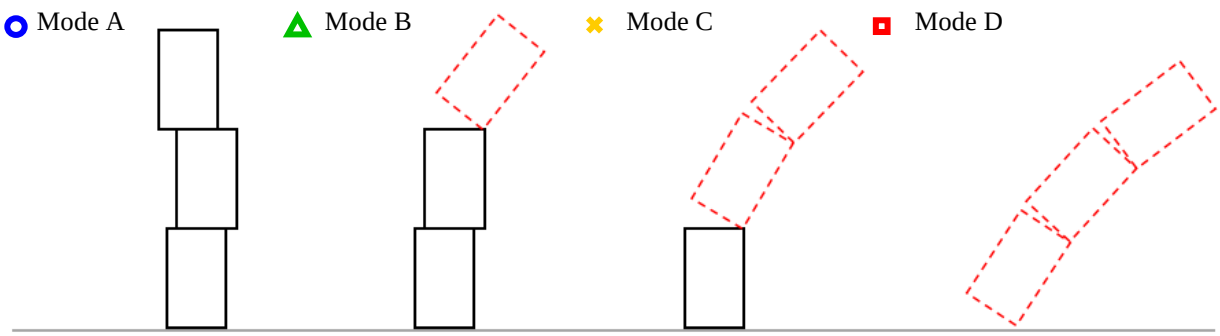
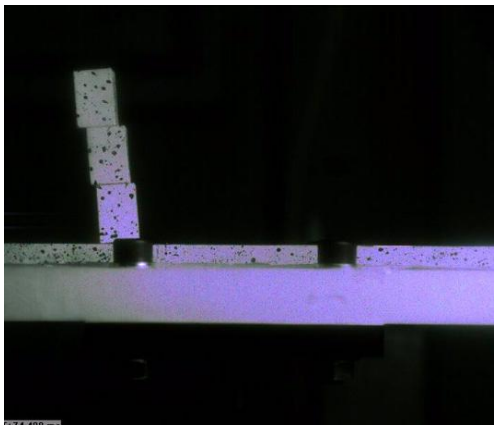
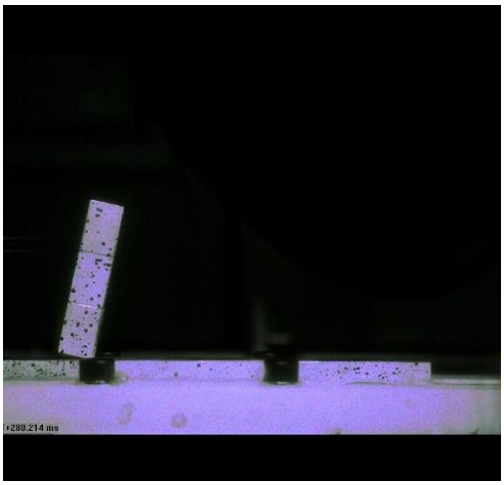


Figure 5: Possible overtopping modes of the stack of three blocks

Deformation of the spring in pin-ball mechanism (IM) induces kinetic energy put into system via the initial impact between the projectile and the aluminium base. The subsequent impact of the aluminium base with the stopper (via foam cushion) completes the pulse by a counter shock. The counter shock depends on the distance between aluminium base and the stopper (BD), as well as the amplitude of the initial impact. Due to the friction between the aluminium base plate and the teflon subsurface, there are experimental scenarios where the base comes to a rest before ever reaching the stopper. Typical block centroids horizontal displacement time histories as processed from video images are illustrated below (Fig 6) for pulse experiments for a stack of three blocks with smooth contacts surfaces (predominantly sliding mode) and with non smooth surfaces (predominantly rocking mode).



smooth



nonsmooth

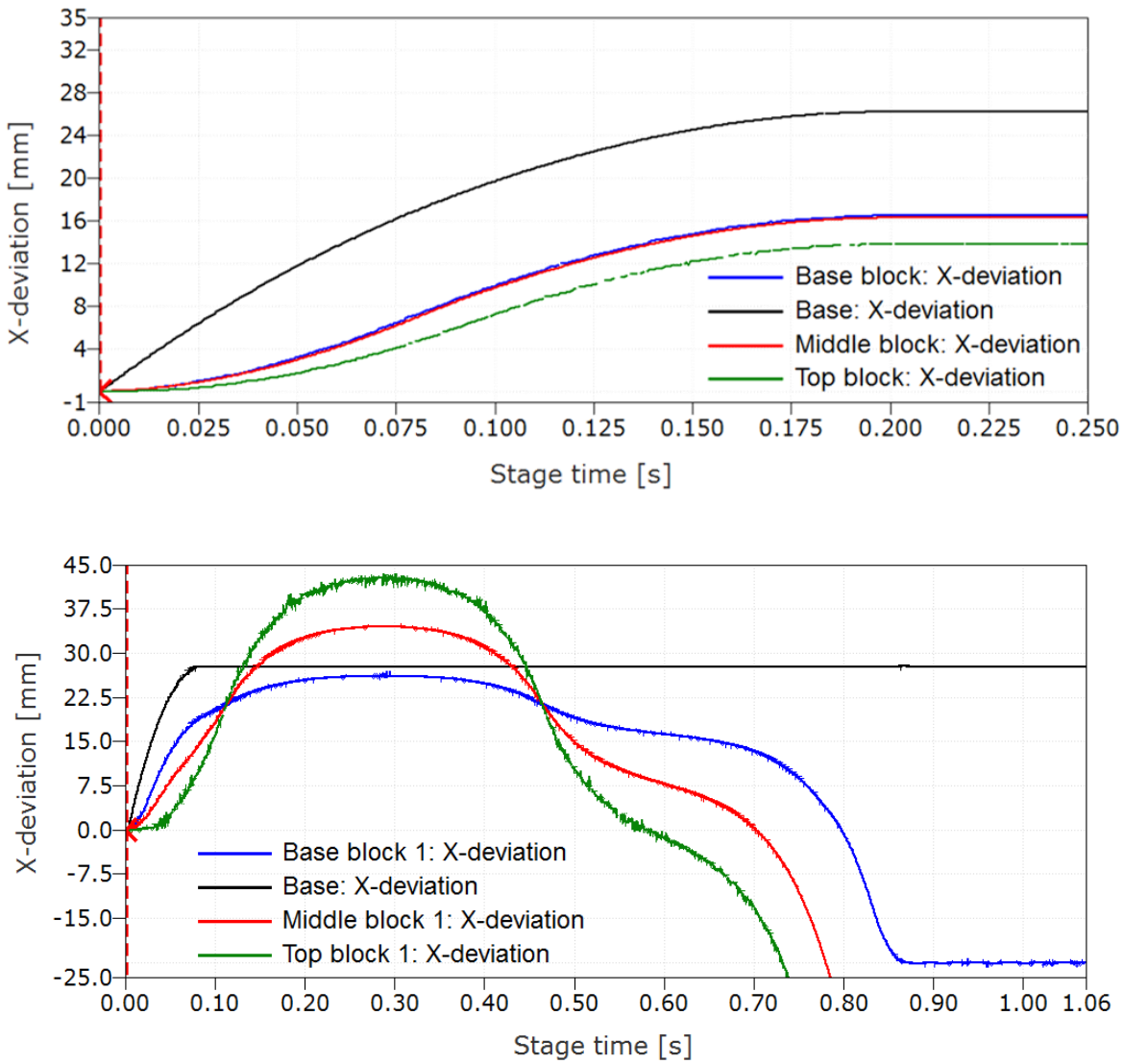
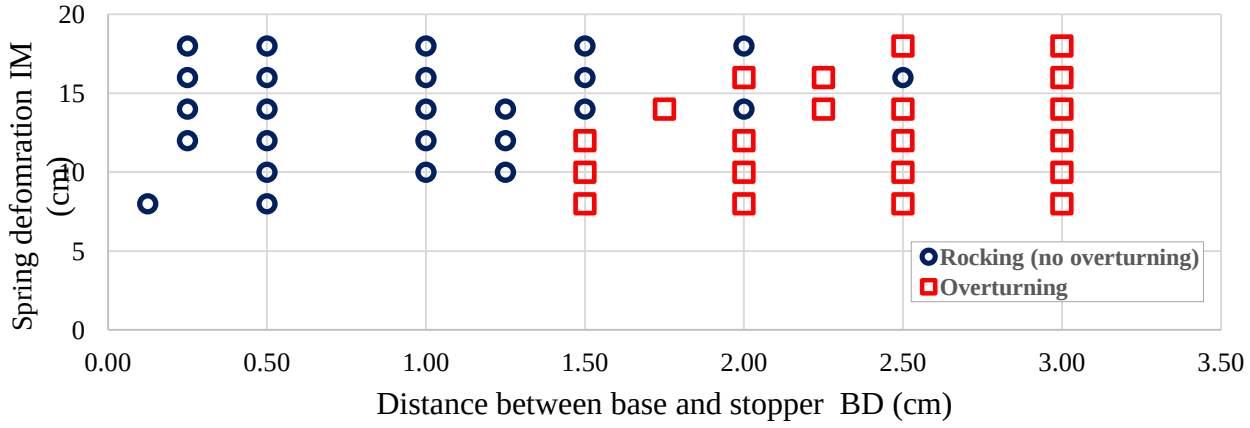
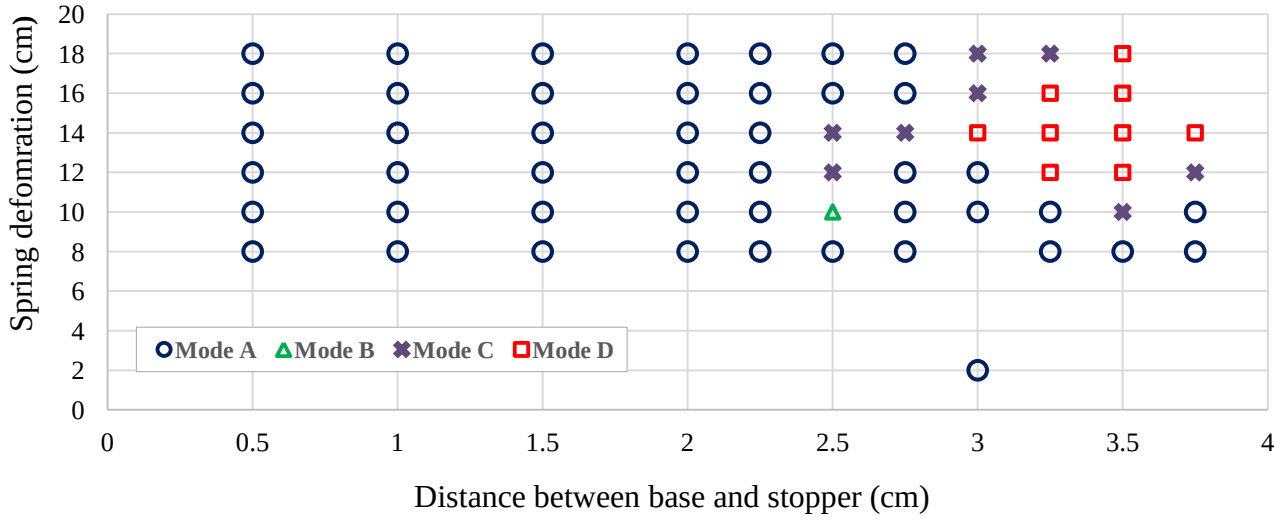


Figure 6: Typical horizontal displacement histories for the base and blocks centroids, for the case of smooth (above) and non smooth (below) contact surfaces, for the experiment with a single impulse, i.e. with no stopper. Note the rocking response for the non smooth case, whilst the smooth case induces block sliding only.

It is reasonable to expect that a mode of overturning is influenced by the amplitude and the duration of the dynamic pulse. Sensitivity of the failure mode following a counter shock for a specific experiment is here noted within the 2D parameter space (Fig 7), defined by the distance between aluminium base and the stopper and the trigger point for the pin ball spring, for the two cases of a single slender block and a stack of three blocks with the same overall dimension, with all non smooth contact surfaces.



(a) Single block 10/10/45 mm



(b) Stack of 3 blocks 10/10/15 mm

Figure 7. Overturning modes for a single block (a) and a stack of same overall dimensions, comprising three blocks (b) with non smooth (below) contacts related to the pin ball spring trigger position (IM) and the distance between the aluminium base and the stopper (BD). Mode A Rocking, Mode B Top block overturning, Mode C Top 2 blocks overturning, Mode D entire stack overturning

2.2 Block stack experiments with lateral constraints

Per analogiam to the series of experiments without lateral restraints, another series of experiments was conducted with a variation of side wall constraints spacing, distance from the aluminium base to the stopper and the level of spring trigger (Fig 8). Every experiment was again recorded with the Phantom video camera with resolution of 800x600 pixels and frame rate of 2000 fps. The camera was again triggered by a laser-beam curtain.

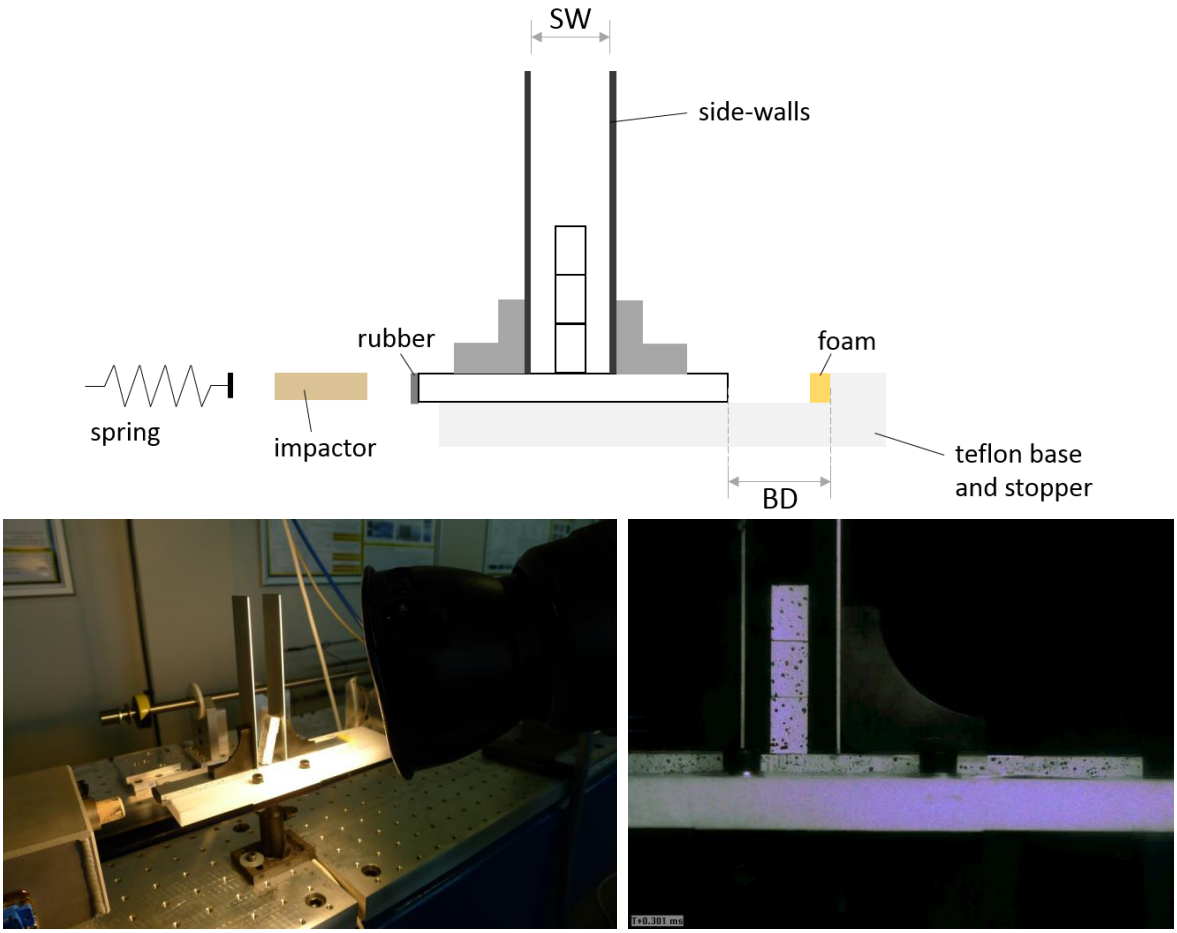


Figure 8: Scheme of series of experiments of dynamic sensitivity of multiblock structures including lateral side-walls constraints

Typical high speed video images and time histories of the block centroids horizontal displacements processed with ARAMIS software are illustrated below, Fig 9.

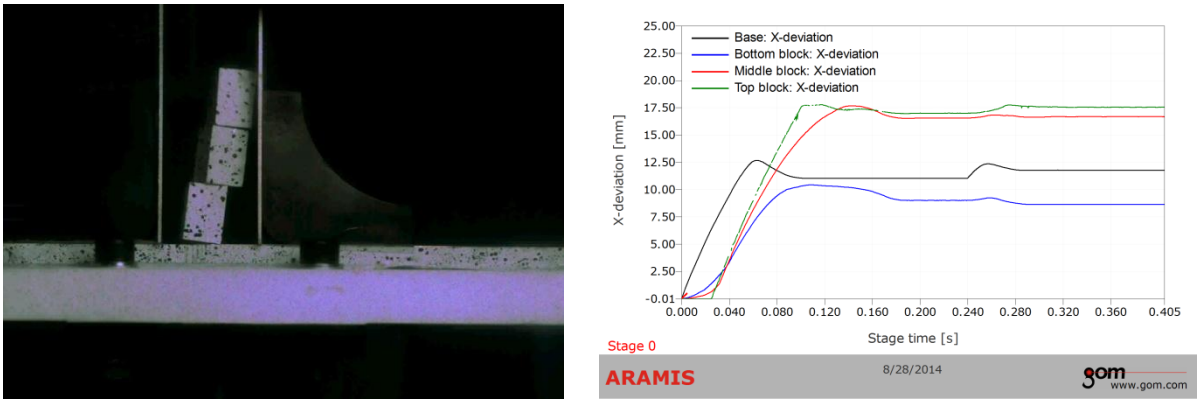


Figure 9: Time histories of the block centroids horizontal displacements, indicating intermittent contacts with lateral constraints

Fuller results are available on the project website http://mbsdynamics-ukf.gradri.uniri.hr/.

3 NSCD SIMULATIONS

Comparative Non Smooth Contact Dynamics studies were conducted with SOLFEC http://code.google.com/p/solfec/ [3]. For the simulations (Fig 10), the base was subjected to a constant acceleration (linear rise of velocity) over a fixed finite time (0.005 sec), giving rise to a series of different peak base velocities. All blocks were assumed to be rigid. Coefficient of restitution for both normal and tangential direction were set to zero. Coefficient of friction (base/Teflon base) is adopted as 0.26. In the experiment, the surface of the blocks is either smooth or non smooth after sandblasting. The coefficient of friction between blocks is taken as 1.3 when the blocks are smooth, whereas for the non smooth case, the simulations were made with the coefficient of friction in the range of 1.3 to 2.7. Simulation consequences of a series of different block and base grid subdivisions were explored (for the purpose of contact detection, as all the blocks are assumed rigid) on Fig 12 .

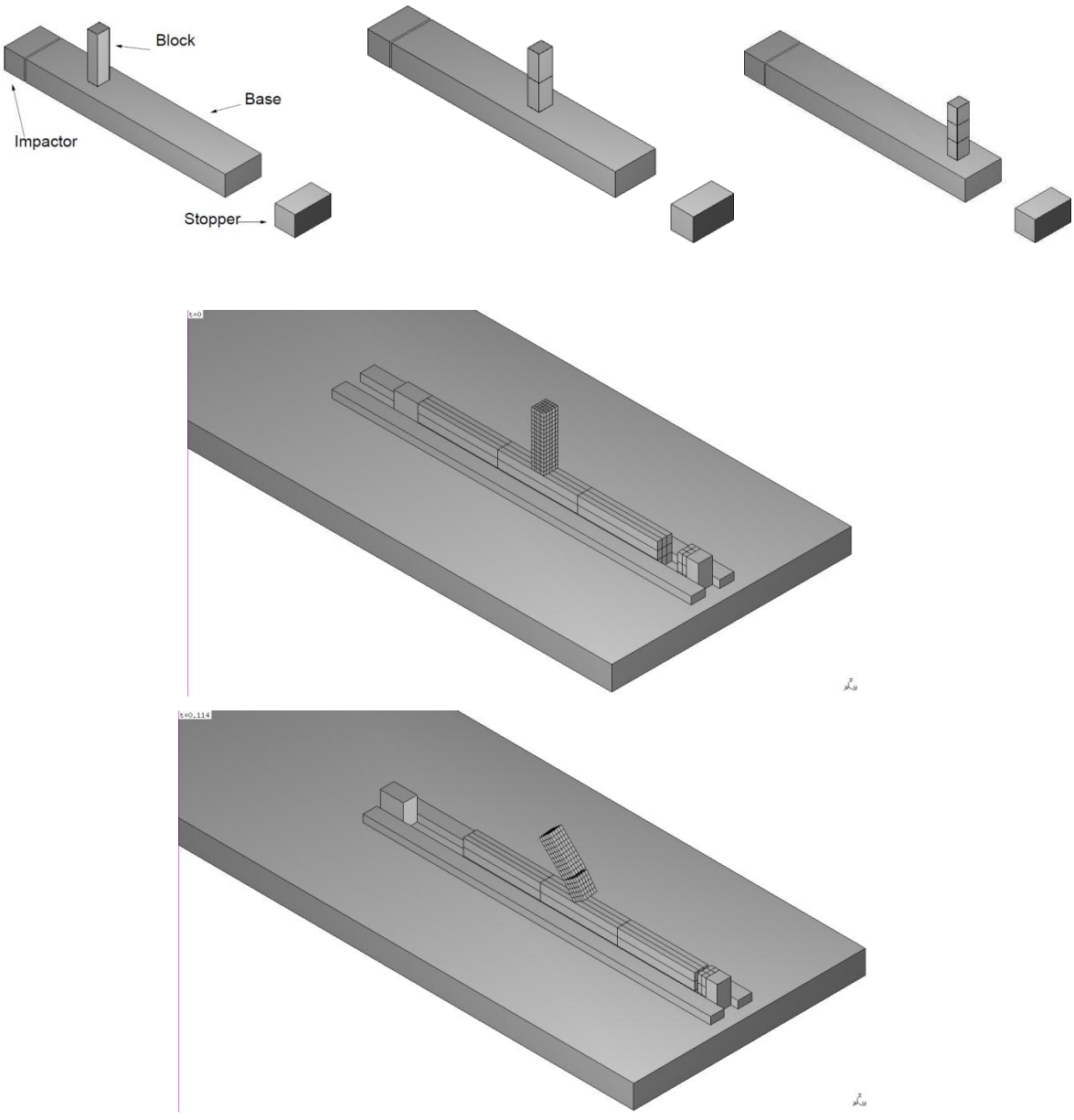


Figure 10: SOLFEC NSCD simulations of the ROORI-1 experimental set up

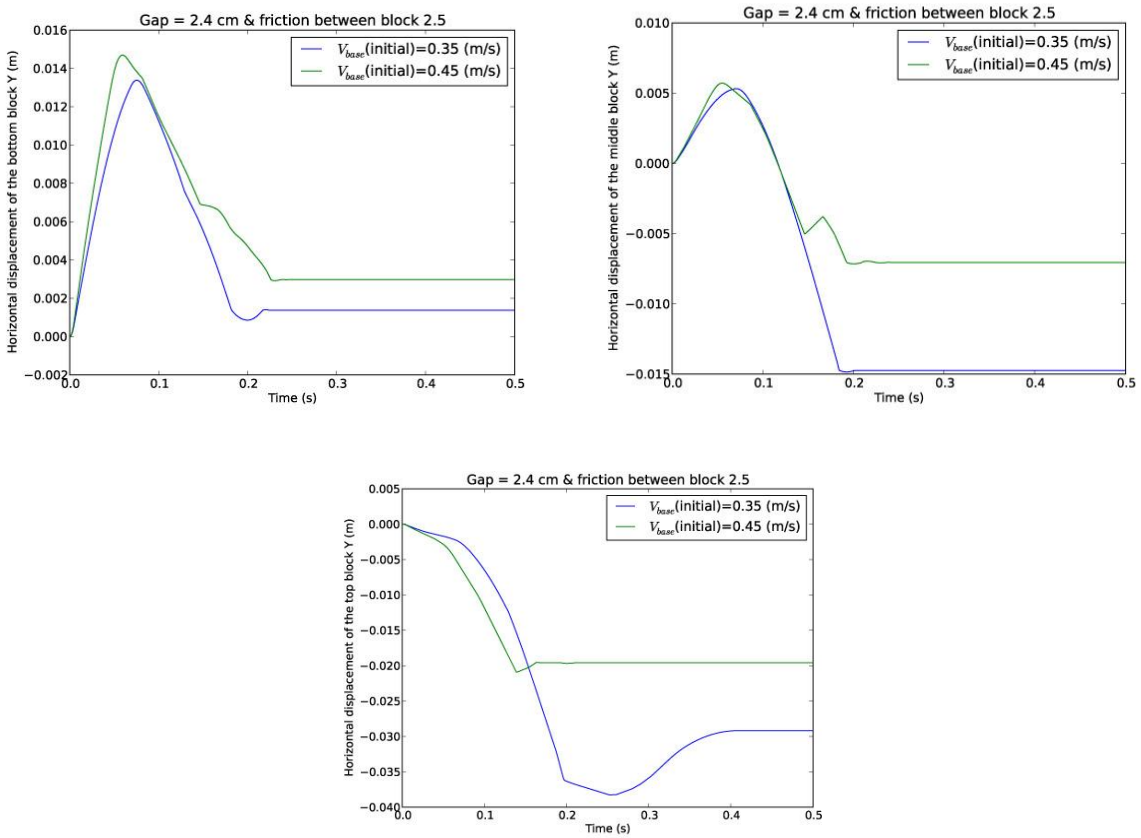


Figure 11: Horizontal displacement time histories for the block centroids (top, middle and bottom) for the two pulse excitation scenarios with peak base velocities (0.35 m/sec and 0.45 m/sec)

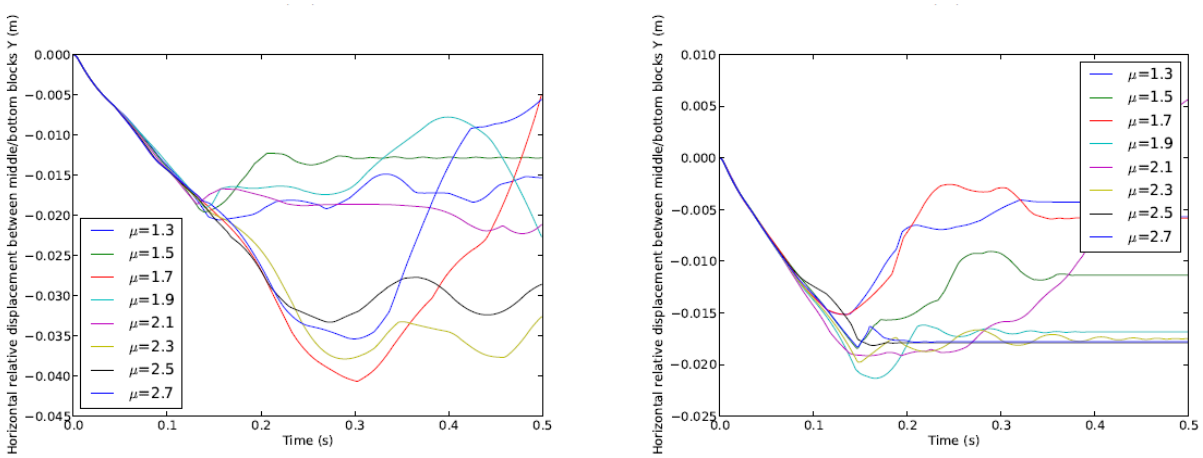


Figure 12: Time evolution of the horizontal relative horizontal displacement between the middle and bottom blocks, with the grid on the left (1, 1, 1) and a finer grid on the right (3, 3, 3).

Based on an extensive series of analyses, a qualitative characterisation of the multi block stack tumbling modes of failures (global or partial) are illustrated (Fig 13), due to various conditions of pulse excitation (parametrised here by the peak base velocity and the distance between the base and the stopper). Different states of the block stack system (or modes of

failure) at the end of simulations were distinguished (Mode A - block stack remains stable on the base, Mode B - overturning of the top block, Mode C - overturning of the top and middle blocks - mode C, Mode D - overturning of the entire stack).

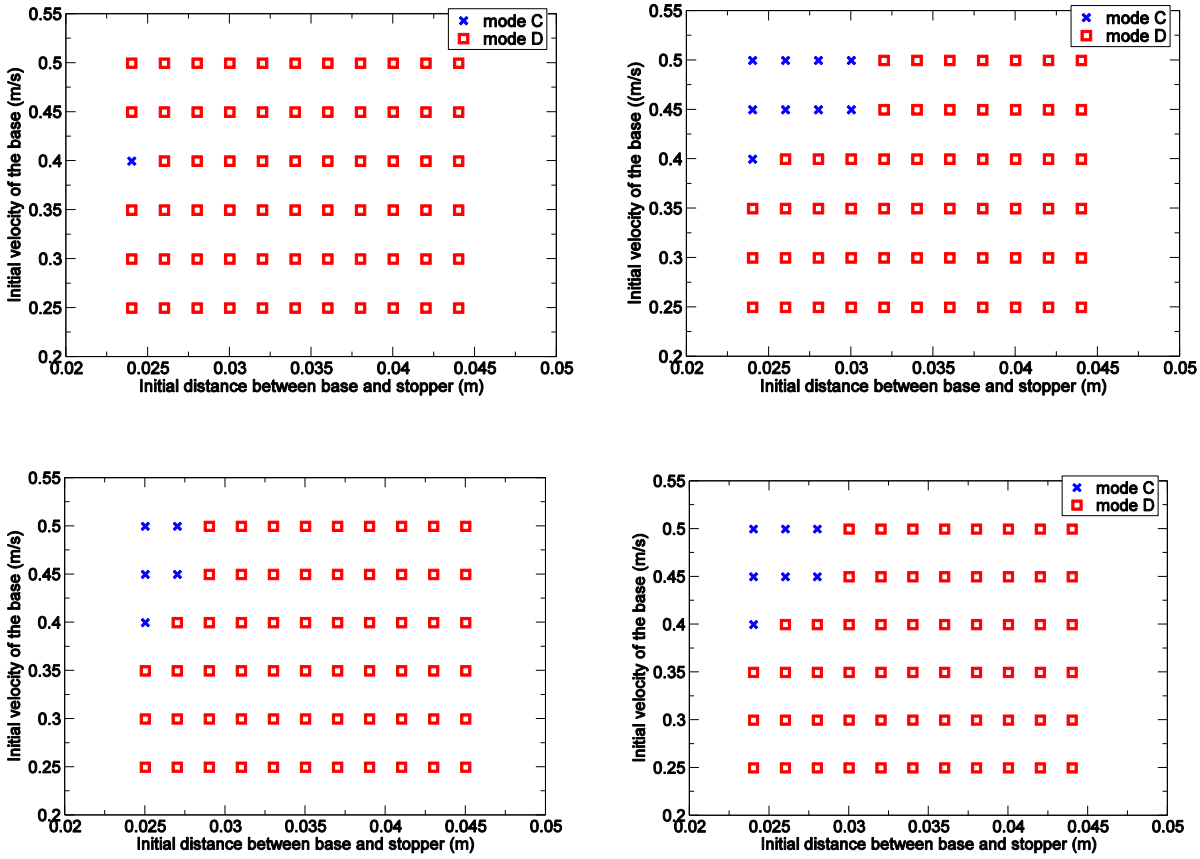


Figure 13: Three Blocks Stack Overturning Mode Characterisation

Several NSCD SOLFEC analyses for the stack overturning study with lateral constraints at different distances (Fig 14) were also conducted

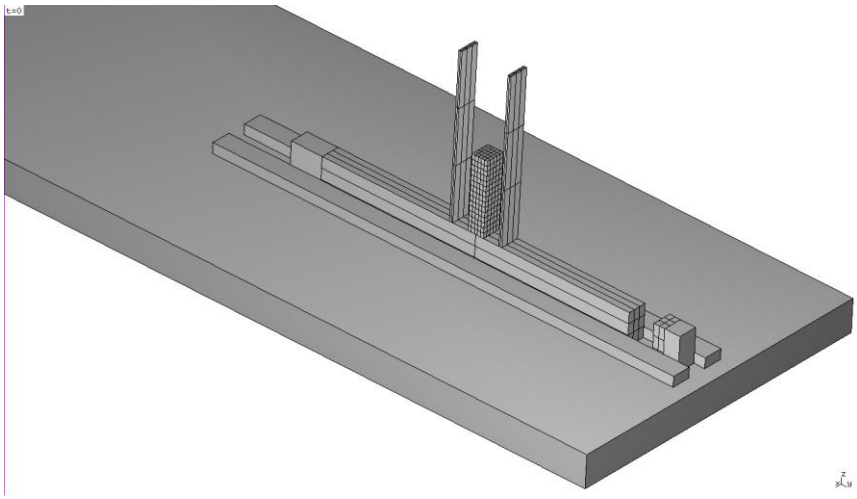


Figure 14: Three Blocks Stack Study with Lateral Constraints

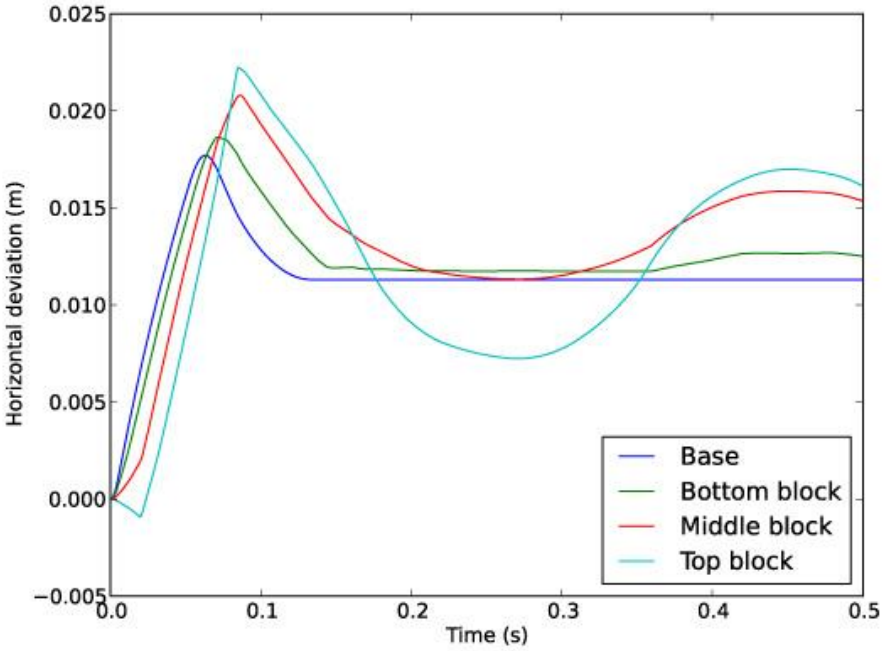


Figure 15 Block Centroids Horizontal Displacements Time Histories for the three Blocks Stack Study with Lateral Constraints

Figs 15 illustrates the three block centroids time histories, as well as the base time history for a double pulse experiment the constraint wall gap of 3 cm, stopper distance of 2.3 cm, and the peak base velocity of 0.4 m/s. Coefficient of restitution is set to zero. Fig 16 illustrates the final stack configuration.

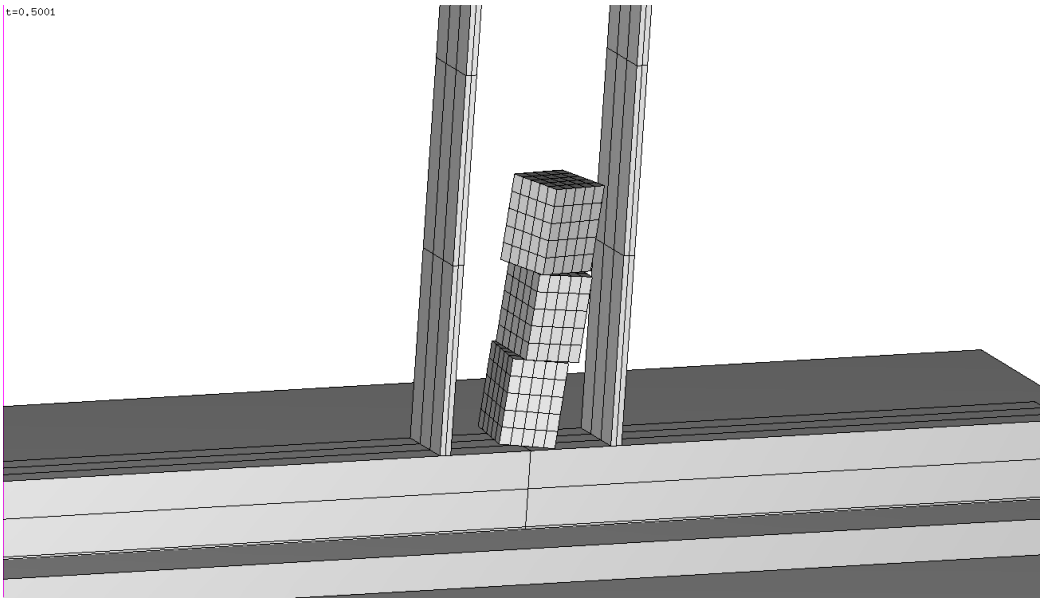


Figure 15 Final post impulse configuration for the three Blocks Stack Study with Lateral Constraints

4 CONCLUDING REMARKS

Apart from very specialist benchmarks, there is a general lack of suitable, well controlled benchmarks problems to validate predictive capabilities of non smooth contact dynamics simulations relevant for multi block structural configurations, with a regular construction pattern and/or clearances. Closed form analytical benchmarks are largely restricted to two dimensional single or double rigid block structural assemblies [5], typically concerned with rocking and overturning conditions due to harmonic or step base excitation of specific amplitudes. In addition, computational intricacies of non smooth dynamics problems are considerable [6].

The presented novel small scale benchmarks aim to expand on the limited database of suitable benchmarks for discontinuous blocky assemblies under dynamic conditions, and to eventually contribute to a library of well documented and well controlled experimental evidence to support and validate computational simulation paradigms (non smooth contact dynamics, discrete elements, discontinuous deformation analysis) as well as to inform the design of larger scale experimental programmes.

It is believed that the creation of a well documented set of benchmarks for the validation of simulation paradigms for discontinuous media will be extremely valuable for researchers and code developers, as well as for safety case engineers and industry regulators. Evidence on dynamic performance attributes and quasi resonance sensitivities for multi body structural assemblies will facilitate better understanding of their structural performance, and will be used as a design and/or forensic tool, as well as a rational basis for the risk assessment. Advanced engineering simulations in industry and regulatory bodies will directly benefit from research results.

REFERENCES

[1] V. Picker, Optimisation and Validation of the ARAMIS Digital Image Correlation System for use in Large-scale High Strain-rate Events. *Maritime Division, Defence Science and Technology Organisation*, Australia, 2013.

[2] M. Jean, The non-smooth contact dynamics method. *Computer Methods in Applied Mechanics and Engineering*, 177(3-4):235–257, 1999.

[3] T. Koziara, N. Bićanić, Semismooth Newton method for frictional contact between pseudo-rigid bodies. *Computer Methods in Applied Mechanics and Engineering* **197**(33-40): 2763–2777, 2008.

[4] M. Qamaruddin, B. Chandra, A. S. Arya, Dynamic testing of brick building models, *Proc. Instn Civ. Engrs*, Part 2, 77, Sept., 353-365, 1984.

[5] A. N. Kounadis, G. J. Papadopoulos and D. M. Cotsovos, Overturning instability of a two-rigid block system under ground excitation, *ZAMM ·Z. Angew. Math. Mech*. 92, No. 7, 536 – 557, 2012.

[6] F. Pfeiffer, M. Foerg, H. Ulbrich, Numerical aspects of non-smooth multibody dynamics. *Computer Methods in Applied Mechanics and Engineering* 195(50-51):6891-6908, 2000.

[7] G. W. Housner, "The Behavior of Inverted Pendulum Structures During Earthquakes," *Bulletin of the Seismological Society of America*, Vol. J3, no. 2, pp. 403, Feb 1963.

COMPDYN 2015
5th ECCOMAS Thematic Conference on
Computational Methods in Structural Dynamics and Earthquake Engineering
M. Papadrakakis, V. Papadopoulos, V. Plevris (eds.)
Crete Island, Greece, 25–27 May 2015

ADAPTIVE CONTROL OF THE ROCKING MOTION OF ART OBJECTS

Rosario Ceravolo [1], Marica L. Pecorelli [1], and Luca Zanotti Fragonara[1]

[1] Politecnico di Torino
Corso Duca degli Abruzzi, 24 -10129 Torino, Italy
{rosario.ceravolo,marica.pecorelli,luca.zanottifragonara}@polito.it

Keywords: Art objects, Rocking, Adaptive control, Non-linear response system.

Abstract. *The seismic behaviour of many art objects and obelisks can be analysed in the context of the seismic response of rigid blocks. Starting from the pioneering works by Housner (1963), a large number of analytical studies of the rigid block dynamics were proposed. In fact, despite its apparent simplicity, the motion of a rigid block involves a number of complex dynamic phenomena such as impacts, sliding, uplift and geometric nonlinearities. Methods that prevent the possible overturning were also presented in the past years, especially to protect statues and art objects with respect to seismic events. In the more general context of control, to date a current strategy is represented by base isolation.*

In this paper a novel adaptive control strategy for protecting monolithic art objects was investigated. The control under study follows a feedback-feedforward scheme that is realised by adjusting the stiffness of anchorages with adaptive stiffness located at the two corners of the block. A numerical comparison was made between the behaviour of the unanchored block, the anchored block with a system having constant stiffness and the anchored block with adaptive stiffness. Finally, numerical investigations were carried out in order to verify the expected efficiency of the proposed control system, and to validate simple control laws.

1 INTRODUCTION

Many studies and codes are devoted to the seismic protection of existing buildings and in particular of museum buildings. On the other hand, the protection of the contents of museums, e.g. art objects on display or kept in storage, has received much less attention by earthquake engineering standards. In fact, the protection of museum collections against seismic hazard is increasingly attracting interest among the governments and the scientists, since their damage could irreparably affect the cultural heritage worldwide.

The past and recent seismic events have clearly shown the high vulnerability of art objects and of museum contents even in case of moderate earthquakes. Indeed, the art objects in many museums are displayed in a way that does not ensure stability during a seismic event. The storage areas are often overloaded without any consideration for the seismic risk. The seismic mitigation of art objects requires a multidisciplinary approach in order to find a compromise between safety and conservation. In addition, the objects on display need to take into account the issues of aesthetic enjoyment of artefacts as well as constraints related to space.

From a structural point of view, the seismic behaviour of art objects in many cases can be analysed within the context of the dynamic response of rigid blocks. The literature counts a large number of analytical studies on the non-linear dynamics of the rigid block, starting from the pioneering work by Housner in 1963 [1]. The motion of rigid blocks on a rigid plane, can be classified into six types: rest, slide, rotation, slide-rotation, translation jump and rotation jump. The equations of motions, transition of motions and motions after the impact between the block and the floor, in the presence of horizontal and vertical accelerations, was investigated by Ishiyama in 1982 [2]. Depending on the form and magnitude of the excitation [2-3] and on the geometry and mass distribution of the objects, the artefacts can experience all the types of motion mentioned above. Among different cases, a particular and fundamental role is covered by the rocking motion, that cause objects to fall from their supports or to collide with other objects.

To mitigate the damage due to rocking motion and limit the probability of overturning, four different strategies are currently used [4]. They consist of lowering the centre of gravity of the artefacts, adjusting the base-to-height ratio proportions of the art objects, fixing the objects to the floor/wall or separating the objects from the ground using base isolation devices. The efficacy of the first two strategies is strictly connected with the dynamics of rigid block motion. During the rocking motion of a rigid block the restoring force is originated by its own rotational inertia. Lowering the centre of gravity of the artefact allows increasing the restoring force of the system and consequently its stability. The second strategy, adjusting the base-to-height ratio proportions, can be easily explained with regard to the effect of slenderness on overturning, studied for the first time by Housner [1] and investigated subsequently by several authors [5-6]. These two strategies, as well as anchoring the objects to the ground, must be used carefully because by moving the objects together with the ground, the amount of forces transmitted to the artefact can be very high. In this case, the art object is forced to bend and deform, instead of oscillating rigidly around the two corners, so an accurate evaluation of the stress level is required. To avoid mechanical failure of the artefacts indeed the mechanical limit of the material must not be reached during the entire seismic event. Stress failure occurring at the area of load concentration or at the area of material weakness is highly likely.

In contrast to the significant amount of basic analytical theoretical research on the response of stand-alone rocking structures, there are relatively few theoretical studies on the response of structures retrofitted against rocking. The seismic isolation of rocking objects was considered in several recent works concerning the behaviour of the anchored blocks [7-8]. In particular Dimentberg et al. [9] investigated the behaviour of an anchored block excited by white

noise, while Makris et al. [10] studied its response to pulse-type ground motions. Makris et al. showed that there is a finite frequency range where the conclusions drawn by Dimentberg et al. [9] do not hold. The study demonstrates that for most of the loading frequency range anchored blocks survive higher acceleration than free-standing blocks. However, there is a frequency range where the opposite happens.

Most retrofitting strategies to avoid toppling of structures that exhibit rocking behaviour during earthquakes consist in preventing this type of motion instead of limiting it or controlling it. The aim of this paper is to allow rocking motion as a means of seismic isolation, and to use a control strategy to enhance its performances. Rocking as a seismic isolation technique is currently proposed for bridges [11] and building [12]. Starting from the idea that a controlled rocking motion, far from the overturning condition, can be a good way to reduce the vulnerability and the stress transmitted to the artefacts, a deformable anchorage, with constant and adaptive stiffness, is examined in this paper. Using the example of Michelangelo's San Matteo sculpture allocated in the "Galleria dei Prigioni" in Florence, whose dynamics has been studied by other authors [13], this paper investigates the behaviour of the free-standing block and the anchored block utilising springs having different stiffness.

2 MODEL OF THE BLOCK

The governing equations of rocking motion of unanchored (Figure 1a) and anchored (Figure 1b) rigid blocks received a special attention in the literature. Housner in [1] defined the governing equations of rocking motion of a rigid block subjected to horizontal and vertical base excitations, taking into account the nonlinear effects. These equations were then modified by Makris et al. [10] in order to consider the presence of unilateral restraints placed at the corners of the rigid block. A brief summary of the two dynamic models is reported hereinafter.

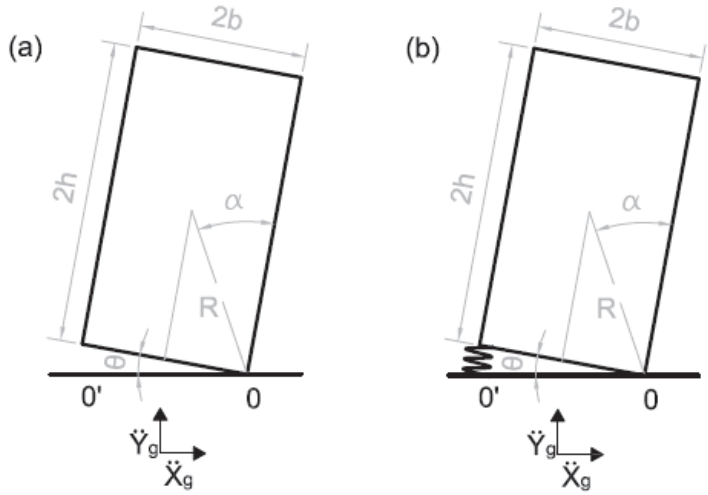


Figure 1: Idealization of the artefact as rigid rocking object, subjected to horizontal and vertical excitation (a) unanchored artefact (b) anchored artefact.

2.1 Initial response

Figure 1a and Figure 1b show an unanchored and anchored rigid block resting on horizontal rigid supporting base subjected to horizontal and vertical base excitations. The block remains at rest for small base excitations and starts to oscillate around the corner 0 or 0' when the base excitation increases and Equation (1) is satisfied:

$$\left|m\ddot{X}_g\right|h > b\, m\left(g + \ddot{Y}_g\right) \tag{1}$$

Three different types of motion may characterize the initial response of a rigid block: pure rocking, pure sliding and slide-rock motion [14-15]. In this work the coefficient of friction (μ_s) between the block and its base is assumed to be sufficiently large so that the object enters in a pure rocking motion without experiencing any sliding. Therefore, the coefficient of friction is assumed to satisfy the following conditions:

$$\left|m\ddot{X}_g\right| \leq \mu_s m\left(g + \ddot{Y}_g\right) \tag{2}$$

$$\frac{3\gamma g - 3\gamma\ddot{Y}_g + 4\ddot{X}_g + \gamma^2\ddot{X}_g}{3\gamma\ddot{X}_g + g + 4\gamma^2 g - \ddot{Y}_g - 4\gamma^2\ddot{Y}_g} \leq \mu_s \tag{3}$$

where: $g =$ the gravitational acceleration; $m =$ the mass of the block; $\mu_s =$ the coefficient of static friction; $\ddot{X}_g =$ horizontal base excitation; $\ddot{Y}_g =$ vertical base excitation; $\gamma = h/b$ is the slenderness of the block (see Figure 1).

2.2 Governing equations of the unanchored rigid block

The governing equation of motion for the rigid object with positive angular rotation can be derived by the rotational equilibrium about the corner 0:

$$I_0\ddot{\theta}(t) + mR\ddot{X}_g cos(\alpha - \theta) + m\left(g + \ddot{Y}_g\right)Rsin(\alpha - \theta) = 0 \tag{4}$$

where: $I_0 =$ moment of inertia of the block about 0; $R =$ the distance from 0 and the centre of mass of the block; $\alpha = cot^{-1}(h/b)$ is the critical angle beyond which the overturning will occur to the object under gravity alone. Similarly, the rocking about 0 is governed by the equation:

$$I_0\ddot{\theta}(t) + mR\ddot{X}_g cos(\alpha + \theta) - m\left(g + \ddot{Y}_g\right)Rsin(\alpha + \theta) = 0 \tag{5}$$

Introducing the frequency parameter of the rectangular block, defined as:

$$p = \sqrt{\frac{mgR}{I_0}} \tag{6}$$

the Equations (4) and (5) can be expressed in the compact form:

$$\ddot{\theta}(t) + p^2\left\{\left(1 + \frac{\ddot{Y}_g(t)}{g}\right)sin\left(sgn[\theta(t)]\alpha - \theta(t)\right) + \frac{\ddot{X}_g(t)}{g}cos\left(sgn[\theta(t)]\alpha - \theta(t)\right)\right\} = 0 \tag{7}$$

where $sgn[\ \ ]$ denotes the signum function.

An additional equation, connecting the angular velocities immediately before and after the impact, must couple with Equation (7), to derive the motion of a rigid block to a generic external excitation.

2.3 Governing equations of the anchored rigid block

In order to consider the presence of the unilateral anchorages at the two corners of the block (Figure 2), an additional term needs to be introduced in Equation (7). This term represents the resisting moment of the spring in tension and can be assumed to be:

$$M_{s,k} = K \cdot 4btan\left|\frac{\theta(t)}{2}\right| \cdot 2bcos\left|\frac{\theta(t)}{2}\right| = 8R^2 sin^2\alpha\, Ksin\left|\frac{\theta(t)}{2}\right| \quad (8)$$

where K = the stiffness of the anchorage.

By substituting Equation (8) into Equation (7) the rocking of the rectangular block will be described by:

$$\ddot{\theta}(t) + p^2\left\{\left(1 + \frac{\ddot{Y}_g(t)}{g}\right)sin\big(sgn[\theta(t)]\alpha - \theta(t)\big) + \frac{\ddot{X}_g(t)}{g}cos\big(sgn[\theta(t)]\alpha - \theta(t)\big) + \frac{M_{s,k}}{I_0 p^2}f_{L,1}(\theta)f_{L,2}(\theta) + \frac{M_{s,k}}{I_0 p^2}f_{R,1}(\theta)f_{R,2}(\theta)\right\} = 0 \quad (9)$$

where $f_{R,1}(\theta)$ and $f_{L,1}(\theta)$ are fracture functions for the right and the left springs, respectively, and are defined as:

$$f_{R,1}(\theta) = f_{L,1}(\theta) = \begin{cases} 1 & if \quad |\theta(t)| \le \theta_y \\ 0 & if \quad |\theta(t)| > \theta_y \end{cases} \quad (10)$$

where $f_{R,2}(\theta)$ and $f_{L,2}(\theta)$ are two functions used to establish which of the two springs is working during the rocking motion, and are defined as:

$$f_{R,2}(\theta) = \left(\frac{1 - sgn[\theta(t)]}{2}\right) \quad (11)$$

$$f_{L,2}(\theta) = \left(\frac{1 + sgn[\theta(t)]}{2}\right) \quad (12)$$

Equation (8) reflects a large displacement formulation, accounting for a spring elongation equal to $4b\ tan|\theta/2|$ and an eccentricity of $2b\ cos|\theta/2|$with respect to the rotation corner.

2.4 Impact energy dissipation

The angular velocity decreases when the angle of rotation reverses and the rotation centre swaps from points 0 to 0' and vice versa, due to energy loss during the impact. Housner [1] derived a model to calculate the angular velocity of the rigid body immediately after the impact and the energy dissipated during the impact. This model uses the following assumptions: (1) the impact is punctual; (2) the impact time t_I is very short; (3) the block remains at the same position during the impact time. Under these assumptions the relation between the two angular velocities, immediately before the $\dot{\theta}(t_I^-)$ and after the impact $\dot{\theta}(t_I^+)$ can be derived by means of the principle of conservation of the angular moments. Writing the momentum equation just before the impact and immediately after:

$$I_0\dot{\theta}(t_I^-) - m\dot{\theta}(t_I^-)2bRsin\alpha = I_0\dot{\theta}(t_I^+) \quad (13)$$

the following relationship between $\dot{\theta}(t_I^-)$ and $\dot{\theta}(t_I^+)$ is obtained for the rectangular block as:

$$e = \frac{\dot{\theta}(t_I^+)}{\dot{\theta}(t_I^-)} = 1 - \frac{2mR^2}{I_0}sin^2\alpha = 1 - \frac{3}{2}sin^2\alpha \quad (14)$$

In the literature e^2, or r, is referred to as "coefficient of restitution" and it is a measure of the energy dissipated at the impact. The value of e given by Equation (14) reflects the maximum value of the coefficient of restitution for a block with slenderness α under rocking motion. In this study, it is assumed that the coefficient of restitution fits exactly the value of Equation (14), even if in real practice additional energy is lost also due to interface mechanisms. Therefore the real value of the coefficient of restitution is generally smaller than e^2.

In order to evaluate whether after the impact the object will maintain a full contact with the base or will undergo uplift on the other corner, the overturning moment M_o and the resisting moment M_s should be compared. The object will rest if the following condition is satisfied:

$$|M_s| > |M_o| \tag{15}$$

2.5 Condition to sustain rocking motion

In order to avoid sliding during the entire duration of the rocking motion, the ratio between horizontal reaction $f_x(t)$ and vertical reaction $f_y(t)$ at the contact points between the block and the base, points 0 and 0' in Figure 1, must always satisfy the following condition:

$$\left|\frac{f_x(t)}{f_y(t)}\right| < \mu_s \tag{16}$$

The horizontal and vertical reactions at contact points 0 or 0' will fluctuate with time, and their value can be derived from the dynamic equilibrium in the horizontal and vertical directions:

$$f_x(t) = m\left[\ddot{X}_g(t) + \ddot{x}(t)\right] \tag{17}$$

$$f_y(t) = m\left[\ddot{Y}_g(t) + g + \ddot{z}(t)\right] \tag{18}$$

where $x(t)$ = horizontal displacement and $z(t)$ = vertical displacements of the centre of mass of the block.

2.6 Sources of nonlinearity

There are four different sources of nonlinearity in the equation of the rocking object described in Equation (7): the transition from one governing equation to the one at the instant of impact (when the centre of rotation changes from one edge to the other); the impact energy dissipation (which induces a jump discontinuity in the angular velocity); the geometric effect of the slenderness ratio of the object and last but not least the coupling of the vertical excitation with the rocking response.

These different sources of nonlinearity were investigated by several authors [16-17].

3 NUMERICAL ANALYSES

3.1 Geometry of the rigid block

Equation (7) is solved hereinafter referring to block dimensions that are of special interest for cultural heritage. More general conclusions would require the non-linear equation of motion to be solved for different values of parameter p. However, the results obtained for art objects, while being useful in themselves, may still support qualitative interpretations and extensions to more general sizes of blocks.

The geometric dimensions chosen for the block are: 2b = 0.60 m; 2h = 2.72 m, with a mass

of 3361 Kg, which matches the scale of the equivalent symmetric rectangular block of the Michelangelo's San Matteo sculpture [13]. The excitation applied to the block is always a one-sine pulse, which represents a typical choice in literature on rocking [1]. The sculpture object of the study is represented in Figure 2.

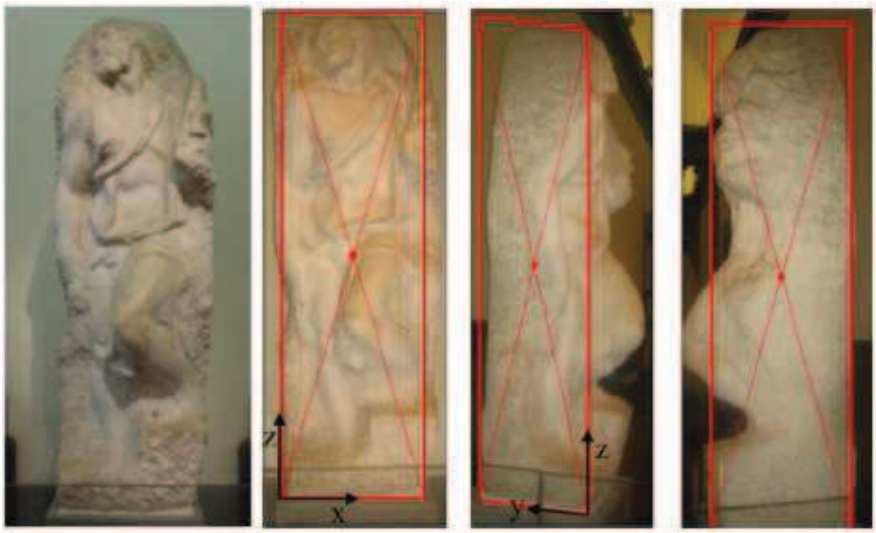


Figure 2: S. Matteo sculpture and equivalent rectangular block [13].

3.2 Numerical algorithm description

Closed form solutions for the rocking response to simple excitation forms are only found in the small displacement range. Therefore, the dynamic response of the rigid block subjected to one-sine pulses were determined numerically in Matlab ®, by integrating Equations (7) and (9) through a fourth-order Runge-Kutta scheme. The time-step used in the numerical integration was set to 0.0025 s [18]. Starting from the rest state of the rigid block, the actual corner of rotation, and therefore the reference equation to integrate, is determined from the sign of the horizontal base excitation. For positive value of $\ddot{X}_g(t_0)$, the block starts to rotate around the left corner (negative rotation), while for negative value it rotates around the right corner (positive rotation). The same equation is used for subsequent time steps until the sign of rotation θ changes. At each step, the condition $\theta_i \cdot \theta_{i+1} \geq 0$ is checked in order to establish the changes of rotation corner. If this condition is not satisfied, the velocity immediately before the impact, $\dot{\theta}(t_I^-)$, is evaluated and the velocity just after the impact, $\dot{\theta}(t_I^+)$, is determined by means the Equation (14). With the initial condition $\theta(t_I) = 0$ and $\dot{\theta}(t_I) = \dot{\theta}(t_I^+)$ the equation of motion on the other corner is used to evaluate the motion of the block in the subsequent time interval until the rotation angle θ will change its sign. The accuracy of the numerical procedure for the free-standing and for the anchored block has been validated for different types of base excitation. The response of the free-standing block under constant excitation, pulses and harmonic loadings were compared with the results found by Housner (linearized equations) [1], Makris et al. [19] and Spanos et al. [20], respectively. Similarly, the behaviour of the anchored block has been validated by implementing a numerical work of Markis et al.[10]. For instance, the S. Matteo equivalent rectangular block overturned when subjected to a constant acceleration of 0.2822g applied for 0.6380 s, but did not topple with a slightly shorter excitation, for example 0.6300 s (Figure 3), this being in agreement with Housner's formulas about overturning by constant acceleration [1].

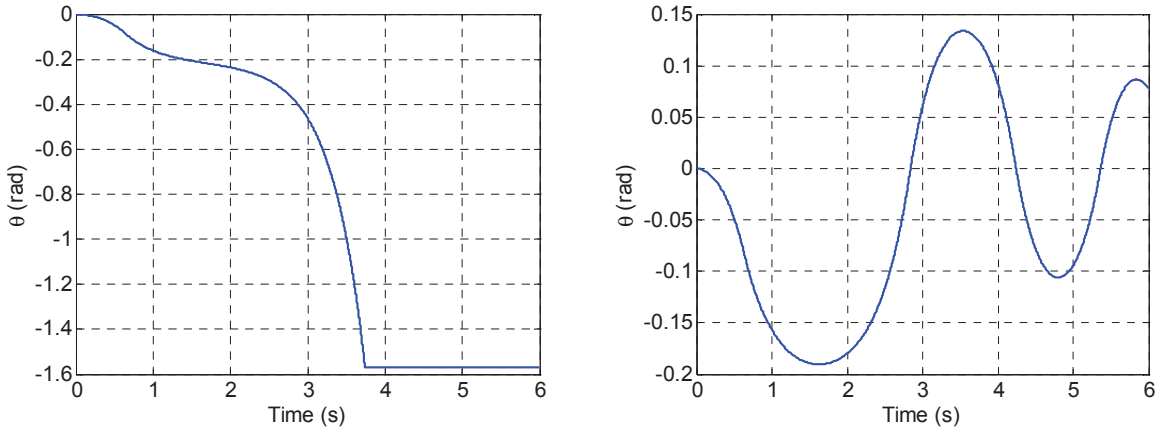


Figure 3: Linearized dynamic responses of S. Matteo equivalent rectangular rigid block subjected to a constant acceleration of 0.2822g applied for 0.6380s (left) and 0.6300 s (right).

3.3 S. Matteo block: free-standing conditions

The dynamic behaviour of S. Matteo equivalent rectangular block subjected to a generic base excitation cannot be established in advance, if not at a statistical level [5]. Indeed, the response of the system not only depends on the amplitude and frequency content of the excitation but also on its particular time-history. The same value of accelerations in a different succession can overturn the rigid block or not.

Aiming to improve the seismic behaviour of a rigid block, the response under one-sine pulse excitation is studied, characterized by different amplitudes a_{p0} and frequencies ω_p. Focusing on the dynamic response of the rigid block subjected to one-sine excitation constitutes the first step for controlling the dynamic behaviour of the block under a generic loading (e.g. earthquake).

In accordance with the studies conducted by Makris et al. [19], in the overturning spectra of the free-standing S. Matteo rectangular block (Figure 4) it is possible to distinguish between two overturning modes. The first mode occurs when there is an impact between the block and the floor before toppling, while in the second one the overturning occurs without any impact. In the frequency range examined in this study, overturning with impact, for a given value of ω_p/p, is typically observed for smaller amplitude of one-sine pulse, if compared with amplitudes that characterize overturning without impact.

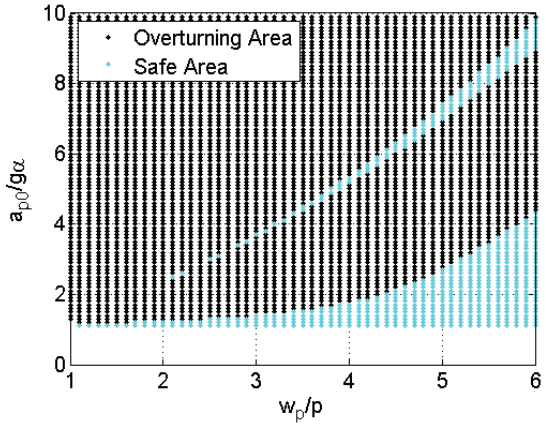


Figure 4: Overturning spectra of free-standing S. Matteo block ($p = 2.2985$) subjected to one-sine pulse.

3.4 S. Matteo block: anchored conditions with constant stiffness

The presence of anchorages provides additional resistance against toppling, compared to the free-standing block. Until the failure of the restrainers, indeed, the restoring force due to the self-weight of the block (see Figure 5) is supplemented by the restoring force engaged by the elastic-brittle anchorage in tension, as given in Equation (8).

In the following, the behaviour of the block anchored with restrainers, having different values of stiffness K, is determined and compared. K is chosen assuming that the failure of the restrainer occurs for a fix value of strength, but for different values of elongation. Failure strength is taken as equal to $0.4\,mg$ while the ultimate rotations are respectively α, $\alpha/2$, $\alpha/3$ and $\alpha/4$. The strength of the anchorage must be chosen as a function of the localized stress and the internal stress that the artefact is able to resist; in this study it was set in accordance with the work of Makris [10]. The first value of θ that brings the restrainers to failure is named θ_f, that corresponds to the angle α beyond which the overturning would occur for the object under gravity load alone. The other values examined were chosen as fractions of the first one. In Figure 6 the total restoring force is reported for the four types of anchorages under study.

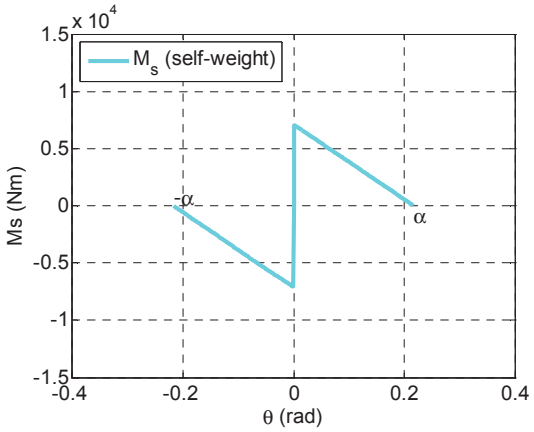


Figure 5: Restoring force due to self-weight.

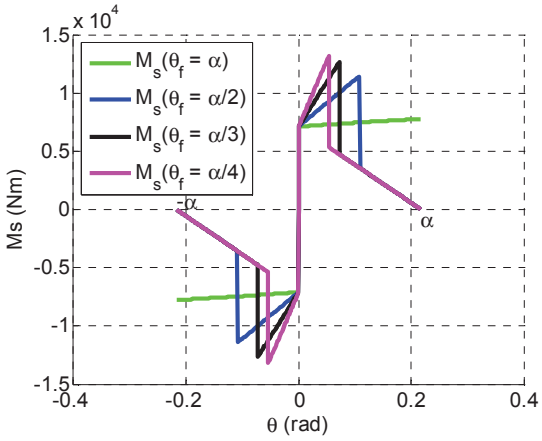


Figure 6: Total restoring force.

The basins of attraction of the rest state, i.e. $\theta = 0$, and of the overturning one, i.e. $\theta = |\pi/2|$, have been calculated for all the values considered for K (Figure 7). Each boundary of a basin of attraction has been determined by equating the total energy of the block at the generic time t to the potential one at the position $\theta = \alpha$ (corresponding to the minimum energy for block overturning). The equations of the boundary for each of the two overturning modes (without and with impact) read:

$$\dot{\theta}_1(t) = sgn[\alpha - \theta(t)]\, p \sqrt{2\big[1 - cos\big(\alpha - \theta(t)\big)\big] + \frac{b\,K}{2p^2 I_0}\left(tan\left|\frac{\alpha}{2}\right| - tan\left|\frac{\theta}{2}\right|\right)} \quad (19)$$

$$\dot{\theta}_1(t) = sgn[\alpha - \theta(t)]\, p \sqrt{2\left[\frac{1 - cos\alpha}{r}\right] + cos\alpha - cos(\alpha - |\theta|) + \frac{b\,K}{2p^2 I_0}\left(tan\left|\frac{\alpha}{2}\right| - tan\left|\frac{\theta}{2}\right|\right)} \quad (20)$$

Figure 7 reports the basins of attraction of S. Matteo block, for both the anchored and unanchored condition. It is worth noticing that in the range $-\alpha \leq \theta \leq \alpha$ the velocity required for the block to overturn increases with the stiffness of the restrainers.

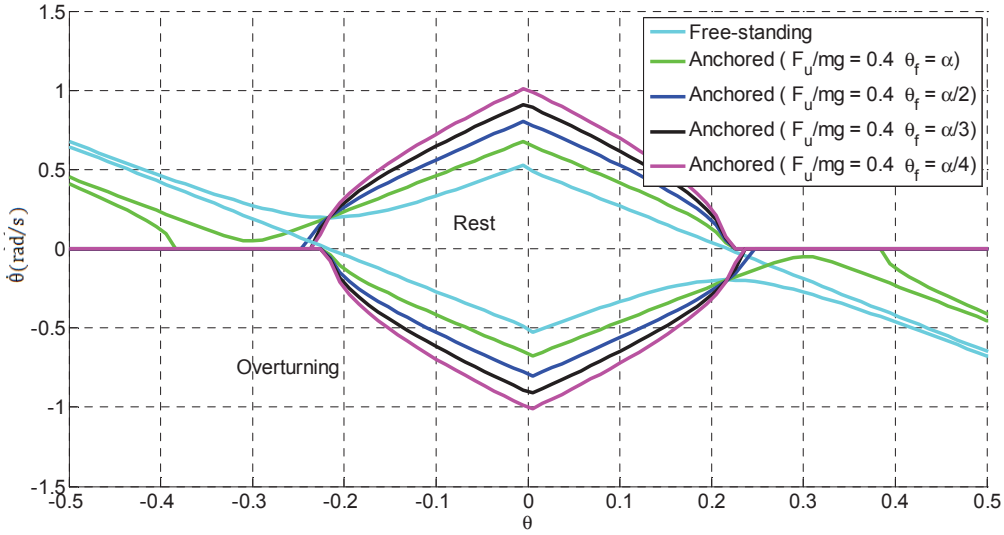


Figure 7: Basins of attraction in the state space for the investigated cases.

With a more rigid anchorage, an expansion of the basin of attraction of the rest state is observed in Figure 7. However, an increase of K does not imply a reduction of overturning risk for the block. In fact, the overturning spectra of the block (see Figures 8-11) reflect a more complex behaviour. The amplitude activating the second overturning mode (without any impact with the floor) is regardless from the stiffness of the anchorage. The value of K, instead, affects significantly the shape and the size of the overturning area associated to the overturning with impact mode. In that case, the amplitude requested, for a given value of ω_p, decreases or remains constant when increasing stiffness. This behaviour, which may seem counterintuitive, can be explained observing the dynamics of the system in the state space: the stiffness of the anchorage not only affects the basins of attraction, but it also influences the history of $(\theta, \dot{\theta})$, thus increasing the vulnerability of the object with respect to the second mode of overturning.

The different shape and size of overturning areas, as depending on the different connection to the floor, entails the possibility to select a value of stiffness that keeps the object within the safety domain. This can be realised when the one-sine pulse excitation is known both in terms of amplitude and frequency. In the next section, a strategy based on an adjustable anchorage is investigated to keep the system stable with respect to a measured excitation.

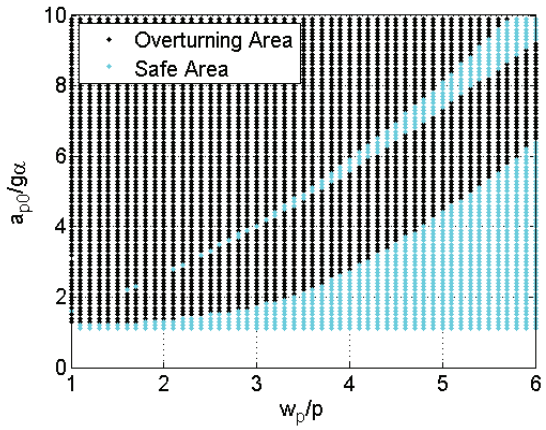


Figure 8: Overturning spectra of S. Matteo block

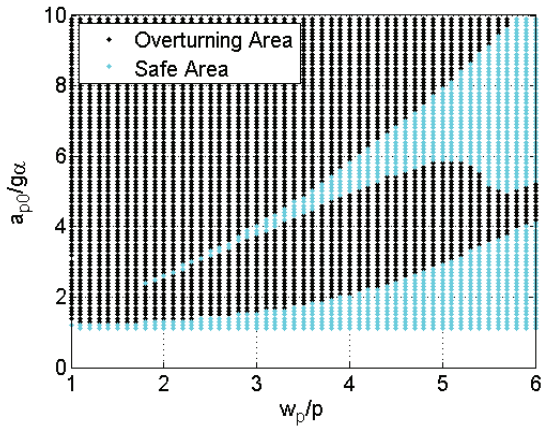


Figure 9: Overturning spectra of S. Matteo block

for $\theta_f = \alpha$ due to one-sine pulses.

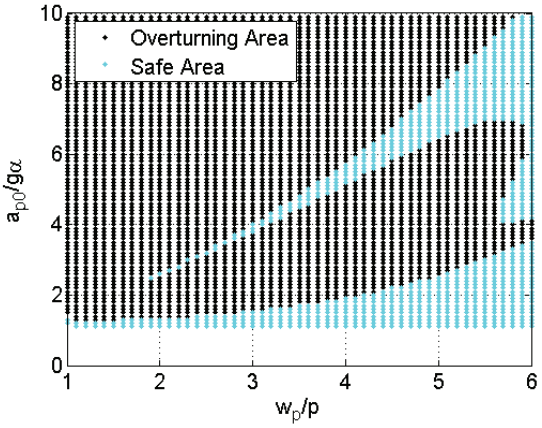


Figure 10: Overturning spectra of S. Matteo block for $\theta_f = \alpha/3$ due to one-sine pulses.

for $\theta_f = \alpha/2$ due to one-sine pulses.

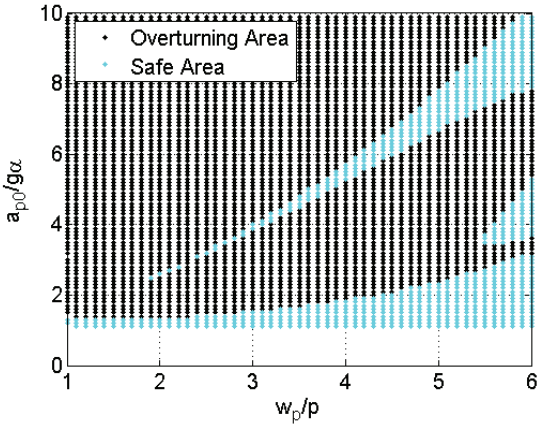


Figure 11: Overturning spectra of S. Matteo block for $\theta_f = \alpha/4$ due to one-sine pulses.

3.5 S. Matteo block: anchored conditions with adaptive stiffness

The performance of a control law applied to an adaptive anchorage is finally investigated. The stiffness of the anchorage/restrainer is assumed to switch between two fix values, K_{max} and K_{min}, as a function of the excitation and of the state of the rigid block. In order to evaluate the benefit of using an adaptive stiffness for the restrainer, the higher value of the stiffness, K_{max}, was chosen to correspond to the value of the less rigid spring examined in Section 3.4 $\left(F_u/mg = 0.4\ \theta_f = \alpha\right)$. Two different values, $K_{min} = 0.5\ K_{max}$ and $K_{min} = 0.1\ K_{max}$, were investigated.

Two different strategies are employed for setting the value of K at the generic time t. The first strategy consists in minimising the absolute value of the total work, and it applies when the block is excited. The second strategy, which applies in free oscillations conditions, consists in minimising the work done by the anchorage, this time in its signed value. Therefore, during the excitation, the stiffness is assigned using the following law:

$$K(t+1) = \begin{cases} K_{max} & if \quad -a_g(t)\cdot\theta(t) > 0 \\ K_{min} & if \quad +a_g(t)\cdot\theta(t) < 0 \end{cases} \tag{21}$$

Instead, during the free oscillations, the law to be used is:

$$K(t+1) = \begin{cases} K_{max} & if \quad |\theta(t)| - |\theta(t-1)| > 0 \\ K_{min} & if \quad |\theta(t)| - |\theta(t-1)| < 0 \end{cases} \tag{22}$$

The work done at time t by the excitation and by the unilateral anchorage can be written accordingly as follows:

$$W_p(t) = -m\ddot{X}_g R cos(\alpha - |\theta(t-1)|)\cdot[\theta(t) - \theta(t-1)] \tag{23}$$

$$W_a(t) = -8b^2 K sin\left|\frac{\theta}{2}\right|\cdot[\theta(t) - \theta(t-1)] \tag{24}$$

In Figures 12 and 13 the overturning spectra are reported for $K_{min} = 0.5\ K_{max}$ and $K_{min} = 0.1\ K_{max}$: the two diagrams show how reduced values of K_{min} can positively affect the response of the block (e.g., the overturning with impact disappears for $\omega_p/p > 3.7$). In particular, the use of an adjustable anchorage, adapted in accordance with Equations (21) and (22), improves the dynamic behaviour of the block independently of the characteristics of the

one-sine pulse excitation.

In order to show the performances of the control of the block in a sample excitation case ($w_p/p = 4$ $a_{p0}/\alpha g = 2.7$), Figures 14 and 15 compare on the time-histories of rotation angle and angular velocity of S. Matteo block, equipped with constant and adaptive anchorage ($K_{min} = 0.5\,K_{max}$), respectively. Correspondingly, Figure 16 depicts the normalised time-history of the values assumed by the stiffness of the adaptive anchorage in order to control the block. It is worth to highlight that the stiffness of the anchorage at the rotation pole in ineffective, thus in the plots it was assigned a zero value.

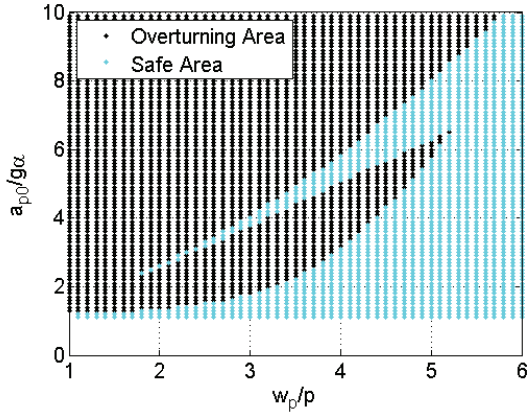


Figure 12: Overturning spectra for $K_{min} = 0.5\,K_{max}$.

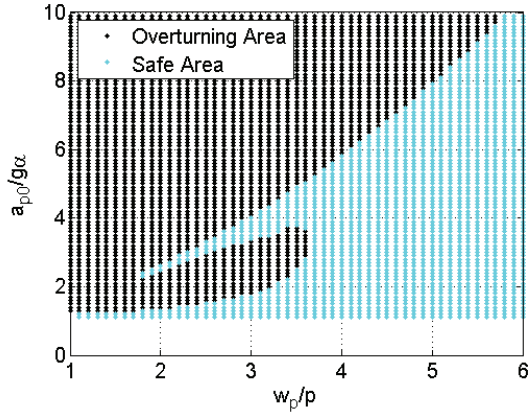


Figure 13: Overturning spectra for $K_{min} = 0.1\,K_{max}$.

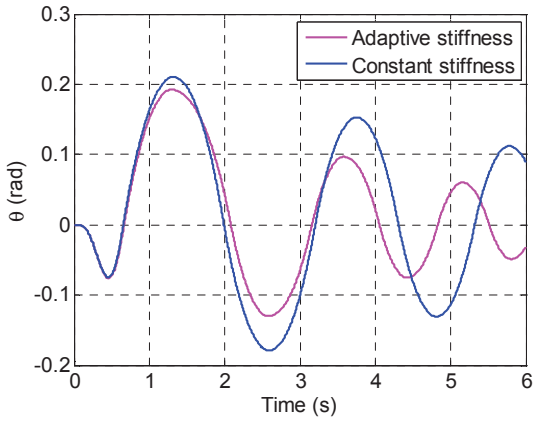


Figure 14: Time-history of the rotation angle for the S. Matteo block: with and without control.

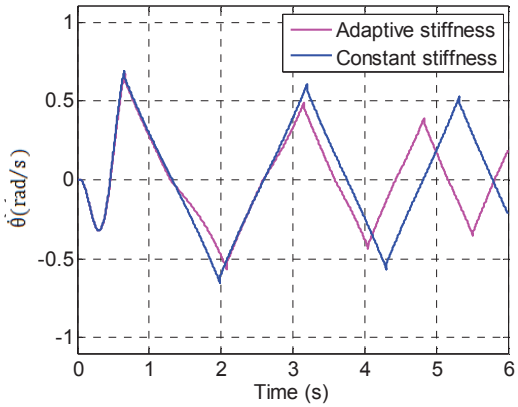


Figure 15: Time-history of the angular velocity for the S. Matteo block: with and without control.

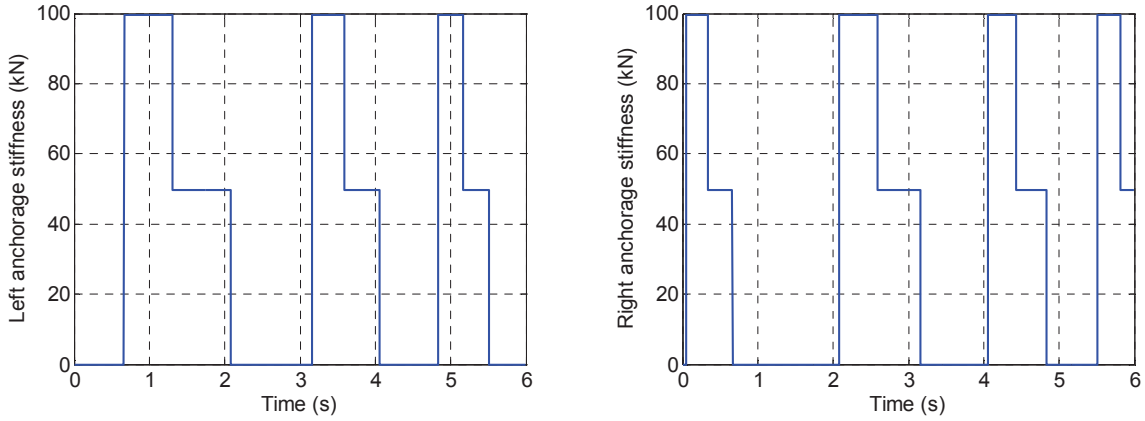


Figure 16: Time-history of the stiffness on the left and right corner of the block.

4 CONCLUSIONS

This paper examined a simple strategy for controlling the rocking response of art objects. The assumed control devices consist in adaptive unilateral restrainers connected to the ground, whose stiffness can be adjusted according to simple energetic laws. A few numerical investigations that regarded a famous statue located in the "Galleria dei Prigioni" in Florence were reported. At first, the overturning spectra, calculated for one-sine pulse excitations, of the statue were analysed with constant stiffness of restrainers. Such diagrams show that: (i) the first mode of overturning (with impact) is significantly affected by the characteristics of the anchorage; (ii) the second mode of overturning (without impact) is not influenced by the stiffness of the anchorage, since in this case the overturning of the block occurs for a fixed amplitude depending only on the loading frequency; (iii) the different shape and size of the overturning area of the same block with different connections suggests that an appropriate value of stiffness can actually prevent overturning of the block under one-sine pulse excitation.

In accordance with the previous observations, a strategy for adjusting the stiffness of the restrainers was proposed that minimise the total work done by the external excitation and by the anchorage system. The simulations performed on the statue showed that the first mode of overturning (with impact) can be appreciably reduced by such type of control. Thus a practical implementation of the presented control strategy can potentially reduce the vulnerability of artefacts that exhibit rigid block behaviour.

REFERENCES

[1] G.W. Housner, The behaviour of inverted pendulum structures during earthquakes. *Bulletin of the Seismological Society of America*, **53**, 403-417, 1963.

[2] Y. Ishiyama, Motion of rigid bodies and criteria for overturning by earthquake excitations. *Earthquake Engineering and Structural Dynamics*, **10**, 635-650, 1982.

[3] T. Taniguchi, Non-linear response analyses of rectangular rigid bodies subjected to horizontal and vertical ground motion. *Earthquake Engineering and Structural Dynamics*, **31**, 1481-1500, 2002.

[4] M. Lowry, B.J. Farrar, D. Armendariz, J. Podany, Protecting collection in the J. Paul Getty Museum from earthquake damage. *Western Association for Art Conservation (WAAC) Newsletter*, **29**, September 2007.

[5] C.S. Yim, A.K. Chopra, J. Penzien, Rocking response of rigid block to earthquakes. *Earthquake Engineering and Structural Dynamics*, **8**, 565-587, 1980.

[6] A.N. Kounadis, Parametric study in rocking instability of rigid block under harmonic ground pulse: A unified approach. *Soil Dynamics and Earthquake Engineering*, **45**, 125-143, 2013.

[7] I. Caliò, M. Marletta, Passive control of the seismic rocking response of art objects. *Engineering Structures*, **25**,1009-1018, 2003.

[8] A. Contento, A. Di Egidio, Investigations into the benefits of base isolation for non-symmetric rigid blocks. *Earthquake Engineering and Structural Dynamics*, **38**, 849-866, 2009.

[9] M.F. Dimentberg, Y.K. Lin, R. Zhang, Toppling of computer-type equipment under base excitation. *Journal of Engineering Mechanics*, **119**, 145-160, 1993.

[10] N. Makris, J. Zhang, Rocking response of anchored blocks under pulse-type motions. *Journal of Engineering Mechanics*, **127**, 484-493, 2001.

[11] Y.H. Chen, W.H. Liao, C.L. Lee, Y.P. Wang, Seismic isolation of viaduct piers by means of a rocking mechanism. *Earthquake Engineering and Structural Dynamics*, **35**, 713-736, 2006.

[12] H.Roh, A. M. Reinhorn, Nonlinear static analysis of structures with rocking columns. *Journal of Engineering Mechanics*, **136**, 532-542, 2010.

[13] L. Berto, T. Favaretto, A. Saetta, F. Antonelli, L. Lazzarini, Assessment of seismic vulnerability of art objects: The "Galleria dei prigioni" sculptures at the Accademia Gallery in Florence. Journal of Cultural Heritage, **13**, 7-21, 2012.

[14] H.W. Shenton, Criteria for initiation of slide, rock and slide-rock rigid-body modes. *Journal of Engineering Mechanics*, **122**, 690-693, 1996.

[15] A. Pompei, A. Scalia, M.A. Sumbatyan, Dynamics of rigid block due to horizontal ground motion. *Journal of Engineering Mechanics*, **124**, 713-717, 1998.

[16] S.C.S. Yim, H. Lin, Nonlinear impact and chaotic response of slender rocking objects, *Journal of Engineering Mechanics*, **117**, 2079-2100, 1991.

[17] F. Prieto, P.B. Lourenço, On the rocking behaviour of rigid objects. *Meccanica*, **40**, 121-133, 2005.

[18] S.C.S. Yim, A.K. Chopra, J. Penzien, Rocking response of rigid block to earthquakes. *Earthquake Engineering and Structural Dynamics*, **8**, 565-587, 1980.

[19] N. Makris, Y. Roussos, Rocking response and overturning of equipment under horizontal pulse-type motions. *Pacific Earthquake Engineering Research*, **5**, 1998.

[20] P.D. Spanos, A.S. Koh, Rocking of rigid block due to harmonic shaking, *Journal of Engineering Mechanics*, **110**, 1627-1642, 1984.

COMPDYN 2015
5th ECCOMAS Thematic Conference on
Computational Methods in Structural Dynamics and Earthquake Engineering
M. Papadrakakis, V. Papadopoulos, V. Plevris (eds.)
Crete Island, Greece, 25–27 May 2015

REDUCED ORDER MODEL OF CIRCULAR FLANGE-BOLTED CONNECTION AND ITS APPLICATION TO DYNAMIC SUBSTRUCTURING OF TELECOMMUNICATION TOWERS

Bartlomiej D. Blachowski[1], Witold Gutkowski[2] and Piotr Wisniewski[1]

[1] Institute of Fundamental Technological Research
Pawinskiego 5b, 02-106 Warsaw, Poland
e-mail: {bblach, pwisn}@ippt.gov.pl

[2] Institute of Mechanized Construction and Rock Mining
Racjonalizacji 6/8, 02-673 Warsaw, Poland
wgutkow@ippt.gov.pl

Keywords: Reduced order modeling, Circular flange-bolted connections, Dynamic substructuring, Nonlinear contact and friction effects, Telecommunication towers.

Abstract.

The paper deals with a nonlinear analysis of a tall tower, with Circular Flange Bolted Connections (CFBC), in which friction and contact effects are taken into account. Due to these nonlinearities, a detailed dynamic model of the whole structure would lead to very complex computational problem, unable for practical solutions. To overcome these difficulties a reduced order model of CFBC is proposed. Such a model enables the simulation of the whole tower including nonlinearities in connections. The paper is illustrated with an example of model reduction and dynamic calculations for a contemporary telecommunication tower. The tower is assembled of 4 truss segments, of triangular cross section, interconnected with CFBCs. Finally, the influence of the number of modes, included in the reduced order model, on the accuracy and computational effect, is discussed.

1 INTRODUCTION

Telecommunication towers, guyed masts and other engineering structures are made of circular hollow profiles. Tower sections welded in the factory, are on site, assembled with circular flange bolted connection (CFBC) shown on Fig. 1.
In a global analysis of tall structures, the mechanical properties of CFBCs are often neglected, under assumption, that they are rigid. However, how it was shown by Blachowski and Gutkowski [1], the influence of the their flexibility on the dynamic response of the structures can not be neglected.
According to the recent trends in structural health monitoring (SHM) it is necessary, among others, to monitor and detect structural damages. Two main methods in SHM can be recognized: local methods [2,3,4] and global ones [5-6]. In local methods connections are monitored directly at the vicinity of the damage. However, the local data don't give information about the health of the whole structure. In the global methods we are monitoring the response of the whole structure by measuring only selected quantities, such as accelerations of assumed structural points. The global methods require precise FE model of the entire structure, which may require a significantly great numerical effort. It is then useful, in such cases, to apply, either simplified [7] or detailed joint models [8]. In the former, connections are considered in a, more or less, approximate way. The latter require sophisticated computer clusters analyzing global behavior of the entire structure. Practical reasons push us, then towards reduced order modeling (ROM).

In this work, a reduced order model (ROM) of the circular flange-bolted connection is presented. The model takes into account the inherent nonlinearity of the connections, consisting of contact and friction forces between adjacent circular flanges and pre-tensioning of bolts. Having the model, describing behavior of CFBC, it is possible to work on a dynamic model of the whole tower. For that purpose the Ritz Vectors as a reduction basis [10] is applied. The paper is illustrated with an example of ROM applied to dynamic simulation of a contemporary telecommunication tower. The tower is assembled of 4 truss segments, of triangular cross section, jointed with CFBCs. One of the connections is assumed to be damaged. Finally, the influence of the number of modes, included in the ROM, on the accuracy and computational effort, is discussed.

2 SUBSTRUCTURING OF A TELECOMUNICATION TOWER

The tower (Fig.1) is composed of two kinds substructures: truss/frame segments (segment substructure) and circular flange connections (connection substructure). One the flange is welded to the segment end. Brought on the side, the segments are assembled together with, bolts passing through the adjacent flanges. Bolts are pre-stressed to given forces, assumed by a designer. A segment with welded flanges constitutes a structure made of a linear material. However, the assembled tower must be considered as a nonlinear system. This is due the contact and friction forces taking place between flanges and bolts.

In Fig 2, a CFBC consisting of pre-tensioned bolts and contacting flanges is presented.

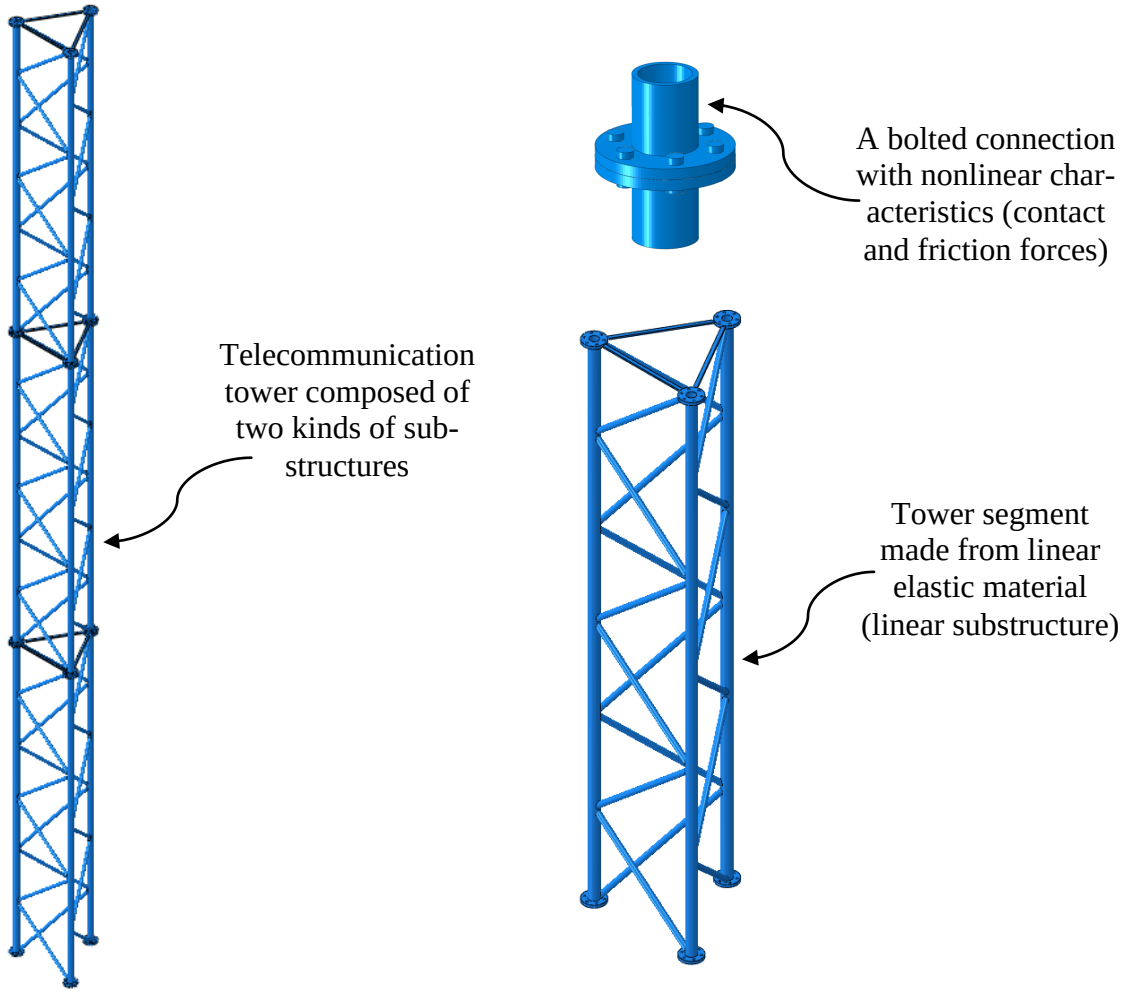


Figure 1. Telecommunication tower and its substructures

3 REDUCED MODEL OF A CFBC

In modeling the CFBC, *isoparametric* elements of 3D FEM are applied. The model is created using a *substructuring* technique [9]. Each of the connection components are modeled separately, and then joined together, they constitute a model of one structure.

After defining the stiffness matrices of the components, the model contact between them is performed, leading to the equilibrium equations of the CFBC in the form:

$$\begin{cases} \mathbf{K}^{(c)}\mathbf{u}^{(c)} = \mathbf{f}^{(c)} + \mathbf{g}^{(c)}(\mathbf{u}^{(c)}) & \\ \mathbf{B}\mathbf{u}^{(c)} = \mathbf{0} & \text{- Compatibility condition} \\ \mathbf{L}^{\mathbf{T}}\mathbf{g}^{(c)}(\mathbf{u}^{(c)}) = \mathbf{0} & \text{- Equilibrium of contact (interface) forces} \end{cases} \tag{1}$$

where : $\mathbf{K}^{(c)}$ is the connection stiffness matrix, $\mathbf{f}^{(c)}$ is the vector of external forces applied to the connection, and $\mathbf{g}^{(c)}$ contains interface, contact and friction forces.

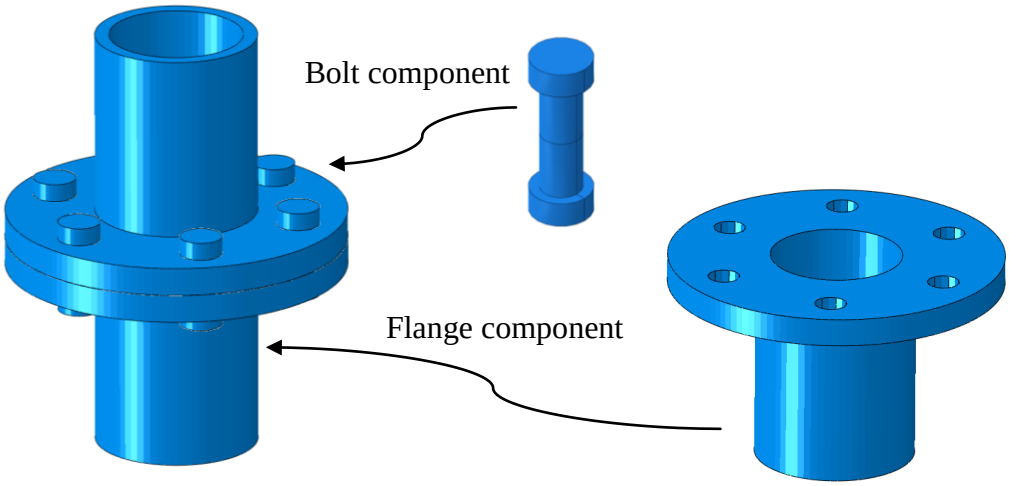


Figure 2. Circular flange-bolted connection and its components

Now, the simulation finding the rigidity of the CFBC is performed with axial forces *f* applied to the ends of the flanges. The connection is assumed to be composed of 30mm thick flanges and bolts of M20. Each connection is welded to the tubes of 114.3mm diameter and wall thickness of 10mm.

The analysis is performed for four different values of pre-stressing bolt force; namely: 100; 80; 60; 40 kN. The force-deformation diagrams for all mentioned cases are presented in Fig 3. The above diagrams allow representing the particular CFBC by nonlinear elastic elements, which will be applied in the reduced tower model. If connections are damaged they can be represented by the mentioned above nonlinear element but of the much smaller stiffness.

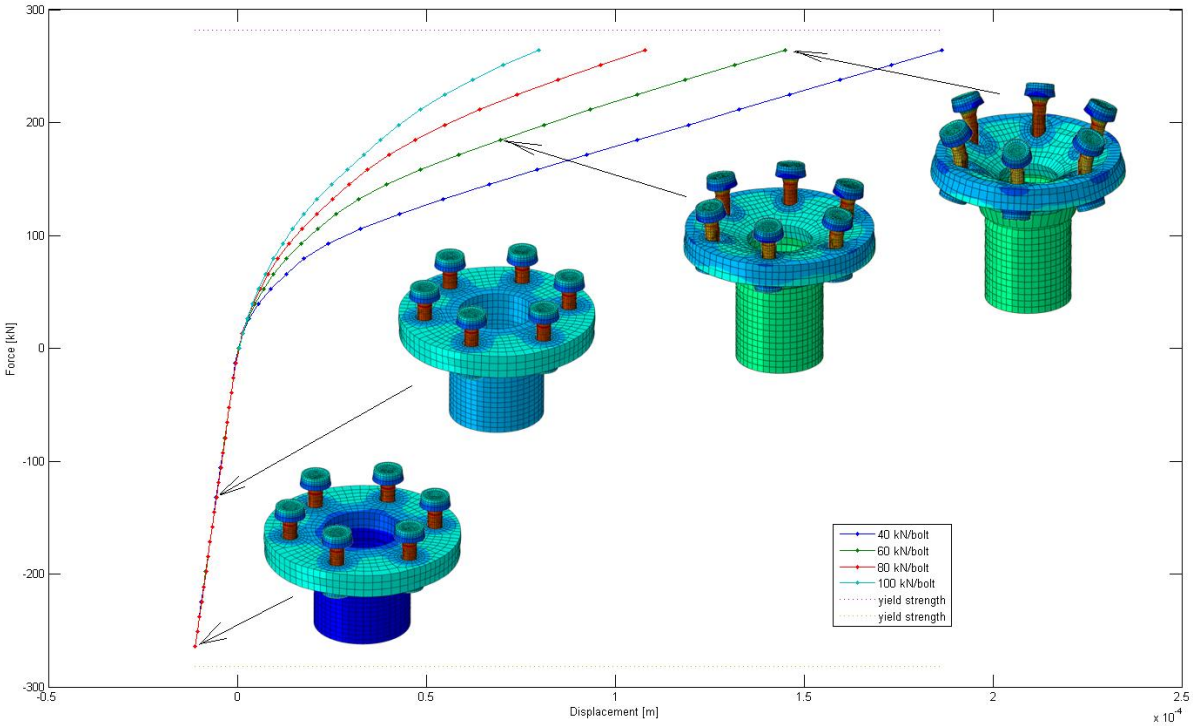


Figure 3. Force-deformation relation for CFBC with four different bolt pre-tension

4 RESPONSE OF AN ASSAMBLED TELECOMUNICATION TOWER TO EXTERNAL DYNAMIC FORCES

Equations of motion for a nonlinear structure have the following form

$$\mathbf{M}\ddot{\mathbf{q}}(t)+\mathbf{r}(\mathbf{q}(t),\dot{\mathbf{q}}(t))=\mathbf{f}^{ext}(t) \tag{2}$$

where: $\mathbf{M}$ - mass matrix, $\mathbf{q}(t)$, $\dot{\mathbf{q}}(t)$, $\ddot{\mathbf{q}}(t)$ are respectively displacement, velocity and acceleration vectors, $\mathbf{r}(\mathbf{q}(t),\dot{\mathbf{q}}(t))$ - nonlinear internal forces including damping and elastic forces, $\mathbf{f}^{ext}(t)$ - external force and t denotes time. The above equations should be considered together with compatibility and interface equilibrium conditions, similarly to equations (1).
Taking into account the nonlinear forces occurring at the tower connections, equations of motion for i-th segment (substructure) can be presented as follows

$$\begin{bmatrix}\mathbf{M}_{uu} & \mathbf{M}_{um} & \mathbf{0}\\ \mathbf{M}_{mu} & \mathbf{M}_{mm} & \mathbf{M}_{ml}\\ \mathbf{0} & \mathbf{M}_{lm} & \mathbf{M}_{ll}\end{bmatrix}^{(i)}\begin{bmatrix}\ddot{\mathbf{q}}_u\\ \ddot{\mathbf{q}}_m\\ \ddot{\mathbf{q}}_l\end{bmatrix}^{(i)}+\begin{bmatrix}\mathbf{K}_{uu} & \mathbf{K}_{um} & \mathbf{0}\\ \mathbf{K}_{mu} & \mathbf{K}_{mm} & \mathbf{K}_{ml}\\ \mathbf{0} & \mathbf{K}_{lm} & \mathbf{K}_{ll}\end{bmatrix}^{(i)}\begin{bmatrix}\mathbf{q}_u\\ \mathbf{q}_m\\ \mathbf{q}_l\end{bmatrix}^{(i)}+\begin{bmatrix}\mathbf{f}_u^{NL}\\ \mathbf{0}\\ \mathbf{f}_l^{NL}\end{bmatrix}^{(i)}=\begin{bmatrix}\mathbf{f}_u^{ext}\\ \mathbf{f}_m^{ext}\\ \mathbf{f}_l^{ext}\end{bmatrix}^{(i)} \tag{3}$$

where: subscripts *u,l* denote upper and lower nodes. The subscript *m* denotes all other nodes. With above notation the equations (3) can be presented shortly as

$$\mathbf{M}^{(i)}\ddot{\mathbf{q}}^{(i)}+\mathbf{K}^{(i)}\mathbf{q}^{(i)}+\mathbf{f}^{NL(i)}=\mathbf{f}^{ext(i)} \qquad i=1,2,\ldots,n_S, \tag{4}$$

where: $\mathbf{M}^{(i)},\mathbf{K}^{(i)}$ - mass and stiffness matrices of i-th tower segment, $\mathbf{f}^{NL(i)}$ - nonlinear forces coming from contact and friction with neighboring segments, n_S - number of the tower segments. The above set of equations is now solved using direct integration approach.

5 DIRECT INTEGRATION OF NON-LINEAR MODEL OF THE TOWER

Combining all n_s equations (4) we come to the full order mode (*FOM*) of the tower

$$\mathbf{M}_{FOM}\ddot{\mathbf{q}}_{FOM}+\mathbf{K}_{FOM}\mathbf{q}_{FOM}+\mathbf{f}_{FOM}^{NL}=\mathbf{f}^{ext} \tag{5}$$

Applying substructuring method for the contact forces, we can represent stiffness matrix and nonlinear internal forces in the following form

$$\mathbf{K}_{FOM}=\begin{bmatrix}\mathbf{K}^{(1)} & \mathbf{0} & \cdots & \mathbf{0}\\ \mathbf{0} & \mathbf{K}^{(2)} & \cdots & \mathbf{0}\\ \vdots & \vdots & \ddots & \vdots\\ \mathbf{0} & \mathbf{0} & \cdots & \mathbf{K}^{(n_S)}\end{bmatrix} \qquad \mathbf{f}_{FOM}^{NL}=\begin{bmatrix}\begin{bmatrix}\mathbf{f}_u^{NL}\\ \mathbf{0}\\ \mathbf{f}_l^{NL}\end{bmatrix}^{(1)}\\ \begin{bmatrix}\mathbf{f}_u^{NL}\\ \mathbf{0}\\ \mathbf{f}_l^{NL}\end{bmatrix}^{(2)}\\ \vdots\\ \begin{bmatrix}\mathbf{f}_u^{NL}\\ \mathbf{0}\\ \mathbf{f}_l^{NL}\end{bmatrix}^{(n_S)}\end{bmatrix}$$

where $\mathbf{f}_{FOM}^{NL}$ represents terms, coupling stiffness matrices of elements in contact.

6 REDUCED ORDER MODEL OF THE TOWER BASED ON SUBSPACE PROJECTION

Let now reduce the *FOM* to a simpler model. It consists in dividing the dynamic problem in two steps. The first one is based on nonlinear static analysis giving the response of the tower to mean (static) value of the dynamic loading. In the second step, we are reducing the system of dynamic equations by applying Ritz vector approach. In this way we obtain a smaller number of coupled equations, representing dynamic modes of the vibrating tower.

Based on the above assumption we formulate the problem as follows:

Step 1

We perform static analysis with the following equation

$$\mathbf{K}_0(\mathbf{q}_0)\mathbf{q}_0 = \mathbf{f}_0^{ext} \tag{6}$$

Step 2

We reduce the number of dynamic equations starting with static response $\mathbf{v}_1 = \mathbf{q}_0$, as the first vector of the reduced basis. Next, we apply the Gram-Schmidt orthogonalization for finding whole set of vectors $\mathbf{V} = [\mathbf{v}_1, \mathbf{v}_2, ..., \mathbf{v}_{n_R}]$. This way we get a reduced order model (*ROM*)

$$\ddot{\eta}_{FOM} + \mathbf{K}_{ROM}\eta_{ROM} + \mathbf{f}_{ROM}^{NL} = \mathbf{V}^T\tilde{\mathbf{f}}^{ext} \tag{7}$$

where

$$\begin{aligned} \mathbf{V}^T\mathbf{M}_{FOM}\mathbf{V} &= \mathbf{I} \\ \mathbf{K}_{ROM} &= \mathbf{V}^T\mathbf{K}_0\mathbf{V} \\ \mathbf{f}_{ROM}^{NL} &= \mathbf{V}^T\mathbf{f}_{FOM}^{NL} \end{aligned} \tag{8}$$

and $\tilde{\mathbf{f}}^{ext}$ denotes fluctuating part of external loading and η_{ROM} modal amplitude vector.

7 NUMERICAL EXAMPLE – SIMULATION OF THE TOWER DYNAMIC RESPONSE WITH DAMAGED CONNECTIONS

The tower is assembled of 4 truss segments, of triangular cross section, interconnected with CFBCs. The dimension of the triangular cross section of the tower's segment is 1.2 m, and the height of the segment is 6 m. The segment is made of 114.3 mm diameter tubes, having 8 mm wall thickness. CFBCs are composed of two 3 cm thick circular flanges, assembled with 6 pre-tensioned bolts of 20 mm diameter. Bolts in all connections are pre-tensioned, with the 400 Nm torque. It is assumed that one connection located between first and second truss segment (Figure 4), may be partially damaged. It means, that their stiffness for tension is smaller than those of healthy ones.

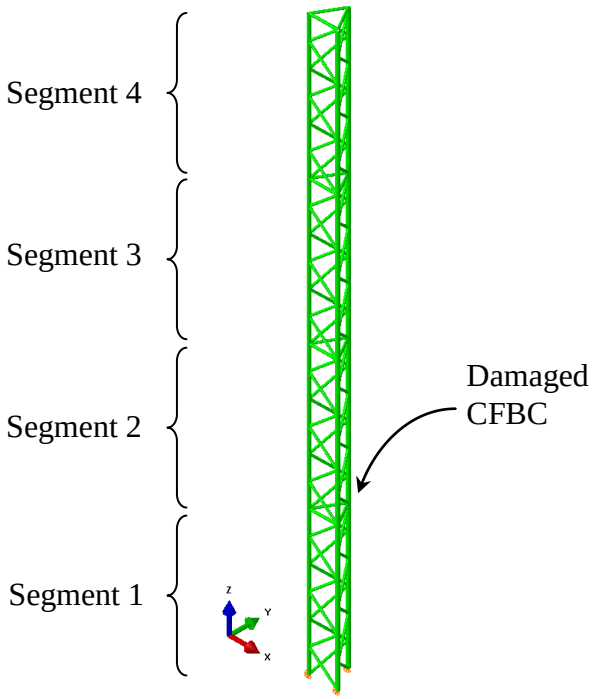


Figure 4. Telecommunication tower under investigation.

As it was mentioned in chapter 3, damaged CFBC exhibits strongly nonlinear behavior. It can be observed from Fig 3, that compression stiffness can be few orders of magnitude higher than for tension. For that reason, two cases of the dynamic response of the tower with a damaged connection are considered. It is assumed that in both of them, forces acting on the tower have the time history, as shown in Fig 5 and are composed of two parts. The first one is the long-term wind pressure causing static deformation of the tower. The second one is the instantaneous wind gusts, inducing oscillations of the tower.
Depending on the direction of the forces acting on the tower, the damaged CFBC is either in compression, or in tension (Fig 6).

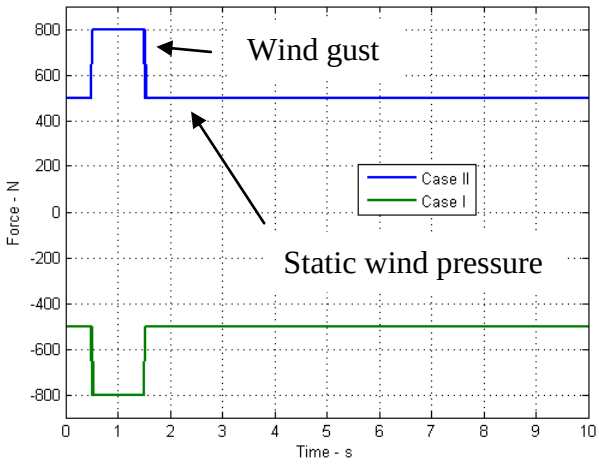


Figure 5. Time history of the forces in dynamic analysis

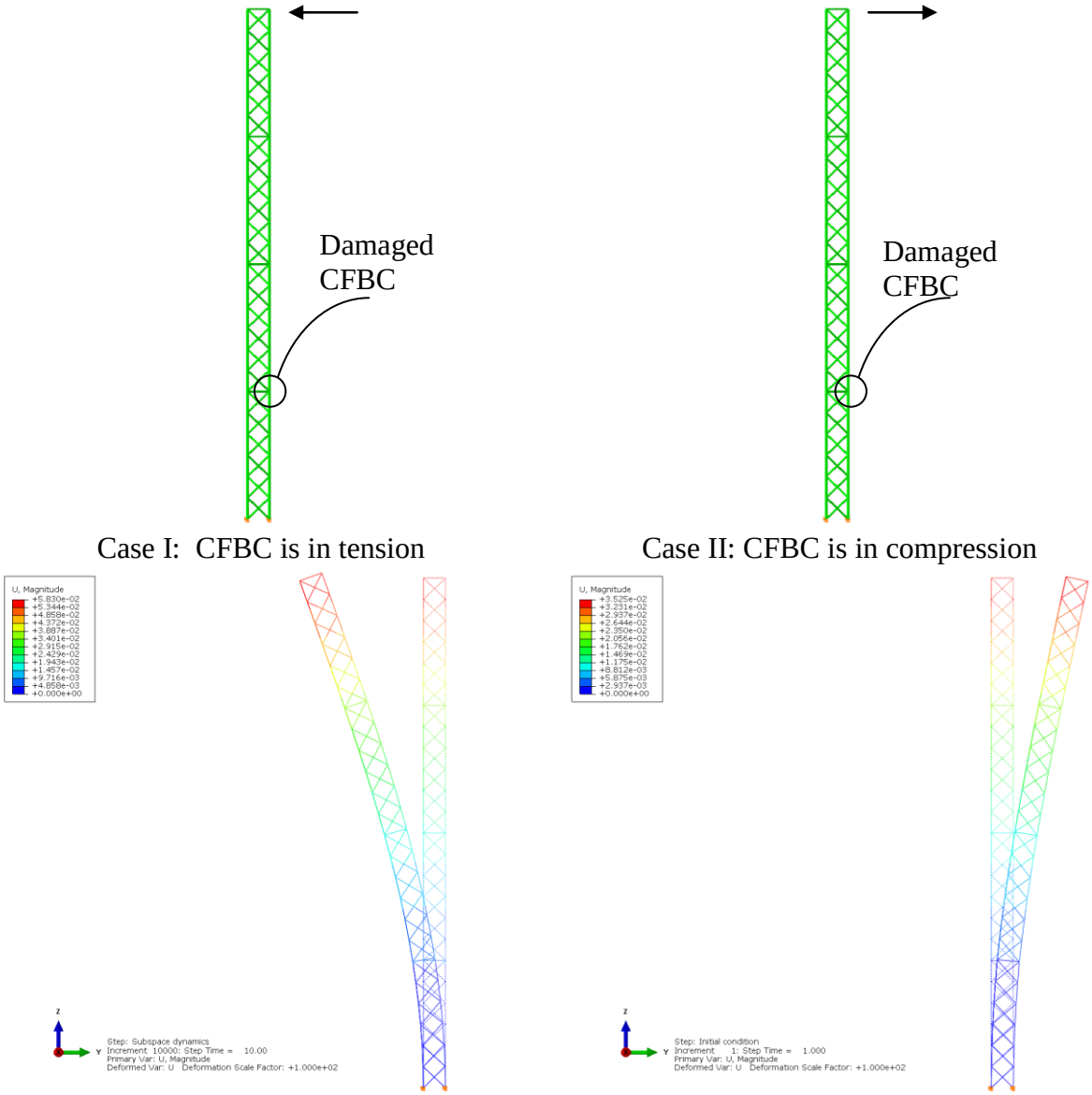
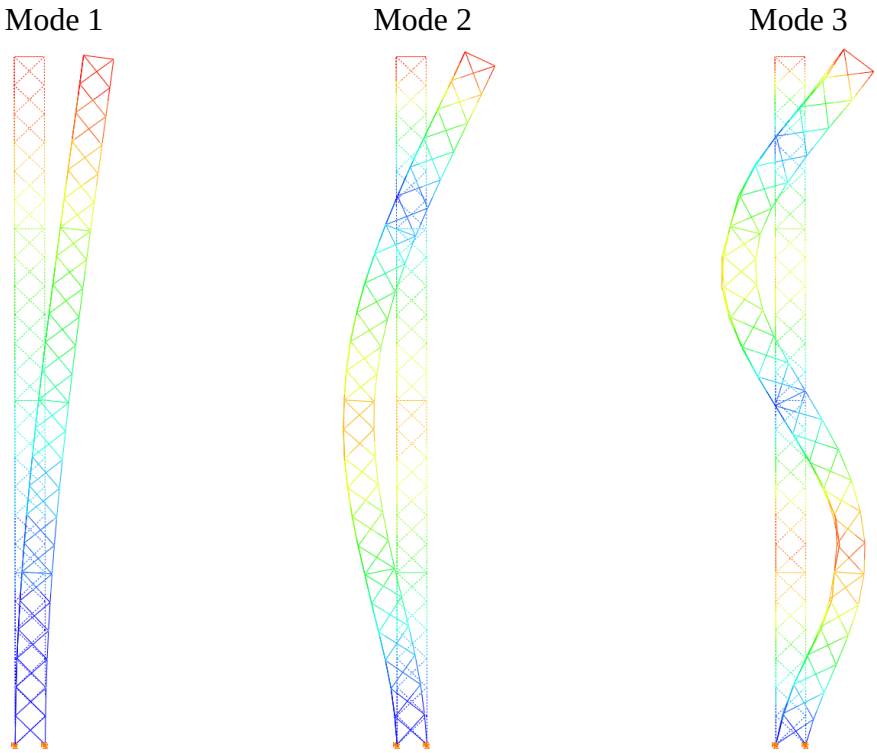


Figure 6. The damaged CFBC in tension (case I) and in compression (case II).
The tower deformation is magnified 100 times.

Unsymmetrical response of the tower under static wind pressure, depending on its direction can be observed on Fig 6. This is caused by much lower stiffness of CFBC in tension, than in compression.

After determining initial static deformation of the tower, the natural frequencies and mode shapes for both cases are discussed.

The first three mode shapes for both discussed cases are shown in Fig 7. One can observe differences in the corresponding natural frequencies. Comparing first frequencies for both cases, we find that first natural frequency for the case II is smaller than in the case I.



Case I	1.6267 Hz	9.6388 Hz	24.743 Hz
Case II	1.5508 Hz	9.6182 Hz	24.008 Hz

Figure 7. Comparison of the natural frequencies in both cases.

After having determined the mode shapes of the tower with damaged CFBC, the response time history of the tower is found and shown on Figures 8 and 9.
Time responses for both cases have been obtained using techniques described in chapters 5 and 6, namely: Direct Integration and Reduced Order Model. In the latter one, a different number of modes are included into analysis, showing their influence on accuracy of calculations (Figure 8 and 9).

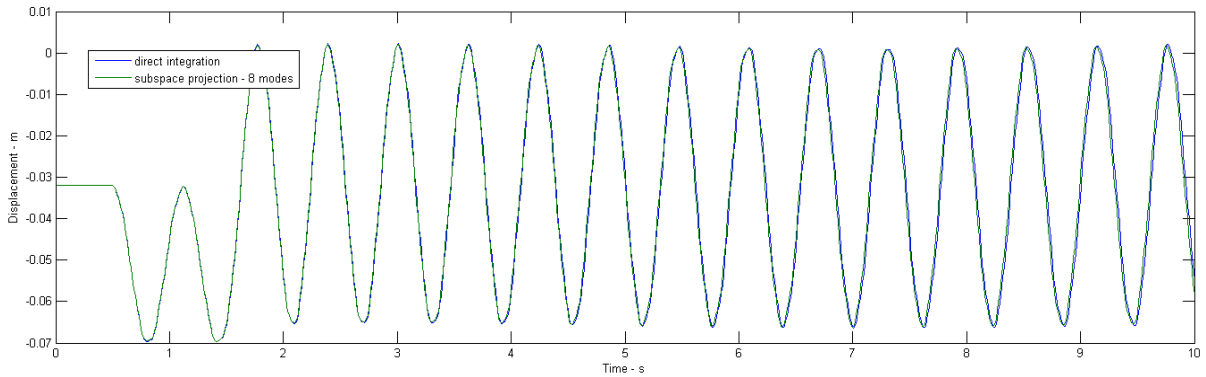


Figure 8. Displacement of the top of the tower (Case I).

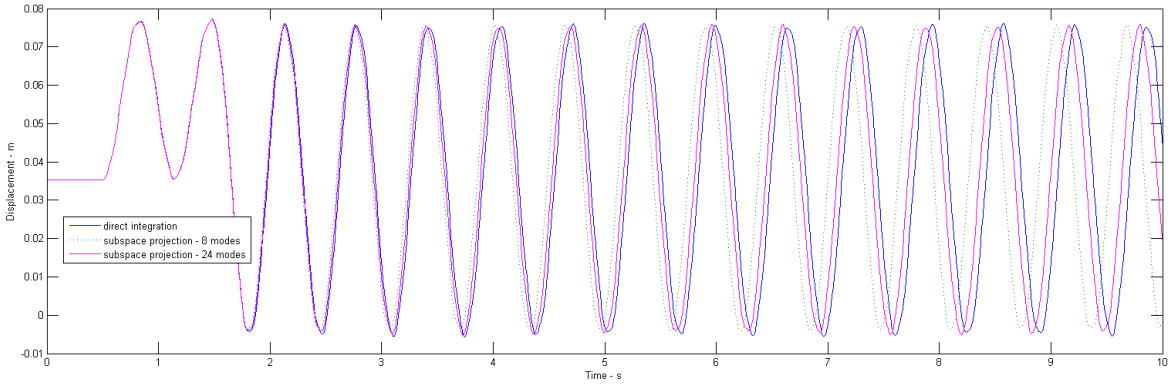


Figure 9. Displacement of the top of the tower (Case II).

Comparing Figures 8 and 9 we conclude that 8 modes are enough to estimate the tower response, in the Case I. The displacement responses obtained with the aid of both methods are almost the same. This is showing that with ROM, significant computational efforts can saved. However, this is not the case, when CFBC is in compression. Up to 24 modes have to be used, in order to obtain better estimation of the direct integration solution. Using only 8 modes in ROM, it is insufficient to estimate the response of the structure with assumed accuracy.
Finally, in the figure 10, the Fourier transform of displacements in both cases is compared. It confirmed, that the in the Case II structure vibrates with fundamental frequency, lower than in the Case I.

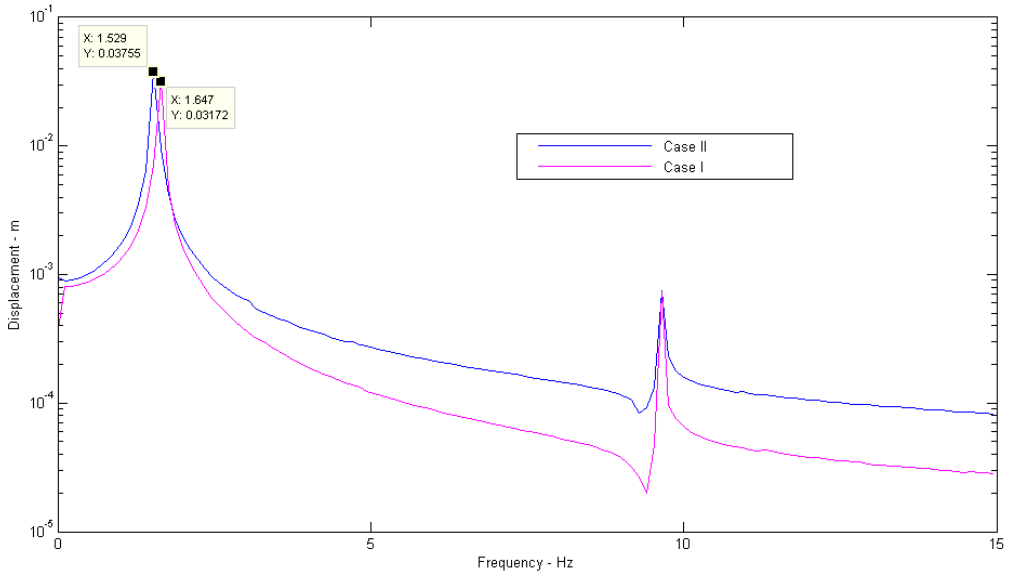


Figure 10. Fourier transform of the displacements.

8 CONCLUSIONS

A Reduced Order Model of vibrating telecommunication tower is presented. The model is composed of two parts. In the first one, applying substructuring approach, the reduced model of a CFBC, including contact and friction forces, is discussed (Section 3). The connection composed of flanges and bolts is here reduced to a nonlinear elastic element.

In the second part, tower segments are considered as substructures, and then the CFBC structure is replaced by mentioned above nonlinear elastic elements (Section 6). This approach allows diminishing the numerical efforts by reducing the model to few important modal shapes.
The direct integration of non-linear, whole model of the tower (Section 5), in turn, gives a view how much results obtained by the reduced model differs from exact ones. This can be observed in the numerical example (Section 7).
Moreover, in the example, a notion of a damaged connection is introduced. The damage is represented by an elastic nonlinear element of stiffness, several times smaller than stiffness of healthy connections. The tower is subjected to dynamic wind forces, which are decomposed in long-term wind pressure, causing static deformation of the tower and instantaneous wind gusts, inducing oscillations of the tower.
The differences in the deformations of a tower, with all healthy CFBCs, and one damaged don't look very significant from the structural point of view. Nevertheless, in some cases, when the damage consists in failure of one or more bolts the stress in nonlinear connection can significantly increase.

ACKNOWLEDGEMENTS

The authors are grateful for financial support from the National Science Centre of Poland (grant N N501 0494 40).

REFERENCES

[1] B.Blachowski, W.Gutkowski, *Revised assumptions for monitoring and control of 3D lattice structures*. 11th Pan-American Congress of Applied Mechanics PACAM XI, Foz do Iguassu, Brasil, 2010.

[2] F. Amerini, and M. Meo., Structural health monitoring of bolted joints using linear and nonlinear acoustic/ultrasound methods. *Structural Health Monitoring - An International Journal*, **10(6)**, 659-672, 2011.

[3] I. Pavelko, V. Pavelko, S. Kuznecovs, I. Ozolins, Bolt-Joint Structural Health Monitoring by the Method of Electromechanical Impedance. Aircraft Engineering and Aerospace Technology, **86(3)**, 207-214. ISSN 0002-2667. Available from: doi:10.1108/AEAT-01-2013-0006, 2014.

[4] T. Wang, G. Song, S. Liu, Y. Li, and H. Xiao, Review of Bolted Connection Monitoring, *International Journal of Distributed Sensor Networks*, (**2013**), Article ID 871213, 8 pages, http://dx.doi.org/10.1155/2013/871213, 2013.

[5] J. N. Yang; Y. Xia; and C.H. Loh, Damage Identification of Bolt Connections in a Steel Frame, *ASCE Journal of Structural Engineering*, **140(3)**, 04013064, 2014.

[6] K. He, W.D. Zhu, A vibration-based structural damage detection method and its applications to engineering structures, *International Journal of Smart and Nano Materials*, 09/2011, **2:3**, 194-218, DOI: 10.1080/19475411.2011.594105, 2011.

[7] Y. Luan, Z.Q. Guan, G.D. Cheng, S. Liu, A simplified nonlinear dynamic model for the analysis of pipe structures with bolted flange joints, *Journal of Sound and Vibration*, **331,** 325-344, 2012.

[8] V. Roulet, L. Champaney, P.A. Boucard, A parallel strategy for the multiparametric analysis of structures with large contact and friction surfaces, *Advances in Engineering Software*, **42(6)**, 347–358, 2011.

[9] D. de Klerk, D. J. Rixen, and S. N. Voormeeren, General Framework for Dynamic Substructuring: History, Review, and Classification of Techniques, *AIAA Journal*, **46(5)**, 2008.

[10] R.K. Kapani and C. Byun, Reduction methods based on eigenvectors and Ritz vectors for nonlinear transient analysis, *Computational Mechanics*, **11**, 65-82, 1993.

COMPDYN 2015
5th ECCOMAS Thematic Conference on
Computational Methods in Structural Dynamics and Earthquake Engineering
M. Papadrakakis, V. Papadopoulos, V. Plevris (eds.)
Crete Island, Greece, 25–27 May 2015

COMPARATIVE STUDY OF THE WIND AND EARTHQUAKE DYNAMIC RESPONSES OF FIRE EXPOSED STEEL FRAMED BUILDINGS

Fabio Mazza[1] **and Marco Fiore**[2]

[1]Dipartimento di Ingegneria Civile, Università della Calabria
Via P. Bucci, 87036 Rende (CS), Italy
fabio.mazza@unical.it

[2]Dipartimento di Ingegneria Civile, Università della Calabria
Via P. Bucci, 87036 Rende (CS), Italy
fioremarco1989@libero.it

Keywords: Steel Framed Structures, Fire Scenarios, Time-Temperature Curves, Along-wind loads, Seismic Loads, Dynamic Analysis.

Abstract. *Wind design of steel-framed buildings aims to provide appropriate stiffness and strength properties of the structural elements, so as to obtain an elastic behaviour, at the same time as controlling floor displacements and accelerations. On the other hand, in a seismic design it is commonly accepted that the structural members can undergo inelastic deformations under strong ground motions, provided that these deformations be kept within an acceptable threshold; moreover, deformability thresholds are also imposed at the serviceability limit state. Nevertheless, knowledge on the wind and seismic responses in the case of fire is lacking and an amplification of the structural response is expected in the case of existing structures exposed to fire. To evaluate the wind and seismic responses following a fire, a numerical investigation is carried out with reference to the steel framed structure of a ten-storey office building, which was designed for a low-risk zone under the former Italian seismic code and in line with Eurocodes 1 and 3. More specifically, the dynamic response of the test structure in a no fire situation, along the in-plan principal directions, is compared with what would happen in the event of fire, at 500°C, 550°C and 600°C fire temperatures, hypothesizing a reduction of stiffness and strength due to fire. Four fire scenarios have been considered on the assumption that the fire compartment is confined to the area of the first level (i.e. F1), the first two (i.e. F1/2) and the upper (i.e. Fi, i=5, 10) levels, with the parametric temperature-time fire curve evaluated in accordance with Eurocode 1. Dynamic analyses are carried out in the time domain using a step-by-step initial stress-like iterative procedure. Along-wind loads are considered assuming, at each level, time histories of the wind velocity for two return periods (i.e. T_r=10 or 50 years), based on an equivalent spectrum technique. Real accelerograms, whose response spectra match those adopted by Italian seismic code for a medium-risk seismic zone and a medium subsoil class, are considered to simulate the seismic loads.*

1 INTRODUCTION

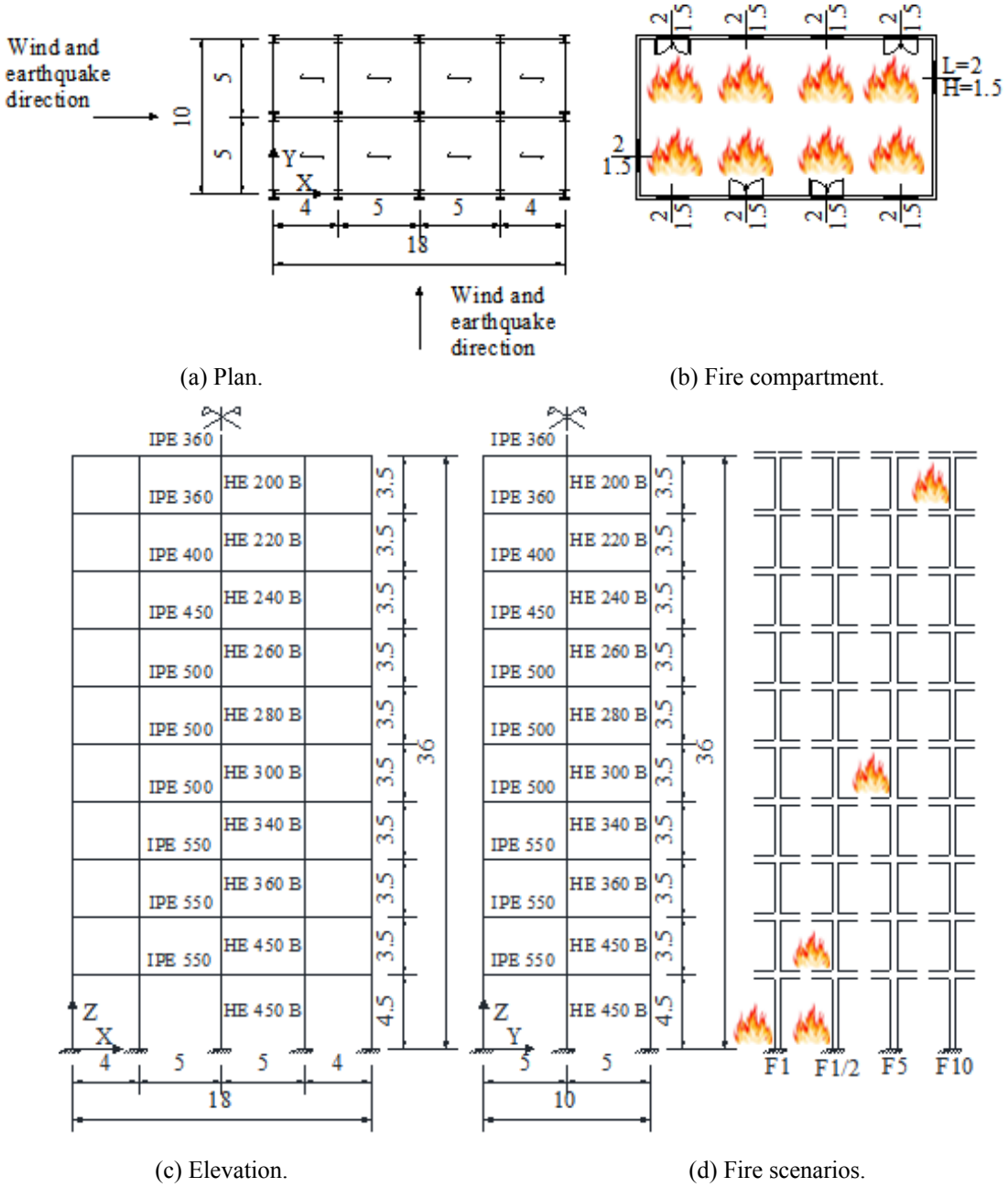
The conventional design of steel framed buildings subjected to wind loads aims to provide stiffness and strength properties of the structural elements to control floor displacements and accelerations, such that an efficient use of the structure and suitable living comfort are guaranteed; in addition, there are provisions to avoid buckling and excessive deformability. On the other hand, in the aseismic design it is commonly accepted that the structural steel members can undergo inelastic deformations under strong ground motions, provided that be kept within an acceptable threshold, while damage limitation requirements are also imposed at the serviceability limit state. However, stiffness and strength properties of steel degrade at high temperatures and this deterioration needs to be properly accounted for in the design of steel structures in the event of fire [1]. The occurrence of fire following earthquake has gained attention of many recent numerical and experimental studies into the nonlinear response of steel [2-5] and composite steel-concrete [6] structures. Nevertheless, knowledge on the wind and seismic dynamic responses of steel framed buildings damaged by fire is lacking and an amplification of the structural response for the serviceability and ultimate limit states is to be expected in such cases. Moreover, little attention has been paid to the influence of fire scenarios on the structural behaviour of steel framed buildings.

In the present work, the wind and earthquake responses of steel framed structures in a no fire situation, along the in-plan principal directions, are compared with those in which fire occurs, at 500°C, 550°C and 600°C temperatures, assuming stiffness and strength properties of the frame members in line with the reduction factors proposed by Eurocode 3 [7]. To this end, ten-storey steel office buildings are designed in line with the previous Italian seismic code [8] for a low-risk zone, as well as the provisions of Eurocode 3. Wind actions are evaluated in compliance with Eurocode 1 [9]. Four fire scenarios are hypothesized assuming the fire compartment confined to the area of the first level (i.e. F1), the first two (i.e. F1/2) and the upper (i.e. Fi, i=5, 10) levels, with the parametric temperature-time fire curve evaluated in line with Eurocode 1. In order to consider along-wind loads, at each storey, time histories of the wind velocity for two return periods (i.e. T_r=10 or 50 years) are assumed, in accordance with an equivalent spectrum technique [10]. Then, real accelerograms, whose response spectra match those adopted by the current Italian seismic code [11] for a medium-risk seismic zone and a medium subsoil class, are considered to simulate seismic loads. Finally, dynamic analyses are carried out in the time domain through a step-by-step initial stress-like iterative procedure [12, 13]. For this purpose, the frame members are idealized by a bilinear model, which allows the simulation of the nonlinear behaviour under seismic loads [14, 15].

2 STEEL TEST STRUCTURE: DESIGN AND FIRE MODELLING

The symmetric steel structure, with a rectangular plan (Figure 1a), of a ten-storey office building (Figure 1c) is considered as test structure in this study. More precisely, moment resisting frames are placed to carry (horizontal) wind or seismic loads, while a grid of main and secondary girders support at the floor levels a composite deck with horizontal bracing. A simulated design of the test structure is carried out in line with the previous Italian seismic code (DM96, [8]), for a low-risk seismic region (degree of seismicity S=6, which corresponds to a coefficient of seismic intensity C=0.04), a medium subsoil class (subsoil parameter ε=1) and a coefficient of seismic protection equal to 1.2. Wind actions are evaluated in compliance with Eurocode 1 [9], assuming: flat terrain with a roughness length of 0.30 m; urban area (class B of terrain roughness) with a reference velocity of 28 m/s, which represents a mean value of those assumed for the nine zones of the Italian wind map; altitude of 500 m above sea level. Moreover, the test structure also satisfies the ultimate limit states for strength and

buckling evaluated in accordance with Eurocode 3 [7]. An ultimate strength of 510 N/mm^2 is assumed for the steel frame members, for which ductile cross-sections regularly tapering in elevation are selected in accordance with class 1 of Eurocode 3 (Figure 1c). For the sake of simplicity, the plane frames orientated along the horizontal earthquake and wind directions (i.e. X and Y shown in Figure 1a) are considered as a reference scheme.



(a) Plan. (b) Fire compartment.

(c) Elevation. (d) Fire scenarios.

Figure 1: Steel test structure (dimensions in m).

The gravity loads considered in the design are represented by dead loads of 3.66 and 4.51 kN/m^2 for the top floor and the others, respectively, and a live load of 3 kN/m^2 for all floors. The weight of sandwich panels, regularly distributed in elevation as external cladding of the building, is taken into account with a dead load of 1.4 kN/m. The dynamic properties of the six main vibration modes are reported in Table 1: i.e. vibration period (T_i); effective masses in the X ($m_{E,X}$) and Y ($m_{E,Y}$) directions, expressed as percentage of the total mass (m_{tot}).

Vibration Mode	T_i [s]	$m_{E,X}$ [%m_{tot}]	$m_{E,Y}$ [%m_{tot}]
1	1.938	80.5	0
2	1.402	0	72.3
3	0.787	13.1	0
4	0.549	0	15.2
5	0.475	3.6	0
6	0.330	0	5.8

Table 1: Dynamic properties of the test structure (m_{tot}= 10.6 kNs^2/cm).

Four fire scenarios have been reported in Figures 1b and 1d, assuming the fire compartment confined to the area of the first level (i.e. F1), the first two (i.e. F1/2) and the upper (i.e. Fi, i=5, 10) levels. It is worth noting that F1/2 fire scenario is obtained from the F1 and F2 ones, which are assumed to occur simultaneously. The geometric properties of the fire compartment are reported in Table 2, assuming three values of the maximum temperature (i.e. T=500°C, 550°C and 600°C) for the first and the upper levels: i.e. L, D and H representing length, depth and height, respectively; A_f, floor area; A_t, total area of enclosure (i.e. walls, ceiling and floor, including openings); A_v, total area of vertical openings; h_{eq}, weighted average height of windows. From these values it is possible to define an opening factor, representing the amount of ventilation:

$$O = A_v h_{eq}^{\ 0.5} \Big/ A_t \tag{1}$$

Fire compartment	L [m]	D [m]	H [m]	A_f [m^2]	A_t [m^2]	h_{eq} [m]	T [°C]	A_v [m^2]	O [m$^{0.5}$]
First level	18	10	4.5	180	612	1.5	500	9	0.018
							550	12	0.024
							600	15	0.030
Upper levels	18	10	3.5	180	556	1.5	500	9	0.020
							550	12	0.026
							600	12	0.026

Table 2: Geometric properties of fire compartment.

As an example, the distribution of windows opened at the upper levels, corresponding to A_v= 12m^2, is shown in Figure 1b. It is worth noting that the uniform temperature in the selected compartment is considered to be the most severe condition for the fire before wind or earthquake. Several models can be used to simulate the time-temperature evolution during an actual fire, from the flashover to the full development: conventional fire curves (e.g. the standard ISO-834 curve [16]), in which temperature monotonically increasing with time represents the heating phase only when the fuel supply is assumed to be inexhaustible; natural fire curves (e.g. the EC1 curve [9]), in which temperature depends on the ventilation and fire load in the compartment and the cooling phase is represented, based on the assumption that, at a certain point, either the air or the combustible material will diminuish.

The EC1 parametric fire curve is used in the present study, on the assumption that the fire load of the compartment is completely burnt out. In the heating phase, the gas temperature (in °C)

$$\theta_g = 20 + 1325\left(1 - 0.324e^{-0.2t^*} - 0.204e^{-1.7t^*} - 0.472e^{-19t^*}\right) \tag{2}$$

is a function of a fictitious time t^* obtained considering the time t (in hours) multiplied by a dimensionless parameter equal to

$$\Gamma = \left(O/b\right)^2 \Big/ \left(0.04/1160\right)^2 \tag{3}$$

where b is the thermal absorptivity of surrounding surfaces of the compartment

$$b = \sqrt{\rho c \lambda} \tag{4}$$

ρ being the density, c the specific heat and λ the thermal conductivity of boundary of enclosure.

The gas temperature in the cooling phase is given by

$$\begin{aligned} & t^*_{\max} \le 0.5\ h \rightarrow \theta_g = \theta_{\max} - 625\left(t^* - t^*_{\max}\right) \\ & 0.5\ h < t^*_{\max} < 2\ h \rightarrow \theta_g = \theta_{\max} - 250\left(3 - t^*_{\max}\right)\left(t^* - t^*_{\max}\right) \\ & t^*_{\max} \ge 2\ h \rightarrow \theta_g = \theta_{\max} - 250\left(t^* - t^*_{\max}\right) \end{aligned} \tag{5}$$

where the maximum temperature θ_{max} in the heating phase happens for

$$t^*_{\max} = \left(0.2 \cdot 10^{-3} q_{t,d} / O\right) \Gamma \tag{6}$$

being the design fire load density

$$q_{t,d} = q_{f,d}\ A_f / A_t \tag{7}$$

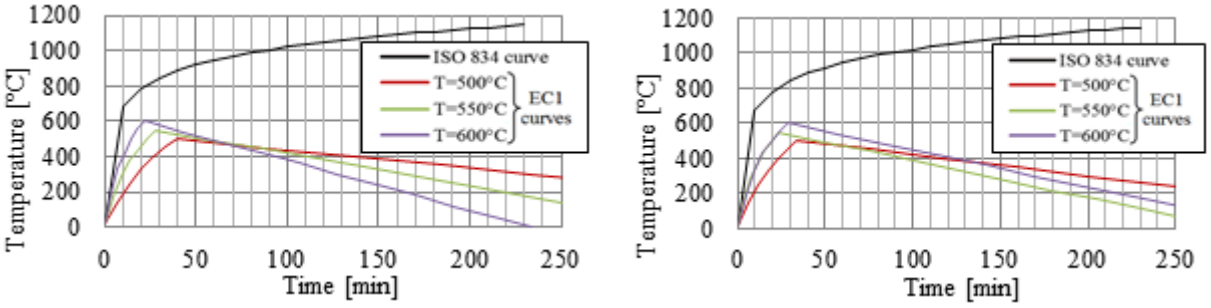
related to the value $q_{f,d}$ corresponding to the surface area of the floor (A_f). Further details on fire modelling can be found in [17, 18].

Finally, the standard ISO-834 curve is defined as [16]

$$\theta_g = 20 + 345 \log_{10}\left(8t + 1\right) \tag{8}$$

where t is expressed in hours.

With reference to the fire scenarios shown in Figure 1, the ISO and EC1 time-temperature curves are compared in Figure 2 in the case where a fire compartment is confined to the area of the first level (Figure 2a) and the upper ones (Figure 2b). Fire parameters, for the opened-plan office building, are reported in Table 3 assuming three values of the maximum temperature (i.e. T=500°C, 550°C and 600°C) in the EC1 time-temperature curves.



(a) Fire compartment at 1st level. (b) Fire compartment at upper levels.

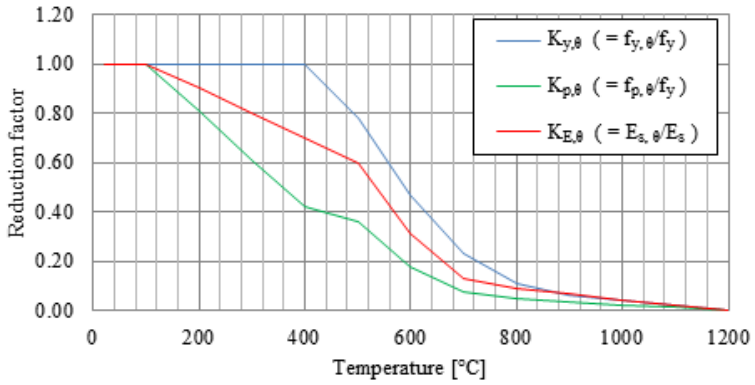
Figure 2: Conventional (ISO 834) and natural (EC1) fire curves.

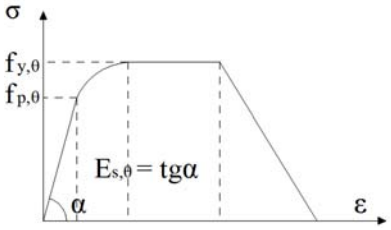
	First level			Upper levels		
T (°C)	$q_{f,d}$ (MJ/m^2)	b (J/m^{2}s$^{1/2}$K)	t^*_{max} (h)	$q_{f,d}$ (MJ/m^2)	b (J/m^{2}s$^{1/2}$K)	t^*_{max} (h)
500	203.44	1660	0.07	174.43	1692	0.07
550	186.91	1666	0.08	160.47	1699	0.08
600	186.21	1671	0.10	198.11	1696	0.10

Table 3: Fire parameters in the EC1 time-temperature curves [9].

3 NUMERICAL RESULTS: FIRE BEFORE WIND AND EARTHQUAKE

Once the time-temperature curve of the fire compartment is determined with the EC1 model, it becomes possible to evaluate the reduction factors (K) of effective yield strength ($f_{y,\theta}$), proportional limit ($f_{p,\theta}$) and slope of the linear elastic range ($E_{s,\theta}$) of stress-strain law of the steel at the maximum temperature (T) of 500 °C, 550°C and 600°C (Figure 3). As can be observed, a decrease of stiffness (i.e. $K_{E,\theta}$) and yield strength (i.e. $K_{y,\theta}$) from a minimum, of about 40% and 22% at T=500°C, and a maximum, of about 69% and 53% at T=600°C, respectively, is obtained in line with Eurocode 3 [7].

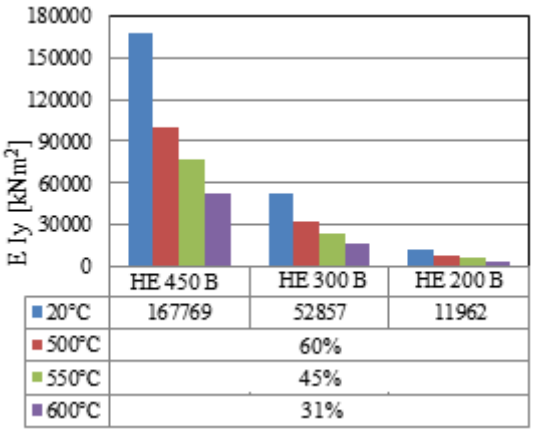




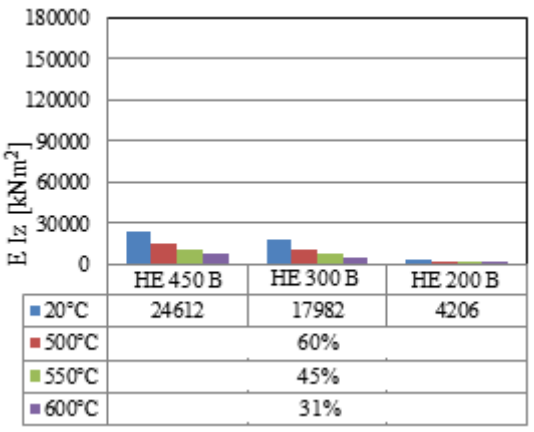
T	500°C	550°C	600°C
$K_{y,\theta}$	0.78	0.63	0.47
$K_{p,\theta}$	0.36	0.27	0.18
$K_{E,\theta}$	0.60	0.46	0.31

Figure 3: Reduction factors for the steel stress-strain law at high temperatures [7].

Subsequently, the residual seismic load capacity of the cross-sections after fire, in terms of stiffness and strength reductions, is evaluated. In detail, columns and girders are considered exposed to fire on all sides in accordance with the assumption of uniform temperature distribution in cross-section. This hypothesis is justified by the high thermal conductivity of steel and the thinness of the cross-sections. In Figure 4, flexural stiffness of steel columns is reported along the building height, assuming a direct correspondence between the examined level and the fire compartment. In particular, major (i.e. EI_y in Figure 4a) and minor (i.e. EI_z in Figure 4b) axes of bending are examined at the maximum temperatures T=500°C, T=550°C and T=600°C. Note that a local decrease in stiffness from a minimum of about 40% to a maximum of about 69% is obtained in comparison with the no-fire condition. Similar results are reported in Figure 5a with reference to the longitudinal and transversal girders.

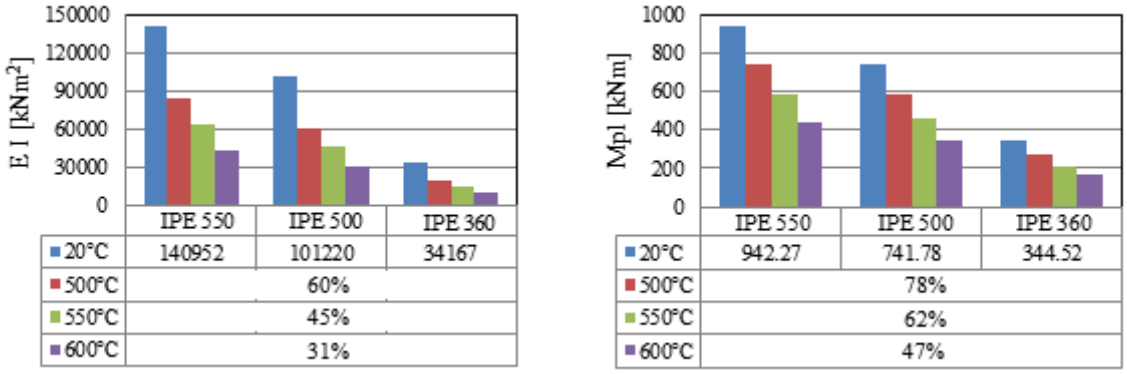


(a) Major bending axis.



(b) Minor bending axis.

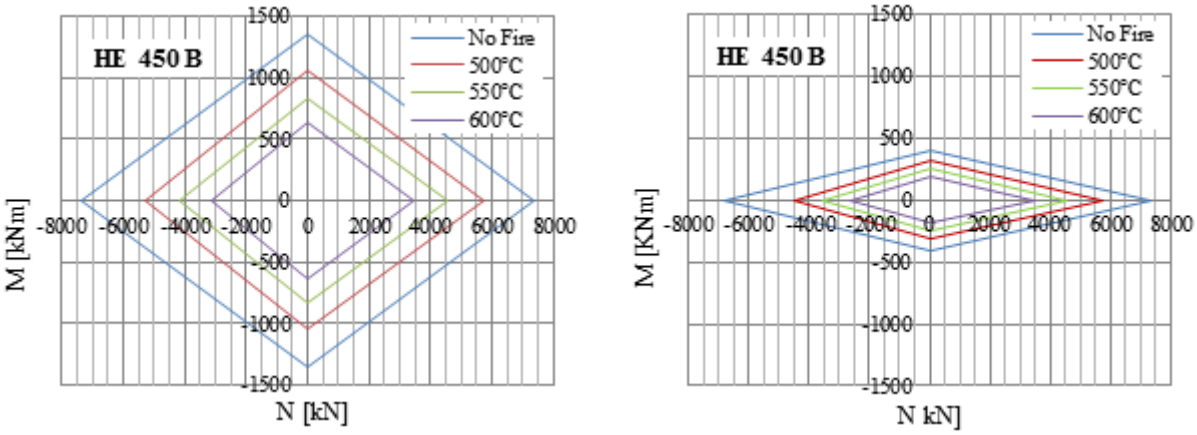
Figure 4: Flexural stiffness of steel columns exposed to fire.



(a) Flexural stiffness. (b) Plastic moment.

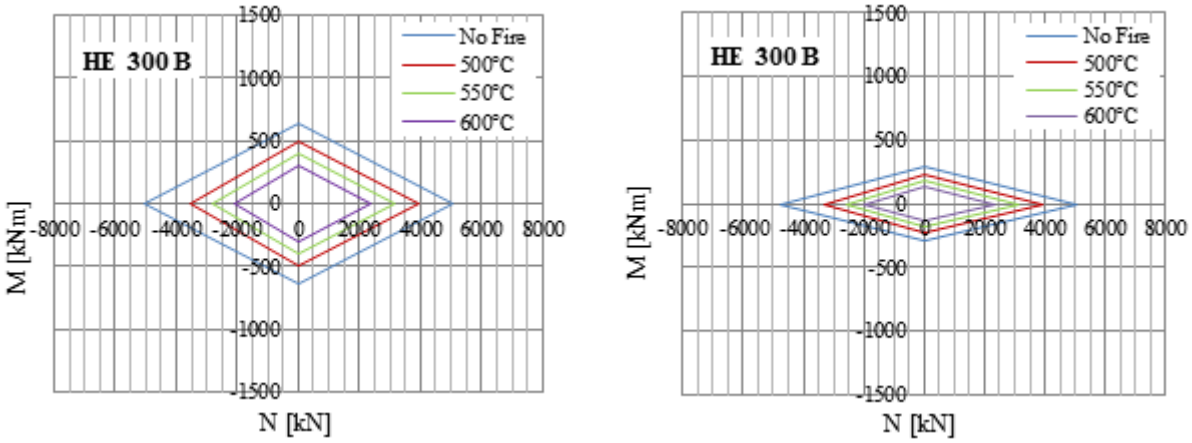
Figure 5: Mechanical properties of steel girders exposed to fire.

Finally, results are reported for the plastic bending moment (*M*) of girders (Figure 5b) and plastic interaction domain between axial load (*N*) and bending moment (*M*) of columns (Figure 6). A simplified calculation is carried out based on an elastic-perfectly plastic stress-strain law of the steel with reduced values of elasticity modulus and yield strength. Moreover, the *N*-*M* domain is obtained analogously to the provisions of EC3, simply by replacing the plastic axial load under uniform compression with the buckling load.



(a) Major bending axis (1st storey/F1).

(b) Minor bending axis (1st storey/F1).



(c) Major bending axis (5th storey/F5).

(d) Minor bending axis (5th storey/F5).

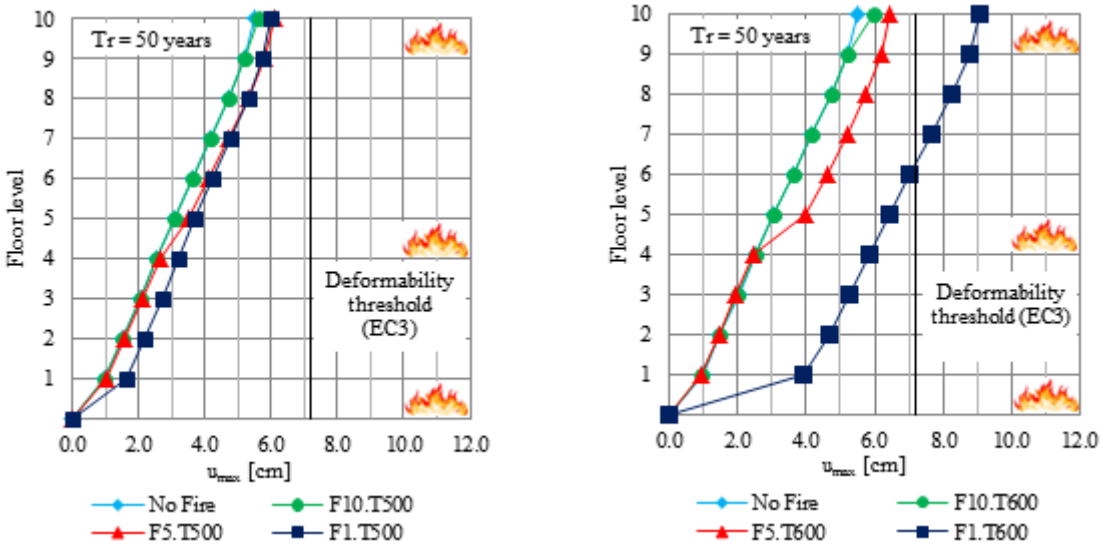
Figure 6: Plastic *N*-*M* domains of steel columns exposed to fire.

Only the fire compartments at the first (i.e. F1 scenario in Figures 6a and 6b) and fifth (i.e. F5 scenario in Figures 6c and 6d) levels are examined for the columns. As can be observed, a significant decrease in strength is observed for the girders, with a maximum local reduction of about 53% in the case of T=600°C (Figure 5b). On the other hand, the columns exhibit a marked narrowing of their N-M domains, especially for the buckling load showing a maximum reduction of 29% and 34%, at the first storey, and 57% and 61%, at the fifth storey, along major (Figures 6a and 6c) and minor (Figures 6b and 6d) axes of bending, respectively.

4 NUMERICAL RESULTS: WIND LOADING FOLLOWING FIRE

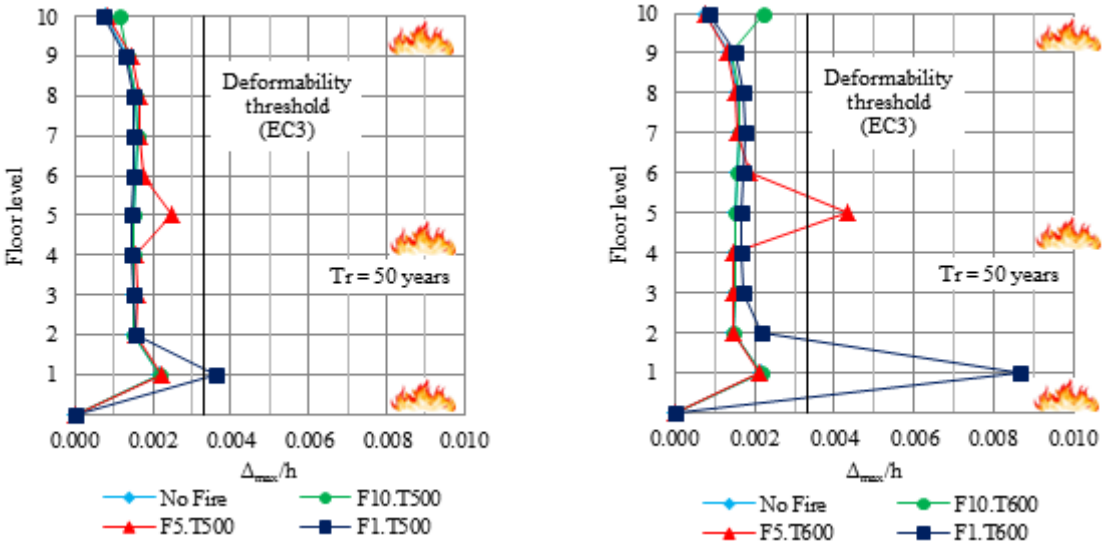
In order to study the dynamic behaviour of the steel structures damaged by the fire loading proposed in Section 3, whose properties are illustrated in Section 2, a computer code for time-domain analysis of frames subjected to wind pressure is adopted [12, 13]. For the sake of simplicity, only the along-wind component of the velocity is taken into account in the in-plan X and Y principal directions (Figure 1a). The instantaneous wind velocity at each floor level of the building is given by the superimposition of a mean wind velocity, with a logarithmic profile along the height depending on the surface roughness, and a zero mean velocity fluctuation, corresponding to a stochastic stationary Gaussian process. More precisely, wind loads are schematized by means of the equivalent wind spectrum technique [10]. The equivalence criterion is formulated by defining a fictitious velocity fluctuation, which is a random function of time but invariant and perfectly cross-correlated in space. A Monte Carlo simulation is adopted to generate time histories of the wind velocity at each floor level: a duration of 600 s and a step Δt=0.2 s are assumed for two return periods (i.e. T_r=10 or 50 years).

At first, maximum values of floor displacement (u_{max}) and storey drift (Δ_{max}/h) are plotted along the frame height in Figures 9 and 10, respectively, comparing steel structures in no-fire condition and fire exposed at a maximum temperature of 500 °C (i.e. T500 in Figures 9a and 10a) and 600 °C (i.e. T600 in Figures 9b and 10b). At the same time, three fire scenarios are examined on the assumption that the fire compartment is confined to the area of the first (i.e. F1), fifth (i.e. F5) and tenth (i.e. F10) levels. A black line reports the deformability limits imposed by EC3 [7] on the top displacement (i.e. 1/500 of the building height) and storey drift (i.e. 1/300 of the storey height).



(a) T=500°C. (b) T=600°C.

Figure 9: Maximum floor displacement for three fire scenarios: wind loads along X direction.

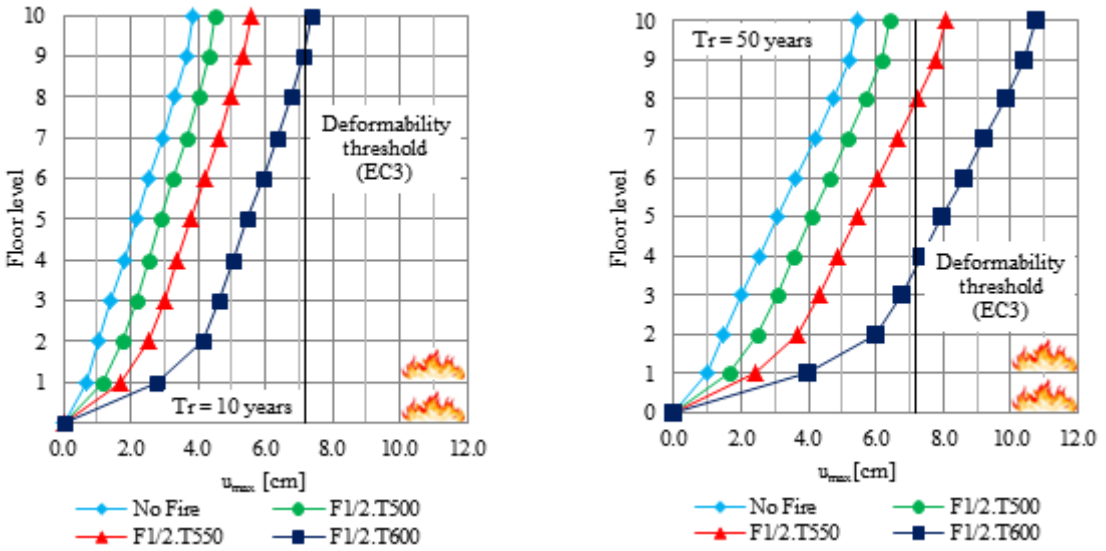


(a) T=500°C. (b) T=600°C.

Figure 10: Maximum storey drift for three fire scenarios: wind loads along X direction.

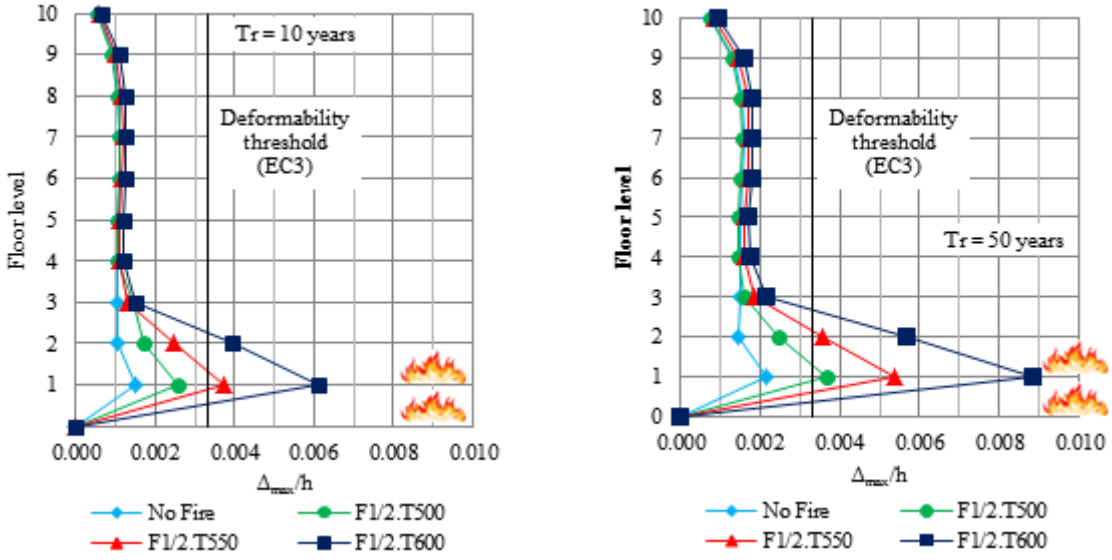
For the sake of brevity, only results in the flexible direction of the building plan (i.e. the X direction) are reported. As can be observed in Figure 9b, the maximum top lateral displacement of the F1.T600 structure has exceeded the corresponding deformability threshold imposed by EC3. This behaviour is due to a soft-storey mechanism at the first level when the fire scenario F1 is assumed, with a lateral displacement curve similar to that of the structure in the no-fire condition at the upper floors. Moreover, the maximum storey drift of the F1.T500 structure (Figure 10a) and F1.T600 and F5.T600 structures (Figure 10b) exceeds the deformability threshold imposed by EC3 only at the levels where the fire compartment occurs.

Thereafter, analogous curves to those reported above are shown in Figures 11 (i.e. u_{max}) and 12 (i.e. Δ_{max}/h), where fire compartment is confined to the area of the first two levels (i.e. F1/2), comparing the no-fire condition with results for three values of the maximum fire temperature (i.e. T=500°C, 550°C and 600°C).



(a) T_r=10 years. (b) T_r=50 years.

Figure 11: Maximum floor displacement for three fire temperatures: wind loads along X direction.

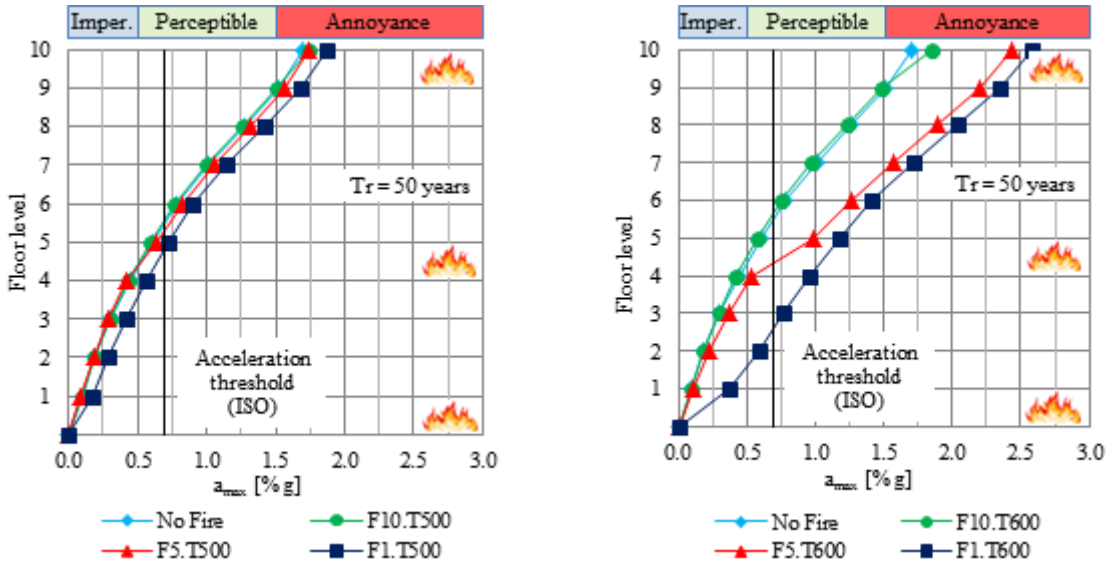


(a) T_r=10 years. (b) T_r=50 years.

Figure 12: Maximum storey drift for three fire temperatures: wind loads along X direction.

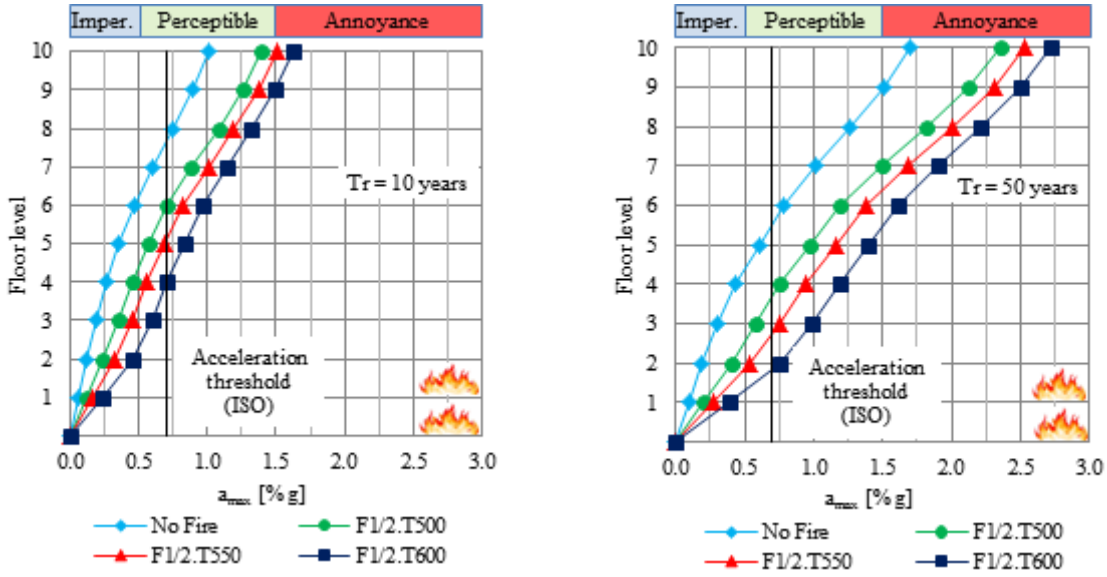
More specifically, effects of wind loads with return period of T_r=10 years (Figures 11a and 12a) and T_r=50 years (Figures 11b and 12b) are compared along the X direction. As can be observed, when T_r=50 years is assumed, it is not possible to obtain values of the top floor maximum displacement below the EC3 threshold for the F1/2.T550 and F1/2.T600 structures (Figure 11b). On the other hand, the maximum storey drift exceeds the EC3 threshold at the first level of the F1/2.T550 and F1/2.T600 structure, even if T_r=10 years is assumed (Figure 12a), and also at the second level, when T_r=50 years is considered (Figure 12b).

Finally, maximum floor acceleration (i.e. a_{max}) along the frame height is plotted in the stiff direction of the building plan (i.e. the Y direction), for both T_r=10 years (Figures 14a) and T_r=50 years (Figures 13a,b and 14b), comparing three fire scenarios (i.e. F1, F5 and F10 for fire temperatures of 500°C and 600°C: Figure 13) and three fire temperatures (i.e. T=500°C, 550°C and 600°C for fire scenario F1/2: Figure 14).



(a) T=500°C. (b) T=600°C.

Figure 13: Maximum floor acceleration for three fire scenarios: wind loads along Y direction.



(a) T_r=10 years. (b) T_r=50 years.

Figure 14: Maximum floor acceleration for three fire temperatures: wind loads along Y direction.

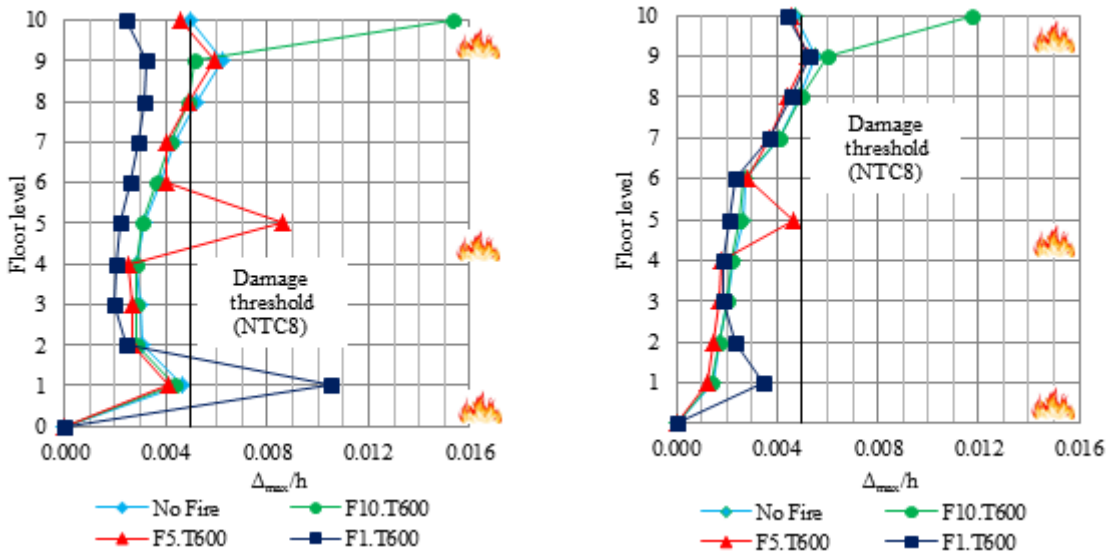
As a reference, the perception thresholds associated with various degrees of human discomfort are formulated in terms of critical values of the wind-induced building acceleration, expressed as percentage of the gravity acceleration g (e.g. [19], the maximum acceleration, a_{max}, can be assumed as: imperceptible, for a_{max}< 0.5%g; perceptible, for a_{max}=0.5%g÷1.5%g; annoyance, for a_{max}=1.5%g÷5%g). The ISO code threshold is also shown [20], which assigns a value of 0.7%g to the standard deviation at the top floor of office buildings. For all fire scenarios, note that the number of levels where the ISO discomfort threshold is exceeded increases for increasing values of fire temperature (Figures 13 and 14) and return period of the wind loads (Figure 14). Moreover, it is not possible to obtain values of a_{max} lower than the annoyance range in the event of fire at the first two levels and T_r=50 years (Figure 14b).

5 NUMERICAL RESULTS: EARTHQUAKE LOADING FOLLOWING FIRE

In order to study the seismic response of the steel framed building along the in-plan X and Y principal directions, nonlinear dynamic analyses are carried out through a step-by-step procedure based on a two parameter implicit integration scheme [21-24]. At each step of the analysis, the final state, satisfying the equilibrium equations within an assigned tolerance, is determined using an initial stress-like iterative procedure [14, 15]. To account for the inelastic deformation due to the seismic loads, the frame members are idealized by a lumped plasticity model constituted of two components, one elastic-perfectly plastic and the other simply elastic, assuming a hardening ratio of 2%. Moreover, the influence of both axial load and slenderness on the yield moment of the columns is considered over time. The axial-force bending moment interaction domain is obtained analogously to the provisions of EC3 [7], simply by replacing the plastic axial load under uniform compression with the buckling load.

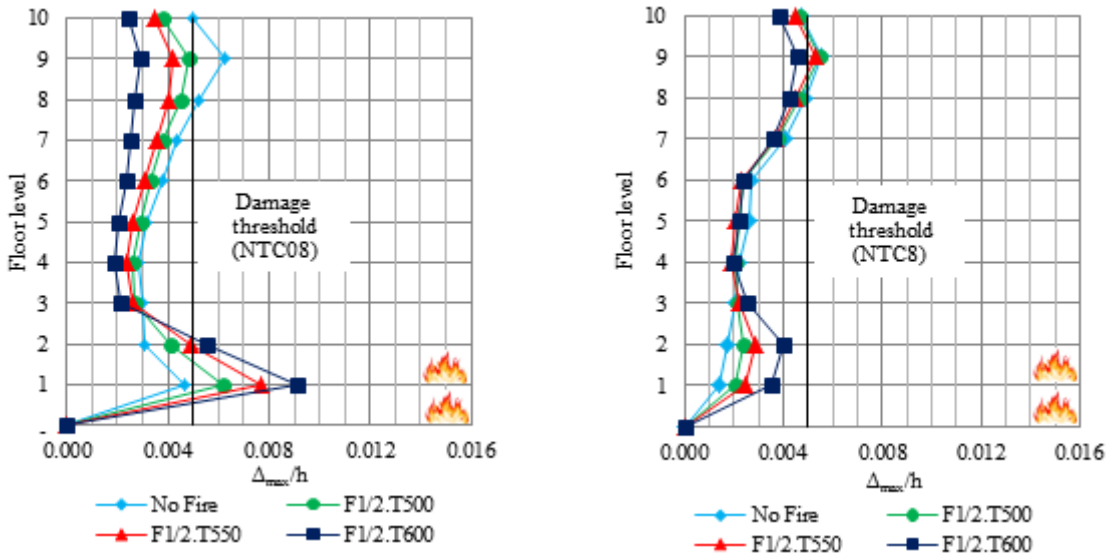
Seven recorded accelerograms, corresponding to a medium-risk seismic region provided by the current Italian seismic code (NTC08, [11]) and a design subsoil class *B* (i.e. subsoil stratigraphic parameter S_S=1.2), are selected by the computer code REXEL [25]. The corresponding elastic response spectra of normalized acceleration match, on average, NTC08 spectrum for the serviceability (i.e. damage) limit state, based on an equivalent viscous damping ratio in the horizontal direction equal to 2%. All the following results are obtained as an average of those separately obtained for the real motions.

Maximum storey drift along the in-plan X (Figure 15a) and Y (Figure 15b) directions are plotted for the fire temperature T=600°C, comparing framed structures both in the no-fire condition and on the assumption that fire scenarios on the first (i.e. F1), fifth (i.e. F5) and tenth (i.e. F10) levels are considered. Moreover, curves analogous are also shown in Figure 16, where the fire compartment is confined to the area of the first two levels (i.e. F1/2 scenario) at three fire temperatures (i.e. T=500°C, 550°C and 600°C). A black line plots the damage limitation requirement imposed by NTC08 (i.e. 1/200 of the storey height). As can be observed, an amplification in the structural response of fire-exposed structures is localized to the level of the fire compartment involved, where the damage threshold is exceeded, while it declines, in comparison with the no-fire condition, on the other levels where fire is not considered. This behaviour is amplified when the F1.T600 (Figure 15a) and F1/2.T600 (Figure 16a) structures are considered in the X direction.



(a) Seismic loads along X direction. (b) Seismic loads along Y direction.

Figure 15: Maximum storey drift for three fire scenarios: T=600°C.



(a) Seismic loads along X direction. (b) Seismic loads along Y direction.

Figure 16: Maximum storey drift for three fire temperatures: fire scenarios F1/2.

6 CONCLUSIONS

The dynamic response of a ten-storey steel office building in a no fire situation is compared, along the in-plan principal directions, with that in the event of fire, at 500°C (i.e. T500), 550°C (i.e. T550) and 600°C (i.e. T600) temperatures. Four scenarios have been considered assuming the fire compartment confined to the area of the first floor (i.e. F1), the first two (i.e. F1/2) and the upper (i.e. Fi, i=5,10) floors. At each storey, along-wind loads are considered based on time histories of the wind velocity for two return periods, in accordance with an equivalent spectrum technique. Real accelerograms, whose response spectra match those adopted by Italian seismic code for a medium-risk seismic zone and medium subsoil class, are considered to simulate seismic loads at the damage limit state.

The numerical results for fire before wind and earthquake show a decrease of the flexural stiffness of the frame members of up to 69% of the value in the no-fire condition. A significant decrease in plastic moments and a marked narrowing of plastic *N-M* domains are also observed for the girders and columns, respectively. Under wind loads, the maximum horizontal acceleration exceeds the ISO discomfort threshold at the upper floors, reaching the annoyance range; moreover, the deformability limits imposed by Eurocode 3 on the maximum top displacement and storey drift are not respected. Under seismic loads, the maximum storey drift exceeds the damage threshold imposed by NTC08 at the levels where the fire occurs, while it declines, in comparison with the no-fire condition, on the other levels where the event of fire is not considered.

ACKNOWLEDGEMENTS

The present work was partially financed by Re.L.U.I.S. (Italian network of university laboratories of earthquake engineering), according to "Convenzione D.P.C.–Re.L.U.I.S. 2014–2016, WPI, Isolation and Dissipation".

REFERENCES

[1] W.-Y. Wang, B. Liu, V. Kodur, Effect of temperature on strength and elastic modulus of high-strength steel. *Journal of Materials in Civil Engineering*, **25**(2), 174-182, 2013.

[2] C. Scawthorn, J.M. Eidinger, A. Schiff, Fire following earthquake. New York, NY *American Society of Civil Engineers*, 2005.

[3] G. Della Corte, R. Landolfo, F.M. Mazzolani, Post-earthquake fire resistance of moment resisting steel frames. *Fire Safety Journal*, **38**, 593-612, 2003.

[4] R. Zaharia, D. Pintea, Fire after earthquake analysis of steel moment resisting frames. *International Journal of Steel Structures*, **9**(4), 275-284, 2009.

[5] B. Behnam, H.R. Ronagh, Post-earthquake fire performance-based behavior of unprotected moment resisting 2d steel frames. *KSCE Journal of Civil Engineering*, **19**(1), 274-284, 2015.

[6] E. Nigro, A. Ferraro, G. Cefarelli, The influence of fire scenarios on the structural behaviour of composite steel-concrete buildings. *Applied Mechanics and Materials*, **82**, 368-373, 2011.

[7] Eurocode 3. Design of steel structures – Part 1-1: General rules and rules for buildings. Part 1-2: General rules, structural fire design. *C.E.N, European Committee for Standardization*, December 2005.

[8] Italian Ministry of Public Works (DM96). Norme tecniche per le costruzioni in zone si-

smiche e relative istruzioni, D.M. 16-01-1996 and C.M. 10-04-1997, n. 65/AA.GG..

[9] Eurocode 1. Actions on structures – Part 1-2: General actions, actions on structures exposed to fire. *C.E.N., European Committee for Standardization*, October 2004.

[10] G. Solari, Equivalent wind spectrum technique: theory and applications. *Journal of Structural Engineering*, **114**: 1303-1323, 1998.

[11] Italian Ministry of Infrastructures (NTC08). Nuove norme tecniche per le costruzioni e relative istruzioni, D.M.14-01-2008 e Circolare 02-02-2009, n. 617/C.S.LL.PP..

[12] F. Mazza, A. Vulcano, Control of the along-wind response of steel framed buildings by using viscoelastic or friction dampers. *Wind and Structures*, **10**(3), 233-247, 2007.

[13] F. Mazza, A. Vulcano, Control of the earthquake and wind dynamic response of steel-framed buildings by using additional braces and/or viscoelastic dampers. *Earthquake Engineering and Strucural Dynamics*, **40**(2), 155-174, 2011.

[14] F. Mazza, M. Mazza, Nonlinear analysis of spatial framed structures by a lumped plasticity model based on the Haar-Kàrmàn principle. *Computational Mechanics*, **45**, 647-664, 2010.

[15] F. Mazza, A distributed plasticity model to simulate the biaxial behaviour in the nonlinear analysis of spatial framed. *Computers and Structures*, **135**, 141-154, 2014.

[16] ISO 834 International Standard, Fire resistance tests, ISO 834-1 Test conditions. *Provided by IHS under license with ISO: 31*, Genève, Switzerland, 1999.

[17] F. Mazza, F. Alesina, Incremental dynamic analysis of fire-exposed base-isolated r.c. framed buildings subjected to near-fault ground motions. *COMPDYN 2015, 5th ECCOMAS Thematic Conference on Computational Methods in Structural Dynamics and Earthquake Engineering*, Crete Island, Greece, May 25–27, paper n. 492, 2015.

[18] F. Mazza, A. De Luca, Seismic vulnerability in case of fire of existing r.c. framed buildings: modelling and nonlinear dynamic analysis. *COMPDYN 2015, 5th ECCOMAS Thematic Conference on Computational Methods in Structural Dynamics and Earthquake Engineering*, Crete Island, Greece, May 25–27, paper n. 491, 2015.

[19] E. Simiu, R. Scanlan, *Wind effects on Structures*, John Wiley & Sons, New York, U.S.A., 1996.

[20] ISO/TC 98/SC 3 International Standard Organization, Wind loads on structures, Berlin, Germany, 1990.

[21] F. Mazza, A. Vulcano, Nonlinear dynamic response of r.c. framed structures subjected to near-fault ground motions. *Bulletin of Earthquake Engineering*, **8**, 1331-1350, 2010.

[22] F. Mazza, M. Mazza, Nonlinear modeling and analysis of R.C. framed buildings located in a near-fault area. *The Open Construction & Building Technology Journal,* **6**, 346-354, 2012.

[23] F. Mazza, Modelling and nonlinear static analysis of reinforced concrete framed buildings irregular in plan. *Engineering Structures*, **80**, 98-108, 2014.

[24] I. Iervolino, G. Maddaloni, E. Cosenza, Eurocode 8 compliant record sets for seismic analysis of structures. *Journal of Earthquake Engineering*, **12**, 54–90, 2008.

[25] F. Mazza, M. Mazza, Nonlinear modeling and analysis of r.c. spatial frames to study the effects of the vertical component of near-fault ground motions. *COMPDYN 2015, 3rd ECCOMAS Thematic Conference on Computational Methods in Structural Dynamics and Earthquake Engineering*, Corfù, Greece, May 25–28, paper n. 322, 2013.

COMPDYN 2015
5th ECCOMAS Thematic Conference on
Computational Methods in Structural Dynamics and Earthquake Engineering
M. Papadrakakis, V. Papadopoulos, V. Plevris (eds.)
Crete Island, Greece, 25–27 May 2015

ESTIMATING OF OVERSTRENGTH FACTOR OF CONCENTRICALLY X-BRACED STEEL FRAMES

T. Branci[1] **and D. Yahmi**[2]

[1] Departement of Civil Engineering, Hassiba Benbouali University of Chlef
Hai Es-Salam, B.P. 151, Route de Senjas, 02000 Ech Chlef, Algeria.
e-mail: brancit@yahoo.fr

[2] Departement of Civil Engineering, Hassiba Benbouali University of Chlef
Hai Es-Salam, B.P. 151, Route de Senjas, 02000 Ech Chlef, Algeria.
e-mail: yahmi_djamel@hotmail.fr

Keywords: Frame, Steel, Inelastic Deformation, Overstrength, Brace, Pushover.

Abstract. *The inelastic deformation of structural elements is generally permitted in the case of the design of structures subjected to earthquakes. In this context, the resistance of such structures increases when plastic hinges are formed in their structural elements. The resistance that occurs during the formation of plastic hinges is none other than the overstrength that plays a significant role in the seismic design of structures. As a result, their overstrength and the influence of X-braces on this overstrength are not well understood. This present study tries to evaluate the overstrength factor obtained from inelastic pushover analyses of concentrically X-braced steel frames. The effects of some parameters influencing the value of overstrength factor, including the number of stories, are investigated. The results show that overstrength factor depends closely on this parameter. Finally, based on the findings presented in the study, tentative of overstrength factors are proposed for X-braced steel frames.*

1 INTRODUCTION

The purpose of this work is to study the influence of of x-braces on the structural overstrength in the seismic design of steel structures. Current seismic codes do not mention very clearly the value to be assigned to the overstrength because in reality this one depends on several factors related to the nature and behavior of the material of the structure. After reviewing European (EC8) [1] and Algerian (RPA) [2] code expressions for seismic design base shears, the lateral load responses of four two-dimensional x-braced frames steel structures, designed according to European seismic code, are presented.

2 OVERSTRENGTH IN SEISMIC DESIGN CODES

All the seismic codes allow the structures to enter in inelastic range of deformations during the design earthquake, for energy dissipation, introducing the structural behavior factor.

2.1 Algerian seismic code (RPA99/2003)

The minimum design base shear, V, required by the Algerian seismic code RPA is:

$$V = \frac{V_e}{R} \tag{1}$$

where V_e is the maximum elastic base shear, and R is the behaviour factor (or reduction factor) of the structure and reflects the capability of a structure to dissipate energy through inelastic behaviour. R depends on the ductility capacity of the structural system and the type of material and was chosen to account for many factors cited in many investigations [3-5]. The magnitude of R varies from 6 to 2 for steel structures, 5 to 2 for reinforced concrete, 2.5 for masonry, and 2 to 4 for other systems. But the disadvantage of this code is that it gives no precision on the contribution of the overstrength and ductility on the behaviour factor R.

2.2 European seismic code (EC8)

The EC8 [1] is based on the capacity design approaches, with its associated procedure in terms of failure mode control, force reduction and ductility requirements. The code suggests the reduction of the design seismic, resulting from idealized elastic response spectra, through the behavior factor generally called the q-factor. For steel structures, the upper value of the behavior factor q to account for the effects of ductility, redundancy and member overstrength is defined as follow [11]:

$$q = q_0 \frac{\alpha_u}{\alpha_1} \tag{2}$$

where q_0 is the basic value of the behaviour factor, α_u/α_1 is the overstrength/redundancy coefficient, α_u represents the horizontal force multiplier corresponding to the maximum lateral strength and α_1 the multiplier corresponding to first yielding in the structure.

3 LATERAL CAPACITY

3.1 Role of factor q (or R) in design

Overstrength (or reserve strength) that develops a structure during an earthquake is the most important characteristic of all the others characteristics. As observed after strong earthquakes, It seems that the buildings structures are able to resist forces greater than those for which they were calculated. The presence of significant reserve of strength that was not accounted in design, explains this phenomenon [7]. In this approach, it assumed that the actual strength of structure is higher than the design strength and the structure is able to dissipate energy through yielding. As shown in figure 1, seismic design of structures leads to reducing the forces, V_e, obtained from the linear elastic response spectra by a behaviour factor, q, in European code or coefficient behaviour, R, in Algerian code (or response modification factor in other codes) to achieve design forces. In this figure, the real nonlinear behaviour is idealized by a bilinear elasto-plastic relation. In addition of the overstrength the seismic codes consider a design loads, taking advantage of the fact that the structure possesses significant capacity to dissipate energy (ductility).

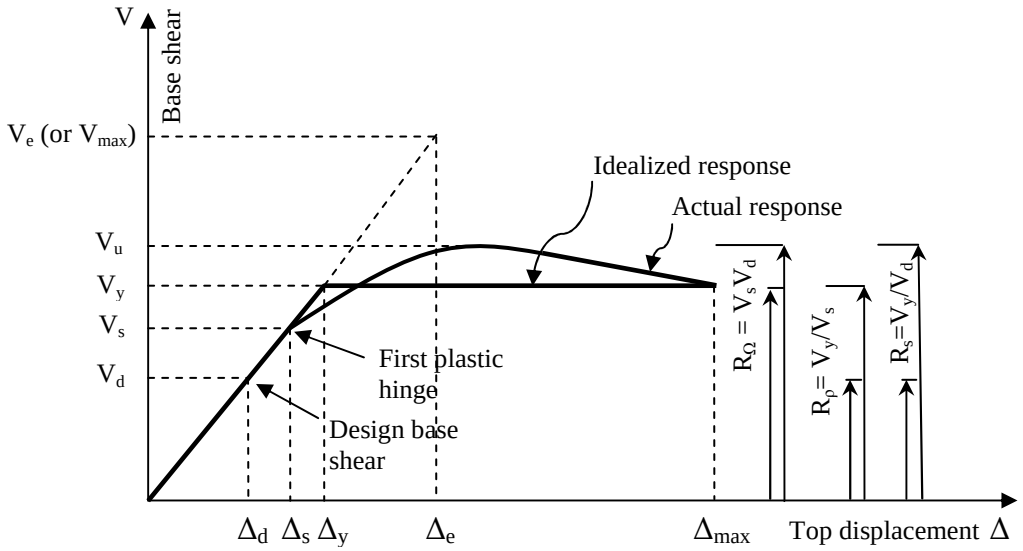


Figure 1: Relation between top displacement and base shear.

3.2 Relation between R, ductility and overstrength

According to many researches [6-11], the presence of behaviour factor, R, implies the existence of three different factors R_μ, R_ρ, and R_Ω:

$$R = R_\mu . R_\rho . R_\Omega \tag{3}$$

- The first, R_μ, is the reduction factor due to ductility [7], 12]:

$$R_\mu = (\mu - 1)\frac{T}{T_C} + 1 \quad \text{if } T < T_C \tag{4-1}$$

$$R_\mu = \mu \quad \text{if } T \geq T_C \tag{4-2}$$

where T and T_c are the fundamental period and the characteristic of ground motion respectively. μ is the structural ductility factor defined as:

$$\mu = \frac{\Delta_{max}}{\Delta_y} \tag{5}$$

where Δ_{max} is the maximum displacement and Δ_y is the yield displacement. Otherwise:

$$R_\mu = \frac{V_e}{V_y} \tag{6}$$

- The second, R_ρ, is the redundancy factor depending on the plastic redistribution capacity of the structure:

$$R_\rho = \frac{V_y}{V_1} \tag{7}$$

- The third, R_Ω, is the overstrength factor and represents the ratio of the lateral strength corresponding to the onset of the first plastic hinge to the one corresponding to the lateral design strength required by code:

$$R_\Omega = \frac{V_1}{V_d} \tag{8}$$

where V_y is the idealized yield strength, V_1 is the first significant yield strength and V_d the allowable stress design strength.

A strength reduction factor, R_s, defined as the product between the redundancy factor and the overstrength factor, is expressed as follows:

$$R_s = R_\rho . R_\Omega = \frac{V_y}{V_d} \tag{9}$$

The comparison between equation (2) and equation (3) leads to:

$$q_0 = R_\mu . R_\Omega \quad \text{and} \quad \frac{\alpha_u}{\alpha_1} = R_\rho \tag{10}$$

3.3 Factors influencing overstrength due to redistribution

Overstrength values associated with redistribution of internal forces strongly depend on : 1) structural type, 2) the load combinations, 3) material proprieties, and 4) the criteria used to determine when the ultimate lateral strength is reached [5].

4 DESCRIPTION OF ANALYTICAL MODELS

4.1 Structural system

In order to assess the range of overstrength associated with redistribution which may present in buildings with concentrically x-braced steel frames (CBFs), a group of such buildings is analyzed. The frames were three, six, nine, and 12 stories tall and were symmetric and regular with the floor plan and geometry illustrated in figure 2. The storey height was 4.5 m for the bottom storey and 3.0 m for all others. The numbers of bays were identical in all frames and were equal to three with 5.5 m in length. The lateral loads were resisted entirely

by the perimeter frames and the response of the frame with axis D is considered. Each frame was designed according to European steel design code (EC3) [13] and designed to satisfy the seismic design requirements of EC8 for structures classified as high ductility (DCH) with reference to a PGA of 0.25g, a soil class A (hard soil type), behaviour factor q = 6.5, damping ratio ξ = 5% and steel members are made of grade S275 steel (f_y=275 Mpa). Column dimensions are kept larger than beam ones in order take into account capacity design. Gravity loads attributable to frames are evaluated according to conventional design rules, while the lateral loads, assumed to represent the seismic action, are derived using the equivalent static method according to EC8. The member sizes of the frames are provided in table 1. The inelastic static push-over analysis involving P-Δ effect and using Sap2000 software [14] is employed for obtaining the effects of height on overstrength factors of these steel frames.

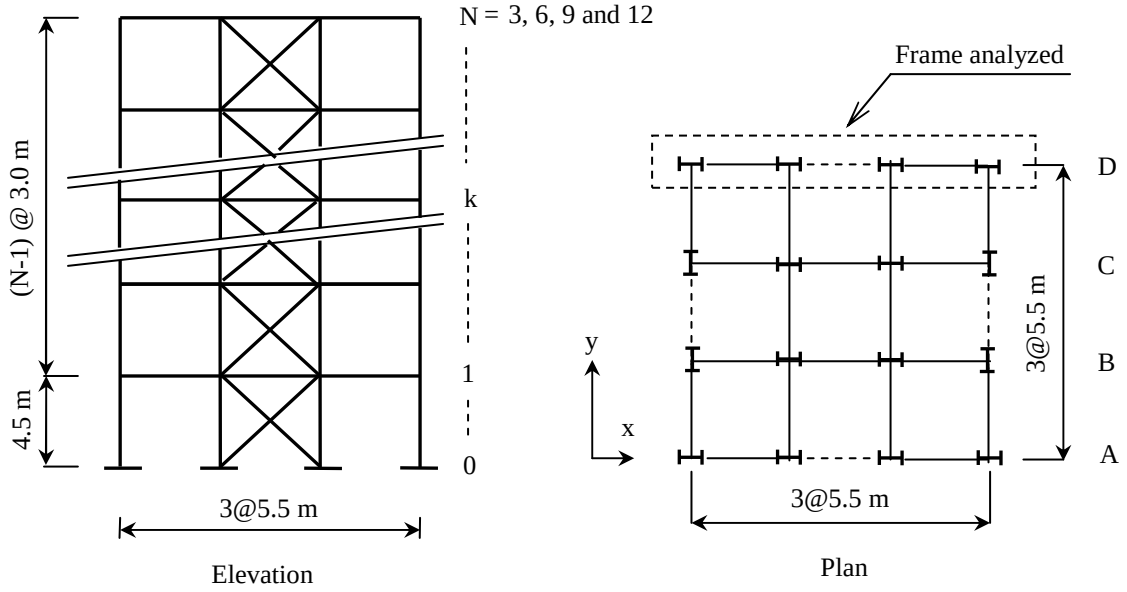


Figure 2: Configuration of x-braced frames systems.

FRAME with	COLUMN HEB section (n° of story)	BEAM IPE section (n° of story)	BRACE TUBO section (n° of story)
3 stories	220 (1 to 3)	300 (1 to 3)	127X4 (1), 108X3.6 (2), 101.6X3.6 (3)
6 stories	240 (1-2), 220 (3-4), 200 (5-6)	300 (1 to 3)	127X4 (1-3), 108X3.6 (4), 101.6X3.6 (5), 82.5X3.2 (6)
9 stories	260 (1-3), 240 (1-6), 220 (7-9)	300 (1 to 3)	127X4 (1-4), 108X3.6 (5-6), 101.6X3.6 (7), 88.9X3.2 (8), 76.1X3.2 (9)
12 stories	320 (1-3), 300 (4-6), 280 (7-9), 260 (10-12)	300 (1 to 3)	127X4 (1-5), 108X3.6 (6-7), 101.6X3.6 (8-10), 82.5X3.2 (11), 76.1X3.2 (12)

Table 1: Dimensions of the members used for the frames.

5 EVALUATION AND COMPARISON

The four frames were subjected to incremental lateral loads using the triangular distribution, which is closer to the first mode distribution. The lateral forces are monotonically increased with a combination of load and displacement control until the target displacement is reached. The target displacement has been considered the 5% of the total height of the building. The results of the inelastic pushover are present for the fourth frames in figure 3, 4 and table 2. The main results of this study can be summarized as follow:

- The three factors, R_ρ (redundancy), R_Ω (strength) and their product, R_s, decrease with an increase in the height of frames. This result was apparent in all frames analyzed.
- The factors, R, are in range of 19 to 4.05 with the average of 8.86. By comparison of these factors with system overstrengh factor suggested by EC8, it is understood that the CBFs-x have higher overstrengh factors.
- With increasing in number of stories the ductility of structure decreases. Therefore, the decrease in ductility causes to decrease the response modification factor, R.
- The ductility factor, R_μ, decreases more rapidly compared to overstrengh factor, R_ρ, with an increase in the number of story.
- In the general state, the overstrengh factor, R_s and R, for this type of structures (CBFs) is suggested as 3.0 and 6.5 respectively.

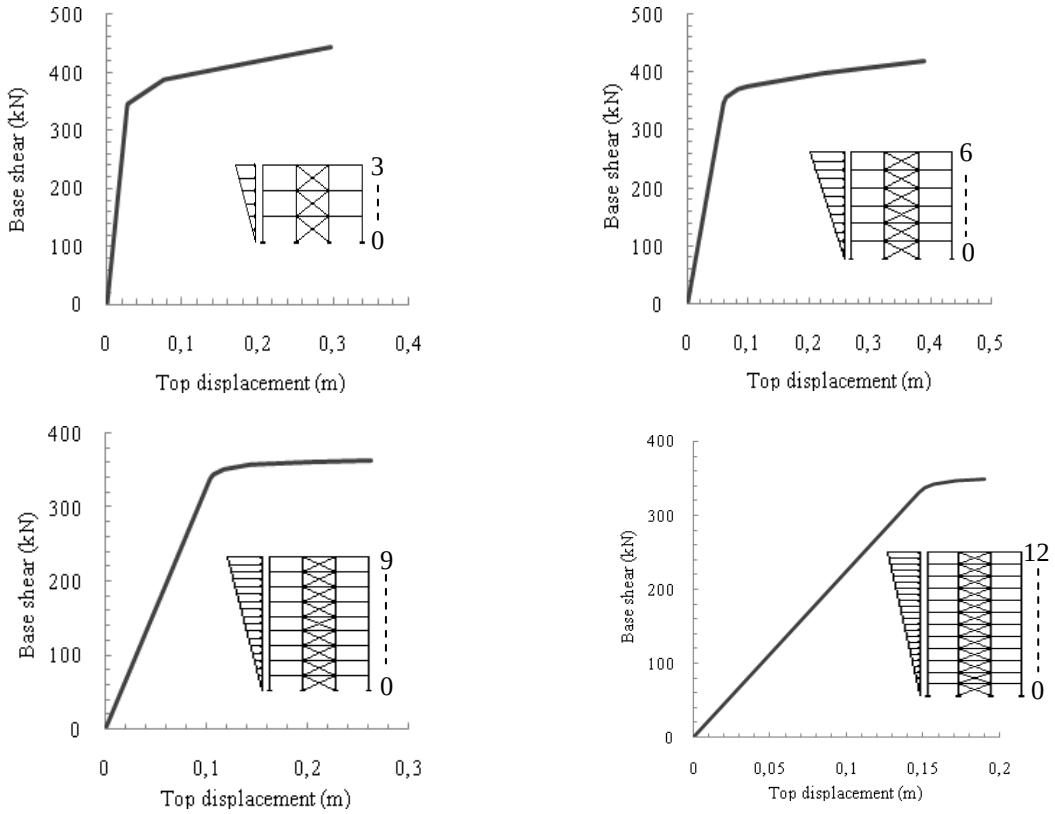


Figure 3: Roof story displacement-base shear curve for frames analyzed.

Frame With	V_y (kN)	Δ_y (m)	Δ_{max} (m)	μ	R_μ	R_ρ	R_Ω	R_s	R
3 stories	344.37	0.028	0.297	10.6	3.23	1.80	3.25	5,85	19.0
6 stories	346.14	0.059	0.390	6.61	2.70	1.60	1.70	2,72	7,34
9 stories	339.20	0.104	0.554	5.33	2.50	1.55	1.30	2,02	5,05
12 stories	329.71	0.147	0.659	4.48	2.25	1.40	1.25	1.80	4,05

Table 2: Results of the inelastic pushover analysis.

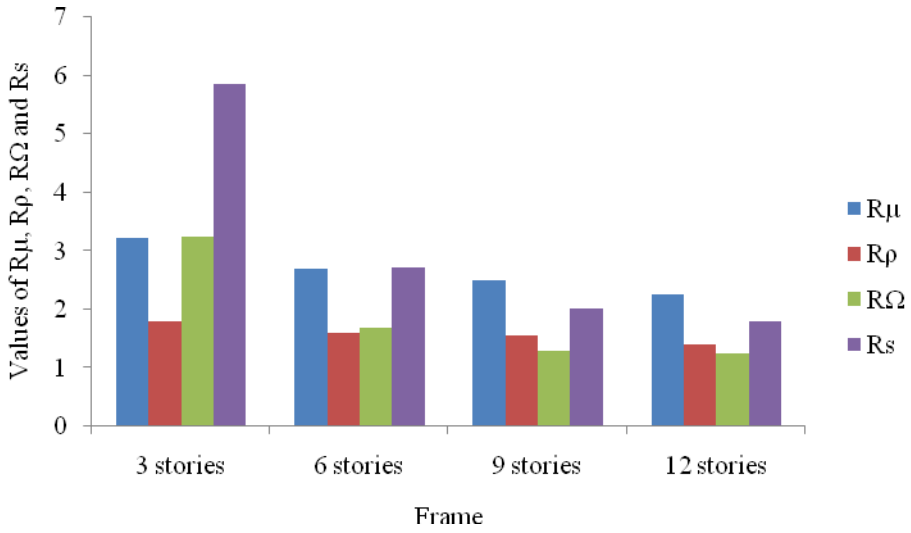


Figure 4: Comparaison between overstrength factors for frames analyzed.

6 CONCLUSION

In the present study, the nonlinear response of concentrically x-braced steel frames, from 3 to 12 stories, using the nonlinear analysis program SAP2000 under incremental lateral loading has been carried out with the intention to assess the presence of overstrength attributable to different factors such as ductility, redundancy and overstrengh. The main observations and conclusions drawn are summarized below:

- The ductility, the redundancy and the overstrengh factors decrease with an increase in the number of stories.
- Redistribution of internal forces in the inelastic range due to redundancy in structural system is probably the most dependable estimate of overstrength.
- The global overstrengh due to ductility, redundancy and strength increases with a decrease in the design seismic load.
- Behaviour factor, R, for this type of frames is suggested as 6.5. The estimate of this value of R presented in this study is applicable only for the group of frames analyzed.

REFERENCES

[1] EN 1998-1. Eurocode 8: Design of structures for earthquake resistance - Part 1: General rules, seismic actions and rules for buildings, *European Committee for Standardization, CEN*, 2004.

[2] RPA99/Version 2003, Règles parasismiques Algériennes, *Document Technique Règlementaire DTR B C 248, Centre de Recherche Appliquée en Génie Parasismique*, Alger, 2003.

[3] A. Osman, A. Ghobarah, R. M. Korol, Implification of design philosophies for seismic response of steel moment frames, *Earthquake Engineering and Structural dynamics*, **24**, 127-143, 1995.

[4] D. Mitchell, P. Paultre, Ductility and overstrength in seismic design of reinforced concrete structures, *Canadian Journal of Civil Engineering*, **21**, 1049-1060, 1994.

[5] M.A. Rahgozar and J.L.Humar, Accounting for overstrength in seismic design of steel structures, *Canadian Journal of Civil Engineering*, **25**(1), 1-15, 1998.

[6] A. Y. Elghazouli, Assessment of capacity design approaches for steel-framed structures, *Steel Structures*, **5**, 465-475, 2005.

[7] M. Mahmoudi, M. Zaree, Determination the modification factors of buckling restrained braced frames, *Procedia Engineering*, **54**, 222-231, 2013.

[8] C. D. Annan, M. A. Youssef, M. H. El Nagger, Assessment of overstrength and ductility of a four-story modular steel building braced frame, *2nd Canadian Conference on Effective Design of Structures McMaster*, University Hamilton, Ontario, Canada, May 20-23, 2008.

[9] A.S. Elnashai and A.M. Mwafy, Overstrength and force reduction factors of multistory reinforced concrete buildings, *The structural design of tall buildings*, **11**(5), 329-351, 2002.

[10] C. Uang, Establishing R (or R_w) and C_d factors for buildings seismic provisions, *Journal of Structural Engineering*, ASCE, **117**(1), 19-28, 1991.

[11] M. Ferraioli, A. Lavino, A. Mandara, Behaviour factor of code-designed steel moment-resisting frames, *International Journal of Steel Structures*, **14**(2), 234-254, 2014.

[12] P. Fajfar, Structural analysis earthquake engineering, A breakthough of simplified non-linear methods, *12th European Conference On Earthquake Engineering*, 2002.

[13] EC3, Eurocode 3, Design of steel structures, *European Committee for standardization*, 1st Draft, prEN 1993-3:2000, 6th December, 2000.

[14] SAP 2000_14.2, Integrated finite element analysis and design of structures reference manual. Berkeley (CA, USA): *Computers and Structures INC*, 2009.

COMPDYN 2015
5th ECCOMAS Thematic Conference on
Computational Methods in Structural Dynamics and Earthquake Engineering
M. Papadrakakis, V. Papadopoulos, V. Plevris (eds.)
Crete Island, Greece, 25–27 May 2015

SENSOR PLACEMENT OPTIMIZATION USING ENSEMBLE KALMAN FILTER AND GENETIC ALGORITHM

Dana E. Nasr[1], **George A. Saad**[2]

[1] American University of Beirut
Beirut, Lebanon
den01@mail.aub.edu

[2] American University of Beirut
Beirut, Lebanon
george.saad@aub.edu.lb

Keywords: Structural Health Monitoring, Optimal Sensor Locations, Ensemble Kalman Filter, Genetic Algorithm.

Abstract. *A robust methodology is proposed in this study for determining the optimal locations of sensors in a structure to extract the most informative measurement data for the purpose of parameter estimations. First, the Ensemble Kalman Filter (EnKF) is used as a history matching method to predict and update the state and model parameters of the system. Then, a Genetic Algorithm (GA) approach is applied to determine the best locations of the sensors in the system through a minimization procedure, where the objective function to be minimized is represented by the mismatch between the predicted values and the actual measurements. The robustness and efficiency of the proposed method are demonstrated by developing the optimal sensor configuration for a shear building subjected to El Centro earthquake excitation at its base and using synthetic measurements of displacements and velocities of different floors.*

1 INTRODUCTION

With the development of sensors and other monitoring devices, detecting the damage in structures became an easier task. Using sensor based structural health monitoring (SHM) made data abundantly available and continuously obtained in real time. As such, one of the main challenges that remain lies in post processing this data. Therefore to save money and get only the necessary data, this study deals with optimizing the sensor locations to efficiently use the generated data for system identification and damage detection.

Many methods were proposed in the literature to determine the optimal sensor placement for damage detection and parameter estimation. These methods can be classified into two main categories: Optimization-based and Selection-based procedures [1]. The most common optimization-based methods used in the literature include the Genetic Algorithm (GA), the Simulated Annealing (SA), the Tabu Search (TS) and their different variations. The GA is a search technique used to solve optimization problems using random operations based on natural evolution operations (selection, crossover, and mutation). The algorithm starts by generating a possible set of solutions, called "population of chromosomes", each having a certain fitness function. After performing a series of natural operations on the initial population, a new better population is created. The algorithm is repeated, each time starting with the new created population, until some predefined end condition is satisfied. L. Yao et al. used the GA for sensor placement optimization for a space structure and a photo-voltaic array, and suggested to use the determinant of the Fisher information matrix as the fitness function in the algorithm [2]. H. Y. Guo et al. proposed to use an improved version of the GA (improved crossover and mutation) to determine the optimal locations of sensors in a SHM system consisting of a 2D truss structure [3]. The SA is an optimization method, named after the physical process of annealing in thermodynamics and used for finding a global minimum or maximum for problems having multiple local minima and maxima [4, 5]. P. L. Chiu et al. proposed to use the SA algorithm to solve the problem of sensor placement and tested it on small and large sensor fields [6]. The TS is a "meta-heuristic" optimization procedure used to avoid being trapped at a local optimum in neighborhood search problems [7, 8, 9][7]. The algorithm creates and updates a "tabu list" of previously visited solutions to prohibit (Tabu means something prohibited) considering them again. The second class of methods, selection-based procedures, consisting mainly of selecting the best sensor locations, is facilitated using information theory measures (i.e. entropy or mutual information) which quantify the uncertainty associated with random variables. Therefore locations where sensors have low information content are eliminated and locations where sensors have good information content are considered optimum. In [10][10], K Yuen et al. used the Bayesian framework to compute the uncertainty in model parameters, then used the information entropy to determine the optimal sensor locations. They applied their method on two numerical examples, an 8 DOF chain mass-spring model and a 40 DOF truss model, having uncertain excitations.

Combined approaches, based on both optimization (more specifically GA) and selection methods, are extensively used in the literature for determining the optimal sensor locations. C. Papadimitriou et al. proposed a methodology where the Bayesian approach is used to compute the uncertainty in the parameters, then the GA is applied to minimize the information entropy over the set of possible sensor configurations [11]. The methodology proposed was applied on two numerical examples, a 9-story building and a 29-DOF truss structure. C. Papadimitriou also used the information entropy to determine the optimal sensor configuration in [12]. In this work, he compared the GA with the sequential sensor placement (SSP) approach based on the computational burden needed to determine the optimal sensor locations and applied his methodology on two numerical examples, a 10 DOF chain-like spring-mass model and a 240

DOF 3D truss structure. E. B. Flynn et al. also combined the Bayesian framework with the GA approach to determine the best locations of sensors and applied their approach to active sensing field [13]. H. M. Chow et al. used a combination of the Bayesian statistical framework, the information entropy and the GA to determine the optimal sensor configuration of a 3D finite element model of a transmission tower modeled in ANSYS [14, 15].

In this paper, a combination between the GA and the Ensemble Kalman Filter (EnKF) is presented to tackle the problem of optimal sensor placement. The EnKF is a sequential data assimilation technique, used in the literature for structural health monitoring (SHM) purposes. R. Ghanem et al. showed the ability of the EnKF to be a good estimator of the system state in [16]. It is combined with a non-parametric modeling technique and applied to a four story shear building subject to El Centro earthquake excitation at its base. G. Evensen provided an overview on the EnKF method and its use for state and parameter estimation problems, then illustrated the advantages of using this filter when dealing with high-dimensional or non-linear systems [17]. To the authors' knowledge, this paper is considered as a first attempt to combine the GA and the EnKF for the purpose of optimal sensor placement, but it should be noted here that these two techniques were used together for other purposes in the past few years. H. Li et al. combined the GA with the EnKF for optimal permeability distribution of a 3D model of landfills [18]. The GA was first used to generate initial ensembles of the permeability distribution of the landfill model. The EnKF was then used to estimate this distribution and update it based on synthetic real-time measurements. The algorithm was repeated till it converged to the optimal distribution. J. Lyons et al. used the EnKF for history matching and updating a reservoir model, then combined it with the GA for well placement optimization [19].

The paper is divided into five sections. Section 2 describes the methodology used, combination between GA and EnKF, and the mathematical formulation of each of the two techniques separately. The third section presents the numerical example consisting of a four story building subjected to seismic excitation at its base. Section four exposes and discusses the results. Finally, a general conclusion is drawn in section five.

2 GA-ENKF METHODOLOGY FOR OPTIMAL SENSNOR PLACEMENT

The methodology proposed in this paper starts by randomly selecting an initial population of sensor locations as a first step for applying the GA. The next step is to determine the objective function of the problem, which is taken to be the difference between the actual sensor measurements and the predicted values. The role of the EnKF starts at this point, it is used to estimate and update the system state and get the needed predicted values to calculate the objective function. The fitness of each individual is next evaluated and preference is given to the ones with the least mismatch between the measured and predicted data. These individuals will be selected as the parents from which GA will give birth to better offsprings (new sensor locations) after performing the crossover and mutation operations. Selection of the best individuals from the new solutions will then be based on their fitness values. The algorithm will be repeated until the convergence condition is satisfied and the best locations of the sensors are determined.

The next sub-section presents a summary about the definition of the GA and its different operations, followed by a sub-section describing a brief mathematical formulation of the EnKF method.

2.1 The Genetic Algorithm (GA)

The GA is a search technique that uses the theory of natural evolution to solve optimization problems. It was first introduced by John Holland in 1975 [20]. The algorithm starts by randomly creating a population of individuals, from which two fittest parents are selected. These initial parents undergo a series of natural evolution operations to create new better offsprings, from which the best two new parents are selected based on their fitness. This is repeated until a certain termination criterion is satisfied.

The GA can be summarized in the following outline [14, 15, 21]:

1. Initialization: The algorithm starts by randomly generating an initial set of individuals or solutions (Population), where each individual is represented by a chromosome. There are many encoding methods in the literature to represent the individuals of a population, but the most used way is the binary string (1 or 0) where each chromosome is represented by one binary string. For the case of optimal sensor location problems, if for example two sensors are available to be placed on a four-story building and the individual is encoded as 1010, this means that one sensor is placed on the first floor and the second sensor is placed on the third floor.
2. Fitness evaluation: The next step is to determine the fitness or objective function to be optimized, that is problem dependent, and evaluate the fitness of each individual of the initial population.
3. Creation of new solutions: The following steps must be repeated until convergence:
    i. Selection: In this step, two parents (sub-population) are selected from the population based on their fitness values to produce new offsprings (children). The fitter the chromosome, the better it has chance to be selected to propagate its genetic information.
    ii. Crossover (Recombination): This operation is used to create new offsprings by recombining genes from the selected parent chromosomes. A crossover point or site should be randomly selected, the part of the strings before this point of the first parent is combined with the part of the strings after this point of the second parent to create the first offspring, whereas the second offspring is created by combining the remaining two parts of the strings from the two parents.

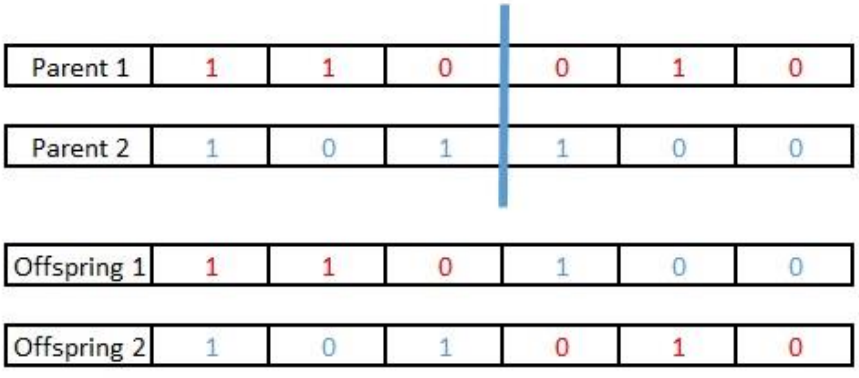


Figure 1: Crossover Example.

    iii. Mutation: This operation randomly changes some of the portions of the new individuals to avoid being trapped into a local optimum. For binary encoding, mutation randomly flips some bits from 0 to 1 or from 1 to 0.

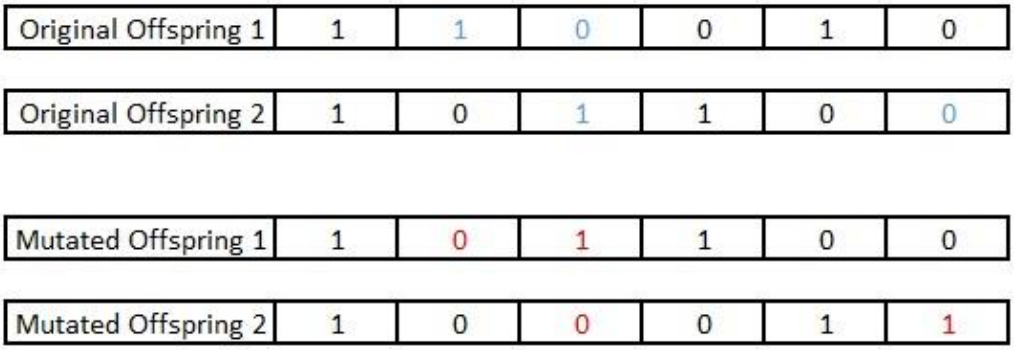


Figure 2: Mutation Example.

iv. The new, hopefully better, solutions are used as parents now. The fitness of the new offsprings should be evaluated and the loop should be repeated until convergence to the best individuals.

4. Termination conditions: For each problem, many termination conditions can be predefined, those may include: number of generations, time of the run, plateau (no more improvement of the best solution), and many others.

2.2 The Ensemble Kalman Filter (EnKF)

The standard Kalman Filter (KF) [22] is an optimal estimator used for the state approximation of linear dynamic systems perturbed by Gaussian white noise using observations subjected to Gaussian error statistics. For the case of large and nonlinear systems, the Ensemble Kalman Filter (EnKF) is widely used in the literature to overcome most of the drawbacks of the standard KF. The EnKF was first introduced by Evensen in 1994 [23] as a Monte Carlo approximation of the ordinary KF. It consists of a forecast step where an ensemble of realizations is propagated forward in time and then corrected in the analysis step, whenever observation data are recorded.

The first step in the EnKF is to evaluate the ensemble matrix A, holding the ensemble members x_i,

$$A = (x_1, x_2, ..., x_N) \quad A \in R^{n \times N}, x_i \in R^n \tag{1}$$

where, n is the size of the model state vector and N is the number of ensemble members.

The next step is to evaluate the ensemble mean and the ensemble perturbation matrices as follows,

$$A = A1_N \, \overline{A} \in R^{n \times N} \tag{2}$$

$$A' = A - \overline{A} = A(I - 1_N) \quad A' \in R^{n \times N} \tag{3}$$

where, $1_N \in R^{N \times N}$ is a matrix having all its elements equal to 1/N.

Consequently, the ensemble covariance matrix is defined as,

$$P = \frac{1}{N-1} A' A'^{T} \quad P \in R^{n \times n} \tag{4}$$

Let D be an ensemble of observation matrix holding the measurement vectors $d \in R^m$

$$D = \left(d_1, d_2, ..., d_N\right) \quad D \in R^{m \times N} \tag{5}$$

where m is the number of measurements at each occurrence, and

$$d_j = d + \in_j \quad j = 1,...N \tag{6}$$

where, ϵ is the measurement noise vector.
The measurement error covariance matrix is defined as,

$$R = \frac{1}{N-1} \gamma \gamma^{T} \quad R \in R^{m \times m} \tag{7}$$

where, γ is the ensemble of perturbations expressed as

$$\gamma = \left(\in_1, \in_2, ..., \in_N\right) \quad \gamma \in R^{m \times N} \tag{8}$$

The assimilation equation in matrix form is expressed as,

$$A^a = A^f + KG\left(D - HA^f\right) \tag{9}$$

where, the superscripts f and a represent the forecast and analysis states respectively, H is the observation matrix connecting the true state to the observations and KG is the Kalman Gain defined as follows,

$$KG = P^f H^T \left(HP^f H^T + R\right)^{-1} \tag{10}$$

3 NUMERICAL EXAMPLE

The numerical problem in this paper is similar to the one found in [16, 24, 25] with some slight modifications. It consists of a four-degree-of-freedom shear building, as shown in figure 1 below, and subjected to El-Centro earthquake excitation at its base. The stiffness is assumed to be constant and equal to $K = 7.5 \times 10^6 N/m$ on all the floors, the damping ratio is also assumed to be constant with a value of 5% for all modes, the mass for each floor is taken to be 5000 Kg.

A predefined change in the hysteretic behavior of the first floor of the system is imposed after the earthquake excitation hits the structure.

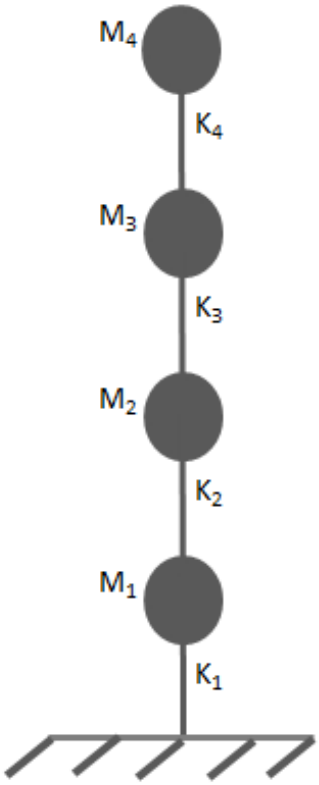


Figure 3: Four-story shear building.

It is assumed that only two sensors are available, therefore the purpose of this numerical problem is to determine the optimal locations of these two monitoring devices.

The first and second floors are randomly selected as an initial population of sensor locations. The next step consists of determining the fitness function, which is the difference between the measured displacements and velocities of each floor and their respective predicted values.

For this problem, the measurements data are synthetically generated by the Bouc-Wen model. Therefore the equation of motion is expressed as

$$M\ddot{u}(t)+C\dot{u}(t)+\alpha K_{el}u(t)+(1-\alpha)K_{in}z(x,t)=-M\ddot{u}_g(t) \tag{11}$$

where M is the mass matrix, C is the damping matrix, K_{el} and K_{in} are respectively the elastic and inelastic stiffness matrices, α is ratio of the post yielding stiffness to the elastic stiffness, τ is an influence vector, u is the displacement vector, x is the inter-story drift vector, and z is the evolutionary hysteretic vector of dimension n and whose ith component is expressed by the Bouc-Wen model by

$$\dot{z}_i = A_i\dot{x}_i - \beta_i|\dot{x}_i||z_i|^{n_i-1}z_i - \gamma_i\dot{x}_i|z_i|^{n_i} \; i=1,...n \tag{12}$$

where A, β, γ are the Bouc-Wen model parameters, whose values are shown in the table below

Model Parameter	Pre-Change (before 5 sec.)	Post-Change (after 5 sec.)
α	0.15	0.15
β	0.1	1000
γ	0.1	1000
A	1	1
n	1	1

Table 1: Bouc-Wen model parameters.

On the other side, the predicted values of the displacements and velocities are calculated using an inverse model that is used to detect the behavior of the system under consideration. The inverse model is expressed by the following equation

$$M\ddot{u}(t)+F(u,\dot{u})=-M\ddot{u}_g(t) \tag{13}$$

where F is the non-parametric representation of the non-linearity (non-linear restoring force), whose ith component for the case of the Ensemble Kalman Filter is given by

$$\begin{aligned}F_i(u,\dot{u}) &= a_i(u_i-u_{i-1})+a_{i+1}(u_i-u_{i+1})+b_i(u_i-u_{i-1})^3+b_{i+1}(u_i-u_{i+1})^3+c_i(\dot{u}_i-\dot{u}_{i-1}) \\ &+c_{i+1}(\dot{u}_i-\dot{u}_{i+1})+d_i(u_i-u_{i-1})(\dot{u}_i-\dot{u}_{i-1})+d_{i+1}(u_i-u_{i+1})(\dot{u}_i-\dot{u}_{i+1})\end{aligned} \tag{14}$$

where $\{a_i\},\{b_i\},\{c_i\},and\{d_i\}$ are the chaos coefficients of the unknown parameters to be identified.

Based on the fitness value of each individual, the ones having the lowest mismatch between the predicted and actual data have a better chance to be selected, hoping they will produce better offsprings after undergoing the crossover and mutation processes.

4 RESULTS

The problem is solved using the Matlab's genetic algorithm function (*ga*) [26],

$$X = ga(@FitnessFunction, N\text{var}s, A, b, A_{eq}, b_{eq}, LB, UB, options) \tag{15}$$

This function is part of the global optimization toolbox in Matlab, it is used for minimization purposes. In this case, *ga* function is used to give the optimal sensor locations as an output (vector *X*). The inputs of this function are the following:

1. The fitness function: for this problem, the fitness function is the mismatch between the measured displacements and velocities synthetically generated by the Bouc-Wen model, and their predicted values generated by applying the EnKF method.
2. The number of variables present in the problem are $N\text{var}s = 2$.
3. Linear constraints represented by the linear inequalities $A \times X \le b$ and the linear equalities $A_{eq} \times X = b_{eq}$. There are no constraints for this special problem.
4. Variables' bounds: a lower bound $LB = 1$ (story 1) and an upper bound $UB = 4$ (story 4) are used.

5. Options: the Matlab function *gaoptimset* is used to impose customized options to the GA. The following table lists the optimization parameters used as inputs for *gaoptimset* function.

Parameter	Value
Number of Population	3
Number of Elite individuals	2
Number of Generations	20
Stall Generations	10
Function Tolerance	10^{-10}
Initial Population	[1 2]

Table 2: Genetic Algorithm parameters.

where, the elite individuals represent the individuals having the best fitness function and consequently having the highest chance to be selected.

The algorithm stops if the number of generations is exceeded or if the average change in the fitness function value is less than the function tolerance over the stall generations. Figure 5 shows the stopping criteria of this numerical problem. It seems that the algorithm has stopped before the number of generations is reached, which means that the change in the fitness function over 10 successive generations is less than 10^{-10}. For this problem, the time and the Stall time limit (Stall (T)), which is the time over which the fitness function exhibits no improvement, are not included as stopping criteria.

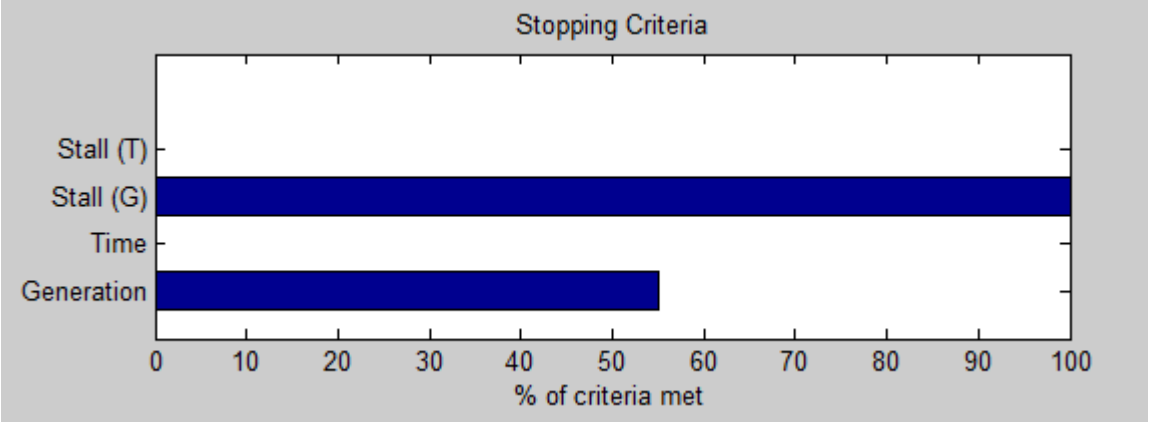


Figure 5: Stopping Criteria.

The default mutation and crossover operations, embedded within Matlab, are applied on this example [26]. The default mutation function is a Gaussian mutation that adds a random Gaussian number with zero mean to each entry of the population. The default crossover function creates a random binary vector (for example, for the four-story example, the random binary vector can be [1001]), and combines the genes of parent 1 at the locations of the ones and the genes of parent 2 at the locations of the zeros (for example, if for the first parent of chromosomes the sensors are placed at floors 1 and 3, parent 1 = [1010], and if the sensors for the second parent are placed at floors 2 and 4 , parent 2 = [0101], the offspring becomes [1100], so the sensors will be placed at floors 1 and 2).

The best fitness values (black dots) and the mean fitness values (blue dots) are represented at each generation in figure 6. It can be seen that the best and the mean values of the fitness function coincide at generation 4. As mentioned before, the algorithm converged before at-

taining the maximum number of generations because there was no improvement in the value of the fitness function for 10 successive generations.

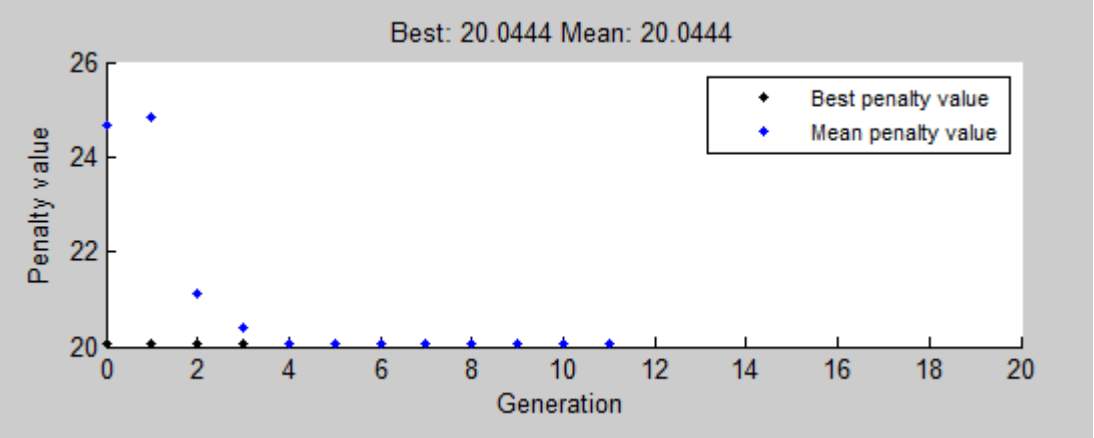


Figure 6: Best fitness value at each generation.

At the end of each generation, the best two locations of the sensors are determined based on their penalty value, the mismatch between the predicted and the measured displacements and velocities is minimal. This penalty value is calculated using the EnKF, which is a sequential data assimilation method that estimates the previously mentioned parameters *a*, *b*, *c* and *d* and the system state at each loop of the proposed algorithm. Figures 7 and 8 show the displacement and velocity estimates of floor 3 at the first generation and last generation, respectively. The comparison between these two figures shows the clear improvement in the mismatch between the EnKF predictions and the Bouc-Wen values for both the displacement and the velocity when sensors are placed at their optimal locations. The best locations of the two sensors are found to be on floors 2 and 3.

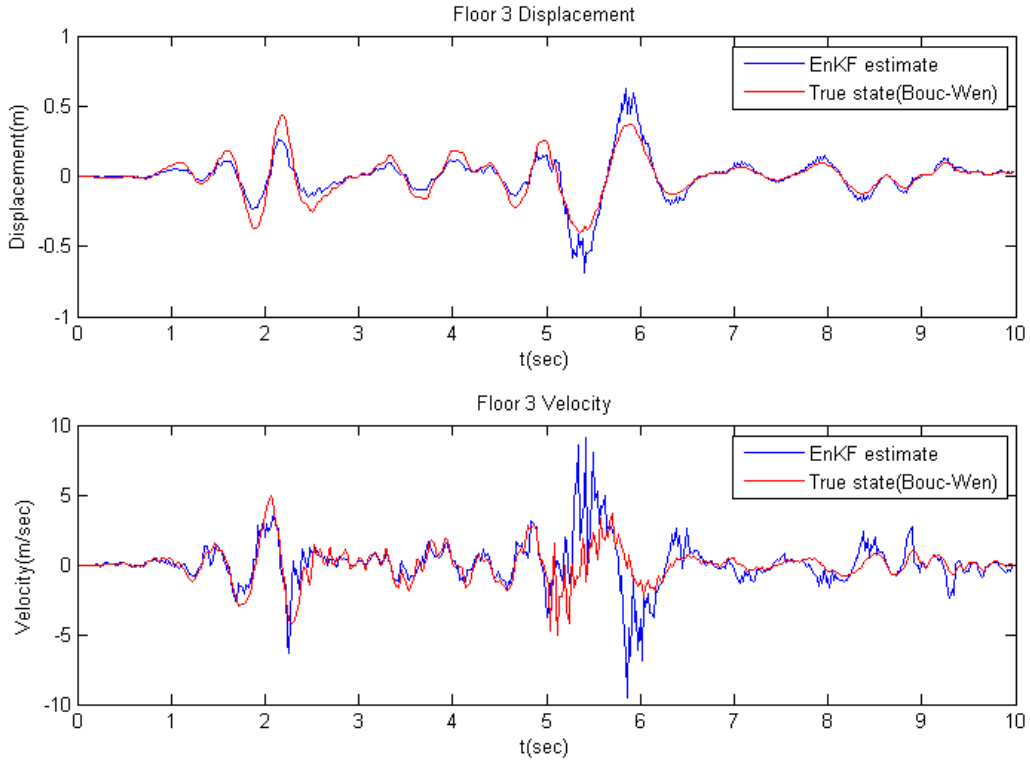


Figure 7: Estimates of the floor 3 displacement and velocity (at first generation).

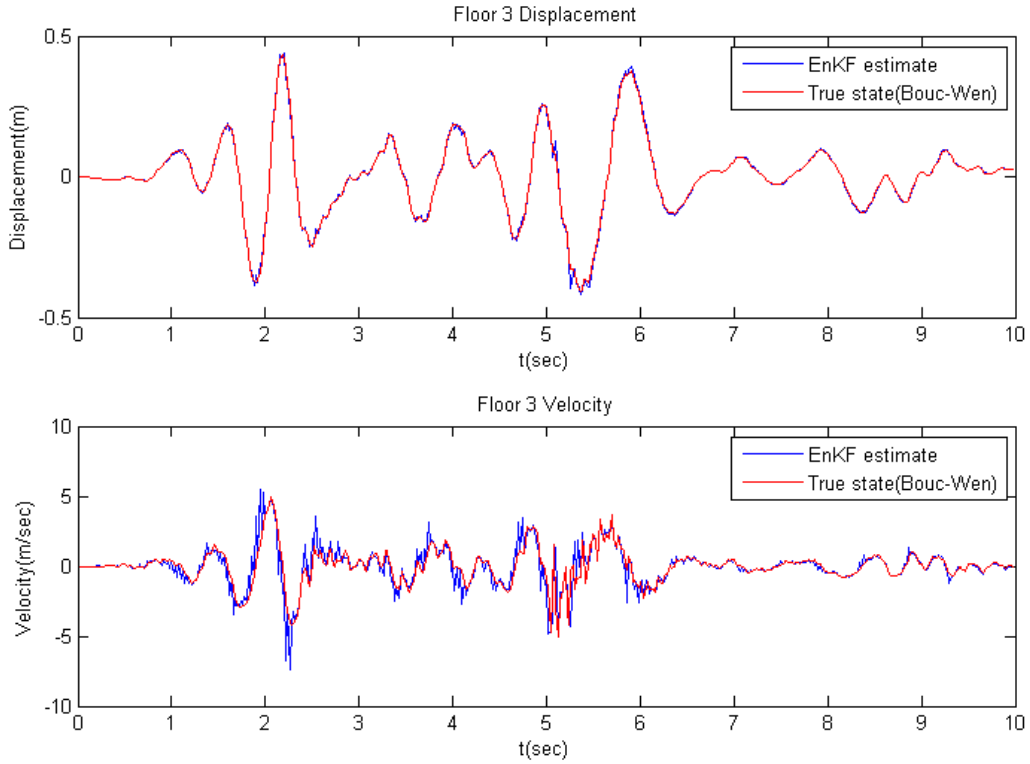


Figure 8: Estimates of the floor 3 displacement and velocity (at final generation).

5 CONCLUSIONS

This paper presented a new methodology for determining the optimal sensor locations to get the most necessary data for the purpose of system identification. This methodology is a combination between the genetic algorithm and the ensemble Kalman filter methods. The efficiency of the method was tested on a numerical example, consisting of determining the best locations of two available sensors on a four-story shear building. First the GA was used to generate an initial population of sensor locations from which the fittest individuals were selected as the best parents. The fitness function in this paper was assumed to be the difference between the synthetically generated measurements data and their respective predicted data from the EnKF. New better solutions resulted from applying some natural evolution operators on the parents chromosomes. The algorithm was repeated till convergence and the best locations of the two sensors were presented.

Future work will include a more complicated high-dimensional structure, to test the efficiency and the robustness of the proposed methodology in optimizing the sensors locations as well as their number for system identification and state estimation purposes.

REFERENCES

[1] W. J. Staszewski, K. Worden, Overview of optimal sensor location methods for damage detection. International Society for Optics and Photonics. *SPIE's 8th Annual International Symposium on Smart Structures and Materials*, August, 2001.

[2] L. Yao, W. A. Sethares, D. C. Kammer, Sensor placement for on-orbit modal identification via a genetic algorithm. *AIAA journal*, **31**, 1922-1928, 1993.

[3] H. Y. Guo, L. Zhang, L. L. Zhang, J. X. Zhou, Optimal placement of sensors for structural health monitoring using improved genetic algorithms, *Smart Materials and Structures*, **13**, 528, 2004.

[4] S. Kirkpatrick, C.D. Gelatt Jr, M.P. Vecchi, Optimization by Simulated Annealing. *Science*, **220**, 671-680, 1983.

[5] V. Cerny, Thermodynamical approach to the traveling salesman problem: An efficient simulation algorithm. *Journal of Optimization Theory and Applications*, **45**, 41-51, 1985.

[6] P. L. Chiu, F. Y. Lin, A simulated annealing algorithm to support the sensor placement for target location. *Electrical and Computer Engineering, 2004. Canadian Conference on*, IEEE, May, 2004.

[7] F. Glover, Future paths for integer programming and links to artificial intelligence. *Computers and Operations Research*, **13**, 533-549, 1986.

[8] F. Glover, Tabu search: Part I. *ORSA J Computing*, **1**, 190-206, 1989.

[9] F. Glover, Tabu search: Part II. *ORSA J Computing*, **2**, 4-32, 199090.

[10] K. V. Yuen, L. S. Katafygiotis, C. Papadimitriou, N. C. Mickleborough, Optimal sensor placement methodology for identification with unmeasured excitation. *Journal of Dynamics Systems, Measurement, and Control*, **123**, 677-686, 2001.

[11] C. Papadimitriou, J. L. Beck, S. K. Au, Entropy-based optimal sensor location for structural model updating. *Journal of Vibration and Control*, **6**, 781-800, 2000.

[12] C. Papadimitriou, Optimal sensor placement methodology for parametric identification of structural systems. *Journal of sound and vibration*, **278**, 923-947, 2004.

[13] E. B. Flynn, M. D. Todd, A Bayesian approach to optimal sensor placement for structural health monitoring with application to active sensing. *Mechanical Systems and Signal Processing*, **24**, 891-903, 2010.

[14] H. M. Chow, H. F. Lam, T. Yin, S. K. Au, Optimal sensor configuration of a typical transmission tower for the purpose of structural model updating. *Structural Control and Health Monitoring*, **18**, 305-320, 2011.

[15] H. F. Lam, J. H. Yang, Q. Hu, How to install sensors for structural model updating?. *Procedia Engineering*, **14**, 450-459, 2011.

[16] R. Ghanem, G. Ferro, Health monitoring of strongly nonlinear systems using the ensemble Kalman filter, *Structural Control and Health Monitoring*, **13**, 245-259, 2006.

[17] G. Evensen, The Ensemble Kalman Filter for combined sate and parameter estimation, *IEEE Control Systems Magazine*, June 2009.

[18] H. Li, S. J. Qin, T. T. Tsotsis, M. Sahimi, Computer simulation of gas generation and transport in landfills: VI—Dynamic updating of the model using the ensemble Kalman filter, *Chemical Engineering Science*, **74**, 69-78, 2012.

[19] J. Lyons, H. Nasrabadi, Well placement optimization under time-dependent uncertainty using an ensemble Kalman filter and a genetic algorithm, *Journal of Petroleum Science and Engineering*, **109**, 70-79, 2013.

[20] J.H. Holland, *Adaptation in natural and artificial systems: An introductory analysis with applications to biology, control, and artificial intelligence*. Oxford, England: U Michigan Press, 1975.

[21] J. H. Chou, J. Ghaboussi, Genetic Algorithm in structural damage detection, *Computers and Structures*, **79**, 1335-1353, 2001.

[22] R. Kalman, A new approach to linear filtering and prediction problems, *Journal of Basic Engineering*, Series D, **82**, 35-45, 1960.

[23] G. Evensen, Sequential Data Assimilation with a nonlinear quasi-geostrophic model using Monte Carlo to forecast error statistics. *Journal of Geophysical Research*, **99**, 10143-10162, 1994.

[24] G. Saad, R. Ghanem, Robust structural health monitoring using a polynomial chaos based sequential data assimilation technique. *3th International Conference on Computational Methods in Structural Dynamics and Earthquake Engineering (COMPDYN 2011)*, Corfu, Greece, May 25-28, 2011.

[25] G. Saad, R. Ghanem, *Robust structural health monitoring using a polynomial chaos based sequential data assimilation technique*. In Computational Methods in Stochastic Dynamics, pp. 203-213. Springer Netherlands, 2013.

[26] Mathworks. Retrieved from http://www.mathworks.com/help/gads/genetic-algorithm-options.html/

COMPDYN 2015
5th ECCOMAS Thematic Conference on
Computational Methods in Structural Dynamics and Earthquake Engineering
M. Papadrakakis, V. Papadopoulos, V. Plevris (eds.)
Crete Island, Greece, 25–27 May 2015

TOPOPLOGY OPTIMIZATION OF TWO-DIMENSIONAL WAVE BARRIERS FOR THE REDUCTION OF GROUND VIBRATION TRANSMISSION

Cédric Van hoorickx[1], Ole Sigmund[2], Mattias Schevenels[3], Boyan S. Lazarov[2], and Geert Lombaert[1]

[1]KU Leuven, Department of Civil Engineering, Structural Mechanics Section
Kasteelpark Arenberg 40, 3001 Leuven, Belgium
e-mail: {cedric.vanhoorickx, geert.lombaert}@bwk.kuleuven.be

[2]DTU, Department of Mechanical Engineering, Solid Mechanics
Nils Koppels Allé, Building 404, 2800 Lyngby, Denmark
e-mail: {sigmund, bsl}@mek.dtu.dk

[3]KU Leuven, Department of Architecture, Architectural Engineering
Kasteelpark Arenberg 1, 3001 Leuven, Belgium
e-mail: mattias.schevenels@asro.kuleuven.be

Keywords: Topology optimization, Elastodynamic wave propagation, Vibration reduction measures, Wave barriers

Abstract. *This paper studies topology optimization as a tool for designing barriers for ground vibration transmission. A two-dimensional problem is considered where material is stiffened in the design domain, located in the transmission path between the wource and the receiver. The two-dimensional homogeneous halfspace is excited at the surface. The response at the receiver is minimized for a harmonic load by distributing a stiffened material in the design domain using topology optimization. The performance is compared to a wall barrier which has the same volume of material and has a depth equal to the depth of the design domain. At low frequencies, where the wavelengths are large compared to the height of the domain, the optimized wave barrier reflects and guides waves away from the surface. At high frequencies, destructive interference is obtained that leads to high values of the insertion loss. The presence of small features in the designs makes the performance sensitive to deviations in the geometry. In order to obtain a design which is robust with respect to geometric imperfections, a worst case approach is followed. The resulting design not only outperforms the wall barrier, but is also robust with respect to deviations in the geometry. This paper also shows that the robust design can be used to develop simplified design solutions.*

1 INTRODUCTION

Vibrations in the built environment are a matter of growing concern. Railway induced vibrations may lead to malfunctioning of sensitive equipment, discomfort to people and, at high vibration levels, damage to structures. Furthermore, noise can be re-radiated from floors and walls when local modes are excited. More and more research is performed to search for efficient and cost-effective vibration mitigation measures. Three categories of mitigation measures can be distinguished: at the source (the railway track) [1], on the transmission path (the ground) [2], and at the receiver (the building) [3]. The present work considers wave barriers to hinder propagation of ground vibration from source to receiver.

Until now, only a limited number of simple design geometries for mitigation measures has been investigated. However, current flexibility in construction methods such as jet grouting leaves much room for improvement. To discover novel design geometries, topology optimization [4] is applied. Topology optimization was originally developed for static mechanical problems, but has since then been used for a variety of applications including problems governed by wave propagation. Topology optimization has been applied to problems with electromagnetic (photonic crystal waveguide designs [5]), elastodynamic (design of phononic band-gap materials and structures [6]), and acoustic waves (noise barriers [7, 8]). In this study, topology optimization is used to develop novel design geometries for barriers impeding elastodynamic wave transmission.

Since structural optimization is often found to lead to designs which are very sensitive to geometrical imperfections [9], a worst case approach is adopted where the worst performance of some (extreme) cases is optimized. This paper demonstrates the importance of considering robustness in the optimization process, and shows that the robust designs can be used to develop simplified design solutions.

The paper is organized as follows. First, the optimization problem is introduced and the topology optimization approach is briefly presented. Second, results for optimized wave barriers are discussed. Third, robust topology optimization is applied to obtain designs less sensitive to geometric imperfections and a simplified design is presented.

2 THE OPTIMIZATION PROBLEM

Figure 1 shows the considered optimization problem. A two-dimensional homogeneous elastic halfspace is considered which is excited at the surface by a vertical harmonic load.

The goal is to minimize the response at an output point (the receiver), located at the surface of the halfspace, at a distance of $15\,\mathrm{m}$ from the excitation point. The effectiveness of the wave barrier is quantified by the insertion loss (IL) in this output point:

$$\mathrm{IL} = 20 \log \left(\frac{\left| \hat{u}_{\mathrm{out}}^{\mathrm{orig}} \right|}{|\hat{u}_{\mathrm{out}}|} \right) \tag{1}$$

with $\left| \hat{u}_{\mathrm{out}}^{\mathrm{orig}} \right|$ the norm of the displacement vector in the output point in the case of the original homogeneous halfspace without the wave barrier and $|\hat{u}_{\mathrm{out}}|$ the norm of the displacement vector in the case with wave barrier.

The displacements are obtained using the finite element method with two-dimensional four-node elements in plane strain. An element size of $0.25\,\mathrm{m}$ is used for the mesh, corresponding to ten elements per shear wavelength λ_s at a frequency of $80\,\mathrm{Hz}$, which is the upper limit considered in this work. At the boundaries of the finite element mesh, appropriate radiation boundary

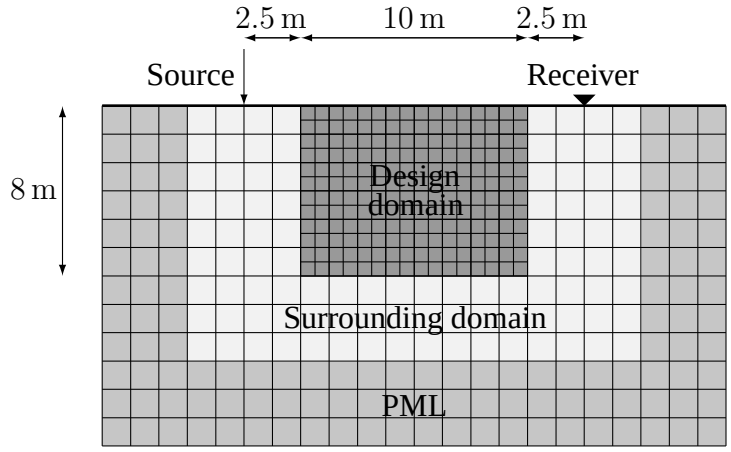


Figure 1: The considered optimization problem.

conditions have to prevent spurious wave reflections. The Perfectly Matched Layers (PML) of Harari and Albocher [10] are applied. The resulting finite element equilibrium equations can be written as:

$$\hat{\mathbf{K}}\hat{\mathbf{u}} = \hat{\mathbf{p}} \tag{2}$$

where $\hat{\mathbf{p}}$ is the load vector, $\hat{\mathbf{u}}$ is the displacement vector, and $\hat{\mathbf{K}}$ is the dynamic stiffness matrix.

The material is stiffened in a design domain which is located between the source and the receiver. The design domain has a cross-sectional area of $10 \times 8\,\mathrm{m}^2$ and is located at a distance of $2.5\,\mathrm{m}$ from both the excitation point and the receiver. The properties of the original material 1 of the homogeneous halfspace and the stiffened material 2 are summarized in table 1.

Property	Original material 1	Stiffened material 2
Material density ρ	$2000\,\mathrm{kg/m^3}$	$2000\,\mathrm{kg/m^3}$
Longitudinal wave velocity C_p	$400\,\mathrm{m/s}$	$950\,\mathrm{m/s}$
Shear wave velocity C_s	$200\,\mathrm{m/s}$	$550\,\mathrm{m/s}$

Table 1: The considered material properties.

The optimal distribution of the stiffened material in the design domain is determined using topology optimization [4]. The material distribution is parameterized using so-called element densities $\bar{\rho}_e$ for each element e in the design domain. The value $\bar{\rho}_e = 0$ indicates that element e has the properties of the homogeneous halfspace, while the value $\bar{\rho}_e = 1$ corresponds to the properties of the stiffened material. The densities are allowed to vary continuously between 0 and 1, making it possible to solve the optimization problem with a gradient based approach.

A Solid Isotropic Material with Penalization (SIMP) interpolation is used to interpolate the material properties α:

$$\alpha = \alpha_1 + \bar{\rho}_e^p \left(\alpha_2 - \alpha_1\right) \tag{3}$$

where α_1 and α_2 are the properties of the original and stiffened material, respectively. The penalization factor $p \geq 1$ avoids so-called gray designs with intermediate densities. A value

$p = 1$ is used for the material density ρ while $p = 3$ is used for the constrained modulus ρC_{p}^2 and the shear modulus ρC_{s}^2. Note that the penalization only works if the volume constraint in Eq. (6) is active.

In order to achieve a design with sufficient detail, the finite element mesh of the design domain is finer than the one of the surrounding domain, following the method proposed by Kristensen [11]. The horizontal and vertical displacements of the intermediate nodes are coupled to the nodes of the surrounding domain and the resulting constraint equations are added to the finite element equilibrium equations.

The (physical) element densities $\bar{\rho}_e$ are obtained from the design variables ρ_e of the optimization problem by applying a projection filter [12]:

$$\bar{\rho}_e = \frac{\tanh(\beta\eta) + \tanh(\beta(\tilde{\rho}_e - \eta))}{\tanh(\beta\eta) + \tanh(\beta(1-\eta))} \tag{4}$$

where β is a sharpness parameter, controlling the smoothness of the projection, η is the projection threshold, and the densities $\tilde{\rho}_e$ are obtained from:

$$\tilde{\rho}_e = \frac{\sum_{i=1}^{N} w_{ei} v_i \rho_i}{\sum_{i=1}^{N} w_{ei} v_i} \tag{5}$$

where v_i is the volume of element i and the weight $w_{ei} = \max(R - r_{ei})$ depends on the filter radius R and the center-to-center distance r_{ei} between the elements e and i. In the present work, the filter radius is taken to be $R = 2.5$ elements, the projection threshold value is set to $\eta = 0.5$ and the sharpness parameter β has an initial value equal to 1 and is doubled every 50 iterations until the value of 32 is reached.

The aim is to maximize the insertion loss in Eq. (1). The problem is reformulated as a minimization problem, by defining the objective function $\Phi = -\mathrm{IL}$. The optimization problem is also subjected to a volume constraint and can be summarized as:

$$\begin{aligned} \min_{\rho_e} \quad & \Phi = 20 \log \left(\frac{|\hat{u}_{\mathrm{out}}(\bar{\rho}_e)|}{\left|\hat{u}_{\mathrm{out}}^{\mathrm{orig}}\right|} \right) \\ \text{s.t.} \quad & \sum_{e=1}^{N} v_e \bar{\rho}_e \leq V^*, \quad e = 1 \ldots N \\ & 0 \leq \rho_e \leq 1, \qquad e = 1 \ldots N \end{aligned} \tag{6}$$

where N is the number of elements in the design domain and the upper limit for the volume V^* is set to 10% of the total volume. The displacements are computed using the finite element method. This problem is not convex, and multiple local minima may exist.

The optimization problem is solved using the method of moving asymptotes (MMA) [13]. This gradient-based approach necessitates the calculation of the derivatives of the objective function. To enable an efficient calculation of the sensitivities, the adjoint method is used (see, e.g. [4, p. 17]). The sensitivities are calculated as follows:

$$\frac{\partial \Phi}{\partial \bar{\rho}_e} = 2\mathrm{Re}\left\{ \boldsymbol{\lambda}^T \frac{\partial \hat{\mathbf{K}}}{\partial \bar{\rho}_e} \hat{\mathbf{u}} \right\} \tag{7}$$

where the vector $\boldsymbol{\lambda}$ is computed from the adjoint equation, which can be written in the following simplified form:

$$\hat{\mathbf{K}} \boldsymbol{\lambda} = -\frac{\partial \Phi}{\partial \hat{\mathbf{u}}} \tag{8}$$

3 TOPOLOGY OPTIMIZATION RESULTS

The wave designs obtained by topology optimization are compared with the reference design of a wall barrier which has the same volume of material and has a depth equal to the depth of the design domain: a rectangular design with dimensions $1\,\mathrm{m} \times 8\,\mathrm{m}$, located in the design domain at the side closest to the source. This reference design is shown in figure 2a. The optimization starts with an initial design where all element densities are assigned a value $\rho_e = 0.2$.

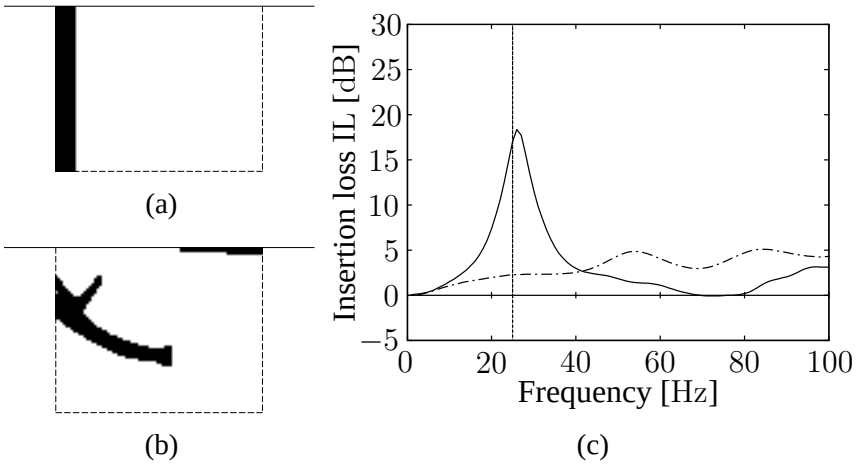


Figure 2: (a) Reference design, (b) optimized design maximizing the insertion loss at $25\,\mathrm{Hz}$, and (c) resulting insertion loss IL as a function of the frequency for the reference design (dash-dotted line) and the optimized design (solid line).

Maximizing the insertion loss in Eq. (1) for harmonic excitation at $25\,\mathrm{Hz}$ results in the design and corresponding insertion loss in figure 2. The optimized design leads to an insertion loss of $17.0\,\mathrm{dB}$ compared to the original situation which is $14.8\,\mathrm{dB}$ higher than the insertion loss of the reference design. Figure 3 shows the vector norm of the real and imaginary part of the displacement field at $25\,\mathrm{Hz}$ for the homogeneous halfspace and after the introduction of the reference barrier and the optimized barrier. The reference barrier mainly reflects the incoming waves and therefore reduces the amplitude of the Rayleigh waves travelling along the free surface from the source to the receiver. The optimized design, however, does not only reflect the incoming waves, but also directs them downwards into the soil, reducing the response at the surface.

The optimized design and its performance change significantly when the wavelength becomes smaller than the half of the depth of the design domain. Figure 4 shows the design and corresponding insertion loss when maximizing the insertion loss for harmonic excitation at $50\,\mathrm{Hz}$. The insertion loss of the optimized design is again compared to the insertion loss of the reference design of $1\,\mathrm{m} \times 8\,\mathrm{m}$. At $50\,\mathrm{Hz}$, the insertion loss reaches a very high value of $50.1\,\mathrm{dB}$, which is $45.7\,\mathrm{dB}$ higher than the insertion loss of the reference design. Figure 5 shows the vector norm of the real and imaginary part of the displacement field at $50\,\mathrm{Hz}$ for the homogeneous halfspace and after the introduction of the reference barrier and the optimized barrier. The reference barrier again primarily reduces the amplitude of the Rayleigh waves. The optimized design, however, moves the incoming waves away from the surface. This effect is caused by destructive interference of the waves transmitted by the top part of the optimized design and the waves reflected by the bottom part.

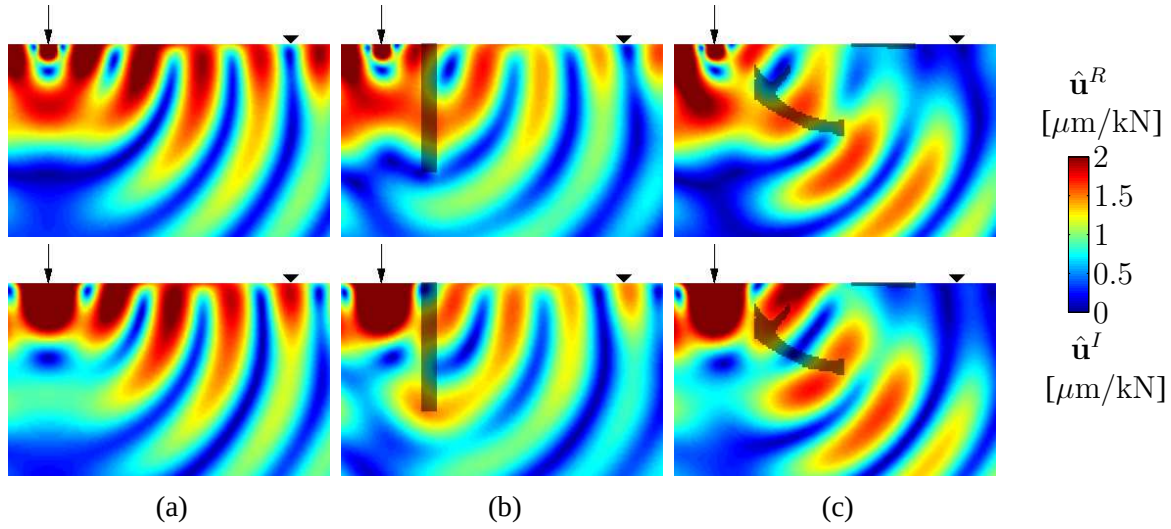


Figure 3: Vector norm of the real part $\hat{\mathbf{u}}^R$ (top) and imaginary part $\hat{\mathbf{u}}^I$ (bottom) of the displacement field at $25\,\mathrm{Hz}$ (a) for the homogeneous halfspace and after the introduction of (b) the reference design (figure 2a), and (c) the optimized design maximizing the insertion loss IL at $25\,\mathrm{Hz}$ (figure 2b).

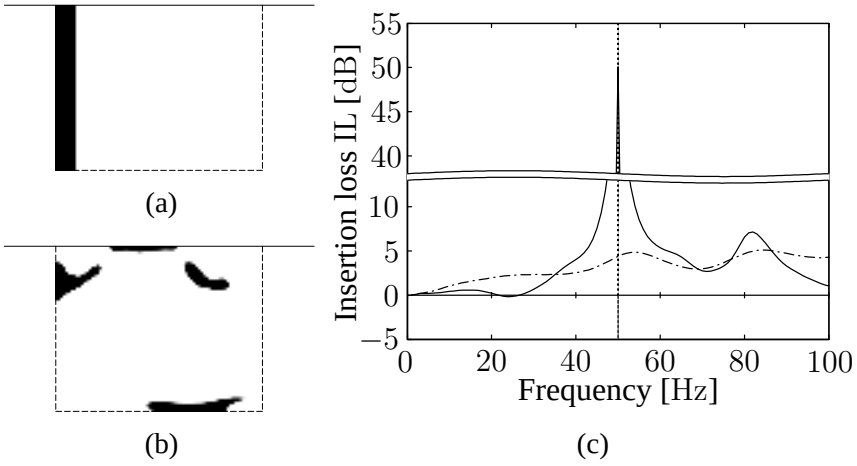
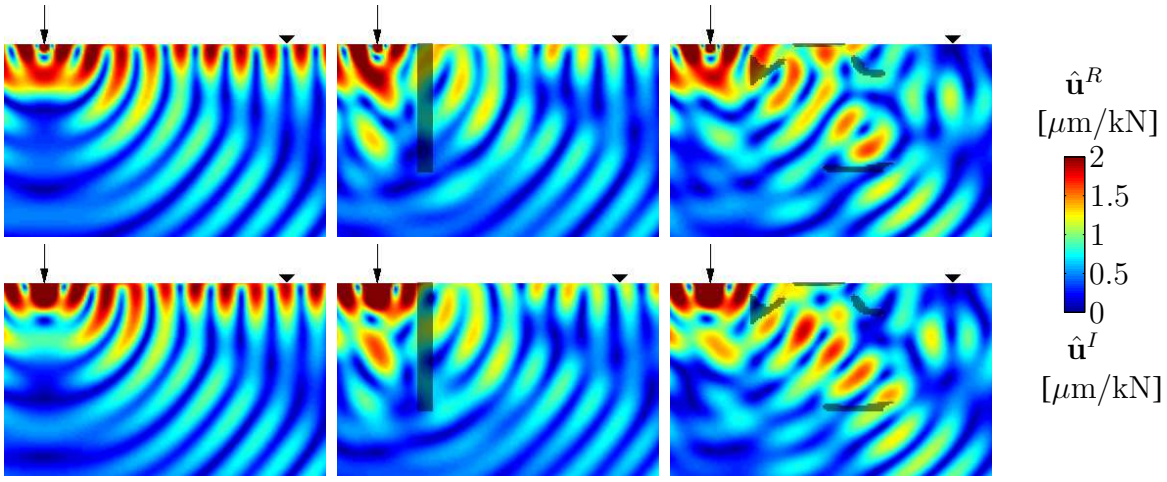


Figure 4: (a) Reference design, (b) optimized design maximizing the insertion loss at $50\,\mathrm{Hz}$, and (c) resulting insertion loss IL as a function of the frequency for the reference design (dash-dotted line) and the optimized design (solid line).

4 GEOMETRIC IMPERFECTIONS

The design in figure 4b contains some small features, making it very sensitive to deviations in the geometry. The performance of the actual wave barrier in case of geometric imperfections may therefore be far from optimal. The influence of errors in the (in-plane) dimensions of the stiffened material can be modeled by varying the projection threshold η in Eq. 4 [14].

Figure 6 shows the influence of the projection threshold η for the design optimized for reducing transmission at a frequency of $50\,\mathrm{Hz}$ (figure 4). For low values of the projection threshold (e.g. $\eta = 0.25$), lower values of the filtered densities are projected to the stiffened material as well, and the dimensions of the stiffened material increase, leading to so-called dilated designs. For high values of the projection threshold (e.g. $\eta = 0.75$), only the higher values of the filtered



(a) (b) (c)

Figure 5: Vector norm of the real part $\hat{\mathbf{u}}^R$ (top) and imaginary part $\hat{\mathbf{u}}^I$ (bottom) of the displacement field at $50\,\mathrm{Hz}$ (a) for the homogeneous halfspace and after the introduction of (b) the reference design (figure 4a), and (c) the optimized design maximizing the insertion loss IL at $50\,\mathrm{Hz}$ (figure 4b).

densities are projected to the stiffened material, and the dimensions of the stiffened material decrease, leading to so-called eroded designs.

A high value for the insertion loss is found for the value $\eta = 0.5$ (intermediate design). The performance is therefore very sensitive to thickness variations. For the dilated design ($\eta = 0.25$), a high performance is still obtained thanks to the top part of the design. This top part is, however, largely affected for the eroded design ($\eta = 0.75$). The upper value $\eta = 1$ removes all stiffened material from the design ($\hat{u}^{\mathrm{out}} = \hat{u}^{\mathrm{out}}_{\mathrm{orig}}$), and the insertion loss (Eq. (1)) becomes equal to zero.

In order to obtain a design which is less sensitive to this type of geometric imperfections, a robust topology optimization approach is used. The interval of the projection threshold is set to $[0.25, 0.75]$ and a worst case formulation is adopted. In the worst case formulation, the minimal insertion loss for different values of the projection threshold is maximized. The robust optimization problem is formulated as follows:

$$\begin{aligned} \min_{\rho_e} \quad & \max_{q} \left\{ \Phi\left(\bar{\rho}_e(\eta^q)\right) \right\}, && q = 1 \ldots Q \\ \text{s.t.} \quad & \sum_{e=1}^{N} v_e \bar{\rho}_e^i \leq V^*, && e = 1 \ldots N \\ & 0 \leq \rho_e \leq 1, && e = 1 \ldots N \end{aligned} \tag{9}$$

where Q is the number of values considered for the projection threshold η and $\bar{\rho}_e^i$ are the element densities of element e in the case of the intermediate design ($\eta = 0.5$).

Figure 7 shows the resulting robust design and insertion loss for $Q = 3$ equidistant values of the projection threshold η. The deterministic performance decreases from $50.1\,\mathrm{dB}$ to $40.6\,\mathrm{dB}$. The robust design is, however, less sensitive to thickness variations. There are some small peaks at $\eta = 0.25$, $\eta = 0.5$ and $\eta = 0.75$ but these are not as distinct as the peak at $\eta = 0.5$ in figure 6d. The insertion loss at a frequency of $50\,\mathrm{Hz}$ is therefore larger than $26.5\,\mathrm{dB}$ for the entire range $\eta = [0.25, 0.75]$.

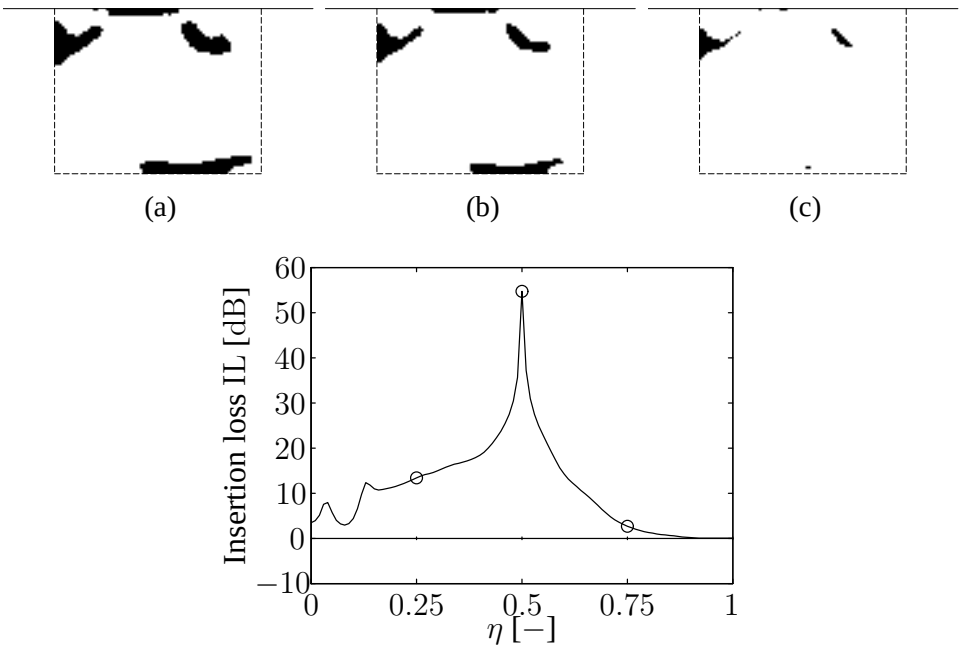


Figure 6: The (a) dilated ($\eta = 0.25$), (b) intermediate ($\eta = 0.5$), and (c) eroded ($\eta = 0.75$) version of the optimized design maximizing the insertion loss IL at a frequency of $50\,\mathrm{Hz}$ and (d) the influence of the projection threshold η on the insertion loss IL at $50\,\mathrm{Hz}$.

Because of buildability constraints, it may be difficult to reproduce the design in figure 7b. Since the design is robust to thickness variations, a simplification of the geometry is not expected to significantly affect the performance of the design. Figure 8 shows a manually simplified design and the corresponding insertion loss. The performance of this simplified design is similar to the performance of the design obtained with deterministic and robust topology optimization. The insertion loss at $50\,\mathrm{Hz}$ is equal to $33.0\,\mathrm{dB}$ and is therefore lower than the insertion loss of the robust design, but the simplified design still outperforms the reference design, which has an insertion loss equal to $4.4\,\mathrm{dB}$ at $50\,\mathrm{Hz}$.

5 CONCLUSIONS

Topology optimization is a powerful tool for finding novel design geometries. In this paper, topology optimization is used to design wave barriers that reduce ground transmission vibration. An optimization problem is considered where a homogeneous halfspace is excited at the surface. The response at a receiver point is minimized by stiffening material in the design domain between the source and receiver.

Harmonic excitation is considered and the optimized designs are shown at two frequencies ($25\,\mathrm{Hz}$ and $50\,\mathrm{Hz}$). At lower frequencies, the incoming waves are directed downwards away from the surface. At higher frequencies, destructive interference is observed, resulting in a peak at the targeted frequency.

Geometric imperfections can lead to an important deterioration of the performance. A worst case approach is therefore used to obtain a robust design, where the lowest performance of some values of the projection threshold is maximized. The resulting design is less sensitive to errors in the dimensions of the wave barrier. Simplifying the topology of the robust design leads to a

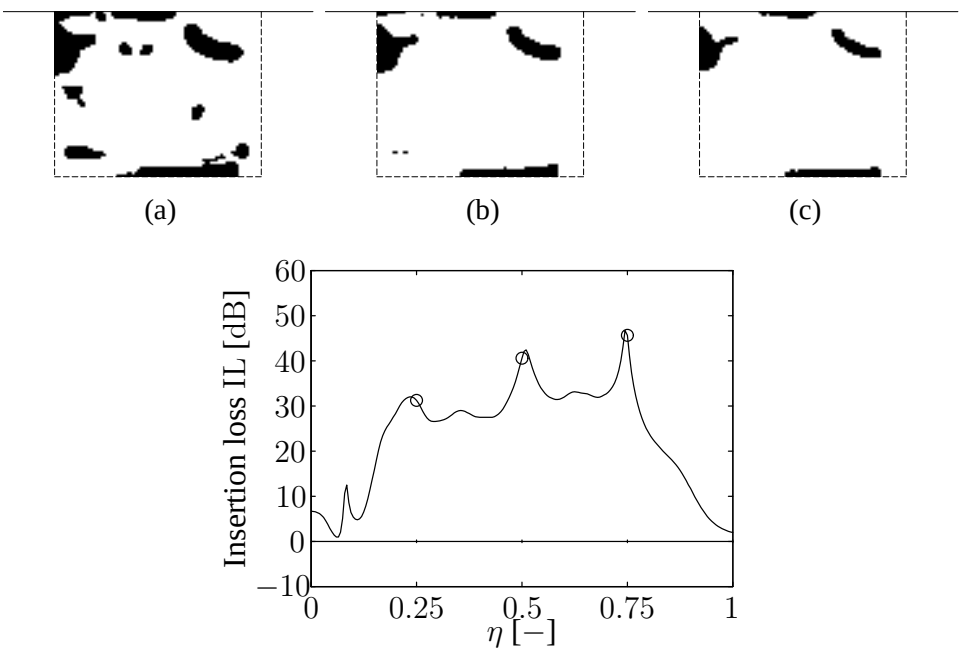


Figure 7: The (a) dilated ($\eta = 0.25$), (b) intermediate ($\eta = 0.5$), and (c) eroded ($\eta = 0.75$) version of the robust optimized design maximizing the minimal insertion loss IL for 3 equidistant values of the projection threshold η in the range $[0.25, 0.75]$ at a frequency of $50\,\mathrm{Hz}$ and (d) the influence of the projection threshold η on the insertion loss IL at $50\,\mathrm{Hz}$.

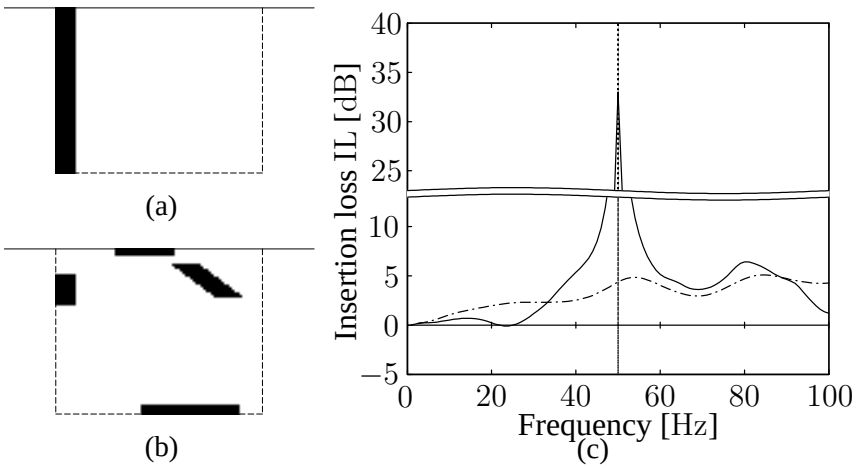


Figure 8: (a) Reference design, (b) simplified design after a manual post-processing of the robust optimized design maximizing the insertion loss at a frequency of $50\,\mathrm{Hz}$ using a worst case robust approach (figure 7b), and (c) resulting insertion loss IL as a function of the frequency for the reference design (dash-dotted line) and the post-processed optimized design (solid line).

slightly reduced performance, but the resulting design significantly outperforms the wall barrier.

ACKNOWLEDGEMENTS

The first author is a doctoral fellow of the Research Foundation Flanders (FWO). The financial support is gratefully acknowledged. The first, second and last authors are members of the KU Leuven-BOF PFV/10/002 OPTEC-Optimization in Engineering Center.

REFERENCES

[1] G. Lombaert, G. Degrande, B. Vanhauwere, B. Vandeborght, S. François, The control of ground-borne vibrations from railway traffic by means of continuous floating slabs. *Journal of Sound and Vibration*, **297**, 946–961, 2006.

[2] P. Coulier, S. François, G. Degrande, G. Lombaert, Subgrade stiffening next to the track as a wave impeding barrier for railway induced vibrations. *Soil Dynamics and Earthquake Engineering*, **48**, 119–131, 2013.

[3] J.P. Talbot, H.E.M. Hunt, A generic model for evaluating the performance of base-isolated buildings, *Journal of Low Frequency Noise, Vibration and Active Control*, **22**, 149–160, 2003.

[4] M.P. Bendsøe, O. Sigmund, *Topology optimization: theory, methods and applications*, Springer, Berlin, 2003.

[5] P. Borel, A. Harpøt, L. Frandsen, M. Kristensen, P. Shi, J. Jensen, O. Sigmund, Topology optimization and fabrication of photonic crystal structures, *Optic Express*, **12**, 1996–2001, 2004.

[6] O. Sigmund, J.S. Jensen, Systematic design of phononic band-gap materials and structures by topology optimization, *Philosophical Transactions of the Royal Society of London Series A: Mathematical, Physical and Engineering Sciences*, **361**, 1001–1019, 2003.

[7] M. Dühring, J. Jensen, O. Sigmund, Acoustic design by topology optimization, *Journal of Sound and Vibration*, **317**, 557–575, 2008.

[8] J. Kook, K. Koo, J. Hyun, J. Jensen, S. Wang, Acoustical topology optimization for Zwickers loudness model – Application to noise barriers, *Computer Methods in Applied Mechanics and Engineering*, **237**, 130–151, 2012.

[9] M. Jansen, G. Lombaert, M. Schevenels, Robust topoplogy optimization of structures with imperfect geometry based on geometric nonlinear analysis. *Computer Methods in Applied Mechanics and Engineering*, **285**, 452–467, 2015.

[10] I. Harari, U. Albocher, Studies of FE/PML for exterior problems of time-harmonic elastic waves. *Computer Methods in Applied Mechanics and Engineering*, **195**, 3854–3879, 2006.

[11] S.S. Kristensen, *Topology optimization for damping of ground vibration*, Master's thesis, DTU, 2012.

[12] J.K. Guest, J.H. Prévost, T. Belytschko, Achieving minimum length scale in topology optimization using nodal design variables and projection functions. *International Journal for Numerical Methods in Engineering*, **61**, 238–254, 2004.

[13] K. Svanberg, The method of moving asymptotes – a new method for structural optimization. *International Journal for Numerical Methods in Engineering*, **24**, 359–373, 1987.

[14] M. Schevenels, B.S. Lazarov, O. Sigmund, Robust topology optimization accounting for spatially varying manufacturing errors. *Computer Methods in Applied Mechanics and Engineering*, **200**, 3613–3627, 2011.

COMPDYN 2015
5th ECCOMAS Thematic Conference on
Computational Methods in Structural Dynamics and Earthquake Engineering
M. Papadrakakis, V. Papadopoulos, V. Plevris (eds.)
Crete Island, Greece, 25–27 May 2015

MULTI-OBJECTIVE OPTIMIZATION UNDER UNCERTAINTY WITH REAL-TIME INTEGRATED DECISION MAKING APPLIED TO STRUCTURAL ENGINEERING

Mariapia Marchi[1], **Mauro Munerato**[1], **Luca Rizzian**[1] **and Stefano Costanzo**[1]

[1] ESTECO S.p.A.
Padriciano 99, 34149 Trieste (Italy)
e-mail: marchi,munerato,rizzian,costanzo@esteco.com

Keywords: Multi-Objective Optimization, Multi-Criteria Decision Making, Interactive Optimization, Robust Design Optimization, Reliability-Based Design Optimization, Reliability Assessment of Structures

Abstract. *One of the major tasks of structural engineering design optimization is the handling of uncertainties (such as variations in material properties, loading conditions, unknown environmental conditions or even uncertainties in modeling assumptions), which affect system performance in terms of robustness and reliability (or, in other words, the ability to respond to input variations with minimal alteration, loss of functionality or damage). This task is usually tackled with Optimization Under Uncertainty (OUU) methods[1], like robust design optimization and reliability-based design optimization. In most cases, the optimization has to deal with multi-objective problems (such as maximizing the performance while minimizing costs, system response variations, etc). These problems do not have a unique solution, but a set of tradeoff optimal solutions (the so-called Pareto front). The action of a decision maker (DM) is necessary for choosing the final optimal design according to some (pre-defined) preferences or criteria. Multi-Criteria Decision Making (MCDM) techniques[2] have been developed over the past years to try to make these choices objective and rational. In most MCDM methods, the preferences are usually taken into account during some a-posteriori analyses of the optimization outcomes.*

Here we address both OUU and MCDM problems with an approach that integrates directly the action of the DM with the optimization process. The DM is asked to express their preferences (based on their previous experience) to drive the optimization towards the most preferred regions of the Pareto front. This can lead to a more efficient exploration of specific regions of the Pareto front and reduce the computational cost of finding desirable solutions. Interactive MCDM approaches have been recently given more attention in the multi-objective optimization community [3, 4, 5]. A validation of this approach on simple test-cases is shown as well as its application to the design of a simple building structure under uncertainties with seismic hazard and snow loads.

1 INTRODUCTION

Some of the main challenges in the field of structural engineering design include the handling of uncertainties arising, e.g., from variations in material properties, loading conditions, unknown environmental conditions or even uncertainties in modeling assumptions, and the multi-objective nature of design problems requiring a trade-off between several (conflicting) objectives (such as performance maximization, cost minimization, variation minimization, etc.).

Uncertainties affect system robustness and reliability, i.e. the ability to respond to input variations with minimal alteration, loss of functionality or damage. Thus in the past decades a number of Optimization Under Uncertainty (OUU) methods[1], like Robust Design Optimization (RDO) and Reliability-Based Design Optimization (RBDO), have been developed to find designs, which are robust and reliable unlike those sometimes found with deterministic optimization methods.

Multi-objective optimization (MO) problems do not have a unique solution, but a set of tradeoff optimal solutions (the so-called Pareto front). Hence a compromise between conflicting requirements is sought. The intervention of a decision maker (DM) is necessary for choosing the final optimal design according to some (pre-defined) preferences or criteria. Multi-Criteria Decision Making (MCDM) techniques[2] have been developed over the past years to make these choices objective and rational. In many MCDM methods, the preferences are taken into account during a-posteriori analyses of the optimization results. Other techniques include the preferences directly in the optimization phase, usually by rewriting the multi-objective problem as a single-objective problem, where a function of the preferences has to be optimized.

The importance of MO in real-world structural engineering problems was highlighted for instance by Papadrakakis et al. in Ref. [6]. Structural sizing examples were studied and optimized with Evolutionary Algorithms (EAs). EAs are more efficient than gradient-based methods for these kinds of problems, because they rely on the evolution of a population of optimal candidate designs. Furthermore EAs are robust global search algorithms (they need no derivatives), which are less likely to be trapped in local optimal regions of large and complex search spaces. Ref. [7] addressed a reliability-based multi-objective sizing optimization of a multi-storey steel frame under seismic loading, where probabilistic constraints were introduced to account for the system reliability. Failure probabilities were computed with the Latin Hypercube Sampling (LHS)[8]. Beck et al. [9] developed a software to find the tradeoff between conflicting design criteria while accounting for modeling and loading uncertainties. They turned the MO into a Single-objective Optimization (SO) of the aggregation of the preference functions. Frangopol[10] reviewed the relevance of using MO and decision making in civil infrastructure maintenance management under uncertainty, while Caterino et al. [11] focused on *a posteriori* MCDM techniques applied to the specific problem of seismic structural retrofitting. Jensen et al. [12] developed a method for efficiently obtaining compromise design solutions and tradeoff information between objectives in the optimization of structural systems under stochastic excitations by introducing an auxiliary variable to solve the MO problem as a SO by means of line search techniques. In Ref. [13] certain authours of this paper studied a structural sizing MO under uncertainty (MOUU) problem by using Polynomial Chaos[14] Expansion (PCE) techniques to determine the system reliability with a method already applied in Refs. [15, 16].

Motivated by the growing interest shown by structural engineering specialists in MCDM and MO techniques, in this paper we address both MOUU and MCDM problems with an approach that integrates directly the action of the DM with the optimization process. For this purpose, a novel algorithm has been developed: the DM is asked to express their preferences (based on

their previous experience) as target points to drive the optimization towards the most preferred regions of the Pareto front. In principle this can lead to a more efficient exploration of specific regions of the Pareto front and reduce the computational cost of finding desirable solutions.

Interactive MCDM techniques have been recently given more attention in the MO community. Two approaches have been explored: direct integration of the DM in the optimization process[3, 4], by giving them the possibility to insert some reference point, and real-time interaction with the optimization algorithm[5], by expressing their preference each time after a defined number of iterations. The target point method follows the first approach. A validation of this approach on simple test-cases is shown as well as its application to the design of a simple building structure under uncertainties with seismic hazard and snow loading. A comparison with the reference-point method of Refs. [3, 4] is also provided.

All the simulations presented below were done with the modeFRONTIER[17] integration platform for multiobjective and multidisciplinary optimization. A significant advantage of this software is that it enables the automation and execution of complex design simulation process chains represented with graphical workflows.

In Section 2 we summarize the key ideas of the MOUU method used in the paper and introduce the MCDM techniques used in the present study as well as a benchmark of the MCDM methods on mathematical test cases. In Section 3 we describe the structural engineering application and the MO we performed (deterministic, with integrated DM and under uncertainties). *A posteriori* checks on the reliability of the solutions are also presented. Conclusions are discussed at the end.

2 TECHNIQUES

In this section we highlight a few key concepts of the theoretical background behind this work and summarize the main ideas of the computational techniques used in this paper.

2.1 Multi-Objective Optimization under Uncertainty

A general multi-objective optimization problem can be formulated in mathematical terms as (see e.g. Ref. [18])

$$\begin{cases} \text{Minimize} & \mathbf{F}(\mathbf{x}) = f_1(\mathbf{x}), ..., f_I(\mathbf{x}), \\ \text{subject to} & g_j(\mathbf{x}) \leq 0,\ j = 1, ..., J \\ & h_k(\mathbf{x}) = 0,\ k = 1, ..., K \\ \text{with} & x_m \in [x_m^L, x_m^U],\ m = 1, ..., M \end{cases} \tag{1}$$

where $\mathbf{x} = (x_1, ..., x_M)$ represents a vector of M independent input variables x_m with lower and upper bounds respectively equal to x_m^L and x_m^U, $\mathbf{F}$ is a vector of I objective functions f_i, while g_j and h_k respectively are a set of J inequality and K equality constraints that define the feasible design space region (i.e. designs satisfying the constraints). If $I > 1$ and the objectives are in contrast, then the problem is multi-objective and has an infinite set of Pareto optimal solutions. A point $\mathbf{x}^*$ is Pareto optimal if and only if there is no other point $\mathbf{x}$ such that $\mathbf{F}(\mathbf{x}) \leq \mathbf{F}(\mathbf{x}^*)$, and $f_i(\mathbf{x}) < f_i(\mathbf{x}^*)$ for at least one function, that is: a point is Pareto optimal if there is no other point that improves at least one of the objectives without deteriorating another. The vector of objectives $\mathbf{F}(\mathbf{x}^*)$ is said to be non-dominated.

Multi-objective optimization problems can be directly solved by means of evolutionary and genetic algorithms. A set of optimal solutions is found starting from an initial set of candidate

solutions (population), which evolve in an iterative process by following mechanisms inspired by biological evolution, like selection, crossover, mutation (see e.g. [18] and references therein).

In MOUU different types of uncertainties can be encountered: random or probabilistic (due to an inherent variability of physical systems and consequently irreducible) and epistemic or imprecise uncertainties (due to a lack of knowledge or information and, in principle, reducible at some stage of the modeling activity) (see e.g. Ref. [1]). Here we consider only the first type. Probabilistic uncertain input parameters are modeled by random input variables following certain probability density functions (PDFs), which represent the probability of occurrence of an event. Because of the input stochasticity, the system response is also stochastic, but its PDF is not known *a priori*. Given that objectives and constraints in optimization problems are often defined in terms of output variables, quantifying the uncertainty on system responses becomes extremely important. This task is accomplished with so-called Uncertainty Quantification (UQ) techniques. Distribution moments, like mean and variance that can be used as robustness measures in RDO, can be estimated with many techniques, e.g. Monte Carlo (MC) or LHS, or the more efficient PCE[14, 19]. The latter is accurate and usually requires a smaller number of function evaluations than the sampling techniques, at least in the case of small-medium problem dimensions. This is a crucial advantage, since computational time is one of the major bottlenecks in design optimization processes. In RBDO instead one is more interested in finding probability tails to determine the failure probability w.r.t. predefined performance or limit state functions (LSFs). The failure probability can be computed with different approaches: (advanced) sampling strategies, FORM and SORM approximations, etc. (see e.g. Ref. [1]). Then it can be minimized or used as a constraint in RBDO problems (see e.g. [1] but also [20, 21] that highlight the effectiveness of using evolutionary algorithms in both single or multi-objective RBDO problems).

For this work we used an OUU method recently introduced by the authors. For a more detailed description, see Refs. [15, 16, 13] and references therein. For each optimization step, a nested UQ flow is executed to compute the statistical output properties to be used as objectives or constraints of the main optimization process. To be specific, in the UQ loop we can compute mean values and standard deviations of output properties with MC, LHS or PCE methods. We can also use the PCE as a stochastic response surface to determine the cumulative distribution function (CDF) and percentile values of output responses that represent probabilistic (or chance) constraints to be optimized in the main loop within a given reliability threshold (with the so-called performance-measure RBDO approach). The use of the PCE for reliability assessments has been growing in recent years (see e.g. Refs. [22, 23, 24, 25]).

For each optimization step, the principal steps in the nested uncertainty quantification flow with percentile calculations are[15, 16]:

- Generation of an MC or LHS sample
- Evaluation of the sample (*real* function evaluations)
- Computation of PCE coefficients via least square minimization
- Estimation of mean and variance
- Generation of an LHS sample for percentile calculations
- Evaluation of the sample (PCE *virtual* function evaluations)
- Determination of CDF and percentiles

The determination of the CDF and percentiles on empirical samples evaluated with the PCE as a stochastic response surface model (*virtual* function evaluation) is clearly an advantage in terms of computational time unlike a pure sampling approach requiring *real* function evaluations, which in real-world applications are often made with calls to finite element or other computationally demanding simulation solvers.

The important parameters for the above-described UQ process are the chaos order k (polynomial degree of the truncated polynomial chaos expansion), the size N of the first sample to determine the PCE coefficient[1], and the size N_{perc} of the sample for the computation of the CDF.

This technique has been benchmarked in Refs. [15, 16, 13, 26] on several test–cases with particular attention to the optimal choice of the sample sizes and k. Our method does not depend on the optimization algorithm used, which can be chosen on the basis of the optimization problem and other necessities. However, evolutionary multiobjective algorithms (e.g. genetic algorithms) are quite beneficial due to their robustness and ability of finding accurate Pareto fronts.

2.2 Optimization with user preferences

One of the major optimization challenges is to generate solutions in a precisely defined region of the Pareto frontier, without wasting computational time to identify the entire set of optimal solutions. For this reason, we tried to directly integrate user preferences (in our case the decision maker, or DM) in the optimization process by implementing an *a priori* approach based on the DM's knowledge of the location of the desirable region. In this way the generated designs can be automatically ordered according to user preferences.

In this paper we studied two different approaches:

NSGA-III, reference point-based algorithm: NSGA-III[3, 4] is a many-objective[2] evolutionary optimization algorithm. NSGA-III does not add any new genetic operator to NSGA-II[27]. Its fundamental quality is the use of reference points that act as attractors driving the optimization towards optimal regions. The *reference points* are objective space points distributed on a grid. They can either be provided by the user or computed by the algorithm. Since the authors of NSGA-III released no official source code, we developed our own prototype following the quoted references. To allow for more freedom in the exploration of *a priori* unknown objective spaces, we chose to provide no explicit reference points. Their number H is

$$H = \binom{M + p - 1}{p}, \tag{2}$$

where M is the number of objectives and p the number of divisions of each objectives (we took $p = 16$).

Since NSGA-III is expected to exhibit better performance on many-objective problems with respect to NSGA-II, we decided to apply it to a structural sizing problem with a discretized Pareto frontier (see Section 3). The expectations were entirely justified.

[1] This sample is used for the least square minimization and can be arbitrarily chosen, with the exception of its minimum size N_{min}, which must be equal to the number of unknown parameters in the PCE, i.e. $N \geq N_{min} = \frac{(k+d)!}{k!d!}$. Thus in the single–variate case the number of coefficients equals $k + 1$, but in the multivariate case it also depends on the stochastic input space dimension d and grows fast as d increases. This is the real bottleneck of this method.

[2] An optimization problem is *many-objective* when the number of objectives $n \geq 3$.

Target point-based algorithm: we modified the NSGA-II algorithm in such a way to ask the user before the start of the optimization to provide a *target point*, i.e. an objective space point that should be reached by the optimizer. Moreover, we modified the solution-sorting mechanism as explained below. The algorithm steps, which initially require an interaction with the user, are the following:

- the user is asked to provide a target point objective values
- the user is asked to provide a tolerance value for each objective in order to define a tolerance hypervolume
- the user is asked to provide a target number of points that the algorithm has to find inside the tolerance hypervolume. Here the interaction with the user ends
- the optimization process starts. It consists in two phases, i.e. reaching the target point and an NSGA-II based optimization for further improvements:
  - In the first phase, to reach the region of the target point, all the solutions generated in the current generation are first ordered using the Pareto sorting criterion according to the value of their absolute distance from the target point. Within each front we apply a modified selection mechanism, based on the so-called controlled elitism[28], which avoids a premature convergence of the algorithm by keeping a percentage of information from lower rank fronts. For each new point, the algorithm checks whether it falls within the tolerance hypervolume. If it does, the target point number counter is decreased. When it becomes zero, the first phase stops
  - In the second phase the relative distance from the target point is used to sort new designs until the specified number of generations is achieved. In our implementation all objectives have to be minimized. Hence, a solution with a negative relative distance is better than a solution with a positive distance.

The target point initially drives the optimization. In particular, if the target point belongs to the Pareto front, then in the second phase the algorithm will start populating the front further. We developed this strategy to prevent the natural tendency of EA evolution to be driven by the simplest objectives rather than those in which the DM is most interested.

We believe that there is a slight but important difference between target and reference points. A target point is a point that the DM wants to reach with the optimization, whereas reference points are points distributed in the objective space that determine only the direction of the optimization, i.e. they have the role of attractors.

These two methods are not mutually exclusive. In fact, the target point is useful when the user wishes to find more points in a "gap" region, while our use of NSGA-III, without any provided reference points, helps finding the whole Pareto frontier.

More in general, within the Multi-Criteria Decision Making field different approaches to design optimization problems are possible as described in Ref. [29]:

1. $a\ priori$: preferences are asked before the optimization;
2. $a\ posteriori$: preferences are expressed after the optimization;
3. interactive: the optimization algorithm asks the DM to express their preferences during the optimization process.

Historically *a posteriori* approaches have been the standard choice for decision making: the DM runs the optimization and then uses MCDM techniques to find the best Pareto front solution in accordance with their preferences. However, *a priori* and (above all) interactive methods have been recently stirring up great interest in the MCDM community.

We believe that interactive methods, like the one presented in Ref. [5], are in principle the most accurate, because the algorithm is able to calculate the most representative value function with respect to the user preferences. DM preferences are specified at each interaction. The more frequent the interactions, the more accurate the algorithm. However each interaction requires a lot of effort from the DM's side, since, for example, an optimization with many generations implies many interactions. In our opinion, this is the most important disadvantage of interactive approaches. Hence we decided to investigate the above-described *a priori* approaches to reduce the DM effort and stress.

2.3 Mathematical test problem

Both the target point-based and the reference point-based algorithms are prototypes. In order to see differences between them, we tested them on two mathematical benchmark problems: the Constrained Test Problem 7 (CTP7)[30] and the unconstrained Zitzler Deb Thiele 1 (ZDT1) problem[31].

The first problem is construed as follows:

$$\textbf{CTP7:}\begin{cases}\text{Minimize } f_1(\mathbf{x}) = x_1 \\ \text{minimize } f_2(\mathbf{x}) = g(\mathbf{x})\left(1 - \dfrac{f_1(\mathbf{x})}{g(\mathbf{x})}\right) \\ \text{subject to } c(\mathbf{x}) = \cos(\theta)(f_2(\mathbf{x}) - e) - \sin(\theta) f_1(\mathbf{x}) \geq \\ \quad a|\sin(b\pi(\sin(\theta)(f_2(\mathbf{x}) - e) + \cos(\theta) f_1(\mathbf{x}))^c)|^d\end{cases} \tag{3}$$

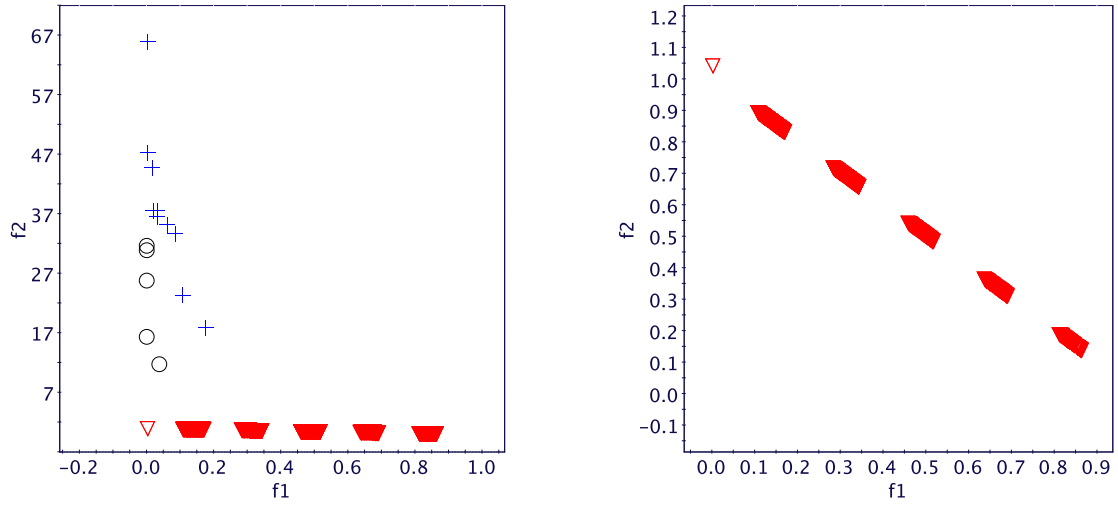
where $\theta = -0.05\pi, \quad a = 40, \quad b = 5, \quad c = 1, \quad d = 6, \quad e = 0$. CTP7 has a discontinuous Pareto frontier.

We performed three optimization runs: one with the standard NSGA-II algorithm and the other two with the target-point and the reference-point algorithms respectively. In each simulation we started from an initial population of 100 individuals and set the number of generations to 1000. We used crossover and mutation probabilities respectively equal to 0.9 and the reciprocal of the number of input variables, and distribution index values set to 20.

On Figure 1 we can see the efficiency of the reference-point NSGA-III algorithm to find the entire Pareto frontier owing to the ability of the reference points to attract the optimization towards the disconnected Pareto front regions. On the other hand NSGA-II and the target-based algorithm are not able to find any points on the true Pareto front, even though we set a target point located on the exact Pareto front. For this problem, the target-point algorithm is still influenced by NSGA-II.

The second test problem is unconstrained and has a continuous Pareto front. It is construed as follows:

$$\textbf{ZDT1:}\begin{cases}\text{Minimize } f_1(\mathbf{x}) = x_1 \\ \text{minimize } f_2(\mathbf{x}) = g(\mathbf{x})\left(1.0 - \sqrt{\dfrac{f_1}{g}}\right) \\ \text{with } g(x_1, x_2, \cdots, x_n) = 1.0 + \dfrac{9.0}{n-1}\displaystyle\sum_{i=2}^{n} x_i\end{cases} \tag{4}$$



(a) (b)

Figure 1: (a): Pareto front designs found with a deterministic optimization of the CTP7 problem with NSGA-II (circles), NSGA-III (downward triangles) and the target-point (plus symbols) algorithm described in Section 2.2. (b): detail of the NSGA-III Pareto front.

We used ZDT1 to test the algorithms with a smaller number of generations in order to see if the target-point method is able to focus on the desired region from the very beginning. We performed again three optimization runs with the same three algorithms and parameters as for CPT7, but with a number of generations equal to 40. Results are shown on Figure 2. We started with the original NSGA-II simulations and we noted that a gap appears in the Pareto frontier. With the target-point algorithm we tried to drive the optimization precisely towards the middle of the gap region (target point values set to the middle of the gap, tolerance values around 20% and maximum points in the tolerance hypervolume equal to 50). As a result, the target point-based algorithm was able to find several designs in the desired region at the expense of the exploration of the Pareto frontier tails. NSGA-III performed slightly better than NSGA-II both in the upper left tail of the Pareto region and in the gap region, but it was not able to extensively explore the right bottom corner with the given number of generations. This is not entirely unexpected because that region is influenced by the most complex objective of the problem (minimization of f_2) and NSGA-III does not use the crowding distance strategy to increase the population diversity. Finally, we observe that both new algorithms present small convergence problems (the attainment of the true Pareto front is not perfect), which can be overcome by increasing the number of generations.

A comparison of the performance of these algorithms on a many-objective optimization problem is provided in Section 3.

3 STRUCTURAL ENGINEERING APPLICATION

In this paper we further analyzed a structural engineering design problem, presented in Ref. [13], with the aim of showing the effects of the dynamic use of MCDM algorithms on the optimal solutions found during the design optimization phase (with or without uncertainty).

We considered the same building structure and model as in Ref. [13] with minor changes. It

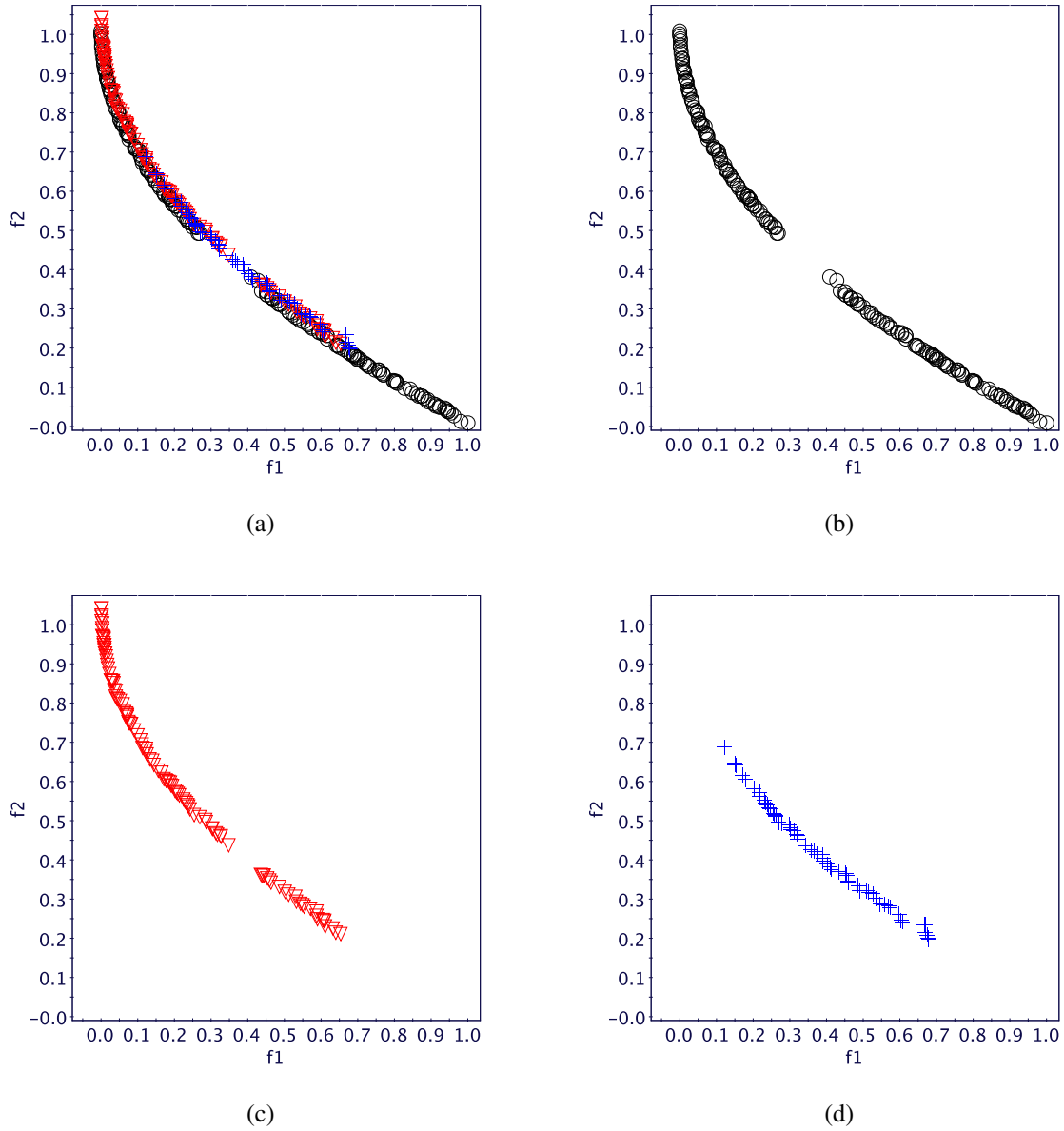


Figure 2: Pareto front designs found with a deterministic optimization of the ZDT1 problem with NSGA-II (b), NSGA-III (c) and the target-point algorithm described in Section 2.2 (d). All the Pareto frontiers are shown on the same graph in (a).

is a two-storey building formed by four 3-bay frames made of reinforced concrete[3] beams and columns, and ceilings/floors made of reinforced concrete joists and hollow flooring blocks. The three-dimensional building frame is shown on Figure 3.

As the location we chose the Italian town of Forni di Sopra (UD) that is characterized by a maximum horizontal ground acceleration $a_g = 0.175g$ and an elevation greater than 1500 m above mean sea level. This enables the statistical analysis of the snow load present on the building flat roof (the worst possible case in the presence of snow) on a site with significant seismic hazard. Wind loads are not relevant for this location and type of structure.

[3]Concrete of type C25/30, i.e. confined characteristic compressive strength $f_{ck} = 25$ MPa and design compressive strength $f_{cd} = 14.17$ MPa.

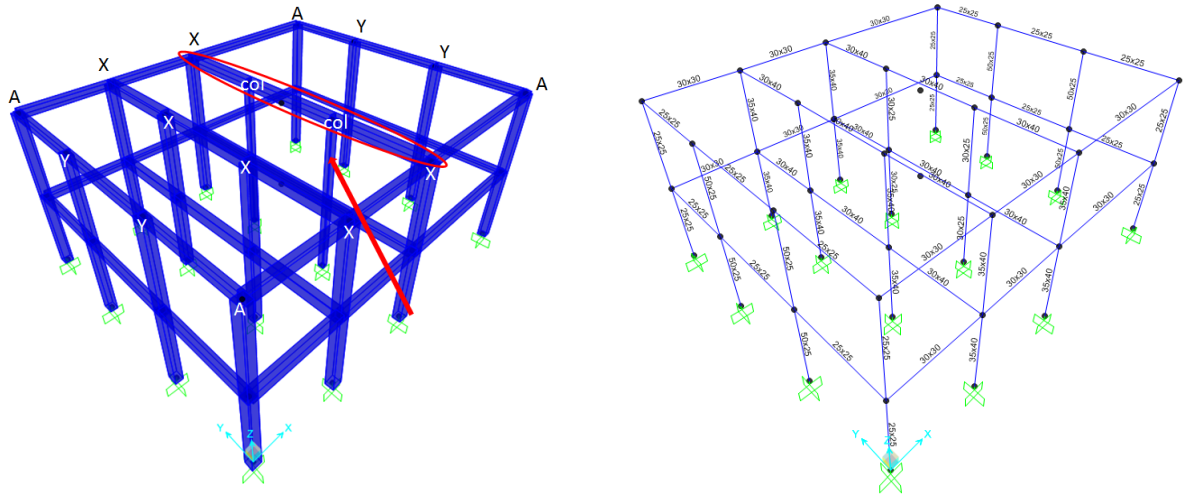


Figure 3: 3D view of the building frame. On the left: extruded view (the different labels denote the different types of column sections. The investigated most loaded beam and column are respectively circled and marked with an arrow). On the right: standard view, with an example of design sections.

To reduce the computational effort, we fully designed only the most loaded coverage beam and the most stressed column (out of the four columns supporting the beam) of the structure (see Figure 3) with the aim of determining the optimal size of their sections and reinforcement content to achieve minimum weight and seismic displacement while respecting the constraints required by the Italian law and considering variations in other column sections.

The stresses for the vertical loads and seismic actions were simulated with SAP2000[32], a finite element analysis general-purpose civil-engineering software. We considered the envelope[4] of vertical load (permanent, variable and snow) combinations at ultimate limit state (ULS) with the seismic combinations in the x and y directions as required by the Italian law for construction engineering (NTC2008: DM 14.1.2008).

For the seismic displacements we used the serviceability limit state (SLS) with an "SLD" (i.e. "Damage Control" performance level) seismic elastic response spectrum.

The framed supporting structure composed of beams and columns was represented with one-dimensional finite elements. Since the perimeter walls were not directly included in the structure model, we introduced them in terms of an additional mass contribution for the seismic actions in the SAP model, also to mimic the effect of any masses not explicitly taken into account. However, the results illustrated below are only intended as guidelines for designers, since we did not consider the shear reinforcements of the structure. In fact, our work was mainly focused on the applicability (and effect) of MOUU and real-time integrated MCDM techniques to structural design optimization problems.

The following sections illustrate the details of the optimization problem, simulations and results.

[4]The envelope merged four terms: two vertical load combinations (one with a dominant variable load and the other with a dominant snow load) and two ULS seismic load combinations (with seismic components $E_X + 0.3E_Y$ and $E_Y + 0.3E_X$, where E_Y and E_Y denotes respectively the seismic action along x and y). Here, we used the seismic project response spectrum "SLV" (corresponding to a "Life Safety" performance level) for the town considered.

3.1 Optimization problem and workflow

To illustrate the effectiveness of the above-illustrated MCDM algorithms on many-objective problems we chose *three objectives*: weight minimization of the most loaded beam and stressed column (see Figure 3) and seismic displacement minimization in the x direction (for a "LSD" seismic spectrum with dominant action along x) by varying the sections of the two elements and their content of reinforcing bars, as well as the sections of all the other columns.

We considered *twelve input variables* and *three constant input parameters*. The input variables are: (1) the most loaded beam section, (2) four types of column sections (denoted with different labels on Figure 3), (3) the three longitudinal reinforcements in the three lower spans of the beam, (4) the three upper longitudinal reinforcements in the three spans of the beam, and (5) the longitudinal reinforcement of the column. The reinforcements are given in terms of steel sections and their number. All the mentioned inputs have discrete values (from a list of sections available in commercial catalogs). The three constant input parameters are: (1) the snow load value provided by the law for 1500 m above sea level, equal to 5.83 kN/m^2 - this value, like the other vertical loads of the two floors, was transformed into linear load and applied to the beams; (2) the additional mass term of 600 kN; (3) the structure factor q = 3.9 (necessary for the conversion from the elastic to the project spectrum) as expected for "Frame structures with multiple floors and spans, of class B" (see NTC2008: DM 14.1.2008).

The most loaded beam and column sections and reinforcement contents were subject to *fourteen input constraints* as required by the law (see NTC2008, paragraphs 7.4.6.2.1 and 7.4.6.2.2).

In output, we monitored several properties, such as the beam and column weights, their total weight, seismic displacements, first-mode eigenperiod, bending moments, etc.

We also considered *nine output constraints*: six ULS compliance checks of load and resistance effects on the beam (beam moment resistances greater than stress moments), one constraint on the column (compliance with the limits on compressive and flexural strengths due to the loads) and two constraints for the seismic displacements along x and y (relative inter-store displacement in both directions smaller than the maximum allowed displacement).

Given the high number of constraints present on both input (geometric constraints for section sizes and reinforcing bar content) and on output variables (seismic displacements, constraints on the most loaded beam and column loads), this is a hyper-constrained problem. The presence of discrete input variables makes its solution even harder from a mathematical point of view. Thus, this example is an interesting benchmark for the performance of the algorithms described in Section 2 on complex and realistic structural design optimization problems.

All simulations were performed with the modeFRONTIER integration platform and optimization software. As said in the previous paragraph, we computed the stresses caused by vertical and seismic loads with SAP2000. The SAP2000 inputs are the structure geometry and constraints, the frame sections, the linear loads, the seismic analysis type, etc. modeFRONTIER was integrated with SAP2000 by means of an Excel file, which controlled the SAP2000 model with a Visual Basic macro. The macro was used for a dual purpose: to update the SAP2000 model parameters (the central beam and column variable sections) with the values provided by modeFRONTIER for each proposed configuration and to extract the output variable values calculated by SAP2000 and write them in the Excel file to be read by modeFRONTIER.

Figure 4 shows the modeFRONTIER optimization workflow. From top to bottom we can follow the optimization data flow: at the top we find input variables, constant parameters and constraints, whereas at the bottom we find the monitored output variables, objectives and constraints on the output variables. The green icons (square boxes with an incoming arrow) in the

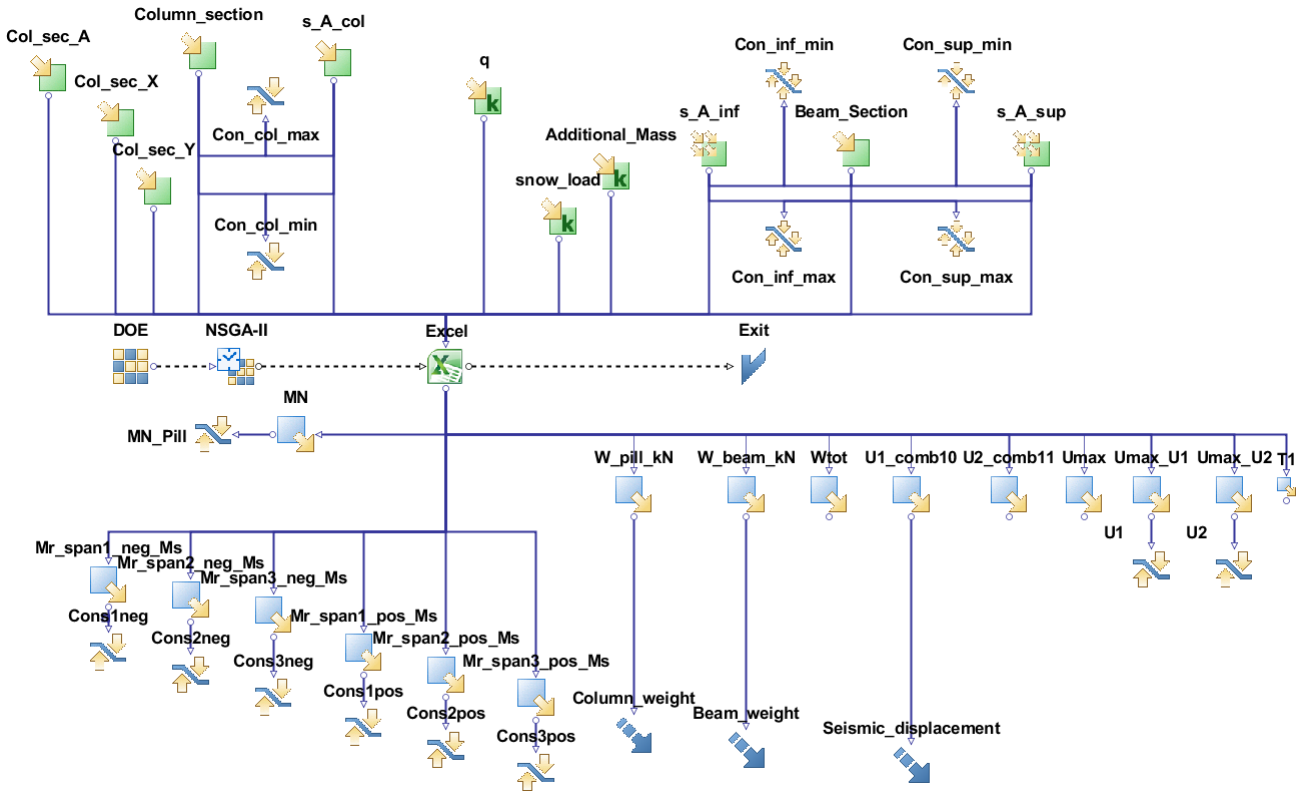


Figure 4: Optimization workflow.

top part of the figure represent the input variables and constants, while the blue icons (square boxes with an outcoming arrow) at the bottom represent the output variables. Constraints are represented by opposing arrows separated by a line, while objectives are represented by an arrow icon. In the center, from left to right we find icons representing the logic flow of the process, with the generation of the initial sample by means of a design of experiment algorithm node (DOE), followed by the optimization algorithm node, an Excel node (interface between modeFRONTIER and SAP) and the logic end of the process.

3.2 Simulation details

We ran the following simulations:

1. deterministic optimization with NSGA-II
2. deterministic optimization with the target point-based algorithm (described in Section 2.2) starting from the deterministic Pareto front of point 1.
3. stochastic optimization starting from the Pareto front found in point 2.
4. stochastic optimization with the target point-based algorithm to improve the stochastic Pareto front found in 3.
5. reliability assessment of representative solutions found in the previous points
6. deterministic optimization with the reference point-based algorithm (i.e. NSGA-III based, see Section 2.2) starting from the Pareto front found in 1.

7. encouraged by the results obtained in the previous point, we used the NSGA-III based algorithm starting from the same random DOE as in 1. to compare its performance against NSGA-II

More details are provided in the following paragraphs.

3.2.1 Deterministic optimization with standard NSGA-II

The problem described in Section 3.1 was optimized with the NSGA-II genetic algorithm, with an initial input population of 360[5] candidate designs (generated with a uniform random algorithm) crossover and mutation probability values respectively equal to 0.9 and the reciprocal of the number of input variables, and an allowed budget of 50 generations.

During the optimization, many unfeasible designs (i.e. designs that violate at least one constraint) were found. Remarkably, no seismic displacement constraints were violated within the explored input variable ranges. The most critical constraints appeared to be those on the most loaded beam.

The Pareto front is shown on Figure 5 (cross symbols). By inspecting the variable values of Pareto front designs, we noticed that all the designs had the same beam section, a square section of dimensions equal to 0.30×0.30 m^2. The range of the column section spanned over almost all the available values in the catalog list, but the majority of designs preferred either square columns or along the x direction (with only few designs preferring the rectangular section directed along y). The first mode eigenperiod appeared to be almost perfectly linearly correlated with the seismic displacement objective.

3.2.2 Deterministic optimization with target-point integrated MCDM

We decided to apply the target point-based algorithm to drive the optimization toward low values of the beam weight, or to be specific toward the objective space region close to beam and column weight and seismic displacement values of respectively 26.35 kN, 14 kN and 0.0203 m^2. We used a maximum number of points inside the tolerance hypervolume equal to 20.

We started the algorithm with an initial population composed of the Pareto front designs found in Section 3.2.1 and other randomly selected feasible designs from that previous run in order to reach 200 elements (since the starting points were already good, it was not necessary to apply the rule of thumb described in footnote 5).

The objective values of the Pareto front designs found after 45 generations are shown on Figure 5 (empty squares), where they are compared with the Pareto front designs found with the standard NSGA-II algorithm in Section 3.2.1 (cross symbols). It can be observed that the target-point algorithm found at least three new points in the target region of the objective space. These objective space points correspond to several designs in the input variable space that differ for their reinforcement content. The new designs tended to have square column sections, while they all had a beam section equal to 0.30×0.30 m^2 as in Section 3.2.1.

Once again, no violation of the seismic displacement was found. The most violated constraints were still those on the beam compliance checks.

[5]This high value was chosen by a rule-of-thumb according to which the input population size should be greater than the number of input variables multiplied by 2 and by the sum of the number of objectives and constraints.

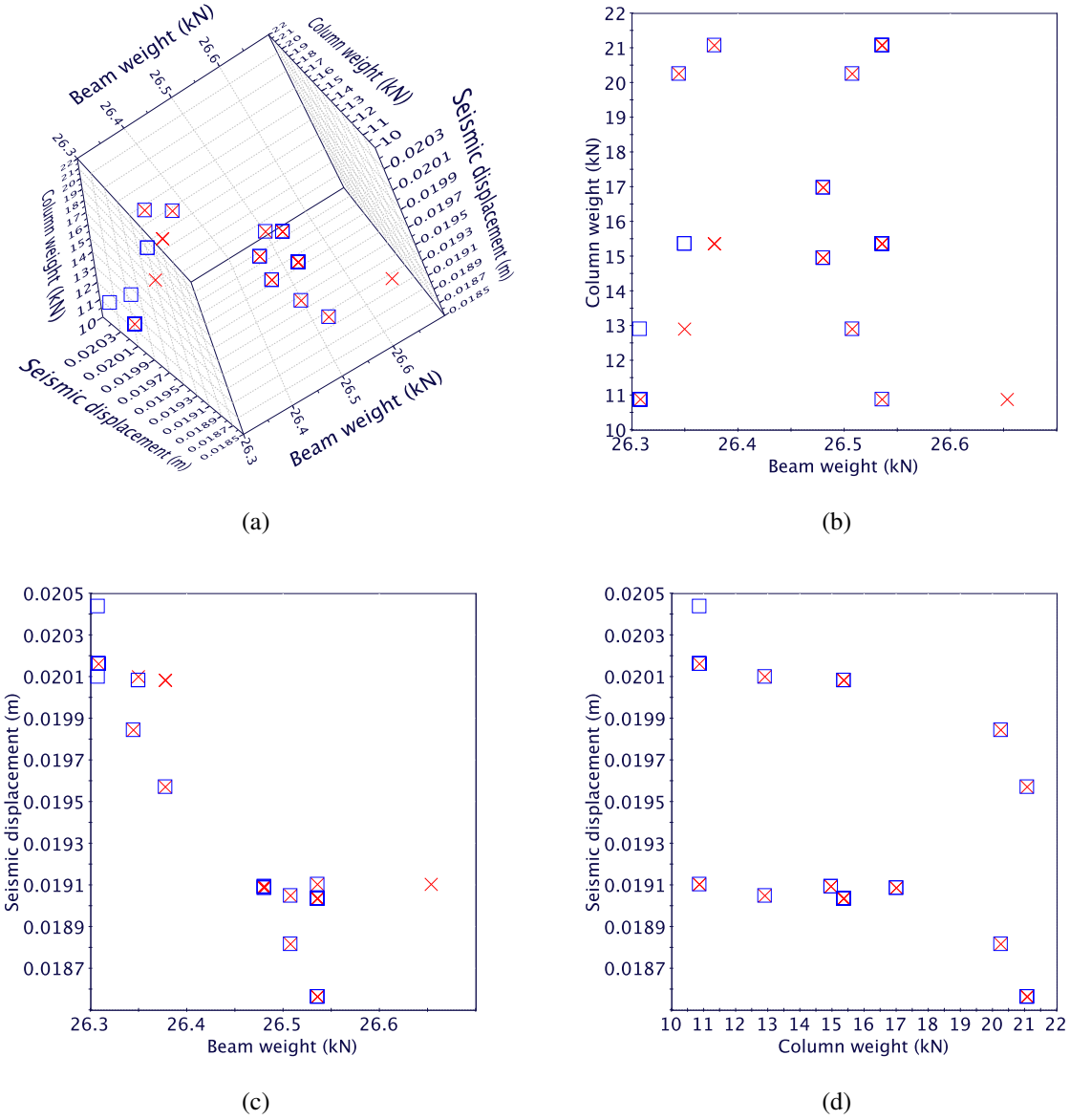


Figure 5: Pareto front designs found with a deterministic optimization with NSGA-II (cross symbols) and with the target-point algorithm described in Section 2.2 (empty squares).

3.2.3 Optimization under uncertainty

To improve the reliability of Pareto optimal designs w.r.t. to the most violated constraints found in the previous sections, we decided to perform a reliability-based design optimization with the technique explained in Section 2.1.

In all the OUU simulations we considered the snow load and the additional mass as uncertain parameters respectively defined by an exponential PDF, with location parameter 5.83 and scale parameter 0.5, and a log-uniform PDF, with location parameter equal to 600 kN and scale parameter of 60 kN (i.e. the underlying uniform distribution is in the range from 600 kN to 660 kN).

To determine the optimal PCE sample size we performed some uncertainty quantification checks with sizes $N = 11,\ 13,\ 20,\ 30,\ 50,\ 100$ and PCE degree $k = 3$ and compared the results obtained with LHS data found with sample sizes $N = 13,\ 20,\ 30,\ 50,\ 100,\ 200,\ 500,\ 1000$.

Figure 6 shows results for two of the most important constraints on the beam, denoted with Cons1neg and Cons3neg in the workflow of Figure 4. As is evident, for these properties the PCE reached convergence with the smallest sample size for the mean values and the second smallest for the standard deviation, at variance with LHS data, which converged for $N = 200$ or 500. Therefore, we chose to perform the stochastic optimization with a PCE sample of 13 designs.

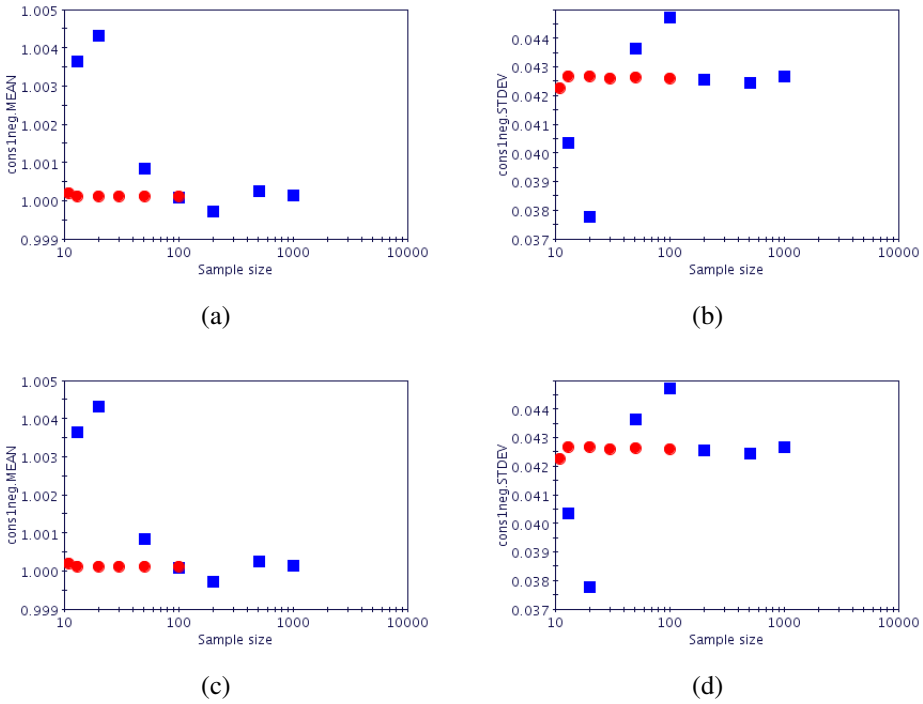


Figure 6: (a) and (b): estimates of the mean values and standard deviation of ultimate limit state compliance checks for the first span of the most loaded beam; (c) and (d): same properties for the third span. Mean values are shown on the left, while standard deviations on the right. PCE data are represented with circles, while LHS data with squares.

We considered the same optimization problem as in the previous sections, but for the introduction of probabilistic constraints. We aimed at achieving a reliability of 99.9%. Therefore we computed the 99.9-th percentile of the six constraints on the beam (called Cons1pos, Cons1neg, Cons2pos, Cons2neg, Cons3pos, Cons3neg in the workflow of Figure 4). All other constraints were treated as deterministic and checks on the design feasibility w.r.t. them were made *a posteriori*.

As an optimizer, we used the NSGA-II algorithm with the same parameters as in the deterministic simulations and an initial population of 200 designs composed of the Pareto front designs found in Section 3.2.2 plus other randomly selected feasible designs. For each design we computed its statistical properties with a third-order PCE determined on a sample of 13 elements generated around the current design by a LHS based on the PDFs of the snow load and additional mass parameter. The computation of these samples requires real function evaluations (i.e. calls to the SAP software). Percentiles were determined with negligible computational cost on new LHS samples with 1000 designs evaluated with the so determined PCE functions. We ran 8 generations of NSGA-II, which correspond approximately to the total number of real function evaluations made in the deterministic optimization in Sections 3.2.1 and 3.2.2.

In the RBDO run, the seismic displacement constraint along the x direction was occasionally violated, due to the output dispersion introduced by the input stochasticity (in practice, violations sometimes occurred in the internal samples of the 13 designs used for the determination of the PCE). However, no design in the samples drawn around the Pareto front designs turned out to be unfeasible.

The column constraint was also occasionally violated for geometric reasons. In fact, in most cases, if a design was violated, all the designs in the sample generated to compute the PCE were also unfeasible.

The stochastic Pareto front is shown in Figure 7 (empty diamonds), where it is compared with the Pareto front found with the target-point deterministic optimization in Section 3.2.2 (empty squares). Like the deterministic optimization, all the OUU Pareto front designs have the same beam section, which this time is rectangular and equal to 0.30×0.40 m^2. Unlike in the case of the deterministic simulations (especially the one of Section 3.2.1) where almost the entire column section range was explored, here most designs have square column sections (of dimension 0.25×0.25 m^2) and only few of them are rectangular (directed along y and of dimension 0.30×0.25 m^2). Apparently the reliability requirement has driven the optimization to this input space region. In the objective space it is striking that the reliability has been reached at the expense of the beam weight (determined not only by the beam section but also by its reinforcement content), which notably increased in the stochastic Pareto front.

3.2.4 Stochastic run with target-point algorithm

To drive the optimization in the gap which appears in the stochastic Pareto front in the seismic displacement range $[0.0195, 0.0215]$ m (see Figure 7), we ran the target point-based algorithm on the OUU problem for 8 generations starting from an initial population of 200 designs (composed of the Pareto front designs found in Section 3.2.3 plus other randomly selected feasible designs). The new stochastic Pareto front (empty triangles) is compared with the stochastic Pareto front found with the standard NSGA-II algorithm (empty diamonds) and with the deterministic target-point results (empty squares) on Figure 7. The Pareto front found with the target point optimization is located in a smaller region w.r.t. the other fronts. The new front presents only one new seismic displacement value in the desired region, given by two different designs in the input variable space.

3.2.5 Reliability assessments

To double check the effectiveness of our MOUU method for finding reliable optimal solutions, we made a posteriori uncertainty quantification checks. In this section we show outcomes for selected solutions, though the trend found can be considered generally valid. Table 1 contains input/output values of four representative optimal designs found in Sections 3.2.1 (**DN**), 3.2.2 (**DT**), 3.2.3 (**SN**) and 3.2.4 (**ST**). The objective-space representation of these points is shown on Figure 8.

We generated samples of 200 points centered on the selected designs with the same uncertainty distributions as those considered in Sections 3.2.3 and 3.2.4. Then we checked whether any of the constraints was violated. The amount of designs violating some of the most critical constraints can be seen for instance by looking at the empirical PDFs of those constraints computed on the generated samples. An example for each representative design is shown on Figure 9. PDFs for the deterministic Pareto-optimal designs are shown at the top of the figure.

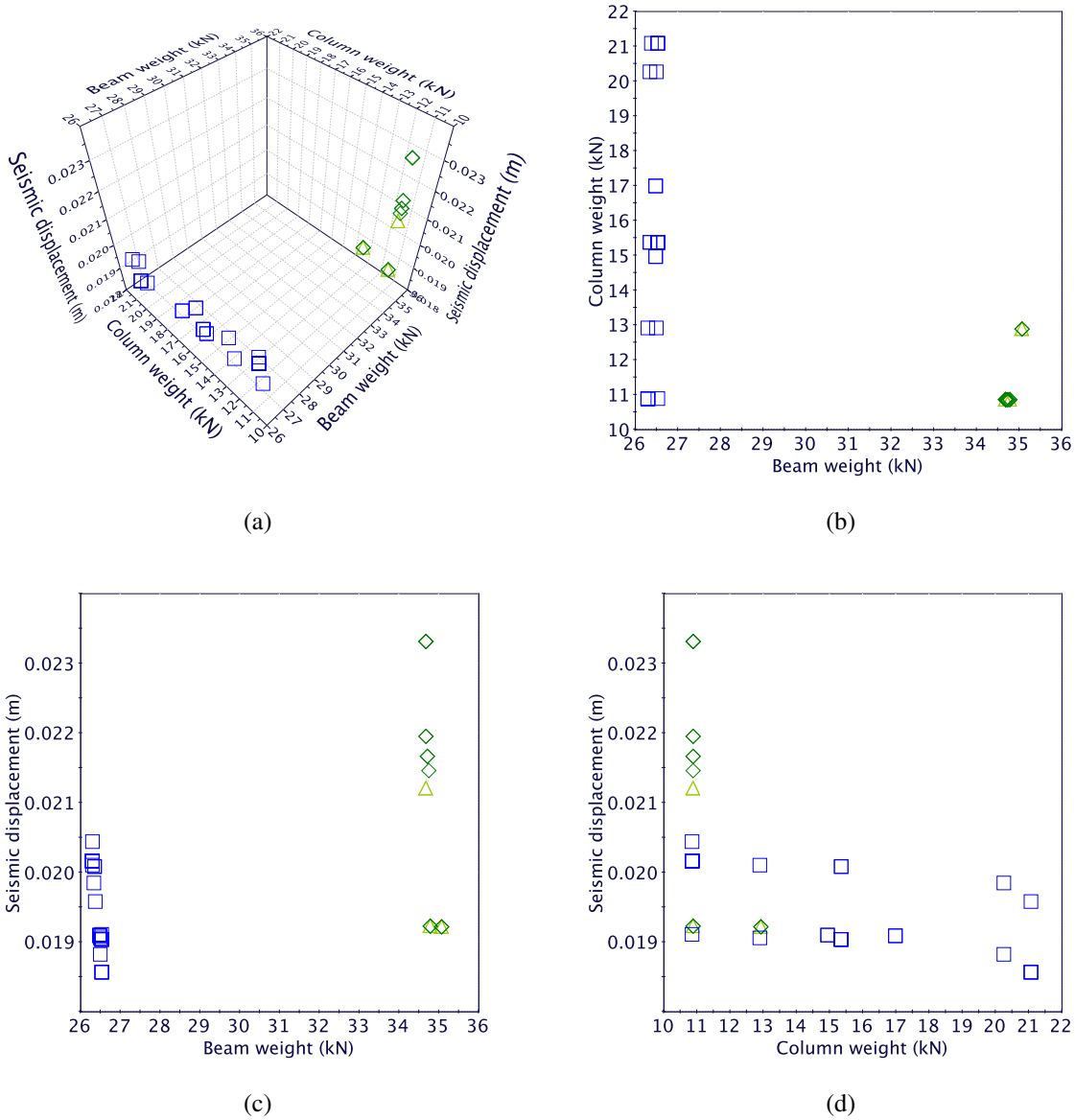


Figure 7: Pareto front designs found with a stochastic optimization with NSGA-II (empty diamonds), stochastic optimization with the target-point algorithm (empty triangles) and results from Section 3.2.2 (empty squares).

For these designs the empirical PDFs of the most violated constraints are shown. The constraint violation is indicated by the light-colored (orange online) part of the histograms. PDFs for the stochastic optimization optimal solutions are shown at the bottom. Since no constraint violation was observed in the samples around **SN** and **ST**, we randomly chose to show Cons2neg for **SN** and Cons3neg for **ST**. This confirms our expectations. Optimal solutions found with deterministic MO methods (with or without MCDM) have a non-negligible probability to violate critical constraints (indeed the largest part of the empirical PDFs lies below the constraint threshold, which equals 1). On the other hand, optimal solutions found with the RBDO methods have a negligible probability of violating the chance constraints.

	DN	**DT**	**SN**	**ST**
Beam_section (m^2)	0.30×0.30	0.30×0.30	0.30×0.40	0.30×0.40
Column_section (m^2)	0.35×0.25	0.25×0.30	0.25×0.25	0.25×0.25
s_A_sup (1) (m^2)	0.001521	0.001357	0.001521	0.001357
s_A_inf (1) (m^2)	0.000763	0.000603	0.000763	0.000603
s_A_sup (2) (m^2)	0.001357	0.001357	0.001357	0.001357
s_A_inf (2) (m^2)	0.001257	0.00076	0.000804	0.00076
s_A_sup (3) (m^2)	0.001257	0.001257	0.001257	0.001257
s_A_inf (3) (m^2)	0.000603	0.000603	0.000763	0.000603
s_A_col (m^2)	0.002714	0.002281	0.001885	0.001885
Col_sec_A (m^2)	0.40×0.40	0.40×0.40	0.40×0.40	0.35×0.35
Col_sec_X (m^2)	0.25×0.50	0.35×0.40	0.25×0.50	0.35×0.40
Col_sec_Y (m^2)	0.40×0.35	0.40×0.35	0.40×0.35	0.40×0.30
T1 (s)	0.598	0.628	0.603	0.667
Beam_weight (kN)	26.48	26.307	34.77	34.659
Column_weight (kN)	14.951	12.911	10.871	10.871
Seismic_displacement (m)	0.019	0.02	0.019	0.021
MN	0.751	0.482	0.514	0.493
Cons1neg	1.157	1.069	1.623	1.504
Cons2neg	1.027	1.006	1.436	1.467
Cons3neg	1.0004	1.029	1.417	1.458
Cons1pos	1.217	1.066	1.522	1.347
Cons2pos	1.853	1.094	1.613	1.469
Cons3pos	1.026	1.139	1.617	1.445
U1 (m)	0.005	0.004	0.005	0.004
U2 (m)	0.006	0.006	0.006	0.007

Table 1: List of some input and output values for the designs chosen for the reliability checks. **DN** is a Pareto optimal design found with the deterministic NSGA-II optimization of Section 3.2.1, **DT** is one of the target point solutions of Section 3.2.2, **SN** was found with the NSGA-II MOUU of Section 3.2.3 and **ST** with the refinement target point stochastic optimization in Section 3.2.4. In the first column, input variable names are written in italics. From top to bottom: beam section, column section, reinforcement content of the three beam bay frames ("*s_A*" stands for "steel area"), reinforcement content for the column, sections of the other type of columns (see labels in Figure 3), first mode eigenperiod, the three objectives, and the constraints (from MN to U2: the constraint on the column, the six constraints on the beam and the seismic displacement constraints).

3.2.6 Deterministic optimization with the reference-point algorithm based on NSGA-III

We used the structural optimization problem described in the previous sections to test the reference-point algorithm based on the NSGA-III algorithm[3, 4] (see Section 2.2). This algorithm is expected to perform better than NSGA-II on many-objective optimization problems.

We began by applying the reference-point algorithm to refine the results found with the deterministic optimization with the standard NSGA-II algorithm in Section 3.2.1. We started from an initial population composed of 200 elements (the NSGA-II Pareto front designs and other randomly selected feasible designs) and ran the reference point algorithm for 20 generations (with the same crossover and mutation probability parameters as in Section 3.2.1).

On Figure 10 we compare the deterministic Pareto front designs found with the reference-point algorithm (downward triangles) and the Pareto front found with the target-point algorithm

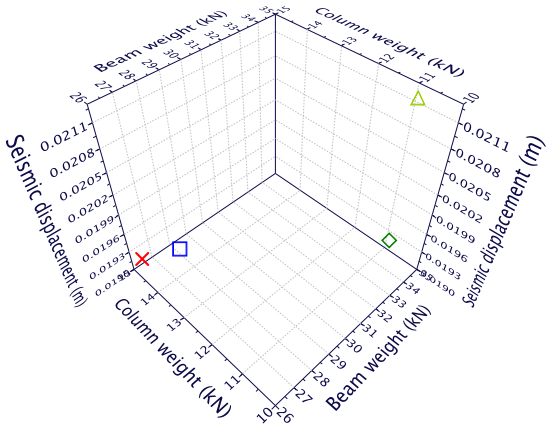


Figure 8: Designs selected for the reliability checks. The cross symbol was found with the deterministic optimization with NSGA-II (**DN** in Table 1 notation), the empty square with the deterministic target point-based optimization (**DT**), the empty diamond with the stochastic optimization with NSGA-II (**SN**) and the triangle with the stochastic target-point optimization (**ST**).

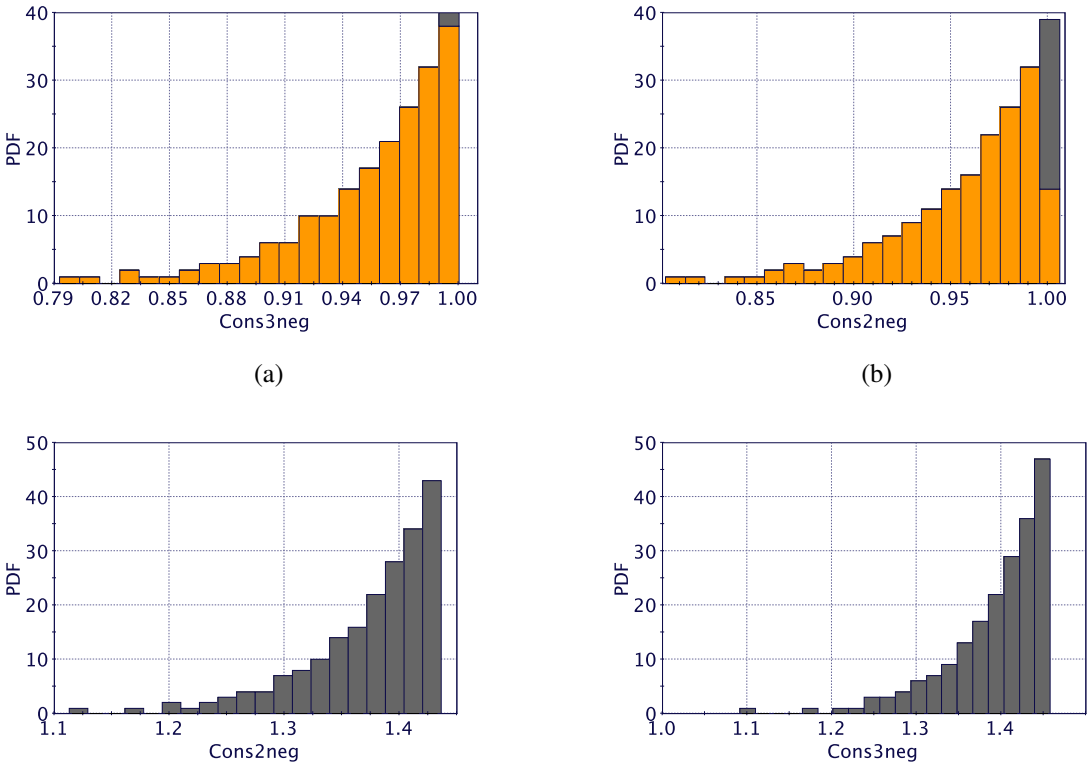


Figure 9: Empirical probability density functions (PDFs) of critical output constraints of selected designs. (a): **DN**, (b): **DT**, (c): **SN**, (d): **ST**. The light-colored (orange online) boxes denote violated constraint values.

in Section 3.2.2 (cross and square symbols, where the crosses represent the points already found with the initial NSGA-II simulation in Section 3.2.1 and the squares the new designs found with

the target-point refinement). The reference point algorithm was capable of finding a well distributed Pareto front. This illustrates well the difference of aims of the target-point algorithm (that drives the simulation process towards a target region) and the reference-point algorithm. It also confirms the good behavior of NSGA-III on many-objective problems. The reference-point algorithm was capable of finding some solutions with better values for the beam weight objective than NSGA-II. An inspection of the input variable values of the reference-point algorithm optimal solutions revealed that all designs had the same beam section as the solutions obtained with the other deterministic optimization runs (hence the smaller weight was obtained with a smaller reinforcement content). However, most designs have either square or rectangular column sections along x.

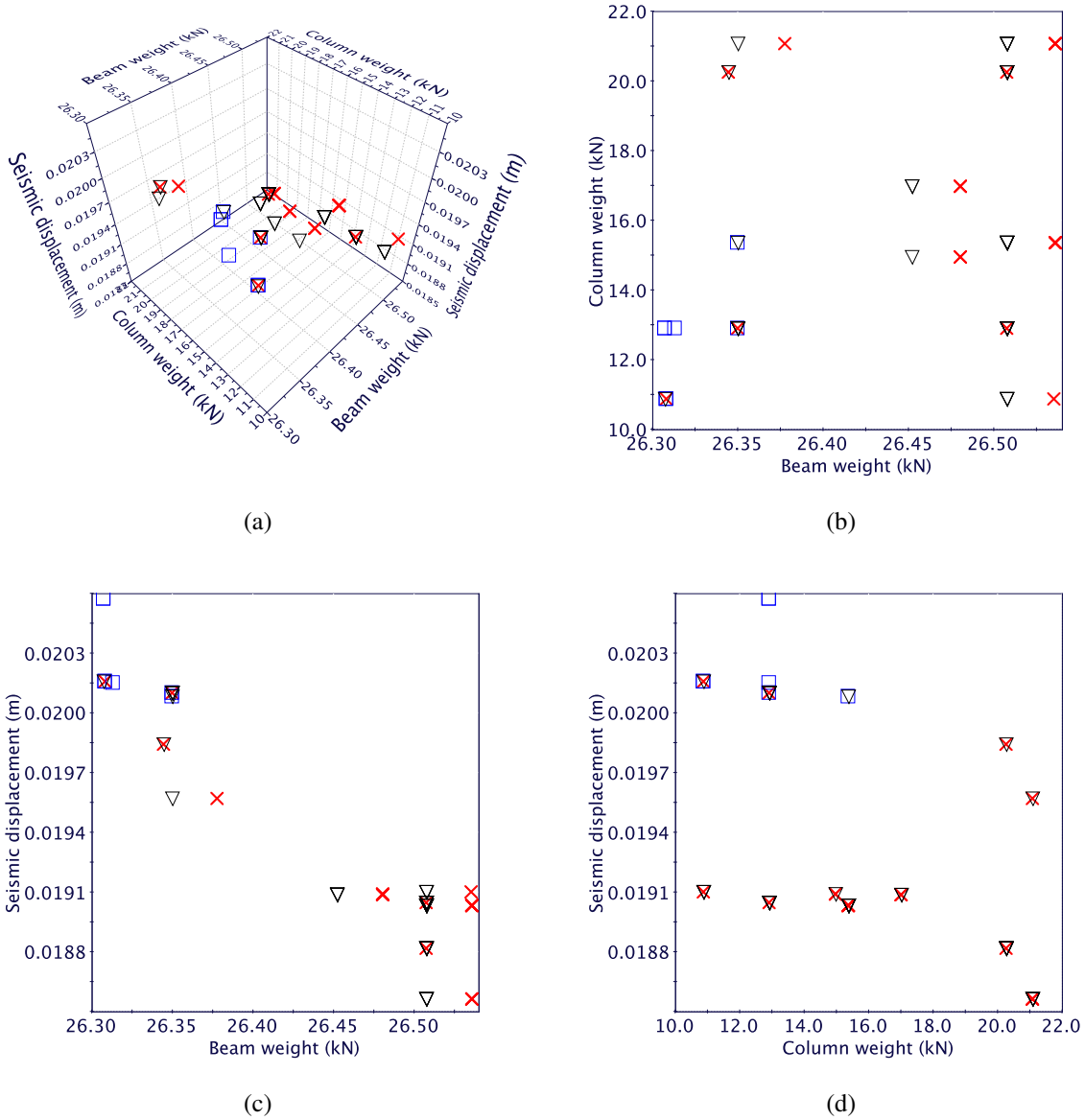
Encouraged by the good results, we decided to rerun the reference-point algorithm from scratch to compare its performance with the deterministic optimization made with NSGA-II and check whether the results shown on Figure 10 depended on the already good initial population used for that run. We started from the same random DOE used for NSGA-II in Section 3.2.1 and ran the algorithm for the same number of iterations, i.e. 50 generations. Results are shown on Figure 11. It is even clearer from these figure than from Figure 10 that the NSGA-III based algorithm is capable of finding nondominated solutions with much smaller weight values for the beam. This demonstrates the very good performance of the reference-point method for this problem.

An analysis of the input variable values of the Pareto front designs found with this simulation from scratch shows that other beam sections were taken into consideration as well (0.30×0.25 m^2 and 0.35×0.25 m^2). However, there seemed to be no preference between the different types of column sections.

4 CONCLUSIONS

In this paper we have addressed a structural optimization problem by combining recently developed strategies for multi-objective optimization under uncertainty and multi-criteria decision making incorporated in the optimization process following the *a priori* approach. A new decision making strategy based on target-points has been developed and benchmarked in combination with the NSGA-III algorithm (based on reference points) of Ref. [3, 4] on mathematical test-cases. We applied these strategies to a real-world case study, i.e. the sizing optimization of a three-dimensional building structure under seismic and snow loads. Many-objective deterministic and stochastic optimizations were performed, both with and without the integrated user preference methods.

The different strategies considered confirmed our expectations even on the structural optimization case, which is very challenging due to its discrete input variable space and a consequently discretized Pareto front. The MOUU provided reliable solutions with a negligible probability of violating critical chance constraints unlike the solutions obtained with the deterministic optimization. The target-point algorithm was used to refine the NSGA-II results and to drive the optimization towards specific regions of the objective space, while with the reference point method we obtained well-distributed optimal solutions, with some striking improvements over the standard NSGA-II algorithm. However, both user-preference algorithms are prototypes and there is still space for further improvements, from both the algorithmic and the methodology points of view. Our goal is to investigate the Pareto frontier as thoroughly as possible to achieve better decision making using the new solutions with the aim of reducing the computational cost which arises from the exploration of undesired objective space regions, and concentrating on specific regions. Another important line of investigation is the development of techniques to



(a) (b)

(c) (d)

Figure 10: Comparison of the Pareto front designs found with the target-point algorithm and the reference-point (NSGA-III based) algorithm described in Section 2.2. Reference-point results are represented by empty downward triangles. Target-points results are represented by cross symbols (which are points already found with the original NSGA-II algorithm, before launching the MCDM optimization) and empty squares (which represent the *new* designs found with the target point algorithm).

efficiently determine the PCE coefficients also in the case of a large number of uncertain input variables, like e.g. Ref. [24].

Acknowledgments

L. Rizzian and ESTECO S.p.A. gratefully acknowledge CSI Italia s.r.l. for providing the SAP2000 license. We thank Maja Engel (ESTECO S.p.A.) for the manuscript revision.

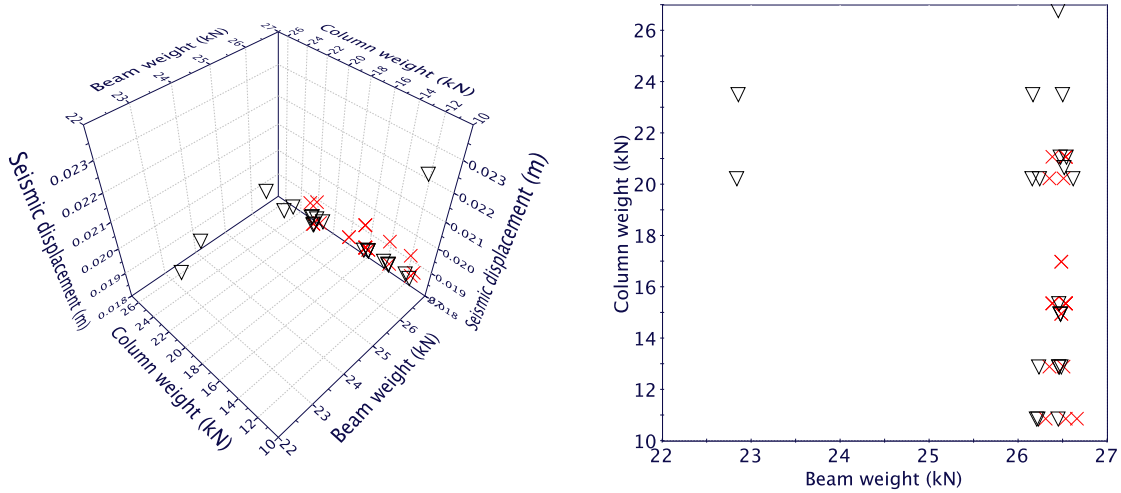


Figure 11: Pareto front designs found with NSGA-II (cross symbols) and with the reference-point algorithm described in Section 2.2 (empty downward triangles).

REFERENCES

[1] G.I. Schuëller and H.A. Jensen, Computational methods in optimization considering uncertainties - An overview. *Comput. Methods Appl. Mech. Engrg.*, **198**, 2–13, 2008.

[2] J. Figueira, S. Greco, M. Ehrgott (eds.), *Multiple criteria decision analysis: state of the art surveys*. Springer Verlag, Berlin, Heidelberg, New York, 2005.

[3] K. Deb, H. Jain, An evolutionary many-objective optimization algorithm using reference-point-based nondominated sorting approach, part I: solving problems with box constraints. *IEEE transactions on Evolutionary Computation*, **18**(4), 577–601, 2014.

[4] H. Jain, K. Deb, An evolutionary many-objective optimization algorithm using reference-point based nondominated sorting approach, part II: handling constraints and extending to

an adaptive approach. *IEEE transactions on Evolutionary Computation*, **18**(4), 602–622, 2014.

[5] J. Branke, S. Greco, R. Slowinski, P. Zielniewicz, Learning value function in interactive evolutionary multiobjective optimization. *IEEE Transactions on Evolutionary Computation*, **19**(1), 88–102, 2014.

[6] M. Papadrakakis, N.D. Lagaros, V. Plevris, Multi-objective optimization of skeletal structures under static and seismic loading conditions. *Engineering Optimization*, **34**, 645–669, 2002.

[7] M. Papadrakakis, Y. Tsompanakis, N.D. Lagaros, M. Fragiadakis, Reliability based optimization of steel frames under seismic loading conditions using evolutionary computation. *Journal of Theoretical and Applied Mechanics*, **42**(3), 585–608, 2004.

[8] M.D. McKay, W.J. Conover, R.J. Beckman, A comparison of three methods for selecting values of input variables in the analysis of output from a computer Code. *Technometrics*, **21**(2), 239–245, 1979.

[9] J.L. Beck, E. Chan, A. Irfanoglu, C. Papadimitriou, Multi-criteria optimal structural design under uncertainty. *Earthquake Engineering and Structural Dynamics*, **28**, 741–761, 1999.

[10] D.M. Frangopol, Life-cycle performance, management, and optimisation of structural systems under uncertainty: accomplishments and challenges. *Structure and Infrastructure Engineering*, **7**(6), 389-413, 2011.

[11] N. Caterino, I. Iervolino, G. Manfredi, E. Cosenza, Comparative analysis of multi-criteria decision-making methods for seismic structural retrofitting. *Computer-Aided Civil and Infrastructure Engineering*, **24**, 432–445, 2009.

[12] H.A. Jensen, D.S. Kusanovic, M.A. Valdebenito, Compromise design of stochastic dynamical systems: A reliability-based approach. *Probabilistic Engineering Mechanics*, **29**, 40–52, 2012.

[13] M. Marchi, L. Rizzian, E. Rigoni, R. Russo, A. Clarich, Combining robustness and reliability with polynomial chaos techniques in multiobjective optimization problems: use of percentiles. A. Cunha, E. Caetano, P. Ribeiro, G. Müller eds. *Proceedings of the 9th International Conference on Structural Dynamics, EURODYN 2014*, Porto, Portugal, 30 June-2 July 2014.

[14] N. Wiener, The homogeneous chaos, *Amer. J. Math.* **60**, 897–936, 1938.

[15] A. Clarich, R. Russo, M. Marchi, E. Rigoni, Reliability-based design optimization applying polynomial chaos expansion: theory and applications. *10th World Congress on Structural and Multidisciplinary Optimization*, Orlando, Florida, USA, 19–24 May, 2013.

[16] M. Marchi, E. Rigoni, R. Russo, A. Clarich, Percentile via polynomial chaos expansion: bridging robust optimization and reliability. *International Conference EVOLVE 2013, A Bridge between Probability, Set Oriented Numerics, and Evolutionary Computation*, July 10–13, Leiden, NL, Extended Abstract Proceedings, ISBN 978-2-87971-118-8, ISSN 2222-9434, 2013.

[17] www.esteco.com

[18] R.T. Marler, J.S. Arora, Survey of multi-objective optimization methods for engineering. *Structural Multidisciplinary Optimization*, **26**, 369–395, 2004.

[19] D. Xiu, G.E. Karniadakis, The Wiener–Askey polynomial chaos for stochastic differential equations. *SIAM J. Sci. Comput.* **24**, 619–644, 2002.

[20] K. Deb, D. Padmanabhan, S. Gupta, A.K. Mall, Handling uncertainties through reliability-based optimization using evolutionary algorithms, *Fourth International Conference on Evolutionary Multi-Criterion Optimization (EMO 2007)*, *LNCS* **4403**, 66–68, 2007.

[21] K. Deb, S. Gupta, D. Daum, J. Branke, A.K. Mall, D. Padmanabhan, Reliability-based optimization using evolutionary algorithms. *IEEE Transactions on Evolutionary Computation*, **13**, 1054–1074, 2009.

[22] B. Sudret, A. Der Kiureghian, Comparison of finite Element Reliability Methods, *Probabilistic Engineering Mechanics*, **17**, 337–348, 2002.

[23] B. Sudret, M. Berveiller, M. Lemaire, A stochastic finite element procedure for moment and reliability analysis. *European Journal of Computational Mechanics/Revue Européenne de Mécanique Numérique*, **15**(7-8), 825–866, 2006.

[24] G. Blatman, B. Sudret, An adaptive algorithm to build up sparse polynomial chaos expansions for stochastic finite element analysis. *Probabilistic Engineering Mechanics*, **25**, 183–197, 2010.

[25] R. Filomeno Coelho, P. Bouillard, Multi-objective reliability-based optimization with stochastic metamodels. *Evolutionary Computation*, **19**(4), 525–560, 2011.

[26] M. Marchi, E. Rigoni, R. Russo, A. Clarich, Guideline identification for optimization under uncertainty through the optimization of a boomerang trajectory. To appear in *Seventh International Conference on Evolutionary Multi-Criterion Optimization (EMO 2015).*

[27] Deb, K., Pratap, A., Agarwal, S., Meyarivan, T.: A fast and elitist multiobjective genetic algorithm: NSGA–II. *IEEE Transactions on Evolutionary Computation*, **6**, 182–197, 2002.

[28] K. Deb, T. Goel, Controlled elitist non-dominated sorting genetic algorithms for better convergence. *First International Conference On Evolutionary Multi-Criterion Optimization (EMO)*, *LNCS*, **1993**, 67–81, 2001.

[29] M. Luque, F. Ruiz, K. Miettinen, Global formulation for interactive multiobjective optimization. *OR Spectrum*, **33**(1), 27–48, 2011.

[30] K. Deb, A. Pratap Mathur and T. Meyarivan, Constrained test problems for multi-objective evolutionary optimization, *First International Conference On Evolutionary Multi-Criterion Optimization (EMO)*, *LNCS*, **1993**, 284–298, 2001.

[31] E. Zitzler and K. Deb and L. Thiele, Comparison of multiobjective evolutionary algorithms: empirical results. *Evolutionay Computation*, **8**(2), 173–195, 2000.

[32] SAP2000 Ultimate 16.0.1, 2013, www.csiamerica.com

COMPDYN 2015
5th ECCOMAS Thematic Conference on
Computational Methods in Structural Dynamics and Earthquake Engineering
M. Papadrakakis, V. Papadopoulos, V. Plevris (eds.)
Crete Island, Greece, 25–27 May 2015

A CODE COMPATIBLE APPROACH TO JUSTIFY THE SEISMIC DESIGN OF SIMPLIFIED STRUCTURES

H.F. Karadogan[1], Y. Durgun[2], I.E. Bal[3], S. Z. Yuce[4], E. Yuksel[5], C. Soydan[6]

[1] Emer. Prof.
Faculty of Civil Engineering, Istanbul Technical University (ITU), Istanbul, Turkey,
karadogan@itu.edu.tr

[2] Dr., [5]Assoc. Prof
Faculty of Civil Engineering, ITU, Istanbul, Turkey
durgunya@itu.edu.tr, yukselerc@itu.edu.tr

[3]Asst. Prof
Earthquake Eng. & Disaster Management Institute, ITU, Istanbul, Turkey
iebal@itu.edu.tr

[4]Dr. , [6] Ph.D. Candidate
Graduate School of Science Engineering and Technology of ITU, Istanbul, Turkey
yuceser@itu.edu.tr, cihansoydan@gmail.com

Keywords: Column Design, Precast Structures, Single Story Frames, Buckling, NTHA

Abstract

An attempt to find out the most probable displacement demands of precast cantilever columns has been presented here. The purpose of the findings presented is to set up a more reliable design philosophy based on dynamic displacement considerations instead of using acceleration spectrum based design which initiates the action with unclear important assumptions such as the initial stiffness, displacement ductility ratio etc. The sole aim of this paper is to define a procedure for overcoming the difficulties rising right at the beginning of the traditional design procedure. For that purpose first 12 groups of earthquake records cover the cases of far field, near field, firm soil, soft soil possibilities for 2/50, 10/50 and 50/50 earthquakes with minimum scale factors are identified associated to the present fundamental period of structure. And they are reselected for each new period of structure during the iterative algorithm presented here and they are used to remove the displacement calculations based on static consideration.

Nonlinear Time History Analysis (NLTHA) are employed within the algorithm presented here which takes into account the strength and stiffness degradations of structural elements and the duration of records which are ignored in the spectrum based design philosophy.

1 INTRODUCTION

Single story precast frame type structures are widely used in the construction of industrial facilities and commercial malls in Turkey. The non-moment resisting *beam-to-column connections* are all wet connections. The lateral strength and stiffness of the structure depend entirely on the cantilevered columns, see. Fig. 1.

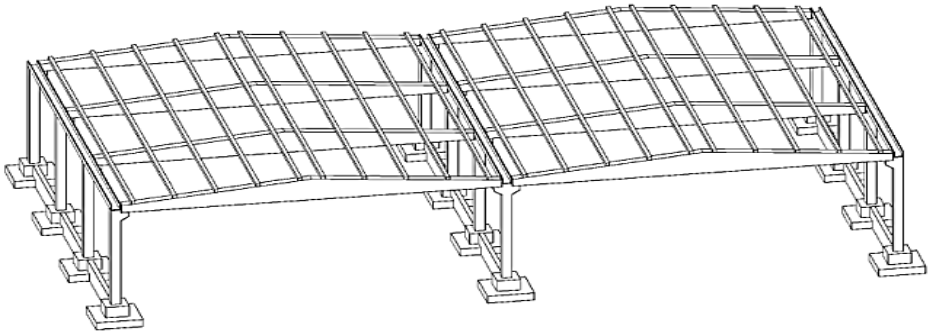


Fig. 1 Single story precast frame type structure

After August 1999 Kocaeli and November 1999 Düzce Earthquakes, site investigations revealed that structural *damage* and *collapse* of one-story precast structures were common especially in uncompleted structures, [1,2,3,4,5]. Various types of structural damage were frequently observed in one-story precast structures, such as plasticized zones at the base of the columns, axial movement of the roof girders that led to pounding against the supporting columns or falling of the roof girders, [6]. The post-earthquake observations of one-story precast frame type structures indicate also that

- Lateral stiffness may not be high enough to limit the lateral displacement of column tops which may differ from peripheral columns to center columns simply because of the lack of in-plane rigidity of roofing system, Fig. 2a,
- Hence the excessive top rotations of columns and the relative displacement in the plane of roof become perfect reasons to dislocate the long span heavy slender roof beam together with the other two component of earthquake, Fig. 2b. They are creating perfect imperfections as well, for out of plane buckling of beams which have very simple insufficient hinge connections to the columns.
- Incompatible column displacement ductility achieved in the field and the lateral load reduction factor used in design, Fig. 2c.



(a) (b) (c)

Fig. 2 Observed damages

In addition to the observations listed above it is also known that, structural alterations done after construction, the effects of nonstructural elements used unconsciously, oversimplified details of connections can be counted among the other important deficiencies of these buildings which causes severe damages.

At the design stage of that type of buildings, the seismic weight coming from the tributary area of columns are determined easily for predicting the earthquake loads. However the *Lateral Displacement Ductility Ratio* which is the main parameter of *Lateral Load Reduction Factor* has to be selected at the beginning of design which is not an easy estimation and has its own uncertainties. Another difficulty is to estimate the lateral rigidity of column which is going to be used to calculate the fundamental period of vibration to go to the spectrum curves. Finally the proposed displacement limits based on static considerations are no longer satisfying the requirements of dynamic displacement calculations.

Those are the factors which are being discussed following experimental and theoretical primary works, [7,8,9]. This Chapter is the scrutinized summary of the findings of the earlier works of the Authors and is aimed to establish a conclusive design algorithm as proposed below.

2 BASIC STRUCTURAL FEATURES OBSERVED IN THE FIELD AND BASIC FEATURES OF THE CURRENT DESIGN PRACTICE

It is strongly probable that all the above mentioned damaged and collapsed buildings they have been neither designed nor manufactured nor mounted properly. From structural engineering point of view, the following facts are important to critic the present design practice:

- Generally there exist almost no in–plane rigidity in the roof and in the sides of the examined precast buildings.
- Generally the connections between the long span beams and columns are almost hinged and they are vulnerable to different types of failure modes in addition to shear strength deficiency such as rupture of concrete around the shear studs etc.
- Generally the tributary areas of columns are used to define the earthquake design forces. When this come along the lack of in-plane rigidity of roof then columns in different location with different dynamic characteristics starts to behave independently hence top displacements and top rotations in opposite direction becomes an important issue to keep the long span and heavy roof beam in the required position. Because all kind of imperfection to destabilize the roof beam appears in addition to the inherent tendency towards out of plane buckling.

In local design practice generally un-cracked sections are used to calculate the fundamental period of the structure. Static calculations are required for determination of displacements and a lateral load reduction factors suggested by codes are used to define the design loads.

One of the main issues in precast structures is that the top displacement of center columns in precast single story industrial buildings may not have synchronized seismic oscillations with the perimeter columns despite the fact that they often have the same cross sectional dimensions. The precast industrial structures do not possess in-plane rigidity at roof level in most cases leading thus to lack of load path among the columns resulting individual shaking of each column [10]. The displacement time-history plots of Column #1, the details of which are given below in the section of *Numerical Analyses*, are presented in Fig. 3. The bottom plot in Fig. 3 presents that the maximum center column displacement is 26 cm, while the middle column maximum displacement is 20 cm. These two numbers may mislead the engineer to a

wrong conclusion that the differential displacement between the perimeter and center columns is just 26-20=6 cm. If the top plot with the differential displacement between the two columns in time domain is observed, however, it can be seen that the maximum differential (i.e. asyncronized) displacement reaches up to level of 33 cm. The main reason for that is because the top displacement of each individual column may occur at different time steps thus the phase alteration may cause large asyncronized displacements. In other words, the top displacement of a center and of a perimeter column may have opposite signs.

The top displacement of individual cantilever columns exhibiting opposite signs may lead to instability of the beams which are hinged to the column tops in existing practice. It can be seen in Fig. 4 following analyses of perimeter and center columns of a single-story precast structure with 20 code-compatible records that the tip rotation is always higher than the chord rotation (please note that the chord rotation is equal to drift in cantilever systems). In other words, the tip of the column where hinged beams are connected rotates more than the column itself. This is a major parameter neglected in design.

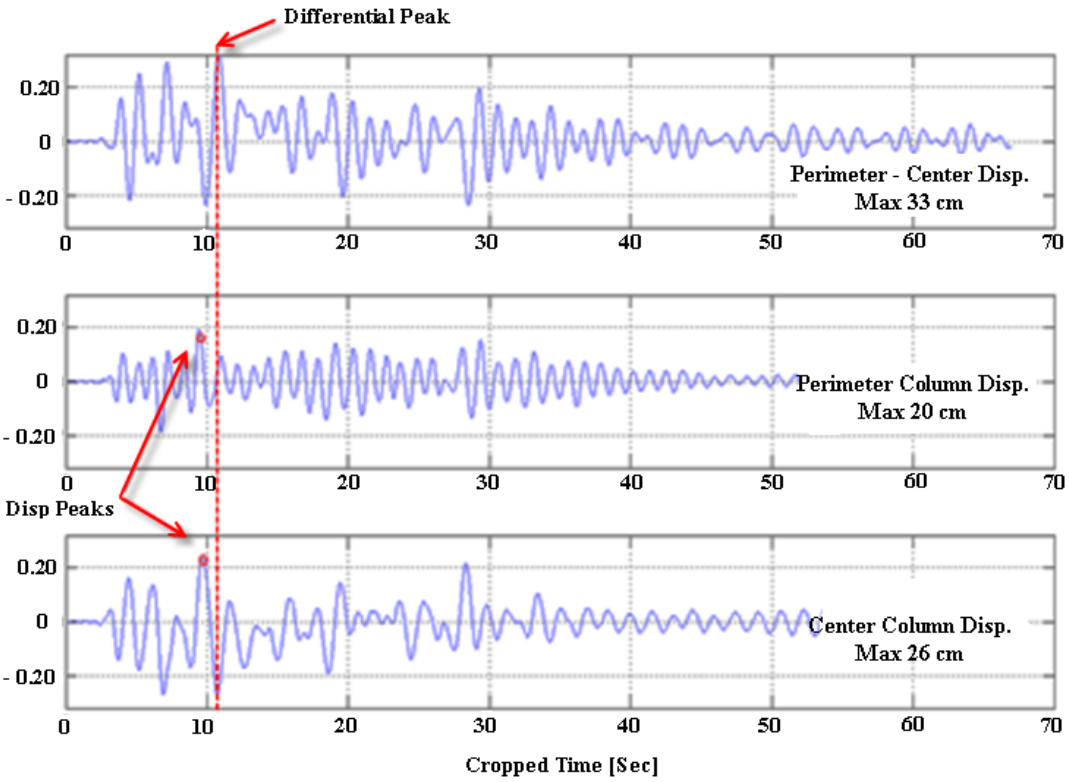


Fig. 3 Asynchronized displacement time histories for center and perimeter columns of a single-story precast Structure

3 WHY JUSTIFICATION OF CODE BASED DESIGN PROCEDURE IS NEEDED?

Even if the damaged or collapsed buildings shown in Fig. 2 had been designed properly, been manufacured properly and been mounted properly, unless the assumptions done at the beginning of design are not justified at the end, one should have rigth to keep suspition about the safety of building.

The basic questions to be kept in mind till the satisfactory design has been reached, are as follows:

- What should be the initial period of the structure on which the fundamental period will be based?
- What should be the displacement ductility factor or lateral load reduction factor on which the design forces will be based?
- To what extent is valid the story drift calculation based on static considerations?

One of the other deficiencies of spectrum based design technique is the length of the record which is not taken into account and the other one is the stiffness and strength deterioration of structure: Unfortunately they are not embedded in the procedure widely used by existing codes.

In order to satisfy the suspicions from which all those questions are arising, an algorithm to justify the design procedures used at the beginning, is presented in the following paragraphs.

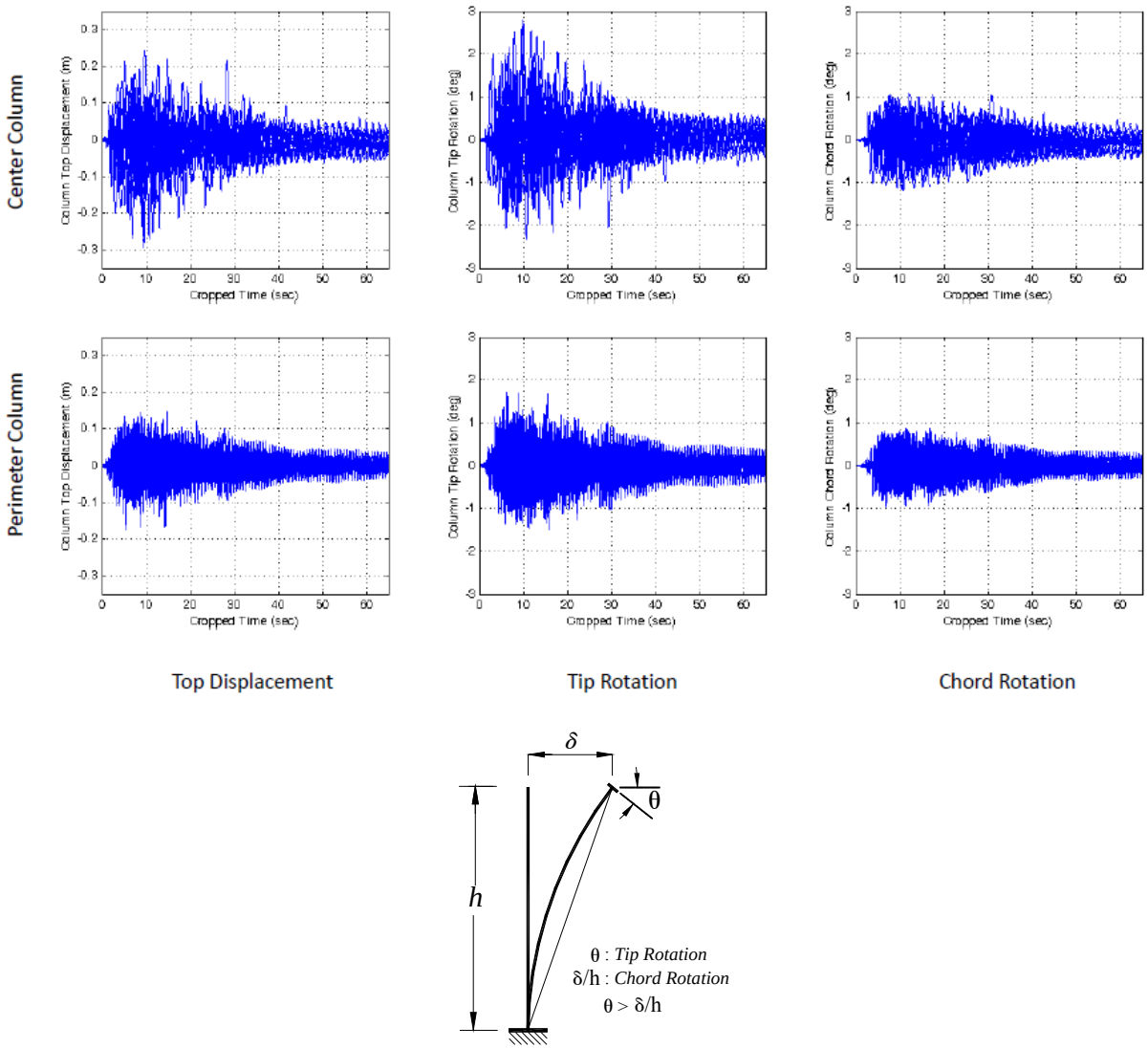


Fig. 4 Definition of *chord rotation* and *tip rotations* (top), comparison of top displacement, tip rotation and chord rotation quantities for an example precast industrial structure (bottom)

4 SELECTION OF PARTIALLY CODE COMPATIBLE RECORDS

A simple engineering approach is used here for the selection of records used in nonlinear analyses. The record selection has been done by using the PEER NGA database [11] where 7025 recorded motions were available. An in-house developed software was used to list and download the record automatically and plot the spectra for acceleration at 5% damping, velocity and displacement.

Twelve bins of records, [12], are created where:

1. Earthquake intensity (2/50, 10/50 or 50/50 earthquakes, 3 bins)
2. Far field or near field issue (2 bins)
3. Soil type (firm soil and soft soil, 2 bins)

parameters are checked. Each of these 12 bins have 20 records,

In terms of the selection algorithm, first the acceleration spectrum of the original record is compared to that of the target, in the period window of 0.2 to 2.0 sec. A scale factor is applied to the ordinates. Then the near field vs. far field comparison is made where the distances above 15 km are assumed as far field. Finally a comparison is made in terms of the soil type where the records taken on soil with Vs30 higher than 300 m/sec are assumed to be recorded on firm soil while records taken on soils with Vs30 lower than 700 m/sec are assumed to be recorded on soft soil. There is certainly an overlap in the soil criteria; this is nevertheless unavoidable if one checks the firm and soft soil borders in the guidelines and codes.

The intensity levels of 2/50, 10/50 and 50/50 are defined to represent 2, 10 and 50% probabilities of exceedance in 50 years, respectively. The criteria applied have resulted the number of available records, but it should be mentioned that some each bin does not return the same number of available records. For instance, records which are recorded on soft soil and farm field consist of more than 60% of the record pool, thus the rest is shared between three different groups which are far field – firm soil, near field – soft soil, and near field – firm soil. As a result, selection criteria have to be loosened in some cases.

The scale factors are set such that average of 20 records does not go below the target spectrum in certain percentages and most of the cases the average spectrum is not allowed to go below the target spectrum at all. Similarly, the average spectrum is not allowed to go above 30% of the target spectrum in any point within the period window. In order to control the difference of the positive and negative peaks, where positive peaks refer to the peaks above the target spectrum and vice versa, another criterion is also applied to check the individual records. According to this, the individual record is not allowed to go below the target spectrum less than 50%, or above more than 200-300% in any of the peaks. This criterion dictates to select rather smooth records with less peaks, however it is a very harsh criterion to be satisfied. The scale factors in overall are not allowed to be below 0.5 and above 2 in any of the selected records so that the energy content can be controlled.

Two more criteria have been applied to control the energy content, one is the PGV and the other is the Arias Intensity. The purpose of the inclusion of these two criteria is to decrease the scatter, i.e. record-to-record variability of the selected records. In order to do so, a record that fits the target spectrum with the least error has been assigned as the best record, and the selected records are not allowed to have PGV or Arias Intensity values above or below certain ratios as compared to those obtained from the best record. The limits for these criteria had be set so high in some of the bins that they were practically not much effective because the number of available records was already low even without these criteria. Generally, the selected

records are not allowed to have PGV and Arias ıntensity values, after scale factors are applied, above 1/0.6 – 1/0.7 and below 0.6-0.7 of that of the best record.

The selection of records has been done by using acceleration spectra, however similar procedures may and should be produced for velocity and displacement spectra as well. As an example, acceleration spectra and displacement spectra are given Fig. 5. Please note that the differences among the selected records are much higher in displacement spectra when long-period structures are considered, such as the single-story precast structures as presented here.

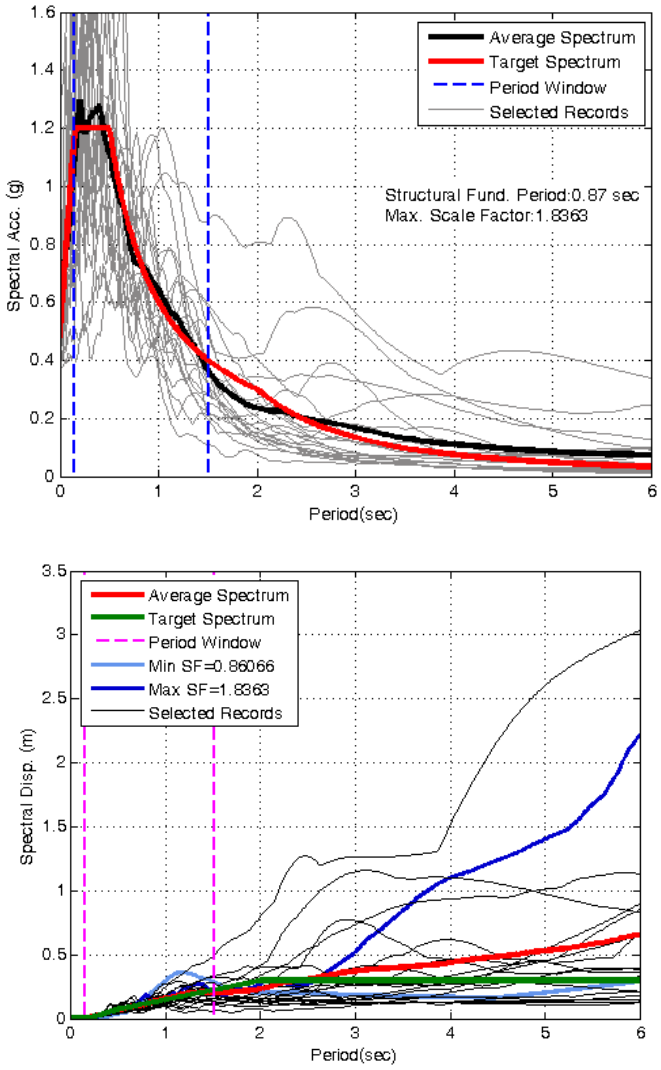


Fig. 5 Acceleration spectra and displacement spectra for an example selection

5 PROPOSED ALGORITHM

The following steps are identified in the proposed algorithm; see the flow chart given in Fig. 6 a,b &c and illustrative description presented in Fig. 7:

- It is assumed that the preliminary design of the structure has been completed so that all requirements in the selected seismic code have been satisfied such as strength and displacement limitations etc. There is no need to discuss what should be initial

stiffness or what is the most suitable lateral load reduction factor or the displacement equality principal is valid or not.

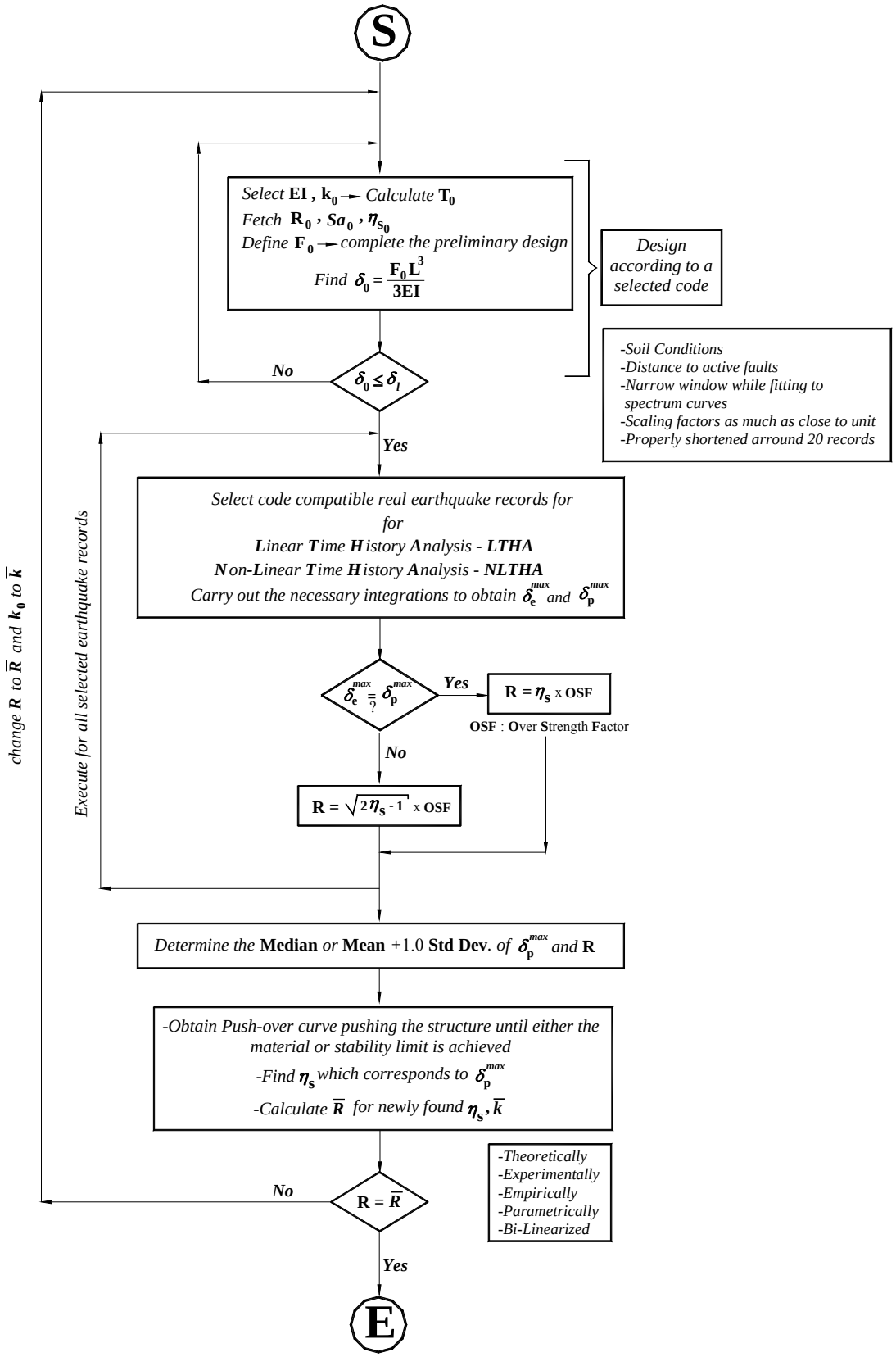


Fig. 6,a - Flow chart of the proposed algorithm : first stage

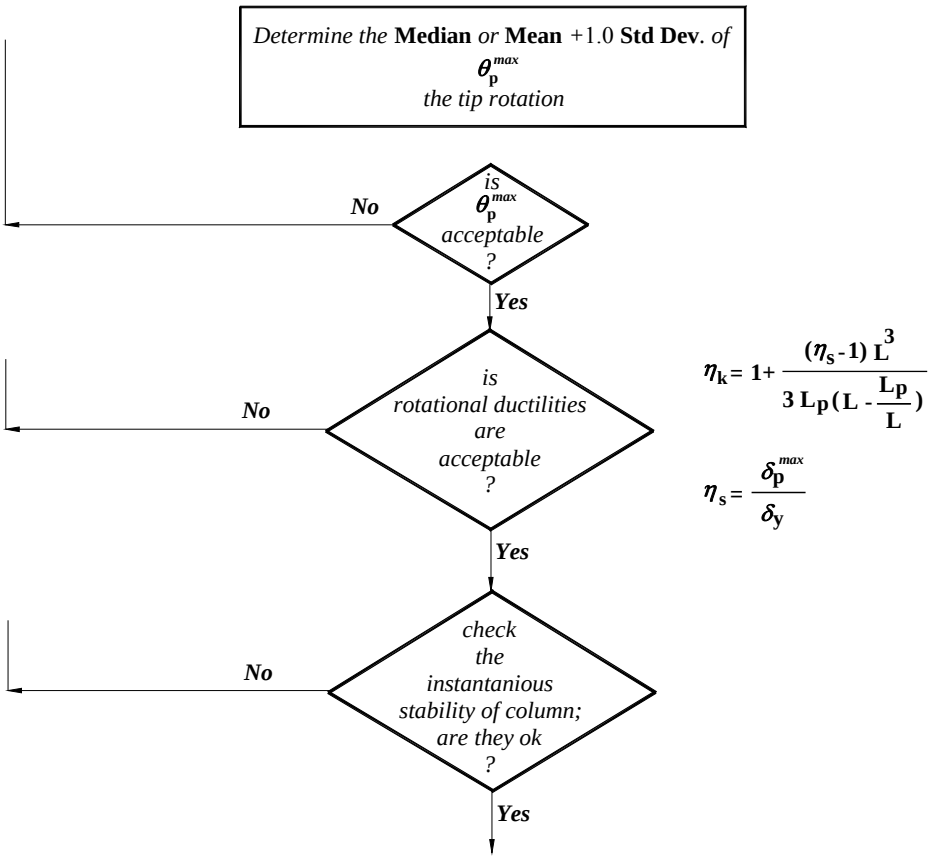


Fig. 6, b - Flow chart of the proposed algorithm: second stage

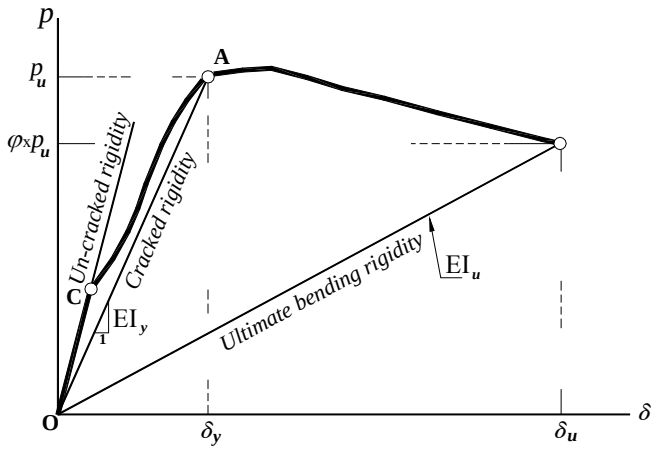


Fig. 6, c – Un-cracked, cracked and ultimate bending rigidities

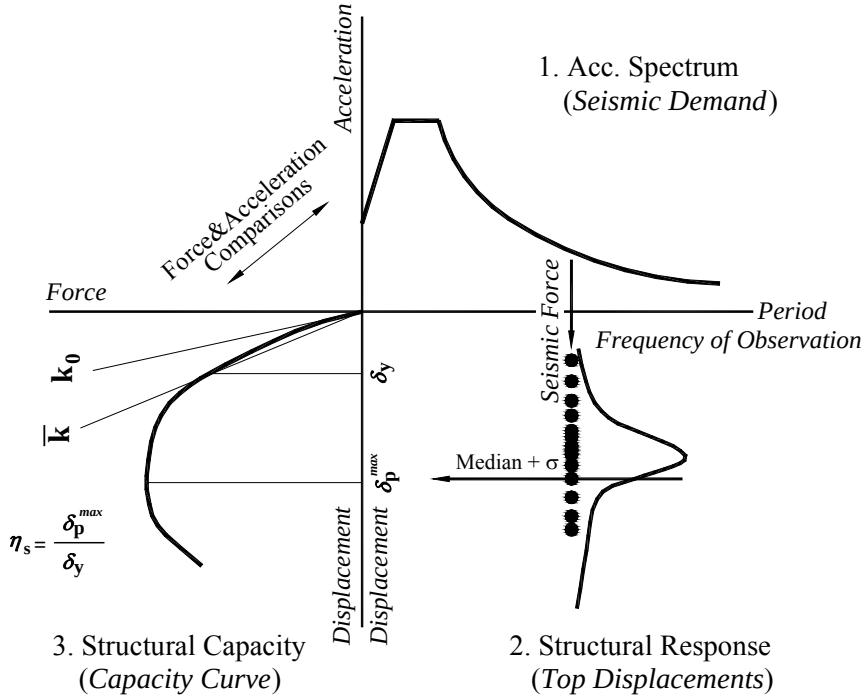


Fig. 7 Description of the proposed procedure

- Real earthquake records are selected so that the parameters like soil conditions, distance to active faults, and the required intensities such as 2/50-10/50-50/50 are all satisfied with reasonable tolerances and scaling factors are chosen as much as close to unity to make the acceleration curves close to the curve provided by codes in a narrowest window around the fundamental period of the structure. The selected earthquakes should be around 20 and the most meaningful part of the records should be identified to shorten the NLTHA analysis which will be used for all records. The details of this topic is discussed below in another sub section.
- The selected partially code compatible earthquakes are used for linear and non-linear analysis of the structure to check which one of the *displacement or energy equality assumption* is valid for the specific structure under consideration. It is also important to have an idea about what could be the tolerance to accept the validity of one of these equalities.
- Depending on the decision done at the end of last step one can calculate the lateral load reduction factor accordingly using the proper formula given in the flow chart.
- Mean plus one standard deviation of maximum displacement obtained through NLTHA and lateral load reduction factors are calculated.
- Capacity curve of the structure is obtained using any one of the known technique. These curves cannot be only obtained theoretically but also experimentally, empirically, parametrically, they can be in a continuous form or in the bilinear form etc.
- Yielding point and the point corresponds to maximum inelastic displacement found are taken into consideration for defining the *lateral rigidity* and the *achieved displacement ductility* of the structure from where the more realistic lateral load reduction factors will be calculated referring to the same formula used in the previous step.

- It is expected to have almost equal lateral load reduction factors in last two cycles of iterations. If they are not at the close proximity then another step of iteration will be carried out.

This will be the end of first stage justification of design. In fact *tip rotations, rotational ductility capacity of critical bottom sections* where the plastic deformations are accumulated and *possible loss of safety against overall and local stability of columns* should be checked as it is proposed in the second stage of the justification process presented in Fig 6,b.

The expected rotational ductility of the critical section can simply and roughly be given as follows [13] for symmetrically reinforced rectangular sections,

$$\mu_k \cong 227 \times \left(\frac{\varepsilon_{cu}}{n} \right)$$

where ε_{cu} and n indicate the maximum concrete strain in uppermost concrete fiber and the dimensionless axial load, $N/(b \times h \times f_{ck})$ respectively. For the derivation of formula presented above it has been assumed that not only the reinforcement bars under tension but the reinforcement bars under compression both are yielded and f_{yk} is around 420 MPa.

The theory which covers the second order effect of axial force on the tip rotation which is significantly different than chord rotation, the tip displacement is summarized in Appendix - 1 together with the overall stability criterion of column considering the material nonlinearity exist in the critical region. The material nonlinearity is simply imparted into the second order analysis by means of the decrements in bending rigidities shown in Fig.6 c. Numerical examples indicate that especially the loss of overall stability of the column cannot be neglected and the excessive tip rotations may become a good reason to destabilize the roof beams sitting on the columns.

In the following paragraphs several definitions and explanations are given and some complementary results of early experimental and theoretical findings for *over strength factor, lateral load reduction factors and capacity curves* are summarized for the sake of having complete information together with this justification procedure.

6 OVER STRENGTH AND LATERAL LOAD REDUCTION FACTORS

For the sake of completeness the early results achieved by reviewing the experimentally obtained and theoretically examined column behavior has been added into this paragraph [9,10].

The 4.0 m high column having a cross section of 40×40 cm, Fig. 8a, subjected to displacement reversals exposed the structural response shown in Fig. 8b. The same hysteresis loops have been obtained theoretically and compared in Fig. 8c with the experimental results. Then the material coefficients have been reduced from 1.15 and 1.4 to unity for steel and concrete respectively before the similar theoretical works carried out. The envelope of hysteresis curves are compared in Fig. 8d.

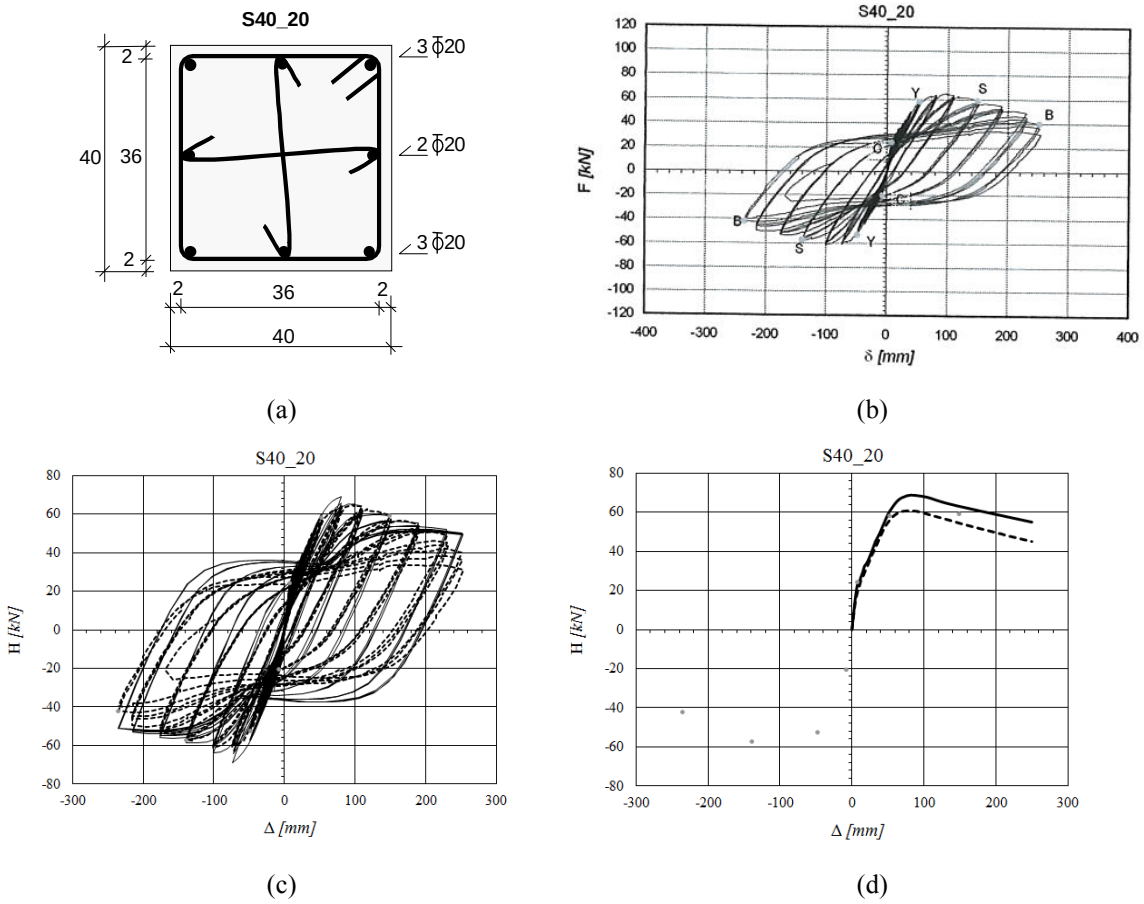


Fig. 8 Experimental and analytical evaluation of 40×40 cm column

Similar 12 more tests have been completed and similar analyses have been carried out depending on the results obtained and Table 1 is prepared, [10]. One can found the ultimate loads of the columns when the material coefficient is taken as unity or different than unity, in the first two lines, respectively. The ratio of these two lines give the approximate over-strength factors. It can be concluded that for these type of columns the over-strength factors can be taken as 1.10. If the displacement ductilities obtained from the same tests which are given in the fourth line of Table 1 are multiplied by over strength factor the lateral load reduction factors on the fifth line will be achieved.

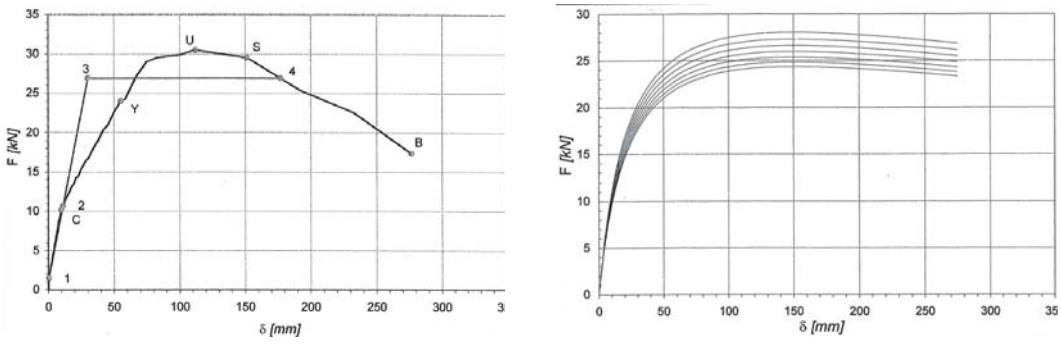
SPECIMEN	1	2	3	4	5	6	7	8	9	10	11	12	13
	S30_14	S30_14M	S30_16	S30_18	S30_18Z	S35_1416	S35_18	S35_20	S35_20Z	S40_16	S40_20	S40_2020	S40_2020Z
$P_{u(\gamma=1)}$	21.30	21.00	29.10	32.60	30.40	33.50	42.50	50.40	48.00	49.30	68.50	88.30	89.76
$P_{u(\gamma\neq1)}$	19.00	19.50	25.20	28.60	26.80	29.70	37.70	44.30	42.20	43.70	60.70	77.73	77.40
OSF	1.12	1.08	1.15	1.14	1.13	1.13	1.13	1.14	1.14	1.13	1.13	1.14	1.16
μ	5.30	3.20	5.10	3.70	3.00	5.80	5.50	4.60	3.90	5.20	5.50	3.00	3.40
OSF × μ	5.94	3.44	5.89	4.22	3.40	6.54	6.20	5.23	4.44	5.87	6.21	3.41	3.94

Table 1 Overstrength factors, displacement ductility ratios and possible lateral load reduction factors

7 CAPACITY CURVES

Capacity curves used in the above explained algorithm can be obtained either by means of a theoretical manner or it can be obtained by any one of the known simplified technique. They can be in a continuous form or in bi-linear form.

Sometimes for the same size same quality concrete but for different reinforcement ratios simple ready charts can be utilized for that purpose. An example of a capacity curve for 30×30 cm C25 square column obtained experimentally, theoretically and parametrically is presented in Fig. 9, as well, [9].



(a) (b)

Fig. 9 Determination of the column capacity curve

8 NUMERICAL EXAMPLES

The presented algorithm has been used to make clear the following issues;

- To what extent the assumptions made at the beginning of preliminary design are satisfied? Namely, have the strength, the lateral load reduction factor and /or the displacement ductility assumptions as well as the stiffness values used in design been checked?
- The design is accepted when one or several of parameters are satisfied. What are the tolerance limits for satisfaction of the design criteria?

The initial design parameters and the findings are presented for three columns, Column #1 to #3. The Column #1 is extracted from the benchmark structure of Safecast Project, [14]. Column # 2 is one of the prefabricated columns tested at ITU laboratories [9]. The Column # 3 is extracted from a real structure currently in use in Kocaeli, Turkey.

The algorithm proposed above was run for each of the columns mentioned here. The algorithm has converged in three steps for all columns. The results as well as the key parameters per each analysis step have been presented in Table 2.

The results presented in Table 2 are based on the assumption that the change of R factor in two consecutive steps will not exceed a tolerance, which is 10% in this study. This tolerance as well as tolerance limits of other parameters may be adjusted by the user depending on parametric studies and findings.

Parameter	Unit	Soil Type B 60×60 Column	Soil Type C 40×40 Column	Soil Type B 70×70 Column
m	tonnes	33	20.4	43.4
K_0	kN/m	2230	1946	582.1
T_0	sec	0.75	0.64	1.54
$Sa(T=T_0)$	g	0.61	0.95	0.34
R		3	3	3
F_{design}	kN	65.80	63.40	36.70
K_1	kN/m	1453	829	349
T_1 (yield)	sec	0.93	0.98	1.99
Sa ($T=T_1$)	g	0.51	0.66	0.28
R_1		2.26	2.02	1.97
$\lvert(R_1-R_0)/R_0\rvert$	>10%	0.25	0.33	0.34
F_{design} (m+s)	kN	73.10	65.40	60.60
K_2	kN/m	1671	1129	379
T_1 (yield)	sec	0.87	0.84	1.91
Sa ($T=T_1$)	g	0.54	0.76	0.29
R_2		2.43	2.05	2.14
$\lvert(R_2-R_1)/R_1\rvert$	OK	0.08	0.01	0.09
F_{design} (m+s)	kN	71.90	74.20	57.70

Table 2 Progress of the algorithm and the change of key design parameters for the case study columns

Comparison of the assumed capacity curve with the pushover and time history analyses results for columns are presented in Figs. 10, 11 and 12.

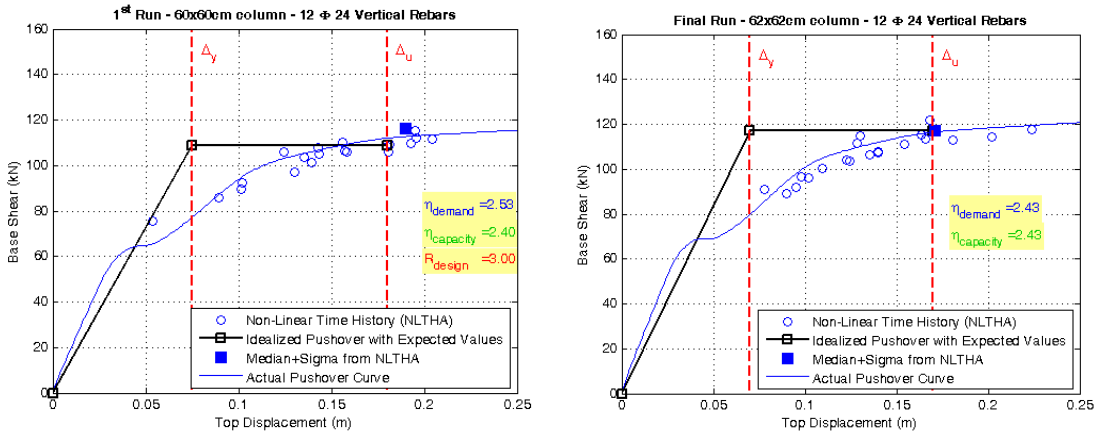


Fig. 10 Comparison of the assumed capacity curve with the pushover and time history analyses results for the **Column #1**

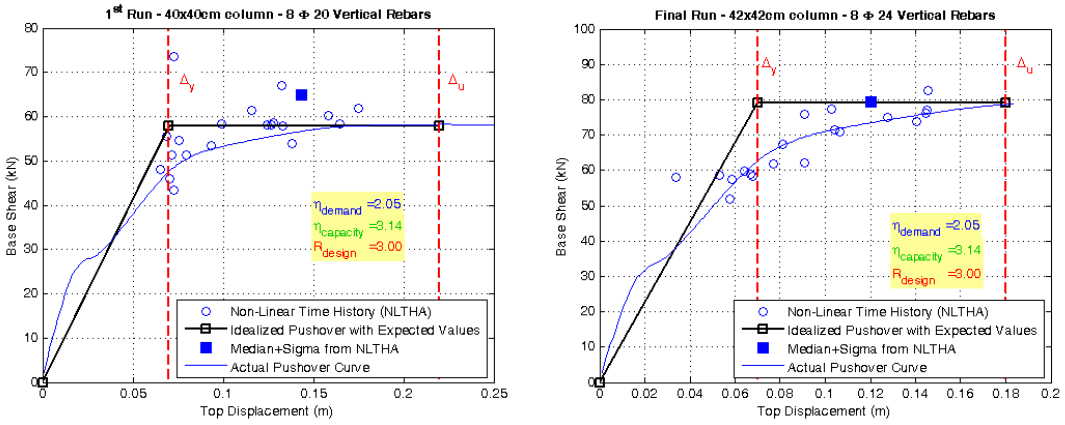


Fig. 11 Comparison of the assumed capacity curve with the pushover and time history analyses results for the **Column #2**

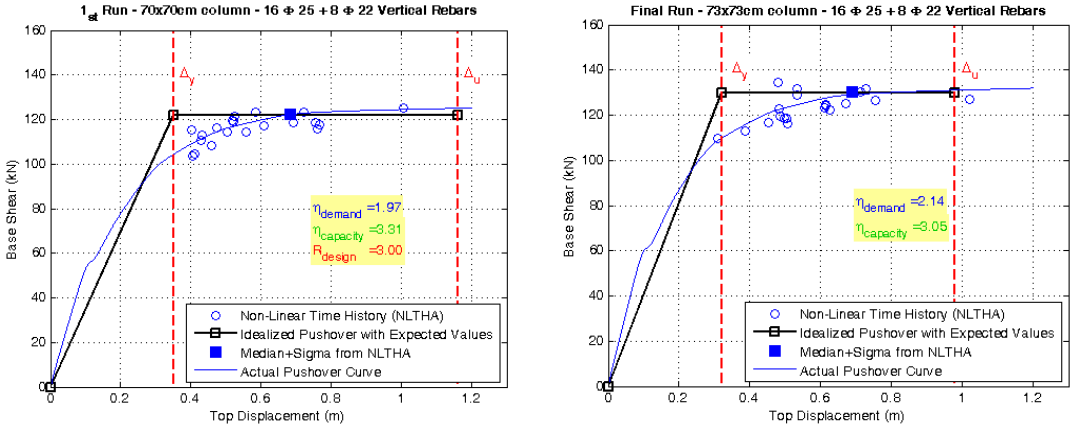


Fig. 12 Comparison of the assumed capacity curve with the pushover and time history analyses results for the **Column #3**

The results presented in Figs. 10, 11 and 12 are representative of all possible cases in design iterations when the proposed algorithm is used. In the first example, the displacement condition is not satisfied (i.e. the displacement demand of the original column is higher than the displacement capacity of the structure). The strength is not satisfied in the second example. The third example satisfies both conditions but the algorithm was still run in order to see how the design would change. It can be observed in these figures that the column dimensions and/or reinforcement need to be changed in all cases in order to satisfy the design algorithm proposed here.

Please note that the scale factors for some of the records listed in Table 3 are higher than 2. These are the cases where the number of available records for the set of criteria used was not high thus the scale factor condition was loosened.

One of the key points of the algorithm proposed here, which is also one of the main motivations of the study, is that the spectral displacement equality (i.e. equal displacement rule) which is the basis of the conventional design is not valid in most of the cases. The analyses show that for the examined three columns, the average plastic displacements calculated by applying selected 20 records on the columns is always higher than the spectral displacements found from the displacement spectra of the selected records. In other words, the equal displacement rule certainly does not work for the cases examined.

60×60 cm Column		40×40 cm Column		70×70 cm Column	
Record	**SF**	**Record**	**SF**	**Record**	**SF**
CHICHI03_TCU129-E	**1.25**	CHICHI06_TCU078-E	**1.31**	CHICHI03_TCU122-E	**2.42**
HECTOR_HEC090	**0.98**	CHICHI03_TCU129-E	**0.99**	CHICHI_TCU136-W	**2.16**
CHICHI_TCU047-N	**1.25**	CHICHI_CHY046-N	**1.58**	CHICHI_TCU128-N	**1.57**
CHICHI_CHY035-N	**0.96**	BIGBEAR_DHP090	**1.44**	CHICHI_TCU116-N	**1.83**
CHICHI_CHY034-W	**0.90**	MORGAN_G06090	**0.97**	CHICHI_TCU106-N	**1.74**
NORTHR_PKC360	**0.86**	HECTOR_HEC000	**1.47**	CHICHI_TCU087-N	**2.15**
NORTHR_STN110	**1.03**	CHICHI_TCU-E	**1.32**	CHICHI_TCU063-N	**1.35**
NORTHR_PEL360	**1.28**	CHICHI_CHY074-E	**1.36**	CHICHI_TCU054-N	**1.97**
LOMAP_G03090	**1.22**	CHICHI_ALS-E	**1.43**	CHICHI_TCU039-N	**1.85**
LOMAP_CYC285	**1.04**	NORTHR_PKC090	**0.91**	CHICHI_TCU029-N	**1.77**
CHICHI_TCU138-N	**1.04**	NORTHR_MRP090	**1.53**	CHICHI_CHY029-N	**1.73**
CHICHI_TCU116-E	**1.24**	NORTHR_0141-270	**1.01**	CHICHI_TCU136-N	**1.99**
CHICHI_TCU063-E	**1.26**	LANDERS_MVH000	**1.45**	CHICHI_TCU107-E	**1.75**
CHICHI_TCU047-E	**0.91**	LOMAP_SLC270	**1.27**	CHICHI_TCU082-E	**1.96**
CHICHI_TCU045-E	**1.19**	WHITTIER_A-CAS000	**1.09**	CHICHI_TCU054-E	**2.39**
CHICHI_CHY024-E	**1.28**	WESTMORL_PTS225	**1.49**	CHICHI_TCU039-E	**1.72**
NORTHR_PKC090	**1.04**	CORINTH_COR--L	**1.33**	CHICHI_TCU-E	**2.04**
NORTHR_LOS000	**0.99**	VICT_CPE045	**0.8**	CHICHI_CHY074-E	**1.78**
LOMAP_STG000	**1.04**	TABAS_DAY-LN	**1.58**	CHICHI_ALS-E	**1.92**
VICT_CPE045	**0.93**	FRIULI_A-TMZ000	**1.45**	KOBE_KBU000	**1.31**

Table 3 Selected earthquake records and scale factors (SF)

The displacement equality is the base of the conventional design because the behavior factor, R, is the most important assumption of the conventional design. A graphical description of the terms and the design assumption are presented in Fig. 13.

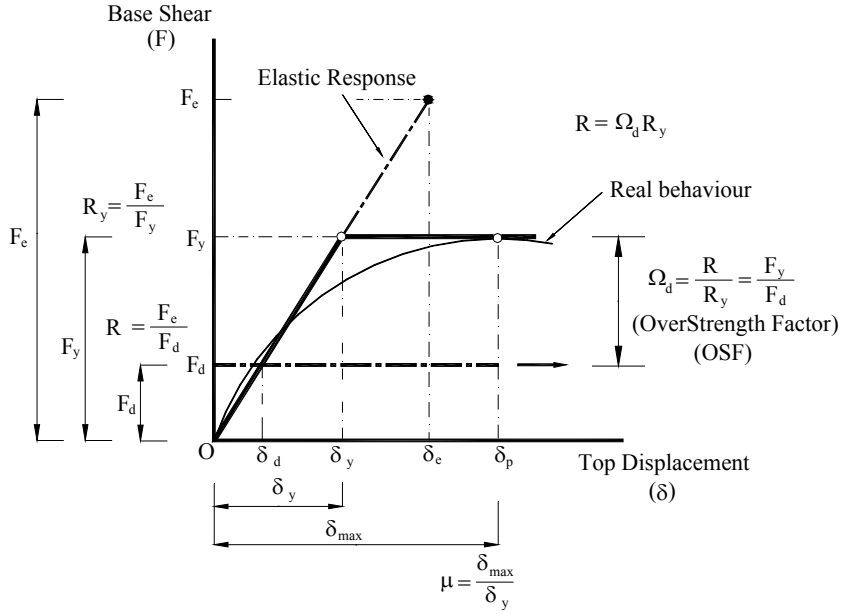


Fig. 13 The use of equal displacement rule in design

The results shown in Fig. 14 indicate a significant disagreement between the spectral and real displacement demands. Please note that the period of the three columns presented in the

plot shown in Fig. 14, columns of 40×40, 60×60 and 70×70, are 0.64 sec, 0.75 sec and 1.54 sec, respectively. As it can be seen in Fig. 14, as the period of the system increases, the disagreement becomes even more evident.

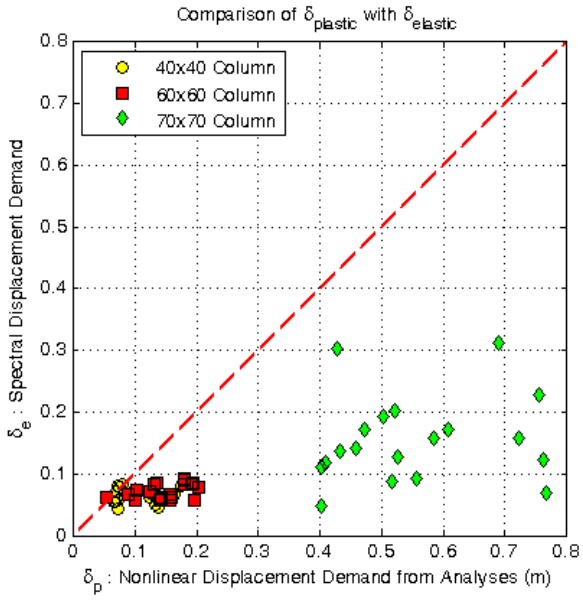


Fig. 14 Comparison of the elastic spectral displacements with the plastic displacement demands obtained from the nonlinear dynamic analyses

The stability analyses of one of the columns have been examined in Table 4. In the analysis, three critical stages namely un-cracked, yielding and ultimate state have been accounted. The equations presented in Appendix I are utilized for the stability analysis. It can be considered that the stability check of a column in the different stages of nonlinear phase is an essential matter.

			40 x 40 Column (L=4.00m) - Stability Checks			
	Lateral Stiffness [kN/m]		Buckling Load [kN]		Buckling Length [m]	
			Fixed Based	Partially Fixed	Fixed Based	Partially Fixed
Un-Cracked	K_0	1946	6394	6394 (γ=0)	8.00	8.00 (γ=0)
Yielding	K_y	829	2724	1185	8.00	12.19 (γ=0.581)
Ultimate	K_u	264	867	162	8.00	18.56 (γ=1.838)

Table 4 Stability analyses of Column 40×40 cm

9 CONCLUSIONS

The following conclusions are drawn:

- Design verification is needed and if necessary redesign step of iterations are carried out.
- It is possible to overcome the inherently existing deficiencies of spectrum based design by the algorithm presented; namely the strength and stiffness degradations and

time duration effects can be considered which are not considered in the code specified spectrum analyses. In this technique, at the beginning of design stage, there is no need to make a series of assumptions such as the initial stiffness of the structure, displacement ductility of the structure and lateral load reduction factor which are all effective on the results. It becomes possible to trace the actual behavior of structure during the iteration steps.

- The top displacements obtained by NLTHA which are based on nearly code compatible real earthquake records are generally bigger than code limits and they are practically not equal to the elastic displacements obtained by linear time history analyses. Therefore the widely utilized assumption of *displacement equality* cannot be generalized for the columns analyzed and *equality of velocities* or *energies* should be considered wherever is needed. The algorithm presented here is providing a versatile tool for that purpose.
- The proposed procedure can be used not only for single story precast buildings but it can be generalized by minor alterations for the design of bridge columns or piers and for the critical columns of piloty type building structures where all the nonlinear behavior is observed only in one of the generally lower stories.
- The execution time for nonlinear time history analyses needed in the proposed algorithm is not a big issue because of the speed reached by computers but more discussions should be done on the selection of real records and their optimal numbers.

- Several more checks has been added to the flow chart presented in [15] to have more refined one for controlling the sufficiency of sectional ductility needed to provide the required displacement ductility and to check the allowable tip rotations to keep the top beams stable in their original position and check for the overall stability of the columns. The algorithm proposed may be supported depending on new research in the field of defining reasonable limits for tip rotations and loss of safety against overall stability of the structure.

10 REFERENCES

[1] Saatcioglu M., Mitchell D., Tinawi R., Gardner N.J., Gillies A.G., Ghobarah A., et al. "The August 17, 1999, Kocaeli (Turkey) Earthquake – Damage to Structures", *Can J Civ Eng* 28: 715-37, 2001.

[2] Ataköy H., "17 August Marmara Earthquake and the Precast Structures Built by TPCA Members", *Turkish Precast Concrete Association*, Ankara, Turkey, 1999.

[3] Sezen H., Elwood K.J., Whitaker A.S., Mosalam K.M., Wallace J.W., Stanton J.F., "Structural Engineering Reconnaissance of the August 17, 1999, Kocaeli (Izmit), Turkey", Earthquake Rep No 2000/09. Pacific Engineering Research Center. University of California, Berkeley, CA, 2000.

[4] Bruneau M., "Building Damage from the Marmara, Turkey Earthquake of August 17, 1999", *J Seismo* 6(3): 357-77, 2002.

[5] Sezen H., Whittaker A.S., "Seismic Performance of Industrial Facilities Affected by the 1999 Turkey Earthquake", *J Per Const Fac* ASCE 20(1): 28-36, 2006.

[6] Wood S.L., "Seismic Rehabilitation of Low-Rise Precast Industrial buildings in Turkey", In: Wasti T, Ozcebe G (eds), *Advances in Earthquake Engineering for Urban Risk*

Reduction. NATO Science Series. IV. Earth and Environmental Sciences: Kluwer Academic Publishers 66: 167-77, 2003.

[7] Karadogan F., "Prefabricated Industrial Type Structures of Adapazarı", *Irregular Structures*, European Association of Earthquake Engineering, Task Group 8, Asymmetric and Irregular Structures, Istanbul, Vol. 2, October 1999.

[8] Karadogan F., Yuksel E., Ilki A., "Deformability Limits and Ductility of Reinforced Concrete Bare Frames", *First Japan – Turkey Workshop on Earthquake Engineering*, Istanbul, Vol.1, March 1997.

[9] Karadogan F., Yuksel E., Yuce S., Taskın K., Saruhan H., "Experimental Study on the Original and Retrofitted Precast Columns", Technical Report (in Turkish), Istanbul Technical University, 2006.

[10] Karadogan, F., Yuce, S., Yuksel, E., Bal, I.E., Hasel, F.B., "Single Story Precast Structures in Seismic Zones-I", COMPDYN 2013, 4th ECCOMAS Thematic Conference on Computational Methods in Structural Dynamics and Earthquake Engineering, Kos Island, Greece, 12–14 June 2013.

[11] PEER NGA Database. Pacific earthquake engineering research center: NGA database. (http://peer.berkeley.edu/peer_ground_motion_database/)

[12] http://web.itu.edu.tr/~iebal/Dr_Ihsan_Engin_BAL/SafeCladding_EU_Project.html

[13] Çakıroğlu A., Karadoğan F., "Plastic Hinge Capacities, Curvature and Structural Ductilities of RC Structures", First Japan-Turkey Workshop on Earthquake Engineering, March, 1997, Istanbul, Vol I.

[14] SAFECAST FP7 Project "Performance of innovative mechanical connections in precast building structures under seismic conditions", Coordinated by Dr. Antonella Colombo.

[15] Karadogan, F., "An algorithm to justify the design of single storey precast structures", Theme Lecture, Second European Conference on Earthquake Engineering, 2ECEES 2014, Istanbul.

[16] Karadogan F., Pala S., Yuksel E., Durgun Y., "Yapı Mühendisliğine Giriş Yapısal Çözümleme Cilt III Hiperstatik Sistemler Yerdeğiştirme Yöntemleri", Istanbul, 2015, *in Turkish.*

[17] Çakıroğlu A., "Kayma Şekildeğiştirmeleri Gözönünde Tutulan II.Mertebe Teorisine Ait Çubuk Sabitleri, Teknik Rapor No: 32, 1978, Istanbul, *in Turkish.*

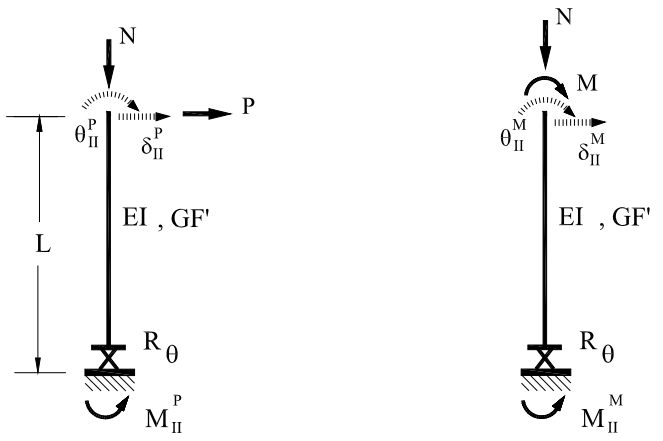
APPENDIX I

Second order effect of axial force on tip rotation and tip displacement and the stability of column with plastic deformations in critical zone

The plastic deformations of a column subjected to conservative axial force and lateral load reversals are accumulated generally slightly above the bottom critical sections. This is a realistic assumption to simplify the design and its justification. It is possible to obtain the exact tip rotation and tip deflection of a semi rigid supported column or a pier which is subjected to single moment M or single lateral load P on top, according to the second order theory without omitting the shear deformations which may accompany with flexural deformations see Fig. A

a&b and Fig. B. It will be assumed that the flexural EI, and shear GF', rigidities of the column are both constant along the height of the element. Since the stiffness coefficients of such a member can be derived easily, the case with variable EI and/or GF' can be handled easily as well [15,16, 17].

The following paragraphs not only outlines the derived necessary equations for tip rotations and tip displacements for several cases but also include the characteristic equation for the stability of the element.



a- Lateral single load on top **b - Single moment on top**

Fig. A

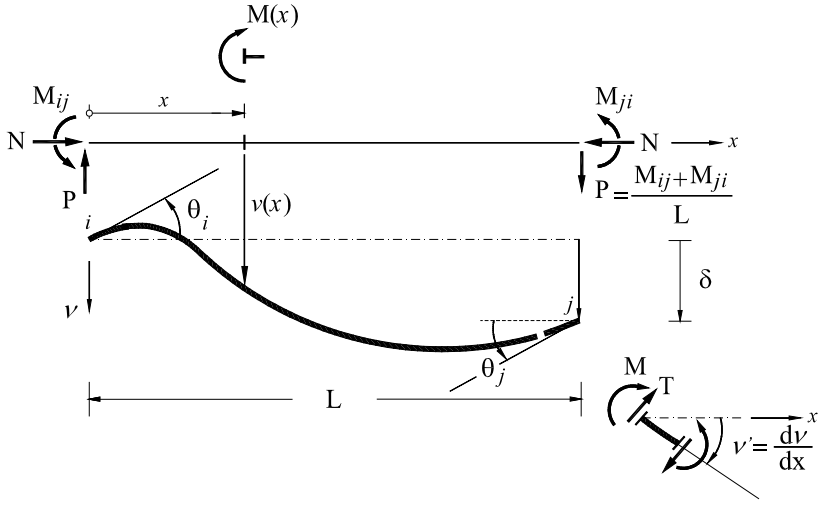


Fig. B

i- General abbreviations and differential equilibrium equation of the problem

$$EI^* = EI \times \left(1 - \frac{N}{GF'}\right) \quad , \quad \left(1 - \frac{N}{GF'}\right) = 1 - \beta \times (\alpha L)^2 \quad , \quad \beta = \frac{EI}{L^2 GF'} \quad , \quad \gamma = \frac{EI}{L\,R_\theta}$$

$$\alpha L = L \times \sqrt{\frac{N}{EI}} \quad , \quad \bar{\alpha} L = L \times \sqrt{\frac{N}{EI^*}} = \alpha L \times \sqrt{\frac{1}{1 - (\alpha L)^2 \times \beta}}$$

$$\bar{R}_\theta = R_\theta \times (1 - \frac{N}{GF'})$$

Subscripts I and II are referring to first and second order theories respectively

$$M(x) = -\left(M_{ij}\right) + \left(\frac{M_{ij} + M_{ji}}{L}\right)x + |N| \times \nu(x) \quad , \quad P = \left(\frac{M_{ij} + M_{ji}}{L}\right)$$

$$\frac{d^2\nu(x)}{dx^2} + \frac{M(x)}{EI^*} = 0 \;\Rightarrow\; \nu''(x) + \bar{\alpha}^2 \times \nu(x) = \left(\frac{M_{ij}}{EI^*}\right) - \left(\frac{P}{EI^*}\right)x$$

$$\nu(x) = C_1 \sin\bar{\alpha}x + C_2 \cos\bar{\alpha}x + \left(\frac{M_{ij}}{|N|}\right) - \left(\frac{P}{|N|}\right)x$$

ii- Single concentrated lateral load P on top together with a conservative single axial load N, Fig Aa

General solution of differential equation and the boundary conditions

$$\nu(x) = C_1 \sin\bar{\alpha}x + C_2 \cos\bar{\alpha}x + \left(\frac{M_{ij}}{\bar{\alpha}^2 \times EI^*}\right) - \left(\frac{P}{\bar{\alpha}^2 \times EI^*}\right)x \tag{1}$$

$$\nu(0) = 0 \quad , \quad \left(\frac{d\nu}{dx}\right)_{x=0} = \frac{M_{ij}}{\bar{R}_\theta} + \frac{P}{GF' \times (1 - \frac{N}{GF'})} \tag{2a}$$

and the constants C_1 and C_2 becomes

$$C_1 = \left(\frac{P}{\bar{\alpha}^2 \times EI^*}\right) + \left(\frac{M_{ij}}{\bar{\alpha} \times \bar{R}_\theta}\right) + \left(\frac{P}{\bar{\alpha} \times GF' \times (1 - \frac{N}{GF'})}\right), \quad C_2 = -\left(\frac{M_{ij}}{\bar{\alpha}^2 \times EI^*}\right) \tag{2b}$$

Hence the general expresssion for *displacements* will be obtained as follows

$$\nu(x) = \left(\frac{P}{\bar{\alpha}^2 \times EI^*} + \frac{M_{ij}}{\bar{\alpha} \times \bar{R}_\theta} + \frac{P}{\bar{\alpha} \times GF' \times (1 - \frac{N}{GF'})}\right)\sin\bar{\alpha}x - \left(\frac{M_{ij}}{\bar{\alpha}^2 \times EI^*}\right)\cos\bar{\alpha}x + \left(\frac{M_{ij}}{\bar{\alpha}^2 \times EI^*}\right) - \left(\frac{P}{\bar{\alpha}^2 \times EI^*}\right)x \tag{3}$$

The bending moment at the critical bottom section can be determined simply by moment equilibrium equation written down considering the deformed shape of the column

$$M_{II}^{(P)} = P \times L + N \times \nu(L) = M_I^{(P)} + N \times \nu(L) \tag{4a}$$

where $M_I^{(P)} = P \times L$

If it is required Equation (4a) can be rearranged in terms of the following definition

$$\varphi^{(P)} = \left(\frac{1 + \beta \times (\bar{\alpha}L)^2}{\cos\bar{\alpha}L - \gamma \times (\bar{\alpha}L) \times \sin\bar{\alpha}L} \times \frac{\sin\bar{\alpha}L}{(\bar{\alpha}L)}\right)$$

$$M_{II}^{(P)} = M_I^{(P)} \times \varphi^{(P)} \tag{4b}$$

The tip displacement $\delta_{II}^{(P)}$ can be extracted from the following equilibrium equation

$$M_{II}^{(P)} = M_I^{(P)} + N \times \delta_{II}^{(P)}$$

as

$$\delta_{II}^{(P)} = \frac{\left(M_{II}^{(P)} - M_I^{(P)}\right)}{N} \tag{5}$$

If Eq. (4b) is used in Eq.5 then $\delta_{II}^{(P)}$ will be

$$\delta_{II}^{(P)} = M_I^{(P)} \times \frac{L^2}{EI^*} \times \frac{1}{(\bar{\alpha}L)^2}(\varphi^{(P)} - 1) \tag{5a}$$

obtained.

The first derivative of the Eq.(3) at $x=L$ will be the required tip rotation according to the second order theory :

$$\theta_{II}^{(P)} = P\left(\frac{\cos\bar{\alpha}L}{GF'} + \frac{\cos\bar{\alpha}L - 1}{\bar{\alpha}^2 \times EI^*}\right) + M_{II}^{(P)}\left(\frac{\cos\bar{\alpha}L}{\bar{R}_\theta} + \frac{\sin\bar{\alpha}L}{\bar{\alpha} \times EI^*}\right) \tag{6}$$

iii- Single concentrated moment M on top together with a concervative single axial load N, Fig A.b

The general solution of the equilibrium equation written according to the second order theory is as follows

$$v(x) = C_1 \sin\bar{\alpha}x + C_2 \cos\bar{\alpha}x + \left(\frac{M_{ij}}{\bar{\alpha}^2 \times EI^*}\right) \tag{7}$$

and with the boundary conditions given below

$$v(0) = 0 \quad , \quad \left(\frac{dv}{dx}\right)_{x=0} = \frac{M_{ij}}{\bar{R}_\theta} \tag{7a}$$

one can determine the constants C_1 and C_2

$$C_1 = \left(\frac{M_{ij}}{\bar{\alpha} \times \bar{R}_\theta}\right) \quad , \quad C_2 = -\left(\frac{M_{ij}}{\bar{\alpha}^2 \times EI^*}\right) \tag{7b}$$

and hence the following general solution is achieved;

$$v(x) = \left(\frac{M_{ij}}{\bar{\alpha} \times \bar{R}_\theta}\right)\sin\bar{\alpha}x - \left(\frac{M_{ij}}{\bar{\alpha}^2 \times EI^*}\right)\cos\bar{\alpha}x + \left(\frac{M_{ij}}{\bar{\alpha}^2 \times EI^*}\right) \tag{8}$$

The bending moment at the critical section according to the second order theory can be simply derived by the moment equilibrium equation of the column as follows

$$M_{II}^{(M)} = M + N \times v(L) = M_I^{(M)} + N \times v(L) \tag{9a}$$

If the following two definitions are used

$$M_I^{(M)} = M$$

$$\varphi^{(M)} = \left(\frac{1}{\cos\bar{\alpha}L - \gamma \times (\bar{\alpha}L) \times \sin\bar{\alpha}L}\right)$$

then

$$M_{II}^{(M)} = M_{I}^{(M)} \times \varphi^{(M)} \tag{9b}$$

can be written.

For the tip displacement and for the tip rotations $\delta_{II}^{(M)}$ ve $\theta_{II}^{(M)}$ due to the tip monet M one can derive the following two expressions

$$\delta_{II}^{(M)} = M_{I}^{(M)} \times \frac{L^2}{EI^*} \times \frac{(\varphi^{(M)} - 1)}{(\bar{\alpha}L)^2} = M_{I}^{(M)} \times \frac{L^2}{EI \times \left(1 - \frac{N}{GF'}\right)} \times \frac{1}{(\bar{\alpha}L)^2} \left(\frac{1 - \left(\cos \bar{\alpha}L - \gamma \times (\bar{\alpha}L) \times \sin \bar{\alpha}L\right)}{\left(\cos \bar{\alpha}L - \gamma \times (\bar{\alpha}L) \times \sin \bar{\alpha}L\right)} \right) \tag{10}$$

$$\theta_{II}^{(M)} = M_{I}^{(M)} \times \frac{L}{EI \times \left(1 - \frac{N}{GF'}\right)} \times \left(\frac{\gamma \times \cos \bar{\alpha}L + \frac{\sin \bar{\alpha}L}{\bar{\alpha}L}}{\left(\cos \bar{\alpha}L - \gamma \times (\bar{\alpha}L) \times \sin \bar{\alpha}L\right)} \right) \tag{11}$$

It is interesting to note that if the moment which makes the tip rotation $\theta_{II}^{(M)} = 1$ is searched this can be achieved through the Eq.10 as follows

$$\bar{m}_{j_{\theta j}} = \bar{k}_{22} = \frac{EI}{L} \times \left(1 - \frac{N}{GF'}\right) \times \left(\frac{\left(\cos \bar{\alpha}L - \gamma \times (\bar{\alpha}L) \times \sin \bar{\alpha}L\right)}{\gamma \times \cos \bar{\alpha}L + \frac{\sin \bar{\alpha}L}{\bar{\alpha}L}} \right) \tag{12}$$

This is a special *rotational stiffness coefficient* by definition and it is going to be used as the characteristic equation for stability. In other words $\bar{\alpha}L$ which makes zero the Eq. 12 will define the stability load of the column with concentrated plastic deformation at the critical section. It should be kept in mind that the buckling length of the cantilever shown in Fig. C.b may even bigger than two times the height of the column.

When the effect of shear deformation is neglected in Equation 4b, one can reach Equation 13. It is important to review the *chord rotations* and *tip rotations* simply comparing the exact values of them obtained through the above summarized formulations. If once again the column given in Fig. C.a is considered and if

$$\varphi^{(P)} = \left(\frac{1}{\cos \alpha L - \gamma \times (\alpha L) \times \sin \alpha L} \times \frac{\sin \alpha L}{(\alpha L)} \right)$$

is defined then tip displacement and associated *chord rotations* are given as follows

$$\delta_{II}^{(P)} = \frac{PL^3}{EI} \times \frac{1}{(\alpha L)^2} (\varphi^{(P)} - 1) \quad \Rightarrow \quad \theta_{II,chord}^{(P)} = \left(\frac{\delta_{II}^{(P)}}{L} \right) = \left(\frac{PL^2}{EI} \right) \times \frac{1}{(\alpha L)^2} (\varphi^{(P)} - 1) \tag{13}$$

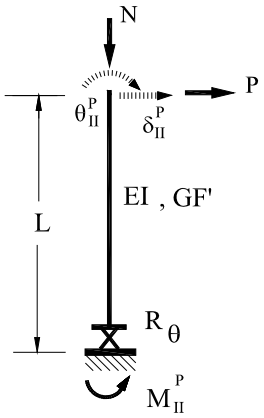
On the other hand tip rotation is given as

$$\theta_{II}^{(P)} = \left(\frac{PL^2}{EI} \right) \times \left[\left(\frac{\cos \alpha L - 1}{(\alpha L)^2} \right) + \varphi^{(P)} \times \left(\gamma \cos \alpha L + \frac{\sin \alpha L}{(\alpha L)} \right) \right] \tag{14}$$

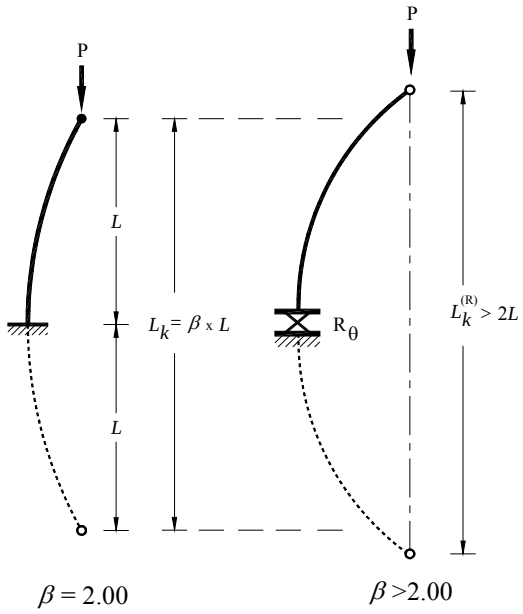
Shortly the ratio of these two expressions yield the following formula

$$\frac{\theta_{II}^{(P)}}{\theta_{II,chord}^{(P)}} = \left(\frac{\cos \alpha L - 1}{\varphi^{(P)} - 1} \right) + \varphi^{(P)} (\alpha L) \left(\frac{\gamma (\alpha L) \cos \alpha L + \sin \alpha L}{\varphi^{(P)} - 1} \right) \tag{15}$$

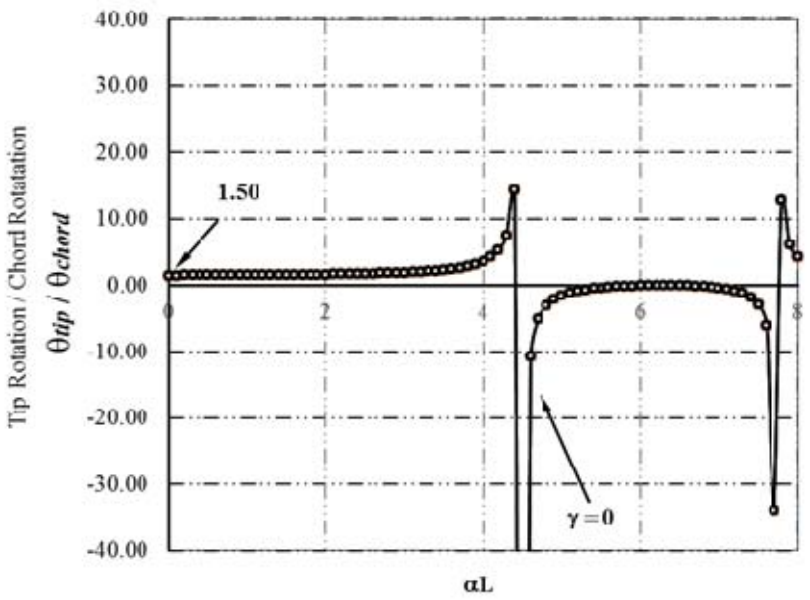
The graphical representation of this ratio is presented in Fig. C.c



a. Column subjected to P and N : second order analysis



b. Graphical representation



c. Ratio of Tip Rotation to Chord Rotation for fully restrained Cantilever Column (γ=0)

Fig C

COMPDYN 2015
5th ECCOMAS Thematic Conference on
Computational Methods in Structural Dynamics and Earthquake Engineering
M. Papadrakakis, V. Papadopoulos, V. Plevris (eds.)
Crete Island, Greece, 25–27 May 2015

DESIGN OF "DOG-BONE" CONNECTION: THE ROLE OF VERTICAL LOADS

Rosario Montuori[1]

[1] University of Salerno

Via Giovanni Paolo II - ITALY
e-mail: r.montuori@unisa.it

Keywords: Reduced Beam Section, "Dog-Bone" connections, Beam to column connection.

Abstract. *A lot of efforts have been made in the last years in order to set up a valid methodology for the design Reduced Beam Section (RBS) connection. The research activity has been devoted both to analytical and to the experimental aspect. In particular, different experimental tests showed that RBS connections designed according to the most modern seismic codes are able to safeguard the connection due to the yielding of the adjacent RBS. But in all the past researches and experimental tests the role that vertical loads can play was neglected or not properly accounted for. This study proposes a new procedure for accurately computing the relation between RBS location, vertical load and amount of section reduction for ensuring that the yielding of beam-column connections is always avoided. This goal can be realized by requiring that plasticization occur in the reduced sections or in a reduced section and in an intermediate section of the beam.*

1 INTRODUCTION

In the seismic design of moment resisting frames it is universally suggested the use of full-strength connections able to develop sufficient overstrength with respect to the connected beam to allow the complete development of the plastic rotation capacity of the beam. This design goal can be achieved provided that the connection overstrength is properly selected accounting for the strain-hardening occurring before flange local buckling and considering also the influence of random material variability [1].

Such high overstrength significantly affects the connection structural detail requiring strengthening elements such as reinforcing ribs, cover plates, haunches, etc; which significantly affects the cost of connections. For this reason experimental investigations on the cyclic response of partial-strength connections have gained new attention [2-11]. RBS connections can be considered a particular typology within the framework of partial-strength connections, because their flexural resistance is less than the one of the connected beam. RBS connections are also known with the name of “dog-bones” due to the reduction of the beam flange width by means of a "dog-bone" shape at a proper distance from the column flange.

The first idea of RBS was due to A. Plumier in 1980s [12] during a research project financed by the Luxembourg steel producer ARBED and the European Union with the aim of increasing the ductility of the structure by promoting the development of plastic hinges in the beams rather than in the columns. At that time the idea was patented by ARBED.

In 1994 Northridge earthquake and in 1995 Kobe earthquake a lot of unexpected damages to steel moment-resisting frames were observed. These damages were mainly due to the failure of welded beam-to-column connections. For these reasons ARBED waived any licensing fees and claims and RBS connections started to be investigated by a lot of researchers [13-29]

Since that time one of the main objective of the research concerning the “dog-bone” connections has been the development of design rules able to promote the beam yielding for safeguarding the beam-to-column connections. [13-33]

In the following research activity, “dog-bone” connections have been used also for promoting the development of a collapse mechanism of global type. In fact, according to the traditional seismic design philosophy, structures have to remain in elastic range during seismic events having a return period comparable with the service life of the structure. On the contrary, in the case of destructive earthquakes, i.e. events with a return period of 475 years and as a consequence having low probability of occurrence, it is accepted the damage of both structural and nonstructural elements due to the development of dissipative mechanisms. Therefore, the plastic reserves of the structure have to be exploited, only in the case of rare major earthquakes, to dissipate the earthquake input energy in some zones (dissipative zones) of the structure which have to be properly selected. The column yielding has to be absolutely avoided, because, due to the action of axial forces and the premature occurrence of local buckling, they have a low available ductility. In addition, the failure modes which can result from column hinging could involve a limited number of dissipative zones. For these reasons, aiming at the complete development of the plastic reserves of the structure, modern seismic codes provide simple design criteria whose goal is the prevention of local failure modes and, instead, the promotion of a global mechanism, i.e. a collapse mechanism characterised by the hinging of all the beam ends and the hinging of the base sections of the first storey columns. So, it can be concluded that structures in high seismicity zones are normally designed to resist severe earthquakes by dissipating the input energy by means of inelastic deformations and, in order to maximize this effect, plastic hinges need to be developed at beam ends rather than in the columns in case of moment resisting frames (MRFs) [34-43]. However also in the case of

other structural typologies the need to avoid the yielding of columns is always the desired goal and the development of a global mechanism is the main design objective [44-63].

In this paper the role played by the vertical load, the amount of the resistance reduction of the weakened section and the distance of RBS from the beam-to-column connection is clearly investigated. In particular, with the aim of obtaining the yielding of both “dog-bones”, i.e. the safeguards of beam-to-column connections, the relations occurring among the three quantities above recalled are investigated, pointing out that during the experimental tests on the classical cantilever scheme (where just one “dog-bone” and just one beam-to-column connection are present, Fig.(1)) the obtained results can be affected by an error which could be avoided only by replacing the cantilever scheme with a structural scheme where the whole beam with both dog-bones, both beam-to-column connections and vertical loads are present. In the case of moment resisting frames, the design criterion suggested by seismic codes is the adoption of columns having a flexural resistance greater than that of the connected beams.

Even if the fulfilment of this design criterion, the so-called member hierarchy criterion, is generally able to prevent the development of storey mechanisms, but not sufficient to guarantee the formation of a collapse mechanism of global type, the respect of this hierarchy criterion often causes column oversize leading to design an uneconomical structure.

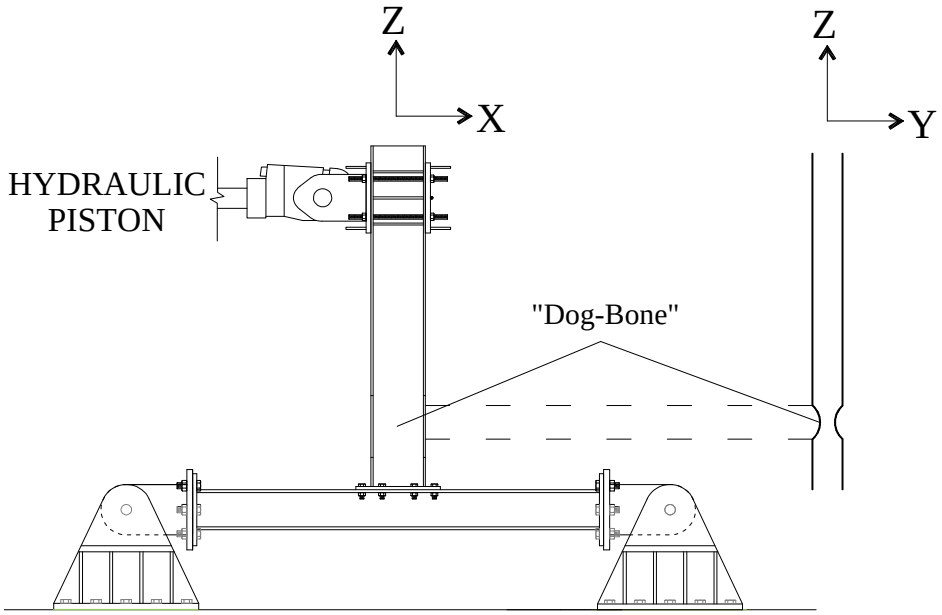


Figure 1:. Typical cantilever scheme for “dog-bone” experimental tests

The use of RBS connections can help to realize a more economical structure. In fact, the maximum moment transmitted by the beam to the column is reduced due to the yielding of “dog-bone”, and, as a consequence, the maximum moment transmitted to the column is lower than the beam plastic moment. Finally, we can summarize the advantages which could come from the use of ”dog-bone” connections:

a) the collapse of beam-to-column connections can be prevented assuring the yielding of the beam in a pre-defined location which acts as a fuse;

b) the weakened beam section is characterized by the decrease, with respect to the original section, of the width-to-thickness ratio of the flanges, i.e. a reduced local slenderness, which leads to the improvement of the plastic rotation capacity;

c) for given beam sections, the use of "dog-bones" allows the development of a dissipative mechanism by means of columns having a section smaller than that required in the case of unweakened beams.

The above advantages are accompanied by design difficulties regarding both the definition of the "dog-bone" location, with respect to the beam-to-column connection, to prevent connection yielding and the definition of the magnitude of the weakening to be conferred to the beam section. The developed research is aimed to overcome such design difficulties. The goal of the work herein presented is the setting up of design rules regarding the magnitude of the weakening to be realised and the location of the weakened beam sections. In particular, the location of the weakened section has to be selected in order to assure the development of the plastic hinges in "dog-bones" and/or in intermediate beam sections, while the yielding of the beam-to-column connections has to be prevented.

2 LOCATION OF FIRST PLASTIC HINGE

One of the most important problem to be solved in seismic design of MRFs is the location of plastic hinges in the beams. Regarding this issue, considering that seismic action can be represented by means of an appropriate distribution of increasing horizontal forces, it is preliminarily necessary to observe which is the shape of the bending moment diagram of a generic beam subjected to both horizontal forces and vertical loads (Figure 2)).

We can apply the superposition principle by considering separately the effect of vertical loads and the effect of horizontal forces (Figure 2)). Therefore, the resulting bending moment diagram is given (Figure 3), where the sections corresponding to the beam ends (sections 1 and 5), those corresponding to the "dog-bone" locations (section 2 and 4) and that corresponding to the maximum bending moment (section 3) have been pointed out.

It is evident that the design parameters are the location of the "dog-bones" (which is denoted with the distance a in (Figure 3), and the magnitude of the weakening characterising the "dog-bones". This second parameter can be expressed in non-dimensional form as:

$$m_{db} = \frac{M_{p.db}}{M_p} \tag{1}$$

where $M_{p.db}$ is the plastic moment of the weakened beam section and M_p is the plastic moment of the complete beam section. In this phase of the design procedure the m_{db} value can assumed as fixed, while the location a of the "dog-bones" is to be properly selected. It is important to note that at the left side of the beam (beam sections 1 and 2) the bending moments due to vertical loads and horizontal forces have an opposite sign (one is anticlock-wise and another is clock-wise), while at the right side (beam sections 3 and 4) they have the same sign (clock-wise). Due to this consideration it is obvious that for increasing values of horizontal forces the first plastic hinge develops in beam section 4 or 5 rather than in beam section 1 or 2.

So the first problem to be solved is to find the conditions assuring that sections 1, 2, 3 and 5 remain in elastic range, while section 4 yields when seismic horizontal forces increase.
To this aim it is useful to consider the expression of bending moment at the generic section x:

$$M(x) = M_A + T_A x - q\frac{x^2}{2} = M_A + \left(q\frac{L}{2} - \frac{M_A + M_B}{L}\right)x - q\frac{x^2}{2} \tag{2}$$

and the value of x_{max} representing the abscissa where the bending moment has its maximum value:

$$x_{\max} = \frac{L}{2} - \frac{M_A + M_B}{qL} \tag{3}$$

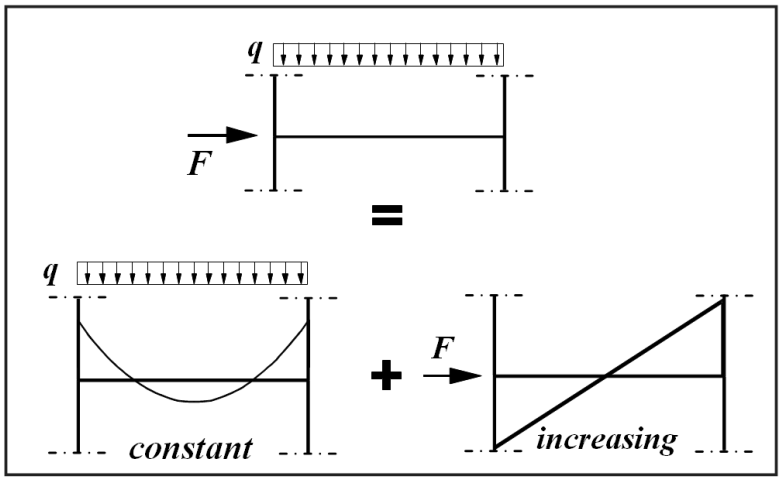


Figure 2. Bending moment due to vertical loads and seismic forces

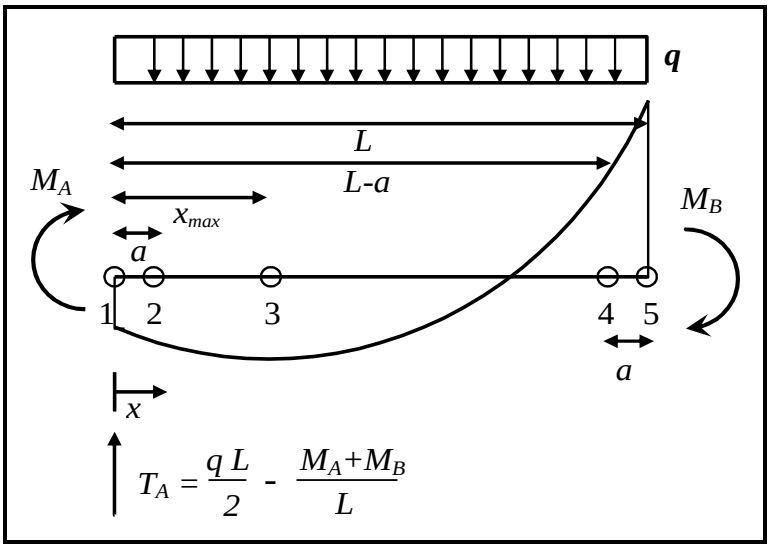


Figure3. Total beam bending moment diagram.

Using Eq. (2) and (3) the bending moment in sections 1,2,3,4 and 5 can be expressed as:

Section 1 $$M(0) = M_A \tag{4}$$

Section 2 $$M(a) = q\frac{a(L-a)}{2} - M_B\frac{a}{L} + \left(1-\frac{a}{L}\right)M_A \tag{5}$$

Section 3 $$M(x_{\max}) = \frac{qL^2}{8} + \frac{M_A - M_B}{2} + \frac{(M_A + M_B)^2}{2qL^2} \tag{6}$$

Section 4 $$M(L-a) = q\frac{a(L-a)}{2} + M_A\frac{a}{L} - \left(1-\frac{a}{L}\right)M_B \tag{7}$$

Section 5 $$M(L) = -M_B \tag{8}$$

The conditions to be fulfilled in order to assure that sections 1, 2, 3 and 5 remain in elastic range, while section 4 yields when seismic horizontal forces increase are given by the following relationships:

Section 1 $$M_A < M_p \tag{9}$$

Section 2 $$M(a) < m_{db} M_p \tag{10}$$

Section 3 $$M(x_{\max}) < M_p \tag{11}$$

Section 4 $$M(L-a) = -m_{db} M_p \tag{12}$$

Section 5 $$M(L) > -M_p \Rightarrow -M_B > -M_p \Rightarrow M_B < M_p \tag{13}$$

It is easy to recognize that by combining the yielding condition of "dog-bone" of the right side (Eq. (12), section 4) with the value of bending moment at the abscissa $x=L-a$ given by Eq.(7), an expression of M_B as a function of M_A can be obtained:

$$M_B = M_A \frac{a}{L-a} + q\frac{La}{2} + \frac{L}{L-a} m_{db}\, M_P \tag{14}$$

This expression represents the relation occurring between the end moments when the first plastic hinge develops at section 4 corresponding to the right "dog-bone".

By means of Eqs. (14) and (2), it is possible to express the design requirements (9), (10), (11) and (13) as follows:

$$M_A < M_{A1} \quad \text{with} \quad M_{A1} = M_p \tag{15}$$

$$M_A < M_{A2} = \frac{m_{db} L}{L-2a} M_p - q\frac{a(L-a)}{2} \tag{16}$$

$$M_A < M_{A3} \quad \text{with} \quad M_{A3} = \sqrt{2\, q(L-a)^2 (1+m_{db}) M_p} - \left(\frac{q(L-a)^2}{2} + m_{db} M_p \right) \tag{17}$$

$$M_A < M_{A5} \quad \text{with} \quad M_{A5} = \frac{(1-m_{db})L - a}{a} M_p - q\frac{L(L-a)}{2} \tag{18}$$

Obviously, the first plastic hinge develops in the right "dog-bone" provided that Eq. (12) is satisfied. Under this condition, it is required that the second plastic hinge develops either in the left "dog-bone" or an intermediate beam section. On the contrary, the yielding of the beam ends close to the beam-to-column connections has to be prevented, because, as already stated, the use of "dog-bones" is also aimed at the protection of beam-to-column connections.

It is easy to recognise that increasing the seismic horizontal forces, i.e. increasing M_A, relationships (15), (16), (17) and (18) allow to identify the section where the second plastic hinge develops. To this scope, it is sufficient to control what is the minimum limit value among M_{A1}, M_{A2}, M_{A3}, M_{A5}. In other words, it is sufficient to identify the first relationship to be unsatisfied as far as M_A increases. Therefore, all the yielding conditions can be expressed by means of the limit values M_{Ai} (with i=1,2,3,5) of the bending moment M_A occurring at the first beam end. In particular, the condition:

$$M_{A3} < M_{A2} \qquad \textbf{condition A} \tag{19}$$

identifies the *a* values assuring that the yielding of the beam in the section where the maximum sagging moment occurs (section 3) precedes the yielding of the left "dog-bone" (section 2); the condition:

$$M_{A3} < M_{A5} \qquad \textbf{condition B} \tag{20}$$

identifies the *a* values assuring that the beam yielding (section 3) precedes the yielding of the connection B (section 5); the condition:

$$M_{A2} < M_{A5} \qquad \textbf{condition C} \tag{21}$$

identifies the *a* values assuring that the left "dog-bone" yielding (section 2) precedes the yielding of the connection B (section 5); the condition:

$$M_{A3} < M_{A5} \qquad \textbf{condition D} \tag{22}$$

identifies the *a* values assuring that the beam yielding (section 3) precedes the yielding of the left connection A (section 1); finally, the condition:

$$M_{A2} < M_{A1} \qquad \textbf{condition E} \tag{23}$$

identifies the *a* values assuring that the yielding of the left "dog-bone" (section 2) precedes the yielding of the left connection A (section 1).

It is evident that conditions (20), (21), (22), (23) have to be absolutely satisfied, because they assure the development of the second plastic hinge either in the left "dog-bone" or in the intermediate beam section where the maximum sagging moment occurs, while the yielding of the connections at the beam ends is prevented. In other words, relationships (20), (21), (22) and (23) are the design requirements.

Conversely, condition (19), depending on its fulfilment or not, can be used to discern if the second plastic hinge develops in the left "dog-bone" or in the intermediate beam section. Such conditions give rise to the following non-dimensional relationships:

- **condition A**:

$$4\left(\frac{a}{L}\right)^3 + \left(4\sqrt{2(1+m_{db})\frac{M_p}{qL^2}} - 8\right)\left(\frac{a}{L}\right)^2 + \left(5 + 4m_{db}\frac{M_p}{qL^2} - 6\sqrt{2(1+m_{db})\frac{M_p}{qL^2}}\right)\left(\frac{a}{L}\right) + \\ - 4m_{db}\frac{M_p}{qL^2} - 1 + 2\sqrt{2(1+m_{db})\frac{M_p}{qL^2}} < 0 \tag{24}$$

whose solutions are:

$$\frac{a}{L} < \frac{a_3}{L} \qquad \text{and} \qquad \frac{a_2}{L} < \frac{a}{L} < \frac{a_1}{L} \tag{25}$$

where:

$$\frac{a_1}{L} = 1 \qquad ; \qquad \frac{a_2}{L} = \frac{1}{2} - \sqrt{\frac{(1+m_{db})}{2}\frac{M_p}{qL^2}} + \sqrt{\frac{(1-m_{db})}{2}\frac{M_p}{qL^2}} \\ \frac{a_3}{L} = \frac{1}{2} - \sqrt{\frac{(1+m_{db})}{2}\frac{M_p}{qL^2}} - \sqrt{\frac{(1-m_{db})}{2}\frac{M_p}{qL^2}} \tag{26}$$

- **condition B:**

$$-\left(\frac{a}{L}\right)^3+\left(1-2\sqrt{2(1+m_{db})\frac{M_p}{qL^2}}\right)\left(\frac{a}{L}\right)^2+\left(2(1-m_{db})\frac{M_p}{qL^2}+2\sqrt{2(1+m_{db})\frac{M_p}{qL^2}}\right)\left(\frac{a}{L}\right)+ \\ -2(1-m_{db})\frac{M_p}{qL^2}<0 \tag{27}$$

whose solution are:

$$\frac{a_6}{L}<\frac{a}{L}<\frac{a_5}{L} \qquad \text{and} \qquad \frac{a}{L}>\frac{a_4}{L} \tag{28}$$

where:

$$\frac{a_4}{L}=1 \;;\; \frac{a_5}{L}=-\sqrt{2(1+m_{db})\frac{M_p}{qL^2}}+2\sqrt{\frac{M_p}{qL^2}} \;;\; \frac{a_6}{L}=-\sqrt{2(1+m_{db})\frac{M_p}{qL^2}}-2\sqrt{\frac{M_p}{qL^2}} \tag{29}$$

- **condition C:**

$$-2\left(\frac{a}{L}\right)^4+5\left(\frac{a}{L}\right)^3-4\left(1+\frac{M_p}{qL^2}\right)\left(\frac{a}{L}\right)^2+\left(1+2(3-m_{db})\frac{M_p}{qL^2}\right)\frac{a}{l}-2(1-m_{db})\frac{M_p}{qL^2}<0 \tag{30}$$

whose solutions are:

$$\frac{a}{L}<\frac{a_8}{L} \qquad \text{and} \qquad \frac{a}{L}>\frac{a_7}{L} \tag{31}$$

where:

$$\frac{a_7}{l}=1 \qquad ; \qquad \frac{a_8}{l}=\frac{1}{2}+\frac{1}{6}\sqrt[3]{T}-6\frac{\frac{2}{3}\frac{M_p}{ql^2}-\frac{1}{12}}{\sqrt[3]{T}} \tag{32}$$

with:

$$T=-108m_{db}\frac{M_p}{qL^2}+3\left[-3+72\frac{M_p}{qL^2}-576\left(\frac{M_p}{qL^2}\right)^2+ \right. \\ \left. +1296{m_{db}}^2\left(\frac{M_p}{qL^2}\right)^2+1536\left(\frac{M_p}{qL^2}\right)^3\right]^{1/2} \tag{33}$$

- **condition D:**

condition D can be written as follows (by expressing relationship (22) by means of M_{A1} and M_{A3} values given by Eqs. (15) and (17), respectively):

$$-\left[\frac{a}{L}+\left(1-\sqrt{2(1+m)\frac{M_p}{qL^2}}\right)\right]^2<0 \tag{34}$$

therefore, condition *D* is always satisfied.

- **condition E:**

By means of Eq.(15) and (16) this condition provides:

$$2\left(\frac{a}{L}\right)^3-3\left(\frac{a}{L}\right)^2-\left(4\frac{M_p}{qL^2}-1\right)\left(\frac{a}{L}\right)+2(1-m)\frac{M_P}{qL^2}>0 \tag{35}$$

In order to show that this condition is always verified when the condition C is verified, it is useful to write the condition C (Eq.(31)) in the following way:

$$\left(\frac{a}{L}-1\right)\left[-2\left(\frac{a}{L}\right)^3+3\left(\frac{a}{L}\right)^2-\left(1+4\frac{M_p}{qL^2}\right)\left(\frac{a}{L}\right)+2(1-m)\frac{M_p}{qL^2}\right]<0 \tag{36}$$

Being *a/L<1* this relation is equivalent to require:

$$\left[-2\left(\frac{a}{L}\right)^3+3\left(\frac{a}{L}\right)^2-\left(1+4\frac{M_p}{qL^2}\right)\left(\frac{a}{L}\right)+2(1-m)\frac{M_p}{qL^2}\right]>0 \tag{37}$$

Now it is easy to verify that the first member of Eq. (35) is greater than the first member of Eq.(37) when the following relation is satisfied:

$$-4\left(\frac{a}{L}\right)^3+6\left(\frac{a}{L}\right)^2-2\left(\frac{a}{L}\right)<0 \tag{38}$$

The solutions of Eq. (38) are:

$$\frac{a}{L}>1 \qquad \text{and} \qquad 0<\frac{a}{L}<\frac{1}{2} \tag{39}$$

Now it can be observed that, being *a/L < 1/2* (which means that a “dog-bone” cannot be located beyond the midspan), Eq. (38) is always true, and so condition *E* is always satisfied if condition *C* is satisfied. Therefore, in the range *0<a/L<1/2*, which is the significant one from the design point of view, only the three conditions *A*, *B* and *C* remain to be analysed. These three remaining condition provide the following significant solutions (32):

$$\textbf{condition A} \quad \frac{a}{L}<\frac{a_3}{L} \qquad \text{and} \qquad \frac{a}{L}>\frac{a_2}{L} \tag{40}$$

which is obtained from Eqs. (25) and (26);

$$\textbf{condition B} \quad \frac{a}{L}<\frac{a_5}{L} \tag{41}$$

which is obtained from Eqs. (28) and (29) by observing that a_6 provides negative values which are not significant;

$$\textbf{condition C} \quad \frac{a}{L}<\frac{a_8}{L} \tag{42}$$

which is obtained from Eqs. (31) and (32). Therefore, taking into account that condition *A* has to be used only to recognise the location of the second plastic hinge which can develop either at the left “dog-bone” or at an intermediate beam section, it means that conditions *B* and *C* show the existence of an upper bound concerning the parameter *a* expressing the "dog-bone" location (this upper bound value is given by the minimum value between a_5 and a_8).

Therefore, the design solution concerning the "dog-bone" location can be expressed as follows: the smallest value between a_5 and a_8 is the upper bound of a, while the location of the second plastic hinge depends on a_2 and a_3 value; in particular, according to Eq. (40), if $a < a_3$ or $a > a_2$ the second plastic hinge develops in the intermediate beam section, where the maximum sagging moment occurs, otherwise the second plastic hinge occurs at the left "dog-bone". In addition, when relation (40) is satisfied, the location x_{max} of the second plastic hinge where the maximum sagging moment occurs can be determined by solving the following equation:

$$T(x) = T_A - qx = \frac{qL}{2} - \frac{M_A + M_B}{L} - qx = 0 \tag{43}$$

which provides:

$$x_{\max} = \frac{L}{2} - \frac{M_A + M_B}{qL} = \frac{L-a}{2} - \frac{M_A}{q(L-a)} - \frac{m_{db} M_p}{q(L-a)} \tag{44}$$

The value of M_A to be used in relationship (43) is equal to M_{A3} consistently with condition A expressed by Eq. (19). By substituting the M_{A3} value in Eq. (44) x_{max} becomes:

$$x_{\max} = L - a - \left(\frac{2M_p (1 + m_{db})}{q} \right)^{1/2} \tag{45}$$

3 LOCATION OF THE SECOND PLASTIC HINGE:

As the expression for computing a_8/L is particularly complex, in order to identify the governing limit value of a/L, a numerical analysis has been carried out. For any given value of m_{db}, by varying the non-dimensional parameter M_p/qL^2 in the range between 1/16 and zero, which covers all the possible design situations, the values of a_2, a_3, a_5 and a_8 have been computed. The results of this numerical analysis is presented in Tables 1,2 and 3 for m_{db} equal to 0.4, 0.5, 0.6, 0.7, 0.8, and 0.9 respectively. In addition, the curves representing the values of a_2, a_3, a_5 and a_8 are plotted in figures 4,5,6,7,8 and 9. From the analysis of the above recalled figures it is evident the existence of two limit values of qL^2/M_p which are $q_{lim1}L^2/M_p$ and $q_{lim2}L^2/M_p$. The first one represents the value for which a_2, a_5 and a_8 are coincident while the second one represents the value for which a_3, a_5 and a_8 are coincident. These values have been highlighted in bold type in Tables 1-6. Such limit values can be easily determined by means of relationships (26) and (29) providing a_2, a_3, and a_5. In fact, q_{lim1} can be obtained by equating a_2 and a_5, while q_{lim2} can be obtained by equating a_3 and a_5. The following relationships are thus obtained:

$$q_{\lim 1} = \frac{4M_p}{L^2} \left(5 - \sqrt{8(1-m_{db})} - 2\sqrt{2(1+m_{db})} + \sqrt{1-m_{db}^2} \right) \tag{46}$$

$$q_{\lim 2} = \frac{4M_p}{L^2} \left(5 + \sqrt{8(1-m_{db})} - 2\sqrt{2(1+m_{db})} - \sqrt{1-m_{db}^2} \right) \tag{47}$$

As a conclusion, the design solution concerning the "dog-bone" location and its influence on the location of the second plastic hinge can be expressed as follows:

case $q<q_{lim1}$: the design requirement is $a < a_8$, while, regarding the development of the second plastic hinge, if $a < a_2$ the yielding of the second "dog-bone" occurs, otherwise the yielding of the beam develops;

case $q_{lim1} < q < q_{lim2}$: the design requirement is $a < a_5$, while, regarding the development of the second plastic hinge, if $a > a_3$ the yielding of the second "dog-bone" occurs, otherwise the yielding of the beam develops;

case $q > q_{lim2}$: the design requirement is $a < a_8$, while, regarding the development of the second plastic hinge, it always develops at the intermediate beam section where the maximum sagging moment occurs.

The result above reported clarifies the role played by the vertical load q concerning the "dog-bone" location. In particular, it can be noted that, for a given value of the "dog-bone" non-dimensional resistance m_{db}, the increase of the vertical load q causes a decrease of the maximum allowed value of a/L.

Similarly, for a given value of the vertical load q, the increase of m_{db} leads to the decrease of the admissible range for a/L. In addition, by means of the described figures, it is possible to understand what happens when the a/L upper limit for the location of the "dog-bones" is not respected. In fact, it is sufficient to observe which are the conditions providing the limit value of a_8/L and a_5/L.

When $q_{lim1} < q < q_{lim2}$, then the design limit of a/L is given by a_5/L, i.e. condition *B* (Eq. (41)) which identifies the a values assuring that the beam yielding (section 3) precedes the yielding of the right connection (section 5). It means that, if a/L is greater than a_5/L the second plastic hinge occurs in the beam-to-column connection located at section 5.

When $q < q_{lim1}$ or $q > q_{lim2}$ the governing condition is the one corresponding to a_8/L limit, i.e. condition *C* which identifies the a values assuring that the left "dog-bone" yielding (section 2) precedes the yielding of connection *B* (section 5). It means that, if a/L is greater than a_8/L, the second plastic hinge occurs in the beam-to-column connection located at the *B* end.

$m_{db} = 0.4$					$m_{db} = 0.5$				
qL^2/M_p	a_2/L	a_3/L	a_5/L	a_8/L	qL^2/M_p	a_2/L	a_3/L	a_5/L	a_8/L
0.01	-2.3894	-13.3438	3.2668	0.2998	0.01	-3.1603	-13.1603	2.6795	0.2498
0.50	0.0914	-1.4578	0.4620	0.2892	0.50	0.1340	-1.4319	0.2679	0.2260
1.00	0.2111	-0.8844	0.3267	0.2777	1.00	0.2412	-0.8660	0.1895	0.2020
1.52	***0.2653***	***-0.6244***	***0.2653***	***0.2653***	***1.61***	***0.2113***	***-0.5774***	***0.2113***	***0.2113***
2.00	0.2957	-0.4789	0.2310	0.2533	2.00	0.2887	-0.4659	0.1547	0.1792
3.00	0.3332	-0.2993	0.1886	0.2282	3.00	0.3170	-0.2887	0.1340	0.1588
4.00	0.3555	-0.1922	0.1633	0.2039	4.00	0.3363	-0.1830	0.1198	0.1412
5.00	0.3708	-0.1191	0.1461	0.1817	5.00	0.3506	-0.1109	0.1094	0.1263
6.00	0.3820	-0.0652	0.1334	0.1623	6.00	0.3617	-0.0577	0.1013	0.1137
7.00	0.3908	-0.0232	0.1235	0.1457	7.00	0.3706	-0.0163	0.0947	0.5000
8.00	0.3979	0.0106	0.1155	0.1316	8.00	0.3780	0.0171	0.0893	0.0942
9.00	0.4037	0.0386	0.1089	0.1197	9.00	0.3843	0.0447	0.0847	0.0866
10.00	0.4086	0.0622	0.1033	0.1095	10.00	0.3896	0.0680	0.0808	0.0800
11.00	0.4129	0.0826	0.0985	0.1009	***10.68***	***0.3880***	***0.0820***	***0.0820***	***0.0820***
11.71	***0.4156***	***0.0955***	***0.0955***	***0.0955***	11.00	0.3943	0.0881	0.0774	0.0743
12.00	0.4166	0.1004	0.0943	0.0934	12.00	0.3985	0.1057	0.0743	0.0693
13.00	0.4199	0.1161	0.0906	0.0869	13.00	0.4022	0.1211	0.0716	0.0650
14.00	0.4228	0.1300	0.0873	0.0812	14.00	0.4055	0.1349	0.0692	0.0611
15.00	0.4254	0.1426	0.0843	0.0762	15.00	0.4085	0.1473	0.0670	0.0577
16.00	0.4278	0.1539	0.0817	0.0718	16.00	0.3525	0.1585	0.1080	0.1242

Table 1. Values of a_2, a_3, a_5 and a_8 for $m_{db} = 0.4$ and $m_{db} = 0.5$.

m_{db} = 0.6					m_{db} = 0.7				
qL^2/M_p	a_2/L	a_3/L	a_5/L	a_8/L	qL^2/M_p	a_2/L	a_3/L	a_5/L	a_8/L
0.01	-3.9721	-12.9164	2.1115	0.1998	0.01	-4.8466	-12.5925	1.5609	0.1498
0.50	-0.1325	-1.3974	0.2986	0.1881	0.50	-0.2561	-1.3516	0.2207	0.1392
1.00	0.0528	-0.8416	0.2111	0.1765	1.00	-0.0347	-0.8093	0.1561	0.1291
1.73	***0.1604***	***-0.5189***	***0.1604***	***0.1604***	***1.91***	***0.1130***	***-0.4477***	***0.1130***	***0.1130***
2.00	0.1838	-0.4487	0.1493	0.1548	2.00	0.1219	-0.4258	0.1104	0.1115
3.00	0.2418	-0.2746	0.1219	0.1359	3.00	0.1913	-0.2559	0.0901	0.0970
4.00	0.2764	-0.1708	0.1056	0.1198	4.00	0.2327	-0.1546	0.0780	0.0853
5.00	0.3000	-0.1000	0.0944	0.1064	5.00	0.2609	-0.0855	0.0698	0.0757
6.00	0.3174	-0.0477	0.0862	0.0953	6.00	0.2817	-0.0345	0.0637	0.0679
7.00	0.3310	-0.0071	0.0798	0.0861	7.00	0.2979	0.0051	0.0590	0.0615
8.00	0.3419	0.0257	0.0746	0.0783	8.00	0.3110	0.0371	0.0552	0.0560
9.00	0.3509	0.0528	0.0704	0.0717	***8.59***	***0.3176***	***0.0533***	***0.0533***	***0.0533***
9.65	***0.3560***	***0.0680***	***0.0680***	***0.0680***	9.00	0.3218	0.0636	0.0520	0.0515
10.00	0.3586	0.0758	0.0668	0.0661	10.00	0.3309	0.0860	0.0494	0.0475
11.00	0.3652	0.0955	0.0637	0.0612	11.00	0.3388	0.1053	0.0471	0.0442
12.00	0.3709	0.1127	0.0609	0.0570	12.00	0.3457	0.1221	0.0451	0.0412
13.00	0.3760	0.1279	0.0586	0.0534	13.00	0.3517	0.1369	0.0433	0.0386
14.0	0.3805	0.1414	0.0564	0.0501	14.00	0.3571	0.1501	0.0417	0.0363
15.0	0.3845	0.1536	0.0545	0.0472	15.00	0.3620	0.1620	0.0403	0.0343
16.0	0.3882	0.1646	0.0528	0.0446	16.00	0.3663	0.1727	0.0390	0.0325

Table 2. Values of a_2, a_3, a_5 and a_8 for m_{db} = 0.6 and m_{db} = 0.7

m_{db} = 0.8					m_{db} = 0.9				
qL^2/M_p	a_2/L	a_3/L	a_5/L	a_8/L	qL^2/M_p	a_2/L	a_3/L	a_5/L	a_8/L
0.01	-5.8246	-12.1491	1.0263	0.0998	0.01	-7.0107	-11.4829	0.5064	0.0499
0.50	-0.3944	-1.2889	0.1451	0.0915	0.50	-0.5622	-1.1946	0.0716	0.0451
1.00	-0.1325	-0.7649	0.1026	0.0840	1.00	-0.2511	-0.6983	0.0506	0.0410
2.00	0.0528	-0.3944	0.0726	0.0715	2.00	-0.0311	-0.3473	0.0358	0.0345
2.16	***0.0698***	***-0.3604***	***0.0698***	***0.0698***	***2.58***	***0.0316***	***-0.2473***	***0.0316***	***0.0316***
3.00	0.1349	-0.2303	0.0593	0.0619	3.00	0.0664	-0.1918	0.0292	0.0297
4.00	0.1838	-0.1325	0.0513	0.0543	4.00	0.1245	-0.0991	0.0253	0.0260
5.00	0.2172	-0.0657	0.0459	0.0482	5.00	0.1641	-0.0359	0.0226	0.0231
6.00	0.2418	-0.0164	0.0419	0.0433	6.00	0.1934	0.0108	0.0207	0.0208
7.00	0.2610	0.0219	0.0388	0.0392	***6.24***	***0.1993***	***0.0203***	***0.0203***	***0.0203***
7.48	***0.2688***	***0.0375***	***0.0375***	***0.0375***	7.00	0.2161	0.0471	0.0191	0.0189
8.00	0.2764	0.0528	0.0363	0.0358	8.00	0.2345	0.0764	0.0179	0.0173
9.00	0.2892	0.0784	0.0342	0.0330	9.00	0.2497	0.1006	0.0169	0.0159
10.00	0.3000	0.1000	0.0325	0.0305	10.00	0.2625	0.1211	0.0160	0.0147
11.00	0.3093	0.1186	0.0309	0.0284	11.00	0.2736	0.1387	0.0153	0.0137
12.00	0.3174	0.1349	0.0296	0.0266	12.00	0.2832	0.1541	0.0146	0.0129
13.00	0.3246	0.1492	0.0285	0.0249	13.00	0.2917	0.1677	0.0140	0.0121
14.00	0.3310	0.1620	0.0274	0.0235	14.00	0.2993	0.1798	0.0135	0.0114
15.00	0.3367	0.1734	0.0265	0.0222	15.00	0.3061	0.1906	0.0131	0.0108
16.00	0.3419	0.1838	0.0257	0.0210	16.00	0.3122	0.2004	0.0127	0.0102

Table 3. Values of a_2, a_3, a_5 and a_8 for m_{db} = 0.8 and m_{db} = 0.9.

The above observations show that experimental tests on the classical cantilever scheme, as depicted in Figure 1 cannot be completely exhaustive, because the information coming from these tests are not able to assure that the second plastic hinge develops in the beam section, where the maximum bending moment occurs, or in the second dog-bone rather than in the beam-to-column connection located at the *B* end close to the tested "dog-bone". It is interesting to note that the q_{lim} value already found in [34] for full-strength beam-to-column joints can be obtained as a particular case from Eqs. (46) and (47). In fact, for $m_{db} = 1$, i.e. in absence of "dog-bones", the above equations provide:

$$q_{\lim 1} = q_{\lim 2} = q_{\lim} = \frac{4M_p}{L^2} \tag{48}$$

Comparing figures 3-9 it is evident that the range where "dog bones" can be located, assuring the protection of the beam-to-column connections, decreases as m_{db} increases. In particular, for high values of m_{db} the width of such range is so limited that it could be incompatible with the length of the weakened beam zone required for an appropriate spreading of plasticity.

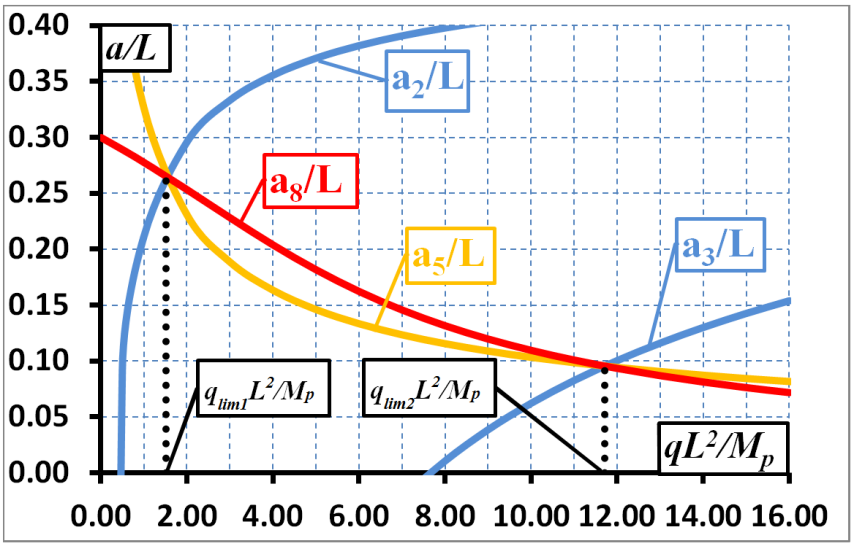


Figure 4: Limit values a_2/L, a_3/L, a_5/L and a_8/L *for* $m_{db} = 0.4$

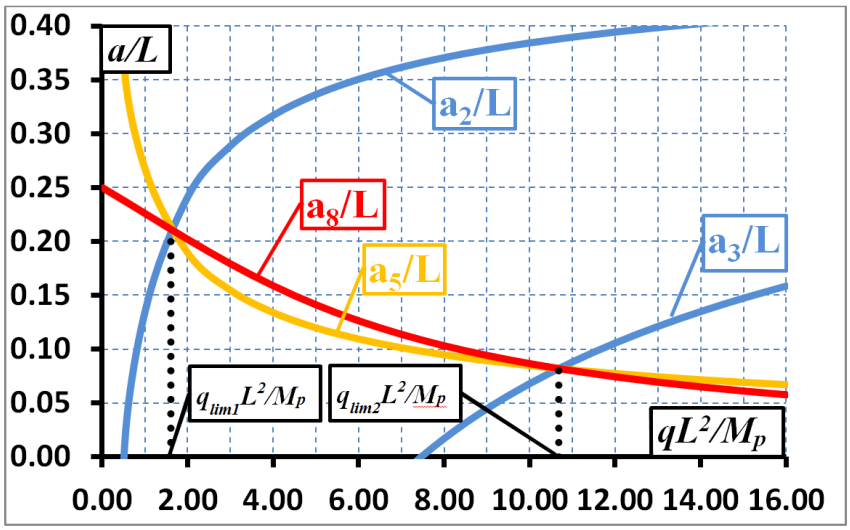


Figure 5: Limit values a_2/L, a_3/L, a_5/L and a_8/L *for* $m_{db} = 0.5$

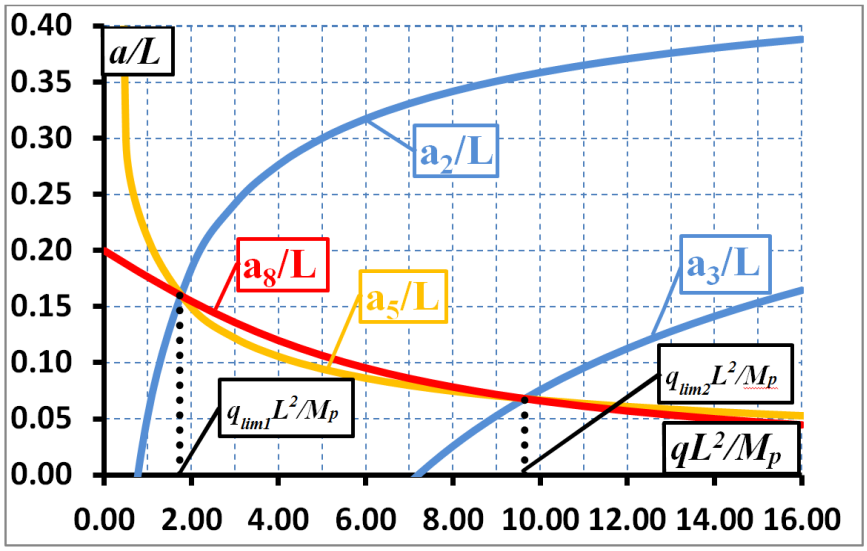


Figure 6: Limit values a_2/L, a_3/L, a_5/L and a_8/L *for* m_{db} = 0.6

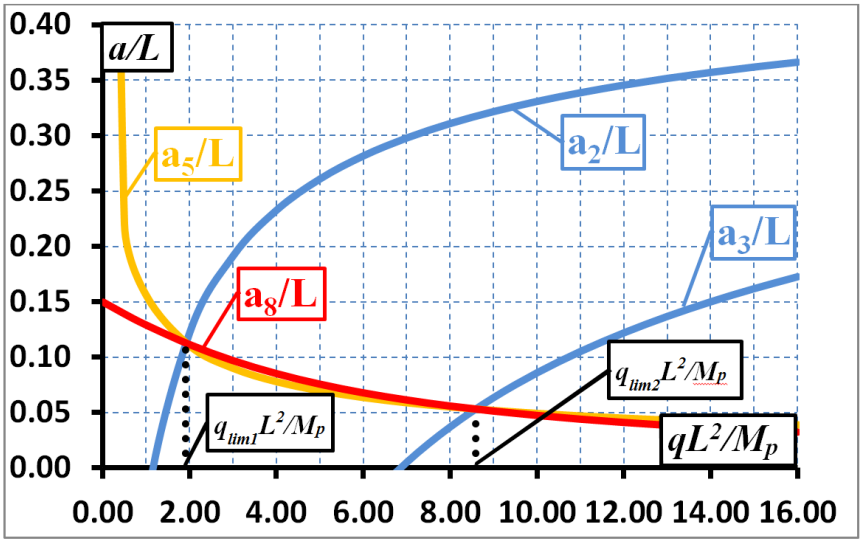


Figure 7: Limit values a_2/L, a_3/L, a_5/L and a_8/L *for* m_{db} = 0.7

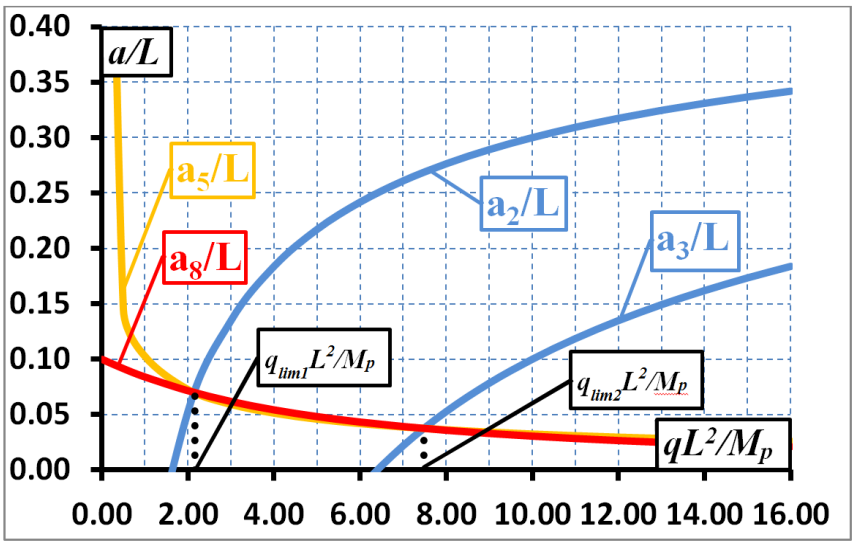


Figure 8: Limit values a_2/L, a_3/L, a_5/L and a_8/L *for* m_{db} = 0.8

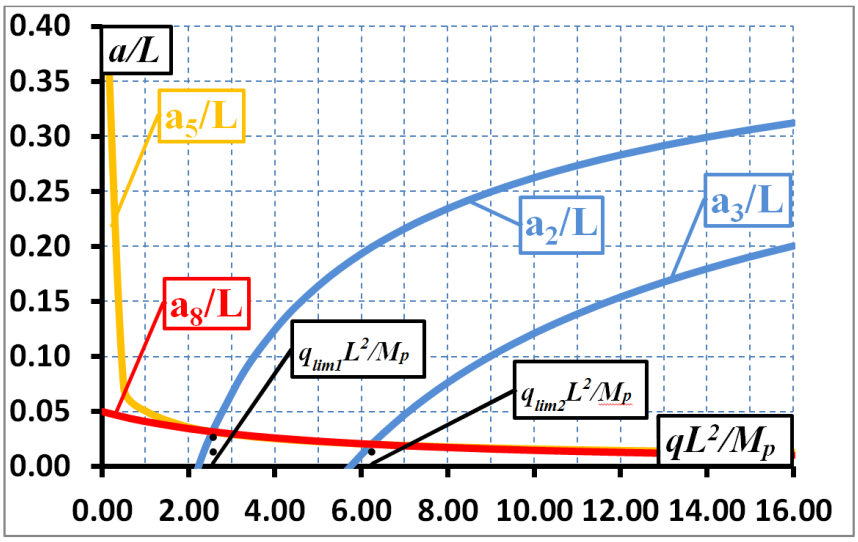


Figure 9: Limit values a_2/L, a_3/L, a_5/L and a_8/L *for* m_{db} = 0.9.

4 DESIGN ABACUS FOR "DOG-BONE" LOCATION

The solution obtained in the previous section, needs the evaluation of q_{lim1}, q_{lim2}, a_5/L, a_8/L and at least one between a_2/L and a_3/L.

From a practical point of view, it could appear too complex. In order to simplify the solution of the problem, it is of fundamental importance to highlight that the design goal consists in the protection of the beam-to-column connections, i.e. yielding of both "dog-bones" or yielding of one "dog-bone" and of a beam cross section. With the aim of obtaining this design objective it is sufficient to consider only the limit value of a/L provided by the minimum between a_5/L and a_8/L. This value can be obtained varying m_{db} for a fixed vertical load q and beam plastic moment M_p. In other words, for a given qL^2/M_p the curve representing the upper limit of a/L as a function of m_{db} can be obtained as depicted in Figure 10). This figure is, substantially, a design abacus for "dog-bone" location.

m_{db}	$\frac{qL^2}{M_p}=0$	$\frac{qL^2}{M_p}=1$	$\frac{qL^2}{M_p}=2$	$\frac{qL^2}{M_p}=3$	$\frac{qL^2}{M_p}=4$	$\frac{qL^2}{M_p}=5$	$\frac{qL^2}{M_p}=6$	$\frac{qL^2}{M_p}=7$	$\frac{qL^2}{M_p}=8$
0.30	0.350	0.331	0.274	0.224	0.194	0.173	0.158	0.146	0.137
0.35	0.325	0.304	0.252	0.206	0.178	0.160	0.146	0.135	0.126
0.40	0.300	0.278	0.231	0.189	0.163	0.146	0.133	0.123	0.116
0.45	0.275	0.252	0.210	0.171	0.149	0.133	0.121	0.112	0.105
0.50	0.250	0.226	0.189	0.155	0.134	0.120	0.109	0.101	0.095
0.55	0.225	0.201	0.169	0.138	0.120	0.107	0.098	0.090	0.085
0.60	0.200	0.176	0.149	0.122	0.106	0.094	0.086	0.080	0.075
0.65	0.175	0.153	0.130	0.106	0.092	0.082	0.075	0.069	0.065
0.70	0.150	0.129	0.110	0.090	0.078	0.070	0.064	0.059	0.055
0.75	0.125	0.106	0.091	0.075	0.065	0.058	0.053	0.049	0.046
0.80	0.100	0.084	0.072	0.059	0.051	0.046	0.042	0.039	0.036
0.85	0.075	0.062	0.053	0.044	0.038	0.034	0.031	0.029	0.026
0.90	0.050	0.041	0.034	0.029	0.025	0.023	0.021	0.019	0.017
0.95	0.025	0.020	0.017	0.015	0.013	0.011	0.010	0.009	0.008
1.00	0.000	0.000	0.000	0.000	0.000	0.000	0.000	0.000	0.000

Table 4. Limit values of a/L for "dog-bone" location

In fact, it includes all the design variables expressed in non-dimensional form.The abacus can be useful also to understand the role played by several parameters. The numerical values used to build Figure 10) are reported in Table 4 and Table 5. In particular, it is important to underline that, for a given value of qL^2/M_p, an increase of m_{db} causes the decrease of the admissible value of a/L and, in the case $m_{db} = 1$, an a/L value equal to zero is provided independently of qL^2/M_p. In addition, increasing the vertical load, the admissible a/L value decreases.

Table 5. Limit values of a/L for "dog-bone" location

m_{db}	$\frac{qL^2}{M_p}=9$	$\frac{qL^2}{M_p}=10$	$\frac{qL^2}{M_p}=11$	$\frac{qL^2}{M_p}=12$	$\frac{qL^2}{M_p}=13$	$\frac{qL^2}{M_p}=14$	$\frac{qL^2}{M_p}=15$	$\frac{qL^2}{M_p}=16$
0.30	0.129	0.123	0.117	0.112	0.107	0.099	0.093	0.087
0.35	0.119	0.113	0.108	0.103	0.096	0.090	0.084	0.079
0.40	0.109	0.103	0.098	0.093	0.087	0.081	0.076	0.072
0.45	0.099	0.094	0.090	0.084	0.078	0.073	0.069	0.065
0.50	0.089	0.085	0.080	0.074	0.069	0.065	0.061	0.058
0.55	0.080	0.076	0.070	0.065	0.061	0.057	0.054	0.051
0.60	0.070	0.066	0.061	0.057	0.053	0.050	0.047	0.045
0.65	0.061	0.057	0.053	0.049	0.046	0.043	0.041	0.038
0.70	0.051	0.048	0.044	0.041	0.039	0.036	0.034	0.032
0.75	0.042	0.039	0.036	0.034	0.032	0.030	0.028	0.027
0.80	0.033	0.031	0.028	0.027	0.025	0.023	0.022	0.021
0.85	0.024	0.022	0.021	0.020	0.018	0.017	0.016	0.016
0.90	0.016	0.015	0.014	0.013	0.012	0.011	0.011	0.010
0.95	0.008	0.007	0.007	0.006	0.006	0.006	0.005	0.005
1.00	0.000	0.000	0.000	0.000	0.000	0.000	0.000	0.000

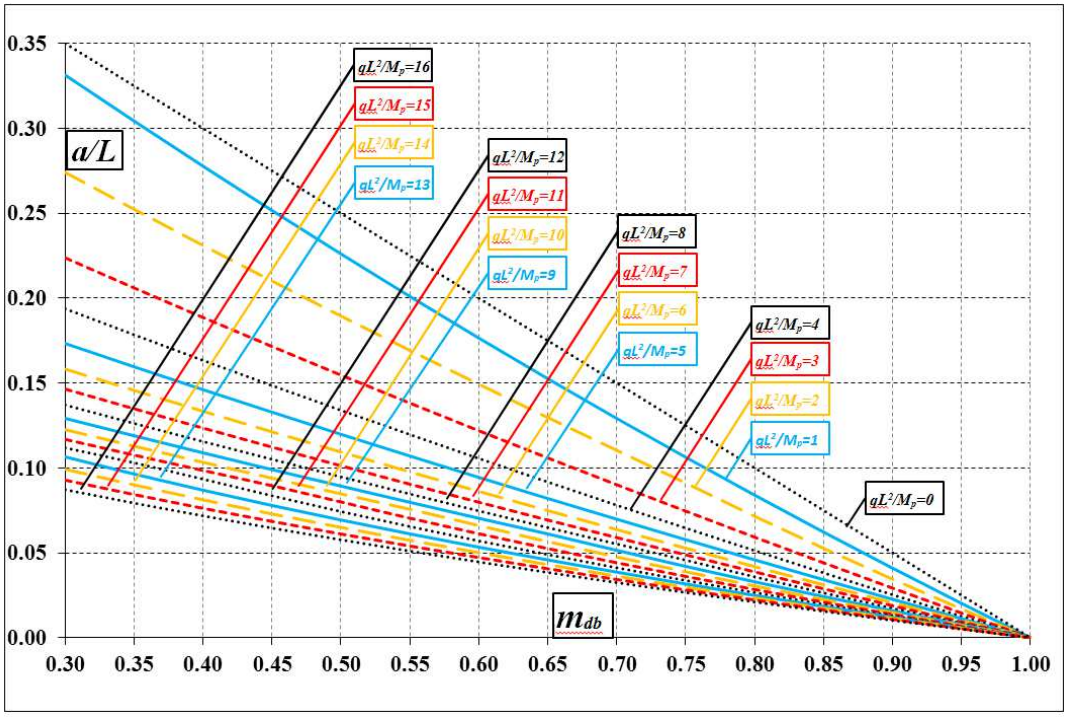


Figure 10: Design abacus for "dog-bone" location

5 CONCLUSIONS

The traditional design philosophy of seismic-resistant structures requires that, in case of seismic events having a return period comparable with the average life of the construction, the structure has to remain in elastic range and has to develop limited lateral displacements in order to determine the minimum discomfort to the activities developed in the construction. Conversely, in the case of destructive seismic events, having a return period of about 500 years, the structure has to be able to dissipate the earthquake input energy by means of plastic excursions whose magnitude has to be limited to values compatible with the local and global ductility which the structure is able to supply. In other words, even though the structure is significantly damaged, collapse has to be prevented aiming to assure the safeguard of the human lives. Therefore, seismic-resistant structures have to be designed to obtain two goals; on one hand, they have to possess sufficient strength and stiffness to fulfil the requirements concerning the serviceability limit state and, on the other hand, adequate ductility and energy absorption capacity to fulfil the requirements regarding the ultimate limit state. While the fulfilment of the first goal is easy to be obtained, the latter generally requires more troublesome design procedures which should account for the structural behaviour in plastic range.

In particular, it is universally recognized the need to prevent collapse mechanisms having limited dissipation capacity, such as storey mechanisms, and to promote the development of a collapse mechanism of global type. Moreover, it is always necessary the design of structural details, i.e. connections between dissipative zones and non-dissipative zones, able to guarantee an high local ductility supply. In this paper the criteria for designing "dog-bone" connections have been analysed. In particular, depending on the magnitude of the weakening of the beam section, the "dog-bone" location has to be properly selected in order to protect the beam-to-column connections which is one of the goals to be achieved in designing frames adopting such a structural detail. In addition, the obtained results show that the smallest m_{db} value provides the widest range where it is possible to locate the "dog-bones"; in fact, increasing m_{db} the range identified by a reduces up to zero for $m_{db} = 1$.

The provided design abacus for RBS location represents a useful tool to easily understand if the beam-to-column connections are protected or not by the realization of a "dog-bone" having a non-dimensional resistance m_{db}, a non-dimensional distance from the beam-to-column connection a/L and a non-dimensional value of vertical load qL^2/M_P.

REFERENCES

[1] Piluso, V. & Rizzano, G., 2007. Random material variability effects on full-strength end-plate beam-to-column joints. *Journal of Constructional Steel Research*, 63(5), pp. 658-666

[2] Bernuzzi, C., Zandonini, R. & Zanon, P., 1996. Experimental analysis and modelling of semi-rigid steel joints under cyclic reversal loading. *Journal of Constructional Steel Research*, Volume 2, pp. 95-123.

[3] Faella, C., Piluso, V. & Rizzano, G., 1997. A new method to design extended end plate connections and semirigid braced frames. *Journal of Constructional Steel Research,* 41(1), pp. 61-91.

[4] Iannone, F., Latour, M., Piluso, V. & Rizzano, G., 2011. Experimental Analysis of Bolted Steel Beam-to-Column Connections: Component Identification. *Journal of Earthquake Engineering,* 15(2), pp. 214-244.

[5] Latour, M., Piluso, V. & Rizzano , G., 2011b. Cyclic Modeling of Bolted Beam-to-Column Connections: Component Approach. *Journal of Earthquake Engineering,* 15(4), pp. 537-563.

[6] Latour, M., Piluso, V. & Rizzano G, 2013b. Experimental behaviour of friction T-stub beam-to-column joints under cyclic loads. *Steel Construction* (1).

[7] Latour, M., Piluso, V. & Rizzano, G., 2011a. Experimental analysis of innovative dissipative bolted double split tee beam-to-column connections. *Steel Construction*, June, 4(2), pp. 53-64.

[8] Latour, M. & Rizzano, G., 2012. Experimental Behavior and Mechanical Modeling of Dissipative T-Stub Connections. *Journal of Structural Engineering*, 138(2), pp.170-182.

[9] Latour, M. & Rizzano, G., 2014c. Innovative Connections for timber panel buildings. *International Journal of Earthquake Engineering*.

[10] Latour, M. & Rizzano, G., 2015a. Cyclic Behavior of Dissipative X-shaped Double Split Tee Joints. Journal of Constructional Steel Research.

[11] Piluso, V. & Rizzano, G., 2008. Experimental Analysis and modelling of bolted T-stubs under cyclic loads. *Journal of Constructional Steel Research*, Volume 64, pp. 655-669.

[12] Plumier A. New idea for safe structures in seismic zones. *IABSE Symposium*, Mixed structures including new materials, Brussels, 1990.

[13] Wilkinson S. et al, A moment resisting connection forearthquake resistant structures *Journal of Constructional Steel Research* vol. 62, pp. 295–302. 2006.

[14] Iwankiw, N. Seismic design enhancement and the reduced beam section detail for steel moment frames, PracticePeriodical on *Structural design and Construction*, ASCE 9, 87-92. 2004.

[15] Engelhardt MD, Venti M, Fry GT, Jones S, Holliday S. Behavior and design of radius cut reduced beam section connections. A draft report of SAC task 7.07a. SAC Joint Venture; 2000.

[16] Chen, S.-J., Chu, J.M., & Chou, Z.L. (1997). Dynamic Behaviour of Steel Frames with Beam Flanges Shaved Around Connection. *Journal of Constructional Steel Research*, Vol 42, No.1, pp.49-70.

[17] Ivankiw, N.R., Carter, C.J. (1998): Improved Ductility in Seismic Steel Moment Frames with Dogbone Connections, *Journal of Constructional Steel Research*, Vol 46:1-3, Paper No 253.

[18] N. Iwankiw, S. Zoruba (2002). Steel moment frames: resolution of recent seismic detailing and material shape issues *Journal of Constructional Steel Research* 58 495–510

[19] K. Lee, D. A. Foutch (2002). Performance evaluation of new steel frame buildings for seismic loads *Earthquake Engng Struct. Dyn.* 31:653–670 (DOI: 10.1002/eqe.147)

[20] Brandon Chi, Chia-Ming Uang (2002). Cyclic Response and Design Recommendations of Reduced Beam Section Moment Connections with Deep Columns *Journal of Structural Engineering*

[21] Ardeshir Deylami, Afshin Moslehi Tabar (2004) Effect of Column Panel Zone Characteristics on Instability of Beams with RBS Moment Resisting Connections. *13th World Conference on Earthquake Engineering* Vancouver, B.C., Canada, Paper No. 31

[22] M. Ohsakia, H. Tagawab, P. Panc, (2009). Shape optimization of reduced beam section under cyclic loads. *Journal of Constructional Steel Research* Vol. 65, Issue 7, Pages 1511–1519

[23] Sang-Whan Hana, Ki-Hoon Moonb, Bozidar Stojadinovic c (2009) Design Equations for Moment Strength of RBS-B Connections. *Journal of Constructional Steel Research* 65 10871095.

[24] Amir A. Hedayat, Murude Celikag (2009). Post-Northridge Connection with Modified Beam end Configuration to Enhance Strength and Ductility. *Journal of Constructional Steel Research*. Vol. 65, Issue 7, July 2009, Pages 1413–1430

[25] D.T. Pachoumis, E.G. Galoussis, C.N. Kalfas, A.D. Christitsas (2009). Reduced beam section moment connections subjected to cyclic loading: Experimental analysis and FEM simulation. *Engineering Structures* 31, 216 – 223.

[26] Ajay Kulkarni Swati, Vesmawala Gaurang, (2014) Study of steel moment connection with and without reduced beam section. *Case Studies in Structural Engineering*, Volume 1, Pages 26-31

[27] C.E. Sofias, C.N. Kalfas, D.T. Pachoumis (2014). Experimental and FEM analysis of reduced beam section moment endplate connections under cyclic loading *Engineering Structures*, Volume 59, Pages 320-329.

[28] D.T. Pachoumis, E.G. Galoussis, C.N. Kalfas, I.Z. Efthimiou (2010). Cyclic performance of steel moment-resisting connections with reduced beam sections — experimental analysis and finite element model simulation. *Engineering Structures*, Volume 32, Issue 9, Pages 2683-2692

[29] Sang Whan Han, Ki-Hoon Moon, Seong-Hoon Hwang, Bozidar Stojadinovic (2012). Rotation capacities of reduced beam section with bolted web (RBS-B) connections. *Journal of Constructional Steel Research*, Volume 70, Pages 256-263

[30] CEN 2003. PrEN 1998-1. Eurocode 8: Design of Structures for Earthquake Resistance. Part 1: General Rules, Seismic Actions and Rules for Buildings.

[31] CEN 1993. PrEN 1993-1. Eurocode 3: Design of Steel Structures. Part 1: General Rules and Rules for Buildings.

[32] FEMA 302. NEHRP recommended provisions for seismic regulations for new buildings and other structures, part 1—provisions. Federal Emergency Management Agency, Washington, DC; 1997.

[33] FEMA 350. Recommended seismic design criteria for new steel moment-frame buildings. Prepared by the SAC Joint Venture for the Federal Emergency Management Agency, Washington, DC; 2000.

[34] Mazzolani, F.M., Piluso, V., "Plastic Design of Seismic Resistant Steel Frames", *Earthquake Engineering and Structural Dynamics*, Vol. 26, pp. 167-191, 1997.

[35] Longo, A.; Montuori, R.; Piluso, V. Theory of Plastic Mechanism Control for MRF-CBF dual system and its validation. *Bulletin of Earthquake Engineering* (BEEE). 2014.

[36] Giugliano M.T., Longo A., Montuori R., Piluso V. Failure mode and drift control of MRF-CBF dual systems *The Open Construction and Building Technology Journal*, 4, 121-133, 2010.

[37] Montuori R., Piluso V., Troisi M. Theory of plastic mechanism control of seismic-resistant MR-frames with set-backs. *Open Construction and Building Technology Journal*, vol. 6, pp. 404-413 , 2012.

[38] Longo A., Montuori R., Piluso V., Theory of Plastic Mechanism Control of Dissipative Truss Moment Frames, *Engineering Structures*, Vol. 37, pp. 63-75, 2012.

[39] Longo A., Montuori R., Piluso V., Failure Mode Control and Seismic Response of Dissipative Truss Moment Frames, *Journal of Structural Engineering*, Vol. 138, pp.1388-1397, 2012.

[40] Montuori R., Piluso V., Troisi M. Innovative structural details in MR-frames for free from damage structures *Mechanics Research Communications* – Vol. 58 pp. 146-156. 2014.

[41] Montuori, R., Muscati R., "Plastic Design of Seismic Resistant Concrete Frame", *Earthquakes and Structures*, (2015).

[42] Montuori, R., Nastri, E., Piluso, V., "Advances in Theory of Plastic Mechanism Control: Closed Form Solution for Mr-Frames", *Earthquake Engineering and Structural Dynamics*. (2015)

[43] Montuori R., Piluso V., Plastic Design of Steel Frames with Dog-Bone Beam-to-Column Joints, Third *International Conference on Behaviour of Steel Structures in Seismic Areas, STESSA 2000*.

[44] Longo A., Montuori R., Piluso V. Failure mode control of X-braced frames under seismic actions. *Journal of Earthquake Engineering*, 12: 728-759, 2008

[45] Longo A, Montuori R, Piluso V. Plastic design of seismic resistant V-Braced frames. *Journal of Earthquake Engineering*, vol. 12: 1246-1266, 2008.

[46] Longo A, Montuori R, Piluso V. "Influence of design Criteria on the seismic Reliability of X-Braced Frames", *Journal of Earthquake Engineering*, Vol. 12, Issue 3– p.406-431. 2008

[47] Montuori, R., Nastri, E., Piluso, V.,"Rigid-plastic analysis and moment–shear interaction for hierarchy criteria of inverted Y EB-Frames" *Journal of Constructional Steel Research* vol. 95 71-80. 2014.

[48] Montuori, R., Nastri, E., Piluso, V., Theory of Plastic Mechanism Control for Eccentrically Braced Frames with inverted Y-scheme, *Journal of Constructional Steel Research*, Volume 92, pp. 122-135, 2014.

[49] Giugliano M.T., Longo A., Montuori R., Piluso V., Plastic design of CB-frames with reduced section solution for bracing members. *Journal of Constructional Steel Research.* Vol. 66 pp 611-621. 2010.

[50] Montuori R., Nastri E., Piluso V. Theory of plastic mechanism control for the seismic design of braced frames equipped with friction dampers - *Mechanics Research Communications* – Vol. 58. pp. 112-123 2014.

[51] Longo A., Montuori R., Piluso V. Seismic reliability of V-braced frames: Influence of design methodologies. *Earthquake Engineering and Structural Dynamics*, vol. 38 p. 1587-1608, 2009.

[52] Longo A., Montuori R., Piluso V. Seismic Reliability of Chevron Braced Frames with Innovative Conception of Bracing Members, *Advanced Steel Construction, an International Journal* - Vol. 5, No. 4, December 2009.

[53] Montuori, R., Nastri, E., Piluso, V. Rigid-plastic analysis and moment–shear interaction for hierarchy criteria of inverted Y EB-Frames. *Journal of Constructional Steel Research*, vol. 95 pp.71-80, 2014.

[54] Longo A., Montuori, R., Nastri, E., Piluso, V. On the use of HSS in seismic-resistant structures *Journal of Constructional Steel Research*, Vol. 103, p. 1-12, 2014.

[55] Montuori, R., Nastri, E., Piluso, V., "Seismic Design of MRF-EBF Dual Systems with Vertical Links: Ec8 Vs Plastic Design", *Journal of Earthquake Engineering*, (2015)

[56] Montuori, R., Nastri, E., Piluso, V., "Seismic Response of EB-Frames with Inverted Yscheme: TPMC Versus Eurocode Provisions", *Earthquakes and Structures*, (2015)

[57] Longo A., Montuori, R., Piluso, V., Moment Frames - Concentrically Braced Frames Dual Systems: Analysis of Different Design Criteria, *Structure and infrastructure engineering*, (2015)

[58] Montuori, R., Muscati V., Plastic design of seismic resistant reinforced concrete frame, *Earthquakes and Structures*, Vol. 8, No. 1, January 2015 Pages 205-224 http://dx.doi.org/10.12989/eas.2015.8.1.895

[59] Montuori, R., Nastri E., Piluso V. Advances in theory of plastic mechanism control: closed form solution for MR-Frames. *Earthquake Engineering & Structural Dynamics*, DOI: 10.1002/eqe.2498

[60] Montuori, R. The Influence of Gravity Loads on the Seismic Design of RBS Connections". *Open Construction and Building Technology Journal*, January 2015 Pages 248-261 DOI: 10.2174/1874836801408010241

[61] R. Montuori, V. Piluso, A. Tisi. Comparative analysis and critical issues of the main constitutive laws for concrete elements confined with FRP. *Composites: Part B, Engineering* Vol.438, Issue 8, 2012. ISSN:1359-8368, doi: 10.1016/j.compositesb.2012.04.001.

[62] R. Montuori, V. Piluso, A. Tisi. Ultimate behaviour of FRP wrapped sections under axial force and bending: Influence of stress-strain confinement model. *Composites: Part B, Engineering* Vol. 548 (2013) pp.85–96. ISSN: 1359-8368, doi: http://dx.doi.org/10.1016/j.compositesb.2013.04.059.

[63] R. Montuori, V. Piluso. "Analysis and modelling of CFT members: Moment curvature analysis". *Thin-Walled Structure.* Volume 86, January 2015, Pages 157–166. DOI:10.1016/j.tws.2014.10.010

COMPDYN 2015
5th ECCOMAS Thematic Conference on
Computational Methods in Structural Dynamics and Earthquake Engineering
M. Papadrakakis, V. Papadopoulos, V. Plevris (eds.)
Crete Island, Greece, 25–27 May 2015

NON-LINEAR ANALYSES OF SEISMIC RESISTANT CONCRETE FRAME FOR THE VALIDATION OF A FAILURE MODE CONTROL METHODOLOGY

Roberta Muscati[1]

[1]Ph. D. student, Department of Civil Engineering, University of Salerno – Italy
E-mail: rmuscati@unisa.it

Keywords: Global Mechanism, Concrete Moment Resisting Frames, Plastic Collapse Theory.

Abstract. *Nowadays, the collapse mechanism control is universally recognized as one of the primary goals of the structural design process. The primary purpose consists in avoiding collapse mechanisms characterized by poor energy dissipation capacity, such as "soft-storey" mechanisms, assuring the development of a collapse mechanism of global type. In particular, such kind of mechanism is characterized by the location of plastic hinges at all the beam ends and at the base sections of first storey columns. In the present work a rational design approach aiming to control the failure mechanism in seismic resistant concrete frame is applied. In particular, column sections are dimensioned by means of the Theory of Plastic Mechanism Control (TPMC) to guarantee structures failing according to a global type mechanism. In past researches, this procedure has been applied to several steel structure typologies. In this paper for the first time it is presented and applied to a concrete moment resisting frame. In the paper the theory is recalled and a worked example is reported in order to show that its application is very easy. In addition both push-over analyses and non-linear dynamic analyses have been made to investigate the actual collapse mechanism of the designed structure. All the obtained results confirm the ability of the design procedure to obtain a collapse mechanism of global type.*

1 INTRODUCTION

In order to avoid undesired collapse mechanisms hierarchy criterion, reported in all the modern seismic codes, suggests that at any joint, the sum of the flexural strength of the columns is greater than the sum of the flexural strength of the beams converging in the same joint [1, 2]. In a collapse mechanism of global type the energy dissipation capacity and global ductility supply are maximized because all the dissipative zones are involved in the corresponding pattern of yielding. Conversely, all the other structural parts remain in elastic range. In fact, relatively to the moment resisting frames, the maximum number of plastic hinges is obtained when two plastic hinges develops in each bay and they are usually located at beam ends. However, for particular load conditions, plastic hinges can develop also in the mid span of the bay. Nowadays, in the design of structures, is important to differentiate on one hand, dissipative zones, designed according to the internal actions arising from the seismic forces provided by the codes, and on the other hand non-dissipative zones, proportioned on the basis of the maximum internal actions transmitted by the dissipative zones. In a seismic resistant concrete frame, beams and columns are identified as dissipative and non-dissipative zones, respectively. These are the basic principles of capacity design approach, independently of the structural scheme and the constructional material [3 - 5].

Unfortunately, the beam-column hierarchy criterion, being based on simple joint equilibrium, is only able to prevent “soft-storey” mechanisms, but it does not assure the development of a collapse mechanism of global type; in fact it is a non-rigorous application of capacity design principles [6,7]. For this reason, a more sophisticated design procedure, based on the kinematic theorem of plastic collapse and on second order plastic analysis (i.e. the concept of mechanism equilibrium curve) has been presented in 1997 [8]. Starting from this first work, the “Theory of Plastic Mechanism Control” (TPMC) has been obtained as a powerful tool for the seismic design. In particular, it consists on the extension of the kinematic theorem of plastic collapse to the concept of mechanism equilibrium curve. In fact, for any given structural typology, the design conditions to be applied in order to prevent undesired collapse mechanisms can be derived by imposing that the mechanism equilibrium curve corresponding to the global mechanism has to be located below those corresponding to all the other undesired mechanisms up to a displacement level compatible with the local ductility supply of dissipative zones.

This design approach was successively extended to MRFs with RBS connections, EB-Frames with horizontal links (i.e. split-K scheme and D-scheme), EB-frames with inverted Y scheme, dissipative truss-moment frames DTMFs, MRF-CBF dual systems and, finally, in MRFs equipped with friction dampers.

So, it can be concluded that structures in high seismicity zones are normally designed to resist severe earthquakes by dissipating the input energy by means of inelastic deformations and, in order to maximize this effect, plastic hinges need to be developed at beam ends rather than in the columns in case of moment resisting frames (MRFs) [9-16]. However also in the case of other structural typologies the need to avoid the yielding of columns is always the desired goal and the development of a global mechanism is the main design objective [17-33].

Starting from the above background, in this paper a new application of the “Theory of Plastic Mechanism Control” is developed with reference to the reinforced concrete frames [34]. Furthermore, the simplicity of the proposed method will be emphasized by means of a worked example aiming to show its practical application which can be carried out even by means of hand calculations. In addition, static inelastic analyses are carried out to control the fulfilment of the desired collapse mechanism typology, i.e. a collapse mechanism of global type.

1. THEORY OF PLASTIC MECHANISM CONTROL

TPMC allows the theoretical solution of the problem of designing a structure failing in global mode, i.e. assuring that plastic hinges develop only at beam ends while all the columns remain in elastic range with the only exception of base sections at first storey columns. In general, three main collapse mechanism typologies that the structure is able to exhibit can be recognized: these mechanisms, depicted in Figure 1, are to be considered undesired because they do not involve all the dissipative zones. Type-1 mechanism starts from the first storey level and involves an i_m-th number of storeys, for this reason plastic hinges develop at the beam ends of all the storeys involved, at the base section of the first storey columns and at the top section of the i_m-th storey columns. Type- 2 mechanism is a particular kind of mechanism which starts to the top of the structure and involves an i_m-th number of storey. In particular, all the beam ends and the base section of the i_m-th storey columns develop plastic hinges. The global mechanism, representing the design goal, is a particular case of type-2 mechanism involving all the storeys. Finally, type-3 mechanism involves only one storey, so that plastic hinges develop at the base and top section of the same storey columns. It has to be considered the worst mechanism because involves only the columns which are to be considered less dissipative than the beam sections. In order to apply the TPMC it is of paramount importance the introduction of the concept of linearized mechanism equilibrium curve for each considered mechanism. The mathematical expression of this curve can be written as:

$$\alpha = \alpha_0 - \gamma\delta \tag{1}$$

W here α_0 is the kinematically admissible multiplier of horizontal forces and γ is the slope of the mechanism equilibrium curve. Both parameters can be derived, according to rigid-plastic theory, using the principle of virtual work. Within the framework of a kinematic approach, for any given collapse mechanism, the mechanism equilibrium curve can be easily derived by equalling the external work to the internal work. In addition, in order to account for second order effects, the external second-order work due to vertical load is also evaluated.

Concerning the evaluation of the kinematically admissible multiplier of horizontal forces corresponding to the generic mechanism, it is easy to recognise that, in the case of global type mechanism, for a virtual rotation $d\theta$ of plastic hinges of the columns at first storey (Figure 1), the internal work can be expressed as:

$$W_i = \left[\sum_{i=1}^{n_c} M_{c,i,1} + 2\sum_{k=1}^{n_s}\sum_{j=1}^{n_b} M_{b.jk}\right] d\theta = \left[M_{c,1} + M_{b,Rd}\right] d\theta \tag{2}$$

For the better comprehension of the adopted notation reference is made to Table 1. The external work due to the horizontal forces can be written as:

$$W_e = \left[\alpha \sum_{k=1}^{n_s} F_k h_k\right] d\theta = [\alpha M_F] d\theta \tag{3}$$

Therefore the application of the virtual work principle provides the kinematically admissible multiplier as:

$$\alpha_0^{(g)} = \frac{\left[M_{c,1} + M_{b,Rd}\right]}{M_F} \tag{4}$$

In order to compute the slope of the mechanism equilibrium curve, it is necessary to evaluate the second-order work due to vertical loads.

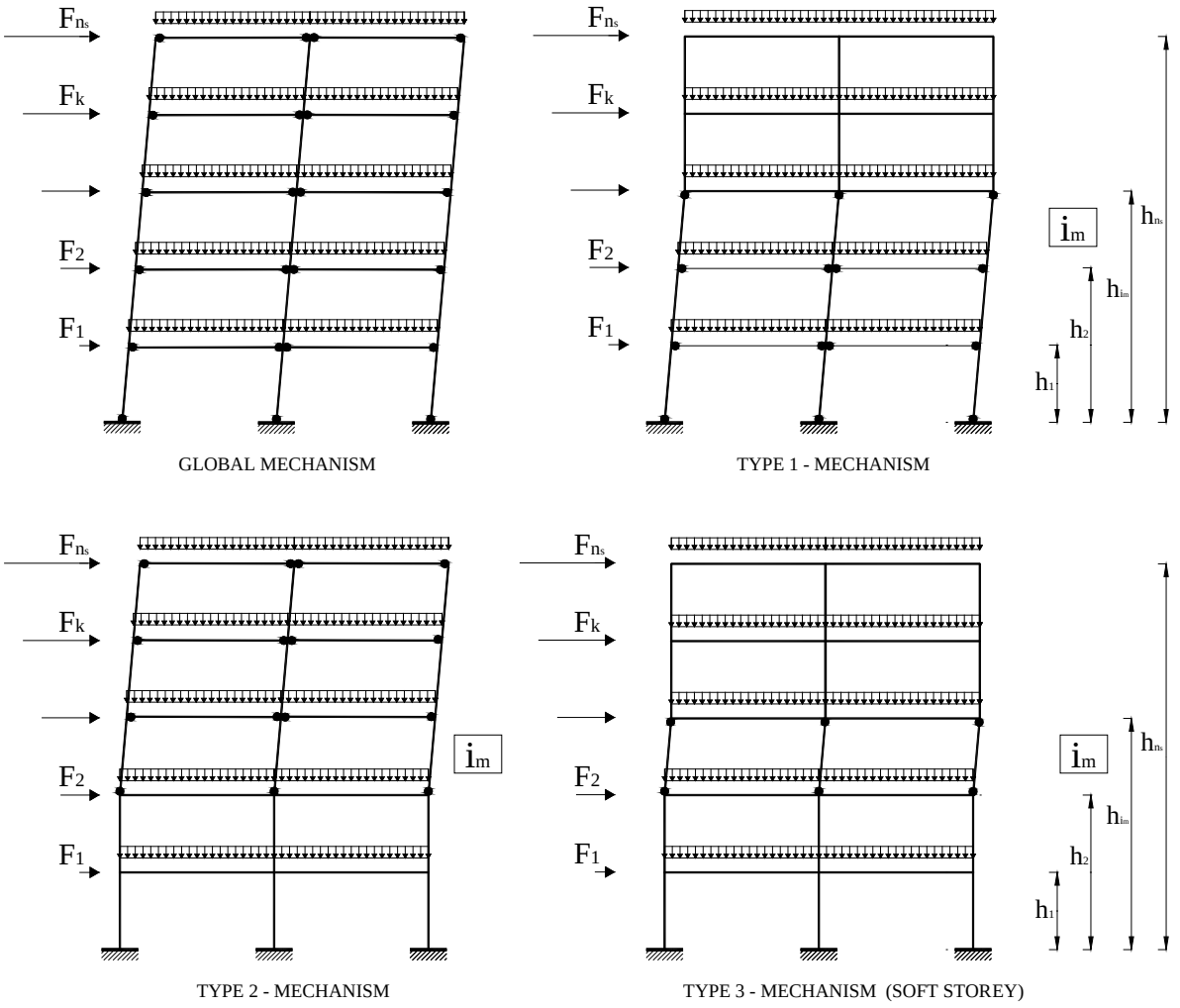


Figure 1: Collapse mechanism typologies

With reference to Figure 2, it can be observed that the horizontal displacement of the k-th storey involved in the generic mechanism is given by $u_k = r_k sin\theta$, where r_k is the distance of the k-th storey from the centre of rotation C and θ the angle of rotation.

n_c	number of columns	$M_{c,im} = \sum_{i=1}^{n_c} M_{c,i,im}$	sum of plastic moments of columns at i_m-th storey
n_b	number of bays	$M_V = \sum_{k=1}^{n_s} V_k h_k$	second-order work due to vertical loads in global mechanism
n_s	number of storeys	$M_F = \sum_{k=1}^{n_s} F_k h_k$	external work due to horizontal forces in the global mechanism
i_m	index of mechanism	$M_{b.jk}$	plastic design resistance of beam at j-th bay of the k-th storey

H_o	sum of the interstorey heights of the storeys involved by the generic mechanism	$M_{b,Rd} = 2\sum_{k=1}^{n_s}\sum_{j=1}^{n_b} M_{b.jk}$	sum of the plastic design resistances of beam ends
h_k	height of the k-th storey (with k=1, 2, .., n_s)	$F = \sum_{k=1}^{n_s} F_k$	sum of the horizontal forces
$M_{c,i,im}$	plastic moment of the i-th column at i_m-th storey		

Table 1: Notation

The top sway displacement is given by $\delta = H_o sin\theta$, where H_o is the sum of the interstorey heights of the storeys involved by the generic mechanism. In the case of global type mechanism, as shown in Figure 1, all the storeys participate to the collapse mechanism, so that $H_o = h_{ns}$. The relationship between vertical and horizontal virtual displacements is given by (Figure 2):

$$dv_k = du_k tan\theta \approx du_k sin\theta = du_k \frac{\delta}{H_o} \tag{5}$$

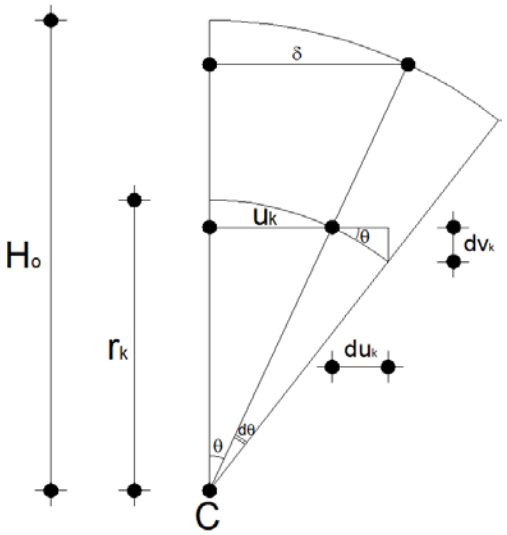


Figure 2: Second order vertical displacements

It shows that, as the ratio dv_k/du_k is independent from the considered storey, vertical and horizontal virtual displacement vectors have the same shape. In fact, the virtual horizontal displacements are given by:

$$du_k = r_k cos\theta d\theta \approx r_k d\theta \tag{6}$$

By substituting Eq. (6) in Eq. (5), the virtual vertical displacements are given by:

$$dv_k = \frac{\delta}{H_o} r_k d\theta \tag{7}$$

and, therefore, they have the same shape r_k of the horizontal ones. As a consequence, the second-order work due to vertical loads for the global mechanism is given by:

$$W_v = \sum_{k=1}^{n_s} V_k h_k \frac{\delta}{H_o} d\theta = M_V \frac{\delta}{H_o} d\theta \tag{8}$$

By accounting for this value, the virtual work principle can be written as:

$$W_i = W_e + W_v \tag{9}$$

By substituting Eqs. (2), (3) and (8) in Eq. (9) the following relation can be obtained:

$$\left[M_{c,1} + M_{b,Rd}\right] d\theta = [\alpha M_F] d\theta + M_V \frac{\delta}{H_o} d\theta \tag{10}$$

By means of simple steps it is immediately recognized the form of the linearized mechanism equilibrium curve expressed by Eq. (1):

$$\alpha = \frac{M_{c,1} + M_{b,Rd}}{M_F} - \frac{\frac{1}{H_o} M_V}{M_F} \delta \tag{11}$$

Therefore, the slope of the mechanism equilibrium curve γ, can be easily obtained. In the case of global mechanism it is given by:

$$\gamma^{(g)} = \frac{\frac{1}{H_o} M_V}{M_F} = \frac{\frac{1}{h_{n_s}} M_V}{M_F} \tag{12}$$

Therefore, the linearized mechanism equilibrium curve of global mechanism $\alpha_0 = \alpha_0^{(g)} - \gamma^{(g)} \delta$ is completely defined. It can be useful to underline that the linearization of equilibrium curve is due to the small displacement theory adopted in Eq. (6). In fact, due to this assumption, second-order work of to vertical loads is linear and as a consequence, also the mechanism equilibrium curve is linear.

For each considered mechanism (Figure 1) a mechanism equilibrium curve can be obtained. In particular, for the i_m-th mechanism ($i_m = 1, 2, \dots, n_s$) of the t-th mechanism typology ($t = 1, 2, 3$) the application of kinematic theorem of plastic collapse provides:

$$\alpha_{im}^{(t)} = \alpha_{0,im}^{(t)} - \gamma_{im}^{(t)} \delta \qquad t = 1,2,3 \qquad i_m = 1,2, \dots n_s \tag{13}$$

Where $\alpha_{0,im}^{(t)}$ and $\gamma_{im}^{(t)}$ represent, respectively, the kinematically admissible multiplier and the slope of mechanism equilibrium curve of the i_m-th mechanism of the t-th mechanism typology. In the proposed method the beam section properties are assumed to be known quantities because they are designed to resist vertical loads. As a consequence, the unknowns of the design problem are the column sections. They could be determined by means of design conditions expressing that the kinematically admissible multiplier corresponding to the global mechanism is the minimum among all kinematically admissible multipliers corresponding to all other mechanisms (Figure 1). Obviously, this design condition is able to assure the desired collapse mechanism only in case of rigid-plastic behaviour, while actual structures are characterized by elastic displacements before the development of a plastic mechanism. Due to these elastic displacements, second-order effects of vertical loads cannot be neglected. These effects can be taken into account by imposing that the mechanism equilibrium curve corresponding to the global mechanism has to lie below those corresponding to all other

mechanisms i.e. the upper bound theorem of plastic design is to be satisfied for each value of the displacements δ (Figure 3). However, the fulfilment of this requirement is necessary only up to a selected ultimate displacement δ_u, which has to be compatible with the ductility supply of structural members.

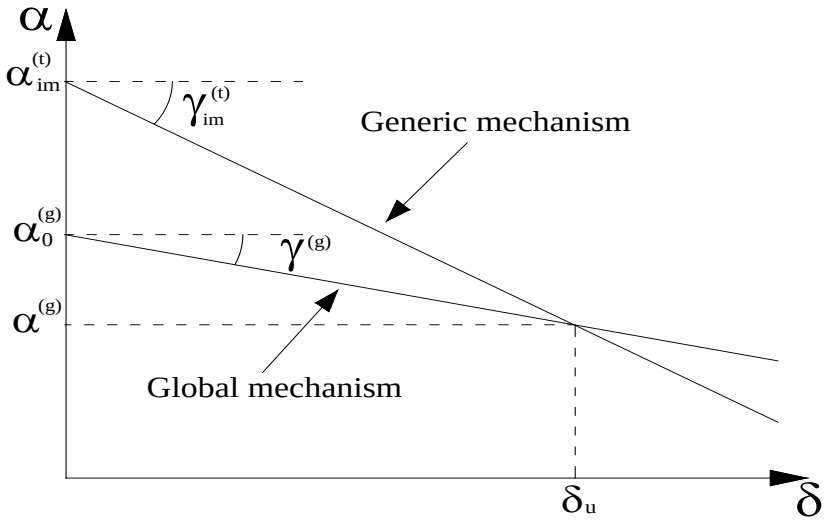


Figure 3: Design condition

This corresponds to impose the following conditions:

$$\alpha_0^{(g)} - \gamma^{(g)}\delta_u \leq \alpha_{0,im}^{(t)} - \gamma_{im}^{(t)}\delta_u \tag{14}$$

for $i_m = 1, 2\ 3, \dots, n_s$ and $t = 1, 2, 3$.

It is important to underline that, for any given geometry of the structural system, the slope of mechanism equilibrium curve attains its minimum value when the global type mechanism is developed. This issue assumes a paramount importance in TPMC allowing the extension of the kinematic theorem of plastic collapse to the concept of mechanism equilibrium curve by simply checking the equation for the value $\delta = \delta_u$, as depicted in Figure 3. Therefore, there are $3n_s$ design conditions to be satisfied for a structural scheme having n_s storeys. With reference to i_m-th mechanism of type-1, the kinematically admissible multiplier of seismic horizontal forces is given by:

$$\alpha_{0,i_m}^{(1)} = \frac{M_{c,1} + 2\sum_{k=1}^{i_m-1}\sum_{j=1}^{n_b} M_{b.jk} + M_{c,im}}{\sum_{k=1}^{i_m} F_k h_k + h_{i_m}\sum_{k=i_m+1}^{n_s} F_k} \tag{15}$$

while the slope of the mechanism equilibrium curve is:

$$\gamma_{i_m}^{(1)} = \frac{1}{h_{i_m}} \frac{\sum_{k=1}^{i_m} V_k h_k + h_{i_m}\sum_{k=i_m+1}^{n_s} V_k}{\sum_{k=1}^{i_m} F_k h_k + h_{i_m}\sum_{k=i_m+1}^{n_s} F_k} \tag{16}$$

With reference to i_m-th mechanism of type-2 the kinematically admissible multiplier of seismic horizontal forces is given by:

$$\alpha_{0,i_m}^{(2)} = \frac{M_{c,im} + 2\sum_{k=i_m}^{n_s}\sum_{j=1}^{n_b} M_{b.jk}}{\sum_{k=i_m}^{n_s} F_k (h_k - h_{i_m-1})} \tag{17}$$

while the slope of the mechanism equilibrium curve is:

$$\gamma_{i_m}^{(2)} = \frac{1}{h_{n_s} - h_{i_m-1}} \frac{\sum_{k=i_m}^{n_s} V_k\left(h_k - h_{i_m-1}\right)}{\sum_{k=i_m}^{n_s} F_k(h_k - h_{i_m-1})} \tag{18}$$

It is useful to note that, for $i_m = 1$ Eq. (17) and Eq. (18) are coincident with Eq. (4) and Eq. (12) respectively, because in such case the mechanism is coincident with the global one. In addition, these relations for $i_m = 1$ include the term $h_{i_m-1} = h_0$ which is to be assumed equal to zero. Finally, with reference to i_m-th mechanism of type-3, the kinematically admissible multiplier of horizontal forces, is given by:

$$\alpha_{0,i_m}^{(3)} = \frac{2M_{c,im}}{\left(h_{i_m} - h_{i_m-1}\right)\sum_{k=i_m}^{n_s} F_k} \tag{19}$$

In addition, the corresponding slope of the mechanism equilibrium curve is given by:

$$\gamma_{\mathrm{i_m}}^{(3)} = \frac{\sum_{\mathrm{k=i_m}}^{\mathrm{n_s}} \mathrm{V_k}}{\left(\mathrm{h_{i_m}} - \mathrm{h_{i_m-1}}\right)\sum_{\mathrm{k=i_m}}^{\mathrm{n_s}} \mathrm{F_k}} \tag{20}$$

2. DESIGN ALGORITHM

The above mentioned relations can be used to design concrete frames failing in global mode and, therefore, having a mechanism equilibrium curve given by Eq. (1), with the kinematically admissible multiplier of horizontal forces given by Eq. (4) and the slope given by relation (12). The design algorithm is constituted by the following steps:

a) Selection of a design top sway displacement δ_u compatible with the ductility supply of structural members. To this scope the plastic rotation capacity of beams can be assumed equal to 0.04 rad so that $\delta_u = 0.04 \cdot h_{ns}$ where h_{n_s} is the height of the structure.

b) Design of beam sections to withstand vertical loads acting in the non-seismic load combination. The preliminary design of beam can be made by considering a bending moment belonging to the range $qL^2/8 \div qL^2/10$ being q the load acting on the beam in the vertical load combination (see worked example). It is important to underline that the presented procedure, considers only symmetric structures characterized by symmetrical beam sections with symmetrical reinforcement. This limitation allows to consider for each beam just one plastic moment.

c) Computation, by means of Eqs. (16), (18) and (20), of the slopes of mechanism equilibrium curves $\gamma_{i_m}^{(t)}$ which are known quantities because they depend on loads (vertical and horizontal) and frame geometry.

d) For each considered i_m value, Eq. (14) provides the following relations where the unknown quantities are represented by $M_{c,im}$ and $M_{c,1}$, which are the sum of plastic moments of columns at i_m-th storey and at first storey, respectively. It is important to note that for $t = 2$ Eq. (14) is an identity because global mechanism is obtained by type 2 mechanism for $i_m = 1$. Furthermore, for $i_m = 1$, type 1 and type 3 mechanisms are coincident. This observation can be immediately derived from Figure 1 and, in addition, it is easy to check that $\alpha_{0,1}^{(1)} = \alpha_{0,1}^{(3)}$ and $\gamma_1^{(1)} = \gamma_1^{(3)}$.

As a consequence, for $i_m = 1$ there is only a design condition where the only unknown is represented by $M_{c,1}$. This value can be found by substituting the values of $\alpha_0^{(g)}, \gamma^{(g)}, \alpha_{0,1}^{(1)}\left(or\ \alpha_{0,1}^{(3)}\right)$ and $\gamma_1^{(1)}\left(or\ \gamma_1^{(3)}\right)$ in Eq. (14) that gives:

$$M_{c,1} \geq \frac{M_{b,Rd} + \left(\gamma_1^{(3)} - \gamma^{(g)}\right) \cdot \delta_u \cdot M_F}{2\frac{M_F}{h_1 F} - 1} \tag{21}$$

The above relation is of paramount importance from the practical point of view, because it allows to design first storey columns by means of a closed form solution easy to be applied by hand calculations.

e) The sum of the required plastic moments of columns can be distributed among the columns in different ways which are at the discretion of the designer. In this case, the following simple rule can be adopted:

$$M_{c,i,1} = \frac{M_{c,1}}{n_c} \tag{22}$$

for $i = 1, \ldots, n_c$.

It is important to underline that the way of distributing the sum of required plastic moments expressed by Eq.(22) is not mandatory, in fact, any other distribution among the columns of storey 1 having as sum the value $M_{c,i,1}$ is perfectly equivalent. The choice has been made according to several analyses carried out on different structures in order to provide a cheaper solution.

f) Design of the columns at first storey. It starts by considering a section able to resist to vertical loads at ultimate limit state ($N_{V,SLU}$). The base of the section is, initially, assumed equal to $b = 30$cm and the height is calculated with the following equation:

$$h = \frac{N_{V,SLU}}{\nu \cdot b \cdot f_{cd}} = \frac{N_{V,SLU}}{0.5 \cdot b \cdot f_{cd}} \geq 30cm \tag{23}$$

For a given value of b and h, the reinforcements of the section are to be designed. At this aim it is very important to consider the shape of the M-N interaction domain. In fact, for a concrete frame, the maximum axial force does not necessarily implicate the worst condition, as happens in steel members, because it depends on the zone of the domain where the design point is located. If the design condition falls at the left of the M-N interaction diagram peak, there is a resistant moment increasing with the increase of axial load (Figure 4(a)). Conversely, at the right of the peak the dual condition is noted (Figure 4(b)).

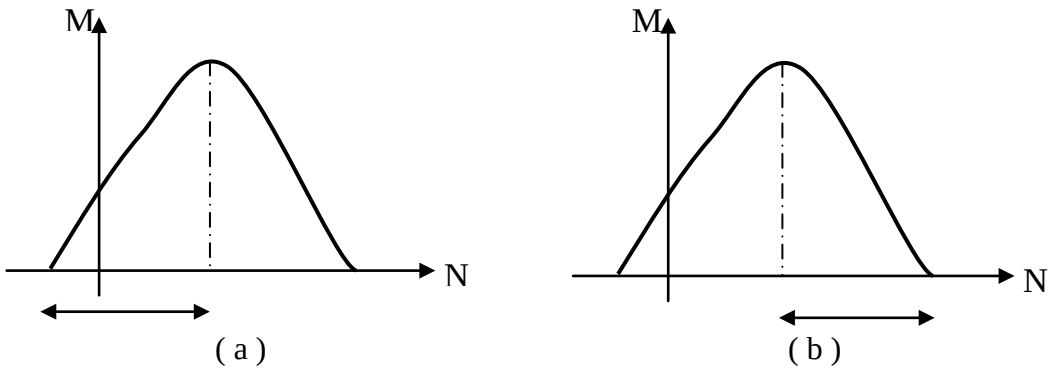


Figure 4: M-N interaction domain

The main problem affecting the M-N interaction domain configuration is that it is impossible to immediately obtain the value of the design axial force. The problem can be solved by considering two values of axial force:

- a maximum value N_{max}, given by the sum of the axial forces due to vertical loads, in the seismic load combination ($N_{q,E}$) and the maximum of the axial force related to the shear actions due to the plastic hinges developed at the beam ends ($N_{M,E}$):

$$N_{max} = N_{q,E} + N_{M,E} \tag{24}$$

- a minimum value N_{min}, obtained by subtracting the same terms mentioned above:

$$N_{min} = N_{q,E} - N_{M,E} \tag{25}$$

For a generic column and for a fixed direction of the earthquake, if the axial load is given by Eq. (24), then, for the opposite direction of horizontal forces, the axial load contribution is given by Eq. (25). Consequently, a design moment must be associated with those axial forces.

In particular the proposed design procedure considers, for both values of the axial forces, the value of the design moment obtained with the Eq. (22), namely M_{PR}. In conclusion the design points are:

$$A\ (N_{min}, M_{PR}) \qquad\qquad B\ (N_{max}, M_{PR}) \tag{26}$$

Anyway, this aspect will be better clarified in the worked example (Figure 6).

g) Design of the reinforcement of columns at first storey. The process consists, essentially, in assuming an initial quantity of reinforcement (corresponding to the minimum value allowed by the adopted code) which is increased until the design points fall into the internal side of the M-N performance domain. If the maximum percentage of reinforcement prescribed by the regulations is reached, then the procedure is repeated by increasing the section dimensions. Once the columns are designed the obtained value of $M_{c,1}$, namely $M_{c,Rd,1}$, is generally greater than the required minimum value provided by Eq. (21). Therefore, the kinematically admissible multiplier $\alpha_0^{(g)}$ corresponding to the global mechanism is to be evaluated accordingly, i.e. by means of Eq. (4) by replacing the term $M_{c,1}$, with the value $M_{c,Rd,1}$ resulting from designed sections.

h) Computation of the required sum of plastic moments of columns $M_{c,im}$ for $i_m > 1$ imposing that the i_m-th mechanism equilibrium curves of type 1, 2 and 3 have to be located above the curve of global one, i.e. by applying relation (14). In fact, for a fixed value of i_m, relation (14) provides three values of $M_{c,im}$, namely $M_{c,im}^{(t)}$ for $t = 1,2,3$. In particular, in order to avoid the i_m-th mechanism of type 1, the minimum required value of $M_{c,im}$ is:

$$M_{c,im}^{(1)} \geq \left(\alpha_0^{(g)} + \gamma_{i_m}^{(1)}\delta_u\right)\left(\sum_{k=1}^{i_m} F_k h_k + h_{i_m}\sum_{k=i_m+1}^{n_s} F_k\right) - M_{c,Rd,1} - 2\sum_{k=1}^{i_m-1}\sum_{j=1}^{n_b} M_{b.jk} \tag{27}$$

In addition, in order to avoid the i_m-th mechanism of type-2, the minimum required value of $M_{c,im}$ is:

$$M_{c,im}^{(2)} \geq \left(\alpha_0^{(g)} + \gamma_{i_m}^{(2)}\delta_u\right)\sum_{k=i_m}^{n_s} F_k(h_k - h_{i_m-1}) - 2\sum_{k=i_m}^{n_s}\sum_{j=1}^{n_b} M_{b.jk} \tag{28}$$

Finally to avoid the i_m-th mechanism of type-3, the minimum required value of $M_{c,im}$ is:

$$M_{c,im}^{(3)} \geq \left(\alpha_0^{(g)} + \gamma_{i_m}^{(3)}\delta_u\right)\frac{\left(h_{i_m} - h_{i_m-1}\right)}{2}\sum_{k=i_m}^{n_s} F_k \tag{29}$$

Eqs. (27), (28) and (29) have been derived from Eq. (14) for $i_m > 1$ and $t = 1$, $t = 2$ and $t = 3$, respectively.

i) Computation of the required sum of the plastic moments of columns for each storey as the maximum value among those coming from the above design conditions:

$$M_{c,im} = max\left\{M_{c,im}^{(1)}, M_{c,im}^{(2)}, M_{c,im}^{(3)}\right\} \qquad \text{per} \quad i_m > 1 \tag{30}$$

j) The sum of the required plastic moments of columns at each storey, is distributed among all the storey columns with the same procedure as for the columns on the first storey i.e. according to the following relation:

$$M_{c,i,im} = \frac{M_{c,im}}{n_c} \qquad \text{for } i = 1, \dots, n_c. \tag{31}$$

k) Design of columns at each storey. The procedure is the same as that explained in the points f) and g).

l) If necessary, a technological condition is imposed by requiring, starting from the base, that the column sections cannot increase along the building height. If this condition requires the change of sections at first storey then the procedure needs to be repeated from point f). In fact, in this case, a new value of $M_{c,Rd,1}$ is obtained and, as a consequence, also a new value of $\alpha_0^{(g)}$ is to be evaluated. As a consequence the values $M_{c,im}^{(1)}, M_{c,im}^{(2)}, M_{c,im}^{(3)}$ obtained by relations (27), (28), (29) also change. On the contrary, if the condition only requires the change of sections at the upper storeys, i.e. without the involvement of first storey columns, then the design step k) is to be repeated in order to consider the new section dimensions.

The check of technological condition could look redundant because it is common for both axial force and shear demand to increase gradually in lower stories but ,when the proposed procedure is applied, as reported in the worked example, the required sum of plastic moments of j-th storey can be bigger than the required sum of plastic moments at $(j-1)$-th storey.

3. WORKED EXAMPLE

In order to show the practical application of the proposed design procedure, the seismic design of a four-bay five-storey moment resisting frame is presented in this section. The inelastic behaviour of the designed structure is successively examined by means of a push-over static inelastic analysis, confirming the fulfilment of the design goal, i.e. the location of the yielding zones at the beam ends with the only exception of the base section of first-storey columns. The structural scheme of the frame to be designed is shown in Figure 5. The structural scheme is symmetric: the external bay span is equal to 5m and the internal bay span is equal to 6m. The interstorey height is equal to 3m. The characteristic values of the vertical loads acting on the beams are equal to 19.5 kN/m and 12 kN/m for permanent (G_k) and live (Q_k) actions, respectively.

The structural materials adopted are concrete C25/30 and reinforcement of steel grade B450C. According to Eurocode 8, the value of the period of vibration to be used for preliminary design is:

$$T = 0.075\, H^{3/4} = 0.075 \cdot 18^{3/4} \approx 0.65\, s \tag{32}$$

where H is the total height of the frame.

With reference to the design spectrum for stiff soil conditions (soil class A of Eurocode 8) and by assuming a behaviour factor q equal to 3.9, the horizontal seismic forces are those depicted in Figure 5.

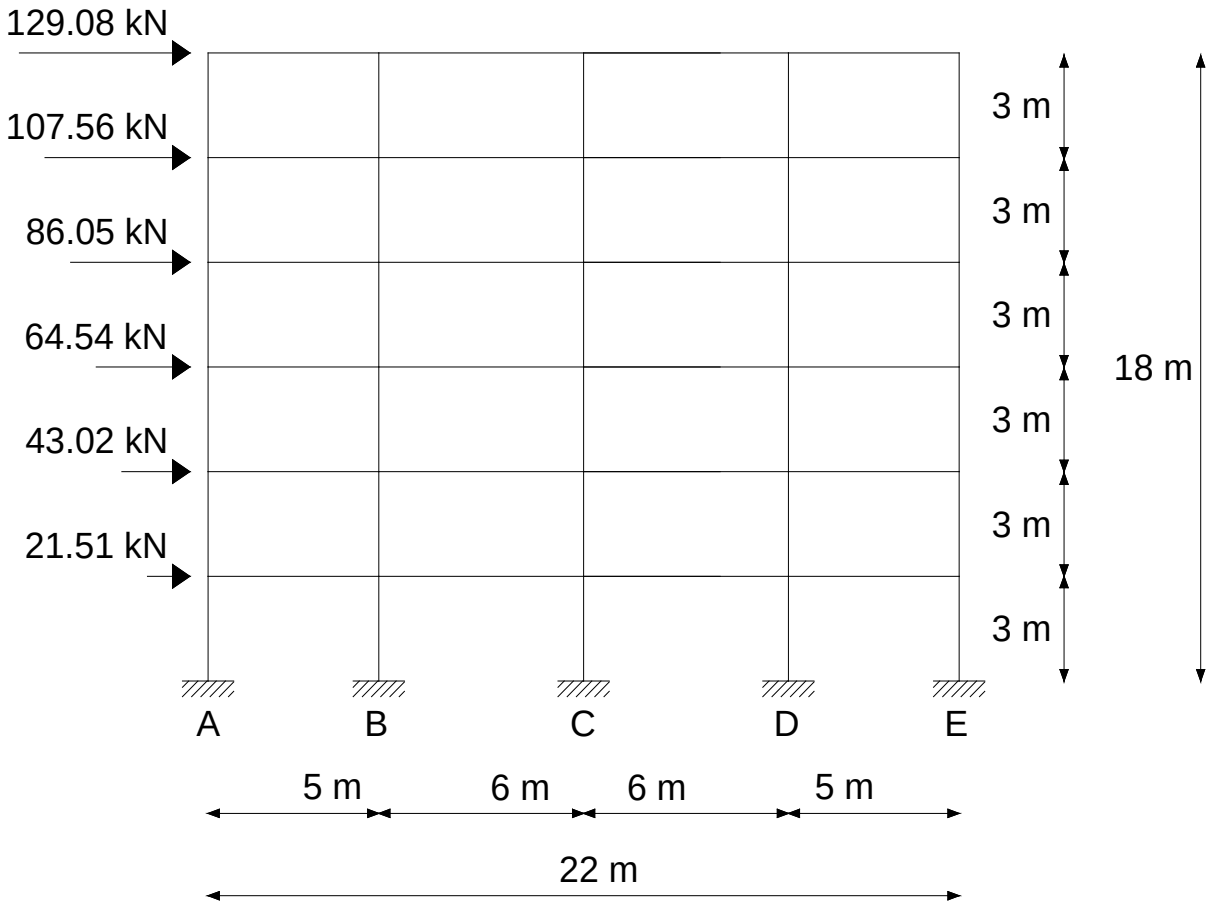


Figure 5: Structural scheme of the designed frame

In the following, the numerical development of the design steps for the structural scheme described above is provided.

a) Selection of the design top sway displacement

The selection of the maximum top sway displacement up to which the global mechanism has to be assured is a very important design issue, because the value of this displacement governs the magnitude of second order effects accounted for in the design procedure. A good criterion to choose the design ultimate displacement δ_u is to relate it to the plastic rotation supply of beams or beam-to-column connections by assuming $\delta_u = \theta_u \cdot h_{ns}$ (where θ_u can be assumed equal to 0.04 rad).

As a consequence, the design value of the top sway displacement has been assumed equal to:

$$\delta_u = 0.04 \cdot h_{ns} = 0.04 \cdot 18 = 0.75\ m \tag{33}$$

b) Design of beam sections to withstand vertical loads.

The load acting on the frame in the vertical load combination is:

$$Q_{SLU} = 1.3\ G_k + 1.5\ Q_k = 43.35\ kN/m \tag{34}$$

For the design of the beams has been considered a bending moment equal to:

$$M_{max} = \frac{Q_{SLU} \cdot L^2}{8} \tag{35}$$

Therefore, by imposing the base of the section equal to b=30 cm, is possible to calculate the height of the beam through the following design relation:

$$d = r\sqrt{\frac{M_{Sd}}{b}} \tag{36}$$

Assuming $\xi = 0.25$ and $\rho = 0.25$ a value of $r = 0.19$ is obtained. As a consequence the amount of reinforcement is given by:

$$A_s = A'_s = \frac{M_{Sd}}{0.85 \cdot h \cdot f_{sd}} \tag{37}$$

Obviously the number of steel bars in the beam is such that:

$$M_{Rd} > M_{Sd} \tag{38}$$

c) Computation of the axial load acting at collapse state in the columns.

According to the global mechanism, axial forces in the columns at collapse state depend both from the distributed loads acting on the beams and from the shear action due to the development of plastic hinges at the beam ends, as depicted in Figure 6 (with reference to the earthquake from left to right).

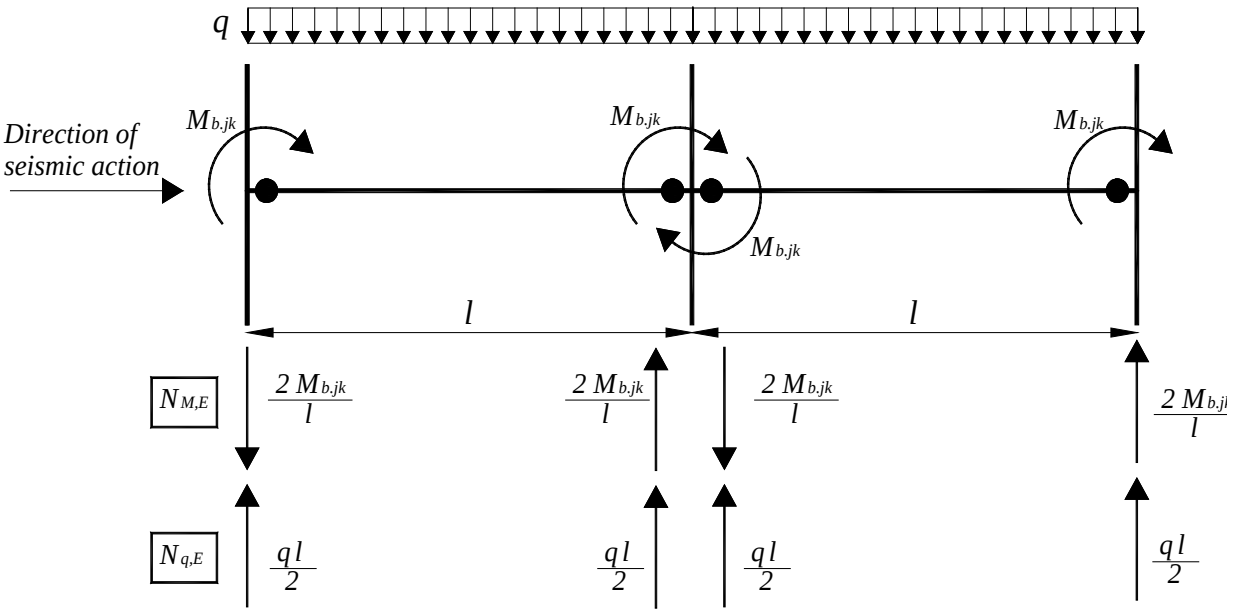


Figure 6: Loads transmitted by the beams to the columns at collapse state

So that, the total load transmitted by the beams to the columns is the sum of two contributions. The first one, $N_{q,E}$, is related to the vertical loads acting in the seismic load combination (i.e. the sum of $ql/2$ type contributions). The second one, $N_{M,E}$, is related to the shear actions due to the plastic hinges developed at the beam ends (i.e. the sum of $2M_{b,jk}/l$ type contributions). In Table 2, the two contributions $N_{q,E}$, $N_{M,E}$ are reported for each storey both for internal columns and for external columns.

STOREY	Columns A and E		Columns B and D		Column C	
i_m	$N_{q,E}$ [kN]	$N_{M,E}$ [kN]	$N_{q,E}$ [kN]	$N_{M,E}$ [kN]	$N_{q,E}$ [kN]	$N_{M,E}$ [kN]
1	346.50	523.55	762.30	143.73	831.60	0
2	288.75	436.29	635.25	119.78	693.00	0
3	231.00	349.03	508.20	95.82	554.40	0
4	173.25	261.77	381.15	71.87	415.80	0
5	115.50	174.52	254.10	47.91	277.20	0
6	57.75	87.26	127.05	23.96	138.60	0

Table 2: Axial forces acting at collapse state in the columns

d) Computation of the slopes of mechanism equilibrium curve $\gamma_{i_m}^{(t)}$.

By means of Eqs. (16), (18) and (20) the slopes of mechanism equilibrium curves are computed. These values are reported in Table 3:

STOREY i_m	$\gamma_{i_m}^{(1)}$	$\gamma_{i_m}^{(2)}$	$\gamma_{i_m}^{(3)}$
1	0.0225	0.0030	0.0225
2	0.0106	0.0034	0.0197
3	0.0067	0.0039	0.0175
4	0.0048	0.0049	0.0157
5	0.0037	0.0069	0.0143
6	0.0030	0.0131	0.0131

Table 3: Slopes of mechanism equilibrium curves (cm^{-1})

In particular it is important to underline that the slope value corresponding to the global mechanism $\gamma^{(g)} = \gamma_1^{(2)}$, is the minimum among all the $\gamma_{i_m}^{(t)}$ values:

$$\gamma^{(g)} = 0.003029\ cm^{-1} \tag{39}$$

e) Computation of the required sum of plastic moments of columns at first storey $M_{c,1}$.

As previously pointed out, the required sum of plastic moments of columns at first storey is provided by Eq. (21). In the examined case, this sum is equal to $M_{c,1} = 2801.17\ kNm$ and has to be distributed among the columns proportionally to their number. Therefore the required bending moment for each column $M_{c,i,1}$, the section, the upper and lower reinforcement, the axial force for both directions of the earthquake are reported in Table 4.

STOREY	Column	$M_{c,i,1}$ [kNm]	$b\ x\ h$	$A_s = A'_s$	N_{min} [kN]	N_{max} [kN]
1°	A	560.23	30x60	5 Φ 28	-177.05	870.05
	B		30x70	5 Φ 20	618.57	906.03
	C		30x80	6 Φ 16	831.60	831.60
	D		30x70	5 Φ 20	618.57	906.03
	E		30x60	5 Φ 28	-177.05	870.05

Table 4: Design of the column sections at first storey

The sum of obtained column plastic moments at first storey is: $M_{c,Rd,1} = 3206.08\ kNm$ which is greater than the required one.

f) Computation of seismic horizontal forces corresponding to the ultimate design displacement.

The value of $\alpha_0^{(g)}$ obtained from Eq. (4) is equal to $\alpha_0^{(g)} = 2.8165$.

g) Computation of the required sum of plastic moments of columns $M_{c,im}^{(t)}$ at any storey, to avoid undesired mechanism by means of equations (27) (28) and (29).

STOREY i_m	$M_{c,im}^{(1)}$ [kNm]	$M_{c,im}^{(2)}$ [kNm]	$M_{c,im}^{(3)}$ [kNm]
1	<u>3206.08</u>	-	3206.08
2	<u>3433.29</u>	1729.90	2581.60
3	<u>4043.52</u>	420.41	2231.96
4	<u>4153.69</u>	-555.71	1798.98
5	<u>3597.12</u>	-1031.79	1282.66
6	<u>2207.14</u>	-841.13	683.00

Table 5: Sum of plastic moments of column required at each storey to avoid undesired mechanism

h) Computation of the maximum value of $M_{c,im}$.

The sum of the plastic moments of columns governing the column design at each storey is given in Table 5 by the underlined values. It can be recognized that, in the examined case, the need to avoid type-1 mechanism always governs the design of columns.

i) Design of column sections at each storey.

The required sum of column plastic moments M_{c,i,i_m}, the section, the upper and lower reinforcement, the axial force for both directions of the earthquake are reported in Table 6.

STOREY	Column	$M_{c,im}$ [kNm]	$b\ x\ h$	$A_s = A'_s$	N_{min} [kN]	N_{max} [kN]
2°	A	686.65	30x70	5 Φ 28	- 147.54	725.04
	B		30x60	6 Φ 24	515.47	755.03
	C		30x70	7 Φ 20	693.00	693.00
	D		30x60	6 Φ 24	515.47	755.03
	E		30x70	5 Φ 28	- 147.54	725.04
3°	A	808.70	30x70	5 Φ 32	- 118.03	580.03
	B		30x70	5 Φ 28	412.38	604.02
	C		30x60	4 Φ 32	554.40	554.40
	D		30x70	5 Φ 28	412.38	604.02
	E		30x70	5 Φ 32	- 118.03	580.03
4°	A	830.73	30x70	5 Φ 32	- 88.52	435.02
	B		30x70	5 Φ 28	309.28	453.02
	C		30x70	5 Φ 28	415.80	415.80
	D		30x70	5 Φ 28	309.28	453.02
	E		30x70	5 Φ 32	- 88.52	435.02
5°	A	719.42	30x70	5 Φ 28	- 59.02	290.02
	B		30x60	4 Φ 32	206.19	302.01
	C		30x60	5 Φ 28	277.20	277.20
	D		30x60	4 Φ 32	206.19	302.01
	E		30x70	5 Φ 28	- 59.02	290.02
6°	A	441.42	30x50	6 Φ 24	- 29.51	145.01
	B		30x50	6 Φ 24	103.09	151.01
	C		30x50	6 Φ 24	138.60	138.60
	D		30x50	6 Φ 24	103.09	151.01
	E		30x50	6 Φ 24	- 29.51	145.01

Table 6: Design of column sections at each storey

j) Checking of technological condition

By observing Table 4 and Table 6 it can be noted that there are some column sections at the first storey which are smaller than the corresponding ones required at the second storey, therefore, this condition generates a technological condition at the first storey. As a consequence, the value of $M_{c,Rd,1}$ needs to be updated and the procedure needs to be repeated from the step e). In Table 7 the new value of required sum of plastic moments of columns $M_{c,im}^{(t)}$ at any storey are reported:

STOREY i_m	$M_{c,im}^{(1)}$ [kNm]	$M_{c,im}^{(2)}$ [kNm]	$M_{c,im}^{(3)}$ [kNm]
1	3299.17	-	3299.17
2	3382.14	1801.51	2591.83
3	4010.78	471.55	2241.17
4	4136.30	-522.98	1806.65
5	3590.98	-1014.40	1288.29
6	2207.14	-834.99	686.07

Table 7: Sum of plastic moments of column required at each storey to avoid undesired mechanism

With reference to Figure 6, that is, to the earthquake from left to right, the axial force corresponding $N_{LR,i,im}$ and the obtained bending resistance $M_{c,Rd,i,im}$ are reported in Table 8.

STOREY	Column	$M_{c,i,im}$ [kNm]	$b\ x\ h$	$A_s = A_s'$	$N_{LR,i,im}$ [kN]	$M_{c,Rd,i,im}$ [kNm]
1°	A	560.23	30x70	6 Φ 24	- 177.05	624.88
	B		30x70	5 Φ 20	618.57	564.77
	C		30x80	6 Φ 16	831.60	600.50
	D		30x70	5 Φ 20	906.03	613.87
	E		30x70	6 Φ 24	870.05	895.14
2°	A	676.42	30x70	5 Φ 28	- 147.54	725.52
	B		30x70	7 Φ 20	515.47	699.78
	C		30x70	7 Φ 20	693.00	736.67
	D		30x70	7 Φ 20	755.03	747.81
	E		30x70	5 Φ 28	725.04	962.94
3°	A	802.15	30x70	5 Φ 32	- 118.03	970.87
	B		30x70	6 Φ 24	412.38	804.06
	C		30x70	6 Φ 24	554.40	837.54
	D		30x70	6 Φ 24	604.02	848.21
	E		30x70	5 Φ 32	580.03	1170.38
4°	A	827.26	30x70	5 Φ 32	- 88.52	980.27
	B		30x70	5 Φ 28	309.28	867.90
	C		30x70	5 Φ 28	415.80	896.16
	D		30x70	5 Φ 28	453.02	905.33
	E		30x70	5 Φ 32	435.02	1136.93
5°	A	718.19	30x70	5 Φ 28	- 59.02	753.74
	B		30x60	4 Φ 32	206.19	736.41
	C		30x60	5 Φ 28	277.20	724.63
	D		30x60	4 Φ 32	302.01	759.55
	E		30x70	5 Φ 28	290.02	862.57
6°	A	441.42	30x50	6 Φ 24	- 29.51	462.44
	B		30x50	6 Φ 24	103.09	491.33
	C		30x50	6 Φ 24	138.60	499.05
	D		30x50	6 Φ 24	151.01	501.73
	E		30x50	6 Φ 24	145.01	500.43

Table 8: Design of column sections at each storey for earthquake from left to right

With reference to the earthquake from right to left, the axial force corresponding $N_{RL,i,im}$ and the obtained bending resistance $M_{c,Rd,i,im}$ are reported in Table 9.

STOREY	Column	$M_{c,i,im}$ [kNm]	$b\ x\ h$	$A_s = A'_s$	$N_{RL,i,im}$ [kN]	$M_{c,Rd,i,im}$ [kNm]
1°	A	560.23	30x60	5 Φ 28	870.05	895.14
	B		30x70	5 Φ 20	906.03	613.87
	C		30x80	6 Φ 16	831.60	600.50
	D		30x70	5 Φ 20	618.57	564.77
	E		30x60	5 Φ 28	- 177.05	624.88
2°	A	686.65	30x70	5 Φ 28	725.04	962.94
	B		30x60	6 Φ 24	755.03	747.81
	C		30x70	7 Φ 20	693.00	736.67
	D		30x60	6 Φ 24	515.47	699.78
	E		30x70	5 Φ 28	- 147.54	725.52
3°	A	808.70	30x70	5 Φ 32	580.03	1170.38
	B		30x70	5 Φ 28	604.02	848.21
	C		30x60	4 Φ 32	554.40	837.54
	D		30x70	5 Φ 28	412.38	804.06
	E		30x70	5 Φ 32	- 118.03	970.87
4°	A	830.73	30x70	5 Φ 32	435.02	1136.93
	B		30x70	5 Φ 28	453.02	905.33
	C		30x70	5 Φ 28	415.80	896.16
	D		30x70	5 Φ 28	309.28	867.90
	E		30x70	5 Φ 32	- 88.52	980.27
5°	A	719.42	30x70	5 Φ 28	290.02	862.57
	B		30x60	4 Φ 32	302.01	759.55
	C		30x60	5 Φ 28	277.20	724.63
	D		30x60	4 Φ 32	206.19	736.41
	E		30x70	5 Φ 28	- 59.02	753.74
6°	A	441.42	30x50	6 Φ 24	145.01	500.43
	B		30x50	6 Φ 24	151.01	501.73
	C		30x50	6 Φ 24	138.60	499.05
	D		30x50	6 Φ 24	103.09	491.33
	E		30x50	6 Φ 24	- 29.51	462.44

Table 9: Design of column sections at each storey for earthquake from right to left

4. VALIDATION OF THE DESIGN PROCEDURE

In order to validate the design procedure, a static non-linear analysis (push-over) has been carried out to investigate the actual seismic response of the designed frame by means SAP2000 computer program [36]. This analysis has the primary aim to confirm the development of the desired collapse mechanism typology and to evaluate the obtained energy dissipation capacity, testing the accuracy of the proposed design methodology.

Regarding the structural modelling, the mechanical non-linearities, have been concentrated at beam and column ends by means of plastic hinge elements. The constitutive law of such plastic hinge elements is provided by a rigid plastic moment-rotation curve. The type of hinge depends on the element considered i.e. by its internal action. In fact, for the beams and the columns M3 and P-M3 hinge type have been considered, respectively. In case of P-M3 hinge type, the interaction domain P-M has been evaluated for each column and used in SAP2000 computer program. The results of the push-over analysis are mainly constituted by base shear – top sway displacement curve which is depicted in Figure 7.

In the same figure also a straight line is given, i.e. the one corresponding to the linearized mechanism equilibrium curve of global mechanism whose expression, for the designed frame, is:

$$\alpha = 2.8165 - 0.003029\ \delta \tag{40}$$

Obviously, the base shear depicted in Figure 7 is, in this case, obtained by multiplying the value of α, given by Eq. (40), for the design base shear corresponding to $\alpha = 1$. The comparison between the capacity curve and the above straight line provides a first confirmation of the accuracy of the proposed design procedure.

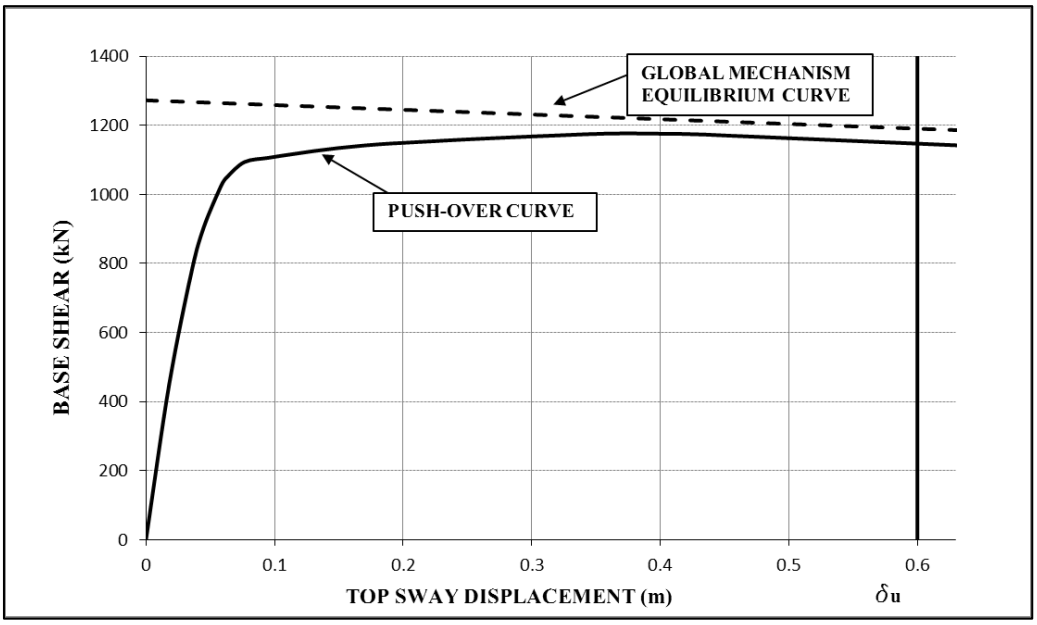


Figure 7: Push-over curve with the global mechanism equilibrium curve

A further confirmation, even the most important, of the fulfilment of the design objective is represented by the pattern of yielding developed at the occurrence of the design ultimate displacement. In fact, developed plastic hinges are shown in Figure 8 and their pattern is in perfect agreement with the global mechanism.

In order to fulfill the serviceability requirements the interstorey drift have been checked with reference to the limit reported in the Eurocode 8. In particular the considered limit refers to buildings having non structural elements of brittle materials attached to the structure:

$$d_r\ \nu \leq 0.005\ \text{h} \tag{41}$$

If this serviceability requirement is not verified the structural stiffness can be improved by increasing the beam sections or the ultimate design displacement. In fact, in both cases the final results will be a more rigid structure with respect to the one obtained in the worked example herein presented. In Table 10 the final results are reported.

STOREY	d_s [mm]	d_r [mm]	υ	$d_r\ \upsilon$	0.005 h
1°	6.9238	0.8140	0.5	0.4070	1.5
2°	6.1097	1.0598		0.5299	1.5
3°	5.0499	1.2805		0.6402	1.5
4°	3.7693	1.4740		0.7370	1.5
5°	2.2953	1.4624		0.7312	1.5
6°	0.8328	0.8328		0.4164	1.5

Table 10: Limitation of interstorey drift

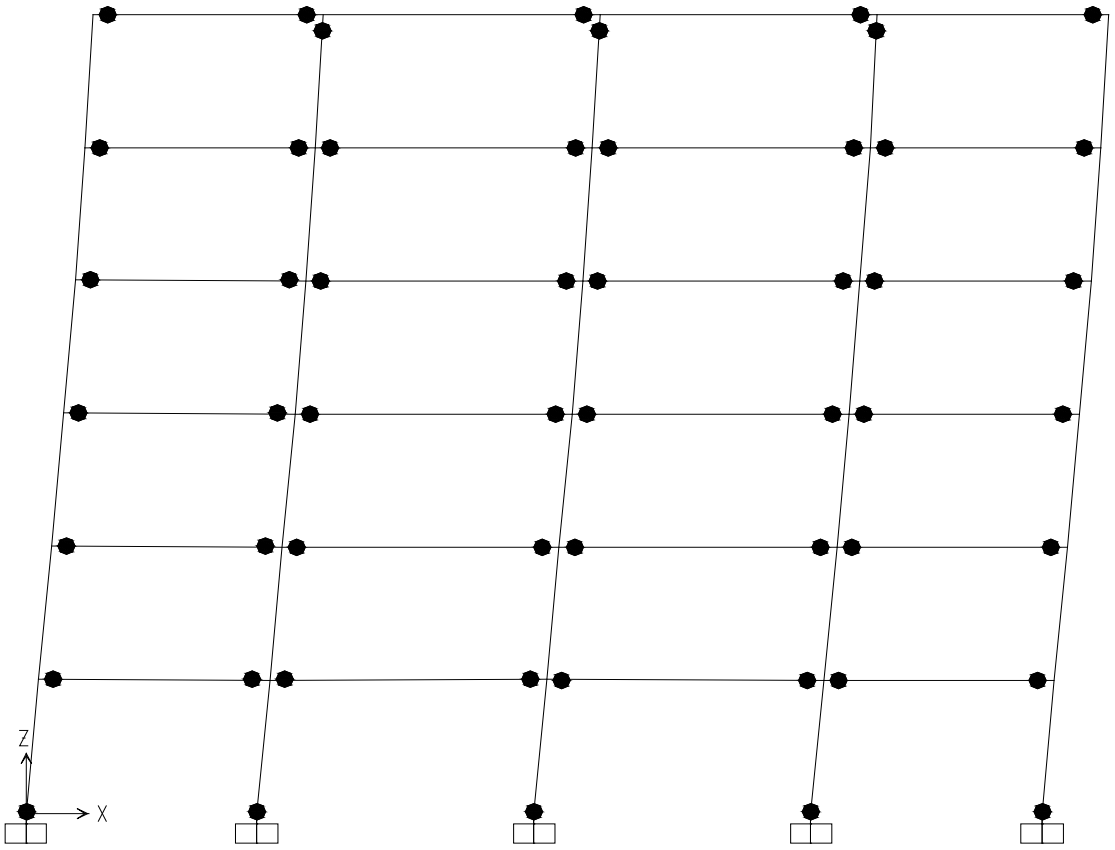


Figure 8: Pattern of yielding of the designed frame at $\delta = \delta_u$

To provide a more robust validation of the design methodology, non-linear incremental dynamic analyses have been developed with reference to the same structural model used for push-over analyses.

Record-to-record variability has been accounted for considering 7 recorded accelerograms selected from PEER data base [37].

In Table 11 main features of the records (name, date, magnitude, ratio between PGA and gravity acceleration, length and step recording) are given. These earthquake records have been selected to approximately match the linear elastic design response spectrum of Eurocode 8, for type A soil.

Moreover, in order to perform IDA analyses, each ground motion has been scaled to obtain the same value of the spectral acceleration $S_a(T_1)$ corresponding to the fundamental period of vibration T_1 of the structure ($T_1 = 0.65$).

Earthquake (record)	Component	Date	PGA/g	Length	Step recording
Coalinga (Slack Canion)	H-SCN045	1983/05/02	0.166	29.99	0.01
Imperial Valley (Agrarias)	H-AGR003	1979/10/15	0.370	28.35	0.01
Kobe (Kakogawa)	KAK000	1995/01/16	0.251	40.95	0.01
Palm Springs (Soboba)	H08000	1986/07/08	0.250	26.00	0.005
Santa Barbara (Courthouse)	SBA132	1978/08/13	0.102	12.57	0.01
Spitak Armenia (Gukasian)	GUK000	1988/07/12	0.199	19.89	0.01
Victoria Mexico (Chihuahua)	CHI102	1980/06/09	0.150	26.91	0.01

Table 11: *Accelerogram characteristics*

This is the seismic intensity measure (IM) adopted for IDA analyses where $S_a(T_1)$ values have been progressively increased until the occurance of structural collapse, corresponding to anyone of the following ultimate limit states: column buckling or to the complete development of a collapse mechanism, attainment of the limit value of plastic rotation of beams or columns. In Figure 9, the maximum interstorey drift ratio (MIDR) versus spectral acceleration curve is reported. MIDR curves appears quite regular and increasing without dynamic instability. In addition, for each record the obtained pattern of yelding has been monitored for increasing values of $S_a(T_1)$ by checking that plastic hinge development is always in perfect agreement with the global mechanism. This results testifies the accuracy of the proposed design procedure even under actual seismic actions.

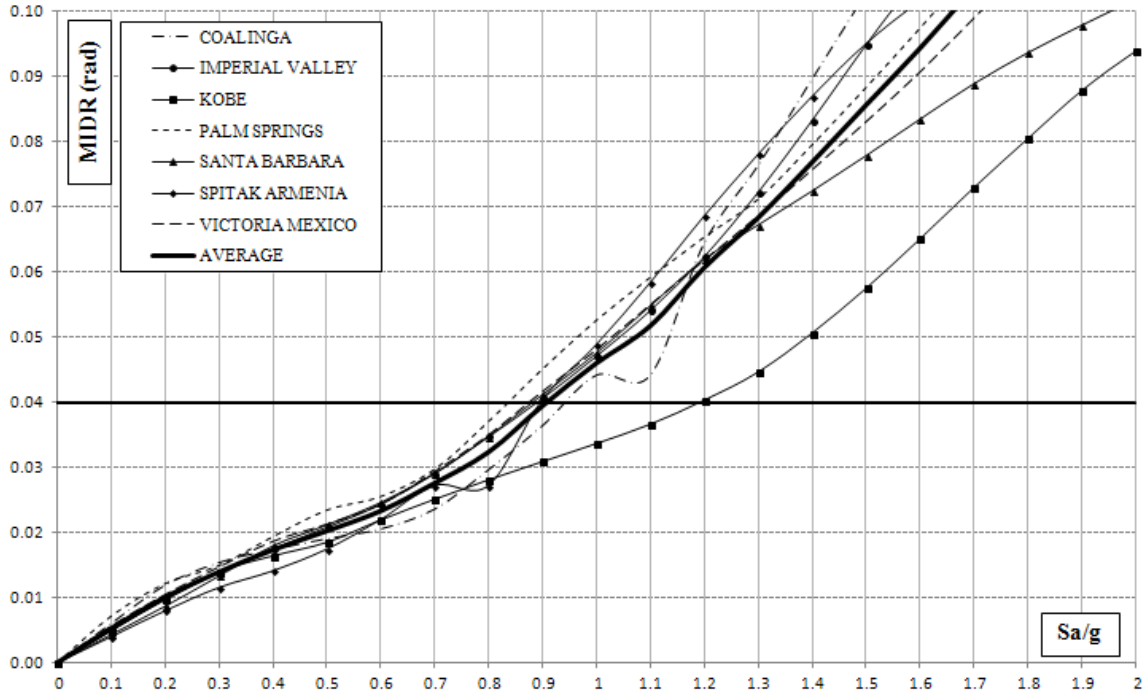


Figure 9: *Maximum interstorey drift ratio versus* $S_a(T_1)$

As an example, Figure 10 provides the distribution of plastic hinges for increasing value of $S_a(T_1)$ with reference to Santa Barbara earthquake record. As a consequence of the obtained design goal, the spectral acceleration values leading to collapse, given in Table 12, are very high and compatible with the adoption of the designed structure even in the case of destructive earthquakes.

Earthquake (record)	**Sa_c/g**	**PGA_c/g**
Coalinga (Slack Canion)	0.94	0.52
Imperial Valley (Agrarias)	0.89	0.73
Kobe (Kakogawa)	1.10	0.83
Palm Springs (Soboba)	0.84	1.51
Santa Barbara (Courthouse)	0.88	0.63
Spitak Armenia (Gukasian)	0.89	0.52
Victoria Mexico (Chihuahua)	0.87	0.32
Mean value	**0.91**	**0.72**

Table 12: $S_a(T_1)$ *and PGA values corresponding to attainment of the structural collapse*

As depicted in Figure 10 the frames present some spurious hinges at the column ends of some storeys. Indeed these hinges are displayed by the SAP but their plastic rotation is very close to zero then they do not partecipate in the development of the collapse mechanism of global type. In paticular, drawn the limit line of the ultimate plastic rotation provided by hinges (0.04 rad). In addition the average value of $S_a(T_1)$ leading to collapse is near to 0.91g while the average PGA is about 0.72g.

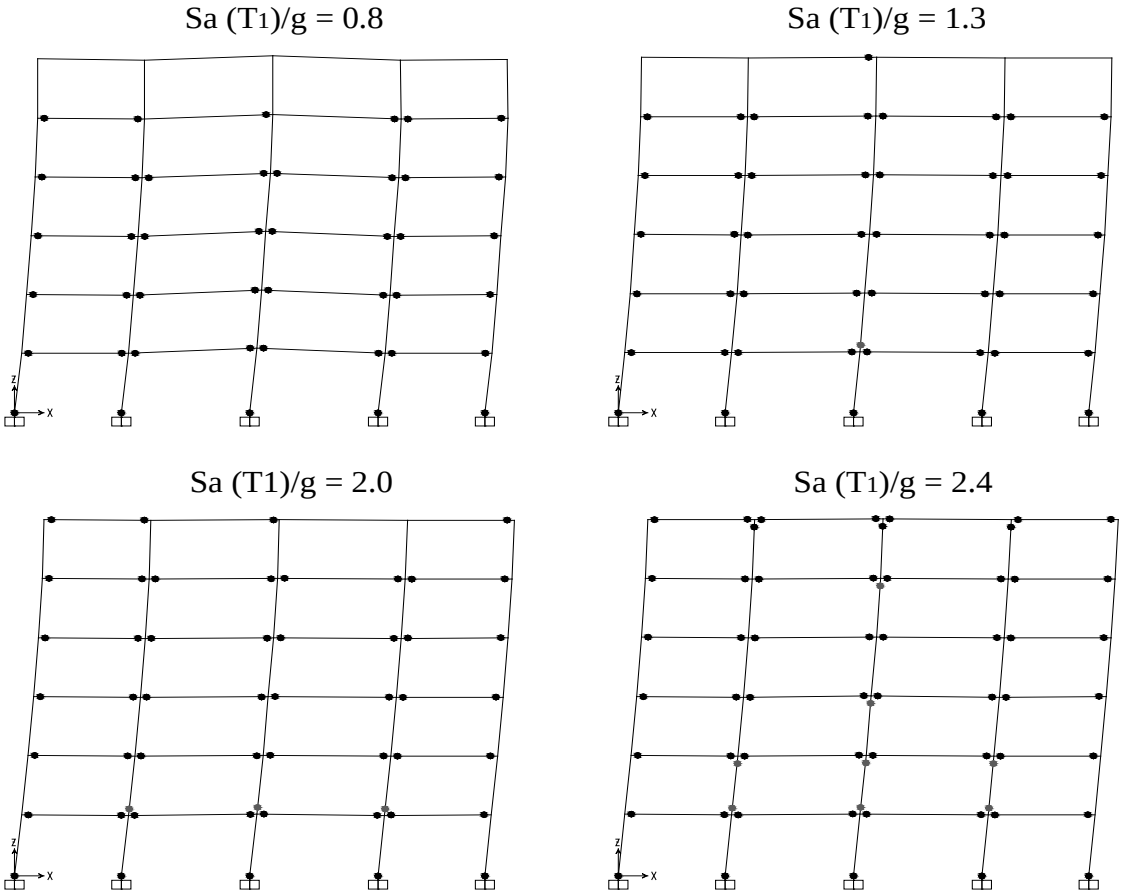


Figure 10: Pattern of yielding of the designed frame for increasing value of $S_a(T_1)$ with reference to Santa Barbara earthquake record

5. CONCLUSIONS

In this paper a methodology called “Theory of Plastic Mechanism Control” for the design of reinforced concrete moment resisting frames has been presented. On the base of the extension of the kinematic theorem of plastic collapse to the concept of mechanism equilibrium curve, the Theory of Plastic Mechanism Control allows to evaluate the sum of plastic moments of the columns required at each storey in order to develope a collapse mechanism of global type. The closed form solution of the design conditions makes the design procedure very easy to be applied even by means of hand calculations and, therefore, it could also be suggested for code purpose by definitely solving the problem of collapse mechanism control whose importance in seismic design is universally recognised. Beam-column hierarchy criterion, commonly suggested by seismic codes, appears only as a very rough approximation when compared to TPMC and its theoretical background. The reliability of the proposed design procedure has

been also demonstrated through its application to a four-bays, five-storeys frame, leading to the fulfilment of the design objective, i.e. the development of a collapse mechanism of global type, as it has been confirmed by the results of both push-over static inelastic analysis and incremental dynamic analyses. The proposed methodology can be considered as belonging to the Performance Based Seismic Design philosophy [38]. In fact, in order to satisfy the limit states of "Life Safe" or "Near Collapse" the designer has to promote a dissipative collapse mechanism avoiding the so called "soft storey mechanism". In addition, it is useful to underline that the proposed procedure constitutes a rigorous application of the capacity design principles. In fact, beams are designed in order to bear external loads, while columns are designed according to the maximum internal actions transmitted by the dissipative zones. As already stated in point b) of the design algorithm, the limit of the procedure herein presented is constituted by the simmetry considered both for the structural scheme and for the beam sections. In fact, only symmetric structures characterized by symmetrical beam sections with symmetrical reinforcement have been considered. This represents the main limit of the procedure and the its overcoming is the main objective of the future developments of the work.

REFERENCES

[1] EN 1998-1, "Eurocode 8: Design of Structures for Earthquake Resistance – Part 1: general Rules, Seismic Actions and Rules for Buildings", CEN, 2004.

[2] New Zealand Standard Code of Practice for the Design of Concrete Structures, NZS 3101: Part 1; Commentary NZS 3101: Part 2; Standard Association of New Zealand, Wellington, New Zealand, 1982.

[3] Lee H.S., "Revised rule for concept of strong-column weak-girder design", J. struct. eng. ASCE, 122, 359-364, 1996.

[4] Paulay T., "Seismic design of ductile moment resisting reinforced concrete frames, columns: evaluation of actions", Bull. New Zealand Natl. Soc. Earthquake Eng., 10, 85-94, 1977.

[5] Paulay T., "Deterministic Design Procedure for Ductile Frames in Seismic Areas", ACI Publication SP-63, American Concrete Institute, Detroit, pp. 357-381, 1980.

[6] Kappos A.J., "Evaluation of the Inelastic Seismic Behaviour of Multistorey Reinforced Concrete Buildings", PhD Thesis (in Greek), Scientific Annual of the Faculty of Engineering, Aristotle University of Thessaloniki, 1986.

[7] Panelis G.G., Kappos A.J., "Earthquake-Resistant Concrete Structures", E&FN Spon, an imprint of Chapman & Hall, 1997.

[8] Mazzolani F.M:, Piluso V., "Plastic Design of Seismic Resistant Steel Frames", Earthquake Engineering and Structural Dynamics, Vol. 26, pp. 167-191, 1997.

[9] Longo A.; Montuori R.; Piluso V., Theory of Plastic Mechanism Control for MRF-CBF dual system and its validation. Bulletin of Earthquake Engineering (BEEE), 2014.

[10] Giugliano M.T., Longo A., Montuori R., Piluso V., Failure mode and drift control of MRF-CBF dual systems The Open Construction and Building Technology Journal, 4, 121-133, 2010.

[11] Montuori R., Piluso V., Troisi M., Theory of plastic mechanism control of seismic-resistant MR-frames with set-backs. Open Construction and Building Technology Journal, vol. 6, pp. 404-413, 2012.

[12] Longo A., Montuori R., Piluso V., Theory of Plastic Mechanism Control of Dissipative Truss Moment Frames, Engineering Structures, Vol. 37, pp. 63-75, 2012.

[13] Longo A., Montuori R., Piluso V., Failure Mode Control and Seismic Response of Dissipative Truss Moment Frames, Journal of Structural Engineering, Vol. 138, pp.1388-1397, 2012.

[14] Montuori R., Piluso V., Troisi M., Innovative structural details in MR-frames for free from damage structures Mechanics Research Communications – Vol. 58 pp. 146-156, 2014.

[15] Montuori R., Nastri E., Piluso V., "Advances in Theory of Plastic Mechanism Control: Closed Form Solution for Mr-Frames", Earthquake Engineering and Structural Dynamics, 2015.

[16] Montuori R., Piluso V., Plastic Design of Steel Frames with Dog-Bone Beam-to-Column Joints, Third International Conference on Behaviour of Steel Structures in Seismic Areas, STESSA 2000.

[17] Longo A., Montuori R., Piluso V. Failure mode control of X-braced frames under seismic actions. Journal of Earthquake Engineering, 12: 728-759, 2008.

[18] Longo A, Montuori R, Piluso V., Plastic design of seismic resistant V-Braced frames. Journal of Earthquake Engineering, vol. 12: 1246-1266, 2008.

[19] Longo A, Montuori R, Piluso V., "Influence of design Criteria on the seismic Reliability of X-Braced Frames", Journal of Earthquake Engineering, Vol. 12, Issue 3– p.406-431, 2008.

[20] Montuori R., Nastri E., Piluso V., "Rigid-plastic analysis and moment–shear interaction for hierarchy criteria of inverted Y EB-Frames" Journal of Constructional Steel Research vol. 95 71-80, 2014.

[21] Montuori R., Nastri E., Piluso V., Theory of Plastic Mechanism Control for Eccentrically Braced Frames with inverted Y-scheme, Journal of Constructional Steel Research, Volume 92, pp. 122-135, 2014.

[22] Giugliano M.T., Longo A., Montuori R., Piluso V., Plastic design of CB-frames with reduced section solution for bracing members. Journal of Constructional Steel Research. Vol. 66 pp 611-621, 2010.

[23] Montuori R., Nastri E., Piluso V. Theory of plastic mechanism control for the seismic design of braced frames equipped with friction dampers - Mechanics Research Communications – Vol. 58. pp. 112-123, 2014.

[24] Longo A., Montuori R., Piluso V., Seismic reliability of V-braced frames: Influence of design methodologies. Earthquake Engineering and Structural Dynamics, vol. 38 p. 1587-1608, 2009.

[25] Longo A., Montuori R., Piluso V., Seismic Reliability of Chevron Braced Frames with Innovative Conception of Bracing Members, Advanced Steel Construction, an International Journal - Vol. 5, No. 4, December 2009.

[26] Montuori R., Nastri E., Piluso V., Rigid-plastic analysis and moment–shear interaction for hierarchy criteria of inverted Y EB-Frames. Journal of Constructional Steel Research, vol. 95 pp.71-80, 2014.

[27] Longo A., Montuori R., Nastri E., Piluso V., On the use of HSS in seismic-resistant structures Journal of Constructional Steel Research, Vol. 103, p. 1-12, 2014.

[28] Montuori R., Nastri E., Piluso V., "Seismic Design of MRF-EBF Dual Systems with Vertical Links: Ec8 Vs Plastic Design", Journal of Earthquake Engineering, 2015.

[29] Montuori R., Nastri E., Piluso V., "Seismic Response of EB-Frames with Inverted Yscheme: TPMC Versus Eurocode Provisions", Earthquakes and Structures, 2015.

[30] Longo A., Montuori R., Piluso V., Moment Frames - Concentrically Braced Frames Dual Systems: Analysis of Different Design Criteria, Structure and infrastructure engineering, 2015.

[31] Montuori R., Nastri E., Piluso V., Advances in theory of plastic mechanism control: closed form solution for MR-Frames. Earthquake Engineering & Structural Dynamics, DOI: 10.1002/eqe.2498

[32] Montuori R., The Influence of Gravity Loads on the Seismic Design of RBS Connections". Open Construction and Building Technology Journal, January 2015 Pages 248-261 DOI: 10.2174/1874836801408010024.

[33] Montuori R., Piluso V., "Analysis and modelling of CFT members: Moment curvature analysis". Thin-Walled Structure. Volume 86, January 2015, Pages 157–166. DOI:10.1016/j.tws.2014.10.010.

[34] Montuori R., Muscati R., "Plastic Design of Seismic Resistant Concrete Frame", Earthquakes and Structures, Vol. 8, No. 1, pp. 205-224, January 2015.

[35] Park R., "Ductile Design Approach for Reinforced Concrete Frames", Earthquake Spectra, EERI, 2(3), pp. 565-619, 1986.

[36] CSI 2007. SAP 2000: Integrated Finite Element Analysis and Design of Structures. Analysis Reference. Computer and Structure Inc. University of California, Berkeley.

[37] Pacific Earthquake Engineering Research Center, PEER Strong Motion Database, http://peer.berkeley.edu.

[38] SEAOC. Vision 2000 - A Framework for Performance Based Design, Volumes I, II, III. Structural Engineers Association of California, Vision 2000 Committee. Sacramento, California, 1995.

COMPDYN 2015
5th ECCOMAS Thematic Conference on
Computational Methods in Structural Dynamics and Earthquake Engineering
M. Papadrakakis, V. Papadopoulos, V. Plevris (eds.)
Crete Island, Greece, 25–27 May 2015

FEASIBILITY STUDY ON OFFSHORE SOLAR UPDRAFT TOWER POWER PLANT(COMPDYN 2015)

Hayami Sato[1], Yasuo Suzuki[1] and Kunitomo Sugiura[1]

[1] Dept. of Civil and Earth Resources Engineering, Kyoto University,Kyoto 615-8540, JAPAN
e-mail: sugiura.kunitomo.4n@kyoto-u.ac.jp, suzuki.yasuo.7c@kyoto-u.ac.jp,
sato.hayami45v@st.kyoto-u.ac.jp

Keywords: Solar updraft tower, Floating structure, Marine environment.

Abstract. *Studied in this paper, is "Solar Updraft Tower Power Plant" in marine environment from the aspect of structural form. Solar updraft tower is a thermal power plant combined with two main components; that is, the collector which collects all solar radiation and the thermal tube which guides the warm air from the collector to the upper sky more than 200m high. The conventional solar updraft tower, however, requires vast land to collect enough solar radiation, so the idea herein is to build solar updraft tower over the sea. Our goal is to stabilize 1000m high tower against the loadings in the marine environment. To accomplish this goal, the following steps were set. At first, the design of the tower is discussed. Steel tower is designed based on Japanese Structural Design Recommendation for Chimneys. Alternatively, the existing plan of RC Solar updraft tower is referred and the two designs are compared each other. From the aspect of weight, RC tower is applied for the following analysis. Next, the buoy for the 1000 m RC tower is assessed. Here, the buoy geometry is set to be cylinder, for the sake of simplicity. From the calculation of buoyancy and stability, it is recommended that the range of radius is 60 m ~ 124 m and that the range of buoy height is 26 m ~ 311 m. Again, for the simplicity, the buoy with radius is set to be 60 m, same with tower, and the height is set to be 311 m. Finally, one prototype of offshore solar updraft tower is modelled. The static analysis in the marine environment is carried out. To calculate the model's stability, the vibration analysis and stress analysis are done with either rigid body model or elastic model. With respect of natural frequency, the first natural frequency is very small, although the third mode may cause resonance with wind or wave. From the view of working stress, a part of tower base is yielded so that at least the thickness of shell should be carefully considered. Dynamic load such as wind load has considerable effect; however, especially the dead load has most effect. In conclusion, one simple model for Offshore Solar Updraft Tower is proposed and its requirements are shown. This assessment can be utilized for the further light and more complicate model.*

1 INTRODUCTION

From the world trend of reducing CO^2 and the nuclear hazard occurred in Japan, shifting energy resources, especially into renewable energies is an imminent issue in Japan. Clean energies such as solar energy, wind energy, bio energy and so on, usually requires vast land because its solar radiation and blowing winds contain little energy per unit area. Therefore, in Japan, how to utilize the ocean will be the key issue. Here we suggest solar updraft tower as the renewable energy to bring into the offshore surrounding Japan islands. Solar updraft tower is a thermal power plant combined with two main components; that is, as shown in the figure, the collector which collects all solar radiation using the Green House effect, and the thermal tube, expected to be as 1000 m tower which guides the warm air from the collector to the upper sky [1]. One prototype existed in Manzanares, Spain, with the tower height of 200 m and energy output of 50 KW, but now it is shut down due to its structural failure. After the one from Manzanares, there are no one tested with higher energy output.

There exist many problems to make use of this structure. Especially, it is difficult to find a land big enough to assure safety, and its height is considered to be a problem inducing high stress concentration at the bottom of the tower. Proposed herein is a floating solar updraft tower, shown in Figure 1, so that the stress concentration at the bottom can be reduced. In the floating system, tower is supported by the buoy but the collector is considered to be floating by its own and merely connected with hinge, not a stiff connection.

In this paper, the floating stability and structural stability of tower structure and buoy structure are assessed for the feasibility of Solar Updraft Tower in the marine environment, with the use of numerical models.

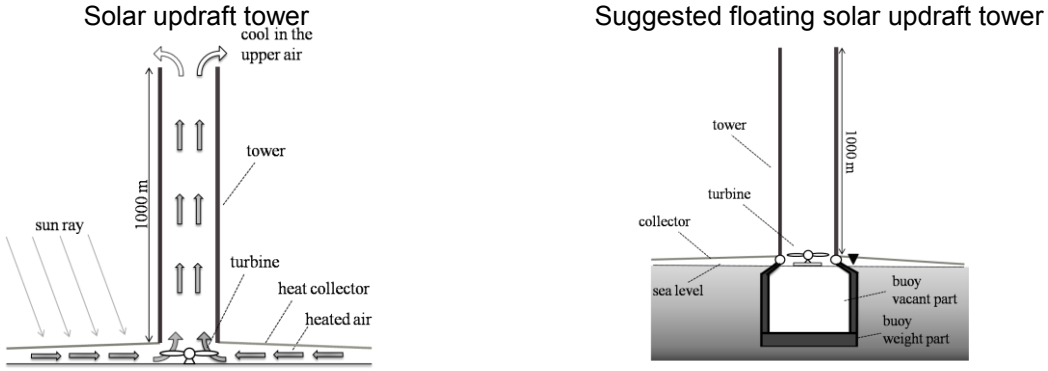


Figure 1: Solar Updraft Tower and a model proposed in this paper

2 TOWER DESIGN

The Solar Updraft Tower with nominal power of 200MW was planned by Schlaich Bergermann & Partner, and from its thermal calculation, it is concluded that the radius of 120 m and height of 1000 m is required. The tower is designed with reinforced concrete and maximum thickness is 1.3 m, minimum thickness is 0.3 m and the total weight is 527,030 tons.

In this paper, the preliminary design of steel tower is carried out. The section of the steel tower is designed based on Structural Design Recommendation for Chimneys [2]. Tower is divided into 10 segments and the thickness is uniform in the each segment as shown in Figure 2. For steel tower, the weight is considered to be 7.85 ton/m^3 and the yield strength is given as 400 N/m^2. The design loads such as wind load and dead load are considered. Distribution of wind speed is given by power law profile, Eq. (1) [3].

$$U(z) = \left(\frac{z}{10}\right)^p U_{10} \tag{1}$$

z m denotes height, *U(z)* m/s denotes wind velocity at each height, U_{10} denotes the wind speed at 10 m height and exponent *p* is a factor that represents air stability and terranean conditions. Here, U_{10} is 30 m/s which is an average wind speed of large typhoons in Japan and *p* is 0.096 assuming the sea surface and the instable air condition. In this calculation, maximum wind speed is 45 m/s at 1000 m height. According to the field research [4], they have observed typhoon with wind speed of 18 m/s on 10 m height and its wind speed was 29 m/s around 1000 m height. Calculation from the above equation, the wind speed at 1000 m height will be 28 m/s .

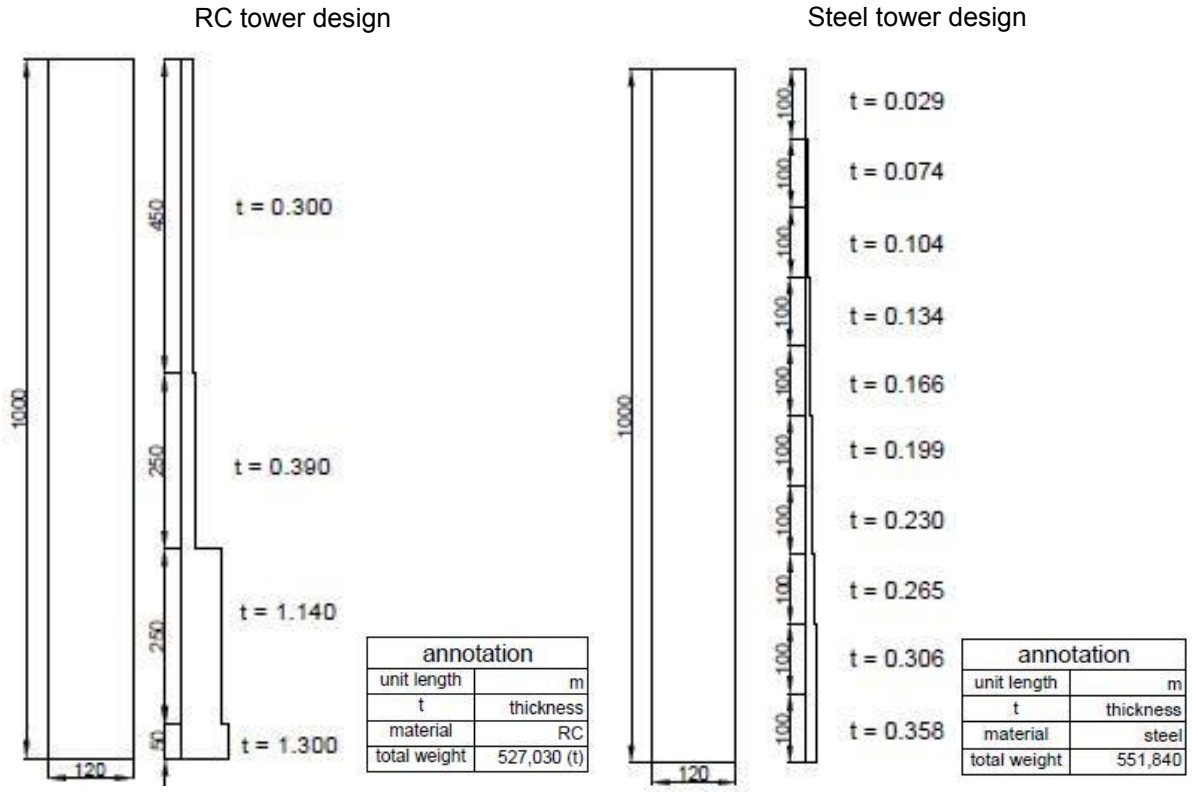


Figure 2: Section design of a 1000 m tower

As a result, the steel tower designed in this paper weighs 551,840 ton and it turned out to be heavier than the RC tower. This difference could be caused because of the considered safety factor and loads. Steel tower is designed with safety factors up to 2.25, in a condition that it will be constructed near towns. So when constructing in isolated area, the safety factor could be rather lowered. For the load difference, since in Japan with lots of typhoon attack, so peak wind load is much higher. Even in Japan, if wind speed could be set to be smaller, the designed wind load will possibly be lowered. So it could be concluded that, from revision of design wind speed and safety factors, steel tower can be designed thinner and lither.

Since the thousand meter steel tower designed in this chapter turned out to be heavier than the RC tower, based on the dimensions of the RC tower further assessment is carried out in the following chapters.

3 BUOY DESIGN

In this chapter, the buoy size and its weight are discussed to make float the thousand meter tower and followings are the design conditions. The applied tower design is referred from Chapter 2. The wind load is also referred from Chapter 2, which uses power law, Eq.(1) so if

the wind speed on 10 meter height is set as 30 m/s, then the wind speed will be 45 m/s at the 1000 m height. As it is shown in Figure 1, the buoy consists of two parts, the hollow and filled parts so that it could assure its buoyancy and stability. The hollow part is made by RC and filled part consists of a concrete block as a solid. Considering the coverage of concrete, the thickness of the shell is set as 0.6 m. After all, two conditions are given to assure its buoyancy and stability (2). M_{tower} and M_{buoy} is a mass of tower, ρ is a density of sea water, 1.062 ton/m^3 and g is an acceleration of gravity. MG is a distance between centre of gravity G and meta centre M, centre of rotation of the hull structures, and h_{buoy} is the height of the whole buoy.

$$M_{tower} + M_{buoy} = \rho \times V_{buoy} \times g$$
$$MG - 0.05\, h_{buoy} = 0 \tag{2}$$

First equation indicates that the mass of the full structure is sustained by the volume of the buoy. Second equation, is for that the centre of gravity is positioned lower than meta centre and the distance is around 5% of the height of buoy. There is a discussion for the length of MG, but in the hull structure, it must be larger than 5% of buoy height.

Let the height of the buoy part h_b, the height of filled part h_w and the radius of the buoy to be r_b. When r_b is set to be 60, 90, 120, 124 m, the h_b and h_w that satisfies equations (2) are shown in table 1.

r_b (m)	h_b (m)	h_w (m)	GM (m)
60	196	115	9.84
90	104	65.0	5.24
120	36.7	19.6	1.83
124	19.2	6.76	0.96

Table 1: Profiles of buoy to make the tower float.

When the radius of the buoy is set to be 60 m, the same with that of the tower, its total length will be 311 m. When assumed to minimize the length of buoy, the total buoy height is 26 m and the radius will be 124 m. However, considering the stress concentration in structural discontinuity of tower and buoy, the radius of 60 m is considered in the following discussions.

4 STATIC CALCULATION OF THE FLOATING UPDRAFT TOWER

The wind load and the dead load are applied to the tower and the maximum tilt of the whole structure including its buoy is discussed here. First, the rigid body model is considered. RC tower design is referred to Chapter 2 and the buoy design with radius of 60 m is referred to Chapter 3 and its whole profile is shown in Figure 3. First the rigid body estimation is done. More precisely, calculation of the equilibrium point of wind energy and energy of the righting moment of the buoyancy is done. For the wind load, the power law above is given, and for moment force, the calculation of distance between meta centre and centre of gravity is multiplied by the total weight of the structure. The torque center is set to be meta centre, and it is 160.15 m from the bottom of the buoy. Here, the distribution of the dead load is not considered and only the centre of gravity is applied in to the calculation. From this calculation, the tower will tilt 29.9 degree when maximum wind speed of 45 m/s is given.

Next, the elastic body analysis is carried out, with applying wind load and dead load on the structure in Abaqus/Standard 6.12-3 [5]. As it could be seen in Figure 3, the structure is fixed

at meta centre except the rotation DOM. To substitute the moment of the buoyancy, torsion spring is adapted to the meta centre and its spring constant is 38 GNmm/rad. This constant is acquired from the calculation of the moment for the rigid body analysis. The tower part and buoy part consists of S4R shell element and the filled part consists of solid element. As a result the maximum tilt is 29.1 degrees and it differs 2% from the rigid body analysis. The stress distribution is given as contour in Figure 3 as well. The highest stress of 287 MPa is obtained in left part of tower base as the compression. This value is over the strength of concrete, so the shell thickness or changing the member into steel should be considered. And as it could be seen in the figure, the top part of the tower is largely deformed in the circumferential direction. So it is sure that the ring stiffeners should be applied to such a cylinder structure as it could be seen in the former researches.

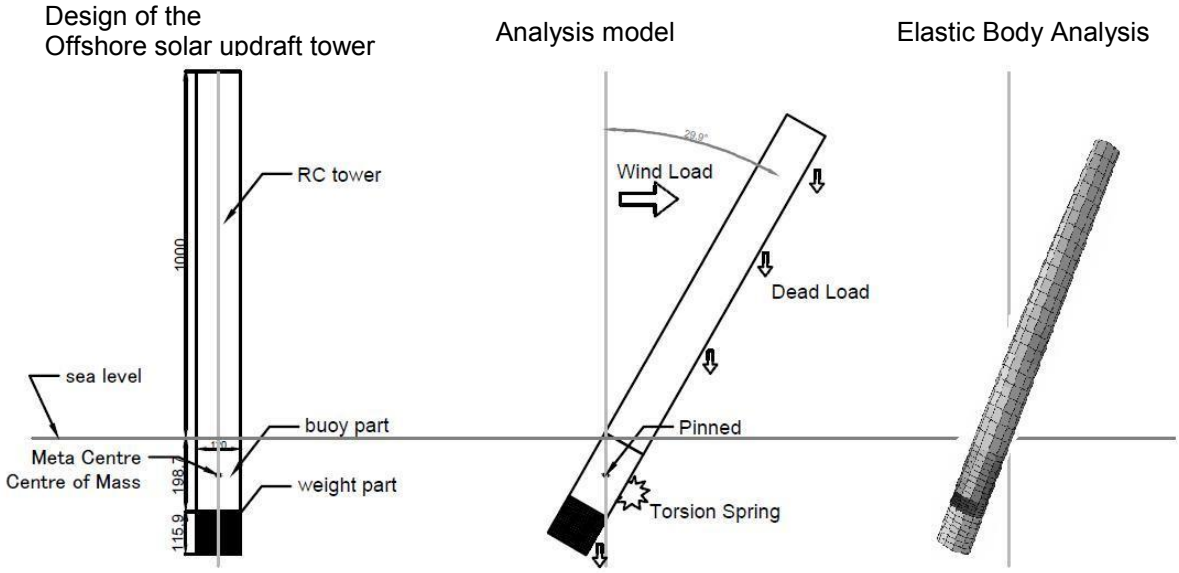


Figure 3: Static analysis conditions

5 DYNAMIC RESPONSE OF THE UPDRAFT TOWER

In Chapter 4, the static calculation has been done for the structure, however, its maximum tilt was estimated to be 29.1, so dynamic response is also considered here. First, frequency analysis is carried out. The same model is used with Figure 3, and without any loads, its natural frequency is calculated with Abaqus, and the result is shown in Figure 4. The first natural frequency is 2.16×10^{-3} Hz. Since it is very low, it is concluded that the wave frequency or wind frequency may not affect. However, the second and third frequency are around 0.1~0.18 so that it could cause the resonance with the wind and wave.

The transient response analysis is carried out to assure the safety against the dynamic loads. Condition assumed here is when the strong wind such as typhoon, it is assessed whether the structure comes back to its original position. In the first step, the tower is rotated 29.1 degrees, and in the following step, the free vibration of the tower is considered. As for calculation method, the direct integration of equation of motion is employed in which time increment is set to be 0.1 (sec). The velocity observed at the tip of the tower is 0.425 m/s and its frequency is also 2.12×10^{-3} Hz which is nearly equal to the first natural frequency. The working stress is merely 2.4 MPa; then, it could be concluded that dynamic loading effect is far smaller compared to the response by the dead load and wind load.

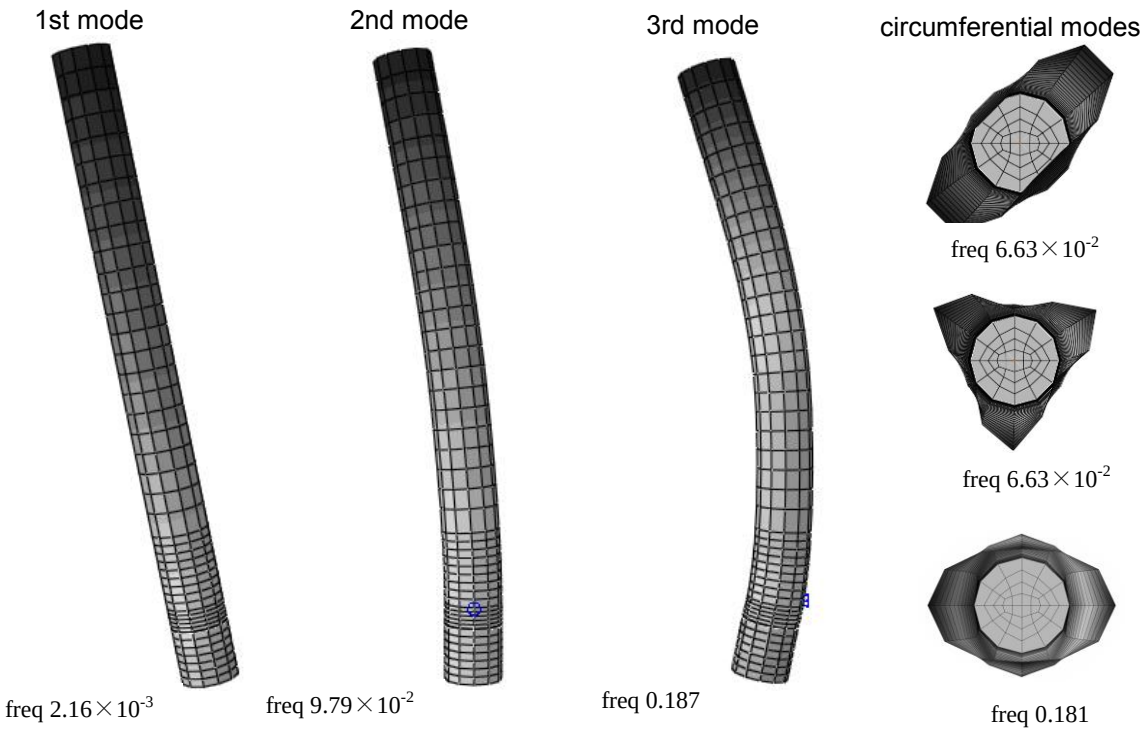


Figure 4: Natural Frequency modes of the structure

6 CONCLUSIONS

- Buoy for tower of 1000 meter height has been designed, considering the stability and the buoyancy. Total mass of the buoy is 3.25×10^{6} ton ; therefore, the total mass of the structure becomes 3.78×10^{6} ton.
- Wind load is applied on the tower structure with static analysis and its maximum tilt is calculated to be up to 29.1 degrees.
- Dynamic load is assessed in a free vibration analysis; then, it is understood that its maximum velocity was merely 0.45 m/s, and that the dead load turned out to be the critical load in this structural design after all.
- From this research, it is concluded that the design of the floating updraft tower is feasible with the existing RC tower design; however, the lighter tower design is recommended.

REFERENCES

[1] Jörg Schlaich, Rudolf Bergermann, Wolfgang Schiel, Gerhard Weinrebe, Sustainable Electricity Generation with Solar Updraft Towers, *Structural Engineering International, Volume 14, Number 3,* 225-229, 2004.

[2] Architectural Institute of Japan. *Structural Design Recommendation for Chimneys,* 114-116, 2007.11.

[3] Japanese Society of Steel Construction. *Wind Resistant Engineering on Structures*, 376, 1997.

[4] Takenaka Corporation. *Wind Velocity in Typhoon at the Height of 250 m ~ 3000 m*, 2001.8.

[5] ABAQUS

COMPDYN 2015
5th ECCOMAS Thematic Conference on
Computational Methods in Structural Dynamics and Earthquake Engineering
M. Papadrakakis, V. Papadopoulos, V. Plevris (eds.)
Crete Island, Greece, 25–27 May 2015

IMPLEMENTATION OF ROBUST CONTROL THEORY IN SMART STRUCTURE DESIGN USING FREQUENSY DOMAIN DATA

A. J. Moutsopoulou[1*], A. D. Pouliezos[2] and G. E. Stavroulakis[3]

[1]Department of Civil Engineering Technological Educational Institute of Crete

Estavromenos Heraklion Crete, amalia@staff.teicrete.gr

[2,3]Department of Production Engineering and Management,

Technical University of Crete, Kounoupidianna GR-73100 Chania, Greece,

gestavr@dpem.tuc.gr, tasos@dpem.tuc.gr

Key words: *H infinity* control, structural control, frequency domain data, smart beam

Abstract. *This paper presents an implementation of a design method of robust H_∞ optimal control to a structural control system. To obtain the best possible performance in the face of uncertainties, robust H_∞ optimal control for the active control structure is used. Relevant numerical techniques, which have been implemented with the help of MATLAB routines, are applied to solve the formulated structural control problem. By proper selection of the weight factor, the seismic response of the building structure can be reduced considerably. Numerical results show high robust performance of the proposed method.*

1. INTRODUCTION

The control of structural vibrations is an important goal for the structural engineer. Several control techniques have been developed for these purposes. Classical engineering design based on appropriate choice of materials and of dimensions of the structure provides only a partial solution to the problem because of their limited control action. The aim of this research is to design a robust controller to suppress adverse vibrations of smart structures due to earthquake and wind excitations. The design specifications of H_∞ control are given in the frequency domain, and thus it is easy for H_∞ control to deal with the uncertainty at high frequencies and to guarantee the robust stability and robust performance [10, 11, 23].

A short literature review gives a deep insight into the research work done on the smart structures so far. Culshaw [1] discussed the concept of smart structure, its benefits and applications. Rao and Sunar explained the use of piezo materials as sensors and actuators in sensing vibrations in their survey paper [2]. Hubbard and Baily [3] have studied the application of piezoelectric materials as sensor / actuator for flexible structures. Hanagud et.al. [4] devel-

oped a Finite Element Model (FEM) for a beam with many distributed piezoceramic sensors/ actuators.

Hwang and Park [5] presented a new finite element (FE) modeling technique for flexible beams. Continuous time and discrete time algorithms were proposed to control a thin piezoelectric structure by Bona, et.al. [6]. Schiehlen and Schonerstedt [7] reported the optimal control designs for the first few vibration modes of a cantilever beam using piezoelectric sensors/ actuators. S.B. Choi et.al. [8] have shown a design of position tracking sliding mode control for a smart structure. Distributed controllers for flexible structures can be seen in Forouza Pourki [9].

2. MODELLING

The dynamical description of the system is given by,

$$\boldsymbol{M}\ddot{\boldsymbol{q}}(t)+\boldsymbol{D}\dot{\boldsymbol{q}}(t)+\boldsymbol{K}\boldsymbol{q}(t)=\boldsymbol{f}_m(t)+\boldsymbol{f}_e(t) \tag{1}$$

Where $\boldsymbol{M}$ is the generalized mass matrix, $\boldsymbol{D}$ the viscous damping matrix, $\boldsymbol{K}$ the generalised stiffness matrix, $\boldsymbol{f}_m$ the external loading vector and $\boldsymbol{f}_e$ the generalised control force vector produced by electromechanical coupling effects. For a model simplified beam model of a composite beam with piezoelectric sensors and actuators the independent variable vector $\boldsymbol{q}(t)$ is composed of transversal deflections w_i and rotations ψ_i, i.e for [10, 11],

$$\boldsymbol{q}(t)=\begin{bmatrix} w_1 \\ \psi_1 \\ \vdots \\ w_n \\ \psi_n \end{bmatrix}$$

where n is the number of finite elements used in the analysis. Vectors $\boldsymbol{w}$ and $\boldsymbol{f}_m$ are positive upwards.

To transform to state-space control representation, let (in the usual manner),

$$\boldsymbol{x}(t)=\begin{bmatrix} \boldsymbol{q}(t) \\ \dot{\boldsymbol{q}}(t) \end{bmatrix}$$

Furthermore to express $\boldsymbol{f}_e(t)$ as $\boldsymbol{B}\boldsymbol{u}(t)$ we write it as $\boldsymbol{f}_e^*\boldsymbol{u}$, where $\boldsymbol{f}_e^*$ is the piezoelectric force for a unit applied on the corresponding actuator, and $\boldsymbol{u}$ represents the voltages on the actuators. Lastly $\boldsymbol{d}(t)=\boldsymbol{f}_m(t)$ is the disturbance vector. Then,

$$\dot{\boldsymbol{x}}(t)=\begin{bmatrix} 0_{2n\times 2n} & I_{2n\times 2n} \\ -\boldsymbol{M}^{-1}\boldsymbol{K} & -\boldsymbol{M}^{-1}\boldsymbol{D} \end{bmatrix}\boldsymbol{x}(t)+\begin{bmatrix} 0_{2n\times n} \\ \boldsymbol{M}^{-1}\boldsymbol{f}_e^* \end{bmatrix}\boldsymbol{u}(t)+\begin{bmatrix} 0_{2n\times 2n} \\ \boldsymbol{M}^{-1} \end{bmatrix}\boldsymbol{d}(t)$$

$$= \boldsymbol{A}\boldsymbol{x}(t) + \boldsymbol{B}\boldsymbol{u}(t) + \boldsymbol{G}\boldsymbol{d}(t)$$

$$= \boldsymbol{A}\boldsymbol{x}(t) + [\boldsymbol{B}\ \boldsymbol{G}]\begin{bmatrix}\boldsymbol{u}(t)\\ \boldsymbol{d}(t)\end{bmatrix}$$

$$= \boldsymbol{A}\boldsymbol{x}(t) + \tilde{\boldsymbol{B}}\tilde{\boldsymbol{u}}(t) \tag{2}$$

We can augment this with the output equation. For example, if we assume that displacements are only measured then,

$$\boldsymbol{y}(t) = [x_1(t)\ x_3(t)\ \ldots\ x_{n-1}(t)]^{\mathrm{T}} = \boldsymbol{C}\boldsymbol{x}(t) \tag{3}$$

with,

$$\boldsymbol{C} = \left[\begin{array}{cccc:c:c} 1 & 0 & \cdots & 0 & 0 & \\ 0 & 0 & 1 & \cdots & & \vdots \\ & & \ddots & & & \vdots \\ 0 & \cdots & 0 & 1 & & 0 \end{array}\right]$$

In this formulation $\boldsymbol{u}$ is $n\times 1$ (at most, but can be smaller), while $\boldsymbol{d}$ is $2n\times 1$. The units used are m, rad, sec and N.

The *control problem* is to keep the beam in equilibrium (: zero displacements and rotations) in the face of external disturbances, noise and model inaccuracies, using the available measurements (displacement) and controls [12, 13].

3. CLASICAL CONTROL

In the sequel we will analyse the behaviour of a cantilever beam, with four pairs of piezoelectric patches bonded symmetrically at the top and bottom surfaces of each beam element [14, 23].

The open loop system is as shown in Fig. 1. Using (2), (3) the transfer function from disturbance to position is,

$$\boldsymbol{H_o}(s)=\boldsymbol{C}(s\boldsymbol{I}-\boldsymbol{A})^{-1}\boldsymbol{G} \tag{4}$$

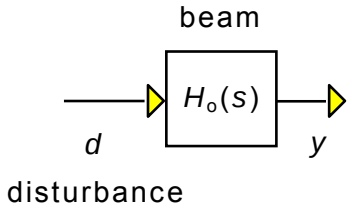


Figure 1 Open loop system

Firstly we note that the ***A*** matrix is badly conditioned with condition number = 5.624703967123330e-013 Fig. 2. This means some preconditioning would be beneficiary to sensitive calculations (like pole placement). A way around this problem is to balance the system matrix. MATLAB provides the routine[15],

$$\textbf{[T, S] = }\boldsymbol{balance}\textbf{(A)}$$

which produces a diagonal transformation matrix ***T*** whose elements are integer powers of 2, and matrix B such that,

$$\boldsymbol{A}=\boldsymbol{TST}^{-1}$$

In this way some of the bad conditioning is transferred to ***T***. Letting,

$$\boldsymbol{z}=\boldsymbol{T}^{-1}\boldsymbol{x}\Rightarrow\boldsymbol{x}=\boldsymbol{Tz}$$

(2) becomes,

$$\begin{aligned}\boldsymbol{T}\dot{z}(t)&=\boldsymbol{ATz}(t)+\boldsymbol{Bu}(t)+\boldsymbol{Gd}(t)\\ \Rightarrow \dot{\boldsymbol{z}}(t)&=\boldsymbol{T}^{-1}\boldsymbol{ATz}(t)+\boldsymbol{T}^{-1}\boldsymbol{Bu}(t)+\boldsymbol{T}^{-1}\boldsymbol{Gd}(t)\\ &=\boldsymbol{Sz}(t)+\hat{\boldsymbol{B}}\boldsymbol{u}(t)+\hat{\boldsymbol{G}}\boldsymbol{d}(t)\end{aligned}$$

Another problem arises from the very small size of the minimum eigenvalue which defines the smallest time constant of the system, which in turns dictates sampling intervals used in simulations. These sampling intervals should be smaller than the smallest time constant. When this happens, arrays involved for example in **lsim** simulations get very big, and special care must be taken if the simulation time is large[15,16].

Also the system is both controllable and observable (in fact the system is both controllable and observable with fewer inputs and measurements).

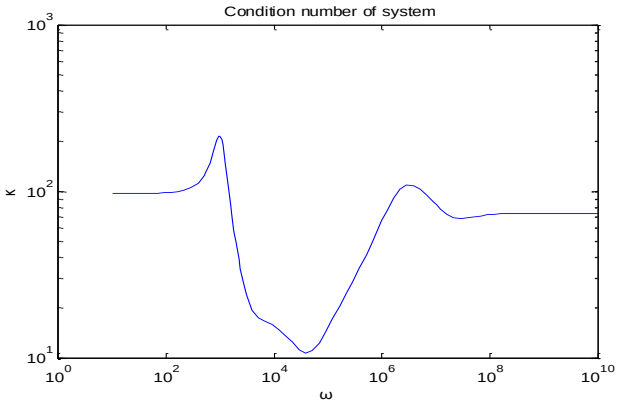


Figure 2 Condition number of the system

Responses to various inputs are in Figs. 2, 4, 5, 6.

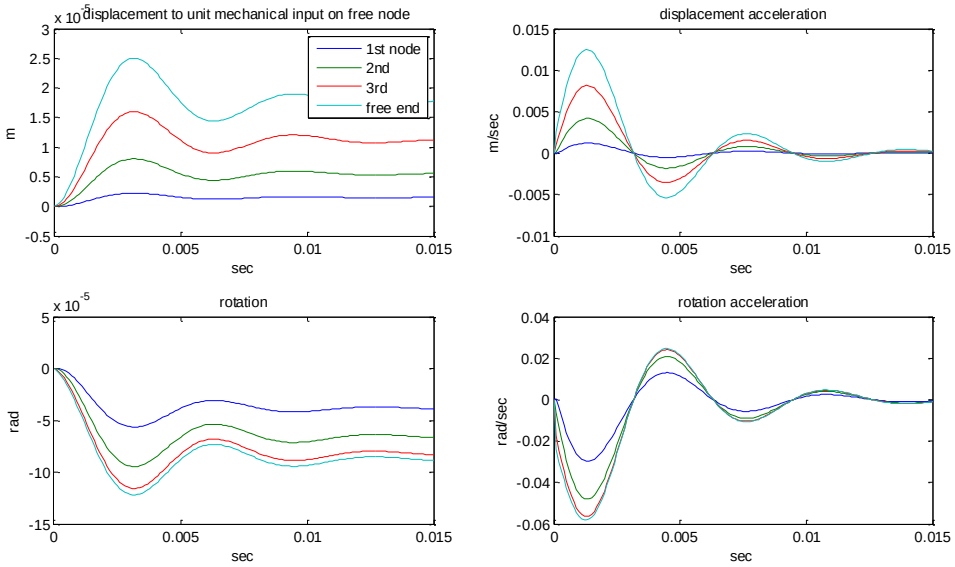


Figure 2 Responses to various mechanical inputs at free end of the beam

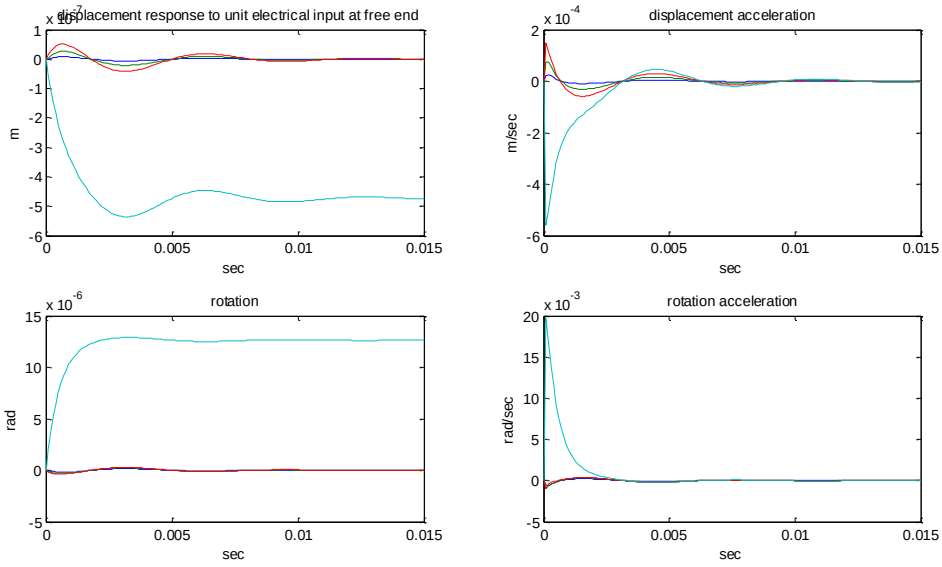


Figure 3 Responses to various electrical inputs at the free end of the system

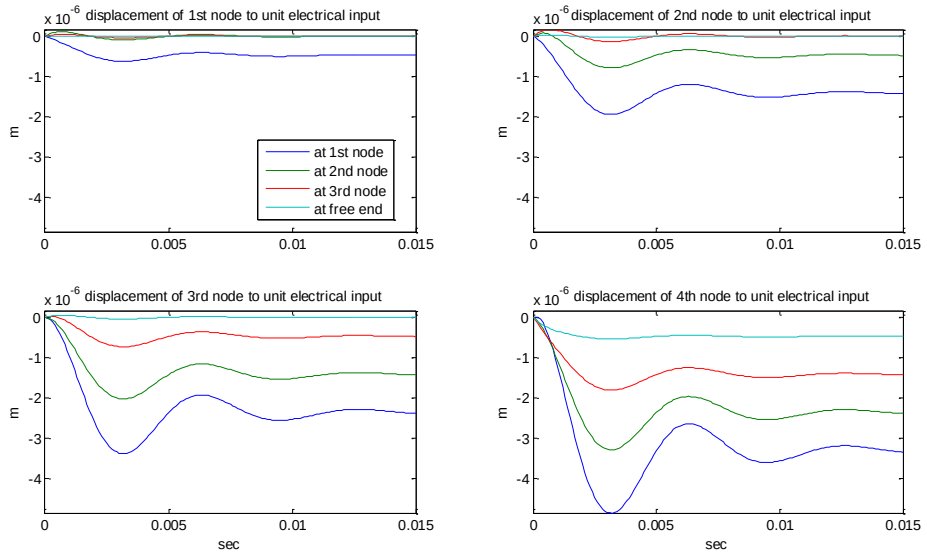


Figure 5 Responses to various electrical inputs at each node of the system

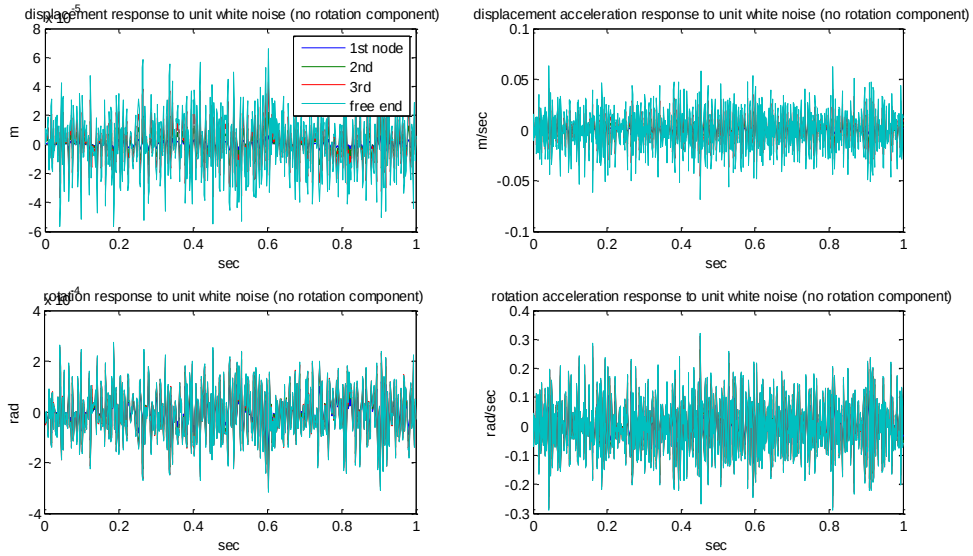


Figure 6 Responses to unit white noise us inputs at each node of the system

3. $H_{infinity}$ CONTROL

To relate the structures used in classical and $\boldsymbol{H}_\infty$ control, let's look at Fig. 4 :

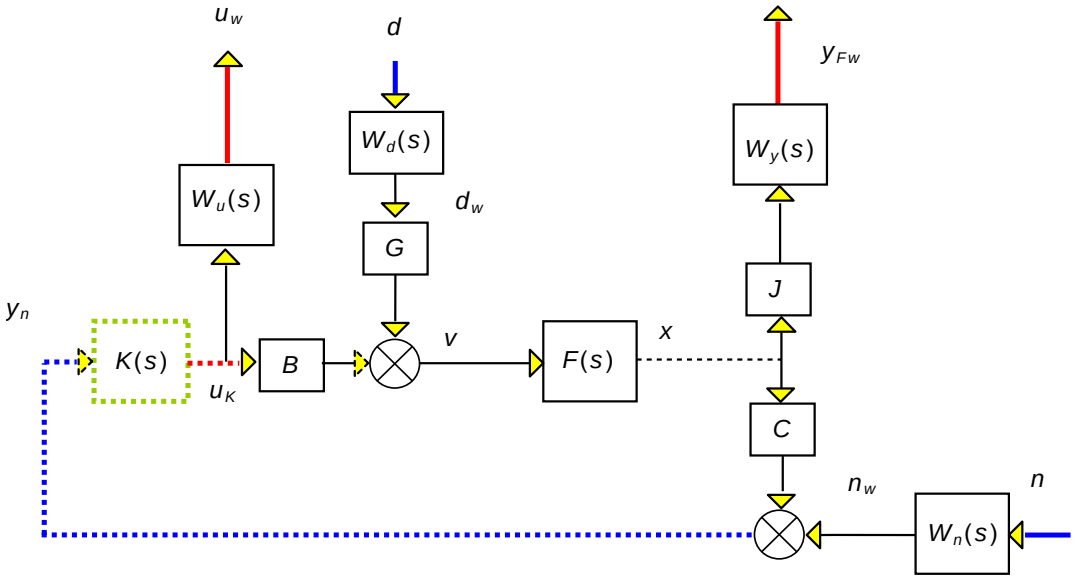


Figure 4 Closed loop diagram in the frequency domain

In this diagram are included all inputs and outputs of interest, along with their respective weighs.

To find the necessary transfer functions [17, 18]:

$$y_{Fw}=W_yJx= W_yJFv=W_yJF(GW_dd+Bu_K)=W_yJFGW_dd+W_yJFBu_K$$

$$u_w=W_uu_K$$

$$y_n=Cx+W_nn=CFv+W_nn=CF(GW_dd+Bu_K)+W_nn=CFGW_dd+CFBu_K+W_nn$$

Combining all these gives,

$$\begin{bmatrix} u_w \\ y_{Fw} \\ \hdashline y_n \end{bmatrix} = \left[\begin{array}{ccc:c} 0 & 0 & W_u \\ W_yJFGW_d & 0 & W_yJFB \\ \hdashline CFGW_d & W_n & CFB \end{array}\right] \begin{bmatrix} d \\ n \\ \hdashline u_K \end{bmatrix} \tag{4}$$

Note that the plant transfer function matrix, $F(s)$, is deduced from the suitably reformulated plant equations,

$$\dot{x}(t) = Ax(t) + Iv(t)$$

$$y(t)=Ix(t)$$

where $v(t)=Gd+Bu_k$. Hence,

$$F(s)=(sI-A)^{-1}$$

The equivalent two-port diagram in the closed loop system is fig. 4,

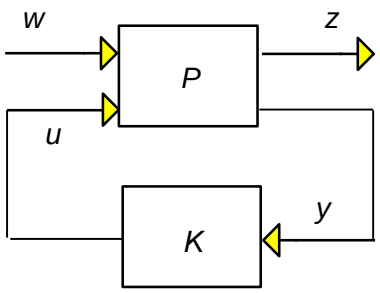


Figure 5 Closed loop system, two port diagram

with,

$$z=\begin{bmatrix} u_w \\ y_{Fw} \end{bmatrix},\quad w=\begin{bmatrix} d \\ n \end{bmatrix},\quad y=y_n,\quad u=u_K$$

where z are the output variables to be controlled, and w the exogenous inputs.

Given that P has two inputs and two outputs it is, as usual, naturally partitioned as,

$$\begin{bmatrix} z(s) \\ y(s) \end{bmatrix} = \begin{bmatrix} P_{zw}(s) & P_{zu}(s) \\ P_{yw}(s) & P_{yu}(s) \end{bmatrix} \begin{bmatrix} w(s) \\ u(s) \end{bmatrix} \overset{\text{o}\rho}{=} P(s) \begin{bmatrix} w(s) \\ u(s) \end{bmatrix} \tag{5}$$

Also,

$$u(s)=K(s)y(s) \tag{6}$$

Using (4) the transfer function for P is,

$$P(s) = \left[\begin{array}{cc:c} 0 & 0 & W_u \\ W_y JFGW_d & 0 & W_y JFB \\ \hdashline CFGW_d & W_n & CFB \end{array}\right] \tag{7}$$

while the closed loop transfer function $M_{zw}(s)$ is,

$$M_{zw}(s)=P_{zw}(s)+P_{zu}(s)K(s)\,(I-P_{yu}(s)K(s))^{-1}P_{yw}(s) \tag{8}$$

Equation (8) is the well known lower LFT for M_{zw}.

To express P in state space form, the natural partitioning [19, 20],

$$P(s) = \left[\begin{array}{c|cc} A & B_1 & B_2 \\ \hline C_1 & D_{11} & D_{12} \\ C_2 & D_{21} & D_{22} \end{array}\right] = \begin{bmatrix} P_{zw}(s) & P_{zu}(s) \\ P_{yw}(s) & P_{yu}(s) \end{bmatrix} \tag{9}$$

is used (where the packed form has been used), while the corresponding form for K is,

$$K(s) = \left[\begin{array}{c|c} A_K & B_K \\ \hline C_K & D_K \end{array}\right]$$

Eq. (10) defines the equations,

$$\dot{x}(t) = Ax(t) + \begin{bmatrix} B_1 & B_2 \end{bmatrix} \begin{bmatrix} w(t) \\ u(t) \end{bmatrix}$$

$$\begin{bmatrix} z(t) \\ y(t) \end{bmatrix} = \begin{bmatrix} C_1 \\ C_2 \end{bmatrix} x(t) + \begin{bmatrix} D_{11} & D_{12} \\ D_{21} & D_{22} \end{bmatrix} \begin{bmatrix} w(t) \\ u(t) \end{bmatrix}$$

and,

$$\dot{x}_K(t)=A_K x_K(t)+B_K y(t)$$

$$u(t)=C_K x_K(t)+D_K y(t)$$

To find the matrices involved, we break the feedback loop and use the relevant equations.

Therefore the equations relating the inputs, outputs, states and input/output to the controller are[21]:

$$\begin{aligned}
\dot{x}_F &= Ax_F + (Gd_w + Bu), \qquad y_F = x_F \\
\dot{x}_u &= A_u x_u + B_u u, \qquad u_w = C_u x_u + D_u u \\
\dot{x}_{yF} &= A_{yF} x_{yF} + B_{yF} J y_F, \quad y_{Fw} = C_{yF} x_{yF} + D_{yF} y_F \\
\dot{x}_n &= A_n x_n + B_n n, \qquad n_w = C_n x_n + D_n n \\
\dot{x}_d &= A_d x_d + Gd, \qquad d_w = C_d x_d + D_d d \\
y_n &= Cy_F + n_w
\end{aligned} \tag{10}$$

$$x=\begin{bmatrix} x_F \\ x_u \\ y_{Fw} \\ x_n \\ x_d \end{bmatrix}, \quad y = y_n, \quad w=\begin{bmatrix} d \\ n \end{bmatrix}, \quad z=\begin{bmatrix} u_w \\ y_{Fw} \end{bmatrix}, \quad u = u_K$$

By taken d_w, n_w και y_F from equation (11) we have,

$$\dot{x}=\begin{bmatrix} A_G & 0 & 0 & 0 & GC_d \\ 0 & A_u & 0 & 0 & 0 \\ BC_F & 0 & A_{yF} & 0 & 0 \\ 0 & 0 & 0 & A_n & 0 \\ 0 & 0 & 0 & 0 & A_d \end{bmatrix} x + \begin{bmatrix} GD_d & 0 \\ 0 & 0 \\ 0 & 0 \\ 0 & B_n \\ B_d & 0 \end{bmatrix} w + \begin{bmatrix} B \\ B_u \\ 0 \\ 0 \\ 0 \end{bmatrix} u$$

$$z=\begin{bmatrix} 0 & C_u & 0 & 0 & 0 \\ D_{yF}C_F & 0 & C_{yF} & 0 & 0 \end{bmatrix} x + 0w + \begin{bmatrix} D_u \\ 0 \end{bmatrix} u$$

$$y=\begin{bmatrix} C_F & 0 & 0 & C_n & 0 \end{bmatrix} x + \begin{bmatrix} 0 & D_n \end{bmatrix} w + 0u$$

Therefore the matrices are:

$$A_1 = \begin{bmatrix} A_F & 0 & 0 & 0 & GC_d \\ 0 & A_u & 0 & 0 & 0 \\ BC_F & 0 & A_{yF} & 0 & 0 \\ 0 & 0 & 0 & A_n & 0 \\ 0 & 0 & 0 & 0 & A_d \end{bmatrix}, \quad B_1 = \begin{bmatrix} GD_d & 0 \\ 0 & 0 \\ 0 & 0 \\ 0 & B_n \\ B_d & 0 \end{bmatrix}, \quad B_2 = \begin{bmatrix} B \\ B_u \\ 0 \\ 0 \\ 0 \end{bmatrix}$$

$$C_1 = \begin{bmatrix} 0 & C_u & 0 & 0 & 0 \\ D_{yF}C_F & 0 & C_{yF} & 0 & 0 \end{bmatrix}, \quad D_{11} = 0, \quad D_{12} = \begin{bmatrix} D_u \\ 0 \end{bmatrix}$$

$$C_2 = \begin{bmatrix} C_F & 0 & 0 & C_n & 0 \end{bmatrix}, \quad D_{21} = \begin{bmatrix} 0 & D_n \end{bmatrix}, \quad D_{22} = 0$$

4. RESULTS

Various tests were performed with disturbance and noise profiles (used in time responses) as shown in Fig. 9.

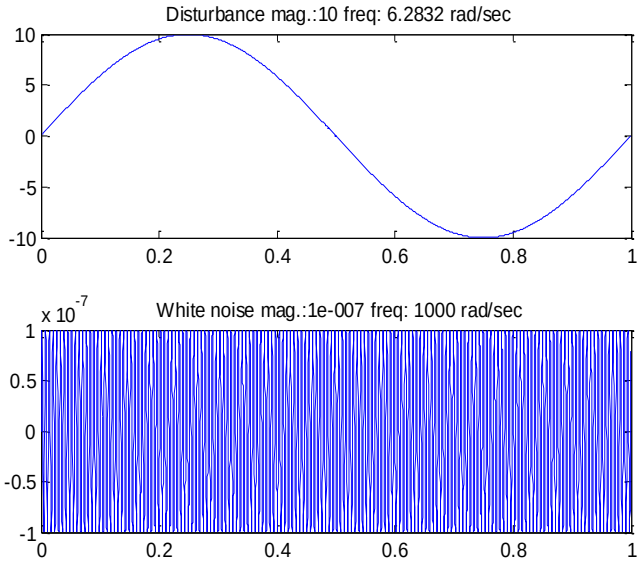


Figure 9 Disturbances of the system

To evaluate robustness we use m_p=10^{-5}, k_p=10^{-10}, d_p=0.005(m_p+k_p).

4.1 Without weights

In the simplest approach no weights are placed on any of the input/output quantities. This means that the H_∞ controller ensures [21, 22],

$$\left\| \begin{bmatrix} e \\ u \end{bmatrix} \right\|_2 \leq 1$$

as long as,

$$\left\| \begin{bmatrix} d \\ n \end{bmatrix} \right\|_2 \leq 1$$

Figs. (10)-(11) show the results of this run.

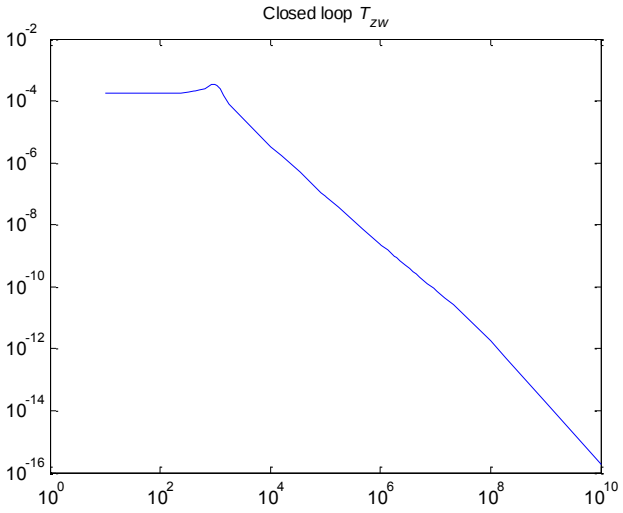


Figure 10 Closed loop T_{zw} for all frequencies

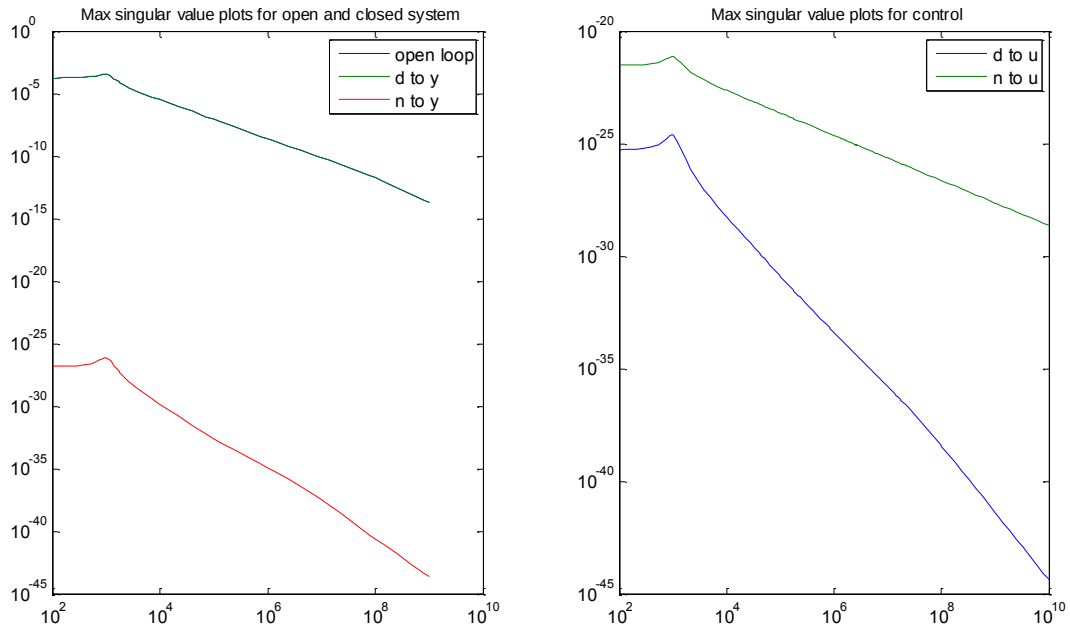


Figure 11 Max singular values for closed and open loop

Figure 10 shows that the price of the singular value of the un weighted system is very small for all frequencies (much lower than one). Fig 11 shows a satisfactory effect of the disturbance on the size of the control scheme (the design could be improved, if it were possible to reduce noise effect for frequencies of 1000 Hz). There are no difference is observed between the frequency plots of open and closed loop for the unweighted system.

4.2. With weights

Next we try constant weights, in particular let,

$$W_n=10^{-8},\ W_u=1/500,\ W_e=10^{3}$$

Figure 12 and 13promises a marked improvement in performance

Figures 12 shows that the value of T_{zw} is low then one for all frequencies.

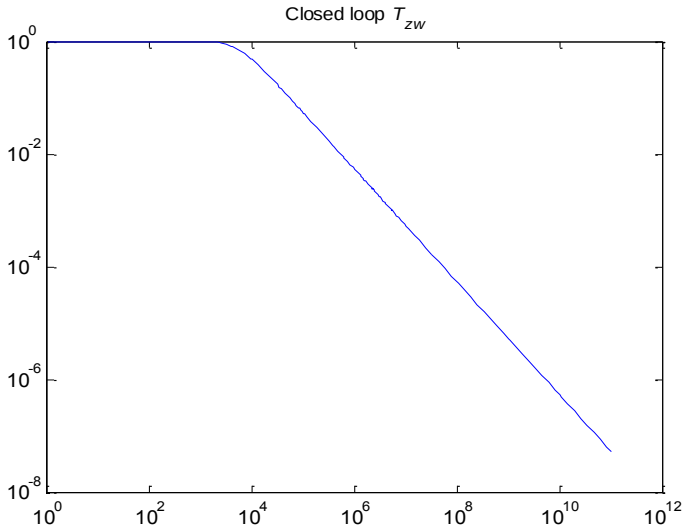


Figure 12 Closed loop T_{zw} for all frequencies

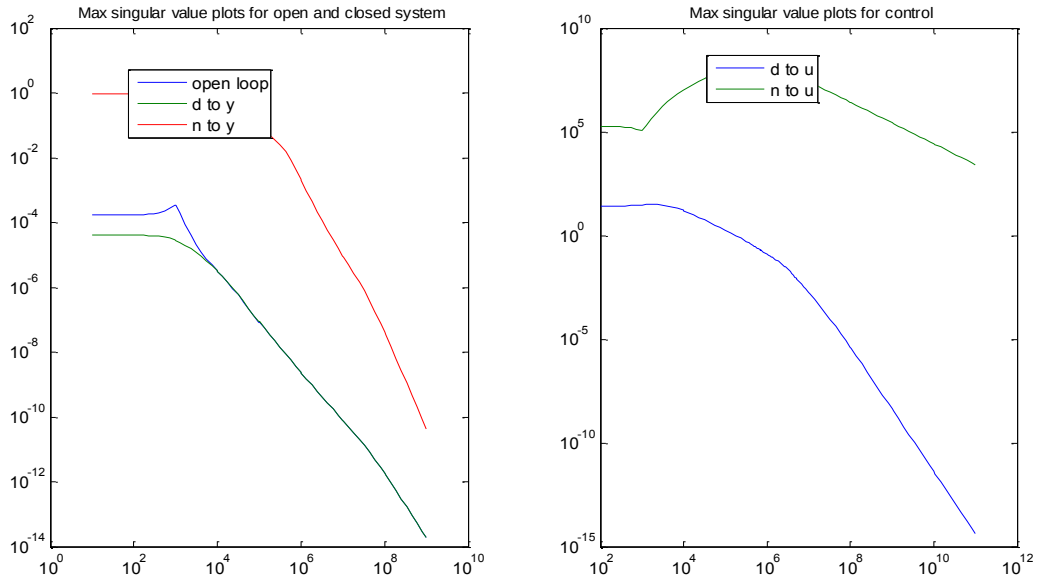


Figure 13 Max singular values for closed and open loop

Fig. 13 shows a satisfactory effect of the disturbance on the size of the control scheme (the design could be improved, if it were possible to reduce noise effect for frequencies of 1000 Hz). There are no difference is observed between the frequency plots of open and closed loop system.

As shown in Fig. 13 a, there is a significant improvement in the effect of disturbance on error up to the frequency of 1000 Hz. In Fig. 13a , there seems to be little effect of noise on error for frequencies beyond 1000 Hz. In Fig. 13b, shows a satisfactory effect of the disturbance on the size of the control scheme (the design could be improved, if it were possible to reduce noise effect for frequencies of 1000 Hz).

CONCLUSIONS

In this paper, a robust control design problem has been formulated within a linear fractional transformation framework using the $H_{infinity}$ technique. The $H_{infinity}$ norm of the closed loop transfer matrix from all disturbances to the errors to be minimized has been chosen as the cost functional. A suboptimal controller has been used for numerical modeling. The open loop and the closed-loop controlled system has been simulated using a periodic impulsive command input, periodic isolated influences. $H_{infinity}$ techniques have the advantage over classical control techniques in that they are readily applicable to problems involving multivariate systems with cross-coupling between channels. Simultaneously optimizing robust performance and robust stabilization is difficult. One method that comes close to achieving this is $H_{infinity}$ loop-shaping, which allows the control designer to apply classical loop-shaping concepts to the multivariable frequency response to get good robust performance, and then optimizes the response near the system bandwidth to achieve good robust stabilization. It must be emphasized that the framework of the structural control employed in this paper is quite general and covers interesting cases of practical importance.

REFERENCES

[1] B. Culshaw, *Smart structures: A concept or a reality*, Journal of Systems and Control Engg, Vol. 26, No. 206, 1992.

[2] S. Rao, M. Sunar, (994), *Piezoelectricity and its uses in disturbance sensing and control of flexible structures: A survey*, Applied mechanics Review, Vol. 17, No..2, pp. 113-119.

[3] T. Baily, J. E. Jr. Hubbard, *Distributed piezoelectric polymer active vibration control of a cantilever beam*, Journal of Guidance, Dynamics and Control, Vol. 8, No. 5, pp. 605-611, 1985.

[4] S. Hanagud, M. W. Obal, and A. J. Callise, *Optimal vibration control by the use of piezoelectric sensors and actuators*, J. Contr. Guidance, Vol. 15, No. 5, pp.1199-1206, 1992.

[5] W. S. Hwang and H. C.l Park, *Finite element modeling of piezoelectric sensors and actuators*, AIAA journal J, Vol. 31, No. 5, pp. 930-937, 1993.

[6] B. Bona, M. Indri, A. Tornamble), *Flexible piezoelectric structures approximate motion equations and control algorithms*, IEEE Auto. Contr., Vol. AC-42, No. 1, pp. 94-101, 1997.

[7] W. Schiehlen, and H. Schonerstedt, *Controller design for the active vibration damping of beam structure*, Proc. Smart Mechanical Systems Adaptronics SAE International. USA, pp. 137-146, 1998 .

[8] S.-Bok Choi, Chae-Cheon Cheong, and C.-Hea Lee, *Possition tracking control of a smart flexible structure featuring a piezofilm actuator,* Journal of Guidance and Control, Vol. 19, No. 6 , pp. 1364-1369, 1996.

[9] Forouza Pourki, , *Distributed controllers for flexible structures using piezoelectric actuators/ sensors*, Proc. 32nd IEEE CDC Conf., Texas, USA, pp. 1367-1369, 1993.

[10] A. J. Moutsopoulou, A. Pouliezos, and G. E. Stavroulakis, *Modelling with Uncertainty and Robust Control of Smart Beams*, Paper 35, Proceedings of the Ninth International Conference on Computational Structures Technology. B.H.V. Topping and M. Papadrakakis, (Editors), Civil Comp Press, 2008.

[11] B. Miara, G. E. Stavroulakis, V. Valente, *Topics on mathematics for smart systems*, Proceedings of the European Conference. Rome, Italy, 26-28 October 2006, World Scientific Publishers, Singapore, International, 2007.

[12] B. Bandyopadhyay, T.C. Manjunath, and M. Unapathy, *Modeling, Control, and Implementation of Smart Structures*, Springer ISBN-10 3-540-48393-4, 2007.

[13] A.J. Moutsopoulou, A. Pouliezos, G. E. Stavroulakis, *Nonsmooth and nonconvex optimization for the design and order reduction of robust controllers used in smart structures*, In: M. Papadrakakis et all., *Computational Methods in Erthquake Engineering*, Vol. 2, Springer ,2012.

[14] Benjeddou, M.A. Trindade, and R. Ohayon, *New shear actuated smart structure beam finite element*, Journal of Guidance. Dynamics and Control.37, 378-383, 1999.

[15] B. Bona, M. Indri, and A. Tornamble, *Flexible piezoelectric structures approximate motion equations and control algorithms*, IEEE Auto.Control 42(1), 94-101, 1997.

[16] O. Bosgra, and H. Kwakernaak, *Design methods for control systems*, Course notes, Dutch Institute for Systems and Control 67, 2001.

[17] J. Burke, A. Lewis, and M.L. Overton, A *robust gradient sampling algorithm for nonsmooth nonconvex optimization*, Siam Journal on Optimization 15, 751-779, 2005.

[18] H. Kimura, *Robust stability for a class of transfer functions*, IEE Transactions on Automatic Control 29, 788–793, 1984.

[19] H. Kwakernaak, *Robust control and H1 optimization*, Tutorial hper JFAC. Automatica, 29(2), 255-273, 1993.

[20] M. Millston, *HIFOO 1.5: Structured control of linear systems with a non trivial feedthrough*, M.S. thesis, Courant Institute of Mathematical Sciences, New York University, 2006.

[21] A. Packard, J. Doyle, and G. Balas, *Linear, multivariable robust control with a μ perspective*, ASME Journal of Dynamic Systems, Measurement and Control, 50th Anniversary Issue, 115(2b), 310–319, 1993.

[22] G. Zames, *Feedback minimax sensitivity and optimal robustness*, IEE Trans. Autom. Control, 28, 585–601, 1983.

[23] G. Foutsitzi, G. Stavroulakis and E. Hadjigeorgiou, *Modelling and Simulation of Controlled Smart Structures*, Proceedings of the 9th HSTAM International Congress on Mechanics pp. 511-518 , Limassol, Cyprus, 2010.

COMPDYN 2015
5th ECCOMAS Thematic Conference on
Computational Methods in Structural Dynamics and Earthquake Engineering
M. Papadrakakis, V. Papadopoulos, V. Plevris (eds.)
Crete Island, Greece, 25–27 May 2015

AN ENHANCED COMPONENT BASED MODEL FOR STEEL LINKS IN HYBRID STRUCTURES: DEVELOPMENT, CALIBRATION AND EXPERIMENTAL VALIDATION

M. Manfredi[1], **F. Morelli** [1] **and W. Salvatore**[1]

[1] Department of Civil and Industrial Engineering - University of Pisa
largo Lucio Lazzarino 1, 56122, Pisa
martin.doc@hotmail.it, francesco.morelli@dic.unipi.it, walter@ing.unipi.it

Keywords: steel-concrete hybrid structures, steel structures, concrete shear walls, experimental test, dissipative systems, component-based model.

Abstract. *In the present paper the development, calibration and experimental validation of an enhanced component based model of a dissipative steel link connecting a reinforced concrete wall and a steel gravity frame is presented. The structural consists in an hybrid coupled shear wall (HCSW), developed within the INNOHYCO project (Dall'Asta et al., 2014), obtained coupling an RC wall with two side steel columns by means of steel links where the energy dissipation takes place. The experimental results carried on a subsystem representing a portion of the shear wall, the dissipative link and one side column, showed that the global dissipative behavior is strongly affected by the characteristics of the link-to-column connection. In particular the prestressing force of the seat angle connection bolts influence in a decisive way the dissipative capacity of the system, especially for the low amplitude cycle. For this reason, an experimental campaign on two different hybrid system containing the dissipative element and the aforementioned connections has been carried out. A non-linear cyclic component-based model of the entire sub-assemblage is then developed and calibrated on the base of experimental results.*

1 INTRODUCTION

During the last decades, several researches have been conducted in order to find structural solutions capable to resist to the seismic lateral loads, assuring the life safety in case of strong intensity earthquakes and minimizing the damages to structural and non structural elements in case of low-to-mid earthquakes. In order to reach these goals, particular attention has been given to dissipative structures that allows the realization of building characterized by relatively small element section, if compared to the structures designed to resist elastically to the seismic action, but with a comparable, if not even greater, safety level. Generally speaking, the optimal solutions should be so characterized by suitable stiffness, resistance, global and local ductility. In order to minimize the damages to the non structural elements and the gravity resisting system and, at the same time, to allow a fast recover after low-to-mid intensity earthquakes, the dissipation of energy should be localized in suitable elements easy to replace after the seismic event.

An effective structural solution capable of offering significant advantages in terms of resistance and lateral stiffness are composite constructions. They have been common in Europe and US for over half a century through the use of composite beam and joist floor systems [3].

In these pioneer experiences only the steel components of the structure were considered to resist loads while the concrete encasement was functional for protection. Although these structures were not designed for seismic loads, they behaved better under strong earthquakes than pure steel structures, thus demonstrating that inadvertent composite action probably contributed to the good performance. For these reason, today, many engineers believe that composite and hybrid systems offer an economical method to develop the strength and stiffness required for seismic design, and many systems have been developed [4] such as unbraced moment frames consisting of steel girders with concrete-filled steel tube (CFT), steel reinforced concrete (i.e. encased steel section) beam-columns, braced frames having concrete-filled steel tube columns and a variety of composite and hybrid wall systems [4]. Several research were also carried out in order to evaluate the dissipative capacity of composite structures [5] [6].

Within the European project INNO-HYCO (INNOvative HYbrid and COmposite steel-concrete structural solutions for building in seismic area) [1], funded by the Research Fund for Coal and Steel (RFCS), steel-concrete hybrid systems obtained by coupling reinforced concrete elements (e.g., walls and shear panels) with steel elements (e.g., beams) were studied. These systems permit to exploit i) the stiffness of reinforced concrete elements, necessary to limit building damage under low-intensity earthquakes, and ii) the ductility of steel elements.

In particular, in the present paper, the attention is focused on the innovative hybrid coupled shear wall (HCSW) systems, obtained coupling an RC wall with two side steel columns by means of steel links where the energy dissipation takes place.

In the following paragraphs, a general description of the solution studied, the experimental campaign on the dissipative element and connection and the results obtained are presented. A component-based model of the concrete-to-column link is then proposed, each component calibrated and the numerical results compared to the experimental ones. The present paper is based upon the work of Manfredi et al. [2], but it includes also a more detailed description of the methodology adopted and of the component model developed.

2 INNOVATIVE HYBRID COUPLED SHEAR WALL SYSTEMS

Generally, hybrid systems may suffer from some drawbacks distinctive of concrete walls and steel frames. In fact, shear walls are low redundant structures; their post-yielding behavior is characterized by deformations localized at the base and expensive detailing is required to avoid concrete crushing. Moreover, due to the excessive overturning moment generated by seismic forces at the base of the wall, expensive foundations are often required. On the other hand, steel moment resisting frames are characterized by expensive connections and dissipative elements coincide with the gravity resisting ones, making their repair difficult after the earthquake.

For these reasons, several hybrid solutions have been studied in the last decade with the aim of overcoming these drawbacks. In figure 1, the structural scheme and a detail of the dissipative element (replaceable link beam) of the HCSW system proposed and developed within the INNO-HYCO project [1], and studied within this paper, are reported.

The system studied is composed by a seismic resistant structure, constituted by a reinforced concrete wall linked to two side columns by steel elements, and by a gravity frame. In this way, the reinforced concrete wall, thanks to its high stiffness, resists almost all the horizontal shear while the overturning moment is divided partially by the individual flexural action of the wall and partially by a couple of axial forces developed within the two side columns for the benefit of the foundation and of the flexural demand on the wall base. If correctly designed, the reinforced concrete wall should remain elastic (or undergo limited damages) while dissipation should be concentrated at the steel links (dissipative elements). For this reason and in order to allow an easy repairing, the link beams should be designed to guarantee the formation of the dissipative mechanism without involving the r.c. wall or the connection system embedded on the concrete, taking into account a suitable over-strength factor of the link elements.

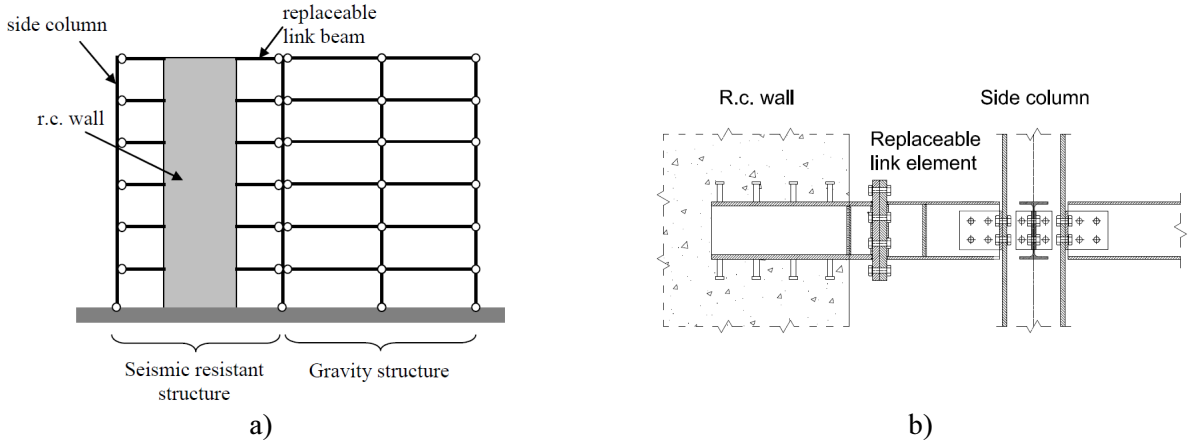


Figure 1: Innovative hybrid coupled shear wall system: a) structural scheme; b) replaceable link

A correct capacity design would allow the activation, in case of high intensity earthquakes, of a global mechanism where almost all the links would dissipate the seismic energy transmitted to the structure, containing so the forces on all the other structural elements. Such capacity design should take in particular account all the elements involved in the transmission of force from the r.c. wall to the steel column, including so the joint between wall and link and between link and steel column.

3 OBJECTIVE AND METHODOLOGY

The optimal seismic behavior of the hybrid system presented is strictly conditioned by the real behavior of the dissipative elements that, within this work, are designed to be realized by simple I profiles. Given that the hysteretic behavior and its dependence from the element mechanical and geometrical characteristics is, nowadays, well known, the main source of uncertainties is related to the characteristics of the wall-to-link and link-to-column connections. The principal objective of this article is to develop a suitable mechanical parametric model able to reproduce, in a precise and reliable manner, the cyclic behavior of the dissipative system (considering so also the presence of the connections) taking into account the influence of the mechanical and geometrical characteristics of the dissipative and connecting elements. The methodology used to develop the aforementioned mechanical model is resumed in figure 2.

In order to take into account the real hysteretic behavior of the dissipative system, an experimental campaign on two sub-systems representing two different connection typologies were carried out. For each connection typology, a total number of 5 tests were executed: 1 monotonic and 4 cyclic (2 with constant amplitude and 2 with increasing amplitude). Within this article, only the cyclic test

results were considered. The experimental behavior of the specimens allowed to select the main mechanical components that influence the global behavior of the dissipative system. Each component selected was then included in a mechanical model implemented in the OpenSEES software [7] and calibrated, in the first phase, using the experimental data and models available in the state-of-the-art literature. After a comparison between the mechanical model results and the experimental ones, a more refined calibration, using the results of the cyclic tests with increasing amplitude, was carried out allowing so to obtain a reliable mechanical model able to reproduce, in a very precise way, the experimental results obtained on the tests with constant amplitude.

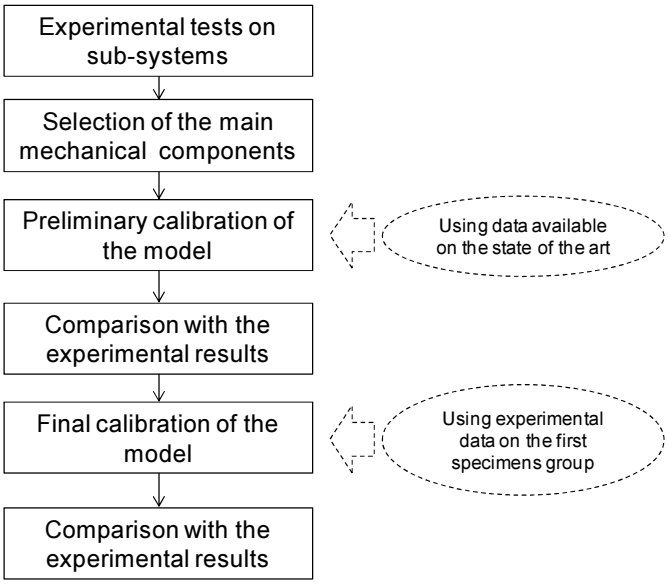


Figure 2: Methodology

4 EXPERIMENTAL CAMPAIGN

4.1 Specimens design

Within the INNO-HYCO project, 2 different case studies were designed in order to evaluate the suitable characteristics of the link element. In particular were considered a 4-storey case and a 8-storey case [1], obtaining the profile reported in table 1 for the dissipative elements.

Table 1: steel link profile (steel S355) [1]

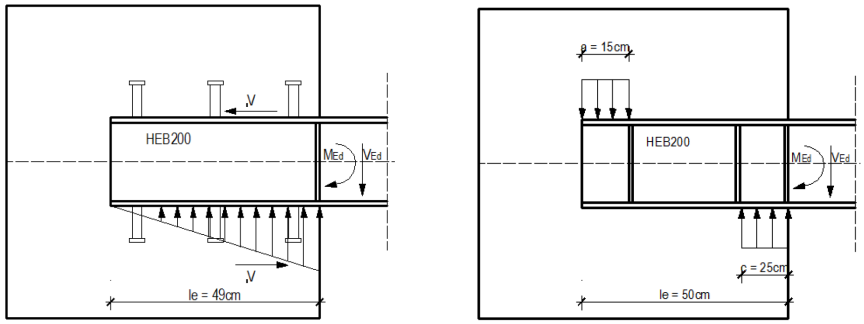
4-storey case			8-storey case		
Floor	Link section	Link length [mm]	Floor	Link section	Link length [mm]
1st floor	IPE550	700	1st and 2nd floor	IPE550	660
2nd floor	IPE500	700	3rd and 4th floor	IPE500	660
3rd floor	IPE450	700	5th and 6th floor	IPE450	660
4th floor	IPE400	700	7th and 8th floor	IPE400	660

Starting from the obtained steel link profile obtained and considering the loading limits of the testing facility, the specimens representing the dissipative zone were downscaled. Considering an arbitrary safety factor equal to 1.5 with respect to the jack capacity, the designed intermediate link of length 660mm with section IPE500 steel S355, determined a down-scaled link with section IPE200, length equal to 360mm and steel grade S275.

Starting from the downscaled link specimens, two different typologies of link-to-wall connection have been considered: in the first case (typology 1) the bending moment is transferred by the link

to the wall primarily by the shear action of shear studs, see figure 3a; in the second case (typology 2) the moment is balanced by a couple of forces orthogonal to the embedded element axis line, see figure 3b. In both cases the configuration of the link fixed to the wall and pinned to the steel column was assumed.

Moreover, two different solutions were considered for the link splice: in one case it was placed at a distance from the concrete wall considered sufficient to allow an easy bolting of the replaceable part (solution associated to typology 1), while, in the other case, the splice connection was placed in correspondence of the face of the wall and threaded bushings were placed to allow the fasten of the link (solution associated to typology 2). Both solutions have been designed following the capacity design concept, allowing the formation of the plastic hinge on the link element without damage to the concrete wall, embedded element and joint. In both cases the link is connected to the steel column by an angle joint.



a) b)

Figure 3: Connection typology 1(a) and 2(b) [1] with the associated transmission force mechanism assumed

In figures 4 and 5, the geometrical characteristic and the realized specimens are shown. Within this paper, the experimental results and the component based model of the first connection typology is presented given that the extension to the second one is straightforward to obtain.

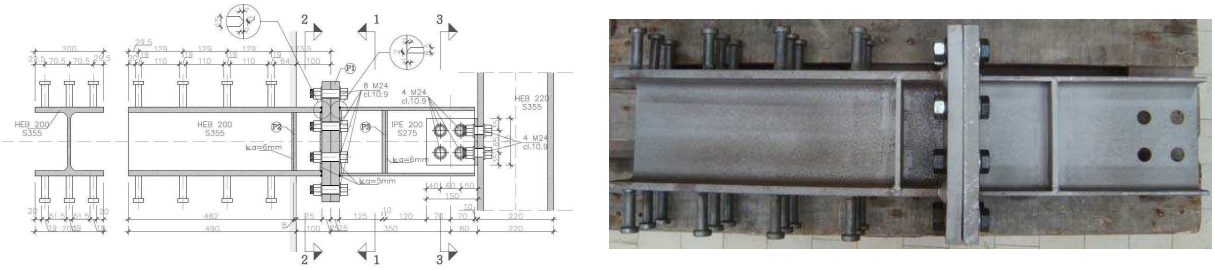


Figure 4: Connection typology 1

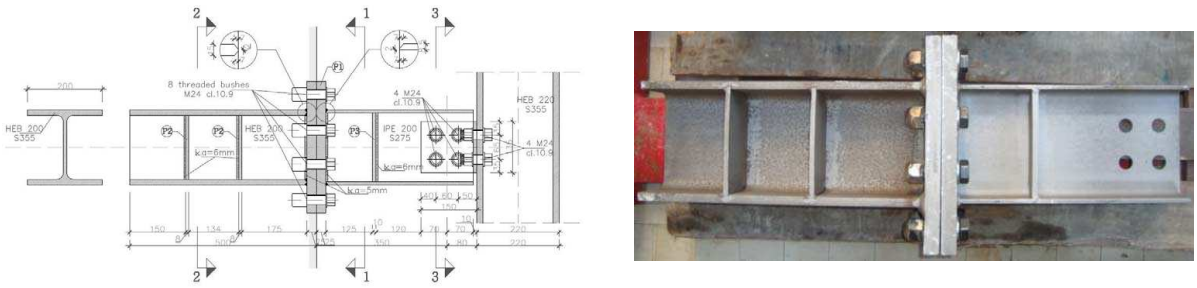


Figure 5: Connection typology 2

4.2 Test setup

In order to evaluate the behaviour of the dissipative zone as close to the real one as possible, for each connection typology, a subsystem representing the portion of the wall interested, the link-to-wall connection, the link, the link-to-column connection and the column were realized.

In figure 6, the global test setup is shown. The r.c. wall is firmly connected to the lab strong floor in order to minimize its vertical and horizontal displacement, while the shear force is transmitted to the link by an hydraulic actuator connected to the element representing the column.

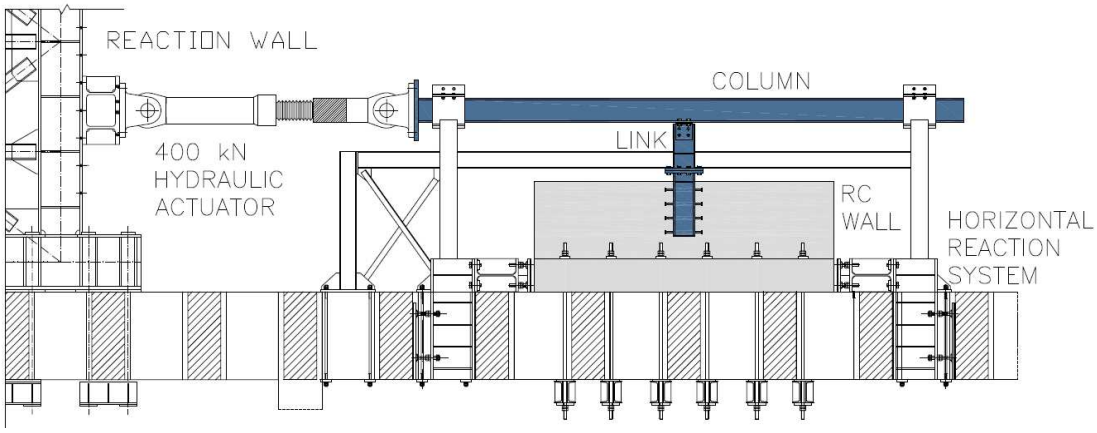


Figure 6: Global test setup

The force transmitted by the actuator was recorded by a load cell, while the displacements and the strains of the steel and concrete element by displacement sensors and strain gauges. In figure 7 the sensors position for the connection typology n°1 is shown.

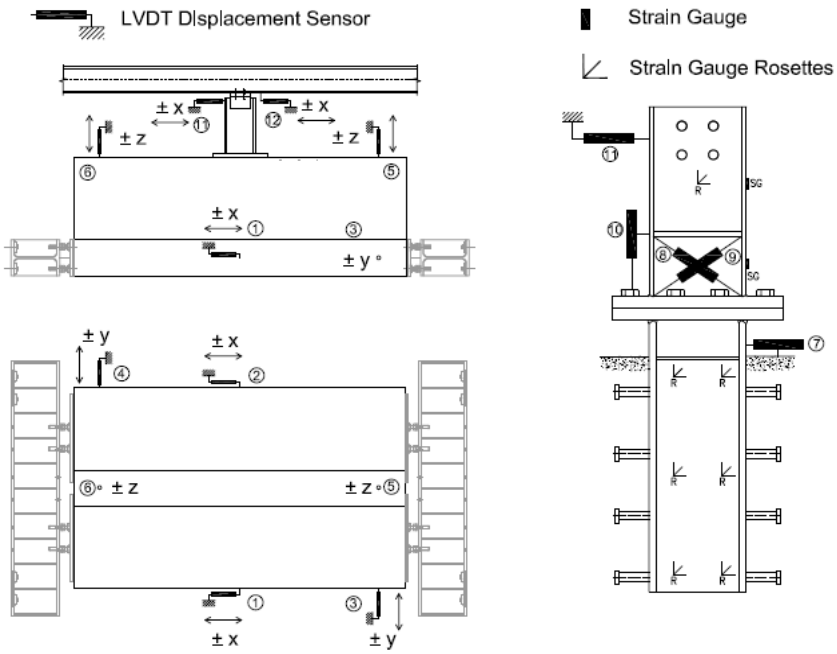


Figure 7: Sensors position

For each connection typology, 5 tests were executed, one monotonic and 4 cyclic. The first specimens couple was subjected to increasing displacement and in particular equal to 0.1 d, 0.2 d, 0.3 d, 0.5 d, 0.7d and 1.0 d (d is the displacement expected at failure). Five cycles were repeated for each intermediate step while ten cycles for the last step (1.0d). A constant amplitude, corresponding to the

design displacement d up to failure, was imposed to the second links couple with a maximum number of imposed cycles equal to 20.

4.3 Test results

In figure 8 the results of the tests, in terms of force-displacement curves, are reported. In particular, the force – link displacement (blue line) and the force – column displacement (red line) are shown.

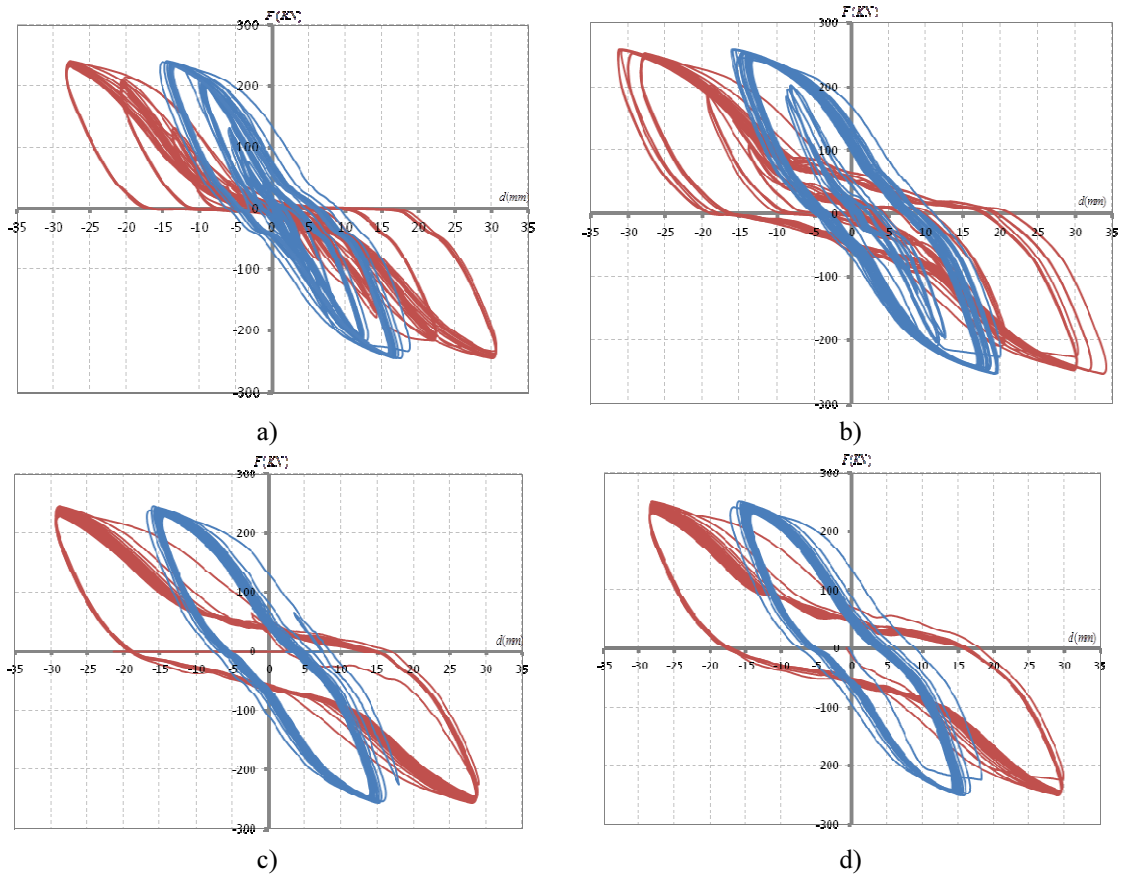


Figure 8: Force – displacement graphs with increasing amplitude (a,b) and constant amplitude (c,d) on the connection typology 1

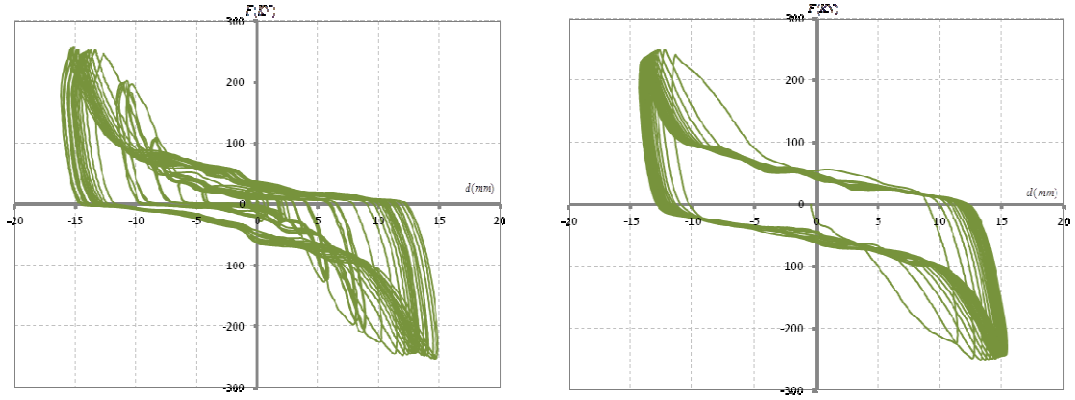
During the first test, figure 8a, problems with the correct fastening of the bolts occurred, determining so different results from the other tests where the problem was fixed. It can be see that, while the first one is characterized by a relative "fat" hysteretic cycle, the latter one is characterized by pinching phenomena, mainly due to the gap associated to the seat joint between the link element and the column. In figure 9a, it can be seen the accentuated eccentricity of the seat angle during the test due to the gap. Moreover, the pinching phenomenon slightly increases as the maximum imposed displacement increases. In fact, due to the excessive relative rotation between the link end and the column, the link web near the seat angle plasticizes, increasing the gap between link and seat angle. In figure 9b, the ovalized holes of the link after the end of the fourth test are shown.



a) b)

Figure 9: a) Position of the seat angle during the test n°4; b) plasticization of the link web at the end of test n°4

In figure 10, the link force versus the relative displacement between the dissipative link and the column element relationships are shown. Two different phenomena can be individuated: 1) a linear variable friction between the angle profile and the link or column element that causes energy dissipation; 2) the pinching due to the contact and consequent ovalization of the dissipative link web holes. During the tests, no damage signs on the concrete wall were detected.



a) b)

Figure 10: Force versus link-to-column relative displacement for the test a) n° II with increasing amplitude and b) n°IV with constant amplitude.

5 COMPONENT-BASED MODEL

5.1 Definition of the model

In order to extend the experimental results obtained to joints characterized by different mechanical and geometrical characteristics and so to establish the link effective capacity to dissipate seismic energy under the action of the cyclic load, a component-based model has been developed for Connection typology 1. The model has been implemented in OpenSEES ("The Open System for Earthquake Engineering Simulation" [7]) and each component, as already specified in § 3 was calibrated, initially, using the experimental data available in the literature and compared with the experimental results obtained with the first group of specimens (tests with increasing amplitude). The global model calibration was then refined and validated using the ones of the second group (tests with constant amplitude).

Analyzing the connection configuration it is possible to subdivide it in four main zones: the embedded part, the bolted joint, the dissipative element and the connection between the dissipative element and the column.

In figure 11, the scheme of the assumed constitutive model is shown. The embedded profile, designed to remain elastic even if the dissipative element undergoes plastic deformations, was mod-

elled as an elastic beam coincident with the element axis (with reference to figure 11, element I-C). The shear studs were represented by nonlinear springs connected to the embedded element trough rigid links representing the eccentricity between the embedded profile axis and the base of the shear studs. The contact between the concrete and the embedded profile flange were modelled using unilateral extensional springs. Both the embedded element-dissipative link joint and the dissipative link-column joint were represented by rotational springs. Finally , the dissipative link was modelled using two elements: a rotational spring representing the zone where plasticization is expected and an elastic beam for the remaining zone. To each element, a suitable constitutive model was assigned and calibrated, in a first phase, on the base of the experimental results available in literature.

Embedded zone

As already mentioned, the three elements/mechanisms considered within the embedded zone were the flexural behavior HEB200 profile, the shear studs and the contact between the concrete and the steel profile flange.

The embedded element was modeled as a simple elastic beam (with reference to figure 11, element C-I). On both sides of this element were introduced 4 rigid links representing the eccentricity between the shear studs base and the HEB200 axis.

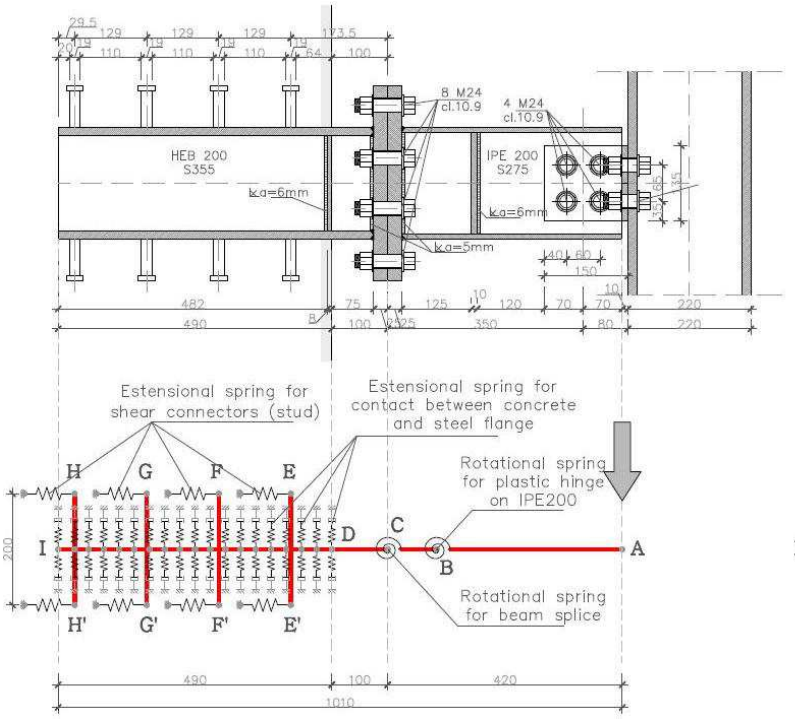


Figure 11: Constitutive model for HCSW connection typology 1

The shear studs were modeled with linear spring elements. The relation between force and slip (F-γ), for the single equivalent spring behavior formed by three connectors arranged in parallel series, was obtained processing experimental tests conducted by Aribert et al. 2000 [11]. The force-displacement relationship is schematically shown in figure 12a for the single shear stud and in figure 12b for the row composed by three shear studs.

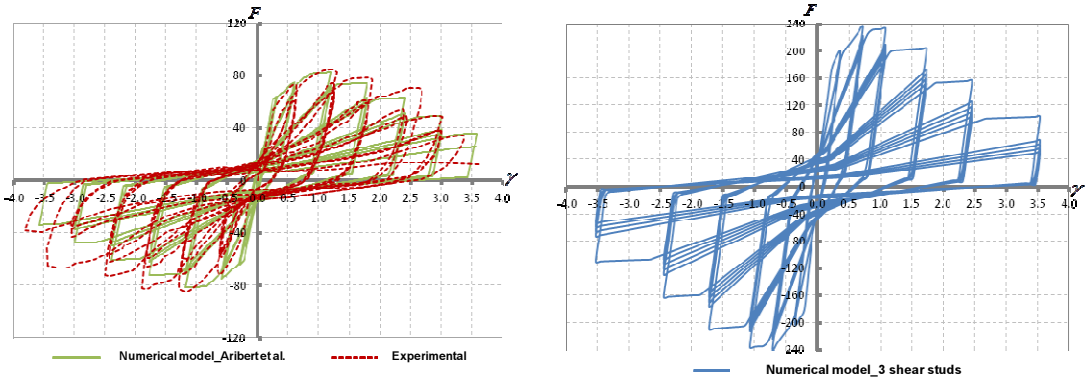
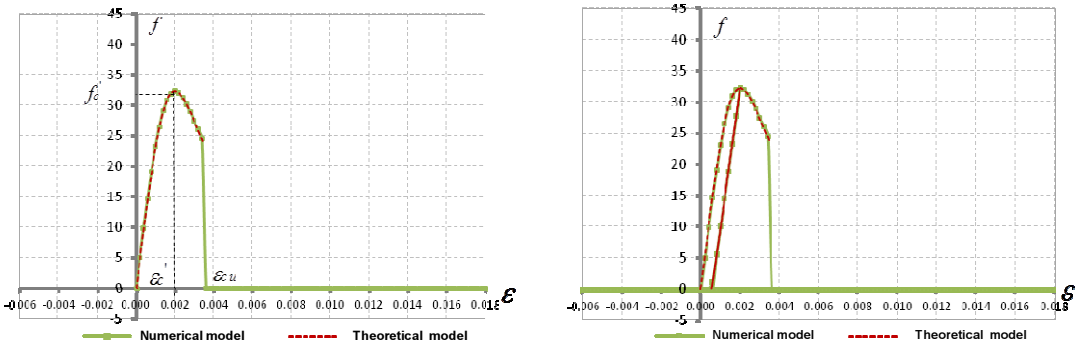


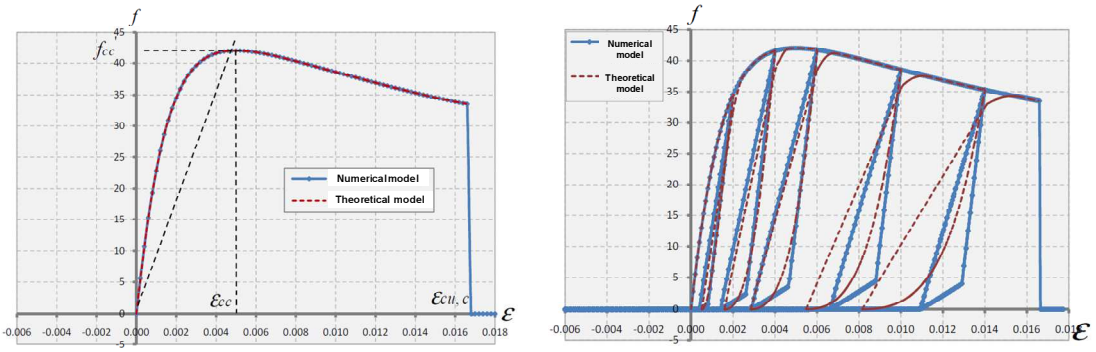
Figure 12 Force-slip relationship [11] for the a) single shear stud; b) three shear stud in a row.

Along the embedded zone, among points D-I, on the both sides of the HEB200 profile axis, a group of extensional springs placed with an inter-axis of 1cm was considered in order to represent the contact between the steel flange and the concrete wall. The concrete stress-strain relationship was evaluated in the zone comprised between the E-E' section and the I point (confined concrete) using the relation suggested by Mander et al. 1988 [12], while in the remaining zone (unconfined concrete) using the relation developed by Popovic 1973 [13], as schematically shown in figures 13 and 14. In order to take into account only the compressive reaction of the concrete, a no-tension element was associated to each spring representing the concrete. The concrete models were calibrated using the results of compression tests executed on three specimens realized with the same concrete of the r.c. wall.



a) b)

Figure 13 Stress-strain relationship for the unconfined concrete: a) monotonic model [13]; b) cyclic model



a) b)

Figure 14 Stress-strain relationship for the confined concrete [12]: a) monotonic model; b) cyclic model.

Extended end plate joint

The rotational spring placed in point C represents the flexural behavior of the beam splice and its behavior was obtained using the "Components Method" described in EN 1993-1-8:2005 [8]. The joint was originally designed as full-strength. However, in order to take into account eventual plasticization of the joint itself, the complete plastic behavior was considered. In figure 15 the theoretical behavior obtained applying the component method and the tri-linear model implemented in OpenSEES are shown. It can be seen the good approximation of the tri-linear model.

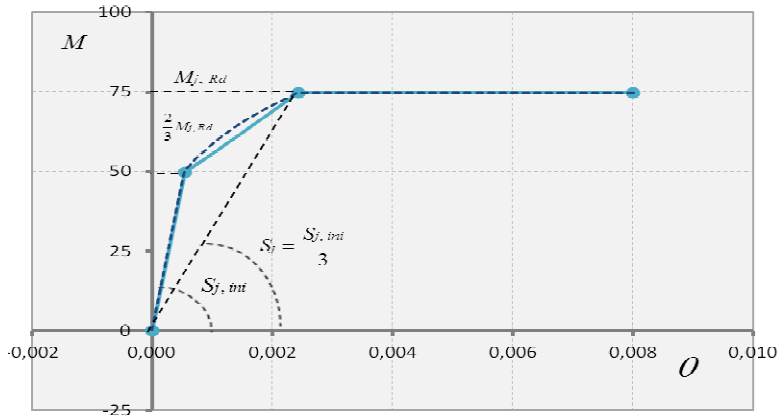


Figure 15 Moment-rotation relationship for the extended end plate joint: theoretical behavior obtained with the component method (dashed line) and numerical approximation (solid line).

Dissipative link

As already mentioned, the dissipative link was modeled using two elements: an elastic beam (element AB of figure 11) and a rotational spring (point B of figure 11) placed coincident with the center of the stiffened zone of the dissipative element. The relation between the moment and chord rotation (M-θ) was obtained processing the data of the experimental tests available on technical literature. In particular, given the lack of tests on IPE200 profiles, both the monotonic and cyclic behavior were calibrated first for an IPE300 profile and then scaled in order to obtain an estimation of the IPE200 behavior.

Both monotonic and cyclic curve for the IPE300 profile were obtained using the experimental data and the procedure described in Landolfo et al. [8].

In Landolfo et al. [8] an experimental program on a wide range of cross section typologies, comprising I sections, under monotonic and cyclic loading was carried out and a methodology for the estimation of the main parameter affecting the non-linear behavior of the section are provided. In particular, the flexural overstrength, *s*, and the rotation capacity, *R*, are evaluated through two different empirical expression, reported hereafter, functions of the geometrical and mechanical characteristics of the section.

$$1/s = C_1^{(s)} + C_2^{(s)} \cdot \lambda_f^2 + C_3^{(s)} \cdot \lambda_w^2 + C_4^{(s)} \cdot \frac{b_f}{L_v} + C_5^{(s)} \cdot \frac{E}{E_h} + C_6^{(s)} \cdot \frac{\varepsilon_h}{\varepsilon_y} \tag{1}$$

$$R = C_1^{(R)} + C_2^{(R)} \cdot \frac{1}{\lambda_f^2} + C_3^{(R)} \frac{1}{\lambda_w^2} + C_4^{(R)} \frac{b_f \cdot h}{L_v^2} + C_5^{(R)} \frac{b_f \cdot t_f}{h \cdot L_v} + C_6^{(R)} \frac{A_f}{A_{TOT}} + C_7^{(R)} \frac{L_m}{L_v} + C_8^{(R)} s \tag{2}$$

The values of the coefficients $C^{(R)}$ and $C^{(s)}$ as well as the meaning of the terms in (1) and (2) are reported in Landolfo et al [8]. Using this approach, the IPE200 monotonic and cyclic behavior was modelled in the following steps:

1) Evaluation of s_{IPE300} and R_{IPE300} for the IPE300 profile using (1) and (2)
2) Calibration of the numerical multi-linear model of the IPE300 using the experimental data available on Landolfo et al. [8].

It was assumed a multi-linear model defined using 6 points, as schematically shown in figure 16.

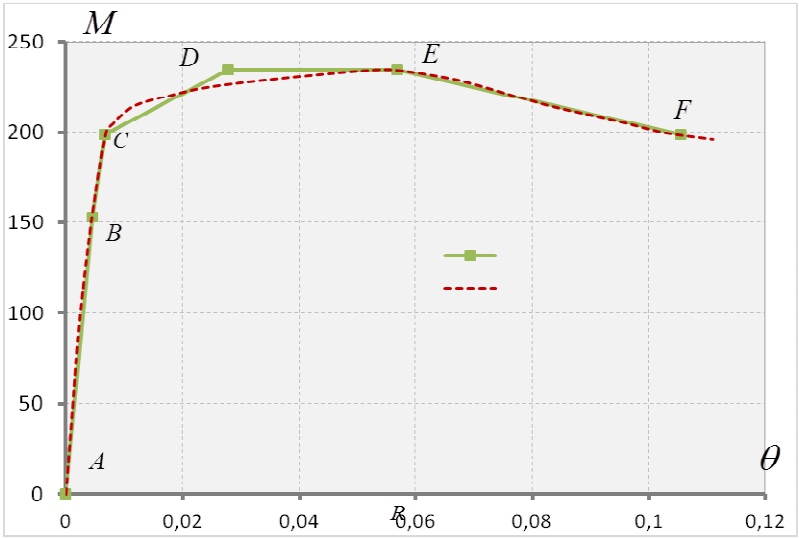


Figure 16: Moment-rotation curve for the IPE300 profile: experimental curve (dashed line) extrapolated from [8] and multi-linear model (solid line).

3) Evaluation of s_{IPE200} and R_{IPE200} for the IPE200 profile using (1) and (2)
4) Scaling of the IPE300 multi-linear curve in order to fit the IPE200 characteristics.

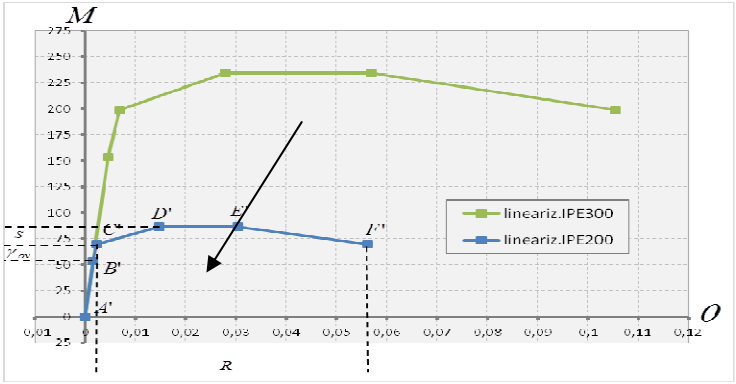
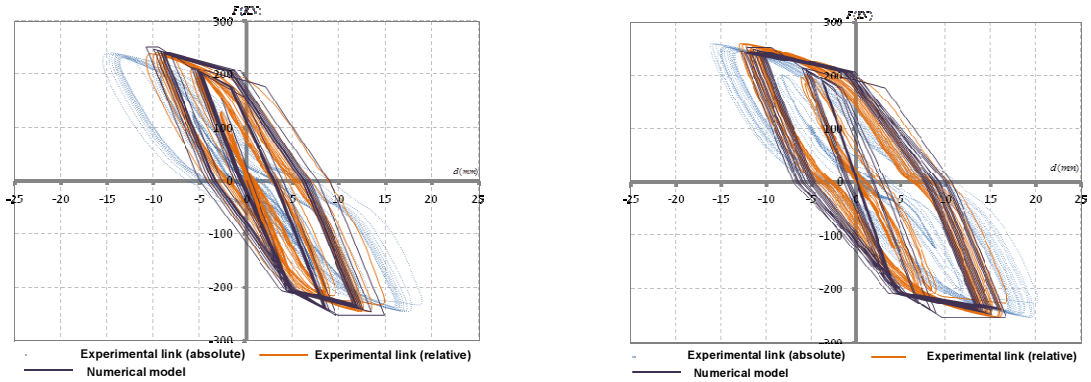


Figure 17: Moment-rotation curve for the IPE300 and IPE200 profiles

5.2 Numerical results

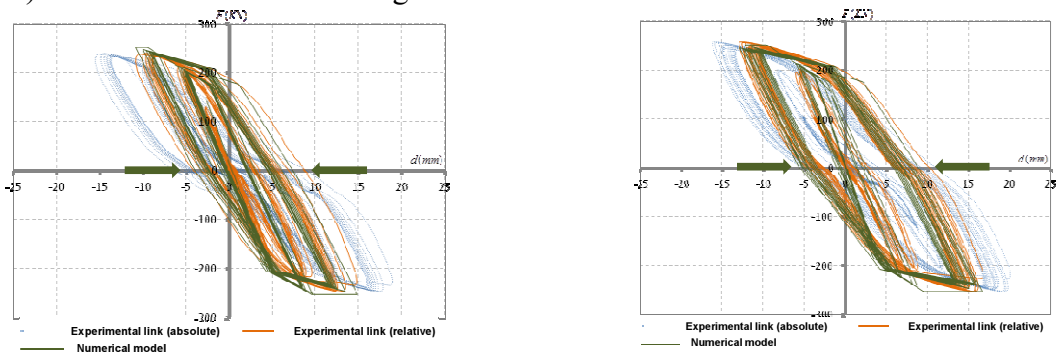
The comparison between the theoretical model (calibrated considering only experimental data present in literature) and the experimental results showed a good agreement in terms of strength and stiffness, but the energy dissipated by the theoretical model resulted to be higher, as schematically shown in figure 18.



a) b)

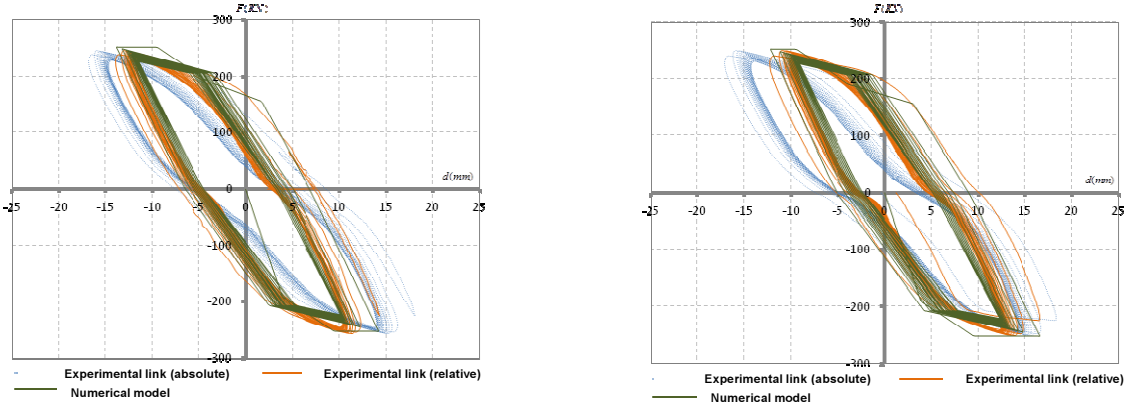
Figure 18: comparison between the link force-displacement curve of the theoretical model (purple line) and the experimental results (orange line) of the first test group.

In order to improve the developed model, the parameter determining the stiffness degradation was calibrated using the experimental results of the first tests group (increasing amplitude). The results are shown in figures 19 and 20.



a) b)

Figure 19: comparison between the link force-displacement curve of the updated theoretical model (green line) and the experimental results (orange line) of the first test group



a) b)

Figure 20: comparison between the link force-displacement curve of the updated theoretical model (green line) and the experimental results (orange line) of the second test group

In figure 21 the comparison between the energy dissipated during the four tests and the numerical results obtained by the theoretical model and the calibrated one is shown. It can

be noticed that, after the calibration, the results obtained with the calibrated model are practically coincident with the experimental one even for the III° and IV° tests.

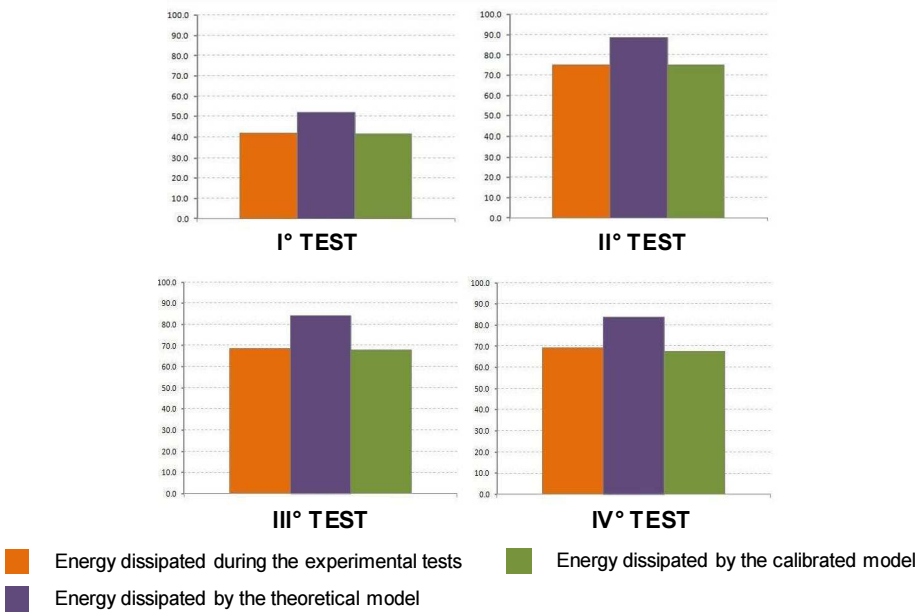


Figure 21: comparison between the energy dissipated during the four tests and the numerical results obtained by the theoretical model and the calibrated one

6 CONCLUSIONS

In the present paper, the behavior of the dissipative link of an innovative hybrid coupled shear wall systems (HCSW), obtained coupling an RC wall with two side steel columns, was studied.

The experimental results obtained from 4 downscaled specimens highlighted the good dissipative capacity of the links, but also the necessity to take into account the pinching phenomena due to the gap between the link and the column. In fact, the experimental hysteretic curves showed that the seat angle connection, commonly modelled as a perfect pin, is characterized by pinching phenomena that increases as the maximum drift increases due to the plasticization of the link web. This pinching phenomena can lead, if not correctly taken into account, to a wrong esteem of the system dissipative capacity.

Starting from the observation made during the experimental tests on 4 downscaled specimens of the dissipative link, a component-based plan model was proposed. In this first version of the model, the angle connection was not taken into account.

A first calibration of the model components was carried out using the experimental data present in literature, especially regarding the plastic hinge zone and the shear studs. From the comparison between the experimental results and the numerical ones in terms of dissipated energy, a slight adjustment of the stiffness degradation parameter was required. So, a second calibration was carried out using the experimental results of the first tests group (tests characterized by an increasing imposed amplitude). The numerical results obtained from the calibrated model were then compared to the experimental ones of the second tests group (constant imposed amplitude), showing a very good capacity of the model to predict the experimental behavior.

The obtained results permits to evaluate the dissipative behavior of the link even for different loading scenarios and set the ground for the development of a model that can take into account also the influence of the angle connection between the link and the column.

Acknowledgment

The research leading to these results has received funding from the European Union's Research Fund for Coal and Steel (RFCS) research programme under grant agreement n° [RFSR-CT-2010-00025].

References

[1] A. Dall'Asta, G. Leoni, A. Zona, B. Hoffmeister, H. Bigelow, H. Degée, C. Braham, T. Bogdan, W. Salvatore, F. Morelli, T. Prokopis, S.A. Karamanos, G. Varelis, A. Galazzi, E. Medici, P. Boni, "INNOvative HYbrid and COmposite steel-concrete structural solutions for building in seismic area – RFSR-CT-2010-00025 project – Final Report", European Commission, Brussels, 2014.

[2] M. Manfredi, F. Morelli, W. Salvatore, "Component-Based Model and Experimental Behavior of a Dissipative Steel Link for Hybrid Structures", in B.H.V. Topping, P. Iványi, (Editors), "*Proceedings of the Twelfth International Conference on Computational Structures Technology*", Civil-Comp Press, Stirlingshire, UK, Paper 165, 2014. doi:10.4203/ccp.106.165

[3] J. F. Hajjar, "Composite steel and concrete structural systems for seismic engineering", *Journal of Constructional Steel Research*, 2002.

[4] C. W. Roeder, "Overview of hybrid and composite systems for seismic design in the United States", *Engineering Structures*, 1998.

[5] A.Braconi, O.S. Bursi, G. Fabbrocino, W. Salvatore, F.Taucer, R. Tremblay "Seismic performance of a 3D full-scale high-ductility steel-concrete composite moment-resisting structure - Part II: Test results and analytical validation". *Earthquake Engineering & Structural Dynamics*, 37:1635–1655, Wiley InterScience, DOI: 10.1002/eqe.843, John Wiley & Sons, 2008

[6] A. Braconi, O. S. Bursi, G. Fabbrocino, W. Salvatore, R. Tremblay, "Seismic performance of a 3D full-scale high-ductility steel-concrete composite moment-resisting structure - Part I: Design and testing procedure", *Earthquake Engineering & Structural Dynamics*, 37:1609–1634, Wiley InterScience, DOI: 10.1002/eqe.829, John Wiley & Sons, 2008

[7] S. Mazzoni, F. McKenna, M.H. Scott, G.L.Fenves *et al.*, "Opensees Command Language Manual", 2006.

[8] M. D'Aniello, R. Landolfo, V. Piluso, G. Rizzano " Ultimate behavior of steel beams under non-uniform bending", *Journal of Constructional Steel Research*, 78, 2012.

[9] CEN (European Communities for Standardization), "EN 1993-1-8 Eurocode 3: design of steel structures -- part 8: Design of joints", 2005.

[10] A. Braconi, W. Salvatore, R. Tremblay, O.S. Bursi, "Behaviour and modelling of partial-strength beam-to-column composite joints for seismic applications", *Earthquake Engineering & Structural Dynamics*, John Wiley & Sons, 36: 142–161, 2007

[11] J. M., Aribert, O. N. Dinga, A. Lachal, "Modélisation et étude expérimentale d'assemblages de type poutre mixte-poteau en acier", *Construction Metallique*, N°1, 2000.

[12] J.B. Mander, M.J.N. Priestley, R. Park, "Theoretical Stress-Strain Model for Confined Concrete". *Journal of Structural Engineering*, Vol. 114, n°8, pagg. 1804-1825, 1988.

[13] S. Popovic, "A numerical approach to the complete stress-strain curves for concrete". *Cement and Concr. Res*., Vol. 3, n°5, pagg. 583-599, 1973.

COMPDYN 2015
5th ECCOMAS Thematic Conference on
Computational Methods in Structural Dynamics and Earthquake Engineering
M. Papadrakakis, V. Papadopoulos, V. Plevris (eds.)
Crete Island, Greece, 25–27 May 2015

ROBUST CONTROL OF SMART STRUCTURES WITH OPTIMALLY PLACED ACTUATORS AND SENSORS

Amalia G. Moutsopoulou[1], Georgia Foutsitzi[2], Christos Gogos[3] and Georgios E. Stavroulakis[4]

[1]Department of Civil Engineering, Technological Educational Institute of Crete,

Estavromenos Heraklion Crete, Greece

e-mail: amalia@staff.teicrete.gr

[2,3]Department of Accounting and Finance, Technological Educational

Institution of Epirus, TEI Campus−Psathaki, GR-48100 Preveza, Greece

e-mails: gfoutsi@teiep.gr , cgogos@teiep.gr

[4]Department of Production Engineering and Management,

Technical University of Crete, GR-73100 Chania, Greece

e-mail: gestavr@dpem.tuc.gr

Keywords: Robust Control, Vibration Control, Piezoelectric beam, Actuator Placement

Abstract.
The objective of this work is to design robust controller for smart structures to control its response under the influence of external excitation. An accurate model for the analysis of smart composite beams with surface bonded piezoelectric sensors and actuators patches is considered. Optimal placement of five piezoelectric sensor/actuator pairs are found, by exhaustively examining all possible configurations in order to suppress the first six modes of vibration. The LQR performance index is used as objective function to locate the sensor/actuator pairs. Vibration reduction for the cantilever beam with piezoelectric patches bonded in the optimal location was investigated to attenuate the first six modes of vibration using a $H_{infinity}$ scheme. After modeling multiplicative uncertainty, the augmented uncertain plant is obtained; an optimal robust controller is designed using $H_{infinity}$. A robust controller is designed based on the augmented plant composed of the nominal model and it's accompanied uncertain. Robust and nominal performances of designed controllers are achieved for perturbed plants and results were compared.

1. INTRODUCTION

The trend of civil engineering design requires structures to become lighter, more flexible and stronger, so in recent years, the light structures have been widely used in various engineering applications [1]. The use of active control techniques for the suppression of vibrations of very light structures is a very important target in many applications, where the additional masses of stiffeners or dampers should be avoided. Active techniques are also more suitable in cases where the disturbance to be cancelled or the properties of the controlled system vary with time [2]. In practice, any structure that deforms under some loading can be regarded as flexible structure and is a distributed parameter system. This implies that vibration at one point is related to vibration at the rest of the points over the structure [3]. Thus, it is desirable to use appropriate sensors and actuators. Piezoelectric sensors and actuators are extensively employed in many practical applications such as smart structures due to their lightness and their capability of coupling strain and electric fields. In order to control structural vibrations, piezoelectric sensors and actuators can be easily bonded on the vibrating structure [4]. Vibration suppression of a flexible structure can be optimized by locating piezoelectric sensors and actuators in efficient locations.

This work is concerned with active vibration reduction of a beam, mounted rigidly along one edge to form a cantilever. Optimal placement of five piezoelectric sensor/actuator pairs to thirty possible locations in order to suppress the first six modes of vibration is obtained by fully examining all possible configurations. The LQR performance index is used as objective function to locate the sensor/actuator pairs. The beam, with piezoelectric sensor/actuator pairs bonded to its surfaces, is modelled using the super-convergent FE approach which includes extension, bending and rotation degrees of freedom [10]. Vibration reduction for the cantilever beam with piezoelectric patches bonded in the optimal location was investigated to attenuate the first six modes of vibration using an $H_{infinity}$ control scheme.

2. DYNAMIC MODELING OF STRUCTURE

For designing a controller, a structure consists of a cantilever beam with five surface bonded piezoelectric pairs is considered. The patches are used as actuators and sensors and they are attached symmetrically to either side of the beam, thus collocating the actuator and sensor. For the analysis of the cantilevered composite structure, a super-convergent finite element (FE) model is used [10].

3.1 Modelling

The dynamical description of the system is given by

$$M\ddot{\chi}(t)+D\dot{\chi}(t)+K_{uu}\chi(t)=f_m(t)+f_e(t) \tag{1}$$

where M is the generalized mass matrix, D is the viscous damping matrix, K_{uu} is the generalized stiffness matrix, f_m is the external loading vector and f_e is the generalized control force vector produced by electromechanical coupling effects. The independent variable $\chi(t)$ is composed of the axial displacements u_i, transversal deflections w_i and rotations ψ_i, [10].

Furthermore to express $f_e(t)$ as $Bu(t)$ we write it as $f_e^* u$, where f_e^* is the piezoelectric force for a unit applied on the corresponding actuator, and u represents the voltages on the actuators. Lastly $d(t)=f_m(t)$ is the disturbance vector.

Generally, the number of degrees of freedom of the system in the FE dynamic model is very large. The mode transform can be used to reduce the size of the structural system by using the most significant equation of motions in the new, modal coordinate system. Assume that modal matrix composed of the first *m* order eigenvectors is Φ, the modal transform can be expressed as

$$\chi = \Phi q$$

where $[\Phi]$ is the modal matrix and q is the modal coordinate vector. Substituting the above equation into equations (1) leads to

$$\overline{M}\ddot{q}(t) + \overline{K}q(t) = \overline{f_m}(t) + \overline{f_e}(t) \qquad (1)'$$

where $\overline{M} = \Phi^T M \Phi$, $\overline{K} = \Phi^T K_{uu} \Phi$ are *m*x*m* diagonal matrices due to the orthogonality of the mode shapes with respect to the mass and stiffness matrices, and $\overline{f_m} = \Phi^T f_m$, $\overline{f_e} = \Phi^T f_e$.
The state space form of the system can be expressed as

$$\dot{x} = Ax + Bu$$

where x is the state vector, A is the system matrix, B is the control matrix and u is the input vector.

3.2 Optimization of Sensors/Actuators Location in Vibration Control

In active control of smart structures, placement of actuators and sensors (S/A) on the structure is a very important issue in order to achieve most effective actuation. Optimal placement of sensors and actuators over a structure can be different for different criteria. Next, in order to propose performance criteria for S/A locations a criterion based on LQR performance index has been considered.
In this work, it is assumed that every actuator covers exactly the length of one element and possible actuator locations are described through the elements of a vector α of binary variables, whose elements α_i are 1 to indicate the presence and 0 the absence of an actuator.

The control vector u can be expressed, using the LQR method, as

$$u = -R^{-1}B^T P,$$

where P satisfying the following matrix Ricatti equation

$$A^T P + PA - PBR^{-1}B^T + Q = 0$$

where Q is a positive semi-definite output weighting matrix and R is a positive input weighting matrix. Since the input matrix B is a function of the locations of the actuators, the system will be changed if the locations of actuators will be changed. in this work, the objective function (criterion) which have been used for the locations of the sensors/actuators pairs is given by [11]

$$J_{opt}(a) = trace\left[P(a)\right]$$

where α represents the location of the actuator–sensor pairs.

Since in this problem setting, there are thirty possible locations and the positions of only five actuators have to be decided, a full enumeration scheme that examined all possible 142506

combinations was used. In case that the number of actuators or locations gets bigger, then other techniques that handle better the combinatorial explosion problem like Genetic Algorithms and Local Search can be used instead.

4. STATEMENT OF THE ROBUST CONTROL PROBLEM

The optimal control problem is initially studied for the nominal system, i.e., the beam with known elastic and piezoelectric properties. A more realistic question concerning the robustness of the control in the presence of defects is also addressed. The fact that the system is influenced by disturbances, such as the wind power, as well as the noise of measurements, is taken into account. The mathematical pattern being used in the designing is an approximation of the real one. Further, a robust control law for the composite beam are designed in order to suppress the vibrations. The response of the controlled nominal and damaged beams is investigated. In order to take into account the incompleteness of the information about the eventual damages and external additional influences a robust $H_{\mathbf{infinity}}$ controller is designed. A system analysis is made on condition that the system is not accurate but includes uncertainty that may be related to some kind of damage [7, 8].

For practical applications the algorithm requires several trial-and-error design iterations in order to provide appropriate control voltages, since the piezoelectric actuators can be depolled by high oscillating voltages. The effectiveness of the proposed control strategies is investigated with the help of numerical simulations.

5. CONTROL DESIGN

We solve a regulator problem for the smart beam with piezoelectric patches. The objective in this section is to determine the optimal vector of active control forces *u(t)* subjected to performance criteria and satisfying the dynamical equations of the system, such that to reduce in an optimal way the external excitations. We consider the steady state (infinite time) case, i.e. the optimization horizon is allowed to extend to infinity. We seek a linear state feedback [9]

$$u = -Kx, \quad \text{with constant gain } K.$$

The *control problem* is to keep the beam in equilibrium which means zero displacements and rotations in the face of external disturbances, noise and model inaccuracies, using the available measurements (displacements and rotations) and controls [14, 15].

5.1 Robustness analysis

The following three steps are taken in the robustness analysis:

1. Expression of *uncertainty set* by a mathematical model.
2. *Robust stability* (RS): check if the system remains stable for all plants within the uncertainty set.
3. *Robust performance* (RP): if system is robustly stable, check whether performance specifications are met for all plants within the uncertainty set. [15, 16]

To perform the robustness analysis, the interconnection of Figure 1a,b will be used.

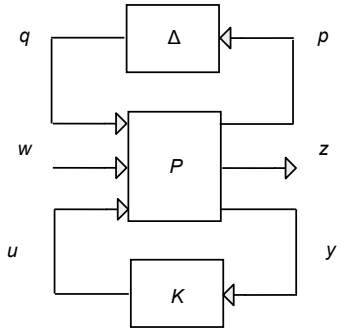


Figure 1a Uncertainty modeling

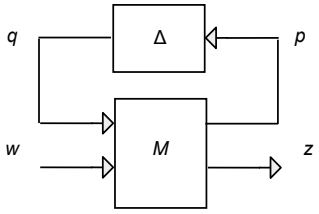


Figure 1b Uncertainty modeling

Here P is the nominal plant defined by figure 1 which includes the uncertainty modelling and K is the calculated H_∞ controller. The uncertainty included in Δ satisfies $\|\Delta\|_\infty \leq 1$. Since K is known, figure 1a can be simplified to figure 1b. [6, 13]

Given this structure it is known that,

I. The system (M, Δ) is *robustly stable* if,

$$\sup_{\omega \in R} \mu_\Delta \left(\mathrm{M}_{11}(j\omega) \right) < 1 \tag{2}$$

where $\dfrac{1}{\mu_{\mathrm{B}}(M)} = \left\{ \inf_{\Delta \in \mathrm{B}_\Delta, \det(I - M\Delta)=0} \bar{\sigma}(\Delta) \right.$ is the *structured singular value* of M given the structured uncertainty set B_Δ.

II. The system (M, Δ) exhibits *robust performance* if,

$$\sup_{\omega \in R} \mu_{\Delta_a} \left(\mathrm{M}(j\omega) \right) < 1, \text{ where } \Delta_a = \begin{bmatrix} \Delta_p & 0 \\ 0 & \Delta \end{bmatrix}$$

and Δ_p has the same structure as Δ but dimensions corresponding to (w, z).

Unfortunately, only bounds on μ can be estimated. To proceed let us assume uncertainty in the M, D and K_{uu} matrices of the form,

$$\overline{M} = M_0(\mathrm{I} + m_p \delta_M) D = D_0(\mathrm{I} + d_p \delta_D)$$

$$\overline{K}_{uu} = K_0(\mathrm{I} + k_p \delta_K)$$

with

$$\|\Delta\|_\infty \overset{def}{=} \left\| \begin{bmatrix} \delta_{\mathrm{M}} & & \\ & \delta_D & \\ & & \delta_K \end{bmatrix} \right\|_{¥} < 1$$

This means we are allowing a percentage deviation from the nominal values. With these definitions Equation (1) becomes,

$$\Rightarrow M_0 \ddot{\quad} \quad \dot{\quad} \quad (t) = \tilde{L} \quad m(t) + f_e(t) \tag{3}$$

where,

$$q_u(t) \overset{def}{=} \begin{bmatrix} \ddot{q}(t) \\ \dot{q}(t) \\ q(t) \end{bmatrix} \quad \begin{bmatrix} M_0 m_p & D_0 d_p & K_0 k_p \end{bmatrix} \begin{bmatrix} I_{2n\times 2n}\delta_M & & \\ & I_{2n\times 2n}\delta_D & \\ & & I_{2n\times 2n}\delta_K \end{bmatrix}$$

Writing Equation (3) in state space form, gives,

$$\dot{x}(t) = \begin{bmatrix} 0_{2n\times 2n} & I_{2n\times 2n} \\ -M^{-1}K & -M^{-1}D \end{bmatrix} x(t) + \begin{bmatrix} 0_{2n\times n} \\ M^{-1} f_e^* \end{bmatrix} u(t) + \begin{bmatrix} 0_{2n\times 2n} \\ M^{-1} \end{bmatrix} d(t) + \begin{bmatrix} 0_{2n\times 6n} \\ M^{-1}\tilde{L} \end{bmatrix} q_u(t)$$

$$= Ax(t) + Bu(t) + Gd(t) + G_u q_u(t)$$

6. RESULTS

For the numerical simulations a composite beam with piezoelectric layers bonded on its top and bottom is used. The cantilever beam is of dimension 300×25×0.5 mm. The host beam is made of aluminum and the piezoceramic is PZT. The material constants for the aluminum and the piezoceramic are: Q_{11}=60.0 GPa, Q_{55}=40.0 GPa and Q_{11}^P=62.0 GPa, Q_{55}^P=30.0 GPa. The piezoelectric constant is d_{13}= 247×10^{-12}. The thickness of each PZT is h_p= 0.35 mm. The length of one piezoelectric patch is assumed to be equal to the length of one finite element. For the finite element analysis the beam is divided into 30 elements and the total number of piezo pairs is assumed to be five. Structural damping is not included in the formulation so that the effectiveness of only the active control in the vibration response can be assessed.
The beam model with the optimal locations of the five sensor–actuator pairs is shown in Fig.2.



Figure 2. Optimal locations of five sensor–actuator pairs based on the LQR norm.

Next, our aim is to study the response of the composite beam in the presence of defects and damages.

Two kinds of loading are used as disturbances:

- Transient force 4*N* distributed in the free end of the plate.
- Periodic sinusoidal loading pressure acting on every node on one side of the structure simulating a strong wind.

Let us first investigate the response of the free and LQR-controlled laminated plate with piezoelectric and viscous layers for various parameters of the glue layer. A vertical impulsive

load is applied at the free-end of the beam. Figures 2a,b show the response of the beam's free end to a constant external force of 4N applied to the free end.

The control effort is shown in Figure 2c, where it is seen that both controllers use comparable voltage and are well within the 500V limit of piezoelectric actuators. With finer tuning (perhaps by adding a D term also), the speed of response and other transient characteristics (overshoot) can of course be improved control strategy. The nominal performance is depicted in Figure 3, which shows the response of the uncontrolled and controlled structure using H_∞

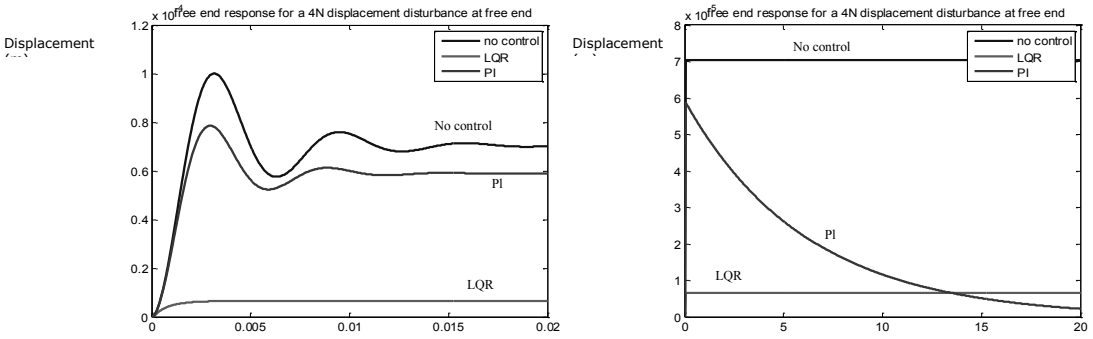


Figure 2a.b. Response of the free vibrating beam with and without control

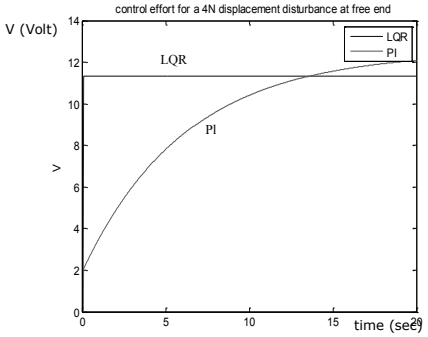


Figure 2c. Control Voltages

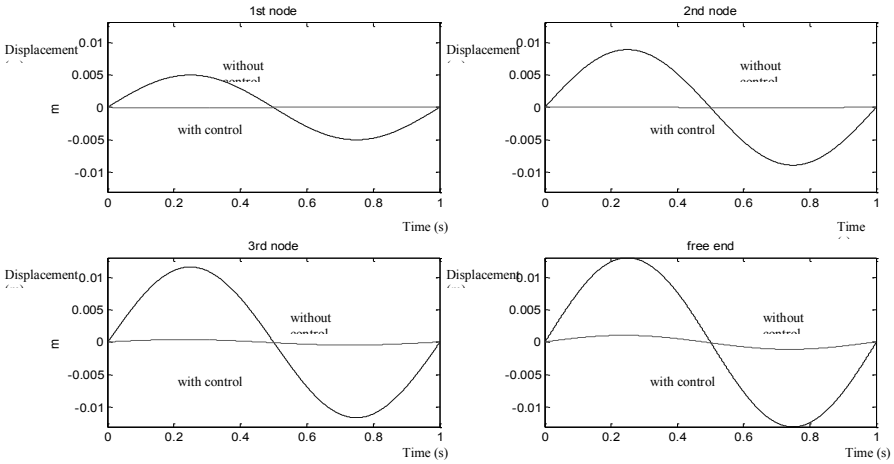


Figure 3 Response of the four nodes vibrating beam with and without control

The H_∞ controller found is of order 36. The fact that controller order, which is equal to the order of the system, is relatively higher than the order of classical controllers such as LQR has led a number of researchers to develop order reduction algorithms. The most widely used such algorithm, known as HIFOO, has been implemented in a Matlab environment, and is the one used in the following procedure [6, 14, 15]. The general problem is to compute a controller of reduced order n< 36 while retaining the performance of the H_∞ criterion as well as the behaviour of a full order controller for the given system [6, 14]. Nonsmooth variation analysis and related computational methods are powerful tools that can be effectively applied to identify local minimizers of the nonconvex optimization problems arising in fixed-order controller design.

The results are shown in Figure 4, where we can see the displacement of the free end of the structure for the open and the closed loop using the H_∞ criterion and nonconvex optimization. The results are very satisfactory; we reduced vibrations with a lower order controller. In Figure 5, we take the maximum value of the stress of the structure in the frequency domain.

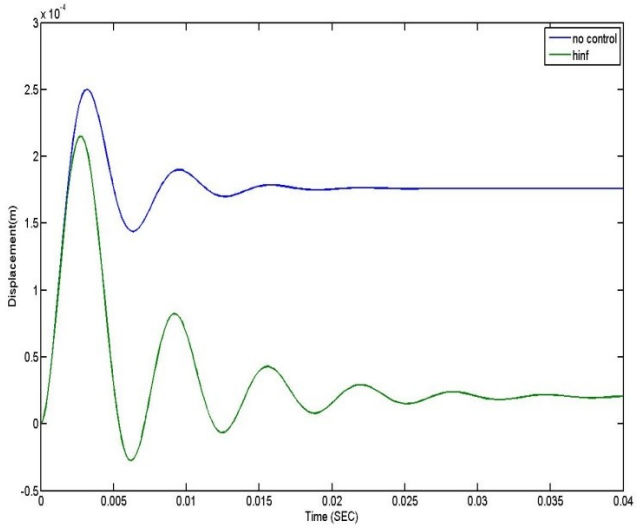


Figure 4 The displacement of the free end of the structure

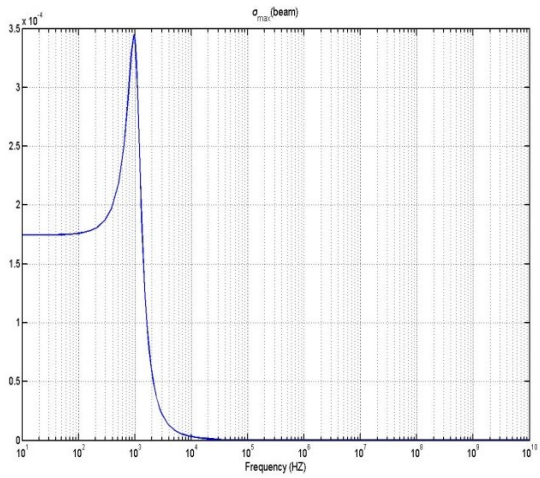


Figure 5 The σ_{max} value for all frequencies

7. CONCLUSIONS

Vibration control of a smart structure with collocated piezoelectric actuator and sensor as a general smart structure has been achieved using optimally placed piezoelectric S/A pairs. The design of the piezoelectric active control using $H_{\mathbf{infinity}}$ control theory for the nominal and damaged laminated plate has been studied. The results show that the proposed model and method are effective and the control behaviour of the beam achieves the predicted characteristics. After the analysis of the system we check the robust stability and system performance. The introduction of uncertainty permits us to keep the structure in service up to given limits of uncertainty.

Acknowledgements: This research has been co-financed by the European Union (European Social Fund – ESF) and Greek national funds through the Operational Program "Education and Lifelong Learning" of the National Strategic Reference Framework (NSRF) - Research Funding Program: ARCHIMEDES III. Investing in knowledge society through the European Social Fund. The authors gratefully acknowledge this support.

REFERENCES

[1] Y.K. Lee, D. Halim, L. Chen and B. Cazzolato, "Design and Implementation of Spatial Feedback Control on a Flexible Plate", *Proceedings of Acoustics,* 2004.

[2] Zh.Q. Gu, K.G. Ma, W.D. Chen, *"Active vibration control",* Beijing: National Defense Industry Press, 1997.

[3] G. Song, V. Sethi, H.N. Li, "Vibration control of civil structures using piezoceramic smart materials: a review", *Eng. Struct.,* vol.28, pp.1513-1524, 2006.

[4] S. Cen, A.K. Soh, Y.Q. Long, et al., "A new 4-node quadrilateral FE model with variable electrical degrees of freedom for the analysis of piezoelectric laminated composite plates", *Compos. Struct,* vol.58, pp.583-599, 2002.

[5] B. Bandyopadhyay, T.C. Manjunath, M. Unapathy, *Modeling, Control, and Implementation of Smart Structures*, Springer, 2007.

[6] J.V. Burke, D. Henron, A.S. Kewis, M.L. Overton, Stabilization via Nonsmooth, Nonconvex Optimization. *Automatic Control IEE.* 2006, Vol. 5, Issue 11, pp. 1760–1769.

[7] S.M. Yang, Y.J. Lee, Optimization of non collocated sensor, actuator location and feedback gain and control systems. *Smart Materials and Structures J.* 1993; 8, 96-102.

[8] B. Miara, G.E. Stavroulakis, V. Valente (eds), *Topics on mathematics for smart systems. Proceedings of the European Conference.* Rome, Italy, 26-28 October 2006, World Scientific Publishers, Singapore, International, 2007.

[9] A. Moutsopoulou, A. Pouliezos, G.E. Stavroulakis, Modelling with Uncertainty and Robust Control of Smart Beams. Paper 35, *Proceedings of the Ninth International Conference on Computational Structures Technology.* B.H.V. Topping and M. Papadrakakis, (Editors), Civil Comp Press, 2008.

[10] G. Foutsitzi, E. Hadjigeorgiou, C. Gogos, G.E. Stavroulakis, "Modal shape control of smart composite beams using piezoelectric actuators," in *10th HSTAM (Hellenic Society*

for Theoretical and Applied Mechanics) 2013 International Congress on Mechanics, D. Beskos, G.E. Stavroulakis (Editors), Technical University of Crete Publishing House, Chania 2013.

[11] K.R. Kumar, S. Narayanan, "Active vibration control of beams with optimal placement of piezoelectric sensor/actuator pairs", *Smart Mater. Struct.* 17 055008 (2008)

[12] G.E. Stavroulakis, G. Foutsitzi, E. Hadjigeorgiou, D. Marinova, C.C. Baniotopoulos, Design and robust optimal control of smart beams with application on vibrations suppression *Advances in Engineering Software*, Volume 36, Issues 11-12, Pages 806-813, November-December 2005.

[13] J.V. Burke, D. Henrion, M.L. Lewis, Overton.HIFOO-a MATLABpackage for fixed-ordercontroller design and Hinf. optimization. *Proceedings of the IFAC Symbosium on Robust Control Design,* Toulouse, France, 2006. www.cs.nyu.edu/overton/software/hifoo

[14] O. Bosgra, H. Kwakernaak, *Design methods for control systems*, Course notes, Dutch Institute for Systems and Control, p.69, 2001.

[15] M. Hou, P.C. Muller, Design of observers for linear systems with unknown inputs, *IEEE Trans. on Automatic Control,* 37: 871-875, 1992.

[16] D. Marinova, G.E. Stavroulakis, G. Foutsitzi, E. Hadjigeorgiou, E.C. Zacharenakis, *Robust design of smart structures taking into account structural defects*, Summer School Conference Advanced Problems in Mechanics Russian Academy of Sciences, Editor: D.A. Indeitsev, 288-292, 2004.

COMPDYN 2015
5th ECCOMAS Thematic Conference on
Computational Methods in Structural Dynamics and Earthquake Engineering
M. Papadrakakis, V. Papadopoulos, V. Plevris (eds.)
Crete Island, Greece, 25–27 May 2015

OPTIMAL DESIGN OF STRUCTURAL INTERFACES BY A POWER FLOW MODE APPROACH

Thomas Weisser[1], **Noureddine Bouhaddi**[2]

[1]MIPS Laboratory, Université de Haute-Alsace
12 rue des Frères Lumière, 68093 Mulhouse, FRANCE
thomas.weisser@uha.fr

[2] Applied Mechanics Department, FEMTO-ST Institute
24 chemin de l'Épitaphe, 25000 Besançon, FRANCE
noureddine.bouhaddi@univ-fcomte.fr

Keywords: Structural Dynamics, Complex Structures, Power Flow, Optimization, Robustness.

Abstract. *Complex mechanical structures usually encountered in the automotive or aerospace industries are composed of an assembly of several components, often exhibiting different mechanical properties and joined at their interfaces by different junction types. The various dynamic behaviors of these substructures and the applied external loadings may generate important forces on the main structure, resulting in high acceleration responses of the on-board equipment, potentially affecting their performance, reliability and security. It is therefore necessary to protect these components from these harsh interface loadings by isolating them from the rest of the structure.*

A variant of power flow mode methods, dedicated to low frequency vibrations, is presented which enables to dynamically characterize these structural interfaces. It is based on the imaginary part of the dynamic flexibility matrix, allowing to determine eigenvalues and eigenforces which represent qualitative and quantitative information on the power flowing inside the structure, respectively. This method is applied to study the power transmitted at the interface, making it possible to identify the direction associated to some dominant power flow patterns and to quantify their contributions. An optimal design procedure of such interfaces, with regard to their mechanical parameters (i.e. stiffness), is further proposed. Both mono-objective and robust multi-objective procedures are implemented and compared to optimize the derived power flow variables. The whole procedure is applied to a simplified coupled structure illustrating structural vibration phenomena on space-launchers.

1 INTRODUCTION

From the early stages of the design process of industrial mechanical structures, such as encountered in the aerospace or automotive sectors, it is necessary to ensure the correct dimensioning of their various components as well as their assembly, to satisfy the expected performance criteria. Given the diversity of the associated structural dynamic behaviors, vibration isolation issues are likely to occur which may finally impact the performance, reliability and security of the whole structure.

The vibration transmission between the boosters and the rocket core of the European space launcher *Ariane 5* perfectly illustrates this stake. During the atmospheric flight, combustion of the solid propellant excites acoustic modes of the boosters resulting in harmonic oscillations of their structures. One of these modes induces an important dynamic response at the junction with the rocket core, which could have an impact on the dynamic environment [2]. For such reasons, industrials need to have access to design procedures to determine optimal power flow paths and thus to ensure vibration isolation.

Such procedures consist in defining one or several cost functions, which are often complex with regard to the design parameters (multi-modal, non-convex,...) and usually contradictory. While eventually convincing, the derived solutions may be particularly sensitive to even small perturbations: it is thus necessary to consider the robustness of these solutions. This can be handled by simultaneously minimizing both average μ_f and standard deviation σ_f of a cost function f, using a vulnerability function f_v defined by

$$f_v = \frac{\sigma_f}{\mu_f} = \frac{1}{f_r} \tag{1}$$

and corresponding to the inverse of the robustness function f_r [1]. The optimization problem thus becomes a multi-objective one, consisting in minimizing one or several cost functions and their associated vulnerability functions, to derive a set of Pareto-optimal (non-dominated) solutions. As genetic algorithms seem particularly well adapted to such problems, a Non Sorted Genetic Algorithm (NSGA) initially developed by Srinivas [9] will be further used in this study.

As previously exposed, vibration isolation problems amount to minimizing the vibration transmitted from a source substructure to a receiver one. The computations exposed in this study are based on a power flow mode approach, as initially proposed by Su *et al.* [10]. Deriving from the seminal works of Goyder and White [4] and Miller *et al.* [7] concerning power flow analysis, the authors have complemented these approaches by the multipole method developed by Pinnington [8] and frequency synthesis techniques to propose a mobility-based power flow mode method. This method mainly consists in transforming a set of source forces or velocities into a new set of power flows: these are associated to modal forces or velocities weighted by orthogonal functions derived from the eigenproblem of a mobility matrix [10].

The targeted applications of this study mainly refer to low frequency structural vibrations of complex structures. Hence, the power flow mode approach has been adapted to combine the advantages of both finite element analysis, *i.e.* fine spatial description, complex geometry handling, vector quantities, and power flow analysis, *i.e.* quadratic variables and scalar characteristic quantities: based on a displacement formulation, this aims to derive power flow modes to qualitatively and quantitatively characterize interface forces in order to estimate their ability to transmit power flow between components[12]. This method is briefly presented in the next section and will be further integrated into the optimization procedure.

2 POWER FLOW MODE METHOD

2.1 Theoretical formulation

The proposed power flow mode method aims to characterize the interface forces between two components of a coupled structure: a source substructure, denoted (*S*), submitted to an external loading $\mathbf{f}^{(S)}$ and a passive receiver substructure, denoted (*R*). The dynamic equilibrium equation of the whole structure is given by:

$$\begin{bmatrix} \mathbf{Z}_{ii}^{(S)} & \mathbf{Z}_{ij}^{(S)} & \mathbf{0} \\ \mathbf{Z}_{ji}^{(S)} & \mathbf{Z}_{jj}^{(S)} + \mathbf{Z}_{jj}^{(R)} & \mathbf{Z}_{ji}^{(R)} \\ \mathbf{0} & \mathbf{Z}_{ji}^{(R)} & \mathbf{Z}_{ii}^{(R)} \end{bmatrix} \begin{pmatrix} \mathbf{x}_i^{(S)} \\ \mathbf{x}_j \\ \mathbf{x}_i^{(R)} \end{pmatrix} = \begin{pmatrix} \mathbf{f}_i^{(S)} \\ \mathbf{0} \\ \mathbf{0} \end{pmatrix} \tag{2}$$

where subscripts *i* and *j* respectively denote internal and junction degrees of freedom (*DOFs*), $\mathbf{Z}^{(.)}$ is the frequency dependent dynamic stiffness matrix of a substructure and $\mathbf{x}^{(.)}$ its dynamic response.

To determine the power flow modes associated to the junction *DOFs*, the power transmitted between both substructures must be expressed with regard to the interface variables. As classically detailed in the work of Bobrovnitskii [3] this average power flow, in harmonic state at a given frequency ω_0, can be derived from the real part of the complex power:

$$P_j^{tr}(\omega_0) = \frac{1}{2}\Re\mathrm{e}\left\{\mathbf{f}_j^H \mathbf{v}_j\right\} = \frac{j\omega}{4}\left(\mathbf{f}_j^H \mathbf{x}_j + \mathbf{x}_j^H \mathbf{f}_j\right) \tag{3}$$

By decoupling equation (2) and considering the classic compatibility equations, this average power flow can be expressed as a quadratic form,

$$P_j^{tr}(\omega_0) = -\frac{\omega_0}{2}\mathbf{f}_j^H \Im\mathrm{m}\left\{\mathbf{\Gamma}_{jj}^{(R)}(\omega_0)\right\}\mathbf{f}_j \tag{4}$$

where $\mathbf{\Gamma}_{jj}^{(R)} \in \mathbb{C}^{(N_j,N_j)}$ corresponds to the dynamic flexibility matrix of the receiver substructure, restricted to its junction *DOFs*:

$$\mathbf{\Gamma}_{jj}^{(R)} = \left[\mathbf{Z}_{jj}^{(R)} - \mathbf{Z}_{ji}^{(R)}\left[\mathbf{Z}_{ii}^{(R)}\right]^{-1}\mathbf{Z}_{ij}^{(R)}\right]^{-1} \tag{5}$$

Hence, minimizing equation (4) at each considered frequency with regard to the interface forces amounts to solving the following equivalent eigenproblem:

$$\left[\Im\mathrm{m}\left\{\mathbf{\Gamma}_{jj}^{(R)}(\omega_0)\right\} - s_\nu \mathbf{I}_{N_j}\right] g_\nu = 0\,, \quad \nu = 1, \ldots, N_j \tag{6}$$

where N_j denotes the number of junction *DOFs*[1]. This equation only depends on the physical parameters of the receiver and the frequency: the derived power flow modes, comprising the eigenvalues s_ν and the associated eigenforces g_ν, are independent of the interface forces applied by the source substructure to the receiver one, thus allowing to characterize the power potentially transmitted at the interface.

[1]To ease further readability, the following notation is adopted: $\mathbf{\Gamma}^{\Im} = \Im\mathrm{m}\left\{\mathbf{\Gamma}_{jj}^{(R)}\right\}$.

Therefore, at each considered frequency, the basis of the eigenforces spans the whole power flow pattern space associated to the interface: these eigenvectors represent the prevailing directions or paths through which the power proportional to the associated eigenvalues will flow. It is thus possible to decompose the actual interface forces $\mathbf{f}_j \in \mathbb{C}^{(N_j,1)}$ as a linear combination:

$$\mathbf{f}_j = \sum_{\nu=1}^{N_j} \alpha_\nu \mathbf{g}_\nu \tag{7}$$

where α_ν are complex projection coefficients representing the contribution of each eigenforces $\mathbf{g}_\nu$ in $\mathbf{f}_j$. This allows to express the power transmitted at the interface (equation (3)) as the sum of the power independently transmitted by each of the N_j power flow modes,

$$P_j^{tr}(\omega_0) = -\frac{\omega_0}{2}\mathbf{f}_j^H \, \mathbf{\Gamma}^{\Im}(\omega_0) \, \mathbf{f}_j = -\frac{\omega_0}{2}\sum_{\nu=1}^{N_j} |\alpha_\nu|^2 s_\nu > 0 \tag{8}$$

where $P_\nu(\omega_0) = -\frac{\omega_0}{2}|\alpha_\nu|^2 s_\nu$ is referred to as the modal power flow.

2.2 Application

To illustrate the previously described industrial context, a finite element model representing a simplified space launcher structure, depicted figure 1 (a), has been designed. The junction between the different cylinders representing the main core and each booster are modeled by three translational springs along the global coordinate system axis. Their location respects the topology of the actually adopted technical solutions, corresponding to three junctions at each of the lower interface and one junction at each upper interface. To simplify the model and to limit the number of design parameters (12 instead of 24), the junctions are supposed symmetrical about the main core axis. However, considering the difficulty to estimate values of these stiffness parameters and to avoid saturation effects resulting in insensitive dynamic responses, a sensitizing input procedure [11] has been used to determine there initial values, given table 1.

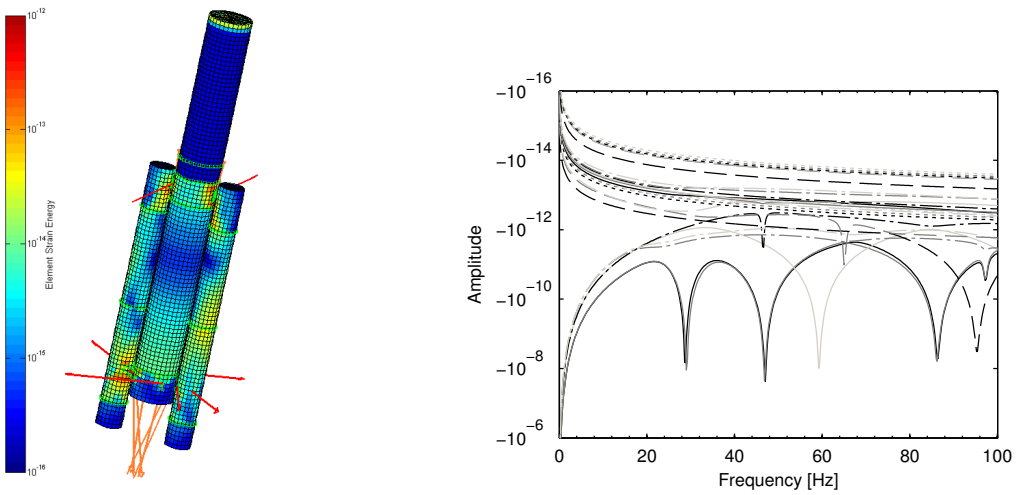
Dir.	Junction 1	Junction 2	Junction 3	Junction 4
T_x	2.9315e9	1.2328e9	2.1963e9	1e12
T_y	5.8617e9	1.404e11	1.394e10	1e12
T_z	1.7433e9	2.1963e9	2.4652e9	1e12

Table 1: Initial values of the interface stiffness parameters (N/m)

Moreover, for practical considerations the structure, including junctions, is globally submitted to a proportional damping hypothesis. Finally, to observe a dynamic behavior similar to the actual one, a harmonic in-phase load is applied to the boosters as a unitary axial force distributed between the lower and upper junctions, coupled to a small out-of-phase transverse perturbation.

Figure 1 (a) shows the evolution of the 24 power flow eigenvalues associated to the interface *DOFs*. The presence of amplitude resonances confirms the important amount of power

transmitted over this frequency band, especially between 45 Hz and 55 Hz where two normal vibration modes are located. These correspond to flexural modes of the boosters as depicted figure 1 (b) by the colormap representing the strain energy distribution. Moreover, only a third of these eigenvalues exhibits a frequency behavior between 0-100 Hz: these may constitute a dominant subspace. This figure also shows the eigenvectors associated to the 3^{rd} power flow mode at 52 Hz, depicting the strain loading of the interfaces, and the 7^{th} one which is orthogonal by definition and whose power flow pattern is less active (*cf.* associated eigenvalue).



(a) Eigenforces g_3 and g_7 at 52 Hz (b) Power flow eigenvalues of the receiving substructure $-$ s_1, $-$ s_2, $-$ s_3, $--$ s_4, *etc.*

Figure 1: Initial power flow modes at the interface of the test-structure

Finally, figure 2 shows the frequency evolution of each modal power flow, whose summed amplitudes have been unitary normalized. It can be observed that the subspace spanned by power flow modes 3, 6 and 8 comprises more than 60 $\%$ of the power transmitted bewteen the boosters and the main core of the test-structure. As a result, these quantities associated to the dominant power flow paths seem particularily relevant in the context of a design optimization procedure.

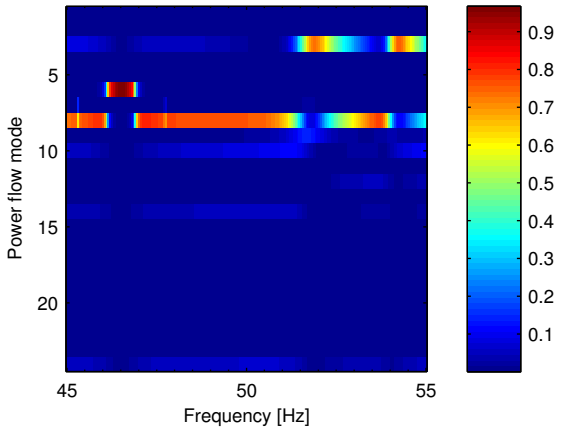


Figure 2: Initial modal power flows P_ν

3 TRANSMITTED POWER FLOW OPTIMIZATION

3.1 Determination of the cost function

According to the previous comments, the cost function f_c to be minimized during the optimization process is defined as:

$$\min_{\mathbf{X}} f_c = \min_{\mathbf{X}} \left(\max_{\omega} \frac{\sum_{\nu=1}^{6} P_\nu(\omega)}{P_j^{tr}(\omega)} \right) = \min_{\mathbf{X}} \left(\max_{\omega} \frac{\sum_{\nu=1}^{6} |\alpha_\nu|^2 s_\nu}{\sum_{\nu=1}^{24} |\alpha_\nu|^2 s_\nu} \right) \tag{9}$$

where $\mathbf{X} \in \mathbb{R}^{(12,1)}$ denotes the vector of the design parameters (*i.e.* junction stiffnesses). This function represents the maximum contribution of the power flow paths spanning the subspace comprising the six first power flow modes. Minimizing this function amounts to projecting the real interface forces along the directions associated to the less important power flow paths. However it must be noticed that the 8^{th} mode has not been retained to avoid over-constraining the optimization problem: although part of the prevailing paths, it potentially concentrates the smaller power flow as $|s_8| < \ldots \ll |s_1|$ while remaining sensitive to the design parameters. It thus constitutes an effective alternative for the power flow diverted from the other dominant paths, which could lower the power transmission.

3.2 Mono-objective approach

The first proposed approach consists in a deterministic optimization procedure whose flowchart is detailed figure 3. A preliminary Monte-Carlo analysis based on 300 samples has been performed to determine some relevant starting points. Based on the obtained initial parameter sets, the gradient-based nonlinear programming algorithm *fmincon* included in the Matlab Optimization Toolbox [5] is used to minimize the cost function: at each iteration the most sensitive direction is sought to converge toward a local minimum.

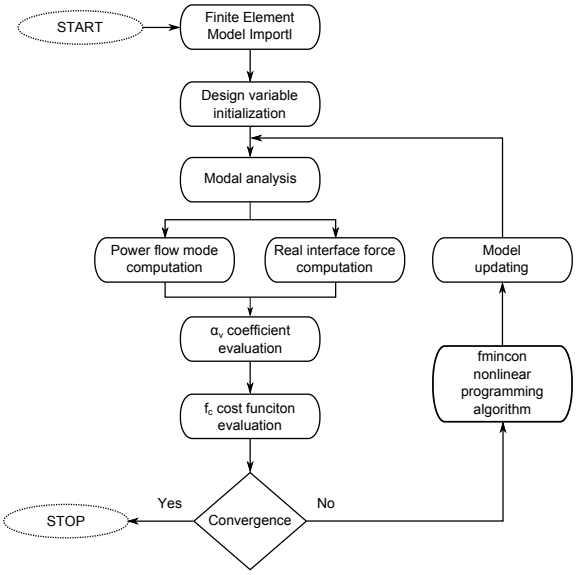
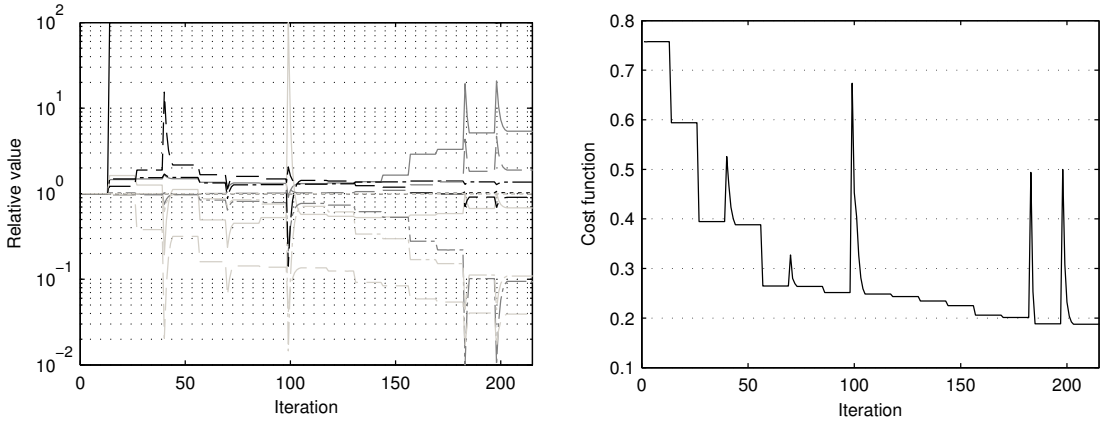


Figure 3: Flowchart of the mono-objective optimization procedure

As an example, figures 4 (a) and (b) respectively represent the evolution of the design variables and the cost function for a starting point with $f_c = 75.75\%$. The different steps of the local sensitivity analysis can be observed before each drop of the cost function, which convergences

after 215 iterations. The results derived from each of the three retained starting points are given table 2 in relative terms. It can be noticed that the final values reached by the cost function are independent of the initial ones, as these do not guarantee the accuracy of the closest local minimum: it may be possible to reach a better solution starting from a worse initial point. The resolution will however be more time consuming and computationally cost effective.



(a) Evolution of the design parameters (b) Evolution of the cost function

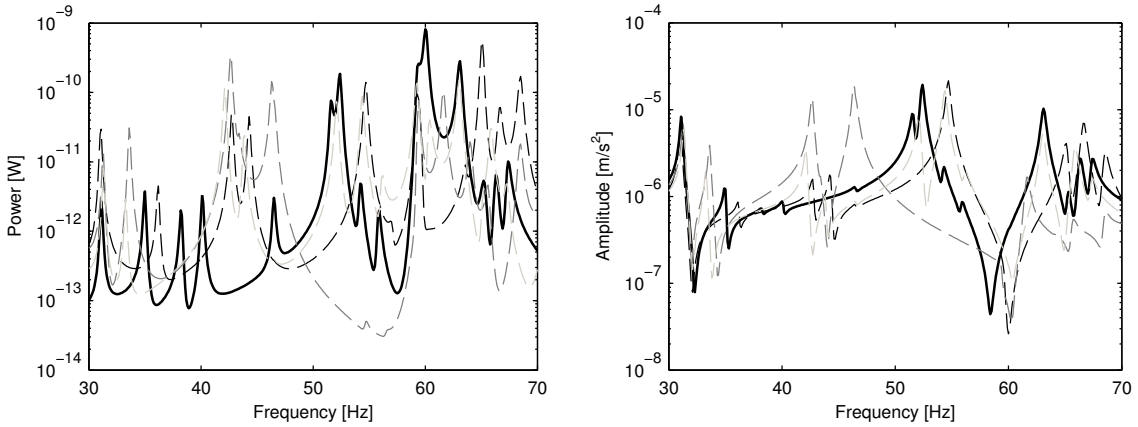
Figure 4: Evolution of the mono-objective optimization starting from point 195

Point	f_c (%)	**Direction**	**Junction 1**	**2**	**3**	**4**
238	45.15 → 23.64	T_x	8.19	95.79	5.77	0.01
		T_y	1.26	1.38	79.2	2.78
		T_z	8.17	0.47	10.07	0.02
262	70.63 → 27.91	T_x	4.82	61.5	11.68	3.5
		T_y	0.03	0.16	0.01	7.86
		T_z	2.28	14.77	20.6	0.52
195	75.75 → 18.74	T_x	100	54.2	0.8	13.64
		T_y	55.36	0	0.05	6.62
		T_z	2.02	5.74	0.01	25.61

Table 2: Relative values of the optimal interface stiffness parameters (mono-objective optimization)

At first sight, these results do not look very similar to one another. Moreover, some design variables have reached the bounds of their dispersion interval: such design points may be standing on a slope leading to a better solution. It can be verified, figure 5 (a), that the derived optimal values of the design parameters actually lower the maximum amplitude of the power flow transmitted at the interface, between $45 - 55\ Hz$. However the associated frequency evolutions tend to be quite different in each case. The same applies to the acceleration response levels displayed figure 5 (b). While a reduction of the amplitude is locally achieved, considerable modifications of the dynamic response can be observed at other frequencies: some power flow resonances

tend to vanish, others are amplified and similarly some vibration modes are highly shifted in frequency. This could possibly lead to new unwanted adverse effects perturbing the structure.



(a) Power flow transmitted at the interface

(b) Acceleration response level of the main core (vertical direction)

Figure 5: Results of the mono-objective optimization procedure:
— initial ; optima _ 1, −− 2, −− 3

Hence, while all these solutions verify the optimization problem and minimize the cost function f_c, it is necessary for the designer to choose the best one considering the global frequency behavior of the coupled structure. Therefore, it may be appropriate to add some design constraints, for example concerning the maximum frequency shift of sensitive vibration modes or response levels not be exceeded, in order to avoid particular types of solutions.

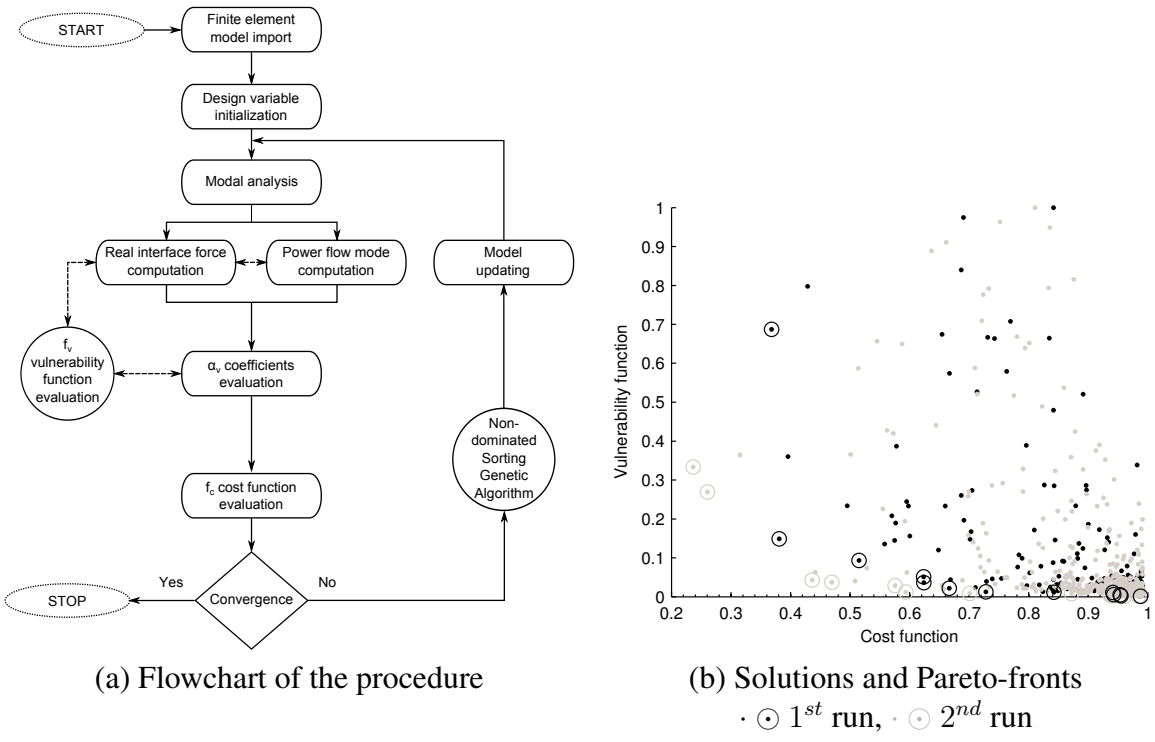
3.3 Robust multi-objective approach

In this section, a robust multi-objective approach is applied to optimize both the cost function f_c and its vulnerability function f_v, defined equation 1. This numerical procedure is detailed in the flowchart figure 6 (a). As previously emphasized, it is based on a genetic algorithm whose parameters have been set as follows [9]: 50 individual solutions per generation; a crossover probability $p_c = 0.8$; a mutation probability $p_m = 0.1$; a parameter of niche function $\sigma = 0.2$.

The major drawback of this approach stems from the evaluation of the vulnerability function. Indeed, it is necessary to locally determine, for each individual, the average and standard deviation of the cost function. These computations are performed considering 50 Monte-Carlo samples, with a uniform distribution and a dispersion of 10 $\%$. However, it implies to successively derive the associated real interface forces: computational costs are thus reduced by using a modal superposition approach, coupled to an approximated realanalysis technique based on an enrichment of the initial basis with static residuals [6].

The results from this robust multi-objective optimization are illustrated figure 6 (b), for two different runs: the first one converged after only 7 generations (16 hours) and the second one after 14 generations (24 hours)[2]. Both complete sets of solutions are depicted. At first, it can be noticed that a large amount of inefficient but robust individuals has been derived, while only a few ones verify $f_c < 40\%$. Moreover, the obtained Pareto fronts turn out to be relatively sparse (with respectively 13 and 14 individuals) but quite homogeneous.

[2]All numerical simulations have been performed using a 3 GHz dual-core processor with 1.96 $Go\ RAM$.



(a) Flowchart of the procedure

(b) Solutions and Pareto-fronts
$\cdot \odot$ 1^{st} run, $\cdot \odot$ 2^{nd} run

Figure 6: Robust multi-objective optimization procedure

The values of the design parameters associated to the four points belonging to the Pareto fronts and constituting the best trade-off between performance and robustness are given table 3, in relative terms. Once again these solutions seem to differ from one another and some design variables have reached the bounds of their dispersion interval. However, figure 7 (a) clearly shows that each of them leads to a reduction of the transmitted power on the considered frequency band, as well as a lowering of the acceleration response level at the top of the main core, figure 7 (b). It can be noticed that these optimal designs seem to modify the global dynamic behavior of the coupled structure in the same way, corresponding to a stiffening of the vibration modes initially located around 55 Hz, with a significant reduction of the power flow resonance at 60 Hz (excepted for solution 3).

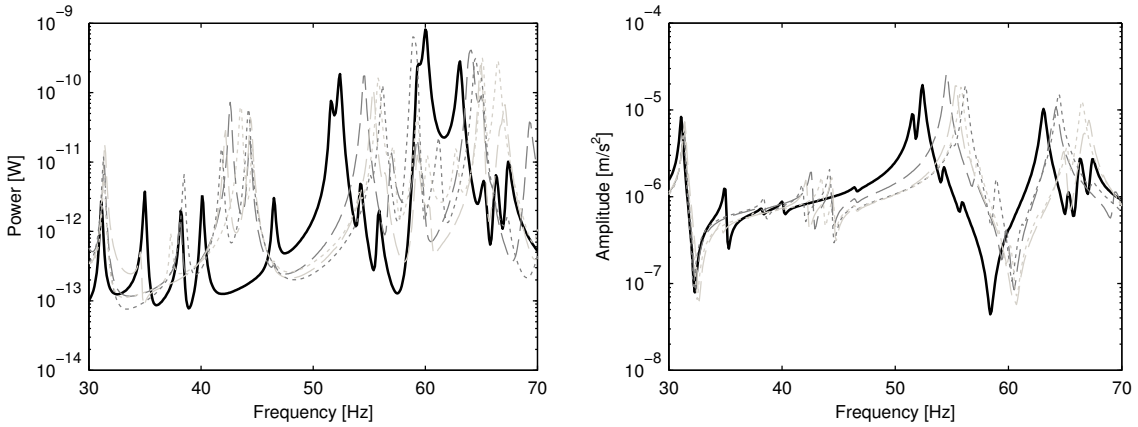
This procedure thus managed to find efficient solutions to the optimization problem, which are also different from the previous ones derived by the mono-objective approach. These solutions tend to be more conservative with regard to the initial dynamic behavior of the structure.

4 CONCLUSION

A robust design approach has been presented to optimize structural interfaces between a source and a receiver substructure of a complex mechanical structure. The obtained results have shown an interest in using power flow modes to derive solutions that minimize the transmitted power flow. Indeed, this method allows to identify interface force distributions constituting prevailing power flow paths which can be avoided by appropriately tuning the interface stiffness parameters. A mono-objective procedure based on a deterministic algorithm has been compared to a multi-objective one, taking into account the vulnerability of the solutions, using Non-Sorted Genetic Algorithm. Both have been applied to a representative complex structure and have achieved interesting designs which actually reduce the vibration response level of the receiver substructure.

Point	$[f_c - f_v]$ (%)	Dir.	Junction 1	Junction 2	Junction 3	Junction 4
428	23.63 - 33.32	T_x	4.4	52.54	1.82	6.8
		T_y	5.7	3.43	1.02	100
		T_z	48.07	3.15	13.97	0.13
505	26.04 - 26.93	T_x	22.63	100	5.94	63.85
		T_y	0.42	4.96	37.49	2.16
		T_z	2.27	0.53	0.15	74.77
157	38.09 - 14.87	T_x	70.48	87.12	0.01	1.01
		T_y	41.8	0.01	18.56	14.91
		T_z	39.81	7.04	2.85	0.91
176	43.63 - 4.28	T_x	17.42	74.21	2.07	0.35
		T_y	16.96	1.83	0.01	2.33
		T_z	0.11	53.86	1.42	0.24

Table 3: Relative values of the optimal interface stiffness parameters (multi-objective optimization)



(a) Power flow transmitted at the interface

(b) Acceleration response level of the main core (vertical direction)

Figure 7: Results of the robust multi-objective optimization procedure : — initial ; optima —— 1, —— 2, ··· 3, ··· 4

Acknowledgments

This work has been funded by the Future Preparation - Research and Technology Sub-Directorate of the *Centre National d'Études Spatiales* (*CNES*) - Launchers Directorate (Paris, France).

REFERENCES

[1] B. Ait-Brik Une mthodologie de conception robuste en dynamique des structures. *European Journal of Computational Mechanics*, **15**, 15–27, 2006.

[2] L.-O. Gonidou, Dynamic characterization of structural interfaces. *Proceedings of the Spacecraft and Launch Vehicle Dynamic Environments Workshop*, 2007.

[3] Y.I. Bobrovnitskii, Some energy relations for mechanical systems. *IUTAM Symposium on Statistical Energy Analysis*, Southampton, United-Kingdom, 1997.

[4] H.G.D. Goyder and R.G. White, Vibrational power flow from machines into built-up structures, Part III: Power flow through isolation systems. *Journal of Sound and Vibration*, **68**, 97–117, 1980.

[5] MathWorks, *Optimization Toolbox - User's guide, R2012a*, 2012

[6] G. Masson, B. Ait Brik, S. Cogan and N. Bouhaddi, Component mode synthesis (CMS) based on an enriched Ritz approach for efficient structural optimization. *Journal of Sound and Vibration*, **296**, 845–860, 2006.

[7] D.W. Miller, S.R. Hall, A.H. von Flotow, Optimal control of power flow at structural junctions. *Journal of Sound and Vibration*, **140**, 475–497, 1990.

[8] R.J. Pinnington and D.C.R. Pearce, Multipole expansion of the vibration transmission between a source and a receiver. *Journal of Sound and Vibration*, **142**, 461–479, 1990.

[9] N. Srinivas and K. Deb, Multiobjective optimization using nondominated sorting in genetic algorithms. *Evolutionary Computation*, **2**, 221–248, 1994.

[10] J. Su, A.T. Moorhouse and B.M. Gibbs, Towards a practical characterization for structure-borne sound sources based on mobility techniques. *Journal of Sound and Vibration*, **185**, 737–741, 1995.

[11] P. Vinot and S. Cogan, Procedure for initializing interface stiffness based on sensitizing inputs. *AIAA Journal*, **42**, 1246–1251, 2004.

[12] T. Weisser, E. Foltête, N. Bouhaddi and L.-O. Gonidou A power flow mode approach dedicated to structural interface dynamic characterization. *Jounral of Sound and Vibration*, **334**, 202–218, 2015.

COMPDYN 2015
5th ECCOMAS Thematic Conference on
Computational Methods in Structural Dynamics and Earthquake Engineering
M. Papadrakakis, V. Papadopoulos, V. Plevris (eds.)
Crete Island, Greece, 25–27 May 2015

CONTROL METHOD FOR ADJACENT BUILDINGS CONSIDERING SOIL STRUCTURE INTERACTION

Luis Pérez[1*], Suzana Avila[2], Graciela Doz[3]

[1]University of Brasilia - UnB
Campus Universitário Darcy Ribeiro, Brasilia, Brazil
alejandrop@unb.br

[2]University of Brasilia - UnB
Campus Gama
avilas@unb.br

[3]University of Brasilia - UnB
Campus Universitário Darcy Ribeiro, Brasilia, Brazil
graciela@unb.br

Keywords: vibration control; structural coupling; soil-structure interaction; optimization

Abstract.
In recent years a vibration control technique, called structural coupling, has been studied. This technique consists on linking two neighboring buildings, through a coupling device, with the purpose of reducing dynamic response. It is possible to control both structures response simultaneously, which is precisely the attractiveness of the technique. Several researchers explored the effectiveness of various seismic control devices, in connecting two adjacent buildings, considering they are supported on a fixed base. However, in general, all structures interacts with the surrounding soil, what substantially affects the dynamic response, it is called soil-structure interaction (SSI). Considering SSI on structural coupling is still incipient in literature. This work aims to evaluate SSI influence on the performance of this control technique, besides of presenting a simple analysis methodology to this type of problem. The results found show that SSI effects cannot be neglected on dynamic analysis of coupled structures. It was verified that changes on system natural frequencies due to SSI are important since, depending on earthquake frequency components, it modifies also the dynamic response of the system. All analysis were performed using MATLAB software.

1 INTRODUCTION

The impact between two neighboring high buildings, during severe earthquakes in the past, caused significant damages and loss of lives. In order to avoid these impacts, in the beginning of seventies various researchers proposed to connect neighboring structures using cable connecting devices. This technique called structural coupling [1] has proved to be effective on minimizing impact possibilities between two neighboring structures, besides of mitigating it dynamical responses.

From the 90s, it has been performed theoretical, numerical and experimental approaches of coupled structures using various control strategies, which showed positive results [1-11]. One of the main conclusions was that the connecting devices are effective if the two adjacent structures have different dynamic properties. In addition, these elements can increase the energy dissipation capacity of the structural system according to its mechanical properties and its position between adjacent structures.

Every structure generally interacts with the surrounding soil. This process is known as soil-structure interaction (SSI) [12]. During earthquakes, structures interact with soil in its surroundings, imposing strains to it. These deformations, however, cause movements in the supports or in the interface region between the ground and the structure, which are different from the movement of the free ground surface.

These interactions change significantly the structural response. In order to a correct evaluation of the dynamic response, taking into account the SSI effects, it is necessary to incorporate the soil dynamic properties on the mathematical formulation of the adopted physical model. There are several methods to solve this kind of problem. Noteworthy are the Direct Method and the Substructure Method, the latter being more computationally efficient [13].

There are still few studies in the literature about SSI influence on the coupling technique. Recently Farghaly [14] analyzed SSI effects on coupling technique performance, through finite element method. The author proposed to link two buildings with fixed mechanical properties using as connecting device like a viscous damper with known properties. All the analyses were performed with SAP2000 [15]. The results showed that the coupled system response is critical for soft soils, considering the types of soils taken into account on the study.

Given that the coupling technique considering SSI has been little studied, this work aims to evaluate SSI influence on the performance of this technique, besides of proposing a simple analysis methodology to this problem. For this purpose it is compared a two structure connected model supported on a fixed and flexible base. The structures are linked through a spring-dashpot device.

The numerical analysis was performed in two stages. On the first stage it was performed an optimization study, using the Particle Swarm Optimization (PSO) [16], in a way to set the connecting device properties, calculating the minimum dynamic responses of the coupled system on a fixed base.

A second stage is performed, now considering a flexible basis to the coupled system and setting the optimum properties calculated previously. Finally, all the results are compared in a way to evaluate SSI influence on coupled structures dynamic behavior. The El Centro earthquake is considered and all analyses are performed with MATLAB [17]. The results obtained in this study show how it is important to consider SSI effects on coupled structures dynamic analysis. Changes in the system natural frequencies were observed due to SSI, it affects the structure dynamic behavior depending on the earthquake frequencies components.

2 MATHEMATICAL FORMULATION

2.1 SSI Model

Consider the single degree-of-freedom (SDOF) system showed in Figure 1(a), supported through a rigid base on an elastic homogeneous isotropic medium [12]. Structure and foundation masses are, respectively, m_b and m_f and I_b e I_f are structure and foundation moments of inertia, respectively.

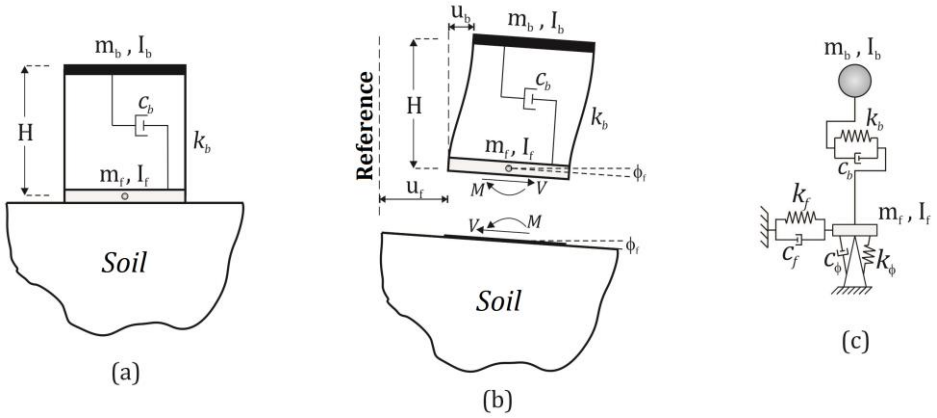


Figure 1: Soil interaction models

It can be observed on Figure 1(b) that structure induces occurrence of two forces at the base, a horizontal shear force (V) and a rocking moment (M). These forces generate a horizontal displacement (u_f) and a rotation (ϕ_f). Thus, in addition to the structure equilibrium equation, two additional equations must be satisfied due to these additional quantities. Thereby the equations of motion of the system of Figure 1(b) are given by

$$\mathbf{M}_{bs}\,\ddot{\mathbf{u}}_{bs}(t)+\mathbf{C}_{bs}\dot{\mathbf{u}}_{bs}(t)+\mathbf{K}_{bs}\,\mathbf{u}_{bs}(t)=-\mathbf{v}_{bs}\,\ddot{\mathbf{u}}_{g}(t) \tag{1}$$

$$\begin{bmatrix} m_b & m_b & m_bH \\ m_b & m_b+m_f & m_bH \\ m_bH & m_bH & I_f+m_bH^2 \end{bmatrix}\begin{Bmatrix} \ddot{u}_b \\ \ddot{u}_f \\ \ddot{\phi}_f \end{Bmatrix}+\begin{bmatrix} c_b & 0 & 0 \\ 0 & C_f & 0 \\ 0 & 0 & C_\phi \end{bmatrix}\begin{Bmatrix} \dot{u}_b \\ \dot{u}_f \\ \dot{\phi}_f \end{Bmatrix}+\begin{bmatrix} k_b & 0 & 0 \\ 0 & K_f & 0 \\ 0 & 0 & K_\phi \end{bmatrix}\begin{Bmatrix} u_b \\ u_f \\ \phi_f \end{Bmatrix}=-\begin{Bmatrix} m_b \\ m_s+m_f \\ m_bH \end{Bmatrix}\ddot{\mathbf{u}}_g(t) \tag{2}$$

In this work SSI is represented by Winkler discrete model, presented on Figure 1(c). In this model, the soil stiffness is represented by springs with constants K_f and K_φ and damping soil effect is modeled by dampers with constants C_f e C_φ. These coefficients are called impedance coefficients and can be obtained through the solution of a boundary value mixed problem in elastodynamics. In general it depends on soil properties, base dimensions and excitation frequency.

It can be found in literature several correlations to consider impedance coefficients in time domain [18-19]. One of the advantages of modeling the problem in time domain is that K_f, K_φ, C_f e C_φ values can be calculated through soil mechanical problems, lixe shear modulus (G) and Poisson´s ratio (ν). In this way Gazetas [18] and Mulliken and Karabalis [19] provide various graphics and tables to estimate impedance coefficient values to different types of foundations and soil conditions.

2.2 Coupled models with fixed base

The model presented on Figure 2 consists of two SDOF structures with fixed base, with masses (m_{b1}, m_{b2}), stiffness (k_{b1}, k_{b2}) and damping (c_{b1}, c_{b2}) associated to each structure, and a spring and a dashpot (k_3, c_3) placed between the two structure masses, acting as a connection device. When the two structures are connected, it represents a two degree of freedom system.

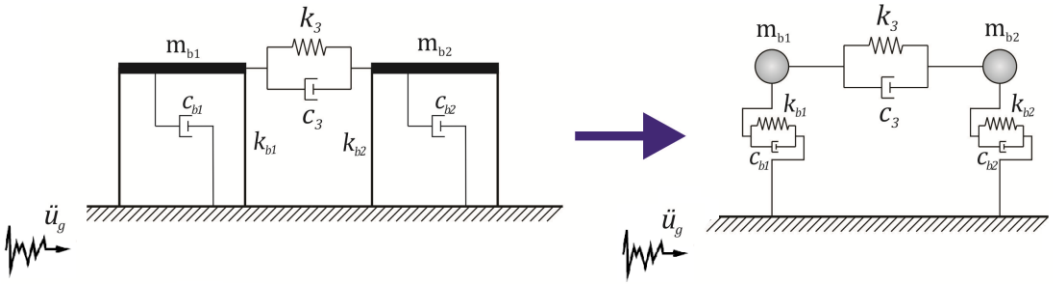


Figure 2: Two degree of freedom coupled system.

The coupled system motion equation, when it is subjected to a seismic base acceleration base $\ddot{\mathbf{u}}_g(t,)$ is given by Eq. (3) where $\mathbf{M}_{bb}$, $\mathbf{C}_{bb}$ *e* $\mathbf{K}_{bb}$ are respectively the mass, damping and stiffness matrices of the coupled system (Eq. (4)), $\mathbf{u}_{bb}(t)$ is the structure displacement vector.

$$\mathbf{M}_{bb}\,\ddot{\mathbf{u}}_{bb}(t)+\mathbf{C}_{bb}\dot{\mathbf{u}}_{bb}(t)+\mathbf{K}_{bb}\,\mathbf{u}_{bb}(t)=-G\,\ddot{\mathbf{u}}_g(t) \tag{3}$$

$$\mathbf{M}_{bb}=\begin{bmatrix} m_{b1} & 0 \\ 0 & m_{b2}\end{bmatrix},\mathbf{K}_{bb}=\begin{bmatrix} k_{b1}+k_3 & -k_3 \\ -k_3 & k_{b2}+k_3\end{bmatrix},\mathbf{C}_{bb}=\begin{bmatrix} c_{b1}+c_3 & -c_3 \\ -c_3 & c_{b2}+c_3\end{bmatrix},G=\mathbf{M}_b\begin{Bmatrix}1\\1\end{Bmatrix} \tag{4}$$

In order to reduce the data processing time, real models of multiple degrees of freedom (MDOF) can be reduced to a two degree of freedom model (2DOF) using modal analysis techniques. For each one of the coupled buildings, natural frequencies, associated vibration modes, modal effective mass (M_i^*), not considering coupling are calculated. With mass M_i^*value, effective stiffness (K_i^*) and effective damping (C_i^*) can be calculated, those are the properties of the reduced SDOF system.

2.3 Coupled models considering SSI

Consider now the 2DOF system of Figure 2, supported by an elastic homogeneous isotropic medium, as shown in Figure 3. Thus the system motion equation can be written:

$$\mathbf{M}_{bsb}\,\ddot{\mathbf{u}}_{bsb}+\mathbf{C}_{bsb}\,\dot{\mathbf{u}}_{bsb}+\mathbf{K}_{bsb}\,\mathbf{u}_{bsb}=-(\mathbf{M}_{bsb}\mathbf{v}_{bsb}+\mathbf{v}_{fbsb})\,\ddot{\mathbf{u}}_g(t) \tag{5}$$

where: $\mathbf{M}_{bsb}$, $\mathbf{C}_{bsb}$ e $\mathbf{K}_{bsb}$ are mass, damping and stiffness matrices of the coupled system considering SSI effects (Eq. 6); $\ddot{\mathbf{u}}_{bsb}$, $\dot{\mathbf{u}}_{sbs}$ e $\mathbf{u}_{bsb}$ are 4x1 vectors with accelerations, velocities and displacement of the structures and surrounding soil; $\mathbf{v}_{bsb}$ is the soil influence vector and $\mathbf{v}_{fbsb}$ is the mass foundations vector.

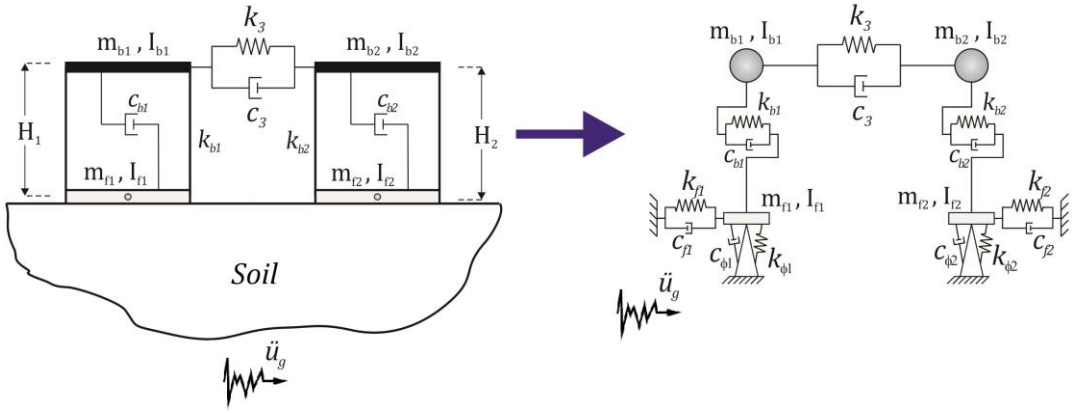


Figure 3: 2DOF coupled system

$$\mathbf{M}_{bsb}=\begin{bmatrix}\mathbf{M}_{bs1} & 0\\ 0 & \mathbf{M}_{bs2}\end{bmatrix},\mathbf{v}_{bsb}^{T}=\{1\ \ 0\ \ 0\ \ 1\ \ 0\ \ 0\},\mathbf{v}_{fbsb}^{T}=\{0\ \ 0\ \ m_{f1}\ \ 0\ \ 0\ \ m_{f1}\}$$

$$\mathbf{C}_{bsb}=\begin{bmatrix}c_{b1}+c_3 & 0 & 0 & -c_3 & 0 & 0\\ 0 & C_{f1} & 0 & 0 & 0 & 0\\ 0 & 0 & C_{\phi 1} & 0 & 0 & 0\\ -c_3 & 0 & 0 & c_{b2}+c_3 & 0 & 0\\ 0 & 0 & 0 & 0 & C_{f2} & 0\\ 0 & 0 & 0 & 0 & 0 & C_{\phi 2}\end{bmatrix},\mathbf{K}_{bsb}=\begin{bmatrix}k_{b1}+k_3 & 0 & 0 & -k_3 & 0 & 0\\ 0 & K_{f1} & 0 & 0 & 0 & 0\\ 0 & 0 & K_{\phi 1} & 0 & 0 & 0\\ -k_3 & 0 & 0 & k_{b2}+k_3 & 0 & 0\\ 0 & 0 & 0 & 0 & K_{f2} & 0\\ 0 & 0 & 0 & 0 & 0 & K_{\phi 2}\end{bmatrix} \quad (6)$$

3 NUMERICAL ANALYSIS

The structural system studied in this work is shown in Figure 4(a) [1,2]. On both buildings it was considered a mass of 30000 kg per floor. The steel columns have a height of 3,0 m with the same stiffness in all floors $k_1^1 = k_1^2 = k_2^2 = k_3^2 = 12{,}58$ MN/m. A damping ratio of 3% was taken into account. El Centro base acceleration (North-South component) was considered. Widely used in literature, this earthquake has a frequency range varying from 0,14 Hz to 2,1 Hz.

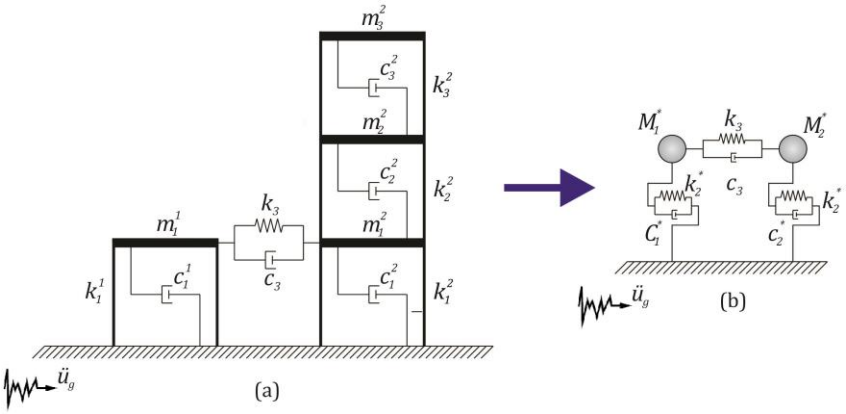


Figure 4: (a) MDOF model; (b) Equivalent reduced model.

In order to reduce computational cost, the MDOF system of Figure 4(a) was reduced to a two degree of freedom model (2DOF), shown in Figure 4(b), using modal analysis techniques. For each one of the uncoupled buildings, natural frequencies, associated vibration modes, modal effective mass (M_i^*) are calculated. According to Paz and Leigh [20] the more influent vibration modes are those, which the adding of its effective masses reach about 90 % of the total structure mass. With mass M_i^*value, effective stiffness (K_i^*) and effective damping (C_i^*) can be calculated, they are shown on Table 1.

Structure	Vibration Mode	ω_i [rad/s]	f [Hz]	M^*_i [kg]	% mass	K_i^* [N/m]	C_i^* [Ns/m]
1	1	20.478	3,2592	30000	100	$1.25800.10^7$	$3.68604.10^4$
3	1	9.1137	1.4505	82267.154	91.4	$6.83307.10^6$	$4.49855.10^4$
	2	25,5352	4,0641	6738.928	98.9		
	3	36,8994	5,8727	993.918	100		

Table 1: Natural frequency, modal mass, effective stiffness and effective damping of uncoupled structures.

3.1 First stage

On this stage it was performed an optimization study, using PSO method [16] in a way to set up connection device properties, calculating minimum coupled response with a fixed base.

The first step was to calculate the dynamical response of each reduced structure alone, *rms* values are shown on Table 2.

Structure	x_{rms} [m]	v_{rms} [m/s]	a_{rms} [m/s²]
1 floor	0.00437	0.08573	1.73199
3 floors	0.02409	0.22198	2.10129

Table 2: Reduced structures *rms* response

Following, k_3 and c_3 values were optimized though PSO technique, with an objective function of the summation of coupled model *rms* accelerations. Stiffness value k_3 varied from zero to 6.10^6 N/m. The same way, damping coefficient c_3 varied from 0 to 6.10^6 Ns/m. These values were based on passive dampers properties available commercially (Taylor Device, Inc.).

One of the advantages of PSO algorithm is that the processing time needed to minimize the objective function is small. In this work various simulations were performed in a way of testing PSO technique and obtain suitable k_3 and c_3 values. On Table 3 it is presented results obtained with three different PSO numerical simulations.

c_3 [Ns/m]	k_3 [N/m]	$f_{objective}$ [m/s²]	a_{rms_E1} [m/s]	a_{rms_E2} [m/s²]
$3.30675x10^5$	$9.58930x10^{-7}$	1.7197	0.75990	0.95982
$3.30359x10^5$	$3.72651x10^{-4}$	1.7197	0.75989	0.95982
$3.31336x10^5$	$3.18925x10^{-4}$	1.7197	0.75990	0. 95982

Table 3: Connection device properties and *rms* response.

It can be observed on the above table that k_3 and c_3 had a very little variation. It also can be noticed that to control dynamic response on both structures, it is necessary to use a connection device with $c_3 = 3.30359 \times 10^5$ Ns/m and $k_3 = 0$. It can be said that the best connection device to the analyzed model is using only a viscofluid damper.

Next, the *rms* response is obtained to the coupled system, using the optimized values of k_3 and c_3. These values are compared with those from Table 1, in order to verify response reduction. The results are presented in Table 4.

It is also compared time history of displacements, velocities and accelerations of coupled and uncoupled systems, the results are shown on Figure 5.

Structure 1								
uncoupled			*coupled*			*Reduction*		
x_{rms} [m]	v_{rms} [m/s]	a_{rms} [m/s²]	x_{rms} [m]	v_{rms} [m/s]	a_{rms} [m/s²]	*x [%]*	*v [%]*	*a [%]*
0.00437	0.08573	1.73199	0.0040	0.0517	0.7599	8.5	39.7	56.2

Structure 2								
uncoupled			*coupled*			*Reduction*		
x_{rms} [m]	v_{rms} [m/s]	a_{rms} [m/s²]	x_{rms} [m]	v_{rms} [m/s]	a_{rms} [m/s²]	*x [%]*	*v [%]*	*a [%]*
0.02409	0.22198	2.10129	0.0083	0.0832	0.9598	65.6	62.5	54.3

Table 4: *Rms* response of coupled and uncoupled systems.

Analyzing the above results it is possible to notice that all responses presented a significant reduction due to the connection device installation. It can also be observed that the better response reductions occurred on structure 2, being displacement the parameter with greater reduction. However, in structure 1 displacement presented a low reduction, being acceleration the parameter with a better response control.

It is noteworthy that PSO optimization presented good performance, however to optimize k_3 and c_3 values it is necessary to define a proper objective function depending on the design and construction conditions, besides the type of response to be reduced.

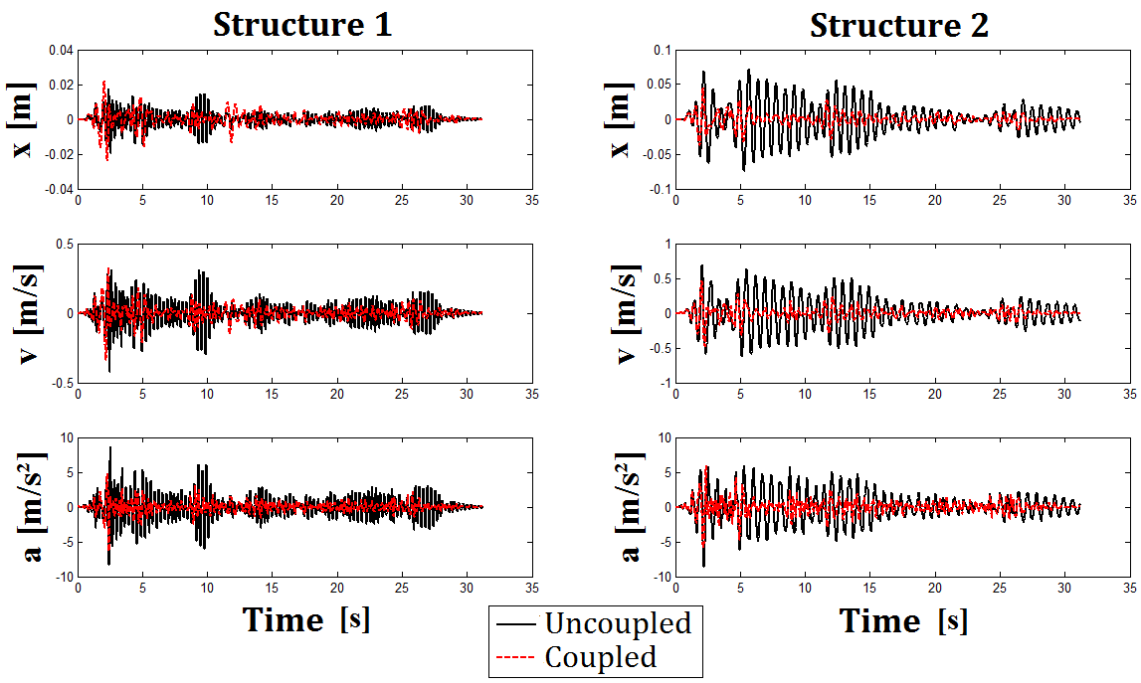


Figure 5: Displacement, velocity and acceleration time histories of coupled and uncoupled systems

3.2 Second stage

At this stage the coupled model with flexible base dynamical responses are obtained making use of the optimum parameters of the connecting device calculated before. Next, the responses obtained on the first and second stages are compared, in order to evaluate SSI effects on coupled structures analysis.

The coupled model considering SSI is similar to the one shown on Figure 3. The optimum values of k_3 e c_3 and only the soil mechanical properties are varied.

Consider the buildings supported on circular superficial foundation or 1.0 m of radius (a = 1.0 m). It is considered three types of soil with different mechanical properties, shown on Table 5. The more resistant the soil is, higher the velocity of propagation of seismic waves V_s is. Thus, it can be said that these soils presented in Table 5 can be classified as: soft (No.1), semi-rigid (No. 2) and rigid (No. 3).

Soil	*Es[Mpa]*	*G [Mpa]*	*ρ [t/m³]*	*Vs [m/s]*	*ν*
No. 1	0.3	0.11	1.3	9.20	0.3
No. 2	15	5.76	1.9	55,10	0.3
No. 3	30	10.71	1.9	75.09	0.4

Table 5: Soil mechanical properties [21].

Soil impedance coefficients proposed by Kennedy and Eberhart [16] are considered and shown on Table 6, they are valid for rigid foundations supported on an homogeneous elastic linear soil.

	Mass	*Damping*	*Stiffness*
Horizontal	$m_f = 4.37\frac{(1-\nu)}{(7-8\nu)}\frac{Ga^3}{V_s^2}$	$C_f = 1.50\frac{1}{(2-\nu)}\frac{Ga^2}{V_s}$	$K_f = 9.2\frac{1}{(2-\nu)}Ga$
Rocking	-	$C_\phi = 2.40\frac{1}{(1-\nu)}Ga^4$	$K_\phi = 4.0\frac{1}{(1-\nu)}Ga^3$

Table 6: Damping impedance coefficients [16].

Following, the responses considering SSI are compared with those with rigid base. On Table 7 natural frequencies and corresponding periods for both cases are presented.

Natural frequencies and vibration periods				
Coupled fixed base		*Coupled (SSI)*		
f [Hz]	*T [s]*	*Soil*	*f [Hz]*	*T [s]*
1,4504	0,6894	No. 1	0.1254	7.9747
		No. 2	0.7759	1.2889
		No. 3	0.9985	1.0015

Table 7: Natural frequencies and vibration periods of coupled system with and without SSI

It can be observed that SSI affects the dynamics behavior of the coupled system, reducing its frequencies and consequently increasing vibration periods. The coupled model based on soil No 1 (soft soil) presented the greater reduction on frequency value, it was about 91,3 %. In the same way, the models based on soils No. 2 and No. 3 (semi-rigid and rigid soils) reduced its frequencies on 46,5% and 31,2%, respectively.

Next, displacement, velocity and acceleration time histories for the three cases, using optimum values of k_3 e c_3 were obtained, they are presented on Figures 6 to 8.

Soil characteristics influence frequency and duration of the earthquake. In general, rock foundations are exposed to high frequency excitation (low periods), but if they are on a weak or soft soil, they will be exposed to low frequency excitation (long periods). Knowing that El Centro earthquake frequency band varies from 0,14 to 2,4 Hz and taking into account the above said, it can be deduced that the coupled model when based on soil No. 1 won't suffer considerable shock since the frequency of this model is outside the earthquake frequency band. In this case, it can be observed on Figure 6 that the response considering SSI has lower amplitudes than the fixed base model.

Coupled models based on soils No. 2 and 3 presented frequencies within the El Centro earthquake frequency band. Observing Figures 7 and 8 that show displacement, velocity and acceleration time histories for both cases, it can be observed that response amplitudes for soil 2 were reduced compared to those of the fixed base model. Finally for soil No. 3 responses considering or not SSI were very similar, what was expected since this soil is considered rigid according to Table 5 classification.

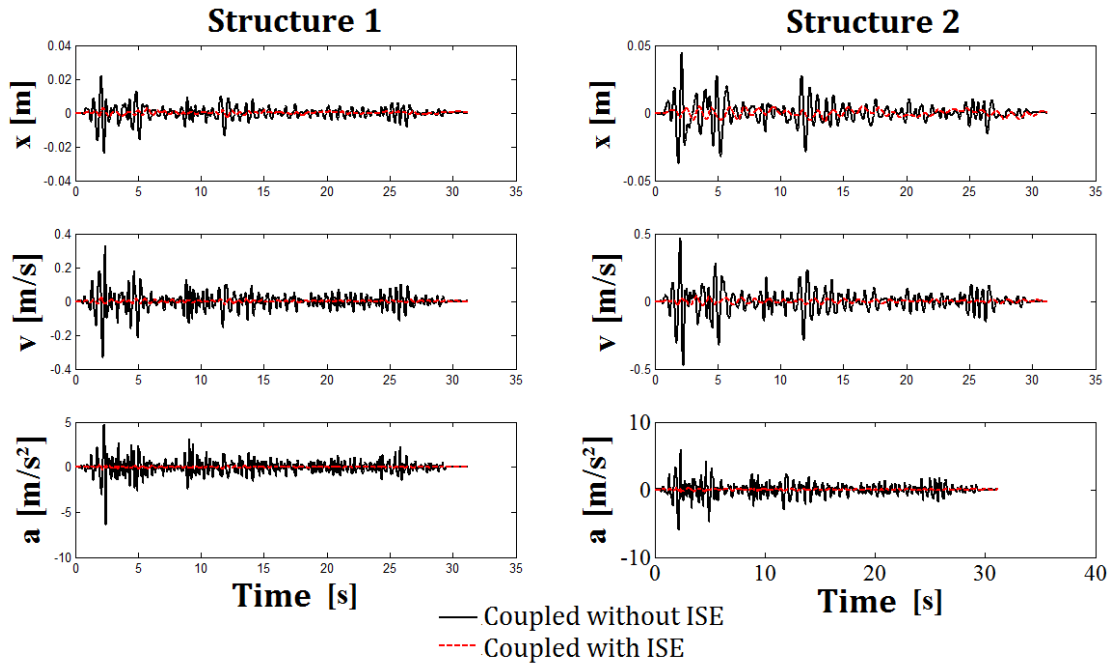


Figure 6: Displacement, velocity and acceleration time histories of coupled structures with and without SSI consideration – Soil No. 1.

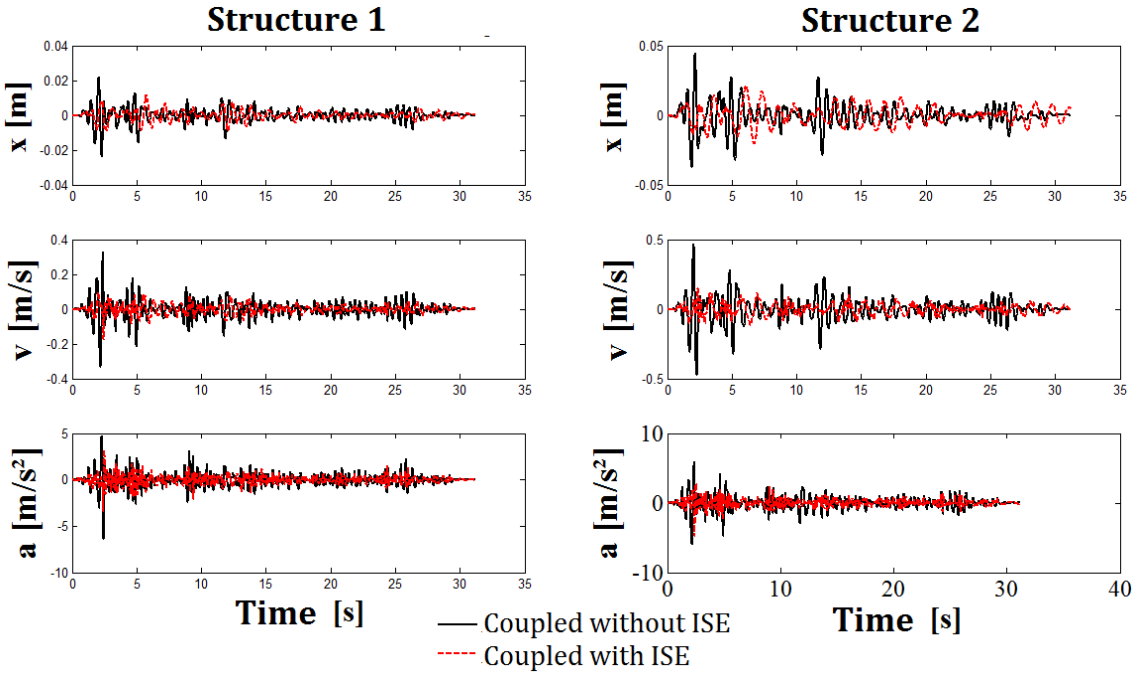


Figure 7: Displacement, velocity and acceleration time histories of coupled structures with and without SSI consideration – Soil No. 2.

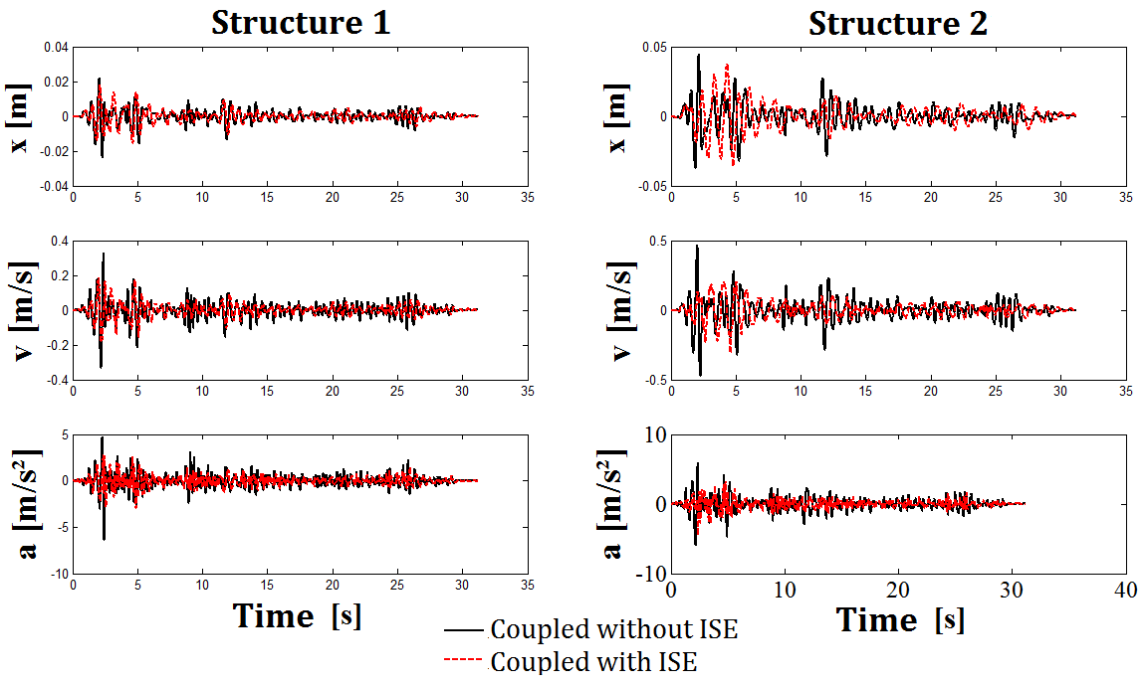


Figure 8: Displacement, velocity and acceleration time histories of coupled structures with and without SSI consideration – Soil No. 3.

4 CONCLUSIONS

It was presented the influence of soil structure interaction on the behavior of two connected structures by passive dampers. Two structures with known and fixed mechanical properties were considered. The SSI was expressed by the discrete model of Winkler and considered that the structures were supported by circular superficial foundations.

On SSI problems the dynamics responses depend on the type of structure and also on the foundation base type. It was verified that considering SSI effects modifies the system natural frequencies. This change affects the structural response to earthquakes, depending on the seismic frequency components associated.

As the soil stiffness decreases, the frequencies of the coupled system with SSI decrease considerably comparing to those of the coupled model with fixed base.

The more rigid the soil is, the behavior of the coupled model resembles to that of the fixed base model.

The results found in this paper show the importance of considering SSI effects on dynamic analysis of coupled structures. It can be verified that changes on system natural frequencies due to the soil stiffness is important since it modifies its response depending on earthquake frequencies. It was observed that models based on soft soils collaborate on reducing amplitude response acting as an energy dissipator. Additional studies on setting connecting device properties are necessary, considering on optimization procedures the SSI effects.

AKNOWLEDGEMENTS

The authors acknowledge CNPq Brazilian Council of National Scientific and Technological Development for the financial support of this research.

REFERÊNCIAS BIBLIOGRÁFICAS.

[1] R.E. Klein, C. Cusano, J. Stukel, Investigation of a method to stabilize wind induced oscillations in large structures. *ASME Winter Annual Meeting*, Paper No. 72, New York, USA, 1972.

[2] L.A. Pérez, S. Avila, G. Doz, Coupled structural dynamic response using passive dampers. *17th International Symposium on Dynamic Problems of Mechanics (DINAME)*, Natal, Brazil, February 22-27, 2015.

[3] L.A. Pérez, S. Avila, G. Doz, Seismic response control of adjacent buildings connected by viscous and hybrid dampers. *Dynamics of Civil Structures*, Vol. 4, pp 433-440, Springer International Publishing, 2014.

[4] C.C. Patel, R.S. Jangid, Seismic response of dynamically similar adjacent structures connected with viscous dampers. *The IES Journal Part A: Civil & Structural Engineering*, 3(1):1–13, 2013.

[5] F. Palacios-Quiñonero, J. Rubió-Masse, J.M. Rossell, R. Pons-López, Active–passive control strategy for adjacent buildings. *Proceedings of the 8th International Conference on Structural Dynamics*, EURODYN, Leuven, Belgium, 2011.

[6] R.E. Christenson, B.F. Spencer Jr, E.A. Johnson, K. Seto, Coupled building control considering the effects of building configurations. *ASCE Journal of Structural Engineering*, 132(6):853–863, 2006.

[7] K. Gurley, A. Kareem, L.A. Bergman, E.A. Johnson, R.E. Klein, Coupling tall buildings for control of response to wind, *Structural Safety & Reliability*, Balkema, Rotterdam, 1553-1560, 1994.

[8] J.E. Luco, H.L. Wong, Control of the Seismic Response of Adjacent Structures, Proc. *1st World Conference on Structure Control*, TA2-21-30, Pasadena, CA, August, 1994.

[9] A.V. Bhaskararao, R.S. Jangid, Seismic analysis of structures connected with friction dampers. *Journal Engineering Structures*, 28:690-703, 2006.

[10] G.C. Kim, J.W. Kang, Seismic Response Control of Adjacent Building by using Hybrid Control Algorithm of MR Damper. *The Twelfth East Asia-Pacific Conference on Structural Engineering and Construction*, 4:1013-1020, 2011.

[11] M.K. Shrimali, S.D. Bharti, Eartjquake Performance of Coupled Building by VF Damper. *The 14th World Conference on Earthquake Engineering (WCEE)*, 2008.

[12] R.W. Clough, J. Penzien, Dynamics of Structures, McGraw Hill, New York, 2003.

[13] J.O. Wolf, Foundation Vibration Analysis Using Simple Physical Models. Prentice Hall, 1994.

[14] A.A. Farghaly, Optimization of viscous dampers with the influence of soil structure inter-action on response of two adjacent 3-D buildings under seismic load. *IOSR Journal of Engineering (IOSRJEN)*, vol. 04, issue 01, pp 18-27, 2014.

[15] Computers and Structures, INC. SAP2000: Integrated finite element analysis and design of structures. *Computers and Structures Inc*, Berkeley, California, U.S.A, 2002.

[16] J. Kennedy, R. Eberhart, Particle swarm optimization. *Proceedings of IEEE International Conference on Neural Networks*, IV: 1942–1948, 1995.

[17] MATLAB. Matrix Laboratory - R2009b. MathWorks - MATLAB and Simulink for Technical Computing. Massachusetts, U.S.A, 2009.

[18] G. Gazetas, Analysis of machine foundation vibrations: state of the art review. *Soil Dynamics and Earthquake Engineering* 2(1): 2–42, 1983.

[19] J. S. Mulliken, D.L Karabalis, Discrete model for dynamic through-the-soil coupling of 3D foundations and structures. *Earthquake Engineering and Structural Dynamics* 27(7): 687–710, 1998.

[20] M. Paz, W.E. Leigh, Structural Dynamics: Theory and Computation. *Springer*, 5th ed., 2006.

COMPDYN 2015
5th ECCOMAS Thematic Conference on
Computational Methods in Structural Dynamics and Earthquake Engineering
M. Papadrakakis, V. Papadopoulos, V. Plevris (eds.)
Crete Island, Greece, 25–27 May 2015

HOW TO ACHIEVE REGULAR SEISMIC BEHAVIOR OF IRREGULAR BRIDGES WITH UNEQUAL HEIGHT PIERS?

Mena. G. Ishak[1*], Sameh. S.F. Mehanny[2]

[1*] Bridge Design Engineer, Dar Al-Handasah, Smart Village, Egypt

& M.Sc. Graduate student, Cairo University, Egypt

Mena.Gerges@dargroup.com

[2] Professor of Structural Engineering, Faculty of Engineering, Cairo University, Egypt

sameh.mehanny@stanfordalumni.org

Keywords: Seismic Analysis, bridge regularity, inelastic analysis, unequal pier heights, EC8.

Abstract. *EuroCode 8 simplistically addresses the seismic behavior of irregular bridges. The proposed criterion for regularizing the response depends on the ratio between the moment demand and moment capacity on each pier aiming to regularize the distribution of seismic design demand among, and ultimately guarantee synchronized failure of, all piers irrespective of their different heights. This criterion may not be effective in addressing some pier height ratios within the same bridge, hence results may not be as expected by code developers. The present paper scrutinizes and evaluates the validity of the criterion proposed by EC8, where the seismic response of four types (featuring a permutation of elastomeric and/or pot bearings along with monolithic pier-to-deck connections) of three-span continuous bridges with one short and one long pier designed to satisfy EC8 regularity condition are compared. Each bridge type has been investigated for four different pier height ratios. Several nonlinear static and dynamic analyses have been performed on each of the total sixteen schemes (namely, four pier height ratios for each of the four bridge types). Nonlinear analysis has resulted in different bridge behavior from that mentioned (and expected) by EC8. The study has led to evidence of realizing somehow regular seismic behavior by altering EC8-design obtained steel reinforcement ratios in either piers of each bridge scheme. It has been also noted that bridge regularity is achieved more efficiently in bridges with elastomeric bearings on shorter piers rather than bridges without elastomeric bearings.*

** The asterisk denotes the presenting author.*

1. INTRODUCTION

Seismic behavior of bridges has been an important topic addressed in most codes and design references worldwide. EuroCode 8 [1 & 2] has demonstrated design guidelines for bridges under seismic loads, and one of these guidelines is determining bridge uniformity in order to estimate the actual bridge behavior when exposed to seismic loading. According to EC8 [1 & 2], bridges satisfying regularity criteria (namely, demonstrating $\rho < 2$ as per Equation 1) are considered uniform; hence, reaching a value of $\rho=1$ implicitly means that the bridge will have strictly uniform response and anticipated perfect synchronized failure of all its piers.

$$\rho = \frac{r\ max}{r\ min} < \rho_0 = 2, \text{ where } r = q\frac{M_{Edi}}{M_{Rdi}} \quad (1)$$

For bridges with uniform ductile behavior, q is assumed to have a value of 3.5 as per code recommendations, M_{Edi} is the design moment already reduced by the behavior factor q, and the value of M_{Rdi} is the resistance moment determined from moment curvature relation. Accordingly, strict uniformity of behavior should imply that all piers reach their M_{Rdi} values somehow simultaneously which leads to a value of ρ of approximately 1. Bridges violating the criterion of Equation (1) shall be designed in accordance to irregular behavior in the designated direction and hence, shall be designed with a reduced behavioral factor value (i.e., $q < 3.5$). EC8 regularity criteria can be modified as proposed herein where we can compare values of curvature demand to curvature capacity at critical sections in piers while computing r_{max} and r_{min} as per Equation 2 rather than moment in order to appropriately capture inelastic effects on the response. An enhanced regularity index, ρ_ϕ, is then calculated using this improved curvature-based r values instead of the codified ρ index relying on moment-based r values.

$$r = \frac{Curvature\ Demand\ of\ column,\ \emptyset Edi}{Curvature\ Capacity\ of\ column,\ \emptyset Rdi} \quad (2)$$

Pushover analysis is performed in the present research adjacent to nonlinear dynamic analysis in order to provide accurate results for verifying EC8 regularity criteria. Building on a previous research effort by Guirguis and Mehanny (2012) [3], this paper further scrutinizes and evaluates the validity of the proposed code criterion for bridge uniformity and suggests effective, smart and economic means to provide uniform seismic response of apparently irregular bridges.

2. MODELING AND DESIGN

Implementing previous work in [3], our case study bridge consists of three equal spans with a total length of 84m (refer to figure 1) divided into four categories, all of which were designed according to EC8 thus satisfying uniformity condition ($\rho < 2$) and hence anticipating somehow "near" synchronized behavior of unequal height piers. Each of the four categories has a pre-stressed deck with both ends resting on abutments connected to the bridge via sliding elastomeric bearings, while the two intermediate piers feature different pier-to-deck connections with various permutations as illustrated in table 1. Both piers are assumed to have equal dimensions regardless of the pier height despite the fact that perfect state material economy can be achieved through differentiating short and long pier cross-section dimensions for each bridge scheme. Such assumption is in line with previous researches in the literature

[4-6] that were largely focusing on piers with equal cross-section dimensions irrespective of their heights for aesthetical and practical – from constructability perspective – purposes.

Category / Piers Cross-section	Short Pier-to-Deck Connection (Height =7m, 9m, 10.5m & 12m)	Long Pier-to-Deck Connection (Height =14m)	Category Symbol
1 / 3.5m x 1.4m	non sliding Elastomeric bearing	non sliding Pot bearing	E-P
2 / 3.5m x 1.4m	non sliding Elastomeric bearing	Monolithic connection	E-M
3 / 3.5m x 1.8m	non sliding Pot bearing	Monolithic connection	P-M
4 / 3.5m x 1.8m	non sliding Pot bearing	non sliding Pot bearing	P-P

Table 1 – The sixteen case-study bridge schemes under investigation with categories description.

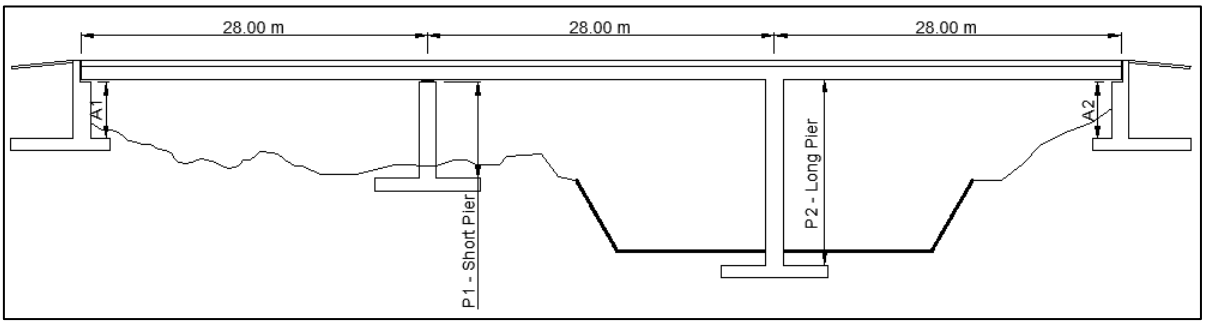


Figure 1a – Case Study Bridge General Arrangement

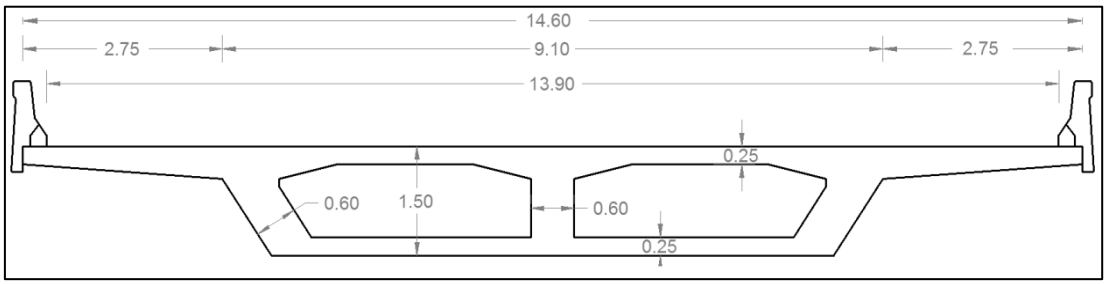


Figure 1b – Typical Bridge Deck Cross-section (dimensions in meters)

Static inelastic pushover and nonlinear dynamic analyses are performed on categories 1 and 2 using Opensees software [7], while only pushover analysis is performed on categories 3 and 4. Piers are assumed to have a fixed connection to the ground ignoring the effect of soil-structure interaction. Piers are modeled as fiber sections possessing two characteristic zones with different properties (confined zone and unconfined zone). Abutments featuring a gap of 200 mm to the deck are considered and modeled according to [8] after gap closure due to deck movement under seismic events. Accordingly, as a result of the movement of sliding elastomeric bearings on abutment's shelf closing the 200 mm gap to the abutment's back wall, passive earth pressure behind abutment is mobilized as shown in figure 2 and is considered in the model through an effective stiffness, K_{eff}.

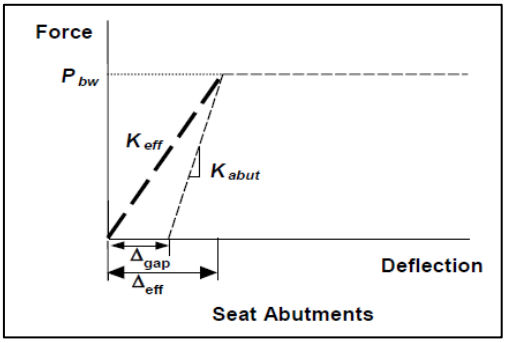


Figure 2 – Abutment effective stiffness after gap closure [8].

As stated above, concrete of the pier was utilized into two zones. The confined concrete zone has an expected compressive strength of 45 MPa, a characteristic ultimate compressive strain of 0.014 and no tensile strength, while the unconfined concrete zone possesses a nominal cylinder strength of 28 MPa, and an expected strength of 36 MPa (f'_{ce}=1.3 f'_c). Reinforcing steel is modeled as uniaxial bilinear material and is characterized by initial elastic behavior with modulus of elasticity E_s=200GPa, followed by strain hardening region after reaching an expected yield stress f_y=475MPa and hardening modulus of 4.75 MPa, with a failure strain of 0.09. The usage of "expected" material properties while performing nonlinear inelastic analysis of the bridge up to collapse limit state is recommended rather than nominal (i.e., design) material properties to get a better estimate of the capacity of structural components. This assumption does not apply to shear for which we still rely on nominal material properties since shear leads to brittle failure. In the current study, piers capacity is assumed to be controlled by "axial-flexure" behavior and piers are hence not prone to shear failure. Furthermore, Fiber Section Analysis (FSA) is performed for piers where each bridge pier cross-section is divided into an array of confined and unconfined concrete and steel fibers according to the design requirements in order to generate moment-curvature capacity curves (refer to Fig. 3 for a sample) as well as to check relevant failure criteria (stated in a following section of the paper) at the material stress-strain level either for confined concrete or reinforcing bars.

Non-sliding pot bearings are modeled by simply introducing moment release at top of pier at its junction with the deck. On the other hand, non-sliding elastomeric bearings atop of pier are modeled primarily as an elastic material. Horizontal spring (in the deck longitudinal direction) modeling the shear stiffness of the elastomeric bearing is hence introduced and assigned a stiffness value that is equal to the shear modulus of the elastomer material, G_b, multiplied by the foot print area of the bearing, A_b, and divided by the total thickness of the elastomer, t_b. The shear stiffness of all elastomeric bearings supporting the deck (represented by a single spine in the current computational model) at the pier location is hence the stiffness of a single bearing estimated as above multiplied by their number, n. As per EN 1998-2 (2005) - Cl. 7.5.2.4 (5), G_b has been taken in the present research with the value proposed for short term (i.e., seismic) response as 1.485 MPa [G_b = 1.1 x (1.15MPa+0.2MPa)]. Elastomeric bearings dimensions used were 550 mm x 500 mm with a total thickness of 150 mm. It has to be finally noted that the equivalent lateral stiffness of the "pier-elastomeric bearing" supporting system as captured by the model throughout the analysis is that of two springs in series: one of them corresponds to the elastomeric bearings themselves deforming in transverse shear mode, while the other corresponds to the pier lateral stiffness, and hence the combined stiffness is less than the least of the two values.

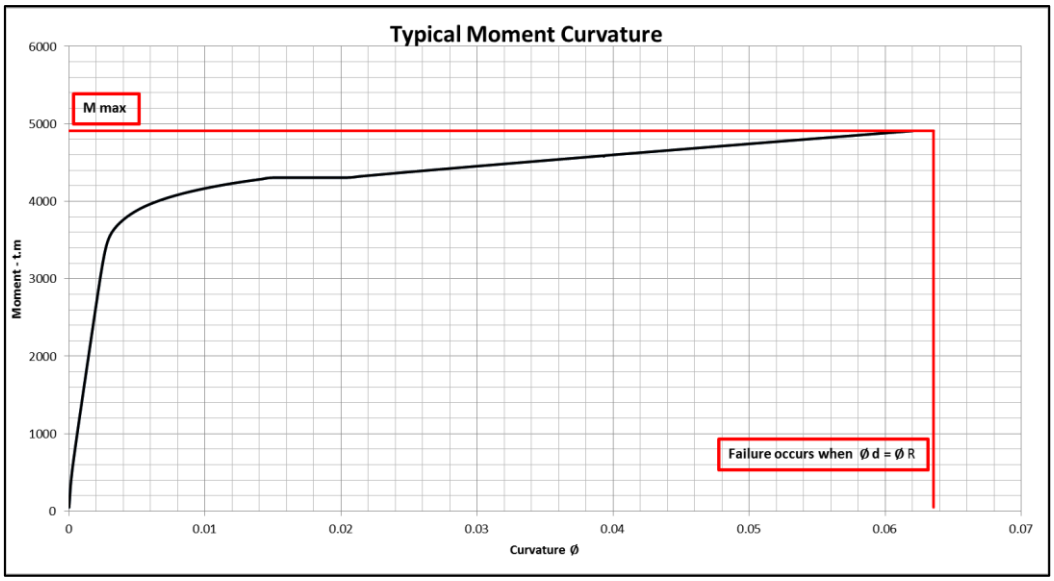


Figure 3 – Typical (sample) moment-curvature graph resulting from FSA.

A flow chart is implemented (figure 4) to organize the design hierarchy and provide systematic loop in order to converge results as possible to match research purpose. The cycle starts with designing the – on scope – bridge according to EC8. All bridges in this research satisfy EC8 regularity condition and other code recommendations. After that, pushover analysis is performed which in most cases show signs of irregularity, then a modification in steel reinforcement is performed –without violating code minimum requirements – in order to reach most possible regular behavior. Finally, a time history analysis is performed to confirm the analysis results from the pushover analysis.

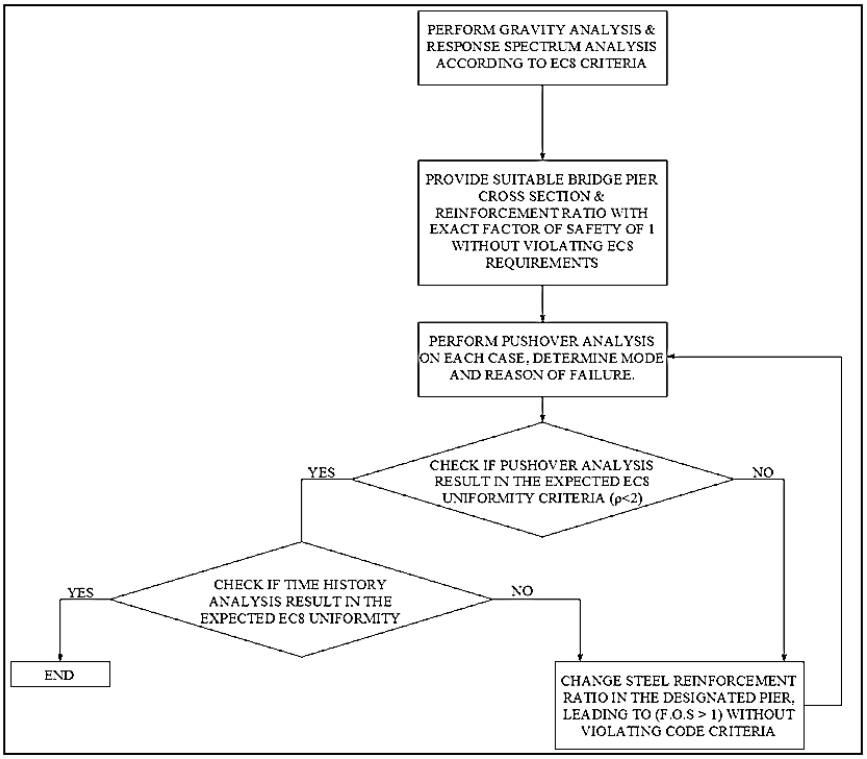


Figure 4 – Flow chart illustrating current research investigation (design/analysis) hierarchy.

3. FAILURE CRITERIA

Key failure criteria in this research are identified as whichever occurs first: a ductile mode of failure when steel reaches ultimate strain versus a brittle mode of failure when confined concrete reaches its ultimate strain. Bridge piers are considered to have reached their ultimate curvature when either outermost confined concrete fibers reach a strain of 0.014 or steel bars reach a strain of 0.09. However, for conservatism in predicting ductility capacity (and consequently curvature at failure) we could consider SCDOT (2008) [9] assumption that ultimate curvature of the piers cross section corresponds to the maximum moment the cross section can bear provided that neither of the above two conditions on material strains occurs prior to this. FSA plays a key role in determining the exact values of stress and strain in each partition of the critical section of the pier in order to identify the precise cause of failure.

Another modes of failure away from bridge piers that are further checked for completeness are (a) when a total longitudinal displacement of the bridge deck exceeds a given limiting displacement at abutment leading to deck falling off abutment ledge, and (b) when non sliding elastomeric bearings – whenever used atop of pier – reaches their maximum shear deformation. This maximum (limiting) lateral deformation within the bearing is specified herein as three times the elastomer thickness t_b and is assumed to demarcate "full" tearing of the elastomeric bearing based on scattered information gathered from experimental and analytical results in the literature [10 & 11]. However, this criterion by itself is not strictly marking a collapse state of the bridge as a whole. Total bridge failure will not happen unless there is an off-seating of the deck from the abutments' shelves, i.e., maximum deck displacement exceeds off-seating limiting values. Hence, tearing of bearings without off-seating may be considered a "weak/soft" mode of failure that could be restored by bearing replacement [12] and therefore the bridge is further investigated in the present research after reaching this *weak* failure state.

4. IMPLEMENTING EC8 UNIFORMITY CRITERIA ON CASE STUDY BRIDGES

Elastic analysis according to EC8 is performed in order to design the unequal height bridge piers cross sections. Response spectrum analysis is hence conducted for a ground acceleration a_g = 0.3g representing moderate to high seismicity, soil type B with the following relevant factors (S=1.2, Tb=0.15, Tc=0.5, Td=2), and a high importance factor of 1.3; and the design of piers is carried out for a behavior factor q=3.5 (ductile response) with pier effective inertia of 50% of pier gross inertia which was recommended in EN 1998-1 article 4.3.1. Table 2a summarizes the required steel percentage for each investigated bridge category and for each pier. A likely live load (20% of the total) is used in the seismic mass as well as in the seismic design load combination according to EC8 design requirements. The main concept followed herein in the piers design is to guarantee a factor of safety against flexure of exactly 1.0 relying on the generated "axial force-bending moment" interaction diagram for each pier and the design values retrieved from the elastic response spectrum analysis after being reduced by q. However, in order for all design scenarios generated in the current research to represent realistic cases that do not violate code rules, it has been decided to increase design-obtained reinforcement ratios in case they do not satisfy minimum reinforcement ratio determined as per EN 1992-1-1 (2004) - Cl. 9.5.2 [13] which has resulted in a factor of safety against flexure that is larger than 1.0 for these specific cases. This has been reflected in the values reported in table 2a. For completeness, table 2b converts reinforcement ratios given in table 2a into actual reinforcement steel tonnage to facilitate comparisons of the different design schemes.

Short pier Height	Cat 1 (E-P) 3.5m x 1.4m		Cat 2 (E-M) 3.5m x 1.4m		Cat 3 (P-M) 3.5m x 1.8m		Cat 4 (P-P) 3.5m x 1.8m	
	short	long	short	long	short	long	short	long
7m	0.200%	1.042%	0.200%	1.363%	1.780%	0.407%	1.880%	0.200%
9m	0.200%	1.077%	0.200%	1.403%	1.320%	0.661%	1.580%	0.405%
10.5m	0.250%	1.122%	0.200%	1.443%	1.060%	0.842%	1.270%	0.538%
12m	0.280%	1.128%	0.200%	1.443%	0.840%	0.966%	1.068%	0.686%

Note: minimum computed steel reinforcement ratio according to EC2 is 0.2%

Table 2a – Steel reinforcement ratios in piers of different investigated bridge categories as per design conforming to EC8 requirements (without steel reinforcement alterations for optimal uniform seismic response).

Short pier Height	Cat 1(E-P) 3.5m x 1.4m	Cat 2(E-M) 3.5m x 1.4m	Cat 3(P-M) 3.5m x 1.8m	Cat 4(P-P) 3.5m x 1.8m
7m	614	788	898	790
9m	649	825	1045	984
10.5m	706	857	1133	1032
12m	737	870	1167	1109

Table 2b – Steel reinforcement total weight (in tons) used in design version/trial 1

Table 3 summarizes the values of ρ computed as per Equation (1) for the different schemes reported in table 2. Referring to table 3, all ρ values appear to satisfy the regularity criteria (namely, demonstrating $\rho < 2$) spelled out in EC8 and in most cases are even too close to a

value of 1 corresponding to perfect anticipated fully synchronized seismic behavior of unequal height piers up to failure. However, further investigation through nonlinear static and dynamic analysis shall be carried out in order for such conclusion of satisfying seismic response regularity to be either approved or denied.

It is nonetheless worth noting from table 3 that best uniform seismic behavior among unequal height piers for very short pier bridge schemes (namely, 7m- and 9m-high) is anticipated for category 2 (ρ is very close to 1.0) apparently followed by category 4, while best regular behavior for relatively long pier bridge schemes (namely, 10.5m- and 12m-high) is expected for categories 1, 2 and 4 (ρ is practically 1.0). However, detailed nonlinear analysis scrutinizing relative curvature demand-to-capacity ratios among piers up to failure – and not only looking into strength as suggested by code recommendations – is yet to be performed for validation of the seismic response regularity of the different categories.

Short pier Height	Cat 1(E-P) 3.5m x 1.4m	Cat 2(E-M) 3.5m x 1.4m	Cat 3(P-M) 3.5m x 1.8m	Cat 4(P-P) 3.5m x 1.8m
7m	1.235	1.010	1.624	1.087
9m	1.030	1.005	1.355	1.021
10.5m	1.013	1.016	1.251	1.007
12m	1.015	1.026	1.195	1.017

Table 3 - Values of ρ (Equation 1) for the sixteen investigated bridge schemes designed as per EC8 requirements

Moreover, despite that categories 4 and 3 as designed per EC8 recommendations may provide reliable seismic response similar to code compliant categories 1 and 2 (but not necessarily in terms of anticipated regularity in seismic behavior), one should realize that this is achieved at the expense of larger concrete dimensions of piers (and somehow generally higher reinforcement quantities); refer to table 2 and compare design data for category 1 versus category 4 and category 2 versus category 3.

5. PUSHOVER ANALYSIS AND DESIGN OPTIMISATION FOR REGULARIZED RESPONSE

Various design trials/alterations are performed starting from EC8 compliant designs (table 2) ending with most suitable version with reasonable steel reinforcement ratios to approach regularity (and synchronized failure of piers) as shown in table 4a. Version/trial 1 denotes pushover analysis performed on bridges with steel reinforcement according to EC8 design requirement as reported in table 2. Increasing either short or long pier steel reinforcement can lead to better uniformity in bridge behavior, where *perfect* uniform behavior is achieved when proposed ρ_ϕ calculated at failure reaches a value of 1. It is noted that global bridge behavior approaches regularity whenever the difference between pier heights decreases. Altering steel reinforcement in short pier can improve uniformity in seismic response such as in categories 1, 2 and 4, while altering steel reinforcement in long pier in category 3 demonstrates better behavior in terms of uniformity. Steel reinforcement alteration applied herein does not violate EC8 recommendations (i.e. minimum or maximum steel reinforcement, etc.) but it also provides better performance and over strength (to be discussed in details later).

In case of category 1 bridges, it is noticed that investigated bridges start with design version 1 (EC8 compliant as per table 2) from a state far from regularity compared to categories 2, 3 & 4. This means that different pier-to-deck connections could affect the bridge uniformity drastically regardless of design requirements and recommendations. Category 2 bridges possess a better starting behavior than category 1 as demonstrated in figure 5, which is due to the fact that monolithic connection atop of the long pier provides better force redistribution among both piers than pot bearing pier-to-deck connection. Category 3 has a different trend in the behavior than the other versions as the steel reinforcement ratio in long piers rather than short piers is altered to target more uniform response at failure. It is noticed that this scheme may provide good solution in case of large difference between pier heights, while its benefits are diminished when the gap between both pier heights decreases, which then results in unpractical solution. A radically different behavior appears in category 4 starting from short pier height of 7m; it is impossible to reach reasonable values of regularity by just altering steel reinforcement ratios of the two piers. This is due to the fact that the stated EC8 design recommendation provides the most likely uniform behavior that could be achieved tied with the section minimum steel reinforcement requirement; if we can override this minimum reinforcement we can achieve better uniformity as noted in dashed lines in figure 5. This behavior further improves dramatically when short pier height increases from 7m to 9m but it is still away from regularity. The regularity/uniformity of response improves among pier heights of 10.5m and 12m but still no synchronization of failure of piers is achievable for this category of the case-study bridges.

As outlined above, the results obtained from pushover analysis showed a clear variation in seismic behavior among investigated categories. Thus, further nonlinear hysteretic time history analyses are performed herein on both “category 1” and “category 2” in order to validate the significance of the pushover analysis results. Time history analysis of categories 3 and 4 is still ongoing by the authors and results are not presented in this manuscript. Shown in table 4a are the optimal reinforcement ratios (retrieved through pushover analysis effort) that *more-or-less* satisfy regularity condition and that are considered throughout the time history analysis. Note the difference between these values in table 4a and those calculated by simply satisfying EC8 design requirements in table 2 without focusing on achieving regular seismic response of piers at failure. For completeness, table 4b converts these reinforcement ratios in table 4a of the optimized design for uniform seismic response into actual reinforcement steel tonnage to facilitate comparisons.

Short pier Height	Cat 1(E-P) 3.5m x 1.4m		Cat 2(E-M) 3.5m x 1.4m		Cat 3(P-M) 3.5m x 1.8m		Cat 4(P-P) 3.5m x 1.8m	
	short	long	short	long	short	long	short	long
7m	1.900 %	1.042%	1.000%	1.363%	1.780%	0.500%	1.880%	0.200%
9m	2.290%	1.077%	0.460%	1.403%	1.320%	1.100%	2.000%	0.405%
10.5m	2.000%	1.122%	0.400%	1.443%	1.060%	1.800%	1.880%	0.538%
12m	1.300%	1.128%	0.280%	1.443%	0.840%	2.000%	2.000%	0.686%

Table 4a – Steel reinforcement ratios used to comprehend best achievable uniform behavior (retrieved from pushover analysis successive trials)

Short pier Height	Cat 1(E-P) 3.5m x 1.4m	Cat 2(E-M) 3.5m x 1.4m	Cat 3(P-M) 3.5m x 1.8m	Cat 4(P-P) 3.5m x 1.8m
7m	1072	1003	962	790
9m	1373	915	1349	1171
10.5m	1412	939	1797	1348
12m	1208	906	1883	1662

Table 4b – Steel reinforcement total weight (in tons) for the two piers resulting from the optimized design

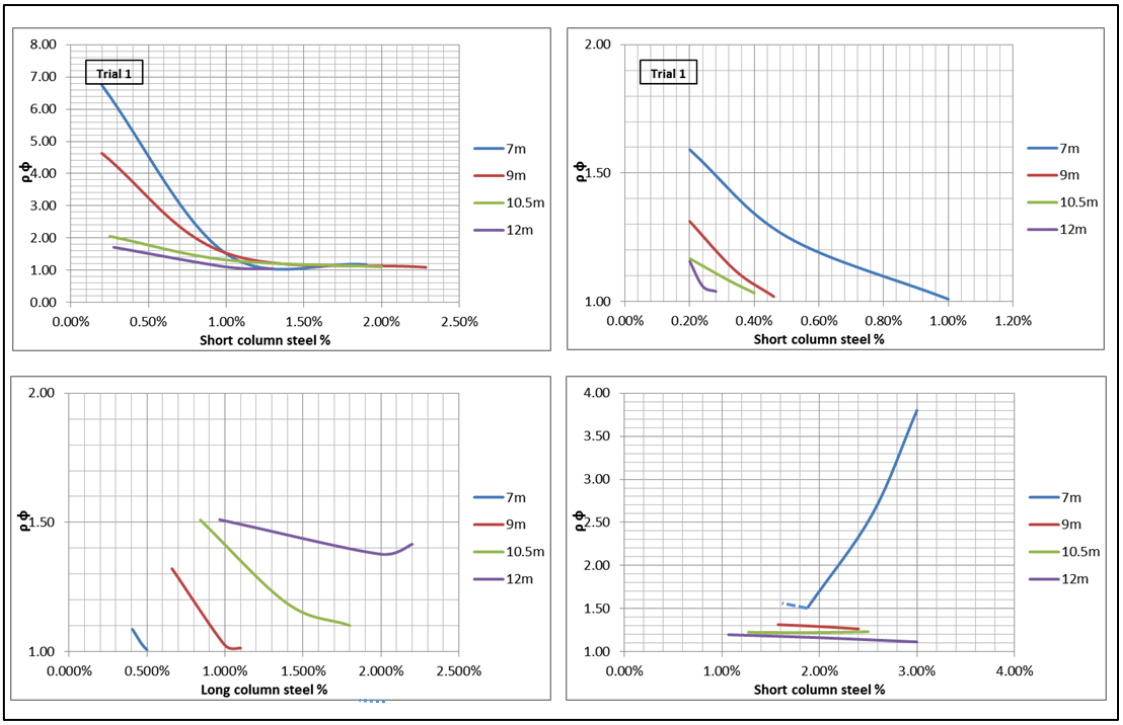


Figure 5 – Uniformity behavior from pushover analysis successive trials, top left: category 1, top right: category 2, bottom left: category 3, bottom right: category 4 [ρ_ϕ values are calculated at failure state].

Table 5a reports ρ_ϕ values computed for version (i.e., trial) 1 corresponding to EC8-based design without steel reinforcement alterations. Comparing EC8-calulcated ρ values (as per Equation 1) in table 3 to proposed curvature-based ρ_ϕ values in table 5a retrieved from pushover analysis at failure as specified above, one could notice that even when a bridge scheme complies with EC8 uniformity behavior it still has the possibility of acting somewhat non-uniform at failure limit state. For completeness, table 5b also reports ρ_ϕ values at failure but for the bridge schemes featuring reinforcement ratios (table 4a) that have been optimized to attain *more-or-less* best regular response at failure based on pushover analysis results. It is hereby clear that categories 1 and 2 are capable of providing satisfactory uniform/regular seismic response at failure for all investigated pier height ratios while this is not strictly the case for all design schemes in categories 3 and 4 with various investigated pier height ratios.

Short pier Height	Cat 1(E-P) 3.5m x 1.4m	Cat 2(E-M) 3.5m x 1.4m	Cat 3(P-M) 3.5m x 1.8m	Cat 4(P-P) 3.5m x 1.8m
7m	6.740	1.590	1.090	1.520
9m	4.631	1.312	1.321	1.314
10.5m	2.060	1.170	1.510	1.230
12m	1.710	1.160	1.510	1.200

Table 5a – Actual values of ρ_ϕ denoted as resulting from pushover analysis (at failure) for version/trial 1 of the sixteen investigated bridge schemes. (Trial 1 corresponds to strict EC8-based design without reinforcement alteration/optimization)

Short pier Height	Cat 1(E-P) 3.5m x 1.4m	Cat 2(E-M) 3.5m x 1.4m	Cat 3(P-M) 3.5m x 1.8m	Cat 4(P-P) 3.5m x 1.8m
7m	1.180	1.010	1.010	1.520
9m	1.093	1.020	1.014	1.266
10.5m	1.110	1.034	1.100	1.220
12m	1.050	1.040	1.420	1.120

Table 5b – Actual values of ρ_ϕ at failure (pushover analysis) for all investigated bridge schemes with optimized reinforcement ratios (Table 4a).

6. TIME HISTORY ANALYSIS

A series of 7 real earthquake records have been used and incrementally scaled up in terms of the spectral acceleration at the fundamental period of vibration of the subject bridge scheme to cover various seismic demands ranging from design level earthquake, passing through limit of elastic response until reaching failure of the bridge under investigation as per the failure criteria previously stated. Each earthquake has a different behavior and effect on each bridge, but the overall behavior will be reported in what follows only based on average results of the seven records. The earthquakes considered are LP89CAP, LP89G03, LP89HDA, NR94NYA, NR94STC, SF71PEL, and SH87WSM – refer to figure 6 showing records acceleration elastic response spectra. These records were extensively used in several other earlier studies (e.g. [12 & 14 – 17]) to which the reader is referred for complete details.

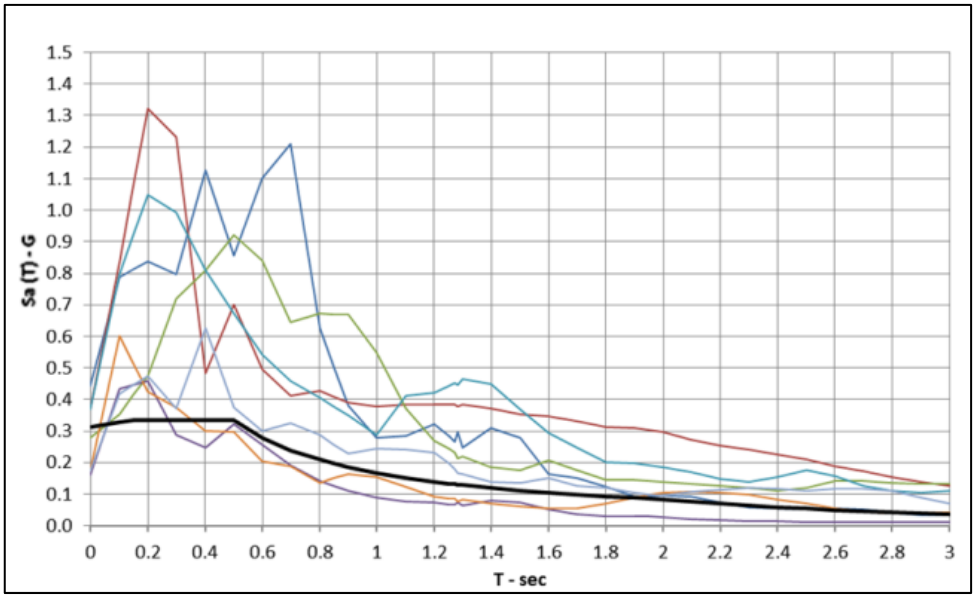


Figure 6 – Design acceleration response spectrum according to EC8 (q=3.5) in Bold, compared to the seven earthquakes elastic response spectra before re-scaling them to design level.

The bridge piers undergo a typical moment-curvature hysteretic loop under inelastic time history analysis until either the end of the event or when failure is imminent at the stress-strain level of confined concrete and/or reinforcing bars as described before. The values of curvature at failure are determined according to failure criteria previously mentioned. Figure 7 displays a typical moment-curvature hysteretic loop for a sample bridge pier.

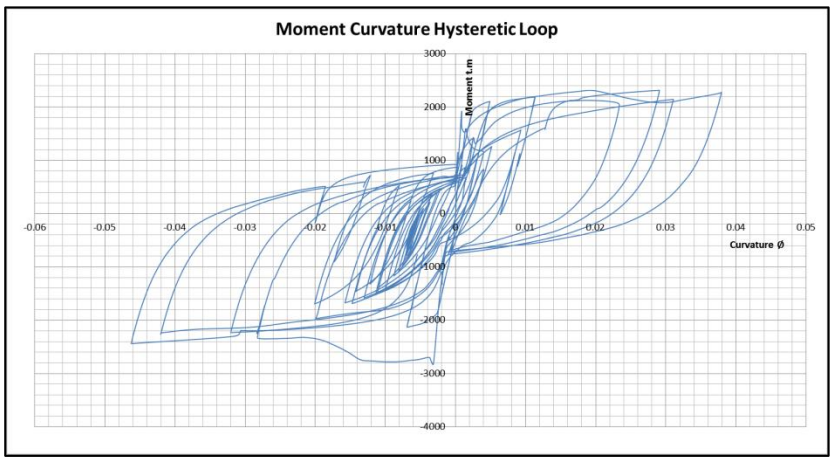


Figure 7 – Sample bridge pier Moment-Curvature hysteretic loop from time history analysis

6.1 CATEGORY 1 TIME HISTORY ANALYSIS RESULTS

In category 1, short pier behavior is influenced by the elastomeric bearing connection to the deck. Thus it is noticed that failure is governed by deck total displacement exceeding a seating width of 1m at abutment. This – of course – occurs after a "weak/soft" mode of failure (as previously defined) takes place, where net transverse shear deformation in the elastomeric bearing exceeds a maximum value of 0.45 m (refer to figure 8) for bridges with 7m or 9m-high short piers. Steel reinforcement strain values corresponding to this failure state are far

less than the maximum strain demarking failure of reinforcement. Average of the maximum achieved stress-strain values for the seven considered earthquake records is denoted in figure 9.

Concrete stress-strain relation to incrementing earthquakes is not shown since concrete strain values retrieved from inelastic time history analyses were far below maximum allowed strain values up to failure state of all studied bridges falling under this category 1. Most achievable bridge uniform behavior from various trials through altering reinforcement ratio of the short pier has resulted in much better performance than the original code-based design (table 2) previously denoted by trial 1. This difference is more obvious when comparing values of back calculated curvature-based ρ_ϕ at failure (averaged over the seven considered earthquake records) as shown in figure 10 to those of the original EC8-based design (retrieved from pushover analysis and corresponding to trial 1) illustrated in table 5a.

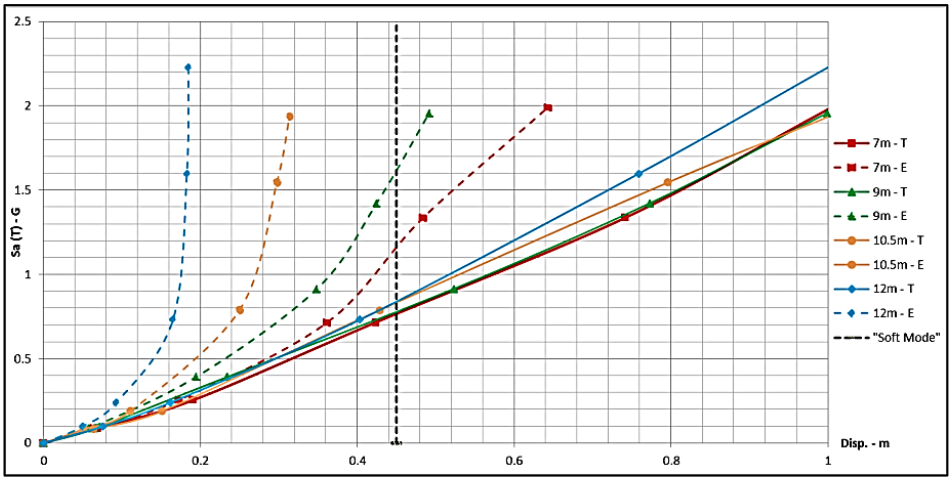


Figure 8 – Net elastomeric bearing displacement (E) and Total deck displacement (T) of all category 1 bridges. Values in the figure are average of the seven selected records.

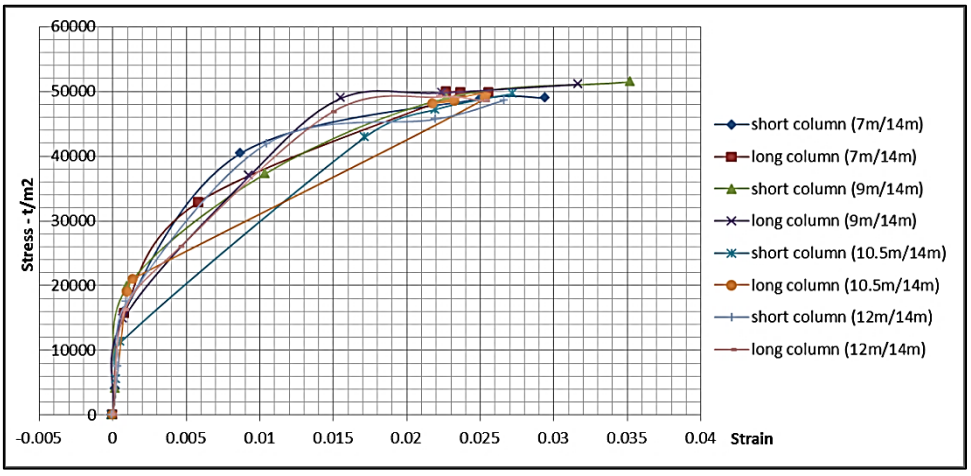


Figure 9 – Maximum stress-strain values resulting from increasing earthquake scale factor until failure – averaged over all seven earthquake records considered.

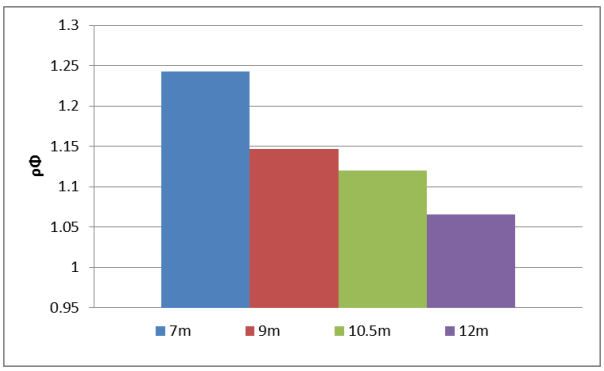


Figure 10 – Uniformity index, curvature-based, ρ_ϕ for category 1 at failure for the four different heights of the short pier after optimizing EC8 original design through reinforcement ratio alteration (Table 4a) – reported values are averaged over the seven considered earthquake records.

An over strength value Ω_R of the bridge is introduced and is defined as the ratio between the actual total base shear of the two piers at *failure level* resulting from time history inelastic analysis averaged over all seven considered earthquake records and the total design base shear of both bridge piers according to EC8 *design* response spectrum. The over strength Ω_R (computed at failure limit state) of the bridge tends to decrease as the ratio between the height of the long to short piers decreases as shown in figure 11 (i.e., when piers tend to be of near height). Similarly, another strength response index denoted by Ω_d is defined and computed but at the *design demand* level rather than at the failure level. Ω_d is simply defined as the total base shear carried by both unequal height piers (averaged over the seven considered earthquakes) corresponding to the design level demand divided by the base shear the actual bridge piers are designed for in order to sustain EC8 seismic demands. As the value of Ω_d decreases and is less than 1.0, the as-designed bridge has higher design strength than expected. On the other hand, when the value of Ω_d becomes greater than 1.0, the bridge as-designed is exposed to actual earthquake forces at *design level* higher than its design ability to resist. Referring to figure 11, it is clear that the case study bridges of category 1 are all featuring Ω_d remarkably less than 1.0 irrespective of the ratio of their unequal height piers. They thus feature a reasonable built-in over strength and are hence *on average* capable of sustaining EC8 seismic design loads when hit by design level earthquake records.

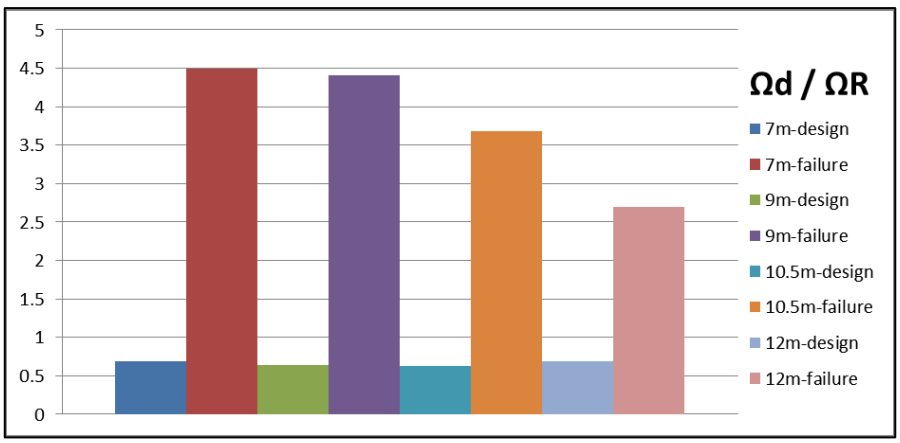


Figure 11 – Over strength values (Ω_d at design level and Ω_R at failure level) retrieved averaged over all considered seven earthquake records for category 1 bridges – design data are as per Table 4a.

6.2 CATEGORY 2 BRIDGE BEHAVIOR

Category 2 is distinguished from category 1 at many features. First of all, the bounding failure criteria here is the ultimate steel strain as opposed to maximum deck displacement and off-seating as shown in figures 12 and 13. The total deck displacement has never exceeded the preset seating width of 1m and the net elastomeric bearing transverse shear deformation has not reached the weak mode of failure demarcated by elastomer shear deformation of $3xt_b$.

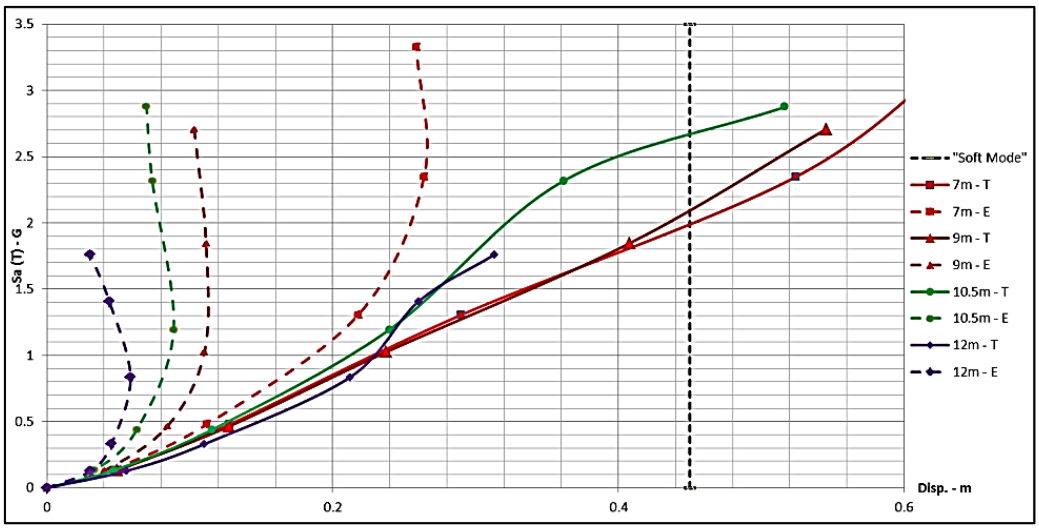


Figure 12 – Net elastomeric bearing displacement (E) and Total deck displacement (T) of all category 2 bridges. Values in the figure are average of the seven selected records.

Steel strain controlled failure mode is governing all studied bridges of this category, as in most notable cases short pier tends to fail first for heights 7m and 9m while this effect diminishes whenever we approach cases with close pier heights, i.e., 12 m-high short pier (refer to figure 13).

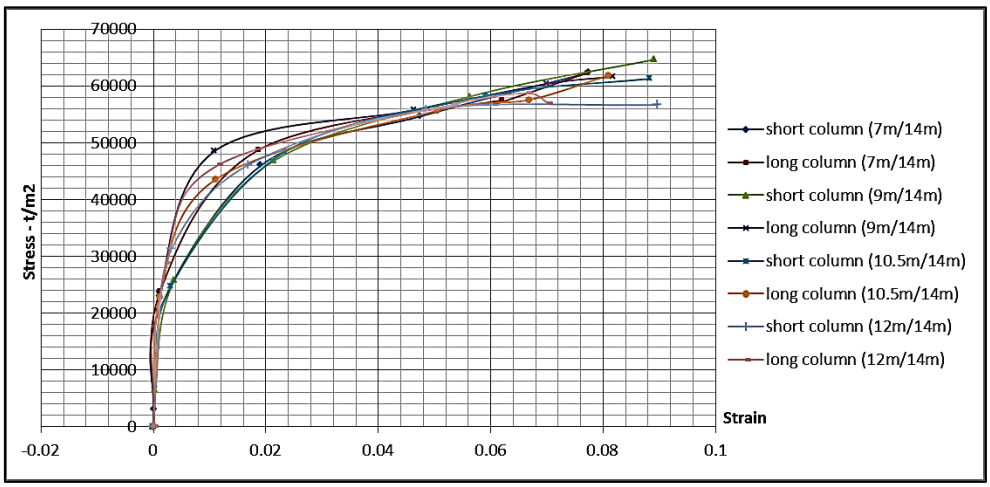


Figure 13 – Maximum stress-strain values resulting from increasing earthquake scale factor until failure of category 2 bridges – averaged over all seven earthquake records considered.

From a seismic response uniformity/regularity perspective, category 2 bridges possess less uniform behavior – especially at failure – than category 1. One can also note that there is a

reversal in behavior in terms of uniformity (and synchronized failure of unequal height piers) when short pier height exceeds 9m. In other words, the scheme with 12m-high short pier possesses low uniformity behavior nearly similar to the scheme with the 7m-high short pier already featuring some inherent non-uniform seismic behavior particularly at failure (refer to figure 14). This is due to some intrinsic effect of monolithic pier-to-deck connection. To conclude, when we have bridge schemes with close heights of piers, it is recommended to consider category 1 instead as its inherent features provide overall better uniformity in seismic response than category 2.

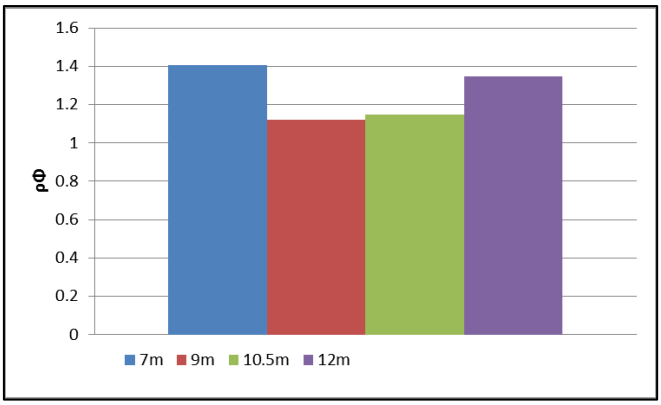


Figure 14 – Uniformity index, curvature-based, ρ_ϕ for category 2 at failure for the four different heights of the short pier after optimizing EC8 original design through reinforcement ratio alteration (Table 4a) – reported values are averaged over the seven considered earthquake records

Regarding built-in over strength, category 2 bridges possess lower over strength at failure than their corresponding versions of category 1 as reflected by Ω_R values in figure 15 versus figure 11, while they possess critical values of *design* strength index, Ω_d that are very close to 1.0 which denotes that these bridges – as-designed – can sharply withstand design earthquakes.

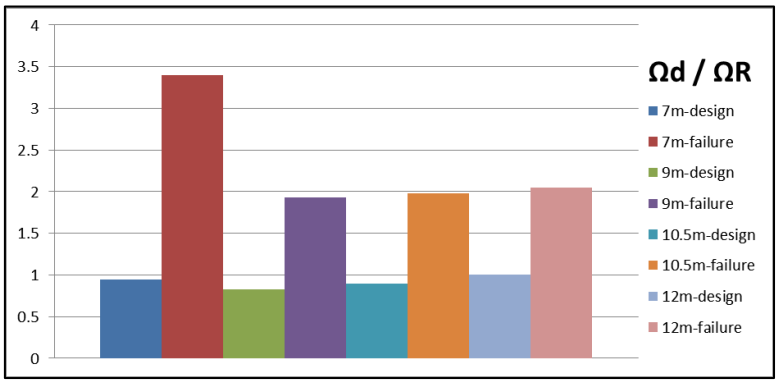


Figure 15 – Over strength values (Ω_d at design level and Ω_R at failure level) retrieved averaged over all considered seven earthquake records for Category 2 bridges – design data are as per Table 4a.

7. MATERIAL ECONOMY AMONG CATEGORY 1 AND CATEGORY 2

Material economy - besides uniformity of seismic response and over strength (both at design and at failure states) - plays a key role in determining the most suitable system according to the available scheme conditions. The designer may sometimes favor bridge material economy over uniformity of behavior. To unify a measurement technique to address and assess the economy of the as-designed bridge, βc and βs are two proposed *dimensional* indexes deemed suitable to compare various studied bridge schemes in terms of concrete and reinforcing steel quantities, respectively.

$$\beta c = \frac{Total\ base\ \text{shear}\ force}{Total\ piers\ cross\ section\ area}\ ,\ \beta s = \frac{Total\ base\ \text{shear}\ force}{Total\ reinforcement\ area\ in\ both\ \text{piers}}\ (t/m^2) \qquad (3)$$

These indexes ignore piers height and are hence used only to compare similar bridge schemes but with different pier-to-deck connections. Higher values of β means better material economy, since higher forces can be sustained for a given quantity of material (be it concrete or reinforcing steel). However, high β values do not necessarily illustrate a better design in terms of uniformity of seismic behavior, redundancy and/or over strength capability. Figures 16a and b denote a comparison between category 1 and category 2 bridges in terms of economy and material utilization.

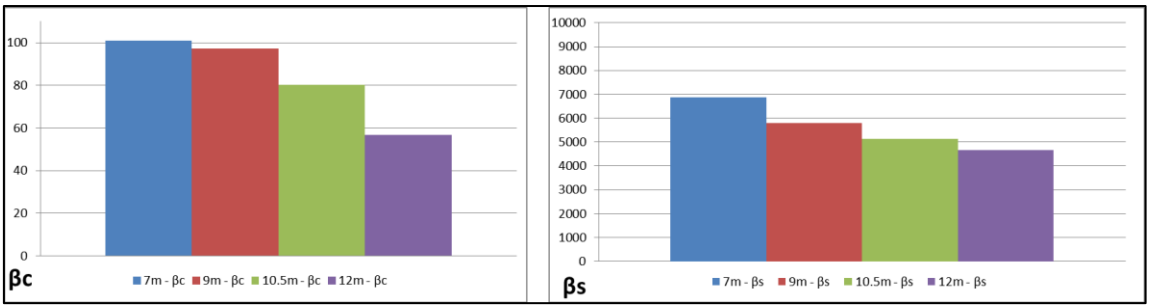
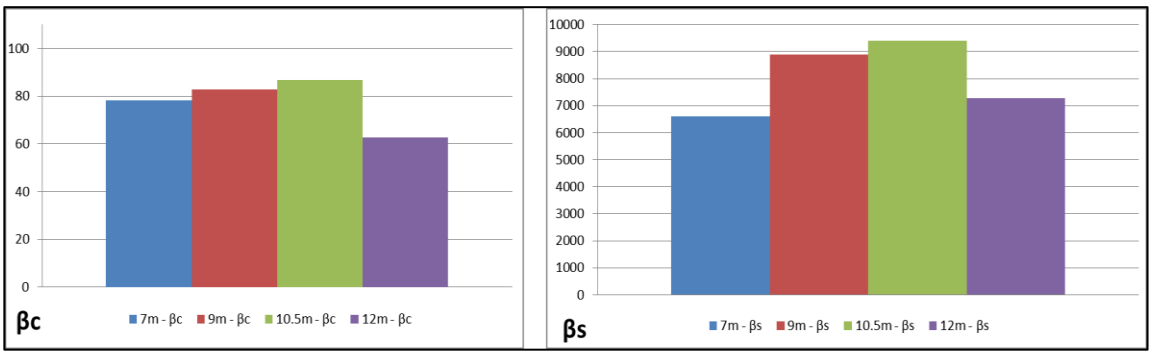


Figure 16a – βc and βs for category 1 bridges – averaged over the seven selected records



.Figure 16b – βc and βs for category 2 bridges – averaged over the seven selected records.

It is obvious that in terms of better concrete utilization, category 1 outnumbers category 2 just for bridge schemes with short pier heights of 7m and 9m (i.e., remarkably different from the height of the longer pier that is 14m), but both categories possess nearly same utilization

for short pier heights of 10.5m and 12m. In terms of steel utilization and excluding short pier of height 7m, category 2 far outnumbers category 1 which denotes that steel reinforcement used in category 2 sustains much more shear force than reinforcement used in category 1. It is worth noting that values in figure 16 reflect results averaged over the seven selected earthquake records and correspond to bridge schemes with steel reinforcement ratios tailored to comprehend best achievable uniform behavior as per table 4a.

8. CONCLUSIONS

Current EC8 criteria in addressing bridge uniformity shall hold further investigation, as the only factor to determine uniformity ($\rho<2$) is force/moment-based and hence is not enough to assess actual bridge behavior and might be misleading in some cases as discussed herein and in the literature. A curvature-based uniformity index such as ρ_ϕ proposed in the present research has been shown to be more appropriate to address and verify this seismic regularity issue for bridges.

Common construction practice might force designers to choose one type of bearing to be used across bridge piers, which is good from aesthetic point of view and constructability but may be a bad option in terms of design optimization targeting utmost uniformity of seismic response. For instance, pot bearings when used on all piers of the same bridge irrespective of their relative height could lead to *less* economic and/or *less* effective design to overcome seismic loads for one case or the other, while still providing *some* uniform behavior among unequal height bridge piers (refer to tables 4b and 5b). Further altering pier-to-deck connections can provide better uniform behavior. Such conclusion based on pushover analysis results is under further investigation by the authors through applying more sophisticated inelastic time history analyses.

Usage of elastomeric bearing on short pier and pot bearing on long pier possesses an effective solution for bridge uniformity under seismic events up to failure in addition to overall material optimized utilization. On the other hand, usage of monolithic connection instead of pot bearing for the long pier is not recommended, as it sustains low over strength characteristics although it still offers uniform seismic behavior close to that provided through the pot bearing solution.

In the case with elastomeric bearing on the short pier, concrete usage economy is better when pot bearing is mounted on long pier, especially when the gap between pier heights is large. But when both piers have closer heights, the monolithic pier-to-deck connection for the long pier along with elastomeric bearing on the short pier shows slightly better concrete utilization. Also, the monolithic connection possesses generally much higher steel reinforcement utilization than the pot bearing pier-to-deck connection for the long pier except for the bridge schemes with 7m-high short pier. However, this benefit effect is diminished when comparing this scheme to the pot bearing connection scheme in terms of seismic behavior uniformity and over strength.

Finally, usage of pot bearings on both piers is not highly recommended, same as usage of pot bearing on short pier and monolithic connection for long pier. Both schemes show very rigid solution attracting significantly higher seismic demands, and may have unexpected *"hard to minimize"* non-uniform seismic behavior. Nonetheless, further extensive investigations through inelastic time history analysis are a must to determine their exact behavior and to weigh their effectiveness in terms of regularity/uniformity of seismic

response, in addition to their built-in overstrength, versus quantities of structural materials (concrete and reinforcement steel) used. This is currently an ongoing research by the authors.

ACKNOWLEDGMENTS

The research reported here was supported by the European Union Project PIRSES-GA-2010-269222: Analysis and Design of Earthquake Resistant Structures (ADERS) of the FP7-PEOPLE-2010-IRSES, Marie Curie Actions. This support is gratefully acknowledged by the authors.

REFERENCES

[1] EN 1998-1 Eurocode 8 (2005): "Design of Structures for Earthquake Resistance. Part 1: General Rules, Seismic Actions and Rules for Buildings," *ComitéEuropéen de Normalisation*, Brussels, Belgium.

[2] EN 1998-2 Eurocode 8 (2005) "Design of Structures for Earthquake Resistance, Part 2: Bridges," *ComitéEuropéen de Normalisation*, Brussels, Belgium.

[3] Guirguis, J.E.B. and Mehanny, S.S.F. (2013), "Evaluating Codes Criteria for Regular Seismic Behavior of Continuous Concrete Box Girder Bridges with Unequal Height Piers," *ASCE Journal of Bridge Engineering*, DOI 10.1061/(ASCE)BE.1943-5592.0000383, Vol. 18, No. 6, June 2013, pp 486-498.

[4] Mohammadi-Tamanani, M and Ayoub, A. (2014), "Design of Bridges with Unequal Pier Heights," *Structures Congress*, Boston, Massachusetts, USA April 3-5, 2014.

[5] Reza, S.M. (2012), "Seismic Performance of Multi-Span RC Bridge with Irregular Column Heights," *Master of Applied Science Thesis*, The University of British Columbia, Canada.

[6] Tehrani, P. (2012), "Seismic Analysis and Behavior of Continuous Reinforced Concrete Bridges," *Ph.D. Thesis*, McGill University, Montreal, Quebec, Canada.

[7] OpenSees 2.0.0 [Computer software]. Berkeley, CA, Pacific Earthq. Engrg. Res. Center, Univ. of California.

[8] Caltrans (SDC) Seismic Design Criteria, Version 1.7 - September 2013.

[9] South Carolina Department of Transporation (SCDOT). (2008). "Seismic Design Specifications for Highway Bridges," version 2.0, SCDOT,Columbia, SC.

[10] Konstantinidis, D., Kelly, J.M. and Makris, N (2009), "Experimental Investigation of the Seismic Response of Bridge Bearings", 3rd International Conference on Advances in Experimental Structural Engineering, San Francisco, CA, 15-16 October, 2009Manos et al. (2011)

[11] Manos, G.C., Mitoulis, S.A. and Sextos, A.G. (2011), "Preliminary Design of Seismically Isolated R/C Highway Overpasses – Features of Relevant Software and Experimental Testing of Elastomeric Bearings," COMPDYN 2011, III ECCOMAS Thematic Conference on Computational Methods in Structural Dynamics and Earthquake Engineering, Corfu,Greece, 26-28 May, 2011.

[12] Farag, M.M.N., Mehanny, S.S.F. and Bakhoum, M.M. (2015), "Establishing optimal gap size for precast beam bridges with a buffer-gap-elastomeric bearings system" *Earthquakes and Structures*, accepted for publication.

[13] EN 1992-1-1 Eurocode 2 (2004), "Design of Concrete Structures. Part 1-1: General Rules and Rules for Buildings," *ComitéEuropéen de Normalisation*, Brussels, Belgium.

[14] Mehanny, S.S.F. (2009), "A Broad-Range Power-Law Form Scalar-Based Seismic Intensity Measure," *Engineering Structures*, Vol. 31, Issue 7, pages 1354-1368, July 2009.

[15] Chenouda, M. and Ayoub, A. (2009), "Probabilistic collapse analysis of degrading multi degree of freedom structures under earthquake excitation," Eng. Struct. 2009; 31(12), pp. 2909-2921.

[16] Mehanny, S.S.F., and Ayoub, A.S. (2008), "Variability in Inelastic Displacement Demands: Uncertainty in System Parameters versus Randomness in Ground Records," *Engineering Structures*; 30(4): 1002-1013.

[17] Mackie K.R. and Stojadinović B. (2005), "Fragility Basis for California Highway Overpass Bridge Seismic Decision Making," *PEER Report 2005/02*, University of California, Berkeley, CA, USA.

COMPDYN 2015
5th ECCOMAS Thematic Conference on
Computational Methods in Structural Dynamics and Earthquake Engineering
M. Papadrakakis, V. Papadopoulos, V. Plevris (eds.)
Crete Island, Greece, 25–27 May 2015

OPTIMIZATION OF QUATROPOD JACKET SUPPORT STRUCTURES FOR OFFSHORE WIND TURBINES SUBJECT TO SEISMIC LOADS USING GENETIC ALGORITHMS

Mohammad H. AlHamaydeh[1], Samer A. Barakat[2], and Omar M. Nassif[2]

[1] Department of Civil Engineering
American University of Sharjah
P.O. Box 26666, Sharjah
United Arab Emirates
e-mail: malhamaydeh@aus.edu

[2] Department of Civil Engineering
University of Sharjah
P.O. Box 27272, Sharjah
United Arab Emirates
{sbarakat,onaseef}@sharjah.ac.ae

Keywords: Offshore Support Structures, Genetic Algorithms, Optimization.

Abstract. *This paper presents evolutionary-based least-weight topology and size optimization procedure for designing offshore wind turbine supporting structures. A modified version of Genetic Algorithms is presented herein. The GA technique is used for solving the nonlinear constrained optimization problem of 3D quatropod jacket offshore support structure. In this optimum design formulation, the objective function is the material weight of the supporting truss; the design variables are the locations of the ends of the truss members as well as the cross-sectional areas of the truss members. The constraints are the stresses in members and the displacements of the joints. The constraints are handled using non-stationary (dynamically modified) penalty functions. The quatropod jacket, one of the most commonly used design alternatives for offshore supporting structures is presented as demonstration to the efficiency of the presented GA algorithm. The quatropod jacket test problem is subjected to gravity, wind, wave and earthquake loading conditions. The results show that the GA method is efficient in finding the best discovered optimal solution [structural topology and weight].*

1 INTRODUCTION AND BACKGROUND

Often times, the individual design solutions (typically, a range of possible feasible design solutions exist for a given engineering problem) significantly influence the structural response to the environmental loads and thus impose additional constraints to the design. For example, the type, configuration, and structural member sizes of the supporting offshore structure, could potentially have a dramatic impact on marine growth size which greatly impacts the hydrodynamic drag forces. As a result, the nonlinearities associated with fluid-structure interaction may be substantial and no longer be admissible to dismiss during the design stage [1].

In the presence of multiple optima and non-smooth constraints in the design variable space, it is difficult to obtain a set of optimum values using member-level optimization formulations. This shortcoming inspired researchers to explore using the relatively new and innovative evolutionary-based optimization techniques. For example, the following methods have been used recently to address structural engineering optimization problems: Shuffled Complex Evolution Optimizer (SCEO), Ant Colony Optimization (ACO), the Genetic Algorithms (GA), and Particle Swarm Optimizer (PSO) (e.g. [2]–[12]).

Many structural optimization problems involve problem-specific constraints applicable to the solutions limiting the feasible search space. In these types of problems, it is challenging to adapt traditional optimization techniques to handle constraints. One of the most popular constraint handling methods is through penalty functions due to the relative simplicity and ease of implementation. Topology optimization was used by many researchers to generate alternative structural design concepts for benchmark wind turbine blades. In these studies, the focus is alternative structural layout for wind turbine blades with the aim of improving its design, minimizing weight and ultimately, wind energy cost reduction (e.g. [13]–[23]).

This study presents an efficient Genetic Algorithm with Domain Trimming (GADT) optimization technique to achieve superior optimization. The GADT scheme is used to solve a typical least-weight design for offshore wind turbine supporting structures through topology and member size optimization. The algorithm is coded using the MATLAB commercial software package [24] and its built-in GA libraries; while the structural analysis and design for the different topology and loading configurations is performed using the SAP2000 commercial software package [25]. The linkage and automation of the structural analysis and design tasks are initiated from within the MATLAB code and established through the Open Application Programming Interface (OAPI) capabilities of the SAP2000 software.

2 GENETIC ALGORITHM WITH DOMAIN TRIMMING (GADT)

To begin GA optimization, a population of N_p (population size) solution alternatives are generated randomly using a uniform probability distribution; each solution of the GA consists of a combination of variables (x_1, x_2, x_3, …, x_n) which has its own fitness value. In cases where the optimization is performed to find the minimum of a given problem, lower fitness is preferable. Solutions that yield low objective values would have better fitness as long as they are not penalized for violating the constraints which would result in increasing the fitness value. Populations of solutions are represented by chromosomes or variable strings. In this research, a variable string is used instead of a binary string because the design variables are discrete. Once the fitness for every solution in the current population is calculated using the fitness function $\boldsymbol{F_j(X)}$, unfit solutions are eliminated. Any solution whose fitness is greater than the average, $\boldsymbol{F_{ave}}$, of the population is reassigned a fitness of zero:

$$F_j(X) = \begin{cases} \mathrm{F_{ave}} - F_j(X) & \text{for } F_j(X) < \mathrm{F_{ave}} \\ 0 & \text{for } F_j(X) \geq \mathrm{F_{ave}} \end{cases} \qquad \mathrm{j} = 1,2,\ldots,\mathrm{N_p} \tag{1}$$

where ($\boldsymbol{X}$) is the vector of the design variables.

The three basic operations of a GA, reproduction, crossover, and mutation, are used to improve the fitness of each population from one generation (iteration) to the next (

Figure). The reproduction operation selects the better fit designs, copies them and places them into a mating pool allowing each to mate and reproduce. Different selection methods are available in the literature. The roulette wheel selection method is used in this study for its simplicity and popularity. The uniform crossover operation is used to combine genetic information between two parent solutions. Uniform crossover selects two parent solutions at a time from the mating pool and swaps variables corresponding to zeros in a binary string known as a mask.

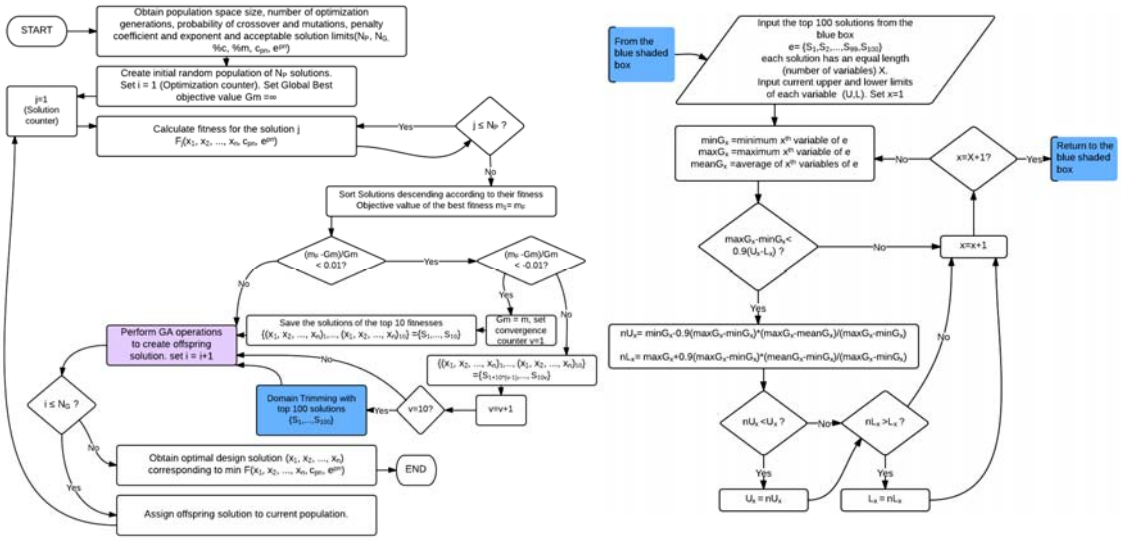


Figure 1: Flow chart of general GADT optimization [26]

A major shortcoming of GA optimization is that while it is good in global search of the optimum solutions, it is weak in local search; meaning that it will converge to the optimum solution but will not locate it with high precision especially if the population size is small. The reason is that initially, the solution variables are selected randomly from a pre-specified range (domain), those variables do not change but relocate from one solution to another, with the exception when mutation occurs which introduces new variables from the specified domain. However, the probability of mutation is generally kept low (2%-5%) in order to increase the solution stability. Another shortcoming of the GA approach is the choice of domain; a poor choice of the domain (e.g.: [1, 1000] when the optimum value is 2) dramatically impacts convergence. In this study, a new technique that addresses these GA shortcomings is presented. The technique is to trim the domain so that the chance of selecting the optimal variable is enhanced (e.g.: trimming a domain from [1, 1000] to [1, 10] would increase the probability of selection of the optimal variable by 200 times). After trimming, the GA is reinitiated and continues to do so until the optimum solution is found. Figure 1 shows the flowchart for the GADT Method. For more details about GADT algorithm the reader is referred to [26].

2.1 Constraints handling

One of the most common constraint–handling techniques is through penalty functions. In such approaches, the problem is solved as an unconstrained one, where the constraints are penalized (such that non–feasible solutions are characterized by high function values). This allows for a single objective function to be formulated and in turn minimized using an unconstrained optimization algorithm. The penalty functions can either be stationary or non-stationary (dynamically modified). It is observed that non-stationary penalty functions are almost always superior to stationary penalty functions. A non-stationary penalty function is, generally, defined as

$$f(X) = F(X) + p(X, c_{pn}, e_{pn}) \tag{2}$$

Where *F(x)* is the original objective function of the constrained optimization problem; $p(\bullet)$ is a dynamically modified penalty value, defined as

$$p\left(X, c_{pn}, e_{pn}\right) = \begin{cases} \left(c_{pn} r_i\right)^{e_{pn}}, & r \geq 1 \\ 0, & r < 1 \end{cases} \tag{3}$$

Where, $\boldsymbol{r_i}$ is the individual member's demand over capacity ratio according to the design code. $\boldsymbol{c_{pn}}$ and $\boldsymbol{e_{pn}}$ are the penalty coefficient and exponent, respectively. As their name implies, they provide means to penalize the optimization objective if the ratio $\boldsymbol{r}$ exceeded unity. $\boldsymbol{e_{pn}}$ serves as efficient means to greatly increase the penalty as $\boldsymbol{r}$ gets farther from unity while $\boldsymbol{c_{pn}}$ ensures that values of $\boldsymbol{r}$ get farther away from unity. In this study, the empirically-selected values of the penalty coefficient and exponent are 2.5 and 2, respectively.

3 PROBLEM FORMULATION FOR OFFSHORE JACKET STRUCTURE

The proposed optimization problem for the wind turbine supporting truss structure is quite complex as it aims at discovering the optimum geometrical configuration and shape as well as member sizes. The mathematical form of the problem can be expressed as follows:

$$\begin{aligned} &\text{Find} && A^T = \{A_1, \ A_2, ...A_n, x_s, y_s, z_s\} \\ &\text{To Minimize} && F = W(A, x_s, y_s, z_s) = \rho \sum_{i=1}^{n} L_i A_i \\ &\text{Subject to} && g_j^L \leq g_j(A) \leq g_j^U \qquad j = 1,2,...m \\ &\text{and} && A_i^{\min} \leq A_i \leq A_i^{\max} \qquad i = 1,2,...n \end{aligned} \tag{4}$$

Where Ai = the design variable i (member i cross-sectional area), (xs, ys, zs) are the members' end nodes coordinates, n = the number of the design variables, W(A) = the objective function (the structural weight), ρ = the material density, Li = the member length, m = the number of inequality constraints (g), $A_i^{\min}$ and $A_i^{\max}$ are the lower and the upper bound of the i^{th} variable respectively. The lower and upper bounds posed by Eq.(4) on the constraints include truss member stresses and joint displacements according to the specified design code.

Combining the objective and penalty functions together would yield the fitness function used in GADT:

$$\text{Min } F\left(A_i, x_i, y_i, z_i, c_{pn}, e_{pn}\right) = f(A_i, x_i, y_i, z_i) + p\left(A_i, x_i, y_i, z_i, c_{pn}, e_{pn}\right) \tag{5}$$

For practicality and to constraint the structure's space, the locations of the nodes in the x-y plane are, not allowed to change. Instead, the vertical location z of the node along the legs is allowed to change (see Figure 2b). Consequently, the slope of the legs, the length of members, and the weight of the structure are changing as well.

3.1 Quatropod Jacket

One of the most commonly used offshore wind turbine support systems is used herein to demonstrate the efficiency of the GADT algorithm. The developed code is applied to design a 3D quatropod jacket trusses subjected to various loading conditions. A total lumped mass of 3.4×10^5 kg representing the turbine mass is assumed on the top of the tower. The design constraints include truss joint displacements and member stresses. The supporting truss systems are analyzed for load combinations and designed for conditions specified according to the 2010 AISC-LRFD design code [27].

4 RESULTS AND DISCUSSION

The GADT algorithm is applied to the quatropod structure. The effect of the GADT control parameters (population size, penalty coefficient and exponent) on the optimum solutions is explored and the combination producing the best results are adopted. This 64-bar 3D truss structure is doubly-symmetric about the x- and y-axes. Thus, the truss members are linked in 14 member groups. Figure 2 shows the detailed description of these groups. Therefore, the optimization problem has 33 independent design variables and 32 (13 tension stresses, 13 compression stresses, and 6 displacements) constraints. Table 1 gives the best discovered solutions for the structure.

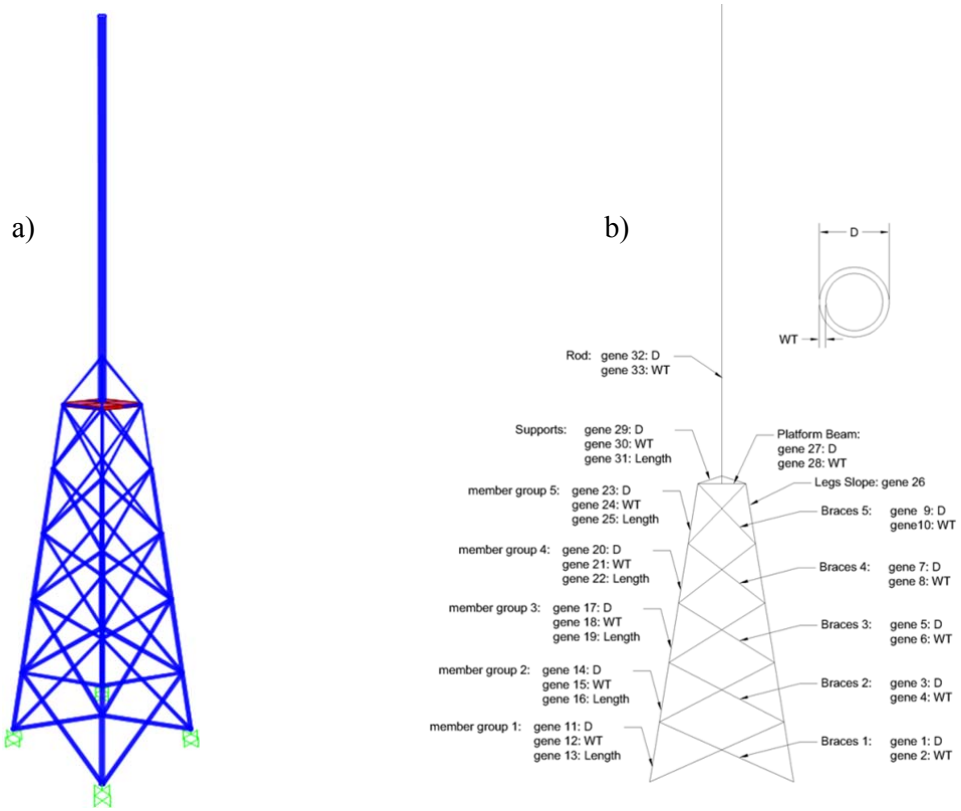


Figure 2: Wind turbine supporting truss structures: a) 3D View b) Description of the design groups (variables).

The best discovered optimum weight via GADT algorithm is found to be 4,227,300 kgf. The best solution is obtained after approximately 500 searches shown in Figure 3. The optimal solutions found by the GADT meet all constraints and have no active constraints.

Table 1: Optimal Design values for the 3D 64-bar space truss (quatropod jacket).

Optimal Design Variables (m)								
Variable		**BDV**	**Variable**		**BDV**	**Variable**		**BDV**[5]
1	D[1]	0.74	12	WT[2]	0.14	23	D	0.57
2	WT	0.055	13	L	13.53	24	WT	0.08
3	D	0.71	14	D	0.96	25	L[3]	13.50
4	WT	0.047	15	WT	0.12	26	S[4]	8.00°
5	D	0.64	16	L	11.75	27	D	0.59
6	WT	0.036	17	D	0.74	28	WT	0.07
7	D	0.55	18	WT	0.13	29	D	0.45
8	WT	0.037	19	L	13.91	30	WT	0.07
9	D	0.54	20	D	0.59	31	L	5.10
10	WT	0.035	21	WT	0.12	32	D	1.80
11	D	0.84	22	L	9.80	33	WT	0.06
Minimum Discovered Total Weight = 4,227,300 kgf								

[1]D: Diameter (outer); [2]WT: Wall Thickness; [3]L: Length; [4]S: Slope; [5]BDV: Best Discovered Value

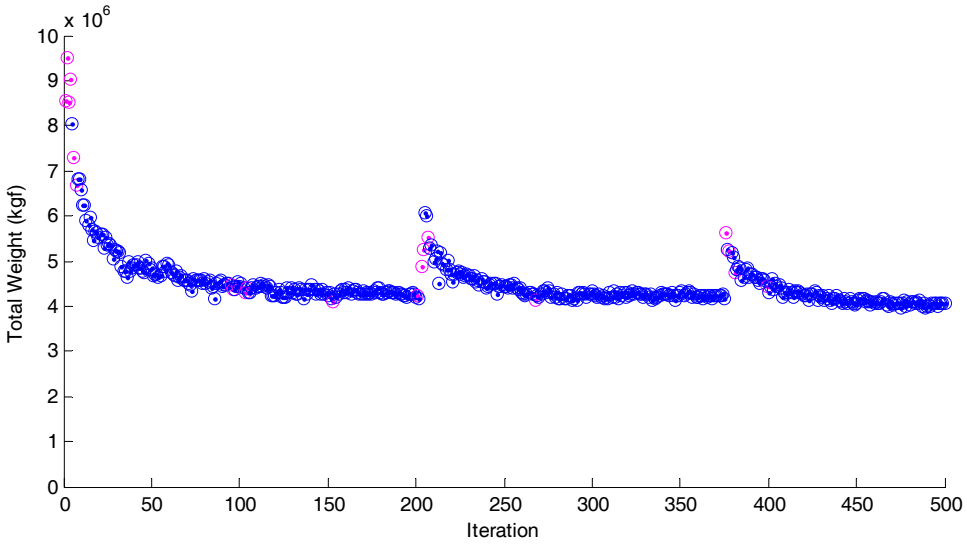


Figure 3: Path to convergence for the minimum weight of the quadropod structure.

5 SUMMARY AND CONCLUSIONS

A modified version of Genetic Algorithm with Domain Trimming (GADT) is presented in this study. The innovative technique is used to solve a least-weight topology and size optimization problem in the design of offshore wind turbine supporting structures. The GADT is used for solving the nonlinear optimization problem of 3D quatropod jacket offshore structure. In this optimum design formulation, the objective function is the material weight of the supporting truss; the design variables are the locations of the ends of the truss members as well as

the cross-sectional areas of the truss members; the constraints are the stresses in members and the displacements of the joints. The constraints were handled using non-stationary (dynamically modified) penalty functions. The quatropod jacket problem is subjected to gravity, wind, wave and earthquake loading conditions. The results show that the (GADT) method is efficient in finding the best discovered optimal solution.

REFERENCES

[1] N. Haritos, "Introduction to the Analysis and Design of Offshore Structures – An Overview," *Electronic Journal of Structural Engineering (EJSE)*, no. Special Issue: Loading on Structures, pp. 55–65, 2007.

[2] Q. Y. Duan, V. K. Gupta, and S. Sorooshian, "Shuffled complex evolution approach for effective and efficient global minimization," *Journal of Optimization Theory and Applications*, vol. 76, no. 3, pp. 501–521, Mar. 1993.

[3] N. D. Lagaros, M. Papadrakakis, and G. Kokossalakis, "Structural optimization using evolutionary algorithms," *Computers & Structures*, vol. 80, no. 7–8, pp. 571–589, Mar. 2002.

[4] Q. S. Li, D. K. Liu, A. Y. T. Leung, N. Zhang, and Q. Z. Luo, "A multilevel genetic algorithm for the optimum design of structural control systems," *International Journal for Numerical Methods in Engineering*, vol. 55, no. 7, pp. 817–834, Nov. 2002.

[5] Q. S. Li, D. K. Liu, J. Tang, N. Zhang, and C. M. Tam, "Combinatorial optimal design of number and positions of actuators in actively controlled structures using genetic algorithms," *Journal of Sound and Vibration*, vol. 270, no. 4–5, pp. 611–624, Mar. 2004.

[6] R. J. Balling, R. R. Briggs, and K. Gillman, "Multiple Optimum Size/Shape/Topology Designs for Skeletal Structures Using a Genetic Algorithm," *Journal of Structural Engineering*, vol. 132, no. 7, pp. 1158–1165, Jul. 2006.

[7] R. E. Perez and K. Behdinan, "Particle swarm approach for structural design optimization," *Computers & Structures*, vol. 85, no. 19–20, pp. 1579–1588, Oct. 2007.

[8] S. A. Barakat and S. Altoubat, "Application of evolutionary global optimization techniques in the design of RC water tanks," *Engineering Structures*, vol. 31, no. 2, pp. 332–344, Feb. 2009.

[9] G.-C. Luh and C.-Y. Lin, "Structural topology optimization using ant colony optimization algorithm," *Applied Soft Computing*, vol. 9, no. 4, pp. 1343–1353, Sep. 2009.

[10] S. Barakat and H. Ibrahim, "Application of shuffled complex evolution global optimization technique in the design of truss structures," in *2011 Fourth International Conference on Modeling, Simulation and Applied Optimization*, 2011, pp. 1–6.

[11] B. Zhang, Y. Wu, J. Lu, and K.-L. Du, "Evolutionary Computation and Its Applications in Neural and Fuzzy Systems," *Applied Computational Intelligence and Soft Computing*, vol. 2011, pp. 1–20, 2011.

[12] M. Kahraman and F. Erbatur, "A GA approach for simultaneous structural optimization," in *Structural engineering mechanics and computation International conference, Structural engineering mechanics and computation*, 2001, pp. 1147–1154.

[13] H. A. Eschenauer and N. Olhoff, "Topology optimization of continuum structures: A review," *Applied Mechanics Reviews*, vol. 54, no. 4, p. 331, Jul. 2001.

[14] M. P. Bendsoe and O. Sigmund, *Topology Optimization: Theory, Methods, and Applications*, 2nd ed. Berlin, Heidelberg: Springer Berlin Heidelberg, 2003.

[15] S. Joncas, M. J. de Ruiter, and F. van Keulen, "Preliminary Design of Large Wind Turbine Blades Using Layout Optimization Techniques," in *10th AIAA/ISSMO multidisciplinary analysis and optimization conference*, 2004.

[16] M. Jureczko, M. Pawlak, and A. Mężyk, "Optimisation of wind turbine blades," *Journal of Materials Processing Technology*, vol. 167, no. 2–3, pp. 463–471, Aug. 2005.

[17] R. Zakhama, M. M. Abdalla, Z. Gürdal, and H. Smaoui, "Wind load effect in topology optimization problems," *Journal of Physics: Conference Series*, vol. 75, no. 1, p. 012048, Jul. 2007.

[18] P. Brøndsted, J. W. Holmes, and B. . Sørensen, "Wind rotor blades materials technology," *European Sustainable Energy Review*, vol. 2008, no. 2, pp. 36–41, 2008.

[19] S. Joncas, "Thermoplastic composite wind turbine blades; an integrated design approach," Technische Universiteit Delft, 2010.

[20] L.-C. Forcier and S. Joncas, "New Structural Design Concepts for Large Thermoplastic Wind Turbine Blades Using Structural Optimization Techniques," in *51st AIAA/ASME/ASCE/AHS/ASC Structures, Structural Dynamics, and Materials Conference*, American Institute of Aeronautics and Astronautics, 2010.

[21] W. LIU and Y. Zhang, "Network Study of Plant Leaf Topological Pattern and Mechanical Property and its Application," *Advances in Natural Science*, vol. 3, no. 2, pp. 82–92, 2010.

[22] N. Buckney, A. Pirrera, S. D. Green, and P. M. Weaver, "Structural efficiency of a wind turbine blade," *Thin-Walled Structures*, vol. 67, pp. 144–154, Jun. 2013.

[23] N. Buckney, S. Green, A. Pirrera, and P. M. Weaver, "On the structural topology of wind turbine blades," *Wind Energy*, vol. 16, no. 4, pp. 545–560, May 2013.

[24] "MATLAB Release 2013a." The MathWorks, Inc., Natick, Massachusetts, United States, 2013.

[25] "SAP2000 ver. 16." Computers and Structures, Inc., Berkeley, California, USA, 2014.

[26] O. M. M. Nassif, "Optimization of Natural Rubber Seismic Isolation Systems with Supplemental Viscous Damping for Near-Field Ground Motion," College of Higher Studies and Research, University of Sharjah, 2014.

[27] American Institute of Steel Construction (AISC), "Specification for Structural Steel Buildings," *ANSI/AISC 360-10*, 2010.

COMPDYN 2015
5th ECCOMAS Thematic Conference on
Computational Methods in Structural Dynamics and Earthquake Engineering
M. Papadrakakis, V. Papadopoulos, V. Plevris (eds.)
Crete Island, Greece, 25–27 May 2015

EVALUATION OF SEISMIC RESPONSE OF BUILDINGS USING DYNAMIC ANALYSIS ON STICK MODELS

Marco Bovo[1], **Marco Savoia**[2]

[1] DICAM - University of Bologna
Viale Risorgimento, 2 - 40136 Bologna (BO)
marco.bovo@unibo.it

[2] DICAM - University of Bologna
Viale Risorgimento, 2 - 40136 Bologna (BO)
marco.savoia@unibo.it

Keywords: Stick model, Equivalent structural model, Seismic response evaluation, Time-history procedures, FEMA440.

Abstract. *A new methodology for the study and evaluation of the seismic response of buildings is presented in this paper. The method involves the use of nonlinear time-history analysis on equivalent multi-degrees of freedom stick models, defined according to the classification given in FEMA440 Report. The steps for implementing the method and obtaining the equivalent model are described in the article. For the validation of the method, the results obtained from the stick models were compared to that obtained by time-history analysis on detailed finite element models of the structures (using the definition of detailed model described in FEMA440). The engineering parameters considered in the comparison are top displacements, interstorey drifts, forces at the floor and base shear. The results of the conducted analyses on the equivalent stick models match satisfactorily, in an excellent way in certain cases, those of the analyses carried out on detailed models. The time-history analyses on the stick models, allowing a considerable saving in terms of both computational effort and time for numerical solution and post-processing of results, could make this kind of analysis more attractive and feasible for a daily design, and comparable in terms of costs with pushover procedures.*

1 INTRODUCTION

The evaluation of dynamic response of a structural system and the interpretation of results obtained are the key aspects in the study of a building subjected to seismic action, both in the case of new building design and for the seismic assessment of existing buildings. To this regard, in the early nineties, innovative design criteria based on respect of structural performance criteria were introduced, not only for ultimate limit state analysis but also related to the containment of damage resulting from seismic events [1].

In the light of this, the design criteria based on performance requirements related to the displacements, have led to the definition of "displacement-based design" procedures [2]. The need to properly estimate the displacements resulting from the seismic action, using simplified models of the structure, however, is an issue introduced earlier.

Linked to the problem of limiting the computational efforts in the study of inelastic structures, the attention of researchers was soon addressed to look for simplified equivalent methods able to correctly represent the global response of structures. To this regard it seems useful to quote the Substitute Damping Method proposed in [3], the Method of the Substitute Structure introduced in [4], the Q-Model [5] and the Multi-Rigid-Body Method [6] which, starting from the theory of rigid bodies, defines an equivalent discrete multi-degrees of freedom (MDOF) model for the study of dynamic response of shear-type frames.

Between the various simplified model proposed from the researchers, one of the recurring assumption is to search for an equivalent single-degree of freedom (SDOF) model, that usually is adopted instead of the complete model in the seismic analysis, with the objective to estimate, albeit approximately, the maximum displacements at the top of the structure and the maximum (positive or negative) value of shear force at the base of the structure. This simple model, if on one hand allows an important save of computational efforts, on the other can sometimes introduce considerable errors due to the MDOF effects usually not considered in the SDOF model.

The equivalent model proposed here is a MDOF model with three degrees of freedom associated to each floor: the allowed movements are two translations in the plane of the slab and one rotation around the vertical axis, orthogonal to the mid-plane of the floor. In summary, being N the number of floors of the structure at hand, the numerical model has a total of 3N degrees of freedom.

2 DESCRIPTION OF THE EQUIVALENT STICK MODEL METHOD

The present paper describes a new structural model for the evaluation of nonlinear seismic behavior of framed buildings. The method involves the definition of an inelastic equivalent model characterized by few degrees of freedom, classified as stick model in the FEMA440 Report [7], and obtained starting from a detailed model of the same structure.

The Equivalent Stick Model (ESM), introduced in [8], is based on the determination of the capacity curves of each floor by incremental static analysis, and assigning each curve to the corresponding degree of freedom. The proposed model is then incorporated in a broader context of a procedure called Equivalent Stick Model Method (ESMM), implementing the ESM model in the resolution of nonlinear time-history analysis. The new methodology proposed here consists of the following main steps:

1) Implementation of the structural detailed model;
2) Determination of the capacity curves for each floor;
3) Definition of the cyclic (hysteretic) behaviour of each degree of freedom;
4) Determination of the mass to be assigned to each degree of freedom;
5) Assembling the equivalent stick model (ESM);

6) Time-history analysis on stick model;
7) Determination of dynamic structural response;
8) Estimation of local parameters from the detailed model.

The first five steps lead to the determination of the equivalent model; the other three provide the procedure for the application of the model in the proposed method. In the following, the procedure to achieve the ESM model will be first described and, subsequently, that for its application in the framework of the proposed methodology used for the assessment of structural seismic response. Furthermore, for a first validation of the method, two case studies are described and analyzed. The results reported provide useful indication on the reliability of the proposed method.

2.1 Implementation of the structural detailed model

The implementation of the detailed model, in accordance with the classification given in [7], allows to assess the dynamic parameters of the real structure (frequencies, periods, modal shape, participation factors). The detailed model must fit in terms of distribution of stiffnesses, masses and strengths, with the real structure since, from it, the capacity curves of each floor will be then achieved.

2.2 Determination of the capacity curves for each floor

As one of the fundamental aspects of the procedure, the seismic induces horizontal displacements of each point of a floor are determined by the generalized displacements (displacements and rotation) of a node identified as representative of the floor. The movements of a floor will be two translations in the horizontal plane and a rotation around the vertical axis. The idea of statically condensing the movements of an entire floor in the movements of a single point, considered as representative, is correct only if the floor has a sufficiently high (theoretically infinite) in-plane stiffness.

The selected representative point is the geometric center of mass CM of the floor. It is also assumed that the centers of mass of all the floors are aligned along the axis perpendicular to the slab. The behavior of each floor is identified by three inelastic curves, obtained by nonlinear static incremental analysis, with a prescribed force distribution. In [8] different types of forces distribution were tested: proportional to the translational mass; proportional to a uniform accelerations distribution; proportional to the shear distribution obtained from one or more vibration modes.

The capacity curves related to each floor are in the form "Force-Displacement" for the two translational degrees of freedom while in the form "Torque-Rotation" for the rotational degree of freedom. Force and torque of the curve are those statically applied in the incremental analysis, while displacement and rotation are those registered at the representative point.

2.3 Definition of the behaviour of each degree of freedom

After determining the three backbone capacity curves for each storey, must be defined a damage criteria to take into account the degradation behavior of the structure due to cyclic action. The choice of the most suitable hysteretic model to be adopted depends on the damaging phenomena to be included. In the present work, in order to simplify the capacity curves obtained via incremental analysis, a tetra linear polygonal curve has been adopted. In addition, to represent the cyclic degradation effects, a peak-oriented hysteretic behaviour has been chosen. With the described assumptions, the response of the structural system is calculated by moving along the backbone curve during virgin loading with unloading and reloading process

that moving through the opposite side of the diagram, points to the value of maximum (or minimum) displacement reached in the past steps of the analysis (see Figure 1).

2.4 Determination of the mass assigned to each degree of freedom

The mass values attributed to the three nodal degrees of freedom of each floor are the translational mass and the rotational moment of inertia of the storey. The calculation of the translational mass of each floor is carried out according to the following rules:

- the mass relative to dead load and live load directly applied on the floor are attributed to the floor itself;
- the mass of structural elements that connect two consecutive storeys is divided equally on two storeys;
- the mass of non-structural elements between two consecutive storeys is attributed equally if they are firmly fixed at both ends, otherwise they are entirely allocated to the underlying floor.

The calculation of rotational moment of inertia to be attributed to the considered floor is made in respect of the following rules:

- the mass considered is the same determining the translational mass;
- the rotational moment of inertia is obtained considering the various distances computated from the center of mass to the actual geometrical position of the elements in the floor.

2.5 Assembling the equivalent stick model (ESM)

The finite element adopted in the definition of the equivalent stick model is a classical lumped plasticity element, having a linear elastic component in series with two inelastic hinges to the extremities. The capacity curves previously obtained are used to define the properties of the elastic portion and the behaviour of inelastic hinges. The boundary conditions adopted are total restraint prescribed at the base section of the model and rotational restraint (along the X-dir and Y-dir) prescribed at each floor level. The generic stick model resulting is schematically shown in Figure 2.

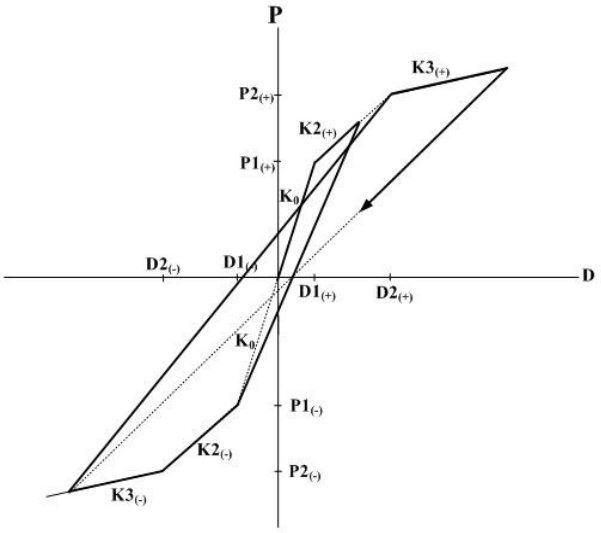


Figure 1: Peak-oriented tetra linear curve modeling the cyclic behaviour of a floor.

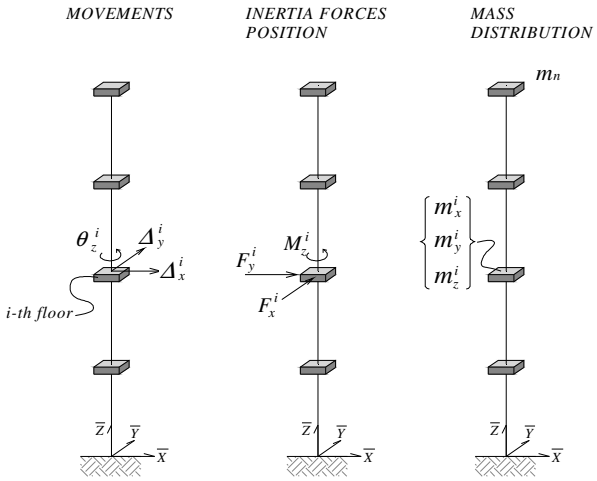


Figure 2: Assembling of the stick model.

2.6 Time-history analysis on stick model

After defined the equivalent structural model, the next step is to conduct the nonlinear time-history analysis for the determination of the seismic response of the structure. The seismic input is a accelerogram applied to the base section of the model, or a pair of accelerograms if the effects of bi-directionality of the earthquake are of interest.

2.7 Determination of dynamic structural response

By means of time-history analysis, the displacements history of each degrees of freedom of the model can be derived, and consequently, the history of global parameters of interest (i.e. referring to the structure) be obtained, such as absolute displacements or interstorey displacements; the same applies to the torsional rotations that provide an estimate of the inelastic seismic demand of rotation on the various floors. Similar considerations can be made with reference to the forces since, from the time-history analysis, it is possible to obtain the storey shear (or storey force) rather than the base shear.

2.8 Estimation of local parameters from the detailed model

The dynamic seismic demand for the individual elements (beams or columns) both in terms of displacements and forces, can be obtained from the detailed model discussed before. In fact, starting from the maximum (or minimum) value of displacement or storey shear required by the seismic input to the stick model, it is possible to determine the corresponding step of the incremental analysis, conducted on the detailed model and discussed at Section 2.2. The value of parameters of interest at that specific step can be considered as an estimate of the value that would be obtained by solving the time-history analysis directly on the detailed model. To set up the structural verification, if of interest, the determination of displacement capacity or strength capacity for the elements, may be obtained following one of the methods prescribed by codes, as well as from the elaboration of data obtained by experimental tests available in the literature [9].

3 VALIDATION OF THE MODEL BY NUMERICAL ANALYSIS ON CASE STUDIES

3.1 Case studies description

For the validation of the reliability of the procedure ESMM and of the adequacy of the ESM to predict the seismic demand, two buildings were selected and time-history analyses were conducted on both equivalent stick models and detailed models. The latter are considered as the reference solutions, able to provide the "correct" seismic response of the structures. In the present work, the two case studies are presented: a one-storey structure, symmetrical in both directions; a three-storey structure, symmetrical in both directions. The two buildings have the same plan, with dimensions of 6.0m x 6.0m and interstorey height of 3.0m. A total fixed constraint was prescribed at the base of the columns of the structures.

3.2 Modelling assumption

The detailed model of the structure was built by means of distributed plasticity finite elements, with transversal fibers section. Four integration points for each element have been used. For confined and not confined concrete the model of Kent and Park [10] was adopted as modified in [11]. The model, adequate for monotonically and increasing load, is completed with the unloading and reloading model of Karsan and Jirsa [12], suitable for analyses with cyclic loading. For the steel of reinforcement bars the model of Menegotto and Pinto [13] was used. Table 1 and Table 2 show the properties of the materials adopted and the coefficients used to define the inelastic behavior of the sections according to the mentioned models.

CONCRETE	f'_c [MPa]	K	ε_{co}	ε_{cu}	Z
Confined concrete	25.0	1.0	0.002	0.006	266.67
Not confined concrete	25.0	1.0	0.002	0.0035	1600.0

Table 1: Adopted parameters for the definition of cyclic behaviour of concrete according to [11,12].

STEEL	f_y [MPa]	E [MPa]	b	R_o	a_1	a_2
Steel	500	200000	0.005	20	18.5	18.5

Table 2: Adopted parameters for the definition of cyclic behaviour of steel according to [13].

3.3 Selection of the seismic input

In the present paper, four registered accelerograms have been used (see Table 3). Not scaled, rather than scaled in terms of PGA (Peak Ground Acceleration), were applied to both models (detailed and ESM), to test the reliability of the ESMM procedure for different intensities of the seismic event. The modeling and the dynamic analyses were carried out by means of software MIDASGen [14].

Seismic input id.	Earthquake	Registration station	Year	PGA [g]
Earthquake n.1	El Centro	El Centro Site, 270 deg	1940	0.3569
Earthquake n.2	Loma Prieta	Oakland Outer Wharf, 0 deg	1989	0.2199
Earthquake n.3	Taft	Lincoln School, 69 deg	1952	0.1557
Earthquake n.4	Northridge	City Hall, 0 deg	1994	0.3703

Table 3: Seismic input adopted in the time-history analysis.

4 CASE STUDY N.1: ONE-STOREY SYMMETRICAL STRUCTURE

The structure has columns with 60cm × 25cm transversal dimensions of and beams with cross section of 50cm × 25cm (WxH). In the detailed model, the sections have the fibers division shown in Figure 3, while the force distribution on the floor is shown in Figure 4. The floor is modeled by reinforced concrete shells element with 20cm thickness. In the analysis of the detailed model, the following vertical loads were considered: for the elements of RC frames a specific weight of 25kN/m³ was assumed; a dead load uniformly distributed on the floor of 6 kN/m²; a live load of 0.6 kN/m².

Since the structure has a single floor, the capacity curves to be determined for the stick model are three, one for each degree of freedom of the stick model. In the simplified case of unidirectional earthquake acting in X direction, the only kinematic parameter to be considered is the displacement Δ_x in X-dir.

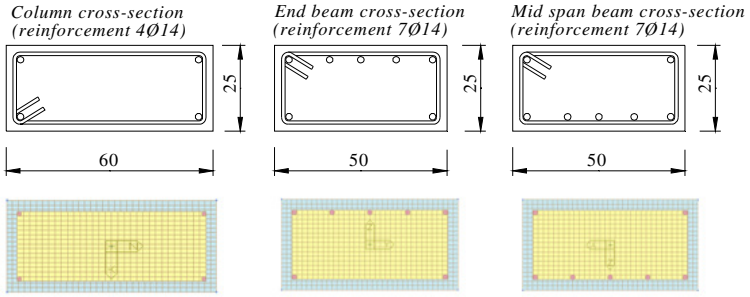


Figure 3: Case study n.1: cross section of columns and beams and their fiber discretization adopted in the detailed model.

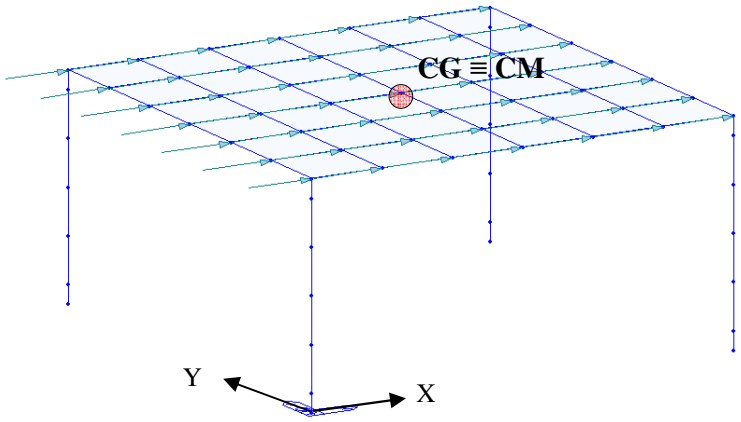


Figure 4: Case study n.1: force distribution applied to obtain the capacity curve of floor.

The capacity curve in the X-dir is obtained by applying an increasing horizontal forces distribution applied at the floor level (see figure 4), proportional to the storey shear resulting from the first mode of vibration in the X-dir. The capacity curve F_X-Δ_X, obtained by increasing the force distribution and conducting a nonlinear static analysis, is shown in Figure 5. The curve, gives on the abscissa axis the displacement in the X-dir of the representative point of the floor (center of mass CM of the floor) and on the ordinate axis the resultant of the distribution of forces acting on X-dir.

In Figure 5, the polygonal tetra linear curve used to approximate the numerical one is superimposed. This curve is then used to obtain the relation to be assigned to the plastic hinges of the stick model. The mass allocated to the single degree of freedom of the stick model is equal to m_X^1=35811.8kg. The elastic properties of the finite elements of the stick model are defined in such a way to obtain an equivalent model with the same frequencies of the detailed model. Figure 6 summarizes the key features of the equivalent stick model obtained.

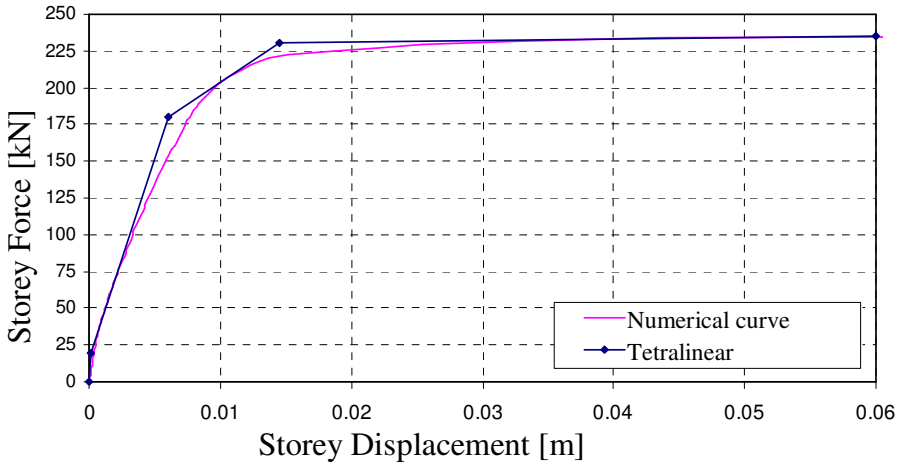


Figure 5: Case study n.1: capacity curve Fx-Δx and tetra linear approximation.

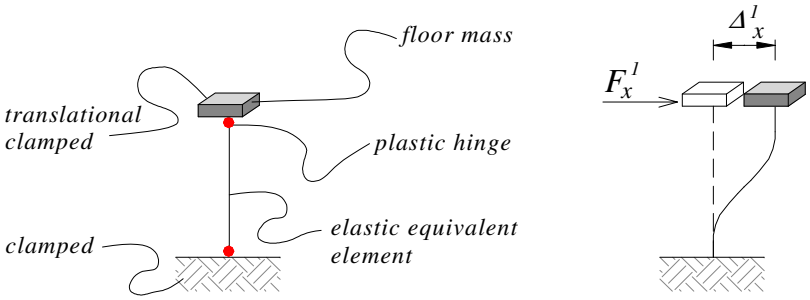


Figure 6: Case study n.1: equivalent stick model.

To validate the model, dynamic analyses were performed on both models (stick and detailed) and the results obtained were compared. The parameters of interest and used in the comparison, are the displacements of the representative node of the floor monitored on the detailed model (displacement of CM) and the displacements of the top node of the stick model. Moreover, the base shear forces are compared. For the specific cases, the sum of the base shear force of each column for the detailed model and the base shear force registered at the single vertical element for the stick model were compared. In Figure 7 and Figure 8, the results in terms of "storey shear-storey displacement" are shown with reference to the Earth-

quake n.1 and Earthquake n.2 in Table 3. For the Earthquake n.2, the result obtained using a Scale Factor SF=2.65 is shown in Figure 9. Figure 10 and Figure 11 show, respectively, the trend of displacement and storey shear, during the time, for Earthquake n.1. The results show that, even for dynamic actions that impose to the structure a strongly inelastic deformation scenarios, the stick model provides accurate results when compared with those of the detailed model. The comparison in terms of "storey shear-storey displacement" is also reported in Figure 12, obtained by superimposing the structural response of dynamic analysis (time-history) and that of nonlinear static analysis both conducted on the detailed model.

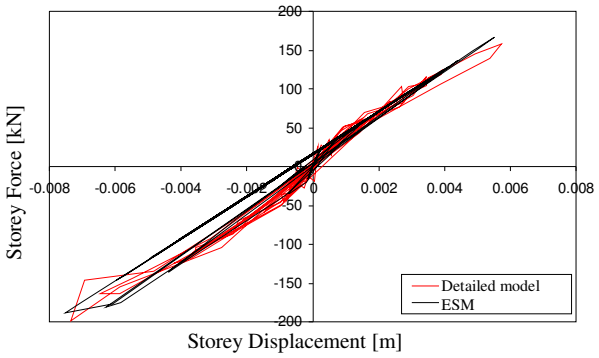


Figure 7: Case study n.1: storey shear-Storey displacement for the Earthquake n.1

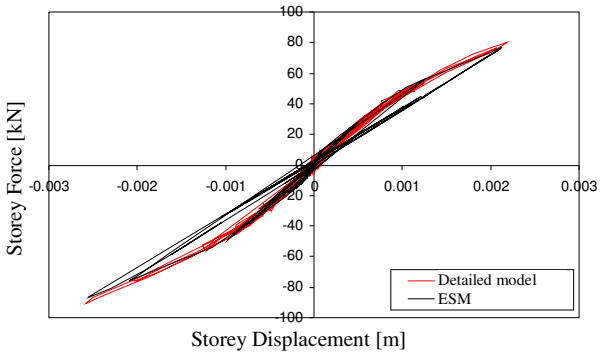


Figure 8: Case study n.1: storey shear-Storey displacement for the Earthquake n.2 - SF=1

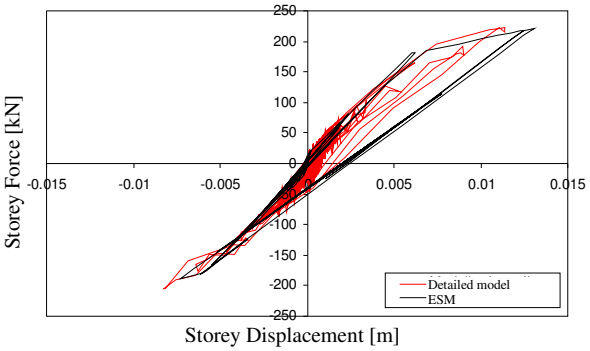


Figure 9: Case study n.1: storey shear-Storey displacement for the Earthquake n.2 - SF=2.65

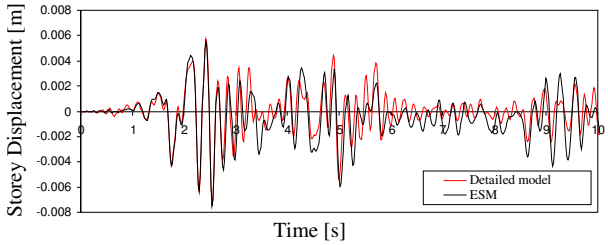


Figure 10: Case study n.1: storey displacement - time for the Earthquake n.1.

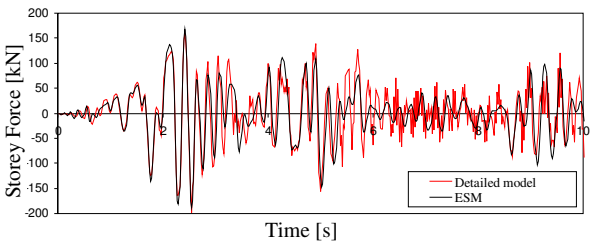


Figure 11: Case study n.1: storey shear - time for the Earthquake n.1.

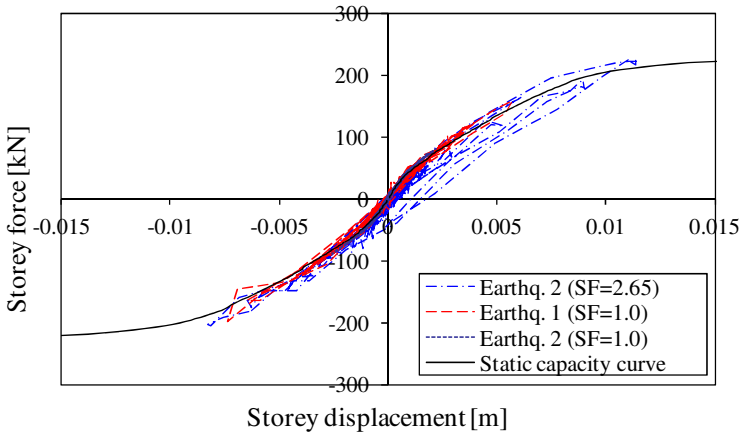


Figure 12: Case study n.1: static capacity curve and dynamic demand (Earthquake n.1 and Earthquake n.2) from the analysis on detailed model.

This comparison suggests that the curve obtained via static analysis (capacity curve) is a satisfactory approximation of the dynamic request (seismic demand) of the seismic action on the structure. The values of the quantities determined by stick model allow to obtain, for the individual seismic input, the dynamic request in terms of shear and displacement to the storey. The seismic request can be used to set the necessary verification from both local (element or section) and global (structure) point of view. In fact, it is possible to set a procedure for the determination of stress and deformation of a single element rather than a section. For example, with reference to the maximum (positive and negative) horizontal displacement imposed to the representative node of the slab and in the absence of torsional rotations (as in the present case), the displacement imposed at the top of each column is known. Reporting this displacement value on the floor capacity curve, it is possible to pick out the load step of the incremental analysis where this displacement is reached. From the analysis of force and deformations obtained on the detailed model for that load increment, it is possible to determine the structural response at the instant of maximum displacement demand. The values of force and displacement by static analysis may be regarded as an estimate of that obtained for the element (or section) from a time-history on the detailed model.

5 CASE STUDY N.2: THREE-STOREY SYMMETRICAL STRUCTURE

The structure has columns with 60cm × 25cm cross-section and beams with 50cm × 25cm (WxH) cross-section. The sections were divided into fibers in both directions, as shown in Figure 13. The slab modeling is the same of the previous case study.

Since three floors are present, the capacity curves to be determined in order to define the stick model are nine. For a unidirectional earthquake acting in X-direction, the determination of the three capacity curves in the X-dir are enough for the description of the structure. The three curves at hand were obtained again by a static incremental analysis with the application of a distribution of forces proportional to the distribution of the storey shear forces calculated by linear dynamic modal analysis. In the present case, the force distribution from principal vibration mode in the X-dir was considered (see Figure 14).

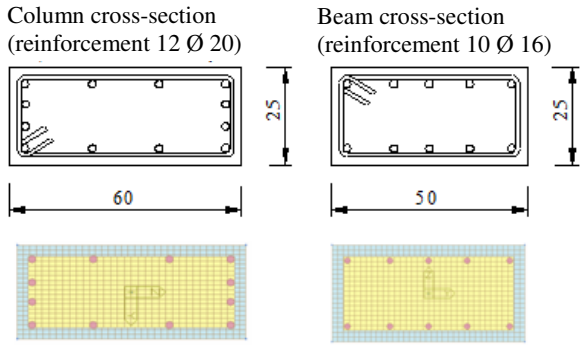


Figure 13: Case study n.2: cross-section of columns and beams and their fiber discretization adopted in the detailed model.

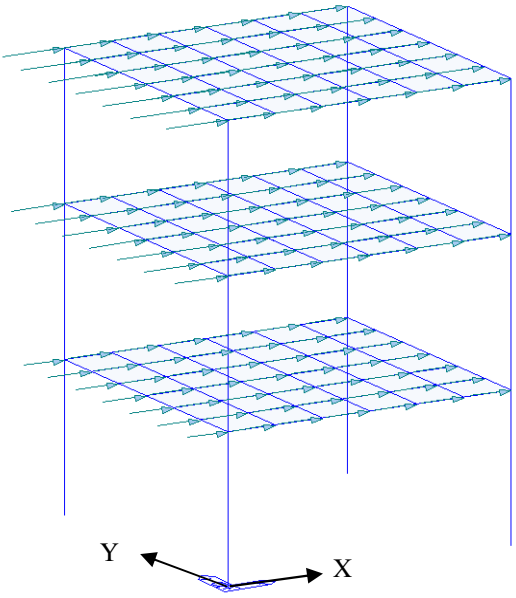


Figure 14: Case study n.2: force distribution applied to obtain the capacity curves of each floor.

The capacity curve "storey force-interstorey displacement" $SF_X^{(1)}$-$\Delta_X^{(1)}$, obtained for the floor n.1 (the lower of the three), is shown in Figure 15 as an example. In the same figure, the tetra linear approximating curve used for the set up of the stick model is superimposed.

The mass located at each one of the three degrees of freedom is considered equal to $m_X^{(1)}=m_X^{(2)}=35940$kg and $m_X^{(3)}=33690$kg. Even in this case, the elastic properties of the finite elements of the stick model are established in such a way to obtain, the same frequencies of the detailed model. Figure 16 summarizes the key features of the equivalent stick model.

In the following, some results of time-history conducted on both the structural models (detailed and stick) are reported.

Figures 17a, 17b, 17c and 17d show the results for the floor n.1 in terms of "storey shear-interstorey displacement" with reference to the four earthquakes considered (see Table 3).

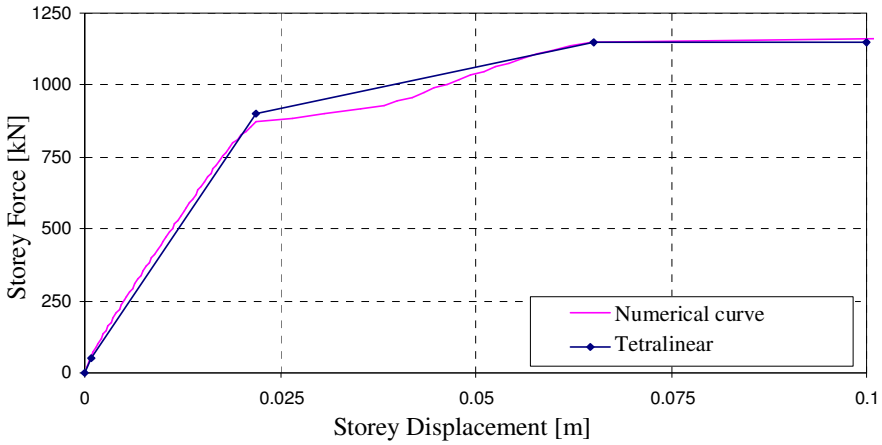


Figure 15: Case study n.2: capacity curve SF_x-Δ_x of floor n.1and tetra linear approximation.

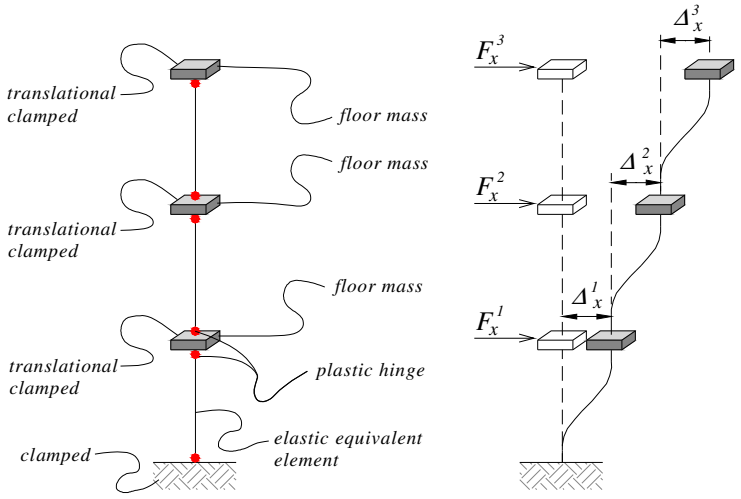


Figure 16: Case study n.2: equivalent stick model.

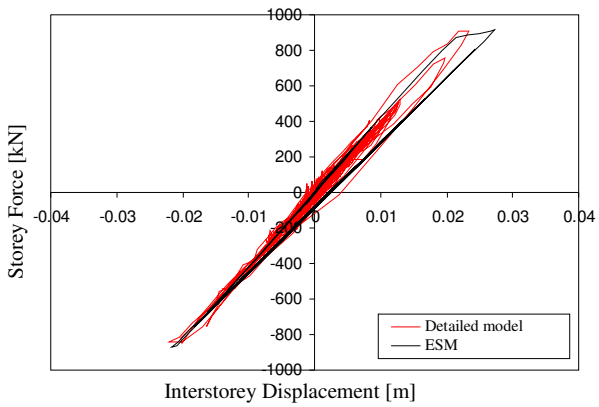


Figure 17a: Case study n.2: storey shear -interstorey displacement of floor n.1 for the Earthquake n.1 (SF=1.5)

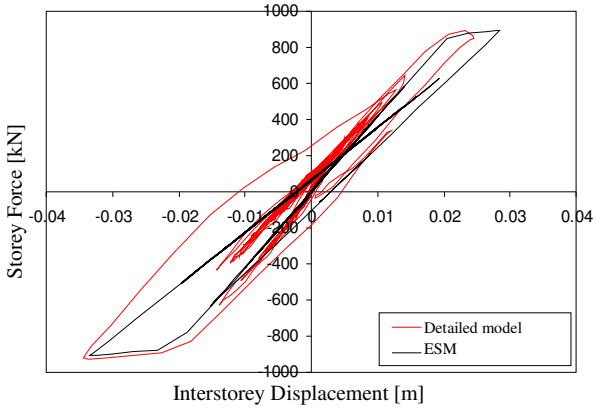


Figure 17b: Case study n.2: storey shear - interstorey displacement of floor n.1 for the Earthquake n.2 (SF=3)

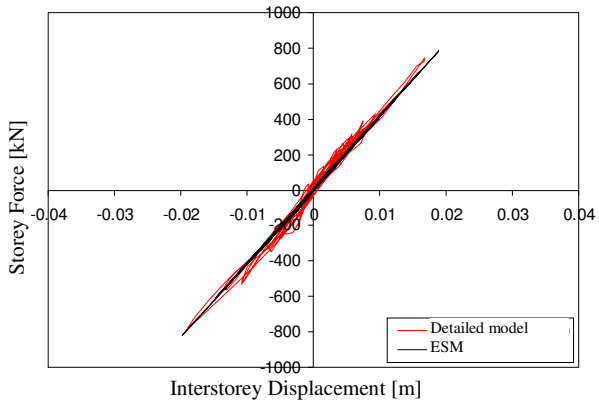


Figure 17c: Case study n.2: storey shear -interstorey displacement of floor n.1 for the Earthquake n.3 (SF=3)

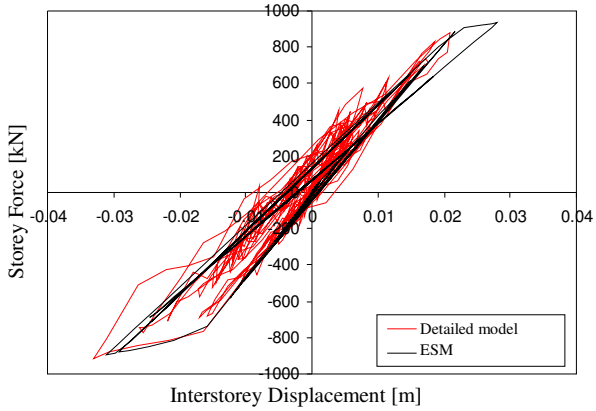


Figure 17d: Case study n.2: storey shear - interstorey displacement of floor n.1 for the Earthquake n.4 (SF=2.5)

Figure 18 and Figure 19 show the same quantities, but referred respectively to floor n.2 and floor n.3 for the Earthquake n.1.

In Figure 20 and Figure 21 the time-variation of displacement and storey shear, for the floor n.1 under the action of Earthquake n.1 are illustrated. Such figures show that ESM is able to reproduce, with good approximation, the dynamic global behavior of the structure, matching satisfactorily with the maximum values required at various levels from the "reference" solution, both in terms of displacement and force estimation. The results obtained show that, even for seismic excitations imposing to the structure a deformation scenarios abundantly beyond the elastic range, the model maintains good precision. It is also to be noted that a very simple hysteretic law, such as that adopted, appears to represent with enough accuracy the dynamic behavior of the structure at hand.

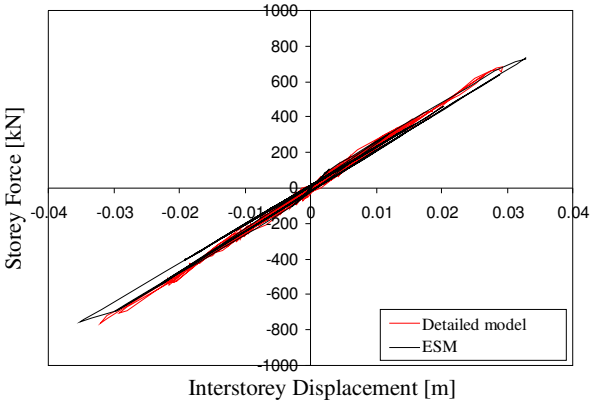


Figure 18: Case study n.2: storey shear -interstorey displacement of floor n.2 for the earthq. 1 (SF=1.5).

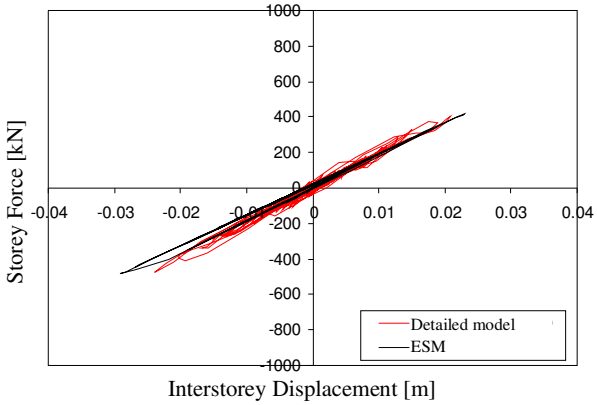


Figure 19: Case study n.2: storey shear - interstorey displacement of floor n.3 for the earthq. 1 (SF=1.5).

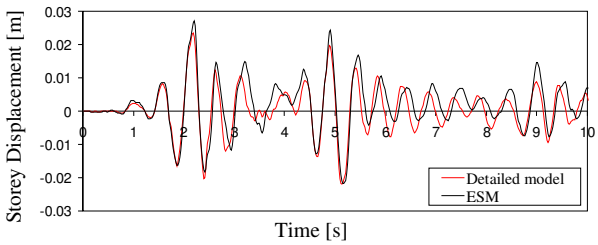


Figure 20: Case study n.2: interstorey displacement VS time for floor n.1 for the Earthquake n.1 (SF=1.5).

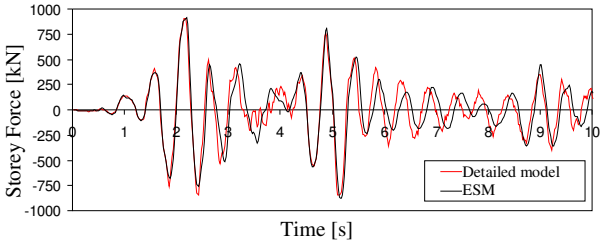


Figure 21: Case study n.2: storey shear VS time for the floor n.1 for the Earthquake n.1 (SF=1.5).

Finally, Figure 22 summarizes the comparison in terms of "storey shear-interstorey displacement", for floor n.1, superimposing the responses obtained by time-history analyses and static incremental analysis both conducted on detailed model. As for the previous case, the capacity curve obtained by static analysis represents an acceptable approximation of the seismic dynamic demand both in terms of force and displacements. More faithful is the static curve matching the dynamic response, more accurate will be the equivalent stick model obtained by the procedure.

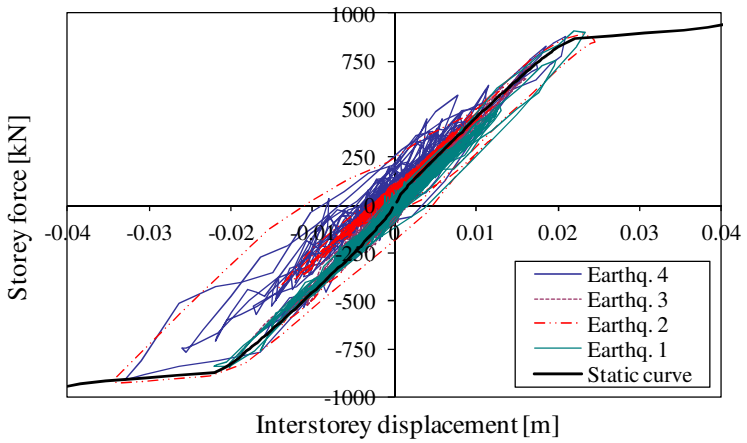


Figure 22: Case study n.2: static capacity curve and dynamic demand (Earthquake n.1, n.2, n.3, n.4) for the analysis on detailed model.

6 COMPARISON IN TERMS OF COMPUTATIONAL EFFORTS

The particular benefits and peculiarities of the proposed method lies in the fact that, leading to the definition of a numerical model with reduced number of degrees of freedom allows to set up dynamic analyses extremely advantageous from a computational point of view. Table 4 and Table 5 show the comparison between the computational time needed to solve the nonlinear time-history, presented earlier. The computational time and post-processing necessary to obtain time-history results on the structural stick model turn out to be far fewer than those required to perform the same analysis on the detailed model. The computational time required by the ESMM procedure, and consisting in the definition of the equivalent stick model, is negligible if compared to the computational savings, even if a limited number of time-history is to be performed.

	Detailed model			ESM
Seismic input	Solving [s]	Post-processing [s]	Total time [s]	Total time [s]
Earthq. n.1 (SF=1)	1026	1022	2048	0.37
Earthq. n.2 (SF=1)	700	838	1538	0.28
Earthq. n.2 (SF=2.65)	717	764	1481	0.29

Table 4. Case study n.1: computational time required to solve the time-history analysis.

	Detailed model			ESM
Seismic input	Solving [s]	Post-processing [s]	Total time [s]	Total time [s]
Earthq. n.1	2927	2081	5008	0.80
Earthq. n.2	2229	1556	3785	0.57
Earthq. n.3	2990	2062	5052	0.73
Earthq. n.4	3547	5580	9127	0.70

Table 5. Case study n.2: computational time required to solve the time-history analysis.

7 CONCLUSIONS

For the considered case studies, used for a preliminary validation of the method, the results obtained by the ESMM procedure are generally in good agreement, excellent in some cases, with those obtained by the same analysis but conducted on a structural detailed model. The engineering parameters assessed by the described procedure, both global (with reference to the entire structure or its floor) and local (with reference to an element or a section), can be used effectively to set verification in terms of strength or displacement. As regard the choice of the hysteretic behaviour of a floor, the numerical results presented show that a simple model, computationally cheap, such as the adopted peak-oriented type, leads to good results. This aspect will be further investigated in future research.

The lower computational efforts, if compared to time-history analyses on detailed models, and the lower level of uncertainty with respect to other seismic analysis methods (pushover), place the ESMM procedure in an interesting intermediate position between the existing procedures usually adopted to assess the seismic response of buildings.

The ESM model and the proposed ESMM methodology seem therefore suitable to be used, as new tools of analysis and design, for the estimation of the dynamic response of framed structure buildings.

ACKNOWLEDGEMENTS

The present investigation was developed within the activities of the (Italian) University Network of Seismic Engineering Laboratories - ReLUIS in the research program funded by the (Italian) National Civil Protection - Progetto Esecutivo 2014 - Research Line “Reinforced Concrete Structures”, WP2.

REFERENCES

[1] T.F. Paret, K.K. Sasaki, S.A. Freeman, Performance-based engineering: can the engineering profession deliver the goods?. *Proc. 6th U.S. National Conference on Earthquake Engineering*, Seattle, Washington, May 31-June 4, 1998.

[2] J.P. Moehle, Displacement-Based Design of RC Structures Subjected to Earthquakes, *Earthquake Spectra*, **8**(3), 403-428, 1992.

[3] P. Gulkan, M.A. Sozen, Inelastic responses of reinforced concrete structure to earthquake motions. *ACI Structural Journal,* **71**(12), 604-610,1974.

[4] A. Shibata, M.A. Sozen, Substitute-Structures Method for Seismic Design in R/C. *Journal of the Structural Division*, ASCE **102**(1), 1-18, 1976.

[5] M. Saiidi, M.A. Sozen, Simple and Complex Models for Nonlinear Seismic Response of Reinforced Concrete Structures. Civil Engineering Studies. *Technical Report No. UILU-ENG-79-2013. Structural Research Series No. 465*, University of Illinois, Urbana-Champaign, 1979.

[6] M. Lai, Y.L. Zhang, C. Zhang, Analysis method of multi-rigid-body model for earthquake responses of shear-type structure. *Proc. 10th World Conference on Earthquake Engineering*, Madrid, Spain, 1992.

[7] FEMA440, *Improvement of Nonlinear Static Seismic Analysis Procedures*. Federal Emergency Management Agency. Washington D.C., June 2005.

[8] M. Bovo, *Inelastic equivalent model for the evaluation of seismic response of buildings.* PhD Dissertation. University of Bologna, 2013.

[9] T.B. Panagiotakos, M.N. Fardis, Deformations of reinforced concrete members at yielding and ultimate. *ACI Structural Journal*. **98**(2), 135-148, 2001.

[10] D.C. Kent, R. Park, Flexural Members with Confined concrete. *Journal of the Structural Division*, ASCE **97**(7), 1969-1990, 1971.

[11] B.D. Scott, R. Park, M.J.N. Priestley, Stress-strain behavior of concrete confined by overlapping hoops at low and high strain rates. *ACI Structural Journal*, **79**(1), 13-27, 1982.

[12] I.D. Karsan, J.O. Jirsa, Behavior of concrete under compressive loading. *Journal of the Structural Division*, ASCE **95**(12), 2543-2563, 1969.

[13] M. Menegotto, P.E. Pinto, Method of analysis for cyclically loaded R.C. plane frames including changes in geometry and non-elastic behavior of element under combined normal force and bending, *Proc. IABSE Symp. of Resistance and Ultimate Deformability of Structures Acted on by Well-Defined Repeated Loads*. International Association of Bridge and Structural Engineering, Lisbon, Portugal, 1973.

[14] MIDAS, *http://eng.midasuser.com* (web site), 2012.

COMPDYN 2015
5th ECCOMAS Thematic Conference on
Computational Methods in Structural Dynamics and Earthquake Engineering
M. Papadrakakis, V. Papadopoulos, V. Plevris (eds.)
Crete Island, Greece, 25–27 May 2015

A PROCEDURE FOR THE DETAILING DESIGN OF SIMPLY SUPPORTED R.C. BRIDGE DECKS SUBJECTED TO IN-PLANE ACTIONS

F. Palmisano[1] **and A. Elia**[2]

[1] Politecnico di Bari
Via E. Orabona 4, Bari, Italy
e-mail: fabrizio.palmisano@poliba.it

[2] PPV Consulting
Via G. Matteotti 37, Bari, Italy
a.elia@ppvconsulting.it

Keywords: Strut-and-Tie Model, Load Path Method, optimization method, bridge, R.C. structures.

Abstract. *Even though nowadays the Strut-and-Tie Model (STM) is widely used, several difficulties can be encountered when dealing with the choice of the model that best fits the actual configuration. This paper proposes a step-by-step procedure, based on the Strut-and-Tie Model, for the design of R.C. girder bridge decks subjected to in-plane seismic actions. The aim is to verify the reliability of the common practitioner design attitude to neglect the evaluation of the effects of seismic action on the decks of multi-girder bridges because it is thought that seismic code prescriptions in addition to ultimate limit state reinforcement dimensioning for permanent and variable load, do not justify more accurate analyses aimed to check and/or optimize reinforcement layout.*

1 INTRODUCTION

The Strut-and-Tie Model (STM), conceived by Ritter [1] on the basis of the construction method by F. Hennebique as a simple representation of a reinforced concrete member subjected to shear and bending, was developed by Mörsch. In the twentieth century, several studies were carried out on the STM and the results constitute the fundamentals of some prescriptions in many international codes.

Schlaich et al. [2] proposed a global approach to the structural design by means of STM. The Strut-and-Tie Model implies that the structure is designed according to the lower bound theorem of plasticity [2]. Since concrete allows for only limited plastic deformations, the STM has to be chosen in a way that the deformation limit is not exceeded at any point within the structure before the assumed state of stress is reached in the rest of the structure. In absence of either nonlinear analyses or specific test evidence for the case under study, this ductility requirement can be considered as fulfilled by adapting each element of the model to both the direction and size of the internal forces as they would come from the theory of elasticity (e.g. [2], [3]).

It is often not necessary to have a deep knowledge of the Strut-and-Tie Model to find the truss that best fits the regions under study. This is also due to the fact that often it is possible to adapt well-known pre-solved examples to the case being analysed.

In non-standard cases the development of the 'optimum' truss model may require not only an expert designer but it could also be extremely time consuming. This is the why many procedures (e.g., the Load Path Method, optimization criteria), that aim to find the most 'accurate' solution with the minimum 'effort', have been proposed in the last few decades.

In this article, a procedure, based on the Strut-and-Tie Model, for the design of R.C. girder bridge decks subjected to in-plane seismic actions is proposed.

The procedure is based on the following steps:

- Step 1: linear elastic analysis;
- Step 2: from the similarity with standard and well-known examples, definition of a tentative STM in which applied loads are substituted by few point loads;
- Step 3: updating of the tentative STM by application of distributed loads and comparison with cases which have been solved in the available literature;
- Step 4: updating of the obtained STM by comparison with principal stress lines resulting from a linear elastic analysis;
- Step 5: updating of the obtained STM by using the Load Path Method;
- Step 6 (optional): validation of the obtained STM by using evolutionary optimization procedures.

In this paper, as a first application, the proposed procedure is used for a single span deck composed of a 0.25 m thick slab with girders and cross-beams. For the sake of simplicity, but without any loss of generality, girders and cross-beams have a rectangular cross section. The slab is characterised by a characteristic compressive cylinder strength of the concrete f_{ck} = 35 MPa, a secant modulus of elasticity E_{cm} =34 GPa and a Poisson's ratio ν = 0.1. The beams are characterised by a characteristic compressive cylinder strength of the concrete f_{ck} = 45 MPa, a secant modulus of elasticity E_{cm} = 36 GPa and a Poisson's ratio ν = 0.1. The following cases have been analysed (Figs. 1, 2):

- *2TBA*: 30.75 m long, 13.25 m wide, 9 girders, 2 cross-beams;
- *5TBA*: 30.75 m long, 13.25 m wide, 9 girders, 5 cross-beams;
- *2TBB*: 30.75 m long, 10.25 m wide, 7 girders, 2 cross-beams;
- *5TBB*: 30.75 m long, 10.25 m wide, 7 girders, 5 cross-beams.

Such typology and dimensions represent the most widespread type within the Italian territory for both existing and new bridges. Even though bridge decks with a span of approximately 30 m have, in general, at least three cross-beams, in this paper the cases of 2 and 5 cross-beams have been studied to immediately highlight the influence of the number and distribution of cross-beams on the behaviour of bridge decks subjected to horizontal actions. Moreover, two different widths have been considered in order to verify the tendency of the deck to behave like a horizontal beam for higher span/width ratios.

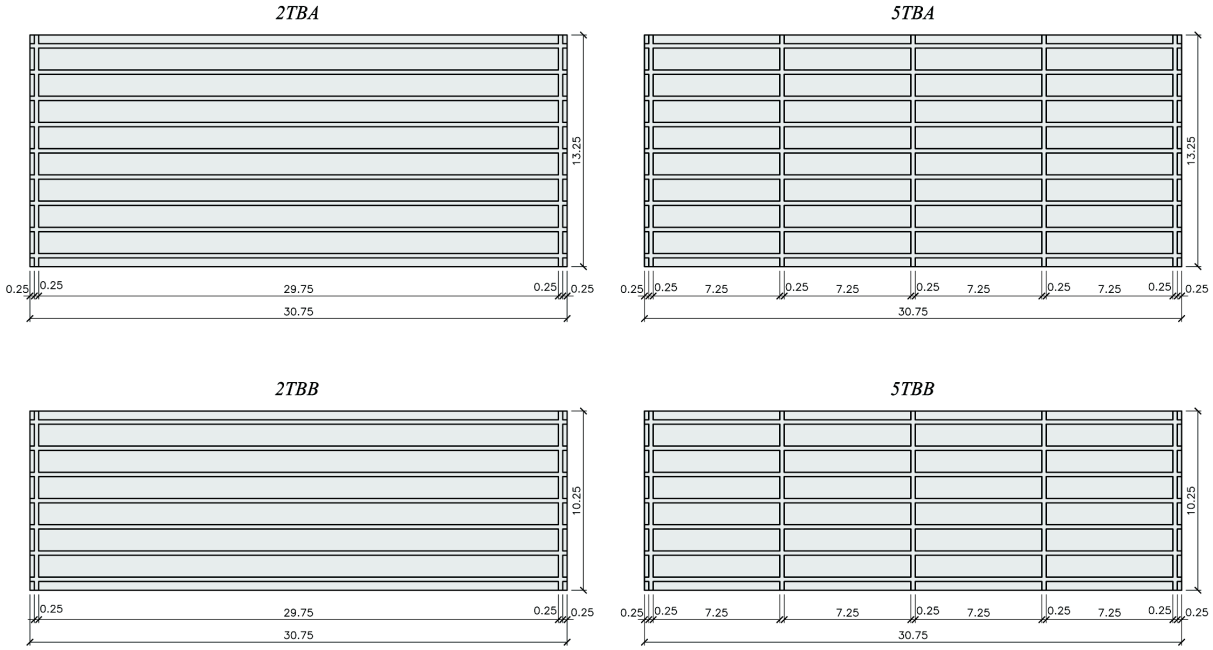


Figure 1: Plan view of the reference bridge decks (unit: m).

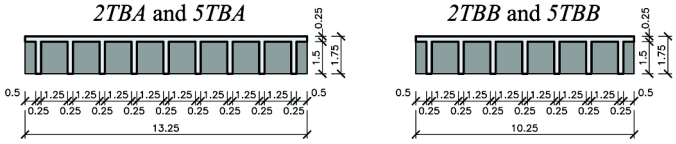


Figure 2: Cross section of the reference bridge decks (unit: m).

The following assumptions have been made:

- the peak ground acceleration is 0.2g (moderate seismicity);
- the vibration periods of the bridges correspond to the 'plateau' of the acceleration response spectrum, hence the seismic elastic design acceleration a_d can be assumed as equal to $2.5 \cdot 0.2g = 0.5g$;
- the behaviour factor is $q = 3.5$;
- the overstrength factor $\gamma_o = 1.3$.

Taking into account that, for the analysed cases, the total permanent load in the seismic combination is w = 18-19 kPa, the seismic horizontal load on the deck is $a_d \cdot \gamma_o \cdot w / q$ = 3.34-3.52 kPa. Hence the bridge decks have been considered as subjected to a 3.5 kPa static transversal load applied to the slab.

The following boundary conditions (*BC*, hereafter) have been assumed:

- *BC1*: the bottom intersections between girders and end diaphragms are vertically fixed;
- *BC2*: the bottom intersections between girders and the left end diaphragm are fixed in

the longitudinal direction;

- *BC3*: the bottom intersections between the end diaphragms and the central girder are fixed in the transversal direction.

These boundary conditions are the most widespread within the Italian territory for both existing and new girder bridges with a single span of about 30 m. In particular, *BC3* is relevant to the presence of shear keys (i.e. stoppers) at the bottom of the central girder.

Other possible transversal restraints could be either shear keys at both ends of each support lines or elastomeric bearings under end diaphragms. In Italy both solutions are not widespread either because of aesthetical aspects (the first solution) or because they have not been recommended (the second solution), for bridge spans of about 30 m, by the Italian organization for construction and management of national roads (i.e. ANAS).

2 STM FROM STANDARD EXAMPLES AND LINEAR ELASTIC STRESS DISTRIBUTION

The first step consists in determining the boundary forces by a linear elastic analysis. In the cases under study the finite element code ABAQUS 6.7-EF1 has been used. The domain has been subdivided into a regular mesh (0.25 m x 0.25 m x 0.25 m size) using the linear hexahedron (type C3D8) finite element (Figs. 3, 4, 5, 6). The uniform applied load has been transformed into many point loads (Figs. 3 and 5), in order to be consistent with the analysis performed using the BESO method and described as follows.

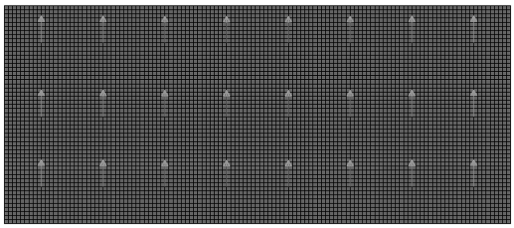


Figure 3: Analysis *5TBA* - plan view of the finite element model.

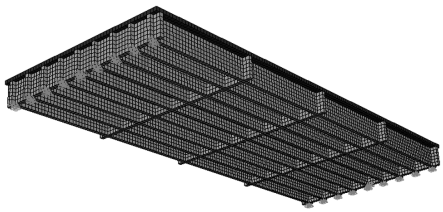


Figure 4: Analysis *5TBA* - axonometric view of the finite element model.

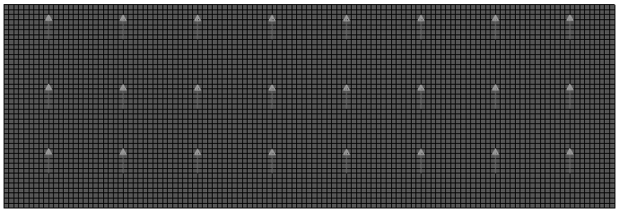


Figure 5: Analysis *5TBB* - plan view of the finite element model.

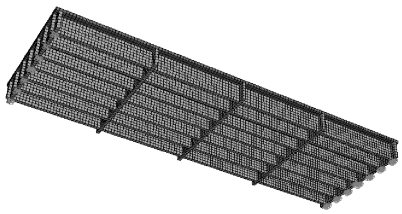


Figure 6: Analysis *5TBB* - axonometric view of the finite element model.

Since the bottom intersections between girders and the left end diaphragm are fixed in the longitudinal direction (see *BC2*), the behaviour of the slab in the horizontal plane has to be intermediate between a simply supported beam and one totally fixed on the left side and simply supported on the right side.

The elastic finite element analysis results highlight that due principally to the transversal/torsional flexibility of the diaphragm beams, the behaviour of the slab is very similar to that of a simply supported beam. Such findings appear to be also confirmed by the strict similarity between the left and right side reactions in the transversal direction (Table 1). This simi-

larity allows for the assumption of perfectly symmetric behaviour of the slab with respect to its transversal centre line.

The simplest way to define a STM for a given geometry and load condition is to try to make reference to standard, well-known examples. For the case under study, the case of a deep beam with distributed loads could be taken as reference.

It could be very useful to first solve the case in which distributed loads are substituted by few point loads (step 2 of the proposed procedure). Thanks to this assumption, the STM can be obtained by applying the similarity to the solution of a beam with dapped ends (compare Figures 7 and 8). The model corresponding to the case with a distributed load (i.e. step 3 of the proposed procedure) can be found by considering that the boundary part of the slab is similar to the case of Figure 8 and the middle part of the slab can be analysed as a deep beam with loads only on the extrados by 'suspending' the total distributed load (Fig. 9).

Analysis	Left side transversal reaction (kN)	Right side transversal reaction (kN)
2TBA	728	700
5TBA	731	696
2TBB	560	532
5TBB	563	528

Table 1: Transversal reactions evaluated by using a linear elastic finite element analysis.

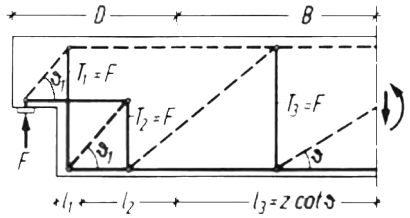


Figure 7: STM of a beam with dapped ends according to [2].

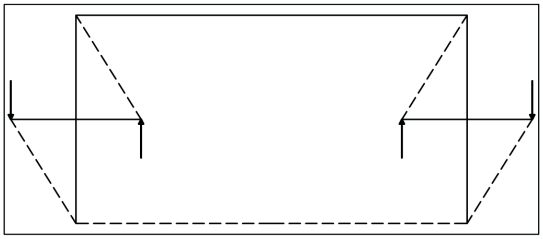


Figure 8: STM of the bridge slab obtained by the analogy with the case in Figure 7.

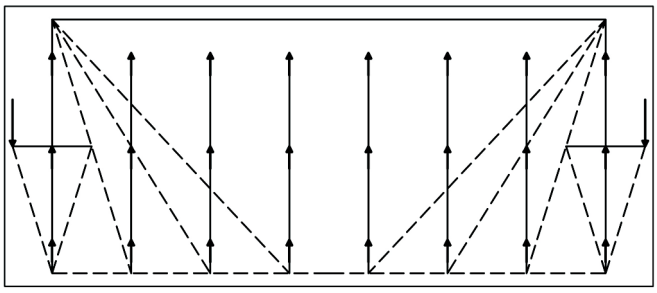


Figure 9: STM of the bridge slab obtained by the solution in Figure 8 and by the analogy with a deep beam with loads on the extrados.

The STM sketched in Figure 9 is valid for all of the four cases under study. In fact, taking account only of the analogy with well-known examples, it is very difficult to analyse the influence of the differences between the four cases on the shape of the STM. Moreover, the assumption of a shape which is based only on the superimposition of standard examples, cannot

guarantee the fulfilment of the ductility check. It follows that, in the absence of either nonlinear analyses or specific test evidence for the case under study, both struts and ties of the model have to be changed according to the direction and size of the internal forces resulting from a linear elastic analysis (i.e. step 4 of the proposed procedure).

It is worth noting that, regarding the design of seismic resistant bridges, modern technical standards require that the entire structure should be designed in such a way that under the seismic action of high reference return period (i.e. the one associated with the ultimate limit state) energy dissipation should occur by flexural yielding of specific sections (i.e. the formation of plastic hinges) in piers and/or by the activation of specific damping systems. The bridge deck should in general be designed to avoid damage, other than locally to secondary components.

These considerations imply that even under seismic action of high reference return period the bridge deck should remain within the elastic range. This approach should also be taken into account when vulnerability evaluation of existing bridges shows capacity deficits that require retrofitting interventions.

In the analysed cases, it can be considered that the deck remains within the elastic range. In fact, even in the worst condition (i.e. *2TBA*), the slab does not suffer any cracking due to the seismic action since the maximum principal tensile stress is equal to 1.31 MPa, lower than the characteristic axial tensile strength of concrete (i.e f_{ctk} = 2.2 MPa according to [3]). Even though this observation is sufficient to justify that the deck remains within the elastic range, another consideration needs to be made. In all the analysed cases, the above mentioned peak values of principal tensile stress are reached in the area where the point loads have been applied, i.e. these peak values are only due to the transformation of the uniform load into point loads. Hence it is plausible not to take account of these peak values and consequently, in the analysed cases, the maximum values of the tensile stress to be considered is equal to 0.50 - 0.62 MPa, significantly lower than f_{ctk}.

The elastic finite element analysis highlights that the STM in Figure 9 is not consistent with the principal stress lines. This is mainly due to the following aspects. Firstly the STM shown in Figure 9 is based on the assumption of cracked concrete; secondly the central part of the slab has 45° inclined stress lines. Thus the shape of the STM that best fits the elastic finite element analysis could be the one shown in Figure 10.

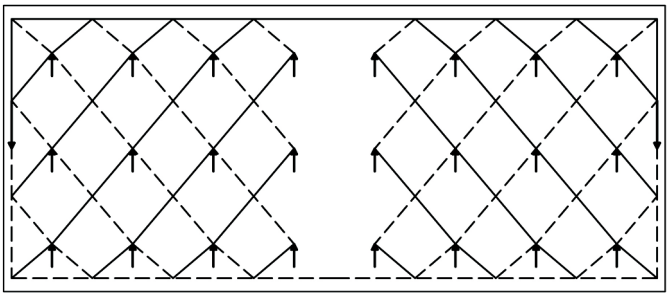


Figure 10: STM of the bridge slab obtained by linear elastic analysis.

There are at least two significant differences between the two models (compare Figures 9 and 11). The first difference is on the safe side because the adoption of the model of Figure 9 implies the assumption of a constant tensile action in the top chord. The second difference regards the ‘web’ tensile action; in fact in the model of Figure 9 there are only transversal tensile actions while in the one of Figure 10 these are inclined in the plane of the slab. This means that according to the latter model either diagonal distributed reinforcement or transversal and longitudinal distributed reinforcement should be provided in the slab.

Therefore, it is worth noting that from the analysis of the elastic solutions, the geometry of the bridge slab as well as the distribution of longitudinal and transversal beams do not seem to influence, to any great degree, the STM.

3 STM FROM LOAD PATH METHOD

Born as a method to design Strut-and-Tie Models in reinforced concrete structures, the Load Path Method (LPM) was introduced by Schlaich et al. [2] and then developed mainly by Palmisano and Vitone (e.g. [4], [5]). So far the Load Path Method has been used for a wide range of applications: conceptual and detailing design [6], reinforced concrete structures [2], special structures [7], optimum design [5], masonry structures [8-11], assessment of existing constructions [12-15].

The Load Path Method is a clear and effective tool of investigation and judgement. It is not only a numerical but also a geometrical method that predicts calculation results disclosing the shape aspects from which it is possible to recognise the real structural behaviour.

The Load Path Method is based on the respect of equilibrium and consistency. Among infinite paths in equilibrium, loads have to choose the one in which their vectors invest the minimum quantity of strain energy, that is the only one consistent and in equilibrium.

The total invested strain energy is

$$D = \frac{1}{2}\int_V \boldsymbol{\sigma}\boldsymbol{\varepsilon} dV \tag{1}$$

where V is the integration domain, $\boldsymbol{\sigma}$ and $\boldsymbol{\varepsilon}$ are the stress and the strain vector respectively.

Along a generic path (polygonal in this model), the calculus of the invested strain energy (D) is simplified in the summation of the terms which are relative to each side of the truss:

$$D = \sum_i D_i \tag{2}$$

where i is the generic side of the load path.

For linearly elastic materials, the elementary strain energy D_i can be expressed, for some typical cases, by means of the relations reported in Figure 11. An immediate consequence is that loads cannot follow a path which is orthogonal to the direction of the travelling load because it would imply a vector of infinite magnitude and a consequent infinite invested strain energy.

In general, the application of the LPM consists in finding the ‘optimum’ path, i.e. the only one, among different equilibrated load paths, to which the lowest value of the total strain energy corresponds . Figure 11 clearly shows that the total strain energy depends fundamentally on the length and on the stress intensity of the paths. It follows that the ‘optimum’ Load Path is characterised by the right balance between the length of all the paths (including those of the thrusts) and the stress level.

In the STM obtained in the previous paragraph and shown in Figure 10, the paths of the loads from the application point to the support are significantly long. This is the immediate consequence of the assumption that all the loads have to reach the two longitudinal chords as in the case of a beam.

Shorter paths can be obtained if the so-called arch-behaviour (see [4], [16]-[18]) is activated. The difference between an arch-shaped path and a beam-shaped path is sketched in Figure 12. For a point load F the arch-shaped path is a direct path (6-1) from the application point to the support; the path 6-5-4-3-2-1 is, on the other hand, a beam-shaped path.

Figure 12 highlights the following differences between the two paths:

- the total length of the diagonal compressive sides (1-2, 3-4, 5-6) of the beam-shaped path is larger than the one of the arch-shaped path (1-6);
- the action in the diagonal compressive sides of the beam-shaped path is lower than the one of the arch-shaped path;
- only the beam-shaped path has 'web' tensile sides;
- only the beam-shaped path has a compressive longitudinal chord (2-6);
- the action in the bottom chord is constant in the arch-shaped path whereas it varies within the beam-shaped path.

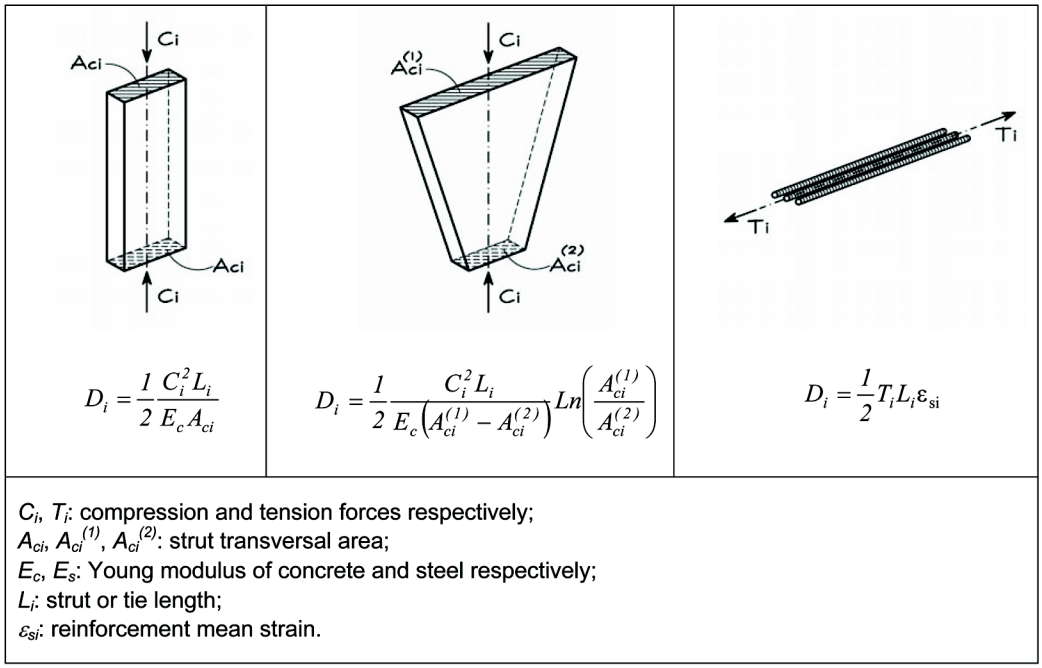


Figure 11: Elastic strain energy in some typical cases of struts and ties.

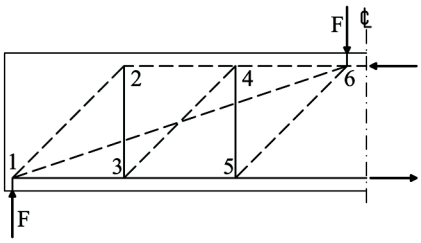


Figure 12: Arch-shaped and beam-shaped path.

Taking into account what is mentioned above about the arch-behaviour and considering that the 'optimum' Load Path is the one associated with the lowest value of the total strain energy, the following considerations can be made for the case under study:

- the proximity of the application point of the load to the support encourages the arch-shaped path;
- the increase of the stiffness of the compressive longitudinal chord encourages the beam-shaped path;
- the increase of the stiffness of the 'web' tensile sides encourages the beam-shaped path.

In the examined cases, loads are very close to the support so an arch-shaped path has to be activated (step 5 of the proposed procedure). In particular, considering the antisymmetry with

respect to the central girder, two main arch-shaped paths can be drawn (Fig. 13); loads on the central girder go towards the arch-shaped paths with 45° inclined paths (according to the results of the linear elastic finite element analyses). Even though the loads near the outer girders are actually in the width of the arch-shaped paths, in the wire frame model of Figure 13, transversal paths towards the arch-shaped paths have been assumed. It is worth noting that the shape of the arches can be drawn from equilibrium conditions simply assuming the position of the crowns (see [4], [16]-[18]).

According to the LPM, assuming the configuration shown in Figure 13, and by modifying the shape of the arches (i.e. changing the position of the crowns) as well as the inclination of the paths of the central loads, the 'optimum' Load Path can be found. For the sake of brevity, in this paragraph these calculations are not reported thanks to the results obtained using the BESO method and illustrated in the next paragraph.

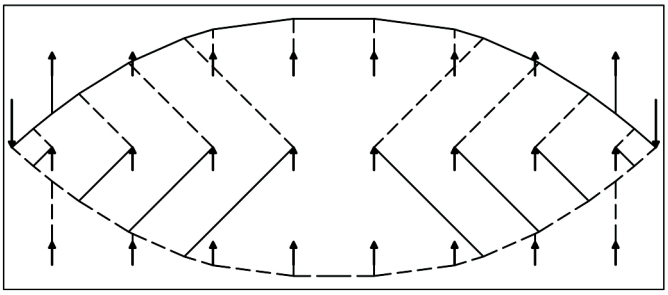


Figure 13: STM of the bridge slab obtained by the LPM.

4 STM FROM THE BESO METHOD

4.1 The application of the Beso Method

Step 6 of the proposed procedure implies the use of evolutionary optimization procedures and is aimed at validating the results obtained by the LPM. Because of the time needed to perform such analyses, this step is optional and, for complex cases, it could be applied only to limited parts of the structure under study.

Shape optimization is a method that enables designers to find a suitable structural layout for the required performances. The 'Evolutionary Structural Optimization' (ESO) method was first proposed by Xie and Steven [19] in the early 1990s and it has been used to solve a variety of size and shape optimization problems. The basic concept of such a method is that by slowly removing inefficient materials, the structure evolves towards an optimum. This method has been already applied to design Strut-and-Tie Models (e.g. [20]-[23]). The validity of the ESO method depends, to a large extent, on the assumptions that the structural modification (evolution) at each step is small and the mesh for the finite element analysis is dense. If too much material is removed in one step, the ESO method is unable to restore the elements which might have been prematurely deleted at earlier iterations. In order to make the ESO method more robust, a Bi-directional ESO method (BESO) was proposed by Yang et al. [24]. It allows for efficient materials to be added to the structure at the same time as the inefficient ones are being removed. For further details concerning the BESO algorithm used in the analyses presented in this paper see Huang and Xie [25].

In order to assist the selection of optimal shapes for the minimum-weight design of continuum structures with stiffness constraints, the performance of the resulting shape at each iteration can be evaluated by a Performance Index *PI* defined as:

$$PI = \frac{C_0 W_0}{C_i W_i} \tag{3}$$

where W_0 is the actual weight of the initial domain, C_0 is the strain energy of the initial design under the applied loads, while W_i and C_i are the same quantities of the current design at the *i-th* iteration. It follows that to the optimal configuration will correspond the highest *PI*.

In the following, the application of the BESO method to the aforementioned four cases of bridge deck is presented. According to [25], the Evolutionary Ratio *ER* and the Filter Radius *FR* have been set to be 0.5% and 0.25 m respectively while the maximum admission volume ratio AR_{max} and the allowable convergence error τ have been assumed as equal to 1.0% and 0.1% respectively. In Figures 14-17 the optimal shape is represented; for each case the maximum value PI_{max} of the performance index as well as the corresponding value V_f of the volume fraction of the initial domain are indicated.

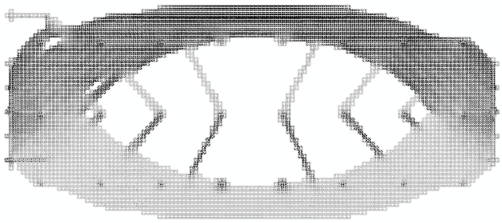


Figure 14: Optimal shape of *2TBA* (PI_{max} = 1.92; V_f = 33%; light grey = compression; dark grey = tension).

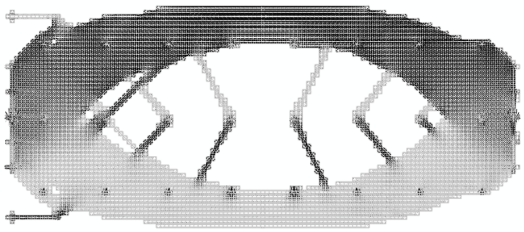


Figure 15: Optimal shape of *5TBA* (PI_{max} = 2.01; V_f = 34%; light grey = compression; dark grey = tension).

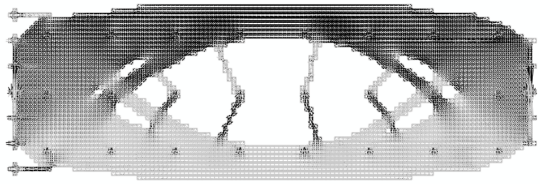


Figure 16: Optimal shape of *2TBB* (PI_{max} = 1.72; V_f = 42%; light grey = compression; dark grey = tension).

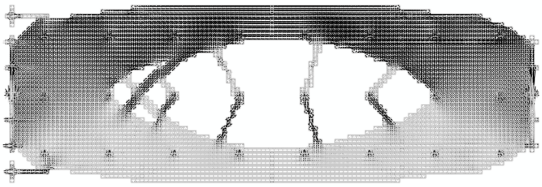


Figure 17: Optimal shape of *5TBB* (PI_{max} = 1.79; V_f = 41%; light grey = compression; dark grey = tension).

Figures 14-17 confirm that the solution is almost perfectly symmetrical with respect to the transversal centre line. Only a slight deviation from such symmetry can be found on the lateral transversal boundaries because of the small stiffness to the horizontal displacement of the slab given by the left end diaphragm. Moreover the validity of the LPM approach has been confirmed by the strict similarity between the four optimal shapes and the STM represented in Figure 13.

It has to be underlined that the BESO method, which has been applied in the assumption of homogeneous and isotropic material, also seems to confirm that the geometry of the bridge slab as well as the distribution of girders and cross-beams does not seem to influence, to any great degree, the STM. This aspect has been investigated more in depth by re-running the BESO analyses for *5TBA* and *5TBB* (see analyses *5TBAS* and *5TBBS* in Figures 18 and 19). In such analyses only for the part of the slab above the girders and cross-beams, a modulus of elasticity E =200 GPa has been used. This assumption is aimed at overestimating the contribution of the reinforcement at the top of the beams.

For the case of a 13.25 m wide slab (analysis *5TBAS*; Fig. 18) the overestimation of the slab stiffness above the beams causes a slight change in the STM with little concentration of stresses at the top of the beams. On the other hand, for the case of a 10.25 m wide slab (analysis *5TBBS*; Fig. 19) the overestimation of slab stiffness causes the following modifications in the STM:

- there is a little concentration of stresses at the top of the beams;
- the central loads follow a transversal path (instead of an inclined one) towards the arch-shaped path;
- each arch-shaped path is subdivided into three parts; the inner ones do not arrive directly at the end diaphragms but in the opposite outer girders (i.e. a partial activation of the STM shown in Figure 10).

The results obtained in the 'limit' analyses *5TBAS* and *5TBBS* demonstrate that, in the cases under study, the geometry of the bridge slab as well as the layout of the girders and cross-beams do not seem to influence, to any great degree, the STM.

Finally, it has to be added that after having obtained the 'optimum' STM from the above mentioned approaches it is necessary to check the strengths of struts, ties and nodal zones and eventually to modify the model in order to satisfy all of the checks.

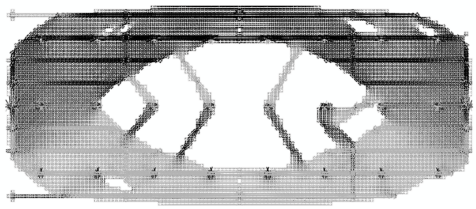


Figure 18: Optimal shape of *5TBAS* (PI_{max} = 2.09; V_f = 36%; light grey = compression; dark grey = tension).

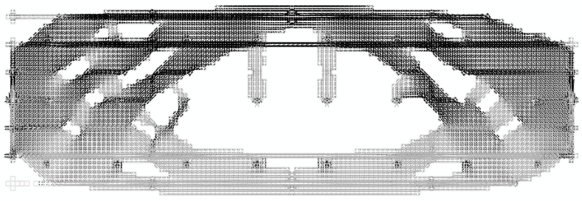


Figure 19: Optimal shape of *5TBBS* (PI_{max} = 1.92; V_f = 36%; light grey = compression; dark grey = tension).

4.2 Some considerations regarding the results

According to [2], a Strut-and-Tie Model is constructed by orientating struts and ties to the mean direction of principal stress trajectories, which are obtained by performing a linear elastic finite element analysis (FEA) on an uncracked homogenization concrete member. However, due to the uncracked assumption of concrete in the linear elastic FEA, the Strut-and-Tie Model obtained by this approach may differ from the actual load transfer mechanism at the ultimate limit states, as reported by Schlaich and Schäfer [26]. The Strut-and-Tie Model obtained on the basis of the elastic stress analysis in order to realize the real behaviour of cracked structural concrete often needs to be be adjusted.

Elia et al. [27] delineated an interactive procedure to design Strut-and-Tie Models using ESO; in this methodology the difference between the strain energy of the design Strut-and-Tie Model and the optimal solution, is measured and it allows an evaluation of the ductility demand of the structure.

Vitone et al. [28] showed the necessity to analyse the physical transformations that a structure undergoes from the uncracked phase to the ultimate load stage in order to verify whether the structure is capable of reaching the ultimate design configuration.

In this scenario, the case under study is particularly important. In the literature it is very common to find solutions for similar cases based on the assumption of cracked concrete. For instance Figure 20 shows the STM of a building diaphragm according to Fardis [29]. This

model has been obtained from the superimposition of the deep beam behaviour as described in paragraph 2 and the arch-behaviour (only for the compression cord) as described in paragraph 3.

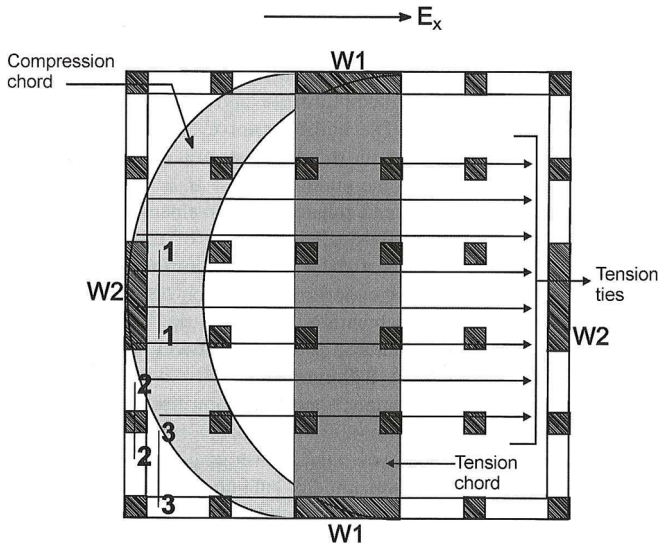


Figure 20: STM of a building diaphragm according to [29].

The analysis performed by the LPM and the BESO have confirmed that the optimum STM obtained from a linear elastic analysis is the one represented in Figure 13.

This means that, due to the lack of ductility of r.c concrete structures, if the diaphragm is designed at the ultimate limit state according to the STM in Figure 20, reinforcement should be designed or checked according to the model in Figure 13, in order to allow the considerable redistribution of internal stresses immediately after cracking. Such findings highlight the necessity of the proposed approach.

It is worth noting that when dealing with single span decks, the design of deck reinforcement is often conditioned by either dimensioning at the ultimate limit state for permanent and variable loads or minimum reinforcement prescriptions. This means that the above mentioned check could be unnecessary. However, this consideration is not so obvious when dealing with girder bridges with jointless concrete decks or with link slabs. These two kinds of bridges are widely used in Italy to economically solve typical problems inherent to the durability of precast beam ends and maintenance of joints and bearing systems that have been noticed in single span decks built in the '60s, '70s and '80s of the last century.

In these cases the behaviour of decks subjected to in-plane seismic action is conditioned by the effective stiffness of each pier (that also depends on footing and bearings), transversal restraints on the abutments, ratio of length to the width of each span, total length of deck slab between two adjacent joints. This is why further work is needed to apply the proposed procedure to these kinds of decks in order to verify whether the check of the deck reinforcement for in-plane seismic action is still unnecessary and whether the assumption of uncracked deck under seismic action is still valid.

Finally, regarding the single span deck under study, as mentioned in paragraph 2, bridge deck, at the seismic ultimate limit state, should remain within the elastic range in order to avoid damage. This means that the model in Figure 13 becomes the only reference for the ultimate limit state design.

5 CONCLUSIONS

The Strut-and-Tie Model is a very powerful tool with which to design reinforced concrete structures.

For standard cases it could be a hand-calculation design procedure, in which the structural engineer uses his experience and intuition to find the truss model that best fits the region under study. For unconventional cases the development of the 'optimum' STM could require not only an expert designer but also the use of special tools for the analysis.

In this paper, a step-by-step procedure based on the Strut-and-Tie Model has been proposed for the design of R.C. girder bridge decks subjected to seismic in-plane actions.

The efficacy of the proposed approach has been shown for the case of a single span girder bridge deck. Moreover, for the case under study, the influence on the model of geometry of the bridge deck as well as of the layout of girders and cross-beams has been investigated.

Further work is needed to apply the method to girder bridges with jointless concrete decks or with link slabs.

ACKNOWLEDGMENTS

The BESO3D software has been developed and provided by the 'Innovative Structures Group, RMIT University, Australia www.isg.rmit.edu.au'.

REFERENCES

[1] W. Ritter, Die Bauweise Hennebique. *Schweizerische Bauzeitung*, 7 (33), 59-61, 1899.

[2] J. Schlaich, K. Schafer, M. Jennewein, Toward A Consistent Design of Structural Concrete. *PCI Journal*, 32 (3), 74-150, 1987.

[3] CEN (European Committee for Standardization), *EN 1992-1-1:2004 Eurocode 2. Part. 1-1 Design of concrete structures. General rules and rules for buildings*. 2004.

[4] F. Palmisano, A. Vitone, C. Vitone, Load path method in the interpretation of the masonry vault behaviour. C.A. Brebbia, A. Torpiano eds. *Structural Studies, Repairs and Maintenance of Heritage Architecture IX (Advances in Architecture Series 20)*, WITpress, 155-167, 2005.

[5] F. Palmisano, A. Vitone, C. Vitone, A first approach to optimum design of cable supported bridges using load path method. *Structural Engineering International*, 18 (4), 412-420, 2008.

[6] F. Palmisano, Form and structure in the harmonious complexity of the building process: from conceptual design to detailing in some reinforced concrete works. *Structural Concrete*, 6 (3), 122-130, 2005.

[7] H. Shi, Q. Wang, F. Wei, L. Shen, Load path analysis of a floating concrete gate using finite element method. *Structural Engineer*, 6 (91), 38-41, 2013.

[8] F. Palmisano, A. Elia, Masonry buildings subjected to foundation settlements due to landslide: a preliminary study on the interpretation of structural behaviour using load path method. C.A. Brebbia ed. *Structural Studies, Repairs and Maintenance of Heritage Architecture XI (WIT Transactions on the Built Environment 109)*, WITpress, 141-150, 2009.

[9] F. Palmisano, A. Elia, Analysis of the structural behaviour of masonry buildings subjected to landslide by using the Load Path Method. *International Journal of Earth Sciences and Engineering*, 6 (1), 39-49, 2013.

[10] F. Palmisano, A. Elia, Structural behaviour of masonry buildings subjected to landslide: load path method approach. P.J.S. Cruz ed. *Structures and Architecture: New concepts, applications and challenges (proc. of the 2nd International Conference on Structures & Architecture, Guimarães, Portugal, 24-26 July 2013)*. CRC Press/Balkema, 888-895, 2013.

[11] F. Palmisano, A. Elia, Behaviour of masonry buildings subjected to landslide-induced settlements. *International Journal of Structural Engineering*, 5 (2), 93-114, 2014.

[12] F. Palmisano, A. Vitone, C. Vitone, V. Vitone, Collapse of the Giotto Avenue Building in Foggia. *Structural Engineering International*, 17 (2), 166-171, 2007.

[13] F. Palmisano, Mitigation of progressive collapse by the activation of the elasto-plastic catenary behaviour of R.C. slab structures. *The Open Construction & Building Technology Journal*, 8, 122-131, 2014.

[14] F. Palmisano, A. Vitone, Partial collapse of one of the most important historical buildings in Salerno, Italy. *Journal of Performance of Constructed Facilities*, published on-line on the 25th September 2014, DOI 10.1061/(ASCE)CF.1943-5509.0000658, 13 pages, in print.

[15] F. Palmisano, Rapid diagnosis of crack patterns of masonry buildings subjected to landslide-induced settlements by using the Load Path Method. *International Journal of Architectural Heritage*, published on-line on the 31st September 2014, DOI 10.1080/15583058.2014.996922, in print.

[16] F. Palmisano, A. Totaro, Load path method in the interpretation of dome behaviour. P.J.S. Cruz ed. *Structures & Architecture (proc. of the 1st International Conference on Structures & Architecture, Guimarães, Portugal, 21-23 July 2010)*, CRC Press/Balkema, 1826-1833, 2010.

[17] F. Palmisano, Interpretation of the behaviour of masonry arches and domes by simple models. C.A. Brebbia ed. *Structural Studies, Repairs and Maintenance of Heritage Architecture XIII (WIT Transactions on the Built Environment 131)*, WITpress, 233-244, 2013.

[18] F. Palmisano, Assessment of masonry arches and domes by simple models. *International Journal of Structural Engineering*, 5 (1), 63-75, 2014.

[19] Y.M. Xie, G.P. Steven, A simple evolutionary procedure for structural optimization. *Computers & Structures*, 49, 885–886, 1993.

[20] Q.Q. Liang, Y.M. Xie, G.P. Steven, L.C. Schmidt, Topology Optimization of Strut-and-Tie Models in Non-Flexural Reinforced Concrete Members. *Proc. of the International Conference on Mechanics of Structures, Materials and Systems*, Wollongong, Australia, 309-315, 1999.

[21] F. Palmisano, A. Elia, Assessment of masonry buildings subjected to landslide by using the Load Path Method. *International Journal of Civil Engineering*, 12(14), 312-330, 2014.

[22] F. Palmisano, G. Alicino, A. Vitone, Nonlinear analysis of R.C. discontinuity regions by using the bi-directional evolutionary structural optimization method. M.G. Karlaftis, N.D. Lagaros, M. Papadrakakis eds. *Proc. of the OPT-I, An International Conference on Engineering and Applied Sciences Optimization*, 749-758, 2014.

[23] F. Palmisano, A. Elia, Shape optimization of strut-and-tie models in masonry buildings subjected to landslide-induced settlements. *Engineering Structures*, 84, 223-232, 2015.

[24] X.Y. Yang, Y.M. Xie, G.P. Steven, O.M. Querin, Bidirectional evolutionary method for stiffness optimization. *AIAA Journal*, 37 (11), 1483–1488, 1999.

[25] X. Huang, Y.M. Xie, Convergent and mesh-independent solutions for the bi-directional evolutionary structural optimization method. *Finite Elements in Analysis and Design*, 43, 1039-1049, 2007.

[26] J. Schlaich, K. Schäfer, Design and detailing of structural concrete using strut-and-tie models. *The Structural Engineer*, 69 (6), 113–125, 1991.

[27] G. Elia, F. Palmisano, A. Vitone, C. Vitone, An interactive procedure to design strut and tie models in reinforced concrete structures using the 'evolutionary structural optimisation' method. P. Gosling ed. *Engineering Design Optimization. Product and Process Improvement*, 60-66, 2002.

[28] A. Vitone, F. Palmisano, C. Vitone, Load path method (LPM) in detailing design. *Proc. 2nd International fib Congress*, Naples, Italy, 11 pages, 2006.

[29] M.N. Fardis, *Seismic Design, Assessment and Retrofitting of Concrete Buildings: based on EN-Eurocode 8*, Springer, 2009.

COMPDYN 2015
5th ECCOMAS Thematic Conference on
Computational Methods in Structural Dynamics and Earthquake Engineering
M. Papadrakakis, V. Papadopoulos, V. Plevris (eds.)
Crete Island, Greece, 25–27 May 2015

MULTI-OBJECTIVE STRUCTURAL OPTIMIZATION UNDER STRESS CRITERIA BASED ON MIXED PLATE FEM AND GENETIC ALGORITHMS

Pierre Garambois[1], Sebastien Besset[1], and Louis Jézéquel[1]

[1]Laboratoire de Tribologie et Dynamique des Systèmes, UMR CNRS 5513
Ecole Centrale de Lyon, 36 avenue Guy de Collongue, 69134 Ecully Cedex, France
e-mail: {pierre.garambois,sebastien.besset,louis.jezequel}@ec-lyon.fr

Keywords: Structural optimization, multi-objective optimization, mixed FEM, Genetic Algorithms(GA), stress criteria

Abstract. *The purpose of this study is to implement a powerful multi-objective (MO) genetic algorithm(GA)-based optimization technique for structural problems, based on the use of displacement-generalized stress Dynamic Mixed plate Finite Element Model (DM-plate-FEM). The idea is to optimize different thickness parameters of a plate structure in order to minimize antagonist objectives among these stress criteria under dynamic loads. In this article, the optimization is performed with a GA-based iterative method and propose a set of Pareto-optimal solutions, leaving the final choice to the user. The repetitions of the calculations in this method is offset by the use of the displacement-stress mixed plate FEM. Such a model discretizes both displacements and generalized stresses in the same model, in order to get the latter directly and increase the efficiency of the method. The implementation of the Kirchoff-Love (KL) plate theory also improve the work of the GA as it allows a quick change of the thickness structure parameters without rebuilding the whole assembly. The number and complexity of calculations needed by the GA is thus smaller and the speed of the method highly improved. A few numerical investigations are made with both simple and complex test examples in order to validate the methods and show its relevance. This work shows efficient and promising results that may turn out to be interesting regarding industrial optimization cases with plate structures.*

1 Introduction

The purpose of this study is to implement a powerful MO-GA-based optimization technique for structural dynamic plate problems, based on the use of mixed displacement-generalized stress plate FEM. This method has been imagined in the context of plate structure with at least one stress objective and thickness parameters.

The optimization of a structure's parameters in order to prevent damages is a major concern in mechanical engineering but can only be achieved at the expense of others essential criteria. Even though often carried out manually, MO-optimization methods also naturally appear in the literature, such as gradient-based method [1, 2] and MO-GA-based methods [3, 4]. In this study, the optimization is performed with a classical GA-based NSGA-II method [5, 6], as it permits to dispense with any weighting of criteria. This kind of method enables to find a set of Pareto-optimal solutions, which are all optimal compared to each other, for at least one criterion. Nevertheless, an inconvenient lies in the repetitions of the criteria's evaluation, depending on the chosen method and theory.

Despite the power of those methods, a major inconvenient lies in the repetitions of the criteria's evaluations for each solution, each generation. In the case where some of the criteria are stresses, their calculations are crucial. Usually, it necessitates to find the displacements first through a primal FEM (in which the parameters are displacements), and then access to the stress fields with extra calculations. Another original method, used in this paper, consists in building a mixed FEM which discretizes both the displacements and the stresses in the same model, in order to get the latter directly.

In the literature, many different formulations for mechanical problems permit to access to different parameters in the same model. Washizu's book [7] gives a good insight of all the variational methods with different fields. Among these, the Hellinger-Reissner's, imagined by Hellinger [8] and later by Reissner [9, 10, 11], describes both displacements and stresses. Its application to FEM is well explained by Wriggers' book [12]. It is widely used in static for plate problems, but more rarely for in dynamics [13, 12, 14]. In this work, we establish a displacement-generalized stress dynamic mixed FEM (DM-FEM) for structural studies, based on Kirchoff-Love thin plate theory [15]. This model allows a direct access to the generalized stresses within the plate, and highly simplifies the work of the GA under stress criteria, compared to a regular primal displacement FEM that need an extra work.

Moreover, the plate theory implementation gives us the opportunity to act on the thicknesses of the plate structure without building a whole new assembly, which offset the numericaly bigger size of such a model. This also improves the performances of the optimization techniques with some thickness parameters as we can act on them directly and independently, and change the whole structure in a simple manner.

In this way, a few investigations are made, using a GA-based optimization improved by the DM-plate-FEM, with stress criteria and thickness parameters. The idea is to split the test structure into smaller ones with their own thicknesses, and try to optimize them, so as to reduce the maximum Von Mises (VM) stress within the plate structure under a dynamic harmonic load, and the mass of the structure.

This original method shows promising results as it is able to satisfy multiple damage criteria with different thickness distributions within the structure, and decrease the number and complexity of calculations needed in the iteration of the algorithm thanks to the DM-FEM.

In the first part, we present the type of optimization problem we study. Then we give a quick description of the GA used. We continue with the implementation of the mixed FEM, and finally get to the principal relevant examples.

2 Optimization problem

The two "example" structures we want to optimize are built up with thin Kirchhoff-Love plate elements (see figure 1 and 2, respectively composed of 256 and 512 elements). They are separated in a few zones with their own thicknesses (respectively 8 and 7 zones in the figures), which are the parameters of the optimization. The range of the parameters, as well as the number of zones and their positions are defined by the user.

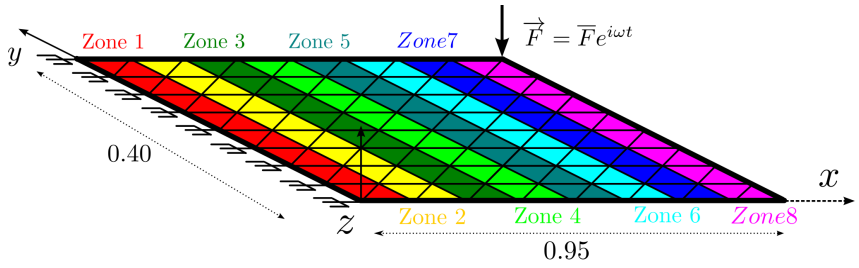


Figure 1: Plate structure "1" composed of 8 sub-structures with their own thicknesses

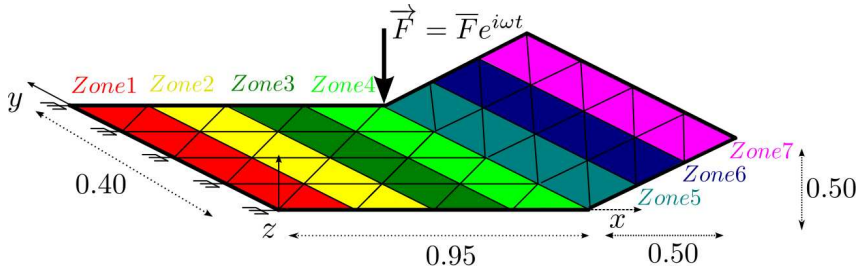


Figure 2: Plate structure "2" composed of 7 sub-structures with their own thicknesses

The problem we try to solve is the minimization of both:

- the maximum Von Mises (VM) stress within the whole plate structure for a given n^{th} mode. In other words, we want to decrease the maximum VM stress within the whole structure under a dynamic load $\overrightarrow{F}$ (see figure 1 and 2) considering:

$$\overrightarrow{F} = \overline{F}e^{i\omega t} \tag{1}$$

  and $\omega = \omega_n$ the pulsation of the n^{th} mode

- the mass of the structure, in a bid of cost

These two objectives being antagonistic, the goal is to find some thickness distributions (set of parameters) that are good compromises between the mass and the maximum stress undergone by the structure. As such, the GA method quite naturally appears.

3 Genetic Algorithm method

The GA methods can be compared to the evolution of species in their natural environment. It consists in making evolve a population, whose individuals, solutions of the problem, tend to improve for the purpose of our objectives as the generations follow. In this context, the word used to explain its functioning are taken from biology domain, namely:

- an "individual" is a solution to the problem (here, a combination of "n" thicknesses (one each zone) that gives a compromises between the objectives)
- a "population" is a group of "individuals" (here, a set of thickness combinations, that forms a Pareto front with one compromises per thickness distribution)
- a "generation" is an iteration of the algorithm and correspond to a population

The functioning of the algorithm is summarized in figure 3). It is composed of 5 different stages (stages 2 being the most costly).

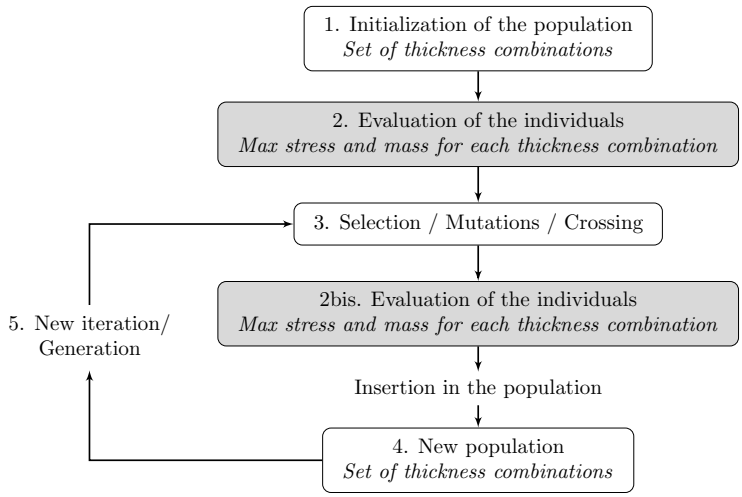


Figure 3: Principle of the genetic algorithm

4 Dynamic Mixed Finite Element Model for thin Kirchhoff-Love plate

In our studies, the "evaluation step" (step 2 in figure 3) is by far the most costly because we need to evaluate the stress within the whole plate structure, identify the maximum, and it eventually necessitate to rebuild the assembly with the new structure parameters. The classical method consists in building a primal FEM to access the displacement in a first step when computing the response of the structure. Then we reach the stress field through matrix calculations, and repeat it each iteration. It's the most common and intuitive method, but it appears to be heavy going because of the extra calculations, the rebuilding and its repetition in our GA case. The main idea of this paper is to delete those

extra calculations and enhance the rebuilding. The originality of our method consists in the construction of a displacement-generalized stress DM-plate-FEM that permits a direct access to both displacements and stress fields in the response of the structure. The features of such a FEM permits to avoid the extra work needed by a primal FEM and replace it by a simple scalar calculation. Furthermore, the implementation of the Kirchhoff-Love thin plate theory in the mixed FEM allows to build each zone of a constant thickness regardless of this inherent parameter, when separating the bending phenomenon. That added features permits to act on the thickness of each zone without having to rebuild it from the beginning which considerably improve the method.

4.1 Hellinger-Reissner mixed formulation

The displacement-generalized stress mixed FEM we implement is based on the HR mixed functional [8, 9] expressed for dynamics problems. It may correspond to the regular Lagrangian used in dynamics, but computed with mixed component, both functions of displacements and stresses, as follows:

$$\Pi_{HRD} = \iiint_V -\boldsymbol{\sigma}_{ij}\boldsymbol{e}_{ij}(\boldsymbol{u}_i) + \frac{1}{2}\boldsymbol{\sigma}_{ij}\boldsymbol{S}_{ijkl}\boldsymbol{\sigma}_{kl} + \boldsymbol{b}_i\boldsymbol{u}_i + \frac{1}{2}\rho\dot{\boldsymbol{u}}_i^2 \,\mathrm{dV} \tag{2}$$

considering $\boldsymbol{\sigma}_{ij}$ the stress, $\boldsymbol{u}_i$ the displacement, $\boldsymbol{e}_{ij}(\boldsymbol{u}_i)$ the strain (function of the displacement $\boldsymbol{u}_i$), $\boldsymbol{b}_i$ the body force, ρ the density and $\boldsymbol{S}_{ijkl}$ the elastic compliance matrix. The stationary condition or Euler-Lagrange equations can then be applied to the functional so as to conventionally solve a dynamic structure problem.

4.2 Discretization of displacements and generalized stress

The discretization of the generalized stresses (according to figure 4a) with plate elements using Kirchhoff-Love (KL) thin plate is made as follows:

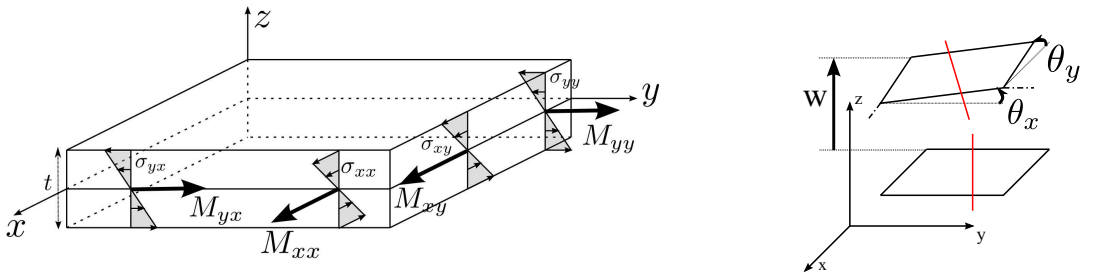
$$\boldsymbol{\sigma}_{ij} = \begin{Bmatrix} M_x & M_y & M_{xy} \end{Bmatrix}^T = \boldsymbol{P}\boldsymbol{\beta} \tag{3}$$

with $\begin{Bmatrix} M_x, M_y, M_{xy} \end{Bmatrix}^T$ respectively the bending moments in the x, and y direction, and the twisting moment within the plate (thickness t). $\boldsymbol{P}$ is the generalized stresses shape function matrix and $\boldsymbol{\beta}$ the generalized stress parameters vector within the plate. The shape functions are linear in functions of x and y. The discretization of the displacements (see figure 4)b for a thin plate elements using Kirchhoff-Love (KL) theory is made as follows:

$$\boldsymbol{u}_i = \begin{Bmatrix} w & \theta_x & \theta_y \end{Bmatrix}^T = \boldsymbol{N}\boldsymbol{U} \tag{4}$$

with $\begin{Bmatrix} w & \theta_x & \theta_y \end{Bmatrix}^T$ being respectively the transverse displacement of the plate, and the section rotations around x and y. $\boldsymbol{N} = \begin{Bmatrix} \boldsymbol{N}_w, \boldsymbol{N}_\theta \end{Bmatrix}^T$ is the displacements shape function matrix and $\boldsymbol{U} = \begin{Bmatrix} \boldsymbol{U}_w, \boldsymbol{U}_\theta \end{Bmatrix}^T$ the displacements parameters vector. For triangular elements and cinematically admissible displacements, the functions are quadratic in function of x and y. The strain depending on the displacement is written as follows:

$$\boldsymbol{e}_{ij} = \begin{Bmatrix} \epsilon_{xx} & \epsilon_{yy} & \gamma_{xy} \end{Bmatrix}^T = \boldsymbol{D}\,\boldsymbol{u}_i = \boldsymbol{D}\boldsymbol{N}\boldsymbol{U} \tag{5}$$



(a) (b)

Figure 4: Displacements & stress in the plate Kirchhoff-Love theory: (a) Bending and twisting moment, (b) Transverse displacement and rotation section

with $\boldsymbol{D}$ the following displacement-strain tensor-operator:

$$\boldsymbol{D} = \begin{Bmatrix} 0 & 0 & \frac{\partial}{\partial x} \\ 0 & -\frac{\partial}{\partial y} & 0 \\ 0 & \frac{\partial}{\partial x} & \frac{\partial}{\partial y} \end{Bmatrix} \tag{6}$$

The elastic compliance matrix $\boldsymbol{S}_{ijkl}$ is given by:

$$\boldsymbol{S}_{ijkl} = \frac{1}{t^3}\tilde{\boldsymbol{S}}_{ijkl} = \begin{Bmatrix} \frac{12}{Et^3} & -\frac{12\nu}{Et^3} & 0 \\ -\frac{12\nu}{Et^3} & \frac{12}{Et^3} & 0 \\ 0 & 0 & \frac{24(1+\nu)}{Et^3} \end{Bmatrix} \tag{7}$$

4.3 Matrix formulation

The application of the Euler-Lagrange equations leads us to the following matrix formulation of the dynamic mixed FEM (for one plate element of surface S and thickness t):

$$\underbrace{\begin{Bmatrix} t\tilde{\boldsymbol{M}}_{F_w} & \boldsymbol{0} & \boldsymbol{0} \\ \boldsymbol{0} & t^3\tilde{\boldsymbol{M}}_{F_\theta} & \boldsymbol{0} \\ \boldsymbol{0} & \boldsymbol{0} & \boldsymbol{0} \end{Bmatrix}}_{\boldsymbol{M}_{mix}} \begin{Bmatrix} \ddot{\boldsymbol{U}}_{F_w} \\ \ddot{\boldsymbol{U}}_{F_\theta} \\ \ddot{\boldsymbol{\beta}} \end{Bmatrix} + \underbrace{\begin{Bmatrix} \boldsymbol{0} & \boldsymbol{0} & \boldsymbol{G}_w^T \\ \boldsymbol{0} & \boldsymbol{0} & \boldsymbol{G}_\theta^T \\ \boldsymbol{G}_w & \boldsymbol{G}_\theta & \frac{1}{t^3}\tilde{\boldsymbol{H}} \end{Bmatrix}}_{\boldsymbol{K}_{mix}} \begin{Bmatrix} \boldsymbol{U}_{F_w} \\ \boldsymbol{U}_{F_\theta} \\ \boldsymbol{\beta} \end{Bmatrix} = \begin{Bmatrix} \boldsymbol{F}_w \\ \boldsymbol{F}_\theta \\ \boldsymbol{0} \end{Bmatrix} \tag{8}$$

with

$$\tilde{\boldsymbol{M}}_{F_w} = \iint_S {\boldsymbol{N_w}}^T \rho \boldsymbol{N_w} \mathrm{dS} \quad \text{et} \quad \tilde{\boldsymbol{M}}_{F_\theta} = \iint_S {\boldsymbol{N_\theta}}^T \frac{\rho}{12} \boldsymbol{N_\theta} \mathrm{dS} \tag{9}$$

$$\boldsymbol{G_w} = \iint_S \boldsymbol{P}^T \boldsymbol{D} \boldsymbol{N_w} \mathrm{dS} \quad \text{et} \quad \boldsymbol{G_\theta} = \iint_S \boldsymbol{P}^T \boldsymbol{D} \boldsymbol{N_\theta} \mathrm{dS} \tag{10}$$

$$\tilde{\boldsymbol{H}} = \iint_S -\boldsymbol{P}^T \tilde{\boldsymbol{S}}_{ijkl} \boldsymbol{P} \mathrm{dS} \tag{11}$$

with $\boldsymbol{G} = \{\boldsymbol{G}_w, \boldsymbol{G}_\theta\}$, $\tilde{\boldsymbol{S}}_{ijkl} = t^3 \boldsymbol{S}_{ijkl}$ and $\boldsymbol{F} = \{\boldsymbol{F}_w, \boldsymbol{F}_\theta\}^T$ being the nodal forces (splitted for w and θ parameters).
When carefully developing the discretization of each component of the displacements and

generalized stresses, it appears that we can split the whole matrices into smaller ones independent on the thicknesses: $\tilde{\boldsymbol{M}}_{F_w}$ representing the mass in the sense of the transverse displacement w, $\tilde{\boldsymbol{M}}_{F_\theta}$ representing the mass in the sense of the rotation section around x and y (respectively θ_x and θ_y) and $\tilde{\boldsymbol{H}}$ representing the stiffness in the meaning of the stress parameters. $\boldsymbol{G}$ is intrinsically independent from the thickness of the element. That features permits to build an assembly of a given structure (or specific zone of it in our case) regardless of its thickness (as long as it is constant in the zone). Thus, we can build the assembly of each q zone of the structure, attribute their own thicknesses, and afterwards assemble the q zones in order to build the "total" assembly.

In the rest of the article, the superscripts $.^{(q)}$ and $.^{tot}$ are added to the matrices in order to make the distinction between respectively the matrices of the zone q and the ones of the "total" structure.

4.4 Computation of the response and the Von Mises stress

The computation of the response of the "total" structure is made with a global viscous damping proportional to the stiffness features, as follows:

$$\boldsymbol{C}_{mix}^{tot} = \alpha \boldsymbol{K}_{mix}^{tot} \tag{12}$$

Thus, the mixed response of the "total" structure is computed as follows:

$$\begin{Bmatrix} \overline{\boldsymbol{U}} \\ \overline{\boldsymbol{\beta}} \end{Bmatrix} = (-\omega^2 \boldsymbol{M}_{mix}^{tot} + (1 + i\alpha\omega)\boldsymbol{K}_{mix}^{tot})^{-1} \begin{Bmatrix} \overline{\boldsymbol{F}} \\ 0 \end{Bmatrix} \tag{13}$$

with $\omega = \omega_n$ the pulsation of the n^{th} mode in our case. The VM stress in then computed as follows:

$$\sigma_{VM} = \frac{1}{\sqrt{2}} \sqrt{(\sigma_{xx} - \sigma_{yy})^2 + \sigma_{yy}^2 + \sigma_{xx}^2 + 6\sigma_{xy}^2} \tag{14}$$

4.5 Implementation in the genetic algorithm, features and advantages

The figure 5 shows the implementation of the DM-FEM in the GA, with a population of p individuals, g generations, and q different parameters (zones' thickness). This type of mixed model coupled with the thin plate theory puts forward two clear advantages comparing to primal FEM:

- a direct access to the generalized stress within the plate (see operation "2.c" in schema figure 5) and the suppression of the extra calculation needed by a primal FEM. Basically, we replace a complex matrix calculation (for example with Gauss points and smoothing methods) by a simple scalar and almost instantaneous calculation (equation 14). Even though the response calculation (equation 13) is a bit heavier than for a primal model because of its size, the global operation remains more efficient with a mixed model

- the thickness parameters of each q zone of the structure are easily mutable (operation "2.a" in schema figure 5), before assembling them (operation 2.b in schema figure

5). Even though such models are numerically bigger than a classical FEM, the "pre-assembly" of $\boldsymbol{M}_{mix}^{(q)}$ and $\boldsymbol{K}_{mix}^{(q)}$ for each q zone regardless of the thickness parameters (operation 0 in schema figure 5) leaves us the opportunity to allocate them separately for each q zone each iteration (operation "2.a") and afterwards assemble the "total" structure's matrices $\boldsymbol{M}_{mix}^{tot}$ and $\boldsymbol{K}_{mix}^{tot}$ (operation 2.b). The replacement of a "global assembly" by a simple assembly of q zones, each iteration each generation, highly increases the performance of the method.

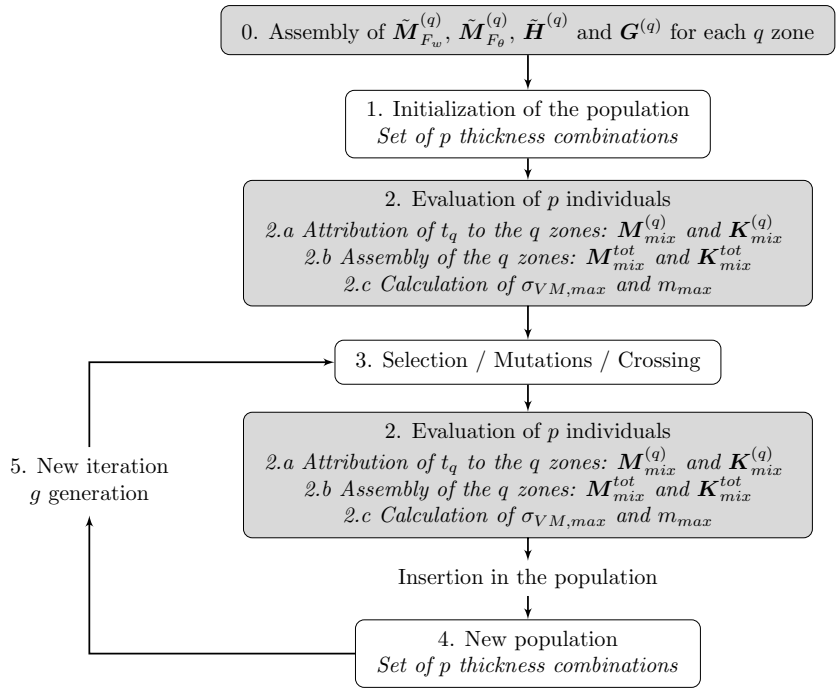


Figure 5: Implementation of the mixed FEM in the genetic algorithm, with a population of p individuals, g generations, and q different parameters (*zones*)

5 Example: optimization of the thickness combination to minimize the mass & the maximum stress for one selected mode

The examples we use to test our method are schematized in figure 1 and 2 in section 2. We want to minimize the maximum VM stress ω_{VM} within the whole structure for a given mode n (see figure 6.c, 7.c and 8c/f), and the mass m of it. The parameters we consider are the thicknesses of each "zone" (see thickness zones in figures 6b, 7b and 8b/e). The range chosen for the different parameters is 1 to 2mm. The plate is made of $S210$ steel (see characteristics in table 1).

The results are presented as "Pareto Front" (black points in figures 6.a, 7.a and 8a/d). These points are defined by the right ordinate axis and the abscissa axis representing respectively the mass of the structure and the maximum VM stress. Each of these optimal

Table 1: Steel characteristics

Young Modulus (Pa)	2.1×10^{11}
Poisson ratio	0.33
Density ($kg.m^{-3}$)	7.5×10^{3}

points are better than the others in the sense of at least one of the two objectives. In that way they are all compromises we can select to design our structure, depending on the objective we want privilege. Once a Pareto point chosen, the parameters corresponding to the point are defined by the colored curves plotted in addition to the Pareto Front in figures 6.a, 7.a and 8a/d. They are determined by the left ordinate axis and the abscissa axis representing respectively the thickness of each of the sub-structures for the chosen Pareto point (with the same abscissa) and the maximum VM stress in the whole structure for this optimal point. Basically, when selecting a point of the Pareto Front, the corresponding thicknesses to design the structure correspond to ordinate of the colored three points with the same abscissa.

Those results were obtained with NSGA-II with a population of p individuals and g generations (depending on the case) following the schema figure 5. It is to be noted that the genetic algorithm has been compiled several times with the same population and generation, in order to check the convergence of the results.

The first subsection deals with the optimization of structure 1 for the mode 1 and constitutes a simple example whose sketch of the results could easily be intuitive, while the second one treats of the optimization of the more complex structure 2 for the mode 3. in the end, subsection 3 shows results for the mode 4 of structure 1 and tricky results.

5.1 Structure 1, Mode 1: Validation / Simple example

This subsection shows a simple intuitive example with structure 1, in order to show the qualitative relevance of such a method. It presents the results obtained with the pulsation ω_1 of the mode $n = 1$ (bending mode), a damping coefficient $\alpha = 2e^{-2}$ and for a stress distribution divided in $q = 8$ zones. The structure is composed of 256 elements. In the genetic algorithm, the population is composed of $p = 50$ individuals and the results presented in figure 6 are obtained with $g = 500$ generations.

This example shows some thickness combinations that allows us to have a VM stress between 17 and 142 MPa, with a mass of the structure between 2.85 and 4.8 Kgs. In this case, more than the steadiness of the Pareto Front itself, the most relevant is the evolution of the thicknesses in function of the VM stress (see colored curves in figure 6a). In fact, we can observe that the most important zones to "reinforce" in order to decrease damages are the closest to the housing. Indeed, the closer to the housing the zone is, the more it needs to be thick. When taking a look at the stress distribution for the first mode (see figure 6c), this evolution of the thicknesses in function of the stress seems coherent. Intuitively, in order to decrease the mass and keep a low stress, we would have decrease

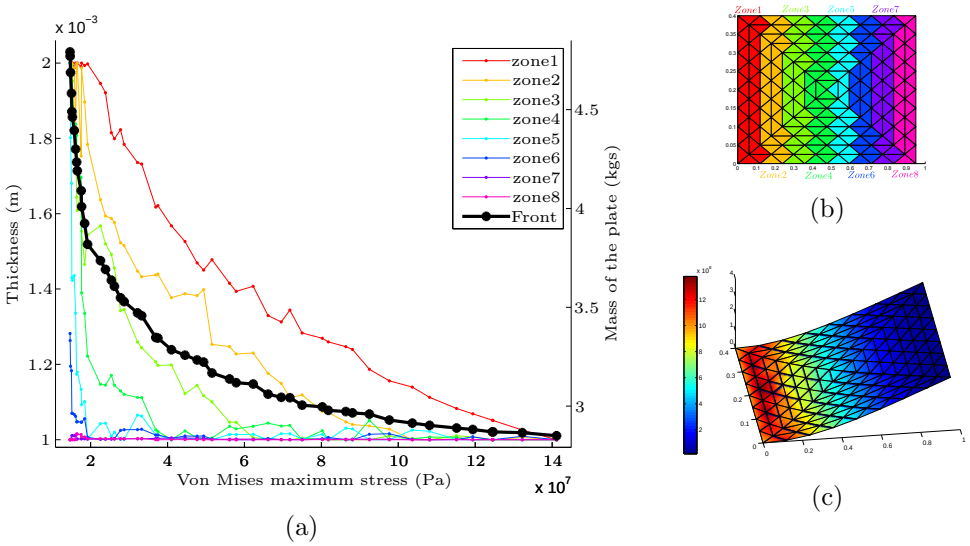


Figure 6: Optimization results for "structure 1" and mode 1: a/ Pareto Front (black) & thicknesses (m) for each point (colored), b/ Independent thickness zones, c/ Stress distribution on mode 1 (Pa)

the thickness where the stress is low, and increase it where it is high. This example puts forward the qualitative relevance of the method, and also gives a quantitative aspect to the thickness parameters with numerical precise values.

5.2 Structure 2, Mode 3: Validation / Complex example

This subsection presents intuitive results with a less simple example with the structure 2 (see figure 2). It presents the results obtained with the pulsation ω_3 of the mode $n = 3$ (bending mode), a damping coefficient $\alpha = 2e^{-3}$ and for a stress distribution divided in $q = 10$ zones. The structure is composed of 512 elements. In the genetic algorithm, the population is composed of $p = 100$ individuals and the results presented in figure 7 are obtained with $g = 500$ generations.

This example shows some thickness combinations that allows us to have a VM stress between 14 and 142 MPa, with a mass of the structure between 4.95 and 8.3 Kgs. In the same way as section 5.1, the most interesting is the evolution of the thicknesses in function of VM stress (see colored curves in figure 7a). In fact, when observing the stress distributions for this mode (see figure 7c), we note that the most stressed zones (see figure 7b) are the zones 1, 5, 6 and 7. It seems intuitive to reinforce these zones specifically in order to decrease the VM stress within the structure. Indeed, the evolutions of the thicknesses 7a) follows this intuition, as these zones look to be the most important, stress wise. In this way, this example, even though more complex than the first one, also puts forward the relevance of the method, in a qualitative manner.
Besides the evolution of the stress distribution that is intuitively predictable, as for the last example, our method still add a qualitative interest as figure 7a gives precise values to the thickness parameters we need to select in order to get the corresponding maximum VM stress and mass of the selected point.

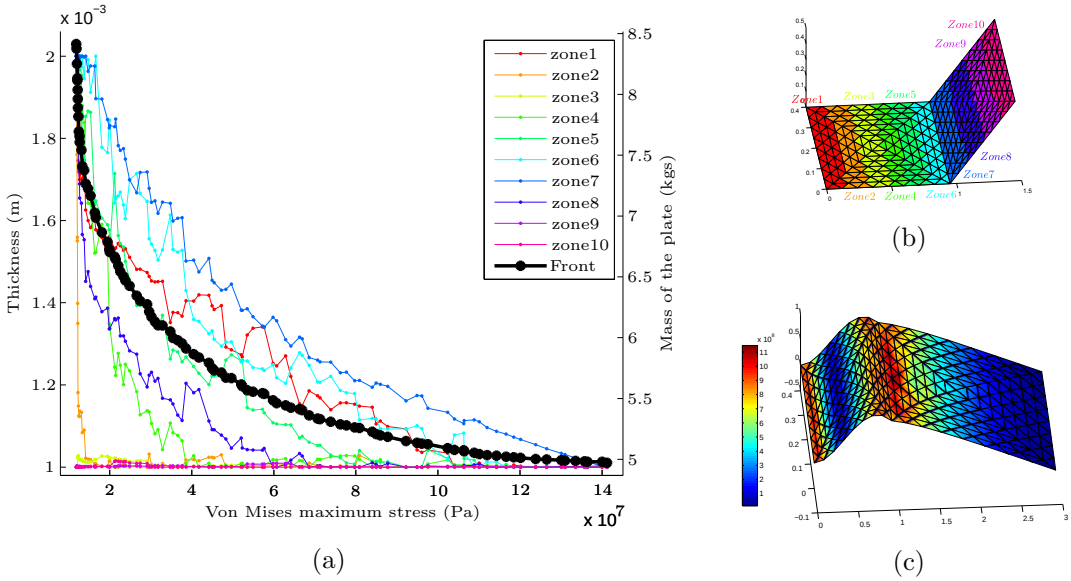


Figure 7: Optimization results for "structure 2" and mode 3: a/ Pareto Front (black) & thicknesses (m) for each point (colored), b/ Independent thickness zones, c/ Stress distribution on mode 1 (Pa)

5.3 Structure 1, Mode 4

This section focus on the 2^{nd} twisting mode of the structure 1. It presents the results obtained with the pulsation ω_4 of the mode $n = 4$ (twisting mode), a damping coefficient $\alpha = 1e^{-4}$. We implemented two cases both divided in 4 zones, with a different repartition of the zones (see figure 8b and 8e). The results are summed up for this two configurations respectively in figure 8a and 8d. In both cases, the structure is composed of 256 elements, the population is made with $p = 50$ individuals and the number of generations is $g = 500$.

The Pareto Front in both cases are not as well-defined and steady as for the last cases. In the first configuration, it allows us to have a VM stress between 3.4 and 170 MPa, with a mass of the structure between 2.85 and 4.23 Kgs. In the second one, the VM stress goes from 3.3 up to 170 MPa, with a mass of the structure between 2.85 and 4.24 Kgs. We note that the Pareto Front both presents some specificity we didn't observe in the optimization of the 1^{st} mode (see section 6), as in both cases:

- the Pareto front shows a large set of solutions that have almost the same VM stress for wide range of mass (low stress domain). This domain is interesting stress wise, because it allows the user to choose this low stress, and dispose of a many different solutions parameters wise. We could call that phenomenon "stress typing"
- the Pareto front shows a large that have a mass between 3.35 and $2.85kgs$ for the first configuration and 3.46 and $2.85kgs$. In this low mass domain, the VM stress varies a lot between respectively 6.6 and $170MPa$, and 6.8 and $170MPa$. This domain is interesting mass wise, because it allows the user to choose a low mass in this domain, and dispose of a a large set of parameters possibility. We could call that phenomenon "mass typing"

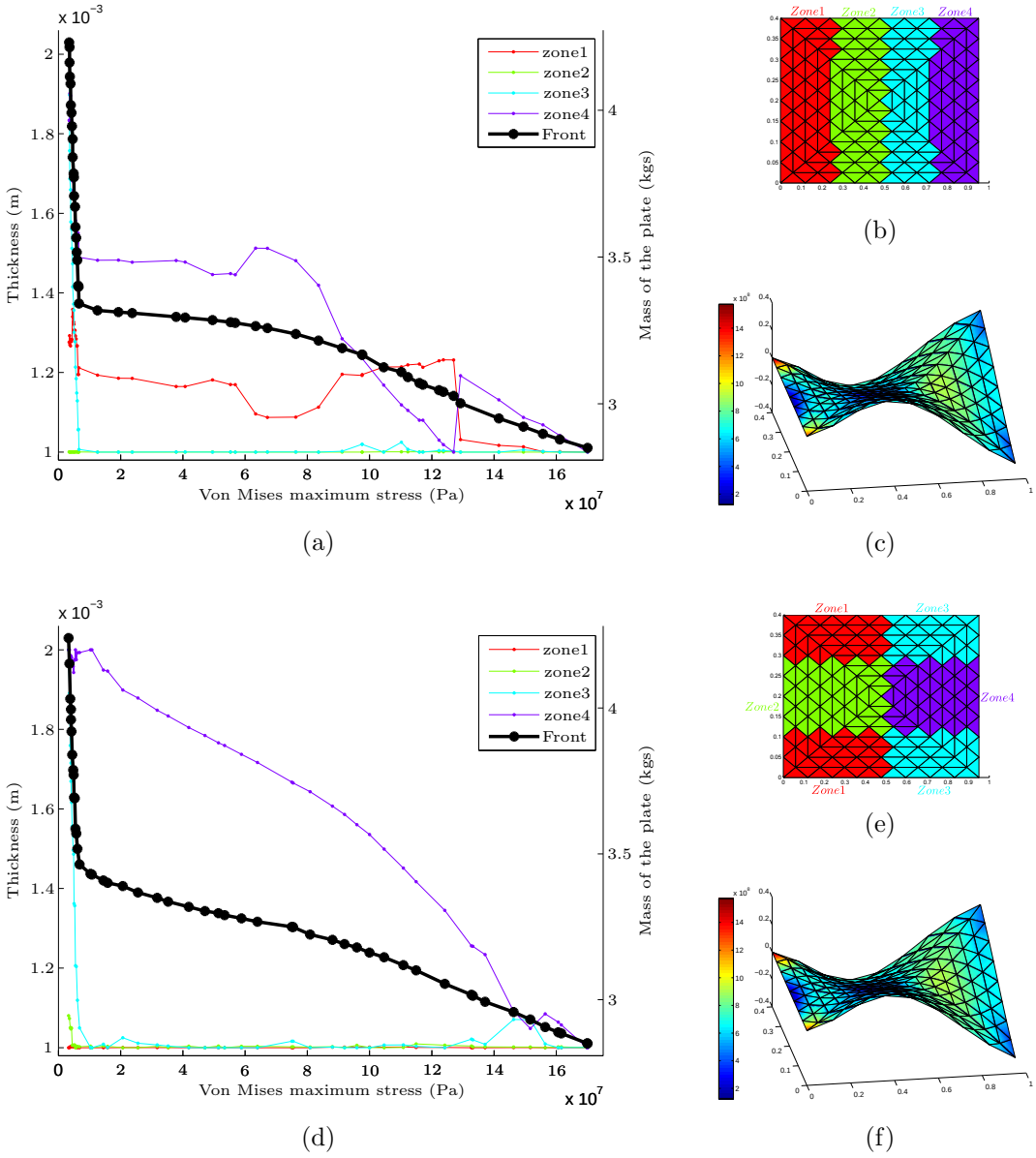


Figure 8: Optimization results for "structure 1" and mode 5: a/ Pareto Front (black) & thicknesses (mm) for each point (colored), b/ Independent thickness zones, c/ Stress distribution on mode 5 (MPa)

When observing the stress distribution within the plate for the 4^{th} mode (see figure 8c/f), it seems tricky to define intuitively which zones need reinforcement. Nevertheless, a first guess would be to increase the thickness either of the first zone (red) in the second configuration (figure 8d/e) or the first zone (red) in the first configuration figure 8a/b). Nevertheless, the two Pareto front show different results, as the second configuration prescribes to pay attention to the 4^{th} central violet zone (almost exclusively), whereas the first configuration focus more on its 4^{th} violet zone and a bit on the 1^{st} red one. Furthermore, the first configuration shows a parameters typing with a switching between the 1^{st} and 4^{th} zones in the high stress domain. This phenomenon can present a high interest in an industrial case as it means that different set of parameters leads to the same stress and mass configuration.

The results described here puts forward the importance of the choice of the distribution of the zone at the beginning of the study, and the relevance of the method in non-intuitive cases. These unexpected results could be interesting in a complex non-predictable industrial case, and puts forward the interest of such a method, in addition to the simplicity and efficiency highlighted in section .

6 Conclusion

This paper introduces a methodology of MO optimization for structural dynamic plate problems with stress criteria and thickness parameters. It is based on a classical NSGA-II method based on compromises and Pareto-optimal solutions, but presents the particularity of using a displacement-generalized stress DM-plate-FEM. Such a model permits a direct access to the stress criteria compared to a primal FEM that needs extra complex calculation. Furthermore, when implementing a KL plate theory, this mixed FEM is featured by a linear dependence to the thickness parameters which facilitates the work of the repetitive algorithm as a whole new assembly is not necessary. These two features combined permits to improve the costly "evaluation step" of the GA and to make it more efficient than classical methods.

This article shows three practical cases, using two different plate structures under a dynamic harmonic load. They are divided into a few zones and each of them has a thickness that is a parameter of the optimization. The goals of the studies are to minimize the maximum VM stress and the mass of the whole structure in function of the thicknesses of each zone, for a harmonic dynamic load of a selected mode. Our optimization technique permits to find a whole group of compromises between the maximum stress and the mass for different thickness distributions, with a different a simpler FEM model. The first examples focus on two different structures and show simple results that could be found intuitively. They put forward the qualitative relevance of the model for a simple example and a more complicated one, and also add a qualitative interest of the method. The third example, deals with a twisting mode and show interesting results. In fact, the qualitative and quantitative evolutions of the parameters of the optimal points were unpredictable, and the Pareto Front presents both stress and mass typing. These kind of results could be interesting to observe in a complex industrial case, and puts forward the interest of such a simple method, in addition to the simplicity and efficiency previously highlighted.

REFERENCES

[1] A.L Araujo, P Martins, C.M Mota Soares, Mota Soares C.A, and J Herskovits. Damping optimization of viscoelastic laminated sandwich composite structures. Structural and Multidisciplinary Optimization, 39:569–579, 2009.

[2] N.D Lagaros and V Papadopoulos. Optimum design of shell structures with random geometric, material and thickness imperfections. International Journal of Solids and Structures, 43:6948–6964, 2006.

[3] R Kudikala, K Deb, and B Bhattacharya. Multi-objective optimization of piezoelectric actuator placement for shape control of plates using genetic algorithms. Journal of Mechanical Design, 131:091007–1–11, 2009.

[4] B Paluch, M Grédiac, and A Faye. Combining a finite element programme and a genetic algorithm to optimize composite structures with variable thickness. Composite and Structures, 83:284–294, 2008.

[5] N Srinivas and K Deb. Multiobjective optimization using nondominated sorting in genetic algorithms. Journal of Evolutionary Computation, 2:221–248, 1994.

[6] K Deb, S Agrawal, A Pratap, and T Meyarivan. A fast elitist non-dominated sorting genetic algorithm for multi-objective optimization: Nsga-ii. Notes in Computer Science, 2000.

[7] Washizu. Variational methods in elasticity and plasticity, 2nd edition. Pergamon Press, 1975.

[8] E Hellinger. Die allgemeinen ansatze der mechanik der kontinua. Encyklopadie der mathematischen Wissenschaften, 4, 1914.

[9] E Reissner. On a variational theorem in elasticity. Journal of Mathematics and Physics, 29:90–95, 1950.

[10] Reissner. On a certain mixed variational theorem and a proposed application. International Journal For Numerical Methods In Engineering, 20(7):1366–1368, 1984.

[11] E Reissner. On a mixed variational theorem and on shear feformable plate theory. International Journal For Numerical Methods In Engineering, 23(2):193–198, 1986.

[12] P Wriggers and C Cartsensen. Mixed Finite Element Technologies. Applied Mathematics/Computational Methods of Engineering, 2009.

[13] M.H Omurtag and F Kadioglu. Free vibration analysis of orthotropic plates resting on pasternak foundation by mixed finite element formulation. Computers and Structures, 67:253–265, 1998.

[14] P Garambois, S Besset, and L Jézéquel. Modal synthesis applied to a reissner mixed plate finite element dynamic model. Proceedings of the 9th International Conference on Structural Dynamics, EURODYN 2014, 2014.

[15] J. N. Reddy. Theory and Analysis of Elastic Plates and Shells. 2007.

COMPDYN 2015
5th ECCOMAS Thematic Conference on
Computational Methods in Structural Dynamics and Earthquake Engineering
M. Papadrakakis, V. Papadopoulos, V. Plevris (eds.)
Crete Island, Greece, 25 27 May 2015

THE STUDY OF X-BRACING ON LIMIT STATE BEHAVIOR OF BUCKLING RESTRAINED BRACE (BRB) IN STEEL FRAMES USING PUSHOVER ANALYSIS

Pe. Sh. Heidari [1], A. Golara [2*], Po. Sh. Heidari [3] and R. A. Jazany [4]

[1] East Tehran Branch, Azad University, e-mail: peyman_shademan@yahoo.com

[2*] National Iranian Gas Company (NIGC), e-mail: a.golara@gmail.com

[3] Central Branch, Azad University, e-mail: pouya_civil1@yahoo.com

[4] International Institute of Earthquake Engineering and Seismology, e-mail: roohollah_ahmady@yahoo.co.uk

Keywords: Buckling restrained brace, Plasticity index, Behavior & resistance coefficient, Plastic joints

Abstract. *Using energy dampers in structures is highly considered for the dissipation and absorption of earthquake energy. The main advantage of using energy dampers is absorbing the earthquake energy in some sections apart from the structure. Among different types of dampers, hysteresis dampers are of special place because of low cost, high reliability and the lack of mechanical parts. In this paper, a special kind of hysteresis damper is considered under the name of buckling brace, which is provided with the aim of the study and investigation of X-brace in the seismic behavior of the steel framed buildings and for pipe and equipment racks that are extensively used in the oil and gas industry. In this paper, 62 models of steel frames with X-brace and buckling type damper are processed with different bays and heights. The frames' plasticity index, behavior coefficient, distribution type and the number of plastic hinges formed were calculated. Furthermore, suitable locations of braces for improving nonlinear behavior and suitable distribution of plastic hinges were presented and it was determined that for some models, the behavior coefficient of structure will increase to 1.5 times.*

1 INTRODUCTION

One of the simple ways for static non-linear analysis of complex structures is gradual increase of lateral load statically. The presented methods are part of a seismic design and structure evaluation, which are based on three-dimensional mathematical model of the structure in nonlinear range. Most of behavioral defects of common converged braces are the result of difference between compressive and tensile capacity of these braces and decline of their resistance under cyclic loading. Therefore, many researches are devoted to optimize these braces in order to make them show an ideal elast-o-plastic behavior. To achieve this goal, it is required to prevent the compressive buckling of braces using a suitable mechanism and provide the steel compressive yield. The method considered was encapsulating a ductile metallic core among a mass of concrete, covered with a metal membrane.

The basics of this damper's function are preventing the buckling of the steel core in order to produce the compressive yield phenomenon in it and as a result absorb the energy in this member of the structure. It is possible through covering the whole length of steel core by a steel pipe filled with concrete or mortar. In this system, there is a need to provide a sliding surface or discontinuity layer between metal core and confining concrete. The main aim of this process is to make the bracing force be tolerated just through the steel core. The sliding layer materials and geometry should be in such a way that provides a relative movement between steel core and concrete, which are created because of shear and Poisson effect and as a result provides its yield in compressive loading mode besides preventing local buckling of the core. Concrete and steel tubular casings provide the required stiffness and bending resistance to prevent general buckling of braces and provide the conditions of load tolerance by the steel core up to yield limit without decreasing the stiffness and resistance of braces during loading cycles. In addition, concrete and steel casings prevent the local buckling of the core.

During the systematic multiplier analysis, showing the distribution of the plastic joints creation method is possible in steel structures. Non-linear static analysis by gradual increase of lateral load or location change on top of the structure is part of the new methods, which present a good and simple estimation of nonlinear function of the structure. Most of the researches show that the multiplier nonlinear static analysis methods properly match with nonlinear dynamic analysis results in evaluating the structures (e.g. [1]). Pushover analysis can provide good information about the structure's resistance-capacity, deformation demand, and discontinuity in the distribution of resistance and the areas with energy absorption potential in the structure [2]. In this study, pushover nonlinear static method is used for seismic evaluation and determination of plasticity index, behavior and resistance coefficient, plastic joints distribution mode, and studying the location of the braces.

2 MODEL SELECTION, MODEL'S LOADING AND SECTIONS

Here, there is a close match among the geometric dimensions of the sections in models and oil and gas industrial frames and structural frames of ordinary building in Iran. For created models, the bays distance is considered 5 metres and the height stories are 3 metres. The aim of this study is modeling and analyzing the structures with different heights and bays by using buckling braces to provide the possibility of studying and observing the effects of the type of braces and the number of braces spans. So the steel frames with 3, 5 and 7 bays and the height of 6, 12 and 18 stories are used. In order to determine the effect of buckling braces location on boundary behavior of braced framed, it has tried to create bracing in different bays. Therefore, in three-bay frames, the braced spans were created as one-bay and two-bays together. In addition, in five-bay frames, the braced spans are used as two-bays, the location of which is different among models. For seven-bay frames the braced spans are used as two-bays

and three-bays, where the side by side symmetric form is used for two-bays and single, double and triple forms are used for three bays next to each other.

In naming the braced frames, a special trend is used. Therefore, in the frame considered, numbering of the bays is from left to right in such a way that the first braced span on the left receives number 1 and the last one on the left receives number 7 for those frames with highest number of bays. Thus, the naming trend for braced frames is as *WS*(X, Y, Z). *W* is the number of the bays in regarded frame and *S* is for bay. X, Y and Z are the number of the first, second and third braced spans, respectively. For instance, 7S (1, 4, 7) means a seven-bay frame where the first, fourth and seventh bay of it is braced from the left, respectively. In Figure 1, a frame sample is shown, which is named in the form of 7S (1, 4, 7).

The composite roof details are used to determine the gravity dead load. Lateral loading of frames is calculated based on the regulations of seismic design with the design basis acceleration of 0.35 for South Pars region [3] and soil period of 0.5 second for soil type II. The design of steel structures was according to AISC89-ASD. The connections between beams and braces are simple joint and columns' connections to the foundation are simple support. The effective length of braces for out of plane buckling is considered equal to 0.67; this value for in plane is 0.5 for IPE sections for beams and IPB section for columns. Also double L sections were employed for braces. Material properties assumed compatible with ST-37 steel grade.

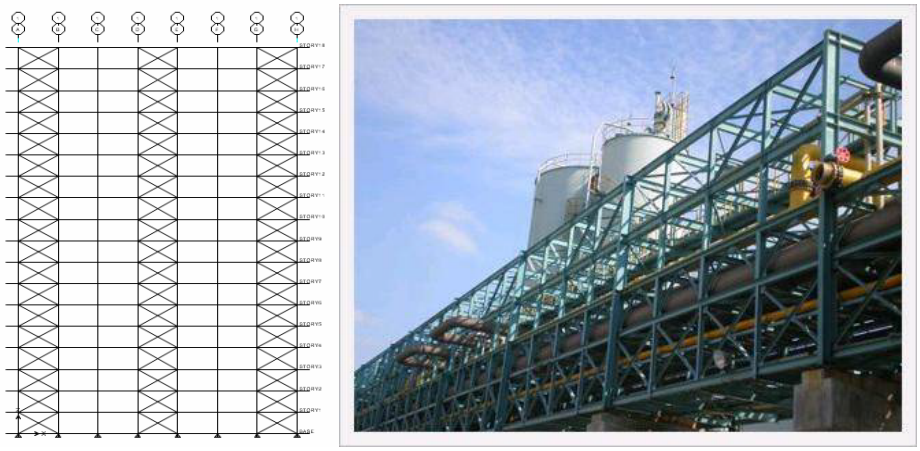


Fig. 1 7S (1,4,7) Steel Framed Building and a 4 Story Pipe Rack Structure

3 BASICS OF INELASTIC CYCLIC BEHAVIOR OF BUCKLING BRACES

Buckling-Restrained Braced Frames (BRBFs), as can be shown in Figure 2, are a relatively new type of concentrically braced system characterized by the use of braces that yield inelastically both in tension and compression at their adjusted strengths [4]. Despite their being a relatively new system, BRBFs in the United States have, to date, been subjected to numerous analytical and experimental studies that have demonstrated their robustness when subjected to code-type ground motions (e.g. [5], [6], [7]).

The brace component of BRBFs is known as the Buckling Restrained Brace (BRB). BRBs have full, balanced hysteresis loops as illustrated in Figure 3, with compression-yielding similar to tension-yielding behavior. They achieve this through the decoupling of the stress-resisting and flexural buckling resisting aspects of compression strength. Axial stresses are resisted by a shaped steel core. Buckling resistance is provided to that core by a casing, which may be of steel, concrete, composite, or other construction. Because the steel core is re-

strained from buckling, it develops almost uniform axial strains. Plastic hinges associated with buckling do not form in properly designed and detailed BRBs.



Fig. 2 Buckling Brace in Stories' Height and Details of Bracing

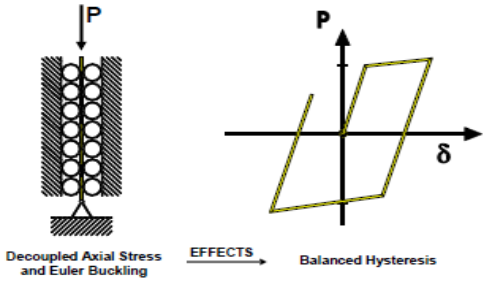


Fig. 3 Mechanics of a Buckling-Restrained Brace

The inelastic cyclic behavior of these braces is studied through many experiences (e.g [8], [9] and [10]). These experiences, matching with finite element studies, showed that unlike common braces, the stable hysteresis cycles can be obtained in tension and pressure, therefore a high capacity of earthquake energy absorption is obtained in the structure. The behavior of the frames with buckling braces shows considerable difference with common coaxial bracing frames despite apparent similarities. In buckling–restrained braces, the hysteresis loops are stable and no resistance or curve decline is observed in the system during loading and unloading cycles.

In this study, after determining the loads applied on the structure and analyzing the frame under them, the force created in braces can be calculated and shown as P'_{br} . Therefore, the section required for yielding area of the buckling equals:

$$A'_{br} = \frac{P'_{br}}{1.25 \times 0.6 F_y} \alpha \qquad (1)$$

In which α is considered between one and final resistance relative to the maximum load resulted from analysis in members to which the load of brace is transferred (such as columns). Higher values of this coefficient increase the stiffness and energy absorption capacity of the system. *Fy* equals the steel core yield resistance of bracing. Coefficient 1.25 is for considering the strain hardening of steel. Because the cross section of the central core is considerably smaller than the cross section of the final area of the connection, most of the elastic and even plastic displacements happen in this area. With regard to this fact, the axial stiffness of each buckling brace equals:

$$K_{br} = \frac{EA'_{br}}{L'_{br}} \tag{2}$$

In which L'_{br} is the length of the central core and E is the elasticity module of the core steel materials. Furthermore, the axial strain of yielding area is:

$$\varepsilon_{br} = \frac{\delta_{br}}{L'_{br}} \tag{3}$$

In which δ_{br} is the axial deformation of the brace. By reducing L'_{br}, the brace's stiffness increases and as a result, the relative displacement of the story decreases. As the above relation shows, this is independent from the brace resistance.

In order to prevent buckling in pressure, the metal core is placed inside a metal sheath filled with concrete or mortar. Before filling the sheath with concrete, a few separating material or vacuum is placed between metal core and mortar to prevent the axial force transfer from metal core to concrete covering or at least to minimize it. The effect of Poisson coefficient also causes the metal core to expand in pressure and this requires a distance to be created (Figure 4).



Fig. 4 Components of Buckling –Restrained Brace

When these braces designed properly with details, the steel sheath should not bear any axial force. To prevent the buckling of BRBs, the metal sheath should be designed for the following stiffness of bending:

$$\frac{P_e}{P_y} \geq 1.0 \tag{4}$$

In which P_y is the flowing resistance of the flowing confined part and P_e is the elastic buckling resistance of the metal sheath.

$$P_e = \frac{\pi^2 EI_{sc}}{L^2_{sc}} \tag{5}$$

E is Yang module, EI_{sc} is the inertia momentum of steel sheath section and L_{sc} is the length of the sheath. In using these equations, it should be noted that the effects of steel strain stiffness is omitted under cyclic loading. In this case, steel strain stiffness increases the pressure resistance of the brace up to 30% and a resistance coefficient of $\varphi = 0.85$ is used in numerator.

$$\frac{\varphi P_e}{1.3 \times P_y} \geq 1.0 \longrightarrow \frac{P_e}{P_y} \geq 1.5 \tag{6}$$

In designing process, it has been tried to change the dimensions and thickness of BRB sections to have a more uniform energy absorption in height. The characteristics of plastic joints of BRB are the same as tensile section of the braces in pressure section (Figure 5).

Point	Force/SF	Disp/SF
E-	-0.8	-14
D-	-0.8	-11
C-	-1.33	-11
B-	-1	0.
A	0	0.
B	1	0.
C	1.33	11
D	0.8	11
E	0.8	14

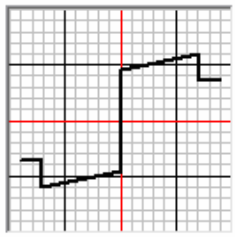


Fig. 5 The Plastic Joints Characteristics of BRB in Pressure and Tensile Section of the Brace

4 RESULTS FROM NONLINER STATIC ANALYSIS

After the two dimensional nonlinear static analysis of each one of the models, the results from base shear–roof displacement for lateral push expressed through a curve. The incremental load curve includes horizontal and vertical axes, which show roof displacement and base shear resulted from lateral push respectively. Information retrievable from these diagrams is yield displacement *Dy*, yield base shear *Fy*, final displacement *Du* and final base shear *Fu*. Displacement and yield base shear are a point on pushover diagram in which the linear an elastic behavior of the structure has terminated and the structure enters the nonlinear area. Displacement and final base shear are a point on this diagram in which the structure's resistance has extensively decreased and in fact this is the result of the structure's destruction, decreases in the structure's stiffness and the lack of tolerance of the loads applied to it.

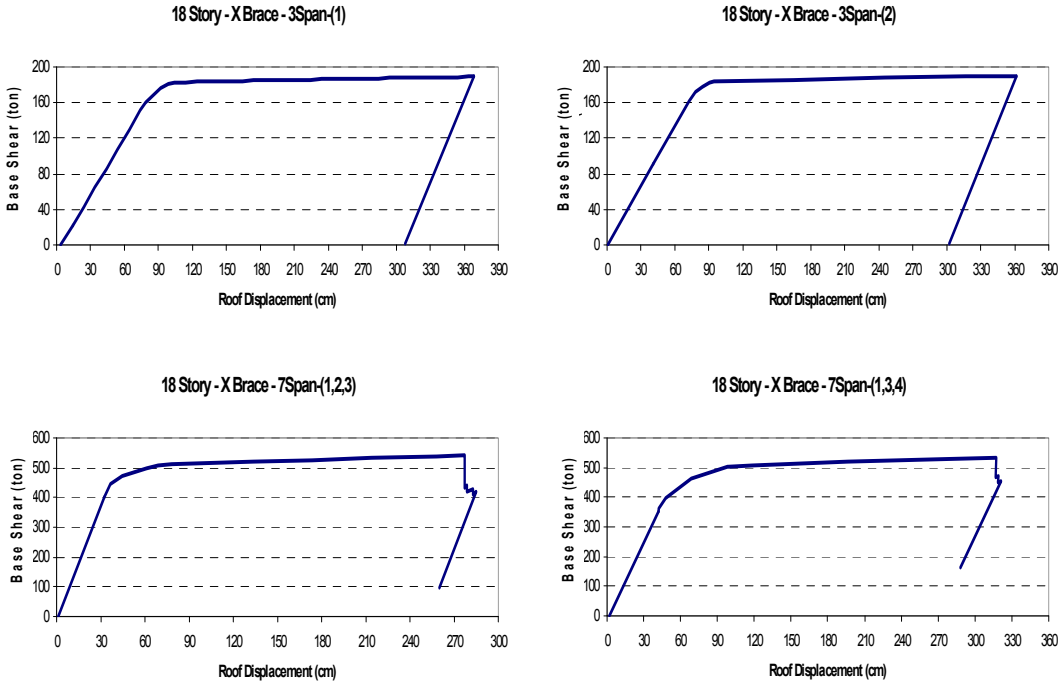


Fig. 6 Roof Story Displacement for 18 Stories Frames for Example for Models 3S(1), 3S(2), 7S(1,2,3) and 7S(1,3,4)

In this paper, computation of R can be carried out using the following method but there are some essential values to be derived first. These values include: yield and ultimate displacements; also yield force and elastic strength demand force. R can be performed by defining two factors: strength demand reduction factor R_d and overstrength factor Ω. Figure 7 shows parameter derived for evaluation of R-values. The results from all models are illustrated in Figure 8, 9 and listed in Table I, II.

$$R_d = \frac{Elastic\ \ Strength\ \ Demand}{Real\ \ Strength} \quad (7)$$

$$\Omega = \frac{Real\ \ Strength}{Design\ \ Strength} \quad (8)$$

$$R = R_d . \Omega \quad (9)$$

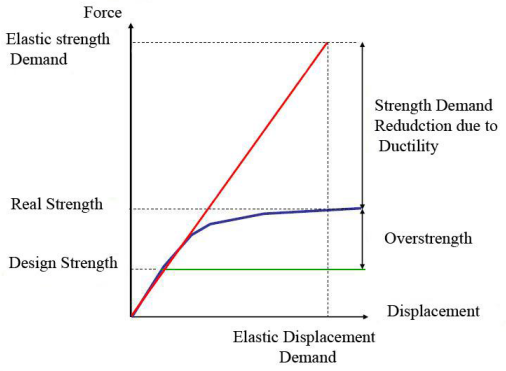


Fig. 7 Parameters Employed in Determined Behavior Coefficient

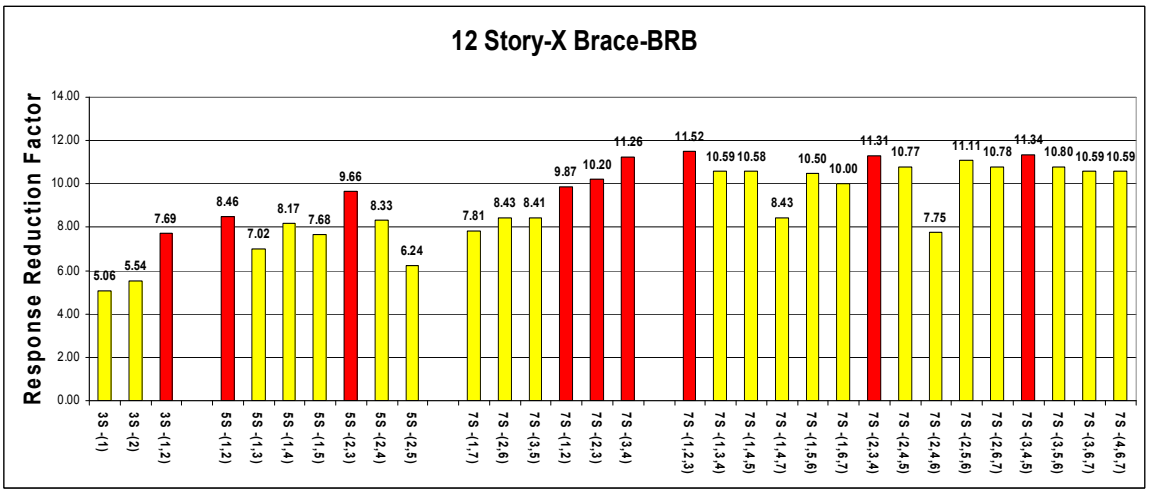


Fig. 8 Computed R-Values for 12-Story Frame and Different Braced Bays

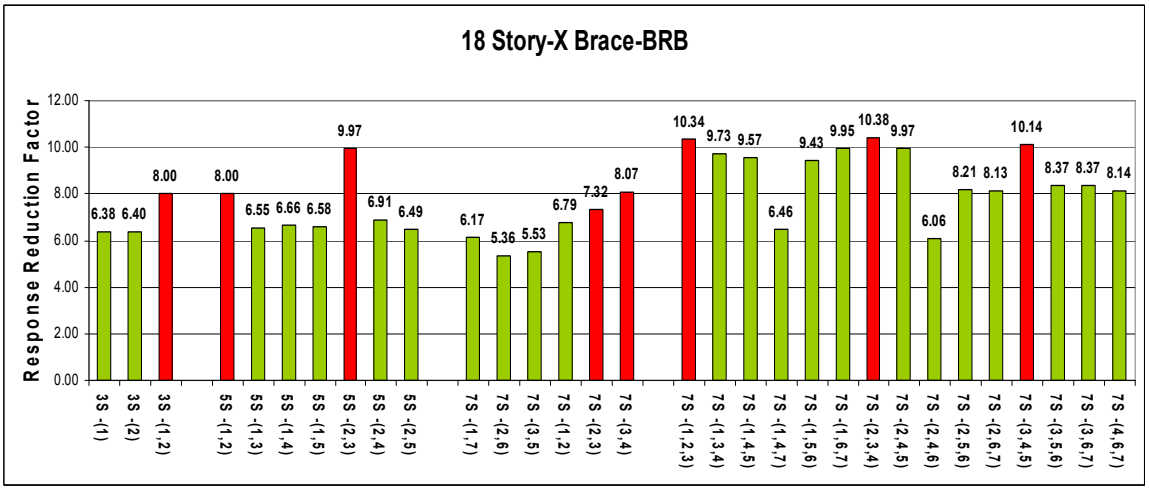


Fig. 9 Computed R-Values for 18-Story Frame and Different Braced Bays

TABLE I
BEHAVIOR COEFFICIENT AND RESISTANCE COEFFICIENT COMPUTATION FOR 6, STORIES FRAMES
UNIT: TON,CM

6 storey - X Brace - BRB			
Span	Initial Stiffness	R	O.S
3S -(1)	11.97	8.20	1.29
3S -(2)	12.26	8.23	1.29
3S -(1,2)	26.80	8.46	1.32
5S -(1,2)	27.53	9.50	1.44
5S -(1,3)	20.53	7.56	1.44
5S -(1,4)	20.25	7.48	1.45
5S -(1,5)	20.25	8.77	1.72
5S -(2,3)	26.34	9.76	1.46
5S -(2,4)	21.34	7.87	1.46
5S -(2,5)	22.52	8.69	1.50
7S -(1,7)	19.75	8.89	1.47
7S -(2,6)	20.72	9.00	1.50
7S -(3,5)	22.69	9.84	1.49
7S -(1,2)	26.00	11.37	1.50
7S -(2,3)	27.48	11.47	1.52
7S -(3,4)	26.96	11.56	1.53
7S -(1,2,3)	43.23	10.24	1.50
7S -(1,3,4)	37.09	8.67	1.43
7S -(1,4,5)	35.17	8.31	1.44
7S -(1,4,7)	28.86	7.34	1.50
7S -(1,5,6)	35.74	8.62	1.47
7S -(1,6,7)	33.77	10.49	1.59
7S -(2,3,4)	40.48	11.86	1.54
7S -(2,4,5)	37.15	11.00	1.59
7S -(2,4,6)	32.86	9.79	1.64
7S -(2,5,6)	36.54	11.10	1.60
7S -(2,6,7)	36.93	10.36	1.60
7S -(3,4,5)	43.73	11.44	1.55
7S -(3,5,6)	38.67	9.84	1.63
7S -(3,6,7)	34.15	8.15	1.47
7S -(4,6,7)	36.89	8.66	1.46

TABLE II
BEHAVIOR COEFFICIENT AND RESISTANCE COEFFICIENT COMPUTATION FOR 12, STORIES FRAMES
UNIT: TON,CM

12 storey - X Brace - BRB			
Span	Initial Stiffness	R	O.S
3S -(1)	4.32	5.06	1.26
3S -(2)	4.64	5.54	1.29
3S -(1,2)	11.05	7.69	1.34
5S -(1,2)	10.84	8.46	1.39
5S -(1,3)	8.31	7.02	1.39
5S -(1,4)	8.43	8.17	1.62
5S -(1,5)	7.96	7.68	1.61
5S -(2,3)	10.88	9.66	1.40
5S -(2,4)	8.56	8.33	1.40
5S -(2,5)	7.98	6.24	1.29
7S -(1,7)	7.79	7.81	1.41
7S -(2,6)	7.73	8.43	1.56
7S -(3,5)	8.36	8.41	1.43
7S -(1,2)	10.72	9.87	1.40
7S -(2,3)	11.89	10.20	1.37
7S -(3,4)	12.98	11.26	1.37
7S -(1,2,3)	18.77	11.52	1.55
7S -(1,3,4)	15.84	10.59	1.55
7S -(1,4,5)	15.82	10.58	1.55
7S -(1,4,7)	11.67	8.43	1.55
7S -(1,5,6)	15.74	10.50	1.57
7S -(1,6,7)	14.99	10.00	1.55
7S -(2,3,4)	18.82	11.31	1.52
7S -(2,4,5)	16.56	10.77	1.51
7S -(2,4,6)	11.72	7.75	1.40
7S -(2,5,6)	16.57	11.11	1.56
7S -(2,6,7)	16.51	10.78	1.52
7S -(3,4,5)	18.83	11.34	1.52
7S -(3,5,6)	16.56	10.80	1.51
7S -(3,6,7)	16.18	10.59	1.52
7S -(4,6,7)	16.22	10.59	1.53

5 CONCLUSION

In conducting this research, many results are obtained. The mail results are as follows:
1- Yield displacement of frames braced by buckling-retrained X-brace is decreased when the bracing spans are approaching each other

2- Final displacement of braced frames is minimized when the bracing spans are approaching each other in all bays and heights.

3- The yield base shear and final force increases when the bracing spans are approaching each other in all bays and heights. Therefore, the lateral loading increases and maximum capacity of the sections can be employed to bear the lateral loads.

4- Primary stiffness decreases with an increase in the number of stories. But by creating the stiff spans in the bays, which are located next to each other, the primary stiffness also increases.

5- By increasing the number of the stories' dispersion, behavior coefficient values increases. Therefore, it shows the sensitivity of behavior coefficient value to the structure height and the criticality of behavior coefficient effect in designing steel joint frames.

6- To improve the behavior coefficient of steel frames with buckling retrained X- bracing, the distance between bracing spans should be decreased and they should be even placed next to each other if it's possible.

7- The resistance coefficient of frames braced with buckling-retrained X-brace can be increased to 1.5 times and improved as well relative to the situation of braces.

ACKNOWLEDGMENTS

We would like to thank National Iranian Gas Company (NIGC) for finical support of this paper.

REFERENCES

[1] G. Gregory, A.M. Reinhorn, and R.M. Willford, *Nonlinear structural analysis for seismic design*, NEHRP Seismic Design Technical Brief No 4, 2010.

[2] H. Kayhani, A. Golara, and R.A. Jazany, Comparison of Modal Pushover Analysis and Nonlinear Time History Analysis Using Precedence List Record Selection Method, *the First Makassar International Conference on Civil Engineering* (MICCE2010-No SCE 67) ISBN 978-602-95227-0-9, 2010.

[3] A. Golara, Probabilistic seismic hazard analysis of interconnected infrastructure: a case of Iranian high-pressure gas supply system. *Natural hazards*, 73(2), 567-577, 2014.

[4] P. Clark, I. Aiken, K. Kasai, E. Ko, and I. Kimura, Design procedures for buildings incorporating hysteretic damping devices, *Proceedings of the 69th Annual Convention*, SEAOC, Sacramento, CA., 1999.

[5] L.A. Fahnestock, R. Sause and J.M. Ricles, Seismic response and performance of BRBFs, *Journal of Structural Engineering*, 9, 1195-1204, 2007.

[6] W.A. López, D.S.Gwie, C.M. Saunders, and T.W. Lauck, Lessons learned from large-scale tests of unbonded braced frame subassemblages, *in Proceedings of the 71st Annual Convention,* 171-183, Structural Engineers Association of California, Sacramento, 2002.

[7] R. Sabelli, S.A. Mahin, and C. Chang, Seismic demands on steel braced-frame buildings with bucklingrestrained braces, *Eng. Struct.*, 25, 655–666, 2003.

[8] M. Hosseini, P.S. Heidari, M. Heravi, Analytical and experimental study of the effect of bracing pattern in the lateral load bearing capacity of concentrically braced steel frames, *The 14thWorld Conference on Earthquake Engineering, Beijing, China*, October 2008.

[9] P. Heidari, H. Kayhani, R.A. Jazany, Experimental Study on the Effects of Different Concentric Bracing Configuration on Steel Frames Inelastic Behavior, *Australian Journal of Basic and Applied Sciences*, 5(12): 2716-2728, 2011 ISSN 1991-8178, 2011.

[10] P.S. Heidari, H. Kayhani, R.A. Jazany, An Investigation on Bracing Configuration Effects on Behavior of Concentrically Braced Steel Frames, *World Applied Sciences Journal* 17(9): 1095-1108, 2012 ISSN 1818-4952, 2012.

COMPDYN 2015
5th ECCOMAS Thematic Conference on
Computational Methods in Structural Dynamics and Earthquake Engineering
M. Papadrakakis, V. Papadopoulos, V. Plevris (eds.)
Crete Island, Greece, 25–27 May 2015

OPTIMIZED RETROFIT OF SEISMICALLY DESIGNED STRUCTURES TO WITHSTAND PROGRESSIVE COLLAPSE

Georgios S. Papavasileiou and Dimos C. Charmpis

Department of Civil and Environmental Engineering, University of Cyprus,
75 Kallipoleos Str., P.O. Box 20537, 1678 Nicosia, Cyprus,
E-mails: papavasileiou.georgios@ucy.ac.cy, charmpis@ucy.ac.cy

Keywords: Progressive collapse, robustness, damage tolerance, local failure, alternate load path, column loss, seismic design, structural optimization, retrofit.

Abstract. *Seismically designed buildings possess the necessary properties to withstand the design earthquake excitations and limit structural damage to the desired level. This is achieved by appropriately defining individual member capacities, interstorey and global stiffnesses and energy dissipation mechanisms based on the provisions of current design codes. However, such provisions do not suffice, in order to protect a structure from disproportional extent of damage when a local failure occurs. Hence, in order to increase their progressive collapse resistance, existing seismically designed buildings need to be appropriately retrofitted.*
This paper presents an optimization procedure for the retrofit of seismically designed buildings, in order to increase their capacity to sustain local damage without extensive propagation leading to severe structural failure (partial/full collapse). Two retrofit methods for seismically designed steel-concrete composite buildings are presented and assessed with respect to their cost-effectiveness. The retrofit methods are based on: (a) the strengthening of beams in the structure or (b) the installation of bracings in the horizontal direction. Structural optimization aims to minimize the total retrofit cost, in order to determine the lowest possible need for retrofit material, enabling at the same time the comparative assessment of the two retrofit methods on a 'fair basis'.

1 INTRODUCTION

Design against progressive collapse has been a concern for engineers since the Ronan Point collapse in London on May 16, 1968, as its results are disproportionate to the cause: small scale damage triggers extended damage or failure of a number of neighboring structural elements, which might result in collapse of a part –if not of the whole– of the building. However, intensive investigation of such phenomena, as well as of methods to reduce their effects, started only after the collapse of the World Trade Center towers in September 11, 2001. Design strategies to control the damage propagation or reduce the probability of occurrence of the initial failure have been proposed [1-8]. Up to now, due to the non-compulsory nature of the design strategies, a very limited number of existing buildings has been designed against progressive collapse. Hence, certain buildings may need to be retrofitted appropriately, in order to reduce the risk of progressive collapse, when they sustain small-scale damage. Thus a corresponding need to develop and examine retrofit methods arises. The preference of a retrofit method over another depends on the cost over effectiveness attained by each one, since the cost induced plays a key role in deciding for and realizing a retrofit solution. Even when progressive collapse resistance is taken into consideration in the design phase of a building, the additional cost to achieve such resistance is considerable.

Over the last decades, structural design optimization has progressed to a valuable computational tool, which assists the engineer in making best use of structural material, in order to detect a feasible and cost-effective design satisfying certain pre-specified constraints. The present work presents an optimization procedure for the retrofit of composite steel-concrete buildings in order to resist earthquake actions and progressive collapse. The Evolution Strategies optimization algorithm is employed in order to minimize the total retrofit cost, subject to constraints on (a) the safety of structural members, (b) the structural system resistance against earthquake and (c) the building's capacity to sustain failure of load-bearing elements without disproportionate propagation of the structural damage. Structural optimization approaches to achieve progressive collapse resistance in a cost-effective manner in the design phase of a building have been presented in [7,8].

Various retrofit methods for existing structural systems are provided in the literature (e.g. [9-14]). Two retrofit approaches for composite buildings are examined in this work: (a) strengthening of beams by welding additional elements (plates or members with I-shaped sections) at their lower flanges and (b) installation of additional bracings to form external horizontal trusses at predefined storeys. A numerical application involving the retrofit of a 6-storey composite steel-concrete building demonstrates the effectiveness of the proposed optimization approach and illustrates the comparative effectiveness of the two retrofit approaches.

2 THE ALTERNATE LOAD PATH METHOD

One of the measures proposed to reduce the potential for progressive collapse is the alternate load path method [2,5-8]. According to this method, the assessed structural design should be able to redistribute successfully the acting loads when local failure takes place, without extensive propagation of structural damage, which indicates the initiation of a chain reaction that might lead to collapse. Thus, alternate load paths, which utilize undamaged members to transfer the loads to the ground, need to be available after the initial failure occurs.

The alternate load path method is implemented by artificially removing certain structural members from the structural system [2,5,7,8]. The gravitational loads are then applied incrementally on the damaged building by means of a non-linear structural analysis. As this type of analysis is considered to be equivalent to a nonlinear pushover analysis in the vertical direction, it is usually referred to as 'pushdown analysis'. Such analyses are associated with considerable

uncertainties on the performance of structural systems under the large deformations that develop, when e.g. a column member is removed from a system. Hence, a building's progressive collapse resistance is quantified using specific indicators, such as the plastic rotation θ of the steel beams above the 'damaged' area of the building (Fig. 1). In [5], 'high requirements' on progressive collapse resistance are related to the limitation of the plastic rotation of the steel beams below 6°. In this work, the relative vertical displacement of the two ends of a beam normalized by its length (vertical drift) can be used as an equivalent alternative to plastic rotation. As a rotation of 6° corresponds to a vertical drift of about 10.5%, the maximum admissible vertical drift is taken 10% and is imposed through a related constraint for beam deformation in the optimization procedure presented herein.

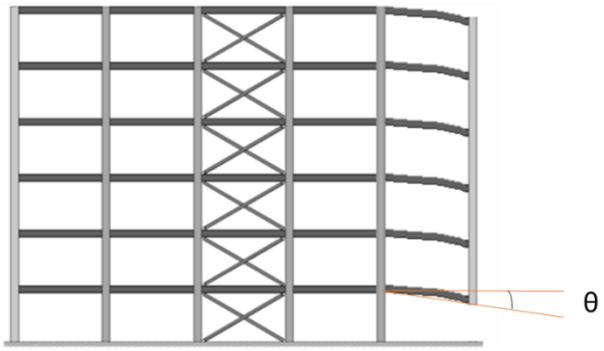


Figure. 1. Deformed shape of a frame under a base corner column loss scenario.

3 RETROFIT METHODS

In this section, two retrofit methods are presented. The first method aims to increase the stiffness of the beams, so that deflections caused by the sudden loss of a column are reduced. An alternative to the aforementioned approach, in order to increase the building's progressive collapse resistance, is to introduce a set of bracings placed in the horizontal direction at predefined storeys.

3.1 Beam retrofit with plates and I-shaped sections

When designing against progressive collapse, of particular significance are the horizontal elements, which are inevitably involved in the redistribution of the gravitational loads from the affected bays to the undamaged structural elements and, thereafter, to the ground. Whether they are the main elements of the intended alternate path or they play a secondary role in realizing it, their integrity is crucial for the successful employment of the alternate path method. By strengthening the steel beams, their stiffness is enhanced and, consequently, deflections due to additional loads and support condition alteration are reduced.

The flanges of an I-shaped beam are the parts of the section with the largest distance from the section's centroid and, therefore, they provide almost all of its stiffness about the major axis. Hence, a method commonly used to increase an I-shaped beam's stiffness about the major axis is the installation (welding) of steel plates at its flanges. Increasing the flanges' area results in a considerable enhancement to the beam's flexural capacity. In an existing building, steel beams are typically connected at their top flange to a composite or reinforced concrete slab using shear studs. Therefore, the external surface of the beam's top flange cannot be accessed, which means that any additional plates would have to be welded at the flange's internal surface (two parts

around the section's web). Such a procedure is considerably more difficult to execute than operating on the external flange surface. Moreover, the top flange may be inaccessible due to other components connected to the beam's web or running parallel to it (e.g. hydraulic or electrical installations, horizontal bracings, etc.). Thus, only the welding of a plate at the external surface of the beam's bottom flange is considered in this work.

Instead of installing a flange plate, an additional I-shaped section can be welded or bolted to the bottom flange of the existing beam, as illustrated in Fig. 2. This approach aims to significantly move the centroid of the beam's steel section and achieve large flange distance in the vertical direction, increasing this way the beam's flexural capacity and improving the effectiveness of the steel material used. It should be noted that the efficiency of the particular method in retrofitting reinforced concrete beams has been investigated in [12]. For the purposes of the present work, IPE sections have been used as additional components attached to existing steel beams.

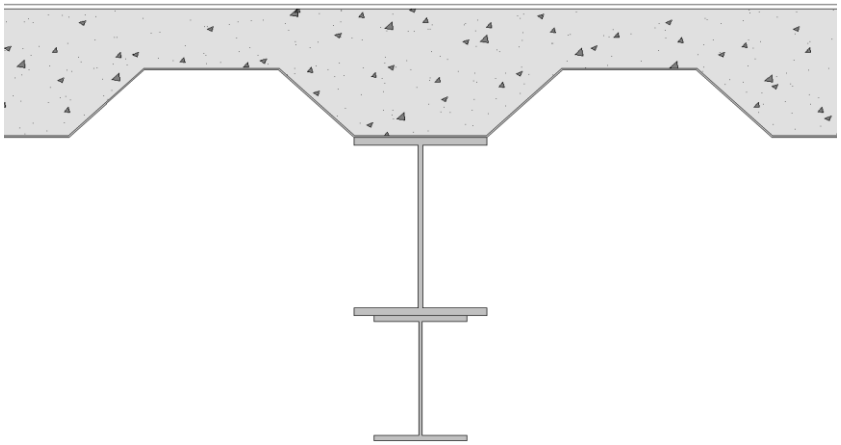


Figure. 2. Cross-section of a steel beam connected to a composite slab, retrofitted with an additional I-shaped steel section.

3.2 Installation of bracings in the horizontal direction

A method often proposed in practice for high-rise buildings, aiming to reduce the effects of damage in load bearing elements, is the creation of reinforced zones along the height by installing steel bracings across predefined storeys. Such bracings, in combination with neighboring beams and columns, form a truss-like mechanism, which receives the gravitational loads from the damaged bays and transfers them to the undamaged section of the building. In order to distinguish the particular bracings configuration from the ones used against horizontal loads, in the remainder of this work they are referred to as 'horizontal bracings' and 'vertical bracings', respectively, with regard to the direction along which they are installed.

Despite their effectiveness, the use of horizontal bracings is often avoided by designers, as long as the building's susceptibility to collapse can be dealt with alternative methods. A zone of horizontal bracings occupies the facade of an entire storey, which is undesirable for residential or office buildings. Since this is a purely architectural issue, the particular retrofit approach cannot be injudiciously rejected; therefore, its cost-effectiveness is investigated herein and compared against beam strengthening. A typical configuration of horizontal bracings is illustrated in Fig. 3. For the purposes of this study, installation of horizontal bracings is allowed to take place at three locations: at the second, fourth and sixth storey of the building.

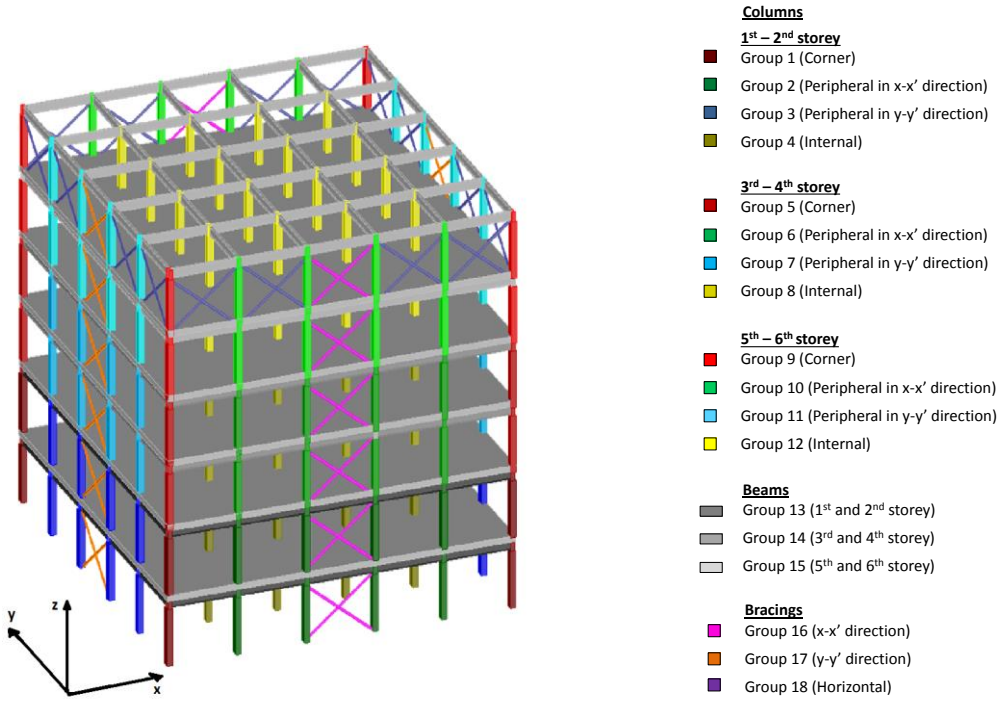


Figure. 3. Building model retrofitted with horizontal bracings (top slab removed for visualization purposes).

4 STRUCTURAL MODELLING & ANALYSIS

All structural analyses were performed using the OpenSEES software [15]. Beams, columns and bracings are simulated as distributed plasticity (fiber) elements. A 'rigid diaphragm' is used for the simulation of the composite slabs. Beam-column joints are considered to be able to transfer the full bending moment developed. Column base connections are modelled as fixed supports. A bilinear material model ('Steel01') is used for the structural steel components, while the 'ReinforcingSteel' material type is used for the longitudinal and transversal reinforcement bars of the composite columns. The 'Concrete01' material type is employed for all concrete regions of the composite columns.

As illustrated in Fig. 3, the structural elements are grouped according to their location on the floor layout, as well as the storey they belong to. In particular, for the initial optimization performed disregarding progressive collapse resistance constraints, columns are divided into: (a) corner, (b) peripheral in *x*-direction, (c) peripheral in *y*-direction and (d) internal columns. Moreover, different groups are defined every two storeys, generating in total 12 element groups for columns. Beams are also grouped every two storeys, but they are not further divided within the same storey, i.e. 3 element groups are produced in total for beams. Finally, two element groups are defined for the vertical bracings: in *x*- and *y*-directions. For the retrofit optimization, the same grouping defined earlier for the columns and beams applies for the column and beam retrofit, respectively; three additional element groups are defined for the horizontal bracings, one for each storey they are allowed to be installed at (i.e. second, fourth and sixth storey).

In order to evaluate the performance of each candidate optimum structural design of the structure under retrofit, six analyses are performed: (a) a linear static analysis under gravitational loads, (b) two eigenvalue analyses (one for each horizontal direction), (c) two nonlinear pushover analyses (one for each horizontal direction) and (d) a nonlinear pushdown analysis.

5 CONFIGURATION OF THE OPTIMIZATION PROBLEM

Instead of applying each retrofit method independently and designing based on a trial-and-error procedure, in this work, an optimization procedure similar to [7] is applied. Its aim is to minimize the total cost of the retrofit materials. The advantage of this procedure is that it does not dictate a particular strategy, such as a localized 'bridge'-type strengthening over the artificially damaged area, which might not be the most cost-effective strategy [8]. Additionally, it allows the utilization of multiple methods in one retrofit design.

Since the unit cost of steel C_S is related to its mass (€/tn), while the unit cost of concrete C_C depends on its volume (€/m^3), the Cost Ratio $CR=C_C/C_S$ is introduced, in order to convert concrete volume into equivalent steel mass. Hence, the objective function minimized is calculated as the total equivalent steel mass of the retrofit materials:

$$M_S^{tot} = CR \cdot V_C + M_S \,. \tag{1}$$

The design variables of the optimization procedure are the section details of the beam retrofit and the horizontal bracings. For the strengthening of beams, plates with thickness from 5mm up to 40mm and sections with sizes from IPE80 up to IPE600 are considered. For horizontal bracings, a total number of 18 standard L-shaped sections are available in the respective database. In the two databases, a 'zero option' to avoid the use of either retrofit method is also provided.

The performance criteria used in this work, which play the role of the constraints of the optimization problem, can be divided in two groups; the first group includes all individual member checks, while the second group explicitly refers to the structural system behavior. Based on the internal forces yielded by the linear static analysis under gravitational loads, steel beams are checked according to the provisions of Eurocode 3 [16] for their capacity in bending moment, shear and their combination, as well as the respective local and global buckling types; composite columns are evaluated according to Eurocode 4 [17] against biaxial bending, shear force (steel core only), compression and their combination. As the bracings are not considered to participate in the load-bearing system of the undamaged building, their assessment is based on the building's behavior under the pushover and pushdown analyses. Seismic assessment of the buildings is performed by means of a displacement-controlled pushover analysis up to a targeted top displacement (Δ_{target}). For the collapse prevention limit state, the maximum inter-storey drift should not exceed the limit value of 4% [18].

The constructed discrete optimization problem is solved with a discrete Evolution Strategies algorithm [19], which can effectively handle the discrete design options available. The optimizer is linked with OpenSees to automatically obtain the results from structural analyses needed for the evaluation of the constraints.

6 APPLICATION

A six-storey 5×5-bay composite building is selected for the application of the optimization procedure (Fig. 3). Vertical bracings are installed in both directions at the middle bays. At first, the building is optimally designed by disregarding progressive collapse resistance constraints. Its columns are designed as concrete-encased I-shaped sections. A concrete layer of 5cm around the steel core is assumed, while its reinforcement consists of 10mm longitudinal bars and 8mm stirrups with 10cm spacing. The beams and bracings are modelled as pure steel elements. The section grouping illustrated in Fig. 3, corresponding to equal number of design variables, is used for columns and beams. Instead of retrofit section characteristics, the particular variables take values from two standard section databases: HE100B-HE1000B sections are used for col-

umns and IPE80-IPE600 sections for beams. L-shaped sections are used for the vertical bracings in both directions. Hence, 17 design variables are utilized in total (corresponding to the 17 first groups depicted in Fig. 3, i.e. except for group 18) to produce an initial optimized design for the composite building. Table 1 provides the characteristics of the seismically designed building yielded by the optimization procedure.

		Storeys 1-2	Storeys 3-4	Storey 5-6
Columns	Corner	HE280B	HE220B	HE200B
	Peripheral, *x*-direction	HE340B	HE260B	HE200B
	Peripheral, *y*-direction	HE400B	HE260B	HE200B
	Internal	HE280B	HE280B	HE200B
		Storeys 1-2	Storeys 3-4	Storey 5-6
Beams		IPE330	IPE330	IPE330
Vertical bracings	*x*-direction	L90x90x7		
	y-direction	L90x90x7		
Total equivalent steel mass		182.46 tn		

Table 1: Optimized seismic design of the composite building disregarding progressive collapse resistance constraints.

As the provisions against progressive collapse were deactivated for the determination of the initial design, its performance under various damage scenarios needs to be evaluated. Three element removal scenarios (Fig. 4) are selected to simulate structural damage. In the first two scenarios, an accident (e.g. collision of a heavy truck on the building) that would result in the loss of a corner and one (ERS1) or two (ERS2) consecutive peripheral columns is assumed. A more destructive event, such as an explosion at the base of the building, is simulated in the third damage scenario (ERS3). The explosion is considered to have affected the first two storeys of the building near its corner. As a result, a number of columns and beams are assumed to be severely damaged and are consequently removed from the model. Referring to the seismically optimized design of Table 1, the maximum vertical drift recorded for scenarios ERS1, ERS2 and ERS3 is 10.6%, 10.8% and 14.6%, respectively. Thus, the maximum admissible vertical drift of 10% set in Section 2 is exceeded, since progressive collapse resistance has not been accounted for obtaining the design of Table 1. It is noted that another damage scenario with only one corner column removed results in a maximum vertical drift of 6.6%, which indicates a sufficient collapse resistance.

In order to be able to sustain the aforementioned damage scenarios without excessive extent of structural damage, the building needs to be appropriately retrofitted. In order to improve its performance under the three element removal scenarios, the retrofit methods described in Section 3 are utilized. Thus, the optimized design of Table 1, which has been identified based on Eurocode 3 and 4 provisions and seismic resistance constraints, is optimally retrofitted to resist also progressive collapse with respect to the three aforementioned damage scenarios.

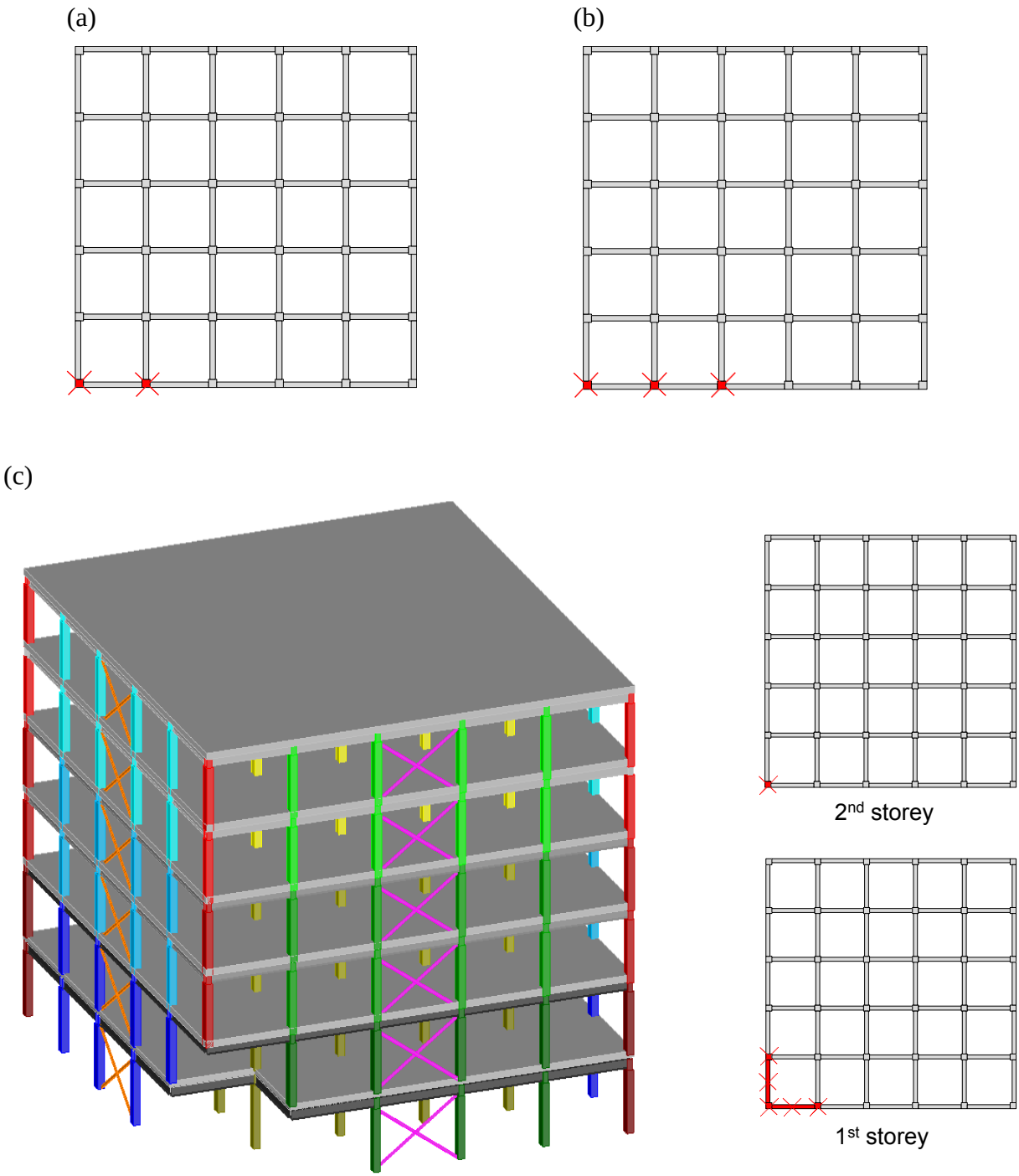


Figure. 4. The three element removal scenarios considered: (a) ERS1 (layout of storey 1 showing the two base columns removed), (b) ERS2 (layout of storey 1 showing the three base columns removed) and (c) ERS3 (three-dimensional view of 'damaged' building and layout of storeys 1 and 2 showing the structural members removed).

It should be mentioned, however, that retrofitting against progressive collapse should not be limited to the strengthening of the horizontal structural elements or the installation of additional ones. In general, particular attention needs to be paid to the columns as well. Considering the actions the building is required to resist, columns may also need strengthening due to requirements for additional stiffness or tensile force capacity. Hence, in the seismic analysis of the retrofitted building, an increased total mass needs to be taken into account, which is due to the

additional material of the retrofit; to avoid a very large fundamental period, an increase in the building's stiffness may be needed. Moreover, when horizontal bracings are installed at a storey, there is a large increase in the stiffness of the particular storey; if the stiffness of this storey is much larger than that of the storey below, it could result in huge drifts of the columns of the storey below. Furthermore, it was noticed in preliminary analyses that, when buildings with strong beams at the top floors are subjected to element removal scenarios, they seem to develop a 'suspension mechanism', in order to transfer the loads from the damaged bays through the undamaged elements to the ground. More specifically, the alternative load path formed utilizes the columns over the bays directly affected by the artificial damage to transfer the loads to the strong top beams and, through them, to the undamaged columns.

The above discussion reveals that the retrofit methods described in Section 3, which actually aim at establishing adequate horizontal load paths over the 'damaged' area, may not be adequate for the overall structural system, since strengthening of the vertical load paths may also be needed. Therefore, the option to retrofit the building's composite columns by means of concrete-covered steel cages, as described in [11], is given to the optimization procedure. Thus, a total of 18 design variables are considered based on corresponding section groups: variables 1-12 control the retrofit of columns, variables 13-15 control the retrofit of beams and variables 16-18 control the placement of horizontal bracings. Fig. 3 illustrates 16 of these 18 design variables; groups 16 and 17 (vertical bracings) are set in the initial optimization for the seismically designed building (Table 1); in retrofit optimization, groups 16 and 17 correspond to the horizontal bracings at storeys 2 and 4, respectively.

Table 2 illustrates the optimized retrofit designs obtained when considering each of the three element removal scenarios. For ERS1 and ERS2, the most cost-effective retrofit is achieved by adequately increasing the stiffness of beams. In these two scenarios, a 'bridge'-type alternate load path is formed by strengthening only the beams of storeys 1-2. The additional steel mass required for ERS1 is particularly high considering the limited extent of the 'damage'. However, such a result can be anticipated due to the change of the support and loading conditions the beams directly over the 'damage'. Moreover, the grouping of the beams every two storeys results in a retrofit requirement for both storeys 1 and 2 regardless of the location and extent of the damage. This retrofit requirement could be possibly reduced by defining a different beam group for each storey. When an additional neighboring column is removed for ERS2, only about 30% additional steel mass is needed compared to the requirement for ERS1. Apparently, the loss of an additional peripheral column in ERS2 is a less significant 'damage' compared to the members lost in ERS1. Finally, for the significantly more severe 'three-dimensional' damage scenario ERS3, beam retrofit appears to be less cost-effective than the use of horizontal bracings. For this rather aggressive damage scenario, more than double retrofit material is required than for ERS2.

To gain better insight on the effectiveness of the retrofit methods, sub-optimal designs are presented in Table 3 for the three damage scenarios. The designs this table are obtained by allowing only beam retrofit for ERS3 (the option to install horizontal bracings is deactivated), while only horizontal bracings are allowed for ERS1 and ERS2 (the option to retrofit beams is deactivated). Thus, Table 3 gives retrofit designs using alternative methods to the ones identified in Table 2. A comparison between the designs of Tables 2 and 3 reveals that, for ERS2, the two retrofit methods produce practically the same total retrofit cost. For ERS1, installing horizontal bracings induces a material cost that is about 35% more costly than the one corresponding to beam retrofit. For ERS3, the retrofit of beams costs about 60% more that the placement of horizontal bracings. Despite the architectural and operational implications introduced by horizontal bracings, this is a much more cost-effective solution for ERS3 and cannot be easily rejected for non-structural reasons. It is also interesting to notice that the designs for ERS1 and

ERS2 in Table 3 activate a ‘suspension mechanism’ by introducing horizontal bracings at the top storey. For ERS3, an overall structural system upgrade is realized by strengthening all beams along the building’s height, avoiding just the activation of a ‘bridge’ over the ‘damaged’ area.

	Beam retrofit			**Horizontal bracings**			Total equiva-lent steel mass
Storeys of application	1-2	3-4	5-6	2	4	6	
Group number	13	14	15	16	17	18	
ERS1	10mm plate	-	-	-	-	-	15.2 tn
ERS2	IPE180	-	-	-	-	-	19.8 tn
ERS3	-	-	-	L90x90x7	L90x90x7	-	40.9 tn

Table 2. Optimized retrofit designs.

	Beam retrofit			**Horizontal bracings**			Total equiva-lent steel mass
Storeys of application	1-2	3-4	5-6	2	4	6	
Group number	13	14	15	16	17	18	
ERS1	-	-	-	-	-	L90x90x7	20.5 tn
ERS2	-	-	-	-	-	L90x90x7	20.5 tn
ERS3	30mm plate	10mm plate	25mm plate	-	-	-	65.3 tn

Table 3. Sub-optimal retrofit designs.

An important observation regarding all retrofit designs of Tables 2 and 3 is that columns do not actually require strengthening. Despite the increase of the total seismic mass due to the added retrofit material of beams or horizontal bracings, the additional stiffness introduced in the structural system either by the beam retrofit or by the horizontal bracings seems to balance the effect of the additional mass. Moreover, in the optimized designs of Table 2 for ERS1 and ERS2, the ‘bridge’-type strengthening of the beams directly over the location of the ‘damage’ serves as a ‘support’ for all storeys above and leaves the respective load paths unaffected. This mechanism prevents the development of tensile forces at the columns over the ‘damaged’ area, so the column sections identified for seismic demands suffice also for progressive collapse resistance. It is finally emphasized that the fact that column strengthening is not required for the particular retrofit cases of the present study does not imply that the same applies generally, as each building’s performance and retrofit requirements may vary significantly.

7 CONCLUSIONS

In this paper, two retrofit methods for steel-concrete composite buildings to resist progressive collapse were assessed. A building previously optimized to satisfy Eurocode 3 and 4 provisions and seismic resistance constraints was optimally strengthened to meet requirements on progressive collapse resistance. Optimized retrofit designs have been identified using beam strengthening or installation of horizontal bracings, in order to provide the structure with sufficient collapse resistance with respect to three element removal scenarios corresponding to artificially introduced damage of varying extent. The patterns of the optimized retrofit designs verify the findings of previous studies [7,8], according to which the establishment of adequate horizontal load paths within a locally damaged building is a key aspect in attaining progressive collapse resistance.

Inevitably, additional design requirements on progressive collapse resistance lead to increased structural costs due to the need for extra material. The results obtained in this study demonstrate that the structural optimization approach presented is capable of producing cost-effective retrofit designs. Coping with progressive collapse in an optimal way is critical, in order to maintain the extra cost induced as low as possible, hopefully within affordable limits.

REFERENCES

[1] B.R. Ellingwood, D.O. Dusenberry, Building design for abnormal loads and progressive collapse. *Computer-Aided Civil and Infrastructure Engineering*, **20**, 194-205, 2005.

[2] U. Starossek, M. Wolf, Design of collapse-resistant structures. In: *Proceedings of JCSS and IABSE Workshop on Robustness of Structures*, Building Research Establishment, Garston, Watford, UK, 2005.

[3] R.S. Nair, Preventing disproportionate collapse. *Journal of Performance of Constructed Facilities*, **20**, 309-314, 2006.

[4] J.D. Sørensen, H.H. Christensen, Danish requirements for robustness of structures: Background and implementation. *Structural Engineering International*, **16**, 172-177, 2006.

[5] Department of Defense (DoD), *Unified Facilities Criteria (UFC) – Design of buildings to resist progressive collapse*. UFC 4-023-03, Washington, DC, USA, 2009.

[6] M.H. Faber, *Robustness of structures – Final report of COST action TU0601*. COST (European Cooperation in Science and Technology), EU, 2011.

[7] D.C. Charmpis, G.S. Papavasileiou, Designing against earthquake and progressive collapse – A structural optimization approach applied to composite steel-concrete buildings. In: *Proceedings of 7th European Conference on Steel and Composite Structures (EUROSTEEL 2014)*, Naples, Italy, 2014.

[8] D.C. Charmpis, A. Kontogiannis, The cost of satisfying design requirements on progressive collapse resistance – Investigation based on structural optimization. *Structure and Infrastructure Engineering*, 2015, http://dx.doi.org/10.1080/15732479.2015.1038725.

[9] Y.-F. Wu, T. Liu, D.J. Oehlers, Fundamental principles that govern retrofiting of reinforced concrete columns by steel and FRP jacketing. *Advances in Structural Engineering*, **4**, 507-533, 2006.

[10] K.G. Vandoros, S.E. Dritsos, Concrete jacket construction detail effectiveness when strengthening RC columns. *Construction and Building Materials*, **22**, 264-276, 2008.

[11] G. Papavasileiou, D.C. Charmpis, N.D. Lagaros, Optimized seismic retrofit of steel-concrete composite frames, In: *Proceedings of 3rd ECCOMAS Thematic Conference on Computational Methods in Structural Dynamics and Earthquake Engineering (COMPDYN 2011)*, Corfu, Greece, 2011.

[12] X.S. Ren, B. Zhou, Design and analysis of reinforced concrete beam retrofitted by externally bonded H-type steel member. *Procedia Engineering*, **14**, 2133-2140, 2011.

[13] G.E. Thermou, S.J. Pantazopoulou, A.S. Elnashai, Global interventions for seismic upgrading of substandard RC buildings. *ASCE Journal of Structural Engineering*, **138**, 387-401, 2012.

[14] D.C. Charmpis, M.C. Phocas, P. Komodromos, Optimized retrofit of multi-storey buildings using seismic isolation at various elevations: assessment for several earthquake excitations. Bulletin of Earthquake Engineering, 2015, http://dx.doi.org/10.1007/s10518-015-9737-y.

[15] S. Mazzoni, F. McKenna, M. Scott, G.L. Fenves, *Open System for Earthquake Engineering Simulation*, OpenSees Command Language Manual, PEER Center, California, USA, 2006.

[16] EN 1993-1-1, *Eurocode 3: Design of steel structures – Part 1-1: General rules and rules for buildings*. European Committee for Standardization (CEN), Brussels, Belgium, 2005.

[17] EN 1994-1-1, *Eurocode 4: Design of composite steel and concrete structures – Part 1-1: General rules and rules for buildings*. European Committee for Standardization (CEN), Brussels, Belgium, 2004.

[18] American Society of Civil Engineers (ASCE), *Seismic rehabilitation of existing buildings*. Standard ASCE/SEI 41-06 (including Supplement No. 1), Reston, Virginia, USA, 2006.

[19] N.D. Lagaros, M. Papadrakakis, G. Kokossalakis, Structural optimization using evolutionary algorithms. *Computers and Structures*, **80**, 571-589, 2002.

COMPDYN 2015
5th ECCOMAS Thematic Conference on
Computational Methods in Structural Dynamics and Earthquake Engineering
M. Papadrakakis, V. Papadopoulos, V. Plevris (eds.)
Crete Island, Greece, 25–27 May 2015

ASSESSMENT OF OPTIMUM STRENGTHENING DESIGN OF A REINFORCED CONCRETE BUILDING WITH VULNERABILITY CRITERIA

Evangelia G. Skoulikari[1], Vissarion Papadopoulos[2], and Nikos D. Lagaros[3]

Institute of Structural Analysis & Seismic Research,
National Technical University of Athens,
9, Iroon Polytechniou Str.,
Zografou Campus, 157 80 Athens, Greece

[1] e-mail: vskoulikari@gmail.com
[2] e-mail: vpapado@central.ntua.gr
[3] e-mail: nlagaros@central.ntua.gr

Keywords: Nonlinear Static (Pushover) Analysis, Incremental Dynamic Analysis (IDA), RC jacketing, CFRP wrapping, Fragility Curves, Optimum Design.

Abstract. *This research deals with the assessment of the seismic behavior and capacity of a reinforced concrete building in order to examine the possibility of strengthening. This process is achieved by using the Nonlinear Static Analysis (Pushover Analysis) and is based also on performance criteria. In case of damages two different methods of strengthening are implemented: the reinforced concrete jacketing and the carbon fiber reinforced polymer wrapping (CFRP). Afterwards, the determination of the optimum strengthening design is performed, thanks to metaheuristic optimization algorithms, aiming at the minimization of the cost. Subsequently, the retrofitting measures are evaluated through a methodology defined by vulnerability criteria and fragility curves, produced either by the Incremental Dynamic Analysis (IDA) or by using Eurocode8 Regulations, the Method of Coefficients as well as the Hazus Methodology. The fragility curves refer to different earthquake performance levels and as a result they express the probability of excess of the different target damage states. A comparison between these curves, before the intervention and after that, indicates the effectiveness of the selected strengthening techniques.*

1 INTRODUCTION

The strengthening of structures has become frequent in recent years. Lots of problems arise due to failed initial design or bad application of it. Other significant factors are the materials used and the construction and maintenance conditions. Moreover, earthquakes and strong winds have an important impact on the structures and cause often damages.

For the assessment of an existing building's seismic capacity there are some determinate methods of analysis [1, 2] that can be used; linear and non-linear. To the linear category belong the elastic static analysis and the elastic dynamic one, whereas the inelastic static (Push-over Analysis) and the inelastic time history dynamic (Incremental Dynamic Analysis) belong to the non-linear category. The strong difference between the non-linear and linear analyses is that in the non-linear framework the structure continues to receive seismic loads of different intense levels even if some elements have exceeded the yield point, through their deformation, a fact that is not taken into consideration within linear analyses. Very important is to define the non-linear characteristics of the materials (concrete and steel) used [3]. For concrete the following deformation values are valid: ε_c=2‰ και ε_{cu}=3,5‰, for steel: ε_{su}=0,02. The non-linear behavior of a building is equivalent with the appearance of plastic hinges at the nodes. The determination of the plastic hinges' characteristics and the calculation of specific performance criteria in terms of chord rotation, through which the assessment of the seismic behavior of the building is achieved, are crucial.

Pushover Analysis [1] is implemented by using many seismic load combinations concerning two directions X, Y: ±X±0.3Y and ±0.3X±Y. The seismic loads are imposed to the building as acceleration in various ways: uniform and modal form. A target displacement is defined relying on ATC-40 [4] or Coefficient Methodology [1] by using the equivalent SDOF system. The acceleration increases incrementally, while the displacement at the roof of the building is recorded. At the point, that the top displacement reaches the target displacement (performance point), the increase of the acceleration is interrupted. The capacity curve V-D is produced and the yield situation of the plastic hinges is examined according to the performance criteria. Thus, an assessment of the structural capacity can be carried out.

Incremental Dynamic Analysis (IDA) [1, 5] uses a variety of accelerograms of earthquakes that have taken place in the past. Moreover, a proper scaling of each earthquake accelerogram is proceeded relatively to the selected intense levels. These scaled time history accelerograms of all the earthquakes act as seismic loads for the structure. Meanwhile, the response of the structure is monitored and expressed in terms of maximum interstorey drift. The goal is the formation of an IDA curve for each seismic record, displaying the relation between the seismic intensity measurement and the maximum interstorey drift.

Vulnerability analysis [5, 6, 7, 8] of a structure can have a great influence on the evaluation of its seismic capacity. It can be applied in two alternative ways: based on IDA curves [5] or on theoretical methods (Coefficient, Hazus) incorporating Eurocode8 assumptions [7, 8]. Vulnerability analysis aims at the construction of fragility curves; they demonstrate the probability of excess for different damage states, e.g. slight, moderate and heavy damage, while the intense of the imposed seismic effect is amplified.

The assessment of the seismic response of a structure often proves its inability to meet the demands and points out the need for repair. In fact there are many retrofitting methodologies [1, 9, 10] that are divided into two main categories: strengthening by section enlargement and strengthening by confinement. In the first kind are included the Reinforced Concrete (RC) Jackets, made of cast concrete, shotcrete or cement mortars. In the second kind of strengthening are contained the following techniques: steel angles and strips, steel collars, spiral rein-

forcement, steel jackets, fiber reinforced polymer laminates or sheets made of carbon, glass or aramid.

This study [11, 12] is about the assessment of the seismic capacity of an existing 4-storey reinforced concrete building through Pushover Analysis and the examination of retrofit need's existence. As strengthening methods RC Jackets and carbon fiber reinforced polymer (CFRP) wrapping are used. With purpose of cost minimization of the strengthening measures, an optimization process [13, 14, 15], based on metaheuristic algorithms and in particular on Differential Evolution, is performed. Subsequently, the optimum retrofit design is evaluated by means of IDA and in relation with the established vulnerability criteria.

2 ASSESSMENT OF THE STRUCTURE WITH PERFORMANCE CRITERIA

First and foremost to assess the capacity of a building it is necessary to define its seismic behavior and resistance to the design earthquake. In this particular study, numerous regulations and restrictions, implied by the Interventions Regulation in Buildings of Reinforced Concrete (KANEPE) [1], are followed, according to which a methodology, based on specific performance criteria, is implemented through the Pushover Analysis.

2.1 Adjustment to KANEPE

Distinction between primary and secondary structural elements

Primary elements [1] are the elements that participate in the stiffness of the structure and in the redistribution of the loads by receiving, apart from vertical loads, also horizontal seismic loads. On the contrary the secondary elements [1] are characterized by lower stiffness, capacity or ductility and therefore they contribute to the absorption only of the vertical loads. As a result the damage restriction for the primary elements is more crucial. In this research all of the structural elements of the building are considered as primary.

Structural performance states and hazard levels

There are three basic Performance States (PS) [1, 2, 7, 16] of a structure, which correspond actually to the expected damage states: a) Immediate Occupancy (IO): The damage is very light, none of the operations of the structure is prevented and only hairline cracks are allowed. b) Life Safety (LS): The damage is moderate and repairable, no death or serious injury is expected. c) Collapse Prevention (CP): Severe damage is inevitable and no satisfactory safety is ensured.

As far as the hazard levels are concerned, there are three: a) Occasional Earthquake: with excess probability 50% in a life cycle of 50 years. That means that the period of reoccurrence amounts to 72 years. b) Rare Earthquake: with excess probability 10% in 50 years and period of reoccurrence 475 years. c) Maximum Considered Earthquake: with excess probability 2% in 50 years and period of reoccurrence 2475 years. In the present study as assessment target is considered the performance state "Life Safety" for the Rare Earthquake.

Data reliability levels and proposed methods of analysis

For the assessment of an existing building, important data about materials, construction details and geometrical properties of the structural elements are needed and collected in order to achieve the most successful estimation of its available capacity. The quantity and quality of these data define the data reliability levels (DRL) [1, 2]: high, satisfying and low, according to which the proper safety factors are selected. Depending on the available DRL there are some methods of analysis, proposed by KANEPE: Linear Static Analysis or Linear Dynamic Anal-

ysis regardless of the DRL and Non Linear Static Analysis (Pushover Analysis) or IDA in case the DRL is at least satisfying.

2.2 Pushover analysis

First of all it is essential to determine the plastic hinges of the building. Possible position of a plastic hinge‘s appearance is each edge of the structural elements, so it is significant to form the deformation curve of each element. Subsequently the performance criteria for each section, in terms of the chord rotation θ, are calculated through the following expressions [1], where γ_{Rd}=1.80 :

$$\theta < \delta_y = \theta_y \quad \text{for Immediate Occupancy} \tag{1a}$$

$$\theta < \delta_d = 0.5 \cdot \left(\theta_y + \theta_u\right)/\gamma_{Rd} \quad \text{for Life Safety} \tag{1b}$$

$$\theta < \delta_d = \theta_u/\gamma_{Rd} \quad \text{for Collapse Prevention} \tag{1c}$$

The horizontal seismic load is imposed in two ways, as uniform load and as inverted triangular load along the building height [1]. There are several load combinations used concerning the load direction along the axes X and Y. In fact the implemented load combinations are ±X±0.3Y and ±0.3X±Y. The load V is gradually incremented and simultaneously the displacement of a check node D is monitored until the target displacement is reached. The check node is on the top of the building and very close to the center of gravity. The target displacement corresponds to the performance point, which is calculated through the methodology ATC-40 [4] and by means of Acceleration – Displacement Response Spectrum ADRS (Sa-Sd:) that refers to the equivalent SDOF system. Finally the Capacity Curve (V- Δ_{TOP}) is formed and the situation of the plastic hinges of the structure at the performance point for all the load combinations is examined.

Load Shape	Load Comb	V (KN)	Δ_{TOP} (m)	A to B	B to IO	IO to LS	LS to CP	CP to C	Total Number
Uniform	+X+0,3Y	2635,24	-0,063	201	30	57	0	0	288
	-X-0,3Y	-2637,13	0,063	199	32	57	0	0	288
	+Y+0,3X	2570,65	-0,061	186	12	88	2	0	288
	-Y-0,3X	-2586,55	0,063	182	17	87	2	0	288
Inverted Triangular	+X+0,3Y	-2364,99	0,067	191	28	69	0	0	288
	-X-0,3Y	2340,15	-0,065	193	30	65	0	0	288
	+Y+0,3X	-2275,06	0,070	161	33	93	1	0	288
	-Y-0,3X	2270,29	-0,068	172	37	79	0	0	288

Table 1: Situation of the plastic hinges of the initial building at the performance point [11].

In case a plastic hinge has exceeded the PS “Life Safety”, it is considered that the particular element has been damaged and needs to be retrofitted. As a consequence, from the analysis results [11] it is proved that 5 of the columns have exceeded LS and have to be strengthened.

3 OPTIMUM STRENGTHENING DESIGN OF THE STRUCTURE

3.1 Strengthening techniques

In case of structural elements' damages numerous strengthening techniques can be implemented aiming at the retrieval of the initial capacity of the structure. In this particular study [11, 12] two different techniques are selected for the column strengthening: the reinforced concrete jacketing and the carbon fiber reinforced polymer wrapping (CFRP).

Reinforced concrete jacketing

Reinforced Concrete Jacketing [9, 10] is a strengthening method that requires sectional increase of the damaged element and is realized through additional concrete layers and reinforcement. Reinforced Concrete Jackets are usually produced by cast concrete, shotcrete or cement mortars. They contribute to the increase of the stiffness and also to the reduction of the slenderness and do not influence the architecture of the building.

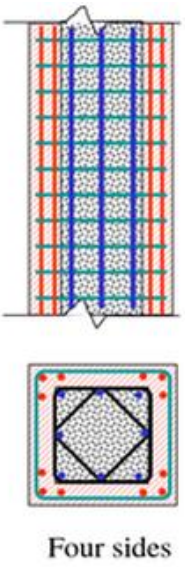


Figure 1: Simulation of reinforced concrete jackets [17].

Fiber reinforced polymer wrapping

Fiber Reinforced Polymer Wrapping [9, 10] is another strengthening method, which is succeeded through confinement of the existing section. This confinement can be achieved by means of fiber sheets of carbon, glass or aramid. They have low weight and can be easily installed. In addition they have high corrosion resistance and conduce not only to the reduction of the slenderness but also to the increase of the compression strength and ductility.

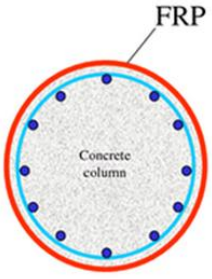


Figure 2: Simulation of CFRP wrapping [17].

3.2 Initial building strengthening

A random building strengthening is initially attempted [11] that includes RC Jackets with 7cm thickness and quality C30/37 as well as 8 additional longitudinal reinforcement bars with diameter 20mm and quality S500. A wrapping retrofitting technique, using CFRP, is also tested. The characteristics of the carbon fiber sheet are the following: layer thickness 0.275mm, modulus of elasticity E_f=240GPa, tensile strength $f_{u,f}$=3500MPa and ultimate deformation $\varepsilon_{f,u}$=0,015. For the columns C1 and C15, 9 CFRP layers are used, whereas for the columns C4, C13 and C14, 8 CFRP layers are chosen. Comparing with the original column section (unconfined concrete), the confined with FRP concrete demonstrates a definitely improved behavior since its failure stress and strain reach much higher values, according to KANEPE [1].

After the implementation of the two different retrofitting techniques and the application of the Pushover analysis on the building, the new performance points (V, Δ_{TOP}) and the new situation of the plastic hinges are defined [11].

Load Shape	Load Comb	V (KN)	Δ_{TOP} (m)	A to B	B to IO	IO to LS	LS to CP	CP to C	Total Number
Uniform	+X+0,3Y	3138,59	-0,060	186	27	75	0	0	288
	-X-0,3Y	-3148,96	0,060	200	37	51	0	0	288
	+Y+0,3X	3053,86	-0,057	185	27	76	0	0	288
	-Y-0,3X	-3053,33	0,059	184	31	73	0	0	288
Inverted Triangular	+X+0,3Y	-2852,53	0,064	186	46	56	0	0	288
	-X-0,3Y	2810,37	-0,064	182	35	71	0	0	288
	+Y+0,3X	-2775,29	0,067	169	45	74	0	0	288
	-Y-0,3X	2780,54	-0,065	163	43	82	0	0	288

Table 2: Situation of the plastic hinges of the strengthened with RC jackets building at the performance point [11].

Load Shape	Load Comb	V (KN)	Δ_{TOP} (m)	A to B	B to IO	IO to LS	LS to CP	CP to C	Total Number
Uniform	+X+0,3Y	2735,01	-0,063	198	15	75	0	0	288
	-X-0,3Y	-2752,14	0,064	198	20	70	0	0	288
	+Y+0,3X	2649,53	-0,062	201	36	51	0	0	288
	-Y-0,3X	-2644,72	0,063	190	41	57	0	0	288
Inverted Triangular	+X+0,3Y	-2441,56	0,067	184	32	72	0	0	288
	-X-0,3Y	2412,81	-0,066	187	34	67	0	0	288
	+Y+0,3X	-2345,56	0,070	171	54	63	0	0	288
	-Y-0,3X	2333,64	-0,069	184	47	57	0	0	288

Table 3: Situation of the plastic hinges of the strengthened with CFRP wrapping building at the performance point [11].

According to the Pushover analysis' results [11], the solution of RC jackets show a larger increase and decrease of the base shear force V and top building displacement Δ_{TOP} respectively, at the performance point, which means that they offer larger carrying capacity than the CFRP sheets. On the other hand, the situation of the plastic hinges seems to be better in case of CFRP sheets' exploitation and that is due to the further ductility they provide. Generally speaking, both of the methods are effective since the situation of the plastic hinges is undoubtedly improved, none of them has exceeded the PS "Life Safety" and as a result no damage appears.

3.3 Building strengthening optimization

Optimization Process

The goal of the building strengthening optimization is the minimization of the cost in a way that the seismic behavior of the structure is absolutely safe. The first step is the definition of the problem [13, 14, 15]. The cost, concerning both materials and labor, is set as *objective function*, the comparison criterion between the optimum and the other possible solutions. Afterwards, the *design variables* are determined: The thickness t and the quality of the jacket concrete as well as the mechanical reinforcement ratio ρ_s are set for the RC Jacketing, whereas the number of fiber sheet layers is set for the CFRP Wrapping. As *restriction* of the problem functions the fact that all of the plastic hinges must not exceed the PS "Life Safety".

The optimum design is performed thanks to a metaheuristic optimization algorithm, based on a methodology of Differential Evolution [13, 14, 15]. The algorithm produces generations of solutions until the optimum one is achieved. In fact the algorithm includes 10 parametric vectors for each generation, where the first one of the first generation is equal with the initial strengthening and the others have random prices. The design variables change, satisfying the restrictions and the minimum objective function is determined for each generation. The optimization comes to the end and the optimum design is reached when the same price of the objective function arises for 4 consecutive generations and this is actually the final one.

Optimization Results

The metaheuristic optimization algorithm [11] for the RC Jacketing produces finally 15 generations and concludes to the following strengthening for the damaged building: RC Jackets, only for columns C1, C4 and C15, with thickness 7cm, concrete quality C30/37 and 4 additional longitudinal reinforcement bars with diameter 22mm and quality S500. This solution ensures the normal operation of the structure and reduces the retrofitting cost from 3170 € regarding the initial design, to 1163€ regarding the optimum design.

The optimum strengthening design through CFRP Wrapping according to the metaheuristic optimization algorithm [11], respectively, contains: 6 fiber sheet layers for columns C1 and C15, 7 fiber sheet layers for column C4 and none for columns C13 and C14. In this case the retrofitting cost declines from 3441 € regarding the initial design, to 2338€ regarding the optimum design.

4 VULNERABILITY ANALYSIS

4.1 Vulnerability analysis through Incremental Dynamic Analysis

Incremental Dynamic Analysis

In the beginning, [12] 12 real accelerograms from different places of the world, most of them from Greece, are collected via PEER Strong Motion Database. The Spectral Acceleration for the first eigenperiod of the structure and damping 5% ($Sa(T_1,5\%)$) and the Peak

Ground Acceleration (PGA) are defined as Intensity Measures (IM). As Damage Measure (DM) is considered the maximum interstorey drift θ_{max}. In order to examine the structural seismic response to lots of different intensity levels IM_i, the original accelerogram of each earthquake has to be scaled depending on the proper Scale Factor (SF). SF is equal with IM_i / IM_o [5,6], where IM_o is the IM corresponding to the original Response Spectrum. Afterwards, all of the scaled accelerograms of each earthquake are enforced to the building in a non-linear way, through IDA, and the structural performance is recorded in terms of the maximum interstorey drift θ_{max}. Thus, the IDA curves can be formed by correlation between IM_i and $\theta_{max,i}$.

Fragility Curves IDA

The performance of the structure is assumed by comparing the resulting interstorey drift $\theta_{max,i}$ of each IDA with the minimum interstorey drift limits θ_{PS} [7] that correspond to the PS: Immediate Occupancy, Life Safety and Collapse Prevention. In case $\theta_{max,i} > \theta_{PS}$ the building has exceeded the particular PS.

Performance State	**Interstorey drift θ_{PS}**
Immediate Occupancy	$0{,}002 < \theta < 0{,}004$
Life Safety	$0{,}010 < \theta < 0{,}018$
Collapse Prevention	$\theta > 0{,}03$

Table 4: Interstorey drift limits for each performance state.

The target of the vulnerability analysis is to define the possibility $P(\theta_{max,i}>\theta_{PS})$, for every intensity level, which is determined according to the following relationship [5, 6]:

(2)

where m is the average and sd is the standard deviation of the IM_{PS} of all the seismic records for each PS. The IM_{PS} of each seismic record is identified through the IDA curves in relation to the limits of θ_{PS}. The fragility curves express the relation between the possibility $P(\theta_{max,i}>\theta_{PS})$ and the IM_i. It is noted that in order to form the fragility curves referring to the retrofitted structure, the optimized strengthening characteristics [11] are taken into consideration for both RC jackets and CFRP wrapping.

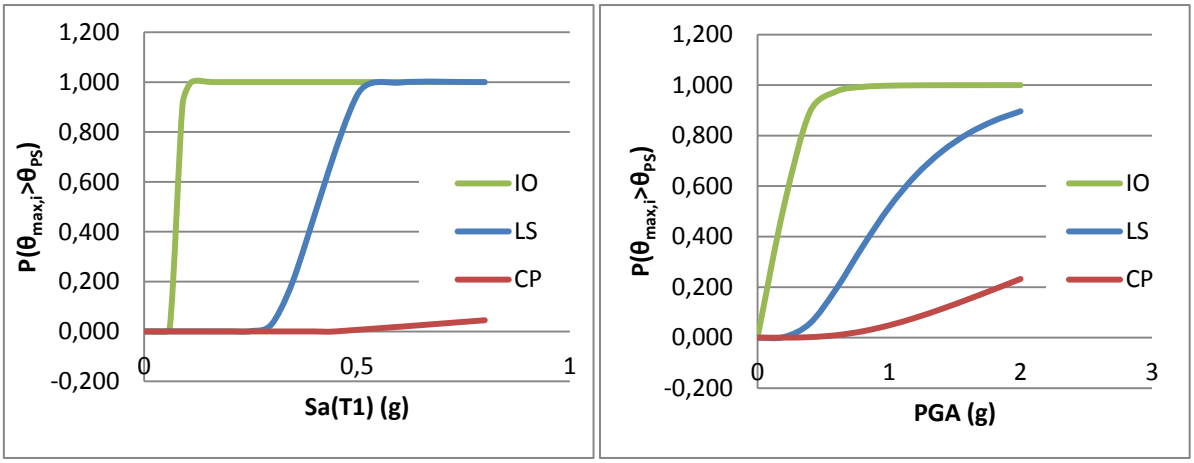


Figure 3: IDA fragility curves for the initial building considering IM= Sa(T1,5%) and PGA respectively [12].

4.2 Vulnerability analysis through EC8

Coefficient Method

The capacity curves of the initial and strengthened structure are formed based on the results of Pushover Analysis. The output of the Pushover Analysis constitutes the seismic response of the building in terms of displacement. Nonetheless it is possible to convert these terms to terms of maximum interstorey drift for each step of the Pushover Analysis and relate the top responding displacements Δ_{TOP} to the θ_{max} values. As a consequence, the interstorey drift limits θ_{PS} can be easily transformed to top displacement limits $\Delta_{TOP,PS}$ [12].

Using the Coefficient method [1, 18] it is feasible to construct a bilinear approximation of the capacity curves. Furthermore, the target displacement can be obtained from the relationship:

$$\Delta_t = C_0 \cdot C_1 \cdot C_2 \cdot C_3 \cdot Sa \cdot \frac{T_e^2}{4\pi^2} \tag{3}$$

where C_0 is the factor that relates the top building displacement to the spectral displacement, C_1 is the factor that relates the displacements of the inelastic system to those of the respective elastic one, C_2 is the factor that accounts the effect of the hysteresis shape on the maximum displacement response and C_3 figures the displacement increase due to P-Δ effects. Sα is the response spectrum acceleration for the effective fundamental period of the building T_e. Using this formula the top displacement limits $\Delta_{TOP,PS}$ can be finally transformed to response spectrum acceleration limits $S\alpha_{PS}$. The SF_{PS} is calculated for each PS as follows: $S\alpha_{PS}/S\alpha(T_e,5\%)$, where $S\alpha(T_e,5\%)$ is acquired from the design response spectrum [19]. Relatively to the SF_{PS} the elastic response spectrum is scaled.

Fragility Curves based on Hazus Methodology

The possibility $P(\theta_{max,i}>\theta_{PS})$, for every intensity level, according to the Hazus Methodology [8] is defined through the formula:

(4)

where (5)

The factors β_C, β_D and $\beta_{T,PS}$ refer to uncertainties about the shape of the capacity curve and other assumptions. The value $CONV[\beta_C,\beta_D]$ is estimated through tables of Hazus Methodology and $\beta_{T,PS}$ is considered due to simplification equal with 0.2, 0.4 and 0.6 for the PS: Immediate Occupancy, Life Safety and Collapse Prevention respectively. Thus the following fragility curves arise [12].

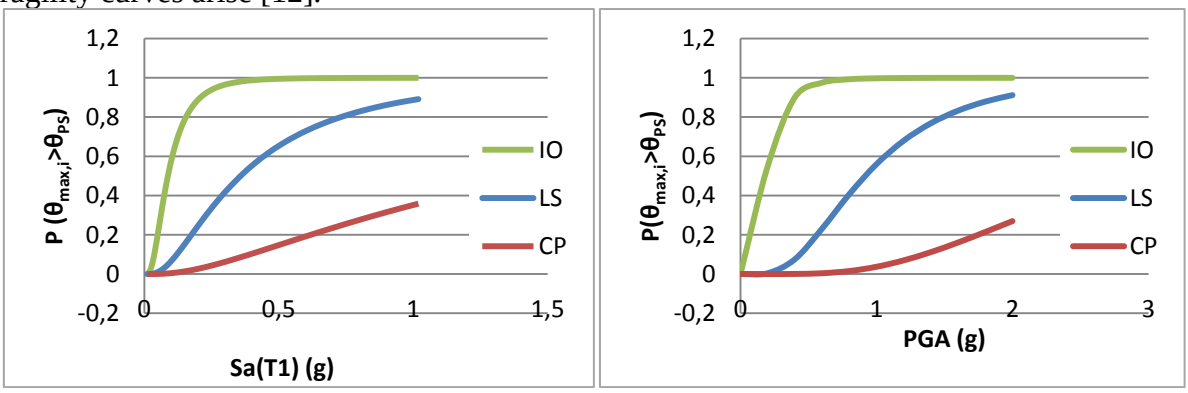


Figure 4: Hazus fragility curves for the initial building considering IM= $Sa(T_1,5\%)$ and PGA respectively [12].

5 ASSESSMENT OF THE OPTIMUM STRENGTHENING DESIGN WITH VULNERABILITY CRITERIA

The assessment of the optimum retrofitting measures is achieved by plotting the IDA fragility curves corresponding to a particular PS on a common diagram for all phases of the structure: initial, strengthened with RC jackets and strengthened with CFRP sheets [12]. The effectiveness of each strengthening technique can be easily evaluated by a comparison between the relative fragility curves and those reflecting the original building.

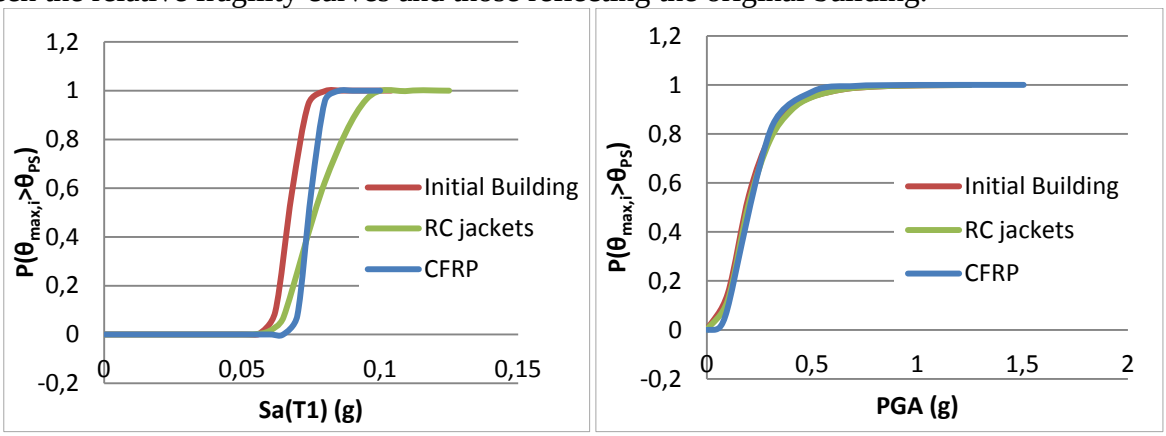


Figure 5: IDA fragility curves for Immediate Occupancy considering IM= Sa(T1,5%) and PGA respectively[12].

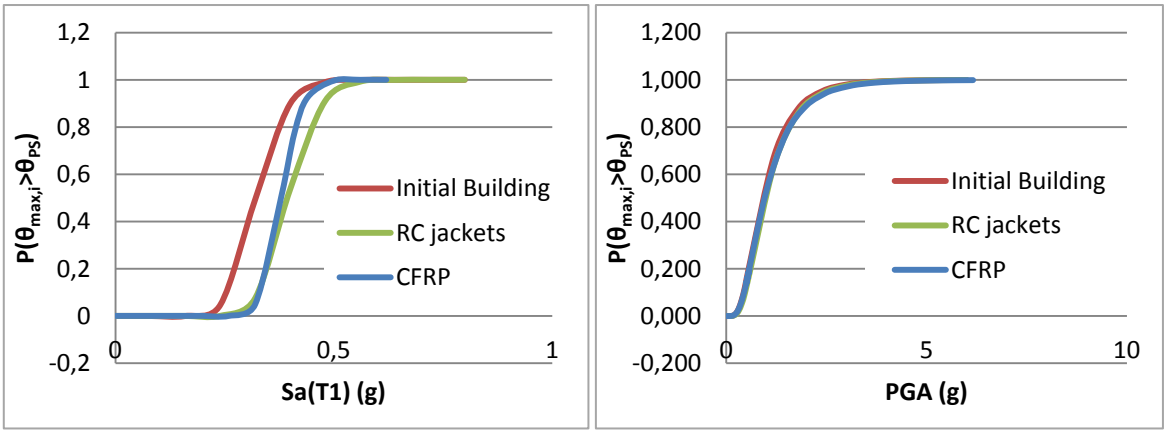


Figure 6: IDA fragility curves for Life Safety considering IM= Sa(T1,5%) and PGA respectively[12].

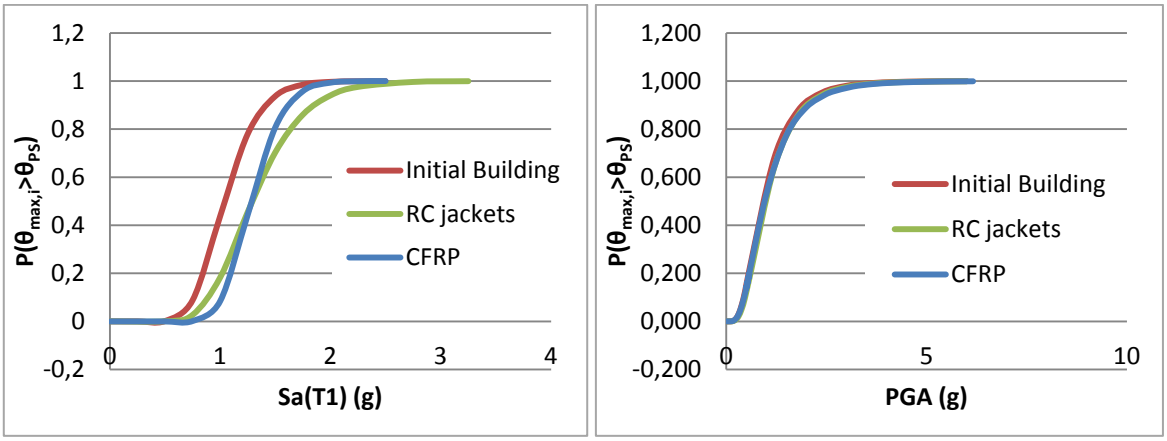


Figure 7: IDA fragility curves for Collapse Prevention considering IM= Sa(T1,5%) and PGA respectively[12].

As a first notice, the Sa(T_1,5%) seems to be a more representative criterion as IM than PGA, since the corresponding fragility curves offer a more distinct image about the difference of the structural behavior before and after the strengthening, as well as the deviation of contribution between the two different techniques. It is also clear that both of the strengthening techniques are productive and help the building respond more effectively to seismic forces, either by entering to a PS ($P(\theta_{max,i}>\theta_{PS})\geq 0$) or by exceeding it ($P(\theta_{max,i}>\theta_{PS})\leq 1$) because of more intense seismic loads (IM_i) than previously. Another verification, additionally, is that CFRP wrapping influences more positively the structure in case of low intense level, when the value of $P(\theta_{max,i}>\theta_{PS})$ fluctuates around zero. On the other hand, RC jackets are more satisfying in case of high intense level, when the value of $P(\theta_{max,i}>\theta_{PS})$ is around one. That can be explained by the fact that CFRP sheets confer further ductility to the structural elements, whereas RC jackets increase the capacity of the building, as it is proven through the Pushover Analysis [11], too. The exact profits of the strengthening are displayed below.

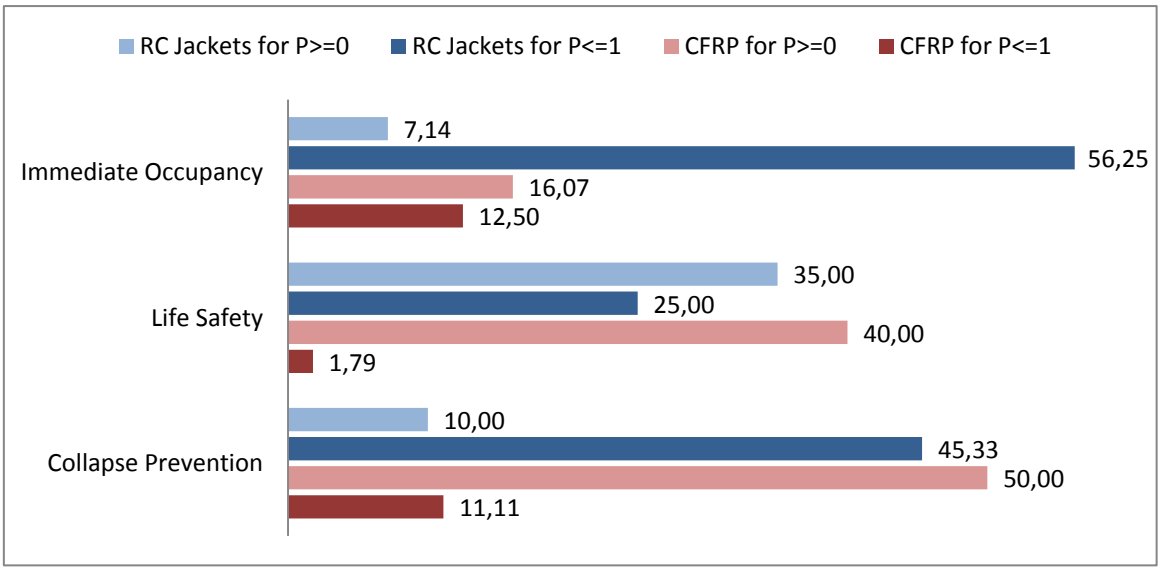


Figure 8: Structural Response Profit (%) thanks to retrofitting measures for IM= Sa(T_1,5%) [12].

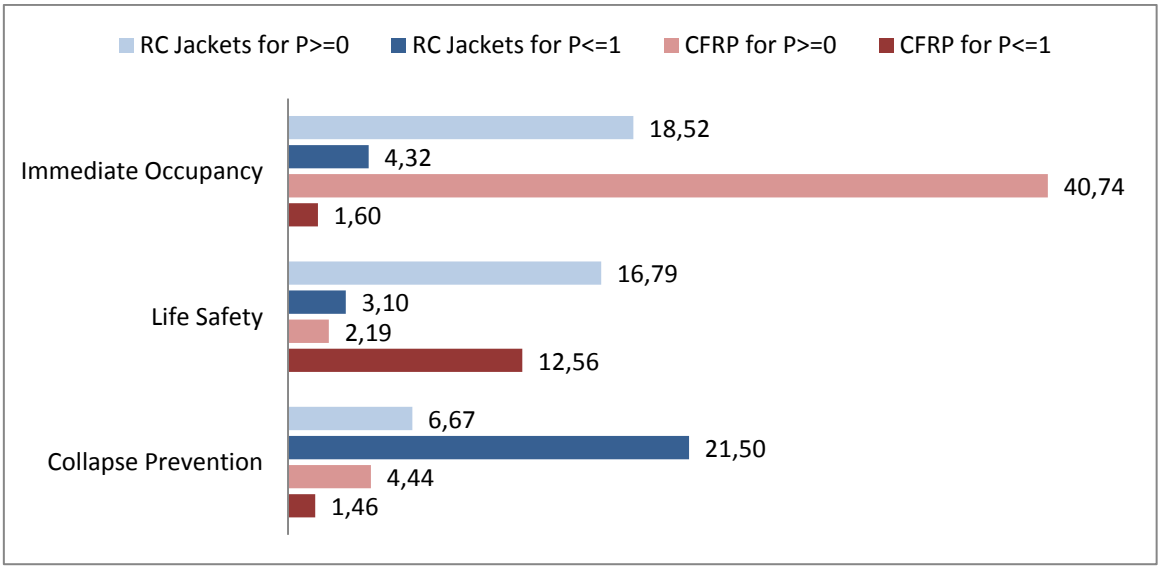


Figure 9: Structural Response Profit (%) thanks to retrofitting measures for IM= PGA [12].

6 CONCLUSIONS

In this work, the assessment of the seismic behavior of a 4-storey reinforced concrete building is attempted by using Pushover Analysis and performance criteria. The inadequate seismic response of the structure and the appearance of damages at 5 columns lead to strengthening solutions through RC jackets and CFRP wrapping. Their minimized cost is set as target; therefore, an optimization process is proposed to define the optimum characteristics of the strengthening measures. Another non-linear analysis, specifically the IDA is performed to assess the retrofitted building. IDA is based on accelerograms of real earthquakes that are imposed to the building in order to monitor its reaction. Afterwards, the IDA curves can be constructed. Different intense levels of the seismic loads are implemented in order to cover as many possible seismic effects as possible. The reliability of IDA results is directly connected with the number of seismic records taken into account. If this number is large, the results approach the real situation; however the computational length of time is huge due to the large amount of data being processed. Subsequently, vulnerability criteria are proposed for the assessment through fragility curves, which can be formed either by means of IDA curves or by applying regulations of EC8 and methods, like Coefficient and Hazus. The two methodologies vary greatly, because the first one is based on real data, whereas the second one follows widespread methodologies, assumptions and codes.

Finally, the results of this study indicate that the optimization process is successful, since the goal of cost reduction is reached and the retrofitting measures satisfy the seismic demands. The superiority of any technique is not clear, because each technique seems to have privileges towards the other in different sectors. For instance, carrying capacity of the building increases more thanks to RC jackets, but CFRP sheets amplify more the ductility. In general, both of them are characterized as effective since they combine low cost and total restitution of the existing damages.

REFERENCES

[1] Earthquake Planning and Protection Organization (EPPO), *Interventions Regulation in Buildings of Reinforced Concrete (KAN.EPE.)*, 2011.

[2] CEN, *European Standard EN 1998-3:2005 Eurocode 8: Design of structures for earthquake resistance – Part 3: Assessment and retrofitting of buildings,* 2005.

[3] EPPO, *Greek Regulation of Reinforced Concrete (EKOS-2000),* 2006.

[4] Applied Technology Council (ATC), *ATC-40 Seismic Evaluation and Retrofit of Concrete Buildings, Vol. I,* Seismic Safety Commission, 1996.

[5] T. Panagopoulos, Investigation of the vulnerability criteria values' influence on the structural design, Diploma thesis NTUA, 2011.

[6] N.D. Lagaros, Probabilistic fragility analysis: A tool for assessing design rules of RC buildings, *Earthquake Engineering and Engineering Vibration*, **7** (1), 45-56, 2008.

[7] V. Papadopoulos, N.D. Lagaros, Performance-based optimum design of structures with vulnerability objectives. *Int. J. Reliability and Safety,* **7** (1), 75-94, 2013.

[8] V. Siormpa, Study on the effect of FE Simulation on Fragility Analysis of RC Structures , Graduate thesis NTUA, 2012

[9] K. Spyrakos, *Retrofitting of Structures for Seismic Loads*, Technical Chamber of Greece, 2004.

[10] EPPO, *Recommendations for pre-earthquake and post-seismic interventions in buildings*, 2001.

[11] E.G. Skoulikari, Optimum Strengthening Design of Reinforced Concrete Structures, Diploma thesis NTUA, 2012.

[12] E.G. Skoulikari, Assesment of Reinforced Concrete Building's Strengthening with Vulnerability Criteria, Graduate thesis NTUA, 2014.

[13] N.D. Lagaros, Structural design optimization based on evolutionary algorithms and neural networks, Doctoral Thesis NTUA, 2000.

[14] V. Plevris, Innovative Computational Techniques for the Optimum Structural Design Considering Uncertainties, Doctoral Thesis NTUA, 2001.

[15] N.D. Lagaros, A general purpose real-world structural design optimization computing platform, *Structural and Multidisciplinary Optimization*, **49**, 1047–1066, 2014.

[16] EPPO, *Greek Seismic Code (EAK - 2000)*, 2006.

[17] N. Mezaini, Repair and Strengthening of Reinforced Concrete Structures, Presentation available online: http://www.docstoc.com/docs/73275011/Repair-and-Strengthening-of-Reinforced-Concrete-Structures#, 2011.

[18] A. Chopra, *Dynamics of Structures Theory and Applications to Earthquake Engineering, Vol. I, 2nd Greek Edition*. M.Giourdas, 2010.

[19] CEN, *European Standard EN 1998-1:2005 Eurocode 8: Design of structures for earthquake resistance – Part 1: General Rules, Seismic Actions and Rules for Buildings*, 2005.

COMPDYN 2015
5th ECCOMAS Thematic Conference on
Computational Methods in Structural Dynamics and Earthquake Engineering
M. Papadrakakis, V. Papadopoulos, V. Plevris (eds.)
Crete Island, Greece, 25–27 May 2015

ENERGY BASED OPTIMUM DESIGN OF TUNED MASS DAMPERS

G.C. Marano

DICAR, Department of civil Engineering and Architecture, Technical University of Bari
via Orabona 4 - 70125, Bari -Italy. Tel. ++39 0805963875, Fax ++39 0805963875, email
g.marano@poliba.it

Keywords: Tuned Mass Damper, optimum design, dissipated energy, vibration control performance.

Abstract. *Vibrations reduction in engineering systems, such as civil, mechanical and aeronautical, can be achieved by modifying rigidities, masses, damping or shape and by providing passive or active counter forces. Among the various control methods, the Tuned Mass Damper is one of the simplest and the most reliable control device. The present study focuses on optimum design of Tuned Mass Dampers based on an energy approach. For this aim, a simple one degree of freedom system subject to a seismic action and equipped with a Tuned Mass Damper is examined. The effectiveness of the control device in reducing the vibration level induced by seismic action is expressed in terms of reduction of the dissipated energy into the primary system with respect to the uncontrolled case. This index is assumed as the objective function to develop an optimum design to achieve Tuned Mass Damper optimum parameters, which give the best performances in vibration control. A comparison with the most common optimization based on displacement reduction is performed.*

1 INTRODUCTION

Passive seismic devices are extensively used to reduce damage induced in structures by earthquakes [1, 2, 3]. The Tuned Mass Damper TMD technology uses a weight, which oscillates at the same period as the main system, and an additional damper that connects two relatively moving points, when the system oscillates. Since the natural frequency of TMD is tuned in resonance with the fundamental mode of the primary system, a large amount of the main system vibrating energy is transferred to the TMD, and then dissipated by the damping, when the primary system is subjected to external disturbances. After the work of Ormondroyd and Den Hartog [4], different optimum design approaches of TMD have been developed to reduce vibration level induced in mechanical systems by various types of excitation sources [5, 6]. In [7] and [8], the TMD protection efficiency for a simple system excited at the support is investigated, considering also different environmental conditions. Performance of TMD in vibration reduction from an energy point of view was studied in [9]. In [10], the authors analyzed the seismic energy dissipation of inelastic structures with multiple TMDs. Some other studies have been developed for optimum design of TMD [11, 12]. This paper aims at evaluating the performance of TMD from the energy point of view. For this purpose, the performance of TMD is estimated the reduction of the energy dissipated by the main system. This index is used as objective function to perform an optimum design of TMD.

2 BASIC EQUATIONS AND COVARIANCE ANALYSIS

The TMD device is composed by a mass, a spring and a damper attached to the main system, as shown in Figure 1.

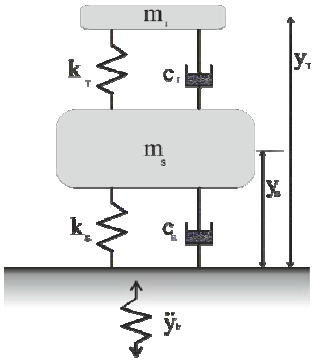


Figure 1: Mechanical model of a linear TMD system

The dynamic response of this system is governed by the dynamic equilibrium equation:

$$\mathbf{M}\ddot{\mathbf{y}}+\mathbf{C}\dot{\mathbf{y}}+\mathbf{K}\mathbf{y}=-\mathbf{M}\mathbf{r}\ddot{y}_g \tag{1}$$

where $\mathbf{y}=(y_T,y_S)^T$ is the relative base displacement vector, and **M**, **C** and **K** are the mass, the damping and the stiffness matrices.

$$\mathbf{M}=\begin{pmatrix} m_T & 0 \\ 0 & m_s \end{pmatrix};\ \mathbf{C}=\begin{pmatrix} c_T & -c_T \\ -c_T & c_T+c_s \end{pmatrix};\ \mathbf{K}=\begin{pmatrix} k_T & -k_T \\ -k_T & k_T+k_s \end{pmatrix};\ \mathbf{r}=\{1 \quad 1\}^T$$

Introducing the state space vector $\mathbf{z}_s=(y_T,y_S,\dot{y}_T,\dot{y}_S)^T$ the equation (1) becomes:

$$\dot{\mathbf{z}}_s=\mathbf{A}\mathbf{z}_s+\mathbf{r}_z\ddot{y}_g(t) \tag{2}$$

$$\mathbf{A}_s=\begin{pmatrix} \mathbf{0} & \mathbf{I} \\ \mathbf{H}_s^1 & \mathbf{H}_s^2 \end{pmatrix} \tag{3}$$

is the state matrix, $\mathbf{r}_z=(0,0,1,1)^T$, **I** and **0** are the unit and zero 2x2 matrices, and:

$$\mathbf{H}_s^1 = -\mathbf{M}^{-1}\mathbf{K} = \begin{pmatrix} -\omega^2_T & +\omega^2_T \\ +\delta_T\omega^2_T & -\left(\delta_T\omega^2_T+\omega^2_s\right) \end{pmatrix} \qquad \mathbf{H}_s^2 = -\mathbf{M}^{-1}\mathbf{C} = \begin{pmatrix} -2\xi_T\omega_T & +2\xi_T\omega_T \\ +\delta_T 2\xi_T\omega_T & -\left(\delta_T 2\xi_T\omega_T+2\xi_s\omega_s\right) \end{pmatrix} \quad (4)$$

The mechanical parameters are introduced:

$$\omega_T = \sqrt{\frac{k_T}{m_T}}\,,\ \omega_s = \sqrt{\frac{k_S}{m_S}}\,,\ \xi_T = \frac{c_T}{2\sqrt{m_T k_T}}\ \xi_s = \frac{c_S}{2\sqrt{m_S k_S}}\ \delta_T = \frac{m_T}{m_S}$$

In equation (1) $\ddot{y}_g(t)$ is the acceleration that excites the system at its support. In this study, in order to consider the intrinsic probabilistic nature of seismic motion, the Kanai-Tajimi model is adopted [12]. The space state covariance matrix $\mathbf{R_{zz}} = \mathrm{E}\left[\mathbf{z}\mathbf{z}^{\mathrm{T}}\right]$, where the symbol $\mathrm{E}[\ ]$ denotes the mathematical expectation, is obtained by the *Lyapunov equation* [19]*:*

$$\mathbf{A}\mathbf{R_{zz}}+\mathbf{R_{zz}}\mathbf{A}^{\mathrm{T}}+\mathbf{B}=0 \quad (6)$$

where **A** is the state matrix. Matrix **B** has all null elements except $[\mathbf{B}]_{6,6}=2\pi S_0$.

The response of the unprotected system is given by the covariance matrix $\mathbf{R}_{\mathbf{z}_0\mathbf{z}_0}$, which can be evaluated by solving the following equation:

$$\mathbf{A}_0\mathbf{R}_{\mathbf{Z}_0\mathbf{Z}_0}+\mathbf{R}_{\mathbf{Z}_0\mathbf{Z}_0}\mathbf{A}_0{}^{\mathrm{T}}+\mathbf{B}_0=\mathbf{0} \quad (7)$$

3 THE ENERGY EQUATIONS

For the system in Figure 1, the energy balance for unit of time, i.e. the power balance, is:

$$\dot{\mathbf{y}}^{\mathrm{T}}\mathbf{M}\ddot{\mathbf{y}}+\dot{\mathbf{y}}^{\mathrm{T}}\mathbf{C}\dot{\mathbf{y}}+\dot{\mathbf{y}}^{\mathrm{T}}\mathbf{K}\mathbf{y}=-\dot{\mathbf{y}}^{\mathrm{T}}\mathbf{M}\mathbf{r}\ddot{x}_g \quad (8)$$

Introducing the power terms, equation (30) becomes:

$$P_k(t) + P_D(t) + P_S(t) = P_I(t) \quad (9)$$

$P_k(t)=\dot{\mathbf{y}}^{\mathrm{T}}\mathbf{M}\ddot{\mathbf{y}}$ is the kinetic power at the time *t,* $P_D(t)=\dot{\mathbf{y}}^{\mathrm{T}}\mathbf{C}\dot{\mathbf{y}}$ is the dissipated power at the time *t,* $P_S(t)=\dot{\mathbf{y}}^{\mathrm{T}}\mathbf{K}\mathbf{y}$ is the elastic power at the time *t* , $P_I(t)-\dot{\mathbf{y}}^{\mathrm{T}}\mathbf{M}\mathbf{r}\ddot{y}_g$ is the input power at the time *t.*

After some rearranging, from equation (31) one obtains:

$$m_T\dot{y}_T\ddot{y}_T+m_s\dot{y}_S\ddot{y}_S+c_S\dot{y}_S^2+c_T(\dot{y}_T-\dot{y}_S)\dot{y}_T+k_T(\dot{y}_T-\dot{y}_S)y_T+k_s\dot{y}_S y_S=-m_T\dot{y}_T\ddot{y}_g-m_s\dot{y}_S\ddot{y}_g \quad (10)$$

By dividing for m_s and by introducing the mass ratio $\delta_T=m_T/m_s$, one obtains:

$$\delta_T\dot{y}_T\ddot{y}_T+\dot{y}_S\ddot{y}_S+2\xi_S\omega_S\dot{y}_S^2+2\delta_T\xi_T\omega_T(\dot{y}_T-\dot{y}_S)\dot{y}_T+\delta_T\omega_T^2(\dot{y}_T-\dot{y}_S)y_T+\omega_S^2\dot{y}_S y_S=-\delta_T\dot{y}_T\ddot{y}_g-\dot{y}_S\ddot{y}_g \quad (11)$$

In stationary condition, the power balance is:

$$2\xi_s\omega_s\dot{y}_S^2+2\delta_T\xi_T\omega_T(\dot{y}_T-\dot{y}_S)\dot{y}_T-\delta_T\omega_T^2\dot{y}_S y_T=-\delta_T\dot{y}_T\ddot{y}_g-\dot{y}_S\ddot{y}_g \quad (12)$$

and, considering the power flow in mean value one obtains:

$$2\delta_T\xi_T\omega_T\sigma^2_{\dot{y}_T}+2\xi_s\omega_s\sigma^2_{\dot{y}_S}-2\delta_T\xi_T\omega_T\gamma_{\dot{y}_T\dot{y}_S}-\delta_T\omega_T^2\gamma_{\dot{y}_S y_T}=-\delta_T\gamma_{\dot{y}_T\ddot{y}_b}-\gamma_{\dot{y}_S\ddot{y}_b} \quad (13)$$

In equation (13) $\sigma^2_{\dot{y}_T}$ and $\sigma^2_{\dot{y}_S}$ are the variances of $\dot{y}_T$ and $\dot{y}_S$, respectively, whereas $\gamma_{\dot{y}_T\dot{y}_S}$ and $\gamma_{\dot{y}_S y_T}$ are the cross-correlations. In the following, the attention will be focused on the dissipated terms: P_{Dsyst} and P_{Ddevic} i.e. the power dissipated by the main system and the power dissipated by the TMD device. As well known, the dissipative term of the main system is strictly related to its damage, whereas the amount of the power dissipated by the device points out on its performance.

If the dissipative terms are evaluated in mean value, then they assume the form:

$$\mu_{P_{Dsyst}}=2\xi_s\omega_S\sigma^2_{\dot{y}_s} \quad (14)$$

$$\mu_{P_{Ddevict}} = 2\delta_T \xi_T \omega_T \sigma^2_{\dot{y}_T} - 2\delta_T \xi_T \omega_T \gamma_{\dot{y}_T \dot{y}_S} \tag{15}$$

4 OPTIMUM DESIGN OF TDM DEVICES

In this section the optimum design [13] of TMD is developed. The main goal of optimization is to define the TMD mechanical characteristics that reduce the amount of the energy dissipated by the primary system. The Factor Reduction of Dissipated Power (FRDP) is then introduced:

$$\text{FRDP} = \frac{\mu_{P_{Dsyst}}}{\mu_{P_{Dsyst0}}} \tag{16}$$

where $\mu_{P_{Dsyst}}$ is the mean of the power dissipated by the main system when it is equipped with the TMD, and $\mu_{P_{Dsyst0}}$ is the same quantity for the uncontrolled system. In addition, the power flow dissipated by the device $\mu_{P_{Ddevic}}$ will be considered in the following. After the stochastic index is introduced, the optimum TMD parameters are evaluated by performing the solution of the optimum problem. In detail, for the TMD the optimum design is formulated as the evaluation of Design Vector $\mathbf{b} = (\omega_T, \xi_T)$, which is able to minimize the Objective Function (OF), represent by the TMD performance index:
The following optimum design problem is then formulated:

Find $\mathbf{b} = (\omega_T, \xi_T)$ (45)

Which Minimizes $OF = \text{FRDP} = \frac{\mu_{P_{Dsyst}}}{\mu_{P_{Dsyst0}}}$ (17)

The optimization problem is formulated as an uncostrained minimization, so that an Evolutive Alghoritm has been used. In details, the standard Genetic Algorithm (GA) has been used to solve numerically the problem [14, 15, 16, 17, 18].

5 NUMERICAL ANALYSIS UNDER STOCHASTIC INPUT

In this section, the results of optimum design of TMD are presented and discussed. The system damping is $\xi_s = 2\%$, the frequency $\omega_S = 2\pi (\text{rad/sec})$ and the mass ratio is $\delta_T = 0.01$. Input is characterized by the following parameters: $\omega_f = 20 \text{rad/sec}$ and $\xi_f = 0.5$.

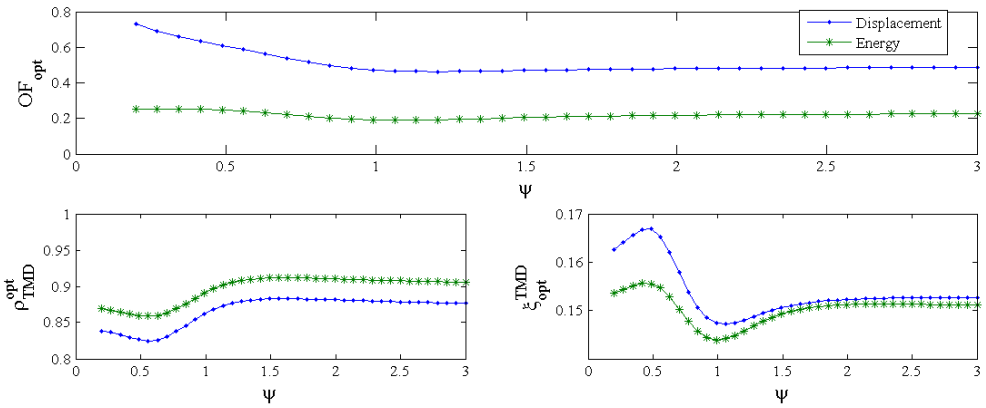


Figure 2: Comparison between the two optimization criteria. Plots represent minimized OFs and optimum design variables versus ψ. The mass ratio is δ_T is 0.01, and $\xi_S = 2\%$.

Optimum design developed considering the energy criterion is compared with results obtained considering the approach based on displacement reduction [12]. In figure 2 performance indices (energy reduction ad displacement reduction) are plotted versus $\psi = \omega_f / \omega_s$, both in the cases of displacement criterion and energy criterion. On the y-axis the symbol OF appears, whereas the demarcation between the two criteria is pointed out by different line types. In addition, also the TMD optimum parameters ρ_{opt}^{TMD} - ξ_{opt}^{TMD} that give the optimum TMD efficiency in two performance criteria are shown. One observes that in case of optimum design developed by the energy approach the FRDP assumes approximately a constant value, equal to 0.2, over the entire range of frequency investigated. This means a reduction of the 80% of the energy dissipated by the main system with respect to the uncontrolled case.
This result is of great relevance, especially when a hysteretic behaviour takes place into the structure. As well known, the amount of the energy dissipated is strictly correlated to the global and local damage level of the vibrating system.
However, exactly a minimum of FRDP is observed around $\psi = 1$, i.e. if the dominant frequency of the excitation matches the resonance frequency of the system to which the TMD frequency is tuned. This means, obvious, that the maximum effectiveness of TMD is reached when the main system is in resonance with the ground motion frequency. An important outcome is that the efficiency of TMD from the energy point of view is earthquake independent if TMD parameters are suitably chosen by optimum design strategy.
If the displacement criterion is considered, the TMD performances are more manifestly earthquake dependant, and a variability of the versus ψ is noticeable. The minimum of the OF, equal almost to 0.45, is reached for $\psi = 1$; then, for $\psi > 1$ the performance is almost constant, whereas for $\psi < 1$ the TMD effectiveness decreases and becomes inefficient when ψ decreases. With regard to the optimum parameters which let the best TMD performance, the variability towards the frequency content of ground motion is similar in the two examined optimum criteria. However, one can notice that the energy criterion gives greater ρ_{opt}^{TMD} values. Moreover, ρ_{opt}^{TMD} approaches to unit near to the resonance condition, even if, in the analyzed case this happens not exactly at $\psi = 1$, because the excitation here considered is not a narrow band one.

REFERENCES

[1] A. Fiore, P. Monaco. Earthquake-induced pounding between the main buildings of the "Quinto Orazio Flacco" school. *Earthquakes and Structures*, **1**(4), 371-390, 2010.

[2] A. Fiore, G.C. Marano, P. Monaco. Earthquake-Induced Lateral-Torsional Pounding between Two Equal Height Multi-Storey Buildings under Multiple Bi-Directional Ground Motions. *Advances in Structural Engineering*, **16**(5), 845-865, 2013.

[3] G.C. Marano, R. Greco. Damage and ductility demand spectra assessment of hysteretic degrading systems subject to stochastic seismic loads. *Journal of Earthquake Engineering*, **10,** 615-640, 2006.

[4] S.H. Crandall, W.D. Mark. *Random vibration in mechanical system*, Academic Press Inc. 1973.

[5] R. Rana, T.T. Soong. Parametric study and simplified design of tuned mass dampers. *Engineering Structures*, **20**, 193-204, 1998.

[6] G.C. Marano, R. Greco, B. Chiaia. A comparison between different optimization criteria for tuned mass dampers design. *Journal of Sound and Vibration*, **329**(23), 4880-4890, 2010.

[7] G.C. Marano, R. Greco. Optimization criteria for tuned mass dampers for structural vibration control under stochastic excitation. *Journal of Vibration and Control*, **17**(5), 679-688, 2011.

[8] F. Pellicano, F.S. Samani. Vibration reduction on beams subjected to moving loads using linear and nonlinear dynamic absorbers, *Journal of Sound and Vibration*, **325**, 742–754, 2009.

[9] K.K.F Wong, J. Johnson. Seismic energy dissipation of inelastic structures with multiple tuned mass dampers. *Journal of Eng. Mech. Asce*, **135** (4), 265-275, 2009.

[10] G.C. Marano, R. Greco. Robust Optimum design of tuned mass dampers for high-rise buildings under moderate earthquakes. *Structural Design of Tall and Special Buildings*, **18**(8), 823-838, 2009.

[11] R. Greco, G.C. Marano. Optimum design of tuned mass dampers by displacement and energy perspectives. *Soil Dynamics and Earthquake Engineering*, **49**, 243-253, 2013.

[12] R. Greco, G.C. Marano. Site based stochastic seismic spectra. *Soil Dynamics and Earthquake Engineering*, **55**, 288-295, 2013.

[13] G.C. Marano, F. Trentadue, R. Greco. Optimum design criteria for elastic structures subject to random dynamic loads. *Engineering Optimization*, **38**(7), 853-871, 2006.

[14] G. Quaranta, A. Fiore, G.C. Marano. Optimum design of prestressed concrete beams using constrained differential evolution algorithm. *Structural and Multidisciplinary Optimization*, **49** (3),441–453, 2014.

[15] A. Fiore, L. Berardi, G.C. Marano, Predicting torsional strength of RC beams by using Evolutionary Polynomial Regression. *Advances in Software Engineering*, **47**(1), 178-187, 2012.

[16] A. Fiore, G. Quaranta, G.C. Marano, G. Monti. Evolutionary Polynomial Regression–Based Statistical Determination of the Shear Capacity Equation for Reinforced Concrete Beams without Stirrups", *Journal of Computing in Civil Engineering*, ASCE, doi:10.1061/(ASCE)CP.1943-5487.0000450, 2015.

[17] G.C. Marano, R. Greco, G. Quaranta, A. Fiore, J. Avakian, D. Cascella. Parametric identification of nonlinear devices for seismic protection using soft computing techniques. *Advanced Materials Research*, **639-640** (1), 118-129, 2013.

[18] A. Fiore, G.C. Marano, D. Laucelli, P. Monaco. Evolutionary Modeling to Evaluate the Shear Behavior of Circular Reinforced Concrete Columns. *Advances in Civil Engineering*, Vol. 2014, Article ID 684256, 14 pages, 2014.

[19] G.C. Marano, G. Acciani, A. Fiore, A. Abrescia. Integration algorithm for covariance non-stationary dynamic analysis of SDOF systems using equivalent stochastic linearization. *International Journal of Structural Stability and Dynamics*, **15**(2), 1450044 (17 pages), 2015.

COMPDYN 2015
5th ECCOMAS Thematic Conference on
Computational Methods in Structural Dynamics and Earthquake Engineering
M. Papadrakakis, V. Papadopoulos, V. Plevris (eds.)
Crete Island, Greece, 25–27 May 2015

A PRELIMINARY ASSESSMENT OF SLENDERNESS AND OVERSTRENGTH HOMOGENEITY CRITERIA USED IN THE DESIGN OF CONCENTRICALLY BRACED STEEL FRAMES IN MODERATE SEISMICITY

Alper Kanyilmaz[1], Carlo A. Castiglioni[2], Hervé Degèe[3], Pierre-Olivier Martin[4]

[1,2]Department of Architecture, Built Environment and Construction Engineering
Politecnico di Milano
Via Ponzio 31, 20133 Milano, Italy
alper.kanyilmaz@polimi.it, carlo.castiglioni@polimi.it

[3]Hasselt University, Belgium
herve.degee@uhasselt.be

[4]CTICM, France
pmartin@cticm.com

Keywords: Moderate seismicity; steel structures; concentrically braced frames, slenderness, overstrength homogeneity

Abstract: *Concentrically braced frames (CBF) represent a very effective structural form against horizontal loading. They provide high lateral resistance at the same time limiting lateral displacements. Thanks to their simpler connection details and smaller cross sections, they are economic alternatives to the costly moment resisting frames. Nevertheless, concerning the seismic design, current Eurocode 8 provisions require a quite high level of complexity for the dissipative design of CBF structures. The global aim of this research is to find an optimal balance between safety and economy for the design of CBF structures, located in low-to-moderate seismic regions. New design rules will be proposed which will have less stringent local ductility and structural homogeneity requirements than current medium ductility class (DCM), and provide necessary safety level limiting the complexity and costs associated with anti-seismic design. This paper presents the results of the preliminary numerical analysis that has been realized thanks to the research fund received from European commission with the contract MEAKADO RFSR-CT-2013-00022.*

1. INTRODUCTION

The general philosophy of the most recent seismic design codes is mainly based on the assumption of providing the structure with global and fully developed plasticity, through the application of capacity design principles. However, the application of these principles in low-to-moderate seismic zones often leads to complex solutions, which are difficult to implement and usually results in significant increases in the construction costs. For this reason, building designers often neglect the capacity design principles, and apply low ductility design (DCL with q=1.5) in low-to-moderate seismic zones [1]. Given the unpredictable behaviour of low or moderate seismic actions, this approach does not always provide safe and economic solutions.

The ductility classifications are based on the rules developed in the 80s which led to the first official publication of Eurocode 8 (May 1988 edition). The behavior factors defined in this edition remained nearly unchanged since then, only some restrictions between moderate ductility design (DCM) and high ductility design (DCH) were introduced. A common aim of almost all research projects carried out since then was to verify and validate the behaviour factors as assessed in 1988.

Regarding the strict application of current Eurocode 8 [2] for regions presenting a low-to-moderate seismicity level (Belgium, Spain, Germany, France, Austria, Portugal and some parts of Italy) the following observations can be made:

- The use of DCL principle is only recommended for low seismicity regions in which the design ground acceleration on type A ground, a_g, is not greater than 0.08g, or those where the product $a_g.S$ is not greater than 0.1g. National authorities in Europe tend to increase PGA values beyond 0.1g (Latest example, France).

- The use of DCM principle requires the application of all design rules prescribed to provide ductility to the structure (same rules as DCH principle).

In this case, designers have two options in low-to-moderate seismicity regions:

i) Design according to DCM, using high q factors to reduce the design forces. In this case, significant local ductility and structural homogeneity requirements have to be fulfilled. Furthermore, the over assessed behaviour factor needs to be corrected by the global over-strength factor Ω which leads to even more complex design.

ii) Design according to DCL, which means design for unreduced seismic actions, without any guarantee and control of ductility and thus a very limited reliability level. Although DCL method is not recommended, it is allowed by Eurocode for moderate seismic zones.

The first approach, if applied accurately, leads to reliable and safe structures, but the cost may be too high since no distinction is made with respect to the design of structures to be built in high seismic zones. The second approach is clearly unreliable, because not even a minimum effort is paid for the control of ductility. It can be also expensive because of limited values allowed for the behavior factor.

Research in earthquake engineering has been essentially realized for applications in regions exhibiting a very significant seismicity level, with the aim of preventing brittle collapses, and maximizing the capacities in terms of energy dissipation. There are very few research projects, which investigate the problem in moderate seismic zones. Some of them provide new approaches for reinforced concrete structures, some suggest considering the contribution of gravity systems to the lateral system, and some gives design tips using the available standards (mostly US standards) to come up with safer and economic design. Pinto (2000) [3], emphasizes the fact that seismic design in low/moderate hazard regions cannot have a single, rational solution applicable to all cases. Application of seismic design principles requires a compromise to be reached based on each specific situation according to physical, quantitative knowledge of

the hazard and awareness of it from the public, capacity on the part of the authorities to regulate the construction process and to impose the use of anti-seismic standards, and availability of the resources necessary for ensuring protection against different levels of damage. Dominic et al. (2006) [4], highlight the fact that in United States, building designers and constructors based in moderate seismic areas do not have extensive experience with earthquake-resistant construction. The consequence of misusing complicated seismic provisions could result in unsafe and unnecessarily costly buildings. Therefore the authors provide design tips which include determining site class and seismic design category, selecting a steel seismic-force-resisting system, and applying detailing requirements according to the American standards. Hines and Fahnestock (2010) [5], point out that from low seismic design to high seismic, the costs of design and fabrication and probability of making mistakes in both processes increase. They suggest that having a flexible reserve system in moderate seismic areas can provide a moderate ductility, which can improve the seismic behavior of steel structures in these zones while keeping the design as simple as possible. Their proposals are addressed to the designers who use American Standards. Hines et.al (2009) [6], propose an independent seismic design philosophy for low-ductility structures in moderate seismic regions. They use the concepts of reserve capacity and elastic flexibility, which should complement better-established concepts of strength, ductility and capacity design. The paper focuses specifically on the concept of reserve capacity and its ability to improve collapse performance for chevron braced steel frames not specifically detailed for seismic resistance. They keep the behavior factor small as possible (R=3, according to American Standards) and try to exploit the energy dissipation characteristics of the gravity system which serves as reserve capacity, although this is not permitted by the standards. They also make an interesting comparison between a low ductility system with R=3 and high ductility system with R=5 in terms of economy. They find that the system with high ductility design costs 82% more. Although an $R = 3$ design may not safely conform to the seismic design philosophy for moderate seismic regions, this comparison shows whether increased ductility is really the most economical approach to ensuring collapse resistance in moderate seismic regions. Elghazouli (2008) [7] explains the necessity of using over-strength homogeneity rule which is not considered explicitly in other codes, however he also accepts that this requirement in isolation cannot eliminate the problem even when the 25% limit is reduced. Moreover, he also mentions that this rule imposes additional design effort and practical difficulties in the selection of brace sizes. He believes that relaxing this limit can be possible by increasing the continuity and stiffness of the columns. Gioncu And Mazzolani (2014) [8] in their new book "Seismic Design of Steel Structures", dedicated an entire section "Low-to-Moderate Seismic regions", which represents a large area of the world, under the chapter of "Challenges in Seismic Design". They explain the main issues regarding the seismic design in these areas, which include main characteristics of low-to-moderate ground motions and structural design problems in these regions. They underline the fact that seismic risk in regions with low-to-moderate seismicity is an important question without clear answers. Murty and Malik (2008) [9] raises the challenges in the current design practice in the large low-to-moderate seismic regions of India, where over the last decade; there has been a sudden surge in the construction activity. Among their proposals for the future are the new design strategies suited for low-to-medium seismic regions, in particular implementing an awareness campaign for all stakeholders especially in low-to-moderate seismic regions, and developing and updating seismic design provisions towards improving earthquake safety, especially for the low-to-moderate seismic regions. The paper published By Elghazouli (2003) [10] deals with the main behavioral issues of seismic design of concentrically braced frames. Eurocode 8 recommendations on ductility demand and inelastic distribution are examined through dynamic nonlinear analysis on idealized frame configurations. Finally, several code modifications are

proposed in order to ease causes of undesirable performance and to facilitate a rational implementation of capacity design concepts.

An extensive literature review makes it evident that low-to-medium seismicity is currently a fresh topic in the research field, with many promises but very few accomplishments. Researches all around the world accept the problem, and are trying to develop solutions. However, so far the achievements are quite limited. Most of the research in earthquake engineering focuses on applications in regions exhibiting a very significant seismicity level, with the aim of preventing brittle collapses and maximizing the capacities in terms of energy dissipation. Among the few researches on low-to-medium seismicity, some of them are providing new approaches for reinforced concrete structures, some suggest to consider the contribution of gravity systems to the lateral system, and some gives design tips using the available standards (mostly US standards) to come up with safer and more economic design. In Europe, only a few researches raised the moderate seismic design necessity. There is an ongoing European RFCS research project MEAKADO, which is investigating the moderate seismic design rules for concentrically braced frames (CBF) and moment resisting frames (MRF), as being the most relevant typologies in the European construction market.

2. METHOD AND ADVANCEMENTS

According to current version of Eurocode 8, a considerable behaviour factor for CBF structures bigger than 1,5 or 2 can only be taken into account if stringent rules on the bracing slenderness and on the over-strength homogeneity are fulfilled. In practice, these requirements are actually very difficult, and sometimes even impossible to meet. In this research, alternative design solutions are being developed with relaxed over-strength homogeneity and slenderness criteria.

By means of nonlinear transient dynamic analysis under several accelerograms, performance of case studies designed according to Eurocodes, and with relaxed capacity design rules, are evaluated. These case studies are designed by project partner CTICM (within Task 3.2 of MEAKADO project). The types of bracing considered include (figure 1):

- X bracings where diagonals in tension and diagonals in compression are in the same span;
- N bracings where diagonals in tension and diagonals in compression are in two different spans;
- V bracings.

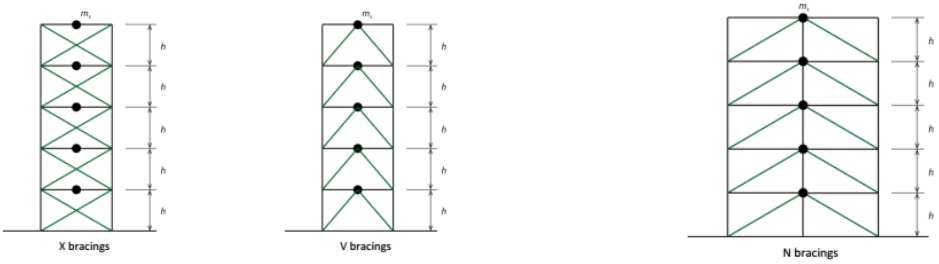


Figure 1 Frame types used in case studies by CTICM

First of all, influence of different modeling parameters has been studied on the case study frames. The parameters studied are beam end boundary conditions, initial imperfection, and presence of rigid links, damping values, and load distribution schemes. The results obtained from the numerical analysis have been compared with those provided by CTICM, which were

obtained from linear static analysis with response spectrum. Following observations can be made:

i) **Effect of initial imperfection amount:** In general, with smaller imperfections, maximum compression forces achieved in bracings are higher, the maximum displacements achieved at each floor level is smaller (the rate of difference changes randomly at each floor), maximum base shear is not very different for 4N-CHS frame, but can be quite higher in case of 4V-UPE frame. All the noted differences (compression forces in bracings, floor displacements and maximum base shear) is much higher when the 4V-UPE frame is modelled with simpler boundary conditions (beam-ends and column bases hinged, no rigid links at the frame).

ii) **Presence of Rigid links at the connections:** In general, presence of rigid links at connections increase the lateral stiffness of the structure, decreases floor displacements, increases base shears and maximum compression forces achieved in bracings. In case of 4V-UPE frame, the differences observed in floor displacements are higher when the frame is modelled with simpler boundary conditions (beam ends and column bases hinged).

iii) **Damping value:** With more damping in numerical analysis, floor displacements, base shear and maximum forces obtained in the bracings are lower.

iv) **Load distribution on beams:** Distribution of gravity loads either on beams, or concentrated on columns directly, do not have an important effect for 4N-CHS frame. 4V-UPE frame had differences in the order of 10%, in terms of displacements and base shears depending on how the gravity loads are imposed (concentrated on columns, or distributed on beams)

v) **Frame effect:** In general, important differences are observed when these two different approaches are adapted to simulate the boundary conditions: i) basic boundary conditions with beam ends, column bases are hinged and no rigid links at connections and ii) boundary conditions with beam ends and column bases are fixed, and rigid links are used to simulate gusset plates and offsets. The comparisons between numerical models and experiments showed that latter boundary conditions can be more realistic. This is probably because with basic boundary conditions, the "frame effect" provided by CBF structure is neglected, while in reality it has a quite important participation in the overall behaviour. Also a linear static analysis on 4N-CHS frame showed that, contribution of "frame effect" on the overall stiffness can be in the order of 15%. Studies on this issue are still underway, and will be validated by experimental work during the research project.

In the FE model, 3 sets of artificial accelerograms have been considered. Input for the target response spectrum can be seen in Table 1.

PGA (for soil type A)	0.15g
Soil Type for target response spectrum	B
Spectrum Type	2

Table 1 Input for target response spectrum

Following assumptions have been made during FE modeling:

i. Columns are continuous along the height
ii. Bracings are pinned at their ends. Beam ends and column bases are pinned.
iii. Rigid links are used at the end of bracings to take into account gusset plates (with 34 cm length, accounting for L_{cr}=0.9L design assumption)

iv. Lumped dynamic masses are used in the middle of beam elements
v. Material and geometrical nonlinearities have been taken into account
vi. Bracings are modelled with fiber-based nonlinear elements with distributed plasticity. Numerical validation studies have been performed on the use of fiber-based nonlinear beam elements with distributed plasticity approach, which are presented in separate articles [11, 12].
vii. Column and beam elements are modelled as elastic
viii. Initial imperfections of L/250 have been used for CHS bracing elements.
ix. The beam cross sections are divided into 16 fibers as circumferential divisions, each fiber is monitored independently with respect to its position on the stress-strain table and the integration of all the fibers over the length, determines effective beam properties. 5 integration points have been used for every section.
x. Bracing and beam elements are subdivided into 20, columns are subdivided into 8, beams are subdivided into 16 elements (meshes) along their length
xi. The analysis is made in three steps: First, a linear static analysis is performed with a displacement applied in the middle of the bracing which is equal to L/250, then based on the deformed shape of this model, nonlinear static analysis is performed only under vertical loads, and finally nonlinear transient dynamic analysis is performed starting from the last step of the nonlinear static analysis.
xii. A viscous damping is usually adopted for nonlinear dynamic analyses, which require a direct integration of the uncoupled motion equations. A particular model of viscous damping, which finds applications in large commercial softwares such as Straus7, is the Rayleigh damping. In the Rayleigh damping model, damping matrix c is a linear combination of the mass matrix m and stiffness matrix k:

a. $$\boldsymbol{c} = a_0\boldsymbol{m} + a_1\boldsymbol{k}$$

b. Where a_0 [1 / s] and a_1 [s] are proportionality constants, which depend on the first two natural frequencies of the structure. In this equation, the stiffness matrix is updated at each step, keeping constant a_0 and a_1.
c. In the models, 2% Rayleigh damping has been used.

xiii. S275 steel has been used with elasto-plastic material with kinematic strain hardening of 1% (ref. eurocode 3)

Strain	Stress (MPa)
0	0
0	275
0,075	430
0,15	430

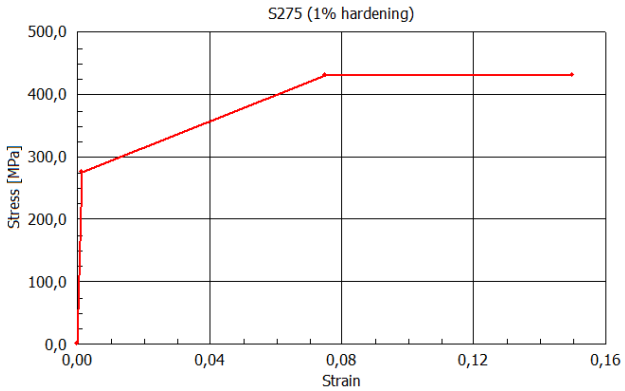


Table 2 Material properties S275

xiv. Design aacceleration inputs have been multiplied by 1.18 to take into account the effect of accidental torsion

The objective of this analysis is to assess the impact of the relaxation of slenderness and overstrength limits of Eurocode 8, on the seismic performance of CBF buildings under moderate seismic actions.

Overstrength criterion for CBF structures is defined as follows in EC8:

$$\Omega_i \leq 1{,}25\ \Omega$$

For buildings with more than two levels, slenderness criterion for CBF structures is defined as follows in EC8:

$\bar{\lambda} \leq 2{,}0$ for N and V bracings

$1{,}3 \leq \bar{\lambda} \leq 2{,}0$ for X bracings

The target of the parametric study is to assess the effect of relaxed criteria on the behaviour of steel structures in moderate seismicity areas. This study proposes some case studies to be considered.

The two following criteria will be assessed, first alone and secondly coupled:

Overstrength criterion: $\Omega_i \leq 1{,}50\ \Omega$

Slenderness criterion: $\bar{\lambda} \leq 2{,}5$

The review of the regulatory limits proposal is shown in Table 2:

EN1998-1 rules	$\Omega_{max} <$ **1,25** Ω_{min} **1,3** $< \lambda <$ **2**
Relaxed overstrength homogenity (**Ω**) criterion	$\Omega_{max} <$ **1,50** Ω_{min} **1,3** $< \lambda <$ **2**
Relaxed overstrength homogenity (**Ω**) & Relaxed slenderness (**λ**) criterion	$\Omega_{max} <$ **1,50** Ω_{min} **1,3** $< \lambda <$ **2,5**

Table 3 Design approaches

Case studies are proposed by CTICM for different “border line” cases, taking into account only circular hollow sections, as this class of sections fulfills the best all the requirements.

It is considered here that the worst situation in seismic design is to have the weak brace at the first level and strong braces at all other levels. So that case studies are studied where

$$\Omega_1 = 1{,}00 \text{ and } \Omega_i = 1{,}50 \text{ for } i > 1.$$

For all cases, theoretical cross-sections are considered (diameter and thickness) to obtain a targeted reduced slenderness of 2 for N bracings.

So far, only 4-level frames with N bracings have been analyzed. Numerical analyses have been performed with Straus7 software [13]. Figure 2 shows the numerical model of case study 4N-CHS case study.

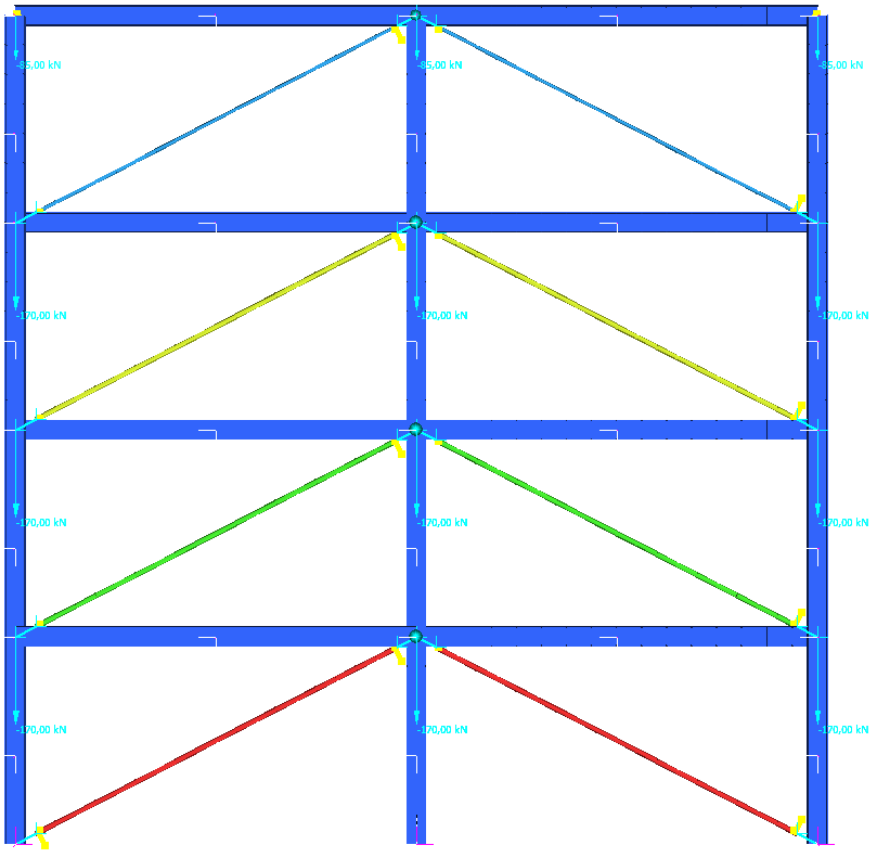


Figure 2 Analysis model of 4N-CHS case study

Three frames have been analyzed, which are designed according to the abovementioned principles (table 2). Bracings considered in different models can be seen in tables 4,5 and 6, which show that relaxation of the EC8 rules permits the adoption of lighter profiles.

Level	Section	Area	Ωi	kbuckl	λmin	λmax	Imin	Imax
1	CHS139.7*5.0	21.2	2.09	0.90	1.47	1.47	481	481
2	CHS114.3*5.0	17.2	2.07	0.90	1.81	1.81	257	257
3	CHS114.3*3.6	12.5	2.00	0.90	1.79	1.79	192	192
4	CHS76.1*4.0	9.1		0.90			59	59

Table 4 4N-CHS EC8 design

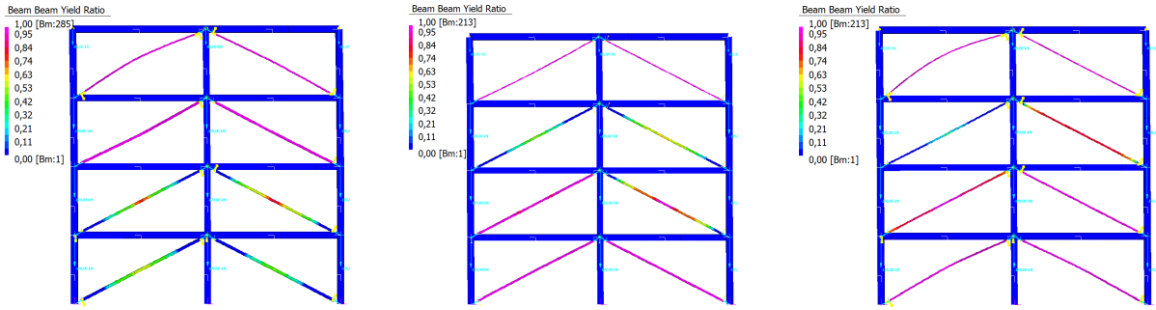
Level	NEd	Ad	Ωi	Dext	t	Imin	Imax
1	229.0	8.3	1.00	101.7	2.7	102	102
2	197.8	10.8	1.50	102.5	3.5	132	132
3	140.0	7.6	1.50	101.5	2.5	94	94
4	70.8	3.4		55.9	2.0	7	4155

Table 5 4N-CHS modified EC8 design with relaxed overstrength homogeneity

Level	NEd	Ad	Ωi	Dext	t	Imin	Imax
1	229.0	8.3	1.00	82.6	3.3	65	65
2	197.8	10.8	1.50	83.5	4.3	85	85
3	140.0	7.6	1.50	82.3	3.1	60	60
4	70.8	3.4		55.9	2.0	7	4155

Table 6 4N-CHS modified EC8 design with relaxed overstrength homogeneity & relaxed slenderness

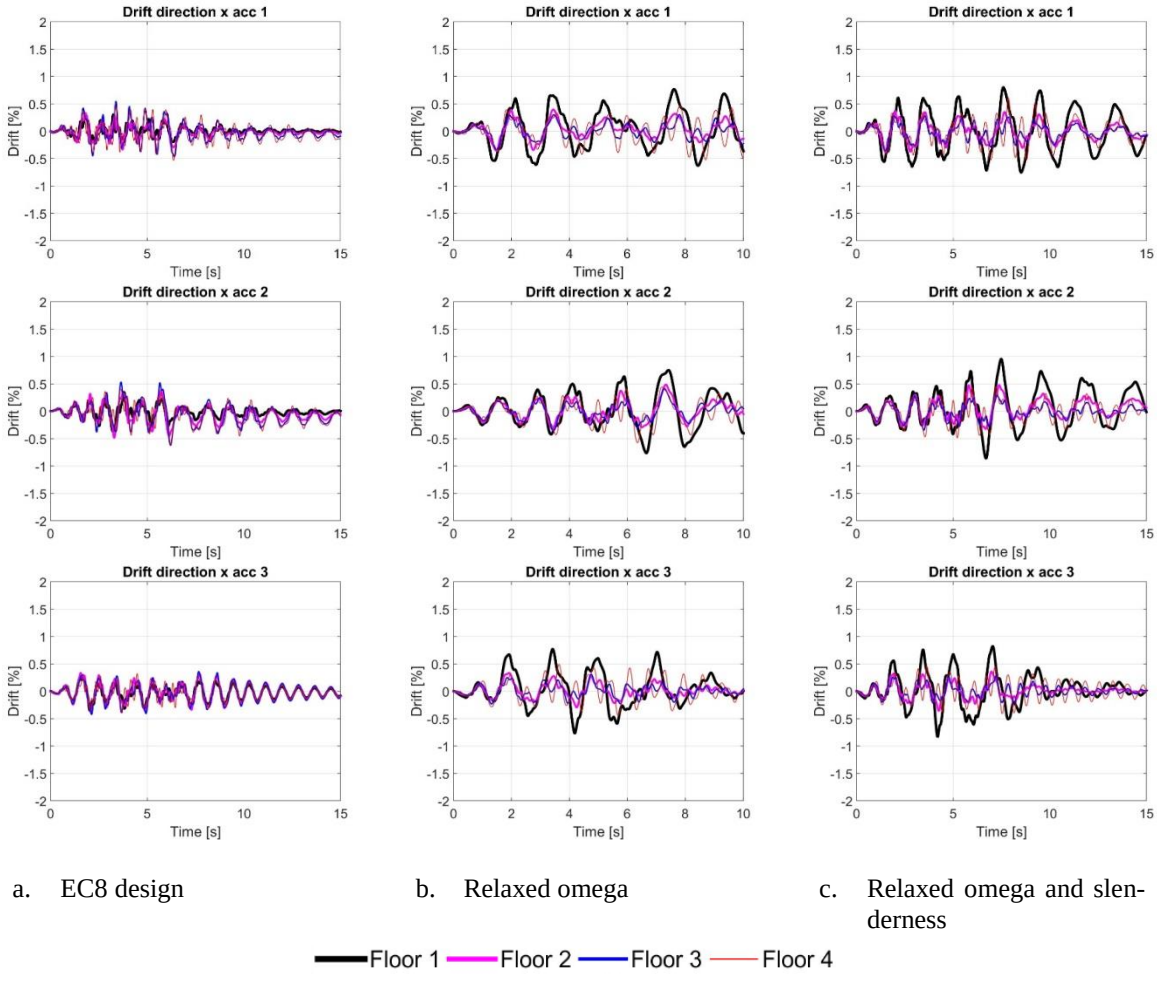
Preliminary results show that with relaxed rules, maximum drifts obtained at each floor are far below the damage limits indicated by Eurocode 8 (figure 4). Although the general distribution of plasticity is quite homogeneous (figure 3), in some cases, there is an initiation of soft-storey floor, but since the seismicity is moderate, drift levels remain small, and do not seem to cause global problems.



a. EC8 Design b. Relaxed omega c. Relaxed omega and slenderness

Figure 3 Cumulative beam yield ratios and deformed shapes at the last step of accelerogram 1

It should also be noted that bracing sections are smaller in when the rules are relaxed, which means a saving in the steel amount used in the building.



a. EC8 design b. Relaxed omega c. Relaxed omega and slenderness

Figure 4 Comparison between results in terms of floor drift ratios

3. CONCLUSIONS

In this article, the outcomes of relaxing the stringent slenderness and overstrength homogenity criteria of Eurocode 8 have been investigated numerically. Nonlinear time history analyses have been performed on the case studies designed according to following design criteria:

i. EN 1998 overstrength homogeneity ($\Omega_{max} < 1{,}25\ \Omega_{min}$) and slenderness limits ($1{,}3 < \lambda < 2$)
ii. Relaxed slenderness (λ) rule ($1{,}3 < \lambda < 2{,}5$)
iii. Combination of relaxed slenderness (λ) ($1{,}3 < \lambda < 2{,}5$) and overstrength homogenity (Ω) rules $\Omega_{max} < 1{,}50\ \Omega_{min}$

Case studies provided by project partner CTICM, are composed of 3 CBF structures, designed with abovementioned three design approaches, using linear static analysis with response spectrum approach. NLTHA have been performed under 3 artificial records, typical for moderate seismic zones. From the results of these analyses, preliminary observations have been made on the seismic performance of the frames designed according to different approaches.

This preliminary work showed that a certain amount of relaxation of slenderness and overstrength homogeneity rules permits designer to choose lighter profile sections from a larger profile database, though not worsening the seismic performance significantly. The research project is underway, and these investigations are currently being made with a broader range of case studies and acceleration time histories, and the results will be verified after experimental studies.

4. ACKNOWLEDGMENT

This study has been realized thanks to the research fund received from European commission with the contract MEAKADO RFSR-CT-2013-00022.

5. REFERENCES

[1] H. Degèe, C.A. Castiglioni, P.O. Martin, I. Calderon, B. Hoffmeister, Eight International Conference on Advances in Steel Structures

[2] Eurocode 8, Design of structures for earthquake resistance, 2003.

[3] P. Pinto, Design for Low-Moderate Seismic Risk, 2000

[4] K. Dominic and J. J. Zona, Design Tips for Steel in Low or Moderate Seismic Regions, 2006

[5] E.M. Hines and L.A. Fahnestock, Design Philosophy for Steel Structures in Moderate Seismic Regions (2010)

[6] E.M Hines, M. E. Appel and P. J. Cheever Collapse Performance of Low Ductility Chevron Braced Steel Frames in Moderate Seismic Regions, 2009

[7] A. Elghazouli, Assessment of European seismic design procedures for steel framed structures, 2008

[8] Gioncu and Mazzolani, Seismic Design of Steel Structures, 2014

[9] Murty and Malik, Challenges of Low-to-Moderate Seismicity in India, 2008

[10] A. Elghazouli, Seismic Design Procedures for Concentrically Braced Frames, 2003

[11] A. Kanyilmaz, C.A. Castiglioni, Performance of Multi-level Composite Steel-Concrete Frames with Dissipative Devices, *COMPDYN 2015, 5th ECCOMAS Thematic Conference on Computational Methods in Structural Dynamics and Earthquake Engineering, Crete Island, Greece, 2015*

[12] A. Kanyilmaz, Inelastic Cyclic numerical analysis of steel struts using distributed plasticity approach, *COMPDYN 2015, 5th ECCOMAS Thematic Conference on Computational Methods in Structural Dynamics and Earthquake Engineering, Crete Island, Greece, 2015*

[13] *G+D Computing Pty Limited*, Straus7. Theoretical Manual. Sydney (Australia), 2004.

COMPDYN 2015
5th ECCOMAS Thematic Conference on
Computational Methods in Structural Dynamics and Earthquake Engineering
M. Papadrakakis, V. Papadopoulos, V. Plevris (eds.)
Crete Island, Greece, 25–27 May 2015

SIMPLE FORMULAE FOR DAMAGE ESTIMATION OF COMPOSITE STEEL/CONCRETE MOMENT RESISTING FRAMES

George S. Kamaris[1], Konstantinos A. Skalomenos[2], George D. Hatzigeorgiou[3], and Dimitri E. Beskos[2,4]

[1] School of Engineering, University of Warwick
Coventry CV4 7AL, United Kingdom
G.Kamaris@warwick.ac.uk

[2] Department of Civil Engineering, University of Patras
Patras GR-26500, Greece
{skalomenos,d.e.beskos}@ upatras.gr

[3] School of Science and Technology, Hellenic Open University
Patras GR-26335, Greece
hatzigeorgiou@eap.gr

[4] Office of Theoretical and Applied Mechanics, Academy of Athens
Athens GR-11527, Greece
d.e.beskos@upatras.gr

Keywords: Steel/concrete moment resisting frames, Damage indices, Far-fault ground motions.

Abstract. *Simple empirical expressions to estimate maximum seismic damage on the basis of three well known damage indices for planar regular steel/concrete composite moment resisting frames are presented. They are based on the results of extensive parametric studies concerning the inelastic response of a large number of frames to a large number of ordinary far-field type ground motions. Thousands of nonlinear dynamic analyses are performed by scaling the seismic records to different intensities in order to drive the structures to different levels of inelastic deformation. The statistical analysis of the created response databank indicates that the number of stories, beam strength ratio, material strength and the ground motion characteristics affect structural damage. Nonlinear regression analysis is employed in order to derive simple formulae, which offer a direct estimation of the damage indices used in this study. More specifically, given the characteristics of the structure and the ground motion, one can calculate the maximum damage observed in column bases and beams. Finally, one example serves to illustrate the use of the proposed expressions and demonstrates their efficiency and accuracy.*

1 INTRODUCTION

Damage in a structure under loading can be defined as the degradation or deterioration of its integrity resulting in reduction of its load capacity. In earthquake-resistant design of structures, some degree of damage in the structural members is generally accepted. This is done because the cost of a structure designed to remain elastic during a severe earthquake would be very large. Thus, existing seismic codes, e.g., EC8 [1], in an implicit way and more recent performance-based seismic design methods [2,3,4] in an explicit and more systematic way employ the concept of damage to establish structural performance levels corresponding to increasing levels of earthquake actions. These performance levels mainly describe the damage of a structure through damage indices, such as the interstory drift ratio, or the member plastic rotations.

Several methods to determine damage indices as functions of certain response parameters have been presented in the literature. In general, these methods can be noncumulative or cumulative in nature. The most commonly used parameter of the first class is ductility, which relates damage only to the maximum deformation and is still regarded as a critical design parameter by codes. To account for the effects of cyclic loading, simple rules of stiffness and strength degradation have been included in various noncumulative indices [5,6,7], mainly referred to reinforced concrete members. Cumulative-type indices can be divided in deformation based [8] or hysteresis based [9,10] formulations and methods that consider the effective distribution of inelastic cycles and generalize the linear law of low-cycle fatigue of metals through a hypothesis of linear damage accumulation [11]. Sucuoğlu and Erberik [12] developed low-cycle fatigue damage models for deteriorating systems on the basis of test data and analysis and Kamaris et al. [13] proposed a new damage model exhibiting strength and stiffness degradation which takes into account the phenomenon of low-cycle fatigue and the interaction between axial force and bending moment at a section of a beam-column steel member. Combinations of deformation and energy dissipation have been also proposed to establish damage indices [14]. In these methods damage is expressed as a linear combination of the damage caused by excessive deformation and that due to repeated cyclic loading effects [14]. An extensive review of damage indices used in the literature can be found in Powell and Allahabadi [15]. Finally, the concept of continuum damage mechanics [16] in conjunction with the finite element method of concentrated inelasticity has been employed in the analysis of steel and reinforced concrete structures [17,18] for the determination of their damage.

The main objective of this paper is to study the seismic inelastic behavior of plane steel/concrete composite moment resisting frames (MRFs) and quantify their damage through simple expressions that relate the most commonly used damage indices of the literature with the characteristics of the frames and the ground motions. Similar expressions have been proposed by the authors for steel MRFs [19], but research on steel/concrete composite MRFs is still missing. For that reason, a large number of steel/concrete composite MRFs consisting of I steel beams and concrete filled steel tube (CFT) columns are subjected to an ensemble of 100 ordinary (i.e. without near-fault effects) ground motions scaled to different intensities. A response databank is created and a regression analysis is performed in order to derive simple formulae that can be used for the prediction of damage. Finally, one example is utilized to illustrate the use of the proposed formulae and demonstrate their efficiency and accuracy.

2 DAMAGE INDICES USED IN THIS STUDY

The proposed damage expressions are associated with three damage indices existing in the literature. These are the damage indices of Park and Ang [14], Roufaiel Meyer [6] and Banon and Veneziano [5]. These indices have been selected here because i) are the most widely used

in applications and ii) can be easily employed with the aid of the Ruaumoko 2D program [20]. In the following, a brief description of all these three damage indices will be given for reasons of completeness.

The damage index D_{PA} of Park and Ang [14] is expressed as a linear combination of the damage caused by excessive deformation and that contributed by repeated cyclic loading effects, as shown in the following equation:

$$D_{PA} = \frac{\delta_m}{\delta_u} + \frac{\beta}{Q_y \delta_u} \int dE \tag{1}$$

In the above, the first part of the index is expressed as the ratio of the maximum experienced deformation δ_m to the ultimate deformation δ_u under monotonic loading. The second part is defined as the ratio of the dissipated energy $\int dE$ to the term $(Q_y\, \delta_u)/\beta$, where Q_y is the yield strength and the coefficient β is a non-negative parameter determined from experimental calibration. In this paper β is taken equal to 0.025, which is a typical value for steel structures [21].

Roufaiel and Meyer [6] proposed that the ratio between the secant stiffness at the onset of failure M_m/φ_m and the minimum secant stiffness reached so far M_x/φ_x, can be used as a good indicator of damage. Based on that, they defined the modified flexural damage ratio (MFDR) or D_{RM} as

$$D_{RM} = MFDR = \max[MFDR^+, MFDR^-] \tag{2}$$

$$MFDR^+ = \frac{\phi_x^+}{M_x^+} - \frac{\phi_y^+}{M_y^+} \Bigg/ \frac{\phi_m^+}{M_m^+} - \frac{\phi_y^+}{M_y^+}, \quad MFDR^- = \frac{\phi_x^-}{M_x^-} - \frac{\phi_y^-}{M_y^-} \Bigg/ \frac{\phi_m^-}{M_m^-} - \frac{\phi_y^-}{M_y^-} \tag{3}$$

where φ is the beam curvature due to a bending moment M, the term M_y/φ_y is the initial elastic stiffness and subscripts + and – denote the loading direction.

The Banon and Veneziano [5] analysis is set in a probabilistic context and their model has been calibrated on the basis of 29 different tests on reinforced concrete elements and structures, selected from among the most representative ones in the technical literature. In particular, the damage parameters d_1 and d_2 are defined, respectively, as the ratio of stiffness at yielding point to secant stiffness at failure, and the plastic dissipated energy E_h normalized with respect to the absorbed energy at the elastic limit. If the elastic-plastic model is used, d_1 is obviously equal to the ratio of the maximum displacement x_{max} to the displacement at the elastic limit x_y. Therefore, according to the notation introduced above, parameters d_1 and d_2 can be expressed as

$$d_1 = x_{\max} / x_y, \quad d_2 = E_h / (1/2) F_y x_y \tag{4}$$

where F_y is the yield strength. Furthermore, modified damage parameters d_1^* and d_2^* are introduced of the form

$$d_1^* = d_1 - 1 \tag{5}$$

$$d_2^* = a d_2^b \tag{6}$$

where a and b are two parameters which characterize the structural problem and are defined experimentally. For flexure, x and F are replaced by θ and M, respectively. Thus, the damage index D_{BV} is defined as

$$D_{BV} = \sqrt{(d_1^*)^2 + (d_2^*)^2} \tag{7}$$

3 PLANE REGULAR CFT-MRFS USED IN THIS STUDY

3.1 Design and Characteristics

A family of 48 plane regular (orthogonal without setbacks) along their height CFT-MRFs are designed for the parametric studies of this work aiming to cover a wide range of structural characteristics of this type of composite structures. These frames have storey height and bay width equal to 3 m and 5 m, respectively and CFT column sections, as shown in Fig. 1. Moreover, the frames have the following structural characteristics: number of stories, n_s, with values 1, 3, 6, 9, 12, 15, 18 and 20, number of bays, $n_b = 3$, steel yielding stress ratio $e_s = 235 / f_s$ with the yielding stress f_s taking the values of 275 and 355 MPa, concrete strength ratio $e_c = 20 / f_c$ with the compressive strength f_c taking the values 20 MPa. Additionally, the beam-to-column stiffness ratio, ρ and column to beam strength ratio, α, taking various values within practical limits are also considered. The beam-to-column stiffness ratio ρ of a frame is based on the beam and column properties in the storey closest to the mid-height of the frame and calculated by

$$\rho = \frac{\sum (I/l)_b}{\sum (I/l)_c} \tag{8}$$

where I and l are the second moment of inertia and length of the steel member (column c or beam b), respectively. The concrete core is considered as cracked and the effective second moment of inertia for the composite section is defined according to EC4 [22]. The parameter ρ definitely controls the behavior of the frame in the elastic range of the response [23]. As ρ increases, the behavior of the frame moves from pure flexural ($\rho = 0.0$) to pure shear ($\rho = \infty$) behavior. In the inelastic range of the response and especially at higher values of ductility, the influence of ρ is lost since the structure behaves in a mechanism type of mode. Furthermore, Karavasilis et al. [24] have introduced during the investigation of the inelastic seismic response of steel MRFs the beam strength ratio, α, which indicates how much stronger are the beams in comparison with the base columns. According to that work [24], the parameter α adopted here is defined as

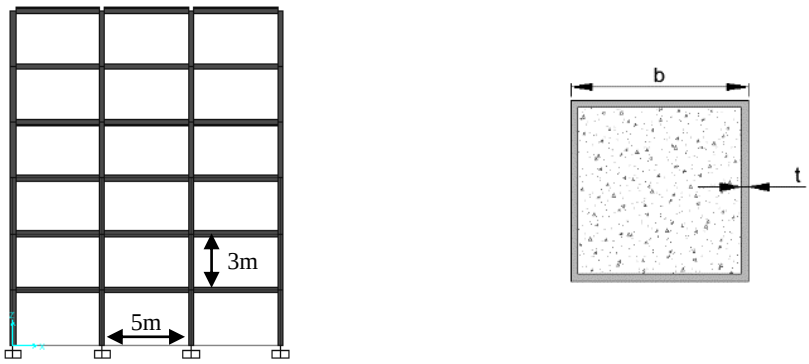
$$\alpha = M_{RC,1,av} / M_{RB,av} \tag{9}$$

where $M_{RC,1,av}$ is the average of the plastic moments of resistance of the columns of the first storey and $M_{RB,av}$ is the average of the plastic moments of resistance of the beams of all the stories of the frame. This parameter quantifies the structural capacity to avoid the formation of a global plastic mechanism which is developed when plastic hinges occur at the base of columns of the first floor and at the ends of beams.

The CFT-MRFs are designed according to the structural Eurocodes 3 [25], 4 [22] and 8 [1] with the aid of the computer programs SAP2000 [26] and MATLAB [27]. The seismic load combination consists of the gravity load G + 0.3Q = 27.5 kN/m on beams plus the earthquake load and the gravity load combination 1.35G + 1.5·Q = 42.6 kN/m with G = 26 kN/m and Q = 5 kN/m being the dead and live floor loads, respectively. Data for 24 of the 48 frames considered here, are given in [28]. The sectional dimensions of the frames with 355 MPa yield steel stress remain the same in order to clarify the effect of that material parameter.

Every frame is designed for vertical static loads according to Eurocodes 3 [25] and 4 [22] and for seismic loads according to Eurocode 8 [1] using design ground acceleration α_g =

0.30g, soil type B (soil factor S = 1.2) and Spectrum Type 1 with behavior factor q = 4. In addition to the satisfaction of the seismic strength demands in members, other seismic design checks include compliance with stability and drift criteria as well as capacity design considerations (Eurocode 3 [25]; Eurocode 4 [22] and Eurocode 8 [1]. Finally, it should be noted that the assumed building configurations, material properties, member section dimensions, loading conditions, e.t.c., are compatible with the everyday engineer practice.



(a) (b)

Figure 1: Typical geometry of frames considered (a) with columns of square concrete filled steel tube (CFT) sections (b).

3.2 Modelling for nonlinear analysis

The 48 CFT-MRFs mentioned in the previous section, are subject to a set of 100 accelerograms and their response to those motions is determined through inelastic dynamic time-history analyses using Newmark's constant average acceleration method with the aid of the computer analysis program RUAUMOKO 2D [20]. Diaphragm action is assumed at every floor due to the presence of the slab. The effect of large deformations is taken into account and therefore, the moment amplification in columns caused by the eccentricity of the axial load is considered in the analyses. Rayleigh type damping corresponding to 3% of the critical damping in the first and second mode is assumed. The deteriorating inelastic behavior of all the frame members is modeled by means of zero-length plastic hinges. The effect of panel zones is taken into account but the connections are assumed to be rigid. All the analytical models of frame components utilized are presented in detail in Skalomenos et al. [28, 30].

4 GROUND MOTIONS CONSIDERED

An ensemble of 100 ordinary (far-field type) ground motions recorded at soils with average shear wave velocity $v_{s,30}$ in the range between 360 and 800 m/s (classified according to Eurocode 8 [1] as soil type B) are selected from the PEER [31] database and are employed for the nonlinear time history analyses of this study. Another constraint on the selection of the earthquakes is that their geometric average spectrum be as near as possible to the Eurocode 8 [1] elastic spectrum for ground acceleration 0.30 g and soil type B, without any scaling. A full list of all these ground motions with their characteristics can be found in Skalomenos [28].

5 METHODOLOGY FOR COMPUTATION OF DAMAGE EXPRESSIONS

In the present work, an extensive parametric study was conducted for the 48 CFT-MRFs of described in section 3, which were subjected to the 100 ground motions section 4 for the evaluation of the damage expressions. The frames were analyzed with the program Ruaumoko

2D [20] using the incremental dynamic analysis method [32]. Thus, approximately 72000 analyses (=48 frames x 100 ground motions x 15 analyses on the average for every frame) were conducted in this work. These 15 on the average analyses for every frame correspond to 15 different PGA values for every ground motion.

The ground motion intensity level was measured here by an intensity measure (IM) equal to the spectral acceleration S_a, of the motion corresponding to the fundamental period of each frame. The structural response was measured by a damage measure (DM) equal to the maximum damage index among all storeys that was recorded during the time history of the analysis. More specifically, each ground motion was continuously scaled by increasing its S_a until the frame to become dynamically unstable and collapse. The results of the analysis were post-processed in order to create a databank with the response quantities of interest.

The created databank is actually a spreadsheet with rows equal to the number of nonlinear analyses and columns equal to the response quantities of interest in columns and beams of a CFT-MRF along its height. Those response quantities are the maximum values of the following damage indices:1) Park and Ang damage index, D_{PA}, 2) Roufaiel and Meyer damage index, D_{RM}, 3) Banon and Veneziano damage index, D_{BV}. Moreover, the columns of the databank were increased by adding the characteristics of the frames (n_s, ρ, α) and the spectral acceleration S_a.

6 DAMAGE FORMULAE FOR COMPOSITE STEEL/CONCRETE MOMENT RESISTING FRAMES

In this section, simple formulae to estimate seismic damage, through three well known damage indices, of CFT-MRFs are proposed. Thus, with the aid of these simple expressions one can determine the maximum damage of column bases or beams, D, of this type of frames in terms of characteristics of the structure and the ground motions that excite them.

By analyzing the response databank, the proposed relationship was identified and thus the expression

$$D = b_1 \cdot n_s^{b_2} \cdot \alpha^{b_3} \cdot \left(\frac{S_a}{g}\right)^{b_4} \left(\frac{235}{f_s}\right)^{b_5} \tag{10}$$

with b_1, b_2, b_3, b_4 and b_5 constants to be determined, was selected as a good candidate for approximating the response databank. The aforementioned relation is relatively simple and satisfies the physical constraint D=0 for S_a=0. However, there are values of S_a that give 0 values of damage either at columns or beams and for this reason this equation fails to estimate the real value of damage which is 0. Thus, before using it, one can check the internal forces of the columns or beams by performing a linear analysis and find if their values are in the elastic range. If this is the case the value of damage is equal to zero by default, otherwise the proposed relationship can be used. Use of the Levenberg–Marquardt algorithm [27] for nonlinear regression analysis of the results of parametric studies, led to the following expressions for each one of the three damage indices

a) for column bases:

$$D_{PA}^{c} = 0.24 \cdot n_s^{0.16} \cdot \alpha^{-0.30} \cdot \left(\frac{S_a}{g}\right)^{0.39} \left(\frac{235}{f_s}\right)^{0.05} \tag{11}$$

$$D_{RM}^{c} = 0.45 \cdot n_s^{0.16} \cdot \alpha^{-0.46} \cdot \left(\frac{S_a}{g}\right)^{0.36} \left(\frac{235}{f_s}\right)^{0.45} \tag{12}$$

$$D_{BV}^{c} = 0.33 \cdot n_s^{0.12} \cdot \alpha^{-0.33} \cdot \left(\frac{S_a}{g}\right)^{0.39} \left(\frac{235}{f_s}\right)^{0.02} \tag{13}$$

b) for beams:

$$D_{PA}^{b} = 0.31 \cdot n_s^{0.33} \cdot \alpha^{-0.12} \cdot \left(\frac{S_a}{g}\right)^{0.43} \left(\frac{235}{f_s}\right)^{-0.08} \tag{14}$$

$$D_{RM}^{b} = 0.38 \cdot n_s^{0.27} \cdot \alpha^{-0.15} \cdot \left(\frac{S_a}{g}\right)^{0.37} \left(\frac{235}{f_s}\right)^{0.004} \tag{15}$$

$$D_{BV}^{b} = 0.40 \cdot n_s^{0.27} \cdot \alpha^{-0.06} \cdot \left(\frac{S_a}{g}\right)^{0.36} \left(\frac{235}{f_s}\right)^{-0.10} \tag{16}$$

With D being any damage index of interest, the mean, median and standard deviation of the ratio of the "exact" value of D obtained from inelastic dynamic analyses over the approximate one calculated from Eqs (11) to (16), respectively., i.e., D_{exact}/D_{app}, are used in order to express the central tendency and the dispersion of the error introduced by the proposed relations. Thus, for the Park and Ang [14] damage index, the ratio $D_{PA,c.exact}/D_{PA,c,app}$, for column bases, corresponds to a mean value equal to 1.0, a central value equal to 0.96 and a standard deviation equal to 0.29. Furthermore, this ratio corresponds to a mean value equal to 1.0and 0.99, a central value equal to 0.93 and 0.97 and a standard deviation equal to 0.37 and 0.27 for the Roufaiel and Meyer [6] and Banon and Veneziano [5] damage indices, respectively. The above ratio for beams corresponds to a mean value equal to 0.99, 1.0 and 0.99, a central value equal to 0.96, 0.96 and 0.98 and a standard deviation equal to 0.27, 0.28 and 0.23 for the Park and Ang [14], the Roufaiel and Meyer [6] and Banon and Veneziano [5] damage indices, respectively. Those values show that the proposed formulae are of high accuracy.

7 EXAMPLE OF APPLICATION

A three storey-three bay CFT-MRF is examined, with a geometrical configuration similar to the one shown in Fig. 1. The seismic load combination consists of the gravity load G + 0.3Q = 27.5 kN/m on beams plus the earthquake load and the gravity load combination 1.35G + 1.5·Q = 42.6 kN/m. The frame has been designed in accordance with the provisions of structural Eurocodes, using design ground acceleration α_g = 0.30g, soil type B (soil factor S = 1.2) and Spectrum Type 1 with behavior factor q = 4. The yielding stress f_s takes the value of 275 MPa. The design yielded CFT columns with square steel tubes of width b = 300 mm and thickness t = 12.5 mm and IPE 240 beams for all the floors.

The characteristic value α of the frame was computed on the basis of Equation (6) and found to be equal to 2.322. The expected ground motion was defined by the acceleration response spectrum of EC8 [1] with a PGA equal to 0.35 g and a soil of class B. The fundamental period of vibration, T, of the frame is equal to 0.844 s, while its spectral acceleration S_a corresponding to this period, derived in the basis of EC8 [1] spectrum, equals 0.64 g.

Eight semi-artificial accelerograms compatible with the EC8 [1] spectrum were generated via a deterministic approach [33] on the basis of eight real seismic records of the database used herein. The response spectra of these motions, in comparison with the EC8 [1] spectrum, are depicted in Fig. 2. Nonlinear time history analyses of the designed frame under these motions were performed. The three damage indices used here and observed in column bases and beams of the frame were computed with the aid of the program Ruaumoko 2D [20]. Then, the

mean value of the maximum damage values for the eight semi-artificial accelerograms was evaluated for each damage index. Moreover, the approximate values of the damage indices were computed with the aid of Eqs (11) to (16) and recorded together with the exact ones in Tables 1 and 2 for column bases and beams, respectively. The proposed relations predict very well the damage of the beams (error = 5.6-9.5%) for all kinds of indices. A similar trend is observed for the columns (error = 4.7-16.0%) for all kinds of indices. Thus, the predictions of the proposed formulae are quite close to the "exact" ones and they are as far as the columns, in most of cases, in the safe (conservative) side.

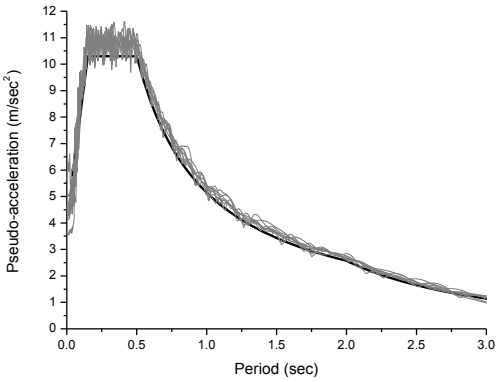


Figure 2: Response spectra of ground motions used in example of sec 7.

Damage Index	"Exact" Value	Approximate Value	Error(%)
D_{PA}	0.157	0.187	16.0
D_{RM}	0.273	0.287	4.7
D_{BV}	0.203	0.240	15.6

Table 1: Comparison between "exact" and approximate values of damage indices for columns of the CFT-MRF of the example of sec 7.

Damage Index	"Exact" Value	Approximate Value	Error(%)
D_{PA}	0.355	0.335	5.6
D_{RM}	0.408	0.384	5.9
D_{BV}	0.494	0.447	9.5

Table 2: Comparison between "exact" and approximate values of damage indices for beams of the CFT-MRF of the example of sec 7.

8 CONCLUSIONS

A procedure in terms of simple formulae for estimating the maximum damage in regular multi-storey CFT-MRFs subjected to ordinary (i.e. without near-fault effects) ground motions has been presented. Particularly, simple and easy to use relationships were derived for the computation of three damage indices of the literature, which take into account the influence of basic characteristics of CFT-MRFs and ground motions, such as the number of stories, beam strength ratio, steel yielding stress ratio and the spectral acceleration. It should be noticed

herein that the proposed relations are valid for frames with characteristics similar to those of the frames used in the parametric studies and for seismic sites where ordinary ground motions are expected. These expressions give a good approximation of damage and provide a rapid damage assessment of existing structures without the use of the more sophisticated and time consuming non-linear dynamic analysis.

REFERENCES

[1] EC8. *Design of structures for earthquake resistance, Part 1: General rules, seismic actions and rules for buildings*, European Committee for Standardization (CEN), Brussels, Belgium, 2004.

[2] P. Fajfar and H. Krawinkler, *Seismic Design Methodologies for the Next Generation of Codes.* Bled, Balkema, Rotterdam, 24-27 June 1997.

[3] FEMA. *FEMA-273 Building Seismic Safety Council, NEHRP guidelines for the seismic rehabilitation of buildings*, Federal Emergency Management Agency, Washington (DC), 1997.

[4] G.S. Kamaris, G.D. Hatzigeorgiou, D.E. Beskos, Direct damage controlled seismic design of plane steel degrading frames. *Bulletin of Earthquake Engineering*, in press.

[5] H. Banon, D. Veneziano, Seismic safety of reinforced concrete members and structures. *Earthquake Engineering and Structural Dynamics*, **10**, 179-173, 1982.

[6] M.S. Roufaiel C. Meyer, Analytical modeling of hysteretic behavior of R/C frames. *Journal of Structural Engineering, ASCE*, **113**, 429-444, 1987.

[7] E. Cosenza, G. Manfredi, R. Ramasco, The use of damage functionals in earthquake engineering: A comparison between different methods. *Earthquake Engineering and Structural Dynamics*, **22,** (10), 855-868, 1993.

[8] J.E. Stephens, J.T.P. Yao, Damage assessment using response measurements. *Journal of Structural Engineering, ASCE*, **113**, 787-801, 1987.

[9] S.L. McCabe, W.J. Hall, Assessment of seismic structural damage. *Journal of Structural Engineering, ASCE*, **115**, 2166-2183, 1989.

[10] J.M. Bracci, A.M. Reinhorn, J.B. Mander, *Deterministic model for seismic damage evaluation of reinforced concrete structures*, Technical Report NCEER 89-0033, State University of New York at Buffalo, 1989.

[11] H. Krawinkler, M. Zohrei, Cumulative damage in steel structures subjected to earthquake ground motions. *Computers and Structures*, **16**, 531-541, 1983.

[12] H. Sucuoğlu, A. Erberik, Energy-based hysteresis and damage models for deteriorating systems. *Earthquake Engineering and Structural Dynamics*, **33**, 69-88, 2004.

[13] G.S. Kamaris, G.D. Hatzigeorgiou, D.E. Beskos, A new damage index for plane steel frames exhibiting strength and stiffness degradation under seismic motion. *Engineering Structures*, **46**, 727-736, 2013.

[14] Y-J. Park, AH-S. Ang, Mechanistic seismic damage model for reinforced concrete. *Journal of Structural Engineering, ASCE*, **111**, 722-739, 1985.

[15] G.H. Powell, R. Allahabadi, Seismic damage prediction by deterministic methods: concepts and procedures. *Earthquake Engineering and Structural Dynamics*, **16**, 719-734, 1988.

[16] J. Lemaitre, *A Course on Damage Mechanics*. Springer-Verlag, Berlin, 1992.

[17] G.D. Hatzigeorgiou, D.E. Beskos, Direct damage controlled design of concrete structures. *Journal of Structural Engineering, ASCE*, **133**, 205-215, 2007.

[18] G.S. Kamaris, G.D. Hatzigeorgiou, D.E. Beskos, Direct damage controlled design of plane steel-moment resisting frames using static inelastic analysis. *Journal of Mechanics of Materials and Structures*, **4**, 1375-1393, 2009.

[19] G.S. Kamaris, Y.-M. Vallianatou, DE. Beskos, Seismic damage estimation of in-plane regular steel moment resisting and x-braced frames. *Bulletin of Earthquake Engineering*, **10**, (6), 1745-1766, 2012.

[20] A.J. Carr, RUAUMOKO-2D. *Inelastic Time-History Analysis of Two-Dimensional Framed Structures*, Department of Civil Engineering. University of Canterbury, New Zealand, 2006.

[21] C.A. Castiglioni, R. Pucinotti, Failure criteria and cumulative damage models for steel components under cyclic loading. *Journal of Constructional Steel Research*, **65**, 751-765, 2009.

[22] EC4: *Design of composite steel and concrete structures - Part 1.1: General rules and rules for buildings*, European Committee for Standardization (CEN), Brussels, Belgium, 2004.

[23] S. Akkar, U. Yazgan, and P. Gülkan, Drift estimates in frame buildings subjected to near-fault ground motions, *Journal of Structural Engineering*, **131**, 1014–1024, 2005.

[24] T.L. Karavasilis, N. Bazeos, DE. Beskos, Drift and Ductility Estimates in Regular Steel MRF Subjected to Ordinary Ground Motions: A Design-Oriented Approach. *Earthquake Spectra*, **24**, (2), 431-451, 2008.

[25] EC3. *Design of steel structures - Part 1.1: General rules and rules for buildings*, European Committee for Standardization (CEN), Brussels, Belgium, 2005.

[26] SAP2000. *Static and Dynamic Finite Element Analysis of Structures - V16*. Computers and Structures Inc., Berkeley, California, 2013.

[27] MATLAB. *The language of technical computing, Version 5.0*. The Mathworks Inc., Natick, Mass, 2009.

[28] K.A. Skalomenos, *Seismic performance of plane moment resisting frames with concrete filled steel tube columns and steel I beams*. Ph.D. Dissertation, Department of Civil Engineering, University of Patras, Greece, 2014.

[29] K.A. Skalomenos, G.D. Hatzigeorgiou, D.E. Beskos, Parameter identification of three hysteretic models for the simulation of the response of CFT columns to cyclic loading. *Engineering Structures*, **61**, 44-60, 2014.

[30] K.A. Skalomenos, G.D. Hatzigeorgiou, DE. Beskos, Modelling level selection for seismic analysis of CFT/MRFs by using fragility curves. *Earthquake Engineering Structural Dynamics*, in press.

[31] NGA *Strong ground motion database*. Pacific Earthquake Engineering Research Center, /http://peer.berkeley.edu, 2011.

[32] D. Vamvatsikos, CA. Cornell, Incremental dynamic analysis. *Earthquake Engineering Structural Dynamics*, **31**, (3), 491-514, 2002.

[33] D.L. Karabalis, G.J. Cokkinides, D.C. Rizos, *Seismic Record Processing Program-Ver.1.03*, Report of the College of Engineering, University of South Carolina, Columbia, 1992.

COMPDYN 2015
5th ECCOMAS Thematic Conference on
Computational Methods in Structural Dynamics and Earthquake Engineering
M. Papadrakakis, V. Papadopoulos, V. Plevris (eds.)
Crete Island, Greece, 25–27 May 2015

RENEWABLE ENERGY TENSEGRITY STRUCTURES

F. Fraternali[1], E. De Chiara[1], A. Fortunato[1], E. Sicignano[1], and R. E. Skelton[2]

[1]Department of Civil Engineering, University of Salerno, 84084, Fisciano (SA), Italy.
f.fraternali@unisa.it (F. Fraternali), elenadechiara@gmail.com (E. De Chiara), a.fortunato@unisa.it (A. Fortunato), e.sicignano@unisa.it (E. Sicignano)

[2] Department of Mechanical and Aerospace Engineering, University of California at San Diego, La Jolla, California 92093-0411, USA. bobskelton@ucsd.edu (R. E. Skelton)

Keywords: Renewable Energy, Tensegrity Structures, Morphing Lattices, Shading Screens.

Abstract. *We design novel sun barriers of energy efficient buildings. Making use of morphing lattices, we design sun screens that can be opened and closed during different hours of the day and periods of the year, by controlling the stretching of a limited number of cables. The struts of the screens remain undeformed during the opening and closure operations and can therefore support rigid plates, such as, e.g., solar panels and/or shading panels. Such morphing abilities lead us to the design of lightweight sun screens whose actuation requires reduced low energy consumption and minimal friction effects. We end with a review of novel "responsive architectures" for energy efficient buildings, which make use of tensegrity structures at different levels (primary and secondary structures) in order to respond to the natural environment by changing their mechanical and heating, ventilating and air-conditioning properties.*

1. INTRODUCTION

It is known that the construction industry significantly contributes to overall energy consumption (up to 40% in the European Union, cf. [1], and directive 31/2010/UE) and there is an urgent need for sustainable buildings that are able to reduce CO2 emissions by 90% and energy consumption by as much as 50% [2]. Renewable energy technologies have significant deployment potential as resources are spread globally, in contrast to the conventional sources such as gas, coal and oil, which are more geographically concentrated. Globally, renewable generation is estimated to rise to 25% of gross power generation in 2018, up from 20% in 2011 as deployment spreads out globally [1] (Figure 1).

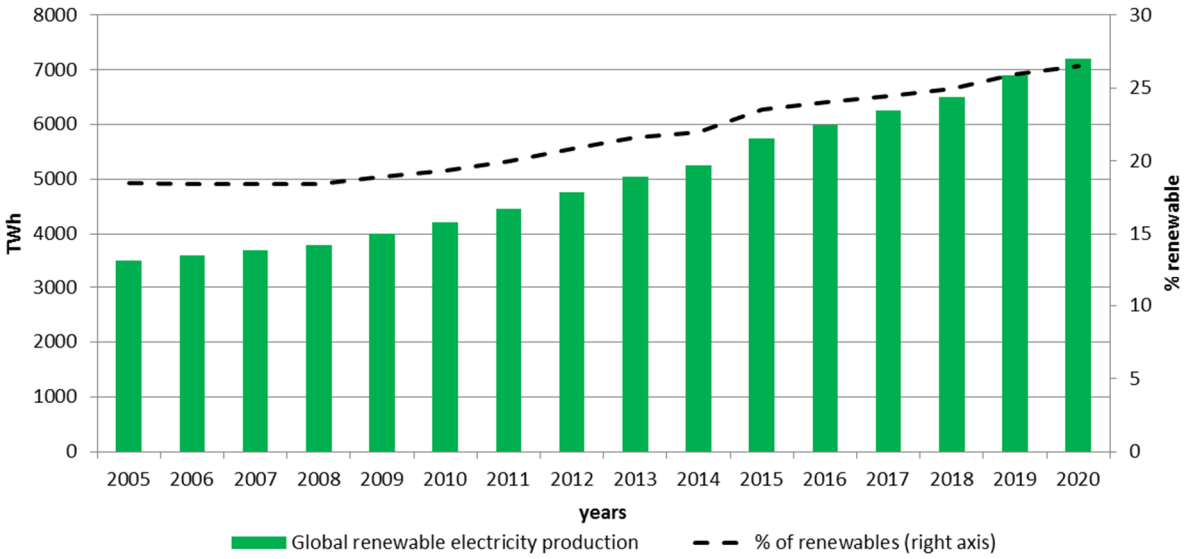


Figure 1: Global renewable electricity production by region, historical and projected (source: ref. [1]).

The demand for energy efficient buildings calls for the adoption of active façades that are able to mitigate air conditioning consumption resulting from direct exposure to solar rays, and to harvest wind and solar energy through on-site wind power generators [3], building integrated photovoltaic (BIPV) systems, and/or solar hot water panels [4]. The building of the future also needs to be safer with respect to natural hazards, such as earthquakes and high winds, and more energy efficient in terms of making components and subsystems multidisciplinary (e.g., combining structural design with heating, ventilation and air conditioning design) [5].

Tensegrity structures are prestressable truss structures, which are obtained by connecting compressive members (bars or struts) through the use of pre-stretched tensile elements (cables or strings) [6]. Motivated by nature, where tensegrity concepts appear in every cell, in the microstructure of the spider silk, and in the arrangement of bones and tendons for control of locomotion in animals and humans [7], engineers have only recently developed efficient analytical methods for exploiting tensegrity concepts in engineering design [8-10]. Form-finding of truss-like structures continues to be an active research area, due to both their easy control (geometry, size, topology and prestress control), and the fact that tensegrity structures provide minimum mass systems under different loading conditions [6,7,11]. The use of tensegrity structures for the construction of renewable energy supplies requires further attention, due to the special ability of tensegrity systems to convert the strain energy stored in cables into electrical energy [7]. There is also the question of their easy integration into solar

and acoustical panels, which can be physically identified with special rigid members of the structure.

The present work deals with the design of novel lattices with morphing abilities, to be used as cost-effective shading screens for energy efficient buildings. A tensegrity solution for the actuated façade panels of the well-known Al Bahar Towers in Abu Dhabi is presented. Designed recently by Aedas Architects, using a different technology [12], this façade mimics the shading lattice-work "mashrabiya". The "origami" tensegrity panels designed in the present work are opened (i.e., folded out) at night, and are progressively closed during daylight hours by controlling the tension in selected cables. Such lightweight morphing lattices require minimal storage of internal energy, and lighter friction between parts, as compared, for instance, to the piston-actuated technology adopted by Aedas Architects [12].

2. ON THE ACTUATION OF MORPHING LATTICES

Let us examine the motion of the elementary truss lattice shown in Figure 2. The axial strain rate of the *k*-th element connecting nodes *i* and *j* is given by:

$$\dot{\varepsilon}_k = \frac{1}{\ell_k} (\dot{\boldsymbol{u}}_j - \dot{\boldsymbol{u}}_i) \cdot \boldsymbol{k} \tag{1}$$

where $\boldsymbol{k}$ is the unit vector parallel to the element at the current time t (pointing towards node *j*); $\dot{\boldsymbol{u}}_i$ and $\dot{\boldsymbol{u}}_j$ are the velocity vectors of the nodes *i* and *j*, respectively; and ℓ_k is the length of the element at time t.

On introducing a Cartesian frame $\{0, x_1, x_2, x_3\}$, and letting *N* denote the total number of nodes of the lattice, it is convenient to collect the Cartesian components of the velocity vectors of the different nodes into the following array with *3N* entries:

$$\dot{\boldsymbol{u}} = [\dot{u}_{1,1}\ \dot{u}_{1,2}\ \dot{u}_{1,3}\ \ldots\ \dot{u}_{N,1}\dot{u}_{N,2}\dot{u}_{N,3}]^{\boldsymbol{T}} \tag{2}$$

$\dot{u}_{i,n}$ being the component of $\dot{\boldsymbol{u}}_i$ with respect to the x_n-axis ($n = 1,2,3$), and *T* denoting the transposition symbol. Similarly, said *M* the total number of truss elements composing the lattice, it is useful to collect the axial strain rates of all lattice elements into the following array with *M* entries:

$$\dot{\boldsymbol{\epsilon}} = [\dot{\varepsilon}_1\ \ldots\ \dot{\varepsilon}_M]^{\boldsymbol{T}} \tag{3}$$

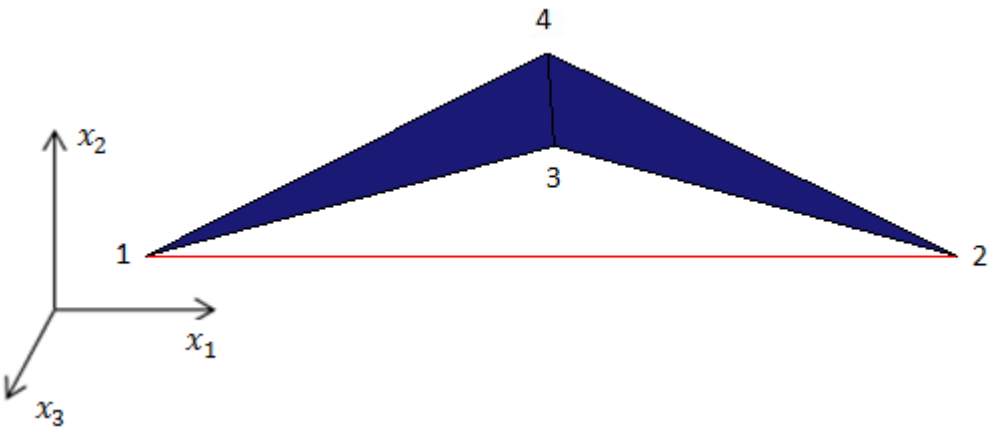


Figure 2: Elementary truss lattice.

It is an easy task to cast the compatibility equations (1) pertaining to all the lattice elements into the following matrix form

$$\boldsymbol{C}\,\dot{\boldsymbol{u}} = \dot{\boldsymbol{\varepsilon}} \tag{4}$$

$\boldsymbol{C}$ denoting the M × N compatibility matrix such that its *k*-th row has entry $-k_{\mathrm{n}}/\ell_{\mathrm{k}}$ in correspondence with $\dot{u}_{\mathrm{i,n}}$; entry $k_{\mathrm{n}}/\ell_{\mathrm{k}}$ in correspondence with $\dot{u}_{\mathrm{j,n}}$ (n = 1,2,3), and all the remaining entries equal to zero.

We now assume that a given number *P* of velocity components are forced to be zero, due to the presence of externals constrains that limit the possibilities of motion of the lattice. By suitably sorting the velocity vector $\dot{\boldsymbol{u}}$, we can rewrite the matrix equation (4) as follows

$$[\boldsymbol{C_1} \quad \vdots \quad \boldsymbol{C_2}] \begin{bmatrix} \dot{\boldsymbol{u}}_1 \\ \cdots \\ \dot{\boldsymbol{u}}_2 \end{bmatrix} = \dot{\boldsymbol{\varepsilon}} \tag{5}$$

where $\dot{\boldsymbol{u}}_1$ is the array with *Q=(3N-P)* entries that collects the unconstrained velocity components of the nodes; $\dot{\boldsymbol{u}}_2$ is the *P*-dimensional array collecting the nodal velocity components constrained to zero; $\boldsymbol{C_1}$ is a $M \times Q$ submatrix of $\boldsymbol{C}$; and $\boldsymbol{C_2}$ is the complementary $M \times P$ submatrix of $\boldsymbol{C}$. In minimal coordinates, the compatibility equations of the constrained lattice are written as follows

$$\mathbf{B}\,\dot{\boldsymbol{q}} = \dot{\boldsymbol{\varepsilon}} \tag{6}$$

with $\mathbf{B} = \boldsymbol{C_1}$ (*kinematic matrix*) [13], and $\dot{\boldsymbol{q}} = \dot{\boldsymbol{u}}_1$.

We say that the lattice is *morphing* [14], if it results:

$$r = M = Q \tag{7}$$

r denoting the rank of the kinematic matrix **B**. The assumption (7) implies that the system of compatibility equations (6) has a unique solution $\dot{\boldsymbol{q}} \in \mathbb{R}^{\boldsymbol{Q}}$ for any given $\dot{\boldsymbol{\varepsilon}} \in \mathbb{R}^{\boldsymbol{M}}$, $\mathbb{R}$ denoting the set of real numbers. It is worth noting that, in a morphing lattice, one can produce the motion of the structure by actuating a single element, i.e., by prescribing that a single entry of $\dot{\boldsymbol{\varepsilon}}$ is nonzero. As a consequence, the actuation of morphing lattices requires minimal storage of internal energy [14]. Given an "actuation" history $\dot{\boldsymbol{\varepsilon}} = \dot{\bar{\boldsymbol{\varepsilon}}}$, the positons of the vertices of a morphing lattice at the current time *t* are computed from the integral equation

$$\boldsymbol{q} = \int_0^t \dot{\boldsymbol{q}}\, dt = = \int_0^t \mathbf{B}^{-1}\, \dot{\bar{\boldsymbol{\varepsilon}}}\, dt \tag{8}$$

$\mathbf{B}^{-1}$ denoting the inverse of the kinematic matrix **B**, which there exists and is unique under the assumption (7).

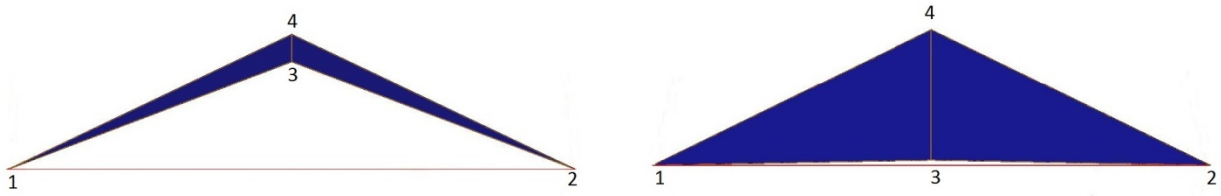
Assuming the action of quasi-stating loading and making use of the principle of virtual work, it is an easy task to obtain the following expression of the equilibrium problem of the lattice [7,13]

$$\mathbf{A}\,\boldsymbol{t} = \boldsymbol{f} \tag{9}$$

where $\boldsymbol{A} = \mathbf{B}^{\boldsymbol{T}}$ is the *static* (or *equilibrium*) *matrix*; $\boldsymbol{t} \in \mathbb{R}^{\boldsymbol{M}}$ is the array collecting the axial forces carried the lattice elements (or *bar tensions* [13]), and $\boldsymbol{f} \in \mathbb{R}^{\boldsymbol{Q}}$ is the array of the active nodal forces. It follows from (7) that a morphing lattice is statically and kinematically determinate (or *isostatic*) [13].

We now get back to the lattice structure in Figure 2, assuming that nodes 1 and 2 are constrained to move along the lines 1-4 and 2-4, respectively, and that node 4 is constrained to move along the x_3-axis. Under such assumptions, it is not difficult to show that the structure in Figure 2 is morphing and can be controlled by actuating only the string 1-2, that

is, prescribing nonzero axial strain in such an element, and zero axial strains in all the remaining elements. This actuation mechanism leaves unchanged the lengths of the edges of the triangles 1-3-4 and 2-3-4, which therefore move rigidly over time (Figure 3).



(a) (b)

Figure 3: Motion produced by the actuation of the string 1-2: (a) string 1-2 unstretched; (b) string 1-2 stretched to 6.25%.

3. "MASHRABIYA" SHADING SCREENS

The morphing abilities of the elementary lattice structure illustrated in Figure 3 can be exploited to design a tensegrity solution for the actuated façade panels of the well-known Al Bahar Towers in Abu Dhabi. Designed recently by Aedas Architects, using a different technology, such panels are intended to mimic the shading lattice-work "mashrabiya" [12].

Let us assume that the x_3-axis of the elementary lattice in Figure 2 is perpendicular to the building façade to be shaded, and that such a façade is placed at the quote $x_3 = -2.00$ m. Let us also suppose that the nodes of such a structure have the following position vectors $\boldsymbol{n}_i$ ($i = 1,..,4$) in correspondence with the open configuration of the lattice (Figure 3a)

$$\boldsymbol{n}_1 = \begin{bmatrix} 0.125 \\ 0.057 \\ 0.045 \end{bmatrix} \text{m}, \quad \boldsymbol{n}_2 = \begin{bmatrix} 3.875 \\ 0.057 \\ 0.045 \end{bmatrix} \text{m}, \quad \boldsymbol{n}_3 = \begin{bmatrix} 2.000 \\ 0.738 \\ -0.262 \end{bmatrix} \text{m}, \quad \boldsymbol{n}_4 = \begin{bmatrix} 2.000 \\ 1.000 \\ 0.968 \end{bmatrix} \text{m} \tag{10}$$

By inserting shading panels in correspondence with the triangular facets 1-4-3 and 2-4-3 of the elementary lattice, and replicating such a structure over space as shown in Figure 4, we can form mashrabiya-like shading screens that can be opened and closed by actuating a single string for each elementary module.

The shading mechanism played by such screens, which is graphically illustrated in Figure 4, assumes that the actuated strings are unstretched in correspondence with the open configuration of the screens, and subject to a 6.25% axial strain in correspondence with the fully-closed configuration. Such a mechanism has been numerically studied by integrating Eqn. (8) through an explicit 4th order Runge-Kutta scheme with step size $\Delta\boldsymbol{\varepsilon} = 0.01\%$. An animation of the mechanism in Figure 4 is given in [15]. The force vectors depicted in Figure 4 are proportional to the amplitude of the elongations of the perimeter strings. The elongations of the actuated strings placed in the interior of the screens are not shown for visual clarity.

4. CONCLUDING REMARKS

We have presented an application of morphing lattices with tensegrity architecture to design adaptable envelopes for energy efficient buildings. We have designed "origami" panels of shading screens that can be opened (i.e., folded out) at night (configuration on top-left of Figure 4), and can be progressively closed during daylight hours (cf., e.g., the fully closed configuration on bottom-right of Figure 4), by controlling the elongation in selected strings.

The operation mechanisms of such screens can be powered by the renewable energy derived from photovoltaic panels and/or microeolic power generators. Their aim is to markedly mitigate air conditioning consumption resulting from direct exposure to solar rays, reducing carbon dioxide emissions. Common issues discussed by architects and engineers are the relative importance of a façade's U-value (the insulation characteristics) versus its G-value (the shading coefficient). The cable-actuated shading screens illustrated in Figure 4 require minimal storage of internal energy [14], and reduced operation costs (due to lighter friction between parts and reduced mass), as compared, for instance, to the piston-actuated technology adopted by Aedas Architects [12]. They offer portable applications for small spans, and can be easily assembled for prefabricated component parts in the case of large spans.

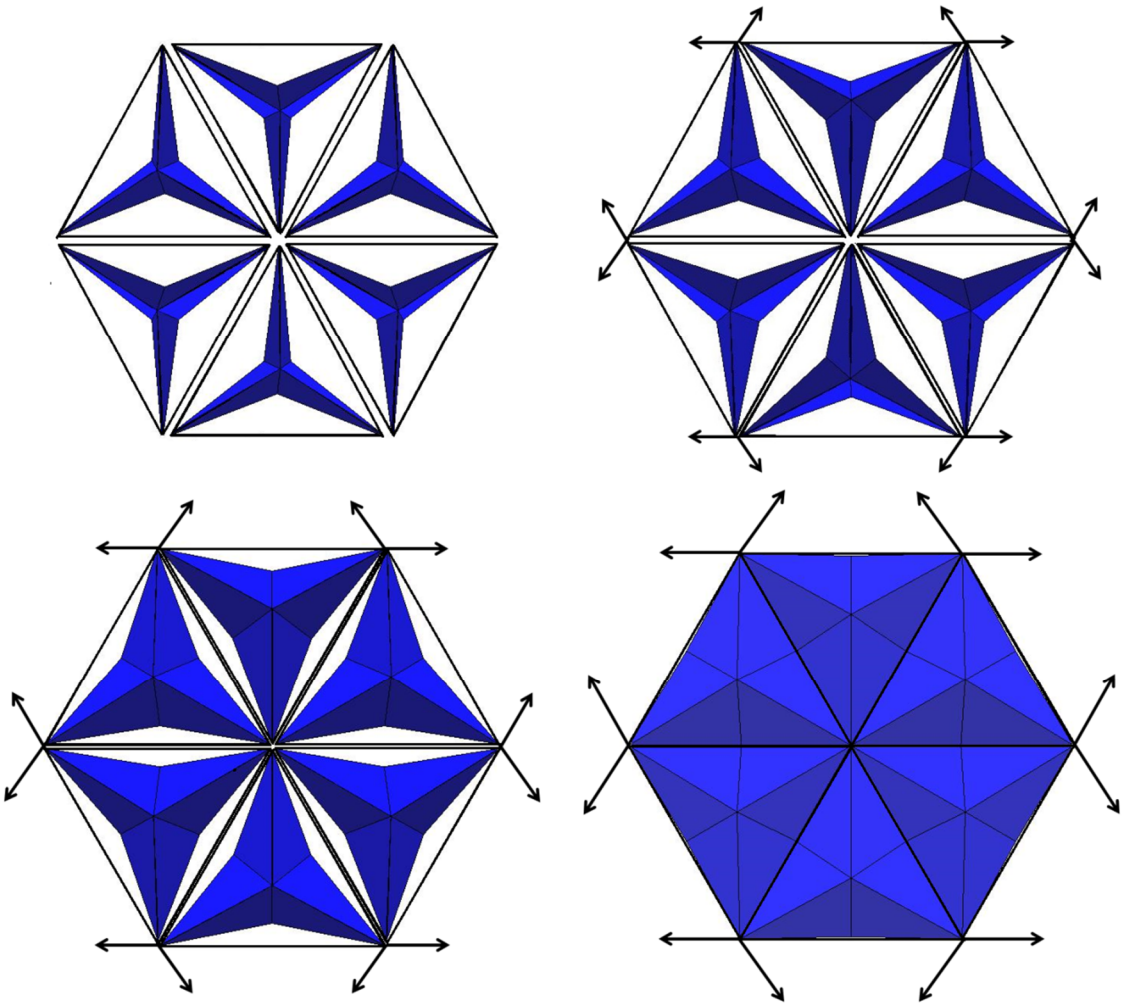


Figure 4: Actuation mechanism of mashrabiya shading screens with tensegrity architecture (an animation of such mechanisms is given in [15]).

Extensions of the present study dealing with bioinspired membranes [16-19], which are able to orient solar panels towards the sun, to adjust the thickness of ventilated walls, and to form innovative microeolic power generators will be addressed in future work. Such structures will assemble tensegrity units, whose rigid parts will consist either of 1D struts, or 2D/3D solid elements of various shape and material (floor slabs, airfoil ribs, solar panels, acoustical panels, etc.). The tensile elements of the tensegrity units will instead consist of cables of various dimensions. Each unit will be equipped with sensors and actuators in

correspondence with selected elements, which will be connected by wires or wireless devices to a data transfer system. Its operation will be controlled by external motors and generators, or by a single apparatus that alternatively works as generator or motor (Figure 5). Some preliminary results and animations related to this ongoing research project are given in [15].

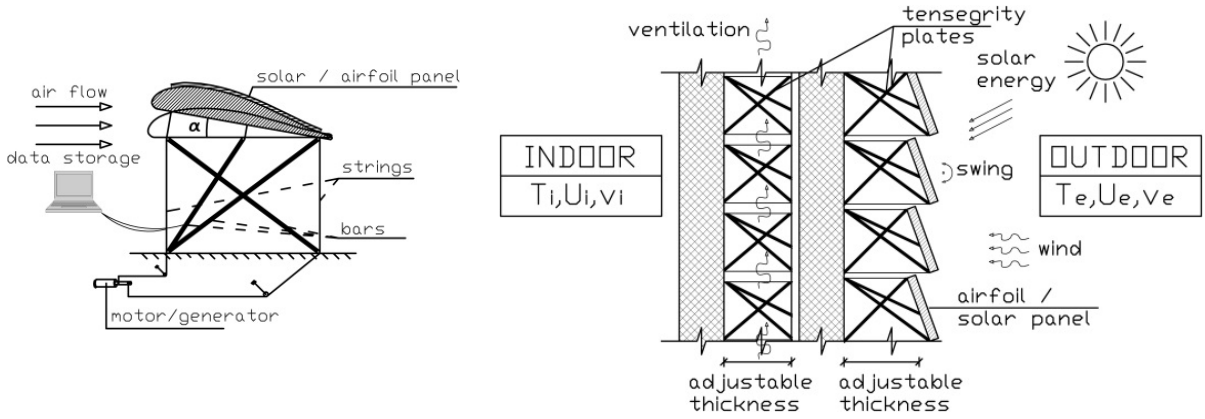


Figure 5: Morphing skins of energy efficient buildings based on tensegrity structures: (a) tensegrity unit; (b) responsive solar façade and ventilated wall [15].

ACKNOWLEDGMENTS

Support for this work was received from the Italian Ministry of Foreign Affairs, Grant no. 00173/2014, Italy-USA Scientific and Technological Cooperation 2014-2015.

REFERENCES

[1] L.P. Lombard, J. Ortiz , C. Pout, A review on buildings energy consumption information. Energy and Buildings, **40**,394-398, 2010.

[2] European Commission, HORIZON 2020 Work Programme 2014-2015, PART 5.ii, Page 98, 2014.

[3] F. Balduzzi, A. Bianchini, L. Ferrari, Microeolic turbines in the built environment: Influence of the installation site on the potential energy yield. *Renewable Energy*, **45**, 163-174, 2012.

[4] T.E. Kuhn, S. Herkel, H-M. Henning, Active solar facades (PV and solar thermal). In: PALENC 2010, http://publica.fraunhofer.de/documentsN-161087.html , 2010

[5] R.E. Skelton, Structural systems: a marriage of structural engineering and system science. *Journal of Structural Control*, **9**,113-133, 2002.

[6] R.E Skelton, F. Fraternali, G. Carpentieri, A. Micheletti, Minimum mass design of tensegrity bridges with parametric architecture and multiscale complexity. *Mechanics Research Communications*, **58**, 124-132, 2014.

[7] R.E. Skelton, M.C. de Oliveira, *Tensegrity Systems.* Springer,2010

[8] F. Fraternali, G. Carpentieri, A. Amendola, On the mechanical modeling of the extreme softening/stiffening response of axially loaded tensegrity prisms. *Journal of the Mechanics and Physics of Solids*, **74**, 136-157, 2014.

[9] F. Fraternali, L. Senatore, C. Daraio, Solitary waves on tensegrity lattices. *Journal of the Mechanics and Physics of Solids*, **60**, 1137-1144, 2012.

[10] F. Fraternali, G. Carpentieri, A. Amendola, R.E. Skelton, V.F. Nesterenko, Multiscale tunability of solitary wave dynamics in tensegrity metamaterials. *Applied Physics Letters*, **105**, 201903, 2014.

[11] A.G. Tilbert, S. Pellegrino, Review of form-finding methods for tensegrity structures. *International Journal of Space Structures* ,**18**, 209–223, 2011.

[12] Aedas Architects website, http://www.aedas.com/

[13] Hutchinson, R.G., Fleck, N.A., The structural performance of the periodic truss. *Journal of the Mechanics and Physics of Solids*, **54**, 756-782, 2012.

[14] N.A. Fleck ,V.S Deshpande, M.F. Ashby, Micro-architectured materials: past, present and future. *Proceedings of the Royal Society A: Mathematical, Physical and Engineering Sciences*, **466**, 2495–2516, 2010.

[15] Project webpage: http://www.fernandofraternaliresearch.com/MAE_project.asp?pg=7

[16] F. Fraternali, C.D Lorenz, G. Marcelli, On the estimation of the curvatures and bending rigidity of membrane networks via a local maximum-entropy approach. *Journal of Computational Physics*, **231**, 528-540, 2012.

[17] F. Fraternali, G.Marcelli, A multiscale approach to the elastic moduli of biomembrane networks. *Biomechanics and Modeling in Mechanobiology*, **11 (7)**, 1097-1108,2012

[18] B. Schmidt, F. Fraternali, Universal formulae for the limiting elastic energy of membrane networks. *Journal of the Mechanics and Physics of Solids*, **60**, 172-180, 2012.

[19] F. Fraternali, I. Farina, G. Carpentieri. A discrete-to-continuum approach to the curvatures of membrane networks and parametric surfaces. *Mechanics Research Communications*, **56**, 18-15, 2014.

COMPDYN 2015
5th ECCOMAS Thematic Conference on
Computational Methods in Structural Dynamics and Earthquake Engineering
M. Papadrakakis, V. Papadopoulos, V. Plevris (eds.)
Crete Island, Greece, 25–27 May 2015

SEISMIC PERFORMANCE OF INNOVATIVE STEEL AND CONCRETE HYBRID COUPLED SHEAR WALLS

Luca Tassotti[1], Alessandro Zona[2], Graziano Leoni[2] and Andrea Dall'Asta[2]

[1] Dept. of Civil and Building Engineering and Architecture, Università Politecnica delle Marche
Via Brecce Bianche, 60131 Ancona, Italy.
e-mail: l.tassotti@univpm.it

[2] School of Architecture and Design, University of Camerino
Viale della Rimembranza, 63100 Ascoli Piceno, Italy
{ alessandro.zona, graziano.leoni, andrea.dallasta }@e-mail.address

Keywords: Coupled shear walls, Nonlinear finite element models, Performance-based design, Seismic design, Steel and concrete hybrid structures, Steel dissipative links.

Abstract. *Steel and concrete hybrid systems are obtained through a combination in series of steel elements and reinforced concrete elements with the aim of exploiting at their best the potentialities of each material. This concept differentiates steel and concrete hybrid structures from steel and concrete composite structures, where steel and concrete are working in parallel in the same structural element, e.g. concrete filled hollows steel columns and steel profiles embedded in reinforced concrete elements. In this work the seismic behaviour of an innovative hybrid coupled shear wall (HCSW) system, developed in the European research project INNO-HYCO (INNOvative HYbrid and COmposite steel-concrete structural solutions for building in seismic area), is investigated. Such earthquake resistant solution is composed by a reinforced concrete wall coupled to steel side columns by means of steel links with the objective to exploit both the stiffness of reinforced concrete wall, necessary to limit building damage under low-intensity earthquakes, and the ductility of steel links, necessary to dissipate energy under medium- and high-intensity earthquakes. The seismic behaviour of the system is assessed through multi-record nonlinear incremental dynamic analysis (IDA). For this purpose, first a set of realistic case studies is designed, then a finite element model is developed into the platform OpenSees and validated through comparisons against experimental tests including local and global responses quantities. The outcomes of the numerical analyses show that the proposed innovative system is actually able to effectively dissipate the energy through the activation of the inelastic behaviour of the steel links before yielding in the reinforced concrete wall.*

1 INTRODUCTION

Recent advances in the field of structural engineering were more that ever oriented towards economically and technically efficient as well as sustainable solutions. Specific attention was given to structural systems capable of offering significant advantages in terms of seismic protection through the structural fuse concept, i.e. the dissipation of seismic energy is concentrated only in sacrificial elements in order to preserve the integrity of the primary load-resisting structural components and to allow a rapid repair even after major earthquakes. Many systems were developed following this concept, and, among them, steel and concrete hybrid structures, i.e. combination in series of steel elements and reinforced concrete (RC) elements, appear to be a rather promising a competitive solution both in structural and economical terms. During the 2010-2013 European research project INNO-HYCO [1] innovative seismic-resistant steel concrete hybrid systems obtained by coupling RC elements with steel elements were developed. Although these systems were subjected to extensive numerical and experimental studies, more investigations are indeed required in order to gain more insight into their seismic performance and consequently produce better performing designs.

The objective of this work is to investigate the seismic behaviour of an innovative hybrid coupled shear wall (HCSW) system developed in the INNO-HYCO project by means of the analysis and assessment of its ductile behaviour, an indispensable step towards the possible use in real applications. The investigated solution is composed by a RC wall coupled to two steel side columns by means of steel links. Such a structural system was conceived with the objective to exploit both the stiffness of RC wall, necessary to limit building damage under low-intensity earthquakes, and the ductility (necessary to dissipate energy under medium- and high-intensity earthquakes) and replaceability of steel links, necessary to easily repair the seismic-resistant components of the structure when damaged after seismic events. In order to analyse the seismic performance of the innovative hybrid systems, a parametric analysis was performed on a set of realistic case studies. The benchmark cases are characterised by a gravity-load resistant steel structure in which the HCSW solution is employed as bracing system. The seismic behaviour of the system is assessed through multi-record nonlinear incremental dynamic analysis (IDA). For this purpose, a finite element fibre-based model is developed into the platform OpenSees and validated through comparisons against experimental tests including local and global responses quantities. In the performed parametric study, global and local engineering demand parameters are monitored in order to obtain a thorough description of the failure mechanisms of the system. The outcomes of this study constitute a contribution for the optimal design selection of the propose innovative HCSW system and a for further possible researches on steel and concrete hybrid systems.

2 DESIGN OF INNOVATIVE COUPLED WALL SYSTEMS

2.1 Resisting mechanism of the system and design procedure

Horizontal actions in the HCSW system generate the forces and moments highlighted in Figure 1. A significant part of the overturning moment is resisted by means an axial compression – tension couple N_c exerted by the two lateral side columns while almost of the all horizontal shear and only a fraction of the overturning moment are sustained by the RC wall (V_w and M_w respectively). The axial forces at the base of the side columns N_c are the summation of the shear forces in the links $V_{link,i}$ (i = 1, …, n_{links}) with n_{links} the number of links for each column (typically equal to the number of storeys). A parameter significantly influencing the structural behaviour of the considered HCSW is the coupling ratio CR [2], defined as the ratio

between the base moment resisted by the lateral columns M_c and the total overturning moment M_c+M_w.

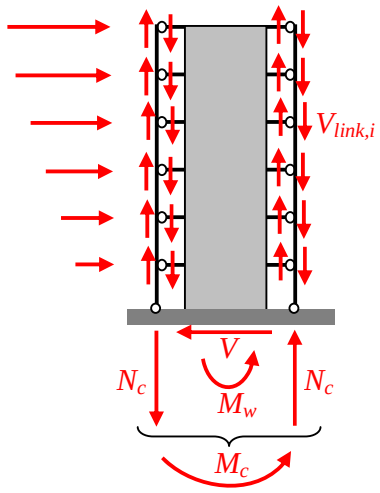


Figure 1: Resisting mechanism of the innovative hybrid coupled shear wall

The procedure adopted in this work for the design of the case studies was developed during the INNO-HYCO research project [1] and takes inspiration from the ASCE recommendations [2] for conventional hybrid coupled shear walls [3].

2.2 Benchmark cases selected and design results

The case studies were defined starting from the plant configuration reported in Figure 2, taken from [1]. The benchmark case is a residential building located in Camerino, Italy, (elevation 670 m). The building was designed as a steel frame with pinned beam-to-column joints resisting to the gravity loads connected to two HCSW systems for each direction as the only horizontal resisting structural elements. The case studies were obtained by varying the number of levels (from 4 to 12 with increasing of 2) and the coupling ratio CR (from 0.40 to 0.80 with increasing of 0.10) for a total of 25 cases. For each case study the gravity resistant system and the innovative earthquake resistant systems, highlighted in Figure 2, were designed following the Eurocode 3 [5] and Eurocode 8 [6] prescriptions. Regarding to the HCSW systems, concrete C30 (f_{ck} = 30 MPa) and reinforcements B450C (f_{yk} = 450 MPa) were used for the wall designed by selecting an aspect ratio (ratio between the overall height and base of the wall h_w/l_w) equal to 10 and a thickness b_w of 0.36 m for each case. The design of the longitudinal reinforcements was performed in order to maximize the wall flexural capacity. For this objective the Eurocode 8 [6] DCM rules (geometric percentage ratio in the confined edges just below 4%) were used. Selecting commercial IPE profiles in order to guarantee short links, according to the Eurocode 8 [6] classification for links used in eccentrically braced frames, the design results summarized in the Table 1 are obtained. Further results can be found in [4].

No. levels	Wall	CR 0.40		CR 0.60		CR 0.80	
	$b_w \times l_w$ [m]	Section	length [mm]	Section	length [mm]	Section	length [mm]
4	0.36×1.40	IPE140	140	IPE220	225	IPE360	360
6	0.36×2.10	IPE140	140	IPE200	200	IPE360	360
8	0.36×2.80	IPE120	120	IPE200	200	IPE360	360
10	0.36×3.50	IPE120	120	IPE200	200	IPE360	360
12	0.36×4.20	IPE120	120	IPE200	200	IPE360	360

Table 1: Design results of the RC wall and the dissipative links.

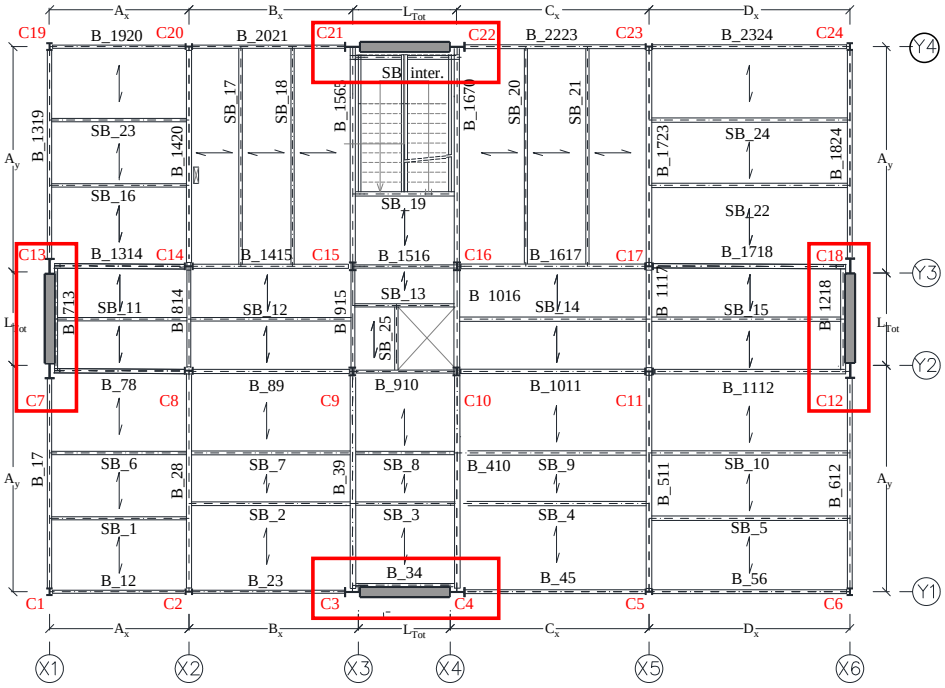


Figure 2: Plant configuration of the case study and positions of the HCSW systems.

3 MODELLING OF HCSW SYSTEMS

The finite element models of the investigated earthquake-resistant system were developed into the platform OpenSees [7]. These models derive from the assembly of different types of finite elements employed to describe each system component. The dissipative link was modelled on the basis of the model proposed for steel links used in eccentrically braced frames in [8] based on the constitutive model presented in [9], modified according to the static scheme of the considered steel links and to improve the computational efficiency. In particular, the finite element model of the steel link is composed by four elements connected in series (EL0, EL1, EL2 and ES1). The central element (EL0) is a displacement-based formulation element with length equal to link length l_{link}, measured from the steel plate of the link-to-wall connection to the centre of the double-angle link-to-column connection. The Gauss-Lobatto formulation was adopted and five integration points were inserted in the element. The flexural and shear stiffness of this element were posed equal to infinity since the behaviours of the link were concentrated in the zero-length elements EL1 and EL2 while the axial stiffness is computed from the link section. The elastic and inelastic flexural behaviour of the link were assigned to the EL2 zero length element, while the shear behaviour was modelled in the EL1 element. The "Steel01" material models were defined to describe the flexural and shear behaviour. ES1 is a zero-length element added to the elements series in order to model the link-to-column connection. From trial analyses conducted by accounting for the connection flexural behaviour it was observed that its contribution on the local and global response of the system is negligible. In the EL1 element the initial elastic shear stiffness corresponds to $k_v = GA_v/l_{link}$, where A_v is the shear area of the link cross-section and G is the tangential modulus of elasticity. Yield shear force of the same material corresponds to the plastic shear computed according to Eurocode 8 Part 1 [6] by using the average value of the resistance. The same reference was adopted for computing the yield moment. Initial flexural stiffness is defined as $k_m = 3EI_z/l_{link}$, where E is the steel Young's modulus and I_z the moment of inertia of the cross-

section**.** Strain hardening ratio (ratio between post-yield tangent and initial elastic tangent, "$b") and isotropic hardening parameters of both the materials were calibrated to obtain the best fit of the simulated results to the experimental results obtained from the experimental campaign carried out in [1].

The RC wall was modelled using fibre-based frame elements by employing the force based formulation element ("nonlinearBeamColumn" element). Five integration points were inserted in each element and the Gauss-Lobatto element integration method was used to integrate the curvatures. The "Steel01" material was defined to describe stress – strain behaviour of the steel bars and two "Concrete04" material models, based on the Popovics work [10], were created to describe both the unconfined and confined concrete, respectively. The validation of the proposed model was performed through the comparison between the simulated and experimental results in [11] where down-scaled wall specimens were constructed and tested.

The global model was obtained by assembling the single components models above de-scribed. Figure 3 shows the numerical description of the system and the single components employed. Since the influence of the beam-to-column connections can be neglected, a material with null flexural stiffness was as-signed at the ES1 element. Elements were placed in their actual positions and connected each other by means of rigid elastic displacement-based formulation elements. Beam elements with null flexural stiffness connect the HCSW system with an equivalent column that simulates the presence of the gravity-resistant frame.

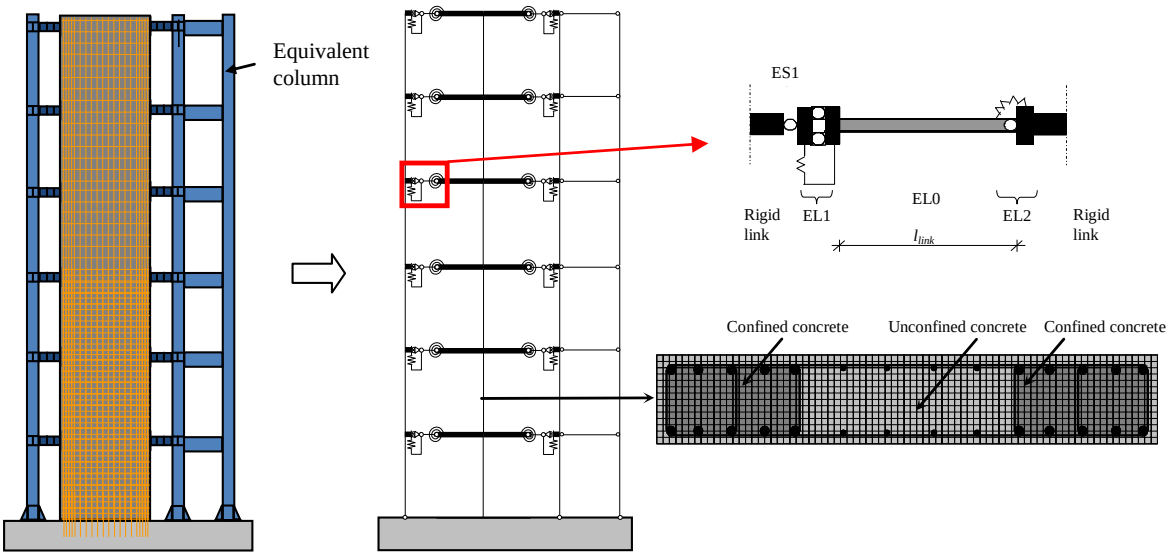


Figure 3: FE model of the innovative hybrid coupled wall system.

The inertia properties are modelled via translational horizontal masses lumped at the DOFs of the frame elements' external nodes. In particular, the tributary deck mass of the coupled wall is concentrated in each floor node, at the wall elements ends. The gravity–vertical loads, deriving by floor loads and self-weight elements, are applied at the top of each wall and column element.

The Rayleigh damping model [12] was used to model structural damping other than the one produced by the hysteretic behaviour of materials. The Rayleigh damping matrix is proportional to the mass matrix and initial stiffness matrix. The mass and stiffness related coefficients calibrated such that the values of the damping factor of 5% are obtained for the first two vibration modes.

4 ANALYSIS RESULTS

The seismic performance of the innovative HCSW systems was investigated on the basis of multi-record nonlinear incremental dynamic analysis. For this purpose, a set of 7 natural ground motion records compatible to the Eurocode 8 type I soil type A (soil factor S = 1.0) pseudo-acceleration response spectrum [6] were selected**.** Figure 4 reports the acceleration response spectrum of the records, the mean spectrum, and the code spectrum relative to the building site.

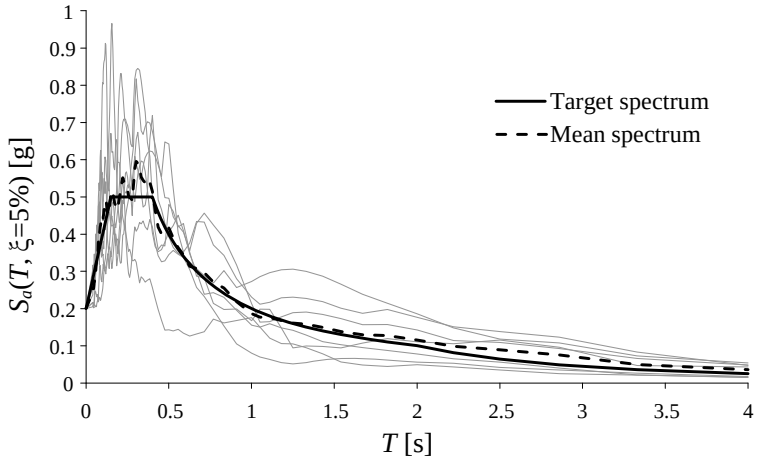


Figure 4: Acceleration response spectra of code spectrum-compatible natural records

Figure 5 shows the IDA curves up to PGA 0.30g for the case studies with 6 (Figure 5a) and 12 floors (Figure 5b), having CR 0.80. In the same figure, it possible to observe the evolution of yielding when increasing the seismic intensity. White triangles indicate shear yielding in the link while the white rhombus represent the bars yielding. Almost all links yield in shear when the wall was still undamaged. On the other hand, the reinforcements yield only at the wall base. This can be explained by noting that the seismic performance is dominated by the cantilever behaviour of the RC wall. Moreover, it is observed that increasing the coupling ratio causes an decreasing of the lateral displacements and, thus, of the interstorey drifts.

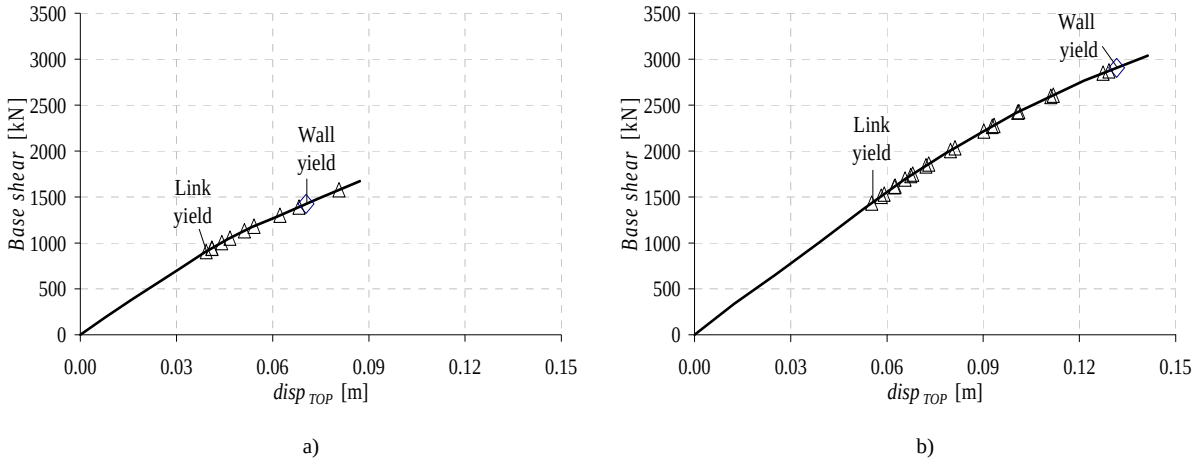


Figure 5: Comparison between IDA and pushover curves for the case study: a) with 6 floors; b) with 12 floors.

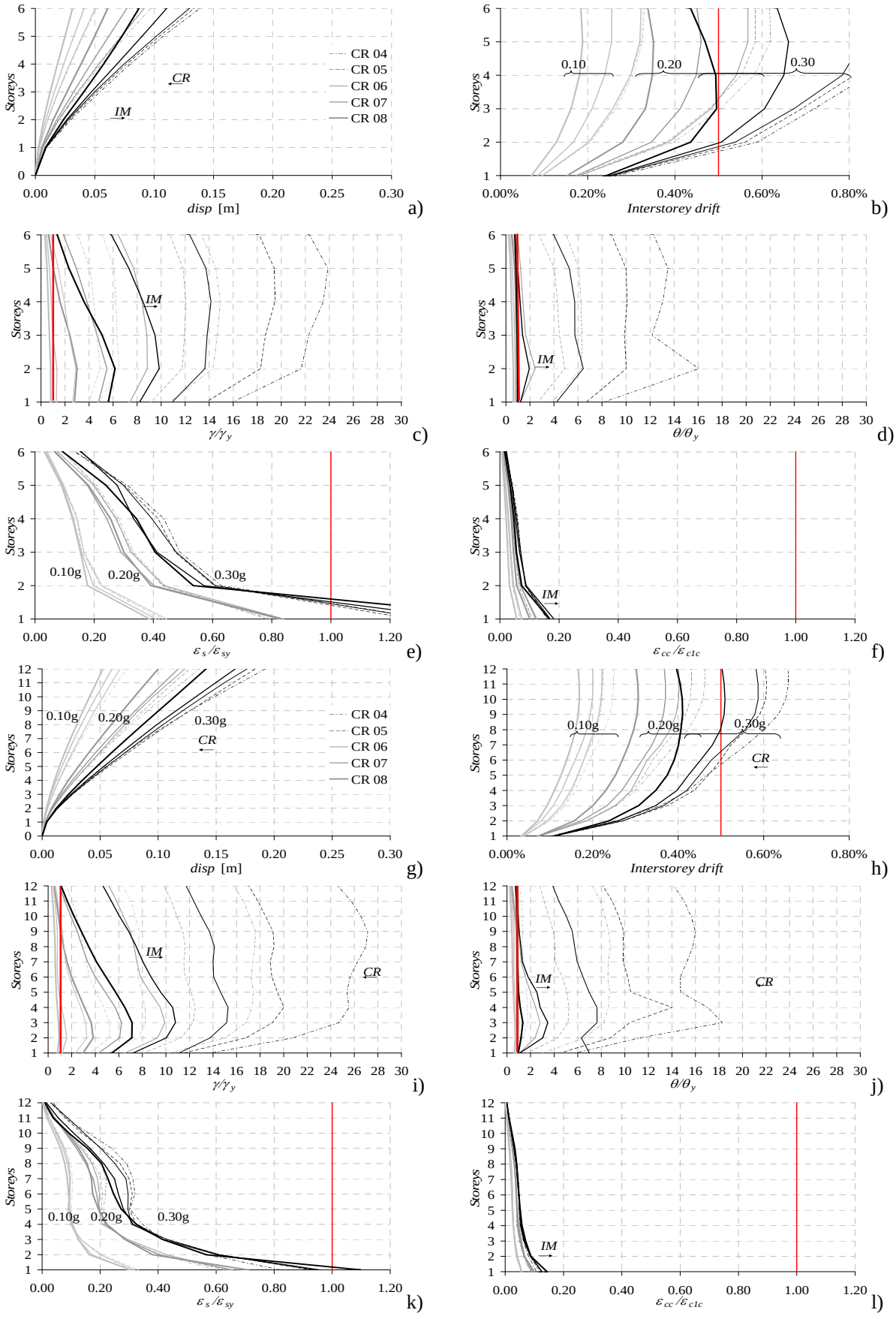


Figure 6: Mean values of the global and local response parameters for selected intensity measures.

The trend of a selection of engineering demand parameters EDPs averaged over the considered accelerograms for the case studies with 6 and 12 floors is reported in Figure 6 for peak ground acceleration (PGA) values 0.10g, 0.20g, and 0.30g and for each considered CR. Figure 6a-b and Figure 6g-h show the floor displacements and the interstorey drifts for the cases with 6 and 12 floors, respectively. From these figures it is noted that the displacement and the interstorey drifts decrease with the increasing of the coupling ratio. Figure 6c-d and Figure 6i-j plot the normalized average values of the shear rotation angle γ and of the chord rotation angle θ for the cases with 6 and 12 floors, respectively. The shear rotation angle γ was evaluated a posteriori by dividing the local transverse relative displacement, recorded in the zero length element EL1 of the link, by the link length l_{link}. Shear and flexural plastic deformations in the steel links are very notable although do not exceed the ultimate deformations assumed equal to those for the steel links in bracing steel frames [6]. Figure 6e-f and Figure 6k-l report the normalized steel bars strains ε_s and the confined concrete strains ε_{cc} in the wall for the case studies with 6 and 12 floors, respectively. The normalized concrete strains are small while the normalized steel strains are larger than one even if the ultimate condition is not attained. These deformations appear not sensitive to the value of CR.

5 CONCLUSIONS

This work analyzed the seismic performance of an innovative hybrid coupled shear wall system (HCSW) made by a single reinforced concrete (RC) wall coupled to two side steel columns by means of dissipative and replaceable steel links. A refined finite element model capable of simulating the nonlinear seismic response for increasing level of the seismic intensity and of monitoring specific global and local EDPs, was developed in OpenSees. A wide set of case studies was adopted in order to evaluate the influence of various geometric and design parameters. With reference to the seismic behaviour, the following conclusions are drawn based on the seismic response averaged over the considered accelerograms for the case studies with 6 and 12 floors: (1) the proposed structural system is able to dissipate the seismic energy through the activation of the inelastic behaviour of the steel links before yielding in the reinforced concrete wall; (2) the coupling ratio notably influence the structural behaviour.

REFERENCES

[1] A. Dall'Asta et al. *Innovative hybrid and composite steel-concrete structural solutions for building in seismic area*, Final Report, EUR 26932 EN, European Commission, 2015. DOI:10.2777/85404.

[2] S. El-Tawil, K. Harries, P. Fortney, B. Shahrooz, Y. Kurama, Seismic Design of Hybrid Coupled Wall Systems: State of the Art. *Journal of Structural Engineering*, **136**(7), 755–769, 2010.

[3] A. Zona, G. Leoni, H. Degée, A. Dall'Asta, Design procedure and analysis of innovative hybrid coupled shear walls. Eds R. Landolfo and F.M. Mazzolani, *7th European Confernce on Steel and Composite Structures*, Naples, Italy September 10-12, 2014.

[4] L. Tassotti, *Seismic analysis and design of innovative steel and concrete hybrid coupled wall systems*. Ph.D. thesis, Marche Polytechnic University, Italy, January 2015.

[5] European Committee for Standardisation, *Eurocode 3: design of steel structures, Part 1.1: general rules and rules for buildings, EN 1993-1-1*, 2005.

[6] European Committee for Standardisation, *Eurocode 8: Design of structures for earthquake resistance", Part 1: General rules, seismic actions and rules for buildings, EN 1998-1*, 2004.

[7] S. Mazzoni, F. McKenna, M.H. Scott, G.L. Fenves, et al., *Opensees Command Language Manual*, PEER, 2007, (http://opensees.berkeley.edu/wiki/index.php/MainPage).

[8] M. Bosco, M.M. Edoardo, P. Rossi, Modelling of Steel Link Beams of Short, Intermediate or Long Length. *Engineering Structures*, **84**(2), 406–418, 2015.

[9] A. Zona, A. Dall'Asta, Elastoplastic model for steel buckling-restrained braces. *Journal of Constructional Steel Research*, **68**(1), 118–125, 2012

[10] S. Popovics, A Numerical Approach to the Complete Stress-Strain Curve of Concrete. *Cement and Concrete Research*, **3**(5), 583–599, 1973.

[11] K. Orakcal, L.M. Massone, J.W. Wallace, *Analytical Modeling of Reinforced Concrete Walls for Predicting Flexural and Coupled–Shear-Flexural Responses*. PEER Report 2006/2007, Pacific Earthquake Engineering Research Center, University of California, Berkeley, CA, 2006.

[12] A.K. Chopra, *Dynamic of Structures, 4th Edition*. Prentice Hall, 2011.

COMPDYN 2015
5th ECCOMAS Thematic Conference on
Computational Methods in Structural Dynamics and Earthquake Engineering
M. Papadrakakis, V. Papadopoulos, V. Plevris (eds.)
Crete Island, Greece, 25–27 May 2015

DAMAGE DETECTION AND MONITORING OF COMPOSITE STRUCTURES WITH THE USE OF PIEZOELECTRIC SENSORS

Piotr Kędziora[1], Adam Stawiarski[2] and Marek Barski[3]

Cracow University of Technology
31-155 Kraków, ul. Warszawska 24, Poland
[1] kedziora@mech.pk.edu.pl

[2] asta@mech.pk.edu.pl

[3] mbar@mech.pk.edu.pl

Keywords: Damage Detection, Composite Materials, Delamination, Piezoelectric Sensors and Actuators, Lamb Wave.

Abstract. *Damage detection in fiber-reinforced composite laminated panels using Lamb waves (wave propagation) is demonstrated with the use of a sensor array. Experiments are conducted to empirically characterize the wave propagation behavior in a manufactured laminate. Piezoelectric patches are used as sensors and actuators in the experiments. Composite laminates are manufactured with an embedded defect to simulate inter-ply delamination. Delaminations are one of the most severe defects associated with multilayered laminated composite structures. The experimental results are also compared with a numerical analysis for cylindrical panels with the use of 3D finite elements. A lot of numerical results allow us to understand better the influence of various parameters on the form of wave propagation in cylindrical multilayered shells. Based on numerical results it is possible to determine the effect of the delamination on the guided wave propagation in curved structures.*

1 INTRODUCTION

The increasing demand in lowering maintenance costs in engineering structures made of composite materials contributes to the growing development of structural health monitoring systems. Such systems would insure continuous knowledge of the structural state of the monitored structural components, possibly allowing directed maintenance and maintenance task optimization. Techniques used to realize the checking must obviously not damage these structures. Many methods have been developed during recent decades, and they have all been grouped under the term of Non-Destructive Testing (NDT) methods, such as: e.g.: mechanical (ultrasonic, acoustic emission), thermal (thermography), magnetic (Eddy current), X-ray (tomography) and visual (penetrant testing, CCD camera) optical fiber methods. The number of inspection methods grow and depends on application in particular type of construction [1-3]. The principles, application, advantages and limitations of those methods has been described by Hellier [4]. Kuhn et al. [5] have been shown and discussed some characteristics of the most common NDT methods used in industry.

Few methods are able to monitoring the structure in real time. One of this is the Acoustic Emission (AE) method, that has long been recognized as a viable technique for real-time monitoring of metallic and composite structures, giving useful information not only on the presence of defects, but also on their evolution and position [6–11]. Structural health monitoring (SHM) techniques based on guided waves propagation have been the subject of interest for researchers since 1980. A literature review of the most salient studies on ultrasonic guided waves was presented by Su, Ye and Lu [12]. A classification of dynamic-based SHM techniques as a relationship between interrogation frequency and damage size was presented by Gopalakrishnan et al. [13]. Guided waves are able to propagate for relatively long distance and have high sensitivity to both surface and embedded structural damage. Accordingly, guided waves have been widely used to develop various damage identification algorithms.

The efficient and effective use of composite materials in design applications is directly connected with the good knowledge of the static and fatigue strengths of the material. There is a variety of failure modes associated with static and/or fatigue damage, including: 1) matrix cracking, 2) interfacial debonding, 3) fiber breakage, and 4) delaminations.

There have been many works on wave propagation problems related to composite shells. The first work (Lord-Rayleigh [14]) of this field dealt with wave propagation in a semi-infinite solid. In 1917 Lamb published the first work [15] of dealing with guided wave propagation in thin elastic specimens. Mirsky [16] and Nowinski [17] solved for axially symmetric waves in orthotropic shells. Chou and Achenbach [18] provided a three-dimensional solution for orthotropic shell as well. Nayfeh [19] discussed scattering of horizontally polarized elastic waves from multilayered anisotropic cylinders embedded in isotropic solids. Yuan and Hsieh [20] proposed an analytical method for the investigation of free harmonic wave propagation in laminated shells. The numerical description of the waves traveling into waveguides and slen-der structures has also raised many interests – information about those problems is discussed in Ref. [21].

The first introduction of Lamb waves as a means of damage detection was made by Worlton [22] in 1961. He noticed that distinguish characteristics of the various modes of Lamb waves can be useful in nondestructive testing applications. Prosser et al. [23] used acoustic emission to identify cracking of thin composite specimens; also outlined the difficulties associated with acoustic emission. Wevers [24] outlined the advantages of acoustic emission techniques over other NDE methods for identifying damage in a loaded composite component. Lakshmanan and Pines [25] used and developed a wave propagation method to identify delaminations and transverse cracks in Gr/Ep composite rotorcraft. Ihn and Chang [26] used

spectrograms to process guided wave signals obtained from an array of piezoelectric transducers to detect and monitor fatigue crack growth.

In this study, damage detection in fiber-reinforced composite laminated panels using Lamb waves is demonstrated with the use of a sensor array. Experiments are conducted to empirically characterize the wave propagation behavior in a manufactured laminate. Piezoelectric patches are used as sensors and actuators in the experiments. Experiments were conducted to detect the presence of damage in a composite laminate. These results are used to quantify the difference in the cases of perfect and defected structures. The experimental results are also compared with a numerical analysis for cylindrical panels with the use of 3D finite elements. A lot of numerical results allow us to understand better the influence of various parameters on the form of wave propagation in cylindrical multilayered shells. The problems of optimization and positioning sensors were also discussed due to possibility of detecting damage the laminate, in which the location of the defect is unknown. Then, the results are compared with the FE model.

2 DETECTION OF DAMAGE

Elastic waves are generated by an actuator (one of the grid piezoelectric transducers (PZT)) and recorded using the remaining PZT transducers (from the same grid – Figure 1). The shape of system of PZT transducers, shape and number of PZT influence on the quality (sensitivity) and accuracy of detection of defects in the test of composite structures. An additional issue is the control and detection of failure sensors, which is discussed among other in the works [27, 28].

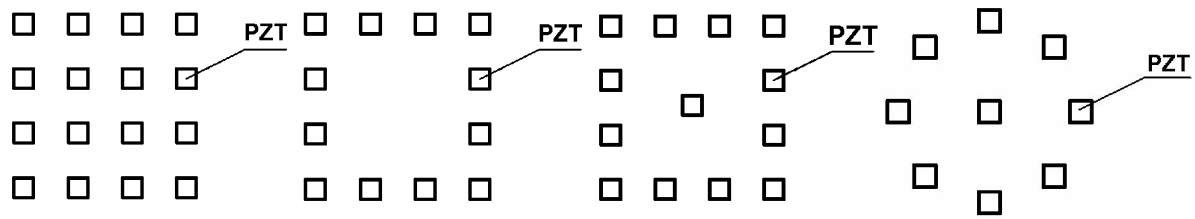


Figure 1: Examples of systems of PZT transducers.

A comparison of the wave signal for the structure without any damage and disturbance in the propagation of the wave induced by delamination. The location of this damage is defined as follows:

$$d = \frac{v_g \Delta T}{2} \tag{1}$$

where v_g is the velocity of wave propagation, ΔT is the difference between the signal of the incident wave and the wave disturbed by the damage.

The correlation coefficient ρ_{ab} between the original and distorted signals was calculated for individual sensing paths in the time domain to get the perception to damage near the sensing paths. The damage index (D) is defined as:

$$D = 1 - \rho_{ab} \tag{2}$$

3 OPTIMIZATION PROBLEMS

Optimization problems deal with the analysis of structures with some response (denoted by *R*) requirements. In general structures with actuators can be optimized using three computationally different strategies. In the first, the most common optimization problem the objective function to be minimized is the response of the system, i.e.:

$$\underset{\mathbf{s}}{Min}\, R(\mathbf{s}) \tag{3}$$

The vector *s* denotes the set of design variables.

The response tuning is the second problem. It can be treated as the alternative or sometimes equivalent optimization problem to the above:

$$\underset{\mathbf{s}}{Min}\left[R_l(\mathbf{s}) - R_{l-1}(\mathbf{s})\right], l = 2,3,... \tag{4}$$

In addition, as the third problem volume or weight minimization of a structure has been considered here, in which:

$$\underset{\mathbf{s}}{Min}\, V(\mathbf{s}) \tag{5}$$

The problem of shape optimization of piezoelectric transducers has been discussed among others in the works [29–34].

Optimal location of sensors concerns the best location of sensors and their required number. To solve this problem, the optimization procedures have been applied. In addition, the information of composite structures and wave propagation in the material has been used.

Simple methods have been used to find the best configuration of transducers. This is done by adding or removing one or more sensors and evaluated the relationship between the transducers, signal quality and accuracy of fault location in order to find the best combination. Development of methods of combinatorial optimization based on biological and physical analogy allows the use of such genetic algorithms, neural networks, simulated annealing, etc.

Optimal location of sensors and actuators over a structure can be different for different criteria based upon: maximization of modal forces/moments applied by the PZT actuator, maximization of deflection of the host structure, minimal change in host structural dynamics, desired host structural dynamics, minimization of control effort/maximizing energy dissipated, minimization of host vibrations, maximization of degree of controllability/observability of modes of interest, etc.

4 EXPERIMENTAL ANALYSIS

4.1 Piezoelectric transducers

Piezoelectric materials are characterized as being able to produce a mechanical strain when an electrical field is applied to the piezoelectric actuator. The converse effect has also been observed, which has led to their use as sensors. Sensors respond to a physical stimulus and transmit a resulting impulse. When a device is actuated by power from one system and supplies power, than it is called as piezoelectric transducer.

Piezoelectric transducers are usually made in the shape of rectangular (Fig. 2) or round plane-parallel plates (see Ref. [35]), cut from a piezoelectric crystal so that the plate has been properly oriented with respect to the crystallographic axis, in particular in relation to the polar axis. Along this axis, the effect is highest for the longitudinal deformation, and therefore the plate, which has ultrasonic transducer longitudinal waves, is cut perpendicular to the polar axis.

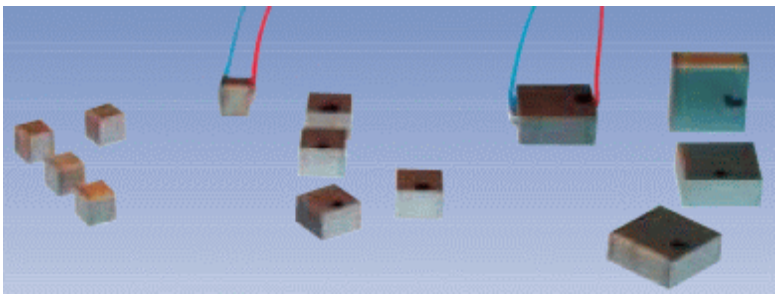


Figure 2: Piezoelectric transducers.

Piezoelectric transducers are made of ceramic materials often. These generally have better hardness and high-temperature strength. In the micro electromechanical systems it is also used the thick ceramic film and tree-dimensional ceramic structures. More information of piezoelectric transducers we can be find in the works [35, 36].

4.2 Damage detection

Damage detection in composite laminated panels using Lamb waves is demonstrated with use of a sensor array. Experiments were conducted to characterize empirically the wave propagation behavior in a manufactured laminate. Piezoelectric patches were used as sensors and actuators in the experiments. Sensor arrays and associated processing were used for wave number decomposition and filtering of the Lamb wave modes. Composite laminates were manufactured with an embedded defect to simulate inter-ply delamination– see Fig. 3. Experiments were conducted to detect the presence of delamination damage in a composite laminate.

A cylindrical panel made of glass woven roving having the mechanical and geometrical parameters was made of 8 layers and had the following geometrical parameters: L=298 [mm], R=92 [mm], t=1.8 [mm] , $h_1=h_2=t/2$ – Fig. 3. An excitation signal took the form of sine wave function was modulated with the Hanning window and was applied at the left piezoelectric actuator in Fig. 4 (piezoelectric transducer No. 1); its frequency is varies from 50-500 [kHz]. The piezoelectric sensors (on the right side in Fig. 4 - piezoelectric transducer Nos. 2-5) were placed close to the local square delamination having the size 10 [mm] and being in the middle of the laminate – see Fig. 3.

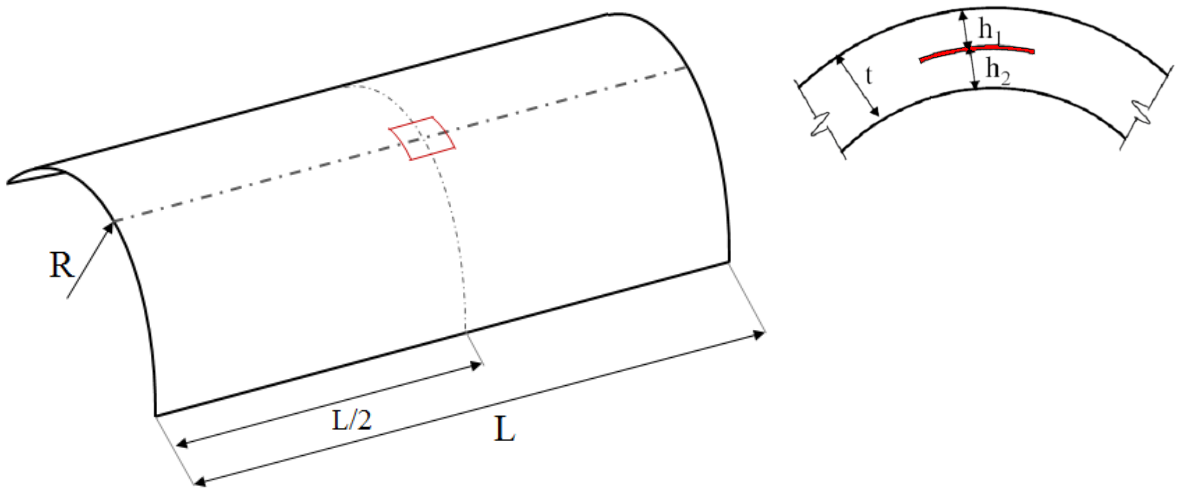


Figure 3: A cylindrical panel with a single delamination.

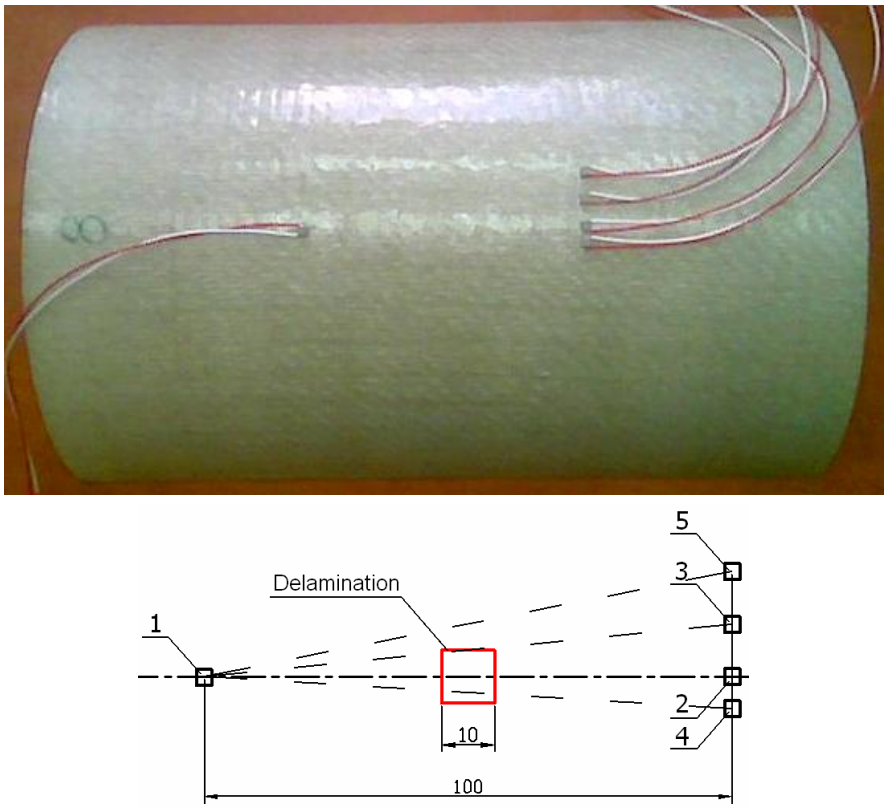


Figure 4: General configuration of the cylindrical panel with one actuator No. 1 and sensors Nos. 2-5 – they are located parallel to the delaminated area.

The wave propagation in the panel with local delamination was analyzed experimentally. The excitation signal and the response signal were generated and collected by the analyzer and then those signals were converted to digital ones with the use of MATLAB package.

Figure 5 demonstrates the response signals obtained experimentally for the perfect and imperfect (with the single delamination) cylindrical panel. As it may be seen there is a visible difference between response signals for perfect and imperfect shells for excitation signal frequency 100 [kHz]. Various excitation signal frequency was considered in Ref. [37].

However, the reasonable detection of the size and the location of delamination require the careful analysis and optimal design of the location and number of piezoelectric sensors and actuator. In addition, in the delaminated region the interference between generated and reflected waves is observed that affects the signal collected by the sensor (see Figs 7). In order to obtain better experimental results it is necessary to conduct further work dealing particularly with the optimal design of sensors number, locations and the frequency of the excitation signal.

The locations of piezoelectric sensor and actuator have significant effects on the displacement response. Different locations are presented in Figs 6 and 8. The response result (Figs 7 and 9) are plotted for one value of the signal excitation frequency equal to 100 [kHz]. The amplitude of response displacement is strongly affected by the distance between sensor and actuator – compare results plotted in Figs 5 and 9. The growth of the distance reduces the amplitudes. For the sensor and actuator located in the parallel direction to the delamination the amplitude for imperfect shell is lower than for perfect one, whereas for other locations the amplitude is higher – compare the results presented in Figs 5 and 7, 9.

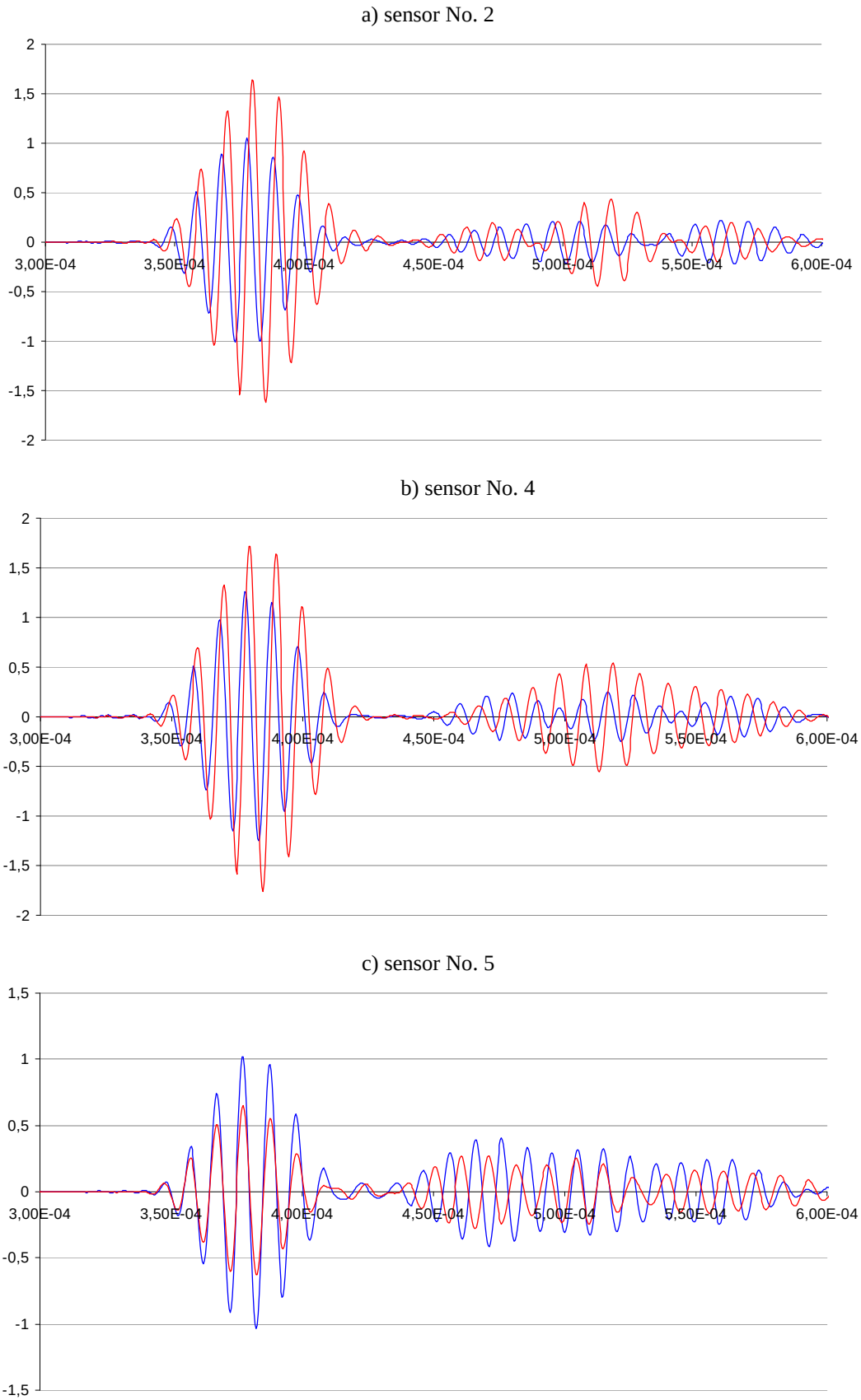


Figure 5: Experimental wave propagation results (blue line – without delamination, red line – with delamination); for frequency equal to 100 [kHz].



Figure 6: Configuration of the cylindrical panel with the sensor and actuator – they are located below delaminated area 5 [cm] from the panel edge.

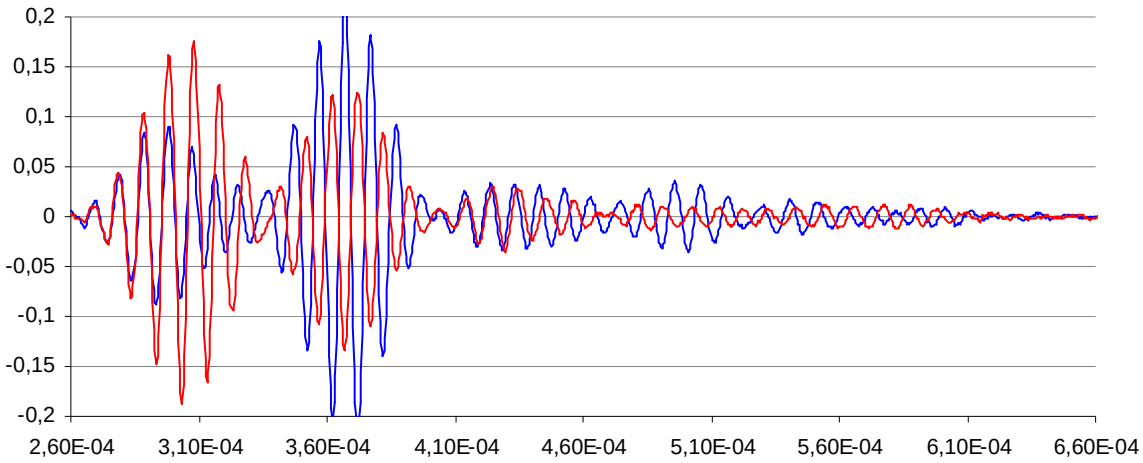


Figure 7: Experimental wave propagation results (blue line – without delamination, red line – with delamination); frequency is equal to 100 [kHz].



Figure 8: Configuration of the cylindrical panel with the sensor and actuator – the actuator is located above delaminated area 5 [cm] from the upper panel edge and the sensor 5 [cm] from lower panel edge.

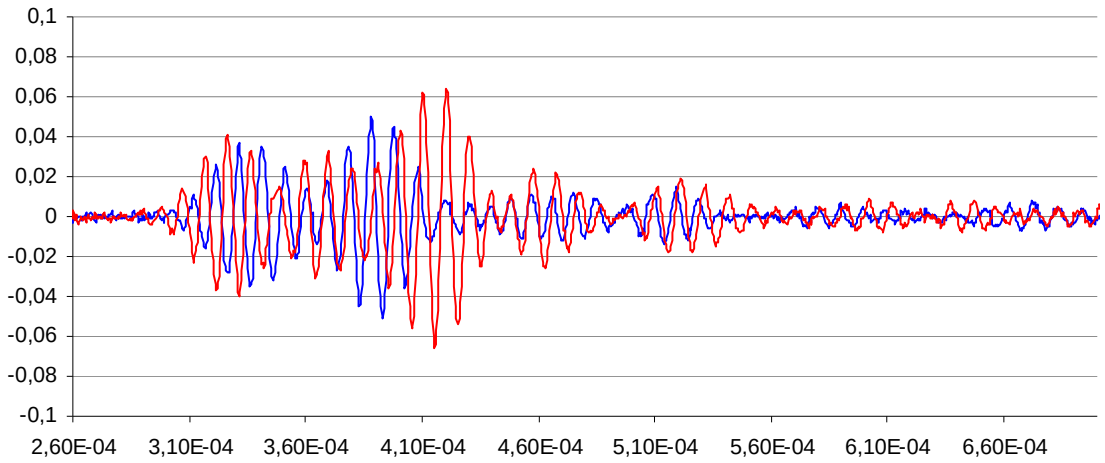


Figure 9: Experimental wave propagation results (blue line – without delamination, red line – with delamination); frequency is equal to 100 [kHz].

5 FINITE ELEMENT MODELING

5.1 Finite element modeling and simulation of guided wave propagation

Modeling methods and sensing technologies are the crucial areas of SHM. In fundamental axioms of SHM defined by Worden [38] the damage detection analysis is possible by comparison of two state system (intact and defected) because a sensors cannot measure flaws. The system of sensors applied to the structure gives a set of raw data which have to be processed to identification and localization of potential damage. It indicates to importance of modeling of damage and a damage detection algorithms. Common modeling techniques like the finite element method, spectral finite element method, finite difference techniques, boundary element methods and other were successful applied to SHM. The choice of accurate and efficient computational method depends on the size of damage that needs to be detected.

5.2 Finite Element Method modeling assessments

Among all numerical methods FEM is one of the most versatile, powerful and widespread due to its ability to model complex geometries. In this study the FE ANSYS package was applied to evaluate dynamic behavior of composite structure. FE modeling of composites is more complex than of isotropic materials, particularly due to the presence of complex stiffness and variety of failure modes. An appropriate finite element model of structural damage have to fulfill a several requirements which have been pointed out by Ye, Su [39]. The size of finite elements used to model a geometry of the structure depends on the speeds of the medium in which the signal is propagating and on the signal frequency. The mesh density should feature at least 8 nodes per wavelength to deliver good spatial precision. The time step for dynamic calculation should be less than the ratio of the minimum distance of any two adjoining nodes to the maximum wave velocity. The laminate should be divided into sub-laminates in thickness to characterize individual laminae especially when we consider interlaminar delamination in composite structure. In the present study the 3D solid95 finite element type with a 20-nodes was used in modeling a structure. A higher order version of a classical 8-nodes solid element with three degrees of freedom per node and fulfillment of presented requirements allow to obtain an accurate results of the numerical analysis.

Modeling of structural damage is crucial for the development of dynamic-based damage identification. The number of different modes of failure cause that this subject has attracted intensive research efforts over long period. Considered in this study delamination can be modeled by stiffness reduction method, kinematics based method or duplicate node method. the most adequate technique based on completely model the entire of the defect can be used either the 1D beam elements or 2D and 3D finite elements. Detailed information of the modeling of delamination we can be find in the works [36, 40, 41].

The most common techniques for the generation and receiving of guided waves is the use of piezoelectric elements. A PZT patches can deliver wide frequency responses with low power cost. A light and small structures are suitable for integration into a structures with good coupling capacity. Moreover, the sensor network can be configured by application a number of PZT elements to achieve a multi-point measurements for reliable analysis. In FEM model a concentrated force applied to the considered composite cylindrical panel varies with time function and simulate the load generated by real PZT element with 100kHz excitation frequency. The excitation signal was generated by one actuator and the data from the sensors placed after defected zone was compared with the results from an intact structure.

5.3 Results of numerical analysis

In this study a cylindrical panel with a single delamination in the middle (Fig. 3) is considered. A cylindrical panel was made of glass woven roving having the following properties: $E_{long}=E_{circumf}=13.14$ [GPa], $G_{12}=4.1$ [GPa], $\nu_{12}=0.25$, $\rho=1100$ [kg/m^3].

As it has been mentioned the any observations of waves is strongly dependent both on locations of the actuator/s and sensors (Fig. 1). Let consider the actuator and sensors configuration in the form presented in Fig. 4. Various localization of the sensors are taken into account to determine the influence zone of delamination on wave propagation path.

The wave propagation for construction is disturbed by the delamination. We can observe the defect influence zone after delamination which broaden with the distance between propagating waves and the delamination. The influence of delamination on wave propagation can be observed by comparison signal of the intact and defected structure.

Figure 10 illustrates the response signals obtained for the perfect and imperfect (with a single delamination) structures. Even if the signal passes through the whole delaminated area (sensor No. 2) the difference between displacement for the defected and perfect structures is small. The most significant difference between response signals is observed by sensors placed outside of the defect influence zone (sensor No. 5). The signal observed by sensor No. 5 is going near the corner of the delamination. The greater distance from defected area cause a lower disturbance of response signals.

The experimental results are also compared with a numerical analysis for cylindrical panels for the signal excitation frequency equal to 100 [kHz]. The difference between the perfect and imperfect (with the single delamination) cylindrical panel plotted in Figs 5 and 10 demonstrate very good agreement. The form of response signal is strongly affected by the location of sensor and actuator.

The size of the defect influences on wave propagation. To the effect of delamination size on the dynamic behavior of the structure (a cylindrical panel with a square delaminations of different sizes) is analyzed in the work [40].

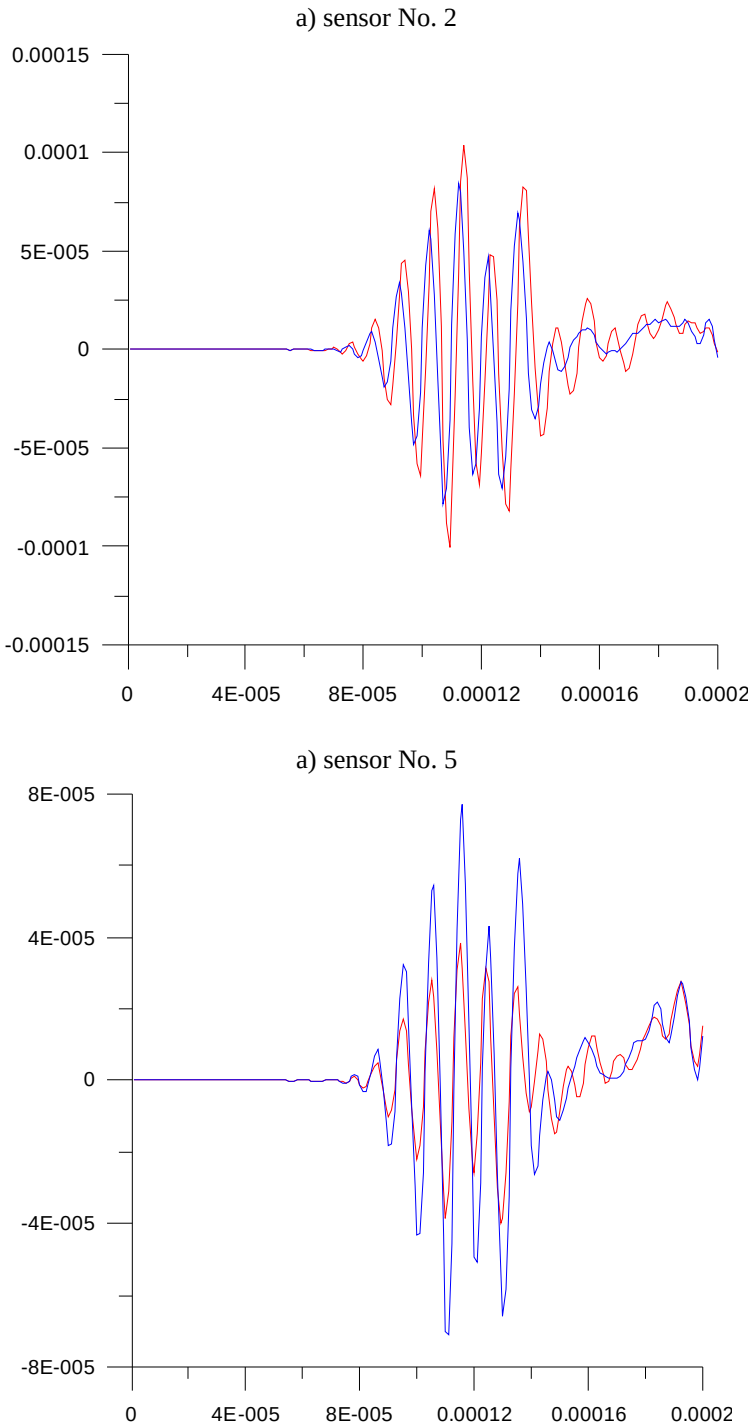


Figure 10: Numerical wave propagation results (blue line – without delamination, red line – with delamination); for frequency equal to 100 [kHz].

6 CONCLUSIONS

- Results of damage detection in composite laminated panels are demonstrated with use of piezoelectric patches.

- The amplitude of the response is strongly affected by the excitation signal frequency and location of sensor and actuator; therefore, the optimization of they location and number is required.
- Modeling of composite structures having smart piezoelectric sensors or actuators are very similar to conventional composite layered structures, however, there is one difference reflected in the constitutive laws in the form of the electromechanical coupling.
- Optimal location of sensors and actuators over a structure can be different for different criteria.
- The composition of experimental and numerical results demonstrates very good agreement.
- A lot of numerical results allow us to understand better the influence of various parameters on the form of wave propagation in cylindrical multilayered shells.
- Based on numerical results it is possible to determine the effect of the delamination on the guided wave propagation in curved structures.
- The shape of system of piezoelectric transducers, the shape and the number of PZT sensors have a great influence on the quality and accuracy of damage detection.

ACKNOWLEDGMENTS

The support from the NCN under the grant UMO-2013/09/B/ST8/00178 is gratefully acknowledged.

REFERENCES

[1] J. Hoła, K. Schabowicz, State-of-the-art non-destructive methods for diagnostic testing of building structures – anticipated development trends, *Archives of Civil and Mechanical Engineering*, **10**, 5–18, 2010.

[2] R. Raišutis, E. Jasiūnienė, R. Šliteris, A. Vladišauskas, The review of non-destructive testing techniques suitable for inspection of the wind turbine blades, *Ultrasound Journal*, **63**, 26–30, 2008.

[3] D. Rao, M.R. Pawar, *Review of nondestructive evaluation techniques for FRP composite structural components*, Civil Engineering, 2007.

[4] C. Hellier, *Handbook of Nondestructive Evaluation*, McGraw-Hill, 2001.

[5] E. Kuhn, E. Valo, P. Herve, A comparison between thermosonics and thermography for delamination detection in polymer matrix laminates, *Composite Structures*, **94**, 1155–1164, 2012.

[6] T.F. Drouillard, A history of acoustic emission, *Journal of Acoustic Emission*, **14**, 1–34, 1996.

[7] R.K. Miller, E.V.K. Hill, *Acoustic emission testing, Nondestructive testing handbook, third edition, vol. 6*, ASNT, 2005.

[8] Z. Su, L. Ye, Lamb wave-based quantitative identification of delamination in CF/EP composite structures using artificial neural algorithm, *Composite Structures*, **66**, 627–637, 2004.

[9] S.K. Seth, S.M. Spearing, S. Constantinos, Damage detection in composite materials using Lamb wave methods, *Smart Materials and Structures*, **11**, 269–278, 2002.

[10] T.P. Philippidis, T.T. Assimakopoulou, Using acoustic emission to assess shear strength degradation in FRP composites due to constant and variable amplitude fatigue loading, *Composites Science and Technology*, **68**, 840–847, 2008.

[11] C. Leone, V. Lopresto, L. Papa, G. Caprino, Triangulation method as a valid tool to locate the damage in unidirectional CFRP laminates, *Composite Structures*, **94**, 2418–2423, 2012.

[12] Z. Su, L. Ye, Y. Lu, Guided Lamb waves for identification of damage in composite structures: A review, *Journal of Sound and Vibration*, **295**, 753–780, 2006.

[13] S. Gopalakrishnan, M. Ruzzene, S. Hanagud, *Computational techniques for structural health monitoring*, Springer, 2011.

[14] Lord-Rayleigh, On the free vibrations of an infinite plate of homogeneous isotropic matter, *Proc. of the London Mathematical Society*, **20**, 225–234, 1889.

[15] H. Lamb, On Waves in an elastic plate, *Proc. of the Royal Society*, London, **93**, 114–128, 1917.

[16] I. Mirsky, Axisymmetric vibrations of orthotropic cylinders, *Journal of the Acoustical Society of America*, **36**, 2106, 1964.

[17] J.L. Nowinski, Propagation of longitudinal waves in circular cylindrical orthotropic bars, *Journal of Engineering for Industry*, **89**, 408, 1967.

[18] F.H. Chou, J.D. Achenbach, Three-dimensional vibrations of orthotropic cylinders, *Journal of Engineering Mechanics (ASCE)*, **98**, 813, 1981.

[19] A.H. Nayfeh, *Wave propagation in layered anisotropic media with applications to composites*, Elsevier, 1995.

[20] F.G. Yuan, C.C. Hsieh, Three-dimensional wale propagation in composite cylindrical shells, *Composite Structures*, **42**, 153, 1998.

[21] M.N. Ichchou. J.L. Mencik, W. Zhou, Wave finite elements for low and mid-frequency description of coupled structures with damage, *Computer Methods in Applied Mechanics and Engineering*, **198**, 1311–1326, 2009.

[22] D.C. Worlton, Experimental Confirmation of Lamb Waves at Megacycle Frequencies, *Journal of Applied Physics*, **32**, 967, 1961.

[23] W.H. Prosser, K.E. Jackson, S. Kellas, B.T. Smith, J. McKeon, A. Friedman, Advanced, waveform based acoustic emission detection of matrix cracking in composites, *Materials Evaluation*, **53**, 1052–1058, 1995.

[24] M. Wevers, Listening to the sound of materials: acoustic emission for the analysis of material behavior, *NDT&E International*, **30**, 99–106, 1997.

[25] K.A. Lakshmanan, D.J. Pines, Modeling damage in rotorcraft flex beams using wave mechanics, *Smart Materials and Structures*, **6**, 383–392, 1997.

[26] J.B. Ihn, F.K. Chang, Detection and monitoring of hidden fatigue crack growth using a built-in piezoelectric sensor/actuator network: I. Diagnostics, *Smart Materials and Structures*, **13**, 609–620, 2004.

[27] K. Worden and W.J. Staszewski and G.R. Tomlinson, Smart systems – the role of signal processing, *Proc. of CEAS International Forum on Aeroelasticity and Structural Dynamics*, Rome, Italy, 17–20 June, 1997.

[28] W.J. Staszewski, Intelligent signal processing for damage detection in composite materials, *Composites Science and Technology*, **62**, 941–950, 2002.

[29] A. Muc, P. Kędziora, Variational approach in optimal design of piezoelectric sensors & actuators, *Advanced Materials Research*, **47-50**, 1258–1261, 2008.

[30] P. Kędziora, A. Muc, Optimal shapes of PZT actuators for laminated structures subjected to displacement or eigenfrequency constraints, *Composite Structures*, **94**, 1224–1235, 2012.

[31] P. Kędziora, A. Muc, Optimal piezoelectric location for composite structures, Ryszard Pecherski, Jerzy Rojek, Piotr Kowalczyk (Editors), *38th Solid Mechanics Conference*, Warszawa, 284–285, 2012

[32] P. Kędziora, Optimal design of PZT actuators and sensors in composite structural elements, *Key Engineering Materials*, **542**, 59–73, 2013.

[33] A. Muc, P. Kędziora, Free vibrations of cylindrical shells with delaminations, *Shell Structures, Theory and Applications (SSTA 2009)*, Taylor & Francis Group, Wielka Brytania, 187–190, 2010.

[34] P. Kędziora, Optimization and modeling composite structures with PZT Layers, *Advanced Materials Research*, **849**, 108–114, 2014.

[35] P. Kędziora, M. Barski, M. Chwał, Piezoelectric Transducers, *Key Engineering Materials*, **542**, 75-80, 2013.

[36] M. Barski, P. Kędziora, A. Muc, P. Romanowicz, Structural health monitoring (SHM) methods in machine design and operation, *Archive of Mechanical Engineering*, **LXI**, 653–677, 2014.

[37] P. Kędziora, Detection of interlaminar cracks in composite structures with the use of piezoelectric sensors and thermography, *III ECCOMAS International Conference on Computational Methods in Structural Dynamics and Earthquake Engineering (COMPDYN 2011)*, Greece, 26–28 May, 2011.

[38] K. Worden, C.R. Farrar, G. Manson, G. Park, A fundamental axioms of structural health monitoring, *Proc. R. Soc. A*, **463**, 1639–1664, 2007.

[39] L. Ye, Z. Su, *Identification of damage using Lamb waves*, Springer, 2009.

[40] A. Stawiarski, A. Muc, P. Kędziora, Damage detection, localization and assessment in multilayered composite structure with delaminations, *Key Engineering Materials*, **542**, 193–204, 2013.

[41] A. Muc, A. Stawiarski, Wave propagation in composite multilayered structures with delaminations, *Mechanics of Composite Materials*, **48**, 101–106, 2012.

COMPDYN 2015
5th ECCOMAS Thematic Conference on
Computational Methods in Structural Dynamics and Earthquake Engineering
M. Papadrakakis, V. Papadopoulos, V. Plevris (eds.)
Crete Island, Greece, 25–27 May 2015

INFLUENCE OF CONNECTIONS MODELING ON THE SEISMIC BEHAVIOUR OF INDUSTRIAL BUILDINGS

Luca Tassotti, Mohammed Radi, Fabrizio Gara and Laura Ragni

Dept. of Civil and Building Engineering and Architecture, Università Politecnica delle Marche
Via Brecce Bianche, 60131 Ancona, Italy.
{l.tassotti, m.radi, f.gara, laura.ragni}@univpm.it

Keywords: Dowel connections, Precast structures, Push-over analysis, Seismic vulnerability assessment, Shear-displacement relation.

Abstract. *Many industrial buildings with a precast concrete structure have been designed in accordance with non-seismic provisions by considering only gravity loads or, in some other cases, in accordance with not adequate seismic detailing requirements .In particular, seismic events that occurred in the recent past have shown that the connections between the main structural elements play an important role on the dynamic and seismic behaviour of the precast concrete structure. Nowadays, the more advanced technical standards require mechanical connections between the precast elements; however codes do not furnish exhaustive information about the design and modelling of these connections neither in the seismic vulnerability assessment of existing buildings nor in the design of new constructions. In this work, the role of dowel connections between beams and columns elements in the seismic behaviour of one-storey precast concrete industrial building is investigated and a simple modelling procedure is proposed for both the seismic vulnerability assessment of existing buildings and the design of new constructions. The applicability of the proposed methodology is tested through linear dynamic analysis and non linear static analysis carried out on two real case studies. In particular, different finite elements models are developed for the benchmark cases, both considering or omitting the rigid floor constrain and both assuming rigid or flexible connections. The results show that the modelling strategy strongly influences the seismic response and thus the safety verifications of the structural typologies considered.*

1 INTRODUCTION

Since the second post-war period single-storey precast structures represent a structural typology widely used for the construction of industrial and commercial buildings. Nowadays, in the Italian and European context, a large part of these buildings are characterized by a outdated and inadequate structure compared to structures which meet current seismic criteria, resulting therefore exposed to high seismic hazard.

There are many evidences about the behaviour of precast structures during past earthquakes; the main causes associated to the damage of the precast structures were constituted by the failure of connections. In particular, the recent earthquake that hit Emilia in 2012 highlighted the importance of the role that the connecting systems play in the global behaviour of prefabricated structures [1]. Specifically, in the older precast buildings, collapses due to mere loss of seating among the elements were observed where the connections were entrusted only to the resources of friction.

Recent Italian regulations, in force until a few years ago, allowed the realization of friction based connections between structural elements [2] for areas classified non-seismic while the latest standards ([3], [4]) require that the connection is secured by mechanical devices properly dimensioned. However, serious damages due to inadequacy of the connections were also observed in more recent buildings, complying with the latest standard indications. In some cases, the cause can be traced to reduced resistance of the same, to the absence of the rigid diaphragm behaviour or abnormal rigid floor behaviour induced by particular configurations of connection between the structural elements (main and secondary) that generated forces concentrations in some connections determining the rupture. Therefore, these issues have highlighted a deficiency of the current rules that, although requiring the use of mechanical connections, do not furnish exhaustive information for designing [1] and modelling of the same.

Connections by means of pin or dowel are the most common connection system in the single-storey industrial buildings in Europe for their effectiveness and practicality of realization. The aim of this paper is to propose a procedure for modelling the dowel connections that is easy to use both for the evaluation of the seismic vulnerability of existing buildings and for the design of new buildings. Modelling aspects of dowel connections between beams and columns and between main beams and secondary elements are investigated with reference to single storey buildings with precast structure frame (beams, columns, and roof secondary elements). For these purposes, in a first step, the analysis of the state of the art is carried out, through investigation of the scientific literature and available codes, then the proposed method for modelling the dowel connections is applied to two real case studies consisting of buildings with single level precast structure with dowel connections. The structures are modelled by means finite element method both by considering and by omitting the rigid floor constraint. The procedure is tested through nonlinear static analysis and the main results are discussed. In particular, it is emphasized how the strategy for connection modelling affects the seismic response of the structure and, consequently, the results of the safety verifications.

2 BACKGROUND

The dowel or pinned connections sustain shear forces through a mechanism known in the literature as dowel action (Figure 1), discovered in the 30s [5].

The resistance of the connection can be governed by three different failure mechanisms: pure shear failure of the pin (steel shear failure), concrete splitting failure and yield of the bar and concrete crushing of the contemporary concrete around the dowel (combined steel and concrete failure).

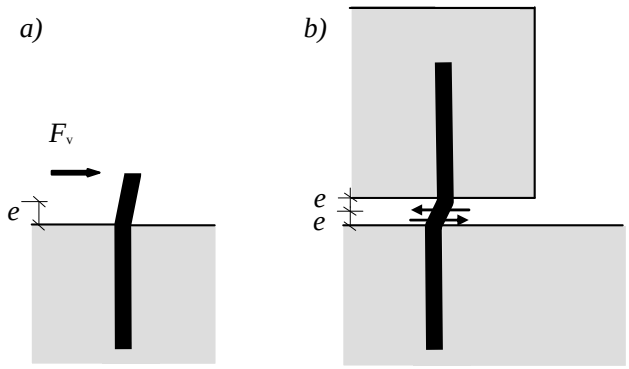


Figure 1: Transfer of shear force through the dowel action: *a*) one-sided dowel; *b*) double-sided dowel [7]

The shear failure is not very applicant; it can be determined by means the Von Mises criterion.

The concrete splitting failure is a brittle mechanism that can arise if the bar acts against the concrete cover characterized by a reduced thickness *c* and not provided with adequate confinement bars. Various authors conducted experimental investigations with the aim of estimating the splitting resistance. Vintzeleou and Tassios (1986) [6] provide expressions derived from analytical models and show that the failure may happen for side splitting or bottom splitting in relation to the diameter of the pin and to the ratio between the concrete cover *c* and the lateral cover b_{ct}, measured along the orthogonal direction of the acting force. The splitting failure can be avoided if adequate bars are foreseen and dimensioned by means strut and ties models, according to the fib bulletin n.43 document [7].

The combined steel and concrete failure mechanism is a ductile mechanism because it occurs together with the formation of plastic hinges in the pin. This mechanism was widely investigated by the scientific community since the beginning of the last century. In the first half of the previous century simple models based on linear elastic behaviour of materials were used [8]; however the linear model proved unsuitable for such purposes since the materials exhibit a plastic behaviour in conditions close to collapse. For these reasons, the beginning of the second half of the last century models based on the theory of plasticity were adopted. Rasmussen (1963) [9] was among the firsts to propose a plastic model; other authors investigated the same failure mechanism by calibrating the analytical model on the basis of experimental results, including [10]. Subsequently, Vintzeleou and Tassios [6], [11], applied the Brom's model [12] of free-headed pile in cohesive soil for the definition of the pin resistance and the response curve of the same. On the basis of the theory of plasticity, Engström (1990) [13] proposed further formulations for the determination of the parameters of dowel displacement. An exhaustive summary of the studies conducted on the connection strength governed by the pin yielding is available in fib bulletin n.43 document [7].

3 PROPOSED METHODOLOGY

3.1 Ultimate strength

The ultimate strength is assumed equal to the minor among the resistance values associated to rupture mechanisms discussed in the previous paragraph.

As previously reported, pure shear resistance of the pin is determined via Von Mises criterion whereas concrete splitting failure follows indications proposed by Vintzeleou and Tassios in [6]. This collapse mechanism can occur if the cover *c* of the pin is less than 6 to 8 times its diameter *d*. In particular, the resistance is determined as the smaller value between

the side splitting resistance and the bottom splitting resistance, reported in this order in the Equation (1) where f_{ct} indicates the tensile strength of the concrete.

$$F_{V,cr} = \min\left(2b_{ct} d f_{ct}; 5 f_{ct} d \frac{c^2}{0.66 + d} \right) \tag{1}$$

In the case of covers smaller than limits reported above and equipped with confinement bars, splitting failure can not be considered. Therefore, by considering that the precast elements are provided of bars in the connection areas, the connection rupture can be assumed as the minor value between the pin shear strength and the dowel yielding resistance. Resistance associated to the last collapse mechanism is determined through the following Equation, according to the requirements set out in [7],

$$F_{V,Rd} = \alpha_0 \alpha_e d^2 \sqrt{f_{cc} f_y} \tag{2}$$

where f_{cc} and f_y represent the materials strengths, while α_0 and α_e are the parameters evaluated respectively according to the Equations (3) and (4)

$$\alpha_0 = \sqrt{\frac{\beta_c}{3}}, \qquad \text{where} \quad \beta_c = \frac{f_{cc}^*}{f_{cc}} = 4 \tag{3}$$

$$\alpha_e = \sqrt{1 + \left(3\frac{e}{d}\sqrt{\frac{f_{cc}}{f_y}}\alpha_0 \right)^2} - 3\frac{e}{d}\sqrt{\frac{f_{cc}}{f_y}}\alpha_0 \tag{4}$$

in which f_{cc}^* indicates the concrete strength in the triaxial stress state.

3.2 Shear-displacement law

The force-displacement law is proposed on the basis of the information given in [7] and of the results of research performed in the literature. Such relationship is determined with reference to the ductile failure mechanism. In particular, the ultimate strength is evaluated from Equation (2) by assuming, in the case of double – sided dowel configuration, a concrete strength f_{cc} equal to the maximum value between the resistances of the two connected elements.

The yielding point is considered reached to a level of strength equal to half of the ultimate strength, while the displacement at yield is evaluated on the basis of the following formula

$$s_y = \frac{2F_{VRd}\beta_e\left(e\beta_e + 1\right)}{E_c} \tag{5}$$

in which β_e is the stiffness parameter defined as

$$\beta_e = \left(\frac{E_c}{8E_s I_s} \right)^{0.25} \tag{6}$$

where E_c and E_s are the Young's moduli of the concrete and steel, respectively, while I_s is the moment of inertia of the dowel cross-section. Displacement corresponding to the ultimate plasticization of the pin s_{max} is evaluated by means the following expression:

$$s_{max} = \theta_{cr} l_p \tag{7}$$

where θ_{cr} represents the critical rotation, which is assumed proportional to the curvature of the pin cross-section when this latter reaches the yield strength. This rotation is estimated as $1.75\varepsilon_{sy}/d$. The l_p parameter corresponds to the distance of the plastic hinge from the external edge x_0 in the case of one sided dowel configuration whereas, in the case of double sided dowel configuration, l_p represents the distance between the two plastic hinges. The distance from the outer edge of the element to the plastic hinge x_0 is determined via the following expression.

$$x_0 = \frac{F_{VRd}}{3\alpha_0^2 f_{cc} d} \tag{8}$$

Figure 2 illustrates an example of the force-displacement curve proposed.

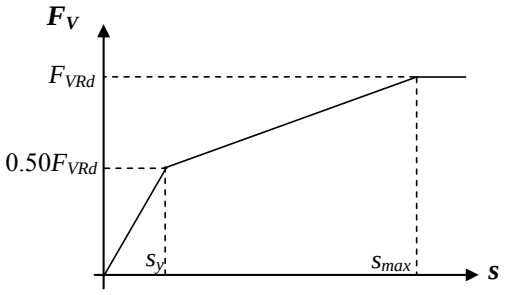


Figure 2: Example of the force-displacement curve proposed.

4 CASE STUDIES

In this section, the proposed procedure is illustrated by considering two real existing buildings that belong to the same industrial complex, but built in different years in Italy. The seismic action for the structures site is defined by the NTC08 soil type E (soil factor S = 1.524) spectrum [4], for a peak ground acceleration PGA = 0.174 g and period of return T_R = 475 years. The Figure 3 shows the seismic action for the selected case studies.

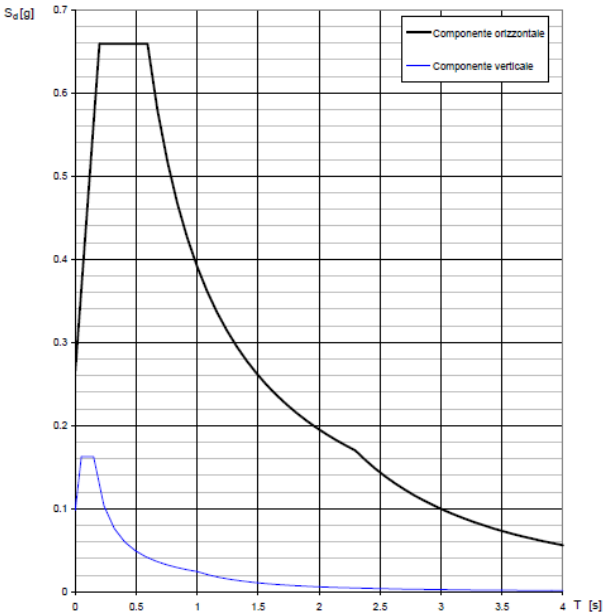
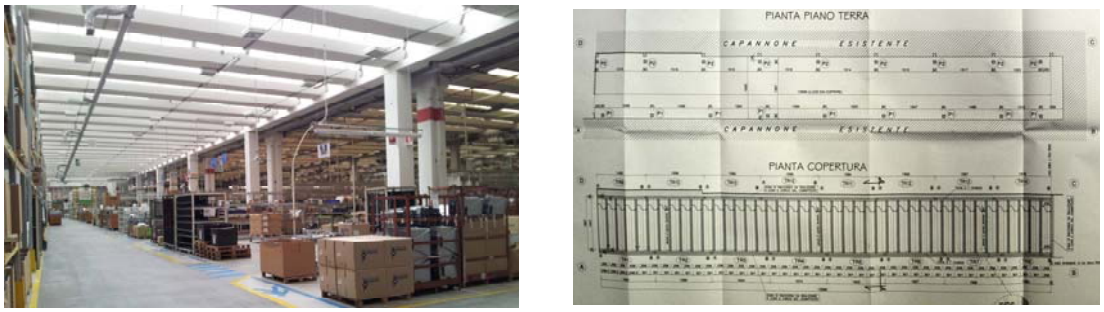


Figure 3: Vertical and horizontal elastic pseudo-acceleration response spectrum of the buildings site

4.1 Case study 1

The first case study concerns a structure with an elongated rectangular plan built in 2005; it consists of equal columns with square cross-section of 0.80 x 0.80m and main beams with an "inverted T" cross-section with a height of 1.65 m. These beams support secondary beams that complete the roof. These latter have the typical shed cross-section, largely diffused in Italy. Beam-column and beam to shed connections are dowel connections, made with Italian FeB44k steel. Figure 4 shows a photo of the building and an excerpt of the original project while Figure 5 shows the details of the connections.

First analyses are carried out by adopting dynamic linear models with rigid connections. Since the real degree of stiffness of the roof floor is not known, two global models of the structure are defined, with and without the rigid diaphragm constraint for the roof. Additionally, the analyses are conducted by adopting a confidence factor equal to 1.0 (due to the nature of the prefabricated structure) and 1.35 (given the lack of knowledge of the structure details). Structure factors of 1.5 and 3, as contemplated by the Italian current regulations for existing buildings [4], are chosen to take into account the dissipation capacity of the structure.



a) *b)*

Figure 4: Case study 1: a) photo taken from the inside; b) excerpt of the originate projects

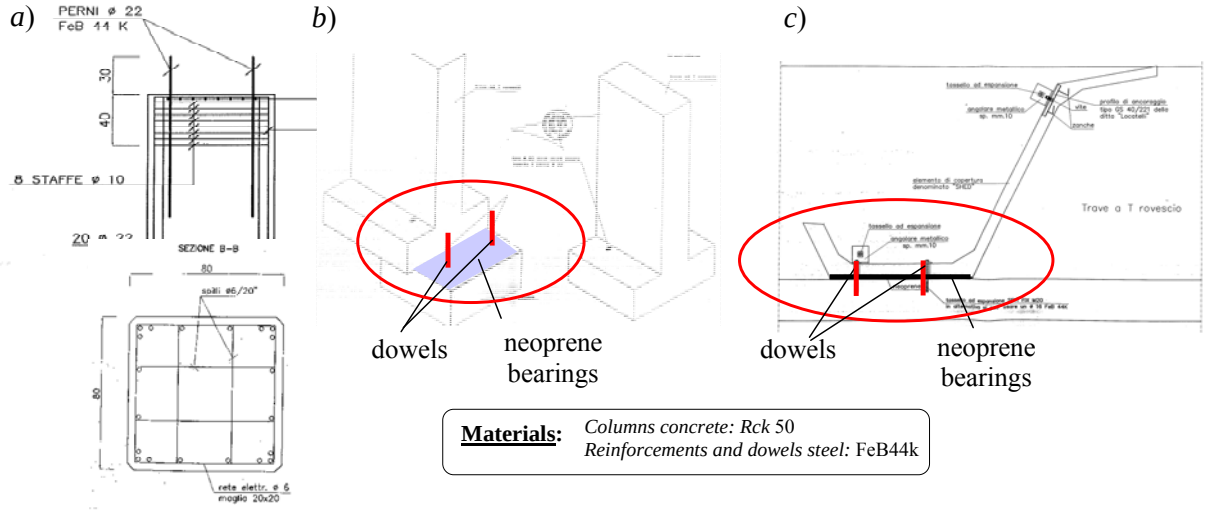


Figure 5: a) Detail of dowels; b) beam-column connections; c) beam-shed connections

It should be observed that the linear analyses are characterized by some limits. First off all the evaluation of the seismic vulnerability of the investigated structure carried out via linear analysis is excessively precautionary, since it is necessary to refer to the first element in which capacity is exceeded, thus in some cases the seismic action sustained by the building is very low. Additionally, it should be noted that the analyses are conducted by assuming over-

resistant and rigid connections, i.e. not-deformable and able to allow the columns plasticization, and thus the adoption of the behaviour factors.

In order to investigate the behaviour of the structure beyond the elastic limit non-linear analysis are performed. Also for these analyses both the case of deformable deck and infinitely rigid roof are considered. Figure 6 shows the comparison between the elastic and inelastic spectra relative to a period of return T_R = 475 years and the capacity curve of the structure obtained by applying a distribution of forces proportional to the masses along the direction +x and +y (the results obtained by applying the same distribution along the negative direction and by assuming a rigid deck are similar and for reasons of synthesis are not reported). It is possible to observe that in both analyses the structure ductility (μ_c) is high (about 3) and greater than the value required to sustain the design earthquake (R_μ). Therefore, it can be concluded that safety verifications are satisfied because, in each case, the ductility demand is less than the available ductility. Also in this case, it should be emphasized that the results obtained are valid only in the event that the connections between the structural elements are over-resistant with respect to the columns. So, it is necessary to check the full strength of the dowels, by comparing the demand, expressed in terms of internal forces, with the resistance provided by the pins at each connection.

From non-linear static analysis a maximum shear force of 234 kN in beam-to-column connections and a maximum action of 232 kN in the beam-to-shed connections are obtained. Collapses for splitting does not take place because the cover thickness is greater than the limit of 6-8 *d* as shown by Figure 7. Therefore, the possible local collapse mechanisms can be induced by shear failure or flexural yielding of the dowel. The pure shear strength of the couple of dowels in the beam-column connection amounts to 203.8 kN. The flexural resistance of the connection, obtained by substituting in the Equation (2) the value of the materials resistance and by assuming α_0 = 1 and α_e = 0, is equal to 144.6 kN. From the results it can be noted that the resistance of the connection is governed by the flexural failure mechanism of the dowel and that the resistance of the connections is lower than the acting shear forces, thus they are not over resistant.

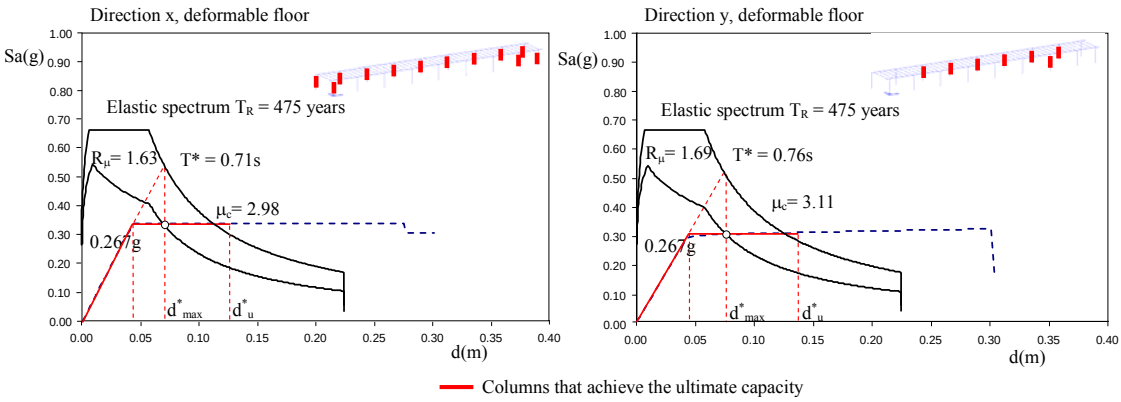


Figure 6: Curve capacity relating to the analysis of push-over (with forces proportional to the masses) both in the longitudinal direction x and transverse direction y

However, it should be noted that the deformability of the connections could result in a reduction of the forces acting on the same. Therefore, a proper assessment of the local demand on the connections and the comparison with their capacity can only be performed in terms of displacements in a model with deformable connections, as shown below.

Figure 7 shows the force-displacement law adopted to describe the behaviour of the connections in the non-linear model of the industrial building, without rigid diaphragm constraint.

Non-linear static analyses carried out both in the transverse (y) and longitudinal (x) direction have provided deformation levels much lower than those for which the dowels plasticization occurs, for both main beams-secondary beams and beam-columns connections.

In Figure 8 the comparison between the capacity curve and the demand curve is depicted. It is possible to note that, in both the directions, the earthquake sustained by the structure is higher than design one (period of return T_R greater than 475 years) and the risk index is greater than 1.

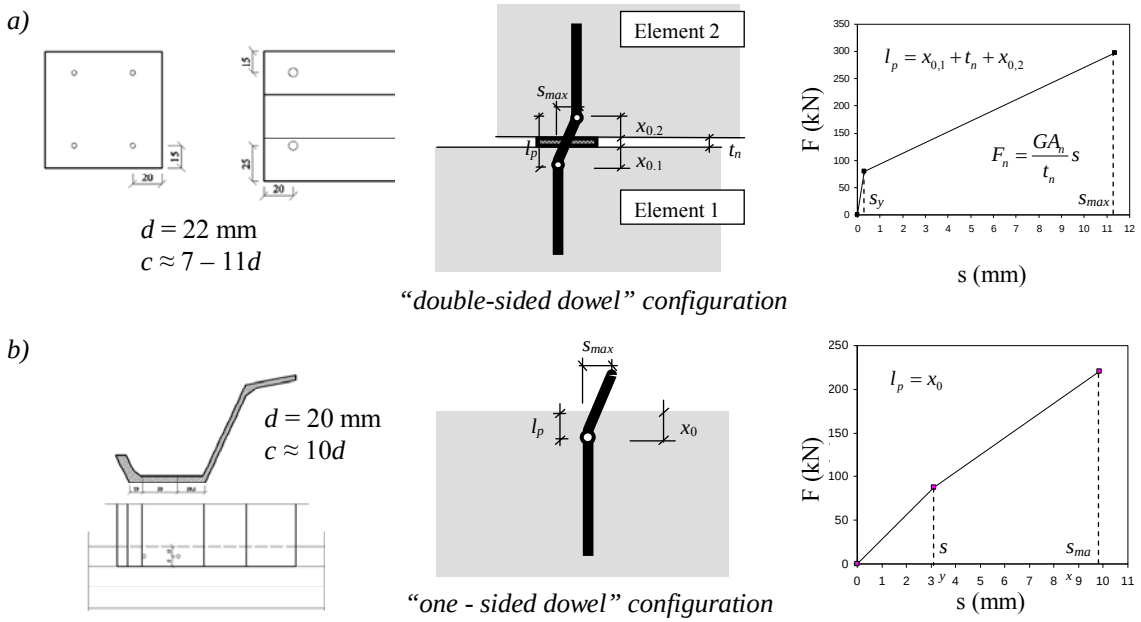


Figure 7: Shear-displacement relations of a) beam-column connections and b) beam to shed connections

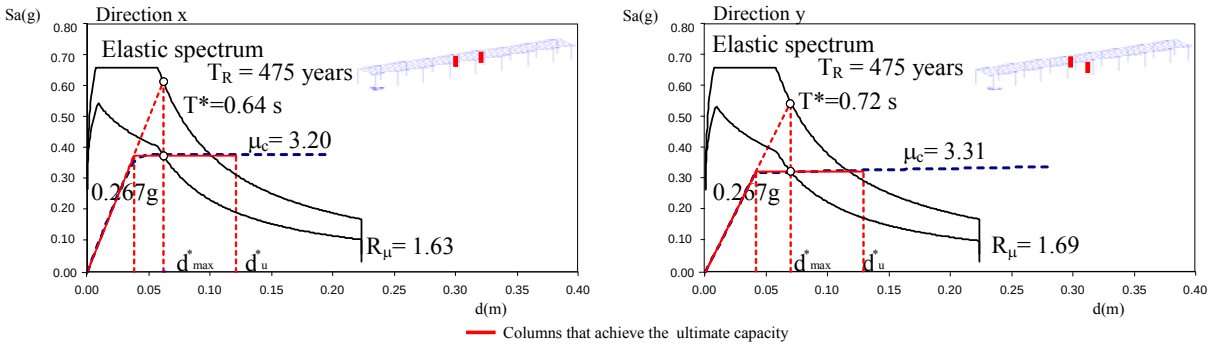


Figure 8: Push-over analysis results: comparison between demand and capacity curves in the ADRS plane for both the directions of analysis

4.2 Case study 2

The second case study concerns an irregular building in plan and elevation, built in 1981 and adjacent to the building previously analyzed. The building is characterized by precast columns of variable dimensions, from 0.90 x 0.90m to 0.30 x 0.40m, while the beams have "inverted T" and "Omega" cross-section. As regards the materials, the resistances are lower than those of the first case study. The beam-column connections and beams-shed connections consist of steel dowels, whose configurations are shown in Figure 9.

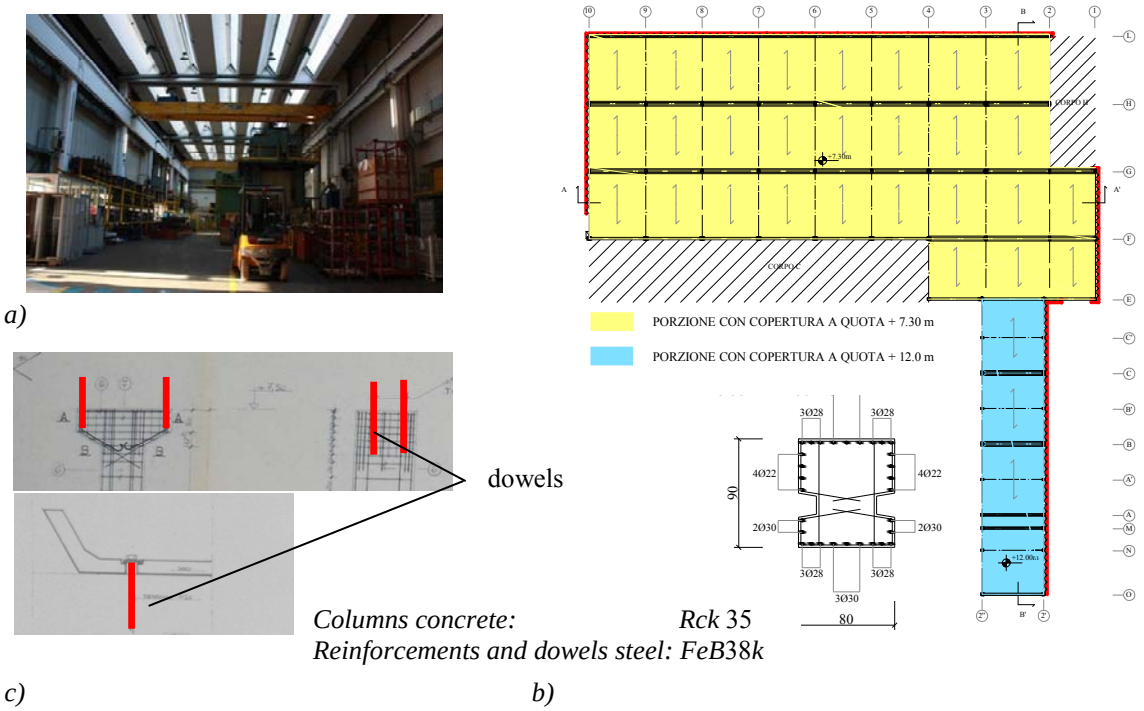


Figure 9: Case study 2: a) photo taken from inside; b) write-off of project; c) write-off of the executive details of beam-to-column and beam-to-shed connections

Also in this case dynamic linear analyses are carried out by adopting models with rigid connections and both by considering and by disregarding the rigid plane behaviour of the roof. Same confidence factors and behaviour factors employed in the previous case study are used for performing the safety verifications. In many cases the checks are not satisfied. Also in this case, since the linear analyses are considerably prudential non-linear static analyses are performed in order to take into account the behaviour of the structure beyond the elastic range. From the comparison between the elastic and inelastic demand spectrum and the structure capacity curve it is possible to observe that the verifications are satisfied in that, in each case, the demand in terms of ductility (R_μ) is less than the available ductility (μ_c). With the objective of checking whether the connections over strength hypothesis is satisfied, dowels forces are compared with the strengths. The analysis carried out in both directions have shown that the shear forces on the various types of beam-column connections were greater than the dowels resistances, calculated by assuming the same assumptions of the previous case study. Moreover, it was observed that the dowel resistance is governed by the combined steel and concrete failure. Splitting verification was not conducted because, despite the covers result smaller the limit of 6-8 *d*, they are equipped with confinement bars. Since, as explained in the previous case study, the analysis conducted by considering rigid connections lead to an overestimation of the forces, the same analyses are carried out by modelling the connections as deformable. The assumed force-displacement law is depicted in Figure 10.

Non-linear static analyses carried out both in the transverse (y) and longitudinal (x) direction have provided for both beams-shed connections and beams-columns displacement levels much higher, in some cases, than the displacement at which the ultimate plasticization occurs. However, the obtained displacements are always lower than the seating extension of the supported elements. Therefore, it is possible to state that important damages occur in the connections, but seating losses of the main and secondary beams do not occur.

In Figure 11 the comparison between the capacity curve and the demand curve is depicted; from the comparison it is possible to note that, in all cases, the earthquake sustained by the

structure is higher than design one (with period of return T_R = 475 years) and the risk index is greater than 1.

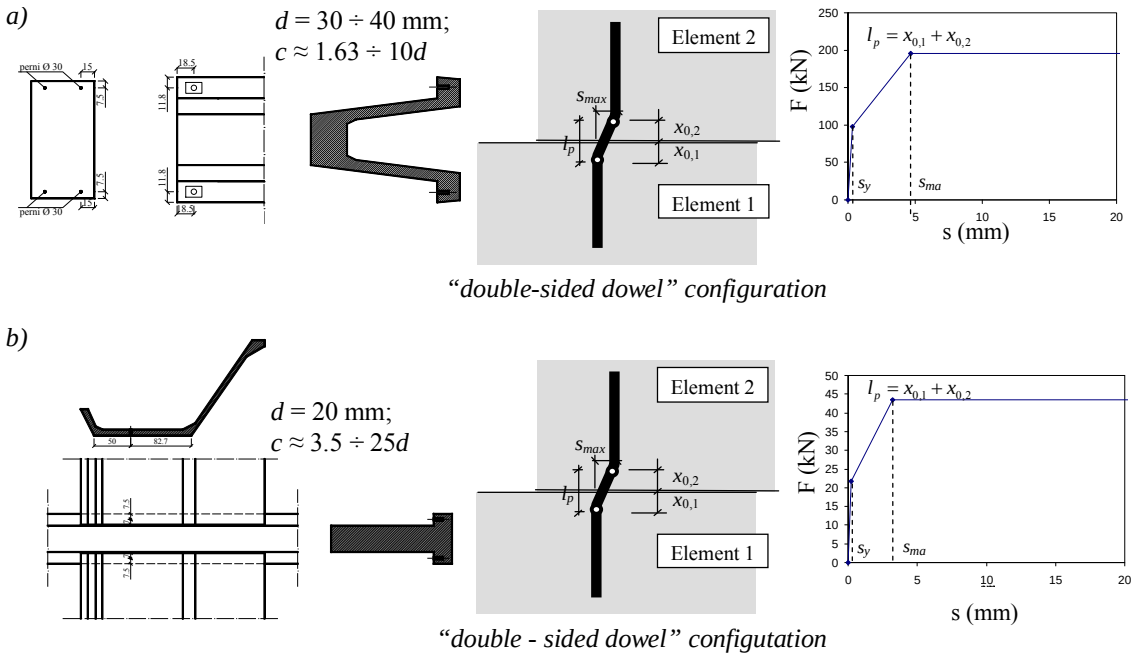


Figure 10: Force–displacement relations of a) beam-to-column connections and b) beam–to-shed connections

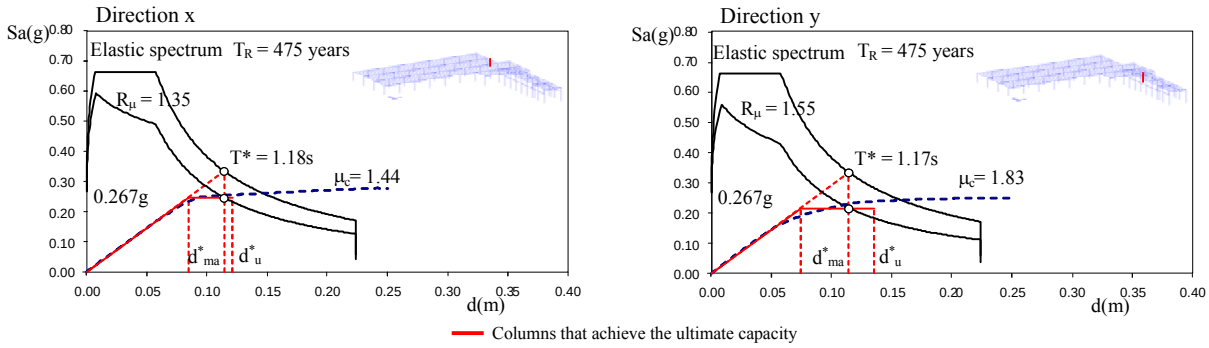


Figure 11: Push-over analysis results: comparison between demand and capacity curves in the ADRS plane for both the directions of analysis

5 CONCLUSIONS

In the present work a procedure for modelling the dowel connections between prefabricated elements of single level buildings was proposed for assessing the seismic vulnerability of existing buildings and for the new buildings design. The proposed shear force-displacement law refers to the ultimate flexural dowel resistance and its applicability is tested by performing non-linear static analysis conducted on two real industrial buildings.

The analyses are carried out both by considering the rigid and the deformable behaviour of the connections and both by omitting and by considering the rigid diaphragm constraint. The results have shown that the seismic response of the structure and thus the safety verifications are strongly influenced by the modelling strategy adopted for describe the connections. In particular, in both the study cases, it is observed that the shear forces on the beam-to-column connections and shed-beams connections reach significantly higher values in the models with rigid connections with respect to the models with deformable connections. Moreover, for both the study cases, the investigated structures are able to sustain the design earthquake only if

elastic and inelastic connection behaviour is modelled, because the connections are adequately resistant and allow the formation of the dissipative mechanism in the columns.

Finally, it was noted that in the first case study, of more recent realization, the structure is able to withstand the design action without to undergo significant damage of the connections, while in the second case the dowels of many connections are plasticized undergoing elevated plastic displacements, but minor of the available seating length.

REFERENCES

[1] D. A. Bournas, P. Paolo Negro, F. Taucer, The Emilia Earthquakes: Report and analysis on the behaviour of precast industrial buildings from a field mission. M. Papadrakakis, V. Papadopoulos, V. Plevris eds. *4th ECCOMAS Thematic Conference on Computational Methods in Structural Dynamics and Earthquake Engineering (COMPDYN 2013)*, Kos, Greece, June 12-14, 2013.

[2] Ministero dei Lavori Pubblici, *Norme tecniche per la progettazione, esecuzione e collaudo delle costruzioni prefabbricate*, Roma, Italia, 1987.

[3] European Committee for Standardisation, *Eurocode 8: Design of structures for earthquake resistance, Part 1: General rules, seismic actions and rules for buildings*, EN 1998-1, 2004.

[4] Ministero delle Infrastrutture, *Norme Tecniche per le costruzioni*, Roma, Italia, (2008).

[5] S. Dei Poli, M. M. Di Prisco, P.G. Gambarova, Dowel action as a means shear transmission in RC Elements: a state of the art and new test results. *Studi e Ricerche*, School for the Design of R/C Structures, Milan University of Technology, **9**(87), 217-303, 1988.

[6] E.N. Vintzeleou, T.P. Tassios, Mathematical models for dowel action under monotonic and cyclic conditions, *Magazine of Concrete Research*, **38**(134), 13-22, 1986.

[7] fib (Fédération international de bèton) *Structural connections for precast concrete buildings, Guide to good practice*, (Bullettin 43), Lausanne, Swisse, 2008.

[8] B.F. Friberg, Design of dowels in transverse joints of concrete pavements. *Proceedings of the American Society of Civil Engineers*, **64**(2), 1809-1828, 1938.

[9] B.H. Rasmussen, The carrying capacity of transversely loaded bolts and dowels embedded in concrete, *Bygninynysstatiske Medddelilser*, **34**(2), 34-55, 1963.

[10] H. Dulácska, Dowel action of reinforcement crossing cracks in concrete. *ACI Journal*, **69**(12), 754-757, 1972.

[11] E.N. Vintzeleou, T.P. Tassios, Behaviour of dowels under cyclic Deformations. *ACI Structural Journal,* **84**(1), 18-30, 1987.

[12] B.B. Broms, Lateral resistance of piles in cohesive soils. *Proceedings of the American Society of Civil Engineers*, **90**(2), 27-63, 1964.

[13] B. Engström, Combined effects of dowel action and friction in bolted connections. Nordic Concrete Research. *The Nordic Concrete Federation*, **9**, 14-33, 1972.

COMPDYN 2015
5th ECCOMAS Thematic Conference on
Computational Methods in Structural Dynamics and Earthquake Engineering
M. Papadrakakis, V. Papadopoulos, V. Plevris (eds.)
Crete Island, Greece, 25–27 May 2015

INELASTIC CYCLIC NUMERICAL ANALYSIS OF STEEL STRUTS USING DISTRIBUTED PLASTICITY APPROACH

Alper Kanyilmaz[1]
[1]Department of Architecture, Built Environment and Construction Engineering
Politecnico di Milano
Via Ponzio 31, 20133 Milano, Italy
alper.kanyilmaz@polimi.it

Keywords: Distributed plasticity, inelastic cyclic modeling, fiber based beam elements

Abstract: *This paper presents a comparison between two different modeling approaches: Refined FE modeling using volumetric elements, and fiber modeling using beam elements with distributed plasticity. The numerical models calibrated with the experimental result from existing literature, reproduce the behavior of cold formed SHS40, and hot rolled DUPE100 steel elements under inelastic cyclic loading. The hysteresis loops obtained from two models show that the accuracy obtained by simpler fiber-element formulation is quite close to the more refined volumetric model. In terms of computation time, distributed plasticity model is much more efficient, and can be a good option to perform nonlinear analysis of multi-level buildings, which would be quite cumbersome with volumetric modeling approach. This study has been realized thanks to the research fund received from European commission with the contract MEAKADO RFSR-CT-2013-00022.*

1. MODELING OF CYCLIC BEHAVIOUR OF BRACING ELEMENTS

Inelastic deformation of bracing elements is the main parameter affecting the seismic performance of braced frames during a seismic event.

The objective of this study is to explore accurate and time efficient modelling ways to simulate inelastic behaviour of steel bracings under cyclic loading by means of validation studies based on experimental data and refined finite element models.

Validation studies shown in this report has been performed in two stages:

i) Numerical model of various steel struts made of cold formed square hollow sections have been developed and calibrated with the inelastic cyclic load tests carried out by [1]. Continuum finite element modelling approach is used (CFEM)

ii) Fiber based distributed plasticity modelling approach has been validated against calibrated continuum finite element model of steel struts (DPE).

In order to obtain experimental data to validate numerical models, Goggins et. al have performed several cyclic tests on cold-formed square and rectangular hollow steel section bracing elements, according to the provisions of the ECCS (1986) [2]. 1 Fifteen specimens have been tested which are fabricated from 20x20x2.5SHS, 40x40x2.5SHS and 50x25x2.5 RHS sections with two different lengths: intermediate (1100mm) and long (3300mm).

We focus on intermediate (Model 1) and long length (Model 2) steel struts of 40x40x2.5 SHS cross- sections as shown in Table 1. A general layout of the test specimens is shown in Figure 1.

Test ID	Section Size	$\bar{\lambda}$	d/t	F_y kN	δ_y mm	F_{max} kN	δ_u mm	μ_Δ
Series1								
CyIS1	40x40x2.5	0.4	13.1	100.4	2.4	112.9	20.7	8.7
CyIS2	40x40x2.5	0.4	13.1	101.5	2.4	112.4	17.8	7.5
CyIS3	20x20x2.0	0.9	6.7	26.0	1.2	45.4	35.3	29.7
CyIS4	20x20x2.0	0.9	6.7	29.8	1.1	46.0	22.6	20.9
CyIS5	50x25x2.5	0.6	17.1	78.1	1.6	111.5	23.0	14.3
CyIS6	50x25x2.5	0.6	17.1	83.1	1.8	111.5	21.8	12.2
Series2								
CyLS1	40x40x2.5	1.3	12.9	123.1	4.3	143.9	–	9.5*
CyLS2	40x40x2.5	1.3	12.9	124.1	4.4	143.8	–	9.2*
CyLS3	40x40x2.5	1.3	12.9	126.5	5.7	142.5	–	7.2*
CyLS4	20x20x2.0	3.2	6.5	63.1	7.0	70.2	16.0	2.3
CyLS5	20x20x2.0	3.0	6.0	64.4	7.9	69.3	15.2	2.0
CyLS6	20x20x2.0	3.0	6.0	63.6	6.0	72.3	16.7	2.8
CyLS7	50x25x2.5	1.9	17.3	99.4	4.6	117.7	–	8.8*
CyLS8	50x25x2.5	2.2	16.9	162.6	7.3	187.7	–	5.6*
CyLS9	50x25x2.5	2.2	16.9	165.4	7.0	190.1	–	5.8*

Cyclic test programme

Cross section:	**40x40x2.5 mm**
E=	**210000 MPa**
Poisson's ratio:	**0.3**
f_y =	**343 MPa**
f_u =	**393 MPa**
ε_u =	**0.15**
Element length (model 1)	**1100 mm**
Element length (model 2)	**3300 mm**

Material properties

Table 1 Test program and material properties (Goggins J.M, 2006).

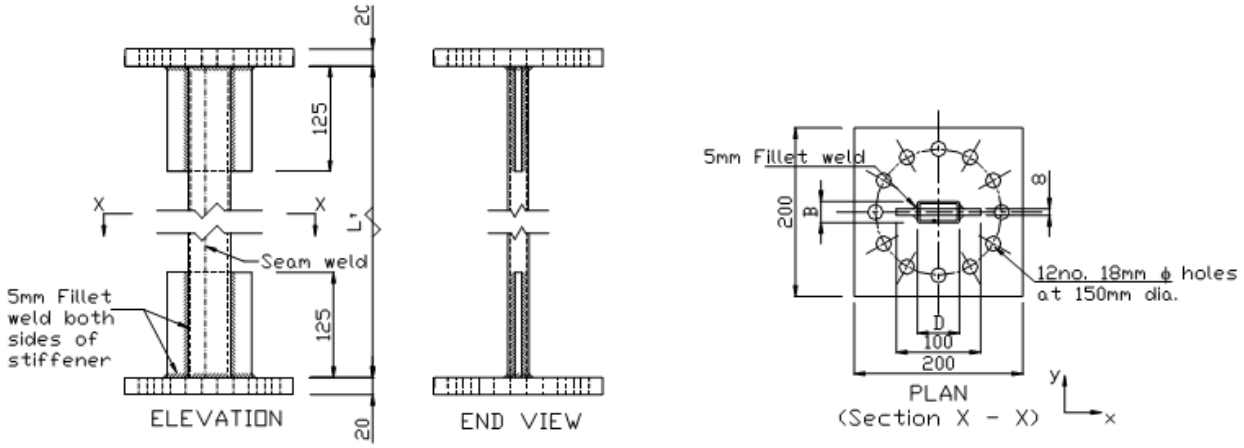


Figure 1 Test specimen (Goggins J.M, 2006)

Numerical model developed with software package (ABAQUS) [3], has the following features:

- 8-node solid elements with 6 DOF,
- elastic-plastic behavior with Von Mises Criteria,
- kinematic hardening,
- great displacement and strain.

Calculation procedure is composed of two steps:

- Buckling modes obtained from linear buckling analysis,
- Then inelastic cyclic analysis has been performed considering an initial imperfection based on first and/or second buckling mode shape.

One end of the steel strut is fully fixed, while the other end is fully fixed except for the axial degree of freedom, to which the cyclic displacement loads are applied (figure 2).

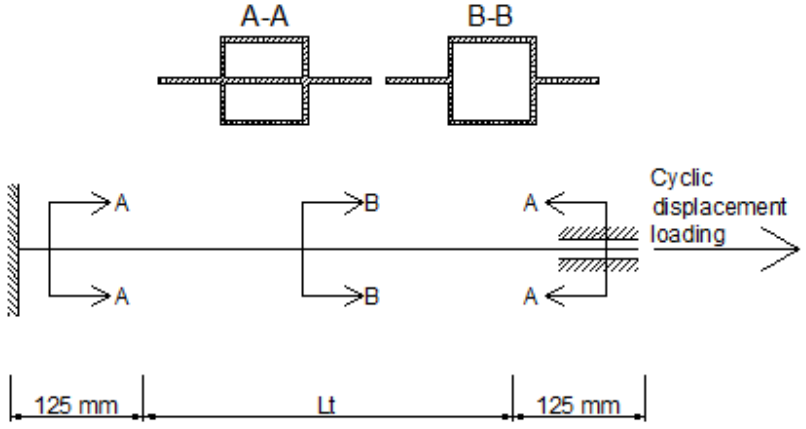


Figure 2 Setup and loading direction of the numerical model

For the element with 1100 mm length (model 1) and 3300 mm length (model 2), cyclic displacements applied with same amplitudes but with different number of cycles (Table 2).

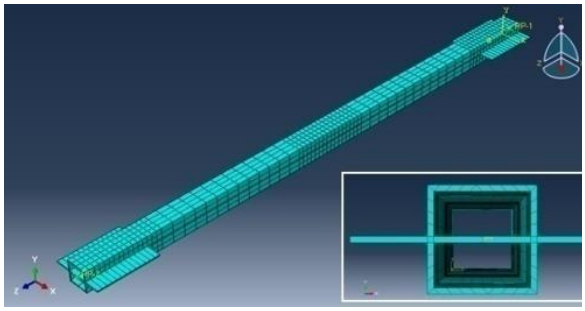
Model 1 (1100 mm)	
one cycle	+/- 0.625 mm
one cycle	+/- 1.25 mm
one cycle	+/- 2.5 mm
Three cycles	+/- 5 mm
Three cycles	+/- 10 mm
Three cycles	+/- 15 mm
Three cycles	+/- 20 mm
Three cycles	+/- 25 mm

Model 2 (3300 mm)	
one cycle	+/- 0.625 mm
one cycle	+/- 1.25 mm
one cycle	+/- 2.5 mm
Three cycles	+/- 5 mm
Three cycles	+/- 10 mm
Three cycles	+/- 15 mm
Three cycles	+/- 20 mm
Three cycles	+/- 25 mm
Three cycles	+/- 30 mm
Three cycles	+/- 40 mm

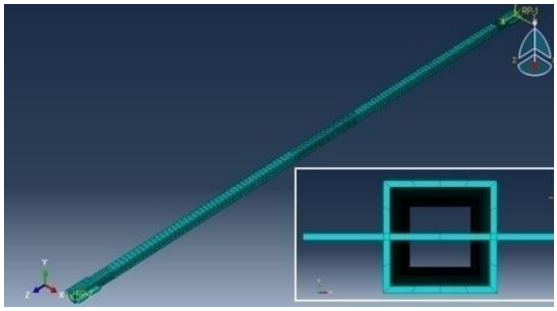
Table 2 Loading procedure (displacements are in mm)

Mesh properties are shown in figure 3. In areas where local buckling is expected, refined meshes were used (at the ends and at the center of the member). The size and the length of refined mesh areas are decided after sensitivity analysis.

Initial imperfections that are present in the structural members trigger out-of-plane deformations under forces lower than their critical buckling values. To be able to trigger this initial buckling in the inelastic cyclic analysis, initial imperfections have been incorporated in the numerical model of bracing elements. For this purpose, a linear buckling analysis has been performed, and inelastic cyclic analysis has started on the base of the deformed shapes obtained from the first and/or second linear buckling modes.



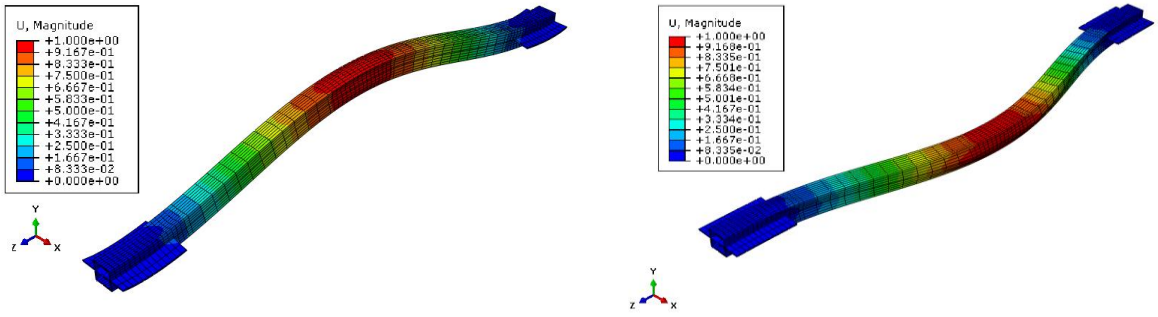
Tube 1100 mm: 2376 linear hexahedral, 444 linear wedge elements (At the mid-height and at end of the tube, for a length of 160 mm, mesh is denser).



Tube 3300 mm: 5340 linear hexahedral elements (At the mid-height and at end of the tube, for a length of 480mm and 225mm, respectively, mesh is denser).

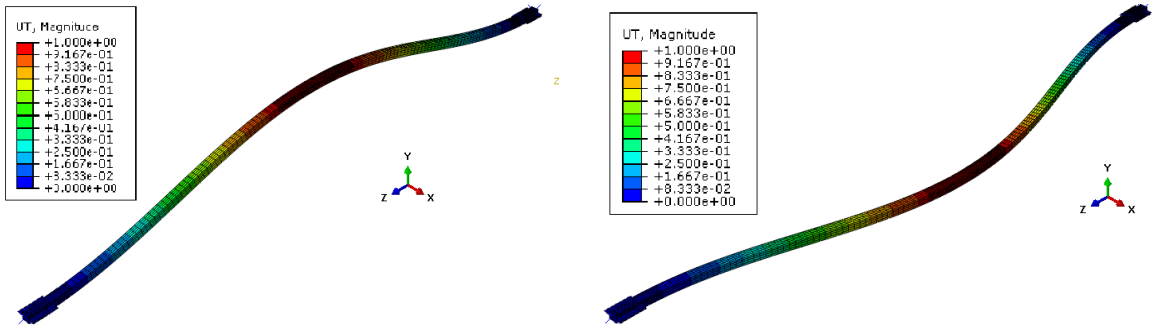
Figure 3 Mesh model 1 and model 2

In Figure 4 and Figure 5, first two linear buckling mode shapes are shown. According to the results of the experimental studies, only first mode deformed shape has been used in model 1, and both first and second mode shapes have been used for the model 2. Initial imperfection value is considered as L/150 according to Eurocode 8, however for the longer element convergence could be obtained by a larger value (L/120).



First global buckling mode shape **Second global buckling mode shape**

Figure 4 First and buckling mode shapes – model 1



First global buckling mode shape **Second global buckling mode shape**

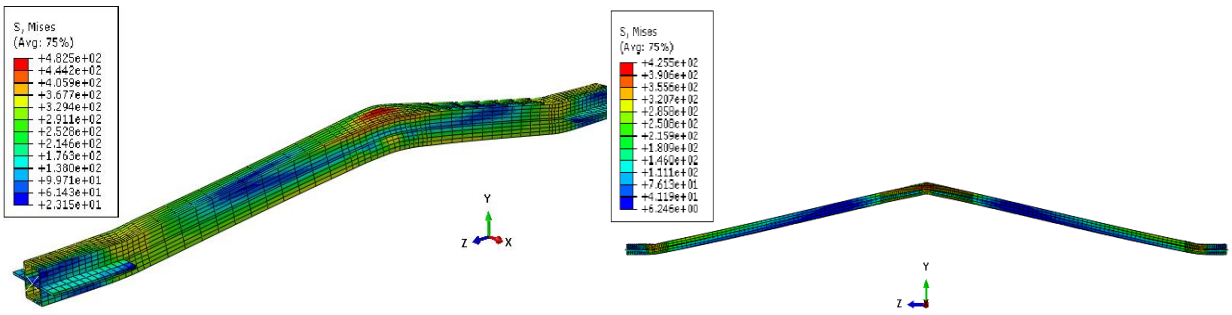
Figure 5 First and second buckling mode shapes – model 2

Critical buckling loads obtained from linear buckling analysis are almost coincident with the Euler buckling loads (Table 3).

		Tube 1100mm	**Tube 3300mm**
Critical Buckling Load	**Numerical model**	**573.75 KN**	**66.03 KN**
	Euler critical load	**563.20 KN**	**62.58 KN**

Table 3 Comparison of critical buckling loads obtained numerically and analytically

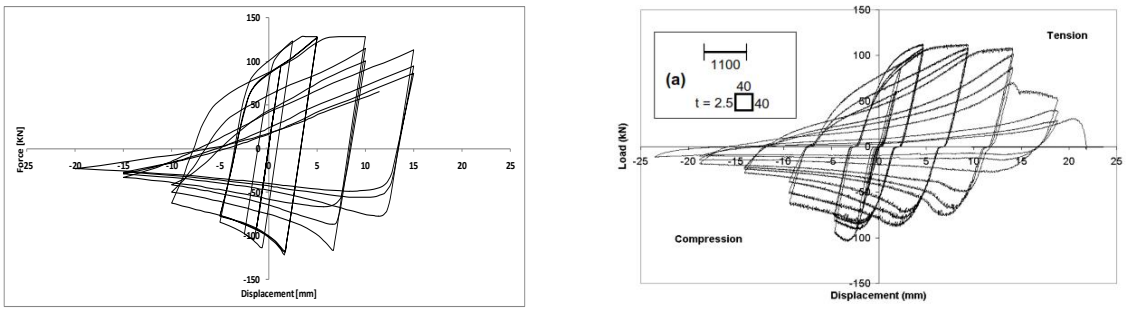
Figure 6 shows the plastic deformations concentrated at the beam ends and at the centre of the braces, as happens during the experimental tests.



Deformed shape of tube1100 at ultimate load **Deformed shape of tube3300 at ultimate load**

Figure 6 Deformed shape of tube elements under ultimate load

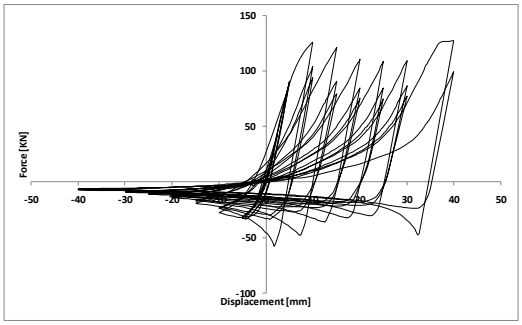
A good agreement between numerical model and experimental results has been obtained, except for the last three cycles of the displacement loading due to impossibility to reproduce local buckling fractures experienced by test specimens (figure 7). In the numerical simulation of both models, after the first buckling in compression takes place, compressive strength decreases because of plastic hinges formed at the center of the brace and next to the end plates. Then the compressive strength continues to degrade due to Baushinger effect.



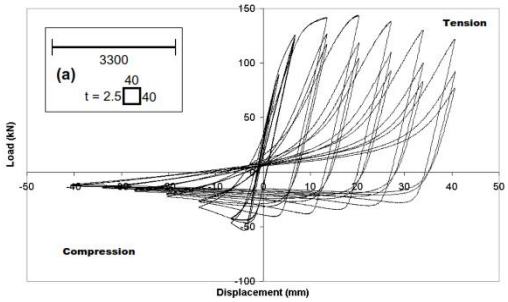
a. Numerical model (Abaqus) b. Experimental result

Figure 7 Load-displacement curve - Model 1

In the case of model 2, the convergence between the experimental and numerical curve is much better, since no local buckling fracture occurred during the test (figure 8). The decrease in the global tensile and compression resistance is well visible in the numerical curve, with the exception of the last cycle. The maximum compression force recorded by the numerical model is 57.49 KN, while the experimental value is 52.30 KN. Maximum tensile force recorded by the numerical model is 127.20 KN, while the experimental value is 143.80 KN. Furthermore, in agreement with the experimental results, the numerical model provides global biaxial instability (figure 9).



a. Numerical model (Abaqus)



b. Experimental result

Figure 8 Load-displacement curve - Model 2

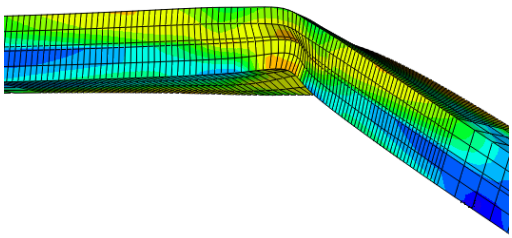


Figure 9 Biaxial instability model 2

In Table 4, comparisons are shown in terms of inelastic buckling and ultimate tensile loads according to numerical model, Eurocode 3, and experimental results. In general, it is seen that numerical simulation of more slender element gives better results.

		Tube 1100mm	Tube 3300mm
Inelastic Buckling Load	**Numerical model**	**121.66 KN**	**57.49 KN**
	Eurocode	**109.85 KN**	**43.51 KN**
	Experiment	**105.50 KN**	**52.30 KN**
Ultimate tensile load	**Numerical model**	**128.46 KN**	**127.20 KN**
	Eurocode	**147.38 KN**	**147.38 KN**
	Experiment	**112.40 KN**	**143.80 KN**

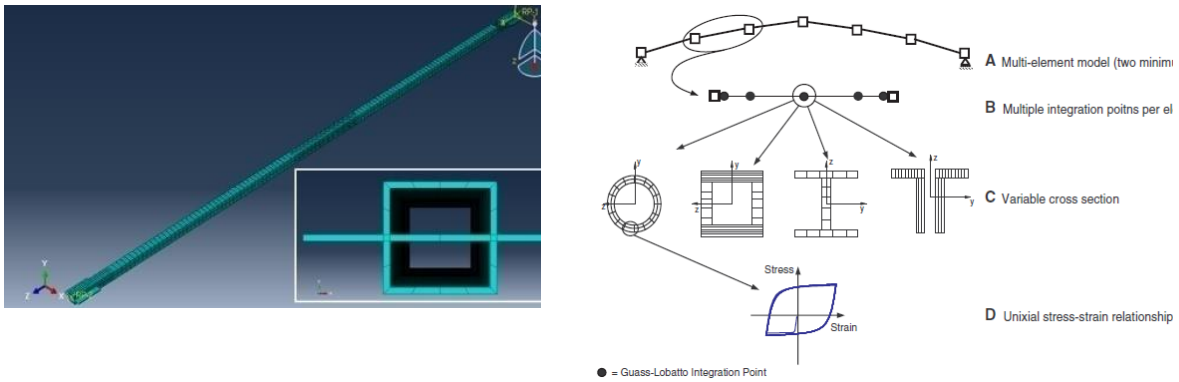
Table 4 Comparison of major loading limits between numerical analysis, experiments and code

2. CALIBRATION OF FIBER BASED DISTRIBUTED PLASTICITY APPROACH FOR MODELLING CBF STRUCTURES

Continuum finite element modeling (CFEM) based on shell or solid elements is currently the most efficient numerical modeling method, which is able to reproduce, with a minimum margin of error, even complex phenomena such as local buckling, distortion and changes in shape of the cross section [4]. However, this is not a common approach to study the global behavior of multistory buildings subject to seismic actions, due to its inherent complexity, computational expense, and difficulty in preparing and calibrating the models. For this reason, the CFEM method is mostly used to study the response of individual profiles or to represent details such as connection parts of global structures.

To study the global nonlinear response of multi-story buildings, most common alternatives are concentrated plasticity and fiber-based modeling approaches. Former one concentrates the inelastic deformations in individual parts of the structural system (as plastic hinges) with the rest of the structure remaining elastic. This method better captures the nonlinear response of members through calibration using test data on moment-rotation or hystereis curves. Fiber based modelling on the other hand, distributes plasticity by numerical integrations through the member cross sections and along the member length, and with a "plane sections remain plane" assumption [5]. Uniaxial material models are used to capture the nonlinear hysteretic axial stress-strain characteristics in the element cross sections. Fibers are numerically integrated over the cross section to monitor the axial force and moments, incremental moment-curvature and axial force-strain relations. The cross section parameters are numerically integrated at several sections along the member length, using displacement or force interpolation functions. This approach allows performing nonlinear analysis considering both geometric and material nonlinearity, within a time much more limited than a 3D continuum finite element analysis. However, using this approach local behaviour such as degradation due to local buckling is difficult to capture without sophisticated models. Fiber-based modeling approach with distributed plasticity (DPE) offers a good compromise in terms of accuracy and computational time to model hysteresis behavior of steel struts. Application example of this approach in moment-resisting frames is presented by Kanyilmaz et. al [6].

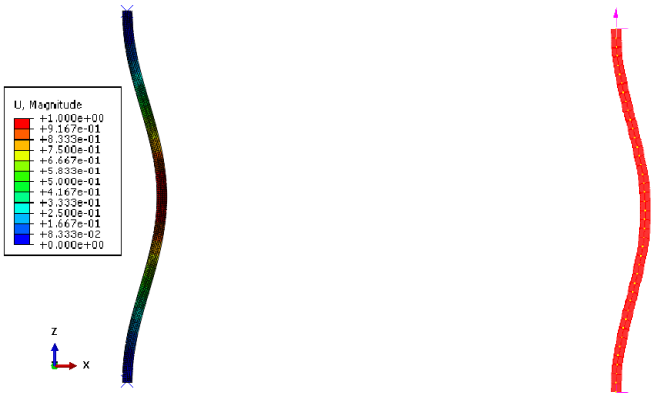
At this section, comparisons are shown between the results obtained from a CFEM model developed using Abaqus, and a fiber-based model developed using (Straus7) [7]. First, hysteresis response of the model 2 of section 1 has been compared, and then the same comparison has been made for an open section (Figure 10).



a. CFEM approach **b. Fiber based distributed plasticity approach [8]**

Figure 10 CFEM vs Fiber based approach

Linear buckling analysis results are very similar as can be seen in Figure 11.



Abaqus 1° buckling mode: 66 kN **Straus7 1° buckling mode: 67 kN**

Figure 11 Comparison in terms of 1st linear buckling mode

From the comparison of two hysteresis curves obtained from an inelastic cyclic analysis, it is evident how DPE model is able to reproduce the nonlinear response of the profile under cyclic loading (Figure 12). Both models show a gradual reduction in the maximum compression resistance at later cycles, which is in line with the actual behavior of the specimens observed during the experiments performed by [1].

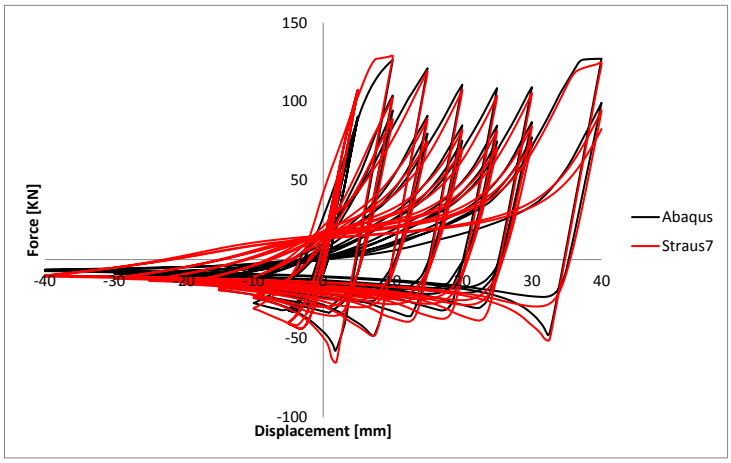


Figure 12 Comparison of hysteretic response of two modelling approaches

Maximum and minimum values achieved by the two curves are also coincident. However, in terms of dissipated energy, represented by the area enclosed by the hysteresis curves, there is a slight difference between the two models. DPE model dissipates slightly more, since DPE modeling cannot capture local instabilities that can be captured by a refined FE model with shell elements. Yet, considered the time required for the analysis and the satisfactory accuracy of DPE model, it can be concluded that the modeling with distributed plasticity (DPE) represents a good compromise between the validity of the results and analysis time.

Another comparison has been made with an open section. A DUPE100 section with 4310mm length has been analyzed. Boundary conditions are fixed on both ends for all degrees of freedom, except the axial translational degree of freedom in one end to impose the axial displacement.

Material properties are shown in Table 5. Linear buckling analysis give similar results (figure 13).

Cross section	DUPE100
E: Young's modulus	210000 MPa
υ: Poisson coefficient	0,30
f_y: yield strength	343 MPa
f_u: ultimate strength	393 MPa
ε_u: ultimate strain	0.15

Table 5 Material properties



Abaqus 1° buckling mode: 720 kN **Straus7 1° buckling mode: 740 kN**

Figure 13 Comparison of two approaches in terms of critical buckling load

Also in this case, results of DPE model and CFEM model are very similar. The observations made in the calibrated tube model are valid also for this case (Figure 14).

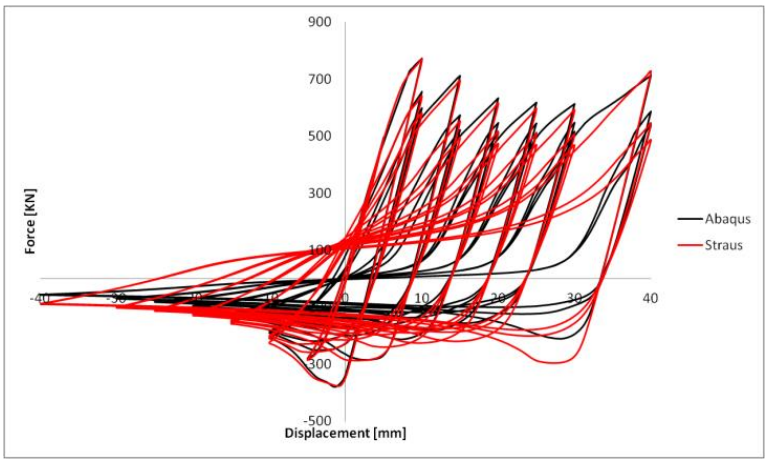


Figure 14 Comparison of hysteretic response of two modelling approaches

Local instabilities that cannot be captured by fiber-based approach are seen in Figure 15.

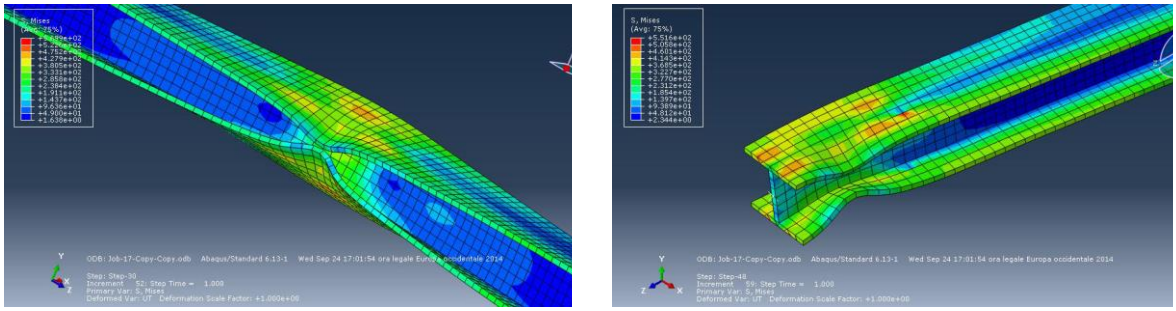


Figure 15 Local deformations at the centre and end of the strut that cannot be simulated by fiber-based approach

3. CONCLUSIONS

Seismic response of a concentrically braced frame mainly depends on the behaviour of its bracing elements. An accurate numerical simulation of inelastic behaviour of a braced frame is a complex matter, for which specific tools and methods are needed.

The focus of this study was to come up with an accurate and time efficient way modelling approach for the simulation of steel bracings under inelastic cyclic and seismic loading, which can be used in the modelling of multi-storey structures. Therefore, a comparative numerical study has been presented to validate the suitability of fiber based distributed plasticity modelling approach, to simulate inelastic cyclic response of bracing elements of concentrically braced frame (CBF) buildings. The simulations are based on previous experimental data and refined finite element models.

For the validation purposes, first nonlinear cyclic behaviour of various steel struts made of cold formed square hollow sections have been analyzed and calibrated with the inelastic cyclic load tests carried out by Goggins et. al. [1]. Then fiber based distributed plasticity modelling approach has been validated against calibrated continuum finite element model of steel struts.

The comparison of the hysteresis curves of several elements, evaluated for different boundary conditions shows that results obtained by fiber based approach are almost coincident with those obtained by continuum based modelling. The drawback is that fiber based modelling approach is not capable of obtaining local effects, however for a global analysis of a multi-storey building, the accuracy obtained without considering these local effects can be acceptable. The results of these analyses are used as benchmark for the simulation of braced frames within the research program MEAKADO [9,10].

4. ACKNOWLEDGMENT

This study has been realized thanks to the research fund received from European commission with the contract MEAKADO RFSR-CT-2013-00022.

The contribution of MSc thesis student Alex Belingheri, in performing the numerical analysis shown in this paper is deeply acknowledged.

5. REFERENCES

[1] J.M Goggins, B.M Broderick, A.Y Elghazouli. and A.S Lucas, Behaviour of Tubular Steel Members under Cyclic Axial Loading. *Journal of Constructional Steel Research,* **62**, 121-131, 2006

[2] ECCS (1986), Technical Committee 1. Structural Safety and Loadings -Technical Working Group 1.3. Seismic design recommended testing procedure for assessing the behaviour of structural steel elements under cyclic loads, 1st ed. Brussels

[3] ABAQUS. Analysis User's Manual. Version 6.12 ABAQUS, Inc., Dassault.

[4] S. Salawdeh, Seismic Design of Concentrically Braced Steel Frames. *PhD thesis, National University of Ireland, Galway (NUI Galway),* 2012

[5] R. Sabelli, Research on Improving the design and analysis of earthquake resistant steel braced frames, *The 2000 NEHRP Professional Fellowship Report*, 2001

[6] A. Kanyilmaz, C.A. Castiglioni, Performance of Multi-level moment resisting composite frames with dissipative devices, *COMPDYN 2015, 5th ECCOMAS Thematic Conference on Computational Methods in Structural Dynamics and Earthquake Engineering, Crete Island, Greece, 2015*

[7] *G+D Computing Pty Limited*, Straus7. Theoretical Manual. Sydney (Australia), 2004.

[8] P. Uriz, S.A Mahin, Toward Earthquake-Resistant Design of Concentrically Braced Steel Frame Structures. *PEER Report 2008/08.* Pacific Earthquake Engineering Research Center, University of Berkeley, 2008

[9] H. Degee, C.A. Castiglioni, P.O. Martin, I. Calderon, B. Hoffmeister, Eight International Conference on Advances in Steel Structures, Lisbon, Portugal, 2015

[10] A. Kanyilmaz, C.A. Castiglioni, H. Degèe, P.O. Martin, A Preliminary assessment of slenderness and overstrength homogeneity criteria used in the design of concentrically braced steel frames in moderate seismicity, *COMPDYN 2015, 5th ECCOMAS Thematic Conference on Computational Methods in Structural Dynamics and Earthquake Engineering, Crete Island, Greece, 2015*

COMPDYN 2015
5th ECCOMAS Thematic Conference on
Computational Methods in Structural Dynamics and Earthquake Engineering
M. Papadrakakis, V. Papadopoulos, V. Plevris (eds.)
Crete Island, Greece, 25–27 May 2015

SIMPLIFIED SEISMIC COLLAPSE ASSESSMENT OF GENERIC FRAME STRUCTURES SUBJECTED TO PDELTA AND MATERIAL DETERIORATION

David Kampenhuber[1] **and Christoph Adam**[2]

[1] Unit of Applied Mechanics, University of Innsbruck, Innsbruck, Austria
e-mail: david.kampenhuber@uibk.ac.at

[2] Unit of Applied Mechanics, University of Innsbruck, Innsbruck, Austria
e-mail: christoph.adam@uibk.ac.at

Keywords: Generic frame structures, material deterioration, PDelta effect, seismic excitation, simplified collapse assessment

Abstract. *In this paper the influence of material deterioration on the seismic collapse capacity of PDelta vulnerable frame structures is quantified. The main objective is to reveal and to validate the range of applicability of the proposed equivalent single-degree-of-freedom (ESDOF) system for assessment of the global collapse capacity. This is achieved through comparison of the median collapse capacity of PDelta vulnerable generic frame structures that exhibit material deterioration in strength and stiffness with outcomes of the corresponding ESDOF system based on the derived transformation rules. Sets of planar generic frame structures are compiled varying the governing structural parameters for seismic collapse independently. In all cases, the collapse capacity is calculated using incremental dynamic analysis. Record-to-record variability of the collapse capacity is studied using a set of ordinary earthquake records compiled in FEMA-P695.*

1 INTRODUCTION

For professionals in engineering practice it is desirable to have simplified methods for the seismic assessment of structures available. An example is the response spectrum method, where the effect of inelastic structural behavior and overstrength is considered via a reduction of the pseudo-acceleration demand leaving the seismic analysis completely elastic. In a more recent development the collapse capacity spectrum method [4] aims at assessing the seismic collapse capacity of highly inelastic PDelta vulnerable frame structures without conducting nonlinear time history analysis. The main assumptions of the latter method are that the impact of material deterioration on seismic sidesway collapse of moment resisting frame structures is negligible compared to the destabilizing effect of gravity loads, and that collapse is governed by the fundamental mode. The application of all of these methods requires the engineer to examining carefully the underlying assumptions and restrictions for the considered structure to be assessed. Based on the modified Ibarra-Medina-Krawinkler deterioration model [14], Kampenhuber, Adam [17] quantified the effect of material deterioration on the collapse capacity of PDelta vulnerable single-degree-of-freedom (SDOF) systems considering different material deterioration modes. As a result, for SDOF systems exhibiting nonlinear cyclic behavior sets of parameter combinations have been identified, where PDelta, material deterioration, or a combination of both effects simultaneously governs seismic collapse. To include this knowledge into the framework of the collapse capacity spectrum methodology, Kampenhuber, Adam [16] proposed a procedure how the deterioration parameters of the modified Ibarra-Medina-Krawinkler model [14] assigned to the nonlinear components of a frame structure can be transformed into the domain of the corresponding equivalent SDOF (ESDOF) system. Based on regression analyses, the present contribution describes an enhanced version of the transformation rules for these material parameters. A validation is provided for a set of generic planar multi-degree-of-freedom (MDOF) frame structures subjected to the 44 ordinary earthquake records of FEMA-P695 report [11]. Incremental dynamic analysis (IDA) up to collapse is conducted both for each frame structure and the corresponding ESDOF model, and the resulting median collapse capacities are set in contrast. The results presented here aim at assessing the accuracy and the range of applicability of the proposed simplified collapse prediction procedure. Note that in this contribution the expression "deterioration" only refers to the successive reduction of material/component quantities such as strength and unloading stiffness as a result of cyclic deformation. The degrading effect of PDelta on the structure is not addressed with this expression. Moreover, superscript $(\cdot^{wG})$ refers to quantities considering gravity loads (read: "with gravity"), whereas superscript $(\cdot^{woG})$ represents parameters disregarding gravity loads (read: "without gravity").

2 GENERIC FRAME STRUCTURES AND STRUCTURAL MODELING STRATEGY

The investigated multi-story frame structures are based on the ones presented in Medina, Krawinkler [22], which have already been used in other studies such as in Ibarra, Medina, Krawinkler [14], Lignos, Krawinkler [19], Jäger [15], and Adam, Jäger [4]. These n story generic moment-resisting single-bay frame structures of uniform story height h, designed according to the weak beam-strong column design philosophy, are composed of rigid beams, elastic flexible columns, and inelastic rotational springs at the beam ends and the base according to a concentrated plasticity formulation. To each joint of the frames an identical point mass $m_i/2 = m_s/2$, $i = 1, \ldots, n$, and an identical gravity load is assigned. Figure 1 shows exemplarily a four-story frame.

The targeted straight-line fundamental mode shape is the governing condition for adjusting

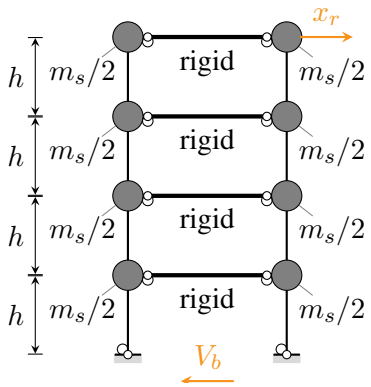


Figure 1: Mechanical model of e. g. a four-story MDOF system.

the bending stiffness of the columns and the initial stiffness of the springs. Coefficient τ relates the fundamental period without gravity loads, T_1^{woG}, and the number of stories of the frame structures, n,

$$T_1^{woG} = \tau n \tag{1}$$

and thus, quantifies the global lateral stiffness of the structure. According to Ibarra, Medina, Krawinkler [14], periods $T_1^{woG} = 0.10n$ and $T_1^{woG} = 0.20n$ are a reasonable lower and upper bound for moment-resisting frames, representing stiff and flexible structures, respectively.

The strength of the rotational springs is tuned with the result that in a first mode pushover analysis without taking into account gravity loads yielding is initiated at all springs simultaneously. A predefined base shear coefficient γ of 0.10, i. e. the base shear without gravity loads at the onset of yielding $V_{b,y}^{woG}$ over the total structural weight $W = Mg$, $M = \sum_{i=1}^{n} m_s$, governs the magnitude of the yield strength [22]. To the rotational springs a bilinear backbone curve is assigned. That is, a linear elastic branch of deformation is followed by a linear inelastic branch with reduced stiffness, characterized by the strain hardening coefficient α_s, which is the same for all springs of the considered MDOF models: $\alpha_s = 0.03$.

The hysteretic response of the springs is assumed to be bilinear. Deterioration of the bilinear hysteretic cyclic behavior is simulated with the modified Ibarra-Medina-Krawinkler deterioration model [13]. This bilinear constitutive model exhibits unloading stiffness deterioration and cyclic strength deterioration, controlled by deterioration parameters Λ_K and Λ_S, respectively. The further deterioration modes *accelerated reloading stiffness deterioration* and *post-capping strength deterioration*, which may be captured by the modified Ibarra-Medina-Krawinkler deterioration model, do not apply in this case. For details it is referred to [14, 13, 19]. For the sake of simplicity, unloading stiffness deterioration and cyclic strength deterioration parameters Λ_K and Λ_S, respectively, are assumed to be equal, $\Lambda_S = \Lambda_K$. To all springs of a frame the same deterioration parameters Λ_K and Λ_S are assigned. Lignos, Krawinkler [19, 18] compiled a database of experimental cyclic studies on steel components, which allowed to identify the significant parameters affecting the cyclic moment-rotation relationship at plastic hinge regions in beams. Based on this study, in the present publication three different levels of deterioration, representing slow, medium, and rapid deterioration, have been defined.

The PDelta effect on the frame structures is quantified by two base shear-roof drift (V_b–x_r) relations (referred to as global pushover curves) resulting from two different first mode pushover analyses [4]. In one pushover analysis the constant gravity loads are applied to the model, whereas the second pushover analysis is conducted without gravity loads. For the present

generic frame structures both global pushover curves are bilinear, because at all springs yielding is initiated simultaneously. As depicted in Figure 2, the PDelta effect leads for a given roof displacement to a reduction of the base shear, and thus, to an apparent reduction of the lateral stiffness.

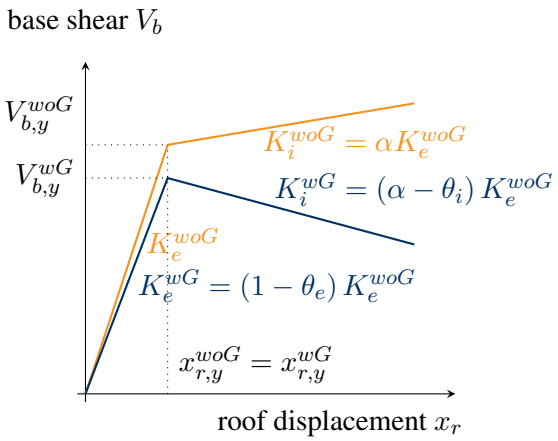


Figure 2: Global pushover curves of MDOF system considering and disregarding gravity loads

It has already been shown by Medina, Krawinkler [22] that for multi-story frame structures this stiffness reduction is different in the elastic and inelastic deformation branch of the global pushover curve. Consequently, additionally to the lateral global hardening coefficient α, an elastic and an inelastic stability coefficient, θ_e and θ_i, respectively, which characterize the magnitude of the stiffness reduction in these branches, can be identified from the pushover curves,

$$\theta_e = 1 - \frac{K_e^{wG}}{K_e^{woG}} \quad , \quad \theta_i = \alpha - \frac{K_i^{wG}}{K_e^{woG}} \tag{2}$$

Note that in general the lateral global hardening coefficient α is not the same as the strain hardening coefficient α_s assigned to each rotational spring.

In the present study the difference $\theta_i - \alpha$, i. e. the normalized slope of the inelastic deformation branch (also referred to as negative post-yield stiffness ratio), is the target variable that characterizes the PDelta effect on the frame structure (compare with Figure 2) [6]. Thus, for each structure with different properties but the same $\theta_i - \alpha$ value, the ratio ν of total gravity load over dead weight is in general different. This is a contrast to previous studies of the authors [17, 15, 6], where the PDelta effect was characterized by a constant gravity load coefficient ν.

Rayleigh type damping enforcing $5\,\%$ viscous damping of the first mode and of the mode, where $95\,\%$ of the total mass is included, is considered. The corresponding damping matrix is proportional to the mass matrix and the current stiffness matrix.

All predefined basic model parameters of the considered generic frame structures are summarized in Table 1.

3 EQUIVALENT SINGLE-DEGREE-OF-FREEDOM SYSTEM

If the response is dominated by the first mode of vibration, it is reasonable to assume that an ESDOF system captures the global seismic response. This is in general the case for low- to medium-rise regular planar frame structures up to nine stories. However, Adam, Jäger [4] have shown that an ESDOF system even can be used to estimate the seismic collapse capacity of high-rise frame structures if collapse is primarily governed by PDelta.

Table 1: Summary of basic model parameters of the considered frame structures

Variable	Description	Range of values
n	Number of stories	1 to 20
τ	Global stiffness quantification factor	$0.10, 0.12, 0.14, 0.16, 0.18, 0.20$
$\Lambda_K = \Lambda_S$	Deterioration parameter representing slow, medium and rapid deterioration, respectively	$2.0, 1.0, 0.5$
α_s	Strain hardening coefficient of rotational springs	0.03
$\theta_i - \alpha$	Negative post-yield stiffness ratio	$0.03, 0.04, 0.05, 0.06, 0.10, 0.20, 0.30, 0.40$
γ	Base shear coefficient at yield	0.10

The basic assumption of most ESDOF models is that the vertical distribution of the horizontal deformations of the MDOF structures does not change during the cyclic excitation. That is, the deflected shape remains constant throughout the time history regardless of the amount of inelastic deformations. This assumption can be expressed as

$$\mathbf{x} = \boldsymbol{\psi} x_r \tag{3}$$

where $\mathbf{x}$ is the displacement vector of the story masses, x_r denotes the roof displacement, and $\boldsymbol{\psi}$ is a time independent shape vector, which describes the horizontal displacement pattern according to a fundamental mode approximation. Consequently, if the real behavior of the MDOF differs significantly from this assumption, an ESDOF system will be in general less appropriate for predicting the seismic collapse capacity.

In this section it is described how the parameters of a generic frame structure can be transformed into the domain of the corresponding ESDOF system, based on a shape vector that is identical with the first mode: $\boldsymbol{\psi} = \boldsymbol{\phi}_1$. With increasing complexity of the MDOF model this transformation becomes more and more tricky. In particular, when strength and stiffness of the components deteriorate, additional considerations are required that are not treated in the literature yet.

Subsequently, parameters with a superscript $(\cdot^*)$ represent quantities of the ESDOF system. The ESDOF model and the underlying MDOF model used in this study is sketched in Figure 3. It is characterized by a rigid, massless rod of length h^* with a lumped mass L^* [2, 8, 9],

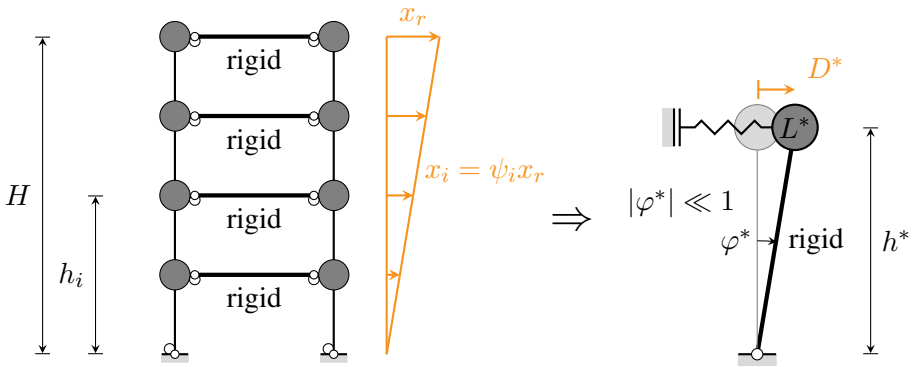


Figure 3: Utilized equivalent single-degree-of-freedom model

$$h^* = \frac{\sum_{i=1}^{n} h_i m_i \phi_{1,i}}{\sum_{i=1}^{n} m_i \phi_{1,i}} = \frac{\sum_{i=1}^{n} h_i \phi_{1,i}}{\sum_{i=1}^{n} \phi_{1,i}} \quad , \quad L^* = \sum_{i=1}^{n} m_i \phi_{1,i} = m_s \sum_{i=1}^{n} \phi_{1,i} \tag{4}$$

at its tip, and a horizontal translational spring attached to the lumped mass with assigned nonlinear material properties. In equation (4) h_i represents the height of the ith story with respect to the base (see Figure 3), and $\phi_{1,i}$ is the ith element of shape vector $\boldsymbol{\phi_1}$. In accordance with Chopra [8], h^* represents the first mode modal height h_1^* and L^* the modal mass of the first mode of vibration of the MDOF model. It is recalled that equation (4) simplifies because the mass matrix of the considered generic frames is diagonal with equal mass coefficients $m_s = m_i$ for each story i.

According to Adam, Krawinkler [5] earthquake induced collapse is sufficiently accurate represented by small displacement theory, and thus, the geometric linearized horizontal tip displacement $D^* = \varphi^* h^*$ serves as engineering demand parameter (EDP). Defining equilibrium on the deformed shape, vertical forces (i. e. gravity loads) affect the horizontal displacement, referred to as PDelta effect. Note that the post-buckling behavior of the considered model is equivalent to an inverted mathematical pendulum with a rotational spring at its base (as used in Adam, Krawinkler [5]) because small displacement theory is employed [10].

The backbone curve of the ESDOF system is based on the base shear-roof drift relations from a first mode pushover analysis, as shown in orange color in Figure 2. Accordingly, yield strength $f_y^{*,woG}$, yield displacement D_y^*, elastic stiffness $K_e^{*,woG}$, and period $T^{*,woG}$ of the ESDOF model without gravity loads reads as [4]

$$f_y^{*,woG} = \frac{V_{b,y}^{woG}}{\Gamma^*} \quad , \quad D_y^* = \frac{x_{r,y}}{\Gamma^*} \quad , \quad K_e^{*,woG} = \frac{f_y^{*,woG}}{D_y^*} \quad , \quad T^{*,woG} = 2\pi \sqrt{\frac{L^*}{K_e^{*,woG}}} \tag{5}$$

$V_{b,y}^{woG}$ represents the base shear, and $x_{r,y}$ the roof displacement at the onset of yielding of the MDOF model subjected to a first mode pushover analysis, and Γ^* is the effective participation factor,

$$\Gamma^* = \frac{L^*}{m^*} \quad , \quad m^* = \sum_{i=1}^{n} m_i \phi_{1,i}^2 = m_s \sum_{i=1}^{n} \phi_{1,i}^2 \tag{6}$$

3.1 Incorporation of the PDelta effect into the ESDOF system

In the present study the PDelta effect is incorporated into the ESDOF system depicted in Figure 3 as proposed by Adam, Ibarra, Krawinkler [2] and Ibarra, Krawinkler [13]. Basis of quantification of PDelta are the global pushover curves from first mode pushover analyses with and without considering gravity loads as shown in Figure 4.

Since in a real SDOF system PDelta is governed by a single stability coefficient [21], the bilinear pushover curves of the MDOF model, however, exhibit an elastic and an inelastic stability coefficient [22], Ibarra, Krawinkler [13] derived an auxiliary ESDOF system with a uniform (auxiliary) stability coefficient $\theta^{*,a}$. $\theta^{*,a}$ is a function of θ_e, θ_i and α^* [13],

$$\theta^{*,a} = \frac{\theta_i - \theta_e \alpha^*}{1 - \theta_e + \theta_i - \alpha^*} \tag{7}$$

Stiffness $K_e^{*,a,woG}$, and the yield strength $f_y^{*,a,woG}$ of this auxiliary ESDOF system is derived from the corresponding parameters of the ESDOF system that is not affected by PDelta [2, 13],

$$K_e^{*,a,woG} = \frac{1 - \theta_e + \theta_i - \alpha^*}{1 - \alpha^*} K_e^{*,woG} \qquad f_y^{*,a,woG} = \frac{1 - \theta_e + \theta_i - \alpha^*}{1 - \alpha^*} f_y^{*,woG} \tag{8}$$

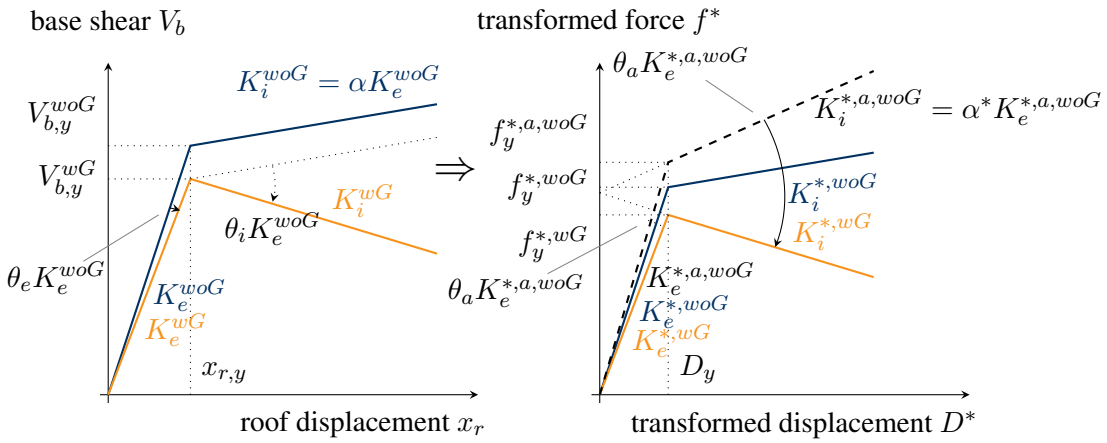


Figure 4: Transformation of global pushover curves of the MDOF model (left subplot) into the domain of the ESDOF system. Right subplot: backbone curve of the auxiliary ESDOF system (black graph), and of the ESDOF system considering gravity loads (orange graph) .

For the period $T^{*,a,woG}$ of the auxiliary ESDOF system the following relation holds:

$$T^{*,a,woG} = T^{*,woG}\sqrt{\frac{1-\alpha^*}{1-\theta_e+\theta_i-\alpha^*}} \tag{9}$$

To simulate the PDelta effect, this auxiliary ESDOF system with stiffness $K_e^{*,a,woG}$ is loaded by the gravity load $P^{*,a}$, which is related to the auxiliary stability coefficient $\theta^{*,a}$ according to MacRae [21]

$$P^{*,a} = \theta^{*,a} K_e^{*,a,woG} h^* \tag{10}$$

The right subplot of Figure 4 shows in black the backbone curve of the auxiliary ESDOF system, and in orange of the ESDOF system considering gravity loads. The blue graph refers to the transformed pushover curve disregarding gravity loads.

3.2 Transformation of the deterioration parameters into the ESDOF domain

Based on cyclic pushover analyses and subsequent optimization analyses [7, 12], Kampenhuber, Adam [16] identified in a previous study a relation between the component deterioration parameters Λ_K and Λ_S assigned to the rotational springs of the considered generic frame structures and the corresponding parameters Λ_K^* and Λ_S^* of the ESDOF system. The resulting median deterioration parameter ratios Λ_K^*/Λ_K and Λ_S^*/Λ_S are depicted in Figure 5 by markers.

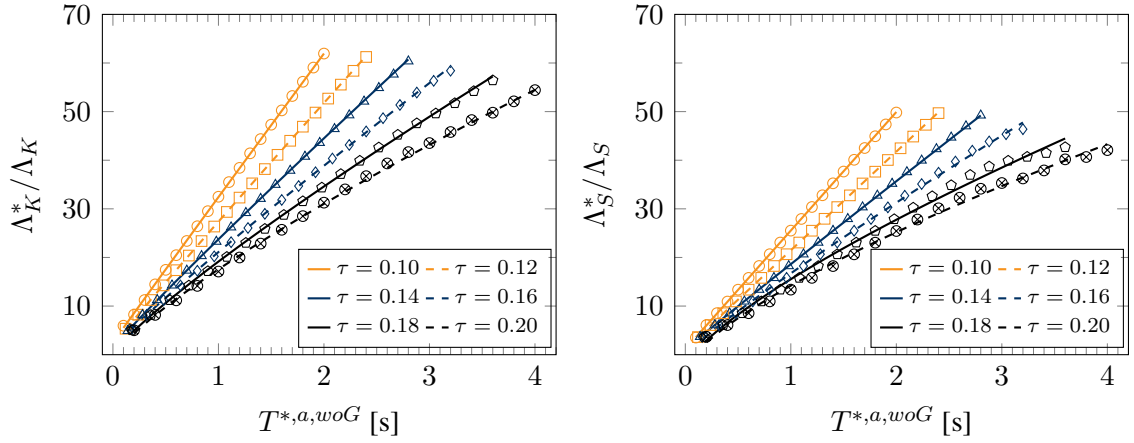
It is readily observed that these ratios become larger with increasing period $T^{*,a,woG}$ and stiffness quantification coefficient τ. The full lines represent the corresponding regression curves, which can be expressed as a function of $T^{*,a,woG}$ as follows:

$$\Lambda_m^*/\Lambda_m = a\left(T^{*,a,woG}\right)^b + c \quad , \quad m = K, S \tag{11}$$

Coefficients a, b, and c listed in Table 2 are different for unloading stiffness (Λ_K^*) and cyclic deterioration (Λ_S^*), and depend on the global stiffness coefficient τ of the MDOF system.

With given stiffness quantification coefficient τ of the MDOF model, $T^{*,a,woG}$, and coefficients a, b, c, the deterioration parameter ratio according to equation (11) can be evaluated.

In an analysis disregarding PDelta, the deterioration parameter should be read at the ESDOF model period $T^{*,woG}$. Subsequent multiplication of this ratio with the deterioration parameter



(a) (b)

Figure 5: Relation between deterioration parameters of the ESDOF and the MDOF model based on the period of the ESDOF model: median and regression curve

Table 2: Coefficients for evaluation of equation (11)

	$\tau = 0.10$			$\tau = 0.12$			$\tau = 0.14$		
	a	b	c	a	b	c	a	b	c
Λ_K^*/Λ_K	29.96	0.99	2.45	25.48	0.97	1.88	22.30	0.95	1.43
Λ_S^*/Λ_S	24.39	1.00	1.14	20.30	1.00	1.17	17.55	0.98	1.07
	$\tau = 0.16$			$\tau = 0.18$			$\tau = 0.20$		
	a	b	c	a	b	c	a	b	c
Λ_K^*/Λ_K	19.90	0.92	1.21	18.96	0.86	0.19	18.18	0.80	-0.62
Λ_S^*/Λ_S	16.79	0.90	-0.06	17.94	0.75	-2.41	16.99	0.72	-2.79

assigned to the rotational springs (Λ_K, Λ_S) in the frame structure renders the corresponding quantity ($\Lambda_K^{*,a}$, $\Lambda_S^{*,a}$) for the auxiliary ESDOF system.

4 COLLAPSE CAPACITY, GROUND MOTION SELECTION, AND GROUND MOTION SCALING

In the present study the global seismic collapse capacity of the MDOF frame structures and the corresponding ESDOF systems is determined performing incremental dynamic analyses (IDA) [25]. In an IDA nonlinear response history analyses are conducted repeatedly, increasing in each subsequent run the ground motion intensity. As an outcome an appropriate measure of the intensity of the earthquake record is plotted against the EDP. The analysis is stopped when the structure collapses. In this study collapse is assumed to be indicated when an incremental increase of the intensity leads to an unbounded structural response. The corresponding intensity of the ground motion record is referred to as global seismic collapse capacity. For details of seismic collapse assessment it is referred to Adam, Ibarra [1]

In this contribution in the MDOF domain the 5 % damped spectral pseudo-acceleration S_a at the fundamental structural period (considering gravity loads) T_1^{wG} normalized with respect to the base shear coefficient γ^{wG} (considering gravity loads) at yield and acceleration of gravity g

is used as characteristic relative intensity of an earthquake record [24],

$$IM = \frac{S_a(T_1^{wG}, \zeta = 5\%)}{g\gamma^{wG}} \quad , \quad \gamma^{wG} = \frac{V_{b,y}^{wG}}{W} \tag{12}$$

As discussed in Tsantaki [24] it is beneficial to utilize in this definition of the relative intensity the structural quantities affected by gravity. The relative collapse capacity is therefore given by

$$CC = IM|_{collapse} \tag{13}$$

Accordingly, the relative collapse capacity in the ESDOF domain reads as

$$CC^{ESDOF} = \left.\frac{S_a(T^{*,a,wG}, \zeta = 5\%)}{g\gamma^{*,a,wG}}\right|_{collapse} \quad , \quad \gamma^{*,a,wG} = \frac{f_y^{*,a,wG}}{L^* g} \tag{14}$$

When transformed into the domain of the MDOF structure,

$$CC^* = \frac{CC^{ESDOF}}{\lambda^{IM}} \tag{15}$$

CC^* is assumed to be a reasonable approximation of the collapse capacity CC. Transformation coefficient

$$\lambda^{IM} = \frac{L^{*2}}{Mm^*} \tag{16}$$

relates collapse capacity of the MDOF and the ESDOF domain [4].

To capture the inherent record-to-record variability of the collapse capacity, in this study the 44 ordinary ground motions compiled in the far-field set of the FEMA P-695 report [11] are used, and subsequently median and dispersion of the 44 corresponding collapse capacities of each structure are evaluated.

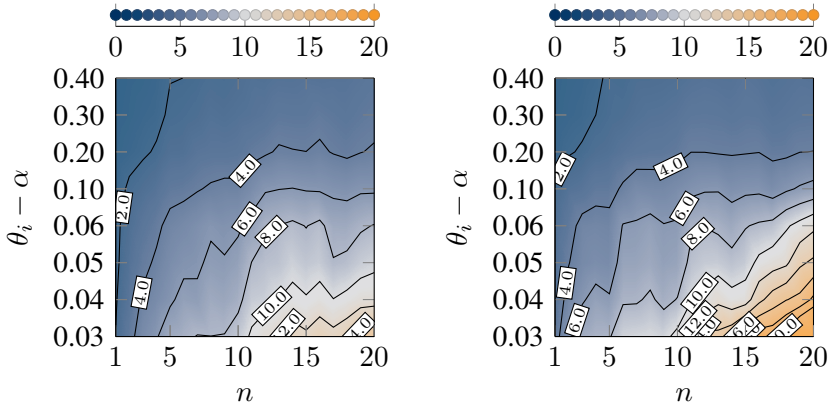
5 EXACT VERSUS SIMPLIFIED COLLAPSE ASSESSMENT

5.1 Non-deteriorating frame structures ("base case")

At first the global seismic collapse capacity of frame structure that exhibit a negative post-yield stiffness ratio but no material deterioration is discussed. These structure are referred to as "base case", because the corresponding collapse capacities are compared with the ones of material deteriorating structures. Some of the presented results can also be found in Jäger [15].

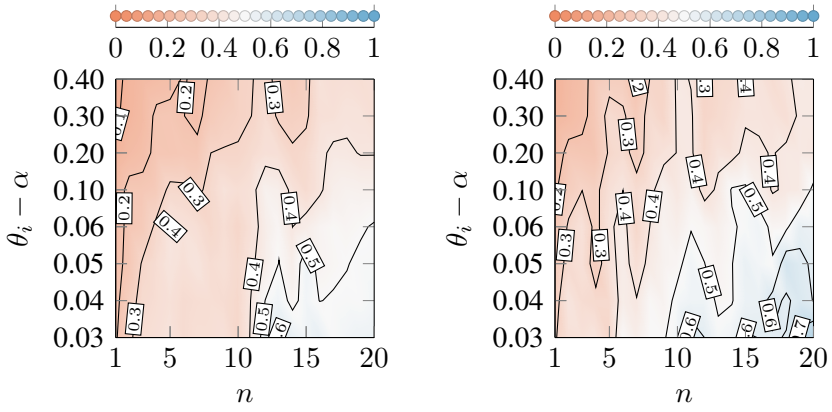
Figure 6 shows contour plots of the median collapse capacity of non-deteriorating frame structures vulnerable to PDelta as a function of the number of stories n and the negative post-yield stiffness ratio $\theta_i - \alpha$.

The left subplot corresponds to stiff frames with a stiffness quantification coefficient $\tau = 0.10$, and the right subplot refers to flexible frames with $\tau = 0.20$. It can be seen that structures with a large negative post-yield stiffness ratio, i. e. $\theta_i - \alpha = 0.20$ to 0.40, the median collapse capacity is almost constant independently of the number of stories and stiffness quantification coefficient τ. In contrast, with decreasing PDelta vulnerability, i. e. $\theta_i - \alpha$ in the range of 0.03 to 0.05, the median collapse capacity varies with the number of stories and the structural stiffness. It is also observed that the magnitude of the median collapse capacity becomes larger with increasing number of stories and flexibility, and thus, with increasing fundamental structural period, compare with equation (1).



(a) $\tau = 0.10$; base case (b) $\tau = 0.20$; base case

Figure 6: Median collapse capacities (CC_{p50}) of non-deteriorating PDelta vulnerable frame structures (base case) for two stiffness quantification coefficients τ.

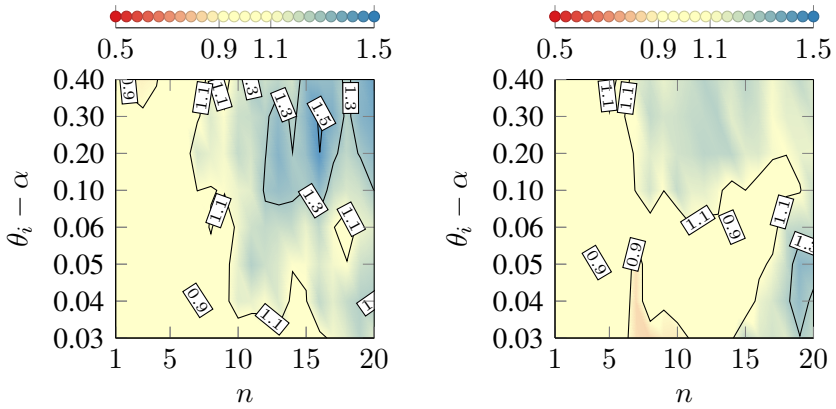


(a) $\tau = 0.10$; base case (b) $\tau = 0.20$; base case

Figure 7: Measure of dispersion (σ) of non-deteriorating PDelta vulnerable frame structures (base case) for two stiffness quantification coefficients τ.

For the same structural configurations, in Figure 7 the corresponding measure for the record-to-record dispersion $\sigma = \ln \sqrt{CC_{p84}/CC_{p16}}$ [20], where CC_{p84} and CC_{p16} denotes the 84th and 16th percentile, respectively, of the collapse capacity, is depicted. σ is a meaningful measure of dispersion because the record-to-record variability of the collapse capacity can be in general approximated by a log-normal distribution [23], confirmed in [4, 3] for PDelta sensitive structures. The outcomes show that σ is proportional to the building flexibility τ and the number of stories n, and it increases as τ and n increases. σ is inversely proportional to the vulnerability to PDelta expressed by $\theta_i - \alpha$, and it decreases as $\theta_i - \alpha$ increases. For instance, for a stiff one-story frame ($\tau = 0.10$, $n = 1$) highly vulnerable to PDelta ($\theta_i - \alpha = 0.40$), σ is 0.08. In contrast, a 20-story frame with the same negative post-yield stiffness ratio $\theta_i - \alpha = 0.40$ and the same stiffness quantification factor $\tau = 0.10$ the dispersion increases to $\sigma = 0.37$. For a very flexible ($\tau = 0.20$) 20-story highly structure highly vulnerable to PDelta ($\theta_i - \alpha = 0.40$), the dispersion becomes even larger, i. e. $\sigma = 0.42$. A slightly PDelta vulnerable flexible one-story building ($\theta_i - \alpha = 0.03$, $\tau = 0.20$, $n = 1$) exhibits the largest collapse capacity dispersion of $\sigma = 0.78$.

Each considered non-deteriorating MDOF structure is now transformed into the ESDOF domain according to the relations presented in section 3 for simplified collapse assessment. In an effort visualize domains, where the simplified predictions of the ESDOF system match the more time-consuming collapse predictions of the actual MDOF frame, in Figure 8 median collapse capacity ratios of the MDOF structure with respect to the ESDOF model, i. e. CC_{p50}/CC^*_{p50}, are plotted. A ratio of 1.0 implies that the "simplified" collapse capacity prediction based on



(a) $\tau = 0.10$; base case (b) $\tau = 0.20$; base case

Figure 8: "Exact" median collapse capacity over the median collapse capacity of the ESDOF system (CC_{p50}/CC^*_{p50}) of non-deteriorating frame structures (base case) for two stiffness quantification coefficients τ.

the ESDOF system coincides with the "exact" counterpart. If the median collapse capacity of the MDOF system is smaller than the median collapse capacity of the corresponding ESDOF model (i. e. $CC_{p50} < CC^*_{p50}$), the ratio is smaller than 1.0. In this figure the domain of $CC_{p50}/CC^*_{p50} < 0.90$ is plotted in red. Blue domains characterize those parameter configurations where the median collapse capacity of the MDOF structure is larger than the one of the ESDOF model: $CC_{p50} > CC^*_{p50}$.

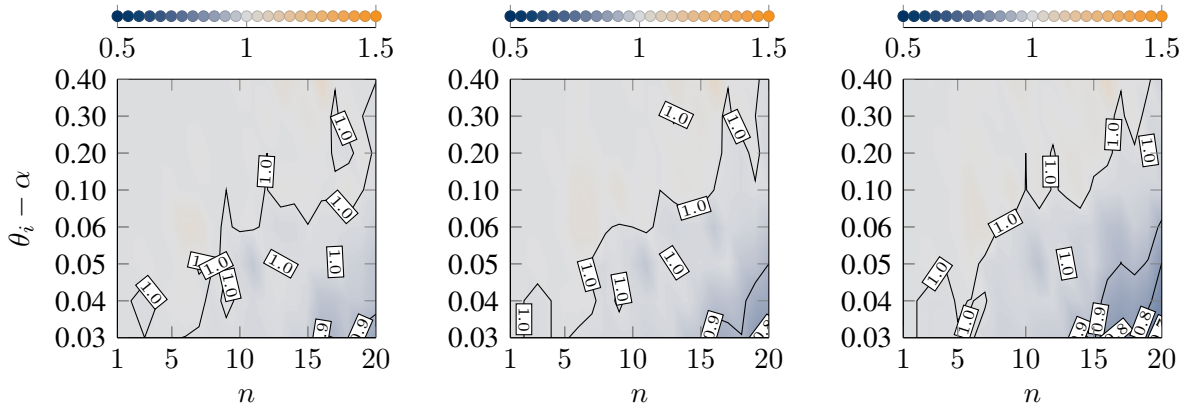
The results of Figure 8a demonstrate that for stiff frame structures ($\tau = 0.10$) up to 10 stories the ESDOF system slightly overestimates the median collapse capacity by $10\,\%$ at most. With increasing number of stories ($n \geq 10$) and increasing negative post-yield stiffness ratio ($\theta_i - \alpha \geq 0.10$) the ESDOF system, however, underestimates this collapse quantity. For instance, for a 20-story stiff structure ($\tau = 0.10$) with $\theta_i - \alpha = 0.40$ the collapse capacity ratio CC_{p50}/CC^*_{p50} is 1.46. More flexible systems as shown in Figure 8b exhibit the same trend, however, in general the deviation between both predictions is smaller. From these results it can be concluded that global collapse of PDelta vulnerable frames up to 10 stories is primarily governed by the first mode, as it is assumed for simplified ESDOF system based collapse assessment.

5.2 Deteriorating frame structures

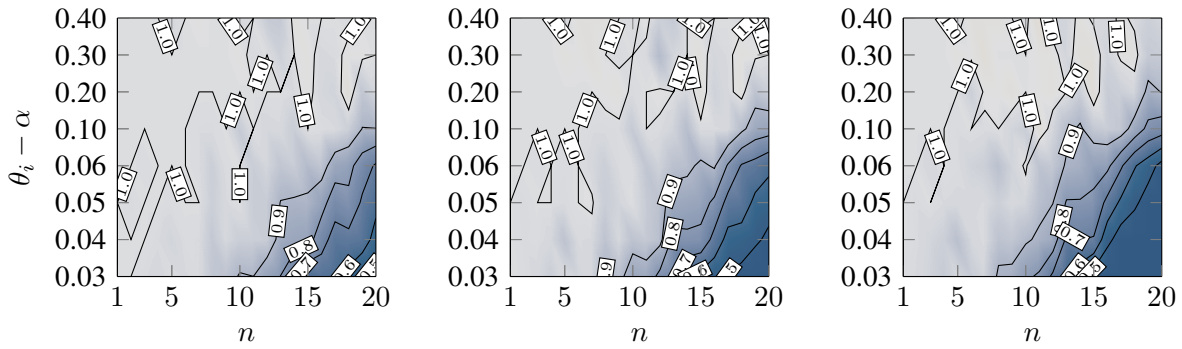
To assess the effect of material deterioration on the median collapse capacity of the considered frame structures, and in further consequence on the predictions based on the corresponding ESDOF systems, three different speeds of component deterioration are taken into account. As shown in Table 1 the deterioration speed effects the choice of the deterioration parameters Λ [13, 19].

In Figure 9 the derived median collapse capacities $CC^{deteriorating}_{p50}$ of these structures are

compared with the outcomes $CC_{p50}^{basecase}$ of the base case frames through representation of the collapse capacity ratios $CC_{p50}^{deteriorating}/CC_{p50}^{basecase}$. In the first row of Figure 9 (Figures 9a



(a) $\tau = 0.10$; slow (b) $\tau = 0.10$; medium (c) $\tau = 0.10$; rapid



(d) $\tau = 0.20$; slow (e) $\tau = 0.20$; medium (f) $\tau = 0.20$; rapid

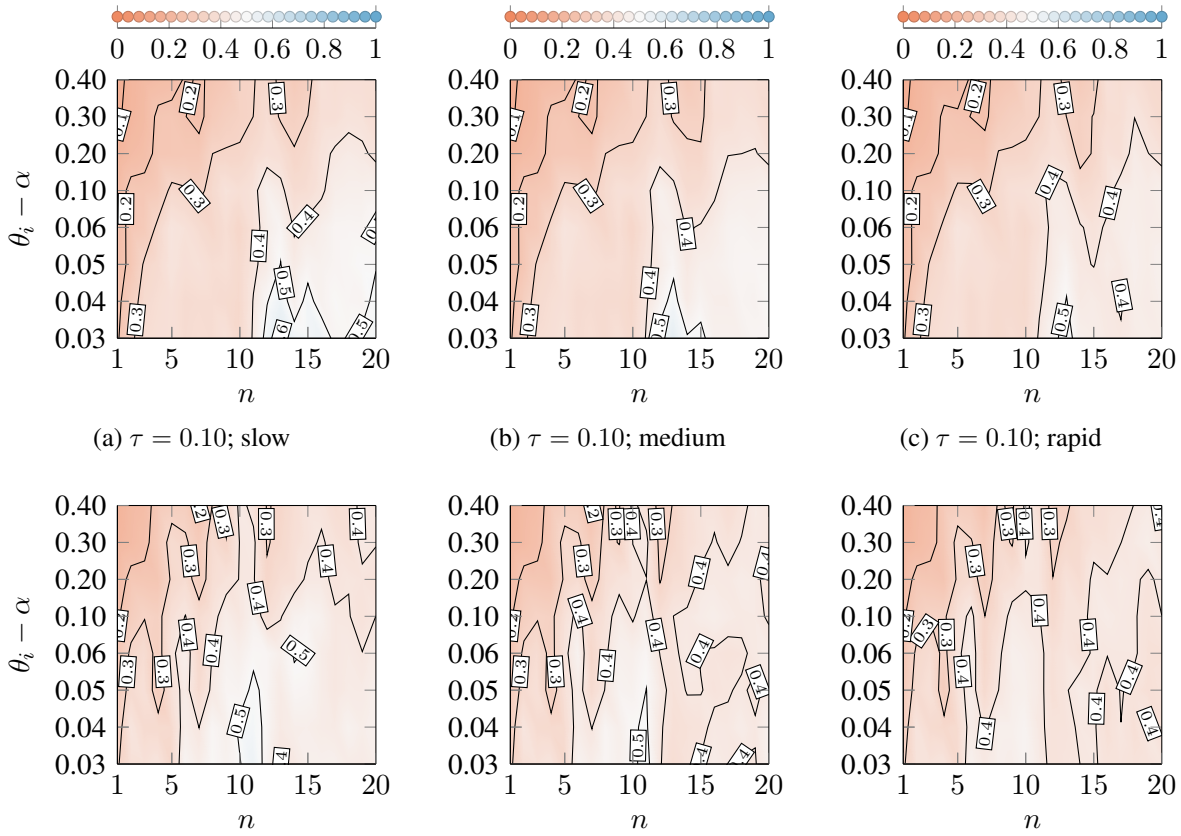
Figure 9: Median collapse capacity of deteriorating over the median collapse capacity of non-deteriorating frame structures ($CC_{p50}^{deteriorating}/CC_{p50}^{basecase}$) for two stiffness quantification coefficients τ and three "speeds" of component deterioration.

to 9c) the effect of three deterioration speeds on the collapse capacity ratios of *stiff* structures ($\tau = 0.10$) is visualized. It is readily observed that for the depicted structural domain the ratio is close to 1.0. That is, in these domains material deterioration does not affect significantly the median collapse capacity. Only for high-rise frames with small negative post-yield stiffness ratio $\theta_i - \alpha$ deterioration becomes more significant, in particular for rapid material deterioration. For instance, for a 20-story frame with $\theta_i - \alpha = 0.03$ the ratio $CC_{p50}^{deteriorating}/CC_{p50}^{basecase}$ is 0.68, which means that that material deterioration reduces the median collapse capacity by 32 %. From these results it can be concluded that collapse of the considered stiff structures is primarily governed by PDelta.

The subplots of the second row of Figure 9 (Figures 9d to 9f) representing flexible frame structures ($\tau = 0.20$) show a different picture. It can be seen that material deterioration plays a more prominent role compared to stiff structures. For those *flexible* frames a significant influence of material deterioration on the median collapse capacity is observed if PDelta is less pronounced (i. e. $\theta_i - \alpha < 0.06$) and the number of stories is larger than 10. Here, the median collapse capacity ratio $CC_{p50}^{deteriorating}/CC_{p50}^{basecase}$ of the 20-story frame with $\theta_i - \alpha = 0.03$ is 0.23, which is about 66 % smaller than for the stiff counterpart structure.

Both stiff and flexible groups of frame structures have in common that the collapse capacity is only negligibly influenced by material deterioration if the structures are highly vulnerable to PDelta, i. e. the negative post-yield stiffness ratio $\theta_i - \alpha$ is larger than 0.20. Consequently, in this parameter domain the collapse capacity ratios shown in Figure 9 are close to 1.0.

In Figure 10 the measure of dispersion σ of the collapse capacity of the same group of material deteriorating PDelta vulnerable frame structures is depicted. The results of this figure



(a) $\tau = 0.10$; slow (b) $\tau = 0.10$; medium (c) $\tau = 0.10$; rapid

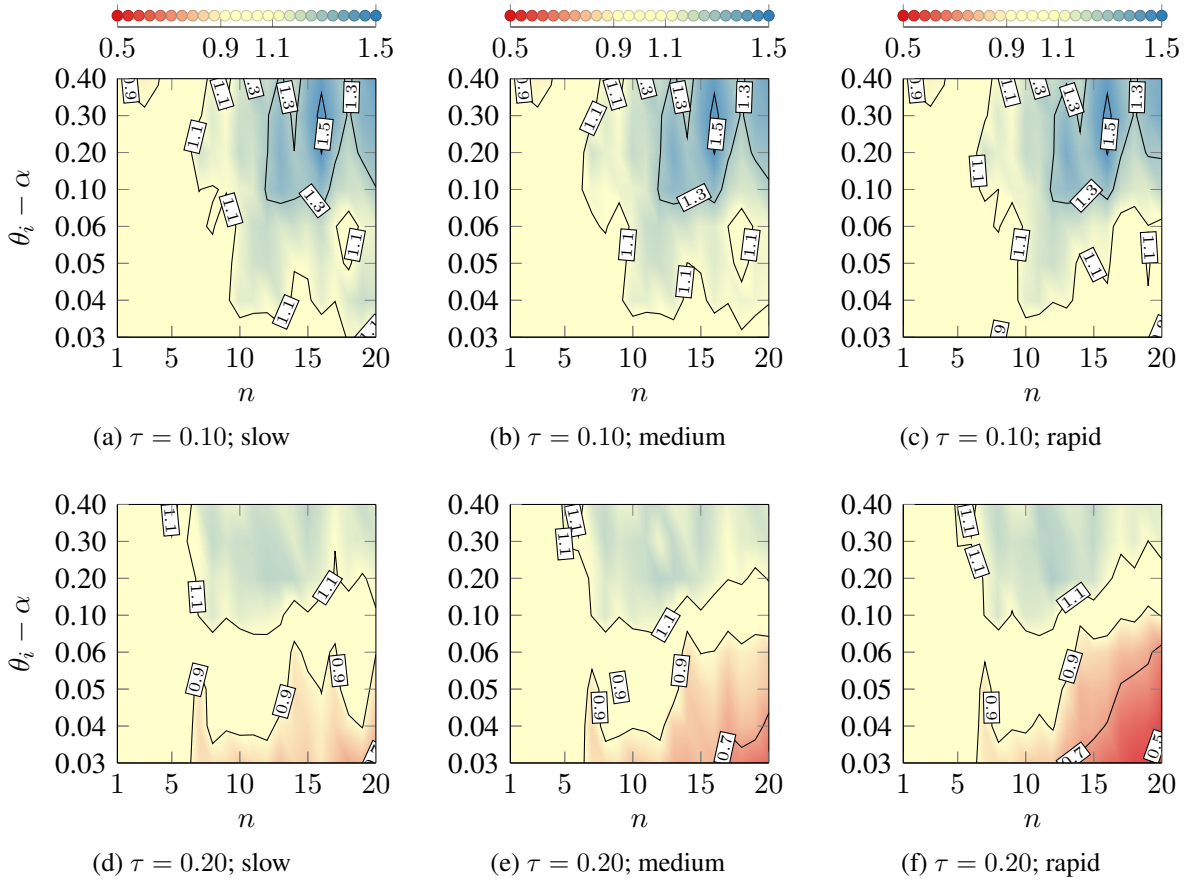
(d) $\tau = 0.20$; slow (e) $\tau = 0.20$; medium (f) $\tau = 0.20$; rapid

Figure 10: Measure of dispersion σ of deteriorating frame structures (corresponding to Figure 9) for two stiffness quantification coefficients τ and three "speeds" of deterioration.

reflect the trend of σ with respect to the number of stories and the negative post-yield stiffness ratios as observed for non-deteriorating structures, see Figure 7. Comparing the subplots of Figure 10 reveals that σ is not significantly affected by the deterioration speed. The difference between the outcomes of stiff and flexible structures is also small. For instance, for 10-story stiff deteriorating frames with $\theta_i - \alpha = 0.10$ dispersion measure σ is 0.36 for slow and medium deterioration and 0.37 for rapid deterioration. Flexible but otherwise frames with the same parameters exhibit a σ of 0.40 for slow, 0.39 for medium, and 0.41 for rapid deterioration. For these cases the corresponding dispersion ratios $\sigma^{deteriorating}/\sigma^{basecase}$ are close to 1.0, i. e. 1.006, 1.009, 1.042, 0.990, 0.967, and 1.018, respectively.

Next, simplified collapse capacity predictions based on the proposed ESDOF system, which captures also material deterioration, are evaluated. For each frame structure deterioration parameters have been calculated based on equation (11) and Table 2. The basic equivalent model parameters are defined as described in section 5.1. Figure 11 shows for the same structural

configurations as described before the ratio "exact" median collapse capacity CC_{p50} to the simplified prediction CC^*_{p50}: CC_{p50}/CC^*_{p50}. The yellow domain indicates ratios in the range of 0.9



(a) $\tau = 0.10$; slow (b) $\tau = 0.10$; medium (c) $\tau = 0.10$; rapid

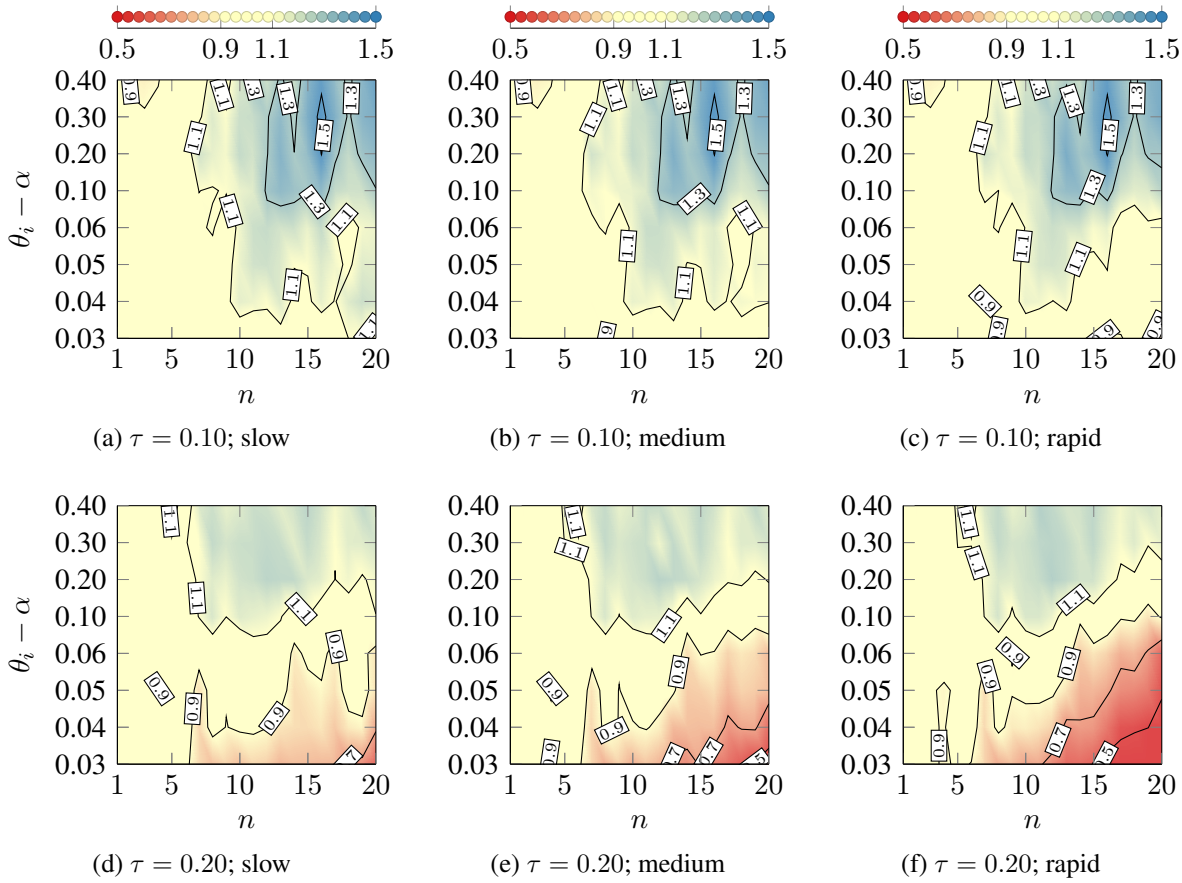
(d) $\tau = 0.20$; slow (e) $\tau = 0.20$; medium (f) $\tau = 0.20$; rapid

Figure 11: Deviation of the median collapse capacity of deteriorating frame structures based on an ESDOF model ($CC^{deteriorating}_{p50}/CC^{*,deteriorating}_{p50}$) for two stiffness quantification factor τ and three "speeds" of deterioration.

to 1.1. It can be seen that for frames up to 6 stories the median collapse capacity of the simplified model approximates the median collapse capacity of the MDOF model ($CC_{p50} \approx CC^*_{p50}$) within the accepted bounds. For a six-story structure the minimum ratio $CC_{p50}/CC^*_{p50}\Big|_{min}$ is 0.88 and the maximum one is 1.17. However, for stiff high-rise frames highly vulnerable to PDelta, the equivalent SDOF model underestimates the collapse capacity of the MDOF model, i. e. $CC_{p50}/CC^*_{p50} = 1.54$, or alternatively, $CC^*_{p50} = 0.65CC_{p50}$. This domain is depicted in blue. The results for stiff frames (Figures 11a to 11c) also reveal that the ESDOF system does not overestimate the median collapse capacity for any parameter combination. This holds, however, not true for flexible frames. Here the collapse capacity ratio becomes smaller than 1.0 if the negative post-yield ratio $\theta_i - \alpha$ is smaller than 0.06 and the number of stories exceeds 6. It is seen that the over-prediction of the collapse capacity increases with increasing deterioration speed. For instance, the extreme case is the 20-story frame with rapid deterioration and a negative post-yield stiffness ratio $\theta_i - \alpha = 0.03$, where the collapse capacity ratio CC_{p50}/CC^*_{p50} drops to a value of 0.47. That is an overestimation of the MDOF collapse capacity by a factor of about two.

5.3 Assessment of the proposed ESDOF model

The improvement of the simplified collapse assessment based on the novel deteriorating ESDOF model system compared to a non-deteriorating counterpart [4] is studied subsequently. Therefore, in Figure 12 the ratio of the exact median collapse capacity CC_{p50} of PDelta vulnerable "deteriorating" frame structures to the median collapse capacity of the corresponding "non-deteriorating" ESDOF model ($CC_{p50}^{*,basecase}$) is depicted. It is readily observed that the difference



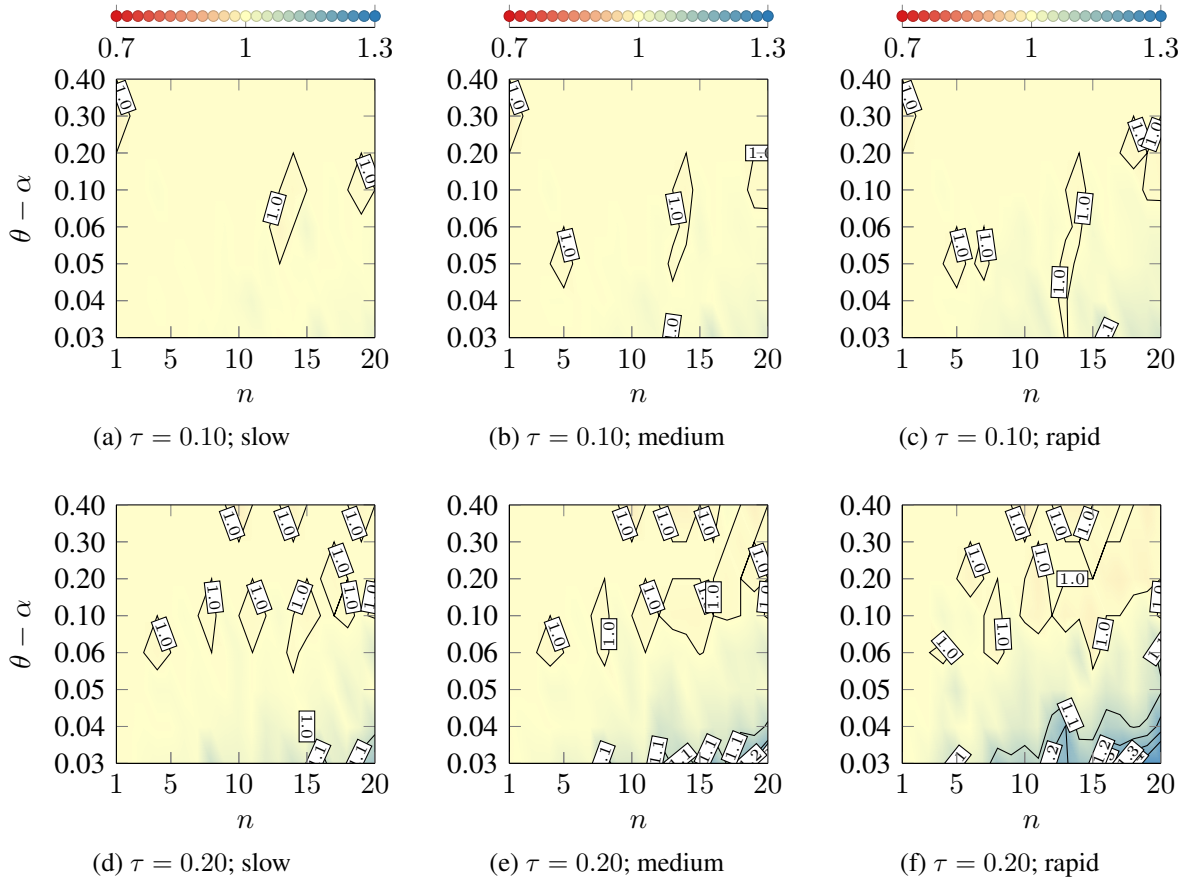
(a) $\tau = 0.10$; slow (b) $\tau = 0.10$; medium (c) $\tau = 0.10$; rapid

(d) $\tau = 0.20$; slow (e) $\tau = 0.20$; medium (f) $\tau = 0.20$; rapid

Figure 12: Efficiency of proposed ESDOF model for two stiffness quantification factor τ and three "speeds" of deterioration: median collapse capacity of deteriorating MDOF structure in relation to the outcome of non-deteriorating ESDOF system ($CC_{p50}^{deteriorating}/CC_{p50}^{*,basecase}$).

of Figure 12 and Figure 11 (non-deteriorating case) is comparatively small. In particular, when comparing the outcomes of the simplified assessment for stiff frame structures the results are of the same order. For instance, for a stiff 15-story building ($\tau = 0.10$) with $\theta_i - \alpha = 0.10$ the collapse capacity ratio is 1.31 for slow, 1.32 for medium, and 1.31 for rapid material deterioration. When using a non-deteriorating ESDOF system for the collapse assessment of a deteriorating frame structure, the accuracy of the collapse prediction decreases for high buildings that are less vulnerable to PDelta, in particular when they are flexible (Figures 12d to 12f). There the ratio $CC_{p50}/CC_{p50}^{*,basecase}$ is significantly smaller than 1.0 (highlighted in red color). In the extreme case of a 20-story rapid deteriorating frame structure with $\theta_i - \alpha = 0.03$, this ratio decreases to a minimum of 0.29, see Figure 12f. Thus, the collapse capacity of ESDOF model is 3.5 times larger than the "exact" one.

To visualize this loss of accuracy, the ratios of the ESDOF system based predictions without and with considering material deterioration, $CC_{p50}^{*,basecase}/CC_{p50}^{*,deterioration}$, are shown in Figure 13. It is observed that for PDelta vulnerable systems in the range $\theta_i - \alpha$ from 0.10 to 0.20



(a) $\tau = 0.10$; slow (b) $\tau = 0.10$; medium (c) $\tau = 0.10$; rapid

(d) $\tau = 0.20$; slow (e) $\tau = 0.20$; medium (f) $\tau = 0.20$; rapid

Figure 13: Efficiency of proposed ESDOF model ($CC_{p50}^{*,basecase}/CC_{p50}^{*}$) for a fixed stiffness quantification factor τ and different "speeds" of deterioration: non-deteriorating ESDOF system versus deteriorating ESDOF system

the prediction of the median collapse capacity is not affected by consideration of material deterioration, both for stiff and flexible frame structures. This result is desired because in this parameter domain material deterioration has no significant influence on the "exact" collapse prediction. Material deterioration has the largest impact on the median collapse capacity of high-rise flexible buildings with small negative stiffness ratio $\theta_i - \alpha$, i. e. $\tau = 0.20$, $\theta_i - \alpha = 0.03$ to 0.06, and $n = 10$ to 20. For this parameter set the proposed deteriorating ESDOF model should yield closer approximation of the collapse capacity than the non-deteriorating ESDOF model, which considers PDelta only. As it has already been discussed before, Figures 11d to 11f show that the proposed ESDOF model overestimates the collapse capacity of the MDOF system. Figures 13d to 13f illustrate that an ESDOF system without considering material deterioration would lead to a much larger overestimation of the median collapse capacity. For instance, in the worst case for a 20-story flexible building ($\tau = 0.20$) with $\theta_i - \alpha = 0.03$ the collapse capacity ratio $CC_{p50}^{*,basecase}/CC_{p50}^{*}$ is 1.63. Thus, it can be concluded that the proposed ESDOF system considering material deterioration improves the accuracy of simplified collapse prediction of PDelta vulnerable deterioration frame structures.

6 SUMMARY AND CONCLUSION

In this paper the influence of component deterioration on the collapse capacity of PDelta vulnerable frame structures has been quantified. The main objective has been to reveal and to validate the range of applicability of a proposed equivalent single-degree-of-freedom (ESDOF) system for simplified assessment of the global seismic collapse capacity. From the results of this study it can be concluded that component deterioration hardly reduces the median collapse capacity of highly PDelta vulnerable frame structures with a negative post-yield stiffness ratio between 0.10 and 0.40. Therefore, in those cases it is sufficient to use a non-deteriorating ESDOF constitutive model for a simplified collapse assessment. In general for low to moderate rise MDOF frame structures up to seven stories the collapse capacity predictions based on the proposed ESDOF model are reasonably accurate, independently of the significance of component deterioration. In high-rise frame structures with 10 to 20 stories, where PDelta leads to a small negative post-yield stiffness ratio in the range of 0.03 to 0.06, component deterioration has the largest effect on the median collapse capacity. For structures within this parameter range the proposed ESDOF system overestimates the median collapse capacity up to a factor of 2.12. This could be an indicator that the identified deterioration parameters of the ESDOF system are too large for flexible and high-rise structures. However, the collapse prediction using the proposed ESDOF model is much more accurate compared to a classical non-deteriorating one. For a non-deteriorating ESDOF model this factor increases to 3.5.

ACKNOWLEDGEMENT

This work was supported by the Austrian Ministry of Science BMWF as part of the UniInfrastrukturprogramm of the Focal Point Scientific Computing at the University of Innsbruck.

REFERENCES

[1] C. Adam, L.F. Ibarra, Seismic collapse assessment. *Earthquake Engineering Encyclopedia*. Accepted for publication, Springer Berlin Heidelberg. 2014.

[2] C. Adam, L.F. Ibarra, H. Krawinkler, Evaluation of P-delta effects in non-deteriorating MDOF structures from equivalent SDOF systems. *Proceedings of the 13th World Conference on Earthquake Engineering (13WCEE)*, Vancouver, B.C., Canada, Aug. 1-6, Paper No. 3407, 2004.

[3] C. Adam, C. Jäger, Seismic collapse capacity of basic inelastic structures vulnerable to the P-delta effect. *Earthquake Engineering & Structural Dynamics*, **41**, 775–793, 2012.

[4] C. Adam, C. Jäger, Simplified collapse capacity assessment of earthquake excited regular frame structures vulnerable to P-delta. *Engineering Structures*, **44**, 159–173, 2012.

[5] C. Adam, H. Krawinkler, Large displacement effects on seismically excited elastic-plastic frame structures. *Asian Journal of Civil Engineering (Building and Housing)*, **5**, 41–55, 2004.

[6] C. Adam, S. Tsantaki, L. Ibarra, D. Kampenhuber, Record-to-record vulnerability of the collapse capacity of multi-story frame structures vulnerable to P-Delta. *Proceedings of the Second European Conference on Earthquake Engineering and Seismology (2ECEES)*, Istanbul, Turkey, Aug. 24-29, Paper No. 132, 2014.

[7] C. Chintanapakdee, A. Jaiyong, Estimation of peak roof displacement of degrading structures. *Proceedings of the 15th World Conference on Earthquake Engineering (15WCEE)*, Lisboa, Portugal, Sept. 24-28, DVD–ROM paper 835, 2012.

[8] A.K. Chopra, *Dynamics of Structures. 3rd Edition*. Pearson Education. 2012.
[9] P. Fajfar, Structural analysis in earthquake engineering – a breakthrough of simplified non-linear methods. *Proceedings of the 12th European Conference on Earthquake Engineering (12ECEE)*, London, UK, Sept. 9-13, CD–ROM paper 843, 2002.
[10] C. Felippa, *Introduction to Aerospace Structures (ASEN 3112)*, Lecture notes, University of Colorado at Boulder. 2014.
[11] FEMA-P695, *Quantification of Building Seismic Performance Factors*. Federal Emergency Management Agency (FEMA), 2009.
[12] F. Graziotti, A. Penna, G. Magenens, Use of equivalent SDOF systems for the evaluation of displacement demand for masonry buildings. *Proceedings of the Vienna Congress on Recent Advances in Earthquake Engineering and Structural Dynamics 2013 (VEESD 2013)*, ed. by C. Adam, R. Heuer, W. Lenhardt, C. Schranz. Vienna, Austria, Aug. 28-30, Paper No. 347, 2013.
[13] L.F. Ibarra, H. Krawinkler, *Global collapse of frame structures under seismic excitations*. Report No. 152, The John A. Blume Earthquake Engineering Research Center, Department of Civil and Environmental Engineering, Stanford University, Stanford, CA., 2005.
[14] L.F. Ibarra, R.A. Medina, H. Krawinkler, Hysteretic models that incorporate strength and stiffness deterioration. *Earthquake Engineering & Structural Dynamics*, **34**, 1489–1511, 2005.
[15] C. Jäger, *The collapse capacity spectrum method. A methodology for rapid assessment of the collapse capacity of inelastic frame structures vulnerable to P-delta subjected to earthquake excitation (in German)*. PhD thesis, University of Innsbruck, 2012.
[16] D. Kampenhuber, C. Adam, Degradation parameter for equivalent SDOF systems obtained from cyclic pushover analysis and parameter optimisation. *Proceedings of the Second European Conference on Earthquake Engineering and Seismology (2ECEES)*, Istanbul, Turkey, Aug. 24-29, Paper No. 275, 2014.
[17] D. Kampenhuber, C. Adam, Vulnerability of collapse capacity spectra to material deterioration. *Proceedings of the Vienna Congress on Recent Advances in Earthquake Engineering and Structural Dynamics 2013 (VEESD 2013)*, ed. by C. Adam, R. Heuer, W. Lenhardt, C. Schranz. August 28-30. Vienna, Austria, Paper No. 424, 2013.
[18] D. Lignos, H. Krawinkler, Deterioration modeling of steel components in support of collapse prediction of steel moment frames under earthquake loading. *Journal of Structural Engineering*, **137**.11, 1291–1302, 2011.
[19] D. Lignos, H. Krawinkler, *Sidesway collapse of deteriorating structural systems under seismic excitations*. Report No. 177, The John A. Blume Earthquake Engineering Research Center, Department of Civil and Environmental Engineering, Stanford University, Stanford, CA., 2012.
[20] E. Limpert, W.A. Stahel, M. Abbt, Log-normal distributions across the sciences: keys and clues. *BioScience*, **51**, 341–352, 2001.
[21] G.A. MacRae, P-Δ effects on single-degree-of-freedom structures in earthquakes. *Earthquake spectra*, **10**, 539, 1994.
[22] R.A. Medina, H. Krawinkler, *Seismic demands for nondeteriorating frame structures and their dependence on ground motions*. Report No. 144, The John A. Blume Earthquake Engineering Research Center, Department of Civil and Environmental Engineering, Stanford University, Stanford, CA., 2003.
[23] N. Shome, C.A. Cornell, P. Bazzurro, J.E. Carballo, Earthquakes, records, and nonlinear responses. *Earthquake spectra*, **14**.3, 469–500, 1998.

[24] S. Tsantaki, *A contribution to the assessment of the seismic collapse capacity of basic structures vulnerable to the destabilizing effect of gravity loads*. PhD thesis, University of Innsbruck, 2014.

[25] D. Vamvatsikos, C.A. Cornell, Incremental dynamic analysis. *Earthquake Engineering & Structural Dynamics*, **31**, 491–514, 2002.

COMPDYN 2015
5th ECCOMAS Thematic Conference on
Computational Methods in Structural Dynamics and Earthquake Engineering
M. Papadrakakis, V. Papadopoulos, V. Plevris (eds.)
Crete Island, Greece, 25–27 May 2015

DISTRIBUTED AND CONCENTRATED INELASTICITY BEAM-COLUMN ELEMENTS: APPLICATION TO REINFORCED CONCRETE FRAMES AND VERIFICATION

Armin Gharakhanloo[1], Amir M. Kaynia[1,2], and Georgios Tsionis[3]

[1] Norwegian University of Science and Technology
e-mail: armin.ghar@gmail.com

[2] Norwegian Geotechnical Institute
e-mail: amir.kaynia@ntnu.no

[3] European Laboratory for Structural Assessment (ELSA), Joint Research Centre, Italy
e-mail: georgios.tsionis@jrc.ec.europa.eu

Keywords: Inelasticity, beam-column, displacement-based element, force-based element, discretization, earthquake engineering.

Abstract: *Inelastic beam elements are widely used in the analysis of structures subjected to seismic actions. These elements are capable of describing the linear and nonlinear force-displacement and moment-rotation response of beams, columns and shear walls. However, there are numerical inaccuracies associated with these element formulations, as well as differences in computational effort. In this paper, the fundamentals of displacement-based and force-based elements are briefly presented, with emphasis on localization issues due to strain softening, and regularization procedures necessary to achieve convergence to single solutions. The modelling criteria regarding the number of integration points, the number of elements in each member and the length of the prescribed plastic hinges are also discussed. A one-story reinforced concrete frame, representing industrial buildings, has been modelled in a finite element software with the objective of studying the efficiency of three element types: displacement- and force-based distributed plasticity elements and concentrated plasticity ones. The running times of the analyses confirm that the computational demand of models with displacement-based elements is larger than that of models with force-based elements. Analysis results have then been compared to the experimental values obtained from a series of pseudo-dynamic tests performed with increasing seismic intensity. All element formulations showed very good approximation of the global response. Overall, force-based and plastic hinge models performed slightly better than the displacement-based model.*

1 INTRODUCTION

Distributed and concentrated inelasticity beam-column elements are used for the assessment of structural response to strong ground motions. These elements are usually based on one of two formulations; the displacement-based stiffness method (DB), or the force-based flexibility method (FB). The DB formulation is the familiar textbook finite element method, with approximated interpolation functions for axial and transverse displacements. In contrast, the FB formulation is based on interpolation functions for the internal forces, which are chosen to represent the exact solution. While members modelled with the FB formulation only require a single element per member, DB members require several elements to obtain sufficient accuracy. Distributed inelasticity elements commonly have their sections discretized into several fibres with different material properties. This is called fibre modelling, and enables representing inhomogeneous element sections with reasonable accuracy. The first concentrated inelasticity elements where designed with nonlinear springs at the member ends [1]. However, it is now more common to use fibre modelling in the plastic hinge lengths to achieve better numerical results.

Both DB and FB element formulations experience localization issues for strain-softening, called non-objective response. This is a numerical failure issue due to the analysis not converging into one single solution as the member is further discretized. In the case of DB elements, this implies the increased number of elements in the member, while for FB elements it is the increased number of integration points. Several regularization procedures have been proposed to achieve objective response for strain-softening. DB elements can be regularized by adjusting the extremity element lengths, or by adding a damage variable to the constitutive relation [2, 3]. The regularization of FB elements is often done by adjusting stress-strain relationships by a constant fracture energy criterion, and by post-processing moment-curvature response based on plastic hinge lengths [4]. One of the most recent methods to achieve objective response is using the Improved Gauss-Radau integration scheme for concentrated inelasticity elements; thus reducing computational power as well as gaining increased accuracy [5].

The objective of the research presented in this paper is to compare the efficiency of the aforementioned modelling approaches for the analysis of reinforced concrete (RC) frame structures subjected to earthquakes. A single-storey industrial building was analysed using displacement- or force-based elements with distributed inelasticity and concentrated inelasticity ones. The analytical results were compared to experimental data obtained from a series of pseudo-dynamic tests of a full-scale model.

2 SEISMIC TEST

The Joint Research Centre of the European Commission has performed several experiments on the seismic behaviour of buildings and other structures. A full-scale one-story RC industrial building is examined in this paper [6]. The prototype was made of cast-in-situ beams and columns, consisting of two two-bay frames connected by a slab (Fig. 1). The column heights were 5050 mm, while the beams were 8300 mm long. The prototype was designed for a dead load equal to 27 kN/m^2, including the self-weight of the slab. All six columns were identical with section dimensions 300x300 mm, having 8Ø14 longitudinal reinforcement throughout their whole length (Fig. 2). The transverse reinforcement consisted of 6 mm bars. In the critical regions, which are 1 m from the bottom and top cross sections, stirrups were placed with 50 mm spacing. Outside these regions, the spacing was 150 mm. The beams had 600x300 mm sections, with such reinforcement that the plastic hinges form in

the columns. Concrete cube specimen test gave cylindrical compressive strengths of f_{cm} = 42.7 MPa for the columns and f_{cm} = 47.2 MPa for the beams. The longitudinal steel reinforcement had a yielding strength of f_y = 550 MPa, and a tensile strength of f_y = 657 MPa.

Seismic tests of the cast-in-situ prototype were performed using the pseudo-dynamic method. Horizontal displacements were applied with the use of hydraulic jacks. In addition, vertical jacks were used to apply additional load on the slab, in total approximately 600 kN including the self-weight of the slab. The vertical jacks were always oriented towards a fixed base point, thus not producing any second-order P-delta effects. These effects were taken into account in the dynamic equilibrium model employed for the control of the pseudo-dynamic tests. The seismic ground motion was simulated by an artificial accelerogram (Fig. 3), which was generated to yield a response spectrum similar to the Type 1 response spectrum of Eurocode 8 [7] for ground type B. The prototype was subjected to four different acceleration time-histories based on the scaling of the ground motion for peak ground acceleration (PGA) equal to 0.05g, 0.32g, 0.64g, and 0.80g. The acceleregram with PGA = 0.05g was applied to calibrate the testing devices. The time-histories of top displacement measured during the tests are plotted in Fig. 4.



Figure 1: One-story RC frame [6].

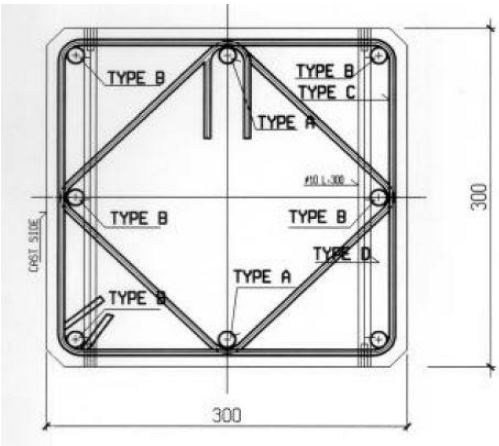


Figure 2: Column geometry and reinforcement [6].

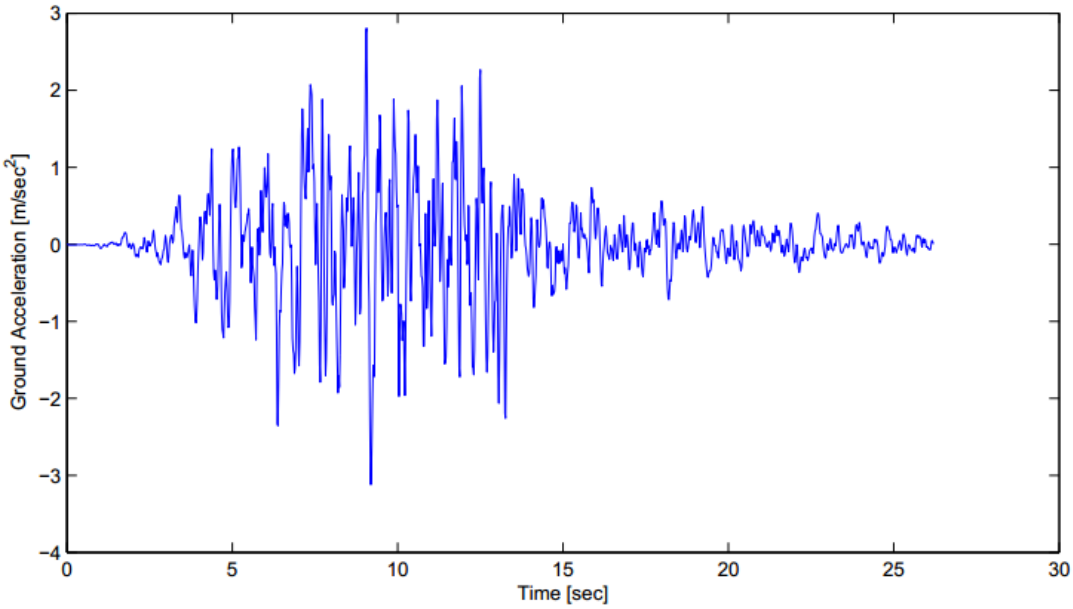


Figure 3: Artificial ground motion time-history with PGA 0.32g.

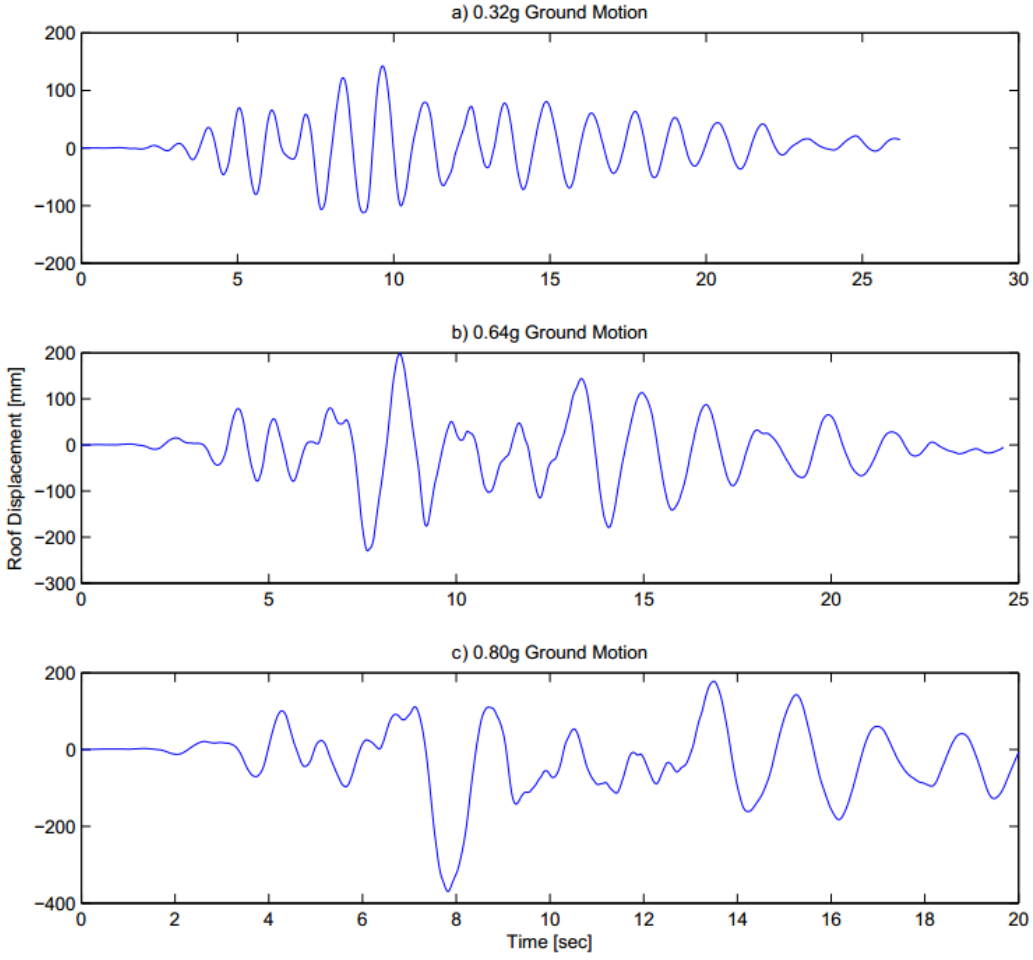


Figure 4: Displacement time-histories from pseudo-dynamic tests.

3 NUMERICAL MODELING

3.1 General

The numerical analysis has been performed in the finite element software SeismoStruct. It provides all the element types discussed in this paper, as well as options to modify their discretization properties. Because the structure is symmetric, only one of the frames has been modelled, carrying half of the total distributed vertical load, which is 300 kN including the self-weight of the slab. The column bases were fixed, with their heights set to 5350 mm, such that the structural nodes were situated in the centre of the beam section. The models developed by Chang and Mander [8] and Menegotto-Pinto [9] were used for the concrete and steel reinforcement elements respectively. The material properties were set equal to the ones measured from the prototype, with confinement factors calculated in SeismoStruct based on the amount of transverse reinforcement. The beams were modelled with large amounts of reinforcement, such that they had a significant overstrength compared to the columns. A static analysis was then performed by imposing the top displacement time-history provided from the experiment.

3.2 DB distributed inelasticity

The discretization of the columns for the different element types is illustrated in Figure 5. Based on earlier research, objective hardening response is expected when using a minimum of six DB elements per structural member with a two-point Gauss-Legendre integration scheme [10, 11]. Fewer elements tend to produce overly stiff solutions. In an effort to also achieve objective response in the case of strain-softening, the extremity elements of the column member have their lengths adjusted such that localization concentrates in one single integration point. This was done by choosing the element length as double the predetermined plastic hinge length, and was calculated as 1.146 m [12].

3.3 FB distributed inelasticity

Due to the fact that FB element members have exact solutions of the internal forces, it is not necessary to divide structural members into several elements [13]. A five-point Gauss-Lobatto integration scheme was used to achieve objective hardening response. Since no information on the concrete fracture energy was available for the prototype, no regularization procedure was applied for the FB element member.

3.4 FB concentrated inelasticity

The concentrated inelasticity members employed FB fibre modelling of the prescribed plastic hinges, with a linear elastic interior span. To ensure objectivity for both strain-hardening and strain-softening, the Modified Gauss-Radau integration scheme was used for the plastic hinges. It consists of two integration points: one is situated at the member end, and the second in the element interior.

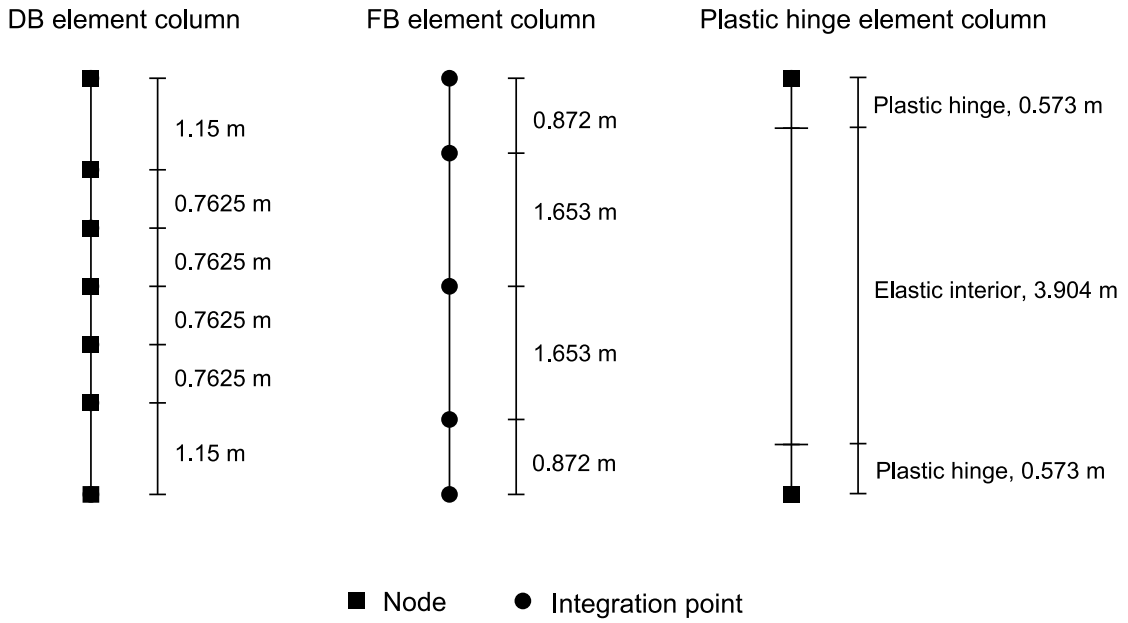


Figure 5: Discretization of RC columns.

4 COMPARISON OF EXPERIMENTAL AND NUMERICAL RESULTS

The frame prototype was subjected to the acceleration input motions without any repair between the tests. Thus, to obtain the most realistic numerical results, the 0.32g, 0.64g, and 0.80g motions have been applied consecutively in one single run. The computation times for each of these analyses are listed in Table 1. As expected, the frame modelled with the DB formulation requires more computational effort than the FB formulation elements. This is because of the higher number of nodes required for the DB beam-column members.

Element formulation	Elements	Integration points per element	Total time
DB distributed inelasticity	6	2	00:02:58
FB distributed inelasticity	1	5	00:02:33
FB plastic hinge	1	4	00:02:11

Table 1: Element discretization and computation times of analysis.

Due to the small number of structural nodes in the examined frame models, the differences between the computation times are not that significant. Indeed, the studied frame is very small compared to common residential and industrial buildings. The finite element models for these structures often consist of several thousands of nodes, which increase immensely if DB element members are used instead of FB elements. The fastest known matrix multiplication and inversion algorithms have running times of $n^{2.373}$ for a square a n x n matrix [14]. This means that a large number of nodes causes a significant increase in computational effort.

The base shear time-histories from the analysis are compared to the experimental data in Figs. 6, 7 and 8. All element types result in identical response paths as the experimental results for all three ground motion intensities. There is however, overestimation of the force

values at some cycles. The difference is larger for the DB elements and smaller for the FB distributed and plastic hinge elements, which is reasonable because the DB formulation tends to provide stiffer solutions. The time histories from the analysis with the 0.64g and 0.80g ground motions do not start at zero force. This is due to the fact that, as the three time-histories were applied consecutively, the base shear at the first time step was equal to the force at the last analysis step of the previous time history. The peak base shear values from the time-histories are listed in Table 2. The overestimation of force by the DB formulation is confirmed. It also shown that the FB distributed inelasticity and the plastic hinge elements result in almost identical values of base shear.

The modelling issues and the comparison of analytical and experimental results are discussed in detail elsewhere [11].

Peak base shear [kN]							
					Error (%)		
PGA	Experimental	DB	FB	Plastic hinge	DB	FB	Plastic hinge
0.32g	109.4	138.4	116.0	115.2	26.5	6.0	5.3
0.64g	122.0	145.7	117.0	117.4	18.9	-3.9	-3.8
0.80g	118.3	143.5	115.7	114.8	23.4	-0.9	-0.8

Table 2: Peak base shear values from analysis.

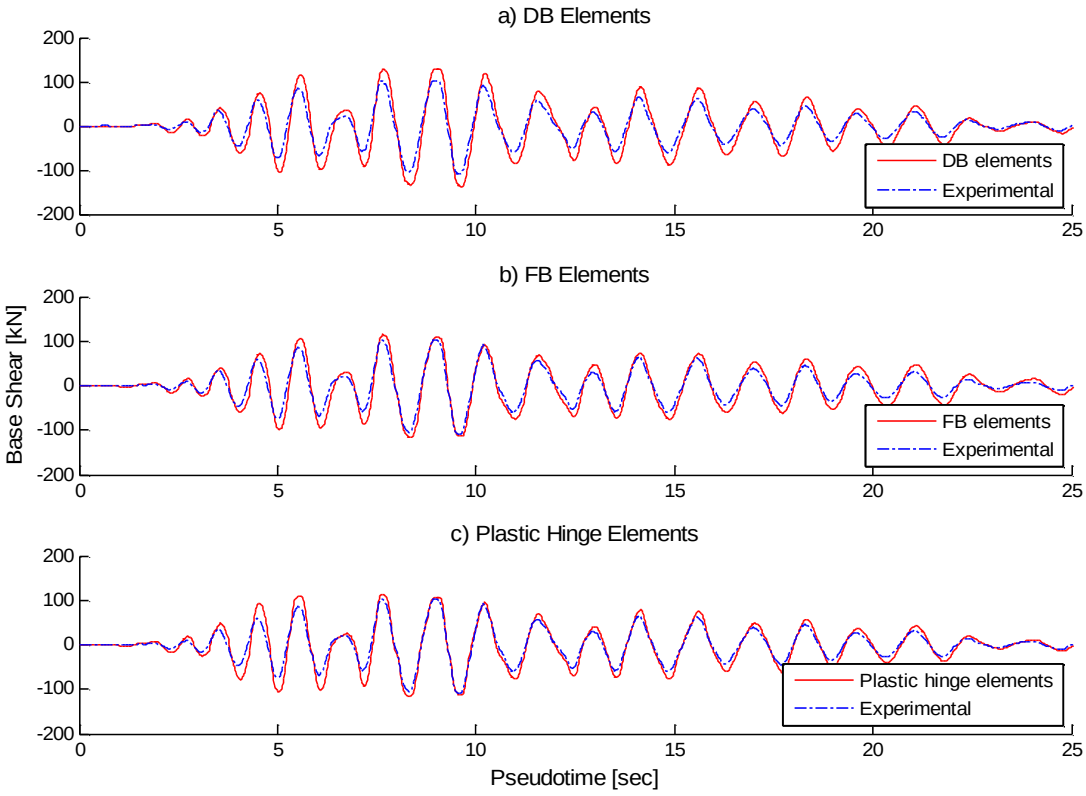


Figure 6: Base shear time-histories for 0.32g ground motion.

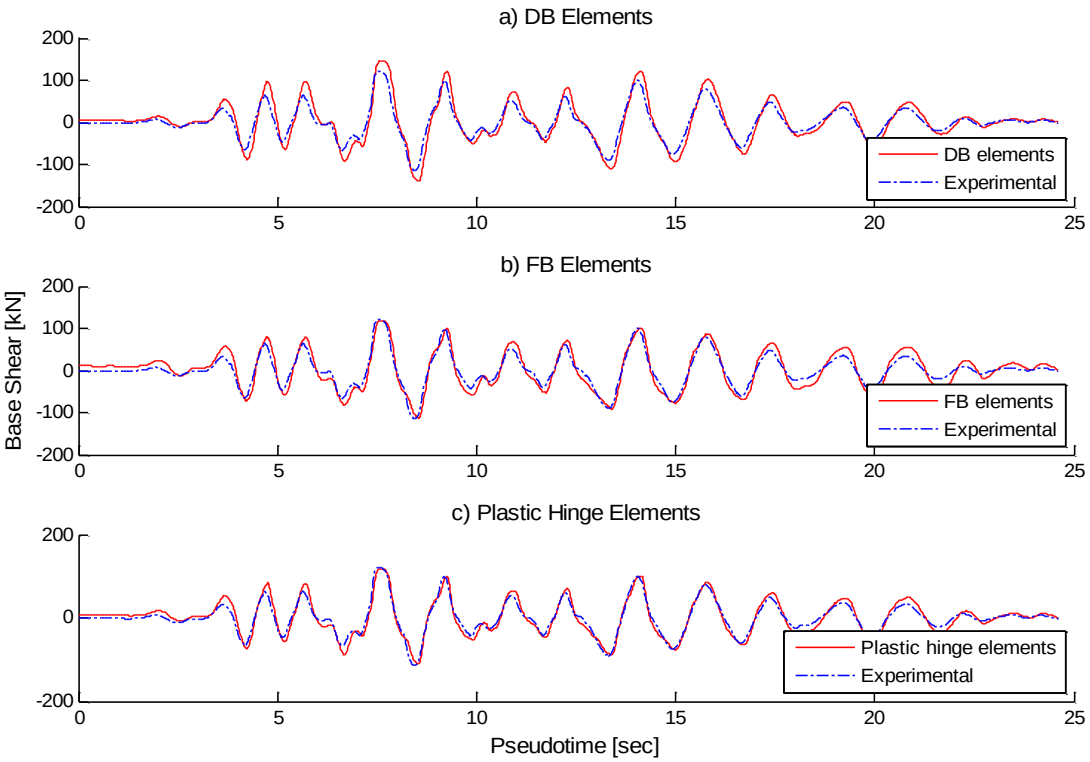


Figure 7: Base shear time-histories for 0.64g ground motion.

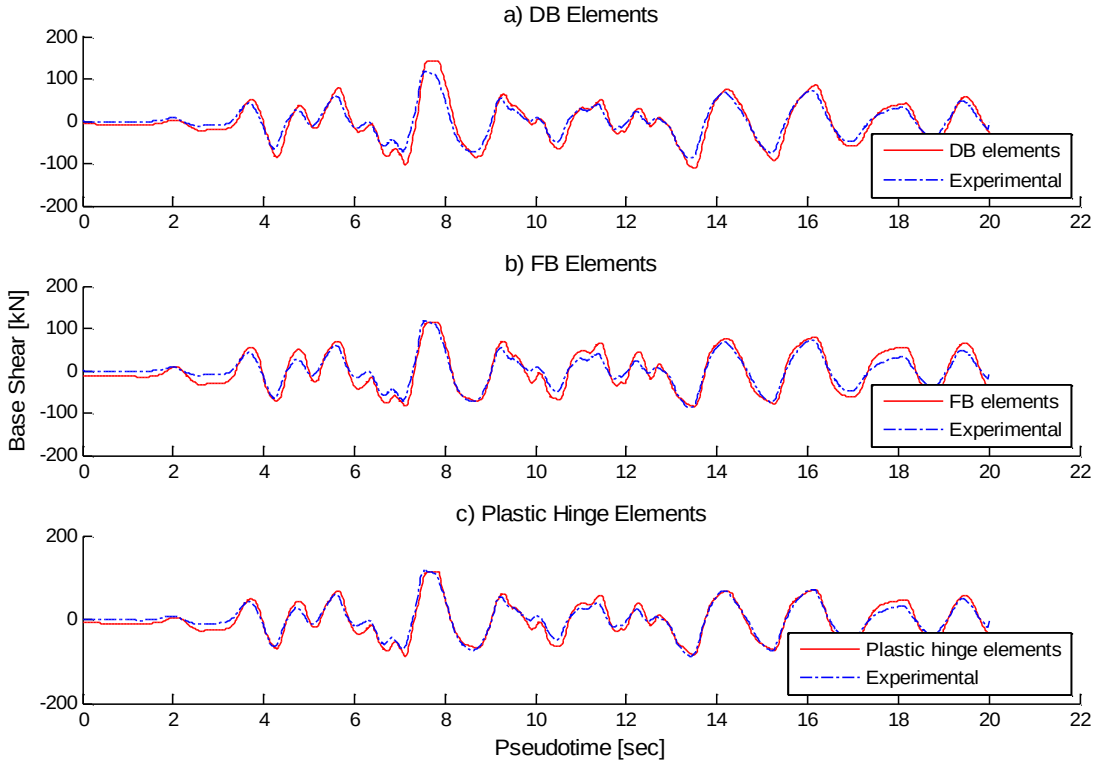


Figure 8: Base shear time-histories for 0.80g ground motion.

5 CONCLUSIONS

The running times of the different analyses clearly show that the computational effort of models with DB elements is higher than the one of FB elements. In addition, concentrated-inelasticity elements require fewer calculations than distributed-inelasticity elements, resulting in decreased computation time. While all three element types display satisfactory accuracy compared to experimental values for a simple RC frame, the FB elements offer a slightly better approximation of the response. Thus, the analyses confirm that both FB distributed- and concentrated-inelasticity elements achieve greater accuracy and require less computational effort than DB elements.

REFERENCES

[1] R.W. Clough, K.L. Benuska, E.L. Wilson, Inelastic earthquake response of tall buildings. *3rd World Conference on Earthquake Engineering*, Wellington, New Zealand, 1965.

[2] C.A. Zeris, S.A. Mahin, Analysis of reinforced concrete beam-columns under uniaxial excitation. *Journal of Structural Engineering*, **114**, 804-820, 1988.

[3] D. Addessi, V. Ciampi, A regularized force-based beam-column element with a damage-plastic section constitutive law. *International Journal for Numerical Methods in Engineering*, **70**, 610-629, 2007.

[4] J. Coleman, E. Spacone, Localization issues in force-based frame elements. *Journal of Structural Engineering*, **127**, 1257-1265, 2001.

[5] M.H. Scott, G.L. Fenves, Plastic hinge integration methods for force-based beam-column elements. *Journal of Structural Engineering*, **132**, 244-252, 2006.

[6] L. Ferrara, P. Negro, *Seismic behaviour of reinforced concrete structures: Test of the cast-in-situ prototype*. European Laboratory of Structural Assessment, Ispra, Italy, EUR 21097 EN, 2004.

[7] CEN, *Eurocode 8: Design of structures for earthquake resistance - Part 1: General rules, seismic actions and rules for buildings*. European Committee for Standardization, Brussels, 2004.

[8] G.A. Chang, J.B. Mander, Seismic Energy Based Fatigue Damage Ananlysis of Bridge Columns:Part 1 – *Evaluation of Seismic Capacity, NCEER Technical Report No. NCEER-94-0006,* State University of New York, Buffalo, N.Y.M, 1994.

[9] Menegotto, P.E. Pinto, Method of analysis for cyclically loaded reinforced concrete plane frames including changes in geometry and nonelastic behaviour of elements under combined normal force and bending. *IABSE Symposium on Resistance and Ultimate Deformability of Structures Acted On by Well-defined Repeated Loads*, Lisbon, Portugal, 1973.

[10] A. Calabrese, J.P. Almeida, R. Pinho, Numerical issues in distributed inelasticity modeling of RC frame elements for seismic analysis. *Journal of Earthquake Engineering*, **14**, 38-68, 2010.

[11] A. Gharakhanloo, *Distributed and concentrated inelasticity beam-column elements used in earthquake engineering*. MSc thesis, Norwegian University of Science and Technology, Trondheim, 2014.

[12] T. Paulay, M.J.N. Priestley, *Seismic design of reinforced concrete and masonry buildings*. John Wiley & Sons, New York, 1992.

[13] A. Neuenhofer, F.C. Filippou, Evaluation of nonlinear frame finite-element models. *Journal of Structural Engineering*, **123**, 958-966, 1997.

[14] S. Robinson, Toward an optimal algorithm for matrix multiplication. *SIAM News*, **38**, 2005.

COMPDYN 2015
5th ECCOMAS Thematic Conference on
Computational Methods in Structural Dynamics and Earthquake Engineering
M. Papadrakakis, V. Papadopoulos, V. Plevris (eds.)
Crete Island, Greece, 25–27 May 2015

A GROUPED MAXIMAL CONDITIONED SPECTRAL ORDINATE METHOD (MCSO) FOR GROUND MOTION SELECTION

Ahmad Nicknam[1], Ehsan Yousefi Dadras[2], Mohammad Javad Asgari[3]

[1] faculty of Civil and environmental engineering school,

Iran University of Science and Technology, Tehran, Iran

a_nicknam@iust.ac.ir

[2] PhD candidate of Civil and environmental engineering school,

Iran University of Science and Technology, Tehran, Iran

Ehsan_yousefi_dadras@civileng.iust.ac.ir

[3] graduate of Civil and environmental engineering school,

Iran University of Science and Technology, Tehran, Iran

mj_asgari@civileng.iust.ac.ir

Keywords: MCSO, CMS, CS, GMSM, non-linear dynamic analysis, target scenario.

Abstract. *This article intends to present a computationally simple ground motion selection method (MCSO) whose spectral accelerations are matched at specified period in the desired uniform hazard spectrum (UHS). The deficiencies of the Conditional Mean Spectrum and Conditional Spectrum (CS) approaches are monitored. MCSO benefits from the advantages of consistency with the predefined target Magnitude-Distance. It comes up with positive epsilons, scaling factors close to one, larger magnitudes than those of the two mentioned methods, and associated with the actual earthquake variability. The seismic demands of the three reinforced concrete structures are calculated and compared with those of MCSO, POC, CMS, and CS.*

1 INTRODUCTION

Relating regional hazard curve to mean structural collapse capacity by providing a suite of strong motion (e.g., [1] due to its ability in reducing the strong motion scaling factors is a promising approach in earthquake engineering. Recently, two techniques in the context of GMSM, termed the Conditional Mean Spectrum (CMS) and the Conditional Spectrum (CS) approach, have been proposed [2, 3]. These two methods are developed on the basis of epsilon (ε) at the spectral ordinate at the first mode vibration and relating it to those of the multiple spectral ordinates at the other periods to form the mean spectral values termed "Conditional Mean Spectrum".

The key feature of these methods are the scaling spectral acceleration at the fundamental period Sa(T1) to the desired hazard level (e.g., 2% in 50 years) and selecting sets of ground motions compatible with the predefined conditioned mean spectrum [2]. As mentioned by Jayaram et al [3], matching the selected ground motions only to a predefined mean-response-spectrum and ignoring the inherent variability existing in the ground motions is not sufficient for appropriately selecting sets of ground motions.

We believe that the two approaches especially CMS method suffer from being associated with: (a) small earthquakes likely to be associated with negative epsilons; (b) considerably large scaling factors;, and (c) ground motions associated with mean magnitude and distance different from those of the target magnitude M and distance R. The two above-mentioned methods have been cited by many researchers (e.g., [4, 5, 6, 7]), despite their deficiencies that will be discussed later. These points have been the main motivation of this article.

2 OBJECTIVE AND SCOPE

The major purposes of this article are to present a simple methodology for selecting suites of appropriate ground motions, including the following characteristics:

- Associated with scaling factor close to one i.e., not being suffered from large scaling factor.
- Correspond to magnitude (M) and distance (R) and consistent with the desired hazard level.

3 PROPOSED APPROACH

A simplified GMSM for selecting suites of ground motions being matched at a specific period (T*) in the desired hazard level termed the Maximal Conditioned Spectral Ordinate (MCSO) is proposed.

In this approach, the process of computing the mean target response spectrum $\mu_{lnSa}(\bar{M},\bar{R},T^*)$ established by $\bar{M}$, $\bar{R}$ and $\bar{\varepsilon}(T^*)$, given Sa(T*), through a disaggregation process is similar to the two above mentioned methods. It will be demonstrated that this approach results in the selection of suites of large ground motions associated with positive epsilons, scaling factors close to one, and correspond to the target magnitude and distance.

4 SUCCESSIVE STEPS OF THE METHOD

The mathematic formulation and the successive steps of the proposed algorithm are:

(I) For each ground-motion candidate, the Scaling Factor Effect (SFE) is calculated by Eq. 4 expressed as:

$$scaling\ factor\ effects = \left| \frac{\ln sa_{hazard}(T^*)}{\ln sa(T^*) - \ln sa_{hazard}(T^*)} \right| \quad (1)$$

Where $\ln sa_{hazard}(T^*)$ and $\ln sa(T^*)$ are the logarithmic response spectrum in the hazard curve and that of the candidate at the fundamental period T*, respectively

(II) The Selection Criterion Function (SCF) for each individual candidate is calculated by Eq. 5 expressed as:

$$SCF = scaling\ factor\ effects * \sum_{i=1}^{n} (element_mean(i) * element_drop(i)) \quad (5)$$

Where Element-Mean (i) for each candidate is calculated by Eq. 6 (see Fig. 1) expressed as:

$$element_mean(i) = \left(\frac{\ln Sa_{scaled}(T_i) + \ln Sa_{scaled}(T_{i+1})}{2} - \frac{\mu_{\ln Sa}(T_i) + \mu_{\ln Sa}(T_{i+1})}{2} \right) \quad (6)$$

Where $\ln Sa_{scaled}$ is the scaled logarithmic spectral acceleration corresponding to each ground motion candidate (i.e., each candidate is scaled in the hazard curve at T*), μ_{lnSa} is the logarithm of the mean hazard spectral acceleration. The Element-Drop(i) is calculated by Eq. 7 expressed as:

$$element_drop(i) = \left(\ln Sa_{scaled}(T_i) - \ln Sa_{scaled}(T_{i+1}) \right) + \left(\mu_{\ln Sa}(T_i) - \mu_{\ln Sa}(T_{i+1}) \right) \quad (7)$$

Where Element-Drop(i) determines the difference between the logarithmic spectral accelerations for each element.

(III) The selected ground motion candidates are listed in a descending order on the basis of their SCF values, i.e., larger SCF value is placed at the upper numbers of the list as the more appropriate candidate place.

Lastly, the orderly listed desired numbers of strong motions are selected as the most appropriate suite of ground motion candidates.

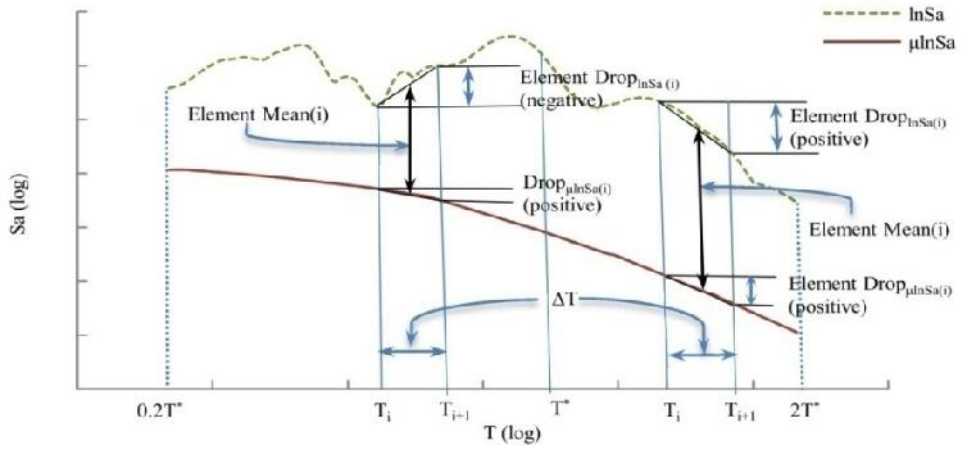


Figure 1: Graphical illustration of the Element-Mean and the Element-Drop associated with a typical response spectrum. Note that Element-Drop at the left side of the element has a negative sign, whereas that of the right side is positive. The vertical line (termed T* line) drawn from the fundamental period of the structure under study (T*) is also shown.

Table 1: The selected structures used, along with the corresponding code compliances, and their three natural periods.

Building	No. of Story	Type	Code compliance	Period
A	4	Modern RC special moment frame	2003 IBC, ASCE 7-02, ACI 318-02	0.97, 0.35, 0.18
B	12	Modern RC special moment frame	2003 IBC, ASCE 7-02, ACI 318-02	2.01, 0.68, 0.39
C	20	Modern RC special moment frame	2003 IBC, ASCE 7-02, ACI 318-02	2.63, 0.85, 0.46

5 EXAMPLES: MODELED STRUCTURES

As mentioned earlier, the selected three reinforced concrete special-moment frames used are those previously used by Haselton and Deierlein [8]. The 4-story, 12-story, and 20-story R/C structures used (see Table 1) have been previously designed according to modern building codes and checked by practicing engineers as part of the Applied Technology Council Project [9]. Table 1 lists the three buildings (A, B, and C), number of stories, structural resisting systems, code compliances, and the three successive natural periods of the structures. The structures subjected to the selected suite of ground motions are dynamically analyzed using the proposed method. The resulting response histories are evaluated by comparing to those of the POC [10]. The process implicitly compares and evaluates the results of MCSO algorithm to those of the CMS and CS. The Open-SEES software [11] is used for modeling the structures and performing dynamic analysis procedure. The structural deterioration is taken into account, and the structural collapse is assumed to occur once dynamic instability is reached [12], i.e., a large increase in drift as the result of a small increase in the applied loading. Tables 2,3, and 4 compare the maximum inter-story drift ratios (MIDR) obtained from POC and those of the MCSO, CMS, and CS methods in the form of mean values. The number of the selected ground motions, the MIDR ratios to POC, the dispersions, and lastly the collapse probabilities corresponding to each method are also shown.

Table 2: The maximum inter-story drift ratio (MIDR) corresponding to the 4-story building

method	POC	No. Of Rec.	Median MIDR	Ratio to POC	Dispertion MIDR	Collapse probability
Conditional Mean Spectrum	0.027	28	0.0274	1.014	-	-
		40	0.0279	1.033	0.28	0.1
Conditional Spectrum	0.027	40	0.0237	0.87	0.46	0.2
Proposed algorithm	0.027	28	0.0293	1.08	0.44	0.035
		40	0.0287	1.06	0.43	0.025

6 GROUND-MOTION SELECTION

For demonstrating the reliability of the proposed algorithm, the following circumstances are made aimed at comparing the structural response histories as the result of implementing the proposed algorithm with those of the POC [10] under the same conditions:

--A total of 7102 single components from the Next Generation Attenuation (NGA) [13] were used as a database. Each horizontal component (recorded at the same station) in the NGA database is treated as an individual ground motion.

--The Campbell and Bozorgnia ground-motion prediction model [14] was used to estimate the target scenario using the disaggregation method, i.e., a mean with magnitude = 7; distance to rupture of 10 km, assuming Vs30 = 400 m/s; and a strike-slip mechanism, which is the same as those of Haselton et al. [10].

--Each ground-motion candidate is preliminarily scaled at the fundamental period of the three selected structures in the probabilistic hazard curve [14] with $\varepsilon(T^*) = 2$. This step is the same as that of Haselton et al. [10]).

The proposed algorithm is used for selecting three sets of appropriate ground motions (e.g., 28 and 40 in this study) for the purpose of dynamically analyzing the three structures. The sets of ground motions in orderly descending SCFs are selected following the above-mentioned steps. Lastly, the first three sets of 28 and two sets of 40 single strong motions were selected.

Table 3: The maximum inter-story drift ratio (MIDR) corresponding to the 12-story building

method	POC	No. Of Rec.	Median MIDR	Ratio to POC	Dispertion MIDR	Collapse probability
Conditional Mean Spectrum	0.022	28	0.0199	0.90	-	-
		40	-	-	-	-
Conditional Spectrum	0.022	40	-	-	-	-
Proposed algorithm	0.022	28	0.0227	1.03	0.41	0.10
		40	0.0247	1.12	0.43	0.075

Table 4: The maximum interstory drift ratio (MIDR) corresponding to the 20-story building

method	POC	No. Of Rec.	Median MIDR	Ratio to POC	Dispertion MIDR	Collapse probability
Conditional Mean Spectrum	0.019	28	0.0186	0.98	-	-
		40	0.0186	0.98	0.25	0
Conditional Spectrum	0.019	40	0.0196	1.03	0.43	0.05
Proposed algorithm	0.019	28	0.0192	1.01	0.37	0.10
		40	0.0192	1.01	0.40	0.125

7 DYNAMIC ANALYSIS PROCEDURE

In POC procedure, the accuracy of each GMSM method has been evaluated by comparing the results of the nonlinear response histories of each structure with the true response, or, alternatively, the high-end prediction [10]. The CMS approach [1] has been recognized as the most appropriate approach among the 16 GMSMs [10]. The reader is referred to Haselton et

al. [10] for more information. The proposed method is also evaluated by comparing the nonlinear responses of the same structures subjected to the same number of the selected ground motions as those of POC [10]. To this end, the 2-dimensional forms of the selected frames having 4, 12, and 20 stories are dynamically analyzed calculating the response histories. The dynamic nonlinear analysis of the structures subjected to the following strong motions are performed using CMS, CS, and MCSO methods.

(a) Sets of 28 and 40 selected earthquakes.

(b) sets of 7, 14, and 21 selected earthquakes

Furthermore, the median, the dispersion of response histories of each structure, and the probability of collapses are calculated and explicitly compared with those of the POC [10], while implicitly are compared to those of the CMS and the CS methods.

8 RESULTS AND COMPARISON

The Maximum Inter-story Drift Ratio (MIDR), defined as the relative displacement between two consecutive story levels normalized by the story height, is used as the primary measurement of the structural response history. The mean MIDR of the three selected structures subjected to the set of 28 selected records, among 7102 single components, are calculated. The obtained seismic demands of the structures having 4, 12, and 20 stories are explicitly compared with those of POC [10] and implicitly with those of CMS and CS [3].

The statistical characteristics of the obtained MIDRs, in the median and dispersion forms of the non-collapse response histories and the probability of collapse (i.e., counted as the fraction of response histories indicating collapse), are also calculated and compared. Similar comparisons are performed between the selected 28 strong motions and those of the Haselton's are made [10]. The selected ground motions, as listed in Table A-1, are in the form of four sets of seven ground motions obtained from the CMS method and this study along with PEER-NGA Filenames and PEER-NGA Numbers for the structures B and C. The scaling factors associated with the individual ground motions as well as the mean value of sets of the seven earthquakes are also shown.

The agreement of the target scenario (M-R) with those of the average magnitude M and distance R, the positive epsilons, and the scaling factors, having values close to one as the objectives of the article, confirm the reliability of the proposed technique in selecting the appropriate suite of ground motions. Notably, the resulted scaling factors, as our objective, imply that the method does not suffer from scaling-factor problems. The comparison of the selected suite of strong motions obtained from this study along with those of the CMS (left-hand side plots), and CS (right-hand side plots) are shown in Fig. 3. The response spectra (from 0.2T*-2T*), corresponding to the selected sets of 28 and 40 ground motions which are scaled at the fundamental periods of the three structures (T*) in the hazard curve using the proposed method, along with those of the CMS, and CS methods are also shown.

Moreover, median plus two standard deviations (from Campbell and Bozorgnia GMPE 2008), at: (a) 4 stories; (b) 12 stories; and (c) 20 stories are displayed in the Figure 2. The right panel three figures, b, d, and f show the comparison of the standard deviation variations versus the period obtained from this study and the CS as the results of applying the sets of 28 and 40 selected strong motions upon the three structures. The differences of standard deviation variations at periods in the two methods are quite visible. As seen, the mean nonlinear responses have slight differences with those of the CMS, especially CS, whereas the dispersions are closer to those of the CS than to the CMS. The latter result implies that the inherent variances existing in the spectral ordinates of the selected ground motions selectd by the proposed MSCO are sufficiently accounted for.

Furthermore, a series of dynamic analyses on the structural types B and C subjected to the sets of 7, 14, and 21 numbers of the selected strong motions are performed to better understand the effects of increasing the strong motion numbers on the mean MIDRs (see Table 5).

Table 5: Comparison of the MIDR's median results for 2 structural types, B and C, obtained from the CMS and this study.

No. Of records	Structure B (8 story)			Structure C (20 story)		
	CMS	This study (MSCO)	MSCO/CMS ratio	CMS	This study (MSCO)	MSCO/CMS ratio
7	0.0224	0.0159	0.7	0.0173	0.0207	1.19
14	0.0199	0.022	1.1	0.0178	0.0197	1.1
21	0.0185	0.182	0.98	0.0182	0.0192	1.05
28	0.0199	0.0227	1.14	0.0185	0.0192	1.03

9 DISCUSSION

As mentioned earlier, the two CMS and CS methods are developed to select those candidates whose spectral ordinates are restricted to the predefined mean spectrum ignoring their intensity, frequency content, and duration [15]. Additionally, their restriction at periods smaller than T* causes the selection of candidates associated with small spectral ordinates at the periods smaller than T* where the demands of irregular structures are influenced by the higher modes [16]. Figure 2 shows the selected sets of 28 earthquakes in the forms of epsilons versus periods obtained from the CMS (right-hand side) and this study (left-hand side). The trends of the mean responses because of the above-mentioned restriction are quite visible. The problem is also confirmed by showing the mean responses of the structures A, B, and C subjected to the sets of 28 and 40 earthquakes obtained from CMS, CS, and this study (see Fig.3). The three dashed lines in the left-hand side figures at periods larger than T* (this study) are associated with spectral ordinates equal to or smaller than those of the CMS's, whereas those at smaller periods are larger. On the other hand, the spectral ordinates associated with smaller periods are closer to those in the hazard curve, compared to those of the CMS, meaning that use of the MCSO method, to some extent, provides earthquakes more sensitive to the structural higher mode. Because regular structures are used in this study (i.e., the responses are less influenced by the higher-mode effects). This problem notably has no significant impact on the response histories.

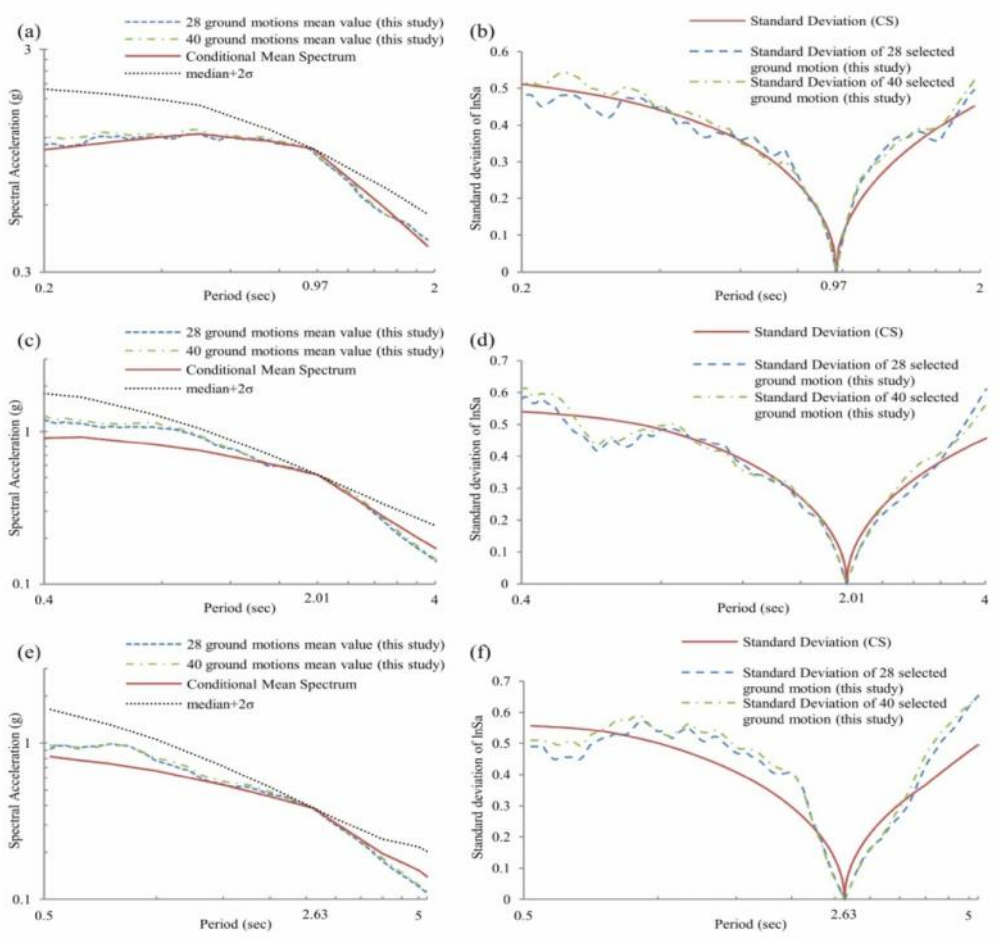


Figure 2: Comparison illustration of the selected suit of earthquakes (in logarithmic form) obtained from this study as compared with those of CMS (left-hand side plots) and CS (right-hand side plots). The left three figures, a, c, and e, display the comparison of the median response spectra (from 0.2T* -2T*) corresponding to the selected 28 and 40 ground motions scaled at the fundamental periods of the three structures (T*) using the proposed method, CMS, and CS methods. The median plus two standard deviations (from Campbell and Bozorgnia GMPE, 2008) are also shown in the three left-hand sides. The examined structures are (a) 4 stories, (b) 12 stories, and (c) 20 stories. The right-hand side three figures, b, d, and f, show a comparison of the standard deviation variations versus the periods obtained from this study and those of CS as the results of applying 28 and 40 selected ground motions to the three structures. The standard deviation variations at different periods in the two methods are quite visible.

The right-hand side plots in Fig. 3 show the comparison of the response history standard deviations obtained from this study and those of the CS. As seen, the standard deviation obtained from this study, which reflects the dispersions of the three structures' response histories, poses similar and, to some extent, more standard deviation than those of the CS reflecting more-realistic data.

the proposed method, in addition to its simplicity, is free from the above mentioned shortcomings, The reasons are: its very small scaling factors (close to one), selecting more real earthquakes, achieving the target magnitude, distance, and positive epsilon (M-R-ε) considerably higher than those of the CMS and CS (see Table 6), and finally accounting for the ground motion variability.

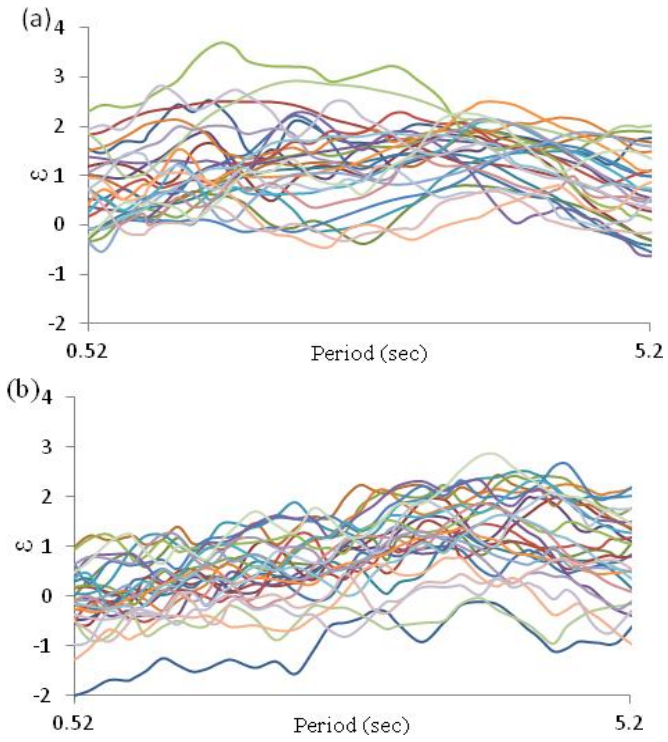


Figure 3: Illustration of the epsilon's trends associated with the selected set of 28 earthquakes for the 20-story frame: (a) MCSO method, and (b) CMS method. The downward trends of CMS (right-hand side) earthquakes are quite visible.

Tables 2, 3, and 4 compare the median MIDRs and their ratios to POC obtained from the dynamic analysis of the three selected structures subjected to the selected sets of 28 and 40 ground motions as the result of using the proposed algorithm, CMS, and CS. The average magnitudes M, distances R, and epsilon of the sets of seven ground motions and their total averages are listed in Table 6 demonstrating the M-R-ε (Richter-Km-dimensionless) values of 6.85-94.25-0.13, 6.75-71-0.43 (by CMS) against 7.1-8.8-1.46, 7-5.75-1.25 (by this study), respectively. As seen, this study has produced results more consistent with those of the target moment, distance, and epsilon with no suffering from scaling problems.

Table 6: Comparison illustration of the mean magnitude M, distance R, and epsilon ε corresponding to the ground motions selected by the MSCO and CMS methods.

	Mean M-R-ε (Richter-Km)	
Method \ Structural Type	B	C
CMS	6.85-94.25-0.13	6.75-71-0.43
This Study	7.1-8.8-1.46	7-5.75-1.25

10 CONCLUSION

A computationally GMSM, termed MCSO, is proposed to select suites of appropriate ground motions that, in addition of its simplicity, emerges with earthquakes associated with positive epsilons, have scaling factors close to one, consistent with the target magnitude-

distance M-R, and provide real ground-motion variability. The selected ground motions are matched in a predefined Uniform Hazard Spectra, (UHS) (e.g., 10% or 2% in 50 years) at a specified period (T*) (fundamental period of the structure under study). The basic concept of the method and its mathematic formulations are comprehensively declared, tested, and evaluated. The effectiveness of the Selection Criteria Function "SCF," whose value reflects the appropriateness of the ground-motion candidate, is evaluated through a selection of four couples of the candidate ground motions provided by MCSO and CMS and their influences in the selection procedure are compared. The MCSO performance is evaluated through a comparison process by intentionally selecting the same assumptions made by Haselton and his co-workers. These assumptions are: the three special reinforced concrete structures having 4, 12, and 20 stories; the 7102 single ground motions obtained from the Next Generation Attenuation (NGA) database; the Campbell and Bozorgnia ground-motion prediction equation [14]; a mean target scenario with magnitude = 7; distance of 10 km to rupture (as the result of using the disaggregation method; the Vs30 = 400 m/s, and the strike-slip mechanism. The traditional CMS and the CS methods and their deficiencies are briefly explained, aimed at posing the simplicity and merits of the proposed method. The 2-dimensional form of the selected three reinforced concrete structures are dynamically analyzed, and the MIDR response histories are calculated taking into account the structural deterioration. Two series of dynamic analyses of the three structures having 4, 12, and 20 stories subjected to 28 and 40 sets of the selected ground motions are performed using the successive steps of the proposed algorithm (see Fig 2). The Point Of Comparison (POC) procedure, by which the accuracies of the 16 GMSMs have been evaluated, as the high-end prediction [16], are followed as the comparison purpose for evaluating the results of the proposed method. Comparison of the results are explicitly made between those of the MCSO and the POC methods and implicitly with those of the CMS and CS. These are as follows:

-The median of Maximum Inter-story Drift Ratios (MIDRs) and their ratios to those of the POCs.

-The corresponding dispersions and the scaling factors associated with each selected set of ground motions.

-The magnitudes and distances (M-R), the epsilons, the dispersions, and the probability of collapse.

Stricktly speaking, the suite of ground motions selected by the proposed approach and its simplicity (i.e., free from calculating the correlation at multiple vibration periods as a necessary step in CMS and CS), benefits from the following major advantage:

(a) Coming up with a very small scaling factor, thus keeping up the natural links between the signal amplitudes and associated frequencies; (b) good consistency with the target earthquake scenario (M-R of 6.85-94.25 and 6.75-71 from the CMS against 7.1-8.8 and 7.5-5.75 from this study); (c) ending up with higher positive epsilons (see Table 6); (d) and lastly, providing the natural variability of the suites of earthquake.

The aforementioned points are quantitatively demonstrated through calculating and comparing the response histories (MIDR) of the three R/C frames subjected to 28 and 40 sets of the selected ground motions as the result of implementing the CMS, CS, and MCSO methods.

The material in this article is meant to be neither comprehensive nor complete, and more structures including different types of irregularities are necessary for analysis to more-convincing results.

REFERENCES

[1] Baker, J. W. and Cornell, C. A. [2006] "Spectral shape, epsilon and record selection", Earthquake Engineering & Structural Dynamics 35, 1077–1095.

[2] Baker, J. W. [2011] "The conditional mean spectrum: A tool for ground motion selection", ASCE Journal of Structural Engineering 137, 322–331.

[3] Jayaram, N. and Lin, T. and Baker, J. W. [2011] "A computationally efficient ground-motion selection algorithm for matching a target response spectrum mean and variance", Earthquake Spectra 27, 797-815.

[4] Tothong, P. and Luco, N. [2007] "Probabilistic seismic demand analysis using advanced ground motion intensity measures", Earthquake Engineering & Structural Dynamics 36, 1837–1860.

[5] Hancock, J. and Bommer, J.J. and Stafford, P.J. [2006] "Numbers of scaled and matched accelerograms required for inelastic dynamic analyses", Earthquake Engineering & Structural Dynamics 37, 1585-1607.

[6] Corigliano, M. and Lai, C. G. and Rota, M. and Strobbia, C. L. [2012] "ASCONA: Automated Selection of Compatible Natural Accelerograms", Earthquake Spectra 28, 965-987.

[7] Giaralis, A. and Spanos, P.D. [2012] "Derivation of response spectrum compatible non-stationary stochastic processes relying on Monte Carlo-based peak factor estimation", Earthquakes and Structures 3, 581-609.

[8] Haselton, C.B. and Deierlein, G.G. [2007] "Assessing seismic collapse safety of modern reinforced concrete frame buildings", Technical report, Pacific Earthquak Engineering Research Center, University of California, Berkeley, CA.

[9] Applied Technology Council (ATC) [2009]. Guidelines for Seismic Performance Assessment of Buildings ATC-58 50% Draft, the Applied Technology Council, Redwood City, CA.

[10] Haselton, C. B. and Baker, J. W. and Bozorgnia, Y. and Goulet, C. A. and Kalkan, E. and Luco, N. and Shantz, T. J. and Shome, N. and Stewart, J. P. and Tothong, P. and Watson-Lamprey, J. A. and Zareian, F. [2009] "Evaluation of ground motion selection and modification methods: Predicting median inter-story drift response of buildings", Technical report, Report 01, Pacific Earthquake Engineering Research Center, University of California, Berkeley, CA.

[11] Open System for Earthquake Engineering Simulation (OpenSEES) [2007]. Pacific Earthquake Engineering Research Center, University of California, Berkeley.

[12] Ibarra, L. F. and Medina, R.A. and Krawinkler, H. [2005] "Hysteretic models that incorporate strength and stiffness deterioration", Earthquake Engineering & Structural Dynamics 34, 1489–1511.

[13] Chiou, B.S.J. and Darragh, R.B. and Gregor, N.J. and Silva, J.W. [2008] "NGA project strong motion database, Earthquake Spectra 24, 23–44.

[14] Campbell, K.W. and Bozorgnia, Y. [2008] "NGA ground motion model for the geometric mean horizontal component of PGA, PGV, PGD and 5% damped linear elastic response spectra for periods ranging from 0.01 to 10s", Earthquake Spectra 24, 139–171.

[15] Bradley, B. A. [2010] “A generalized conditional intensity measure approach and holistic ground-motion selection”. Earthquake Engineering & Structural Dynamics 39, 1321-1342.

[16] Chopra, A. K. [2001] “Dynamics of Structures. Theory and application to Earthquake Engineering”, Prentice-Hall, Upper Saddle River, N.J.

COMPDYN 2015
5th ECCOMAS Thematic Conference on
Computational Methods in Structural Dynamics and Earthquake Engineering
M. Papadrakakis, V. Papadopoulos, V. Plevris (eds.)
Crete Island, Greece, 25–27 May 2015

ADVANCED MODELS FOR THE LIMIT ANALYSIS OF MASONRY STRUCTURES

A. Fortunato[1], E. De Chiara[1], F. Fraternali[1], and M. Angelillo[1]

[1]Department of Civil Engineering,
University of Salerno
84084, Fisciano (SA), Italy
e-mail: a.fortunato@unisa.it (A. Fortunato), elenadechiara@gmail.com (E. De Chiara),
{f.fraternali, mangelillo}@unisa.it (F. Fraternali, M. Angelillo)

Keywords: Structural capacity, Masonry walls, Limit analysis, Free discontinuities.

Abstract. *We formulate a novel procedure for the limit analysis of masonry structures subject to horizontal loads. The proposed approach works in the framework of free discontinuity methods, on examining collapse mechanisms that exhibit free crack opening discontinuities. Numerical examples illustrate the practical application of the proposed procedure to the limit analysis of masonry structures subject to seismic actions, within a conventional static approach.*

1 INTRODUCTION

In the present work we describe a procedure for determining the ground acceleration that activates the in-plane mechanism of a wall panel with openings. The method generalizes and extends a numerical model proposed in [1], based on the (crude) assumption that the material is unilateral (namely a No-Tension material in the sense of Heyman [2]), leans on the kinematic theorem of limit analysis.

The unilateral model for masonry was first rationally introduced by Heyman in [2]. Several authors of the Italian school of Structural Mechanics has divulgated and extended such model [3–17]. The analysis of masonry-like materials can be conducted within the frame of limit analysis, specifically by applying the static and kinematic theorems on the basis of admissible stress and strain fields (see [18]). The first tool that can be introduced for applying the unilateral No-Tension model to masonry structures is the systematic use of singular stress and strain fields, within the framework defined by the two theorems of Limit Analysis [19, 20]. The use of singular equilibrated stresses for approximating plane equilibrium problems can be traced in [17, 21–23]. In particular, in the application we present, we focus on the kinematic approach. By working with the kinematic theorem, we admit singular strains representing concentrated fractures; in other words we allow for strong discontinuities in the displacements. A recent computational model for fracture nucleation and propagation in 2d brittle solids, based on variational fracture is proposed in [24–26]. Essentially the analysis is based on the variational formulation of Griffith–type fracture [27], the main difference being the fact that we rely on local rather than on global minimization. Nucleation and propagation of fracture is obtained by minimizing in a step by step process a form of energy that is the sum of bulk and interface terms. In the present paper we adopt a similar, though simplified, strategy to explore compatible mechanisms having free discontinuities. The practical implementation of the proposed approach is illustrated through a collection of numerical examples dealing with masonry structures subject to vertical and horizontal loads.

2 THE BOUNDARY VALUE PROBLEM FOR RIGID NO-TENSION MATERIALS

2.1 Constitutive restrictions and equilibrium problem

We consider a body $\Omega \in \mathbb{R}^n$ (here $n = 2$), loaded by the given tractions $\underline{\mathbf{s}}$ on the part $\partial\Omega_{\mathrm{N}}$ of the boundary, and subject to given displacements $\underline{\mathbf{u}}$ on the complementary, constrained part of the boundary $\partial\Omega_{\mathrm{D}}$, is in equilibrium under the action of such given surface displacements and tractions, besides body loads $\mathbf{b}$ and distortions $\underline{\mathbf{E}}$ (the set of data being denoted: $(\underline{\mathbf{u}}, \underline{\mathbf{E}}; \underline{\mathbf{s}}, \mathbf{b})$), and undergoes small displacements $\mathbf{u}$ and strains $\mathbf{E}(\mathbf{u})$[1].

The body Ω is composed of Rigid No-Tension material, that is the stress $\mathbf{T}$ is negative semidefinite

$$\mathbf{T} \in \mathrm{Sym}^{-} \ , \tag{1}$$

the effective strain $\mathbf{E}^* = \mathbf{E}(\mathbf{u}) - \underline{\mathbf{E}}$ is positive semidefinite

$$\mathbf{E}^* \in \mathrm{Sym}^{+} \ , \tag{2}$$

and the stress $\mathbf{T}$ does no work for the corresponding effective strain $\mathbf{E}^*$

$$\mathbf{T} \cdot \mathbf{E}^* = 0 \ . \tag{3}$$

[1]When eigenstrains are considered, under the small strain assumption, the total strain $\mathbf{E}(\mathbf{u})$ is decomposed additively as follows: $\mathbf{E}(\mathbf{u}) = \mathbf{E}^* + \underline{\mathbf{E}}$, $\mathbf{E}^*$ being the *effective* strain of the material.

In order to avoid trivial incompatible loads $(\underline{\mathbf{s}}, \mathbf{b})$, it is assumed that the tractions $\underline{\mathbf{s}}$ satisfy the condition

$$\underline{\mathbf{s}} \cdot \mathbf{n} < 0 \ , \ \text{or} \ \underline{\mathbf{s}} = \mathbf{0}, \ \forall \mathbf{x} \in \partial\Omega_{\mathrm{N}} \ . \tag{4}$$

2.2 Admissible fields

For RNT materials is natural to define the sets of statically admissible stress fields $\mathcal{H}$ and kinematically admissible displacement fields $\mathcal{K}$, as follows

$$\mathcal{H} = \left\{ \mathbf{T} \in \mathcal{S}(\Omega) \text{ s.t. } \mathrm{div}\mathbf{T} + \mathbf{b} = \mathbf{0} \ , \ \mathbf{T}\mathbf{n} = \underline{\mathbf{s}} \text{ on } \partial\Omega_{\mathrm{N}} \ , \ \mathbf{T} \in \mathrm{Sym}^{-} \right\} \ , \tag{5}$$

$$\mathcal{K} = \left\{ \mathbf{u} \in \mathcal{T}(\Omega) \text{ s.t. } \mathbf{u} = \underline{\mathbf{u}} \text{ on } \partial\Omega_{\mathrm{D}} \ , \ (\mathbf{E}(\mathbf{u}) - \underline{\mathbf{E}}) \in \mathrm{Sym}^{+} \right\} \ , \tag{6}$$

where a convenient choice for the function spaces $\mathcal{S}(\Omega)$ and $\mathcal{T}(\Omega)$ is

$$\mathcal{S}(\Omega) = SMF(\Omega) \ , \qquad \mathcal{T}(\Omega) = \{ \mathbf{u} \ , \text{s.t. } \mathrm{grad}\, \mathbf{u} \in SMF^{*}(\Omega) \} \ , \tag{7}$$

$SMF(\Omega)$ being the set of Special Measures (that is measures with null Cantor part) whose jump set is finite, in the sense that the support of their singular part consists of a finite number of regular $(n-1)$d arcs. With $SMF^{*}(\Omega)$ we denote the subset of $SMF(\Omega)$ for which the support of the singular part is restricted to a finite number of $(n-1)$d segments.

3 COMPATIBILITY CONDITIONS

3.1 Compatibility and incompatibility of loads and distortions

The data of a general BVP for a RNT body can be split into two parts

$$\ell \ \leftrightarrow \ (\underline{\mathbf{s}}, \mathbf{b}) \ \approx \ \text{loads} \ , \qquad \ell^{*} \ \leftrightarrow \ (\underline{\mathbf{u}}, \underline{\mathbf{E}}) \ \approx \ \text{distortions} \ . \tag{8}$$

The *equilibrium problem* and the *kinematical problem* for RNT materials, namely the search of admissible stress or displacement fields for given data, are essentially independent, in the sense that they are uncoupled but for condition (3).

It has to be pointed out that, for RNT bodies, there are non-trivial compatibility conditions, both on the loads and on the distortions; that is the existence of statically admissible stress fields for given loads, and the existence of kinematically admissible displacement fields for given distortions, is submitted to special conditions on the data (for a thorough study of compatibility conditions on the loads see [7, 28]).

The definition of compatible loads and distortions is rather straightforward:

$$\{\ell \text{ is compatible}\} \ \Leftrightarrow \{\mathcal{H} \neq \emptyset\} \ , \qquad \{\ell^{*} \text{ is compatible}\} \ \Leftrightarrow \{\mathcal{K} \neq \emptyset\} \ . \tag{9}$$

Therefore the more direct way to prove compatibility, both for loads and distortions, is to construct a s.a. stress field or a k.a. displacement field, as done in the previous examples.

To prove the existence of a solution to the BVP for a No-Tension body, the compatibility of ℓ and ℓ^{*} is necessary but not sufficient, since the further condition

$$\mathbf{T} \cdot \mathbf{E}^{*}(\mathbf{u}) = 0 \ , \tag{10}$$

must be satisfied (this is the material restriction (3)). Then one can say that a possible solution to the BVP is given, if there exist a s.a. stress field and and a k.a. displacement field, which are reconcilable in the sense of condition (3).

The way to verify the incompatibility of the data is less straightforward [20].

$$\{\ell \text{ incompatible}\} \Leftarrow \left\{\exists \mathbf{u}^0 \in \mathcal{K}^0 \text{ s.t. } \left\langle \ell, \mathbf{u}^0 \right\rangle > 0\right\} \ , \tag{11}$$

$$\{\ell^* \text{ incompatible}\} \Leftarrow \left\{\exists \mathbf{T}^0 \in \mathcal{H}^0 \text{ s.t. } \left\langle \ell^*, \mathbf{T}^0 \right\rangle > 0\right\} \ , \tag{12}$$

where $\mathcal{H}^0$ and $\mathcal{K}^0$ are the same as defined in (5) and(6) but with set of data $(\underline{\mathbf{u}}, \underline{\mathbf{E}}; \underline{\mathbf{s}}, \mathbf{b}) = (\mathbf{0}, \mathbf{0}; \mathbf{0}, \mathbf{0})$, and $\langle \ell, \mathbf{u}^0 \rangle$, $\langle \ell^*, \mathbf{T}^0 \rangle$ represent the work of the loads and distortions for $\mathbf{u}^0$, $\mathbf{T}^0$, respectively.

4 LIMIT ANALYSIS

We concentrate on necessary or sufficient conditions for the compatibility of a given set of loads $(\underline{\mathbf{s}}, \mathbf{b})$, restricting to the case of zero kinematical data $(\underline{\mathbf{u}}, \underline{\mathbf{E}})$.

4.1 Theorems of Limit Analysis.

Strictly admissible stress fields and load classification. On denoting $\langle \ell, \mathbf{u} \rangle$ the work of the load $\ell = (\underline{\mathbf{s}}, \mathbf{b})$ for the displacement $\mathbf{u}$, the load can be classified as follows:

$$(\ell \text{ is a collapse load}) \Leftrightarrow (\exists \mathbf{u}^* \in \mathcal{K} \text{ s.t. } \langle \ell, \mathbf{u}^* \rangle > 0) \tag{13}$$

$$(\ell \text{ is a limit load}) \Leftrightarrow (\langle \ell, \mathbf{u} \rangle \leq 0, \ \forall \mathbf{u} \in \mathcal{K} \text{ and } \exists \mathbf{u}^* \in \mathcal{K} - \mathcal{K}^{00} \text{ s.t. } \langle \ell, \mathbf{u}^* \rangle = 0) \tag{14}$$

$$(\ell \text{ is a safe load}) \Leftrightarrow (\langle \ell, \mathbf{u} \rangle < 0 \ , \ \forall \mathbf{u} \in \mathcal{K}) \tag{15}$$

where $\mathcal{H}^{00}$ and $\mathcal{K}^{00}$ are the sets $\mathcal{H}^0$ and $\mathcal{K}^0$ corresponding to null stress and strain fields, depending on the geometry of the boundary, of the loads and of the constraints. A stress field $\mathbf{T} \in \mathcal{H}$ such that tr$\mathbf{T} < 0$ and det$\mathbf{T} > 0$, $\forall \mathbf{x} \in \Omega$, is said to be *strictly admissible*.

Notice that, if $\mathbf{T}$ is strictly admissible, then at each point of Ω (that is the open set $\dot{\Omega}$ to which the fixed part of the boundary $\partial\Omega_{\mathrm{D}}$ is added) it results: $\sigma_1 < 0$, $\sigma_2 < 0$, σ_1, σ_2 being the eigenvalues of $\mathbf{T}$ at the point $\mathbf{x}$.

Kinematic Theorem. If ℓ is a collapse load (in the sense of item (1) above) then $\mathcal{H}$ is void.

Static Theorem. If a strictly admissible stress field $\mathbf{T}$ exists, then the load ℓ is safe (in the sense of item (3) above).

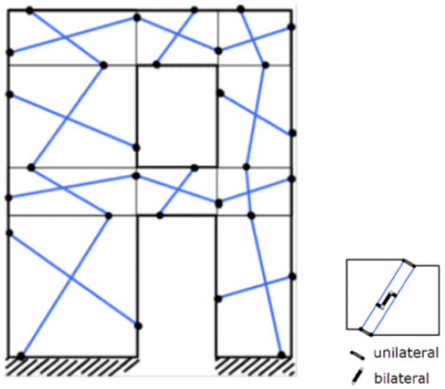
Limit Theorem. If $\mathcal{H}$ is not void and there exists $\mathbf{u}^* \in \mathcal{K} - \mathcal{K}^{00}$ such that $\langle \ell, \mathbf{u}^* \rangle = 0$, then the load ℓ is limit (in the sense of item (2) above).

For the proof of these theorems we refer to the paper [18]. The reader must be warned that the proofs given by Del Piero refer to a similar function space for the displacement but to a different functional setting for the stress (namely $L^2(\Omega)$). In the present paper we assume that these theorem are still valid in the present larger setting for the stress [20].

4.2 Formalization of the kinematical problem

We focus on the formalization of the kinematical problem under the effect of kinematical data (such as settlements and distortions). By restricting to displacement fields characterized by strain fields that are, purely, line Dirac deltas with support on a finite number of segments, the body Ω can be divided into a finite number, say n, of domains Ω_i (forming a partition of Ω) each exhibiting a rigid body motion. Under the assumption of small strains, for each element Ω_i, such rigid body motion, that is the displacement $\mathbf{u}^i$ of any point of Ω_i, can be described in terms of three displacement parameters u^i, v^i, ϕ^i, as follows

$$u_1^i(x_1, x_2) = u^i - \phi^i x_2, \qquad u_2^i(x_1, x_2) = v^i + \phi^i x_1. \tag{16}$$



a) b)

Figure 1: The Rigid–Block Masonry Model with Fixed and Floating Interface

Under these restrictive assumptions the generalized displacement of the structure, denoted $\hat{\mathbf{u}}$ is a vector of $3n$ components, namely the three displacement parameters per each element Ω_i:

$$\hat{\mathbf{u}} = \{u^1, v^1, \phi^1, \ldots, u^i, v^i, \phi^i, \ldots, u^n, v^n, \phi^n\} \ . \tag{17}$$

5 A METHOD FOR KINEMATIC COLLAPSE ANALYSIS

In our method, the three basic assumptions of Heymans model for masonry are adopted, i.e. *i*) Tensile stresses (forces) are forbidden and, therefore, the material can separate freely (with zero energy expended); *ii*) the material can withstand stresses of infinite intensity (infinite strength to compression, i.e. no possibility of crushing); and *iii*) friction coefficient is infinite: no sliding on separation lines. We, also, restrict to deformations represented by line Dirac deltas on a finite number of segments. In Fig.1 the main idea is depicted for simple plane wall with regular openings: thick solid lines represent the boundary; thin solid lines represent fixed interfaces; grey lines represent moving interfaces.

The movement of the interfaces is controlled by the movement of their end nodes constrained along fixed interfaces and boundary segments. In 1b the constraints that are assumed along the interfaces are reported. The unilateral constraint considered along the interfaces, incorporates the incompenetrability condition. The normality condition (2), (3) (that is the non-sliding assumption along the interface) is enforced by the bilateral pendulum (see 1b). The kinematical and statical problems for such a structure are coupled, in the sense that, given the assumption of zero dissipation on any interface (Assumption *i*)), the work of the reactions for the displacements both at the internal and at the boundary interfaces must be zero. In general there will be infinite elements $\hat{u} \in \mathcal{K}$ and infinite elements $\hat{R} \in \mathcal{H}$, and the no–work assumption gives a criterion to select (may be not uniquely), among them, a couple $(\hat{u}^0, \hat{R}^0)$, that is called: solution of the kinematical and statical problem. (Notice that, restricting to a finite number of rigid blocks, having fixed or moving interfaces, the sets $\mathcal{H}$ and $\mathcal{K}$ become finite dimensional). There is a way to select variationally such a couple. The idea is to introduce the potential energy of the structure, that is minus the potential energy of the loads, i.e. the scalar product of the loads and couples applied at the centroids of the pieces, collected in a generalized force vector $\hat{f}$, for the generalized displacement $\hat{u}$ collecting the parameters of translation and rotation of each piece of S). Call it $E(\hat{u})$, and minimize $E(\hat{u})$ over the set $\mathcal{K}$. Can write

$$E(\hat{u}) = -\left\langle \hat{f}, \hat{u} \right\rangle \ , \tag{18}$$

a linear function of the generalized displacement u of the structure, and

$$E(\hat{u}^0) == \min_{\hat{u}\in\mathcal{K}} E(\hat{u}) \ . \tag{19}$$

This is a linearly constrained minimization problem for a linear function if the interfaces are not moving, that is the pieces are fixed. In such a simplified case the problem can be solved by using the Simplex Method. If both the load data and the distorsion data are fixed, the minimum criterion selects, among all the kinematically admissible displacements $\hat{u}$ the displacement $\hat{u}^0$ that is more convenient on an energetical ground. If the load is assigned with a load parameter λ (say: the vertical component of the load is fixed and the horizontal component is gradually increased with λ), at each stage of the loading program (that is at any given value of λ) the minimal displacement can be calculated through the minimum condition. The limit value λ^0 of the load parameter is obtained when a mechanism (that is an indefinite increase of the displacement) for which the loads perform zero work is detected.

6 NUMERICAL RESULTS

6.1 A simple case study

As a first case study, we analyze the masonry wall in Fig. 2 under the action of the self-weight and a settlement of the central base panel. On assuming that the adopted mesh is fixed, we regard the analyzed structure a set S of $n = 8$ rigid bodies connected by unilateral and bilateral constraints (Fig. 2a). An arbitrary generalized displacement of the wall is given by

$$\hat{u} = \{u(1), v(1), \phi(1), , u(n), v(n), \phi(n)\}. \tag{20}$$

with the displacement parameters being referred to the centroid of mesh elements. The corresponding generalized dual force is as follows

$$\hat{F} = \{H(1), V(1), M(1), , H(n), V(n), M(n)\}. \tag{21}$$

Assuming pure dead loads due to the self-weight of the wall, we have: $H(i) = 0,\ V(i) = P(i),\ M(i) = 0$, for any $i = 1, 2, ..., n$, where $P(i)$ is the self–weight of the panel i. The bilateral and unilateral constraints depicted in Fig.1b are considered to be active on all the mesh interfaces, which leads us to the following system of equality and inequality constraints:

$$\Gamma'\hat{u} = 0 \ , \qquad \Gamma''\hat{u} \leq \delta \ , \tag{22}$$

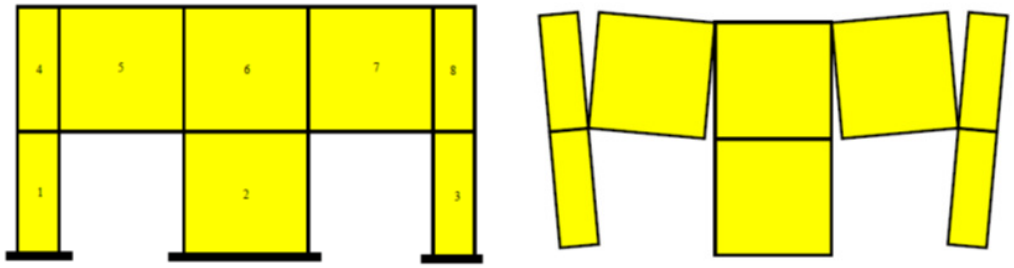
δ being the vector of the applied settlements. In the present case, the latter accounts for a translational vertical settlement the center base panel, which we assume equal to $-0.06L$. The set of kinematically admissible generalized displacement is given by

$$\mathcal{K} = \{\hat{u} : \Gamma'\hat{u} = 0 \ , \Gamma''\hat{u} \leq \delta\}, \tag{23}$$

and the collapse mechanism $\hat{u}^0$ is found via a simplex algorithm, by minimizing the following objective function

$$E(\hat{u}) = -\hat{F} \cdot \hat{u} \ , \tag{24}$$

over $\mathcal{K}$ (Fig.2b).

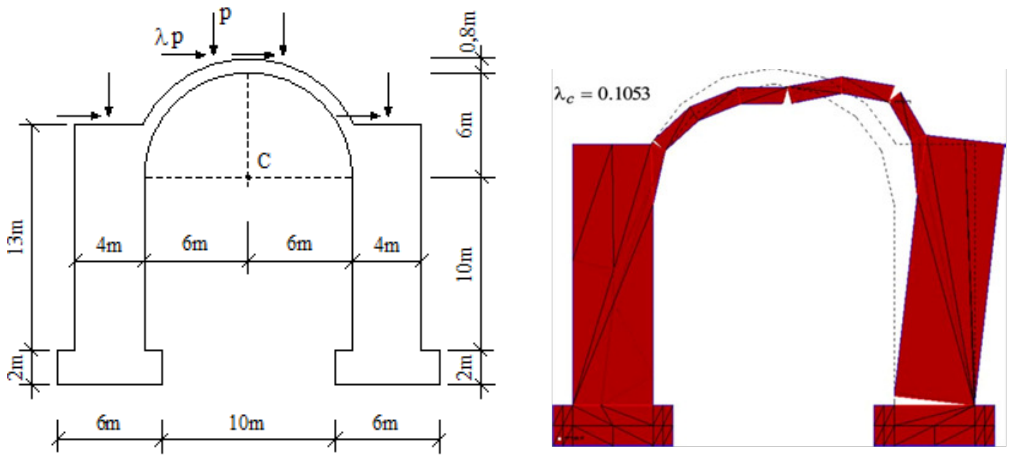


a) b)

Figure 2: A simple case study: a) Geometry and notation, b) collapse mechanism

6.2 Collapse mechanism of a barrel vault subject to seismic loading

A second example deals with the collapse analysis of the monumental masonry structure shown in Fig.4-left, consisting of a barrel vault resting on thick buttresses [34]. The loading condition is represented by the self–weight p of the structure (masonry unit weight equal to $17KN/m^3$), and horizontal forcesλp (static seismic loading, cf. Fig.3a). We estimate the collapse multiplier λ^0 of the horizontal forces by analyzing a $1.0m$ long slice of the structure. Fig.3b shows the collapse mechanism obtained for the present example through the self-adaptive mesh depicted in the same figure ($\lambda^0 = \lambda_c = 0.1053$, cf. [34]). Such a mechanism shows four opening hinges (cracks) in the masonry, one of which is located in a buttress and the other three in the vault (semi-global mechanism).

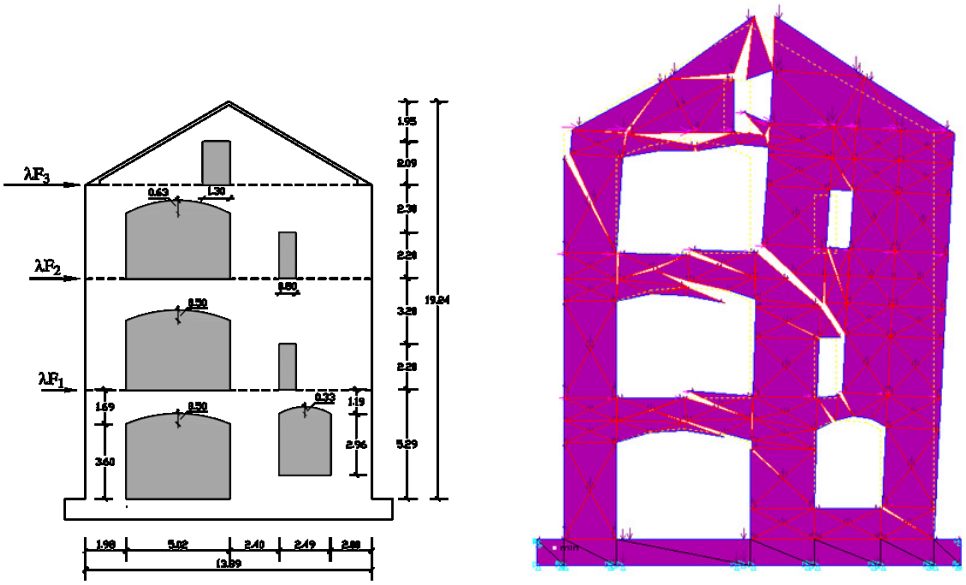


a) b)

Figure 3: Masonry structure covered with a barrel vault a) and corresponding collapse mechanism b)

6.3 Collapse mechanism of a multi storey masonry wall subject to seismic loading

Our final example is concerned with a three storey masonry wall subjected to fixed vertical loads and variable horizontal forces (Fig.4a). The wall is made up of tufe stones with 1.0 m thickness (constant over the height) and $18kN/m^3$ unit weight. A permanent loading of $7.5kN/m$ is acting in correspondence with each storey level. The base values of horizontal forces are: $F_1 = 33.82kN$; $F_2 = 45.58kN$; $F_3 = 70.31kN$ [34]. Fig.4b shows the employed mesh and the corresponding collapse mechanism ($\lambda^0 = 3.9827$).



a) b)

Figure 4: Masonry wall with openings subjected to fixed vertical loads and variable horizontal forces a) and corresponding collapse mechanism b).

7 CONCLUDING REMARKS

The free-discontinuity model presented in this work can be used to predict the ultimate load carrying capacity of masonry structures under vertical and horizontal loads, with the latter describing seismic excitations within a simplified static approach. We address a generalization of the present theory dealing with the limit behavior of vaults, membranes, and structural networks; and the inclusion of different free-discontinuity approaches to the variational theory of fracture, crushing and fracturing of masonry, as well as interface debonding and ripping (FRP-reinforced structures) to future work [22, 25, 29–34].

REFERENCES

[1] M. Como, A. Grimaldi, A unilateral model for the limit analysis of masonry walls. G. Del Piero, F. Maceri eds, *Unilateral problems in structural analysis, CISM Courses and Lectures*, **288**, 25–45, Springer, 1985

[2] J. Heyman, The stone skeleton. *International Journal of Solids and Structures*, **2**, 249–279, 1966

[3] S. Di Pasquale, Statica dei solidi murari. *Atti Dipartimento Costruzioni*, University of Firenze, 1984

[4] G. Romano, M. Romano, Sulla soluzione di problemi strutturali in presenza di legami costitutivi unilaterali. *Rendiconti Accademia Nazionale dei Lincei*, **67**, 104–113, 1979

[5] A. Baratta, R. Toscano, Stati tensionali in pannelli di materiale non resistente a trazione. *Atti del VI AIMETA Congress*, Genova, 1982

[6] M. Giaquinta, E. Giusti, Researches on the equilibrium of masonry structures. *Archive for Rational Mechanics and Analysis*, **88**, 359–392, 1985

[7] G. Del Piero, Constitutive equation and compatibility of the external loads for linear elastic masonry–like materials. *Meccanica*, **24**, 150–162, 1989

[8] M. Como, Equilibrium and collapse of masonry bodies. *Meccanica*, **27**(3), 185–194, 1992

[9] M. Angelillo, Constitutive relations for no-tension materials. *Meccanica*, **28**(2), 195–202, 1993

[10] M. Angelillo, L. Giliberti, Statica delle strutture murarie. *Giornale del Genio Civile*, 1988 (in Italian)

[11] M. Angelillo, R.S. Olivito, Experimental analysis of masonry walls loaded horizontally in plane. *Masonry International*, **8**(3), 91–100, 1995

[12] M. Angelillo, A. Fortunato, Equilibrium of masonry vaults. M. Fremond, F. Maceri eds. *Lecture Notes in Applied and Computational Mechanics*, **16**, 105–111, Springer–Verlag, 2002

[13] M. Angelillo, L. Cardamone, A. Fortunato, A numerical model for masonry-like structures, *Journal of Mechanics of Materials and Structures*, **5**, 583–615, 2010.

[14] A. Fortunato, Elastic solutions for masonry-like panels. *Journal of Elasticity*, **98**, 87–110, 2010

[15] M. Angelillo, E. Babilio, A. Fortunato, Singular stress fields for masonry-like vaults. *Continuum Mechanics and Thermodynamics*, **25**:423–441, 2013

[16] Mechanics of masonry structures. *Series: CISM International Centre for Mechanical Sciences*, **551**, M. Angelillo eds., 2014

[17] F. Fraternali, A Mixed Lumped Stress–Displacement Approach to the Elastic Problem of Masonry Walls. *Mechanics Research Communications*, **38**, 176–180, 2011

[18] G. Del Piero, Limit analysis and no–tension materials. *International Journal of Plasticity*, **14**, 259–271, 1998

[19] M. Angelillo, A. Fortunato, M. Lippiello, A. Montanino. Singular stress fields for masonry walls: Derand was right. *Meccanica*, **49**(5), 1243–1262, 2014

[20] A. Fortunato, M. Angelillo, F. Fraternali, Structural capacity of masonry walls under horizontal loads. *Ingegneria Sismica*, **1**, 41–49, 2014

[21] F. Fraternali, M. Angelillo, A. Fortunato, The lumped stress method and the discrete-continuum approximation. *International Journal of Solids and Structures*, **39**, 6211–6240, 2002

[22] F. Fraternali, A Thrust Network Approach to the Equilibrium Problem of Unreinforced Masonry Vaults via Polyhedral Stress Functions. *Mechanics Research Communications*, **37**, 198–204, 2010

[23] P. Block, J. Ochsendorf, Thrust network analysis: A new methodology for three-dimensional equilibrium. *Journal of the International Association for Shell and Spatial Structures*, **48**(3), 167-173, 2007

[24] M. Angelillo, E. Babilio, A. Fortunato, Folding of thin walled tubes. *Journal of Elasticity*, **82**, 243–271, 2006

[25] M. Angelillo, E. Babilio, A. Fortunato, Numerical solutions for crack growth based on the variational theory of fracturre. *Computational Mechanics*, **50**(3), 285–301, 2012

[26] M. Angelillo, E. Babilio, A. Fortunato, A numerical model for fracture of rods. M. Fremond, F. Maceri eds. *Lecture Notes in Applied and Computational Mechanics*, **23**, 277–292, Springer–Verlag, 2005

[27] G.A. Francfort, J.J. Marigo, Revisiting brittle fracture as an energy minimization problem *Journal of the Mechanics and Physics of Solids*, **46**(8), 1319–1342, 1998

[28] M. Angelillo and F. Rosso, On statically admissible stress fields for a plane masonry-like structure. *Quarterly of Applied Mathematics*, **53**(4), 731–751, 1995

[29] T. El Sayed, W. Mock, A. Mota, F. Fraternali, M. Ortiz, Computational assessment of ballistic impact on a high strength structural steel/polyurea composite plate. *Computational Mechanics*, **43**(4), 525–534, 2009

[30] B. Schmidt, F. Fraternali, Universal formulae for the limiting elastic energy of membrane networks. *International Journal of Solids and Structures*, **60**, 172–180, 2012

[31] F. Fraternali, L. Senatore, C. Daraio, Solitary waves on tensegrity lattices. *Journal of the Mechanics and Physics of Solids*, **60**, 1137-1144, 2012

[32] F. Fraternali, I. Farina, G. Carpentieri. A discrete-to-continuum approach to the curvatures of membrane networks and parametric surfaces. *Mechanics Research Communications*, **56**, 18-15, 2014

[33] F. Fraternali, Free Discontinuity Finite Element Models in Two-Dimensions for In-Plane Crack Problems. *Theoretical and Applied Fracture Mechanics*, **47**, 274–282, 2007

[34] L. Ascione, L. Feo, F. Fraternali, Load Carrying Capacity of 2D FRP/Strengthened Masonry Structures. *Composites Part B: Engineering*, **36**, 619–626, 2005

COMPDYN 2015
5th ECCOMAS Thematic Conference on
Computational Methods in Structural Dynamics and Earthquake Engineering
M. Papadrakakis, V. Papadopoulos, V. Plevris (eds.)
Crete Island, Greece, 25–27 May 2015

DYNAMIC RESPONSE OF A GOTHIC CATHEDRAL IN CYPRUS

Zehra Cagnan[1], **Christis Z. Chrysostomou**[2], **Nicholas Kyriakides**[3], **Renos A. Votsis**[4]

[1] Department of Civil Engineering, Faculty of Engineering and Architecture, TED University, Ziya Gokalp Caddesi No: 48, Kolej, Ankara, TURKEY
e-mail: zehra.cagnan@tedu.edu.tr

[2] Department of Civil Engineering and Geomatics, Faculty of Engineering and Technology, Cyprus University of Technology, Archbishop Kyprianou Street No: 30, 3036 Lemesos, CYPRUS
e-mail: c.chrysostomou@cut.ac.cy

[3] Department of Civil Engineering and Geomatics, Faculty of Engineering and Technology, Cyprus University of Technology, Archbishop Kyprianou Street No: 30, 3036 Lemesos, CYPRUS
e-mail: nicholas.kyriakides@cut.ac.cy

[4] Department of Civil Engineering and Geomatics, Faculty of Engineering and Technology, Cyprus University of Technology, Archbishop Kyprianou Street No: 30, 3036 Lemesos, CYPRUS
e-mail: renos.votsis@cut.ac.cy

Keywords: Unreinforced masonry structure, System identification, Seismic assessment, Historical structure.

Abstract. *Within the scope of this study, dynamic response of the St. Nicholas Cathedral in Cyprus that dates back to the 13th century was assessed based on obtained earthquake records. This structure resembles to the Rheims Cathedral of France with a nave of seven bays ending in a polygonal apse, together with flanking aisles ending in apsidal chapels of similar shape. According to historical records, it sustained heavy earthquake damage twice to its roof structure and flying buttresses. The main construction material used at this structure is calcarenite. Back in 2011, a strong-motion network was installed at the cathedral, which recorded a series of small to moderate magnitude events since then. This strong motion network consisting of 10 tri-axial accelerometers is the only active structural health monitoring system in Cyprus. In this article, the time-domain and frequency-domain analysis of this data is presented.*

1 INTRODUCTION

St. Nicholas Cathedral, one of the architectural landmarks of Cyprus, is located at the Gothic city center of Famagusta on the Eastern coast line of the island. The earliest documents that mention this structure go back to 1300 [1]. The era during which the cathedral was under construction corresponds to the first period of Lusignan rule on the island that is characterized by differentiable economic prosperity [2] which was reflected to the quality of monuments produced in that period. The architectural style of the cathedral heavily corresponds to the Rayonnant style in Gothic architecture that was developing in Europe during that very same period; an indication that developments in Europe were closely followed on the island during this period. St. Nicholas Cathedral was the appointed location for the coronation of the Lusignan kings as Kings of Jerusalem after they had been crowned in Nicosia (Capital of Cyprus) as Kings of Cyprus. According to [1], it is because of this functionality that St. Nicholas Cathedral imitates architecturally Rheims Cathedral of France.

St. Nicholas Cathedral has a plan area of 24mx50m, and a height of 29m (Figure 1a). It consists of a nave of seven bays ending in a polygonal apse flanked by aisles ending in apsidal chapels of similar shape. The last bay of the north aisle communicates with a sacristy composed of two roughly rectangular rib vaulted bays (Figure 1a). Enlart [1] indicates that from this sacristy, one could go down into a cistern however the passage way to the cistern is not open today. Also being mentioned in [1] is the fact that when the author visited Cyprus in late 1890s, the northern chapel of St. Nicholas Cathedral, which was added to the building after the initial construction of the main structure, was not in place (Figure 1a). In 1571, with Cyprus entering the Ottoman rule, a minaret was added to the cathedral, interior walls were white washed with gypsum and it has been in service as a mosque since then (Figure 2a).

Today the monuments of the Gothic city center of Famagusta are in a very deprived state due to decades long lack of maintenance. The deterioration of the masonry of these monuments is due to wind carrying sea salts, considerable temperature cycles between day and night, plant and animal ingress and drainage problems. St. Nicholas Cathedral is unfortunately one of the structures at which severe effects of this decay are visible (Figure 2b and 2c). In addition to this rather poor state of the structure, it is under the risk of earthquakes. The Cathedral being located close to the eastern arm of the Cyprus Arc (main seismic source for the island), it sustained severe structural damage caused by earthquakes a number of times throughout its history: 1546 [1, 3], 1568 [1, 3], 1735 [4], and 1941 [5]. It should be underlined that there are varying accounts in the literature regarding which structural elements of St. Nicholas Cathedral sustained damage throughout its history and what caused this damage; the flying buttresses and roof structure of St. Nicholas suffered severely due to 1546 and 1568 earthquakes according to [1, 3] and were tastelessly repaired. According to the British consul Alexander Drummond [4] the 1735 earthquake damaged 2/3 of the cathedral and over 200 people were buried under its ruins as a result. By [5] it was documented that the tremor of 1941 opened up cracks between the vaulting of the nave and the main walls at the St. Nicholas Cathedral. In 1951 and 1963, the cathedral was repaired and strengthened by constructing a concrete collar and a cross tie at the roof level [6].

Within the scope of European Union funded 'Earthquake Vulnerability Assessment of Historical Monuments in Cyprus' project that was active between 2009-2011, a strong motion network was developed at the St. Nicholas Cathedral with the aim of recording this structure's behavior under future earthquakes. This network is composed of 10 Guralp CMG-5TDE triaxial accelerometers (with sampling rate 100 sps, frequency band dc to 100Hz, full scale low gain sensitivity 4g to 0.1g) that are simultaneously triggered to provide a continuous record with a common time basis. Locations of these instruments are indicated in Figure 1b and 1c.

In this article, the time-domain and frequency-domain analysis of data recorded at the St. Nicholas Cathedral between 2011-2014 is presented.

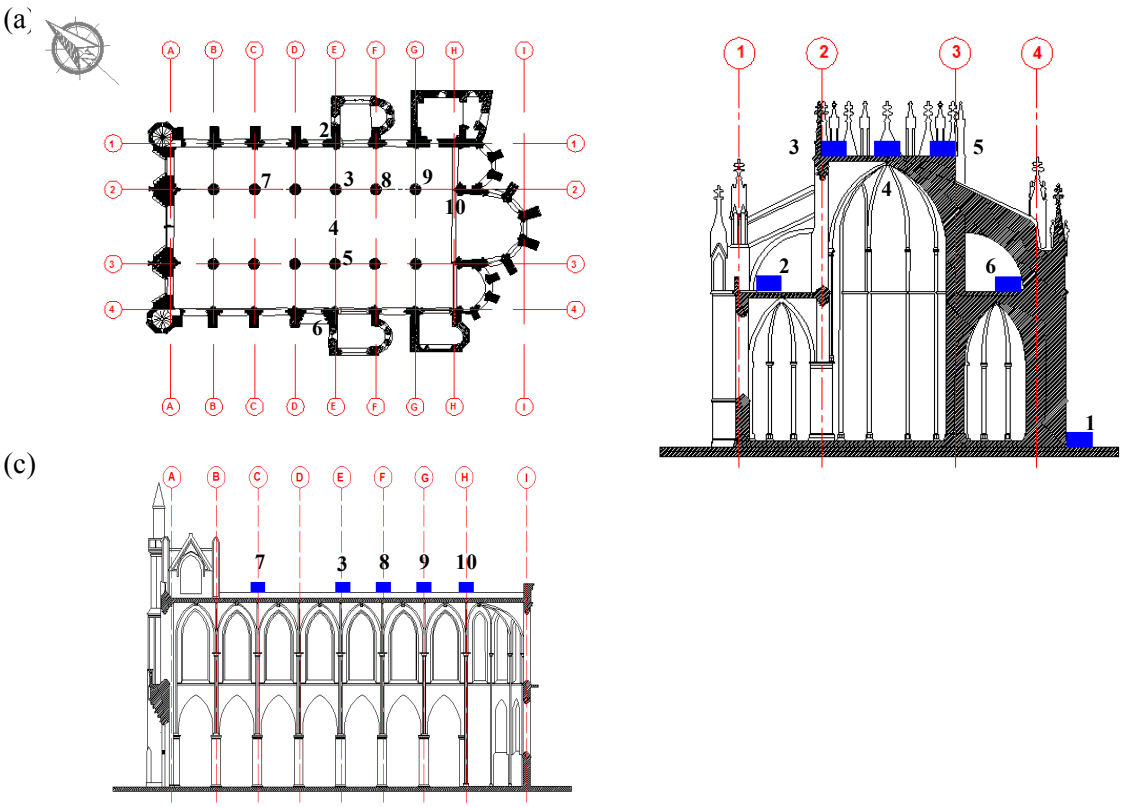


Figure 1: (a) Plan view of St. Nicholas Cathedral. (b) Transverse Section along Axis E and (c) Longitudinal Section along Axis 2 of the structure. Blue boxes indicate locations of 10 strong motion instruments installed to the St. Nicholas Cathedral for monitoring.

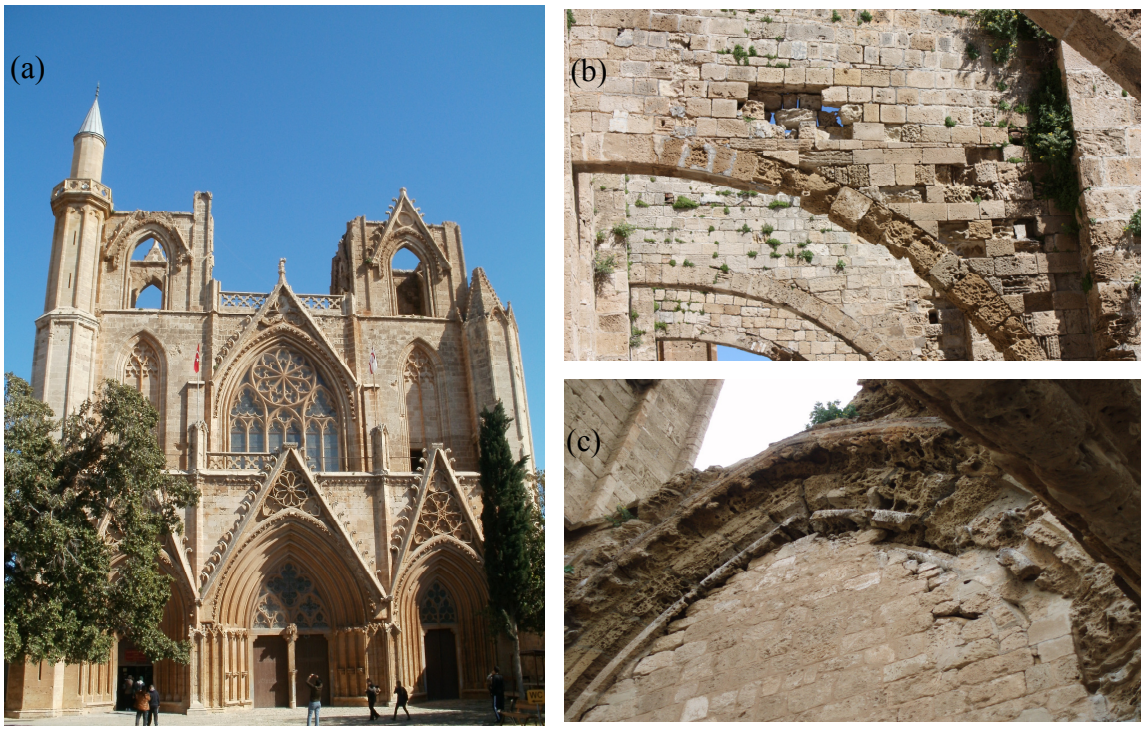


Figure 2: (a) Front (Western) façade of St. Nicholas Cathedral, (b) a close up on one of the flying buttresses of Southern façade, (c) a close up on the peripheral walls of the Northern façade. In both cases severe decay of masonry, gave the material a 'sponge like' appearance.

2 STRONG MOTION DATA

Between 2011-2014, the response of the St. Nicholas Cathedral was captured under 22 small to moderate regional events with magnitudes changing between M_d 3.1-6.0 and epicentral distances varying between 6-669 km (Table 1). Within the scope of this study all the acceleration records obtained were processed by using the USDP software [7] and following the filtering procedure suggested by [8] (a bi-directional 4 pole-4 pole Butterworth filter was used in this study; low pass and high pass cut-off frequencies were determined by observing regions of deviation of FAS computed for the accelerograms under consideration from the theoretical source spectra). The two highest acceleration values measured on the structure are 3.20 cm/s^2 and 2.28 cm/s^2 as a result of the 18 October 2012 (event 7) and 01 April 2011 (event 2) earthquakes respectively (Table 2). Based on these earthquake-recordings made at the St. Nicholas Cathedral, behavior at the locations of stations 5 and 8 were observed to be unexpected. These stations that are sitting on top of columns E3 (and southern façade axis E flying buttress), F2 (and northern façade axis F flying buttress) respectively, were observed to be associated with higher levels of acceleration when compared with data from stations at the same level such as 3, 9 and 10 (Figure 3). Different frequency characteristics were also observed in the case of recordings of these stations (Figure 4). Mainly these differences were observed for the N-S components of records that are aligned with the transverse direction of the structure.

Event No.	Date	Time	Lat	Long	Depth (km)	Magnitude (M_d)	Epicentral Distance (km)
1	26.03.2011	16:25:13	34.373	32.111	12.0	4.2	187
2	01.04.2011	13:29:07	35.514	26.580	57.1	6.0‡	669
3	18.04.2011	12:50:42	35.048	34.444	36.7	3.7	47
4	19.09.2012	09:17:46	37.320	37.116	8.1	4.7‡	376
5	26.09.2012	01:28:28	34.719	29.973	12.3	4.7	364
6	30.09.2012	15:52:34	34.988	33.639	54.0	3.4	31
7	18.10.2012	06:46:38	34.852	34.003	31.6	3.7	6
8	14.11.2012	23:55:48	37.266	37.100	14.8	4.9	371
9	30.11.2012	19:27:25	34.844	34.038	22.9	3.1	32
10	02.12.2012	00:21:55	34.393	32.933	5.0	3.5	123
11	12.12.2012	01:18:13	37.300	36.271	10.7	4.1	320
12	14.12.2012	00:31:19	35.409	33.336	12.0	3.3	64
13	03.03.2013	11:22:24	35.962	34.635	8.0	4.1	113
14	25.04.2013	22:54:15	37.315	37.137	6.0	4.3	377
15	10.07.2013	21:22:44	35.021	34.184	7.6	3.1	25
16	12.07.2013	08:57:38	35.179	33.897	11.2	3.2	8
17	12.07.2013	08:57:36	35.094	34.038	8.8	3.2	9
18	12.07.2013	08:58:42	34.719	34.240	25.2	3.5	52
19	08.08.2013	08:25:39	34.438	34.421	13.2	3.3	88
20	03.02.2014	18:29:44	34.833	32.560	24.8	4.1	130
21	14.02.2014	00:33:38	36.722	36.027	17.5	4.5	259
22	02.03.2014	04:25:57	36.776	35.159	7.5	4.1	214

Table 1: Recorded earthquakes at St. Nicholas Cathedral. Seismological data corresponding to recorded earthquakes was taken from Kandilli Observatory and Earthquake Research Institute's recent earthquakes database. M_d is duration magnitude. ǂMagnitude values given represent moment magnitude values taken from the European-Mediterranean Seismological Center database.

Event No.	PGA_{ground} $(gal)_{obs}$	$Direction_{ground}$	$PA_{structure}$ $(gal)_{obs}$	Location	$Direction_{structure}$
1	0.10	N-S	0.52	H2	N-S
2	0.36	N-S	2.28	H2	N-S
3	0.20	N-S	1.34	H2	N-S
4	NA	NA	0.22	G2	N-S
5	NA	NA	0.12	G2	N-S
6	NA	NA	0.17	G2	N-S
7	0.50	N-S	3.20	G2	N-S
8	NA	NA	0.08	G2	N-S
9	NA	NA	1.29	F2	N-S
10	0.02	N-S	0.12	F2	N-S
11	0.03*	N-S	0.04	H2	N-S
12	0.03*	N-S	0.09	G2	N-S
13	0.11*	N-S	0.69	F2	N-S
14	0.01*	N-S	0.17	E3	N-S
15	NA	NA	0.23	E3	N-S
16	0.02*	N-S	0.08	G2	N-S
17	NA	NA	0.35	G2	N-S
18	NA	NA	0.35	H2	N-S
19	0.07*	N-S	0.18	H2	N-S
20	NA	NA	0.53	G2	N-S
21	0.04	N-S	0.28	E3	N-S
22	0.1	N-S	0.32	G2	N-S

Table 2: Main peak acceleration characteristics of records obtained at St. Nicholas Cathedral: $PGA_{ground}(gal)_{obs}$ – Geometric mean of horizontal peak ground acceleration values recorded outside St. Nicholas Cathedral, NA – No ground level records are available, * – No ground level records are available from St. Nicholas Cathedral site however ground level accelerations measured by a nearby station (1.4km away with similar soil conditions) at Famagusta are given for comparison, $Direction_{ground}$ – direction in which maximum peak ground acceleration value was observed at St. Nicholas Cathedral site ((N-S, north-south direction which also corresponds to the transverse direction of the structure; E-W, east-west direction which also corresponds to the longitudinal direction of the structure), $PA_{structure}(gal)obs$ – Geometric mean of horizontal peak acceleration values recorded on the St. Nicholas Cathedral, Location – location at which these horizontal peak ground acceleration values were recorded on St. Nicholas Cathedral (Please refer back to Figure 1 for these exact locations), $Direction_{structure}$ – direction in which maximum peak acceleration value was observed on St. Nicholas Cathedral (N-S, north-south direction which also corresponds to the transverse direction of the structure; E-W, east-west direction which also corresponds to the longitudinal direction of the structure).

The unexpected behavior above columns E3 and F2 (as detected by stations 5 and 8) are likely to be caused by deteriorated flying buttresses of Northern and Southern facades along axes E and F and to a lesser extent by poor material properties at these columns as was documented by [9] during past studies on St. Nicholas Cathedral.

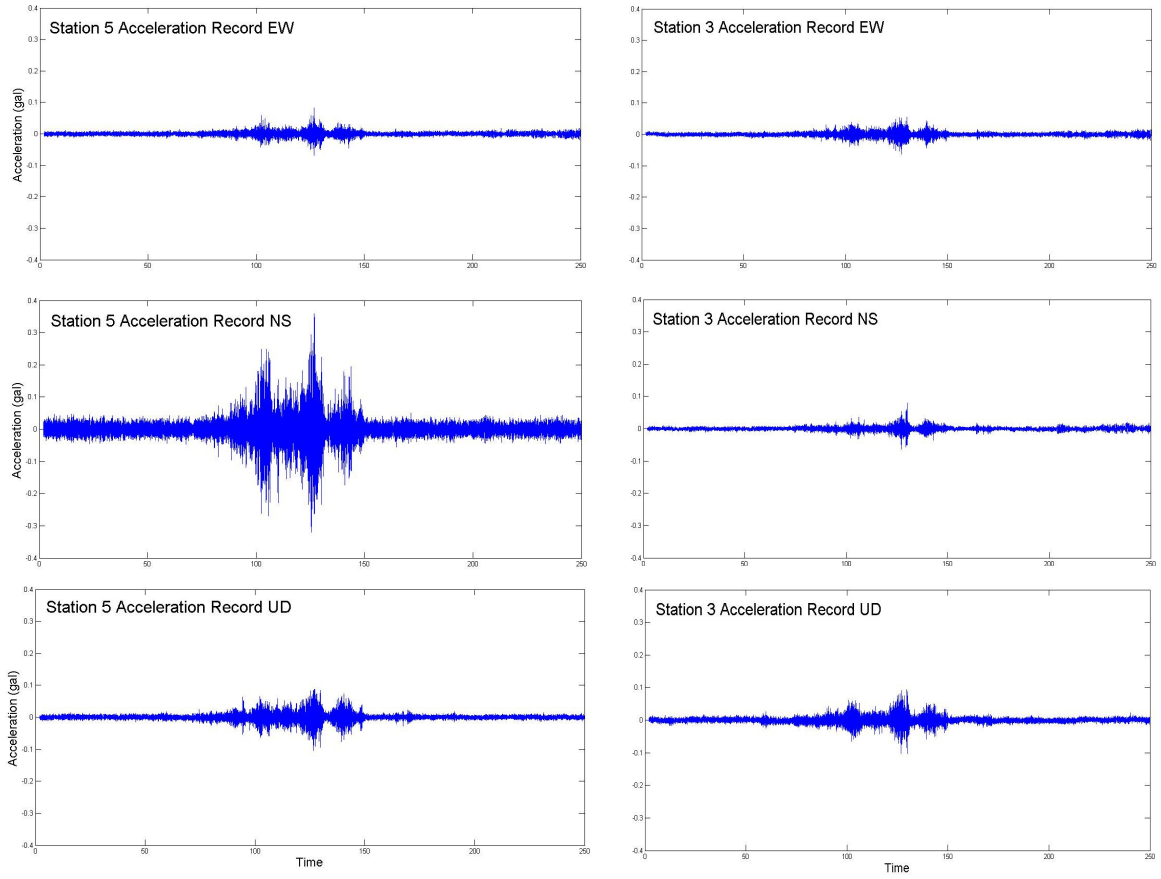


Figure 3: Acceleration records obtained at St. Nicholas Cathedral stations 3 and 5 during the 25 April 2013 Earthquake (N-S direction corresponds to the transverse direction of the structure; E-W direction corresponds to the longitudinal direction of the structure).

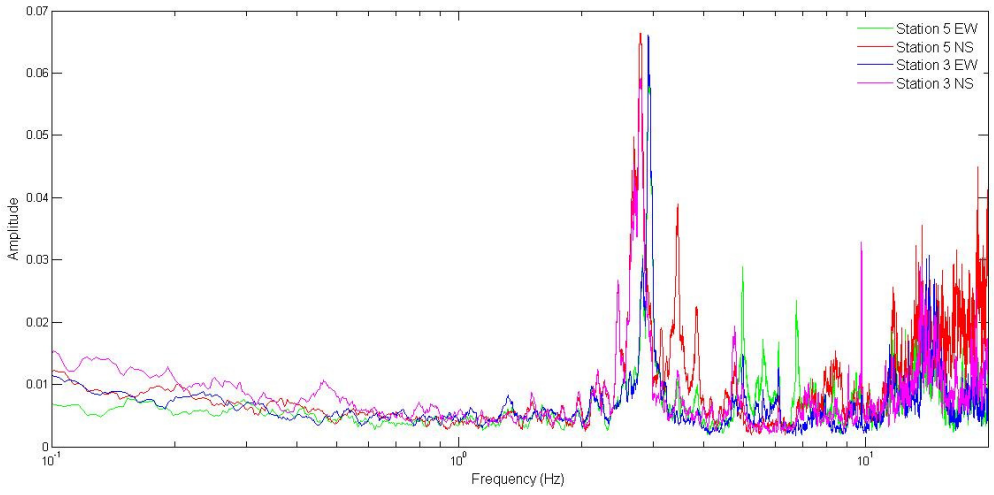


Figure 4: Comparison of Fourier Amplitude Spectra for stations 3 and 5 obtained from 25 April 2013 Earthquake acceleration records (N-S direction corresponds to the transverse direction of the structure; E-W direction corresponds to the longitudinal direction of the structure).

3 SPECTRAL ESTIMATIONS

Within the scope of this study, spectral techniques were applied to the records obtained from the 22 events given in Table 1 to identify dynamic system properties of the St. Nicholas Cathedral. Transfer functions were utilized in case of the events for which ground station of the network (station 1) yielded acceptable records (adequate signal to noise ratio values). As can be seen from Table 2, such events are rather limited in number. For the rest of the events, the power spectral density approach was preferred and only upper level stations of St. Nicholas Cathedral were utilized in this part of the study. Power spectral densities (PSD) were estimated on the basis of averaging of 10 sec. long windows with 50% overlapping. In Figure 6, the determined transfer functions based on each record (in grey) together with the overall average transfer function for each event (in red) are given. These computations were repeated for E-W and N-S direction records separately. In Figure 7, average PSDs computed for each event in E-W and N-S directions are given separately. Both in the case of Figure 6 and 7, N-S direction records yielded first vibrational modal frequencies and E-W direction records yielded second vibrational modal frequencies. Identified modal frequencies within the scope of this study from the 22 events for the presumed first and second modes are summarized in Table 3 below.

Event No.	1st Modal Frequency (Hz) Direction N-S	2nd Modal Frequency (Hz) Direction E-W
1	2.63	2.90
2	2.68	2.95
3	2.75	2.98
4	2.81	2.98
5	2.78	2.93
6	2.76	3.00
7	2.64	2.86
8	2.69	2.93
9	2.73	2.95
10	2.68	2.89
11	2.81	2.93
12	2.83	2.93
13	2.69	2.83
14	2.95	3.08
15	2.78	3.00
16	2.81	3.05
17	2.81	3.05
18	2.81	3.05
19	2.83	3.05
20	2.64	2.86
21	2.78	2.93
22	2.78	2.93

Table 3: Modal frequencies associated with the 1st and 2nd dominant vibrational modes at St. Nicholas Cathedral .

Based on the data given in Table 3, it can be stated that a correlation exists between 1st and 2nd modal frequencies determined and amplitude of recorded accelerations on the St. Nicholas Cathedral as well as between 1st and 2nd modal frequencies and event durations although the latter observed to be a weaker correlation (Figure 5). Also it should be noted that measured modal frequencies are under the effect of ambient temperature as well, as measurements were

taken in different seasons and times. As temperature at the St. Nicholas Cathedral site was not recorded at the time of events, the relationship between the measured modal frequencies and temperature could not be studied in detail within the scope of this study.

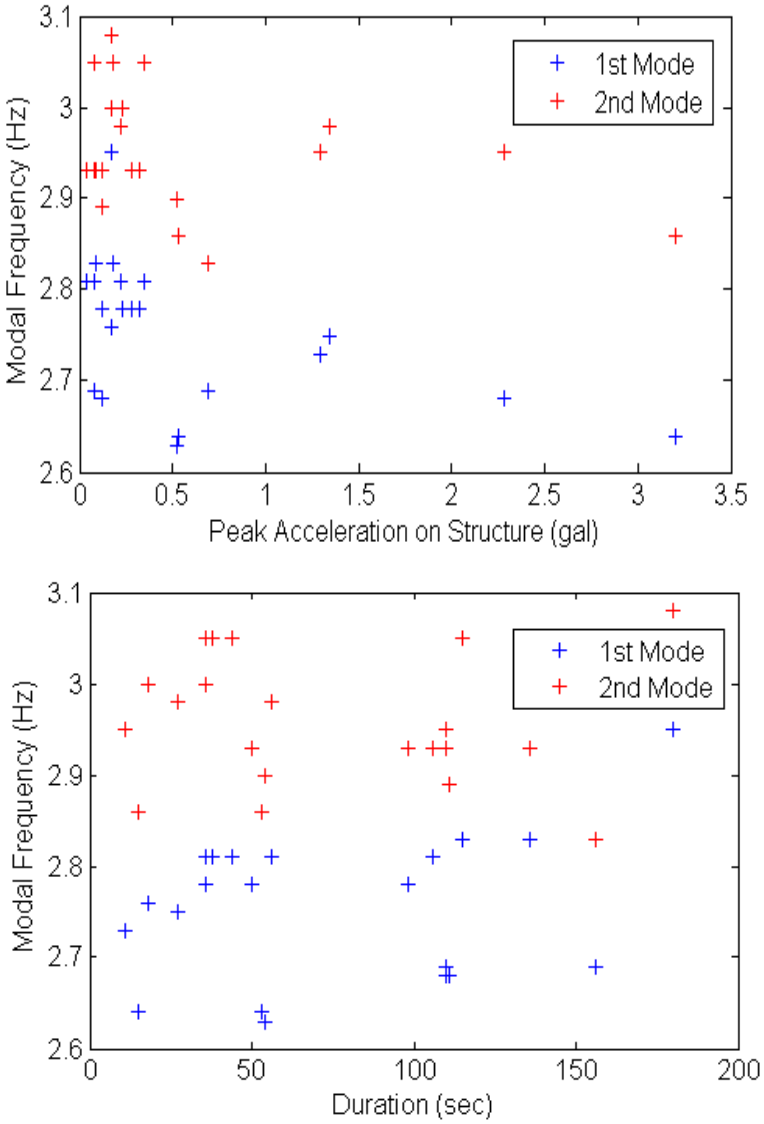


Figure 5: Relationship between measured 1st and 2nd modal frequencies and (a) observed peak acceleration values on the St. Nicholas Cathedral and (b) event durations.

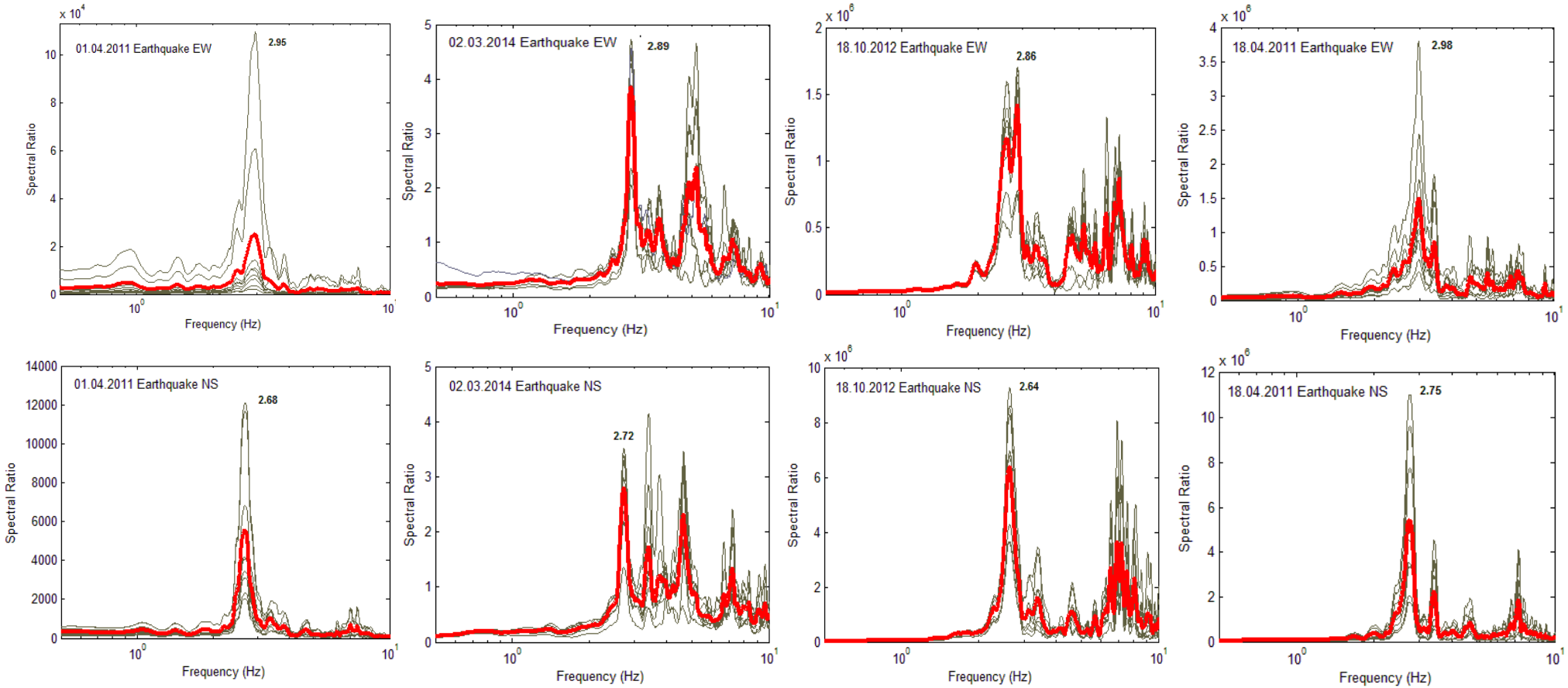


Figure 6: Estimated transfer functions for the E-W and N-S directions of St. Nicholas Cathedral for the events of 01 April 2011, 02 March 2014, 18 October 2012 and 18 April 2011. Transfer functions obtained based on individual station records are represented by grey lines. Red lines represent average transfer functions computed for each event (N-S direction corresponds to the transverse direction of the structure; E-W direction corresponds to the longitudinal direction of the structure).

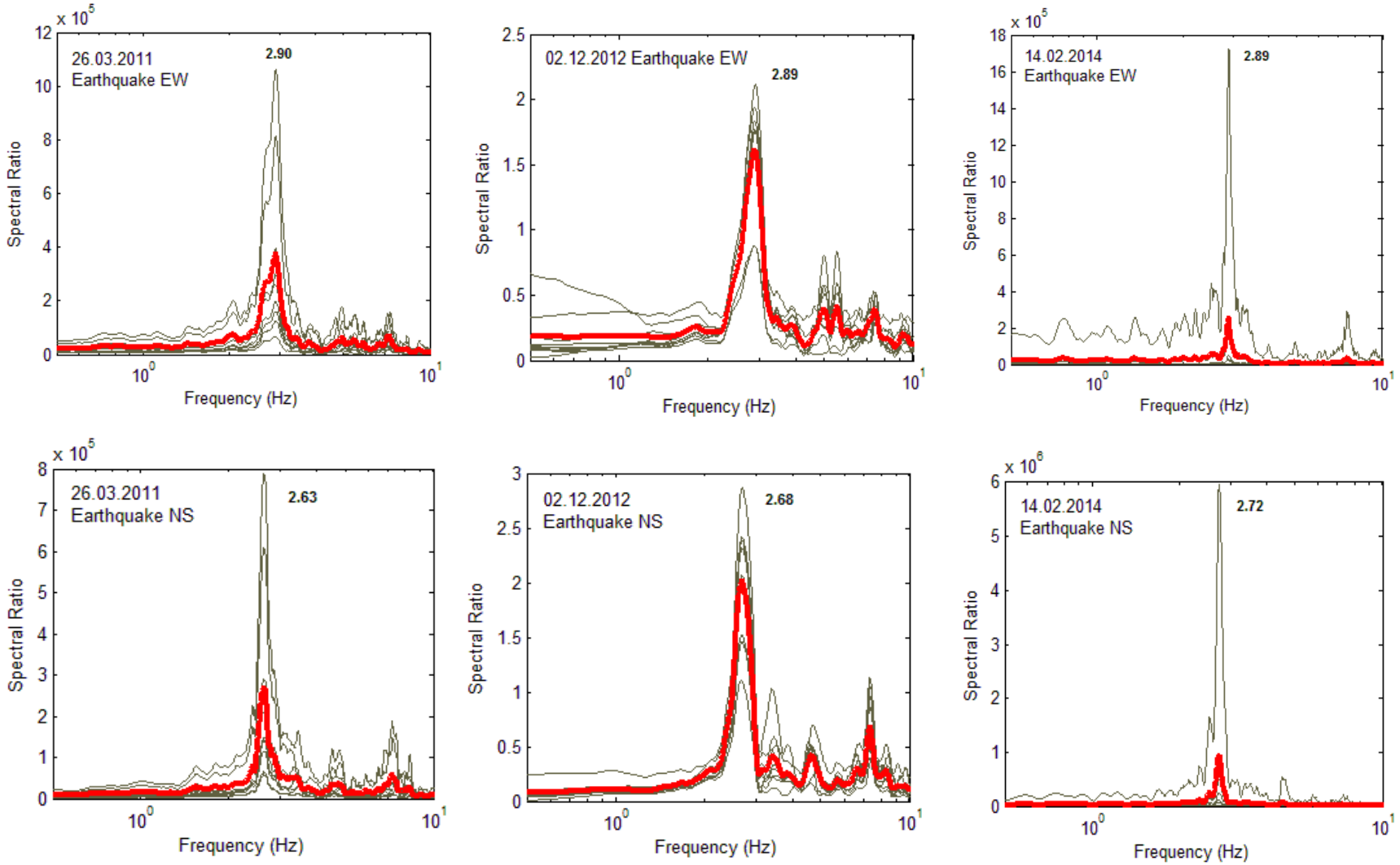


Figure 6 cont.: Estimated transfer functions for the E-W and N-S directions of St. Nicholas Cathedral for the events of 26 March 2011, 02 December 2012 and 14 February 2014. Transfer functions obtained based on individual station records are represented by grey lines. Red lines represent average transfer functions computed for each event (N-S direction corresponds to the transverse direction of the structure; E-W direction corresponds to the longitudinal direction of the structure).

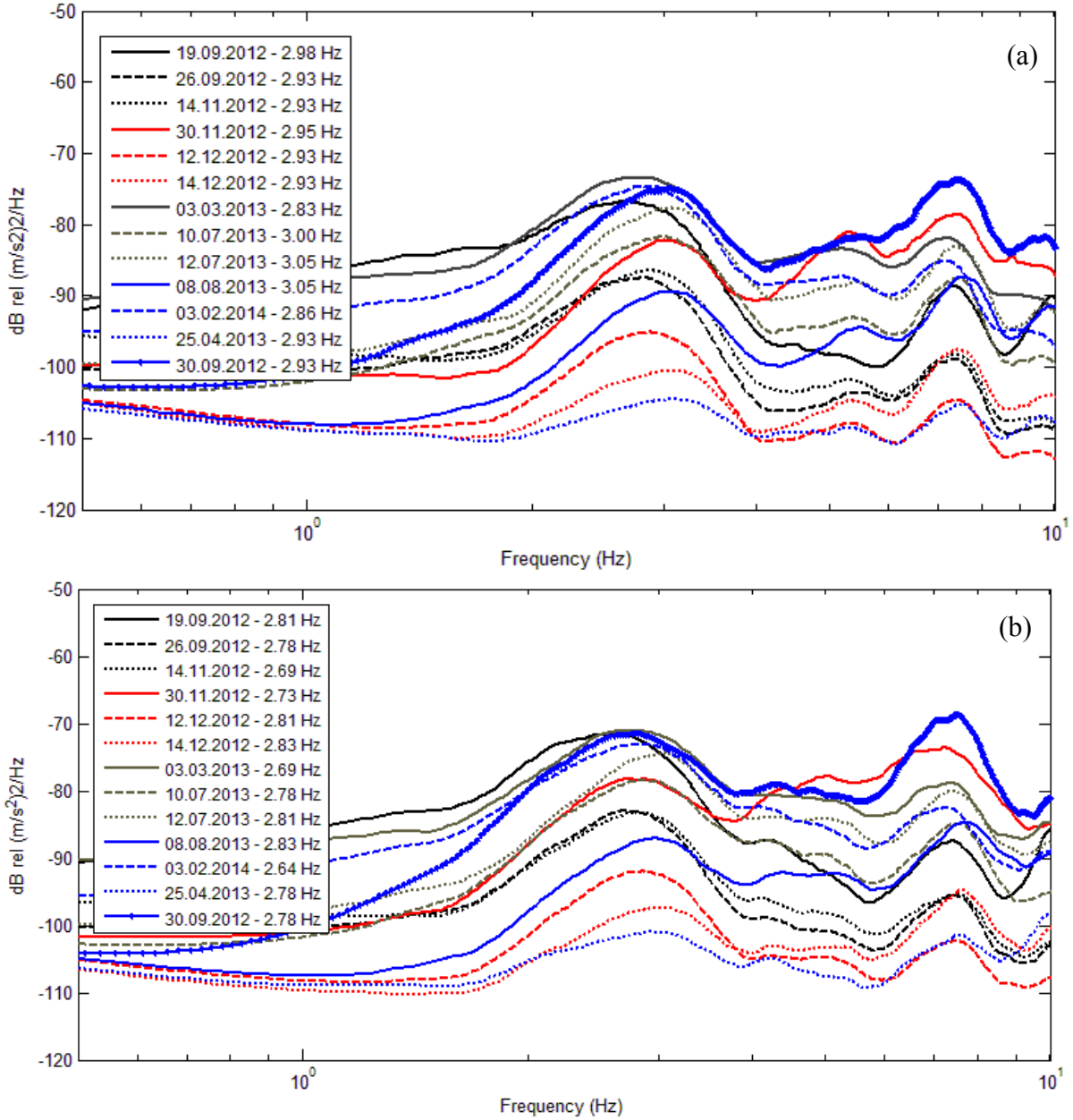


Figure 7: (a) Average power spectral densities computed for 19.09.2012, 26.09.2012, 14.11.2012, 30.11.2012, 12.12.2012, 14.12.2012, 03.03.2013, 10.07.2013, 12.07.2013, 08.08.2013, 03.02.2014, 25.04.2013, 30.09.2012 events for the E-W direction of St. Nicholas Cathedral, (b) average power spectral densities computed for 19.09.2012, 26.09.2012, 14.11.2012, 30.11.2012, 12.12.2012, 14.12.2012, 03.03.2013, 10.07.2013, 12.07.2013, 08.08.2013, 03.02.2014, 25.04.2013, 30.09.2012 events for the N-S direction of St. Nicholas Cathedral.

4 CONCLUSIONS

Within the scope of this study, the time domain and frequency domain characteristics of 22 earthquake records detected by the strong motion network at St. Nicholas Cathedral were assessed. These events that were recorded between 2011 and 2014 are rather small local and moderate distant events hence observed peak acceleration values on the St. Nicholas Cathedral remained below the 3.5 gal level. As a result processing of the obtained records proved to be rather challenging.

Based on the records obtained, it was detected that above columns E3 and F2 (at locations of station 5 and 8) the structure underwent unexpectedly high accelerations. As the N-S components of the obtained records especially observed to be unexpectedly high, it is believed that this behavior is associated with deteriorated Northern and Southern façade flying buttresses of St. Nicholas Cathedral around axes E and F of the structure (Figure 1).

Based on frequency domain analyses of obtained records, 1st and 2nd vibrational modal frequencies were detected for the St. Nicholas Cathedral. Previously, a finite element model of the structure was developed and calibrated based on ambient vibration tests conducted on the structure [10] and [11]. Findings of these previous studies do not fully agree with the results reached within the scope of this study based on small to moderate magnitude events recorded. In [11], the first four vibrational frequencies and their associated mode shapes were identified at 0.98 Hz, 1.04 Hz, 1.28 Hz and 1.40 Hz. Both [11] and analytical model of [10] yielded translation along the longitudinal axis of the St. Nicholas Cathedral as the 1st dominant mode for the structure and translation along the transverse axis of the structure as the 2nd dominant mode. Based on frequency domain analyses of this study, we did not observe peaks around 1 Hz but rather later between 2.63 Hz-2.83 Hz for the 1st vibrational mode and between 2.83 Hz-3.08 Hz for the 2nd vibrational mode. This study also implies that the 1st vibrational mode is dominated by translation along the transverse direction of the structure and it is the 2nd vibrational mode being dominantly translation along the longitudinal axis of the structure. These differences can be due to record high temperatures experienced and documented in [11] during ambient vibration tests. Also the lateral stiffness provided by the flying buttresses of the structure is probably not correctly reflected to the FEM model in [10] (modeled as higher than what the structure possess in reality). Exact conclusions, however, will be drawn when the mode shapes are extracted from the current records, so that the vibrational modes identified in both studies can be appropriately correlated.

The 22 small to moderate events recorded by the St. Nicholas Cathedral strong motion network provided valuable insight into the behavior of this structure. Before more firm conclusions can be drawn on the dynamic behavior of this structure local moderate to large events that would yield higher acceleration levels at the site of St. Nicholas Cathedral have to be recorded by this network. Nevertheless this preliminary data obtained indicates clearly the importance of such networks for fully understanding complex behavior of historical structures such as the cathedral under consideration.

5 ACKNOWLEDGEMENTS

The St. Nicholas Cathedral strong motion network was financed by the European Union within the scope of Cypriot Civil Society in Action Program under the award no. CRIS 2008/172-607 within the scope of the project ‘Earthquake Vulnerability Assessment of Historical Monuments in Cyprus’, however the views expressed in this publication do not necessarily reflect the views of the European Union.

REFERENCES

[1] C. Enlart, *L'Art gothique et la Renaissance en Chypre (2 vols, Paris) (English translation: Gothic Art and the Renaissance in Cyprus, trans. And ed. D. Hunt (London, 1987)*. Trigraph, p. 215, 1899.

[2] E. Solsten, *Cyprus: a country study*. Washington: GPO for the Library of Congress, 1991.

[3] B. Stewart, *My experiences of Cyprus*. Routledge, 1908.

[4] CD. Cobham, *Experta Cypria: materials for a history of Cyprus*. Cambridge University Press, 1908.

[5] *Cyprus: annual report of the director of antiquities*. Nicosia, 1951.

[6] *Cyprus: annual report of the director of antiquities*. Nicosia, 1968.

[7] S. Akkar, Ö. Ay, Ö. Kale and O. Pekcan, *Utility software for data processing (USDP)*, http://web.boun.edu.tr/sinan.akkar/usdp1.html, last accessed 30.01.2015. Bogazici University, Turkey, 2012.

[8] D. Boore and S. Akkar, Effects of causal and acausal filters on elastic and inelastic response spectra. *Earthquake Engineering and Structural Dynamics*, **32**, 1729-1748, 2003.

[9] Z. Cagnan, *Report on structural properties of St. Nicholas Cathedral Famagusta and St. Mamas Church Morpou, An earthquake vulnerability of historical monuments in Cyprus project report of KTTMOB*. Nicosia, Cyprus, 2010.

[10] Z. Cagnan, Numerical models for the seismic assessment of St. Nicholas Cathedral, Cyprus, *Soil Dynamics and Earthquake Engineering*, **39**, 50-60, 2012.

[11] R.A Votsis, N. Kyriakides, C.Z. Chrysostomou, E. Tantele, Ambient vibration testing of two masonry monuments in Cyprus, *Soil Dynamics and Earthquake Engineering*, **43**, 58-68, 2012.

COMPDYN 2015
5th ECCOMAS Thematic Conference on
Computational Methods in Structural Dynamics and Earthquake Engineering
M. Papadrakakis, V. Papadopoulos, V. Plevris (eds.)
Crete Island, Greece, 25–27 May 2015

APPLICATION OF THE PUSHOVER-BASED PROCEDURE TO PREDICT THE LARGEST PEAK RESPONSE OF ASYMMETRIC BUILDINGS WITH BUCKLING-RESTRAINED BRACES

Kenji Fujii

Department of Architecture and Civil Engineering, Chiba Institute of Technology
2-17-1 Tsudanuma, Narashino, Chiba 275-0016, Japan
e-mail: kenji.fujii@it-chiba.ac.jp

Keywords: Pushover Analysis, Asymmetric Buildings, Bidirectional Excitation, Buckling-restrained Braces

Abstract. *Asymmetric buildings are known to be vulnerable to earthquakes. This is because excessive deformation may occur at the frame of the flexible and/or weak side owing to an unfavourable torsional effect. Such deformation may lead to premature failure of the brittle members and finally to the collapse of whole buildings. To reduce the unfavourable torsional effect, one promising method is to install dampers to the frame in which excessive deformation is expected. The buckling-restrained brace (BRB) is widely used as a hysteresis damper in new buildings and for the seismic upgrading of existing buildings. For the evaluation of the peak seismic response of buildings, a pushover-based simplified procedure, which is often referred to as the nonlinear static procedure (NSP), has been developed and adopted to seismic design codes. In the case of reinforced concrete asymmetric buildings with BRBs, the first mode shape may notably change in the nonlinear range. This change may be critical in the accurate prediction of the peak response employing the NSP. However, there have been few studies on the applicability of NSPs to asymmetric buildings with BRBs. In this paper, the applicability of the simplified procedure proposed by the author to four-storey reinforced-concrete asymmetric buildings with BRBs is numerically investigated. In the simplified procedure presented in the previous study, the largest peak response is predicted from (a) the response of two independent equivalent single-degree-of-freedom models representing the first and second modes, considering the change in the first mode shape in each nonlinear stage, and (b) the envelope obtained from the combination of four pushover analyses considering the effect of bidirectional excitation. The predicted largest peak response is compared with the nonlinear time-history analysis results considering various directions of incidence of seismic input. The results show that the largest peak response of asymmetric buildings with BRBs is satisfactorily predicted by the procedure presented in the previous study. The effect of the change in mode shape on the accuracy of the NSP is also investigated and shown to be important in the accurate prediction of the peak response.*

1 INTRODUCTION

Asymmetric buildings are known to be vulnerable to earthquakes. This is because excessive deformation may occur at the frame of the flexible and/or weak side edge owing to an unfavourable torsional effect. This may lead to premature failure of the brittle members and finally to collapse of whole buildings. In general, the excessive deformation at the flexible and/or weak side frame can be reduced by relocation of frames and/or members. However, such relocation may not be feasible for existing buildings because of difficulties arising from architectural and functional constraints.

In recent years, the seismic rehabilitation of existing buildings using energy dissipative devices has been widely studied, and the seismic behaviour of asymmetric buildings with viscous, viscoelastic and elasto-plastic devices has been investigated [1–7]; the seismic behaviour of asymmetric buildings with viscous dampers has been investigated by Goel [1–3] and Chopra [4], while Landi [5] discussed the seismic design scheme of viscous dampers for the rehabilitation of an asymmetric building. De la Llera [6] discussed torsional balance, which is defined as the property of an asymmetric structure that leads to similar deformation demand in structural members equidistant from the geometric centre of the building plan, for elastic asymmetric structures with a friction damper. Mazza [7] discussed a displacement-based seismic design scheme of hysteresis dampers for rehabilitation of in-plan irregular reinforced concrete (RC) buildings. The results of these studies suggest that installation of dampers to the frame in which excessive deformation is expected is a promising method of reducing the unfavourable torsional effect of asymmetric buildings. However, in most of the above studies [1–6], asymmetric buildings are assumed to have linear (elastic) behaviour. Although Mazza [7] investigated the nonlinear behaviour of asymmetric buildings with a hysteresis damper by conducting nonlinear static (pushover) analyses, the results of pushover analyses and nonlinear dynamic (time-history) analyses have not been compared. Therefore, more investigations on the nonlinear behaviour of asymmetric buildings with various dampers are needed.

The pushover-based simplified nonlinear analysis procedure, which is often referred to as the nonlinear static procedure (NSP), has been developed by several researchers since the 1980s (e.g., [8], [9]). Although the application of the earlier version of the NSP is limited to planar frame analysis of buildings with regular elevation, the extension of the NSP to asymmetric buildings has been widely investigated in recent years (e.g., [10–16]). It would be valuable if these extended versions of the NSP were applicable to asymmetric buildings with dampers; however, there are problems. One critical problem, from the author's point of view, is that the unfavourable torsional effect is estimated from the linear elastic behaviour in most studies [10–13]. In the case of RC buildings with dampers, the first mode shape may change notably in the nonlinear range. Therefore, the estimation of the torsional effect based on linear elastic behaviour would lead to notable error in case of asymmetric buildings with dampers. In contrast, Bosco et al. [14] proposed a procedure of estimating the horizontal displacement distribution of asymmetric buildings from the envelope of two pushover analyses, using "corrective eccentricities". Even though this idea is attractive, proposed equations for the calculation of corrective eccentricities are based on numerical analyses of asymmetric structures without dampers. Therefore, it may be difficult to apply the idea directly to such asymmetric buildings with dampers. The author has investigated the development of the advanced NSP for asymmetric buildings considering by-directional excitation [15]. The author then proposed a simplified procedure that predicts the largest peak response of an asymmetric building to horizontal bidirectional ground motion acting at an arbitrary angle of incidence [16]. In this procedure, the largest peak response is predicted from (a) the response of two independent

equivalent single-degree-of-freedom (SDOF) models representing the first and second modes, considering the change in the first mode shape in each nonlinear stage, and (b) the envelope obtained from the combination of four pushover analyses considering the effect of bi-directional excitation. Because the effect of the change in mode shape in the nonlinear stage is considered in this procedure, the procedure has promise for application to an asymmetric building with dampers.

In this paper, the applicability of the simplified procedure proposed by the author [16] to four-storey RC asymmetric buildings with a hysteresis damper (buckling-restrained brace (BRB) [17, 18]) is numerically investigated. The predicted largest peak response is compared with the nonlinear dynamic (time-history) analysis results considering various directions of the incidence of seismic input. Note that the asymmetric buildings are limited to torsionally stiff (TS) buildings in this study.

2 DESCRIPTION OF THE SIMPLIFIED PROCEDURE TO PREDICT THE LARGEST PEAK RESPONSE

The simplified procedure presented by the author [16] is outlined in Figure 1. The asymmetric building considered in this study is an N-storey building, with $3N$ degrees of freedoms ($3N$-DOFs). All frames of the asymmetric building are oriented either the X- or Y-direction, which are mutually orthogonal. Another set of orthogonal axes U and V in the X–Y plane is considered, with the U-axis being the principal axis of the first modal response [15, 16]. This simplified procedure is detailed below on the basis of reference [16].

2.1 Step 1: Pushover analysis of the asymmetric building model (first mode)

A pushover analysis of an asymmetric building is carried out considering the change in the first mode shape. In this study, the displacement-based mode-adaptive pushover analysis (DB-MAP analysis presented in [16]) is applied. The nonlinear properties of the equivalent SDOF model and the relationship of the equivalent acceleration A_{1U}^{*} and equivalent displacement D_{1U}^{*}, referred to as the capacity curve, are then determined from the pushover analysis results.

The displacement vector at each loading stage $_{n}\mathbf{d}$ is assumed to be proportional to the first mode vector at each loading stage $_{n}\Gamma_{1U\,n}\boldsymbol{\varphi}_{\mathbf{1}}$. The equivalent displacement and acceleration at each loading step n, $_{n}D_{1U}^{*}$ and $_{n}A_{1U}^{*}$, are then determined as

$$ {}_{n}D_{1U}^{*} = \frac{{}_{n}\Gamma_{1U\,n}\boldsymbol{\varphi}_{\mathbf{1}}^{\mathrm{T}}\mathbf{M}_{n}\mathbf{d}}{{}_{n}M_{1U}^{*}} = \frac{\sum_{j}\left(m_{j\,n}x_{j}^{2} + m_{j\,n}y_{j}^{2} + I_{j\,n}\theta_{j}^{2}\right)}{\sqrt{\left(\sum_{j}m_{j\,n}x_{j}\right)^{2} + \left(\sum_{j}m_{j\,n}y_{j}\right)^{2}}}, \tag{1} $$

$$ {}_{n}A_{1U}^{*} = \frac{{}_{n}\Gamma_{1U\,n}\boldsymbol{\varphi}_{\mathbf{1}}^{\mathrm{T}}{}_{n}\mathbf{f}_{\mathbf{R}}}{{}_{n}M_{1U}^{*}} = \frac{\sum_{j}\left({}_{n}f_{RXjn}x_{j} + {}_{n}f_{RYjn}y_{j} + {}_{n}f_{MZj\,n}\theta_{j}\right)}{\sqrt{\left(\sum_{j}m_{j\,n}x_{j}\right)^{2} + \left(\sum_{j}m_{j\,n}y_{j}\right)^{2}}}, \tag{2} $$

where

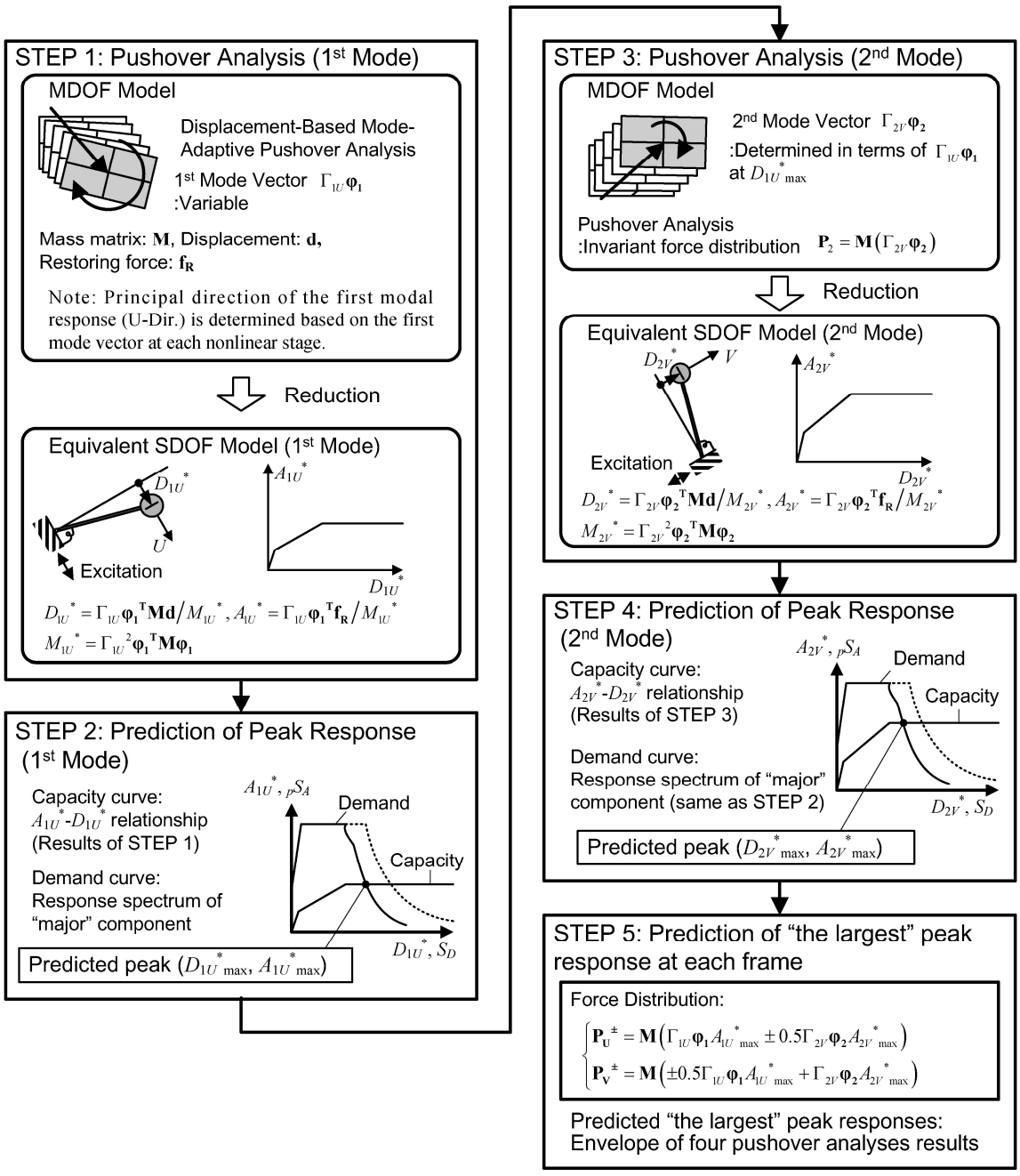


Figure 1: Outline of the simplified procedure

$$ {}_nM_{1U}^* = {}_n\Gamma_{1U}^2\,{}_n\boldsymbol{\varphi}_1^T\mathbf{M}_n\boldsymbol{\varphi}_1 = \frac{\left(\sum_j m_{j\,n}x_j\right)^2 + \left(\sum_j m_{j\,n}y_j\right)^2}{\sum_j\left(m_{j\,n}x_j^2 + m_{j\,n}y_j^2 + I_{j\,n}\theta_j^2\right)}, \tag{3} $$

$$ {}_n\Gamma_{1U} = \frac{{}_n\boldsymbol{\varphi}_1^T\mathbf{M}_n\boldsymbol{\alpha}_U}{{}_n\boldsymbol{\varphi}_1^T\mathbf{M}_n\boldsymbol{\varphi}_1} = \frac{\sqrt{\left(\sum_j m_{j\,n}x_j\right)^2 + \left(\sum_j m_{j\,n}y_j\right)^2}}{\sum_j\left(m_{j\,n}x_j^2 + m_{j\,n}y_j^2 + I_{j\,n}\theta_j^2\right)}, \tag{4} $$

$$\mathbf{M}=\begin{bmatrix}\mathbf{M_0} & \mathbf{0} & \mathbf{0}\\ \mathbf{0} & \mathbf{M_0} & \mathbf{0}\\ \mathbf{0} & \mathbf{0} & \mathbf{I_0}\end{bmatrix},\mathbf{M_0}=\begin{bmatrix}m_1 & & 0\\ & \ddots & \\ 0 & & m_N\end{bmatrix},\mathbf{I_0}=\begin{bmatrix}I_1 & & 0\\ & \ddots & \\ 0 & & I_N\end{bmatrix}, \tag{5}$$

$${}_{\mathbf{n}}\mathbf{d}=\left\{{}_nx_1 \quad \cdots \quad {}_nx_N \quad {}_ny_1 \quad \cdots \quad {}_ny_N \quad {}_n\theta_1 \quad \cdots \quad {}_n\theta_N\right\}^{\mathbf{T}}, \tag{6}$$

$${}_{\mathbf{n}}\mathbf{f_R}=\left\{{}_nf_{RX1} \quad \cdots \quad {}_nf_{RXN} \quad {}_nf_{RY1} \quad \cdots \quad {}_nf_{RYN} \quad {}_nf_{MZ1} \quad \cdots \quad {}_nf_{MZN}\right\}^{\mathbf{T}}, \tag{7}$$

$${}_{\mathbf{n}}\boldsymbol{\varphi}_{\mathbf{1}}=\left\{{}_n\phi_{X11} \quad \cdots \quad {}_n\phi_{XN1} \quad {}_n\phi_{Y11} \quad \cdots \quad {}_n\phi_{YN1} \quad {}_n\phi_{\Theta 11} \quad \cdots \quad {}_n\phi_{\Theta N1}\right\}^{\mathbf{T}}, \tag{8}$$

$${}_{\mathbf{n}}\boldsymbol{\alpha}_{\mathbf{U}}=\left\{\cos{}_n\psi_1 \quad \cdots \quad \cos{}_n\psi_1 \quad -\sin{}_n\psi_1 \quad \cdots \quad -\sin{}_n\psi_1 \quad 0 \quad \cdots \quad 0\right\}^{\mathbf{T}}, \tag{9}$$

$$\cos{}_n\psi_1=\frac{\sum_j m_j{}_n\phi_{Xj1}}{\sqrt{\left(\sum_j m_j{}_n\phi_{Xj1}\right)^2+\left(\sum_j m_j{}_n\phi_{Yj1}\right)^2}}=\frac{\sum_j m_j{}_nx_j}{\sqrt{\left(\sum_j m_j{}_nx_j\right)^2+\left(\sum_j m_j{}_ny_j\right)^2}}, \tag{10}$$

$$\sin{}_n\psi_1=\frac{-\sum_j m_j{}_n\phi_{Yj1}}{\sqrt{\left(\sum_j m_j{}_n\phi_{Xj1}\right)^2+\left(\sum_j m_j{}_n\phi_{Yj1}\right)^2}}=\frac{-\sum_j m_j{}_ny_j}{\sqrt{\left(\sum_j m_j{}_nx_j\right)^2+\left(\sum_j m_j{}_ny_j\right)^2}}. \tag{11}$$

In Eqs. (1)–(11), m_j and I_j are the mass and mass moment of inertia of the jth floor, respectively, ${}_nM_{1U}^{*}$ is the equivalent first modal mass with respect to the U-axis in each nonlinear stage, and ${}_n\psi_1$ is the angle of incidence of the U-axis in each nonlinear stage. Note that the reference axis considering the first modal response (U-axis) depends on the displacement; it changes in each nonlinear stage as the first mode vector changes.

2.2 Step 2: Prediction of the peak response of the equivalent SDOF model (first mode)

The largest peak equivalent displacement $D_{1U}{}^{*}{}_{\max}$ and equivalent acceleration $A_{1U}{}^{*}$ are obtained using the equivalent linearization technique [19]. The equivalent period and the equivalent damping ratio of the equivalent SDOF model in each loading stage n, ${}_nT_{1eq}$ and ${}_nh_{1eq}$ respectively, are determined as

$${}_nT_{1eq}=2\pi\sqrt{\frac{{}_nD_{1U}{}^{*}}{{}_nA_{1U}{}^{*}}}=2\pi\sqrt{\frac{\sum_j\left(m_j{}_nx_j{}^2+m_j{}_ny_j{}^2+I_j{}_n\theta_j{}^2\right)}{\sum_j\left({}_nf_{RXj}{}_nx_j+{}_nf_{RYj}{}_ny_j+{}_nf_{MZj}{}_n\theta_j\right)}}, \tag{12}$$

$${}_nh_{1eq}=\frac{\sum_k{}_nh_{eqFk}{}_nW_{eFk}+\sum_l{}_nh_{eqDl}{}_nW_{eDl}}{\sum_k{}_nW_{eFk}+\sum_l{}_nW_{eDl}}, \tag{13}$$

where

$$ {}_{n}h_{eqFk} = \begin{cases} h_0 \sqrt{\dfrac{{}_{n}K_{EQFk}}{K_{EFk}}} & : {}_{n}\mu_{Fk} \le 1 \\ 0.25\left(1 - \dfrac{1}{\sqrt{{}_{n}\mu_{Fk}}}\right) + h_0 \sqrt{\dfrac{{}_{n}K_{EQFk}}{K_{EFk}}} & : {}_{n}\mu_{Fk} \ge 1 \end{cases}, \tag{14} $$

$$ {}_{n}h_{eqDl} = \begin{cases} 0 & : {}_{n}\mu_{Dl} \le 1 \\ 0.6 \times \dfrac{2}{\pi}\left(1 - \dfrac{1}{{}_{n}\mu_{Dl}}\right) & : {}_{n}\mu_{Dl} \ge 1 \end{cases}. \tag{15} $$

In Eqs. (12)–(15), ${}_{n}h_{eqFk}$, ${}_{n}W_{eFk}$ and ${}_{n}\mu_{Fk}$ are the equivalent damping ratio, potential energy, and ductility ratio of the kth nonlinear spring of the RC member, respectively; ${}_{n}h_{eqDl}$, ${}_{n}W_{eDl}$ and ${}_{n}\mu_{Dl}$ are the equivalent damping ratio, potential energy, and ductility ratio of the lth nonlinear spring of the hysteresis damper, respectively; and h_0 is the initial damping ratio, which is assumed to be 0.03 in this study.

The spectral reduction factor relating to the equivalent damping ratio, $F({}_{n}h_{1eq})$, is determined as

$$ F\left({}_{n}h_{1eq}\right) = \frac{{}_{p}S_A\left({}_{n}T_{1eq}, {}_{n}h_{1eq}\right)}{{}_{p}S_A\left({}_{n}T_{1eq}, 0.05\right)} = \frac{S_D\left({}_{n}T_{1eq}, {}_{n}h_{1eq}\right)}{S_D\left({}_{n}T_{1eq}, 0.05\right)} = \frac{1.5}{1 + 10\,{}_{n}h_{1eq}}, \tag{16} $$

where ${}_{p}S_A$ (${}_{n}T_{1eq}$, ${}_{n}h_{1eq}$) and S_D (${}_{n}T_{1eq}$, ${}_{n}h_{1eq}$) are the psuedo spectral acceleration and the spectral displacement of ground motion, respectively. In this study, the curve of the ${}_{p}S_A$ (${}_{n}T_{1eq}$, ${}_{n}h_{1eq}$)–S_D (${}_{n}T_{1eq}$, ${}_{n}h_{1eq}$) relationship is referred to as the demand curve.

For the prediction of the "largest" peak response, it is assumed that the spectra of two horizontal ground motion components are identical: the spectrum of the horizontal minor component is assumed to be the same as that of the major component. Therefore, the same response spectra are used to predict the peak responses of the first and second modes.

The predicted peak response ($D_{1U}{}^{*}{}_{\max}$, $A_{1U}{}^{*}{}_{\max}$) is obtained as the intersection point of the capacity curve and demand curve.

2.3 Step 3: Pushover analysis of the asymmetric building model (second mode)

From the results of Steps 1 and 2, the first mode vector corresponding to $D_{1U}{}^{*}{}_{\max}$, $\Gamma_{1Uie}\boldsymbol{\varphi}_{\mathbf{1ie}}$, is obtained. The second mode vector, $\Gamma_{2Vie}\boldsymbol{\varphi}_{\mathbf{2ie}}$, is then determined in terms of $\Gamma_{1Uie}\boldsymbol{\varphi}_{\mathbf{1ie}}$ and the second mode vector in the elastic range, $\boldsymbol{\varphi}_{\mathbf{2e}}$, considering the orthogonal condition of the mode vector, as

$$ \Gamma_{2Vie} = \frac{\boldsymbol{\varphi}_{\mathbf{2ie}}{}^{\mathrm{T}}\mathbf{M}\boldsymbol{\alpha}_{\mathbf{Vie}}}{\boldsymbol{\varphi}_{\mathbf{2ie}}{}^{\mathrm{T}}\mathbf{M}\boldsymbol{\varphi}_{\mathbf{2ie}}}, \boldsymbol{\varphi}_{\mathbf{2ie}} = \boldsymbol{\varphi}_{\mathbf{2e}} - \frac{\boldsymbol{\varphi}_{\mathbf{2e}}{}^{\mathrm{T}}\mathbf{M}\boldsymbol{\varphi}_{\mathbf{1ie}}}{\boldsymbol{\varphi}_{\mathbf{1ie}}{}^{\mathrm{T}}\mathbf{M}\boldsymbol{\varphi}_{\mathbf{1ie}}}\boldsymbol{\varphi}_{\mathbf{1ie}}, \tag{17} $$

where

$$ \boldsymbol{\alpha}_{\mathbf{Vie}} = \left\{\sin\psi_{1ie} \;\cdots\; \sin\psi_{1ie} \;\; \cos\psi_{1ie} \;\cdots\; \cos\psi_{1ie} \;\; 0 \;\cdots\; 0\right\}^{\mathrm{T}}, \tag{18} $$

$$\cos\psi_{1ie}=\frac{\sum_j m_j\phi_{Xj1ie}}{\sqrt{\left(\sum_j m_j\phi_{Xj1ie}\right)^2+\left(\sum_j m_j\phi_{Yj1ie}\right)^2}},\ \sin\psi_{1ie}=\frac{-\sum_j m_j\phi_{Yj1ie}}{\sqrt{\left(\sum_j m_j\phi_{Xj1ie}\right)^2+\left(\sum_j m_j\phi_{Yj1ie}\right)^2}}. \quad (19)$$

Next, another pushover analysis of the asymmetric building is carried out to obtain the force–displacement relationship representing the second mode response by applying the invariant force distribution $\mathbf{P_2}$ determined as

$$\mathbf{P_2}=\mathbf{M}\left(\Gamma_{2Vie}\boldsymbol{\varphi}_{\mathbf{2ie}}\right). \quad (20)$$

The equivalent displacement ${}_nD_{2V}{}^*$ and acceleration ${}_nA_{2V}{}^*$ of the equivalent SDOF model representing the second mode response at each loading step n are determined as

$${}_nD_{2V}{}^*=\frac{\Gamma_{2Vie}\boldsymbol{\varphi}_{\mathbf{2ie}}{}^{\mathbf{T}}\mathbf{M}_{\mathbf{n}}\mathbf{d}}{M_{2Vie}{}^*},\ {}_nA_{2V}{}^*=\frac{\Gamma_{2Vie}\boldsymbol{\varphi}_{\mathbf{2ie}}{}^{\mathbf{T}}{}_{\mathbf{n}}\mathbf{f}_{\mathbf{R}}}{M_{2Vie}{}^*}, \quad (21)$$

$$M_{2Vie}{}^*=\Gamma_{2Vie}{}^2\boldsymbol{\varphi}_{\mathbf{2ie}}{}^{\mathbf{T}}\mathbf{M}\boldsymbol{\varphi}_{\mathbf{2ie}}. \quad (22)$$

In Eq. (22), $M_{2Vie}{}^*$ is the equivalent second modal mass with respect to the V-axis determined in terms of $\Gamma_{2Vie}\boldsymbol{\varphi}_{\mathbf{2ie}}$.

2.4 Step 4: Prediction of the peak response of the equivalent SDOF model (second mode)

The largest peak equivalent displacement $D_{2V}{}^*{}_{\max}$ and the equivalent acceleration $A_{2V}{}^*{}_{\max}$ for the second mode response are obtained using the equivalent linearization technique as discussed in Step 2. Note that for the calculation of the equivalent damping ratio of the second mode, the initial damping ratio used in Eq. (14), h_0, is assumed to be the same as that assumed in Step 2 for the first mode. The same spectrum used in Step 2 is used again for the prediction of the second mode response.

2.5 Step 5: Prediction of the largest peak response at each frame

The four force distributions are determined as the sum of the contributions of the first and second mode responses. The largest peak response is predicted as the envelope of the four pushover analyses results. Details of the largest peak response prediction at each frame are described as follows.

1) Determine the four combined forces $\mathbf{P_U}^+$, $\mathbf{P_U}^-$, $\mathbf{P_V}^+$, $\mathbf{P_V}^-$, according to

$$\begin{cases}\mathbf{P_U}^{\pm}=\mathbf{M}\left(\Gamma_{1Uie}\boldsymbol{\varphi}_{\mathbf{1ie}}A_{1U}{}^*{}_{\max}\pm 0.5\Gamma_{2Vie}\boldsymbol{\varphi}_{\mathbf{2ie}}A_{2V}{}^*{}_{\max}\right)\\ \mathbf{P_V}^{\pm}=\mathbf{M}\left(\pm 0.5\Gamma_{1Uie}\boldsymbol{\varphi}_{\mathbf{1ie}}A_{1U}{}^*{}_{\max}+\Gamma_{2Vie}\boldsymbol{\varphi}_{\mathbf{2ie}}A_{2V}{}^*{}_{\max}\right)\end{cases}. \quad (23)$$

2) Perform pushover analyses using $\mathbf{P_U}^+$, $\mathbf{P_U}^-$ until the equivalent displacement ${}_nD_U{}^*$ calculated using Eq. (24) reaches $D_{1U}{}^*{}_{\max}$, obtained from Step 2 (referred to as Pushover-1U and 2U, respectively); similarly, $\mathbf{P_V}^+$, $\mathbf{P_V}^-$ are used in the analysis until the equivalent displacement ${}_nD_V{}^*$ calculated from Eq. (24) reaches $D_{2V}{}^*{}_{\max}$, obtained from Step 4 (referred to as Pushover-1V and 2V, respectively). Equation (24) is

$$ {}_nD_U^* = \frac{\Gamma_{1Uie}\boldsymbol{\varphi}_{\mathbf{1ie}}^{\mathrm{T}}\mathbf{M}_{\mathbf{n}}\mathbf{d}}{M_{1Uie}^*}, \; {}_nD_V^* = \frac{\Gamma_{2Vie}\boldsymbol{\varphi}_{\mathbf{2ie}}^{\mathrm{T}}\mathbf{M}_{\mathbf{n}}\mathbf{d}}{M_{2Vie}^*}, \tag{24} $$

where

$$ M_{1Uie}^* = \Gamma_{1Uie}^2\boldsymbol{\varphi}_{\mathbf{1ie}}^{\mathrm{T}}\mathbf{M}\boldsymbol{\varphi}_{\mathbf{1ie}}. \tag{25} $$

In Eq. (24), M_{1Uie}^* is the equivalent first modal mass with respect to the U-axis determined in terms of $\Gamma_{1Uie}\boldsymbol{\varphi}_{\mathbf{1ie}}$.

3) Determine the largest peak response at each frame from the envelope of (a) Pushover-1U and 2U and (b) Pushover-1V and 2V.

3 BUILDING AND GROUND MOTION DATA

3.1 Building data

3.1.1. Building model without BRBs

The building investigated in this study is a four-storey asymmetric building model as shown in Figure 2. This building model, with bi-directional eccentricity, is the same as Model-B1 in the previous study [16]. In the present study, this building model (without BRBs) is referred to as Model-O.

The floor mass m_j and moment of inertia I_j (j = 1–4) are assumed as 525t and 4.37×10^4 tm^2, respectively. The columns are assumed to have fixed ends supported by the foundation. The compressive strength of concrete, σ_B, is assumed to be 24 N/mm^2. In addition, SD345 steel (yield strength σ_y = 345 N/mm^2) is used for the longitudinal reinforcement, and SD295 steel (σ_y = 295 N/mm^2) is used for the shear reinforcement and wall and slab reinforcement. Each frame structure was designed according to the weak-beam, strong-column concept; the longitudinal reinforcement of the concrete section is determined so that potential hinges are located at the beam ends and the bottoms of the columns and the structural walls in the first storey. Sufficient shear reinforcement is assumed to be provided to prevent premature shear failure. Table 1 gives the longitudinal reinforcement for each member. The crack moment M_c and yield moment M_y of each member are calculated according to the AIJ Design Guideline [20]. The base shear coefficients obtained from the planar pushover analysis in the X- and Y-directions, which are the values when the roof displacement reaches 1% of the total height H_N (= 14.8 m), were 0.522 and 0.455, respectively.

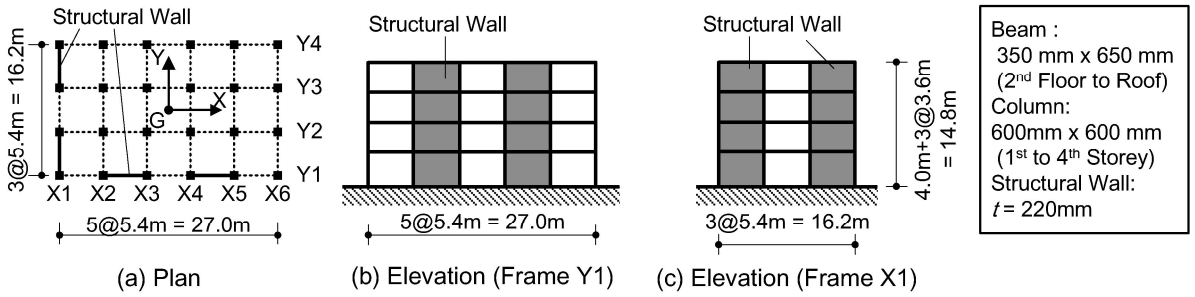
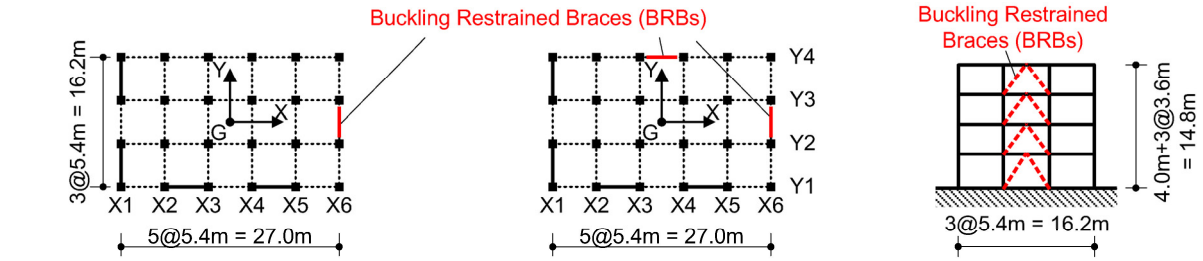


Figure 2: Model building without BRBs (Model-O)

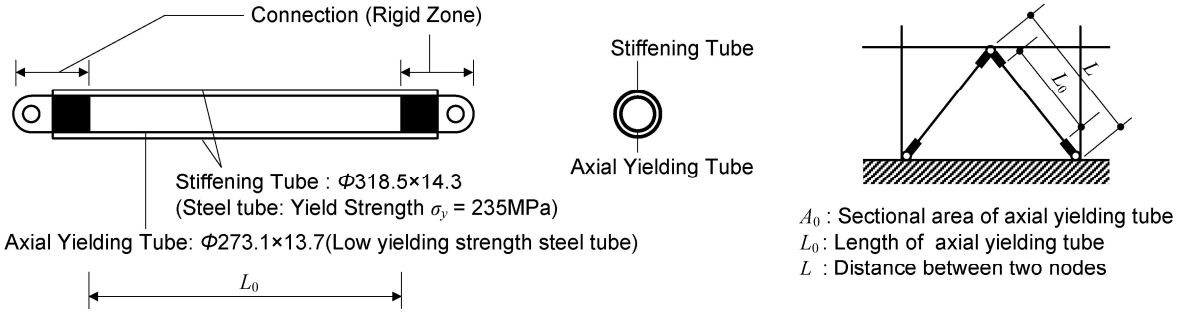
Member	Location	Reinforcement
Boundary beam	2nd to roof floor	6-D25 (top and bottom)
Beam	4th and roof floor 2nd to 3rd floor	3-D25 (top and bottom) 4-D25 (top and bottom)
Column	2nd to 4th storey 1st storey	20-D29 (top and bottom) 20-D29 (top), 8-D29 (bottom)
Structural Wall	All storey	D10@200Double

Table 1: Longitudinal reinforcement of each member



(a) Plan (Model-BRB1L, Model-BRB1H) (b) Plan (Model-BRB2L, Model-BRB2H) (c) Elevation (Frame X6)

Figure 3: Model building with BRBs (Model-BRB1L, BRB1H, BRB2L and BRB2H)



(a) Buckling Restrained Brace (BRB) (b) Frame with BRBs

Figure 4: Configuration of BRB

3.1.2. Building models with BRBs

In this study, Model-O was rehabilitated by installing BRBs, and the four rehabilitated building models shown in Figure 3 were investigated: two rehabilitated building models with BRBs in Frame X6, which is the flexible edge frame in the Y-direction (Model-BRB1L, BRB1H), and two with BRBs in Frames Y4 and X6, which are the flexible edge frames in both X- and Y-directions, respectively (Model-BRB2L, BRB2H). Figure 4 shows the configuration of BRBs installed in the rehabilitated model. As shown in Figure 4 (a), the tube-in-tube BRB [17, 18] was used in this study. In this brace, an axial yielding tube (a steel tube with low yielding strength) inside the brace yields and absorbs the hysteresis energy, while a stiffening tube outside the brace prevents the premature buckling of the axial yielding tube. The dimensions of the axial yielding tube were the same for all storeys. In this study, two grades of yield strength σ_y were assumed for the axial yielding tube: σ_y was assumed as 80 N/mm^2 for Model-BRB1L and BRB2L and 205 N/mm^2 for Model-BRB1H and BRB2H. Therefore, the yield axial force, N_y, of the BRBs used in Model-BRB1L and BRB2L is 893 kN while that of the BRBs used in Model-BRB1H and BRB2H is 2290 kN.

Figure 4(b) shows the frame with BRBs. Because the end connection of the BRB is considered a rigid zone, the axial stiffness of the BRB is increased by the ratio (L/L_0), where L

and L_0 are the distance between two nodes and the length of the axial yielding tube (shown in Figure 4), respectively. In the case of actual BRBs, there is "deformation loss" due to, for example, gaps of pin connections and deformations of joints. In this study, the axial stiffness of the BRB is determined from the sectional area of the axial yielding tube A_0 and L, for the simplicity of analysis.

3.1.3. Modelling of building structures

The building structures are modelled as a psuedo three-dimensional frame model in which the floor diaphragms are assumed to be rigid in their own planes with no out-of-plane stiffness, and the frames oriented in the X- and Y-directions are modelled independently. One-component model, with one nonlinear flexural spring at both ends and one nonlinear shear spring in the middle of the line element, is used for all concrete beams, columns and structural walls. At the end of each member, rigid zones are assumed, and the rigid zone length is determined as follows. For the beams (except the boundary beam) and columns, the rigid zone length is assumed as half the depth of the intersecting member minus one-fourth of the depth of the considered member itself, and the rigid zone length on the wall-side of the boundary beam is assumed as half the column-centre to column-centre length of the structural wall. For the structural walls, no rigid zone is considered at either end. To determine the flexibility of the nonlinear flexural springs, an anti-symmetric curvature distribution is assumed for the beams and columns, and a uniform curvature distribution is assumed for the structural walls. The BRBs are modelled as a line element with a pin at both ends, and a nonlinear axial spring in the middle of the line element.

Figure 5 shows the envelope curve for the force–deformation relationship of each nonlinear spring. The envelopes are assumed to be symmetric in both the positive and negative loading directions. In Figure 5(a), the secant stiffness degradation ratio of the flexural spring at the yield point, α_y, is assumed to be 0.25 for all beams and columns. For the structural walls at the bottom of the first storey, α_y is assumed to be 0.12. At all other ends of structural walls, α_y is assumed to be 0.19. In Figure 5(b), the secant stiffness degradation ratio of the shear spring at the "yield point" β_y is assumed to be 0.16. The axial behaviour of the concrete columns and structural walls is assumed to remain elastic, and the effects of the biaxial bending and axial-flexural interaction are ignored. Braces (BRBs) are modelled as a line element with a pin connection at both ends, and the envelope of the axial force (N)–axial deformation (e) relationship is shown in Figure 5(c). The torsional stiffness of the members is ignored. No second-order effect (e.g., the P-Δ effect) is considered.

Figure 6 shows the hysteresis model used for each nonlinear spring. The Muto hysteretic model [21] with one modification is used to model the flexural spring, as shown in Figure 6 (a). Specifically, the unloading stiffness after yielding decreases in proportion to $\mu^{-0.5}$ (where μ is the ductility ratio of the flexural spring) to represent the degradation of the unloading stiffness after yielding of the RC members, as in the model of Otani [22]. The origin-

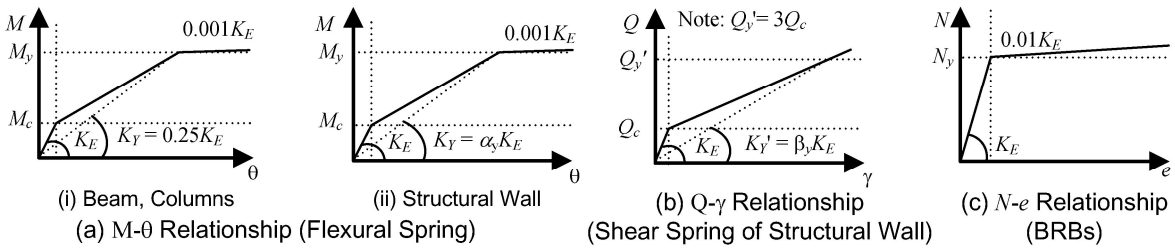


Figure 5: Envelope of the force–deformation relationship of nonlinear springs

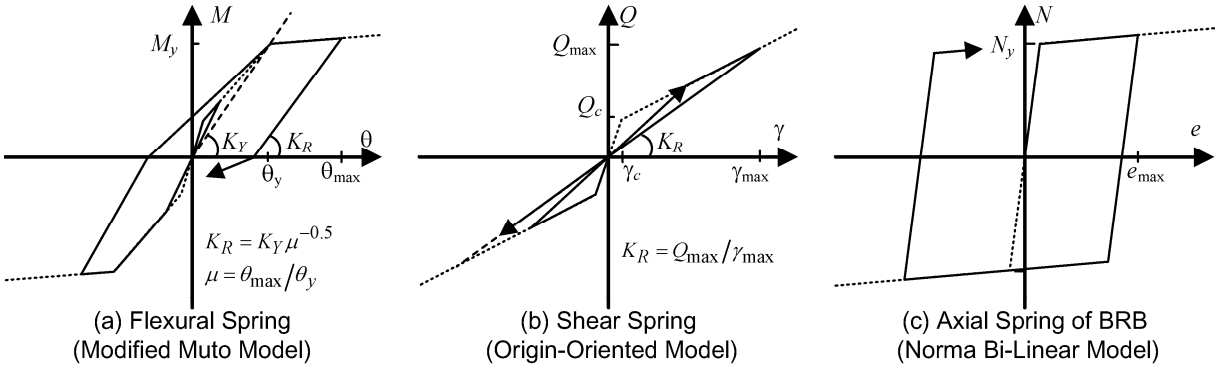


Figure 6: Hysteresis model for the nonlinear springs

oriented model (Figure 6 (b)) is used to model the shear spring of the structural wall. The shear spring of the beams and columns is assumed to be elastic. The normal bilinear hysteretic model (Figure 6 (c)) is used to model the axial spring of the BRBs.

In this study, the damping matrix at time t, $\mathbf{C}(t)$, is assumed to be proportional to the instant stiffness matrix without BRBs $\mathbf{K_{Tf}}(t)$ as expressed by

$$\mathbf{C}(t) = \left(2h_{1f}/\omega_{1ef}\right)\mathbf{K_{Tf}}(t), \tag{26}$$

where ω_{1ef} and h_{1f} are the elastic natural circular frequency and damping ratio of the first mode of the model without BRBs, respectively. In this study, h_{1f} is assumed to be 0.03.

3.1.4. Natural modes of the building models

Figure 7 shows the natural modes of the building models in the elastic range. Here, T_{ie} is the ith natural period in the elastic range, ψ_{ie} is the angle of incidence of the principal direction of the ith modal response in the elastic range with its tangent given by

$$\tan\psi_{ie} = -\sum_j m_j\phi_{Yjie} \Big/ \sum_j m_j\phi_{Xjie}, \tag{27}$$

and $R_{\rho ie}$ is the torsional index of the ith mode [23] in the elastic range, as defined by

$$R_{\rho ie} = \sqrt{\sum_j I_j\phi_{\Theta jie}{}^2 \Big/ \left(\sum_j m_j\phi_{Xjie}{}^2 + \sum_j m_j\phi_{Yjie}{}^2\right)}. \tag{28}$$

Note that, in the elastic range, the natural modes of Model-BRB1L and BRB1H are mutually the same, and those of Model-BRB2L and BRB2H are also mutually the same. This is because the elastic axial stiffness is the same for all BRBs used in this study. As shown in Figure 7, the principal direction of the first three modes is not along the X- and Y-axes in any of the building models, and the differences in natural modes among building models are very small; a significant difference can be found only in the natural period of the first mode. In all building models, the first mode is predominantly translational $\left(R_{\rho 1e} < 1\right)$, the second mode is almost purely translational $\left(R_{\rho 2e} \ll 1\right)$, while the third mode is predominantly torsional $\left(R_{\rho 3e} > 1\right)$, and the angle between the principal directions of the first two modes is close to 90° (within 90.2°–99.7°). Because the first and second modes are predominantly translational

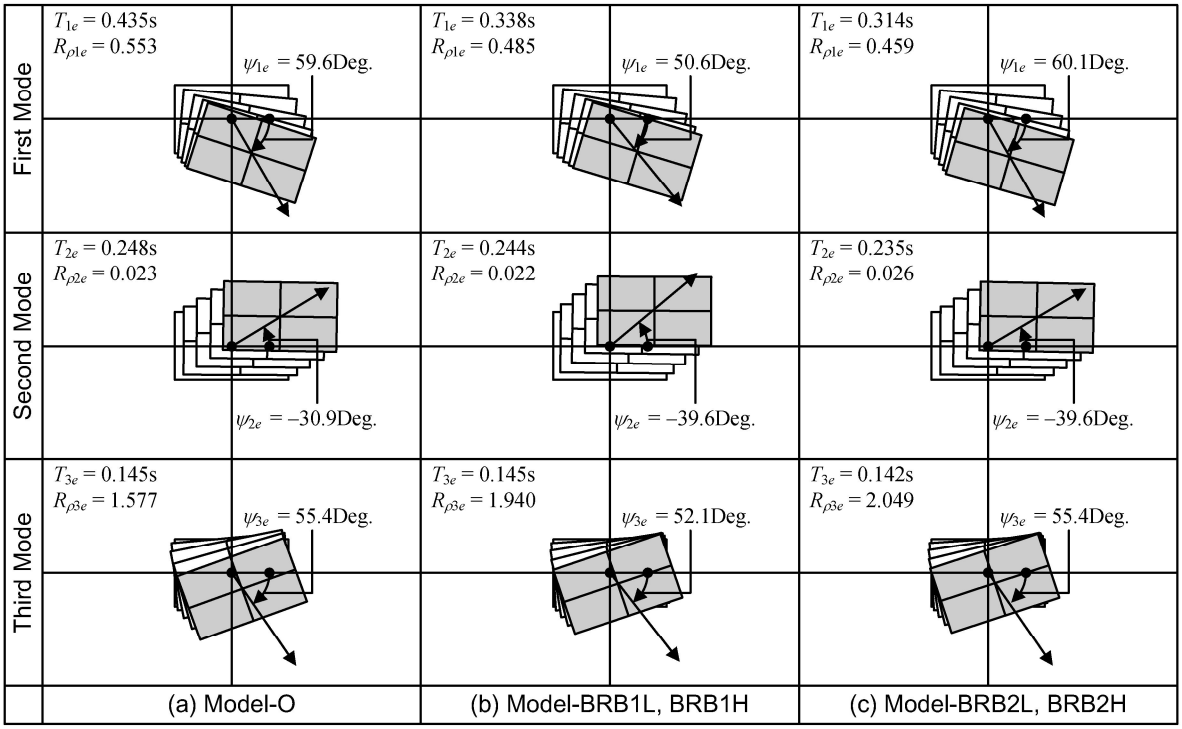


Figure 7: Shapes of the first three modes of the building models in the elastic range

in all the building models, the models are classified as TS systems in this study. Further discussions can be found in references [16], [23] and [24].

3.2 Ground motion data

In this study, the seismic excitation was considered to be bidirectional in the X–Y plane, and three sets of artificial ground motions were generated. Note that the three sets of artificial ground motions were the same as those used in the previous study [16].

The target elastic spectrum of the "major" components with 5% critical damping, ${}_pS_{A\xi}(T,0.05)$, determined from the Building Standard Law of Japan [25] considering soil conditions, is calculated as

$${}_pS_{A\xi}(T,0.05)=\begin{cases}4.8+45T \quad \mathrm{m/s^2} & :T\le 0.16\mathrm{s}\\ 12.0 & :0.16\mathrm{s}\le T\le 0.576\mathrm{s}\\ 12.0(0.576/T) & :T\ge 0.576\mathrm{s}\end{cases}, \tag{29}$$

where T represents the natural period of the SDOF model.

The target spectrum of the "minor" components ${}_pS_{A\zeta}(T,0.05)$ is reduced by the parameter γ. Here, the parameter γ is set to 0, 0.5, 0.7, and 1.0; the ground motion is considered unidirectional for $\gamma=0$ whereas the spectra of the two horizontal components are identical when $\gamma=1.0$, as is assumed for the prediction of the largest peak response. According to López et al. [26], this ratio varies between 0.63 and 0.81 and the average ratio is 0.70. Therefore, the case $\gamma=0.7$ may be considered the most realistic case for real ground motion.

The phase angle is given by uniform random values and the Jenning type envelope function $e(t)$ proposed by the Building Centre of Japan:

$$e(t)=\begin{cases}(t/5)^2 & :0\text{s}\le t\le 5\text{s}\\ 1 & :5\text{s}\le t\le 35\text{s}\\ \exp\{-0.027(t-35)\} & :35\text{s}\le t\le 120\text{s}\end{cases}. \quad (30)$$

Figure 8 shows the elastic response spectra of artificial ground motions with 5% critical damping.

4 APPLICABILITY OF THE SIMPLIFIED PROCEDURE TO AN ASYMMETRIC BUILDING WITH BUCKLING-RESTRAINED BRACES

4.1 Prediction of the peak response

4.1.1. Prediction of the peak response of the first and second mode responses

Figure 9 shows the prediction of the peak response of the first and second mode responses employing equivalent linearization. It is seen that the intersection points of the capacity curve and demand curve represent the predicted peak response. Figure 10 shows the relationship of equivalent damping versus the equivalent displacement of the first and second modes for each model. The dots "●" in the figure represent the predicted peak responses of the first and second modes.

Figure 10 (a) shows that the equivalent damping ratios of the first and second modes at the predicted peak, h_{1eq} and h_{2eq}, respectively, are very close in the case of the asymmetric building model without BRBs (Model-O): h_{1eq} = 0.091 and h_{2eq} = 0.094. In contrast, the trends of the equivalent damping ratios of the two modes at the predicted peak are different for each model in the case of the asymmetric building model with BRBs. In the case of Model-BRB1L and BRB2L (Figure 10 (b) and (d)), h_{1eq} is larger than h_{2eq}; in case of Model-BRB1L, h_{1eq} = 0.130 and h_{2eq} = 0.094; while in the case of Model-BRB2L, h_{1eq} = 0.144 and h_{2eq} = 0.104. Meanwhile, h_{1eq} is smaller than h_{2eq} in the case of Model-BRB1H (Figure 10 (c)), and h_{1eq} is very close to h_{2eq} in the case of Model-BRB2H (Figure 10 (e)); in case of Model-BRB1H, h_{1eq} = 0.104 and h_{2eq} = 0.130, while in case of Model-BRB2H, h_{1eq} = 0.122 and h_{2eq} = 0.115.

4.1.2. Change in mode shape based on pushover analysis results

To evaluate the change in mode shape, the principal direction and torsional index based on mode shape for the first three modes were investigated using the pushover analyses results obtained in Step 2. The second and third modes at loading step n, ${}_n\boldsymbol{\varphi}_2$ and ${}_n\boldsymbol{\varphi}_3$ respectively, were calculated in terms of the displacement vector at loading step n, ${}_n\mathbf{d}$, and the second and

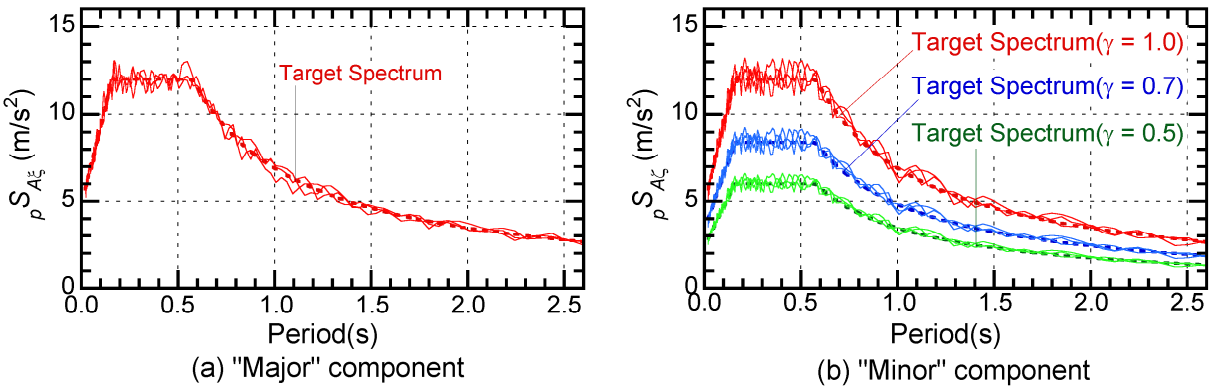


Figure 8: Elastic pseudo acceleration response spectra for simulated ground motion

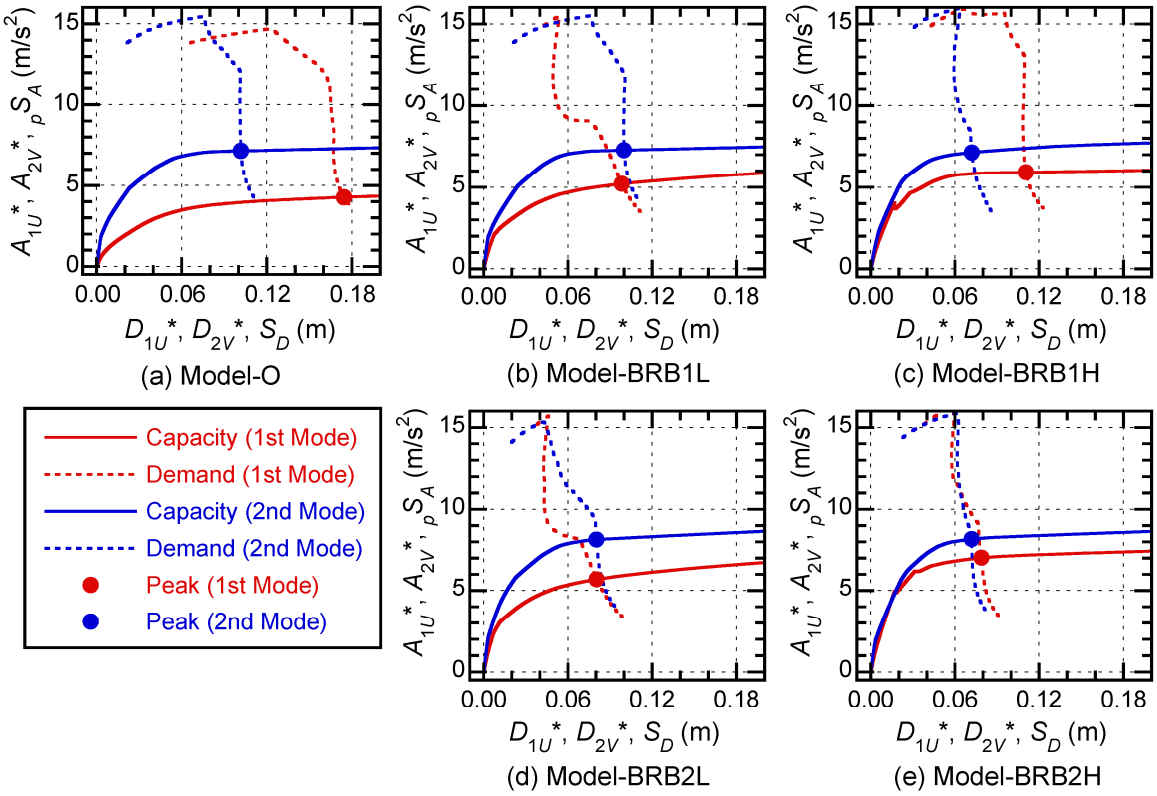


Figure 9: Prediction of the peak response of equivalent SDOF models

third mode vectors in the elastic range, $\boldsymbol{\varphi}_{2e}$ and $\boldsymbol{\varphi}_{3e}$ respectively, as

$$ {}_n\boldsymbol{\varphi}_2 = \boldsymbol{\varphi}_{2e} - \frac{\boldsymbol{\varphi}_{2e}^{\mathrm{T}}\mathbf{M}_n\boldsymbol{\varphi}_1}{{}_n\boldsymbol{\varphi}_1^{\mathrm{T}}\mathbf{M}_n\boldsymbol{\varphi}_1}\,{}_n\boldsymbol{\varphi}_1 = \boldsymbol{\varphi}_{2e} - \frac{\boldsymbol{\varphi}_{2e}^{\mathrm{T}}\mathbf{M}_n\mathbf{d}}{{}_n\mathbf{d}^{\mathrm{T}}\mathbf{M}_n\mathbf{d}}\,{}_n\mathbf{d}, \tag{31} $$

$$ {}_n\boldsymbol{\varphi}_3 = \boldsymbol{\varphi}_{3e} - \frac{\boldsymbol{\varphi}_{3e}^{\mathrm{T}}\mathbf{M}_n\boldsymbol{\varphi}_1}{{}_n\boldsymbol{\varphi}_1^{\mathrm{T}}\mathbf{M}_n\boldsymbol{\varphi}_1}\,{}_n\boldsymbol{\varphi}_1 - \frac{\boldsymbol{\varphi}_{3e}^{\mathrm{T}}\mathbf{M}_n\boldsymbol{\varphi}_2}{{}_n\boldsymbol{\varphi}_2^{\mathrm{T}}\mathbf{M}_n\boldsymbol{\varphi}_2}\,{}_n\boldsymbol{\varphi}_2 = \boldsymbol{\varphi}_{3e} - \frac{\boldsymbol{\varphi}_{3e}^{\mathrm{T}}\mathbf{M}_n\mathbf{d}}{{}_n\mathbf{d}^{\mathrm{T}}\mathbf{M}_n\mathbf{d}}\,{}_n\mathbf{d} - \frac{\boldsymbol{\varphi}_{3e}^{\mathrm{T}}\mathbf{M}_n\boldsymbol{\varphi}_2}{{}_n\boldsymbol{\varphi}_2^{\mathrm{T}}\mathbf{M}_n\boldsymbol{\varphi}_2}\,{}_n\boldsymbol{\varphi}_2 . \tag{32} $$

Next, the tangent of the angle of the principal direction of the ith mode at loading step n, $\tan {}_n\psi_i$, and the torsional index of the ith mode at loading step n, ${}_nR_{\rho i}$, were calculated as

$$ \tan {}_n\psi_i = -\sum_j m_j\,{}_n\phi_{Yji} \Big/ \sum_j m_j\,{}_n\phi_{Xji}, \tag{33} $$

$$ {}_nR_{\rho i} = \sqrt{\sum_j I_j\,{}_n\phi_{\Theta ji}{}^2 \Big/ \left(\sum_j m_j\,{}_n\phi_{Xji}{}^2 + \sum_j m_j\,{}_n\phi_{Yji}{}^2 \right)}. \tag{34} $$

Figure 11 shows the changes in ${}_n\psi_i$ and ${}_nR_{\rho i}$ at each loading step for all building models. The dots "●" in this figure correspond to the points of the predicted peak response of the first mode.

Figure 11(a) shows that the changes in ${}_n\psi_i$ and ${}_nR_{\rho i}$ are very small in the case of Model-O. In contrast, the changes in ${}_n\psi_i$ and ${}_nR_{\rho i}$ are small in the case of Model-BRB1L and BRB2L (Figure 11 (b) and (d), respectively), and significant in the case of Model-BRB1H and BRB2H (Figure 11 (c) and (e), respectively); in particular, in the case of Model-BRB1H, the

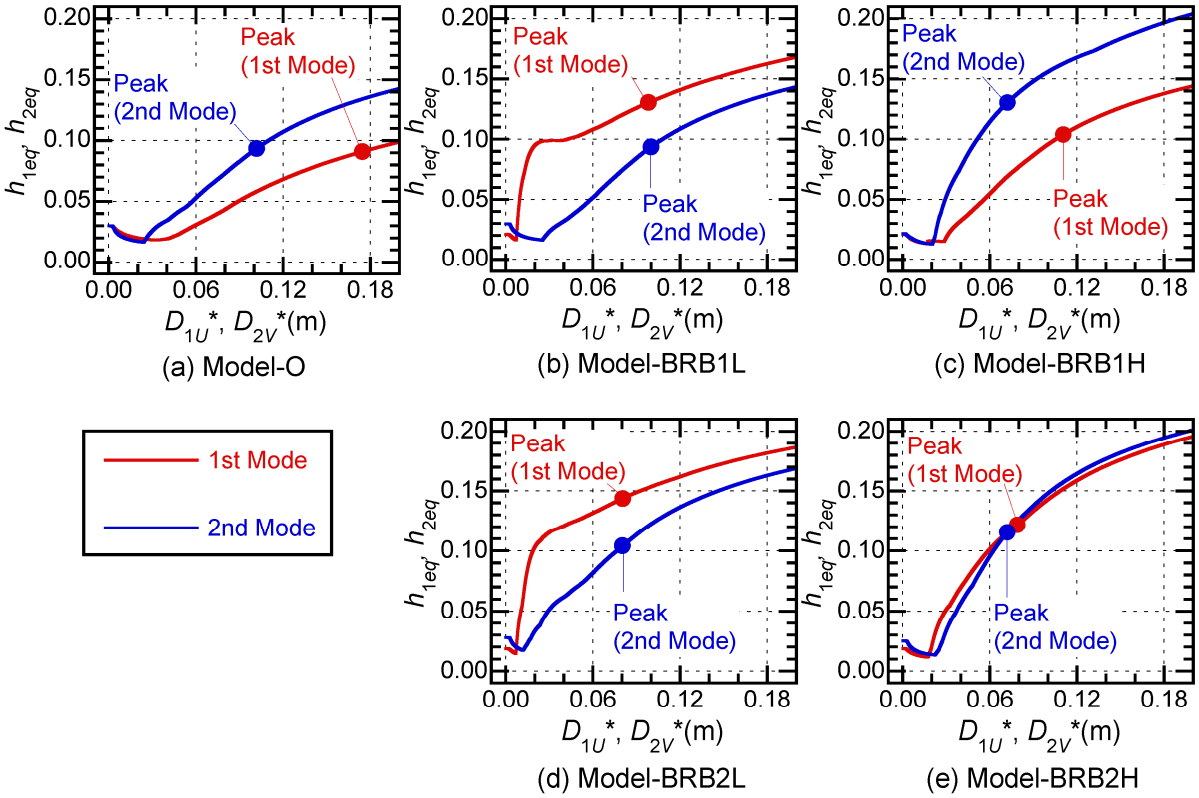


Figure 10: Equivalent damping ratio–equivalent displacement relationship of equivalent SDOF models

change in ${}_n\psi_i$ is about 50° from the elastic stage ($\psi_{1e} = 50.6^\circ$) to the predicted peak response ($\psi_1 = 2.2^\circ$). Figure 11 (c) and (e) shows that ${}_nR_{\rho 1}$ and ${}_nR_{\rho 2}$ decrease as ${}_nR_{\rho 3}$ increases rapidly as the equivalent displacement ${}_nD_1{}^*$ increases, in the case of Model-BRB1H and Model-BRB2H. This implies that the first two modes become almost purely translational modes when the building models respond in the nonlinear range.

4.2 Comparisons of the predicted results with the results of time-history analyses

4.2.1. Time-history analysis cases

The applicability of the simplified procedure to asymmetric buildings with BRBs was evaluated as follows. First, nonlinear dynamic (time-history) analyses were carried out for fixed values of γ, various spectral ratios of "minor" to "major" components (γ = 0, 0.5, 0.7, and 1.0) and various directions of the incidence of seismic input. Then, from the results of each set of artificial ground motions, the envelope of the peak response of various directions of incidence was obtained for the cases γ = 0, 0.5, 0.7, while for the case γ = 1.0, the average of the peak response in directions of incidence was obtained. Finally, the averages of the results for the three sets of artificial ground motions were compared with the predicted "largest" peak response. Note that the angle of incidence of the "major" component with respect to the X-axis, ψ, varied at 15° intervals from $(\psi_1 - 90)^\circ$ to $(\psi_1 + 90)^\circ$, where ψ_1 is the angle of incidence of the U-axis corresponding to the predicted peak equivalent displacement of the first mode, $D_{1U}{}^*{}_{\max}$, shown in Figure 11. Therefore, $4 \times 3 \times 13 = 156$ cases were considered for the nonlinear time-history analyses of each building model.

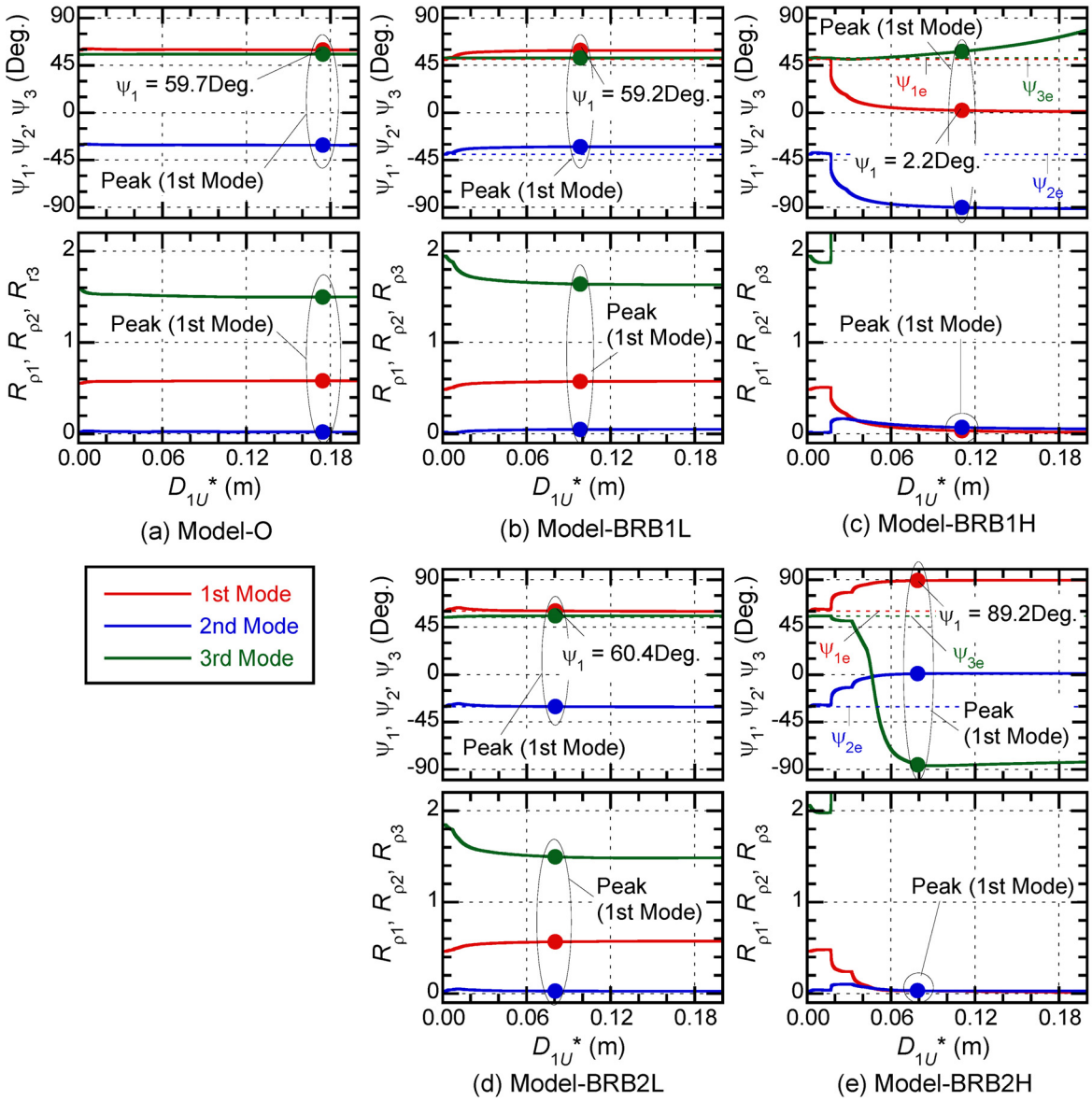


Figure 11: Change in the principal direction of modal responses and torsional indices in the nonlinear stage evaluated by pushover analysis

4.2.2. Accuracy of the results predicted using the simplified procedure

Figure 12 compares the peak displacement at the roof obtained from dynamic analysis results and the predicted peak response for each building model. In this figure, the plot "Envelope" for the cases γ = 0, 0.5 and 0.7 shows the average of the envelope of three sets of artificial ground motions (for each set, 13 directions are considered) for each γ, while the plot "Ave. (γ = 1.0)" indicates the average of 36 cases (three sets of artificial ground motions × 12 directions) of the results for γ = 1.0.

In the case of Model-O, as shown in Figure 12 (a), the predicted results approximate the upper bound of the dynamic analysis results in the X-direction, while in the Y-direction, the predicted results are conservative relative to the time-history analysis results except for Frame X1. In the case of building models with BRBs, the trends strongly depend on each model; in the cases of Model-BRB1L (Figure 12 (b)), BRB1H (Figure 12 (c)) and BRB2H (Figure 12

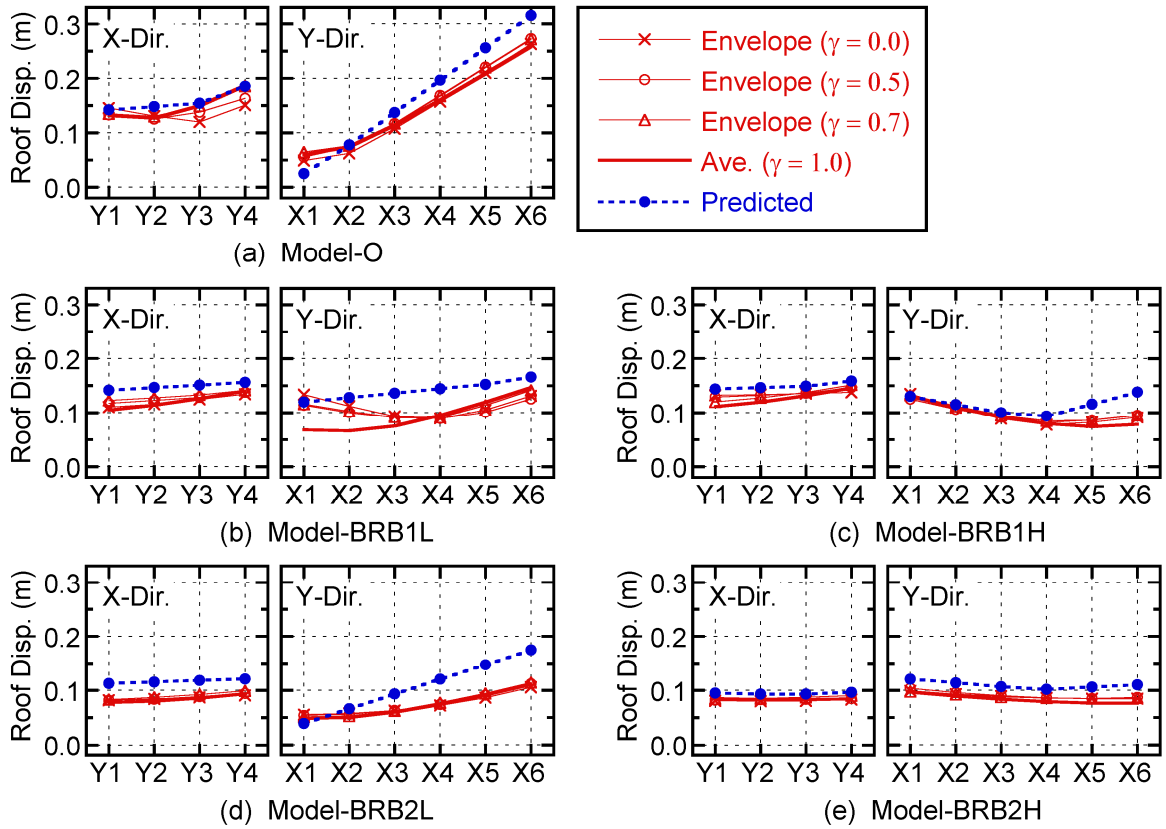


Figure 12: Prediction of "the largest" peak displacement at roof and comparisons with dynamic analyses results

(e)), the predicted results approximate the upper bound of the dynamic analysis results of all frames, while trends similar to those seen in Figure 12 (a) are observed in the case of Model-BRB2L (Figure 12 (d)).

Figure 13 compares the peak storey drift at edge frames (Frames Y1, Y4, X1 and X6) obtained from time-history analyses and the predicted peak response for each building model. As shown in this figure, the predicted results satisfactorily agree with the dynamic analysis results of all models, except Frame X1 of Model-O (Figure 13(a)) and BRB2L (Figure 13(d)). According to these results, the simplified procedure presented in reference [16] may be applicable to asymmetric buildings with BRBs.

Figure 14 shows the effect of the direction of incidence of the "major" component on the peak roof displacement at edge frames (Frames Y1, Y4, X1 and X6). In this figure, the "normalized displacement" indicates the peak roof displacement in various directions for $\gamma = 0$, 0.5 and 0.7 divided by the average for $\gamma = 1.0$.

Also shown is the predicted peak response, and ψ_{1e} and ψ_1, the angles of incidence of the principal direction of the first modal response with respect to the X-axis, in the elastic range and corresponding to $D_{1U}{}^{*}{}_{\max}$, respectively.

Figure 14(a) shows that, in the case of Model-O and for $\gamma = 0$, 0.5 and 0.7, the normalized displacement at edge frames is less than 1 in most cases, as expected. This point is important because it is assumed the ratio γ equals 1.0 in the simplified procedure for the prediction of the "largest" peak response. In Frame X6, the flexible edge frame in the Y-direction, the normalized displacement is the largest and close to 1.0 when ψ is close to ψ_1. However, as is seen in Figures 14(b) to (e), the trend strongly depends on the building model; trends similar

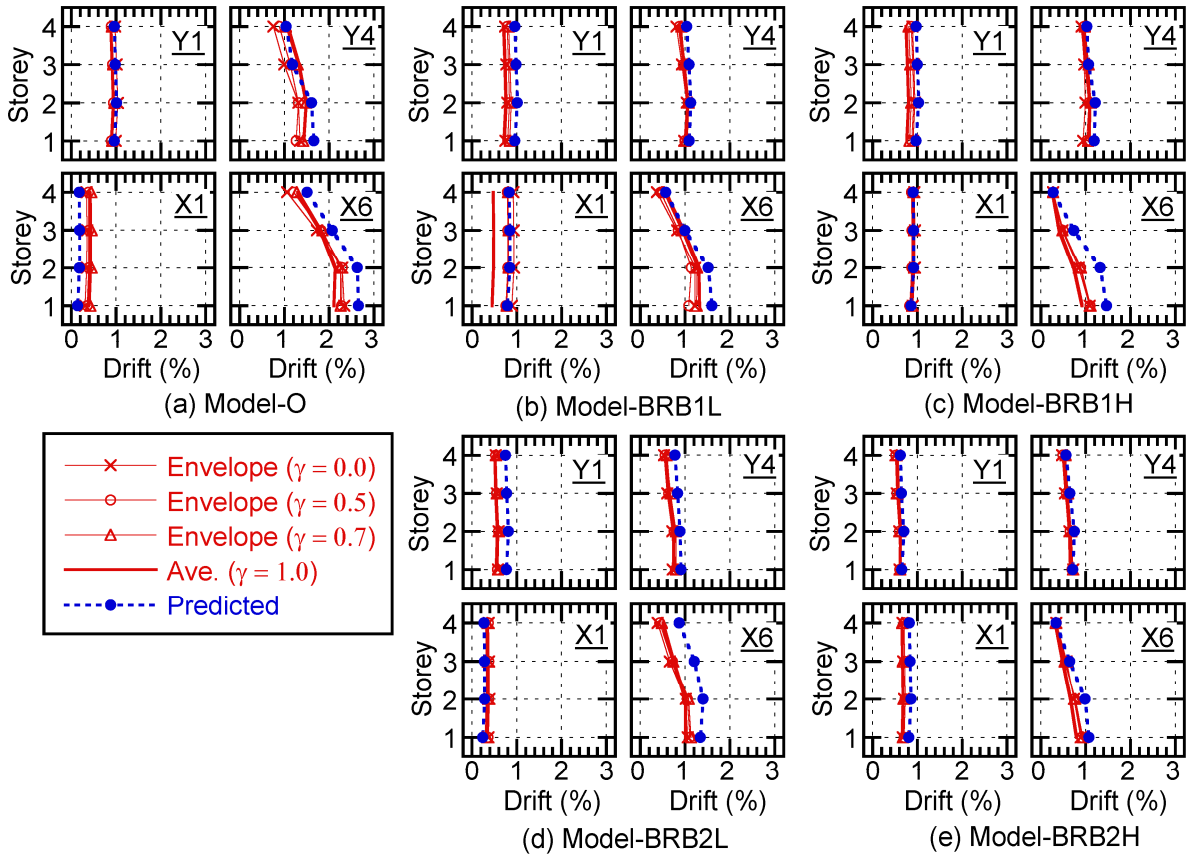


Figure 13: Prediction of "the largest" peak storey drift at edge frames (frames Y1, Y4, X1 and X6) and comparisons with dynamic analysis results

to those for Model-O are observed for Model-BRB1L and BRB2L (Figures 14(b) and (d), respectively) except for Frame X1 of Model-BRB1L, the normalized displacement of which is much larger than 1 in some cases. By contrast, in the case of Model-BRB1H (Figure 14(c)), the normalized displacement of Frame Y4, where the largest roof displacement occurs in this building model, is the largest and close to 1.0 when ψ is close to ψ_1, not ψ_{1e}. Meanwhile, in the case of Model-BRB2H (Figure 14(e)), the normalized displacement of Frame X1, where the largest roof displacement occurs in this building model, is the largest and close to 1.0 when ψ is close to ψ_1, not ψ_{1e}. These results imply that the most critical direction of incidence of the seismic input is different from that in the elastic range, in the case of asymmetric buildings with BRBs responding beyond the elastic range.

5 EFFECT OF THE CHANGE IN MODE SHAPE ON THE ACCURACY OF THE NONLINEAR STATIC PROCEDURE

5.1 Prediction cases

In the simplified procedure presented in reference [16], there are two main differences from conventional pushover analyses [10–13]. One is that the change in the mode shape in nonlinear range is considered, and the other is that the combination of two modal responses is considered by the force distributions used in pushover analyses for the prediction of peak responses (referred to as the envelope method). In contrast, especially in modal pushover analy-

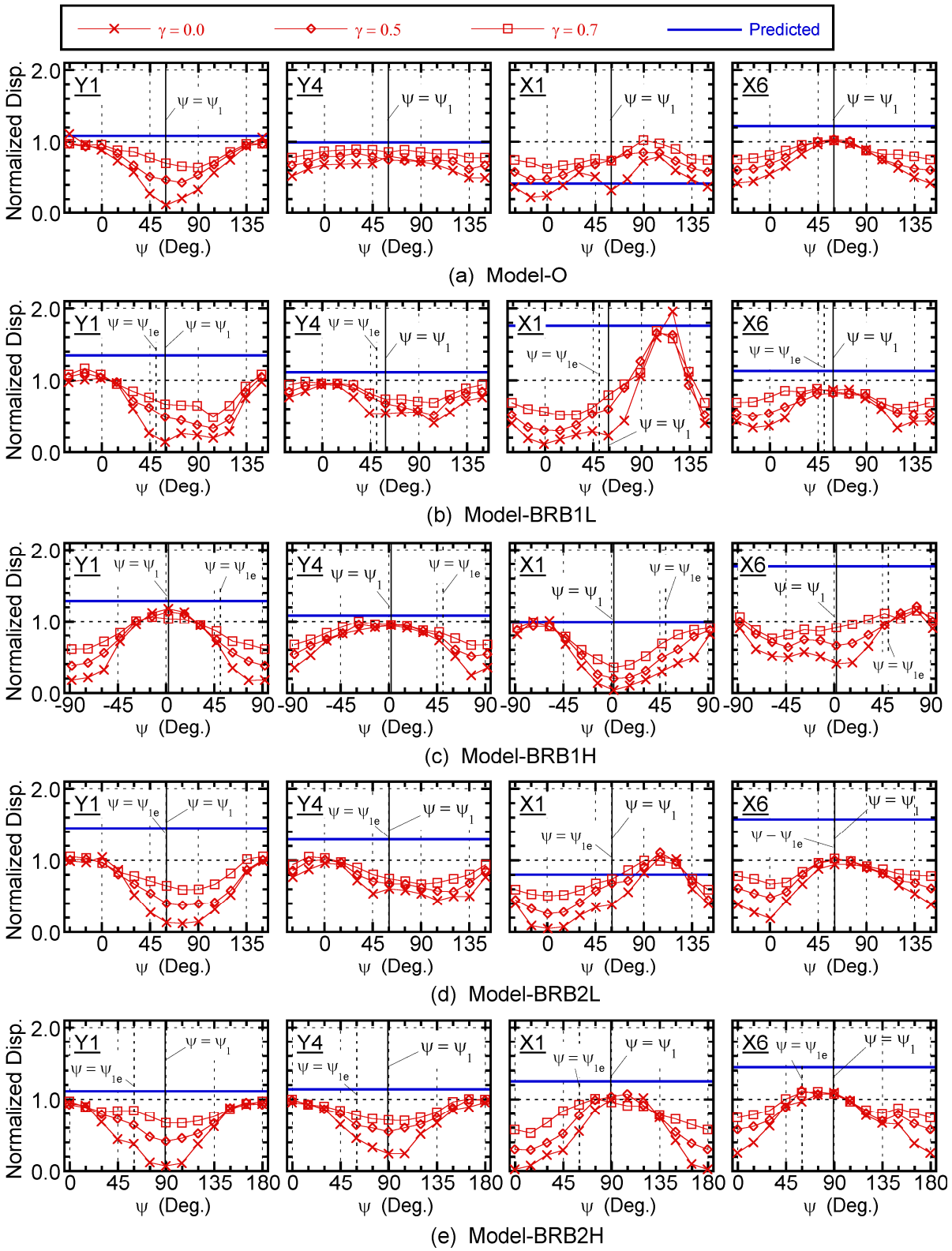


Figure 14: Effect of the direction of incidence of the "major" component on the peak roof displacement at edge frames (Frames Y1, Y4, X1 and X6)

sis in [13], the mode shape is assumed as that in the elastic range, and the square root of the sum of squares (SRSS) rule or CQC rule is applied as the combination rule.

In this section, the effects of the change in mode shape and the combination rule on the accuracy of the NSP for asymmetric buildings with BRBs are investigated.

The parameters in the prediction cases are (i) consideration of the change in mode shape (variant/invariant) and (ii) the combination rules (envelope method/SRSS method).

5.1.1. Parameter (i): consideration of the change in mode shape

In the case of the "invariant" mode shape, pushover analyses in Steps 1 and 3 are based on invariant force distributions; force distributions used in Steps 1 and 3, $\mathbf{P_{1e}}$ and $\mathbf{P_{2e}}$ respectively, are calculated as

$$\mathbf{P_{1e}} = \mathbf{M}\left(\Gamma_{1Ue}\boldsymbol{\varphi}_{\mathbf{1e}}\right), \mathbf{P_{2e}} = \mathbf{M}\left(\Gamma_{2Ve}\boldsymbol{\varphi}_{\mathbf{2e}}\right). \tag{35}$$

From the displacement vector at loading step n, ${}_n\mathbf{d}$, the equivalent displacement and acceleration of the first mode, ${}_nD_{1Ue}{}^*$ and ${}_nA_{1Ue}{}^*$ respectively, and those of the second mode, ${}_nD_{2Ve}{}^*$ and ${}_nA_{2Ve}{}^*$ respectively, are calculated as

$${}_nD_{1Ue}{}^* = \Gamma_{1Ue}\boldsymbol{\varphi}_{\mathbf{1e}}{}^{\mathrm{T}}\mathbf{M}\,{}_n\mathbf{d}/M_{1Ue}{}^*, {}_nA_{1Ue}{}^* = \Gamma_{1Ue}\boldsymbol{\varphi}_{\mathbf{1e}}{}^{\mathrm{T}}\,{}_n\mathbf{f_R}/M_{1Ue}{}^*, \tag{36}$$

$${}_nD_{2Ve}{}^* = \Gamma_{2Ve}\boldsymbol{\varphi}_{\mathbf{2e}}{}^{\mathrm{T}}\mathbf{M}\,{}_n\mathbf{d}/M_{2Ve}{}^*, {}_nA_{2Ve}{}^* = \Gamma_{2Ve}\boldsymbol{\varphi}_{\mathbf{2e}}{}^{\mathrm{T}}\,{}_n\mathbf{f_R}/M_{2Ve}{}^*, \tag{37}$$

where

$$M_{1Ue}{}^* = \Gamma_{1Ue}{}^2\boldsymbol{\varphi}_{\mathbf{1e}}{}^{\mathrm{T}}\mathbf{M}\boldsymbol{\varphi}_{\mathbf{1e}}, M_{2Ve}{}^* = \Gamma_{2Ve}{}^2\boldsymbol{\varphi}_{\mathbf{2e}}{}^{\mathrm{T}}\mathbf{M}\boldsymbol{\varphi}_{\mathbf{2e}}, \tag{38}$$

$$\Gamma_{1Ue} = \frac{\boldsymbol{\varphi}_{\mathbf{1e}}{}^{\mathrm{T}}\mathbf{M}\boldsymbol{\alpha}_{\mathbf{Ue}}}{\boldsymbol{\varphi}_{\mathbf{1e}}{}^{\mathrm{T}}\mathbf{M}\boldsymbol{\varphi}_{\mathbf{1e}}}, \Gamma_{2Ve} = \frac{\boldsymbol{\varphi}_{\mathbf{2e}}{}^{\mathrm{T}}\mathbf{M}\boldsymbol{\alpha}_{\mathbf{Ve}}}{\boldsymbol{\varphi}_{\mathbf{2e}}{}^{\mathrm{T}}\mathbf{M}\boldsymbol{\varphi}_{\mathbf{2e}}}, \tag{39}$$

$$\begin{cases} \boldsymbol{\alpha}_{\mathbf{Ue}} = \{\cos\psi_{1e} \quad \cdots \quad \cos\psi_{1e} \quad -\sin\psi_{1e} \quad \cdots \quad -\sin\psi_{1e} \quad 0 \quad \cdots \quad 0\}^{\mathrm{T}} \\ \boldsymbol{\alpha}_{\mathbf{Ve}} = \{\sin\psi_{1e} \quad \cdots \quad \sin\psi_{1e} \quad \cos\psi_{1e} \quad \cdots \quad \cos\psi_{1e} \quad 0 \quad \cdots \quad 0\}^{\mathrm{T}} \end{cases}. \tag{40}$$

The peak equivalent displacement and acceleration of the first and second models are predicted from the ${}_nA_{1Ue}{}^*$–${}_nD_{1Ue}{}^*$ curve and ${}_nA_{2Ve}{}^*$–${}_nD_{2Ve}{}^*$ curve, respectively.

In the case of the "variant" mode shape, pushover analyses in Steps 1 and 3 are carried out according to section 2.

5.1.2. Parameter (ii): combination rule

In the case of the envelope method, the peak response at each frame in Step 5 is predicted according to section 2.5. Note that, in the case of the invariant mode shape, Eq. (23) is rewritten considering the elastic mode shapes instead of inelastic mode shapes at peak response:

$$\begin{cases} \mathbf{P_{Ue}}^{\pm} = \mathbf{M}\left(\Gamma_{1Ue}\boldsymbol{\varphi}_{\mathbf{1e}}A_{1Ue}{}^*{}_{\max} \pm 0.5\Gamma_{2Ve}\boldsymbol{\varphi}_{\mathbf{2e}}A_{2Ve}{}^*{}_{\max}\right) \\ \mathbf{P_{Ve}}^{\pm} = \mathbf{M}\left(\pm 0.5\Gamma_{1Ue}\boldsymbol{\varphi}_{\mathbf{1e}}A_{1Ue}{}^*{}_{\max} + \Gamma_{2Ve}\boldsymbol{\varphi}_{\mathbf{2e}}A_{2Ve}{}^*{}_{\max}\right) \end{cases}. \tag{41}$$

In the case of the SRSS method, the peak response at each frame in Step 5 is predicted from the SRSS rule as follows. Let $d_{Xmj1U\max}$ and $d_{Ynj1U\max}$ be the peak displacement of the mth frame in the X-direction and nth frame in the Y-direction at the jth floor, respectively, obtained from the first mode response in Step 1, while $d_{Xmj2V\max}$ and $d_{Ynj2V\max}$ are those obtained from the second mode response in Step 3. The peak displacement of the mth frame in the X-direction at the jth floor, $d_{Xmj\max}$, and nth frame in the Y-direction at the jth floor, $d_{Yn\max}$, are calculated according to

$$d_{Xmj\max} = \sqrt{d_{Xmj1U\max}{}^2 + d_{Xmj2V\max}{}^2}, d_{Ynj\max} = \sqrt{d_{Ynj1U\max}{}^2 + d_{Ynj2V\max}{}^2} . \quad (42)$$

5.2 Comparisons of the predicted results

5.2.1. Comparisons of peak roof displacement

Figure 15 compares the peak displacement at the roof obtained from dynamic analyses and the predicted peak response in the case of the envelope method. Figure 15(a) reveals that the difference in the predicted results using invariant and variant mode shapes is negligibly small in the case of Model-O. This is because, as shown in Figure 11(a), the change in the first mode shape is very small. In contrast, the effect of the consideration of the change in mode shapes on the accuracy of the predicted results strongly depends on the building model, in the case of asymmetric building models with BRBs in this study; in the case of Model-BRB1L and BRB2L (Figures 15(b) and (d), respectively), the difference in the predicted results is very small, while it is significant in the case of Model-BRB1H (Figure 15(c)), and moderate in the case of Model-BRB2H (Figure 15(e)).

Note that in the case of Model-BRB1H, the results predicted from the variant mode shape are closer than those predicted from the invariant mode shape to the dynamic analysis results except for Frames X5 and X6. In the case of Model-BRB2H, the predicted peak response at Frame X1 obtained from the invariant mode shape is unconservative in comparison with the dynamic analysis results, while the predicted response obtained from the variant mode shape agrees satisfactorily with the dynamic analysis results. Therefore, the predicted peak responses obtained from the variant mode shape are more accurate than those obtained from the in-

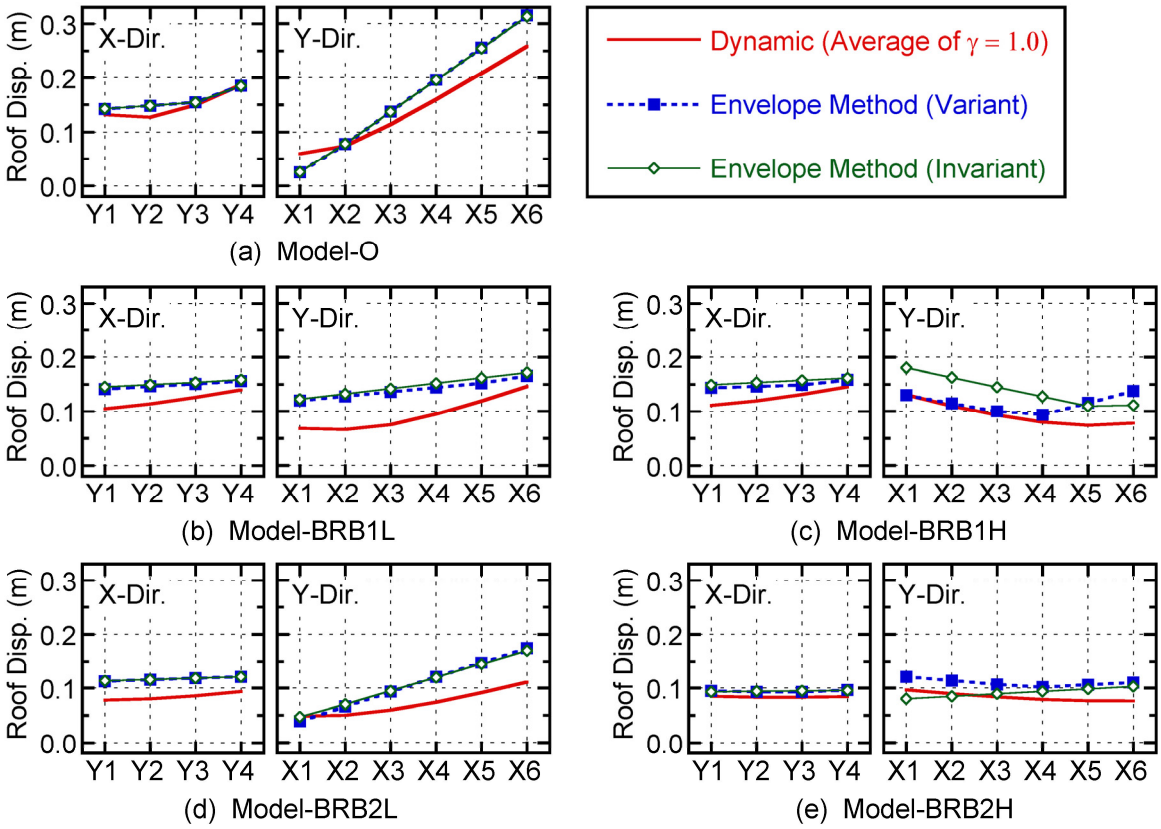


Figure 15: Comparisons of the peak response predicted from variant and invariant mode shapes and dynamic analysis results (envelope method)

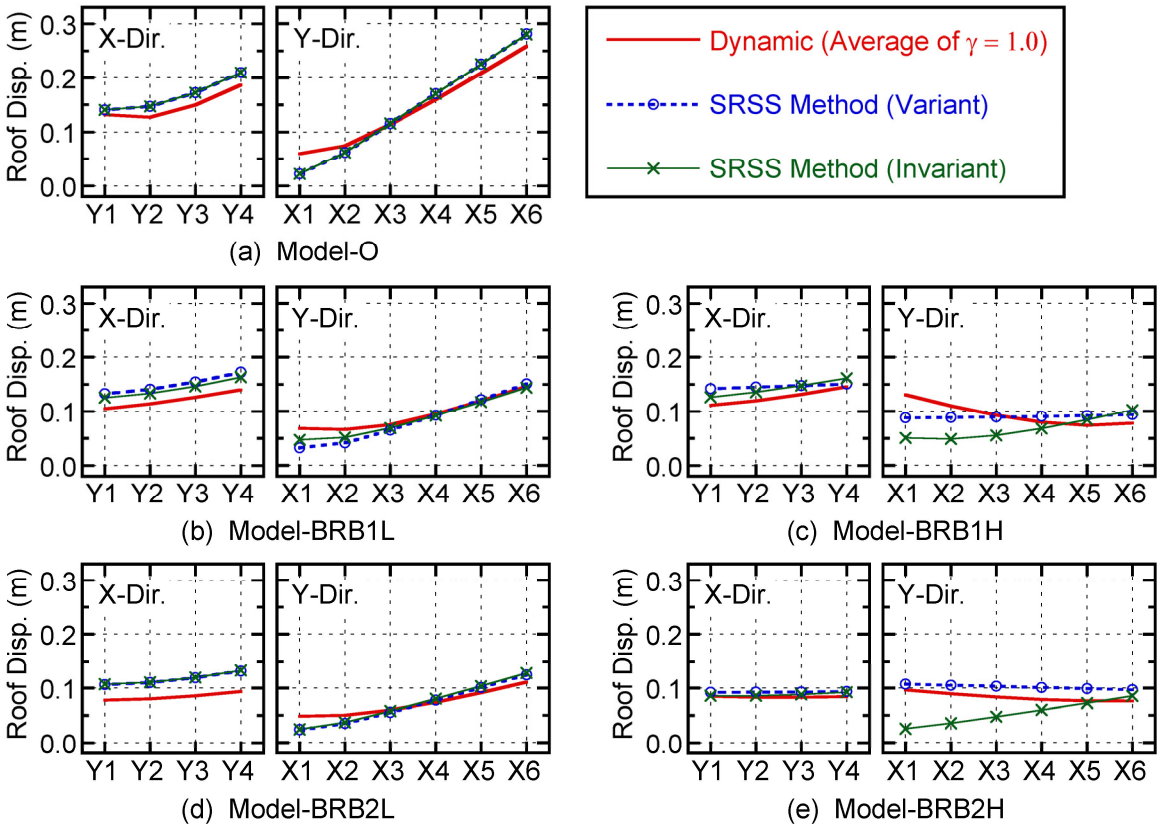


Figure 16: Comparisons of predicted peak response using "variant" and "invariant" mode shapes and dynamic analyses results (SRSS method)

variant mode shape.

Figure 16 compares the peak displacement at the roof obtained from dynamic analyses and the predicted peak response in the case of the SRSS method. It is seen that the predicted peak responses are less conservative than those in the case of the envelope method shown in Figure 15. As shown in Figures 16 (a), (b) and (d), the differences in the prediction results obtained with invariant and variant mode shapes are negligibly small in the cases of Model-O, Model-BRB1L, and Model-BRB2L, and these predicted results agree well with the dynamic analysis results except for Frame X1. In contrast, the accuracy of the results predicted with invariant mode shapes is very poor in case of Model-BRB1H (Figure 16 (c)) and Model-BRB2H (Figure 16 (e)), while the results predicted with the variant mode shape are closer to the dynamic analysis results; however, in the case of Model-BRB1H, the predicted peak displacement at Frame X1 is unconservative in comparison with the dynamic analysis results, even if the change in mode shape in the nonlinear stage is considered.

5.2.2. Comparisons of the amplification of roof displacement

To evaluate the amplification of displacement due to the unfavourable torsional effect, the normalized roof displacement, which is defined as the ratio of the displacement at each frame to that of the centre of mass, has been studied often (e.g., [11] and [12]). Figure 17 compares the normalized roof displacement obtained from dynamic analysis results (average for $\gamma = 1.0$) and results predicted employing two methods (i.e., the envelope method and SRSS method) and using the variant mode shape.

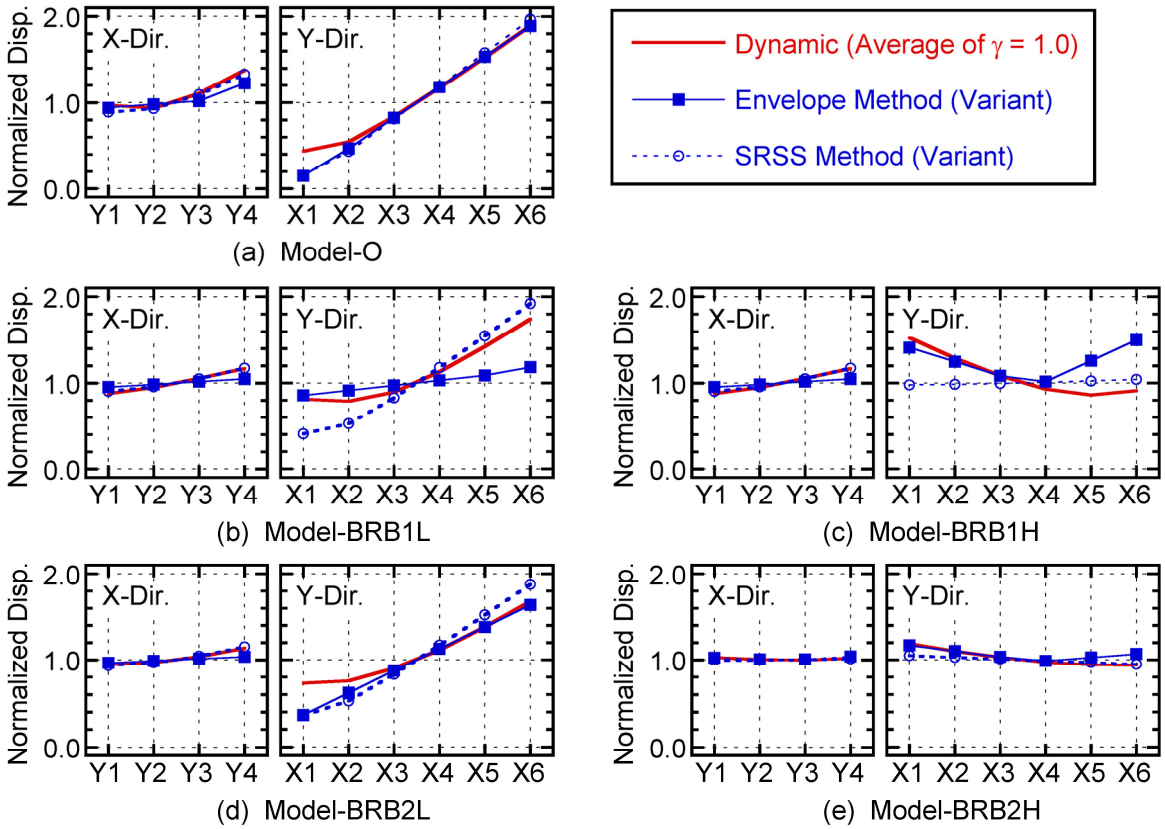


Figure 17: Comparisons of normalized roof displacement with dynamic analysis and results predicted using the envelope method and SRSS method (variant mode shape)

In the case of Model-O (Figure 17(a)), the differences in results predicted with the two methods are negligible and the results agree well with the dynamic analysis results, except for Frame X1.

However, the trends of the asymmetric building models with BRBs strongly depend on the model. In the case of Model-BRB1L (Figure 17(b)), the differences in results predicted with the envelope method and SRSS method are notable; the normalized displacement at Frame X6 obtained using the envelope method is smaller than the dynamic analysis result, while that obtained using the SRSS method agrees well with the dynamic analysis result. By contrast, in the case of Model-BRB1H (Figure 17(c)), the normalized displacement obtained using the envelope method agrees well with the dynamic analysis results for Frame X1, while the results obtained using the SRSS method fail to fit the dynamic analysis results. The trends of Model-BRB2L (Figure 17(d)) are similar to those of Model-O. In the case of Model-BRB2H (Figure 17(e)), the results predicted using the envelope method fit the dynamic analysis results for all frames, while the normalized displacement at Frame X1 obtained using the SRSS method is lower than the dynamic analysis result.

Note that the centre of mass at the roof is *not* the reference point for pushover analysis in the envelope method, which is one of the largest differences from other pushover-based simplified procedures (e.g., [14]). Therefore, underestimation of the amplification ratio due to the torsional effect at the flexible/weak side frame itself does not directory lead to underestimation of the peak displacement at the flexible/weak side frame in this simplified procedure [16], as is seen for the case of Model-BRB1L in Figure 15 (c).

Figure 18 compares the normalized roof displacement obtained from dynamic analyses and predicted using the two methods and the invariant mode shape. Trends similar to those in Fig-

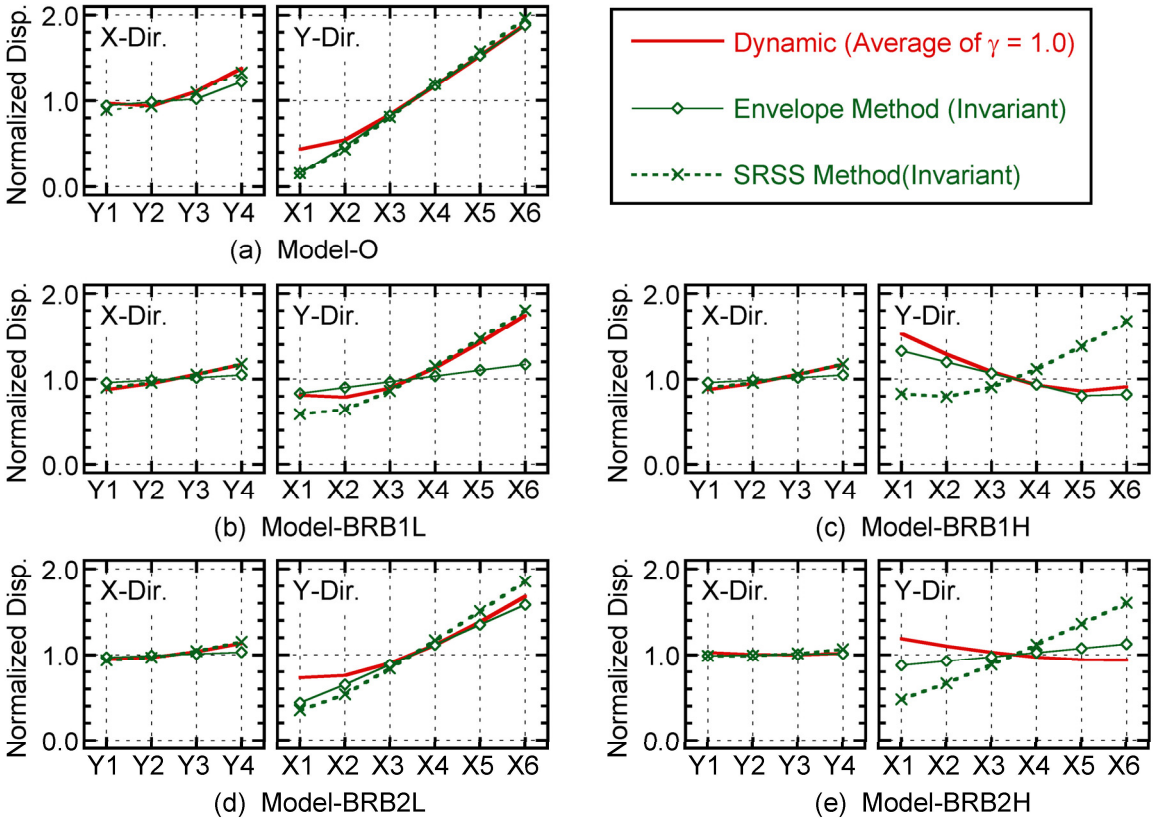


Figure 18: Comparisons of normalized roof displacement with dynamic analysis and results predicted using the envelope method and SRSS method (invariant mode shape)

ure 17 are seen in the case of Model-O (Figure 18(a)), Model-BRB1L (Figure 18(b)), and BRB2L (Figure 18(d)). However, in case of Model-BRB1H (Figure 18(c)) and Model-BRB2H (Figure 18(e)), the results predicted using the invariant mode shape fail to fit the dynamic analysis results. In particular, the results predicted using the SRSS method fail to show the frames in which the largest displacement occurs; as shown in Figures 18(c) and (e), the normalized displacement obtained from dynamic analyses is largest at Frame X1, while that predicted using the SRSS method is largest at Frame X6. Similarly, inaccurate prediction due to the assumption of the invariant mode shape has been pointed out by Isakovic and Fischinger in the case of bridge structures [27]. Although the normalized displacement predicted using the envelope method agrees well with the dynamic analysis results in the case of Model-BRB1H (Figure 18(c)), it fails to fit the dynamic analysis results in the case of Model-BRB2H (Figure 18(e)). Therefore, for the better prediction of peak displacement in each frame, the effect of the change in mode shape at each nonlinear stage should be properly considered.

5.2.3. Comparisons of the properties of equivalent SDOF models

To investigate the effect of the change in mode shape in each nonlinear stage on the properties of equivalent SDOF models, Figures 19 and 20 compare the equivalent acceleration–equivalent displacement curve and the equivalent damping–equivalent displacement curve of Model-O, Model-BRB1L, and Model-BRB1H. The figures show that the differences in properties of equivalent SDOF models are (a) negligible for Model-O, (b) small for Model-BRB1L, and (c) notable for Model-BRB1H. In particular, for Model-BRB1H, the peak response of the first mode predicted using the invariant mode shape is smaller than that predicted using the variable mode shape, because the equivalent damping obtained using the

invariant mode shape is significantly larger than that obtained using the variant mode shape (Figure 19(c)). In contrast, the peak response of the second mode predicted using the invariant mode shape is larger than that predicted using the variable mode shape (Figure 20(c)). These results may explain the difference in the predicted results shown in Figure 16 (c); i.e., the peak response predicted with the SRSS method and invariant mode shapes having poorer accuracy than that predicted with the variant mode shapes.

In conclusion, for a more accurate NSP, consideration of the change in mode shape in each nonlinear stage is essential in the case of asymmetric buildings with BRBs, and according to the combination rule, the envelope method may provide results that are more conservative than the SRSS rule applied in references [11–13].

6 CONCLUSIONS

The applicability of the simplified procedure previously proposed by the author [16] to four-storey RC asymmetric buildings with a hysteresis damper (BRB) was numerically investigated. The predicted largest peak response was compared with nonlinear dynamic (time-history) analysis results considering various directions of the incidence of the seismic input. Although the number of building models considered in the study was limited, the following primary findings were made.

1. The simplified procedure proposed by the author [16] is applicable to asymmetric buildings with BRBs that are classified as TS buildings. The predicted "largest" peak responses of all four asymmetric buildings with BRBs satisfactorily enveloped the results obtained in dynamic analyses.
2. The effect of the change in mode shape in each nonlinear stage on the accuracy of the NSP may be important in the case of asymmetric buildings with BRBs. In this study, there were cases in which the accuracy of the predictions based on an elastic mode shape was poor.
3. For the combination rule considering bidirectional excitation, the envelope method, which is one of the prediction steps in the simplified procedure [16], provides more conservative results than the SRSS method; the responses predicted with SRSS methods may be unconservative, especially when the change in the mode shape is not considered. Meanwhile, the response predicted using the envelope method satisfactorily approximates the envelope of dynamic analysis results.

Note that the discussions above focus only on TS asymmetric buildings. The author concluded in reference [24] that the applicability of the simplified procedure to a torsionally flexible (TF) asymmetric building is questionable. However, the applicability to TF asymmetric buildings with hysteresis dampers in outermost frames remains unknown. This is a problem that should be investigated in future work.

REFERENCES

[1] R. K. Goel, Effects of supplemental viscous damping on seismic response of asymmetric-plan systems, Earthquake Engineering and Structural Dynamics, **27**, 125-141, 1998.

[2] R. K. Goel, Seismic behaviour of asymmetric buildings with supplemental damping, Earthquake Engineering and Structural Dynamics, **29**, 461-480, 2000.

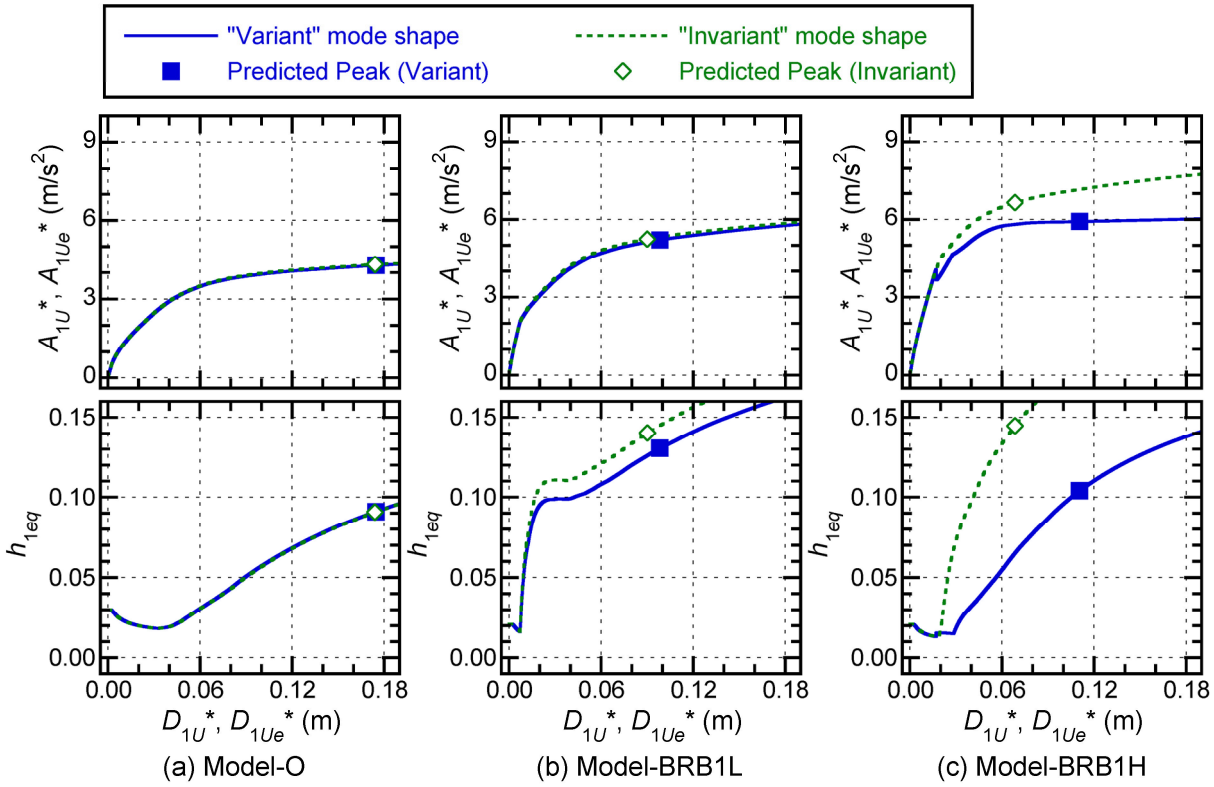


Figure 19: Comparisons of the properties of equivalent SDOF models (first mode)

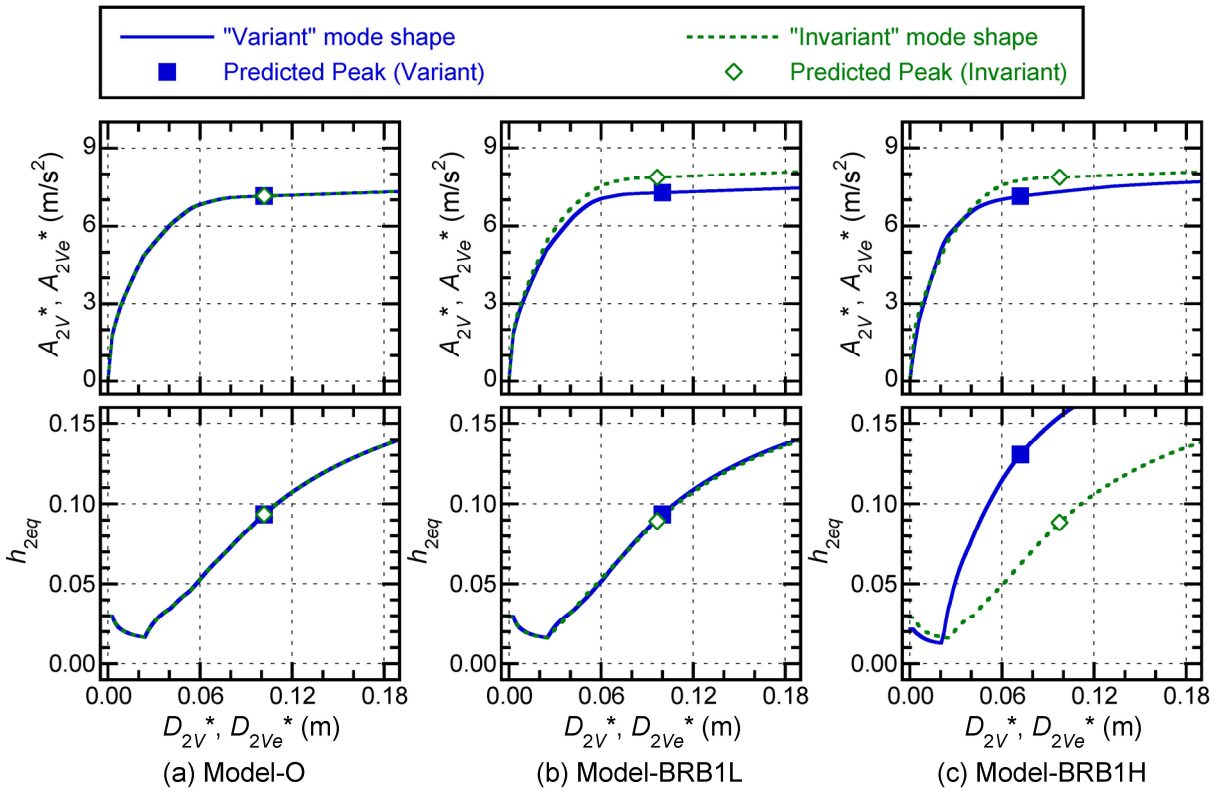


Figure 20: Comparisons of the properties of equivalent SDOF models (second mode)

[3] R. K. Goel and C. A. Booker, Effect of supplemental viscous damping on inelastic seismic response of asymmetric systems, Earthquake Engineering and Structural Dynamics, **30**, 411-430, 2001.

[4] W. Lin, and A. K. Chopra, Understanding and predicting effects of supplemental viscous damping on seismic response of asymmetric one-storey systems, Earthquake Engineering and Structural Dynamics, **30**, 1475-1474, 2001.

[5] L. Landi, P. P. Diotallevi and G. Castellari, On the Design of Viscous Dampers for the Rehabilitation of Plan-Asymmetric Buildings, Journal of Earthquake Engineering, **17**, 1141-1161, 2013.

[6] J. C. De la Llera, J. L. Almazán, and I. J. Vial, Torsional balance of plan-asymmetric structures with friction dampers: analytical results, Earthquake Engineering and Structural Dynamics, **34**, 1089-1108, 2005.

[7] F. Mazza, Displacement-based seismic design of hysteretic damped braces for retrofitting in-plan irregular r.c. framed structures, Soil Dynamics and Earthquake Engineering, **66**, 231-240, 2014.

[8] M. Saiidi, M. A. Sozen, Simple nonlinear seismic analysis of R/C structures, Journal of Structural Division, ASCE, **107**, 937–952, 1981.

[9] P. Fajfar, M. Fischinger, N2-a method for non-linear seismic analysis of regular buildings. In: Proceedings of ninth world conference on earthquake engineering, **5**, 111–116, Tokyo-Kyoto, Japan, 1988.

[10] P. Fajfar, D. Marusić, I. Perus, and G. Magliulo, The extension of The N2 method to asymmetric buildings, Proceedings of the Fourth Forum on Implications of Recent Earthquakes on Seismic Risk, Technical Report TIT/EERG 02/1, 291–308, 2002.

[11] P. Fajfar, D. Marusić, I. Perus, Torsional effects in the pushover-based seismic analysis of buildings. Journal of Earthquake Engineering, **9**, 831–854, 2005.

[12] C. Bhatt, R. Bento, Assessing the seismic response of existing RC buildings using the extended N2 method. Bulletin of Earthquake Engineering, **9**, 1183–1201, 2011.

[13] A. K. Chopra, and R. K. Goel, A modal pushover analysis procedure to estimate seismic demands for unsymmetric-plan buildings, Earthquake Engineering and Structural Dynamics **33**, 903–927, 2004.

[14] M. Bosco, A. Ghersi, E. M. Marino, Corrective eccentricities for assessment by nonlinear static method of 3D structures subjected to bidirectional ground motion. Earthquake Engineering and Structural Dynamics, **41**, 1751–1773, 2012.

[15] K. Fujii, Nonlinear static procedure for multi-story asymmetric frame buildings considering bidirectional excitation. Journal of Earthquake Engineering, **15**, 245–273, 2011.

[16] K. Fujii, Prediction of the largest peak nonlinear seismic response of asymmetric buildings under bi-directional excitation using pushover analyses, Bulletin of Earthquake Engineering, **12**, 909-938, 2014.

[17] R. Kinoshita, K. Miyagawa, M. Haginoya, K. Fujisawa, K. Imai, Y. Ohtani, I Mitani, Study on seismic retrofit for existing R/C buildings by using CHS bracing, Proceedings of First fib Congress, 505-514, Osaka, Japan, October 13-19, 2002.

[18] T. Ishiii, T. Mukai, H. Kitamura, T. Shimizu, K. Fujisawa, and Y. Ishida, Seismic retrofit for existing R/C building using energy dissipative braces, Proceedings of 13th World Conference on Earthquake Engineering, paper no. 1209, Vancouver, Canada, August 1-6, 2004.

[19] S. Otani, New seismic design provision in Japan, Proceeding of the Second U.S.-Japan Workshop on Performance-Based Earthquake Engineering Methodology for Reinforced Concrete Structures. PEER report, 10, 3–14, 2000.

[20] AIJ, Design guidelines for earthquake resistant reinforced concrete buildings based on inelastic displacement concept. Architectural Institute of Japan, Tokyo, 1999. (Japanese)

[21] K. Muto, T. Hisada, T. Tsugawa, and S. Bessho, Earthquake resistant design of a 20 story reinforced concrete buildings. Proceedings of the 5th World Conference on Earthquake Engineering, 1960–1969, Rome, Italy, 1974.

[22] S. Otani, Hysteresis models of reinforced concrete for earthquake response analysis, Journal of Faculty of Engineering University of Tokyo, **36(2)**, 407–441, 1981.

[23] K. Fujii, T. Ikeda, Shaking table test of irregular buildings under horizontal excitation acting in an arbitrary direction, Proceedings of 15th World Conference on Earthquake Engineering, paper no. 0439, Lisbon, Portugal, September 24-28, 2012.

[24] K. Fujii, Torsional Index of asymmetric building based on mode shape, Proceedings of the 7th European Workshop on the Seismic Behaviour of Irregular and Complex Structures, paper no. 14, Faculty of Civil Engineering, Opole University of Technology, Poland, October 17-18, 2014.

[25] BCJ, The building standard law of Japan on CD-ROM. The Building Center of Japan, Tokyo, 2010.

[26] A. López, JJ. Hernández, R. Bonilla, A. Fernández, Response spectra for multicomponent structural analysis, Earthquake Spectra, **22**, 85–113, 2006.

[27] T. Isakovic, M. Fischinger, Applicability of pushover methods to the seismic analysis of an RC bridge, experimentally tested on three shake tables. Journal of Earthquake Engineering, **15**, 303–320, 2011.

COMPDYN 2015
5th ECCOMAS Thematic Conference on
Computational Methods in Structural Dynamics and Earthquake Engineering
M. Papadrakakis, V. Papadopoulos, V. Plevris (eds.)
Crete Island, Greece, 25–27 May 2015

SEISMIC LOSS OPTIMIZATION OF FRAME BUILDINGS USING VISCOUS DAMPERS

Arun M. Puthanpurayil[1], Oren Lavan[2], and Rajesh P. Dhakal[3]

[1] Department of Civil and Natural Resources engineering
University of Canterbury
e-mail: ama299@uclive.ac.nz

[2] Technion, Israel institute of Technology
Haifa, Israel
e-mail: lavan@cv.technion.ac.il

[3]Department of Civil and Natural Resources engineering
University of Canterbury
e-mail: rajesh.dhakal@canterbury.ac.nz

Keywords: Gradient optimization, Viscous dampers, Passive control, Sequential linear programming, Earthquake engineering.

Abstract. *The effectiveness of control strategies in achieving the objectives of a performance-based-design is well accepted in the earthquake engineering community. Consequently, various methods have been proposed for optimal design of dampers and their distribution along the building height. Most of the formulated methods concentrate mainly on reducing the responses with no explicit consideration of their long-term economic impact. In this study, an optimization problem is formulated for optimally distributing viscous dampers by minimizing the initial cost subject to a constraint on the total expected seismic loss. An intensity based assessment is used for the computation of the total expected loss. A generic Sequential Linear Programming procedure is employed to solve the formulated optimization problem. Implementation scheme of the optimization procedure is outlined in detail. The efficacy of the proposed procedure is illustrated by applying it on a four story reinforced concrete frame. It has been shown that the optimization procedure results in the optimal quantity and distribution of viscous dampers along the height of the case study building.*

1 INTRODUCTION

Conventional capacity design strategy relies on the philosophy of "dissipation with degradation" as seismic energy is dissipated by inelastic deformation. Due to the reliance of this philosophy on inelastic deformations, this incurs heavy damage to the parent structure making it non-functional after most major seismic events. A more rational approach to reduce damage would be to rely on "dissipation without degradation" rather than "evasion/dissipation" of seismic induced forces by degradation. One way to achieve this is by increasing the amount of effective damping in the system by introducing control strategies. The introduction of control techniques in structural engineering was mainly necessitated due to the growing demand for minimizing damage during a seismic event. Among the different control techniques implemented in structures to reduce seismic responses, application of viscous dampers seems to be more common; especially from a retrofitting perspective. This is mainly attributed to the fact that the damper force is linearly or nonlinearly proportional to velocity and is out of phase from the column displacements. As a result, the columns or foundations are not subjected to additional demand, and may not need to be strengthened [1-3]. This paper is mainly concerned with the seismic performance enhancement of existing frames using viscous dampers.

The main task needed to be addressed by the engineer in the retrofitting design using viscous dampers is to efficiently allocate and size the dampers. This should take into account both the initial cost that needs to be invested and the achievement of the performance objective. Various optimal design methodologies for retrofitting are available in the literature. Many of them primarily address the problem of distributing a given total added damping to achieve the best performance (minimize damage measures). Some of the works in this direction presented very efficient methods [4-12]. Note that in these works the total added damping is predetermined. The algorithms are thus used to determine the optimal positioning of this quantity along the height of the building. In some of these works, approaches to estimate a reasonable total added damping were also proposed.

From a different perspective, Lavan and Levy [13-15] minimized the total added damping subject to a constraint on the performance of the structure (allowable inter-story drifts). They also present a practical analysis/redesign procedure for arriving at the optimal designs exploiting the advantage of the fully stressed characteristics of the optimal solution [16, 17]. While this formulation lends itself to the performance-based-design framework, the allowable inter-story drifts, or performance measures, are determined based on code requirements. These drifts are usually not determined explicitly based on the economic consequences.

In the present paper a novel optimization scheme is developed in which the total initial cost is minimized while explicitly constraining on the total expected loss. One of the ways of measuring the economic consequences can be in terms of expected annual loss which actually corresponds to the economic loss that, on an average, occurs every year in the building [18, 19]. A more simplified version of this measure could be the use of the total expected loss which is actually the loss that the building incurs for a specific intensity of earthquake. In this study this approach of measuring the economic consequences is adopted. The formulated problem thus directly incorporates the economic impact, and the optimization scheme proposed reflects the economic aspect of the response optimization. The parent frame is assumed to remain linear. The framework developed is generic and is easily extendable to nonlinear frames.

2 PROBLEM FORMULATION

When the optimization is used for strengthening existing buildings using viscous dampers, the stiffness and the mass of the building to be retrofitted are known (and do not vary for different combinations of the damper amount and configuration). Therefore the initial cost in the case of enhancing seismic performance with viscous dampers can be assumed as the cost of added dampers and their installation. A component based loss computation methodology is adopted for calculating the total expected loss. As the parent frame is assumed to remain linear after retrofitting, the computed loss is due to non-structural component damage only. In this study, seismic losses due to downtime and injury are not accounted for; thereby resulting in underestimation of the benefits of optimal intervention.

2.1 Linear frame

In this paper, it is assumed that a linear analysis reasonably predicts the behavior of the damped frame. This does not necessarily require a strict linear behavior of the structure. Nonetheless, a strict linear behavior can be ensured by limiting the damage to drift sensitive components in a prescriptive manner by specifying an allowable/acceptable total expected loss.

2.1.1. Equations of motion

The equations of motion of the linear frame with added dampers are given as,

$$\begin{aligned} &\mathbf{M}\ddot{\mathbf{u}}(t)+\left[\mathbf{C}+\mathbf{C}_{damper}(\mathbf{c}_d)\right]\dot{\mathbf{u}}(t)+\mathbf{K}\mathbf{u}(t)=-\mathbf{M}\mathbf{i}\ddot{u}_g(t) \\ &\mathbf{u}(0)=0;\dot{\mathbf{u}}(0)=0 \end{aligned} \tag{1}$$

In eq. (1), **M** represents the mass matrix and **K** represents the stiffness matrix; in the case of a linear frame both the matrices remain constant. Similarly, **C** represents the inherent damping matrix, $\mathbf{C}_{damper}(\mathbf{c}_d)$ is the added supplemental damping matrix, $\mathbf{c}_d$ is the added damping vector, **i** represents the ground motion directional vector, $\ddot{\mathbf{u}}(t),\dot{\mathbf{u}}(t)$ and $\mathbf{u}(t)$ represent the relative acceleration, relative velocity and relative displacement, and $\ddot{\mathbf{u}}_g(t)$ represents the acceleration due to gravity.

2.2 Loss computation

In classical detail loss assessment framework, the expected annual loss or the loss expected over a period of time is computed as [18, 19],

$$E[L_T]=\frac{1-e^{-\lambda t}}{\lambda}\int_0^{\infty}E[L_T\mid IM]\,dv(IM) \tag{2}$$

where $E[L_T]$ is the expected annual loss, λ is the discount rate (to convert the future loss to net present value), t is the period for which the rate is applied, $E[L_T\mid IM]$ is the expected loss conditioned on the intensity measure *IM*, and *v(IM)* is the mean annual rate of exceedance of the intensity measure. As this study aims to present the optimization methodology, the expected loss is computed only at a single value of intensity measure. Hence, the computed loss is independent of period *t*; thereby making eq. (2) not readily usable. Hence, in the present study, the total expected loss in no-collapse scenario conditioned on the mean engineering demand parameter ($\overline{EDP}$) which in turn is conditioned on the selected intensity measure (IM_1) is used and is assumed to be [18],

$$E\left[L_T \mid NC, \overline{EDP}_{IM_1}\right] = \sum_{j=1}^{N} a_j \left(E\left[L_j \mid NC, \overline{EDP}_{IM_1}\right]\right) \tag{3}$$

Over here, a_j is the cost of a new j^{th} component and *NC* refers to no-collapse state, *N* refers to the number of components. Eq. (3) is period independent and $\overline{EDP}$ is computed for the specific intensity measure (IM_1). As dampers are added into the structure and the structure is assumed to behave linearly, collapse probability can be argued to be zero. Hence, only the no-collapse state is used for estimating loss in this paper.

2.3 Optimization problem

The optimization problem is formulated as,

$$min\, J(\mathbf{c}_d) = \mathbf{c}_d^T \mathbf{1} \tag{4}$$

Subject to:

$$\sum_{i=1}^{N_d} (\theta_i) \le \Theta_{allowable} \tag{5}$$

Over here θ_i refers to the expected loss at the i^{th} degree of freedom computed based on the maximum peak response. Mathematically θ_i is given as,

$$\left.\begin{aligned} &\theta_i = \chi(max(abs(\mathbf{r}_i(t)))) \\ &\textit{where } \chi \textit{ represents a function form and } \mathbf{r}_i(t) \textit{ is the response vector} \\ &\textit{and satisfies the following equation,} \\ &\mathbf{M}\ddot{\mathbf{u}}(t) + \left[\mathbf{C} + \mathbf{C}_{damper}(\mathbf{c}_d)\right]\dot{\mathbf{u}}(t) + \mathbf{K}\mathbf{u}(t) = -\mathbf{M}\mathbf{r}\ddot{\mathbf{u}}_g(t) \\ &\mathbf{u}(0) = 0; \dot{\mathbf{u}}(0) = 0 \\ &0 \le \mathbf{c}_d \end{aligned}\right\} \forall \ddot{\mathbf{u}}_g(t) \tag{6}$$

Eq. (5) can be re-written as,

$$\Pi = \frac{\sum_{i=1}^{N_d} (\theta_i)}{\Theta_{allowable}} \le 1.0 \tag{7}$$

where Π is called the performance index and $\Theta_{allowable}$ is the allowable (i.e. acceptable) total expected loss.

3 OPTIMIZATION ALGORITHM

This section gives stepwise implementation scheme of the optimization procedure. The algorithm employs intensity based assessment for loss computation. A target mean spectrum corresponding to a specific intensity is selected and a suite of ground motion pair is matched to the target spectrum. Following steps are involved in the proposed optimization scheme.

Step 1: Computation of mean responses

Perform linear time domain analysis of the system with an initial amount of damping vector $\mathbf{c}_d$ for all the matched ground motions and compute the mean responses. The initial amount of $\mathbf{c}_d$ vector can be computed using any of the approximate methods available in the literature [20].

Step 2 Evaluation of the total expected loss and performance index Π

Compute the total expected loss and performance index Π by using eqs. (3), (6) and (7). No dispersion is applied in this study to the mean responses obtained and hence the expected total loss can be treated as a deterministic scalar value. In a more generic study the dispersion can also be taken into account within this framework.

Step 3 Computing the gradient of the performance index Π and the objective function *J*

Gradient for the objective function *J* is trivial as it is a direct function of the damping vector $\mathbf{c}_d$ and the sensitivity will return a vector **1.** But the gradient of the performance index Π is not trivial. In this study gradient is derived using the classical finite difference scheme and it is given as below,

$$\frac{\partial \Pi}{\partial c_{dj}} \approx \frac{\Pi_{new} - \Pi}{\Delta c_{dj}} \tag{8}$$

where Π_{new} is the new performance index computed with perturbed $\mathbf{c}_d + \Delta\mathbf{c}_{dj}$ where $\Delta\mathbf{c}_{dj}$ is the perturbed vector with Δc_{dj} at the j^{th} location and zero elsewhere in the vector. Eq. (8) has some limitations especially when applied to large systems as it requires *n+1* analysis for *n* design variables. But as the main intention of this paper is to illustrate the optimization procedure incorporating the loss methodology, finite difference scheme is deemed to be sufficient.

Step 4 Estimating a new guess for the optimal design using Sequential Linear Programming (SLP)

The original optimization problem is given in eqs. (4) and (7) through (6). This is a nonlinear programming problem. SLP is chosen to solve this problem as other nonlinear schemes require the estimation of Hessian matrices which can pose serious difficulties in the vicinity of the optimum solution. So linearizing the objective function given by eq. (4) at the i^{th} iteration gives,

$$J^i(\mathbf{c}_d) = J(\mathbf{c}_d^i) + \{\nabla_{\mathbf{c}_d} J(\mathbf{c}_d^i)\}\{\Delta\mathbf{c}_d^i\} \tag{9}$$

and linearizing the constraint at the i^{th} iteration satisfying eq. (6) is given as,

$$\Pi^i(\mathbf{c}_d) = \Pi(\mathbf{c}_d^i) + \{\nabla_{\mathbf{c}_d} \Pi(\mathbf{c}_d^i)\}\{\Delta\mathbf{c}_d^i\} \tag{10}$$

In order to solve eqs. (9) and (10), an additional side constraints of '*move limits'* limiting the damper step size has to be introduced. So the linearized optimization problem for the i^{th} iteration is given as,

$$\left.\begin{aligned} &min\, J^i(\mathbf{c}_d) \\ &Subject\ to: \\ &\Pi^i(\mathbf{c}_d) \le 1.0 \\ &\Delta\mathbf{c}_d^{low} \le \Delta\mathbf{c}_d^i \le \Delta\mathbf{c}_d^{upper} \end{aligned}\right\} \forall i \tag{11}$$

Solving the eq. (11) gives the $\Delta\mathbf{c}_d$ required for the next iteration. Update the damping vector $\mathbf{c}_d$ as,

$$\mathbf{c}_d + \Delta\mathbf{c}_d \tag{12}$$

Step 5 Check for termination condition

The iteration is terminated if the change in added damper vector $\Delta\mathbf{c}_d$ is less than the tolerance or maximum number of iterations has been reached. Otherwise, update the iteration number as *i=i+1* and proceed to step 1.0. The optimization algorithm when $\Delta\mathbf{c}_d^i \ge \varepsilon_{tolerance}$ is illustrated in Fig. 1.

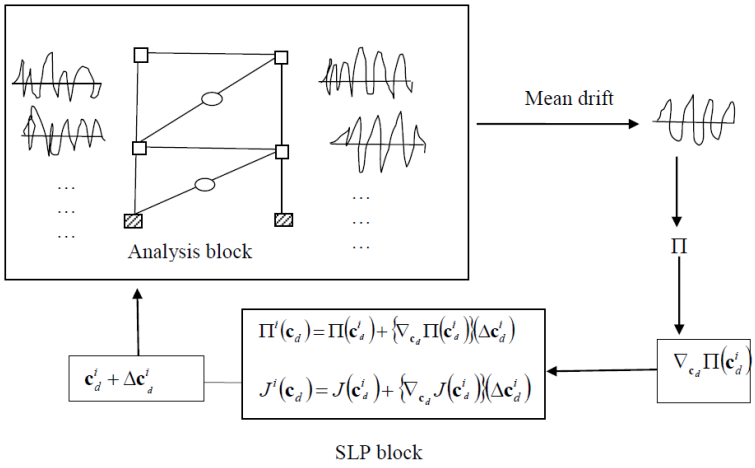


Fig.1 Schematic representation of the optimization procedure for $\Delta\mathbf{c}_d^i \ge \varepsilon_{tolerance}$

4 NUMERICAL STUDY

A four story reinforced concrete frame described in [21], designed in accordance with Eurocode 8 (EC8) and Eurocode 2(EC2) is used to illustrate the proposed optimization procedure. The frame is designed for high seismicity assuming a PGA of 0.3g. The details of the frame and the arrangement of the dampers are given in appendix A.

As the whole purpose of this paper is to demonstrate the optimization procedure, a suite of 7 artificial ground motions scaled to match a Eurocode 8 design spectra with PGA adopted as 1.5 times the design PGA is used for the present study. Un-controlled frame analysis has revealed that this level of ground motion intensity can incur inelastic excursions in the parent frame [21]. The allowable expected loss in eq. (5) is computed by assuming an allowable inter-story drift of 0.5% which ensures elastic frame behavior [12]. Only drift sensitive non-structural loss is accounted in the present study. Figs. 2a and 2b illustrate the constraint error and the performance index. As SLP is used, in order to ensure better convergence an adaptive *move limits scheme* had to be introduced. A *move limit* of 1% of the design damping vector is

used for the first iteration. This is the reason for the steep slope of the line shown in the plots depicted in Figs. 2a and 2b. An initial *move limit* of 0.1% of the design damping vector is used for the rest of the iterations. In the neighborhood of the optimum the initial *move limit* is adaptively updated for better convergence.

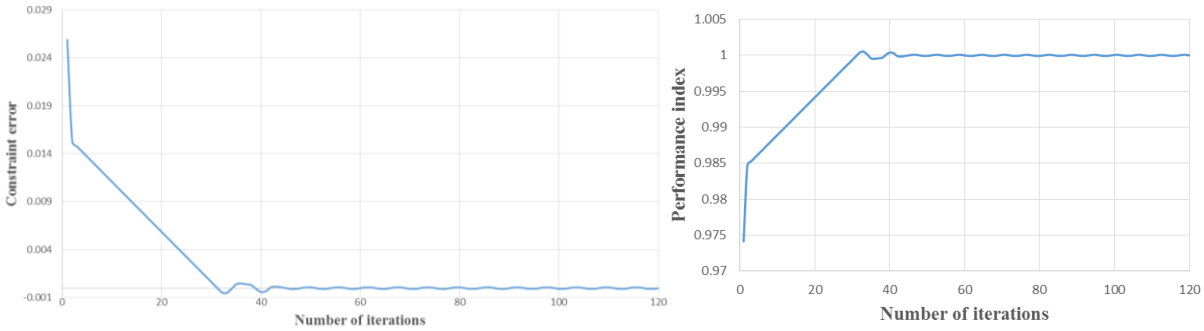


Fig. 2 (a) Constraint error plot, (b) Performance index plot, illustrating convergence to optimum.

Fig. 3 gives the optimum distribution of the damping coefficients along the height of the building. The initial uniformly distributed total damping vector used in this study for starting the optimization procedure is 101.92 kN-sec/m.

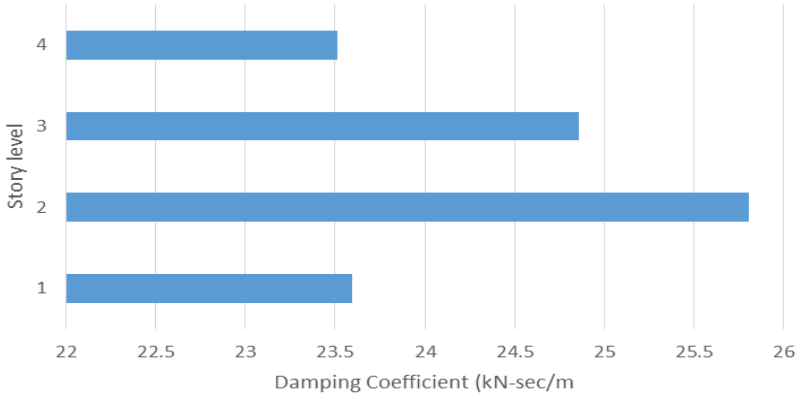


Fig. 3 Optimum damper distribution

The present optimization problem is formulated in such a way that the total expected loss of the building is less than a certain allowable value. In this study *no story level constraints* on the expected loss is considered. So in order to understand the localized effect of the distribution of dampers achieved in Fig. 3 a disaggregation of the total expected loss per story is also conducted.

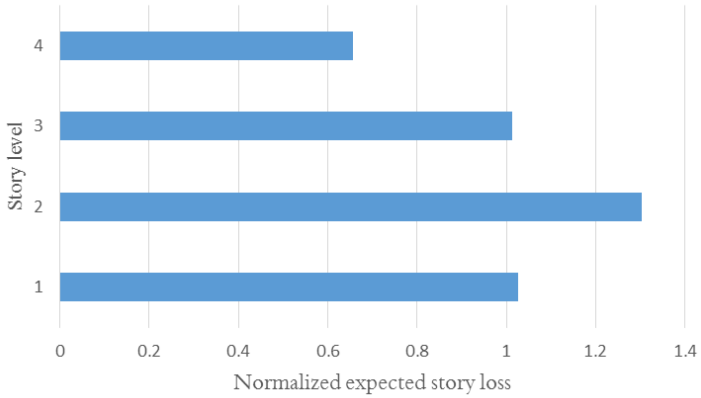


Fig. 4 Disaggregation of the expected loss per story

Fig. 4 shows the story level expected normalized losses. Normalized loss is obtained by dividing the computed story level loss to the allowable story level loss. In a realistic scenario, the allowable loss at story level should be determined based on the performance criterion to be satisfied for the story. Since Fig. 4 is plotted simply to understand the distribution of the expected loss per story, the allowable value of the loss at story level is assumed to be obtained by dividing the total allowable value by the number of stories. From Fig. 4 it could be clearly seen that with the optimum damper distribution shown in Fig. 3, the second story loss exceeds the assumed allowable limit. *This is to be expected as no story level constraint on the expected loss is applied in the optimization procedure*. Fig. 4 suggests that in the present study if we had adopted a constraint on the allowable story level loss limit in addition to the constraint on the total allowable expected loss, more damping would have to be allocated to the second story. But, as the total expected loss is of more concern for engineers and other stakeholders only this is considered as the constraint in the present study. However, if desired the story level constraints can be easily added by specifying the allowable story loss based on the specific requirements of the building. This gives more flexibility in the algorithm and allows the functional requirements of different stories of the building to be accounted for.

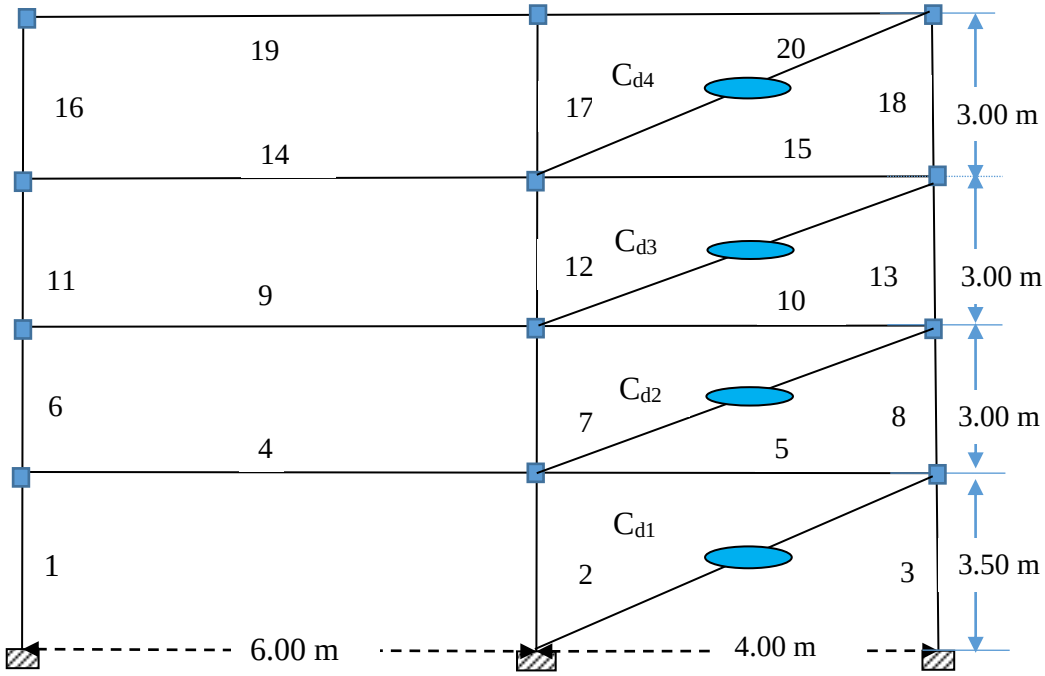
5 CONCLUSIONS

A gradient based sequential linear programming (SLP) optimization methodology is adopted to optimally quantify and optimally position added viscous dampers in multi-story frames. The optimization problem addressed is to minimize the amount of added damping subject to a constraint on the total expected seismic loss. Details of the optimization algorithm is presented and its application is illustrated using a four story reinforced concrete frame subjected to a suite of ground motions scaled to a specific target spectra. It is shown that the proposed procedure is capable of arriving at an optimal quantity of dampers and also simultaneously optimally distributes the dampers along the height of the building.

ACKNOWLEDGEMENTS

The first author gratefully acknowledges the support provided for this research by the NZ Earthquake Commission (EQC) in the form of postgraduate research scholarship.

APPENDIX A: DETAILS OF THE FOUR STORY FRAME



C_{di} refers to added dampers and $i=1....4$

Material Property

Dynamic Young's modulus $=3.5\times10^{10}\ N/m^2$

Geometric Properties

Member number	Width of the member (mm)	Depth of the member(mm)
1,6,11,16,17,12,7,2,3,8,13,18	450	450
4,5,9,10,14,15,19,20	300	450

Nodal Mass

Floor level	Mass per node (kg)
1st floor	29800
2nd -4th floor	29500

REFERENCES

[1] Constantinou MC, Syman MD, Tsopelas P, Taylor DP *Fluid viscous dampers in applications of seismic energy dissipation and seismic isolation.* ATC-17-1:581-591, 1993

[2] Miyamoto HK, Scholl RE Case study: seismic rehabilitation of non-ductile soft story concrete structure using viscous dampers. *11th World Conference on Earthquake Engineering* , Acapulco, Mexico (1996).

[3] Lavan O., On the efficiency of viscous dampers in reducing various seismic responses of wall structures. *Earthquake and Structural Dynamics,***41**, 1673-1692, 2012.

[4] Zhang, R.H., & Soong T.T. Seismic design of visco-elastic dampers for structural applications. *Journal of Structural Engineering*, **118 (5)**, 1375-1392, 1992.

[5] Tsuji, M. & Nakamura, T. Optimum viscous dampers for stiffness design of shear buildings. *Journal of the Structural Design of Tall Buildings*, **5,** 217-234, 1996.

[6] Takewaki, I. Optimal damper placements for minimum transfer functions. *Earthquake Engineering & Structural Dynamics,* **26 (11),** 1113-1124, 1997a.

[7] Takewaki, I. Efficient redesign of damped structural systems for target transfer functions. *Computer Methods in Applied Mechanics & Engineering,* **147(3-4),** 275-286,1997b.

[8] Takewaki, I. Optimal damper positioning in beams for minimum dynamic compliance. *Computer Methods in Applied Mechanics & Engineering,* **156(1-4),** 363-373, 1998.

[9] Takewaki, I. Displacement-acceleration control via stiffness-damping collaboration. *Earthquake Engineering & Structural Dynamics,* **28,** 1567-1585, 1999.

[10] Singh M.P., & Moreschi, L.M. Optimal seismic response control with dampers. *Earthquake and Structural Dynamics,* **30 (4),** 553-572, 2001.

[11] Singh M.P., & Moreschi, L.M. Optimal placement of dampers for passive response control. *Earthquake and Structural Dynamics,* **31 (4),** 955-976, 2002.

[12] Garcia, D.L., A simple method for the design of optimal damper configuration in MDOF structures. *Earthquake Spectra,* **17(3),** 38-398, 2001.

[13] Lavan, O., & Levy, R., Optimal design of supplemental viscous dampers for irregular shear frames in the presence of yielding. *Earthquake Engineering & Structural Dynamics,* **34(8),** 889-907, 2005.

[14] Lavan, O., & Levy, R., Performance based optimal seismic retrofitting of yielding plane frames using added viscous damping. *Earthquakes & structures,* **3,** 307-326, 2010

[15] Lavan, O., Optimal Design of Viscous Dampers and Their Supporting Members for the Seismic Retrofitting of 3D Irregular Frame Structures. *Journal of Structural Engineering*, 2015 (Article in press, DOI: 10.1061/(ASCE)ST.1943-541X.0001261).

[16] Levy, R. & Lavan, O., Fully stressed design of passive controllers in framed structures for seismic loadings. *Structural Multidisciplinary Optimization*, **32**, 485-498, 2006.

[17] Lavan, O., A methodology for the integrated seismic design of nonlinear buildings with supplemental damping. *Structural Control and Health Monitoring*, 22 (3), pp 484–499, 2015.

[18] Aslani, H. & Miranda E., *Probabilistic earthquake loss estimation and loss disaggregation in buildings*, Research report No:15, University of Stanford, 2005.

[19] Bradley B.A., Dhakal R.P., Cubrinovski M., MacRae G.A., Lee S.D., Seismic loss estimation for efficient decision making. *Bulletin of the New Zealand Society of Earthquake Engineering*, **Vol 42 No. 2**, pp 96-110, 2009.

[20] Liang Z.,Lee G.C.,Dargush G.F., Song J., *Structural Damping: Applications in seismic response modification*, CRC press, 2012.

[21] Arede A.J.C.D., *Seismic assessment of reinforced concrete frame structures with a new flexibility based element*, Research Thesis, Universidade Do Porto, 1997.

COMPDYN 2015
5th ECCOMAS Thematic Conference on
Computational Methods in Structural Dynamics and Earthquake Engineering
M. Papadrakakis, V. Papadopoulos, V. Plevris (eds.)
Crete Island, Greece, 25–27 May 2015

HOW CAN INSURERS GET PREPARED TO CATASTROPHES? ASSESSING EARTHQUAKE EXPECTED LOSSES FROM HISTORICAL CATALOGUE.

Anna Bozza[1], Domenico Asprone[1], Fatemeh Jalayer[1], Gaetano Manfredi[1]

[1] Department of Structures for Engineering and Architecture,
University of Naples "Federico II",
Via Claudio 21 – 80125 Naples, Italy.
{anna.bozza, domenico.asprone, fatemeh.jalayer, gaetano.manfredi}@unina.it

Keywords: PBEE, economic resilience, insurance industry, probability-based loss assessment, earthquake simulation.

Abstract. *Countries around the world have had to face huge economic losses due to natural disasters over the past decade. This, of course represents a source of great concern for National Governments and even more so for the insurance industry. In the aftermath of a natural disaster, insurance and reinsurance markets are prone to severe insolvencies and destabilization. Therefore, the finance industry is looking for more reliable loss estimation procedures and insurance models, as effective means for resilience improvement.*

The present paper proposes an engineering-based methodology as a support for innovative insurance models. The study aims at defining a scientific instrument supporting insurers and reinsurers in forecasting expected losses and in mitigating the potential lack of financial capacity. This allows for catastrophe-linked modeling to be performed according to a risk-based framework. The proposed methodology is applied to the Italian residential building stock subjected to seismic risk. Expected losses are evaluated following the procedure outlined in Asprone et al. (2013)[1] for earthquake scenarios from the catalogue of historical earthquakes, of the National Institute of Volcanology and Geology (INGV) [2] and assuming present-day exposure characteristics. Hence the procedure can be implemented anywhere else a detailed catalogue collecting information about earthquakes from the past is available, as for Italy.

Statistical simulations of ground motion intensity (peak ground acceleration, PGA) using multivariate normal distributions are performed for each earthquake. The simulated PGA values are calculated based on the ground motion prediction equation of Sabetta and Pugliese (1996)[3], whose coefficient are re-estimated by Bindi et al. (2009)[4], for each Italian Municipality.

A set of different fragility curves from the literature has been selected and averaged for each building type, also accounting for seismic and non-seismic design. In the next step, the annual expected losses for insurers are evaluated and the results are aggregated in order to calculate total losses for the entire National building stock. Linear regression analysis is performed for predicting the expected loss as a function of earthquake magnitude. The resulting loss model can be used for efficient and rapid loss estimation for a given earthquake scenario.

1 INTRODUCTION

In last decades the rate of occurrence and the severity of natural catastrophes around the world have seriously increased. Hence the probability of severe losses is getting ever higher for homeowner, Governments and insurance industry, affecting simultaneously local and urban communities. This is also due to the growing urbanization in hazard-prone areas and to the existence of many old, non-seismic buildings, especially in European countries.

An effective and widely accepted means to mitigate seismic risk is the private insurance. Unfortunately, efforts for the roll-out of the insurance systems for residential buildings against natural disasters and, particularly, against seismic risk, are related to several different issues.

On the householder side, there is a widespread low risk perception, hence low willingness of people to voluntarily adopt cost-effective protective measures and to purchase insurance.

At the same time, insurance and reinsurance industry are not willing to promote and to sell coverage against such events, due to the high risk of exceeding their financial capacity.

According to Kunreuther [5], the challenges associated with reducing losses from natural hazards is attributed to "the natural disaster syndrome", which consists of two strictly interrelated components: the limited interest in adopting pre-event protections and the high costs to the Governments and insurers following a catastrophe.

The optimization of engineering-based procedures to assess expected losses from disasters, has got the potential to meet the needs of householder and insurers, and is also an effective means for supporting mitigation actions. Reinsurers and Governments can then be represented just as bounds on the insurer-insured interactions, without being directly involved with catastrophic losses [6].

Different scientific studies focus on probability-based means aiming at estimating expected losses from earthquakes [26][27][28].

The integration of catastrophe modelling with insurance management is very popular in the modern insurance systems. Such methodology is usually highly conservative and prevent insurers to get an adequate gain mark up, in order to fix a high leeway to avoid insurers to get financial problems due to catastrophic losses.

Actually, a more precise assessment of expected losses allow insurers to know better the magnitude of losses they will have to face whenever a disaster occurs. Moreover, being losses not overestimated due to the conservatism of catastrophe modelling, insurers can sell insurance products at much lower premiums.

The present work proposes an engineering-based methodology to be used as a support for insurance systems modelling, based on the Italian territory hazard, on the vulnerability of its built environment and on its actual exposure. Such a methodology can potentially be implemented also for the insurance premium evaluation in other countries threatened by seismic risk. Two fundamental requirements are needed in order to effectively implement the procedure, that is, a detailed inventory of past earthquakes and a dataset containing information about the location of buildings in each municipality and their structural typology.

Peak ground acceleration (PGA) values are simulated based on the attenuation law of Bindi et al. (2009) [4]. Selected seismic events are the Italian historical earthquakes from the Catalogue of the National Institute of Geophysics and Volcanology (INGV). Intra-event and inter-event residuals are simulated in consistency with the log-normal attenuation law, using a multivariate normal distribution for the statistical simulation of PGA fields.

Fragility curves are selected from literature and averaged on each building type to evaluate the structural performance in terms of structural limit state exceedance probability given ground motion intensity.

Annual expected losses are estimated through the scenario analysis referring to the actual Italian building stock, according to data supplied by the National Institute of Statistics (ISTAT) [8]. Results are then aggregated to compute the total expected National loss.

Linear regression analysis are then performed on 50°, 16° and 84° percentile values, for each simulated PGA field (100 values for each simulation) in order to obtain predictive expected loss versus event magnitude relationships.

2 EARTHQUAKES SCENARIO ANALYSIS AND SIMULATIONS

All historical earthquakes are selected, whose epicentre was located within the Italian frontier. Hence, 970 earthquakes on 1172 events are investigated from the updated catalogue of INGV [2], from 217 b.C. until 2002 and with magnitude larger than 4.

The catalogue provides some parameters which are fundamental for the implementation of the scenario analysis: geographical coordinates of epicentre and magnitude.

The ground motion equation used in this work for PGA estimate is outlined in Bindi et al. (2009) [4]. It adopts the same functional form of Sabetta and Pugliese (1996) [3], and updates its coefficients, as follows:

$$\log_{10}(PGA) = -1.344 + 0.328 \cdot M - \log_{10}\sqrt{(R^2 + h^2)} + 0{,}262 S_i \pm \sigma \qquad (1)$$

Some assumptions are made in the context of the present study: M is assumed to be equal to Msp, according to the INGV's historical catalogue, R is the epicentral distance from the centre of each municipality [km]. Other parameters are assumed to be the same as suggested by Bindi et al.. In this first step, S_i is assumed to be equal to zero, which means that PGA is evaluated assuming rock soil conditions. σ is the standard deviation of the log of PGA and is given by the following:

$$\sigma^2 = \sigma_{inter}^2 + \sigma_{intra}^2 = (0.174)^2 + (0.222)^2 \qquad (2)$$

where σ_{inter} is the inter-event standard deviation and σ_{intra} is the intra-event standard deviation. According to such distinction, to evaluate the differences attained in the evaluation of expected losses, in this study two limit cases are investigated when performing scenario simulations: PGA fully uncorrelated, assuming $\sigma=\sigma_{,}$ and PGA partially correlated, considering only the inter-event correlation in the residuals of the ground motion prediction equation. 100 values are simulated for each earthquake, drawn from the attenuation law.

The attenuation law is calculated for each seismic event with different magnitude, as shown in Figure 1, for each Italian municipality.

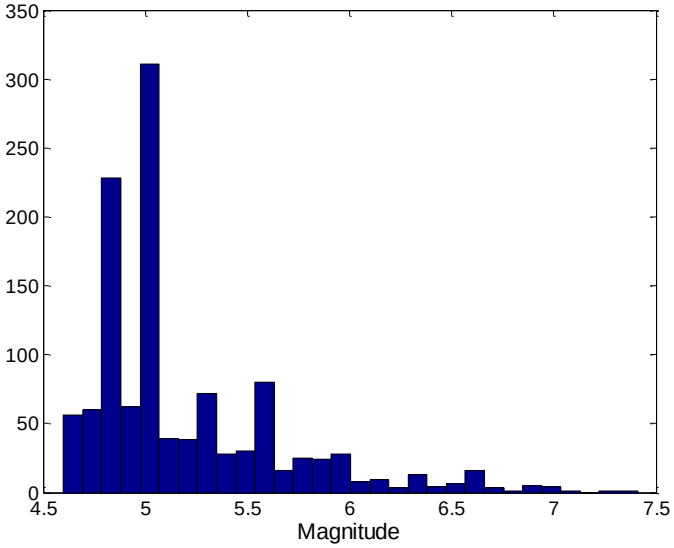


Figure 1 – Histogram of magnitude values of the simulated seismic events

For municipalities at distances lower than 5 km from the epicentre, PGA is assumed to be equal to the epicentral one. For municipalities at distances larger than 100 km from the epicentre PGA is assumed to be equal to zero.

In the case of both fully correlated PGA and partially correlated PGA, error simulations according to a multivariate normal distribution are performed, whose median is equal to the PGA calculated according to the attenuation law from Bindi et al. (2009), given in equation (2).

Regarding the standard deviation, Σ, of the multivariate normal distribution, it is differently calculated for the two limit cases.

In the case of PGA fully uncorrelated it is given by a covariance matrix, which accounts for the total standard deviation as it is given by Bindi et al., and is defined as follows:

$$\Sigma = \sigma^2 \begin{bmatrix} 1 & 0 & \cdots & \cdots & 0 \\ 0 & \ddots & & & 0 \\ \vdots & & 1 & & \vdots \\ \vdots & & & \ddots & \vdots \\ 0 & \cdots & \cdots & 0 & 1 \end{bmatrix}_{8101X8101} \qquad (3)$$

The histogram of sample simulations based on the fully uncorrelated assumption is shown for Benevento municipality for Molise 2002 (Msp=5.59) in Figure 2-(a). Conversely, in the case of partially correlated PGA, standard deviation for multivariate normal distribution for simulations is evaluated from a covariance matrix, Σ, accounting only for the inter-event correlation, as follows:

$$\Sigma = \sigma^2 \begin{bmatrix} 1 & \sigma^2_{inter}/\sigma^2 & \cdots & \sigma^2_{inter}/\sigma^2 & \sigma^2_{inter}/\sigma^2 \\ \sigma^2_{inter}/\sigma^2 & \ddots & & & \sigma^2_{inter}/\sigma^2 \\ \vdots & & 1 & & \vdots \\ \sigma^2_{inter}/\sigma^2 & & & \ddots & \sigma^2_{inter}/\sigma^2 \\ \sigma^2_{inter}/\sigma^2 & \sigma^2_{inter}/\sigma^2 & \cdots & \sigma^2_{inter}/\sigma^2 & 1 \end{bmatrix}_{8101X8101} \quad (4)$$

The histogram of sample simulations based on the partially correlated assumption is shown for Benevento municipality for Molise 2002 (Msp=5.59) in Figure 2-(b).

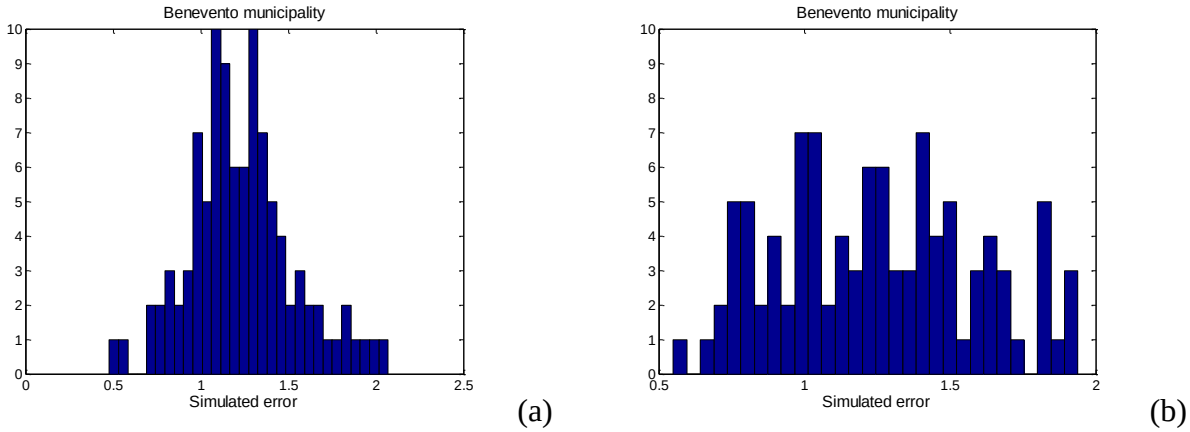


Figure 2 - Error simulated (Nsim=100) for Molise 2002 (Msp=5.59) for Benevento municipality in the case of fully uncorrelated PGA (left side), and in the case of partially correlated PGA (right side)

Once the PGA field, derived from each earthquake, is evaluated for the entire Italian territory (assuming rock as soil type), PGA values are amplified according to the topographical and stratigraphic coefficient of each municipality, as defined by Colombi et al. (2010) [7].

3 FRAGILITY CURVE DATASET SELECTION

Seismic fragility curves define the probability of exceedance of a discrete set of limit states, as a function of an intensity measure of the earthquake (IM).

In this paper, the considered intensity measure is the PGA, hence the cumulative distribution function (CDF) representing each set of fragility curves is defined as:

$$F_{j,i} = \Phi\left(\frac{\log(PGA) - \log\mu(i,j)}{\sigma(i,j)}\right) \quad (5)$$

Being i the structural typology, j the number of limit states and Φ is the standard normal distribution function. Several studies have been investigated from the literature among which those referring to structural typologies which are more similar to the Italian ones, have been selected ([10]). Six structural typologies have been identified from ISTAT dataset: seismic and non-seismic reinforced concrete, seismic and non-seismic masonry and seismic and non-seismic mixed buildings.

The probability of the exceedance of limit state *sl* given PGA is evaluated as:

$$P\left[SL = sl / PGA\right] = F_{SL,i}(PGA) - F_{SL+1,i}(PGA) \qquad with \qquad 1 \le sl \le j \qquad (6)$$

Actually a vulnerability assessment considering spectral acceleration, Sa, rather than PGA is more precise from a structural point of view and respects the ground motion IM as meant by the Italian building code. Unfortunately, to evaluate spectral acceleration at least the number of storeys of each residential building should be known. Such an information, which allow to estimate the fundamental period, T, of the buildings, is not given by the ISTAT database.

4 LOSS ESTIMATION MODEL

In this paper, a discrete version of the Performance-based Earthquake Engineering (PBEE) framework equation (e.g., [9]) is used (see Asprone et al. (2013) for more details):

$$l_i = \sum_{LS=1}^{n} RC(LS) \cdot [F_{SL,i}(\overline{\mathrm{PGA}}) - F_{SL+1,i}(\overline{\mathrm{PGA}})] \qquad [€ / sqm] \qquad (7)$$

where l_i is the expected loss given PGA per square meters of residential units; $\overline{\mathrm{PGA}}$ is the earthquake IM evaluated for each municipality through the attenuation law and then amplified for the stratigraphic and topographical coefficients, S_S and S_T.

The specific loss expected values, l_i, are averaged on all considered curves (i=1:N) for each structural typology and the resulting mean value, $l_m = 1/N \sum_{i=1}^{N} l_i$, is then integrated on the square meters amount. Hence, the total expected loss, L_m, is evaluated, which represents an indicator of mean losses on the overall municipal territory. By summing up L_m for all municipalities, the National expected loss, L, is computed.

Some assumptions are made regarding the unit cost of reconstruction/restoration. Being n the number of limit states for each vulnerability curve, the reconstruction cost, $RC_{collapse}$, is assumed to be equal to 1500 €/sqm. It corresponds to the collapse limit state and its amount comes from the estimates of CRESME (2011) [25] regarding mean costs for new constructions in Italy.

Furthermore, according to the scenario analysis by Asprone et al. (2013), the reconstruction/restoration costs for residential buildings are assumed to have a linear trend against the limit states, i, as in the following:

$$RC(LS) = \left(\frac{i}{n}\right) \cdot RC_{collapse} \qquad (8)$$

Such relationship allows to evaluate the unit loss also for intermediate limit states and to keep this invariant for the assumptions made.

Expected National Losses are evaluated for each earthquake simulation performed, and plotted against magnitude, in the case of PGA fully uncorrelated (Figure 3) and PGA partially correlated (Figure 4).

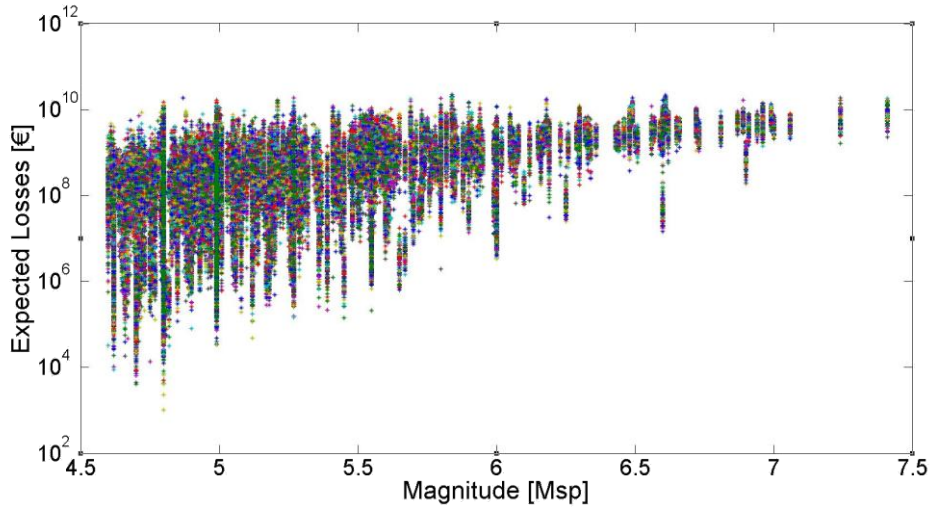


Figure 3 – Expected National Losses for each simulated earthquake, in the case of PGA fully uncorrelated

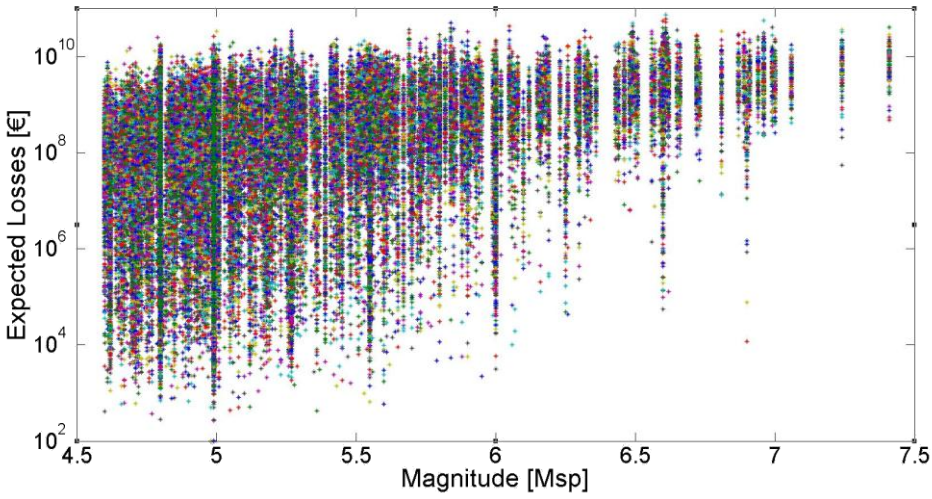


Figure 4 - Expected National Losses for each simulated earthquake, in the case of PGA partially correlated (considering only the inter-event correlation)

The results demonstrate more scatter in expected loss given magnitude for the case when PGA values are partially correlated (with respect to the uncorrelated case). Figure 5 below shows the histogram of expected loss for the Italian built environment (residential) for two historic events of Messina (1908, Msp=7.24) and Irpinia-Basilicata (1980, Msp=6.89).

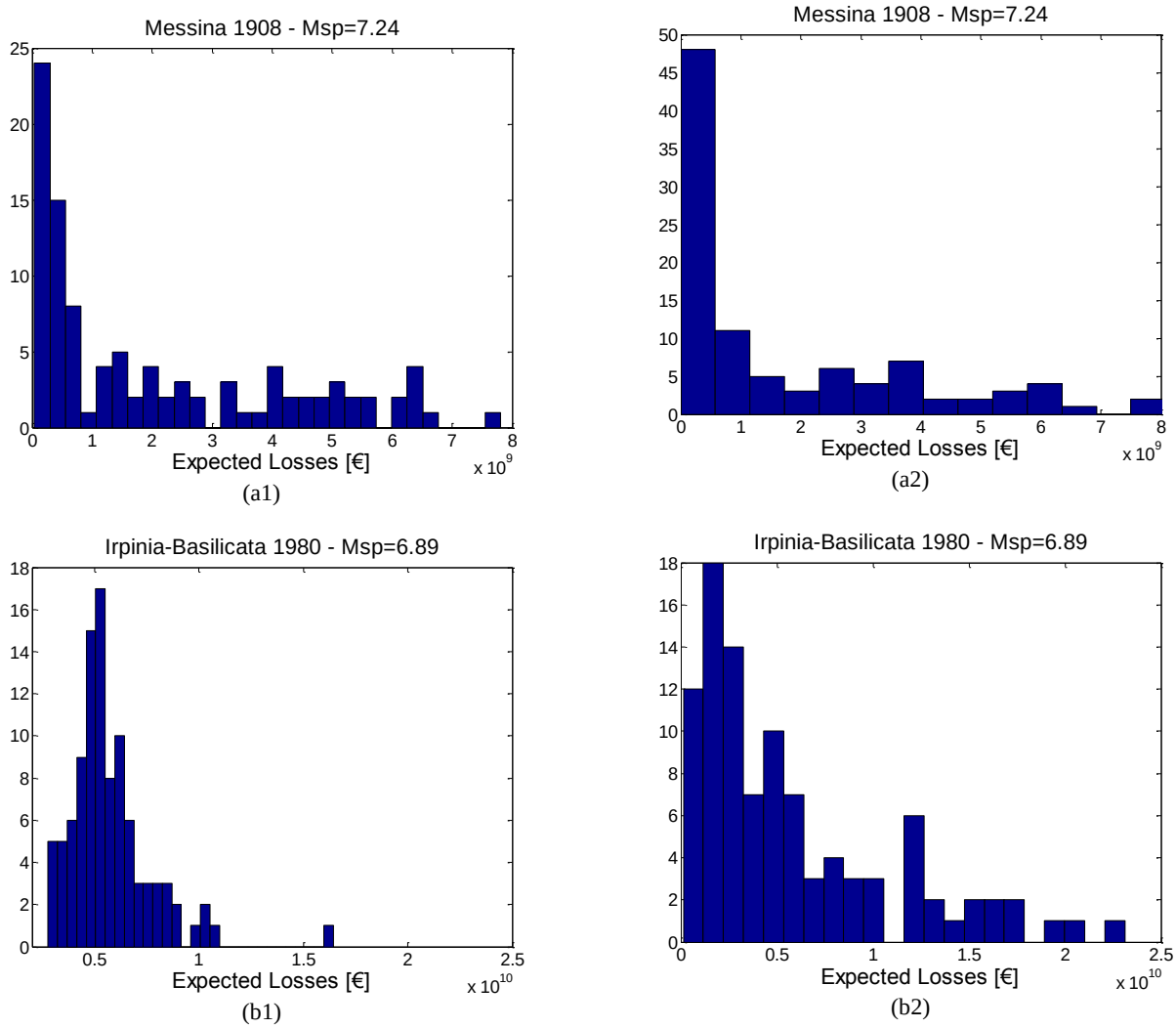


Figure 5 – Examples of total losses evaluated for the Italian built environment in the case of PGA fully uncorrelated (left side) and PGA partially correlated (right side). Analysis results refers to the following seismic events: 6.a1- 6.a2 Messina 1908, 6.b1 – 6.b2 Irpinia-Basilicata 1980.

5 PBEE SUPPORTING INSURANCE INDUSTRY: RESULTS AND DISCUSSION

Seismic insurance is a potential tool for seismic risk mitigation, whose modeling is currently of great concern.

Dealing with the Italian building stock, one has to consider that the set of residential buildings is a spatially distributed system. Hence, the joint distribution of ground motion parameters at different sites is needed when performing a scenario simulation. Since, the entire Italian built environment is investigated, and the spatial modeling of ground motion at the level of each municipality rather than the single building is performed. This is done based on the working assumption that PGA values are constant within the single municipality's area.

Once scenario simulations are executed, linear regression analysis are implemented according to the least square method. These leads to a predictive model for expected loss given magnitude .

First a linear regression on logarithms of 50th percentile of estimated losses for both the case of PGA fully uncorrelated and PGA inter-event correlated is performed:

$$\log_{10} L^{50th} = \log_{10} a + b \cdot \log_{10} M_{sp} \quad (9)$$

where L^{50th} is the median value of evaluated expected losses for each earthquake simulation, M_{sp}, is the magnitude according to the INGV catalogue, and $\log_{10}$a and b are the coefficients of the regression curve (the intercept and the slope, respectively). The regression can be seen also as a probabilistic model for the residuals (errors), where the assumption of having constant dispersion, i.e. the homoskedasticity assumption, subsists. The sample variance can be then estimated as:

$$\sigma^2 \approx s^2 = \frac{\sum_{i=1}^{n} e_i^2}{n-2} \quad (10)$$

where the numerator represents the residual sum of squares and the denominator is the degree of freedom remaining, since the predicted values are calculated using two statistics, namely, the slope and the intercept of regression. Hence, the 16th and 84th percentiles for loss given magnitude according to the regression predictive model are calculated as:

$$STD(L \mid \mathrm{M}) = \mathrm{s} = \sqrt{\frac{\sum_{\mathrm{i=1}}^{\mathrm{n}} [\log_{10} L^{50th}{}_i - (\log_{10} a + b \cdot \log_{10} M_{sp,i})]^2}{\mathrm{n-2}}} \quad (11)$$

$$\log_{10} L^{16th} = \log_{10} a + b \cdot \log_{10} M_{sp} - s$$

$$\log_{10} L^{84th} = \log_{10} a + b \cdot \log_{10} M_{sp} + s$$

Where L^{16th} and L^{84th} are the 16th and 84th percentiles of the loss. Alternatively, logarithmic linear regression is also performed taking the 16th and 84th percentile expected loss values as the dependent variables (in exactly the same manner described above for the case of the 50th percentile), for the cases of PGA fully uncorrelated and PGA inter-event correlated. The resulting predictive equations are plotted in Figure 6 and Figure 7. The black curves demonstrate the regression curve and its 84th and 16th percentiles; the blue curves demonstrate the regression curves fitted to the 16th and 84th percentiles of the expected loss values. It can be observed that the blue curves capture the fact that there are less data (less number of very big earthquakes) for very large magnitudes. On the other hand, the black lines are based on a homoskedastic regression model (constant dispersion) and cannot capture this trend.

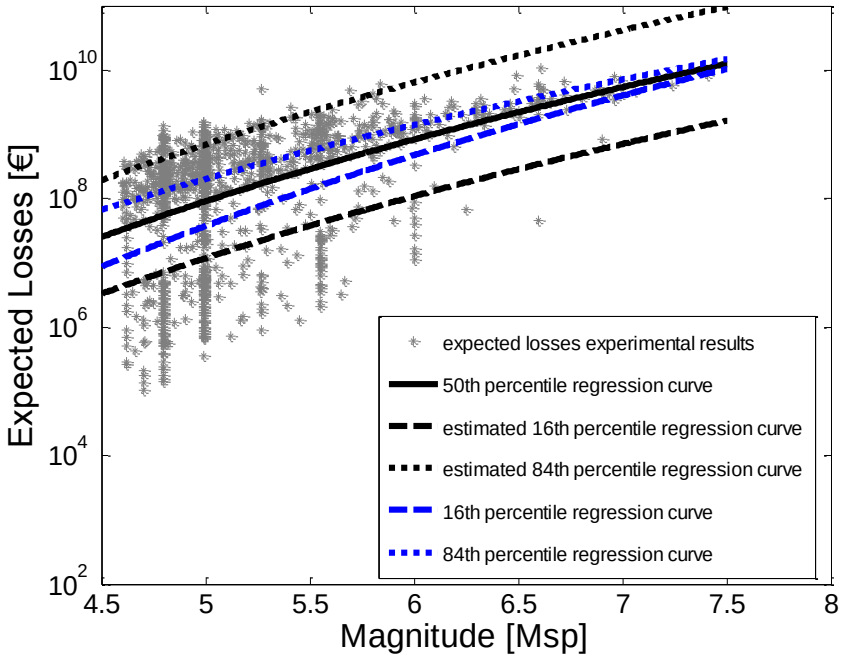


Figure 6 – Expected losses against magnitude and regression curves for the case of PGA fully uncorrelated

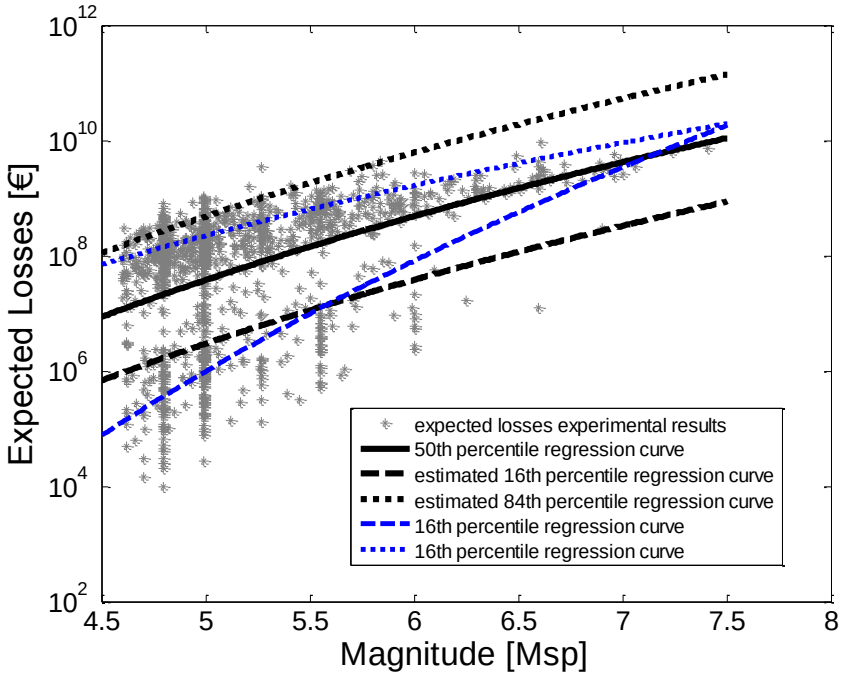


Figure 7 – Expected losses against magnitude and regression curves for the case of PGA partially correlated

In both Figure 6 and Figure 7, the expected losses are calculated for each historical event with a given magnitude for the built environment in the entire Italian territory. Table 1 below shows the statistics of the loss values simulated for a given historic event (Venafro 1873, Msp=4.99). It can be observed that the mean loss values are almost equal (something that is expected); whereas the partially correlated case shows a significantly higher dispersion.

ex. 500th earthquake [Venafro 1873 – Msp=4.99]	PGA FULLY UNCORRELATED	PGA INTER-EVENT CORRELATED
Mean	1.0646e+009	0.93656e+009
Standard deviation	5.7097e+008	1.2162e+009
Median	1.0205e+009	0.49394e+009

Table 1: statistics of expected loss distribution according to the two studied PGA limit case

Figues 8a,b below show the regression curves fitted to the median (Figure 8a) and the mean values (Figure 8b) for losses calculated for the two cases of uncorrelated (dashed dot) and partially correlated (dashed) PGA values. As it is expected the mean values curves are almost identical (the expected value for total losses over the entire territory does not depend on the correlation structure); whereas, the median values for the partially correlated case are lower (this is reasonable since the partially correlated case is associated with higher standard deviations, the median should be smaller so that the expected values are equal).

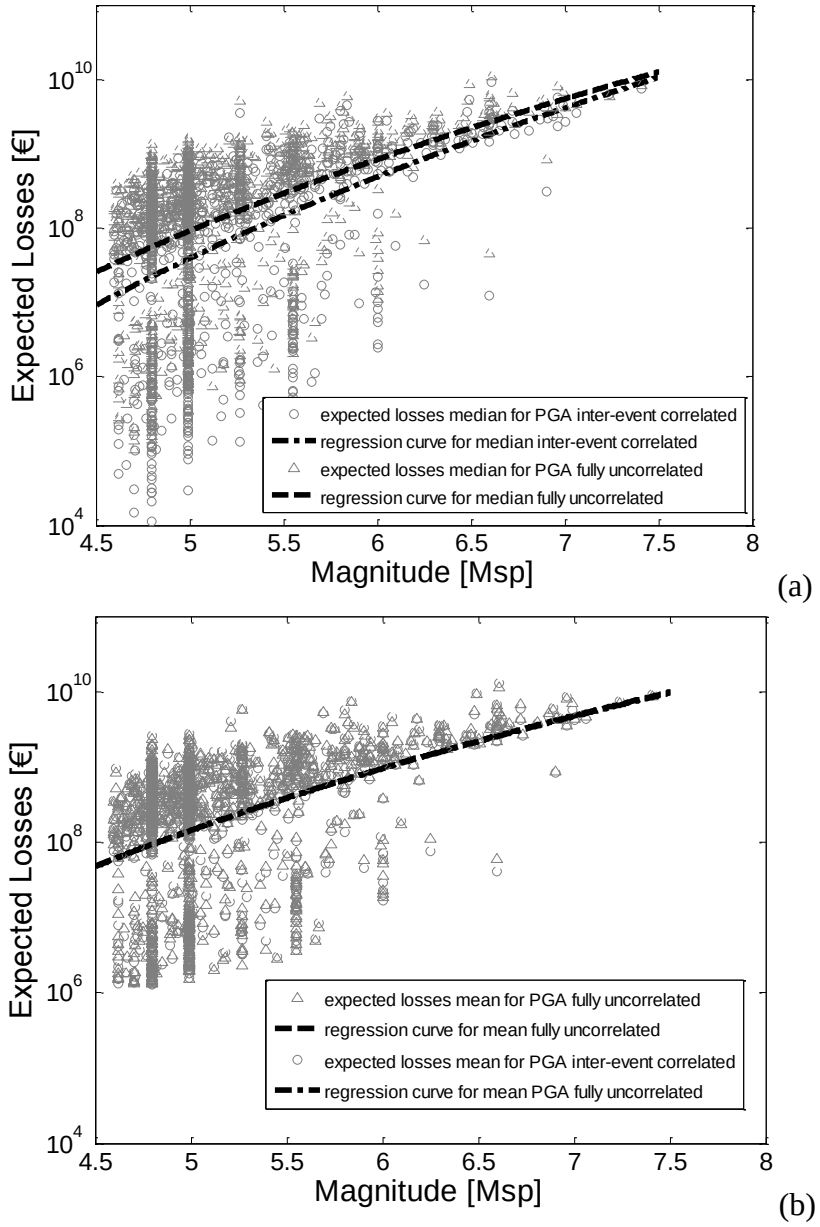


Figure 8 – Regression curve for expected losses against magnitude on median (a) and mean (b) values, showing almost complete correspondence between PGA fully uncorrelated and PGA partially correlated in the case of mean regression

6 CONCLUSIONS

The main criticality that insurers have to face when dealing with private seismic insurance is related to the knowledge of effective economic resources needed. It is fundamental to cope with the insurers' need to pay the insured, without incurring in insolvency, and also to cover expenses without getting into cash flow problems. Collecting information about past earthquakes and information about the population of residential buildings and their construction in the present, this study proposes predictive relationships for the expected economic losses given the magnitude. The procedure employed for deriving these predictive relationships takes into account (partially) the spatial correlation in the residuals of the ground motion prediction equation. The results are presented in terms of the 16th, median and 84th percentiles for ex-

pected loss curves given magnitude based on two distinct assumptions regarding the spatial correlation structure in PGA values (uncorrelated and partially correlated considering only the inter-event correlation). The above-mentioned percentile curves are calculated based on both homoskedastic (constant dispersion) linear regression and also by directly calculating the percentiles from the data. It can be observed that the 16^{th}/84^{th} percentiles' confidence interval around the median is larger in the case of partially correlated PGA values. This observation is in agreement with similar results in the literature (e.g., Goda and Hong 2008). Moreover, it is observed that the simple linear logarithmic regression based on the assumption of constant dispersion cannot capture the fact that there are less historical earthquakes available for the very large magnitudes (also reflecting the fact that there are fewer faults that are physically capable of producing very large events). The seismic events collected by the historical catalogue are, in fact, in higher number for lower magnitudes. In general, the predictive relationships derived for the expected loss given magnitude clearly show significant dependence on how the correlation in the peak ground acceleration is modeled (with the exception of the mean curve that demonstrates a certain insensitivity to spatial correlation). This confirms further (see e.g. see for example Yoshikawa and Goda 2014) that the choice of a suitable risk metric for insurers is of extreme importance for decision-making.

REFERENCES

[1] Asprone, D., Jalayer, F., Simonelli, S., Acconcia, A., Prota, A., Manfredi, G. Sesimic insurance model for the Italian residential building stock. *Structural Safety, 44, pp. 70-79,* 2013.

[2] A. Rovida, R. Camassi, P. Gasperini and M. Stucchi (eds.), "CPTI11, the 2011 version of the Parametric Catalogue of Italian Earthquakes.", Milano, Bologna, *http://emidius.mi.ingv.it/CPTI, DOI: 10.6092/INGV.IT-CPTI11*, 2011.

[3] Sabetta, F., and Pugliese, A., "Estimation of response spectra and simulation of nonstationary earthquake ground motions.", *Bulletin of the Seismological Society of America* 86.2 , 1996.

[4] Bindi, D., Luzi, L., Pacor, F., Sabetta, F., Massa M., "Towards a new reference ground motion prediction equation for Italy: update of the Sabetta-Pugliese (1996)", *Bulletin of Earthquake Engineering ,* 2009.

[5] Kunreuther H., "Mitigating Disaster Losses though Insurance", ..., 1996.

[6] Kesete , …, ..., 2014.

[7] Colombi M., Crowley H., Di Capua G., Peppoloni S., Borzi B., Pinho R., Calvi G.M., "Mappe di Rischio Sismico a Scala Nazionale con Dati Aggiornati sulla Pericolosità Sismica di base e locale". *Progettazione Sismica, 1, ISSN 1973-7432*, 2010.

[8] ISTAT - Istituto nazionale di statistica, 14° Censimento generale della popolazione e delle abitazioni, *http://dawinci.istat.it/MD/dawinciMD.jsp*, 2001.

[9] Goulet, Christine A., et al. "Evaluation of the seismic performance of a code-conforming reinforced-concrete frame building—from seismic hazard to collapse safety and economic losses.", *Earthquake Engineering and Structural Dynamics 36.13*, 2007.

[10] Ahmad N., H. Crowley, R. Pinho, "Analytical fragility functions for reinforced concrete and masonry buildings aggregates of euro-mediterranean regions – UPAV methodology" *Internal report, Syner-G Project, 2009/2012,* 2011.

[11] Borzi, B., Crowley, H., Pinho, R., "SP-BELA: Un metodo meccanico per la definizione della vulnerabilità basato su analisi pushover semplificate." *Proceedings of XII Convegno L'Ingegneria Sismica in Italia ANIDIS 2007, Pisa, paper no. 160 (in Italian),* 2007.

[12] Borzi B, Crowley H, Pinho R., "The influence of infill panels on vulnerability curves for RC buildings." *Proceeding. 14th World Conference on Earthquake Engineering, Beijing, China,* 2008.

[13] Crowley H., Borzi B., Pinho R., Colombi M., Onida M., "Comparison of two mechanics-based methods for simplified structural analysis in vulnerability assessment." *Adv Civil Eng 2008, Article ID 438379,* 2008.

[14] M.A. Erberik., "Generation of fragility curves for Turkish masonry buildings considering in-plane failure modes." *Earthquake Eng. and Str. Dyn., 37,* 2008.

[15] A. J. Kappos, C.Panagiotopoulos, G. Panagopoulos, El. Papadopoulos. "WP4 – Reinforce Concrete Buildings (Level 1 and Level 2 analysis)." *RISK-UE*, 2003.

[16] A. J. Kappos, G. Panagopoulos, C.Panagiotopoulos, G. Penelis, "A hybrid method for the vulnerability assessment of R/C and URM buildings" *Bulletin of Earthquake Engineering, 4, 391-413*, 2006.

[17] M. Kostov, E. Vaseva, A. Kaneva, N. Koleva, G. Varbanov, D.Stefanov, E. Darvarova, D. Solakov, S. Simeonova & L. Cristoskov,"Application to Sofia", *RISK-UE WP13,* 2004.

[18] Kwon OS, Elnashai A. "The effect of material and ground motion uncertainty on the seismic vulnerability curves of RC structure." *Engineering Structures, 28(2):289–303,* 2006.

[19] S. Lagomarsino & S. Giovinazzi. "Macroseismic and mechanical models for the vulnerability and damage assessment of current buildings." *Bulletin of Earthquake Engineering 4(4), 415-443*, 2006,

[20] H.B. Ozmen, M. Inel, E. Meral and M. Bucakli, "Vulnerability of Low and Mid-Rise Reinforced Concrete Buildings in Turkey", *14ECEE, Ohrid, Turkey,* 2010.

[21] M. Rota, A. Penna, C.L. Strobbia, "Processing Italian damage data to derive typological fragility curves", *Soil Dynamics and Earthquake Engineering 28(10-11), 933-947,* 2008.

[22] M. Rota, A, Penna, G. Magenes, "A methodology for deriving analytical fragility curves for masonry buildings based on stochastic nonlinear analyses", *Engineering Structures 32, 1312-1323,* 2010.

[23] Spence, R., ed. 2007. "Earthquake disaster scenario predictions and loss modelling for urban areas". *In LESSLOSS Report 7, Pavia, , Italy: IUSS Press.*, 2007.

[24] G. Tsionis A. Papailia M.N. Fardis, "Analytical fragility functions for reinforced concrete and masonry buildings aggregates of euro-mediterranean regions – UPAT methodology" *Internal report, Syner-G Project, 2009/2012,* 2011

[25] CRESME IL MERCATO DELLE COSTRUZIONI 2011-2015, "Rapporto congiunturale e previsionale Novembre 2011", 2011.

[26] K. Goda, H. P. Hong, *"Estimation of Seismic Loss for Spatially Distributed Buildings",* Earthquake Spectra, Volume 24, No. 4, pages 889–910, November 2008.

[27] H. Yoshikawa, K. Goda., *"Financial Seismic Risk Analysis of Building Portfolios."* Natural Hazards Review, Volume 15, Issue 2, 1 May 2014, Pages 112-120.

[28] Jaiswal, Kishor, and David J. Wald. *"Estimating economic losses from earthquakes using an empirical approach."* Earthquake Spectra 29.1 (2013): 309-324.

COMPDYN 2015
5th ECCOMAS Thematic Conference on
Computational Methods in Structural Dynamics and Earthquake Engineering
M. Papadrakakis, V. Papadopoulos, V. Plevris (eds.)
Crete Island, Greece, 25–27 May 2015

APPLICATION OF INCREMENTAL DYNAMIC ANALYSIS TO SEISMIC EVALUATION OF UNDERGROUND STRUCTURE

Tong LIU[1], Yong YUAN[2], Zhiyi Chen[1]

[1] Department of Geotechnical Engineering, Tongji University
1239 Siping Road, Shanghai, China, 200092
262liut@tongji.edu.cn

[2] State Key Laboratory of Disaster Reduction in Civil Engineering, Tongji University
1239 Siping Road, Shanghai, China, 200092
yuany@tongji.edu.cn

Keywords: Performance-based Earthquake Engineering, Incremental Dynamic Analysis, Underground Structure, Intensity Measure, Damage Measure, Daikai Subway Station.

Abstract. *Based on the IDA method for seismic evaluation of superstructure, an IDA method for seismic evaluation of underground structure was proposed in this paper. The feature of IDA and its implementation procedures were introduced in detail. Combined with an engineering project, a two-dimensional finite element numerical model was proposed to analyze structural seismic response through finite element analysis software ABAQUS. 10 ground motion records were selected to provide sufficient accuracy in the estimation of seismic demands. Analysis result shows that IDA method can be applied successfully to underground structure and the difference between superstructure and underground structure using IDA method was also presented. Furthermore, the efficiency of different intensity measures was investigated. Two intensity measures were used, namely, Peak Ground Acceleration (PGA), Peak Ground Velocity (PGV) , and* θ *max was selected as the damage measure. The analytical progress and results are helpful for the performance-based seismic design of underground structure and a wide application of IDA in other complex underground structures.*

1 INTRODUCTION

With the rapid development of science and technology, underground structure becomes more and more important in our daily life. Therefore, the security of underground structure under seismic loads should be ensured. In early years, many researchers believed that because of the restraint of surrounding soil, the seismic performance of underground structure could be better than that of superstructure. However, from the damage phenomenon in the earthquakes happened in recent years, we know that the existing underground structures are not security enough, which can also cause great earthquake damage sometimes. Especially in the Kobe earthquake at Japan in 1995, the Daikai subway station was suffered from serious earthquake damage, and more than 30 columns of the central section of the station completely collapsed over a total length of about 110m [1]. This event also aroused many researchers' awareness to do research on seismic performance of underground structure.

Nowadays, the concept of performance-based earthquake engineering is the most popular seismic design theory in recent years. This concept is also considered as the major guiding ideology for seismic design in the future. The aim of this concept is to make sure the structures designed can have the anticipative functions [2]. During the design life of architectural structure, specific performance levels should be provided when it endures different earthquake levels, which should also make the costs lower enough over the structures' life cycle.

There are several methodologies proposed to fulfill this aim, but undoubtedly, the most promising method is incremental dynamic analysis (IDA) or dynamic pushover, which can estimate the seismic performance of structures accurately and is of great contribution in performance-based earthquake engineering. It takes the old concept of scaling ground motion records and develops it into a way to accurately describe the full range of structural behavior, from elasticity to collapse [3]. In the concrete, IDA is a parametric analysis method, which involves performing a series of nonlinear dynamic analyses of a suite of ground motion records, each scaled to multiple levels of intensity, thus producing dynamic capacity curves of response parameterized versus intensity level. The concept has been provided as early as 1977 by Bertero [4], and has been used by several authors, such as Luco and Cornell [5, 6], Bazurro and Cornell [7, 8], Mehanny and Deierlin[9], Nassar and Krawinkler[10]. The method was well documented and introduced by Vamvatsikos and Cornell in 2000[11]. With the rapid spread of IDA among researchers all over the world, this method has already been used to many different kinds of structures in recent years, including the use to high-rise towers by Behrouz and Mahmood et al [3], the use to hybrid structure by Zhou Ying et al [12], the use to steel moment resisting frames by Behrouz and Hamideh et al [13] and the use to multi-column bridge bents by A.H.M and M. Shahria [14]. From the content mentioned above, we can find that IDA is mostly used to evaluate the performance of superstructure.

In this paper, IDA is applied to the underground structure. An introduction of the method of IDA is presented specifically and its available application to underground structure is shown through the representative example of Daikai subway station. The analytical process and results are helpful for the performance-based seismic design of underground structure and capacity estimation of underground structure.

2 INCREMENTAL DYNAMIC ANALYSIS

2.1 Basic concepts [11]

1. Original ground motion records:

The original ground motion records a_1 are selected from the ground motion database, which can represent the structure's site conditions.

2. Scale factor (SF)

The scale factor λ is a nonnegative number, which can produce ground motion a_λ with different intensity levels ranging from structure's elasticity to collapse by multiplying original acceleration time history a_1. A value of $\lambda=1$ signifies the original record, $\lambda<1$ means a scaled-down record, while $\lambda>1$ is a scaled-up one. A common method is to determine one intensity level, which can be used for initial elastic analysis, and then enhance the intensity level one-to one through multiplying the SF.

3. Intensity measure (IM)

Intensity Measure is a parameter that can signify the ground motion intensity and should be scalable. There are many quantities proposed to characterize the intensity of a ground motion record. Common examples of scalable IMs are the Peak Ground Acceleration (PGA), Peak Ground Velocity (PGV), the $\xi=5\%$ damped Spectral Acceleration at the structure's first-mode period ($S_a(T_1,5\%)$), and the yield reduction R-factor, et al.

4. Damage Measure (DM)

Damage Measure or Structural State Variable is a parameter that can deduced from the output of the corresponding non-linear dynamic analysis. It can characterize the additional response of the structural model due to a prescribed seismic loading. Common examples of DMs are maximum base shear, node rotations, peak story ductility, various proposed damage indices (e.g. a global cumulative hysteretic energy), peak roof drift, the floor peak inter story drift angles, the maximum peak inter story drift angle.

The selection of a suitable DM depends on the application and the structure itself. For structural damage of frame buildings, θ_{max} relates well to joint rotations and both global and local story collapse, thus becoming a strong DM candidate.

2.2 Basic steps

The basic steps of IDA described in FEMA-350/351 are [15, 16]:

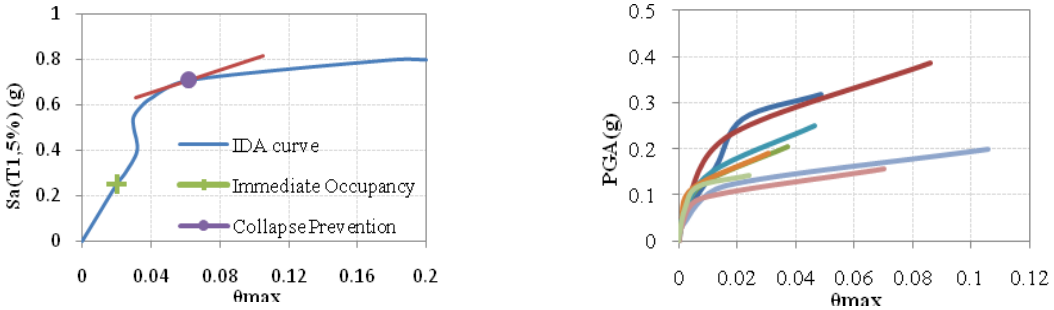
1. Establish the calculation model which can be used for both elastic analysis and elastic-plastic analysis of the structure.

2. Choose the ground motion records which can be representative of events likely to cause severe ground motions in the site on which structures are located. Around 10 to 20 records are usually enough to provide sufficient accuracy in the estimation of seismic demands for mid-rise building [17]. Choose suitable IM and DM.

3. Get a series of ground motion records through monotonously scaling the original ground motion records.

4. A single-record IDA study, as shown in Figure 1(a). Choose a little scaled record for elastic time history analysis, getting the first point of IM-DM, which is denoted as Δ_1; the elastic slope of the ligature between the origin and Δ_1 is denoted as K_e; continue dynamic analysis for the next scaled ground motion record to get the second point of IM-DM, which is denoted as Δ_2; if the slope of the ligature between Δ_1 and Δ_2 is larger than $0.2K_e$, continue elastic-plastic dynamic analysis for the next scaled ground motion record until the slope of the ligature between Δ_i and Δ_{i+1} is lower than $0.2K_e$, at which point the structure is considered being collapse. Δ_{i+1} is the ultimate value of DM; if Δ_{i+1} is larger than 0.1, the ultimate value of DM is considered as 0.10; the ligature of all points is the IDA curve.

5. Exchange the original ground motion record and repeat step3 and step4 to get an IDA curve set, which is a collection of IDA curves of the same structural model under different ground motion records, as shown in Figure 1(b). Conduct statistic according to a specific method and get the statistical IDA curves.



(a) A single-record IDA study [18] (b) A multi-record IDA study

Figure 1: IDA curves.

3 THE APPLICATION OF IDA TO UNDERGROUND STRUCTURE

In order to show the available application of IDA to the underground structure, the Daikai subway station at Japan which suffered from strong seismic loads in 1995 is taken as a typical example according to the steps introduced above.

3.1 General profile [1]

The Daikai subway station was built between 1962 and 1964 by cut-and-cover which belongs to the privately owned Kobe Rapid Transit System. The distance between the station and the epicenter of the earthquake is about 15 km. The Daikai station can be divided into three sections as follows: (1) the main section of the station that collapsed; (2) the subway tunnels section with no severe damage occurred; and (3) the access station section that had two underground levels, where no severe damage occurred. The main structure considered in this paper is the first section, as shown in Figure 2. The rectangular reinforced concrete box is of 17m wide and 7.17m high, and the space of central columns is 3.5m in the longitudinal direction. The columns which are about 5m high had a rectangular reinforced concrete cross section of 0.4m by 1.0m. The soil condition applied in this paper can be got from the reference [19], which is shown in Table1.

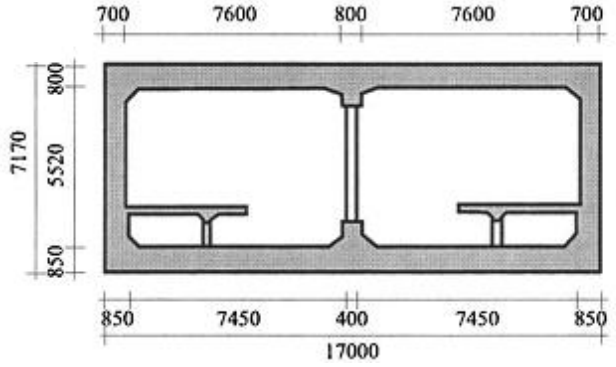


Figure 2: Section one that collapsed [1].

Soil layer	Depth(m)	Unit weight(t/m^3)	Shear wave velocity(m/s)	Poisson ratio
1	0~2.04	1.9	140	0.333
2	2.04~5.10	1.9	140	0.488
3	5.10~8.21	1.9	170	0.493
4	8.21~11.45	1.9	190	0.494
5	11.45~17.20	1.9	240	0.490
6	17.20~39.20	2.0	330	0.487
7	-	2.1	500	0.470

Table 1: Soil condition of the site where Daikai subway station is located.

3.2 Analytical modeling

The two dimensional finite element model with both soil and subway station is established according to the general profile mentioned above through the finite element software ABAQUS, as shown in Figure 3. To model the behavior of reinforced concrete accurately, both concrete damage plasticity model and steel model are all considered in this detailed numerical model. With the help of SHAKE, soil's equivalent linearization is considered. The boundary of soil in this model is considered through infinite element.

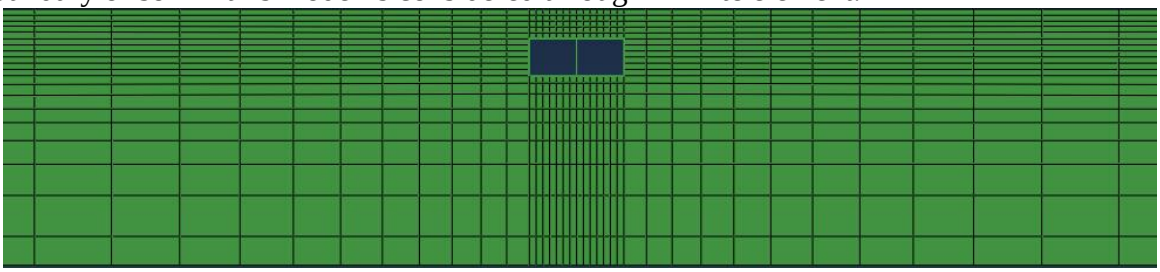


Figure 3: Finite element model.

3.3 Selection of ground motion records

The ground motion records selected from the ground motion database should be able to represent the structure's site conditions. According to the United States Geological Survey, USGS, the site condition can be divided into four groups, denoted as S_1, S_2, S_3, S_4 respectively. The shear wave velocity of each group is greater than 750m/s, 360~750m/s, 180~360m/s and less than 180m/s in turn. The character of the site where Daikai subway station is located is similar to S_3 group. Therefore, the ground motions selected all come from S_3 group. As mentioned above in 2.2, ten to twenty records are usually enough to provide sufficient accuracy in the estimation of seismic demands [17]. Consequently, a set of ten ground motion records that belong to a bin of relatively large magnitudes of 7.5-8.0 and near-fault, all recorded on soil type S_3 are selected from the Pacific Earthquake Engineering Research Center [20], as shown in Table2. The selected ground motions are effectively presumed to be able to cause severe ground motions in the site where structure is located.

No	Event	Station	Φ[01]	Soil[2]	M[3]	PGA(g)	PGV(cm/s)
1	Kocaeli Turkey, 1999	ERD 99999 Duzce	DZC180	S_3	7.51	0.312	58.86
2	Kocaeli Turkey, 1999	ERD 99999 Duzce	DZC270	S_3	7.51	0.358	46.40
3	Kocaeli Turkey, 1999	KOERI 99999 Yarimca	YPT060	S_3	7.51	0.268	65.75
4	Kocaeli Turkey, 1999	KOERI 99999 Yarimca	YPT330	S_3	7.51	0.349	62.18
5	Chi-Chi, Taiwan, 1999	CWB 99999 CHY101	CHY101-E	S_3	7.62	0.353	70.64
6	Chi-Chi, Taiwan, 1999	CWB 99999 CHY101	CHY101-N	S_3	7.62	0.439	115.0
7	Chi-Chi, Taiwan, 1999	CWB 99999 TCU050	TCU050-E	S_3	7.62	0.147	36.91
8	Chi-Chi, Taiwan, 1999	CWB 99999 TCU050	TCU050-N	S_3	7.62	0.130	42.36
9	Denali, Alaska, 2002	TAPS Pump Station #10	PS10047	S_3	7.9	0.138	134.8
10	Denali, Alaska, 2002	TAPS Pump Station #10	PS10317	S_3	7.9	0.318	76.99

[1] Component [2] USGS [3] Magnitude

Table 2: Set of ten ground motion records.

3.4 Selection of IM and DM

The most important issues to perform an IDA are selecting a suitable IM and DM. The basic principle of IM selection is to truly reflect the potential damage effect under seismic loads in the future and make the discrepancy of DM under different ground motions as small as possible. In this paper, Peak Ground Acceleration (PGA), Peak Ground Velocity (PGV), which are common examples of scalable IMs are selected. The spectral acceleration at the

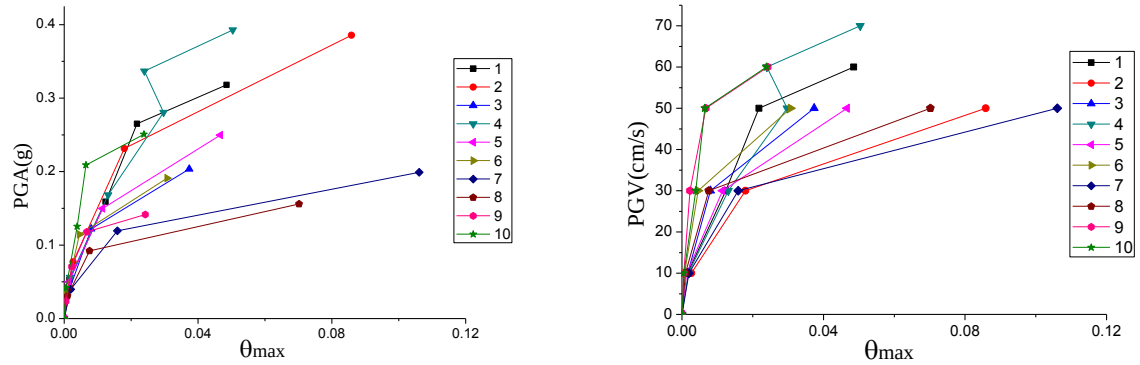
structure's first-mode period $S_a(T_1,5\%)$ may not be suitable for underground structure, which will not be discussed in this paper.

The basic principle of DM selection is to truly reflect the damage of structures, including the structural components, non-structural components and in-house facilities. This progress also depends on the application and the structure itself. As mentioned above, θ_{max} relates well to joint rotations and both global and local story collapse, thus θ_{max} is selected as DM in this paper.

In order to cover the entire range of the structural response from elasticity to global dynamic instability, the original ground motion records are scaled with the value of PGV as 10, 30, 50, 60, 70, 80, 90, 100 cm/s in turn. The model is conducted with one-way ground motion input of X axis along the structural plane. When it comes to PGA as IM, there is no need to do another large number of calculations, but just replace the value of PGV with the corresponding PGA and then get the IM versus DM curves.

3.5 IDA analysis results

IDA analysis of Daikai subway station subjected to ground motion is performed using ABAQUS software. IDA result of studied structure in terms of IM and DM is presented in Figure 4. The figures present the IDA curves for 10 ground motion records shown in Table 2.



(a) Using the PGA as IM (b) Using the PGV as IM

Figure 4: The 10 IDA curves analysed.

As can be seen, for a specific numerical model, the IDA curves under different ground motion records have significant differences, especially the variation of slope. For example, the slope of curve (1-3) is decreasing gradually while the slope of curve (4) presents the trend of decreasing firstly, increasing secondly, and then decreasing. The latter phenomenon is due to period elongation or the so-called structural resurrection [11]. The slopes of the straight lines from the origin of the axes to the first IM-DM points on the graphs are referred to as the elastic slope. These trends mentioned above are nearly the same as IDA analysis results for the superstructure.

What is more, the IDA graphs also bring a fresh perspective to an important question of the effective IM choice for the underground structure. As mentioned above, IM selection is to make the discrepancy of DM under different ground motions as small as possible. Smaller dispersion of DM given IM implies that fewer nonlinear runs and a smaller sample of ground motion records are enough to estimate structure's performance. Therefore, a desirable property of a candidate IM is small dispersion. From the graphs in Figure 4, it is obvious that the latter produces a lower dispersion over the full range of DM values. PGV appears preferable to PGA for the subway station.

4 CONCLUSIONS

- IDA can be applied successfully to underground structure, especially the Daikai subway station. The trend of IDA curves for the underground structure is nearly the same as the superstructure.
- For the IM selection of underground structure, PGV is better than PGA for its smaller dispersion, which may also be the difference between underground structure and superstructure.

REFERENCES

[1] H. Huo, A. Bobet, et al, Load transfer mechanisms between underground structure and surrounding ground: evaluation of the failure of the Daikai station. *Journal of Geotechnical and Geoenvironmental Engineering*, Vol.**131** (12), 1522-1533, 2005.

[2] MA Hong- wang, Lu Xi- lin, Some problems about performance-based seismic design. *Journal of Tongji University*, Vol.**30** (12), 1429-1434, 2002.(in Chinese)

[3] Behrouz Asgarian, Mahmood Yahyai, et al, Incremental dynamic analysis of high-rise towers. *The Structural Design of Tall and Special Buildings*, **19**, 922-934, 2010.

[4] Bertero VV, Strength and deformation capacities of buildings under extreme environments. *Structural Engineering and Structural Mechanics*, Pister KS, ed. Prentice Hall: Englewood Cliffs, NJ, 211-215, 1977.

[5] Luco N, Cornell CA, Effects of connection fractures on SMRF seismic drift demands. *ASCE Journal of Structural Engineering*, **126**, 127-136, 2000.

[6] Luco N, Cornell CA, Effects of random connection fractures on demands and reliablilty for a 3-storey pre-Northridge SMRF structure. *Proceeding of the 6th U.S. National Conference on Earthquake Engineering*, Paper 244. EERI: E1 Cerrito, CA: Seattle, Washington, 1-12, 1998.

[7] Bazzurro P, Cornell CA, Seismic hazard analysis for non-linear structures. I: Methodology. *ASCE Journal of Structural Engineering*, Vol.**120** (11), 3320-3344, 1994.

[8] Bazzurro P, Cornell CA, Seismic hazard analysis for non-linear structures. Ⅱ: Applications. *ASCE Journal of Structural Engineering*, Vol.**120** (11), 3345-3365, 1994.

[9] Mehanny SS, Deierlein GG, Modeling and assessment of seismic performance of composite frames with reinforced concrete columns and steel beams. *Report No. 136*, The John A. Blume Earthquake Engineering Center, Stanford University, Stanford, 2000.

[10] Nassar AA, Krawinkler H, Seismic demands for SDOF and MDOF systems. *Report No. 95*, The John A. Blume Earthquake Engineering Center, Stanford University, Stanford, 1991

[11] Vamvatsikos D., Cornell C.A, Incremental dynamic analysis. *Earthquake Engineering and Structural Dynamics*, Vol.**31** (3), 491-514, 2002.

[12] ZHOU Ying, LU Xilin, et al, Application of incremental dynamic analysis to seismic evaluation of hybrid structure. *Journal of Tongji University (National Science)*, Vol.**38** (2), 183-187, 2010. (in Chinese)

[13] Behrouz Asgarian, Hamideh Khazaee, et al, Performance evaluation of different types of steel moment resisting frames subjected to strong ground motion through incremental dynamic analysis. *International Journal of Steel Structures*, Vol.**12** (3), 363-379, 2012.

[14] A.H.M. Muntasir Billah, M. Shahria Alam, Seismic performance evaluation of multi-column bridge bents retrofitted with different alternatives using incremental dynamic analysis. *Engineering Structures*, **62-63**, 105-117, 2014.

[15] FEMA, Recommended seismic design criteria for new steel moment-frame buildings. *Report No. FEMA-350*, SAC Joint Venture, Federal Emergency Management Agency, Washington DC, 2000.

[16] FEMA, Recommended seismic evaluation and upgrade criteria for existing welded steel moment-frame buildings. *Report No. FEMA-351*, SAC Joint Venture, Federal Emergency Management Agency, Washington DC, 2000.

[17] Shome N, Cornell CA, Probabilistic seismic demand analysis of nonlinear structures. *Report No. RMS-35*, RMS Program, Stanford University, Stanford, 1999.

[18] Dimitrios Vamvatsikos, C. Allin Cornell, The incremental dynamic analysis and its application to performance-based earthquake engineering. *12th European Conference on Earthquake Engineering*, Paper reference 479, 2002.

[19] Teruo YAMATO, Toshio UMEHARA, et al, Damage to Daikai subway station of Kobe rapid transit system and estimation of its reason during the 1995 hyogoken-nanbu earthquake. *Proceeding of the civil society*, 537, 303-320, 1996. (in Japanese)

[20] Pacific Earthquake Engineering Research Center, PEER strong motion database [DB/OL]. California: Berkley, http://peer.berkeley.edu/peer_ground_motion_database.

COMPDYN 2015
5th ECCOMAS Thematic Conference on
Computational Methods in Structural Dynamics and Earthquake Engineering
M. Papadrakakis, V. Papadopoulos, V. Plevris (eds.)
Crete Island, Greece, 25–27 May 2015

GRAPHICAL DYNAMIC TRENDS FOR EARTHQUAKE INCIDENCE RESPONSE OF PLAN-ASYMMETRIC SYSTEMS

M. Faggella[1], R. Gigliotti[1], G. Mezzacapo[1], and E. Spacone[2]

[1] Sapienza University of Rome
Via Eudossiana 18, 00184 Rome, Italy
e-mail: marco.faggella@uniroma1.it, rosario.gigliotti@uniroma1.it

[2] University of Chieti-Pescara
Viale Pindaro 42, 65129, Pescara
e-mail: espacone@unich.it

Keywords: asymmetric structures, irregularity, torsion, earthquake incidence response, graphic dynamics, modal analysis.

Abstract. *A Graphical Dynamic model is derived to describe the directional earthquake response of two-ways plan-asymmetric systems, which retains the insightful educational evidence of traditional graphical static methods and the accuracy of computational methods of analysis. The dynamic directional response is expressed in terms of modal rotational kinematics about modal centers of rotation, referred to as modal torsional pivots. Seismic forces and response decomposition are handled through geometric modal torsional trends and the earthquake incidence response envelopes are described through directional modal participation radii and graphic spectrum-based "8-shaped" directional influence circles. The graphic approach provides good predictions of the maximum response and of the critical angle computed through CQC3 and other directional analysis methods.*

1 INTRODUCTION

This paper presents an application of Graphic Dynamics for predicting the response of plan irregular structures with changing angle of earthquake attack. The method is based on the Graphic Response History Analysis (GRHA) and Graphic Response Spectrum Analysis (GRSA) and on the definition of directional modal participation radii, [1], computing the dynamics through the Graphic Modal Analysis (GMA), and the Ellipse of Elasticity Modal Analysis (EEMA), described in [2], [3], [4], and [5]. The approach uses the results of [6], [7], and [8], where the response of irregular buildings is treated in terms of rotational kinematics about torsional pivots. Some authors have proposed synthetic parameters for describing the torsional response of eccentric systems, [9], which provide improved prediction with respect to code-based formulae. The method used here is based on the GRSA, and provides an improved rational description accounting for both the complete structural parameters and the input motion information. It is suited for full graphic development, providing increased control and insight into the dynamic behavior of irregular systems. The identification of synthetic structural and modal parameters in the linear range can be critical for the choice of spectrum-based intensity measures governing the response of building systems also in the nonlinear range, [10], [11]. New graphical features are presented as well as a validation of the GRSA method for predicting the directional response in terms of 'eight-shaped' modal influence circles. A graphical relation is presented which links the modal torsional pivots to the eigenvectors of the equivalent translational system. The effectiveness of the predictive graphical method is shown with reference to a numerical application of a two-ways plan asymmetric building system with eccentric infills.

2 GRAPHIC DYNAMIC TORSIONAL TRENDS

Graphic dynamic methods make use of global diaphragm systems properties such as the mass circle of gyration and the ellipse of elasticity, which are centered in the center of mass G and in the center of stiffness K respectively.

$$\rho = \sqrt{I_p/m}, \quad \rho_x = \sqrt{k_\theta/k_x}, \quad \rho_y = \sqrt{k_\theta/k_y}, \quad \alpha = \frac{\rho_y}{\rho_x} = \sqrt{\frac{k_x}{k_y}}, \quad d_{xy} = \sqrt{e_x^2 + \rho_y^2 + (\alpha e_y)^2} \tag{1}$$

These graphic figures are defined by the mass gyrator ρ, and by the semi-axes ρ_x and ρ_y. The position of K with respect to G is the two ways eccentricity with components e_x and e_y.

$$\ddot{\mathbf{u}}_\rho + \frac{1}{m}\mathbf{k}_\rho \mathbf{u}_\rho = \mathbf{0}$$

$$\text{where} \quad \mathbf{u}_\rho = \sum_{n=1}^{3} \begin{Bmatrix} y_{c,n} \\ -x_{c,n} \\ \rho \end{Bmatrix} \theta_n(t) \quad \text{and} \quad \frac{1}{m}\mathbf{k}_\rho = \omega_y^2 \begin{bmatrix} \alpha^2 & 0 & -\alpha^2 \dfrac{e_y}{\rho} \\ 0 & 1 & \dfrac{e_x}{\rho} \\ -\alpha^2 \dfrac{e_y}{\rho} & \dfrac{e_x}{\rho} & \left(\dfrac{d_{xy}}{\rho}\right)^2 \end{bmatrix} \tag{2}$$

It was shown, [1], that a graphic indicator of the torsional character is the 'coupled stiffness radius' d_{xy}, which represents the diagonal built starting from the eccentricity e_x and the rotated semi-axis of the Ellipse of elasticity ρ_y, and accounts for both the torsional coupling induced

by the eccentricity and the in-plan irregular distribution of the lateral load resisting elements. The parameter d_{xy} figures in the rotational diagonal term of the dynamic stiffness matrix $\mathbf{k}_\rho/m$ associated with the vector $\boldsymbol{u}_\rho$ of the equivalent translational degrees of freedom u_x, u_y and $\rho\theta$, which are the displacement at the center of mass G and the floor rotation multiplied by ρ, as it is evident from the Equations (2). The ratio $(d_{xy}/\rho)^2$ is related to the 'translationality' of the torsionally coupled system. It can be show that a generic floor deformation corresponds a rigid rotation with center C given as the intersection of the vector $\boldsymbol{u}_\rho$ with a horizontal floor plane placed at a height equal to ρ, as it is shown in Figure 1. Since the system of dynamic equations is in the standard form, i.e. the mass matrix is diagonal, the eigenvectors $\Phi_{1\rho}$, $\Phi_{2\rho}$, and $\Phi_{3\rho}$ are three orthogonal axes and intersect the idealized horizontal floor plane in correspondence of the three torsional modal pivots C_1, C_2 and C_3.

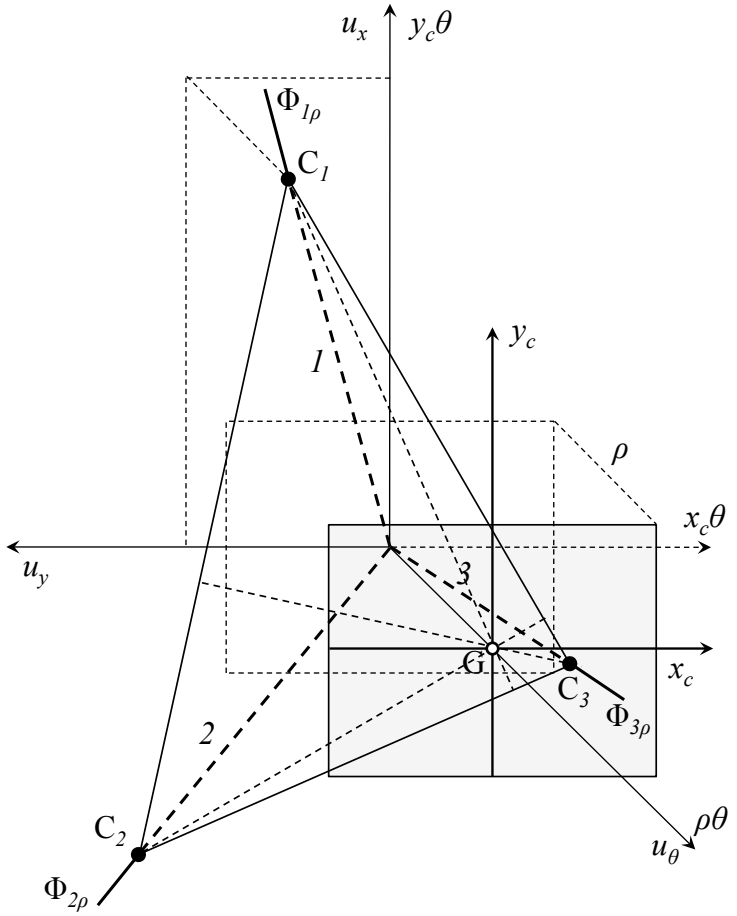


Figure 1: Graphic identification of the modal torsional pivots C_1, C_2 and C_3 corresponding to the classical eigenvectors $\Phi_{1\rho}$, $\Phi_{2\rho}$ and $\Phi_{3\rho}$ of the equivalent translational stiffness matrix.

3 EARTHQUAKE RESPONSE AND INCIDENCE ANGLE

The GRHA and GRSA approaches for determining the maximum response of irregular systems have been introduced in [1] and [5]. In general the elastic response of a system to earthquake loads is obtained starting from the results of the modal analysis, [12], expressing the mass proportional static earthquake forces **mr** in terms of their modal components. The approach based on the modal decomposition of the forces and of the response has been found to be accurate enough also in the case of weakly coupled nonlinear systems [13]. The overall response is traditionally expressed as the sum of the products of N modes shapes times the

time-dependent amplification functions. If the rotational mode shapes are scaled so to have a unit rotation angle, the corresponding time-dependent functions are the actual rotation histories θ_n(t). The graphic visualization of the modal expansion of the earthquake forces is the basis for the GRHA and for the related GRSA procedures. The graphic dynamic approaches translate the modal response decomposition in terms that are easy to visualize on the floor plan of a two-ways asymmetric system.

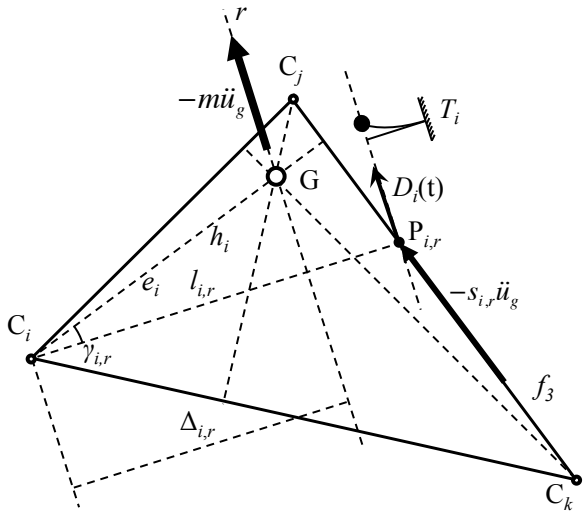


Figure 2: GRHA, Mode *i* component of the earthquake force, directional modal participation radius $l_{i,r}$ and modal sampling point $P_{i,r}$.

An important feature are the so called 'directional modal participation radii' $l_{i,r}=1/\Gamma_{i,r}$, which represent the inverse of the directional participation factors, and describe the contribution of each mode to the overall response. The radii $l_{i,r}$ are the distance of the modal nodes from the line of modal earthquake forces drawn orthogonal to the direction of earthquake attack.

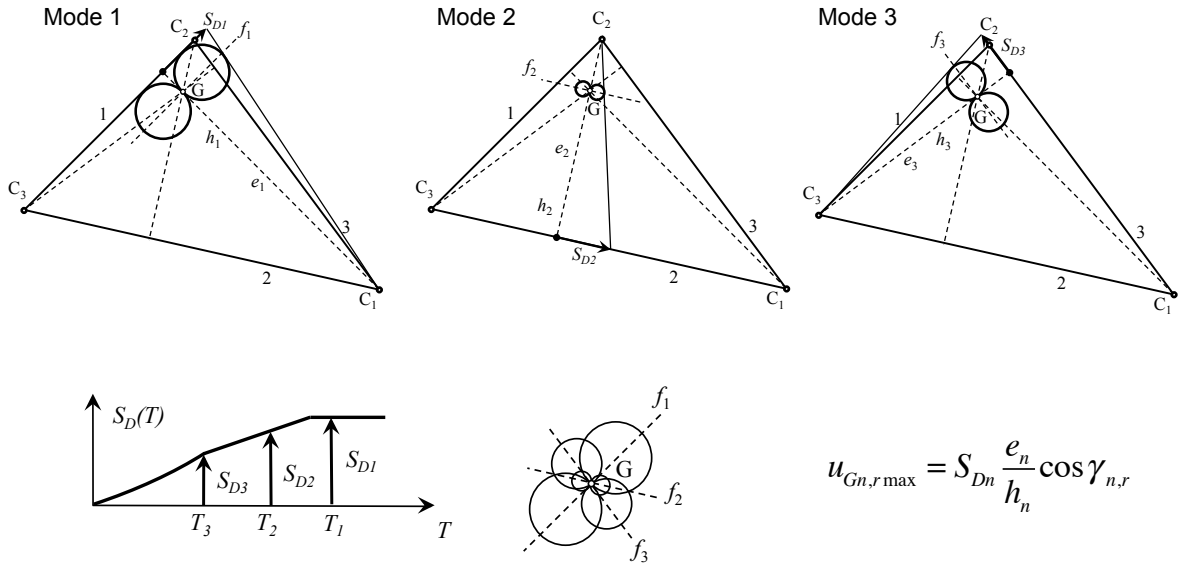


Figure 3: GRSA, displacement spectrum-based directional modal influence circles of the response at the center of mass G.

The graphical modal expansion of the earthquake forces is made based on the polygonal force decomposition rule of the directional seismic force on the lines of action of the modal forces. The directional effective modal masses are viewed as the projections of the modal seismic forces on the direction of earthquake attack. The GRSA completes this graphical construction with the intensity of the maximum response coming from the displacement response spectrum. The construction of the maximum directional modal response of the center of mass G is shown building on the triangle of modal pivots and on the ordinates $S_D(T_i)$. This construction yields the envelope of the directional modal response in form of two 'eight-shaped' circles, referred to as 'directional spectral influence circles', which match well the response envelopes described in other studies, [14], [15].

4 NUMERICAL EXAMPLE

The graphic GRSA construction of the directional response is illustrated with reference to an example of single-story R/C frame structure with masonry infills. The structure is two-ways plan-asymmetric due to eccentric placement of the infills in the left two bays and in the bottom three bays. The linear analysis is carried out considering the initial elastic properties of the structure and of the infills, and yields the modal periods T_1 = 0.21s, T_2 = 0.14s, and T_3 = 0.09s.

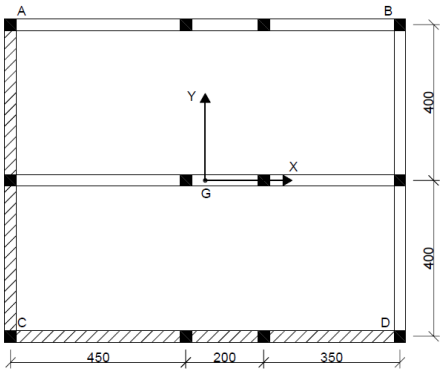


Figure 4: Plan layout of two-ways asymmetric single story structure with eccentric infills.

The corresponding mode shapes are represented in figure through the rotational modal nodes C1, C2 and C3. The RHA is carried out with a single natural ground motion extracted from a set of motions consistent with the design spectrum.

NODE	RHA	CQC3	Graphic Angle
G	119°	117°	120°
A	118°	120°	120°
B	117°	120°	120°
C	33°	35°	36°
D	121°	120°	120°

Table 1: Critical angles for displacement response at different nodes with RHA, CQC3 and graphic prediction.

The x-component of the Gazli 17/05/76 record is used, with PGA=0.6g. The displacement spectrum modal ordinates are $S_D(T_1)$=1.25cm, $S_D(T_2)$=0.61cm, $S_D(T_3)$=0.35cm. The GRSA determination of the modal response envelope is reported in Figure 5 drawing the modal re-

sponse influence circles for the floor corner points and for the center of mass, which clearly indicate the torsional gradients of the modal response component along the floor.

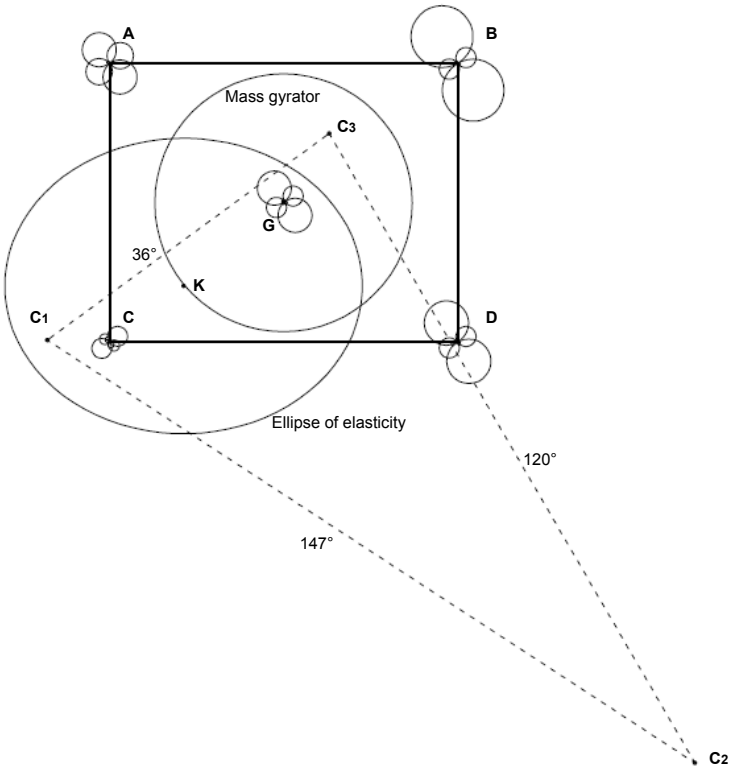


Figure 5: Plan schematic with Ellipse of Elasticity, Mass circle of gyration, modal torsional pivots and triangle of forces, and GRSA construction of the directional influence circles at corner points.

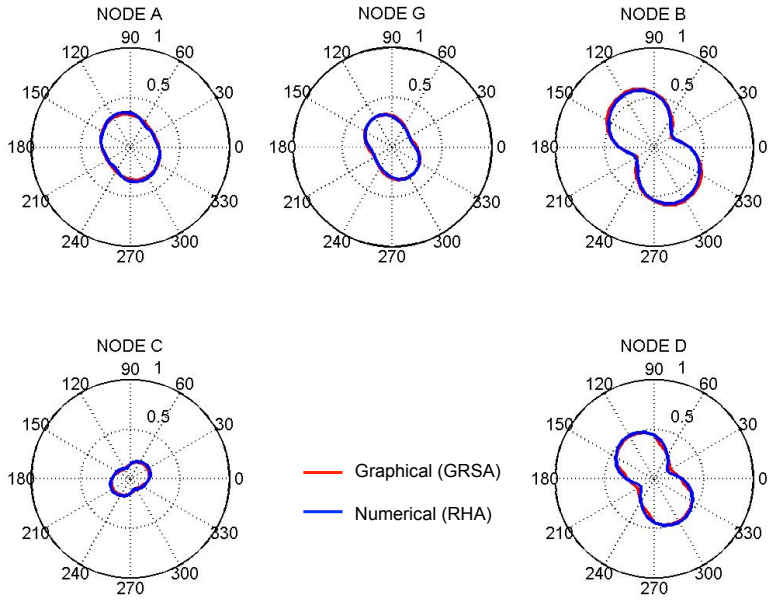


Figure 6: Displacement response at the corner nodes and center of mass, matching of numerical RHA (blue line) with the GRSA graphical prediction (red line).

In Figure 6 the modal contributions obtained with the GRSA are combined with a CQC rule, and their directional response envelopes compared with those obtained with the RHA using

the input ground motion. The comparison of the critical earthquake angle for the displacement response at different locations is reported in Table 1. Results indicate that the directions of the graphical modal trends given by the triangle of modal pivots/forces provide an accurate enough prediction of the critical angle as compared with the CQC3 rule [16], and with the RHA directional response envelope.

5 CONCLUSIONS

This paper presented further insight on torsional coupling from graphical dynamic methods, and on graphic directional response envelope prediction of torsionally coupled systems subjected to unidirectional earthquake with rotating angle of attack. The method was applied to an example of two-ways asymmetric R/C single story building with irregular infills layout. Results have shown that: a graphical correspondence can be drawn between orthogonal eigenvectors of the torsional dynamic stiffness matrix and the floor modal torsional centers of rotation (pivots). The graphical methods provide valuable insight into the torsional coupling trends of two-ways asymmetric systems, and match well the numerical response. The graphic GRSA directional response envelopes based on directional modal participation radii predict well the dynamic torsional trends and the critical angle of incidence obtained through the CQC3 rule.

REFERENCES

[1] M. Faggella, "Graphical Dynamic Earthquake Response of Two-ways Asymmetric Systems based on Directional Modal Participation Radii". CST2014, The Twelfth International Conference, on Computational Structures Technology, Naples, Italy, 2-5 September 2014.

[2] M. Faggella, “Graphical Modal Analysis and Earthquake Statics of Linear One-way Asymmetric Single-Story Structure”, COMPDYN 2013 4th ECCOMAS Thematic Conference on Computational Methods in Structural Dynamics and Earthquake Engineering. Kos Island, Greece, 2013.

[3] M. Faggella, “The Ellipse of Elasticity and Mohr Circle-based Graphic Dynamic Modal Analysis of Torsionally Coupled Systems”, Proceedings of the 9th International Conference on Structural Dynamics, EURODYN 2014, 30th June – 2nd July, Porto, Portugal, 2014.

[4] M. Faggella, “Graphic Dynamic Earthquake Response Analysis of Linear Torsionally Coupled 2DOF Systems”, Proceedings of the 9th International Conference on Structural Dynamics, EURODYN 2014, 30th June – 2nd July, Porto, Portugal, 2014.

[5] M. Faggella, “ Graphical Dynamic Earthquake Response Analysis of One-way Asymmetric Systems”, Proceedings of the 10th National Conference in Earthquake Engineering, Earthquake Engineering Research Institute, Anchorage, AK, 2014.

[6] K.M. Dempsey, H.M. Irvine, “Envelopes of maximum seismic response for a partially symmetric single storey building model”, Earthquake Engineering & Structural Dynamics, 7(2), 161-180, 1979.

[7] A.M. Athanatopoulou, T. Makarios, K. Anastassiadis, “Earthquake analysis of isotropic asymmetric multistory buildings”, The Structural Design of Tall and Special Buildings, 15(4), 417-443, 2006.

[8] K. Anastassiadis, “Caracteristiques elastiques des batiments a etages”, Annales de l’ITBTP no. 435, 1985.

[9] T.L. Trombetti, J.P. Conte, “New insight into and simplified approach to seismic analysis of torsionally coupled one-story, elastic systems”, Journal of Sound and Vibration, 286: 265-312, 2005.

[10] M. Faggella, A.R. Barbosa, J.P. Conte, E. Spacone, J.I. Restrepo, "Probabilistic Seismic Response Analysis of a 3D Reinforced Concrete Building", Structural Safety, 44, 11-27, 2013.

[11] M. Faggella, G. Mezzacapo, R. Gigliotti, and E. Spacone, “Significance of Earthquake Incidence on Response Plan-irregular Infilled R/C Buildings”, COMPDYN 2015, 5th ECCOMAS Thematic Conference on Computational Methods in Structural Dynamics and Earthquake Engineering, Crete Island, Greece, 25–27 May 2015. (Submitted).

[12] A.K. Chopra, “Dynamics of Structures: Theory and Applications to Earthquake Engineering”, Prentice Hall: Englewood Cliffs, New Jersey, 2012.

[13] A.K. Chopra, & R.K. Goel, “A modal pushover analysis procedure to estimate seismic demands for unsymmetric-plan buildings”. Earthquake Engineering & Structural Dynamics, 33(8), 903-927, 2004.

[14] M. Paparoni, O. Paz, O. Peña, I. Carbonell, “The Culmann Ellipse as a Strategic tool for seismic grading of structural configurations”, 15WCEE, 15th World Conference in Earthquake Engineering. Lisbon, Portugal, 2012.

[15] J.C. Reyes, E. Kalkan, “Significance of rotating ground motions on behavior of symmetric-and asymmetric-plan structures: Part 1. Single-story structures”, Earthquake Spectra, 2012.

[16] C. Menun C, A. Der Kiureghian, “A replacement for the 30%, 40% and SRSS rules for multicomponent seismic analysis”, Earthquake Spectra, 14(1):153–63, 1998.

COMPDYN 2015
5th ECCOMAS Thematic Conference on
Computational Methods in Structural Dynamics and Earthquake Engineering
M. Papadrakakis, V. Papadopoulos, V. Plevris (eds.)
Crete Island, Greece, 25–27 May 2015

SIGNIFICANCE OF EARTHQUAKE INCIDENCE ON RESPONSE OF PLAN-IRREGULAR INFILLED R/C BUILDINGS

M. Faggella[1], G. Mezzacapo[1], R. Gigliotti[1], and E. Spacone[2]

[1] Sapienza University of Rome
Via Eudossiana 18, 00184 Rome, Italy
e-mail: marco.faggella@uniroma1.it, rosario.gigliotti@uniroma1.it

[2] University of Chieti-Pescara
Viale Pindaro 42, 65129, Pescara
e-mail: espacone@unich.it

Keywords: plan-irregular structures, infilled frames, earthquake incidence response, graphic dynamic torsional trends, Incremental Dynamic Analysis.

Abstract. *Masonry infilled R/C buildings present a number of complexities inherent to in-plan eccentricities and asymmetric layout of infills. Their dynamic earthquake response cannot generally be characterized in terms of principal directions of deflection as for plan-regular structures. The response is then complicated by nonlinear frame-infill interaction, which makes the resulting collapse mechanism particularly sensitive to local shear failures. A three-dimensional nonlinear model is developed incorporating frame elements, eccentric infill struts, and shear-prone short columns. Results from nonlinear Response History Analyses (RHA) changing the earthquake incidence are analyzed starting from Graphic-Dynamic modal torsional trends and directional inelastic response envelopes. Directional Incremental Dynamic Analyses (IDA) and Uncoupled Modal Response History Analyses (UMRHA) over a range of hazard levels (OP, DL, SD, NC) highlight the polarization of the elastic and inelastic modal response.*

1 INTRODUCTION

This paper investigates the estimation of the nonlinear seismic response of plan irregular buildings under unidirectional earthquakes with changing angle of attack based on Graphic Dynamics and nonlinear Response History Analyses (RHA). The elastic modal torsional trends computed from Graphic Dynamics, [1] - [7], are used as a basis to highlight the inelastic contribution to the overall response and the relevant polarization with the earthquake angle. In performance-based earthquake engineering, the identification of synthetic structural and modal parameters in the linear range is critical for the choice of optimal spectrum-based intensity measures, [8]. The importance of earthquake directionality has been addressed by several researchers, in particular [9] and [10] showed that the response of uniformly plan-

asymmetric multi-story buildings can be expressed in terms of a multi-story system and a rigid-diaphragm single-story torsional system. The work of [11] introduced the CQC3 rule for maximum directional response computation under concurrent seismic components and for determination of the critical response angle. More recently [12] pointed out the importance of seismic incidence in the context of performance-based assessment of plan-asymmetric buildings through nonlinear RHA.

The objective of this work is to investigate the directional nonlinear response of a plan-asymmetric building based on the in-plan torsional trends and the effect of the modal contributions in terms of polarization of the inelastic response. Incremental Dynamic Analyses (IDA) are performed on a nonlinear model of an irregular one-story R/C building with masonry infills in two consecutive open sides. The model includes nonlinear frame behavior, eccentric hysteretic infill struts and nonlinear shear in short columns. The graphical modal torsional trends and the elastic response predictors based on the 8-shaped modal influence circles, are used to further investigate the nonlinear response through Uncoupled Modal Response History Analysis (UMRHA), [13], [14].

2 DIRECTIONAL NONLINEAR RESPONSE HISTORY ANALYSES

The case study structure is a two-ways plan-asymmetric building with eccentric infills in the left and bottom frames, used also in [7]. Previous studies have pointed out the influence of the infills-induced shear failure of the columns, resulting in increased strength and stiffness at low hazard levels, and triggering shear-dominated story mechanisms [15], [16], while the response of the bare frames is characterized by increased flexibility due to bond slip effects [17], [18]. These additional mechanisms and components result in increased plan irregularity both in terms of stiffness and strength. The structure modal periods computed with the initial elastic frame and infill properties are $T_1 = 0.21$s, $T_2 = 0.14$s, and $T_3 = 0.09$s.

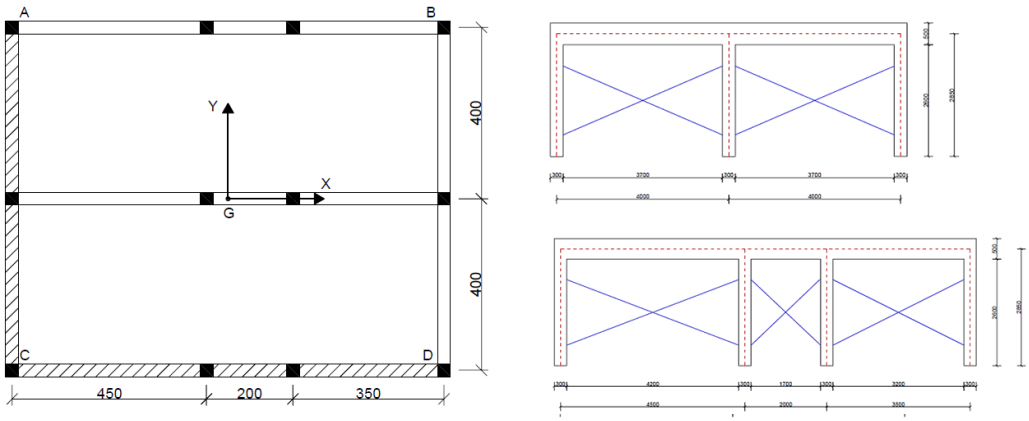


Figure 1: (a) Plan layout of two-ways asymmetric single story building structure with eccentric infills, (b) R/C frames with eccentric infill struts and shear-prone short columns.

Figure 2 shows the results of RHA at the Operational (OP), Damage Limitation (DL), Significant Damage (SD) and Near Collapse (NC) limt states, obtained with the actual nonlinear model and with the elastic model based on initial elements stiffness. It is evident how the maximum directional nonlinear response is polarized along the direction of the elastic modal torsional trends, indicated by the internal 8-shaped figures. Plan-irregular infills induce a change of polarization and of the critical angle with respect to the geometric axes of the bare frame, particularly at lower hazard levels.

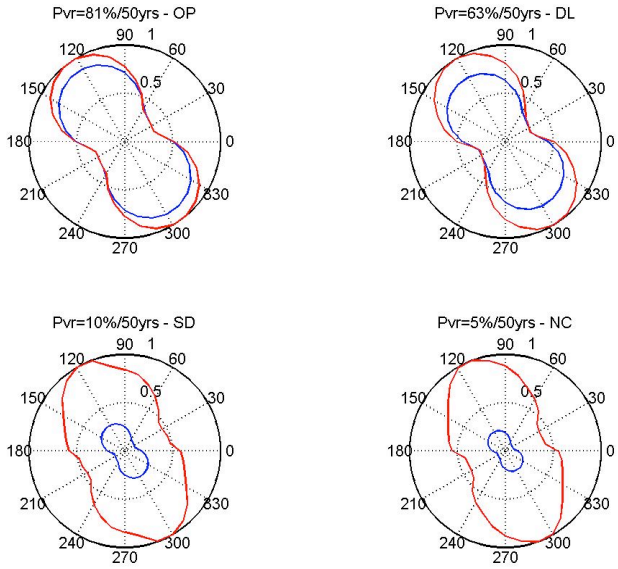


Figure 2: Directional RHA response at the center of mass with linear (blue line) and nonlinear (red line) structure models at OP, DL, SD and NC limit states.

3 DIRECTIONAL MODAL RESPONSE DECOMPOSITION

Modern seismic codes prescribe the use of complete NL RHA to simulate the earthquake response of structures subjected to damage or equipped with protection devices. In fact the robustness of NL RHA allows accounting for the nonlinear coupling of the modal response, which in some cases has been observed also experimentally [19]. It has been shown that in some cases the nonlinear modal coupling may be neglected, [14], and the results of NL RHA may be approximated by the so-called Uncoupled Modal Response History Analysis (UMRHA). In Figures 3,4 and 5 we show the results of directional UMRHA carried out using the modal forces obtained from the initial stiffness elastic analysis.

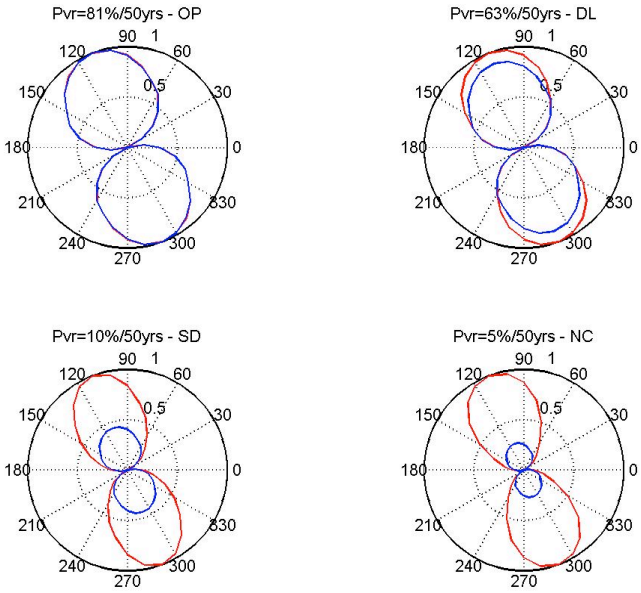


Figure 3: Directional Mode 1 RHA response at the center of mass with linear (blue line) and nonlinear (red line) structure models at OP, DL, SD and NC limit states.

It is evident how the directional response obtained with the elastic model and at the lower hazard level match well and are well described by the 8-shaped circle directional envelopes.

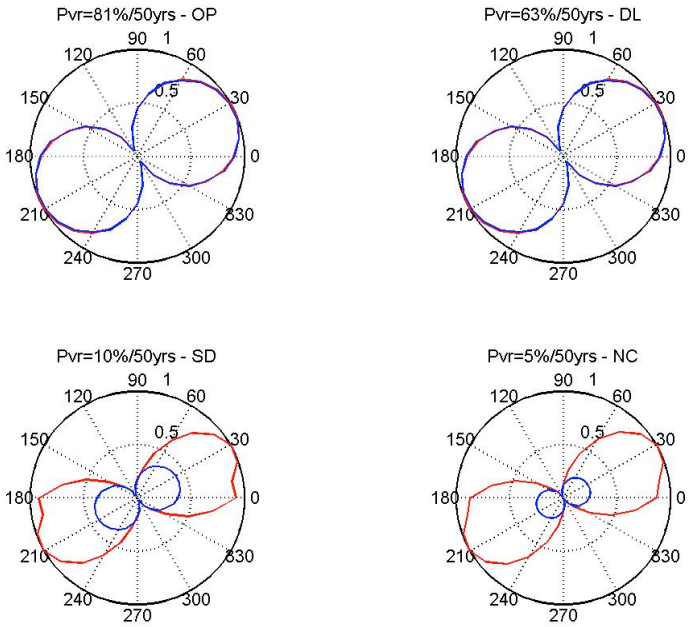


Figure 4: Directional Mode 2 RHA response at the center of mass with linear (blue line) and nonlinear (red line) structure models at OP, DL, SD and NC limit states.

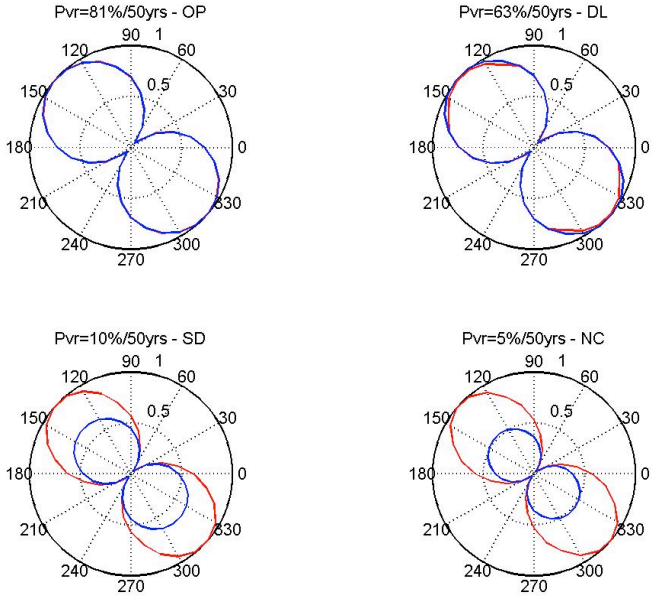


Figure 5: Directional Mode 3 RHA response at the center of mass with linear (blue line) and nonlinear (red line) structure models at OP, DL, SD and NC limit states.

At the higher hazard levels the system nonlinearities cause the response to deviate from the elastic prediction. The inelastic response is maximum along the critical directions of each modes, and is zero along the mode-orthogonal directions. The comparison of Figure 6 indicate a generally good agreement between the RHA and the total UMRHA summed over all

modes, and therefore a weak influence of nonlinear modal coupling on maximum response envelopes along most of the incidence angles.

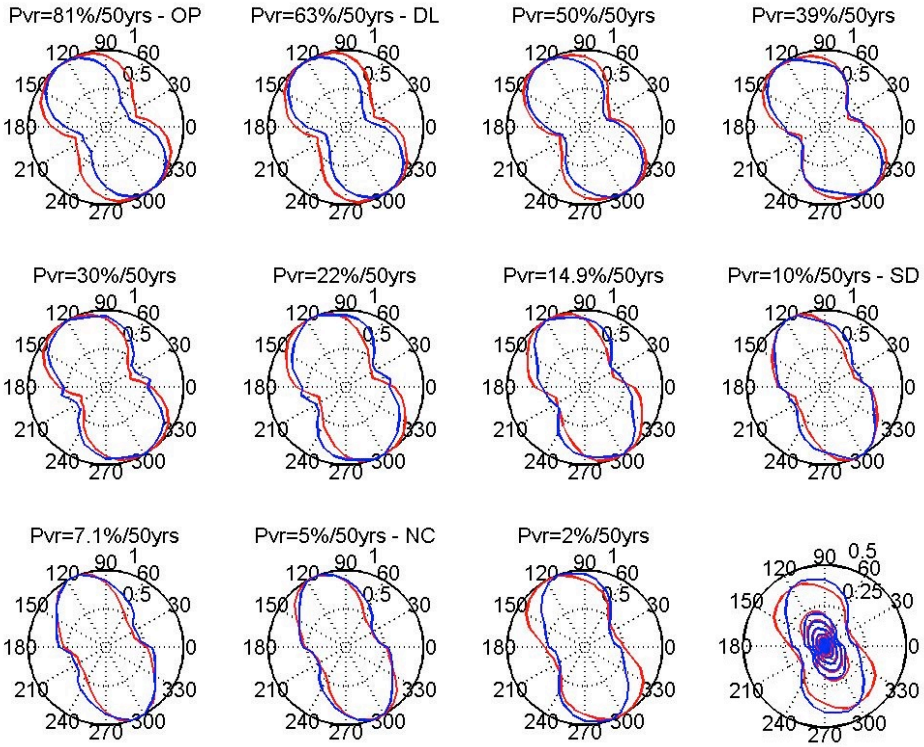


Figure 6: Directional Incremental Dynamic Analyses (IDA) response at the center of mass at 81% through 2%PoE/50yrs hazard levels with coupled RHA (blue line) and uncoupled UMRHA (red line).

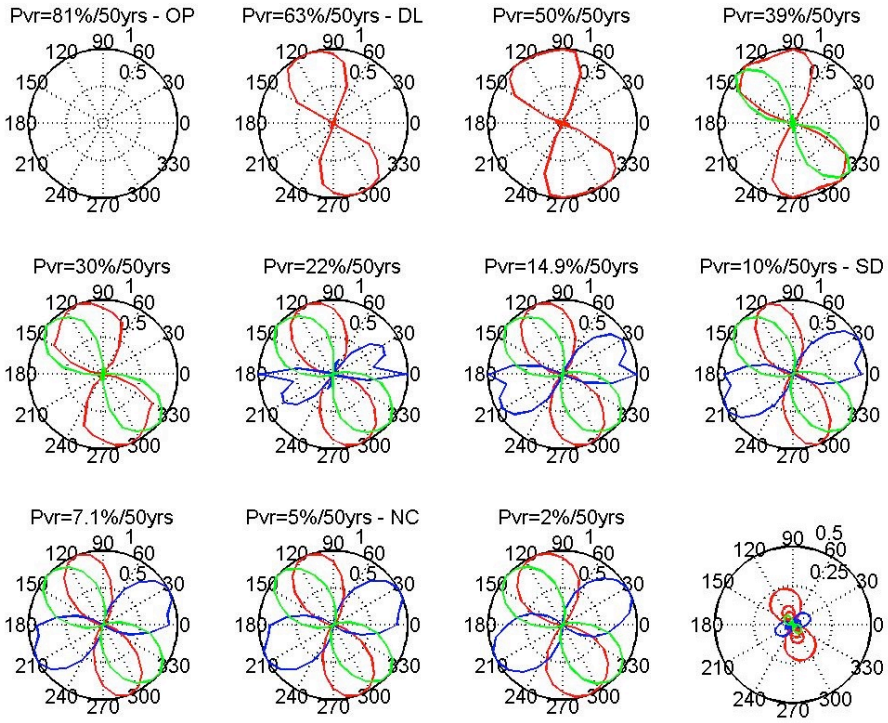


Figure 7: Inelastic contributions to the response at the center of mass from directional Modal IDA at 81% through 2%PoE/50yrs hazard levels based on Mode 1 (red line) Mode 2 (blue line) and Mode 3 (green line).

Finally Figure 7 shows the radial plots of the inelastic contribution of the response obtained from each modal RHA at the different hazard levels. The inelastic contributions are obtained as the difference between the total response of the RHA and the response from the elastic analysis.

4 CONCLUSIONS

This paper investigated the graphic directional response envelope prediction for torsionally coupled systems subjected to unidirectional earthquake with rotating angle of attack. Numerical nonlinear analyses were performed on an example of two-ways asymmetric R/C single story building with irregular infills layout. Results show that: plan-irregular placement of infills can induce a change of polarization and of the critical angle with respect to the geometric axes, particularly at lower hazard levels. Graphic dynamic in-plan torsional trends and modal pivots can be used to predict the direction of polarization of the overall response and the critical angle. The Modal decomposition of the response through UMRHA and comparison of response with RHA indicate a weak influence of nonlinear modal coupling on response envelopes, and highlight the directions of polarization of the inelastic component of the response.

REFERENCES

[1] A.F. Mohammad, M. Faggella, R. Gigliotti, E. Spacone, 2014. "Influence of bond-slip effect and shear deficient column in the seismic assessment of older infilled frame R/C structures". Proceedings of the 9th International Conference on Structural Dynamics, EURODYN 2014, 30th June – 2nd July, Porto, Portugal, 2014.

[2] M. Faggella, "Graphical Dynamic Earthquake Response of Two-ways Asymmetric Systems based on Directional Modal Participation Radii". CST2014, The Twelfth International Conference, on Computational Structures Technology, Naples, Italy, 2-5 September 2014.

[3] M. Faggella, "Graphical Modal Analysis and Earthquake Statics of Linear One-way Asymmetric Single-Story Structure", COMPDYN 2013 4th ECCOMAS Thematic Conference on Computational Methods in Structural Dynamics and Earthquake Engineering. Kos Island, Greece, 2013.

[4] M. Faggella, "The Ellipse of Elasticity and Mohr Circle-based Graphic Dynamic Modal Analysis of Torsionally Coupled Systems", Proceedings of the 9th International Conference on Structural Dynamics, EURODYN 2014, 30th June – 2nd July, Porto, Portugal, 2014.

[5] M. Faggella, "Graphic Dynamic Earthquake Response Analysis of Linear Torsionally Coupled 2DOF Systems", Proceedings of the 9th International Conference on Structural Dynamics, EURODYN 2014, 30th June – 2nd July, Porto, Portugal, 2014.

[6] M. Faggella, " Graphical Dynamic Earthquake Response Analysis of One-way Asymmetric Systems", Proceedings of the 10th National Conference in Earthquake Engineering, Earthquake Engineering Research Institute, Anchorage, AK, 2014.

[7] M. Faggella, R. Gigliotti, G. Mezzacapo, E. Spacone, 2015. "Graphical Dynamic Trends for Earthquake Incidence Response of Plan-Asymmetric Systems". COMPDYN 2015, 5th ECCOMAS Thematic Conference on Computational Methods in Structural Dynamics and Earthquake Engineering, Crete Island, Greece, 25–27 May 2015. (Submitted).

[8] M. Faggella, A.R. Barbosa, J.P. Conte, E. Spacone, J.I. Restrepo, "Probabilistic Seismic Response Analysis of a 3D Reinforced Concrete Building", Structural Safety, 44, 11-27, 2013.

[9] R. Hejal, A.K. Chopra, "Earthquake analysis of a class of torsionally-coupled buildings", Earthquake Engineering and Structural Dynamics 1989; 18: 305-323.

[10] A.M. Athanatopoulou, T. Makarios, K. Anastassiadis, "Earthquake analysis of isotropic asymmetric multistory buildings", The Structural Design of Tall and Special Buildings, 15(4), 417-443, 2006.

[11] Menun C, Der Kiureghian A. A replacement for the 30%, 40% and SRSS rules for multicomponent seismic analysis. Earthquake Spectra, 14(1):153–63, 1998.

[12] J.C. Reyes, E. Kalkan, "Significance of rotating ground motions on behavior of symmetric-and asymmetric-plan structures: Part 1. Single-story structures", Earthquake Spectra, 2012.

[13] A.K. Chopra, "Dynamics of Structures: Theory and Applications to Earthquake Engineering", Prentice Hall: Englewood Cliffs, New Jersey, 2012.

[14] A.K. Chopra, & R.K. Goel, "A modal pushover analysis procedure to estimate seismic demands for unsymmetric-plan buildings". Earthquake Engineering & Structural Dynamics, 33(8), 903-927, 2004.

[15] A.F. Mohammad, M. Faggella, R. Gigliotti, E. Spacone, "Influence of bond-slip effect and shear deficient column in the seismic assessment of older infilled frame R/C structures." EURODYN 2014 9th International Conference on Structural Dynamics. Vol. 30. 2014.

[16] A.F. Mohammad, M. Faggella, R. Gigliotti, E. Spacone, "Probabilistic Seismic Response Sensitivity of Nonlinear Frame Bending-Shear and Infill Model Parameters for an Existing Infilled Reinforced Concrete Structure". In Proceedings of the Twelfth International Conference on Computational Structures Technology 2014.

[17] M. D'Amato, F. Braga, R. Gigliotti, S. Kunnath, M. Laterza, "Validation of a modified steel bar model incorporating bond-slip for seismic assessment of concrete structures", Journal of Structural Engineering, 138(11), 1351-1360, 2012.

[18] F. Braga, R. Gigliotti, M. Laterza, M. D'Amato, S. Kunnath, "Modified steel bar model incorporating bond-slip for seismic assessment of concrete structures", Journal of Structural Engineering, 138(11), 1342-1350, 2012.

[19] F. Braga, M. Faggella, R. Gigliotti, M. Laterza, "Nonlinear dynamic response of HDRB and hybrid HDRB-friction sliders base isolation systems", Bulletin of Earthquake Engineering, 3(3), 333-353, 2005.

5th ECCOMAS Thematic Conference on
Computational Methods in Structural Dynamics and Earthquake Engineering
M. Papadrakakis, V. Papadopoulos, V. Plevris (eds.)
Crete Island, Greece, 25–27 May 2015

BEHAVIOUR OF NON-CONFORMING R.C. MEMBERS UNDER COMPRESSIVE AXIAL LOAD AND BIAXIAL BENDING

Marta Del Zoppo[1], **Marco Di Ludovico**[2] **and Aurelio Ghersi**[3]

[1] Ph.D. Student, Department of Engineering
University of Naples "Parthenope"
e-mail: marta.delzoppo@uniparthenope.it

[2] Assistant Professor, Department of Structures for Engineering and Architecture
University of Naples "Federico II"
e-mail: diludovi@unina.it

[3] Full Professor, Department of Civil and Environmental Engineering
University of Catania
e-mail: aghersi@dica.unict.it

Keywords: existing building; biaxial bending; ultimate curvature domain; yielding curvature; rotational capacity; chord rotation.

Abstract. *Under seismic actions, the structures undergo two simultaneous horizontal components of the ground motion, which cause a structural response in an oblique direction and biaxial bending in the columns. The current approach to the seismic design of new structures or the assessment of existing ones points out the need of taking into account the contemporaneous presence of the two components of ground motion, in order to make a good prediction of the real structural behaviour, both in terms of strength and deformation capacity. The paper analyses the influence of the two components of bending moment on the deformation capacity of reinforced concrete (r.c.) cross-sections and r.c. members (i.e. columns) by using a specific fibre model. The behaviour of the generic member is expressed in terms of ultimate/yielding curvature domain for the cross-section and ultimate/yielding rotational capacity domain for the column. The study underlines the influence of the two components of biaxial bending on the deformation capacity of r.c. cross-sections and r.c. members.*

1 INTRODUCTION

During a seismic event, the structures are subjected to two simultaneous horizontal components of the ground motion, which cause a structural response in an oblique direction and biaxial bending on the columns.

In XX century, the usual approach for the evaluation of the capacity of structures under seismic excitations was based on the analysis of two unidirectional independent actions. Several experimental researches have been carried out under this simplified hypothesis, assuming the structural elements (i.e. columns) mainly subjected to compressive axial load and uniaxial bending. According to the current seismic codes provisions [1, 2], it is possible to analyse and design the structure assuming two unidirectional independent actions and then combining the results of the two separate analyses. In order to refine the prediction of the structural capacity, both in term of strength and deformation capacity, the contemporaneous presence of the two components of ground motion should be taken into account in structural analysis.

The strength capacity of reinforced concrete (r.c.) cross-sections subjected to compressive axial load and biaxial bending has been widely investigated in literature. The most general approach to the analysis of cross-sections subjected to two components of bending moment is the numerical procedure, which discretizes the cross-section in fibres and integrates the stress distribution over the cross-section area [3, 4, 5, 6]. An alternative and simplified approach is the definition of analytical formulations for the evaluation of the failure surface N-M_x-M_y for a generic r.c. cross-section. The most diffused analytic formulation is the Load Contour method [7], which describes the strength domain M_x-M_y for square/rectangular cross-sections as a function of the uniaxial flexural strength (Eq. 1).

$$\left(\frac{M_{Ed,x}}{M_{Rd,x}}\right)^{\alpha_1}+\left(\frac{M_{Ed,y}}{M_{Rd,y}}\right)^{\alpha 2}\leq 1 \tag{1}$$

Recently, the attention have been focused on the behaviour of r.c. cross-sections in terms of deformation (i.e. curvature) capacity. Based on the results of numerical analysis, some authors proposed the cross-section failure domain $\phi_{u,x}$-$\phi_{u,y}$ in terms of ultimate curvature achieved before the failure [5, 8]. In [9] a simplified procedure for the evaluation of the ultimate curvature of doubly symmetric r.c. cross-sections is proposed. Nevertheless, general analytical formulations for the ultimate curvature in biaxial conditions are still lacking.

Similarly, a lack of investigation has been found about the deformation (i.e. rotational) capacity of r.c. members subjected to two components of bending moment. Several studies investigated on the experimental evaluation of the chord rotation for r.c. members under uniaxial bending [10, 11, 12, 13]. Analytical formulations for the chord rotation at ultimate conditions under uniaxial bending are provided by codes [1, 14].

Experimental studies on the behaviour of r.c. members subjected to different and oblique loading paths have been proposed in literature by [15, 16, 17, 18].

The experimental results confirm that the biaxial bending action affects the rotational capacity of r.c. members more than their strength and underline the need for numerical and analytical models, which relate biaxial bending and axial load in the evaluation of the deformation capacity of r.c. members.

Some authors performed numerical analyses with specific fibre models extended to the member length [6, 19, 20] in order to evaluate the theoretical rotational capacity of the biaxially loaded members.

The purpose of this study is to show the behaviour of r.c. members under simultaneous compressive axial load and biaxial bending, focusing particular attention on the reduction of

deformation capacity due to the two components of bending. The analysis on the generic r.c. member is performed with a specific numerical model, which takes into account the tension shift phenomenon due to the simultaneous presence of shear and bending moment, the deformation of anchorage bars at the joint and the softening branch in the Moment-Curvature diagram.

2 RESEARCH SIGNIFICANCE

The influence of bi-directional seismic excitations on the inelastic behaviour of r.c. members is a crucial aspect to correctly predict the structural behaviour. Taking into account the two components of ground motion, the columns are subjected to combined compressive axial load and biaxial bending, which reduces significantly the deformation capacity of r.c. members. In particular, the study focuses on the behaviour of non-conforming r.c. columns, typical of existing buildings. The present paper proposes curvature domains and chord rotation domains, obtained performing nonlinear analyses with a specific numerical model. The reduction of deformation capacity due to the two components of bending underlines the need of new formulations able to take into account the behaviour of members under biaxial actions.

3 NUMERICAL MODEL FOR THE ANALYSIS OF R.C. MEMBERS

The present research is carried out by using a specific numerical procedure for the evaluation of the nonlinear behaviour of r.c. members under combined axial load and biaxial bending moment [6]. As aforementioned, the behaviour of an r.c. member is strictly related to the behaviour of its cross-section. In a generic r.c. cross-section subjected to axial load N and two components of bending moment M_x-M_y, the inclination angle α_n of the neutral axis n is different from the inclination angle β (Eq. 2) of the bending axis m (Fig. 1a).

$$\beta = \tan^{-1}\frac{M_y}{M_x} \tag{2}$$

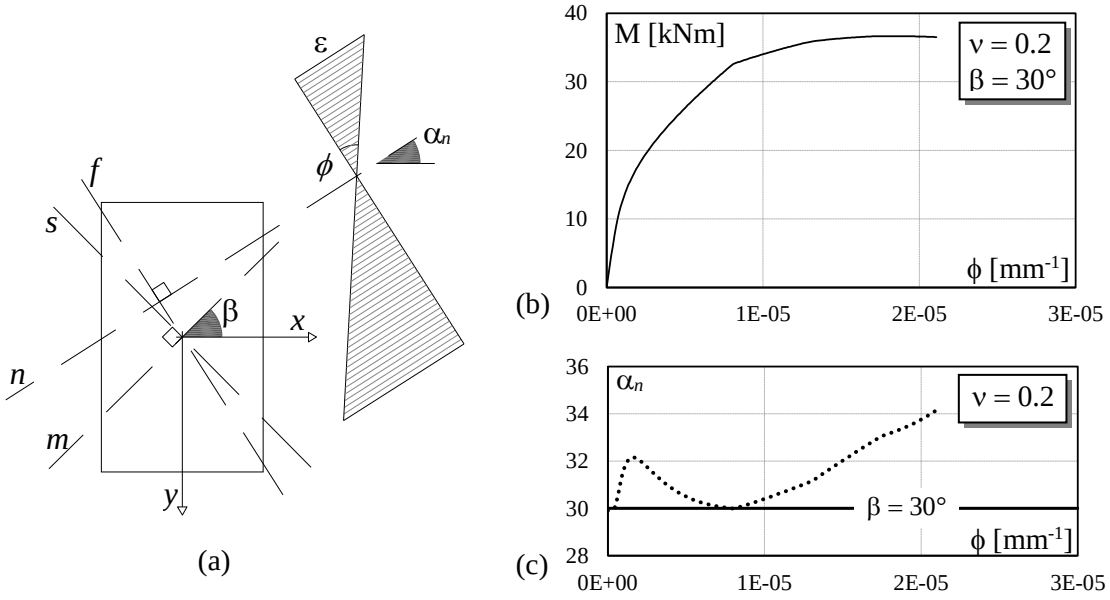


Figure 1: (a) Cross-section under biaxial bending (b) Moment-Curvature relationship for a given β and ν and (c) α_n - ϕ relationship for a given β.

The cross-section curvature ϕ is a function of the neutral axis inclination angle α_n, which in case of biaxial bending could be evaluated only by iterative procedures. Performing a moment-curvature analysis on a generic r.c. cross-section assuming a constant inclination angle β of the bending axis *m* (Fig. 1b), the value of the inclination angle α_n is different from β (Fig. 1c). Moreover, the relation between the two angles α_n and β, which is a function of the value of β and of the normalised axial load ν, is not analytically predictable.

The deflection of three-dimensional members is strictly related to the inclination angle α_n of the neutral axis. In general, the deflection of an r.c. member subjected to biaxial bending is three-dimensional. However if the direction of displacements is imposed, as in conventional pushover analysis, the deflection of the member will be plane along this direction. In other words, if the inclination of the deflection axis *f* (i.e. the inclination angle α_n) is assumed constant during the load history, the deflection of the member is plane.

The adopted numerical procedure performs the analysis of r.c. members for a fixed inclination angle α_n of the neutral axis, in order to guarantee a plane deflection of the generic three-dimensional member. The model replicates an experimental test on an r.c. cantilever subjected to compressive axial load and oblique loading path [18].

The analysis is performed on the cross-section firstly and then on the member. The generic r.c. cross-section is analysed using a specific fibre model. The cross-section is divided in a finite number of triangles and then each triangle is discretized in a finite number of fibres (i.e. strips) parallel to the direction α_n of the neutral axis. At each fibre is assigned a nonlinear constitutive law for concrete. The steel reinforcement properties are assumed to be concentrated at the location of each steel bar. The Moment-Curvature relationship for the generic cross-section is obtained by an iterative procedure with increasing curvature ϕ until the failure. At each step of curvature, the procedure finds the neutral axis depth able to satisfy the equilibrium between external and internal actions.

The generic r.c. member is herein analysed as the basic scheme of cantilever with constant cross-section along its length L_V (i.e. the shear span of the member), subjected to a horizontal force *F* at the free end. Displacements and rotations for the cantilever are obtained by integration of the curvatures along the member length, including the deformation of steel bars inside the joint. The numerical procedure adopted consists in applying an external curvature ϕ_{fix} at the fixed end of the cantilever. Since the Moment-Curvature relationship for the cross-section is known, the bending moment M_{fix} at the fixed end is easily evaluated, as well as the value of the external force $F=M_{fix}/L_V$ applied at the fixed end.

The diagram of the bending moment along the member length takes into account the tension shift phenomenon, due to the simultaneous presence of bending moment and shear. The *effective bending moment diagram* is obtained shifting the bending diagram of the quantity Δz (Fig. 2a). The consequence of the tension shift is that part of the member near the fixed end is characterized by constant bending moment. The value of curvature in this portion of member is constant and equal to the curvature at the fixed end, so that it behaves as a unique element subjected to the same curvature. Then the wider part of the flexural deformation is here concentrated, so this zone becomes naturally a plastic hinge of length $L_{pl,flex}$ equal to Δz (Eq. 3). The quantity Δz is a function of the internal lever arm *z* and of the compressive strut inclination angle ϑ, according to the variable strut inclination truss model.

$$L_{pl,\,flex} = \Delta z = 0.5 z \cot \vartheta \tag{3}$$

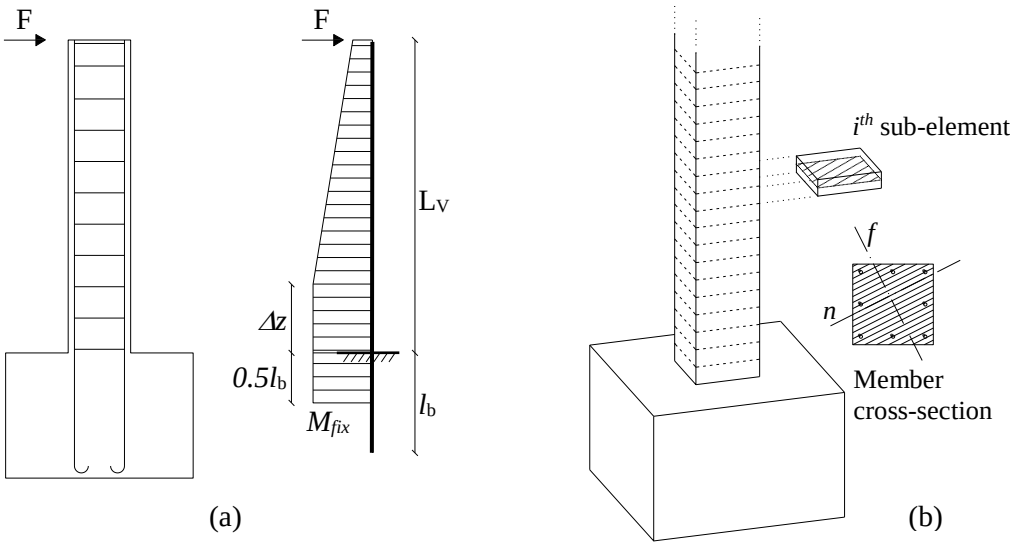


Figure 2: (a) Effective ending moment diagram (b) Cross-section and member discretization

As aforementioned, the model takes also into account the contribution of the tensile reinforcement deformation inside the joint to the rotation of the fixed end. The bending moment is maximum at the fixed end of the cantilever then decreases slowly (it is assumed a linear decreasing) inside the joint becoming null at a distance equal to the steel anchorage length l_b. The bending moment diagram inside the joint could be assumed constant and equal to the bending moment at the fixed end M_{fix}, for a length equal to a half of the anchorage length of steel reinforcement l_b (Fig. 2a). In case of frames, the point of null of bending diagram is at the middle span of the joint, then the bending moment could be considered constant for at least a quarter of the joint global length.

This portion of the joint behaves as a plastic hinge of length $L_{pl,slip}$ equal to a half of the anchorage length of the steel bars l_b (Eq. 4), which is a function of the reinforcement tensile stress σ_s, the bars diameter d_b and the bond stress f_b.

$$L_{pl,\text{slip}} = 0.5 l_b = \frac{\sigma_s d_b}{8 f_b} \qquad f_b = 2.25 \eta_1 \eta_2 f_{ct} \tag{4}$$

The bond stress f_b is evaluated according to the Eurocode [21], as a function of the concrete tensile strength f_{ct}, reduced by two coefficients η_1 and η_2 which take into account respectively the quality of bond conditions due to smooth/deformed bars and the bars diameter.

The concept of plastic hinge is a natural consequence of the two aforementioned phenomena and the plastic hinge global length L_{pl} is given by the sum of the flexural and slip contributions (Eq. 5). The shear deformation is here neglected.

$$L_{pl} = L_{pl,\text{flex}} + L_{pl,\text{slip}} \tag{5}$$

Once the distribution of bending moment along the cantilever is defined (Fig. 2a), the value of curvature at each section of the cantilever could be evaluated from the cross-section M-ϕ relationship. Herein the cantilever is discretized along its length in a finite number of sub-elements and the curvature is evaluated only at the centroid of each sub-element, in order to reduce the computational effort (Fig 2b). The bending diagram is considered constant along

the generic sub-element and the value of bending is assumed equal to the bending moment at its centroid.

The Force-Drift relationship for the member is obtained by iterative procedure with increasing external curvature ϕ_{fix} applied at the fixed end until the failure of the member, due to the achievement of the cross-section ultimate curvature.

4 BEHAVIOUR OF R.C. MEMBERS UNDER BIAXIAL ACTIONS

4.1 Analysis of r.c. cross-section

A sample of the procedure for evaluating the behaviour of r.c. members under biaxial actions is herein explained. In particular, the study focuses on the behaviour of non-conforming r.c. columns, typical of existing buildings.

Two kind of cross-sections are analysed: a square cross-section and a rectangular one. The geometrical percentage of reinforcement, the aspect ratio of the section and the mechanical properties of materials are not significant in this phase since the general trend of the domain curves is analysed independently from these parameters. Nevertheless, the influence of these factors on the reduction of deformation capacity will be evaluated in further studies.

The nonlinear behaviour of concrete is taken into account by adopting the nonlinear stress-strain relationship provided by Eurocode [21], which is a simplification of the model proposed in literature by Sargin [22]. The tensile strength of concrete is neglected so as to the effect of confinement. Then the confined core is assumed to have the same mechanical properties of the unconfined concrete. This assumption is conservative, but is in accordance with the usual hypothesis for existing buildings, in which a lack of stirrups anchorage is always recognized. The mechanical behaviour of reinforcement steel is assumed elastic-perfectly plastic and the contribution of hardening in neglected, as in standard analysis. Moreover, steel bars are considered plain.

The cross-section failure (i.e. the ultimate curvature) corresponds to the achievement of the maximum compressive strain of unconfined concrete $\varepsilon_{cu} = 0.0035$ at the most compressed vertex of the cross-section.

Firstly, the behaviour of the r.c. cross-section subjected to combined compressive axial load and biaxial bending is evaluated by plotting the Moment-Curvature curves for several values of ν. The M-ϕ curves obtained performing the analysis with constant inclination of the neutral axis $\alpha_n = 0°$ (Fig. 3a) show a nonlinear trend with a softening branch for higher values of axial load. In case of softening branch, the ultimate curvature for the cross-section is assumed as the value corresponding to 80% of the maximum bending moment.

The maximum value of resisting bending moment corresponds to a normalized axial load ν equal to 0.4÷0.5, whereas for higher values of ν the bending capacity of the cross-section decreases. However, this reduction is not so alarming in consideration of the fact that the usual range of normalized axial load for columns is about $\nu = 0.1 \div 0.5$ both for new structures (due to current codes design provisions) and existing structures (as a consequence of typical design old approaches). It is worth noting the influence of the axial stress level on the cross-section ductility under uniaxial bending. The ultimate curvature between the curves at $\nu = 0.1$ and $\nu = 0.5$ decreases significantly.

Assuming a fixed value of ν and several values of α_n, the Moment-Curvature curves show the same global trend and initial stiffness (Fig. 3b). The effect of biaxial bending (i.e. inclination α_n of the neutral axis) affects more the cross-section ultimate curvature than the cross-section strength. Indeed the reduction in terms of resisting bending moment is quite negligible if compared with the reduction in terms of ultimate curvature and ductility.

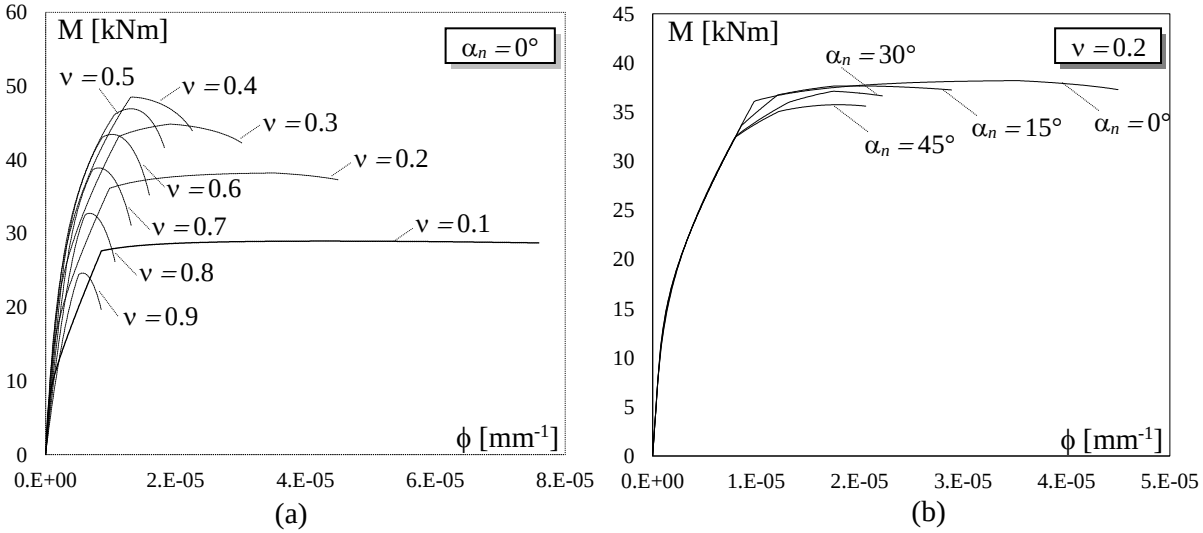


Figure 3: Moment-Curvature curves for different values of (a) ν and (b) α_n.

The cross-section behaviour under biaxial bending is expressed in terms of ultimate curvature domains and yielding curvature domains. The yielding curvature is here evaluated assuming a bilinear curve for the Moment-Curvature relationship, using the approach suggested for the evaluation of the capacity curves by Fajfar [23].

The analysis has been performed on the generic r.c. cross-section, varying the inclination of the neutral axis between $\alpha_n = 0° \div 90°$ and the normalized axial load in the range $\nu = 0.1 \div 0.9$. Starting from the Moment-Curvature curves, the interaction surfaces in terms of yielding curvature and ultimate curvature could be evaluated.

The curvature domain is represented by plotting the two components of yielding/ultimate curvature with respect to the neutral axis inclination angle α_n (Eq. 6)

$$\begin{aligned} \phi_{u(y),x} &= \phi_{u(y)} \cos \alpha_n \\ \phi_{u(y),y} &= \phi_{u(y)} \sin \alpha_n \end{aligned} \tag{6}$$

The ultimate curvature domains have the same global trend for squared and rectangular cross-sections (Fig. 4a-b). Indeed the only difference is the asymmetry of the rectangular cross-section, which is characterized by a lower stiffness along the weak axis, whereas the square section with symmetric reinforcement has the same ultimate curvature under uniaxial bending along the *x*-*y* axis.

The global trend of the curves depends on the normalized axial load, ν. For high values of axial load ($\nu = 0.6 \div 0.9$) the curves are characterized by a concavity faced to the origin of the reference system, whereas for lower values of compressive load ($\nu \leq 0.4$) the concavity of the curves is inverted. Moreover, the trend is approximately linear between $\nu = 0.4 \div 0.5$. It is worth noting that the reduction of ultimate curvature due to the biaxial bending is much relevant for $\nu \leq 0.4$.

In doubly symmetric cross-sections, as the square sections with symmetric reinforcement, the minimum value of the ultimate curvature is always achieved at $\alpha_n = 45°$. This condition is independent from the axial load and depends only from the geometry.

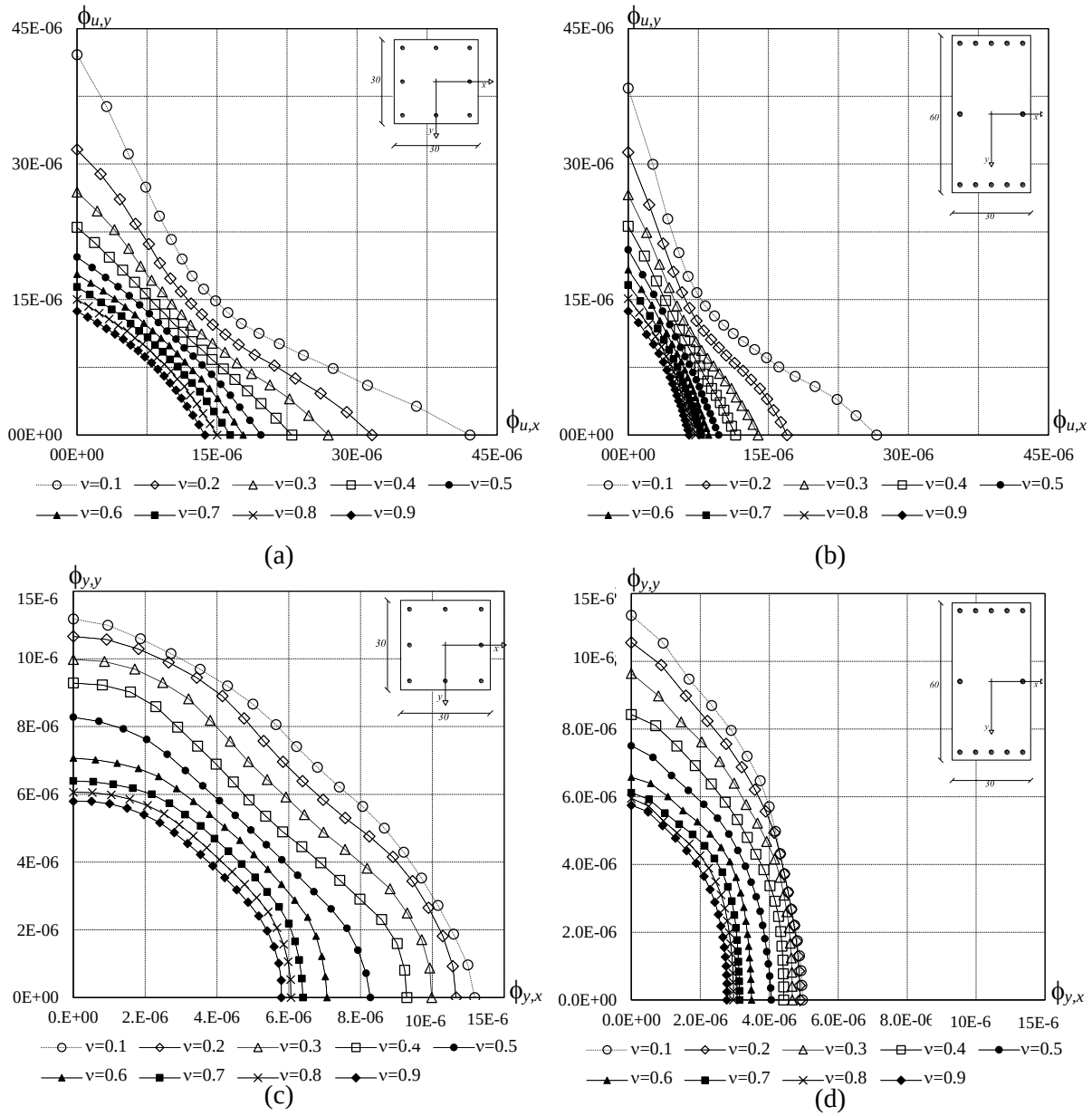


Figure 4: Ultimate curvature domain for (a) square cross-section and (b) rectangular cross-section and yielding curvature domain for (c) square cross-section and (d) rectangular cross-section.

Differently, in case of rectangular cross-sections, the inclination α_n for which the minimum value of ultimate curvature is achieved depends on several factors as the axial load, the cross-section aspect ratio and the location of steel bars. By this, the inclination of neutral axis corresponding to the minimum value of ultimate curvature in case of rectangular cross-section is not predictable.

Similar considerations could be carried out for the yielding curvature. However, the yielding curvature curves (Fig. 4c-d) obtained for square and rectangular cross-sections show the concavity faced to the origin of the reference system, independently from the value of the normalized axial load ν. Moreover, similarly to the case of ultimate curvature, the reduction of yielding curvature due to the axial stress is relevant for low values of ν, whereas for higher values of axial load ($\nu > 0.5$), the reduction is quite negligible.

This is a preliminary step for the evaluation of the redaction of ductility due to the two components of bending moment.

4.2 Analysis of r.c. member

The definition of the Moment-Curvature relationship for the cross-section of the r.c. member is necessary for evaluating the member deflection. As before mentioned, the deflection of an r.c. member subjected to biaxial bending is three-dimensional. Nevertheless, if the two components of bending increase in a way that allow to have a constant inclination angle α_n of the neutral axis (i.e. for a fixed direction of displacement path), the deflection of the member is plane over the plane of deflexion.

The member behaviour under biaxial bending is expressed in terms of ultimate chord rotation domains and yielding chord rotation domains. Analogously to the case of cross-section, the yielding rotation is evaluated assuming a bilinear curve for the Moment-Rotation relationship using the approach suggested for the evaluation of the capacity curves by Fajfar [23].

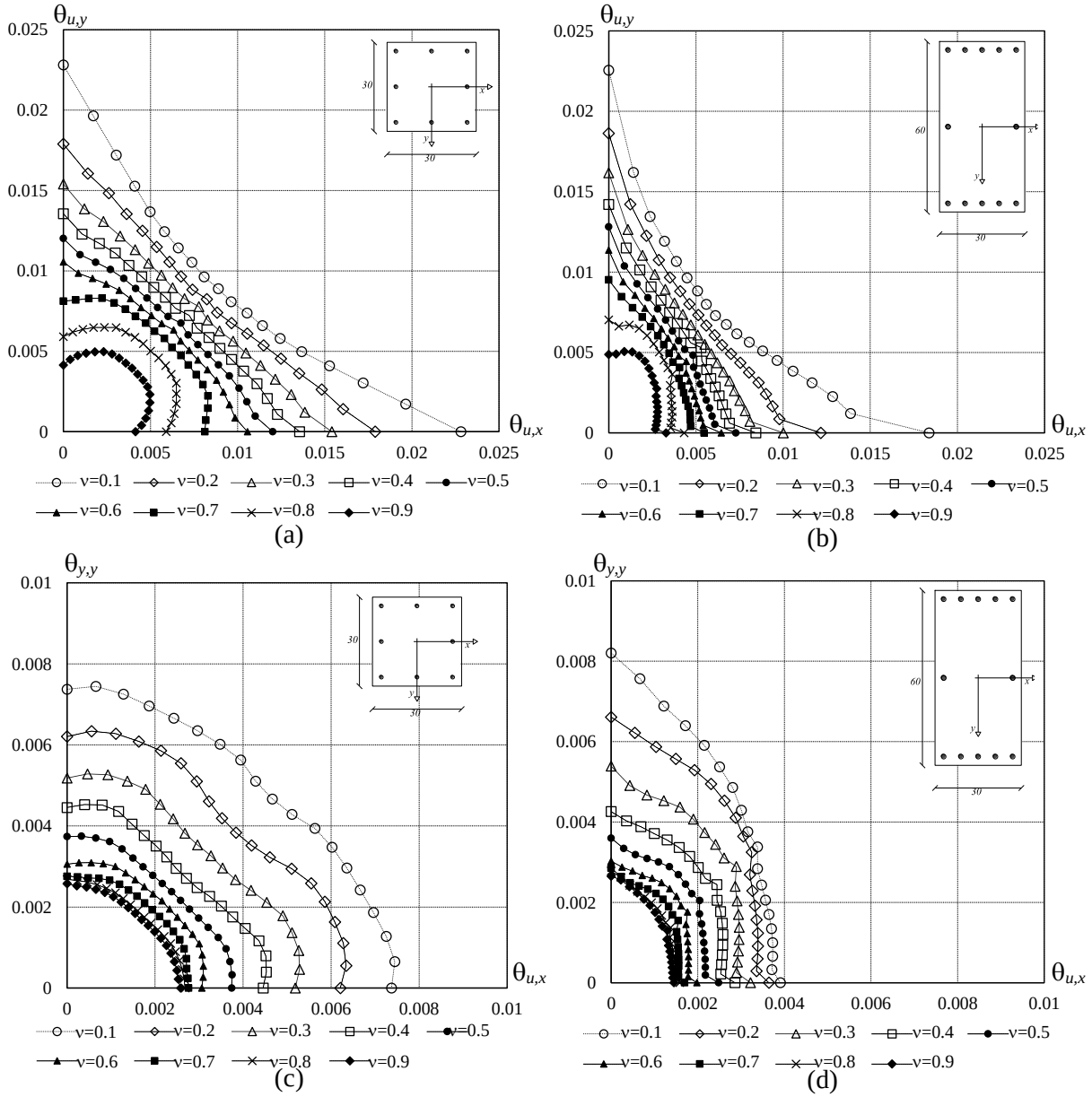


Figure 5: Ultimate rotation domain for (a) squared cross-section and (b) rectangular cross-section and yielding rotation domain for (c) squared cross-section and (d) rectangular cross-section.

The Moment-Rotation relationship is calculated for several inclination of the neutral axis between $\alpha_n = 0° \div 90°$ and varying the normalized axial load in the range $\nu = 0 \div 0.9$. Then the three-dimensional ultimate/yielding chord rotation domain is obtained (Fig. 5).

The general trend of ultimate rotation domain curves is very close to the ultimate curvature domain (Fig. 5a-b). For high values of axial load the concavity of the curves is faced to the origin but the ultimate rotation under biaxial bending is higher than the uniaxial one. It is observed that for values of $\alpha_n \cong 0°$ the failure is caused by achievement of 20% reduction of the strength capacity. For $\nu = 0 \div 0.3$ the concavity is in the opposite direction and the reduction of the capacity due to the biaxial bending is evident.

On the contrary, the concavity of yielding rotation domain curves is always faced to the origin, independently from the entity of ν (Fig. 5c-d). For normalized axial load higher than 0.6 the difference between the curves is negligible.

The representation of the curvature and rotation domains for the generic r.c. member confirms the strong correlation between the behaviour of the member and the behaviour of its cross-section.

5 COMPARISON BETWEEN NUMERICAL RESULTS AND CODE PROVISIONS

The evaluation of the ultimate and yielding rotation of r.c. members is crucial for defining the deformation capacity of existing buildings or new constructions.

The current European code [14] provides a specific formulation for calculating the yielding and ultimate rotation of r.c. member under uniaxial actions. In particular, the expression of the yielding rotation is given by the sum of three contribution: (i) the flexural rotation, (ii) the shear deformation and (iii) the deformation due to the bond slip (Eq. 7). It is a function of the mechanical properties of materials (i.e. steel yielding strength f_y and concrete compressive strength f_c) and geometrical characteristic of the member (i.e. shear span L_V and cross-section depth h)

$$\theta_y = \phi_y \frac{L_V}{3} + 0.0013\left(1 + 1.5\frac{h}{L_V}\right) + 0.13\phi_y \frac{d_b f_y}{\sqrt{f_c}} \tag{7}$$

A critical aspect of this formulation is the accuracy in the evaluation of the yielding curvature ϕ_y for elements subjected to compressive axial load and bending moment. Usually, the yielding curvature is associated to the yielding of tensile reinforcement. Nevertheless, this value of yielding curvature is not representative for sections subjected to compressive axial load and biaxial bending and implies an underestimation of the yielding rotation. A more accurate procedure is the evaluation of the bilinear curve of Moment-Curvature relationship for the cross-section. Therefore, this method requires a higher computational effort and generally is not used in standard applications. For the following examples, the yielding curvature is calculated with a simplified approach, assuming both steel reinforcement yielded.

According to the codes provisions [14, 24], the ultimate chord rotation could be calculated choosing between the two formulations provided (Eq 8a). The first one is an additive formulation where the yielding rotation is increased by the plastic rotation above a reduced plastic hinge. The second expression is based on results of experimental tests [25] and takes into account the effectiveness of confinement α_c, which increases the rotational capacity (Eq 8b).

$$\theta_u = \frac{1}{\gamma_{el}}\left(\theta_y + (\phi_u - \phi_y)L_{pl}\left(1 - \frac{0.5L_{pl}}{L_V}\right)\right)$$
$$\theta_u = \frac{1}{\gamma_{el}} 0.016(0.3)^{\nu}\left[\frac{\max(0.01;\omega')}{\max(0.01;\omega)} f_c\right]^{0.225}\left(\frac{L_V}{h}\right)^{0.35} 25^{\left(\alpha_c \rho \frac{f_{yw}}{f_c}\right)}\left(1.25^{100\rho_d}\right) \quad (8)$$

In case of members characterized by ties not closed with 90-degree hooks at both ends, the code suggests to neglect the effectiveness of confinement, assuming $\alpha_c = 0$ in the second expression. Moreover, in case of elements without seismic details, the ultimate rotation is 85% of the value obtained previously assuming $\alpha_c = 0$.

The results provided by the numerical procedure herein described are here compared with the results of codes formulations under uniaxial bending (Fig. 6a). For values of normalized axial load $\nu \leq 0.5$, the trend of the numerical results under uniaxial bending (i.e. $\alpha_n = 0°$) is very close to the results of (Eq. 8a). In case of biaxial bending (i.e. $\alpha_n = 45°$), the ultimate rotation is strongly reduced in case of low normalized axial loads. The codes formulations, (Eq. 8a) and (Eq. 8b), provide different results. In particular, the (Eq. 8a) provides results more conservative than (Eq. 8b), even though the reductions applied at (Eq. 8b) in case of non-conforming elements. Nevertheless, also (Eq. 8a) overestimates the rotational capacity, if the effect of biaxial bending is considered.

Moreover, for higher values of ν, the strong compressive stress reduces significantly the rotational capacity, but the (Eq. 8a) is not able to catch this phenomenon, in part due to the approximation in the evaluation of the yielding rotation and in part due to the evaluation of the plastic hinge length.

The plastic hinge length L_{pl} is calculated according to the equation provided by [14] Eq. 9). In particular, the global plastic hinge length is given by the sum of three contributions (Fig. 6b): (i) the flexural contribution $L_{pl,flex}$, (ii) the shear contribution $L_{pl,shear}$ and (iii) the bond slip contribution $L_{pl,slip}$.

$$L_{pl} = 0.1L_V + 0.17h + 0.24\frac{d_b f_y}{\sqrt{f_c}} \quad (9)$$

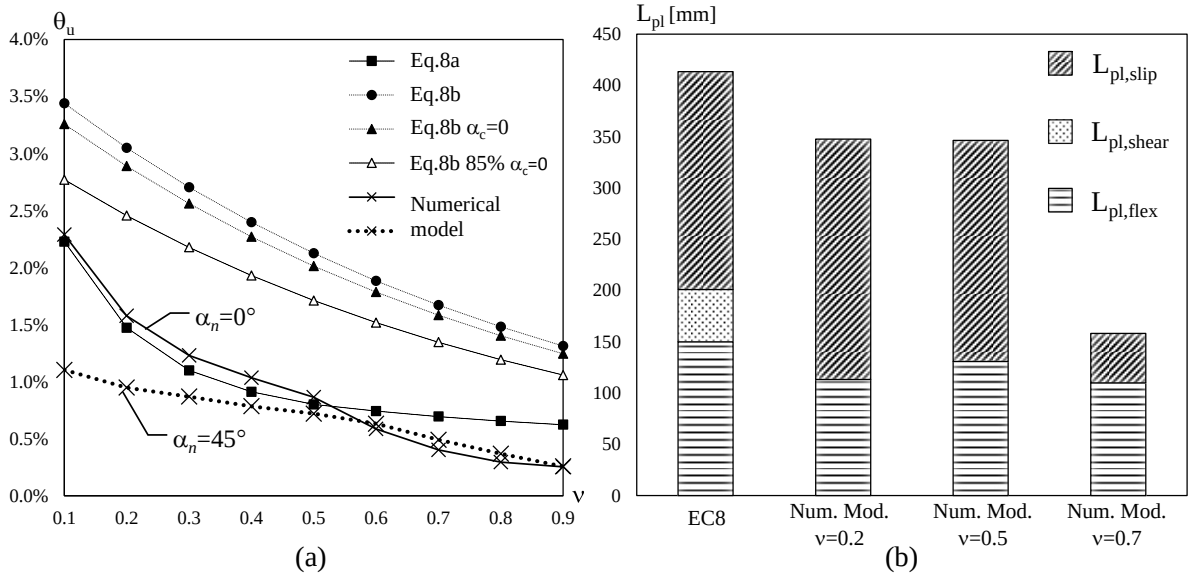


Figure 6: (a) Comparison between codes provisions and numerical model results in uniaxial conditions (b) Comparison of plastic hinge length calculated with EC8 formulation and with the numerical model.

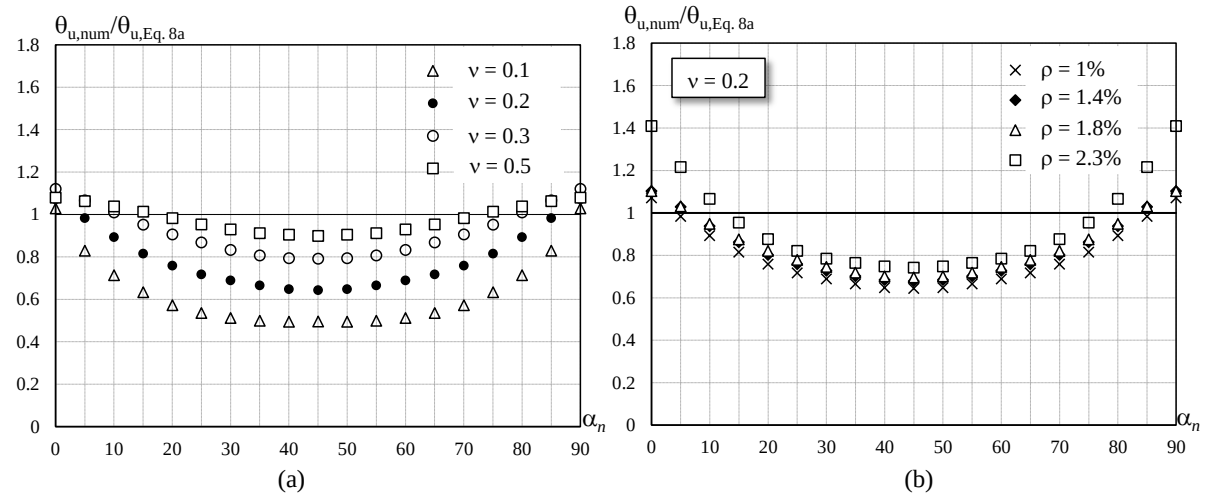


Figure 7: (a) Comparison between codes provisions and numerical results under biaxial actions for several ν and (b) Comparison between codes provisions and numerical results under biaxial actions for several ρ.

The numerical model is able to catch both the flexural and anchorage bars contributions. The shear deformation, neglected in the model, is smaller than the other two contributions. Moreover, the effect of the compressive axial load reduces the plastic hinge length (in particular the component due to the deformation of reinforcement in tension inside the joint), but the formulation provided by the code is independent from ν.

The ratio between the ultimate rotation capacity computed by the numerical procedure and that provided by (Eq. 8a) for uniaxial bending is plotted as a function of α_n in (Fig. 7a). The Figure shows that, if biaxial action are neglected, the capacity of the cross-section is overestimated. Moreover, the reduction of ultimate rotation is stronger for low values of axial load, arriving at 50% of the uniaxial ultimate rotation.

In conclusion, the axial load strongly affects the trend of the deformation capacity curves. Nevertheless, other parameters, like the geometric percentage of reinforcement (Fig. 7b) or the mechanical properties influence the reduction due to the biaxial bending. The analysis of such influence is outside the scope of the present research, but will be the goal of further studies.

6 CONCLUSIONS

The deformation capacity of r.c. members subjected to compressive axial load and biaxial bending has been evaluated using a specific numerical procedure. Firstly, the yielding and ultimate curvature domains for the r.c. cross-section of non-conforming elements have been evaluated and discussed. Then, the yielding and ultimate rotation domains for the r.c. member have been plotted, taking into account the nonlinear behaviour of concrete, the softening branch of the Moment-Curvature relationship, the tension shift phenomenon and the deformation of anchorage bars.

The results of the numerical analyses confirm the reduction of deformation capacity due the two components of bending, in terms of both ultimate curvature and rotational capacity. In particular, the reduction is stronger in the range of normalized axial load value $0.1 \leq \nu \leq 0.5$, typical of columns.

The expressions provided by the Eurocode 8 [14] for the evaluation of the ultimate rotation under uniaxial actions provide different results. In particular, the additive formulation (Eq. 8b) is particularly conservative but it is also widely used in standard applications. The results of

the numerical procedure under uniaxial bending have a good agreement with the (Eq. 8a) for normalized axial load lower than 0.6.

Moreover, assuming the rotational capacity of the member constant for each direction and equal to the uniaxial one, estimated by (Eq. 8a), the ultimate rotation under biaxial actions in the examined cases is overestimated up to 50%.

This research underlines the need of further investigation on the behaviour of non-conforming r.c. member subjected to biaxial bending, in order to provide new formulations able to easily and reliably predict the rotation capacity in biaxial conditions.

REFERENCES

[1] ASCE, Seismic rehabilitation of existing buildings, *ASCE SEI/41, ASCE, Reston, VA*, 2007.

[2] European Standard, Eurocode 8: Design of structures for earthquake resistance. Part 1: General rules, seismic actions and rules for buildings, *EN 1998-1*, Brusselles, Belgium, 2003.

[3] M. G. Sfakianakis, Biaxial Bending with Axial Force of Reinforced, Composite and Repaired Concrete Section of Arbitrary Shape by Fiber Model and Computer Graphics, *Advanced in Engineering Software*, **33**, 227-242, 2002.

[4] M. Di Ludovico, G. P. Lignola, A. Prota, E. Cosenza, Nonlinear analysis of cross-sections under axial load and biaxial bending, *ACI Structural Journal*, **107**(4), 390-399, 2010.

[5] M. Fossetti, M. Papia, Dimensionless analysis of RC rectangular sections under axial load and biaxial bending, *Engineering Structures*, **44**, 34-45, 2012.

[6] M. Bosco, M. Del Zoppo, A. Ghersi, E. M. Marino, A model for the analysis of reinforced concrete cross-sections and members under biaxial bending and axial force, *proposed to Computers and Structures*, 2015.

[7] B. Bresler, Design criteria of reinforced columns under axial load and biaxial bending, *ACI Journal*, **57**(5), 481-490, 1960.

[8] M. Di Ludovico, G. P. Lignola, A. Prota, E. Cosenza, Analisi non lineare di sezioni in c.a. soggette a pressoflessione deviata, *ANIDIS XII Convegno, L'Ingegneria sismica in Italia*, Pisa, Italy, 2007.

[9] M. Di Ludovico, G. M. Verderame, I. Iovinella, E. Cosenza, Domini di curvatura di sezioni in c.a. in pressoflessione deviata. Parte II, *ReLuis Convegno*, Rome, Italy, 2008.

[10] M. N. Fardis, D. E. Biskinis, Deformation capacity of RC members, as controlled by flexure or shear, *Performance based engineering for earthquake resistant reinforced concrete structures: A volume honoring Shunsuke Otani, T. Kabeyasawa and H. Shiohara, eds.*, University of Tokyo, Tokyo, 511–530, 2003.

[11] M. Berry, M. Eberhard, Performance models for flexural damage in reinforced concrete columns, *Rep. No. 2003/18*, PEER Center, University of California, Berkeley, CA, 2003.

[12] M. Eberhard, *Structural Performance Database*, Dept. of Civil and Environmental Engineering, Univ. of Washington, *http://www.ce.washington.edu/peera1/last*, 2005.

[13] M. Di Ludovico, G. M. Verderame, A. Prota, G. Manfredi, E. Cosenza, Cyclic behavior of nonconforming full-scale RC columns, *J. Struct. Eng.*, **140**(5), 2014.

[14] European Standard, Eurocode 8: Design of structures for earthquake resistance. Part 3: Assessment and retrofitting of buildings, *EN 1998-3*, Brusselles, Belgium, 2004.

[15] S. N. Bousias, G. Verzeletti, M. N. Fardis, M., E. Gutierrez, Load path effects in column biaxial bending with axial force, *J. Eng. Mech.*,**121**(5), 596–605, 1995.

[16] F. Qiu, W. Li, P. Pan, L. Qian, Experimental tests on reinforced concrete columns under biaxial quasi-static loading, *J. Eng. Struct.*, 24(4), 419–428, 2002.

[17] H. Rodrigues, A. Arede, H. Varum, A. G. Costa, Experimental evaluation of rectangular concrete column behaviour under biaxial cyclic loading, *Earthquake Engng Struct. Dyn.*, **42**, 239-259, 2013.

[18] M. Di Ludovico, G. M. Verderame, A. Prota, G. Manfredi, E. Cosenza, Experimental behaviour of nonconforming RC columns with plain bars under constant axial load and biaxial bending, *J. Struct. Eng.*, **139**, 897-914, 2013.

[19] C. A. Christos, S. A. Mahin, Behavior of reinforced concrete structures subjected to biaxial excitation, *J. Struct. Eng*., **117**, 2657-2673, 1991

[20] G.G. Wang, C. T. Hsu, Complete biaxial load-deformation behaviour of RC columns, *J. Struct. Eng.*, 118:2590-2609, 1992.

[21] European Standard, Eurocode 2: Design of concrete structures. Part 1-1: General rules and rules for buildings, *EN 1992-1-1*, Brussels, Belgium, 2004.

[22] M. Sargin, Stress-Strain Relationships for Concrete and the Analysis of Structural Concrete Sections, *SM Study 4, Solid Mechanic Division*, University of Waterloo, 1971.

[23] P. Fajfar, M.EERI, A nonlinear analysis method for performance-based seismic design, *Earthquake Spectra*, **16**(3), 573-592, 2000.

[24] D. M. 14 Gen. 2008, Norme tecniche per il calcolo, l'esecuzione, ed il collaudo delle strutture in conglomerato cementizio armato normale e precompresso e per le strutture metalliche [*Technical guidelines for the design and contruction of reinforced concrete, prestressed concrete and steel structures*], 2008 (in Italian).

[25] T. B. Panagiotakos, M. N. Fardis, Deformations of Reinforced Concrete Members at Yielding and Ultimate, *ACI Structural Journal*, **98**(2), 135-148, 2001.

COMPDYN 2015
5th ECCOMAS Thematic Conference on
Computational Methods in Structural Dynamics and Earthquake Engineering
M. Papadrakakis, V. Papadopoulos, V. Plevris (eds.)
Crete Island, Greece, 25–27 May 2015

STIFFNESS MODELING OF RC COLUMNS REINFORCED WITH PLAIN REBARS

Okan Ozcan[1]

[1] Akdeniz University, Department of Civil Engineering, 07058, Antalya, Turkey
e-mail: ookan@akdeniz.edu.tr

Keywords: Reinforced concrete; columns; effective stiffness; plain rebars; guidelines

Abstract. *Inaccurate predictions of effective stiffness for reinforced concrete (RC) columns having plain (undeformed) longitudinal rebars may lead to unsafe performance assessment and strengthening of existing deficient frames. Currently utilized effective stiffness models cover RC columns reinforced with deformed longitudinal rebars. A database of 47 RC columns (33 columns had continuous rebars and the remaining had spliced reinforcement) that were longitudinally reinforced with plain rebars was compiled from literature. The existing effective stiffness equations were found to overestimate the effective stiffness of columns with plain rebars for all levels of axial loads. A new approach that considers the contributions of flexure, shear and bond slip to column deflections prior to yielding was proposed. The new effective stiffness formulations were simplified without loss of generality for columns with and without lap-spliced plain rebars. In addition, the existing stiffness models for the columns with deformed rebars were improved while taking poor bond characteristics of plain rebars into account.*

1 INTRODUCTION

Effective stiffness predictions in performance based seismic assessment of existing structures primarily affect the dynamic characteristics of structures via structural demand estimations (lateral deformations and shear) and consequently the cost of seismic retrofit. In this respect, the strong dependence of effective stiffness on column axial load level was recognized by various researchers [1-8].

In addition, the influence of other parameters such as shear span to depth ratio, eccentricity and longitudinal reinforcement on effective stiffness was investigated and proposed stiffness formulations were modified accordingly [3, 5, and 9]. Moreover, simplified design implications were imposed in various structural guidelines [10-14] using the axial load level as the main design parameter. The literature study conducted on the effective stiffness reveals that all effective stiffness formulations are for columns longitudinally reinforced with deformed rebars. ASCE/SEI 41 update report [15] states that lower effective stiffness values might be attained for the structural components with plain rebars due to the reduced bond stress levels without further elaboration. Thus, it is expected that the effective stiffness recommended in assessment guidelines may show a tendency to overestimate the effective stiffness of vertical load bearing members having plain reinforcement. In addition, since the effective stiffness estimations substantially influence the anticipated seismic deformation demands, internal force distribution and dynamic response [3, 5, 7 and 8], special attention should be paid especially for the performance based assessment of structures reinforced with plain rebars. Therefore, the aim herein is to propose sound column effective stiffness estimations for columns having plain rebars.

2 COLUMN DATABASE

In order to examine the stiffness properties of RC columns with plain rebars, a database including 47 RC columns was formed [16] in which 33 of the columns were continuously reinforced and the remaining columns were spliced with various splice lengths. The database consisted of monotonic and cyclic lateral force – tip deflection responses of rectangular RC columns that were tested in single curvature. The axial load upper limit as taken from the database is 63% of the axial load carrying capacity with a shear span to depth ratio range of 2.8 to 9.2. In addition, longitudinal reinforcement ratios ranging between 0.6% and 2.5% were used with splice lengths from 15 to 40 bar diameters. The monitored failure mechanisms for the columns in the database were flexure dominant (i.e. longitudinal rebar yielding in tension accompanied by other limit states such as concrete crushing, rebar buckling and rebar fracture) in addition to lap-splice failures for inadequate splice lengths.

2.1 Spliced Steel Model

Instead of a constitutive steel model that was used for continuous rebars a spliced steel model was generated for plain rebars considering the failure mechanism as pull-out rather than splitting failure that is usually observed in columns with deformed reinforcing bars. For the spliced steel model, the strain decomposition method was implemented in which the total strain was assumed to be decomposed into elongation and slip components. The strain components were calculated iteratively while satisfying equilibrium and bond stress equations concurrently [16]. The adopted constitutive relationship of bond stress and slip depends on maximum bond stress and maximum slip [17]. Since the confining stresses primarily affect the bond stresses and corresponding slips for deformed reinforcement pertinent to splitting type of bond failure, the confining stresses were taken as zero as it would merely affect the bond behavior of plain rebars.

In addition, the maximum bond stress expression was modified for plain rebars using the lap-spliced beam database that was obtained from literature [18]. The splices were located at

the bottom tension reinforcement with various splice lengths in the middle of the beams. Analytical calculations were based on standard section analysis carried out by the constitutive models of concrete [19] and spliced steel [16]. In the analyses, the analytically obtained beam moment capacities were compared with experimental moment capacities in order to acquire the maximum bond stress expression for plain rebars. Hereby, the maximum bond stress was determined as $\tau_{max} = 0.5\sqrt{f_c'}$ while providing the analytical to experimental moment capacity ratio close to unity.

2.2 Stiffness Approximations and Code Comparisons

The experimental effective stiffness calculations for the columns were based on estimated yield deflections ($\Delta_{y,exp}$) according to the yield forces (f_{fy}) that were determined by either standard section analysis (SSA) or load deflection curves due to the unavailability of the measured strain data for longitudinal reinforcement. Thus, the incipient yield deflections (Δ_{fy}) were determined initially as corresponding to the preceding lateral force (F_{fy}) at which the tensile reinforcement yielded or concrete compressive strain reached 0.002 by using standard section analysis with the constitutive models for concrete, steel and spliced steel. In accordance with Elwood and Eberhard [7], for the cases where the experimental lateral strength ($F_{max,exp}$) did not exceed the calculated yield force by a minimum 7%, the yield force was assumed as 80% of the experimental lateral strength concerning the influence of axial load and shear induced failure mechanisms.

The experimental yield deflections were acquired by extrapolating the attained incipient yield deflections in proportion to the ratio of the lateral force at which the strain at extreme concrete fiber reached 0.004 ($F_{0.004}$) to the incipient yield force (Eq. 1a). The yield curvatures (κ_y) were determined similarly (Eq. 1b). The experimental effective stiffness ($EI_{eff,exp}$) is defined in Eq. 2a assuming a linear curvature distribution over the column shear span (L) and the flexural stiffness (EI_{flex}) is calculated as shown in Eq. 2b.

$$\Delta_{y,exp} = \Delta_{fy} F_{0.004} / F_{fy} \tag{1a}$$

$$\kappa_y = \kappa_{fy} M_{0.004} / M_{fy} \tag{1b}$$

$$EI_{eff,exp} = F_{0.004} L^3 / 3\Delta_{y,exp} \tag{2a}$$

$$EI_{flex} = M_{fy} / \kappa_{fy} = M_{0.004} / \kappa_y \tag{2b}$$

11 columns out of the database were identified as not yielding while the experimental lateral strength was not monitored to exceed the calculated yield force at least by 7%. Herein, 2 beams and 7 columns were not identified to yield due to the relatively low shear span to depth ratio of 2.8 and high axial load ratio beyond 30% that introduced the effect of shear and axial load induced failure mechanisms, respectively. The remaining 2 columns (1 lap-spliced column and 1 column with relatively low axial load ratio of 12%) were observed to exceed the calculated yield force by approximately 5%. In reference to the measured effective stiffnesses for continuous and lap-spliced columns, the influences of key parameters ranging in investigation limits are presented in Figs. 1a - 1i.

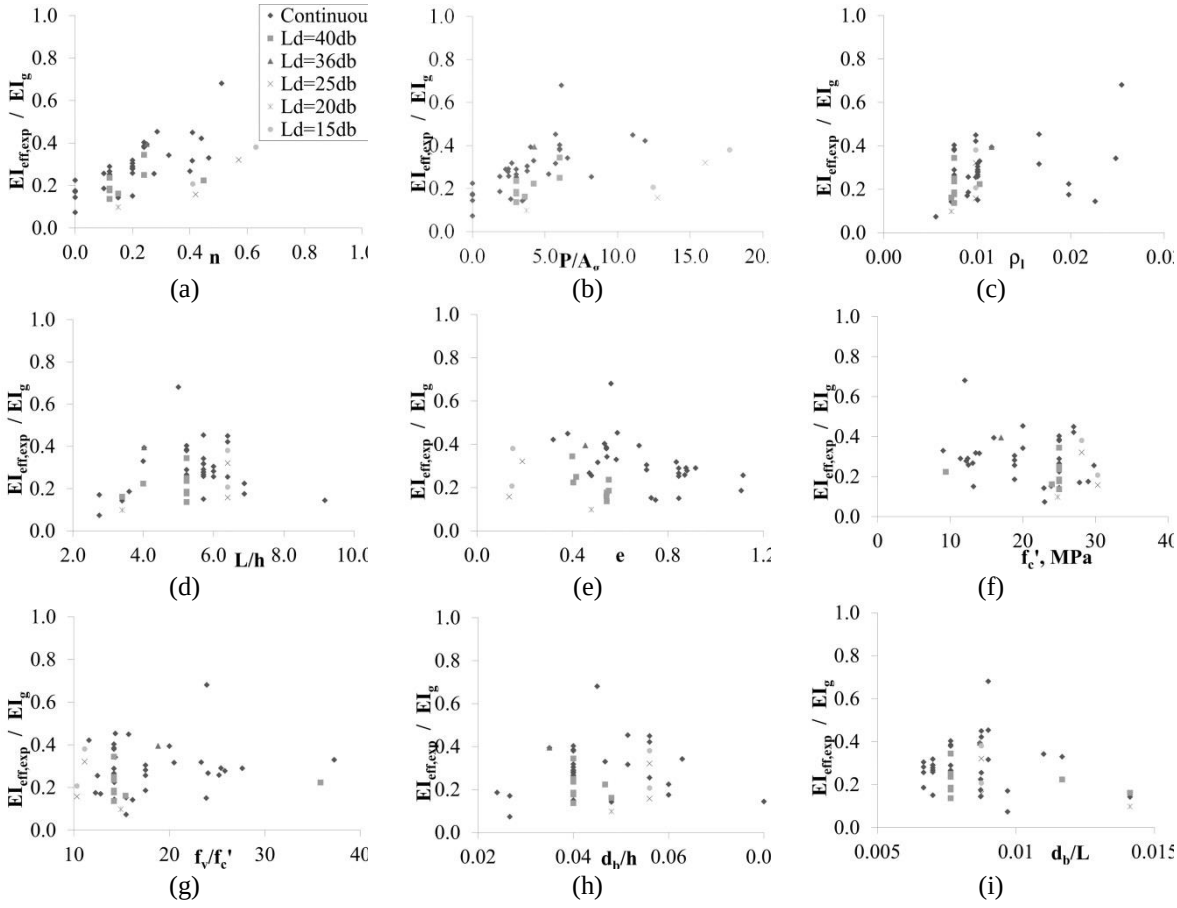


Figure 1 Experimental effective stiffness variations according to key parameters.

The most significant dependence can be observed for axial load level ($P/A_g f_c'$) in which P and A_g specify the axial load and gross cross-section area, respectively (Fig. 1a). However, due to the cluster of data below 7 MPa and increasing scatter beyond that region impeded the interpretation of the dependence of effective stiffness on mean axial stress (P/A_g) (Fig. 1b), additional tests to investigate the column performances beyond 7 MPa are needed for more reliable evaluation. Since the stiffening effect of axial compression on effective stiffness was verified among many researchers in the literature [3, 5-8], a similar response was observed for the columns longitudinally reinforced with plain rebars (Figs. 1a and 1b). The direct correlation between longitudinal reinforcement ratio (ρ_l) and effective stiffness can be attributed to the comparative increase in moment capacity rather than yield deflection with increasing reinforcement ratio (Fig. 1c) [5-8] however additional tests for longitudinal reinforcement ratios beyond 1% can provide better interpretation.

A slight influence of shear span to depth ratio (L/h) [6, 7 and 9] and eccentricity ratio ($e = M_{0.004}/Ph$) [5, 9] on the effective stiffness can be observed (Figs. 1d - 1e). Since the eccentricity ratio is infinite for the beams, the cases with no axial load were not included in Fig. 1e. The weakest interrelation with the column effective stiffness was examined for concrete compressive strength (f_c'), steel yield stress to concrete compressive strength ratio (f_y/f_c'), bar diameter to depth (d_b/h) and shear span ratios (d_b/L) as similar symptoms were attained in literature (Figs. 1f - 1i) [6, 7].

Guideline	Expression (EI_{eff}/EI_g)
ACI 318 [10]	$\begin{cases} 0.35, n < 0.1 \\ 0.70, n \geq 0.1 \end{cases}$
FEMA 356 [11]	$0.5 \leq n + 0.2 \leq 0.7$
ASCE 41 [12]	$0.3 \leq n + 0.2 \leq 0.7$
TEC-07 [13]	$0.4 \leq 4/3n + 0.8/3 \leq 0.8$
EC-8 [14]	$\frac{M_y L}{3EI_g\theta_y}, \theta_y = \frac{\kappa_y L}{3} + 0.013\left(1 + 1.5\frac{h}{L}\right) + 0.13\kappa_y \frac{d_b f_y}{\sqrt{f_c'}}$
Elwood and Eberhard [6]	$0.2 \leq 5/3n + 0.4/3 \leq 0.7$
Biskinis and Fardis [22]*	$a\left(0.8 + \ln\left(\max\left(\frac{L}{h}, 0.6\right)\right)\right)\left(1 + 0.048\min\left(50MPa, \frac{P}{A_g}\right)\right)$

* a is 0.081 for columns and 0.10 for beams.

Table 1 The guideline expressions for effective stiffness.

In line with the experimental data obtained from the column database, the stiffness approximations for columns with deformed rebars given in structural assessment guidelines (Table 1) were evaluated regarding the Figs. 2a and 2b. Since all guidelines predicted effective stiffness of the columns presuming deformed rebars as longitudinal reinforcement, a significant overestimation in effective stiffnesses was monitored for the columns longitudinally reinforced with plain rebars for all levels of axial load as shown in Fig. 2a. Herein, FEMA 356 [11] and TEC-07 (Turkish Earthquake Code – 2007) [13] gave the almost upper bound predictions of effective stiffness for low and high axial load ratios that represent the actual cases for beams and columns, respectively. For Eurocode 8 [14], the moments and curvatures at yield were computed according to the guideline provisions and compared with the aforementioned results of standard section analysis as shown in Figs. 3a - 3b. Herein, the overestimated yield moments were observed to have an increasing dispersion with the axial load as similar to the underestimated yield curvatures. Since the lower bond stress levels of plain rebars and poor bond slip performance enhanced the slip component of the yield deflections, the effective stiffnesses were monitored to be overestimated particularly for low axial load levels. However, for the columns under high axial load ratio, the development of slip induced deflections was not permitted as much as the columns under low axial load and the slip contribution can be expected to be higher for lap-spliced columns regarding the lower bond stress levels. The outcomes of the previous research [20-22] claimed the influence of poor bond performance of plain rebars on the yield deflection, yield strength and effective stiffness of RC columns to be insignificant considering a database including 20 columns reinforced with plain rebars.

Considering the inadequate bond strength along plain rebars that inhibited the full mobilization of yield strength, the yield moments were overestimated with an experimental to prediction ratio of 0.95 [20] and it can be anticipated that the development of yield strength can be inhibited further for lap-spliced columns as compared to the columns with continuous rebars. Thus, this phenomenon was found to be responsible for the reduced mean levels for yield moments (0.92 and 0.69 for continuous and lap-spliced, respectively) with a low scatter as shown in Fig. 3a. Further, the suggested empirical formulation by Biskinis and Fardis [22] (Table 1) was observed to underestimate the effective stiffnesses as compared to EC8-3 while satisfying slightly higher mean and standard deviation (Figs. 3c - 3d). However, the effective stiffness and yield properties of the columns should be evaluated while preventing shear force underestimations or displacement demand overestimations for low effective stiffnesses [7, 20].

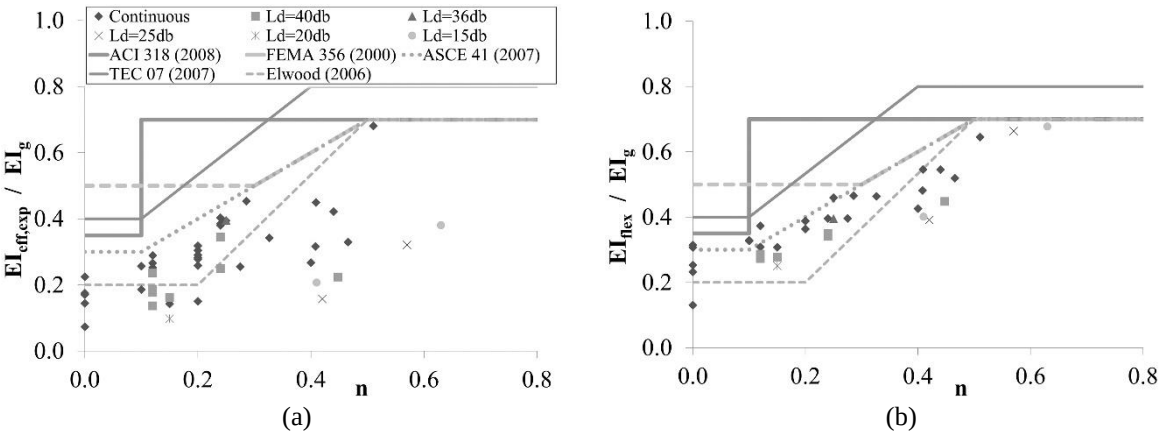


Figure 2 The normalized (a) experimental effective stiffness and (b) flexural stiffness variations

The chord rotations at yield (θ_y) were computed accordingly with the components of flexure, shear and bond slip (Table 1) in order to determine the effective stiffnesses that were overestimated beyond axial load ratios of approximately 0.2 (Fig. 3c) while ignoring the effect of plain rebars. The closest and most reliable estimations were obtained by Elwood et al. [6] for low axial load levels up to the ratio of approximately 0.3, above which the effective stiffness was still overestimated. For all the investigated guidelines, effective stiffness overestimations can be attributed to the consideration of deformed rebars. Regarding the normalized flexural stiffness (EI_{flex}/EI_g), the most consistent predictions were obtained by ASCE 41 [12] and Elwood et al. [6] as shown in Fig. 2b. Since the other tip deflection contributors of shear and bond slip were not accounted, overestimations were majorly observed for the other guidelines (ACI 318, FEMA 356 and TEC-07) for all levels of axial load. Thus, the flexural stiffness estimations were reduced using the three component approach in order to provide more reliable predictions for the effective stiffness of the columns that were longitudinally reinforced with plain rebars.

3 EFFECTIVE STIFFNESS MODELING

The effective stiffness modeling estimations were based on the idea of reducing the flexural stiffness that was computed by standard section analysis pursuant to the adverse effects of shear and bond slip deformations. Since this phenomenon was a consequence of the three component approach in order to estimate column tip deflections, the same idea was utilized in effective stiffness computations for columns. The flexural component (Δ_{flex}) of the column yield deflection (Δ_y) (Eq. 3a) was computed as shown in Eq. 3b by integrating the curvature distribution which was assumed to be linear over the column shear span (L). Eq. 3c enables the calculation of the shear term (Δ_{shear}) of the yield deflection while being comparatively lower regarding the other sources of deformation such as flexure and bond slip. The effective shear area (A_v) and the effective shear modulus (G_{eff}) terms were concerned in order to reflect the deteriorating impact of shear cracking on column stiffness. Bond slip deflections (Δ_{slip}) were computed considering the rigid body rotation of the column as a result of elongation and slip of longitudinal rebars at the interface of column base and footing. Thereby, as shown in Eq. 3d, the bond slip component of yield deflection was calculated using the yield curvature (κ_y), rebar diameter (d_b) and column shear span (L). The bond strength for plain rebars was calculated by recalibrating maximum bond stress as ($\tau_{max} = 0.5\sqrt{f_c'}$). The experimental and analytical yield deflections are compared in Fig. 3e while providing close estimations except five lap-spliced columns for which the yield deflections were underestimated by a factor of 1.58 to 2.31.

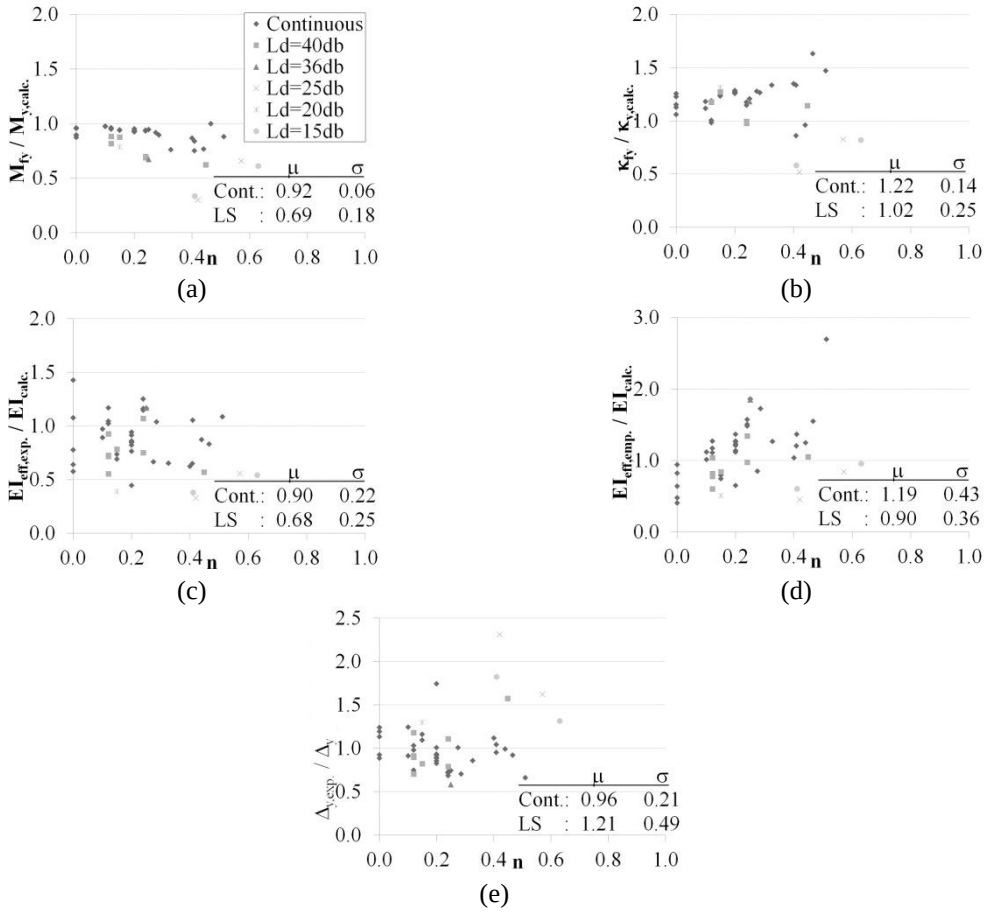


Figure 3 The comparison of experimental to calculated (a) yield moments, (b) yield curvatures, (c) effective stiffnesses according to Eurocode 8 (EC-8, 2005), (d) Biskinis and Fardis [22] and (e) yield deflections

$$\Delta_y = \Delta_{flex} + \Delta_{shear} + \Delta_{slip} \tag{3a}$$

$$\Delta_{flex} = \frac{\kappa_y L^2}{3} = \frac{M_{0.004}}{3EI_{flex}} \tag{3b}$$

$$\Delta_{shear} = \frac{M_{0.004}}{A_v G_{eff}} = \frac{4.8 M_{0.004}}{A_v E_c} \tag{3c}$$

$$\Delta_{slip} = \kappa_y \frac{f_s d_b L}{8\tau_{max}} = \kappa_y \frac{d_b L}{4} \frac{f_y}{\sqrt{f_c'}} \frac{f_s}{f_y} \tag{3d}$$

Further, Eq. 2a was rewritten in terms of dimensionless parameters encapsulating Eq. 2b and Eqs. 3a - 3d that yielded Eq. 4 where $\alpha = EI_{flex}/EI_g$ denotes normalized flexural stiffness and $r_v^2 = I_g/A_g$ is the radius of gyration in loading direction. I_g and A_g denote the gross moment of inertia and gross cross-section area, respectively. The experimental and calculated effective stiffnesses are compared in Table 2.

$$\frac{EI_{eff,calc}}{EI_g} = \frac{\alpha}{1+17.28\alpha\left(\frac{r_v}{L}\right)^2 + 0.75\frac{f_s}{f_y}\frac{f_y}{\sqrt{f_c'}}\frac{d_b}{L}} \tag{4}$$

4 STIFFNESS MODELS

The aforementioned stiffness model acquired by Eq. 4 was further simplified in order to eliminate the need of standard section analysis. Considering design simplifications, the parameters of α and f_s/f_y were estimated in terms of only axial load (n) (Eqs. 5a - 5b) for continuous ($cont$) columns as shown in Fig. 4. However, for lap-spliced columns, the parameters of splice length (L_d/d_b) and shear span to depth ratio (L/h) were embodied in addition to the axial load as presented in Eqs. 6a and 6b.

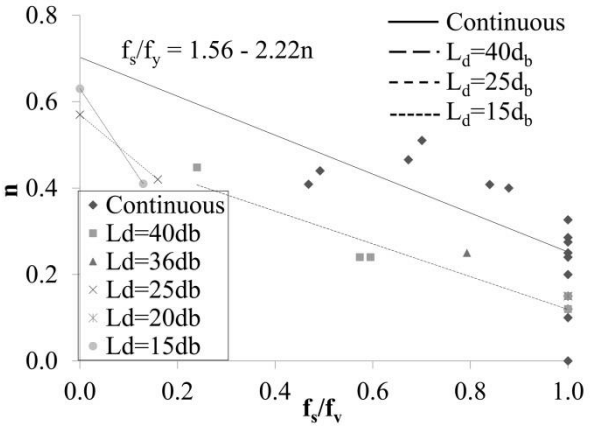


Figure 4 The variation of steel stress with axial load.

For Eqs. 6a - 6b, since the database did not include lap-spliced beams, the equations were valid within database limitations for axial loads in the range between 12 to 63% for lap-spliced columns and between 0 and 51% for the columns with longitudinal rebars. Table 2 demonstrates that reliable estimations could be obtained for the effective stiffnesses. As can be observed in Table 2, the introduced design formulations for continuous and lap-spliced columns had a good correlation with the analytical results. Furthermore, the predicted yield curvatures ($\kappa_{y,cont}$) [4] by Eq. 7a were monitored to correlate well with the continuously reinforced columns.

$$\alpha_{cont} = 0.26 + 0.65n \tag{5a}$$

$$\left(\frac{f_s}{f_y}\right)_{cont} = 1.56 - 2.22n \leq 1.0 \tag{5b}$$

$$\alpha_{LS} = 0.39n^{0.5}\left(\frac{L_d}{d_b}\right)^{0.05}\left(\frac{L}{h}\right)^{0.25} \tag{6a}$$

$$\left(\frac{f_s}{f_y}\right)_{LS} = 0.18n^{-1}\left(\frac{L_d}{d_b}\right)^{0.25}\left(\frac{L}{h}\right)^{-0.8} \leq 1.0 \tag{6b}$$

$$\kappa_{y,cont} = 2.1\frac{\varepsilon_y}{d} \tag{7a}$$

$$\kappa_{y,LS} = \kappa_{y,cont}\left(0.75n^{-0.06}\left(\frac{L_d}{d_b}\right)^{0.16}\left(\frac{L}{h}\right)^{-0.37}\right) = 1.575\left(\frac{\varepsilon_y}{d}\right)^{-0.06}\left(\frac{L_d}{d_b}\right)^{0.16}\left(\frac{L}{h}\right)^{-0.37} \tag{7b}$$

$$\frac{EI_{eff,calc}}{EI_g} = \frac{\alpha}{1+\beta\frac{d_b}{L}} \tag{8}$$

However, since this formulation tended to yield overestimated results for lap-spliced columns, Eq. 7a was modified for lap-spliced columns with regard to axial load, splice length and shear span to depth ratio (Eq. 7b). For the equations, ε_y and d identify the steel yield strain and column effective depth, respectively. In addition, Eq. 4 can be further simplified to yield Eq. 8 by ignoring the shear term in the denominator since it constitutes at most 3% of the tip deflection. In Eq. 8, α can be obtained by Eqs. 5a, 6a and the β constant has a value of 50 for plain reinforcement. Thus, Eq. 8 gave more realistic estimations (Table 2) as compared to the effective stiffness predictions of the previous studies that were related to the RC columns reinforced with deformed rebars [6, 7]. For the Eq. 8, the difference between two cases was ignored and a more general formula was suggested for the sake of simplicity.

Column Type	*	$\frac{EI_{eff,calc}}{EI_{eff,\exp}}$					$\frac{\Delta_{y,\exp}}{\Delta_y}$	$\frac{\alpha_{calc}}{\alpha_{pred}}$	$\frac{\kappa_{y,calc}}{\kappa_{y,pred}}$
		EC-8	a	b	c	d	e	f	g
Continuous (Cont.)	μ	0.90	1.19	1.08	1.04	1.02	0.96	0.97	1.02
	σ	0.22	0.43	0.21	0.25	0.26	0.21	0.12	0.11
Lap-Spliced (LS)	μ	0.68	0.90	0.95	0.91	0.98	1.21	1.06	1.02
	σ	0.25	0.36	0.36	0.35	0.32	0.49	0.12	0.09
Average	μ	0.83	1.10	1.04	1.00	1.01	1.04	1.00	1.02
	σ	0.25	0.43	0.27	0.28	0.28	0.33	0.13	0.10

* μ and σ: Mean and standard deviations for experimental to calculated ratios.
a. Biskinis and Fardis [22]
b. SSA: Standard section analysis
c. $\alpha, f_s/f_y$: Cont: Eqs. 5a - 5b, LS: Eqs. 6a - 6b
d. α : Cont: Eq. 5a, LS: Eq. 6a, $\beta = 50$
e. Eq. 1a, Eq. 3a - 3d
f. Cont: Eq. 5a, LS: Eq. 6a
g. Cont: Eq. 7a, LS: Eq. 7b

Table 2 Mean and standard deviation variations.

Herein, the suggested values for $\alpha = 0.45 + 2.5\text{n}$ and $\beta = 110$ in literature [7] were shown to overestimate the effective stiffness of RC columns reinforced with plain rebars since the formulations were suggested primarily for RC columns with deformed rebars. In comparison with Eq. 5a, it can be inferred that the use of plain longitudinal rebars induced a lower rate of increase of flexural stiffness with axial load as compared to the deformed longitudinal rebars. All design formulations were compared in Table 2 and good estimations were provided since the terms of $\Delta_y, \alpha, \kappa_y$ could be predicted contiguous to experimental measurements. The recommended effective stiffness predictions for continuous columns were defined for upper and lower bounds for force based and displacement based analysis in case of either underestimating shear demands or overestimating displacement demands, respectively. Considering 90% of confidence level, the upper and lower bounds for effective stiffness were defined as shown in Eqs. 9a - 9c (Fig. 5a). For lap-spliced columns, the ratio of effective stiffness to gross stiffness was recommended to have a constant value of 0.2, since no significant trend was observed for varying splice lengths used in the database (Fig. 5b).

$$\left(\frac{EI_{eff}}{EI_g}\right)_{lowerbound} = 0.15 \leq \frac{1}{4}n + \frac{1}{8} \leq 0.25 \quad (9a)$$

$$\left(\frac{EI_{eff}}{EI_g}\right)_{mean} = 0.20 \leq \frac{5}{8}n + \frac{11}{80} \leq 0.45 \quad (9b)$$

$$\left(\frac{EI_{eff}}{EI_g}\right)_{upperbound} = 0.25 \leq n + \frac{3}{20} \leq 0.65 \quad (9c)$$

As a final remark, in common practice, the circular and rectangular cross sections generally pertain to RC bridge and building columns with low to high axial load level, respectively. Thus, circular columns are liable to possess lower axial load and d_b/L values with shear spans generally longer than ordinary building columns. Therefore, although all the formulations implemented in this research were based on a database of rectangular columns, the suggested formulations can also be utilized for circular columns regarding the range of variables under investigation.

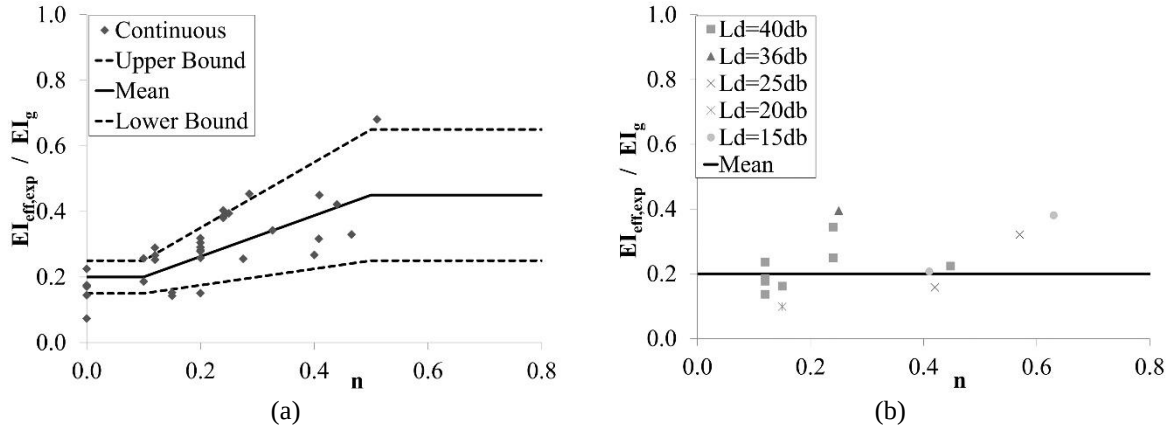


Figure 5 The effective stiffness recommendations for (a) cont. and (b) LS columns with plain rebars.

5 CONCLUSIONS

Predicting the effective stiffness for RC members is crucial in assessment and strengthening since the seismic characteristics and consequent response of RC structures is majorly influenced by cracking under gravity and lateral forces. The current guideline recommendations on effective stiffness of RC columns may mislead for plain reinforcement due to the major postulation of deformed rebars as longitudinal reinforcement. Thus, a RC column database was constituted by monotonic and reversed cyclic tests of 47 columns in which 33 columns were continuously reinforced and the remaining were spliced with various splice lengths. In the analysis of lap-spliced columns, the adopted spliced steel model from literature was modified using a lap-spliced beam database reflecting the failure mechanism of plain rebars. The analyses approved the dependence of effective stiffness on axial load and longitudinal reinforcement ratio as compatible with previous researches on deformed rebars. In this sense, it was ascertained that due to the shortcomings of the current structural guidelines upon utilization of longitudinal plain rebars, column effective stiffnesses were overestimated. Therefore, more reliable effective stiffness predictions were obtained by reducing the flexural stiffness of the columns regarding the deflection constituents of shear and bond slip on the basis of the three component approach while taking plain rebars into account. In addition, upper and lower bound effective stiffness expressions were recommended that can be utilized for force and displacement based assessment of RC structures, respectively.

REFERENCES

[1] Hage SE, MacGregor JG. *Second Order Analysis of RC Frames.*Univ. of Alberta; 1974.

[2] Paulay P, Priestley MJN. *Seismic Des. of RC and Masonry Buildings.* NY: J. Wiley; 1992.

[3] Mehanny SSF, Kuramoto H, Deierlein GG. Stiffness Modeling of RC Beam-Columns for Frame Analysis. *ACI Str. J.*; 98 (2): 215-25, 2001.

[4] Priestley MJN. *Myths and Fallacies in Earthq. Eng., Rev*. 9 M.Milne Lec.; Italy: 2003.

[5] Khuntia M, Ghosh SK. Flexural Stiffness of Reinforced Concrete Columns and Beams: Analytical Approach. *ACI Structural Journal*; 101 (3): 351-63, 2004.

[6] Elwood KJ, Eberhard MO. *Effective Stiffness of RC Columns*; Univ. of Calif., 2006.

[7] Elwood KJ, Eberhard MO. Effective Stiffness of Reinforced Concrete Columns. *ACI Structural Journal*; 106 (4): 476-83, 2009.

[8] Kumar R, Singh Y. Stiffness for RC Members for Seismic Analysis. *ACI Str.J.*; 107 (5): 607-15, 2010.

[9] Mirza SA., Flexural Stiffness of Rectangular RC Columns. *ACI Str.J*; 87(4): 425-35, 1990.

[10] ACI Committee 318. *Building Code Requirements for Structural Concrete and Commentary*. American Concrete Institute; Farmington Hills; MI: 2008.

[11] FEMA 356. *Prestandard and Commentary for Seismic Rehabilitation of Buildings. Federal Emergency Management Agency*; Washington; DC: 2000.

[12] ASCE 2007b. *Seismic Rehabilitation of Existing Buildings*, ASCE/SEI 41, Supplement I. American Society of Civil Engineers; Reston; VA: 2007.

[13] Turkish Earthquake Code (TEC). *Regulations on Structures Constructed in Disaster Regions*. Ministry of Public Works and Settlement; Ankara: 2007.

[14] European Committee for Standardization. *Design Provisions for Earthquake Resistance of Structures* EC-8; Brussels: 1994-2003.

[15] Elwood KJ, Matamoros A, Wallace JW, Lehman D, Heintz J, Mitchell A et al. Update to ASCE/SEI 41 Concrete Provisions. *Earthquake Spectra*; EERI; 23 (3): 493-523, 2007.

[16] Ozcan, O. Stiffness Modeling of RC Columns Reinforced with Plain Rebars, *Structural Engineering and Mechanics*, 50 (2), 163-180, 2014.

[17] Xiao Y, Ma R. Seismic Retrofit of RC Circular Columns using Prefabricated Composite Jacketing. *ASCE Journal of Structural Engineering*; 123 (10): 1357-64, 1997.

[18] Hassan MN. *Splice Tests of Plain Steel Bars in Concrete*. PhD Th.; Univ. of Sask.: 2011.

[19] Mander JB, Priestley MJN, Park R. Theoretical Stress-Strain Model for Confined Concrete. *Journal of Structural Engineering*; 114 (8): 1804-26, 1988.

[20] Fardis, M.N., Seismic Design, Assessment and Retrofitting of Concrete Buildings Based on EN-Eurocode8, Springer Geotechnical, Geological and Earthquake Eng., V8, 2009

[21] Fardis, M.N., Performance and displacement based seismic design and assessment of concrete structures in the model code 2010, *Struct. Concrete*, 14(3), 215-229, 2013

[22] Biskinis, D.E. and Fardis, M.N., "Deformations at flexural yielding of members with continuous or lap-spliced bars", *Struct. Concrete*, 11(3), 127-138, 2010.

COMPDYN 2015
5th ECCOMAS Thematic Conference on
Computational Methods in Structural Dynamics and Earthquake Engineering
M. Papadrakakis, V. Papadopoulos, V. Plevris (eds.)
Crete Island, Greece, 25–27 May 2015

CORRELATION BETWEEN THE PROBABILISTIC SEISMIC ASSSMENT OF FRAME STRUCTURES WITHOUT AND WITH ADDED DAMPERS

L. Landi[1], C. Vorabbi[1], and P.P. Diotallevi[1]

[1] Department of Civil, Chemical, Environmental and Materials Engineering-DICAM, University of Bologna
Viale Risorgimento, 2 - 40136 Bologna - Italy
e-mail: l.landi@unibo.it, cristina.vorabbi@studio.unibo.it, Pierpaolo.diotallevi@unibo.it

Keywords: Nonlinear fluid viscous dampers, Nonlinear dynamic analyses, Probabilistic method, Median, Dispersion, SAC/FEMA.

Abstract. *This paper deals with the parameters which influence the probability of reaching the near collapse limit state of RC frame structures equipped with nonlinear fluid viscous dampers. The study can be divided into two steps. The first aims to assess how the median and the dispersion of seismic demand can vary in the RC frame structures equipped with nonlinear fluid viscous dampers, considering a wide set of ground motions; these parameters have been compared with those obtained for RC structures without dampers. The second step evaluates the expression in closed form given in the 2000 SAC/FEMA method to assess the annual probability of failure of RC structures. This calculation has been performed using the parameters obtained in the previous step. The annual probability of failure has been estimated for the RC frame structures with and without dampers, considering a wide set of ground motions and different method to approximate the hazard curve. The adopted case study is a frame configuration characterized by three bays and six floors. The analyses have allowed to evaluate the variability of the terms of the closed form expression proposed in the 2000 SAC/FEMA method, and their influence on the definition of the annual probability of failure.*

1 INTRODUCTION

Motivated by the recent seismic events, there has been an increase of concern towards seismic assessment and retrofit of existing buildings [1-3]. One of the innovative technique of seismic retrofit is the insertion of supplemental damping systems in existing buildings. They are activated by the movement of the main structural system and reduce the overall dynamic response of the structure. The dissipation of energy is diverted to these mechanical devices that can be inspected and even replaced after an earthquake [1]. Among them, those considered in this paper are passive energy dissipation systems, which dissipate a portion of the seismic energy input to a structure without external power source. An efficient passive energy dissipation system is made by nonlinear fluid viscous dampers, which have been also considered in this paper. They are rate dependent devices which provide a velocity dependent force. The typology considered is orificed fluid dampers, which dissipate energy by a flow of fluid inside a cylindrical closed container, which is forced to flow through the action of a piston. Nonlinear fluid viscous dampers have the characteristic of having a lower velocity exponent than the unity. In this way, in the event of a velocity spike, the force in the viscous damper is controlled to avoid overloading the dampers or the bracing system to which it is connected [1, 4]. Their advantages are the reduction of damper forces at high velocities, the supply of higher dampers forces at low speed and the dissipation of a larger amount of energy than the other dampers. Since the assessment of seismic response is considerably complex for the presence of a large number of uncertainties, it is better to adopt a probabilistic approach. For this reason, a probabilistic approach has been followed in this paper, in particular the 2000 SAC/FEMA method [5]. This approach provides a closed form expression to evaluate the annual probability of exceeding a specified performance level for a given structure. The variability of terms inside the closed form expression and their influence on the probability of exceeding a specified performance level, have been analyzed here, considering the near collapse limit state, a wide set of ground motions and different methods to approximate the hazard curve. The study has been performed without applying scaling factors to the earthquake records, but considering different records for increasing values of seismic intensity.

The considered case study is a RC frame, characterized by three bays and six floors, designed to resist only gravity loads; nonlinear fluid viscous dampers have been inserted for the seismic retrofit. The seismic demand parameters here considered are the maximum displacement at the top of the structure and the maximum interstorey drift. The probabilistic assessment on the basis of the results obtained from nonlinear dynamic analyses has been performed for those parameters. Nine return periods have been chosen to identify nine values of seismic intensity and twenty ground motions have been selected for each of them. The analyses have been reported considering two different models for the plastic hinges behaviour: the first model with post peak strength deterioration, the second model without it. In the first case the results have been obtained only for the records which converged for both structures, in the second case the results have been obtained for all the records considered, that is 180 for both structures.

2 PROBABILISTIC APPROACH

Among the probabilistic approaches there is the 2000 SAC/FEMA method, which thanks to its mathematical simplicity and comparatively light computational effort, provides directly a measure of the unconditional risk for a given structures located in a known seismic environment. The original formulation of the method was developed for steel moment resisting frames [5].

2.1 Description of the basis method

The 2000 SAC/FEMA method is based on the realization of a performance objective expressed as a specified performance level. Performance levels are quantified as expressions relating to generic structural variables "demand" and "capacity" [5].

2.1.1 Probability assessment formulation

The probability theory is applied through the representation of the three random elements of the problem:

1) the ground motion intensity, represented by the spectral acceleration S_a calculated approximately at the first natural period of the structure and for 5% or higher damping;
2) the displacement demand D;
3) the displacement capacity C.

Both displacement demand and capacity are measured in terms of maximum interstorey drift angle. The likelihood of various levels of future intense ground motions at the site is represented in the standard way by the function $H(s_a)$, which gives the annual probability that the (random) intensity S_a at the site will equal or exceed level s_a [5]. In order to obtain criteria based on required performance objectives, the probabilistic representation of S_a, D and C must be folded together. This folding together takes place in three phases; the first relates S_a and D to produce a drift hazard curve $H_D(d)$, which provides the annual probability that the drift demand D exceeds any specified value d. The second combines the curve obtained in the previous phase with the displacement capacity C, giving rise to P_{PL}, which is the annual probability that the performance level is not being met (e.g., the annual probability of collapse or the annual probability of exceeding the life safety level). Using the total probability theorem, $H_D(d)$ becomes, in discrete form:

$$H_D(d) = P[D \geq d] = \sum_{allx_i} P[D \geq d \mid S_a = x_i] P[S_a = x_i] \tag{1}$$

The second factor within the sum, that is the likelihood of a given level of spectral acceleration $P[S_a=x]$, can be easily obtained from the standard hazard curve $H(S_a)$. The first factor, that is the likelihood $P[D \geq d]$ that the drift exceeds d given that the value of S_a is known, can be obtained through structural response analysis [5]. In continuous, Eq. (1) becomes:

$$H_D(d) = \int P[D \geq d \mid S_a = x] \left| dH(x) \right| \tag{2}$$

where $|dH(x)|$ is the absolute value of the differential of the spectral acceleration hazard curve. Using the total probability theorem again P_{PL} becomes in discrete form:

$$P_{PL} = P[C \leq D] = \sum_{alld_i} P[C \leq D \mid D = d_i] P[D = d_i] \tag{3}$$

The second factor, the likelihood of given displacement demand level $P[D=d]$, can be determined by the drift hazard curve derived in Eq. (2). The first factor, the likelihood that the drift capacity is less than a specified value d given that the drift demand equals that value, $P[C \leq D | D=d]$ can be assumed, in a first approximation, independent of the information about the drift level itself, permitting this term to be simplified as below. The continuous form is:

$$P_{PL} = \int P[C \leq d] \left| dH_D(x) \right| \tag{4}$$

The second factor $|dH_D(d)|$ is defined as the absolute value of the differential of the drift demand hazard curve.

2.1.2 Probability assessment in closed form

In principle, Eqs. (2) and (4) can be solved numerically for any assumption about the form of the probabilistic representation of the three elements $H(s_a)$, D and C. Three approximations of the probabilistic representations of the three terms above have been proposed in order to obtain a closed form expression of Eq. (4).

The first assumes that the site hazard curve can be approximated in the region around P_{PLSa} (in the region of hazard levels close the limit state probability P_{PL}) by the form:

$$H(s_a) = P[S_a \geq s_a] = k_o s_a^{-k} \tag{5}$$

which implies that the hazard curve is linear on a log-log plot in the region of interest. The second assumes that the median drift demand $\hat{D}$ can be represented approximately in the region around P_{PLSa}, by the form:

$$\hat{D} = a(S_a)^b \tag{6}$$

Lastly, the third assumes that the drift demand D is lognormally distributed about the median with the standard deviation of the natural logarithm, $\beta_{D|Sa}$; this definition will be considered as dispersion. Also the drift capacity C is assumed to be lognormally distributed with dispersion β_C. Making use of Eq. (6) and of the lognormal distribution, the first factor in Eq. (2) can be assumed as:

$$P[D \geq d \mid S_a = x] = 1 - \Phi\left(\ln\left[d/ax^b\right]/\beta_{D|S_a}\right) \tag{7}$$

in which Φ is the widely tabulated standardized Gaussian distribution function. Using this result and Eq. (5), Eq. (2) becomes:

$$H_D(d) = P[D \geq d] = H(s_a^d)\exp\left[\frac{1}{2}\frac{k^2}{b^2}\beta_{D|S_a}^2\right] \tag{8}$$

in which s_a^d is defined as the spectral acceleration corresponding to the drift level d, that is the inverse of Eq. (6):

$$s_a^d = (d/a)^{1/b} \tag{9}$$

Assuming that the drift capacity C has a median value $\hat{C}$ and that is lognormally distributed with dispersion β_C, the first factor of Eq. (2) becomes:

$$P[C \leq d] = \Phi\left(\ln\left[d/\hat{C}\right]/\beta_C\right) \tag{10}$$

Substituting and carrying out the integration of Eq. (2), it can be obtained the required relation, i.e. the expression in closed form of Eq. (4):

$$P_{PL} = H\left(s_a^{\hat{C}}\right)\exp\left[\frac{1}{2}\frac{k^2}{b^2}\left(\beta_{D|S_a}^2 + \beta_C^2\right)\right] \tag{11}$$

where s_a^C is the spectral acceleration associated to the attainment of the capacity. From Eq. (11) it is possible to note how the effect of the dispersion increases the P_{PL} through the exponential correction factor $\exp[(1/2)(k^2/b^2)\ (\beta_{D|Sa}^2+\beta_C^2)]$. It is so called because it corrects the total randomness, both in drift and in capacity.

3 THE CONSIDERED CASE STUDY

The considered case study is a RC frame characterized by three bays and six floors (Fig. 1). This frame has been designed to resist only gravity loads. Nonlinear fluid viscous dampers have been inserted so that the structure can sustain a high level of seismic action. Dampers of mechanical properties already known have been considered in this paper [6], since its aim is the study of the parameters which affect the property of reaching the near collapse limit state for RC structure equipped with given nonlinear fluid viscous dampers. With regard to the mechanical properties of dampers, the exponent of velocity is α=0.5, the supplemental damping provided by the damping system is equal to 24.5% and the damping coefficient corresponds to 556 kN $(s/m)^{0.5}$. As for the geometry of the structure, each bay is 6 m wide and each interstorey is 3.2 m high. The beams are 30 cm wide and 60 cm deep in all floors. On the ground floor the columns at the edges have a square cross section with a 40 cm side length, while the central ones with a 45 cm side length; on the first floor both columns have square cross section 40x40 cm; on the third floor 35x35 and on the last three floors 30x30 cm. A concrete with a cylinder strength equal to 28 MPa and a steel with a yield strength equal to 450 MPa have been assumed in this study. The seismic weights are 561.6 kN for the sixth floor, 833.4 kN for the fifth and fourth floor, 838.6 kN for the third floor, 849.8 kN for the second floor and 859.2 kN for the first floor. The structure is assumed to be located in Santa Sofia, Italy.

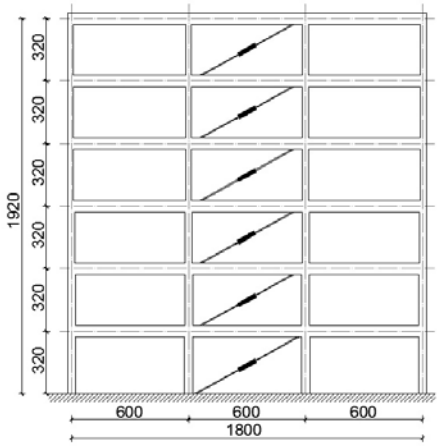


Figure 1: Geometrical characteristics of the considered RC frame (dimensions in cm).

Since the aim of this paper is the probabilistic assessment of the seismic response of RC structures equipped with nonlinear fluid viscous dampers, it is necessary to carry out a wide number of nonlinear dynamic analysis and consequently to select a high number of spectrum-compatible recorded ground motions. Nine return periods have been considered in this study (T_R=30, 50, 101, 201, 475, 664, 975, 1950 and 2475 years) and for each of them, 20 recorded ground motions characterized by an elastic acceleration response spectrum compatible with the code spectrum [7] have been selected through the software Rexel [8].

The code elastic response spectrum for the assumed site and for a soil type C has been determined for each considered return period [7]. Given the site and the soil type, the PGA for T_R=475 is equal to 0.29 g. Each record has been scaled to the code design value of PGA. Figure 2 shows the spectra [9] of the 20 selected records for T_R=475years and their average spectrum compared to the code spectrum.

The nonlinear dynamic analyses have been performed using a concentrated plasticity model implemented in a FE computer program (SAP2000) [10]. A moment-rotation curve has

been assigned to the plastic hinges, located at the ends of each element. The moment-rotation curve has been identified by assigning the yielding and the ultimate bending moments and the corresponding chord rotations, which have been provided by empirical relations given in the Commentary to the National code and similar to those of Panagiotakos and Fardis [11].

In order to carry out assessments with a different number of results, two different moment-rotation curves have been considered. At first, a moment rotation curve with post peak strength deterioration has been used (bilinear moment rotation curve, Figure 3a); then a moment-rotation curve without post peak strength deterioration (trilinear moment rotation curve, Figure 3b) has been considered to ease the convergence of the large number of analyses and to obtain a greater number of results for the probabilistic assessment.

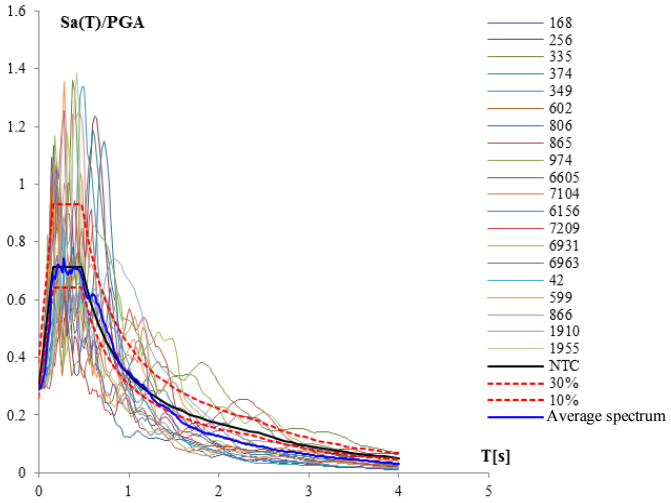


Figure 2: Spectra of the 20 selected compatible records for T_R=475 years, average spectrum of the selected records, code spectrum and tolerance limits (30 % and 10%).

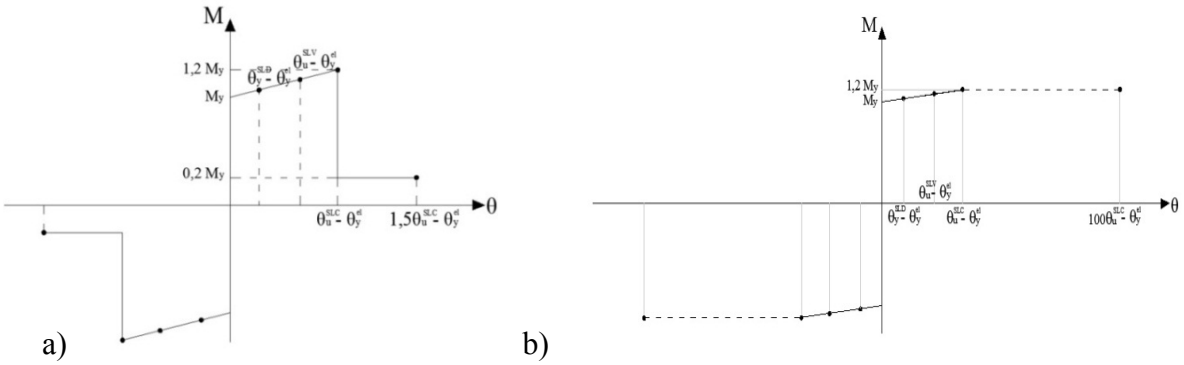


Figure 3: a) bilinear moment-rotation curve with post peak strength deterioration, assigned to plastic hinges ; b) trilinear moment-rotation curve without strength deterioration, assigned to plastic hinges.

The obtained results are grouped in three cases, as shown in Table 1. In the first case a bilinear moment rotation curve (Figure 3a) is considered and the probabilistic assessment is made on 170 and 104 records respectively for the structure with and without dampers. In the second case the same plastic hinge model of the first case is adopted, but the probabilistic assessment is made on the same number of records, i.e. 104, for both structures. In the third case a trilinear moment rotation curve (Figure 3b) is assumed and the probabilistic assessment is performed on 180 records for both structures.

Case 1)	Bilinear moment-rotation curve with post peak strength deterioration	
	Structure with dampers	Structure without dampers
	170 results	104 results
Case 2)	Bilinear moment-rotation curve with post peak strength deterioration	
	Structure with dampers	Structure without dampers
	104 results	104 results
Case 3)	Trilinear moment-rotation curve without post peak strength deterioration	
	Structure with dampers	Structure without dampers
	180 results	180 results

Table 1: The three cases in which the performed analyses have been grouped.

4 RESULTS AND COMMENTS

4.1 Probabilistic seismic demand analysis

The following parameters have been examined for each nonlinear dynamic analysis:

- profiles of maximum displacement, obtained by the envelope of the maximum displacements which occur on each floor during the seismic event;
- profiles of maximum interstorey drift, which represent the envelope of maximum interstorey drifts occurring during the seismic event.

Once obtained the maximum displacement and maximum interstorey drift profiles, the maximum displacement on the top of building (D_{roof}) and the maximum interstorey drift (δ_{max}) along the height have been determined for each record and each return period. The values thus obtained have been plotted in graphs, which have a parameter representing the seismic intensity ($S_a(T_1)$, spectral acceleration at the first natural period of the structure and for 5% damping) as abscissa and a parameter representing the seismic demand (D_{roof} or δ_{max}) as ordinate. In Figures 4 and 5 the points D_{roof}-$S_a(T_1)$ and δ_{max}-$S_a(T_1)$ obtained with each record have been represented for the structure with and without dampers, respectively.

In order to perform the probabilistic assessment, the median and the dispersion values have been determined. As for the median, it is assumed from the scientific literature [5] that the distribution of median values of the seismic demand parameters follows the relation:

$$MeD = a\left(S_a(T_1)\right)^b \tag{12}$$

where MeD is the median value of demand parameter D, $S_a(T_1)$ is the spectral acceleration and a, b are constants deriving from a regression analysis. These constants have been identified for D_{roof} and δ_{max} once the points MeD_{roof}-$S_a(T_1)$ and $Me\delta_{max}$-$S_a(T_1)$ have been determined for each return period.

As for the dispersion, two different dispersion formulations have been considered. The first considers a variable dispersion with the seismic intensity. The dispersion for each return period is obtained through the formulation proposed from scientific literature: standard deviation of demand parameters of natural logarithm; it is indicated with the notation β_{regr} and it is obtained through the expression:

$$\beta_{D|S_a} = \sqrt{\frac{\sum_k \left(\ln x_k - \hat{\mu}\right)}{n}} \tag{13}$$

where n is the number of values and $\hat{\mu}$ is the median, determined as the mean of the natural logarithm of the results:

$$\hat{\mu} = \frac{\sum_k \ln x_k}{n} \tag{14}$$

A regression analysis has been carried out on the obtained dispersion values determining the parameters of the straight line which interpolates the dispersion values best:

$$\beta_{D|S_a} = a + bS_a(T_1) \tag{15}$$

In order to evaluate the accuracy of the obtained correlation, the parameters R^2 (determination index) and the errors (mean and standard deviation of residues) have been considered. The second formulation, denoted with β_{cost}, considers a parameter of constant dispersion with seismic intensity. This is obtained performing a regression analysis of ln$D$ on lnS_a on the totality of the results. The value thus obtained is the standard deviation of the residues.

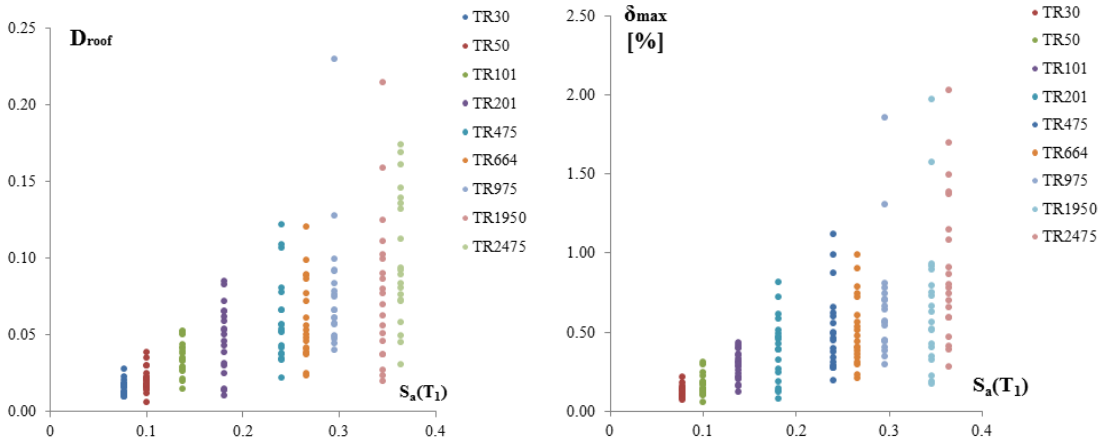


Figure 4: D_{roof} - $S_a(T_1)$ and δ_{max} - $S_a(T_1)$ points for the structure with dampers.

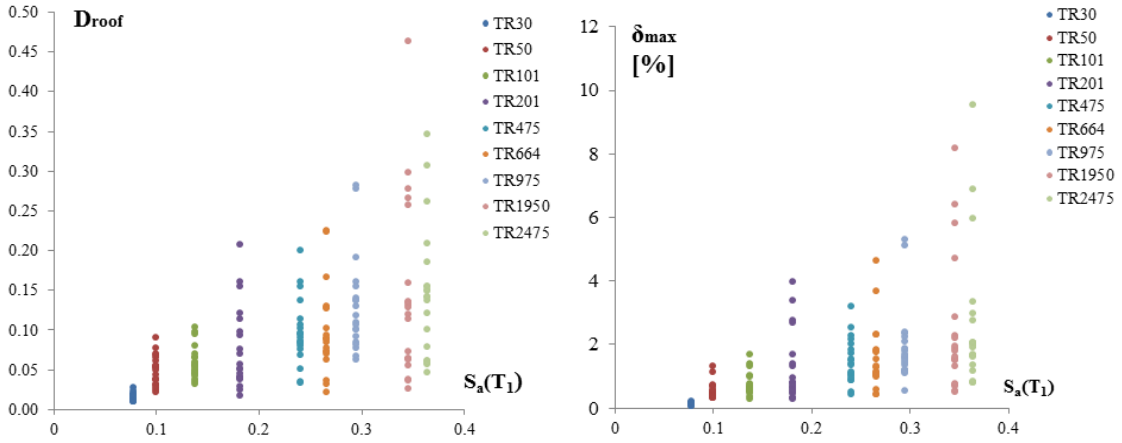


Figure 5: D_{roof} - $S_a(T_1)$ and δ_{max} - $S_a(T_1)$ points for the structure without dampers.

Table 2 shows the expressions of median and dispersion of demand parameters for the analyses of Case 1 (see Table 1). Figures 6 and 7 illustrates for the same case the graphs of median and dispersion of demand parameters as a function of seismic intensity. The same results are reported in Table 3, Figures 8 and 9 for the analyses of Case 2, and in Table 4 and Figures 10 and 11 for the analyses of Case 3. Figure 6 shows that the median roof displacements (D_{roof}) of the structure without dampers are greater than those of the structure with dampers, as expected. With regard to the dispersion values (β_{regr}, Figure 6b) both for the structure with dampers and without dampers, it increases with seismic intensity.

D_{roof}		δ_{max}	
Structures with dampers 170 records	Structures without dampers 104 records	Structures with dampers 170 records	Structures without dampers 104 records
$MeD_{roof} = 0.2114 \cdot S_a^{0.9872}$	$MeD_{roof} = 0.2129 \cdot S_a^{0.8059}$	$Me\delta_{max} = 2.041 \cdot S_a^{1.0755}$	$Me\delta_{max} = 4.1216 \cdot S_a^{1.1327}$
$\beta_{regr}=0.3385+0.3894S_a$	$\beta_{regr}=0.3274+0.2272S_a$	$\beta_{regr}=0.3359+0.4341S_a$	$\beta_{regr}=0.4016-0.2375S_a$
$\beta_{cost} = 0.4523$	$\beta_{cost} = 0.5252$	$\beta_{cost} = 0.4595$	$\beta_{cost} = 0.56296$

Table 2: Expressions of median and dispersion for D_{roof} and δ_{max}, Case 1.

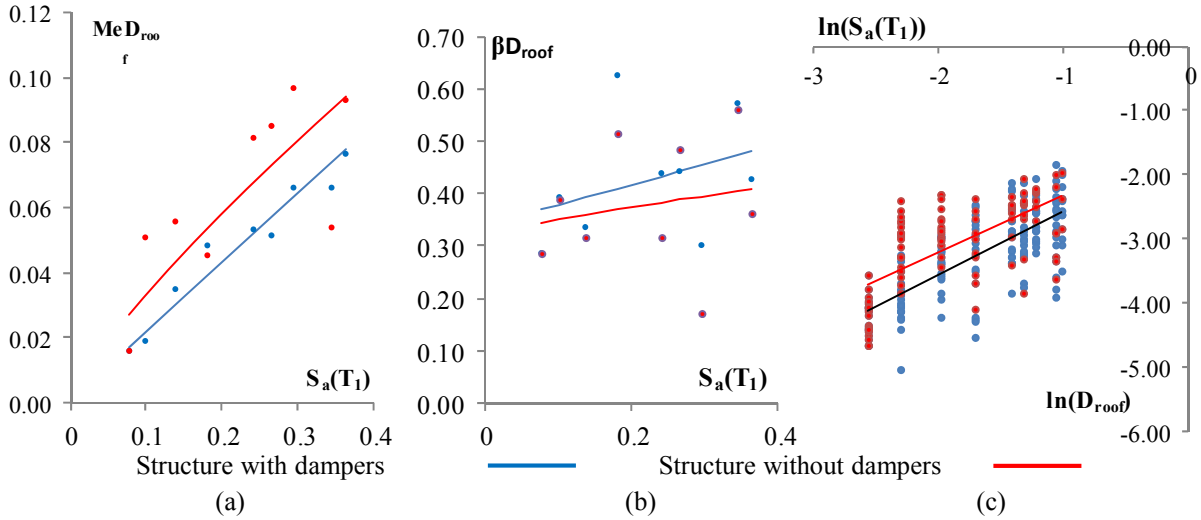


Figure 6: Case 1: a) MeD_{roof}- $S_a(T_1)$; b) βD_{roof}- $S_a(T_1)$; c) $\ln D_{roof}$-$\ln S_a(T_1)$

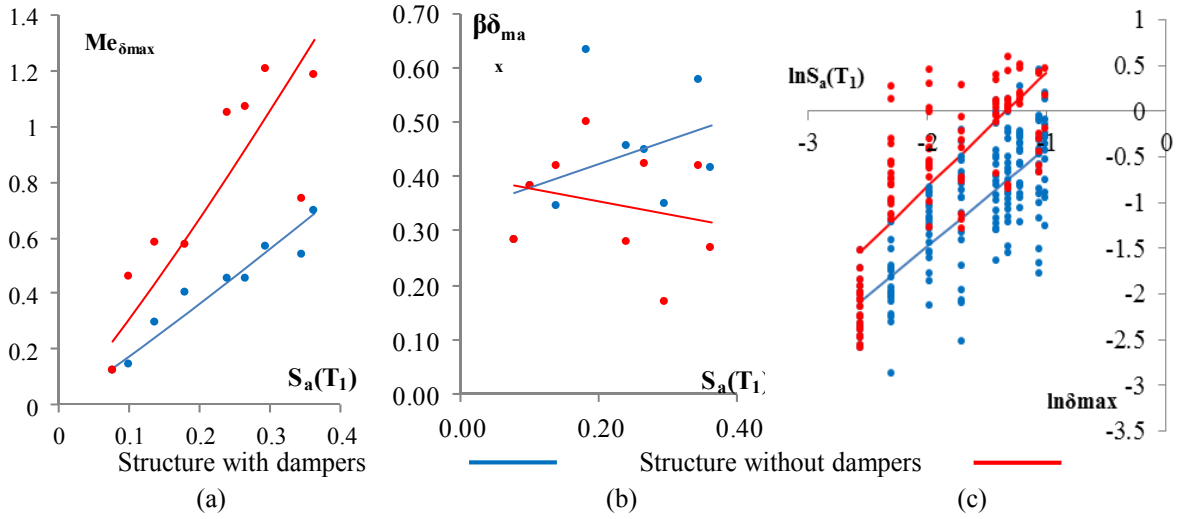


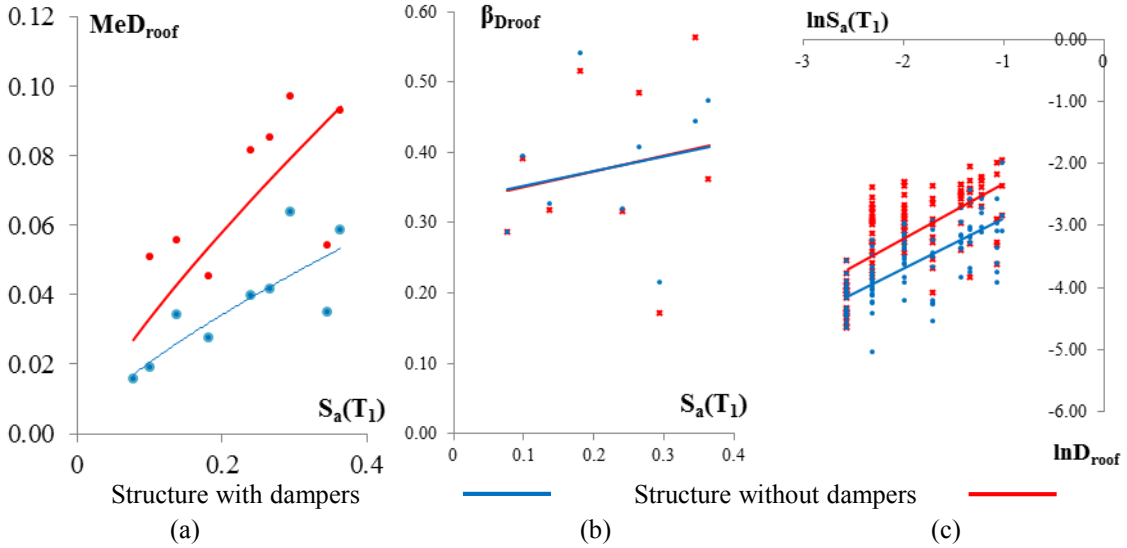
Figure 7: Case 1: a) $Me\delta_{max}$- $S_a(T_1)$; b) $\beta\delta_{max}$- $S_a(T_1)$; c) $\ln\delta_{max}$-$\ln S_a(T_1)$

Moreover, the dispersion of the structure with dampers is greater than that without dampers; this is a trend not in line with the expectations. Lastly, Figure 6c illustrates that, in accordance with Figure 6a, the displacements of the structure with dampers are smaller than those obtained for the structure without dampers. Considering the parameter of constant dispersion (β_{cost}, Table 2), the dispersion of the structure without dampers is greater than that with dampers; therefore the trend of β_{cost} is in line with the expectations. As regards Fig. 7 the same remarks are made for the maximum interstorey drifts (δ_{max}); in addition it is possible to observe that: the variable dispersion (β_{regr}) decreases for the structure without dampers when seismic

intensity increases and this trend is not in line with the expectations; as for the parameter of constant dispersion (β_{cost}), the values of dispersion are slightly higher than those obtained for the maximum displacement at the top of the building (D_{roof}).

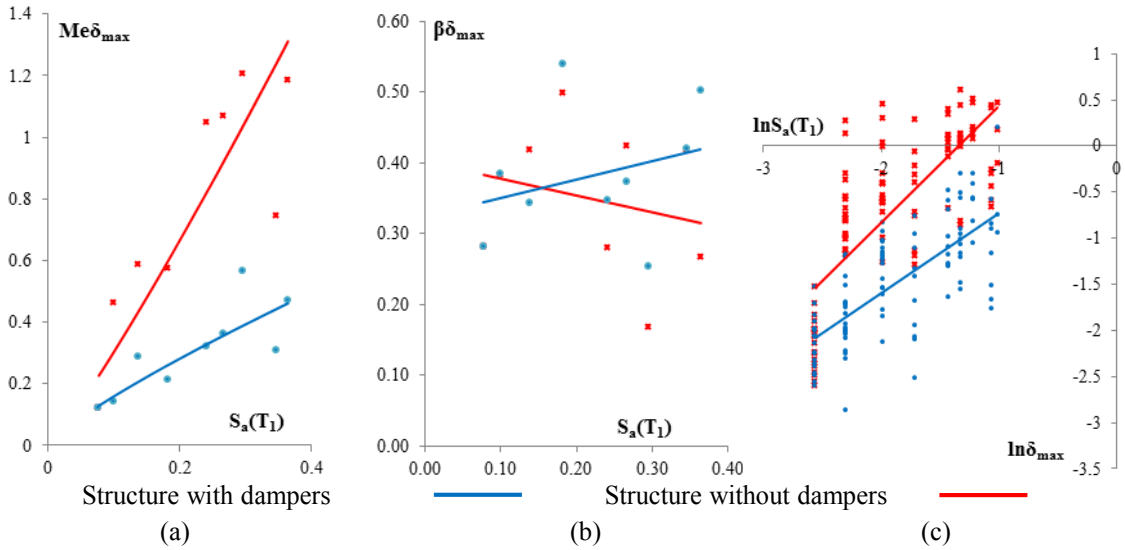
D_{roof}		δ_{max}	
Structures with dampers 104 records	Structures without dampers 104 records	Structures with dampers 104 records	Structures without dampers 104 records
$MeD_{roof} = 0.1127 \cdot S_a^{0.7398}$	$MeD_{roof} = 0.2129 \cdot S_a^{0.8059}$	$Me\delta_{max} = 1.0595 \cdot S_a^{0.8221}$	$Me\delta_{max} = 4.1216 \cdot S_a^{1.1327}$
$\beta_{regr}=0.3306+0.2143 S_a$	$\beta_{regr}=0.3274+0.2272\ S_a$	$\beta_{regr}=0.3254+0.257\ S_a$	$\beta_{regr}=0.4016-0.2375\ S_a$
$\beta_{cost} = 0.42236$	$\beta_{cost} = 0.5252$	$\beta_{cost} = 0.42239$	$\beta_{cost} = 0.56296$

Table 3: Expressions of median and dispersion for D_{roof} and δ_{max}, Case 2.



(a) (b) (c)

Figure 8: Case 2: a) MeD_{roof}- $S_a(T_1)$; b) βD_{roof}- $S_a(T_1)$; c) $\ln D_{roof}$-$\ln S_a(T_1)$



(a) (b) (c)

Figure 9: Case 2: a) $Me\delta_{max}$- $S_a(T_1)$; b) $\beta\delta_{max}$- $S_a(T_1)$; c) $\ln\delta_{max}$-$\ln S_a(T_1)$

D_{roof}		δ_{max}	
Structures with dampers 180 records	Structures without dampers 180 records	Structures with dampers 180 records	Structures without dampers 180 records
$MeD_{roof} = 0.2421 \cdot S_a^{1.0523}$	$MeD_{roof} = 0.44 \cdot S_a^{1.1357}$	$Me\delta_{max} = 2.2724 \cdot S_a^{1.1285}$	$Me\delta_{max} = 9.8605 \cdot S_a^{1.5088}$
$\beta_{regr} = 0.3145 + 0.5809 S_a$	$\beta_{regr} = 0.2626 + 1.0257 S_a$	$\beta_{regr} = 0.2975 + 0.7001 S_a$	$\beta_{regr} = 0.2906 + 1.1428 S_a$
$\beta_{cost} = 0.4696$	$\beta_{cost} = 0.5651$	$\beta_{cost} = 0.4803$	$\beta_{cost} = 0.6389$

Table 4: Expressions of median and dispersion for D_{roof} and δ_{max}, Case 3.

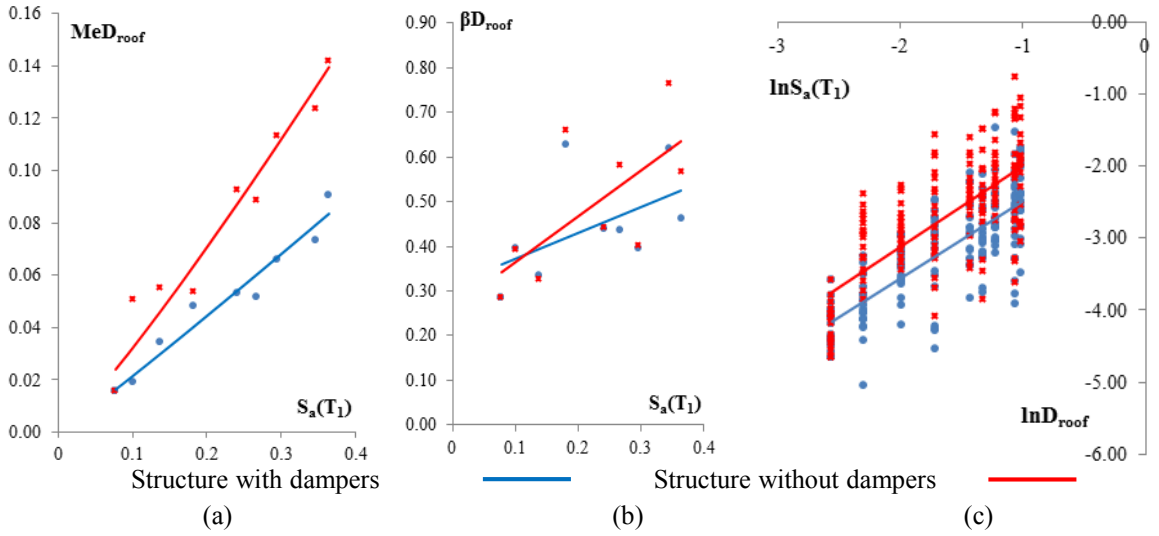


Figure 10: Case 3: a) MeD_{roof}- $S_a(T_1)$; b) βD_{roof}- $S_a(T_1)$; c) $\ln D_{roof}$-$\ln S_a(T_1)$

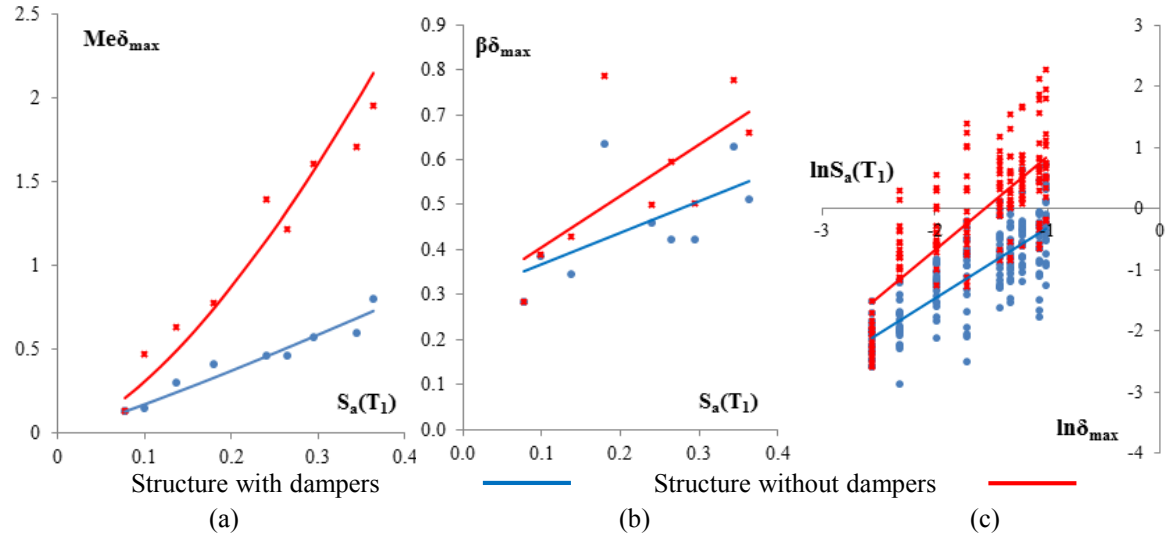


Figure 11: Case 3: a) $Me\delta_{max}$- $S_a(T_1)$; b) $\beta\delta_{max}$- $S_a(T_1)$; c) $\ln\delta_{max}$-$\ln S_a(T_1)$

Figure 8a shows smaller values of median D_{roof} than for case 1. Figure 8b confirms that the dispersion (β_{regr}) always increases for both the structure when the seismic intensity increases. Moreover, the values of dispersion (β_{regr}) decrease for the structure with dampers if we consider a smaller number of records. Lastly, Figure 8c and Table 4 illustrate that also a smaller value of dispersion (β_{cost}) is obtained for the structure with dampers if we consider a smaller number of records. Figure 9 shows that the same remarks made for the maximum roof displacement (D_{roof}) can be made for the maximum interstorey drift, i.e. both the values of medi-

an and dispersion decrease for the structure with dampers, considering a smaller number of records. However, passing from the structure with damper to the one without damper, a trend in lines with the expectations is not obtained yet for β_{regr}.

If we consider a greater number of records for both the structures (Case 3), a trend in line with the expectations is obtained. As for the maximum roof displacement (D_{roof}) one can note that (Figure 10):

- the median values for the structure without dampers are greater than those obtained for the structure with dampers (Figure 10a);
- the dispersion β_{regr} always increases for both the structures when seismic intensity increases and the expected trend is obtained, that is the dispersion of the structure without dampers is greater than that with dampers (Figure 10b);
- the dispersion β_{cost} is greater for both structures than the previous cases but it always maintains the same trend, that is the dispersion for the structure without dampers is greater than that for the structure with dampers (Figure 10c).

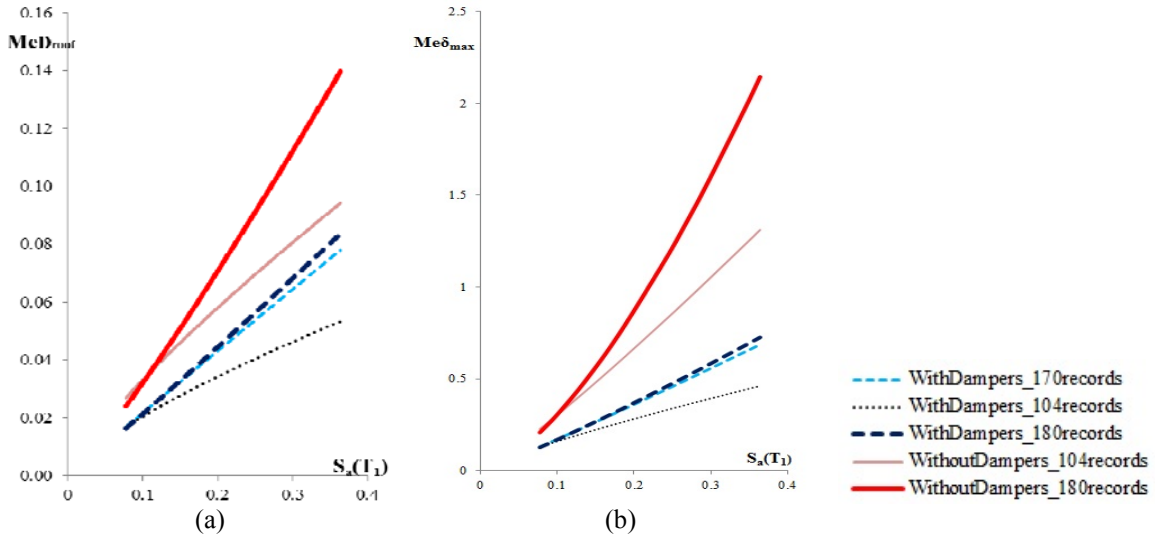
The same remarks can be made for the maximum interstorey drift (δ_{max}, Figure 11), with the additional observation that the decreasing trend disappears for β_{regr}, which always increases with seismic intensity.

Figure 12,13 and 14 compare, for the three cases of Table 1, the curves of median and dispersion of maximum roof displacement and interstorey drift as functions of the seismic intensity. Figure 12 shows that both for D_{roof} and δ_{max}:

- the median values of displacement for the structure without dampers are greater than those for the structure with dampers;
- the values of D_{roof} and δ_{max} increases when the number of records increases and the accuracy of the correlation increases.

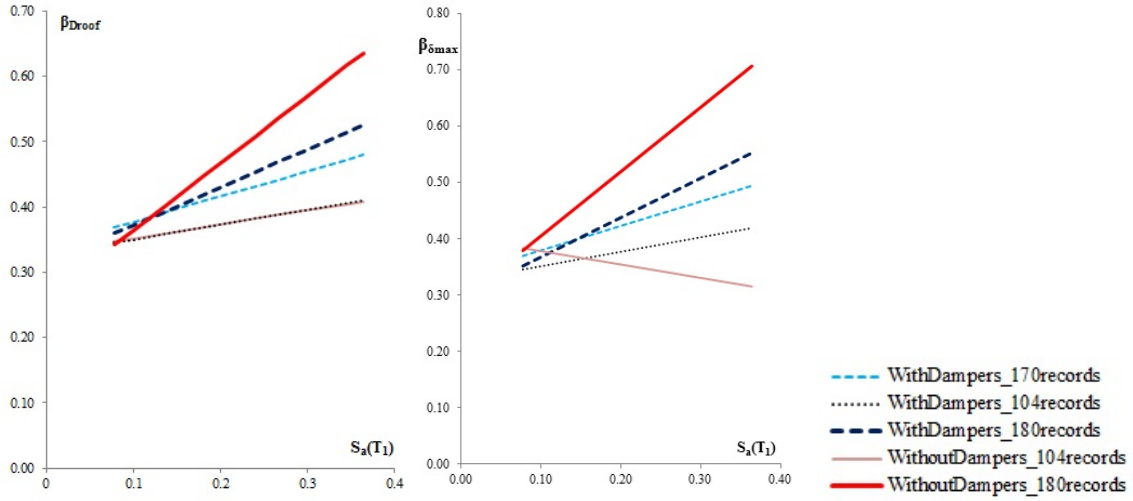
Figure 13 illustrates the trend of the dispersion variable with the seismic intensity. It is possible to observe that:

- the variable dispersion (β_{regr}) increases with the increasing of seismic intensity, with the exception of δ_{max} with 104 records;
- the variable dispersion (β_{regr}) increases for both structures and the accuracy of the correlation increases when the number of records increases. With 180 records for both structures the expected trend is obtained, that is the dispersion for the structure without damper is greater than that for the structure with dampers.



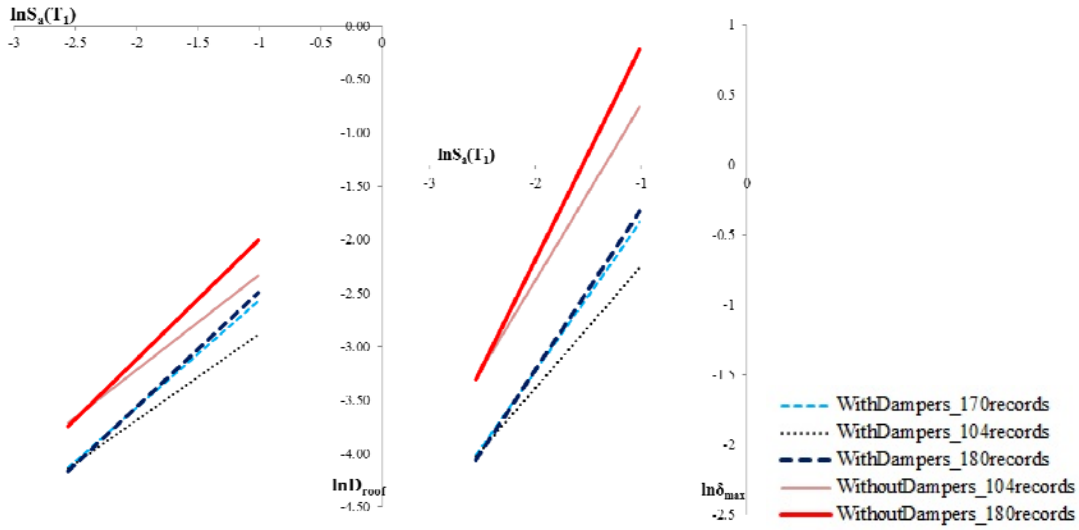
(a) (b)

Figure 12: Comparison of cases 1, 2 and 3: a) MeD_{roof}- $S_a(T_1)$; b) $Me\delta_{max}$ -$S_a(T_1)$



(a) (b)

Figure 13: Comparison of cases 1, 2 and 3: a) βD_{roof}- $S_a(T_1)$; b) $\beta\delta_{max}$- $S_a(T_1)$



(a) (b)

Figure 14: Comparison of cases 1, 2 and 3: a) lnD_{roof}-ln$S_a(T_1)$; b) $ln\delta_{max}$-ln$S_a(T_1)$

	Structure with dampers			Structure without dampers	
	104 records	170 records	180 records	104 records	180 records
$\beta_{cost}D_{roof}$	0,42236	0,4523	0,4696	0,5252	0,5651
$\beta_{cost}\delta_{max}$	0,42239	0,4595	0,4803	0,5629	0,6389

Table 5: β_{cost} with the increasing of the number of records for D_{roof} and δ_{max}.

Table 5 illustrates that the parameter of constant dispersion (β_{cost}) increases when the number of records increases for both structures and for both demand parameters (D_{roof} and δ_{max}). Lastly, with regard to dispersion, it is useful to perform some evaluations. By calculating the ratio between the parameter of constant dispersion obtained for both structures with and without dampers in the three cases, it comes out that the dispersion of the structure with dampers is about 80% of the dispersion of the structure without dampers (Table 6). By calculating the ratio between the coefficients of the regression lines obtained for the structures with and without dampers in the three cases, one gets the relation which allows to obtain the dispersion of the structure with dampers, knowing that for the structure without dampers (Table 7). The

most reliable correlations are all obtained for Case 3, characterized by a greater number of records (180).

		Case 1	Case 2	Case 3
D_{roof}	$\beta_{Dam}/\beta_{WithoutDam}$	0.8612	0.8042	0.831
δ_{max}	$\beta_{Dam}/\beta_{WithoutDam}$	0.8162	0.7503	0.7518

Table 6: $\beta_{cost,}$ ratio between the parameters of constant dispersion, obtained for both structures with and without dampers in the three cases.

	D_{roof}		δ_{max}	
$\beta=\alpha+\lambda S_a$; $\alpha = a_{Dam}/a_{WithoutDam}$; $\lambda = b_{Dam}/b_{WithoutDam}$				
	α	λ	α	λ
CASE 1	1.714	1.034	-1.828	0.836
CASE 2	0.943	1.009	-1.082	0.810
CASE 3	0.566	1.198	0.613	1.024

Table 7: $\beta_{regr,}$ ratio between the coefficients of the regression lines obtained for the structure with and without dampers in the three cases.

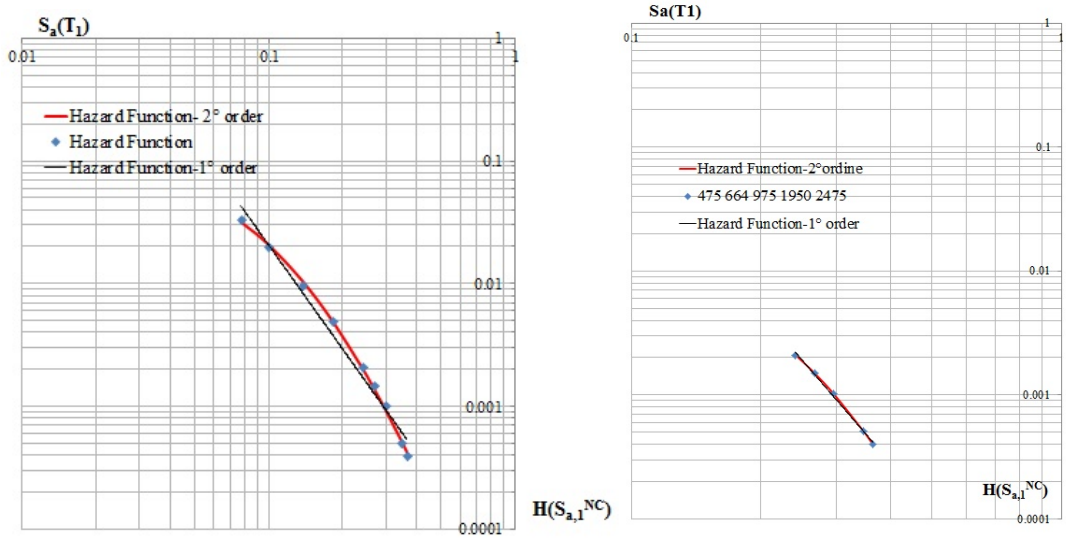
4.2 Evaluation of the annual failure probability

The second step of this research is the study of the simplified formula proposed by the 2000 SAC/FEMA method to assess the annual probability of exceeding a given performance level (Eq. (11)). The following assumptions have been considered in this study:

- consideration of the near collapse limit state;
- adoption of different criteria for approximating the hazard curve: interpolation on the whole range of examined return periods (criterion (a), T_R=30, 50, 101, 201, 475, 664, 975, 1950 and 2475 years); interpolation on a small range close to the return period of 975 years, which is associated in the code [7] to the near collapse limit state (criterion (b) T_R=475, 664, 975, 1950 and 2475 years). Moreover, interpolations of the first and second order have been performed for both the criteria identifying thus four hazard curves. The approximation of the second order has been determined according to the method proposed by Vamvatsikos [12]. The expressions of the obtained hazard curves are reported in Table 8, the graphs of such relations are illustrated in Figure 15.
- determination of the capacity values for the near collapse limit state and for the two considered demand parameters according to two criteria described in the following. In this way two collapse conditions are defined, one based on the ultimate roof displacement ($D_{roof,u}$), the other on the ultimate interstorey drift ($\delta_{max,u}$). $D_{roof,u}$ has been determined through a pushover analysis, under a modal pattern of lateral load, as the roof displacement when the first plastic hinge in a column reaches the collapse rotation. This value is $D_{roof,u}$=0.145 m. $\delta_{max,u}$, to be compared with the demand, evaluated in terms of maximum drift along the height, has been determined through a pushover analysis as the maximum drift along the height when the first plastic hinge in a column reaches the collapse rotation. Since in the pushover analysis a column sway mechanism at the fourth storey has been observed, the mentioned drift corresponds to the ultimate drift of the fourth storey, equal to 2.5375%. It should be noticed also that during the nonlinear dynamic analyses, in all the cases in which the collapse has been reached, a mechanism at the third or fourth storey has been observed.

		Hazard curve criterion a)
Hazard curve criterion (a)	Approximation of the first order	$H\left(S_a^{NC}\right)=3\cdot10^{-5}\left(S_{a,1}^{NC}\right)^{-2.827}$
	Approximation of the second order	$H\left(S_a^{NC}\right)=2.62\cdot10^{-6}\cdot e^{\left(-0.878\ln^2 S_a(T_1)-5.923\ln S_a(T_1)\right)}$
Hazard curve criterion (b)	Approximation of the first order	$H\left(S_a^{NC}\right)=7\cdot10^{-6}\left(S_{a,1}^{NC}\right)^{-4.03}$
	Approximation of the second order	$H\left(S_a^{NC}\right)=3.04\cdot10^{-7}\cdot e^{\left(-2.18\ln^2 S_a(T_1)-9.312\ln S_a(T_1)\right)}$

Table 8: Approximation of the first and second order of the hazard curve, obtained with criterion (a) and (b).



(a) (b)

Figure 15: Approximations of the first and second order for the hazard curve with criterion (a) and (b)

Firstly, the variability of the parameters of the expression of the annual probability of failure is examined, in particular the value $H(S_{a,1}^{NC})$ of the hazard function, the dispersion parameter variable (β_{regr}) with seismic intensity and the constant dispersion (β_{cost}). With regard to the first order approximation of the hazard curve, the results reported in Table 9 show that:

- the spectral acceleration at failure decreases when the number of records increases and consequently the corresponding mean annual frequency increases; moreover, the parameter of constant dispersion also increases.
- comparing the values obtained for the structure with and without dampers, the greatest difference between the spectral acceleration at failure occurs in the second case with a smaller number of records; this shows a great variability of parameters according to the number of considered records; there is also a great variability of the values of mean annual frequency.
- moreover, the dispersion which varies with seismic intensity (β_{regr}), is greater for the structure with dampers than for the structure without dampers; on the contrary the parameter of constant dispersion (β_{cost}) is greater for the structure without dampers.

	$D_{roof,u}$=0.145 m					$\delta_{max,u}$=2.5375%				
	Structure with dampers			Structure without dampers		Structure with dampers			Structure without dampers	
	104	170	180	104	180	104	170	180	104	180
$S_{a,1}^{NC}$	1.41	0.68	0.61	0.62	0.37	2.89	1.22	1.11	0.65	0.41
$H(S_{a,1}^{NC})$ Hazard curve (a)	$1.2\cdot10^{-5}$	$8.8\cdot10^{-5}$	$1.2\cdot10^{-4}$	$1.2\cdot10^{-4}$	$4.7\cdot10^{-4}$	$1.5\cdot10^{-6}$	$1.7\cdot10^{-5}$	$2.3\cdot10^{-5}$	$1.0\cdot10^{-4}$	$3.8\cdot10^{-4}$
$H(S_{a,1}^{NC})$ Hazard curve (b)	$1.8\cdot10^{-6}$	$3.3\cdot10^{-5}$	$4.9\cdot10^{-5}$	$4.7\cdot10^{-5}$	$3.6\cdot10^{-4}$	$9.7\cdot10^{-8}$	$3.1\cdot10^{-6}$	$4.7\cdot10^{-6}$	$3.9\cdot10^{-5}$	$2.6\cdot10^{-4}$
β_{regr}	0.63	0.60	0.67	0.47	0.65	1.07	0.87	1.07	0.25	0.75
β_{cost}	0.42	0.45	0.47	0.52	0.56	0.42	0.46	0.48	0.56	0.64

Table 9: D_{roof} and δ_{max}, variability of the parameters which define the annual probability of failure, varying the number of records for the approximation of the first order of the hazard curve.

Secondly, the variability of the annual probability of failure is examined. With regard to the first order approximation of the hazard curve, the results are reported in Tables 10 to 13, which show the values of probability together with the corresponding values of hazard and dispersion. Tables 10 and 11, relative to the collapse defined by $D_{roof,u}$, shows that:

- under the same conditions of structure and dispersion, the values of annual probability of failure vary considerably depending on the hazard curves (a) or (b);
- under the same hazard curves (a) or (b), a slightly higher value of mean annual frequency and a smaller value of dispersion determine higher values of annual probability of failure; this shows the great influence of the dispersion on the final value of the annual probability of failure.
- as for the parameter of constant dispersion, a much greater annual probability of failure has been obtained for the structure without dampers than for the structure with dampers; this does not always occur when the parameter of variable dispersion is used, as for the Case 2, hazard curve (b).

The same observations can be made for the collapse defined by $\delta_{max,u}$ (Tables 12 and 13) with the additional observation that, when the variable dispersion parameter (β_{regr}) is used, the annual probability of failure is much greater for the structure with dampers than for the structure without dampers. Consequently, the results are in line with the expectations only when the parameter of constant dispersion (β_{cost}) is used.

As for the second order approximation of the hazard curve, for both the demand parameters and for the same structure, there is a smaller difference among the values of $H(S_{a,1}^{NC})$ determined with different intervals for interpolating the hazard curve (criterion (a) or (b)) than with the first order approximation. This is shown in Tables 14 and 15 for the Case 3.

	$D_{roof,u}$=0.145 m					
	Case 1		Case 2		Case 3	
	Dampers 170	Without dampers 104	Dampers 104	Without dampers 104	Dampers 180	Without dampers 180
$H(S_{a,1}^{NC})$ Hazard curve (a)	$8.83\cdot10^{-5}$	$1.15\cdot10^{-4}$	$1.15\cdot10^{-5}$	$1.12\cdot10^{-4}$	$1.19\cdot10^{-4}$	$4.75\cdot10^{-4}$
β_{regr}	0.6043	0.4686	0.6319	0.4686	0.6714	0.6486
$P_{F,NC}$	$5.38\cdot10^{-4}$	$7.05\cdot10^{-4}$	$3.67\cdot10^{-4}$	$7.05\cdot10^{-4}$	$7.95\cdot10^{-4}$	$2.21\cdot10^{-3}$
β_{cost}	0.4523	0.5252	0.4224	0.5252	0.4696	0.5651
$P_{F,NC}$	$2.79\cdot10^{-4}$	$9.96\cdot10^{-4}$	$7.32\cdot10^{-5}$	$9.96\cdot10^{-4}$	$3.46\cdot10^{-4}$	$1.62\cdot10^{-3}$

Table 10: Annual failure probability for the first order approximation of the hazard curve with criterion (a) and for collapse defined by $D_{roof,u}$.

	$D_{roof,u}$=0.145 m					
	Case 1		Case 2		Case 3	
	Dampers 170	Without dampers 104	Dampers 104	Without dampers 104	Dampers 180	Without dampers 180
$H(S_{a,1}^{NC})$ Hazard curve (b)	$3.26\cdot10^{-5}$	$4.76\cdot10^{-5}$	$1.77\cdot10^{-6}$	$4.76\cdot10^{-5}$	$4.98\cdot10^{-5}$	$3.59\cdot10^{-4}$
β_{regr}	0.6043	0.4686	0.6319	0.4686	0.6714	0.6486
$P_{F,NC}$	$1.28\cdot10^{-3}$	$1.89\cdot10^{-3}$	$2.04\cdot10^{-3}$	$1.89\cdot10^{-3}$	$2.37\cdot10^{-3}$	$8.18\cdot10^{-3}$
β_{cost}	0.4523	0.5252	0.4224	0.5252	0.4696	0.5651
$P_{F,NC}$	$3.37\cdot10^{-4}$	$3.82\cdot10^{-3}$	$7.69\cdot10^{-5}$	$3.82\cdot10^{-3}$	$4.37\cdot10^{-4}$	$4.32\cdot10^{-3}$

Table 11: Annual failure probability for the first order approximation of the hazard curve with criterion (b) and for collapse defined by $D_{roof,u}$.

	$\delta_{max,u}$=2.5375%					
	Case 1		Case 2		Case 3	
	Dampers 170	Without dampers 104	Dampers 104	Without dampers 104	Dampers 180	Without dampers 180
$H(S_{a,1}^{NC})$ Hazard curve (a)	$1.69\cdot10^{-5}$	$1.01\cdot10^{-4}$	$1.48\cdot10^{-6}$	$1.01\cdot10^{-4}$	$2.27\cdot10^{-5}$	$3.82\cdot10^{-4}$
β_{regr}	0.867	0.2468	1.0689	0.2468	1.0695	0.7554
$P_{F,NC}$	$2.94\cdot10^{-4}$	$1.54\cdot10^{-4}$	$2.00\cdot10^{-3}$	$1.54\cdot10^{-4}$	$1.04\cdot10^{-3}$	$1.19\cdot10^{-3}$
β_{cost}	0.4595	0.5629	0.4224	0.5629	0.4803	0.6389
$P_{F,NC}$	$4.55\cdot10^{-5}$	$3.42\cdot10^{-4}$	$6.69\cdot10^{-6}$	$3.42\cdot10^{-4}$	$5.95\cdot10^{-5}$	$8.92\cdot10^{-4}$

Table 12: Annual failure probability for the first order approximation of the hazard curve with criterion (a) and for collapse defined by $\delta_{max,u}$.

	$\delta_{max,u}$=2.5375%					
	Case 1		Case 2		Case 3	
	Dampers 170	Without dampers 104	Dampers 104	Without dampers 104	Dampers 180	Without dampers 180
$H(S_{a,1}^{NC})$ Hazard curve (b)	$3.09\cdot10^{-6}$	$3.93\cdot10^{-5}$	$9.67\cdot10^{-8}$	$3.93\cdot10^{-5}$	$4.72\cdot10^{-6}$	$2.63\cdot10^{-4}$
β_{regr}	0.867	0.2468	1.0689	0.2468	1.0695	0.7554
$P_{F,NC}$	$1.02\cdot10^{-3}$	$9.33\cdot10^{-5}$	$2.21\cdot10^{-1}$	$9.33\cdot10^{-5}$	$1.12\cdot10^{-2}$	$2.64\cdot10^{-3}$
β_{cost}	0.4595	0.5629	0.4224	0.5629	0.4803	0.6389
$P_{F,NC}$	$2.31\cdot10^{-5}$	$4.72\cdot10^{-4}$	$2.05\cdot10^{-6}$	$4.72\cdot10^{-4}$	$3.33\cdot10^{-5}$	$1.48\cdot10^{-3}$

Table 13: Annual failure probability for the first order approximation of the hazard curve with criterion (b) and for collapse defined by $\delta_{max,u}$.

Tables 14 and 15 report the values of the annual probability of failure obtained as follows: with the approximation of the first order suggested by the 2000 SAC/FEMA method [5] (Eq.(11)); with the approximation of the second order suggested by Vamvatsikos [12]. The latter can be evaluated as follows:

$$H(S) = k_0 \cdot e^{\left(-k_2 \ln^2 S_a(T_1) - k_1 \ln S_a(T_1)\right)} \tag{16}$$

where $k_1>0$ and $k_2\geq0$. Using the approximation of the second order for the hazard curve, the new closed-form expression of the annual probability of failure [12] becomes:

$$P_{F,NC} = \sqrt{p} \cdot k_0^{1-p} \cdot \left[H\left(S_{a,1}^{NC}\right)\right]^p \cdot e^{\left(\frac{1}{2} p k_1^2 \beta_{sc}^2\right)} \tag{17}$$

where:

$$p = \frac{1}{1 + 2k_2 \beta_{Sc}^2} \qquad 0<p<1 \tag{18}$$

The difference between Eqs. (11) and (17) is the insertion of the factor p. Substituting k_2=0 in Eq. (18), it can be noticed that p becomes equal to unity and that Eq. (17) simplifies as:

$$P_{F,NC} = \left[H\left(S_{a,1}^{NC}\right)\right]^p \cdot e^{\left(\frac{1}{2} p k_1^2 \beta_{sc}^2\right)} \tag{19}$$

It can be observed that the reduction of Eq.(17) to Eq.(19) does not coincide exactly with the original formulation of the SAC/ FEMA [2] , but it is a simplification.

From Tables 14 and 15 it is possible to notice that, considering the second order approximation of the hazard curve (Eq.(17)), the variation, for the same structure and dispersion, of the annual failure probability with the number of values of T_R (9 values of T_R corresponds to criterion (a), 5 values of T_R to criterion (b)) is reduced if compared with the same variation obtained with the first order approximation. This is a consequence of the above mentioned reduction of the variation of the hazard value $H(S_{a,1}{}^{NC})$.

Moreover, considering the second order approximation of the hazard curve, a lower influence of the dispersion on the annual failure probability has been obtained than with the first order approximation. Finally it is possible to observe that, considering the second order approximation and using both the dispersion parameters, the results are in line with the expectations, i.e. the annual failure probability for the structure without dampers is always much greater than that obtained for the structure without dampers.

$D_{roof,u}$ = 0.145 m With Dampers $S_{a,1}{}^{NC}$=0.6144, a=0.2421, b=1.0523, β_c=0.275						
	9 T_R I order (2000SAC/FEMA method)	9 T_R I order (Vamvatsikos)	9 T_R II order (Vamvatsikos)	5 T_R I order (2000SAC/FEMA method)	5 T_R I order (Vamvatsikos)	5 T_R II order (Vamvatsikos)
$H(S_{a,1}{}^{NC})$	$1.189 \cdot 10^{-4}$	$1.189 \cdot 10^{-4}$	$3.81 \cdot 10^{-5}$	$4.985 \cdot 10^{-5}$	$4.985 \cdot 10^{-5}$	$1.69 \cdot 10^{-5}$
			β_{regr} = 0.6717			
$P_{F,NC}$	$7.95 \cdot 10^{-4}$	$7.21 \cdot 10^{-4}$	$7.19 \cdot 10^{-4}$	$2.37 \cdot 10^{-3}$	$1.94 \cdot 10^{-3}$	$4.99 \cdot 10^{-4}$
			β_{cost}=0.4696			
$P_{F,NC}$	$3.46 \cdot 10^{-4}$	$2.87 \cdot 10^{-4}$	$2.49 \cdot 10^{-4}$	$4.37 \cdot 10^{-4}$	$2.98 \cdot 10^{-4}$	$2.20 \cdot 10^{-4}$
Without dampers $S_{a,1}{}^{NC}$=0.3763, a=0.44, b=1.1357, β_c=0.275						
	9 T_R I order (2000SAC/FEMA method)	9 T_R I order (Vamvatsikos)	9 T_R II order (Vamvatsikos)	5 T_R I order (2000SAC/FEMA method)	5 T_R I order (Vamvatsikos)	5 T_R II order (Vamvatsikos)
$H(S_{a,1}{}^{NC})$	$4.75 \cdot 10^{-4}$	$4.75 \cdot 10^{-4}$	$3.70 \cdot 10^{-4}$	$3.6 \cdot 10^{-4}$	$3.6 \cdot 10^{-4}$	$3.4 \cdot 10^{-4}$
			β_{regr} = 0.6486			
$P_{F,NC}$	$2.21 \cdot 10^{-3}$	$2.55 \cdot 10^{-3}$	$2.38 \cdot 10^{-3}$	$8.18 \cdot 10^{-3}$	$1.09 \cdot 10^{-2}$	$1.34 \cdot 10^{-3}$
			β_{cost}=0.5651			
$P_{F,NC}$	$1.62 \cdot 10^{-3}$	$1.70 \cdot 10^{-3}$	$1.81 \cdot 10^{-3}$	$4.32 \cdot 10^{-3}$	$4.80 \cdot 10^{-3}$	$1.21 \cdot 10^{-3}$

Table 14: Annual failure probability for different hazard curve approximations and for collapse defined by $D_{roof,u}$.

$\delta_{max,u}$ = 2.5375% With Dampers $S_{a,1}^{NC}$=1.1027, a=2.27, b=1.1285, β_c=0.275						
	9 T_R I order (2000SAC/FEMA method)	9 T_R I order (Vamvatsikos)	9 T_R II order (Vamvatsikos)	5 T_R I order (2000SAC/FEMA method)	5 T_R I order (Vamvatsikos)	5 T_R II order (Vamvatsikos)
$H(S_{a,1}^{NC})$	$2.27\cdot10^{-5}$	$2.27\cdot10^{-5}$	$1.46\cdot10^{-6}$	$4.72\cdot10^{-6}$	$4.72\cdot10^{-6}$	$1.20\cdot10^{-7}$
			β_{regr}=1.0695			
$P_{F,NC}$	$1.04\cdot10^{-3}$	$2.20\cdot10^{-3}$	$9.76\cdot10^{-4}$	$1.12\cdot10^{-2}$	$5.10\cdot10^{-2}$	$4.21\cdot10^{-4}$
			β_{cost}=0.4803			
$P_{F,NC}$	$5.95\cdot10^{-5}$	$5.72\cdot10^{-5}$	$2.586\cdot10^{-5}$	$3.33\cdot10^{-5}$	$3.073\cdot10^{-5}$	$1.98\cdot10^{-5}$
Without dampers $S_{a,1}^{NC}$=0.4067, a=9.86, b=1.1509, β_c=0.275						
	9 T_R I order (2000SAC/FEMA method)	9 T_R I order (Vamvatsikos)	9 T_R II order (Vamvatsikos)	5 T_R I order (2000SAC/FEMA method)	5 T_R I order (Vamvatsikos)	5 T_R II order (Vamvatsikos)
$H(S_{a,1}^{NC})$	$3.82\cdot10^{-4}$	$3.82\cdot10^{-4}$	$2.66\cdot10^{-4}$	$2.628\cdot10^{-4}$	$2.628\cdot10^{-4}$	$2.27\cdot10^{-4}$
			β_{regr}=0.7554			
$P_{F,NC}$	$1.19\cdot10^{-3}$	$3.73\cdot10^{-3}$	$2.75\cdot10^{-3}$	$2.64\cdot10^{-3}$	$2.70\cdot10^{-2}$	$1.30\cdot10^{-3}$
			β_{cost}=0.6389			
$P_{F,NC}$	$8.92\cdot10^{-4}$	$1.95\cdot10^{-3}$	$1.90\cdot10^{-3}$	$1.48\cdot10^{-3}$	$7.23\cdot10^{-3}$	$1.15\cdot10^{-3}$

Table 15: Annual failure probability for different hazard curve approximations and for collapse defined by $\delta_{max,u}$.

5. CONCLUSIONS

In conclusion, as for the probabilistic assessment we can note that it depends on the number of records considered. In particular, reliable trends have been obtained only for 180 records for both structures with and without dampers. As for the median, the median values for the structure without dampers are greater than those obtained for the structure with dampers regardless of the number of record considered. With regard to β_{regr} it is possible to notice that: it increases with seismic intensity; it depends on the results of the dynamic nonlinear analyses, and in particular on the number of records; the expected trend, i.e. greater dispersion for the structure without dampers than for the structure with dampers, has been determined only for the higher number of results (180 records). As for β_{cost}, we can note that: the expected trend has been obtained also for the lower number of records; the parameter of constant dispersion increases with the number of seismic events both for the structure with and without dampers. Moreover, relations between the expressions of β_{cost} and β_{regr} for the structure without and with dampers have been derived with the purpose to obtain the dispersion for the structure with dampers by knowing that for the structure without dampers.

It is possible to observe that the simplified formula to determine the annual probability of failure $P_{F,NC}$ suggested by the 2000 SAC/FEMA method is strongly sensitive to variations of the hazard curve and of the dispersion. It is possible to note that for the hazard curves determined with the first order approximations, different values of $P_{F,NC}$ have been obtained by changing the interval in which the hazard curve is interpolated. Moreover, the simplified formula for $P_{F,NC}$ is particularly affected by the dispersion. $P_{F,NC}$ values always in line with the expectations have been obtained only using the parameter of dispersion β_{cost}. Considering the second order approximation of the hazard curve, the variation of the annual failure probability when changing the interval for interpolating the hazard curve is reduced if compared with the same variation obtained with the first order approximation. With the mentioned second order

approximation it is also reduced the influence of the values of dispersion and the $P_{F,NC}$ is always greater for the structure without dampers than for the structure with dampers.

Therefore, it is possible to deduce that it is better to use the parameter of constant dispersion β_{cost} when we consider the interpolation of the first order for the hazard curve. Otherwise, using the second order approximations allows to obtain values of probability less sensitive to the interval for interpolating the hazard curve and to the type of dispersion β_{regr} or β_{cost}.

REFERENCES

[1] C. Christopoulos, A. Filiatrault, *Principles of Passive Supplemental Damping and Seismic Isolation*, Pavia, Italy, IUSS Press, 2006.

[2] L. Landi, P.P. Diotallevi, G. Castellari, On the Design of Viscous Dampers for the Rehabilitation of Plan-Asymmetric Buildings, *Journal of Earthquake Engineering,* **17**(8), 1141-1161, 2013.

[3] L. Landi, S. Lucchi, P.P. Diotallevi, A Procedure for the Direct Determination of the Required Supplemental Damping for the Seismic Retrofit with Viscous Dampers, *Engineering Structures*, **71**: 137-149, 2014.

[4] P.P. Diotallevi, L. Landi, A. Dellavalle. A methodology for the direct assessment of the damping ratio of structures equipped with nonlinear viscous dampers. *Journal of Earthquake Engineering*, **16**(3): 350–373, 2012.

[5] C.A. Cornell, F. Jalayer, R.O. Hamburger, D.A. Foutch, Probabilistic Basis for 2000 SAC Federal Emergency Management Agency Steel Moment Frame Guidelines, *Journal of Structural Engineering*, **128**(4): 526-533, 2002.

[6] L. Landi, O. Fabbri, P.P. Diotallevi. A two-step direct method for estimating the seismic response of nonlinear structures equipped with nonlinear viscous dampers. *Earthquake Engineering and Structural Dynamics*, **43**(11): 1641-1659, 2014.

[7] Min. LL PP. Norme Tecniche per le Costruzioni. Italian building code, adopted with D.M. 14/01/2008, published on S.O. n. 30 G.U. n. 29, 04/02/2008.

[8] I. Iervolino, C. Galasso, E. Cosenza, REXEL: computer aided record selection for code-based seismic structural analysis, *Bulletin of Earthquake Engineering*, **8**: 339-362, 2010.

[9] Seismosoft , *SeismoSignal v5.1 – A computer program for signal processing of strong-motion data,* 2013.

[10] CSI. *Analysis Reference Manual for SAP2000. ETABS, and SAFE*, 2009, Berkeley, California, USA.

[11] T.B. Panagiotakos, M.N. Fardis, Deformation of Reinforced Concrete Members at Yielding and Ultimate, *ACI Structural Journal,* **98**(2), 135-148, 2001.

[12] D. Vamvatsikos, Derivation of new SAC/FEMA performance evaluation solutions with second-order hazard approximation, *Earthquake Engineering and Structural Dynamics*, **42**: 1171-1188, 2013.

COMPDYN 2015
5th ECCOMAS Thematic Conference on
Computational Methods in Structural Dynamics and Earthquake Engineering
M. Papadrakakis, V. Papadopoulos, V. Plevris (eds.)
Crete Island, Greece, 25–27 May 2015

NUMERICAL MODELING OF FRP - RETROFITTED CIRCULAR RC COLUMNS INCLUDING SHEAR

Konstantinos G. Megalooikonomou[1], **Giorgio Monti**[2]

[1] Department of Civil and Environmental Engineering, University of Cyprus
P.O. Box 20537, 1687 Nicosia, Cyprus
kmegal01@ucy.ac.cy

[2] Department of Structural and Geotechnical Engineering, Sapienza University of Rome
Via A.Gramsci 53, 00197 Rome, Italy
giorgio.monti@uniroma1.it

Keywords: FRP, RC column, circular section, confinement, shear deformation.

Abstract. *The Fiber Reinforced Polymer (FRP)-confined concrete model contained in a well-known Bulletin by the International Federation for Structural Concrete (fib) has been enhanced to take into account the superposition of the confining effects of the already existing steel reinforcement with that of the FRP jacketing applied when retrofitting reinforced concrete (RC) columns. Columns are here modeled with a fiber-based nonlinear beam- column element (with displacement formulation) in which the constitutive law for concrete presented in this paper is implemented. This allows for the immediate incorporation of shear strains (uncoupled from the normal ones) at the material level. The averaged response of the two different regions -concrete core and concrete cover-in the cross-section allows the assignment of a unique stress-strain law for all the fibers/layers of the circular section. Correlation with an experimental study is performed to validate the proposed iterative procedure.*

1 INTRODUCTION

Several strong earthquakes attacked California U.S.A., Kobe Japan, and Ji-Ji Taiwan. These major earthquakes have caused severe structural damage, and even collapse which have resulted in the necessity of seismic retrofit of existing structures. Confining wraps or jackets to rehabilitate and strengthen existing concrete columns has proven to be an efficient technique for seismic retrofit of structures. Fiber Reinforced Polymers (FRPs) to retrofit RC columns have been found to be beneficial for the compressive strength, shear strength, flexural strength and displacement ductility of RC columns.

It is well known that columns play a key role in determining the overall structural performance. Therefore, it is essential to develop a suitable analytical tool to estimate their structural behavior, able to detect all failure mechanisms such as shear, and bending and possibly to include the effect of FRP confinement as a retrofitting measure.

The behavior of reinforced concrete columns in shear and bending has been studied for decades. In case of flexural behavior, traditional section analysis, or the more precise method, fiber model in one-dimensional stress field gives acceptable predictions in terms of ultimate strength and yielding deformation. Performance of reinforced concrete columns dominated in shear or shear-flexure cannot be estimated by applying only section analysis because shear behavior is not taken into account. For evaluating the shear response of structural elements, such as beams and columns, many analytical models and theories have been conceived in the past [1].

Most of the state-of-the-art on seismic design and assessment procedures proposed recently for common engineering practice requires some kind of nonlinear analysis either static or dynamic. These nonlinear analyses are mostly carried out using frame elements with different levels of accuracy. Two main approaches are traditionally used and classified as lumped-plasticity and distributed-inelasticity models. For the latter, the well known fiber beam elements provide results that are particularly accurate when studying the cyclic behavior of RC structures.

Several fiber beam-column elements have been developed with high capability of reproducing axial force and bending coupling. On the other hand, the coupling between the effects of normal force and shear force is not straightforward and hence only few modeling strategies have successfully dealt with it up to now [1].

The most basic theory capable of analyzing beam-column elements is the Euler-Bernoulli approach. The fundamental assumptions are that cross-sections remain plain and normal to the deformed longitudinal axis. The Euler-Bernoulli theory is capable of reproducing correctly the actual response of a beam under combined axial forces and bending moments, while shear forces are obtained from static equilibrium (the effects of the latter on beam deformations are neglected though). When the effects of tangential stresses are important in the response of the element, more refined Timoshenko-like beam theories are more appropriate. Here cross-sections remain plane but not necessarily normal to the deformed longitudinal axis.

The Timoshenko beam theory allows considering the shear strain effect through a constant shear strain distribution along the cross-section, implying that an effective shear area factor is needed in order to be energetically consistent. This factor depends on the section shape and is usually derived for isotropic materials. This implies that being state-dependent, it is far more complex to use in nonlinear analysis of cracked RC sections.

2 ANALYTICAL INVESTIGATION

The mechanical properties of concrete (strength, pseudo-ductility, energy dissipation) are substantially enhanced under a triaxial stress state. In practice, this is obtained by using closed stirrups or spiral reinforcement or even FRP wraps, so that, together with the longitudinal reinforcement, the lateral expansion of concrete is limited. This kind of (passive) confinement improves the material behavior after the initiation of internal cracking, which gives rise to the initiation of expansion.

For low strain values, the stress state in the transverse steel reinforcement is very small and the concrete is basically unconfined. In this range, steel and FRP jacketing behave similarly. That is, the inward pressure as a reaction to the expansion of concrete increases continuously. Therefore, speaking in terms of variable confining pressures corresponding to the axial strain level in the section and active triaxial models defining axial stress-strain curves for concrete subject to constant lateral pressure, it can be stated following the original approach of [2] that the stress-strain curve describing the stress state of the section has to cross all active confinement curves up to the curve with lateral pressure equal to the one applied by the stirrups at yielding. After yielding of stirrups, the lateral pressure is still increasing only due to the FRP jacketing, while the steel lateral pressure remains constant. The corresponding stress-strain curve of the section throughout this procedure converges to a confined-concrete axial stress-strain curve that is associated with a lateral pressure magnitude equal to the tensile strength of the FRP jacket plus the yielding strength of ties (excluding the strain hardening behavior of steel, since ultimate strains of steel are usually much higher than those of FRP jackets). In order to model this behavior, a well-known FRP-confined concrete model [2] has been enhanced to include the steel ties contribution and thus model in a more consistent way circular columns with transverse steel reinforcement and retrofitted with FRP jacketing. The above model was based on an iteration procedure that needed to be modified as in Figure 1.

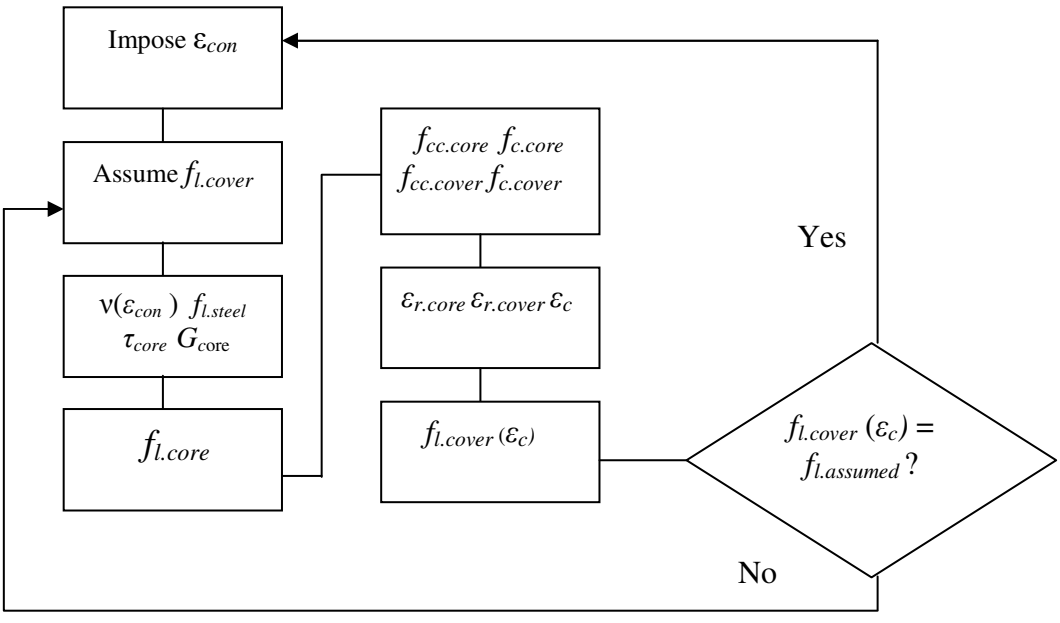


Figure 1: Iterative Procedure.

In the procedure depicted in (Fig.1), after imposing an axial strain on the section, a pressure coming from the FRP jacket is assumed. Then, the Poisson's coefficient until yielding of steel stirrups and the pressure coming from the steel ties is calculated based on the BGL model [3]. Since, this lateral pressure according to BGL model is the solution of the plain stress tensor by the Airy's stress function, the shear stress in the concrete core is also determined along with the shear modulus .Here, also the longitudinal bars' contribution and the arching action between two adjacent stirrups along the column are taken into account (Table 1). Thus, the confining pressure in the concrete core is the summation of the lateral pressures contributed by the two confining systems (FRP and Steel). The fib's model proposal [2] beyond this point is basically used to define the remainder of the parameters declared above, applying that model for the two different regions already mentioned. The focal point of the procedure is in the last step where the confining pressure of the jacket is defined based on the circumferential strain according to Table 1. Finally, cases with partial wrapping have been included too [4] (Table 1). Such approach also permits in cases of repair and retrofit to consider two different concrete strengths, one for the new layer of concrete applied externally and the other for the old existing concrete core which may also be cracked due to former seismic loading [5]. At the end of the procedure, a two-condition failure criterion [5] is incorporated either due to excessive dilation of concrete or due to buckling of longitudinal bars.

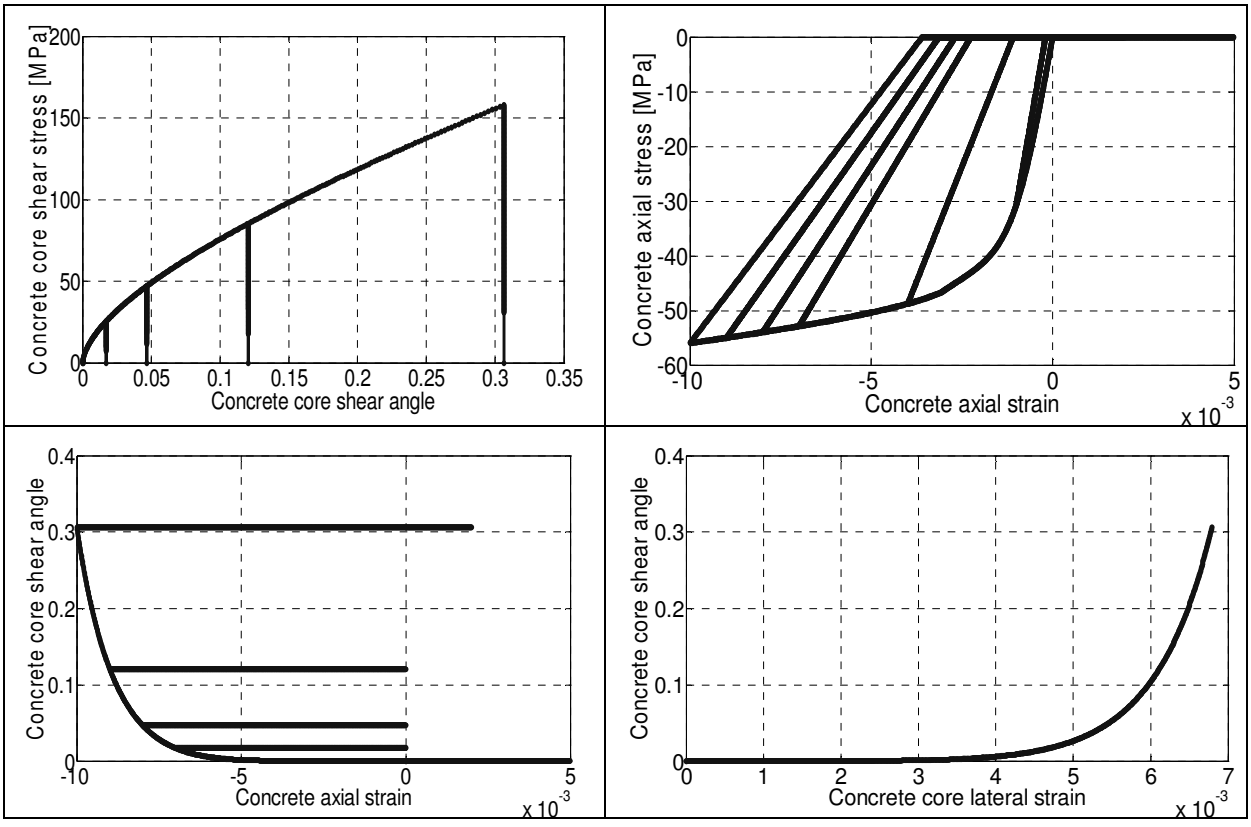


Figure 2: Prediction of concrete behavior with properties similar to ST2NT by Sheikh and Yau [6]

(Braga et al. 2006) [3]	$f_{l.steel}(\varepsilon_{con}) = k_{sl}\dfrac{E_{con}E_s A_{sh}\nu(\varepsilon_{con})}{R_{core}E_{con}S + E_s A_{sh}\left[1-\nu(\varepsilon_{con})\right]\cdot\left[\nu(\varepsilon_{con})\cdot\varepsilon_{con}+1\right]}\cdot\varepsilon_{con}, \varepsilon_{sh} \prec \varepsilon_{yh}$ $f_{l.steel}(\varepsilon_{con}) = k_{sl}\,0.5\rho_{sh}f_{yh}, \varepsilon_{shu} \geq \varepsilon_{sh} \geq \varepsilon_{yh}$ $\rho_{sh} = \dfrac{4A_{sh}}{D_{core}S},\ \varepsilon_{yh} = \dfrac{f_{yh}}{E_s},\ \varepsilon_{sh} = \varepsilon_{c.core} = \varepsilon_{r.core} = \nu(\varepsilon_{con})\cdot\varepsilon_{con}$ $\nu(\varepsilon_{con}) = \nu_0\left[1 + 0.2\left(\dfrac{\varepsilon_{con}}{\varepsilon_{c0}}\right) - \left(\dfrac{\varepsilon_{con}}{\varepsilon_{c0}}\right)^2 + 1.55\left(\dfrac{\varepsilon_{con}}{\varepsilon_{c0}}\right)^3\right],\ \nu_0 = 0.2,\ \varepsilon_{co} = 0.002$ $k_{sl} = \dfrac{45\xi_l{}^3}{45\xi_l{}^3 + \beta\xi_{st}}, \xi_l = \dfrac{D_b}{S}, \beta = \dfrac{D_h}{D_b}, \xi_{st} = \dfrac{2D_h}{\pi R_{core}}$ $\tau_{core} = \dfrac{E_{con}E_s A_{sh}\nu(\varepsilon_{con})}{R_{core}E_{con}S + E_s A_{sh}\left[1-\nu(\varepsilon_{con})\right]\cdot\left[\nu(\varepsilon_{con})\cdot\varepsilon_{con}+1\right]}\cdot\varepsilon_{con}$ $G_{core} = \dfrac{E_{con}}{2\cdot[1+\nu(\varepsilon_{con})]}$
(Spoelstra and Monti 1999) [2]	$f_c = \dfrac{f_{cc}\cdot x\cdot r}{r-1+x^r},\ x = \dfrac{\varepsilon_{con}}{\varepsilon_{cc}},\ \varepsilon_{cc} = \varepsilon_{co}\left[1+5\left(\dfrac{f_{cc}}{f_{co}}-1\right)\right],\ r = \dfrac{E_{con}}{E_{con}-E_{\sec}}$ $E_{\sec} = \dfrac{f_{cc}}{\varepsilon_{cc}},\ \dfrac{f_{cc}(f_l)}{f_{co}} = 2.254\sqrt{1+7.94\dfrac{f_l}{f_{co}}} - 2\dfrac{f_l}{f_{co}} - 1.254,$ $\varepsilon_r(\varepsilon_{con}, f_l) = \dfrac{E_{con}\varepsilon_{con} - f_c(\varepsilon_{con}, f_l)}{2\beta f_c(\varepsilon_{con}, f_l)},\ \beta = \dfrac{5700}{\sqrt{\lvert f_{co}\rvert}} - 500,\ E_{con} = 5700\cdot\sqrt{\lvert f_{co}\rvert}(MPa)$
(14th fib Bulletin) [4]	$k_j = \dfrac{\left(1-\dfrac{S_j}{2D}\right)^2}{1-\dfrac{A_b}{A_g}} \approx \left(1-\dfrac{S_j}{2D}\right)^2$ *(Coefficient for Partial Wrapping)* $f_{l.\mathrm{cover}} = \dfrac{1}{2}k_j\rho_j E_j\varepsilon_c, \rho_j = \dfrac{4t_j}{D}$
Iterative Procedure	$f_{l.core} = f_{l.\mathrm{cover}} + f_{l.steel},\ f_{c.av} = \dfrac{A_{core}}{A_{tot}}f_{c.core} + \dfrac{A_{\mathrm{cover}}}{A_{tot}}f_{c.\mathrm{cover}}$
(Megalooikonomou et. al. 2012) [5]	$\varepsilon_c = \dfrac{\Delta C}{C} = \dfrac{2\pi\left\{\left[R_{core}(1+\varepsilon_{r.core})+c(1+\varepsilon_{r.\mathrm{cover}})\right]-(R_{core}+c)\right\}}{2\pi(R_{core}+c)}$ $= \dfrac{R_{core}(1+\varepsilon_{r.core})+c(1+\varepsilon_{r.\mathrm{cover}})}{(R_{core}+c)} - 1$

Table 1: Equations used in the iterative procedure

Figure 2 depicts a simple run of the material model under axial strain reversals with the same material properties as the specimen ST2NT of the experimental study with FRP- and steel- confined columns performed by Sheikh and Yau [6] . A moment-curvature analysis for the section (with layers/fibers) of the same specimen that provides also the shear force - shear angle diagram has been performed, where the constitutive model by Menegotto and Pinto [7] is used to model the longitudinal steel behavior. Figures 3, 4 and 5 depict the implications of the application of the constitutive relation presented in this paper, where in contrast to the assumption of a Timoshenko beam the shear deformation is not constant along the section. The shear deformation of the section derives as the mean value of the shear deformations of each material fiber/layer. The Bernoulli assumption is bypassed since the shear deformations are included and are uncoupled from the normal ones.

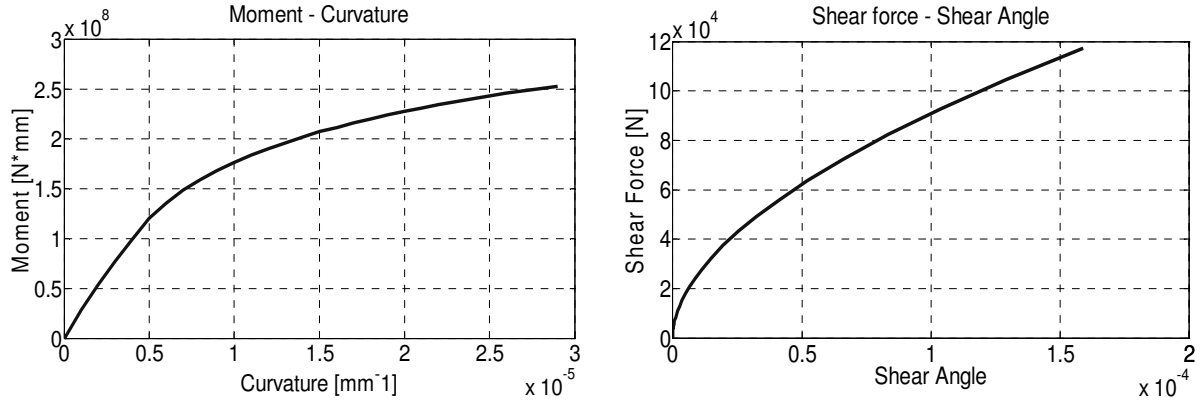


Figure 3: Prediction of section's response with properties similar to ST2NT by Sheikh and Yau [6]

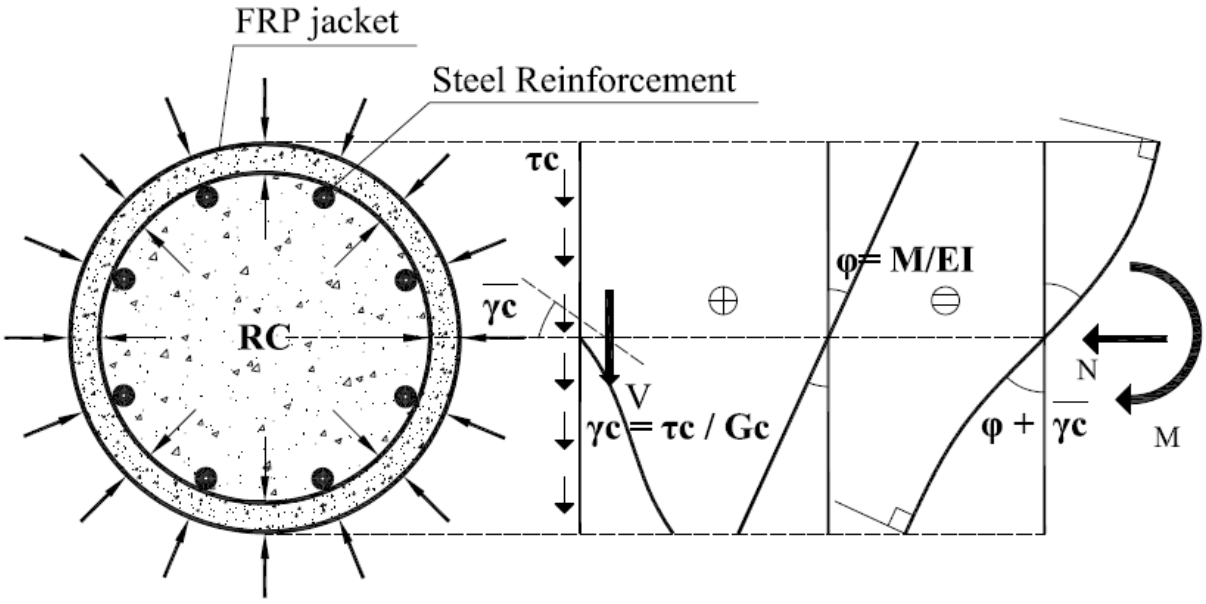


Figure 4: Circular concrete section confined by steel stirrups and FRP jacket under bending and shear.

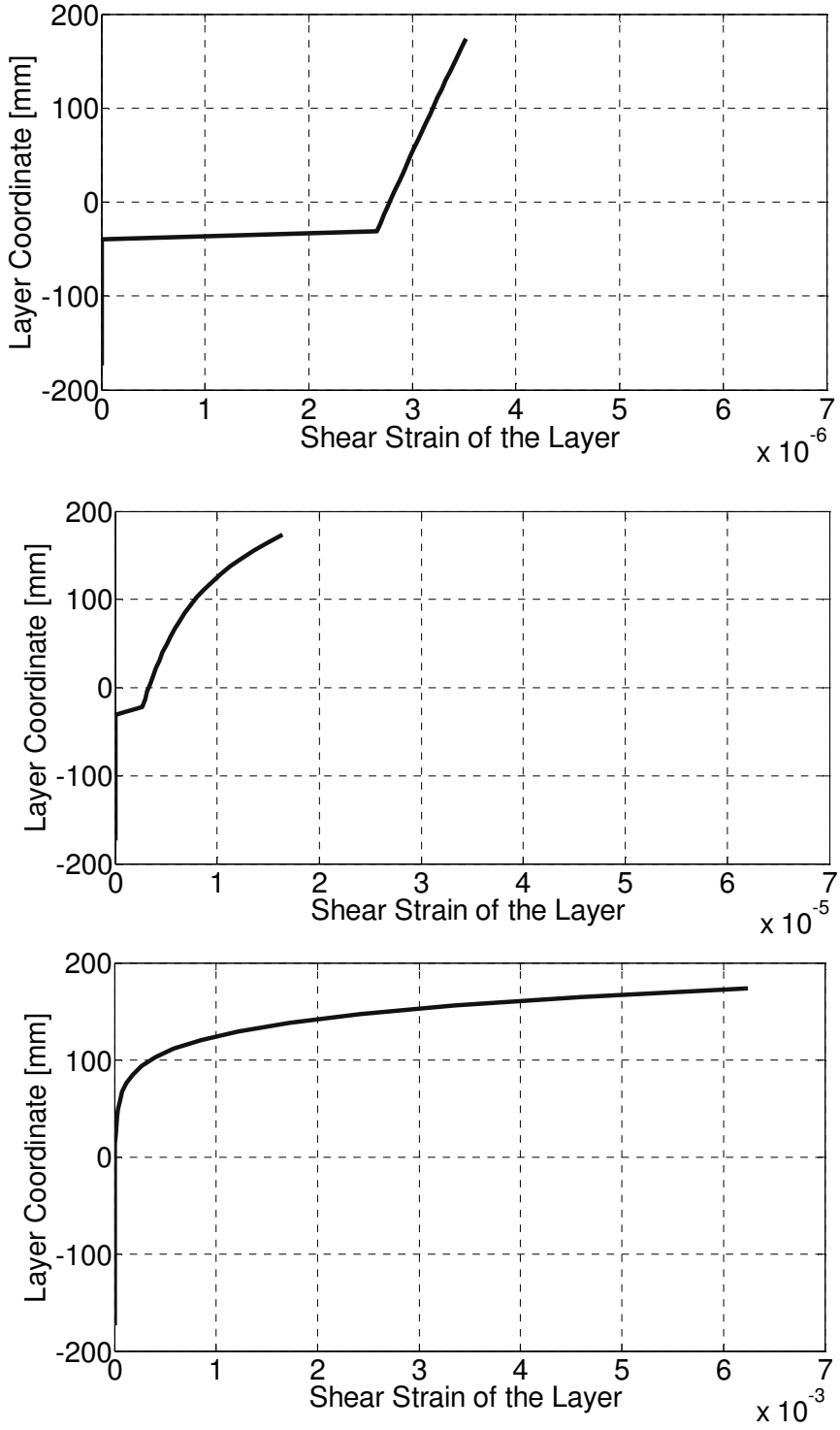


Figure 5: Shear strain profile over the section for the first curvature increment, flexural yielding and ultimate moment (from top to bottom).

3 COMPARISON OF PREDICTIONS AND EXPERIMENTAL RESULTS

The experimental study under consideration was performed by Sheikh and Yau [6] in which twelve 356 mm diameter and 1473 mm long columns were tested under constant axial load and reversed cyclic lateral load that simulated earthquake-induced forces. The test specimens were divided in three groups. The first group consisted of four columns that were conventionally reinforced with longitudinal and spiral steel reinforcement. The second group contained six reinforced concrete columns that were strengthened with carbon fiber-reinforced polymers (CFRP) or glass fiber-reinforced polymers (GFRP) before testing. The last group included two columns that were damaged to a certain extent, repaired with fiber-reinforced polymers (FRP) under axial load and then tested to failure. The correlation with the second group will be provided here. The columns contained six 25M longitudinal steel bars, and the spirals were made of U.S No 3. bars. The latter experimental program was conducted on FRP-retrofitted columns subjected to constant axial load and increasing cycles of lateral deformation in single-curvature setup. Four specimens of identical dimensions and steel reinforcements are used from this study. For each level of applied axial load (27% and 54% of the axial load carrying capacity, Po), two columns were retrofitted using two different types of FRP lamina, carbon (CFRP) and glass (GFRP), prior to testing.

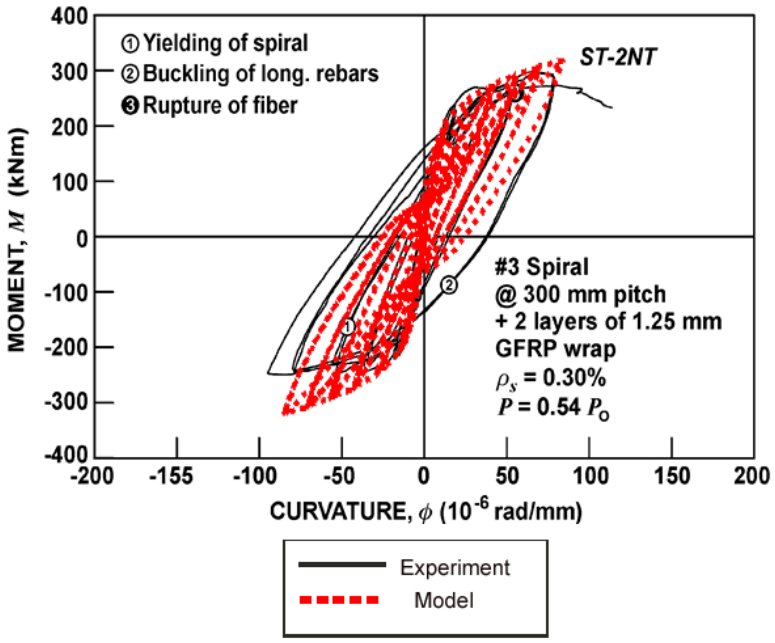


Figure 6: Correlation with experimental results ST-2NT – Sheikh and Yau [6]

The modeling of the RC columns has been performed using the "MatLab Finite Elements for Design Evaluation and Analysis of Structures" (FEDEAS Lab [8]). The experimental moment curvature responses within the plastic hinge regions are reported along with the numerical results in Fig. 6 – 9 (only flexure is considered in this case). The modeling of the cantilever columns has been applied using a unique fiber beam-column element [9] with displacement formulation for the entire column and then reporting the moment curvature response of the most critical section. It can be seen that the agreement is very close to the experimental one, with some deviation concentrated on the parts of reloading after reversal of the imposed displacement. This difference in response in terms of modeling can be explained

based on the way the cracks on the concrete surface are described in the level of the material model. Because the crack is described as a two-event phenomenon (open or closed) (in reality, this is not the case due to imperfect crack closure), the contribution of concrete while the longitudinal steel reinforcement is in compression and the crack is closing gives this deviation in the response. The total moment-curvature response until the last step of numerical convergence is provided here.

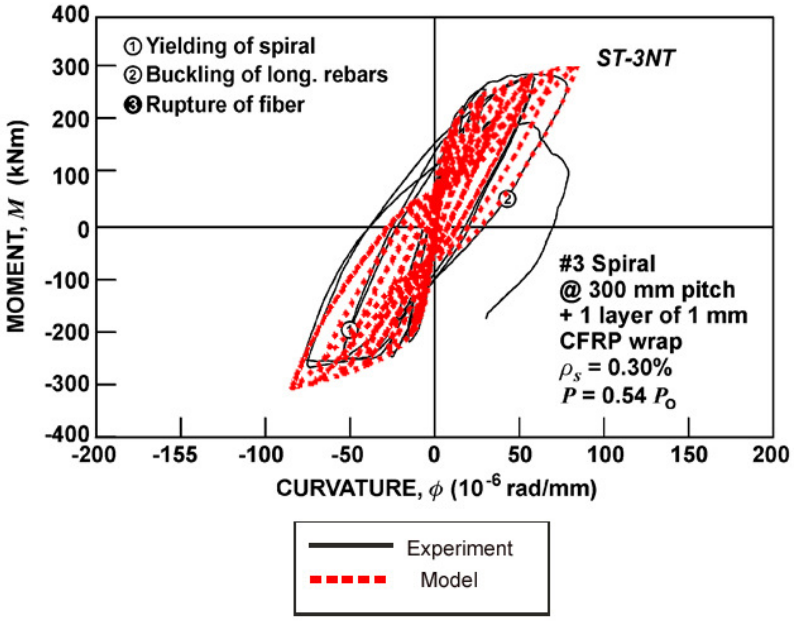


Figure 7: Correlation with experimental results ST-3NT – Sheikh and Yau [6].

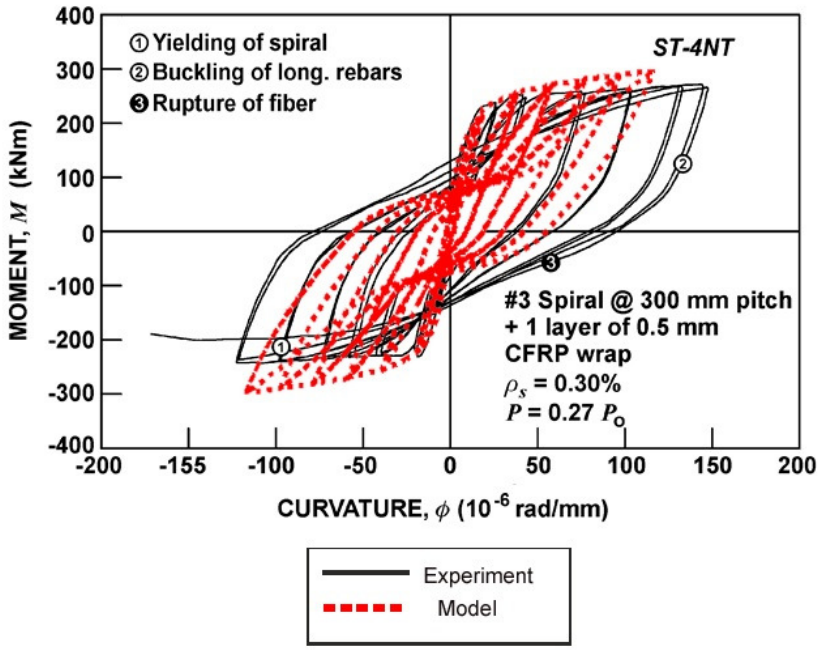


Figure 8: Correlation with experimental results ST-4NT – Sheikh and Yau [6].

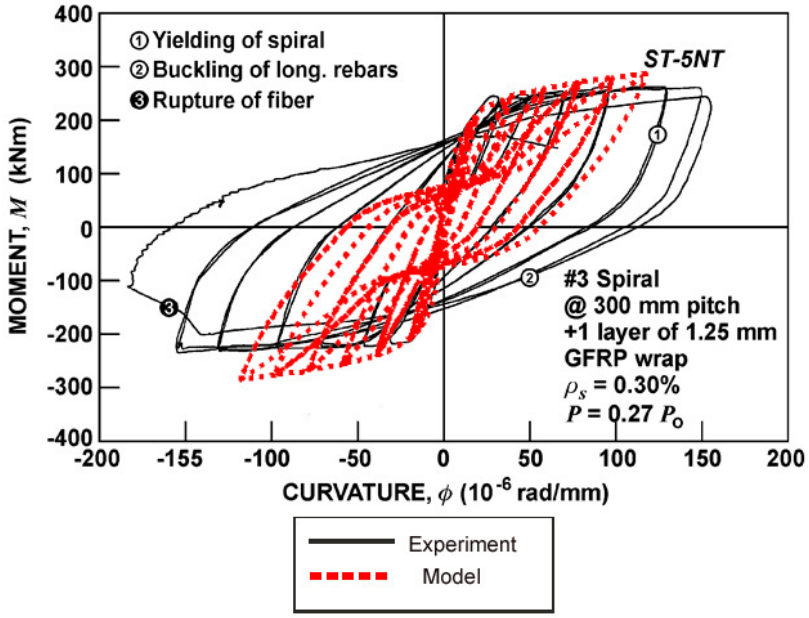


Figure 9: Correlation with experimental results ST-5NT – Sheikh and Yau [6].

4 CONCLUSIONS

Based on the results of this analytical investigation and the comparison of the predictions with the experimental study under consideration, the following conclusions are drawn:

- In case of RC column modeling with a fiber nonlinear beam- column element (displacement formulation) based on the presented constitutive law for concrete, apart from the immediate incorporation of shear deformations (uncoupled from the normal ones) in the material level (and in contrast to the standard fiber beam-column formulation), the averaged response of the two different regions -concrete core and concrete cover- in the cross-section allows the assignment of a unique stress-strain law for all the fibers/layers of the circular section.
- Moreover, in contrast to the assumption of a Timoshenko beam the shear deformation is not constant along the section. Along that line, also Timoshenko's assumption about shear deformation being a result of pure shear is adjusted in this case.
- Finally, another aspect that seems to be valid and important for further thought is that the response of the RC columns based on the model here presented is correct, although they are under cyclic excitation and contrary to the model assumptions, which are clearly static. Moreover, it uses the idea of the superposition of the effects of confinement that extends further of the linear assumptions.

ACKNOWLEDGEMENTS

This work has been carried out with the financial support of the Alexander S. Onassis Public Benefit Foundation.

REFERENCES

[1] P.Ceresa, L.Petrini, R.Pinho, Flexure-shear fiber beam-column elements for modeling frame structures under seismic loading-state of the art, *Journal of Earthquake Engineering*, **11**, 46–88, 2007.

[2] M.R. Spoelstra and G.Monti, FRP-Confined Concrete Model , *Journal of Composites for Construction ASCE* , **3**(3), 143-150,1999.

[3] F.Braga, R.Gigliotti, M.Laterza, Analytical Stress-Strain Relationship for Concrete Confined by Steel Stirrups and/or FRP Jackets, *Journal of Structural Engineering ASCE* , **132**(9), 1-15, 2006.

[4] Technical Report, *Externally bonded FRP reinforcement for RC structures*, 14th fib bulletin, The International Federation for Structural Concrete (fib), Lausanne, Switzerland, 2001

[5] K.G. Megalooikonomou, G.Monti, S.Santini, Constitutive Model for Fiber –Reinforced Polymer - and Tie – Confined Concrete , *ACI Structural Journal*, **109**(4), 569-578, 2012

[6] SA Sheikh, G. Yau, Seismic Behavior of Concrete Columns Confined with Steel and Fiber-Reinforced Polymers, *ACI Structural Journal*, **99**(1), 72-80, 2002.

[7] M. Menegotto, Pinto, P. , Method of analysis for cyclically loaded reinforced concrete plane frames including changes in geometry and non-elastic behavior of elements under combined normal force and bending, *IABSE Symposium on Resistance and Ultimate Deformability of Structures Acted on by Well Defined Repeated Loads*, Lisbon , Portugal, 1973.

[8] F.C. Filippou, M.Constantinides, *FEDEAS Lab – Getting Started Guide and Simulation Examples*, NEESgrid Report 2004-22 and SEMM Report 2004-05, 2004 (http://fedeaslab.berkeley.edu/).

[9] E.Spacone, F.Filippou, F.Taucer, Fiber beam-column model for nonlinear analysis of R/C frames: Part I. Formulation., *Earthquake Engineering and Structural Dynamics*, **25**, 711 – 725, 1996.

NOTATION:

C =*circumference of the circular section*

ΔC =*change in the circumference of the circular section*

ε_r =*radial strain*

ε_c =*circumferential strain*

ε_{con} =*concrete's axial strain*

ε_{co} =*concrete's axial strain at unconfined concrete's strength*

ε_{cc} =*concrete's axial strain at confined concrete's strength*

$\varepsilon_{c.core}$ =*circumferential strain of the core*

$\varepsilon_{r.core}$ =*radial strain of the core*

$\varepsilon_{r.cover}$ =*radial strain of the cover*

R_{core} =*radius of the concrete core*

c =*concrete cover*

f_{co} =*concrete strength*

f_{cc} =*confined concrete strength*

v_o =*initial Poisson's coefficient for concrete*

v =*Poisson's coefficient for concrete*

ρ_{sh} =*steel hoop's volumetric ratio*

ρ_j =*FRP jacket's volumetric ratio*

G_{core} =*shear modulus of concrete core*

G_c =*shear modulus of concrete*

τ_{core} =*shear stress of concrete core*

τ_c =*concrete shear stress*

γ_c =*concrete shear strain*

$\overline{\gamma_c}$ =*mean value of shear strains of the fibers/layers*

φ =*curvature of section*

M =*applied moment*

E = *modulus of elasticity*

I = *moment of inertia*

$f_{l.core}$ =*lateral confining pressure of the concrete core*

$f_{l.cover}$ =*lateral confining pressure of the concrete cover*

$f_{l.steel}$ =*lateral confining pressure of the steel reinforcement*

$f_{c.av}$ =*average axial concrete stress*

$f_{c.core}$ =*axial concrete core stress*

$f_{c.cover}$ =*axial concrete cover stress*

$f_{cc.core}$ =*axial confined concrete core strength*

$f_{cc.cover}$ =*axial confined concrete cover strength*

A_{core} =*area of concrete core*

A_{cover} =*area of concrete cover*

f_l =*lateral confining pressure of concrete*

f_c =*axial concrete stress*

E_{con} =*modulus of elasticity of concrete*

E_{sec} =*secant modulus of elasticity of concrete*

β =*a property of concrete evaluated as a function of the unconfined concrete strength*

D_b =*bar diameter*

E_s =*modulus of elasticity for steel*

A_{tot} =*total area of the circular section*

A_{sh} =*area of steel hoops (ties)*

ε_{sl} =*axial strain in the bar*

ε_{sh} =*steel hoop's strain*

ε_{shu} =*ultimate steel hoop's strain*

ε_{yh} =*steel hoop's strain for yielding*

k_{sl} =*Partial confinement coefficient for steel*

ξ_l =*coefficient taking into account longitudinal bar's confining effect*

ξ_{st} =*coefficient taking into account the confining effect of stirrups' spacing*

D_h =*hoop's diameter*

k_j =*partial wrapping coefficient*

A_b =*total area of longitudinal steel reinforcement*

A_g =*gross area of the section*

S_j =*jacket's clear spacing*

E_j =*jacket's modulus*

t_j =*thickness of the jacket*

P_o =*axial load capacity of column*

P =*axial load on column*

COMPDYN 2015
5th ECCOMAS Thematic Conference on
Computational Methods in Structural Dynamics and Earthquake Engineering
M. Papadrakakis, V. Papadopoulos, V. Plevris (eds.)
Crete Island, Greece, 25–27 May 2015

SEISMIC VULNERABILITY IN CASE OF FIRE OF EXISTING R.C. FRAMED BUILDINGS: MODELLING AND NONLINEAR DYNAMIC ANALYSIS

Fabio Mazza[1] **and Antonio De Luca**[2]

[1]Dipartimento di Ingegneria Civile, Università della Calabria
Via P. Bucci, 87036 Rende (CS), Italy
fabio.mazza@unical.it

[2]Dipartimento di Ingegneria Civile, Università della Calabria
Via P. Bucci, 87036 Rende (CS), Italy
antonioodelucaa@alice.it

Keywords: R.C. Framed Structures, Fire Scenarios, Time-Temperature Curves, Thermal Mappings, Nonlinear Dynamic Analysis.

Abstract. *The seismic vulnerability of reinforced concrete (r.c.) framed buildings designed with inadequate seismic zone classifications and seismic code provisions is recognized to be a serious problem. Nevertheless, knowledge on the seismic response in the case of fire is lacking and an amplification of the structural damage is expected in the case of fire-exposed existing structures not designed to withstand fire. To evaluate the nonlinear seismic response following a fire, a numerical investigation is carried out with reference to a five-storey r.c. framed building, which, primarily designed according to the previous Italian seismic code (DM96) for a medium risk zone, needs to be considered as in a high-risk seismic zone provided by the current Italian seismic code (NTC08). More specifically, the nonlinear seismic response of the test structure in a no fire situation is compared with that in the event of fire, at 45 (i.e. R45) and 60 (i.e. R60) minutes of fire resistance, assuming damaged (i.e. DS) and repaired (i.e. RS) stiffness conditions. Five fire scenarios have been considered on the assumption that the fire compartment is confined to the area of the first level (i.e. F1), the first two (i.e. F1/2) and the upper (i.e. Fi, i=3-5) levels, with the parametric temperature-time fire curve evaluated in accordance with Eurocode 1. The nonlinear dynamic analysis is performed through a step-by-step procedure based on a two-parameter implicit integration scheme and an initial-stress-like iterative procedure. At each step of the analysis, plastic conditions are checked at the critical (end) sections of the girders and columns, where a thermal mapping with reduced mechanical properties is evaluated in line with the 500°C isotherm method proposed by Eurocode 2. Two sets of seven real motions, whose response spectra match on average NTC08 spectra for a subsoil class B, are considered with regard to high-risk seismic zone and two topographic classes.*

1 INTRODUCTION

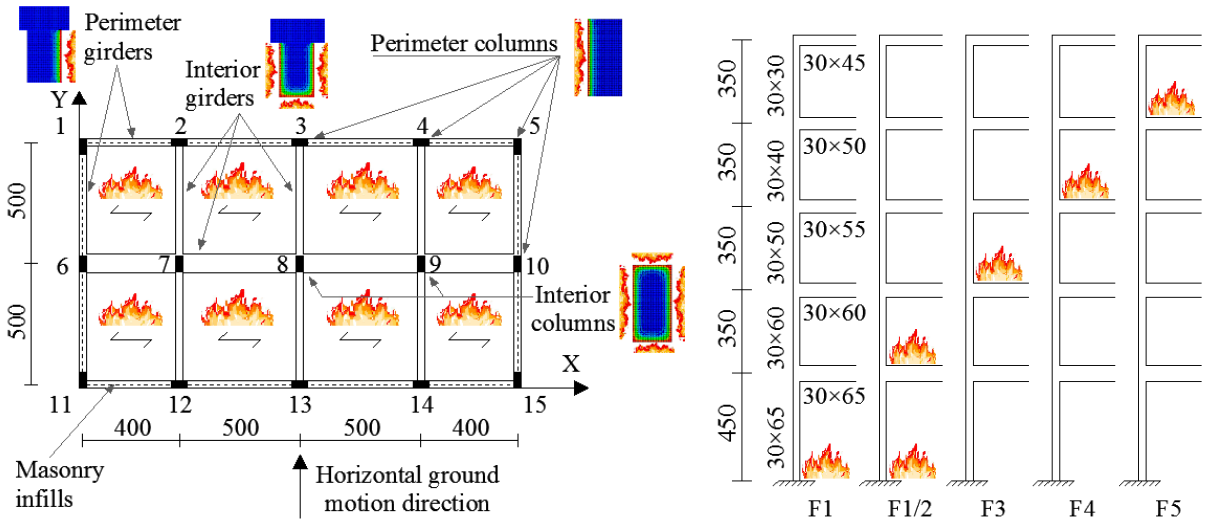
Assessment of the seismic vulnerability of existing structures where fire safety is neglected represents a far-reaching problem especially in the case of reinforced concrete (r.c.) buildings designed for vertical loads only or with inadequate seismic zone classifications and code provisions. In the conventional aseismic design it is accepted that structures can withstand strong ground motions by mainly undergoing inelastic deformations. Consequently, fire can be a serious problem for a structure that has been partially damaged in a prior seismic event, because fire resistance will decrease [1]. More specifically, the fire response of r.c. frame members depends on the thermal (i.e. thermal conductivity, specific heat, thermal diffusivity and mass loss), mechanical (i.e. compressive and tensile strength, modulus of elasticity and stress-strain law) and deformation (i.e. thermal expansion and creep) properties of concrete and reinforcing steel bars, changing substantially with heating rate, strain rate and temperature gradient [2]. The combined effect of earthquake and fire has gained attention of recent studies into the nonlinear response of r.c. framed [3] and frame-wall [4] structures.

On the other hand, earthquakes following fires may find structures whose seismic resistance is considerably reduced. Numerical [5-7] and experimental [8, 9] studies have been carried out on the assessment of the residual seismic load capacity of r.c. structures, in terms of stiffness, strength and ductility after fire. In most cases of fire, structures experience degradation of material properties, due to high temperature, and damage to the structural members, from thermal expansion. In addition, fire induces spalling of concrete that can play a significant role in the seismic performance of r.c. frame members. However, despite the lack of knowledge on the seismic vulnerability of existing framed structures in the event of fire we can expect an amplification of the structural damage in the case of existing structures that have been exposed to fire.

In the present work, the nonlinear seismic response of r.c. framed structures in a no fire situation is compared with that in which fire has occurred, at 45 (i.e. R45) and 60 (i.e. R60) minutes of fire resistance, assuming both damaged (i.e. DS) and repaired (i.e. RS) stiffness conditions in the r.c. frame members. To this end, five-storey r.c. office buildings are designed in line with the previous Italian seismic code [10] for a medium risk zone. A numerical fire investigation is carried out considering a thermal-mechanical mapping analysis, with reduced mechanical properties evaluated in accordance with the 500°C isotherm method proposed by Eurocode 2 [11], followed by a sequentially uncoupled nonlinear dynamic analysis [12, 13]. In order to study the seismic response of the r.c. framed building damaged from fire, real ground motions corresponding to high-risk seismic intensity, provided by the current Italian seismic code [14], and different topographic conditions are considered. Five fire scenarios are hypothesized assuming the fire compartment confined to the area of the first level (i.e. F1), the first two (i.e. F1/2) and the upper (i.e. Fi, i=3-5) levels, with the parametric temperature-time fire curve evaluated in accordance with Eurocode 1 [15].

2 R.C. TEST STRUCTURE: DESIGN AND FIRE MODELLING

A typical five-storey office building with a r.c. framed structure, whose symmetric plan is shown in Figure 1a, is considered as test structure. Perimeter masonry infills, assumed as non-structural elements regularly distributed in elevation, are considered. For the sake of simplicity, the plane frames orientated along the horizontal ground motion direction (*Y*), perpendicular to the floor slab direction (*X*) shown in Figure 1a, are considered as a reference scheme. The dimensions of the cross sections assumed for the columns and the girders, equal at a given level and with a regular tapering in elevation, are reported in Figure 1b.



(a) Plan and fire compartment. (b) Elevation and fire scenarios.

Figure 1: R.c. test structure (dimensions in cm).

A simulated design of the test structure is carried out in line with the previous Italian seismic code (DM96, [10]), for a medium-risk seismic region (degree of seismicity S=9, which corresponds to a coefficient of seismic intensity C=0.07) and a typical subsoil class (subsoil parameter ε=1). The gravity loads are represented by a dead load of 4.48 kN/m^2 on the top floor and 5.18 kN/m^2 on the other floors, and a live load of 3.0 kN/m^2 on all the floors; infill walls, regularly distributed in elevation along the perimeter are considered, assuming an average weight of about 2.7 kN/m^2. A cylindrical compressive strength of 20 N/mm^2 for the concrete and a yield strength of 375 N/mm^2 for the steel are assumed for the r.c. frame members. The design complies with the ultimate limit states satisfying minimum conditions for the longitudinal bars of the girders and columns: at least two 12 mm bars are provided both at the top and bottom throughout the entire length of the frame members; for the girders, a tension reinforcement ratio not less than 0.37% (for the assumed yield strength) is provided and, at their end sections, a compression reinforcement not less than half of the tension reinforcement is placed; minimum steel geometric ratio is 1% for the symmetrically-reinforced section of each column. The dynamic properties of the six main vibration modes are reported in Table 1: i.e. vibration period (T_i); effective masses in the X ($m_{E,X}$) and Y ($m_{E,Y}$) directions, expressed as percentage of the total mass (m_{tot}).

Mode	T_i [s]	$m_{E,X}$ [%m_{tot}]	$m_{E,Y}$ [%m_{tot}]
1	0.808	81.6	0
2	0.749	0	80.4
3	0.326	13.0	0
4	0.302	0	13.5
5	0.195	3.4	0
6	0.183	0	3.8

Table 1: Dynamic properties of the test structure (m_{tot}= 9.35 kNs^2/cm).

Five fire scenarios have been reported in Figures 1a and 1b, assuming the fire compartment is confined to the area of the first level (i.e. F1), the first two (i.e. F1/2) and the upper (i.e. Fi, i=3-5) levels. It is worth noting that F1/2 fire scenario is obtained from F1 and F2, which occur simultaneously. The geometric properties of the fire compartment are reported in Table 2, for the first and the upper levels: i.e. L, D and H representing length, depth and height, respec-

tively; A_f, floor area; A_t, total area of enclosure (i.e. walls, ceiling and floor, including openings); A_v, total area of vertical openings; h_{eq}, weighted average height of windows. From these values it is possible to define an opening factor, representing the amount of ventilation:

$$O = A_v h_{eq}^{0.5} / A_t \tag{1}$$

Fire compartment	L [m]	D [m]	H [m]	A_f [m^2]	A_t [m^2]	A_v [m^2]	h_{eq} [m]	O [m$^{0.5}$]
First level	18	10	4.5	180	612	24	1.5	0.048
Upper levels	18	10	3.5	180	556	24	1.5	0.053

Table 2: Geometric properties of fire compartment.

Depending on combustible contents and relevant combustible parts of the building, the design value of the fire load density is defined as [15]:

$$q_{t,d} = q_{f,d} \, A_f / A_t \tag{2}$$

related to the value $q_{f,d}$ corresponding to the surface area of the floor

$$q_{f,d} = \frac{Q_{f,k}}{A_f} \cdot \delta_{q1} \cdot \delta_{q2} \cdot \delta_n \tag{3}$$

where: $Q_{f,k}$ is the characteristic fire load; δ_{q1} and δ_{q2} are dimensionless factors, taking into account the fire risk due to the size of the compartment and the type of occupancy, respectively; δ_n is a dimensionless factor taking into account the different fire fighting measures. With reference to 45 min (i.e. R45) and 60 min (i.e. R60) of exposure, the design parameters of the fire load reported in Table 3 are obtained, for the first and the upper levels of the test structure.

Fire compartment	Fire resistance [min]	$Q_{f,k}$ [MJ]	δ_{q1}	δ_{q2}	δ_n	$q_{f,d}$ [MJ/m^2]	$q_{t,d}$ [MJ/m^2]
First level	R45	102904	1	1	1	571.7	168.1
Upper levels		102904	1	1	1	571.7	185.1
First level	R60	114102	1	1	1	633.9	186.4
Upper levels		114102	1	1	1	633.9	205.2

Table 3: Design parameters of fire load.

Afterwards, the thermal absorptivity coefficient of the surrounding surfaces in the fire compartment can be calculated as

$$b = \sqrt{\rho c \lambda} \tag{4}$$

ρ being the density, c the specific heat and λ the thermal conductivity of enclosure boundary. More specifically, in the case the j-th enclosure surface is made with different layers of material, b_{1j} and b_{2j} thermal absorptivity coefficients should be adopted to define the design value b_j, where labels 1 and 2 refer to the layer directly exposed to the fire and the next one, respectively. Finally, to account for different thermal absorptivity coefficients in the walls (i.e. masonry infills), ceiling (i.e. top floor slab) and floor (i.e. bottom floor slab), the thermal absorptivity coefficient is modified thus:

$$b = \sum_j \left(b_j \cdot A_j \right) / \left(A_t - A_v \right) \tag{5}$$

A_j being the area of the j-th enclosure surface, openings not included. In Table 4, the main parameters for defining the thermal absorptivity coefficient of the fire compartment are reported for the test structure, with reference to both R45 and R60 at the first and upper levels.

Fire compartment	Enclosure surface	b_{1j} [J/m^{2}s$^{1/2}$K]	b_{2j} [J/m^{2}s$^{1/2}$K]	b_j [J/m^{2}s$^{1/2}$K] R45	R60	A_j [m^2]	b [J/m^{2}s$^{1/2}$K] R45	R60
First level	Masonry infill	1131.37	963.00	1034.14	1030.56	228	1128.3	1125.8
	Top floor slab	1131.37	963.00	1034.14	1030.56	180		
	Bottom floor slab	1341.64	2300.00	1341.64	1341.64	180		
Upper levels	Masonry infill	1131.37	963.00	1034.14	1030.56	172	1138.2	1135.8
	Top floor slab	1131.37	963.00	1034.14	1030.56	180		
	Bottom floor slab	1341.64	2300.00	1341.64	1341.64	180		

Table 4: Thermal absorptivity coefficient of fire compartment.

Assuming closed openings once the fire scenarios have been hypothesized (Figure 1b), the temperature is considered uniform in the selected compartment (Figure 1a) in such a way to be the most severe condition for the fire before an earthquake. Several models can be used to simulate the time-temperature evolution during an actual fire, from the flashover to the full development: conventional fire curves (e.g. the standard ISO-834 curve [16]), in which the temperature monotonically increasing with time represents the heating phase only, when the fuel supply is assumed to be inexhaustible; natural fire curves (e.g. the EC1 curve [15]), in which temperature depends on the ventilation and fire load in the compartment and the cooling phase is represented, based on the assumption that at a certain point, either the air or the combustible material will diminuish.

The EC1 parametric fire curve is used in the present study, on the assumption that the fire load of the compartment is completely burnt out. In the heating phase, the gas temperature θ_g(°C)

$$\theta_g = 20 + 1325\left(1 - 0.324e^{-0.2t^*} - 0.204e^{-1.7t^*} - 0.472e^{-19t^*}\right) \tag{5}$$

is a function of a fictitious time t^* obtained by considering time t (in hours) multiplied by a dimensionless parameter equal to

$$\Gamma = \left(O/b\right)^2 \Big/ \left(0.04/1160\right)^2 \tag{6}$$

The gas temperature in the cooling phase is given by

$$\begin{aligned} &t^*_{\max} \le 0.5\ h \rightarrow \theta_g = \theta_{\max} - 625\left(t^* - t^*_{\max}\right) \\ &0.5\ h < t^*_{\max} < 2\ h \rightarrow \theta_g = \theta_{\max} - 250\left(3 - t^*_{\max}\right)\left(t^* - t^*_{\max}\right) \\ &t^*_{\max} \ge 2\ h \rightarrow \theta_g = \theta_{\max} - 250\left(t^* - t^*_{\max}\right) \end{aligned} \tag{7}$$

where the maximum temperature θ_{max} in the heating phase happens for

$$t^*_{\max} = \left(0.2 \cdot 10^{-3} q_{t,d} / O\right)\Gamma \tag{8}$$

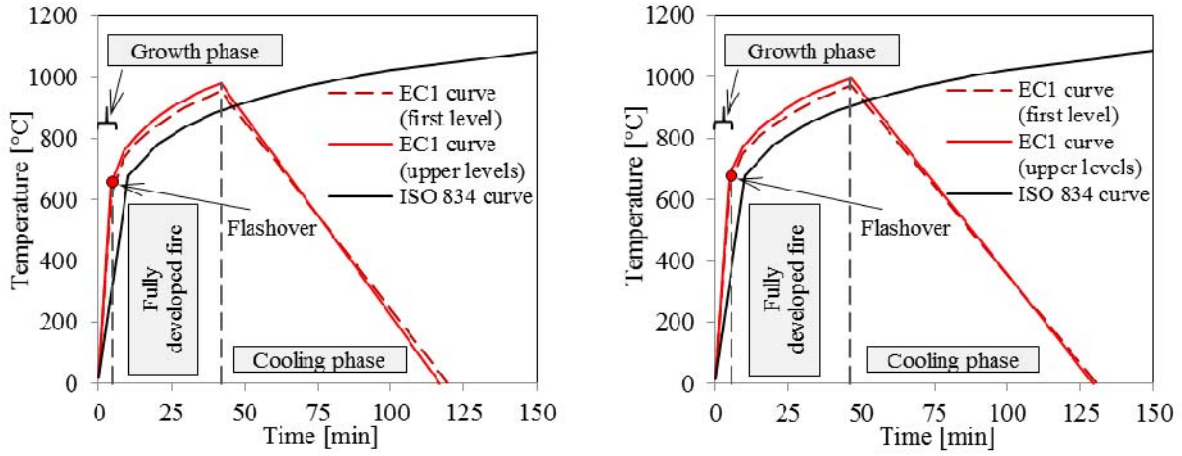
Finally, the standard ISO-834 curve is defined as [16]

$$\theta_g = 20 + 345\log_{10}\left(8t + 1\right) \tag{9}$$

where t is expressed in hours.

With reference to the fire scenarios shown in Figure 1, the ISO and EC1 time-temperature curves are compared in Figure 2 in the case where a fire compartment is confined to the first level and the upper ones. The combination of fire parameters, for the open-plan office building, results in a temperature of 918°C (t^*_{max}=1.07h) and 942°C (t^*_{max}=1.27h) in 45 min (i.e.

fire resistance R45 in Figure 2a) and 816°C (t^*_{max}=1.19h) and 836 °C (t^*_{max}=1.41h) in 60 min (i.e. fire resistance R60 in Figure 2b), at the first and upper floors, respectively.

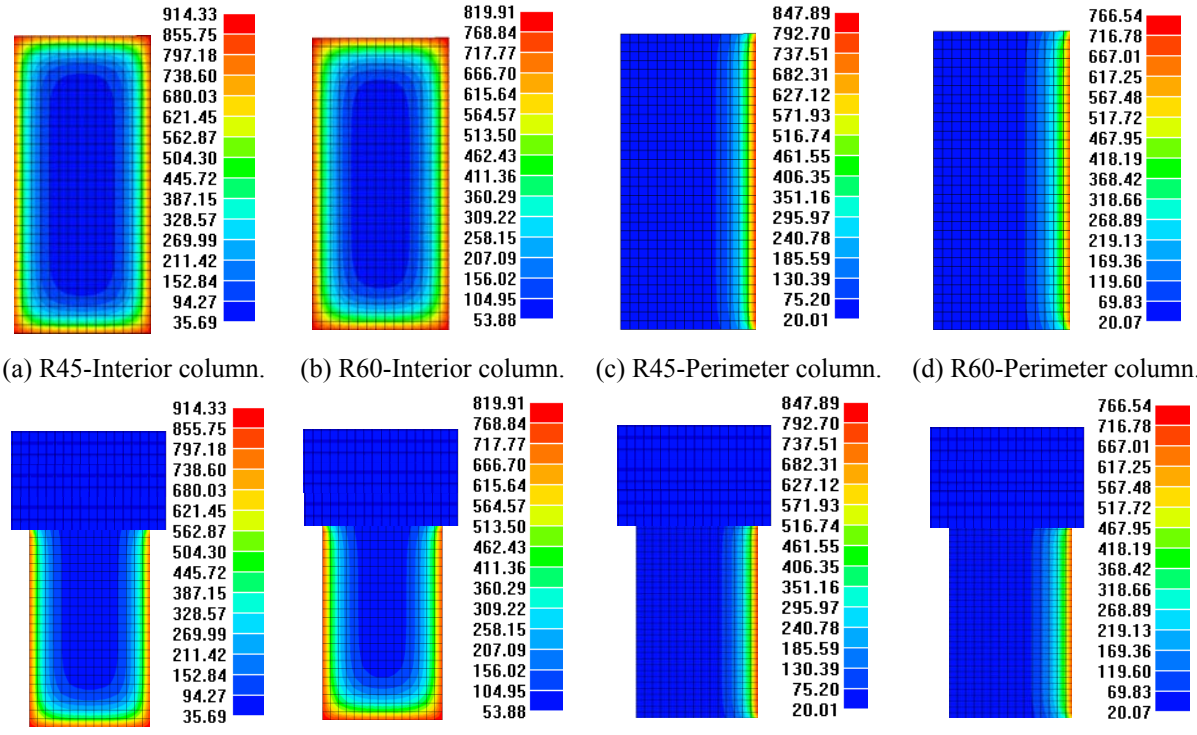


(a) R45. (b) R60.

Figure 2: Conventional (ISO 834) and natural (EC1) fire curves.

3 NUMERICAL RESULTS: FIRE LOADING BEFORE AN EARTHQUAKE

Once the time-temperature curve of the fire compartment is determined with the EC1 model, it is possible to evaluate the temperature distribution in the frame members of the test structure at R45 and R60. As an example, thermal mappings of interior and perimeter r.c. frame members in the first level of the test structure are plotted in Figure 3, considering a convection factor equal to 25 and an emissivity of the concrete surface equal to 0.56.



(a) R45-Interior column. (b) R60-Interior column. (c) R45-Perimeter column. (d) R60-Perimeter column.

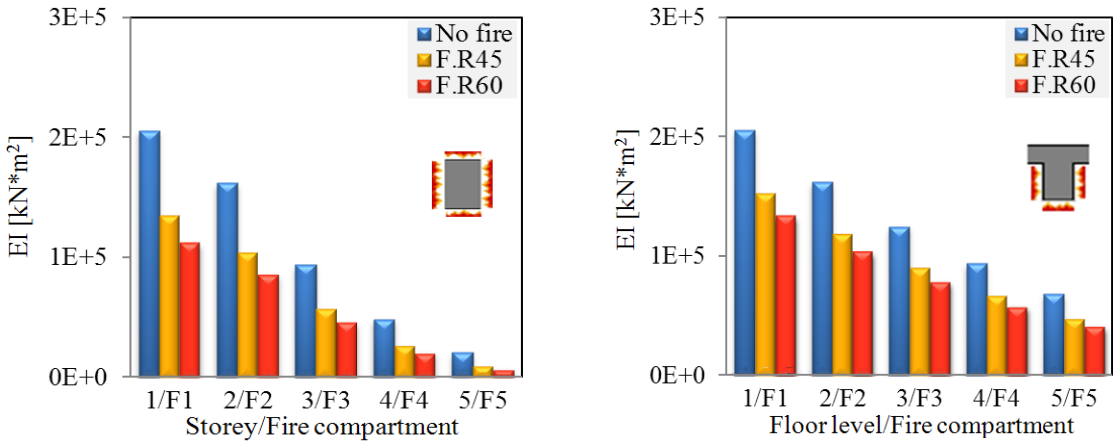
(e) R45-Interior girder. (f) R60-Interior girder. (g) R45-Perimeter girder. (h) R60-Perimeter girder.

Figure 3: Thermal mappings at 1st level of test structure.

In detail, the finite thermal element cross-section model of columns, exposed to fire on four (Figures 3a and 3b) and one (Figures 3c and 3d) sides, and girders, exposed to fire on three (Figures 3e and 3f) and one (Figures 3g and 3h) sides, are considered assuming an ambient tempearture of 20°C for the unexposed cross-section sides. As expected, at the end of 45 and 60 minutes of exposure, the increase in temperature is greater in the case of cross-sections exposed on four or three sides compared to those exposed on one side only. Moreover, the temperature profiles highlight a decrease in the maximum value with the time increment from R45 to R60, in accordance with EC1 natural fire curves shown in Figure 2, but the concrete zone damaged by heat is more extended in the case of R60.

Subsequently, the residual seismic load capacity of the cross-sections after fire is evaluated in accordance with the 500°C isotherm method of Eurocode 2 [11], in terms of stiffness, strength and ductility reductions. The simplified calculation provides for a reduction of the cross-section size, with respect to a heat damaged zone defined by thermal mapping. Concrete with temperatures exceeding 500°C, corresponding roughly to the thickness of the unconfined zone, is not assumed to contribute, while the residual concrete cross-section retains its initial values of strength and modulus of elasticity. On the other hand, the reduced yield strength of each longitudinal reinforcement bar, in the tension and compression zones of the cross-section, is evaluated with respect to the steel temperature profile in the centre of the bar [17]. It is worth noting that some of the reinforcing bars may fall outside the reduced cross-section, but they are included in the calculation of the ultimate values of load bearing capacity and curvature ductility, which is evaluated in line with the provisions of Eurocode 8 for the assessment of existing buildings [18].

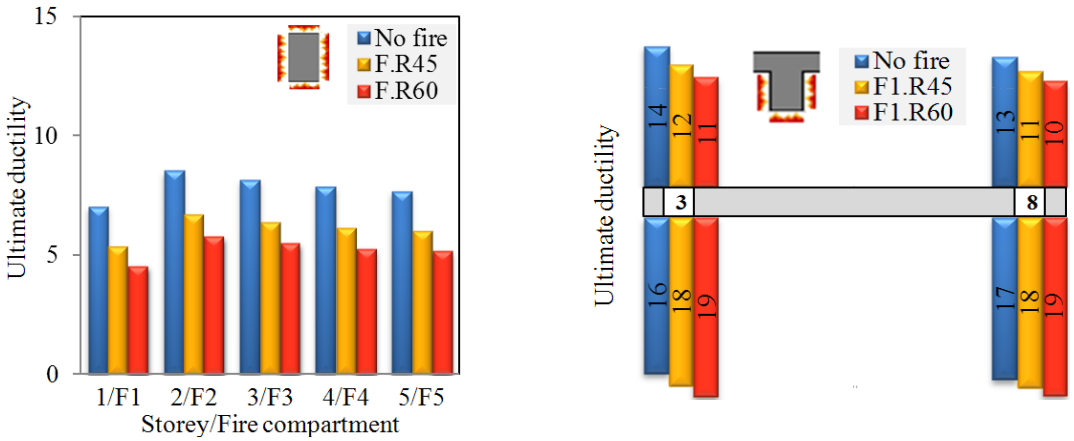
In Figure 4, flexural stiffness in the fire-exposed cross-section of r.c. frame members is reported along the building height, assuming a direct correspondence between the examined level and the fire compartment. In particular, interior columns (Figure 4a) and girders (Figure 4b) are examined at the end of 45 (i.e. F.R45 structure) and 60 (i.e. F.R60 structure) minutes of exposure to fire. As expected, a local decrease in stiffness from a minimum, of about 34% and 26% at the 1st level, and a maximum, of about 52% and 30% at the 5th level, is obtained for the interior columns and girders of the F.R45 structure, respectively, in comparison with the no-fire condition. A further minimum decrease in stiffness, of about 12% and 9% at the 1st level, and maximum, of about 13% and 10% at the 5th level, is obtained after an additional 15 minutes of fire (i.e. F.R60 structure). Further results, which are omitted for the sake of brevity, have confirmed limited fire effects in the perimeter frame members at all levels where the fire compartment is supposed.



(a) Interior column n. 8. (b) Interior girder n. 3-8.

Figure 4: Flexural stiffness of r.c. frame members exposed to fire.

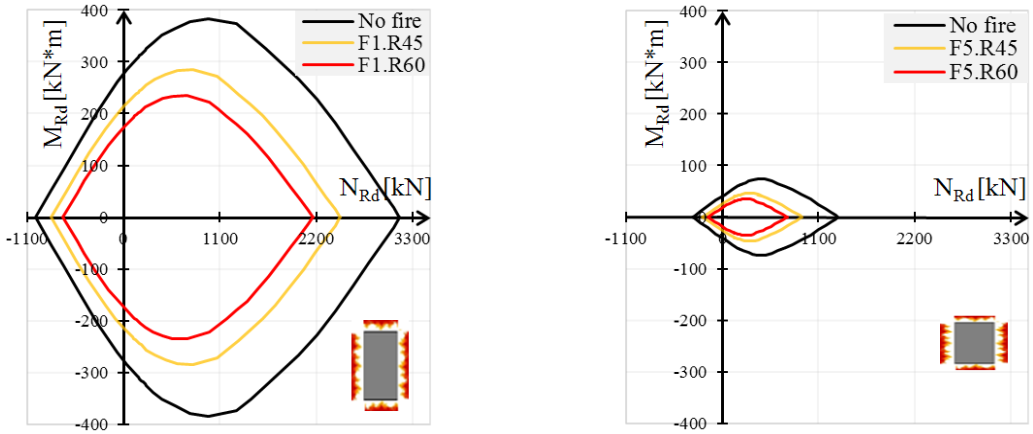
Thereafter, ultimate ductility of the columns, corresponding to the axial force due to the gravity loads, confirmed limited fire effects in the perimeter columns of all storeys where the fire compartment is supposed and a significant reduction only for the interior columns (Figure 5a), of about 22% and 33% for the F.R45 and F.R60 structures, respectively. Moreover, it is interesting to note that an increase of ductility is obtained on the bottom side of the interior girders (Figure 5b), of about 7% (i.e. F.R45) and 13% (i.e. F.R60), due to the fire-reduced yield strength of the longitudinal bars in tension. On the other hand, a decrease in the ultimate ductility at the top, of about 15% (i.e. F.R45) and 29% (i.e. F.R60), is observed because of heat damage to the compression zone of concrete and corresponding longitudinal reinforcement.



(a) Interior column n. 8. (b) Interior girder n. 3-8 (1st floor/F1).

Figure 5: Ultimate ductility of r.c. frame members exposed to fire.

Finally, analogous results are reported for the ultimate interaction domain between axial load (N_{Rd}) and bending moment (M_{Rd}) of columns (Figure 6) and the ultimate bending moment of girders (Figure 7). For clarity, only fire compartments at the first (i.e. F1 in Figures 6a and 7a) and fifth (i.e. F5 in Figures 6b and 7b) level are examined.

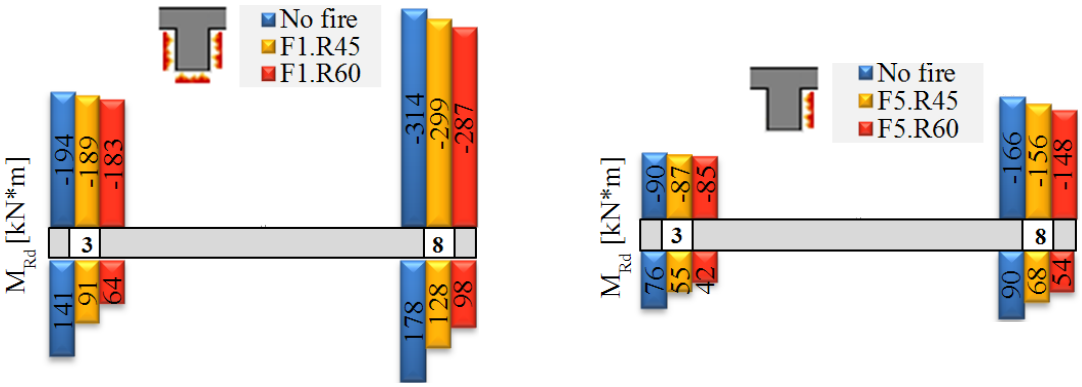


(a) Interior column n. 8 (1st storey/F1). (b) Interior column n. 8 (5th storey/F5).

Figure 6: Ultimate N_{Rd}-M_{Rd} domains of r.c. columns exposed to fire.

As can be observed, interior columns exhibit a marked narrowing of their N_{Rd}-M_{Rd} domains, especially for values of the compressive axial load greater than those corresponding to the balanced compressive load. For this axial load, a local reduction in flexural strength, in com-

parison with the no-fire condition, of about 26% and 39%, at the first storey, and 37% and 53%, at the fifth storey, is found in the F.R45 and F.R60 structures, respectively. On the other hand, a significant decrease in strength is observed on the bottom side of the interior girder 3-8 (see Figure 1a) with a maximum local reduction of about 35% and 55%, at the first floor, and 28% and 45%, at the fifth floor, considering the F.R45 and F.R60 structures, respectively.



(a) Interior girder n. 3-8 (1st floor/F1). (b) Interior girder n. 3-8 (5th floor/F5).

Figure 7: Ultimate bending moments of r.c. girders exposed to fire.

4 NUMERICAL RESULTS: SEISMIC LOADING FOLLOWING FIRE

In order to study the seismic response of the r.c. framed building described in Section 2 and damaged according to the fire loading proposed in Section 3, nonlinear dynamic analyses are carried out. To this end, the r.c. frame members are idealized by means of a two-component model (TCM), constituted of an elastic-plastic component and an elastic component, assuming a bilinear moment-curvature law [19]. The effect of the axial load on the ultimate bending moment of the columns is also considered. At each step of the analysis, the elastic-plastic solution is evaluated in terms of the initial state and the incremental load on the basis of a holonomic law, as a solution of the Haar-Kàrmàn principle [20-22]. In the Rayleigh hypothesis, the damping matrix of the framed structure is assumed to be a linear combination of the mass and stiffness matrices, assuming a damping ratio of 5% with reference to the frequencies of the second and sixth vibration modes in the Y direction (see Table 1). In this way, a somewhat lower value of the damping ratio is achieved for the fourth mode in the same direction, while the higher frequency modes, which do not contribute significantly to the dynamic response, are practically eliminated due to their high damping ratio. The structural damage is evaluated in terms of ductility demand at the critical end sections (i.e. *i* and *j*) of girders and columns. The curvature ductility demand is calculated with reference to the two loading directions, assuming as yielding curvature for the columns that corresponding to the axial force due to the gravity loads.

Real ground motions corresponding to a high-risk seismic region provided by the current Italian seismic code (NTC08, [14]), and a design subsoil class *B* (i.e. subsoil stratigraphic parameter S_S=1.08) are considered. In detail, two sets of seven recorded accelerograms, selected by the computer code REXEL [23], are considered for the topographic classes *T1* and *T2* (i.e. topographic parameters S_{T1}=1.0 and S_{T2}=1.2). The corresponding elastic response spectra of normalized acceleration (S_a/g) are plotted in Figure 8, assuming an equivalent viscous damping ratio in the horizontal direction, ξ_H, equal to 5%, considering different scale factors (SFs). On average, these spectra match the corresponding target NTC08 response spectra for PGA_{T1}=0.34g (Figure 8a) and PGA_{T2}= 0.41g (Figure 8b), in the range of vibration periods 0.05s–4s, which also contains the lower and upper limits of the vibration period (i.e. T_{min}=0.2T_1 and T_{max}=2T_1, where T_1 is the fundamental vibration period of the structure). Thus,

the selected accelerograms can be used for the nonlinear dynamic analysis of structures with $T_1 \leq 1$s. All the following results are obtained as an average of those separately obtained for the sets *T1* and *T2* of real motions.

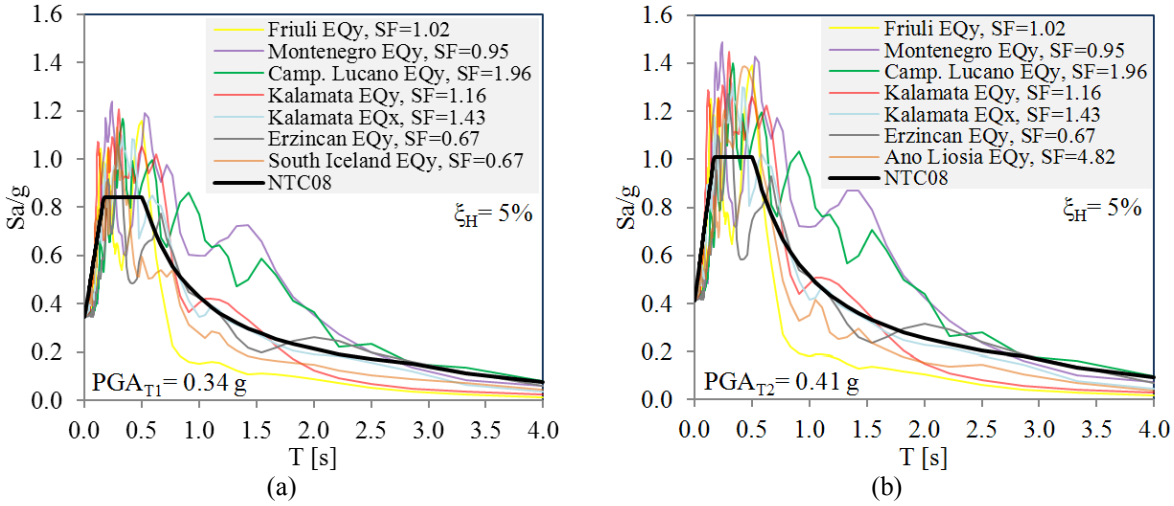


Figure 8: Acceleration (elastic) response spectra for the topographic classes *T1* (a) and *T2* (b).

Firstly, maximum ductility demand of columns and girders along the building height is plotted in Figure 9, for the topographic class *T1* (i.e. PGA_{T1}=0.34g), comparing framed structures both in the no-fire condition and at the end of 45 (i.e. R45) and 60 (i.e. R60) minutes of fire exposure. More specifically, interior columns (Figures 9a and 9c) and girders (Figures 9b and 9d) are examined, on the assumption that the fire compartment is confined to the area of the first (i.e. F1, Figures 9a and 9b) and the fourth (i.e. F4, Figures 9c and 9d) levels.

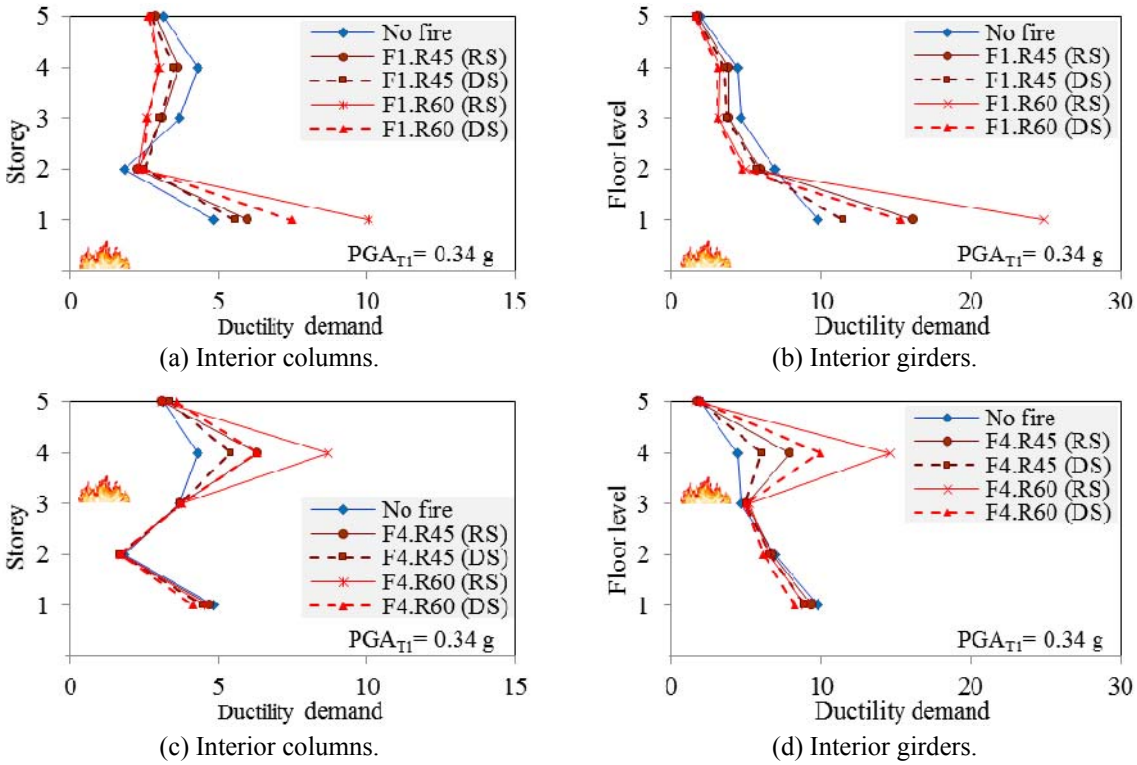
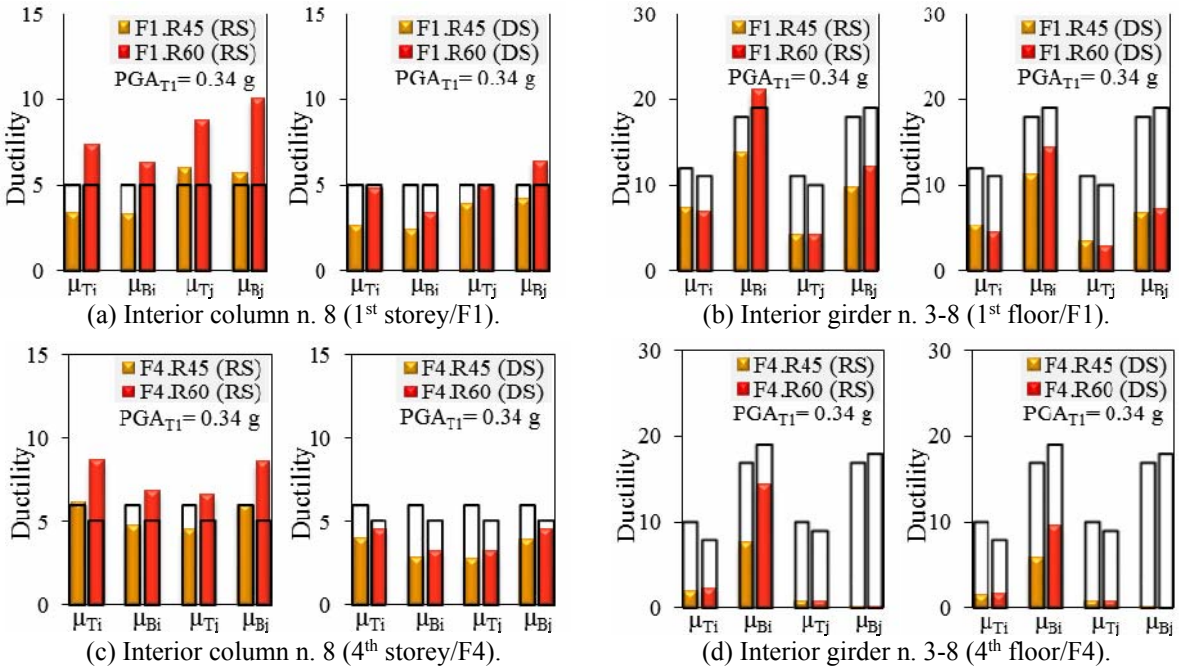


Figure 9: Global ductility demand for the topographic class *T1*:
(a) and (b), fire at the 1st level (fire scenario F1); (c) and (d), fire at the 4th level (fire scenario F4).

Moreover, r.c. frame members are assumed to have been previously damaged by fire, with a reduced cross-section (i.e. in the Damaged Stiffness condition, DS), and later repaired, e.g. using jacketing with thin layers of concrete (i.e. in the Repaired Stiffness condition, RS). As can be observed, an amplification in the structural response of fire-exposed structures is localized to the level of the fire compartment involved. As expected, this result is more marked in the F1.R60 and F4.R60 structures than in the F1.R45 and F4.R45 ones, because the first are characterized by lower strength and ductility. The results also show that the seismic response of the test structures differs in the DS and RS conditions, with higher ductility demand when the initial stiffness is restored (i.e. RS condition).

To better clarify the local damage distribution, top (i.e. μ_{Ti} and μ_{Tj}) and bottom (i.e. μ_{Bi} and μ_{Bj}) maximum ductility demand in the frame members and corresponding ultimate values are reported in Figure 10 for the fire scenarios F1 (Figures 10a and 10b) and F4 (Figures 10c and 10d). In particular, girders and columns exposed to fire on three (e.g. the interior girder 3-8) and four (e.g. the interior column 8) sides are examined. Note that the maximum ductility demand and the number of sections in which the corresponding ultimate value is exceeded increase especially at the first level, with an amplification when the initial stiffness is restored (i.e. RS condition) and R60 is assumed (Figures 10a and 10b). In this case, three interior columns and all interior girders exceed the corresponding ultimate ductility demand at the first level. Moreover, a significant increase of ductility demand on the fourth level is observed only in the interior columns of the F4.R60 structure (Figure 10c), producing a "strong beam-weak column mechanism" at this level. Further results, omitted for the sake of brevity, have confirmed this behaviour also in the case of the F3 and F5 fire scenarios.



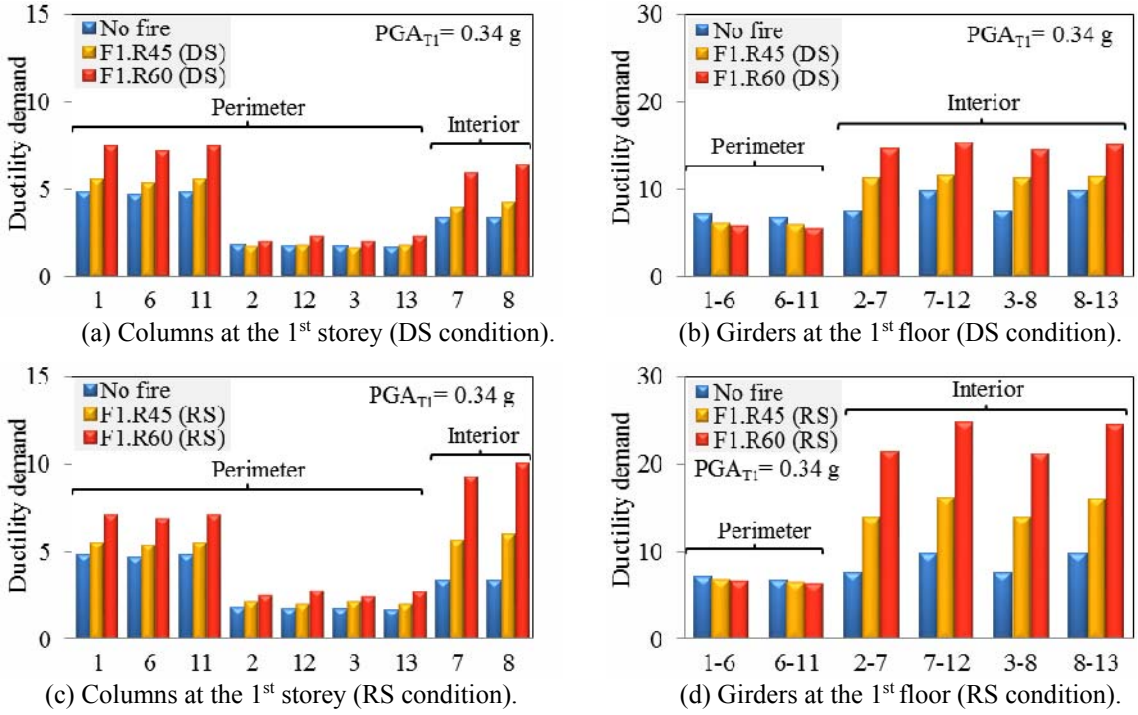
(a) Interior column n. 8 (1st storey/F1). (b) Interior girder n. 3-8 (1st floor/F1).

(c) Interior column n. 8 (4th storey/F4). (d) Interior girder n. 3-8 (4th floor/F4).

Figure 10: Local ductility for the topographic class T1:
(a) and (b), fire at the 1st level (fire scenario F1); (c) and (d), fire at the 4th level (fire scenario F4).

Afterwards, taking into account the symmetric plan shown in Figure 1a, the distribution of maximum ductility demand in the perimeter and interior frame members is investigated in Figure 11. Local maximum ductility demand in the perimeter and interior columns (Figures 11a and 11c) and girders (Figures 11b and 11d) for the DS (Figures 11a and 11b) and RS (Figures 11c and 11d) conditions are plotted at the first level where the fire compartment is

hypothesized. Note that the ductility demand increases especially in the frame members exposed on three (i.e. the interior girders 2-7, 7-12, 3-8 and 8-13) and four (i.e. the interior columns 7 and 8) sides in the RS condition. Moreover, among the columns exposed on one side greater ductility demand is obtained in the perimeter ones of the exterior frames (i.e. the perimeter columns 1, 6 and 11). Further results, omitted for the sake of brevity, confirm an increase of maximum ductility demand and number of frame members in which the corresponding ultimate value is exceeded, especially at the lower storeys.



(a) Columns at the 1st storey (DS condition).

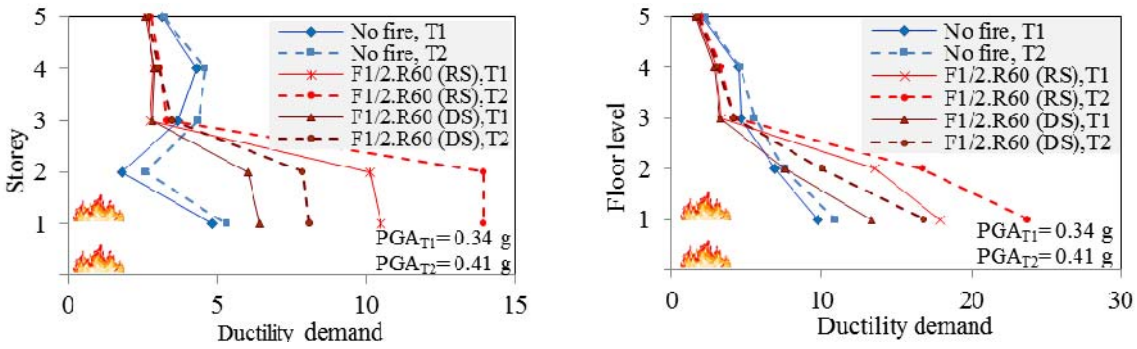
(b) Girders at the 1st floor (DS condition).

(c) Columns at the 1st storey (RS condition).

(d) Girders at the 1st floor (RS condition).

Figure 11: Local ductility demand for the topographic class *T1*: fire at the 1st level (fire scenario F1).

Finally, curves analogous to those above reported are shown in Figure 12 where fire compartment is confined to the area of the first two levels (i.e. F1/2 scenario) and R60 is assumed, with reference to the topographic classes *T1* (i.e. PGA_{T1}=0.34g) and *T2* (i.e. PGA_{T2}=0.41g). As can be observed, a significant increase in ductility is obtained in the frame members of the fire compartment moving from *T1* to *T2* topographic class.



(a) Interior columns.

(b) Interior girders.

Figure 12: Global ductility demand for the topographic classes *T1* and *T2*: fire at the 1st and 2nd levels (fire scenario F1/2).

Moreover, the maximum ductility demand of the interior columns (Figure 12a) and girders (Figure 12b) increases at the levels where the event of fire is hypothesized while it is reduced, in comparison with the no fire conditions, on the other levels. This behaviour is amplified when the RS condition and topographic class *T2* are considered. In this case, the ultimate ductility demand is reached in all the interior columns of the first two levels and all the interior girders of the first one.

5 CONCLUSIONS

The nonlinear seismic response of five-storey r.c. framed buildings, primarily designed in line with the previous Italian seismic code for a medium risk zone, is studied under two sets of seven real motions whose response spectra match, on average, NTC08 spectra with regard to a high-risk seismic zone and two topographic classes. More specifically, the nonlinear dynamic analysis of framed structures in a no fire situation is compared with that in the event of fire, at 45 (i.e. R45) and 60 (i.e. R60) minutes of exposure to fire, assuming both damaged (i.e. DS) and repaired (i.e. RS) stiffness conditions.

The numerical results show that fire safety should also be taken into account when evaluating the seismic vulnerability of existing r.c. framed buildings. Fire results show a significant decrease in stiffness and ultimate values of strength and ductility in the interior columns and girders and negligible effects in the perimeter ones. Seismic results highlight an amplification in the structural response localized to the level where the fire compartment is hypothesized, with a slight reduction on the other levels in comparison with the no fire condition. Moreover, fire scenarios at the upper levels produce "strong beam-weak column" local mechanism at these levels. Finally, the results show that the seismic vulnerability of the test structure differs in the DS and RS conditions, with higher ductility demand in the case where the initial stiffness has been restored.

ACKNOWLEDGEMENTS

The present work was also financed by Re.L.U.I.S. (Italian network of university laboratories of earthquake engineering), according to "Convenzione D.P.C.–Re.L.U.I.S. 2014–2016, WPI, Isolation and Dissipation".

REFERENCES

[1] C. Scawthorn, J.M. Eidinger, A. Schiff, Fire following earthquake. New York, NY *American Society of Civil Engineers*, 2005.

[2] V.K.R. Kodur, M. Garlock, N. Iwankiw, Structures in fire: state-of-the-art, research and training needs, *Fire Technology*, **48**, 825-839, 2012.

[3] H. Mostafaei, T. Kabeyasawa, Performance of a six-story reinforced concrete structure in post-earthquake fire. Institute for Research in Construction, *10th Canadian Conference on Earthquake Engineering*, Toronto, Canada, July 25-29, **1**, 481-490, 2010.

[4] B. Behnam, H. Ronagh, Performance of reinforced concrete structures subjected to fire following earthquake. *European Journal of Environmental and Civil Engineering,* **17**(4), 270-292, 2013.

[5] V.K.R. Kodur, N.K. Raut, X.Y. Mao, W. Khaliq, Simplified approach for evaluating residual strength of fire-exposed reinforced concrete columns. *Materials and Structures*, **46**, 2059-2075, 2013.

[6] H. Mostafaei, F. Vecchio, N. Bénichou, Seismic Resistance of Fire-Damaged Rein-

forced Concrete Columns. *ATC and SEI Conference on Improving the Seismic Performance of Existing Buildings and Other Structures,* San Francisco, California, United States, December 9-11, **1**, 1396-1407, 2009.

[7] F. Mazza, F. Alesina, Incremental dynamic analysis of fire-exposed base-isolated r.c. framed buildings subjected to near-fault ground motions. *COMPDYN 2015, 5th ECCOMAS Thematic Conference on Computational Methods in Structural Dynamics and Earthquake Engineering*, Crete Island, Greece, May 25–27, paper n. 492, 2015.

[8] H. Mostafaei, Hybrid fire testing for assessing performance of structures in fire - Methodology. Fire Safety Journal, **58**, 170-179, 2013.

[9] H. Mostafaei, Hybrid fire testing for assessing performance of structures in fire - Application. Fire Safety Journal, **56**, 30-38, 2013.

[10] Italian Ministry of Public Works (DM96). Norme tecniche per le costruzioni in zone sismiche e relative istruzioni, D.M. 16-01-1996 and C.M. 10-04-1997, n. 65/AA.GG..

[11] Eurocode 2. Design of concrete structures – Part 1-2: General rules, structural fire design. *C.E.N., European Committee for Standardization*, December 2004.

[12] F. Mazza, A. Vulcano, Nonlinear dynamic response of r.c. framed structures subjected to near-fault ground motions. *Bulletin of Earthquake Engineering*, **8**, 1331-1350, 2010.

[13] F. Mazza, M. Mazza, Nonlinear modeling and analysis of R.C. framed buildings located in a near-fault area. *The Open Construction & Building Technology Journal,* **6**, 346-354, 2012.

[14] Italian Ministry of Infrastructures (NTC08). Nuove norme tecniche per le costruzioni e relative istruzioni, D.M.14-01-2008 e Circolare 02-02-2009, n. 617/C.S.LL.PP..

[15] Eurocode 1. Actions on structures – Part 1-2: General actions, actions on structures exposed to fire. *C.E.N., European Committee for Standardization*, October 2004.

[16] ISO 834 International Standard, Fire resistance tests, ISO 834-1 Test conditions. *Provided by IHS under license with ISO: 31*, Genève, Switzerland, 1999.

[17] F. Mazza, M. Fiore, Comparative study of the wind and earthquake dynamic responses of fire exposed steel framed buildings. *COMPDYN 2015, 5th ECCOMAS Thematic Conference on Computational Methods in Structural Dynamics and Earthquake Engineering*, Crete Island, Greece, May 25–27, paper n. 490, 2015.

[18] Eurocode 8. Design of structures for earthquake resistance – Part 3: Assessment and retrofitting of buildings. *C.E.N, European Committee for Standardization*, June 2004.

[19] F. Mazza, Modelling and nonlinear static analysis of reinforced concrete framed buildings irregular in plan. *Engineering Structures*, **80**, 98-108, 2014.

[20] F. Mazza, M. Mazza, Nonlinear analysis of spatial framed structures by a lumped plasticity model based on the Haar-Kàrmàn principle. *Computational Mechanics*, **45**, 647-664, 2010.

[21] F. Mazza, A distributed plasticity model to simulate the biaxial behaviour in the nonlinear analysis of spatial framed. *Computers and Structures*, **135**, 141-154, 2014.

[22] F. Mazza, M. Mazza, Nonlinear modeling and analysis of r.c. spatial frames to study the effects of the vertical component of near-fault ground motions. *COMPDYN 2015, 3rd ECCOMAS Thematic Conference on Computational Methods in Structural Dynamics and Earthquake Engineering*, Corfù, Greece, May 25–28, paper n. 322, 2013.

[23] I. Iervolino, G. Maddaloni, E. Cosenza, Eurocode 8 compliant record sets for seismic analysis of structures. *Journal of Earthquake Engineering*, **12**, 54–90, 2008.

COMPDYN 2015
5th ECCOMAS Thematic Conference on
Computational Methods in Structural Dynamics and Earthquake Engineering
M. Papadrakakis, V. Papadopoulos, V. Plevris (eds.)
Crete Island, Greece, 25–27 May 2015

THE EFFECT OF STEEL SLIT PANELS IN RETROFITTING WEAK BUILDINGS

F. Jamshidzadeh[1], and B. Mohebi[2]

[1] Faculty of Engineering
Imam Khomeini International University, Qazvin, Iran. Postal Code: 34149-16818
e-mail: ff.jam.4@gmail.com

[2] Faculty of Engineering
Imam Khomeini International University, Qazvin, Iran. Postal Code: 34149-16818
mohebi@ENG.ikiu.ac.ir

Keywords: Steel Slit Panel (SSP); Nonlinear Static Analysis; Seismic Rehabilitation; retrofitting.

Abstract. *Due to the importance of Retrofitting and researches done about it, and the importance of selecting a good lateral resisting system, this paper is going to use Steel Slit Panel to retrofit available buildings and see its effect. This is a new system suitable for high seismic region. Some benefits of this system are its ductile behavior and ability to dissipate energy, architectural flexibility, simple fabrication and installation and its easy replacement. In this research the SSP's nonlinear behavior and their effects on retrofitting buildings are studied using nonlinear static analysis and Guidelines for seismic rehabilitation. At first the panel has modeled and analyzed in a finite element software individually and its nonlinear behavior derived to be used in the nonlinear analysis. Then weak structures and retrofitted structures with this panel have modeled and analyzed in analytical software using nonlinear static analysis and the results have compared. This panels will greatly improve the behavior of the structures. The stress ratio of the elements after retrofitting is in allowable ranges and has greatly improved. And also after retrofitting the Performance Level was improved and the life safety was obtained.*

1 INTRODUCTION

Earthquake is one of the greatest hazard of nature. Its impact is sudden and there is little or no time to get ready against damages.

One of the way of preventing the disaster caused by earthquake is to reduce the seismic risk by retrofitting existing buildings. The first step to retrofitting the structures is to strengthen and stiffen them by adding a lateral load resisting system, such as braces, shear walls and etc [1].

Selecting a good system especially in bays with openings (doors, windows, etc) is important and sometimes difficult.

The Steel Slit Panel-Frame is a new resistant system for seismic regions. Its main members are beams and columns that are simply connected and the Steel Slit Panels (SSPs) that are bolted to the beams at the top and bottom of the bays.

The SSPs has a pair of vertical stiffeners at the edge of them and are designed to resist all lateral load [2].

At first in 1969, Muto has studied on the slitted reinforced concrete walls by goal of utilizing elements that would yield at specific regions [3].

In 1991 Whittaker et al. studied the ADAS elements. It also shares the same concept of dissipating energy through yielding of steel.

The steel wall with slits were discussed in 2000 and 2003 by Hitaka and Matsui. It is similar in concept to the SSPs but there are two differences between them: 1) height to with ratio; 2:1 and 2) resisting the entire base shear [4].

McCloskey studied the behavior of SSPs in 2006. He worked on different parameters of the SSPs (b/t, α, m). He also verified formulas presented by Hitaka and Matsui for the SSPs. He presented formulas for failure mechanism of the SSPs. McCloskey also suggested the use of edge stiffeners and studied ways of reducing the gravity loads demands in SSPs [2].

Deierlein et al. in 2007 studied on Self-Centered braced frame that also uses steel plates with slits to dissipate energy [5].

After all Gustavo Cortes with his Professor Judy Liu studied experimental and analytical models of SSPs.

The SSP is a steel plate with vertical slits cut in rows that form a series of flexural members –called links- in it. Under lateral deformations each link behaves as a beam in double curvature. They reach to their plastic moment capacity at both ends.

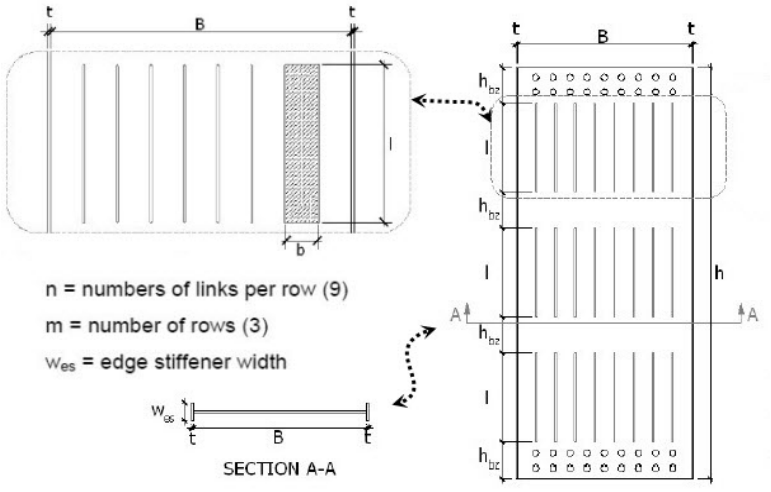


Figure 1: SSP parameters [6].

The parameters to define the geometry of an SSP are B, the width of the panel, h, the height of the panel, t, the thickness of the panel and the edge stiffeners, l, length of the links, b, width of the links, b, m, the number of rows in one panel, n, the number of the links in a row and h_{bz} the height of a band zone that is between the rows of links [2].

There are three types of SSP, T1, T2 and BR panels shown in Figure 2. They are different in their geometry parameters and their behavior [7].

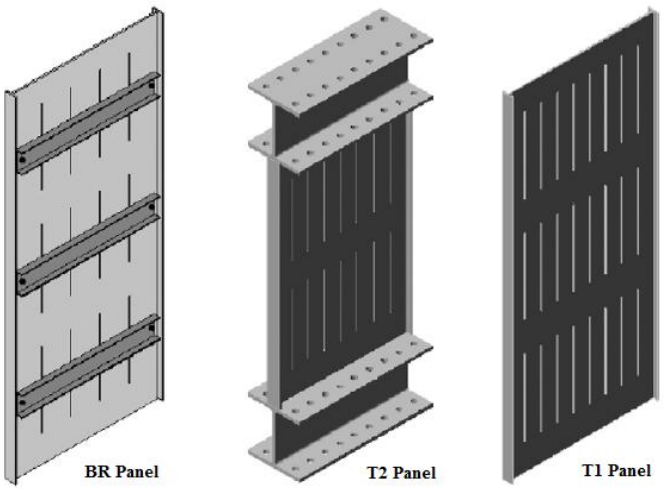


Figure 2: SSP panels [7].

α, β and b/t are three important parameters that are need to considered for ductile behavior of the panels. α (l/b) should be between 2.5 and 5.0. β (ml/h) should be between 0.65 and 0.85. And b/t ratio should be between 10 and 15 [2].

Ductility; Architectural flexibility; Simple fabrication and installation and replacing the panels are some benefits of the Steel Slit Panels. And the easy replacing of the panels makes it possible to use them in retrofitting deteriorated structures.

In this paper it is going to use T1 panel to retrofit available buildings and discuss its effect on the buildings' behavior.

2 RETROFITTING A WEAK BUILDING WITH SSP

2.1 Existing weak building

The existing weak building has three stories. In both X and Y axles moment resisting frames are used as lateral resisting system in the building. The stress ratio of some elements of the building is shown in Figure 3.

As it is obvious, the stress ratio is more than allowable ratio. In nonlinear static analysis the Life Safety Performance Level was not obtained. Figure 4 represent the deformed shape of the one of the frame in target displacement in pushover analysis.

Because of the importance of this building it was decided to retrofit it by adding a lateral resisting system. But the problem choosing one was the existence of openings in most bays. That is why we thought about Steel Slit Panels. So we tried to use T1 panel to retrofit this building. Analysis Software was used to analyze and design the structure [8].

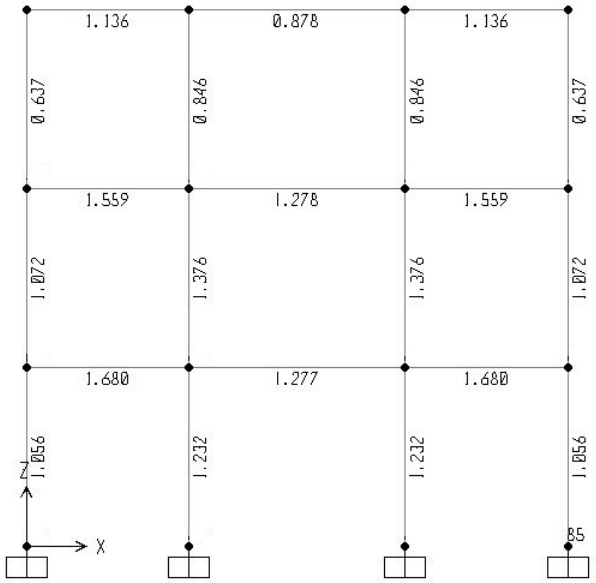


Figure 3: The stress ratio of weak building (beams and columns).

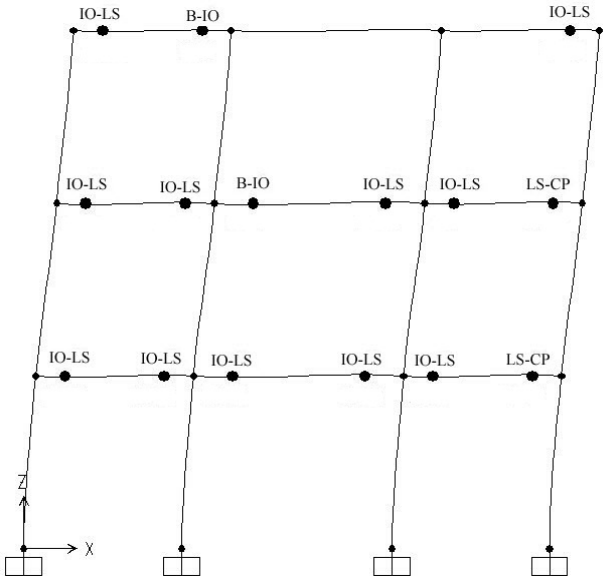


Figure 4: Deformed shape of the Frame 4 in target displacement for weak building.

2.2 Retrofitting existing weak building

As said before due to the existence of openings in most bays the selected lateral resisting element to retrofit this building was T1 panel of SSPs. This panel's parameters are represent in Table 1.

m	n	B	h	t	b	l	β	α	b/t
3	9	59.375	130	0.5	6.375	32	0.72	4.9	12.8

Table 1: T1 panel Parameters (inch).

In X direction, one panel was used in middle bay of the frames from top to bottom of the frames. In Y direction one panel was used in edge bays of the frame from top to bottom. To define SSP behavior, the results of FEM model in Finite Element software [9] was used.

The 1/3 scale of this panel, according to Gustavo Cortes' study, was analyzed in Finite Element software, Figure 5.

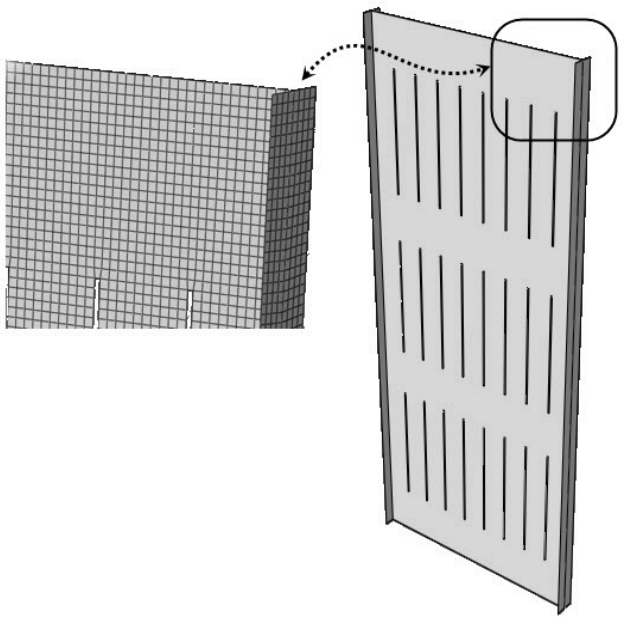


Figure 5: T1 panel model in FE Software.

After adding SSPs to the building its behavior was greatly improved. The stress ratio of the beams and columns are shown in figures 7. As it is clear the stress ratios are in allowable limit.

The life safety level was obtained in all beams and columns. The deformed shape of one of the frame in the target displacement is shown in figure 8.

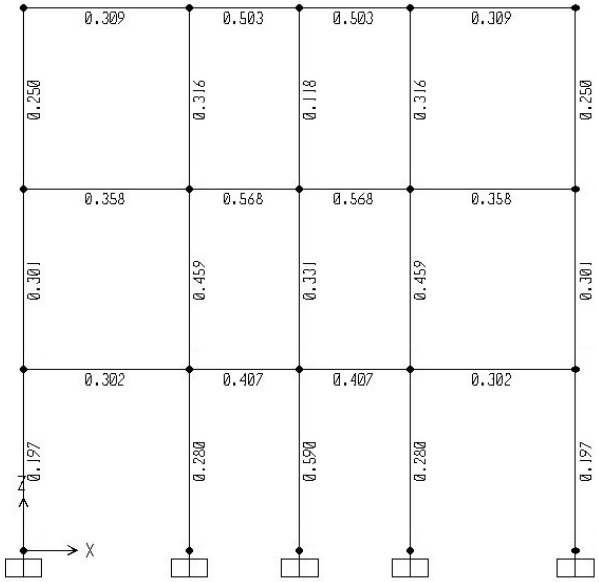


Figure 7: The stress ratio of retrofitted building (beams and columns).

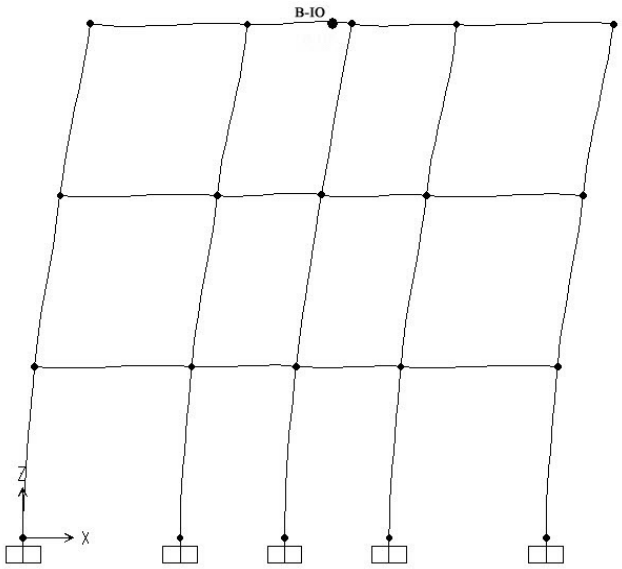


Figure 8. Deformed shape of the Frame in target displacement for retrofitted building.

3 CONCLUSIONS

From the results shown in figures it is obvious that SSP panel added to the building has improved the stress ratio of the elements. The stress ratio after retrofitting is in allowable ranges and has greatly improved.

And also it is clear that in the initial structure the Life Safety Performance Level was not secured but after retrofitting it was improved and the life safety performance level was obtained.

REFERENCES

[1] *Handbook on retrofit seismic building*, Central Public Works Department & Indian Building Congress, Aplril, 2007.
[2] G. Cortes and J. Liu, *Experimental evaluation of steel slit panel-frames for seismic resistance*, Journal of Constructional Steel Research 67, 181-191, School of Civil Engineering, Purdue University, 2011.
[3] Martinez-Rueda JE. *On the evolution of energy dissipation devices for seismic design*, Earthquake Spectra, EERI 2002; 18(2): 309-46.
[4] Hitaka T, Matsui C, *Experimental study on steel shear wall with slits, Journal of Structural Engineering*, ASCE 2003; 1299(5):586-95.
[5] M.R. Eatherton, J.F. Hajjar, G.G. Deirelein, H. Krawinkler, S. Billington, and X. Ma. *Controlled Rocking of Steel-Framed Buildings with Replaceable Energy Dissipated Fuses. The 14th World Conference on Earthquake Engineering*, Beijing, China, October 12-17, 2008.
[6] G. Cortes, *Steel Slit Panel Frames for Lateral Resistance of Building*, Dissertation submitted to the Factually of Purdue University, 2009.
[7] G. Cortes and J. Liu, *Steel slit panel configurations, The 14th World Conference on Earthquake Engineering*, Beijing, China, October 12-17, 2008.
[8] CSI (2010), CSI Analysis Reference Manual, Computers and Structures, Inc., Berkeley, California.
[9] ABAQUS, Version 9.11 Documentation, ABAQUS, Inc., Providence, RI.

COMPDYN 2015
5th ECCOMAS Thematic Conference on
Computational Methods in Structural Dynamics and Earthquake Engineering
M. Papadrakakis, V. Papadopoulos, V. Plevris (eds.)
Crete Island, Greece, 25–27 May 2015

REHABILITATION OF AN EDIFIED BUILDING IN A SEISMIC ZONE IN ALGERIA ACCORDING TO THE EUROCODE 8-3

Amar Kassoul[1] , Abdelkader Zerrouk[2] , and Imane Djafar henni[3]

[1] Laboratory of Structures, Geotechnics and Risks, University of Hassiba Benbouali of Chlef, Algeria
e-mail: amkassoul@hotmail.com

[2] Laboratory of Structures, Geotechnics and Risks, University of Hassiba Benbouali of Chlef, Algeria
e-mail: abdzerrouk@yahoo.fr

[3] Laboratory of Structures, Geotechnics and Risks, University of Hassiba Benbouali of Chlef, Algeria
e-mail: djh-im@hotmail.com

Keys Words: rehabilitation, building, Eurocode 8-3, retrofitting, strengthening

Abstract. *The objective of this paper is to perform a study on rehabilitation of a vital seven-story administrative building located in a low seismic area according to the old Algerian earthquake regulations (RPA88). Modifications were brought to the old code, including the seismic zoning which passed from moderate to high seismicity. The applied rehabilitation standards are based on the recommendations of the Eurocode 8-3 (EC8-3). The assessment of the vulnerability of the existing construction showed that the seismic forces at the base are lower than those required by the Algerian seismic code RPA99/V2003. As a retrofitting measure to strengthen this construction, the addition of new shears walls in both directions of the building was proposed. The dynamic study of the structure with the suggested structural intervention fulfilled all the required dynamic characteristics. For setting evidence of the performance of the proposed strengthening solution for the existing construction, a non-linear static analysis or pushover was accomplished. The obtained results using the SAP 2000 software enable us to make a comparison between the nonlinear behavior of the modified structure and the initial one. Compared to the original structure, from the point of view of the performance status, the strengthened structure showed a marked improvement in the strength and damping exceeding 80% while the overall capacity for resistance is enhanced more than three times.*

1 INTRODUCTION

Many reinforced concrete constructions yet in service in Algeria , especially those built before the enactment of the governing seismic code in 2003[1], were originally designed to support only gravity loads lacking the needed stiffness to deal with even a moderate seismic event. According to the current earthquake standards old reinforced concrete structures were designed and built without essential seismic details deemed vital to withstand large lateral loads. These old buildings could cease their serviceability and seriously jeopardize the safety of occupants because of the influence of complex interacting phenomena such as shear deficient columns which are the most critical elements present substandard shear design to inhibit shear failure, improper splicing of longitudinal reinforcement bars (insufficient lap length, and/or improper lap location), structural system consists of weak columns and strong beams , and finally unsafe design and detailing within the joint region beam-column connection nodes with less shear stress capacity [1].

Usually earthquakes induce damaging lateral forces but may become more deteriorating because of ignorance or lack of effective and integrated rehabilitation. Indeed, precipitated or incorrect design and poor enforcement of building work can lead to widespread damage and even large casualties during future earthquakes. Therefore, the need to disseminate knowledge to engineers regarding the repair of concrete is essential, namely reasonable design, repair or enhancement which includes the assessment of structural and modern knowledge of repair and strengthening techniques and appropriate method of implementing the structural rehabilitation [2].

Many researches were carried out in this area. Sarno et al. [3] have studied a seismic assessment of a reinforced concrete school building retrofitted with innovative braces. The existing frame was retrofitted through innovative buckling restrained braces (BRBs). The seismic performance of the as-built and consolidated structure was investigated through refined static and dynamic analyses, both linear and nonlinear. The nonlinear static analyses demonstrated that the use of BRBs is very efficient to enhance the global over-strength (about 30%) and energy dissipation capacity of the reinforced concrete frame under moderate-to-high magnitude earthquakes.

Hassaballa et al. [4] have conducted a seismic evaluation and retrofitting of existing Hospital building in Sudan. The building was constructed according to the design using one case of loads, this situation needs remedy. This paper suggested two solutions for this problem based on strengthening the weak columns by inserting reinforced concrete shear walls. It was found that solution one solved the problem partially because some columns were still unsafe, but solution two solved the problem completely and all columns were safe. Ahmed et al. [5] have guided a study on the performance and strengthening of non-seismically designed concrete framed structure building under seismic loading conforming to Kingdom of Saudi Arabia`s Code. A shear wall coupled structure system is adopted as seismic strengthening option as the structure of building is found unsafe under the seismic loading. The seismic load and other loadings are adopted as conforming to ACI Code. The shear wall structure analysis results are compared with the complete frame structure building. It was found that the provision of shear wall is an appropriate strengthening technique for the building under seismic loading. Knowing that, there are other works on the rehabilitation of vulnerable structures, namely that of Davidovici [6, 7] on the rehabilitation of existing hospitals and schools as well as their strengthening with reinforced concrete walls. In Algeria, as in other seismic countries, several practical studies have been conducted on the rehabilitation of structures after each earthquake. Two experiences in rehabilitation made after the earthquakes of El Asnam 1980 and Bou-

merdes 2003 are worthy to be cited. In Algeria, despite the existence of recommendations [8] and a technical guide of repair or strengthening methods for structures [9], there is a lack of regulatory support for the study of rehabilitation. It is well known that the measures used to achieve ductility and toughness in structural elements is unique to each construction material and to each type of structural system for each building.

The purpose of this study is to present first, a summary of the rehabilitation method of Eurocode 8-3 [10]. Then we apply the measures indicated in the latter code by proportioning the structure adequately to rehabilitate an office building in Algeria, which was edified in low seismicity zone (zone I) according to the pre-amended Algerian Earthquake Regulations (RPA88) [12]. The amendments to Regulation in 2003 resulted in the production of a new regulatory seismic zoning and the zone was switched at medium scale zone IIa. Finally, the paper highlights the performance of the proposed solution for the strengthening using a nonlinear static analysis.

2 METHOD OF REHABILITATION ACCORDING TO THE EUROCODE 8-3

2.1 Information for structural assessment

According to the steps described by Eurocode 8-3 [10], the first step governing the structural rehabilitation begins with the collection of the general and historical information of the building, especially the required input data to begin the methodology rehabilitation.

2.1.1 General Information and History

In order to assess the earthquake resistance of existing structures, the input data shall be collected from a variety of sources, including:

- Available documentation specific to the building in question,
- Relevant generic data sources (e.g. contemporary codes and standards),
- Field investigations and, in most cases, in-situ and/or laboratory measurements and tests, as described in the following steps.

It should check between the data collected from different sources to minimize uncertainties.

2.1.2 Required Input data

The minimum input data required for the evaluation of the structure according to Eurocode 8-3 [10] are summarized as follow:

a. Identification of the structural system and its compliance with the regularity criteria in EC8-1 [11]. The information should be collected either from on site investigation or from original design drawings, if available. In this latter case, information on possible structural changes since construction should also be collected.
b. Identification of the type of building foundations.
c. Identification of the ground conditions as categorized in EC8-1 [11].
d. Information about the overall dimensions and cross-sectional properties of the building elements and the mechanical properties and condition of constituent materials.
e. Information about identifiable material defects and inadequate detailing.
f. Information on the seismic design criteria used for the initial design, including the value of the force reduction factor (q-factor), if applicable.
g. Description of the present and/or the planned use of the building (with identification of its importance category, as described in EC8-1 [11].
h. Re-assessment of imposed actions taking into account the use of the building.

i. Information about the type and extent of previous and present structural damage, if any, including earlier repair measures.

The different types of analysis and different values of the confidence coefficients must be adopted according to the volume and quality of the gathered information.

2.2 Definition and identification of knowledge levels

The type of allowable analysis and the appropriate confidence factor values, according EC8-3 [10] is based on three knowledge levels, namely limited knowledge (KL1), normal (KL2) and full (KL3). The factors determining the appropriate knowledge level are:

- The geometry of the structural system and non-structural elements,
- Detailing of reinforcement in reinforced concrete and,
- The mechanical properties of the constituent materials.

The identification of the knowledge level of these factors is necessary to examine the following aspects:

i. Physical condition of reinforced concrete elements and presence of any degradation, due to carbonation, steel corrosion, etc.
ii. Continuity of load paths between lateral resisting elements.

2.3 Confidence factors

To determine the properties of existing materials used in the calculation of capacity, and when this one must is to be compared with demand for safety verification, the average values obtained from in-situ tests and from the additional sources of information shall be divided by the coefficient of confidence, CF, given by the EC8-3 [10], which is the appropriate knowledge level that complies with the requirements. However, in order to compute the force capacity in terms of the ductile components, intended to be used in the safety check, the mean value properties of existing materials shall be multiplied by the confidence factor CF for the appropriate knowledge level.

2.4 Vulnerability assessment

Assessment is a quantitative procedure for checking whether an existing undamaged or damaged building will satisfy the required limit state appropriate to the seismic action under consideration, as specified in EC8-1 [11].

3 DESCRIPTION OF BUILDING

From original outline construction built drawings as a source of information the evaluation of the structure can be derived.

3.1 General information and history of the existing building

The basic documentation available of the structure is original design specifications of the structural components shown in Figure 1 and Table 1. The relevant sources of generic data are reached based on Algerian Earthquake Regulations RPA88 [12] and the French Concrete Code CCBA 68 [13] used at the time. Regarding inexistent field investigations, but currently the foundation of the built structure is loose ground soil.

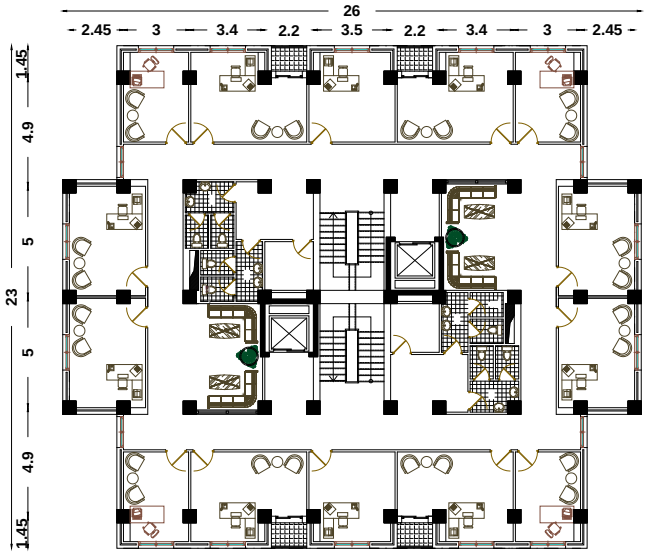


Figure 1: Plan of old building

Components	Storey	Sizes (cmxcm)
Columns	1, 2, 3, 4	40x40
	4, 5, 6, 7	35x35
Beams	Primary	30x40
	Secondary	30x35

Tableau 1: sizes of beams and Columns

3.2 Necessary input data of the existing building

The necessary input data for the structure assessment according to Eurocode 8-3 [10] are:

a. The classification and identification of the structural system1 and of its compliance with the regularity criteria according to Algerian Earthquake Regulations RPA99/V2003 [1], are:
- The administrative building is of vital importance of usage classified in group III.
- its structural system is composed by resisting frames,
- The arrangement of these structural elements largely meets the criteria of regularity in code RPA99 / V2003 [1].

b. The existing foundations of the structure are strip footing
c. The soil is defined as loose soil (S3);
d. The value of the behavior factor (q factor) used in the initial design is equal to 4.

To select the type of permissible analysis and the appropriate values of the confidence factors, according to EC 8-3 [10], the established knowledge level is Level 2 corresponds to the normal knowledge (KL2).

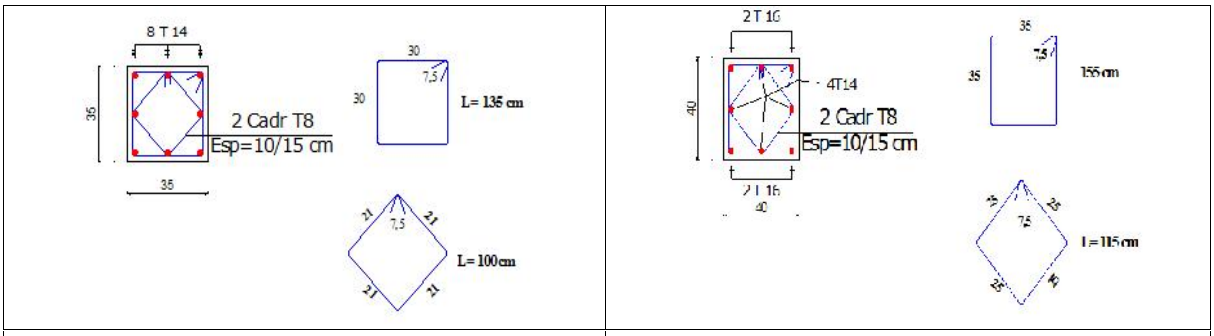
3.3 Identification of geometry, details and materials

3.3.1 Geometry

The bracing system in both directions is provided by the resisting frames systems. The direction of floor slabs considered as rigid diaphragm and the various quotes between axes are illustrated in Figure 1. The dimensions of the existing cross-sectional area of beams and columns are shown in Table 1.

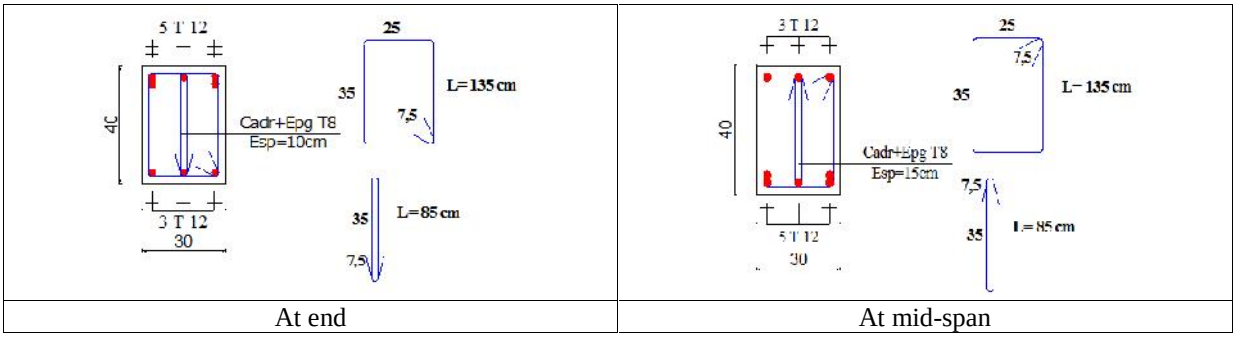
3.3.2 Details

The amounts of longitudinal and transverse reinforcement and their detailing for columns and beams are illustrated in Figures 2 and 3. The percentage of total longitudinal reinforcement in beams is fitting with that required by the RPA99 / V2003 [1].



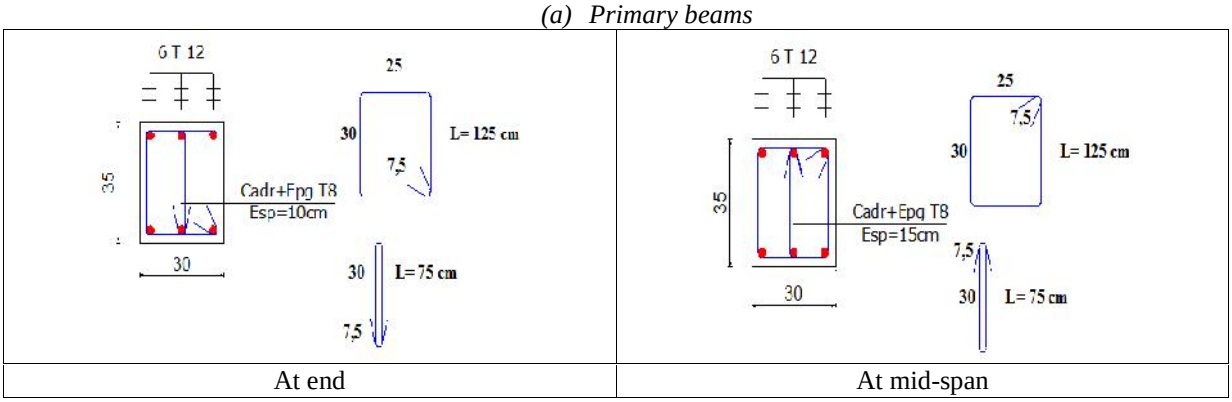
Columns (35x35) cm²	Columns (40x40) cm²

Figure 2: Detailing of columns



At end	At mid-span

(a) Primary beams



At end	At mid-span

(b) Secondary beams

Figure 3: Detailing of beams

3.3.3 Materials

In order to assess the current mechanical properties of concrete, a non-destructive testing has been performed. The measured compressive stress fck is 16 MPa, while the computed value of fck is 25MPa. Moreover, steel offers good resistance to tensile stresses with a value of fcy equal to 400 MPa.

4 EVALUATION OF VULNERABILITY OF BUILDING

The evaluation of the seismic vulnerability of the building is performed using the linear dynamic method with SAP2000 software. After modeling of the structure, the natural periods of vibration, and participation of the masses as well as the Eigen modes are estimated. Then, the seismic force is determined at the base using the equivalent static method. Finally, the inter-storey drifts then the lateral displacement of the whole structure are checked.

4.1 Building modeling

The modeling shown in Figure (4) by SAP2000 software enables to study the elastic structure. Hence, the model considers the selected members of the structure according to the following concept:

- The Beams and columns will be modeled by bars "FRAME";
- The Floors have infinite stiffness in their plane; this is done by assigning an element "DIAPHRAGME";
- The Mass of each floor is concentrated at its gravity center.

The load path due to each structure member allows the weight evaluation of each floor as illustrated in figure (5). The total weight of the structure was found equal to 44619.65 KN.

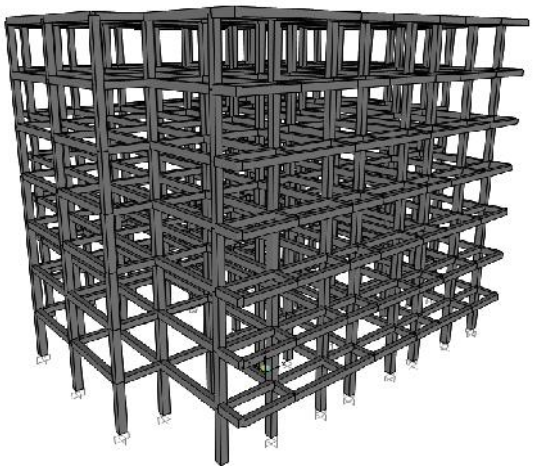


Figure 4 : Building Modeling

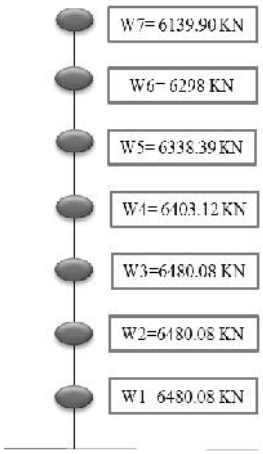


Figure 5 : weight of each floor

4.2 Natural periods

In this section the natural vibration periods are determined, as well as the modal mass participation and mode, using the SAP2000 software. For the three main directions of the structure the values of fundamental periods are:

T_1= 1.31sec for the 1st period
T_2= 1.**2**4sec for the 2nd period
T_3= 1.22 sec for the 3rd period

The first two modes are translational modes (which is acceptable), and the third mode is a torsional mode. These periods shall not exceed the fundamental period of the structure T_{RPA} increased by 30%, which is established from the empirical formula of RPA99 / V2003 [1]. 0.55 sec is the estimated value of the T_{RPA}. The results obtained show that the actual periods in both directions are far beyond $1.3T_{RPA}$. This is due to the flexibility of the construction which confirms its vulnerability.

4.3 Determination of the seismic force

The seismic force evaluation determined by the SAP 2000 software were found equal to 2627,904 kN in the x direction and 2648,089 KN in the y direction. These forces shall not be less than 80% of the prescribed seismic forces V_{RPA} determined by the equivalent static method. The values of these forces are 4747.79 KN in the x direction, and 4945.61 in the y direction. Comparing these forces in each direction with the actual seismic forces shows that they are beneath the values required by RPA99 / V2003. The gap exceeds by 30% of that obtained by the empirical formula. This confirms the vulnerability of the structure as it has been proved in the verification of the fundamental period. This also shows that the original design seismic force in zone I was very low according to former RPA 88 [12] regulation.

According to the study of vulnerability by the linear dynamic analysis, the studied construction showed a glaring deficiency in the period and the design base shear. This requires seismic retrofit of the construction is essential to reduce its vulnerability.

5 STUDY OF THE REHABILITATION OF THE BUILDING

Decision should be focused on how to intervene based on the conclusion of the condition assessment of structural vulnerability. The type of remedial intervention, its technique, scale and urgency, must refer to the report from condition assessment which provides information of the actual condition of the building [10].

5.1 Technical criteria

It should be taken into account the following technical criteria [10]:

a. repair of all identified structural defects in appropriate manner to ensure safety of the structure;
b. In case of highly vertical mass or stiffness irregularity in the existing building, structural regularity should be improved as much as possible, both in elevation and in plan;
c. The required characteristics of regularity and resistance can be achieved by either modification of the strength and/or stiffness of an appropriate number of existing components, or by the introduction of new structural elements;
d. Increase in the local ductility supply should be affected where required;
e. The increase in strength after the intervention should not reduce the available global ductility;

5.2 Type of intervention

An intervention may be selected from the following indicative options [10]:

a. Local or overall modification of damaged or undamaged elements (repair, strengthening or full replacement), considering the stiffness, strength and/or ductility of these elements;
b. Addition of new structural elements (e.g. bracings or infill walls; steel, timber or reinforced concrete belts in masonry construction; etc);
c. Modification of the structural system (removal of some structural joints and vulnerable elements; widening of joints; modification into more regular and/or more ductile arrangements);
d. Addition of a new structural system to sustain some or all of the entire seismic action;
e. Possible conversion of existing non-structural elements into structural elements;
f. Introduction of passive protection devices through either dissipative bracing or base isolation;
g. Mass reduction;

h. Restriction or alteration of the building usage;
i. Partial demolition;

One or a combination of several options of retrofit strategies can be chosen. It should, in any case take into account the effect of changes in structure on the foundation.

5.3 Proposed Solution

In order to increase the resistance capacity and ductility of the structure, the limited funding has restrained the strengthening of the resisting frames of building to the addition of new bracings walls in the original plan of the building as shown in Figure 1. Concrete walls should be integrated at the periphery of the building, so to preserve the integrity of the interior of the building and conserve a reasonable regularity in plan and elevation. The specific concern is to ensure that adjustments brought to the building configurations can satisfactorily carry lateral loads suitably and in harmony with the existing structure. The proposed solution is illustrated in figure (6).

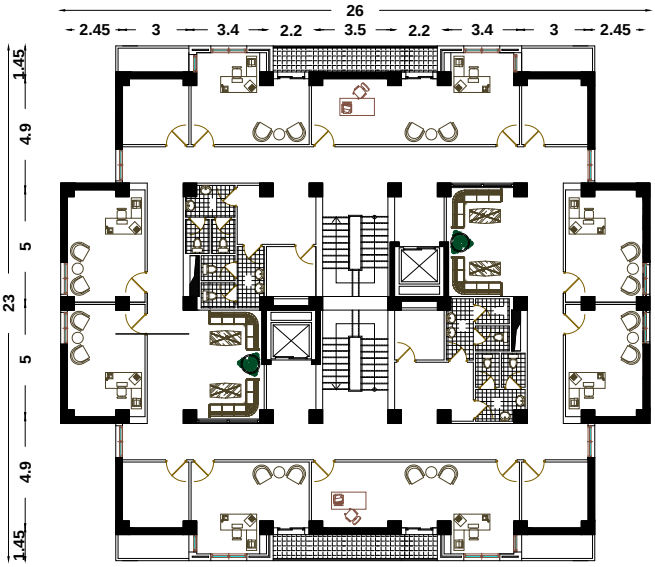


Figure 6: Plan of strengthening building

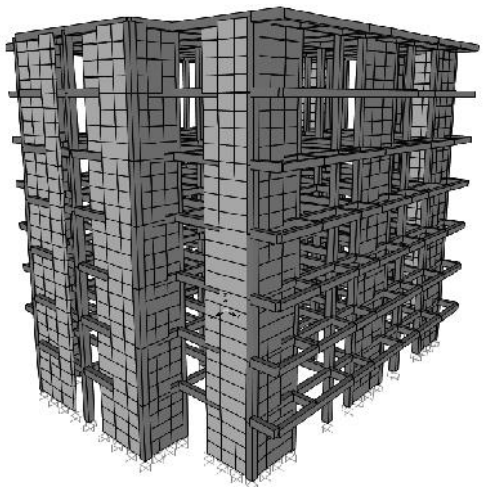


Figure 7: Modeling of strengthening building

5.4 Dynamic Study of the building with the proposed solution

5.4.1 Modeling of the structure

The new shear walls are already integrated and arranged in accordance to the recommendation of the Algerian Earthquake Regulations (RPA 99 / V2003 [1] concerning the stability of the structure (Figure 7). Non-structural elements are considered as dead loads only.

5.4.2 Checking dynamic characteristics of the building

The results obtained using the SAP2000 software have given specific periods $T_x = 0.52$ sec and $T_y = 0.42$ sec for the new structure in x direction, and y direction respectively, While the estimated value of the fundamental period T_{RPA} is 0.46 sec. These results show that the actual periods T_X and T_Y are less than the factored fundamental period by 30%, according to the RPA99 / V2003 code (T_X and $T_Y < 1.3T_{RPA} = 0.56$ sec). This shows that the shear walls placement is improving the resisting capability of the building.

Determined seismic resulting forces of the retrofitted structure are 3420KN and 3603 KN in X and Y directions respectively. These forces must not be less than 80% of the prescribed seismic forces V_{RPA} determined by the equivalent static method. The values of these force are the same in both directions (V_{XRPA} and V_{YRPA}) are equal to 3772 KN. Comparing the forces in each direction shows that the actual resisting seismic forces are greater than those required by RPA99 / V2003. This shows that the undertaken structural interventions aimed at stiffening the building were adequate.

6 PERFORMANCE OF THE STRENGTHENING STUDIED BUILDING

The results obtained by push-over (non-linear static analysis) analysis elucidated as capacity curves using SAP 2000 software enabled a comparison of the nonlinear behavior between the strengthened structure and the old one.

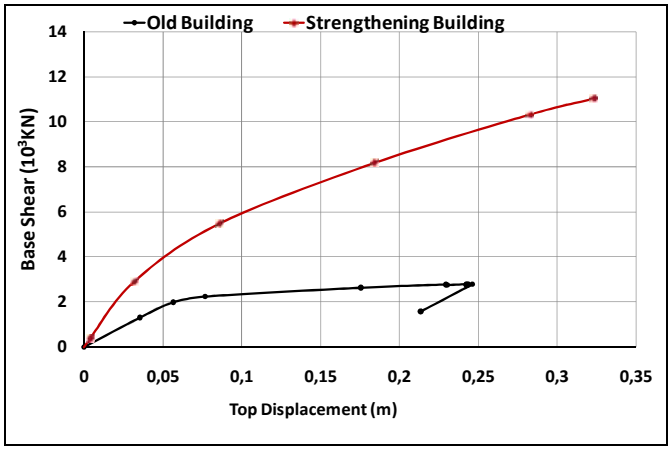
6.1 Shear force

Figure (7.a) highlights a confrontation between the old building capacity curves before and after strengthening the structure by adding reinforced concrete bracing walls in both directions. This figure clearly shows the importance of the adopted strengthening in terms of base shear, where the strengthened structure capacity curve corresponding to that modification is far more exceeding the one of the non strengthened structure. In the original building, the value of the base shear is 2783.031KN which represents less than 65% of the value found using the equivalent static method in the x direction (V_X = 3675,054KN). This value increases to 11020.129KN for the strengthened structure which is about four fold increase in computed force for the original building, and more than three times the strength value when using the equivalent static method for the same direction (V_X = 3772,27KN). The same observation is noticed for improving the behavior of the structure for the y direction in Figure (7.b). Therefore, it can be noticed that the overall resistance capacity of the strengthened structure is improved more than three times compared to the original structure.

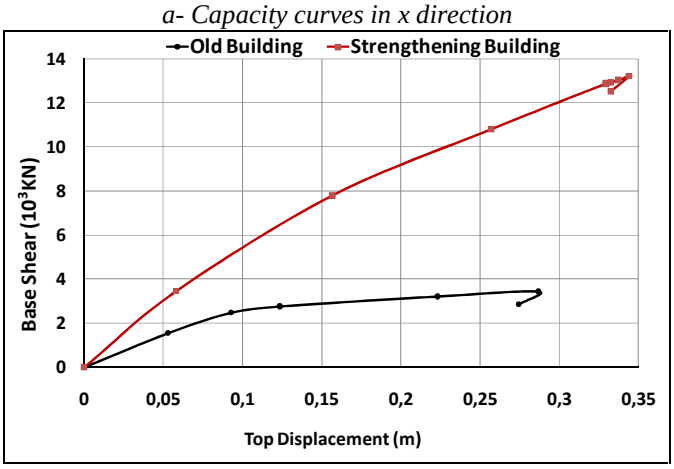
6.2 Displacement

From Figure (8.a), in terms of roof displacement, the capacity curve of the original structure shows that the final displacement reaches a corresponding value of 0.24m, which is enhanced to 0.34m for the strengthened structure, which represents approximately a 15% increase. For the y direction (Figure (8.b)), the displacement reached a value of 0.29 m for the

non strengthened structure, which is increased to 0.33m with a rate of 10% for the strengthened structure. Accordingly, the structure deformation capacity is not greatly improved is still in a range that does not exceed 10 to 15%.



a- Capacity curves in x direction

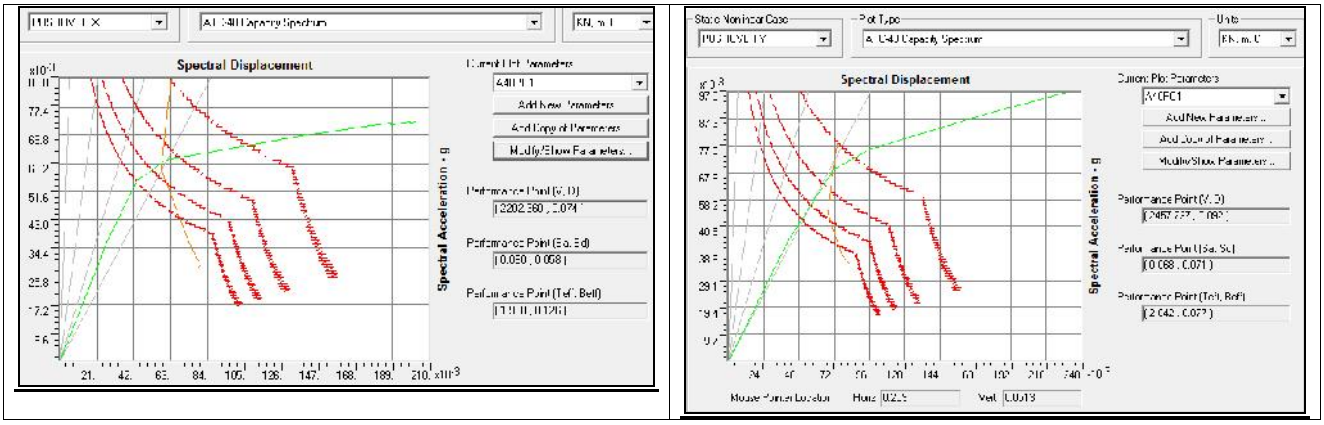


b- Capacity curves in y direction

Figure 8: comparison between the capacity curves before and after strengthening the structure

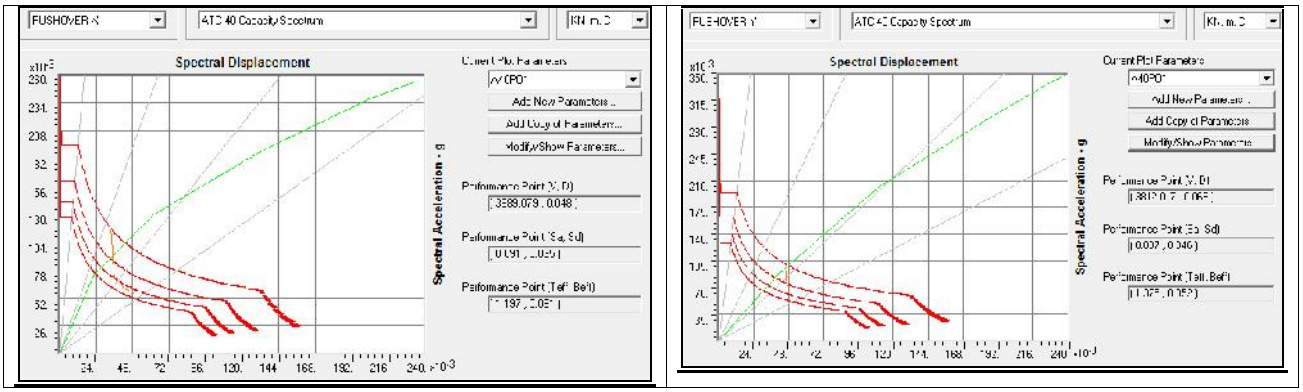
6.3 The structure performance point

The performance point enables to make several considerations on the structure behavior vis a vis of the earthquake from the integration of regulatory spectrum response corresponding to the current seismic zone on the capacity curve of the structure [11]. In this case, the junction is almost at the limit of elastic behavior of the structure in both directions as shown in Figure 9 for the old structure, and Figure 10 for the strengthened one. Table 2 shows a comparison between the performance point values obtained in terms of shear, displacement and damping ε_{eff} for the structure before and after strengthening. According to this table, we observe that the values for the original structure are lower than the ultimate values obtained previously which furthermore confirms that the structure is vulnerable. However, the values obtained for the retrofitted structure is well above that found previously for base shear force and control displacement. As a consequence, the performance point values of the strengthened structure show a clear improvement in the resistance and damping that is greater than the initial values of the original structure by 80%.



a-x direction b- y direction

Figure 9: Performance point for the structure before strengthening



a-x direction b- y direction

Figure 10: Performance point for the structure after strengthening

		Before strengthening	After strengthening
X direction	Shear force V (KN)	2202,36	3689,08
	Damping ε_{eff}	0,126	0,081
Y direction	Shear force V (KN)	2456,74	3812,02
	Damping ε_{eff}	0,077	0,052

Tableau 2: Comparison between the performance point values for the structure before and after strengthening

7 CONCLUSION

The study of vulnerability using the linear dynamic analysis, studied building showed a great deficiency into the dynamic characteristics, namely its natural period and the seismic base shear, which requires rehabilitation. A brief presentation of the rehabilitation method of Eurocode 8-3 [10] was exposed. An adopted strengthening solution of construction was proposed. The highlighting of the performance of the proposed solution for the strengthening is performed using a non-linear static analysis.

The study of the performance of the building before and after strengthening using push-over analysis enables to draw the following conclusions:

- The overall resisting capacity of the strengthened structure is improved by more than three times compared to the old structure.

- The structure deformation capacity is not greatly enhanced, but remains within a range that does not exceed 10 to 15%.
- The performance point values after of the strengthened structure show a clear improvement in the resistance and damping that exceed 80% of the initial values of the original structure.

REFERENCES

[1] RPA-99/ 2003, 2004, *Règles parasismiques Algériennes 1999 - Version 2003*. DTR-BC 248 - Centre National de Recherche Appliquée en Génie sismique (CGS), Alger.

[2] Penelis G.G., Kappos A.J, *Earthquake resistant concrete structures*, Edition E & FN SPON, 1997.

[3] Sarno L. Di and Manfredi G., 2009, *Seismic assessment of a RC school building retrofitted with innovative braces, Concrete Repair,* Rehabilitation and Retrofitting II – Alexander et al (eds), 2009 Taylor & Francis Group, London, pp. 1149-1155.

[4] Hassaballa A. E., Ismaeil M. A., Fathelrahman M. A., 2014, Seismic Evaluation and Retrofitting of Existing Hospital Building in the Sudan, *Open Journal of Civil Engineering*, 4, 159-172.

[5] Ahmed M., Nazar S., Islam S., Khan R. A., 2014, Seismic Performance and Strengthening Study of Concrete Frame Structure Building, *Journal of Multidisciplinary Engineering Science and Technology (JMEST)*, Vol. 1 (5), pp. 478 - 482

[6] DAVIDOVICI Victor, *réhabilitation des hôpitaux existants*, 2007.

[7] DAVIDOVICI Victor, *renforcement par mur en béton armé*, 2006.

[8] Recommandations techniques pour la réparation et le renforcement des ouvrages, Algérie.

[9] Catalogue des méthodes de réparation et de renforcement des ouvrages - CGS- 1992, Algérie.

[10] EN 1998-3:2005 E, Eurocode 8 : *Design of structures for earthquake resistance Part 3 : Assessment and retrofitting of buildings,* European Committee For Standardization, Brussels.

[11] EN 1998-1:2004 E, Eurocode 8 : *Design of structures for earthquake resistance Part 1: General rules, seismic actions and rules for buildings,* European Committee For Standardization, Brussels.

[12] RPA-88, *Règles Parasismiques Algériennes*, Centre National de Research Appliquee en Genie Parasismique (CGS), 1989. DTR, Algiers, (in French).

[13] CCBA 68, Règles techniques de conception et de calcul des ouvrages et constructions en béton armé, PARIS 1968 (in French).

COMPDYN 2015
5th ECCOMAS Thematic Conference on
Computational Methods in Structural Dynamics and Earthquake Engineering
M. Papadrakakis, V. Papadopoulos, V. Plevris (eds.)
Crete Island, Greece, 25–27 May 2015

SEISMIC ANALYSIS AND RETROFIT OF A MID-RISE BUILDING

Fernando Saitta[1], Paolo Clemente[1], Giacomo Buffarini[1], and Giovanni Bongiovanni[1]

[1] ENEA
Casaccia Research Centre, Via Anguillarese 301, 00123 Rome, Italy
e-mail: fernando.saitta@enea.it; paolo.clemente@enea.it; giacomo.buffarini@enea.it; giovanni.bongiovanni@enea.it

Keywords: Experimental analysis, Dynamic analysis, Base isolation, Pile foundations, Structural modelling.

Abstract. *The structural analysis of an about 30 m tall building is presented in this paper. It was constructed in 70s, so its use pointed out the issue of the seismic reliability of existing buildings, especially if considered of strategic importance for civil protection. The structure is composed by two parts, the lower one in reinforced concrete, which contains a theatre room, and an upper in steel. The study allowed defining the seismic vulnerability. A refined finite element model was assembled and updated on the basis of comprehensive experimental analyses on materials and structure and also of experimental modal analysis, highlighting the dynamic effect due to the irregularity of the building and the influence of the adjacent building, the seismic joint is missing. The results pointed out a quite high vulnerability of the building to seismic actions and the inadequacy of the pile foundation to support horizontal seismic loads. A retrofit intervention, based on the insertion of a seismic isolation system and the realization of a seismic joint with the adjacent building, is proposed. It allows reducing the horizontal forces in the piles and the torsional movements of the structure.*

1 INTRODUCTION

The Italian territory seismic classification started after the 1908 Messina and Reggio Calabria earthquake (M=7.1) and was updated only after new seismic events up to recently. So, most of the Italian structures were designed without accounting for the seismic actions or, in some cases, with design earthquake of intensity lower than that required in the present code. This could be very dangerous for strategic structures, such as buildings with civil protection purposes, bridges and railways critical to the transport networks, plants at risk of a major accident, etc., and of relevant structures that can be very crowded, such as schools and hospitals. Also the recent Italian earthquakes pointed out the high vulnerability of a large number of structures and the strategic and relevant ones are no exceptions [1], making the overall improvement of the built very hard. Only recently, the reliability evaluation and the design of improving interventions of existing strategic and relevant structures have been considered compulsory in the framework of a prevention policy.

The improvement process of a singular structure consists essentially in two steps. The first one consists in the evaluation of its structural health status. This can be performed on the basis of an appropriate experimental analysis, which includes material and structural tests, and of an accurate numerical analysis with a suitable model, which accounts for the actual characteristics of the structure obtained experimentally. In the second step a proper intervention should be designed on the basis of the experimental and numerical results of the first step.

In this paper the analysis carried out on an existing building is shown. The original design being available, it was quite easy to perform a suitable finite element model. Then the available experimental results were analyzed and a more detailed experimental campaign was organized, which included test on the soil and foundations, on steel and concrete elements and ambient vibration analysis to extract the dynamic properties of the building. The updated model allowed analyzing the actual capacity of the structure, highlighting the irregular dynamic behavior of the building under seismic load and the inability of the foundation to resist horizontal actions, and designing the most adequate retrofit intervention, which consists in the insertion of a base isolation system.

2 THE BUILDING

The building object of this study, built in the 70s in an area not considered as seismic zone at the time of construction, has eight stories above the ground (floor 0, floors 1 to 7, respectively) and one underground story of shorter height (floor -1). From the architectural point of view the building is composed by two different parts in elevation (Figure 1). The lower part has in-plan squared shape and includes the underground level and three levels above the ground (floors 0 to 2 – Figure 2 left). The upper part, where are located offices, has a T shape covering only a portion of the lower part (floors 3 to 7 – Figure 2 right). The lower part contains an auditorium and a boardroom, therefore the structure should be considered as building of particular relevance. The four steel columns, which are around the auditorium (Figure 2 left), and the corresponding columns at the north and south sides (two for each side) support a spatial Vierendeel system, whose height occupies the entire floor 3. Most of the columns of the seventh level are not in correspondence of other columns but are supported by the lower beams. The stability against horizontal actions and second order effects is guaranteed by concrete shear walls, placed eccentrically with reference to the gravity center at the south side in the WE direction and around the staircase. The presence of stiff end walls leads to the needs of considering in the analysis the floor diaphragm flexibility [2][3].

The structure is adjacent at the south side to another building of lower height. Given that no seismic joint was made at the construction age, the two structures are exposed to the risk of pounding in case of earthquake [4].

The load-carrying structure is mainly constituted by steel members, joined by welding. It was designed according to the Italian code existing at the construction time and therefore without accounting for seismic actions and without adopting usual details for structures in seismic area. In the lower part also concrete members are present. The foundations consist in concrete plinths with piles of about 40 m length, with reinforcing bars only in the first 16 m. The plinths are connected by means of concrete beams.

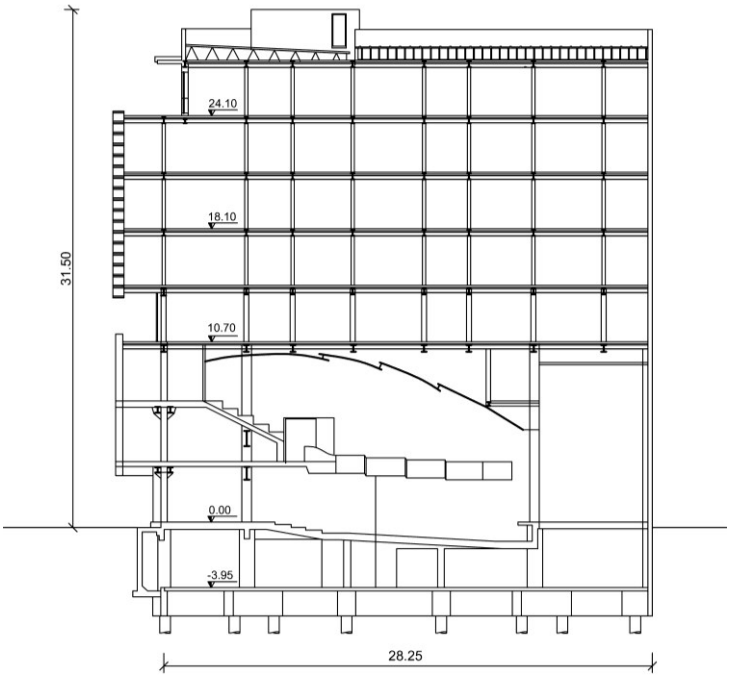


Figure 1 : Vertical section of the building (North side on the left)

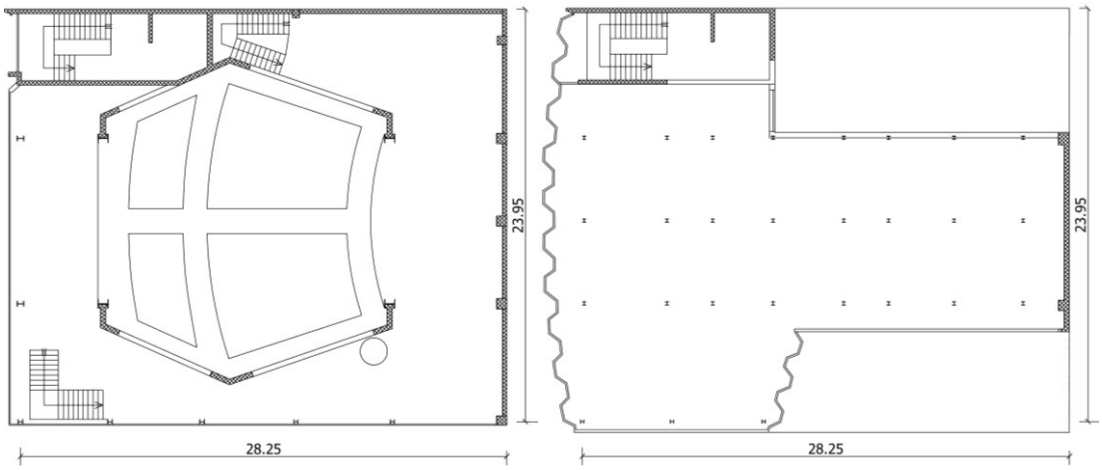


Figure 2 : Plants of floors 0 to 2 (left) and of floors 3 to 6 (right).

In a first step the results of in situ tests, carried out at the construction time, and of one drilling with continuous core were available. Another continuous core drilling was done in the second step and also the result of a SPT was available, made at about 200 *m* from the building. Four layers can be individualized in the subsoil, from the top: a surface layer of about 6 *m*,

with negligible resistance to penetration; a non-cohesive layer up to 15 *m*; a cohesive soil up to 41 *m*, where a gravel deposit is present. The pile head is at 4 *m* from the campaign level and so is the average groundwater level. From the seismic point of view the subsoil can be classified as soil type C, with seismic wave velocity Vs_{30} between 180 *m/s* and 360 *m/s*.

The geometry of the structure was known from the original architectural and executive structural drawings. Furthermore, detailed *in-situ* tests were carried out, so a full knowledge level for the structure was reached and, therefore, no reduction of the average material characteristics obtained from the experimental analyses was considered.

Most of the carrying structure was realized with steel of Fe360 type, with a yield strength $f_{yk} = 235\ N/mm^2$. The tensile tests carried out on a suitable number of specimens pointed out an average strength $f_{ym} = 268\ N/mm^2$. The reinforcing bars for concrete are Aq60-70 type, used at the construction time, having a tensile strength between 600 and 700 N/mm^2. The laboratory tests made on specimens extracted in site gave an average strength of 461 N/mm^2. The compression tests on concrete specimens pointed put an average cube strength $R_{cm} = 28\ N/mm^2$. The corresponding Young's modulus is $E_{cm} = 28300\ N/mm^2$.

The analysis under static loadings, carried out considering the various loading condition of the Italian code, gave positive results both for the superstructure and the foundations.

3 EXPERIMENTAL DYNAMIC ANALYSIS

An output-only strategy with ambient noise excitation was used for modal identification. The instrumentation was composed by 24 short-period seismometers (Kinemetrics SS-1, period = 1 sec), wired to a digital acquisition Kinemetrics Granite with a 24 bit A/D converter, able to simultaneously convert all the 24 channels. Four different sensor configurations were implemented, designed to identify the dynamic behavior of the structure. For the purpose of this paper only one of them (namely C2) was considered, which allowed analyzing the dynamic characteristics of the building. The positions of the sensors are plotted in 0. An acquisition lasting 30 *min* with a sampling frequency of 200 *samples/sec* was performed.

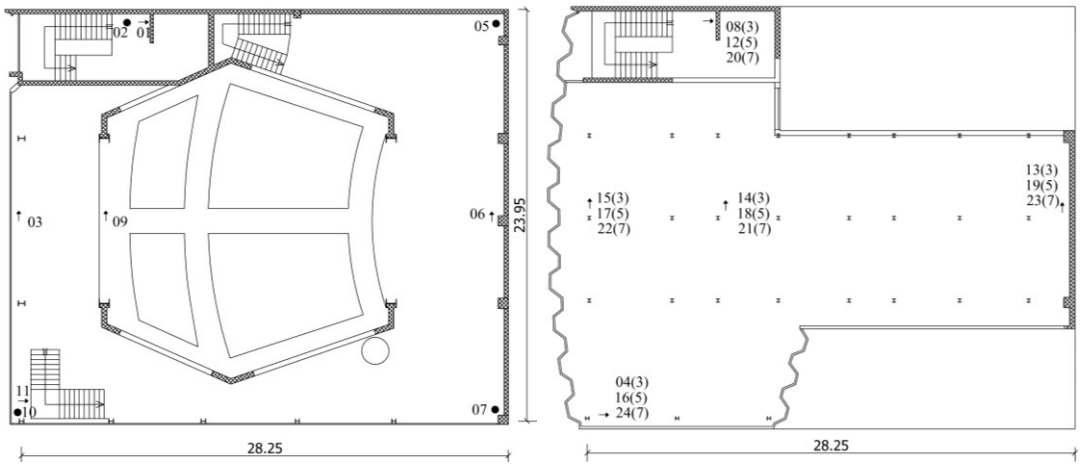


Figure 3 : Sensor configuration on floor 0 (left) and on floors 3, 5 and 7 (right, numbers in () indicate the floor).

The building showed a quite complex behavior mainly related to its irregular shape both in plan and elevation, but also to the presence of the adjacent building at the south side. The power spectral densities (Figure 4) pointed out the presence of two main resonance frequencies, equal to 1.67 *Hz* (0.59 *sec*) and 2.60 *Hz* (0.38 *sec*), respectively. The analysis of the cross spectra, in terms of amplitudes and phase factor, and of the corresponding coherence function, allowed stating that both the modal shapes associated to these frequencies showed rotational

movements. In the first case (1.67 *Hz*) the rotation center is close to the S-E corner of the building, in the second one (2.60 *Hz*) out of the plant of the building in the N-E direction.

The other configurations confirmed the presence of the two modal shapes already described but showed also out of phase signals, probably due to a nonlinear behavior of the building. In one of them most of the sensors were oriented in the vertical direction. The results obtained demonstrated that all the points moved in phase and with the same amplitude, and allowed to exclude the presence of rocking effects in the building. This occurrence guaranteed the good performance of the pile system at least under permanent loadings and ambient vibrations.

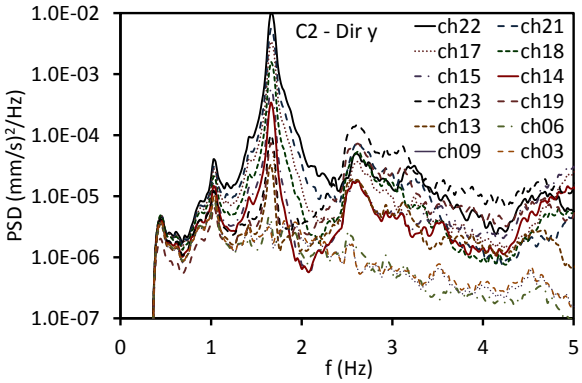


Figure 4 : Power Spectral Densities (PSD) of all the recordings in y direction (C2).

The results of the experimental static and dynamic analyses were used to update the finite element model set up in the first step and based on the original design. The masses related to the dead loads and to a fraction of the variable loads were considered. The structure was modelled by using frame and shell elements.

A good correspondence with the experimental results was obtained only considering the presence of the adjacent building, which, under ambient vibrations, certainly contributed to the dynamic behavior of the structure. This was accounted for in the model by means of horizontal springs, whose stiffness was calibrated in order to obtain the coincidence of the first experimental periods of vibration, equal to 0.58 *sec*, and the associated modal shape (Figure 5). The numerical analysis also revealed the presence of vertical modes, related to the presence of the theater room. This occurrence had been pointed out also by the experimental analysis.

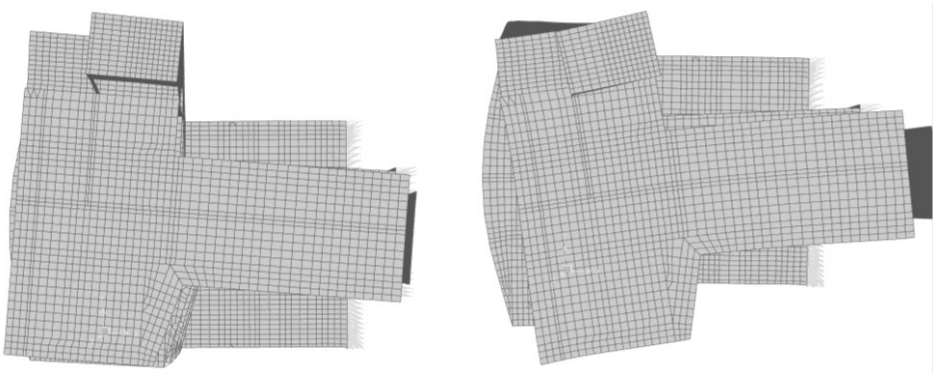
For the model of the building alone, set up just eliminating the horizontal springs, the fundamental period of vibration was about 1.0 *sec*. The seismic analysis was carried out by using the Ritz method that allows reducing the computational burden due to the very high number of degree of freedom and obtaining a participant mass higher that 90% with 50 modes.

4 SEISMIC VULNERABILITY ANALYSIS

As pointed out by the experimental investigations, the types of beam-column connections cannot guarantee a dissipative behaviour. So the seismic analysis was performed as for the static actions, assuming a behaviour factor $q = 1$. The response spectrum analysis was carried out with reference to the spectrum relative to the exceedance probability of 2%. The results were used to individualize all the elements that reach the elastic limit and the corresponding spectral amplitude. The comparison between these amplitudes and those of the elastic spectra relative to the various exceedance probabilities P_{NCR} in 50 years allowed describing the vulnerability of the building.

Mode	Experimental Periods (sec)	Numerical Periods (sec)	Periods without the adjacent building (sec)	Displ.
1	0.59	0.58	1.01	*Horiz.*
2	0.38	0.28	0.44	*Horiz.*
3		-	0.34	*Horiz.*
4	.	0.25	0.25	*Vert.*
5	.	0.19	0.20	*Horiz.*
6	.	0.19	0.19	*Vert.*
7	.	0.18	0.19	*Horiz.*

Table 1 : Periods of vibration of the modes with highest participation mass.



$T_1 = 0.58\ sec$ $T_2 = 0.28\ sec$

Figure 5 : First two modal shapes accounting for the presence of the adjacent building.

The elastic and the plastic analyses (both applicable in this case) were used [7]. It is worth reminding that the first one refers to the ideal stress $\tilde{\sigma}$ at the characteristic points of the cross section, the second to the function $\tilde{M}$ of the demanding moment (Figure 6 left).

In Figure 6 (right) the elements for which the check is not satisfied are pointed out. As one can see, the limit values, both in the elastic and plastic analyses, are overpassed in several elements. The analysis in *x* direction gave similar results but, as one could expect, the worst case is that of seismic action along *y* direction. For all the elements the checks are satisfied up to a PGA = 0.10 g (on rigid soil), equal to 43% of the reference one (P_{NCR}=2%), when for the first element (column) $\tilde{M}$. This corresponds to P_{NCR}=21% in 50 years (T_{NCR}=207 years). If one refers to the acceleration peak on surface (PGA·S) the value for which the first is not verified is about 47% of the reference one, due to the reduction of the amplification factor S when PGA increases.

In the hypothesis of rigid connection with the adjacent building, the period of vibration becomes equal to about 0.58 sec and the spectral amplitude decreases. The situation is worse than in the previous case. All the elements are verified up to PGA = 0.08 g (on rigid soil), equal to 35% of the reference one (P_{NCR}=2%), when the first element (column) in not verified. This corresponds to P_{NCR}=33% in 50 years and T_{NCR}=125 years. It is worth noting these considerations do not account for the effects of pounding between the two buildings.

The comparisons of the internal forces of the shear walls with the interaction domains gave always good results. Bending and shear checks were performed for all the reinforced concrete beams. The capacity moments were always higher than the demanding moments.

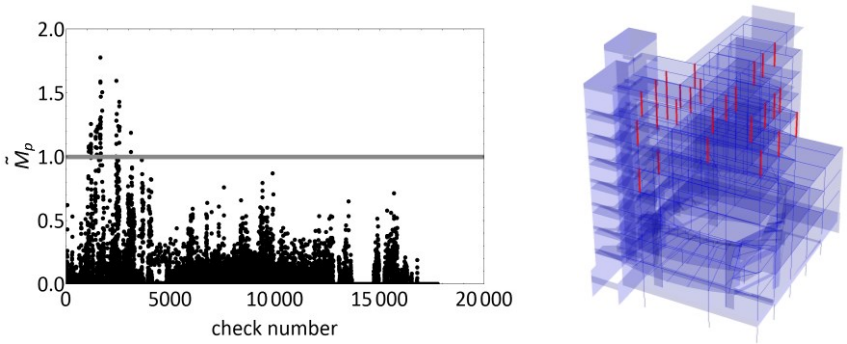


Figure 6 : Plastic checks (left) and steel members (right) that do not satisfy the plastic check for prevalent seismic action in *y* direction.

5 NONLINEAR ANALYSIS OF THE PILE SYSTEM

The foundation are composed of concrete plinths, connected by means of concrete beams and supported by piles of about 40 m length (Figure 7). These have reinforcing bars only in the first 16 m. This unusual situation induced performing a detailed nonlinear analysis of the pile system.

The superstructure base shears and moments corresponding to the first modal shape, with prevalent motion in the *y* direction, were applied at the top of piles and monotonically increased. The behavior of the piles was modeled considering the moment-curvature relationships under constant normal force. Three different cross sections were considered for each pile, due to the variability of the reinforcing bars, which are present up to the depth of 16 m. The corresponding moment-curvature plots are shown in Figure 8 for a given pile.

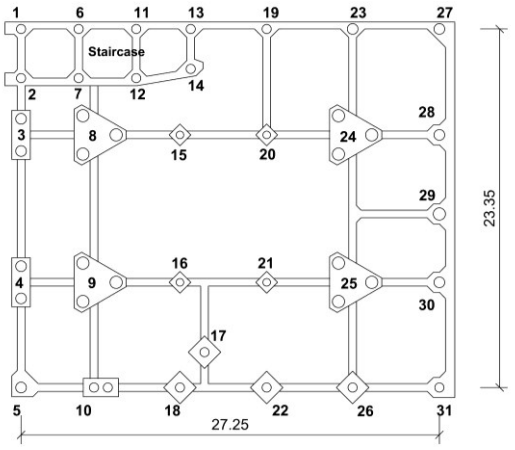


Figure 7 : Scheme of the foundation plinths with pile.

The soil was modeled by means of nonlinear springs, with stiffness deduced by means of the well-known *p-y* method. For the non-cohesive saturated soil, present up to $z = 15$ *m*, the relationships *p(y,z)* suggested by Reese et al. [9]**Errore. L'origine riferimento non è stata trovata.** were adopted; for the cohesive saturated soil, present from $z = 15.0$ *m*, the relationships suggested by Matlock [10] were used, but the contribution of this layer resulted negligible in practice. The model was developed in SAP2000 for the whole foundation. As previously said, modal base forces derived from the superstructure model were applied at the top of the piles, which were supposed to be connected by means of a rigid horizontal diaphragm.

The wall at the south side influences very much the forces distribution and the piles under that wall are much loaded. Bending moments along some piles at three different load steps are reported in Figure 9. They show the increasing moment up to the formation of the plastic hinges at the top and the unloading when the ultimate rotation is reached. The horizontal acceleration, given by the ratio between the horizontal force and the mass of the building, is plotted in Figure 10 versus the displacement of the control point, i.e. the point where the force is applied. The analysis was carried out in two ways, controlling the displacement and the force, respectively. The value of pseudo-acceleration equal to about 0.17 *g* can be assumed as limit one for the elastic behavior of the pile system.

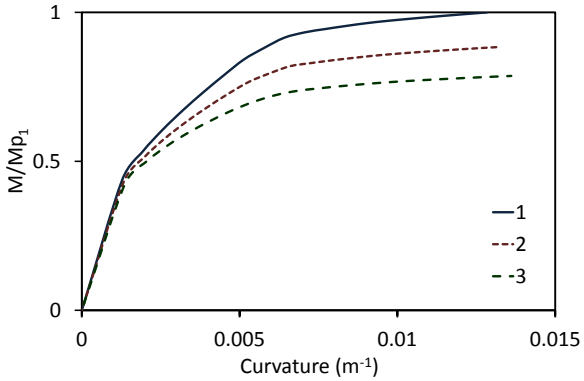


Figure 8 Moment-curvature curves for the three different reinforcing steel sections (Pile n. 27, M_{pl}= 1021 *kNm*).

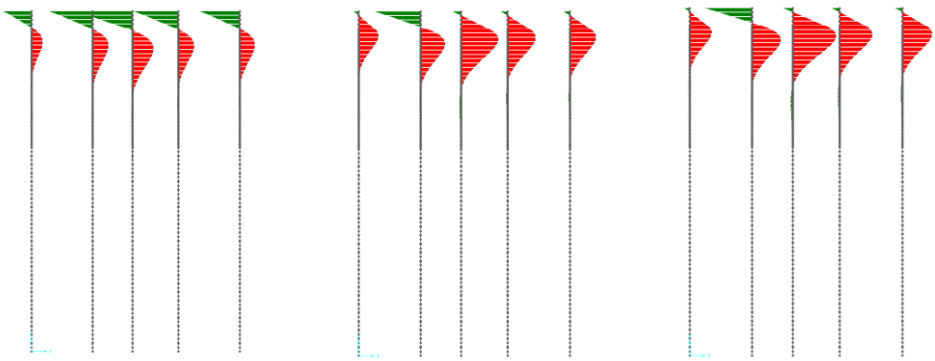


Figure 9 Bending moment in y-z plane at three steps for piles 27, 28, 29, 30 and 31.

6 BASE ISOLATION SYSTEM

A suitable solution, which can satisfy all the requirements, is the base isolation of the building. This allows reducing the seismic actions on the elevation structure and, as a consequence, on the foundation. A wider joint should be realized in this case but this does not represent a problem. In fact the joint should be realized in any case, substituting the south side walls with a new braced steel frame displaced of the needed gap with reference to the adjacent building.

The spectrum relative to P_{NCR} = 2% in 50 years was assumed for the design, with reference to a damping ratio ξ = 15%. Elastomeric isolators (HDRB) and sliders (SD) were considered, whose deployment was chosen with the objective of optimizing the dynamic behaviour of the building, so torsional effects were limited. 15 SD and 16 HDRB were used as shown in Figure 11. The isolator stiffness (K_e = 1250 *kNm*) was chosen in order to obtain a period of vibration of about 3.0 *sec*, which guarantees an adequate decoupling between the motion of the super-

structure with reference to the motion of the soil and also a significant reduction of the acceleration in the structure, much lower than those corresponding to its elastic capacity. The elastomeric isolators can support a displacement of 250 *mm*, which is also the value for the horizontal gaps. The response spectrum analysis was performed, combining the seismic effects according to the Italian code.

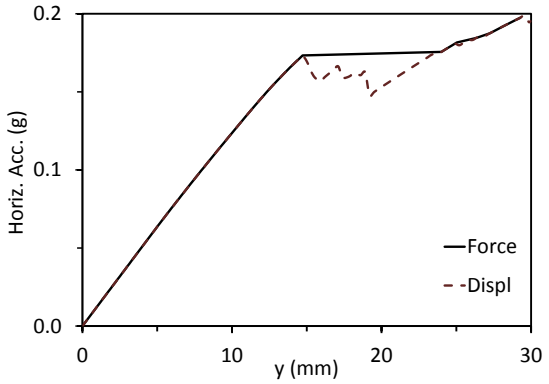


Figure 10 Static horizontal pseudo-acceleration in y direction versus displacement of the control point for the analysis carried out with force control (continuous line) and displacement control (dotted line).

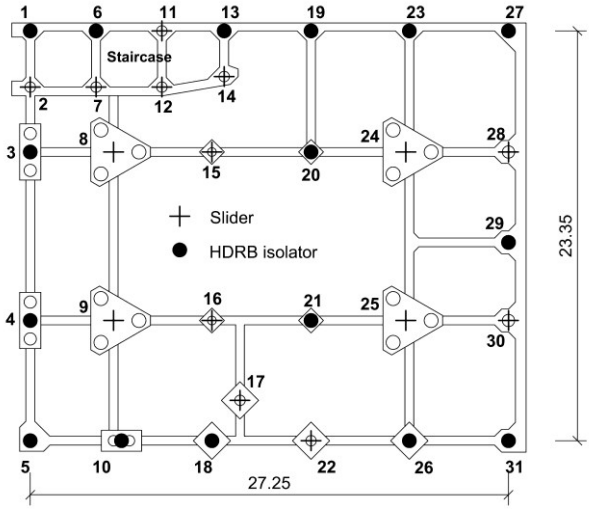


Figure 11 : Isolation system.

7 CONCLUSIONS

The analysis of an existing building, which could be used as strategic one, has been described in this paper. A finite element model was set up based on the original design, and the available experimental results were analyzed. Detailed experimental analysis on the materials and structure were carried out, and the dynamic characterization of the building was also performed by using ambient vibration tests.

The detailed and extended in situ experimental tests allowed assuming a full knowledge level of the structure so to avoid the lowering of the average material strength obtained experimentally. The checks under gravitational loads were satisfied both for the elevation structure and the foundations. The vulnerability analysis pointed out that the elevation structure safety was assured only up to seismic actions equal to 43% of those relative to the minimum exceedance probability of 2% in 50 years. For the foundations the situation is even worse.

The seismic isolation seemed to be the most appropriate retrofitting solution. It allows a significant reduction of the seismic action on the superstructure and the foundation so that to eliminate any structural intervention on them, while the realization of a gap with respect to the adjacent building at the south side should be done in any case to avoid pounding with the adjacent building.

REFERENCES

[1] Çelebi M., Bazzurro P., Chiaraluce L., Clemente P., Decanini L., De Sortis A., Ellsworth W., Gorini A., Kalkan E., Marcucci S., Milana G., Mollaioli F., Olivieri M., Paolucci R., Rinaldis D., Rovelli A., Sabetta F. and Stephens C., (2010). "Recorded Motions of the Mw6.3 April 6, 2009 L'Aquila (Italy) Earthquake and Implications for Building Structural Damage: A Review". *Earthquake Spectra,* Volume 26, No. 3, pages 651–684, August 2010; © 2010, Earthquake Engineering Research Institute.

[2] Basu D. and Jain S.K., Seismic Analysis of Asymmetric Buildings with Flexible Floor Diaphragms. *Journal of Structural Engineering*, **130**, 1169-1176, 2004.

[3] De La Colina J., In-Plane Floor Flexibility Effects on Torsionally Unbalanced Systems, *Earthquake Engng. Struct. Dyn.*, **28**, 1705-1715, 1999.

[4] Karayannis C.G. and Favvata M.J., Earthquake-induced interaction between adjacent reinforced concrete structures with non-equal heights, *Earthquake Engng Struct. Dyn.*, **34**, 1–20, 2005.

[5] Verderame G.M., Stella A. and Cosenza E., Le proprietà meccaniche degli acciai impiegati nelle strutture in c.a. realizzate negli anni '60. *10th Italian National Congress on Seismic Engineering (ANIDIS)*, Potenza-Matera, September 9-13, 2001, (in Italian).

[6] Clemente P., Bongiovanni G., Buffarini G. and Saitta F., Seismic Input in the Structural Design: Considerations and Application to the Italian Territory. *To be published in Int. J. of Safety and Security Eng.*, 2015.

[7] Ballio G., Mazzolani F.M., Strutture in acciaio, Hoepli, 1987, (in Italian).

[8] Meyer B.J. and Reese L.C., *Analysis of single piles under lateral loading, 4th Edition*. Center for Transportation Research Report - University of Texas at Austin, 1979.

[9] Reese L.C., Cox W.R., Koop F.D., Analysis of laterally loaded piles in sand, *Proc. VI Offshore Tech. Conf.*, Houston, Texas, 1974, **2**, 473-483.

[10] Matlock, H. Correlations for Design of Laterally Loaded Piles in Soft Clay, *Proceedings of Second Annual Offshore Technology Conference*, Houston, Texas, April 22-24, 1970.

[11] Chopra A.K. (1995), Dynamic of Structures, *Prentice Hall,* Englewood Cliff, New Jersey.

[12] Clemente P. and Buffarini G., "Base isolation: design and optimization criteria". *SIAPS 1-1(2010) 17--40. DOI 10.2140/siaps.2010.1.17*, Mathematical Science Publisher, 2010.

COMPDYN 2015
5th ECCOMAS Thematic Conference on
Computational Methods in Structural Dynamics and Earthquake Engineering
M. Papadrakakis, V. Papadopoulos, V. Plevris (eds.)
Crete Island, Greece, 25–27 May 2015

ADVANCED NUMERICAL MODELLING FOR DAMAGE ANALYSIS OF RC STRUCTURES: A CASE STUDY ON BEAM-COLUMN JOINTS

C. Del Vecchio[1], M. Di Ludovico[2], A. Prota[3] and G. Manfredi[4]

[1]University of Napoli "Federico II"
Department of Structures for Engineering and Architecture, via Claudio 21, 80125 Napoli, Italy
ciro.delvecchio@unina.it

[2]University of Napoli "Federico II"
Department of Structures for Engineering and Architecture, via Claudio 21, 80125 Napoli, Italy
diludovi@unina.it

[3] University of Napoli "Federico II"
Department of Structures for Engineering and Architecture, via Claudio 21, 80125 Napoli, Italy
aprota@unina.it

[4]University of Napoli "Federico II"
Department of Structures for Engineering and Architecture, via Claudio 21, 80125 Napoli, Italy
gamanfre@unina.it

Keywords: Reinforce concrete, existing building, beam-column joints, numerical modelling, crack pattern, shear.

Abstract. *The structural damage of reinforced concrete (RC) or masonry constructions, is commonly, associated with nonlinear phenomena that make the analysis of the structural behavior a challenging task. This is even more difficult for shear critical structures. Furthermore, the severe cracking may be associated, in these cases, with an incipient collapse, due to the limited ductility of shear critical members. Advanced mechanical-based theories has been developed in order to accurately capture the post-cracking behavior of shear critical structural systems; although accurate, such theories required complex calculations that make their use not suitable for practical applications. Recent technological developments in computational capacity opened to the implementation of accurate and complex theories on the nonlinear behavior of RC structures in software suitable to accurately reproduce the nonlinear behavior of structural systems. Computer-aided nonlinear analyses are nowadays widespread in the practical engineering and, in some cases, they represent an useful tool for forensic engineering. This paper presents a case study on the application of advanced numerical modelling for the damage analysis of poorly detailed beam-column joints. These elements are one of the main source of vulnerability of RC existing buildings subjected to seismic actions and their failure may lead to the collapse of the entire structural system.*

1 INTRODUCTION

The investigation on the seismic behavior of existing structural systems is nowadays a critical issues in the protection of modern societies in seismic-prone areas. Recent earthquakes demonstrated the high vulnerability of reinforced concrete (RC) structures and in particular, those designed not conforming to current seismic codes. Concerning the beam-column joints, the 80' years large earthquakes (El Asnam, 1980, Mexico 1985, Loma Prieta 1989) clearly showed the high vulnerability of these members. Before these events the joint shear reinforcements were almost never provided. This because of the lack of widely accepted theories and formulations on the joint capacity which resulted in a complete overlook in the design and construction practice [1]. Field inspections and experimental evidence demonstrated the high seismic vulnerability of poorly detailed beam-column joints. In certain situations, the premature joint shear failure may lead to the collapse of the entire structural system. Considering that in many countries the largest development of civil infrastructures took place in the 50-80's year, it is notable that many structural systems are vulnerable to seismic action because of the reduced capacity of beam-column joint.
This strongly encouraged the scientific community to investigate the seismic behavior of joint subassemblies. Several experimental tests (an example is reported in Figure 1) pointed out the influence of different parameters (e.g. the concrete mechanical properties, joint dimensions, axial load ratio, longitudinal reinforcement type, anchorage details) on the seismic capacity of beam-column joints [1]–[4].

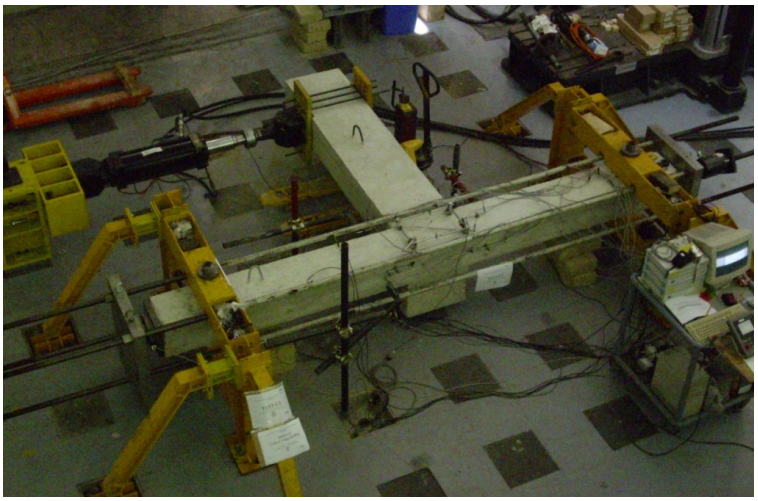


Figure 1: Experimental test on beam-column corner joint.

These observations resulted in several strength capacity models [1], [5] constituting the theoretical basis of modern code provisions for the seismic assessment of existing structures [6], [7]. Among the proposed models, particular emphasis should be given to the principal stresses approach [5]. Its mechanical basis along with the use of empirical coefficients make the model simple and suitable for practical applications. This model have been adopted in several national standards limiting the joint panel strength to the first cracking [6], [7]. Analytical studies pointed out that this limit is detrimental for the global seismic performances [8], [9]. Experimental tests [4] demonstrated that further shear forces can be carried by the joint panel after the first cracking. However, as already formulated by Priestley et al. [10] large shear de-

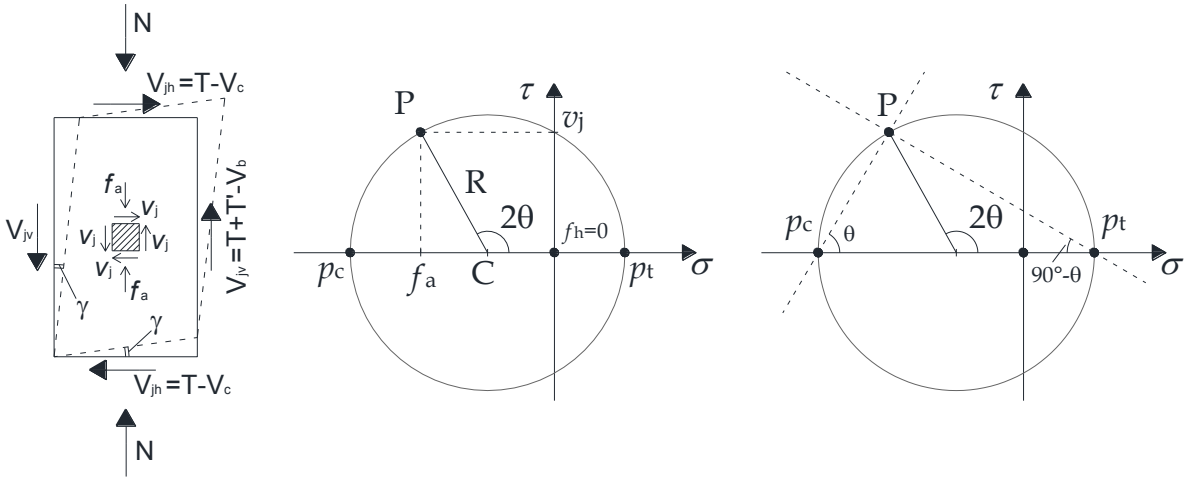
formations are exhibited after the joint panel first cracking. Indeed, to accurately reproduce the joint behavior, the joint shear deformation cannot be neglected. This is also confirmed by several research studies [2], [11] that quantified the effects of joint deformability on the overall seismic behavior.
Although several capacity model have been proposed to predict the joint behavior and the effects on the structural system performances [10]–[14], they are commonly based on empirical approaches or calibrated for specific joint types. Few models can accurately reproduce the joint hysteretic behavior. This because of the significant Strength and Stiffness Degradation (SSD) and pinching phenomena related to the shear cracking that strongly affect the cyclic response. Recent studies, pointed out the importance to accurately reproduce the member hysteretic behavior in the seismic assessment of shear critical structures [15], [16]. However include the effects of SSD in the seismic response of structural member is nowadays a critical issue. Sophisticated numerical models have been proposed to predict the structural response of SSD members for large displacement demand (i.e., the modified compression field theory, MCFT [17] and disturbed stress field model, DSFM [18]), but significant computational demand has limited their application to structures. In recent years, the development of advanced and efficient algorithms in computer programs suitable for practical applications (i.e., Membrane 2000 [19], VecTor programs [18]) promoted their use to reliably simulate the cyclic behavior of SSD RC structural systems.

2 RESEARCH OBJECTIVE

Although the joint behavior analytical modeling assumed significant relevance in the recent years, few capacity models, reliable for poorly detailed beam-column subassembly are nowadays available. The complex hysteretic behavior of these members, characterized by significant strength and stiffness degradation and pinching phenomena related to the shear cracks, makes it difficult to be reproduced.
A new strategy to model the beam-column joint cyclic behavior, based on the recent developments in the analytical models and computer software dedicated to shear critical systems, is presented in this paper. Available finite element method (FEM)-based software, implementing rigorous theoretical approaches (i.e. the MCFT and the DSFM) have been adopted in the model development. The proposed FEM model is described in detail, with particular attention to the material mechanical models and the effects of reinforcement anchorages. The model has been validated with reference to experimental tests; in particular, comparisons between theoretical and experimental outcomes are presented and discussed in the paper in terms of global response, local stress-strain behavior and crack pattern prediction. Further considerations on the joint panel stress levels are also presented.

3 SEISMIC BEHAVIOR OF BEAM-COLUMN JOINTS

Seismic events provide reverse cyclic actions on the beam–column joints transmitted by the adjacent members. Paulay and Priestley [1] summarized the structural behavior of the joint subassemblies with simple mechanical approaches suitable for all joint types (i.e. internal, external, corner, knee). However, the strength capacity and the joint deformability strongly depend on the joint type, confinement pressure, anchorage details and longitudinal reinforcements. A reduced confinement pressure due to the lack of structural members at all the joint faces and the local actions transmitted by the beam longitudinal anchorage make the corner joint the most vulnerable against seismic actions.



(a) (b) (c)

Figure 2: Mohr's circle of stresses for a typical joint panel (a); principal stresses (b) and principal directions (b).

The joint panel is subjected to a significant and complex stress field generated by seismic excitation (bending moment, shear and axial load). The beams and columns introduce large shear forces in the concrete core. Replacing the flexural bending moments with the resulting tension, T, and compression forces, C, the joint shear force in the vertical, V_{jv}, and horizontal, V_{jh}, directions can be computed as shown in Figure 2a [1], [20]. To satisfy rotational equilibrium, the vertical joint shear must be proportional to the horizontal shear; they are approximately in proportion by the joint dimensions, h_b/h_c. These large shear forces lead to diagonal compressive and tensile stresses (Figure 2b) in the joint core that may result in severe joint cracking, especially in the case of under-designed beam–columns joints without a proper amount of internal stirrups (i.e. transverse reinforcement). A diagonal strut can be used to capture this effect. However, in the case of structural members dominated by shear, diagonal tension failure can govern over concrete strut crushing. This is particularly common on beam–column joints with a low amount of transverse reinforcement. These assumptions resulted in an analytical model based on the Mohr's circle of a typical stress field of the joint panels (Figure 2a), characterized by uniform shear stresses, $v_{jh}=V_{jh}\backslash A_{col}$, and axial stresses, $f_a=N\backslash A_{col}$. According to experimental evidence, several authors suggested to limit the average principal stresses in tension Eq. (1) or compression Eq. (2) to values proportional to the concrete compressive strength [2], [5].

$$p_t = -\frac{f_a}{2} + \sqrt{\left(\frac{f_a}{2}\right)^2 + v_{jh}^2} \le k\sqrt{f_c} \tag{1}$$

$$p_c = \frac{f_a}{2} + \sqrt{\left(\frac{f_a}{2}\right)^2 + v_{jh}^2} \le 0.5 f_c \tag{2}$$

Here, k is a numerical coefficient equal to 0.29 for deformed bars (at the joint first cracking) or 0.42 (at the peak strength). For smooth internal reinforcement the maximum peak strength is reached along with the joint cracking and k can be assumed equal to 0.20. Furthermore, with the Mohr's circle approach, the direction of the principal compressive stress, θ, can be computed; this angle represents a fulfilling approximation of the crack inclination. The experimental evidence [2], [4] showed that large diagonal corner-to-corner cracks characterize

the failure mode of beam–column joint under cyclic horizontal actions, regardless of the joint dimensions or longitudinal reinforcement details. In absence of stirrups, the principal compressive stress after cracking, can be assumed to be inclined at a constant angle, θ, and, in turn, the direction of principal tensile stress is inclined at 90-θ. The angle θ can be computed, as proposed by Paulay and Priestley [1], as function of the joint panel dimensions by $\theta = atan(h_b/h_c)$.

Minor importance has been reserved to the joint deformation and its effects on the global seismic response. This because of the predominant brittle failure of these members and the difficulties in handle shear distortions. However, the joints have a key-role in the structural system and small joint shear deformations may have significant effects on the overall structural response. Although this aspect has been introduced by Priestly along with the principal stresses approach [10], only recently, the scientific community focused the attention on the role of joint shear deformations. The joint shear deformations represent the complement of the shear strength. To be more precise, they are the effects of the shear stresses applied on the joint panel (see Figure 2a). An estimation of the magnitude of the shear deformations γ, assumed equal for the horizontal and vertical direction, was introduced by Priestly [10]. Based on experimental evidence, he provided the joint panel shear deformation at different stress levels (cracking, peak strength and joint collapse). Later, this model has been particularized to include the relations for plain internal reinforcements [2].

4 ADVANCED NUMERICAL MODELLING

The advanced numerical models proposed in the recent years improved accuracy in reproducing the behavior of RC structural systems. New mechanical models and solution algorithms have been developed and great effort has been made to combine them with the state-of-the-art knowledge in refined tools suitable for the use in the practical applications (e.g., OpenSees [21], VecTor programs [22], among others).

The continuum element considered in this study is based on the Modified Compression Field Theory (MCFT) [15] and Disturbed Stress Field Model (DSFM)[18]. Both these theories have been developed at University of Toronto and validated through large experimental programs on shear critical RC panel, structural members and entire structural systems. The MCFT is a two-dimensional analytical model in which compatibility, equilibrium, and constitutive relationships were derived based on average stress and strain of concrete. In the MCFT, it is assumed that the directions of averaged stress and strain are identical. The formulation of the model was simplified by assuming cracks are smeared and fully rotating. Local stresses and strains at cracks are computed based on the stress-strain relationship developed for cracked concrete. Out-of-plane and in-plane transverse reinforcements are smeared over the entire concrete core. Such a theory has been later generalized by the DSFM, modifying some basic assumptions (i.e. alignment of shear stress and strain) and enlarging the applicability to more complex stress fields. The complexity of this approach and the number of information contained in the analysis strongly limited its their application in the past year. Recently, it has been implemented in accurate computer tools suitable for practical applications. In this paper, the response of a reference beam-column joint will be reproduced by mean of two different computer software (Membrane 2000, M2k [19], and VecTor2, VT2 [18]). They are characterized by increasing level of difficulty in the modeling and, in turn, higher accuracy in the response prediction.

The joint subassembly selected for the model validation is a poorly detailed corner beam-column joint typical of existing structures designed for gravity load only. The specimen

(named T_C3 in the experimental program carried out at University of Naples and described in Del Vecchio et al. [4]) has no stirrups in the joint panel and geometry and internal reinforcement details typical of existing buildings. It has been tested with an imposed cyclic displacement applied at the beam tip and under constant axial load on the columns (see Figure 1). To simulate gravity loads, a preload of 19.2 kN was applied to the beam along with a constant axial load ($\nu = P/A_g f_c = 0.21$) to the column. The specimen was constrained to the strong floor by two rigid steel frames, with a steel roller placed inside the lower column end to simulate a pin connection. The top column was constrained to a rigid frame by two steel rollers that grabbed the column end externally and allowed top column elongation. The beam and column length were designed to allow for the typical story height and the portion of the beam up to the zero point of the bending moment diagram, respectively. The cylindrical concrete compressive strength is about 16.4 MPa and the longitudinal steel reinforcement yielding stress about 470 MPa. The experimental test pointed out a shear failure of the joint panel before the flexural yielding of longitudinal steel reinforcement of members framing into the joint.

- *Membrane 2000*

Membrane 2000 (M2k) is a simple computer program implementing the MCFT. It allows analysis of reinforced concrete shells subjected to in-plane forces (axial force in X and Y directions and in-plane shear). Internal reinforcement may be in orthogonal directions X and Y with an arbitrary number of bar layers and spacing allowed. Membrane elements subjected to in-plane forces can be found in structural walls, the webs of beams, containment vessels, and cooling towers among many others. This is the type of experimental element tested to develop the modified compression field theory. The complex stress field and geometry of a joint subassembly can be reduced to a simple shell loaded in shear and axial force by using the assumptions reported in the previous paragraph. In particular, the actions transmitted by the member framing in the joint should be reduced to acting shear stress (assumed equal for all the faces of the joint) and axial compression stresses acting on the joint horizontal faces (see Figure 2a). It should be noted that this modeling approach can be extended only to joint subassemblies suffering the premature shear failure of the joint panel without relevant nonlinear phenomena in the adjacent members. According to these assumptions, the selected joint T_C3 has been modeled in M2k by using a shell element 300 mm thick subjected to a constant axial stress of 3.50 MPa (it is obtained spreading the axial load on the joint horizontal surface). The specimen shear strength has been evaluated under monotonic joint shear stresses and the results are plotted in

Figure 3 against the joint shear strain, γ_{xy}. Comparison with available experimental results [4], points out a significant underestimation of the real joint performances in terms of joint panel peak strength (v_{jh}=2.56MPa). The analysis of the Mohr's circle of stress and the crack pattern at the peak strength (

Figure 3b,c) demonstrated that the ultimate joint capacity is reached along with joint panel first cracking, for a principal tensile stress about 1.38MPa. This is in compliance with the stress limit proposed by Priestley [5], $p_t = 0.29\sqrt{f_c}$. Such underestimation is related to the effects of the longitudinal reinforcement anchorages, neglected in the model. In fact, larger shear stress can be achieved in the joint panel if the longitudinal beam reinforcements are bent into the joint [5] ($p_t = 0.42\sqrt{f_c}$).

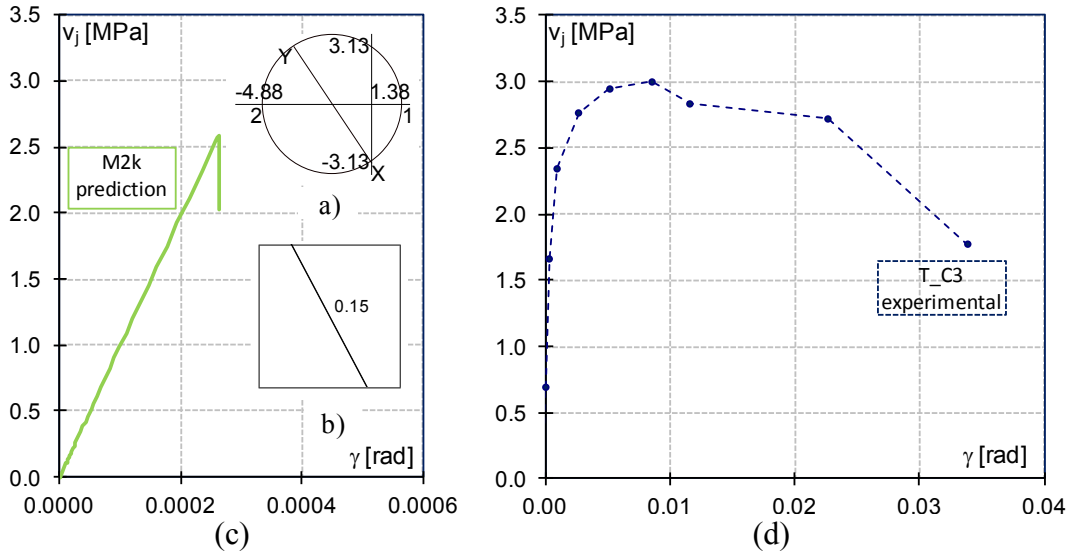


Figure 3: Membrane 2000 (M2k) monotonic response prediction without the anchorage effects: (a) Mohr's circle and (b) crack patter at the peak strength; (c) shear stress-strain behavior.

However there are no simple options to include the effects of beam bar anchorages in the M2k model. To solve this issue, the maximum lateral pressure provided by the bar bents have been computed and an equivalent amount of transverse reinforcement offering the same lateral pressure has been inserted in the model. Details on the modeling procedure are reported in Figure 4.

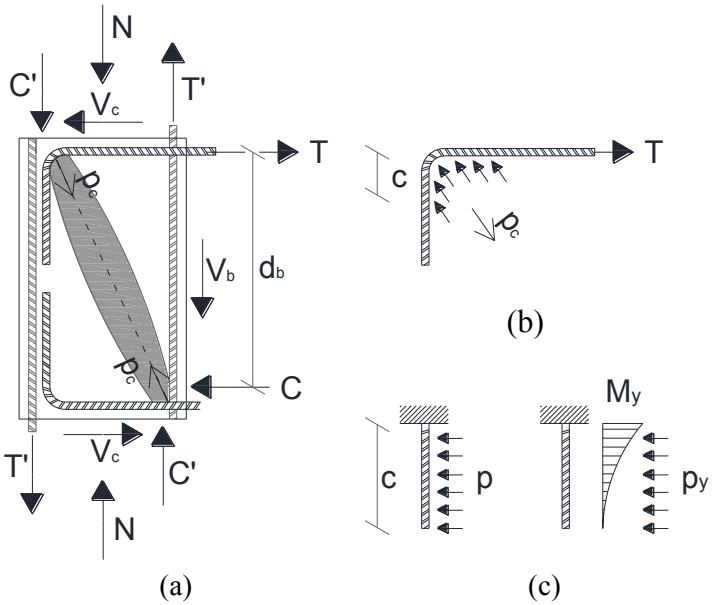


Figure 4: Mechanical model of the anchorage effects.

The lateral pressure of the beam bar anchorages comes from the reaction to the concrete compressive forces developing in the diagonal strut. The maximum pressure carried by the anchorage is assumed equal to the pressure needed to yield the longitudinal reinforcement in

flexure. In the calculation it is assumed that the straight length of the anchorage is fixed in correspondence of the bent. This pressure can be computed with Eq. (3).

$$M_y = \frac{pl^2}{2} \Rightarrow p_y = \frac{2M_y}{c^2} = \frac{2f_{ym} \cdot \pi \cdot r^3}{c^2 \cdot 4} = \frac{2 \cdot 470 \cdot \pi \cdot 8^3}{85^2 \cdot 4} = 52.2 \frac{N}{mm} \quad (3)$$

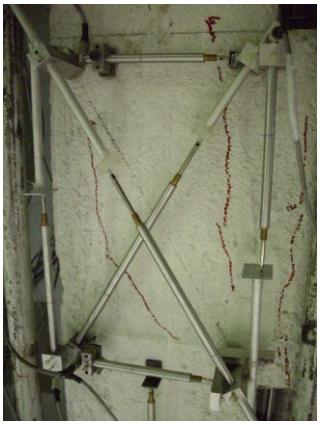
where c is the straight length of the anchorage subjected to the lateral pressure of the concrete compressive strut. It can be assumed equal to the total height of the concrete compressive zone above the longitudinal reinforcement $0.25h\text{-}c_c\text{-}d_b$=125-25-16=85mm, where c_c is the concrete cove and d_b is the diameter of longitudinal reinforcements.
The total pressure acting on the external face of the joint panel can be computed multiplying the maximum pressure of the single anchorage for the number of anchorages and dividing by the joint width:

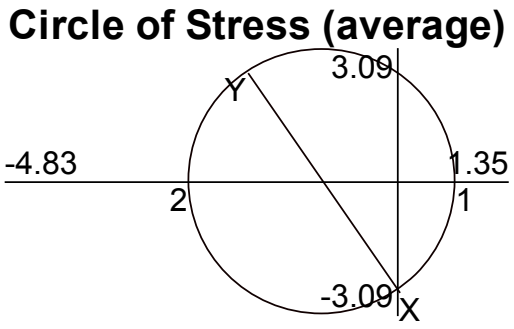
$$p_{t,tot} = \frac{p_y \cdot n_b}{b_j} = \frac{52.2 \cdot 5}{300} = 0.87 \frac{N}{mm^2} \quad (4)$$

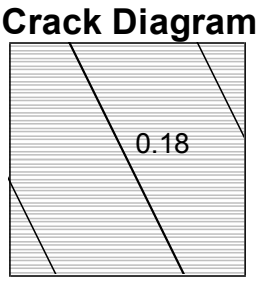
where n_b is the number of beam bars bent into the joint panel, in this case 5, and b_j the joint width assumed equal to the column width, 300mm.
Once that the maximum lateral pressure has been identified, the equivalent amount of joint reinforcement (in terms of percentage of transverse reinforcements) can be derived dividing this pressure for the yield stress of steel:

$$p_{t,tot} = f_{ym} \cdot \rho_s \Rightarrow \rho_s = \frac{p_{t,tot}}{f_{ym}} = \frac{0.87}{470} = 0.186\% \quad (5)$$

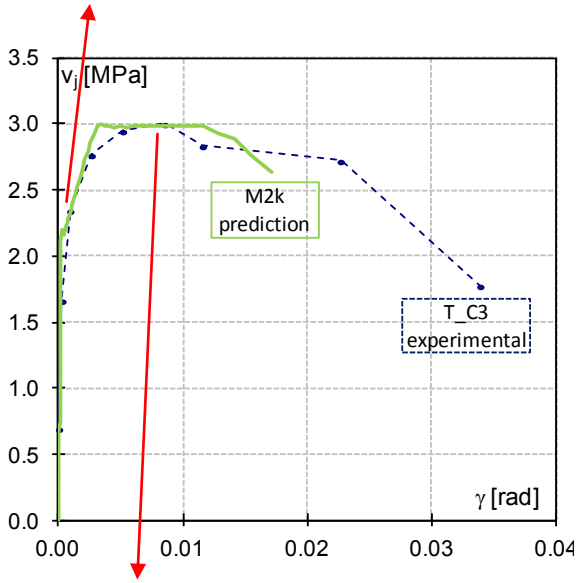
In this case an equivalent amount of joint stirrup, representative of the confinement effects of the beam bar anchorages, will be placed into the joint. This solution has been preferred with respect to a constant value of the lateral pressure in order to be representative of the variability of the confinement pressure, that increases increasing the shear stress.
Comparison between the proposed analytical model and experimental results is reported in Figure 5 in terms of joint shear stress-strain behavior, acting stress field and crack pattern.
The comparison points out the good match of the proposed analytical model in terms of joint panel shear behavior at different levels. In particular, the joint panel first cracking (where hairline cracking was detected during the test) is well predicted by the proposed analytical model in terms of shear strength and crack pattern (see Figure 5, level II). Furthermore, the joint panel circle of stresses highlights the good match in terms of principle tensile stress with the limit proposed by Priestley [5], $p_t = 0.29\sqrt{f_c}$ =1.2MPa. The analytical predictions match well the experimental results also at the peak strength (see Figure 5, level III) in terms of stress strain behavior and crack pattern, where large shear cracks can be detected. The good match in terms of joint panel principal tensile stress with the stress limit proposed by Priestley, $p_t = 0.42\sqrt{f_c}$ =1.7MPa, shows the reliability of the proposed model to account for the effects of anchorages bent into the joint. The full strength degradation cannot be captured by this software and more refined calculations are needed.



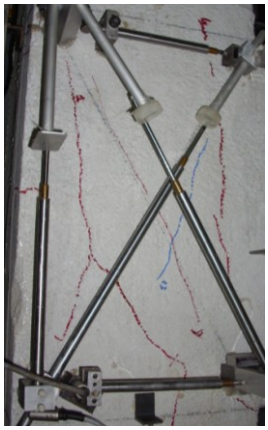


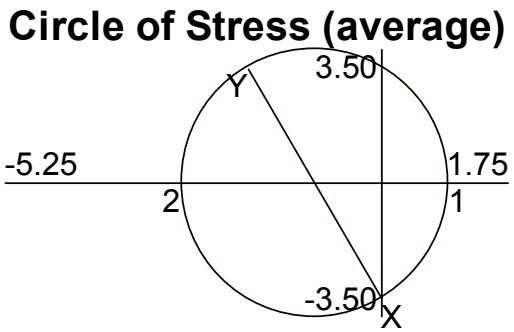


Level II: Joint panel first cracking



Level III: Joint peak strength





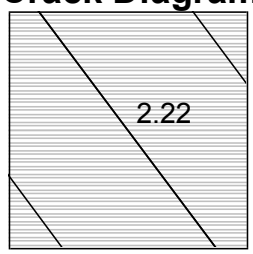


Figure 5: Experimental vs. M2k prediction in terms of shear stress-strain behavior and crack patterns (Crack widths in mm).

- *VecTor2*

VecTor2 is a program based on the MCFT/DSFM for nonlinear finite element (FEM) analysis of reinforced concrete membrane 2D structures that permits accurate assessments of structural performance (strength, post-peak behavior, failure mode, deflections and cracking). The Vector2 bundle [22] includes: FormWorks, a graphics-based preprocessor program that simplifies

the model building; Augustus, a complete VecTor2 post-processor that may pro-vide all the global and local results in useful numeric or graphic formats. It is also able to dis-play the specimen crack pattern at each stage of imposed displacement and this represents a very use-ful tool to detect numerical model failure mode. The FEM elements require a different and more complex modeling approach. The VecTor2 model was developed using a pre-processor unit FormWorks [22] that simplified the meshing and the input of the model parameters. Sim-ilar to other continuum elements, mesh size plays an important role in computational efficien-cy and accuracy. A mesh size in the range of about 25 mm, and approximately square elements have been adopted as suggested in the related studies [18, 25, 27]. The software can accommodate only 2D elements. A specific thicknesses equal to 300 mm has been set for all members. Longitudinal reinforcements are modeled with truss elements. Link elements were adopted to model the bond-slip behavior using the *Embedded deformed bar* option available in the software option [22]. To account for the stress concentration at the anchorages of longi-tudinal beam bars, the *Hooked bar option* has been adopted for the link element in corre-spondence of reinforcements ends. Transverse reinforcements in the beam and columns were modeled as smeared reinforcements with appropriate in-plane (ρ_t) and out of- plane (ρ_z) aver-age ratios. The same approach was used to account for the joint panel internal reinforcement representative of the anchorage effects as determined by Eq. (5).

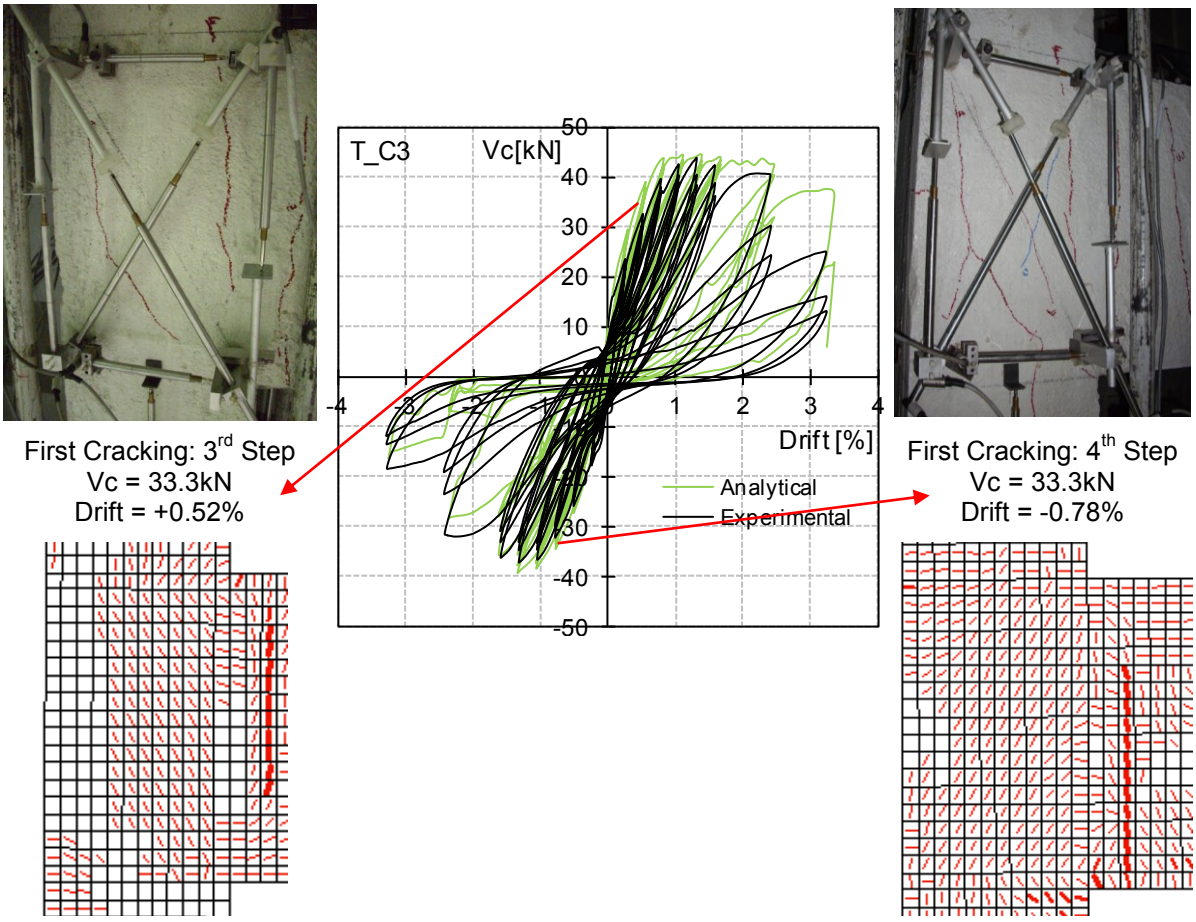


Figure 6: Experimental and analytical crack patterns at the joint panel first cracking
(Crack widths: thin<0.5mm; thick>1mm).

The concrete cover was modeled as unconfined concrete. The material properties are defined in accordance with the material tests reported Del Vecchio et al. [4]. All analyses are performed with the use of basic default material behavior models and analysis options. The concrete constitutive model by Popovic and Mander [19, 37] is adopted to reproduce concrete compressive behavior. A proper representation of the loading/unloading behavior and the cyclic-load induced damage sustained by the concrete is critical in determining the strength and energy-dissipation capacity of the subassembly. Indeed, as suggested by Sagbas et al. [23],The hysteretic model for the concrete employed here was that proposed by Palermo and Vecchio [24].
As in the experimental test, joint models are subjected to cyclic displacement and axial load applied at the beam tip and columns, respectively. The comparisons between the analytical model and experimental results at the significant steps of the test are reported in Figures 6-9.

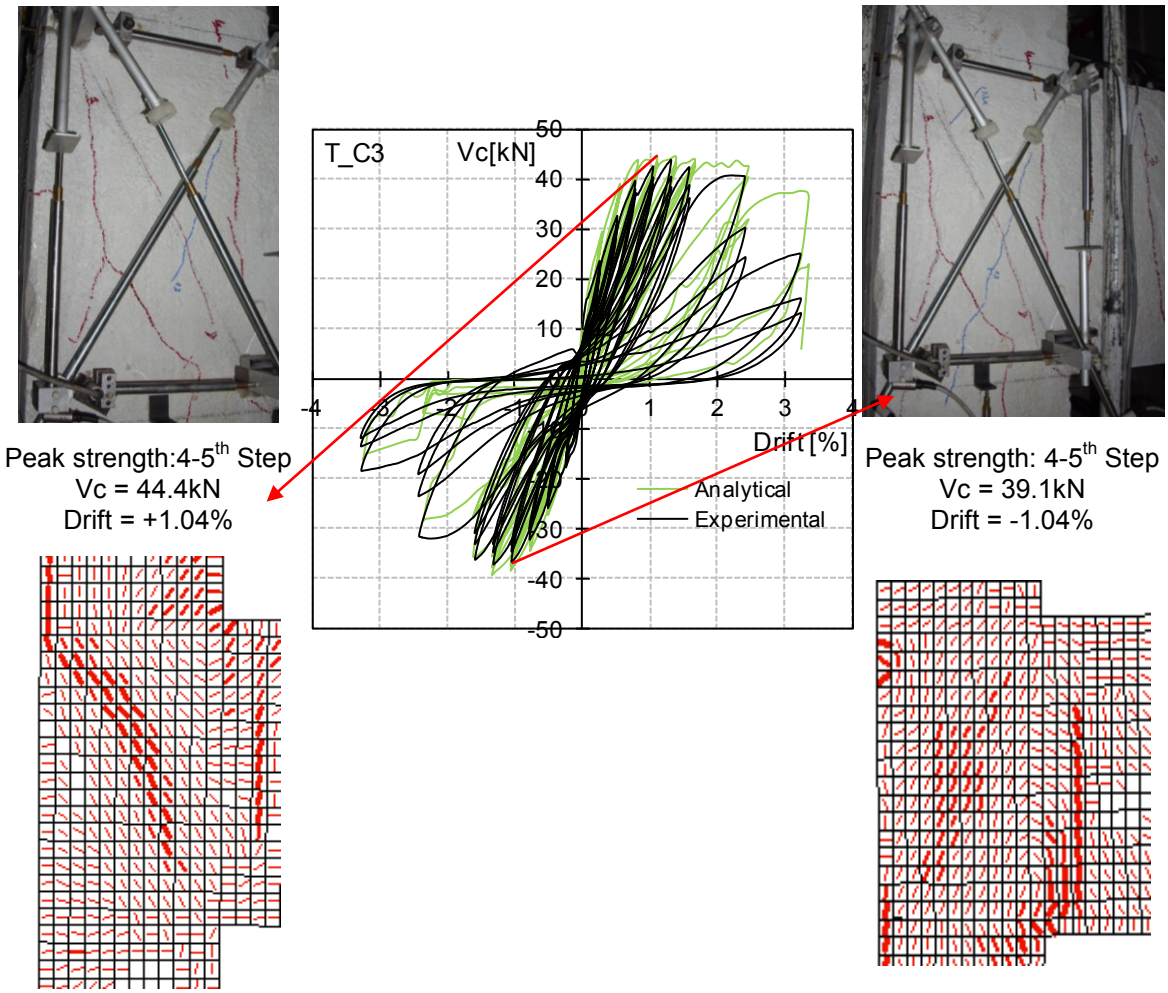


Figure 7: Experimental and analytical crack patterns at the subassembly peak strength (Crack widths: thin<1mm; thick>2mm).

The comparison between the proposed analytical model and experimental results demonstrated the accuracy in predicting the joint subassembly global behavior. The theoretical predictions show a good match with respect to all significant parameters in the seismic assessment, including initial stiffness, peak strength, strength and stiffness degradation, pinch-

ing effects and energy dissipation. Furthermore, a crack pattern very similar to the experimental one is also predicted. In particular, the joint panel first cracking (depicted in Figure 6) occurs for a column shear of about 33kN, significantly lower than the maximum strength. At this step diffused hairline cracks appears in both directions. At the same step, a flexural crack appears on the beam in the section of the maximum bending moment. Because of the higher magnitude of the flexural crack, in the analytical model joint shear cracks are represented with a thin line.

The joint peak strength is characterized by deep and large diagonal cracks in the order of millimeters. As reported in Figure 7 a corner-to-corner diagonal crack appears in the joint panel for the positive loads. Reverse cyclic actions produces a change in the crack orientation; however, due to the strong nonlinear behavior of the cracked concrete, the opposite diagonal cracks are not completely closed.

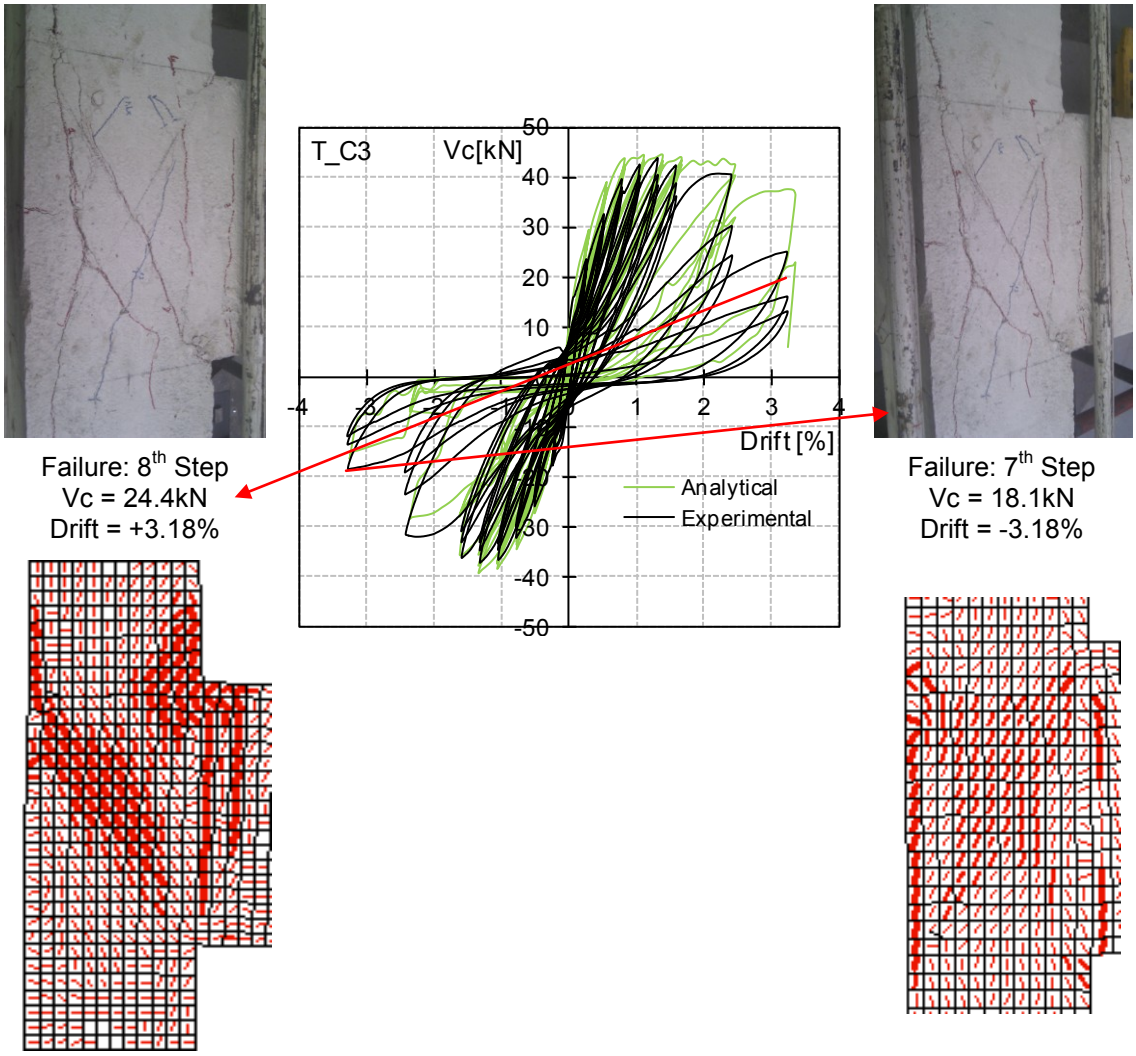


Figure 8: Experimental and analytical crack patterns at joint panel shear failure
(Crack widths: thin<2mm; thick>4mm).

The crack pattern at the joint panel failure, after which a significant drop in the shear strength can be observed, shows marked cracks in both direction and the spalling of concrete cover.

Due to the severe damage of the joint panel, large shear cracks, in the order of centimeters, can be observed in both directions.

Further information on the joint panel failure mode are provided by analyzing the local behavior of members. No relevant damage is detected on columns and beam framing in the joint panel. Analytical prediction confirmed that the internal longitudinal reinforcements are far below the tensile yielding. On the other side the joint panel shear stress-strain behavior shows significant nonlinear phenomena (see Figure 9). In compliance with experimental results, the joint panel first cracking is followed by significant joint shear deformations. Once that the peak strength is achieved, the strength degradation is related to joint shear strains even double respect to the peak strength. The VecTor2 model is able to capture the shear stress-strain behavior with enough accuracy until a significant drop in the shear strength occurs.

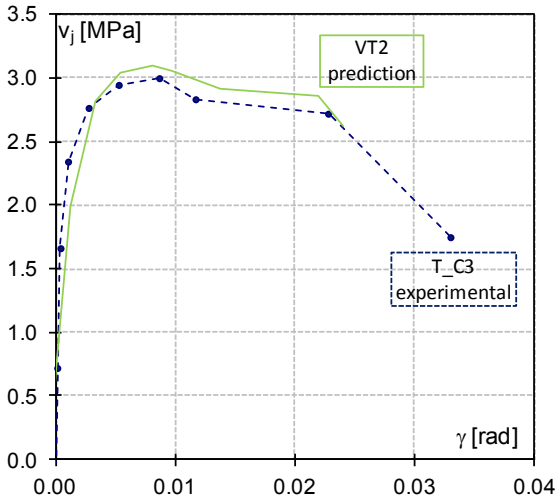


Figure 9: Joint panel shear stress strain behavior.

5 CONCLUSIONS

The seismic behavior of beam-column joint is of paramount importance in the seismic assessment of existing RC structures. In fact, the occurrence the of joint panel premature shear failure is often detrimental for the global seismic response. Several experimental tests have been carried out with the scope to characterize the joint seismic capacity and find the main parameter affecting the cyclic response. Although refined analytical models have been developed, few models are able to reliably predict the joint hysteretic response. This because of the significant strength and stiffness degradation phenomena, complex to be captured with classical modeling approaches. In the present paper, a new modeling approach for poorly detailed beam-column joints is presented. The model has been developed with the recent computer programs (Membrane 2000 and VecTor 2) able to reproduce the cyclic response of shear-critical structural systems based on refined theoretical approaches (MCFT/DSFM). The modeling assumptions on the mesh-size, mechanical model of materials, anchorage details and applied loads are discussed in detail. The comparison with experimental results of a reference tests confirms that, neglecting the confinement pressure provided by the longitudinal reinforcement anchorages in the analytical model, the strength is limited to the joint panel first cracking. The proposed M2k model, comprehensive of the anchorage effects, is able to accurately capture the joint panel shear strength at the first cracking and joint ultimate capacity.

Furthermore, the analytical response in terms of principal stress is in compliance with the limits proposed by Priestley, both at the first cracking and peak strength.

The more refined VecTor2 analytical model provide a good match with experimental results with respect to all significant parameters in the seismic assessment, including initial stiffness, peak strength, strength and stiffness degradation, pinching effects and energy dissipation. Furthermore, the crack pattern at different stress level can be accurately predicted. Concerning the local stress-strain behavior of the joint panel, a surprising match has been also achieved. In conclusion, the proposed analytical model can be employed to accurately predict the response of poorly detailed beam-column joint. However, particular care should be adopted in modeling the anchorage details to avoid significant underestimation of the joint shear capacity.

AKNOWLEDGMENTS

This study was performed in the framework of PE 2015 joint program DPC-Reluis Reinforced Concrete, Task 1.3: Capacity of beam-column joints.

REFERENCES

[1] T. Paulay and M. J. N. Priestley, *Seismic design of Reinforced Concrete and masonry buildings*. U.S.A.: John Wiley & Sons, Inc., 1992, p. 744.

[2] G. M. Calvi, G. Magenes, and S. Pampanin, "Relevance of beam-column joint damage and collapse in RC frame assessment," *J. Earthq. Eng.*, vol. 6, no. Special Issue 1, pp. 75–100, 2002.

[3] A. Prota, A. Nanni, G. Manfredi, and E. Cosenza, "Selective upgrade of underdesigned Reinforced Concrete beam-column joints using carbon Fiber-Reinforced Polymers," *ACI Struct. J.*, vol. 5, no. 101, pp. 699–707, 2004.

[4] C. Del Vecchio, M. Di Ludovico, A. Balsamo, A. Prota, G. Manfredi, and M. Dolce, "Experimental investigation of exterior RC beam-column joints retrofitted with FRP systems," *ASCE J. Compos. Constr.*, vol. 18, no. 4, pp. 1–13, 2014.

[5] M. J. N. Priestley, "Displacement-based seismic assessment of Reinforced Concrete buildings," *J. Earthq. Eng.*, vol. 1, no. 1, pp. 157–192, Jan. 1997.

[6] CEN, *Eurocode 8: Design of structures for earthquake resistance - Part 3: Assessment and reofitting of buildings*. Brussell: European Committee for Standardization, 2005.

[7] MI, *D.M. 14 Gennaio 2008 (D.M. 2008). Technical codes for structures (in Italian)*, GU n°29, F. Rome, Italy, 2008.

[8] M. Di Ludovico, G. Manfredi, E. Mola, P. Negro, and A. Prota, "Seismic behavior of a full-scale RC structure retrofitted using GFRP laminates," *J. Struct. Eng.*, vol. 134, no. 5, pp. 810–821, 2008.

[9] R. Frascadore, M. Di Ludovico, A. Prota, G. M. Verderame, G. Manfredi, M. Dolce, and E. Cosenza, "Local strengthening of RC structures as a strategy for seismic risk mitigation at regional scale," *Earthq. Spectra*, vol. In Press, 2014. http://dx.doi.org/10.1193/122912EQS361M.

[10] M. J. N. Priestley, F. Seible, and G. M. Calvi, *Seismic design and retrofit of bridges*. New York: John Wiley & Sons, Inc., 1996, p. 686.

[11] S. Park and K. M. Mosalam, "Simulation of Reinforced Concrete Frames with Nonductile Beam-Column Joints," *Earthq. Spectra*, vol. 29, no. 1, pp. 233–257, Feb. 2013.
[12] L. N. Lowes and A. Altoontash, "Modeling Reinforced-Concrete Beam-Column Joints Subjected to Cyclic Loading," *J. Struct. Eng.*, vol. 129, no. 12, pp. 1686–1697, 2003.
[13] ASCE/SEI, *ASCE/SEI 41-06. Seismic rehabilitation of existing buildings*. Reston, VA, USA, 2007.
[14] J. M. Lafave and J. Kim, "Joint Shear Behavior Prediction for RC Beam-Column Connections," *Int. J. Concr. Struct. Mater.*, vol. 5, no. 1, pp. 57–64, 2011.
[15] X. Huang and O.-S. Kwon, "Numerical Models of RC Elements and their Impacts on Seismic Performance Assessment," *Earthq. Eng. Struct. Dyn.*, vol. 44, no. 2, pp. 283–298, 2015.
[16] C. Del Vecchio, O. Kwon, L. Di Sarno, and A. Prota, "Accuracy of nonlinear static procedures for the seismic assessment of shear critical structures," *Earthq. Eng. Struct. Dyn.*, vol. (on line published, 2015). doi: 10.1002/eqe.2540.
[17] F. J. Vecchio and M. P. Collins, "The Modified Compression-Field Theory for Reinforced Concrete elements subjected to shear," *ACI J.*, vol. March-Apri, pp. 219–231, 1986.
[18] F. J. Vecchio, "Disturbed Stress Field Model for Reinforced Concrete: Formulation," *ASCE J. Struct. Eng.*, vol. 126, no. 9, pp. 1070–1077, 2000.
[19] E. C. Bentz, "Sectional Analysis of Reinforced Concrete Members," University of Toronto, ON, Canada, 2000.
[20] C. Del Vecchio, M. Di Ludovico, A. Prota, and G. Manfredi, "Analytical model and design approach for FRP strengthening of non-conforming RC corner beam-column joints," *Eng. Struct.*, vol. 87, pp. 8–20, 2015.
[21] The Regents of the University of California, "OpenSees: Open system for earthquake engineering simulation." Pacific Earthquake Engineering Research Center College of Engineering University of California, Berkeley.
[22] P. S. Wong, F. J. Vecchio, and H. Trommels, "VecTor2 & FormWorks User's Manual. Second Edition," Toronto, ON, Canada, 2013.
[23] G. Sagbas, F. J. Vecchio, and C. Christopoulos, "Computational Modeling of the Seismic Performance of Beam-Column Subassemblies," *J. Earthq. Eng.*, vol. 15, no. 4, pp. 640–663, Apr. 2011.
[24] D. Palermo and F. J. Vecchio, "Compression Field Modeling of Reinforced Concrete Subjected to Reverse Loading: Formulation," *ACI Struct. J.*, vol. 100, no. 5, 2003.

COMPDYN 2015
5th ECCOMAS Thematic Conference on
Computational Methods in Structural Dynamics and Earthquake Engineering
M. Papadrakakis, V. Papadopoulos, V. Plevris (eds.)
Crete Island, Greece, 25–27 May 2015

SEISMIC RETROFITTING EFFECT OF 10-STORY RESIDENTIAL BUILDING RETROFITTED USING PASSIVE SEISMIC CONTROL SYSTEM WITH AMPLIFIER MECHANISM

Y. TAKASE[1], T. IKEDA[2], AND T. SUZUMURA[3]

[1] Research Institute of Technology, TOBISHIMA Corporation
Kimagase 5472 Noda-shi Chiba-ken Japan
e-mail: yuya_takase@tobishima.co.jp

[2] Research Institute of Technology, TOBISHIMA Corporation
Kimagase 5472 Noda-shi Chiba-ken Japan
e-mail: takaaki_ikeda@tobishima.co.jp

[3] Nagoya Branch, TOBISHIMA Corporation
Matsubara 3-2-8 Naka-ku Nagoya-shi Aichi-ken Japan
e-mail: takeshi_suzumura@tobishima.co.jp

Keywords: Seismic Retrofitting, The 2011 off The Pacific Coast of Tohoku Earthquake, Modifid Compression Field Theory

Abstract. *In Japan many buildings that were designed by the old code have been retrofitted structurally because lots of buildings designed by the old code were collapsed in the Southern Hyogo prefecture earthquake in 1995. Moreover many retrofitted structures were subject to strong seismic motion in the 2011 off the Pacific coast of Tohoku Earthquake. It was found that seismic retrofitting was very useful for seismically weak structures. In Sendai city, there is the 10-story residential building that was retrofitted using a passive seismic control system with an amplifier mechanism. The nonstructural members (partial walls) of the building had been damaged when Tohoku Earthquake, though their structural members had not been damaged. In order to evaluate the effect of the seismic retrofitting, we investigated the damage of the building after the 2011 off the Pacific coast of Tohoku earthquake. In addition we calculated the story drift angle by seismic response analysis to evaluate from the analytical viewpoint. As a result of the damage investigation of this building, it was obvious that the building was safe structurally. Furthermore, we verified when nonstructural members had been in failure using the modified compression field theory(Vecchio,F.J. and Collins,M.P, 1986). The nonstructural members were in failure before the peak acceleration. Thus, we concluded that the effect of the partial walls on structural performance was very small.*

1 INTRODUCTION

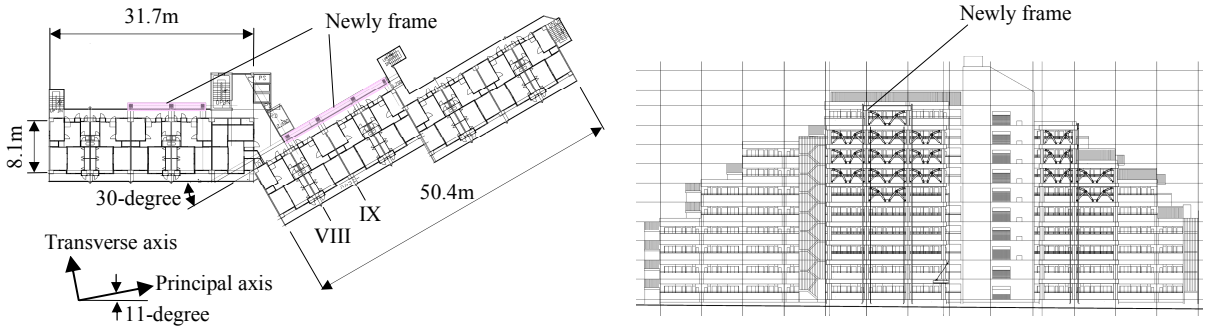
At the time of the 2011 off the Pacific coast of Tohoku Earthquake (the Earthquake below), the City of Sendai near the earthquake source subjected to very strong ground motion. Numerous buildings with poor earthquake resistance had been retrofitted against the Miyagi-ken-oki Earthquake and other active-fault-induced inland earthquakes that were highly likely to occur. The state of the retrofitted buildings were reported[1] after the Earthquake. The effects of and problems of seismic retrofit are gradually being known.

The authors investigated the structural performance and the effects of seismic retrofit in a ten-storied high-rise residential apartments (the Building below) that had been retrofitted using a seismic control systems equipped with amplification mechanism. Damage to nonstructural members was confirmed in numerous buildings including the Building in the wake of the Earthquake. In this study, therefore, the shear stress - deformation relationship in nonstructural members of the building was estimated using an existing theoretical model, and the effects of nonstructural members on the structural performance of the Building were examined based on the shear strength and the time when the shear strength was reached.

2 OUTLINE OF THE BUILDING AND SEISMIC RETROFIT

2.1 Outline of the Building

Figure 1 shows a plan view of the second floor of the retrofitted Building and a northern elevation. The Building was constructed in 1979. At present, buildings are designed to the earthquake resistance standards came into forced in 1981. The Building does not therefore comply with the existing standards. The Building is of a complex shape. In plan, the Building bends sharply at the elevator hall and is of an echelon structure in eastern buildings. In elevation, the Building has setbacks on both sides on the fifth and higher floors. From a structural viewpoint, the Building is made of steel encased reinforced concrete (SRC) on the first to sixth floors and of reinforced concrete (RC) on the seventh to tenth floors. The Building is of a frame structure longitudinally and of a frame structure combined with shear walls in the span direction.



(a) The floor plan (b) The nothern elevation

Figure 1: Views of the building

2.2 Outline of retrofit design

As a result of the seismic diagnosis earthquake resistance diagnosis of the Building, the Is value exceeded 0.6, the level specified in the new earthquake resistance standards, on all floors in the span direction, but was lower than 0.6 longitudinally except on some floors. It was then decided to apply seismic retrofit longitudinally. For retrofit, a seismic retrofit meth-

od using the seismic control systems with amplification mechanism was adopted in view of the post-retrofit usability of habitable rooms, usability of the Building during retrofit work and cost performance. Seismic control systems with amplification mechanism were installed on the side of the side-corridor on the north face. An exterior retrofit method was adopted in which a retrofitted frame composed of steel columns and SRC beams was connected to the existing frame through additional slabs. The additional slabs were connected to the existing frame using post-installed anchors. The objective of retrofit was to prevent the Building from collapsing. The main design criterion was to hold the story drift angle below 1/125 in the SRC structure and below 1/150 in the RC structure against the wave defined by the earthquake motion in notification with a spectrum intensity of an extremely rare earthquake motion and the typical recoded wave. Shear failure of columns was not allowed before the story drift angle reached the angles of the design criteria. Structural slits were made in brittle columns to ensure ductility before retrofit.

2.3 Seismic control system with amplification mechanism

The method of retrofit using seismic control systems equipped with amplification mechanism [5] amplifies the story displacement in the frame and transfers the amplified displacement to the hydraulic damper and thereby doubles the absorption of seismic energy, applying the principle of leverage. In the seismic retrofit, hydraulic dampers with a design marginal damping force of 43 tf were used. The amplification ratio was set at 1.7 to 2.3 times. A total of 32 dampers were installed, four on the sixth floor, ten on the seventh floor, eight on the eighth floor, eight on the ninth floor and two on the tenth floor. The seismic control systems with amplification mechanism were placed only on the sixth through tenth floor. Only retrofitted frames were placed on the first through fifth floors.

3 RESULTS OF POST-EARTHQUAKE FIELD SURVEYS OF THE BUILDING

3.1 Outline of field surveys

Surveys were conducted on April 6 through 8, 2011. Relatively large aftershocks occurred on March 11 when the Earthquake occurred through April 8, the last day of surveys. The results of the surveys therefore include also the results of aftershocks. Investigations were made of (i) existing structural members, (ii) retrofitted frame (newly applied structural members), (iii) nonstructural members and (iv) seismic control systems with amplification mechanism. Only the sections where confirmation was possible from the side corridor were examined. An aftershock with a seismic intensity of 6 upper occurred on April 7. Only item (iv) was investigated after the aftershock and the other items before the aftershock.

3.2 State of existing structural members

Photographs 1 and 2 show an existing column with cracking and a wall with slits on three sides, respectively. Small cracks were confirmed in some of the existing columns and beams, most of which had a width of 0.2 mm or smaller. The damage was classified by the Japanese guidelines for evaluating seismic performance of reinforced concrete structures as the “one that enables continued use of the structure without repair”. Photograph 2 shows that shear cracks occurred in the wall with three slits but that none progressed to existing columns. It was thus determined that the slits worked effectively

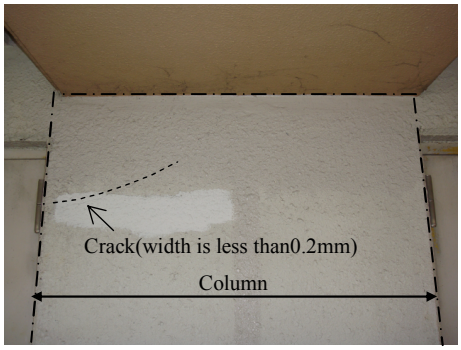


Photo. 1: Example of Columns with cracking

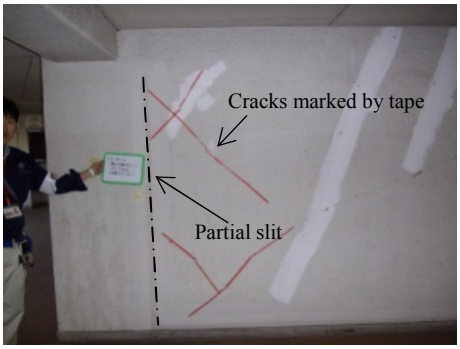


Photo. 2: Shear wall with slit

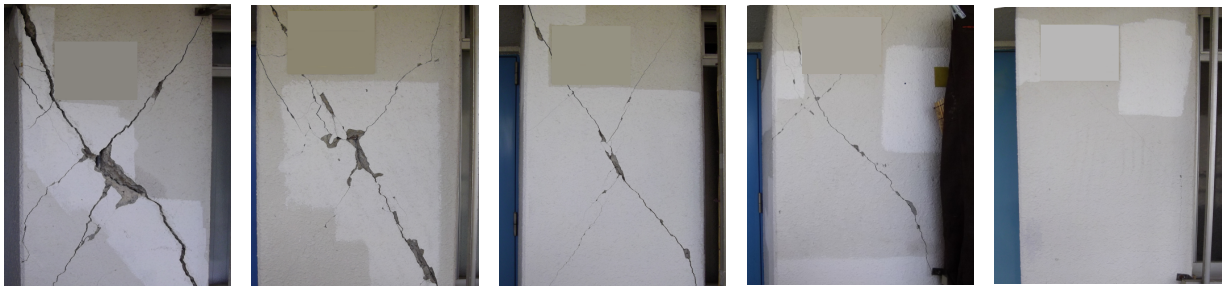
3.3 State of newly applied structural members

Newly applied steel columns were coated with autoclaved lightweight concrete (ALC) plates for fireproofing. No direct observation of the frame was therefore possible. No damage was, however, found in ALC plates. If steel members had yielded and been deformed greatly, ALC place might also suffered damage. It was therefore assumed that there was no serious damage to newly applied columns despite local damage. No damage was confirmed in newly applied beams. No trace was recognized of cracking or slip at the plane of connection at the bond between newly applied and existing frames. It was thus assumed that shear force was appropriately transferred through post-installed anchors, and both frames behaved as one during the Earthquake. The seismic control systems with amplification mechanism that was responsible for absorbing seismic energy, therefore, worked effectively.

No damage was confirmed that required repair in the structural members of the Building as well as in the existing structural members. The Building was found to be fit for continuous use.

3.4 State of nonstructural members

No measures were considered in the retrofit design to avoid or reduce damage to nonstructural members. Shear cracks were confirmed in the partial walls on the side of the side corridor. In the 120-mm-thick partial wall, ϕ=10mm reinforcing bars were arranged at a pitch of 250 mm. Photograph 3 shows the damage to the partial walls between lines (viii) and (ix) on the first through tenth floors. Only moderate shear cracks with a width of approximately 0.2 mm (concrete crack width except spalling) were found in the partial walls on the first and tenth floors. Damage was larger on the middle floors. The spalling of concrete cover was confirmed on the third through fifth floors. In the surveys, the residual crack width was measured with a crack scale in partial walls on each floor. The results are shown in Section 3.5.



(f) 6F (g) 7F (h) 8F (i) 9F (j) 10F



(a) 1F (b) 2F (c) 3F (d) 4F (e) 5F

Photo. 3: Failing of partial walls

3.5 State of seismic control systems with amplification mechanism

In the surveys, total traces of lubricant left each time the hydraulic damper worked during an earthquake were verified. Hydraulic displacement was measured based on the trace. If it was assumed that the hydraulic damper returned to the center after the earthquake, the measurement would have indicated the unidirectional hydraulic displacement (in the direction in which the damper shrank). The maximum hydraulic damper displacements on respective floors are shown in Figure 2 together with the residual crack widths in the partial walls. The figure shows that the hydraulic displacement of damper was largest on the sixth floor and smaller on the upper floors. The tendency was similar to the state of residual crack widths in the partial walls. In the partial walls on the third through fifth floors, no residual crack widths could be measured because of the spalling of concrete.

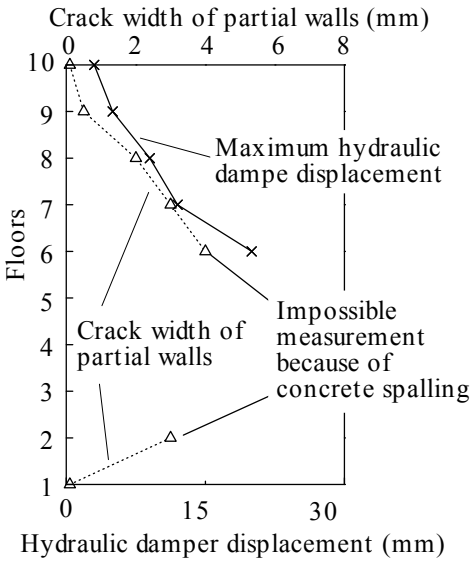


Figure 2: Results of the suvey

4 ESTIMATION OF SEISMIC DEFORMATION BEHAVIOR BASED ON SEISMIC RESPONSE ANALYSIS

4.1 Outline of seismic response analysis

The seismic deformation behavior of the Building was evaluated by nonlinear 3D-frame analysis that considered vertical springs of piles and the seismic control system with amplifi-

cation mechanism. As analysis models, the Takeda model [3] was used for representing force-displacement characteristics of structural members, Maxwell model for hydraulic damper and a slip model considering the displacement loss at the point of attachment for the brackets of the seismic control system with amplification mechanism. Seismic response analysis was made in cases with and without seismic retrofit. The deformation of the Building during the Earthquake was grasped and the effect of seismic retrofit was verified.

4.2 Estimation of input motion

No seismic monitoring were conducted in the Building. The ground motion records obtained at Sendai city hall, approximately 2.6 km south of the study site, were modified for use. To modify, a relatively simple method was used that enabled the estimation of ground motion at the study site with adequate accuracy from an engineering viewpoint. The method uses the H/V spectral ratios at the study site and the site of seismic records based on the microtremer measurement. Specifically, it was assumed that equation (1) could be established based on the works of Seo et al. [2] and the frequency amplitude of observed wave was corrected using the H/V spectral ratios at the two sites. Figure 3 shows *H/V* spectra at the two sites.

$$\frac{A(f)}{B(f)} \approx \frac{A_{H/V}(f)}{B_{H/V}(f)} \tag{1}$$

where, $A(f)$ and $B(f)$ are the Fourier amplitudes of ground motions at the study site and the site of seismological observation, respectively; and $A_{H/V}(f)$ and $B_{H/V}(f)$ are *H/V* spectra at the study site and the site of the Sendai city hall.

In the seismic response analysis, ground motions were in two directions, along and transverse to the principal axis. The ground motions modified using *H/V* spectra were subjected to orientation transform. Figure 4 shows the acceleration time history of input ground motion. Figure 5 shows the pseudo velocity spectrum (h = 5%). The figure also shows the notification of the Japanese ministry spectrum used as level-2 ground motion used in retrofit design.

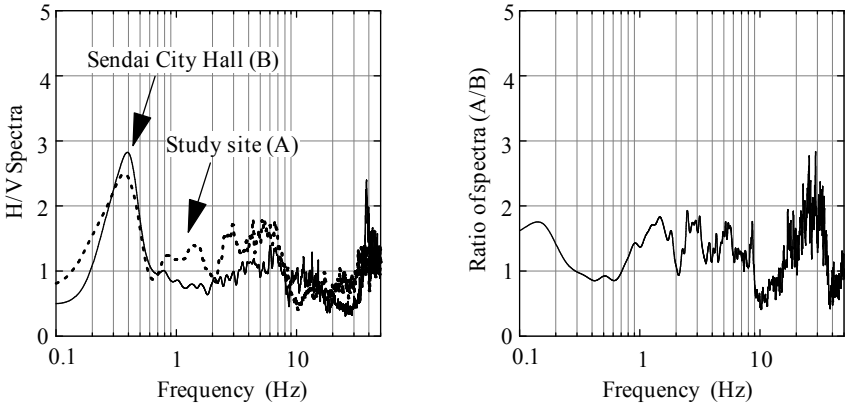


Figure 3: H/V spectra at the two sites

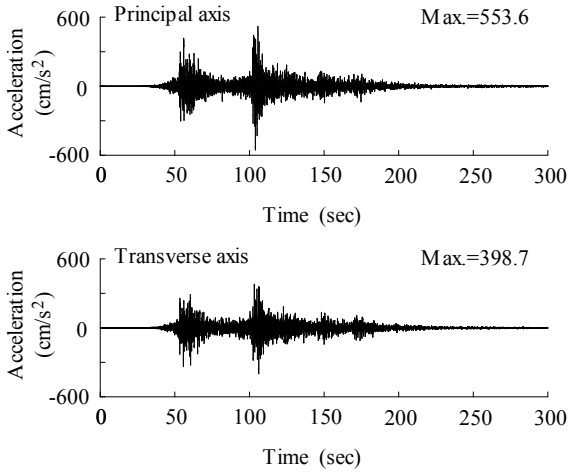


Figure 4: Input ground motions

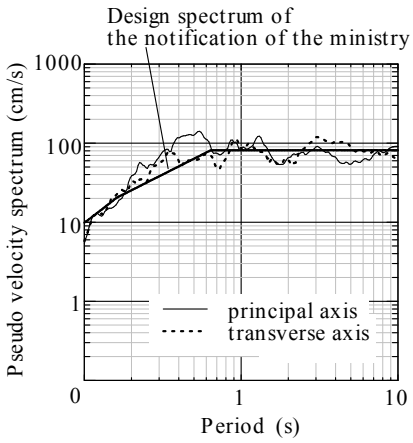


Figure 5: Pseudo velocity spectra

4.3 Behavior in the case with no seismic retrofit

Figure 6 shows the results of analysis of the maximum story drift angle in the longitudinal direction in the case with or without seismic retrofit for comparison. Story drift angle before seismic retrofit exceeded the design criteria (reinforced concrete structure: 1/150, SRC structure: 1/125) on the seventh through ninth floors and increased to 1/115 on the eighth floor. In the case without seismic retrofit, therefore, some damage may have occurred such as the shear failure of structural members on upper floors of the Building. The distribution of story drift angles in the direction of height in the case without seismic retrofit shows that the story drift angle was largest on the eighth floor. The tendency was different from the state of damage to partial walls confirmed by field surveys and described in the previous chapter in which damage was moderate on the lowest and highest floors and damage increased on middle floors.

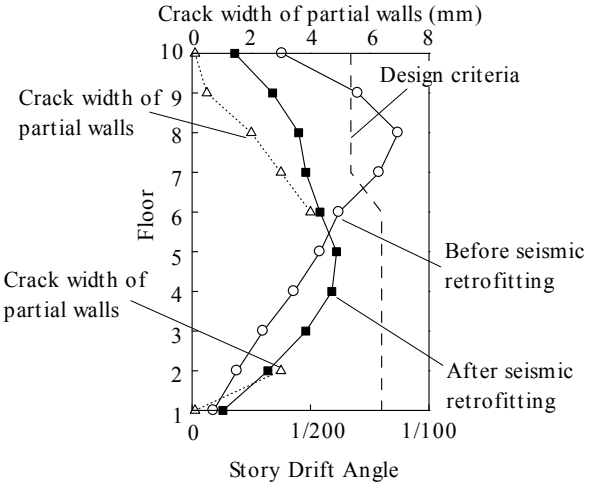


Figure 6: Story Drift Angle

4.4 Behavior in the case with seismic retrofit (actual behavior)

The maximum story drift angle after seismic retrofit was 1/164, approximately 70% of a maximum value of 1/115 in the case without seismic retrofit. Story drift angle after seismic retrofit was smaller than the design criteria on all floors, which was in agreement with the results of field surveys in which no damage was found in structural members.

The distribution of story drift angles in the direction of height after seismic retrofit shows that story drift angle was largest on the fifth floor. The deformation was in agreement with the damage to the partial walls found in the building surveys. Figure 6 also shows the width of the residual crack in the partial wall between lines (viii) and (ix) for comparison with story drift

angle. No measurement could be made on the third through fifth floors. Small cracks on the upper and lower floors and large cracks on the middle floors were in agreement with the distribution of story drift angles. The tendencies of hydraulic displacement and residual crack width (Figure 2) were also similar. Thus, the results of seismic response analysis for evaluating post-seismic-retrofit conditions were also in agreement with hydraulic displacement.

As a result of above discussions, it was assumed that the results of seismic response analysis conducted in this study generally reproduced the seismic behavior of the Building during the Earthquake. Retrofitting the Building using seismic control systems with amplification mechanism greatly reduced story drift angle. Then, the design criteria were satisfied. The vertical distribution of story drift angles was altered owing to seismic retrofit because seismic control systems with amplification mechanism were installed only on upper floors.

5 CONSIDERATIONS CONCERNING THE DAMAGE TO PARTIAL WALLS

5.1 Outline

One of the characteristics of damage to the Building was the confirmation of shear cracking in partial walls despite the soundness of structural members owing to seismic retrofit. Partial walls were nonstructural members. The damage to partial walls was allowable according to the seismic design policy of the Building. Knowing the degree of influence of partial walls on the seismic behavior of the Building provides valuable data for future seismic retrofit design. In this chapter, the maximum shear on the partial wall, shear deformation angle in shear failure is reached and the time of partial wall failure are estimated.

5.2 Method for estimating shear strength of partial walls and deformation

Studies have been made mostly on structural members. Few studies have been conducted concerning partial walls, as nonstructural member. Most of the previous studies were experimental verifications. No works are available that analytically evaluate shear stress - deformation angle relationships in partial walls. In this study, it was assumed that the stress-deformation relationship in partial walls could be estimated using the modified compression field theory (MCFT) [4], one of the reinforced concrete plate constitutive laws because the partial walls in the Building were shaped like a square. Figures 7 shows the stress and displacement fields in the MCFT model, respectively. The MCFT model expresses the stress-deformation relationship in reinforced concrete plane element based on the condition of compatibility of deformation, condition of equilibrium of stress, and material constitutive laws of rebars and concrete.

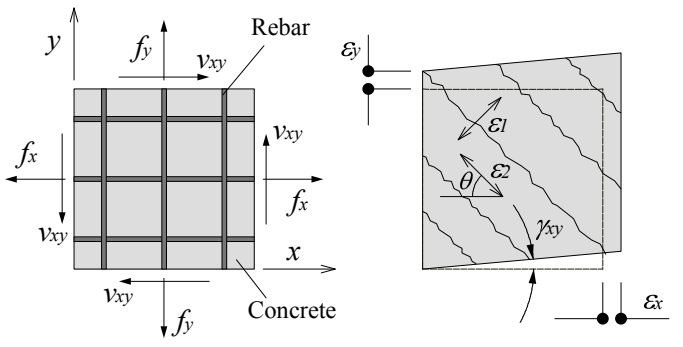


Figure 7: Example of the construction of one table.

5.3 Estimation of shear strength of partial walls and deformation angle at shear strength

Table 1 lists the shear strengths and deformation angle in shear failure on respective floors of the Building calculated using the MCFT model. The shear strength of the partial wall ranged from 111 to 132 kN. Story drift angle when shear strength was reached was approximately 1/330 on each floor. Judging from the fact that the shear strength of a main reinforced column on the seventh floor of the Building was 700 kN to nearly 1000 kN, the shear strength of the partial wall was approximately 10 to 15% of the shear strength of existing columns.

Story	f_c (N/mm^2)	Q_{pw} (kN)	R_{dd} (mm/mm)	R_{cd} (mm/mm)
10	22.50	132	1/333	1/610
9	22.50	132	1/333	1/610
8	11.45	111	1/331	1/608
7	22.50	132	1/333	1/610
6	12.48	113	1/331	1/608
5	15.04	118	1/332	1/610
4	13.47	116	1/331	1/608
3	13.13	114	1/331	1/608
2	15.07	123	1/332	1/610
1	22.50	132	1/333	1/610

f_c: Concrete compressive strength, Q_{pw}: Shear strength of partial wall,
R_{dd}: Dd-Angle(distributed drift angle), R_{cd}: Cd-Angle(concentrated drift angle)

Table 1: Example of the construction of one table.

5.4 Time of shear failure of partial walls during the Earthquake

Figure 8 shows the detail of the partial walls of the Building. In structures of that partial wall is integrated with a hanging wall and a spandrel wall, like the Building, deformation concentrates locally as shown in figure 8. Then, story drift angle is not identical to the deformation angle of the partial wall. No shear cracking was confirmed in hanging walls and spandrel walls of the Building. It is therefore reasonably assumed that no deformation occurred in these sections but that deformation concentrated at the center of the partial wall. In other words, it was assumed that the partial wall suffered shear failure before story drift angle reached the deformation angle at the shear strength of the partial wall. It was assumed that the hanging wall and spandrel wall were subjected to rigid deformation. The story drift angle when the partial wall collapsed was referred to as the Cd-angle (concentrated drift angle), and listed in Table 1. The Cd-angle is the story drift angle at which the partial wall suffered shear failure at the earliest time. The story drift angle that was the same as the deformation angle at the shear strength of the partial wall was referred to as the Dd-angle (distributed drift angle). At which story drift angle the partial wall suffered shear failure was estimated based on the results of time history response analysis and of the surveys of the Building.

Figure 9 shows the time history waveforms of story drift angle on the first, second, third, fifth and tenth floors after seismic retrofit based on the results of seismic response analysis. The time when story drift angle reached the Cd-angle (Cd-angle point) and the time when story drift angle reached the Dd-angle (Dd-angle point) were plotted on the output waveform on the positive and negative sides, respectively. The time history output waveforms of story drift angle were obtained as a result of calculation for the column member (line (viii)) on the west side of the partial wall shown in Photograph 3.

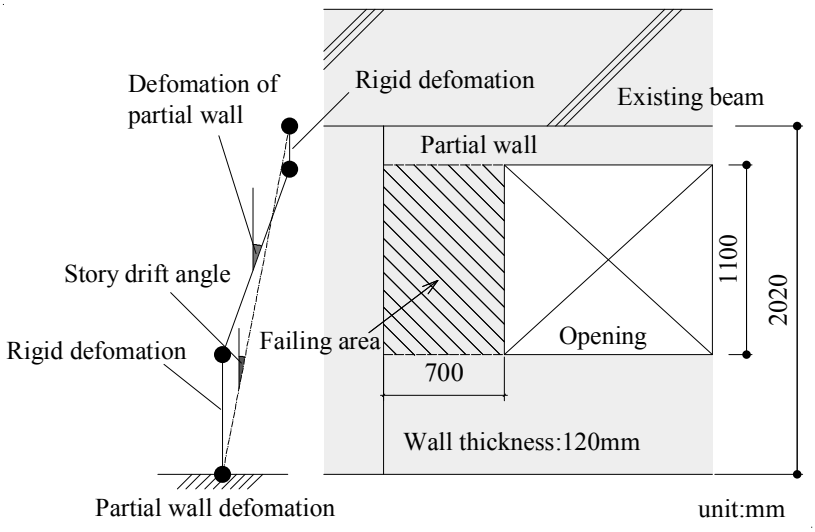


Figure 8: Partial wall derogation when the earthquake.

Figure 9 shows that story drift angle did not reach the Cd-angle during the Earthquake on the first and tenth floors, which confirms that only moderate damage occurred in the partial walls on the first and tenth floors.

Focus is now placed on the second, third and fifth floors in Figure 9. One of the characteristics of the input ground motion is two peaks in the acceleration waveform. On the third and fifth floors, the Cd-angle and Dd-angle points existed before the first peak was reached. On the second floor, the Cd-angle point existed but no Dd-angle point existed before the first peak was reached, which indicates that the Dd-angle was not reached. It was, however, determined that partial walls suffered shear failure on the second floor based on the condition of partial walls on the second floor (Photograph 4 (b)) and 3-mm residual crack width. It is therefore highly likely that partial walls suffer shear failure when the story drift angle reaches the Cd-angle.

The Cd-angle point in the partial wall suggests that the partial wall suffered shear failure in the early stages of the Earthquake because the story drift angle reached the Cd-angle point before the first peak was reached on the second, third and fifth floors. The tendency was similar on the fourth, sixth, seventh and eighth floors. In seismic retrofit design, no seismic energy absorption by partial walls was considered. The partial walls suffered shear failure in the early stages of the Earthquake and it was concluded that seismic energy absorption of partial walls made little contributions to the structural performance of the Building.

6 CONCLUSIONS

The following conclusions were obtained.

- As a result of damage surveys of the Building, it was found that the structural frame of the Building suffered no serious damage and that the Building could be used continuously without any repair.

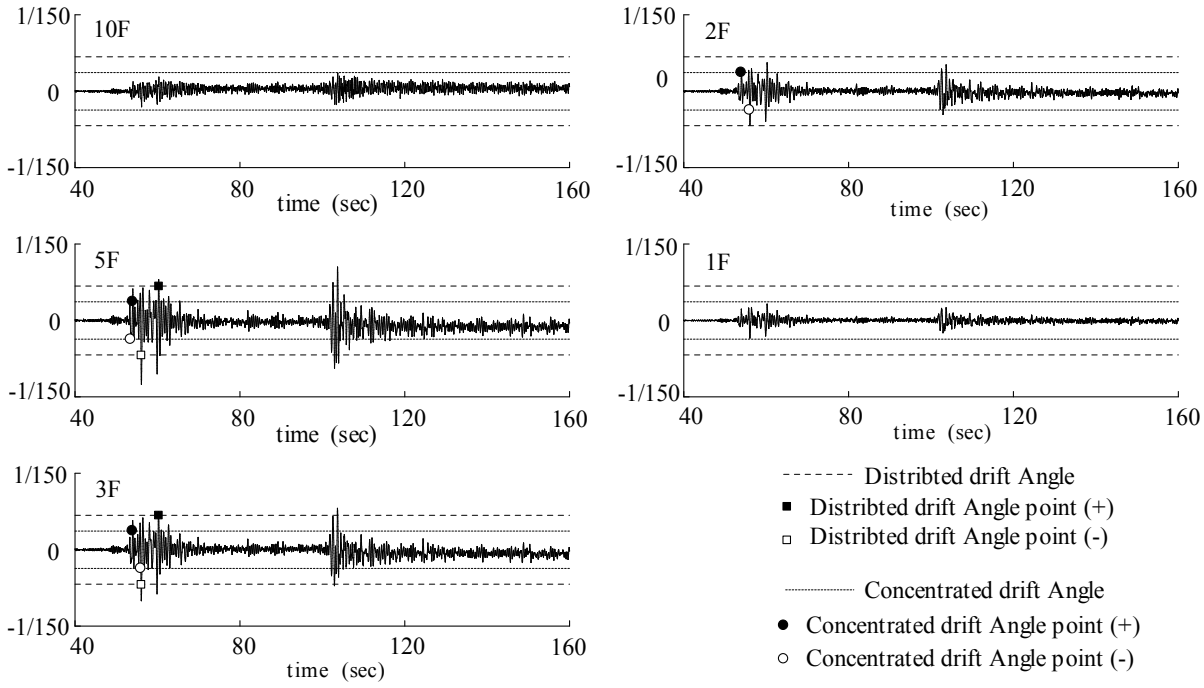


Figure 9: The time history output waveforms of story drift angle after seismic retrofit

- The results of estimation of the maximum story drift angle after seismic retrofit based on the results of seismic response analysis were in agreement with the damage to partial walls and with the action of hydraulic dampers. It was considered based on the analysis results that seismic control systems with amplification mechanism reduced the story drift angle of the Building to approximately 70%, the angle in the case without seismic retrofit, and the design criteria were satisfied. Then, no damage was observed in structural members during the Earthquake.
- It was shown that shear strength and story drift angle when shear strength was reached could be estimated properly using the MCFT model. As a result of calculation for partial walls of the Building, shear strength was 111 to 132 kN and deformation angle when shear strength was reached was approximately 1/330.
- As a result of the time history waveforms of story drift angle during the Earthquake based on seismic response analysis, it was assumed that partial walls collapsed in relatively early stages of earthquake. It was thus concluded that partial walls had little influence on the structural performance of the Building.

ACKNOWLEDGEMENTS

The authors acknowledge K.Satoh (Seki kukan design corporation), T.Horisaki (E&CS corporation), M.Kubota, T.Abe, T.Satoh and T.Miyazato (Tobishima corporation) for their contoribution to the suveys of the building.

REFERENCES

[1] Sasaki, K., Tanaka, R. and Takase: *Seismic Retrofitting Using Vibration Contorol System with Ampifer Mechanism and Effect of Sendai holl, No. 750,* The Kenchiku Gijutu(Architectural technology), July 2012.(in Japanese)

[2] Seo K.: *A Joint Work for Measurements of Microtremors in the Ashigara Valley*, International Symposium the Effect of Surface Geology on Seismic Mortion, ESG1992, pp.43-52, 1992.

[3] Takeda, T.: *Study on Reinforced Concrete Members Subjected to the Alternate Plastic Deformation - Characteristics of Deflection of Reinforced Concrete Frames-*, Anual conference of Architectual Institute of Japan ,pp153, 1964.

[4] Vecchio. F. J.and Collins M. P.: *The Modified Compression Field Theory for Reinforced Concrete Elements Subjected to Shear*, ACI Struct. J., pp.219~231, Mar.-Apr. 1986.

COMPDYN 2015
5th ECCOMAS Thematic Conference on
Computational Methods in Structural Dynamics and Earthquake Engineering
M. Papadrakakis, V. Papadopoulos, V. Plevris (eds.)
Crete Island, Greece, 25–27 May 2015

VERIFICATION OF THE TOGGLE DAMPING SYSTEM FOR THE SRC BUILDING DURING THE 2011 OFF THE PACIFIC COAST OF TOHOKU EARTHQUAKE

Takaaki IKEDA[1], Yuya TAKASE[2], and Yoshiaki SENOO[3]

[1] Dr. Eng., General Manager, Research Institute of Technology, TOBISHIMA Corporation
5472 Kimagase, Noda, Chiba, JAPAN
e-mail: takaaki_ikeda@tobishima.co.jp

[2] Ph.D., Researcher, Research Institute of Technology, TOBISHIMA Corporation
5472 Kimagase, Noda, Chiba, JAPAN
e-mail: yuya_takase@tobishima.co.jp

[3] Senior structural engineer, Seismic solution division, TOBISHIMA Corporation
3-2-1 Sakado, Takatsu, Kawasaki, Kanagawa, JAPAN
e-mail: yoshiaki_senoo@tobishima.co.jp

Keywords: SRC building, Seismic retrofit, damping system with amplification mechanism, 2011 off the Pacific coast of Tohoku Earthquake, Dynamic response analysis

Abstract. *A steel frame reinforced concrete building completed in 1965 was seismically retrofitted using seismic isolation braces with amplification mechanism. The building was subjected to shaking with a seismic intensity of upper 5 during the 2011 off the Pacific coast of Tohoku Earthquake. The seismic retrofit applied, however, minimized damage. The seismic retrofit performance was then examined based on the ground motions recorded in the building and the results of seismic response analysis using the records. As a result, it was revealed that the retrofit design goal was met and that the deformation of the building was controlled considerably as compared with the case with no retrofit.*

1 INTRODUCTION

The off the Pacific coast of Tohoku Earthquake that occurred on March 11, 2011 produced strong ground motions mainly in the areas along the Pacific coast in the Tohoku district near the source area. A maximum seismic intensity of 7 was observed in Kurihara City, Miyagi Prefecture. Seismic intensities of 5^- or greater were observed in areas in 17 prefectures.

Strong ground motions occurred also at around the site of the study building (hereinafter referred to as the Building). Buildings with low seismic performance suffered damage. The Building had been constructed in 1965 and designated as an existing non-conforming building. It had been retrofitted before the huge earthquake using damping system with amplification mechanism (hereinafter referred to as the toggle damping system). Then, the Building suffered only repairable minor damage to some of its nonstructural members.

Earthquake observation has been conducted in the Building since 2009. The seismic behavior of the Building during the main shock has been observed. This study examines the effectiveness of the toggle damping system for enhancing seismic isolation performance during the 2011 off the Pacific coast of Tohoku Earthquake based on the ground motions recorded in the Building and the results of seismic response analysis using the records..

2 OUTLINE OF STUDY BUILDING

The steel reinforced concrete Building was constructed in 1965 and has eight stories above the ground and two underground stories with a three-storied penthouse. It is supported directly on tuff bedrock. It is divided into the higher and lower sections. It can safely be assumed that the Building is structurally monolithic because shear forces can be transferred via slabs. Photo 1 presents a general view of the Building. Table 1 outlines the Building.



Photo 1 Over view of study building

Table 1 Outline of study building

Gross floor area	27,809m^2
Scale	8 stories above ground and 2 below
Structure	Steal Reinforced Concrete structure
Structural Type	Rigid-frame structures with shear wall
Foundation	Directed Independent foundation

3 OUTLINE OF SEISMIC RETROFIT METHOD

The Building was designed to the standards before the present seismic design method was developed. As a result of seismic diagnosis, the seismic retrofit index (Is) was determined to be not more than 0.6. Seismic retrofit was considered necessary. Seismic retrofit was therefore applied using the toggle seismic isolation method in order to enhance Is to 0.6 or higher as provided by present seismic design methods.

The toggle seismic isolation method amplifies the interstory displacement occurring in the building during an earthquake by two to three times and transfers it to the hydraulic damper and thereby efficiently absorbs seismic energy, using an amplification mechanism applying the principle of leverage. Figure 1 presents a schematic view of the toggle seismic isolation method.

In seismic retrofit, the design criterion was specified so as to set interstory displacement at 1/150 or less. The objective was to prevent the collapse threatening the lives of the people in the event of a strong ground motion that was likely to occur once during the service life of the Building (level-2 earthquake) as a minimum requirement. Accordingly, 94 and 88 seismic isolation braces were installed in the longitudinal (along the X axis) and transverse (along the Y axis) directions, respectively. Table 2 outlines seismic retrofit.

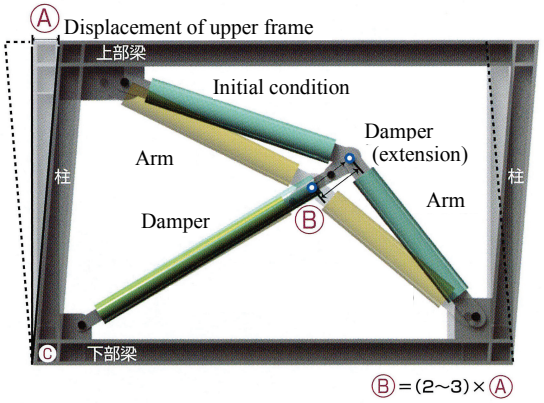


Figure 1 Toggle damping system (damping system with amplification mechanism)

Table 2 Outline of seismic retrofitted

Toggle damping brace	X direction : 94
	Y direction : 88
Shear wall (increased)	2
Structural slit	X direction : 12
Structural Type	Y direction : 8
retrofitting column	12

4 SEISMOLOGICAL OBSERVATION RECORDS

Figure 2 shows the locations of the Building and the assumed source region of the 2011 off the Pacific coast of Tohoku Earthquake. Figure 3 shows the acceleration waveform observed in the Building. Outstanding in the acceleration waveform on the first floor above the ground are two areas with large amplitudes. The source area of the off the Pacific coast of Tohoku Earthquake was assumed to be 450 km x 200 km. It was assumed that large failure occurred at

least three locations. The two large amplitudes found in the acceleration waveform probably represent the effects.

The ground motion lasted a long time. The peak acceleration exceeded 50 cm/s^2 for a duration of approximately 130 seconds on the first floor above the ground and for 150 seconds on the penthouse. The peak acceleration was approximately 413 cm/s^2 on the floor above the ground and 853 cm/s^2 on the penthouse, both of which were observed in the second high-amplitude area starting at approximately 100 seconds.

Figure 4 shows the pseudo velocity response spectra (h = 0.05) on the first floor above the ground and on the penthouse. Shown with the response spectrum on the first floor above the ground is the spectrum of notification wave used as the seismic ground motion for design. It is clear that the ground motion observed on the first floor above the ground was nearly equivalent to level-2 ground motion considered in design. An explicit predominance is found in the pseudo velocity response spectrum on the penthouse near 0.9 second. It was therefore assumed that the Building behaved with the primary mode being predominant.

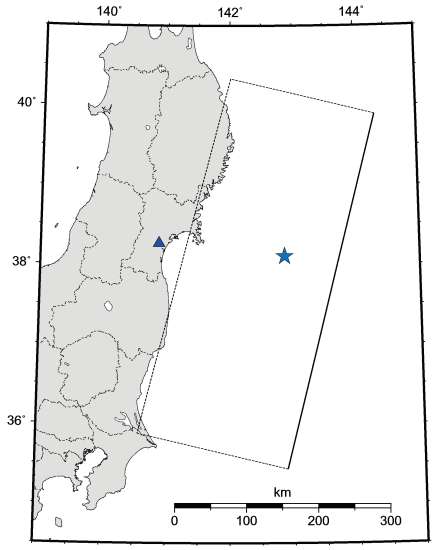


Figure 2 Location of the Building and source area of off the Pacific coast of Tohoku Earthquake

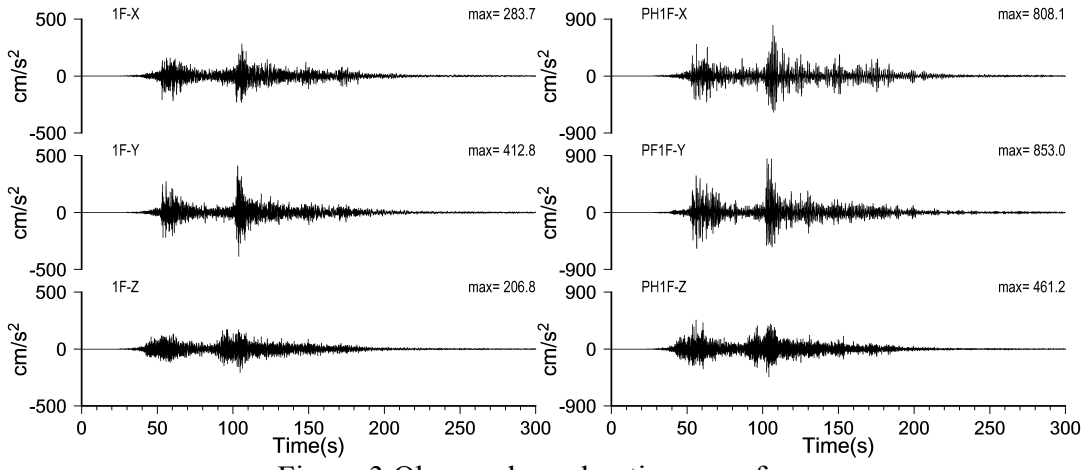
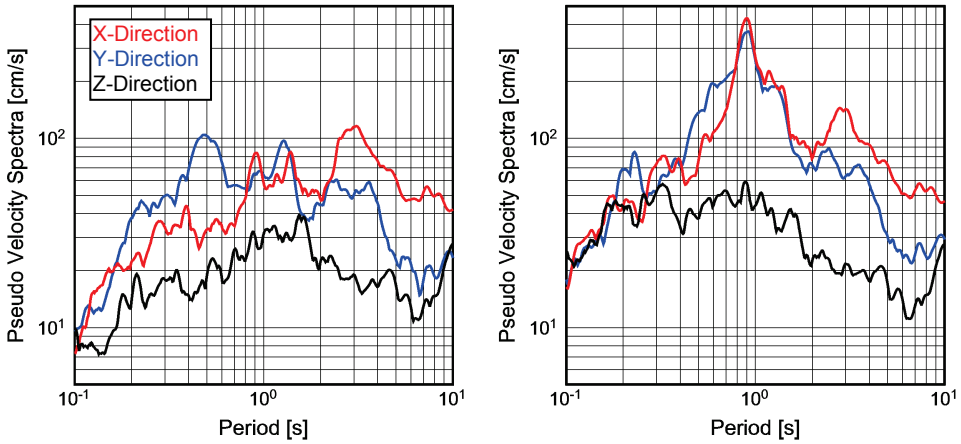


Figure 3 Observed acceleration waveform



(a) 1F (b) PH1F

Figure 4 Pseudo velocity spectra (h=0.05)

5 VERIFICATION OF THE EFFECT OF RETROFIT

The story deformation angle used as a seismic retrofit performance index was adopted as an index for verification. The variance between the behavior during the main shock and that in the case where no retrofit was applied (case with no retrofit) was regarded as the seismic retrofit effect.

Computing story deformation angle required displacement waveforms on respective floors. Seismographs were, however, installed only on the first floor above the ground and on the penthouse, so obtaining story deformation angle based on the seismological observation records was impossible. Then, the building was represented by a mass system model on a fixed foundation. The ground motion observed on the first aboveground floor was input and displacement waveforms on respective floors were computed based on the results of seismic response analysis.

The analysis model was independent in the directions of X and Y axes. It was designed that the predominant period during a strong ground motion matched the predominant period during a strong ground motion obtained based on the seismological observation records.

The accuracy of seismic response analysis was verified based on the reproducibility of observed displacement waveform on the penthouse. Figure 5 shows the observed and analysis displacement waveforms in layers. The observed displacement waveform was computed by applying a band-pass filter of 0.1 to 10 Hz to the observed acceleration waveform and using Fourier integral.

The observed and analysis displacement waveforms were in agreement with each other highly accurately in terms of amplitude and phase. Thus, the observed displacement waveform was accurately reproduced based on the results of seismic response analysis. It was therefore assumed that the displacement waveforms on other floors than the penthouse could be estimated similarly based on the results of seismic response analysis.

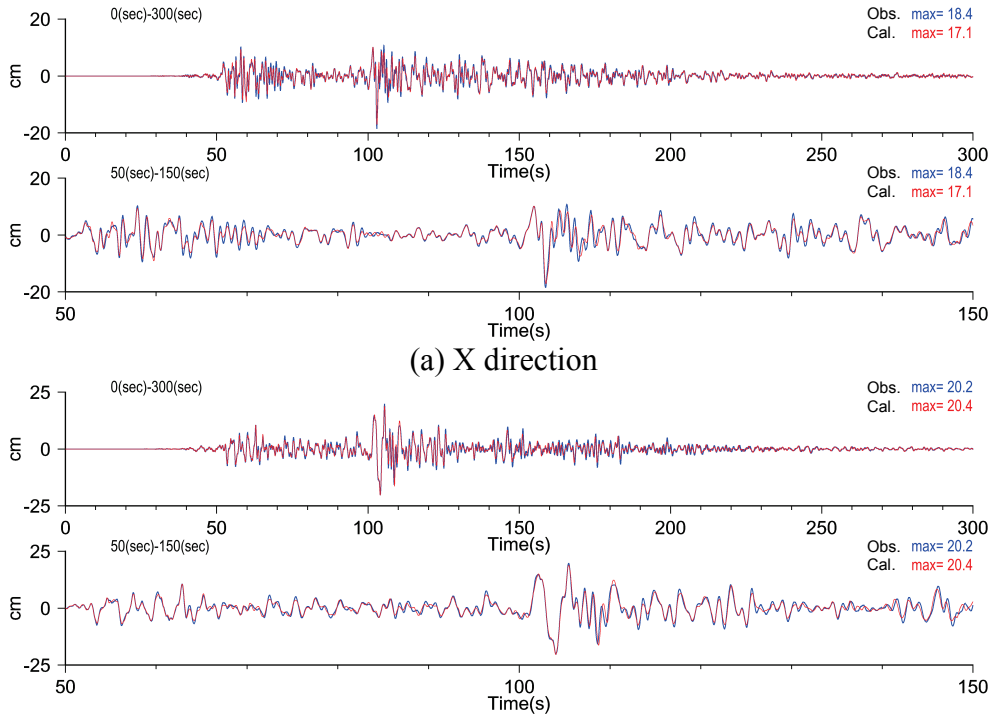
Figure 6 shows story deformation angles computed based on the results of seismic response analysis. Story deformation angle is not more than 1/150, the design criterion, in both directions. The retrofit design goal was thus achieved.

Story deformation angles in the case with no retrofit were estimated also based on the results of seismic response analysis. The analysis model was developed by removing the toggle seismic isolation members from the analysis model used during the main shock. Figure 6 shows the distribution of story deformation angles in the case with no retrofit. Story deformation angle exceeded the design criterion of 1/150 on multiple floors. It increased to 1/61 in

the direction of X axis and to 1/58 in the Y axis direction. It is therefore highly likely that the building suffered great damage in the case with no retrofit.

If the variance from the story deformation angle during the main shock was regarded as the effect of seismic retrofit, it was assumed that seismic retrofit reduced story deformation angle in the building to 1/4 at the maximum and helped avoid great damage.

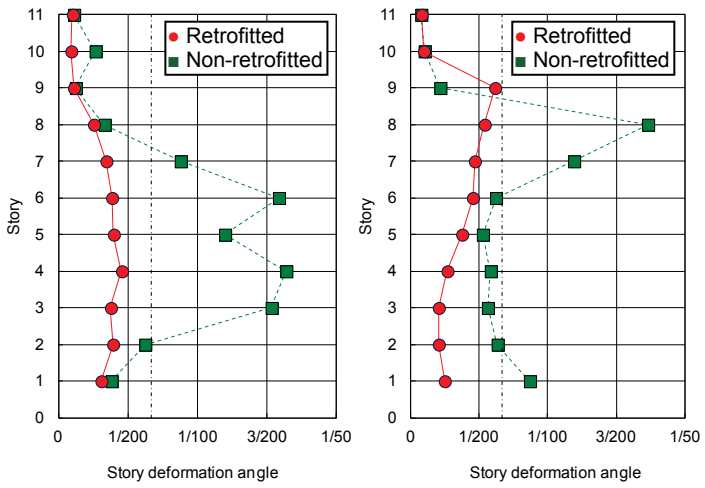
Figure 7 shows the distribution of relative displacements on the first floor above the ground. Seismic retrofit reduced relative displacement to 1/3 at the maximum. It is clear that displacements were controlled considerably throughout the building.



(a) X direction

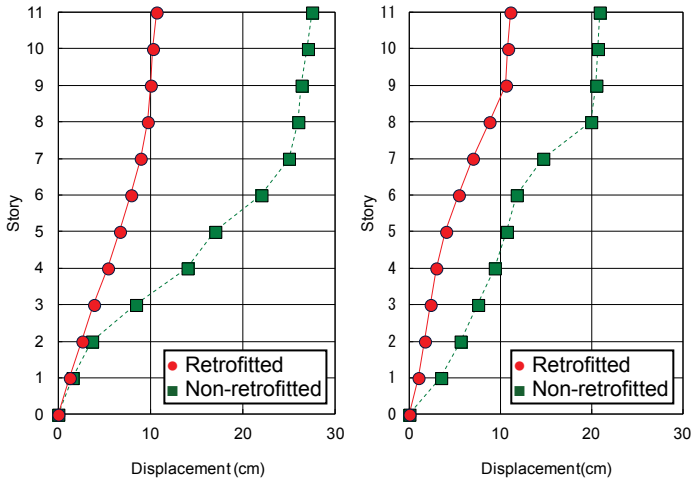
(b) Y Direction

Figure 5 Comparison between calculated displacement waveform of PH1F and observed one



(a) X direction (b) Y Direction

Figure 6 Comparison of story deformation angle distribution (Retrofitted/Non-retrofitted)



(a) X direction (b) Y Direction

Figure 7 Comparison of relative displacement distribution (Retrofitted/Non-retrofitted)

6 CONCLUSIONS

The effectiveness of seismic retrofit of a steel frame reinforced concrete building using a damping system with amplification mechanism was examined based on the seismological observation records during the 2011 off the Pacific coast of Tohoku Earthquake and on the results of seismic response analysis. As a result, the following conclusions were obtained.

- Story deformation angle of the building was not more than 1/150 during the main shock. The seismic retrofit performance goal was therefore achieved.
- Seismic retrofit reduced story deformation angle of the building to 1/4 and relative displacement to 1/3.
- In the case where no seismic retrofit was applied, the building may have suffered great damage.

COMPDYN 2015
5th ECCOMAS Thematic Conference on
Computational Methods in Structural Dynamics and Earthquake Engineering
M. Papadrakakis, V. Papadopoulos, V. Plevris (eds.)
Crete Island, Greece, 25–27May 2015

SEISMIC RESPONSE VERIFICATION AND RETROFITTING OF RC BUILDING SUBJECTED TO 2014, CEPHALONIA EARTHQUAKES

Ioannis E. Kavvadias[1], **Ifigeneia P. Litina**[1], **Varvara C. Kyriakidou**[1], **Fani T. Mamatsopoulou**[1], **Lazaros K. Vasiliadis**[1]

[1] Democritus University of Thrace, Dept. of Civil Engineering,
Institute of Structural Mechanics and Earthquake Engineering
Vas. Sofias 12, 67100 Xanthi, Greece
{ikavvadi, ilitina, varvkyri, fanimama, lvasilia}@civil.duth.gr

Keywords: RC building, assessment, base isolation, metal braces

Abstract. *In early 2014, strong earthquakes occurred on the Island of Cephalonia and buildings with significant design errors were heavily damaged. The building that is being studied is a two-storey reinforced concrete building, which was affected by the specific earthquakes. The structural model of the building is regular in plan as it consists of parallel frames arranged in dense grid but it is non regular in elevation as there are no infill walls located in the down floor. In the first part of this paper, the seismic assessment of the structure is presented. It is an attempt to verify the damages which occurred to the building during the earthquakes. In the second part of this paper, strategies for structural intervention are suggested. Firstly, it is intended to reduce the seismic demand of the structure through the implementation of base isolation systems. Specifically the appliance of lead rubber bearings (LRB) and friction pendulum systems (FPS) has been studied. Secondly, it is intended to increase the stiffness of the ground floor by placing metal braces. The study is based on results from nonlinear analyses. The analyses that have been used are the pushover analysis and the nonlinear time history analysis.*

1 INTRODUCTION

Heavy earthquakes occurred on the Cephalonia Island in early 2014. The RC building studied in this work, is an existing in the area building which was subjected to the earthquakes. After infield investigation enough data have been gathered to assess the building. The basic purpose of the paper is the verification of the actual seismic behavior of the building and afterwards the intervention in its structural system in order to improve its seismic behavior.

A crucial characteristic of the structure that must be taken into consideration is that the building is regular in plan but irregular in elevation. The abrupt reduction of stiffness and resistance of the ground floor determines the seismic behavior of the building. The building is expected to behave as "pilotis" type and to suffer from severe damages in the columns of the ground floor (soft floor). Reinforced concrete buildings with first floor irregularities studied thoroughly by Favvata et al. [1], have showed the increase of the demand for interstory drift at the ground floor. The assessment of the seismic behavior of the building will be carried out using nonlinear methods, which are pushover and time-history analyses.

Having assessed the building, which revealed the weaknesses of the structure, the decision to intervene has been made. The interventions were made to the building without considering the damages from the earthquakes. The purpose was to balance the structural weaknesses with the interventions. Among various alternatives [2], the intervention will take place firstly with the implementation of base isolation systems and afterwards with the implementation of metal braces. The two methods are based on different principles as the base isolation systems aim to isolate the superstructure from the ground motions and to decrease the seismic demand of the superstructure [3, 4] and the metal braces aim to increase the strength and the stiffness of the structure [5].

As concerns the base isolation system, two types of bearings have been studied, Lead Rubber Bearings and Friction Pendulum Systems [6]. A significant amount of both past and recent research has focused on the use of elastomeric and friction bearings [7, 8].The implementation of base isolation systems is expected to increase the fundamental period of the structure and therefore decrease the seismic demand for the structure. Moreover, it is expected that the horizontal displacements will be taken over by the isolation systems and the structure will move as a rigid body without any additional stresses.

As concerns the metal braces, their section has been chosen so that the braces equate the lack of stiffness in the "soft" floor of the building. The implementation of metal braces restricted to the open ground floor is expected to increase the stiffness and the strength of the ground floor and as a result to improve the seismic behavior of the entire building [5].

Finally, conclusions are drawn regarding the effectiveness of the proposed strategies. The seismic performance of the building, before and after retrofitting is evaluated according to the provisions of EC8 Part-3 [9] and the Greek Retrofitting Code [10].

2 BUILDING DESCRIPTION

The under study building is located on the island of Cephalonia. It is situated at the beachfront, approximately 100m from the sea. The construction of the building took place in early 1980 and it was used as a residence. It was built according to the Greek Royal Decree of 1959 [11].

The construction is a two-storey RC building without a basement. The ground plan of the building is rectangular and its surface is reduced to the first floor. The ground floor has a height of 3.30m whereas the first floor a height of 3.00m. The structural model of the building is regular in plan as it consists of parallel frames arranged in a dense and symmetrical grid of

columns but it is non regular in elevation as there are no infill walls located in the ground floor. Consequently the building is expected to response as a “pilotis” type building.

In Figures 1, 2 and 3, a schematic presentation of the structure is displayed. It shows the plan of both floors and the faces of the building. The area of the ground floor is hatched with diagonal lines and the area of the upper floor is located between the infill walls. It also shows the location of the infill walls that have been taken into consideration for the structural model. The beams are shown with dashed lines. The columns which do not continue in the upper floor do not have a solid hatch.

The structural system is made of reinforced concrete. The material types for the model are concrete B225 (f_{ck}=16MPa) and rebar steel StIII (f_{yk}=420MPa). The plates are 18cm thick, horizontal and at the same level. The beams of the building are 50x25cm and the columns are 50x25cm.The columns confinement bars are not anchored properly, so they do not contribute to the ductility and they are not included in the model. All columns are considered to be fully supported to the ground, at the soil level. The data concerning the column reinforcement have been collected from field investigation and they are presented in Table 1. The beam reinforcement has been calculated according to the Greek Royal Decree [11].

The data of the infill walls are simulated according to common practice in the island, where the infill walls usually have a considerably high resistance. The infill walls are considered to be 25cm thick and to be built with clay hollow bricks with dimensions 250x250x240mm and compression strength of 10MPa and with M5 mortar.

Columns	Reinforcement
For columns 0.26mx0.50m	8Φ20+4Φ16
For columns 0.50mx0.26m	18Φ18

Table 1: Reinforcement of the columns

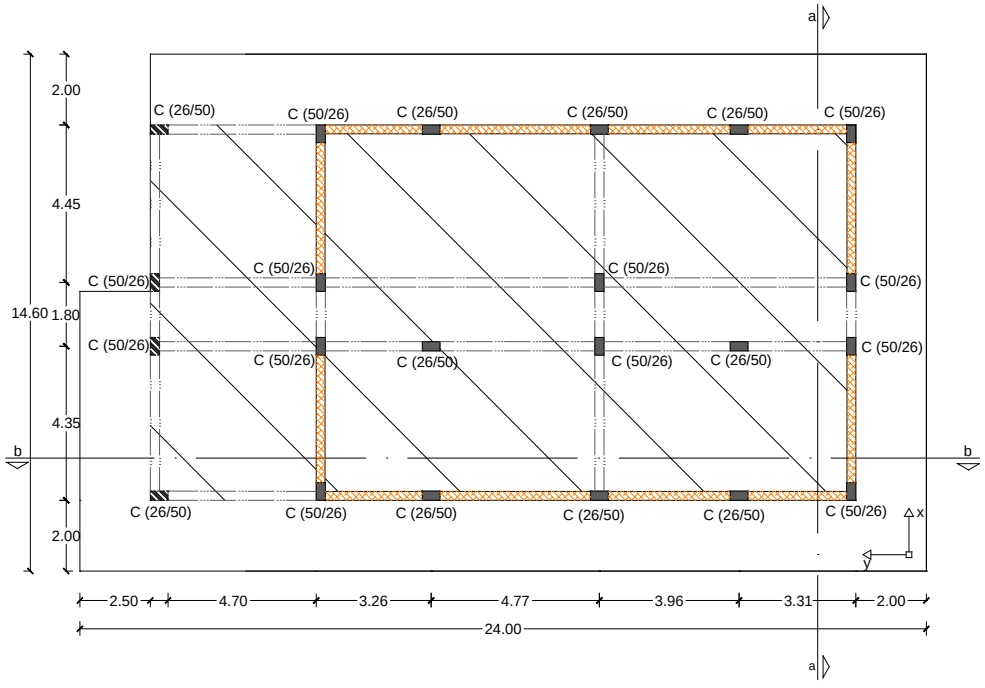


Figure 1: Schematic Plan of the Floors

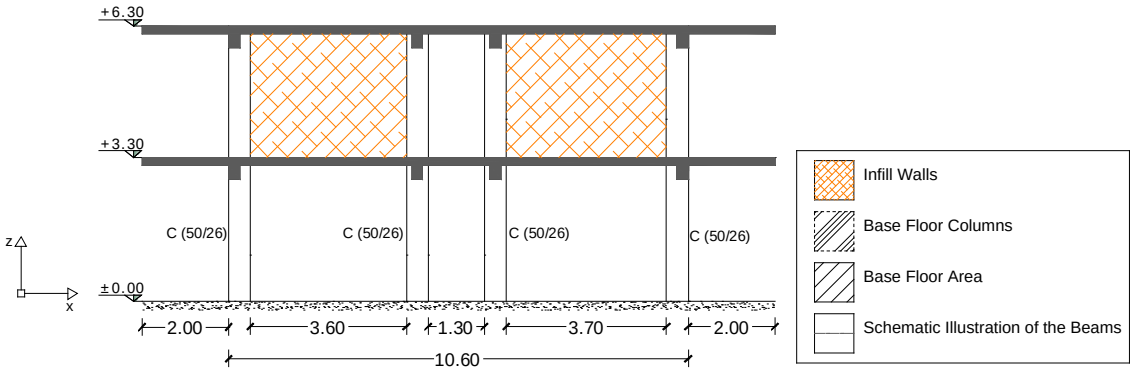


Figure 2: Architectural Section a-a

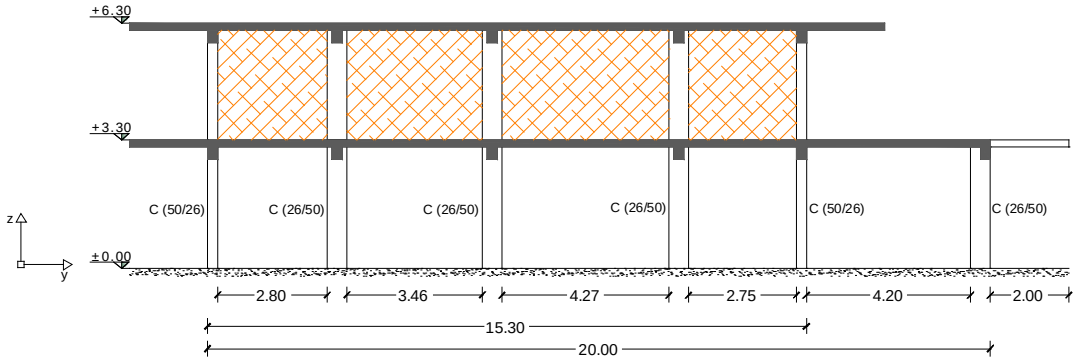


Figure 3: Architectural Section b-b

3 SEISMIC ACTIONS

The earthquake that occurred on the island of Cephalonia on January 26th 2014 and specifically the recorded accelerograms in the Argostoli station were used as the main seismic action. The epicenter of the earthquake was at the southwestern coasts of Cephalonia, about 9 km southwest of the Lixuri town. Its focal depth was 21 km and its magnitude M6.1.The actual accelerograms of the earthquake in x and y directions were used in the analysis, as it is intended to verify the actual behavior of the building. The vertical component of the earthquake was not used as it is not required according to EC8. The accelerograms of the earthquake and the acceleration spectrum are presented in Figures 4 and 5. The east to west axis is parallel to the x – axis of the building and the north to south axis to the y-axis.

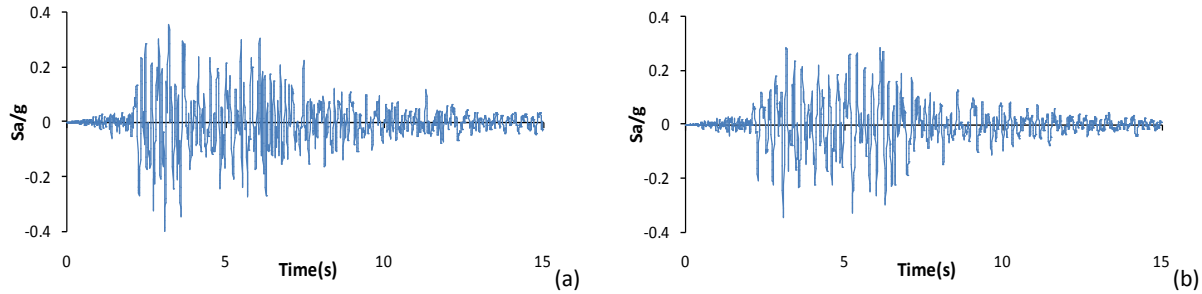


Figure 4: Accelerograms in (a) north to south direction, (b) east to west direction

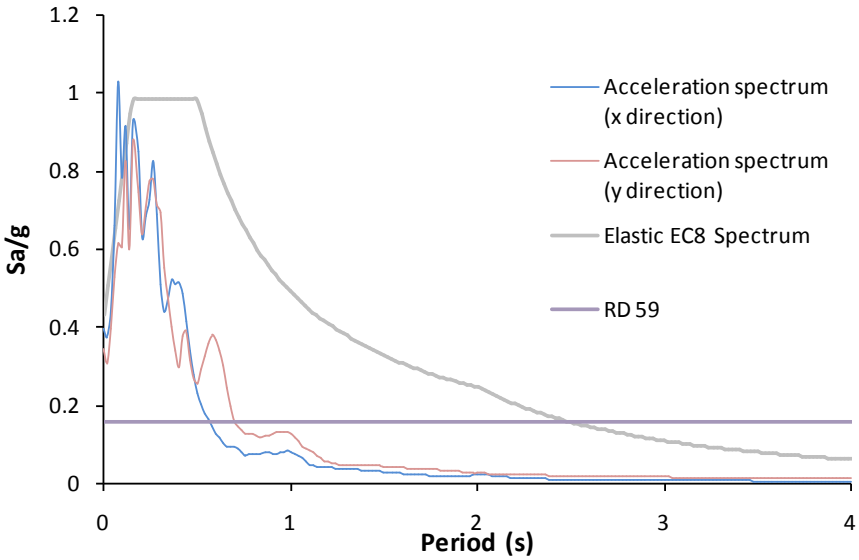


Figure 5: Acceleration Spectrum

4 DAMAGE DISTRIBUTION AFTER THE EARTHQUAKE

As it has been mentioned, the studied building is expected to behave as a “pilotis” type building. The lack of infill walls in the ground floor creates asymmetry in the distribution of stiffness in elevation. As a result, the application of the seismic force causes torsion to the vertical axis and leads to the development of a “soft” floor mechanism. Specifically, the failure is performed with the creation of plastic hinges at the top and base of the columns of the “soft” floor. This mechanism leads to the concentration of all movements in the ground floor, to the development of P-Delta effects and eventually to total or partial collapse.

After conducting field investigation, the type and extent of the present structural damage agrees with the above description. The majority of the ground floor columns have been heavily damaged. Plastic hinges have been created at the top and the base of those columns. The upper floor has reacted as a rigid body with the structural members and the infill walls behaving linearly. Figure 6 is representative of the building situation.



(a) (b)

Figure 6: (a) Photograph of the ground floor, (b) Close up to a damaged column

5 SIMULATION OF THE STRUCTURAL SYSTEM

The building is simulated as a 3D model which includes all the members that contribute to the seismic behavior of the building (beams, columns and infill walls). The nonlinear behavior of the frame members is represented with the assignment of plastic hinges in the critical sections of the members.

5.1 Simulation of the structural members

As regards the beams, the model that is used represents the uniaxial bending of the beam. The used model defines the relation between the bending moment and the rotation of the section. The plasticity is concentrated at the ends of the beams. The hysteresis of the model is determined according to the Takeda hysteresis model [12]. A different type of element is adopted in order to model the columns. This model correlates the biaxial bending with axial force using the fiber model which distributes the plasticity along the column length [13, 14].

5.2 Simulation of the infill walls

The model of equivalent diagonal strut is used in order to simulate the infill walls. It should be noticed that the infill walls are simulated in such a way so that they exhibit axial response only. The diagonal bar is pinned in the nodes of the frame. The dimension of the diagonal bar and the stress – deformation diagram (Figure 7) are calculated according to the Greek Retrofitting Code [10].

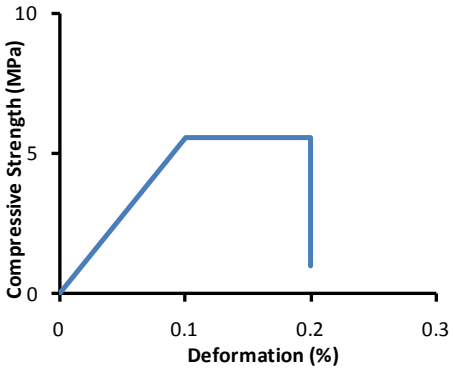


Figure 7: Stress - Deformation Diagram of infill walls

6 ASSESSMENT ANALYSES

6.1 Modal Analysis

Modal analysis is a way to have a better understanding of the behavior of a building. Moreover the periods of the two first modes are necessary clues for the nonlinear dynamic analysis. The results of the modal analysis are shown in Table 2.

Mode	Movement	Period (s)	Mass Participation Ratios
1	translational x axis	0.38	0.828
2	translational y axis	0.374	0.957
3	rotational	0.308	0.605

Table 2: Modal Analysis Results

6.2 Nonlinear analyses

Nonlinear analyses are primarily used for the assessment of existing buildings. Those analysis methods take into account the inelastic response of the used materials and calculate the nonlinear behavior of the member section and therefore the behavior of the member and the whole structure. The nonlinear analyses approach the real behavior of a building in an accurate way. The Greek Retrofitting Code [10] defines two types of nonlinear analysis, pushover analysis and time history analysis.

6.2.1 Pushover analysis

Pushover analysis approaches, by sequential analyses, the nonlinear behavior of the structural system under different distribution of lateral forces. Reinforced concrete frame structure evaluation using nonlinear static analyses has been studied by Karayannis and Favvata [15]. The control of the structure is carried out in the step (performance point) during which the capacity of the building meets the demand of the regulations (in this work the response spectrum of EC8 Part-1 [16]). In this step, the deformations of the critical sections are compared with the defined by the regulations deformations in terms of plastic rotation. The result of the comparison is the expected by the regulation behavior of the critical sections (linear or nonlinear response, performance requirements).

Two different distributions of lateral forces are used. The first is a triangular distribution of the lateral forces and the second a uniform distribution of the lateral forces. The structure is analyzed for combination of the lateral forces which are parallel to the two main directions. These combinations are x+0.3y and y+0.3x.

The results for the structure that is being studied are shown below. Figure 8 presents the local nonlinear behavior of the members of the building in terms of plastic rotational hinge requirement, based on the limit state of the critical sections. The yielded results correspond to the maximum limit state that has been reached between the triangular and the uniform distribution of the lateral forces for both combinations of the lateral forces.

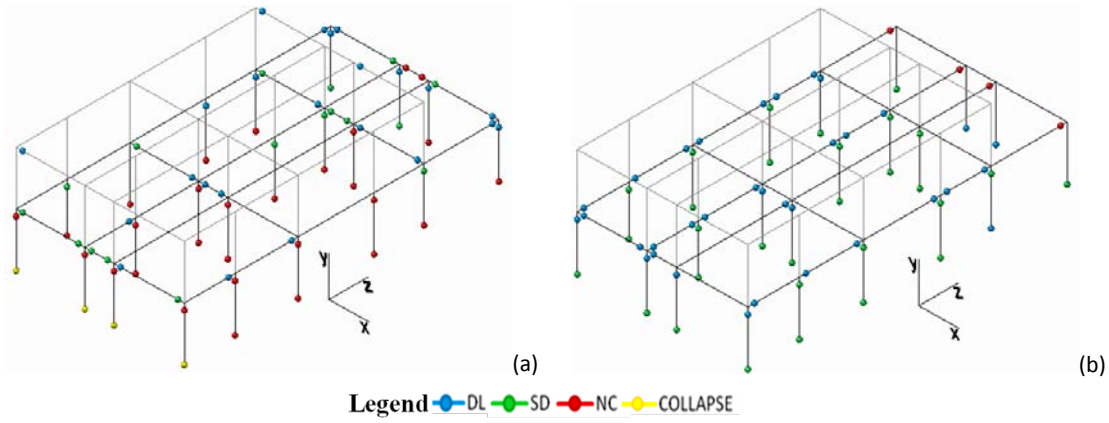


Figure 8: Damage Distribution (a) for combination x+0.3y, (b) for combination y+0.3x

As it is shown in Figure 8, the majority of the critical sections of the columns and beams of the ground floor behaved nonlinearly, while the majority of the upper floor members responded linearly. As regards the combination of the lateral forces x+0.3y the rotation requirement is larger, as the *Near Collapse (NC) limit state* is reached while, as regards the combination y+0.3x, the *Significant Damage (SD) limit state* is reached.

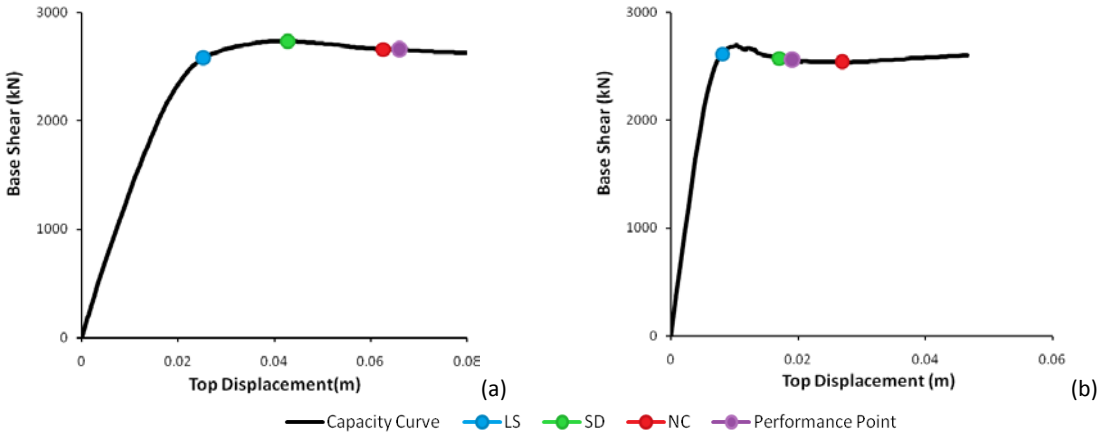


Figure 9: Capacity Curves (a) for combination x+0.3y, (b) for combination y+0.3x

The limit state of the structure can also be observed by the capacity curves of the structure (Figure 9). The capacity curves are almost identical for both distributions of the lateral force. As it is shown by the diagrams, for the combination of the lateral forces x+0.3y, the performance point exceeds the *Near Collapse (NC) limit state* with top displacement equal to 0.067m and for the combination y+0.3x, the performance point exceeds the *Significant Damage (SD) limit state* with top displacement equal to 0.062m.

In Figure 10, the storey drift for both combinations of the lateral force is presented. As it is obvious, the displacement of the down floor is significantly higher than that of the upper floor. Specifically, as regards the combination x+0.3y, the storey drift of the down floor is 2.23%, while the storey drift of the upper floor is 0.06%. As regards, the combination y+0.3x, the storey drift of the down floor is 2.19%, while the storey drift of the upper floor is 0.02%.

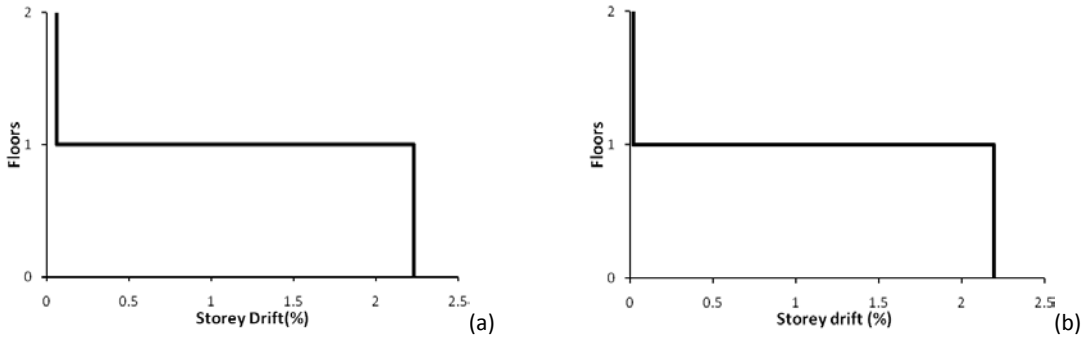


Figure 10: Storey Drift Diagram (a) for combination x+0.3y, (b) for combination y+0.3x

6.2.2 Time history analysis

In time history analysis, a sequential solving of the dynamic problem for every time step of an earthquake is performed. The time history analysis is the most accurate method of analysis, but it is difficult to use because of the great computational cost, the difficulty of processing the huge amount of data and the need of carefully choosing the right accelerograms. The structure is analyzed for combination of the seismic forces parallel to the two main directions. These combinations are x+0.3y and y+0.3x.

The results for the structure that is being studied are shown below. Figure 11 presents the local nonlinear behavior of the building members in terms of plastic rotational hinge requirement based on the limit state of the critical sections.

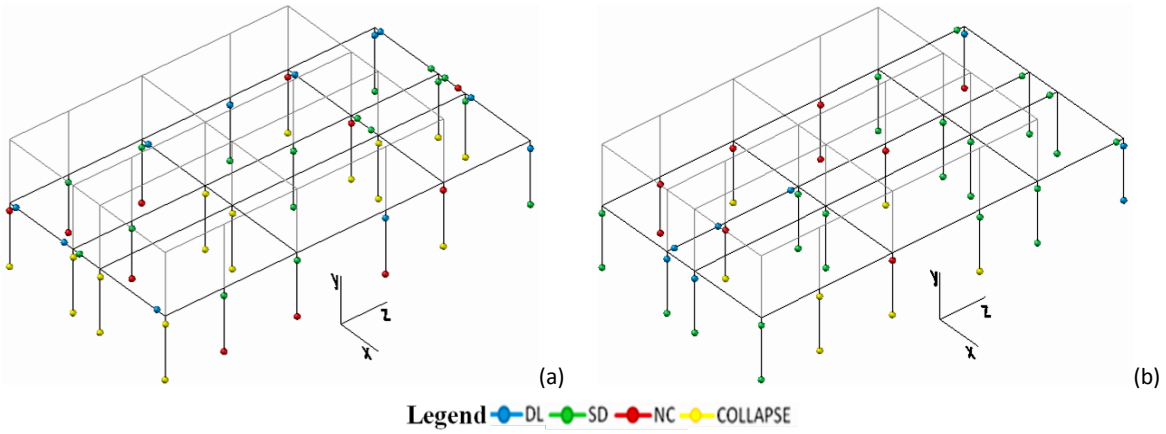


Figure 11: Damage Distribution (a) for combination x+0.3y, (b) for combination y+0.3x

As it is shown in Figure 11, the majority of the critical sections of the columns and beams of the ground floor responded inelastically, while the structural members of the upper floor responded elastically. The majority of the sections either reaches or exceeds the *Near Collapse (NC) limit state* for both combinations.

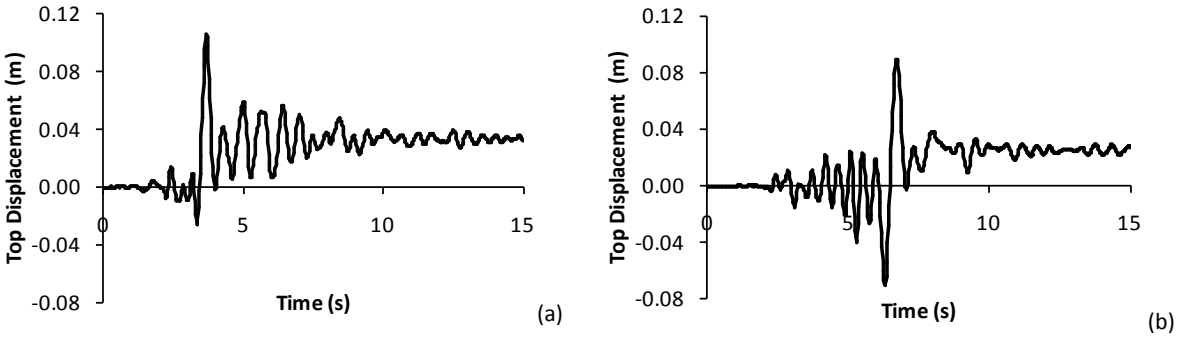


Figure 12: Top Displacement (a) for combination x+0.3y, (b) for combination y+0.3x

In Figure 12, the top displacement of the building per time is shown. The maximum top displacement for the combination x+0.3y is 0.106m and for the combination y+0.3x is 0.089m. For both combinations, at the earthquake end the top displacement of the building is different to zero (in combination x+0.3y is 0.032m and in combination y+0.3x is 0.027m). The reason for that is that the columns of the ground floor are permanently deformed.

In addition, in Figure 13, the storey drift of the building is presented. It can be observed that the relative displacement of the upper floor is considerably less than the displacement of the ground floor. Specifically, as regards the combination x+0.3y, the storey drift of the ground floor is 3.13% while the storey drift of the upper floor is 0.03%. As regards the combination y+0.3x, the storey drift of the ground floor is 2.72% while the storey drift of the upper floor is 0.03%.

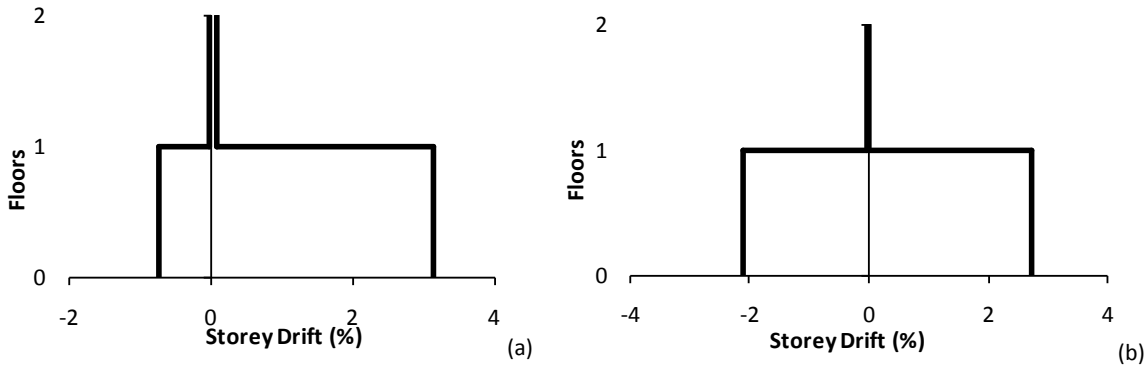


Figure 13: Storey Drift Diagram (a) for combination x+0.3y, (b) for combination y+0.3x

7 BASE ISOLATION

The next phase of the paper is the retrofitting of the existing structure. Firstly, it is intended to reduce the seismic demand for the building with the use of seismic isolation systems. The reduction of the seismic response of the lateral – force resisting system is obtained by increasing the fundamental period of the seismically isolated structure and the damping. As a result, the isolators take over a great percentage of the horizontal displacement. The structure moves like a rigid solid body and does not take over tension from the seismic forces. In this work, two types of isolators have been used, Lead Rubber Bearings (LRB) and Friction Pendulum Systems (FPS).

7.1 Simulation of base isolation systems

According to the Greek Retrofitting Code [10] and EC8 Part-3 [9], the hysteresis diagram of an LRB and an FPS can be modeled as bilinear. In Figures 14 and 16 the typical force – displacement diagrams for an LRB and an FPS is presented, respectively. In this work, the bearings are designed according to the simplified linear analysis method (EC8 Part-1).

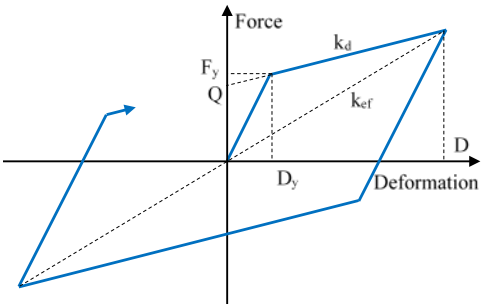


Figure 14: Bilinear Force - Deformation Diagram of LRB

The behavior of an LRB can be defined throughout the yield point load of the lead core (F_y), the lead core contribution to the horizontal stiffness (K_{lead}) and the elastomer contribution to the horizontal stiffness (K_r). The implemented LRB bearing has a diameter of 350mm, elastomer thickness of 112mm and the effective damping takes a value b_{eff}=28%. The shear modulus of the elastomer is equal to G=0.4MPa. The analysis model is based on the hysteresis model which was suggested by Wen [17] and Park et al. [18] (Figure 15).

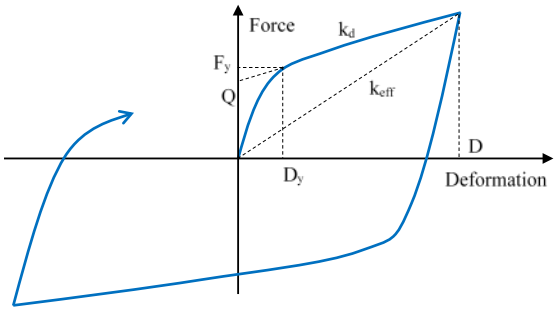


Figure 15: Hysteresis Model of LRB

The response of friction pendulum systems can be described using the radius of curvature (R), the coefficient of friction (μ) and the effective vertical load (V). The implemented FPS bearing has radius of curvature 2.5m, coefficient of friction 0.055 and effective vertical load 560kN. The analysis model is based on the hysteresis model recommended for base isolation analysis suggested by Nagarajaiah et al. [19] and on the sliding behavior suggested by Zayas et al. [20].

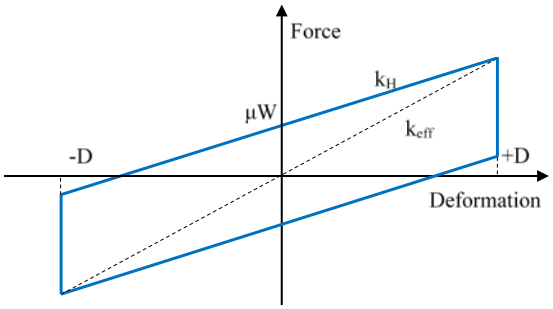


Figure 16: Bilinear Force - Deformation Diagram of FPS

7.2 Results

Mode	Movement	Initial Period (s)	Period LRB (s)	Period FPS(s)
1	translational x axis	0.38	1.936	3.582
2	translational y axis	0.374	1.91	3.538

Table 3: Modal Analysis Results

The implementation of the base isolation systems has successfully increased the fundamental period (Table 3). The period of the first mode increased from 0.38s to 1.936s with the use of LRB. With the use of FPS the period of the first mode increased from 0.38s to 3.58s. The structural members and the infill walls responded linearly for both types of bearings. The hysteresis behavior of the bearings is shown in Figure 17.

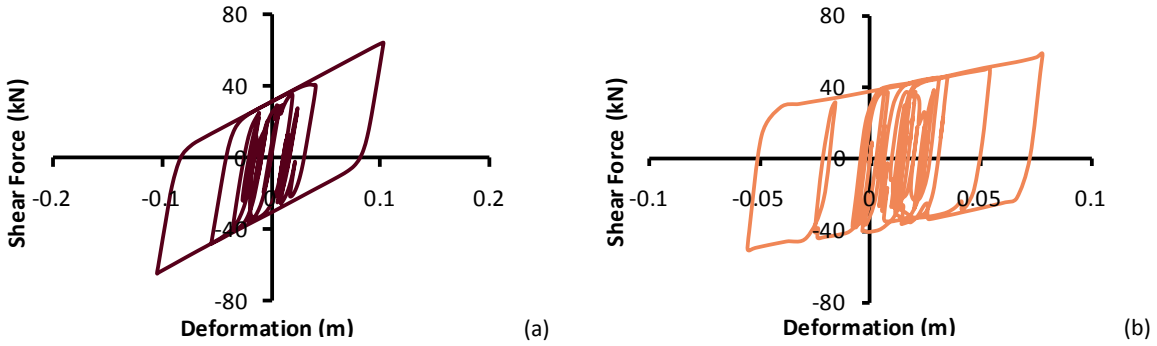


Figure 17: Hysteresis behavior of (a) LRB, (b) FPS

In Figure 18, the relative displacement between the top and the base of the structure is shown. This Diagram represents the behavior of the structure in three different conditions, the initial (without any intervention) and the intervention with each base isolation system (LRB and FPS). In the initial stage, the relative displacement between the top and the base of the building is significantly larger than the displacement which corresponds to the intervention with the base isolation systems. In the first case, the ground floor columns deform and because of that the maximum relative displacement is 0.106m. At the same time, after the base isolation intervention, the horizontal displacement is taken over by the bearings and consequently the member deformations are approximately 10 times less and the maximum relative displacement is 0.017m for the FPS and 0.015m for the LRB. It is also observed that after the intervention with base isolation systems, there is no permanent displacement. Before the intervention the permanent displacement of the structure was for both combinations close to 0.03m.

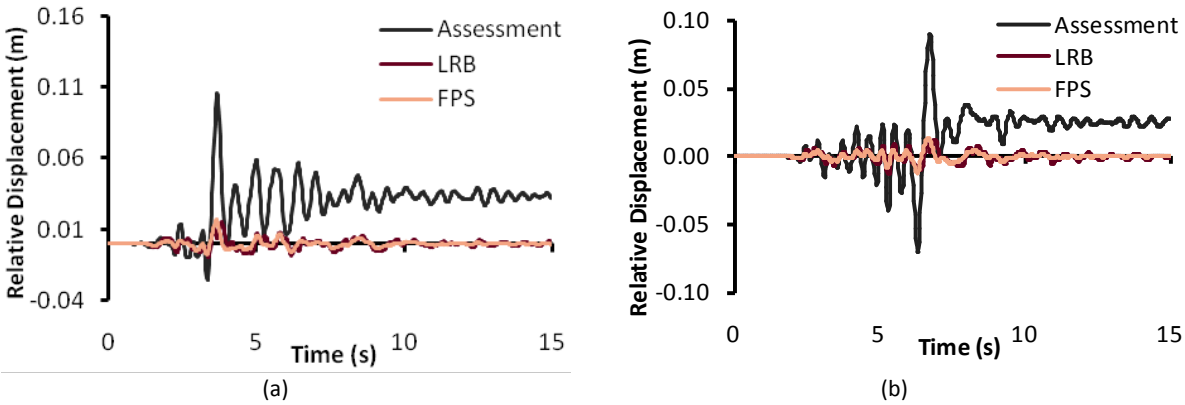


Figure 18: Top to Base Relative Displacement (a) for combination x+0.3y, (b) for combination y+0.3x

In Figure 19, the storey drift for the initial condition and the base isolation intervention (LRB and FPS) is shown. The storey drift is significantly decreased with the use of base isolation systems. Specifically, for the combination x+0.3y before the intervention, the maximum storey drift is 3.13% while after the intervention with LRB, the maximum storey drift is 0.43% and with FPS it is 0.48%. For the combination y+0.3x before the intervention, the maximum storey drift is 2.72% while after the intervention with LRB, the maximum storey drift is 0.36% and with FPS it is 0.37%.

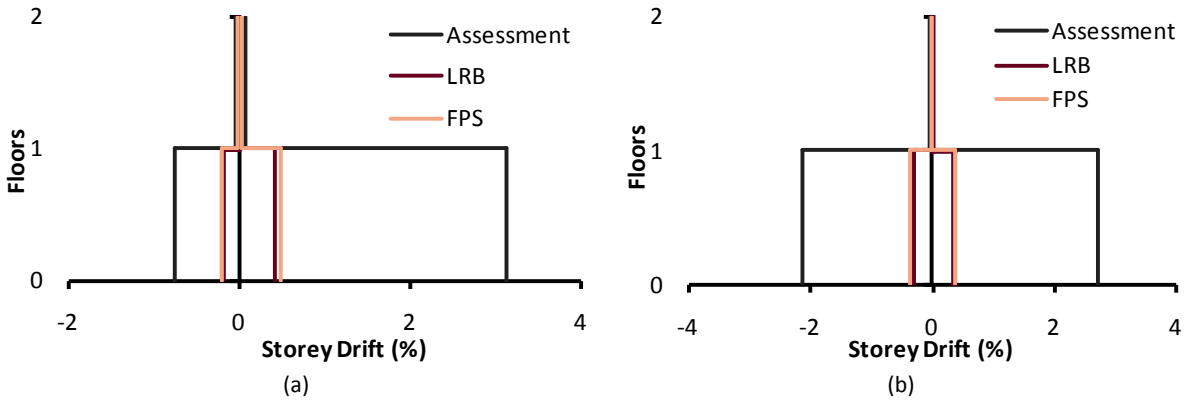


Figure 19: Storey Drift Diagram (a) for combination x+0.3y, (b) for combination y+0.3x

In Figure 20, the shear distribution to the floors for the initial condition and the base isolation intervention (LRB and FPS) is shown. The shear distribution is significantly decreased with the use of base isolation systems. Specifically, for the combination x+0.3y before the intervention, the maximum shear force to the ground floor is near to 2900kN while after the intervention with LRB, the maximum shear force to the ground floor is about 1550kN and with FPS it is close to 1700kN. For the combination y+0.3x before the intervention, the maximum shear force to the ground floor is about 1900kN, while after the intervention with LRB the maximum shear force to the ground floor is about 550kN and with FPS it is close to 600kN.

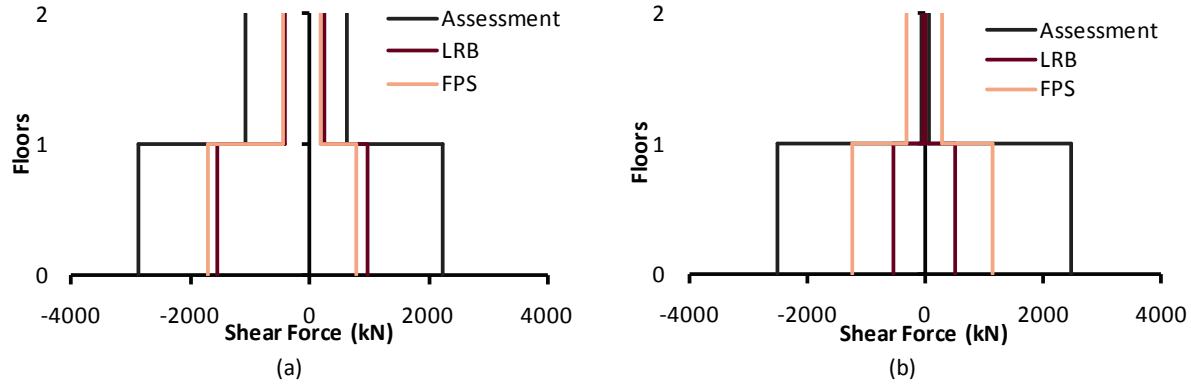


Figure 20: Shear Distribution per floor (a) for combination x+0.3y, (b) for combination y+0.3x

8 METAL BRACES

The second intervention method used is the implementation of metal braces. The metal braces with the beams and columns of the building behave as a truss. The horizontal seismic force is taken over from the diagonal bars of the formed truss (the metal braces). The brace material is chosen to be steel. Steel because of its ductility deforms significantly and observes a great amount of seismic energy.

The section of the metal braces has been chosen so that the additional stiffness to the ground floor balances the initial stiffness lack of that floor. In order to accomplish this, the chosen section is SHSH120x120x10. These braces have been chosen to be placed crosswise, with no eccentricities and pinned to the frame nodes. Moreover, the metal braces have been placed symmetrically in plan, so as not to cause torsional phenomena.

8.1 Simulation

The metal braces simulation has been performed according to the Greek Retrofitting Code [10] model regarding the relation between the axial force and the axial deformation. That diagram is presented in Figure 21. The control of the braces has been performed according to the EC8 Part-3 [9] model for the axial deformation capacity of braces in compression and tension. The location of the metal braces in the building is also presented in Figure 22.

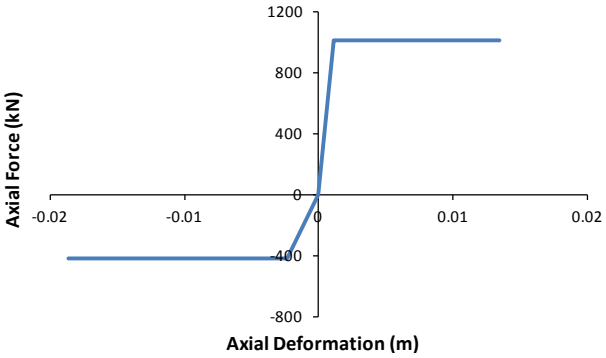


Figure 21: Force - Deformation Diagram for metal braces

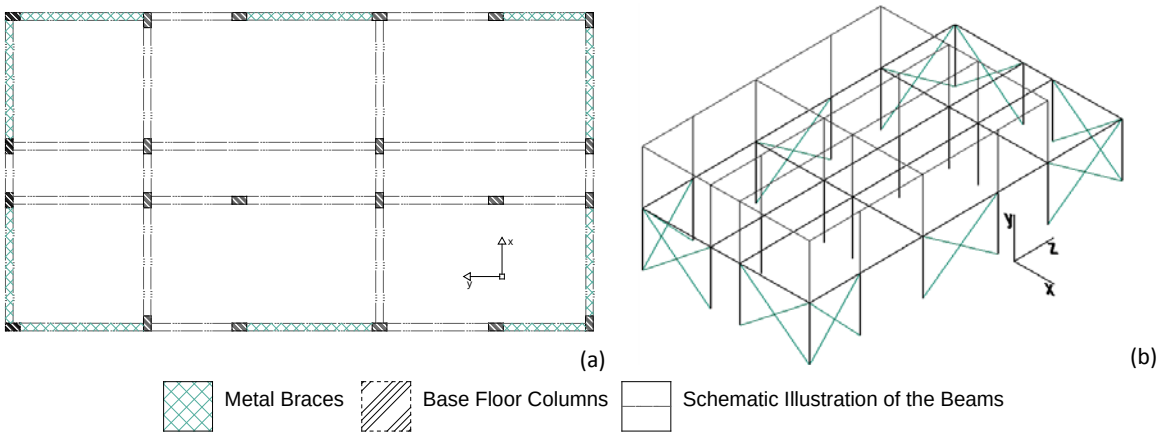


Figure 22: Position of the implemented metal braces (a) in plan, (b) in 3D

8.2 Modal analysis results

Mode	Movement	Initial Period (s)	Period (s) (Metal Braces)
1	translational x axis	0.38	0.267
2	translational y axis	0.374	0.228
3	rotational	0.308	0.174

Table 4: Modal Analysis Results

The implementation of the metal braces has increased the stiffness of the building and decreased the fundamental period of the building. The period of the first mode has decreased from 0.38s to 0.267s with the implementation of metal braces.

8.3 Pushover analysis results

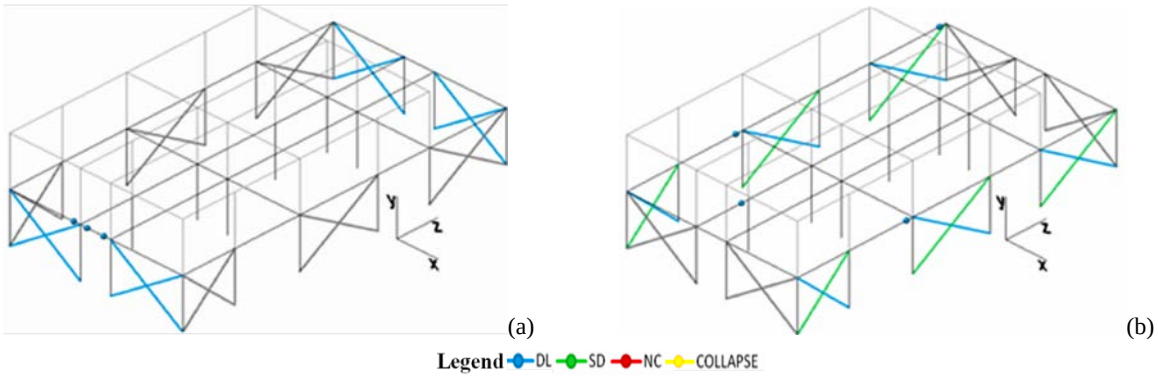


Figure 23: Damage Distribution (a) for combination x+0.3y, (b) y+0.3x

Figure 23 presents the local nonlinear behavior of the structural members in terms of plastic rotational hinge requirement based on the limit state of the critical sections. The results that are being shown correspond to the maximum limit state that has been reached between the triangular and the uniform distribution of the lateral forces for both combinations of the lateral forces. The majority of the structural members responded elastically.

For both combinations, increased performance requirements are observed only in a small number of beam critical sections and to the metal braces that are situated parallel to the direction of the force. For the combination x+0.3y, the sections that behaved nonlinearly reached the *Damage Limitation (DL) limit state, while f*or the combination y+0.3x they reached either the *Damage Limitation (DL) limit state* or the *Significant Damage (SD) limit state*. The metal braces are replaceable, so the damages that occurred to them are considered fixable. The beams are lightly damaged and can also be repaired.

Figure 24 shows a comparison between the capacity curves before and after the implementation of metal braces. The increase of stiffness and strength is obvious. The performance point after the intervention for both combinations is in the elastic part of the capacity curve. The structure behaved elastically. In Figure 25 the storey drift for the initial condition and the intervention with metal braces is shown. The storey drift is significantly decreased with the use of base isolation systems. Specifically, for the combination x+0.3y before the intervention the maximum storey drift is 2.23% while after the intervention the maximum storey drift is 0.15%. For the combination y+0.3x before the intervention the maximum storey drift is 2.19% while after the intervention the maximum storey drift is 0.25%.

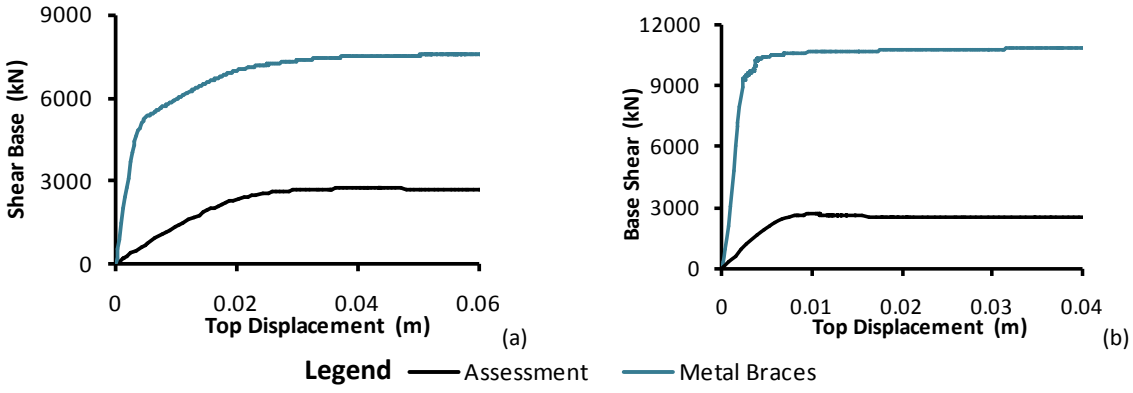


Figure 24: Capacity Curves (a) for combination x+0.3y, (b) for combination y+0.3x

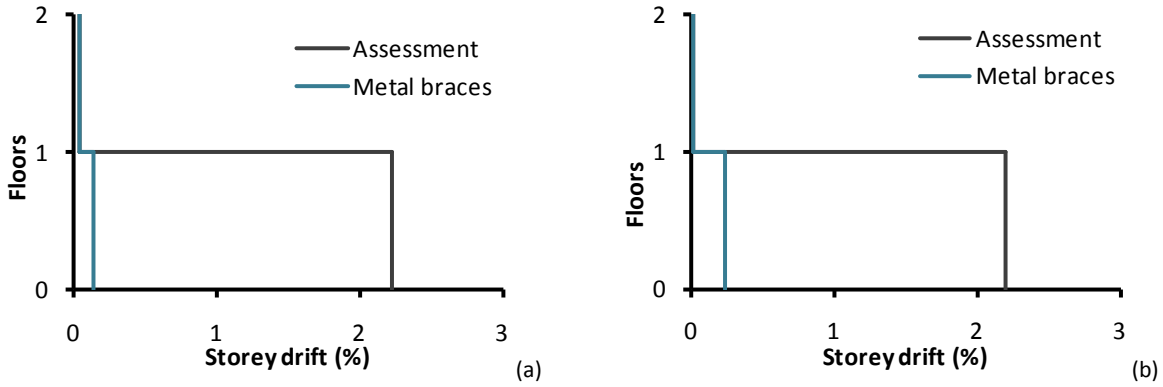


Figure 25: Storey Drift Diagram (a) for combination x+0.3y, (b) for combination y+0.3x

8.4 Time history analysis results

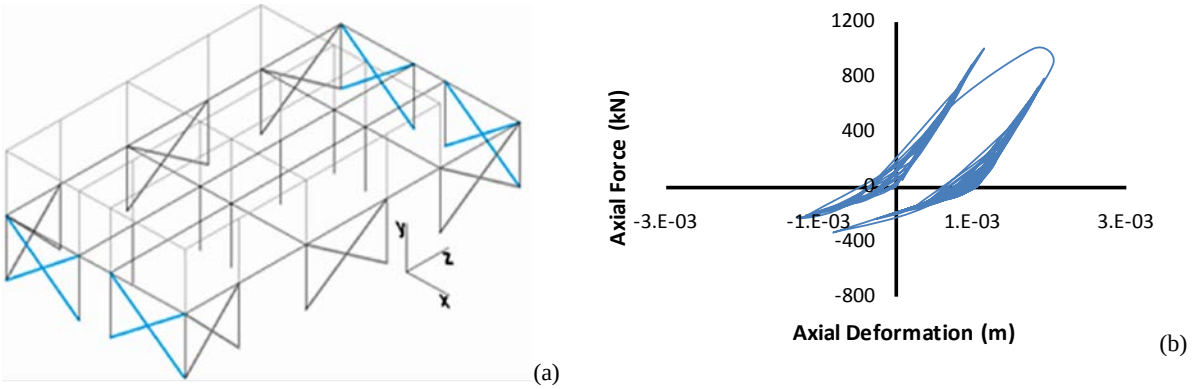


Figure 26: (a) Damage Distribution for combination x+0.3y, (b) Hysteresis Diagram of metal brace

Figure 26(a) presents the local nonlinear behavior of the structural members in terms of plastic rotational hinge requirement based on the limit state of the critical sections. For the combination y+0.3x, all the structural members responded elastically. For the combination x+0.3y, increased demands are shown only to the metal braces that are situated parallel to the direction of the force. The sections that responded nonlinearly reached the *Damage Limitation (DL) limit state.* In Figure 26(b) the hysteresis diagram of a metal brace is shown. The damage to the metal braces can be economically repaired.

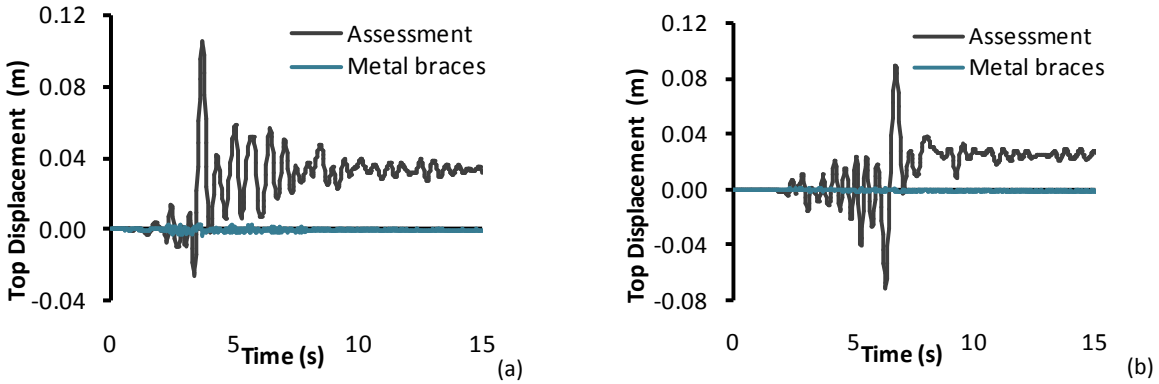


Figure 27: Top Displacement (a) for combination x+0.3y, (b) for combination y+0.3x

In Figure 27 the top displacement of the structure is shown. This diagram represents the behavior of the structure before and after the intervention with metal braces. In the initial stage, the displacements of the top of the building are significantly larger that those after the intervention with the metal braces. In the first case, the maximum top displacement is 0.106m while after the intervention the maximum top displacement is 0.0034m. It is also observed that after the intervention with metal braces, there is no permanent displacement. Before the intervention the permanent displacement of the structure was for both combinations near to 0.03m.

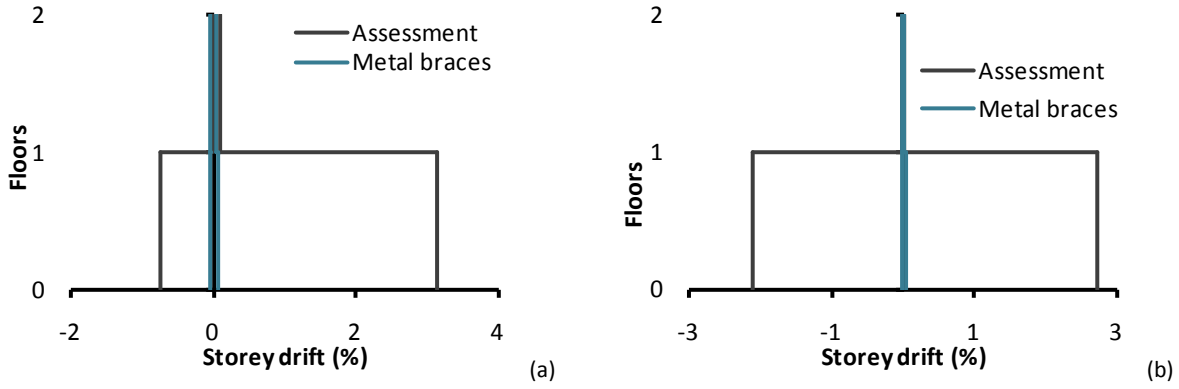


Figure 28: Storey Drift Diagram (a) for combination x+0.3y, (b) for combination y+0.3x

In Figure 28, the storey drift for the initial condition and the metal brace intervention is shown. The storey drift is significantly decreased with the use of metal braces. Specifically, for the combination x+0.3y, before the intervention the maximum storey drift is 3.13% while after the intervention the maximum storey drift is 0.066%. For the combination y+0.3x, before the intervention the maximum storey drift is 2.72% while after the intervention the maximum storey drift is 0.033%.

In Figure 29, the shear distribution to the floors before and after the intervention is shown. The shear distribution is significantly decreased with the use of metal braces. Specifically, for the combination x+0.3y, before the intervention the maximum shear force to the ground floor is near to 2900kN, while after the intervention the maximum shear force to the ground floor is about 320kN. For the combination y+0.3x, before the intervention the maximum shear force to the ground floor is about 1900kN, while after the intervention the maximum shear force to the ground floor is about 80kN.

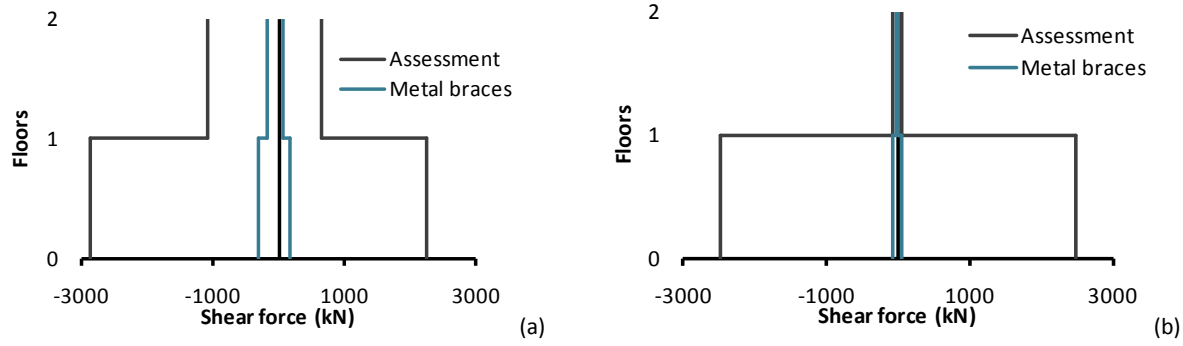


Figure 29: Shear Distribution per floor (a) for combination x+0.3y, (b) for combination y+0.3x

9 CONCLUSION

Firstly, the assessment of the building with nonlinear analysis methods took place. As it was expected the building behaved as “pilotis” type. A “soft” floor mechanism was created in the ground floor because of the lack of infill walls there. The columns majority and a great number of beams of the ground floor responded nonlinearly. The structural members of the first floor remained in the elastic range. It was also observed that, at the end of the earthquake, large permanent drifts were present. Finally, the analyses results verified the actual state that was presented by the building after the earthquakes. A “soft” floor mechanism actually occurred, since the columns of the ground floor were heavily damaged and the second floor responded elastically.

Having the assessment procedure carried out, the need for structural intervention has been decided. The first method to be used was the implementation of LRB and FPS isolation systems. As a result, the period of the building was increased and the seismic force demand was reduced. The structural members of the structure and the walls responded linearly. It was observed that the largest side movements were taken over from the bearings, while the rest of the structure moved as a rigid body. The relative displacement between the top and the base of the building decreased about 10 times, while the storey drift of the ground floor decreased 7 times and the shear force of the ground floor 2 times. Moreover, there were no permanent deformations.

The second intervention method to be used was the implementation of metal braces with a SHSH120x120x10 section. As a result, the stiffness and the strength of the building were increased and consequently the period was reduced. The majority of the structural members responded linearly. The majority of the damages concentrated in the metal braces which are considered replaceable. The top displacement of the building was incomparably reduced, while the storey drift of the ground floor was reduced 8 times and the shear force of the ground floor 9 times.

The assessment of the seismic behavior of the building verified the damages that were observed during the field investigation and were expected also according to the scientific knowledge about the “pilotis” type buildings. The intervention to the building was made with two methods which are based in different principles. Both methods were proved to be equally efficient as they were successful in preventing the structural elements from significant yielding and in decreasing the storey drift to a negligible point. Thus, after the interventions the structure is lightly damaged and does not need any repair measures to be taken.

REFERENCES

[1] M.J. Favvata, M.C. Naoum, C.G Karayannis, Limit States of RC structures with first floor Irregularities. *Structural Engineering and Mechanics,* **47**, 791-818, 2013.

[2] G.E. Thermou, S.A. Elnashai, Seismic retrofit schemes for RC structures and local-global consequences. *Progress in Structural Engineering and Engineering Materials,* **8**, 1-15, 2006.

[3] R.I. Skinner, W.H. Robinson, G.H. McVerry, *An introduction to seismic isolation*. John Wiley and Sons, 1993.

[4] F. Naeim, J.M. Kelly, (1999), *Design of seismic isolated structures*. Wiley, 1999.

[5] T.A. Antonopoulos, S.A. Anagnostopoulos, *Seismic evaluation and upgrading of RC buildings with weak open ground stories*. Earthquakes and Structures, **3**, 611-628, 2012.

[6] L.Su, G. Ahmadi, J.G. Tadjbakhsh, A comparative study of performances of various base isolation systems, part I: Shear beam structures. *Earthquake Engineering and Structural Dynamics*, **18**, 11-32, 1989.

[7] J.M. Kelly, *Earthquake-Resistant Design with Rubber, 2nd Edition.* Springer-Verlag, 1997.

[8] M. Constantinou, A. Mokha, and A. Reinhorn, Teflon bearings in base isolation II: Modeling. *Journal of Structural Engineering*, **116**, 455-474, 1990.

[9] Eurocode 8: Design of structures for earthquake resistance, Part 3: assessment and retrofitting of buildings. EN1998-3-2005, *European Committee for Standardization (CEN)*, 2005.

[10] KAN.EPE., Greek Retrofitting Code. Greek Organization for Seismic Planning and Protection (OASP), *Greek Ministry for Environmental Planning and Public Works*, Athens, 2012.(In Greek)

[11] RD, Earthquake design regulation of building works, Royal Decree (19/26.02.1959), *Ministry of Public Works*, Greece, 1959. (In Greek)

[12] T. Takeda, M.A. Sozen, N.N Nielson, Reinforced concrete response to simulated earthquakes. *Journal of Structural Division ASCE*, **96**, 2557–2573, 1970.

[13] E. Spacone, F.C. Filippou, F.F. Taucer, Fibre beam–column model for non-linear analysis of RC frames: Part I: Formulation. *Earthquake Engineering and Structural Dynamics*, **25**, 711–725, 1996.

[14] E. Spacone, and F.C. Filippou, F.F. Taucer, Fibre beam–column model for non-linear analysis of RC frames: Part II: Applications. *Earthquake Engineering and Structural Dynamics*, **25**,727–742, 1996.

[15] C. Karayannis, M. Favvata, Application of ATC40 and FEMA nonlinear static analysis procedures for the evaluation of RC frame structures. *Scientific Review KTIRIO*, **A-B**, 95-104, 2003.(In Greek)

[16] Eurocode 8: Design of structures for earthquake resistance, Part 1: General rules, seismic actions and rules for buildings. EN 1998-1:2004, *European Committee for Standardization (CEN)*, 2004.

[17] Y.K. Wen, Method for random vibration of hysteretic systems. *Journal of the Engineering Mechanics Division*, **102**, 249–263, 1976.

[18] Y.J Park, Y.K Wen, A.H.S Ang, Random vibration of hysteretic systems under bi-directional ground motions. *Earthquake Engineering and Structural Dynamics*, **14**, 543–557, 1986.

[19] S. Nagarajaiah, A.M Reinhorn, M.C. Constantinou, 3D-Basis: Non-Linear Dynamic Analysis of Three-Dimensional Base Isolated Structures: Part II, Technical Report NCEER-91-0005, *National Center for Earthquake Engineering Research*, State University of New York at Buffalo, Buffalo, USA, 1991.

[20] V.A. Zayas, S.S. Low, S.A. Mahin, A simple pendulum technique for achieving seismic isolation. *Earthquake Spectra*, **6**, 317-334, 1990.

COMPDYN 2015
5th ECCOMAS Thematic Conference on
Computational Methods in Structural Dynamics and Earthquake Engineering
M. Papadrakakis, V. Papadopoulos, V. Plevris (eds.)
Crete Island, Greece, 25–27 May 2015

DESIGN METHODOLOGY FOR SEISMIC UPGRADING OF TORSIONALLY UNBALANCED EXISTING R.C. BUILDINGS

Georgia E. Thermou[1] **and Manousos Psaltakis**[1]

[1]Aristotle University of Thessaloniki
Dept. of Civil Engineering, 54124, Thessaloniki, Greece
gthermou@civil.auth.gr; manousoscivil@hotmail.gr

Keywords: Assessment, Retrofitting, Torsion, Buildings, Reinforced Concrete.

Abstract.

This paper presents a design methodology for the seismic upgrading of rotationally sensitive existing R.C. buildings. The first part of the methodology deals with the elimination of the effect of torsional coupling on modal periods and shapes. The second part aims at the modification of the response shape of the building in each direction so as to achieve a near – uniform distribution of interstorey drift along the building height. A three-storey building constructed in the early 1970s with old type reinforcement detailing is selected as a case study. After being assessed, the proposed methodology is implemented and the various steps involved are described in detail. The validity of the proposed methodology was assessed by carrying out inelastic analyses with the use of a three-dimensional finite element model of the retrofitted structure. The results indicate the efficiency of the proposed design methodology for the seismic upgrading of existing torsionally unbalanced R.C. buildings.

1 INTRODUCTION

The vast majority of existing R.C. buildings stock has been designed with out-of-date codes where seismic detailing was at a primitive stage of knowledge. Recent earthquakes occurred worldwide (e.g. Northridge, California (1994); Kobe, Japan (1995); Chi Chi, Taiwan (1999); Athens, Greece (1999), Izmit and Düzce, Turkey (1999), L' Aquila, Italy (2009), Haiti (2010)) have demonstrated the susceptibility of non-ductile buildings with deficiencies related to member- and/or system-level. Insufficient reinforcement detailing of components (e.g. inadequately anchored transverse and longitudinal reinforcement, sparse and smooth stirrups, lap splices in the region of the plastic hinge, no stirrups in the beam-column joints, bad connection of the ground floor columns to the foundation system) limit the ability of the structure to resist seismic loading. System-level deficiencies such as eccentricities of stiffness and mass in both plan and elevation are common in existing structures leading to severe damage and eventually to collapse. Irregularities along the vertical axis are due to either irregular distribution of mass or stiffness along the height of the building. A special case is the soft-storey formation in pilotis type buildings (i.e. the ground storey used for commercial facilities is an open frame (bare frame), while the storeys above are infilled.). The uneven distribution of stiffness in plan (horizontal irregularities) may be the result of architectural (e.g. L-shaped buildings) or functional (e.g. facade of commercial buildings) features. The position of the elevator shaft walls plays an important role in the distribution of stiffness in plan (Fig. 1).



Figure 1: Collapse of torsionally unbalanced R.C. buildings in the 1999 Athens earthquake.

Different retrofit strategies may be developed for non-ductile R.C. buildings depending among other parameters on the mandated level of the intervention and the financial objectives of the retrofit offer [1]. Thermou et al. [2] developed a retrofit design concept according to which response may be improved by targeting for a fundamental mode shape that would produce a desirable pattern of interstorey drift and therefore damage. This concept was further extended by Pardalopoulos and Pantazopoulou [3] in three-dimensional structures with torsional component in their lateral response, where in the methodology developed the fundamental translational mode shape is approximated by separating the contributions to translation and twisting from the corresponding basic modes of an associated decoupled system.

In the proposed retrofit design methodology the criteria that need be satisfied are correction of any irregularities in plan and in elevation and elimination of mechanisms likely to lead to damage localization. Distribution rather than localization of damage is crucial; otherwise the weakest link will jeopardize the stability of the whole structure [2]. Another important issue is the modification of the structural system so as to achieve increase in the redundancy of the lateral load resisting system.

This paper presents a design methodology for the seismic upgrading of rotationally sensitive existing R.C. buildings. The methodology aims first to eliminate the effect of torsional coupling on modal periods and shapes. After this stage, the building is expected to respond independently in the two lateral directions (since torsional effects have been neglected) following the corresponding fundamental mode shapes. Next, the translational response shape in each orthogonal direction is engineered as to achieve a near – uniform distribution of interstorey drift along the building height [2]. The proposed methodology was implemented to an existing three-storey building constructed in the early 1970s. The validity of the proposed methodology was assessed by carrying out inelastic analyses with the use of a three-dimensional finite element model of the retrofitted structure. The results indicate the efficiency of the proposed design methodology for the seismic upgrading of existing torsionally unbalanced R.C. buildings.

2 FUNDAMENTALS OF THE PROPOSED RETROFIT DESIGN METHODOLOGY

The proposed retrofit design methodology aims to modify radically the response of old substandard R.C. buildings with torsional sensitivity. For this scope a retrofit design methodology has been developed which comprises two design stages (Phase I and Phase II). First, structural eccentricities are minimized and simultaneously torsional resistance and stiffness are enhanced. This is realized by the addition of stiffness at the periphery of the building through adoption of global intervention methods (e.g. R.C. infill walls, R.C. jacketing). At the end of this design stage (Phase I), the building is symmetric in plan and torsionally balanced. Thus, the ground motion in the two orthogonal axes (x and y) will cause only lateral motion, whereas the system will experience no torsional motion unless the base motion includes rotation about the vertical axis. The building is modified further as to respond in each lateral direction according to a target response shape, called hereafter target response shape. The objective is to mitigate damage localization through controlled modification of the lateral response shape. This is achieved by a weighted distribution of additional stiffness along the height of the building ([2], [4], [5]).

2.1 Elimination of the torsional sensitivity – Design Phase I

The unsymmetric plan depicted in Fig. 2(a) corresponds to the constant floor plan of an existing mulitistorey R.C. building. Due to the distance between the center of mass (CM) and the center of stiffness (CS) (i.e. eccentricities e_x and e_y in Fig. 2(a)), the building is expected to simultaneously undergo lateral motion in the two orthogonal directions (x and y) and torsion about the vertical axis whenever subjected to the x- or y-component of ground motion. In case that the origin of the xOy coordinate system is defined at the CM for each vertical member i the translational and rotational stiffness are defined as:

$$\text{Translational stiffness: } K_x = \sum_{i=1}^{n} K_{x,i} \; ; \; K_y = \sum_{i=1}^{n} K_{y,i} \tag{1a}$$

$$\text{Rotational stiffness: } K_z = \sum_{i=1}^{n} \left(K_{y,i} \cdot x_i^2 + K_{x,i} \cdot y_i^2 \right) \tag{1b}$$

where $K_{x,i}$, $K_{y,i}$ are the lateral stiffness of the individual floor elements and x_i, y_i is the distance of the geometrical center of each element from the origin xOy. Note the translational and rotational stiffness as defined in Eqs. (1) correspond to the CM. The floor rotation, θ, as a result of force V_o acting at the CM is:

$$\theta = \frac{M_v}{K_z^{/}} = \frac{-V_o \cdot \cos a \cdot e_y + V_o \cdot \sin a \cdot e_x}{K_z^{/}} \tag{2}$$

where $K_z^{/}$ is the rotational stiffness defined at the CS according to:

$$K_z^{/} = \sum_{i=1}^{n} \left[K_{y,i} \cdot \left(x_i - e_x \right)^2 + K_{x,i} \cdot \left(y_i - e_y \right)^2 \right] \tag{2a}$$

The eigenvalue problem of the existing building whose solution provides the natural frequencies, ω_s, and modes, $\mathbf{\Phi_s}$, is described mathematically by:

$$\left[\underline{\mathbf{K}} - \omega_s^2 \cdot \underline{\mathbf{M}} \right] \cdot \underline{\mathbf{\Phi}} = 0 \Rightarrow \omega_s^2 \cdot \underline{\mathbf{M}} \cdot \underline{\mathbf{\Phi}} = \underline{\mathbf{K}} \cdot \underline{\mathbf{\Phi}} \Rightarrow$$

$$\omega_s^2 \cdot \begin{bmatrix} \mathbf{m} & \mathbf{0} & \mathbf{0} \\ \mathbf{0} & \mathbf{m} & \mathbf{0} \\ \mathbf{0} & \mathbf{0} & \mathbf{J_m} \end{bmatrix} \cdot \begin{Bmatrix} \mathbf{\Phi_x} \\ \mathbf{\Phi_y} \\ \mathbf{\Phi_z} \end{Bmatrix} = \begin{bmatrix} \mathbf{K_x} & \mathbf{0} & -e_y \cdot \mathbf{K_x} \\ \mathbf{0} & \mathbf{K_y} & e_x \cdot \mathbf{K_y} \\ -e_y \cdot \mathbf{K_x} & e_x \cdot \mathbf{K_y} & \mathbf{K_z} \end{bmatrix} \cdot \begin{Bmatrix} \mathbf{\Phi_x} \\ \mathbf{\Phi_y} \\ \mathbf{\Phi_z} \end{Bmatrix} \tag{3}$$

where ω_s (s=x,y,z) is the natural frequency, $\mathbf{K_x}$, $\mathbf{K_y}$, $\mathbf{K_z}$ are the diagonal submatrices of the translational stiffness in x and y direction and of the rotational stiffness of order N/3 (N is the number of storeys). $\mathbf{\Phi_s}^T=[\Phi_{s,1}, \Phi_{s,2},\ldots, \Phi_{s,N}]^T$ (s=x, y, z) are the mode shapes of the system. $\mathbf{m}$, $\mathbf{J_m}$ are the diagonal submatrices of the mass and moment of inertia of order N/3 (N is the number of storeys). The moment of inertia at each storey is defined as:

$$J_m = m_{st} \frac{\left(L_x^2 + L_y^2 \right)}{12} = m_{st} \cdot l_s^2 \tag{4}$$

where m_{st} is the storey mass, L_x, L_y are the in plan dimensions of the building and l_s is the radius of gyration of the floor mass in plan.

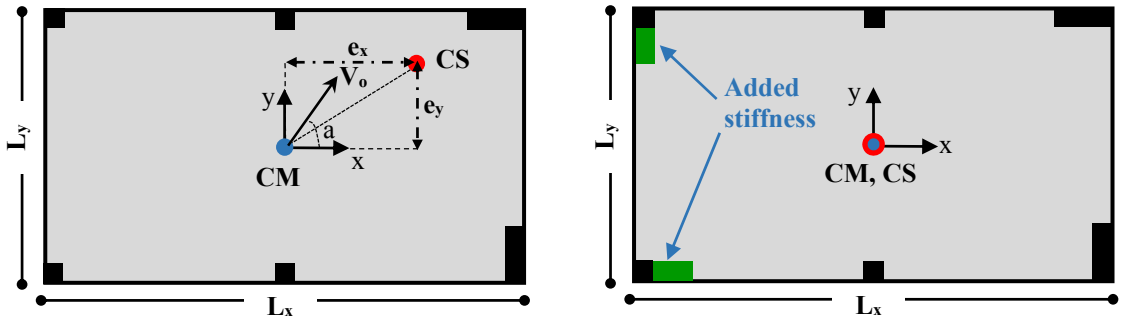


Figure 2: Plan layout (a) of the existing building; (b) of the retrofitted building (eccentricity elimination).

The mode shapes are coupled through the stiffness matrix, **K**, because the stiffness properties are not symmetric about the x and y axes. In case that eccentricity could be eliminated so that $\mathbf{K_{x\theta}=K_{\theta x}=K_{y\theta}=K_{\theta y}=0}$ (i.e. $e_x=e_y=0$ and thus $\theta=0$ (Eq. (2)), then the system would be uncoupled in x, y and z directions. This can be achieved by adding stiffness to the system in strategically selected positions at the periphery of the building as to minimize eccentricity and simultaneously increase torsional resistance (Fig. 2(b)). The translational and rotational stiffness of the modified system are:

$$\text{Translational stiffness: } K_x^R = \sum_{i=1}^{n} K_{x,i} + \sum_{p=1}^{m} K_{x,p} \; ; \; K_y^R = \sum_{i=1}^{n} K_{y,i} + \sum_{q=1}^{\ell} K_{y,q} \tag{5a}$$

$$\text{Rotational stiffness: } K_z^R = \sum_{i=1}^{n} \left(K_{y,i} \cdot x_i^2 + K_{x,i} \cdot y_i^2 \right) + 0.25 \cdot L_x^2 \cdot \sum_{q=1}^{\ell} K_{y,q}^R + 0.25 \cdot L_y^2 \cdot \sum_{p=1}^{m} K_{x,p}^R \tag{5b}$$

where $\sum_{p=1}^{m} K_{x,p}$ and $\sum_{q=1}^{\ell} K_{y,q}$ refer to the additional stiffness required as to remove any eccentricity of the floor plan. The objective is to add such an amount of stiffness as to move the CS to the CM (i.e. $e_x=e_y=0$ in Fig. 2(a)). Hence, the required amount of stiffness in the x direction may be estimated from:

$$x_{CM} = x_{CS} = 0 \Rightarrow \frac{\sum_{i=1}^{n} \left(K_{x,i} \cdot y_i \right) + 0.5 \cdot L_y \cdot \sum_{p=1}^{m} K_{x,p}}{\sum_{i=1}^{n} K_{x,i} + \sum_{p=1}^{m} K_{x,p}} = 0 \Rightarrow \sum_{p=1}^{m} K_{x,p} = -\frac{2}{L_y} \sum_{i=1}^{n} \left(K_{x,i} \cdot y_i \right) \tag{6a}$$

Similarly, the required amount of stiffness in the y direction is:

$$\sum_{q=1}^{\ell} K_{y,p} = -\frac{2}{L_x} \sum_{i=1}^{n} \left(K_{y,i} \cdot x_i \right) \tag{6b}$$

Eq.(3) that describes the eigenvalue problem for the existing building is modified accordingly as to account for the effect of the additional stiffness that lead to elimination of eccentricity and enhancement of the torsional resistance:

$$\omega_s^2 \cdot \begin{bmatrix} \mathbf{m} & \mathbf{0} & \mathbf{0} \\ \mathbf{0} & \mathbf{m} & \mathbf{0} \\ \mathbf{0} & \mathbf{0} & \mathbf{J_m} \end{bmatrix} \cdot \begin{Bmatrix} \mathbf{\Phi_x^R} \\ \mathbf{\Phi_y^R} \\ \mathbf{\Phi_z^R} \end{Bmatrix} = \begin{bmatrix} \mathbf{K}_x^R & \mathbf{0} & \mathbf{0} \\ \mathbf{0} & \mathbf{K}_y^R & \mathbf{0} \\ \mathbf{0} & \mathbf{0} & \mathbf{K}_z^R \end{bmatrix} \cdot \begin{Bmatrix} \mathbf{\Phi_x^R} \\ \mathbf{\Phi_y^R} \\ \mathbf{\Phi_z^R} \end{Bmatrix} \tag{7}$$

Thus, the three uncoupled equations that describe the eigenvalue problem are:

$$\omega_x^2 \cdot \mathbf{m} \cdot \mathbf{\Phi_x^R} = \mathbf{K}_x^R \cdot \mathbf{\Phi_x^R}\,;\ \omega_y^2 \cdot \mathbf{m} \cdot \mathbf{\Phi_y^R} = \mathbf{K}_y^R \cdot \mathbf{\Phi_y^R}\,;\ \omega_z^2 \cdot \mathbf{m} \cdot \mathbf{\Phi_z^R} = \mathbf{K}_z^R \cdot \mathbf{\Phi_z^R} \tag{8}$$

According to Eq. (8) the modified building (Fig. 2(b)) will response independently in the two lateral directions (torsional effects have been neglected) following the corresponding fundamental mode shapes.

2.2 Strengthening for a target response shape – Design Phase II

In the proposed rehabilitation framework, deformation demand is quantified by interstory drift throughout the structure. In a reverse process of redesign, in which the desirable pattern of interstorey drift distribution prescribes the proper morphology of the fundamental mode shape, it is relatively straightforward to evaluate the pattern of stiffness distribution throughout the structure that is required to produce a desirable translational mode ([5], [6], [7]). The retrofit design methodology developed by Thermou et al. [6] is adopted. In the first step of the methodology the target period of the retrofitted building, T_{target}, is defined. It could range between $0.05H_{tot}^{3/4} \leq T_{target} < T_{existing}$. The Yield Point Spectrum (YPS) representation [8] is utilized for defining for a given period value, T_{target}, the total acceleration and relative displacement coordinates of the elastic ADRS spectrum (corresponding to T_{target}) which are simply divided by the behaviour factor, q_{target}, and the corresponding ductility demand, μ_{target}. A ductility value (μ_{target}) between 2 and 3 may be considered achievable for retrofitted buildings. Next, the target response shape, Φ_{shape}, is selected. The driving consideration is the pursuit to obtain as nearly uniform as possible a distribution of drift demand. Alternative options for the selected response shape are presented in Fig. 3. When considering structural vibration in the selected target mode shape, the generalized (effective) SDOF properties of the structure are related to the target period and from there to the required secant-to-yield stiffness of the first floor, K_1, as follows:

$$T_{target} = 2\pi\sqrt{\frac{M^*}{K^*}} = 2\pi\sqrt{\frac{m \cdot w_1}{K_1} \cdot \frac{\sum_{j=1}^{N} \Phi_j^2}{\sum_{j=1}^{N} w_j \cdot \Delta\Phi_j^2}} \Rightarrow K_1 = \frac{4\pi^2}{\left(T_{target}\right)^2}\left(m \cdot w_1 \frac{\sum_{j=1}^{n} \Phi_j^2}{\sum_{j=1}^{n} w_i \cdot \Delta\Phi_j^2}\right) \tag{9a}$$

where K_1 is the stiffness of the first storey, w_1 is the weighting factor value at the first storey, m is the typical storey mass, Φ_j is shape value at the j^{th} storey (N is the total number of storeys) and T_{target} is the target period. Eq. (9a) may be further simplified in case of a triangular response shape with equal storey height to:

$$K_1 = \frac{4\pi^2}{\left(T_{target}\right)^2}\left(m \cdot w_1 \cdot \sum_{j=1}^{N} i\right) \tag{9b}$$

The required stiffness in the *j*-th floor associated with the selected target shape is obtained from:

$$K_j = \frac{w_j}{w_1} K_1 \tag{10}$$

This procedure is repeated in both lateral directions. The additional stiffness required at each storey in both lateral directions as for the lateral response shape to conform to the target shape is distributed along the vertical members of the floor. In the selection of the vertical members to be strengthened attention should be paid as not to modify the center of stiffness.

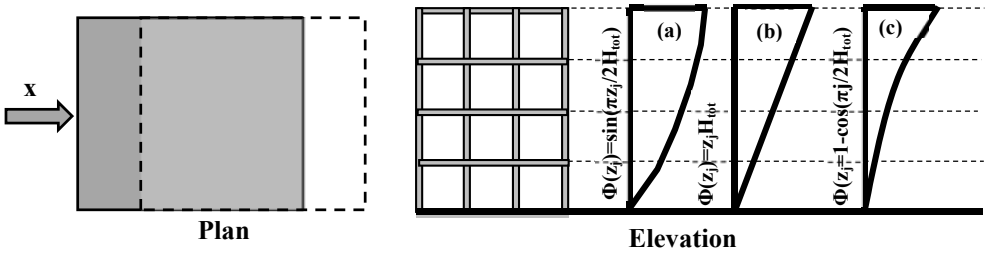


Figure 3: Lateral displacement profiles; (a) shear; (b) triangular; (c) flexural.

3 IMPLEMENTATION OF THE PROPOSED RETROFIT DESIGN METHODOLOGY

3.1 Description of the Existing Building

The building selected as a case study is a 3-storey residential R.C. building constructed in the center of the city of Thessaloniki (North Greece) in the early 1970s according to the provisions of the first Greek Seismic Code [9]. The first storey (ground floor) has a commercial use (windows at the perimeter - open first storey) whereas the other floors are used as apartments. The plan layout of the first storey is differentiated. The first storey height is 4.50 m whereas the height of the other two floors is 3 m. The area of the typical floor is 351.68m^2 and is constant along the height of the building.

The structural system is formed as an orthogonal grid of columns, walls, beams and slabs (Fig. 4). As it is observed there are a few beam to beam connections. Discontinued (cut-off) columns do not exist.

The cross section of the columns is rectangular with varied dimensions along the building's height, generally reducing by 5 cm in each upper floor. The average column in the ground floor is 35cm square and is reduced up to 25cm square in the last floor. Columns longitudinal reinforcement comprises smooth bars of 12 mm ÷ 20 mm diameter and the longitudinal reinforcement over the column section ranged between 6.6‰ ÷ 10.3‰. Column transverse reinforcement comprises stirrups of 6 mm bar diameter spaced at 250 mm anchored with 90° hooks in the ends. The influence of the shear reinforcement is considered negligible, due to the small diameter and the sparse placement of the transverse reinforcement.

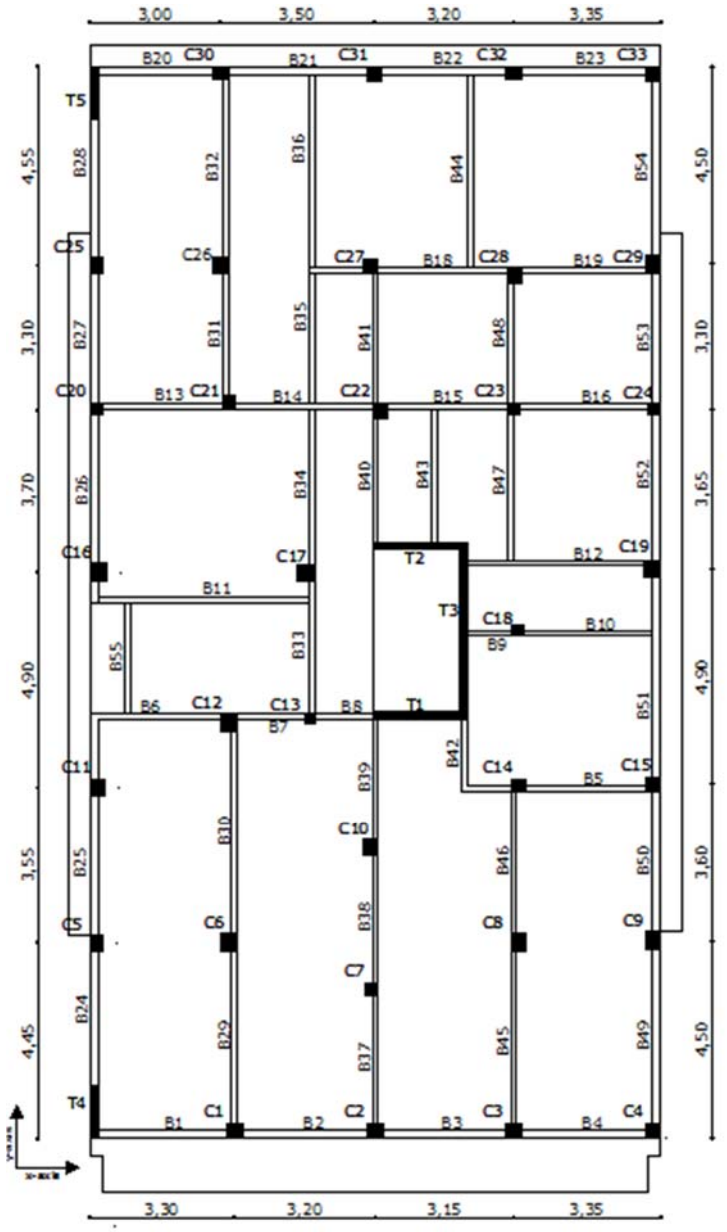


Figure 4: Typical plan layout of the 1st storey.

The geometry and the reinforcement detailing of R.C. walls followed the typical construction practice of that era in Southern Europe. The dimensions of the wall cross section were 1200 mm ÷ 2150 mm long by 150 mm ÷ 250 mm in width. The boundary elements were lightly reinforced by 4∅12 mm longitudinal bars and the web reinforcement comprised of a dual mesh ∅8/250 mm.

The longitudinal reinforcement of the beams comprises smooth bars of varying diameter 10 mm ÷ 20mm and longitudinal reinforcement area ratio tanged between 3.1‰ ÷ 14.7‰ approximately. Note that in a few beams three different bar diameters are placed (e.g. 10 mm, 12 mm and 16 mm). Transverse reinforcement follows the same pattern as in columns. The slab thickness was 0.10 m constant at all floors and considered to offer diaphragmatic action.

The materials considered were B160 concrete quality (which corresponds to f_{ck}=10 MPa) and smooth StI for longitudinal and transverse reinforcement of the structural members (f_{sy}=f_{syw}=250 MPa).

Gravity load was estimated by considering the load combination g+0.3q (dead load and 30% of the live load). Finishing were taken 0.6 kN/m^2 and live load 2 kN/m^2 according to the information found in the folder of the project. The balcony load was applied as uniform load on the external beams providing an additional dead load of 3.40 kN/m and live load of 5.00 kN/m.

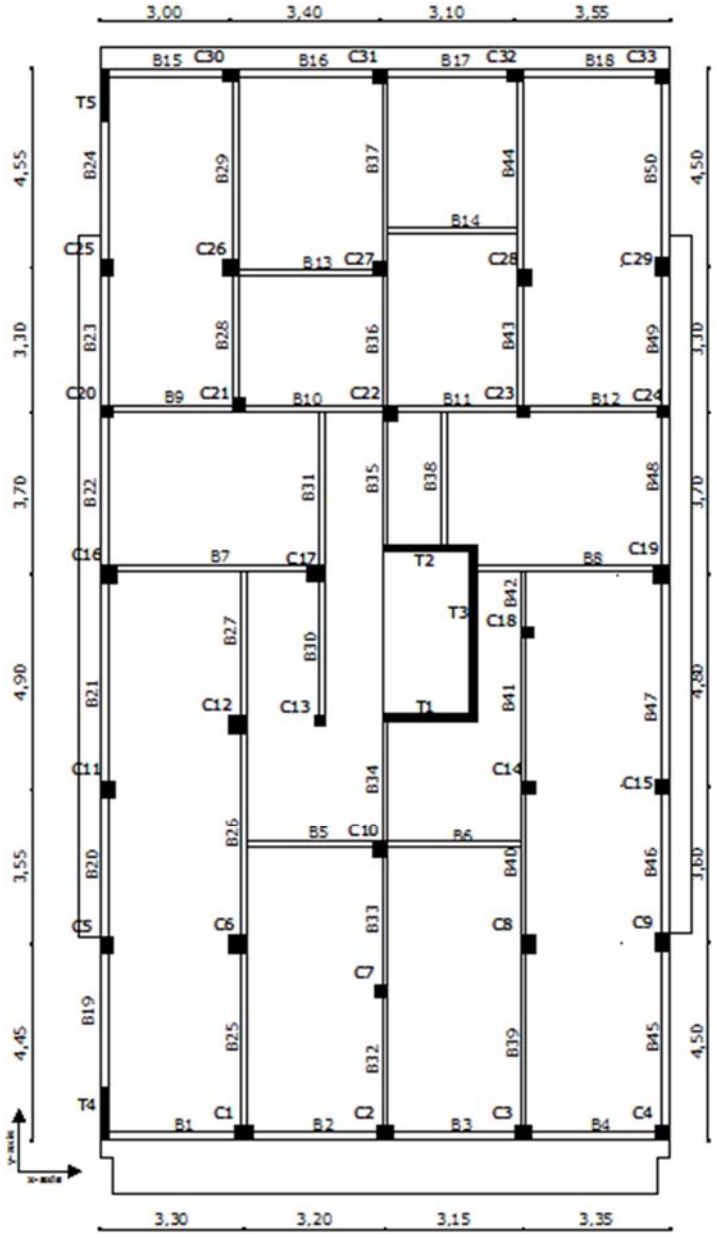


Figure 5: Typical floor plan layout of the 2nd and 3rd storey.

3.2 Assessment of the Existing Building

Before proceeding with the implementation of the proposed retrofit design methodology, a pre-requisite step is the assessment of the existing building. Structural regularity is checked first and then assessment at member level is performed as to define the deformation and strength capacity of all the structural members. Moreover, assessment through detailed analysis was also performed as to verify the results of the hand calculations.

3.2.1 Check of Regularity in Plan and Elevation

The EC8-Part I [10] quantified criteria for assessing structural regularity are implemented. The slenderness, $\lambda(=L_{max}/L_{min})$, of the case study building is 1,90 (λ=1,90<4), thus less than 4,0. The structural eccentricity in both directions x-x and y-y, $e_{o,x}$ and $e_{o,y}$, is smaller than 30% of the torsional radius in both horizontal directions (Table 1). The torsional radius, r_x and r_y, is larger than the radius of gyration in direction x and smaller in direction y. As a result, the building is characterized as being irregular in plan only in the x-x direction.

Table 1: Check of regularity in plan

Direction x-x						**Direction y-y**					
e_{ox}<	0,30 r_x	Check	r_x>	l_s	Check	e_{oy}<	0,30 r_y	Check	r_y>	l_s	Check
1,09<	1,61	√	5,36	7,99	X	0,02	2,53	√	8,43	7,99	√
Conclusion: Irregularity in plan						**Conclusion: Regularity in plan**					

The building evidently fulfills all requirements for regularity in elevation stated in EN 1998-Part I [10]. Specifically, all lateral load resisting systems run without interruption from the foundation to the top of the building. The lateral stiffness and the mass of the individual storeys remain constant from the base to the top of the building.

3.2.2 Assessment at Member Level

The chord rotation at yield and at ultimate, as well as the flexural and shear strength of the existing j^{th} R.C. members (columns, beams, walls) were estimated according to EC8-Part III [11] and the Greek Intervention Code [12]. The following expressions were used:

For beams or rectangular columns:

$$\theta_{y,j} = (1/r)_y \frac{L_S + a_v z}{3} + 0{,}0014\left(1 + 1{,}5\frac{h}{L_S}\right) + \frac{(1/r)_y d_b f_y}{8\sqrt{f_c}} \quad (11a)$$

For walls:

$$\theta_{y,j} = (1/r)_y \frac{L_S + a_v z}{3} + 0{,}0013 + \frac{(1/r)_y d_b f_y}{8\sqrt{f_c}} \quad (11b)$$

For beams or rectangular columns:

$$\theta_{um,j} = 0{,}016(0{,}3^{\nu})\left[\frac{\max(0{,}01;\omega')}{\max(0{,}01;\omega)} f_c\right]^{0.225} (a_s)^{0{,}35} 25^{\left(a\rho_s \frac{f_{sw}}{f_c}\right)} (1{,}25^{100\rho_d}) \quad (11c)$$

, where a_v=1 if the shear force at flexural yielding, M_y/L_s, exceeds the shear at diagonal cracking, or 0 otherwise, z is internal lever arm equal to 0.9d in beams or columns, $0.8l_w$ in walls, d_b: diameter of longitudinal bars, a_w=1 for walls, 0 otherwise; ρ_s: confining reinforcement ratio in the direction of bending; ρ_d is diagonal reinforcement ratio. Material strengths f_y, f_c are in MPa. In members not detailed for earthquake resistance, the right hand of Eq (11c) is reduced by 20%. For every vertical member the flexural strength, V_y, was estimated by considering EC8-III [11] and KANEPE [12] expressions according to which flexural capacities are converted into associated shear forces, $V_y=M_y/Ls$. This may be done assuming attainment of flexural capacity at both ends for the columns (shear span L_s equal to half the clear storey height), or a shear span L_s of walls equal to 2/3 of the total height of the building. The yield moment, M_y, may be computed according to Eq (12).

$$\frac{M_{y,j}}{bd^3} = (1/r)_{y,j} \begin{Bmatrix} E_C \frac{\xi_{y,j}{}^2}{2}\left(0.5(1+\delta') - \frac{\xi_{y,j}}{3}\right) + \left[(1-\xi_{y,j})\rho + (\xi_{y,j}-\delta')\rho' + \frac{\rho_v}{6}(1-\delta')\right] \\ (1-\delta'\frac{E_S}{2} \end{Bmatrix} \quad (12)$$

According to KANEPE [12] the secand-to-yield at each end of a concrete member, EI_{eff}, may be computed from the yield moment, M_y, and the chord rotation at yielding at the end, θ_y, as:

$$EI_{eff,j} = M_{y,j}L_s/3\theta_{y,j} \quad (13)$$

In this study, it is assumed that the columns of the storey are fixed in both ends whereas walls are fixed only at the base. Thus, the shear span for the columns is equal to half the clear storey height whereas for the walls it was taken equal to 2/3 of the total height of the building (i.e. they are considered to behave as cantilevers with a height equal to $2/3H_{tot}$). Thus, the stiffness, K_j, of the i^{th} vertical member is:

For columns: $$K_j = M_{y,j}/\left(2 \cdot \theta_{y,j} \cdot {L_S}^2\right) \quad (14a)$$

For walls: $$K_j = M_{y,j}/\left(\theta_{y,j} \cdot {L_S}^2\right) \quad (14b)$$

From the above, the stiffness at member level is estimated. The total stiffness of each floor is obtained by direct summation of the stiffness of the individual vertical members of each floor (they are considered to function as a sequence of springs in parallel) and presented in Tables 2:

Table 2: Stiffness of the building for each storey and at each direction

Stiffness, K_j (kN/m)		
Storey	direction x	direction y
1st	87077,12	96447,9
2nd	165381,76	181295,15
3rd	127008,98	137747,31

The shear resistance of beams, columns and walls, $V_{R,i}$, with rectangular web (with units: MN and meters) was calculated according to:

$$V_{R,i} = \frac{h-x}{2L_S}\min\left(N; 0{,}55A_{c,i}f_c\right) + \left(1 - 0{,}05\min\left(5, \mu_{\theta,i}^{pl}\right)\right)\left[0{,}16\max\left(0{,}5; 100\rho_{tot,i}\right)(1 - 0{,}16\min(5; a_s))\sqrt{f_c}A_{c,i} + V_{w,i}\right] \quad (15)$$

The shear strength of a concrete wall, $V_{R,i}$, may not be taken greater than the value corresponding to failure by web crushing, $V_{R,max,i}$, which under cyclic loading may be calculated from the following expression (with units: MN and meters):

$$V_{R,max,i} = 0{,}85\left(1 - 0{,}06\min\left(5; \mu_{\theta,i}^{pl}\right)\right)\left(1 + 1{,}8\min\left(0{,}15; \frac{N_i}{A_{c,i}f_c}\right)\right)\left(1 + 0{,}25\max\left(1{,}75; 100\rho_{tot,i}\right)\right)(1 - 0{,}2\min(2; a_s))\sqrt{f_c}b_{w,i}z_i \quad (16)$$

where $\mu_{\theta,i}^{pl}$ is the ratio the plastic part of the chord rotation, θ, normalized to the chord rotation at yielding, θ_y. In the calculations, $\mu_{\theta,i}^{pl}$ was assumed equal to 0. The results of the shear strength assessment of the columns and the walls are presented in Table 3. As it is shown in case of columns premature failure in shear is expected to occur in all the floors. This corresponds to the case that index v ($=V_{shear,c}/V_y$) < 1 (Table 3). This implies that the columns will fail well before reaching yielding and thus the chord rotation at yielding will not be reached. Instead the columns at the time of failure will have a chord rotation significantly reduced (almost half) of the chord rotation at yielding (Table 3). The value of 0.25% can be considered representative for all the floors. Referring to the walls no premature failure is anticipated.

Table 3: Average values of chord rotation at yielding and ultimate and shear resistance of the vertical members

Floor		$\theta_{y,col}^{flex*}$ (%)	$\theta_{u,col}^{flex*}$ (%)	$V_{shear,c}$ (kN)	V_y (kN)	$v=V_{shear,c}/V_y$	Failure	$\theta_{fail}^{*}= v\cdot\theta_{y,col}^{flex}$ (%)
1st	Columns (C1-C33)	0,44	0,61	22,26	38,21	0.58	Shear	0.26
2nd		0,41	0,56	29,75	46,19	0.64	Shear	0.26
3rd		0,41	0,55	21,00	34,79	0.60	Shear	0.25
		$\theta_{y,wall}$ (%)	$\theta_{u,wall}$ (%)	$V_{shear,w}$ (kN)	V_y (kN)	$v=V_{shear,c}/V_y$	Failure	$\theta_{fail}^{*}= v\cdot\theta_{y,col}^{flex}$ (%)
Walls	direction x-x (T1-T2)	0,34	3,19	691,20	127,59	5.42	Flexure	-
	direction y-y (T3-T5)	0,43	3,45	691,20	127,59	5.42	Flexure	-

* The same value applies in both directions x-x, y-y due to the square cross section

3.2.3 Assessment through Detailed Analysis

The finite element analysis program SeismoStruct v6.5 is utilized to perform necessary analysis for the assessment of existing building such as nonlinear static pushover analysis, eigenvalue analysis and incremental dynamic analysis. Both vertical and horizontal elements are modeled with inelastic elements capable of representing progressive cracking and spread of inelasticity. Beam-column joints are assumed rigid and fully-fixed boundary conditions are adopted at the base of the building (Fig. 6).



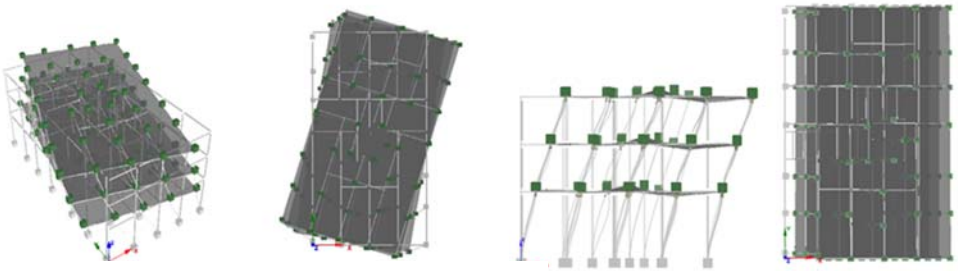
Figure 6: 3D modeling of the existing R.C. building

3.2.3.1. Eigenvalue Analysis

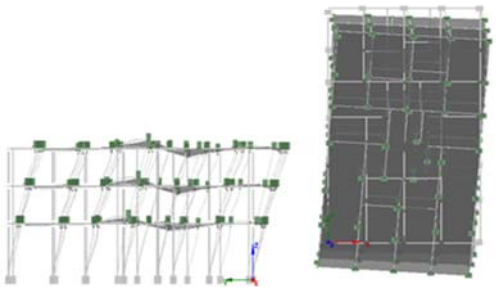
Eigenvalue analysis was performed for determining the periods and mode shapes as presented in Table 4 and Fig. 7. The torsional sensitivity of the building due to the irregularity in plan in x-x direction is verified by the eigenvalue analysis.

Table 4: Elastic periods and modal participation mass ratios of the existing building

Mode shape No.	Period (s)	Modal participation mass ratio		
		Ux	Uy	Rz
1	0,683	0,22%	4,55%	90,43%
2	0,634	84,15%	0,07%	0,13%
3	0,373	0,04%	80,92%	4,53%



(a) 1st mode: T_1=0.68s MPMR=90.43% (b) 2nd mode: T_2=0.63s MPMR=84.15%



(c) 3rd mode T_3=0.37s MPMR=80.92%

Figure 7: Deformed shape, periods and modal participating mass ratio (MPMR) of the existing building: (a) 1st mode; (b) 2nd mode; (c) 3rd mode

3.2.3.2 Pushover Analysis

In case of torsionally sensitive buildings static pushover analysis exhibits shortcomings and limitations that confine its range of application and raise doubts of its effectiveness to accurately estimate structural seismic demand, as demonstrated by a number of researchers [e.g. [13], [14]). However, according to the Greek Code for interventions [11], pushover analysis is permitted to be implemented even in torsionally unbalanced buildings, only when accompanied by a non-linear dynamic analysis for validation reasons. Thus, incremental dynamic analyses are performed for various ground motions in order to assess the level of validity of the pushover analyses results. Incremental dynamic analyses (IDA) are performed only for the direction where the structure is torsionally unbalanced (direction y-y). Eurocode 8-III [11] requires the use of a spatial model in case of building not conforming with the criteria for regularity in plan.

The building was subjected to pushover analyses separately in the two orthogonal directions x-x and y-y. Two different lateral force profiles were adopted, the modal and the uniform shape. From the pushover analyses conducted, it was shown that uniform distribution led always to more unfavorable results as expected. For this purpose, the results from the uniform load profile are presented. The base shear – roof displacement curve of the structure in the x-x and y-y direction is depicted in Fig. 8(a) and 8(b), respectively. The horizontal dashed line indicates the base shear force level at which shear failure is anticipated according to the assessment conducted at member level (Table 2). Hence, from the assessment failure is expected prior to global yielding.

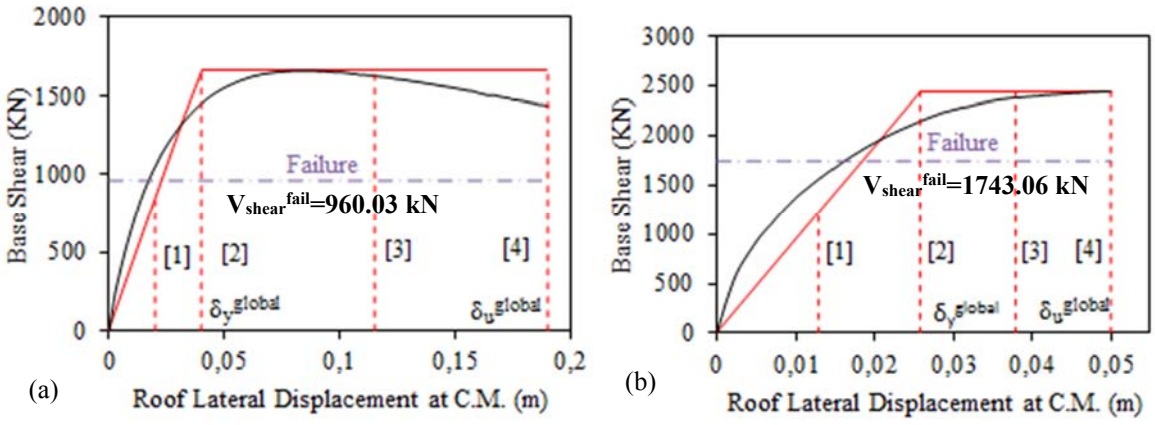


Figure 8: Pushover curves of the existing R.C. building along (a) x-x axis and (b) y-y axis

After bi-linearization of the pushover curve yielding, δ_y^{global}, and ultimate, δ_u^{global}, at global level are defined as shown in Fig. 8. The interstorey drift profile was estimated for four different deformation stages depicted as [1], [2], [3] and [4] (Fig. 8). Stage [2] and Stage [4] correspond to global yielding and ultimate, respectively, whereas Stage [1] corresponds to half the global yielding and Stage [3] to ($\delta_y^{global}+1/2\delta_{pl}^{global}$). Failure is expected when the interstorey drift level reaches a value equal to 0.25% (Fig. 9, see also Table 2). Damage is localized in the columns

of the ground floor. For instance, in direction x-x 85% of the columns in 1st storey fails due to the lack of shear resistance, the same happens in the 2nd and 3rd storey with 48% and 55% of the columns to fail. Consequently, localization of damage in the first storey leads to soft storey mechanism and brittle failure mode.

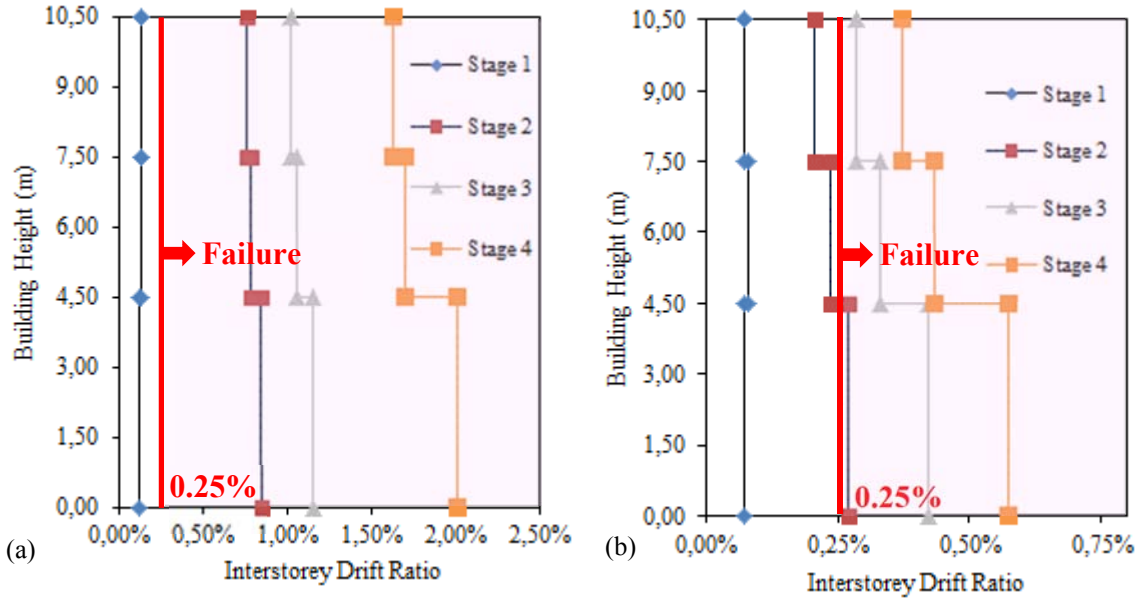


Figure 9: Interstorey drift ratio (a) along x-x axis (b) y-y axis

3.2.4.3 Response to Earthquake Excitation

Incremental dynamic analyses were performed for three different ground motions (El Centro 1940, Northridge 1994 and Loma Prieta 1989). The duration of the records is 40 seconds and the peak ground acceleration is 0.31g, 0.60g and 0.50g, for the El Centro 1940, Northridge 1994 and Loma Prieta 1989 ground motion, respectively. IDA involved performing a series of non-linear dynamic analyses for each record by scaling it to multiple levels of intensity. Five scaling factors (0.1, 0.4, 0.7 and 1.0) are selected in order to represent the seismic intensity at each time of history analysis. The comparison between static pushover curves and IDA curves is depicted in Fig. 10 and it is shown that the behavior of structure along direction y –y under static push-over analysis is similar to the behavior under dynamic analysis. The maximum base shear for the selected ground motion El Centro is 1733.0 kN, Loma Prieta is 2583.0 kN and for the Northridge is 2500.0 kN. The comparison between the pushover and the IDA curves verifies that static pushover analyses can be used for assessment.

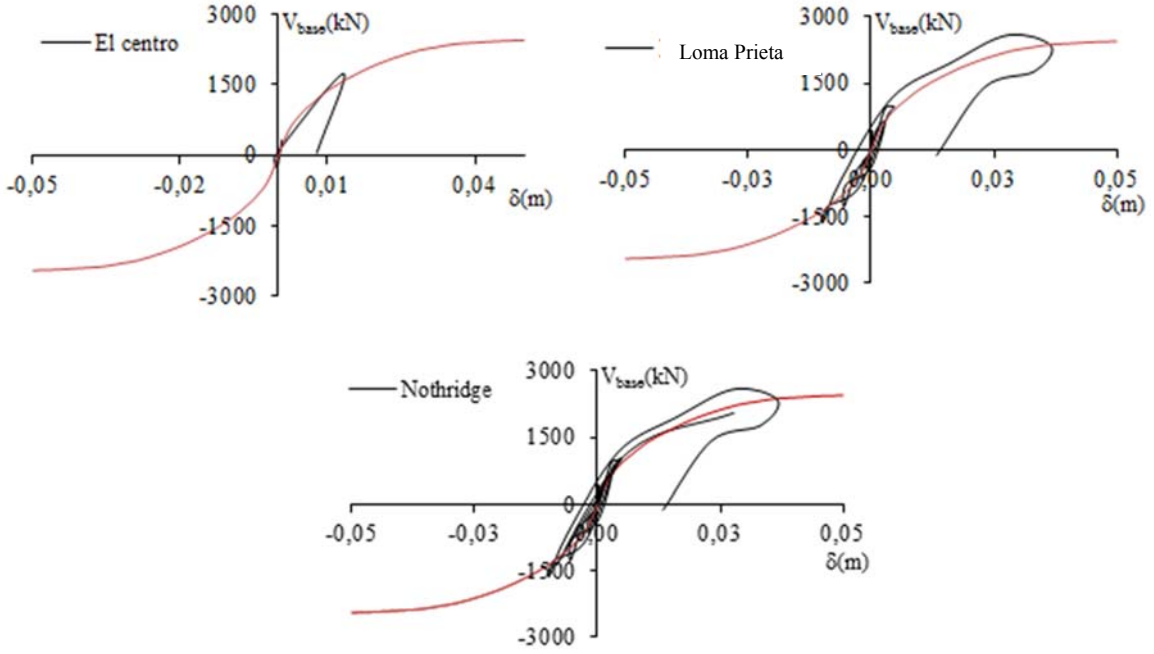


Figure 10: Comparison between static pushover and IDA analysis

3.3 Design of the Retrofit Solution

3.3.1 Elimination of the Torsional Sensitivity

The building according to the regularity in plan check is rotationally sensitive (Table 1). The first phase of the proposed retrofit design methodology involves addition of stiffness in a strategic way at the periphery of the building as to minimize structural eccentricities and increase torsional resistance. Intervention methods that may serve this scope are R.C. jacketing and the addition of R.C. walls. Table 5 indicates the required additional floor stiffness in the x-x and y-y direction for the elimination of the effect of torsional coupling on modal periods and shapes. The most efficient solution is depicted in Fig. 11. Four infill R.C. walls are added at the perimeter of the first storey, two in each direction (T9 and T10 in x-x direction, and T6 and T7 in y-y direction) and one column is jacketed C19 (Fig. 11(a)). The added R.C. walls continue to the second and third floor (Fig. 11(b)). Tables 6 and 7 present reinforcement details of the additional concrete walls and the jacketed members. The material properties of the new added members are concrete compressive strength f_{ck}=30 MPa, and nominal yield strength f_{syk}=500 MPa.

Table 5: Required stiffness for elimination of plan eccentricity

Required stiffness for (e_x=0 και e_y=0)			
	1st Floor	2nd Floor	3rd Floor
direction x-x, K_x (kN/m)	113164,88	108337,22	101868,10
direction y-y, K_y (kN/m)	120650,11	115822,20	109353,08

Table 6: Reinforcement details of the added R.C. walls

R.C. Walls									
	b_x (m)	b_y (m)	Long. Reinforcement (mm)	Stirrups (mm)	h_{fi} (m)	ρ_{itot} (%)	A_{fi} (mm)	K_x (kN/m)	K_y (kN/m)
T6	0,20	3,20	#Ø10/250	Ø10/150	0,35	1,02%	4Ø22	0	66320,0
T7	0,20	3,20	#Ø10/250	Ø10/250	0,35	0,64%	4Ø20	0	43033,1
T9	2,80	0,20	#Ø10/250	Ø10/200	0,35	0,74%	4Ø20	35577,5	0
T10	2,80	0,20	#Ø10/250	Ø10/250	0,35	0,68%	4Ø22	32053,6	0

Table 7: Reinforcement details of the R.C. jacketed members

R.C. Jacketed Columns								
		b_x (m)	b_y (m)	Long. Reinforcement (mm)	Stirrups (mm)	ρ_{itot} (%)	ΔKx (kN/m)	ΔKy (kN/m)
1st		0,55	0,55	8Ø22	Ø16/100	1,01%	4407,0	4407,0
2nd	C19	R.C. jacketing of column C19 in the first floor						
3rd								

3.3.2 Strengthening for a Target Interstorey Drift

Once the torsional effects of the building have been eliminated in the first phase of the methodology, the second phase deals with system-level deficiencies associated with irregular distribution of stiffness along the height of the building. The method assumes that the building responds in a single mode in each direction since twisting rotation along the vertical axis is insignificant. The retrofit scenario adopted aims to reduce the period of the existing building to a period that can range between $0,05H_{tot}^{3/4}=0,05\cdot10,5^{\wedge(3/4)}=0,29s\leq T_{target}<T_{existing}=0,66s$ (average value of the period of the first and the second modes: 1/2(0,68+0,63)=0,66s, see Fig. 7). The target period was selected to be equal to half the period of the existing building $T_{target}=0,33s$. Ductility was assumed equal to 2 which is considered a realistic scenario for a substandard building. The triangular response shape which corresponds to equal distribution of damage along the height of the building was utilized ($\Phi^T=[0,43\ ,\ 0,71,\ 1,00]^T$). The target stiffness of each floor is determined through the use of the weighting factors following the procedure described in Section 2, §2.2.

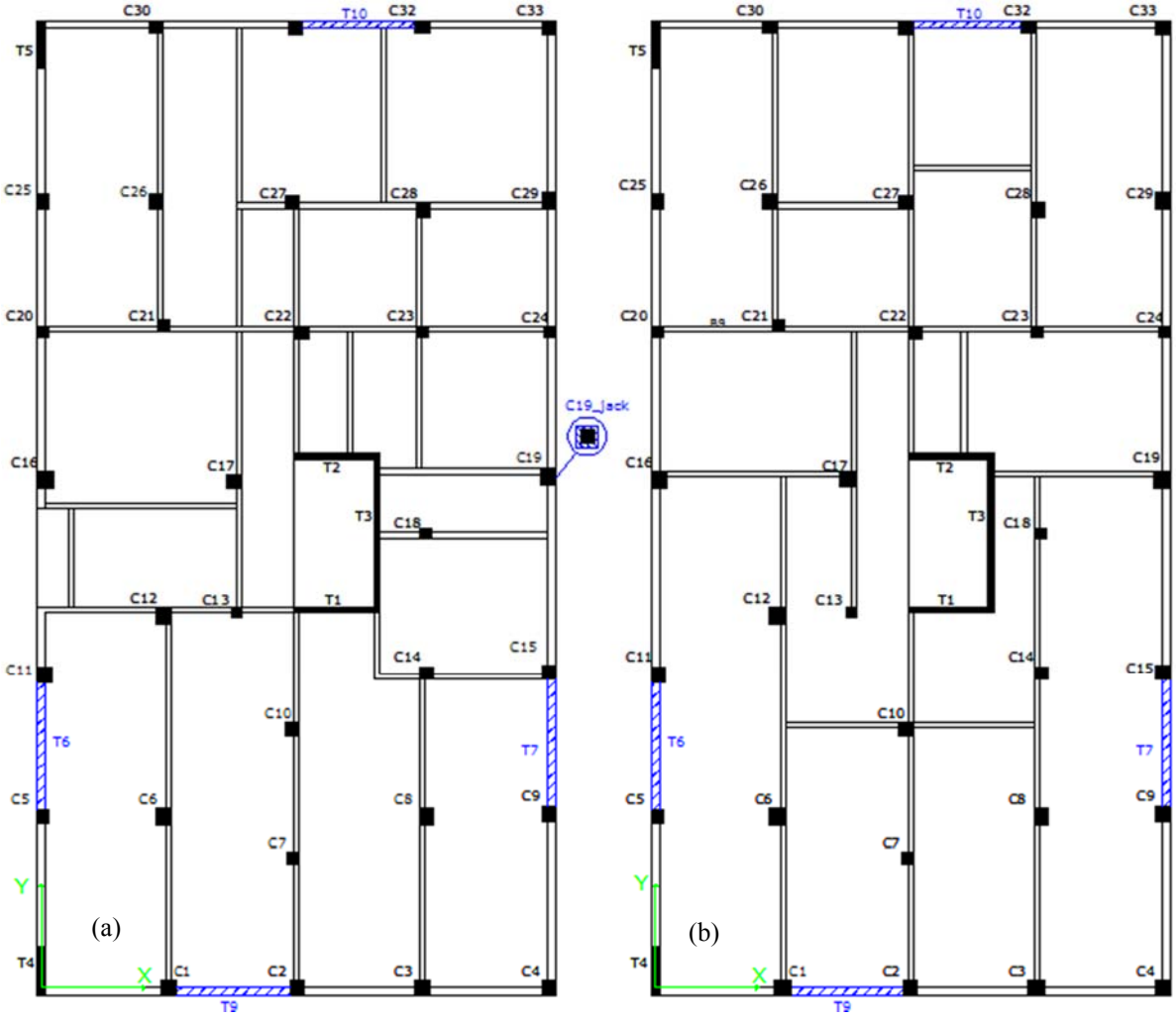


Figure 11: Addition of R.C. walls and R.C. jacketing for the elimination of torsional sensitivity (a) floor plan of first storey (b) floor plan of second and third floor

The MDOF system with storey mass m=136,25t is transformed to ESDOF system with the following characteristics:

$$M^* = \sum_{j=1}^{N} m_j \cdot \phi_j^2 = 230,79t \; ; \; L^* = \sum_{j=1}^{N} m_j \cdot \phi_j = 291,96t \; ; \quad \Gamma = \frac{L^*}{M^*} = 1,27 \tag{17}$$

The Yield Point Spectra (YPS) of Fig. 12 were extracted from the 5% damped elastic spectrum of EC8 (2004) using the equal displacement rule (q=μ) for peak ground acceleration a_g=0.36g, soil class B, S=1.2, with corner point periods defining the various spectrum regions equal to T_B=0.15 s, T_C=0.40s and T_D=2.00s. Given the target period T_{target}=0.33s, the target displacement at yield of the ESDOF, $\delta^*_{y,\,target}$, is estimated through the YPS depicted in Fig. 12 is 14.61mm. Thus, the target drift of the MDOF system is:

$$\theta_{y,target} = \frac{\delta_{y,target}}{H_{tot}} = \frac{\delta^*_{y,target} \cdot \Gamma}{H_{tot}} = \frac{18,55}{10500} = 0.18\% \tag{18}$$

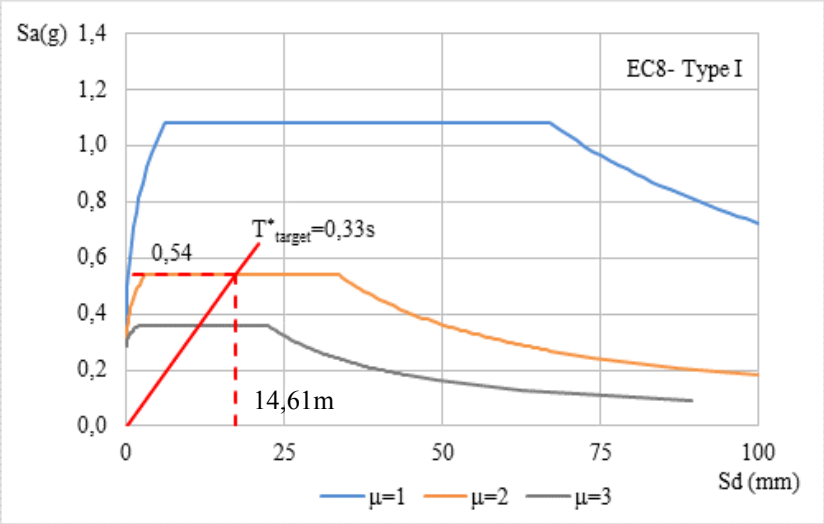


Figure 1: Calculation of the target period of the ESDOF system through ADRS

Table 8: Required stiffness for the correction of the response shape in x-x and y-y direction

Stiffness in x-x direction, K_x (kN)					
Storey	Existing building	Torsionally balanced building (Phase I)	Required Stiffness for target shape (Phase II)	Added stiffness (Design of R.C. jackets)	Stiffness at the end of the retrofit design
1st	87077,1	193352,2	246966,7	49170,8	242523,0
2nd	165381,7	267249,8	296360,0	0,0	267249,8
3rd	127008,9	228877,0	172876,7	0,0	228877,1
Stiffness in y-y direction, K_y (kN)					
Storey	Existing building	Torsionally balanced building (Phase I)	Required Stiffness for target shape (Phase II)	Added stiffness (Design of R.C. jackets)	Stiffness at the end of the retrofit design
1st	96447,9	210207,9	246966,7	43432,2	253660,1
2nd	181295,1	290648,2	296360,0	0,0	290648,2
3rd	137747,3	247100,3	172876,7	0,0	247100,3

The target stiffness of the ESDOF system (K^*) is defined from:

$$K^* = 4 \cdot \pi^2 \frac{M^*}{T_{target}^2} = 83666,26 kN/m \quad (19)$$

The stiffness distribution along the height of the building is estimated according to Eqs. (9), (10):

$$K_1 = 246967 kN/m \; ; \; K_2 = \frac{w_2}{w_1} \cdot K_1 = 296360 kN/m \; ; \; K_3 = \frac{w_3}{w_1} \cdot K_1 = 172877 kN/m$$

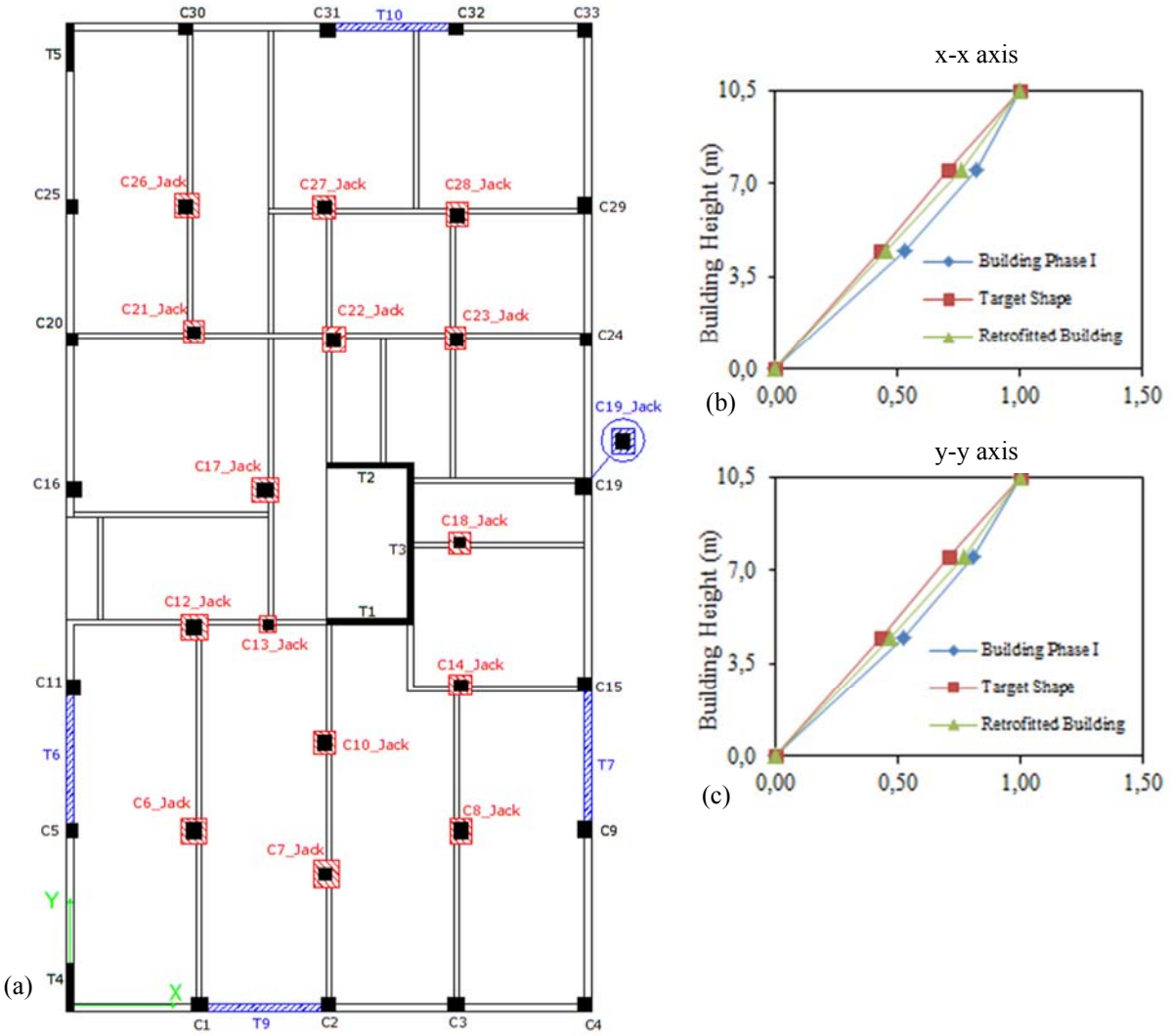


Figure 13: (a) Retrofit solution according to the proposed methodology; Phase I: Elimination of torsional effects through the addition of the blue colored members at the perimeter of the building; Phase II: Strengthening for a target response shape through strengthening of the red colored vertical members. Response Shape of the retrofitted structure according to Rayleigh Method (b) along x-x axis (c) y-y axis.

Table 8 presents information related to the stiffness of the building at each design phase. The required stiffness distribution along the height of the building for the target response shape is also presented. It is observed that only in the first and second floor stiffness addition is required, whereas in the third floor the stiffness of the existing building after design phase I is already higher than the required stiffness for the target response shape. The latter implies that even in the case that the stiffness in the first and second storey are increased as to comply with the stiffness corresponding to the target response, the resulting lateral response shape would slightly deviate from the target one. It was decided to modify only the stiffness of the first storey by the addition of R.C. jackets (i.e. longitudinal bars pass through holes drilled in the slab and anchored in the second storey) due to the cost effectiveness of this solution. The columns to be jacketed at the end of the design phase II are depicted by red colour in Fig. 13(a). The selection of this specific group of columns and the distribution of the target added stiffness along them

did not affect the center of stiffness as defined in design phase I. Details regarding dimensioning of the R.C. jacketed members appear in Table 9. The proposed retrofit solution may lead to a lateral response shape very close to the target one as seen in Fig. 13(b), (c) after applying the Rayleigh iterative method.

Table 9: Reinforcement details of R.C. jacketed members

R.C. Jacketed Columns									
	b_x (m)	b_y (m)	Long. Reinforcement (mm)	Stirrups (mm)	ρ_{itot} (%)	K_x (kN/m)	K_y (kN/m)	ΔK_x (kN/m)	ΔK_y (kN/m)
C21	0,45	0,40	8Ø20	Ø14/100	1,40%	4377,2	3555,5	3076,3	2254,7
C22	0,50	0,45	8Ø22	Ø14/100	1,35%	6347,5	5285,1	4012,4	2950,0
C23	0,45	0,45	8Ø22	Ø14/100	1,50%	5043,7	5043,7	3847,1	3847,1
C18	0,45	0,40	8Ø22	Ø14/100	1,53%	4785,8	3882,7	3692,5	3146,0
C14	0,50	0,50	8Ø22	Ø14/100	1,22%	6322,8	6322,8	4307,1	4858,6
C10	0,50	0,45	8Ø18	Ø14/100	0,90%	4886,7	4076,6	2721,9	1911,8
C12	0,55	0,48	8Ø22	Ø14/100	1,16%	8358,5	6508,9	4253,8	2404,2
C17	0,50	0,45	8Ø16	Ø14/100	0,71%	4321,1	3608,0	985,7	1050,0
C13	0,35	0,35	8Ø22	Ø14/100	1,95%	2847,5	2847,5	2376,1	2376,1
C6	0,55	0,50	8Ø22	Ø16/100	1,11%	8436,6	7177,3	4312,2	3052,9
C7	0,45	0,45	8Ø18	Ø14/100	1,01%	3846,5	3846,5	2653,0	2653,0
C8	0,50	0,50	8Ø22	Ø14/100	1,22%	6510,5	6510,5	3941,9	3162,4
C26	0,45	0,45	8Ø22	Ø14/100	1,50%	5172,4	5172,4	2880,5	2880,5
C27	0,45	0,45	8Ø22	Ø14/100	1,50%	6003,1	6003,1	3155,3	3929,9
C28	0,50	0,50	8Ø18	Ø14/100	0,81%	5655,0	5655,0	2955,0	2955,0

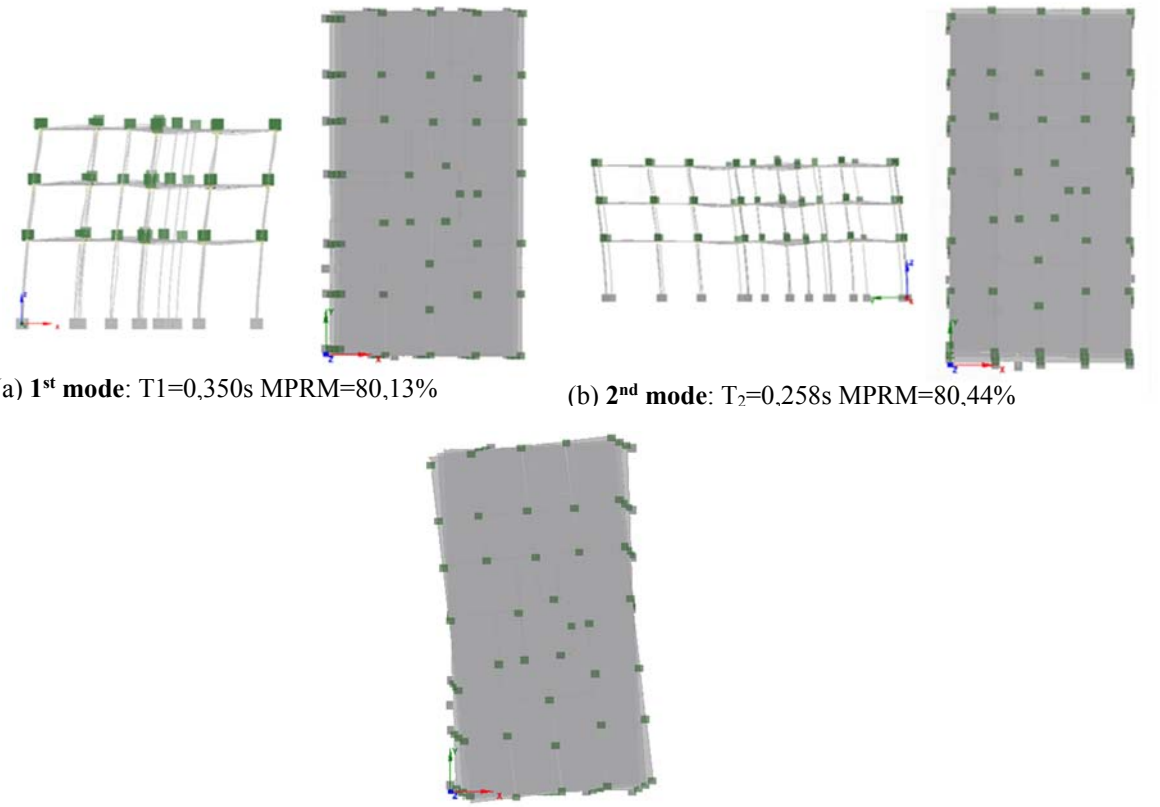
3.4 Assessment of the retrofitted structure

3.4.1 Eigenvalue Analysis

Eigenvalue analysis was performed to the retrofitted structure as to verify the results conducted by hand calculations. The modal response parameters are presented in Table 10, whereas the first three modes are shown in Fig. 14. It is observed that first and second mode are translational with mass participation over 80%. Moreover, the fundamental period (0.35s) is close to the target one (0.33s).

Table 3: Modal response parameters of the retrofitted building

No.	Period (s)	Modal participation mass ratio		
		Ux	Uy	Rz
1	0,350	80,13%	0,00%	0,09%
2	0,258	0,01%	80,44%	0,13%
3	0,235	0,12%	0,14%	79,37%



(a) **1st mode**: T1=0,350s MPRM=80,13%

(b) **2nd mode**: T_2=0,258s MPRM=80,44%

(c) **3rd mode**: T_3=0,235s MPRM=79,37%

Figure 2: Deformed shape, periods and modal participating mass ratio (MPMR) of the retrofitted building: (a) 1st mode; (b) 2nd mode; (c) 3rd mode

3.4.2 Pushover Analysis

Nonlinear static analyses were carried out for the modal and the uniform pattern. The response curve after application of the uniform distribution along the height of the building of the applied lateral load is presented in Fig. 15 along with the response curve of the existing building for the same pattern in the x-x and y-y directions (The blue dot placed on the curve of the existing building corresponds to the point of failure). As it is observed the retrofitted building has increased substantially its strength.

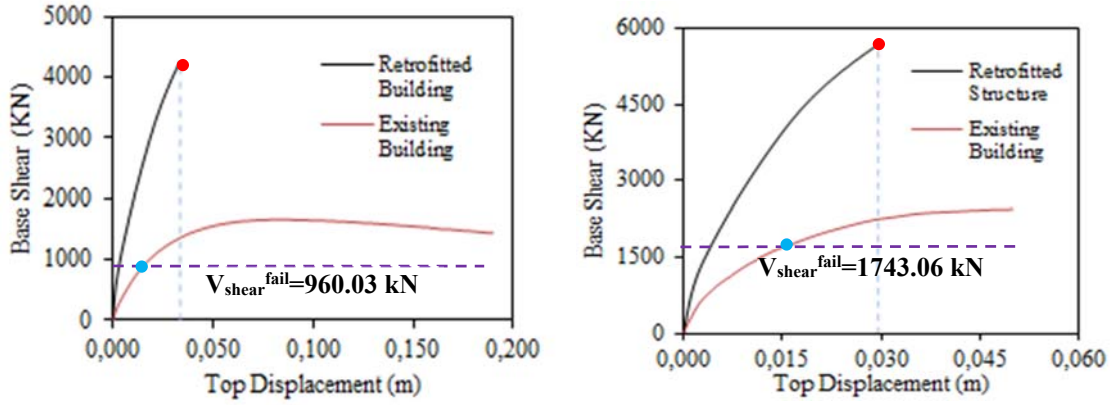


Figure 15: Pushover curves for the existing and the retrofitted building along (a) x-x and (b) y-y axis

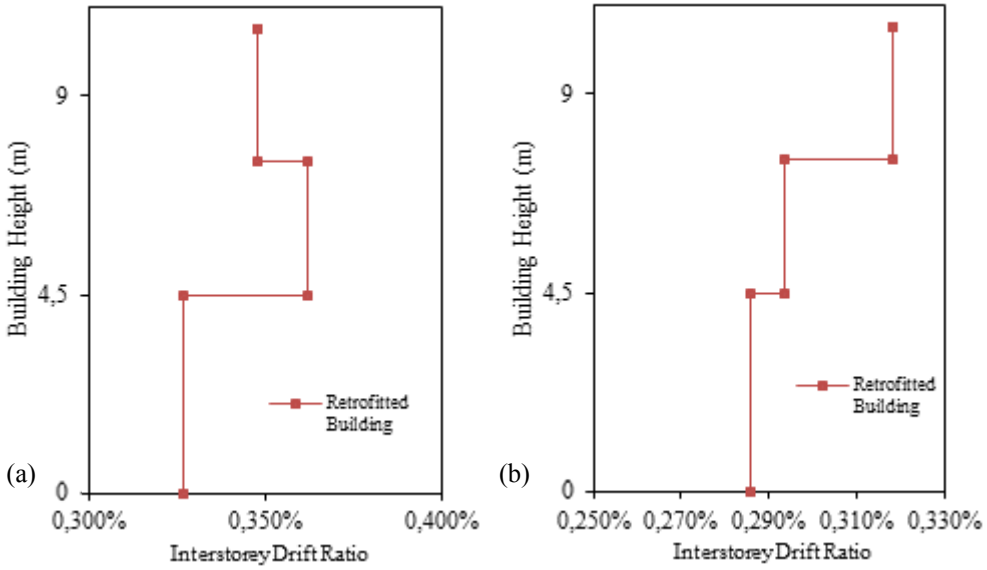


Figure 16: Interstorey drift ratio of the retrofitted and the existing building along (a) x-x and (b) y-y axis

The interstorey drift profiles that correspond to the maximum top displacement of the retrofitted building (red dot in Fig. 15) in x-x and y-y axis are presented in Fig. 16. Moreover, the lateral response shape at the maximum roof displacement is compared to the triangular response shape in Fig. 17.

The proposed retrofit solution manages to keep almost a uniform distribution of interstorey drift along the building height even in the post-yield region. Deviations from the target response shape are justified and expected in the sense that one has to deal with existing buildings which after elimination of torsional sensitivity (design phase I) have a pre-defined distribution of stiffness along the height of the building that may impose limitations when compared to the desirable distribution of stiffness along the height of the building as to comply with the target response shape.

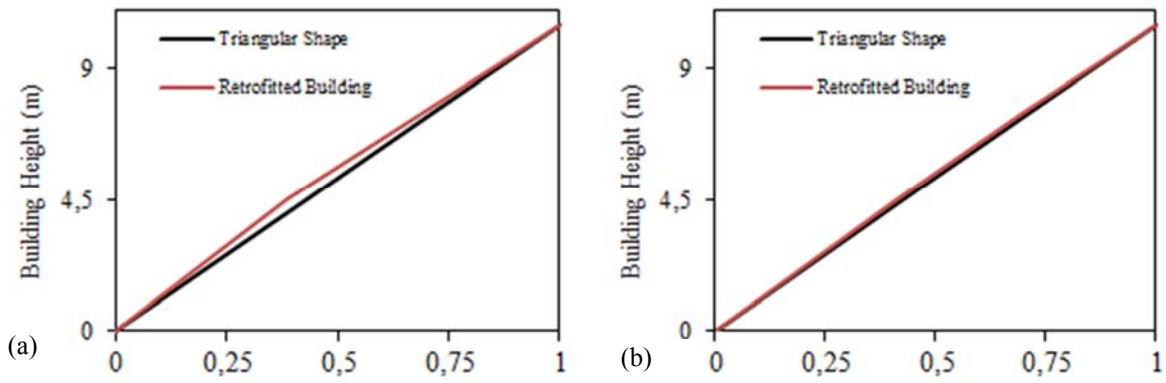


Figure 17: Comparison of the target response shape and the lateral response shape of the retrofitted building along (a) x-x (b) y-y axis

4 CONCLUSIONS

A retrofit design methodology for the seismic upgrading of rotationally sensitive existing R.C. buildings was presented. The proposed methodology aims to modify substantially the response by minimizing structural eccentricities and simultaneously increasing torsional resistance and stiffness. For this purpose, stiffness is added through the adoption of global intervention methods at the periphery of the building so as to provide a building symmetric in plan and torsionally balanced. The lateral response shape in the two orthogonal axes (x-x and y-y) is further modified as to comply with the target response shape. This is achieved by a weighted distribution of additional stiffness along the height of the building. The proposed methodology was implemented to a three-storey building constructed in the early 1970s in North Greece. The validity of the proposed methodology was assessed by carrying out inelastic analyses with the use of a three-dimensional finite element model of the retrofitted structure. The results indicate the efficiency of the proposed design methodology for the seismic upgrading of existing torsionally unbalanced R.C. buildings.

REFERENCES

[1] G.E Thermou, A.S. Elnashai, Seismic retrofit schemes for R.C. structures and local-global consequences. *Journal of Progress in Structural Engineering and Materials*, Wiley InterScience, **8(1)**, 1-15, 2006.

[2] G.E. Thermou, S.J. Pantazopoulou, A.S. Elnashai, Design methodology for seismic upgrading of substandard R.C. structures. Journal of Earthquake Engineering, **4(1)**, 582-606, 2007.

[3] S.J. Pardalopoulos, S. J. Pantazopoulou, Spatial component analysis of 3-D Displacement and Storey Drift in R.C. Buildings Under Seismic Loads. Computational Methods in Earthquake Engineering, (Ed.: M. Papadrakakis et al.), 123-145, 2010. Series: Computational Methods in Applied Sciences 21, DOI 10.1007/978-94-007-0053-6_6, Springer Publishers.

[4] G.E. Thermou, S.J. Pantazopoulou, A.S. Elnashai, Upgrading of R.C. structures for a target response shape. *Thirteenth World Conference on Earthquake Engineering*, Vancouver, Canada, Paper No 1412, 2004.

[5] G.E. Thermou, S.J. Pantazopoulou, A.S. Elnashai, Design methodology for seismic upgrading of existing R.C. structures. *fib Symposium* "Keep Concrete Attractive", Budapest, Hungary, Paper No 302, 2005.

[6] G.E. Thermou, A.S. Elnashai, S.J. Pantazopoulou, Retrofit Yield Spectra–a practical device in seismic rehabilitation. *Earthquake and Structures*, **3(2)**, 141-168, 2012.

[7] G.E. Thermou, S.J. Pantazopoulou, A.S. Elnashai, Global interventions for seismic upgrading of substandard R.C. buildings. *Journal of Structural Engineering*, ASCE, **138(3)**, 387-401, 2012.

[8] M.A. Aschheim, E.F. Black, Yield Point Spectra for seismic design and rehabilitation. *Earthquake Spectra*, EERI, **16(2)**, 317-336, 2000.

[9] Royal Decree, Seismic design of reinforced concrete buildings. Royal Decree (19/26.02.1959), Ministry of Public Works, Greece (in Greek), 1959.

[10] Eurocode 8, Design of structures for earthquake resistance - Part I: General rules, seismic actions and rules for buildings. EN1998-1-2004:E, European Committee for Standardization (CEN), Brussels, 2004.

[11] Eurocode 8, Design of structures for earthquake resistance. Part III: Assessment and retrofitting of buildings. EN 1998-3:2005(E), European Committee for Standardization (CEN), Brussels, 2005.

[12] Greek Code for Interventions (KANEPE). *Earthquake Planning and Protection Organization*, Athens, 2013.

[13] H. Krawinkler, G.D.P.K. Seneviratna, Pros and cons of a pushover analysis of seismic performance evaluation. *Engineering Structures*, **20(4-6)**, 452-464, 1998.

[14] S. Kim, E. D'Amore, Push-over analysis procedure in earthquake engineering. *Earthquake Spectra*, **15(3)**, 417-434, 1999.

COMPDYN 2015
5th ECCOMAS Thematic Conference on
Computational Methods in Structural Dynamics and Earthquake Engineering
M. Papadrakakis, V. Papadopoulos, V. Plevris (eds.)
Crete Island, Greece, 25–27 May 2015

A COMPUTATIONAL INVESTIGATION FOR THE SEISMIC RESPONSE OF RC STRUCTURES STRENGTHENED BY CABLE ELEMENTS

Angelos A. Liolios

Democritus University of Thrace, Department of Civil Engineering,
Division of Structural Engineering, Xanthi, GREECE
e-mail: aliolios@civil.duth.gr

Keywords: Seismic Upgrading and Strengthening of RC Structures, Cable-braced Systems, Damage Indices.

Abstract. *A numerical investigation is presented for the seismic analysis of existing reinforced concrete (RC) structures, which have been damaged due to extreme actions and are seismically upgraded by cable elements (tension-ties). A double discretization, in space by the Finite Element Method and in time by a direct incremental approach, is used. The unilateral behavior of the cable-elements, which can undertake tension stresses only, is strictly taken into account and results to inequality constitutive conditions. So, in a first numerical approach, a non-convex linear complementarity problem is solved in each time-step. Alternatively, in a second numerical approach, an incremental problem formulation and treatment is applied. The decision for the optimal cable-strengthening scheme in praxis problems of RC structures under multiple earthquakes excitation can be obtained on the basis of computed damage indices. A calibration of the numerical approaches is realized in a typical example problem by comparing the computational results with available experimental ones. It is shown that cable strengthening has significant effects on the earthquake response and, hence, can be used effectively for the seismic upgrading of existing RC structures.*

1 INTRODUCTION

In Greece and other seismically active countries, many existing reinforced concrete (RC) frame buildings have been designed and built using the old seismic codes. Such old regulations for reinforcement details are often not adequate for proper seismic structural behavior, local and/or global. An example of inadequate local behavior is the case of the beam-column connections [1,2]. As concerns the global behavior, for such RC frames a need for seismic strengthening often arises. One of the simple, cheap and efficient methods for strengthening of RC frames against lateral induced earthquake load is the use of steel cross X-bracings, see e.g. Massumi [3,4] and the references given therein. The combination of reinforced concrete frame with steel cross X-bracing is not a common practice due to unknown behavior and performance that needs to be investigated. Research, mainly experimental one, on the use of this method of retrofitting has begun since 80s in which cross X-bracings have been used indirectly together with a steel frame confined by a concrete frame. Application of this technique is reported, among others, also in Greece, for the case of improving the seismic performance of existing old pilotis type multi-story RC buildings by strengthening only the ground story [5,6].

In general, seismic upgrading of existing RC structures makes use of well known today repairing and strengthening techniques, see e.g. Bertero et al [7], Penelis & Kappos [8], Dritsos [9], Fardis [10] and Penelis & Penelis [11]. An alternative technique, the one using cable-like members (tension-ties) instead of the mentioned steel cross X-bracing, can be used as a first strengthening and repairing procedure for RC building frames against earthquake actions, see Tegos et al, [12,13]. Cable restrainers are also used for concrete and steel superstructure movement joints in bridges [14]. These cable-members (ties) can undertake tension, but buckle and become slack and structurally ineffective when subjected to a sufficiently large compressive force. Thus the governing conditions take an equality as well as an inequality form and the problem becomes highly nonlinear, see Liolios et al, [15].

Regarding the strict mathematical treatment of the problem, the concept of variational and/or hemivariational inequalities can be used, as it has been introduced and successfully applied in engineering by Panagiotopoulos [16]. As concerns the numerical treatment, non-convex optimization algorithms are generally required [15-17].

On the other hand, current seismic codes, e.g. EC8 [18-22], suggest the exclusive adoption of the isolated and rare "design earthquake", while the influence of repeated earthquake phenomena is ignored. This is a significant drawback for the realistic design of building structures. Despite the fact that the problem has been qualitatively acknowledged, few studies have been reported in the literature, especially the last years, regarding the multiple earthquake phenomena, see e.g. [23].

This study presents a numerical investigation for the seismic analysis of existing reinforced concrete (RC) building frames, which have been strengthened by cable elements. The investigation results to two proposed approaches, one based on linear complementarity problem formulation and treatment [15], and the second based on incremental formulation. The latter procedure uses the Ruaumoko structural engineering software [24]. Damage indices are computed and used for comparing various cable-bracing strengthening versions, in order the optimum one to be chosen, especially under multiple earthquakes. A calibration of the second approach is realized by using available experimental results for a simple typical one-bay one-story RC frame.

2 METHOD OF ANALYSIS

2.1 Formulation of the problem

As is usual in Structural Dynamics [25], a double discretization is applied. First, the structural system is discretized in space by using finite elements. Pin-jointed bar elements are used for the cable-elements. The behavior of these elements can in general include loosening, elastoplastic or/and elastoplastic-softening-fracturing and unloading - reloading effects. All these characteristics, concerning the cable full constitutive law, as well as other general nonlinearities of the RC structure, can be expressed mathematically by using concepts of convex and non-convex analysis, see Panagiotopoulos [16]. So, for the cable-elements behavior, the following relation holds:

$$s_i\,(d_i) \;\in\; \hat{\partial}\, SP_i(d_i) \tag{1}$$

Here s_i and d_i are the (tensile) force (in [kN]) and the deformation (elongation) (in [m]), respectively, of the i-th cable element, $\hat{\partial}$ is the generalized gradient and SP_i is the superpotential function, see Panagiotopoulos [16] and Mistakidis & Stavroulakis [17]. By definition, relation (1) is equivalent to the following hemivariational inequality, expressing the Virtual Work Principle:

$$SP_i^{\uparrow}\,(d_i, e_i - d_i) \;\geq\; s_i(d_i)\cdot(e_i - d_i) \tag{2}$$

where $SP_i^{\uparrow}$ denotes the subderivative of SP_i and e_i, d_i are kinematically admissible (virtual) deformations.

Next, dynamic equilibrium for the assembled structural system with cables is expressed by the usual matrix relation:

$$\boldsymbol{M\,\ddot{u} + C(\dot{u}) + K(u) \;=\; p + A\,s} \tag{3}$$

Here $\boldsymbol{u(t)}$ and $\boldsymbol{p(t)}$ are the displacement and the load time dependent vectors, respectively. The damping and stiffness terms, $\boldsymbol{C(\dot{u})}$ and $\boldsymbol{K(u)}$, respectively, concern the general nonlinear case. When the linear-elastic case holds, these terms have the usual form $\boldsymbol{C\dot{u}}$ and $\boldsymbol{Ku}$. Dots over symbols denote derivatives with respect to time. By $\boldsymbol{s(t)}$ is denoted the cable stress vector. $\boldsymbol{A}$ is a transformation matrix. For the case of ground seismic excitation $\boldsymbol{u_g}$, the loading history term $\boldsymbol{p}$ becomes $\boldsymbol{-M\ddot{u}_g}$.

The above relations (1)-(3), combined with the initial conditions, consist the problem formulation, where, for given $\boldsymbol{p}$ and/or $\boldsymbol{\ddot{u}_g}$, the vectors $\boldsymbol{u}$ and $\boldsymbol{s}$ have to be computed. Regarding the strict mathematical point of view, using (l) and (2), we can formulate the problem as a hemivariational inequality one by following [16, 17] and investigate it.

2.2 Numerical treatment

A numerical treatment of the problem, based on a piecewise linearization of the above constitutive relations as in elastoplasticity [35], is described in Liolios et al [15] for cable-braced RC systems. By using a direct time-integration scheme, in each time-step Δt a relevant nonconvex linear complementarity problem (NC-LCP) of the following matrix form is solved :

$$\mathbf{v} \geq \mathbf{0}\,, \qquad \mathbf{D}\,\mathbf{v} + \mathbf{d} \leq \mathbf{0}\,, \qquad \mathbf{v}^{\mathrm{T}} \,.\, (\mathbf{D}\,\mathbf{v} + \mathbf{d}) = 0\,. \tag{4}$$

Here $\mathbf{v}$ is the vector of unknown unilateral quantities at the time–moment t, $\mathbf{v}^{\mathrm{T}}$ is the transpose of $\mathbf{v}$, $\mathbf{d}$ is a known vector dependent on excitation and results from previous time moments (t- Δt), and $\mathbf{D}$ is a transformation matrix. The problem (4) is solved by using available optimization algorithms [15-17].

So, the nonlinear Response Time-History (RTH) for a given dynamic and/or seismic ground excitation can be computed.

An alternative approach for treating numerically the problem is the incremental one. Now, relation (3), taking into account both, load history and ground seismic excitation, is written in incremental form:

$$\boldsymbol{M}\,\Delta\ddot{\boldsymbol{u}} + \boldsymbol{C}\,\Delta\dot{\boldsymbol{u}} + \boldsymbol{K_T}\,\Delta\boldsymbol{u} \;=\; -\boldsymbol{M}\,\Delta\ddot{\boldsymbol{u}}_{\boldsymbol{g}} + \boldsymbol{A}\,\Delta\boldsymbol{s} \;+\Delta\boldsymbol{p}, \tag{5}$$

Here $\boldsymbol{K_T}$ is the tangent stiffness matrix, by which restoring nonlinear force-displacement relations are taken into account [24, 25].

The structural analysis software Ruaumoko [24], which uses the finite element method, is based on this approach. For the time-discretization, the Newmark scheme is here chosen. Ruaumoko provides results which concern, among others, the following critical parameters: local or global structural damage, maximum displacements, interstorey drift ratios, development of plastic hinges and various response quantities, which allow the using of the incremental dynamic analysis (IDA) method [26].

Further, Ruaumoko has been applied successfully for multiple earthquakes concerning the cases of concrete planar frames [23] and RC frames strengthened by cables [27]. It is reminded that multiple earthquakes consist of real seismic sequences, which have been recorded during a short period of time (up to some days), by the same station, in the same direction, and almost at the same fault distance. In the reported applications [23, 27], complete lists of the used earthquakes sequences were downloaded from the strong motion database of the Pacific Earthquake Engineering Research (PEER) Center [36].

2.3 Damage indices used for assessment and comparison

After the seismic assessment [10,11,22] of the existing RC structure, the choice of the best strengthening cable system can be realized by using damage indices [28-33]. Here the overall structural damage index (OSDI) is used. This parameter summarizes all the existing damages on columns and beams of reinforced concrete frames in a single value, which is useful for comparison reasons [33].

In the OSDI model after Park/Ang [28] the global damage is obtained as a weighted average of the local damage at the section ends of each frame element or at each cable element. The local damage index is given by the following relation:

$$\mathrm{DI_L} = \frac{\mu_{\mathrm{m}}}{\mu_{\mathrm{u}}} + \frac{\beta}{\mathrm{F_y d_u}}\,\mathrm{E_T} \tag{6a}$$

where: $\mathrm{DI_L}$ is the local damage index, μ_{m} the maximum ductility attained during the load history, μ_{u} the ultimate ductility capacity of the section or element, β a strength degrading parameter, $\mathrm{F_y}$ the yield force of the section or element, $\mathrm{E_T}$ the dissipated hysteretic energy.

The modified Park/Ang local damage index as proposed by Kunnath et al. [29] is given by the following relation:

$$DI_{L,M} = \frac{\theta_m - \theta_r}{\theta_u - \theta_r} + \frac{\beta}{M_y \theta_u} E_T \tag{6b}$$

where the deformation ductility was replaced by the rotation; while θ_m is the maximum rotation attained during the loading history; θ_u is the ultimate rotation capacity of the critical region; θ_r is the recoverable rotation after unloading; M_y is the yield moment; and E_T is the dissipated energy in the critical region. The element damage is selected as the largest damage index of the end critical region.

In the global damage index, which is a weighted average of the local damage indices, the dissipated energy is chosen as the weighting function. So, the global damage index is given by the following relation:

$$DI_G = \frac{\sum_{i=1}^{n} DI_L E_i}{\sum_{i=1}^{n} E_i} \tag{7}$$

where DI_G is the global damage index, DI_L the local damage index, E_i the energy dissipated at location i and n the number of locations at which the local damage is computed.

3 CALIBRATION AND APPLICATION OF THE NUMERICAL APPROACH

3.1 The available experimental results

A calibration of the presented numerical approach is realized by using available experimental results for a simple typical one-bay one-storey RC frame strengthened with steel cross X-bracing and investigated by Massumi et al [3,4].The results concern two experimental models of reinforced concrete frames, which have been designed on the basis of old traditional codes. The first of them is a bare-frame and the second is the same frame, but strengthened with steel X-bracing.

The single-bay, one-storey frame and the experimental testing procedure are shown in Figures 1, 2 and 3 adapted from [3,4]. The frame was of concrete C25 and had section dimensions (12cm)x(12cm) for the two columns and the beam. The steel bracings were squared tubes with section (20mm)x(20mm) and thickness t=2mm. Yield strength of steel bracings was 240 MPa. For the details of the experimental program see Massumi et al [3,4].

During the experiments, a lateral additive cyclic static load P was applied to the storey beam in a displacement-controlled mode, see Fig. 3. The relevant diagrammes of the load P versus to the top displacement u hysteretic behavior for the unbraced (bare) frame and the X-braced frame are shown in Fig. 4. Similar hysteretic diagrammes for bare frames are reported in other experimental publications, see e.g. [37].

Based on the above experimental results and using Ruaumoko software, in the next paragraph the finite element model related to these frames is made by using cable-elements and calibrated, and then nonlinear analyses under additive cyclic static loading suggested by the experimental results are performed.

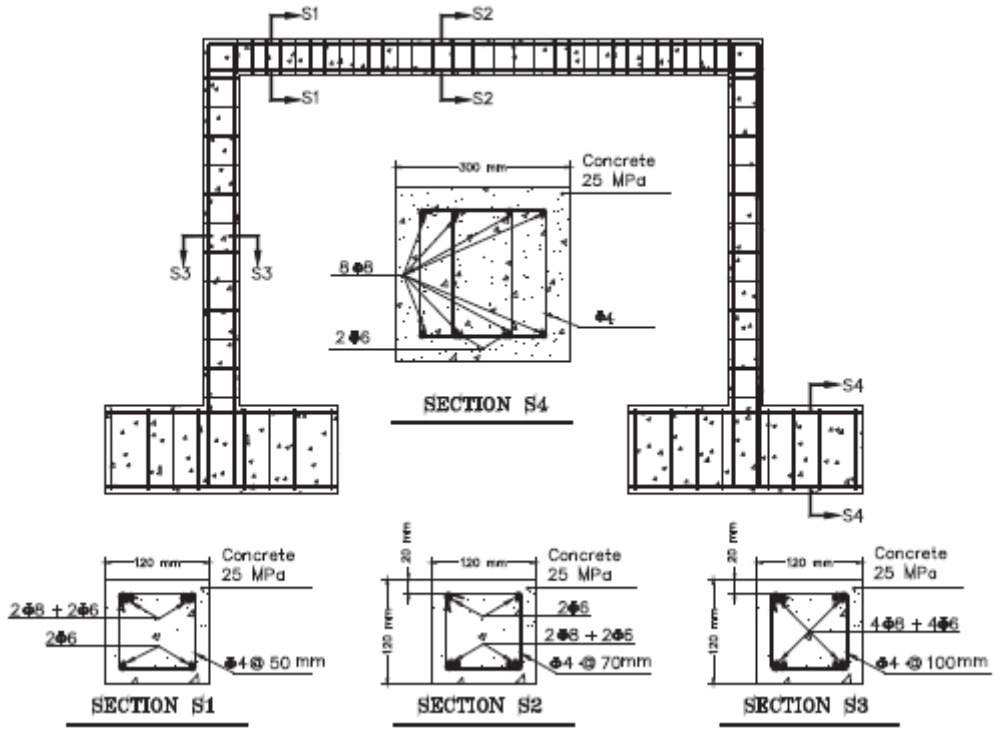


Figure 1. Details of the investigated RC frames (adapted from Massumi et al [4] after permission)

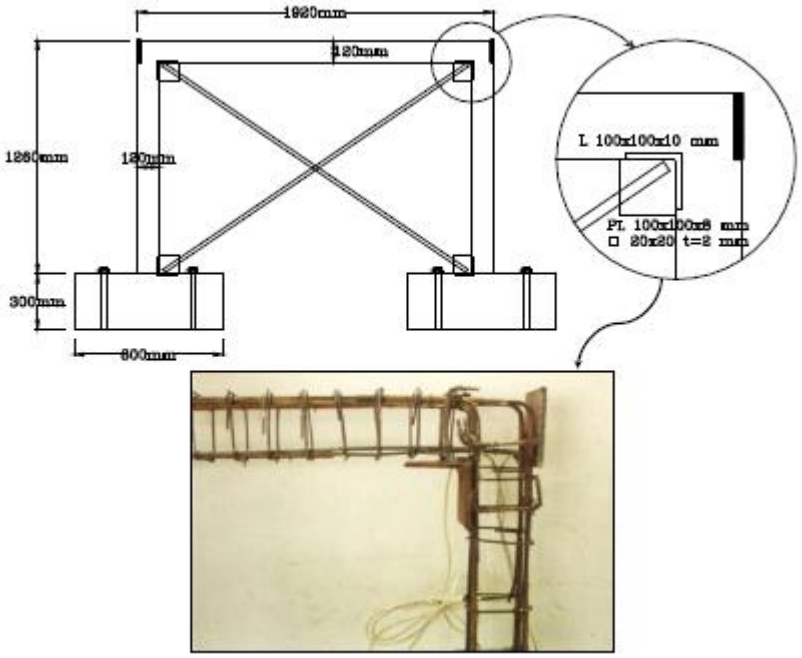


Figure 2. Strengthened RC frame with X-cross bracings and its connection details (adapted from Massumi et al [4] after permission)

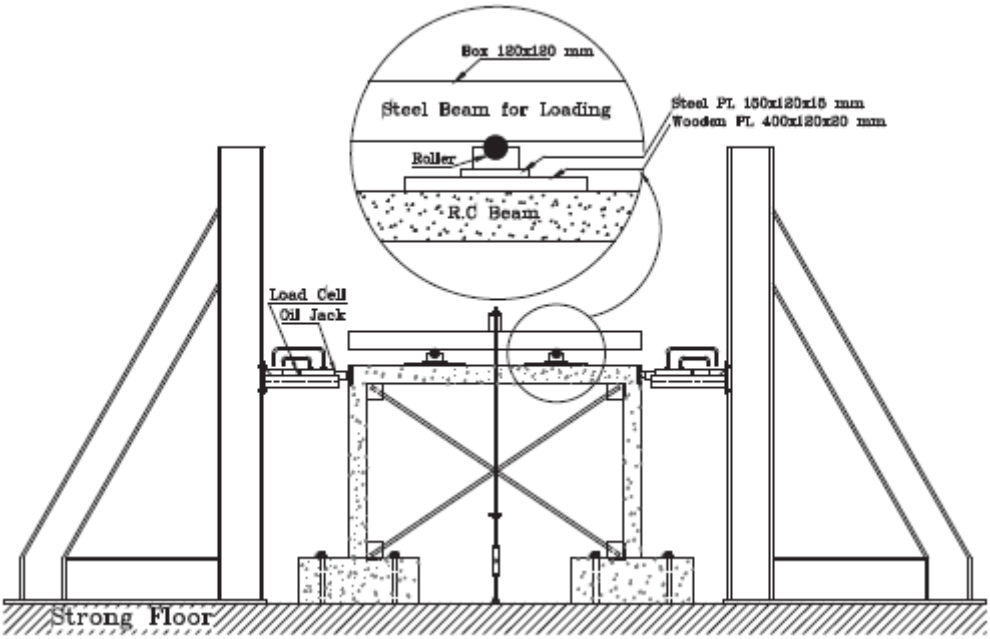


Figure 3. Test setup and loading systems (adapted from Massumi et al [4] after permission)

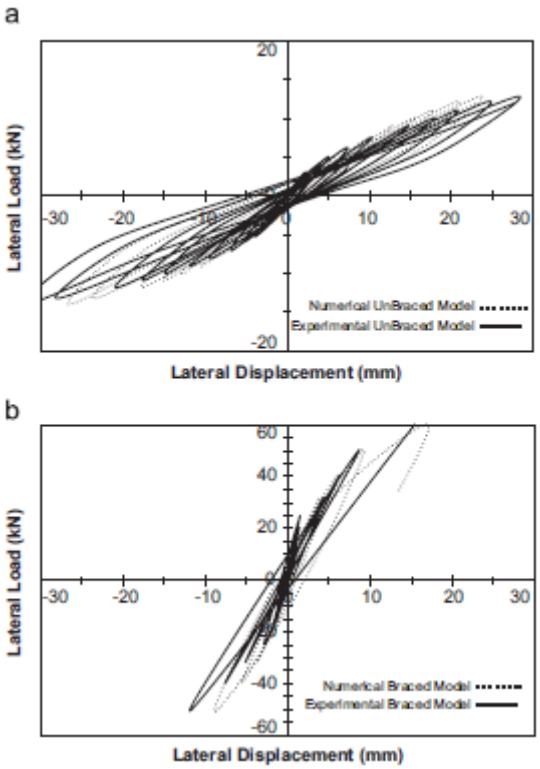


Figure 4. Experimental load-displacement hysteretic behavior for (a) unbraced frame, and (b) X-braced frame (adapted from Massumi et al [4] after permission)

3.2 Simulation of the Massumi et al [3,4] experiments

With respect to above experimental results, the finite element models related to the unbraced and braced frames are made using Ruaumoko software [24]. The two columns and the beam are modeled using prismatic frame elements. Nonlinearity at the two ends of RC members is idealized using one-component plastic hinge models, following the Takeda hysteresis rule. The effects of cracking on columns and beams are estimated by applying the guidelines of EC8-Part3 [10, 18, 19] and KAN.EPE [22]. So, the stiffness reduction due to cracking results to effective stiffness of 0.450 I_g for the columns and 0.225 I_g for the beam, where I_g is the gross inertia moment of the section (12cm)x(12cm).

For the steel bracings simulation, cable-elements are used herein by applying the bilinear with slackness hysteresis rule [24]. These cable elements have a cross-sectional area F_c = 1.44 cm^2, which is equivalent to the cross-sectional area of steel braces tubes with section (20mm)x(20mm) and thickness t=2mm used in Massumi et al [3], see Fig. 2. Yield strength of cable bracings was considered to be also the same one of [3], i.e. 240 MPa. Further, yield strain ε_y = 0.2 %, fracture strain ε_f = 2 % and elasticity modulus E_s = 200 GPa are taken for the cables. So, the cable constitutive law, concerning the unilateral (slackness), hysteretic, fracturing, unloading-reloading etc. behavior, has the diagramme depicted in Fig. 5. Ductility index is $\mu = d/d_y$.

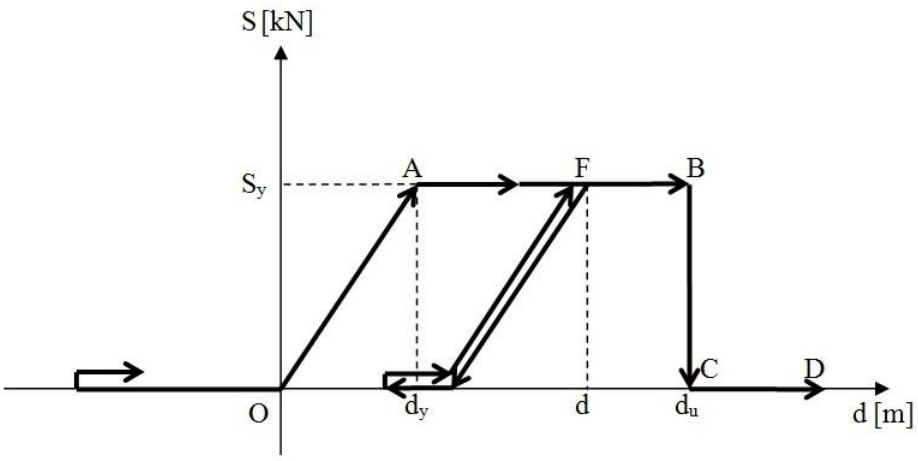


Figure 5. The diagramme for the constitutive law of cable-elements.

Based on the experimental procedure [3,4] and on Fig. 4, the loading history has been simulated as an displacement-controlled multiple earthquake excitation imposed on the top left node of the frame. This loading simulation had full loading steps with maximum displacements ±5, ±10, ±15, ±20, ±25 and ±30 [mm] for the unbraced frame, whereas for the X-braced frame the loading steps had maximum displacements ±2.5, ±5.0, ±7.5, ±10, ±12.5 and ±15 [mm].

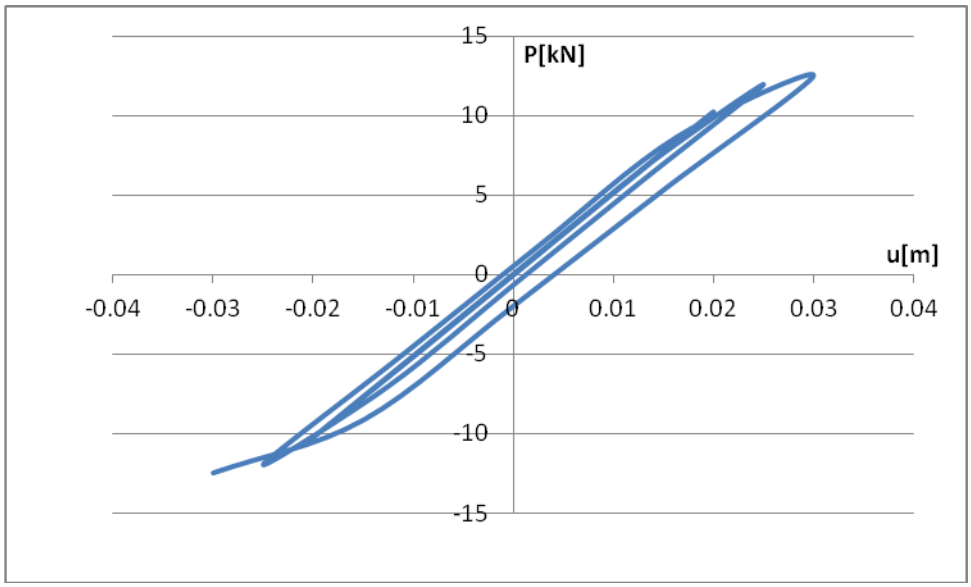


Figure 6. Simulated load-displacement hysteretic behavior for the unbraced frame.

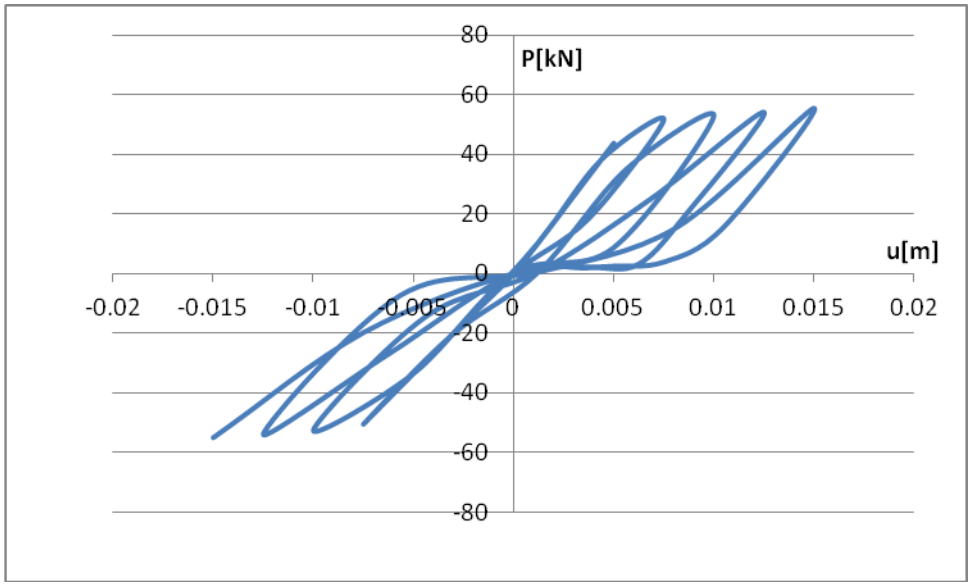


Figure 7. Simulated load-displacement hysteretic behavior for the X-cable braced frame.

The relevant diagrammes of the (load P)-(top displacement u) hysteretic behavior for the unbraced (bare) frame and the X-braced frame are shown in Fig. 6 and Fig. 7, respectively. As these figures show, the computed results are in a good agreement with the experimental ones of Fig. 4.

Some representative results of the numerical simulation are presented in next Table 1. In column (2) the Global Damage Index DI_G and in column (3) the Local Damage Index DI_L for the bending moment at the left fixed support of the frame are given. Finally, in the column (4), the developed maximum horizontal top force P_{top} is given.

FRAME	DI_G	DI_L	P_{top} [kN]
(1)	(2)	(3)	(4)
Unbraced	0.098	0. 201	12.52
X-braced	0.001	0.001	55.40

Table 1. Representative response quantities for the unbraced and braced frames

The table values show, as expected, that cable- strengthening generally on the one hand reduces the damage indices and on the other hand increases the global horizontal frame resistance. So, for the unbraced frame, is P_{max} = 12.52 kN, whereas for the cable-X-braced frame is P_{max} = 55.40 kN. That means that the frame-stiffness is increased by a factor 55.4/12.52 = 4.425. As concerns the damage indices, they are minimized for the cable-strengthened frame. Similar concluding remarks hold for multi-story and multi-bay real praxis RC frames as investigated in [27]. Therein is shown that a further improvement of the seismic behavior of the initial frames can be obtained by trying various cable-bracing schemes and by realizing a parameter sensitivity analysis concerning the cable characteristics, e.g. cross-sectional area F_c or steel class.

3.3 Application for the case of one-tie braced frame

After the previous calibration of the numerical procedure, and in order to clarify the unilateral behavior of the cable-elements and their effects on the structural response, the same frame of Fig. 1 is investigated, but with only one tension-tie, the ascending diagonal cable, as shown in Fig. 8.

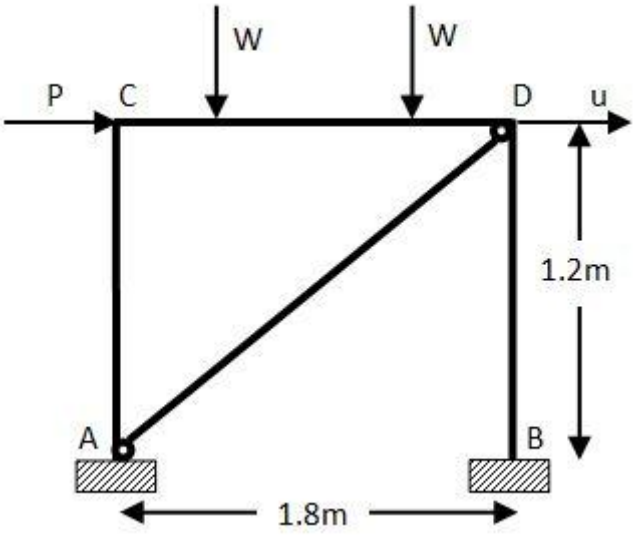


Figure 8. The one-tie braced frame

The loading history had the same full loading steps as for the X-braced frame, i.e. the loading steps had maximum displacements ±2.5, ±5.0, ±7.5, ±10, ±12.5 and ±15 mm.

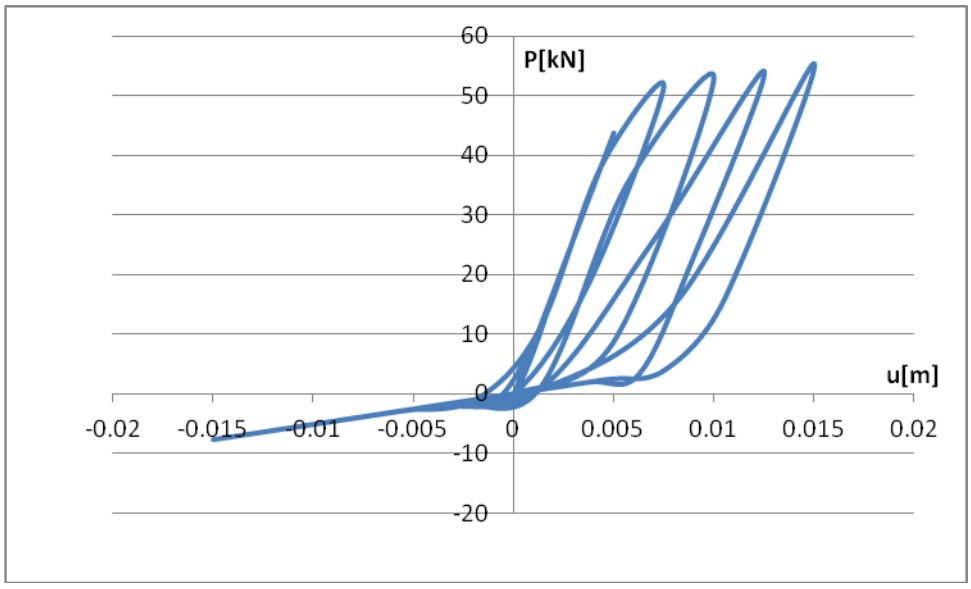


Figure 9. Computed load-displacement hysteretic behavior for the one-tie braced frame

In Fig.8 the relevant diagramme of the load-top displacement hysteretic behavior is shown. As this figure shows, when the loading is in the direction CD, the cable is activated and the system stiffness is increasing about 4.25 times. On the contrary, when the loading is in the inverse direction DC, then the cable becomes slack and so inactivated, and the system stiffness is decreasing and approaching the one of the bare frame.

4 CONCLUSIONS

The seismic inelastic behavior of planar RC frames strengthened by cable elements has been numerically investigated by the herein presented numerical approach. This approach has been calibrated by using available experimental results concerning the case of a single-bay one-storey RC frame, which was subjected to a recycling additive lateral loading in displacement-controlled mode.

The presented numerical approach can be effectively used for the seismic assessment and strengthening of existing RC structures by cable-elements. This holds for general dynamic excitations, as well as for sequential strong ground motions. For the last case of multiple earthquakes, the proposed numerical procedure has been already applied in [27]. Finally, on the basis of computed damage indices, an optimal cable-bracing scheme can be selected among investigated alternative ones by realizing a parameter sensitivity analysis concerning the cable characteristics.

REFERENCES

[1] Chalioris, C. E., Favvata, M. J., & Karayannis, C. G. (2008). *Reinforced concrete beam–column joints with crossed inclined bars under cyclic deformations*. Earthquake Engineering & Structural Dynamics, 37(6), 881-897.

[2] Karayannis, C. G., Chalioris, C. E., & Sirkelis, G. M. (2008). *Local retrofit of exterior RC beam–column joints using thin RC jackets-An experimental study*. Earthquake Engineering & Structural Dynamics, 37(5), 727-746.

[3] Massumi, A. and A.A. Tasnimi, (2008). *"Strengthening of low ductile reinforced concrete frames using steel x-bracing with different details"*, in: Proceedings of the Fourteen World Conference on Earthquake Engineering (14WCEE), Beijing, China, 2008.

[4] Massumi, A., & Absalan, M. (2013). *"Interaction between bracing system and moment resisting frame in braced RC frames".* Archives of Civil and Mechanical Engineering, 13(2), 260-268.

[5] Antonopoulos, T.A., S.A. Anagnostopoulos, F.N. Tsirlis, (2008). *Evaluation of the seismic performance of old reinforced concrete buildings with an open ground storey, simple retrofitting solutions.* Proceedings of the 3rd Greek Conference on Earthquake Engineering and Engineering Seismology, 2061, Athens, Greece, 2008. (In Greek)

[6] Antonopoulos, T.A., S.A. Anagnostopoulos (2013), *Improving the seismic performance of existing old pilotis type buildings by strengthening only the ground story*, In: M. Papadrakakis, V. Papadopoulos & V. Plevris (eds.), *COMPDYN 2013, ECCOMAS: Thematic Conference on Computational Methods in Structural Dynamics and Earthquake Engineering*, Kos Island, Greece, 12–14 June 2013.

[7] Bertero, V. V., & Whittaker, A. S. (1989). *Seismic upgrading of existing buildings*, 5as Jornadas Chilenas de Sismología e Ingeniería Antisísmica, 1, 27-46.

[8] Penelis, G. G. & Kappos, A. J. (2010). *Earthquake resistant concrete structures*. CRC Press, London.

[9] Dritsos, S. E. (2001). *Repair and strengthening of reinforced concrete structures* (in greek). University of Patras, Greece.

[10] Fardis, M. N. (2009). *Seismic design, assessment and retrofitting of concrete buildings: based on EN-Eurocode 8.* Springer, Berlin.

[11] Penelis, G. Gr. & Penelis, Gr. G. (2014). *Concrete Buildings in Seismic Regions*. CRC Press.

[12] Tegos, I., G. Liakos, S. Tegou, G. Roupakias, K. Stilianidis, (2009). *An alternative proposal for the seismic strengthening of existing R/C buildings through tension-ties*, Proceedings, 16th Pan- Hellenic Concrete Conference, Cyprus, 2009.

[13] Markogiannaki, O., & Tegos, I. (2011). *Strengthening of a Multistory R/C Building under Lateral Loading by Utilizing Ties.* Applied Mechanics and Materials, 82, 559-564.

[14] Priestley, M. J. N., Seible, F. C., & Calvi, G. G.. M.(1996). *"Seismic Design and Retrofit of Bridges"*. John Wiley & Sons, Inc..

[15] Liolios Ang., Chalioris C., et al (2012). *"A Computational Approach for the Earthquake Response of Cable-braced Reinforced Concrete Structures under Environmental Actions".* Lecture Notes in Computer Science, LNCS, vol. 7116, pp. 590-597, Springer-Verlag, Berlin Heidelberg.

[16] Panagiotopoulos, P.D., (1993). *Hemivariational Inequalities. Applications in Mechanics and Engineering*. Springer-Verlag, Berlin, New York, (1993).

[17] Mistakidis, E.S. & Stavroulakis, G.E., (1998). *Nonconvex optimization in mechanics. Smooth and nonsmooth algorithmes, heuristic and engineering applications*. Kluwer, London.

[18] EC8-Part 3, Eurocode 8: *Design of structures for earthquake resistance, Part 3: Assessment and retrofitting of buildings.* European Standard EN 1998-3:2005. Comite Europeen de Normalisation. Brussels, 2005.

[19] EC8, Eurocode 8: *Design of structures for earthquake resistance, Part 1: General rules, seismic actions and rules for buildings*, European Standard EN 1998-1:2004. Comite Europeen de Normalisation, Brussels, 2004.

[20] EAK, (2000) *Greek Seismic Design Code*. Greek Organization for Seismic Planning and Protection (OASP), Greek Ministry for Environmental Planning and Public Works, Athens, Greece, 2003. (In Greek): www.oasp.gr

[21] FEMA (Federal Emergency Management Agency) (2000) *FEMA 356: Pre-standard and commentary for the seismic rehabilitation of buildings*, FEMA, Washington, DC.

[22] KAN.EPE., Greek Retrofitting Code. Greek Organization for Seismic Planning and Protection (OASP), Greek Ministry for Environmental Planning and Public Works. Athens, Greece, 2012. (In Greek): www.oasp.gr.

[23] Hatzigeorgiou G. and A. A. Liolios, , (2010). Nonlinear behaviour of RC frames under repeated strong ground motions. *Soil Dynamics and Earthquake Engineering*, vol. 30, 1010-1025, 2010.

[24] Carr A.J., (2008). *"RUAUMOKO - Inelastic Dynamic Analysis Program".* Department of Civil Engineering, University of Canterbury, Christchurch, New Zealand.

[25] Chopra, A.K., (2007) . *Dynamics of Structures: Theory and Applications to Earthquake Engineering*, Pearson Prentice Hall, New York.

[26] Vamvatsikos, D. and C.A, Cornell, (2002). Incremental dynamic analysis. *Earthquake Engineering and Structural Dynamics*, vol. 31, 491–514.

[27] Liolios, Ang., Hatzigeorgiou, G. & Liolios, Ast., (2013). "A numerical approach for estimating the effects of multiple earthquakes to seismic response of structures strengthened by cable-elements". *Journal of Theoretical and Applied Mechanics*, 43(3), 21-32.

[28] Park Y.J. and A.H.S. Ang, (1985). Mechanistic seismic damage model for reinforced concrete, *Journal of Structural Division ASCE*, vol. 111(4), 722–739.

[29] Kunnath, S.K., Reinhorn AM, Lobo RF, (1992). IDARC version 3.0: a program for the inelastic damage analysis of reinforced concrete structures. *Technical report NCEER-92-0022*. National Center for Earthquake Engineering Research, Buffalo, NY; 1992.

[30] Kappos, A. J. (1997). Seismic damage indices for RC buildings: evaluation of concepts and procedures. *Progress in Structural Engineering and Materials*, 1(1), 78-87.

[31] Mergos, P. E., & Kappos, A. J. (2013). A combined local damage index for seismic assessment of existing RC structures. *Earthquake Engineering & Structural Dynamics*, 42(6), 833-852.

[32] Mitropoulou, C. C., Lagaros, N. D., & Papadrakakis, M. (2014). Numerical calibration of damage indices. *Advances in Engineering Software*, 70, 36-50.

[33] Elenas, A., Liolios, Ast., Vasiliadis, L., Favvata, M. & Liolios, Ang., (2012). Seismic intensity parameters as damage potential descriptors for life-cycle analysis of buildings. *IALCCE 2012: Proc. Third Int. Symp. Life-Cycle Civil Engineering*, Vienna, Austria, October 2012, CRC Press, Taylor & Francis, London.

[34] Paulay T. and M.J.N. Priestley, (1992), *Seismic Design of Reinforced Concrete and Masonry Buildings*, Wiley, New York.

[35] Maier, G., (1971). Incremental Elastoplastic Analysis in the Presence of Large Displacements and Physical Instabilizing Effects, *Int. Jnl Solids and Structures*, Vol. 7, 345-372.

[36] PEER (2011). Pacific Earthquake Engineering Research Center. *PEER Strong Motion Database*. http://peer.berkeley.edu/smcat. Last access: 2011/02/15.

[37] Kakaletsis, D. J., & Karayannis, C. G. (2009). Experimental investigation of infilled reinforced concrete frames with openings. *ACI Structural Journal*, 106(2), pp. 132-141.

COMPDYN 2015
5th ECCOMAS Thematic Conference on
Computational Methods in Structural Dynamics and Earthquake Engineering
M. Papadrakakis, V. Papadopoulos, V. Plevris (eds.)
Crete Island, Greece, 25–27 May 2015

INCREMENTAL DYNAMIC ANALYSIS OF FIRE-EXPOSED BASE-ISOLATED R.C. FRAMED BUILDINGS SUBJECTED TO NEAR-FAULT GROUND MOTIONS

Fabio Mazza[1] **and Fabio Alesina**[2]

[1]Dipartimento di Ingegneria Civile, Università della Calabria
Via P. Bucci, 87036 Rende (CS), Italy
fabio.mazza@unical.it

[2]Dipartimento di Ingegneria Civile, Università della Calabria
Via P. Bucci, 87036 Rende (CS), Italy
fabioalesina@yahoo.it

Keywords: Base-Isolated Structures, Fire Scenarios, Thermal Mappings, Near-Fault Ground Motions, Incremental Dynamic Analysis.

Abstract. *It is well known that near-fault ground motions are characterized by long-duration horizontal pulses, which can become critical for base-isolated reinforced concrete (r.c.) structures when the pulse intensity is so strong that the superstructure undergoes plastic deformations. There is, however, a lack of knowledge on the seismic response in case of fire; moreover, an amplification of the structural damage is expected in case of fire-exposed base-isolated structures which are not designed to withstand fire. To investigate the nonlinear seismic response following a fire, an incremental dynamic analysis is carried out with reference to five-storey base-isolated r.c. buildings with fire-protected High-Damping-Laminated-Rubber Bearings (HDLRBs), designed according to the Italian seismic code. Horizontal components of seven near-fault ground motions have been selected according to the design subsoil class C adopted for the test structures. More specifically, the nonlinear seismic response of base-isolated structures in a no fire situation is compared with that in which fire occurs, at 45 (i.e. R45) and 60 (i.e. R60) minutes of fire resistance, assuming both damaged (i.e. DS) and repaired (i.e. RS) stiffness conditions. Five fire scenarios are considered assuming the fire compartment confined to the area of the first level (i.e. F1), the first two (i.e. F1/2) and the upper (i.e. Fi, i=3-5) levels, with the parametric temperature-time fire curve evaluated according to Eurocode 1. The nonlinear seismic analysis is performed by using a step-by-step procedure based on a two-parameter implicit integration scheme and an initial-stress-like iterative procedure. At each step of the analysis, plastic conditions are checked at the critical (end) sections of the girders and columns, where thermal mapping with reduced mechanical properties is evaluated with the 500°C isotherm method proposed by Eurocode 2. A viscoelastic model with variable stiffness properties in the horizontal and vertical directions, depending on the axial force and lateral deformation, simulates the response of an HDLRB.*

1 INTRODUCTION

Fire can be a serious problem for a structure that has been partially damaged in a prior seismic event, because fire resistance will decrease with respect to an undamaged structure [1]. Recent studies have focused the attention on the combined effect of earthquake and fire on the nonlinear response of reinforced concrete (r.c.) [2, 3], steel [4, 5] and composite steel-concrete [6] fixed-base structures. On the other hand, numerical [7] and experimental [8, 9] studies have been carried out on the residual seismic load capacity of fixed-base structures, in terms of stiffness, strength and ductility after fire. In most of cases of fire, framed structures experience degradation of material properties, due to the high temperature, and damage to the structural members, from thermal expansion. There is, however, a lack of knowledge on the seismic response of base-isolated structures in case of fire and an amplification of the structural damage is expected in the case of fire-exposed base-isolated structures not designed to withstand fire.

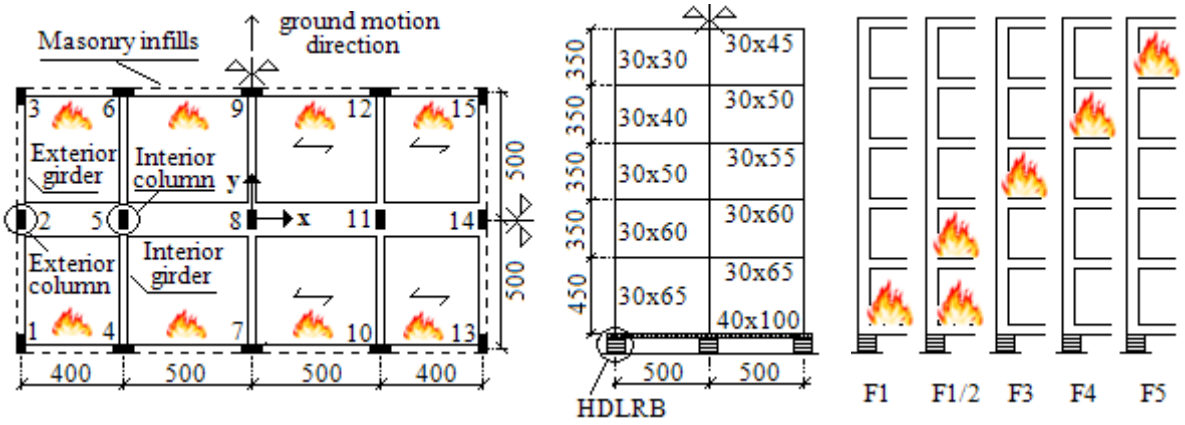
When a base-isolated structure is designed for a sufficiently high strength level, it behaves elastically and the vibration periods of the upper framed structure are shorter than the predominant periods of the motion filtered by the isolators. Nevertheless, the frequency content of the motion transmitted by the isolators to the superstructure can become critical as soon as the strength level of a fire-weakened base-isolated structure is reduced; as a consequence, the superstructure can undergo plastic deformations and the ductility demand can increase much more rapidly for an ever-lower strength level. Moreover, a considerable increase in the deformability of a base-isolated structure, in comparison with that of the corresponding fixed-base structure, may lead to an amplification in the structural response under near-fault ground motions [10, 11], which are characterized by long-duration (horizontal) directivity and fling-step pulses due to fault-rupture directivity and elastic rebound effects, respectively [12].

In the present work, the nonlinear seismic response of base-isolated structures in a no fire situation is compared with that in which fire occurs, at 45 (i.e. R45) and 60 (i.e. R60) minutes of fire resistance, assuming both damaged (i.e. DS) and repaired (i.e. RS) stiffness conditions in the r.c. frame members. To this end, five-storey r.c. office buildings, base-isolated with fire-protected High-Damping-Laminated-Rubber Bearings (HDLRBs), are designed according to the Italian seismic code [13]. A numerical fire investigation is carried out considering a thermal-mechanical mapping analysis, with reduced mechanical properties evaluated according to the 500°C isotherm method proposed by Eurocode 2 [14], followed by a sequentially uncoupled nonlinear incremental dynamic analysis. Horizontal components of seven near-fault ground motions, available in the *Pacific Earthquake Engineering Research center database* [15] and corresponding to both directivity and fling-step pulse-type records, are selected according to the design subsoil class C adopted for the test structures [16]. Five fire scenarios have been considered assuming the fire compartment is confined to the area of the first level (i.e. F1), the first two (i.e. F1/2) and the upper (i.e. Fi, i=3-5) levels, with the parametric temperature-time fire curve evaluated according to Eurocode 1 [17].

2 LAYOUT AND DESIGN OF THE BASE-ISOLATED R.C. FRAMED BUILDING

A typical five-storey office building with an r.c. framed structure isolated at the base by fifteen identical fire-protected HDLRBs is considered for the numerical investigation. The symmetric plan of the building and the elevation of a base-isolated plane frame are shown in Figures 1a and 1b, respectively, where length and cross-sections of the frame members are also shown. Perimeter masonry infills, assumed as non-structural elements regularly distributed in elevation, are considered (Figure 1a). A grid of rigid girders is placed at the base of the framed structure on the HDLRBs (Figure 1b). For the sake of simplicity, the plane frames ori-

entated along the horizontal ground motion direction (y), perpendicular to the floor slab direction (x) shown in Figure 1a, are considered as a reference scheme. Five fire scenarios are reported in Figures 1a and 1c, assuming the fire compartment is confined to the area of the first level (i.e. F1), the first two (i.e. F1/2) and the upper (i.e. Fi, i=3-5) levels.



(a) Plan and fire compartment. (b) Elevation. (c) Fire scenarios.

Figure 1: Base-isolated r.c. test structure (dimensions in cm).

The proportioning of the test structure has been done according to the Italian seismic code (NTC08) assuming, besides the gravity loads, the horizontal seismic loads corresponding to: elastic response of the superstructure (behaviour factor q=1); design subsoil class C (subsoil parameter S=1.41); high-risk seismic region (peak ground acceleration, PGA=0.201gx1.41 =0.283g). The acceleration design spectrum is modified in the period range $T \geq 0.8T_{I,H}$, being $T_{I,H}$ the fundamental vibration period of the base-isolated structure in the horizontal direction, assuming an equivalent viscous damping ratio of the isolation system $\xi_{I,H}$=10%, at shear deformation γ=1. Moreover, NTC08 requires that $3T_{F,H} \leq T_{I,H} \leq 3$s, $T_{F,H}$ being the fundamental vibration period of the same structure on fixed-base. In the present case a reasonable isolation period was $T_{I,H}$=2.5 s having $T_{F,H}$=0.73 s; an isolation degree, in terms of spectral acceleration at the fundament vibration period, equal to α_{Sa}=0.28(=$S_{a,I}/S_{a,F}$) is obtained. Finally, the vibration period with prevailing component in the vertical direction is $T_{I,V}$=0.072 s with the corresponding equivalent viscous damping ratio $\xi_{I,V}$=2%.

The gravity loads used in the design are represented by dead- and live loads, equal respectively to: 4.4 kN/m^2 e 3 kN/m^2, for the top floor; 6.1 kN/m^2 e 3 kN/m^2, for the isolated floor; 5.7 kN/m^2 e 3 kN/m^2, for the other floors. The weight of the perimeter masonry infills is taken into account by considering a gravity load of 2.7 kN/m^2. A cylindrical compressive strength of 25 N/mm^2 for the concrete and a yield strength of 450 N/mm^2 for the steel are assumed for the r.c. frame members. The design of the superstructure has been carried out so as to satisfy minimum conditions for the longitudinal bars of the girders and columns, according to the provisions for low ductility class imposed by NTC08: at least two 14 mm bars are provided both at the top and bottom throughout the entire length of all the frame members; for the girders, a tension reinforcement ratio not less than 0.31% (for the assumed yield strength) is provided and a compression reinforcement not less than half of the tension reinforcement is placed at their end sections; a minimum steel geometric ratio of 1% is assumed for the symmetrically-reinforced section of each column.

The HDLRBs fulfill the ultimate limit state verifications regarding the maximum shear strains: i.e. $\gamma_{tot}=\gamma_s+\gamma_c+\gamma_\alpha \leq 5$ and $\gamma_s \leq 2$, where γ_{tot} represents the total design shear strain, while γ_s, γ_c and γ_α represent the shear strains of the elastomer due to seismic displacement, axial

compression and angular rotation, respectively. Moreover, the maximum compression axial load (P) does not exceed the critical load (P_{cr}) divided by a safety coefficient equal to 2.0. The minimum tensile stress (σ_t) resulting from the seismic analysis is assumed as $2G$(=0.8 MPa, for a shear modulus of the elastomer G=0.4 MPa). A nominal stiffness ratio α_{K0}, defined as the ratio between the nominal value of the vertical stiffness (K_{V0}) and the analogous value of the horizontal stiffness (K_{H0}), equal to 1200 is assumed for the isolators, considering a volumetric compression modulus of the rubber equal to 2000 MPa. In Table 1 initial stiffnesses and corresponding equivalent damping coefficients (i.e. C_H and C_V) are reported together with the results of the ULS verifications for the isolators. It is interesting to note that the design of the isolators depends on the condition imposed on the maximum value of the compression axial load (P). Finally, no tensile forces are found in the isolators. The following geometrical and mechanical properties of the HDLRBs are also reported in Table 2: the diameter of the steel layer (D_s) and that of the elastomer (D_e); the total thickness of elastomer (t_e); primary (S_1) and secondary (S_2) shape factors; compression modulus (E_c).

α_{K0}	K_{H0} (kN/cm)	K_{V0} (kN/cm)	C_H (kNs/cm)	C_V (kNs/cm)	γ_s	$\gamma_{tot,max}$	$(P_{cr}/P)_{min}$
1200	81.30	97522	6.47	44.70	0.96	2.85	2.00

Table 1: Mechanical properties of the base-isolation system.

D_s (cm)	D_e (cm)	t_e (cm)	S_1	S_2	E_c (kN/cm^2)
62.00	66.00	25.00	19.22	2.46	55.34

Table 2: Geometrical and mechanical properties of the HDLRBs.

3 FIRE LOADING BEFORE AN EARTHQUAKE AND NUMERICAL RESULTS

Once the fire scenarios, assuming closed openings, have been hypothesized (Figure 1c), temperature is considered uniform in the selected compartment (Figure 1a) in such a way as to be the most severe condition for the fire before an earthquake. Several fire action models can be used to simulate the time-temperature evolution during an actual fire, from the flashover to the full development: conventional fire curves (e.g. the standard ISO-834 curve [18]), in which temperature monotonically increasing with time represents the heating phase only, when the fuel supply is assumed to be inexhaustible; natural fire curves (e.g. the EC1 curve [17]), in which temperature depends on the actual ventilation and fire load in the compartment and the cooling phase is represented, based on the assumption that at a certain point, either the air or the combustible material will become less.

The EC1 parametric fire curve is used in the present study, on the assumption that the fire load of the compartment is completely burnt out. In the heating phase, the gas temperature θ_g(°C)

$$\theta_g = 20 + 1325\left(1 - 0.324e^{-0.2t^*} - 0.204e^{-1.7t^*} - 0.472e^{-19t^*}\right) \tag{1}$$

is a function of a fictitious time t^* obtained considering the time t (in hours) multiplied by a dimensionless parameter equal to

$$\Gamma = \left(O/b\right)^2 \Big/ \left(0.04/1160\right)^2 \tag{2}$$

where O is an opening factor

$$O = A_v h_{eq}^{\ 0.5} \Big/ A_t \tag{3}$$

depending on the total area of vertical openings (A_v), the weighted average of window heights (h_{eq}) and the total area of the compartment (A_t) and b is the thermal absorptivity of

surrounding surfaces of the compartment

$$b = \sqrt{\rho c \lambda} \tag{4}$$

being: ρ the density, c the specific heat and λ the thermal conductivity of boundary of enclosure.

The gas temperature in the cooling phase is given by

$$\begin{aligned} & t^*_{\max} \le 0.5\ h \rightarrow \theta_g = \theta_{\max} - 625\left(t^* - t^*_{\max}\right) \\ & 0.5\ h < t^*_{\max} < 2\ h \rightarrow \theta_g = \theta_{\max} - 250\left(3 - t^*_{\max}\right)\left(t^* - t^*_{\max}\right) \\ & t^*_{\max} \ge 2\ h \rightarrow \theta_g = \theta_{\max} - 250\left(t^* - t^*_{\max}\right) \end{aligned} \tag{5}$$

where the maximum temperature θ_{max} in the heating phase happens for

$$t^*_{\max} = \left(0.2 \cdot 10^{-3} q_{t,d} / O\right) \Gamma \tag{6}$$

being the design fire load density

$$q_{t,d} = q_{f,d}\ A_f / A_t \tag{7}$$

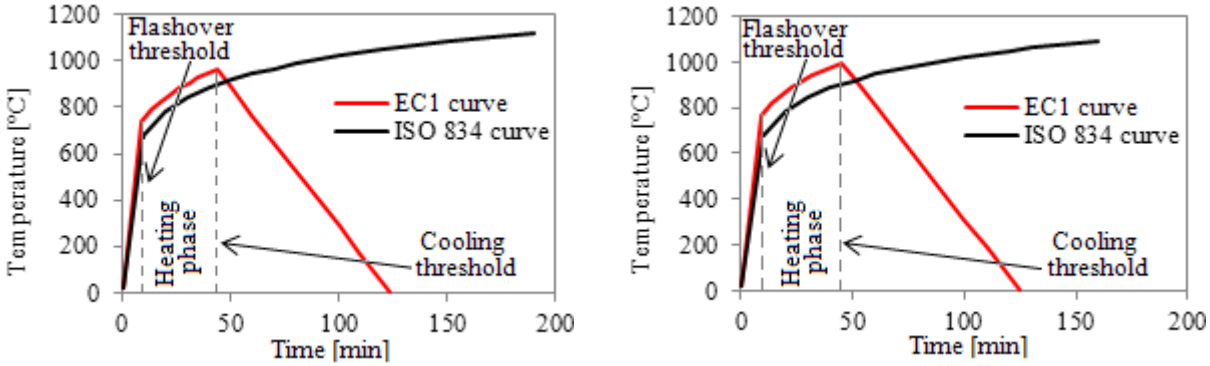
related to the value $q_{f,d}$ corresponding to the surface area of the floor (A_f). Further details on fire modelling can be found in [19].

Finally, the standard ISO-834 curve is defined as [18]

$$\theta_g = 20 + 345 \log_{10}\left(8t + 1\right) \tag{8}$$

where t is expressed in hours.

With reference to the fire scenarios shown in Figure 1, the ISO and EC1 time-temperature curves are compared in Figure 2 in the case of a fire compartment confined to the area of the first level (Figure 2a) and the upper levels (Figure 2b). The combination of fire parameters, for the opened-plan office base-isolated building (see Table 3), results in a temperature of 956 °C and 960 °C in 45 min (i.e. fire resistance R45) and 788 °C and 805 °C in 60 min (i.e. fire resistance R60), on the first level and the upper levels, respectively.



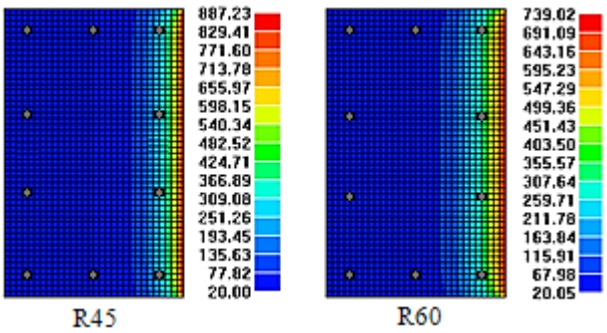
(a) Fire compartment at the 1st level. (b) Fire compartment at the upper levels.

Figure 2: Conventional (ISO 834) and natural (EC1) fire curves.

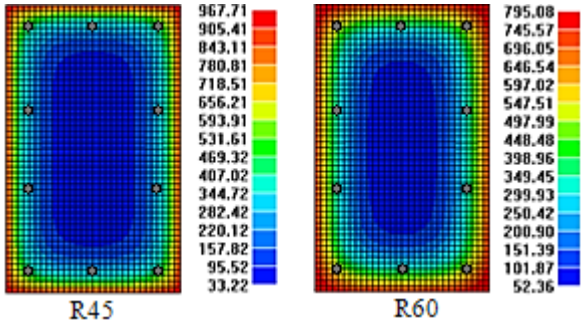
Fire resistance (minutes)	$q_{f,d}$ (MJ/m^2)	O (m$^{1/2}$)	b (J/m^{2}s$^{1/2}$K)	t^*_{max} (h)
R45	595.60	0.05	1127	1.326
R60	612.00	0.05	1137	1.365

Table 3: Fire parameters in the EC1 time-temperature curve [17].

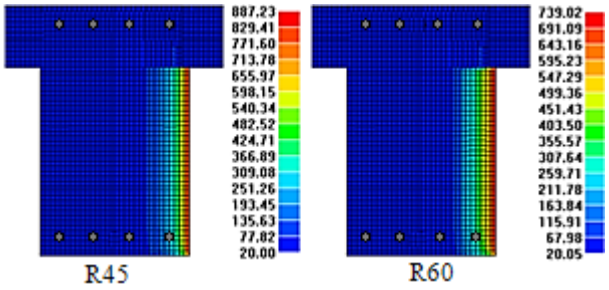
Once time-temperature curve of the fire compartment is determined with the EC1 model, it becomes possible to evaluate the temperature distribution in the frame members of the test structure at R45 and R60. As an example, thermal mappings of exterior and interior r.c. frame members in the first level of the test structure are plotted in Figure 3, considering a convection factor equal to 25 and an emissivity related to the concrete surface equal to 0.56. In detail, the thermal finite element cross-section model of columns, exposed to fire on one (Figure 3a) and four (Figure 3b) sides, and girders, exposed to fire on one (Figure 3c) and three (Figure 3d) sides, are considered assuming an ambient temperature of 20°C for the un-exposed cross-section sides. As expected, at the end of 45 and 60 minutes of fire exposition, the increase in temperature is greater in the case of cross-sections exposed on four (Figure 3b) or three (Figure 3d) sides than those exposed on one side only (Figures 3a and 3c). Moreover, the temperature profiles highlight a decrease in the maximum value with the time increment from R45 to R60, in accordance with EC1 natural fire curves shown in Figure 2, but the concrete zone damaged by heat is more extended in the case of R60.



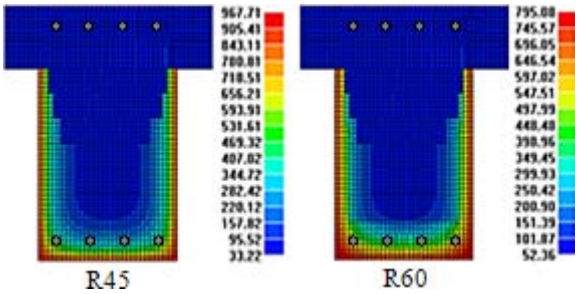
(a) Exterior column exposed to fire on one side.



(b) Interior column exposed to fire on four sides.



(c) Exterior girder exposed to fire on one side.

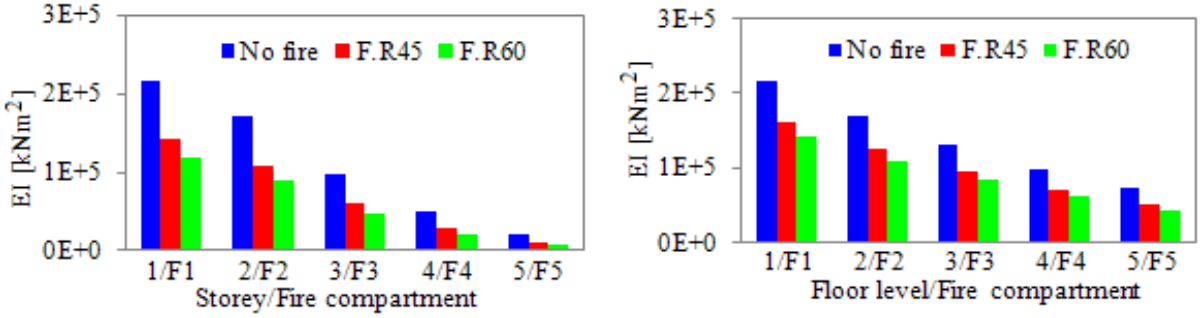


(d) Interior girder exposed to fire on three sides.

Figure 3: Thermal mappings at the 1st level of the test structure.

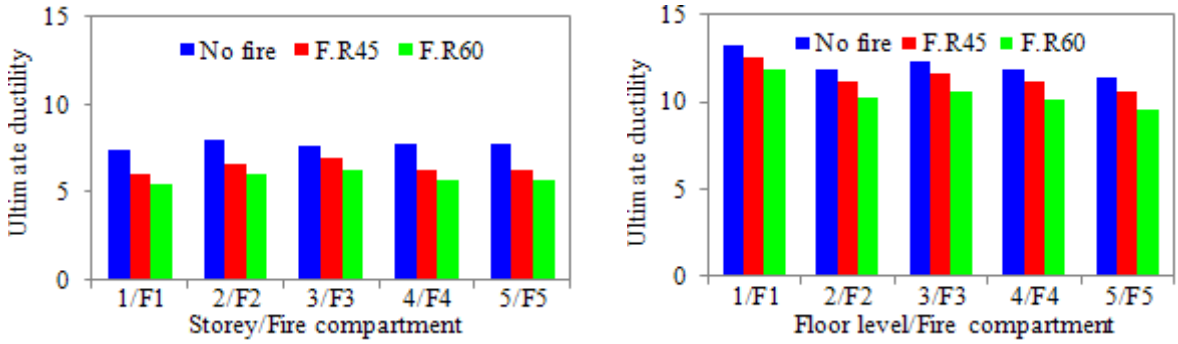
Subsequently, the residual seismic load capacity of the cross-sections after fire occurrence is evaluated with the 500°C isotherm method of Eurocode 2 [14], in terms of stiffness, strength and ductility. The simplified calculation provides for a reduction of the cross-section size, with respect to a heat damaged zone defined by thermal mappings. Concrete with temperatures exceeding 500°C, corresponding roughly to the thickness of the unconfined zone, is assumed not to contribute, while the residual concrete cross-section retains its initial values of strength and modulus of elasticity. On the other hand, a reduced yield strength of each longitudinal reinforcement bar, in the tension and compression zones of the cross-section, is evaluated on the basis of the steel temperature profile in the centre of the bar [20]. It is worth noting that some of the reinforcing bars may fall outside the reduced cross-section, but they are included in the calculation of the ultimate values of load bearing capacity and curvature ductility, which is evaluated according to the provisions of Eurocode 8 for the assessment of existing buildings [21].

In Figures 4 and 5 flexural stiffness and ultimate ductility on the top side, in the fire-exposed cross-section of r.c. frame members, are reported along the building height, respectively, assuming the direct correspondence between the examined level and the fire compartment. In particular, interior columns (Figures 4a and 5a) and girders (Figures 4b and 5b) are examined at the end of 45 (i.e. F.R45 structure) and 60 (i.e. F.R60 structure) minutes of exposure to fire. As expected, a global mean decrease in stiffness, of about 41% and 28%, and ultimate ductility, of about 16% and 6%, is obtained for the interior columns and girders of the F.R45 structure, respectively, in comparison with the no-fire condition. A further global mean decrease in stiffness, of about 12% and 9%, and ultimate ductility, of about 8%, is obtained after an additional 15 minutes of fire (i.e. F.R60 structure). Further results, which are omitted for the sake of brevity, confirm limited fire effects in the perimeter frame members of all levels where the fire compartment is supposed.



(a) Interior columns. (b) Interior girders.

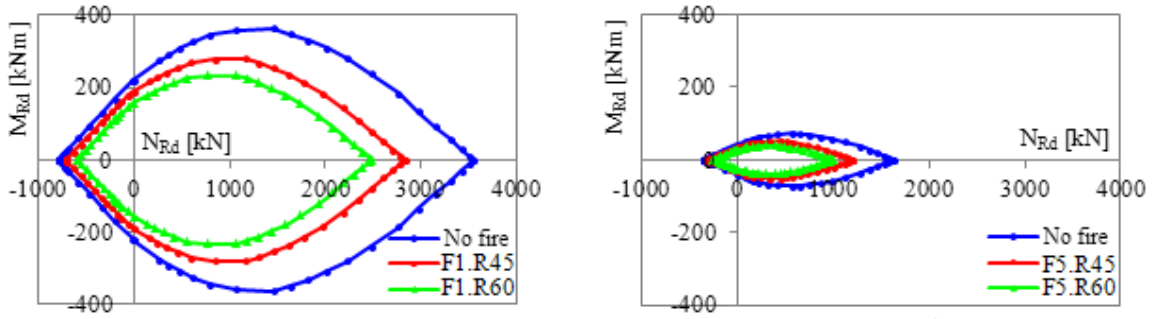
Figure 4: Flexural stiffness of r.c. frame members exposed to fire.



(a) Interior columns. (b) Interior girders (top side).

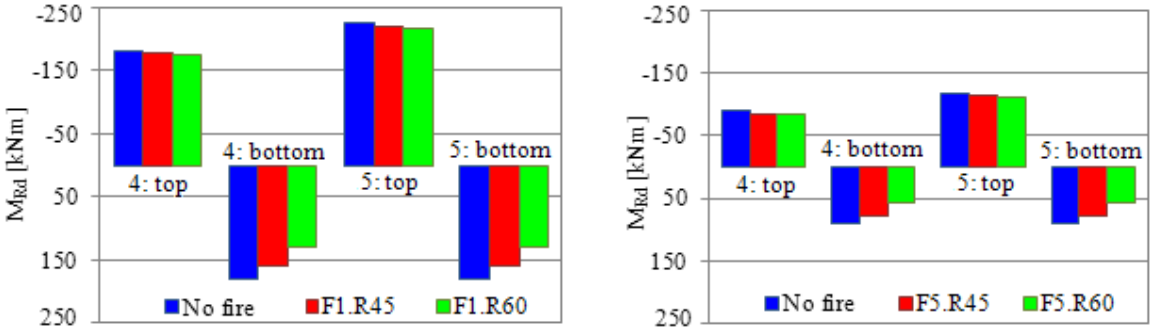
Figure 5: Ultimate ductility of r.c. frame members exposed to fire.

Finally, analogous results are reported for the ultimate interaction domain between axial load (N_{Rd}) and bending moment (M_{Rd}) of columns (Figure 6) and the ultimate bending moment of girders (Figure 7). For the sake of clarity, only the fire compartment at the first (i.e. F1 in Figures 6a and 7a) and fifth (i.e. F5 in Figures 6b and 7b) level are examined. As can be observed, interior columns exhibit a marked narrowing of their N_{Rd}-M_{Rd} domains, especially for values of the compressive axial load greater than that corresponding to the balanced compressive load. For this axial load, a local reduction in flexural strength, in comparison with the no-fire condition, of about 23% and 36%, at the first storey, and 30% and 47%, at the fifth storey, is found in the F.R45 and F.R60 structures, respectively. On the other hand, a significant decrease in strength is observed on the bottom side of the interior girder 4-5 (see Figure 1a) with a global mean reduction of about 13% and 33% considering the F.R45 and F.R60 structures, respectively.



(a) Interior columns (1st storey/F1). (b) Interior columns (5th storey/F5).

Figure 6: Ultimate N_{Rd}-M_{Rd} domains of r.c. columns exposed to fire.



(a) Interior girders (1st floor/F1). (b) Interior girders (5th floor/F5).

Figure 7: Ultimate bending moments of r.c. girders exposed to fire.

4 SEISMIC LOADING FOLLOWING FIRE AND NUMERICAL RESULTS

In order to study the seismic response of the base-isolated r.c. framed building described in Section 2 and damaged by the fire loading proposed in Section 3, near-fault ground motions are considered. Long-duration horizontal pulses due to forward-directivity and fling-step effects characterize these motions [12]. In particular, earthquake rupture towards a site tends to produce a short-duration, but large amplitude, two-sided velocity pulses principally in the horizontal direction normal to the fault strike; on the other hand, fling-step is associated with the permanent displacement that occurs across a ruptured fault and, generally, presents one-sided velocity pulses in the slip parallel direction. Seven near-fault ground motions available in the *Pacific Earthquake Engineering Research center database* [15] have been selected according to the design hypotheses adopted for the test structure (i.e. subsoil class C and high-risk seismic region). For each ground motion attention is focused on the horizontal component showing forward-directivity or fling-step effect [16]. In Table 4 the main data of the selected near-fault ground motions are shown: i.e. date, recording station, component, peak ground acceleration, magnitude, pulse-type and period of the velocity pulse.

Country	Earthquake	Date	Station	Comp.	*PGA*	M_w	Pulse-type	T_p (s)
Taiwan	Chi-Chi	20/09/1999	TCU068	EW	0.566 g	7.3	Fling-step	12.29
USA	Northridge	17/01/1994	Rinaldi	228	0.837 g	6.6	Forward-directivity	1.25
	Superstition Hills	24/11/1987	Parachute	225	0.455 g	6.4	Forward-directivity	2.39
	Cape Mendocino	25/04/1992	Petrolia	090	0.662 g	7.1	Forward-directivity	3.00
Japan	Kobe	16/01/1995	Takatori	090	0.616 g	6.9	Forward-directivity	1.55
Iran	Tabas	16/09/1978	Tabas	TR	0.852 g	7.7	Forward-directivity	6.19
Turkey	Erzincan	13/03/1992	Erzincan	NS	0.515 g	6.7	Forward-directivity	2.70

Table 4: Main data of the selected near-fault ground motions [15, 16].

The corresponding elastic response spectra of normalized acceleration (S_a/g) are plotted in Figure 8, assuming an equivalent viscous damping ratio in the horizontal direction, ξ_H, equal to 10%. The response spectra are compared with the corresponding target NTC08 response spectrum for high-risk seismic region and design subsoil class C adopted for the test structures, assuming PGA_H=0.283g.

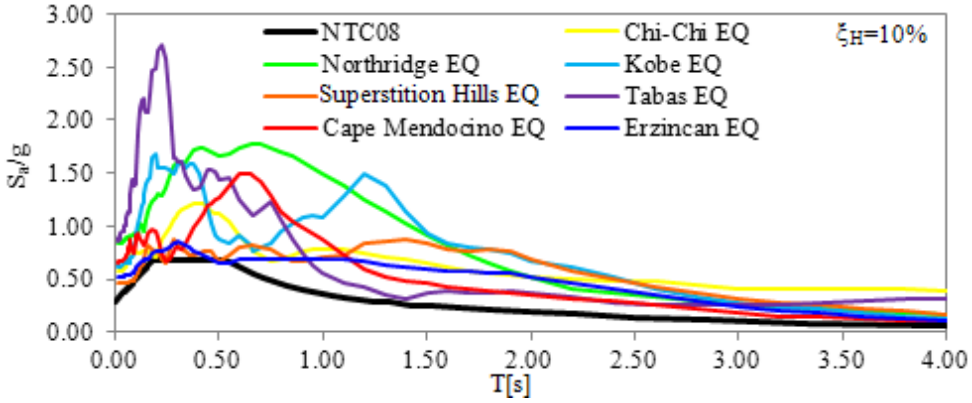


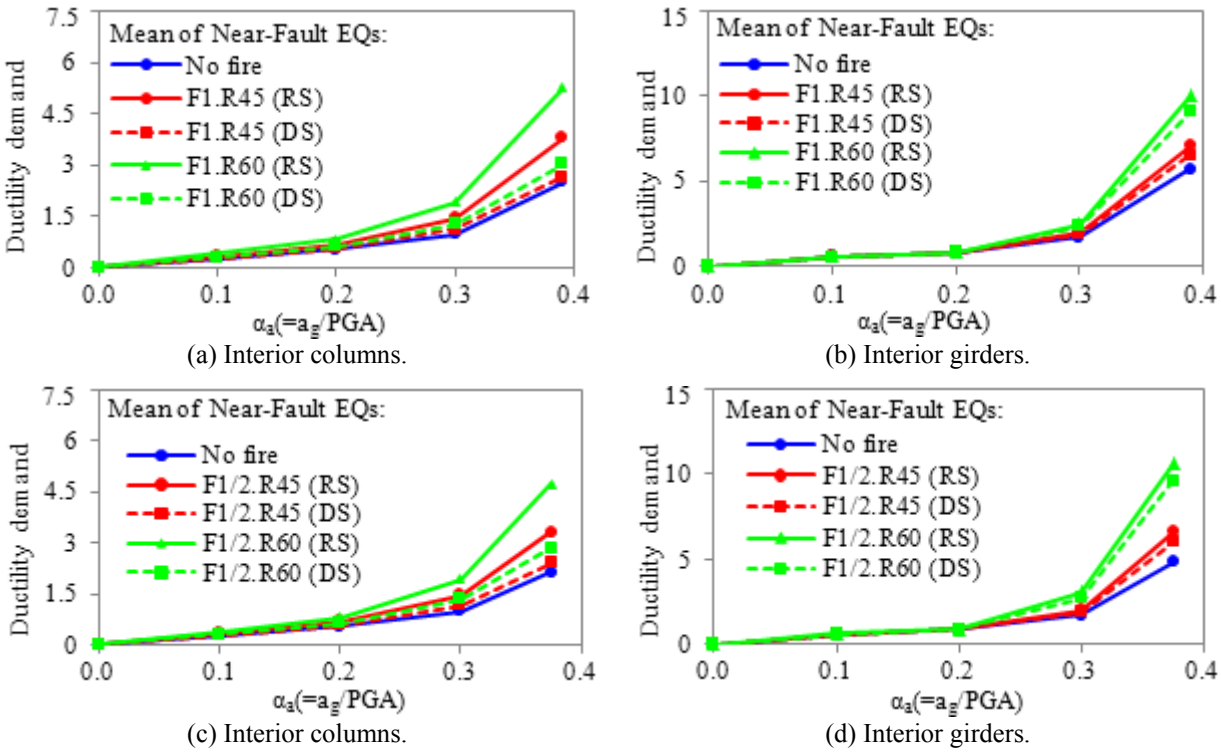
Figure 8: Acceleration (elastic) response spectra.

The r.c. frame members are idealized by means of a two-component model (TCM), constituted of an elastic-plastic component and an elastic component, assuming a bilinear moment-curvature law [22]. The effect of the axial load on the ultimate bending moment of the columns is also considered. At each step of the analysis, the elastic-plastic solution is evaluated in terms of the initial state and the incremental load on the basis of a holonomic law, as a solution of the Haar-Kàrmàn principle [23]. In the Rayleigh hypothesis, the damping matrix of the superstructure is assumed as a linear combination of the mass and stiffness matrices, assuming a viscous damping ratio in the horizontal ($\xi_{S,H}$) and vertical ($\xi_{S,V}$) direction equal to 1% with reference, respectively, to the two fundamental vibration periods $T_{I,H}$ and $T_{I,V}$ reported in Section 3. A two-spring-two-dashpot model (TSTDM), constituted of nonlinear spring acting in parallel with a linear viscous dashpot both in the horizontal and vertical directions, is adopted for modelling a HDLRB [11, 24]. The TSTDM takes into account experimental results, which have pointed out that the horizontal stiffness of a HDLRB (starting from K_{H0}) decreases with increasing vertical load while the corresponding vertical stiffness (starting from K_{V0}) decreases with increasing lateral deformation. Moreover, the equivalent viscous damping ratio of the isolation system is assumed equal to $\xi_{I,H}$=10% and $\xi_{I,V}$=2% with reference to the horizontal motion and the vertical one, respectively.

Incremental dynamic analysis (IDA) of the test structures is carried out by using a series of nonlinear dynamic analyses under the above mentioned set of seven near-fault earthquakes (EQs), each scaled to a submultiple (a_g) of the corresponding *PGA* value reported in Table 4. Afterwards, a mean of the results separately obtained for these ground motions is calculated. The local damage is evaluated in terms of ductility demand at the critical end sections of girders and columns. The curvature ductility demand is calculated with reference to the two loading directions, assuming as yielding curvature for the columns that corresponding to the axial force due to the gravity loads.

Firstly, mean values of maximum ductility demand for increasing values of the dimensionless acceleration α_a(=a_g/PGA) are plotted in Figure 9, comparing base-isolated structures both in no-fire condition and at the end of 45 (i.e. R45) and 60 (i.e. R60) minutes of fire exposure. More specifically, interior columns (Figures 9a and 9c) and girders (Figures 9b and 9d) are examined, on the assumption that the fire compartment is confined to the area of the first level

(i.e. F1, Figures 9a and 9b) and the first two levels (i.e. F1/2, Figures 9c and 9d). Moreover, the r.c. superstructure of the base-isolated building is assumed to have been previously damaged by fire, with a reduced cross-section (i.e. in the Damaged Stiffness condition, DS), and later repaired, e.g. using jacketing with thin layers of concrete (i.e. in the Repaired Stiffness condition, RS). For all the examined cases, the IDAs were interrupted once the ultimate value imposed on the curvature ductility demand in the r.c. frame members was reached, which occurred at different values of α_a. For this reason, the analyses were repeated assuming the minimum dimensionless acceleration ($\alpha_{a,min}$) for all structures corresponding to the same fire-scenario. As can be observed, an amplification in the structural response of fire-exposed base-isolated structures is obtained for increasing values of α_a. As expected, this result is more evident in the Fi.R60 structures than in the Fi.R45 ones, because the first are characterized by lower strength and ductility. The results also show that the seismic response of the test structures differs in the DS and RS conditions, especially with higher ductility demand of the interior columns (Figures 9a and 9c) in the case when the initial stiffness is restored (i.e. RS condition). It is worth noting that, the IDA was interrupted to $\alpha_{a,min}$=0.395 in the fire scenario F1 (Figures 9a and 9b), while when the fire compartment was confined to the area of the first two levels (Figures 9c and 9d) the IDA was limited to $\alpha_{a,min}$=0.375. Further results, omitted for the sake of brevity, confirm negligible effects at the upper storeys when the fire compartment is supposed at these levels.



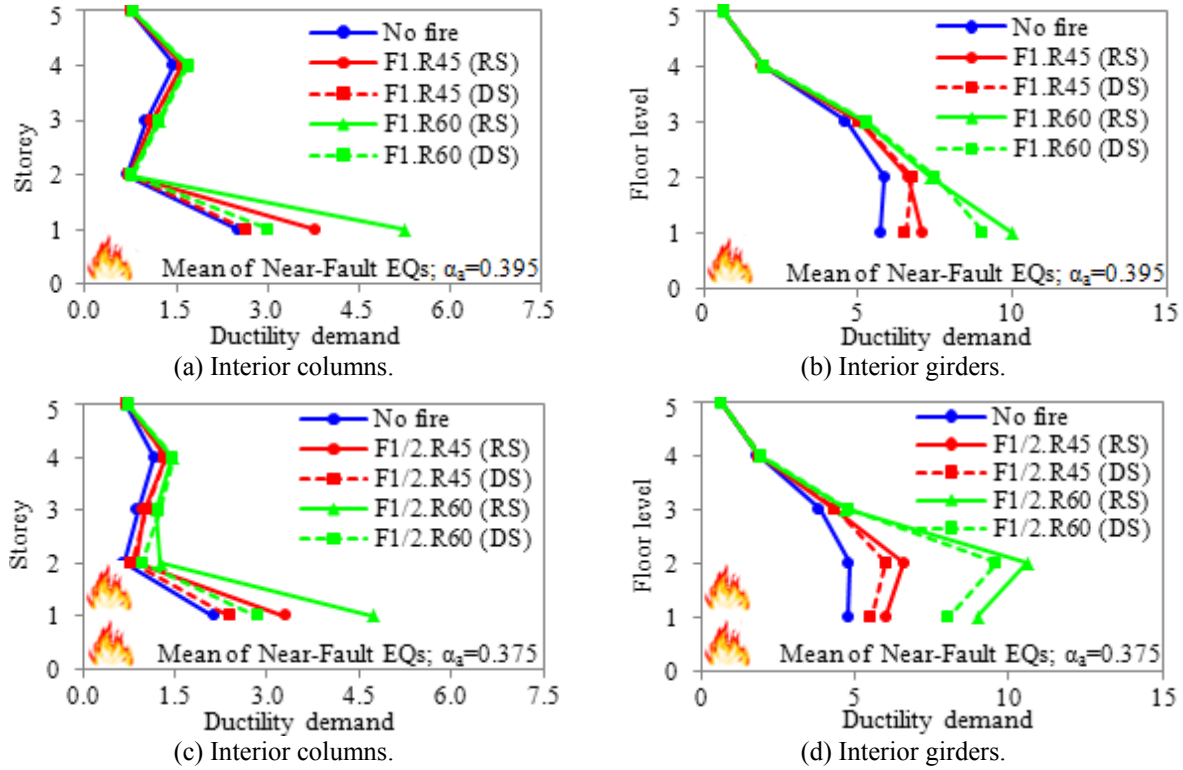
(a) Interior columns. (b) Interior girders.

(c) Interior columns. (d) Interior girders.

Figure 9: Global mean ductility demand for incremental dynamic analysis:
(a) and (b), fire at the 1st level (fire scenario F1); (c) and (d), fire at the 1st and 2nd levels (fire scenario F1/2).

To better clarify the local damage distribution along the building height, mean ductility demand of columns and girders is plotted in Figure 10 at the end of the IDA, in the cases of F1 (i.e. $\alpha_{a,min}$=0.395) and F1/2 (i.e. $\alpha_{a,min}$=0.375) fire scenarios. As can be observed, the pulse-type nature of the horizontal component of near-fault ground motions can induce unexpected ductility demand especially at the lower levels, with an amplification when the fire

compartment at these levels and R60 are assumed. More specifically, the IDAs are interrupted when the ultimate ductility demand of the F1.R60 and F1/2R.60 structures is reached in an interior column on the first storey (Figure 10a) and an interior girder on the second floor (Figure 10d), respectively.



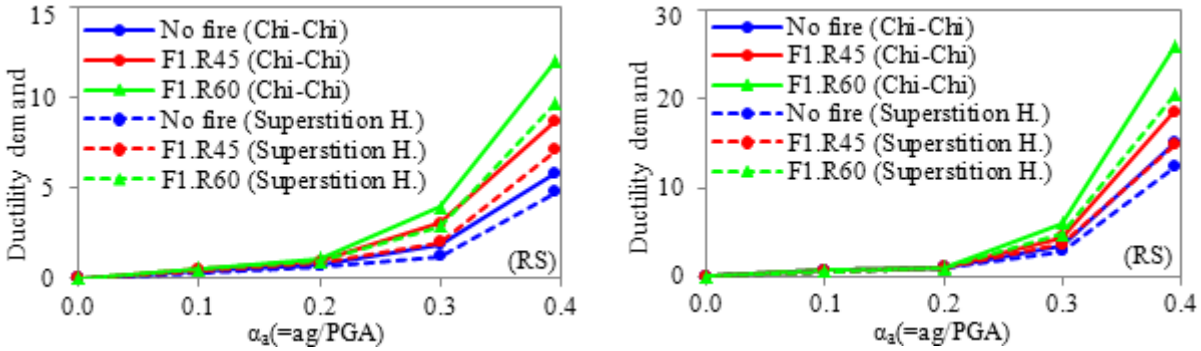
(a) Interior columns. (b) Interior girders.

(c) Interior columns. (d) Interior girders.

Figure 10: Local mean ductility demand at the end of the incremental dynamic analysis: (a) and (b), fire at the 1st level (fire scenario F1); (c) and (d), fire at the 1st and 2nd levels (fire scenario F1/2).

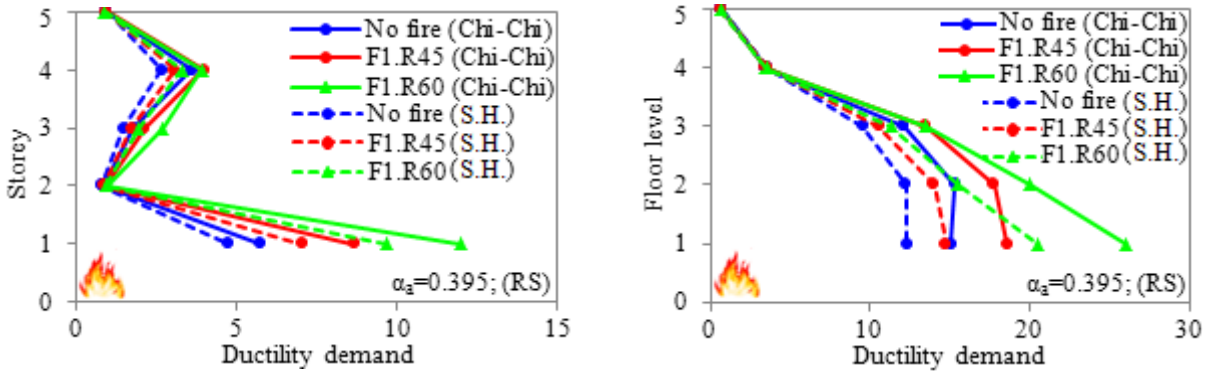
Afterwards, to investigate the effects of forward-directivity and fling-step pulse-type, curves analogous to the previous ones are reported in Figures 11 and 12 with reference to the Superstition Hills and Chi-Chi EQs. Attention is focused on the fire scenario F1, assuming the same final value of the dimensionless acceleration α_a (i.e. $\alpha_{a,min}$=0.395) for both near-fault ground motions. These motions are selected as they are characterized by a comparable value of elastic spectral acceleration (see Figure 8) corresponding to the fundamental vibration period of the base-isolated test structure (i.e. $T_{I,H}$=2.5 s). In all the examined cases, global and local maximum ductility demands of the structures subjected to the Chi-Chi EQ are found to be greater than those observed for the Superstition Hills EQ. This kind of behaviour can be interpreted as an amplification of the inelastic response during the fling-step Chi-Chi EQ due to the long duration of the pulse-velocity (see Table 4).

Finally, taking into account the symmetric plan shown in Figure 1a, the distribution of maximum ductility demand in the exterior and interior frame members is investigated in Figure 13. More specifically, local maximum ductility demand in the columns (Figures 13a and 13c) and girders (Figures 13b and 13d) for the Chi-Chi (Figures 13a and 13b) and Superstition Hills (Figures 13c and 13d) EQs are plotted at the first level where the fire compartment is assumed. Note that the ductility demand increases especially in the frame members exposed on three (i.e. the interior girders 4-5, 5-6, 7-8 and 8-9) and four (i.e. the interior columns 5 and 8) sides. Moreover, among the columns exposed on one side greater ductility demand is obtained in the exterior ones (i.e. 1, 2 and 3).



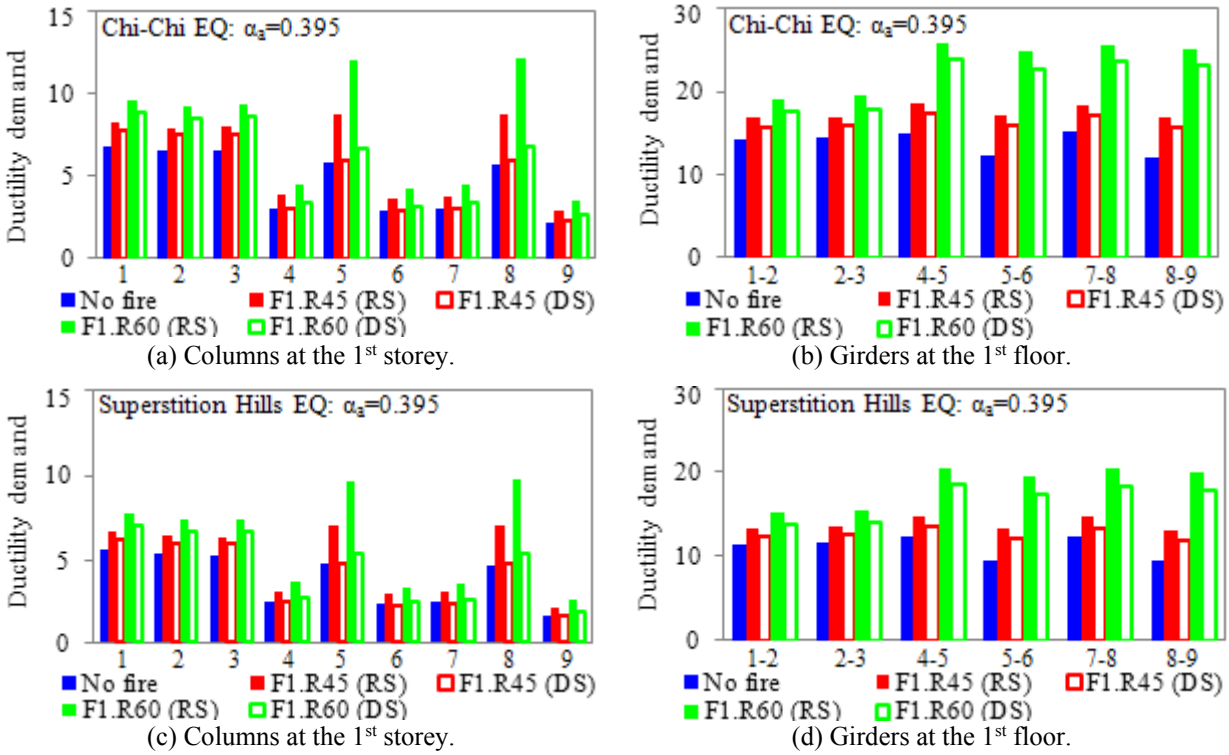
(a) Interior columns. (b) Interior girders.

Figure 11: Global maximum ductility demand for incremental dynamic analysis: fire at the 1st level (fire scenario F1) under Chi-Chi and Superstition Hills EQs.



(a) Interior columns. (b) Interior girders.

Figure 12: Local maximum ductility demand at the end of the incremental dynamic analysis: fire at the 1st level (fire scenario F1) under Chi-Chi and Superstition Hills EQs.



(a) Columns at the 1st storey. (b) Girders at the 1st floor.

(c) Columns at the 1st storey. (d) Girders at the 1st floor.

Figure 13: Local ductility demand in the fire compartment at the end of the incremental dynamic analysis: fire at the 1st level (fire scenario F1) under Chi-Chi (a, b) and Superstition Hills (c, d) EQs.

5 CONCLUSIONS

The nonlinear seismic response of five-storey base-isolated r.c. framed buildings, with fire-protected High-Damping-Laminated-Rubber Bearings, is studied under the horizontal components of seven near-fault ground motions with long-duration velocity pulses due to forward-directivity and fling-step effects. More specifically, the incremental dynamic analysis of base-isolated structures in a no fire situation is compared with that in the event of fire, at 45 (i.e. R45) and 60 (i.e. R60) minutes of fire exposition, assuming both damaged (i.e. DS) and repaired (i.e. RS) stiffness conditions.

The numerical results show that in the case of base-isolated buildings subjected to near-fault motions structural fire safety rules should be taken into account in the design. A significant decrease in stiffness and ultimate values of strength and ductility is obtained in the structural members exposed to fire. Moreover, the pulse-type nature of the horizontal near-fault ground motions induces unexpected ductility demands in the lower levels, which are amplified when the fire compartment is supposed at these levels and R60 is assumed. On the other hand, in all the examined cases the upper storeys are practically independent of this effect. Finally, the ductility demand increases especially in the most fire-exposed r.c. frame members (i.e. the interior girders and columns) in both DS and RS conditions.

ACKNOWLEDGEMENTS

The present work was also financed by Re.L.U.I.S. (Italian network of university laboratories of earthquake engineering), according to "Convenzione D.P.C.–Re.L.U.I.S. 2014–2016, WPI, Isolation and Dissipation".

REFERENCES

[1] C. Scawthorn, J.M. Eidinger, A. Schiff, Fire following earthquake. New York, NY *American Society of Civil Engineers*, 2005.

[2] H. Mostafaei, T. Kabeyasawa, Performance of a six-story reinforced concrete structure in post-earthquake fire. Institute for Research in Construction, *10th Canadian Conference on Earthquake Engineering*, Toronto, Canada, July 25-29, **1**, 481-490, 2010.

[3] B. Behnam, H. Ronagh, Performance of reinforced concrete structures subjected to fire following earthquake. *European Journal of Environmental and Civil Engineering,* **17**(4), 270-292, 2013.

[4] G. Della Corte, R. Landolfo, F.M. Mazzolani, Post earthquake fire resistance of moment resisting steel frames. *Fire Safety Journal*, **38**, 593–612, 2003.

[5] M. Memari, H. Mahmoud, Performance of steel moment resisting frames with RBS connections under fire loading. Engineering Structures, **75**, 126-138, 2014.

[6] E. Nigro, A. Ferraro, G. Cefarelli, R. The influence of fire scenarios on the structural behaviour of composite steel-concrete buildings. *Applied Mechanics and Materials*, **82**, 368-373, 2011.

[7] H. Mostafaei, F. Vecchio, N. Bénichou, Seismic Resistance of Fire-Damaged Reinforced Concrete Columns. *ATC and SEI Conference on Improving the Seismic Performance of Existing Buildings and Other Structures,* San Francisco, California, United States, December 9-11, **1**, 1396-1407, 2009.

[8] H. Mostafaei, Hybrid fire testing for assessing performance of structures in fire - Meth-

odology. Fire Safety Journal, **58**, 170-179, 2013.

[9] H. Mostafaei, Hybrid fire testing for assessing performance of structures in fire - Application. Fire Safety Journal, **56**, 30-38, 2013.

[10] F. Mazza, A. Vulcano, Nonlinear response of r.c. framed buildings with isolation and supplemental damping at the base subjected to near-fault earthquakes. *Journal of Earthquake Engineering*, **13(5)**, 690-715, 2009.

[11] F. Mazza, A. Vulcano, Effects of the near-fault ground motions on the nonlinear dynamic response of base-isolated r.c. framed buildings. *Earthquake Engineering and Structural Dynamics,* **41**, 211-232, 2012.

[12] B.A. Bolt, Seismic input motions for nonlinear structural analysis. *ISET Journal of Earthquake Technology,* **41**(2-4), 223-232, 2004.

[13] Technical Regulations for the Constructions. Italian Ministry of the Infrastructures, January 14, 2008 (in Italian).

[14] Eurocode 2. Design of concrete structures – Part 1-2: General rules, structural fire design. *C.E.N., European Committee for Standardization*, December 2004.

[15] Pacific Earthquake Engineering Research Center database. peer.berkeley.edu/smcat /search.html.

[16] E. Kalkan, S.K. Kunnath, Relevance of absolute and relative energy content in seismic evaluation of structures. *Advances in Structural Engineering*, **11**(1), 17-34, 2008.

[17] Eurocode 1. Actions on structures – Part 1-2: General actions, actions on structures exposed to fire. *C.E.N., European Committee for Standardization*, October 2004.

[18] ISO 834 International Standard, Fire resistance tests, ISO 834-1 Test conditions. *Provided by IHS under license with ISO: 31*, Genève, Switzerland, 1999.

[19] F. Mazza, A. De Luca, Seismic vulnerability in case of fire of existing r.c. framed buildings: modelling and nonlinear dynamic analysis. *COMPDYN 2015, 5th ECCOMAS Thematic Conference on Computational Methods in Structural Dynamics and Earthquake Engineering*, Crete Island, Greece, May 25–27, paper n. 491, 2015.

[20] F. Mazza, M. Fiore, Comparative study of the wind and earthquake dynamic responses of fire exposed steel framed buildings. *COMPDYN 2015, 5th ECCOMAS Thematic Conference on Computational Methods in Structural Dynamics and Earthquake Engineering*, Crete Island, Greece, May 25–27, paper n. 490, 2015.

[21] Eurocode 8. Design of structures for earthquake resistance – Part 3: Assessment and retrofitting of buildings. *C.E.N, European Committee for Standardization*, June 2004.

[22] F. Mazza, M. Mazza, Nonlinear analysis of spatial framed structures by a lumped plasticity model based on the Haar-Kàrmàn principle. *Computational Mechanics*, **45**, 647-664, 2010.

[23] F. Mazza, A distributed plasticity model to simulate the biaxial behaviour in the nonlinear analysis of spatial framed. *Computers and Structures*, **135**, 141-154, 2014.

[24] F. Mazza, M. Mazza, A. Vulcano, Nonlinear Dynamic Response of R.C. Buildings with Different Base-Isolation Systems Subjected to Horizontal and Vertical Components of Near-Fault Ground Motions. *The Open Construction & Building Technology Journal,* **6**, 373-383, 2012.

COMPDYN 2015
5th ECCOMAS Thematic Conference on
Computational Methods in Structural Dynamics and Earthquake Engineering
M. Papadrakakis, V. Papadopoulos, V. Plevris (eds.)
Crete Island, Greece, 25–27 May 2015

ROLLING-BALL RUBBER-LAYER ISOLATION SYSTEM: STATE OF THE ART, PERFORMANCE AND DESIGN PROCEDURE

Marco Donà[1], Giovanni Tecchio[1], Claudio Modena[1], and Alan H. Muhr[2]

[1] Department ICEA - University of Padova
Via F. Marzolo, 9, 35131 Padova (IT)
e-mail:
marco.dona@dicea.unipd.it
giovanni.tecchio@dicea.unipd.it
claudio.modena@dicea.unipd.it

[2] Tun Abdul Razak Research Centre - TARRC
Brickendonbury, Hertford, SG13 8NL (UK)
amuhr@tarrc.co.uk

Keywords: Seismic isolation system, content seismic-protection, rolling on rubber tracks, viscoelastic indentation effect.

Abstract. *A rolling-ball rubber-layer (RBRL) isolation system was developed at TARRC to enable isolation of lightweight structures. The system is very versatile, a great range of equivalent natural frequencies and coefficients of damping being achievable through the independent choice of rubber spring and rubber-layer rolling track. It is suitable for isolating light structures, and much more effective at low excitations than an equivalent sliding system would be. In this paper the state of the art and the dynamic behaviour of RBRL isolation system will be restated. Subsequently, a simple and efficient procedure will be described for the design of the system: this is aimed to get the principal value of the system parameters to meet the chosen values of isolation period and damping ratio. In particular, it will be emphasized that a certain value of rolling resistance of the device could result from different combinations of the device parameters, thus leaving the final specification to be made on the basis also of preferences regarding small-deflection behaviour and cost. Finally, a future application of the isolation system for the seismic protection of a statue is presented and discussed.*

1 INTRODUCTION

While in the last decades the main studies and applications performed in the field of seismic isolation were aimed toward the isolation of structures, in the last few years attention was also dedicated to the protection of the contents, since they may have an extremely high value, sometimes even more than the structure in which they are contained. The lack of effective techniques, which are sufficiently developed and applicable for the seismic risk mitigation of lightweight objects, make the seismic protection of contents a crucial and worldwide issue.

Some data from Taghavi & Miranda [1], reported in Figure 1, illustrate the typical investment in structural framing, non-structural components and building contents, for three common types of commercial construction: office, hotel and hospital. Clearly the investment in non-structural components and building contents is far greater than that for structural components and framing (Whittaker & Soong [2], FEMA E-74 [3]).

The value of the content objects might be high not only from an economical point of view, e.g. for special medical or industrial equipment, but also from a cultural or historical one: this is the case for museum contents and art objects in general. The need to prevent or mitigate the devastating effects of earthquakes on cultural heritage assets is acute for countries in which this heritage is concentrated, and which suffer the highest seismic risk level: such as the case of Italy, and many other sites in the Mediterranean basin. Awareness of this issue has recently grown in Italy too, as a result of the quakes of Umbria-Marche (1997), l'Aquila (2009) and Emilia (2012).

Although the basic theories and concepts of seismic isolation are the same, the isolation techniques to be used for the content are not a mere extension of the ones used for civil structures. Indeed, the following technical peculiarities have to be considered:

- the contents involve masses orders of magnitude smaller than those characteristic of civil structures, whereas the demand for relative displacement is not likewise scaled down, and the combination may fall outside the range feasible with a conventional isolator suitable for large masses;
- lightweight structures are often very vulnerable, even for small seismic actions, since they often are merely supported on the base without possibility to be anchored (because of architectural or preservation requirements); this leads to the necessity to design a base isolation considering the possible rocking/overturning and sliding phenomena;
- besides being technically proficient, the isolation systems at the base of items of content have to observe conservation and aesthetic requirements too.

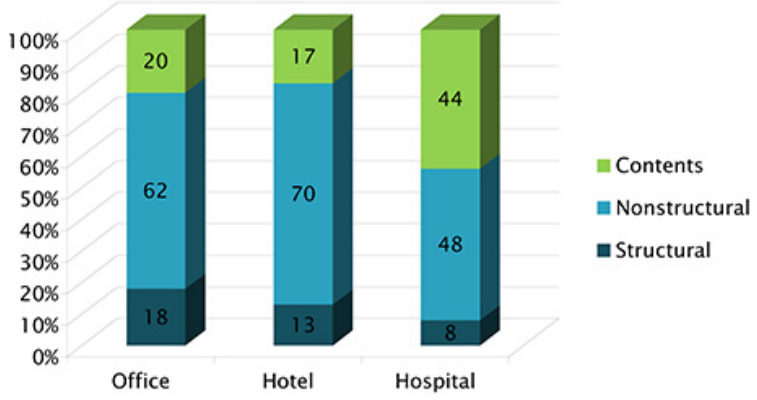


Figure 1: Typical cost breakdown in building construction, according to Taghavi & Miranda [1], for three different occupancies (image from FEMA E-74 [3]).

2 BACKGROUND OF RBRL ISOLATION SYSTEM

2.1 Presentation of the isolation system

The rolling-ball rubber-layer isolation (RBRL) system, originally proposed by Prof. A.G. Thomas, was developed at TARRC to enable isolation of low-mass (< 10 t) structures. The principal system components are visible in Figure 2, from Guerreiro et al. [4], and their principal functions are:

- steel rolling balls system – enables support of gravity loads and accommodation of large horizontal displacements;
- rubber-layer tracks – provide appropriate energy dissipation capacity and adequate resistance for horizontal non-seismic actions;
- rubber springs – provide recentering function and system stiffness in steady-state rolling phase.

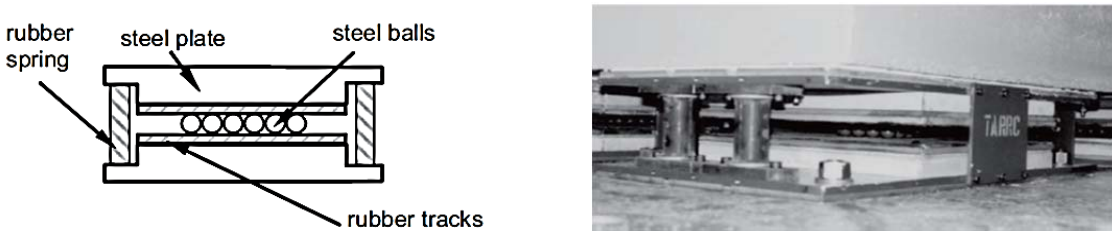


Figure 2: a) Simplified representation and b) image of the RBRL system (from Guerreiro et al. [4]).

Extensive experimental studies of this system were undertaken by TARRC and collaborating research centres in the period 1995 – 2002 (Donà et al. [5]), resulting in four publications on shaking table tests and two more publications restricted to laboratory characterisation of the system itself. A new experimental campaign for the characterization of the system behaviour was performed at TARRC's engineering laboratory in 2014 for a Ph.D. project (Donà [6]), in a collaboration between TARRC and University of Padova.

All these experimental studies are briefly reported in Table 1. The RBRL systems investigated were diverse, involving different design natural frequencies and levels of damping.

2.2 Highlights of the system behaviour

Previous experimental studies have shown that the RBRL isolation system has three key types of behaviour, differentiated according to the magnitude of the displacements relative to the ground.

1. Inside-pit behaviour

For small displacements the system has nonlinear force-displacement characteristics, with high damping and high stiffness, albeit the stiffness declining rapidly as the displacement amplitude is increased. In this regime the behaviour is dominated by the continued location of the balls within a viscoelastic depression, or pit, formed during the long period under static load in the absence of seismic excitation. This behaviour contrasts with that of a sliding system, which presents a very high elastic stiffness, bordering on rigidity, for small excitations.

2. Fuse behaviour

If a characteristic threshold horizontal force is applied, for example by a sufficiently large ground acceleration, the balls will escape from the locality of the viscoelastic depressions, and roll with an approximately constant opposing resistance, significantly lower than the characteristic threshold force. In this regime, the system behaves like a mechanical fuse, the force

Project / Publication	Type of tests	Tracks	Springs	Superstructure
INCLUDING SHAKING TABLE TESTS				
EERC (Foti and Kelly [7])	monoaxial	high damping, Jakarta compound (Lab Rep 96. Compound 009-06)	steel coil, soft	flexible – model building
ENEL/ISMES/TARRC collaboration (Muhr and Bergamo [8])	monoaxial	high damping, probably the same as EERC	steel coil, soft	rigid – concrete slab
REEDS (Bettinali et al. [9])	triaxial	low damping A, inside ϕ of 190 mm; high damping B outside (ball array ϕ ~ 190mm)	rubber B, stiff (1.3Hz)	flexible - electrical substation structure
ECOEST (Guerreiro et al. [4])	monoaxial biaxial triaxial	low damping A, both or upper; high damping B, lower	rubber A, soft and none	rigid or flexible model building
LABORATORY BASED STUDIES				
DEGREE PROJECT (Cook et al. [10])	monoaxial	unfilled NBR	none	none
PhD PROJECT (Muhr et al. [11])	monoaxial	unfilled NR (two levels of curatives) and NBR	none	none
PhD PROJECT (Donà [6]) (Donà et al. [12])	monoaxial	unfilled NR, 3 different compounds: A, A+, A-	rubber A, 3 different diameters	none

Table 1: Summary of experimental studies done by TARRC and collaborators, on RBRL device.

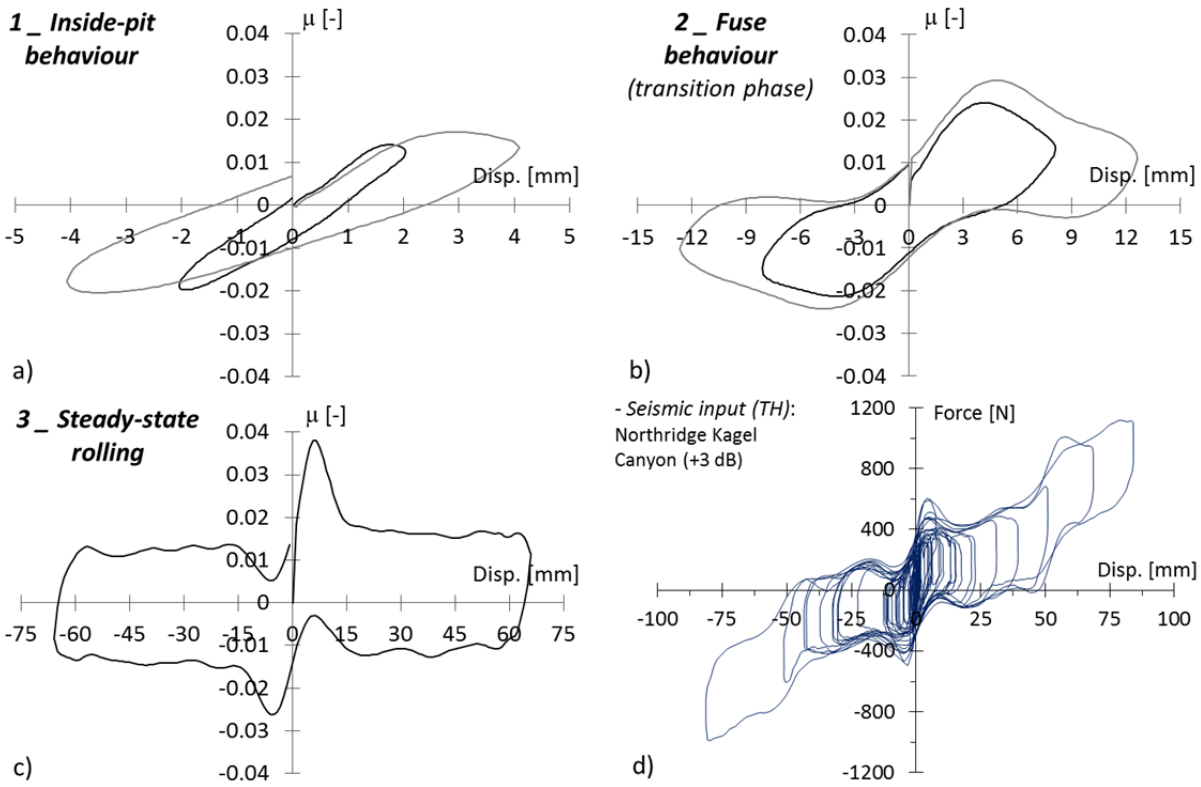


Figure 3: a), b), c) Rolling friction-displacement (μ-Disp) loops, representative of the types of behaviour of the RBRL system without springs (Donà [6]). d) Overall behaviour form a shaking-table test of the ECOEST project.

applied to the superstructure being truncated at the value of the characteristic peak, or threshold, force. This behaviour is akin to that of a sliding system subjected to moderate excitations, but with the additional feature that there is a memory effect of the viscoelastic depressions that tends quite strongly to recapture the rolling balls in their initial reference configuration. The displacement time history of the isolated structure therefore exhibits periods of small displacement, with occasional larger excursions; the force-time history is clipped at the characteristic threshold force.

3. Steady-state rolling behaviour

For strong excitations with many fluctuations (as opposed to a discrete pulse), continuous free rolling will be induced. In this regime, the recentering springs provide a well-defined stiffness so that a natural frequency of isolation may be defined: it is not strongly amplitude-dependent, and can be designed to have any desired value. The equivalent linear damping level can be calculated for the design displacement from the rolling resistance of the balls and the spring stiffness, as will be shown later, and there is very good scope for meeting any desired level of damping. The system thus behaves like a classical linear isolation system, but enables great scope for choice of natural frequency and damping ratio.

These key types of the system behaviour are visible in Figure 3 a, b and c. These rolling friction-displacement (μ-disp) loops, in which μ is the horizontal resistance divided by the vertical load applied on the RBRL system, derive from a new parametric experimentation conducted at TARRC for the Ph.D. project of Donà [6]. These tests involved different RBRL systems and different imposed sinusoidal motions, but only a few representative results of the system behaviour are herein shown, related to a RBRL system so configured:

- rubber tracks, 2 mm thick, of type A - an unfilled natural rubber with low-damping (see Guerreiro et al. [4] and Donà [6]);
- steel balls with 25 mm diameter;
- stress parameter $W/ER^2 = 1.2$, where W = vertical load per ball, E = Young's modulus of the rubber, R = radius of the ball;
- no recentering springs.

The choice to not consider the recentering springs in these tests was for better characterizing the pits effect on the small-deflection behaviour of the system.

Rubber springs provide a recentering stiffness that simply acts in parallel with the behaviour of the RBRL device without springs. The overall behaviour of the isolation system, with springs, is shown in Figure 3 d for a shaking-table monoaxial test of the ECOEST project, considering the RBRL system with rubber A, the "Mass Down" configuration and the real accelerogram of the earthquake "Northridge Canyon" (for more details see Guerreiro et al.[4]).

2.3 Advantages of the RBRL isolation system

- The RBRL system is relatively economical.
- The device assembly is easy to tailor for the specific case, in terms of geometry and performance, a great range of equivalent natural frequencies and coefficients of damping being achievable. Depending on the choice of parameters, the RBRL system provides a rich variety of possibilities, including primary seismic mitigation strategies of isolation, damping or fuse functions.
- The RBRL isolation system provides very effective reduction of excitation of the first mode of the isolated structure for small seismic events, for a wide range of frequency content, despite its being very much stiffer when the deflections across the isolators are small (< 5mm). The primary factor responsible is probably the very high damping, together with the changed

mode shape resulting from the compliance of the isolators, although the non-linear behaviour may also be significant (Donà et al. [5], Donà et al. [12]).

These considerations make the RBRL isolation system very attractive for the protection of works of art in a museum, which are present in large quantity and characterized by very different shapes, dimensions and masses.

3 NEW TESTS: ROLLING FRICTION AND RECENTERING STIFFNESS

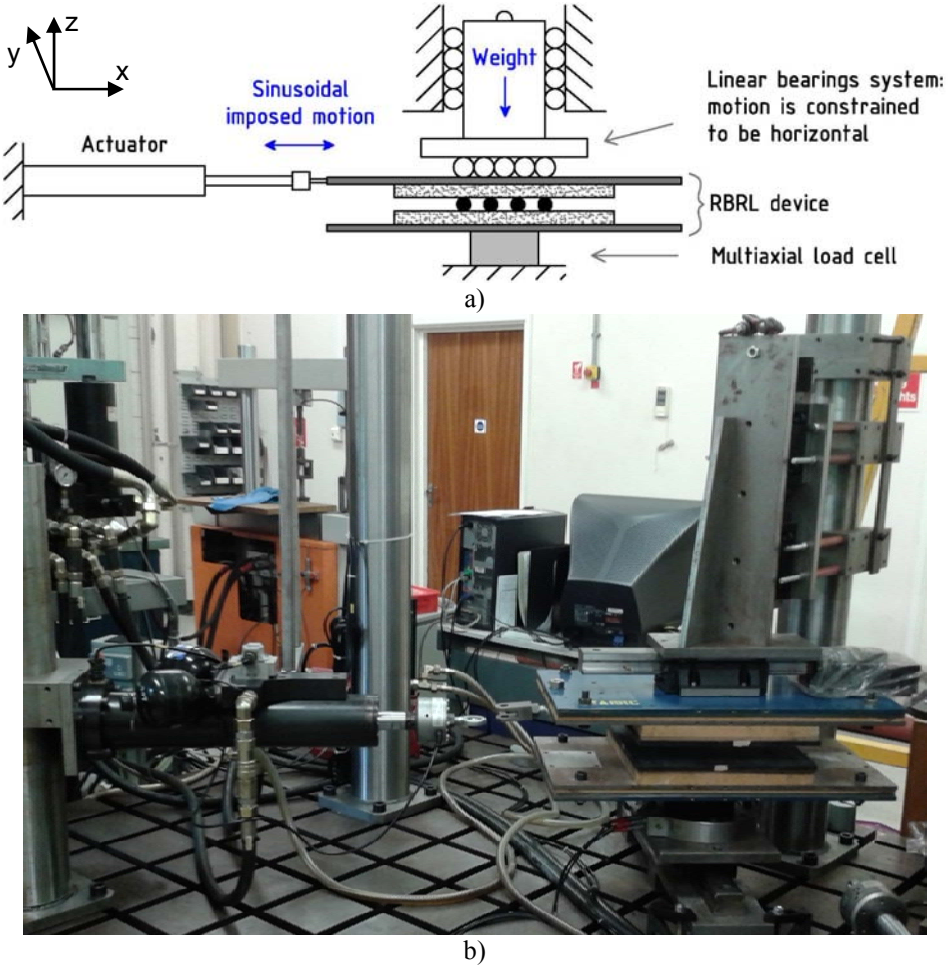
Although the small-deflection behaviour of the RBRL system requires a complicated model, the design of the isolation system is relatively simple, as it can be based only on the main performance parameters: the steady-state rolling force and the stiffness of the recentering rubber springs.

For design purposes, parametric experimentations were carried out at TARRC in 2014 [6] regarding the steady-state rolling and the dynamic behaviour of the recentering rubber springs.

These tests and some useful results for the design of the system are presented below.

3.1 Tests on the RBRL devices for the steady-state rolling friction

All the tests were performed in single shear configuration for one RBRL device with no recentering springs: the test setup is shown in Figure 4.



a)

b)

Figure 4: Setup of the sinusoidal uniaxial tests: a) schematic drawing, b) photo.

The steel linear roller bearings shown in Figure 4 permit translation of the top plate in the x and z directions, but prevent rotation of it about any axis. The sinusoidal motion was controlled by the actuator and transmitted to the top steel plate of the device, that supports the weight, through a rose joint connection that permits small rotations. This connection was necessary to avoid bending stresses related to a non-perfect vertical alignment between actuator and top plate of the device, and to accommodate the small z-displacement as the balls roll out of and into their pits. The horizontal force (x-axis) was measured by the multiaxial load cell placed under the bottom plate of the device, which was fixed on it. This was preferred to the direct measurement of the force by the actuator load cell, to avoid inclusion of the friction inside the linear rolling bearings which constrain the top plate motion.

153 tests have been carried out changing the principal device parameters that control behaviour, i.e. the rubber compound, the thickness t of the rubber layers, the radius R of the balls and the stress parameter W/ER^2 per ball. Each test consisted of 3 sinusoidal cycles, with a displacement amplitude of 65 mm and a frequency of 0.5 Hz.

The rolling friction force in steady state condition was obtained, for each test, from the second of the three sinusoidal cycles performed. These force values were then divided by the vertical load used in the relative test, obtaining the rolling friction coefficients μ.

Some of the obtained results for rubber type A are reported in Figure 5, where the rolling friction μ is plotted versus coefficient t/R (thickness of rubber layers / radius of balls) for chosen values of the stress parameter.

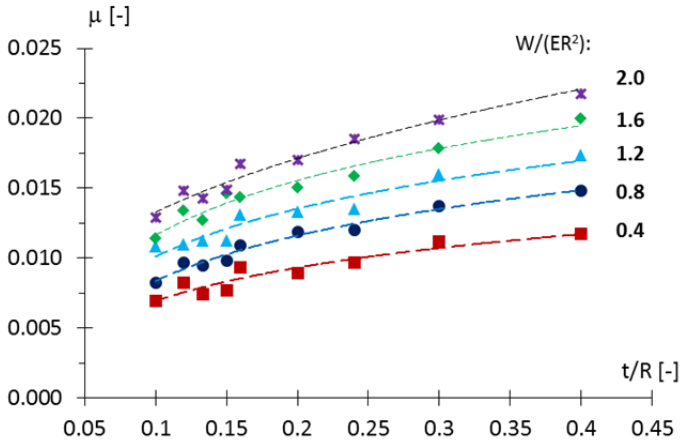


Figure 5: Rolling friction μ values of the RBRL system with rubber A, for different t/R and W/ER^2.

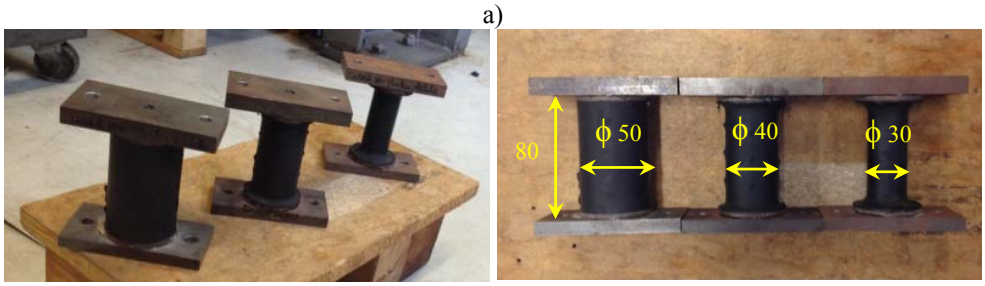
3.2 Tests on the recentering rubber springs for the system stiffness

Figure 6a shows the setup for the double shear tests carried out for the behaviour characterization of the recentering rubber springs. These springs are cylinders of rubber 80 mm long, bonded to steel endplates; they were moulded for the ECOEST Project (Guerreiro et al. [4]) from rubber compound A, in three different diameters: 30, 40 or 50 mm (Figure 6b). Every test was conducted using two springs with the same diameter, constrained into a steel frame appositely designed for this purpose. The steel plate connecting the two spring endplates was linked to the arm of the actuator.

Both sinusoidal and quasi-static tests were considered, according to Table 2. In particular, concerning the imposed sinusoidal motion, tests were carried out with different amplitudes (from 1 to 75 mm) for the same frequency (1 Hz) and with different frequencies (from 0.1 to 2 Hz) for the same amplitude (75 mm).



a)



b)

Figure 6: a) Double shear test setup for the behaviour characterization of the recentering rubber springs. b) Tested recentering rubber springs; diameter (ϕ), from left to right: 50, 40, 30 mm.

Sinusoidal tests *different amplitudes*	*Frequency* *Amplitudes*	**1 Hz** 2.5; 5; 7.5; 10; 20; 30; 40; 50; 60; 75 mm
Sinusoidal tests *different frequencies*	*Amplitude* *Frequencies*	**75 mm** 0.1; 0.5; 1; 2 Hz
Quasi-static tests	*Velocity* *Displacements*	**1 mm/s** from 0 to 150 mm

Table 2: Double shear tests carried out on the recentering rubber springs.

Results from the sinusoidal tests with different frequencies are reported as force-displacement loops in Figure 7a. These show a not significant dependence on the velocity and a negligible hysteretic dissipation for the dynamic behaviour of the recentering springs, in particular for the smaller diameters. Figure 7b presents the results of the quasi-static tests, which were needed to extend the information about the stiffness of the springs for amplitudes bigger than 75 mm, this being the maximum stroke of the actuator in each direction and hence the amplitude limit for the dynamic tests. Both types of test show a slight dependence of the springs behaviour on the amplitude of deflection. The parameter needed for design purposes of the isolation system is the storage stiffness $K^{/}$ (from dynamic tests) or the secant stiffness K_{sec} (from static tests). These values are plotted versus displacement and compared in Figure 8. In particular, the values of the storage stiffness were calculated by the force-displacement loops of the sinusoidal tests with different amplitudes, using the Harmonic method (Ahmadi & Muhr [13]).

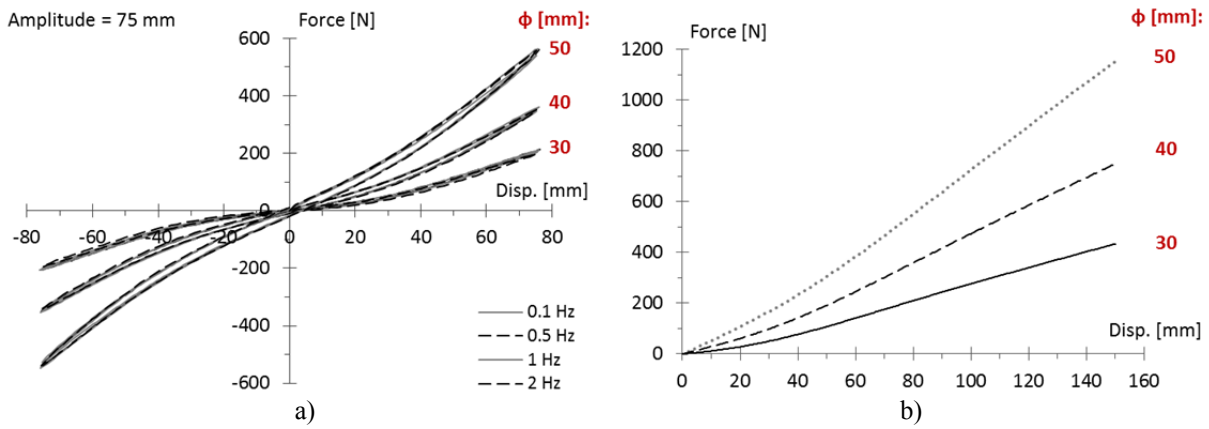


Figure 7: Results from tests for springs of different diameter ϕ: a) dynamic – with different frequencies; b) quasi-static.

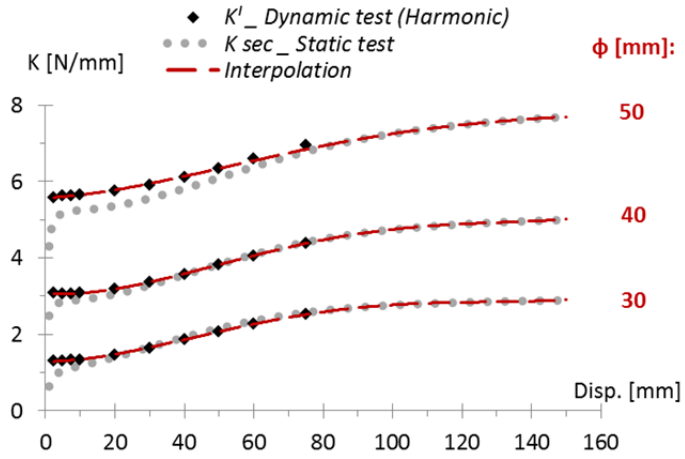


Figure 8: Comparison between the storage stiffness $K^{/}$, from dynamic tests, and the secant one K_{sec}, from quasi-static tests. The stiffness finally considered derives from $K^{/}$ values until 75 mm, and from K_{sec} values for higher deflections (as indicated by the dashed lines).

4 DESIGN PROCEDURE OF THE RBRL SYSTEM

According to Cook et al. [10], the values of the stiffness K and rolling friction coefficient μ of the RBRL system can be determined through the equations reported below, if the values of period T and damping ratio ζ have been decided and if the design displacement D, e.g. from the damped spectrum, and the mass M to be isolated are known.

$$K = \frac{4\pi^2 M}{T^2} \tag{1}$$

$$\mu \equiv \frac{F_R}{Mg} = \frac{1}{g}\,\frac{2\pi^3 D\zeta}{T^2\left(1-\pi\zeta/2\right)} \tag{2}$$

These equations were obtained considering an elasto-plastic hysteresis loop (Figure 9) as dynamic response of the RBRL system, and using the Secant linearization method (Ahmadi & Muhr [13]). These can be used if parameter ζ does not grossly exceed 20% and if the seismic excitation is sufficient for the peak roll-out force to be generated for much of the time history. For lower seismic excitations, the behaviour of the device will be governed by the effective dynamic stiffness of the balls rocking in their static depressions or "pits": for this reason the

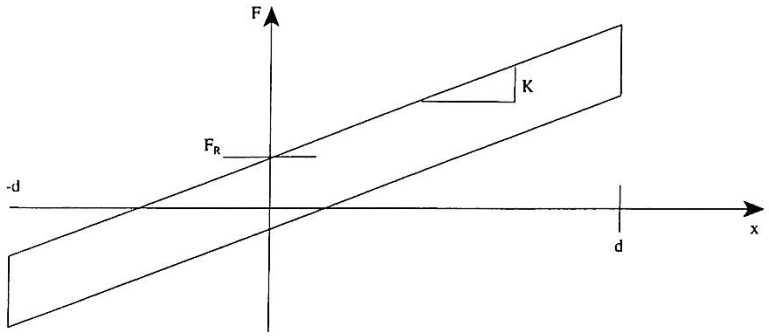


Figure 9: Schematic hysteresis loop for isolation system comprising rolling-ball dissipative-layer isolators and springs (from Cook et al. [10]).

method here presented is proposed for use only for design purposes, considering the maximum response spectrum as the design spectrum.

When the values of K and μ have been calculated, together with the ultimate displacement by the damped response spectrum, the geometric characteristics of the RBRL system can be determined through the previous experimental results. Using the plots of Figure 8, the correct diameter of the recentering springs to achieve the target stiffness of the system can be easily found by entering the figure with the values of displacement and K. Once the stress parameter has been decided, then, the value of the ratio t/R needed to get the correct μ can be obtained using the results as those presented in Figure 5. Finally, after the choice of R, it is possible to determine the number of balls to meet the stress level previously established.

Design procedure calls for two free choices to be made, the values of W/ER^2 and R. A different combination of the stress parameter W/ER^2 with the parameter t/R, that leads to the same μ, does not change the steady-state behaviour of the device. The appropriate value of this stress parameter is thus a compromise between cost and the necessity to avoid the creation of semi-permanent rolling tracks on the rubber layers. Also the choice of R is important from an economic point of view, the steel balls being one of the principal cost components.

Cost consideration is not so significant for a single application of the RBRL system. However, as the system is relatively economical and easy to tailor for the specific case in terms of geometry and performance, it is envisaged to be appropriate for projects such as a museum needing to isolate single artefacts, showcases and podia, where a large number of discrete isolation systems are needed, and hence the total cost becomes a key choice-determining factor.

5 FUTURE APPLICATION: ISOLATION OF THE STATUE "TEMPERANZA"

The University of Padova, in collaboration with TARRC, Numeria s.r.l. and the local authority of Verona, is working on a pilot project that involves the seismic isolation of one of the statues of the Scaliger Tombs (Arche Scaligere). The statue, the "Temperanza", is shown in Figure 10.

The principal features of the statue, with base (see Figure 10 b), are:

- total weight: ≈ 372 kg
- maximum dimension: ≈ 483 x 463 x 1665 mm

The principal features of the statue, without base, are:

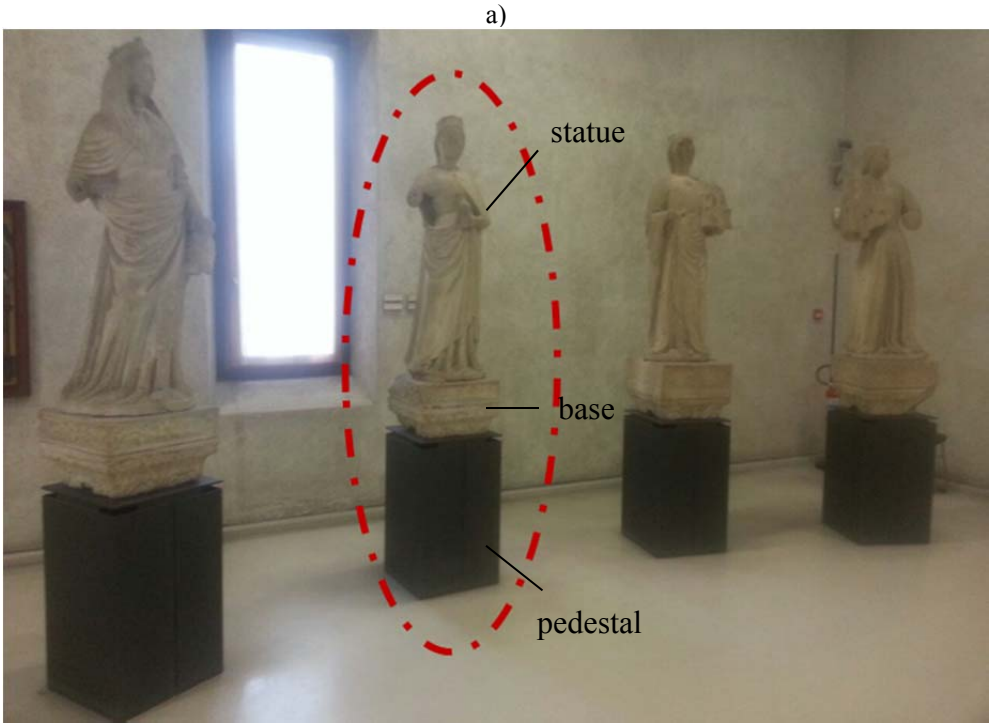
- maximum dimension: ≈ 483 x 455 x 1372 mm
- height of the centre of gravity, relative to the plane between the statue and base: ≈ 536 mm.

The statue is placed in the "Museum of the frescoes of G.B. Cavalcaselle" in Verona (IT); the SLV (Life Safety) seismic response spectrum of that area is shown in Table 3.

Figure 11 presents a possible scheme of the RBRL system for this pilot project.



a)



b)

Figure 10: a) Optical scanning of the statue "Temperanza" (images provided by UNOCAD s.r.l. – Vicenza IT). b) Images of the statues of the Scaliger Tombs in the "Museum of the frescoes of G.B. Cavalcaselle", Verona IT.

Verona Response Spectrum	
Limit state	**SLV**
Reference period (V_R)	50 years
Return Period (T_R)	475years
Exceedance probability in V_R	10%
a_g	0.157
Soil type	B
Topographic height effects	T1
Behaviour factor q	1
PGA [g]	0.188

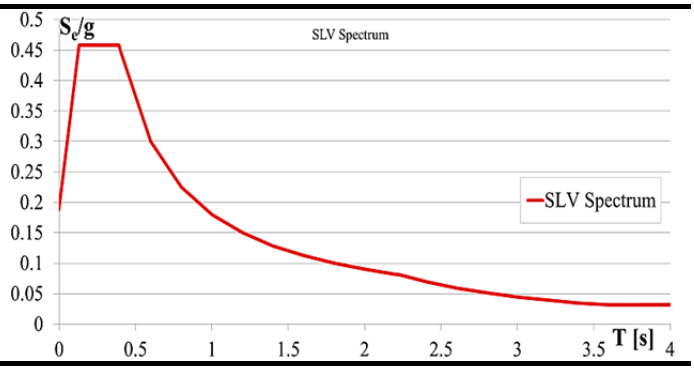


Table 3: SLV (Life Safety) acceleration response spectrum (ARS) of Verona.

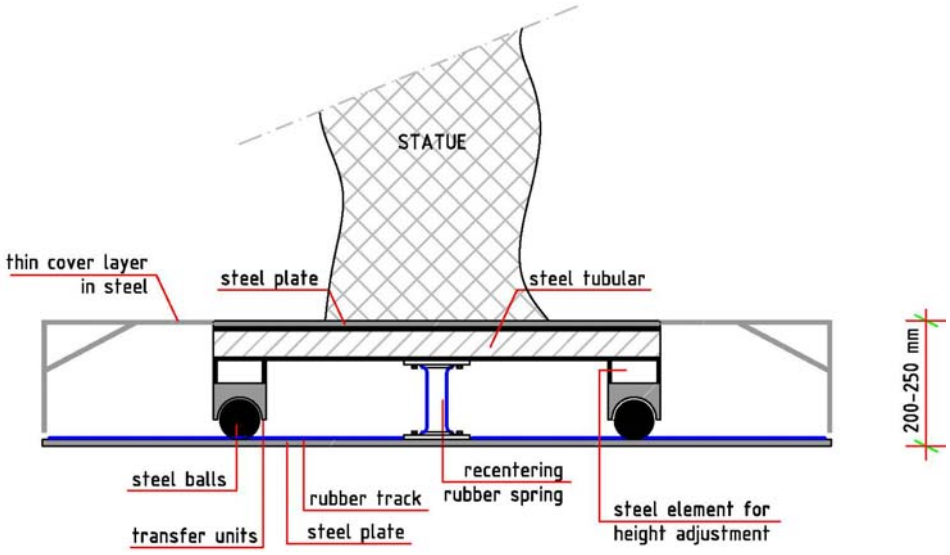


Figure 11: Scheme of the RBRL system (1 rubber layer) for seismic isolation of the statue "Temperanza". The same for both directions.

The choice to use the balls inside transfer units, thus only one rubber track, minimises the vulnerability of the system to the effect of overturning moment. However, it also results in a rolling resistance that is half with respect to the associated RBRL system with a double rubber-layer.

6 CONCLUSIONS

- The state of the art of the RBRL seismic isolation system is reported. The principal components and characteristics are presented. The three key types of its behaviour, differentiated according to the magnitude of the displacements relative to the ground, are shown and discussed.
- The principal advantages of this system, for the seismic isolation of lightweight structures, are highlighted. Briefly: the RBRL system is relatively economical and is easy to tailor for the specific case, in terms of geometry and performance, a great range of equivalent natural frequencies and coefficients of damping being achievable; the RBRL system presents a good performance also for small seismic events, which induce small deflections (< 5 mm) across the isolator, resulting much more effective at low excitations than an equivalent sliding isolation system (Donà et al. [12]).
- Two new experimentations, carried out at TARRC in 2014 for a Ph.D. project (Donà [6]) and addressing the steady-state rolling resistance and the recentering stiffness of the system, are presented. The results of these investigations are presented in a suitable form for the design of the RBRL system.
- A design procedure for the RBRL system is presented, based on that proposed by Cook et al. [10]. This procedure allows the determination of the parameters that influence the system behaviour, for a specific design spectrum and vertical load, starting from the choice of isolation period and damping ratio.
- A future application of the RBRL system for the seismic isolation of a statue is briefly introduced.

REFERENCES

[1] S. Taghavi, E. Miranda, Response Assessment of Nonstructural Building Elements. *PEER Report 2003/05*, University of California Berkeley, 2003.

[2] A.S. Whittaker, T.T. Soong, An overview of nonstructural components research at three U.S. Earthquake Engineering Research Centers. *Proceedings of Seminar on Seismic Design, Performance, and Retrofit of Nonstructural Components in Critical Facilities,* Applied Technology Council Multidisciplinary Center for Earthquake Engineering Research, 29, 271-280, 2003.

[3] FEMA E-74, *Reducing the Risks of Nonstructural Earthquake Damage – A practical Guide*. January, 2011.

[4] L. Guerreiro, J. Azevedo, A.H. Muhr, Seismic Tests and Numerical Modeling of a Rolling-ball Isolation System. *Journal of Earthquake Engineering*, **11**(1), 49-66, 2007.

[5] M. Donà, A.H. Muhr, G. Tecchio, A. Dusi, C. Modena, Isolation of light structures with Rolling-Ball Rubber-Layer system - characteristics and performance. *Proceedings of the Second European Conference on Earthquake Engineering and Seismology*, Istanbul, Turkey, August 25-29, paper 1220, 2014.

[6] M. Donà, *Rolling-Ball Rubber-Layer system for the lightweight structures seismic protection: experimentation and numerical analyses*. Ph.D. Thesis, University of Trento – Dept. of Civil, Environmental and Mechanical Engineering, Italy, 2015 (to be published).

[7] D. Foti, J.M. Kelly, *Experimental study of a reduced scale model seismically base-isolated with Rubber-Layer roller bearings*. Monograph IS-18, (Monograph Series in Earthquake Engineering, ed. A.H. Barbat), International Center for Numerical Methods in Engineering, Barcelona, Spain, 1996.

[8] A.H. Muhr, G. Bergamo, Shaking Table Tests On Rolling-Ball Rubber-Layer Isolation System. *Proceeding of 14th ECEE 2010*, Ohrid, Macedonian, August 30 – September 03, paper 745, 2010.

[9] F. Bettinali, S. Bellorini, G. Bergamo, A.H. Muhr, A. Diehl, Seismic Risk Mitigation of Light Structures by means of novel Rolling-Ball Rubber-Layer Systems. *Proceeding of 5th World Congress on Joints, Bearings and Seismic Systems for Concrete Structures*, Rome, Italy, October 7–11, 2001.

[10] J. Cook, A.H. Muhr, M. Sulong, A. Thomas, Rolling-ball Isolation System for Light Structures. *Proceeding of International Post-SMiRT Conference Seminar on Seismic Isolation, Passive Energy Dissipation and Active Control of Seismic Vibrations of Structures*, Taormina, Italy, August 25-27, 795-811, 1997.

[11] A.H. Muhr, M. Sulong, A.G. Thomas, Rolling-ball Rubber-layer Isolators. *Journal of Natural Rubber Research*, **12** (4), 199-214, 1997.

[12] M. Donà, A.H. Muhr, G. Tecchio, G. Granello, Rolling-Ball Rubber-Layer isolation system – small deflection and vibrational behaviour. *Proceedings of SECED 2015 Conference*, Homerton College, Cambridge, UK, July 9-10, 2015 (to be published).

[13] H.R. Ahmadi, A.H. Muhr, Modelling dynamic properties of filled rubber. *Journal of Plastics, Rubber and Composites Processing and Applications*, **26** (10), 451-461, 1997.

COMPDYN 2015
5th ECCOMAS Thematic Conference on
Computational Methods in Structural Dynamics and Earthquake Engineering
M. Papadrakakis, V. Papadopoulos, V. Plevris (eds.)
Crete Island, Greece, 25–27 May 2015

THE EFFECT OF MODIFIED LINEAR VISCOELASTIC IMPACT MODELS ON THE POUNDING RESPONSE OF A BASE-ISOLATED BUILDING WITH ADJACENT STRUCTURES

Eftychia A. Mavronicola[1*], Panayiotis C. Polycarpou[1], Petros Komodromos[1]

[1] Department of Civil and Environmental Engineering, University of Cyprus
75 Kallipoleos Street, P.O. Box 20537, 1678 Nicosia, Cyprus
{mavronicola.eftychia, ppanikos, komodromos}@ucy.ac.cy

Keywords: Seismic isolation, Structural pounding, Impact models, Kelvin-Voigt model, Seismic gap.

Abstract. *During strong earthquake excitations, base-isolated buildings may collide, either with the surrounding moat wall or with adjacent buildings. This unfavorable possibility has been recently investigated through numerical simulations and parametric studies. A very important issue regarding these numerical studies is the modeling of impacts, which are typically simulated using various types of force-based impact models. This paper parametrically investigates the effects of impact modeling characteristics on the overall structural response of a base-isolated building that is subjected to seismic pounding. Specifically, the Kelvin-Voigt impact model and various other modifications of this linear viscoelastic impact model are considered in the performed analyses. In order to effectively and efficiently conduct this investigation, a specialized software application, which has been specifically developed to simulate buildings subjected to pounding, is employed. A smooth bilinear (Bouc-Wen) model is used for the simulation of the seismic isolation system. The influence of particular impact parameters, as well as the width of the seismic gap, on the dynamic response of the structure under strong excitations is quantified. Furthermore, the effect of using different impact models for the calculation of the impact forces on the overall seismic response during pounding is simulated and discussed, since a reasonable question arises regarding the accuracy of an impact model, which is a simplification of the actually very complicated impact phenomenon.*

1 INTRODUCTION

Seismic isolation is widely considered as an efficient technology to improve the seismic performance of structures [1-3]. Although base isolation decreases the possibility of damage to a building, it induces large relative displacements at the isolation level. To accommodate the expected large relative displacements, a wide seismic gap must be provided around the building. This requirement imposes, a practical constraint for the utilization of seismic isolation, considering that there are often certain restrictions to the size of the available clearance around seismically isolated buildings, especially in cases of retrofitting of existing buildings in densely resided civic centers. Therefore, a reasonable concern is the risk of structural pounding with the surrounding moat wall or adjacent structures during strong earthquakes.

Earthquake-induced structural pounding on base isolated structures has been studied by several researchers the last few years. Nagarajaiah and Sun [4] observed that the response of the base-isolated Fire Command and Control Building in Los Angeles during the 1994 Northridge earthquake was altered significantly due to the occurrence of impact in the one direction, reducing the effectiveness of base isolation in that direction. Malhotra [5] and Tsai [6] examined the response of a base-isolated structure pounding against the surrounding moat wall. The superstructure was idealized as a rigid shear beam structure colliding on an adjacent retaining wall modeled as a spring element. Matsagar and Jangid [7] investigated the seismic pounding of a multi-storey building supported on various base isolation systems during impact with adjacent structures, while impacts were assumed to happen only at the base of the building with the moat wall. Komodromos *et al*. [8] and Komodromos [9] investigated, through parametric studies, the effects of poundings of a base isolated building with the surrounding moat wall, revealing the potentially detrimental effects of structural impact on the effectiveness of seismic isolation. Limited research works have been conducted considering three-dimensional (3D) earthquake-induced structural pounding, apparently because of the involved complexities and the consequently excessive computational cost. Pant and Wijeyewickrema [10, 11] studied seismic pounding of a typical 4-storey base-isolated building with retaining walls at the base using 3D finite element analyses. More recently, Polycarpou *et al.* [12] presented a novel methodology for simulating earthquake-induced pounding of buildings that are modeled as 3D multi-degree of freedom systems.

A critical aspect in numerical simulations of structural pounding is the impact model that is employed and the values of the associated parameters, which may affect the computed results. In most research studies on structural pounding, force-based impact models are used, exerting impact forces to the colliding structures whenever their separation distances are exceeded. Anagnostopoulos [13], Jankowski [14], Komodromos *et al.* [8], Ye *et al.* [15], Pant and Wijeyewickrema [10] and others [16-18], have proposed various methodologies using either a linear or a non-linear impact spring together with an energy dissipation mechanism to model structural pounding.

This paper describes four linear impact models that have been proposed in the literature and contrasts their performances through dynamic analyses of a typical 3-storey seismically isolated building, which is subjected to a set of near-fault ground motions. Simulation results are presented while varying several parameters, such as the size of the seismic gap and impact characteristics. The objective of this research work is to investigate how the peak seismic response of base isolated buildings during pounding may be affected by the type of the incorporated impact model. Therefore, a discussion on the deviation of the peak absolute floor accelerations and inter-storey deflections during poundings is presented, considering as base values the peak response predicted by the classical linear viscoelastic (Kelvin-Voigt) model.

2 MODELING AND SIMULATION ASSUMPTIONS

It is a common practice to consider structural impacts using force-based approaches, also known as penalty methods. These methods allow some interpenetration between the colliding structures, which can be justified by local deformability at the contact point. Contact springs are automatically formed as soon as an impact is detected, kept active while the colliding bodies remain in contact and removed once the bodies are detached from each other. At each time step, the interpenetration depth, $\delta(t)$, is used together with the stiffness of the contact spring to assess, according to the adopted impact model, the contact forces that should be applied to the structures. In this research work, various linear impact models proposed in the literature are used, in order to investigate the effect of the impact model selection on the peak seismic response considering pounding incidences. Specifically, the classical Kelvin-Voigt model has been selected as a base reference, using the formulas provided by Anagnostopoulos [13] for the estimation of the impact damping coefficient. In addition, three variations of the Kelvin-Voigt model are discussed and compared with each other with respect to the computed peak responses through parametric studies under strong earthquake excitations with low frequency content.

2.1 Impact modeling

The classical Kelvin-Voigt model is commonly used to model the impact force generated between two colliding structures. The Kelvin-Voigt model consists of a linear spring and a damper, acting in parallel, in order to simulate the energy loss due to permanent deformation at the contact point, as shown in Figure 2(a). The forces in the contact element, which has been used by Anagnostopoulos [13], can be calculated through the equation:

$$F_{imp}(t) = k_k \cdot \delta(t) + c_k \cdot \dot{\delta}(t) \tag{1}$$

Considering two impacting masses, a relationship may be found between the dashpot constant c_k and the coefficient of restitution e. The resulting mathematical expression for the damping coefficient according to this linear viscoelastic model can be assessed as:

$$c_k = 2 \cdot \xi_k \sqrt{k_k \cdot \frac{m_1 \cdot m_2}{m_1 + m_2}} \tag{2}$$

where the impact stiffness k_k is determined based on the axial stiffness of the colliding bodies and the impact damping ratio ξ_k is given by the following expression:

$$\xi_k = -\frac{ln\,e}{\sqrt{\pi^2 + (ln\,e)^2}} \tag{3}$$

The viscous impact damper of the Kelvin-Voigt element dissipates energy throughout the approach and restitution phases, but in reality, most of the energy dissipation takes place during the approach period and less energy is dissipated during the restitution phase. Furthermore, this model exhibits an initial jump in the impact force values due to the viscous damping term, while the damping force at the end of the restitution phase causes negative (i.e. tensile) impact forces that pull the colliding bodies together, which is unrealistic. However, due to its simplicity this model has been widely used to simulate structural pounding [19-21].

The generation of tensile forces after the detachment of the colliding bodies can be rectified through a slight adjustment of the linear viscoelastic impact model, proposed by Komodromos *et al.*, 2007 [8], as shown in Figure 2(b). The modified viscoelastic impact model

prevents the tensile forces, while introducing permanent plastic deformations, by zeroing the impact force when the contact is lost at the end of the restitution phase of the impact as:

$$F_{imp}\left(t+\Delta t\right)=\begin{cases} k_k\cdot\delta\left(t\right)+c_k\cdot\dot{\delta}\left(t\right) & for \quad F_{imp}\left(t\right)\geq 0 \\ \\ 0 & for \quad F_{imp}\left(t\right)<0 \end{cases} \tag{4}$$

Ye *et al.*, 2009 [15] proposed a different modification to the Kelvin-Voigt impact model, as shown in Figure 2(c), noting that the Kelvin model cannot reasonably reflect the physical nature of structural pounding. That proposed model preserves the convenience in determining the linear impact spring stiffness as in the classical Kelvin-Voigt model, while the damping coefficient $\hat{c}_k$ and the damping constant $\hat{\xi}_k$ are given by the following equations:

$$\hat{c}_k\left(t\right)=\hat{\xi}_k\cdot\delta\left(t\right), \qquad \hat{\xi}_k=\frac{3}{2}\cdot\frac{k_k\cdot\left(1-e\right)}{e\cdot\left(v_1-v_2\right)} \tag{5}$$

Another variation of the Kelvin-Voigt model was proposed by Pant and Wijeyewickrema, 2012 [10] to be used for the seismic pounding between reinforced concrete moment-resisting frame buildings (Figure 2(d)). The main difference with this modified Kelvin-Voigt model lies on the usage of a dashpot, in parallel with the spring in the contact element that is only activated during the approach period, according to the following expressions:

$$F_{imp}\left(t\right)=\begin{cases} k_k\cdot\delta\left(t\right)+\overline{c}_k\cdot\dot{\delta}\left(t\right) & for \quad \delta\left(t\right)>0 \ \ and \ \ \dot{\delta}\left(t\right)>0 \\ \\ k_k\cdot\delta\left(t\right) & for \quad \delta\left(t\right)>0 \ \ and \ \ \dot{\delta}\left(t\right)\leq 0 \\ \\ 0 & for \quad \delta\left(t\right)\leq 0 \end{cases} \tag{6}$$

The following formulas are used for the damping coefficient and the damping constant:

$$\overline{c}_k\left(t\right)=\overline{\xi}_k\cdot\delta\left(t\right), \qquad \overline{\xi}_k=\frac{3}{2}\cdot\frac{k_k\cdot\left(1-e^2\right)}{e^2\left(v_1-v_2\right)} \tag{7}$$

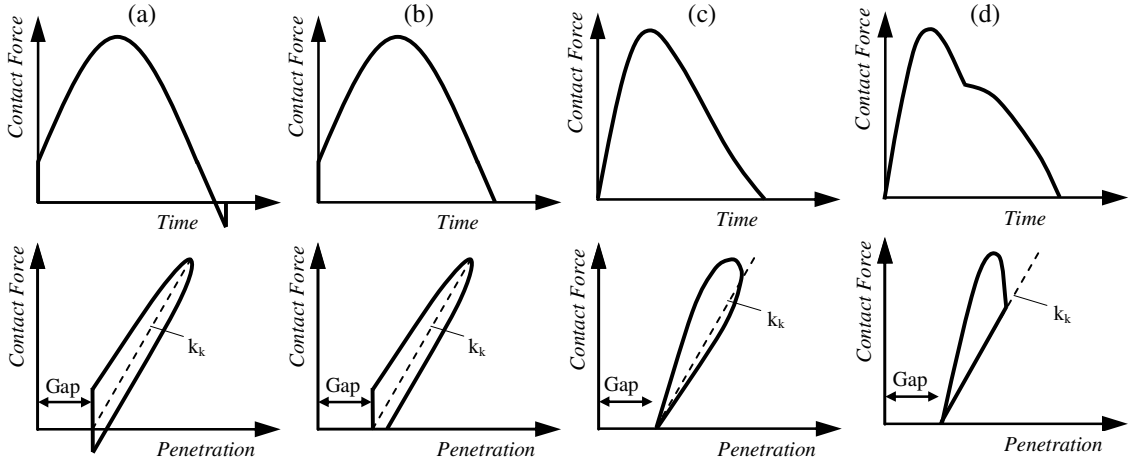


Figure 1: The linear viscoelastic impact models of (a) Anagnostopoulos, and the corresponding modified impact models proposed by (b) Komodromos *et al.*, (c) Ye *et al.*, and (d) Pant and Wijeyewickrema.

Two colliding masses and a range of values of the coefficient of restitution are used in order to assess the accuracy of the aforementioned impact models. For each predefined value of the coefficient of restitution, each of the impact models is used to perform an impact simulation, compute the impact velocity after impact and, thus, the corresponding computed value for the coefficient of restitution. Figure 2 compares the pre-specified (nominal) and the computed values for the impact models under consideration, which ideally should coincide. The results show that the assumption of a direct relationship between the impact velocity and the indentation is reasonable for pre-specified coefficients of restitution larger than 0.5. Considering that for most practical purposes the coefficient of restitution for structural impact varies within the range of 0.5 to 0.75 [14], the accuracy of the proposed formulas is satisfactory.

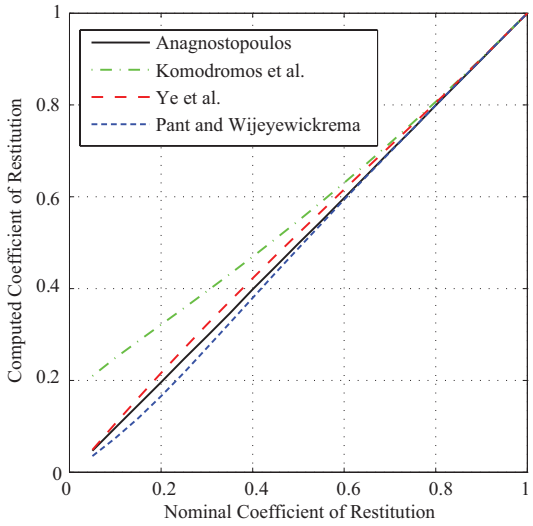


Figure 2: Comparison of the pre-specified (nominal) and computed coefficient of restitution.

2.2 Modeling of seismically isolated buildings considering poundings

In this study, the dynamic analyses of the simulated buildings, taking into account structural pounding, are performed in two dimensions, while the superstructure of the seismically isolated building is modeled as a shear-type structure mounted on LRBs with one lateral degree-of-freedom at each floor and the masses lumped at the floor levels, as shown in Figure 3(a). Poundings are assumed to happen between the moat wall and the base mat at the isolation level, which is the most common case of structural impact for a base isolated building due to the large relative displacements at the isolation level.

The seismically isolated MDOF system is subjected to horizontal components of near-fault ground motions, while it is assumed that the superstructure maintains a linear elastic behavior during the induced earthquake excitations. A typical 3-storey base-isolated building with 340 tons lumped mass at each floor level and a roof mass of 250 tons is used in the simulations, while a finite seismic gap on either of its sides is considered, in order to compare the estimations of the aforedescribed impact models. An additional mass of 340 tons is assumed to be lumped at the seismic isolation level. Each storey has a horizontal stiffness of 600 MN/m, whereas a viscous damping ratio equal to 2.0 % is assumed for the superstructure.

A smooth bilinear inelastic model is used to simulate the base isolation system (Figure 3(b)), with an isolation period based on the post-yield stiffness of 2.0 second, normalized characteristic strength F_{yi}/W_{tot} = 10.0 % and yield displacement equal to 1.0 cm. For all performed dynamic analyses, the values 1.0, 0.5, 0.5 and 2 are adopted for the Bouc-Wen models' parameters A, β, γ and n, respectively [22]. In addition to the hysteretic damping of the

isolation system, a 5.0 % viscous damping ratio has also been considered assuming non-classical damping.

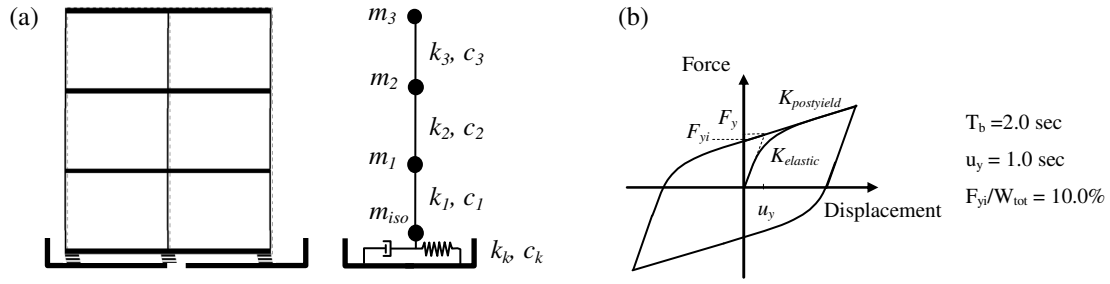


Figure 3: (a) Configuration of a 3-storey seismically isolated building, and (b) smooth bilinear inelastic model for the behavior of the seismic isolation system.

3 PRACTICAL APPLICATION

The linear viscoelastic model and its modifications that have been proposed in the literature are used to compare the response of a 3-storey base-isolated building due to poundings with the surrounding moat wall, under the Loma Prieta (UCSC 16 LGPC Station: Comp FN) and the Northridge (DWP 74 Sylmar - Converter Station: Comp FN) earthquakes. The impact stiffness is considered to be 2500 MN/m, the coefficient of restitution is taken as 0.7 for all cases, while the mass of the surrounding moat wall is set to 500 tons.

Table 1 presents the peak responses of the base isolated structure with the separation gap equal to 20 cm for both excitations, considering the four aforedescribed impact models. The maximum impact velocities (both sides) and the impact incidences are also provided. It shall be noted that the number of impacts may deviate between the various models considered. In general, the differences in the computed responses for the linear viscoelastic and the Komodromos *et al.* models are very small. As expected, the two models have almost identical responses due to the fact that their only difference is in the tensile force during detachment. Nevertheless, there is a considerable variation of the peak base-floor acceleration computed considering the classic Kelvin-Voigt model and the corresponding results of the Ye *et al.* and the Pant and Wijeyewickrema models.

Peak Response		Loma Prieta earthquake 1989-10-18				Northridge-01 earthquake 1994-01-17			
		1	2	3	4	1	2	3	4
Base displacement (cm)		20.47	20.47	20.45	20.39	21.12	21.13	21.06	20.91
Top-floor displacement (cm)		23.60	23.60	23.60	23.56	28.14	28.15	28.11	28.01
Interstorey deflection (cm)		1.82	1.82	1.77	1.77	4.14	4.14	4.02	3.97
Base-floor acceleration (m/sec^2)		34.20	34.20	38.08	42.71	71.88	71.99	80.57	92.07
Top-floor acceleration (m/sec^2)		22.57	22.57	22.30	22.13	49.51	49.51	48.56	47.60
Remaining plastic deform. (cm)		-	0.04	-	-	-	0.11	-	-
Max impact velocity (m/sec)		0.48	0.48	0.48	0.48	1.06	1.06	1.06	1.07
Number of impacts (#)	Left	0	0	0	0	2	3	2	3
	Right	2	2	2	2	2	2	2	2

***1:** Kelvin-Voigt model (Anagnostopoulos, 1988); **2:** Modified Linear viscoelastic model (Komodromos et al., 2007); **3:** Ye et al., 2009, **4:** Pant and Wijeyewickrema,2012.*

Table 1: Peak seismic responses of the 3-storey base isolated building with a seismic gap equal to 20 cm, considering the 4 different impact models, under the Loma Prieta and the Northridge earthquakes.

The origins of the observed variations can be clarified through Figure 4 and Figure 5. Specifically, these two figures present the impact force-indentation diagrams and the time-histories of the impact force at the base of the isolated building for the 4 different impact models, subjected to the Loma Prieta (Figure 4) and Northridge (Figure 5) excitations. Solid lines represent impacts on the left side of the building whereas dashed lines correspond to poundings on the right side. It is observed that the values of the maximum impact force calculated through the Kelvin-Voigt model and the modified version proposed by Komodromos *et al.* are essentially equal. This observation is also valid for the Northridge earthquake responses where the peak response occurs due to the second impact. However, the maximum impact force for the models proposed by Ye *et al.* and Pant and Wijeyewickrema is significantly higher. This deviation justifies the higher discrepancies among model responses observed in the base acceleration results (Table 1). Despite the large differences in the calculated impact forces the displacement response of the structure is found to be relatively insensitive to the actual model used.

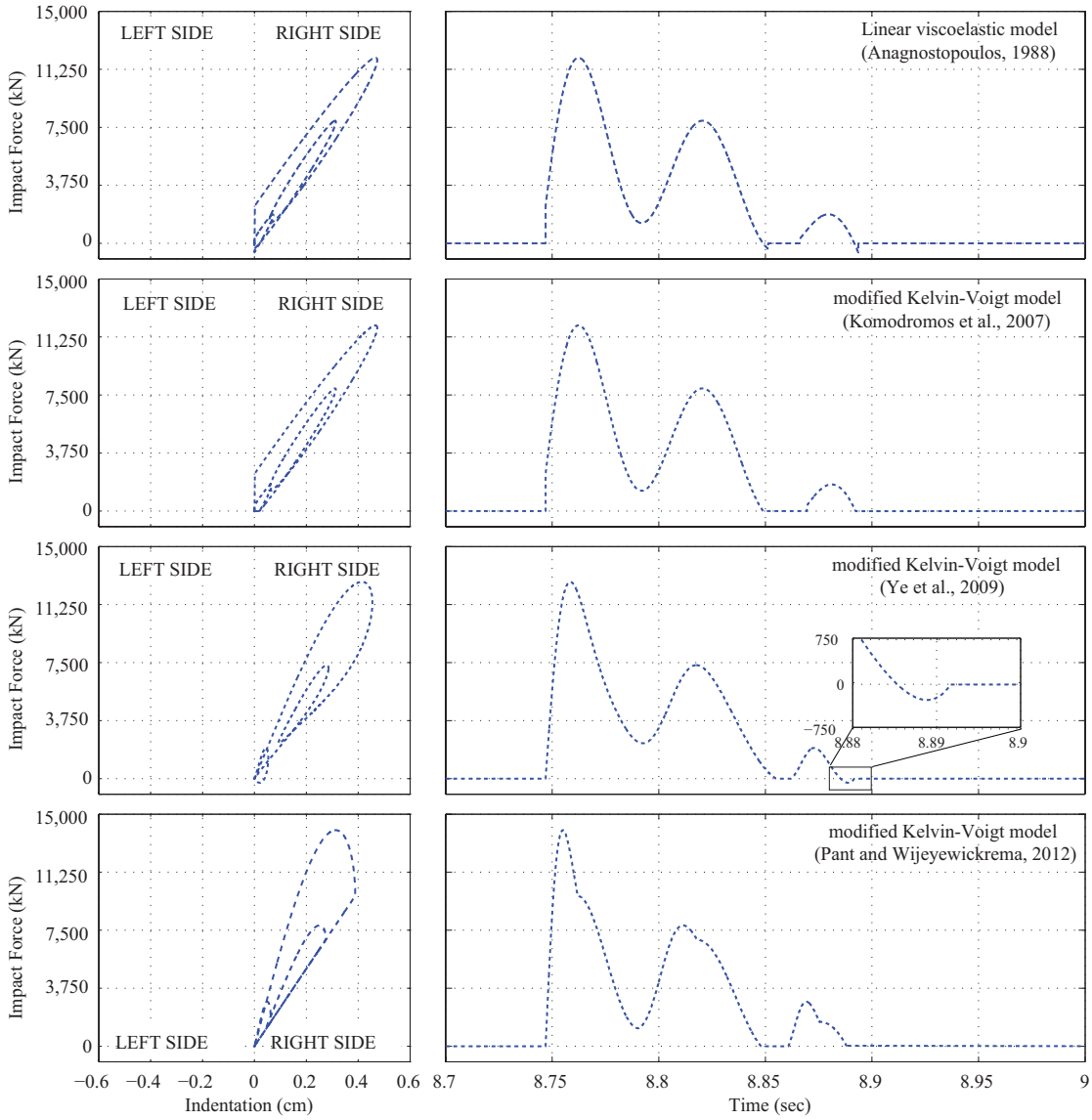


Figure 4: Plots of the impact force in terms of indentation and time-histories of the 3-storey base isolated building, under the Loma Prieta earthquake with a seismic gap equal 20 cm, considering the 4 impact models.

These simulations reveal that the utilization of the Ye *et al.* model does not always avoid the appearance of tensile force immediately before separation, which is consistent with the observations of Pant *et al.* [23]. The existence of tensile forces in the case of the Loma Prieta earthquake, as shown in Figure 4 (third row), is possible due to the activation of the dashpot element, which by definition is included in the restitution phase of contact. It should be noted, however, that in the case of the Northridge excitation (third row of Figure 5) the model does not produce tensile forces.

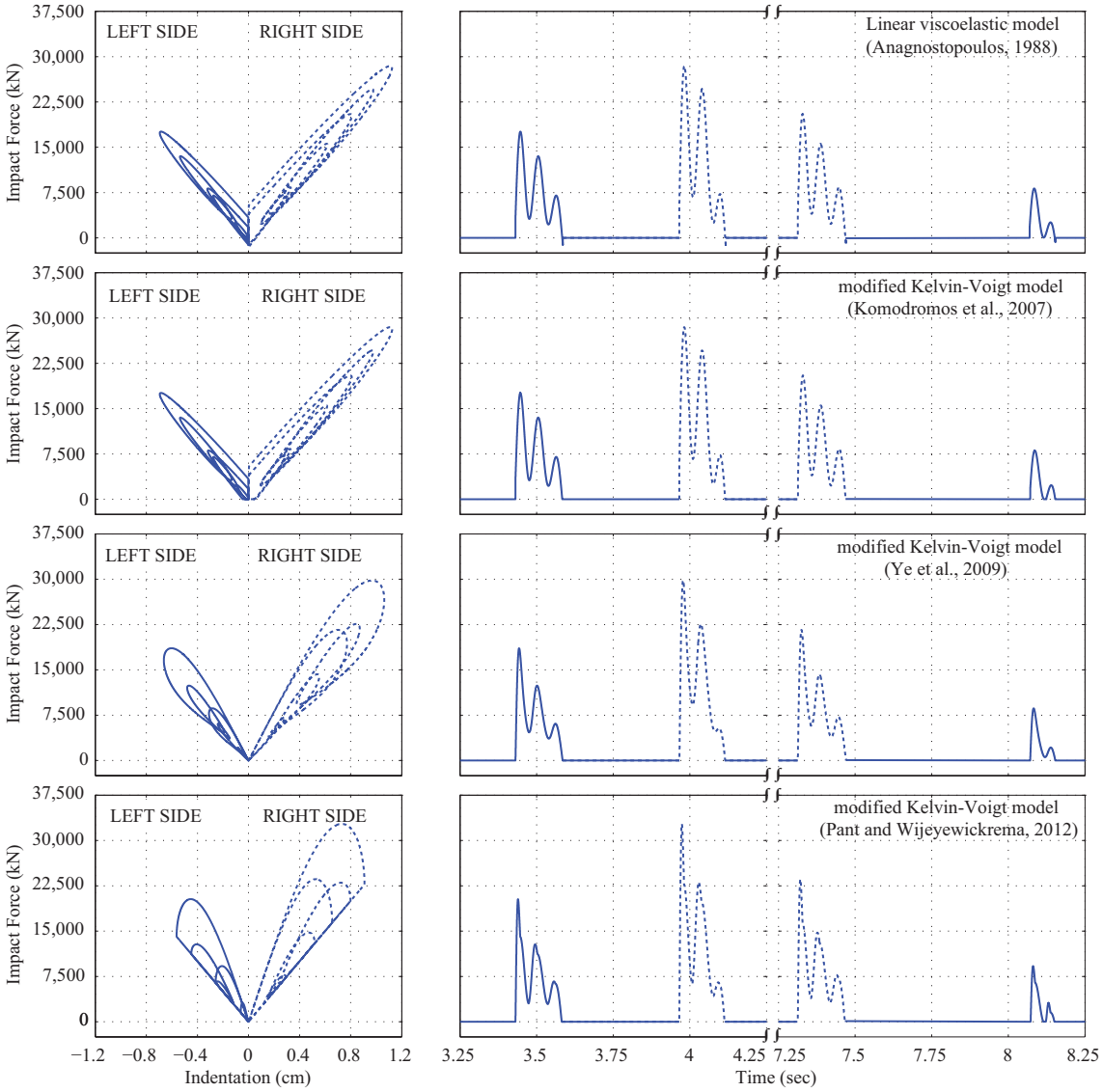


Figure 5: Plots of the impact force in terms of indentation and time-histories; of the 3-storey base isolated building under the Northridge earthquake with a seismic gap equal 20 cm, considering different impact models.

4 PARAMETRIC STUDIES AND NUMERICAL RESULTS

A parametric study has been performed in order to examine the effects of the excitation characteristics on the dynamic response of the simulated base isolated building during poundings. Table 2 shows the five near-fault ground motions that have been used. The selected seismic accelerograms have been taken from the NGA database [24] and are expected to induce large displacements to the seismically isolated building, since they are characterized by low-frequency content, which is one of the most decisive factors for the occurrence of pound-

ings in such structures. The response spectra of the five earthquakes' fault-normal component that has been used in this study are plotted in Figure 6.

NGA#	Event	Station	Mw	PGA (g)
779	Loma Prieta 1989-10-18	UCSC 16 LGPC	6.93	0.944
821	Erzican, Turkey 1992-03-13	95 Erzincan	6.69	0.486
828	Cape Mendocino 1992-04-25	CDMG 89156 Petrolia	7.01	0.615
1084	Northridge-01 1994-01-17	DWP 74 Sylmar - Converter Sta	6.69	0.594
2627	Chi-Chi, Taiwan-03 1999-09-20	CWB 99999 TCU076	6.2	0.524

Table 2: Earthquake records that have been used in the performed simulations.

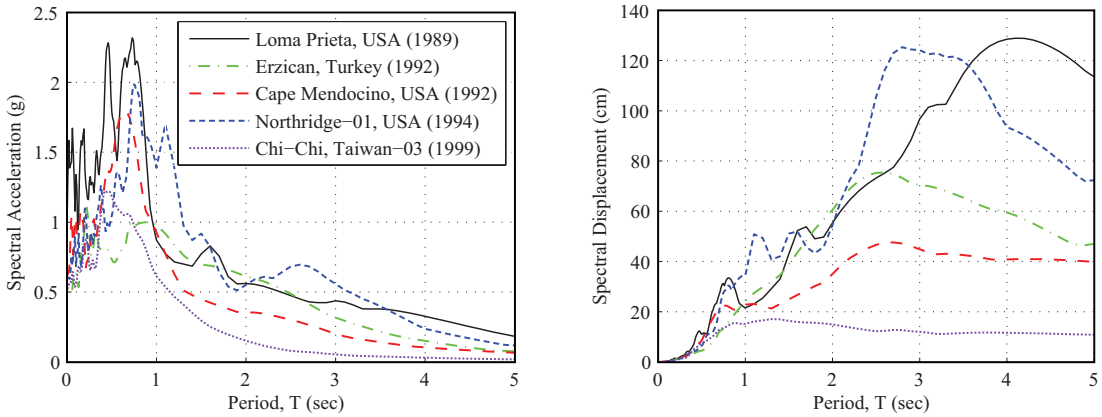


Figure 6: Acceleration and displacement response spectra of the fault normal components for the five earthquake records, considering a viscous damping ratio of 5 %.

4.1 Effect of the gap size and the characteristics of the earthquake excitation

The seismic gap width is systematically varied in the range of 10 to 35 cm with a step of 0.5 cm, in order to investigate its effect on the overall response. The 3-storey base isolated building is analyzed under the selected near-fault ground motions, while the moat wall is assumed to be present on both sides of the building. Figure 7 shows the peak floor accelerations and the maximum inter-storey drifts of the base isolated building under the Loma Prieta earthquake as a function of the seismic gap width considering the four impact models. Each subplot corresponds to the response of a particular floor, or inter-storey response for the case of inter-storey deflections. It is apparent that the most severe peak floor accelerations occur at the base level where poundings occur. Subsequently, the maximum inter-storey deflections occur at the 1-0 interface.

The simulation results indicate that the peak absolute acceleration of the 3-storey base isolated building increase significantly due to structural impact, reaching values that are several times the PGA and can be more than 10 times the corresponding peak accelerations without pounding. The amplification of the inter-storey deflections due to structural poundings reaches values higher than 6 for a seismic gap of 10 cm. Specifically, in that case the peak inter-storey drifts exceed what the corresponding fixed-supported superstructure would experience (0.026 m). Furthermore, as the seismic gap increases, both peak floor accelerations and inter-storey deflections of the superstructure significantly decrease. In particular, for relatively narrow gap widths the response is increasing with the width of the available clearance and, after a certain value, the response of the seismically isolated building begins to decrease as the seismic gap increases.

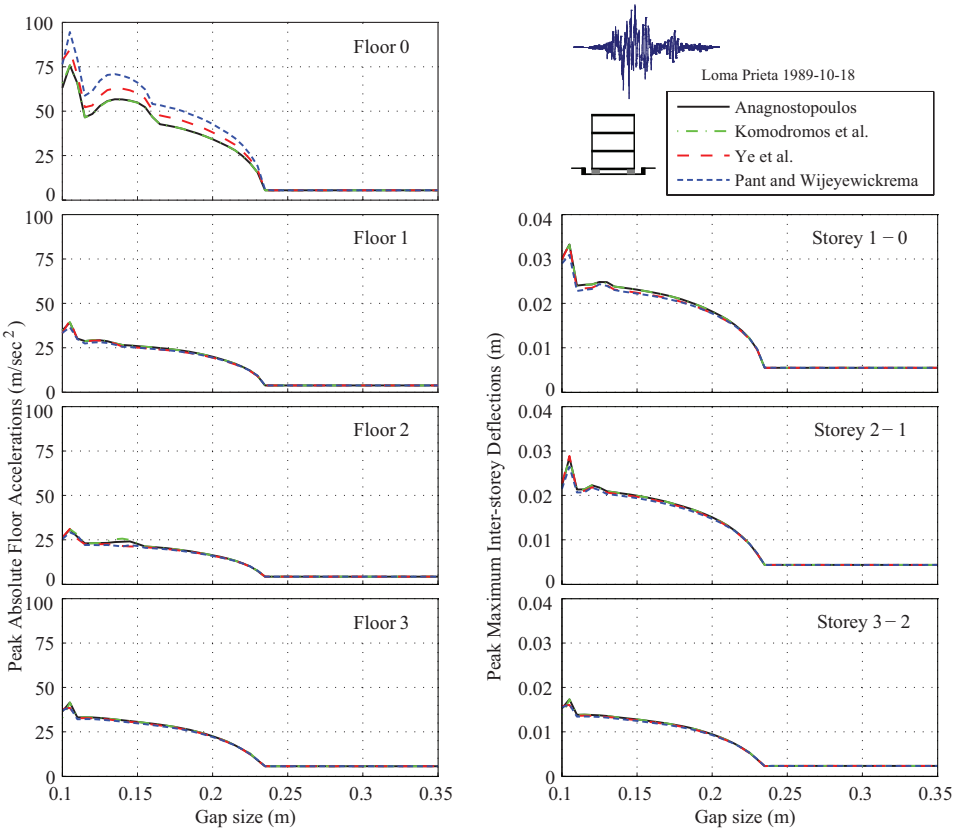


Figure 7: Maximum responses of the 3-storey base isolated building, under the Loma Prieta earthquake in terms of the width of the seismic gap, which varies from 10 to 35 cm.

Figure 8 presents the peak values for indentation, impact velocity and impact force on both sides of the seismically isolated building for the Loma Prieta excitation, in terms of the width of the seismic. It is observed that the trends of the parameters under examination are very similar with the corresponding peak absolute floor acceleration at the impacting floor of the seismically isolated building, indicating that the amplification of the response due to impact is proportional to the impact velocity. It is also observed that, although the maximum impact velocity is relatively consistent between all four impact models considered, the predicted impact forces considering the modified contact models proposed by Ye et *al.* and Pant and Wijeyewickrema are consistently higher.

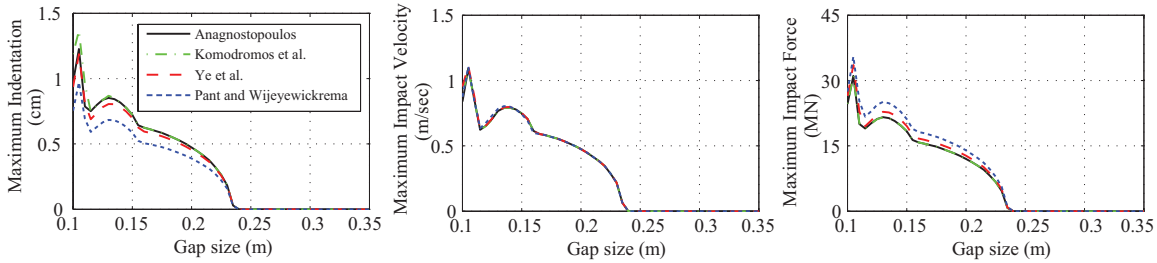


Figure 8: Maximum indentation, impact velocity and impact force of the seismically isolated building induced to the 3-storey structure subjected to Loma Prieta excitation, in terms of the width of the seismic gap.

The variation of the response of the 3-storey seismically isolated building due to the characteristics of the excitation is provided in Figure 9, where the envelope of peak responses is plotted for all considered earthquake excitations. It is observed that, in general and for a range

of values of the width of the seismic gap near the maximum induced displacement, i.e. the critical gap size, the response is decreasing rapidly with the increment of the gap size. Overall, the four linear impact models that have been examined provide similar trends for the peak response of the superstructure.

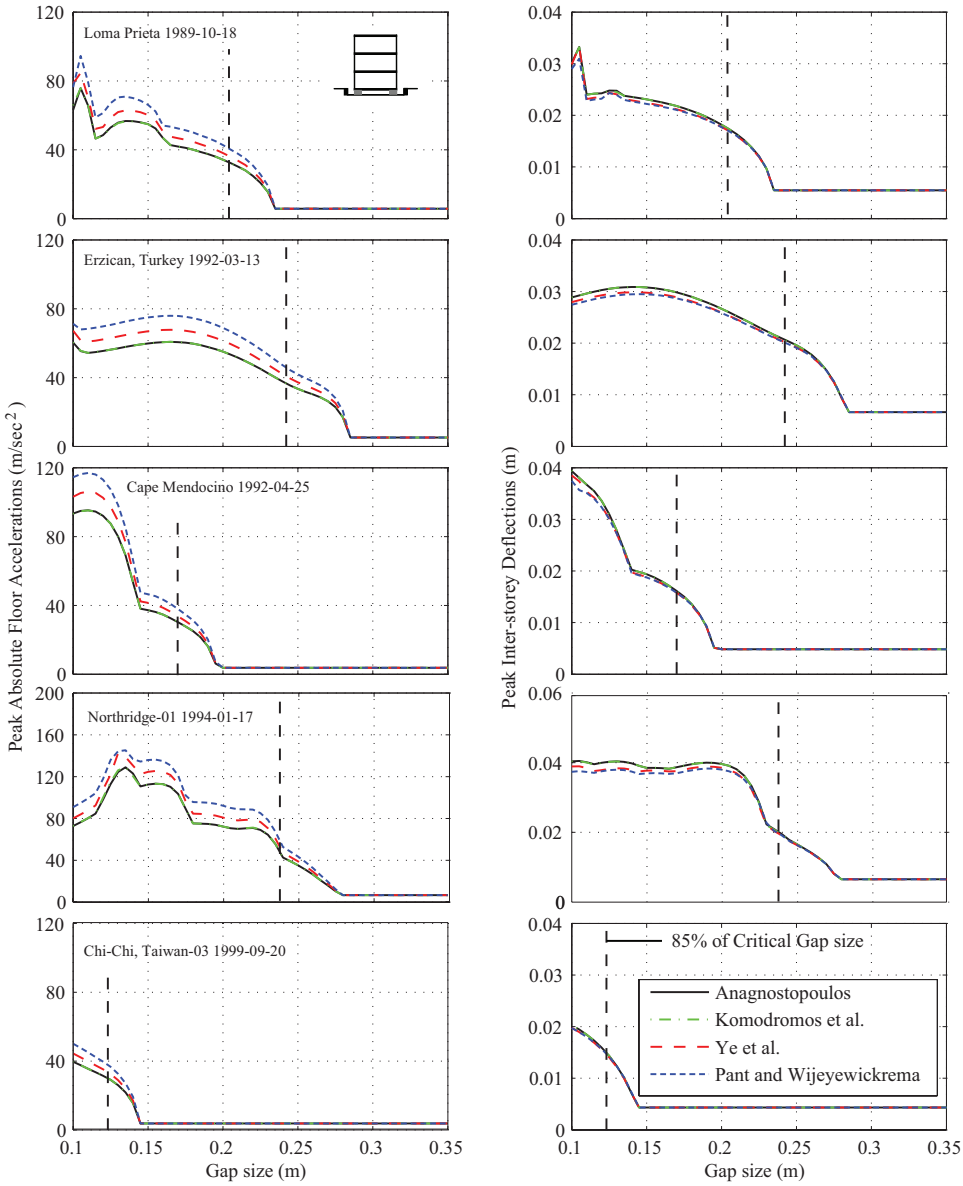


Figure 9: Maximum responses of the base isolated building, in terms of the width of the seismic gap, for the five selected earthquakes considering the 4 impact models under consideration.

In order to compare the results among the four impact models, all peak responses are normalized with respect to the classical Kelvin-Voigt model (i.e. using the formula provided by Anagnostopoulos for the estimation of the impact damping coefficient). Figure 10 presents the normalized peak absolute floor accelerations, showing that the Kelvin-Voigt impact model and the modified linear viscoelastic model proposed by Komodromos *et al.*, in which a permanent deformation is allowed, lead to almost identical responses. The interstorey drifts are, in general, underestimated up to 7.5 % for relatively narrow gap sizes, when the modified linear models proposed by the Ye *et al.* and Pant and Wijeyewickrema are used, compared to the corresponding peak responses computed using the classical Kelvin-Voigt model. In general,

the underestimation of the peak response while using the two modified models tends to decrease with the increase of the width of the seismic gap. Additionally, for a seismic gap 15 % smaller than the maximum unobstructed displacement under each one of the selected near-fault ground motions the deviation of the peak response is similar. The overestimation of the peak accelerations fluctuate around 10.0 and 25.0 % when the contact elements proposed by Ye *et al*. and the Pant and Wijeyewickrema, respectively, are used.

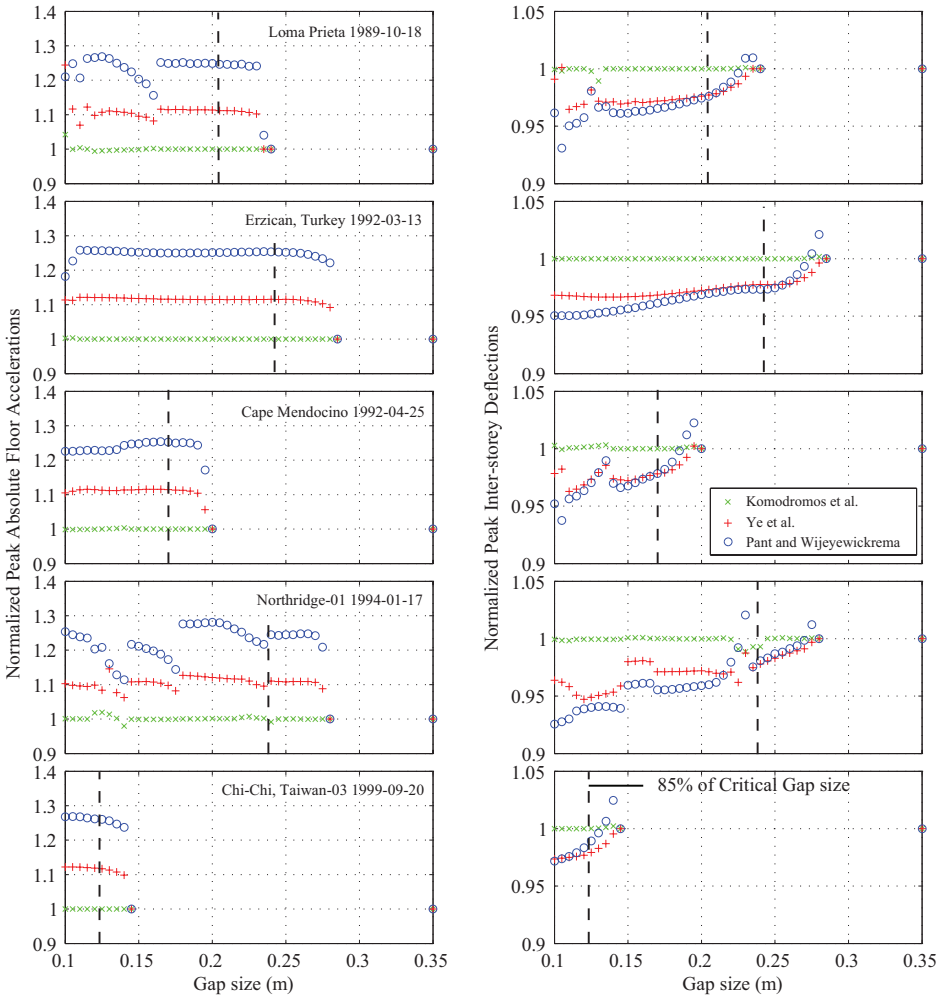


Figure 10: Peak response using the modified linear impact models normalized to the corresponding peak response obtained with the classical Kelvin-Voigt model in terms of the width of the seismic gap.

4.2 Effect of the impact parameters

In order to examine the effect of the impact stiffness and the coefficient of restitution on the peak seismic response of the base isolated building during poundings, another series of parametric studies is performed. For this investigation the 3-storey base isolated building is simulated, assuming a seismic gap 15 % smaller than the maximum unobstructed displacement under each one of the selected near-fault ground motions, in order to ensure structural pounding. The widths of the seismic gap size that have been used in the simulations have been marked in Figure 9. The impact stiffness, k_k of the linear impact spring is varied in the range of 500 to 5000 kN/mm, while the coefficient of restitution is varied between 0.3 and 1.0. The variation of the amplification of peak floor accelerations and peak inter-storey deflections

of the 3-storey base isolated building that are computed considering the classic Kelvin-Voigt model in terms of the two impact parameters, are presented in the next graphs.

The peak absolute floor accelerations due to pounding of the seismically isolated building with the moat wall under each one of the selected near-fault ground motions, as presented in Figure 11(a), tend to increase for high values of the impact stiffness. Please note that there is a correspondence between the line-type used to plot Figure 11(a) with the excitation shown in the subplots of Figure 11(b). The results indicate that when the impact stiffness ranges up to the value of ~1200 kN/mm, which corresponds to 2 times the superstructure's storey stiffness, the inter-storey deflections increase rapidly, while for the rest of the examined range the peak response remain almost insensitive to this parameter. The simulation results also reveal that the excitation characteristics influence considerably the amplification of the peak response.

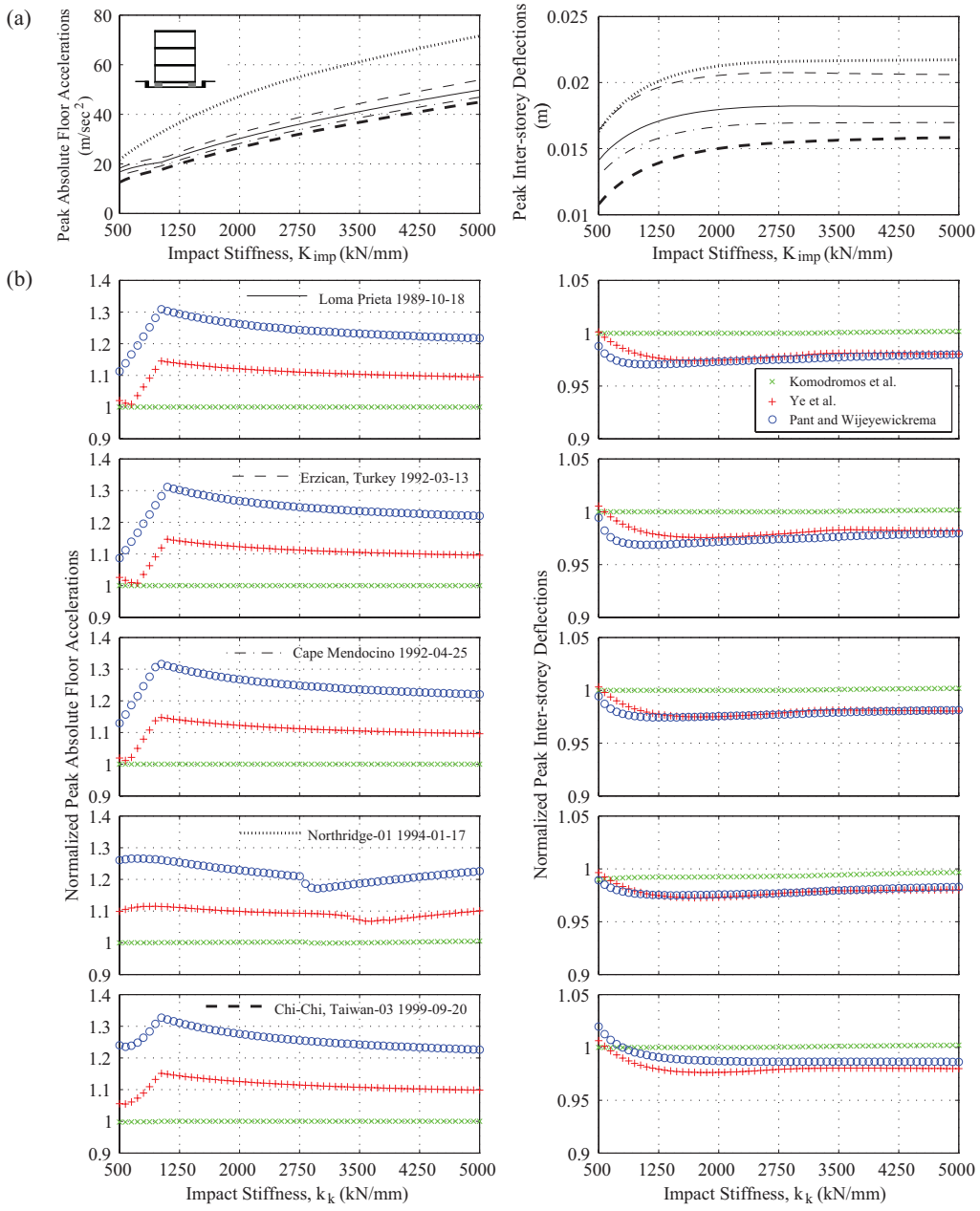


Figure 11: Influence of the impact stiffness on the (a) peak response considering the Kelvin-Voigt contact element and (b) normalized peak response considering modified linear impact models, for each earthquake record.

Figure 11(b) shows the normalized peak response of the modified linear impact models considering as reference model the linear viscoelastic widely used by Anagnostopoulos. The results indicate that the peak responses from the classical Kelvin-Voigt and the modified by Komodromos *et al.* models are similar. Furthermore, the peak inter-storey drifts considering models proposed by Ye *et al.* and Pant and Wijeyewickrema, although they use different methodologies to represent impact, lead to an underestimation of the response of 2.5% for impact stiffness higher than 1200 kN/mm. On the other hand, using the aforementioned models lead to an overestimation of the peak absolute acceleration up to 15 and 33%, respectively. It can be generally observed that the peak floor accelerations are directly proportional to the impact stiffness for low values of k_k (approx. k_k<1000 kN/mm). As the impact stiffness increases this dependency fades away and the peak floor accelerations tend to become constant for all floors with the exception of the base floor response, which maintains a strong dependency. These reported characteristics appear to hold for both Loma Prieta and Northridge excitations, which are presented in Figure 12. Furthermore, these results shed light on the origin of the kinks appearing in Figure 11(b), which relate to an interchange between the floors that dominate the global structural response, i.e. for low values of k_k (Loma Prieta excitation) the third floor appears to deliver the peak floor acceleration, whereas as k_k increases the response is dominated by the base floor accelerations, which is the level impact occurs.

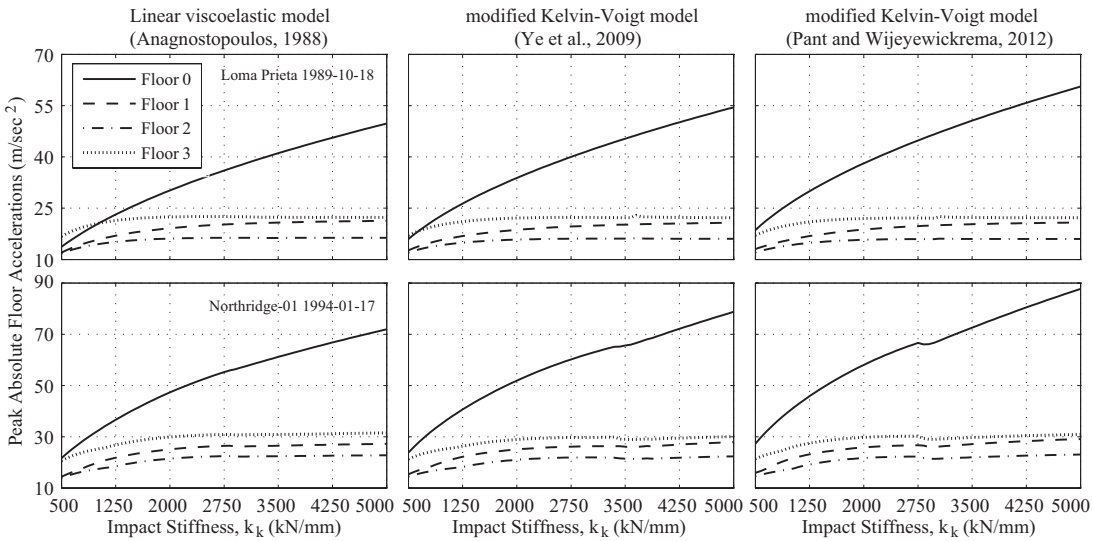


Figure 12: Influence of the impact stiffness on the peak floor accelerations under near-fault ground motions.

Figure 13 presents the first impact incidence obtained from the time-history analysis carried out for the Loma Prieta ground motion considering different linear contact elements for various values of the impact stiffness. It should be noted that for this particular excitation the first impact incidence delivers the peak responses. The results highlight the significant influence of the impact stiffness on the peak impact force due to pounding with the adjacent moat wall. In general, large peak forces are coupled with higher values of the impact stiffness and small deformations across all three impact models. It is apparent that the models proposed by Ye *et al*. and Pant and Wijeyewickrema, produce higher magnitude impact forces than the linear viscoelastic model mainly due to the damping of the contact elements.

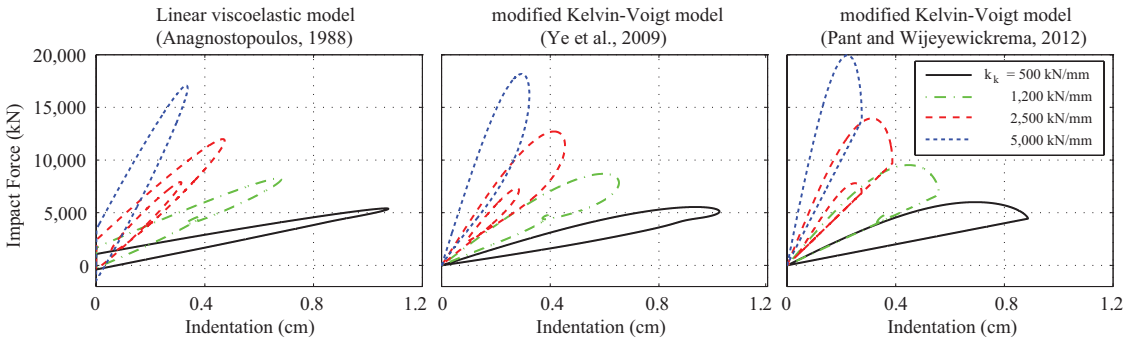


Figure 13: Plots of impact force introduced to the 3-storey seismically isolated building during the first incidence in terms of indentation considering different impact stiffnesses.

The variation of peak responses of the 3-storey base isolated building in terms of the coefficient of restitution under the five ground motions is presented in Figure 14(a). It is observed that for values lower than 0.4, the peak floor accelerations increase, reaching their maximum values when the impact becomes highly overdamped. In general, the excitation characteristics influence considerably the magnitude of the response. Figure 14(b) shows the normalized peak response of the linear impact models with respect to the classical Kelvin-Voigt model.

The results indicate that the minor modification proposed by Komodromos *et al.* does not significantly influence the accuracy of the impact model. Furthermore, the peak inter-storey drifts computed while using the models proposed by Ye *et al.* and Pant and Wijeyewickrema, lead to an underestimation of the response up to 7.5 and 5.0 %, respectively, with respect to the peak responses computed using the classical Kelvin-Voigt model. For all cases, the underestimation of the peak inter-storey deflections tends to decrease with the increase of the coefficient of restitution. On the other hand, employing the aforementioned models lead to a significant overestimation of the peak absolute floor acceleration.

The enclosed areas between the loading and unloading curves of an impact-force vs. indentation curve, define the amount of energy dissipated during the impact. As we can see from the first subplot in Figure 15, the coefficient of restitution does not influence considerably the peak impact force for the linear viscoelastic model. On the other hand, the peak impact force considering the recommended modifications by Ye *et al.* and Pant and Wijeyewickrema depends significantly on the coefficient of restitution (as shown in the second and third columns of Figure 15). Such a deviation of the peak impact force, especially for lower values of the coefficient of restitution, lead to an overestimation of the peak absolute floor acceleration, i.e. of the magnitude of 2.75 and 1.6 for e=0.3, when utilizing the Ye *et al.* and Pant and Wijeyewickrema models, respectively.

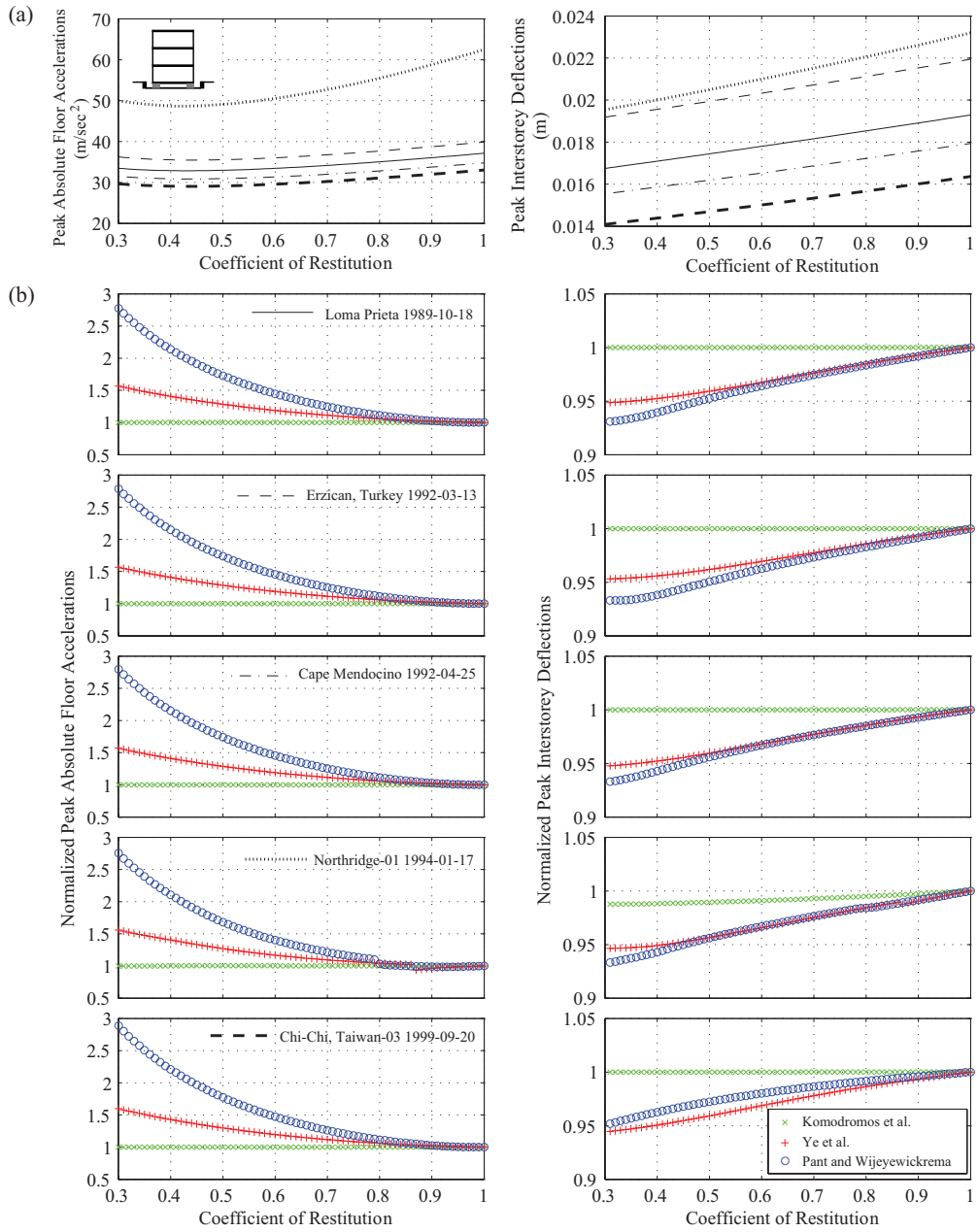


Figure 14: (a) Peak response considering the Kelvin-Voigt contact element and (b) normalized peak response considering modified linear impact models, in terms of coefficient of restitution, e.

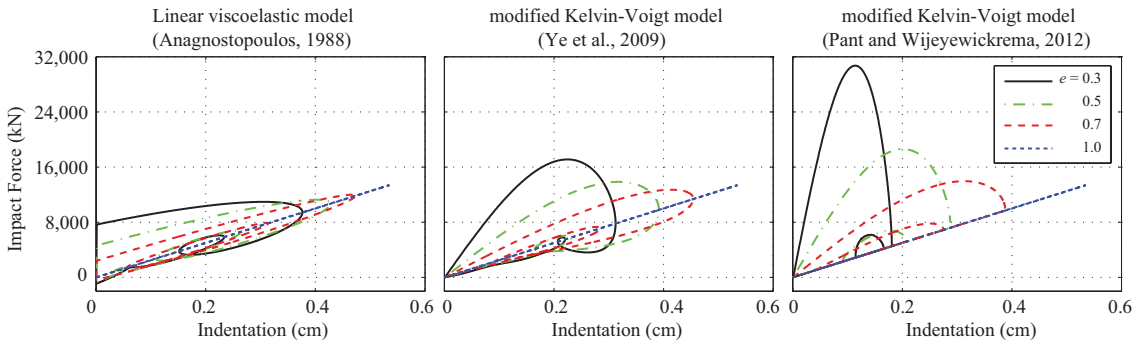


Figure 15: Plots of the impact force introduced to the 3-storey seismically isolated building during the first incidence in terms of indentation, under the Loma Prieta earthquake considering different coefficients of restitutions.

5 CONCLUSIONS

The seismic performance of a typical 3-storey seismically isolated building with the surrounding moat wall has been evaluated using near-fault pulse-like ground motions. Three recently proposed variations of the linear viscoelastic contact model have been compared considering as a base model the classical Kelvin-Voigt model using the formula provided by Anagnostopoulos for the estimation of the impact damping coefficient. The relative performance of the structure has been evaluated based on the peak absolute floor accelerations and inter-storey drifts for various gap sizes and different impact parameters.

The following conclusions are drawn for the building and the ground motions considered in this research study:

- Although the modified linear viscoelastic model by Ye *et al.* was introduced to provide a reasonable physical explanation of the pounding mechanism, it does not always prevent the appearance of tensile force just before the end of the contact.
- The minor modification proposed by Komodromos *et al.* for the linear viscoelastic model does not influence considerably the peak response values.
- The maximum impact forces obtained using the linear impact models proposed by Ye *et al.* and Pant and Wijeyewickrema are much higher than those obtained using the linear viscoelastic model with the formula provided by Anagnostopoulos, leading to a significant overestimation of the peak absolute accelerations.
- The inter-storey deflections of the building are, in general, underestimated when the impact models proposed by Ye *et al.* and Pant and Wijeyewickrema are used. Moreover, the normalized response ratios of the inter-storey drifts appear to increase with a decreasing gap size and coefficient of restitution.

REFERENCES

[1] R. I. Skinner, W. H. Robinson, and G. H. McVerry, *An introduction to seismic isolation*. West Sussex, UK: John Wiley & Sons Ltd, 1993.

[2] F. Naeim and J. M. Kelly, *Design of seismic isolated structures: From theory to practice*. Hoboken NJ, USA: John Wiley & Sons Inc, 1999.

[3] P. Komodromos, *Seismic Isolation for Earthquake Resistant Structures*. Southampton, 2000.

[4] S. Nagarajaiah and X. Sun, "Base-Isolated FCC Building: Impact Response in Northridge Earthquake", *J. Struct. Eng.*, **127** (9), 1063–1075, 2001.

[5] P. K. Malhotra, "Dynamics of seismic impacts in base-isolated buildings", *Earthq. Eng. Struct. Dyn.*, **26** (8), 797–813, 1997.

[6] H. C. Tsai, "Dynamic analysis of base-isolated shear beams bumping against stops", *Earthq. Eng. Struct. Dyn.*, **26** (5), 515–528, 1997.

[7] V. A. Matsagar and R. S. Jangid, "Seismic response of base-isolated structures during impact with adjacent structures", *Eng. Struct.*, **25** (10), 1311–1323, 2003.

[8] P. Komodromos, P. C. Polycarpou, L. Papaloizou, and M. C. Phocas, "Response of seismically isolated buildings considering poundings", *Earthq. Eng. Struct. Dyn.*, **36** (12), 1605–1622, 2007.

[9] P. Komodromos, "Simulation of the earthquake-induced pounding of seismically isolated buildings", *Comput. Struct.*, 86 (7–8), 618–626, 2008.

[10] D. R. Pant and A. C. Wijeyewickrema, "Structural performance of a base-isolated reinforced concrete building subjected to seismic pounding", *Earthq. Eng. Struct. Dyn.*, **41** (12), 1709–1716, 2012.

[11] D. R. Pant and A. C. Wijeyewickrema, "Performance of base-isolated reinforced concrete buildings under bidirectional seismic excitation considering pounding with retaining walls including friction effects", *Earthq. Eng. Struct. Dyn.*, **43** (10), 1521–1541, 2014.

[12] P. C. Polycarpou, L. Papaloizou, and P. Komodromos, "An efficient methodology for simulating earthquake-induced 3D pounding of buildings", *Earthq. Eng. Struct. Dyn.*, **43** (7), 985–1003, 2014.

[13] S. A. Anagnostopoulos, "Pounding of buildings in series during earthquakes", *Earthq. Eng. Struct. Dyn.*, **16,** 443–456, 1988.

[14] R. Jankowski, "Non-linear viscoelastic modelling of earthquake-induced structural pounding", *Earthq. Eng. Struct. Dyn.*, **34** (6), 595–611, 2005.

[15] K. Ye, L. Li, and H. Zhu, "A modified Kelvin impact model for pounding simulation of base-isolated building with adjacent structures", *Earthq. Eng. Eng. Vib.*, **8** (3), 433–446, 2009.

[16] K. Ye, L. Li, and H. Zhu, "A note on the Hertz contact model with nonlinear damping for pounding simulation," *Earthq. Eng. Struct. Dyn.*, **38** (9), 1135–1142, 2009.

[17] S. Muthukumar and R. DesRoches, "A Hertz contact model with non-linear damping for pounding simulation", *Earthq. Eng. Struct. Dyn.*, **35** (7), 811–828, 2006.

[18] R. C. Barros, H. Naderpour, S. M. Khatami, and A. Mortezaei, "Influence of Seismic Pounding on RC Buildings with and without Base Isolation System Subject to Near-Fault Ground Motions", *J. Rehabil. Civ. Eng.*, **1** (1), 39–52, 2013.

[19] S. A. Anagnostopoulos and K. V. Spiliopoulos, "An investigation of earthquake induced pounding between adjacent buildings", *Earthq. Eng. Struct. Dyn.*, **21** (4), 289–302, 1992.

[20] R. Jankowski, K. Wilde, and Y. Fujino, "Pounding of superstructure segments in isolated elevated bridge during earthquakes", *Earthq. Eng. Struct. Dyn.*, **27** (5), 487–502, 1998.

[21] P. Zhu, M. Abe, and Y. Fujino, "Modelling three-dimensional non-linear seismic performance of elevated bridges with emphasis on pounding of girders", *Earthq. Eng. Struct.* Dyn., **31** (11), 1891–1913, 2002.

[22] E. Mavronicola and P. Komodromos, "On the response of base-isolated buildings using bilinear models for LRBs subjected to pulse-like ground motions: sharp vs. smooth behaviour", *Earthq. Struct.*, **7** (6), 1223–1240, 2014.

[23] D. R. Pant, A. C. Wijeyewickrema, and T. Ohmachi, "Seismic Pounding between Reinforced Concrete Buildings: A Study using two recently proposed Contact Element Models", in *14th European Conference on Earthquake Engineering*, 2010.

[24] PEER Pacific Earthquake Engineering Research Center, "Ground motion database," 2011 [Online]. Available: http://peer.berkeley.edu/peer_ground_motion_database.

COMPDYN 2015
5th ECCOMAS Thematic Conference on
Computational Methods in Structural Dynamics and Earthquake Engineering
M. Papadrakakis, V. Papadopoulos, V. Plevris (eds.)
Crete Island, Greece, 25–27 May 2015

ANALYSIS AND EXPERIMENT OF ISOLATED BRIDGES USING POLYNOMIAL ROCKING BEARINGS

T.Y. Lee[1], L.Y. Lu[2], J.H. Tzeng[3] and K.J. Chung[3]

[1] National Central University
Taoyuan County, Taiwan 32001, R.O.C.
tylee@ncu.edu.tw

[2] National Cheng Kung University
Tainan City, Taiwan 701, R.O.C.
lylu@mail.ncku.edu.tw

[3] National Central University
Taoyuan County, Taiwan 32001, R.O.C.
{993202017,100322016}@cc.ncu.edu.tw

Keywords: Variable-Curvature Seismic Isolator, Various-Frequency Seismic Isolator, Rocking Isolator, Near-Field Ground Motion, Shaking Table Test.

Abstract. *This paper is aimed to study the effectiveness of Polynomial Rocking Bearing (PRB), a various-frequency sliding isolator, in decreasing the seismic responses of isolated bridges. Although sliding isolators have been widely used to mitigate seismic hazard, it may be not effective in decreasing the seismic responses of isolated structures subjected to near-field ground motions. Near-field ground motions are of a pulse period which may be close to the natural periods of the isolated structures so as to lead the isolated structures to be resonant. Various-frequency sliding isolators could regulate the natural periods of the structures to avoid resonance under near-field ground motions. However, the key issue is how to choose the geometric shape and friction materials in design of various-frequency sliding isolators. This study adopts PRB to be the various-frequency sliding isolator whose rocking surface consisting of six-order polynomial. The restoring stiffness of the PRB possesses softening section as well as hardening section. The structural acceleration response can be decreased by decreasing the restoring stiffness in softening section while the structural displacement response can be decreased by increasing the restoring stiffness in hardening section. Since the PRB equivalent horizontal friction coefficient can be adjusted via the various geometric shapes, the friction material can be then arbitrarily chosen to increase the bearing reliability and durability. PSO-SA hybrid algorithm is used to find out the optimum parameters of the PRB in this study. A series of shaking table tests are conducted to demonstrate the effectiveness of the PRB in mitigating the dynamic responses of bridges under strong earthquakes. Numerical analysis is also performed to make comparison with the experiments. It shows the numerical results agree with the experimental results very well.*

1 INTRODUCTION

Seismic isolation is one of most effective technologies to protect structural systems and their interior equipment or facilities from earthquakes [1-2]. Different from conventional seismic resistance techniques, seismic isolation is to implement a soft layer under the protected structure, so that the seismic load transmitted onto the structure can be mitigated [3]. A seismic structure with a conventional isolation system is usually designed to be a long-period system with a fixed isolation frequency and damping ratio. Although these constant isolation parameters may be optimally designed for the given design earthquake, the existence of the long-period feature inevitably induces a low-frequency resonant-like response when the isolation system is subjected to a ground motion containing strong long-period components [4]. Many studies have found that an isolated structure with a conventional isolation system will exhibit excessive isolator displacement in near-field ground motions, whose waveforms usually possess a long-period pulse component [5]. Consequently, this will yield an unsuitable isolator design and increase the risk of superstructure pounding effect.

To avoid the low-frequency resonance problem that conventional isolators may encounter in long-period earthquakes, some researchers have suggested using isolators with variable mechanical properties, so the isolation systems may be adaptive to a wider range of earthquakes with different characteristics [6]. A new type of isolator called polynomial rocking bearings (PRB) is adopted for bridges in this study. The PRBs have variable isolation stiffness that can meet the desired design specifications. This study involves the experiment verification and numerical simulation of the seismic responses of an isolated bridge with PRBs. Moreover, the theory and formulas that describe the mechanical properties of a general PRB will be reviewed at the beginning of this paper. Then, based on the general formulas, the PRB used in the shaking table tests can be designed.

2 THEORY OF POLYNOMIAL ROCKING BEARINGS

2.1 Configuration of a PRB

Figure 1 illustrates a PRB installed between the deck and column in a bridge. The PRB has an articular (ball-and-socket) joint on the top and a concave rocking surface with a base plate on the lower part. The articular joint is mounted on the bottom of the deck with the sole plate while on the column with the base plate. In an earthquake, the rocking surface of the bearing will rock back-and-forth on the base plate, which provides an isolation layer to reduce the seismic induced forces transmitted onto the superstructure. The geometry of the rocking surface is usually axially symmetric about the vertical axis and must be concave. In order to provide variable isolation frequencies, the rocking surface may have a variable curvature that can be determined by the designer. However, the radius of the curvature has to be larger than the bearing height to maintain the stability during rocking. Moreover, there are three important design items for the rocking bearing including the bearing height, the radius of the spherical head and the sixth-order polynomial function defining the shape of the rocking surface. [6]

2.2 Mechanism of a PRB

The mechanical properties of an isolator are generally characterized by the relation between its horizontal shear and displacement. The formulas that describe this relation for a general PRB will be discussed below.

Figure 2 depicts the free-body diagram of a PRB where the friction on the spherical head is neglected because of insignificant effect. *xy* coordinate is fixed on the base plate while XY c-

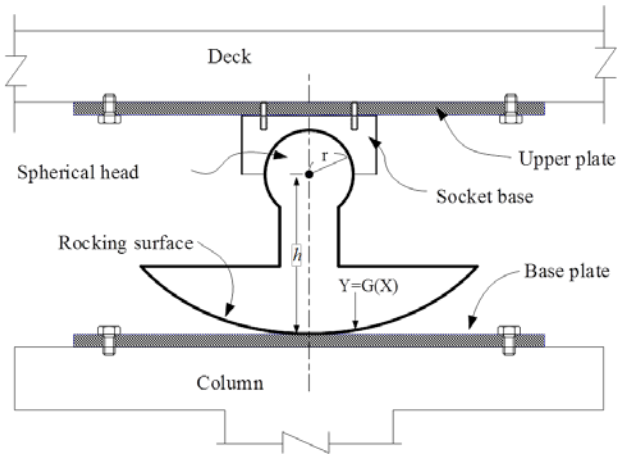


Figure 1: A PRB installed on a column

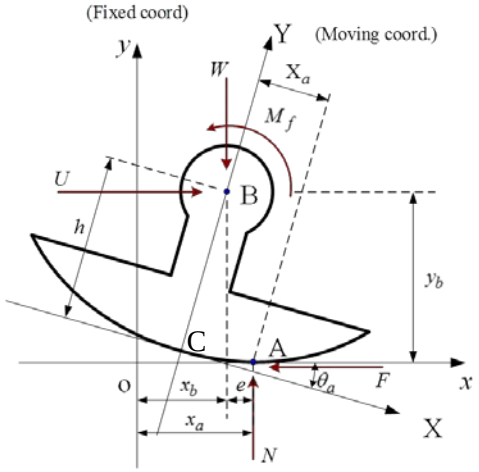


Figure 2: Free-body diagram of a PRB

-oordinate is moving with the rocking body. The rocking surface is defined by a sixth-order polynomial function, $\mathrm{Y} = \mathrm{G}(\mathrm{X})$. Assume that the rocking surface and the base plate intersect at point A. Therefore, the x-axis is always tangent to the rocking surface at the intersect A.

The vertical force W can be determined by the structural weights when neglecting vertical motion. The horizontal shear force U transmitted onto the isolated structure can be calculated by using the equilibrium equation of moments, i.e. $\sum M_A = 0$, as

$$U = u_r = \frac{We}{y_b} = \frac{W\left(x_a - x_b\right)}{y_b} \tag{1}$$

where u_r signifies the bearing restoring force; x_a is the x coordinate of the intersect A in the xy coordinate; x_b and y_b are the x and y coordinates of the point B, respectively. Since it is assumed that there is no relative sliding between the rocking surface and the base plate, x_a is equal to the arc length S_{ac} from point A to point C on the rocking surface. x_a, x_b, y_b and θ_a are determined by the following equations.

$$x_a = S_a = \int ds = \int_0^{\mathrm{X}_a} \left[1 + \left(G'\left(\mathrm{X}_a\right)\right)^2\right]^{1/2} d\mathrm{X} \tag{2}$$

$$x_b = \left(h - G\left(\mathrm{X}_a\right)\right)\sin\theta_a - \mathrm{X}_a\cos\theta_a + x_a \tag{3}$$

$$y_b = \left(h - G\left(\mathrm{X}_a\right)\right)\cos\theta_a + \mathrm{X}_a\sin\theta_a \tag{4}$$

$$\tan\theta_a = G'\left(\mathrm{X}_a\right) \quad , \quad -\frac{\pi}{2} \le \theta_a \le \frac{\pi}{2} \tag{5}$$

where X_a represents the X coordinate of the point A.

Applying Eq. (5), Eqs. (3) and (4) can be rewritten as

$$x_b = \frac{\left(h - G\left(X_a\right)\right)G'\left(\mathrm{X}_a\right)}{\left[1 + \left(G'\left(\mathrm{X}_a\right)\right)^2\right]^{\frac{1}{2}}} - \frac{X_a}{\left[1 + \left(G'\left(\mathrm{X}_a\right)\right)^2\right]^{\frac{1}{2}}} + x_a \tag{6}$$

$$y_b = \frac{\left(h - G\left(X_a\right)\right)}{\left[1+\left(G'\left(\mathrm{X}_a\right)\right)^2\right]^{\frac{1}{2}}} + \frac{X_a G'\left(\mathrm{X}_a\right)}{\left[1+\left(G'\left(\mathrm{X}_a\right)\right)^2\right]^{\frac{1}{2}}} \tag{7}$$

Substituting Eqs. (2), (6) and (7) in Eq. (1) yields

$$u_r = u_r\left(\mathrm{X}_a\right) = \frac{W\left[-\left(h - G\left(\mathrm{X}_a\right)\right)G'\left(\mathrm{X}_a\right) + \mathrm{X}_a\right]}{\left(h - G\left(\mathrm{X}_a\right)\right) + \mathrm{X}_a G'\left(\mathrm{X}_a\right)} \tag{8}$$

Note that the restoring force u_r of a PRB is proportional to the vertical load *W*.

In order to improve the isolation performance for near-field earthquakes, the geometric function $\mathrm{Y} = \mathrm{G}\left(\mathrm{X}\right)$ of the rocking surface may be defined by the following sixth-order polynomial function:

$$G\left(\mathrm{X}\right) = c_1 X^6 + c_2 X^4 + c_3 X^2 \tag{9}$$

where c_1, c_2 and c_3 are three constant coefficients determined by designers. Next, applying Eq. (9) in Eq. (8) yields the fifth-order polynomial function for the isolator restoring force.

The stiffness k_r of a PRB can be defined as the rate of change of the restoring force u_r with respect to the isolator displacement x_b. However, since the restoring force u_r of a PRB is not an explicit function of x_b, the bearing stiffness k_r has to be computed indirectly by using the following equation

$$k_r = k_r\left(\mathrm{X}_a\right) = \frac{du_r\left(\mathrm{X}_a\right)}{dx_b\left(\mathrm{X}_a\right)} = \frac{\left(\frac{du_r\left(\mathrm{X}_a\right)}{d\mathrm{X}_a}\right)}{\left(\frac{dx_b\left(\mathrm{X}_a\right)}{d\mathrm{X}_a}\right)} \tag{10}$$

Once the geometric function G(X) of the rocking surface is defined, the stiffness k_r can be calculated by Eq. (10). The restoring stiffness of the PRB can be divided into softening section and hardening section. The structural acceleration response can be decreased by decreasing the restoring stiffness in softening section while the structural displacement response can be decreased by increasing the restoring stiffness in hardening section. Since the PRB equivalent horizontal friction coefficient can be adjusted via the various geometric shapes, the friction material can be then arbitrarily chosen to increase the bearing reliability and durability.

3 NUMERICAL ANALYSIS

3.1 Simplified numerical model of bridges

Since bracing systems and shear connectors are always used in superstructures to interconnect all the steel girders and slabs as a solid deck, the deck of the typical isolated bridge may be assumed rigid in the longitudinal direction. Therefore, a column with an effective deck mass on the top can be taken apart as a unit for analysis as shown in Fig. 3

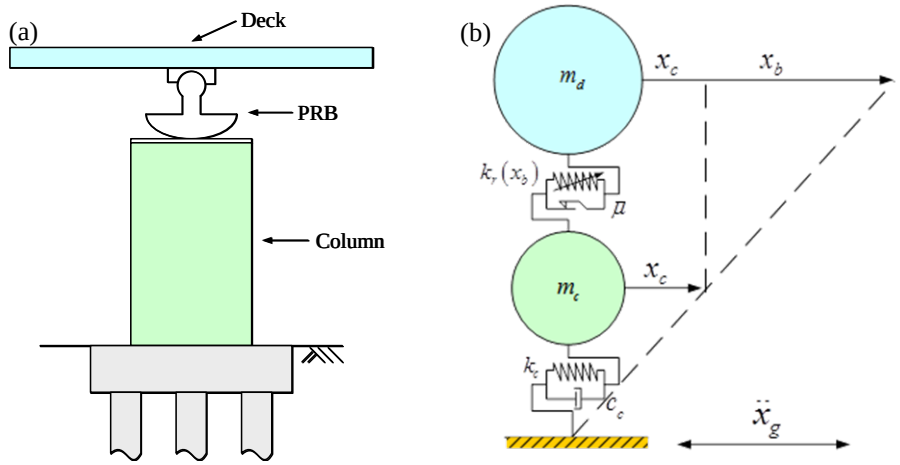


Figure 3: Analytical idealization (a) analytical unit (b) 2DOF system

3.2 Equations of Motion

The equations of motion for the isolated bridge with PRBs may be expressed as

$$\begin{bmatrix} m_d & m_d \\ 0 & m_c \end{bmatrix}\begin{bmatrix} \ddot{x}_b \\ \ddot{x}_c \end{bmatrix}+\begin{bmatrix} 0 & 0 \\ 0 & c_c \end{bmatrix}\begin{bmatrix} \dot{x}_b \\ \dot{x}_c \end{bmatrix}+\begin{bmatrix} 0 & 0 \\ 0 & k_c \end{bmatrix}\begin{bmatrix} x_b \\ x_c \end{bmatrix}=-\begin{bmatrix} m_d & 0 \\ 0 & m_c \end{bmatrix}\begin{bmatrix} 1 \\ 1 \end{bmatrix}\ddot{x}_g+\begin{bmatrix} u_r+u_f \\ -u_r-u_f \end{bmatrix} \tag{11}$$

Let $u(t)=u_r+u_f$ and rewrite Eq. (11) in vector form as:

$$\mathbf{M}\ddot{\mathbf{x}}(t)+\mathbf{C}\dot{\mathbf{x}}(t)+\mathbf{K}\mathbf{x}(t)=-\mathbf{M}_1\mathbf{L}_1\ddot{x}_g(t)+\mathbf{L}_2u(t) \tag{12}$$

where $\mathbf{x}$ is the displacement vector. $\ddot{x}_g$ is the ground acceleration. $\mathbf{M}$, $\mathbf{C}$, $\mathbf{K}$ and $\mathbf{M}_1$ are the mass matrix, damping matrix, stiffness matrix and distribution matrix of mass, respectively. $\mathbf{L_1}$ and $\mathbf{L_2}$ are the distribution matrices of seismic force and horizontal shearing force of PRBs, respectively.

The equations of motion, Eq. (12) can be rewritten in the state space as:

$$\dot{\mathbf{z}}(t)=\mathbf{A}\mathbf{z}(t)+\mathbf{E}\ddot{x}_g(t)+\mathbf{B}u(t) \tag{13}$$

The equations of motion, Eq. (13), in a continuous time system can be expressed in a discrete-time state-space form as

$$\mathbf{z}[k+1]=\mathbf{A}_d\mathbf{z}[k]+\mathbf{E}_0\ddot{x}_g[k]+\mathbf{E}_1\ddot{x}_g[k+1]+\mathbf{B}_0u[k]+\mathbf{B}_1u[k+1] \tag{14}$$

where a variable with [k] denotes the quantity is evaluated at the kth computational time step. All the matrices $\mathbf{A}_d$, $\mathbf{B}_0$, $\mathbf{B}_1$, $\mathbf{E}_0$ and $\mathbf{E}_1$ are constant coefficient matrices that are evaluated by using the following equations.

$$\mathbf{A}_d=e^{A\Delta t}=\sum_{i=0}^{\infty}\frac{\Delta t}{i!}\mathbf{A}^i\ ,\ \mathbf{B}_0=\left(\sum_{i=0}^{\infty}\frac{(\Delta t)^{i+1}}{i!(i+2)}\mathbf{A}^i\right)\mathbf{B}\ ,\ \mathbf{B}_1=\left(\sum_{i=0}^{\infty}\frac{(\Delta t)^{i+1}}{(i+1)!}\mathbf{A}^i-\sum_{i=0}^{\infty}\frac{(\Delta t)^{i+1}}{i!(i+2)}\mathbf{A}^i\right)\mathbf{B},$$
$$\mathbf{E}_0=\left(\sum_{i=0}^{\infty}\frac{(\Delta t)^{i+1}}{i!(i+2)}\mathbf{A}^i\right)\mathbf{E}\ ,\ \mathbf{E}_1=\left(\sum_{i=0}^{\infty}\frac{(\Delta t)^{i+1}}{(i+1)!}\mathbf{A}^i-\sum_{i=0}^{\infty}\frac{(\Delta t)^{i+1}}{i!(i+2)}\mathbf{A}^i\right)\mathbf{E} \tag{15}$$

where Δt denotes the time interval of computation.

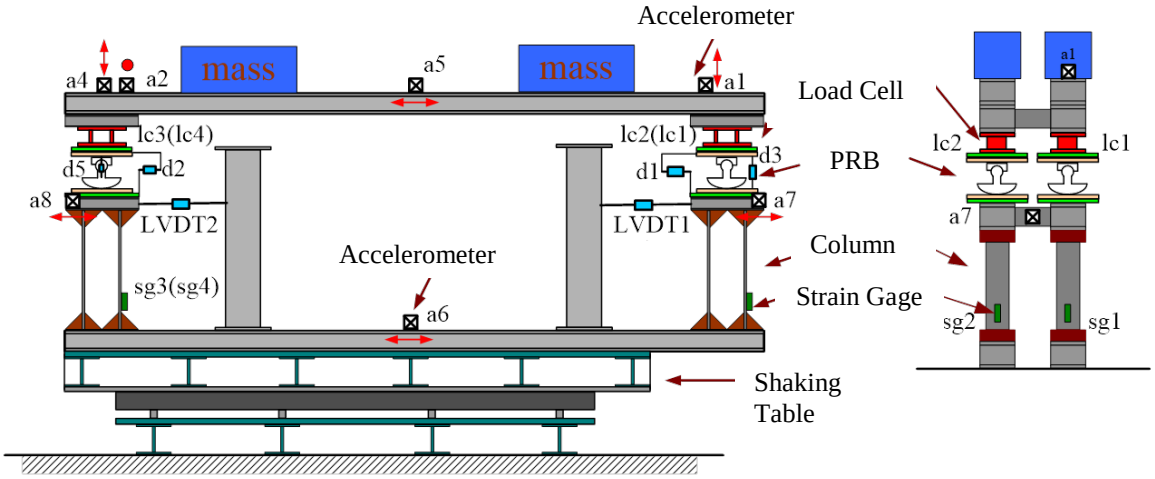


Figure 4: Test setup of a bridge with PRBs

4 EXPERIMENT OF A BRIDGE MODEL WITH PRBS

A series of shaking table tests are conducted to recognize the effectiveness of the PRBs in decreasing the induced seismic force for bridges. The experimental results are compared with the analysis results to verify the accuracy of the numerical model. Since we reused the PRBs studied by Lu et al. for buildings [7], the rocking surface may be not optimum for the bridge test model. However, after proving the feasibility of the PRBs, the optimum rocking surface will be searched by PSO-SA hybrid algorithm. Figure 4 illustrates the setup of the shaking table tests. Two ground motions recorded at El Centro, California 1940 and Imperial Valley 1979 are selected. El Centro records represent the far-field ground motions while Imperial Valley records represent the near-field ground motions.

4.1 Results of numerical analysis and experiment

The experimental and analytical results under El Centro and Imperial Valley ground motions are compared in Figs. 5 and 6. Figures 5(a), 5(b) and 5(c) show the time histories of the deck displacement, bearing displacement and column displacement, respectively, under El Centro ground motion with PGA of 307 gal. Figure 5(d) shows the hysteresis loop of the PRB under El Centro ground motion. Figure 6 shows the comparison under Imperial Valley ground motion with PGA of 350 gal. Observed from the results, the numerical model is able to satisfactorily simulate the dynamic behavior of the isolated bridge with PRBs. Besides, the effectiveness of PRB isolation can be estimated in the experiment. Table 1 shows the comparison between the isolated bridge with PRBs and non-isolated bridge. Obviously, the peak column displacement largely decreases in the isolated bridge with PRBs as compared to the non-isolated bridge under both far-field and near-field ground motions.

Table 1: Comparison between the isolated bridge with PRBs and non-isolated bridge

Ground Motion	PGA (g)	Peak Column Displacement with PRB (cm)	Peak Column Displacement w/o PRB (cm)	Percentage of reduction (%)
El Centro	0.307	1.46	6.33	76.9
Imperial Valley	0.350	1.58	4.62	65.8

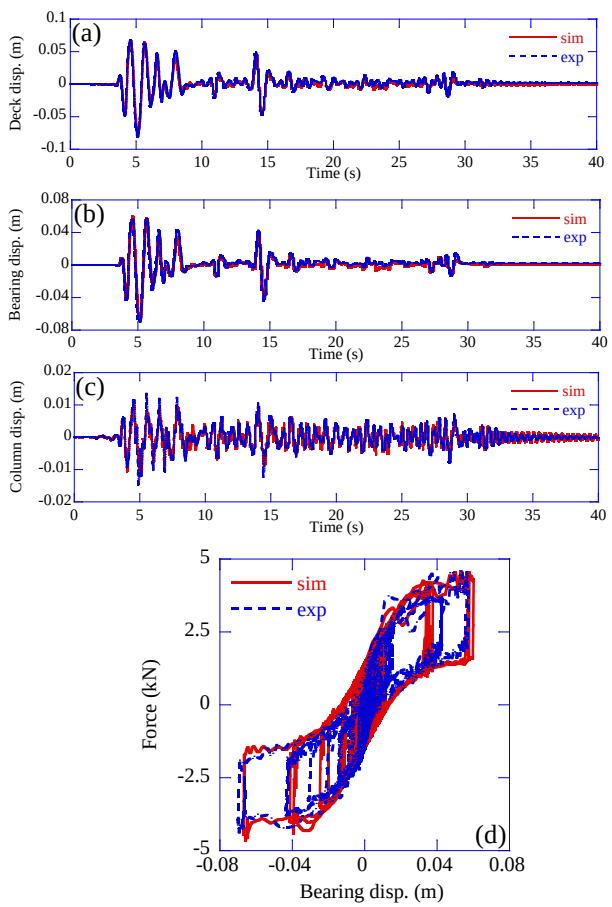


Figure 5: (a) deck displacement (b) bearing displacement (c) column displacement (d) hysteresis loop of PRBs under El Centro ground motion

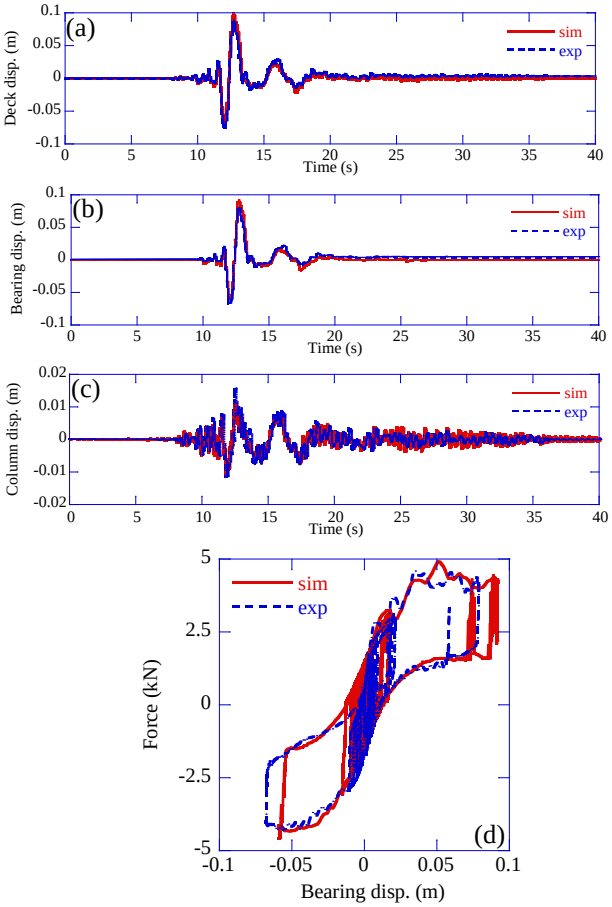


Figure 6: (a) deck displacement (b) bearing displacement (c) column displacement (d) hysteresis loop of PRBs under Imperial Valley ground motion

5 DESIGN OF PRBS

The effect of PRBs on the seismic behavior is influenced by the six-order polynomial of rocking surface, bearing height and equivalent friction coefficient. It is extremely tedious and time-consuming to perform a parametric study for exploring the optimum parameters. Optimization techniques are expected to provide a smart solution to such an optimization problem. In this study, PSO-SA hybrid searching algorithm is adopted to explore the optimum design parameters of PRBs. [8]

In order to reveal the efficiency of the PRBs, a friction pendulum system (FPS), a traditional sliding bearing, is also investigated in this study for comparison. The design parameters of both the PRBs and FPSs are determined by using PSO-SA hybrid searching algorithm. Figures 7 and 8 compare the dynamic responses of the isolated bridges with PRBs and FPSs under El Centro records and Imperial Valley records, respectively. Table 2 shows the peak responses of bridges under two records. The simulation results indicate that the column and deck displacements of the isolated bridge with PRBs are further decreased as compared with FPSs.

Table 2: Peak responses of isolated bridges

Ground Motion	Peak Bearing Displacement (cm)		Peak Column Displacement (cm)		Peak Deck Displacement (cm)	
	PRB	FPS	PRB	FPS	PRB	FPS
El Centro	4.23	4.04	1.91	2.04	4.14	4.24
Imperial Valley	6.29	9.13	2.52	2.59	8.49	10.90

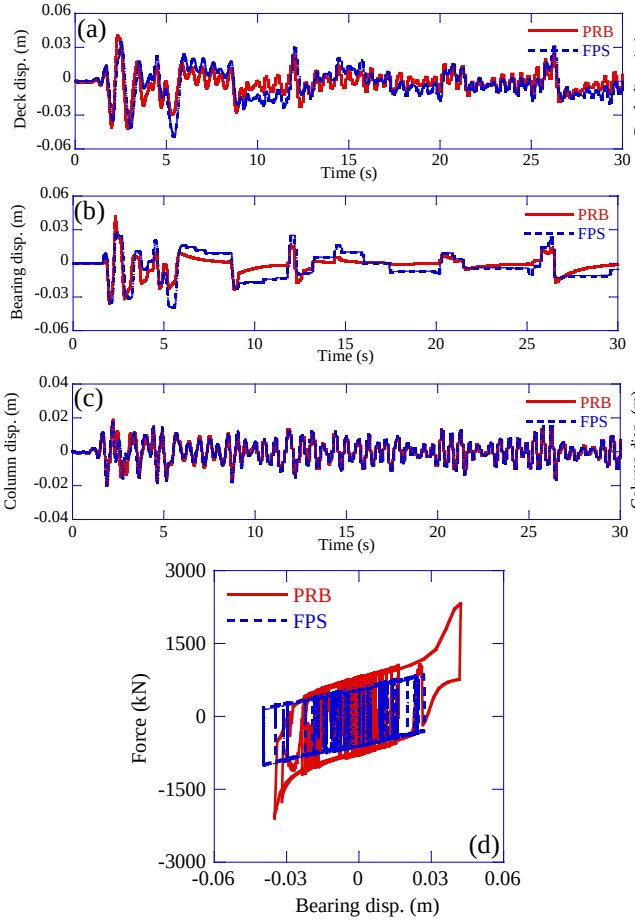


Figure 7: (a) deck displacement (b) bearing displacement (c) column displacement (d) hysteresis loop of PRBs and FPSs under El Centro records

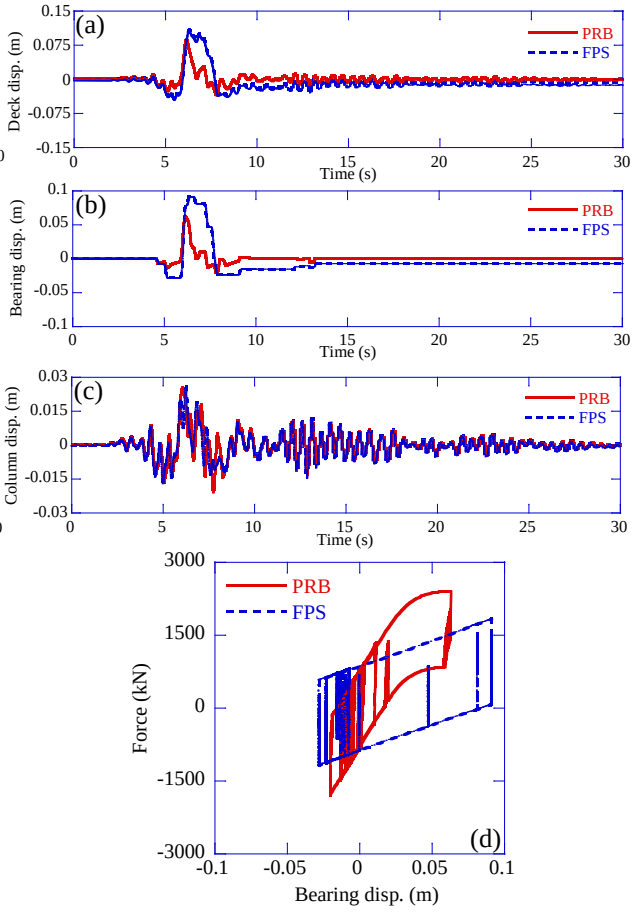


Figure 8: (a) deck displacement (b) bearing displacement (c) column displacement (d) hysteresis loop of PRBs and FPSs under Imperial Valley records

6 CONCLUSIONS

- A new type of isolator called polynomial rocking bearing (PRB) is applied to bridges in this study. Through shaking table tests, the results reveal the feasibility and effectiveness of PRBs in mitigating the dynamic responses of bridges under both near-field and far-field ground motions as compared to the non-isolated bridges. Also, the numerical model is verified to be accurate in simulation of the isolated bridge with PRBs.

- Since the restoring stiffness of the PRB can be divided into softening section and hardening section, the structural acceleration response can be decreased in softening section while the structural displacement response can be decreased in hardening section. As compared to the traditional FPS, the column and deck displacements of the isolated bridge with PRBs can be further improved under both near-field and far-field ground motions.
- The effect of PRBs on the seismic behavior is influenced by the six-order polynomial of rocking surface, bearing height and equivalent friction coefficient. Such design parameters can be determined by using PSO-SA hybrid searching algorithm. From the results of numerical simulations, it is verified that the PRBs can reach the optimum performance in mitigating the seismic responses of bridges.

REFERENCES

[1] C. Christopoulos, A. Filiatrault, Principles of passive supplemental damping and seismic isolation. *IUSS Press*. Pavia, 2006.

[2] F. Naeim, J.M. Kelly, Design of seismic isolated structures: from theory to practice. *John Wiley & Sons*, 1999.

[3] Y.B. Yang, L.Y. Lu, J.D. Yau, C.W. de Silva (Ed.), Structure and equipment isolation, vibration and shock handbook. *CRC Press*, Taylor & Francis Group, 2005.

[4] W.L. He, A.K. Agrawal, Analytical model of ground motion pulses for the design and assessment of seismic protective systems. *J Struct Eng*, **134**, 1177-1188, 2008.

[5] L.Y. Lu, G.L. Lin, M.H. Shih, An experimental study on generalized Maxwell model for nonlinear viscous dampers used in seismic isolation. *Eng Struct*, **34**, 111-123, 2012.

[6] L.Y. Lu, C.C. Hsu, Experimental study of variable-frequency rocking bearings for near-fault seismic isolation. *Eng Struct*, **46**, 116-129, 2013.

[7] L.Y. Lu, T.Y. Lee, I.L. Yeh, H. Chang, Rocking bearings with variable frequency for near-fault seismic isolation (in Chinese). *Journal of the Chinese Institute of Civil and Hydraulic Engineering*, **22**, 283-298, 2010.

[8] T.Y. Lee, P.C. Chen, D.S. Juang, Sliding mode control on isolated bridge with columns of irregular heights using pole assignment and PSO-SA hybrid algorithm. *International Journal of Structural Stability and Dynamics*, **12**, 1250014 (26pages), 2012.

COMPDYN 2015
5th ECCOMAS Thematic Conference on
Computational Methods in Structural Dynamics and Earthquake Engineering
M. Papadrakakis, V. Papadopoulos, V. Plevris (eds.)
Crete Island, Greece, 25–27 May 2015

FINITE ELEMENT INVESTIGATION OF A NEW SEISMIC ENERGY ABSORPTION DEVICE THROUGH SIMOULTANEOUSLY YIELD AND FRICTION

Magdalini D. Titirla[1] **and Panikos K. Papadopoulos**[1]

[1] Department of Civil Engineering
Aristotle University of Thessaloniki, Greece
e-mail: {mtitirla, paniko}@civil.auth.gr

Keywords: Passive Energy Dissipation System, Finite Element Method, Absorption Seismic Energy, Friction.

Abstract. *The aim of this study is to investigate the micro-behavior of the CAR1 device. This device was presented by Papadopoulos et al [1] and has the advantages to (i) provide additional stiffness as well as (ii) absorption of seismic energy, (iii) provide control of the axial forces that are developed at the diagonal steel rods. Last but not least, it has the ability to retain the plastic displacements to a desired level. The first step was to model and analyze the group of superimposed blades in order to ascertain its behavior under monotonic loading, increased step by step until the collapse. To that purpose, Finite Element (FE) models of the system were developed and analyzed using the software ABAQUS. Parametric investigation was conducted to define the optimum combination of number and thickness as well as their elastoplastic properties. Furthermore, the group of superimposed blades was modeled and analyzed under quasi static cyclic loading, in order to ascertain its behavior to absorbed seismic energy. In addition, numerical results were compared with the same experimental so as to validate the model in the software ABAQUS.*

1 INTRODUCTION

The safety of construction (existing or new) is one of the major priorities of engineering globally, because structures often subject to large and often devastating, for their viability, loadings. So, great interest is in the study of the innovations of the design and materials of construction that minimize the probability of failure of the structure in any charging. Therefore, many efforts have been made to create devices that will absorb the majority of the seismic energy but will not belong to the supporting structure of the construction. The main advantages of these, is the easy replaced or repaired. These devices belong to the passive energy dissipation systems, do not require external power to generate system control forces and hence, are easy and cheap to implement in a structure. Passive energy dissipation devices such as visco-elastic dampers, metallic dampers and friction dampers have widely been used to reduce the dynamic response of civil engineering structures subjected to seismic loads [2, 3] Their effectiveness for seismic design of building structures is attributed to minimizing structural damages by absorbing the structural vibratory energy and by dissipating it through their inherent hysteresis behaviour [2].

In order to demonstrate the effectiveness of the devices, many passive energy dissipation systems were studied in experimental research [4, 5, 6, 7], others in numerical research [8, 9, 10] and others in both of these.

The Finite Element Method (FEM) has become the most popular method in both research and industrial numerical simulations. Several algorithms, with different computational costs, are implemented in the finite codes, such as ABAQUS [11], which is commonly used software for finite element analysis. Understanding the nature, advantages and disadvantages of this software, ABAQUS has been chosen to validate the group of the superimposed blades, which is the main element of the investigated device. Numerical analysis was conducted in order to investigate the behavior of the superimposed blades. What is more, a micro-investigation locally in regions of high importance is permissible. In this way, results come out that are harder to obtain experimentally.

In present paper, an analytical investigation of the group of the superimposed blades is presented through finite element analysis with parametric study of material, dimensions and friction coefficient between surface contacts.

2 DESCRIPTION OF THE INVESTIGATED DEVICE CAR1

The device CAR1, presented by Papadopoulos et al [1], is illustrated in Figure 1. The relevant movement between the exterior tube (Element A) and the interior shaft (Element B) is carried out by an elastoplastic bending deformation of the superimposed blades that connect crosswise elements A and B. The number and the dimensions of superimposed blades as well as their elastoplastic properties define the principle of elastoplastic behavior of the diagonal bars on an axial load.

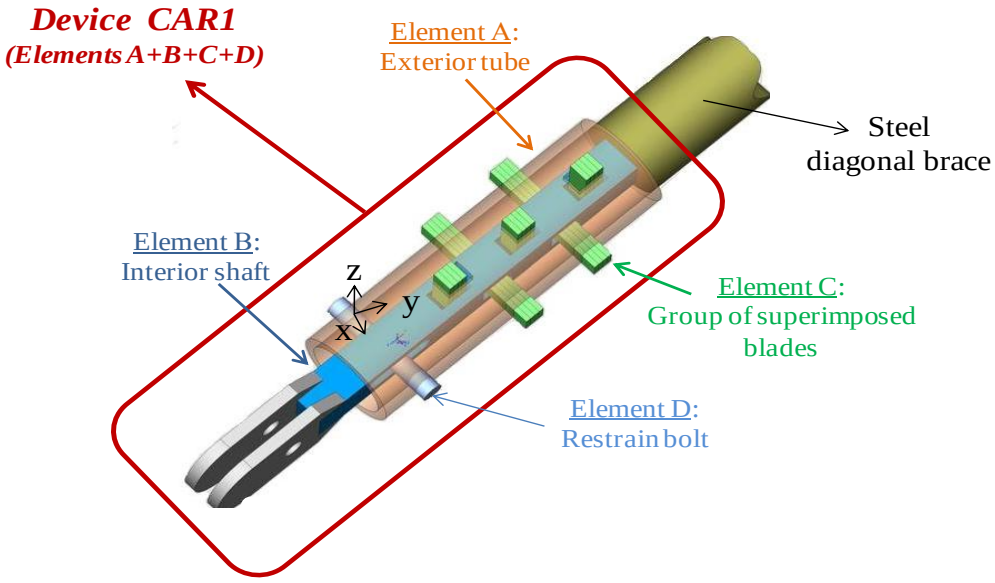


Figure 1: The investigated device CAR1.

3 FINITE ELEMENT MODELING IN ABAQUS

The finite elements analysis calibration study included modeling of a group of superimposed steel blades, with dimensions 125x20x20mm, as illustrated in Figure 2. The group consists of five steel blades with thickness of 4mm each one. Young's modulus is given as E=200GPa, Poisson's ratio is ν=0.30 and Yield strength is F=235MPa. The average coefficient of friction between steel surfaces is equal to μ=0.40 [12].

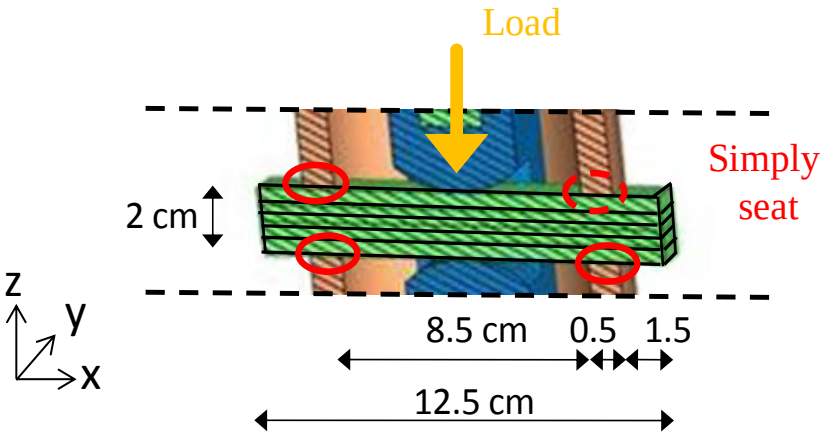


Figure 2: Description of the group of superimposed steel blades.

The superimposed blades are free to move along the axis x-x, independently of each other. The movements along the axis y-y and z-z are prohibited because of the existence of the external tube (Element A). Definition of boundary conditions for the superimposed blades is not considered necessary as simply mounted to the rigid components of the exterior tube A of the device. On the other hand, each rigid element is fixed (all degrees of freedom).

The load is transferred to the center of the top superposed blade through the interior shaft of the device (Element B). The curvature of the interior shaft leading to uniform load transfer small amplitude along the axis x-x and y-y, which be considered as a point load. During the

modeling in order to avoid high stress concentration at individual points, the load introduced as uniform in a small strip (Figure 3a). During the analysis the load imposed at a very slow pace, increased step by step until the collapse.

To simulate the behavior of the group of superimposed steel blades, it was selected to use an explicit dynamic solver because this allows the definition of very general contact conditions for complicated contact problems, without generating numerical convergence difficulties. Moreover, an explicit dynamic solver uses a consistent large-deformation theory that can model large rotations and large deformations, which is beneficial for the analysis of the group of superimposed steel blades.

For the explicit method, 3D reduced integration solid element C3D8R (eight-node bricks) are used. A view of the finite element mesh is displayed in Figure 3b.

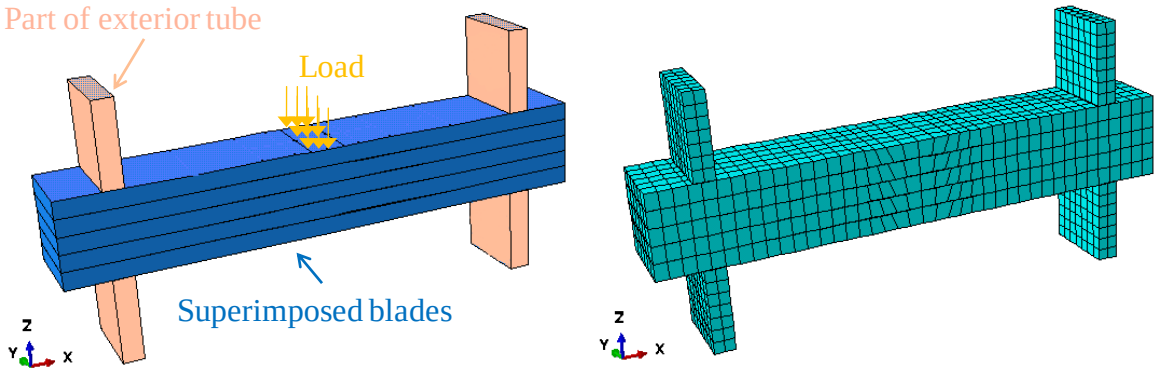


Figure 3: a) Numerical model in ABAQUS, b) Finite element mesh in ABAQUS.

Surfaces in contact are not only the interior surfaces of the superimposed steel blades, but also the part of exterior tube in which blades simply seat. Figure 4 shows all the contact surfaces with green color. To model the contact areas in ABAQUS, surface to surface contact was used with coefficient of friction equal to μ=0.40.

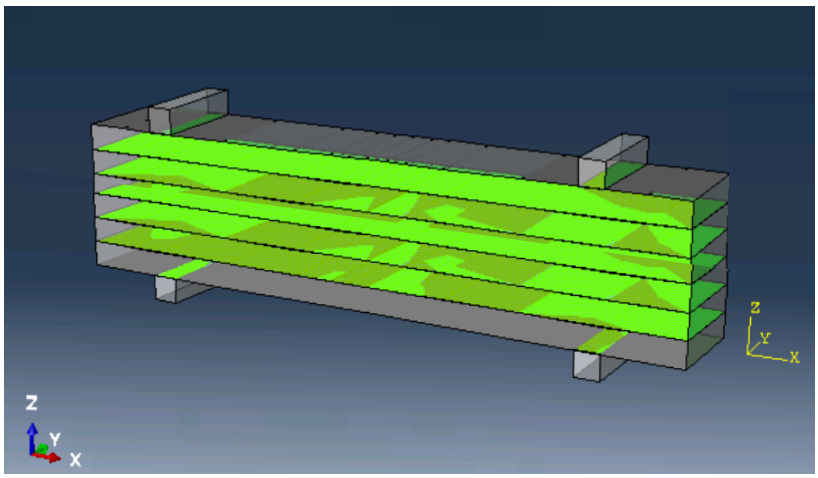


Figure 4: In contact surfaces.

Figure 5 illustrate the force-deformation relation at the central section of the bottom blade, for the group of superimposed which was presented previously, under increasing step by step load until the collapse.

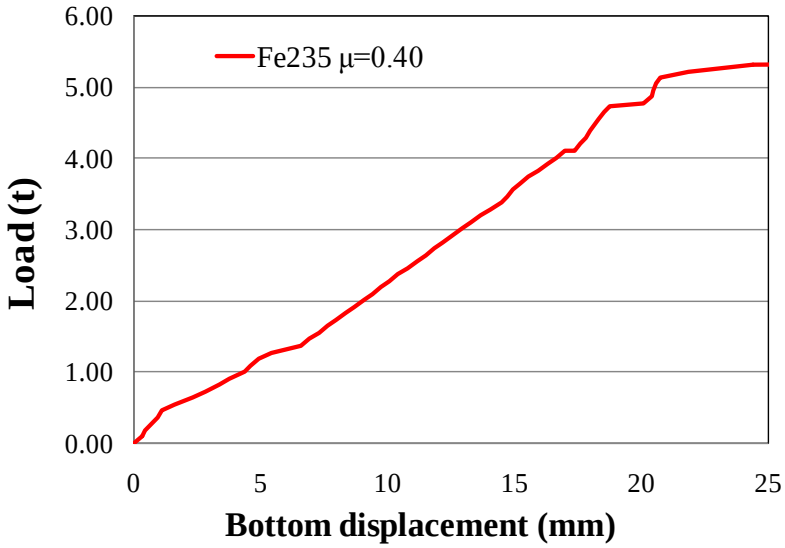


Figure 5: Numerical results with increasing step by step load until the collapse.

4 PARAMETRIC STUDY

In order to investigate the behavior of the superimposed blades 56 parametric numerical analyses have been done. The main parameters for comparison of the group of superimposed blades are: (i) the material of the blades, (ii) their thickness and (iii) the friction coefficient between contact surfaces.

4.1 Material of the blades

Three different qualities of materials were investigated, two steel and one brass. It was chosen soft qualities of steel and brass and particularly qualities that are easily founded in the commercial without order. In ABAQUS software a typical elastic-plastic material was used with properties that are presented in the following Table (Table 1) both for steel and brass.

	Young Modulus (GPa)	**Mass Density x1000 (kg/m^3)**	**Yield Stress (MPa)**	**Plastic Strain (MPa)**
Steel (Fe150)	201	7.85	150	180
Steel (Fe235)	201	7.85	235	340
Brass (Br)	100	8.45	200	370

Table 1: Elastoplastic characteristics of materials.

4.2 Thickness of the blades

The total thickness of the superimposed blades should be equal to 20mm, to satisfy the dimensions of the device CAR1. Thickness and number of the blades was classified into two categories. In the first, the material remained the same throughout the group, while in the second the material was differentiated from blade to blade. The analyzed combinations presented in Table 2. The total number of combination due to the thickness, taking account of the material, is 21.

Thickness and number of blades					Number of combination
Fe150		**Fe235**		**Br**	
20mm (1)	**or**	20mm (1)	**or**	20mm (1)	3
10mm (2)	**or**	10mm (2)	**or**	10mm (2)	3
5mm (4)	**or**	5mm (4)	**or**	5mm (4)	3
4 mm (5)	**or**	4mm (5)	**or**	4mm (5)	3
2 mm (10)	**or**	2mm (10)	**or**	2mm (10)	3
5mm (2)	**or**	5mm(2)	**and**	5mm(2)	2
4mm (3)	**or**	4mm(3)	**and**	4mm(2)	2
5 mm (3)	**or**	5mm(3)	**and**	2.5mm (2)	2

Table 2: Number and thickness of groups of superimposed blades.

4.3 Coefficient of friction

When surfaces in contact move relative to each other, the friction between the two surfaces converts kinetic energy into thermal energy. Friction is not itself a fundamental force but arises from interatomic and intermolecular forces between the two contacting surfaces. The coefficient of friction (COF), often symbolized by the Greek letter μ, is a dimensionless scalar value which describes the ratio of the force of friction between two bodies and the force pressing them together. The coefficient of friction depends on the materials used as Table 3 illustrates.

Surfaces in contact	Coefficient of friction μ
Steel to Steel	0.00 (theoretical smooth)
Steel to Steel	0.40 (standard)
Steel to Steel	0.70 (knurled)
Brass to Brass	0.00 (theoretical smooth)
Brass to Brass	0.40 (standard)
Steel to Brass	0.35 (standard)

Table 3: Coefficient of friction between contact surfaces.

5 DISCUSSION OF PARAMETRIC STUDY

Figure 6 illustrates the observed dependence of load on displacement (at the middle point of the bottom blade) for group of superimposed steel blades for all coefficient friction. The groups, which presented in this Figure, are one blade with thickness 20mm and two blades with thickness equal to 10mm each one. It can be deduced that the blades of both groups entered in the plastic area in small displacements. The behavior of these groups is not compatible with the rationale of the device CAR1, although the large load that can be received.

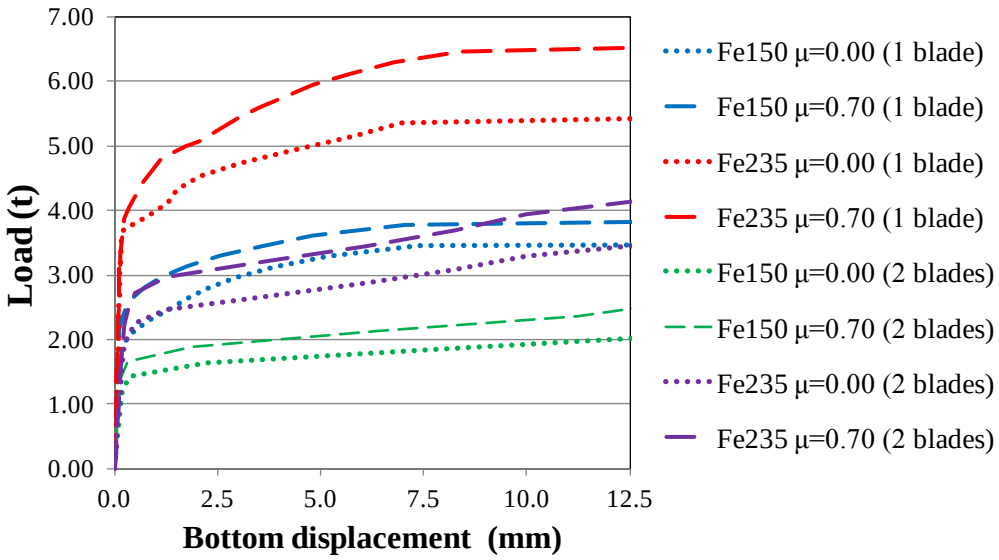


Figure 6: Load versus displacement for group with blade's thickness 20mm and 10mm.

The observed dependence of load on displacement (at the middle point of the bottom blade) for group of superimposed steel blades with thickness 4mm for all coefficient friction is presented in Figure 7. Also for the desirable displacement of 13mm, we can notice the variation of the received load. The choice of movement was indicative in order to observe the influence of the coefficient of friction. Thus creating knurled in blades, such as increasing the friction coefficient to 0.70, the received force for this movement can easily increased around 20%.

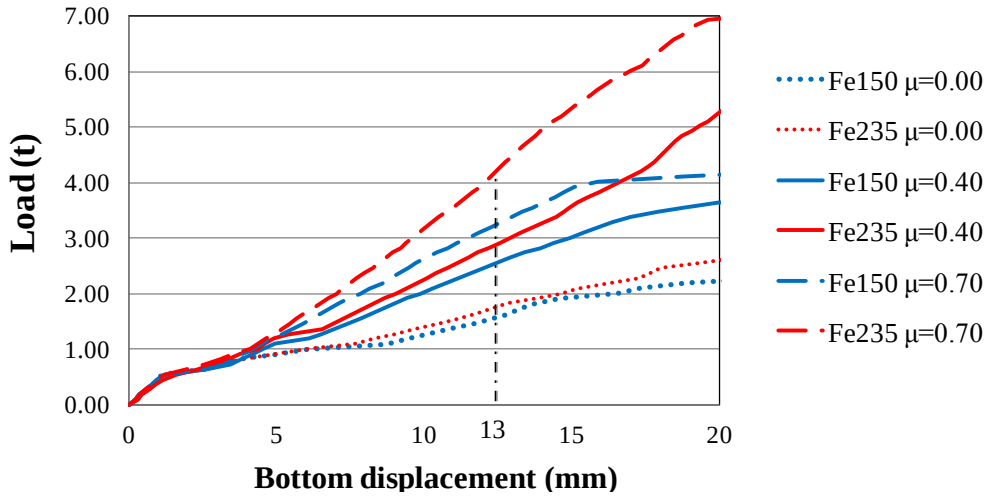


Figure 7: Load versus displacement for group with blade's thickness 4mm.

Figure 8 shows the comparison of maximum load for the desirable displacement equal to 13mm. Three different thicknesses of blades, such as 5mm, 4mm and 2mm, were selected in Figure 8a. The materials of the groups are steel and brass. It is necessary to notice that material and thickness remain the same into the group. The optimum combinations are the groups with blade's thickness 5mm or 4mm and material Fe235. The received load for the brass blades is small due to the Young Modulus. In addition, the material was differentiated from blade to blade in Figure 8b. The received load is smaller than the corresponding with the same material into the group, but it reduces the probability to behavior like one part over time.

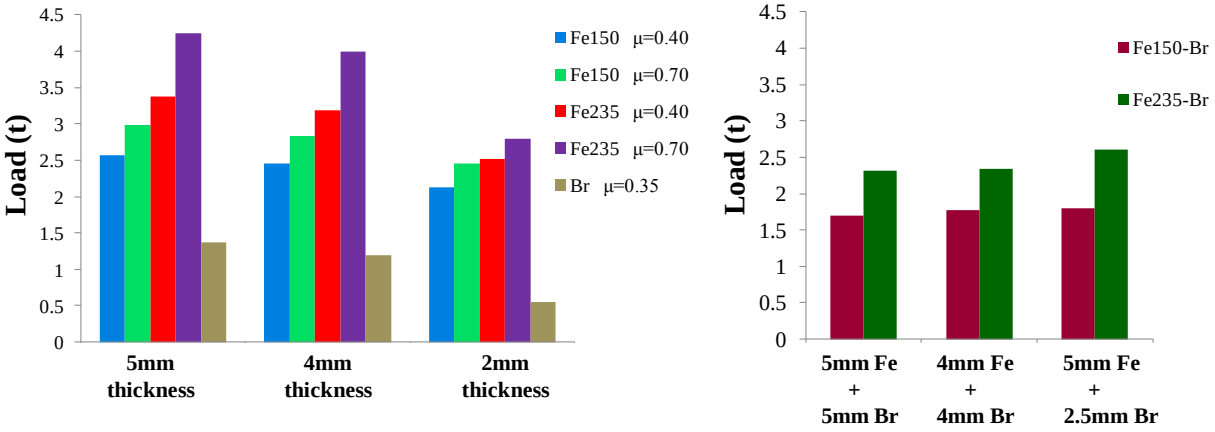


Figure 8: Maximum load for the desirable blades' displacement of 13mm.

One of the optimum combinations was chosen to illustrate the variation of the mises stress according to friction coefficient at a load magnitude corresponding to yield of frictionless group (Figure 9). The thickness of the blades is equal to 5mm and the material is Fe235.

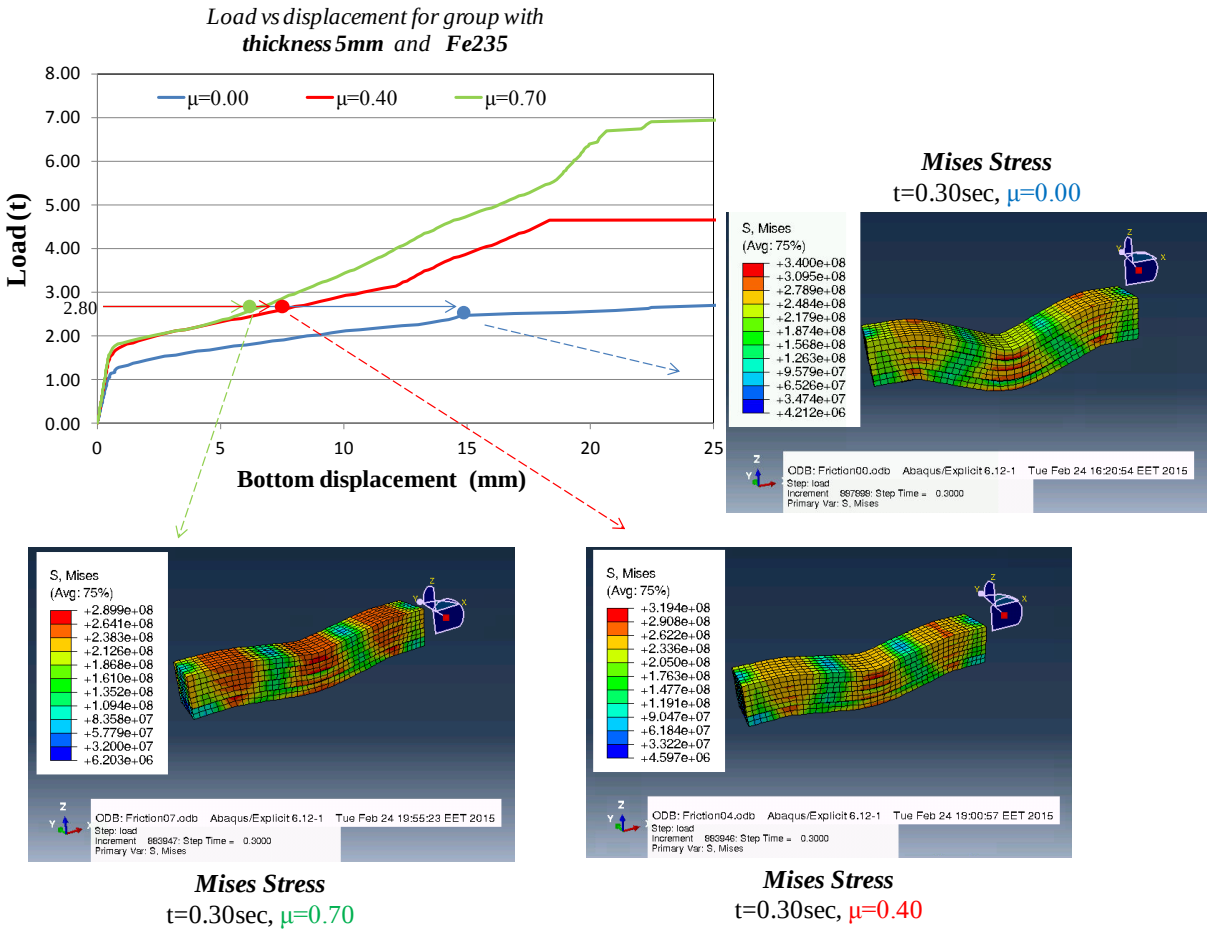


Figure 9: Load versus displacement for superimposed blades with thickness equal to 5mm and Fe235 and mises stress of blades at a load magnitude corresponding to yield of frictionless group.

6 CYCLIC LOADING

Quasi-static cyclic tests were carried out for a group of superimposed steel blades in order to ascertain its behavior to absorbed seismic energy. Multiple dynamic tests were run on each group of superimposed blades under varying load amplitudes and time. In Figure 10 the cycling load versus time, for the group of 4 blades with thickness equal to 5mm, is presented. Blue line illustrate one cycle loading with stable maximum force equal to 2.25t, while red line shows three cycles loading with increasing force cycle by cycle from 1.50t to 2.25t.

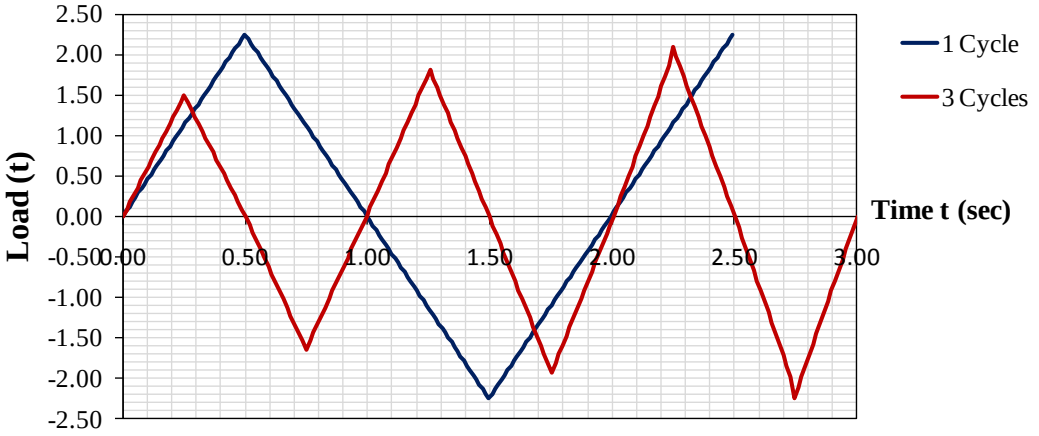


Figure 10: Quasi static cycling load versus time.

Figure 11 illustrates the hysteretic loops of the displacement for the previous cycles loading. As hysteretic loops of the displacement represent the amount of the absorbed energy, we can notice the ability of the device CAR1 to absorb seismic energy. From the shape and consistency of the hysteresis loops, it can be determined that the CAR1 device is effective in dissipating energy. The area within a hysteresis loop is equivalent to the amount of energy that the device is dissipating.

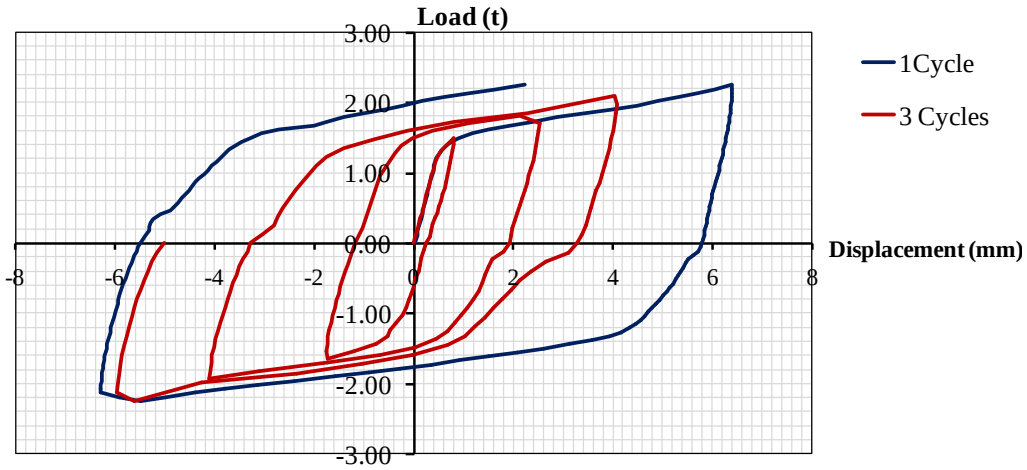


Figure 11: Hysteretic loops.

In addition, tests were run for ten cycles in order to ascertain any degradation in behavior over repeated cycles. To produce these hysteresis loops, load of amplitudes varying from 2.50t-3.00t were applied on group for 10 cycles as shown in Figure 12.

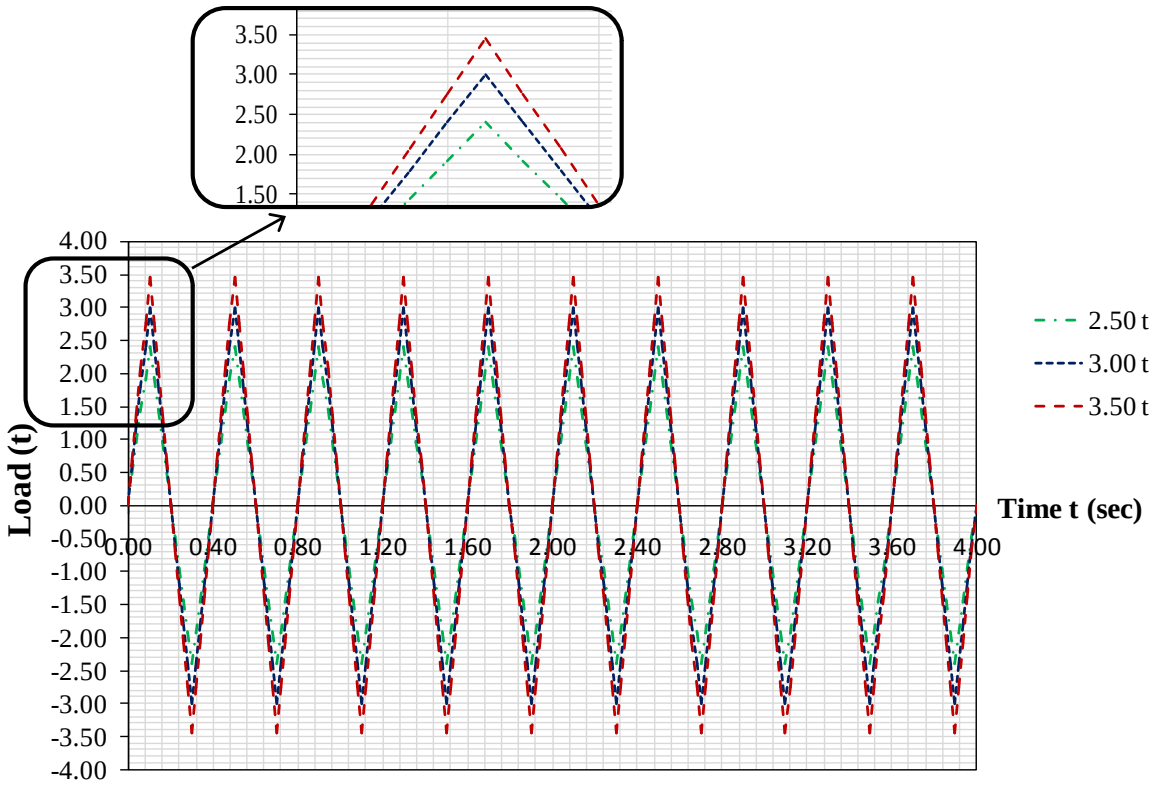


Figure 12: Cycling load versus time for ten cycles.

From the shape and consistency of the hysteresis loops, as illustrated in Figure 13, it can be determined that the CAR1 device is effective in dissipating energy and it will not break down during the course of cyclic loading. Furthermore, it can be seen that CAR1 device has very good energy dissipation potential.

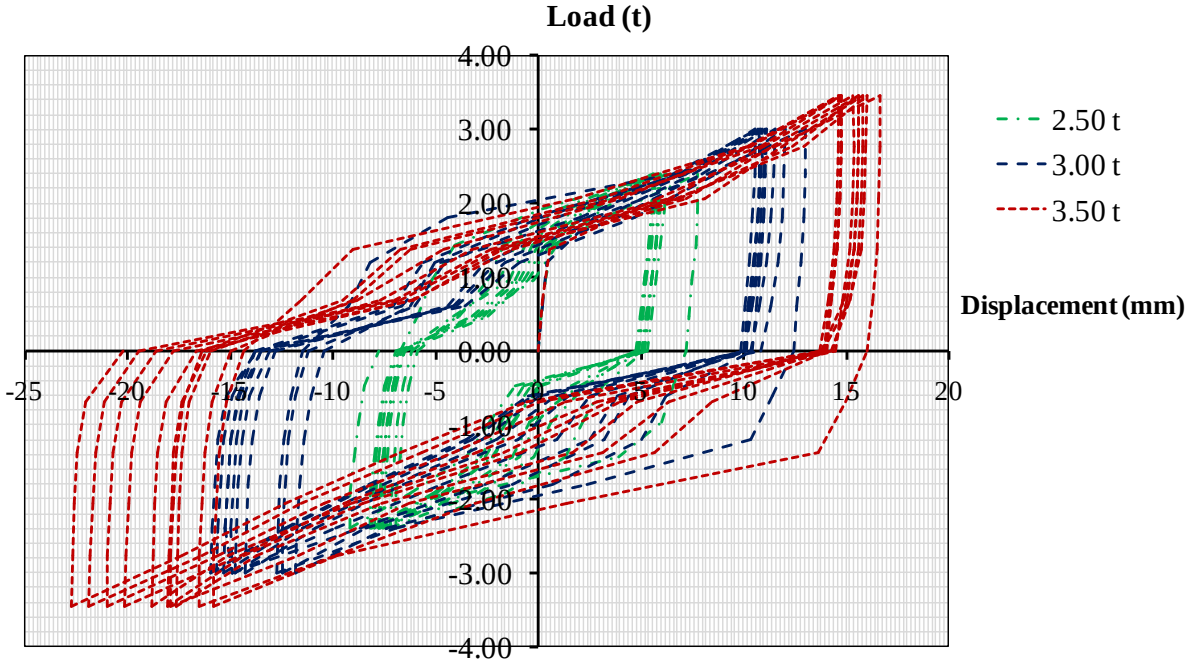


Figure 13: Hysteretic loops.

Figures 14 shows the distribution of plastic equivalent strain and the deformed shape of the 5 superimposed steel blades with thickness 4mm at the end of 10 cycles. It is observed that the nodes with more stress, is the center of the blades and the support points of the blades into the exterior tube.

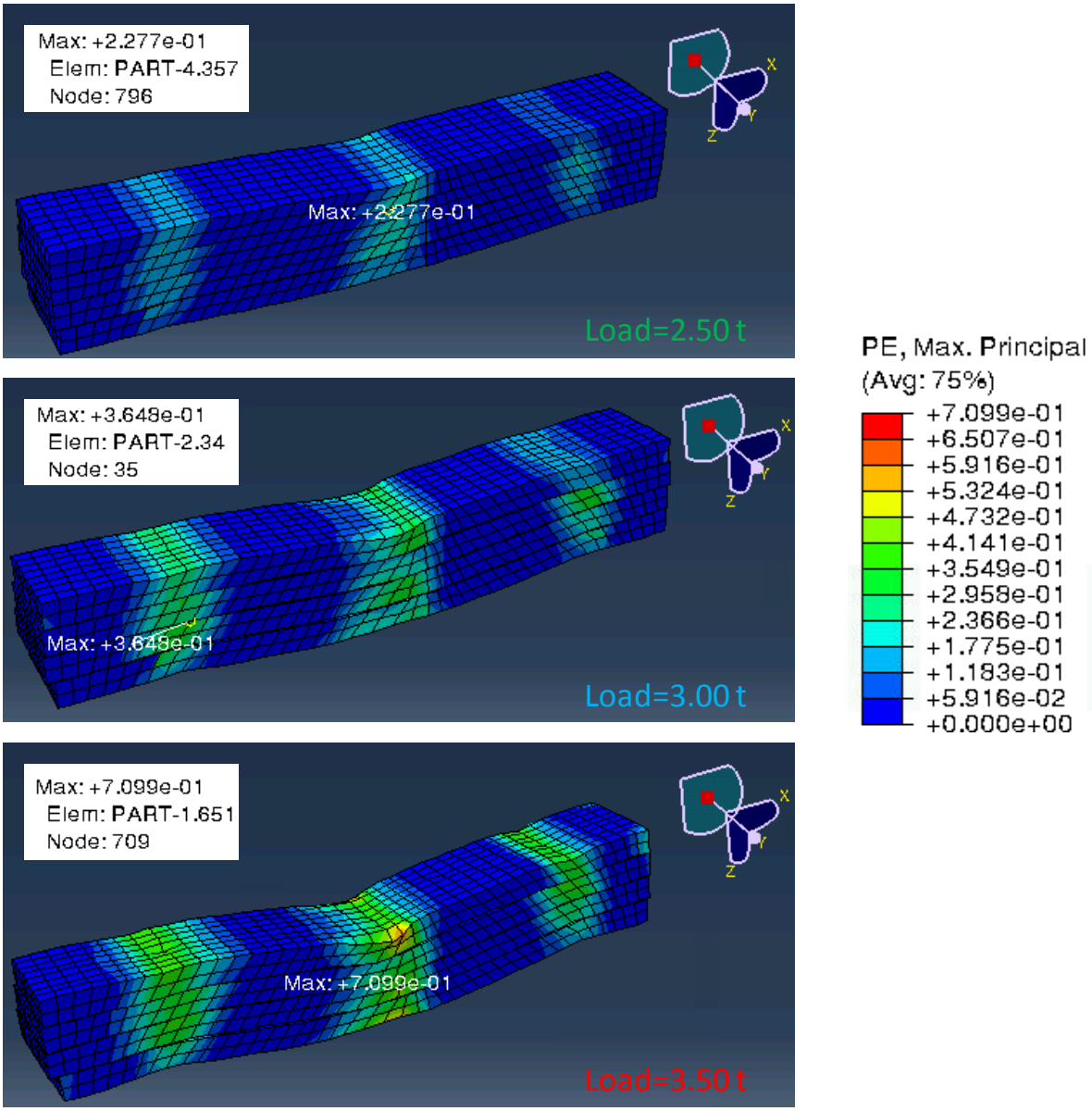


Figure 14: Deformed geometry from a group of 5 superimposed blades at the end of 10 cycles.

7 VALIDATION OF NUMERICAL AND EXPERIMENTAL TEST RESULTS

The finite elements analysis calibration study included: (i) modeling of a group of superimposed steel blades and (ii) comparison of the numerical results with the same experimental. The group consists of five steel blades, 4mm thick each. Young's modulus is given as E=200GPa, Poisson's ratio is ν=0.30 and Yield strength is F=235MPa. The average coefficient of friction between steel surfaces is equal to μ=0.40. During the analysis the load imposed at a very slow pace, increased step by step until the load of 3.60t and then reduced step

by step. As it is shown, in Figure 15, the finite element results are in accordance with the experimental results.

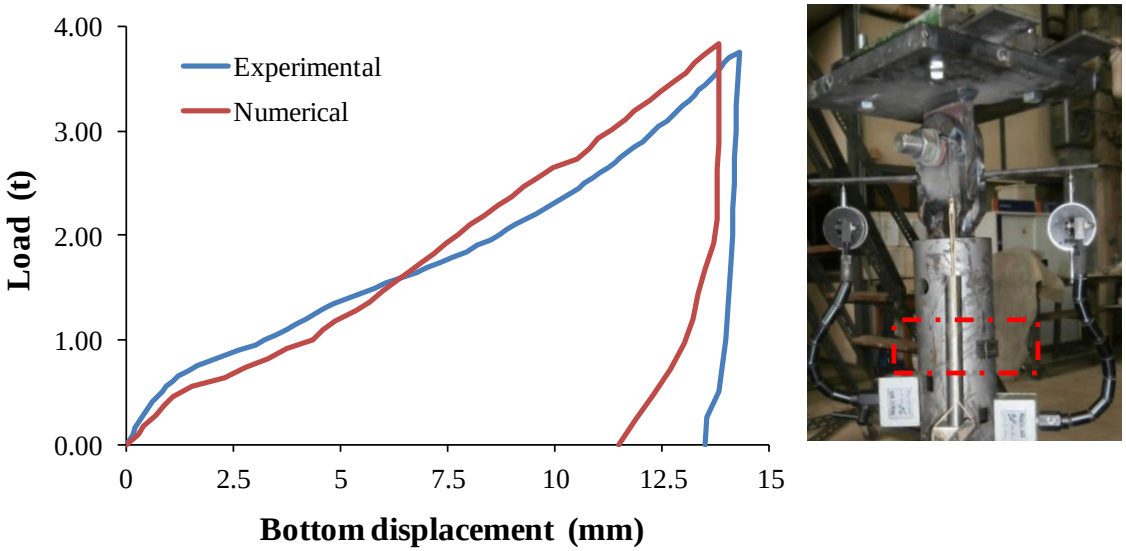


Figure 15: Experimental and numerical test results.

8 CONCLUSION

In this paper, an analytical investigation of the group of the superimposed blades, which is the main element of the device CAR1, was presented. The group analyzed through finite element analysis with parametric study of material, dimensions and friction coefficient between surface contacts. Furthermore, the numerical results reveal some conclusions of the behavior of the superimposed blades, namely that:

- ✓ Group of blades with thickness 20mm and 10mm entered in the plastic area in small displacements. The behavior of these groups is not compatible with the rationale of the device CAR1, although the large load that can be received. While blades with thickness equal to 4mm and 5mm are the optimum combinations.

- ✓ In addition, in group blades where the material was differentiated from blade to blade the received load is smaller than the corresponding with the same material into the group, but it reduces the probability to behavior like one part over time.

- ✓ The hysteresis loops of the displacement for the 10 cycles loading confirm the ability of the device CAR1 to absorb seismic energy. The area within a hysteresis loop is equivalent to the amount of energy that the device is dissipating. From the hysteresis loops, it can be seen that the device CAR1 not only is effective in dissipating energy, but also it will not break down during the course of cyclic loading.

ACKNOWLEDGMENTS

The authors would like to thank Alkis Papadopoulos, PhD Candidate at Aristotle University of Thessaloniki, for his valuable support provided during the experiments. Although the experiments results are thesis of other research, these were helpful to validate the numerical results.

REFERENCES

[1] P.K. Papadopoulos, M.D. Titirla, A.P. Papadopoulos, A new seismic energy absorption device through simultaneously yield and friction used for the protection of structures. *2nd European Conference on Earthquake Engineering and Seismology*, Istanbul, Turkey, August 25-29, 2014.

[2] T.T. Soong, B.F.S Jr, Supplemental energy dissipation: state-of-the-art and state-of-the-practice. *Engineering Structures*, **24**, 243-259, 2002.

[3] I.D. Aiken, D.K. Nims, J.M. Kelly, Comparative study of four passive energy dissipation systems. *Bull. N. Z. Natl. Soc. Earthquake Engineering*, **25**, 175–192, 1992.

[4] I.D. Aiken, D.K. Nims, A.S. Whittaker, J.M. Kelly, Testing of passive energy dissipation systems. *Earthquake spectra*, **9**, 335-370, 1993.

[5] G. Anagnostides, A.C. Hargreaves, Shake table testing on an energy absorption device for steel braced frames. *Soil Dynamics and Earthquake Engineering*, **9**, 120-140, 1990.

[6] P.K. Papadopoulos, T.N. Salonikios, S.A. Dimitrakis, A.P. Papadopoulos, Experimental investigation of a new steel friction device with link element for seismic strengthening of structures. *Structural Engineering & Mechanics*, **46**, 487-504, 2013

[7] A.S. Whittaker, V.V. Bertero, J.L. Alonso, C.L. Thompson, Earthquake Simulator Testing of Steel Plate Added Damping and Stiffness Elements. *Report No. UCB/EERC 89/02*, University of California, Berkley, 1989.

[8] A.S. Pall, Friction devices for aseismic design of buildings, *4th Canadian Conference on Earthquake Engineering*, Vancouver, Canada, 1983.

[9] P. Papadopoulos, New nonlinear anti-seismic steel device for the increasing the seismic capacity of multi-storey reinforced concrete frames. *The structural design of tall and special buildings*, **21**, 750-763, 2012.

[10] J.D.M. Ramirez, L. Tirca, Numerical Simulation and Design of Friction- Damped Steel Frame Structures damped. *15th World Conference in Earthquake Engineering*, Lisbon, Portugal, September 24-28, 2012.

[11] ABAQUS: *Theory and analysis user's manual version 6.12*, Providence, RI, USA: Dassault Systèmes SIMULIA Corp. 2012.

[12] F. Cobb, Structural Engineers' Pocket Book. *2nd Edition, British Standards Edition*, 2008.

COMPDYN 2015
5th ECCOMAS Thematic Conference on
Computational Methods in Structural Dynamics and Earthquake Engineering
M. Papadrakakis, V. Papadopoulos, V. Plevris (eds.)
Crete Island, Greece, 25–27 May 2015

SEISMIC ANALYSIS OF BASE-ISOLATED CYLINDRICAL LIQUID STORAGE TANK USING COUPLED ACOUSTIC-STRUCTURAL INTERACTION

Aruna Rawat[1], Vasant Matsagar[2], and A.K. Nagpal[3]

[1] Research Scholar, Department of Civil Engineering, Indian Institute of Technology (IIT) Delhi, Hauz Khaus, New Delhi – 110 016, India
e-mail: augupta2001@gmail.com

[2] Associate Professor Department of Civil Engineering, Indian Institute of Technology (IIT) Delhi, Hauz Khaus, New Delhi – 110 016, India

[3] Dogra Professor, Department of Civil Engineering, Indian Institute of Technology (IIT) Delhi, Hauz Khas, New Delhi - 110 016, India.

Keywords: Base isolation, Base shear, Coupled acoustic-structure, Finite element, Liquid storage tank, Seismic analysis, Sloshing.

Abstract *Seismic analysis of three-dimensional (3-D) ground-supported base-isolated cylindrical liquid storage tank is investigated using coupled acoustic-structural interaction approach. In this approach of finite element (FE) method the contained liquid in tank is modeled with acoustic elements, having only pressure degree-of-freedom. By using the present approach the impulsive and convective or sloshing components acting on the tank can be evaluated separately by using the appropriate boundary conditions on the top of free liquid surface. The study is performed for two base isolation systems, elastomeric bearing and sliding system, which are modeled as non-linear connectors in the present study. A parametric study is performed to study the effectiveness of the proposed analysis method for broad and slender base-isolated tanks. The sloshing displacement and base shear time history responses are evaluated for 3-D tanks subjected to uni-directional earthquake ground motions. The FE time history responses are compared with the non-isolated 3-D tanks and it is found that the impulsive component of base shear has reduced more as compared to convective component of base shear. It is also seen that sloshing displacement was unaffected by the application of both the isolation systems.*

1 INTRODUCTION

Structures which are in contact with fluids exhibit a different behavior under seismic loads from other structures. The seismically induced motion of the structure causes dynamic pressure in the fluid, which in turn act upon the structure and hence modifies its dynamic response. This complex fluid-structure interaction (FSI) problem which arises not only for liquid storage tanks but also for large water reservoir and their containing structures as shown in Figure 1.

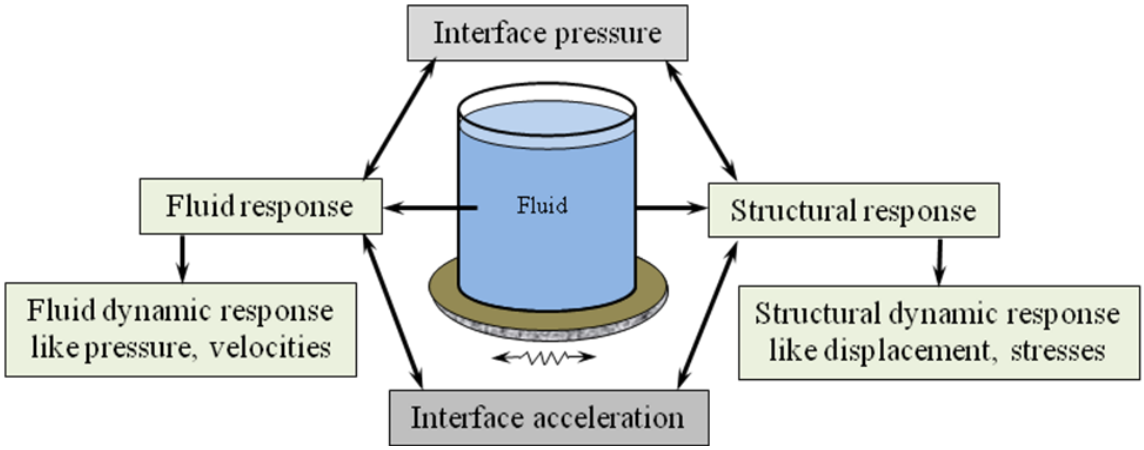


Figure 1 Fluid-structure interaction (FSI) problem.

Liquid storage tanks are the lifeline structures used for storage of various liquids, for example storage of water for drinking, fire-fighting system, industries, nuclear reactors. Failure of these liquid storage tanks were reported in past earthquakes events in the number of forms such as elephant foot buckling, diamond-shaped buckling, sliding of the base, uplifting of base, damage to the roof and the top of the tank wall caused by sloshing and failure of piping systems.

The protection of liquid storage tanks against the possible hazard of earthquakes is the major concern of the present design strategies. Over the three decades the development in the field of seismic control devices has reduced the failure of structure or the risk of damage in structures. Base isolation system has being extensively used to improve the seismic performance of the structures. This is achieved by introducing base isolation system between the foundation and the tank which causes the decoupling of the tank from the damages of earthquake ground motions. The purpose of using base isolation system is to lengthen the fundamental time period of the tank beyond the energy containing periods of earthquake ground motions.

Several researchers have studied base-isolated liquid storage using analytical, experimental and numerical methods. Chalhoub and Kelly [1] carried out several shake table tests on fixed base and base-isolated tanks using elastomeric bearings and observed the reduction in dynamic response but slight increase in the sloshing displacement. Bo and Jia-xiang [2] analyzed the ground-supported base-isolated liquid storage tank using lead rubber bearing (N-Z system) by finite element method. Kim and Lee [3] carried out pseudodynamic test on cylindrical liquid storage tank supported on laminated rubber bearings (LRB). Malhotra [4, 5] proposed a new method for base-isolated liquid storage tank in which the wall of the tank was supported over a flexible rubber bearing subjected to uni-directional and bi-directional components of earthquake. Kim et al. [6] numerically analyzed the three-dimensional (3-D) soil-structure-fluid interaction for base-isolated liquid storage tanks. Shrimali and Jangid [7] used three lumped

mass model for the seismic response of tank with pure-friction (P-F) sliding system under bi-directional ground excitation. Shrimali and Jangid [8] performed a comparative study of various isolation systems for the liquid storage tanks. Cho et al. [9] analyzed the base-isolated liquid storage tank considering the soil-interaction effect using a coupling method that combines the finite element and boundary element methods. Jadhav and Jangid [10, 11] carried out the study on various parameters such as aspect ratio of tank, the period of isolation and the damping of isolation bearings on base-isolated tank. Panchal and Jangid [12, 13] used FPS and variable friction pendulum (VFPI) system for base isolation of liquid storage tank under uni-directional earthquake ground motion. Emre and Eren [14] carried out a parametric study of base-isolated ground supported tanks using curved surface sliding bearings. Christovasilis and Whittaker [15] used mechanical analog and finite element methods, for studying the behavior of isolated liquefied natural gas (LNG) tanks. Calugaru and Mahin [16] conducted experimental and analytical studies on isolated and fixed base liquid storage tanks mounted on triple pendulum system. Shekari et al. [17] investigated the effects of base isolation on the seismic response of cylindrical vertical flexible liquid storage tanks subjected to horizontal seismic ground motion considering the coupled boundary element-fluid element (BE-FE) method. Soni et al. [18] used double variable frequency pendulum isolator (DVFPI) for isolation of liquid storage tank under uni-directional earthquake using three lumped mass model. Ruifu et al. [19] studied the seismic response of an isolated vertical, cylindrical liquefied natural gas (LNG) tank by multiple friction pendulum system (MFPS). Fallahian et al. [20] carried out an analytical study of liquid storage mounted on double concave friction pendulum (DCFP) isolation system. In the present work the seismic analyses of 3-D ground-supported base-isolated cylindrical liquid storage tank is analyzed using coupled acoustic-structural approach of FE method. By the present FE model the effect of impulsive and convective components can be calculated separately.

The objectives of the present study are (i) to compare the sloshing and base shear response of base-isolated cylindrical liquid storage tank with non-isolated 3-D finite element tank subjected to uni-directional earthquake ground motion, (ii) to study the 3-D liquid storage tank isolated using elastomeric bearing LRB and sliding bearing FPS, and (iii) to study seismic response of the tanks with two different aspect ratios, height of liquid to radius of the tank.

2 NUMERICAL MODELING OF BASE-ISOLATED LIQUID STORAGE TANK

Many researchers have modeled fluid with acoustic elements in finite (FE) analyses. Morand and Ohyan [21], Everstine [22], Virella et al. [23] investigated the FSI problems using acoustic elements. In the present study, coupled acoustic-structure approach of FE method is used for the seismic analysis of base-isolated tank. In this approach the liquid content in the tank is modeled using an acoustic element AC3D8R, eight-node 3-D continuum element with reduced integration and hourglass control used for acoustic wave propagation. The tank wall are modeled with shell S4R and S3R elements, four-node quadrilateral and triangular 3-D element with reduced integration and hourglass control, respectively as shown in Figure 2. The base isolation system is modeled using connectors available in Abaqus finite element software [24], which act in horizontal direction. Connectors allow the connection between two points in an assembly or between a point in an assembly and ground. The base isolation system parameters are assigned to connectors.

In the present study boundary impedance interaction is defined at the free surface of acoustic medium to model the sloshing behavior considering the linearized wave condition. For the impulsive component of the liquid response, the boundary condition at free surface of liquid is to be replaced by zero pressure, $p = 0$ at $z = H_L$. The interaction between the tank walls and acoustic liquid elements is defined using a surface-based tie constraint [24].

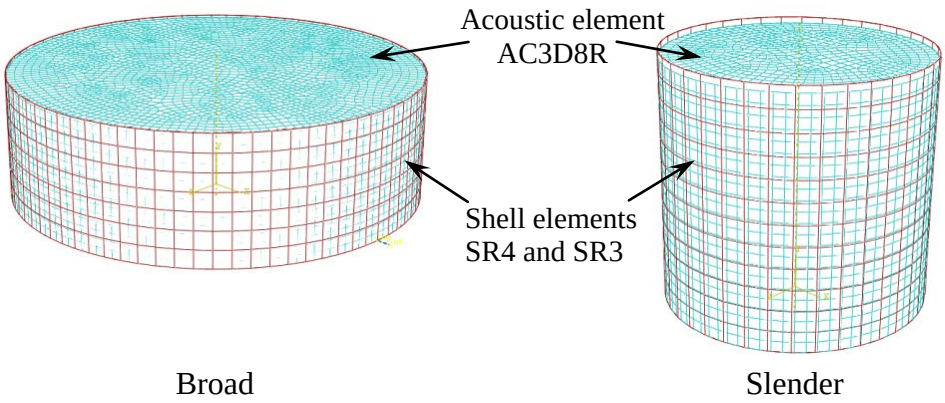


Figure 2 3-D FE model of base-isolated liquid storage tank.

3 NUMERICAL STUDY

In the present study, 3-D FE ground-supported flexible base-isolated tank are investigated under uni-directional earthquake ground motions. The two aspect ratios, $S = H_L/R$ (ratio of liquid height to radius of tank) broad and slender tanks are studied with their geometrical dimensions as given in Table 1.

	Aspect ratio, (H_L/R)	Height of water, H_L (m)	Thickness of tank, t (cm)
Broad	0.6	14.6	9.73
Slender	1.85	11.3	2.44

Table 1 Geometrical dimensions of circular tank.

The steel properties are used for modeling the circular tank and the liquid contained in tank is water having density (ρ_w) 1000 kg/m^3 and bulk modulus (K) is 2.05 GPa. The earthquake motions selected for the study are N00E component of 1940 Imperial Valley earthquake recorded at El Centro and N00S component of 1995 Kobe earthquake recorded at Japan Meteorological Agency (JMA). The peak ground acceleration (PGA) of Imperial Valley and Kobe earthquake motions are 0.348 g and 0.84 g, respectively. The two base isolation systems are used for the present study, elastomeric bearing, laminated rubber bearing (LRB) which is commonly characterized by its isolation time period (T_b) and damping (ξ_b). And sliding system, friction pendulum system (FPS) is characterized by the isolation time period (T_b) and friction coefficient (μ). For the present study, isolator properties for the LRB system T_b = 2 sec and ξ_b = 0.1 and for FPS are T_b = 2 sec and μ =0.05. The LRB is modeled by assigning a cumulative stiffness, k_b and cumulative damping force, c_b by non-linear connector given by Equation (1) and (2), respectively.

$$k_b = M\left(2\pi/T_b\right)^2 \tag{1}$$

$$c_b = 2M\xi_b\left(2\pi/T_b\right)^2 \tag{2}$$

where M is the total mass of liquid storage tank. The FPS is modeled by assigning coefficient of friction and cumulative stiffness to non-linear connector. The stiffness force for FPS

is given by Equation (1). The dynamic analysis is carried for a 20 seconds acceleration time history of earthquake in uni-direction at the rigid base of the tank.

The sloshing displacement is measured at the extreme node from the centre of the tank along the direction of excitation. Figure 3 shows the time history response for broad and slender tank for Imperial Valley, 1940 earthquake ground motion for both LRB and FPS isolation systems compared with the non-isolated tank. Figure 4 shows the time history response for broad and slender tank subjected to Kobe, 1995 earthquake ground motion for isolated and non-isolated tanks. Table 2 gives the peak response values for non-isolated and isolated tank. It can be observed from the responses that due to isolated systems the impulsive component of base shear has reduced more as compared to convective component of base shear. The sloshing displacement is unaffected by both the isolation systems.

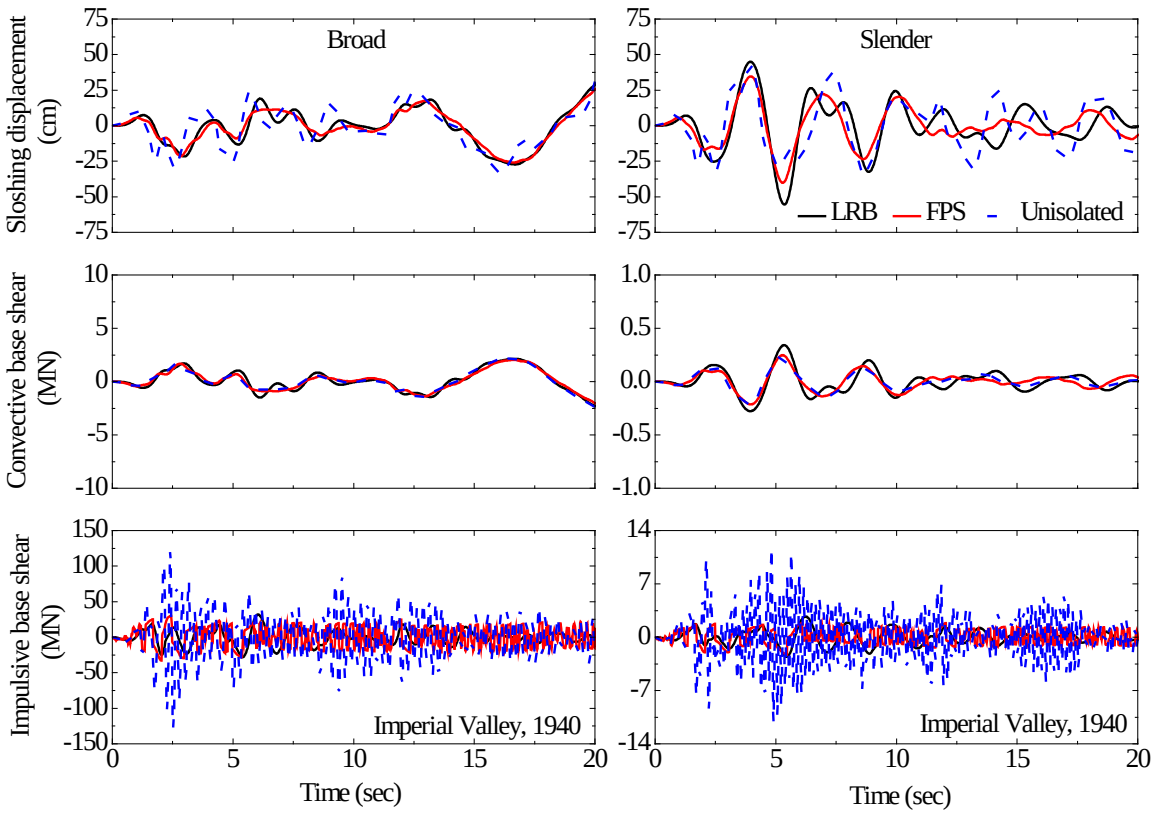


Figure 3 Time history response for 3-D base-isolated circular tanks subjected to Imperial Valley, 1940 earthquake ground motion.

Tank	Earthquake excitation	Isolation system	Sloshing (cm)	Impulsive base shear (MN)	Convective base shear (MN)
Broad	Imperial Valley, 1940	Non-isolated	61.20	127.08	5.06
		LRB	55.94	32.03	4.41
		FPS	52.84	33.02	2.92
	Kobe, 1995	Non-isolated	44.05	258.32	3.62
		LRB	46.75	108.79	3.68
		FPS	49.33	122.55	3.89
Slender	Imperial Valley, 1940	Non-isolated	41.88	12.41	0.34
		LRB	55.42	2.69	0.34

		FPS	40.12	2.29	0.24
	Kobe, 1995	Non-isolated	73.96	21.34	0.42
		LRB	98.73	8.03	0.60
		FPS	95.88	8.54	0.59

Table 2 Peak responses for 3-D base-isolated circular tanks.

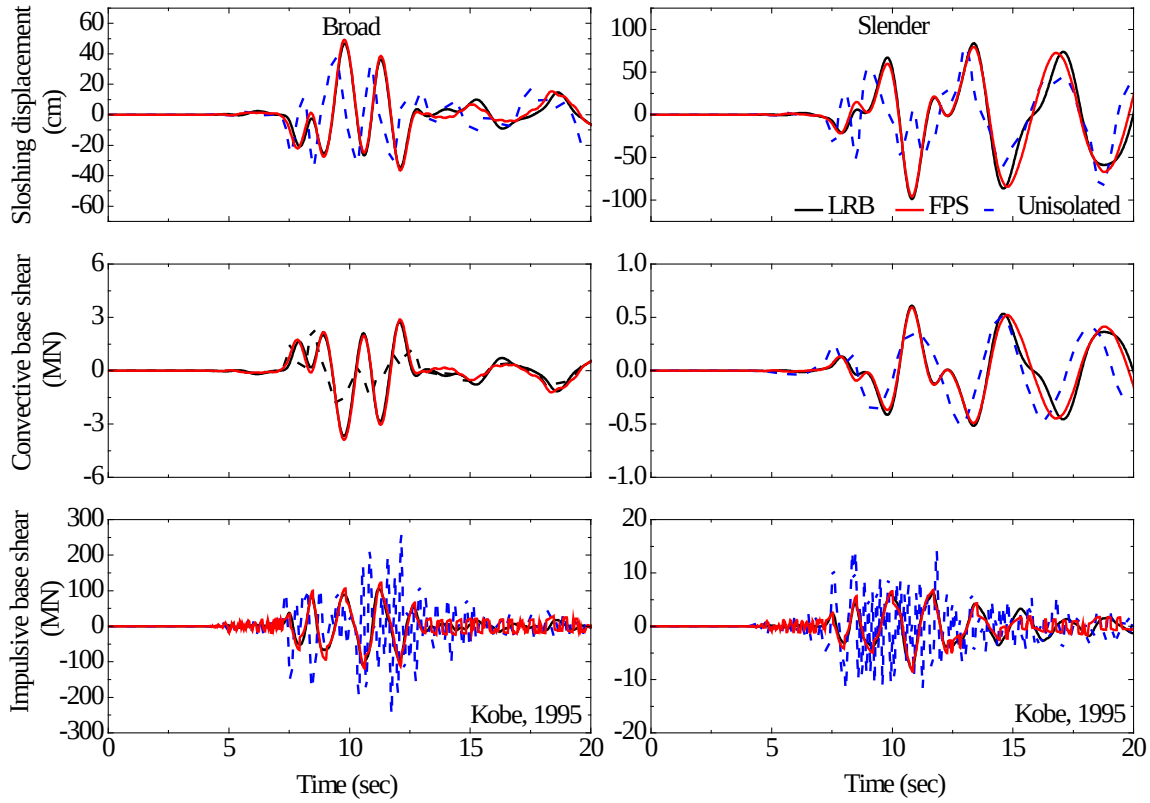


Figure 4 Time history response for 3-D base-isolated circular tanks subjected to Kobe, 1995 earthquake ground motion.

4 CONCLUSIONS

In the present study, 3-D FE ground-supported flexible base-isolated cylindrical tank are investigated under uni-directional earthquake ground motions. The coupled acoustic-structure approach of FE method is used for the analyses of tank. The two aspect ratios, broad and slender tanks are studied. The tanks are isolated using elastomeric laminated rubber bearing (LRB) and sliding systems friction pendulum system (FPS). The following conclusions are arrived.

- Both the isolation systems are found effective in reducing the earthquake forces in liquid storage tanks.
- The base shear response is reduced for both broad and slender tanks on application of isolation systems as compared to non-isolated tanks The impulsive component of base shear has major contribution and which has reduced significantly as compared to convective component of base shear.

- The sloshing displacement response has no significant effect on the introduction of isolation.

REFERENCES

[1] Chalhoub, M. S., Kelly, J. M., Shake table test of cylindrical water tanks in base-isolated structures, *Journal of Engineering Mechanics, ASCE*, 116, 7, 1451-1472, 1990.

[2] Bo, L., Jia-xiang, T., Vibration studies of base-isolated liquid storage tanks, *Computers and Structures*, 52, 5, 1051-1059, 1994.

[3] Kim, N. S., Lee, D. G., Pseudo-dynamic test for evaluation of seismic performance of base-isolated liquid storage tanks, *Engineering Structures*, 17, 3, 198-208, 1995.

[4] Malhotra, P. K., New methods for seismic isolation of liquid-storage tanks, *Earthquake Engineering and Structural Dynamics*, **26**, 839-847, 1997.

[5] Malhotra, P. K., Method for seismic base isolation of liquid storage tanks, *Journal of Structural Engineering, ASCE*, **123**, 1, 113-116, 1997.

[6] Kim, M. K., Lim, Y. M., Cho, S. Y., Cho, K. H., Lee, K. W., Seismic analysis of base-isolated liquid storage tanks using the BE–FE–BE coupling technique, Soil Dynamics and Earthquake Engineering, **22**, 1151-1158, 2002.

[7] Shrimali, M. K., Jangid, R. S., Seismic response of liquid storage tanks isolated by sliding bearings, *Engineering Structures*, **24**, 907-919, 2002.

[8] Shrimali, M. K., Jangid, R. S., A comparative study of performance of various isolation systems for liquid storage tanks, *International Journal of Structural Stability and Dynamics (IJSSD)*, **2**, 4, 573-591, 2002.

[9] Cho, K. H., Kim, M. K., Lim, Y. M., Cho, S. Y., Seismic response of base-isolated liquid storage tanks considering fluid-structure-soil interaction in time domain, *Soil Dynamics and Earthquake Engineering*, **24**, 11, 839-852, 2004.

[10] Jadhav, M. B., Jangid, R. S., Response of base-isolated liquid storage tanks, *Shock and Vibration*, **11**, 33-45, 2004.

[11] Jadhav, M. B., Jangid, R. S., Response of base-isolated liquid storage tanks to near fault motions, *Structural Engineering and Mechanics*, **23**, 615-634, 2006.

[12] Panchal, V. R., Jangid, R. S., Variable friction pendulum system for seismic isolation of liquid storage tanks, *Nuclear Engineering and Design*, **238**, 6, 1304-1315, 2008.

[13] Panchal, V. R., Jangid, R. S., Seismic response of liquid storage steel tanks with variable frequency pendulum isolator, *KSCE Journal of Civil Engineering*, **15**, 6, 1041-1055, 2011.

[14] Emre, A., Eren, U., Parametric analysis of liquid storage tanks base-isolated by curved surface sliding bearings, *Soil Dynamics and Earthquake Engineering*, **30**, 21-31, 2010.

[15] Christovasilis, I. P., Whittaker, A. (2008), Seismic analysis of conventional and isolated LNG tanks using mechanical analogs, *Earthquake Spectra, Earthquake Engineering Research Institute (EERI)*, **24**, 3, 599-616, 2008.

[16] Calugaru, V., Mahin, S., Experimental and analytical studies of fixed-base and seismically isolated liquid storage tanks, *Proceeding of 3rd International Conference on Advances in Experimental Structural Engineering*, October 15-16, San Francisco, 2009.

[17] Shekari, M. R., Khaji, N., Ahmadi, M. T., A coupled BE-FE study for evaluation of seismically isolated cylindrical liquid storage tanks considering fluid-structure interaction, *Journal of Fluids and Structures*, **25**, 567-585, 2009.

[18] Soni, D. P, Mistry, B. B., Panchal, V. R., Double variable frequency pendulum isolator for seismic isolation of liquid storage tanks, *Nuclear Engineering and Design* **241**, 700-713, 2011.

[19] Ruifu, Z., Dagen, W., Xiaosong, R., Seismic analysis of a LNG storage tank isolated by a multiple friction pendulum system, *Earthquake Engineering and Engineering Vibration*, **10**, 253-262, 2011.

[20] Fallahian, M., Mellati, A., Tehrani, H. T., Khoshnoudian, F., Tarverdi, M., Parametric analysis of liquid storage tanks base isolated by double concave friction pendulum system, *Proceeding of the International. Conference on Advances in Structural, Civil and Environmental Engineering (SCEE),* 2013.

[21] Morand, H., Ohayon, R., *Fluid Structure Interaction: Applied Numerical Methods,* Wiley, New York, 1995.

[22] Everstin, G. C., Finite element formulations of structural acoustics problems, *Computers and Structures*, **65**, 3, 307-321, 1997.

[23] Virella, J. C., Prato, C. A., Godoy, L. A., Linear and nonlinear 2-D finite element analysis of sloshing modes and pressures in rectangular tanks subject to horizontal harmonic motions, *Journal of Sound and Vibration*, **312**, 442-460, 2008.

[24] Abaqus User's Manual, Version 6.11, *Dassault Systèmes Simulia Corporation*, Providence, Rhode Island, USA, 2011.

COMPDYN 2015
5th ECCOMAS Thematic Conference on
Computational Methods in Structural Dynamics and Earthquake Engineering
M. Papadrakakis, V. Papadopoulos, V. Plevris (eds.)
Crete Island, Greece, 25–27 May 2015

OPTIMIZATION OF SEISMIC ISOLATION SYSTEMS WITH VISCOUS FLUID DAMPERS USING GENETIC ALGORITHMS

Samer A. Barakat[1], **Mohammad H. AlHamaydeh**[2], **and Omar M. Nassif** [1]

[1] Dept. of Civil and Environmental engineering
University of Sharjah, P.O.Box 27272, Sharjah, UAE
{sbarakat,onaseef}@sharjah.ac.ae

[2] Department of Civil Engineering
American University of Sharjah, P.O.Box 26666, Sharjah, UAE
malhamaydeh@aus.edu

Keywords: Optimization, Seismic Isolation, Viscous Fluid Dampers, Genetic Algorithm.

Abstract. *This paper presents evolutionary-based optimization procedure for designing natural rubber seismic isolation systems with viscous fluid dampers. The proposed technique is applied to the design of seismic isolation systems with viscous fluid dampers. A lumped-mass stick model representing a realistic five-story MDOF system with natural period of vibration ranging between 2.5 to 4.5 seconds. A suite of 24 Near-Field (NF) earthquake records representing different seismic hazard levels are utilized in the analysis and design. The damping coefficient (C), damping exponent (α) and fundamental natural period (T) are used as design variables for the seismic isolation system. The minimization of the key response parameter, the top story acceleration ratio (TSAR) of the isolated structure compared to an identical fixed base structure, is selected as the objective function in this optimization problem. The total maximum displacements (D_{TM}), the peak damper force (P_{DF}), as well as the maximum drift ratio (δ_{max}) are presented as constraints in the optimization problem. In order to achieve global optimum performance [TSAR] while handling competing constraints [D_{TM}, P_{DF}, δ_{max}], the presented GA-based technique is utilized. The commercial structural analysis software SAP2000 is utilized to perform the dynamic analysis for the MDOF system through direct Time-History Analysis (THA). The optimization algorithm is programmed in MATLAB and linked to SAP2000 through its OAPI feature. In agreement with conventional wisdom and sound engineering experience, it is found that combining low values of (C), highly nonlinear (α) [low values] with highly flexible rubber isolators [long T] produces the optimum performance.*

1 INTRODUCTION AND BACKGROUND

Seismic isolation is a protective measure against high earthquake risk exposure and is now seeing increased applications all over the world [1]. Various studies have investigated the different aspects of seismic isolation systems whether pertaining to the theory, development, behavior or the applications of such systems [2]–[6]. These included investigating the feasibility of production and implementation of low cost rubber bearings comparable in efficiency to commercial rubber bearings [7]. In addition, Ge et al. [8] investigated the performance of Viscous Fluid Dampers (VFD) under Near-Field ground motions coupling adjacent structures. A number of simulated ground motions on the structure were run to find the optimal damping coefficient. It was found that adjacent structures greatly reduce the response and the damping coefficient had lesser impact. The use of base isolation systems has been applied to many essential and emergency facilities, such structures have to meet the "Immediate Occupancy" seismic performance requirements [9]. Some designs have utilized NR bearings supplemented by linear VFDs for high-velocity pulses caused by Near-Field ground motions [10]. Similarly, AlHamaydeh & Aly [11] studied the use of a base isolation system to be retrofitted to an existing Reinforced Concrete (RC) bridge. Further research has been conducted using artificial neural network (ANN) to design a base isolation system [12]. The study demonstrated that ANN models are powerful tools that can be utilized early in the design stages. Similarly, the incorporation of Multiple Regression Analysis (MRA) models can also be valuable during preliminary design stages [13].

The modeling and control of Magneto-Rheoliogical (MR) dampers has also been investigated[9]. The studies used system identification techniques to approximate the dynamic behavior of the MR dampers[14], [15]. MR dampers are semi-active control dampers and hence are more effective than their passive counterparts[16]. Others have examined the response of a linear elastic, one-story building with linear and non-linear viscous dampers[17]. It was shown that non-linear viscous dampers are more effective at reducing the responses as well as in decreasing the effects of torsional coupling. Lei and He [18] proposed algorithms to identify the non-linear properties of LR bearings. Other algorithms include a proposed artificial bee colony algorithm for optimization of VFDs sizes and locations in a planar building frame in order to reduce accelerations in structures during ground motions [19].

2 PROBLEM DEFINITION

2.1 Structural model

The objective of this study is property optimization of base isolation system for superstructures that are subjected to near-field ground motions. This optimization is carried out by a modified Genetic Algorithm on a five stories (Figure 1) lumped-mass stick model. The model has a fixed story height of 3.5 m. It should be emphasized that the MDOF model used for the analysis is a simple lumped-mass stick first introduced by Kelly et al. [20] and later used by many other researchers. The same model was replicated by AlHamaydeh et al. [13] and checked to match the natural frequencies of the original model. The same replicated model is used in this research but with variable natural periods.

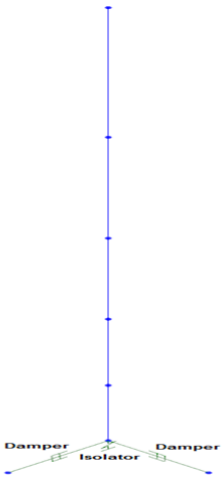


Figure 1: Five-stories lumped-mass stick model with ground excitation.

Model details are shown in Figure 1 above.

Table 1: Five-stories MDOF system parameters with fundamental period 2.5s [20]

Story	Mass (kg)	Stiffness (kN/m)	Mode	Period of vibration (s)
5	5897	19059	6	0.048
4	5897	24954	5	0.057
3	5897	28621	4	0.073
2	5897	29093	3	0.115
1	5897	33732	2	0.313
Isolation System	6800	232	1	2.500

2.2 Ground motion records

This study will use representative Near-Field (NF) ground motion records as excitation to the BI model. Generally speaking, a ground motion is considered near field if it is close to the epicenter of the earthquake and has a high Peak Ground Velocity (PGV). In this research, time history records with a PGV greater than 60cm/s and recorded within 25 km from the epi-center. A total of 24 ground motion records that satisfy these criteria were acquired from PEER ground motion database [21].

Figure 2 shows the 5% damped response spectra for the ensemble of earthquake records.

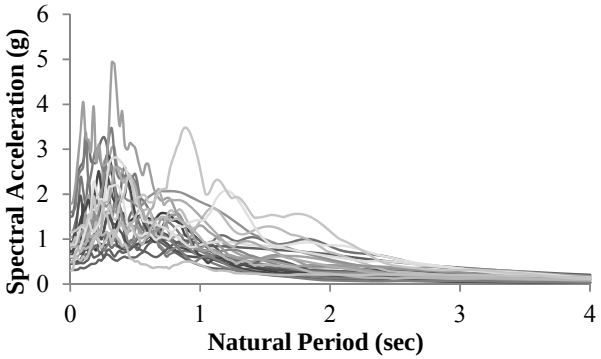


Figure 2: Acceleration Response Spectra (5% damped) for the 24 EQ records considered in the study

2.3 Optimization method: Genetic Algorithm with Domain Trimming (GADT)

To begin GA optimization, a population of N_p (population size) solution alternatives are generated randomly using a uniform probability distribution; each solution of the GA consists of a combination of variables (x_1, x_2, x_3, …, x_n) which has its own fitness value. In cases where the optimization is performed to find the minimum of a given problem, lower fitness is preferable. Solutions that yield low objective values would have better fitness as long as they are not penalized for violating the constraints which would result in increasing the fitness value. Populations of solutions are represented by chromosomes or variable strings. In this research, a variable string is used instead of a binary string because the design variables are discrete. Once the fitness for every solution in the current population is calculated using the fitness function $\boldsymbol{F_j(X)}$, unfit solutions are eliminated. Any solution whose fitness is greater than the average, $\boldsymbol{F_{ave}}$, of the population is reassigned a fitness of zero:

$$F_j(X) = \begin{cases} \mathrm{F_{ave}} - F_j(X) & \text{for } F_j(X) < \mathrm{F_{ave}} \\ 0 & \text{for } F_j(X) \geq \mathrm{F_{ave}} \end{cases} \qquad \mathrm{j} = 1,2,\ldots,\mathrm{N_p} \tag{1}$$

where ($\boldsymbol{X}$) is the vector of the design variables.

The three basic operations of a GA, reproduction, crossover, and mutation, are used to improve the fitness of each population from one generation (iteration) to the next (Figure 3). The reproduction operation selects the better fit designs, copies them and places them into a mating pool allowing each to mate and reproduce. Different selection methods are available in the literature. The roulette wheel selection method is used in this study for its simplicity and popularity. The uniform crossover operation is used to combine genetic information between two parent solutions. Uniform crossover selects two parent solutions at a time from the mating pool and swaps variables corresponding to zeros in a binary string known as a mask.

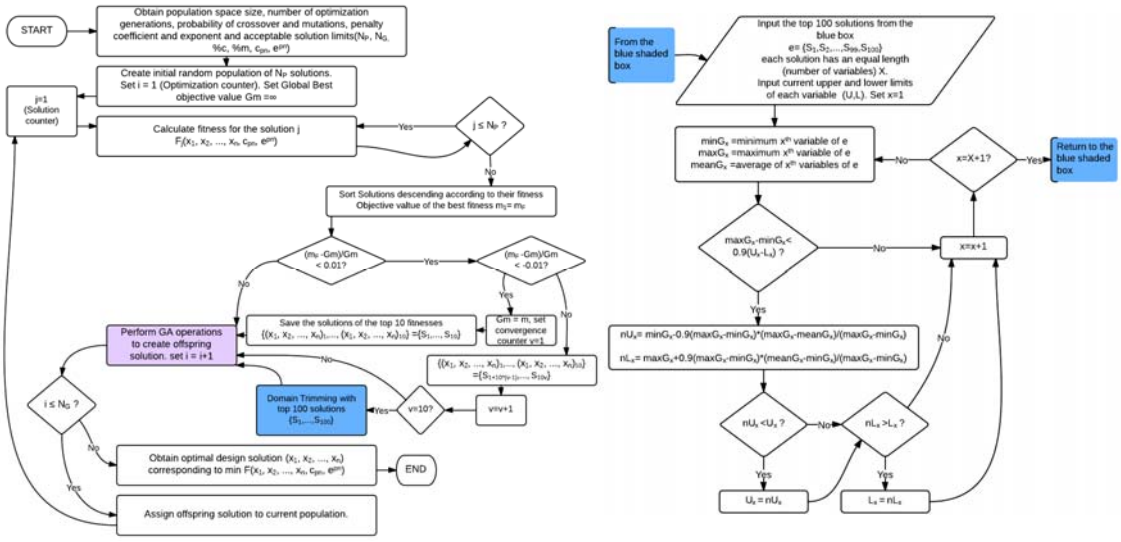


Figure 3: Flow chart of general GADT optimization [22]

A major shortcoming of GA optimization is that while it is good in global search of the optimum solutions, it is weak in local search; meaning that it will converge to the optimum solution but will not locate it with high precision especially if the population size is small. The reason is that initially, the solution variables are selected randomly from a pre-specified range

(domain), those variables do not change but relocate from one solution to another, with the exception when mutation occurs which introduces new variables from the specified domain. However, the probability of mutation is generally kept low (2%-5%) in order to increase the solution stability. Another shortcoming of the GA approach is the choice of domain; a poor choice of the domain (e.g.: [1, 1000] when the optimum value is 2) dramatically impacts convergence. In this study, a new technique that addresses these GA shortcomings is presented. The technique is to trim the domain so that the chance of selecting the optimal variable is enhanced (e.g.: trimming a domain from [1, 1000] to [1, 10] would increase the probability of selection of the optimal variable by 200 times). After trimming, the GA is reinitiated and continues to do so until the optimum solution is found. **Error! Reference source not found.** shows the flowchart for the GADT Method. For more details about GADT algorithm the reader is referred to [22].

2.4 Constraints handling

One of the most common constraint–handling techniques is through penalty functions. In such approaches, the problem is solved as an unconstrained one, where the constraints are penalized (such that non–feasible solutions are characterized by high function values). This allows for a single objective function to be formulated and in turn minimized using an unconstrained optimization algorithm. The penalty functions can either be stationary or non-stationary (dynamically modified). It is observed that non-stationary penalty functions are almost always superior to stationary penalty functions. A non-stationary penalty function is, generally, defined as

$$f(X) = F(X) + p(X, c_{pn}, e_{pn}) \tag{2}$$

Where *F(x)* is the original objective function of the constrained optimization problem; $p(\bullet)$ is a dynamically modified penalty value, defined as

$$p\left(X, c_{pn}, e_{pn}\right) = \begin{cases} \left(c_{pn} r_i\right)^{e_{pn}}, & r \geq 1 \\ 0, & r < 1 \end{cases} \tag{3}$$

Where, $\boldsymbol{r_i}$ is the individual member's demand over capacity ratio according to the design code. $\boldsymbol{c_{pn}}$ and $\boldsymbol{e_{pn}}$ are the penalty coefficient and exponent, respectively. As their name implies, they provide means to penalize the optimization objective if the ratio $\boldsymbol{r}$ exceeded unity. $\boldsymbol{e_{pn}}$ serves as efficient means to greatly increase the penalty as $\boldsymbol{r}$ gets farther from unity while $\boldsymbol{c_{pn}}$ ensures that values of $\boldsymbol{r}$ get farther away from unity. In this study, the empirically-selected values of the penalty coefficient and exponent are 2.5 and 2, respectively.

2.5 Optimization problem formulation

The formulation of the optimization of seismic isolation systems with viscous fluid dampers using GADT Algorithm is as follows:

- The objective function for the optimization problem is the Top Story Acceleration Ratio (*TSAR*) of the isolated-base structure to the fixed base one. Taking the maximum acceleration of the top story of both cases (Figure 4):

$$TSAR = \frac{max(\boldsymbol{a})_{(Isolated)}}{max(\boldsymbol{a})_{(Fixed)}} \tag{4}$$

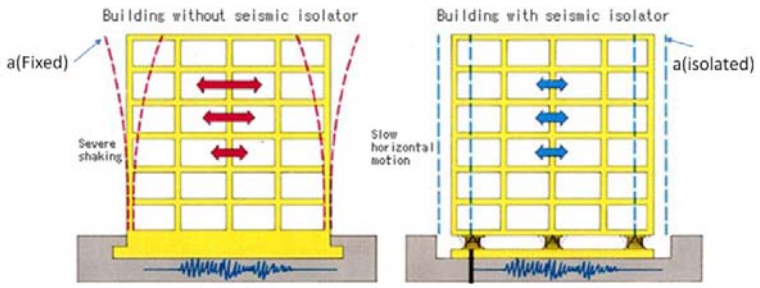


Figure 4: Comparison between the two cases of a fixed-base (left) and isolated-base (right) structures, adopted from [23]

The objective function of the optimization could be expressed as:

$$f(C, \alpha, T) = TSAR \tag{5}$$

Where c is the damping coefficient, α is the damping exponent. Both are specified by the designer to the manufacturer, damping exponent values could range between 0.1 and 1.5. T is the fundamental period of the structure. The range of natural periods considered in this study is between 2.5 and 4.5 seconds. This period is changed in BI system by changing the lateral stiffness of the rubber isolators.

- The constraints of the optimization problem are the Total Maximum Displacements (D_{TM}), the peak damper force (P_{DF}), as well as the maximum drift ratio (δ_{max}). Those constraints are summarized in the constraint function:

$$p(P_{DF}, D_{TM}, \delta_{max}, c_{pn}, e_{pn}) = \begin{cases} (c_{pn} r)^{e_{pn}}, & r \geq 1 \\ 0, & r < 1 \end{cases} \tag{6}$$

Where,

$$r = \max\left(\frac{P_{DF}}{P_{DF_{limit}}}, \frac{D_{TM}}{D_{TM_{limit}}}, \frac{\delta_{max}}{\delta_{max_{limit}}}\right) \tag{7}$$

Where $P_{DF_{limit}}$ is the maximum damping capacity of the VFD which is taken, based on practicality considerations, to range between 450 kN and 4450 kN. $D_{TM_{limit}}$ is the maximum limit at which the base of the structure can displace, further displacement of the base will result in rupture of the rubber isolator and will therefore jeopardize the entire structure. For this study, $D_{TM_{limit}}$ is limited to a maximum value of 1 m. δ_{max} is the maximum amplified story drift ratio, its calculated by finding the maximum value of all individual story drifts and then dividing it by their respective story height, it is then multiplied by the deflection amplification factor $\boldsymbol{C_d}$, the structure is assumed to be in the elastic range if the ratio is less than 2%, IBC'12 [24].

Combining the objective and constraint functions together would yield the fitness function used in GA:

$$Min\ \ F(c, \alpha, T, \delta_{max}, c_{pn}, e_{pn}) = TSAR + p(P_{DF}, D_{TM}, \delta_{max}, c_{pn}, e_{pn}) \tag{8}$$

In calculating the solution fitness, TSAR is selected as the main objective of the optimization as it signifies the effectiveness of the isolation system. The other response parameters ($P_{DF}, D_{TM}, \delta_{max}$) signify practical acceptably limits of the structural response when the BI system is utilized. The BI of design variables to be used in the optimization are $\boldsymbol{C}$,

$\boldsymbol{\alpha}$ and $\boldsymbol{T}$. In this research, a variable string is used instead of a binary string because the design variables are continuous. Once the fitness for every solution in the current population is calculated using the fitness function defined by equation 8, unfit solutions are eliminated using the following equation where any solution, whose fitness is greater than the average, $\boldsymbol{F_{ave}}$, of the population fitness is reassigned a fitness of zero:

$$F_j(c,\alpha,T,\delta_{max},c_{pn},e_{pn}) = \begin{cases} \mathrm{F_{ave}} - F_j(c,\alpha,T,\delta_{max},c_{pn},e_{pn}) & \text{for } F_j(c,\alpha,T,\delta_{max},c_{pn},e_{pn}) < \mathrm{F_{ave}} \\ 0 & \text{for } F_j(c,\alpha,T,\delta_{max},c_{pn},e_{pn}) \geq \mathrm{F_{ave}} \end{cases} \quad (9)$$

$$j = 1,2,\ldots,N_p$$

where the fitness of an individual design solution is denoted by $\boldsymbol{F_j}$.

3 RESULTS

The GADT algorithm is used to carry out the optimization of the lumped-mass stick model (Figure 1) to find the BI parameters that would yield minimum objective function, TSAR subjected to the $\boldsymbol{P_{DF}}$, $\boldsymbol{D_{TM}}$, $\boldsymbol{\delta_{max}}$ constraints. The population size used was 200 solutions, and the GA spanned over 300 generations. Table 2 summarizes the results of the optimization for the five-story model.

In agreement with conventional wisdom and sound engineering experience, it is found that combining low values of $\boldsymbol{C}$, highly nonlinear $\boldsymbol{\alpha}$ [low values] with highly flexible rubber isolators [long $\boldsymbol{T}$] produces the optimum performance [low ***TSAR***].

Table 2: Results of GA optimization of BI system for the 5-story model

Best found optimum solution			Analysis Results			
			Objective	Constraints		
C (kN.(m/s)$^{-\alpha}$)	α	T (sec)	TSAR	P_{DF} (kN)	D_{TM} (m)	δ_{max} (%)
175	0.4	4.5	0.126	22.7	0.59	0.04

4 SUMMARY AND CONCLUSIONS

The aim of the research was to optimize the properties of base isolation systems under Near-Field Ground motions which are characterized by their high velocity demands. Three solution variables are considered as input for the optimization: the damping coefficient $\boldsymbol{C}$, the damping exponent $\boldsymbol{\alpha}$ and the structure's natural period $\boldsymbol{T}$.

As a mean of optimization, a modified GA is presented; the modifications enhance its performance. The enhancements are based on a simple concept which is to eliminate most of the undesirable variables that produce unfit solutions after some generations have been evaluated. The GA is then restarted with the new pool of genes that produced desirable solution. The GA re-initiation increases the probability of finding the optimum solution.

For the representative five-story structure, the BI system is efficiently designed to have optimal performance using the presented GADT. It is found that, for NF ground motions, nonlinear dampers with relatively low damping coefficients are capable of superior performance [produce lower acceleration levels] especially when implemented with soft isolators. Future work may include cost optimization; in the current GADT formulation there is no considera-

tion for the cost of the VFD or the rubber bearings. Also, other structural heights and configurations can be considered for broader implementation.

REFERENCES

[1] S. Hussain, M. AlHamaydeh, and N. Aly, "Jakarta's First Seismic-Isolated Building - A 25 Story Tower," in *The 15th World Conference on Earthquake Engineering (15WCEE), September 24-28*, 2012.

[2] G.-H. Koo and Y. Ohtori, "Loading rate effects of high damping seismic isolation rubber bearing on earthquake responses," *KSME International Journal, Korean Society of Mechanical Engineers*, vol. 12, pp. 58–66, 1998.

[3] J. Eibl, "Dynamic behavior of high damping rubber bearings for building seismic isolation," *Vrancea Earthquakes: Tectonics, Hazard and Risk Mitigation*, pp. 207–214, 1998.

[4] K. Fuller, C. Lim, S. Loo, M. Melkumyan, and K. Muniandy, "Design and Testing of High Damping Rubber Earthquake Bearings for Retrofit Project," in *Armenia Earthquake Hazard and Seismic Risk Reduction*, 2000, vol. 12, pp. 379–385.

[5] R. Jankowski, "Nonlinear Rate Dependent Model of High Damping Rubber Bearing," *Bulletin of Earthquake Engineering*, vol. 1, no. 3, pp. 397–403, 2003.

[6] A. Hameed, M.-S. Koo, T. Do, and J.-H. Jeong, "Effect of lead rubber bearing characteristics on the response of seismic-isolated bridges," *KSCE Journal of Civil Engineering*, vol. 12, no. 3, pp. 187–196, 2008.

[7] M. Garevski, "Development, Production and Implementation of Low Cost Rubber Bearings," *Earthquake Engineering in Europe*, vol. 17, pp. 411–437, 2010.

[8] D. –. Ge, H. –. Zhu, J. –. Zhang, and X. –. Chen, "Performance of viscous fluid dampers coupling adjacent inelastic structures under near-fault earthquakes," *Journal of Central South University of Technology*, vol. 17, no. 6, pp. 1336–1343, 2010.

[9] S. Hussain and M. Al Satari, "Design of a Seismic Isolation System with Supplemental Viscous Damping for a Near-Fault Essential Facility," in *The 14th World Conference on Earthquake Engineering (14WCEE), Oct. 12-17*, 2008.

[10] M. Al Satari and J. Abdalla, "Optimization of A Base-Isolation System Consisting of Natural Rubber Bearings and Fluid Viscous Dampers," in *The 11th World Conference on Seismic Isolation, Energy Dissipation and Active Vibration Control of Structures, November 17-21*, 2009, no. 1.

[11] M. Alhamaydeh and N. Aly, "Optimum Seismic Isolation System Design for Retrofitting and Upgrading Existing Concrete Bridges," in *2014 International*

Conference on Mechanics, Fluid Mechanics, Heat and Mass Transfer (MFMHMT 2014), February 22-24, 2014, pp. 135–139.

[12] S. A. Barakat and M. H. Alhamaydeh, "Preliminary Design of Seismic Isolation Systems Using Artificial Neural Networks," in *2014 International Conference on Neural Networks - Fuzzy Systems (NN-FS 2014), March 15-17*, 2014, pp. 91–95.

[13] M. AlHamaydeh, S. Barakat, and F. Abed, "Multiple Regression Modeling of Natural Rubber Seismic-Isolation Systems with Supplemental Viscous Damping for Near-Field Ground Motion," *Journal of Civil Engineering and Management*, vol. 19, no. 5, pp. 665–682, 2013.

[14] A. H. El-Sinawi, M. H. AlHamaydeh, and A. a. Jhemi, "Optimal Control of Magneto-Rheological Fluid Dampers for Seismic Isolation of Structures," *Mathematical Problems in Engineering*, vol. 2013, pp. 1–7, 2013.

[15] A. H. ElSinawi, A. Jhemi, and M. AlHamaydeh, "Adaptive Seismic Isolation of Structures Using MR-Fluid Dampers," in *The 5th International Conference on Modeling, Simulation and Applied Optimization (ICMSAO), April 28-30*, 2013, pp. 1–6.

[16] A. H. ElSinawi, A. Jhemi, and M. AlHamaydeh, "Linearized State-Space Model of the Behavior of MR-Fluid Dampers," in *The 5th International Conference on Modeling, Simulation and Applied Optimization (ICMSAO), April 28-30*, 2013, pp. 1–5.

[17] S. . Mevada and R. Jangid, "Seismic response of asymmetric systems with linear and non-linear viscous dampers," *International Journal of Advanced Structural Engineering (IJASE)*, vol. 4, no. 5, pp. 1–20, 2012.

[18] Y. Lei and M. He, "Identification of the nonlinear properties of rubber-bearings in base-isolated buildings with limited seismic response data," *Science China Technological Sciences*, vol. 56, pp. 1224–1231, 2013.

[19] M. Sonmez, E. Aydin, and T. Karabork, "Using an artificial bee colony algorithm for the optimal placement of viscous dampers in planar building frames," *Structural and Multidisciplinary Optimization*, vol. 48, no. 2, pp. 395–409, 2013.

[20] J. M. Kelly, G. Leitmann, and A. G. Soldatos, "Robust control of base-isolated structures under earthquake excitation," *Journal of Optimization Theory and Applications*, vol. 53, no. 2, pp. 159–180, 1987.

[21] Pacific Earthquake Engineering Research Center, "PEER Ground Motion Database," 2013. [Online]. Available: http://ngawest2.berkeley.edu/. [Accessed: 15-Jan-2014].

[22] O. M. M. Nassif, "Optimization of Natural Rubber Seismic Isolation Systems with Supplemental Viscous Damping for Near-Field Ground Motion," College of Higher Studies and Research, University of Sharjah, 2014.

[23] Bridgestone Coroporation, "Seismic Isolator for Buildings," 2014. [Online]. Available: http://www.bridgestone.com/products/diversified/antiseismic_rubber/images/img_antiseismic_rubber_10.gif. [Accessed: 10-Feb-2014].

[24] International Code Council (ICC), "International Building Code," Falls Church, Virginia, 2012.

COMPDYN 2015
5th ECCOMAS Thematic Conference on
Computational Methods in Structural Dynamics and Earthquake Engineering
M. Papadrakakis, V. Papadopoulos, V. Plevris (eds.)
Crete Island, Greece, 25–27 May 2015

IN PLAN DISTRIBUTION OF ISOLATORS EFFECTIVE STIFFNESS FOR MINIMIZING THE TORSIONAL RESPONSE OF BASE ISOLATED BUILDINGS

K. Kostinakis[1], A. Athanatopoulou[2], D. Arampatzi[3] and A. Atsalos[4]

[1] Post-Doctoral Researcher, Department of Civil Engineering, Aristotle University of Thessaloniki
Aristotle University campus, 54124, Thessaloniki, Greece
e-mail: kkostina@civil.auth.gr

[2] Professor, Department of Civil Engineering, Aristotle University of Thessaloniki
Aristotle University campus, 54124, Thessaloniki, Greece
e-mail: minak@civil.auth.gr

[3,4] Civil Engineer, Department of Civil Engineering, Aristotle University of Thessaloniki
Aristotle University campus, 54124, Thessaloniki, Greece

Keywords: Base Isolation, Torsional Response, R/C Buildings, Effective Stiffness of Isolators, Time History Analysis.

Abstract. *The present study examines the influence of the isolators' effective stiffness distribution on the torsional response of base isolated structures. To accomplish this purpose two asymmetric in plan R/C buildings are analyzed for two different distributions of isolators' effective stiffness: (a) all the isolators have identical horizontal stiffness and (b) the isolators' effective stiffness is chosen so as the optimum torsion axis of the structure to coincide with the vertical mass axis. The two buildings are subjected to linear as well as nonlinear time history analyses under three bidirectional earthquake ground motions. For each earthquake record the maximum response over all incident angles of seismic motion is determined. The analyses results reveal that the displacements of the structural elements located at the flexible side of the buildings as well as the rotations of the slabs are reduced significantly when the isolators' effective stiffness is chosen so as the optimum torsion axis of the structure to coincide with the vertical mass axis.*

1 INTRODUCTION

Base isolation has been used as one of the most wildly accepted seismic protection system. It consists of a flexible material which is provided at the base of the building in order to reduce the seismic forces induced to the structure. The isolators, which are installed between the ground and the upper structure, are designed to decrease the seismic forces applied to the building under strong ground motions and as a consequence to reduce damage to the primary structural members. In addition base isolation minimizes damage to secondary members as well as to equipment inside the building. The isolators' flexibility increases the vibration period of the total structure and, as a consequence, the seismic forces induced to the building are reduced. Isolators' flexibility also leads to increase of the horizontal displacements. However, it's possible to control them through increase of damping.

Crosbie [1] first reasoned that by designing the centre of yield forces of the base isolation system (CYF) to coincide with the mass centre of the superstructure (CM) results in significant reduction in the post-yield response of asymmetric structures. Lee [2] suggested that the rigidity centre of the base isolation system (CRB) should be designed to coincide with the CM. The above mentioned researchers reached to the conclusion that this design practically eliminates the effects of asymmetry in the elastic range. Moreover for an equal level of yield stresses in all the bearings this is also true in the inelastic range.

Colunga and Cruz [3] studied the seismic codes suggestions concerning the seismic analysis of asymmetric base isolated buildings. They conducted a parametric study in order to evaluate the seismic code provisions regarding the simplified methods of analysis for asymmetric base-isolated buildings. They studied the effects of the following parameters on isolators' response: a) the ratio T_I / T_s (T_I is the effective period of the isolated building at the design displacement and T_s the elastic period of the fixed based building), b) mass eccentricity in the superstructure and c) stiffness eccentricity in the superstructure. With the aid of this study they defined the limits of structural irregularity for base isolated structures regarding the application of linear methods of analysis.

Kilar and Koren [4] conducted a parametric study for three levels of mass asymmetry, three levels of torsional rigidity of the superstructure and six various distributions of bearings in the isolation system. All these variants were applied on a selected realistic RC frame building structure designed according to Eurocodes 2 [5] and 8 [6].They tried to determine the most favourable distribution of isolators that is able to balance the effects of eccentricities in the superstructure. The results obtained by 3D nonlinear dynamic analyses indicate that all six considered distributions of bearings, reduce the unfavourable torsional effects, which are with different extent transferred from the superstructure to the base isolation system. Also it was observed that CI=CM distribution (CI is the center of isolators and CM the mass center of the superstructure), suggested by some building codes does not minimize torsional effects in base isolated buildings.

In a recent study [7] a methodology that leads to optimal torsional control of base isolated buildings is presented. The methodology is based on the assumption that the superstructure acts as a rigid body. The methodology provides a choice of the optimal eccentricity and torsional stiffness parameters of the isolation system that minimize the lateral-torsional response of the superstructure. Results obtained by probabilistic technique show that the response of the superstructure may be substantially improved if the center of stiffness of the isolators lie in the vicinity of the (average) center of stiffness of the superstructure. Therefore in order to minimize torsional effects in base isolated asymmetric structures it is necessary to introduce eccentricity in the isolation system.

From the above mentioned papers it is derived that there is no consensus on the choice of isolators' properties for minimizing torsional effects in base isolated asymmetric buildings. Some codes [8, 9] suggest that the rigidity center of the base isolation system (CRB) should coincide with the mass center (CM). However, as it mentioned above it has not been proved that this coincidence minimizes the torsional response.

In the present study two R/C 3-storey buildings are analyzed under bi-directional earthquake ground motions for the following two distributions of isolators' effective stiffness: (a) all the isolators have identical horizontal stiffness and (b) the isolators' effective stiffness is chosen so as the optimum torsion axis of the structure to coincide with the vertical mass axis. Note that the total horizontal and torsional stiffness of the isolators should remain approximately constant between the cases (a) and (b). Linear and nonlinear time history analyses under three bidirectional earthquake records are performed and the maximum response over all seismic incident angles is determined. The analyses results reveal that the displacements of the structural elements located at the flexible side of the buildings are reduced significantly in case of model (b). However, the displacements of the structural elements located at the stiff side are either smaller or slightly larger. Furthermore, there is a significant reduction of the diaphragm rotations of model (b) compared to the rotations of model (a). As a general conclusion, we can say that distribution (b) minimizes the torsional response of asymmetric buildings.

2 DESCRIPTION OF THE BUILDINGS AND BASE ISOLATORS

2.1 Description and design of the buildings

For the purposes of the present investigation two 3D R/C buildings (Building 1 and Building 2), with data supplied in figure 1, are studied. The buildings have three stories and their structural systems consist of vertical elements in two perpendicular directions (axes x and y). The dimensions of the structural elements' cross section are shown in Tables 1 and 2.

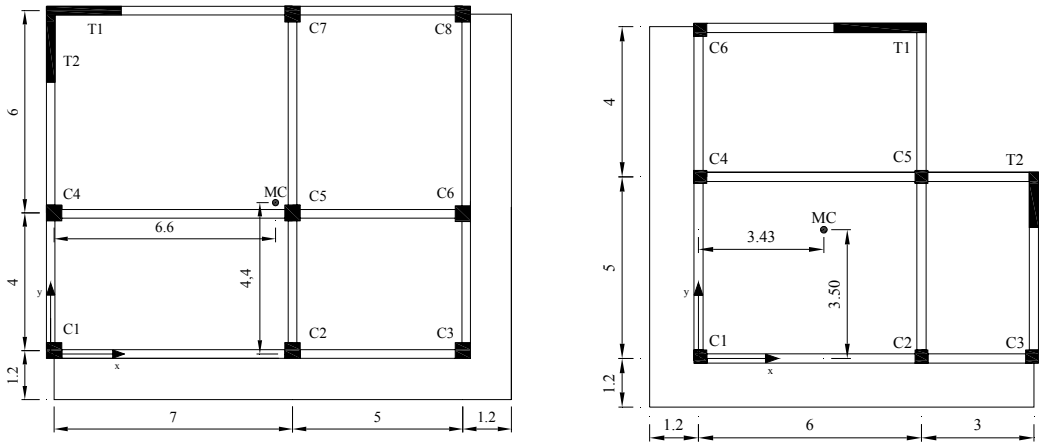


Figure 1. Plan view and geometrical parameters. Building B1 (a) and B2 (b).

For the elastic modeling and design of the buildings, all basic recommendations of EC8 [6] were taken into consideration, such as the diaphragmatic behavior of the slabs, the rigid zones in the joint regions of beams/columns and beams/walls, and the values of flexural and shear stiffness corresponding to cracked R/C elements. The two structures were analyzed using the

modal response spectrum analysis, as described in EC8. The R/C structural elements were designed following the clauses of EC2 [5] and EC8 [6].

	1st Storey	2nd Storey	3rd Storey
Beams (cm)	25/60	25/60	25/60
Columns (cm)	45/45	40/40	30/30
Wall T1 (cm)	25/220	25/220	25/220
Wall T2 (cm)	25/220	25/220	25/220

Table 1: Dimensions of the structural elements' cross sections for building B1.

	1st Storey	2nd Storey	3rd Storey
Beams (cm)	25/60	25/60	25/60
Columns (cm)	35/35	35/35	30/30
Wall T1 (cm)	25/250	25/250	25/250
Wall T2 (cm)	25/150	25/150	25/150

Table 2: Dimensions of the structural elements' cross sections for building B2.

2.2 Isolators' properties

One of the most widely used types of isolators is the Lead Rubber Bearing (LRB), which consists of alternating laminations of thin rubber layers and steel plates, bonded together to provide vertical rigidity and horizontal flexibility. Vertical rigidity assures the isolator will support the weight of the structure, while horizontal flexibility converts destructive horizontal shaking into gentle movement [10]. Moreover, at the centre of laminated natural rubber a lead plug is embedded. Note that the laminated natural rubber demonstrates spring capability, while the lead plug demonstrates damping capability. The seismic response of the isolators depends on their special properties, which are the horizontal effective stiffness, the vertical effective stiffness, as well as the damping. For the two buildings presented in the previous paragraph LRB are used as seismic isolation system. Furthermore, three different models are analyzed:

(a) The buildings are considered as fully fixed to the ground.

(b) All isolators possess the same properties (no eccentricity in the base isolation system exists): The buildings rest on rubber base isolators with vertical effective stiffness k_{veff}=100000 kN/m, horizontal effective stiffness k_{eff}=2000 kN/m and torsional stiffness k_t=5000 kNm/rad. The isolators' damping was taken equal to 30%. Note that the choice of the aforementioned isolators' properties was made bearing in mind that the fundamental period of the base isolated buildings must be approximately three times the fundamental period of the fully fixed to the ground buildings.

(c) Isolators with eccentricity: The buildings rest on base isolators with vertical effective stiffness k_{veff}=100000 kN/m and torsional stiffness k_t=5000 kNm/rad. However, regarding the horizontal effective stiffness, for each building three different types of isolators are available and can be used. For the building B1 the three types of isolators are the following: (i) isolators with k_{eff}=1000 kN/m, (ii) isolators with k_{eff}=1550 kN/m and (iii) isolators with k_{eff}=2950 kN/m. For the building B2 the three available types of isolators are the following: (i) isolators with k_{eff}=1000 kN/m, (ii) isolators with k_{eff}=1400 kN/m and (iii) isolators with k_{eff}=3400 kN/m. The isolators' damping was taken equal to 30% for both the buildings. The distribution of the above three types of isolators in plan was chosen so as the optimum torsion axis (OTA)

of the structures [11, 12] to coincide with the vertical mass axis. Moreover, note that the total horizontal and torsional stiffness of the isolators should remain approximately constant between the cases (b) and (c). For the building B1 the total horizontal and torsional stiffness of the isolators is 20000 kN/m and 893560 kNm/rad for model (b) (772619kNm/rad for model (c)) respectively. For the building B2 the total horizontal and torsional stiffness of the isolators is 16000 kN/m and 469257 kNm/rad for model (b) (462823kNm/rad for model (c)) respectively.

2.3 Determination of the Optimum Torsion Axis

For the two buildings considered the location of the Optimum Torsion Axis (OTA) was determined. Then, the properties of the isolators as well as their in-plan arrangement were determined for case (c) of the previous paragraph. For the determination of the OTA the methodology proposed by Marino and Rossi [11] was used. Then the principal directions under lateral loading were determined using the methodology presented in [12]. According to the aforementioned studies [11, 12] the process of determining the OTA is as follows: Let there be N-storey building system with horizontal rigid floor diaphragms at the floor levels, in a Cartesian global coordinate system Oxyz with a vertical Oz axis (figure 1). Considering as degrees of freedom of the i^{th} floor level the diaphragm rotation θ_{zi} and the horizontal displacements u_{xi} and u_{yi} of a point on the diaphragm, the displacement state of the diaphragms can be characterized by the N-column vectors:

$$\boldsymbol{u}_x = \left[u_{x1}, u_{x2}, \ldots \ldots, u_{xN}\right]^T \tag{1}$$

$$\boldsymbol{u}_y = \left[u_{y1}, u_{y2}, \ldots \ldots, u_{yN}\right]^T \tag{2}$$

$$\boldsymbol{\theta}_z = \left[\theta_{z1}, \theta_{z2}, \ldots \ldots, \theta_{zN}\right]^T \tag{3}$$

Let us also consider the action of a given distribution of horizontal forces:

$$\boldsymbol{F} = \left[F_1, F_2, \ldots \ldots, F_N\right]^T \tag{4}$$

that belong to a vertical loading plane and pass through a vertical loading axis. Note that for the fully fixed to the ground buildings a triangular distribution of horizontal forces is used, whereas in case of base isolated buildings an orthogonal distribution is adopted. The position of the OTA is defined by the coordinates x_T and y_T of its intersection point with the Oxy plane.

$$x_T = \frac{-\boldsymbol{\theta}_{z,y}^T \boldsymbol{\theta}_{z,z}}{\boldsymbol{\theta}_{z,z}^T \boldsymbol{\theta}_{z,z}} \tag{5}$$

$$y_T = \frac{\boldsymbol{\theta}_{z,x}^T \boldsymbol{\theta}_{z,z}}{\boldsymbol{\theta}_{z,z}^T \boldsymbol{\theta}_{z,z}} \tag{6}$$

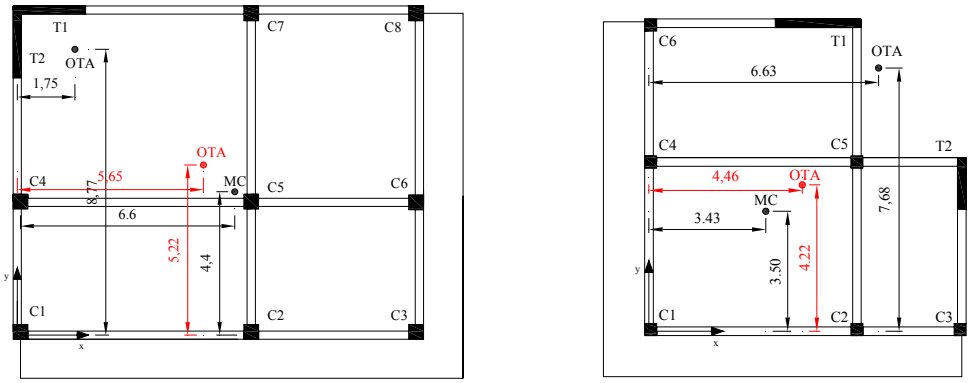
where

$\boldsymbol{\theta}_{z,x}$ are the rotations due to the action of forces $\mathbf{F}_x$, with $\mathbf{F}_x = 1 \cdot \mathbf{F}$ the vector of the forces $\mathbf{F}$ when acting parallel to the axis Ox.

$\boldsymbol{\theta}_{z,y}$ are the rotations due to the action of forces $\mathbf{F}_y$, with $\mathbf{F}_y = 1 \cdot \mathbf{F}$ the vector of the forces $\mathbf{F}$ when acting parallel to the axis Oy.

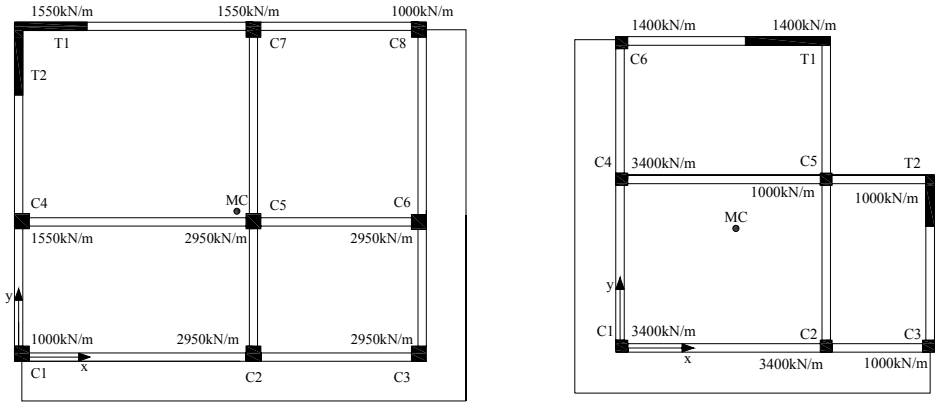
$\boldsymbol{\theta}_{z,z}$ are the rotations due to the action of moments $\mathbf{M}_z$, with $\mathbf{M}_z = 1 \cdot \mathbf{F}$ the vector of the torsional moments $\mathbf{M}$ about axis Oz which have the same distribution with the horizontal forces $\mathbf{F}$.

Based on the above procedure, the OTA for the fully fixed to the ground buildings (case (a)), as well as for the buildings resting on the isolators without eccentricity (case (b)), was determined (figure 2). Moreover, as mentioned before, in case (c), the isolators' effective stiffness was chosen so as the optimum torsion axis of the structure to coincide with the vertical mass axis. In order to fulfill the above criterion the distribution of the isolators' horizontal effective stiffness given in figure 3 is considered.



(a) (b)

Figure 2. Location of the OTA for the fully fixed to the ground buildings and for the buildings resting on the isolators without eccentricity (red color). Building B1 (a) and B2 (b) (MC: Mass Centre)



(a) (b)

Figure 3. Distribution of the isolators' horizontal effective stiffness for model (c) (building B1 (a) and building B2 (b))

3 LINEAR TIME HISTORY ANALYSES

The influence of the two different distributions of isolators' effective stiffness on the linear response of the two buildings considered in the present study (B1 and B2) was evaluated by means of linear analyses. More specifically, linear time history analyses under three bidirectional seismic strong motions (recorded during El Centro, Kobe and Lefkada earthquakes) were performed and the maximum response over all seismic incident angles was determined with the aid of analytical formulae [13]. For each building two different models were considered accounting for the cases (b) and (c) of isolators. The analyses were performed with the aid of the computer program SAP2000 [14]. The base isolators were

modeled using NLink elements of the rubber isolator type. The hysteretic model used to simulate the inelastic behavior of the base isolators along two orthogonal horizontal axes is shown in figure 4. The post-yield stiffness k_2 was taken equal to $0.1k_1$, where k_1 is the elastic stiffness. The yield force V_y was taken equal to 10% of the total weight of the structure.

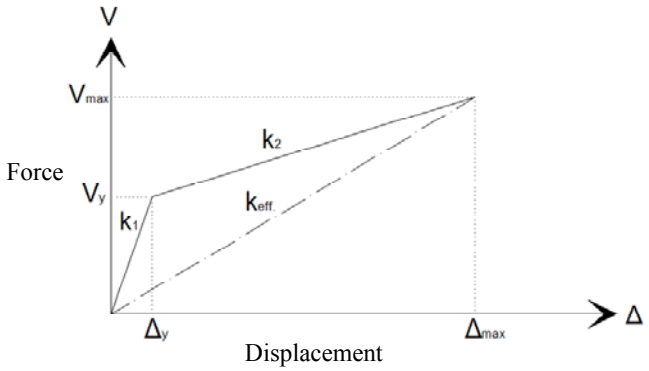


Figure 4. Hysteretic model for the base isolators.

3.1 Critical orientation and maximum response

General

The structure is subjected to bidirectional horizontal seismic motion consisting of the accelerograms $\ddot{u}_{ag}(t)$ and $\ddot{u}_{bg}(t)$. As the direction of the seismic motion is unknown, they can form any angle θ with the x and y structural axes (figure 5a). We consider two orientations of the seismic excitation:

(i) Excitation ‘α0’: The accelerograms $\ddot{u}_{ag}(t)$ and $\ddot{u}_{bg}(t)$ are applied along the axes x and y, respectively, i.e. the angle of seismic incidence is $\theta=0^o$ (figure 5b). A typical response quantity R is denoted as $R_{,\alpha 0}$.

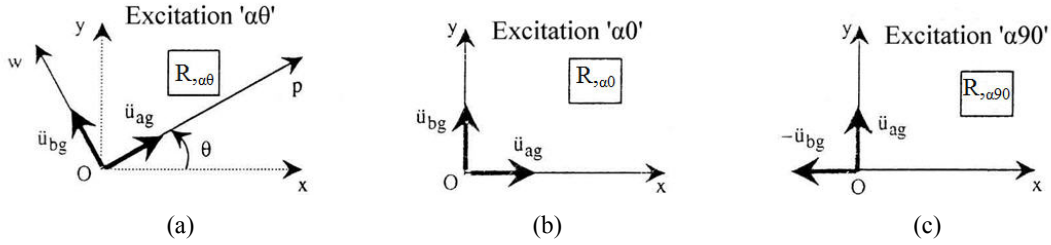


Figure 5. Excitations ‘αθ’ (a), ‘α0’ (b) and ‘α90’ (c)

(ii) Excitation ‘α90’: The accelerograms $\ddot{u}_{ag}(t)$ and $\ddot{u}_{bg}(t)$ are applied along the axes y and x, respectively, i.e. the angle of seismic incidence is $\theta=90^o$ (figure 5c). A typical response quantity R is denoted as $R_{,\alpha 90}$.

It has been proved [13] that the maximum value of a response parameter for any angle θ of seismic incidence is given, as a function of time, by the relation:

$$R_o(t) = \left(R^2_{,\alpha 0}(t) + R^2_{,\alpha 90}(t) \right)^{1/2} \tag{7}$$

The plot of the function $\pm R_0(t)$ provides the maximum/minimum value of the required response parameter as well as the time instant t_{cr} at which the maximum/minimum occurs.

$$\max R = +R_0(t_{cr}) \quad \text{and} \quad \min R = -R_0(t_{cr}) \tag{8}$$

The corresponding critical angles θ_{cr1} (maximum value) and θ_{cr2} (minimum value) are given by the relations [13]:

$$\theta_{cr1} = \tan^{-1}\left(\frac{R_{,\alpha 90}(t_{cr})}{R_{,\alpha 0}(t_{cr})}\right) \text{ and } \theta_{cr2} = \theta_{cr1} - \pi \tag{9}$$

Displacement vector

The horizontal displacements at any point of the building's floors are usually computed along the (ξ, η) axes of an appropriate local reference system. The displacement vector u is related to u_ξ and u_η through the relation: $u^2(t) = u_\xi^2(t) + u_\eta^2(t)$ (figure 6). Subscripts ξ and η characterize the axis along which the displacement is computed.

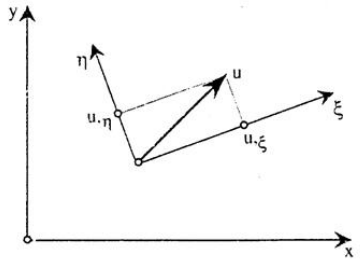


Figure 6. Displacement vector u

Thus, the response quantities $u_{,\alpha 0}^2(t)$ and $u_{,\alpha 90}^2(t)$ are given by the following relations:

$$u_{,\alpha 0}^2(t) = u_{\xi,\alpha 0}^2(t) + u_{\eta,\alpha 0}^2(t) \tag{10}$$

$$u_{,\alpha 90}^2(t) = u_{\xi,\alpha 90}^2(t) + u_{\eta,\alpha 90}^2(t) \tag{11}$$

The meanings of the subscripts remain the same as in the previous paragraph. The parameter u_{xy} is defined as:

$$u_{xy}(t) = u_{\xi,\alpha 0}(t) \cdot u_{\xi,\alpha 90}(t) + u_{\eta,\alpha 0}(t) \cdot u_{\eta,\alpha 90}(t) \tag{12}$$

The plot of the function $u_{,I}(t)$ (equation 13) provides all the information necessary to compute the maximum value of the displacement u_{cr} and the associated time instant t_{cr} [13]:

$$u_{cr}^2 = \max u_{,I}^2(t) = u_I^2(t_{cr}) = \frac{u_{,\alpha 0}^2(t_{cr}) + u_{,\alpha 90}^2(t_{cr})}{2} + \sqrt{\left(\frac{u_{,\alpha 0}^2(t_{cr}) - u_{,\alpha 90}^2(t_{cr})}{2}\right)^2 + u_{xy}^2(t_{cr})} \tag{13}$$

The corresponding critical angle θ_{cr} is determined by the angle θ_o (equation 14) with the aid of figure 7 [13]:

$$\theta_o = \frac{1}{2}\tan^{-1}\left(\frac{2u_{xy}(t_{cr})}{u_{,\alpha 0}^2(t_{cr}) - u_{,\alpha 90}^2(t_{cr})}\right) \tag{14}$$

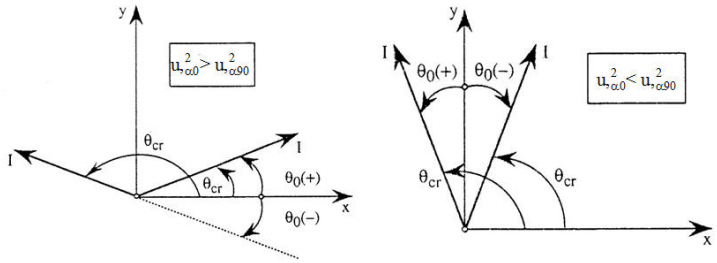


Figure 7. Determination of critical angle θ_o

3.2 Analyses results

Tables 3 and 4 present the displacements $u_{,I}^2$ (see section 3.1) as well as the associated critical time instant t_{cr} and critical incident angle θ_{cr} of the vertical structural elements at the level of the isolators (Table 3) and of the 3rd floor (Table 4). The tables regard the building B1 subjected to the earthquake record of El Centro. Moreover, in table 5 the maximum values of the floor rotations over all incident angles R_z, as well as the floor rotations due to excitations α0 and α90 (see section 3.1) are presented. From these tables we can see that for the same earthquake record different response quantities have different critical incident angles. Furthermore, note that the same response quantities have different critical incident angles for the two cases of isolators, since, as it can be seen from the tables, the critical incident angle of a certain response quantity depends on the distribution of the isolators' stiffness.

	Isolators without eccentricity			**Isolators with eccentricity**		
	$\mathbf{u_{,I}^2}$	$\mathbf{t_{cr}}$	$\boldsymbol{\theta_{cr}}$	$\mathbf{u_{,I}^2}$	$\mathbf{t_{cr}}$	$\boldsymbol{\theta_{cr}}$
C1	0.00481	12.30	79.34	0.00282	2.94	106.48
C2	0.00427	2.30	52.73	0.00264	2.95	2.94
C3	0.00583	2.96	74.10	0.00264	2.95	13.92
C4	0.00371	12.30	65.91	0.00285	2.94	90.80
C5	0.00314	2.95	75.23	0.00301	2.95	32.24
C6	0.00466	2.95	90.36	0.00268	2.95	31.87
C7	0.00310	2.93	134.36	0.00282	2.95	58.83
C8	0.00455	2.94	111.36	0.00277	2.95	45.89
T1	0.00279	12.30	43.79	0.00292	2.95	75.22
T2	0.00308	12.30	49.89	0.00292	2.95	79.29

Table 3: Displacements $u_{,I}^2$ of the vertical structural elements (basement) and critical incident angles in case of building B1 subjected to earthquake record of El Centro

	Isolators without eccentricity			Isolators with eccentricity		
	$u_{,I}^2$	t_{cr}	θ_{cr}	$u_{,I}^2$	t_{cr}	θ_{cr}
C1	0.00765	12.30	89.32	0.00467	2.96	17.99
C2	0.00717	2.98	54.88	0.00471	2.96	56.77
C3	0.00997	2.97	76.09	0.00496	2.96	79.75
C4	0.00578	12.31	71.73	0.00455	2.95	179.49
C5	0.00489	2.95	23.25	0.00478	2.96	56.23
C6	0.00806	2.96	92.75	0.00482	2.96	97.82
C7	0.00541	2.94	134.87	0.00460	2.95	136.17
C8	0.00794	2.95	112.45	0.00479	2.95	119.18
T1	0.00452	2.95	71.39	0.00451	2.95	157.32
T2	0.00470	12.30	51.14	0.00451	2.95	162.52

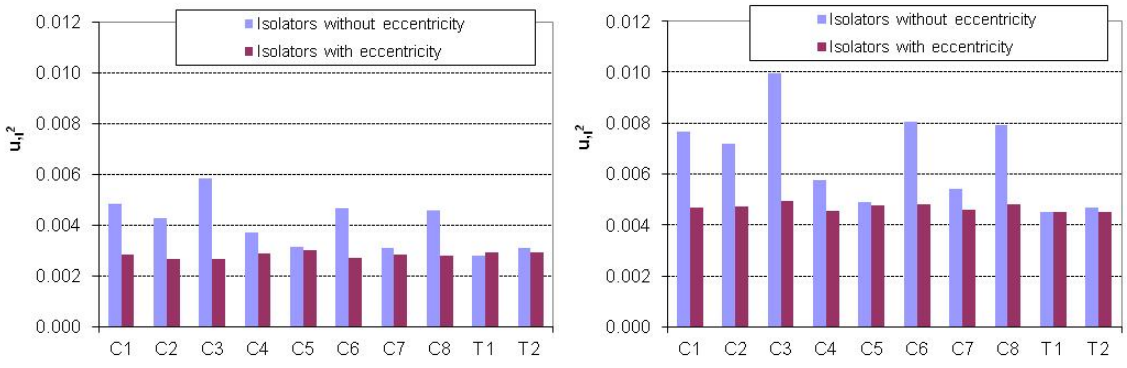
Table 4: Displacements $u_{,I}^2$ of the vertical structural elements (3rd floor) and critical incident angles in case of building B1 subjected to earthquake record of El Centro

	Isolators without eccentricity				
	$R_{z,\alpha 0}$	$R_{z,\alpha 90}$	R_z	t_{cr}	θ_{cr}
Basement	-1.240E-03	-3.670E-03	3.874E-03	2.97	71.33
1st storey	-1.350E-03	-4.060E-03	4.279E-03	2.96	71.61
2nd storey	-1.450E-03	-4.460E-03	4.690E-03	2.96	71.99
3rd storey	-1.530E-03	-4.870E-03	5.105E-03	2.96	72.56

	Isolators with eccentricity				
	$R_{z,\alpha 0}$	$R_{z,\alpha 90}$	R_z	t_{cr}	θ_{cr}
Basement	-1.700E-04	-4.510E-04	4.817E-04	2.33	69.33
1st storey	-1.280E-04	-2.640E-04	2.931E-04	2.33	64.08
2nd storey	-1.720E-04	-2.390E-04	2.946E-04	3.02	54.32
3rd storey	-2.540E-04	-5.360E-04	5.931E-04	3.03	64.68

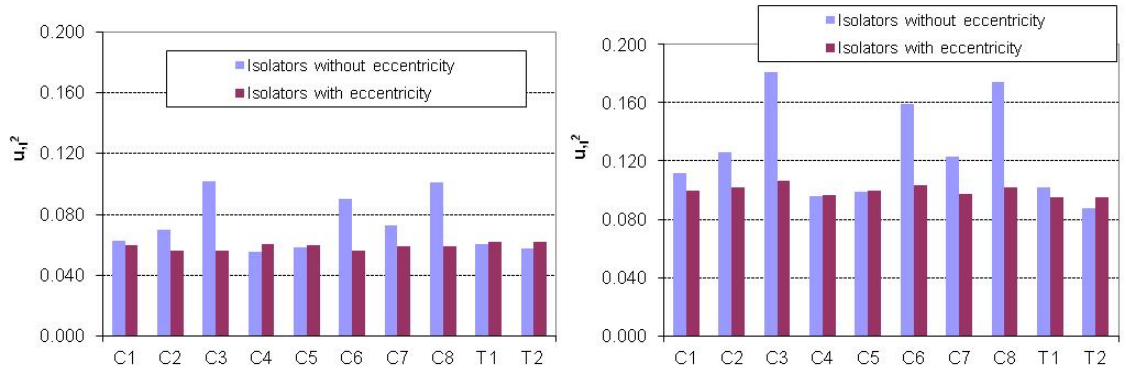
Table 5: Floor rotations R_z and critical incident angles in case of building B1 subjected to earthquake record of El Centro

In order to better illustrate the differences between the two cases of isolators, figures 8-15 present the displacements $u_{,I}^2$ of the vertical structural elements, as well as the maximum floor rotations R_z, computed with the aid of the methodology proposed in [13] (see section 3.1), for the three earthquake records considered. Figures 8-11 correspond to the building B1, whereas figures 12-15 correspond to the building B2.



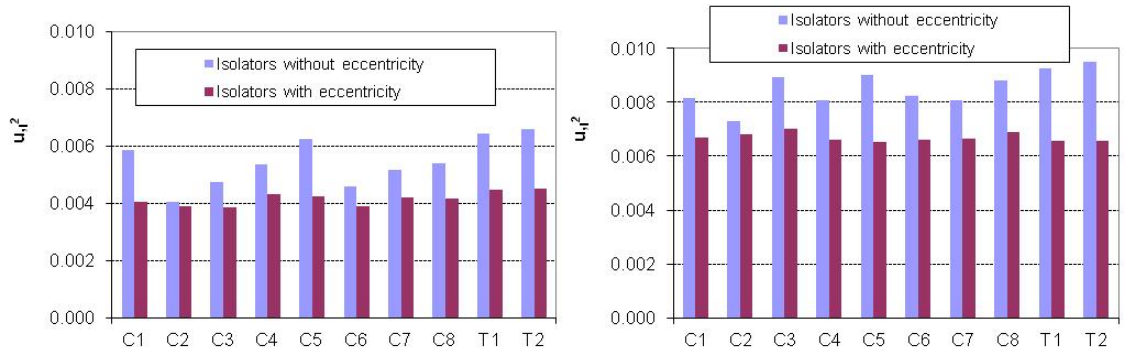
(a) (b)

Figure 8: Displacements $u_{,I}^2$ of the vertical structural elements (basement (a) and 3rd floor (b)) in case of building B1 subjected to earthquake record of El Centro



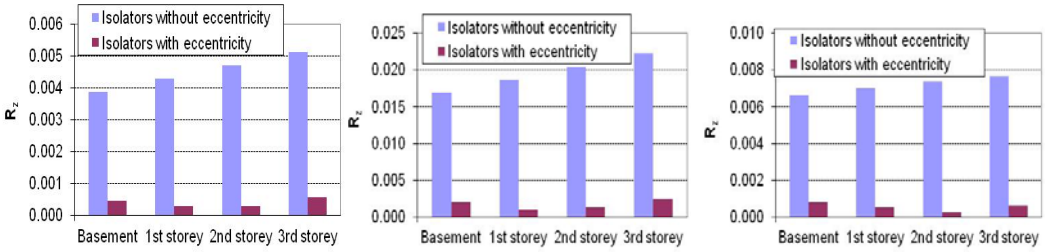
(a) (b)

Figure 9: Displacements $u_{,I}^2$ of the vertical structural elements (basement (a) and 3rd floor (b)) in case of building B1 subjected to earthquake record of Kobe



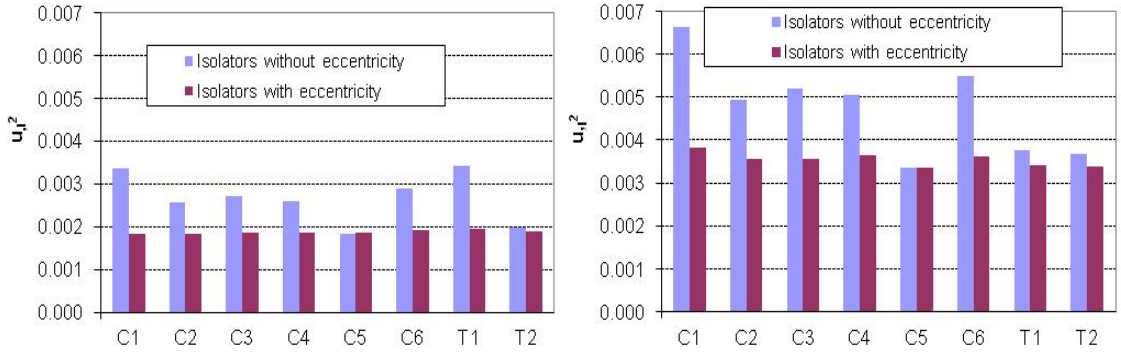
(a) (b)

Figure 10: Displacements $u_{,I}^2$ of the vertical structural elements (basement (a) and 3rd floor (b)) in case of building B1 subjected to earthquake record of Lefkada



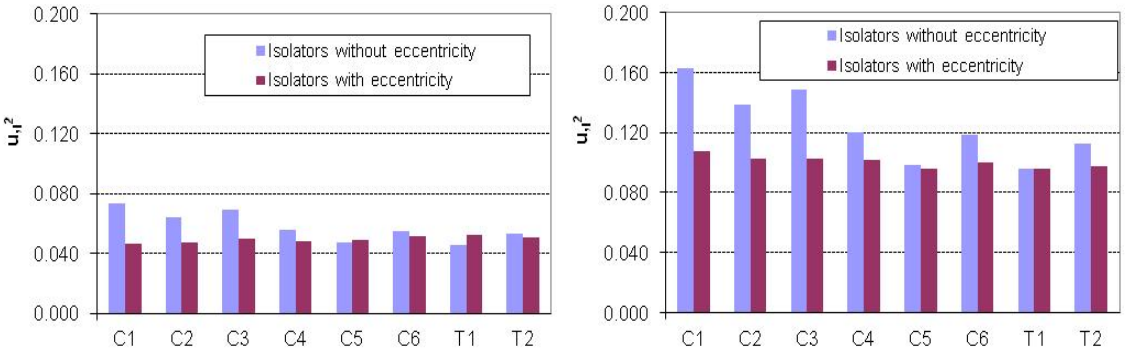
(a) (b) (c)

Figure 11: Floor rotations R_z in case of building B1 subjected to earthquake records of El Centro (a), Kobe (b) and Lefkada (c)



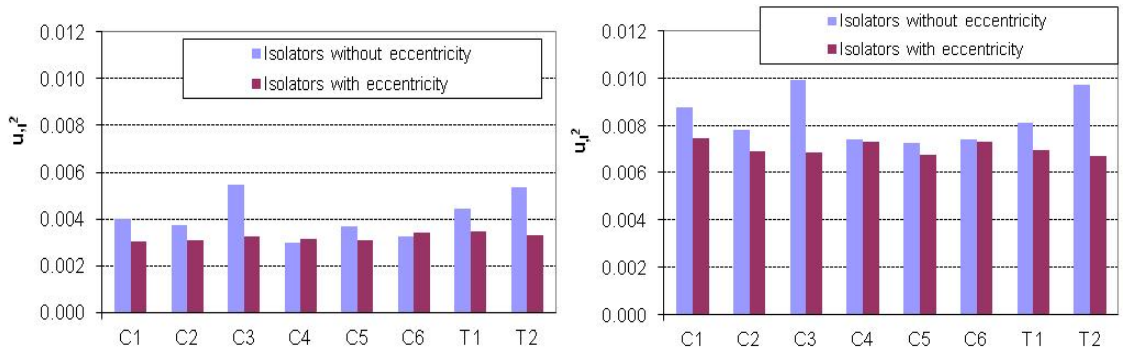
(a) (b)

Figure 12: Displacements $u_{,I}^2$ of the vertical structural elements (basement (a) and 3rd floor (b)) in case of building B2 subjected to earthquake record of El Centro



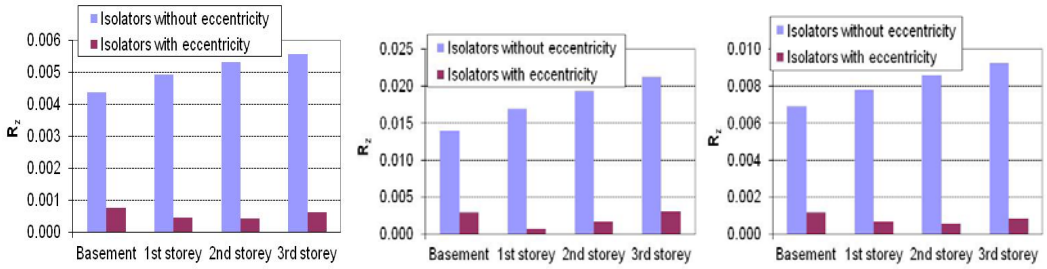
(a) (b)

Figure 13: Displacements $u_{,I}^2$ of the vertical structural elements (basement (a) and 3rd floor (b)) in case of building B2 subjected to earthquake record of Kobe



(a) (b)

Figure 14: Displacements $u_{,I}^2$ of the vertical structural elements (basement (a) and 3rd floor (b)) in case of building B2 subjected to earthquake record of Lefkada



(a) (b) (c)

Figure 15: Floor rotations R_z in case of building B2 subjected to earthquake records of El Centro (a), Kobe (b) and Lefkada (c)

We can see that the displacements of the vertical structural elements in most cases are smaller when the buildings rest on the isolators with eccentricity. Note that the displacements can be up to 55% smaller (column C3 at the level of the isolators) for the building B1 (figure 8a) and up to 46% smaller (column C1 at the level of the isolators) for the building B2 (figure 12a). The reduction of the displacements that is achieved in case of the isolators with eccentricity is larger for the structural elements of the flexible side of the buildings. However, the displacements of the structural elements located at the stiff side can be either reduced or increased depending on the earthquake record. The above conclusion is valid for both the buildings investigated in the present study. For example, note that the displacement of the wall T2 (building B1) is smaller for the isolators with eccentricity in case of the earthquake records of El Centro and Lefkada (figures 8 and 10). The opposite observation can be made when the building is subjected to the earthquake record of Kobe (figure 9). Of great significance is also the fact that when isolators with eccentricity are used the analyses produce displacements which have almost the same value for all the vertical structural elements. With regard to the floor rotations, figures 11 and 15 show that they are much smaller in case of the isolators with eccentricity (up to 25 times smaller for building B1 (figure 11c) and up to 20 times smaller for building B2 (figure 15b).

4 NONLINEAR TIME HISTORY ANALYSES

In order to evaluate the influence of the two different distributions of isolators' effective stiffness on the nonlinear response, the two buildings considered in the present study (B1 and

B2) were analyzed by Nonlinear Time History Analysis (NTHA) for each one of the three earthquake ground motions presented in the previous section. For each building two different models were considered accounting for the distributions (b) and (c) of isolators properties. The analyses were performed with the aid of the computer program SAP2000 [14] and assuming the inelasticity concentrated on the isolators while the superstructure behaves elastically. Furthermore, in order to determine the maximum response over all incident angles, the two horizontal accelerograms of each ground motion were applied along horizontal orthogonal axes forming with the structural axes an angle θ=0°, 30°, 60°, …, 150°. Thus, for each building and each pair of accelerograms six orientations were considered. As a consequence a total of 72 NTHA (2 buildings x 2 cases of isolators x 3 earthquake records x 6 incident angles) were conducted in the present study. For each ground motion and incident angle, the damage state of the two buildings was determined. The seismic response was expressed in terms of the displacements of the vertical structural elements at the level of the isolation (basement), as well as of the floor rotations.

Table 6 presents the maximum displacements of the vertical structural elements over all incident angles at the level of the isolators (basement) and the associated critical time instant and critical incident angle. We can see that the displacements of all the vertical elements are approximately equal when isolators with eccentricity are used.

Figure 16 (building B1) and figure 18 (building B2) present the maximum displacements of the vertical structural elements for the three earthquake records considered. Figure 17 (building B1) and figure 19 (building B2) present the maximum floor rotations for the three earthquake records considered.

	Isolators without eccentricity			**Isolators with eccentricity**		
	maxu	**t_{cr}**	**θ_{cr}**	**maxu**	**t_{cr}**	**θ_{cr}**
C1	0.10996	4.49	0	0.10089	8.80	90
C2	0.14330	2.98	30	0.09913	4.48	120
C3	0.12006	4.51	30	0.09886	4.48	150
C4	0.10425	4.48	150	0.10067	8.80	90
C5	0.10023	4.48	120	0.10023	4.48	90
C6	0.11217	4.51	60	0.09873	4.49	150
C7	0.10282	4.49	120	0.09964	4.48	30
C8	0.11232	4.50	90	0.09933	4.49	0
T1	0.09909	4.48	120	0.10105	4.48	60
T2	0.09962	4.48	150	0.10131	4.48	0

Table 6: Maximum displacements of the vertical structural elements (basement) and critical incident angles in case of building B1 subjected to earthquake record of El Centro

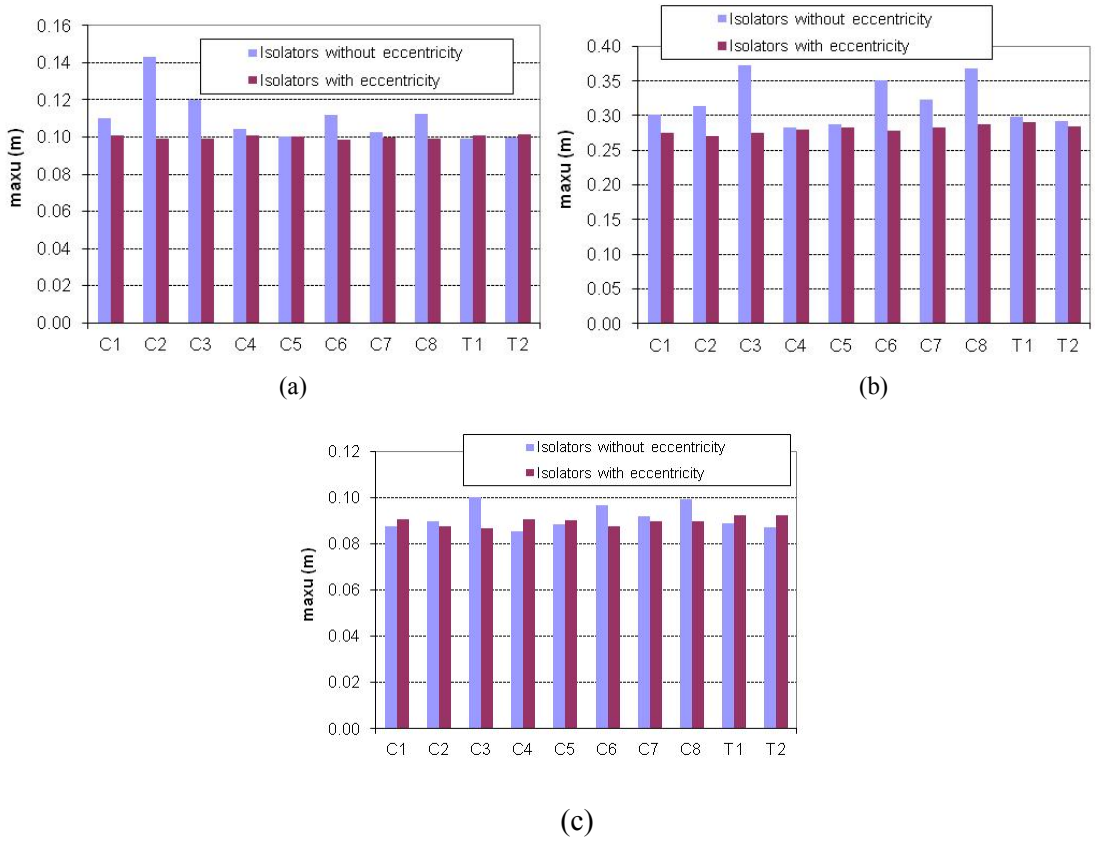
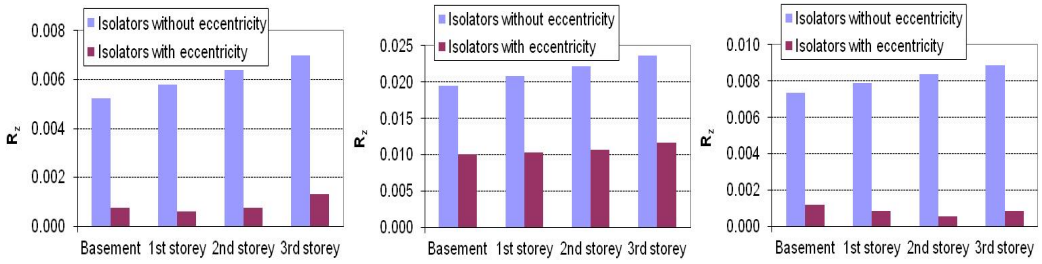


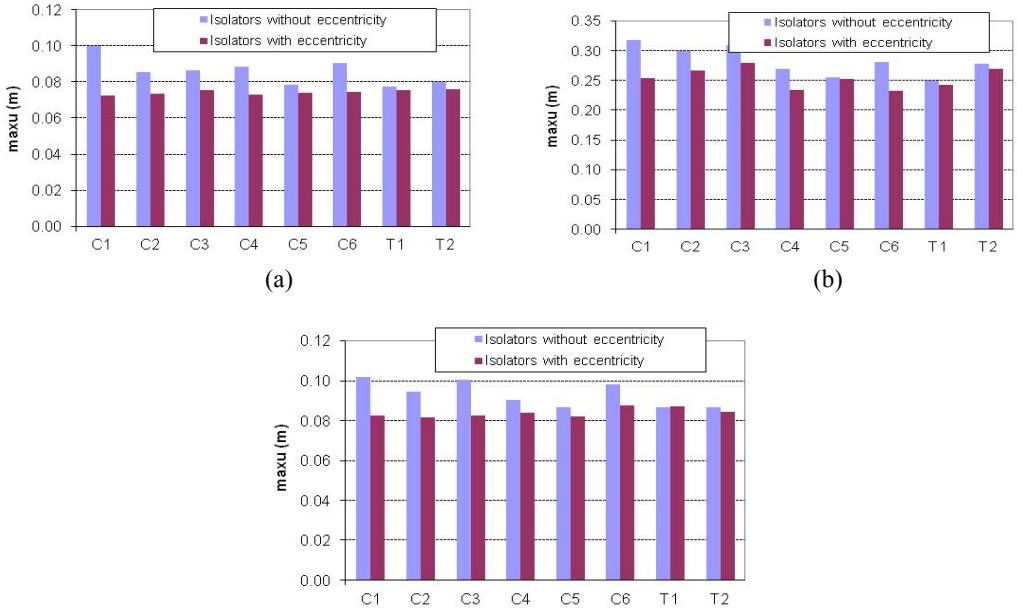
Figure 16: Maximum displacements of the vertical structural elements (basement) in case of building B1 subjected to earthquake records of El Centro (a), Kobe (b) and Lefkada (c)

It can be seen that the displacements of the vertical structural elements located at the flexible side of the building are smaller [up to 45% for the column C2 of the building B1 (figure 16a) and up to 38% smaller for the column C1 of the building B2 (figure 18a)] when the buildings rest on the isolators with eccentricity. Concerning the displacements of the structural elements located at the stiff side, note that they can be either reduced or increased depending on the earthquake record. For example, we can see that the displacement of the column C4 (building B1) is smaller in the case of the isolators with eccentricity for the earthquake record of El Centro (figure 16a). However, when the same building is subjected to the earthquake record of Lefkada, the displacement of the column C4 is smaller in case of the isolators without eccentricity (figure 16c). As it was mentioned in the case of the linear analyses, the displacements produced when isolators with eccentricity are used have almost the same value for all the vertical structural elements. Finally, figures 17 and 19 show that the floor rotations are much smaller in case of the isolators with eccentricity (up to 16 times smaller for building B1 (figure 17c) and up to 8 times smaller for building B2 (figure 19a). The difference between the values of the displacements produced for the two different distributions of isolators' stiffness depends on the earthquake record. See for example that seismic motion of Kobe led to smaller differences among the floor rotations compared to the differences produced when the seismic records of El Centro or Lefkada were used for the analyses.



(a) (b) (c)

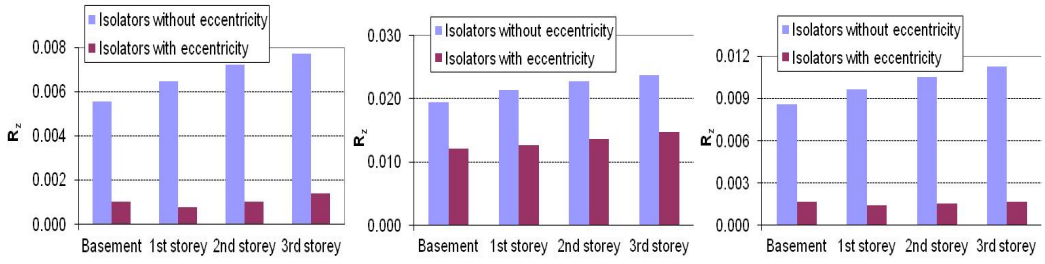
Figure 17: Maximum floor rotations in case of building B1 subjected to earthquake records of El Centro (a), Kobe (b) and Lefkada (c)



(a) (b)

(c)

Figure 18: Maximum displacements of the vertical structural elements (basement) in case of building B2 subjected to earthquake records of El Centro (a), Kobe (b) and Lefkada (c)



(a) (b) (c)

Figure 19: Maximum floor rotations in case of building B2 subjected to earthquake records of El Centro (a), Kobe (b) and Lefkada (c)

5 CONCLUSIONS

The present study examines the influence of the isolators' effective stiffness distribution on the torsional response of base isolated structures. To accomplish this purpose two R/C 3-storey buildings were analyzed under earthquake ground motions for the following two distributions of isolators' effective stiffness: (a) all the isolators have identical horizontal stiffness and (b) the isolators' effective stiffness is chosen so as the optimum torsion axis of the structure to coincide with the vertical mass axis. The two buildings were subjected to linear as well as nonlinear time history analyses under three bidirectional earthquake ground motions. For each earthquake record the maximum response over all incident angles of seismic motion was determined. Based on the analyses results of the study, the following conclusion can be drawn:

- When the isolators' effective stiffness is chosen so as the optimum torsion axis of the structure to coincide with the vertical mass axis (isolators with eccentricity) the analysis produces displacements which have almost the same value for all the vertical structural elements.
- The displacements of the vertical structural elements located at the flexible side of the buildings are smaller in case of the isolators with eccentricity compared to the corresponding ones produced when all the isolators possess the same stiffness. However, the displacements of the structural elements located at the stiff side can be either reduced or increased depending on the earthquake record.
- The floor rotations are much smaller in case of the isolators with eccentricity. The difference between the values of the floor rotations produced for the two different distributions of isolators' stiffness depends on the earthquake record.

It must be noted that the aforementioned conclusions are valid for the buildings and ground motions used in the present study. In order to expand them to other structural systems, further investigation is necessary.

6 ACKNOWLEDGEMENTS

This study was financially supported by "IKY FELLOWSHIPS OF EXCELLENCE FOR POSTGRADUATE STUDIES IN GREECE - SIEMENS PROGRAM".

REFERENCES

[1] R.L. Crosbie, *Base isolation for brick masonry shear wall structures*, MEng Thesis, University of Canterbury, Christchurch, NZ, 1977.

[2] D.M. Lee, Base isolation for torsion reduction in asymmetric structures under earthquake loadings, *Earthquake Engineering and Structural Dynamics,* **8(4)**, 349-359, 1980.

[3] A. Tena-Colunga, J.L. Escamilla-Cruz, Torsional amplifications in asymmetric base-isolated structures, *Engineering Structures*, **29(2)**, 237-247, 2007.

[4] V. Kilar, D. Koren, Seismic behaviour of asymmetric base isolated structures with various distributions of isolators", *Engineering structures*, **31(4)**, 910-921, 2009.

[5] Eurocode 2 (2004) Design of concrete structures, Part 1-1: General rules and rules for buildings, European Committee for Standardization, Brussels, Belgium, 2004.

[6] Eurocode 8 (1998-1), Design provisions for earthquake resistance of structures, European Committee for Standardization, Brussels, Belgium, 2003.

[7] C.E. Seguin, J.L. Almazán, J.C. De la Llera, Torsional balance of seismically isolated asymmetric structures, *Engineering structures*, **46**, 703-717, 2013.

[8] FEMA 356. Prestandard and commentary for the seismic rehabilitation of buildings, Federal Emergency Management Agency, Washington, DC, 2000.

[9] ASCE 41/06. Seismic Rehabilitation of Existing Buildings, American Society of Civil Engineers, 2009.

[10] http://www.bridgestone.com/products/diversified/antiseismic_rubber/principle.html

[11] E.M. Marino, P.P. Rossi, Exact evaluation of the location of the optimum torsion axis. *Structural Design of Tall and Special Buildings*, **13(4)**, 277-290, 2004.

[12] J.N. Doudoumis, A.M. Athanatopoulou, Invariant torsion properties of multistorey asymmetric buildings. *Structural Design of tall and Special Buildings*, **17(1)**, 79-97, 2008.

[13] A.M. Athanatopoulou, Critical orientation of three correlated seismic components. *Engineering Structures*, **27(2)**, 301-312, 2005.

[14] SAP2000, Computers and Structures Inc, CSI, Berkeley.

COMPDYN 2015
5th ECCOMAS Thematic Conference on
Computational Methods in Structural Dynamics and Earthquake Engineering
M. Papadrakakis, V. Papadopoulos, V. Plevris (eds.)
Crete Island, Greece, 25–27 May 2015

THE EFFECTS OF THE SEISMIC INPUT ON THE SEISMIC RESPONSE OF RC BUILDINGS

Maria Pianigiani[1], Valentina Mariani[1], Marco Tanganelli[1] and Stefania Viti[1]

[1] Department of Architecture (DiDA), University of Florence, ITALY
Piazza Brunelleschi, 6 – 50121 Firenze
e-mail: {maria.pianigiani;valentina.mariani;marco.tanganelli;stefania.viti}@unifi.it

Keywords: seismic input, selection criteria for seismic spectra, time history analysis, seismic response of existing RC buildings.

Abstract. *This work is aimed at investigating the variation of the seismic response of RC structures subjected to different ensembles of ground motions in the nonlinear dynamic analysis for the seismic assessment of existing RC buildings. At the current time indeed, all the main International Seismic Codes provide a soil classification which is based on the shear wave velocity, the soil morphology and the assumed distance from the fault source. Depending on the soil properties, a suitable elastic spectrum is provided, defined on the basis of average properties assumed for the soil. To perform a nonlinear dynamic analysis, an ensemble of ground motions compatible to the elastic spectrum must be selected. The ensemble can be made by ground motions compatible to the Code spectrum for the assumed soil-type, or, alternatively, by assuming the ground motions to be consistent with the bed rock Code spectrum and by filtering them according with the specific stratigraphy of the site soil. In this work a comparison among these different approaches, all compatible to the European (Eurocode 8, EC8) and Italian (NTC 2008) Code provisions, has been made on a case-study, i.e. a real irregular RC Italian building. The comparison has been made in terms of seismic response, i.e. by checking the maximum displacement and interstory drift induced by the assumed ensembles of ground motions.*

1 INTRODUCTION

The evaluation of the seismic performance of existing buildings is affected by many uncertainties, both aleatoric or epistemic ones. The seismic input is considered to be the most random quantity involved in such evaluation [1,2,3]. It is commonly accepted, indeed, that the properties of ground motions which will occur in a certain area - i.e. intensity, frequency contents, distance from the source fault, etc. - are not possible to be exactly predicted. In the past years many studies have been made to limit the aleatoric uncertainty, by carefully mapping the entire area of countries affected by seismic hazard and collecting all types of information useful for prediction.

Even the epistemic uncertainty has been strongly reduced. At the current time, all the main International Seismic Codes provide a soil classification which is based on the shear wave velocity *Vs*, the soil morphology and the assumed distance from the fault source. In Italy in the past decades the available information about the seismic hazard of the territory has been largely increased achieving, at the current time, a detailed mapping [4,5,6]. Depending on the soil properties, a suitable elastic spectrum is provided by the seismic codes [7,8], defined on the basis of average properties assumed for the soil. To perform a nonlinear dynamic analysis, an ensemble of ground motions compatible to the elastic spectrum must be selected [9]. The choice of a seismic input as close as possible to the code spectrum is a controversial matter [10]: it helps in limiting the randomness of the response quantities induced by the seismic event, but it introduces a "discretional" limitation of the response itself, which could eventually result to be unconservative [11]. Another controversy about the spectral matching is about the most significant range of periods to check. In fact, while usually the fundamental period characterizing the dynamic response of the structure is assumed to be the one corresponding to the first vibrational mode, alternative assumptions can be made [12], referring to the "non-linear period" of the structure, defined as the one corresponding to the initial branch of the bilinear idealized capacity curve obtained from the non-linear static (pushover) analysis, according to Eurocode 8, which, in turn, depends on the distribution of lateral loads.

This work is focused on the effects of the ground motions selection on the seismic response of real buildings. According to the Code specification, in fact, different choices can be made about the selection of spectrum-compatible ground motions. Moreover, when a real building is considered for analysis, the soil properties can be not so easy to be classified according to the Code criteria, and consequently the ground motions selection should be even more careful.

According to EC8 and NTC 2008, for soil-types different from the bed rock, the ensemble of ground motions to be used for the analysis can be made *i)* by ground motions selected to be consistent to the Code spectrum for the assumed soil-type, or, alternatively, *ii)* by assuming a set of ground motions consistent with the bed rock Code spectrum and by filtering them according with the specific stratigraphy of the site soil. In the first case, the designer can chose natural ground motions from a standard database, or artificial ones, appositely generated to fit the Code-spectrum for the selected soil-type. In the second case, natural and – when it is possible – local ground motions are usually preferred, and the filtering procedure should provide more reliable results in terms of signal representativeness. The two alternative options, whose choice is up to the engineer in charge of the analysis, can induce very different results in terms of seismic performance, depending on the specific soil-type.

In this work, a comparison among these different approaches, all compatible to the EC8 provisions, has been made on a case-study, i.e. a real irregular RC building currently used as a Hospital. A fully satisfactory knowledge of the building has been achieved; all the documents

describing the original design and the foundation soil have been found, and a soil-type B has been assumed for the building, according to the Italian Technical Code NTC 2008.

In the first part of the paper three different selections of ground motions have been described and compared for two different limit states, i.e. a serviceability (Damage Limitation, *DL*) and an ultimate (Significant Damage, *SD*) one, respectively. The adopted ensembles are characterized as follows:

a) A set of 7 artificial accelerograms, all compatible to the elastic spectrum provided by NTC 2008 for the soil-type B, generated by the software SIMQKE [13].
b) A set of 7 real ground motions, taken by the Italian Accelerometric Archive [14] through the adoption of the software REXEL [15,16,17], for a soil-type B.
c) A set of 7 "local" real ground motions chosen through the software SCALCONA 2.0 [18], which selects spectrum-compatible accelerograms by the data-base ASCONA [19] taking into account the position of the case-study area. The elastic spectra have been chosen to fit the NTC 2008 elastic spectrum for a soil-type A; subsequently the time-histories have been filtered by the software Strata [20] on the basis of the specific mechanical properties of the site soil, to obtain a "customized" seismic input compatible with the site.

In the second part of the work the seismic response of the case-study has been found by performing a nonlinear dynamic analysis, for the two considered limit states, for each of the three assumed ground motions ensembles. The results found by the three ensembles, expressed in terms of maximum displacement and interstory drift, have been compared in order to quantify the effects of the different ground motions selection criteria.

2 THE CASE STUDY

The case-study, shown in Figure 1, is a framed 3-storey RC building. It has been designed in 1976, i.e. just after the introduction of the first seismic Italian Technical Code, and it presents some efficient design criterions, like column section reduction from foundation level to the top storey, or solid connection of the beam-column joints, although it is far away from complying the current seismic design criteria.

The dimensions of beams and columns are listed in Table 1, while the reinforcements data can be find in [21,22]. It should be noted that the third floor of the building consists of two different structural layers, partially coinciding. In fact two different floors, 40 cm far away each other, constitute the last storey of the building. In some alignments (*X3*, *Y1* and *Y3*) two layers of beams separately support the two different floors, whilst in the other alignments (*X1*, *X2* and *Y2*) a single beam supports both floors. Therefore the 3rd floor and the related beams will be in the following distinguished with a subscript *a* or *b*, depending on weather they refer to the lower or upper layer respectively. All floors are made by deck and concrete, and they have a total height of 20 cm. The infill panels of the RC frames have a double layer, with an inside casing.

An accurate investigation, including destructive and non-destructive tests [21,22], has been made to characterize the material; the obtained *mean* and design stresses for concrete and steel, together with their Knowledge Level (*KL*), has been listed in Fig.1.

Soil mechanical properties have been determined through a geophysical site investigation, through seismic refraction and down hole techniques. The results, processed using both Generalized Reciprocal Method [23] and Tomographic one, have provided detailed information on the distribution and thicknesses of subsurface layers, rock dynamics and geo-mechanical properties, seismic *S* waves velocity profiles (see Fig. 2) and the consequential value of the average shear wave velocity $V_{s,30}$ [24], which is equal to 390 m/s. Therefore the soil has been

classified as B-type, according to NTC2008 (Sec. 3.2.2, Tab. 3.2.II) and EC8 (Part 1, sec. 3.1.2, Tab. 3.1).

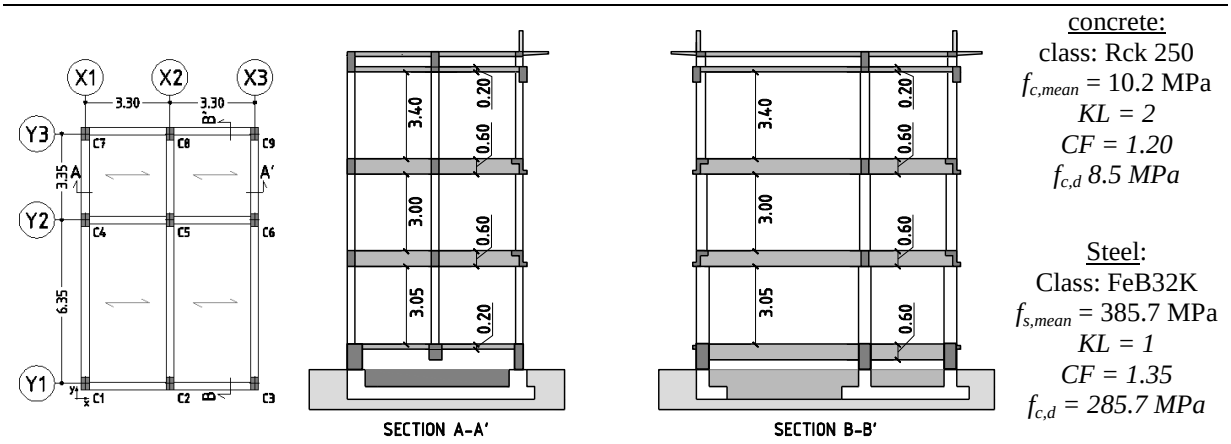


Figure 1. Plan and sections of the RC case-study building.

Table 1. Cross section data of beams and columns.

	beams						columns
	x_1,2; x_2,3; x_7,8; x_8,9	x_4,5; x_5,6	y_1,4; y_2,5	y_3,6	y_4,7; y_5,8	y_6,9	c1-c9
1st st.	Z-shape	30x60	30x60	Z-shape	30x60	Z-shape	30 x 50
2nd st.	Z-shape	30x60	30x60	Z-shape	30x60	Z-shape	30 x 40
3rd st.(a)	30x60	30x80	30x 80	30x60	30x80	30x60	30 x 35
3rd st.(b)	30x20	30x20	-	30x20	-	30x20	

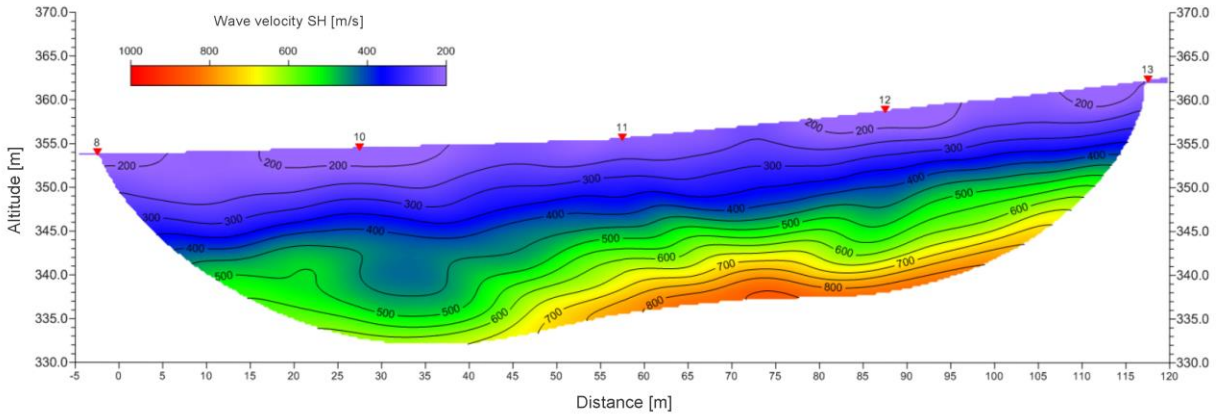


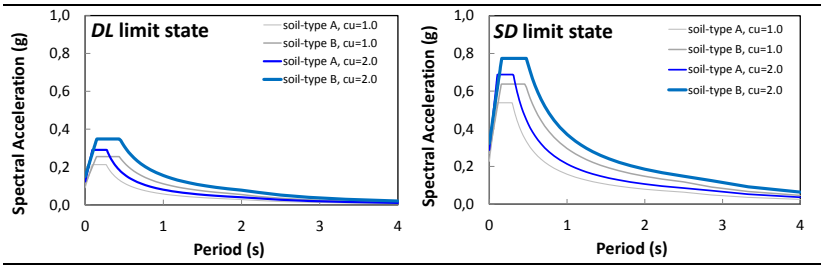
Figure 2. Tomographic section representing the *S* waves profile of the case-study site.

3 THE ASSUMED SEISMIC INPUT

3.1 The elastic spectrum provided by the Code (NTC 2008)

The expected maximum seismic intensity of the area, measured in terms of Peak Ground Acceleration (PGA), has been defined according to NTC 2008. Two Limit States, a serviceability (*DL*) and an ultimate (*SD*) ones, are assumed for analysis. Since the building is current-

ly used as a Hospital, according to NTC 2008, a *coefficient of use* (c_U) equal to 2.0 is assumed, with a consequent doubling of the return period. The main information about the maximum seismic intensity assumed for the two limit states is listed in Tab.2, while the plots of the elastic spectra are shown in Fig. 2.



limit state	*DL*	*SD*
probability of exceedance in 50 years	63%	10%
return period (c_U=1) (in years)	50	475
return period (c_U=2) (in years)	100	950
PGA (g)	0.107	0.227

Figure 2. Elastic spectra provided by NTC 2008.

3.2 Ensemble #1, made of artificial ground motions fitting the B soil-type Code spectrum

A set of 7 artificially generated spectrum-fitting accelerograms, with a duration of 25 s and compatible with the *DL* and *LS* demand spectra respectively provided by the Italian code NTC 2008, have been defined. The time-histories functions have been produced by the software Simqke [13]. The software generates statistically independent artificial ground motions matching a specified response spectrum, through the superposition of sinusoids having random phase angles and amplitudes derived from a stationary power spectral density function. The refinement of the spectral match is done through an iterative procedure. In the present case, ten cycles have been used in the iterative procedure to smoothen the generated response spectra and make them closer to the Code one. The match has been checked in the period range 0-4 s. The generated accelerograms present a stationary part of 10 s, preceded and followed by two branches, increasing and decreasing respectively, of 7.5 s.

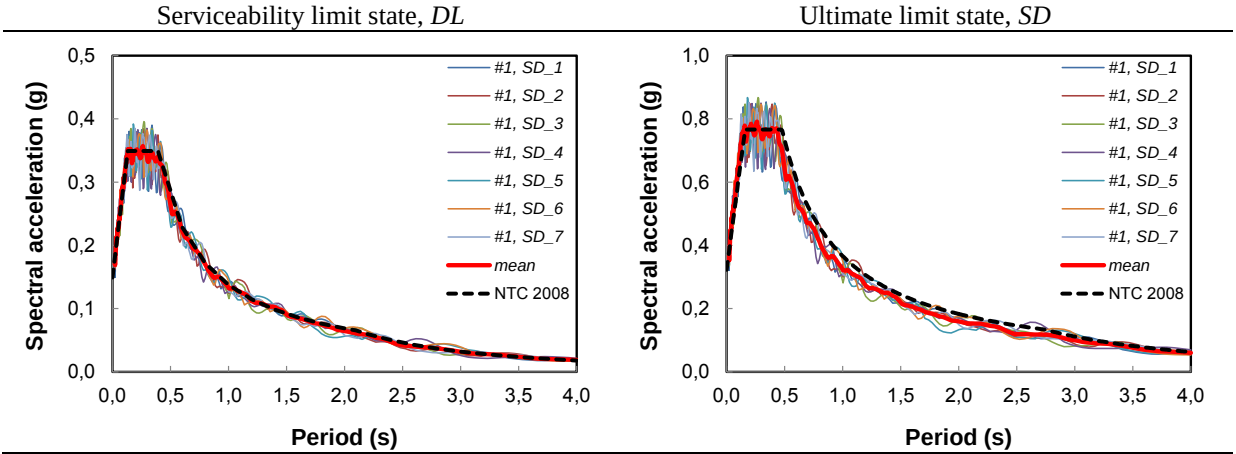


Figure 3. Comparison between the ensemble # 1 elastic spectra and the Code one (soil-type B).

3.3 Ensemble #2, made of natural ground motions fitting the B soil-type Code spectrum

The assumed natural ground motions have been selected, for each limit state, by the Italian Accelerometric Archive [14] through the adoption of the software REXEL [15,16,17], on the basis of the elastic spectrum found for the soil-type B. All ground motions have been used without introducing any scale-factor, i.e. by assuming their effective PGAs. In Figure 4 the

two ensembles of elastic spectra assumed to represent the seismic input for the two limit states have been shown and compared to the ones provided by NTC 2008.

Table 2. Description of the ground motions of the ensemble #2.

	Code	Event	Station Name	Date YYYY-MM-DD	PGA g
DL limit state	#2, DL_1	Friuli Earthquake 3rd Shock	Forgaria Cornino	1976-09-15	0.215
	#2, DL_2	Irpinia Earthquake	Mercato S. Severino	1980-11-23	0.141
	#2, DL_3	Irpinia Earthquake	Mercato S. Severino	1980-11-23	0.107
	#2, DL_4	Umbria-Marche 3rd Shock	Norcia	1997-10-14	0.095
	#2, DL_5	Irpinia Earthquake	Rionero in Vulture	1980-11-23	0.096
	#2, DL_6	Irpinia Earthquake	Rionero in Vulture	1980-11-23	0.099
	#2, DL_7	Irpinia Earthquake	Sturno	1980-11-23	0.225
SD limit state	#2, SD_1	L'Aquila Mainshock	L'aquila - V. Aterno - Colle Grilli	2009-04-06	0.446
	#2, SD_2	L'Aquila Mainshock	L'aquila - V. Aterno - Colle Grilli	2009-04-06	0.489
	#2, SD_3	L'Aquila Mainshock	L'aquila - V. Aterno - Aquil Park Ing.	2009-04-06	0.354
	#2, SD_4	L'Aquila Mainshock	L'aquila - V. Aterno - Centro Valle	2009-04-06	0.657
	#2, SD_5	Irpinia Earthquake	Sturno	1980-11-23	0.316
	#2, SD_6	Irpinia Earthquake	Sturno	1980-11-23	0.225
	#2,SD_7	Friuli Earthquake 1st Shock	Tolmezzo Centrale - Diga Ambiesta 1	1976-05-06	0.346

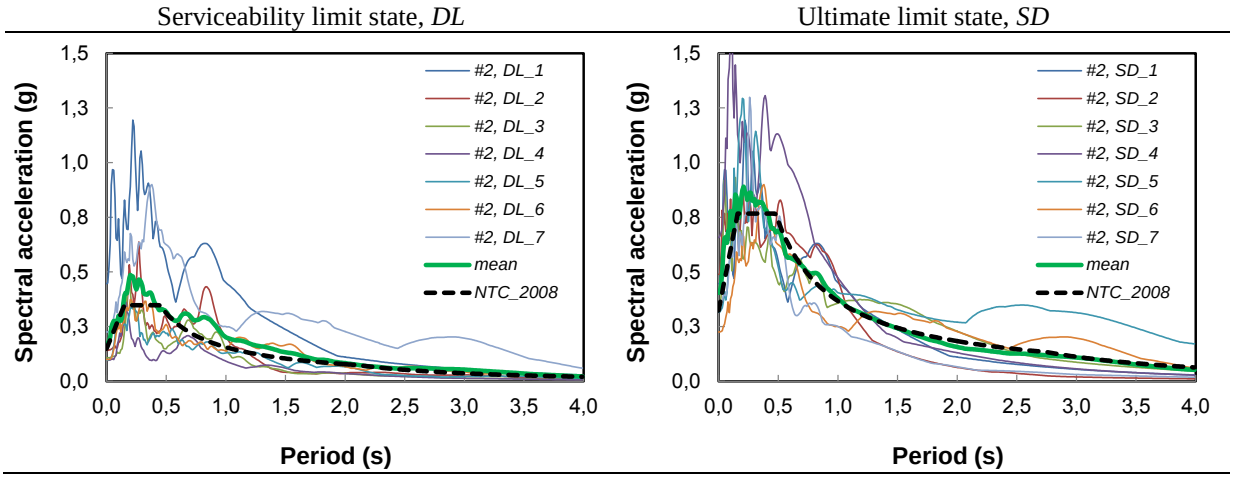


Figure 4. Comparison between the ensemble # 2 elastic spectra and the Code one (soil-type B).

3.4 Ensemble #3, made of natural ground motions fitting the A soil-type Code spectrum

The ensemble #3 is made of seven ground motions for each limit state, fitting the Code spectrum related to the soil-type A (see Fig. 5). The ground motions, whose data are listed in Tab. 3, have been selected through SCALCONA 2.0 [18], which selects natural ground motions, complying to intensity and spectrum-compatibility requirements, taking into account the position (location or geographic coordinates) of the considered site. The time-histories, scaled by two different scale factors to comply the requirements [25], are selected by the database ASCONA [19], which includes ESD (http://www.isesd.hi.is/), PEER-NGA (http://peer.berkeley.edu/nga/) and Itaca [14] databases. The ground motion is applied to the bedrock and the filtering process is performed through the soil, represented as a column of individual layers. Each layer has been characterized according to parameters found by experimental laboratory and *in situ* tests.

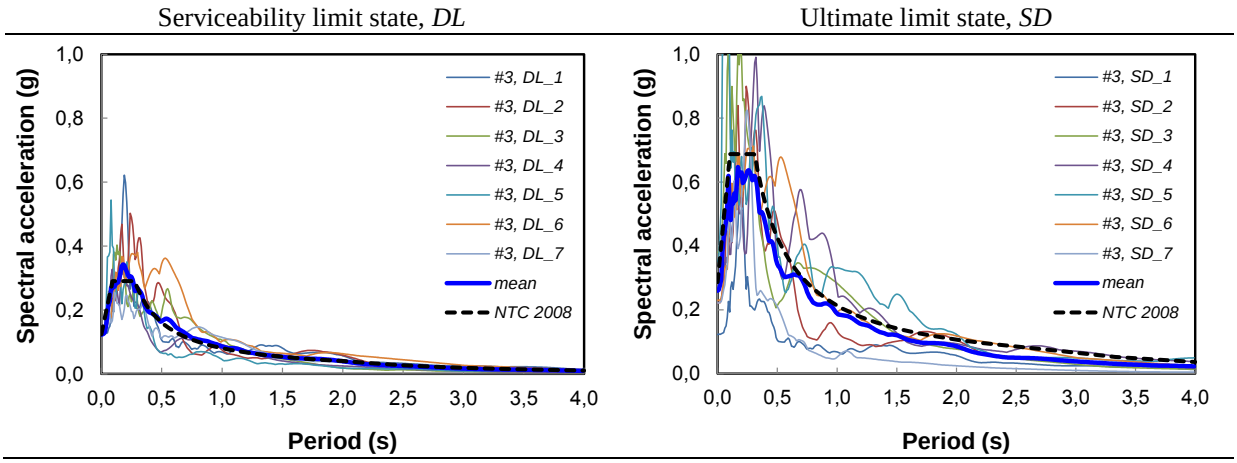


Figure 5. Comparison between the ensemble # 3 elastic spectra and the Code one (soil-type A).

Table 3. Description of the ground motions of the ensemble #3.

	Source file name	Magnitude [Mw]	Epic. Dist. [km]	Total S.F.
DL limit state	ESD 000783ya.cor	5.30	37.00	2.51
	ESD 000234ya.cor	6.20	32.00	1.58
	ESD 000944xa.cor	5.71	37.00	1.48
	NGA 0146y.txt	5.74	12.56	0.92
	NGA 0455x.txt	6.19	38.63	1.78
	ITACA 19971014_152309ITDPC_CSC__WEC.DAT	5.60	22.00	1.94
	ITACA 20090406_013239ITDPC_CLN__NSC.DAT	6.30	31.60	1.35
SD limit state	ESD 000182xa.cor	6.87	11.00	1.16
	ESD 000234ya.cor	6.20	32.00	2.84
	NGA 0146y.txt	5.74	12.56	2.87
	NGA 0804y.txt	6.93	83.53	2.81
	KNET1 SAG0010503201053.NS	6.60	36.18	2.78
	ITACA 19971014_152309ITDPC_CSC__WEC.DAT	5.60	22.00	3.64
	ITACA 20090407_174737ITDPC_AQP__WEC.DAT	5.60	14.40	2.36

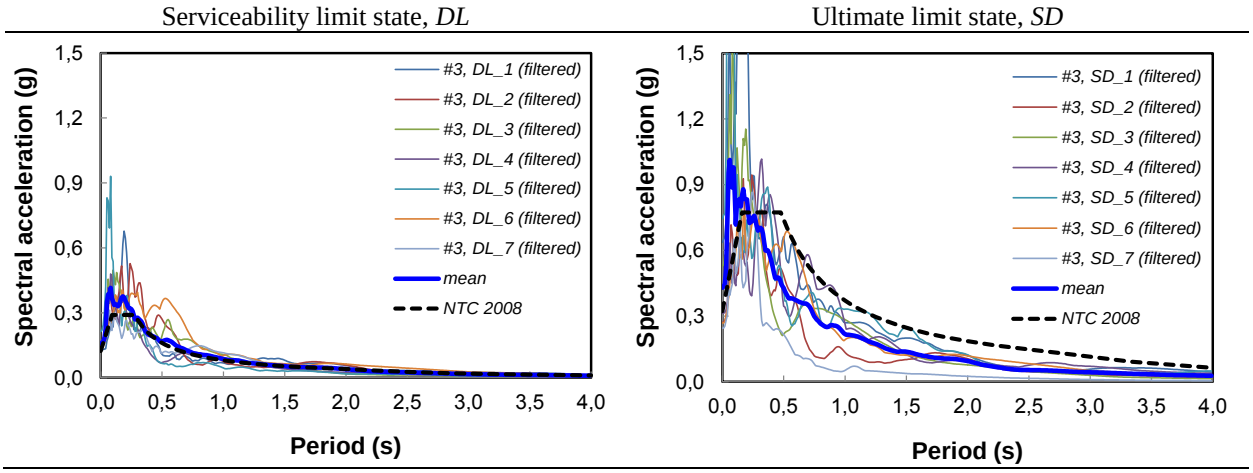


Figure 6. Comparison between the ensemble # 3 elastic spectra and the Code one (soil-type B).

The ground motions constituting the ensemble #3 have been filtered, by assuming the specific soil parameters of the building site, in order to find the expected seismic input as a function of the effective soil properties. The software Strata [20] has been adopted for the filtering phase, by obtaining the elastic spectra shown in Fig. 6.

4 THE STRUCTURAL RESPONSE

All analyses have been performed by using the computer code SAP2000. The two floors of the third level have been modeled according to the real geometry as regards the stiffness and strength distribution, while the mass (both translational and rotational) of the storey has been considered applied at the center of the storey package. The effect of the joint stiffness has been considered by introducing a rigid offset at each element end. A reduced value of the Young modulus of the concrete E_c, i.e. $E_{c,red} = 0.5\ E_c$, has been assumed, as recommended by NTC 2008 (4.1.1.1) and EC8 (part 1, 4.3.1(7)). The floor stiffness has been introduced by assigning the diaphragm constraint to all nodes belonging to the same floor. A lumped plasticity model has been adopted for all RC elements, with one-directional flexural hinges at each element end. After the attainment of the yielding moment, plastic hinges have an almost constant bending moment (hardening ratio between 2% and 6%) till the ultimate rotation is achieved, with a drop of the bending capacity to 20% of the yielding one. Limit values of bending moment and chord rotation have been made according to NTC 2008, which are identical to those provided by EC8.

The seismic response of the building has been measured in terms of displacement and drift, The displacements have been measured at the mass center of each storey of the building, while the drifts have been checked at each column line. Despite being regular both in plan and in elevation, the building evidences some eccentricity along the two main directions. In fact the column distribution is not symmetric in the *Y*-direction, and the infill panels distribution is irregular in both directions. The in-plan eccentricity of the building, expressed in terms of stiffness [23,24,25], is equal to 10.71% (1st st.), 9.41% (2nd st.) and 7.95% (3rd st.) in the *X*-direction and to 2.23% (1st st.), 5.00 (2nd st.) and 3.17% (3rd st.) in the *Y*-direction respectively.

Figs 7 and 8 show, for the two limit states and the three selected ensembles, both the displacements provided by each single ground motion and their *mean*. In this way both the amount of the seismic response found for each ensemble and its dispersion around the *mean* value can be read. The maximum displacements found by using the ensemble #3 are much lower than the other ones, for both the two limit states and direction. The scatter of the results differs very much for the three considered ensembles. The ensemble #1, which is made by artificial ground motions, has the smallest dispersion of the response domain. On the contrary, the response domain found by the #2, made of real non-scaled ground motions taken by [14], has the larger dispersion, especially in the *DL* limit state.

In Fig. 9 the mean values of the maximum displacements found by the three ensembles are compared for the two limit states, in order to evidence the mutual differences.

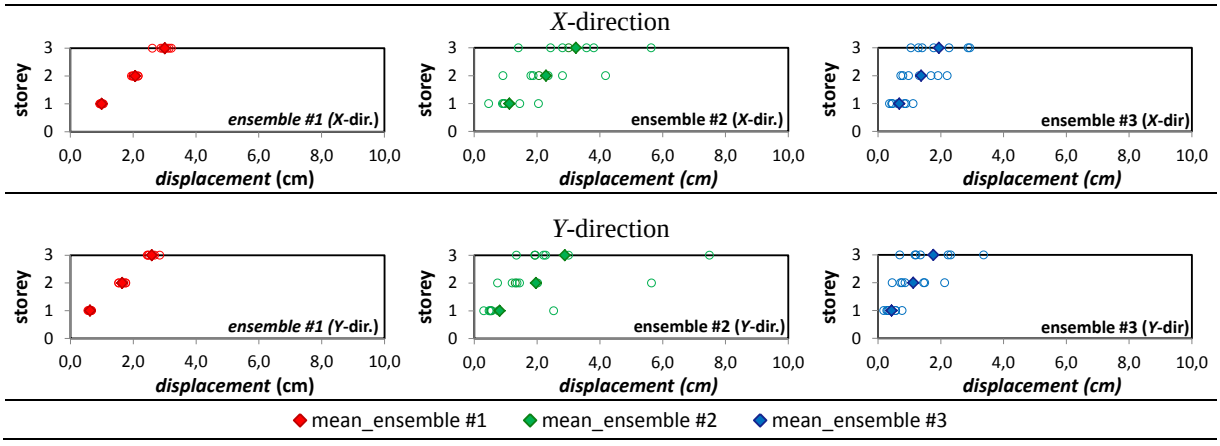


Figure 7. *DL* limit state: displacements profiles provided by the three ensembles.

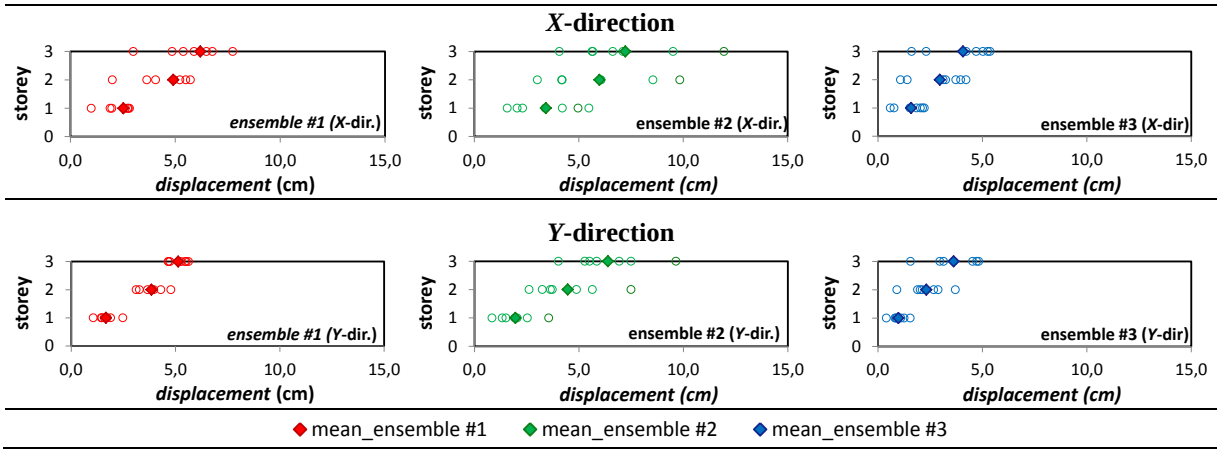


Figure 8. *SD* limit state: displacements profiles provided by the three ensembles.

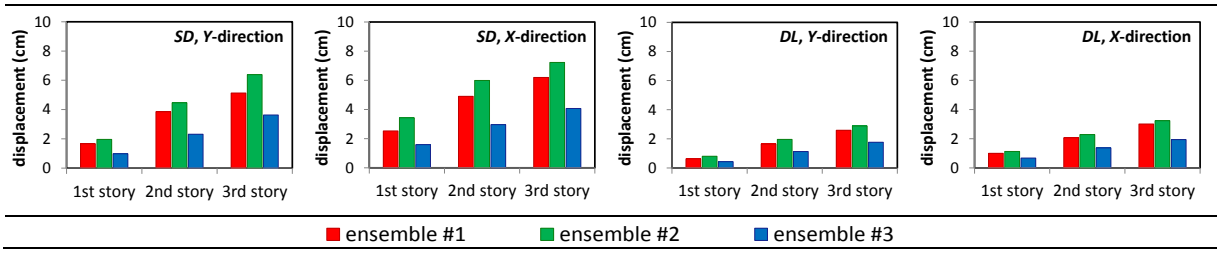


Figure 9. Comparison between the maximum displacement found by the three ensembles.

Figs 10 and 11 show the maximum drift found at each column line of the case-study. The trend found for the drift confirm the displacement one. The ensembles #1 and #2 provide similar results, with the ensemble #2 being the more conservative of the two. The drift found by adopting the ensemble #3, instead, provides the lowest drift, which is even lower than the one provided by the ensemble #1, and up to 54% lower than the one provided by the ensemble #2.

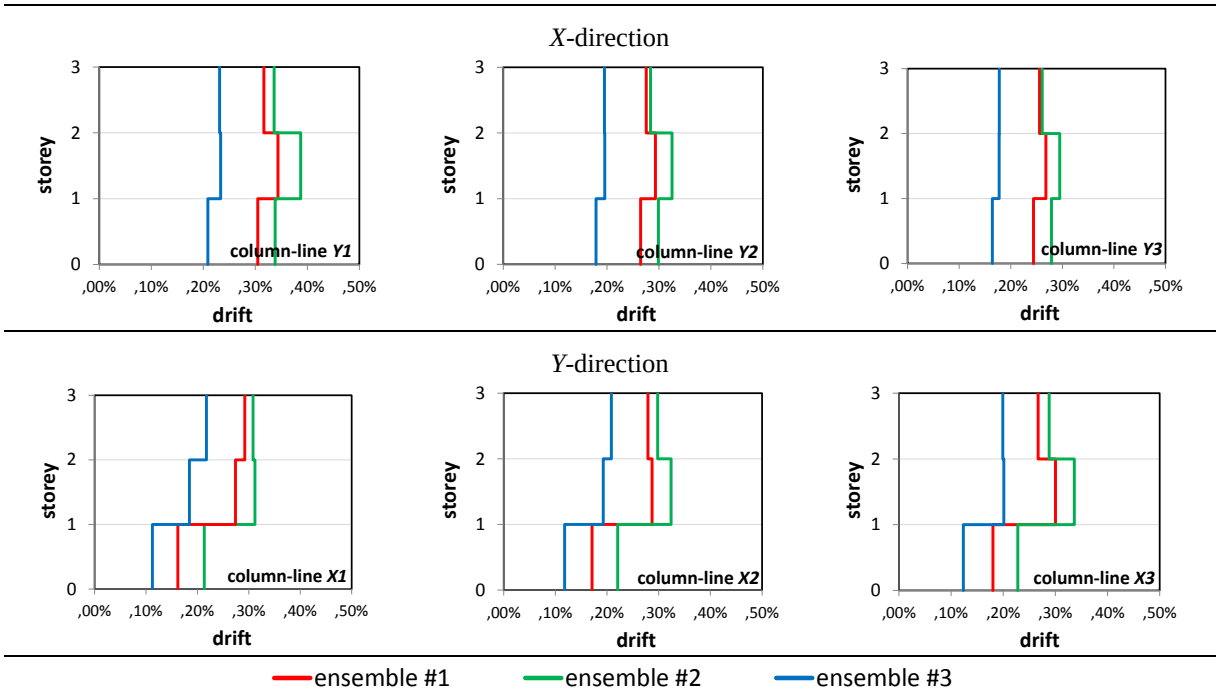


Figure 10. *DL* limit state: maximum drift at each column-line.

The torsional effects due to the eccentricities in the two directions can be evaluated by comparing the maximum drift found at the side column line. As it was expectable, since the only non-negligible (> 5%) eccentricity is along the *Y*-direction, the torsional effects are larger when the seismic analysis in is performed the *X*-direction. In the results found for both the limit states, in fact, the drifts experienced by the structure at the column line *Y1* are larger than the ones at the column line *Y3*. The effects of the different ground motions assumed as seismic input can be read even in the drift profile, especially when the Significant Damage limit state is considered.

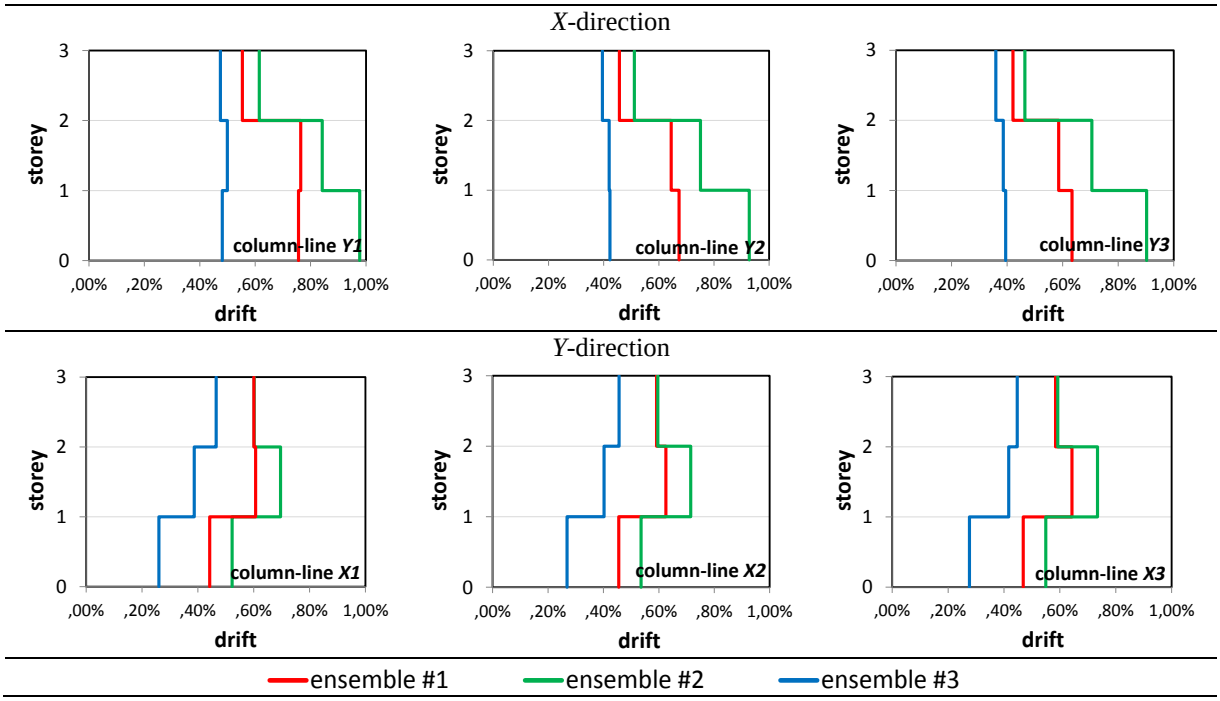


Figure 11. *SD* limit state: maximum drift at each column-line.

5 CONCLUSIONS

In this work the effects of the selection of ground motions to be used as seismic input for nonlinear dynamic analysis have been studied on a case-study, i.e. an existing irregular RC building. A very detailed knowledge has been achieved on the building, including both structural and geological aspects. The site ground have been extensively described, and a soil-type B has been consequently assumed. Three different ensembles of ground motions, all compatible to the Italian Technical Code (NTC 2008), have been selected and compared. Two of them, respectively made of artificial ground motions (#1) and natural ones selected by a National archive (#2), have been set directly on the elastic spectrum provided by the Code for the soil-type B, while the third one (#3), made of natural ground motions taken by a regional database, has been set on the bed rock soil, and then filtered on the base of the specific ground properties.

The three selected ensembles differ very much each other both in terms of dispersion and spectral ordinates. The ensemble #1, in fact, can be generated by imposing different amounts of scatter, all compatible to the Code requirements. The ensemble adopted in the analysis presents a much lower scatter than the other ones. Its spectral ordinates are close enough to the ones of the ensemble #2, which is characterized by a very high scatter. The ensemble #3, in-

stead, differ very much from the other two in terms of spectral ordinates, providing lower values of Spectral Acceleration. These differences among the three considered ensembles can be found even when the seismic response of the building has been checked. Both the results in terms of maximum displacement and drift, in fact, confirm these observations, as regards both the amount of the response and the dispersion of the response domain.

According to this work, the three assumed ensembles of ground motions, despite being consistent to the provisions of the current Technical Code, provide very different results. Further investigations are needed to understand which selection of ground motions can be more appropriate as a function of the soil-type and of the purpose of the analysis.

REFERENCES

[1] K.A. Porter, J.L. Beck and R.V. Shaikhutdinov. Sensitivity of building loss estimates to major uncertain variables, *Earthquake Spectra* ***18(4)***, 719–743, 2002.

[2] T.H. Lee and K.M. Mosalam. Seismic Demand Sensitivity of Reinforced Concrete Shear-Wall Building Using FOSM Method, *Earthquake Engineering and Structural Dynamics* **34(14)**, 1719-1736, 2005.

[3] M. Faggella, A.R. Barbosa, J.P. Conte, E. Spacone and J.I. Restrepo. Probabilistic Seismic Response Analysis of a 3-D Reinforced Concrete Building. *ASCE Journal of Structural Engineering*, 2012.

[4] NTC 2008. Norme tecniche per le costruzioni. D.M. Ministero Infrastrutture e Trasporti 14 gennaio 2008, G.U.R.I. 4 Febbraio 2008, Roma.

[5] Ordinanza PCM 3519 (28/04/2006) criteri generali per l'individuazione delle zone sismiche e per la formazione e l'aggiornamento degli elenchi delle medesime zone (G.U. n.108 del 11/05/2006)

[6] Ordinanza PCM 3274 (20/03/2003) primi elementi in materia di criteri generali per la classificazione del territorio nazionale e di normative tecniche (G.U. n.105 del 08/05/2003)

[7] EC 8-3 (2005). Design of structures for earthquake resistance, part 3: strengthening and repair of buildings, European standard EN 1998-3. European Committee for Standardization (CEN), Brussels.

[8] R.P. Dhakal, S.L. Lin, A.K. Loye, S.J. Evans. Seismic design spectra for different soil classes. *Bulletin of the New Zealand Society for Earthquake Engineering,* ***Vol. 46, No. 2****, June 2013.*

[9] R.L. Gascot and L.A. Montejo. Evaluation of spectrum compatible earthquake records and its effect on the inelastic demand of civil structures. *Proc. 10NCEE*, Anchorage, Alaska, July 21-25, 2014.

[10] I. Iervolino, G. Maddaloni, E. Cosenza. Eurocode 8 compliant real record sets for seismic analysis of structures. *Journal of Earthquake Engineering, Vol. 00, No. 0, June 2007*: pp. 1–30.

[11] A.E. Seifried and J. W. Baker. Spectral variability and its relationship to structural response estimated from scaled and spectrum-matched ground motions *Proc. 10NCEE* Anchorage, Alaska, July 21-25, 2014.

[12] C. Cantagallo, G. Camata, and E. Spacone. Seismic Demand Sensitivity of Reinforced Concrete Structures to Ground Motion Selection and Modification Methods. *Engineering Spectra,* **30(4)**:1449-1465, 2014.

[13] D. Gasparini, E.H. Vanmarcke. SIMQKE: A program for artificial motion generation. Department of Civil Engineering, Massachusetts Institute of Technology, Cambridge, MA, 1976.

[14] Itaca. (2008). Database of the Italian strong motions data. http://itaca.mi.ingv.it.

[15] I. Iervolino, C. Galasso, E. Cosenza. REXEL: computer aided record selection for code-based seismic structural analysis. *Bulletin of Earthquake Engineering,* **8**:339-362, 2009.

[17] C. Smerzini, C. Galasso, I. Iervolino, R. Paolucci. Ground motion record selection based on broadband spectral compatibility. *Earthquake Spectra,* 2013.

[18] E.Zuccolo, M.Corigliano, C.G. Lai. Selection of spectrum- and seismo-compatible accelerograms for the Tuscany region in Central Italy. *Soil Dynamics and Earthquake Engineering*, **vol. 66**, 305-313, 2014.

[19] M. Corigliano, C.G. Lai, M. Rota, C. Strobbia. ASCONA: Automated Selection of COmpatibile Natural Accelerograms. *Earthquake Spectra*, 2012.

[20] A.R. Kottke and E.M. Rathje. Technical Manual for Strata. *PEER Report 2008/10*. University of California, Berkeley (California), 2008.

[21] A. Lo Brusco, V. Mariani, M. Tanganelli, S. Viti and M. De Stefano. Seismic assessment of an existing irregular RC building according to Eurocode 8 methods. *Proc. 7 EWICS*, Oct.17-18, Opole, 2014.

[22] A. Lo Brusco, V. Mariani, M. Tanganelli, S. Viti and M. De Stefano. Seismic assessment of a real RC asymmetric hospital building according to NTC 2008 analysis methods. *Bull. Earth. Eng.* (in print).

[23] D. Palmer. An Introduction to the generalized reciprocal method of seismic refraction interpretation. *Geophysics*, **46(11)**, 1508–1518, 1981.

[24] C. Sirles, A. Viksne. Site-specific shear wave velocity determinations for geotechnical engineering applications. *Geotechnical and Environmental Geophysics*, **Vol. 3**, 121-131, 1990.

[25] E. Zuccolo, M. Corigliano, C.G. Lai. Probabilistic Seismic Hazard Assessment of Italy Using Kernel Estimation Methods. *Journal of Seismology*, **Vol. 17**, 1001-1020, 2013.

[26] M. De Stefano, M. Tanganelli, S. Viti. Variability in concrete mechanical properties as a source of in-plan irregularity for existing RC framed structures. *Engineering Structures*, **Vol. 59**, 161-172, 2014.

[27] M. De Stefano, M. Tanganelli, S. Viti. Torsional effects due to concrete strength variability in existing buildings", *Earthquakes and Structures*, **Vol. 8, No. 2**, 379-399, 2015.

[28] S.A. Anagnastopoulos, C. Alexopoulou, M.T. Kyrkos. An answer to an important controversy and the need for caution when using simple models to predict inelastic earthquake response of buildings with torsion. *Earthquake Engng Struct. Dyn.* 2009.

COMPDYN 2015
5th ECCOMAS Thematic Conference on
Computational Methods in Structural Dynamics and Earthquake Engineering
M. Papadrakakis, V. Papadopoulos, V. Plevris (eds.)
Crete Island, Greece, 25–27 May 2015

BIDIRECTIONAL ANALYSIS OF A REAL RC BUILDING ACCORDING TO THE ITALIAN CODE PROVISIONS

Stefania Viti[1], Valentina Mariani[1], Marco Tanganelli[1] and Mario De Stefano[1]

[1] University of Florence, Department of Architecture (DiDA)
Piazza Brunelleschi, 6 – 50121 Firenze
e-mail: {viti, valentina.mariani, marco.tanganelli, mario.destefano}@unifi.it

Keywords: seismic response under bi-directional ground motions, nonlinear dynamic analysis, seismic assessment of existing RC buildings.

Abstract. *The seismic assessment of existing buildings is an essential issue of seismic engineering. This work is focused on the effects of a bi-directional analysis on the evaluation of the seismic response of existing RC buildings according to the current Italian Technical Code. A nonlinear dynamic (time-history) analysis has been performed with reference to a case-study, that is a real RC hospital building. An accurate knowledge of the building has been achieved, as a result of a collaboration between the University of Florence and the Regional Government. Two different limit states, i.e. a serviceability (Damage Limitation) and a ultimate (Severe Damage) one, have been considered. Two ensemble of ground motions have been selected to represent the seismic action for the two limit states. Each set is made of 14 records, i.e. 7 ground motions with their two (N/S, E/W) components. The seismic response of the case-study has been studied in terms of displacements and interstorey drifts. The drift profile at each column-line of the case-study has been checked in order to evaluate the torsional effects arising by the eccentricities in the two directions.*

1 INTRODUCTION

The assessment of the seismic performance of existing buildings is a crucial issue of seismic engineering. In Italy, as well as in many other European countries, most part of RC buildings have been constructed in the 60s and 70s and therefore they often do not comply with the technical requirements provided by the Codes in force; a reliable evaluation of their seismic capacity is an essential step for a convenient choice about their use and maintenance.

According to the current Italian (NTC 2008, [1]) and European (Eurocode 8, [2]) Technical Codes, a seismic input acting along two different orthogonal directions must be considered for analysis. Usually the wave trains in the two directions are separately considered, and their effects are combined according to the Code' rules. Different combination criteria are provided by the Code, depending on the type of performed analysis.

In this work a bi-directional nonlinear dynamic analysis has been performed on a case-study, i.e. a real RC building, slightly irregular in plan, currently used as a hospital [3-5]. Its numerical modeling is based on a wide knowledge process, that is the result of a joint agreement with the Regional Government of Tuscany. A large number of experimental tests have been performed to evaluate material and ground mechanical properties [6-7].

The seismic response of the building is found with regards to two different limit states, i.e. a serviceability (*Damage Limitation, DL)* and a ultimate one (*Significant Damage, SD*).

For each limit state an ensemble of seven ground motions, spectrum-compatible with the elastic seismic spectrum provided by the Italian Code, has been selected. The orthogonal components of each ground motion, which are also spectrum-compatible, are assumed to represent the ensemble in the orthogonal direction. For each selected seismic event, the two components of the ground motion have been applied in the two main directions of the building and then reversed. Five analyses have been run for each direction and limit state: one with the acceleration trains applied to the mass center and other four by introducing a ±5% eccentricity in the two directions according to the Code prescriptions.

Since the building is irregular the seismic action induces possible torsional effects [8-10]. Therefore the seismic response, expressed in terms of drift and displacement, has been checked both at the mass center and at the side column lines of the structure. Firstly, the results obtained by applying the assumed set of ground motions at the mass center only, have been preliminary discussed, in order to evaluate the influence of the direction of application of the two different components in terms of scatter of the response quantities. Then the enveloped results found by introducing the ±5% eccentricity have been found and shown, in terms of *mean* values only. Finally, the enveloped drift profiles of the building have been shown both at the mass center and at the side column lines, to investigate the torsional effects arising by the in-plan irregularities.

2 THE CASE STUDY

The case-study, shown in Figure 1, is a framed 3-storey RC building. It has been designed in 1976, i.e. just after the introduction of the first seismic Italian Technical Code, and it presents some efficient design criteria, such as column section reduction from foundation level to the top storey and solid joint connection at beam-column intersection, although it is far away from complying the current seismic design criteria. The dimensions of beams and columns are listed in Table1, while the reinforcements data can be find in La Brusco et al. [3-5]. It should be noted that the third floor of the building consists of two different structural layers, partially coinciding. In fact, two different floors, 40 cm far away each other, constitute the last storey of the building. In some alignments (*X3*, *Y1* and *Y3*) two layers of beams separately support

the two different floors, whilst in the other alignments (*X1*, *X2* and *Y2*) a single beam supports both floors. Therefore the 3rd floor and the related beams will be in the following distinguished with a subscript *a* or *b*, depending on weather they refer to the lower or upper layer respectively. All floors are made by deck and concrete, and they have a total height of 20 cm. The infill panels of the RC frames have a double layer, with an inside casing. A in-depth investigation, including destructive and non-destructive tests [3-5], has been made to characterize the material mechanical properties; the obtained *mean* and design strengths for concrete and steel, together with the achieved Knowledge Level (*KL*), have been listed in Fig.1. Even the ground properties have been investigated through seismic refraction and down hole techniques; on the basis of such investigations, the soil has been classified as B-type, according to NTC2008 (Sec. 3.2.2, Tab. 3.2.II) and EC8 (Part 1, sec. 3.1.2, Tab. 3.1).

The case-study building is rectangular in plan, structurally symmetrical about the *Y*-direction, while in the *X*-direction the two spans have different lengths. In order to quantify the in-plan irregularity, the mass-stiffness eccentricity has been determined in the two main directions. At each storey, the mass center has been found by considering the mass of the floors and of the infill panels, while the center of stiffness has been determined by applying the simplified relationship proposed by Anagnastopoulos [11-13].

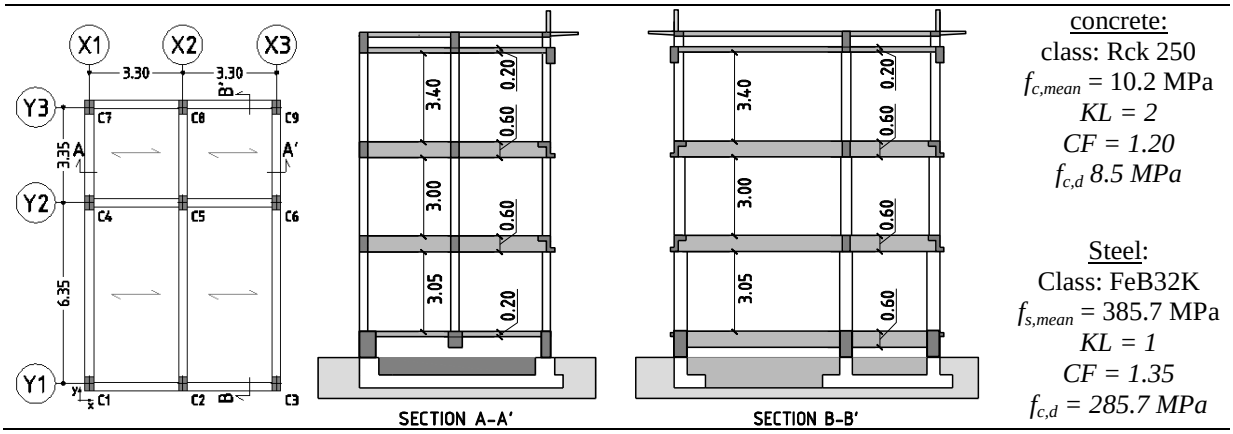


Figure 1. Plan and sections of the RC case-study building.

Table 1. Cross section data of beams and columns.

	beams						columns
	x_1,2; x_2,3; x_7,8; x_8,9	x_4,5; x_5,6	y_1,4; y_2,5	y_3,6	y_4,7; y_5,8	y_6,9	c1-c9
1st st.	Z-shape	30x60	30x60	Z-shape	30x60	Z-shape	30 x 50
2nd st.	Z-shape	30x60	30x60	Z-shape	30x60	Z-shape	30 x 40
3rd st.(a)	30x60	30x80	30x 80	30x60	30x80	30x60	30 x 35
3rd st.(b)	30x20	30x20	-	30x20	-	30x20	

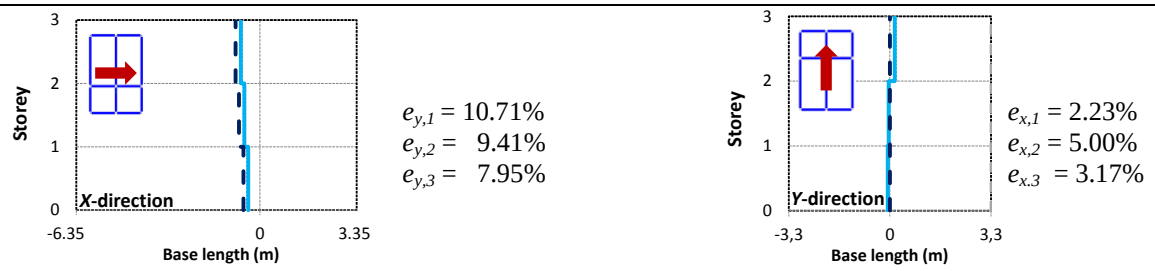


Figure 2. Stiffness eccentricity of the case-study.

Figure 2 shows the positions of the mass and stiffness centers at each storey in the two directions, together with the corresponding eccentricities. It can be noted that, despite the building has a symmetric structure about the *Y*-direction, it presents non-zero eccentricity even in this direction, confirming the role of infill panels distribution on structural regularity [14].

3 ASSUMED GROUND MOTIONS AND SEISMIC ANALYSIS

3.1 The seismic input

A soil-type B has been assumed for the case-study ground, with a maximum PGA equal to 0.32 g and 0.15 g respectively for the two limit states. To perform the nonlinear dynamic analysis, two different sets of ground motions (see Table 2) have been considered, whose average spectra closely approaches the NTC 2008 ones (for both assumed limit states).

Table 2. Ground motions data for the assumed Limit States (soil-type B)

l.s.	Ensemble code	Record code	Event	Station Name	Date YYYY-MM-DD	PGA [g]	scale factor
Damage Limitation (DL)	*DL_E/W DL_N/S*	FRC_HN	FRIULI_EARTHQUAKE_4TH_SHOCK	FORGARIA CORNINO	1976-09-15	0.332	0.45
		SRC0_HN	FRIULI_EARTHQUAKE_4TH_SHOCK	S. ROCCO	1976-09-15	0.249	0.60
		AQK_HN	L_AQUILA_MAINSHOCK	L'AQUILA - V. ATERNO	2009-04-06	0.330	0.45
		CSO1_HN	L_AQUILA_MAINSHOCK	CARSOLI1	2009-04-06	0.018	7.99
		MRT_HN	L_AQUILA_MAINSHOCK	MONTEREALE	2009-04-06	0.044	3.40
		AQK_HN	L_AQUILA_EARTHQUAKE	L'AQUILA - V. ATERNO	2009-04-07	0.090	1.65
		SSU_HN	EMILIA_2ND_MAINSHOCK	SASSUOLO	2012-05-29	0.017	8.54
Severe damage (SD)	*SD_E/W SD_N/S*	SRC0_HN	FRIULI_EARTHQUAKE_4TH_SHOCK	S. ROCCO	1976-09-15	0.249	1.29
		PTT1_HN	PATTI_GULF_EARTHQUAKE	PATTI	1978-04-15	0.163	1.98
		AQK_HN	L_AQUILA_MAINSHOCK	L'AQUILA - V. ATERNO	2009-04-06	0.330	0.98
		MDN_HN	EMILIA_1ST_MAINSHOCK	MODENA	2012-05-20	0.037	8.73
		CNT_HN	EMILIA_2ND_MAINSHOCK	CENTO	2012-05-29	0.224	1.44
		BUI_HN	FRIULI_EARTHQUAKE_3RD_SHOCK	BUIA	1976-09-15	0.093	3.47
		MDN_HN	EMILIA_2ND_MAINSHOCK	MODENA	2012-05-29	0.030	10.69

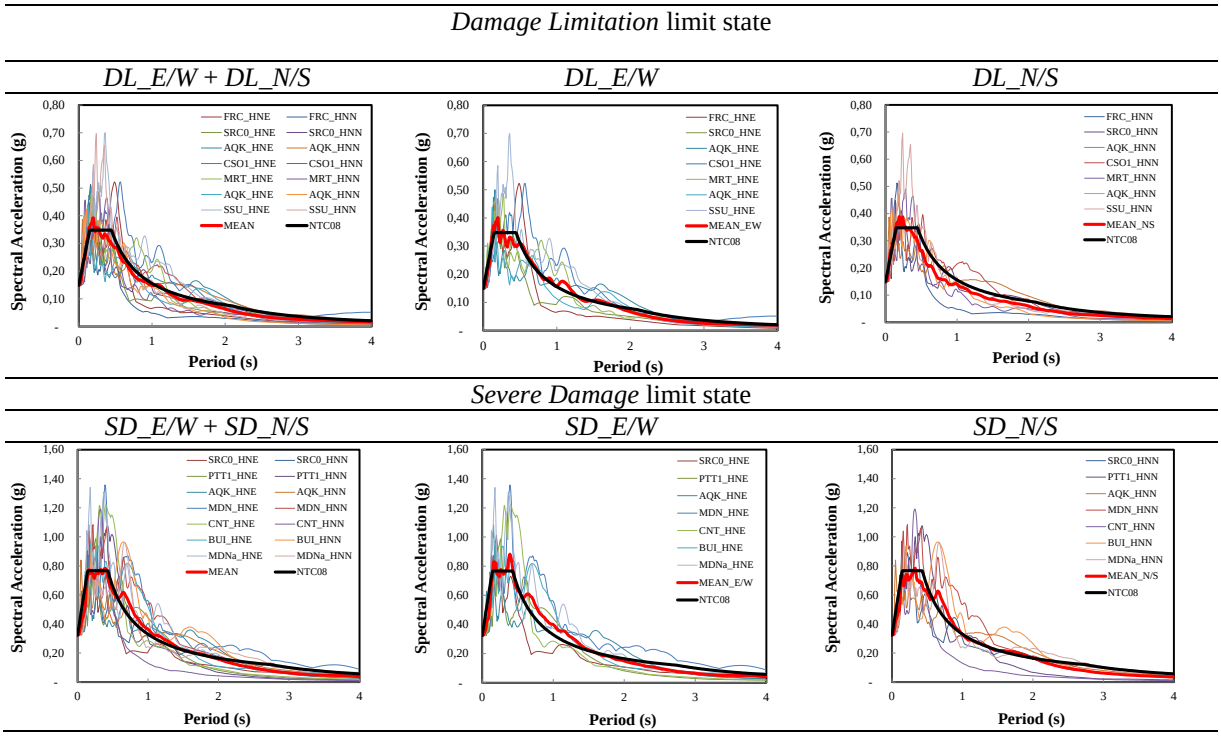


Figure 3 Comparison between the elastic spectra of the assumed ensembles and the NTC 2008 ones.

For each limit state, 7 ground motions, with their two directional components (N/S, E/W) have been selected. Each ensemble has been identified with a code defining the limit state and the direction of application (see Table 2).

The ground motions have been taken by the Italian Accelerometric Archive [15] through the adoption of the software REXEL [16-18], on the basis of a soil-type B, a nominal life of 50 years, a magnitude between 5.5 and 6.5, and a *coefficient of use* equal to 2.0, as required for strategic buildings. In Figure 3 the two ensembles of elastic spectra assumed to represent the seismic input for the two limit states have been shown and compared to the ones provided by NTC 2008.

3.1 The seismic analysis

All analyses have been performed by using the computer code SAP2000 [19]. The two floors of the third level have been modeled according to the real geometry as regards the stiffness and strength distribution, while the mass (both translational and rotational) of the storey has been considered applied at the center of the storey package. The effect of the joint stiffness has been considered by introducing a rigid offset at each element end. A reduced value of the Young modulus of the concrete E_c, i.e. $E_{c,red} = 0.5\ E_c$, has been assumed, as allowed by NTC 2008 (4.1.1.1) and EC8 (part 1, 4.3.1(7)). The floor stiffness has been introduced by assigning the diaphragm constraint to all nodes belonging to the same floor. A lumped plasticity model has been adopted at each end of all structural members, with mono-directional flexural hinges. Plastic hinges have an almost constant bending moment until the ultimate rotation is achieved (hardening ratio between 2% and 6%), and a residual bending moment equal to 20% of the yield one. Limit values of bending moment and chord rotation have been evaluated according to NTC 2008, which are identical to those provided by EC8. The bi-directional analysis has been performed by applying, alternatively reversing the direction of application, 7 ground motions along one direction and the other 7 in the orthogonal direction (see Table 3).

Table 3. Performed analyses.

	Damage Limitation		Severe Damage	
Analysis Code	*DL_1*	*DL_2*	*SD_1*	*SD_2*
Seismic input	*X*-dir: *DL_E/W* *Y*-dir: *DL_N/S*	*X*-dir: *DL_N/S* *Y*-dir: *DL_E/W*	*X*-dir: *SD_E/W* *Y*-dir: *SD_N/S*	*X*-dir: *SD_N/S* *Y*-dir: *SD_E/W*

According to EC8 prescriptions, a ± 5% mass eccentricity has been introduced in both directions. The maximum response in each direction, therefore, is given by the envelope of 5 different cases: besides the one with no eccentricity, where the seismic input is applied to the mass center (*MC*), there are two cases with the 5% introduced along the *X*-direction (*X_E+* and *X_E-*) and two other cases with the 5% eccentricity introduced along the *Y*-direction (*Y_E+* and *Y_E-*).

4. SEISMIC RESPONSE OF THE CASE-STUDY

Figures 4 and 5 show, for the two main directions, the maximum displacements found at the mass center of each storey for the *DL* and *SD* limit states respectively. The diagrams report the maximum responses produced by each record, and their *mean* value, obtained by applying the assumed sets of ground motions to the mass center only. In the *X*-direction the building presents a more scattered response than in the *Y*-direction. This occurrence is expectable, since the building is asymmetric around the *X*-axis; therefore, when the seismic response

is checked in the *X*-direction, some torsional effect can occur, affecting the global response of the structure. Reversing the direction of application of the two components of the ground motions, the displacement patterns show a slight variation. Figures 6 and 7 show the results of the same analyses in terms of interstorey drifts. When the response in the *X*-direction is checked, i.e. at the occurring of torsional effects, the shape of the drift profile is sensitive to the considered limit state: while the drift profile of the *DL* limit state is almost constant, the one obtained for the *SD* limit state achieves its maximum value at the first storey, regularly decreasing along the building height. Even in this case the different scatter associated to each set of ground motions can be noted.

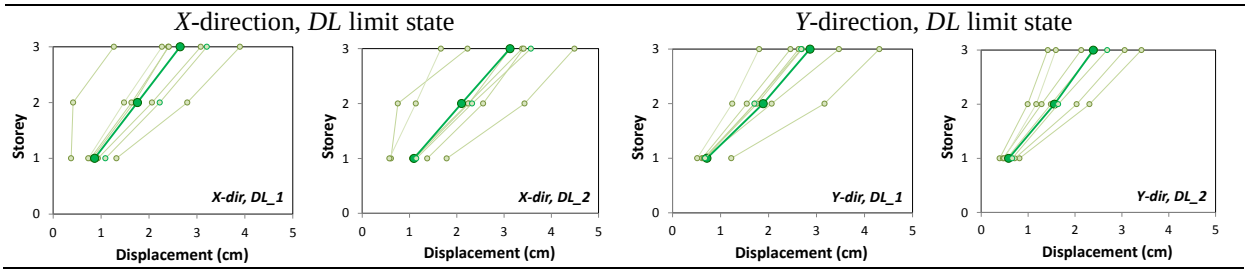


Figure 4. *DL* limit state: maximum displacement at the mass center.

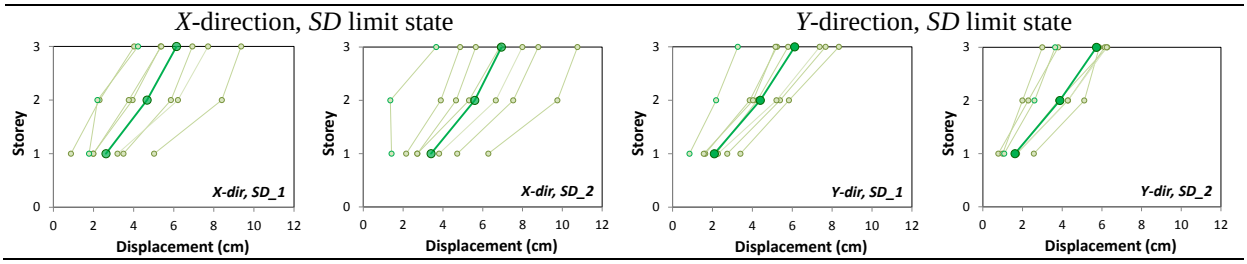


Figure 5. *SD* limit state: maximum displacement at the mass center.

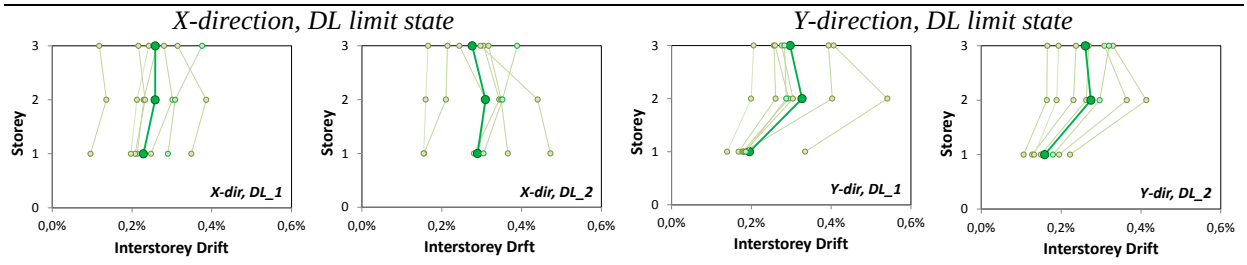


Figure 6. *DL* limit state: maximum Interstorey Drift at the mass center.

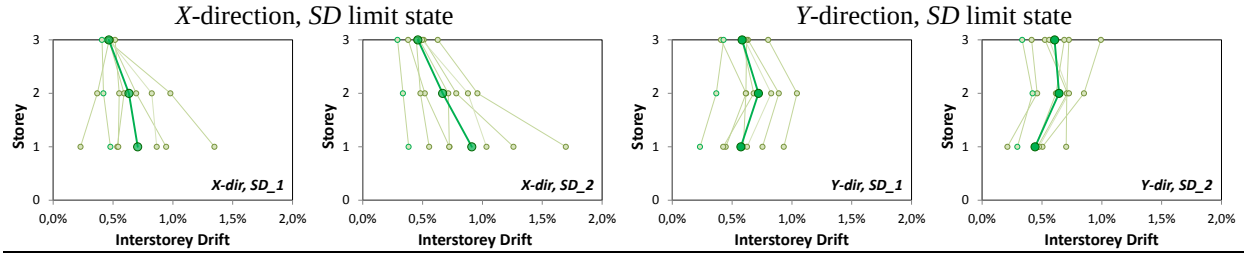


Figure 7. *SD* limit state: maximum Interstorey Drift at the mass center.

Figure 8 shows the response of the structure at the mass center in terms of maximum displacement for all the seismic analyses, comprehensive of the introduced 5% eccentricity in the two directions. As can be noted, the results coming from all the performed analyses are almost coincident with each other, showing that the introduced 5% eccentricity does not affect the displacement profile at the mass center for the present case study. The effects of the introduced 5% eccentricity is more pronounced in the displacement at the two ends of the structures, as can be seen in Figure 9, where the ratio between the maximum displacement experienced by the structure at the side column-lines and the one experienced at the mass center (D_{SIDE}/D_{MC}) is shown.

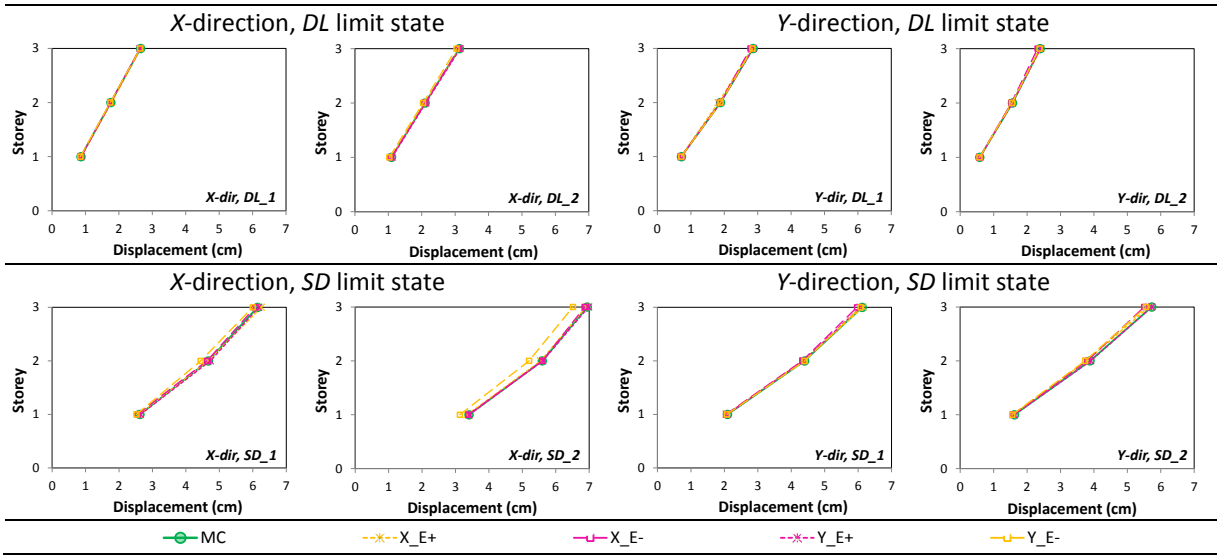


Figure 8. Maximum displacements at the mass center provided by all the performed seismic analyses.

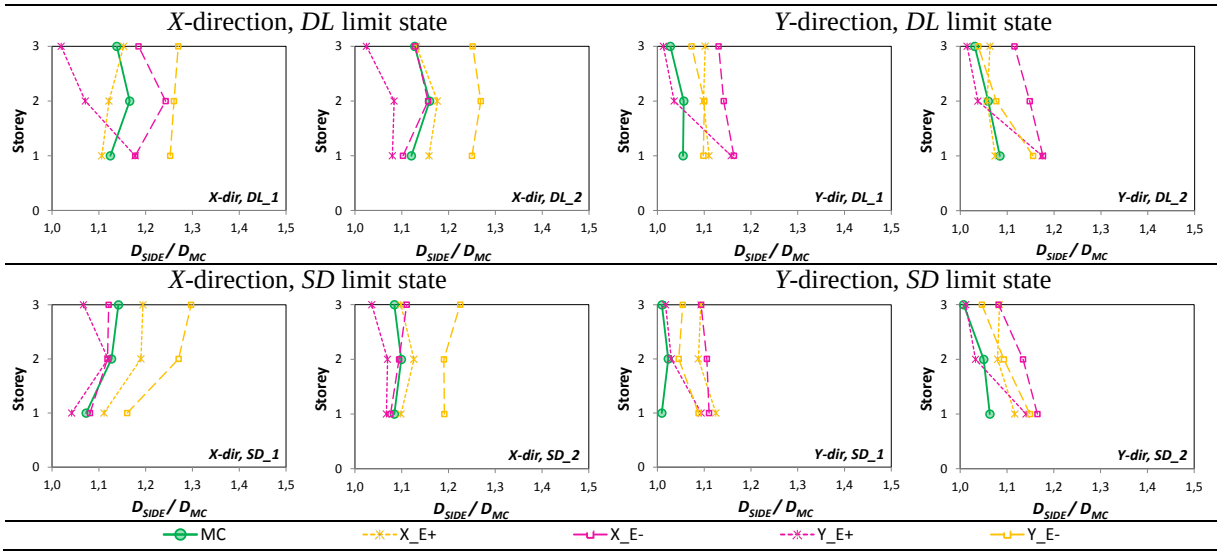


Figure 9. Ratio between the maximum displacement at the building flexible side and the one at the mass center.

Finally, Figures 10 and 11 show the enveloped drift profile related to the 5 analyses, at each column line of the building. As evidenced by the diagrams shown in Figure 9, in fact, the building, under the seismic excitation, exhibits a torsional behavior due to the in-plan eccentricity. The drift occurring at each column line, therefore, can differ from the one observed at the mass center of the building. Diagrams in Figs 10 and 11 show the enveloped drift profile,

i.e. the maximum by the 5 analyses, provided by each set of ground motions. The scatter between the maximum drift at the side column lines is more pronounced in the *X*-direction, due the geometrical non-symmetry of the building along the *X* direction. As already observed in Figs 6 and 7, when the behavior in the *X*-direction is checked, the drift profile is different for the two limit states: in the *DL* limit state, in fact, the maximum drift occurs at the second level, while in the *SD* one it occurs at the first level. To better understand the sensitivity of each performed analysis to the torsional effects, the percentage increase of interstorey drift at the side columns has been found with respect to the one observed at the mass center (Figure 12).

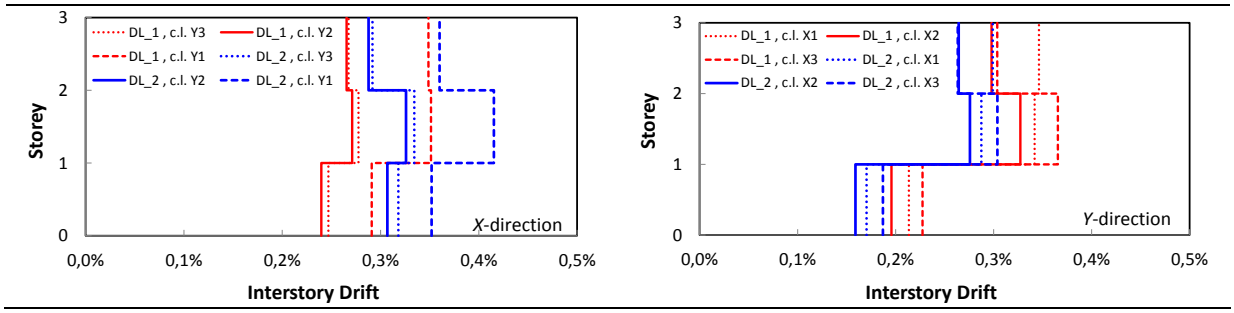


Figure 10. Interstorey Drift envelope at each column line (*DL* limit state).

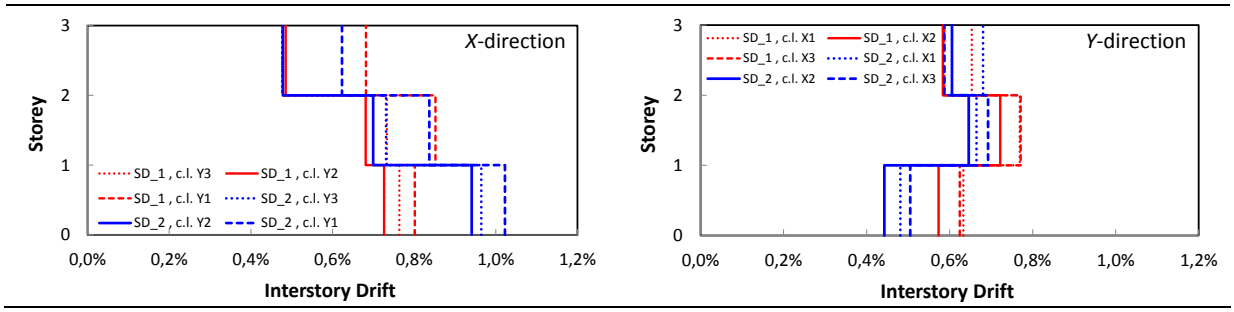


Figure 11. Interstorey Drift envelope at each column line (*SD* limit state).

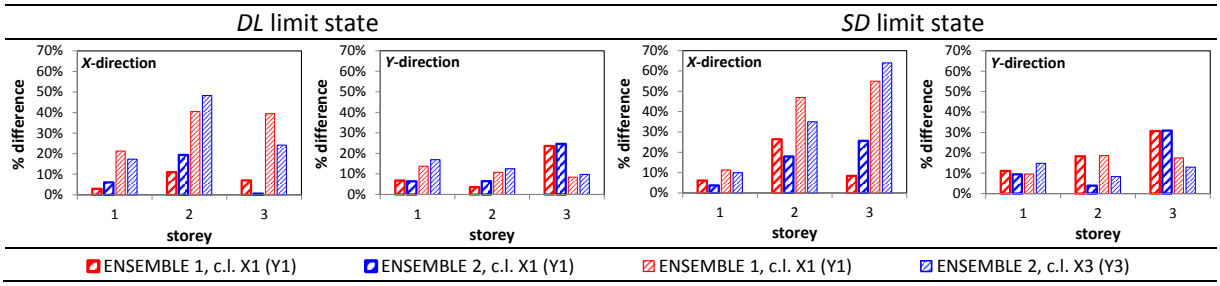


Figure 12. Percentage increase of Interstorey Drift at the side column line with respect to the one at the mass center.

5. CONCLUSIVE REMARKS

In this work a bi-directional nonlinear dynamic analysis has been performed on a real RC framed structure, i.e. a 3-storey existing building currently used as a hospital. Two ensembles of 7 ground motions each, whose both components (N/S, E/W) are compatible with the elastic spectrum provided by the Italian Code for the case-study site, have been selected and used as seismic input for the *Damage Limitation* and *Significant Damage* limit states verification, respectively. Each ground motion has been applied with 2 components oriented on both the

main direction of the building, alternatively, and by introducing the ±5% eccentricity prescribed EC8 and NTC 2008. The structural response has been expressed in terms of displacement and interstorey drift.
Different evaluations have been made on the obtained results. First of all the effects of the choice of the assumed ensembles of ground motions have been checked. The amount and the scatter related to each considered ensemble direction have been shown and compared. The two components of the assumed ground motions, slightly differing each other, produce almost identical results in terms of *mean* response, despite providing a different amount of scatter. The case-study, which is not symmetric around the *X*-axis, shows a different response in the two main directions, evidencing a larger response along the *X*-direction.

The effects of the introduced eccentricity have been checked in terms of maximum displacements only. The maximum displacements found at the mass center by performing the five analyses for each set of ground motions are almost coincident, showing a negligible effect of the introduced 5% eccentricity for the present case study. If the introduced eccentricity does not affect the maximum translational response, it increases the torsional effects arising in the structure as a consequence of the seismic excitation. To evaluate the role of the 5% eccentricity in the torsional response of the structure, the ratio between the maximum displacement experienced by the structure at the side column lines and the one at the mass center has been checked. The increase in displacement due to the 5% eccentricity achieves 30% along the *X*-direction.

Finally, the torsional effects have been observed by checking the maximum enveloped interstorey drift at each column-line of the structure. The comparison among the maximum drift experienced by the building at the flexible side and at the mass center one has evidenced not negligible torsional effects in both the main directions, with an expectable prevalence in the non-symmetric *X*-direction.

ACKNOWLEDGMENTS

This work has been supported by the project DPC-ReLUIS 2010/2013 Task 1.1.2. "Strutture in cemento armato ordinarie e prefabbricate". The Authors also wish to thank the Government of Regione Toscana for providing the building database.

REFERENCES

[1] NTC 2008. Norme tecniche per le costruzioni. D.M. Ministero Infrastrutture e Trasporti 14 gennaio 2008, G.U.R.I. 4 Febbraio 2008, Roma (in Italian).

[2] EC 8-3 (2005). Design of structures for earthquake resistance, part 3: strengthening and repair of buildings, European standard EN 1998-3. European Committee for Standardization (CEN), Brussels.

[3] A. La Brusco, V. Mariani, M. Tanganelli, S. Viti, M. De Stefano. Seismic assessment of an existing irregular RC building according to Eurocode 8 methods. In: Perspectives on European Earthquake Engineering and Seismology, *Series: Geotechnical, Geological and Earthquake Engineering*, Ansal A. Ed. (in press)

[4] A. La Brusco, V. Mariani, M. Tanganelli, S. Viti, M. De Stefano. Seismic assessment of a real RC asymmetric hospital building according to NTC 2008 analysis methods. *Bull. Earth. Eng.* In press.

[5] A. La Brusco, V. Mariani, M. Tanganelli, S. Viti, M. De Stefano. The role of structural modeling on the seismic assessment of existing RC buildings according to Eurocode 8. *Proc.2 European Conference on Earthquake Engineering and Seismology*, Istanbul, 2014.

[6] M.T. Cristofaro. Metodi di valutazione della resistenza a compressione del calcestruzzo di strutture in c.a. esistenti. *PhD Dissertation*, Università di Firenze, 2009. (in Italian)

[7] M.T. Cristofaro, R. Pucinotti, M. Tanganelli, M. De Stefano. The dispersion of concrete compressive strength of existing buildings. Computational Methods. In: Seismic Protection, Hybrid Testing and Resilience in Earthquake Engineering, G.P. Cimellaro et al. (eds), *Geotechnical, Geological and Earthquake Engineering 33*, 2015.

[8] M. De Stefano, M. Tanganelli, S. Viti. Variability in concrete mechanical properties as a source of in-plan irregularity for existing RC framed structures. *Engineering Structures*, **Vol. 59**, 161-172, 2014.

[9] M. De Stefano, M. Tanganelli, S. Viti. On the variability of concrete strength as a source of irregularity in elevation for existing RC buildings: a case study. *Bulletin of Earthquake Engineering*, **Vol. 11 Issue 5**, 1711-1726, 2013.

[10] M. De Stefano, M. Tanganelli, S. Viti. Effect of the variability in plan of concrete mechanical properties on the seismic response of existing RC framed structures. *Bulletin of Earthquake Engineering*, **Vol. 11 Issue 4**, 1049-1060, 2013.

[11] S.A. Anagnastopoulos, C. Alexopoulou, M.T. Kyrkos. An answer to an important controversy and the need for caution when using simple models to predict inelastic earthquake response of buildings with torsion. *Earthquake Engineering and Structural Dynamic*, 2009.

[12] S.A. Anagnastopoulos, M.T. Kyrkos, K.G. Stathopoulos. Earthquake induced torsion in buildings: critical review and state of art. *Proc. ASEM13*, Jeju Korea, 2013.

[13] De Stefano, M., Tanganelli, M., Viti, S. (2015) Torsional effects due to concrete strength variability in existing buildings. Earthquakes and Structures, Vol. 8, No. 2: 379-399.

[14] M. Tanganelli, S. Viti, M. De Stefano and A. Reinhorn. Influence of Infill Panels on the Seismic Response of Existing RC Buildings: A Case Study. *Seismic Behaviour and Design of Irregular and Complex Civil Structures*, 119-133, 2013.

[15] Itaca. (2008). Database of the Italian strong motions data. http://itaca.mi.ingv.it.

[16] C. Smerzini, C. Galasso, I. Iervolino and R. Paolucci. Ground motion record selection based on broadband spectral compatibility. *Earthquake Spectra*, 2013.

[17] I. Iervolino, C. Galasso, E. Cosenza. REXEL: computer aided record selection for code-based seismic structural analysis. *Bulletin of Earthquake Engineering*, **8**, 339-362, 2009.

[18] I. Iervolino, C. Galasso, E. Cosenza. Spettri, Accelerogrammi e le Nuove Norme Tecniche per le Costruzioni. *Progettazione Sismica*, **Vol. I(1)**, 33-50, 2009.

[19] SAP2000 Advanced. Version 14.0.0, Structural analysis program. Analysis reference manual. *Computer and Structures*, Inc. Berkley, California, USA, 2009.

COMPDYN 2015
5th ECCOMAS Thematic Conference on
Computational Methods in Structural Dynamics and Earthquake Engineering
M. Papadrakakis, V. Papadopoulos, V. Plevris (eds.)
Crete Island, Greece, 25–27 May 2015

THE EFFECTS OF THE AXIAL LOAD VARIATION ON THE SEISMIC PERFORMANCE OF EXISTING RC BUILDINGS

V. Mariani[1], M. Tanganelli[1], S. Viti[1], M. De Stefano[1]

[1] University of Florence, Department of Architecture (DiDA)
Piazza Brunelleschi, 6 – 50121 Firenze
e-mail: {valentina.mariani, marco.tanganelli, viti, mario.destefano}@unifi.it

Keywords: RC framed structures, seismic assessment, axial load sensitivity, concrete strength variability.

Abstract. *It is well known that the axial load plays an important role in the evaluation of the structural capacity of RC columns. In existing buildings this problem can be even more relevant than in new ones, since the material can easily present poor mechanical properties. The paper is aimed at investigating the role of the axial load variation on the seismic performance of RC columns, evaluated in terms of limit chord rotation and shear force, according to the EC8 provisions. The study is developed with reference to a case-study, which is a doubly symmetric 4-storey RC building. A dynamic (time history) analysis has been performed by adopting a fiber model for the cross section of the concrete members, to determine the structural response under the assumed seismic excitation. An ensemble of 7 ground motions, spectrum-compatible with the elastic spectrum provided by EC8 has been assumed as seismic input. The combined effects of the strength variability and axial load variation have been checked on the seismic performance of the columns of the 1st storey, which presented the higher levels of compression and axial load variation.*

1 INTRODUCTION

The axial load variation influences both the seismic demand and capacity of RC members [1-3], and therefore it is a relevant factor in the seismic performance evaluation [4-6]. Existing RC buildings are even more sensitive to the axial load variation than the new ones, since the material can easily present poor and uncertain mechanical properties. Moreover, the joints of existing buildings have been usually designed without specific confinement provisions, so resulting very sensitive to the reduction in ductility related to the increase of axial load [7-8].

Both the axial load variation and the concrete strength variability can largely affect the seismic performance of RC buildings. Their combined effect, therefore, can be even more important in such evaluation. This paper is aimed at investigating the combined effect of the concrete strength variability and the axial load variation on the seismic performance of RC structures. The study is carried out with reference to a case-study, i.e. a doubly symmetric 4-storey RC building [9-13], representing a typical example of pre-seismic code structure.

The seismic response of the case-study has been evaluated in terms of chord rotation and shear force of the RC members, by performing a time-history analysis with reference to two different limit states, i.e. the Damage Limitation (*DL*) and the Significant Damage (*SD*). The assumed seismic input is made of seven ground motions, whose elastic spectra fit very closely the elastic spectrum provided by Eurocode 8 (EC8) for the assumed soil type (B type).

The capacity of the structure has been found by accounting for the axial load in each considered member. On the basis of the concrete *mean* strength, two different alternative assumptions have been made to describe the members capacity. In the first one, the design value of compressive strength to be used in the analysis has been found by following the EC8 approach, i.e. by introducing a Confidence Factor (CF) based on the achieved knowledge level. In the second approach, instead, a hypothetical Gaussian distribution of the compressive strength has been assumed, considering the experimental *mean* value and different Coefficients of Variation (*CoV*). Three different *CoV* values, respectively equal to 15%, 30% and 45%, consistent with a large database of experimental values [14-15] have been assumed in the analysis. Each strength distribution has been discretized into seven percentile values, respectively equal to 5%, 10%, 20%, 50%, 80%, 90% and 95% [13, 16].

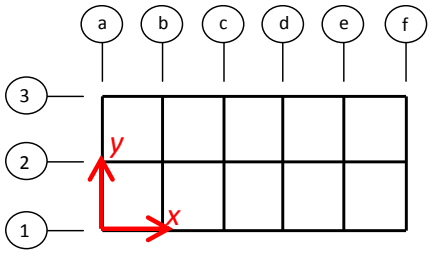
The seismic performance is expressed as the ratio between demand (D) and capacity (C) as a function of the variable axial load in each column. Due to the applied acceleration train, in fact, the axial load in each column ranges around an initial value, i.e. the axial load related to the gravity loads. The range of axial load experienced by each member is considered to define a range of capacity. By comparing the obtained results, the sensitivity of the seismic performance to the axial load variation has been checked, and the role played by the concrete strength assumptions has been discussed.

2. THE ANALYSIS

The sample structure [13], shown in Fig. 1, is a 4-story 3D reinforced concrete frame, symmetric along both *x* and y directions, with two 4.5 m long bays in the *y*-direction and 5 bays 3.5 m long in the *x*-direction, designed for vertical loads only. The concrete has been assumed to have a *mean* strength equal to 19.36 MPa, while for the reinforcement, the Italian FeB38k steel (yield stress over 375 MPa, ultimate stress over 430 MPa) has been assumed.

The *mean* values of concrete and steel strength have been assumed in the analysis for seismic response assessment, while the capacity of the case study has been evaluated considering two different assumptions for the concrete strength: the first one refers to the conventional EC8 approach, which requires to reduce the *mean* strength value by a *CF*, equal to 1.00, 1.20 or 1.35

respectively, depending on the knowledge level (KL3, KL2 and KL1) of the structure. The second one provides for a Gaussian representation of the probabilistic distribution of the concrete strength. In the Gaussian representation, the strength domain is defined [11-13] with reference to an extensive experimental campaign carried out by the Tuscan Regional Government [14-15]; a single *mean* strength, i.e. the EC8 value for *CF*=1.00 has been assumed, while three different *CoVs*, respectively equal to 15%, 30% and 45% have been considered. For each *CoV*, a sample of seven concrete strength values, corresponding to the percentiles of 5%, 10%, 20%, 50%, 80%, 90% and 95% has been assumed for the definition of columns capacity.



columns			beams		
dimensions	reinforcement		dimensions	reinforcement	
(cm)	long	transv.	(cm)	long	transv.
30x30	8 ϕ14	ϕ6/20 cm	30x50	3+3 ϕ12	ϕ8/20’

Figure 1 Plan configuration of the case-study and structural features of the RC members.

The seismic response of the case-study has been found by performing a nonlinear dynamic (time history) analysis through the computer program Seismostruct [17]. A fiber model has been adopted to describe the cross sections; the model by Mander [18] has been assumed for the core concrete, a three-linear model has been assumed for the unconfined concrete, and a bilinear model has been assumed for the reinforcement steel. The stiffness of floor slabs has been modelled by introducing a rigid diaphragm.

The seismic input has been defined by a set of 7 ground motions whose mean spectrum closely fits the EC8 elastic one (soil-type B). The records, described in Table 1, have been selected by the data-base Itaca [19], on the basis of a PGA equal to 0.25g, a nominal life of the structure of 50 years and a magnitude between 5.5 and 6.5.

Table 1. Ground motions data.

Name	Location	Date dd/mm/yyyy	PGA (g)	Duration (sec)
Irpinia	Sturno	23/11/1980	0.225	70.75
Irpinia	Calitri	23/11/1980	0.174	85.99
L’Aquila	Colle Grilli	06/04/2009	0.446	100.00
L’Aquila	Aquil Park Ing 1	06/04/2009	0.353	100.00
L’Aquila	Aquil Park Ing 2	06/04/2009	0.330	100.00
L’Aquila	Centro Valle 1	06/04/2009	0.545	100.00
L’Aquila	Centro Valle 2	06/04/2009	0.657	100.00

Two different limit states have been assumed in the present paper: the Damage Limitation (*DL*) and the Significant Damage (*SD*) limit states. According to EC8 provisions, the response parameter to be checked for the serviceability limit states is the chord rotation only, while both chord rotation and shear force must be checked for ultimate limit states. Therefore, in the present paper, a limit value corresponding to the yield chord rotation has been assumed for the *DL* limit state, while two limit values, based respectively on the ultimate chord rotation and ultimate shear force, have been assumed for the *SD* limit state. Both *DL* and *SD* limit values are strictly dependent on the axial load level in the RC members.

3 THE SEISMIC PERFORMANCE OF THE 1ST STOREY COLUMNS

3.1 The seismic demand

Fig. 2 shows the global response of the case study in terms of maximum drift, maximum shear force and maximum axial load variation (ΔN). All local results refer to the 1st storey columns, since they are the most affected by ΔN. The column drift, under the assumption of shear type behavior, can be assumed as coincident to the chord rotation, i.e. the assumed response quantity. Since the effects of ΔN are very sensitive to the initial amount of compression, it's important to check such variation for each single column.

Fig. 3 shows the maximum N (grey bars) and minimum N (white bars) experienced by each column of the case-study. The horizontal line in each figure represents the reference static axial load. Since, in each frame, the internal columns (column lines *b*, *c*, *d* and *e*) and the side ones (column lines *a* and *f*) respectively experience almost the same ΔN (see [12]), in Fig. 3 only the results of two columns for each frame have been shown, together to the static axial load of the two (side and internal) columns. It should be noted that, despite the building is symmetric along both main axes, ΔN is not the same in the two side frames (frames 1 and 3).

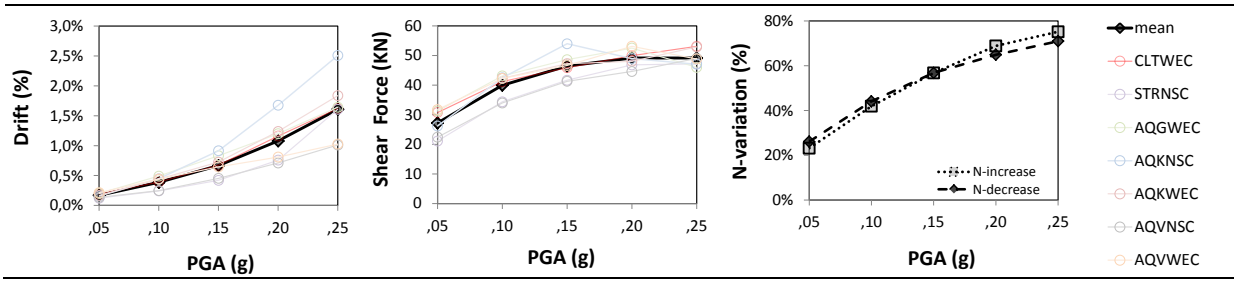


Figure 2. Seismic response of the case study.

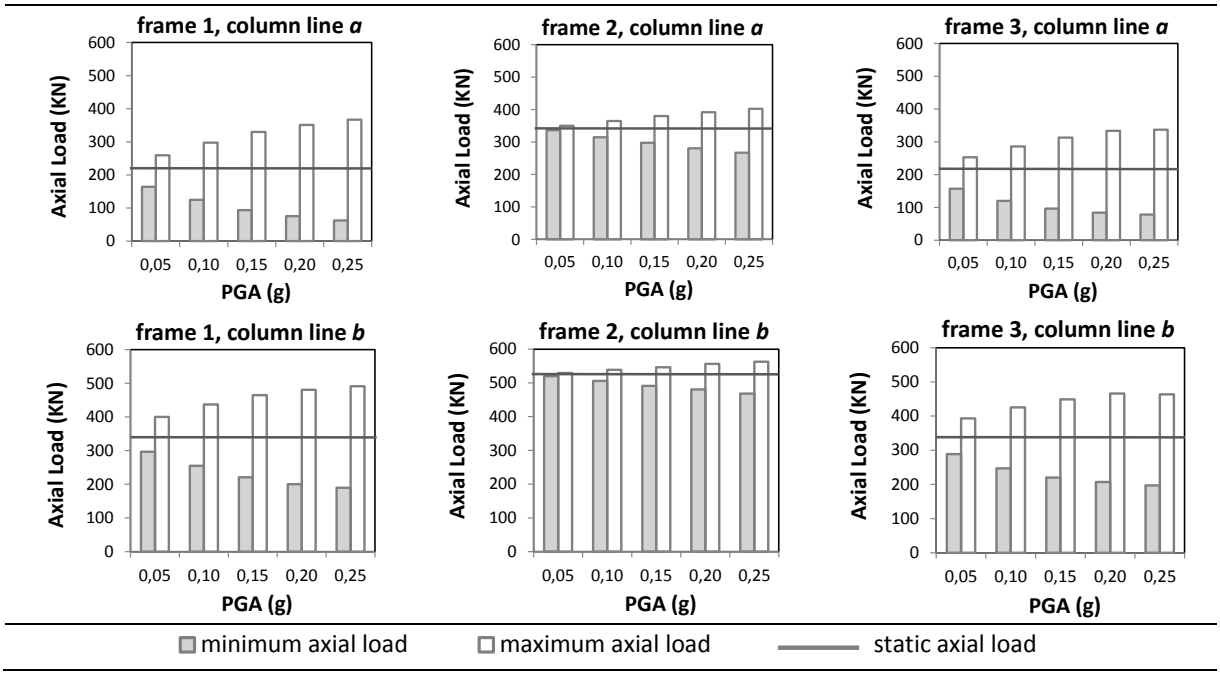


Figure 3. Axial load variation in the columns.

3.2 The seismic capacity

In this section, columns structural capacity is evaluated as a function of the axial load level, assuming both a variable concrete strength and the approach ofEC8 provisions. Figs 4 and 5 show, respectively, the sensitivity of the chord rotation and shear force capacities to the axial load variation for *DL* and *SD* limit states.

In each graph, the colored lines represent the domains related to the percentile values describing the assumed strength distribution related to the three different *CoV* values, while the black dashed ones represent the capacities provided by EC8. The domains have been interrupted in correspondence of the axial force capacity of the structural section. As can be noted, the range of capacities provided by EC8 is relevantly smaller than the one obtained when the probabilistic strength variability is considered, even for the lowest assumed *CoV* (*CoV* = 15%). For higher values of *CoV*, more likely to be found in existing buildings [9-10, 14], the difference between the two ranges is even more relevant.

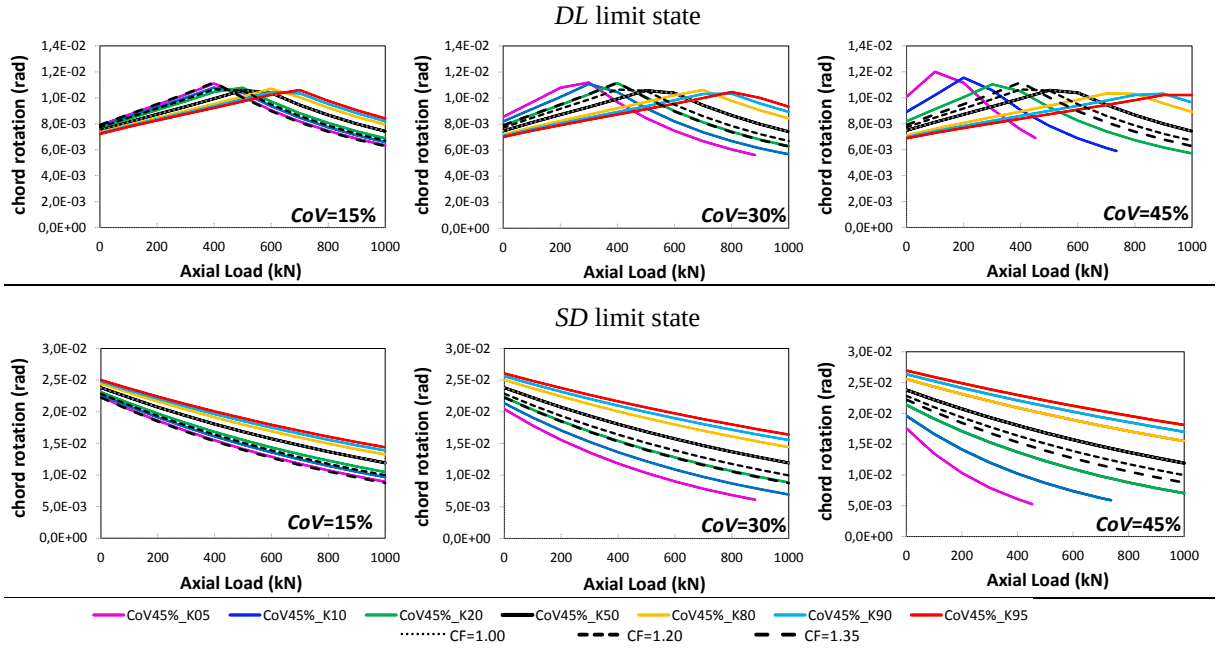


Figure 4. Sensitivity of the *DL* and *SD* chord rotation capacity of columns to the axial load variation.

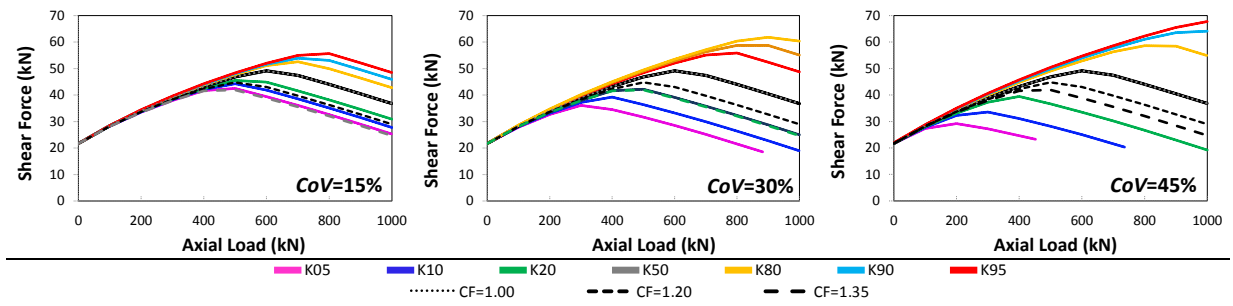


Figure 5. Sensitivity of the Shear Force capacity of columns to the axial load variation (*SD* limit state).

4 THE SEISMIC PERFORMANCE

The seismic performance has been quantified as the ratio between the demand (D) and the capacity (C) of each column at the first storey. The sensitivity of the seismic performance to the axial load variation has been investigated with reference to both *DL* and *SD* limit states.

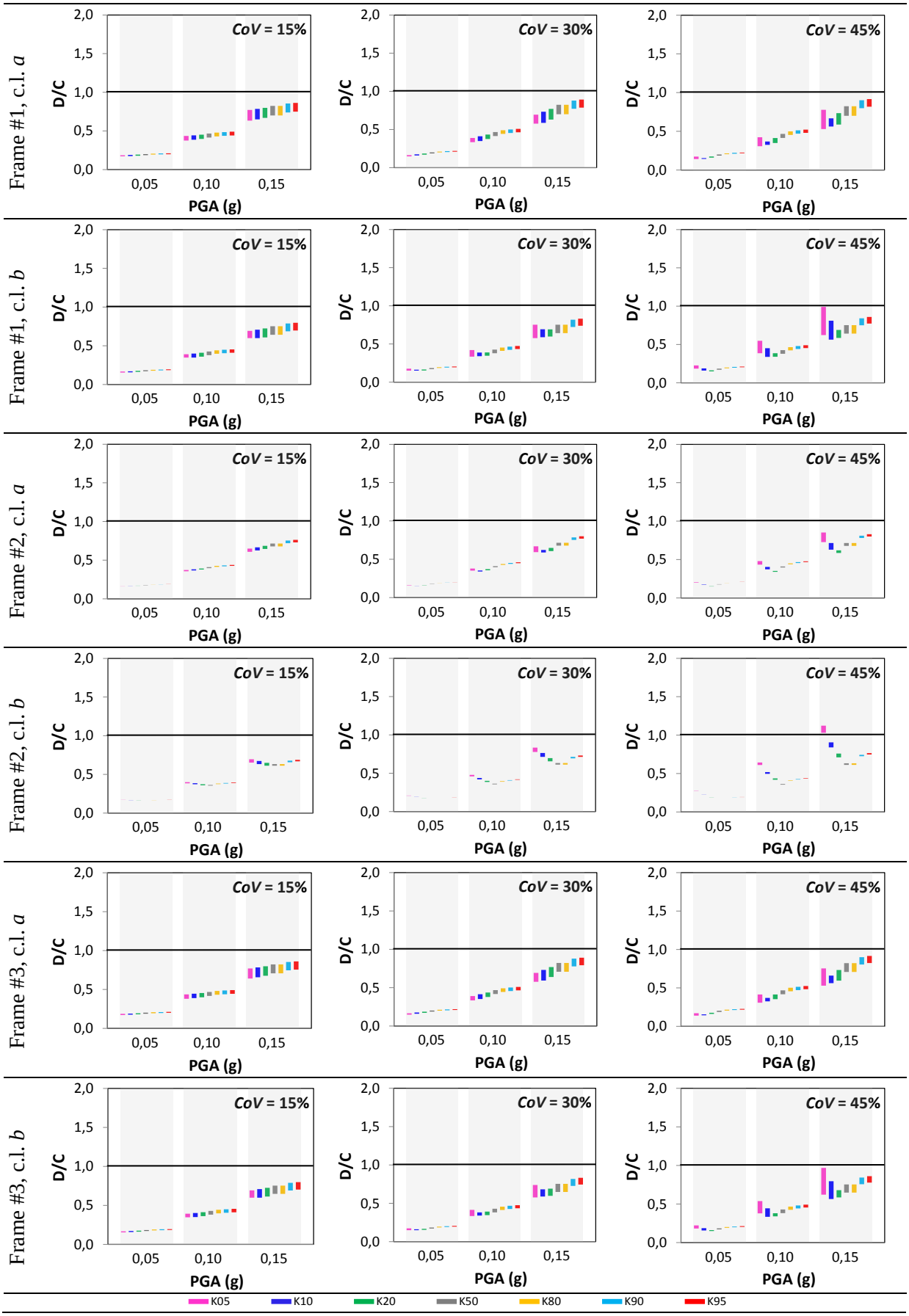


Figure 6. *DL* limit state: performance ranges in terms of chord rotation.

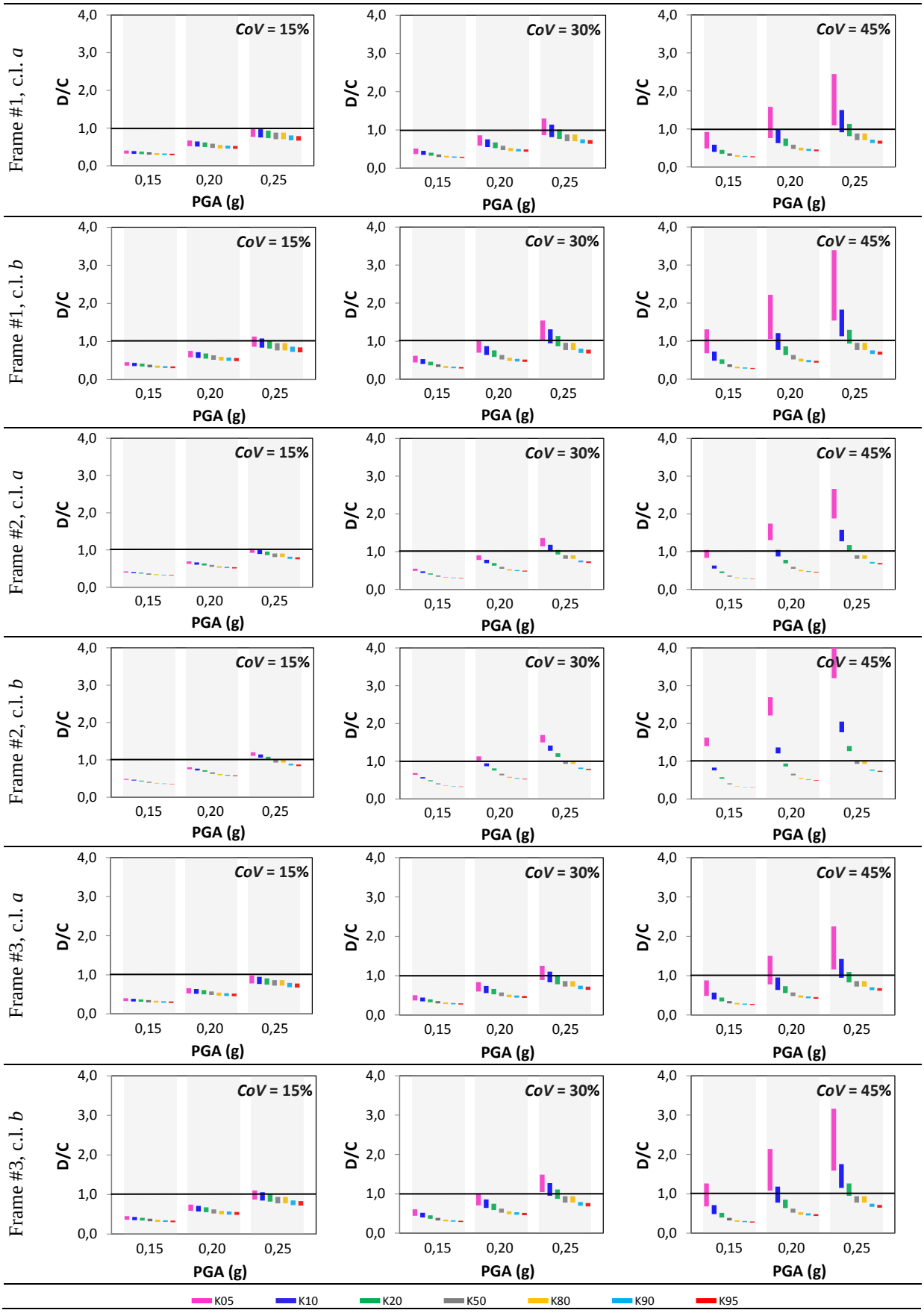


Figure 7. *SD* limit state: performance ranges in terms of chord rotation.

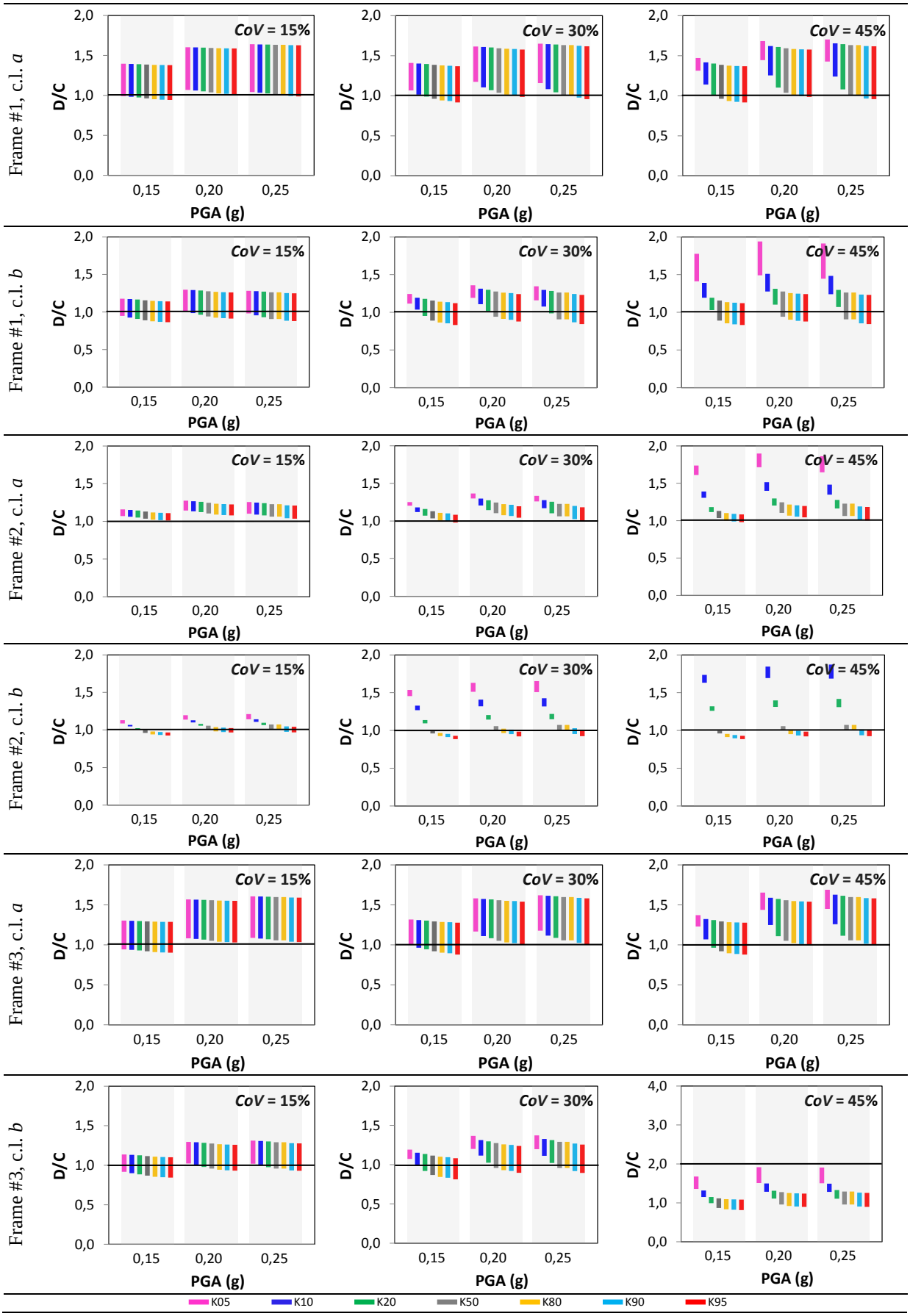


Figure 8. *SD* limit state: performance ranges in terms of shear force.

DL limit state has been verified for PGAs up to 0.15g, while *SD* limit state has been checked for PGA values ranging between 0.15g and 0.25g. For each column the actual range of axial load has been considered in the capacity only, while the seismic demand (chord rotation and shear force respectively) has been assumed with its maximum value. Consequently, for each PGA, a range of values is found for the seismic performance; the amplitude of the range, therefore, can be read as an index of the sensitivity of the seismic performance to ΔN. For sake of brevity, only results referred to two columns for each frame have been shown, belonging to the column lines *a* (side column) and *b* (internal column). Figure 6 shows the D/C ranges found, in terms of chord rotation, for the *DL* limit state. The strength variability largely affects the sensitivity of the seismic performance to the axial load variation. For PGA = 0.15g the case-study exceeds the limit state provided by EC8 only when the lowest percentile of concrete strength and the highest *CoV* are assumed (Frame#2 c.l. b).

The *SD* limit state has been investigated in terms of both chord rotation and shear force. Figure 7 shows the ranges of D/C found for the *SD* limit state in terms of chord rotation. The ranges between minimum and maximum D/C values related to ΔN are much larger than in the *DL* limit state, showing a higher sensitivity of the *SD* seismic performance to the axial load variation. Such sensitivity is relevant especially in the side frames (frames 1 and 3), and it increases when low values of concrete strength are assumed. With reference to the current case-study, when a low concrete strength is assumed, i.e. for high variability (*CoV* = 45%) and low percentiles (K_{05}, K_{10}), ΔN involves an increase of the D/C ratio up to three times the value found by assuming the *mean* strength and exceeding the required limit.

Figure 8 shows the D/C ranges found in terms of shear force. They significantly differ from the ones found in terms of chord rotation as regards the role of the concrete strength on the sensitivity to the axial load variation. The performance ranges expressed in terms of shear force, in fact, are larger for the higher values of concrete strength, especially for high levelsof axial load experienced by the columns.

CONCLUSIONS

In this paper the effects of the axial load variation on the seismic performance of RC structures have been investigated with reference to a case-study, i.e. a 4-storey RC framed building, symmetric about both main directions. The seismic performance, checked at the 1st storey columns, has been measured as the ratio between demand (D) and capacity (C). The capacity of each column has been found at the varying of the axial load and by considering different values of concrete strength, respectively consistent to the EC8 approach and to a probabilistic strength distribution, having the same *mean* value and three different *CoV*s. The capacity has been found for both the *DL* limit state (in terms of chord rotation) and for the *SD* limit state (in terms of chord rotation and shear force).

For each column, a range of D/C has been found by considering the maximum response found by the time-history analysis and the range of capacity corresponding to the axial load range experienced during the seismic response. The width of each D/C range expresses the sensitivity of the column performance to the axial load variation.

As regards the *DL* limit state, the sensitivity of the seismic performance to ΔN is significant only in the side frames for the highest considered PGA (equal to 0.15g), while the value of the concrete strength has a significant effect in most cases. The case-study complies the EC8 requirements in almost all cases; only when the highest value of *CoV* (*CoV* = 45%) is

assumed together with lowest strength percentile (5%), for PGA=0.15g the internal columns belonging to the three frames may present D/C values higher than unity.

The *SD* limit state verification in terms of chord rotation pointed out a high sensitivity of the seismic performance to the axial load variation. Such sensitivity, more relevant in the side frames, increases for low values of concrete strength. For low strength values, i.e. for high variability and low percentiles (K_{05}, K_{10}), the axial load variation plays a crucial role in the seismic performance of the structure, inducing an increase of the D/C ratio up to three times the one obtained adopting the *mean* strength value, i.e. by assuming EC8 procedure. In the internal columns, where the amount of axial load is higher, the D/C ratio varies between 0.7 and 4.0, depending on the assumed concrete strength percentage and the axial load level.

The performance ranges expressed in terms of shear force present a different trend comparing to the other ones, being larger for the higher values of concrete strength, especially for high amount of axial load experienced by the columns.

The obtained results evidenced the important role played by the axial load variation on the evaluation of the seismic performance of structures, underlining the relationship between the effects of axial load variation and the effective concrete strength. Both factors, i.e. the effective amount of axial load during the seismic response of the structure, and a more realistic description of the concrete strength distribution should be carefully evaluated in order to assess the seismic performance of existing buildings.

REFERENCES

[1] M.A. Saadeghvaziri. Nonlinear response and modeling of RC columns subjected to varying axial load. *Engineering Structures*, **Vol. 19, No. 6**, 417-424, 1997.

[2] K. ElMandooh Galal, A. Ghobarah. Flexural and shear hysteretic behaviour of reinforced concrete columns with variable axial load. *Engineering Structures* **Vol. 25, Issue 11**, 1353-1367, 2003.

[3] H. Ousalem, T. Kabeyasawa and A. Tasai. Evaluation of ultimate deformation capacity at axial load collapse of reinforced concrete columns. *13th WCEE*, Vancouver, B.C., (Canada), 2004

[4] R. Abbasnia, N. Mirzadeh and K. Kildashti. Assessment of axial force effect on improved damage index of confined RC beam-column members. *International Journal of Civil Engineering*, **Vol. 9, No. 3**, 237-246, 2011.

[5] Y.J. Kim, H.M. Shin, T.H. Kim. Seismic performance assessment of reinforced concrete bridge columns under variable axial load. *Magazine of Concrete Research* - **59(2)**, 87-96, 2007.

[6] J.K. Elwood and J.P. Moehle. Axial Capacity Model for Shear-Damaged Columns. *ACI Structural Journal* **Vol. 102, Issue 4**, 578-587, 2005.

[7] U. Akguzel, S. Pampanin. Effects of Variation of Axial Load and Bidirectional Loading on Seismic Performance of GFRP Retrofitted Reinforced Concrete Exterior Beam-Column Joints. *Journal of Composites for Construction* **14(1)**, 2010.

[8] A. Masi, G. Santarsiero, A. Mossucca, D. Nigro. Influence of Axial Load on the Seismic Behavior of RC Beam-Column Joints with Wide Beam. *Applied Mechanics and Materials* **Vol. 508**, 208-214, 2014.

[9] M. De Stefano, M. Tanganelli, S. Viti. Effect of the variability in plan of concrete mechanical properties on the seismic response of existing RC framed structures. *Bull Earthquake Eng* **11**, 1049–1060, 2013.

[10] M.De Stefano, M. Tanganelli, S. Viti. On the variability of concrete strength as a source of irregularity in elevation for existing RC buildings: a case study. *Bull Earth. Eng.* **vol. 11 Issue 5**, 1711-1726, 2013.

[11] M. De Stefano, M. Tanganelli, S. Viti. Variability in concrete mechanical properties as a source of in-plan irregularity for existing RC framed structures. *Engineering Structures*, **vol. 59**, 161-172, 2014.

[12] M. De Stefano, V. Mariani, M. Tanganelli, S. Viti. The influence of the axial load variation on the seismic capacity of existing RC buildings. *Proc. 2 European Conference on Earthquake Engineering*, Istanbul 2014.

[13] M. De Stefano, V. Mariani, M. Tanganelli, S. Viti. Torsional effects due to concrete strength variability in existing buildings. *Earthquake and Structures*, **Vol. 8, No. 2**: 379-399, 2015.

[14] M.T. Cristofaro. Metodi di valutazione della resistenza a compressione del calcestruzzo di strutture in c.a. esistenti. *PhD Dissertation*, Università di Firenze, 2009.

[15] M.T. Cristofaro, A. D'Ambrisi, M. De Stefano, R. Pucinotti, M. Tanganelli. Studio sulla dispersione dei valori di resistenza a compressione del calcestruzzo di edifici esistenti. *Il giornale delle prove non distruttive, monitoraggio, diagnostica*, **vol. 2**, pp. 32-39, 2012.

[16] M.,De Stefano, M., Tanganelli, S. Viti. Seismic performance sensitivity to concrete strength variability: a case-study . *Earthquake and Structures* (in press).

[17] Seismostruct Version 5.2.2 - A computer program for static and dynamic nonlinear analysis of framed structures. Available online from URL: www.seismosoft.com.

[18] J.B. Mander, M.J.N. Priestley, R. Park. Theoretical stress-strain model for confined concrete. *Journal of the Structural Division ASCE*, **vol. 114**, 1804-1826, 1988.

[19] Itaca. Database of the Italian strong motions data. http://itaca.mi.ingv.it, 2008.

COMPDYN 2015
5th ECCOMAS Thematic Conference on
Computational Methods in Structural Dynamics and Earthquake Engineering
M. Papadrakakis, V. Papadopoulos, V. Plevris (eds.)
Crete Island, Greece, 25–27 May 2015

IMPROVED FRAGILITY FUNCTIONS FOR RC BRIDGE POPULATIONS

C. Zelaschi[1], R. Monteiro[1] and R. Pinho[2]

[1] IUSS Pavia
Palazzo del Broletto, Piazza della Vittoria n. 15, 27100 Pavia (Italy)
e-mail: ricardo.monteiro@iusspavia.it

[2] University of Pavia, Department of Civil Engineering and Architecture
Via Ferrata n. 1, 27100 Pavia (Italy)
e-mail: rui.pinho@unipv.it

Keywords: Seismic assessment, RC Bridges, Populations, Networks, Fragility curves, Scalar and vector Intensity measures.

Abstract. *When carrying out loss assessment of a road network within a certain region, the characterization of the vulnerability of the existing population of bridges is one of the most relevant aspects. To such extent, in the last decades, the engineering community has recognised fragility curves as one of the fundamental and most effective tools in seismic risk assessment, correlating the probability of exceeding of specific limit states, which can instead be correlated with damage and loss, for different levels of intensity measures (IMs). The available literature mainly provides such curves as function of peak ground acceleration (PGA) or spectral acceleration (S_a), often preferred for the availability of national hazard information in terms of such parameters. However, when dealing with a bridge population of reinforced concrete bridges, Fajfar Index, peak ground velocity and root mean square velocity have been recently identified as the most promising intensity measures, in terms of efficiency, proficiency and sufficiency, notwithstanding the acceptable performance of PGA and S_a. As such, this paper intends to further extend the analysis of RC populations of bridges by providing a statistically sound comparison of analytical fragility curves based on traditional and innovative intensity measures of an extensive bridge population. Nonlinear static analyses of 3D RC bridge models are carried out. The bridge population is randomly generated using Latin Hypercube sampling in order to include geometrical variability, in addition to aleatory and epistemic uncertainties. For what concerns the seismic ground motion, a proper selection of records was performed, according to a recent selection and scaling procedure (Conditional Spectrum Method).*

1 INTRODUCTION

During the last decades, the engineering community has recognized fragility functions as fundamental tools for characterization of structural resilience due to their capability of establishing the link between seismic hazard of a certain site and the level of structural damage related to a certain seismic excitation. Even if the outcome of the most recent research in the structural fragility assessment field led to more complex methodologies for the definition of more accurate fragility curves, the lack of a unique approach for their evaluation leads to discrepancies in the results from varying initial assumptions [1]. In addition to the variability of the procedure itself, significant dispersion in seismic demand, epistemic and aleatory uncertainties are present throughout the entire process of development of fragility curves [2]. A great deal of effort has been witnessed in literature to deal with such sources of uncertainties: the logic trees for both seismic source models definition and the consideration of multiple ground motion prediction equations is only one example of the most popular strategies to face hazard variability problems. Indeed, new seismic record selection and scaling strategies arose from recent research [3] with the goal of reducing the main source of uncertainty associated to the seismic input, the record-to-record variability, which it is well known to have repercussions on the accuracy of seismic structural capacity and demand [1]. Moreover, within the process of fragility curve development, the selection of the intensity measure (IM) to be considered is a crucial aspect. Due to the nature of the earthquake record itself, the conventionally employed IMs, such as peak ground acceleration (PGA) or peak ground velocity (PGV), might not be able to take into account, as single scalars, all the information regarding the seismic signal, resulting in increased variability of the seismic structural demand. Accordingly, with a view to optimize the link between hazard and structural response, recent research [4, 5] considered different scalar IMs or couples of IMs, not only for studying the accuracy of the IM itself, but also for expressing fragility curves as function of such alternative variables.

Furthermore, most of the available literature considers building frames as case study for similar investigations, hence, to fill such gap, the present study focuses on reinforced concrete bridge structures, which are part of a road network system. In particular, a population of reinforced concrete bridges, randomly generated through Latin Hypercube sampling for including geometrical and material properties variability, already successfully employed in previous studies addressing RC bridges [6, 7], is considered to scrutinize the accuracy of fragility estimates as function of certain number of IMs with good performance in terms of efficiency, proficiency and sufficiency, such as Fajfar Index (Iv), peak ground velocity (PGV), root mean square velocity (vRMS) and spectral acceleration (Sa) [8]. Notwithstanding the optimal performance of the aforementioned IMs, the traditionally employed peak ground acceleration (PGA) is also considered as the vast majority of the available hazard information is expressed in terms of such ground motion characteristic.

Nonlinear static analysis was selected as an accurate tool for the identification of the performance point at different demand levels, validated in past studies concerning the seismic assessment of bridges and buildings through nonlinear static procedures [9-12]. As such, a reexamination of the N2 method [13-15] was featured in order to use response spectra derived from a set of selected real records. Fragility curves of the considered bridge portfolio were thus derived with different IMs with multiple stripes analysis, a methodology capable of including the variation of the ground motion records at different IMs levels, which was herein adjusted for application to structural portfolios. Finally, the dispersion level among the bridge portfolio for each IM-based fragility curve was assessed by means of statistical parameters that rapidly estimate the goodness-fit of the obtained fragility curve, enclosing in a single scalar the amount of dispersion between observed and fitted data.

2 BRIDGE POPULATION AND BRIDGE MODELLING

With a view to demonstrate the level of accuracy of different IM-based fragility curves in the expedite risk assessment of road networks, the case study considered in this paper does not focus on individual structural configurations but rather on a population of bridges that could represent a given bridge class, with different, yet statistically correlated, configurations. The endorsed methodology makes use of a parametric statistical characterization of Italian reinforced concrete bridges conducted in recent studies [6, 8]. One hundred bridges were randomly generated thorough Latin Hypercube sampling, which guarantees the reduction of computational onus when compared to other approaches, such as Monte Carlo, on the basis of the statistical distribution associated to the main geometrical and material properties shown in Table 1. As far as longitudinal and transverse reinforcement are concerned, the associated ratios were assumed to vary in the ranges of 0.5% - 1% and 0.08% - 0.1% respectively.

Parameter	Distribution	Distribution parameters
Pier height [m]	Lognormal	Mean (log): 1.95; std: 0.828
Total length of bridges	Lognormal	Mean (log): 5.10; std: 1.145
Span length [m]	Normal	Mean: 31.18; std: 11.527
Section Diameter	Normal	Mean: 2.19; std: 0.969
Reinforcement yield strength [N/mm2]	Normal	Mean: 504.40; std: 157.84
Reinforcement Young Modulus [GPa]	Normal	Mean: 203.82; std: 19.426
Concrete compressive strength [MPa]	Normal	Mean: 40.0; std: 7.44
Superstructure width	Lognormal	Mean: 2.49; std: 0.256
Number of spans	1.5+0.03*(Total length)	

Table 1: Statistical distribution properties [1, 7].

The cross section of the deck takes the form of rectangular reinforced concrete girders, which is consistent with real Italian bridges, in which the deck is simply supported in most cases. The abutments were modeled with bilinear response springs with stiffness sets as 26’329kN/m [16] along horizontal direction. Further details on the remaining modelling assumptions can be found in a previous study [8].

An automatized procedure was coded in Matlab [17] in order to automatically carry out nonlinear static analyses, i.e. pushover analyses, of the considered bridges in OpenSees software package [18]. The analysis considered the transverse direction only, with a load path proportional to the fundamental mode of each structure of the considered bridge population, whose transverse fundamental periods are represented in the histogram in Figure 1.

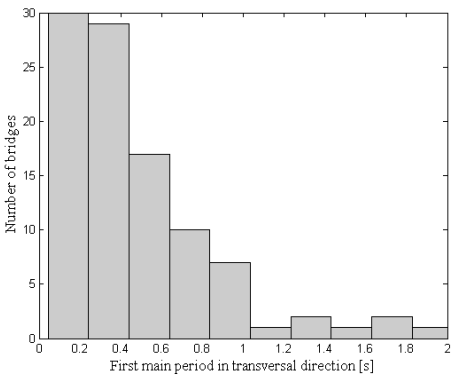


Figure 1: First transversal periods of the randomly generated bridges.

3 GROUND MOTION RECORDS

In addition to the geometrical and material variability, modeled in §2, the record-to-record variability [19] was also included in the computation of the fragility curves. Within an attempt to minimize the effects of such variability in the structural demand, a recent selection and scaling procedure known as conditional spectrum method (CSM) [2] was chosen, especially for its effectiveness in selecting a suite of ground motion records that match the ground motion characteristics at each intensity measure level. Given that the CSM foresees that the record selection is conditioned at the specific structural period, its employment required a certain level of simplification in order to accommodate the analysis of groups of structures with different periods within reasonable computational onus. Accordingly, the randomly generated bridges were grouped in three classes, defined by a central period of 0.2s, 0.3s and 0.75s.

Considering that the majority of the bridges are located in central regions of Italy, the target city of Campobasso (Molise region) was fully characterized in terms of seismic hazard. Hazard curves and disaggregation results conditioned at the spectral acceleration for the selected periods of vibration (0.2s, 0.3s and 0.75s) were undertaken with a ground motion prediction equation suitable for European regions [20] using Openquake [21]. The area source model information provided by the Italian zonation (ZS9) was adopted [22]. Such outcome was used to select and scale a set of 30 records for 15 different assumed intensity measure levels and for each class of fundamental period. The response spectra obtained for T=0.2s and for one of the intensity levels are shown in Figure 2.

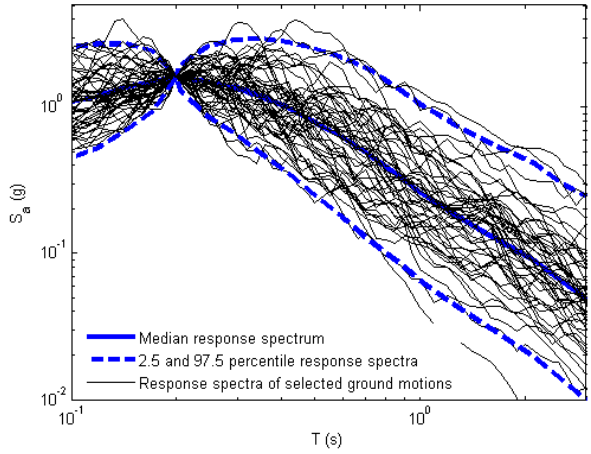


Figure 2: Response spectra of the selected input records with 10% probability of exceedance in 50 years for period bridge class 0.2s.

4 INTENSITY MEASURES

The selection of a proper intensity measure is very important for the reduction of the effects of the uncertainties that surround probabilistic seismic hazard analysis and nonlinear structural analysis. Reducing such uncertainties becomes even more important when dealing with the seismic loss assessment of a road network, in which there is the need to characterize the seismic behavior of different nodes, represented by bridges with different geometrical and material properties.

In line with the main findings of recent research [8], the Fajfar Index (I_v), peak ground velocity (PGV), root mean square velocity (vRMS), peak ground acceleration (PGA) and spectral acceleration (S_a) were selected as IMs to be considered in the derivation of fragility functions, due to their good performance in terms of efficiency, practicality, proficiency and sufficiency for the case of bridge populations. Moreover, the aforementioned IMs have the advantage of being easily obtained from earthquake characteristics. Coupling of IMs in vector

fashion was not taken into account due to the not relevant improvement in terms of efficiency, practicality and proficiency, to justify their employment in the assessment of bridge populations.

5 DAMAGE LIMIT STATES

The definition of the damage limit states is a crucial phase of the process of the fragility curve definition. In literature a wide variety of different damage limit states definitions can be found for seismic assessment of bridges; however, especially in case of the assessment of a bridge population, a global damage indicator seems more appropriate. Following the approach adopted in [23] the ductility in displacement was chosen as engineering demand parameter for the quantification of the damage of each pier and the maximum ductility over all the bridge piers was considered representative of the bridge behavior. Four different values of curvature ductility, shown in Table 2, were used for the definition of the considered levels of damage: slight, moderate, extensive and collapse [24, 25].

Slight (DS1)	Moderate (DS2)	Extensive (DS3)	Collapse (DS4)
1.29	2.10	3.52	5.24

Table 2: Damage limit states in terms of curvature ductility [23].

According to Equation (1) and Equation (2), proposed by Priestley et al. [26], the expected displacement ductility of each bridge pier was calculated as function of curvature ductility, $\mu_{\emptyset}$, and then compared with the values associated to each damage limit state.

$$\mu_{\Delta} = 1 + 3(\mu_{\emptyset} - 1)\left(l_p/l\right)\left[1 - 0.5\left(l_p/l\right)\right] \quad (1)$$

$$l_p = 0.08l + 9d_b \quad (2)$$

Where l_p is the plastic hinge length, l is the pier height and d_b the longitudinal reinforcement bar diameter.

6 NONLINEAR STATIC PROCEDURE

The development of fragility curves for a bridge population requires the allocation of each structure to a certain damage limit state, according to the given definition. As such, when using a nonlinear static procedure (NSP) to estimate the demand, the target displacement corresponding to each couple of the considered pushover curve and response spectrum needs to be identified. Seismic guidelines all over the world are already employing NSPs as simplified approaches for assessing seismic response of structures. A great deal of effort has been done in the last decades to approach with more accuracy the results of dynamic analyses, which, when properly used, is considered the most reliable way for predicting structural response along the entire duration of the seismic excitation. However, required computational time demand could represent an obstacle in the view of the development of rapid methodologies for deriving fragility curves, also when limited information available from national structures inventory.

In agreement with such context and despite the drawbacks of considering simplified approaches rather than dynamic response analyses, such as the impossibility of reproducing phenomena of viscous damping, strength deterioration or of considering deformations, the seismic behavior of the considered bridge population was evaluated through a conventional pushover based nonlinear static procedure – N2. The choice for N2 was based on the findings of a recent study regarding the accuracy in the fragility estimates using different approaches

to derive analytical fragility curves [23], which demonstrated that N2 [15], when compared to nonlinear dynamic analysis, provides accurate results for low and high intensity levels.

Pushover analyses were thus performed for each bridge of the three considered classes applying a load pattern proportional to the first transverse mode and the pier top closest to the deck center of mass as controlling point. The corresponding curves exhibited considerable dispersion, something that strengthens the motivation of modelling a set of bridges with the inclusion of geometrical and material properties variability.

Some specificities of the N2 method are the use of inelastic spectra and the fact that an elasto-perfectly plastic force-displacement relationship for the linearization procedure is assumed. In addition, the definition of the target displacement distinguishes between short-period and medium/long period based on the corner period (T_s), according to Figure 3.

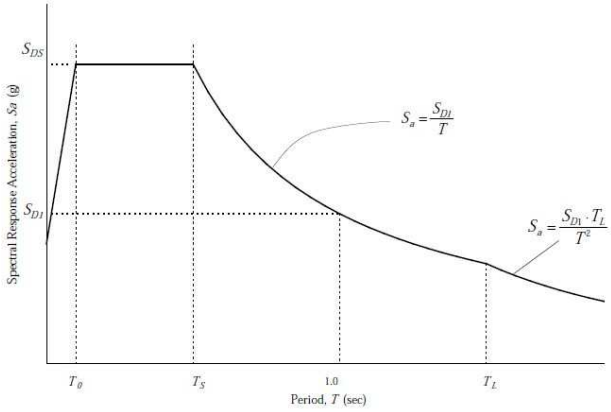


Figure 3: Design response spectrum [27].

Even though the corner period T_S is not easily predictable in a spectrum directly derived from real records, the latter were nevertheless considered for consistency with seismic hazard outcomes and observations regarding record variability. The corner period was identified according to Equations (3) and (4), where S_{DS}, the design spectral response acceleration parameter at short periods, was assumed as the highest spectral acceleration obtained from each real scaled record. S_{D1} is the design spectral response acceleration parameter at 1-second period.

$$T_0 = 0.2S_{D1}/S_{DS} \tag{3}$$

$$T_s = S_{D1}/S_{DS} \tag{4}$$

For each bridge of each period class (0.2, 0.3, 0.75), the steps of the conventional N2 method were followed, transforming the correspondent pushover curve, referred to a multi degree of freedom (MDOF) system, in the equivalent curve of the associated single degree of freedom (SDOF) system. The bilinerization was conducted assuming as the ultimate and yielding force the 0.85 of the peak value, which ensured a more reliable approximation of the first branch of the curve when an automatize procedure is used. The performance points could be identified along the SDOF first and MDOF after, according to the equations proposed in Eurocode 8 [13]. The entire procedure was repeated for each of the 30 selected records and for 15 intensity measure levels.

7 FRAGILITY CURVES FOR BRIDGE POPULATIONS

Once all the performance points are known and compared to the selected damage limit states, a methodology for the derivation of the fragility curve needs to be selected. Among the different approaches that can be found in literature, the multiple stripes analysis [28] tech-

nique was considered the most appropriate. Such procedure is the most suitable when different ground motions at different intensity measure levels are used, which typically occurs when the conditional spectrum method is used: the representative ground motions change at each intensity measure level because the target properties follow the same trend. The main advantage of such approach is that there is no need for reaching the intensity measure level for which structural collapse occurs for all records. The most suitable fitting technique is the maximum likelihood method [29-31], however, also the alternative procedure used for estimating fragility function parameters of multiple stripes analysis, which consists in the minimization of the sum of the squared errors (SSE), was taken into account.

The aforementioned procedure typically considers an individual structure subjected to a certain number of ground motions and, at each intensity measure level, counts the number of collapses out of the total number of ground motions. Given that the objective of the present study was to define a fragility curve referred to a set of bridges of a specific class, the procedure was adapted to fit such need. In fact, the fractions of each damage limit state were obtained counting, for each record of each IML, the number of bridges that attained or exceeded the considered damage limit state out of the total number of bridges of the considered class. Assuming that the observations of the achievement of a certain damage limit state or not for each bridge and for each spectrum is independent of the observations from other bridges and ground motions, the probability attaining or the exceeding the considered damage limit state is given by a binomial distribution, as in Equation 5.

$$P\left(e_{ij}\ exceedances\ DLS\ of\ n_{ij}\ bridges\ for\ record_{ij}\right) = \binom{n_{ij}}{e_{ij}} p_{ij}^{e_{ij}} (1-p_{ij})^{n_{ij}-e_{ij}} \quad (5)$$

Where p_i is the probability that the ground motion *i* at intensity level *j* will cause the attainment or exceedance of damage limit state DLS of the considered structure.

In order to get the highest probability of attaining or exceeding the considered damage limit state obtained from structural analysis, the product of the binomial probabilities of each record at each IML is considered to get the likelihood of the entire data set, which need to be maximize in order to obtained fragility function parameters. More easily, the logarithm of the likelihood function of Equation (6) can be maximized according to Equation (9).

$$Likelihood = \prod_{k=1}^{ij} \binom{n_k}{e_k} p_k^{e_k} (1-p_k)^{n_k-e_k} \quad (6)$$

The likelihood function takes *ij* values, considering each record at each intensity measure and Π indicates the product over all *ij* levels.

Considering that the lognormal cumulative distribution of Equation (7) is commonly used to express fragility functions, when combined with Equation (6), it takes the form of Equation (8), where $P(DS|IM = x)$ is the probability that a certain ground motion with $IM = x$ will cause in the structure the attainment or exceedance of the considered damage state (DS), $\Phi(\cdots)$ is the standard normal cumulative distribution function (CDF), and θ and β are the median of the fragility function and the standard deviation of *ln(IM)* respectively.

$$P(DS|IM = x) = \Phi\left(\frac{\ln\left(x/\theta\right)}{\beta}\right) \quad (7)$$

$$Likelihood = \prod_{k=1}^{ij} \binom{n_k}{e_k} \Phi\left(\frac{\ln\left(x_k/\theta\right)}{\beta}\right)^{e_k} \left(1 - \Phi\left(\frac{\ln\left(x_k/\theta\right)}{\beta}\right)\right)^{n_k-e_k} \quad (8)$$

$$\{\hat{\theta},\hat{\beta}\} = argmax_{\theta,\beta} \sum_{k=1}^{ij} \left\{ \ln \binom{n_k}{e_k} + e_k \ln \Phi\left(\frac{\ln\left(x_k/\theta\right)}{\beta}\right) + (n_k - e_k) \ln\left(1 - \Phi\left(\frac{\ln\left(x/\theta\right)}{\beta}\right)\right)\right\} \quad (9)$$

$\hat{\theta}$ and $\hat{\beta}$ denotes the estimates of fragility function parameters, θ and β respectively.

According to the previous variable definitions, the alternative method adopted, SSE, is given by Equation (10).

$$\{\hat{\theta},\hat{\beta}\} = argmin_{\theta,\beta} \sum_{k=1}^{ij} \left(\frac{e_k}{n_k} - \Phi\left(\frac{\ln\left(x_k/\theta\right)}{\beta}\right)\right)^2 \quad (10)$$

8 RESULTS

8.1 Fragility curves

Fragility function estimates were derived according to either the maximum likelihood algorithm or the minimization of the sum of the squared errors, as described in §7, referring to global displacement ductility as the highest among the piers of each bridge.

Different curves were derived for bridge classes of 0.2, 0.3, 0.75s for five different IMs (I_v, PGV, PGA, PGV, vRMS, S_a) and are illustrated in Figure 4 and 5 for both MLE and SSE fitting algorithms together with fractions, obtained considering each record and counting the number of bridges of a specified class attaining or exceeding the correspondent damage limit state out of the total number of bridges.

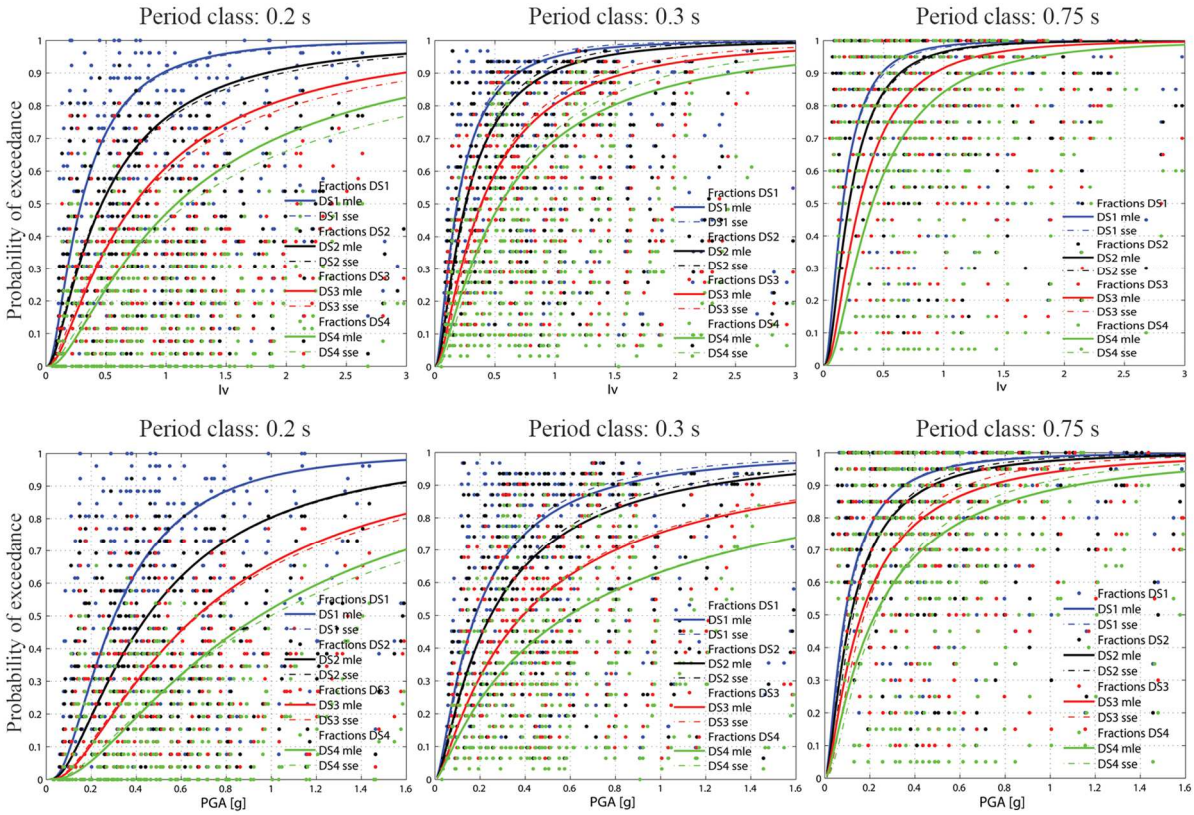


Figure 4: Fragility curves in terms of I_v and PGA for period classes 0.2s, 0.3s and 0.75s.

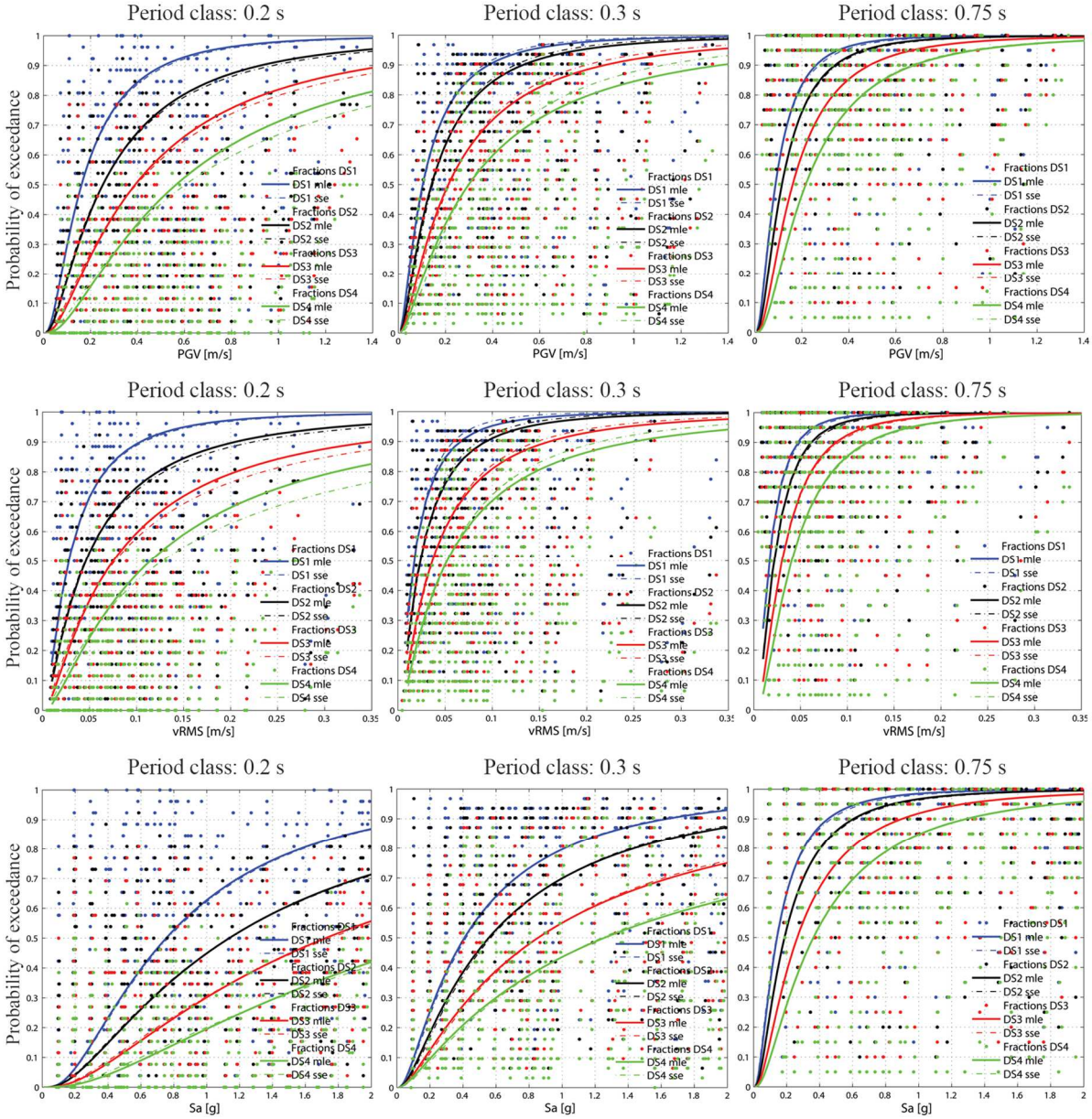


Figure 5: Fragility curves in terms of PGV, vRMS and S_a for period classes 0.2s, 0.3s and 0.75s.

8.2 Measures of dispersion: fragility curves goodness-of-fit

In order to understand which IM-based fragility curve corresponds to lower scatter among the different bridges hence to higher accuracy in representing the bridge class, an analysis of the goodness-of-fit around each IM-based group of curves is carried out.

Statistical analysis of fragility curves has been conducted in the past [32] by defining a specific approach for performing goodness-of-fit tests. The outcome of such tests is the statistical p-value, a function of the observed sample results, typically used for testing statistical hypothesis and compered with a significance level, commonly known as α for claiming if the hypothesis of following a certain model can be accepted or rejected. However, in the order to rapidly compare results with a simple scalar that can provide an immediate idea of the level of dispersion, the coefficient of determination, R^2, was considered for defining the level of dis-

persion of the structural analysis data and the fitted model along y-axis. On the other hand, the dispersion along the x-axis, which represents the quality of the fit curve with respect to the entire set of bridges and records, was analyzed by evaluating the root-mean-square deviation in Equation (11), normalized with respect the difference between the observed maximum (x_{max}) and minimum values (x_{min}), obtaining the normalized root-mean-square deviation of Equation (12), parameters which allows the comparison between datasets with different scales.

$$RMSD = \sqrt{\frac{\sum_i^n (x_{obs,i} - x_{model,i})^2}{n}} \tag{11}$$

$x_{obs,i}$ and $x_{model,i}$ are the observed values and the fitted values, given the same probability of exceedance for each level of observed probability of exceedance and n is the sample size.

$$NRMSD = \frac{RMSD}{(x_{max} - x_{min})} \tag{12}$$

The results in terms of R^2 and NRMSD do not exhibit relevant differences whether MLE or SSE fitting procedures are employed. Accordingly Figure 6 illustrates R^2 values and Figure 7 depicts NRMSD values, both using MLE fitting for each damage state and each class of bridges.

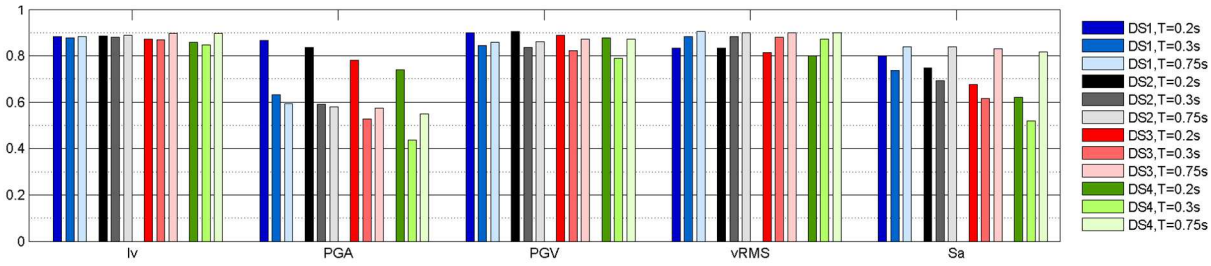


Figure 6: R^2 values associated to MLE fitting for each damage state and each class of bridges.

A lower scatter (R^2 closer to one) means that the model fits better the structural analysis data and, from a bridge population point of view, the IMs which shows less dispersion are Fajfar index (I_v), peak ground velocity (PGV), and root mean square velocity (vRMS). It is worth noting that for such intensity measures the level of accuracy in terms of coefficient of dispersion is essentially constant for all damage states and bridge classes, whereas for peak ground acceleration (PGA) and spectral acceleration (S_a), which denote lower levels of accuracy, the dispersion increases with the damage state i.e. demand level.

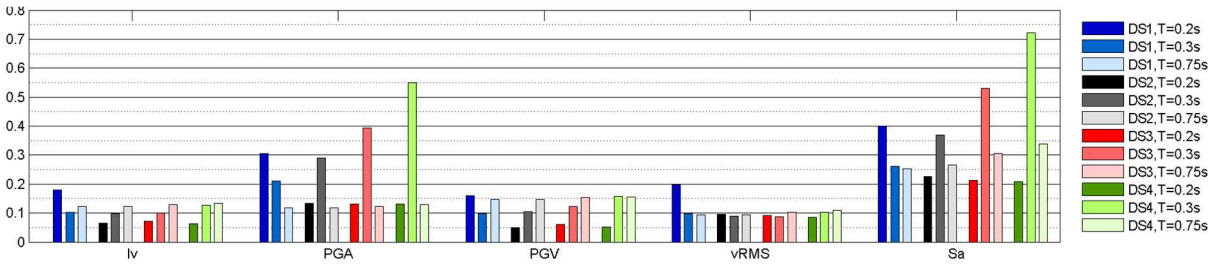


Figure 7: NRMSD values associated to MLE fitting for each damage state and each class of bridges.

When the dispersion along the x-axis is examined, considering that a smaller value of NRMSD indicates a lower dispersion around the different bridges, again, Iv, PGV and vRMS perform better with respect PGA and S_a which, moreover, vary with both bridge class and damage state level.

9 CONCLUSIONS AND FUTURE DEVELOPMENTS

The present study was focused on the development of nonlinear static analytical fragility curves of bridge populations based on traditional and innovative intensity measures, a field of research that has been mainly dedicated to buildings, by means of a statistically sound comparison between fitting and error measures. The adopted structural population was obtained considering a relevant number of structural configurations, randomly generated using Latin Hypercube sampling and grouped in three classes, defined by a central period of 0.2s, 0.3s and 0.75s. To assess the performance of such structural configurations, thirty response spectra, compatible with the seismic hazard of the region of Molise, in Italy, for fifteen levels of intensity measures were employed. The multi stripe analysis method was selected as the most suitable for estimating fragility parameters, through the fitting of the structural dataset.

The results have shown that Fajfar index (I_v), peak ground velocity (PGV), and root mean square velocity (vRMS) lead to less dispersion around the fitted fragility curves, in agreement with the findings of previous studies, which demonstrated that the same IMs exhibited better performance in terms of efficiency, practicality and proficiency in prediction of multiple engineering demand parameters when dealing with bridge populations.

Future developments of the present study will address the validation of the results obtained with nonlinear static analysis with the nonlinear dynamic counterpart. Moreover, the employed nonlinear static procedure can be further scrutinized by adopting different load patterns to better assess the performance of irregular configurations.

REFERENCES

[1] T. Rossetto, A. Elnashai, A new analytical procedure for the derivation of displacement-based vulnerability curves for population of reinforced concrete structures. *Engineering Structures,* **27**: 397-409, 2007.

[2] R. Monteiro, R. Delgado, R. Pinho, Using different uncertainty models for seismic assessment of RC bridges. M. Papadrakakis, V. Papadopoulos, V. Plevris eds. *5th ECCOMAS Thematic Conference on Computational Methods in Structural Dynamics and Earthquake Engineering (COMPDYN 2015)*, Crete Island, Greece, 25–27 May, 2015.

[3] N. Jayaram, T. Ling, M.EERI, J.W. Baker, A computationally Efficient Ground-Motion Selection algorithm for Matching a Target Response Spectrum Mean and Variance. *Earthquake Spectra*, **27**, 797-815, 2011.

[4] P. Gehl, D.M. Seyedi, J. Douglas, Vector-valued fragility functions for seismic risk evaluation. *Bulletin of Earthquake Engineering,* **11**, 365-384, 2013.

[5] L. Sousa, V. Silva, M. Marques, H. Crowley, R. Pinho, Including Multiple IMTs in the Development of Fragility Functions for Earthquake Loss Estimation. *Vulnerability, Uncertainty, and Risk*, 1716-1725, 2014.

[6] C. Zelaschi, R. Monteiro, R. Pinho, Parametric characterization of reinforced concrete Italian bridges for seismic assessment purposes. *Structure and Infrastructure Engineering* (submitted for publication), 2015.

[7] C. Zelaschi, D. Forcellini, G. De Angelis, R. Monteiro, Performance based earthquake engineering approach applied to bridges in a road network, *Proceedings of the 5th*

ECCOMAS Thematic Conference on Computational Methods in Structural Dynamics and Earthquake Engineering (COMPDYN), Crete, Greece, May 25-27, 2015

[8] C. Zelaschi, R. Monteiro, M. Marques, R. Pinho, Comparative analysis of intensity measures for reinforced concrete bridges. *Proceedings of 2nd European Conference on Earthquake Engineering and Seismology (2ECEES)*, Istanbul, Turkey, August 24-29, 2014.

[9] C. Casarotti, R. Monteiro, R. Pinho, Verification of spectral reduction factors for seismic assessment of bridges. *Bulletin of the New Zealand Society for Earthquake Engineering*, **42**, 111-121, 2009.

[10] R. Pinho, R. Monteiro, C. Casarotti, R. Delgado, Assessment of continuous span bridges through nonlinear static procedures. *Earthquake Spectra*, **25**, 143-159, 2009.

[11] R. Monteiro, M. Marques, G. Adhikari, C. Casarotti, R. Pinho, Spectral reduction factors evaluation for seismic assessment of frame buildings. *Engineering Structures*, **77**, 129-142, 2014.

[12] R. Pinho, M. Marques, R. Monteiro, C. Casarotti, R. Delgado, Evaluation of nonlinear static procedures in the assessment of building frames. *Earthquake Spectra*, **29**, 1459-1476, 2013.

[13] CEN Eurocode 8: Design of Structures for Earthquake Resistance - Part 1: General rules, seismic actions and rules for buildings, EN 1998-2, Comité Européen de Normalisation, Brussels, Belgium, 2005a.

[14] CEN Eurocode 8: Design of Structures for Earthquake Resistance - Part 2: Bridges, EN 1998-2, Comité Européen de Normalisation, Brussels, Belgium, 2005b.

[15] P. Fajfar, M.EERI, A Nonlinear Analysis Method for Performance-Based Seismic Design. *Earthquake Spectra*, **16**, 2000.

[16] C. Casarotti, R. Pinho, G.M. Calvi, Adaptive pushover-based methods for seismic assessment and design of bridge structures, ROSE Research Report No. 2005/06, IUSS Press, Pavia, Italy, 2005.

[17] Matlab version 7.1.0.246. Natick, Massachusetts: The MathWorks Inc., 2005.

[18] OpenSees, Open System for Earthquake Engineering simulation, Pacific Earthquake Engineering Research Center, US, available from http://opensees.berkeley.edu/.

[19] N. Shome, C.A. Cornell, Probabilistic seismic demand analysis of nonlinear structures, *Technical report RMS-35*, RMS Program: Standford CA.

[20] S. Akkar, J.J. Bommer, Empirical equations for the prediction of PGS, PGV, and spectral accelerations in Europe, the Mediterranean Region, and the Middle East," *Seism. Res. Lett.*, **81**:195–206, 2010.

[21] OpenQuake, Available from: http://openquake.org/ [12 September 2012], 2012.

[22] C. Meletti, F. Galadini, G. Valensise, M. Stucchi, R. Basili, S. Barba, G. Vannucci and E. Boschi, A seismic source zone model for the seismic hazard assessment of the Italian territory. Tectonophysics, 450, 85-108, 2008.

[23] R. Monteiro, X. Zhang, R. Pinho, Different approaches to derive analytical fragility functions of bridges. *Proceedings of 2nd European Conference on Earthquake Engineering and Seismology (2ECEES)*, Istanbul, Turkey, August 24-29, 2014.

[24] HAZUS, Multi-hazard Loss Estimation Methodology Earthquake Model, *Federal Emergency Management Agency*, Washington, D.C., USA, 2003.

[25] B.G. Nielson, Analytical fragility curves for highway bridges in moderate seismic zones, *Ph.D. Thesis*, School of Civil and Environment Engineering, Georgia Institute of Technology, USA, 2005.

[26] M.J.N. Priestley, F. Seible, G.M. Calvi, *Seismic Design and Retrofit of Bridges, Wiley-Interscience*, New York, 1996.

[27] FEMA P-750, NEHRP Recommended Seismic Provisions for New Buildings and Other Structures, 2009.

[28] J.W. Baker, Efficient analytical fragility function fitting using dynamic structural analysis. *Earthquake Spectra*, (in press).

[29] M. Shinozuka, M.Q. Feng, J. Lee, T. Naganuma, Statistical analysis of fragility curves. *Journal of Engineering Mechanics*, **126**, 1224-1231, 2000.

[30] J.W. Baker, C.A. Cornell, A vector-value ground intensity measure consisting of spectral acceleration and epsilon. *Earthquake Engineering & Structural Dynamics*, **34**, 1193-1217, 2005b.

[31] D. Straub, A. Der Kiureghian, Improved seismic fragility modelling from empirical data. *Structural Safety*, **30**, 320-336, 2008.

[32] M. Shinozuka, M.Q. Feng, H. Kim, T. Uzawa, T. Ueda, Statistical Analisys of Fragility Curves, *Technical Report MCEER*, University of Southern California, Los Angeles, California, 2001.

COMPDYN 2015
5th ECCOMAS Thematic Conference on
Computational Methods in Structural Dynamics and Earthquake Engineering
M. Papadrakakis, V. Papadopoulos, V. Plevris (eds.)
Crete Island, Greece, 25–27 May 2015

SIMPLIFIED CLOSED-FORM SOLUTION FOR THE DETERMINATION OF THE MOMENT-CURVATURE RESPONSE OF A CIRCULAR RC SECTION

Domenico Raffaele[1], **Roberto Gentile**[1], **and Mauro Mezzina**[1]

[1]DICATECh, Politecnico di Bari, Bari, Italy
e-mail: {domenico.raffaele, roberto.gentile, mauro.mezzina}@poliba.it

Keywords: simply supported bridges; reinforced concrete; seismic vulnerability; moment-curvature.

Abstract. *A seismic vulnerability analysis of a multi-span simply supported bridge is often based on the seismic response of the most critical pier. This response is influenced by different collapse modes (flexural, shear, second order effects, lap-splice of longitudinal bars or their buckling). Among these the flexural behaviour is important and it's known if the equivalent plastic hinge length and the Moment-Curvature law of the fixed end are given. This paper provides a closed-form dimensionless solution to obtain a 5 point Moment-Curvature diagram for circular RC section. The solution is based only on three parameters: dimensionless axial force, mechanical percentage of longitudinal reinforcement, geometrical percentage of transversal reinforcement. A numerical example is presented to test the solution comparing it with a FEM analysis.*

1 Introduction

Seismic vulnerability is an actual theme in engineering and in particular great attention has been devoted to bridge structures in order to perform vulnerability inventory at a regional scale. In fact for example the major part of the Italian RC bridges was built around the 1960s referring to codes with no "anti seismic philosophy" [1] and studies based on the monitoring of bridges [2] support the need of the above mentioned inventory. Moreover a bridge can often be a crucial node of a transport web and thus it's performance has to be guaranteed even in the moments next to an earthquake [3]. Hence having an inventory of the structural performances of the bridges in a region is a central question in order to plan mitigation actions. Considering the large amount of the structures to analyze and the shortage of the resources to do that, it is impossible to perform detailed analysis to obtain capacity curves (e.g. Pushover Analysis). Usually regional scale analysis resorts to typological or semi empirical vulnerability methods but in this paper it's used a procedure that is based on rational mechanics with whom the ultimate displacement of a multi span bridge can be obtained with small computational effort and with few input data. Basing on the so called "Simplified Pushover Analysis"[4], instead of performing a full structural analysis under pushing loads, the vulnerability of the bridge is directly expressed by the capacity curve of an equivalent SDoF system. Moreover, given that the energy dissipation capacity of a simply supported bridge is concentrated in the piers and the deck usually remains elastic, in the simplified analysis only the piers contribute to model the SDoF system. The most critical pier of the bridge can be defined as the one that exibits the greater seismic demand/capacity ratio at a given limit state (fig.1). Often the capacity curve of the most critical pier is a good approximation of the capacity curve of the whole bridge. In this procedure [5] the capacity curve of the most critical pier, expressed in terms of Moment-Displacement $(M - \delta)$, is obtained taking into account the flexural behaviour (Moment-Curvature curve of the base section) and all the other collapse modes (shear, second order effects, lap-splice of longitudinal bars or their buckling) that can anticipate the flexural collapse. In this paper is proposed a procedure with which the *Moment-Curvature* $(M - \varphi)$ relationship of an RC section is calculated by defining the position of 5 characteristic points. Each of these is defined in a closed form depending on 3 parameters: dimensionless axial force, mechanical percentage of longitudinal reinforcement, geometrical percentage of transversal reinforcement. The basic concept is that knowing only a few parameters like geometry and amount of reinforcement, for example through a simple inspection, it is possible to perform a first level vulnerability analysis of a group of circular column multi span simply supported bridges. The approach herein proposed is based on realistic stress-strain relationships for both concrete and steel and its reliability is proved analyzing a numerical example and comparing it with a FEM non linear analysis.

2 Summary of the procedure

The Moment-Curvature relationship is obtained defining the position of 5 characteristic points (defined later). Moment and curvature of each of these points are predicted through a 5th grade polynomial. It was created a database of Moment-Curvature analysis conducted with the software *KSU_RC* [6]. The results are processed in *MATLAB* in order to define the characteristic points of each $(M - \varphi)$ curve. Finally the polynomials are obtained with a least squares method linear regression.

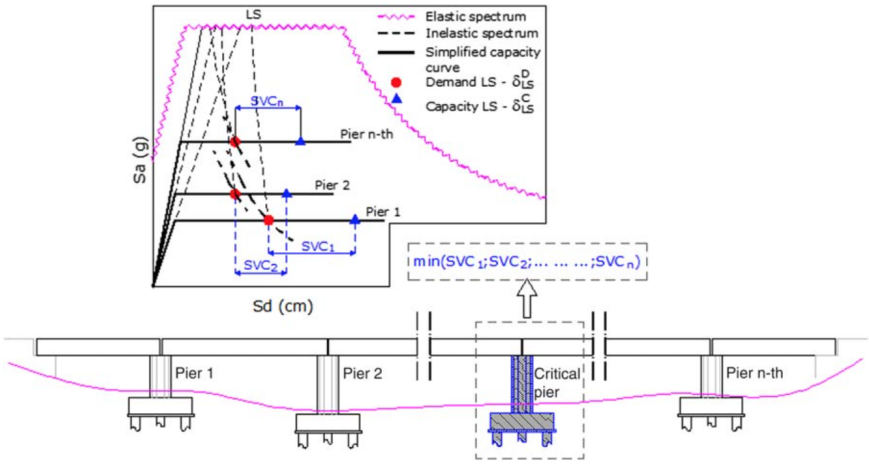


Figure 1: Determination of the critical pier.

3 Selecting the problem parameters

The parameters involved in the definition of the flexural behaviour of an RC circular section are several: radius R, clear cover c, normal force N, compression strength of concrete in unconfined conditions f_c, tension strength of concrete f_{ct}, concrete's modulus of elasticity E_c, yielding strength of longitudinal and transversal reinforcement f_{ys}, f_{yh}, moduli of elasticity of the steel E_s, E_h, number and diameter of longitudinal reinforcement n_l, d_l, diameter and spacing of transversal reinforcement d_h, s. It is clear that, for the scope of this work, it's inconvenient to have a so large number of parameters and for this reason some hypothesis have been made:

- concrete tension strength f_{ct} has been related to its compression strength according to a relationship contained in the Italian code [7]:

$$f_t = 0.3 f_c^{\frac{2}{3}}. \tag{1}$$

  Finally the relation

$$f_{ct} = 1.2 f_t (NTC08) \tag{2}$$

  is used in order to consider the flexural tension strength;

- the transversal reinforcement steel has the same characteristics of the one used for longitudinal reinforcement. So

$$f_{yh} = f_y \quad and \quad E_{sh} = E_s; \tag{3}$$

- longitudinal reinforcement is composed by n_l evenly distributed bars of equal diameter d_l. So the total area of longitudinal steel is

$$A_s = \frac{n_l(\pi d_l^2)}{4}; \tag{4}$$

- the clear cover is proportional to the radius of the section according to:

$$c = 0.05R. \tag{5}$$

The remaining parameters of the problem are grouped into 3 dimensionless parameters (dimensionless axial force ν, mechanical percentage of longitudinal reinforcement ω, geometrical percentage of transversal reinforcement ρ) so that a circular RC section is completely defined by them:

$$\nu = \frac{N}{\pi f_c R^2} \tag{6}$$

$$\omega = \frac{A_s f_y}{\pi f_c R^2} \tag{7}$$

$$\rho_{sp} = \frac{4A_{sp}}{(2R - 2c)s}. \tag{8}$$

The idea is that a variation in ν can be seen as a variation in the normal force N, the concrete compression strength f_c or the radius R and similarly for the equations 7 and 8.

4 Parameters' ranges

In order to create the database cited in par.2 it's been selected a plausible range for each of the three parameters (ν, ω, ρ). Then, picked up enough discrete values in these intervals, it's been conducted a Moment-Curvature analysis for each combination (462 analysis) of them using the software *KSU_RC*.

4.1 Axial force

It's been considerated the entire range of variation for this parameter (from 0 to 1) and the 11 chosen discrete values are:

$$\nu = \{0,\ 0.1,\ 0.2,\ 0.3,\ 0.4,\ 0.5,\ 0.6,\ 0.7,\ 0.8,\ 0.9,\ 1\}. \tag{9}$$

For the analysis in *KSU_RC* it's been fixed $R = 1\,m$ and $f_c = 31.83\,Mpa$ so the value of N corresponding to ν it's been calculated with eq. 6.

4.2 Longitudinal reinforcement

It's been chosen a range between 0.05 and 0.8 and in particular the 6 values:

$$\omega = \{0.05,\ 0.1,\ 0.2,\ 0.4,\ 0.6,\ 0.8\}. \tag{10}$$

For the numerical analysis it's been fixed $f_y = 450\,MPa$ and $n_l = 22$ so the cross sectional area of a single rebar it's been calculated using eqs. 7 and 4.

4.3 Transversal reinforcement

The range of this parameter goes from 0 to 0.01 and in particular the 7 values:

$$\rho_{sp} = \{0,\ 0.001,\ 0.002,\ 0.004,\ 0.006,\ 0.008,\ 0.010\}. \tag{11}$$

Fixing the spacing of the stirrups ($s = 0.1m$), according to the fixed values mentioned in pars.4.1 and 4.2 and knowing the value of the clear cover (eq.5) the cross sectional area of the stirrup has been calculated using eq.8.

5 Execution of the analysis

For each combination of the parameters mentioned in par.4 (hence 11x6x7=462) it's been conducted a Moment-Curvature analysis using the software *KSU_RC* whose reliability has been proved [6]. The cross section is divided into fibers and a stress-strain relationship is assigned to each of them. Concrete follows the relationship proposed by Mander [8] in order to model the different behaviour (fig.2) of concrete in the core (confined) and in the cover (unconfined). In order to model the behaviour of steel *KSU_RC* uses a stress-strain relationship, proposed by the owner of the software, that brings to results in good agreement with the experiments. The curve (fig.3) is assumed linear up to the yielding, has a constant tension until a strain of K_1 times the yielding strain and then is parabolic. The peak of the parabola corresponds to a strain of K_2 times the yielding strain and the ultimate point corresponds to a strain of K_3 times the yielding strain. The peak strength is equal to K_4 times the yielding strength. For this study the values used are such that the curve best approximates the real behaviour of the most common italian steel. In particular: $K_1 = 10$, $K_2 = 30$, $K_3 = 55$, $K_4 = 1.3$.

The output of the software is a 7-column array containing curvature, moment, neutral axis, strain in the furthermost fiber of the concrete core, strain of the extreme tension rebar and axial force.

6 Post processing

It's been projected a *MATLAB* function that analyzes each ($M - \varphi$) curve in order to obtain a 5-point curve (an example can be seen in fig.5). The function input is the 7-column array obtained from the output of *KSU_RC*. The characteristic points of the ($M - \varphi$) curve chosen are:

Cracking If the curve presents a softening branch at cracking this point is exactly the start of this branch. If else this branch isn't appreciable, and this can occur for great values of the axial force, the cracking point assumed is the one that induces a strain of ε_{ct} in the furthermost concrete fibre in the section (fig.4).In particular the function finds the value of ε_c that satisfy eq:

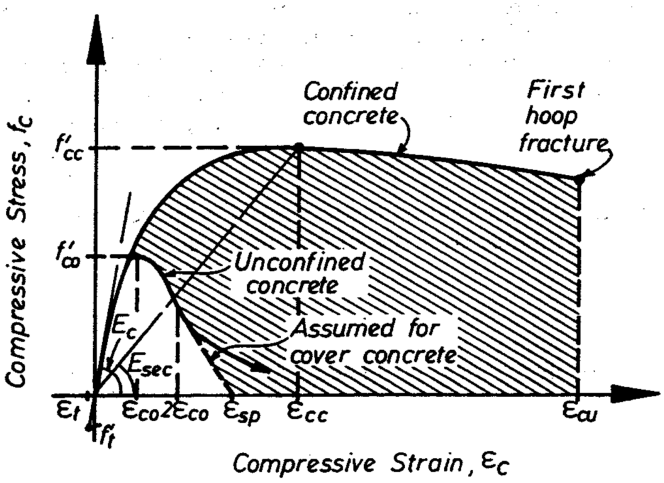


Figure 2: Mander stress-strain relationship for confined and unconfined concrete.

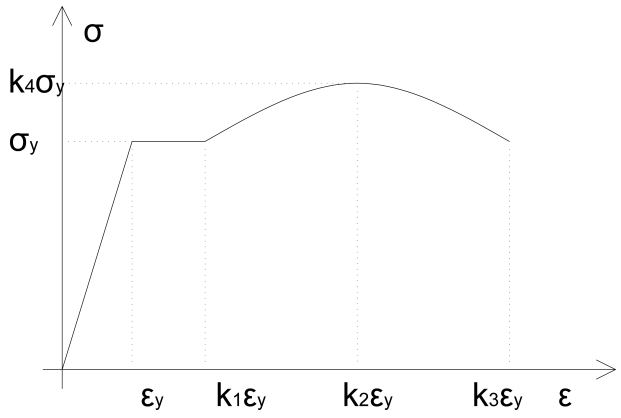


Figure 3: Stress-strain relationship for steel.

$$\frac{D-x}{x-c}\varepsilon_c = \varepsilon_{ct} \tag{12}$$

where

$$\varepsilon_{ct} = \frac{f_{ct}}{E_c}. \tag{13}$$

First Yield This point is defined as the point on $(M-\varphi)$ curve when the reinforcement furthest from the neutral axis attains the first yield, or when extreme concrete compression fibre attains a strain of 0.002, which ever occurs first [9].

Spalling The point of the $(M-\varphi)$ response that induces a strain of 0.0045 in the extreme fiber of the cover concrete (fig. 4) according to eq:

$$\frac{x}{x-c}\varepsilon_c = \varepsilon_{sp}. \tag{14}$$

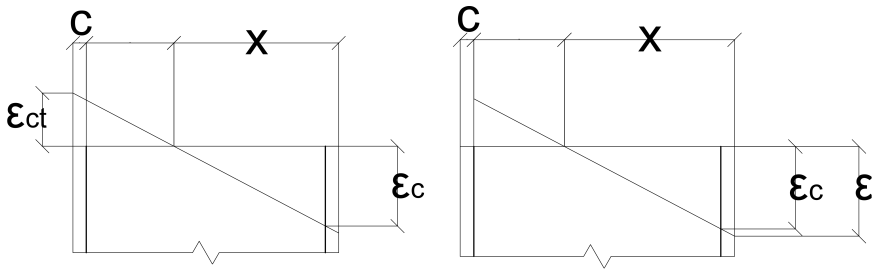


Figure 4: Strain state of the section at cracking and spalling.

Peak of confined concrete Defined as the condition that causes, in the extreme core concrete fibre, a strain corresponding to its peak in the Mander constitutive relation.

Collapse Simply the last point of the $(M - \varphi)$ curve. It can represent both the failure due to reaching the ultimate strain in confined concrete or in the extreme tension rebar.

Finally the curves are tranformed in dimensionless form according to:

$$m = \frac{M}{\pi R^3 f_c} \tag{15}$$

$$\chi = 1000\varphi R. \tag{16}$$

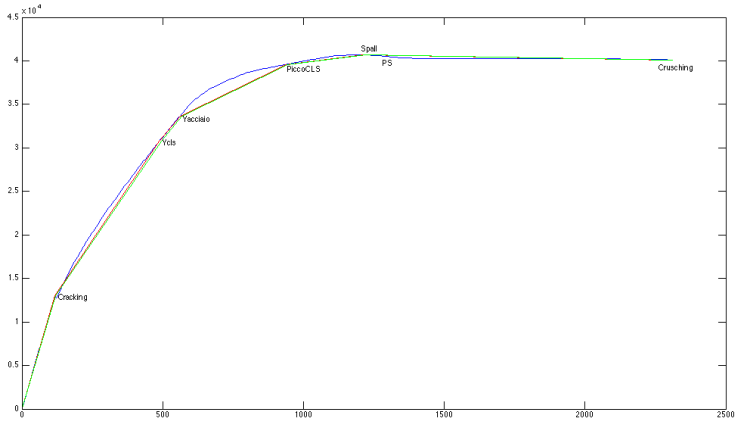


Figure 5: 5-point Moment-Curvature relationship.

7 Curve fitting

Knowing the values of the characteristic moments and curvatures for each tern of parameters ν, ω, ρ it's been possible to find a 5th-grade polynomial in these three variables that best fit the data basing on a least square method linear regression. Notice that the terns with $\rho = 0$ are studied only for control purposes and so they are excluded from the fitting. The structure of the polynomials (eq.17) is shown in appendix A. It is obvious that the manual use of these functions is practically impossible but it will be easy to use them with a simple software.

8 Numerical application

With the aim of demonstrating that the simplified procedure to evaluate the *Moment-Curvature* of an RC section herein proposed can be used as a reliable input for the assessment of a simply supported bridge (e.g. assessing the most critical pier) a numerical validation of it is presented. The response of the base section of the most critical pier is predicted according to the characteristic polynomials of appendix A and compared to a numerical analysis conducted with *KSU_RC* (fig.6). Basing on a linearisation of the $(M - \varphi)$ relationship, the *Moment-displacement* curve of the pier has been calculated according to a simplified procedure proposed by Raffaele et al. [5] named *VulPil*. According to this procedure knowing the $(M-\varphi)$ curve of the base section of the pier and the length of the plastic hinge it can be calculated the flexural $(M-\delta)$ relationship. Then this curve can be "corrected" in order to take into account the different collapse modes. It is important to notice that in this work only the $(M - \varphi)$ curve is to be validated and so the benchmark case is calibrated in such a way that it is only governed by the flexural behaviour. The $(M - \delta)$ curve is compared to the results of a FEM analysis performed using *SAP2000* V17. In SAP the pier has been modeled by means of 12 "beam" elements each one discretized into 52 fibers. It has been conducted a pushover analysis under a single horizontal load on the top of the pier. The constitutive laws used in SAP can be seen in figs.2 and 3. According to the simplified procedure used the behaviour of the pier depends on the presence of seismic restraints and this can be taken into account by considering the effective mass pertaining to the pier. For this reason it is necessary to consider two different models, one for the transversal and one for the longitudinal direction (they differ only for the axial force acting on the pier). In table 1 the geometric and mechanical parameters for the pier chosen for this example. It should be noted that the example chosen is identical to the one chosen by [5]. The reason of doing that is to show the improvement of the $(M - \delta)$ relationship prediction due to the more refined $(M - \varphi)$ curve. In fact the simplified $(M - \delta)$ analysis in this example is different from the *VulPil* analysis only in the definition of the $(M - \varphi)$ curve. The resulting capacity curve for the transversal direction is represented in fig.7 in which the curve calculated with SAP2000 has been transformed in a bilinear curve in order to simplify the comparison.

Looking at the comparison it can be seen that the simplified procedure is close to the refined numerical solution. There is an important improvement in the prediction of the yielding displacement and the maximum moment, with respect to the VulPil procedure, due to the better definition of the $(M-\varphi)$ curve. Conversely it can be seen an over prediction of the ultimate displacement of the pier with respect to the SAP2000 analysis. In table 2 is presented a numerical comparison of the results in terms of ultimate moment, ultimate displacement and displacement ductility.

	L $[m]$	D $[m]$	c $[m]$	n_l $[-]$	d_l $[mm]$	d_h $[mm]$	s $[mm]$
Transversal	6	2	0.05	30	26	10	100
Longitudinal	6	2	0.05	30	26	10	100
	f_c $[MPa]$	f_{ct} $[MPa]$	f_{ys} $[MPa]$	N $[KN]$	ν $[-]$	ω $[-]$	ρ_{sp} $[-]$
Transversal	20	3	450	13870	0.678	0.107	0.009
Longitudinal	20	3	450	17847	0.678	0.107	0.009

Table 1: Geometric and mechanical properties of the pier.

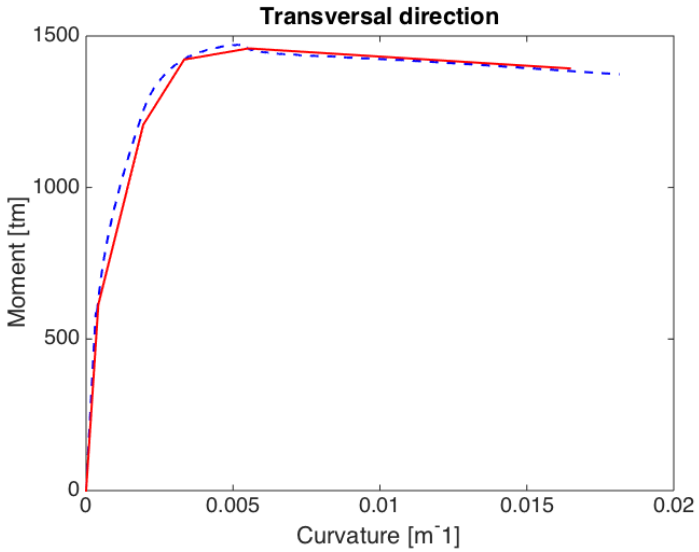


Figure 6: Moment-Curvature: comparison between KSU_RC and the simplified procedure, transversal direction.

	ΔM_u [%]	$\Delta \delta_u$ [%]	$\Delta \mu$ [%]
Transversal	3,23	27,36	13,14
Longitudinal	2,63	17,43	6,82

Table 2: Simplified analysis and refined FEM analysis. Numerical comparison of the results.

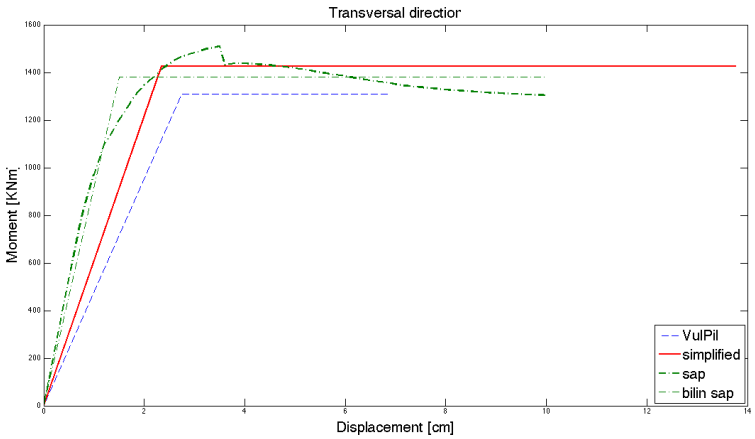


Figure 7: Comparison between capacity curves, transversal direction.

9 Conclusions

The need to develop procedure for performing the vulnerability inventory of the bridges in a specific region is a central question in order to plan mitigation actions. Most of the simplified procedures aimed to the assessment of a simply supported bridge are based on the knowledge of the flexural behaviour of the base section of the most critical pier. In this paper is proposed a polynomial closed form solution to obtain a 5-point *Moment Curvature* curve of an RC section knowing only few parameters. After describing the whole procedure used to obtain the above mentioned polynomials the procedure has been applied to a benchmark case and the solution has been compared to a FEM analysis. The differences in the results found with the simplified procedure and the FEM analysis are quite small, especially because they are obtained with really few input data.

10 Acknowledgements

The research presented in this article was partially funded by the Department of Civil Protection, Project ReLUIS-DPC 2014-2018

REFERENCES

[1] D. Raffaele, F. Porco, G. Uva, A. Fiore, *Simplified assessment of seismic retrofitting interventions on RC circular piers in multi-span simply supported bridges*. Proceedings of the 7th International Conference on Bridge Maintenance, Safety and Management, Shanghai, China; 7-11/07/2014, Taylor and Francis ISBN 978-113800103-9.

[2] G. Uva, G. Porco, F. Porco, A. Fiore, *Monitoring and safety for prestressed bridge girders by SOFO sensors*. Journal of Civil Structural Health Monitoring (2013), vol. 3, N1, p. 3-18, ISSN: 2190-5452, DOI: 10.1007/s13349-012-0029-9.

[3] D. Raffaele, G. Uva, F. Porco, A. Fiore, *About of seismic capacity of bridge piers: A simplified approach*. Proceedings of the 7th International Conference on Bridge Maintenance, Safety and Management, Shanghai, China; 7-11/07/2014, Taylor and Francis ISBN 978-113800103-9.

[4] B. Borzi, R. Pinho, H. Crowley, *Simplified vulnerability analysis for large scale assessment of RC buildings*. Engineering Structures, 2007.

[5] D. Raffaele, F. Porco, A. Fiore, G. Uva, *Simplified vulnerability assessment of reinforced concrete circular piers in multi-span simply supported bridges*, Structure and Infrastructure Engineering, 2014 vol. 10, N8, p. 950-962, ISSN: 1744-8980, DOI:10.1080/15732479.2013.772642.

[6] A. Esmaeily, R.J Peterman *Performance analysis tool for reinforced concrete members*. International Congress on Civil Engineering, 2005.

[7] *DM 14/01/2008, Norme tecniche per le costruzioni*. Gazzetta ufficiale n.29, Roma, Italy, 2008.

[8] J.B. Mander, M.J.N. Priestley, R. Park, *Theoretical stress-strain model for confined concrete*. Journal of Structural Engineering ASCE, 1988.

[9] M.J.N. Priestley, G.M. Calvi, M.J. Kowalsky, *Displacement-based seismic design of structures*. IUSS Press, Pavia, Italy, 2007.

A Characteristic points polynomials

$$\begin{aligned} m_{char}\ (or\ \chi_{char}) = {} & a_1\nu^5 + a_2\nu^4\omega + a_3\nu^4\rho_{sp} + a_4\nu^4 + a_5\nu^3\omega^2 + a_6\nu^3\omega\rho_{sp} + a_7\nu^3\omega + \\ & + a_8\nu^3\rho_{sp}^2 + a_9\nu^3\rho_{sp} + a_{10}\nu^3 + a_{11}\nu^2\omega^3 + a_{12}\nu^2\omega^2\rho_{sp} + a_{13}\nu^2\omega^2 + a_{14}\nu^2\omega\rho_{sp}^2 + \\ & + a_{15}\nu^2\omega\rho_{sp} + a_{16}\nu^2\omega + a_{17}\nu^2\rho_{sp}^3 + a_{18}\nu^2\rho_{sp}^2 + a_{19}\nu^2\rho_{sp} + a_{20}\nu^2 + a_{21}\nu\omega^4 + \\ & + a_{22}\nu\omega^3\rho_{sp} + a_{23}\nu\omega^3 + a_{24}\nu\omega^2\rho_{sp}^2 + a_{25}\nu\omega^2\rho_{sp} + a_{26}\nu\omega^2 + a_{27}\nu\omega\rho_{sp}^3 + a_{28}\nu\omega\rho_{sp}^2 + \\ & + a_{29}\nu\omega\rho_{sp} + a_{30}\nu\omega + a_{31}\nu\rho_{sp}^4 + a_{32}\nu\rho_{sp}^3 + a_{33}\nu\rho_{sp}^2 + a_{34}\nu\rho_{sp} + a_{35}\nu + \\ & + a_{36}\omega^5 + a_{37}\omega^4\rho_{sp} + a_{38}\omega^4 + a_{39}\omega^3\rho_{sp}^2 + a_{40}\omega^3\rho_{sp} + a_{41}\omega^3 + a_{42}\omega^2\rho_{sp}^3 + \\ & + a_{43}\omega^2\rho_{sp}^2 + a_{44}\omega^2\rho_{sp} + a_{45}\omega^2 + a_{46}\omega\rho_{sp}^4 + a_{47}\omega\rho_{sp}^3 + a_{48}\omega\rho_{sp}^2 + a_{49}\omega\rho_{sp} + \\ & + a_{50}\omega + a_{51}\rho_{sp}^5 + a_{52}\rho_{sp}^4 + a_{53}\rho_{sp}^3 + a_{54}\rho_{sp}^2 + a_{55}\rho_{sp} + a_{56}. \end{aligned}$$

COMPDYN 2015
5th ECCOMAS Thematic Conference on
Computational Methods in Structural Dynamics and Earthquake Engineering
M. Papadrakakis, V. Papadopoulos, V. Plevris (eds.)
Crete Island, Greece, 25–27 May 2015

ENERGY DISSIPATION CHARACTERISTICS OF SLAB TYPE BUILDINGS WITH SPECIAL CONNECTORS

Erkan Şenol[1], Ahmet Anıl Dindar[2], Ercan Yüksel[3] and Faruk Karadoğan[4]
[1]Yildiz Technical University, Department of Civil Engineering
Davutpasa, Istanbul, Turkey
e-mail: esenol@yildiz.edu.tr
[2]İstanbul Kültür University, Department Of Civil Engineering
Bakırköy, Istanbul, Turkey
e-mail: adindar@iku.edu.tr
[3]İstanbul Technical University, Department Of Civil Engineering
Maslak, Istanbul, Turkey
e-mail: ercyuksel@itu.edu.tr
[4]İsik University, Department Of Civil Engineering
Şile, Istanbul, Turkey
e-mail: faruk.karadogan@isikun.edu.tr

Keywords: SAFECLADDING, Energy Dissipation, SAP2000 OAPI, Nonlinear Time-History Analysis, Precast RC Systems, SAMA.

Abstract. *The latest developments in the construction technologies and the materials facilitated the practicing engineers to go higher and energy-efficient buildings. However, the safety of the buildings and the residents has been an issue all the time. This is not an exception for the pre-cast structures. The advantages of the precast elements are the quality assurance and the rapid erection on the site and challenged by the connection details and their performances during the extreme loading cases such as earthquakes. The utilization of a special mechanical connection of the precast members have been in the focus of the recent works in Istanbul Technical University (ITU-STEELAB). The prototypes of the proposed special connectors, called as cushion, were tested in STEELAB in order to determine the mechanical properties such as lateral and axial stiffness and the failure modes. Once the properties were determined, a hypothetical building of single story multi-bay slab type structure was modeled in the computer framework capable of substituting various parametric values into the model, processing and extracting the results for statistical analysis, SAMA. SAMA is developed based on the use of SAP2000 OAPI functions called in MATLAB and Python scripts. In the hypothetical model, the cushions were modeled as link elements and placed between all the precast elements including foundation-cladding interface. Extensive non-linear time-history analysis was conducted to identify the damage localization by comparing the energy dissipation at each mechanical connector under ground motion records selected according to focal distance, site conditions and intensity. The preliminary results reveal that the cushions are effectively dissipating a significant amount of energy and mitigating the collapse of the precast elements. The more detailed conclusions will be discussed in the near future.*

1 INTRODUCTION

The current economic conditions demand for minimum cost and shortest period of construction in order to compete in the fierce market. Hence, the precast structures have been the most favorable construction type since the recent developments in the precast member manufacturing and the construction techniques covers the demand of the market. The connection details of the precast members have always been interest of the researchers looking for safer designs against extreme loadings, particularly the seismic loads. The connection of the precast elements (beams, columns, slabs and claddings) should have enough resistance capacity during the ground motions while they must be economical in case of retrofitting after the earthquake. The resistance of the structural members have been defined in terms of strength and deformation, however energy concept, a strong alternative to the current design approaches, can be used in the definition of the seismic resistance.

Kelly et. al. (1972) performed elementary tests on the flat U shaped strip type steel elements, which is presented in Figure 1.6. The relative motion of steel elements is directed parallel between adjacent surfaces, which might be significant energy absorption source by means of rolling, and bending. This study highlighted the significance of steel bent plates, which might be incorporated in structures for absorption of energy generated by earthquake effects.

The energy dissipater type steel members in jointed wall system of two or more precast concrete walls, post-tensioned to the foundation using unbounded tendons, and connected along the vertical joints with special energy dissipating shear connectors were studied in the content of Precast Seismic Structural Systems (PRESSS) program, by Priestley et al, (1991).

A special type of energy dissipative connectors which can be utilized for the all connections mentioned above have been developed in the Structural Dynamics and Earthquake Engineering Laboratory of Istanbul Technical University (ITU-STEELAB) as a part of European FP7 project SAFECLADDING. In this paper, a connector type placed in the precast members' connections was studied to understand the overall response of the one story precast structures subjected to carefully selected and scaled earthquake records [1].

2 ENERGY DISSIPATING DEVICES AND STRUCTURAL MODELS

2.1 ENERGY DISSIPATION DEVICE

The energy dissipation device used in this study is a deformable steel cushion element that is connected to the RC precast members (slab, beam, column, cladding, foundation) with eccentrically placed single bolts, Fig. 1. The thickness of the device named as "Cushion" is taken as 8mm in the study.

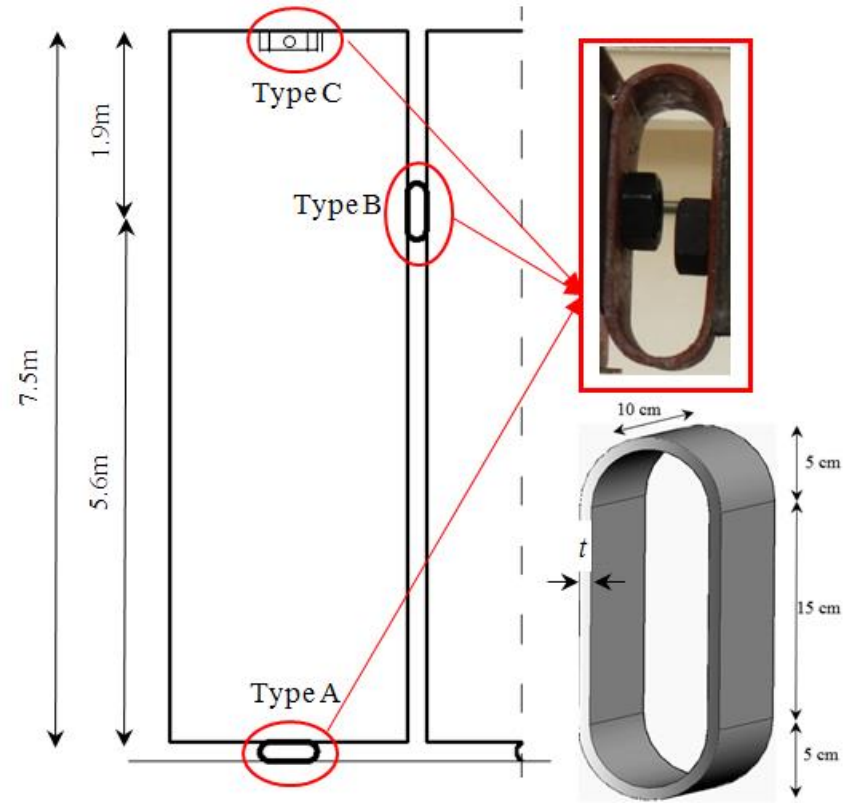


Figure 1: Proposed cushion geometry and their placements between the cladding and the peripheral elements.

The deformation and strength characteristics of the cushion was obtained from the shear tests in ITU laboratories. The displacement based saw teeth test protocol with increasing amplitude up to 20 cm to both directions, was applied to the cushion. The force-deformation curve measured from the material experiment was carefully studied in the Finite Element Analyses numerical modeling program [2] and two mathematical models, namely WEN 1 and WEN 2, were fit to the experimental data in elastic range and plastic ranges, respectively.

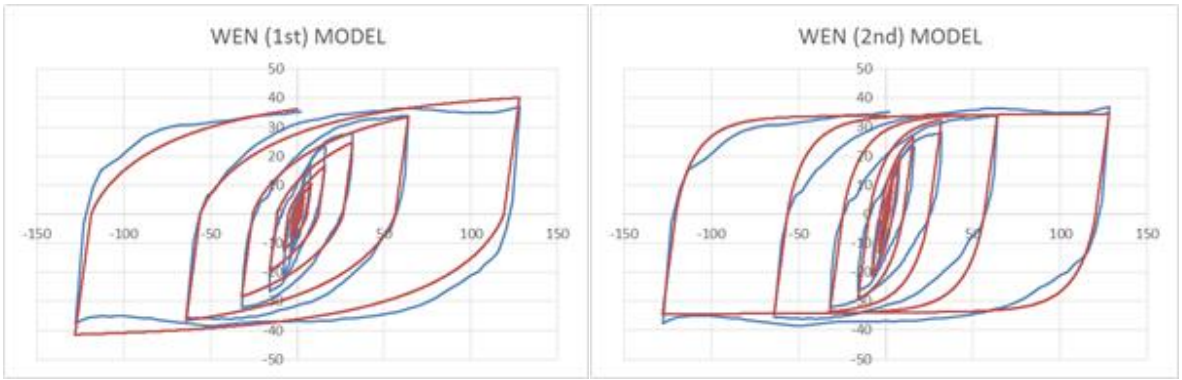


Figure 2: Behavior Models of the cushion.

The fitting success of the all two models were scrutinized in the comparison of the force variation curve on which part of the structural response is achieved, Fig 3. WEN 1 and WEN 2 are in good agreement with experimental data in linear (before #150) and nonlinear (after #150) response, respectively.



Figure 3: Force variation between experimental and numerical models.

The mechanical parameters computed from the FEM analysis for the cushion element are given in Table 1 and the corresponding force-displacement scheme is depicted in Figure 4.

Models/ NL Pros.	**WEN 1**	**WEN 2**
Stiffness (kNm)	4500	4500
Yield F. (kN)	42	34
Stiff. Ratio	0.001	0.001
Yield Exp.	0.12	0.5

Table 1: Parameters for cushion elements

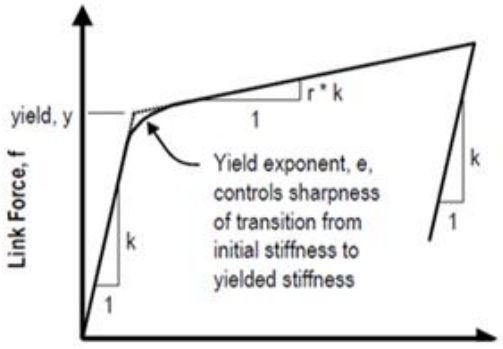


Figure 4.WEN constitutive model based force-displacement relationship.

2.2 STRUCTURAL MODEL AND CONNECTION VARIATIONS

The structural model studied is depicted in Figure 5. The features of the structural model is provided as follows;

- The aspect ratio of this slab type building is three; it means that in-plane deformation of slabs will be effective especially on the behavior of middle frame columns even the slabs are cast in situ slabs. It can easily be estimated that the non-rigid connections and in-plane plastic deformations of slabs will pronounce this expectations.

- There are only two frames running in the long direction and two exterior frames running in transversal short direction. They are consisting of precast columns and beams which may be connected to each other with proposed energy dissipating device. Slab elements and cladding panels are connected to the longitudinal and transversal exterior frames respectively, by means of semi-rigid or rigid connectors.
- Slab elements and cladding panels which are located at the end of building in the short direction, are all connected to each other by steel cushions.
- Cladding panels are connected to the foundation so that this connection will provide both bending hinges and shear dissipations. Those will be parameters of this work.
- Cladding panels are connected to the beams of exterior frames by steel cushions with different strength and rigidities.

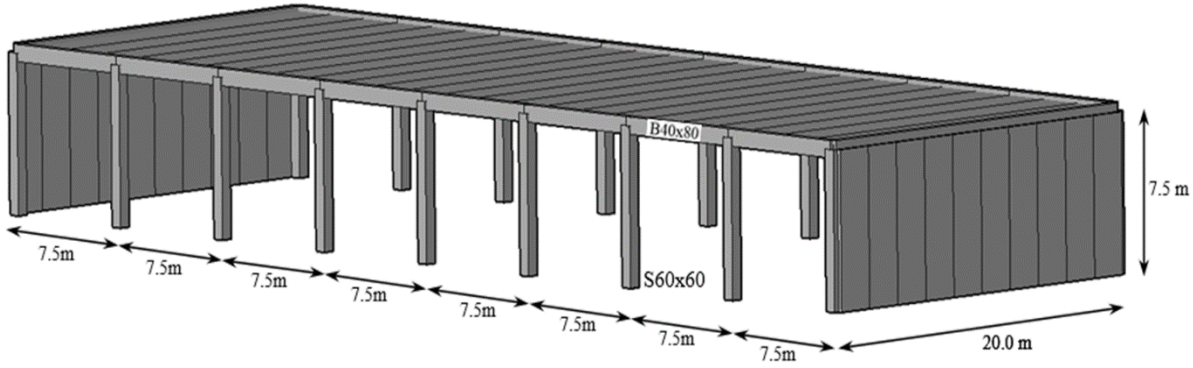


Figure 5. General view of the slab type structure used in the parametric study.

The numerical model constructed in FEM analysis program was taken as the half of the longitudinal direction since the transversal symmetry is provided, Fig. 6. The connection types between the all precast members (columns, beams, slabs, claddings) and the foundation were also shown in Fig. 6.

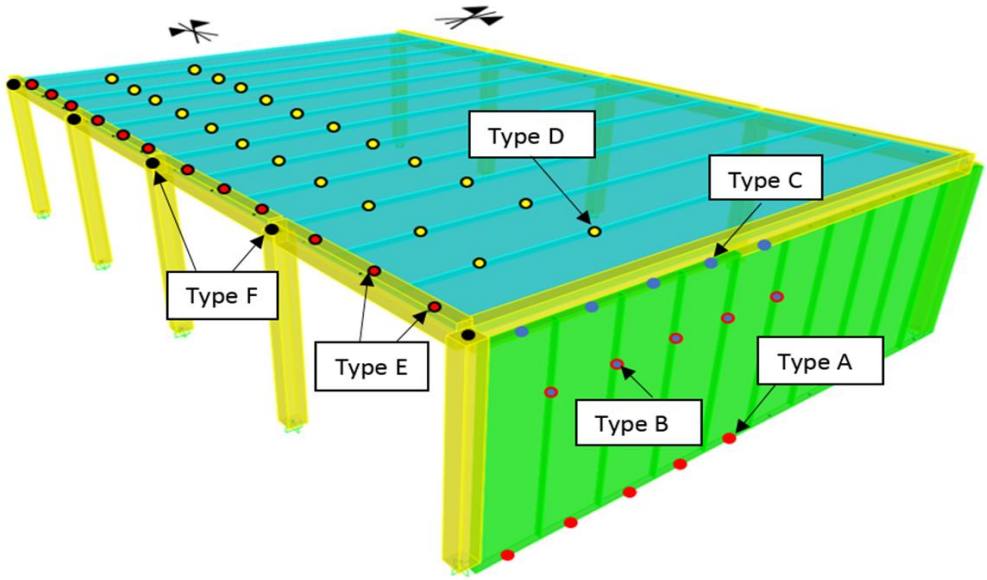


Figure 6. Half of the structural model and designation of connectors.

To study the energy dissipation characteristics of the entire structural model, the connection types were studied in three different variations. Table 2 displays the connection types and the variations.

Structural Model Variation	Cushion Characteristics					
	Type A	Type B	Type C	Type D	Type E	Type F
1	WEN 1	WEN 1	WEN 1	WEN 1	WEN 1	Rigid
2	WEN 2	WEN 2	WEN 2	WEN 2	WEN 2	Rigid
3	WEN 2	WEN 2	WEN 2	WEN 2	Elastic	Rigid

Table 2. Connection variations.

The structural variations are organized in order to observe the distribution of the energy dissipation by the connection types and accordingly which part of the structure is susceptible to the damage. Indeed, this approach is the motivation of the FP7 SAFECLADDING project and in this study, we realized how to manage the energy dissipation location which is the key to understand the energy based design. By means of this and further studies, a provision guideline would be recommended in the selection and the installation of the energy dissipation device for the slab-type precast structures with claddings.

3 GROUND MOTION RECORDS

The earthquake records used in the study was taken from PEER database [3] with respect to the soil conditions and the distance to the station using a selection and scaling procedure [4].

GM Set	Distance	Soil Condition	Probability of exceedance in 50 years (%)	Analyses Set Name	No of Records	Scaling Factors Range
1	Far Field (D_f > 15km)	Firm (Vs > 700m/s)	2	Farfield_Softsoil_0250	16	0.94 - 1.72
2			10	Farfield_Softsoil_1050	16	0.91 - 1.37
3			50	Farfield_Softsoil_5050	15	0.82 - 1.10
4		Soft (Vs < 300m/s)	2	Farfield_Firmsoil_0250	16	0.86 - 1.56
5			10	Farfield_Firmsoil_1050	16	0.61 - 1.04
6			50	Farfield_Firmsoil_5050	16	0.70 - 1.04
7	Near Field (D_f < 15km)	Firm (Vs > 700m/s)	2	Nearfield_Softsoil_0250	16	0.99 - 1.76
8			10	Nearfield_Softsoil_1050	17	0.80 - 1.31
9			50	Nearfield_Softsoil_5050	9	0.81 - 1.12
10		Soft (Vs < 300m/s)	2	Nearfield_Firmsoil_0250	17	0.93 - 1.82
11			10	Nearfield_Firmsoil_1050	18	0.58 - 0.95
12			50	Nearfield_Firmsoil_5050	13	0.67 - 1.09

Table 3: Properties of the ground motions.

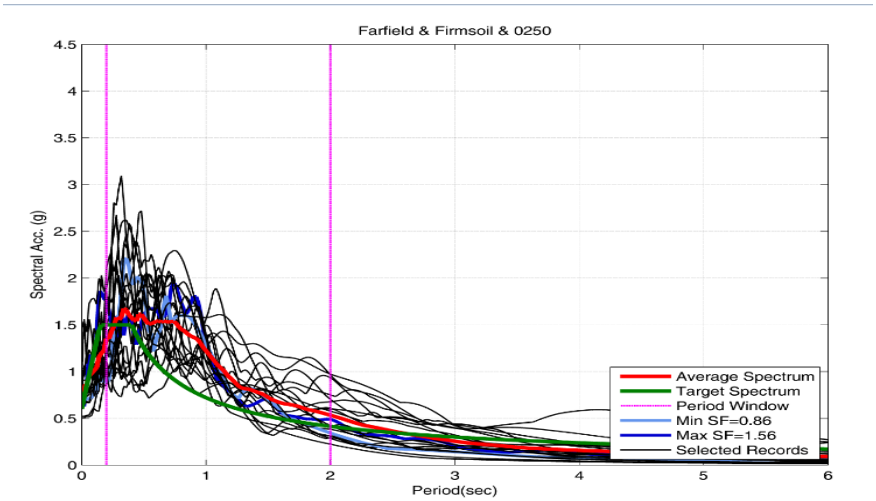


Figure 7: Set of Acceleration Spectrum for Far field-Firm soil 2/50 records.

4 ENERGY CALCULATIONS AND ANALYSIS ALGORITHM

The Energy Input (E_I) to the structures energy dissipation (E_H) values of the proposed device were derived from the results of extensive Nonlinear Time History Analysis (NTHA) repeated for each WEN constitutive models. The Energy Input (E_I) values for Single Degree of Freedom Systems is calculated according to Eq. 1.

$$E_I = -m \times \int_0^t \ddot{u}_g(t)du \tag{1}$$

where m is the assembled mass at the joint, $\ddot{u}_g(t)$is ground acceleration and du is the relative displacement of the joint. The total energy imparted into the structure was taken as the summation of the Energy Input values for each joint element. On the other hand, the Energy Dissipation (E_D) values were computed analytically from the closed force-displacement loop area of the cushions modeled in the FEM program.

To overcome the pre- and post-process of the NTHA, the Open Application Protocol Interface (OAPI) commands of the FEM program were employed into a MATLAB based algorithm (SAMA-SAFECLADDING) that runs in High-Power Computing Server in Istanbul Kultur University [5]. SAMA-SAFECLADDING algorithm starts with copying the structural model, adding dynamic nonlinear time history case with parameters such as acceleration data, duration, sampling time, running the analyses cases and finally extracting the response values. Having all the response and the ground motion data, the energy dissipation values were calculated automatically.

The developed MATLAB scripts those employ OAPI commands were used in the civil engineering education for all degrees and also in the research projects. All the steps for NTHA process preparation of the models, running the analyses, extraction of the responses for energy and engineering parameter calculations for each structural variation was less than the expected duration if one has done all the pre- and post-process steps. Considering the amount of the earthquake records of 185 with different length, this analysis period without any additional human involvement is significantly important in the parametric seismic resistance studies. Because, the effort is paid to the evaluation of the results instead of process run.

5 RESULTS

The energy imparted into the structures and the energy dissipated by the deforming connectors (cushions) were calculated according to the comprehensive NTHA analyses of three structural model variations having different connection types, Table 2. The values presented in the

following results were taken as the arithmetic mean values of all the NTHA for each analyses sets to represent the characteristics of the ground motion records i.e. soil condition, focal distance and seismic intensity.

The first structural model variation was created with all the connectors, except F, of WEN 1 behavior model and the most of the imparted energy dissipated by Type E (connecting slabs to the longitudinal beams) , then Type A (connecting cladding to the foundation) and Type B (connecting the claddings) was computed. As seen in Table 4, the remaining connectors of Type C (connecting the claddings to the transversal beam) and Type D (connecting the slabs) did not dissipate much energy.

Analyses Set Name	EH/EI ratio (%)						ENERGY INPUT (kNm)
	TYPE A	TYPE B	TYPE C	TYPE D	TYPE E	TYPE F	
Farfield_Softsoil_0250	2.23	1.23	0.06	0.02	40.33	0.00	1275.51
Farfield_Softsoil_1050	2.12	1.33	0.06	0.02	45.92	0.00	774.51
Farfield_Softsoil_5050	1.78	1.48	0.08	0.02	60.20	0.00	156.23
Farfield_Firmsoil_0250	2.13	1.22	0.06	0.02	43.43	0.00	1028.47
Farfield_Firmsoil_1050	1.97	1.45	0.07	0.02	51.42	0.00	394.82
Farfield_Firmsoil_5050	1.79	1.56	0.08	0.02	59.49	0.00	96.13
Nearfield_Softsoil_0250	2.50	1.23	0.05	0.03	33.72	0.00	784.76
Nearfield_Softsoil_1050	2.43	1.35	0.06	0.02	39.69	0.00	377.20
Nearfield_Softsoil_5050	2.14	1.24	0.07	0.02	48.82	0.00	156.27
Nearfield_Firmsoil_0250	2.60	1.28	0.06	0.03	36.03	0.00	658.26
Nearfield_Firmsoil_1050	2.26	1.34	0.07	0.02	48.06	0.00	200.95
Nearfield_Firmsoil_5050	1.99	1.27	0.07	0.02	46.54	0.00	139.78

Table 4. Structural Model variation 1

The second structural model variation was created with all the connectors, except F, of WEN 2 behavior model and the most of the imparted energy dissipated by Type E, then Type B and Type A was computed. Contrary to the Variation 1, the energy dissipation ratios for Type A and E will decrease whereas Type B and C will increase, Table 5. Because, the yielding level of the devices in variation 2 is set to higher than the Variation 1 as seen in Fig. 2.

Analyses Set Name	EH/EI ratio (%)						ENERGY INPUT (kNm)
	TYPE A	TYPE B	TYPE C	TYPE D	TYPE E	TYPE F	
Farfield_Softsoil_0250	0.91	2.23	0.09	0.03	27.72	0.00	1283.99
Farfield_Softsoil_1050	0.83	2.29	0.13	0.04	32.09	0.00	794.18
Farfield_Softsoil_5050	0.62	2.67	0.22	0.04	45.31	0.00	151.80
Farfield_Firmsoil_0250	0.81	2.22	0.10	0.03	29.62	0.00	1039.65
Farfield_Firmsoil_1050	0.70	2.31	0.15	0.03	34.52	0.00	403.10
Farfield_Firmsoil_5050	0.64	2.70	0.23	0.03	45.37	0.00	100.07
Nearfield_Softsoil_0250	1.40	2.09	0.09	0.04	24.41	0.00	773.34
Nearfield_Softsoil_1050	1.19	1.92	0.11	0.04	24.85	0.00	367.77
Nearfield_Softsoil_5050	0.90	1.82	0.14	0.04	36.24	0.00	160.88
Nearfield_Firmsoil_0250	1.30	1.87	0.10	0.04	23.19	0.00	653.84
Nearfield_Firmsoil_1050	0.94	1.91	0.14	0.04	32.38	0.00	191.03
Nearfield_Firmsoil_5050	0.93	2.11	0.16	0.04	36.06	0.00	137.42

Table 5: Structural Model variation 2.

The third structural model variation was created with all the connectors, except E and F, of WEN 2 behavior model and so that the most of the imparted energy dissipated by Type B, then

Type A and Type C was computed. Keeping the Type E respond elastic by increasing the yield level, the energy dissipation of the structure has reoriented towards the connectors around the claddings, Type A, B and C.

Analyses Set Name	EH/EI ratio (%)						ENERGY INPUT (kNm)
	TYPE A	TYPE B	TYPE C	TYPE D	TYPE E	TYPE F	
Farfield_Softsoil_0250	0.95	3.63	0.13	0.05	0.00	0.00	1323.79
Farfield_Softsoil_1050	0.95	3.93	0.20	0.05	0.00	0.00	820.71
Farfield_Softsoil_5050	0.89	6.08	0.48	0.06	0.01	0.00	153.21
Farfield_Firmsoil_0250	0.88	3.69	0.15	0.05	0.00	0.00	1070.36
Farfield_Firmsoil_1050	0.88	4.05	0.25	0.05	0.00	0.00	411.37
Farfield_Firmsoil_5050	0.89	6.36	0.54	0.06	0.01	0.00	106.12
Nearfield_Softsoil_0250	1.52	3.53	0.16	0.06	0.00	0.00	785.10
Nearfield_Softsoil_1050	1.38	3.07	0.17	0.05	0.00	0.00	363.01
Nearfield_Softsoil_5050	1.12	3.58	0.27	0.06	0.00	0.00	158.99
Nearfield_Firmsoil_0250	1.43	3.01	0.15	0.05	0.00	0.00	661.74
Nearfield_Firmsoil_1050	1.21	3.37	0.23	0.05	0.00	0.00	185.33
Nearfield_Firmsoil_5050	1.15	4.45	0.34	0.06	0.00	0.00	134.20

Table 6: Structural Model variation 3.

Noticing the Energy Input (EI) values for all structural variations it is clear that inelastic response characteristic of the devices do not significantly affect energy imparted into the structure. However, distribution of the energy dissipation within the structure is absolutely sensitive to cushion response characteristics.

6 CONCLUSIONS

The summary of the study is given in the following;

- One of the cushions studied in SAFECLADDING project, 8mm hollow cushion, was used in the analyses. The shear behavior of the cushion was determined from Material Tests.
- The numerical models of the cushion were defined by using a FEM analysis program. Two different behavior model based on WEN Model. The first model (WEN 1) fits the plastic region of the experimental hysteresis while the second (WEN2) is more consistent in the elastic region.
- Three variation of the structural model which has been used as benchmark case in SAFECLADDING project was studied with different connector types.
- Sets of ground motion records selected and scaled as the test data in SAFECLADDING were used in the Nonlinear Time History Analyses of the each structural variation.
- In total, 185 NTHA for each variation was conducted using a computer algorithm "SAMA-SAFECLADDING" that provides efficiency in the pre- and post-process. SAMA-SAFECLADDING algorithm was developed in MATLAB program using OAPI commands.
- The results of the NTHA were used in the computation of the Energy terms of Input (EI) and Plastic (ED).

According to the results of the study, the conclusions are listed as following;

- Energy dissipation within the structure is partly provided by the devices those can be plastically deformed. The deformation characteristic of these devices are related to the geometric and mechanical properties. Therefore, the behavior numerical model defined to the device influences the energy dissipation characteristics of the entire structure. As observed between the Structural Variation models 1 and 2, the increase in the yielding

level of the cushion (8mm hollow) significantly affects the energy dissipation values of the devices, therefore, higher the yield level results in lower energy dissipation which consequently affect the selection of the device properties.

- On the other hand, the change of the connector's response in one location, here it was the Type E in Structural Variation 3, resulted the reorientation of the energy dissipation values of the cushions. Therefore, it may be possible to control the energy dissipation distribution within the structure if the connectors' energy dissipation and deformation characteristics are predictable. The structural variation 3 clearly reveals the redistribution of the energy dissipation between the different connector locations.
- Comparing the results of the structural variations, the slabs freedom is more provided in the following order variation 1, 2 and 3. Larger drift of the mass is requires higher energy dissipation. Therefore, Type E connector should be taken as criterion in the evaluation of the behavior model for economical and safer design of the slab type structures. WEN 2 behavior model revealed that less amount of energy was dissipated by the cushions. Based on this fact, using WEN 2 model for the 8mm hollow cushions can be recommended for design.

The motivation of the FP7 SAFECLADDING project and also this study is to understand the influence of the cushion characteristic and location on energy dissipation of the structure. Having studied this influence on several numerical models it is highly possible to lead an energy based seismic resistance and design of the slab type precast structures.

In the future studies, the other cushions tested in SAFECLADDING will be included into the structural model variations in order to propose a guideline for optimized the energy distribution in slab type precast buildings.

REFERENCES

[1] SAFECLADDING EU Project - *Improved Fastening Systems of Cladding Panels for Precast Buildings in Seismic Zones*, 2012-2015

[2] SAP2000 v16.0, *Computers & Structures Inc.*, Berkeley, CA, USA

[3] PEER Strong Ground Motion Database, *Pacific Earthquake Engineering Research Center*, California, http://ngawest2.berkeley.edu/

[4] Bal, I. E. et al., "An engineering approach for structural-oriented earthquake record selection", *Second European Conference on Earthquake Engineering and Seismology*, Istanbul, Turkey, August 24-29, 2014.

[5] Dindar, A.A, Önen, Y.H. and Tugan, B., A cloud computer applicaton in civil engineering education and research: SAMA, *In the proceedings of 11th Advances in Civil Engineering*, 21-25 October, Istanbul, Turkey. 2014

[6] Priestley, M. J. N. Overview of PRESSS Research Program. *Journal of Precast Concrete Institute*. Vol. 36, no. 4, pp. 50-57, 1991

[7] Kelly, J. M., Skinner, R. I., and Heine, A. J., Mechanisms of Energy Absorption in Special Devices for use in Earthquake Resistant Structures. Bulletin of the New Zealand Society for Earthquake Engineering. Vol. 5, no. 3, pp. 63-73, 1972

[8] Khajehdehi A., Güllü A., Gökçe T., Özkaynak H., Yüksel E., Karadoğan F., Cyclic test of the precast panels equipped with steel cushions. *Poster Presentation in Second European Conference on Earthquake Engineering and Seismology*, Istanbul, Turkey, August 25-29, 2014

[9] MATLAB Release 2014b, *The MathWorks, Inc.*, Natick, Massachusetts, United States.

5th ECCOMAS Thematic Conference on
Computational Methods in Structural Dynamics and Earthquake Engineering
M. Papadrakakis, V. Papadopoulos, V. Plevris (eds.)
Crete Island, Greece, 25–27 May 2015

SEISMIC FRAGILITY ANALYSIS OF EXISTING URM BUILDINGS: A STUDY ON KATHMANDU VALLEY

Sujan Shrestha[1], Lorenzo Colarusso[2], Domenico Liberatore[3] and Daniela Addessi[4]

[1] Dept. of Structural and Geotechnical Engineering, Sapienza University of Rome
Via Antonio Gramsci 53, 00197 Rome, Italy
e-mail: suzan_sth@yahoo.com

[2] Dept. of Structural and Geotechnical Engineering, Sapienza University of Rome
Via Eudossiana 18, 00184 Rome, Italy
e-mail: lorencola@gmail.com

[3] Dept. of Structural and Geotechnical Engineering, Sapienza University of Rome
Via Antonio Gramsci 53, 00197 Rome, Italy
e-mail: domenico.liberatore@uniroma1.it

[4] Dept. of Structural and Geotechnical Engineering, Sapienza University of Rome
Via Eudossiana 18, 00184 Rome, Italy
e-mail: daniela.addessi@uniroma1.it

Keywords: URM walls, Equivalent Frame Model, Capacity Spectrum Method, Fragility Curves.

Abstract. *Seismic fragility analysis is performed for the assessment of in-plane mechanisms of existing unreinforced masonry (URM) buildings of Kathmandu Valley. The equivalent frame model is used, which has been validated by analyzing the URM prototype tested at the University of Pavia and comparing the analytical results with the experimental outcomes. Existing URM buildings of Kathmandu Valley are firstly investigated by means of a Rapid Visual Screening survey, and the most representative buildings are selected as prototypes for the analysis. Monte Carlo simulation method is used to account for the uncertainty of the mechanical parameters of each prototype. Analyses are carried out both with correlated and uncorrelated distributions of uncertain parameters. Finally, fragility curves are calculated in terms of spectral displacement, according to the capacity spectrum method.*

1 INTRODUCTION

Nepal has a long seismic history due to its location on a very active tectonic zone. Three main fault lines, each running East to West, are causes of major earthquakes in Nepal: the main central thrust (MCT) at the foot of the greater Himalaya joining the midland mountains, the main boundary thrust (MBT) at the junction of the lesser Himalaya and the Siwalik, and the main frontal thrust (MFT) south of the Siwalik [ICIMOD, 2007]. These fault lines are the result of the subduction of the Indian plate under the Eurasian Plate (Figure 1).

Major earthquakes were reported in 1255 AD, 1810 AD, 1866 AD, 1934 AD, 1980 AD and 1988 AD. In 1934, the fault line that runs beneath the Kathmandu valley slipped causing a M 8.4 earthquake which destroyed more than 80,000 buildings and claimed 8,500 lives [United Nation Office for the Coordination of the Humanitarian Affairs (OCHA), 2013]. It was the last major earthquake which shook the city of Kathmandu and the surrounding valley. One of the most detailed studies may be found in the field memoir published by the Geological Survey of India [Jain, 1998].

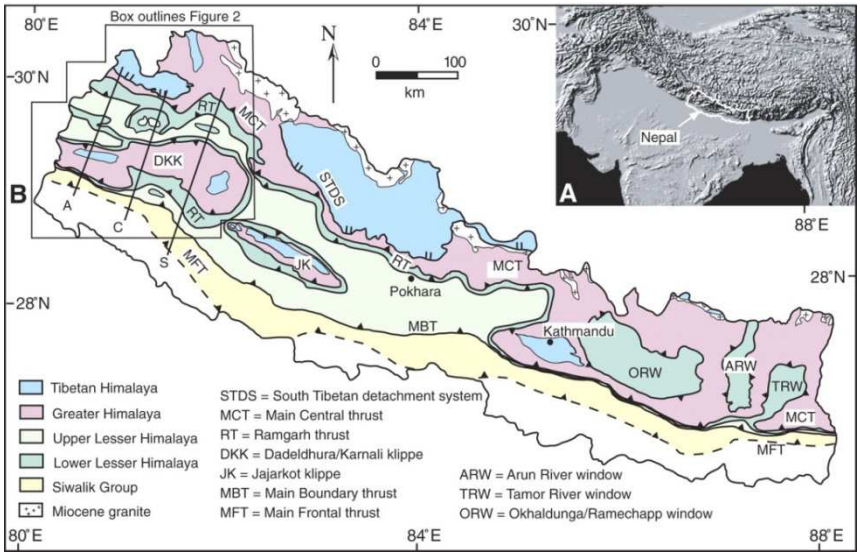


Figure 1: Major thrusts of Nepal (source: http://geosphere.gsapubs.org).

In Nepal, unreinforced brick masonry (URM) construction is the most common type in the historical sites of Kathmandu Valley. UNESCO has already included the historical centres of the three cities (Kathmandu, Bhaktapur, Lalitpur) of Kathmandu Valley into the World Heritage Sites. These sites are enriched with their unique architectural heritage, palaces, temples and courtyards with a symbiosis of Hinduism, Buddism and Tantrism, built between the 12th and the 18th centuries by the ancient Malla kings of Nepal.

Several studies on loss estimations have been carried out for the Kathmandu Valley. Two of such studies are the "Kathmandu Valley Earthquake Risk Management Project" (KVERMP, 1999) and the "Study on earthquake disaster mitigation in the Kathmandu valley, Kingdom of Nepal" carried out in 2002 by the Japan International Cooperation Agency (JICA) and the Ministry of Home Affairs, HMG of Nepal, 2002. Both studies estimate the damage to the buildings and the casualties in the case of repetition of the 1934 earthquake.

However, the definition of the building classes is not completely clear in these studies, as well as the mechanical properties of building materials. The Department of Survey categorizes the buildings into four classes, namely permanent, semi-permanent, temporary and other. Thus, it is difficult to develop fragility curves for such types of buildings.

Today, Kathmandu is a city completely different from that almost levelled in 1934. It has almost 3.0 million inhabitants, many living and working in buildings that will not withstand a significant seismic event. The present study is focused on the systematic categorization of the existing URM buildings, and investigates their in-plane response by means of static nonlinear analysis. Different uncertainty parameters regarding the mechanical properties of unreinforced masonry are considered, and the results are used to develop fragility curves in terms of spectral displacement.

2 EQUIVALENT FRAME MODEL

As shown by recent earthquakes [Penna *et al.*, 2014], [Sorrentino *et al.*, 2014a,b], when the masonry walls are properly constrained by horizontal structures and toothed with orthogonal walls, out-of-plane mechanisms are prevented and in-plane mechanisms can develop.

An equivalent frame model is commonly used by different authors [Magenes and Della Fontana, 1998], [Salonikios *et al.*, 2003], [Kappos *et al.*, 2006], [Pasticier *et al.*, 2008] for the analysis of nonlinear in-plane response of unreinforced masonry walls under horizontal seismic actions. A finite element model is used to define the equivalent frame model, consisting of vertical elements (piers) and horizontal elements (spandrels) (Figure 2). Intersection zones are considered rigid and the effective height of the piers is calculated using the formulation provided by [Dolce, 1991] (Figure 3):

$$H_{eff} = h' + \frac{1}{3h'} D\left(H - h'\right) \tag{1}$$

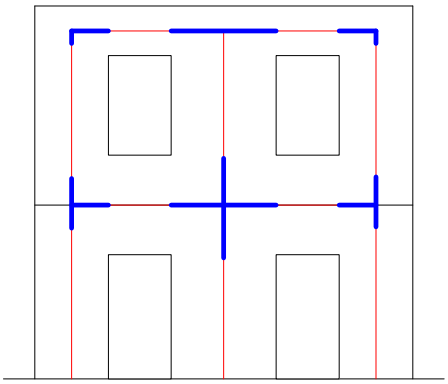


Figure 2: Equivalent frame model.

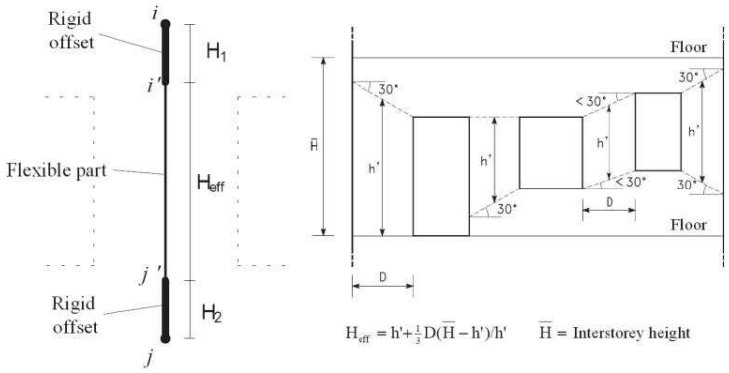
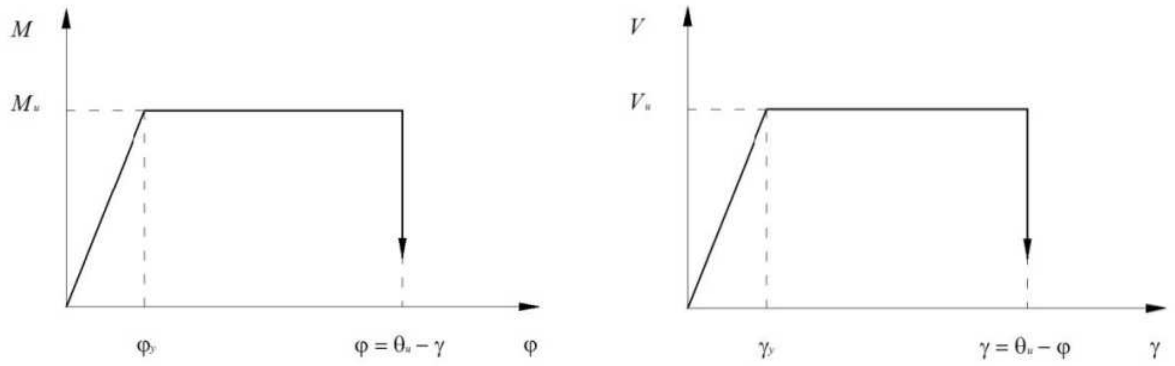


Figure 3: Effective height of piers [Dolce, 1991].

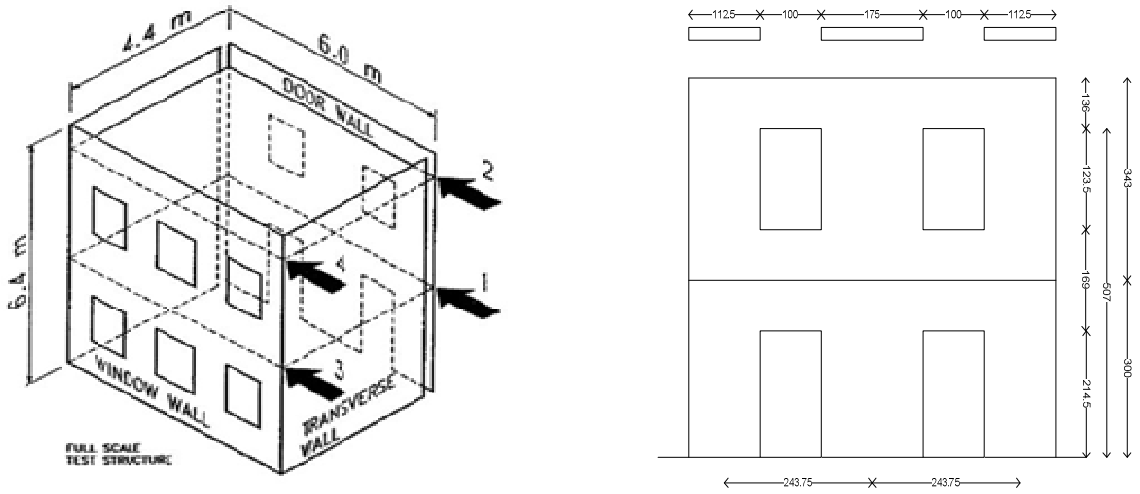
The finite element proposed by [Addessi *et al.*, 2015], [Liberatore and Addessi, 2015] is used in this study. The lumped hinge approach has been adopted in order to model the nonlinear constitutive response of masonry, introducing two flexural hinges at the ends of the element, together with a shear link, with elastic-perfectly plastic behavior (Figure 4).

The finite element is validated by comparing the numerical results on Pavia prototype door wall D with the experimental outcomes [Calvi and Magenes, 1994], [Calvi and Magenes, 1995]. The prototype consists of a two storey wall, with two door openings at the first level and two window openings at the second level (Figure 5).



a) Flexural response b) Shear response

Figure 4: Elastic-perfectly plastic behaviour of flexural hinges and shear link.



a) 3D model of the Pavia prototype b) Pavia door wall D

Figure 5: Geometric configuration of Pavia prototype.

Two uniformly distributed vertical loads are applied at the floor levels. The structural model is subjected to increasing lateral loads, applied at the floor levels, keeping 1:1 ratio between the loads at the first and second floor. In order to follow the softening branches, an external rigid vertical beam is introduced, hinged to the ends of the floors. The analysis is performed by controlling the displacement at the mid-point of the beam, which shares the reactive force in equal parts to the first and second floor.

The mechanical properties, based on the available experimental tests, are reported in Table 1. The FE model of wall D is shown in Figure 6.

E (MPa)	G (MPa)	f_m (kN/m^2)	f_{vk}(kN/m^2)
1900	500	2000	69.3

Table 1: Mechanical properties for Pavia door wall D.

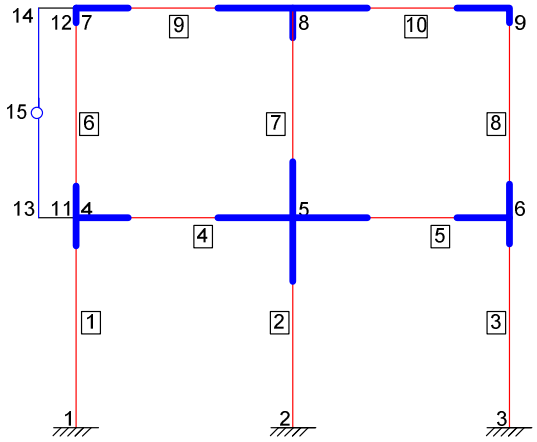


Figure 6: FE model of wall D.

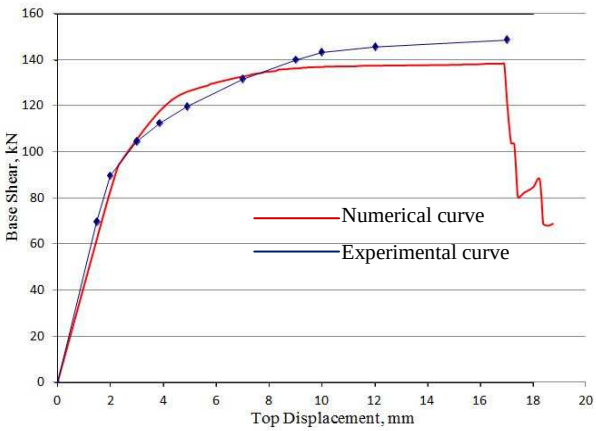


Figure 7: Experimental vs. numerical pushover curve.

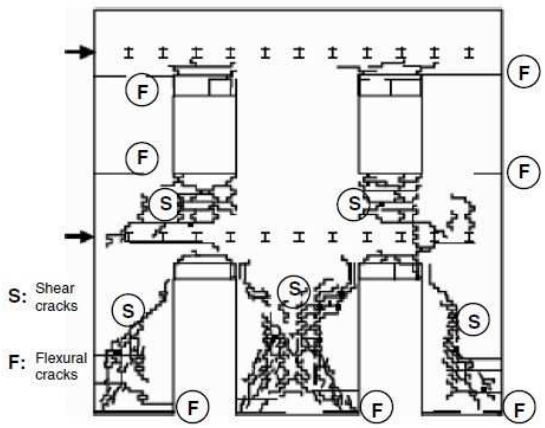


Figure 8: Crack formation from test result.

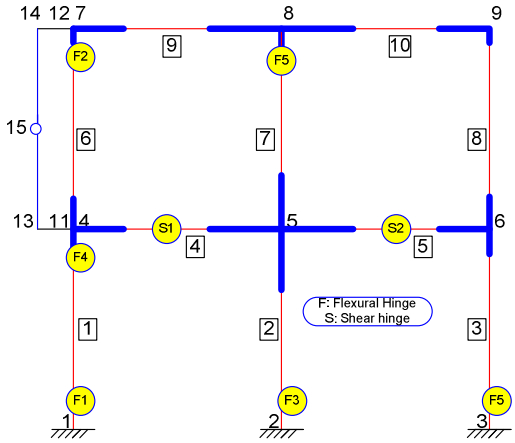


Figure 9: Hinge formation in analytical result.

The comparison between the numerical pushover curve and the experimental envelope curve, reported in Figure 7, shows a good agreement. For further verification of the results, the experimental crack pattern at drift 0.4% (Figure 8) is compared with the formation of hinges in the numerical model (Figure 9), showing again a satisfactory agreement.

3 ANALYSIS OF URM BUILDINGS OF KATHMANDU VALLEY

A preliminary survey was carried out in Bode, one of the historic cities of Kathmandu Valley, located in Madhyapur Thimi Municipality, Bhaktapur, according to the Rapid Visual Screening Method [FEMA, 2002]. Different structural and nonstructural parameters (e.g. storey's number, inter-storey height, materials, openings, age, dimensions of walls, observed damage, number of residents, etc.) of nearly 300 URM buildings were collected, and the buildings were grouped into different classes. Nine prototype walls are selected for the analysis, with storey's number ranging between 2 and 4 (2S, 3S, 4S) and bay's number ranging between 1 and 3(1B, 2B, 3B) (Figure 10).

The uncertainties associated with the mechanical properties of brick masonry are taken into account by deriving a set of variants using Monte Carlo simulation [Rota *et al.*, 2010], [CNR, 2014] The associated mean material properties and coefficients of variation, taken from

literature studies [Jaishi *et al.*, 2003], [Parajuli *et al.*, 2011a,b], [Parajuli *et al.*, 2012], [Parajuli, 2012], are reported in Table 2.

Parameter	Mean	St. Dev.	CoV	Lower bound	Upper bound
E (MPa)	509	101.8	20%	341.55	676.45
G (MPa)	204	40.8	20%	136.89	271.11
f_c (kN/m^2)	1820	364	20%	1221.27	2418.73
f_{v0} (kN/m^2)	100	20	25%	67.10	132.89
drift$_{sh}$ (%)	0.4	–	–	–	–
drift$_{fl}$ (%)	0.6	–	–	–	–

Table 2: Mechanical parameters of masonry adopted for the analysis.

Assuming that the mechanical parameters follow a normal distribution, 30 models of each prototype are generated for Monte Carlo analysis. The analysis has been conducted assuming either correlated or uncorrelated distributions of the parameters. As an example, the pushover curves for 2S2B wall under the hypotheses of correlated and uncorrelated distributions are shown in Figure 11. It has been seen that all pushover curves follow almost the same pattern in the case of correlated distributions, whereas they follow independent patterns, with higher scatter, in the case of uncorrelated distributions. Uncorrelated distributions of mechanical parameters are believed to provide more realistic results.

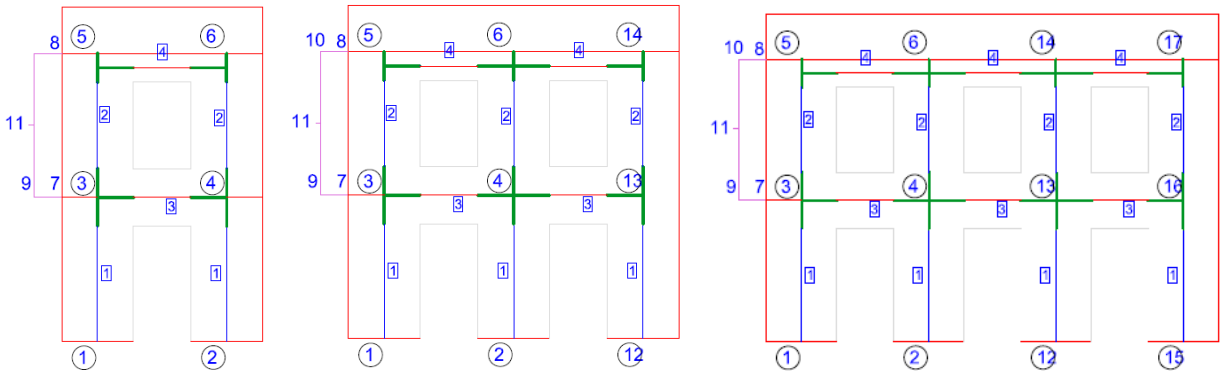
The original pushover curves are converted into capacity spectrum curves, where spectral acceleration (S_a) is plotted vs. spectral displacement (S_d), according to the AD format [ATC, 1996]. The displacement shape, normalized to top displacement, is shown in Figure 12 for different storey's numbers.

Figure 13 shows the capacity curves bi-linearized according to [ATC, 1996], i.e. equalling the area under the bilinear curve to that of the effective capacity curve, and assuming the same initial stiffness. It can be observed that the effect of the variation of storey's number is predominant compared to bay's number. Furthermore, the yielding spectral acceleration is lower for higher storey's number, due to the increase of seismic loads caused by the greater weight of the wall. The numerical values corresponding to the yield point and the ultimate point are shown in Table 3.

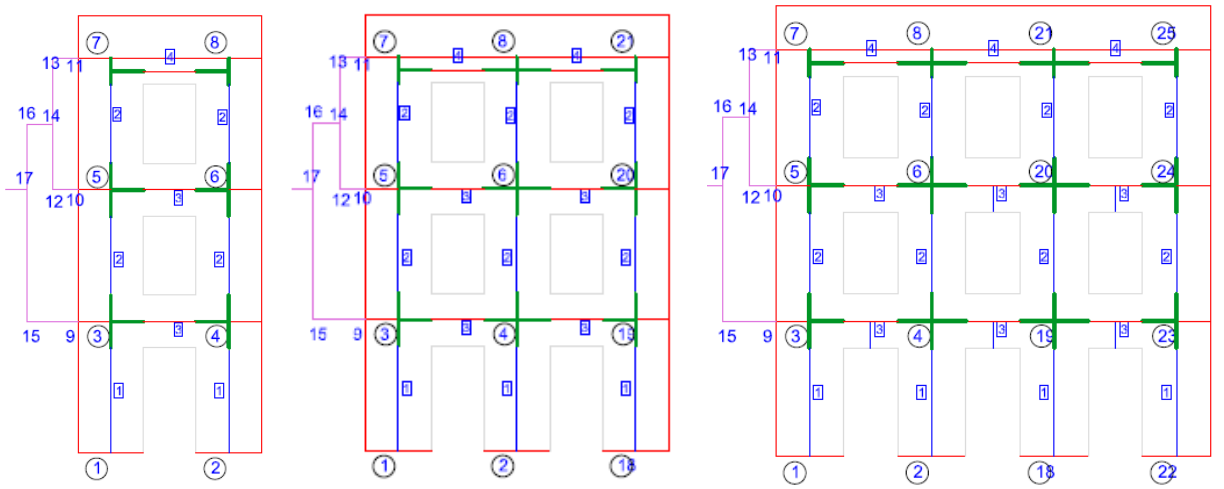
4 FRAGILITY CURVES

The fragility curve represents the conditional probability of being in or exceeding a particular damage state (*ds*), given the seismic ground motion. Different measures of the latter can be adopted: the peak ground acceleration, the spectral acceleration, the spectral displacement, etc.. In this study, the spectral displacement is used, assuming a lognormal cumulative distribution for fragility curves [FEMA, 2003]:

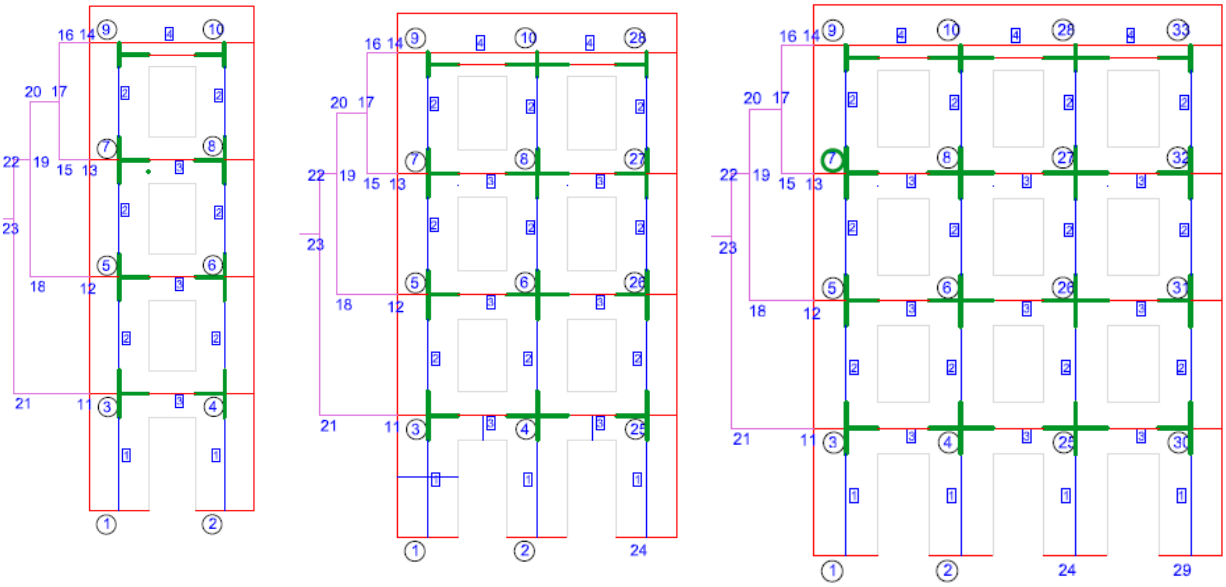
$$P[ds \mid S_d] = \Phi\left[\frac{1}{\beta_{ds}} \ln\left(\frac{S_d}{\overline{S}_{d,ds}}\right)\right] \tag{2}$$



a) 2S1B b) 2S2B c) 2S3B

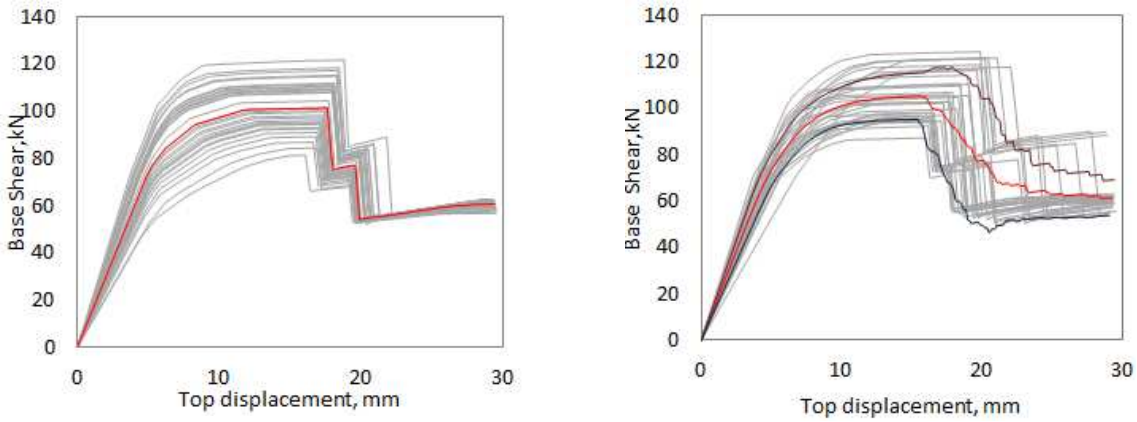


d) 3S1B e) 3S2B f) 3S3B



g) 4S1B h) 4S2B i) 4S3B

Figure 10: Equivalent frame model of prototype wall models.



a) Correlated distributions

b) Uncorrelated distributions

Figure 11: Pushover curves for 2S2B wall for correlated and uncorrelated distributions of mechanical properties.

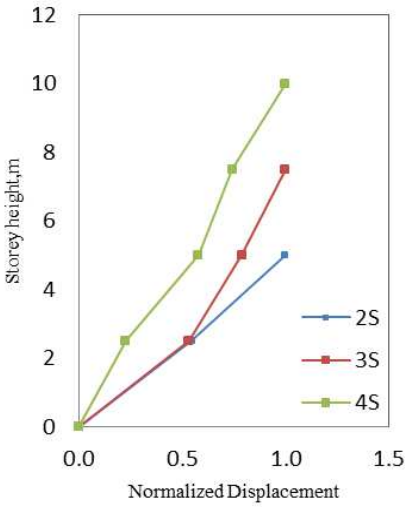


Figure 12: Displacement shapes normalized to top displacement.

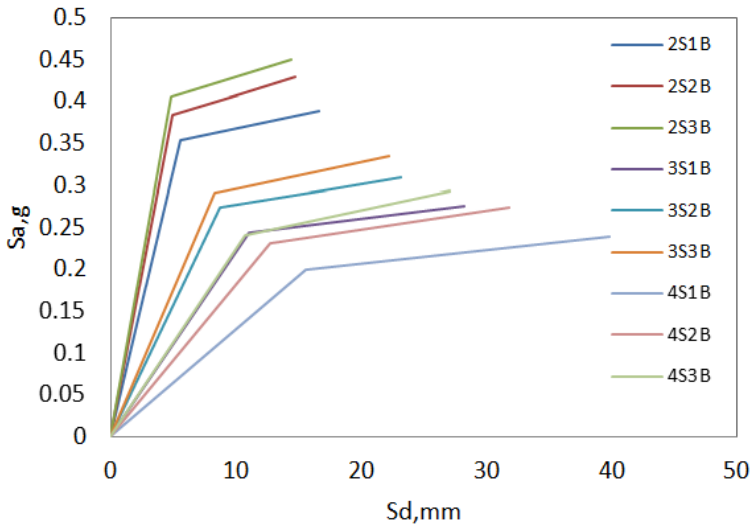


Figure13: Set of idealized bilinear capacity spectrum curves.

Model	S_{dy} (mm)	S_{ay} (g)	S_{du} (mm)	S_{au} (g)
2S1B	5.54	0.353	16.63	0.389
2S2B	4.90	0.383	14.67	0.429
2S3B	4.85	0.405	14.33	0.450
3S1B	11.00	0.244	28.19	0.275
3S2B	8.75	0.274	23.17	0.310
3S3B	8.30	0.290	22.24	0.335
4S1B	15.54	0.199	39.79	0.239
4S2B	12.70	0.231	31.84	0.273
4S3B	10.76	0.293	27.04	0.293

Table 3: Points of idealized bilinear curves.

where, $\overline{S_{d,ds}}$ is the median value of the spectral displacement corresponding to damage state *ds* and β_{ds} its standard deviation. The parameter β_{ds} describes the total variability of the fragility curve for a given damage state and depends on the variability associated with the capacity curve β_C, the demand spectrum β_D and the discrete threshold of the damage state $\beta_{M(ds)}$, and is given by:

$$\beta_{ds} = \sqrt{(CONV[\beta_C \beta_D])^2 + (\beta_{M(ds)})^2} \tag{3}$$

The HAZUS method was originally developed as a tool for estimating seismic scenarios corresponding to a given earthquake; it was later adapted for estimating the loss according to the Probabilistic Seismic Hazard Assessment (PSHA), i.e. considering the occurrence of all possible earthquakes [FEMA, 2003]. In this case the dispersion of the demand is already modelled in the PSHA and shall be removed from the seismic fragility curves to avoid counting it twice; the dispersion becomes accordingly:

$$\beta_{ds} = \sqrt{(\beta_C)^2 + (\beta_{M(ds)})^2} \tag{4}$$

Dispersion values are provided by HAZUS for low rise URM buildings as function of the degradation of the structural system (Table 4).

Capacity curve variability β_C	**Degradation of structural system**								
	Minor			Major			Extreme		
	Damage variability $\beta_{M(ds)}$			Damage variability $\beta_{M(ds)}$			Damage variability $\beta_{M(ds)}$		
	Small (0.2)	Mod (0.4)	Large (0.6)	Small (0.2)	Mod (0.4)	Large (0.6)	Small (0.2)	Mod. (0.4)	Large (0.6)
Very small (0.1)	0.70	0.80	0.90	0.85	0.90	1.00	0.95	1.00	1.10
Small (0.2)	0.70	0.80	0.90	0.85	0.90	1.00	0.95	1.05	1.15
Moderate (0.3)	0.75	0.80	0.95	0.85	0.95	1.05	1.00	1.05	1.15
Large (0.4)	0.80	0.80	0.95	0.90	1.00	1.10	1.05	1.10	1.20

Table 4: Dispersion β_{ds} for URM buildings with degradation [FEMA, 2003].

The damage states can be defined: a) as quantities, local or global, relevant to the model response, or b) from the bilinearized capacity curve.

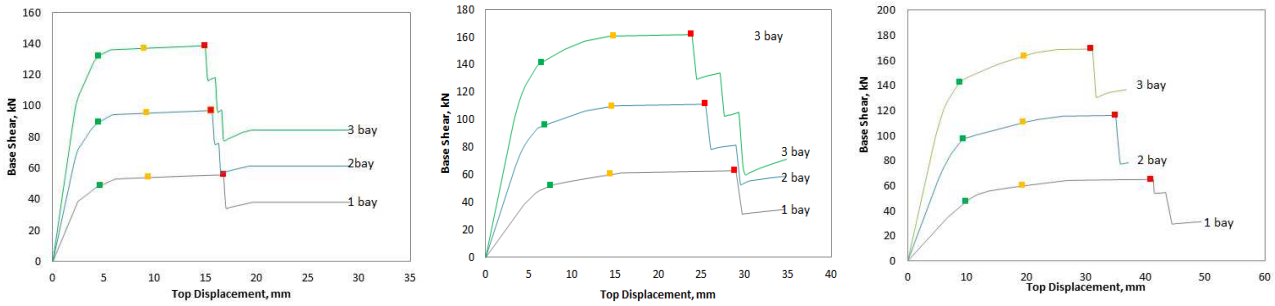
In the first case the damage states are associated with the achievement of predefined values of drift or characteristic points of the capacity curve. We considered four states of damage, or limit states. The Immediate Occupancy (IO) limit state is characterized by the achievement of 0.1% drift. The Damage Limit State (DLS) corresponds to the achievement of 0.2% drift. The third and fourth limit states are associated with the global response, as determined by the capacity curve. The Life Safety (LS) limit state is associated with the maximum base shear and the Collapse Prevention (CP) limit state with the 20% drop of base shear, compared to the maximum.

It can be observed that the 20% drop of base shear always occurs in coincidence with the attainment of the maximum. Therefore, for the models analyzed, the LS and CP limit states

coincide. The pushover curves for the different models, indicating the limit states, are shown in Figure 14, where the horizontal axis reports the mean value of the spectral displacement over the building population. The mean values of the spectral displacement for the different limit states are also given in Table 5 and Figure 15 for each model. It can be noticed that bay's number has negligible effect on the IO and DLS limit states. On the contrary, its influence is significant on the limit state LS. The fragility curves calculated according to this method are shown in Figure 16.

Damage state	2S1B	2S2B	2S3B	3S1B	3S2B	3S3B	4S1B	4S2B	4S3B
IO	3.842	3.704	3.674	6.091	5.527	5.229	7.272	6.969	6.557
DLS	7.671	7.536	7.394	11.685	11.821	11.972	14.304	14.508	14.562
LS	13.701	12.689	12.243	23.256	20.533	19.258	30.377	25.942	22.842

Table 5: Mean spectral displacements for the different limit states [in mm].



a) 2 stories b) 3 stories c) 4 stories

Figure 14: Median pushover curves with indication of the damage states.

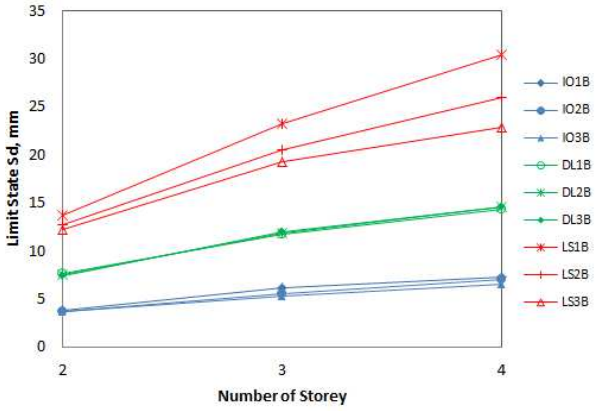
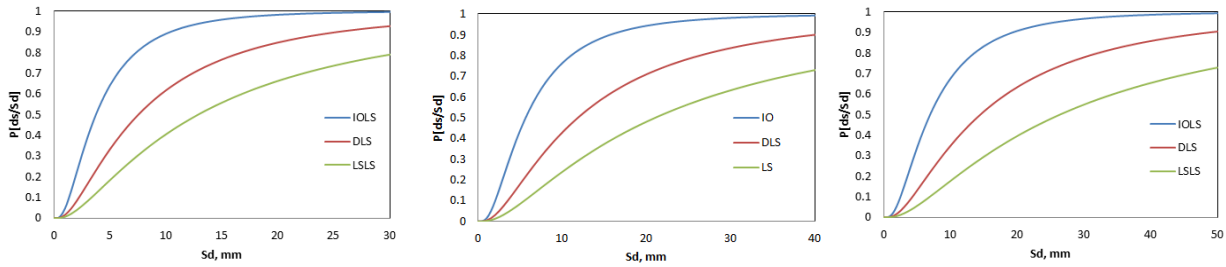


Figure 15: Mean spectral displacements.

The second method [Barbat *et al.*, 2006], [Giovinazzi, 2005], [Kappos *et al.*, 2002] operates on the bilinearized capacity curves. These are calculated on the basis of the median values of yielding acceleration and ultimate displacement. In this study, we adopt the definitions of the mean values corresponding to the damage states proposed by [Kappos *et al.*, 2002] yielding to the results reported in Table 6. The fragility curves obtained according to this method are shown in Figure 17.

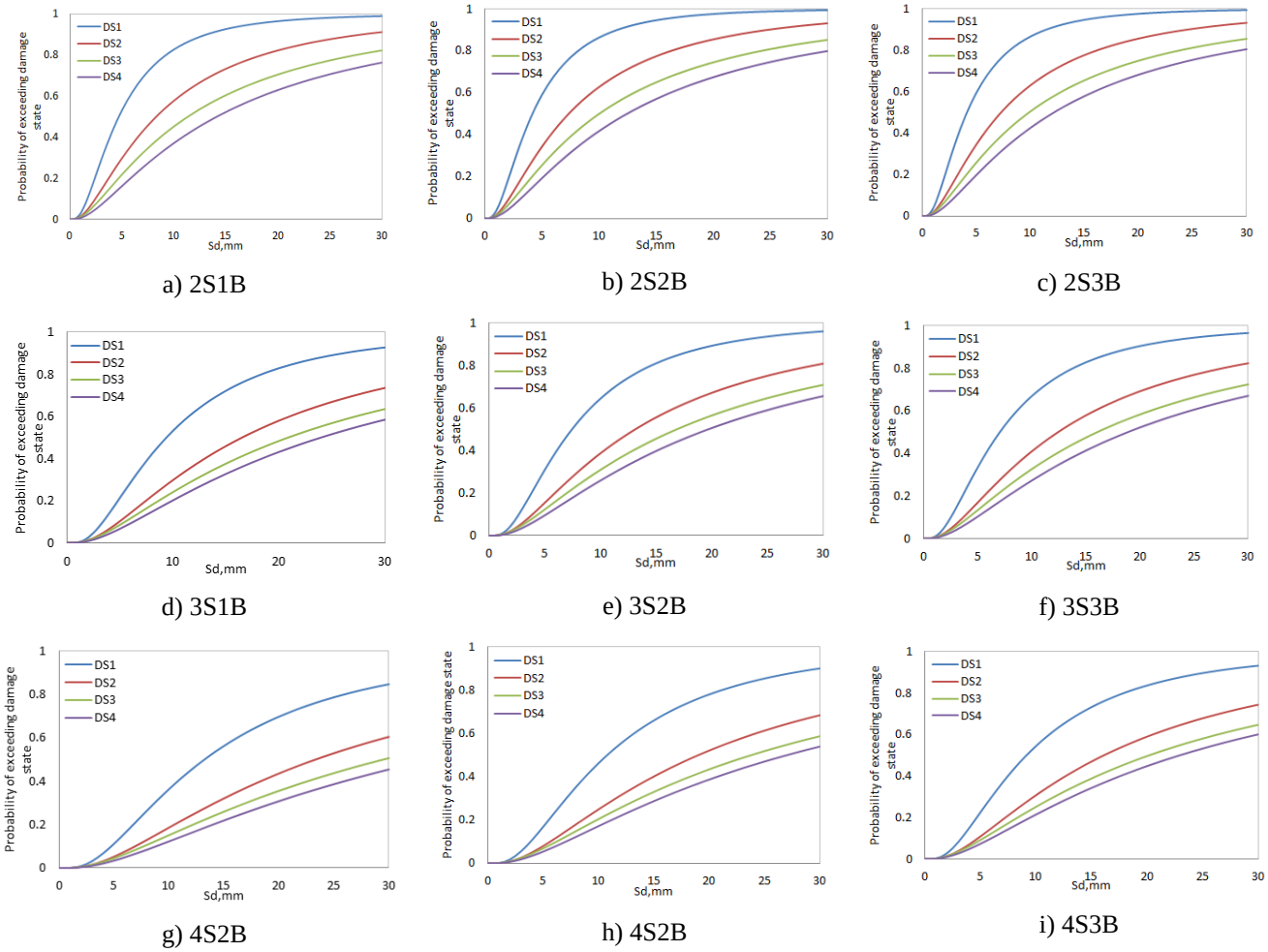


a) 2 stories b) 3 stories c) 4 stories

Figure 16: Fragility curves for URM walls (method a).

Damage state	2S1B	2S2B	2S3B	3S1B	3S2B	3S3B	4S1B	4S2B	4S3B
DS1	4.71	4.17	4.12	9.35	7.44	7.06	13.21	10.80	9.15
DS2	8.31	7.35	7.28	16.50	13.13	12.45	23.31	19.05	16.14
DS3	11.36	10.03	9.87	20.87	16.86	16.08	29.47	23.84	20.23
DS4	14.14	12.47	12.18	23.97	19.69	18.91	33.83	27.07	22.99

Table 6: Median damage state value [in mm].



a) 2S1B b) 2S2B c) 2S3B

d) 3S1B e) 3S2B f) 3S3B

g) 4S2B h) 4S2B i) 4S3B

Figure 17: Fragility curves for URM walls (method b).

5 CONCLUSIONS

This study presents the evaluation of the seismic vulnerability of existing URM buildings of Kathmandu Valley, based on fragility curves and the capacity spectrum method.

A set of prototype walls has been defined on the basis of a Rapid Visual Screening. The prototype walls represent not only the buildings in the surveyed area, but also other historical areas of Kathmandu Valley. A Monte Carlo simulation has been performed for the prototype walls under in-plane seismic actions varying the mechanical properties of masonry.

The prototype walls have been analyzed according to the equivalent frame model. Piers and spandrels are modelled with a central Timoshenko beam element, flexural hinges at the ends and a shear link with elastic-perfectly plastic behaviour. The node zones are modelled by means of rigid offsets. The comparison of the model with the experimental results of the full scale prototype tested at Pavia University showed a good agreement, both in terms of pushover curve and failure mechanism. The equivalent frame model results particularly suited for Monte Carlo simulation thanks to its small computational burden and its satisfying accuracy.

The fragility curves of the prototype URM walls have been derived through a stochastic nonlinear analysis. The uncertainties on the mechanical properties of masonry have been taken into account through Monte Carlo method. The analysis has been performed assuming either correlated or uncorrelated distributions of the mechanical properties. The hypothesis of uncorrelated distributions appears more realistic in describing the post-peak behaviour of the capacity curves.

Finally, the fragility curves have been derived either: a) by defining the damage states through quantities relevant to the model response (drift or capacity curve), or b) by defining the damage states on the bilinearized capacity curve.

ACKNOWLEDGEMENTS

The authors acknowledge the contribution of the European Commission through a PhD fellowship to the first author within the EU-NICE Erasmus Mundus Project.

This study was in part carried out under the programs of the “Dipartimento della Protezione Civile – Consorzio ReLUIS”, signed on 2013-12-27, Research Line Masonry Structures. The opinions expressed in this publication are those of the authors and are not necessarily endorsed by the Dipartimento della Protezione Civile.

REFERENCES

[1] Pradhan BK (2007) Disaster preparedness for natural hazards: current status in Nepal. International Centre for Integrated Mountain Development (ICIMOD), Kathmandu, Nepal.

[2] United Nations Office for the Coordination of Humanitarian Affairs (OCHA) (2013) Nepal: Preparing for an earthquake in the Kathmandu Valley. http://www.unocha.org/top-stories/all-stories/nepal-preparing-earthquake-kathmandu-valley.

[3] Jain SK (1998) Lessons from recent Indian earthquakes. Editorial as Guest Editor of Special Issue on Earthquakes in India. Indian Concrete Journal, 72(11).

[4] Kathmandu Valley earthquake risk management project (KVERMP) (1999) Geohazards International, http://geohaz.org/projects/kathmandu.html.

[5] Japan International Cooperation Agency (JICA), Ministry of Home Affairs, HMG of Nepal (2002) The study on earthquake disaster mitigation in the Kathmandu Valley, Kingdom of Nepal. Final Report.

[6] Magenes G, Della Fontana A (1998) Simplified non-linear seismic analysis of masonry buildings. Proc. of the 5th International Masonry Conference, London, 190-195.

[7] Penna A, Morandi P, Rota M, Manzini CF, da Porto F, Magenes G. (2014) Performance of masonry buildings during the Emilia 2012 earthquakes. Bull Earthquake Eng, 12(5):2255-2273. http://dx.doi.org/10.1007/s10518-013-9496-6.

[8] Sorrentino L, Liberatore L, Decanini LD, Liberatore D. (2014) The performance of churches in the 2012 Emilia earthquakes. Bull Earthquake Eng, 12(5):2299-2331. http://dx.doi.org/10.1007/s10518-013-9519-3.

[9] Sorrentino L, Liberatore L, Liberatore D, Masiani R. (2014) The behaviour of vernacular buildings in the 2012 Emilia earthquakes. Bull Earthquake Eng, 12(5):2367-2382. http://dx.doi.org/10.1007/s10518-013-9455-2.

[10] Salonikios T, Karakostas C, Lekidis V, Anthoine A (2003) Comparative inelastic pushover analysis of masonry frames. Engineering Structures, 25(12): 1515-1523.

[11] Kappos AJ, Penelis GG, Drakopoulos CG (2002) Evaluation of simplified models for lateral load analysis of unreinforced masonry buildings. ASCE, Journal of Structural Engineering, 128(7): 890-897.

[12] Pasticier L, Amadio C, Fragiacomo M (2008) Non-linear seismic analysis and vulnerability evaluation of a masonry building by means of the SAP2000 V.10 code. Earthquake Engineering and Structural Dynamics, 37(3): 467-485.

[13] Dolce M (1991) Schematizzazione e modellazione degli edifici in muratura soggetti ad azioni sismiche. L'Industria delle Costruzioni 242:44-57.

[14] Addessi D, Liberatore D, Masiani R (2015) Force-based beam finite element (FE) for the pushover analysis of masonry buildings. International Journal of Architectural Heritage, 9(3): 231-243. http://dx.doi.org/10.1080/15583058.2013.768309.

[15] Liberatore D, Addessi D (2015) Strength domains and return algorithm for the lumped plasticity equivalent frame model of masonry structures. Engineering Structures. http://dx.doi.org/10.1016/j.engstruct.2015.02.030.

[16] Calvi GM, Magenes G. (1994) Experimental research on response of URM building systems. In: Abrams DP, Calvi GM (Eds.), Proc. of the U.S.-Italy Workshop on Guidelines for Seismic Evaluation and Rehabilitation of Unreinforced Masonry Buildings. State University of New York at Buffalo, Technical Report NCEER-94-0021, 3-41/57.

[17] Calvi GM, Magenes G (1995) Indagine sperimentale e numerica su un prototipo di edificio in muratura: rapporto sullo sviluppo del progetto. Atti del 7° Convegno Nazionale "L'Ingegneria Sismica in Italia", Siena, 291-300.

[18] FEMA (2002) Rapid Visual Screening of Buildings for Potential Seismic Hazards – A Handbook. FEMA 154. Federal Emergency Management Agency, Washington, DC, U.S.A..

[19] Rota M, Penna A, Magenes G (2010) A methodology for deriving analytical fragility curves for masonry buildings based on stochastic nonlinear analyses. Engineering Structures, 32(5): 1312-1323.

[20] CNR (2014) Istruzioni per la valutazione affidabilistica della sicurezza sismica di edifici esistenti. CNR-DT 212/2013, Consiglio Nazionale delle Ricerche, Roma.

[21] Jaishi B, Ren W-X, Zong Z-H, Maskey PN (2003) Dynamic and seismic performance of old multi-tiered temples in Nepal. Engineering Structures, 25(14): 1827-1839.

[22] Parajuli HR, Kiyono J, Tatsumi M, Suzuki Y, Umemura H, Taniguchi H, Toki K, Furukawa A, Maskey PN (2011a) Dynamic characteristic investigation of a historical masonry building and surrounding ground in Kathmandu. Journal of Disaster Research, 6(1): 26-35.

[23] Parajuli HR, Kiyono J, Maskey PN, Taniguchi H (2011b) Investigations of material properties on old brick masonry buildings of Kathmandu. Disaster Mitigation of Cultural Heritage and Historic Cities, 5.

[24] Parajuli HR, Maskey PN, Taniguchi H (2012) Vulnerability assessment of the old brick masonry buildings. Disaster Mitigation of Cultural Heritage and Historic Cities, 6: 61-66.

[25] Parajuli HR (2012) Determination of mechanical properties of the Kathmandu World Heritage brick masonry buildings. Proc. of the 15th World Conference on Earthquake Engineering, Lisboa.

[26] ATC (1996) Seismic Evaluation and Retrofit of Concrete Buildings. Report ATC-40, Applied Technology Council, Redwood City, California, U.S.A..

[27] FEMA (2003) HAZUS MH MR4. Technical Manual. Federal Emergency Management Agency, Washington, DC, U.S.A..

[28] Barbat, AH, Yépez Moya F, Canas JA (1996) Damage scenarios simulation for seismic risk assessment in urban zones. Earthquake Spectra, 12(3): 371-394.

[29] Giovinazzi S (2005) The vulnerability assessment and the damage scenario in seismic risk analysis, PhD Thesis, Technical University Carolo-Wilhelmina at Braunschweig, Braunschweig, Germany and University of Florence, Florence, Italy.

COMPDYN 2015
5th ECCOMAS Thematic Conference on
Computational Methods in Structural Dynamics and Earthquake Engineering
M. Papadrakakis, V. Papadopoulos, V. Plevris (eds.)
Crete Island, Greece, 25–27May 2015

MAPPING HAZARD POTENTIALS IN SEISMIC ZONES BASED ON GEOTECHNICAL DATA FOR DESIGNING TRANSPORTATION NETWORKS INFRASTRUCTURE

Mohamed I.S. Elmasry[1], Tarek M. Abdelaziz[1], and Amr T. Wagdy[1]

[1]Arab Academy for Science & Technology & Maritime Transport
elmasryi@aast.edu, tareqmaziz@yahoo.com, moro_1690@hotmail.com

Keywords: Hazard Potential, Seismic Zones, Geotechnical, Design, Transportation Networks, Infrastructure.

Abstract. *On designing transportation networks, bridges, as infrastructures, are found to be spreading in many locations along freeways and roads. Thus, designing bridges should cover all expected load cases and accounts for various foundation soil profiles in a reliable manner. To achieve that, correct dynamic structural analyses of bridges are required. However, the latter analyses, to be reliable, require the knowledge of the expected dynamic response of the soil-foundation-bridge structure system, which demands the characterization of dynamic soil properties using geophysical methods in advance. Consequently, and with taking into consideration the associated social and economic losses upon having partial or total damage of bridges in vital transportation networks, the effect of having different dynamic behaviors for different soil profiles under seismic actions must be accounted for. In spite of that, a major basic problem that lies in reality is the insufficient knowledge about the soil behavior under seismic waves as well as the scarcity of data for the different sites before designing. This is the case especially when knowing that the national design codes account for large areas per a single seismic zone, which may thus include different soil profiles for different sites, and sometimes in the same site. This should eventually yield an error in estimating the design dynamic loads for different soil profiles and foundation systems lying in a single seismic zone.*
The introduced research herein generally studies the bridge foundations vibrations under seismic events. The paper proposes initiating a map that includes a hazard potential impact factor for the different areas having different soil profiles. The resulting map should categorize the hazard potential as per the geophysical data obtained from site investigations. The case study here is Alexandria Governorate in Egypt, assumed lying within the 2nd seismic zone as per the Egyptian design code. In contrast, the General Egyptian Authority for Educational Buildings, in its soil categorization map, divides this Governorate into nine regions with different soil profiles. The proposed approach counts on actual in-situ investigations, to derive the soil dynamic properties then the results are integrated into a dynamic model for the soil-structure interaction. Finally, the simulation results associated with statistical models for earthquake occurrence are used to obtain a seismic hazard potential impact factor for each region. Results can be used to trace the best locations for infrastructures as bridges lying within transportation networks.

1 INTRODUCTION

Bridge structures during their lifetime may in practice be subjected to severe dynamic excitations as earthquakes. Damage resulting from such excessive lateral loading and its location is usually unexpected. Thus, protection of strategic structures as bridges against excessive loading hazards from earthquakes has become actually one of the very essential targets for civil engineers and seismologists. This is the case especially on knowing that the economic and social effects of earthquake disasters can be efficiently reduced through a comprehensive assessment of seismic hazard and the associated risk for areas that have a history of earthquake occurrence events. Such assessments are usually reflected in design estimates of earthquake intensity loads to achieve a reliable earthquake-resistant design for new structures, and should eventually lead to increased public awareness, with a consequent upgrading of the existing structures and the corresponding engineering works [1].

However, the soil profile properties under any structure cannot be neglected in such an assessment since the soil underneath structures is undoubtedly the medium that transfers the seismic excitation to the structures foundations. The process in which the response of the soil influences the motion of the structure and the motion of the structure influences the response of the soil is termed as soil-structure interaction (SSI) [2]. Moreover, studying the soil formation in any region, one can recognize that the geological conditions, topographic characteristics and climatic conditions play a vital role in such soil formation. Thus, soil is generally considered as a three-phase system (air, water and solid) causing significant changes in the system characteristics due to interaction of these phases under applied dynamic or static loads [3]. Accordingly, determination of dynamic soil properties is a critical requirement in geotechnical-earthquake engineering problems.

Dynamic soil properties namely shear wave velocity, variation of stiffness or modulus reduction and material damping with strain levels, and liquefaction susceptibility parameters are the primary input parameters for various dynamic studies and investigations. Generally, soil properties depend on different state parameters such as the state of stress, void ratio, confining stress and water content, stress history, strain levels, and drainage condition. In addition to the influence of the above mentioned parameters, dynamic soil properties are significantly influenced by the dynamic amplitude and frequency of the applied dynamic load. Thus, estimation of the dynamic soil properties as the shear modulus and damping characteristics requires correct consideration of all the above-mentioned influencing parameters. The latter estimations should thus be the key to both fundamental understanding of soil behavior and subsequently practical application of soil modeling programs.

Moreover, field evaluation of dynamic soil properties predominantly aids in the estimation of the shear wave velocity and implicitly the shear modulus at low strain level. Meanwhile, laboratory based evaluations helps in the estimation of a realistic range of dynamic soil properties (*e.g.* experiments carried out in a specific strain-controlled environment) at varying strain levels [3]. For example, the cyclic triaxial method has been the most widely used to measure the strength, deformation and dynamic characteristics of soils [3].

This paper outlines the effect of the foundation soil profile properties on the seismic response of loaded foundations of bridges. It is shown that this factor, varying from one location to another, requires careful consideration when deriving the design response spectra in national codes. Moreover, stiffness and damping parameters are assumed for different soil profiles and used in a structural dynamic model to observe the response of the soil underneath the foundation together with the foundation itself. This is done in order to see the amplification resulting from different soil profiles lying within a zone that is initially estimated in the national codes to have the same design loads for similar structures. Finally, based on the obtained results, a seismic ha-

zard potential impact factor distribution map is obtained for different regions, categorized as per the soil profiles, lying within a defined single seismic zone in the national codes.

2 PROBLEM DEFINITION

Civil Structures such as bridges in transportation networks may be subjected to severe dynamic excitations as earthquakes. Thus, decent dynamic structural analysis and design of superstructures as bridges requires the knowledge of the dynamic response of the soil structure underneath. This in turn relies on the foundation soil dynamic properties. In spite of that, insufficient knowledge about the soil behavior in different areas under seismic ground waves is an annoying problem that must be better analyzed and well-studied by scientists editing national codes. The problem is even reflected in having a minimum number of categorized seismic zones in the national codes. This is the case such that each zone covers large areas including many regions with different soil profiles.

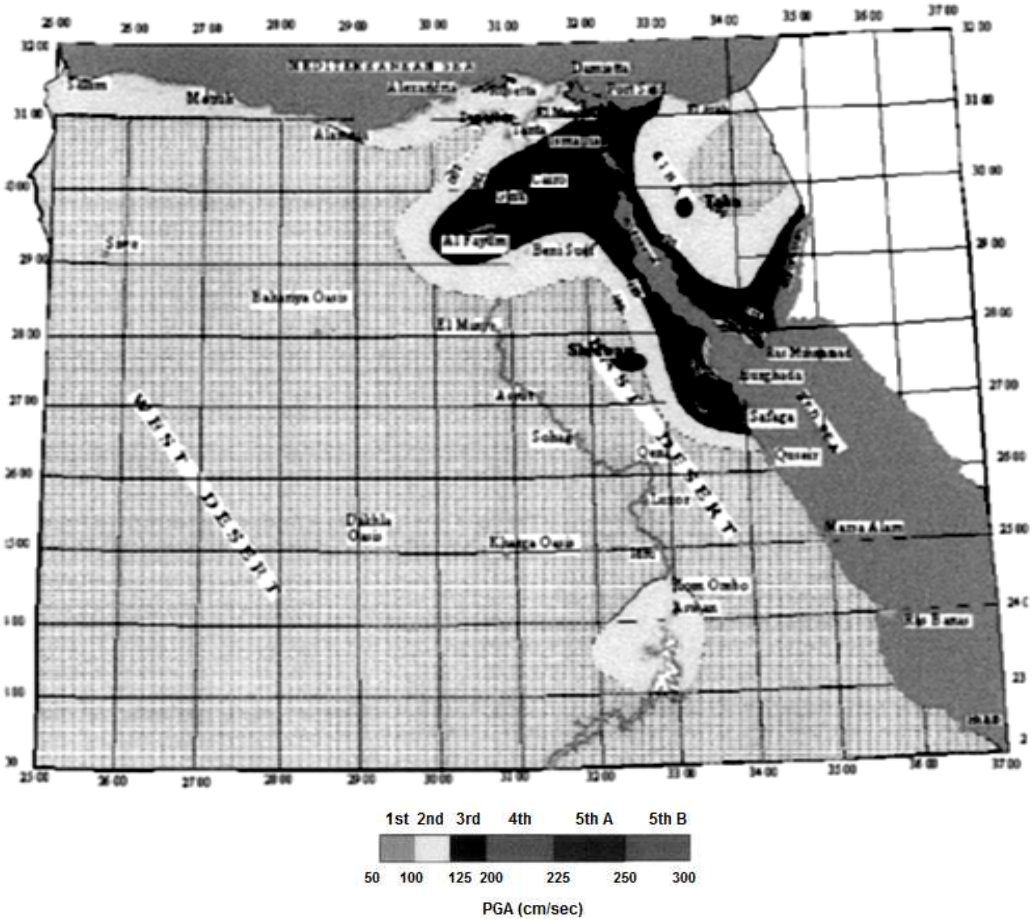


Figure 1: Seismic Zones as per the Egyptian Code of Loads [4]

In Egypt, for instance, the Egyptian Code of Design Loads [4] on designing structures supplies equivalent earthquake loads for defined seismic zones within the Egyptian territories. As shown in Figure 1. Each zone covers wide areas across the Egyptian lands such that it is expected and can be easily verified that many soil profiles with different properties lie undoubtedly in each zone. Consequently, the differences in soil profiles in areas as large as Alexandria Governorate and others are neglected. This is definitely unacceptable where dif-

ferent areas in Alexandria undergo different responses as evident from the descriptions of the buildings' tenants in different areas in the city after each earthquake or tremor occurrence.

Such problem should be urgently solved in order to avoid negative effects on designed and existing structures. Thus, the expected behavior of different soil profiles under seismic effect needs to be verified in advance. This application is important as it affects the design strategy of structures in general but mostly large and strategic ones including bridges. The loss of the latter structures not only would cause considerable life and economic losses but may sometimes initiates environmental hazards and economic impacts.

3 LITERATURE REVIEW

Subjected to similar testing conditions, a significant difference in the dynamic soil properties for characteristically different soils have been observed by earlier researchers[3].It has been observed that the dynamic soil properties are affected by many factors like: method of sample preparation in the laboratory (whether intact and reconstituted samples),relative density, confining pressure, methods of loading, overconsolidation ratio, loading frequency, soil plasticity, percentage of fines and soil type[3]. This should thus raise a flag of how important is considering the soil profile properties as a factor in design. In spite of that, the analysis of the dynamic soil properties is costly and may not be practical to apply for every borehole sample results, yet, using the SPT results may be helpful in anticipating such dynamic properties for the different samples [5].Earlier studies on the methodology of obtaining dynamic soil properties were presented by scientists and researchers to highlight the importance of each influencing parameter [3].

Moreover, over the past 40 years, a considerable progress had been made in understanding the nature of earthquakes and how the resulting damage takes place in structure, and consequently in improving the seismic performance of the built environment [6]. For instance, during a seismic event, ground motions propagating through the foundation soils transmit energy through the piles to the bridge superstructure. In turn, the bridge responds dynamically to these vibrations, and the resulting inertial forces are transmitted back to the soil through the pile foundations. This soil-structure interaction response of the bridge was modeled using foundation springs at the base of the pile caps. Figure 2 shows a schematic of a representative model (bascule pier) for analysis of the soil-foundation interaction and the model representing SSI in the global analysis of the bridge [7].

Furthermore, when subjecting piles to abrupt loads such as the case of seismic loads, piles may suffer structural damage that would threaten the integrity of the supported structures [8,9]. This is reflected in some cases where extreme effects sometimes took place after some seismic events tragically in terms of human lives losses, material and financial losses like what happened in Niigata earthquake (1964) in Japan and Izmit earthquake (1999) in Turkey [8,9].Thus, a suitable model for representing soil-structure interaction is needed in order to obtain the expectations for the transferred excitations to the main structure under seismic event [10].

Furthermore, Egypt is considered to be one of the few countries among the world where earthquake activity has been documented during the past 4200 years (*e.g.* in 1210 and 600 B.C. and A.D. 778,967,1303,1874,and 1899), with earthquakes destroying parts of big cities , such as Cairo and Alexandria [11]. Figure 3 shows the tectonic boundaries and the seismicity data of the Eastern Mediterranean Region [12]. The Acronyms on the map represent: AEG – Aegean Sea; Al – Alexandria City; CY – Cyprus; ERA – Eratosthenes Seamount; FL – Florence; IB – Ionian Basin; MR – Mediterranean Ridge; LEV – Levantine Basin; LF – Levant Fault; ND – Nile Delta. Red diamond indicates the location of Abo-Zenema area

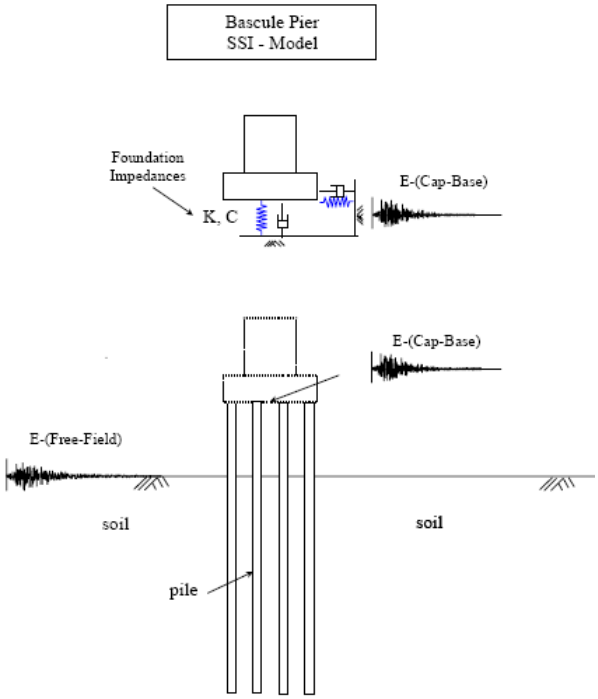


Figure 2: The local model for analysis of the soil-foundation interaction and the model representing SSI in the global analysis of the bridge [7].

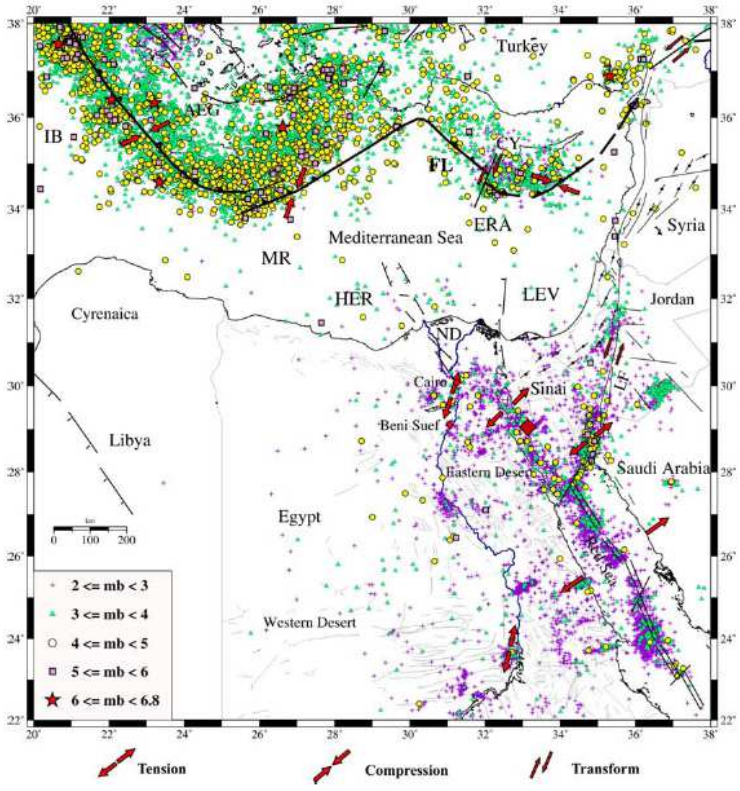


Figure 3: Tectonic boundaries of the Eastern Mediterranean Region [12]

The interaction of the African, Arabian, Eurasian plates and Sinai sub-plate is the main factor behind the seismicity of northern part of Egypt. All earthquakes occur at shallow depth and are concentrated at four seismic zones, these zones including the Gulfs of Suez and Aqa-

ba, around the entrance of the Gulf of Suez and the fourth one is located at the south- west of great Cairo (Dahshour area). The seismicity map of the previous zones shows that the activity is coincided with the major tectonic trends of the Suez rift, Aqaba rift with their connection with the great rift system of the Red Sea and Gulf of Suez- Cairo-Alexandria trend [13]. As shown at figure (1), Egypt's Position on the map is considered to be hazardous seismic activity area.

4 CASE STUDY

The main study herein focuses on the Alexandria Governorate lying in the North West coast of Egypt on the Mediterranean Sea. The reason for that is that Alexandria city used to be the capital of Egypt for centuries ago before building Cairo, the current capital, and because Alexandria city lies close to the active seismic zones of the southern Mediterranean area. The General Egyptian Authority for Educational Buildings [14] in its soil categorization printouts divides the governorate into nine main regions as shown in Figure 4. The categorization comes from the fact that every region has its own soil profile. Thus, if one of the regions is exposed to an earthquake event, it is expected that the profile response across the whole region will be nearly the same but different from other regions. This information was documented for structural engineers to design efficiently the educational structures within each region.

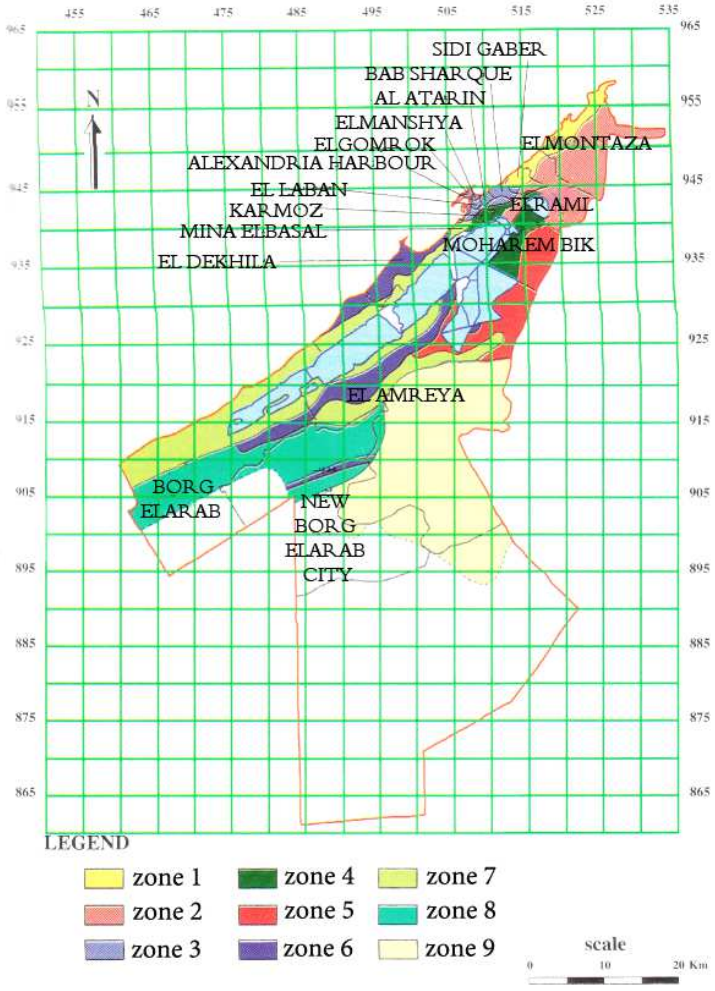


Figure 4: Main nine soil profiles regions across Alexandria governorate [14]

The research herein aims to identify the dynamic soil properties in the different regions in Alexandria city and incorporates the results in designing filters for the expected earthquake intensity in each region. On accomplishing the latter procedure, maps will be prepared for the whole Alexandria Governorate area, showing hazard potential areas for structures in the different regions. Moreover, modified response spectra design curves will be introduced for the design community in Alexandria taking into account the categorization as per the soil profiles. This is done by taking samples of borehole results for the different nine regions then estimating the dynamic soil properties for the studied soil profiles from boreholes results.

5 METHODOLOGY

Within the context of this paper, it is assumed that a set of similar bridges are needed to be built within a desired transportation network lying across Alexandria governorate. Each bridge is assumed bearing on portal frames as its supports. The foundation system of the bridges is assumed composed of piles lying under pile caps supporting the columns of the portal frames. The foundation system is assumed embedded in stratified soil profiles in the form of consecutive layers, as obtained from the borehole tests, as shown in Figure 5.

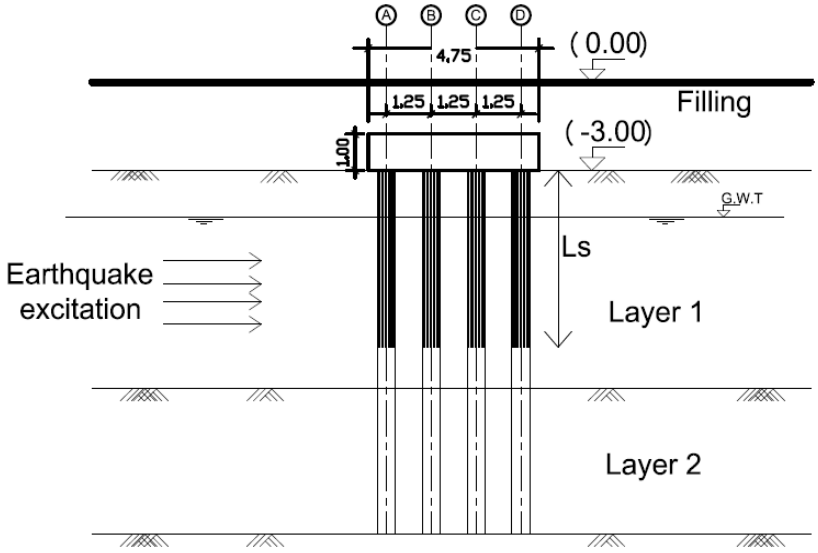


Figure 5: Typical Layout of the studied foundation system

5.1 Modeling

A shear building model, as shown at Figure 6, is chosen to represent the mathematical model of the soil-pile-cap system under earthquake excitation, where piles are divided along the vertical direction into horizontal strips. Moreover, developing the dynamic model for analyzing the soil-Pile-cap interactive response under earthquakes requires calculating stiffness for the pile group together with the soil wedge around it, estimating the mass of the interactive soil wedge surrounding the concrete piles during lateral excitation of the piles-cap system, and estimating the damping coefficients of the soil.

Furthermore, the length of the upper part of the buried pile that can be considered affected by seismic waves is defined as L_s. This affected length varies from soil profile to another according to the type of soil (dense sand, loose sand, soft clay, medium clay or stiff clay). The following Table (1) [15] indicates the design parameters n_h and K_h that are needed to evaluate L_s. This is the case where n_h is the horizontal subgrade reaction in the case of cohesionless soils, and K_h is the horizontal subgrade reaction in the case of cohesive soils.

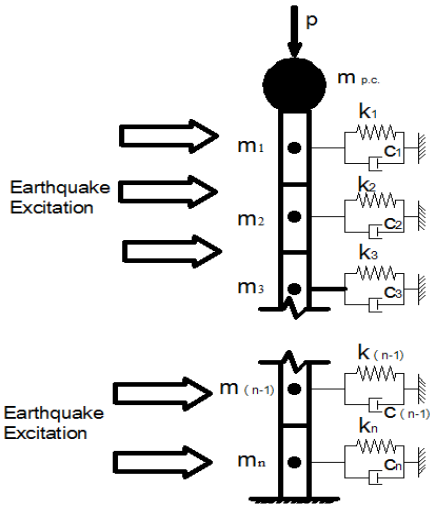


Figure 6: Shear Building model of interactive soil-concrete piles-cap system

Soil type		Site data			Design parameters			
		N	*c*	Ø	n_h (kN/m^3)		K_h	E_s
		Blows/0.3m	(*K*Pa)	degrees	Dry	Submerged	KN/m^2	KN/m^2
Cohesion less soils	Dense	30-50		45°	15×10^3	9×10^3		
	Loose	4-10		30°	2×10^3	1×10^3		
Cohesive soils	Hard	20-60	150-250				18×10^3	25×10^3
	Stiff	8-15	50-100				6×10^3	8×10^3
	soft	2-4	15-30				1.5×10^3	2×10^3

Table 1: Suggested Soil Stiffness Parameters for use in a Preliminary Seismic Analysis [15]

In general, the length of pile shaft between the level of the pile cap and the assumed starting point of fixation, L_s, can be evaluated from the following equations [15] such that in case of cohesionless soil,

$$L_s = 1.8\sqrt[5]{\frac{EI}{n_h}} \tag{1}$$

and in case of cohesive soil,

$$L_s = 1.4\sqrt[4]{\frac{EI}{K_h}} \tag{2}$$

where *E is* the modulus of elasticity of concrete, assumed 24 *G*Pa for a cubic strength of 30 *M*Pa [16], and *I* is the moment of inertia for the concrete pile cross section.

5.1.1. Mass Estimates

The mass of each strip is assumed lumped as shown at Figure 7, where $m_{p.c}$ is the mass of the pile cap, and m_i is the mass of the i^{th} strip. The lumped mass of each strip is evaluated as per the volume of the strips and the surrounding interactive soil wedge, see Figure 7. Each mass is assumed to have a single degree of freedom such that the number of degrees of freedom is relative to the number of masses [10]. It is important to note that not all the full depth of each studied pile undergoes lateral vibration due to earthquake excitation, but rather the affected buried depth only.

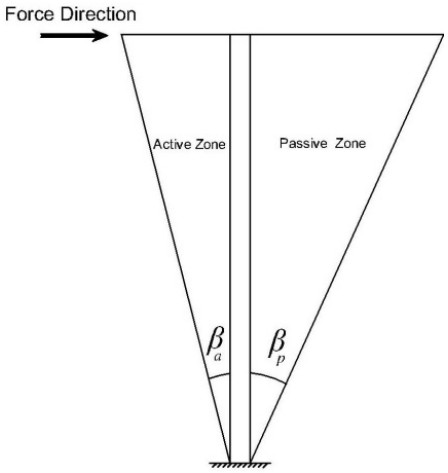


Figure 7: An elevation view showing the projection of the interactive soil wedge surrounding each concrete pile during lateral excitation of the piles-cap system [16]

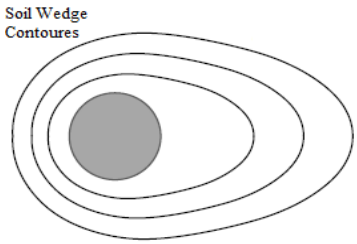


Figure 8: An example plan showing the effective soil wedge around the concrete pile in terms of contour lines [10]

This is the case such that the angles for the active and passive sides of the pile, β_a and β_p respectively, are obtained from,

$$\beta_a = 45 - \frac{\phi}{2} \tag{3}$$

and

$$\beta_p = 45 + \frac{\phi}{2} \tag{4}$$

where ϕ is the angle of friction of the sandy soil, and in the case of clay soil $\beta_a = \beta_P = 45°$.As evident from Figure 7, it can be easily concluded that the cross section of the interactive soil wedge is nearly elliptical or oval [17] such that the longer dimension of the oval ellipse can be obtained from

$$D_y = H \times (\tan \beta_a + \tan \beta_p) + d \tag{5}$$

and the shorter dimension can be assumed from

$$D_x \cong \frac{1}{2} \times H \times (\tan \beta_a + \tan \beta_p) + d \tag{6}$$

where D_x is the shorter oval ellipse dimension in the horizontal X-axis, and D_y is the longer oval ellipse dimension in the perpendicular horizontal Y-axis, and d is the pile diameter, and H is the full height of the concrete pile excluding the fixation length. Note that for large values of D_x and D_y, it is expected that the overlap between the effective soil surrounding each pile is large. Thus, it is advisory to draw the soil wedge for each pile in terms of contour lines as shown in Figure 8 and evaluate soil masses excluding the overlap areas or volumes for each strip.

5.1.2. Stiffness Estimates

To calculate the stiffness parameters for the pile, the equivalent cantilever method of stiffness is used where the buried length of the pile affected by seismic wave is defined as L_s as explained earlier, see Figure 9. Similarly, on calculating the piles group stiffness for each strip, the affected buried pile length, L_s, is divided into strip elements with stiffness each of

$$k_i = \frac{12\,EI}{h^3} \tag{7}$$

where k_i is the single pile strip stiffness, E is the modules of elasticity, and h is the strip element height.

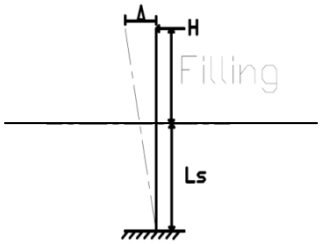


Figure 9: Equivalent Cantilever for foundation stiffness [15].

Moreover, the soil is model used as a linear hysteretic material of Young's modulus, E, Poisson's ratio, ν, material damping ratio, ζ, and shear velocity, v_s. Meanwhile, to calculate the single pile stiffness in the strips embedded in the sandy soil or clay soil, the geotechnical engineering software (*AllPile*) [18] is used. The software (*AllPile)* directly uses COM624S calculation methods for lateral analysis. For details on COM624, please refer to the FHWA publications [18,19]. In summary, COM624S uses the four nonlinear differential equations to perform the lateral analysis,

$$EI\frac{d^4Y}{dZ^4} + Q\frac{d^2Y}{dZ^2} + R - Pq = 0 \tag{8}$$

$$EI\frac{dY}{dZ} + Q\frac{dY}{dZ} = P \tag{9}$$

$$\frac{dY}{dZ} = S_t \tag{1}$$

$$EI\frac{d^2Y}{dZ^2} = M \tag{11}$$

where Q is the axial compression load on the pile, y is the lateral deflection of pile at depth z, z is the depth from top of pile, R is the soil reaction per unit length, E is the modulus of elasticity of the pile, I is the moment of inertia of the pile, and Pq is the distributed load along the length of the pile, P is the shear in the pile, S_t is the slope of the elastic curve defined by the axis of pile, and M is the bending moment on the pile.

5.1.3. Damping Estimates

Dividing the pile shaft length affected by seismic wave height into strips every 0.5m, the damping is assumed to be 3% in case of sandy soil and 2% for clayey soil [20,10]. In case of the presence of soft clay layers surrounding the pile shaft, the damping is assumed to be 1%, and neglected in case of filling layers.

5.1.4. Group interaction effects

Due to the fact that the distances between the piles are relatively small, it is expected that the interference between the soil wedges around the piles should result in reduction of the group total stiffness rather than summing the stiffness for each pile. Thus, a reduction factor for group effect is used [21]. Figure 10 shows the values of the P-multipliers (f_m) [21].

The f_m value, as indicated in Figure 10, decreases as the number of rows of piles increases. In addition, the f_m value decreases as well on decreasing the spacing of the rows. The values of f_m are relative to the load carried by each row of piles. The chart shows that the leading row takes most of the input energy. For piles spaced more than six diameters apart, the values of f_m are equal to 1.0, indicating that group interaction effects are negligible [21].

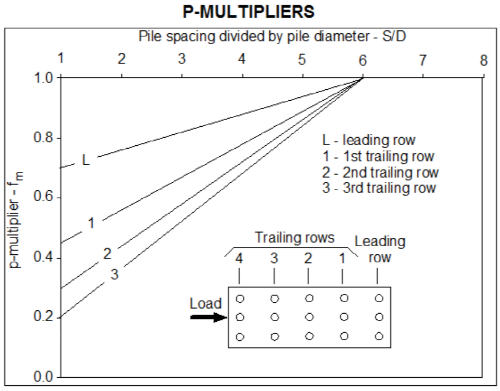


Figure 10: Piles group reduction factors [20].

5.2 Modeling Earthquake Excitation

An analytical model such as the state space model is applied for computing the dynamic response of the soil-piles-cap system studied. The soil-piles-cap system is then considered subjected to an earthquake along the buried depth of the pile. The seismic response of the system in different soil profiles is studied. The applied dynamic forces are assumed transmitted onto each pile through the buried part of the pile. In addition, the earthquake excitation is assumed to affect the piles-cap system along the buried depth of the piles. Thus, all strips under the soil top layer are excited with the same lateral excitation momentarily. This is the case where the seismic wave acting on the pile is assumed to have the same magnitude along the pile depth in the soil. Moreover, since the number of piles in the studied group is relatively large and the pile spacing, S, is equal to three times the pile diameter (relatively small), it is assumed that the lateral responses of all embedded piles will have the same phase. Furthermore, the dynamic time-domain responses of the shear building model of the system is obtained using a linear state space model using Matlab® software [22]. Thus, consider a linear structural model of the form:

$$\mathbf{M}\ddot{\mathbf{x}} + \mathbf{C}_d\dot{\mathbf{x}} + \mathbf{K}\mathbf{x} = \mathbf{b}f\,, \quad \mathbf{y} = \mathbf{C}_1\mathbf{x} + \mathbf{C}_2\dot{\mathbf{x}} + \mathbf{d}f \tag{2}$$

where **M**, **K**, and $\mathbf{C}_d$ are the mass, stiffness and damping matrices of the system, and $\mathbf{C}_1$, $\mathbf{C}_2$, and **d** are the output influence matrices for the displacement, velocity and the external force, *f*. Thus, one can write the model in a state-space form

$$\dot{\mathbf{q}} = \tilde{\mathbf{A}}\mathbf{q} + \tilde{\mathbf{B}}f\,, \qquad \mathbf{y} = \mathbf{C}\mathbf{q} + \mathbf{D}f \tag{3}$$

where

$$\mathbf{q} = \begin{bmatrix}\mathbf{x}^T & \dot{\mathbf{x}}^T\end{bmatrix}^T \tag{4}$$

is the state vector, $\tilde{\mathbf{A}}$ is the system state matrix which is dependent on the mass **M**, damping **C**, and stiffness **K** matrices of the structural system such that,

$$\tilde{\mathrm{A}} = \begin{bmatrix} 0_{\mathrm{nDOF}\times\mathrm{nDOF}} & \mathrm{I}_{\mathrm{nDOF}\times\mathrm{nDOF}} \\ (-\mathrm{M}^{-1}\mathrm{K})_{\mathrm{nDOF}\times\mathrm{nDOF}} & (-\mathrm{M}^{-1}\mathrm{C})_{\mathrm{nDOF}\times\mathrm{nDOF}} \end{bmatrix} \tag{5}$$

where *n*DOF is the number of degrees of freedom of the system. In addition, *f* is an excitation force, and **y** is a vector of measured responses. Moreover, $\tilde{\mathbf{B}}$ is the input influence matrix, **C** is the output influence matrix for the state vector **q,** and **D** is the direct transmission matrix.

5.3 Numerical Example

The main core related to the problem herein is studying the effect of a seismic event on a standard soil-foundation-bridge structure system located in different locations within the Alexandria governorate. The numerical study herein is a pile cap of a bridge as shown in Figure 11, assumed to be located in all various nine soil profile regions around Alexandria governorate, Egypt. The pile cap is assumed carrying a vertical load of 7500*k*N from the frame column which is carrying the main girder of the studied bridge.

The pile cap design foundation level is assumed to be at (-3.00) from ground level, for all the nine assumed soil profile regions, as per the General Egyptian Authority for Educational Buildings [14], see Figure 4. The diameter for each pile is 0.5*m* with a capacity of each assumed to be 500 *k*N. The piles are distributed forming a 4×4 array under the pile cap where the spacing between piles, *s*, equals 2.5 times the pile diameter. Thus, the side dimension of the resulting square pile cap is 4.75*m*, as shown in Figure 11.

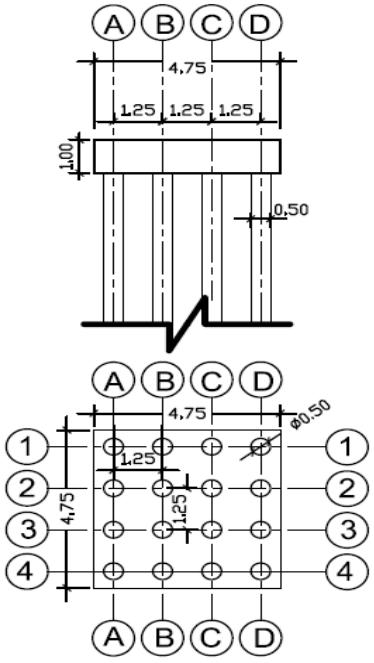


Figure 11: A layout of the studied foundation system

In addition, the studied bridge foundations are assumed to lie all in the same seismic active area as per the Egyptian Code [4], namely the second seismic zone of Egypt, corresponding to Alexandria governorate location on the seismicity map of Egypt, see Figure 1 [4]. The soil-foundation-bridge structure system is assumed subjected to an earthquake such as Aqaba (or Nuwaibaa) earthquake with a scaled max ground acceleration of 0.125*g*, corresponding to the max expected ground acceleration in the second seismic zone [4].

Furthermore, on applying the shear building model, the pile shaft is considered divided into strips of 0.5*m* height. The suggested soil-structure interaction dynamic model is applied on borehole samples taken among the nine zones of Alexandria, as shown in Figure 12. The stiffness factors for each borehole according to the pile length affected by seismic waves, L_s, are calculated as shown in Table 2. It is important to note that the number of strip elements differs from one borehole to another. In addition, on modeling the soil, the upper filling layers are neglected such the affected shaft length, L_s, starts below the filling layers, see Figure 9.

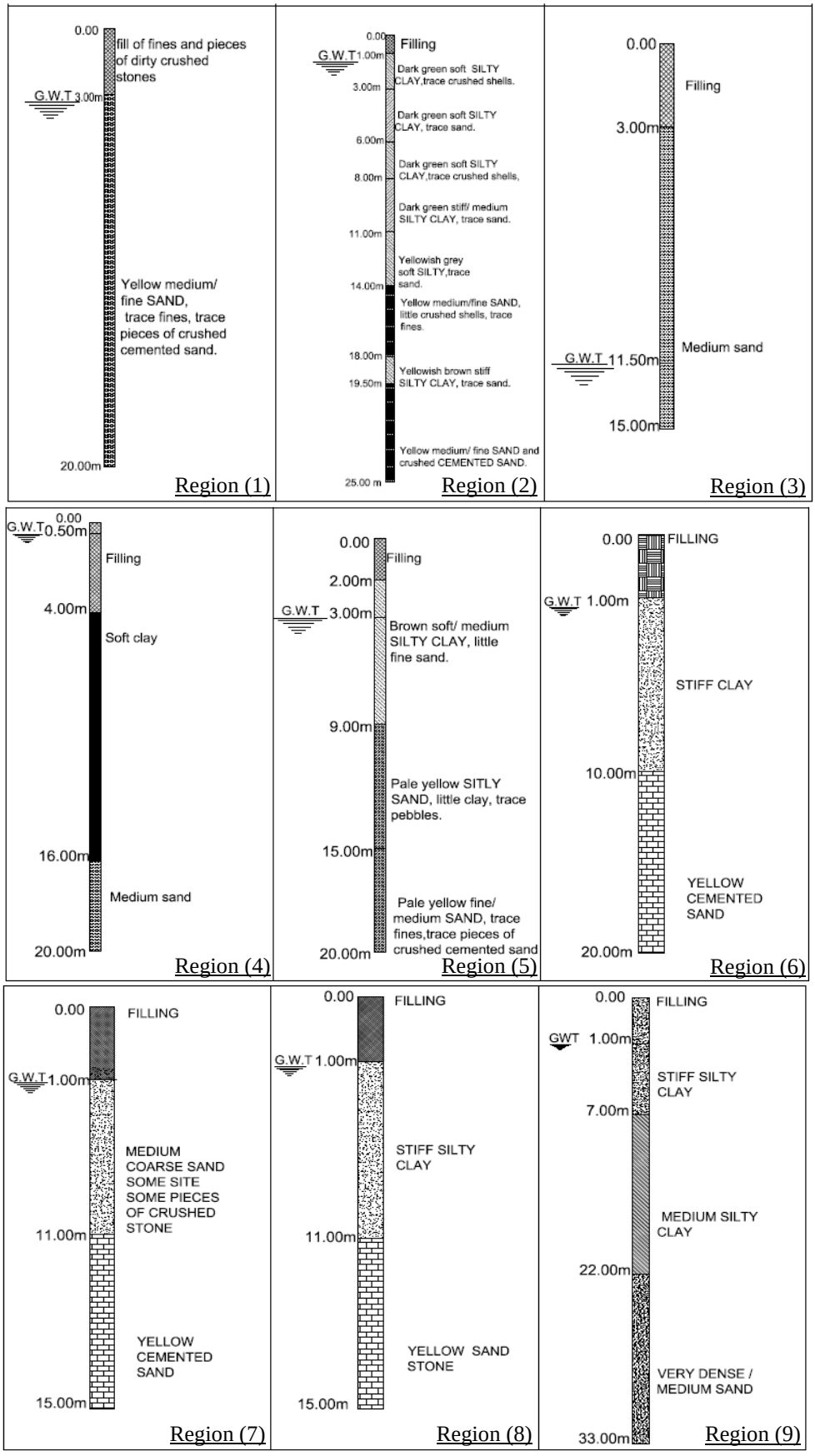


Figure 12: Borehole samples for regions (1 to 9) in the Alexandria governorate

Elements	Region (1) (L_s = 3m)			Region (2) (L_s = 4m)			Region (3) (L_s = 3m)		
	k_i *KN/mm*	m_i *Kg*	*D* %	*ki KN/mm*	m_i *Kg*	*D* %	k_i *KN/mm*	m_i *Kg*	*D* %
Pile cap	-	57498.72	-	-	57498.72	-	-	57498.72	-
1	6187146	32818.8	3.00	651449.5	56152.7	1.00	3444531	69116.1	3.00
2	6120767	26473.2		625519.6	46926.2		3164192	54933.8	
3	5898289	20744.4		594367.5	38596.8		3049068	42070.2	
4	5553329	15341.7		559203.1	30740.6		2870829	30354.8	
5	5117255	846.33		520997.8	23820.7		2645321	16037.9	
6	-	-		480564.9	17595.9		-	-	
7	-	-		427004.2	11977.2		-	-	

Elements	Region (4) (L_s = 4m)			Region (5) (L_s = 4m)			Region (6) (L_s = 3m)		
	k_i *KN/mm*	m_i *Kg*	*D* %	k_i *KN/mm*	m_i *Kg*	*D* %	k_i *KN/mm*	m_i *Kg*	*D* %
Pile cap	-	57498.72	-	-	57498.72	-	-	57498.72	-
piles only	57019.07	-	-	-	-	-	-	-	-
1	92958.67	37826.76	1.00	222969.1	56152.7	1.00	505889.7	35910.6	2.00
2	89858.98	31624.92		198388.6	46926.2		468439.7	28598.6	
3	86144.03	26026.04		180962.5	38596.8		427787.8	22158.3	
4	81877.8	20745.21		162778.6	30740.6		385234.4	16364.7	
5	77194.22	16093.83		144343.2	23820.7		341895.7	11135.3	
6	70253.57	11909.58		126032.7	17595.9		-	-	
7	61832.69	8132.82		108133.6	11977.2		-	-	

Elements	Region (7) (L_s = 3m)			Region (8) (L_s = 3m)			Region (9) (L_s = 3m)		
	k_i *KN/mm*	m_i *Kg*	*D* %	k_i *KN/mm*	m_i *Kg*	*D* %	k_i *KN/mm*	m_i *Kg*	*D* %
Pile cap	-	57498.72	-	-	57498.72	-	-	57498.72	-
1	8354382	43643.4	3.00	328242.3	34721.7	2.00	4574839	33745.8	3.00
2	8264865	34707		303934.7	27653.7		4596255	27172.5	
3	7964271	26601.5		137803.6	21428		5299374	21123.7	
4	7498635	19219.4		124090.3	15827.5		4541985	15534.4	
5	6909680	10198.2		110135.8	10772.5		4472552	7862.2	

Table 2: Model properties for the soil-foundation-structure system in the different 9 regions

6 ANALYSIS OF RESULTS

On subjecting the loaded soil-foundation system with an earthquake loading such as the Aqaba Earthquake (Egyptian Red Sea Coast, 1995), see Figure 14, the different soil profiles effect on the system is studied. The earthquake records are scaled to a maximum ground acceleration of 0.125*g* as per the second seismic zone code assumptions [4], see Figure 1. The nine soil profiles regions as identified by the Egyptian Authority of Educational Buildings [14] were considered on modeling the dynamic model and obtaining the parameters in Table 2. The Power Spectral Density (PSD) of the dynamic response of the assumed pile cap, as shown in Figure 11, when considering each of the nine regions, are obtained and shown in Figure 13. The curves in Figure 13 clearly indicate variation in the response for the different profiles. For clayey soil profiles even with being on top of sandy layers that the piles pene-

trated, yet, the resulting PSD curves show that the vibration transferred to the structure from the loaded soil-foundation system in case of regions 2,4,5,6,8 will excite the lower mode shapes of the overlaying bridge structural system in the frequency domain 0 to 10 Hz. Meanwhile, the vibration transmitted from the loaded soil-foundation system in zones 1,3,7,9 will excite the higher modes indicating lesser risks of excessive excitations of the bridge structure.

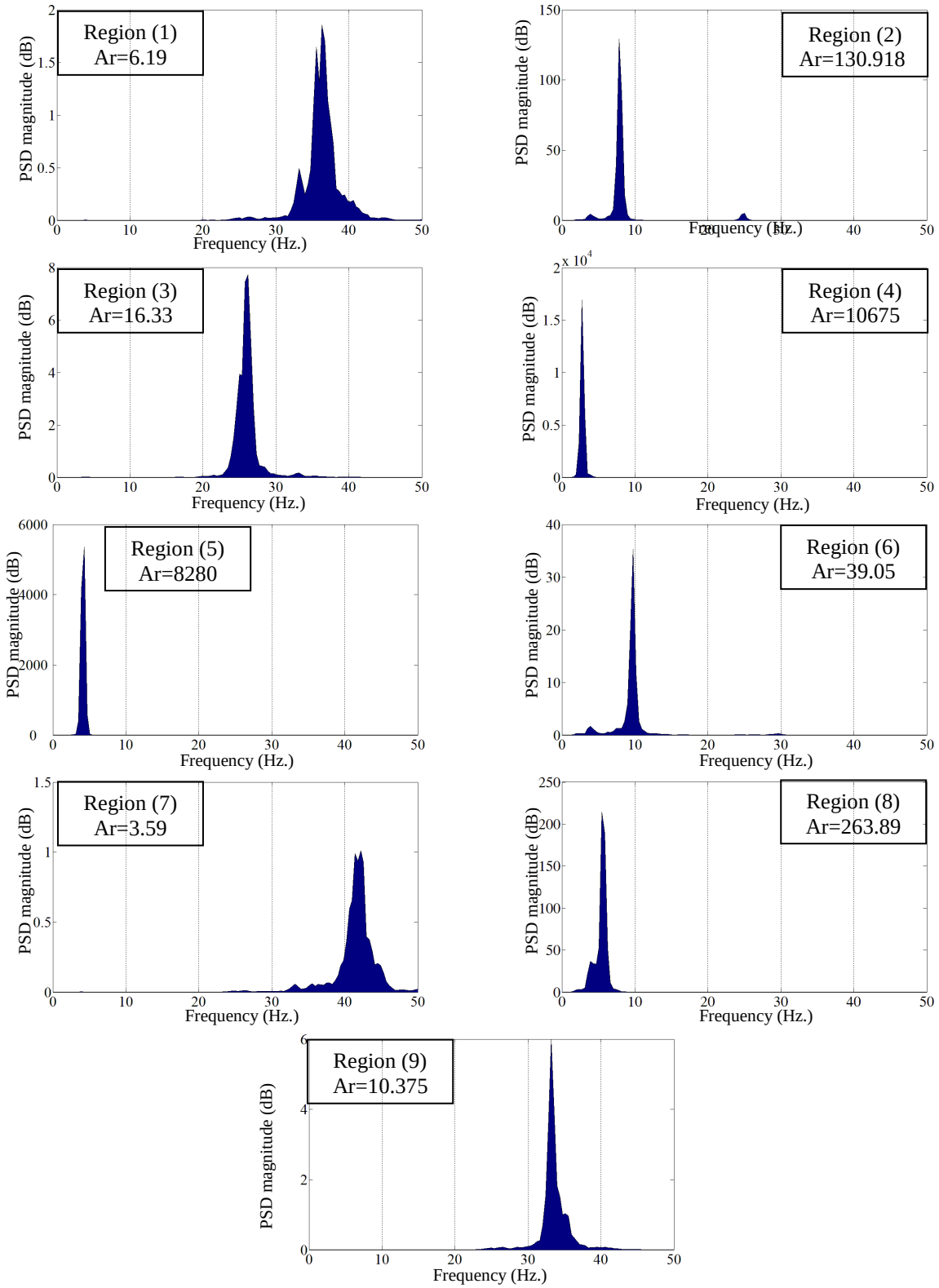


Figure 13: PSD for the loaded soil-foundation system for regions (1 to 9) in the Alexandria governorate

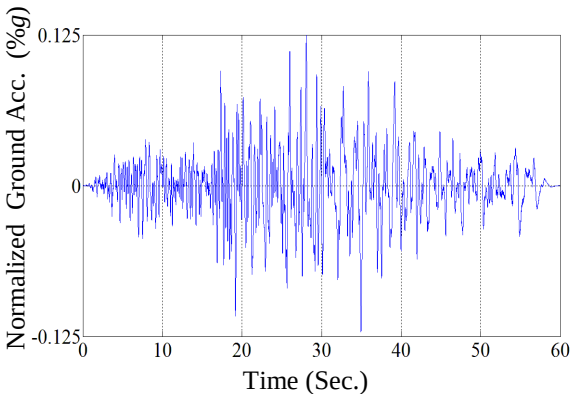


Figure 14: Normalized Aqaba earthquake ground acceleration time history (North-South direction)

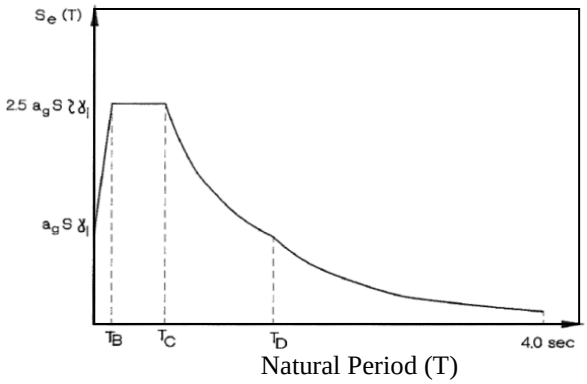


Figure 15: Design Response Spectra (ECOP 201 [4]) for the Egyptian Mediterranean shores

	Reg. (1)	Reg. (2)	Reg. (3)	Reg. (4)	Reg. (5)	Reg. (6)	Reg. (7)	Reg. (8)	Reg.
Fund. Freq.	36.613	8.021	25.929	2.754	4.171	9.662	42.341	5.638	33.607
Energy factor (*E*)	6.194	130.919	16.327	10675	8280.6	39.052	3.591	263.891	10.375

Table 3: Model properties for the soil-foundation-structure system in the different 9 regions

Furthermore, looking at Table 3, one can recognize that the energy output in the vibrations of the loaded soil-foundation system at the pile cap level, in terms of the areas under curves in Figure 13, indicates that the amount of energy released in case of regions 4 and 5 is much larger than the cases of zones 1,3,7,9. This is associated with fundamental frequencies as low as 2.754 Hz and 4.171 Hz for zones 4 and 5 respectively. The latter results in Table 3 should reflect the excessive vibrations for the bridge structures lying in regions 2,6,8, and especially 4 and 5. This is the case in contrast to finding that the national codes for loads, in its evaluation of the level of design forces for the different soil types soil types, assigns only an excess of 35% for the softest soils than the stiffest ones [4]. This is reflected in the design response spectra curve [4] as shown in Figure 15, where the maximum response spectra level is

$$S_e = 2.5 a_g \gamma_I S \eta \tag{6}$$

where a_g is the ground acceleration, γ_I is the structure importance factor, η is the damping factor, and S is the soil factor that ranges between 1 to 1.35 for worst soil type cases in areas as Alexandria Governorate [4]. It is therefore a must to find an alternative indicator that grasps results from similar modeling as shown in this paper and the potential of having earthquakes in the designed bridge area. A seismic hazard potential impact factor (*SHIF)* can be thus evaluated from multiplying both the energy released from the pile cap vibration in the dynamic model, normalized to the energy released from the earthquake in the same frequency domain, and the probability of having an earthquake during the design estimated life time of the bridge structure or the transportation network such that

$$SHIF = E_n \times P(X_{eq} = 1) \tag{18}$$

The latter earthquake occurrence probability can be evaluated from Elmasry (2008), and Elmasry and Elkordy (2010) [23,24]. The probability of earthquake occurrence within a 20 years lifetime estimate of a transportation network is assumed 18.8% yielding Table 4.

	Reg. (1)	Reg. (2)	Reg. (3)	Reg. (4)	Reg. (5)	Reg. (6)	Reg. (7)	Reg. (8)	Reg. (9)
SHIF	0.156	3.299	0.411	268.952	208.6269	0.9839	0.091	6.649	0.261

Table 4: *SHIF* values for the different soil profile regions in Alexandria governorate

7 CONCLUSIONS

- The introduced research herein generally studies the dynamic response under earthquakes of a loaded bridge pile cap system together with the surrounding soil profiles. A dynamic soil-structure interaction model is used and identified.
- A hazard potential impact factor (*SHIF*) is defined and evaluated for different Soil profile regions assumed to be existing within the same defined seismic zone in the national design codes.
- The hazard potential impact factor (*SHIF*) is assumed critical when exceeding a unit value since it is dependent on the output energy amplification and the probability of earthquake occurrence.
- The paper proposes using the map, as shown in Figure 4, to better reflect the distribution of hazard expectations among different soil profile regions, the case study was Alexandria Governorate, Egypt.
- The resulting map should categorize the hazard potential as per the geophysical data obtained from site investigations.
- Actual in-situ investigations were used to derive the soil properties then the results were integrated into a dynamic model for the soil-structure interaction.
- Paper output results can definitely be used to trace the best locations for infrastructures as bridges, lying within national transportation networks, as well as better estimating the resulting hazard so as to raise the level of design forces when this is needed.

REFRENCES:

[1] A.K. Abd El-Aal , Ground motion prediction from nearest seismogenic zones in and around Greater Cairo Area, Egypt. *Natural hazards and earth system science*, **10**, 1495-1511, 2010.

[2] G. kumar, H.K. Shruti, Soil Structure Interaction Effect On 200m Tall Industrial Chimney Under Seismic Load. *International Journal of Civil and Structural Engineering Research*, **2**, *pp.* 111-118, 2014.

[3] S.S. Kumar, A.M. Krishna, A. Dey, Parameters Influencing Dynamic Soil Properties, A Review Treatise. *National Conference on Recent Advances in Civil Engineering*, 2013.

[4] ECP-201, *Egyptian Code for Calculating Loads and Forces in Structural Work and Masonry, Housing and Building National Research Center, Ministry of Housing, Utilities and Urban Planning, Cairo*, Egypt , 2012.

[5] A. Marto, T.C. Soon, F. Kasim , A Correlation of Shear Wave Velocity and Standard Penetration Resistance. *Electronic Journal of Geotechnical Engineering - EJGE*, **18**, 2013.

[6] S.E. Abdel Raheem , M.M. Ahmed and T.M.A. Alazrak, Soil-structure interaction effects on seismic response of multi-story buildings on raft foundation. *Journal of Engineering Sciences, Assiut University, Faculty of Engineering,* **42(**4), *pp*. 905-930, 2014.

[7] M.K. Yegian, S.G. Arzoumanidis, S. Nikolaou et al., Seismic soil-foundation interaction analyses of the new Woodrow Wilson Bridge, *7th US Conference on Earthquake Engineering*, Boston, United States, July 21-25, 2002.

[8] V. Puri, S. Prakash, The Foundations For Dynamic Loads, *Art of Foundation Engineering Practice Congress*, West Palm Beach, Florida, United States, 2010.

[9] S. Prakash , V. Puri, *Piles under Earthquake Loads*, Sacramento, California, United States, 2008.

[10] M.I. Elmasry , T.M. Abd-El-Aziz , A.M. Kamel , Studying the Impact of Using Tubular Concrete-Filled FRP Pile foundations on the Seismic Response of Structures , *Proceedings of the 9th International Conference on Structural Dynamics, EURODYN 2014* , Porto, Portugal, 30 June - 2 July, 2014.

[11] N.N. Ambraseys , C.P. Melville ,R.D. Adams, *The Seismicity of Egypt, Arabia, and the Red Sea: A Historical Review*, Cambridge University Press, ISBN 978-0521020251, 2005.

[12] K. M. AbouElenean , A.M. E. Mohamed, H. M. Hussein, Source parameters and ground motion of the Suez-Cairo shear zone earthquakes, Eastern Desert, Egypt, *Natural Hazards and Earth system Sciences*,**52,** 431-451 , 2010.

[13] S.A. Dahy , Seismic Active Zones and Mechanism of Earthquakes in Northern Egypt, *European Journal of Applied Sciences*,**4 (2)**, 65-71, 2012.

[14] General Authority for Educational Buildings Official Design Handouts, Alexandria governorate, Egypt, 2002.

[15] F. Edmonds, A. Carr, P. Goldsmith et al., Seismic Design of Bridges Section 4 – Bridge Foundations, *Bulletin of NZSEE*, **13**, No.3, Wellington, New Zealand, 1980.

[16] ECP-203, *Egyptian Code for Design and Construction of Concrete Structures*, Housing and Building National Research Center, Ministry of Housing, Utilities and Urban Planning, Cairo, Egypt, 2012.

[17] M. Ashour, G. Norris, S. Elfass, Analysis of Laterally Loaded Long or Intermediate Drilled Shafts of Small or Large Diameter in Layered Soils, *University of Nevada, Reno, Final Report*, Report No. CA04-0252, Chapter 5, 2008.

[18] *AllPile User's Manual*, USA, Volume 2, Chapter 8, 2011.

[19] FHWA-SA-91-048, COM624P– *Laterally Loaded Pile Program for the Microcomputer*, Version 2.0.

[20] I. Ishibashi ,X. Zhang, Unified dynamic shear module and damping ratio of sand and clay. *Soil and Foundations*, **33(**1), *pp.* 182-191, 1993.

[21] J. Clarke and J. Duncan, Revision of the CLM Spreadsheet for Lateral Load Analyses of Deep Foundations, *Virginia Polytechnic Institute*, Virginia, USA, 2001.

[22] MATLAB®. *The Math Works Inc.*, Natick, Massachusetts, 2013.

[23] M.I. Elmasry, Estimating damage potential of structures in active seismic zones. *7th European Conference on Structural Dynamics*, Southampton, UK, 7-9 July, 2008.

[24] M.I. Elmasry and E.A. ElKordy, Vulnerability assessment of older reinforced concrete structures designed for gravity loads only," *Proceedings of the 7th Alexandria International conference for structural and Geo-technical Engineering, Alexandria*, Egypt, 27-29 December, 2010.

COMPDYN 2015
5th ECCOMAS Thematic Conference on
Computational Methods in Structural Dynamics and Earthquake Engineering
M. Papadrakakis, V. Papadopoulos, V. Plevris (eds.)
Crete Island, Greece, 25–27 May 2015

RELIABILITY-BASED METHOD FOR ASSESSING LIQUEFACTION POTENTIAL OF SOILS

M.Naghizaderokni[1], Dr.A.Janalizade[2], M.Naghizaderokni[3] (Corresponding Author)
[1] Department of Civil Engineering, Zanjan Branch, Islamic Azad University, Zanjan, Iran
E-mail: naghizademehran@yahoo,com
[2] Departments of Civil Engineering, Babol Branch, Babol, Iran
[3] Department of Civil Engineering, Zanjan Branch, Islamic Azad University, Zanjan, Iran
E-mail: naghizademohsen@yahoo.com

Keywords: liquefaction; Reliability analysis; Chalos area

Abstract. *This paper explores probabilistic method for assessing the liquefaction potential of sandy soils. The current simplified methods for assessing soil liquefaction potential use a deterministic safety factor in order to determine whether liquefaction will occur or not. However, these methods are unable to determine the liquefaction probability related to a safety factor. A solution to this problem can be found by reliability analysis. This paper presents a reliability analysis method based on the popular certain liquefaction analysis method. The proposed probabilistic method is formulated based on the results of reliability analyses of 190 field records and observations of soil performance against liquefaction. The results of the present study show that confidence coefficient greater and smaller than 1 doesn't mean safety and/ or liquefaction in cadence for liquefaction, and for assuring liquefaction probability, reliability based method analysis should be used. This reliability method uses the empirical acceleration attenuation law in the Chalos area to derive the probability density distribution function and the statistics for the earthquake-induced cyclic shear stress ratio (CSR). The CSR and CRR statistics are used in continuity with the first order and second moment method [8] to calculate the relation between the liquefaction probability, the safety factor and the reliability index. Based on the proposed method, the liquefaction probability related to a safety factor can be easily calculated. The influence of some of the soil parameters on the liquefaction probability can be quantitatively evaluated.*

1 INTRODUCTION

Because of abundant earthquakes which occur in the world every year, numerous problems and damages are created. These damages are divided into two classes of structural and geotechnical damages. Structural damages (problems) are generally resulted from lack of attention and not observing technical principles during construction.

The other class is also resulted from due to geotechnical factors and influencing the building by local soil conditions and interaction between them witch liquefaction incidence, earth sliding, decrease in soil loading, subsidence and/or affecting by earthquake characteristics can be placed in this group. In liquefaction incidence, due to water pressure enhance, an opening is created and as a result of decrease in sandy soils resistance, it is saturated and soil takes a liquefied form which this phenomenon is as significant subsidence, eruption of mud and water and water and water leakage through earth (land) surface pores. [1]

It is very difficult to obtain high-quality intact samples and it costs high, today simple tests (experiments) which are performed in the place, are used which some tests including Standard Penetration Test (SPT), cone penetration Test (BPT), Intact penetration Test (CPT) and shear wave rate (speed) Test (Vs) are used. [2, 3]

In most projects, for obtaining liquefaction potential, Standard Penetration Test (SPT) obtained by seed and Idriss, is used. and cone penetration Test is less used, BPT test is used in Sandy and rubble stone soil.[4] In SPT method, limit conditions are usually (generally) used which separate liquefaction district from non- liquefaction district. These limit conditions (This limit condition) is generally obtained empirically and based on observations in the site which during these limit conditions, many of uncertainties are entered the calculation. While most potential assessment (evaluation) methods are based on crucial analysis which are not able to communicate exactly with liquefaction probability, due to the problems and high costs to prepare the intact and high- quality samples and also the presence of simple methods based on in-site (in- place) tests such as standard penetration test (SPT), geotechnical In most projects, for obtaining liquefaction potential, Standard Penetration Test (SPT) obtained by seed and Idriss, is used. and cone penetration Test is less used, BPT test is used in Sandy and rubble stone soil.[4] In SPT method, limit conditions are usually (generally) used which separate liquefaction district from non- liquefaction district. These limit conditions (This limit condition) is generally obtained empirically and based on observations in the site which during these limit conditions, many of uncertainties are entered the calculation. While most potential assessment (evaluation) methods are based on crucial analysis which are not able to communicate exactly with liquefaction probability, due to the problems and high costs to prepare the intact and high- quality samples and also the presence of simple methods based on in-site (in- place) tests such as standard penetration test (SPT), geotechnical engineers prefer generally these tests for liquefaction potential assessment (evaluation). One of the methods for liquefaction potential assessment (evaluation) is based on SPT (standard penetration test) which was developed by seed and Idriss. This empirical method for limit conditions extension enters crucially many of uncertainties into the calculation. In addition, most evaluation (assessment) methods are based on crucial analysis and don’t consider soil resistance changes and the loads resulted from earthquake and are not able to communicate exactly with liquefaction incidence probability [5].

2 RELIABILITY MODEL FOR SOIL LIQUEFACTION

Advanced first-order second-moment (AFOSM) techniques are used to calculate the reliability index in this study. Specifically, the Hasofer-Lind reliability index is computed as follows [6]:

$$\beta = \min_{x \varepsilon F} \sqrt{(X - m)^T C^{-1} (X - m)} \quad (1)$$

Where X = vector of random variables in the limit state function is given by G(X) = 0; m = vector of mean values; and C = covariance matrix. The minimization in (1) is performed over the failure domain F related to the region G(X) < 0. A number of numerical techniques have been used to solve this minimization problem. The ellipsoid method [7, 8] is used here to perform the minimization and determine the reliability index β [7]. Among the practical advantages of this method are: (1) the solution can be obtained by working in original, rather than in changed or reduced random variable space; (2) it is not necessary to provide or calculate partial derivatives of G(X); and (3) associate and non-normal variables are handled easily through transformations [6].

For a reliability analysis of the liquefaction potential, the limit state may be written as G(X) = CRR/CSR - 1 = 0, where CSR is the cyclic stress ratio that shows the loading burden by an earthquake, and CRR is the cyclic resistance ratio that represents the liquefaction resistance of soil. The period of CRR was first described by Robertson and endorsed by the National Center for Earthquake Engineering Research (NCEER) Workshop on Evaluation of Liquefaction Resistance of Soils [9]. In the present study, CSR is calculated using Seed and Idriss [1, 4] formulation:

$$CSR = \left(\frac{\tau_{av}}{\sigma_v^{'}} \right) = 0.65 \left(\frac{a_{\max}}{g} \right) \left(\frac{\sigma_v}{\sigma_v^{'}} \right) \left(\frac{r_d}{MSF} \right) \quad (2)$$

Where $a_{\max}$ = peak horizontal ground acceleration generated by the earthquake; g = acceleration of gravity; σ_v = total vertical overburden stress; $\sigma_v^{'}$ = effective vertical overburden stress; r_d = stress reduction coefficient; and FMS = magnitude scaling factor.

The term r_d gives a relative repair for the flexibility of the soil profile. Seed and Idriss [10] provide a chart showing the mean and the range of r_d values against depth. Liao and Whitman [11] proposed an excellent access to the Seed and Idriss mean r_d values. The latter method, which was adopted during the NCEER workshop [9], is used in the present study. Note that the certainty with which CSR can be calculated decreases with depth when using mean r_d values in the calculations [9]. Since almost all field liquefaction data available are at shallow depths, where the uncertainty is smaller, r_d is treated as a nonrandom variable, although it is a function of depth.

The term FMS is used to correct the calculated CSR for earthquakes with magnitudes smaller or larger than 7.5. This variable is a function of earthquake magnitude (M). This term is required since Seed and Idriss' [10] simplified method was originally developed for an earth-

quake magnitude of 7.5. In this study, Idriss' new formula $\left(F_{MS} = 10^{2.24} / M^{2.56}\right)$ mention with Youd and Idriss [9] is accepted. With this formula, (2) can be rewritten as follows:

$$CSR = \left(0.65/10^{2.24}\right)\left(a_{\max}/g\right)\left(\sigma_v/\sigma_v^{'}\right)\left(r_d\right)\left(M^{2.56}\right) \quad (3)$$

The variables $a_{\max}$, M, σ_v and $\sigma_v^{'}$ in (3) are the amounts as random variables in the present study. These random variables are all assumed to follow normal distribution. In this study, the reported values of these variables are taken as the means. The coefficients of variation (COV) of the variables $a_{\max}$, M, σ_v, and $\sigma_v^{'}$ are calculated to be 0.15, 0.05, 0.10, and 0.15, respectively. The assessment of COV levels for $a_{\max}$ and M should not be confused with a general liquefaction risk analysis, where the seismic loads are also considered as uncertain, in which case the COV of $a_{\max}$ could easily reach 0.50 or higher [8] due to uncertain attenuation. The COV for σ_v is estimated based on the fact that the unit weight of soils normally falls in the 15–21 kN/m3 range, and thus the COV may be estimated as 0.10, considering the range as the average +/- 2 standard deviations. The COV for $\sigma_v^{'}$ is considered to be somewhat greater than that for σ_v because of the uncertainty in the ground-water table.

A COV of 0.15 for $\sigma_v^{'}$ is considered suitable. As with any geotechnical projects, the responsibility of assessing input uncertainties is on the engineer, and if the understand uncertainties in terms of COVs differ significantly from the foregoing COV values, some regulation to the solution received in the probabilistic analysis is warranted. The CRR may be calculated based on SPT-based methods [12] or the CPT-based methods.

The COV for CRR model uncertainty is assumed to be 0.10, which is estimated based on the standard error of the CRR prediction as deviated from those calculated by Robertson and Wide's method [13]. The communication among the input variables also needs to be considered in the reliability analysis. There is strong communication between σ_v and $\sigma_v^{'}$ between $a_{\max}$ and M, while the communication for all other pairs of variables is weak. The communication coefficient is calculated by using standard statistical methods [14]. Based on the available data, the communication coefficient between σ_v and $\sigma_v^{'}$ is determined to be about 0.95, and a communication coefficient between $a_{\max}$ and M is determined to be about 0.90. These values are used in this paper, while all other variables are assumed to be independent.

The database, including120 liquefied cases and 70nonliquefied cases, is taken from the literature [15]. For each case, the tabulated data include depth of the water table, depth of the liquefaction observation, and the four input variables—$a_{\max}$, M, σ_v and $\sigma_v^{'}$. Here, the reported values of the four input variables are taken as the average values, the afore-mentioned COV values are used, and all random variables are assumed to be normally distributed. The reliability index β is calculated with the following equation, derived from (1) and based on the foregoing communication assumption:

$$\beta^2 = \min_{G(X)=0} \left\{ \begin{array}{l} \left[\dfrac{(x_1 - m_1)^2}{\sigma_1^2} \right] + \left[\dfrac{(x_2 - m_2)^2}{\sigma_2^2} \right] + \left[\dfrac{(x_3 - m_3)^2}{\sigma_3^2} - 2\dfrac{(x_3 - m_3)(x_4 - m_4)\rho_{34}}{\sigma_3\sigma_4} + \dfrac{(x_4 - m_4)^2}{\sigma_4^2} \right] \\ .\left(\dfrac{1}{1-\rho_{34}^2} \right) + \left[\dfrac{(x_5 - m_5)^2}{\sigma_5^2} \right] + \left[\dfrac{(x_6 - m_6)^2}{\sigma_6^2} - 2\dfrac{(x_6 - m_6)(x_7 - m_7)\rho_{67}}{\sigma_6\sigma_7} + \dfrac{(x_7 - m_7)^2}{\sigma_7^2} \right] \\ .\left(\dfrac{1}{1-\rho_{67}^2} \right) \end{array} \right\} \quad (4)$$

Where x_1 = random variable $(N_1)_{60cs}$; x_2 = random variable σ_v; x_3 = random variable $\sigma_v^{'}$; x_4 = random variable $a_{\max}$; x_5 = random variable M_w; m_i = mean value of random variable x_i (i = 1, 5); σ_i = standard deviation of random variable x_i; and ρ_{23}, and ρ_{45} = correlation coefficients between x_2 and x_3, and x_4, x_5. The reliability index β determined from (4) is subjected to the limitation of G(X) = 0. The calculated β values are grouped according to whether or not liquefaction actually occurred at the site. For a case in which a reliability index β has been calculated, the probability that liquefaction will occur would be:

$$P_1 = 1 - \phi(\beta) \quad (5)$$

Figure 1 shows the communication between reliability index and probability of liquefaction as for equation 5.

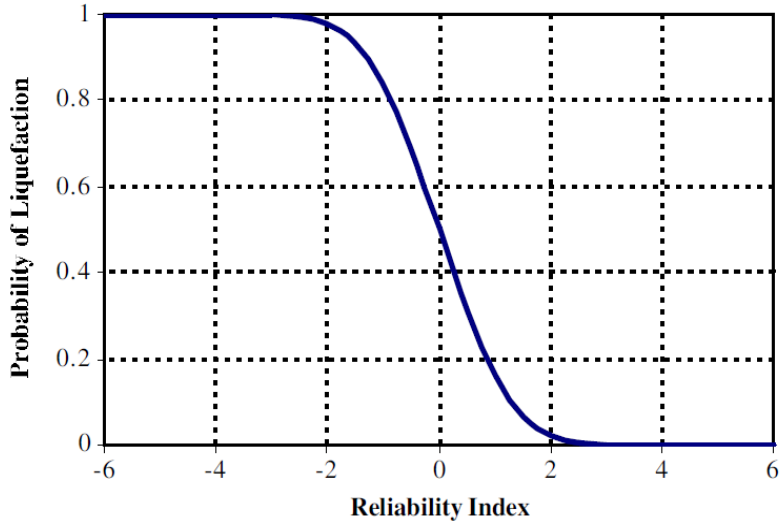


Figure 1: Communication between reliability index and probability of liquefaction [15]

3 CASE STUDY

In the present study, 190 case records from Chalos city have been analyzed. For each case, the CRR and CSR have been calculated, along with the reliability index and probability of liquefaction. Table 1 show a summary of this reliability analysis for all cases at the depths where soil performance against liquefaction was reported. For each of these cases, the CSR, CRR, and the probability of liquefaction (PL) have been calculated continuously at all depths so that a profile of PL could be drawn.

No.	Depth (m)	Soil type	P_L (%)	β	F.S	CSR	CRR	a_{max}	M_W	$(N_1)_{60CS}$	σ'_v T/m^2	σ_v T/m^2
1	2.5	SP-SM	81	-0.88	0.71	0.2	0.14	0.36	6.3	13	4.5	6
2	3	SP	87	-1.14	0.85	0.27	0.23	0.36	6.3	21	2.99	5.49
3	3.5	SP	54	-0.1	0.87	0.2	0.18	0.36	6.3	17	5.04	7.04
4	4	SP	82	-0.9	0.72	0.18	0.13	0.36	6.3	12	6.35	7.8
5	4.5	SM	77	-0.75	0.77	0.17	0.13	0.36	6.3	12	6.59	7.82
6	5	SP	97	-1.9	0.45	0.19	0.09	0.36	6.3	7	6	8
7	5.5	SP	27	0.62	1.08	0.19	0.21	0.36	6.3	19	7.5	10
8	6	SP-SM	99	-2.53	0.31	0.24	0.07	0.36	6.3	5	4.35	7.05
9	6.5	SM	26	0.65	1.09	0.2	0.21	0.36	6.3	20	5.59	11.82
10	7	SM	76	-0.7	0.78	0.2	0.15	0.36	6.3	14	9.5	13
11	8	SP	96	-1.8	0.43	0.22	0.1	0.36	6.3	8	9	14
12	10	SP-SM	32	0.5	1	0.22	0.21	0.36	6.3	20	13	19
13	11	SP-SM	94	-1.59	0.52	0.21	0.11	0.36	6.3	9	14	22
14	11.5	SP-SM	19	0.86	1.12	0.21	0.24	0.36	6.3	22	14	21.9
15	12	SP	56	-0.15	0.82	0.23	0.19	0.36	6.3	18	13	23.4
16	16	SP-SM	77	-0.73	0.74	0.19	0.14	0.36	6.3	13	19	31.9
17	16.5	SP-SM	38	0.3	1.03	0.15	0.16	0.36	6.3	15	22.7	32
18	17	SM	16	1	1.17	0.19	0.22	0.36	6.3	21	18.7	34.19
19	18	SP-SM	12	1.18	0.3	0.19	0.25	0.36	6.3	22	19	36
20	19	SM	50	0	0.85	0.2	0.36	0.36	6.3	16	15.1	33.6

Table 1: The geotechnical parameters of soils in the Chalos area

Figure2 shows a sample output of the PL profile, along with the CSR and CRR profiles and the input SPT profiles. The drawing of the CSR and CRR profiles, such as those shown in figure 3(b), are quite useful, as they show which layers are likely to liquefy. However, this assessment of the liquefaction potential is essentially deterministic. Because of the uncertainties involved in the calculation of CSR and CRR, such a deterministic approach is not always appropriate. The drawing of the PL profile, as shown in figure2 (d), offers an alternative on which engineering decisions may be based.

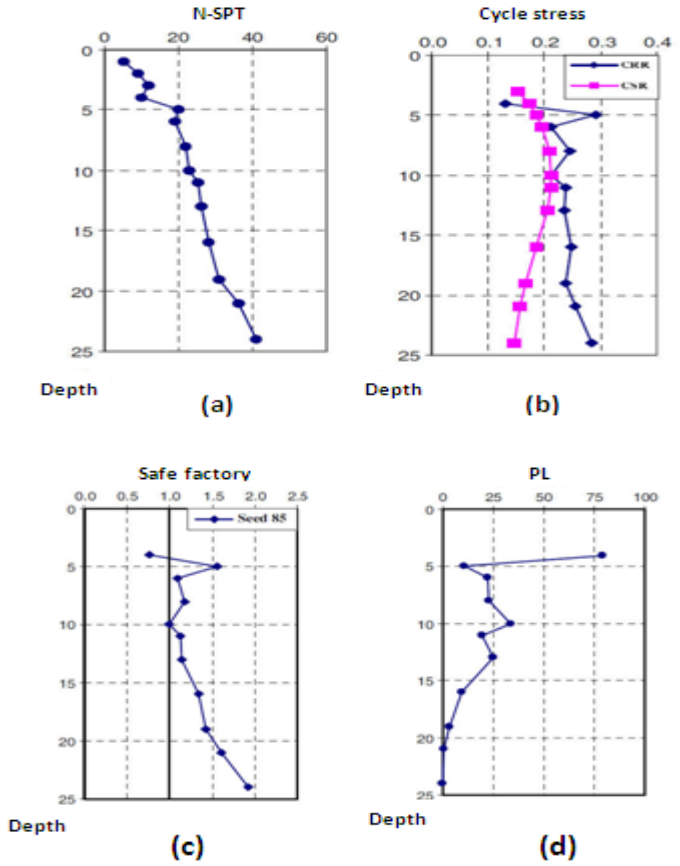


Figure 2: Sample Output of Cyclic Liquefaction Resistance and Probability of Liquefaction

With this profile, the engineer can determine which layers are sensitive to liquefaction from the viewpoint of an acceptable risk level. This advantage is also observed in Table 1. For example, in the case of 12 at the depth of10 m, comparison of calculated CSR and CRR suggests that there would be no liquefaction since CRR > CSR (albeit slightly). However, the field observation indicates the occurrence of liquefaction. The probability of liquefaction for this case is 32, which suggests that liquefaction may be possible. Similar observation was found in the case of 17, in which the deterministic approach shows a CRR of 0.16 and a CSR of 0.15, suggesting that liquefaction will not occur.

However, the field observation indicates the occurrence of liquefaction. For this case, the result of the probability analysis (PL = 38) does not yield a credible support of the occurrence of liquefaction; thus, the probabilistic analysis does not indicate an advantage over the deterministic method. Figure3 shows a plot of the factor of safety (FS)—defined as the simple ratio of CRR over CSR— against the probability of liquefaction for the 190log cases analyzed. It is observed that the PL value is very close to 0 if FS is greater than 2.0. Thus, a conservative and expensive design with a FS of 2 would almost eliminate the chance of liquefaction, even though it is recognized that the FS approach does not account for parameter and model uncertainties. However, if the FS is between 1.0 and 1.5, the effect of uncertainty on the computed FS becomes more significant—the probability of liquefaction can change drastically for a small change in the FS (Fig. 3). Confidence coefficient by liquefaction incidence probability for 190 data related to 19 bores (dipping rods) in the studied district are given in the fig-

ure. The relation between PL-Fs and correlation coefficient of =0.887 can be described as the following relation (equation 6).

$$P_L = \frac{1}{1+\left(F_S / 0.783\right)^{6.63}} \tag{6}$$

The equation 5 shows that when PL approaches zero, confidence coefficient (Fs) doesn't exceed from 25.2, which is a conservative and expensive design. when Fs is between 1 through 1.5 (when Fs ranges 1 to 1.5) , uncertainty effect in the calculations becomes meaningful and liquefaction incidences probability changes effectively for small changes in Fs. For example, if PL < 15, the liquefaction doesn't crucially occur, which equals to confidence coefficient of 1.15.

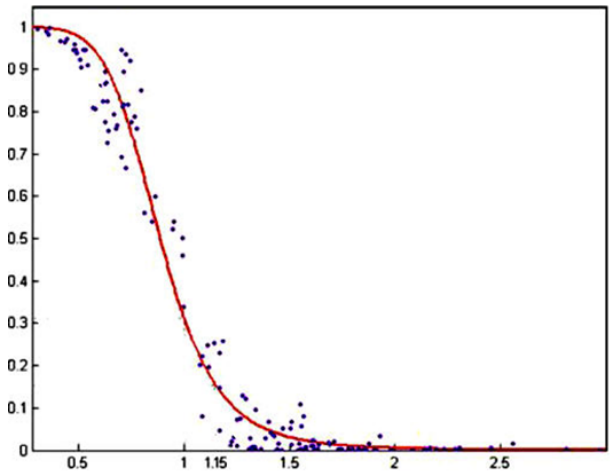


Figure 3: Factor of safety versus probability of liquefaction [15]

4 CONCLUSIONS

A new framework for the reliability analysis of liquefaction potential has been presented in this paper. Excellent results have been obtained in terms of being able to assess the liquefaction potential in a more rational way.

Regarding the performed comparisons between the deterministic method and probabilistic analysis-based method in this research, the efficiency of the probabilistic approach is well shown and it can be applied as a functional tool for application in engineering.

In this research, it was determined that confidence coefficient greater and smaller than 1 doesn't mean safety and/ or liquefaction in cadence for liquefaction, and for assuring liquefaction probability, reliability-based method analysis should be used. Regarding the proposed relationship between PL and FS, liquefaction probability of soil layers can be obtained by deterministic methods. This is a big advantage for geotechnical engineers who use common methods based on confidence coefficient for liquefaction potential assessment.

REFERENCES

[1] M. Bagheripor, M. and H. and M. Mohammadi Zadeh, (1380). Field (desert) operations of standard penetration and potential control, first conference for earth optimization,

university of Amir Kabir J.T. Oden, T. Belytschko, I. Babuska, T.J.R. Hughes, Research directions in computational mechanics. *Computer Methods in Applied Mechanics and Engineering*, **192**, 913-922, 2003.

[2] T. D. Starks, and S. M. Olsen, (1995). *Liquefaction resistance using CPT and field case histories*. J. Geotech. Engrg, ASCE, 121(12), 856–869.

[3] Y. Suzuki, K. Tokimatsu, K. Koyamada, Y. Taya, and Y. Kubota, (1995). *Field correlation of soil liquefaction based on CPT data.Proc*. Int. Symp.on Cone Penetration Testing, CPT 95, Vol. 2, Balkema, Rotterdam, 583–588.

[4] M. Haeri, and M. Zolfaghari, (1372). *Review of liquefaction resulted from 31 khordad, 1369 Manjil earthquake, and report of center for conflict with natural disasters*

[5] A. Hamidi, (1378), liquefaction potential assessment (evaluation) in sandy alluviums of a part of Tehran south missing of permanent state method. *A dissertation (thesis) for geotechnical M.A. Industrial University of Sharif.*

[6] O. Ditlevson, (1981). *Uncertainty modeling*. McGraw-Hill, New York.

[7] B. K. Low, (1996). *Practical probability approach using spreadsheet. Uncertainty in the Geologic Environment: From Theory to Practice: Proc., Uncertainty 96 Geotech. Special Publ*. No. 58, C. D. Shackelford, P. P. Nelson, and M. J. S. Roth, eds., ASCE, New York, 1284– 1302

[8] B. K. Low, and H. Tang, (1997). *Efficient reliability evaluation using spreadsheet*. Engrg. Mech., ASCE, 123(7), 749–752.

[9] T. L. Youd, and I. M. Idriss, (1997). *Evaluation of liquefaction resistance of soils.Proc*. NCEER Workshop on Evaluation of Liquefaction. Resistance of Soils: Tech. Rep. NCEER-97-0022, State University of New York at Buffalo.

[10] H.B. Seed, I.M. Idriss, (1982). *Ground Motion and soil liquefaction during Earth quake*.

[11] S. S. C. Liao, and R. V. Whitman, (1986). *Catalog of liquefaction and non-liquefaction occurrences during earthquake*s. Res. Rep. Dept. of Civ. Engrg. MIT, Cambridge, Mass.

[12] H. B. Seed, K. Tokimatsu, L. F. Harder, and R. M. Chung, (1985). *Influence of SPT procedures in soil liquefaction resistance evaluations*. J. Geotech. Engrg, ASCE, 111(12), 1425–1445.

[13] P. K. Robertson, and C. E. Wride, (1997). *Cyclic liquefaction and its evaluation based on the SPT and CPT. Proc*. NCEER Workshop on Evaluation of Liquefaction Resistance of Soils: Tech. Rep. NCEER-97- 0022, State University of New York at Buffalo, 41–88.

[14] W. Mendenhall, and T. Sincich, (1995). *Statistics for engineering and the sciences, 4th Ed*. Prentice-Hall, Englewood Cliffs, NJ.

[15] M. Naghizade, and A. Janalizade, (2010). *Estimate the potential of liquefaction in sandy soils with reliability method in Chalos city*.

COMPDYN 2015
5th ECCOMAS Thematic Conference on
Computational Methods in Structural Dynamics and Earthquake Engineering
M. Papadrakakis, V. Papadopoulos, V. Plevris (eds.)
Crete Island, Greece, 25–27 May 2015

SEISMIC RESILIENCE OF A BRIDGE BASED ON FUZZY-PROBABILISTIC APPROACH

J. Andrić[1] and D.G. Lü[2]

Group of Reliability and Risk Engineering,
School of Civil Engineering,
Harbin Institute of Technology,
73 Huanghe Road, 150001 Harbin, P.R. China

e-mail: jln.andric@gmail.com, ludagang@hit.edu.cn

Keywords: Seismic Resilience, Fuzzy Set Theory, Fuzzy Probability, Fuzzy Random Variable, Monte Carlo Simulation

Abstract. *In this paper, a new model based on a fuzzy-probabilistic approach for predicting seismic resilience of a bridge is developed. The main purpose is to use seismic resilience in decision making process for disaster management during the pre-disaster period. Another aim is to include contingency in resilience assessment. In previous research, uncertainties have not been fully considered in the proposed models for seismic resilience assessment. Since the residual functionality of bridges depends on its vague damage states, so it is presented by fuzzy triangular numbers. However, the both idle time interval and recovery duration are random in nature, so they are described as random variables. The Monte Carlo simulation is used for generating 10000 samples of these variables. Further, resilience is represented as fuzzy-random variable with corresponding fuzzy mean value and fuzzy standard deviation obtained from the generated and estimated data. The functionality of the system is therefore described as a fuzzy-random function whose shape depends on the disaster preparedness of the system. The resilient curves are illustrated using fuzzy functions. A Java application is developed for purpose of resilience assessment. For a case study, a bridge in Santa Barbara is chosen. The result of resilience assessment process is used for decision making in disaster management and emergency responses.*

1 INTRODUCTION

Transportation systems represent critical infrastructures that play a major role in any country and their failure would have a great impact on the health, safety, economics and social well-being of society [1]. Societies are impacted by natural disasters such as earthquake, hurricane, floods; and man-made disasters. When a disaster strikes, the performance of highway networks is vital for emergency response and recovery activities. Also, the reduced functionality of transportation network caused economic lossess. In recent years, a lot of attention is paid to build resilient infrastructure systems that show reduced failure probabilities, reduced consequences from failure and reduced recovery time [2]. Although in this paper, the focus is on the bridges, since these highway infrastructure components are the most vulnerable and fragile elements of the transportation network in case of seismic event [3]. Earthquakes produce direct and indirect economic losses to bridges [4]. Furthermore, the direct losses include bridge repair, reconstruction and rehabilitation, and the indirect losses are caused by disruption of a traffic flow.

Many studies have been conducted on the topic of seismic resilience assessment. Bocchini and Frangopol (2010, 2011a, 2011b, 2011c, 2012a, 2012b) have studies the reliabilty, fragility and resilience of bridge network [5-10]. They proposed a method using seismic resilience as a criterion in decision making process for optimal restoration process of bridge network. Deco et al (2013) have extended the research by proposing a probabilistic model for seismic resilience assessment of bridge [11]. Karamlou and Bocchini (2014) in their latest research have suggested a new methodology for restoration process of bridges based on Genetic Algorithms, where resilience of the transportation network and the time to connect the critical locations to the infrastructure network are used as a criterion for optimization [12]. Cimellaro et. al. (2005, 2006, 2008, 2010a, 2010b, 2011, 2013) have presented several studies focusing on the seismic resilience of hospitals, health care facilities, and hospital systems with ambulance emergency response [13-19]. In case of infrastructure resilience, Reed et al (2011) have developed a framework and a model for optimizing civil infrastructure resiliency which aim is to increase resiliency [20].

The above research only considered randomness. We noticed that there are many fuzzy uncertain factors in assessment of seismic resilience. For example, the residual functionality of bridges depends on its damage states, while the definition and classification are generally vague and modeled by linguistic variables of experts. The purpose of this research is to include fuzzy uncertainties in resilience assessment considering randomness and fuzziness. An approach for seismic resilience of bridges is developed based on the idea of fuzzy-random variables, where resilience is modeled by random triangular fuzzy numbers, which values correspond to three case scenarios: optimistic, pessimistic and the most probable. The result of resilience assessment process is to represent seismic resilience as a fuzzy random variable, with corresponding fuzzy mean value and fuzzy standard deviation.

The paper is organized into five parts. In the second part, the description and definition of resilience are given. The fuzzy-probability model is illustrated in the third part. The case study is shown in the fourth part, and the conclusion with the suggested further research is presented in the last part.

2 DEFINITION AND MEASURE OF RESILIENCE

Resilience characterizes a system to '*bounce back*' and return its previous state after the disastrous event. In literature, there are different definitions of the term *resilience*. The concept of resilience appears in two different aspects: as outcome and as a process leading to desire outcome [21]. Cimellaro et. al. (2010a) gave a framework for analytical quantification of

disaster resilience and defined resilience as a function indicating the capability to sustain a level of functionality or performance for a given building, bridge, lifeline network, or community, over a period defined as the control time that is usually decided by owners, or society [16]. Terje (2011) explained the concept of resilience as the ability of a system to withstand a major disruption within acceptable degradation parameters and to recover within an acceptable time, and composite costs, and risks [22]. Bocchini and Frangopol (2014) represented resilience as a metric that measures the ability of a system to withstand an unusual perturbation and to recover efficiently from the damage [23]. In civil engineering, resilience represents the ability to deliver a certain service level even after the occurrence of an extreme event, and to recover the desired functionality as fast as possible.

The most widely used definition of resilience is the definition which is given by Bruneau et al (2003). They provided the definition of community seismic resilience as the ability of social units to mitigate hazards, contain the effects of disasters when they occur, and carry out the recovery activities in ways that minimize social disruption and mitigate the effects of future disasters [24]. The characteristics of a resilient system are to robustness, redudancy, resourcefulness, and rapidity.

The resilience is based on the functionality of a system *Q(t)* over the time *t* as shown in Figure 1. It is defined for the quality of service of the infrastructure system. Mathematically, resilience is expressed by:

$$R = \int_0^{t_h} \frac{Q(t)}{t_h} dt \tag{1}$$

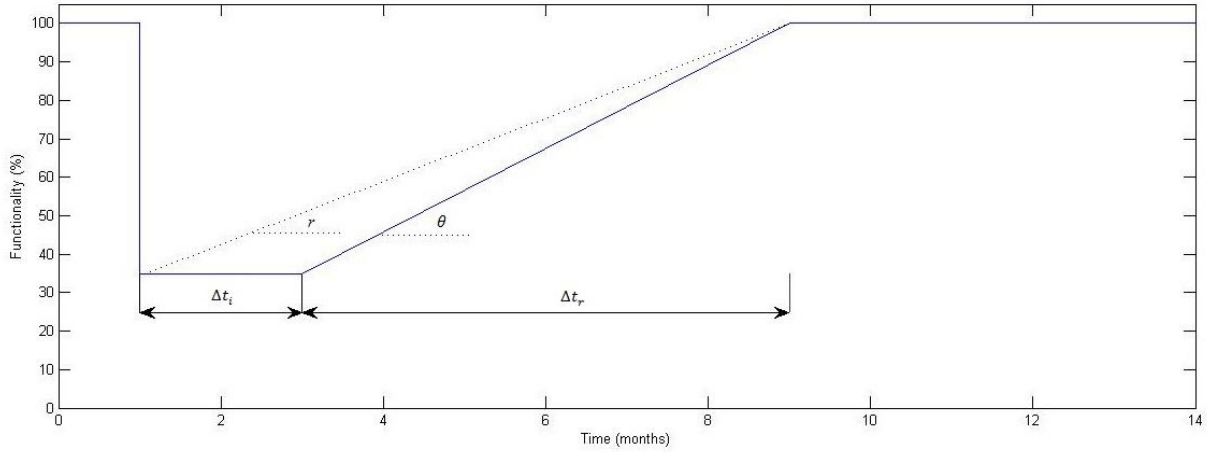


Figure 1: Schematic representation of resilience

After the recovery process, the system can return its previous functionality, or the functionality of the system can be higher or lower than the previous one [25].

3 FUZZY-PROBABILITY MODEL FOR SEISMIC RESILIENCE ASSESSMENT

The resilience is a complex issue which depends on a lot of factors such as residual functionality, target functionality, idle time interval, recovery time and recovery function [11]. Due to this, the prediction of seismic resilience of bridges is a hard task which is determined by many highly uncertain factors. For example, the residual functionality is highly uncertain factor because it is directly associated with the level of bridge damage [11].

The seismic event will cause damages or collapse to bridges. The possible damage states of a bridge are defined in *HAZUS-MR 4* as [26]: no damage, slight/minor damage, moderate damage, extensive damage and complete damage (collapse). The fragility functions are generally used as a tool for evaluating damage states of the bridge. Essentially, the level of the damage is quantified by linguistic variables, thus it represents lexical uncertainty. The residual functionality is directly associated with the levels of bridge damage as the aftermath of the disaster event. According to this, the residual functionality also includes lexical uncertainty. In addition, the characteristics of lexical uncertainty are fuzziness [27]. Hence, the residual functionality can be represented by a fuzzy variable in the model.

In this research, the residual functionality is defined as a convex, normalized fuzzy set $\overline{Q}_r =< Q_{r_1}, Q_{r_2}, Q_{r_3} >$, which is determined by interval bounds of supporting the smallest value Q_{r_1} and the largest value Q_{r_3}, whose membership functions are segmentally continuous and has the functional value $\mu(Q_r)=1$, at exactly one of the value for $Q_r = Q_{r_2}$. For different damage states, they have different values. The membership function for the residual functionality is given as:

$$\mu(Q_{r_i}) = \begin{pmatrix} \dfrac{Q_{r_i} - Q_{r_1}}{Q_{r_2} - Q_{r_1}}, Q_{r_1} < Q_{r_i} < Q_{r_2} \\ \dfrac{Q_{r_3} - Q_{r_i}}{Q_{r_3} - Q_{r_2}}, Q_{r_2} < Q_{r_i} < Q_{r_3} \\ 0, otherwise \end{pmatrix} \tag{2}$$

The recovery path depends on the preparedness for disasters and on the rehabilitation process as well as its techniques and scheduling. The first phase of the recovery is the idle time interval, which is a period between the occurrence of a disaster event and the starting of restoration process on the bridge. During this period, the activities for rehabilitation process are planned. Also, it is used for contacting construction companies and contracting the future reconstruction works. In some cases, during the idle time the restoration activities which do not increase the functionality are finished. In the proposed approach, the idle time interval is a random variable, which follows uniform distribution with values between the minimum and the maximum. Furthermore, the functionality of a bridge in this phase is constant and it is equal to residual functionality.

In the second phase, reconstruction and rehabilitation works are carried out. The recovery time is a period from the beginning of the restoration process until the system gain a desired level of functionality which can be higher, equal or lower than before the disastrous event. The construction industry is more uncertain compare to other industries due to its unique features of construction, reconstruction or repair activities. Usually, these activities are performed outside, so in great extent these processes depend on the weather conditions, soil conditions, and underground water, among others. Bad weather conditions can make delay bridge reconstruction works. Due to this, the recovery period is also modeled by a random variable that follows uniform distribution.

At the end of a restoration process, the system will achieve the target functionality. Generally, the target functionality can be equal to the functionality which the system had before the disaster occurred, lower than before, higher than before, or to totally loose its functionality. The target functionality is defined as a convex, normalized fuzzy set $\overline{Q}_t =< Q_{t_1}, Q_{t_2}, Q_{t_3} >$, that is determined by interval bounds of supporting the smallest value Q_{t_1} and the largest value

Q_{t_3}, whose membership functions are segmentally continuous and has the functional value $\mu(Q_t)=1$, at exactly one of the value for $Q_t = Q_{t_2}$. The membership function for the residual functionality is given as:

$$\mu(Q_{t_i}) = \begin{pmatrix} \dfrac{Q_{t_i} - Q_{t_1}}{Q_{t_2} - Q_{t_1}}, Q_{t_1} < Q_{t_i} < Q_{t_2} \\ \dfrac{Q_{t_3} - Q_{t_i}}{Q_{t_3} - Q_{t_2}}, Q_{t_2} < Q_{t_i} < Q_{t_3} \\ 0, otherwise \end{pmatrix} \tag{3}$$

The shape and the position of the recovery curve depend on the already mentioned factors in previous paragraphs: the residual functionality, the idle time interval, the recovery duration, the target functionality, and the selected recovery function. The residual functionality is modeled as a fuzzy triangular number. However, the idle time and recovery time are treated as independent random variables. Further, the recovery function that covers the recovery pattern depends on the bridge preparedness to disaster. In addition, according to the system preparedness, the system can be classified into three classes: well-prepared systems, average prepared systems and poor-prepared systems. For modeling recovery process, the fuzzy functions are used as fuzziness of recovery process, attributable to a variable of residual functionality which constitutes lexical uncertainties.

If the system is well-prepared to disasters, the recovery process is modeled by a negative-exponential recovery function. The well-prepared systems at the beginning of the restoration process have the recovery speed faster than at the end of the process. The function for functionality of a system for a well-prepared system is proposed as a fuzzy negative-exponential function:

$$\overline{Q}(t) = \begin{pmatrix} \overline{Q_r}, t < t_i \\ -(\overline{Q_t} - \overline{Q_r}) * e^{-\ln(200)*\frac{t-t_i}{t_r}} + \overline{Q_t}, t_i < t < t_i + t_r \\ \overline{Q_t}, t > t_i + t_r \end{pmatrix} \tag{4}$$

where: $\overline{Q_t}$, $\overline{Q_r}$, t_i and t_r are target functionality, residual functionality, idle tme interval and recovery time, respectively.

For the systems which are poor prepared for disasters, the situation is different than from previous case. At the beginning of the restoration process, the recovery speed is less than at the end of the process. To describe the recovery path for this type of systems, the positive-exponential recovery function is proposed. The fuzzy function for a poor-prepared/unprepared system is modeled as a fuzzy positive-exponential function:

$$\overline{Q}(t) = \begin{pmatrix} \overline{Q_r}, t < t_i \\ (\overline{Q_t} - \overline{Q_r}) * e^{\ln(200)*\frac{t-t_i}{t_r}} * \dfrac{1}{200} + \overline{Q_r}, t_i < t < t_i + t_r \\ \overline{Q_t}, t > t_i + t_r \end{pmatrix} \tag{5}$$

The average-prepared systems are modeled by a linear recovery function, because the average-prepared system has uniformly recovery speed during this phase. The fuzzy function for functionality in the case of an average-prepared system is proposed as a fuzzy linear function:

$$\overline{Q}(t)=\begin{pmatrix}\overline{Q_r}, t<t_i\\ (\overline{Q_t}-\overline{Q_r})*\dfrac{t-t_i}{t_r}+\overline{Q_r}, t_i<t<t_i+t_r\\ \overline{Q_t}, t>t_i+t_r\end{pmatrix} \tag{6}$$

In this research, resilience is defined as a fuzzy random variable with fuzzy mean value and fuzzy standard deviation. To model fuzzy mean value and fuzzy standard deviation fuzzy triangular numbers are preferred since they are suitable to describe the three case scenarios (optimistic, the most-probable and pessimistic) of bridge functionality. Mathematically, the resilience can be measured by the fuzzy integral:

$$\overline{R}=\int_0^{t_h}\frac{\overline{Q}(t)}{t_h}dt \tag{7}$$

4 A CASE STUDY

The case study represents a bridge in Santa Barbara in the USA, which is located on a crossroads of Route 217 and Route 101 [9]. The resilience of the bridge is considered for seismic hazards. The research on the risk assessment has been conducted and the expected level of bridge damage is extensive damage [9]. For the expected damage state of the bridge, the resilience assessment is obtained and the possible recovery paths are obtained.

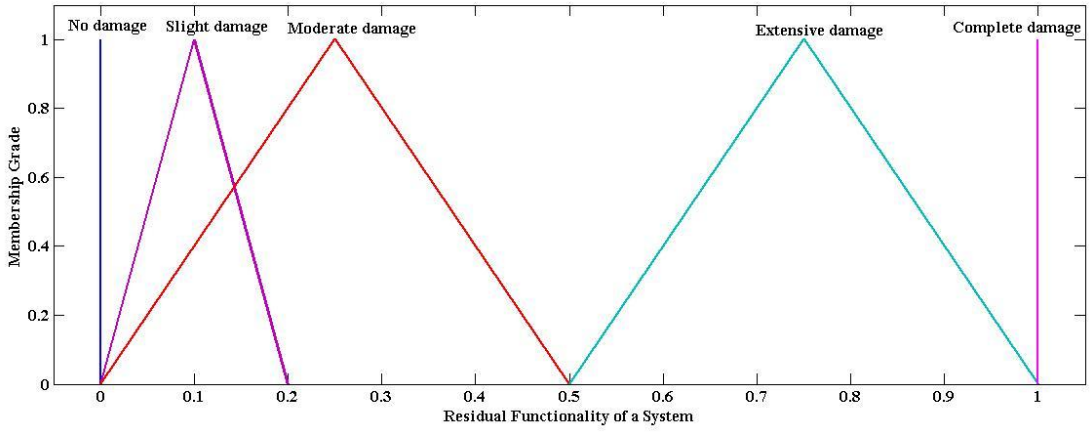


Figure 2:Membership functions for Residual functionality of the bridge

The first step is forming fragility curves for this bridge. In this research, the fragility curves are obtained from FEMA HAZUS-MR4 [26]. According to the damage degree, the residual functionality is estimated and these data is taken from *HAZUS-MR 4*. Furthermore, the residual functionality is represented as fuzzy triangular numbers with the values from *HAZUS MR 4* (Figure 2). Also, this step includes defining the horizon time. The value for time horizon is assumed to be equal to 14 months. Normally, the time horizon value lies between 1 to 2 years.

The estimated values from *HAZUS-MR4* of the residual functionality for each damage state of the bridge are:

1. Residual functionality in case of "no damage": $\overline{Q}_{r_1} = <1,1,1>$
2. Residual functionality in case of "slight damage": $\overline{Q}_{r_2} = <1,0.75,0.50,>$
3. Residual functionality in case of "moderate damage": $\overline{Q}_{r_3} = <0.5,0.25,0>$
4. Residual functionality in case of "extensive damage": $\overline{Q}_{r_4} = <0.2,0.1,0>$
5. Residual functionality in case of "complete damage": $\overline{Q}_{r_5} = <0,0,0>$

The target functionality is 100%. In this case study, we assume that after the rehabilitation process, the bridge returns to its previous functionality, which is the target functionality. According to that, the target functionality is presented as single fuzzy number. The value for the target functionality for each damage state and recovery path is:

$$\overline{Q}_t = <1,1,1>$$

Damage level	Minimum (days/months)	Maximum (days/months)
Slight damage	10/0.333	150/5
Moderate damage	20/0.667	200/6.667
Extensive damage	60/2.0	250/8.333
Complete damage	75/2.5	300/10.0

Table 1: Uniform distribution parameters for recovery time of bridge [1, 28]

Idle time	Min (months)	Max (months)
	1	2

Table 2: Uniform distribution parameters for idle time

The recovery time is given by a uniform probability distribution for each damage state of the bridge, as shown in Table 1. Also, the idle time interval follows uniform distribution between 1 and 2 months (Table 2). The values for the recovery time and the idle time interval are generated by Monte Carlo simulation [29].

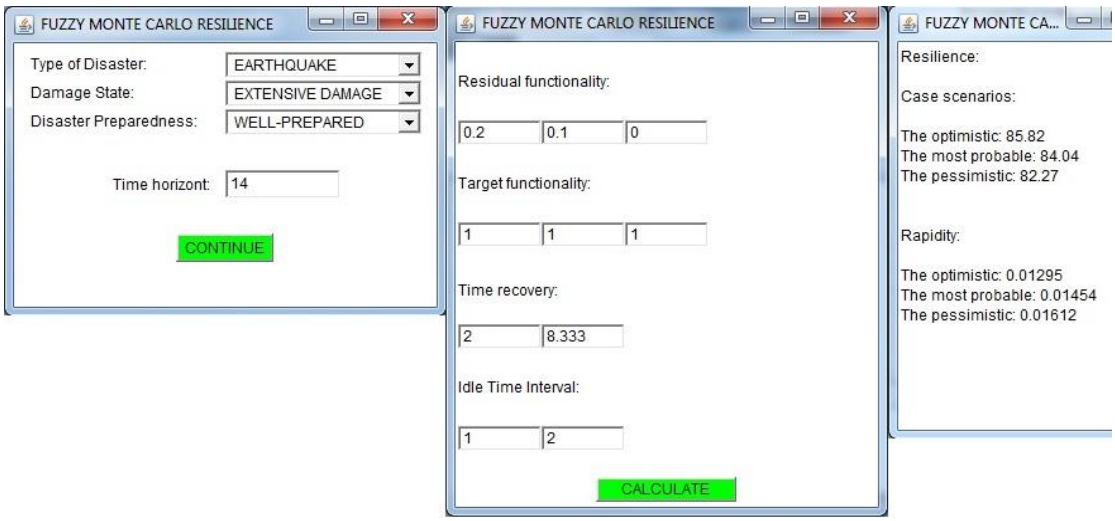


Figure 3: The Fuzzy Resilience - Java application

An In-house application tool has been developed in Java programming language [30] named *Fuzzy Monte Carlo Resilience*, as shown in Figure 3, and it is used for the process of resili-

ence assessment. It contains options to choose the type of disasters: earthquake, tsunami, hurricane, floods, scour, drift, or multiple hazards; the damage states of the bridge: no damage, slight damage, moderate damage, extensive damage and complete damage; the disaster preparedness: well-prepared, average-prepared and poor prepared; and the time horizon given in the first window of application. The input data for the characteristics of bridges is set up in the next step.

In this case study, the residual functionality, and the recovery time are taken considering the state of "extensive" bridge damage. Each bridge damage state has three possible case scenarios for resilience assessment: optimistic, most-probable and pessimistic. The resilience when considering the extensive damage state in the optimistic case scenario takes on a value of the residual functionality after disaster equal to 20%. The most-probable case scenario which contains the values of residual functionality is only 10% of its full functionality. For the pessimistic case scenario, the minimum value of resilience which is obtained by considering the minimum residual functionality after disaster event is taken as 0%.

Then, the random numbers that follow the prescribed uniform distribution for the recovery period and the idle time interval are generated using random number generator from *Java application*. Totally, ten thousand samples in this process are used for resilience assessment in all three case scenarios. The output of the program is an Excel file with the data which contains the residual functionality, the generated idle time interval, the generated recovery time and the calculated resilience. Furthermore, the fuzzy mean value and the fuzzy standard deviation of the resilience are estimated using these 10,000 samples of fuzzy realization. The shape of the fuzzy mean value and the fuzzy standard deviation are fuzzy triangular numbers with corresponding membership functions, as shown in Figure 4. Also, the fuzzy distribution function for the resilience is obtained from these values, as shown in Figure 5. The results for resilience for each seismic damage state are presented by triangular fuzzy numbers, whose values are given in Table 3.

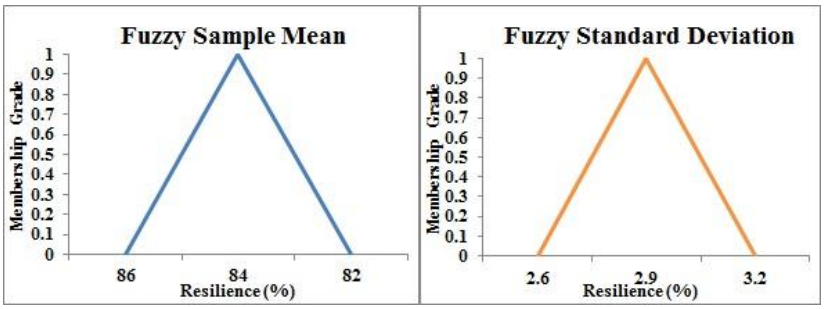


Figure 4: Fuzzy mean and fuzzy standard deviation of Bridge in Santa Barbara

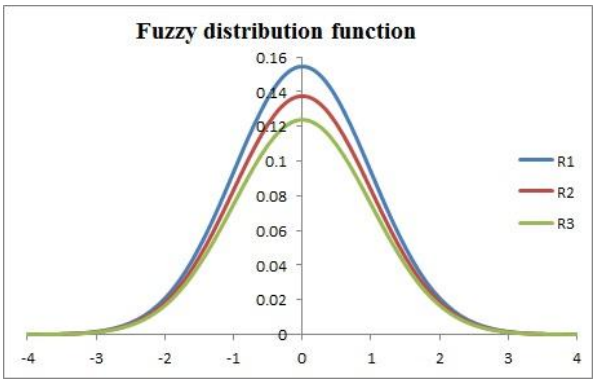


Figure 5 Fuzzy distribution functions for resilience

Damage	Disaster Preparedness	Case scenario	Resilience	
			Mean	Standard deviation
Extensive	Well-prepared	Optimistic	0.86	0.026
		The most probable	0.84	0.029
		Pessimistic	0.82	0.032

Table 3: Resilience of a bridge

The resilience of the bridge in Santa Barbara in the extensive damage state and well-prepared scenario for a future seismic disaster is (0.86, 0.84, 0.82), where the first, second and third value represent optimistic, most-probable and pessimistic case scenarios, respectively. Therefore, the possible values of the resilience lie between the optimistic and pessimistic values.

Matlab [31] is used for obtaining the resilient curves in Figure 6. The curve (1) depicts the optimistic case scenario for the bridge in the extensive damage state in a well-prepared disaster region. The residual functionality in the optimistic case scenario for the extensive damage and well-prepared system is equal to 20%, so the curve (1) begins at this point, and it is horizontal during a 1.5-months idle time. Moreover, the recovery phase follows negative-exponential function, since the bridge is well-prepared for seismic disaster and during the 5.19-months recovery period, the bridge succeeds to return to full functionality of 100%. After this, the curve is straight. The Curve (2) is obtained for the most-probable case scenario with the membership grade equals to 1. The residual functionality for the most-probable case scenario is equal to 10%, and the curve (2) starts from 10%, and it is horizontal during a 1.5-months idle time. Further, the recovery phase follows the negative-exponential function during the recovery period of 5.19-months when the bridge returns its previous functionality of 100%. The curve (3) represents the pessimistic case scenario for the extensive damage and well-prepared system with a membership grade of 0. The residual functionality in the pessimistic case scenario is 0% for a 1.5-months idle time. Also, the recovery phase follows the negative-exponential function, and during the recovery period of 5.19-months, the bridge functionality from 0% gradually proceeds to 100%. All three curves have the same recovery duration, with different starting points, because the residual functionalities are different (20%, 10%, 0%), but the same ending points, because the target functionality in all three cases is the same (100%, 100%, 100%).

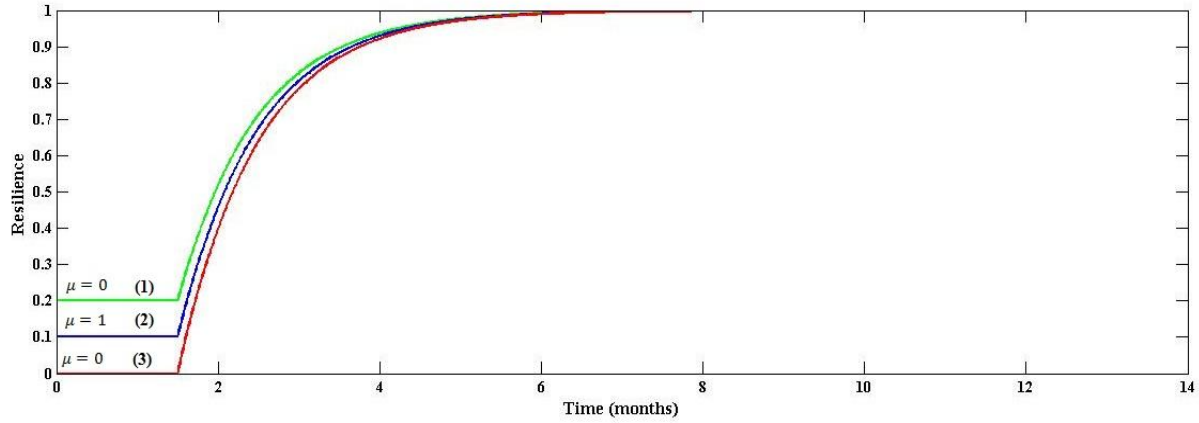


Figure 6: Resilience curves for the bridge in Santa Barbara

5 CONCLUSIONS

This paper presents a model for predicting the seismic resilience of a bridge under uncertainties based on a fuzzy-probabilistic approach. In the proposed model, the residual functionality is represented by a triangular fuzzy number; the idle time interval and the recovery period are represented by random variables that follow the uniform distributions. Compared with other methods and models for resilience assessment, the triangular fuzzy numbers are favorable for the representation of the residual functionality, because they correspond to three case scenarios: optimistic, the most-probable and pessimistic scenario of bridge damage after the disaster. The type of recovery function depends on the disaster preparedness of the bridge and its circumstances. It has been found that the negative exponential recovery functions should be applied for high-resilient, while the linear for average-resilient, and positive exponential recovery function for low-resilient bridges. The resilience is modeled by a fuzzy random variable. Also, the model can be applied to other highway infrastructure components such as tunnels and roadways, only the values for residual functionality, idle time interval and time recovery will be different. The important goal of this research is to use resilience assessment as a criterion for decision making process in disaster risk management. The prediction of resilience is used for development of the optimal strategy for disaster mitigation.

REFERENCES

[1] W. Kröger, and E. Zio. *Vulnerable systems*. Springer Science & Business Media, 2011.

[2] M. Bruneau, A. Reinhorn, Exploring the concept of seismic resilience for acute care facilities, *Earthquake Spectra*, **23(1)**, 41–62, 2007.

[3] M. Shinozuka, Y. Murachi, X. Dong, Y. Zhou, M. J. Orlikowski, Effect of Seismic Retrofit of Bridges on Transportation Networks, *Earthquake Engineering and Engineering Vibrations*, **2(2)**, 35-49, 2003.

[4] S. Banerjee, M. Shinozuka, Uncertainties in Seismic Risk Assessment of Highway Transportation Systems, *Lifeline Earthquake Engineering in a Multihazard Environment (TCLEE2009)*, 79-87, 2009.

[5] P. Bocchini, D.M. Frangopol, On the applicability of random field theory to transportation network analysis, *In Bridge maintenance, safety, management and life-cycle optimization*, CRC, UK, 3018–3026, 2010.

[6] P. Bocchini, D.M. Frangopol, A stochastic computational framework for the joint transportation network fragility analysis and traffic flow distribution under extreme events, *Prob. Eng. Mech.*, **26(2)**, 182–193, 2011a.

[7] P. Bocchini, D.M. Frangopol, A probabilistic computational framework for bridge network optimal maintenance scheduling, *Reliability Engineering and System Safety*, **96(2)**, 332–349, 2011b.

[8] D.M. Frangopol, P. Bocchini, Resilience as Optimization Criterion for the Rehabilitation of bridges belonging to a Transportation Network Subject to Earthquake, *Structures Congress 2011, ASCE*, 2044 – 2055, 2011c.

[9] P. Bocchini, D.M. Frangopol, Restoration of Bridge Networks after an Earthquake: Multicriteria Intervention Optimization, *Earthquake Spectra*, **28(2)**, 427 – 455, 2012a.

[10] P. Bocchini, D.M. Frangopol, Optimal Resilience- and Cost-Based Post-disaster Intervention Prioritization for Bridges along a Highway Segment, *Journal of Bridge Engineering, ASCE,* 117-129, 2012b.

[11] A. Deco, P. Bocchini, D.M. Frangopol, A probabilistic approach for the prediction of seismic resilience of bridges, *Earthquake Engineering & Structural Dynamics*, **42(10)**, 1469 -1487, 2013.

[12] A. Karamlou, P. Bocchini, Optimal Bridge Restoration Sequence for Resilient Transportation Networks, *Structures Congress 2014*, 1437 – 1447, 2014.

[13] G.P. Cimellaro, A.M. Reinhorn, M. Bruneau, Seismic resilience of a health care facility, *In: Proceedings of annual meeting of the Asian Pacific network of Centers for Earthquake Engineering Research (ANCER 2005)*, Korea, 2005.

[14] G.P. Cimellaro, A.M. Reinhorn, M. Bruneau, Quantification of seismic resilience, *In: Proceedings of 8th national conference of Earthquake Engineering,* San Francisco, 2006.

[15] G.P. Cimellaro, C. Fumo, A. Reinhorn, Seismic resilience of health care facilities, *The 14th World Conference on Earthquake Engineering.* Beijing, China, 2008.

[16] G.P. Cimellaro, A.M. Reinhorn, M. Bruneau, Framework for analytical quantification of disaster resilience, *Engineering Structures,* **32**, 3639-3649, 2010a.

[17] G.P. Cimellaro, A.M. Reinhorn, M. Bruneau, Seismic resilience of a hospital system, *Structure and Infrastructure Engineering*, **6**, 127-144, 2010b.

[18] G.P. Cimellaro, A.M. Renschler, A. Frazier, L.A. Arendt, A.M. Reinhorn, M. Bruneau, The State of Art of Community Resilience of Physical Infrastructures, *Structure Congress 2011, ASCE,* 2021 – 2032, 2011.

[19] G.P. Cimellaro, V. Arcidiacono, A.M. Reinhorn, M. Bruneau, Disaster Resilience of hospitals considering emergency ambulance services, *Structures Congress 2013*, 2824-2836, 2013.

[20] D.A. Reed, Z.B. Zabinsky, L.N. Boyle, A Framework for Optimizing Civil Infrastructure Resiliency, *Structures Congress 2011*, 2104 – 2112, 2011.

[21] H.B. Kaplan, Toward an Understanding of Resilience: A Critical Review of Definitions and Models, *In M.D. Glantz and J.L Johnson (eds.) Resilience and Development,* Kluwer Academic, New York, NY, 17–83, 1999.

[22] A. Terje, On Some Recent Definitions and Analysis Frameworks for Risk, Vulnerability, and Resilience, *Risk Analysis,* **4**, 515 – 522, 2011.

[23] P. Bocchini, D.M. Frangopol, T. Ummenhofer, T. Zinke, Resilience and sustainability of Civil Infrastructure: Toward a Unified Approach, *Journal of Infrastructure Engineering, ASCE,* **20(2)**, 2014.

[24] M. Bruneau et. al., A framework to quantitatively assess and enhance the seismic resilience of communities, *Earthquake Spectra,* **19(4)**, 733-752, 2003.

[25] P.N. Priscilla, L.S. Raymond, Sustainability and Resilience of Underground Urban Infrastructure: New Approaches to Metrics and Formalism, *GeoCongress 2012*, 3199-3208, 2012.

[26] FEMA. *HAZUS-MR4 Earthquake model Technical Manual*, Department of Homeland Security, Federal Emergency Management Agency (FEMA): Washington, DC, 2009.

[27] B. Moller, M. Beer, Fuzzy Randomness Uncertainty in Civil Engineering and Computational Mechanics, 2nd Edition. Berlin: Springer, 2004.

[28] M. Shinozuka et. al., *Socio-economic effect of seismic retrofit implemented on bridges in Los Angeles highway network.* Final report to the California Department of Transportation, University of California, Irvine, CA, 2005.

[29] A.H. Ang, W.H Tang, Probability Concepts in Engineering Emphasis on Application in Civil & Environmental Engineering, 2nd Edition, John Wiley and Sons, United States, 2007.

[30] NetBeans. Version NetBeans IDE 7.3.1. JAVA EE 7. Sun Microsystems, 2013.

[31] Matlab. Matlab version 7.8-R2009a, The Mathworks Inc., Natick, MA, 2009.

COMPDYN 2015
5th ECCOMAS Thematic Conference on
Computational Methods in Structural Dynamics and Earthquake Engineering
M. Papadrakakis, V. Papadopoulos, V. Plevris (eds.)
Crete Island, Greece, 25–27 May 2015

NEURAL NETWORKS FOR THE PREDICTION OF MINE-INDUCED VIBRATIONS TRANSMISSION FROM THE GROUND TO BUILDING FOUNDATION

Krystyna Kuzniar

Pedagogical University of Cracow
ul. Podchorazych 2, 30-084 Krakow, Poland
e-mail: kkuzniar@up.krakow.pl

Keywords: Mining tremors, Neural Networks, Transmission of Ground Vibrations, Acceleration of Vibrations, Response Spectra, Building Foundation Vibrations.

Abstract. *This paper deals with the application of neural networks for the prediction of the transmission of mine-induced accelerations of ground vibrations to the foundations of apartment buildings. Results from measurements in situ at the same time on the ground level and on the building foundation were used as the neural networks training and testing patterns. Rockbursts in Legnica-Glogow Copperfield (LGC), the most seismically active mining region in Poland with surface horizontal vibrations reaching 0,2 acceleration of gravity (g) and vertical components reaching 0,3g, were the sources of vibrations. The mining tremors are not subject to human control and they are random events in view of their time, place and magnitude, similarly as earthquakes. Full-scale tests were carried out many times in a period of a few years. Comparison of a huge number of records of vibrations measured at the same time on the ground and on the building foundation level leads to conclusion that they differ generally significantly. However the more precise estimation of harmfulness of the mine-induced vibrations to actual buildings can be performed on the basis of the foundation vibrations. Therefore the prediction of foundation vibrations is necessary if the measured ground vibrations are accessible only. Reduction of maximal values of accelerations of horizontal vibrations as well as differences between non-dimensional ground and foundation acceleration response spectra were taken into account in this paper. Various pre-processing of the experimental data (compression, linguistic variables introduction, scaling of input and output data) is proposed. The influence of some mining tremors as well as ground vibrations parameters (e.g. energy, epicentral distance, direction of wave propagation, direction of vibrations parallel to the transverse or longitudinal axis of the building, values of accelerations of the ground vibrations) on the transmission is considered in the input vectors. The main advantage of the neural approach is that the prediction of the parameters of vibrations of building foundation can be performed on the basis of ground vibrations taken from experimental data. The obtained results show that application of relatively simple neural networks enables us providing for building foundation vibrations based on ground vibrations with satisfactory accuracy.*

1 INTRODUCTION

Soil-structure interaction involves a lot of very difficult problems in the dynamic analysis of structures. Estimation of the way of ground vibrations transmission to building foundations is one of the most important issue among them.

Such problems are mainly analysed with respect to earthquakes. However the ground motion can be induced not only by earthquakes, but also by the so-called paraseismic sources, for instance mining tremors. Although these tremors are strictly connected with human activity, they differ considerably from other paraseismic vibrations. They are not subject to human control and they are random events in view of their time, place and magnitude, similarly as earthquakes whereas some parameters of such ground vibrations (for instance: dominating frequencies, duration) are different from earthquake-induced ground vibrations [11].

Mine-induced seismicity has been recorded in many countries in mining areas with underground exploitation of coal, copper, gold. In Poland, mining tremors resulted from underground raw mineral material exploitations induce the surface horizontal vibrations reaching even 0,2 acceleration of gravity (g) and vertical components reaching 0,3g. Such large values of the peak accelerations are comparable with the peak accelerations of the surface vibrations excited by some weak and shallow earthquakes. It is worth mention that the mining works are run under highly urbanized and heavily populated areas, so the harmful effects of mining seismicity may affect many buildings and people on the surface.

A great number of published papers deal with dynamic soil-structure interaction. The most of them are of theoretical character. A lot of computational models are discussed, cf. e.g. [1, 4, 8, 9, 10, 12]. In spite of extensive development of computational methods (first of all the Finite Element Method) and progress in computer software and hardware, the analysis of soil-structure interaction problems is still far from satisfactory from the structural engineering point of view. That is why there are attempts to explore non-standard, co-disciplinary approaches in the analysis of the dynamic problems. From this point of view artificial neural networks seem to be a tool, very prospective for solving the problems [5, 7].

The comparison of maximal values (amplitudes) of vibrations (accelerations, velocities, displacements) recorded at the same time on the ground and on the foundation level is the simplest and very often employed way of estimation of the vibrations transmission from the ground to the building. The more general way of evaluation the differences between vibrations recorded at the same time on the ground and on the foundation level is the comparison of response spectra from both the vibrations.

This paper deals with the application of neural networks for the prediction of the transmission of mine-induced accelerations of ground vibrations to the foundations of apartment buildings. Rockbursts in Legnica-Glogow Copperfield (LGC), the most seismically active mining region in Poland, were the sources of vibrations. Results from measurements *in situ* at the same time on the ground level and on the building foundation were used as the neural networks training and testing patterns. Reduction of maximal values of accelerations of horizontal vibrations as well as differences between non-dimensional ground and foundation acceleration response spectra were taken into account in this paper. Various pre-processing of the experimental data (compression to principal components by the Principal Component Analysis method – PCA, linguistic variables introduction, scaling of input and output data) is proposed. The influence of some mining tremors as well as ground vibrations parameters (energy, epicentral distance, direction of wave propagation, direction of vibrations parallel to the transverse or longitudinal axis of the building, values of accelerations of the ground vibrations, dominating frequency of ground vibrations) on the transmission is considered in the neural network input vectors. Types of problems analysed with neural networks application are syn-

thetically presented in Table 1. The information about the components of the neural network input and output vectors and variants of the experimental data pre-processing methods is given in the table.

Neural network		Variants of actual data pre-processing
input	output	
- maximal value (amplitude) of ground vibrations - other parameters of ground vibrations - mining tremor parameters	comparison of the maximal value (amplitude) of vibrations recorded at the same time on the ground and on the foundation level	- scaling - introduction of the linguistic variables (fuzzy inputs)
- record of ground acceleration vibrations compressed to the first principal component - mining tremor parameters	comparison of the maximal value (amplitude) of vibrations recorded at the same time on the ground and on the foundation level	- scaling - compression using PCA
- response spectrum from the ground vibrations	response spectrum from the building foundation vibrations	- scaling

Table 1: Types of problems analysed with neural networks application.

2 EXPERIMENTAL DATA

Mining tremors in the most seismically active mining region in Poland with underground copper ore exploitation – Legnica-Glogow Copperfield (LGC), were the sources of ground and buildings vibrations. Full-scale tests were carried out many times in a period of a lot of years. Measurements come from the surface and building seismological measurement stations. The accelerometers were installed on the ground in the front of the building (in six meters distance), at the foundation level in the building and on some floors of the building. The results of long-term experimental monitoring of ground and actual building vibrations were synthetically collected. Simultaneously recorded ground and building foundation accelerograms are useful in the determination of the way of vibration transmission from ground to buildings. The main attention was devoted to measurements of the horizontal vibration components in the directions parallel to the transverse (x) and longitudinal (y) axis of the considered buildings. In this paper two types of typical prefabricated (with load bearing walls) actual buildings were taken into account – medium-height (five-storey) and tall (twelve-storey) buildings founded directly on the ground using concrete strip foundations.

At a contact between the ground and a building foundation, accelerations undergo changes. The building works, to a certain degree, as a low-pass filter for ground accelerations, first of all, with high frequencies. The degree of the acceleration modification depends on the characteristics of the ground accelerograms, intensity of vibrations and the type of the building on which vibrations are transmitted [2, 6].

Comparison of a huge number of records of vibrations measured at the same time on the ground and on the building foundation level leads to conclusion that they differ generally significantly. The similar effect in the corresponding response spectra can be observed. It is the result of soil-structure interaction, which is visible in the transmission of ground vibrations to building foundations. Therefore the responses of buildings determined on the basis of vibra-

tions recorded on the ground may be different than the responses obtained with application of vibrations recorded on the foundation level of the buildings.

Examples which illustrate these significant differences between the simultaneously recorded horizontal components of ground and building foundation accelerations of vibrations in case of medium-height and tall buildings are shown in Fig. 1. Fig. 2 presents the examples of trajectories of the ends of the resultant acceleration vectors at the same time of mine-induced ground and medium-height building foundation vibrations. In Fig. 3 comparisons of non-dimensional acceleration spectra (β) from simultaneously measured ground and foundation vibrations in case of medium-height as well as tall building are performed. With regard to the determined damping, the response spectra are computed with damping ratio $\xi = 3\%$. All these illustrative vibrations were induced by the mining tremors in LGC region with energies (*En*) and epicentral distances (*re*) given below the figures.

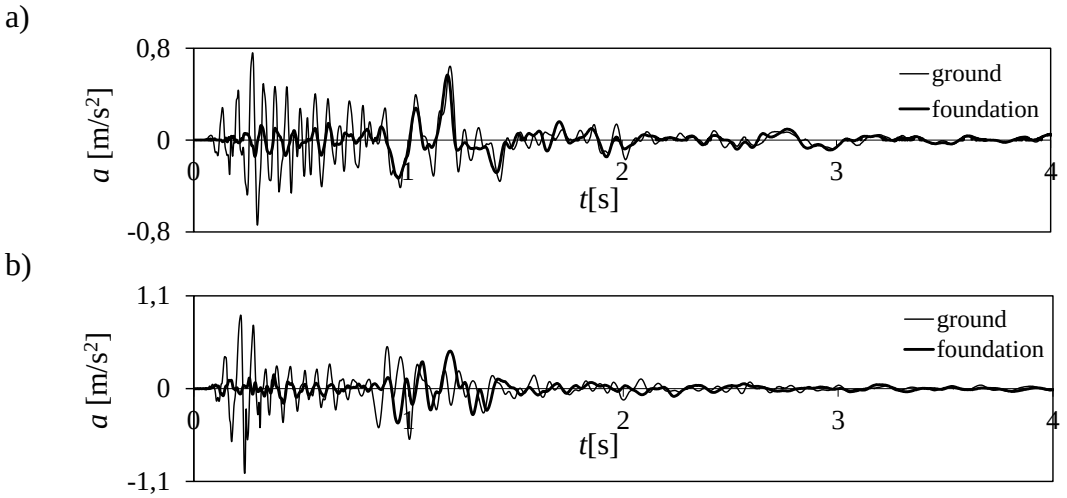


Figure 1: Records of horizontal components of vibrations (accelerations):
a) medium-height building, mining tremor – $En = 1{,}3 \cdot 10^8$J, re = 905m, direction x;
b) tall building, mining tremor – $En = 1{,}3 \cdot 10^8$J, re = 650m, direction y.

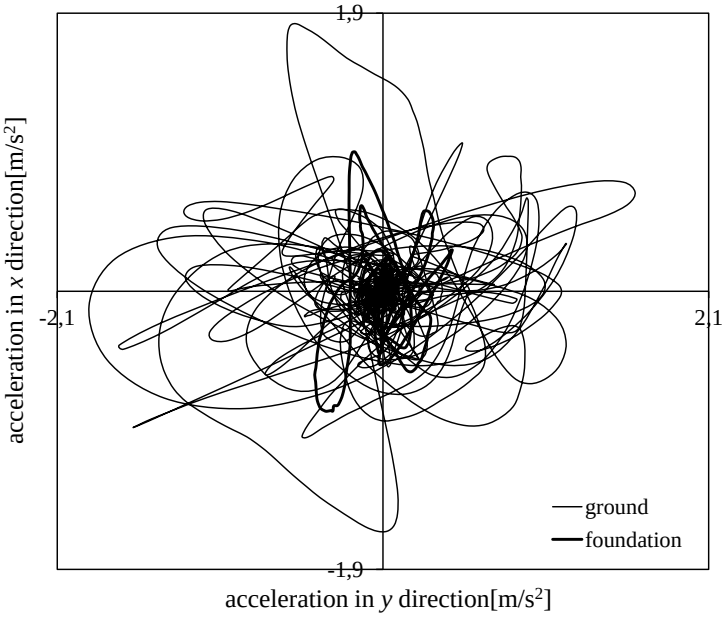
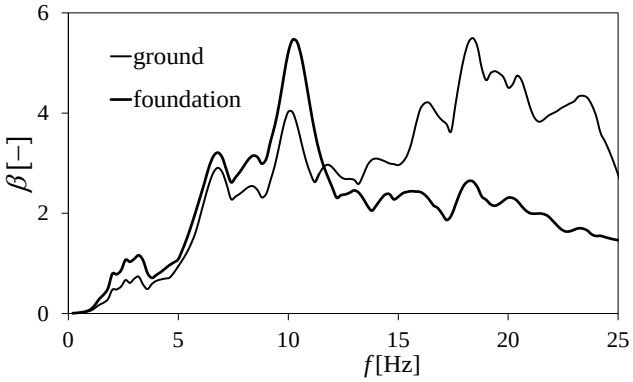


Figure 2: Trajectories of the ends of resultant acceleration vectors at the same time of mine-induced the ground and the medium-height building foundation vibrations: $En = 1{,}9 \cdot 10^9$J, re = 1267m.

a)



b)

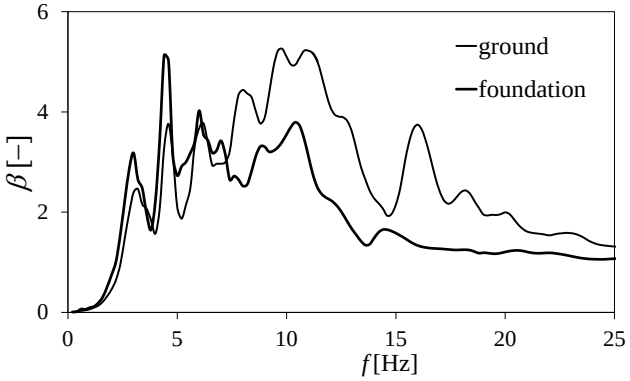


Figure 3: Non-dimension response spectra: a) medium-height building, mining tremor – $En = 8{,}3 \cdot 10^6$J, re = 1569m, direction y; b) tall building, mining tremor – $En = 3{,}5 \cdot 10^7$J, re = 964m, direction x.

The influence of rockbursts parameters as mining tremor energy, epicentral distance, wave propagation direction as well as ground vibrations parameters (amplitude, direction of vibrations, dominating frequency) on the soil-structure interaction effect can be observed. However the prediction of the relation between ground and foundation records of accelerations and the mine-induced vibrations transmission from the ground to the building foundation is very difficult.

3 NEURAL NETWORKS APPLICATION RESULTS

3.1 Introductory remarks

Taking into account the difficulties in the soil-structure interaction analysis in the case of vibrations induced by mining tremors, the application of neural networks for the prediction of building foundation vibrations on the basis of ground vibrations taken from measurements is proposed in the paper.

The database created of the results of long-term experimental monitoring of ground and actual structure vibrations makes it possible to use them as the patterns to design the neural network analysers for considerations of the transmission of ground vibration accelerations induced by mining tremors to building foundation. Pre-processing methods of the experimental data are applied: scaling, introduction of the linguistic variables (fuzzy inputs) and compression.

Back-propagation neural networks (BPNNs) were trained and tested on the basis of experimental data. The results of neural network analysis and the results of experiments were com-

pared. The accuracy of the network approximation was evaluated by the mean-square-error $MSE(Q)$, the standard error $st\varepsilon(Q)$ and the relative errors ep, eQ_{avr}:

$$MSE(Q) = \frac{1}{Q}\sum_{p=1}^{Q}(z^{(p)} - y^{(p)})^2, \tag{1}$$

$$st\varepsilon(Q) = \sqrt{\frac{1}{Q}\sum_{p=1}^{Q}(z^{(p)} - y^{(p)})^2}, \tag{2}$$

$$ep = |1 - y^{(p)}/z^{(p)}| \cdot 100\%, \tag{3}$$

$$eQ_{avr} = \frac{1}{Q}\sum_{p=1}^{Q} ep, \tag{4}$$

where: $z^{(p)}$, $y^{(p)}$– target and neurally computed outputs for p-th pattern, $Q = L, V, T, P$ – number of the learning (L), validating (V), testing (T) and all (P) patterns respectively.

Besides the linear regression coefficient $R(Q)$ was computed for every set of pairs $z^{(p)}$, $y^{(p)}$. The numerical efficiency of the trained network also was evaluated by the success ratio SR. This function enables us to estimate what percentage of patterns SR[%] gives the neural prediction with the error not greater than ep[%].

3.2 Prediction of the maximum accelerations of foundation vibrations based on maximal value (amplitude) of ground vibrations, other parameters of ground vibrations and mining tremors parameters

The first proposition deals with the application of neural networks for the estimation of the way of vibrations transmission from the ground to the building foundation by the evaluation of the reduction of maximal values of the accelerations. Therefore the comparison of maximal values (amplitudes) of accelerations recorded at the same time on the ground (a_{gmax} in x or y directions, respectively) and on the foundation level (a_{fmax}) was necessary. For this purpose the ratios $r = a_{fmax}/ a_{gmax}$ were computed. The value of ratio r was proposed as the output of the corresponding neural network.

The aim of this approach is to apply neural networks for the prediction of ratios r based on the corresponding mining tremor and ground vibration parameters. The following neural network input parameters were taken into consideration: a_{gmax} - maximal value (amplitude) of accelerations recorded on the ground in the case of vibrations in x or y directions, k - parameter related to direction of vibrations (values $k = 0{,}4$ and $k = 0{,}7$ were arbitrarily assumed for the transverse direction x and longitudinal direction y, respectively in order to differentiate the directions), En - mining tremor energy, re - epicentral distance, X and Y - local seismological coordinates, fg - dominating ground vibration (acceleration) frequency. Variant neural network input vectors were analysed taking into account the various combinations of input parameters. Parameters of the neural network pairs of input-output vectors, the neural network structures and the errors corresponding to the networks training, validating and testing processes for selected neural networks designed in case of the ground vibrations transmission to the medium-height building foundation are given in Table 2.

Neural network number	Input parameters	Neural network structure	*MSE*(*Q*)		
			L	*V*	*T*
NN1	$a_{g\max}$, *En*, *re*	3-25-1	0,0194	0,0237	0,0220
NN2	$a_{g\max}$, *En*, X,Y	4-5-1	0,0212	0,0232	0,0236
NN3	$a_{g\max}$, *En*, *re*, *fg*	4-22-1	0,0153	0,0157	0,0166
NN4	$a_{g\max}$, *En*, *re*, *k*	4-7-1	0,0150	0,0148	0,0143
NN5	$a_{g\max}$, *En*, X,Y, *fg*	5-4-1	0,0167	0,0175	0,0175
NN6	$a_{g\max}$, *En*, X,Y, *k*	5-10-1	0,0137	0,0148	0,0140
NN7	$a_{g\max}$, *En*, *re*, *fg*, *k*	5-15-1	0,0095	0,0115	0,0114
NN8	$a_{g\max}$, *En*, *re*, X, Y	5-7-1	0,0229	0,0250	0,0228
NN9	$a_{g\max}$, *En*, X, Y, *fg*, *k*	6-15-1	0,0079	0,0095	0,0104
NN10	$a_{g\max}$, *En*, *re*, X, Y, *fg*	6-5-1	0,0184	0,0174	0,0184
NN11	$a_{g\max}$, *En*, *re*, X, Y, *fg*, *k*	7-4-1	0,0129	0,0120	0,0103

Table 2: BPNNs input parameters, structures and training, validating and testing errors (medium-height building).

The influence of various input parameters on the neural network approximation accuracy is visible. It was stated that certainly the more precise prognosis of ratios *r* is obtained for the richer neural network input information. Moreover an application of neural networks enables to evaluate the influence importance of some mining tremors and ground vibrations parameters on the reduction of maximal foundation acceleration of vibrations vs. maximal ground acceleration of vibrations.

The neural network input parameters, mining tremor energy and epicentral distance among others, are estimated as approximate values found experimentally. The energy of mining tremor and epicentral distance are calculated by the seismologists on the basis of vibrations simultaneously recorded in time of this tremor on a few measuring stations in the underground mine. Then the found experimentally values of *En* and *re* have an approximate character and the ranges of small, medium and large mining tremors energies as well as the ranges of small, medium and large epicentral distances can be defined. This is in fact the introduction of the linguistic variables associated with the fuzzy character of the mining tremor energy {*Enl*} and epicentral distance {*rel*} instead of crisp values *En* and *re*, respectively.Therefore the linguistic variables associated with the fuzzy character of the parameters are introduced in the neural network analysis.

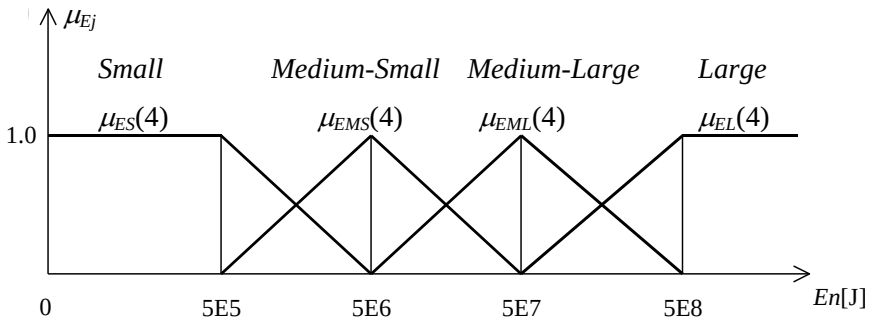


Figure 4: Membership functions for values of mining tremors energies *En* in case of 4 membership functions.

Triangular and trapezoid membership functions are adopted. Then instead of the crisp value of *re* the linguistic variable {*rel*} is introduced in the neural network input vector: {*rel*} = {μ_{rS}, μ_{rM}, μ_{rL}}, where: μ_{rS}, μ_{rM}, μ_{rL} – values of membership functions for small, medium and large epicentral distance, respectively, corresponding to membership functions. Taking into account the wide range of values of energies, three variants of the number of membership functions in case of mining tremors energies are analyzed: three (3), four (4) and five (5) membership functions. These functions adopted in case of four (4) membership functions are shown in Fig. 4 as the example.

Thus eight, nine or ten components in the input vector occur respectively, as the result of introducing the linguistic variables {*rel*} and {*Enl*(3)}, {*Enl*(4)} or {*Enl*(5)} instead of crisp parameters in the neural network input vector composed of parameters: $a_{g\max}$, *En*, *re*, *k*. The errors related to these neural networks in case of the high building are collected in Table 3.

Input parameters	BPNN	*MSE*(*Q*)		eQ_{avr}			st ε	*R*(*P*)
		L	*T*	*L*	*T*	*P*		
$a_{g\max}$, *En*, *re*, *k*	4-5-1	0,00895	0,01900	18,1	33,8	25,9	0,118	0,677
$a_{g\max}$,{*Enl*(3)},{*rel*}, *k*	8-6-1	0,01303	0,01622	22,5	32,5	27,5	0,121	0,639
$a_{g\max}$,{*Enl*(4)},{*rel*}, *k*	9-7-1	0,00599	0,01870	13,3	29,1	21,2	0,111	0,725
$a_{g\max}$,{*Enl*(5)},{*rel*}, *k*	10-7-1	0,00365	0,02131	11,2	34,3	22,7	0,112	0,717

Table 3: BPNNs input crisp and linguistic parameters, structures and errors (tall building).

Additionally, Fig. 5 presents the success ratio *SR* for the neural prediction of the transmission of accelerations of ground vibrations to building foundation obtained using the above-mentioned BPNN: 4-5-1 and BPNN: 10-7-1.

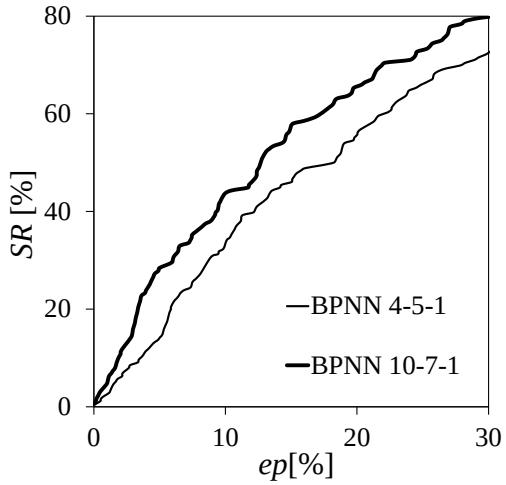


Figure 5: Success ratio *SR* for the neural prediction of the transmission of accelerations of ground vibrations to building foundation in cases of BPNN: 4-5-1 and BPNN: 10-7-1 (tall building).

It can be concluded that the introduction of linguistic variables can lead to a better accuracy of neural identification than that by means of crisp values of epicentral distance and mining tremor energy. These results can also be explained by the increase of the number of network parameters but with no increase of physically interpreted input variables. Three membership functions are not sufficient for describing such large (wide) range of mining tremors energies.

It is visible that the accuracy of network with such linguistic variable is not better than in case of network with crisp values in the input vector.

3.3 Prediction of the maximum accelerations of foundation vibrations based on compressed record of ground vibrations and mining tremors parameters

The aim of the next approach is to apply neural network for the prediction of the ratio *r* on the basis of the corresponding mining tremor parameters and the compressed ground vibration record instead of maximal value of ground acceleration. Compression of the data to principal components by the Principal Component Analysis method (PCA) [3] is proposed.

The carried out analysis leads to conclusion that the introduction of the principal component analysis method enables us to compress vibration data corresponding to the ground records of accelerations. Because of the strong correlation of the successive values of accelerations, the full ground acceleration vibrations in time domain could be compressed to the first principal components only. Hence the design of considerably smaller neural networks than those without data compression for the prediction of building foundation vibrations on the basis of ground vibrations taken from measurements is possible. It results in the reduction of number of network parameters and improvement of the network generalization properties.

The following neural network input parameters were taken into consideration: cag_1, *En*, *re*, *k*, where cag_1 – record of ground acceleration vibrations compressed to the first principal component and *En* – mining tremor energy, *re* – epicentral distance, *k* – parameter related to the direction of vibrations as in chapter 3.2.

The neural network of structure 4 – 6 – 4 – 1 was accepted for the practical applications in case of medium-height building for the sake of the network "size" and good accuracy. Using this network leads to the relative errors less than 30% in the case of 88% of the all patterns: *SR*(30%) = 88%. The comparison of results obtained using neural network with experimental ones is shown in Fig. 6. In this figure the bounds of relative errors *ep* = 30% are marked. The following values of the neural network errors were computed: *MSE*(*L*) = 0,0035, eL_{avr} = 13,5%, *R*(*L*) = 0,941 in case of learning; *MSE*(*T*) = 0,0053, eT_{avr} = 18,9%, *R*(*T*) = 0,883 in case of testing. It should be noted that very simple network with the compressed ground vibration record instead of the maximal value (amplitude) of vibrations causes an increase of accuracy of obtained results.

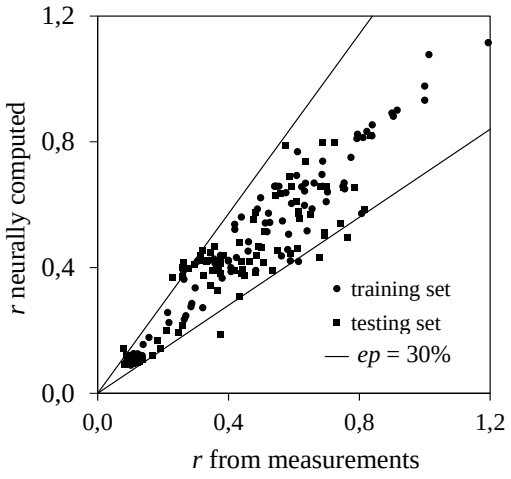


Figure 6: Values of ratio *r* obtained from measurements vs. values computed by the neural network (medium-height building).

3.4 Mapping of response spectra from the ground vibrations into response spectra from foundation vibrations

In the third way of the analysis of the vibrations transmission the acceleration response spectra were considered. The subpicture idea from picture transmission is also adapted for the mapping of response spectra from ground vibrations to response spectra from foundation vibrations of the buildings. Then in the input vector six elements were proposed: $\beta_g(f_{i-2})$, $\beta_g(f_{i-1})$, $\beta_g(f_i)$, $\beta_g(f_{i+1})$, $\beta_g(f_{i+2})$, f_i, where f_{i-2}, f_{i-1}, f_i, f_{i+1}, f_{i+2} – successive vibration frequencies, β_g – non-dimensional acceleration spectrum from ground vibrations. The corresponding value of non-dimensional acceleration spectrum from the vibrations recorded at the foundation level of building $\beta_f(f_i)$ was taken as the output of this neural network. The neural networks of structure 6 – 5 – 1 in case of the medium-height building as well as 6 – 10 – 1 in case of the tall building were formulated after a number of numerical experiments.

The errors corresponding to the training and testing processes of the network applied in case of the medium-height building are put together in Table 4 and the example of comparison of computed on the basis of recorded vibrations and neurally predicted non-dimensional acceleration response spectra from foundation is shown in Fig. 7.

MSE(*L*)	*MSE*(*T*)	eQ_{avr} [%]			stε (*P*)	*R*(*P*)
		L	*T*	*P*		
0,00283	0,01385	9,4	15,9	12,7	0,091	0,766

Table 4: Errors of the training and testing processes of the network applied for mapping of response spectra from the ground vibrations into spectra from foundation vibrations in case of the medium-height building.

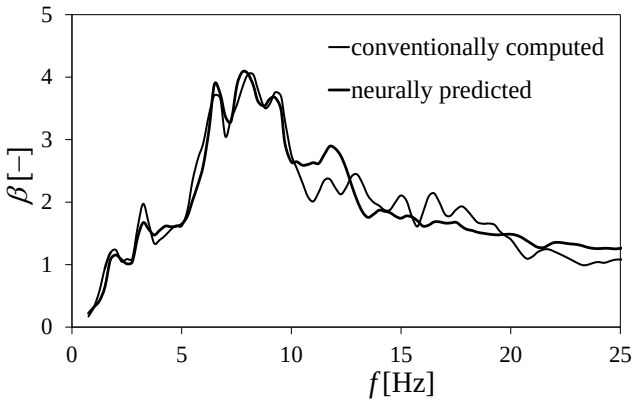


Figure 7: Comparison of computed on the basis of recorded vibrations and neurally predicted non-dimensional acceleration response spectra from foundation vibrations in case of the medium-height building.

Application of simple neural networks enables us to predict the acceleration response spectra from building foundation vibrations with satisfactory accuracy. That is the result of neural mapping of response spectra from ground vibrations to response spectra from foundation vibrations of buildings.

4 CONCLUSIONS

Because of the significant differences of mine-induced ground and building foundation vibrations simultaneously measured and the fact that the more precise estimation of harmfulness of the mine-induced vibrations to actual buildings can be performed on the basis of the foundation vibrations, the prediction of foundation vibrations is necessary if the measured ground vibrations are accessible only (for instance in the design procedure of new structures).

Looking at the difficulties in prognosis of differences between ground and foundation vibrations it is visible from the results obtained that the effects of the transmission of mine-induced ground vibrations to building foundation may be successfully analyzed using neural networks.

The main advantage of the neural approach is that the prediction of the parameters of vibrations of building foundation can be performed on the basis of ground vibrations taken from experimental data. The obtained results show that application of relatively simple neural networks enables us providing for building foundation vibrations based on accelerations of ground vibrations with satisfactory accuracy.

REFERENCES

[1] J. Aviles, M. Suarez, Effective periods and dampings of building-foundation systems including seismic wave effects. *Engineering Structures*, **24**, 553-562, 2002.

[2] W.K. Cloud, Modification of seismic waves by a building. *Proc. 6th European Conference on Earthquake Engineering*, Dubrovnik, Yugoslavia, September 18-22, 1978.

[3] S. Haykin, *Neural networks – a comprehensive foundation*. 2nd Edition, Prentice Hall Intern. Inc., Upper Saddle River, NY, 1999.

[4] J.L. Humar, A. Bagchi, H. Xia, Frequency domain analysis of soil-structure interaction. *Computers and Structures*, **66**, 337-351, 1998.

[5] K. Kuzniar, E. Maciag, Neural network analysis of soil-structure interaction in case of mining tremors. *Proc. 11th International Conference on Soil Dynamics and Earthquake Engineering and the 3rd International Conference on Earthquake Geotechnical Engineering*, Berkeley, USA, vol. 2, 829-836, 2004.

[6] E. Maciag, Experimental evaluation of changes of dynamic properties of buildings on different grounds. *Earthquake Engineering and Structural Dynamics*, **14**, 925-932, 1986.

[7] M. Pala, N. Caglar, M. Elmas, A. Cevik, M. Saribiyik, Dynamic soil-structure interaction analysis of buildings by neural networks. *Construction and Building Materials*, **22**, 330-342, 2008.

[8] M.E. Rodriquez, R. Montes, Seismic response and damage analysis of buildings supported on flexible soils. *Earthquake Engineering and Structural Dynamics*, **29**, 647-665, 2000.

[9] J.P. Stewart, G.L. Fenves, System identification for evaluating soil-structure interaction effects in buildings from strong motion recordings. *Earthquake Engineering and Structural Dynamics*, **27**, 869-885, 1998.

[10] Ch.-B. Yun, D.-K. Kim, J.-M. Kim, Analytical frequency-dependent infinite elements for soil-structure interaction analysis in two-dimensional medium. *Engineering Structures*, **22**, 258-271, 2000.

[11] Z. Zembaty, Rockburst induced ground motion – a comparative study. *Soil Dynamics and Earthquake Engineering*, **24**, 11-23, 2004.

[12] X. Zhang, J.L. Wegner, J.B. Haddow, Three-dimensional dynamic soil-structure interaction analysis in the time domain. *Earthquake Engineering and Structural Dynamics*, **28**, 1501-1524, 1999.

COMPDYN 2015
5th ECCOMAS Thematic Conference on
Computational Methods in Structural Dynamics and Earthquake Engineering
M. Papadrakakis, V. Papadopoulos, V. Plevris (eds.)
Crete Island, Greece, 25–27 May 2015

BAYESIAN IDENTIFICATION OF ELASTIC PARAMETERS IN COMPOSITE LAMINATES APPLYING LAMB WAVES MONITORING

Marek Słoński[1]

[1]Cracow University of Technology
Institute for Computational Civil Engineering
ul. Warszawska 24, Kraków, Poland
e-mail: mslonski@L5.pk.edu.pl

Keywords: Lamb waves, dispersion curves, thin orthotropic plate, Bayesian state estimation, particle filter

Abstract. *In this paper we consider the problem of identification of elastic parameters of homogeneous, elastic and hexagonally orthotropic plates. The proposed solution of the identification problem is based on dispersion curves for Lamb waves propagating in free waveguides and Bayesian inference for sequential estimation of elastic parameters with uncertainty quantification. In particular we solve the problem by treating the unknown elastic parameters as state variables of a stationary dynamic system and formulating the sequential identification problem as a Bayesian state estimation problem. We solve the problem by using sequential Monte Carlo filter (a.k.a. particle filter). Finally, we present two case studies which correspond either to pseudo-experimental computer simulations or laboratory tests in which the elastic parameters of an aluminum thin plate are estimated. The results confirm that the proposed approach allows to find the unknown elastic parameters and that this approach is also useful for quantification of uncertainty with respect to the elastic parameters.*

1 INTRODUCTION

Currently guided Lamb waves are often used for non-destructive identification of elastic constants of materials. In general, the identification procedure is based on minimization of the discrepancy between experimental and numerical or analytical dispersion curves. Rogers in his highly cited paper presents results of identification of elastic properties of several materials (aluminum, steel, glass) using nonlinear least squares method [5].

Recently, Pabisek et al. in [4] proposed reconstruction of elastic moduli of plates based on fundamental symmetric and antisymmetric dispersion curves obtained through a semi-analytical formulation and corresponding experimental curves. The hybrid method coupled with the neural network based inverse procedure was tested by identification of the elastic properties of a thin aluminum plate.

Most of the guided Lamb wave based identification procedures are deterministic in nature and provide only numerical values of the elastic properties. Thus, they are unable to characterize reconstruction uncertainty in a systematic manner. In this context Bayesian methods can be useful by offering systematic approach to uncertainty quantification. Gogu et al. applied Bayesian methods for identification of elastic constants of an orthotropic plate and they found that Bayesian approach offers more accurate representation of the experimental uncertainty [3].

Bayesian methods are also sequential by solving identification problems recursively. Recently, Słoński in his paper applied particle filter in the problem of identification of elastic parameters of aluminum this plates [7].

In this paper an application of particle filter for sequential stochastic identification of elastic parameters of thin plates using Lamb waves monitoring is proposed. The procedure is based on the comparison of numerical and experimental dispersion curves. The identification results are then presented in the form of a posterior probability density distribution over elastic parameters and the posterior describes the uncertainty. The proposed procedure is verified on an example of pseudo-experimental dispersion curves computed for a thin orthotropic plate.

The paper is organized as follows. Section 2 presents the identification algorithm based on Bayesian state estimation and particle filter for sequential stochastic identification of elastic parameters. Section 3 describes numerical experiments for verification of the proposed procedure together with the results and Section 4 presents the final remarks.

2 IDENTIFICATION ALGORITHM

2.1 Bayesian state estimation problem

We formulate the sequential identification problem as a Bayesian state estimation problem. The elastic parameters are assumed to not change in time, so they are treated as time-independent state variables, see [7] for details. Then the transition equation has the following form:

$$\mathbf{x}_{k+1} = \mathbf{x}_k. \tag{1}$$

The equation (1) is further modified as

$$\mathbf{x}_{k+1} = \mathbf{x}_k + \mathbf{w}_{k+1}, \tag{2}$$

where $\mathbf{w}_k$ is a noise random variables added for numerical efficiency of particle filter-based identification. In this work, $\mathbf{w}$ is assumed to be a set of independent and identically distributed (iid) Gaussian random variables

$$p(\mathbf{w}) = \mathcal{N}(\mathbf{w}|\mathbf{0}, \boldsymbol{\sigma}_w^2), \tag{3}$$

where $\boldsymbol{\sigma}_w^2$ is a covariance matrix.

The states are recursively estimated using measurements $\mathbf{y}_{k+1}$ that here are defined as the parameters of fundamental antisymmetric dispersion curves A_0. They are related to state variables $\mathbf{x}_{k+1}$ by the nonlinear observation model $\mathbf{h}(\mathbf{x}_{k+1}, \mathbf{v}_{k+1})$ as

$$\mathbf{y}_{k+1} = \mathbf{h}(\mathbf{x}_{k+1}) + \mathbf{v}_{k+1}, \tag{4}$$

where $\mathbf{v}_{k+1}$ is a noise random variables introduced to account for modeling and measurement uncertainties. Here it is also assumed to be a set of independent and identically distributed (iid) Gaussian random variables

$$p(\mathbf{v}) \propto \mathcal{N}(\mathbf{v}|\mathbf{0}, \boldsymbol{\sigma}_v^2), \tag{5}$$

where $\boldsymbol{\sigma}_v^2$ is a covariance function.

The main goal of Bayesian state estimation is sequential inference of the posterior distribution $p(\mathbf{x}_{k+1}|\mathbf{Y}_{1:k+1})$ starting from a prior distribution $p(\mathbf{x}_k|\mathbf{Y}_{1:k})$. The inference is performed recursively in two steps: prediction step and update (correction) step. In the first step the prediction of state variables distribution $p(\mathbf{x}_{k+1}|\mathbf{y}_k)$ before applying new measurements is done. This distribution is computed using the sum rule of probability and integrating out the state variables as

$$p(\mathbf{x}_{k+1}|\mathbf{Y}_{1:k}) = \int p(\mathbf{x}_{k+1}|\mathbf{x}_k) p(\mathbf{x}_k|\mathbf{Y}_{1:k}) d\mathbf{x}_k. \tag{6}$$

Then the new measurements $\mathbf{y}_{k+1}$ are used to update the prior to obtain the posterior distribution $p(\mathbf{x}_{k+1}|\mathbf{Y}_{1:k+1})$ applying the Bayes' rule

$$p(\mathbf{x}_{k+1}|\mathbf{Y}_{1:k+1}) = \frac{p(\mathbf{y}_{k+1}|\mathbf{x}_{k+1}) p(\mathbf{x}_{k+1}|\mathbf{Y}_{1:k})}{p(\mathbf{y}_{k+1}|\mathbf{Y}_{1:k})}, \tag{7}$$

where the denominator in (7) is computed from

$$p(\mathbf{y}_{k+1}|\mathbf{Y}_{1:k}) = \int p(\mathbf{y}_{k+1}|\mathbf{x}_{k+1}) p(\mathbf{x}_{k+1}|\mathbf{Y}_{1:k}) d\mathbf{x}_{k+1}. \tag{8}$$

The update step in Eq. (7) can be also written in the recursive form that is more useful for obtaining particle filter algorithm. Using Bayes' rule we can rewrite Eq. (7) as

$$p(\mathbf{x}_{k+1}|\mathbf{Y}_{1:k+1}) = p(\mathbf{x}_k|\mathbf{Y}_{1:k}) \frac{p(\mathbf{y}_{k+1}|\mathbf{x}_{k+1}) p(\mathbf{x}_{k+1}|\mathbf{x}_k)}{p(\mathbf{y}_{k+1}|\mathbf{Y}_{1:k})}. \tag{9}$$

2.2 Particle filter

The Bayesian state estimation described above gives the posterior distribution over the states. It does not give however, the way to find the solution efficiently using both equations (6) and (7). In addition, the exact inference is intractable and an approximate method has to be applied. In this work a particle filter (PF) algorithm is used. It is based on sequential Monte Carlo sampling and is described below.

In order to implement Bayesian filtering, we approximate the posterior distribution $p(\mathbf{x}_{k+1}|\mathbf{y}_{k+1})$ using N particles $\mathbf{x}_{k+1}^i, (i = 1, 2, \ldots, N)$, with corresponding importance weights w_{k+1}^i, that is replace the posterior distribution with the empirical distribution

$$P_N(\mathbf{x}_{k+1}) = \sum_{i=1}^{N} w_{k+1}^i \delta(\mathbf{x}_{k+1} - \mathbf{x}_{k+1}^i), \tag{10}$$

where $\delta(\cdot)$ is the Dirac delta function. The weights are computed using sequential importance sampling as

$$w_{k+1}^i = w_k^i \frac{p(\mathbf{y}_{k+1}|\mathbf{x}_{k+1}^i)p(\mathbf{x}_{k+1}^i|\mathbf{x}_k^i)}{\pi(\mathbf{x}_{k+1}^i|\mathbf{x}_k^i, \mathbf{y}_{k+1})}, \tag{11}$$

where $\pi(\mathbf{x}_{k+1}|\mathbf{x}_k, \mathbf{y}_{k+1})$ is the importance distribution such that samples from it can be easily generated.

In general, choosing the optimal importance distribution is rather difficult so for simplicity, the common choice is to apply the transition density as the importance density

$$\pi(\mathbf{x}_{k+1}^i|\mathbf{x}_k^i, \mathbf{y}_{k+1}) = p(\mathbf{x}_{k+1}^i|\mathbf{x}_k^i), \tag{12}$$

that yields a simple equation for computing weights in the next time step as

$$w_{k+1}^i = w_k^i \, p(\mathbf{y}_{k+1}|\mathbf{x}_{k+1}^i). \tag{13}$$

Note that these weights are normalized and satisfy $0 \leq \ w_k^i \ \leq 1$ and $\sum_{i=1}^N w_k^i = 1$.

The initial weights are uniform with values $w_1^i = 1/N$ but later during recursive computations they become far from uniform leading to particles degradation (few particles with large weights). As a result the empirical distribution becomes very poor approximation of the state variables distribution $p(\mathbf{x}_{k+1}|\mathbf{Y}_{1:k+1})$. To overcome this particular degradation problem, a sequential resampling procedure is applied. The resampling procedure regenerates the set of particles by replicating the particles with high importance weights and removing samples with low weights.

Finally, the basic particle filter algorithm is as follows. It starts with a population of N initial-state samples, created by sampling from the prior $p(\mathbf{x}_1)$. Then the prediction-update-resample cycle is repeated for each time step [6]:

1. Each sample is propagated forward by sampling the next state value $\mathbf{x}_{k+1}$, given the current value $\mathbf{x}_k$ for the sample, based on the transition model $p(\mathbf{x}_{k+1}|\mathbf{x}_k)$.

2. Each sample is weighted by the likelihood it assigns to the new evidence, $p(\mathbf{y}_{k+1}|\mathbf{x}_{k+1})$.

3. The population is resampled to generate a new population of N samples. Each new sample is selected from the current population; the probability that a particular sample is selected is proportional to its weight. The new samples are unweighted.

A flowchart of the proposed identification algorithm is shown in Fig. 1.

3 NUMERICAL EXPERIMENTS

The effectiveness of the proposed method is assessed by performing numerical exercises for an orthotropic plate. In the experiments, the material properties of the plate (Young's moduli, Poisson's ratios and mass density) and the plate thickness are taken from [1], see Tab. 1 for exact values of these parameters.

Having defined the plate parameters, a pseudo-experimental fundamental antisymmetric dispersion curves A_0 were computed using numerical approach described in [2]. In this approach it is assumed that the dynamic problem is formulated as a plain strain problem and solved by numerical simulations via commercial finite element code Abaqus in a few series of modal analyzes. The numerical model in Abaqus for a 30mm by 1.2mm plate segment has 3600 square

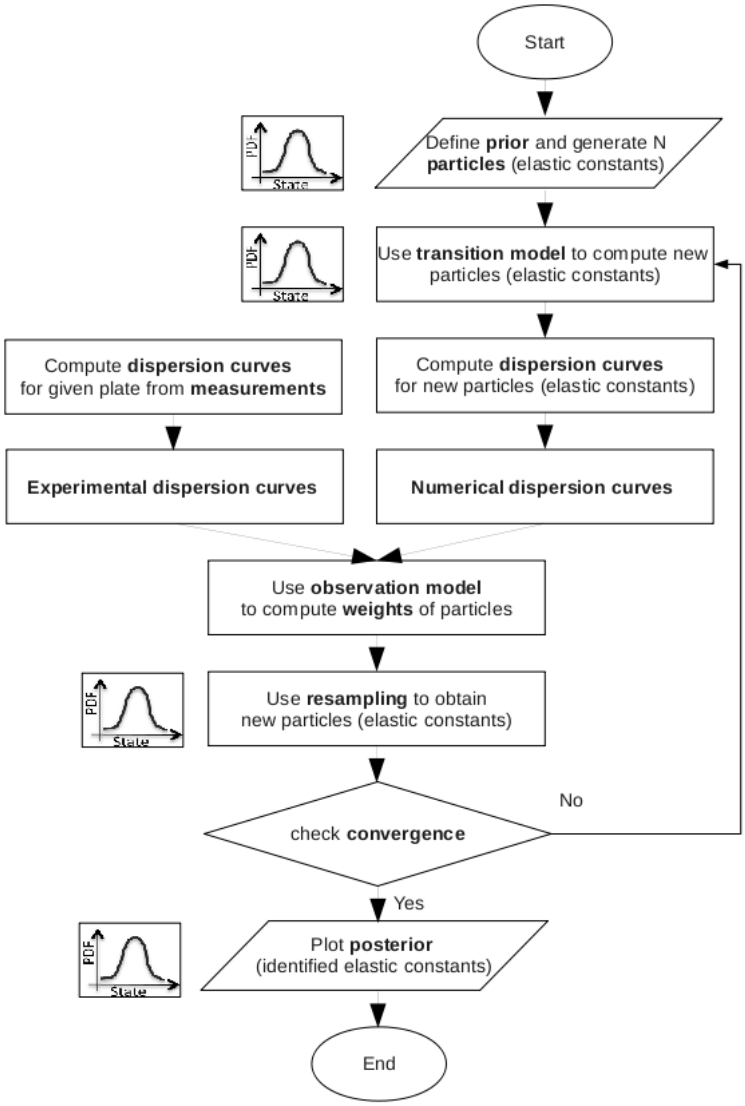


Figure 1: Flowchart of particle filter-based algorithm for elastic parameters identification

CPE4 elements with characteristic length $l_e = 0.1$mm. These dispersion curves were approximated by using basis functions and corresponding parameters that were found with the least squares method. The parameters were treated as the observed variables $\mathbf{y}$. Fig. 2 presents fundamental dispersion curve A0 for the orthotropic plate with elastic constants defined in Tab. 1 and its approximation using 5 basis functions proposed in [4]:

$$k(f) = \phi_0 w_0 + w_1\phi_1 + w_2\phi_2 + w_3\phi_3 + w_4\phi_4, \tag{14}$$

where k denotes wave number corresponding to frequency f and $\phi_i(f)$ denotes i-th basis function. These basis functions are defined as:

$$\phi_0 = 1,\ \phi_1 = f,\ \phi_2 = f^2,\ \phi_3 = 1/f,\ \phi_4 = \tan(0.65f). \tag{15}$$

3.1 Young's modulus E_1 identification

Initial and uncertain knowledge about Young's modulus E_1 is represented by a prior distribution $p(x_0)$. We applied a Gaussian prior probability density distribution $p(x_0) = \mathcal{N}(\mu_0, \sigma_0^2)$,

Table 1: Assumed values of orthotropic plate parameters applied in numerical experiments

Parameter	E_1(GPa)	E_2(GPa)	ν_{12}(-)	ν_{23}(-)	G_1(GPa)	ρ(kg/m^3)	h(mm)
Assumed value	131	8	0.337	0.3	4.23	1560	1.2

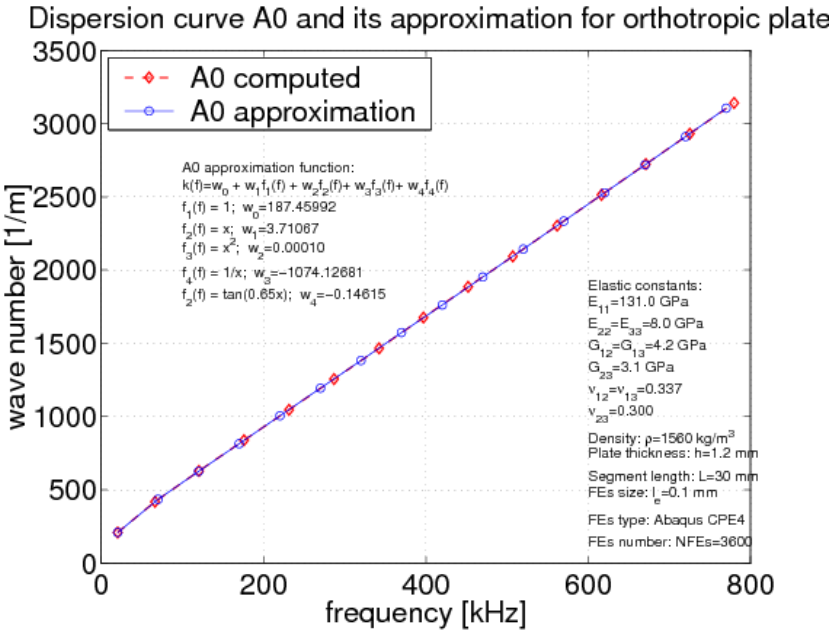


Figure 2: Fundamental dispersion curve for orthotropic plate with thickness h=1.2mm and its approximation using 5 basis functions

with mean value $\mu_0 = 131.0$ GPa and standard deviation σ_0=1.3 GPa (coefficient of variation (CoV) was 1%). Fig. 3 shows the plot of the prior (as a dashed line).

The approximate posterior distribution of Young's modulus given pseudo-experimental dispersion curves $P_N(x_k|\mathbf{y}_k)$ in the k-th step was computed using the particle filter-based identification procedure described above. In experiments, we applied $N = 2000$ particles to obtain the approximate posterior distribution and the number of steps in the sequential identification was set to K=500. Fig. 4 shows the sequential nature of the elastic constant identification process by plotting the evolution of the mean value of the posterior distribution and the corresponding plot for the one-standard deviation error bars as a function of the step number. There is also shown a solid horizontal line representing the reference Young's modulus value (131.0 GPa) applied in numerical experiments. From the plot, it may be observed that the estimation process converged to the reference value quite rapidly (in about 100 iterations).

Tab. 2 presents statistical parameters of prior and posterior distributions in the form of mean values, standard deviations and coefficients of variation (COV) are given. From the table, it can be stated that the final mean value of the posterior distribution is the same as the reference value. Moreover, the coefficient of variation decreased from 1% for the prior distribution to only 0.15% for the final posterior distribution. Fig. 3 shows the final one-dimensional posterior distribution together with the prior distribution.

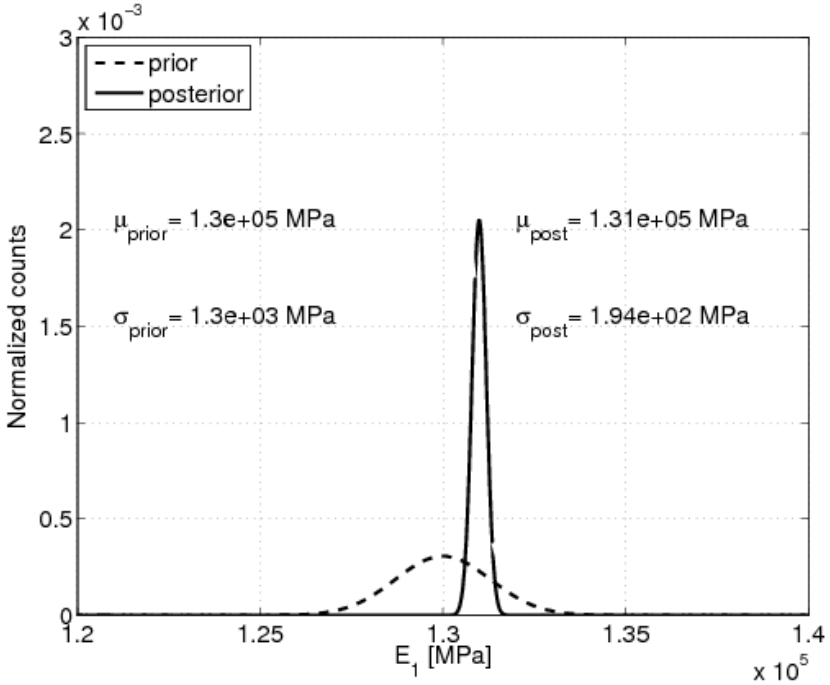


Figure 3: Prior and posterior probability density distributions for Young's modulus E_1. Prior (dashed line) has mean value $\mu_{\text{prior}} = 130.0$ GPa and standard deviation σ_{prior}=1.31 GPa (coefficient of variation (CoV) is 1%). Posterior (solid line) has mean value $\mu_{\text{post}} = 131.0$ GPa and standard deviation σ_{post}=0.19 GPa (coefficient of variation (CoV) is 0.15%)

4 FINAL CONCLUSIONS

This paper presents an application of Bayesian methods and particle filter for reconstruction of elastic parameters of plates. The proposed procedure is based on the comparison of experimental and numerical dispersion curves from guided Lamb waves monitoring.

Taking into account the assumed experimental errors and considering propagation of errors in the sequential estimation, the uncertainty in the identified value of Young's modulus E_1 is less than 0.5%. More results for other elastic parameters will be presented during the conference.

ACKNOWLEDGMENTS

The financial support of the Polish National Science Centre Grant no. 2011/01/B/ST8/07210 "Theoretical basis for structural health monitoring by means of inverse problem solution under uncertainty" is gratefully acknowledged. Author is also very grateful to Prof. T. Uhl, supervisor of the Grant and Prof. Z. Waszczyszyn for their remarks.

Table 2: Statistical parameters of prior and posterior distributions for Young's modulus (mean value, standard deviation and coefficient of variation (COV))

Parameter	Prior	Posterior
Mean value (GPa)	130.0	131.0
Standard deviation (GPa)	1.3	0.19
COV (%)	1.0	0.15

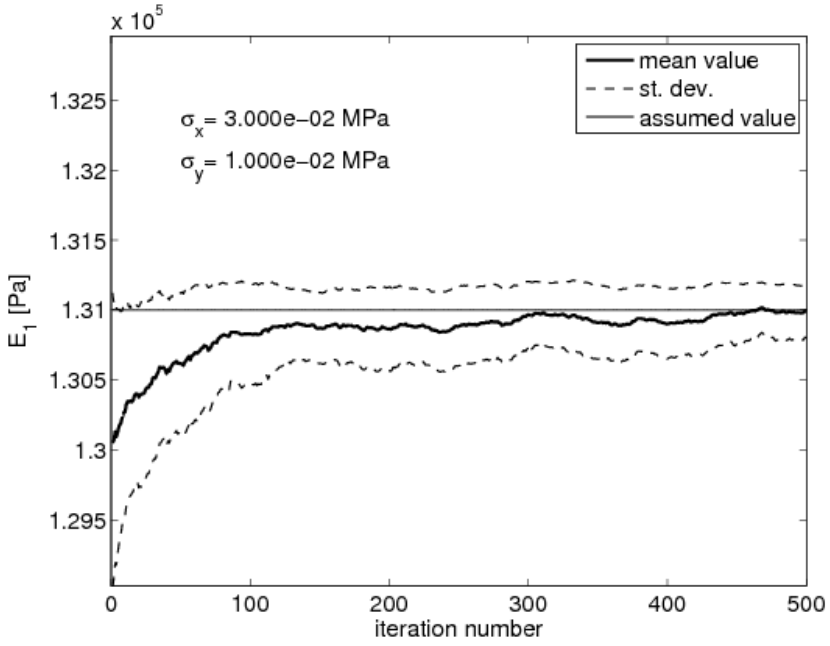


Figure 4: Plot of evolution of mean value of posterior distribution for Young's modulus and corresponding one-standard deviation error bars (solid horizontal line represents Young's modulus value (131.0 GPa) assumed in numerical experiments)

REFERENCES

[1] M. Ce. Finite elements modeling of guided wave propagation in composite laminates for structural health monitoring applications. Master's thesis, Politecnico di Milano, 2010.

[2] Ş. Sorohan, N. Constantin, M. Găvan, and V. Anghel. Extraction of dispersion curves for waves propagating in free complex waveguides by standard finite element codes. *Ultrasonics*, 51(4):503–515, 2011.

[3] C. Gogu, W. Yin, R. Haftka, P. Ifju, J. Molimard, R. Le Riche, and A. Vautrin. Bayesian identification of elastic constants in multi-directional laminate from Moiré interferometry displacement fields. *Experimental Mechanics*, pages 635–648, 2013.

[4] E. Pabisek, Z. Waszczyszyn, and Ł. Ambroziński. A semi-analytical method for identification of thin elastic plate parameters basing on LWM. *Computer Assisted Meth. Eng. Sci.*, 21(1):5–14, 2014.

[5] W. Rogers. Elastic property measurement using Rayleigh-Lamb waves. *Research in Nondestructive Evaluation*, 6(4):185–208, 1995.

[6] S. Russel and P. Norvig. *Artificial Intelligence: A Modern Approach*. Prentice Hall, 3rd Ed., 2010.

[7] M. Słoński. Sequential stochastic identification of elastic constants using Lamb waves and particle filters. *Computer Assisted Meth. Eng. Sci.*, 21(1):15–26, 2014.

COMPDYN 2015
5th ECCOMAS Thematic Conference on
Computational Methods in Structural Dynamics and Earthquake Engineering
M. Papadrakakis, V. Papadopoulos, V. Plevris (eds.)
Crete Island, Greece, 25–27 May 2015

DEVELOPMENT OF A HYBRID SYSTEM FOR IDENTIFICATION OF ELASTIC MATERIAL IN COMPOSITE LAMINA: APPLICATION OF LAMB WAVES AND NEURAL NETWORKS

Zenon Waszczyszyn [1*], **Piotr Nazarko** [2],
Pawel Packo [3], **Lukasz Ambrozinski** [3] **and Tadeusz Uhl** [3]

[1] Cracow University of Technology,
Institute for Computational Civil Engineering,
Warszawska 24, Cracow 31-155, Poland,
e-mail: zenwa@L5.pk.edu.pl

[2] Rzeszow University of Technology,
Chair of Structural Mechanics,
Powstancow Warszawy 12, 35-959 Rzeszow, Poland
email: pnazarko@ prz.edu.pl

[3] AGH University of Science and Technology,
Chair of Mechatronics and Robotics
Al. Mickiewicza 30, 30-059 Cracow, Poland
email: {pawel.packo, ambrozine, tuhl}@agh.edu.pl

Keywords: Hybrid Computational System, Structure Health Monitoring, Lamb waves, Dispersion Curve, Lamb DC, Artificial Neural Network, direct analysis (simulation), reverse analysis (identification), parameter identification.

Abstract. *A new Hybrid Computational System is presented, developed for the identification of homogeneous, elastic, hexagonally orthotropic plate parameters. Attention is focused on the construction of dispersion curves, related to Lamb waves. The main idea of the hybrid system lies in the separation of two essential basic computational stages, corresponding to the direct and inverse analyses. In the frame of the first stage an experimental dispersion curve DC_{exp} is constructed, applying Guided Wave Measurement technique. The other stage is supported on the application of artificial neural network trained 'off line'. Two case studies are presented, corresponding either to pseudo-experimental computer simulations or to laboratory tests.*

1 INTRODUCTION

The presented paper is related to a new area of science and technology, called Structure Health Monitoring (SHM). It has been increasingly developing for some time now. SHM deals with structures and various processes closely connected with the life and maintenance of a variety of engineering structures. An important role for SHM is played by systems which on the base of monitoring or measurements can reflect the actual state (health) of structures. This permits control of the structure and warning against failures or dangerous events. Non-destructive methods of structure examination and 'on line' methods of information transmission are especially valuable for aspect of SHM, see, e.g. [1, 2, 3].

From among non-destructive methods, the application of ultrasonic waves is worth emphasizing for the evaluation of material properties and detection of various defects, cf, references in [2]. In what follows we are discussing a comparatively simple problem of the application of the Lamb Waves (LWs) propagation in thin, elastic and homogeneous plates, cf. [4-6]. These waves are guided in the vibration plane, perpendicular to the plate mid-surface and are propagated over a comparatively long distance.

The presented paper is related to the identification of parameters of anisotropic plates. The formulation of mathematical models of such plates and the identification of 'a priori' unknown parameters or defects is much more difficult than in isotropic plates. In such a situation we can tread the solutions obtained for isotropic plates as a special case, called even "bench mark" solutions for the analysis of orthotropic plates.

The Lamb equations make it possible to formulate the Dispersion Curve (DC). A relation $k(f \mid \mathbf{par})$ can be written, where: k – DC wavenumber, f – frequency of vibrations as an independent variable, **par** – vector of plate parameters. For example, in the case of isotropic, homogeneous plate, this vector is completed from the following constants: **par** = $\{E, \nu, \rho, d\}$, where: k and ν, – Young's modulus and Poisson ratio, ρ and d – plate density and thickness, respectively.

Unfortunately, the Lamb equations can be derived in an implicit and very elegant form (see e.g. books [4, 5] for the case of isotropic plates), but they can be analysed only by numerical methods. There is a variety of such numerical methods based on FEM, BEM and FDM. What seems especially numerically efficient are their modifications and combinations, see e.g. LISA/SIM (Local Interaction Simulation Approach/ Sharp Interface Model), EFIT (Elasto-dynamic Finite Integration Technique), see [7-11]. Unfortunately, these methods are rather "numerical costly" since they need a great number of numerical operations.

What seems to be especially numerically efficient, there is the formulation of semi-analytical methods (SEM) as the application of EFIT/LISA/FDM, with introducing of the Finite Difference Method (FDM) , see [12-14]. Unfortunately, the above listed methods are rather numerical costly since they need a great number of numerical operations.

Another disadvantage of the application of the aforementioned methods appears in the identification analysis, called in mathematics as the reverse approach.

This approach is related to the application of the paradigm of minimizing the difference between the "distance" between known and search states. Let us take as an example the norm of the experimental and numerically simulated values of the dispersion curves:

$$\left\| k_{num}^{(it)} - k_{\exp} \right\| \xrightarrow{it} \cong 0 \ . \tag{1}$$

In fact, the described approach, called in literature Classical Method (CM) of optimization, is refers to a sequence of direct problem solutions, see [14]. In our paper [15] we developed another approach, based on the application of Artificial Neural Networks (ANNs). This ap-

proach is related to the formulation of a corresponding Hybrid Computational Method (HCM). The system is composed of two stages. Stage A relates to the physical tests on material models (laboratory tests or measurements on laboratory models or structures). In Stage B data, satisfying the Lamb equations, are identified by 'off line' trained ANN. Then, preprocessed data of the Stage A are substituted as inputs into the trained network. Thus, the proposed HCS works 'numerically on line' as a method of one substitution of data from Stage A to Stage B.

The sketched HCM was checked in paper [15]. The results, obtained in this paper can also serve us as a "bench mark" in validation of our proposal. The main goal o our paper is a generalization of the approach developed in [15] to the appropriate modification of HCS for the identification of parameters for elastic orthotropic composite materials. In the present paper we adopted a hexagonal (five parameters) orthotropic material, corresponding to the unidirectional reinforced composite lamina.

Obviously, the identification of composite parameters is much more complicated than this applied for the isotropic material. Instead of the Armikulova's dimensionless Lamb equations, see [17], used for isotropic material, we now apply the finite difference equations, formulated in [13]. These equations have been adopted for computing patterns for the orthotropic material in Stage B for generating patterns needed for the 'off line' training and testing ANN as a component of HCS.

The basics on Lamb waves, and corresponding equations for the analysis of a thin plate made of hexagonally orthotropic material, are presented briefly.

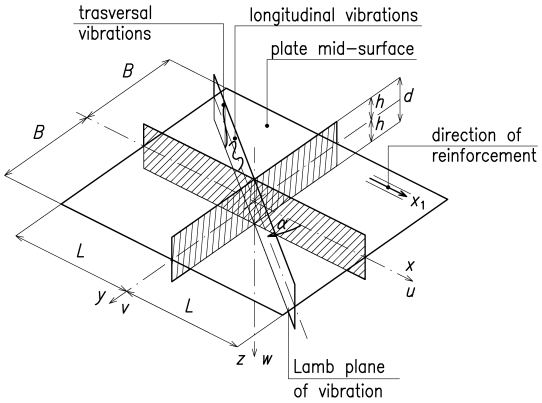
Next, case studies are discussed. The first case refers to pseudo-experimental verification of the identification results, supported on data taken from [4] for hexagonally orthotropic plate. The other case study relates to data taken from laboratory tests on unidirectional reinforced composite lamina, see [17]. In both case studies the results of an extensive numerical analysis are connected with the sensitivity of Lamb dispersion curves to variations of material parameters.

2 LAMB WAVES IN ELASTIC THIN PLATES

2.1 Some basics of LW equations

The Lamb plane of vibrations is shown in Fig. 1.

a)



b)

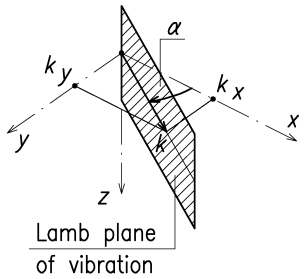


Figure 1: a) Lamb waves propagations with longitudinal, transverse and shear horizontal waves, b) Inclination angle α of vector wave-number $\mathbf{k}$ from reinforcement direction x_1

Fig. 2 illustrates the influences of displacements normal to the plate mid-surface which cause the symmetric and anti-symmetric modes of vibrations. These vibration modes can be drawn as radial in-plane and out of-plane motions, see [5].

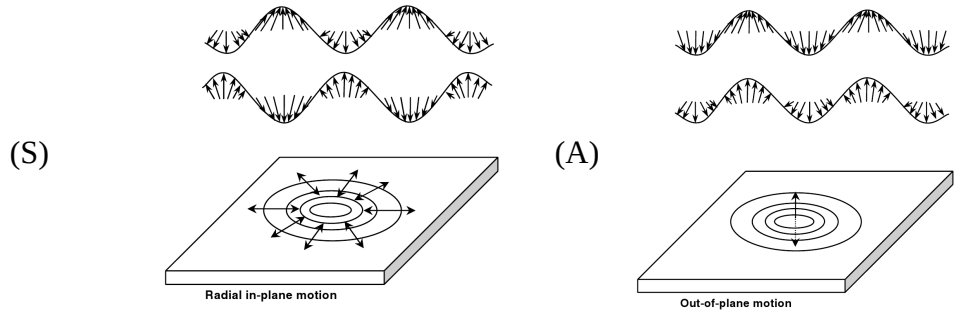


Figure 2. LW modes: (S) Symmetric (radial in-plane motion), (A) Anti-symmetric mode (out of-plane motion)

The adopted elastic, hexagonal, orthotropic material, has five independent elastic constants. The stiffness matrix of this material is shown in Table 1.

$\mathbf{C}_{(6x6)} =$

C_{11}	C_{12}	C_{12}			
C_{12}	C_{22}	C_{23}= $= C_{22} - 2\,C_{44}$			
C_{23}	C_{23}	C_{22}	C_{44}		
				C_{55}	
					C_{55}

Table 1: Stiffness matrix for hexagonal orthotropic material with 5 independent constants

The stiffness matrix of this material corresponds to the unidirectional reinforced composite lamina, see [11].

Two equations, which are the basis for deriving of Lamb equations, are: i) eigenvalue problem equations and ii) dispersion equations cf. e.g. [1, 5, 16].

2.2 Eigenvalue equations for composite lamina

The Cartesian coordinate system is adopted with *z* axis normal to the midsurface of a composite lamina, see Fig. 1. The displacement vector has components on the z distance to the plate midsurface:

$$\mathbf{W} \equiv \{u, v, w\} = \{U(z),\, V(z),\, W(z)\}\, \mathrm{e}^{[(k_x + k_y) - \omega t]} \equiv W\, \mathrm{e}^{\,i[(k_x + k_y) - \omega t]}, \tag{2}$$

where: $\mathbf{k} = [k_x, k_y]^{\mathrm{T}}$ – wave number vector of length $k = |\mathbf{k}| = +\sqrt{k_x^2 + k_y^2} = \omega / c_p$ and ω is angular frequency, c_{p} is phase frequency. The direction of wave propagation depends on the angle α, i.e. $\mathbf{k} = k[\cos\alpha, \sin\alpha]^{\mathrm{T}}$, k_x^2, see Fig. 1b.

The displacement functions (2) can be separated into symmetric and snit-symmetric modes, see [18].

$$U_{\mathrm{s}} \cos \xi z = C_1 \cos \xi z, \quad V_{\mathrm{s}} \cos \xi z = C_2 \cos \xi z, \quad W_{\mathrm{s}} \sin \xi z = C_1 \sin \xi z, \tag{3S}$$

$$U_a \cos \xi z = C_1 \sin \xi z, \quad V_a \sin \xi z = C_2 \sin \xi z, \quad W_{\mathrm{a}} \sin \xi z = C_3 \cos \xi z, \tag{3A}$$

where: ξ_j – eigenvalues that will be computed as solutions of the characteristic equations of the eigenvalue problem

2.3 Eigenvalue equations for composite lamina

From the equations of motion, see [18], we can formulate the following equations of the eigenvalue problem:

$$\mathbf{[\Gamma - \chi^2 I]\, C^T} \equiv \begin{bmatrix} \Gamma_{11} - \chi^2 & \Gamma_{12} & \Gamma_{13} \\ \Gamma_{12} & \Gamma_{22} - \chi^2 & \Gamma_{23} \\ \overline{\Gamma}_{13} & \overline{\Gamma}_{23} & \Gamma_{33} - \chi^2 \end{bmatrix} \begin{bmatrix} C_1 \\ C_2 \\ C_3 \end{bmatrix} = \begin{bmatrix} 0 \\ 0 \\ 0 \end{bmatrix}, \tag{4}$$

where: $\chi^2 = \rho\omega^2$, ρ^2 is the plate density. The expressions for Γ_{ij} can be found in [??]. For instance $\Gamma_{11} = C_{11}k_x^2 + C_{66}k_y^2 + C_{55}\xi^2$.

Characteristic equations related to the eigenvalue analysis Eq. (4) leads to the 6-the order algebraic equations, which can be solved only by means of numerical methods. That is why we apply the finite difference method, see [13], related to the LINSA system, see Appendix.

The Lamb wave equations are derived from the boundary conditions:

$$\sigma_z(\xi z)_{|z=\pm h} = 0, \quad \tau_{zx}(\xi z)_{|z=\pm h} = 0 . \tag{5}$$

From the condition of existence of a non-trivial solution of the set of homogeneous equations (5) the dispersion Lamb function can be found. It has the following implicit form, see [18]:

$$F(k, f, C_{ij}, \chi^2, S \vee A) = 0 . \tag{6}$$

3 BASIC ALGORITHMS FOR PLATE PARAMETERS IDENTIFCATION

3.1 Four essential algorithms for GWM

In the Guided Wave Monitoring or Measurements (GWM) four essential steps can be distinguished, see [2]. The steps are sketched in Fig. 3, underlining Step IV.

Steps I and II correspond to carrying out the experimental test and initial processing of measured responses (signals).

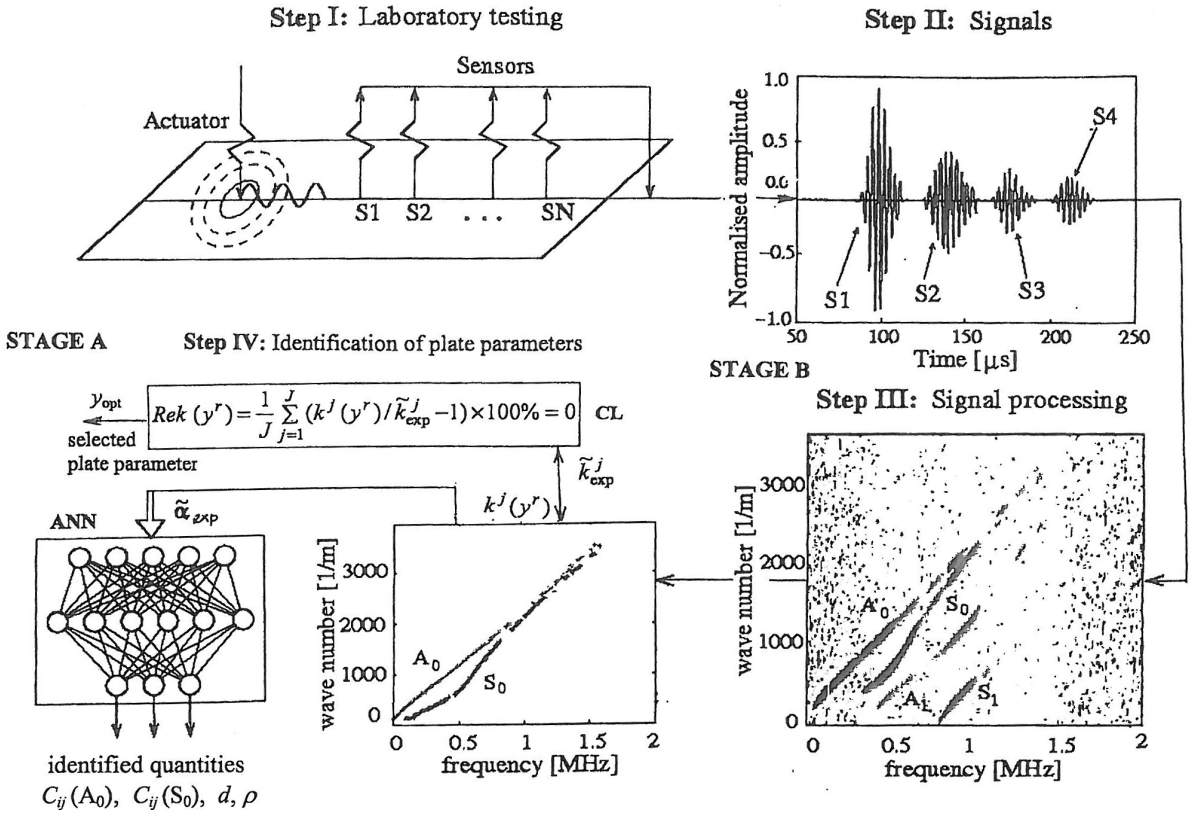


Fig. 3. Four essential steps for identification of plate parameters, applying Lamb wave measurement technique and identification procedures in step IV: CL –Classical approach, ANN – artificial neural network

Step III contains signals processing, applying B-scanning and 2D-FFT transformation [19]. The estimated local maxima on the plane (*f*, *k*) enable us to trace the dispersion curves. In Fig. 3 there are shown DCs, which fulfill symmetric and anti-symmetric modes of DCs. They are, in fact, a set of points $\{f_m^j, k_m^j\}_{j=1}^J$, where $m = 0, 1, 2, \ldots$ are numbers of vibration modes.

Step IV starts from the selection of points which are simulated by numerical methods. In the case presented in Fig.2 only the points related to modes A_0 and S_0 are shown.

This point is based on algorithms developed in [15] for elastic, isotropic plate parameters identification. In the present paper we have introduced some modifications, corresponding to the identification of elastic, hexagonal orthotropic material, see Table 1.

3.2 Hybrid Computational System and corresponding procedures

The Hybrid Computational System is composed of two computational Stages A and B, see Fig.3. Stage A is devoted to the testing analysis, to testing and processing of experimental data. Stage A corresponds to the direct analysis. Step B deals with the inverse analysis, starting from the extended Essential Step IV, see Fig. 3. In beginning the dispersion curves are selected from the spectrum of modes, shown in Essential Step III. In Fig. 3 the selection of two vibration modes was made, corresponding to modes A_0 and S_0.

The basic roles in reverse analysis plays ANNs, see [5, 20-22].The algorithms of Stage B were developed in [15]. In the present paper we discuss briefly only the main algorithms taken from paper aforementioned.

3.2 Algorithms of HCS

In our paper we have decided to restrict our analysis to a range of dispersion curves (DCs), since the considered composite lamina are adopted to be after numerical homogenization and material parameters are constant along the plate length 2 *L*, see Fig. 1. The adopted reference range is related to frequencies of excited vibrations, i.e. $f_{\text{ref}} \in [\, f_{\min}\, ,\, f_{\max}\,]$. The values and forms of corresponding points of experimental curves are processed in order to have experimental approximate dispersion curves related to the formulation processes. The value of f_{ref} is taken from laboratory tests. After numerical processing, an approximate vawenumber function $k_{\exp}\,(\,f \,|\, \mathbf{par})$ is obtained. In what follows the formulated dispersion curves can be written shortly in the form $k\,(\text{X}|\text{Y})$, where: X – independent variable, Y – given values of other variables.

In the presented paper we are discussing hexagonal orthotropic material with the stiffness matrix **C** shown in Table 1. In such a special case, the vector of identified plate parameters is $\mathbf{spar}_{(6\times 1)} = \{C_{11}, C_{22}, C_{44}, C_{66}, C_{12}, d\}$. The following parameters are fixed: $\rho_{\,fixed}$ – density of plate, *N* = number of station in the FDM formulas, see Appendix.

3.2.1 Simulation computation in Stage A

Stage A corresponds to the standard procedure, related to Guided Wave Monitoring GWM) technique, discussed in many books and papers, e.g. see references in [4, 5]. The main attention is focused on Stage B.

After evaluation of reference range $f_{ref}^{\exp}$ for selected modes vibrations, a set of experimental data can be completed.

$$\mathsf{D}_{\exp} = \{\, f^j,\, k^j \,|\, m \,\}_{j=1}^{J},\, {}_{m=1}^{M}\,, \tag{7}$$

where: $j = 1, 2, \ldots, J$ – numbers of dispersion points, m – numbers of vibration modes.

On the basis of data, approximate experimental curves can be formulated. The parameters of these curves are computed by means of the Least Squared Method (LSM):

$$\tilde{k}^{(M=2)} = \left(\, f \,|\, \mathbf{BF}_{\text{ref}}\,(f), D_{\exp}\right) \xrightarrow{\;LMS\;} \tilde{\boldsymbol{\alpha}}_{\exp}\,. \tag{8}$$

In the presented paper, $M = 2$ modes are adopted, i.e. A_0 and S_0. The reference basis function vector $\mathbf{BF}_{\text{ref}}\,(f)$ should corresponds to the adopted reference range $f_{\text{ref}} \in [\, f_{\min}\, ,\, f_{\max}\,]$ and to shape of the dispersion curve, represented by computed values of vector $\tilde{\boldsymbol{\alpha}}_{\exp}$. Components of this vector correspond to internal parameters, which control the transition from Stage A to Stage B.

3.2.3 Identification computation in Stage B

The main part of the stage B corresponds to an ANN, which is a solver of the inverse problems of identification of the plate parameters. Similarly as in [15].the Multi Layered Perceptron (MLP) network, see Haykin [24], of the following architecture can be designed:

$$\text{MLP: } \boldsymbol{\alpha}_{(I\,\times 1)} – \mathbf{H}_{(H\times 1)} – \mathbf{spar}_{(3\times 1)}\,, \tag{9}$$

where: I – number of inputs, H – number of sigmoid functions in the hidden layer designed.

The corresponding set P , composed of P pattern pairs, was adopted for the training of the MLP neural network from the view point of the identification purposes:

$$\mathbf{P} = \{\boldsymbol{\alpha}^p, \mathbf{t}^p = \mathbf{spar}^p\}_{p=1}^{P} . \tag{10}$$

The input vectors $\boldsymbol{\alpha}^p$ can be computed for Armirkulova's approximation in case of isotropic material of the plate, see [17] .We can start from a cloud of P points (f^p, k^p), fulfilling the Lamb dimensionless equations.

In case of the considered orthotropic material, instead of Armikulova's formulas the Finite Difference Method was adopted, see Appendix. These equations can be related to known target values $\mathbf{t}^p$ and the LSM method is applied for the anisotropic materials, computing the p-the input patterns:

$$k \left(f \,|\mathbf{BF}_{\text{ref}}(f), \mathbf{spar}^p \right) \xrightarrow{LMS,\ FDM} \boldsymbol{\alpha}^p . \tag{11}$$

The patterns of the training set are selected from reference ranges of the output vector components of the output vector $\mathbf{spar}^p$. After the training of MLP, relative errors of the neural approximation can be computed:

$$Rey = \frac{1}{P} \sum_{p=1}^{P} (1 - y^p / t^p) \times 100\% \ , \tag{12}$$

where: y and t are computed and target values of the vector **spar** components**.**

The values of components of the vector of experimental curve parameters (11) are substituted into the trained MLP for computing:

$$\tilde{\boldsymbol{\alpha}}_{\text{exp}} \xrightarrow{LMS} \mathbf{spar}_{\text{MLP}} . \tag{13}$$

It should be emphasized that the identification computations in the Stage B are carried out 'off line'. Thus, solution (13) is obtained by patterns corresponding to the exact Lamb dispersion curves. It equals $\mathbf{spar}_{\text{MLP}}$, with the accuracy corresponding to the MLP network errors (12). Thus, we can conclude that

$$\mathbf{spar}_{\text{MLP}} = \mathbf{spar}_{\text{ident}} \approx \mathbf{spar}_{\text{exact}} , \tag{14}$$

The formula (14) gives identification in one substitution, without any iteration. We can call this approach the 'numerically on line' process.

4 CASE STUDIES

4.1 Identification of a pseudo-experimental hexagonal orthotropic composite

In this case study, the material constant values shown in Table 1, were taken from [4]:

C_{11} = 128.2 GPa, $C_{22} = C_{33}$ = 14.95 GPa, C_{44} = 3.81, GPa, $C_{55} = C_{66}$ = 6.73 GPa,
$C_{12} = C_{13}$ = 6.90 GPa, $C_{23} = C_{22} - 2\,C_{44}$ = 7.33 GPa, and ρ = 1.58 g/cm^3, N = 9, (15)
where: N – number of FD stations along the plate thickness.

Data (15) were applied in HCS for three excitations related to different direction of the Lamb planes, see Fig.: 1) $\alpha = 0^{\circ}$, $k_x = k$, $k_y = 0$, 2) $\alpha = 90^{\circ}$, $k_x = 0$, $k_y = k$, 3) $\alpha = 45^{\circ}$, $k_x = k_y = k$.

The computations were made for the reference range $f_{\text{ref}} \in [0.05, 0.5]$ MHz, see Fig. 4. In this Figure four LDCs modes are shown A_0 , SH_0, S_0 and A_1 for the Lamb planes $\alpha = 0^{\circ}$, 90° and 45°.

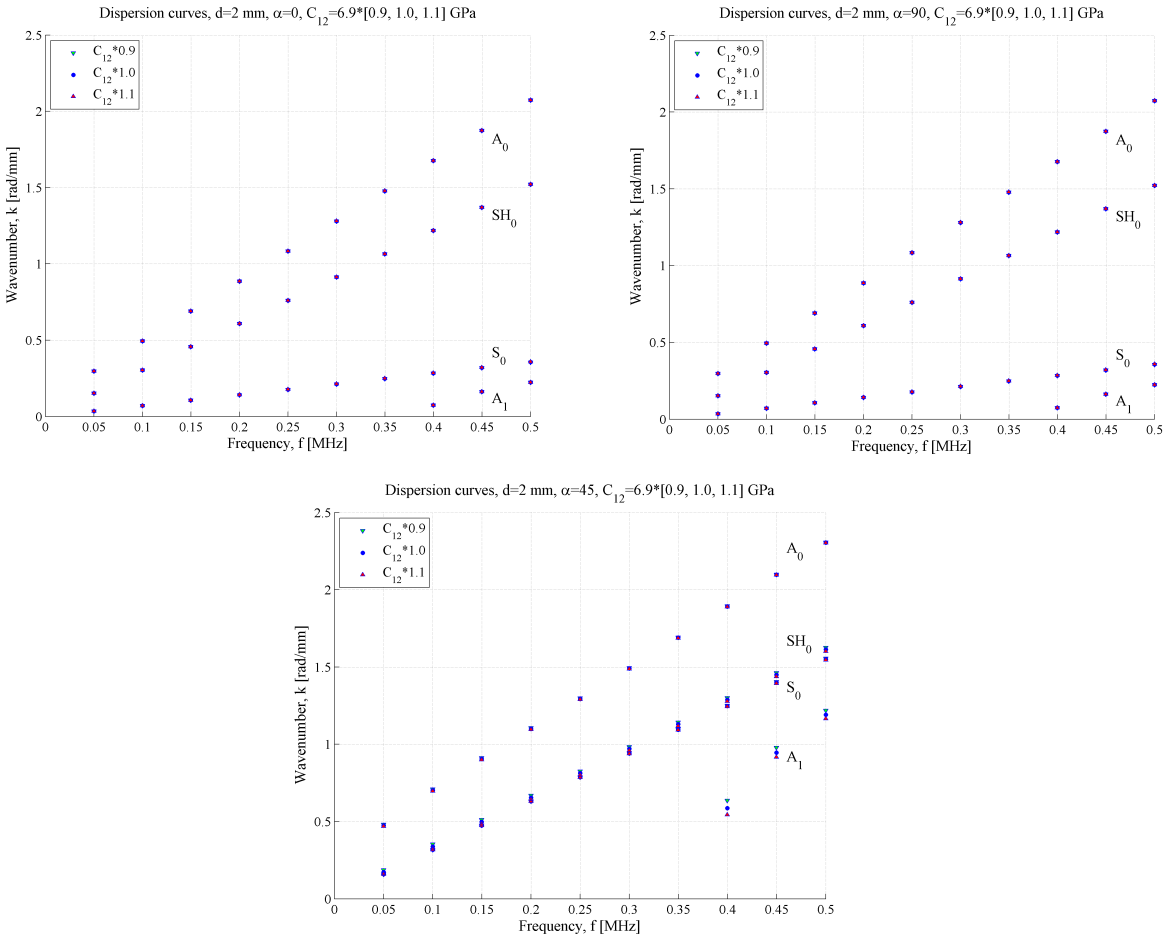


Figure 4. Sensitivity of modes A_0, SH_0, S_0 and A_1 for variations of material parameter C_{12}

The Shear Horizontal mode SH_0 is not dispersive and cannot be reconstructed by standard B-Scans techniques. The corresponding LDCs are close to straight lines. The dispersion curve is a linear functions, see [4], p. 244. The corresponding formula can be used for the calculation of the stiffness C_{66} value:

$$k = 2\pi\sqrt{\rho/C_{66}}\, f \quad \rightarrow \quad C_{66} = 4\pi^2 \rho\, (f/k)^2 \ . \tag{16}$$

For example, if we take the approximate value of wavenumber, $k \approx 1.52 \times 10^{-3}$ m^{-1}, then for $f \approx 0.5$ MHz the stiffness equals $C_{66} \approx 6.74$ MPa.

Similar sensitivity analysis was made for the other four parameters. The recognition of sensitivity of LDCs to perturbations by small values of plate parameters is indispensable for a proper selection of dispersion modes. Such recognition has been taken into account for evalu-

ation of reference ranges of the hexagonal, orthotropic material parameter variations in order to prepare patterns for ANNs training.

The carried out identification of data (15) taken from [4], and treated in the present paper as pseudo-experimental data, gave identified values very close to those in the above mentioned paper.

4.2 Identification by HSM on the base of a laboratory test

Let us start from the Stage A , Essential Step III, see Fig. 3. There are presented Scan-B maps in which LDCs as local maxima, found in the 2D-FTT transform space, see [19]. Corresponding curves were measured on carbon fiber reinforced plastic (CFRP). The Lamb waves propagated in directions α = 0°, 90° and 45°, corresponding to modes A_0, B_0 outlines of A_1 mode.

According to remarks in the previous Case Study, DC of SH_0 could not be reconstructed because it is related to a non-dispersive wave.

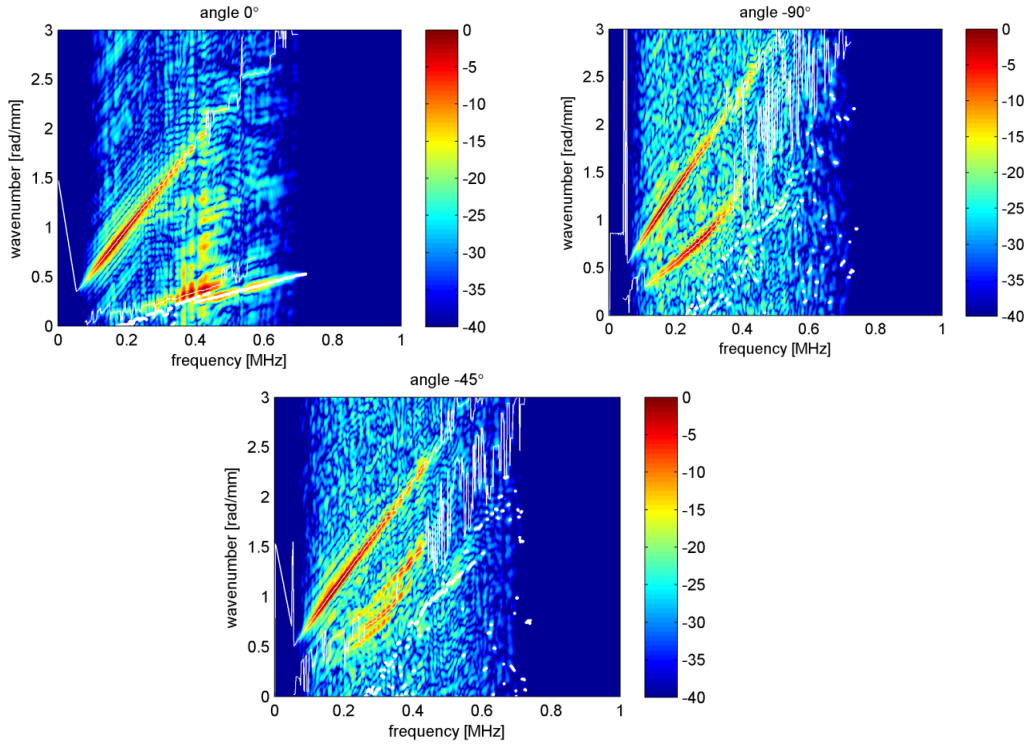


Figure 5. B-Scans and Diffusion Curves in α = 0°, 90° and 45° 2D-direction of vibration in FFT transform space for unidirectional reinforced composite lamina

It is visible that LDCs can be recognized in the reference range $f_{ref} \in [f_{min}, f_{max}]$. Moreover, the CDs shape can be reconstructed in an analytical form with an inaccuracy. We can apply the straight, sloppy lines as approximate LDCs. Such an approximation corresponds to the application of a single basis functions $k(f)$ for $f \in$ [0.2, 0.35] MH, see Fig. 6.

Then we can perturb a selected identified parameter and observe which mode is more sensitive to parameter perturbation.

In this study case, see Fig.6a, the perturbation of the stiffness C_{11} causes larger changes of the mode S_0. Now we can construct a set of points corresponding to 20 regularly placed station

f_j for $j = 1, \ldots, J$. For R changes of the stiffness $C_{11,r}$ we have $J \times R$ patterns for finding an optimal of parameter C_{11} by means of the Mean Square Method.

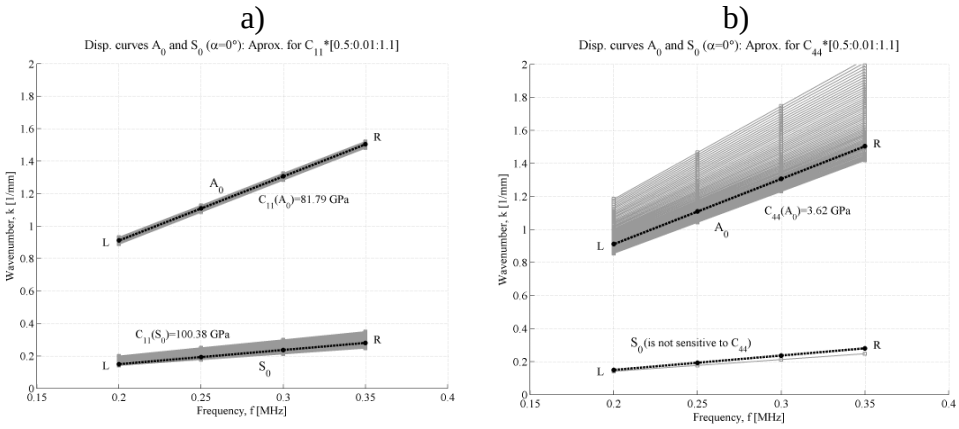


Figure 6. Sensitivity of modes A_0 and S_0 to changes of plate stiffness C_{11} and C_{44}

Optimal value of the parameter C_{11} can be also found by means of the mode A_0 .Similar perturbations of other parameters can points out which of optimal solutions is proper.

There no doubt that in case of identification of the parameter C_{44} the identification by means of the mode A_0 is better than by S_0 .

The approach discussed above fully corresponds to the general method discussed in Point 3.2.3, where the basis functions (BF) are used. In the considered case study a straight BF is used with the left and right bound points are L and R, respectively, see Fig. 6. The vector of parameters is:

$$\boldsymbol{\alpha}_{(4\times 1)} = \{k\,(f = 0.2\,\text{MHz}), k\,(f = 0.25\,\text{MHz}), k\,(f = 0.30\,\text{MHzz}), k\,(f = 0.25\,\text{MHz}), (f = 0.35\,MHz)\} \quad (7)$$

The basis function with parameters (17) was used as a good approximation of LDCs. Selected results of the identification analysis are shown in Table 2. They correspond to the neural network MLP: 4-6-1 with one BF and MLP: 8-6-3 with two BFs.

MLP Neural networks	Number of parameters		Model, α °	Identified parameters		Relative testing errors *ReT* [%]	
	P	L		C_{ij}	MPa	max	mean
8–10–3	2541	847	A_0, S_0, 0 °	C_{11} C_{12} C_{44}	93.00 0.019 3.74	6.11 0.005 12.97	0.64 0.001 4.30
4–6–3	2541	847	A_0, 0 °	C_{11} C_{12} C_{44}	99.45 0.301 3.81	0.65 0.010 19.50	0.059 0.001 8.13
4–6–1	101	34	S_0, 45 °	C_{22}	17.46	0.049	0.003
4–6–1	41	14	A_0, 45°	C_{55}	5.62	0.158	0.008

Table 2. Identified values of stiffness constants

It is worth mentioning that the results shown in Table 2 were obtained for 100 'trained off line' networks. The computed value of the stiffness equals $C_{23} = C_{22} - 2\,C_{44} = 17.46 - 2\times3.74 = 9.98$ GPa. The stiffness C_{55} for computed for wave-number, evaluated from Fib. 4, $\alpha = 45^{o}$, for $f = 0.5$ MHz as $k \approx 1500$ m^{-1}. The stiffness value calculated by formula (16) equals $C_{55} = C_{55} \approx 8.58$ GPa.

5. SOME REMARKS AND FINAL CONCLUSIONS

- The presented paper is a continuation and development of paper [14], where the modeling and analysis are related to an isotropic material. In the presented paper the considered analysis is much more extended than in [15].
- It was proved that the main idea of the Hybrid Computational System (HCS), i.e. separation of direct and reverse analyses can be extended to the analysis of orthotropic material. This can be carried out owing to the application of Artificial Neural Networks (ANN).
- In the present paper the attention was focused on the analysis of the hexagonal model of orthotropic material, useful in the analysis of unidirectional reinforced composites.
- The search for starting values of material constants was based on the sensitivity analysis of the Lamb Dispersion Curves changes of material constants.
- The obtained results seem to be useful for the development of HCS for a numerically efficient analysis of composite plies [16].

A APPENDIX

A semi-analytical method for dispersion curves computation

The regular discrete grid was adopted for the space stations across the plate thickness, see Fig. A1. The regular grid of points is used with spacing $\{\Delta x, \Delta y, \Delta z\}$.

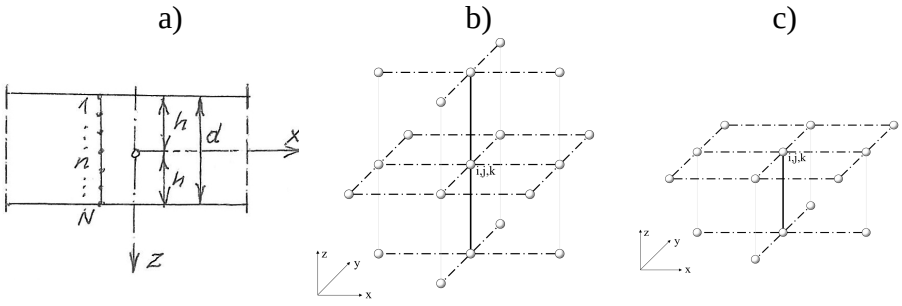


Fig. A1. a) Grid layer stations at plate cross-section, b) internal grid point c) upper boundary grid point.

At each station the elastodynamic equation is discretized. The equilibrium at a station point is given by the semi-analytical LISA equation and, following [13], and it can be expressed as:

$$-\rho_s \frac{\delta^2 \mathbf{W}}{\delta t^2} = \frac{1}{\Delta V} G(\mathbf{W}^{x_1 \pm 1, x_2 \pm 1, x_3 \pm 1}), \tag{A1}$$

where: $G(\mathbf{W})$ – function of material properties, particle displacements and discretizing parameters, ΔV– volume enclosed by neighbouring grid points, ρ_s – sum of density values for all cells surrounding the station point (see Fig. A1).

Subsequently, equation (A1) is re-formulated in the spectral domain along $x_{n=1,2}$ directions. Effectively, grid points adjacent to the considered station point, namely, $\mathbf{W}^{x_1 \pm, x_2 \pm 1, x_3 \pm 1}$ are substituted by $(\tilde{\mathbf{W}}^{(x_1, n \pm, x_2, n \pm 1, x_3 n \pm 1)} e^{\pm i k_x \Delta x \pm k_y \Delta y}$, where $\tilde{\mathbf{W}}$ denotes a discrete-space-Fourier-transformed quantity. It should be noted that the left-hand-side of Eq. (A1) is transformed as, i.e. the time remains as non-discretized (continuous) quantity. Letting $\rho_s \omega^2 \tilde{\mathbf{W}} = \chi^2_{S-A} \tilde{\mathbf{W}}$, where χ^2_{S-A} is the semi-analytical (S-A) counterpart.of $\chi = \Delta t^2 / (\rho_s \Delta V)$,we obtain:

$$-\chi^2_{S-A} \tilde{\mathbf{W}} = \frac{1}{\Delta V} \tilde{G}(\mathbf{W}^{x_3,(n-1,n,n+1)}, e^{i(\pm k_x \Delta x \pm k_y \Delta y)}), \tag{A2}$$

where indices x_n for n = 1, 2 have been omitted for brevity. Formula given by Eq. (6) is the bulk wave dispersion equation of the semi-analytical method and involves only the trans formed displacement values for $x_{3,(n\pm1)}$ grid points.

Manipulating and assembling (A2), using the scheme presented in Fig. 3, leads to an eigenvalue problem analogous to (4). The solution of Eq. (A2) provides the (k, $\chi_{S\text{-}A}$) pairs for the Lamb waves. For the definition and implementation details, the reader is referred to [10].

Acknowledgement

Authors of this paper are gratefully acknowledged, to the Polish National Science Centre, Grant No. UMO-2011/01/B/ST8/ 07210, AGH No.18.18.130.384, "Structural Health Monitoring by means of inverse problem solution under uncertainty", for financial support.

REFERENCES

[1] M.M. Ettoney, S. Alampalli. *Infrastructure Health Monitoring in Civil Engineering: Theory and Components*, vol. 12. CRS Press, Taylor& Francis Group, 2012.

[2] A. Raghavan, C.E.S. Cesnik. Review of guided-wave structural health monitoring. *The Shock and Vibration Digest*, **39**: 91-114, 2007.

[3] Ł. Ambroziński, L. Packo, T. Stepinski, T. Uhl. Ultrasonic guided waves based method for SHM: simulations and an experimental test. *The 5th World Conference on Structural Control and Monitoring* 5WCSCM, pp. 10443-10452, 2010.

[4] G.L. Rose. *Ultrasonic Waves in Solid Media*, Cambridge University Press, 1999.

[5] Z. Su and L. Ye, Identification of damage using Lamb waves: from fundamentals to applications. In F. Pfeifer and P. Wriggers (Series eds), *Lecture Notes in Applied and Computational Mechanics*, vol. 48, Springer, 2009.

[6] P. Packo, L. Ambrozinski, L. Pieczonka, W.J. Staszewski, T. Uhl. The influence of experimental and numerical parameters on the dispersion curves used for elastic constants identification. *Inverse Problems in Sci. and Eng.*, submitted for publishing, 2014.

[7] W. Ostachowicz, J.A.Gűemes (Editors). *New Trends in Structural Health Monitoring.* CISM Courses and Lectures, vol.542. Springer 2013.

[8] P. Fellinger, R. Marklein, S.Klaholz. Numerical modelling of elastic wave propagation

and scattering with EFIT – elastodynamic finite integration technique. *Wave Motion*, **21,** 47-66, 1995.
[9] W. Ostachowicz, P. Kudela, M. Krawczyk, A. Żak. *Guided Waves in Structures for SHM.* J Wiley&Sons, 2012.
[10] P. Packo, T. Bielak, A.B. Spencer, W.J. Staszewski, T. Uhl, K. Worden. Lamb wave propagation modelling and simulation using parallel processing architecture and graphical cards, *Smart Materials*., **21**, 2012.
[11] Packo, L. Pieczonka, L.Ambrozinski, T. Uhl. T 2013 Elastic constants identification for laminated composites based on Lamb waves. *Proceedings of the 9th International workshop on Structural Health Monitoring.* In: Fu-Kuo Chang (ed)., Vol 1, ISBN 978-1-60595-115-7. Stanford, September 10–12, 2010.
[12] M. Sale, P. Rizo, Z. Marzani. Semi-analytical formulation for guided waves-based reconstruction of elastic moduli. *Mech. Systems Signal Processing*, **25,** 2241-2256, 2011.
[13] P. Packo, T.Uhl, WJ. Staszewski. A general semi-analytical difference method for dispersion curves calculation and numerical analysis in Lamb wave propagation. *Journa*l *Acoust. Soc. America,* **136**, 993-1002, 2014.
[14] E. Pabisek, Z. Waszczyszyn, L. Ambrozinski. A semi-analytical method for identification of thin elastic plate parameters basing on LWM. *Computer Assisted Mechanics in Engineering Sciences*, **21**, 5-14, 2014.
[15] E. Pabisek, Z. Waszczyszyn. Identification of thin elastic isotropic plate parameters applying Guided Wave Measurement and Artificial Neural Networks, submitted for publication, *Mechanical Systems Signal Processing*., 2014.
[16] S. Pant, J. Laliberte, M. Martinez, B. Rocha. Derivation and experimental validation of Lamb wave equations for an *n*-layered anisotropic composite lamina. *Computers & Structures,* **111**, 566-579, 2014.
[17] V. Amirkulova. *Dispersion Relations for Elastic Waves in Plates and Rods*. M. Sc. Thesis. The State University of New Jersey, 2011.
[18] Lei Wang, FG. Yuan. Group and characteristic wave curves Lamb waves in composites: Modeling and Experiments. *Composite Science and Technology*, **67** 1370-1384, 2007.
[19] Z. Waszczyszyn, Artificial neural networks in civil and structural engineering: ten years of research in Poland, *Computer Assisted Mech. in Eng. Sci.*, **13**, 489-512, 2006.
[20] Z.Waszczyszyn, Artificial neural networks in civil and structural engineering: another five years of research in Poland, *Computer Assisted Mechanics in Engineering Sciences*.,**18**, 131-146, 2011.
[21] GR. Liu, KY. Lam, X. Han. Determination of elastic constants of anisotropic plates using elastic waves and a progressive neural network. *Journal of Sound Vibrations*, **252**, 239-259, 2002.
[22] D. Alleyne, P. Cawley. A two-dimensional Fourier transform method for the measurement of propagating multimode signals *The Journ. Acoust. Soc. America* ASA. **89:** 1159-1168, 1991.
[23] S.Haykin, *Neural Networks: a Comprehensible Foundations*, 2nd ed., Prentice–Hall, 1999.

COMPDYN 2015
5th ECCOMAS Thematic Conference on
Computational Methods in Structural Dynamics and Earthquake Engineering
M. Papadrakakis, V. Papadopoulos, V. Plevris (eds.)
Crete Island, Greece, 25–27 May 2015

SIMPLIFIED MODEL FOR COUPLED VIBRATION OF ADJACENT STRIP FOOTINGS

Jue Wang[1] , Ding Zhou[2] , Weiqing Liu[3]

[1,2,3] College of Civil Engineering, Nanjing Tech University, Nanjing 211816, P. R. China
e-mail: [1]wjatnjut@gmail.com; [2]dingzhou57@yahoo.com; [3]wqliu@njut.edu.cn

Keywords: foundation-soil-foundation interaction, impedance function, lateral-rocking dynamic, elastic half-space, Green function

Abstract. *A semi-analytical procedure is presented to obtain the coupling lateral-rocking impedances between adjacent strip footings rested on an elastic half space. The interfaces between the footings and the supporting medium are divided into a number of strip elements. Asymmetrical Green functions of the elastic soil medium under lateral and vertical harmonic uniform excitation with infinite length are derived to establish the dynamic-flexibility matric for those strip elements. The intensities of such forces are adjusted so the displacement of the elements are compatible with the rigid body translations or rotations of the footings. The coupled lateral-rocking impedances are solved by adding the bending moments and the contact forces on each element. The accuracy is verified by the comparison study with the rigorous results from the mix-boundary-value method. The influence of the distance ratio S/L on the dynamic cross interaction (DCI) effect between adjacent footings is discussed in detail. It is shown that the lateral-rocking interaction between adjacent strip footings should be taken into consideration when* S/L *less than 5.0.*

1 INTRODUCTION

The substructure method, which enables soil and structure to be considered separately, is widely applied in the Soil-structure interaction (SSI). In practical situations, structures are sometimes placed close to each other due to a limitation of space. Hence, in the realistic evaluation of their dynamic characteristics, it is necessary to consider not only the interaction between the footing and the soil medium but also the interaction between adjacent footings through the soil, which is known as dynamic cross interaction (DCI) problem. Besides experimental investigations and numerical procedures, substructure method is still a powerful and feasible approach to DCI problems. In the substructure method, an important step is the computation of the footing impedances with the consideration of DCI effect.

The analytical solution for footing impedance can be obtained through a stress boundary-value method, which is based on assumptions about stress distributions (static rigidity, uniform, parabolic or their combinations) underneath the footing [1, 2]. However, as the assumed distribution may not satisfy the contact conditions at the footing-soil interface for adjacent footings, the deflected shape of the interface has to be modified based on the averaging techniques. Warburton et al. [3] provided an approximate method based on the relaxed contact assumption to study the dynamic response of two rigid circular footings on soil medium. More rigorous solutions for the impedance of footing can be obtained as a mixed boundary-value problem formulated in terms of dual integral equations [4, 5]. However, as the solutions of dual integral equations cannot be expressed by elementary functions, there are limitations to obtain the contact stress functions for a DCI problem. Otherwise, some semi-analytical approaches make the impedance solve flexibly [6-8]. Savidis and Richter [9] investigated the vertical cross-interference between two rigid, massless, smooth contacting surface footings by boundary integral equations in conjunction with constant elements in soil-footing interface. Dynamic interaction of a group of flexible strip footings resting on smooth contact with a homogeneous elastic half-space was studied by Wang et al. [10] based on a classical Green function for a concentrated vertical line load. It was extended later by Senjuntichai and Kaewjuea [11] to a multilayered poroelastic half-space. Their studies were limited to vertical dynamic interaction. However, the coupling lateral-rocking dynamic holds great significance for earthquake engineering as the largest effects of earthquake are on horizontal ground motion rather than vertical ground motion. In this paper, a discretization method is proposed to evaluate the coupling lateral-rocking impedance of adjacent strip footings intimately attached to an elastic half-space. The influence of the distance ratio S/L on the DCI effect between two footings is discussed in detail.

2 MODEL DESCRIPTION

The lateral-rocking oscillation of two adjacent strip footings with full contact to the free surface of an elastic half-space with different separation distance S is considered as shown in Fig. 1. Footing A with the width L_a is excited by the lateral excitation $P_a e^{i\omega t}$ and the rocking excitation $M_a e^{i\omega t}$. Footing B with the width L_b is excited by the lateral excitation $P_b e^{i\omega t}$ and the rocking excitation $M_b e^{i\omega t}$. For the strip footing such as track foundation, dam or building footing with a high ratio of length to width, it is reasonable to be simplified as a generalized plane strain problem. Considering DCI effect, the dynamic force and deformation relationship of the adjacent footings can be expressed by

$$\begin{Bmatrix} P_a \\ P_b \\ M_a \\ M_b \end{Bmatrix} = \begin{bmatrix} \Re_{\mathrm{hh}} & \Re_{\mathrm{hr}} \\ \Re_{\mathrm{rh}} & \Re_{\mathrm{rr}} \end{bmatrix} \begin{Bmatrix} U_a \\ U_b \\ \Theta_a \\ \Theta_b \end{Bmatrix} = [\Re] \begin{Bmatrix} U_a \\ U_b \\ \Theta_a \\ \Theta_b \end{Bmatrix} \tag{1}$$

where U_a and U_b are the lateral displacements of Footing A and B, respectively. Θ_a and Θ_b are rocking angles of corresponding footings. **[ℜ]** is the impedance matrix of the system consisting of lateral impedance $\Re_{\mathrm{hh}}$, rocking impedance $\Re_{\mathrm{rr}}$ and coupling impedance $\Re_{\mathrm{rh}}$. Each impedance in the **[ℜ]** is a complex number and can be interpreted as a spring with the frequency-dependent coefficient K(ω) and a dashpot in parallel with the frequency-dependent coefficient C(ω). Consequently, a simplified model, as shown in Fig. 2, can be built to simulate the coupled vibration of adjacent strip footings based on the impedance matrix **[ℜ]**.

For the simplification in analysis, the interfaces beneath Footing A and B are divided into *N* and *M* surface strip elements, respectively, as shown in Fig. 1. The widths of all the elements beneath Footing A and B are denoted by $\Delta_a=L_a/N$ and $\Delta_b=L_b/M$, respectively, where *N* and *M* represent the division number of Footing A and B. It is assumed that the *n*-th element (*n*=1，… ，*N*) beneath Footing A is subjected to a uniform lateral traction $p_n^{(a)}\mathrm{e}^{\mathrm{i}\omega t}$ and a vertical traction $q_n^{(a)}\mathrm{e}^{\mathrm{i}\omega t}$. Similarly, the *m*-th element (*m*=1，… ，*M*) beneath Footing B is subjected to a uniform lateral traction $p_m^{(b)}\mathrm{e}^{\mathrm{i}\omega t}$ and a vertical traction $q_m^{(b)}\mathrm{e}^{\mathrm{i}\omega t}$.

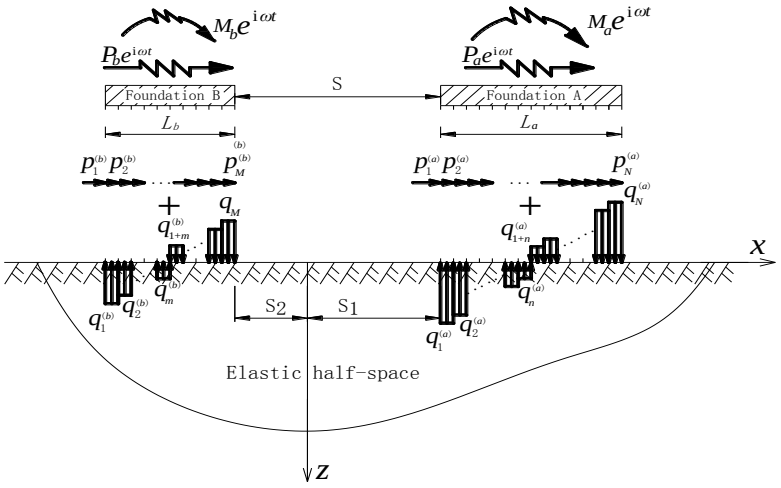


Fig. 1 The dynamic interaction model of the adjacent strip footings attached to an elastic half-space under lateral-rocking harmonic excitations

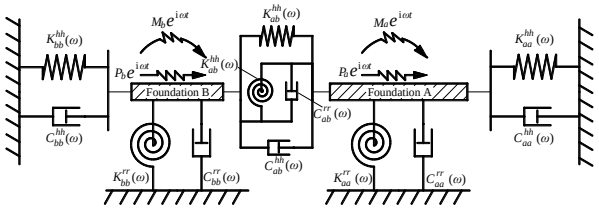


Fig. 2 Equivalent model of two adjacent footings under the lateral-rocking dynamic interaction

3 FORMULATION

3.1 The Half-space Green Function

Based on the Cartesian coordinate system (x-z) with z=0 at the free surface, the wave equations in an elastic half-space of homogeneous solid are given by

$$\begin{cases}(\lambda_s+G_s)\left(\dfrac{\partial^2 u(x,z,t)}{\partial x^2}+\dfrac{\partial^2 w(x,z,t)}{\partial x\partial z}\right)+G_s\nabla^2 u(x,z,t)=\rho_s\dfrac{\partial^2 u(x,z,t)}{\partial t^2}\\ (\lambda_s+G_s)\left(\dfrac{\partial^2 u(x,z,t)}{\partial x\partial z}+\dfrac{\partial^2 w(x,z,t)}{\partial z^2}\right)+G_s\nabla^2 w(x,z,t)=\rho_s\dfrac{\partial^2 w(x,z,t)}{\partial t^2}\end{cases} \tag{2}$$

where ρ_s is the density of the soil, G_s and λ_s are the Lam é constants. $\nabla^2=\left(\dfrac{\partial^2}{\partial x^2}+\dfrac{\partial^2}{\partial z^2}\right)$ denotes the Laplacian operator. u, w are the displacement components in x and z directions. As the footings are excited by harmonic forces, their steady-state vibrations satisfy $u(x, z, t)=U(x, z)e^{i\omega t}$, $w(x, z, t)=W(x, z)e^{i\omega t}$. For brevity, the time dependence $e^{i\omega t}$ is omitted.

Considering the unit lateral uniform traction applied at the interval [x_1, x_2], the boundary conditions at ground surface z=0 are given by

$$\sigma_{zz}(x,0)=0;\ \tau_{xz}(x,0)=\begin{cases}-e^{i\omega t} & x_1\le x\le x_2\\ 0 & \text{Other}\end{cases} \tag{3}$$

Considering the unit vertical uniform traction applied at the interval [x_1, x_2], the boundary conditions at ground surface z=0 are given by

$$\sigma_{zz}(x,0)=\begin{cases}-e^{i\omega t} & x_1\le x\le x_2\\ 0 & \text{Other}\end{cases};\ \tau_{xz}(x,0)=0 \tag{4}$$

The general solutions of Eq. (2) for a half-space can be obtained by the method of separation of variable. The general solutions for stresses σ_{zz} and τ_{xz} can be obtained by the stress-displacement differential relationship. Based on the boundary condition of Eq. (3), the unknown coefficients in the general solutions can be determined. Therefore, the lateral and vertical displacement fields $G_{1,2}(x,0)$ and $G_{2,2}(x,0)$ due to the unit lateral uniform load are as follows

$$G_{1,1}(x,0)=-\frac{V_s}{\pi\omega G_s}\int_0^\infty\frac{\sqrt{\eta^2-1}}{\eta F(\eta)}\left\{\sin\left[\frac{\eta\omega}{V_s}(x-x_1)\right]-\sin\left[\frac{\eta\omega}{V_s}(x-x_2)\right]\right\}d\eta \tag{5}$$

$$G_{2,1}(x,0)=\frac{V_s}{\pi\omega G_s}\int_0^\infty\frac{\left(2\eta^2-1-2\sqrt{\eta^2-\vartheta^2}\sqrt{\eta^2-1}\right)}{F(\eta)}\left\{\cos\left[\frac{\eta\omega}{V_s}(x-x_1)\right]-\cos\left[\frac{\eta\omega}{V_s}(x-x_2)\right]\right\}d\eta \tag{6}$$

Similarly, the lateral and vertical surface displacements $G_{1,2}(x,0)$ and $G_{2,2}(x,0)$ due to the unit vertical uniform traction are as follows

$$G_{1,2}(x,0)=-G_{2,1}(x,0) \tag{7}$$

$$G_{2,2}(x,0)=-\frac{V_s}{\pi\omega G_s}\int_0^\infty\frac{\sqrt{\eta^2-\vartheta^2}}{\eta F(\eta)}\left\{\sin\left[\frac{\eta\omega}{V_s}(x-x_1)\right]-\sin\left[\frac{\eta\omega}{V_s}(x-x_2)\right]\right\}d\eta \tag{8}$$

In Eqs. (5-8), $\eta=\xi V_s/\omega$, $\vartheta=V_s/V_p$, $F(\eta)=(2\eta^2-1)^2-4\eta^2\sqrt{\eta^2-\vartheta^2}\sqrt{\eta^2-1}$, where ξ is the wave number, V_p is the dilatational wave (P wave) velocity with $V_p=\sqrt{(\lambda_s+2G_s)/\rho_s}$; V_s is the shear wave (S wave) velocity with $V_s=\sqrt{G_s/\rho_s}$.

3.2 Coupling Lateral-Rocking Impedance

Based on the superposition principle, the lateral displacement function $U(x,0)$ and the vertical displacement $W(x,0)$ due to the coupling lateral-rocking excitations on the footings are as follows

$$U(x,0)=\sum_{n=1}^{N}p_n^{(a)}G_{1,1}(x,0)+\sum_{m=1}^{M}p_m^{(b)}G_{1,1}(x,0)+\sum_{n=1}^{N}q_n^{(a)}G_{1,2}(x,0)+\sum_{m=1}^{M}p_m^{(a)}G_{1,2}(x,0) \tag{9}$$

$$W(x,0)=\sum_{n=1}^{N}p_n^{(a)}G_{2,1}(x,0)+\sum_{m=1}^{M}p_m^{(b)}G_{2,1}(x,0)+\sum_{n=1}^{N}q_n^{(a)}G_{2,2}(x,0)+\sum_{m=1}^{M}p_m^{(a)}G_{2,2}(x,0) \tag{10}$$

The following flexibility equation of the system can established as follows by substituting the central coordinate of each element into Eqs. (9) and (10)

$$\begin{bmatrix}\boldsymbol{A}_{N\times N}^{(1)} & \boldsymbol{B}_{N\times M}^{(1)} & \boldsymbol{C}_{N\times N}^{(1)} & \boldsymbol{D}_{N\times M}^{(1)}\\ \boldsymbol{A}_{M\times N}^{(2)} & \boldsymbol{B}_{M\times M}^{(2)} & \boldsymbol{C}_{M\times N}^{(2)} & \boldsymbol{D}_{M\times M}^{(2)}\\ \boldsymbol{A}_{N\times N}^{(3)} & \boldsymbol{B}_{N\times M}^{(3)} & \boldsymbol{C}_{N\times N}^{(3)} & \boldsymbol{D}_{N\times M}^{(3)}\\ \boldsymbol{A}_{M\times N}^{(4)} & \boldsymbol{B}_{M\times M}^{(4)} & \boldsymbol{C}_{M\times N}^{(4)} & \boldsymbol{D}_{M\times M}^{(4)}\end{bmatrix}\begin{Bmatrix}\hat{\boldsymbol{p}}^{(a)}\\ \hat{\boldsymbol{p}}^{(b)}\\ \hat{\boldsymbol{q}}^{(a)}\\ \hat{\boldsymbol{q}}^{(a)}\end{Bmatrix}=\begin{Bmatrix}\hat{\boldsymbol{U}}^{(a)}\\ \hat{\boldsymbol{U}}^{(b)}\\ \hat{\boldsymbol{W}}^{(a)}\\ \hat{\boldsymbol{W}}^{(a)}\end{Bmatrix} \tag{11}$$

in which, $\hat{\boldsymbol{p}}^{(a)}=\left\{p_1^{(a)},\ \cdots,\ p_N^{(a)}\right\}^T$; $\hat{\boldsymbol{p}}^{(b)}=\left\{p_1^{(b)},\ \cdots,\ p_M^{(b)}\right\}^T$; $\hat{\boldsymbol{q}}^{(a)}=\left\{q_1^{(a)},\ \cdots,\ q_N^{(a)}\right\}^T$; $\hat{\boldsymbol{q}}^{(b)}=\left\{q_1^{(b)},\ \cdots,\ q_M^{(b)}\right\}^T$; $\hat{\boldsymbol{U}}^{(a)}=\left\{U_1^{(a)},\ \cdots,\ U_N^{(a)}\right\}^T$; $\hat{\boldsymbol{U}}^{(b)}=\left\{U_1^{(b)},\ \cdots,\ U_M^{(b)}\right\}^T$; $\hat{\boldsymbol{W}}^{(a)}=\left\{\hat{W}_1^{(a)},\ \cdots,\ \hat{W}_N^{(a)}\right\}^T$; $\hat{\boldsymbol{W}}^{(b)}=\left\{W_1^{(b)},\ \cdots,\ W_M^{(b)}\right\}^T$. The expressions for every elements ($\boldsymbol{A}^{(i)}$, $\boldsymbol{B}^{(i)}$, $\boldsymbol{C}^{(i)}$, $\boldsymbol{D}^{(i)}$, $i\in1,2,3,4$) in the flexibility matrix are shown in the Appendix.

In consideration of the full contact between the rigid footings and the soil medium, the displacements of all the elements and footings should be satisfied as

$$\begin{Bmatrix}\hat{\boldsymbol{U}}^{(a)}\\ \hat{\boldsymbol{U}}^{(b)}\\ \hat{\boldsymbol{W}}^{(a)}\\ \hat{\boldsymbol{W}}^{(a)}\end{Bmatrix}=\begin{bmatrix}\hat{\boldsymbol{I}}_N & \hat{\boldsymbol{0}} & \hat{\boldsymbol{0}} & \hat{\boldsymbol{0}}\\ \hat{\boldsymbol{0}} & \hat{\boldsymbol{I}}_M & \hat{\boldsymbol{0}} & \hat{\boldsymbol{0}}\\ \hat{\boldsymbol{0}} & \hat{\boldsymbol{0}} & \hat{\boldsymbol{E}}_N & \hat{\boldsymbol{0}}\\ \hat{\boldsymbol{0}} & \hat{\boldsymbol{0}} & \hat{\boldsymbol{0}} & \hat{\boldsymbol{E}}_M\end{bmatrix}\begin{Bmatrix}U_a\\ U_b\\ \Theta_a\\ \Theta_b\end{Bmatrix} \tag{12}$$

where, $\hat{\boldsymbol{I}}_N=\underbrace{\left\{1,\cdots,1\right\}}_{N}^T$; $\hat{\boldsymbol{I}}_M=\underbrace{\left\{1,\cdots,1\right\}}_{M}^T$; $\hat{\boldsymbol{E}}_N=\left\{\frac{2n-1-N}{2N}L_a\right\}^T, n=1,\cdots,N$; $\hat{\boldsymbol{E}}_M=\left\{\frac{2m-1-M}{2M}L_b\right\}^T, m=1,\cdots,M$.

Equating the excitation and the contact tractions for Footing A and Footing B yields

$$\begin{Bmatrix}P_a\\ P_b\\ M_a\\ M_b\end{Bmatrix}=\begin{bmatrix}\Delta_a\hat{\boldsymbol{I}}_N & \hat{\boldsymbol{0}} & \hat{\boldsymbol{0}} & \hat{\boldsymbol{0}}\\ \hat{\boldsymbol{0}} & \Delta_b\hat{\boldsymbol{I}}_M & \hat{\boldsymbol{0}} & \hat{\boldsymbol{0}}\\ \hat{\boldsymbol{0}} & \hat{\boldsymbol{0}} & \Delta_a\hat{\boldsymbol{E}}_N & \hat{\boldsymbol{0}}\\ \hat{\boldsymbol{0}} & \hat{\boldsymbol{0}} & \hat{\boldsymbol{0}} & \Delta_b\hat{\boldsymbol{E}}_M\end{bmatrix}^T\begin{Bmatrix}\hat{\boldsymbol{p}}^{(a)}\\ \hat{\boldsymbol{p}}^{(b)}\\ \hat{\boldsymbol{q}}^{(a)}\\ \hat{\boldsymbol{q}}^{(a)}\end{Bmatrix} \tag{13}$$

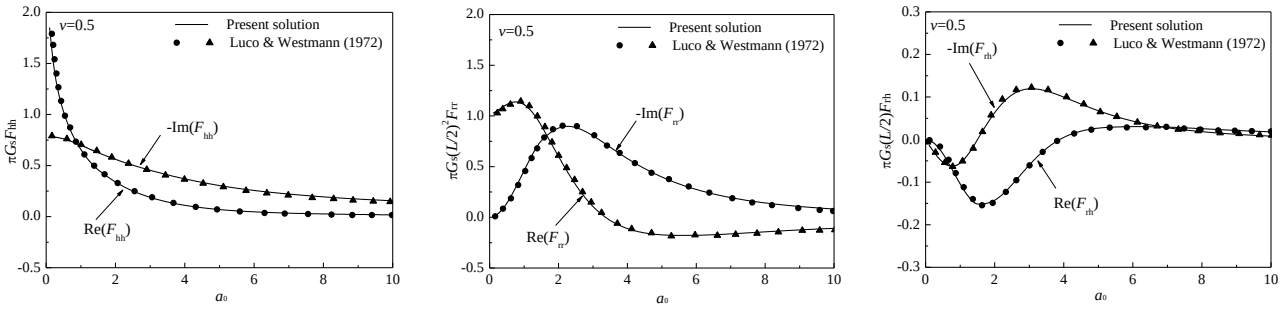
Comparing the force-displacement relationship of Footing A and B, which can be established based on Eqs. (11-13), to the Eq. (1), the coupling lateral-rocking impedance matrix of adjacent footings can be obtained

$$[\mathfrak{R}]=\begin{bmatrix}\Delta_a\hat{\boldsymbol{I}}_N & \hat{\boldsymbol{0}} & \hat{\boldsymbol{0}} & \hat{\boldsymbol{0}}\\ \hat{\boldsymbol{0}} & \Delta_b\hat{\boldsymbol{I}}_M & \hat{\boldsymbol{0}} & \hat{\boldsymbol{0}}\\ \hat{\boldsymbol{0}} & \hat{\boldsymbol{0}} & \Delta_a\hat{\boldsymbol{E}}_N & \hat{\boldsymbol{0}}\\ \hat{\boldsymbol{0}} & \hat{\boldsymbol{0}} & \hat{\boldsymbol{0}} & \Delta_b\hat{\boldsymbol{E}}_M\end{bmatrix}^T\begin{bmatrix}\boldsymbol{A}^{(1)}_{N\times N} & \boldsymbol{B}^{(1)}_{N\times M} & \boldsymbol{C}^{(1)}_{N\times N} & \boldsymbol{D}^{(1)}_{N\times M}\\ \boldsymbol{A}^{(2)}_{M\times N} & \boldsymbol{B}^{(2)}_{M\times M} & \boldsymbol{C}^{(2)}_{M\times N} & \boldsymbol{D}^{(2)}_{M\times M}\\ \boldsymbol{A}^{(3)}_{N\times N} & \boldsymbol{B}^{(3)}_{N\times M} & \boldsymbol{C}^{(3)}_{N\times N} & \boldsymbol{D}^{(3)}_{N\times M}\\ \boldsymbol{A}^{(4)}_{M\times N} & \boldsymbol{B}^{(4)}_{M\times M} & \boldsymbol{C}^{(4)}_{M\times N} & \boldsymbol{D}^{(4)}_{M\times M}\end{bmatrix}^{-1}\begin{bmatrix}\hat{\boldsymbol{I}}_N & \hat{\boldsymbol{0}} & \hat{\boldsymbol{0}} & \hat{\boldsymbol{0}}\\ \hat{\boldsymbol{0}} & \hat{\boldsymbol{I}}_M & \hat{\boldsymbol{0}} & \hat{\boldsymbol{0}}\\ \hat{\boldsymbol{0}} & \hat{\boldsymbol{0}} & \hat{\boldsymbol{E}}_N & \hat{\boldsymbol{0}}\\ \hat{\boldsymbol{0}} & \hat{\boldsymbol{0}} & \hat{\boldsymbol{0}} & \hat{\boldsymbol{E}}_M\end{bmatrix} \quad (14)$$

4 NUMERICAL EXAMPLES AND DISCUSSIONS

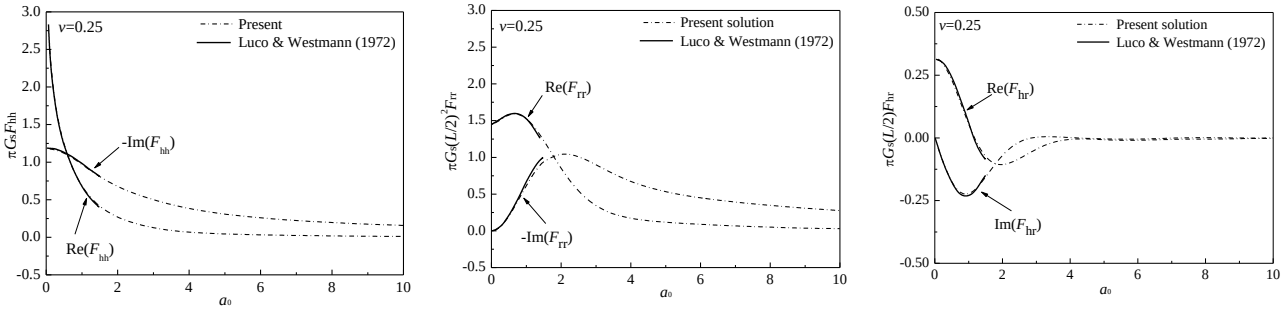
4.1 Comparison Study

Luco and Westmann [4] solved the forced oscillations of a massless rigid strip footing with width L on half-space by using the mixed boundary-value approach. There are considerable difficulties in solving the integral equations numerically or analytically, therefore only a special case for Poisson's ratio ν=0.5 was studied rigorously. The cases with Poisson's ratio ν<0.5 were approximately studied by using the dominant part of the singular integral equation to evaluate the impedances of the strip footing, which is only valid for the low frequency $a_0\leq 1$. In order to compare with the Luco's solutions, the coupling lateral-rocking impedance matrix $\mathfrak{R}$ is transformed into the flexibility by $\boldsymbol{F}=\mathfrak{R}^{-1}$. The flexibility of the footing with respect to dimensionless exciting frequency is plotted in Figs. 3 and 4 for different Poisson's ratios ν=0.5, 0.25. In Figs. 3 and 4, the excellent agreements with Luco's solution approves the correctness and effectiveness of the present method. In addition, Fig. 4 also show that the present method covers a wider range of frequency than Luco's method.



(a) (b) (c)

Fig. 3 Comparison of the present method with mixed boundary-value method for ν=0.5:
(a) Lateral; (b)Rocking; (c)Coupled lateral-rocking

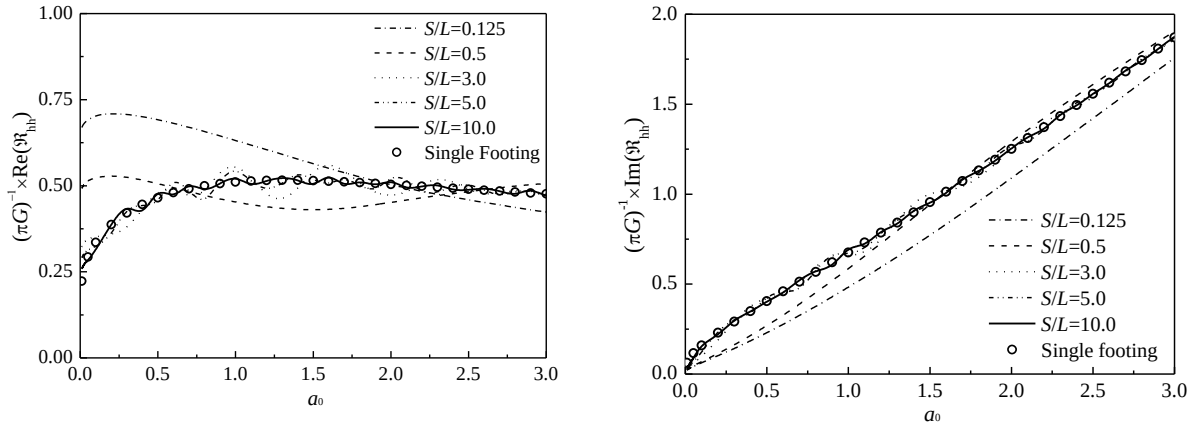


(a) (b) (c)

Fig. 4 Comparison of the present method with mixed boundary-value method for ν=0.25:
(a) Lateral; (b)Rocking; (c)Coupled lateral-rocking

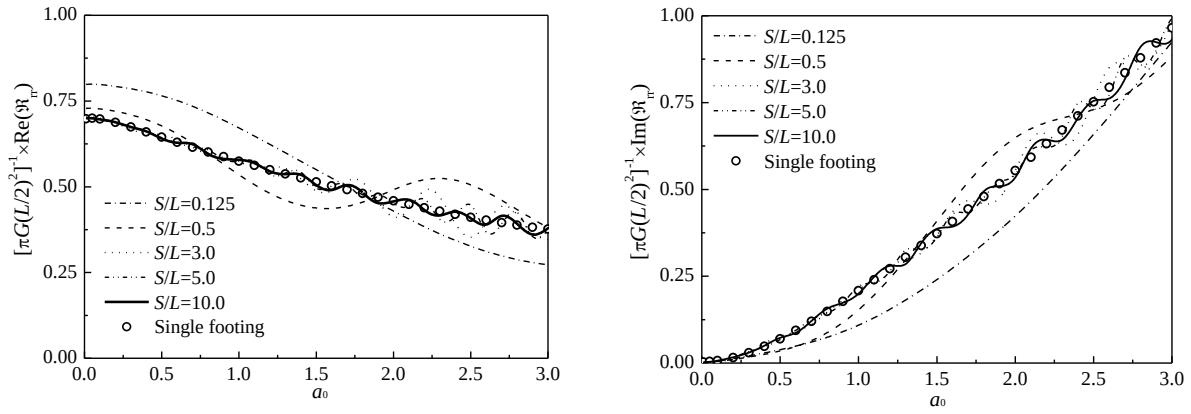
4.2 Influence of the Distance Ratio on Impedances

Two identical strip footings subjected to harmonic lateral-rocking excitations are used to investigate the influence of the ratio between separation distance to footing width *S*/*L* on DCI effect. The variations of lateral and rocking impedances of a footing with respect to different distance ratios (*S*/*L*=0.125, 0.5, 3, 5, 10, ∞) are displayed in Figs. 5 and 6. It can be seen that the lateral and rocking impedances of two footings in the case of closely spaced distance ratio such as *S*/*L*=0.125 fluctuate around that of a single footing. In general, the DCI effect would make the impedances more frequency-dependent. Moreover, the influence from the adjacent footing is not significant in the case of large distance ratio such as *S*/*L*=5.0.



(a) (b)

Fig. 5 Lateral impedance $\mathfrak{R}_{hh}$ for different distance ratio *S*/*L*: (a) Stiffness; (b) Damping



(a) (b)

Fig. 6 Rocking impedance $\mathfrak{R}_{rr}$ for different distance ratio *S*/*L*: (a) Stiffness; (b) Damping

5 CONCLUSION

An efficient semi-analytical method has been presented for obtaining the coupling lateral-rocking impedance of two adjacent footings. The accuracy is verified by the comparison study with the rigorous results from the mix-boundary-value method. Based on the parametric study on DCI effect, the distance ratio *S*/*L* between adjacent strip footings greatly influences the cross dynamic interaction especially for a small ratio less than 5.0. The approach has a definite physical meaning, and is easy to be mastered by technicians for dynamic analysis and seismic design of strip footings with close space, such as parallel tracks or adjacent buildings with a high ratio of length to width.

6 ACKNOWLEDGEMENTS

The financial supports from the Natural Science Foundation of Jiangsu Province, China (SBK201322459) are greatly acknowledged. This work is also supported in part by the scholarship from China Scholarship Council (CSC) under the Grant No. 201408320149.

REFERENCE

[1] T.Y. Sung, Vibration in semi-infinite solids due to periodic surface loadings, Symp. Dyn. Test Soil. 156(1) (1953) 35-64.
[2] I. Anam, J.M. Roësset, Dynamic stiffnesses of surface foundations: an explicit solution, Int. J. Geomech. 4(3) (2004) 216-223.
[3] G.B. Warburton, J.D. Richardson, J.J, Webster. Forced vibrations of two masses on an elastic half space, J. Appl. Mech., ASME, 38 (1971) 148-156.
[4] J.E. Luco, R.A. Westmann, Dynamic response of a rigid footing bonded to an elastic half-space, J. Eng. Mech. Div. ASME. 39(2) (1972) 527-534.
[5] X.H. Ma, Y.M. Cheng, S.K. Au, Y.Q. Cai, C.J. Xu, Rocking vibration of a rigid strip footing on saturated soil, Comput. Geotech. 36(6) (2009) 928-933.
[6] J. Wang, D. Zhou, W.Q. Liu, S.G. Wang, Rocking response of a surface-supported strip foundation under a harmonic swaying force, Appl. Mech. Mat. 226(2012) 1453-1457.
[7] J. Wang, S.H. Lo, D. Zhou. Frequency-dependent Impedance of a Strip Foundation Group and its Representation in Time Domain. Appl Math Model (2014) DOI:10.1016/j.apm.2014.10.062.
[8] G. Lin, Z. Han, H. Zhong, S.G. Wang, D.S. Du, A precise integration approach for dynamic impedance of rigid strip footing on arbitrary anisotropic layered half-space, Soil Dyn. Earthq. Eng. 49(1) (2013) 96-108.
[9] S.A. Savidis, T. Richter, Dynamic interaction of rigid foundations, in: Proceedings of the 9th International Conference on Soil Mechanics and Foundation Engineering, Tokyo, Japan, 1977, pp: 369-374.
[10] Y. Wang, R. Rajapakse, A.H. Shah, Dynamic interaction between flexible strip foundations, Earthq. Eng. Struct. Dyn. 20(5) (1991) 441-454.
[11] T. Senjuntichai, W. Kaewjuea, Dynamic response of multiple flexible strips on a multi-layered poroelastic half-plane, J. Mech. Mat. Struct. 3(10) (2008) 1885-1901.

APPENDIX

The expressions of the elements in the matrix of Eq. (11):

$$A_{ij}^{(1)}=\frac{-1}{\pi G}\int_0^{\infty}\frac{L_a\sqrt{\eta^2-1}}{2F(\eta)\eta a_0}\left\{\sin\left[\eta\frac{2a_0}{L_a}\left(\frac{(i-j)L_a}{N}+\frac{L_a}{2N}\right)\right]-\sin\left[\eta\frac{2a_0}{L_a}\left(\frac{(i-j)L_a}{N}-\frac{L_a}{2N}\right)\right]\right\}d\eta$$

$$B_{ij}^{(1)}=\frac{-1}{\pi G}\int_0^{\infty}\frac{L_a\sqrt{\eta^2-1}}{2F(\eta)\eta a_0}\left\{\sin\left[\eta\frac{2a_0}{L_a}\left((S+L_b)+\frac{(2i-1)L_a}{2N}-\frac{(j-1)L_b}{M}\right)\right]-\sin\left[\eta\frac{2a_0}{L_a}\left((S+L_b)+\frac{(2i-1)L_a}{2N}-\frac{jL_b}{M}\right)\right]\right\}d\eta$$

$$C_{ij}^{(1)}=\frac{-1}{\pi G}\int_0^{\infty}\frac{L_a\left(2\eta^2-1-2\sqrt{\eta^2-\vartheta^2}\sqrt{\eta^2-1}\right)}{2F(\eta)a_0}\left\{\cos\left[\eta\frac{2a_0}{L_a}\left(\frac{(i-j)L_a}{N}+\frac{L_a}{2N}\right)\right]-\cos\left[\eta\frac{2a_0}{L_a}\left(\frac{(i-j)L_a}{N}-\frac{L_a}{2N}\right)\right]\right\}d\eta$$

$$D_{ij}^{(1)}=\frac{-1}{\pi G}\int_0^{\infty}\frac{L_a\left(2\eta^2-1-2\sqrt{\eta^2-\vartheta^2}\sqrt{\eta^2-1}\right)}{2F(\eta)a_0}\left\{\cos\left[\eta\frac{2a_0}{L_a}\left((S+L_b)+\frac{(2i-1)L_a}{2N}-\frac{(j-1)L_b}{M}\right)\right]-\cos\left[\eta\frac{2a_0}{L_a}\left((S+L_b)+\frac{(2i-1)L_a}{2N}-\frac{jL_b}{M}\right)\right]\right\}d\eta$$

$$A_{ij}^{(2)}=\frac{-1}{\pi G}\int_0^{\infty}\frac{L_a\sqrt{\eta^2-1}}{2F(\eta)\eta a_0}\left\{\sin\left[\eta\frac{2a_0}{L_a}\left(-(S+L_b)+\frac{(2i-1)L_b}{2M}-\frac{(j-1)L_a}{N}\right)\right]-\sin\left[\eta\frac{2a_0}{L_a}\left(-(S+L_b)+\frac{(2i-1)L_b}{2M}-\frac{jL_a}{N}\right)\right]\right\}d\eta$$

$$B_{ij}^{(2)}=\frac{-1}{\pi G}\int_0^{\infty}\frac{L_a\sqrt{\eta^2-1}}{2F(\eta)\eta a_0}\left\{\sin\left[\eta\frac{2a_0}{L_a}\left(\frac{(i-j)L_b}{M}+\frac{L_b}{2M}\right)\right]-\sin\left[\eta\frac{2a_0}{L_a}\left(\frac{(i-j)L_b}{M}-\frac{L_b}{2M}\right)\right]\right\}d\eta$$

$$C_{ij}^{(2)}=\frac{-1}{\pi G}\int_0^{\infty}\frac{L_a\left(2\eta^2-1-2\sqrt{\eta^2-\vartheta^2}\sqrt{\eta^2-1}\right)}{2F(\eta)a_0}\left\{\cos\left[\eta\frac{2a_0}{L_a}\left(-(S+L_b)+\frac{(2i-1)L_b}{2M}-\frac{(j-1)L_a}{N}\right)\right]-\cos\left[\eta\frac{2a_0}{L_a}\left(-(S+L_b)+\frac{(2i-1)L_b}{2M}-\frac{jL_a}{N}\right)\right]\right\}d\eta$$

$$D_{ij}^{(2)}=\frac{-1}{\pi G}\int_0^{\infty}\frac{L_a\left(2\eta^2-1-2\sqrt{\eta^2-\vartheta^2}\sqrt{\eta^2-1}\right)}{2F(\eta)a_0}\left\{\cos\left[\eta\frac{2a_0}{L_a}\left(\frac{(i-j)L_b}{M}+\frac{L_b}{2M}\right)\right]-\cos\left[\eta\frac{2a_0}{L_a}\left(\frac{(i-j)L_b}{M}-\frac{L_b}{2M}\right)\right]\right\}d\eta$$

$$A_{ij}^{(3)}=-C_{ij}^{(1)}$$

$$B_{ij}^{(3)}=-D_{ij}^{(1)}$$

$$C_{ij}^{(3)}=\frac{-1}{\pi G}\int_0^{\infty}\frac{L_a\sqrt{\eta^2-\vartheta^2}}{2F(\eta)\eta a_0}\left\{\sin\left[\eta\frac{2a_0}{L_a}\left(\frac{(i-j)L_a}{N}+\frac{L_a}{2N}\right)\right]-\sin\left[\eta\frac{2a_0}{L_a}\left(\frac{(i-j)L_a}{N}-\frac{L_a}{2N}\right)\right]\right\}d\eta$$

$$D_{ij}^{(3)}=\frac{-1}{\pi G}\int_0^{\infty}\frac{L_a\sqrt{\eta^2-\vartheta^2}}{2F(\eta)\eta a_0}\left\{\sin\left[\eta\frac{2a_0}{L_a}\left((S+L_b)+\frac{(2i-1)L_a}{2N}-\frac{(j-1)L_b}{M}\right)\right]-\sin\left[\eta\frac{2a_0}{L_a}\left((S+L_b)+\frac{(2i-1)L_a}{2N}-\frac{jL_b}{M}\right)\right]\right\}d\eta$$

$$A_{ij}^{(4)}=-C_{ij}^{(2)}$$

$$B_{ij}^{(4)}=-D_{ij}^{(2)}$$

$$C_{ij}^{(4)}=\frac{-1}{\pi G}\int_0^{\infty}\frac{L_a\sqrt{\eta^2-\vartheta^2}}{2F(\eta)\eta a_0}\left\{\sin\left[\eta\frac{2a_0}{L_a}\left(-(S+L_b)+\frac{(2i-1)L_b}{2M}-\frac{(j-1)L_a}{N}\right)\right]-\sin\left[\eta\frac{2a_0}{L_a}\left(-(S+L_b)+\frac{(2i-1)L_b}{2M}-\frac{jL_a}{N}\right)\right]\right\}d\eta$$

$$D_{ij}^{(4)}=\frac{-1}{\pi G}\int_0^{\infty}\frac{L_a\sqrt{\eta^2-\vartheta^2}}{2F(\eta)\eta a_0}\left\{\sin\left[\eta\frac{2a_0}{L_a}\left(\frac{(i-j)L_b}{M}+\frac{L_b}{2M}\right)\right]-\sin\left[\eta\frac{2a_0}{L_a}\left(\frac{(i-j)L_b}{M}-\frac{L_b}{2M}\right)\right]\right\}d\eta$$

where， a_0 is the dimensionless frequency $a_0=\omega L_a/(2V_s)$.

COMPDYN 2015
5th ECCOMAS Thematic Conference on
Computational Methods in Structural Dynamics and Earthquake Engineering
M. Papadrakakis, V. Papadopoulos, V. Plevris (eds.)
Crete Island, Greece, 25–27 May 2015

CALIBRATION AND VALIDATION OF A SIMPLIFIED MODEL OF NONLINEAR SOIL-STRUCTURE INTERACTION FOR SHALLOW FOUNDATIONS

Simon Lambert[1], **Charisis Chatzigogos**[1, 2], **and Andrea Godoy**[1]

[1] Géodynamique et Structure
157 rue des Blains, 92220 Bagneux, France
e-mails: {simon.lambert, charisis.chatzigogos, andrea.godoy}@geodynamique.com

[2] Aristotle University of Thessaloniki, Department of Civil Engineering

Keywords: foundation, macroelement, nonlinear soil-structure interaction, calibration, validation.

Abstract. *Modeling of soil-structure interaction for shallow foundations entails three sources of nonlinearities: foundation uplifting, sliding along the soil-footing interface and irreversible displacement due to soil plasticity. Foundation macroelements allow reducing computational efforts in the resolution of seismic response including nonlinear soil-structure interaction. This is achieved by replacing the soil domain and the foundation by a 2-noded element with a sophisticated nonlinear constitutive law reproducing the aforementioned nonlinearities.*

Definition of uplift and soil plasticity models and of the coupling between the two require a set of parameters that depend on the soil characteristics and the foundation geometry. For practical applications, calibration of these parameters is required.

In this paper, calibration tables have been produced for the parameters describing the foundation uplift behavior. In the case of a rectangular foundation (that has been calibrated for the first time), two extra parameters are introduced with respect to the strip and circular footing: the footing aspect ratio and the direction angle of the resultant overturning moment. In addition, a standardized methodology has been proposed to calibrate the parameters describing soil plastic behavior.

The macroelement validation procedure has been carried out in the case of a bridge pier founded on a strip footing. The discrepancy between macroelement calculations and detailed finite element modeling has been evaluated for twenty earthquake records. Prediction of the superstructure maximum displacements (mean error < 10 %, standardized deviation < 20%) and efforts (mean error < 20 %, standardized deviation < 10%) is validated. Macroelement limitations concern the evaluation of foundation residual displacements, suggesting that further development should be focused on the improvement of plasticity model for soil irreversible behavior.

1 INTRODUCTION

Macroelement theory aims at evaluating the nonlinear seismic response of structures founded on shallow foundations. It models the foundation uplift and sliding together with soil plasticity, which represent the three sources of nonlinearity arising at the foundation level in dynamic soil-structure interaction.

In their current state of development macroelements can be used for preliminary seismic design. Further improvements of the macroelement calibration and validation procedures may provide sufficient guarantees for their use as a final justification of a structure. This objective motivates the work presented in sections 3 and 4.

2 THE CONCEPT OF FOUNDATION MACROELEMENT

2.1 Motivations for developing foundation macroelements

The foundation macroelement is a 2-noded linear segment, with a sophisticated constitutive law so as to grasp the nonlinear soil-structure interaction behavior. As illustrated in Figure 1, the advantage of macroelement modeling with respect to finite element modeling is that there is no need to represent explicitly the foundation and soil domain.

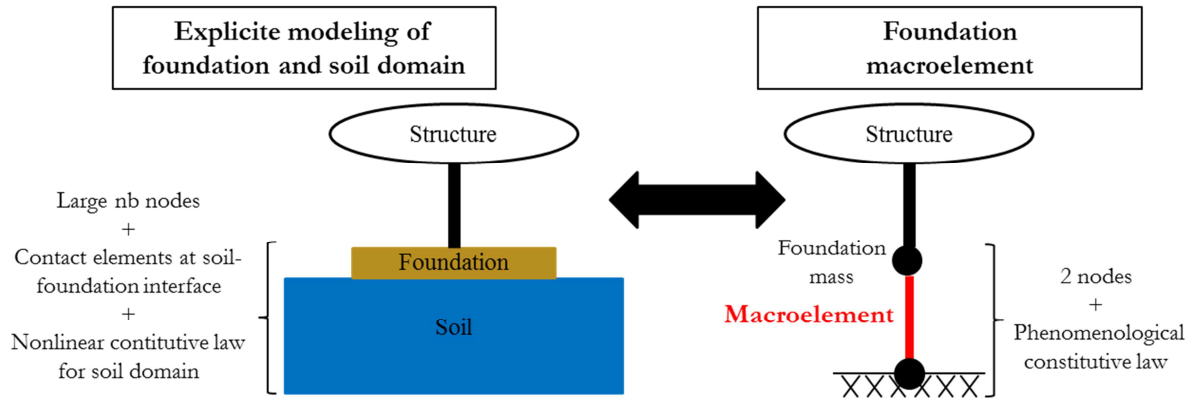


Figure 1: The concept of foundation macroelement

The drastic reduction of the number of degrees-of-freedoms limits significantly computational effort. As a result, two main applications can be mentioned for engineers and researchers:

a) parametric studies, requiring to perform a large number of calculations,
b) and real-time hybrid tests (ref. [8]), when the numerical substructure is the soil and foundation domains.

2.2 Theoretical background

Three hypotheses define the context in which the foundation macroelement can be used: the shallow foundation should be rigid, without embedment and supporting an isolated structure (structure-soil-structure interaction cannot be modeled).

The hypothesis of a rigid foundation allows the description of the foundation kinematics via the displacement and rotation of a single arbitrary point, for example its center of gravity. Figure 2 introduces the notations characterizing the foundation kinematics and load parame-

ters, with B the foundation characteristic dimension and $N_{\max}$ the maximum vertical force supported by the foundation.

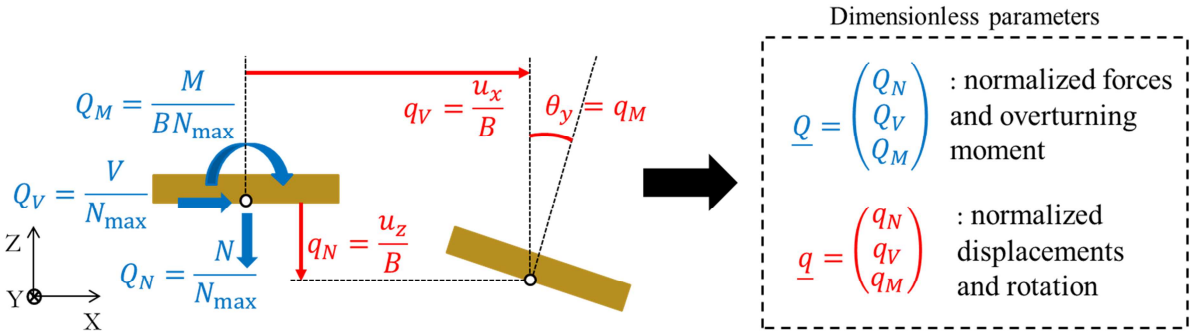


Figure 2: Macroelement formulation - Definition of force and displacement parameters

The main idea for deriving the macroelement constitutive law is the dissociation between reversible and irreversible phenomena. Reversible phenomena regroup the soil elastic behavior and the foundation uplift. Irreversible phenomena entail soil plastic deformations and foundation sliding.

Such a distinction is established by splitting the foundation displacement increment vector $\underline{\dot{q}}$ into an elastic and a plastic component, which are computed at each time step by separate algorithms. Reference [2] details the formulation of the tangent normalized stiffness matrix $\underline{\underline{K}}$ and of plastic modulus $\underline{\underline{H}}$ which are introduced in Figure 3.

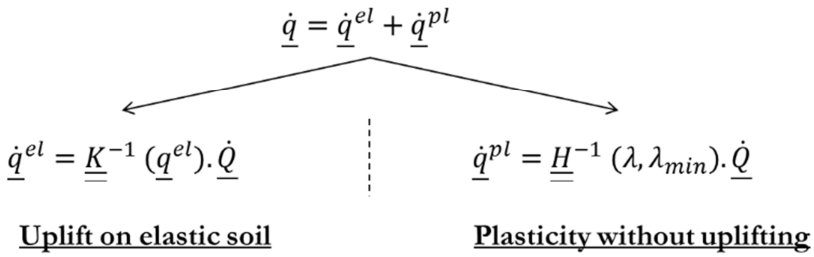


Figure 3: Decomposition of displacement increments

Even though the foundation uplift and soil plasticity are conceptually dealt separately, the numerical implementation of the macroelement associates these two phenomena at each step of calculation of the foundation displacement increment vector $\underline{\dot{q}}$. This operation is performed through an iterative process detailed in ref. [3].

3 MACROELEMENT CALIBRATION

3.1 Objectives

The macroelement theory, as developed in references [2], [3] and [5], introduces six parameters to characterize the formulation of the normalized stiffness matrix $\underline{\underline{K}}$ and the plastic modulus $\underline{\underline{H}}$. Table 1 provides an overview of their definition. Further details are provided in section 3.3 and 3.4.

Footing uplift	p_1^{el}	normalized stiffness matrix $\underline{\underline{K}}$	uplift initiation on elastic soil
	p_2^{el}		overturning moment – rotation diagram
	p_3^{el}		settlement – rotation diagram
Soil plasticity	p_1^{pl}	plastic modulus $\underline{\underline{H}}$	initial loading
	p_2^{pl}		reloading
Uplift-plasticity coupling	p_1^{c}	uplift initiation on plastic soil	

Table 1: Summary of the macroelement parameters requiring specific calibration

The following aims have been addressed:

- Concerning elastic parameters p_1^{el}, p_2^{el} and p_3^{el}: to produce calibration tables for the newly studied case of rectangular footings.
- Concerning plastic parameters p_1^{pl} and p_2^{pl}: to implement the proposals of standardized calibration procedures mentioned in references [2], [3], [5], [6] and [11], so as to provide guidelines to select which is the most appropriate for a given calculation.

3.2 Reference models

The macroelement calibration procedures requires a reference model describing accurately the footing uplift and soil plasticity phenomena. This task is carried out thanks to detailed finite element modeling of the soil and the foundation, implemented on DYNAFLOW software (ref. [12]).

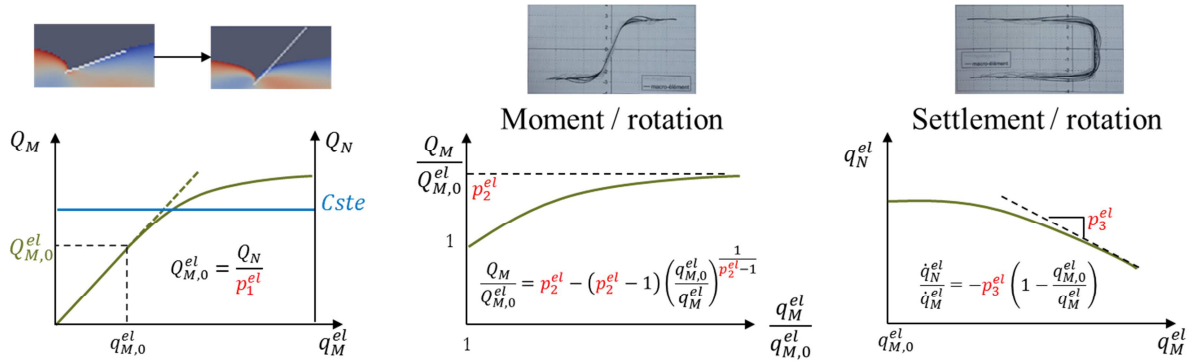
Each calibration objective requires to define a specific DYNAFLOW reference model. Table 2 summarizes the main common features and differences that can be encountered in these models.

Calibration procedure	$\boldsymbol{p_i^{el}}$	$\boldsymbol{p_i^{pl}}$	$\boldsymbol{p_1^{c}}$
Soil domain boundary conditions	identical		
Soil-footing interface	uplift activated	no uplift	uplift activated
Soil constitutive law properties	elastic	plastic	plastic
Loading input data	Q_N = constant q_M linear increase	cyclic loading	Q_N = constant q_M linear increase
Numerical algorithm	Newton-Raphson type		

Table 2: Overview of the reference models used for calibration

3.3 Elastic parameters

Figure 4 illustrates the physical meanings of p_1^{el}, p_2^{el} and p_3^{el} thanks to an approach based on the phenomenological constitutive laws of the footing after uplift initiation. The mathematical equations defining these laws provide a practical means for calibration.



a) Uplift initiation b) Phenomenological constitutive laws after uplift initiation

Figure 4 : Elastic parameters definition

With:

- $Q_{M,0}^{el}$ the normalized overturning moment Q_M of uplift initiation on an elastic soil.
- $q_{M,0}^{el}$ the footing rotational angle of uplift initiation on an elastic soil.

The calibration of the elastic parameters for a rectangular footing requires a significant number of calculations since these parameters depend on:

- The footing rotation axis characterized by the angle ψ.
- The footing aspect ratio R.

Figure 5 details the definition of these parameters.

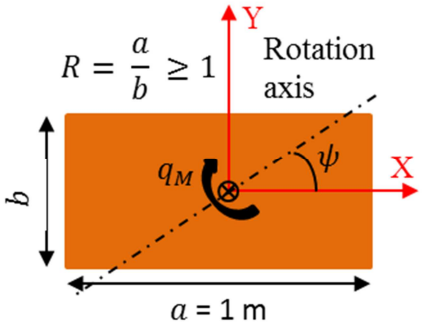


Figure 5: Definition of parameters R and ψ

$R \setminus \psi$	0°	15°	30°	45°	60°	75°	90°
1	4,5	4,7	5,1	5,3	5,1	4,7	4,5
2	8,6	8,8	8,1	6,9	5,8	5,0	4,6
3	12,7	11,9	9,4	7,3	5,9	5,0	4,7
4	16,5	14,3	10,2	7,5	5,9	5,1	4,7

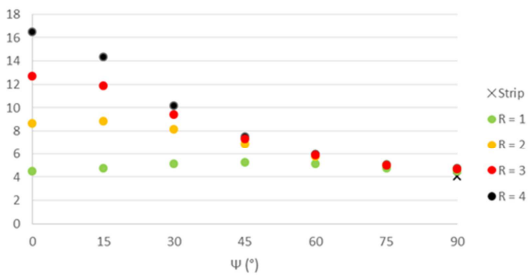
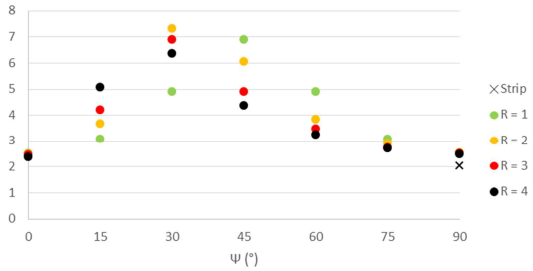


Table 3 & Figure 6: Elastic parameter p_1^{el} calibration

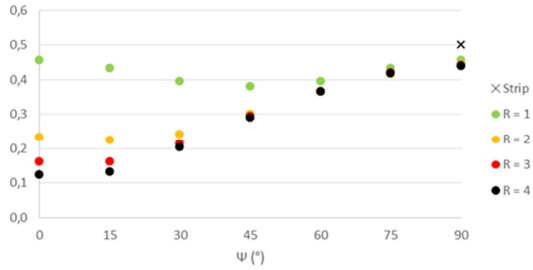
$R \setminus \psi$	0°	15°	30°	45°	60°	75°	90°
1	2,5	3,1	4,9	6,9	4,9	3,1	2,5
2	2,5	3,7	7,3	6,1	3,8	2,9	2,6
3	2,5	4,2	6,9	4,9	3,5	2,7	2,5
4	2,4	5,1	6,4	4,4	3,3	2,7	2,5

Table 4 & Figure 7: Elastic parameter p_2^{el} calibration



$R \setminus \psi$	0°	15°	30°	45°	60°	75°	90°
1	0,46	0,43	0,40	0,38	0,40	0,43	0,46
2	0,23	0,22	0,24	0,30	0,37	0,42	0,44
3	0,16	0,16	0,21	0,29	0,37	0,42	0,44
4	0,12	0,13	0,20	0,29	0,37	0,42	0,44

Table 5 & Figure 8: Elastic parameter p_3^{el} calibration



The elastic parameters for the rectangular footing are calibrated considering the projection of the overturning moment on the rotational axis, as these two directions no longer match for ψ different from 0° and 90°.

3.4 Plastic parameters

Plastic parameters p_1^{pl} and p_2^{pl} characterize the macroelement hypoplastic model. The following physical meanings can be given to these parameters:

- p_1^{pl} characterizes initial loading, in the sense that the plastic increment $\dot{\underline{q}}^{pl}$ linearly increases with $\frac{1}{p_1^{pl}}$.
- p_2^{pl} characterizes the evolution of plastic behavior during the reloading phase. Plastic displacements as in initial loading are developed when $p_2^{pl} = 0$. Elastic response is retrieved when $p_2^{pl} \to \infty$.

Plastic parameters are calibrated to best fit force-displacement and moment-rotation curves between DYNAFLOW reference model and the macroelement. Four methodologies characterized by different loading paths are considered:

I. Cyclic vertical loading.
II. Initial vertical loading followed by horizontal cyclic loading.
III. Initial vertical loading followed by overturning moment cyclic loading.
IV. A combination of the methodologies II and III: initial vertical loading followed by horizontal and overturning moment cyclic loadings such as $M = hV$, with h the superstructure's characteristic height.

Figure 9 illustrates these loading paths in the space of dimensionless force parameters in which the hypoplastic bounding surface is defined.

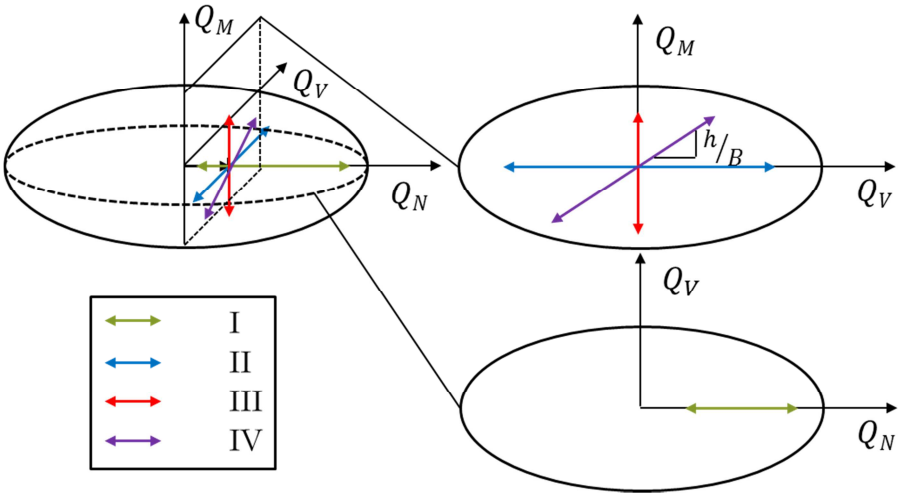


Figure 9: Loading paths considered for plastic parameters calibration methodologies

The four calibration methodologies are carried out for the strip footing case relying on a semi-infinite purely cohesive soil domain. Table 6 summarizes the results obtained under the assumptions of a kinematic and isotropic hardening law for the soil.

Methodology	p_1^{pl}		p_2^{pl}	
	Kinematic	*Isotropic*	*Kinematic*	*Isotropic*
I	1,33	1,33	∞	∞
II	2,29	2,42	0	0,39
III	1,66	1,84	0	2,48
IV	1,82	2,03	0	0,89

Table 6: Plastic parameters calibration

The following points should be noted:

a) The striking variation of p_2^{pl} calibration between the isotropic and kinematic assumptions for the soil hardening law. This observation has no repercussions because separate calibration tables could be considered.

b) The important variation observed between the four calibration methodologies questions the macroelement ability to grasp the soil plastic behavior for all types of loadings with only two parameters.

c) Parameter p_1^{pl} calibration according to methodology IV is predicted by the following linear relation involving the calibration results according to the methodologies II and III:

$$p_{1,\mathrm{IV}}^{pl} = \frac{1}{1+\left(\frac{h}{B}\right)^2} p_{1,\mathrm{II}}^{pl} + \frac{\left(\frac{h}{B}\right)^2}{1+\left(\frac{h}{B}\right)^2} p_{1,\mathrm{III}}^{pl}$$

The coefficient $\alpha_V = \frac{1}{1+\left(\frac{h}{B}\right)^2}$ and $\alpha_M = \frac{\left(\frac{h}{B}\right)^2}{1+\left(\frac{h}{B}\right)^2}$ respectively correspond to the horizontal force and overturning moment proportion of the total normalized load $\sqrt{Q_V^2 + Q_M^2}$.

Knowing that seismic excitation leads to loading histories close to methodology IV, the main conclusion of this section is that methodology III offers the best option to perform plastic parameters calibration for common cases with $\frac{h}{B} > 2$. In that respect, methodology III could be implemented to produce calibration tables for plastic parameters.

4 MACROELEMENT VALIDATION

4.1 General methodology

This section aims at assessing the foundation macroelement qualitative behavior and accuracy when subject to seismic loading. The analysis is carried out for a strip footing. The assumption of a kinematic hardening law for the soil is assessed.

The typical case of a bridge pier founded on a cohesive soil is examined, as presented in Figure 10.

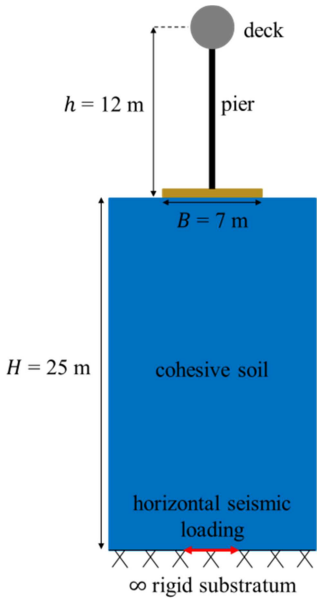


Figure 10: Definition of earthquake engineering context for the validation procedure

Twenty acceleration time histories selected from Project DARE (ref. [4]) are examined. They correspond to a horizontal acceleration imposed at the bedrock level. This selection intends to cover a wide range of frequencies and seismic intensity levels.

The following criteria are considered so as to assess the macroelement precision:

a) The maximum shear force $V_{\max}$ and bending moment $M_{\max}$ developed at the base of the pier.
b) The maximum horizontal displacement $u_{x,\max}^{\text{deck}}$ and rotation $\theta_{y,\max}^{\text{deck}}$ of the deck.
c) The foundation residual displacements and rotation $u_{x,\text{res}}$, $u_{z,\text{res}}$ and $\theta_{y,\text{res}}$.

4.2 Reference model

Footing uplift was modeled in DYNAFLOW (ref. [12]) using contact elements, previously introduced for the calibration of the elastic and uplift-plasticity coupling parameters.

It should be noted that footing sliding is not considered at this stage, i.e. no constitutive law such as Mohr-Coulomb is introduced at the interface to limit the tangential force transferred by the footing to the soil domain. This choice ensures that the footing uplift is not inhibited by the sliding phenomenon.

4.3 Macroelement input data

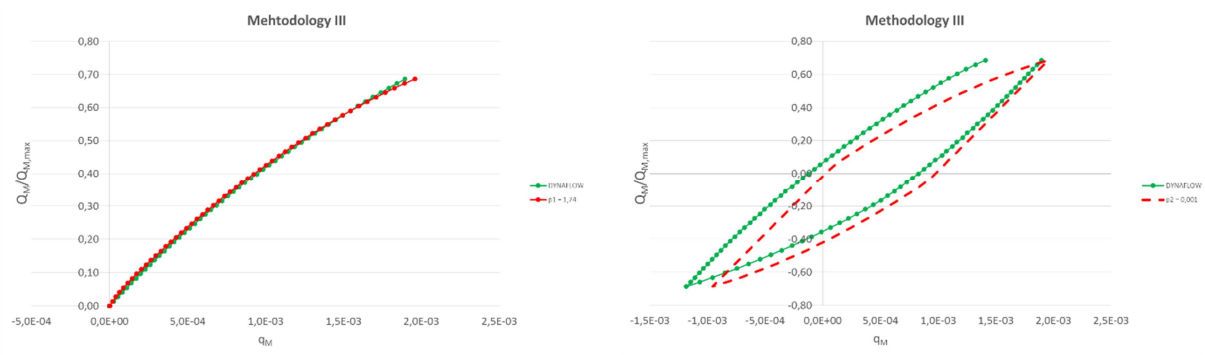
Table 7 details the values of the numerical parameters used in the study.

Type of parameter	Symbol	Definition		Unit	Value	Source
Dimensional	B	Footing characteristic dimension		m	7,00	Design
	$N_{\max}$	Maximum centered vertical load		MN.ml^{-1}	5,397	EC 7
Viscoelastic	K_{NN}^0	Footing normalized dynamic impedance		ml^{-1}	209,3	Gazetas' analytical expressions (ref. [9]
	K_{VV}^0			ml^{-1}	202,9	
	K_{MM}^0			rad^{-1}.ml^{-1}	77,8	
	A_{NN}^0	Footing normalized dashpots		s.ml^{-1}	5,7	
	A_{VV}^0			s.ml^{-1}	3,7	
	A_{MM}^0			s.ml^{-1}	0,068	
Footing uplift	p_1^{el}	Uplift initiation		-	4	§3.3
	p_2^{el}	Constitutive law	Q_M - q_M	-	2	
	p_3^{el}		q_N - q_M	-	0,5	
Soil plasticity	$Q_{V,\max}$	Normalized maximum horizontal force and overturning moment		-	0,195	EC 7
	$Q_{M,\max}$			-	0,111	
	p_1^{pl}	Plasticity modulus	initial loading	-	1,74	§3.4
	p_2^{pl}		reloading	-	0,00	
	n_g	Non associativity plastic law		-	1,00	Von Mises law
Uplift & plasticity coupling	p_1^c	Footing uplift on plastic soil		-	0,90	§3.1
Foundation sliding	φ	Soil friction angle		°	0,00	Cohesive soil

Table 7: Macroelement calibration for the validation procedure

The fictitious zero value attributed to the soil friction angle is a macroelement convention to express that the soil is cohesive.

In compliance with section 3.4, methodology III is implemented to calibrate the plastic parameters for the macroelement validation procedure. Figure 11 shows that the calibration leads to a good matching of moment – rotation curves. However, the macroelement significantly minimizes the foundation settlement produced during the bending moment cyclic loading
(-77 %). As mentioned is section 4.4, this observation is useful to recalibrate macroelement prediction of settlement.



a) p_1^{pl} calibration (initial loading)

b) p_2^{pl} calibration (cyclic loading)

Figure 11: Validation procedure – Plastic parameters calibration curves

4.4 Validation results

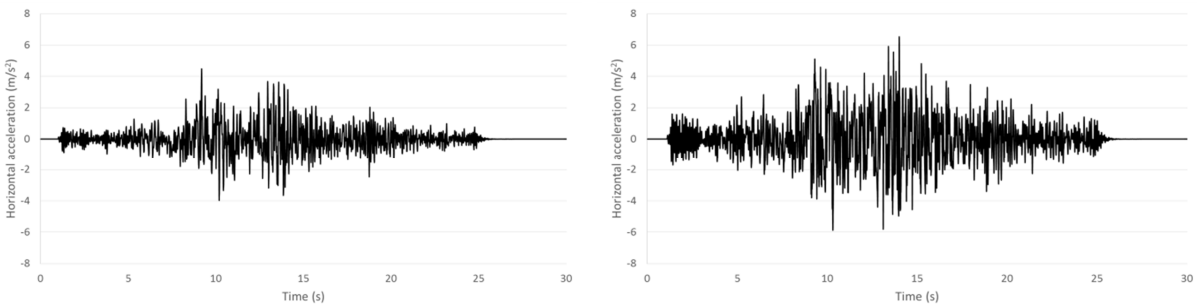
Table 8 establishes the conclusion of the validation procedure.

Criterion	Quantitative assessment	Qualitative assessment
a)	20 % average error with a standard deviation inferior to 10 %.	Very good estimation of the localization of the pic value and of the structure oscillation natural frequency.
b)	Average error inferior to 10 % with a standard deviation inferior to 20 %.	
c)	No satisfactory prediction for the foundation residual horizontal displacement and rotation. After rectifying the foundation settlement according to the error observed during the plastic parameters calibration: average error inferior to 10 % with a standard deviation of 5 %.	The modeling of energy dissipation due to the soil plastic deformation is satisfactory. The macroelement performs well at identifying which earthquakes have the most critical impact on the foundation settlement and residual rotation. This property is less valid concerning the foundation residual horizontal displacement.

Table 8: Summary of the results for the macroelement validation procedure

Figures 14 to 18 illustrate the elements of dynamic response required to assess the macroelement qualitative behavior and precision in the case of Lucerne earthquake (PGA = 0,6 g).

Table 9 and Figure 19 detail the validation results for each acceleration time history.



a) Bedrock level

b) Ground level

Figure 12: Lucerne acceleration time history

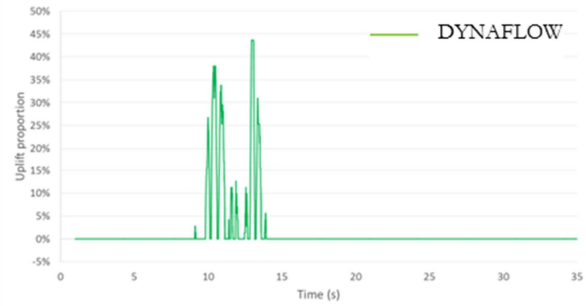
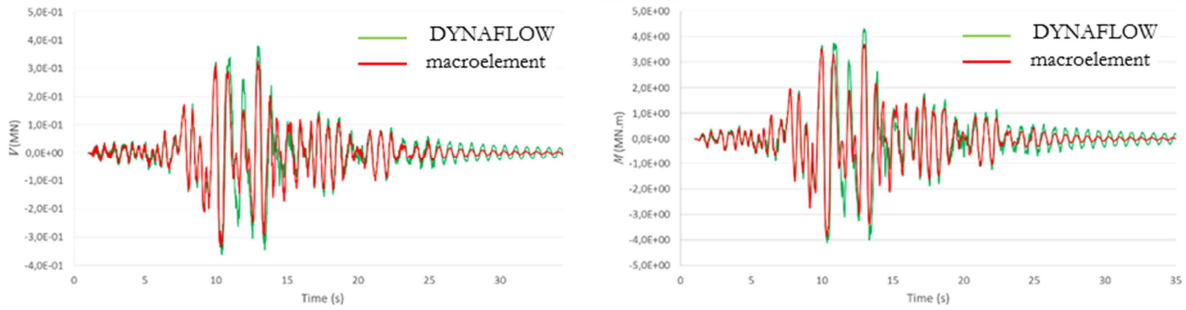


Figure 13: Foundation uplift kinematics



a) Shear force b) Bending moment

Figure 14: Pier base reactions

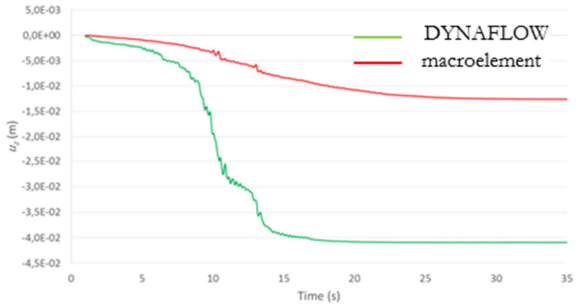
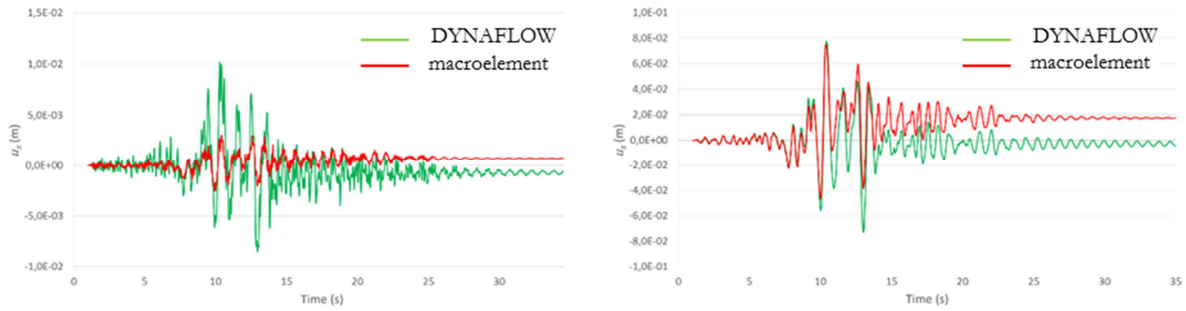
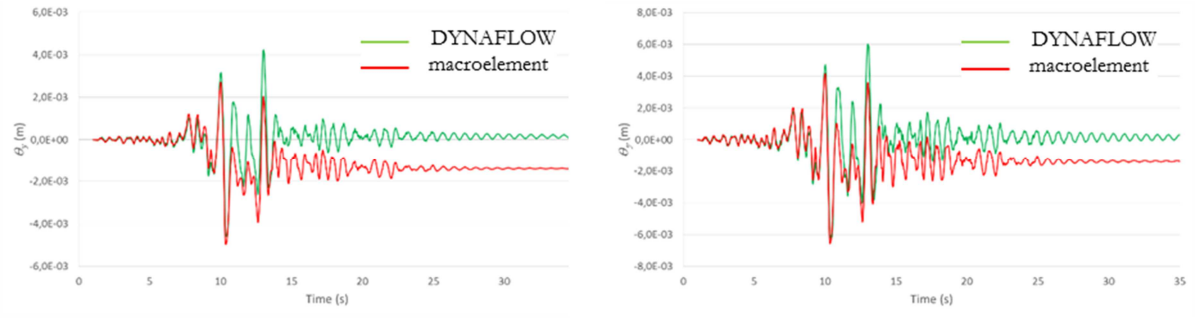


Figure 15: Foundation vertical displacement



a) Foundation b) Deck

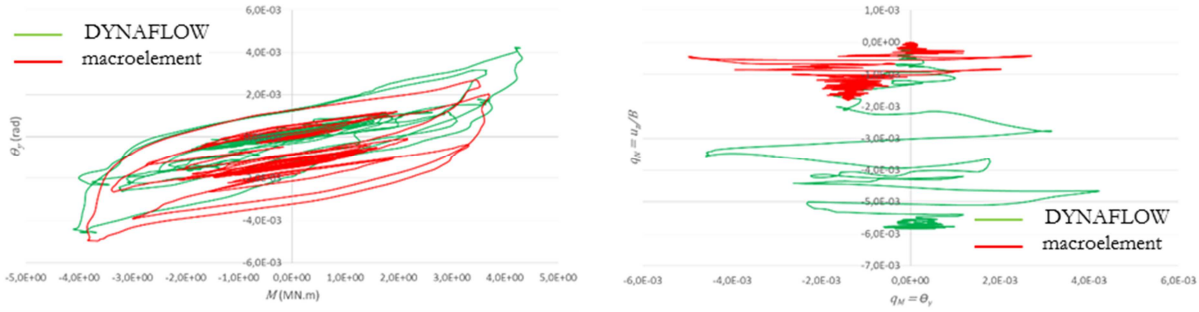
Figure 16: Horizontal displacements



a) Foundation

b) Deck

Figure 17: Rotational displacements



a) Foundation M - θ_y behavior

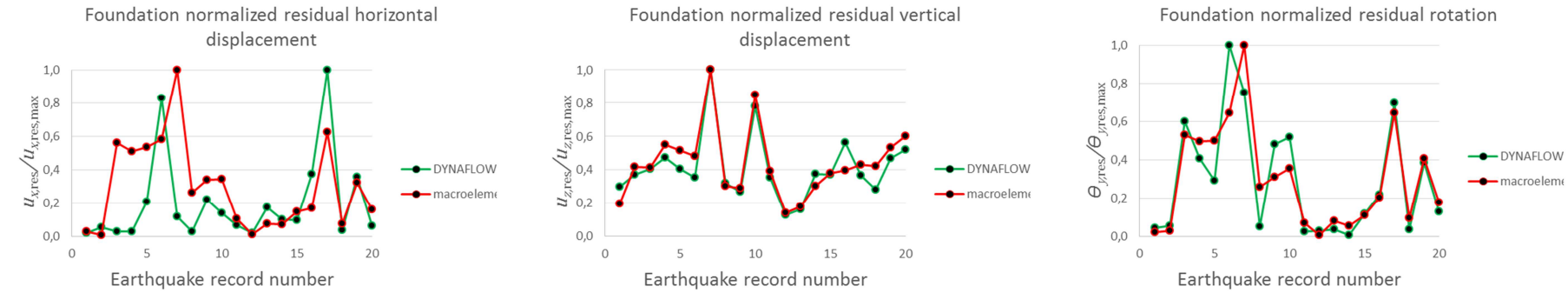
b) Foundation q_N - q_M behavior

Figure 18: Macroelement qualitative assessment

Earthquake record n°	1	2	3	4	5	6	7	8	9	10	11	12	13	14	15	16	17	18	19	20	$\overline{x}$	x_m	σ
$V_{\max}$	-11	-13	-20	-18	-25	-24	-22	-16	-12	-22	-11	-6	-2	-17	-19	-31	-29	-21	-23	-40	-19	-20	9
$M_{\max}$	-12	-14	-19	-19	-23	-24	-21	-13	-14	-20	-11	-8	2	-20	-17	-19	-25	-17	-22	-24	-17	-19	7
$u_{x,\max}^{\text{deck}}$	-2	-22	-3	-7	6	-4	11	34	-9	-5	-3	-7	-3	-32	-3	-7	-27	-5	-2	-27	-6	-4	14
$\theta_{y,\max}^{\text{deck}}$	7	-17	1	-2	17	2	18	38	-2	-2	5	-8	12	-27	5	5	-18	3	2	-20	1	2	15
$u_{x,\text{res}}$	-10	-93	>10²	>10²	64	-55	>10²	>10²	-2	56	1	-65	-73	-54	-3	-71	-60	27	-42	66	>10²	-2	348
$u_{z,\text{res}}$	-82	-68	-71	-68	-64	-62	-72	-74	-70	-69	-69	-69	-69	-77	-71	-80	-67	-58	-68	-68	-70	-69	6
$\theta_{y,\text{res}}$	56	73	>10²	>10²	>10²	>10²	>10²	>10²	>10²	>10²	>10²	-19	>10²	>10²	>10²	>10²	>10²	>10²	>10²	>10²	>10²	>10²	615

Table 9: Assessment of macroelement error (in %)

$\overline{x}$ the average, x_m the median and σ the standard deviation values. The assessment of macroelement error is illustrated in $V_{\max}$ example: $\frac{V_{\max,\text{test}}-V_{\max,\text{ref}}}{V_{\max,\text{ref}}}$, with the tested value corresponding to macroelement calculation.



a) Horizontal direction b) Vertical direction c) Rotation

Figure 19: Foundation normalized residual displacements and rotation

5 CONCLUSION

The analysis of the macroelement current state of development and application domains encouraged further investigations in its calibration and validation procedures.

The following results are obtained concerning the calibration of the macroelement parameters:

- The establishment of calibration tables for the elastic parameters describing the foundation uplift in the case of the rectangular footing.
- The proposal of a standardized methodology to calibrate plastic parameters, characterized by a cyclic overturning moment loading of the foundation.

The macroelement validation procedure is performed using the model of a typical bridge pier structure relying on a strip foundation. Accuracy is evaluated by considering for each criterion two indicators: the average relative error and the standard deviation.

The macroelement ability to predict the maximum displacements/rotation of the superstructure and reaction forces/overturning moment developed at the foundation is demonstrated. Macroelement calculation seems to provide sufficient accuracy for contributing to final justifications of a structure when its design is governed by these criteria.

The macroelement is not that good in predicting the foundation residual displacements and rotation, with the exception of its settlement when its calculation is rectified by the error observed during the calibration of plastic parameters. Nonetheless, the accuracy of the qualitative information provided is sufficient for parametric studies carried out during preliminary design.

Finally, the macroelement calibration and validation procedures highlight the fact that development efforts should be focused on improving the macroelement hypoplastic model, compromising the needs for model simplicity and accuracy in modeling all aspects of dynamic response.

6 REFERENCES

[1] ANASTASOPOULOS I., GAZETAS G., LOLI M., APOSTOLOU M., GEROLYMOS N. – Soil failure can be used for seismic protection of structures. *Bull Earthquake Eng*, 2009, DOI 10.1007/S10518-009-9145-2, 18 p.

[2] CHATZIGOGOS C.T., FIGINI R., PECKER A., SALENÇON J. – A macroelement formulation for shallow foundations on cohesive and frictional soils. *International Journal for Numerical and Analytical Methods in Geomechanics*, 2010, DOI 10.1002/nag.934, 30 p.

[3] CHATZIGOGOS C.T. – Comportement sismique des fondations superficielles: Vers la prise en compte d'un critère de performance dans la conception. Thèse de doctorat, École polytechnique, Octobre 2007, 346 p.

[4] CHATZIGOGOS C.T., PECKER A. – *PROJECT DARE: Soil-Foundation-Structure Systems Beyond Conventional Seismic Failure Thresholds*. Publication interne à GDS, 24/02/2010, 42 p.

[5] CHATZIGOGOS C.T., PECKER A., SALENÇON J. – Macroelement modeling of shallow foundations. *Soil Dynamics and Earthquake Engineering*, 2008, DOI 10.1016/j.soildyn.2008.08.009, 17 p.

[6] CREMER C. – *Modélisation du comportement non linéaire des fondations superficielles sous séisme*. LMT-Cachan, 2001, 162 p.

[7] FIGINI R. – Nonlinear dynamic soil-structure interaction: application to seismic analysis and design of structures on shallow foundations. PhD Thesis, Politecnico di Milano, Italy, 2010.

[8] IGARASHI A., KILUCHI Y., IEMURA H. – Real-time hybrid experimental simulation system using coupled control of shake table and hydraulic actuator. *XIV World Conference on Earthquake Engineering*, Beijing, October 2008. 8 p.

[9] MYLONAKIS G., NIKOLAOU S., GAZETAS G. – Footing under seismic loading: Analysis and design issues with emphasis on bridge foundations. *Soil Dynamics and Earthquake Engineering*, 2005, DOI 10.1016/j.soildyn.2005.12.005, 30 p.

[10] NOVA R., MONTRASIO L. – Settlement of shallow foundations on sand. *Géotechnique* No. 2, 1991, 13 p.

[11] PECKER A., CHATZIGOGOS C.T. – Non linear soil structure interaction: impact on the seismic response of structures. *XIV European Conference on Earthquake Engineering*, Ohrid, August 2010. 26 p.

[12] PREVOST J.H. – *Dynaflow v02 release 08.B*. Department of Civil and Environmental Engineering, Princeton University, October 2008.

COMPDYN 2015
5th ECCOMAS Thematic Conference on
Computational Methods in Structural Dynamics and Earthquake Engineering
M. Papadrakakis, V. Papadopoulos, V. Plevris (eds.)
Crete Island, Greece, 25–27 May 2015

OPTIMIZATION OF WIND TURBINE FOUNDATIONS FOR POOR SOIL

Wael M. Mohamed[1*], **and Per-Erik Austrell** [2]

[1*] PhD student, Department of Construction Sciences, Faculty of Engineering
Lund University, Sweden.
Teaching assistant, Civil Engineering department, Faculty of Engineering,
Suez Canal University, Egypt
E-mail: wael.mahmoud@construction.lth.se & wael.mobarak@gmail.com

[2] Associate professor, Department of Construction Sciences, Faculty of Engineering
Lund University, Sweden

E-mail: per_erik.austrell@construction.lth.se

Keywords: FE analysis, Wind turbine foundations, Circular raft with a water tank, Dynamic analysis.

Abstract. *One of the most important constraints on large-scale civil engineering projects is economic feasibility. All projects are restricted by the cost of construction and materials. A cost analysis of alternative foundation designs for wind turbines is done in this work to aid the choice of design solution. The suitability of different foundation types are compared including a novel solution, with a circular raft surrounded by a water tank for soil with poor properties. In this work cost and behavior comparisons are done for two foundation solutions, namely a piled raft and a circular raft surrounded by a water tank. An observed soil profile found in Gothenburg region, Sweden is used. The soil profile is implemented in the FE software Abaqus to find out the validity of using the different types of foundations on the mentioned type of soil. In terms of settlement and tilting it is shown that there is a good effect of using a water tank surrounding the ordinary circular raft for the actual soil profile in the Gothenburg region. For the cost issue, the analysis was carried out to calculate the whole foundation cost for a circular raft surrounded by a water tank and also for a piled raft. It is shown that using the new foundation system decrease the foundation cost compared to using piled raft with pile length = 28 m and one meter square pile. The effect of dynamic loads was also investigated and the results showed that the complete system, using circular raft surrounded by a water tank as a foundation, successfully avoids resonance through the rotor excitations.*

1 INTRODUCTION

The main aim of this study is: (1) reducing the onshore wind turbine foundation costs for poor soil by using a new foundation system instead of piled raft, and (2) checking the dynamic response of the new foundation system.

As expected the overall weight of wind turbine supporting structure components is reduced due to minimizing the costs. Moreover, the wind turbine supporting structure will be more sensitive to dynamic loads. In addition, soft soils have an influence on the dynamic response of the whole structure system. One of the methods that are used to analyze the soil-structure interaction effects is the finite-element method taking the entire system (structure, foundation and soil) into account. A dynamic FE analysis is presented in this study.

Initially, Gothenburg is considered as one of the best areas with good wind speed to build a wind farm in Sweden. Unfortunately, Gothenburg area has soft clay layer from the ground surface down to 40 m. The problem of soil containing deep clay layers is found in many cities around the world. Examples of cities are London in England, Frankfurt in Germany, Port-Said in Egypt and Taipei in Taiwan. The main conclusion from lots of studies is that the classical foundation solution for soil with poor properties is using a piled foundation. It is expected that the foundation cost percentage will increase a lot if the soil has poor geotechnical properties. Therefore, new solutions may be advantageous economically instead of using piled raft.

A study on cost-benefit analysis of wind energy showed that onshore wind turbine foundation without piling make up about 3% of the total costs [11]. Another study showed that onshore wind turbine supporting structures costs approximately 1% to 9% of the total costs [13]. Considering a piled foundation on the other hand an economic evaluation was made in [6] that showed that the major cost was the wind turbine itself 60% and the piled foundation 28.3%.

According to [2] soil-structure interaction had a significant effect for soils which have shear wave velocity lower than 750 m/s and this effect could lead to reduction in response. A study on soil-structure interaction for wind turbine showed that considering soil-structure interaction is very a vital aspect in order to make it possible stay away from entering the resonance range [7]. According to [3] depending on the output power capacity of the wind turbines, the rotational speeds range for blades are from 30 to 60 rpm, which correspond to maximum operational frequencies from 0.5 to 1 Hz. Moreover, these operational frequencies are close to the soil–structure natural frequency range [3].

In this work a parametric study of cost and behavior of two foundation solutions, a circular raft surrounded by a water tank and a piled raft, are performed. The load conditions are based on usual loads for a 2 MW wind turbine considering Gothenburg ground conditions.

2 MATERIAL PROPERTIES AND LOADS

The main characteristics of soil and load sets will be illustrated in this section. The geotechnical material model adopted in this study is the Mohr-Coulomb model [9]. The soil parameter values of the soil can be seen in Table 1. The values are from an actual case and Poisson's ratio of the soil equals $\nu_s = 0.3$ based on [8]. The backfilled soil (γ =18 kN/m^3) is assumed to be up to natural ground level.

Two sets of loads are given; serviceability limit state (SLS), and ultimate limit state (ULS) loads for Vestas V90-2.0 MW wind turbine. Each set contains a vertical load *N*, a horizontal load *H*, a bending moment *M* and a torsion moment M_z. A three-bladed turbine with a blade

length of 44 m which gives a rotating diameter of 90 m (wind catching area is of 6362 m2) is used [14]. The wind turbine tower height is 80 m [12]. The load sets is presented in Table 1 based on [12], while the definitions of the loads can be seen in Figure 1. Fatigue is not included in this study.

Table 1 Material properties and loads

I. Soil Parameters					
Description	depth Z (m)	Unit weight γ (kN/m^3)	Young's modulus E (KPa)	Internal friction angle Ǿ (^{o})	Cohesion c' (KPa)
Soft clay	40	17	5000	30	1

II. Reinforcement concrete material parameters					
Concrete class is C30/37			Reinforcement		
Young's modulus E_b (kN/m^2)	Poisson's ratio v_b	Unit weight γ_b (kN/m^3)	Yield stress f_{yk} (MPa)	Design Yield stress f_s (MPa)	Young's modulus E_s (GPa)
3.3 * 10^7	0.2	25	500	435	200

III. Tower loads, characteristic values					
Load set	Type of limit state	Load set			
		N (kN)	H (kN)	M (kNm)	M_z (kNm)
I	SLS	3510	482	35108	303
II	ULS	3510	797	63825	1642

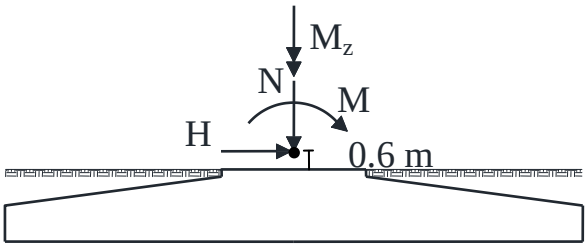


Figure 1 Definition of load denotations [10]

3 FOUNDATION DESCRIPTION

The analysis was carried out for two types of foundation solutions as shown in Figure 2 and Figure 3. It is a piled raft and the new solution is a circular raft surrounded by a water tank. The aim is to check the validity of using a circular raft surrounded by a water tank on a poor soil that contains deep soft clay layer as an alternative to using a piled raft. The new solution is expected to be less expensive in order to pass requirements on settlement and differential settlement.

3.1 Piled raft

A piled raft is a raft foundation that has piles to reduce the settlement. The raft foundation and the piles are designed to cooperate to ensure that the settlement does not exceeded the allowable settlement value. The following characteristics were kept constant in all analysis cases: raft diameter D is equal 22.5 m. square piles are placed below the surface foundations, with a_{pile}= 1.0 m and pile spacing s = 2.4 m. Piles are located symmetrically along one ring with D_{ring} = 18.5 m. However, the analysis was carried out for variations in one foundation variable, namely pile length L_p = 16, 20, 24 and 28 m. Figure 2 shows the geometry and dimensions of the piled raft.

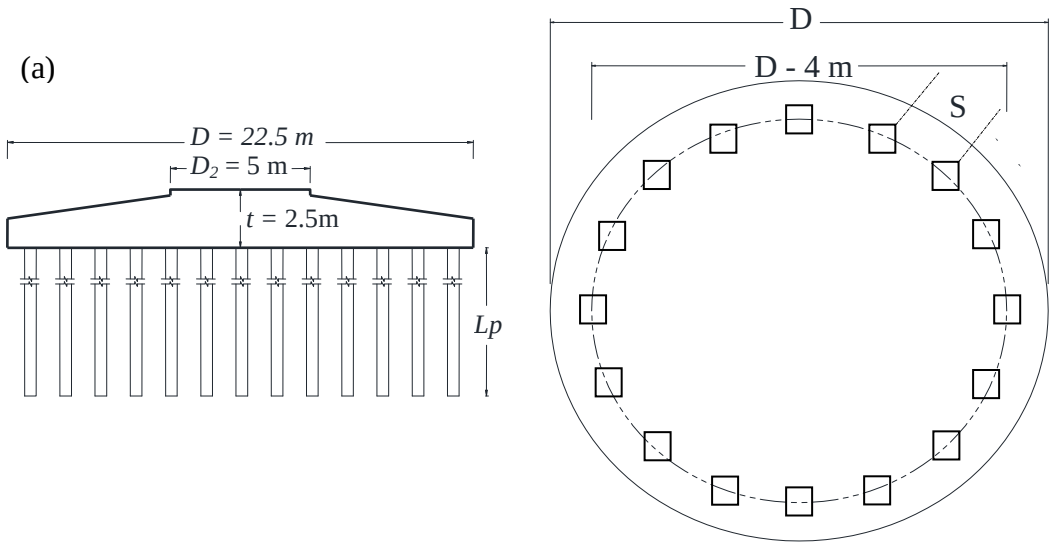


Figure 2 Piled raft

3.2 Circular raft surrounded by a water tank

For a circular raft with a water tank, the idea is to use water as a load to give a stabilizing moment to resist the overturning moment. The reason for using water is the ease of moving water with wind turbine movement. The water tank is divided into four parts and only one or two parts will contain water and all parts are connecting with an active system to move water between parts, see Appendix. To get a big resistant moment with light weight (water load), a big water volume must be used. Figure 3 shows more details of the geometry and dimensions of the circular raft foundation surrounded by a water tank that are used in this study.

The following characteristics were kept constant in all analysis cases: circular raft diameter D equal to 14.5 m, total thickness of the inner part t = 2.50 m and the diameter of upper cylinder equal to D_2 = 5 m. Vertical tank wall thickness increase from 0.25 m in the upper part to 0.75 m for H_{tank} = 5.0 m in the lower part, the upper slab thickness is 0.25 m and the lower slab thickness is 0.75 m. However, the analysis was carried out for variations in one foundation variable, namely the tank width B_{tank} = 4.0 and 5.0 m.

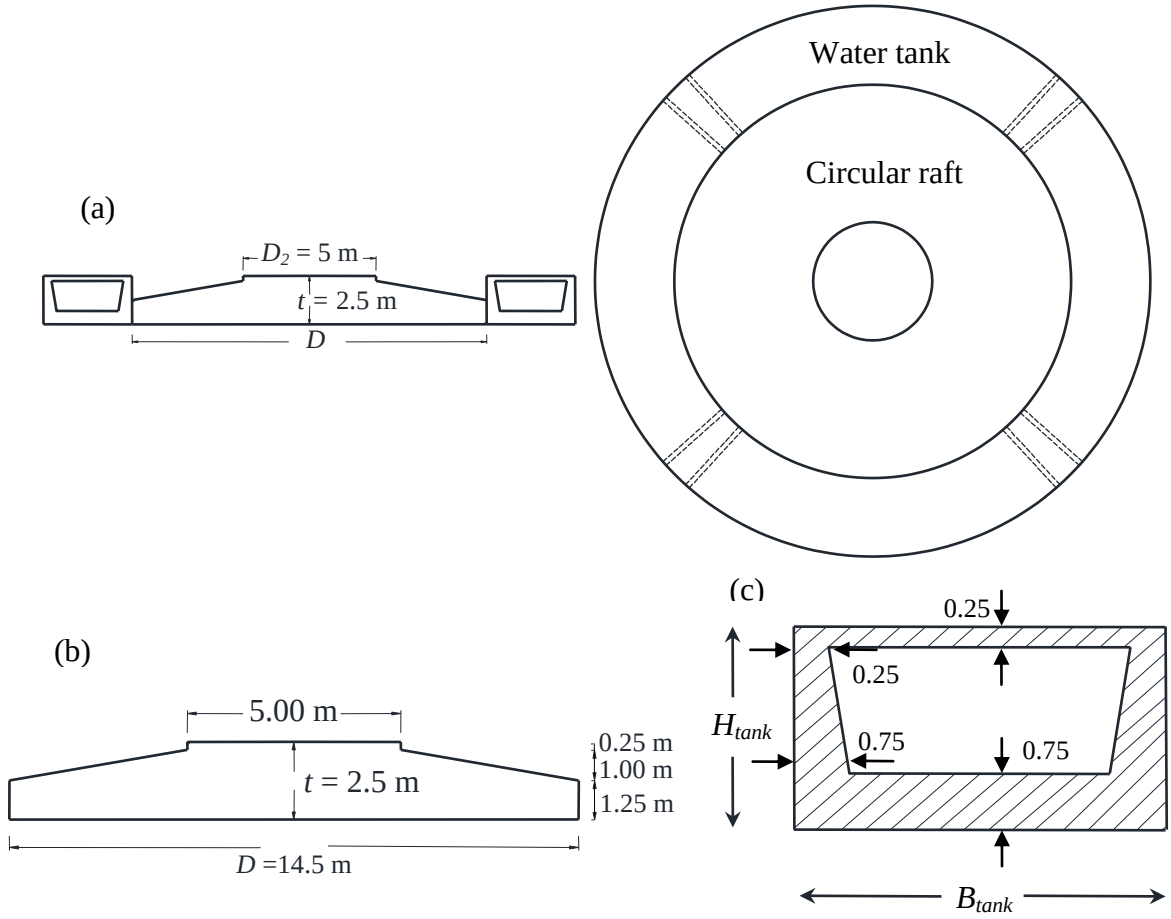


Figure 3 (a) Circular raft surrounded by a water tank, (b) Vertical section for a circular raft, and (c) Vertical section for a water tank

4 FE MODEL

A three dimensional finite element model of the foundation-soil system was created using *ABAQUS* [4]. For the soil model, the computational region chosen is 100*100*50 m where the depth in z direction is 50 m. C3D20R element was selected using a fine grid around the raft and a coarse grid for the far field. The geotechnical material model adopted in this article is the Mohr-Coulomb model [9] with parameters according to Table 1. Full interaction was assumed between the soil and the half of the foundation (the compression side) and surface contact interaction was used between the foundation and the soil in the other half (the tension side) to allow the foundation to elevate without any tension at the interface.

4.1 FE verification for the shallow foundation

One case was studied and compared with the results in figure 5.10 on Svensson work [12]. Svensson analyzed a circular raft on moraine soil using 2D FE model in Plaxis and showed that the tilting for a circular raft on moraine soil equal to 1.25 cm, the maximum settlement equal to 1.3 cm and the minimum settlement is 0.05 cm. In this study, 3D FE model is established in Abaqus with the same foundation dimensions and soil properties. For the soil model, the computational region chosen is 100*100*50 m where the depth in z direction is 50 m. The

FE model result is: tilting equal to 1.13 cm with 9.6% deviation, the maximum settlement equal to 1.24 cm and the minimum settlement is 0.11 cm.

4.2 FE verification for the deep foundation

One case was studied and compared with the results in Figure 9 and Figure 12 on Abdel Glil work [1] for raft thickness equal to 1.1 m, pile length is 24 m, pile spacing is 2 and pile diameter equal to 0.5 m. Abdel Glil calculates the maximum and differential settlements by using ELPLA software. Abdel Glil calculates the maximum settlement (12.6 cm) and the differential settlement (1.89 cm) [1]. In this study, 3D FE model is established in Abaqus with the same foundation dimensions and soil properties. For the soil model, the computational region chosen is 100*100*50 m where the depth in z direction is 50 m. The FE model result is: deferential settlement equal to 2.13 cm with 11.3% deviation, the maximum settlement equal to 13.36 cm with 5.7 % deviation.

5 SETTLEMENT AND DIFFERENTIAL SETTLEMENT

As mentioned above, the maximum settlement and differential settlement ($\Delta S = S_{max} - S_{min}$) for the new system is tested considering specifically the poor ground properties near Gothenburg city, Sweden and compared with a piled raft. Table 2 presents differential settlement and the reduction of differential settlement values for a circular raft surrounded by a water tank and a piled raft. The reduction of differential settlement H_s, which is given by:

$$H_s = [1 - (\Delta S_{rwt} / \Delta S_{pr})] \cdot 100 \quad (2)$$

where ΔS_{rwt} is the differential settlement of the circular raft with a water tank, and ΔS_{pr} is the differential settlement of the piled raft. Figure 4 shows maximum and minimum settlements for the circular raft surrounded by a water tank and the piled raft.

Table 2 Differential settlement (cm) and the reduction of differential settlement

B_{tank}		L_p =16 m		L_p =20 m		L_p =24 m		L_p =28 m	
	ΔS_{rwt}	ΔS_{pr}	H_s %	ΔS_{pr}	H_s %	ΔS_{pr}	H_s %	ΔS_{pr}	H_s %
4 m	2.76	3.76	26.6	3.29	16.1	2.78	0.72	2.27	-21.6
5 m	1.57		58.2		52.2		43.5		30.8

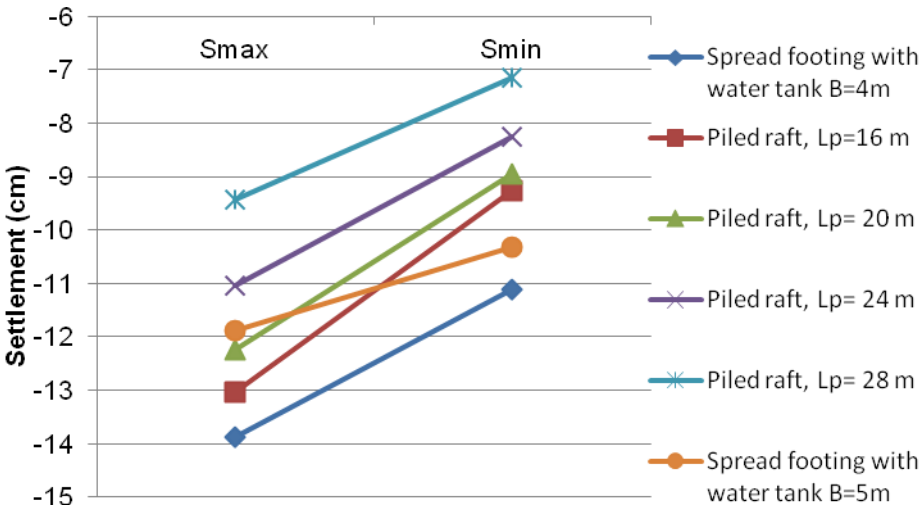


Figure 4 Maximum and minimum settlement for piled raft and circular raft with a water tank

From Table 2 and Figure 4, it can be concluded that

- Using a water tank surrounding a circular raft decreases the differential settlement compared to a piled raft.
- Using a circular raft surrounded by a water tank with B_{tank} = 5 m decreases the differential settlement by 30% compared to a piled raft with pile length L_p = 28 m.
- Using a circular raft surrounded by a water tank with B_{tank} = 5 m increases the maximum settlement by 26% compared to a piled raft with pile length L_p = 28 m but it is lower than the allowable settlement for shallow foundation.

6 COST COMPARISON BETWEEN THE FOUNDATION SYSTEMS

The analysis is carried out to calculate the cost of reinforcement concrete, water system and pilling for spread footing surrounded by water tank and piled raft. For reinforcement in piles, the calculation use 12 bars Ø 16 mm have to provide in a regular pattern and 125 mm for lateral tie spacing. Table 3 shows comparison between the foundation systems. The comparison is depending on estimate cost comparison according to [10] and Peter Alheid (Geoconstructor at Hercules Grundläggning AB).

Table 3 Cost comparison between raft surrounded by water tank and piled raft

	Piled raft	Circular raft surrounded by a water tank	Cost in Sweden (USD)
Volume of Reinforcement concrete (m^3)	670.4	1002	230/m^3
Steel weight (tons)	48	57.5	2167/ton
Pile (drilling + material) (m)	672	0	893/m
Excavation (m^3)	994	1945	17/m^3
Water system	0	8 motors + 12 pipes + 128 electric valves	208000
Total Cost (USD)	876546	596128	

From Table 3, by using the new foundation system in Gothenburg region the foundation cost decreases by 32 % compared to using piled raft with pile length of 28 m and square pile of 1.0 meter square.

7 DYNAMIC ANALYSIS

Wind turbine supporting structure systems are sensitive to dynamic loading conditions. Figure 5 shows a summary of the typical forcing frequencies applied to a Vestas V90-2MW wind turbine system [14]: the 1P frequency means the rotational frequency of the turbine, and the 3P frequency means the blade-passing frequency. A summary of the engineering properties of the turbine is presented in Table 4.

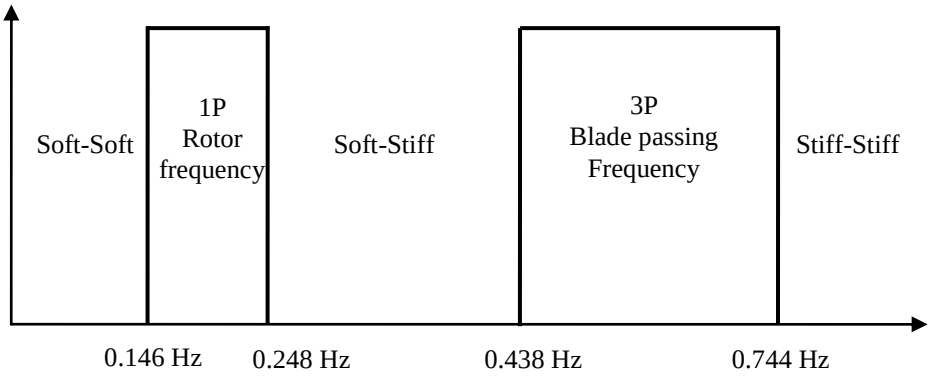


Figure 5 Forcing frequencies plotted against power spectral density for Vestas V90-2.0 MW wind turbine.

Table 4 Turbine Properties.

Property	value
Rated power	2.0 MW
Cut-in wind speed	4 m/sec.
Rotor diameter	90 m
Tower height	80 m
Lower section diameter	4.15 m
Top section diameter	3.15 m
Tower wall thickness	22 mm
Tower mass	156 t
Nacelle mass	68 t
Rotor mass	38 t

A full 3D finite element model of the tower-foundation-soil system was created using ABAQUS [4]. Initially, the soil, foundation and tower were modeled using quadratic 3D stress elements (C3D20). Infinite element (CIN3D12) was used for soil boundary. Nacelle, rotor and blade masses modeled using mass point, see Figure 6. In this case, steady- state dynamics step, which can be used to analyze linear problems, have been used to calculate the first and the second natural frequency for the whole system by putting harmonic loads in three directions at the top of the tower and seeing the response at many points.

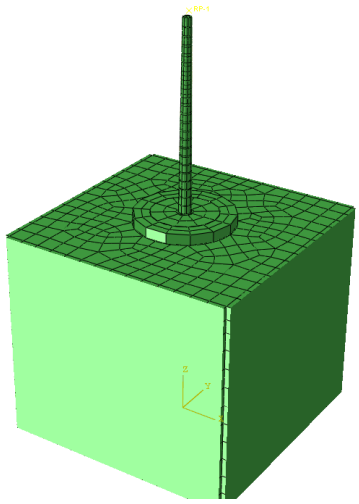


Figure 6 Meshed 3D model using Infinite elements as a boundary condition

Table 5 presents the frequencies for the first and second mode of vibration obtained from the dynamic analysis for a circular raft surrounded by a water tank, and a piled raft with L_p = 28 m. The results show that the structure-foundation-soil system, using the new foundation system, successfully avoids resonance during the rotor excitations.

Table 5 Frequencies and periods of vibration

Mode of vibration	Frequency (Hz)	Frequency +10% (Hz)	Frequency -10% (Hz)	Period of vibration (s)	Rotor frequency (Hz)	Blade passing frequency (Hz)
For a circular raft with a water tank						
1	0.3	0.33	0.27	3.33	0.146-0.248	0.438-0.744
2	1.08	1.188	0.972	0.93		
For a piled raft with L_p = 28 m						
1	0.38	0.418	0.342	2.63	0.146-0.248	0.438-0.744
2	1.23	1.353	1.107	0.81		

8 CONCLUSIONS

In this work, a new solution is developed to decrease the cost of wind turbine foundations for poor soils. Using a water tank surrounding the raft decreases the cost and differential settlement problems compared to using a piled raft. Considering specifically the poor ground properties near Gothenburg city, the whole foundation cost for a circular raft surrounded by a water tank was compared to an ordinary piled raft. In this analysis actual costs were determined considering local Swedish construction cost levels. The results revealed that using the new foundation system in Gothenburg city region can decrease the foundation cost by 32% compared to using a piled raft with pile length of 28 m and square piles of 1.0 m side. Differential settlement problem is one of the biggest challenges for designing wind turbine foundations for poor soils. Using a circular raft surrounding by a water tank with B_{tank} = 5 m decreases the differential settlement by 30% compared to a piled raft with pile length L_p = 28 m. However, the settlement increases by 26% compared to a piled raft with pile length L_p = 28 m but is still lower than the allowable settlement value for a shallow foundation. Secondly, the effect of dynamic loads was also investigated and the results showed that the structure-foundation-soil system, using a circular raft surrounded by a water tank, successfully avoids resonance during the rotor excitations.

REFERENCES

[1] Abdel Glil E., El Gendy M., Ibrahim H. and Reda A. Optimization of piled raft in Port-Said. *Port-Said Engineering Research Journal*. Volume 13, No. 1, pp. 27-45. 2009

[2] Enrique Luco, J. Soil-structure interaction effects on the seismic response of tall chimneys. *Soil Dynamics and Earthquake Engineering* 5(3): 170-177. 1986

[3] Hartmann, F. and Katz C. *Structural analysis with finite elements*, Springer-Verlag, Berlin. 2007

[4] Hibbitt D., Karlsson B., Sorensen P. (2012) Abaqus 6.12-3 Manual.

[5] Larock, B. E., Jeppson R. W. and Watters G. Z. *Hydraulics of pipeline systems*, CRC press LLC. 1999

[6] Manwell, J. F., J. MacLeod, S. Wright, L. DiTullio and J. G. McGowan. Hull Wind II: A Case Study of the Development of a Second Large Wind Turbine Installation in the Town of Hull, MA. American Wind Energy Association. *Windpower 2006 Conference*. 2006

[7] Olariu, C.-P. Soil-structure interaction in case of a wind turbine. *Bul. Inst. Politehnic, Iaşi, LIX (LXIII)* 1: 159-174. 2013

[8] Olsson, M. *Calculating long term settlement in soft clays*, Thesis for the Degree of Licentiate of Eng., Department of Civil & Environmental Eng., Chalmers University of Technology, Gothenburg, Sweden. 2010

[9] Potts D.M. and Zdravkovic L. (1999) *Finite element analysis in geotechnical engineering: theory*. Thomas Telford, London, UK, Section 7, pp.151-155.

[10] Sektionsfakta: kostnadsberäkningar av sektioner för byggbranschen. 13/14. (2014). Växjö: Wikells byggberäkningar. (in Swedish)

[11] Snyder, B. and M. J. Kaiser (2009). Ecological and economic cost-benefit analysis of offshore wind energy. Renewable Energy 34(6): 1567-1578.

[12] Svensson, H. *Design of foundations for wind turbines*. Master's dissertation for structural mechanics. 161 p. 2010 from:

< www. byggmek. lth. se/fileadmin/byggnadsmekanik/publications/tvsm5000/web5173. pdf.

[13] Van Buren, E. Effect of foundation modeling methodology on the dynamic response of offshore wind turbine support structures. ASME 2011 *30th International Conference on Ocean, Offshore and Arctic Engineering, American Society of Mechanical Engineers*.

[14] Vestas Wind Systems. *Vestas V90-2 MW*. 2008 from: http://www.vestas.com/files%2Ffiler%2Fen%2Fbrochures%2Fproductbrochurev901_8_2_0_uk.pdf.

Appendix

Water movement system

The water system depends on 8 motors and 15 pipes (10 inches) with electric valves buried in the tank lower slab, the system is designed with 7 working motors and one motor is for safety to move the half volume of water and pipes will move the other half, see Figure 7. According to [5] required motor horsepower is calculated from the following equation:

$$\text{Motor HP} = \rho\, g\, Q\, H / \mu$$

where: ρ is water density (Kg/m^3), Q is water discharge (m^3/s), H is the total head (m), g is the acceleration due to gravity (m/s^2) and μ is motor efficiency (μ = 0.8).

Water system design is carried out for some constant values such as tank width B_{tank} = 5.0 m, tank depth D_{tank} = 5 m and water volume = 275 m^3. Between all parts there are two pipes to move air from the part which is intended to be filled to the other part which is intended to be emptied. Water movement will depend on rotor hub position which depends on wind direction in Gothenburg city. Figure 8 shows the reference line and angles which used to move water from one part to the other parts. Table 6 presents the location of the water according to the rotor hub position. Control system for the water movement system deals with wind direction and wind speed sensors that used in yaw system in wind turbines. This system needs 7 motors (with flow rate equal 0.33 m^3/s) to move half of the water volume in one minute from one part to the other parts.

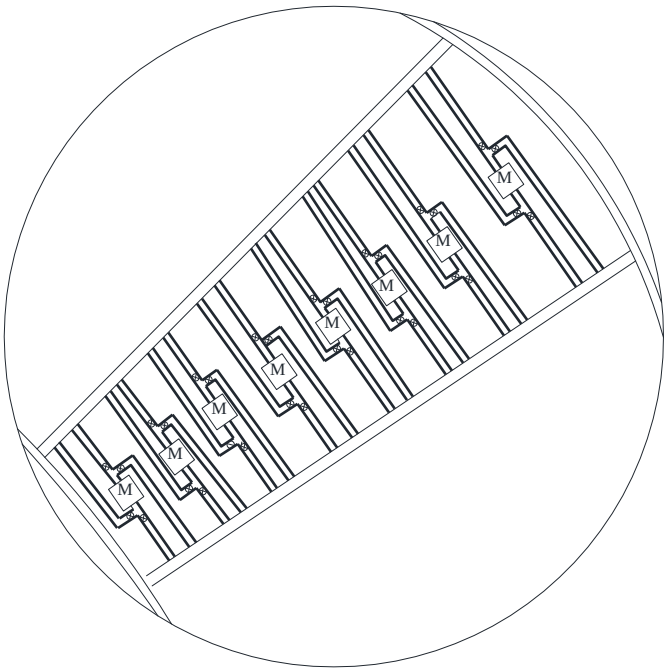


Figure 7 Water movement system between water tank parts

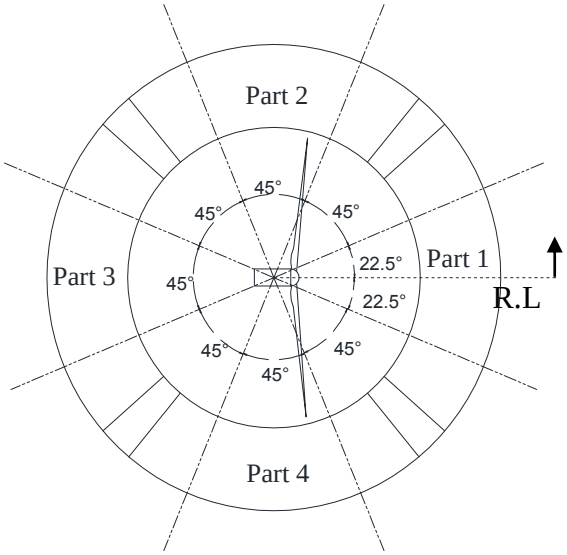


Figure 8 Reference line and angles used to move water from one part to the other parts

Table 6 Location of the water according to rotor hub angle with the R.L.

Rotor hub angle with the R.L.	Water position
0.00 to 22.5 & 337.5 to 360	Part 1
22.5 to 67.5	Part 1 + Part 2
67.5 to 112.5	Part 2
112.5 to 157.5	Part 2 + Part 3
157.5 to 202.5	Part 3
202.5 to 247.5	Part 3 + Part 4
247.5 to 292.5	Part 4
292.5 to 337.5	Part 4 + Part 1

COMPDYN 2015
5th ECCOMAS Thematic Conference on
Computational Methods in Structural Dynamics and Earthquake Engineering
M. Papadrakakis, V. Papadopoulos, V. Plevris (eds.)
Crete Island, Greece, 25–27 May 2015

A SSI NUMERICAL MODEL FOR LAYERED SOILS USING A BEM-FEM FORMULATION IN TIME DOMAIN

A. Romero, P. Galvín

Escuela Técnica Superior de Ingeniería, Universidad de Sevilla Camino de los Descubrimientos 4109, Sevilla (Spain)
e-mail: {aro,pedrogalvin}@us.es

Keywords: BEM-FEM coupling, Layered half-space fundamental solution, Time domain, Soil-structure interaction

Abstract. *This paper presents a numerical method based on a three dimensional boundary element-finite element coupled formulation in the time domain. The proposed model allows studying soil-structure interaction problems. The soil is modelled with the boundary element method, where the radiation condition is implicitly satisfied in the fundamental solution. Layered half-space Green's function including internal material damping is considered as the fundamental solution because of the influence of soil stratification on soil-structure interaction problems is large. This fundamental solution is computed from the exact expressions for the response in the underlying half-space and from a modal solution for the layers. The finite element method is used to represent the structure. In this paper the proposed method is validated by comparison with analytical and numerical results, and an experimental study is done. Afterwards, the dynamic behaviour of a building subjected to an incident wave field is studied.*

1 Introduction

The response of a soil domain to external loads, earthquakes or moving trains, the response of structures to ground-borne waves, and the response of foundations due to static and dynamic loads are some of the problems where soil-structure interaction (SSI) is important [1]. The Boundary Element Method (BEM) and the Finite Element Method (FEM) can be coupled to study SSI problems rigorously. The semi-infinite character of the soil and the Sommerfeld radiation condition [2] are accurately considered by the BEM [3]. Non-linear dynamic behaviour of structures can be represented from the FEM [4].

BEM models are based on full-space or half-space fundamental solutions. Frequency domain models have been proposed from full-space [3, 5], and from homogeneous and horizontally layered half-space fundamental solutions [6, 7]. Time domain models have been developed by full-space [8] and, recently, from homogeneous half-space fundamental solutions [9, 10]; but time domain models based on layered half-space fundamental solutions have not been presented yet.

SSI problems can be studied by numerical models based on a full-space fundamental solution. In this case, an additional discretization of the free field around the soil-structure interface and the discretization of the soil layers are required. The first previously mentioned numerical problem does not appear using a homogeneous half-space fundamental solution since the free field condition is implicitly satisfied, although the discretization of the soil layers is still necessary. Therefore, the computational effort solution could be dramatically increased. Both numerical problems are solved using a layered half-space fundamental solution: soil discretization is limited to soil-structure interfaces.

Shear, dilatational and Rayleigh waves are not dispersive, and their phase velocities are not frequency dependent in the case of a homogeneous half-space. However, the wave propagation in a layered half-space is dispersive, i.e., the wave propagation velocities depend on the frequency. Therefore the influence of soil stratification on soil-structure interaction problems is large. BEM-FEM frequency domain models are frequently used to study SSI problems. Kaynia and Kausel [11] studied horizontal and vertical stiffness and damping of piles and piles groups in homogeneous and layered half-spaces. Lombaert et al. [12] demonstrated that soil stratification has a considerable influence on both the peak particle velocity and the frequency content of the free field vibrations due to road traffic. Auersch [13, 14] concluded from theoretical and experimental results that the dynamic response of the railway track is strongly influenced by the underlying soil. François et al. [15] and Galvín et al. [16] studied the response of a tunnel embedded in a half-space and the influence of the stratification on the tunnel-soil interaction problem.

The soil stratification is normally disregarded when the time domain formulation is considered. Then, the soil is modelled as an equivalent homogeneous half-space. Rizos and Wang [17] studied the dynamic behaviour of a flexible structure on a rigid foundation. Bode et al. [9] analysed the dynamic response of a railway track due to a moving wheel set by demonstrating the influence of the soil-track interaction. Galvín et al. [18] developed a numerical model for the analysis of vibrations due to train traffic and their effects on nearby structures. Romero et al. [8] analysed the soil-foundation interaction accounting for non-linear soil-structure contact. Galvín and Romero [10] studied a soil-structure interaction problem concerning with a building subjected to different incident wave fields.

The present paper proposes a time domain BEM-FEM methodology using the layered half-space fundamental solution presented by Park and Kausel [19, 20]. This solution is computed

from the exact expressions for the response in the underlying half-space and from a modal solution for the layers. The proposed model allows easily considering soil stratification and material damping.

The paper is organized as follows. Firstly, the layered half-space fundamental solution is discussed. Afterwards, the BEM-FEM formulation based on the previous solution is described emphasising in the integration of the Green's function. Then, the proposed model is numerically verified. Afterwards, an experimental study using the proposed methodology is presented. Finally, the dynamic behaviour of a building subjected to an incident wave field is numerically studied.

2 Layered half-space fundamental solution

In this work, the horizontally layered half-space fundamental solution proposed by Park and Kausel [19, 20] is analysed. The fundamental solution is obtained directly in the time domain. It avoids the numerical problems associated with resonances in the layers. Figure 1 shows schematically the problem geometry, where r is the distance between the observation point and the source, and ϕ is the azimuth angle. The solution for displacements is a second order tensor, $\mathbf{g}(\mathbf{x}, t; \mathbf{x}^i)$, that relates displacements at a point $\mathbf{x}$ due to a load applied at $\mathbf{x}^i$. The tensor component g_{lk} represents the k displacement component due to a load applied according to direction l. A point load with a time variation according to a Heaviside function $H(t)$ is considered in this work. It results advantageous for the analytical computation of the BEM time integrals as can be seen in Section 3.

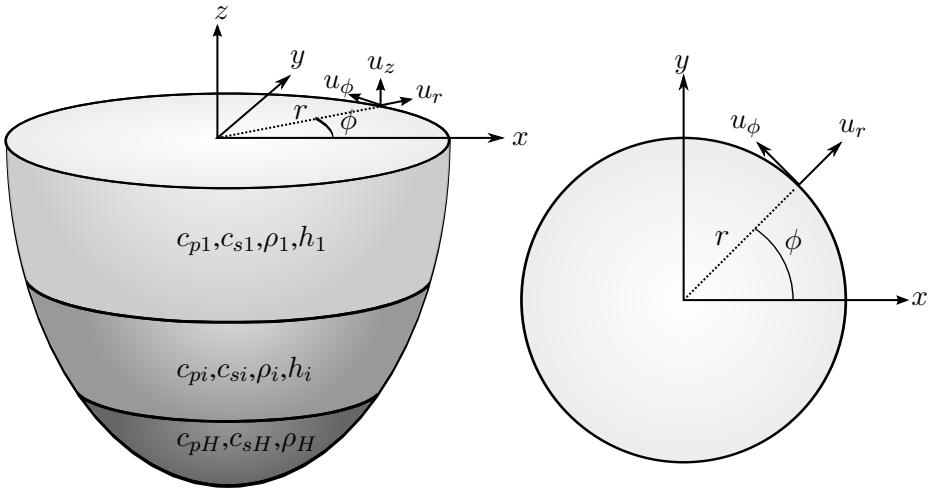


Figure 1: Problem geometry.

The proposed methodology is based on coupling the exact Green's function for a half-space formulated in the wavenumber-time domain [21], with a modal solution for the layers [19, 20]. This topic is briefly summarized in this section.

A homogeneous half-space of mass density ρ_H, damping ratio ξ_H, shear-wave velocity c_{sH}, and dilatational-wave velocity c_{pH} is considered. The displacements in direction k in the half-space at a point due to a load applied at the origin of the cylindrical coordinate system in

direction l are the following [21, 22]:

$$g_{rrH}(r,z,t) = \int_0^\infty \frac{1}{2\pi} H(t) \tilde{G}^{\delta}_{xxH}(k_x,z,t) k J_0(k_x r) dk_x - \tag{1}$$

$$\frac{1}{r}\int_0^\infty \frac{1}{2\pi} H(t) \left[\tilde{G}^{\delta}_{xxH}(k_x,z,t) - \tilde{G}^{\delta}_{yyH}(k_x,z,t)\right] J_1(k_x r) dk_x \tag{2}$$

$$g_{rzH}(r,z,t) = \frac{-1}{i}\int_0^\infty \frac{1}{2\pi} H(t) \tilde{G}^{\delta}_{xzH}(k_x,z,t) k_x \frac{\partial}{\partial k_x r} J_0(k_x r) dk_x \tag{3}$$

$$g_{\theta\theta H}(r,z,t) = -\int_0^\infty \frac{1}{2\pi} H(t) \tilde{G}^{\delta}_{yyH}(k_x,z,t) k_x J_0(k_x r) dk_x - \tag{4}$$

$$\frac{1}{r}\int_0^\infty \frac{1}{2\pi} H(t) \left[\tilde{G}^{\delta}_{xxH}(k_x,z,t) - \tilde{G}^{\delta}_{yyH}(k_x,z,t)\right] J_1(k_x r) dk_x \tag{5}$$

$$g_{zrH}(r,z,t) = -\frac{1}{i}\int_0^\infty \frac{1}{2\pi} H(t) \tilde{G}^{\delta}_{zxH}(k_x,z,t) k_x J_1(k_x r) dk_x \tag{6}$$

$$g_{zzH}(r,z,t) = \int_0^\infty \frac{1}{2\pi} H(t) \tilde{G}^{\delta}_{zzH}(k_x,z,t) k_x J_0(k_x r) dk_x \tag{7}$$

being J_n the Bessel function of the first kind and order n, and $\tilde{G}^{\delta}_{yyH}$ and $\tilde{G}^{\delta}_{mnH}$ are defined as:

$$\tilde{G}^{\delta}_{yyH}(k_x,z,t) = \frac{e^{-\xi_H k_x c_{sH} t}}{c_{sH}\rho_H} J_0\left(k_x c_{sH}\sqrt{1-\xi_H^2}\sqrt{t^2-t_s^2}\right) \tag{8}$$

$$\tilde{G}^{\delta}_{mnH}(k_x,z,t) = \frac{e^{-\xi_H k_x c_{sH} t}}{c_{sH}\rho_H} \left[R_{mn}(k_x,z,t)) - B_{mn}(k_x,z,t)\right] \qquad m,n = x,z \tag{9}$$

where $R_{mn}(k_x,z,t)$ is the Rayleigh pole term, $B_{mn}(k_x,z,t)$ is a branch-cut integral [21], and δ means response to an impulsive load.

Park and Kausel [21] separated the branch-cut integrals in three intervals: $1 \to \sqrt{2}$, $\sqrt{2} \to a$, and $a \to \infty$, where $a = c_{pH}/c_{sH}$. Moreover, they replaced the kernels by their asymptotes from $3a$. Thus, they computed the branch-cut integrals from the sum of their values in the following intervals: $1 \to \sqrt{2}$, $\sqrt{2} \to a$, $a \to 3a$, and $3a \to \infty$.

In this work, it is proposed to separate the branch-cut integrals in two intervals to reduce computational time: $1 \to a$ and $a \to \infty$. The kernels are also replaced by their asymptotes but, in the present methodology, from $5a$. Therefore, the branch-cut integrals are evaluated from the sum of their values in the intervals: $1 \to a$, $a \to 5a$, and $5a \to \infty$. The kernels of the integrals are expressed in a dimensionless form, and the integrals from $1 \to a$, and from $a \to 5a$, are numerically evaluated and saved in a table. The integrals from $5a \to \infty$ are analytically evaluated. This methodology allows to compute the branch-cut integrals with a numerical error lower than 0.25%.

The response of the layered half-space in the wavenumber-time domain for a point located at the layers is obtained as [19, 20]:

$$\tilde{g}_{kl}(k_x,z,t) = \tilde{G}_{klL}(k_x,z,z',t) * \frac{1}{2\pi} H(t) - \tilde{G}_{klL}(k_x,z,0,t) * \tilde{\tau}(k_x,t) \tag{10}$$

where $\tilde{G}_{klL}(k_x,z,z',t)$ is the response of the layer at z due to an Heaviside load applied at z', $\tilde{\tau}(k_x,t)$ are the tractions at the bottom interface which coincides with the top of the half-space, and $*$ means time convolution process. The origin of coordinates, i.e. $z = 0$, is placed at the top of the half-space.

The Green's functions for the layers $\tilde{G}_{klL}(k_x, z, z', t)$ are obtained from a modal superposition with the normal modes of the layer:

$$\tilde{G}_{klL}(k_x, z, z', t) = \sum_{j=1}^{\infty} e^{-\xi_{jL}\omega_{jL}t} \frac{\sin \omega_{djL} t}{\omega_{djL}} \phi_{jL}(k_x, z)\phi_{jL}(k_x, z') \tag{11}$$

The characteristic modal frequencies ω_{jL} and the corresponding modal shapes ϕ_{jL} are computed by making use of the Thin-Layer Method (TLM). The damped modal frequency is obtained from $\omega_{djL} = \omega_{jL}\sqrt{1-\xi_{jL}^2}$, where ξ_{jL} is the damping ratio of the layer.

Tractions at the bottom interface $\tilde{\tau}(k_x, t)$ are obtained from the compatibility of displacements and equilibrium of forces at $z = 0$, i.e., the interface between the layer and the half-space. The response at the interface of the half-space is computed as:

$$\tilde{g}_{kl}(k_x, 0, t) = \tilde{g}_{klH}(k_x, 0, t) * \tilde{\tau}(k_x, t) \tag{12}$$

The response at the bottom interface of the layer can be obtained from:

$$\tilde{g}_{kl}(k_x, 0, t) = \tilde{G}_{klL}(k_x, 0, z', t) * \frac{1}{2\pi} H(t) - \tilde{G}_{klL}(k_x, 0, 0, t) * \tilde{\tau}(k_x, t) \tag{13}$$

Equations (12) and (13) allow to evaluate the tractions $\tilde{\tau}(k_x, t)$. Finally, the response in the space-time domain is obtained from the inverse Hankel transform as [19, 20]:

$$g_{rr}(r, z, t) = \int_0^{\infty} \frac{1}{4\pi}(\tilde{g}_{xx}(k_x, z, t) + \tilde{g}_{yy}(k_x, z, t))k_x J_0(k_x r)dk_x - \tag{14}$$

$$\int_0^{\infty} \frac{1}{4\pi}(\tilde{g}_{xx}(k_x, z, t) - \tilde{g}_{yy}(k_x, z, t))k_x J_2(k_x r)dk_x \tag{15}$$

$$g_{rz}(r, z, t) = -i\int_0^{\infty} \frac{1}{2\pi}\tilde{g}_{xz}(k_x, z, t)k_x J_0(k_x r)dk_x \tag{16}$$

$$g_{\theta\theta}(r, z, t) = -\int_0^{\infty} \frac{1}{4\pi}(\tilde{g}_{xx}(k_x, z, t) + \tilde{g}_{yy}(k_x, z, t))k_x J_0(k_x r)dk_x - \tag{17}$$

$$\int_0^{\infty} \frac{1}{4\pi}(\tilde{g}_{xx}(k_x, z, t) - \tilde{g}_{yy}(k_x, z, t))k_x J_2(k_x r)dk_x \tag{18}$$

$$g_{zr}(r, z, t) = -i\int_0^{\infty} \frac{1}{2\pi}\tilde{g}_{zx}(k_x, z, t)k_x J_1(k_x r)dk_x \tag{19}$$

$$g_{zz}(r, z, t) = i\int_0^{\infty} \frac{1}{2\pi}\tilde{g}_{zz}(k_x, z, t)k_x J_0(k_x r)dk_x \tag{20}$$

Integration kernels appear in Equations (14-20) are smooth and they have not any singularities. The time step should be shorter than the shortest characteristic period of the system layers for stable computations [19, 20].

The fundamental solution is computed considering the cylindrical coordinate system as:

$$\mathbf{g}^{cyl}(r, z, t) = \begin{bmatrix} g_{rr} & 0 & g_{rz} \\ 0 & g_{\phi\phi} & 0 \\ g_{zr} & 0 & g_{zz} \end{bmatrix} \tag{21}$$

Equation (21) represents an antisymmetrical second order tensor. The fundamental solution in the cartesian coordinate system is obtained transforming the Equation (21) as follows:

$$\mathbf{g}(x, y, z, t) = \mathbf{\Omega}\mathbf{g}^{cyl}\mathbf{\Omega}^T \tag{22}$$

where $\mathbf{\Omega}$ is the transformation matrix from cylindrical to cartesian coordinate system:

$$\mathbf{\Omega} = \begin{bmatrix} \cos\phi & \sin\phi & 0 \\ -\sin\phi & \cos\phi & 0 \\ 0 & 0 & 1 \end{bmatrix} \tag{23}$$

Following, the response of a homogeneous and a layered half-space due to a Heaviside point load is studied to validate the proposed methodology. Since analytical solutions of both problems are not available, the MATLAB toolbox EDT 2.1 [26, 27] based on the direct stiffness method [6] in the wavenumber-frequency domain is used to validate the results obtained from the proposed methodology. Moreover, numerical results are also verified by comparison with the explicit displacement solution for a Heaviside load applied at the surface of a homogeneous elastic half-space presented recently by Kausel [23].

First, a homogeneous half-space was assumed with the following properties: $c_{pH} = 300\,\text{m/s}$, $c_{sH} = 150\,\text{m/s}$, $\xi_H = 0.05$, and $\rho_H = 2000\,\text{kg/m}^3$. Figure 2 shows the fundamental solution for displacements at the half-space surface at distance $r = 10\,\text{m}$ from the source. The response shows an initial perturbation at the arrival time of the P-wave ($t = r/c_{pH}$) which it can be clearly identified in the Figures 2.(a,b) where a horizontal load is considered. The maximum displacement is reached between the arrival time of S-wave ($t = r/c_{sH}$) and the arrival time of Rayleigh wave.

The agreement between the computed results and those obtained from EDT 2.1 toolbox [26] is quite good. The mismatches with the analytical solution [23] are due to the internal soil damping induces a smoother behaviour around the different arrival time of the waves.

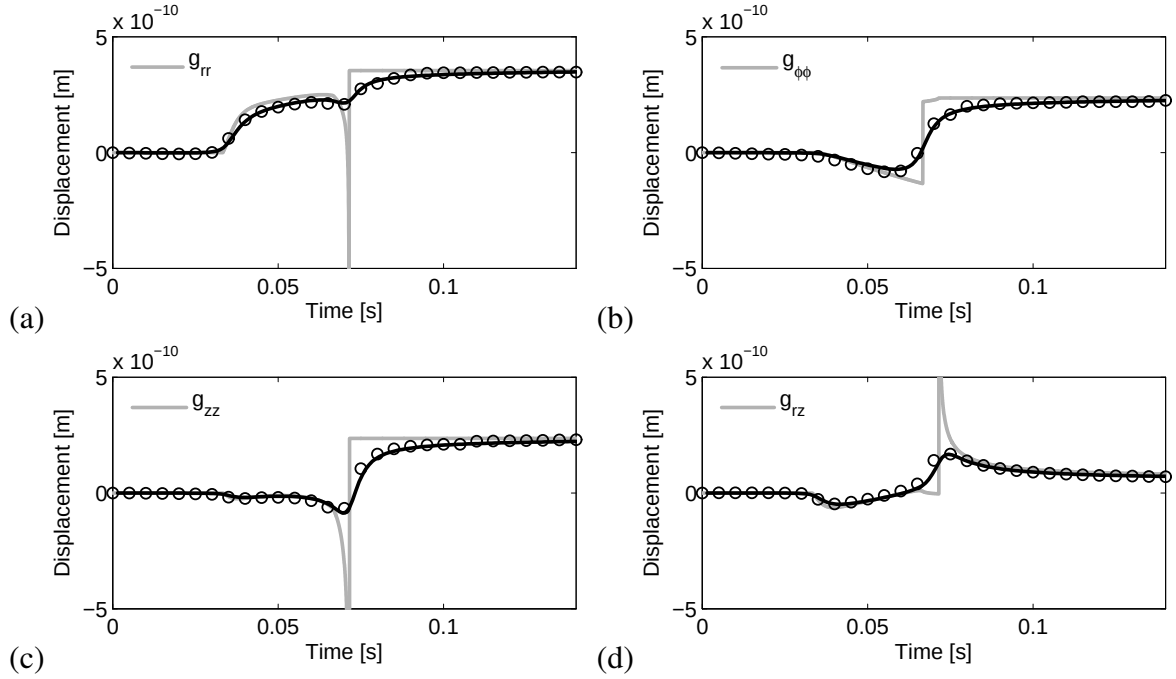


Figure 2: (a) Radial and (b) tangential, and (c) vertical and (d) radial displacements due to a (a,b) horizontal and (c,d) vertical Heaviside load applied at the surface of a homogeneous half-space for a point located at the surface at $r = 10\,\text{m}$ from the source: analytical solution [23] (grey line), EDT 2.1 toolbox [26] (black line) and proposed methodology (black circles).

Next, the response of a layered half-space is studied. A layer with a thickness $h_L = 5\,\text{m}$, and $c_{pL} = 300\,\text{m/s}$, $c_{sL} = 150\,\text{m/s}$, $\xi_L = 0.05$, and $\rho_L = 2000\,\text{kg/m}^3$, on top of a half-space with $c_{pH} = 600\,\text{m/s}$, $c_{sH} = 300\,\text{m/s}$, $\xi_H = 0.05$, and $\rho_H = 2000\,\text{kg/m}^3$ is considered. Figure 3 shows the displacements at a point of the soil surface due to horizontal and vertical loads, and they are compared with the analytical solution for a homogeneous half-space with the same properties that the upper layer of the soil. The mismatches between the numerical results can be neglected. It can be observed in Figure 3 the influence of the soil stratification on the wave propagation from the comparison with the analytical solution for a homogeneous half-space.

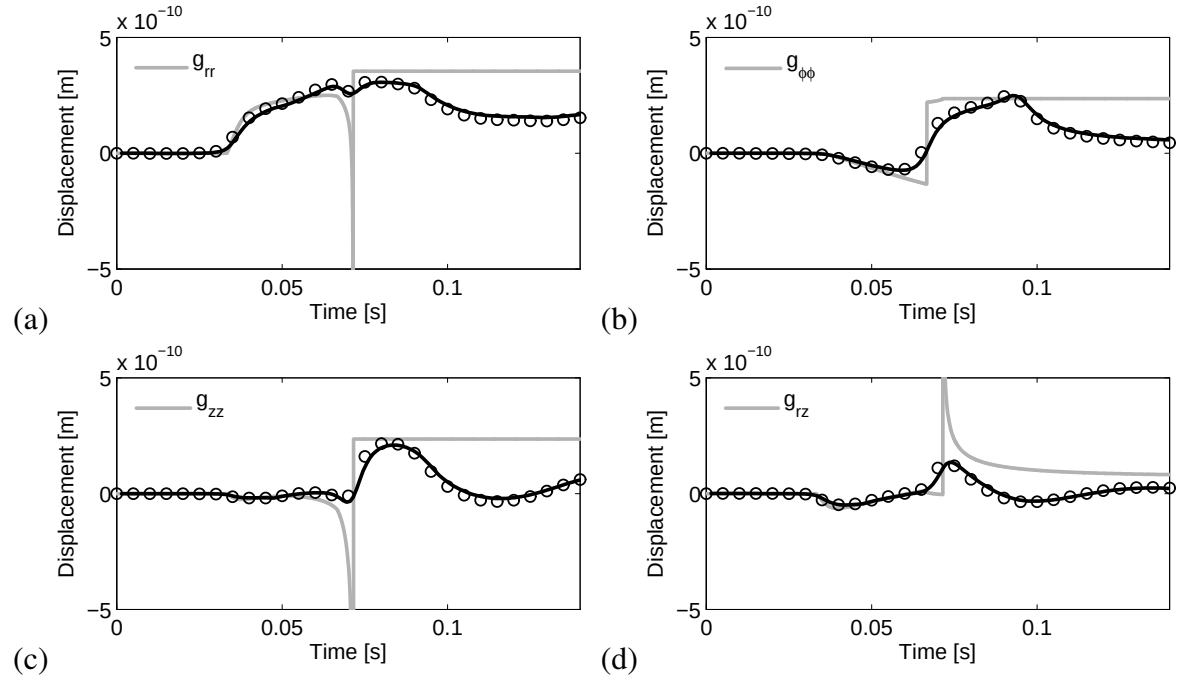


Figure 3: (a) Radial and (b) tangential, and (c) vertical and (d) radial displacements due to a (a,b) horizontal and (c,d) vertical Heaviside load applied at the surface of a layered half-space for a point located at the surface at $r = 10\,\text{m}$ from the source: analytical solution [23] (grey line), EDT 2.1 toolbox [26] (black line) and proposed methodology (black circles).

3 Boundary element formulation

This section presents the three-dimensional (3D) boundary element formulation in time domain based on the half-space fundamental solution previously developed. The integral representation of the displacement u^i for a point i on the soil surface at time t, with zero body forces and zero initial conditions can be written as [3]:

$$\begin{aligned} c^i_{lk} u^i_k(\mathbf{x}^i, t) = &\int_0^{t+} \int_\Gamma u^*_{lk}(\mathbf{x}, t-\tau; \mathbf{x}^i) p_k(\mathbf{x}, \tau) d\Gamma d\tau \\ &- \int_0^{t+} \int_\Gamma p^*_{lk}(\mathbf{x}, t-\tau; \mathbf{x}^i) u_k(\mathbf{x}, \tau) d\Gamma d\tau \end{aligned} \tag{24}$$

where u_k and p_k stand for the k component of the displacement and traction, respectively; $u^*_{lk}(\mathbf{x}, t-\tau; \mathbf{x}^i)$ and $p^*_{lk}(\mathbf{x}, t-\tau; \mathbf{x}^i)$ are the half-space fundamental solution displacement and

traction tensors, respectively, at point $\mathbf{x}$ due to an impulsive load applied at $\mathbf{x}^i$ in l direction. The integral-free term c^i_{lk} depends only on the boundary geometry at point $\mathbf{x}^i$, and its value is unitary at the soil surface for a smooth boundary. For non-smooth boundaries c^i_{lk} is computed as presented in Reference [24].

Half-space fundamental solution for an impulsive load is derived from the solution for a Heaviside load as:

$$u^*_{lk}(\mathbf{x}, t; \mathbf{x}^i) = \frac{\partial g_{lk}(\mathbf{x}, t; \mathbf{x}^i)}{\partial t} \tag{25}$$

$$p^*_{lk}(\mathbf{x}, t; \mathbf{x}^i) = \frac{\partial f_{lk}(\mathbf{x}, t; \mathbf{x}^i)}{\partial t} \tag{26}$$

where the traction solution, f_{lk}, is evaluated using the constitutive law for a linear elastic, homogeneous and isotropic solid by computing the spatial derivatives of the Green's function.

Displacements and tractions over the boundary are approximated at the time step $t = n\Delta t$ from their nodal values u^{mj}_k and p^{mj}_k, using the space interpolation functions $\phi^j(r)$ and $\psi^j(r)$, and the time interpolation functions $\eta^m(\tau)$ and $\mu^m(\tau)$ as:

$$\begin{aligned} c^i_{lk} u^i_k(\mathbf{x}^i, t) = \sum_{m=1}^{n} \sum_{j=1}^{Q} \Bigg\{ & \left[\int_{\Gamma_j} \int_{\Delta t_m} u^*_{lk}(\mathbf{x}, t-\tau; \mathbf{x}^i) \mu^m d\tau \psi^j \, d\Gamma \right] p^{mj}_k \\ & - \left[\int_{\Gamma_j} \int_{\Delta t_m} p^*_{lk}(\mathbf{x}, t-\tau; \mathbf{x}^i) \eta^m d\tau \phi^j \, d\Gamma \right] u^{mj}_k \Bigg\} \end{aligned} \tag{27}$$

where Q is the total number of boundary nodes and Γ_j represents the elements to which node j belongs.

Time kernels in Equation (27) are analytically integrated using constant and linear piecewise time interpolation functions $\mu^m(\tau)$ and $\eta^m(\tau)$ for tractions and displacements, respectively:

$$\begin{aligned} U^{nm}_{lk} &= \int_{\Delta t_m} u^*_{lk}(\mathbf{x}, t-\tau; \mathbf{x}^i) \mu^m d\tau \\ &= g_{lk}(\mathbf{x}, [n-m+1]\Delta t; \mathbf{x}^i) - g_{lk}(\mathbf{x}, [n-m]\Delta t; \mathbf{x}^i) \end{aligned} \tag{28}$$

$$\begin{aligned} P^{nm}_{lk} = \int_{\Delta t_m} p^*_{lk}(\mathbf{x}, t-\tau; \mathbf{x}^i) \eta^m d\tau = 1/\Delta t \, \big\{ & F_{lk}(\mathbf{x}, [n-m+1]\Delta t; \mathbf{x}^i) \\ & -2F_{lk}(\mathbf{x}, [n-m]\Delta t; \mathbf{x}^i) + F_{lk}(\mathbf{x}, [n-m-1]\Delta t; \mathbf{x}^i) \big\} \end{aligned} \tag{29}$$

where $\mathbf{F}(\mathbf{x}, t; \mathbf{x}^i)$ is the time integral of the traction tensor $\mathbf{f}(\mathbf{x}, t; \mathbf{x}^i)$.

After interpolating the boundary variables, the integral equation (27) becomes:

$$c^i_{lk} u^i_k(\mathbf{x}^i, t) = \sum_{m=1}^{n} \sum_{j=1}^{Q} \left\{ \left[\int_{\Gamma_j} U^{nm}_{lk} \psi^j \, d\Gamma \right] p^{mj}_k - \left[\int_{\Gamma_j} P^{nm}_{lk} d\tau \phi^j \, d\Gamma \right] u^{mj}_k \right\} \tag{30}$$

Equation (30) is written in a more compact form as:

$$c^i_{lk} u^{ni}_k = \sum_{m=1}^{n} \sum_{j=1}^{Q} \left[G^{nmij}_{lk} p^{mj}_k - \widehat{H}^{nmij}_{lk} u^{mj}_k \right] \tag{31}$$

Once the integral-free term c_{lk}^{i} is included in the system matrix, the integral representation for point i at time $t = n\Delta t$ becomes:

$$\mathbf{H}^{nn}\mathbf{u}^{n} = \mathbf{G}^{nn}\mathbf{p}^{n} + \sum_{m=1}^{n-1}\left[\mathbf{G}^{nm}\mathbf{p}^{m} - \mathbf{H}^{nm}\mathbf{u}^{m}\right] \tag{32}$$

where H_{lk}^{nmij} collects for c_{lk}^{i} when $i = j$ and $n = m$.

In this work nine-node rectangular quadratic boundary elements are used. Identical space interpolation shape functions $\phi^{j}(r)$ and $\psi^{j}(r)$ are assumed. The spatial integration is done only in those parts of an element under the effects of the fundamental solution waves, according to the causality condition of each term of the fundamental solution [25]. Each side of the element is divided into equal parts in the natural coordinate domain yielding an element subdivision.

Equation (32) yields a system of equations that is solved step by step to obtain the time variation of displacements and tractions at the boundary. After boundary unknowns are solved, the radiated wave field $\mathbf{u}_{r}^{n}$ at any internal point or at the free field is computed by means of the integral representation of the Somigliana identity:

$$\mathbf{u}_{r}^{n} = \sum_{m=1}^{n}\left(\mathbf{G}_{r}^{nm}\mathbf{p}^{m} - \widehat{\mathbf{H}}_{r}^{nm}\mathbf{u}^{m}\right) \tag{33}$$

where $\mathbf{G}_{r}^{nm}$ and $\widehat{\mathbf{H}}_{r}^{nm}$ are the boundary element matrices computed considering only domain point as source points.

The proposed BEM formulation is verified analysing the response of a homogeneous and a layered half-space due to a vertical impulsive point load. The half-space's properties were indicated in Section 2.

Figure 4 shows the vertical and radial response due to a impulsive vertical load at a point of the half-space surface at $r = 10\,\mathrm{m}$ from the source. In this figure can be observed the dispersive character of the wave propagation in the layered half-space mainly for the response at times higher than $t = r/c_{sL}$. The agreement between the computed results and those obtained from EDT 2.1 [26] toolbox is again quite good.

4 Coupled BEM-FEM formulation

This work uses the `SSIFiBo` toolbox[1] for `MATLAB` previously developed by Galvín and Romero [8, 18, 28]. The SSI problem is decomposed in two subdomains represented by the BEM and the FEM. The FEM module of the toolbox does not include any pre-processor. Instead, a gateway for commercial software allows importing directly the structure model. Coupling of both methods requires that the equilibrium of forces and the compatibility of displacements are fulfilled at the interface between the two subdomains. The coupling is performed directly and the equations of both subdomains are assembled into a global system of equations. The FEM equation is solved at each time step following an implicit time integration GN22 Newmark method [4, 29].

5 Experimental study

In this section, the proposed BEM-FEM model is experimentally validated by the measurements recorded at a site located at León, Spain. The dynamic soil characteristics at the measurement site were identified by means of a Spectral Analysis of Surface Waves test (SASW).

[1] http://personal.us.es/pedrogalvin/ssifibo.en.html

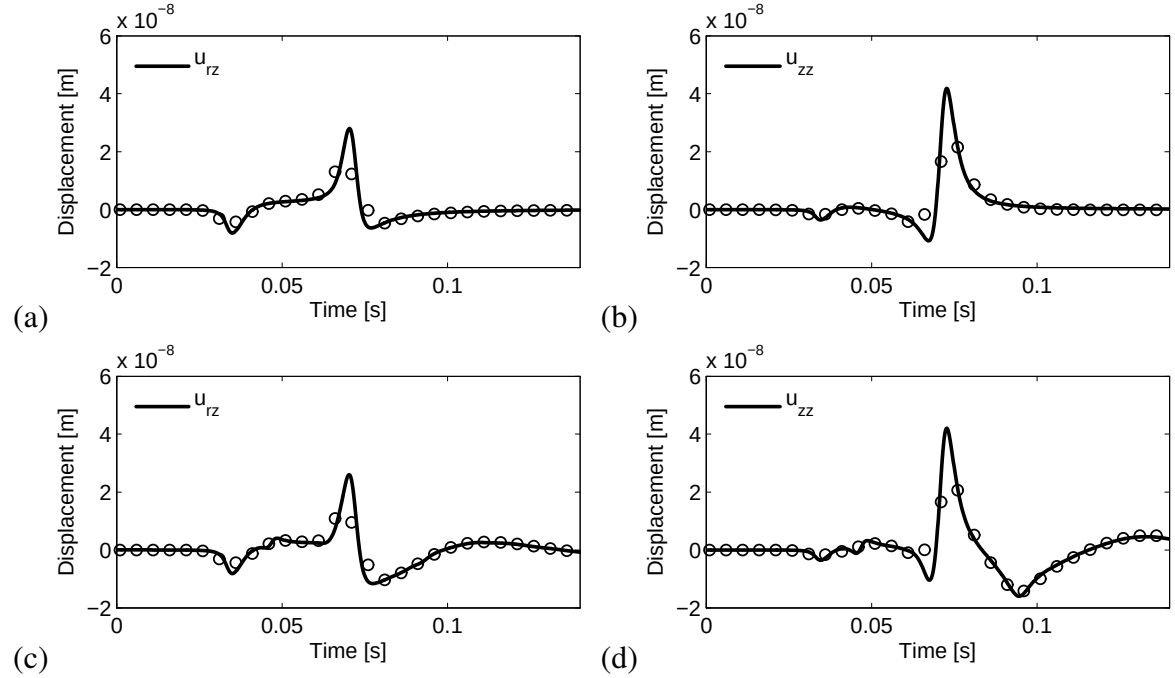


Figure 4: (a,c) Radial and (b,d) vertical displacement due to an impulsive vertical load applied at the surface of a (a,b) homogeneous and (c,d) layered half-space for a point located at the surface at $r = 10\,\mathrm{m}$ from the source: EDT 2.1 toolbox [26] (black line) and proposed method (black circles).

The vertical free field response due to hammer impacts applied to a $0.5\,\mathrm{m} \times 0.5\,\mathrm{m} \times 0.08\,\mathrm{m}$ aluminium foundation was measured using accelerometers located at the soil's surface (Figure 6.(a)). The load was measured by means of a force sensor in the hammer. Figure 6.(b) shows one of the accelerometers used to measure the free field response. Figure 5 shows the location of the aluminium foundation and the measurement line.

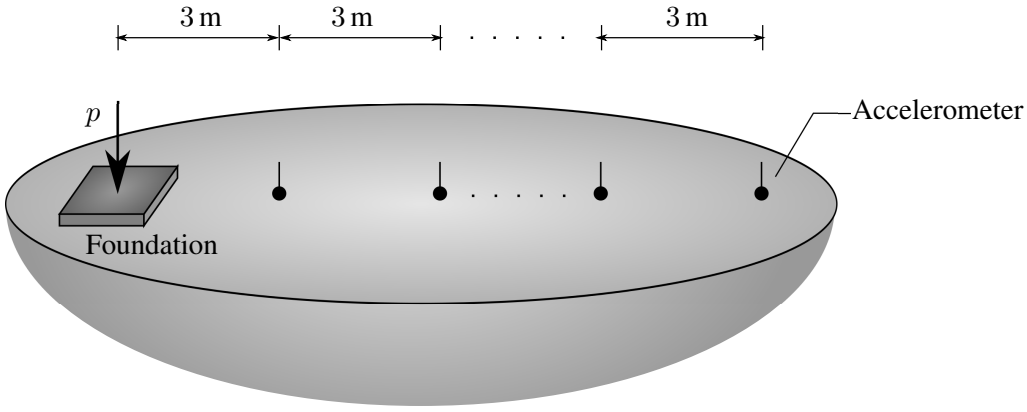


Figure 5: Location of foundation and accelerometers.

The shear wave velocity profile was identified from the SASW test by fitting the computed dispersion curve to the experimental dispersion curve of the fundamental Rayleigh wave at the site [30]. The results show that the soil can be represented by a single layer with a thickness $h_L = 4.1\,\mathrm{m}$ and a shear wave velocity $c_{sL} = 150\,\mathrm{m/s}$ on a half-space with a shear wave velocity $c_{sH} = 495\,\mathrm{m/s}$. A value of $1900\,\mathrm{kg/m^3}$ is assumed for the density of the layer and the half-

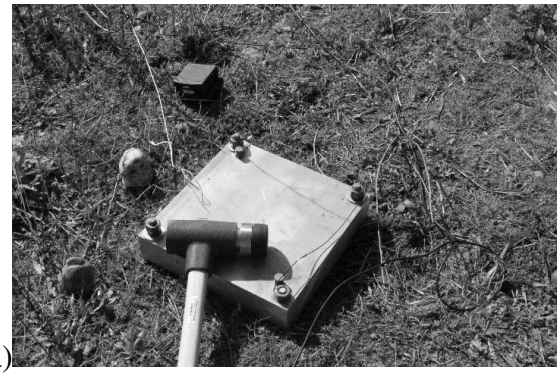
(a)  (b) 

Figure 6: (a) Aluminium foundation and impact hammer and (b) accelerometer anchored in the soil surface.

space. Poisson's ratio has been estimated from the geophysical tests as $\nu = 0.4$. For both, the layer and the half-space, a value of 0.06 was assumed for the material damping ratio ξ. The density was estimated from the geotechnical investigation. Its high value could be due to the soil was saturated. The dynamic soil characteristics are summarized in table 1.

	h [m]	c_p [m/s]	c_s [m/s]	ξ [-]	ν [-]	ρ [kg/m^3]
Layer	4.1	367	150	0.06	0.4	1900
Half-space	∞	1212	495	0.06	0.4	1900

Table 1: Dynamic soil characteristics.

The SASW test was modelled by the proposed numerical model. Figure 7 shows the discretization that it was used to compute the vertical soil displacements. The $0.08\,$m thick aluminium foundation was represented by 4 eight-node solid elements. The aluminium material had the following properties: Young's modulus $E = 70 \times 10^9\,$N/m^2, Poisson's ratio $\nu = 1/3$ and density $\rho = 2700\,$kg/m^3. The soil was represented as a layered half-space according to Table 1. Soil discretization extends only to soil-foundation interface using one nine-node rectangular quadratic boundary elements. A time step $\Delta t = 1 \times 10^{-3}\,$s was chosen according to the soil properties to ensure the stability of the methodology.

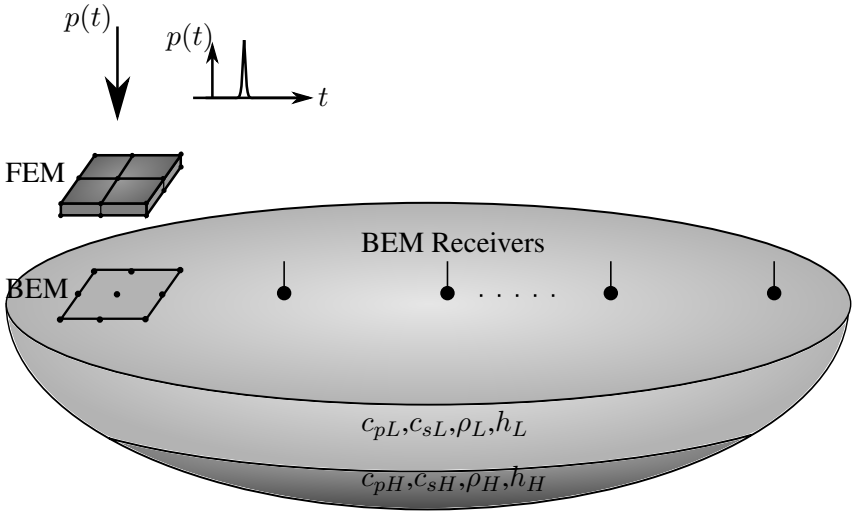


Figure 7: Soil-foundation discretization.

Figure 8 shows the experimental and numerical vertical soil displacements at points located

at the soil surface from $3\,\mathrm{m}$ to $24\,\mathrm{m}$ form the foundation. The signal period as well as its peak value correspond relatively well. However, the agreement between numerical and experimental results is not perfect, and it is required a more comprehensive analysis to explain the mismatches. Therefore, results in the frequency domain were computed.

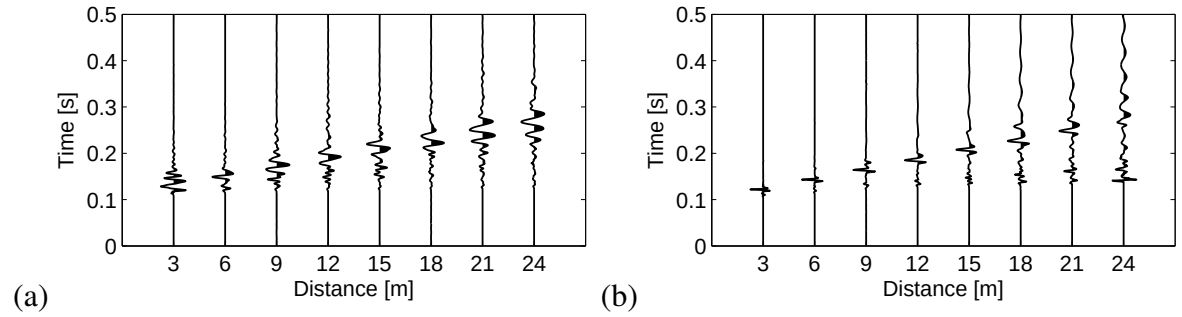


Figure 8: Free field acceleration due to a Ricker pulse: (a) experimental and (b) numerical results.

The transfer function was obtained by the Fourier transform from the numerical and experimental results as [26]:

$$\widehat{H}(r,\omega) = \frac{\widehat{A}(r,\omega)}{\widehat{F}(r,\omega)} \tag{34}$$

where $\widehat{A}(r,\omega)$ and $\widehat{F}(r,\omega)$ mean the soil acceleration and the applied load in the frequency domain.

Figure 9 shows the frequency response function at several points located at the soil surface. At points located at $3\,\mathrm{m}$, $6\,\mathrm{m}$ and $9\,\mathrm{m}$ from source, a relatively good agreement was obtained between the experimental records and the numerical results for frequencies below $70\,\mathrm{Hz}$, but the response was overestimated above $70\,\mathrm{Hz}$. At larger distances from the source, the numerical results underestimates the measured value at the frequency range between $20\,\mathrm{Hz}$ and $50\,\mathrm{Hz}$. This could be due to uncertain in the dynamic soil properties identification for higher frequencies.

Finally, results in the wavenumber-frequency domain were also obtained. The response in the wavenumber-frequency domain was computed by a Hankel transform as:

$$\widetilde{H}(k_r,\omega) = \int_0^\infty \widehat{H}(r,\omega) J_0(k_r,\omega) r dr \tag{35}$$

Figure 10 shows the resulting experimental and numerical wavenumber-frequency spectrum $\widetilde{H}(k_r,\omega)$ in terms of the phase velocity ω/k_r. The maxima in the wavenumber-frequency spectrum are due to the Rayleigh waves and they allow to estimate the dispersion curve. It can be observed from Figure 10.(a) that the experimental dispersion curve at a range from $12\,\mathrm{Hz}$ to $67\,\mathrm{Hz}$ was well-estimated. However, experimental records at frequencies below $8\,\mathrm{Hz}$, and above $70\,\mathrm{Hz}$ are affected by noise. Figure 10.(b) shows the numerical wavenumber-frequency spectrum which it is only correlated with the experimental results in the previously indicated frequency range.

The mismatches between numerical and experimental results could be explained by this analysis.

6 Numerical example

In this section, the dynamic behaviour of a framed wall building subjected to a uniform incident wave field is studied. The analysis of the wave propagation problem is done by decom-

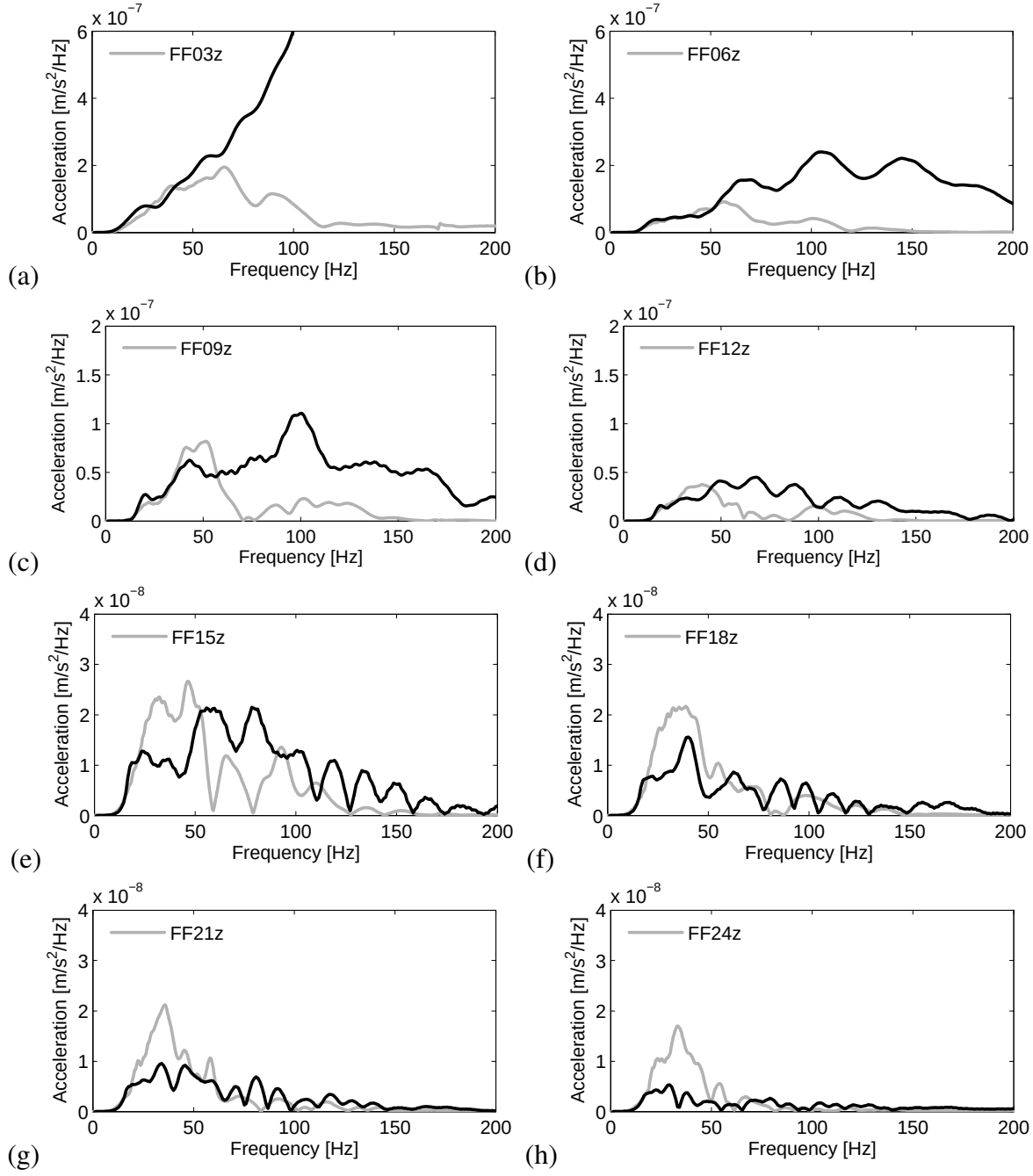


Figure 9: Free field frequency response function at (a) 3 m, (b) 6 m, (c) 9 m, (d) 12 m, (e) 15 m, (f) 18 m, (g) 21 m, and (h) 24 m, from the load: experimental (grey line) and numerical results (black line).

position of the total wave field in two terms: the incident and the scattered fields [3]. The wave propagation is solved by Equation (32). Once the scattered wave field is obtained, the incident wave field is superimposed to the radiation problem (Equation (33)).

The dimensions of the studied twelve-storey building were $12\,\text{m} \times 12\,\text{m} \times 36\,\text{m}$ (Figure 11). The structure consisted of eight concrete columns with $0.6\,\text{m} \times 0.4\,\text{m}$ section, four edge beams with $0.6\,\text{m} \times 0.2\,\text{m}$ section, and two framed concrete wall with $2.4\,\text{m} \times 0.15\,\text{m}$ section. The floors were simply supported concrete slabs with a thickness of $0.2\,\text{m}$. The floors consist of a two-dimensional frame with axial stiffness per unit length $EA = 1.433 \times 10^9$ N/m, bending stiffness

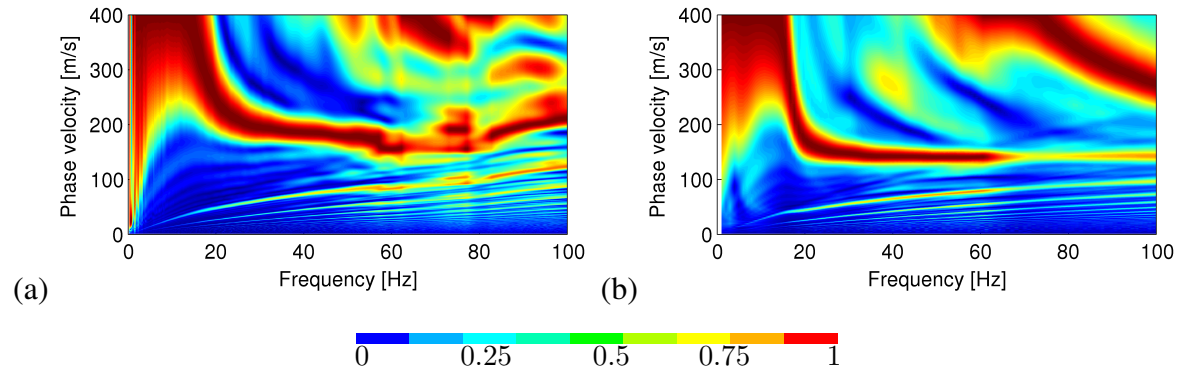


Figure 10: Frequency-wavenumber spectrum of the wave field: (a) experimental, and (b) numerical results.

per unit length $EI = 9.935 \times 10^6$ Nm, and a mass per unit area of $m = 172\,\text{kg/m}^2$. The structure was founded on a 1.0 m thick concrete slab. The concrete material had the following properties: Young's modulus $E = 20 \times 10^9\,\text{N/m}^2$, Poisson's ratio $\nu = 0.2$ and density $\rho = 2400\,\text{kg/m}^3$.

The structural damping was considered by a Rayleigh model [31]. The damping matrix, $\mathbf{C} = a_0\mathbf{M} + a_1\mathbf{K}$, was computed proportional to the mass, $\mathbf{M}$, and the stiffness, $\mathbf{K}$, matrices. A structural damping, $\zeta = 5\,\%$, was set for the first and second mode shapes. Proportional constant values were $a_0 = 0.4193\,\text{s}^{-1}$ and $a_1 = 0.0042\,\text{s}$.

The structure was discretized by 1248 two-node Euler-Bernoulli beam elements to represent columns and beams, and 3072 four-node shell elements for considering the floors and the framed walls. Figure 11.(b) shows the discretization of the building. The element size varies from 0.5 m to 1.25 m. This length was enough to represent adequately the structure dynamic behaviour.

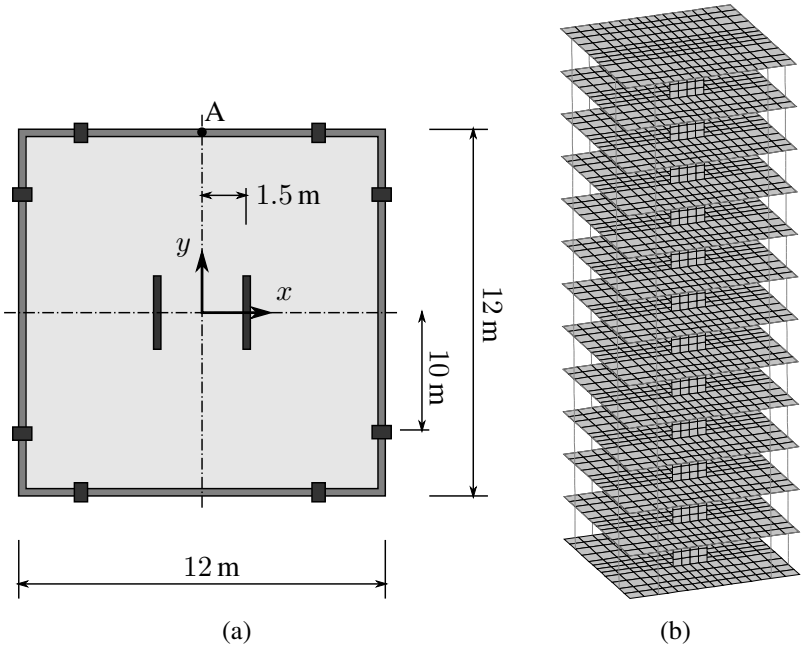


Figure 11: (a) Building plan geometry and (b) discretization.

Soil discretization extends only to soil-structure interface using 48 nine-node rectangular quadratic boundary elements. This problem was previously studied by Galvín and Romero [10] considering the soil as a homogeneous half-space. In this paper, two type of soils are

considered: a homogeneous half-space with $c_{pH} = 300\,\text{m/s}$, $c_{sH} = 150\,\text{m/s}$, $\xi_H = 0.05$, and $\rho_H = 1600\,\text{kg/m}^3$, and a layered half-space with the properties presented in Table 2. A time step $\Delta t = 4.50 \times 10^{-3}\,\text{s}$ was chosen according to each soil properties to ensure the stability of the methodology. Following, the computed results from both cases are compared.

	h [m]	c_p [m/s]	c_s [m/s]	ξ [-]	ρ [kg/m^3]
Layer	2	300	150	0.05	1600
Half-space	∞	600	300	0.05	1600

Table 2: Soil properties considered for the foundation of the building.

In this example, the building response due to a uniform incident wave field is analysed. The incident wave fields corresponded with plane SH propagating along x-axis. The incident waves induced an uniform acceleration at the soil-structure interface, $a(\mathbf{x}, t) = 1\delta(t)\,\text{m/s}^2$, where δ is the Dirac delta function.

Figure 12 shows the time history and frequency content of the horizontal displacement in the y-direction at the ground, and twelfth floors. Frequency response has been obtained by applying a direct Fourier Transform to the time history. Results for the observation point A (Figure 11.(a)) are shown. The floor response amplitudes increased with the level floor. The amplitudes decreased for the building founded on the layered half-space according to the higher stiffness.

The response for the building founded on the layered half-space shows two peaks at the resonance frequencies given by $f_1 = 0.83\,\text{Hz}$ and $f_2 = 2.89\,\text{Hz}$. These frequencies correspond with transversal mode shapes along y-direction. The fundamental period of the building was lightly higher for the homogeneous soil due its higher flexibility. At low frequencies the response is lower if the layered half-space is considered because the wavelength in the soil is large and the properties of the half-space are prevailing. At high frequencies, the wavelength is small compared to the thickness of the layer and the wave propagation in the soil is determined by the characteristics of the top layer.

Figure 13 shows the amplitude at the first resonance frequency at each floor for the different studied soil. The building response at the ground is similar for both considered cases. However, the soil flexibility caused a significantly increment of the amplitude with the story level.

7 Conclusions

This paper has developed a time domain BEM formulation using Green's function for a layered half-space as the fundamental solution. The layered half-space fundamental solution is advantageous because of soil discretization is limited to soil-structure interface and it allows easily considering soil stratification and material damping. The proposed fundamental solution has been verified by a benchmark problem.

The BEM formulation has been coupled with a FEM methodology to study soil-structure interaction problems. The obtained results have demonstrated that the influence of the soil stratification is large.

The proposed BEM-FEM numerical model has been applied to analysed actual ground vibrations. The methodology has been used to modelled a SASW test. The numerical results have been compared with the measured free field response.

The presented results show that the proposed methodology allows describing accurately the dynamic soil-structure interaction considering the influence of the soil stratification.

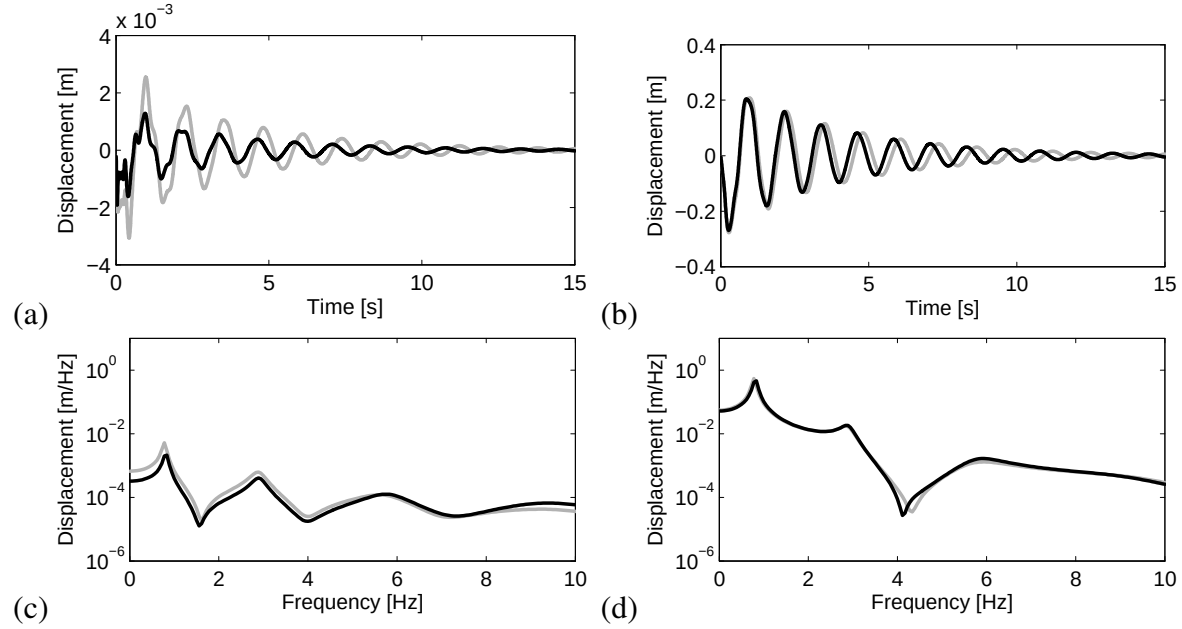


Figure 12: (a,b) Time history and (c,d) frequency content of the horizontal displacement along y-direction at the observation points A located at (a,c) ground floor and (b,d) 12^{th} floor, for a building founded on a homogeneous (grey line) and a layered half-space (black line).

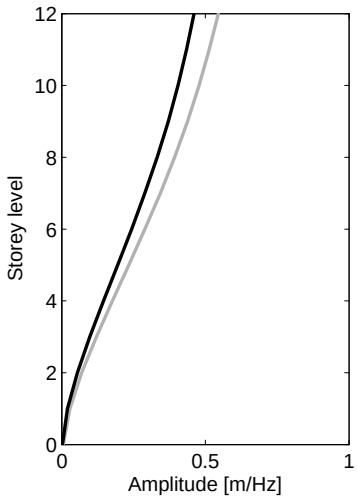


Figure 13: Maximum amplitude at the first resonance frequency at each floor, for a building founded on homogeneous (grey line) and layered half-space (black line).

Acknowledgments

This research was funded by the Spanish Ministry of Economy and Competitiveness (Ministerio de Economía y Competitividad) through research project BIA2013-43085-P. Financial support is gratefully acknowledged. The support given by the Andalusian Scientific Computing Centre (CICA) is also gratefully.

REFERENCES

[1] E. Kausel, Early history of soil-structure interaction. Soil Dynamics and Earthquake Engineering **30**(9), 822-832 (2010)

[2] A.C. Eringen, E.S. Suhubi, Elastodynamics, Volume 2, Linear theory. Academic Press, New York, USA (1975)

[3] J. Domínguez, Boundary elements in dynamics. Computational Mechanics Publications and Elsevier Aplied Science, Southampton (1993)

[4] O.C. Zienkiewicz, R.L. Taylor, The Finite Element Method, Volume I: The Basis. McGraw-Hill, New York (1967)

[5] J.J Aznárez, O. Maeso, J. Domínguez, BE analysis of bottom sediments in dynamic fluid-structure interaction problems. Engineering Analysis with Boundary Elements **30**(2), 124–136 (2006)

[6] E. Kausel, J.M. Roësset, Stiffness matrices for layered soils. Bulletin of the Seismological Society of America **71**, 1743–1761 (1981)

[7] S. François, L. Pyl, H.R. Masoumi, G. Degrande, The influence of dynamic soil-structure interaction on traffic induced vibrations in buildings. Soil Dynamics and Earthquake Engineering **27** 655–674 (2007).

[8] A. Romero, P. Galvín, J. Domínguez, 3D non-linear time domain FEM–BEM approach to soil–structure interaction problems. Engineering Analysis with Boundary Elements **37**(3), 501–512 (2013)

[9] C. Bode, R. Hirschauer, S.A. Savidis, Soil-structure interaction in the time domain using halfspace Green's functions. Soil Dynamics and Earthquake Engineering **22**(4), 283–295 (2002)

[10] P. Galvín, A. Romero, A 3D time domain numerical model based on half-space Green's function for soil-structure interaction analysis. Computational Mechanics **53**, 1073–1085 (2014)

[11] A.M. Kaynia, E. Kausel, Dynamics of piles and pile groups in layered soil media. Soil Dynamics and Earthquake Engineering **10**(8) 386–401 (1991)

[12] G. Lombaert, G. Degrande, D. Clouteau, The influence of the soil stratification on free field traffic-induced vibrations. Archive of Applied Mechanics **71** 661–678 (2001)

[13] L. Auersch, The effect of critically moving loads on the vibrations of soft soils and isolated railway tracks. Journal of Sound and Vibration **310**(3) 587–607 (2008)

[14] L. Auersch, Train induced ground vibrations: different amplitude-speed relations for two layered soils. Proceedings of the Institution of Mechanical Engineers, Part F: Journal of Rail and Rapid Transit **226**(5) 469–488 (2012)

[15] S. François, M. Schevenels, P. Galvín, G. Lombaert, G. Degrande, A 2.5D coupled FE-BE methodology for the dynamic interaction between longitudinally invariant structures and a layered halfspace. Computer Methods in Applied Mechanics and Engineering **199** 1536–1548 (2010)

[16] P. Galvín, S. François, M. Schevenels, E. Bongini, G. Degrande, G. Lombaert, A 2.5D coupled FE-BE model for the prediction of railway induced vibrations. Soil Dynamics and Earthquake Engineering **30** 1500–1512 (2010).

[17] D.C. Rizos, Z. Wang, Coupled BEM-FEM solutions for direct time domain soil-structure interaction analysis. Engineering Analysis with Boundary Elements **26**, 877–888 (2002)

[18] P. Galvín, A. Romero, J. Domínguez, Fully three-dimensional analysis of high-speed train-track-soil-structure dynamic interaction. Journal of Sound and Vibration **329**(24), 5147–5163 (2010)

[19] J. Park, E. Kausel, Response of layered half-space obtained directly in the time domain, Part I: SH sources. Bulletin of the Seismological Society of America **96**, 1725–1809 (2006)

[20] E. Kausel, J. Park, Response of layered half-space obtained directly in the time domain, Part II: SV-P and Three-Dimensional sources Bulletin of the Seismological Society of America **96**, 1810–1826 (2006)

[21] E. Kausel, J. Park, Impulse response of elastic half-space in the wavenumber-time domain. Journal of Engineering Mechanics, ASCE **130**(10) 1211–1222 (2004)

[22] J. Park, Wave Motion in finite and infinite media using the Thin-Layer Method. PhD thesis. Massachusetts Institute of Technology, Department of Civil and Environmental Engineering (2002)

[23] E. Kausel, Lamb's problem at its simplest. Proceedings of the Royal Society A: Mathematical, Physical and Engineering Sciences 469:20120462

[24] V. Mantic, A new formula for the C-matrix in the Somigliana identity. Journal of Elasticity **33**(3), 191–201 (1993)

[25] P. Galvín, J. Domínguez, Analysis of ground motion due to moving surface loads induced by high-speed trains. Engineering Analysis with Boundary Elements **31**(11), 931–941 (2007)

[26] M. Schevenels, S. François, G. Degrande, EDT: An ElastoDynamics Toolbox for MATLAB. Computers & Geosciences **35**(8) 1752–1754 (2009)

[27] M. Schevenels, G. Degrande, S. François, EDT: An ElastoDynamics Toolbox for MATLAB. Proceedings of the Inaugural International Conference of the Engineering Mechanics Institute (EM08), Minneapolis, Minnesota, U.S.A., (2008).

[28] P. Galvín, A. Romero:, A MATLAB toolbox for soil-structure interaction analysis with finite and boundary elements. Soil Dynamics and Earthquake Engineering **57**, 10–14 (2014)

[29] N.M. Newmark, A method of computation for structural dynamics. ASCE Journal of the Engineering Mechanics Division **85**(1), 67–94 (1959)

[30] ADIF, Estudio vibratorio. Línea de alta velocidad Madrid-Asturias. Tramo: Palencia-León. Technical report (in Spanish), (2009)

[31] R.W. Clough, J. Penzien, Dynamic of Structures. McGraw-Hill, New York (1975)

COMPDYN 2015
5th ECCOMAS Thematic Conference on
Computational Methods in Structural Dynamics and Earthquake Engineering
M. Papadrakakis, V. Papadopoulos, V. Plevris (eds.)
Crete Island, Greece, 25–27 May 2015

THE ROLE OF SOIL-STRUCTURE INTERACTION IN THE REDISTRIBUTION OF INTERNAL FORCES IN CONCRETE BUILDINGS DUE TO SEISMIC EXCITATION

George E. Mantzaras[1], and Dimitris L. Karabalis[2]*

[1] Civil Engineer Dipl. MSc.
44 Alexandras Av., 11473 Athens, Greece
e-mail: mantzaras@yahoo.com

[2] Department of Civil Engineering, University of Patras
26504 Rio, Greece
e-mail: karabali@upatras.gr

Keywords: Seismic analysis, concrete structures, soil-structure interaction.

Abstract. *This work studies the role of soil-structure interaction in the redistribution of internal forces among the various vertical load bearing elements of concrete buildings due to seismic excitation. According to the Greek and European Design Codes the columns are designed assuming a fixed base. However, as it is shown in this work, under certain conditions, this is not the critical design state. Soil-structure interaction could lead to redistributed internal forces considerably higher than those predicted under the fixed base assumption. For the purposes of this study a number of "common" simple 3-D concrete frames and their foundations are designed and analyzed according to the specifications of the Greek Earthquake Design Code. Subsequently the foundations are substituted by a system of springs, dashpots and added masses, simulating the phenomenon of soil-structure interaction and the frames are reanalyzed. In both cases, i.e. fixed base or soil-structure interaction, the structures are subjected to artificial seismic motions consistent with acceptable design spectra. Comparison studies between the two assumptions are conducted and conclusions with practical interest are drawn.*

* Correspondence to: Dimitris L. Karabalis, Department of Civil Engineering, University of Patras, 26504 Rio, Greece, e-mail: karabali@upatras.gr

1 INTRODUCTION

According to the Greek Design Codes [1,2] and the equivalent European Codes, e.g. EC8 [3], the analysis and design of structures, especially buildings, due to seismic excitation, should be implemented under the assumption of complete fixity at the base of all vertical elements. This assumption is considered to be on the safe side since, according to this line of thought, it causes maximum internal forces in the vertical load bearing elements. Subsequently the foundations are designed for these internal forces, without taking into consideration the interaction between the soil and the structure. In this work it is shown that, under certain conditions, this assumption does not lead to a critical design state.

In general, soil-structure interaction (SSI) is divided into two components, the kinematic interaction, which is significant in deep and embedded foundations, and the inertial interaction which is always present. In this work only surface foundations are analyzed and, thus, the investigation is limited to inertial interaction. In these cases SSI causes a, usually small, increase, as compared to the fixed base model, of the basic modal period(s) of the structure. Taking under consideration the design spectra used by most design codes, i.e. EC8 [3], Greek Seismic Design Code [2], etc., this usually leads to a reduction of the base shear force while the overall displacements are increased. If the foundation system (soil and structure) of the building is stiff enough, the distribution of internal forces among various vertical elements remains close to that predicted by the fixed base assumption. However, if the soil flexibility allows appreciable deformation under individual footings, in the presence or not of tie beams, then a redistribution of internal forces takes place (as compared to the fixed base assumption), which may lead to a substantial increase of internal forces to some vertical elements and reduction to others, while at the same time the total base shear is actually reduced. In order to specify and quantify the role of SSI in this phenomenon, the following methodology is used.

A. Simple, 3-D concrete framed structures are designed so that they are marginally adequate according to the requirements of the Greek Design Codes [1,2]. The foundation consists of independent footings, under each vertical element, connected with tie beams. The above structures, under the fixed base assumption, are subjected to a seismic motion in the form of an artificial accelerogram, consistent to code specified design spectra [2]. Linear time step analyses are performed to each of these structures and the maximum internal forces of the vertical elements are recorded.
B. In order to take under consideration the deformability of the soil and the SSI effect, the previous fixed foundations are substituted by a system of frequency independent springs, dashpots and lumped masses. The produced structural systems are subjected to the same seismic actions (artificial accelerogram) and the internal forces of the vertical elements are recorded again.
C. Finally the results of the above two analyses, with and without SSI, are compared and conclusions are drawn.

2 METHODOLOGY

2.1 Design of the structures

Fifteen simple structures have been designed, in order to be marginally adequate according to the requirements of the Greek Design Codes [1,2]. Most of them are one-storey structures with the storey high kept constant at h=3m, in all cases.

The internal forces of all vertical elements due to seismic excitation, are computed using modal response spectrum analysis and the CQC method. The elastic pseudo-acceleration design spectrum, as specified by the Greek Earthquake Design Code [2], is used, where the im-

portance factor (γ_I), the foundation factor (θ) and the damping correction factor (n) are equal to unit. The spectrum amplification factor (β_0) is equal to 2,5 and, assuming soil category C with average wave velocity v_s=200m/sec, the characteristic periods T_1 and T_2 are 0,20sec and 0,80sec respectively. The peak ground acceleration (A) is assumed at 0,36g while the behavior factor (q) is taken as unit, since linear analyses are conducted.

The main code requirements can be stated briefly as:

a) Limitation of interstorey drift Δ should be limited as

$$\frac{\Delta}{h} \le 0{,}005 \qquad \frac{N_{st}\Delta}{V_{st}h} \le 0{,}10 \tag{1}$$

where N_{st} and V_{st} are the storey axial and shear forces, respectively.

b) Resistance of vertical elements to shear force and biaxial bending with axial force.

In order to achieve a marginally adequate structure the storey mass and the reinforcement of the vertical elements is altered until all vertical elements acquire a capacity ratio (C.R.) near to unit. In most cases the critical requirement is the resistance to biaxial bending with axial force. Subsequently the required foundations are designed according to the usual fixed base assumption [1].

2.2 Soil-Structure Interaction SSI

The interaction between the soil and the structure is considered via a frequency independent mass-spring-dashpot model representing the interaction forces at the foundation-soil interface. Among the various available such models, simulating a linear elastic, homogeneous, isotropic half space, the one proposed by Mulliken & Karabalis [4] is used in this work and is reproduced in Table 1 for easy reference.

	Equivalent half width, a	Equivalent radius, r_0	Mass (inertia) ratio, β	Soil mass (inertia), m_v	Stiffness, K	Damping, C
Vertical	$0{,}5\sqrt{l_x l_y}$	$\frac{2a}{\sqrt{\pi}}$	$\frac{1-\nu}{4}\frac{m}{\rho r_0^3}$	$\frac{0{,}27m}{\beta}$	$\frac{4{,}7Ga}{1-\nu}$	$\frac{0{,}8a}{V_s}K$
Horizontal	$0{,}5\sqrt{l_x l_y}$	$\frac{2a}{\sqrt{\pi}}$	$\frac{7-8\nu}{32(1-\nu)}\frac{m}{\rho r_0^3}$	$\frac{0{,}095m}{\beta}$	$\frac{9{,}2Ga}{2-\nu}$	$\frac{0{,}163a}{V_s}K$
Rotational about x	$0{,}5\sqrt{l_x l_y^3}$	$\frac{2a}{\sqrt[4]{3\pi}}$	$\frac{3(1-\nu)}{8}\frac{m}{\rho r_0^5}$	$\frac{0{,}24m}{\beta}$	$\frac{4Ga^3}{1-\nu}$	$\frac{0{,}6a}{V_s}K$
Rotational about y	$0{,}5\sqrt{l_x^3 l_y}$	$\frac{2a}{\sqrt[4]{3\pi}}$	$\frac{3(1-\nu)}{8}\frac{m}{\rho r_0^5}$	$\frac{0{,}24m}{\beta}$	$\frac{4Ga^3}{1-\nu}$	$\frac{0{,}6a}{V_s}K$
Torsion	$\max\left\{\begin{matrix}0{,}5\sqrt{l_x l_y^3}\\ 0{,}5\sqrt{l_x^3 l_y}\end{matrix}\right\}$	$\frac{2a}{\sqrt[4]{3\pi}}$	$\frac{m}{\rho r_0^5}$	$\frac{0{,}045m}{\beta}$	$8{,}31Ga^3$	$\frac{0{,}127a}{V_s}K$

Table 1: Mass, stiffness and damping coefficients

For each degree of freedom of the rigid rectangular foundation the adopted model consists of a lumped mass M which is the sum of the total mass (or rotational inertia) of foundation (m) and an interacting soil mass (m_v), a spring with stiffness K and a dashpot with constant C. The produced mass, spring and dashpot constants for the six possible degrees of freedom of each foundation are independent of each other, i.e. relaxed boundary conditions are assumed at the soil-foundation interface.

In Table 1 the values of the proposed coefficients for mass, stiffness and damping coefficients are shown, for a rectangular foundation with sides l_x and l_y. The symbols G, ρ and V_s stand for the shear modulus, mass density and shear wave velocity, respectively, of the soil medium.

2.3 Linear time step analysis

Although the structures used in this work are designed on the basis of the specified design spectrum and the usual design code procedures [1,2] outline previously, the quantities of interest, i.e. internal forces and moments of vertical elements, are obtained via time domain analysis. For this purpose an artificial accelerogram, consistent with design spectra, is produced by processing a random signal in time and frequency domain, with duration of 30 sec. This artificial accelerogram is amplified by 4,4% in order to reach the design code requirement ($E_x \pm 0{,}3E_y$) for a combination of seismic actions in two orthogonal horizontal directions. The same seismic action is applied to all structures analyzed in this work, regardless of the boundary condition at the base, i.e. fixed-base or SSI, in eight distinct directions as shown in Figure 1.

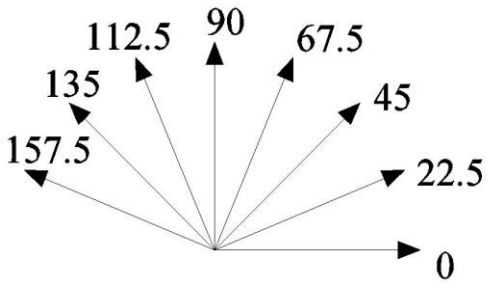


Figure 1: Directions of seismic excitation

The structures are modeled by usual beam and shell finite elements and masses lumped at the nodal points of the finite element mesh. A damping matrix $[C_{sup}]$ proportional to the stiffness matrix $[K_{sup}]$ of the fixed-base superstructure is also assumed. The coefficient of proportionality b, defined in the usual way as

$$b = \frac{\zeta T}{\pi} \tag{2}$$

where ζ=0,05 and T is a weighted average of the mean periods of the structure in two orthogonal directions x and y which are given by

$$T_i = \frac{\sum_{n=1}^{N} T_n M_n^*}{\sum_{n=1}^{N} M_n^*} \quad i = x, y \tag{3}$$

whith the modal periods T_n and effective masses M_n^* computed in the two orthogonal directions of seismic action. The Newmark average acceleration method is used for the computation of the time domain response of each structure and the identification of the maximum internal forces for each vertical element: shear forces in each direction and the capacity ratio in biaxial bending with axial force. Also the maximum total base shear forces in each direction are recorded.

The above procedures are applied to the same structures either under fixed-base conditions or considering the interaction with the soil. Finally, the maximum internal forces recorded in each structure, under both boundary conditions, are compared and conclusions are drawn.

3 NUMERICAL RESULTS

In Figures 2 to 16 the structures designed and analyzed in this work are shown. On the same figures the results obtained from the comparison between the fixed-base and SSI boundary conditions are recorded. Thus, next to each vertical element three coefficients are shown, namely: V_x, V_y and M-N, which reflect, respectively, the variation of shear force in the directions x and y and the capacity ratio in biaxial bending with normal force. Each coefficient is the ratio of the maximum quantity recorded from the analysis with SSI to the respective maximum force from the analysis of the same structure with a fixed-base. In addition, the maximum M-N capacity ratio, of the SSI case only, is shown in brackets, as an indication of the actual structural sufficiency (or insufficiency) of the corresponding vertical element. It should be noted that at the design stage the M-N capacity ratio is kept as close to unity as possible.

The coefficients V_x, V_y shown at the top of each figure designate the ratio of the maximum recorded total base shear force in each direction when SSI is considered to the same maximum quantity when a fixed base boundary condition is implemented..

Structure 1, shown in Figure 2, is a simple, one storey, square structure with basic modal period 0,21sec, when the base is fixed. As expected, a reduction of base shear force appears which is uniformly distributed to all four columns.

Structure 2, in Figure 3, is also a one storey, square structure with eccentricity in the x-axis equal to 25% of the respective length of structure. The basic modal periods are T_x=0,21sec and T_y=0,19sec, for the fixed-based structure. A reduction of base shear force appears in both directions but, as it is expected, it is not distributed uniformly among all columns. Stiffer columns are relieved more than the less stiff. The reduction of the base shear in the x direction is 13%. The respective shear of stiffer columns reduces by 16%, and of the less stiff columns by 9%. The same behavior is observed in the y direction as well, with a reduction of total base shear force reaching 17%, stiffer columns shear 20% and less stiff columns 14%.

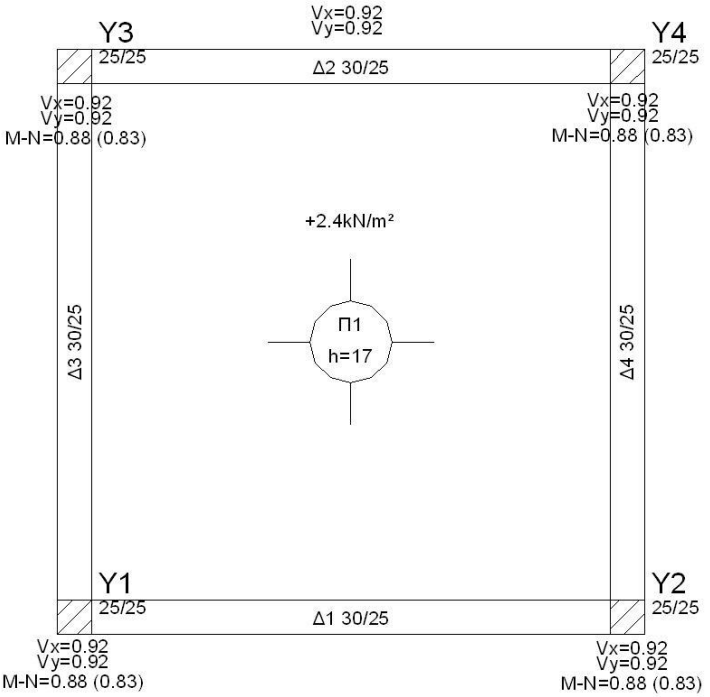


Figure 2: Structure 1

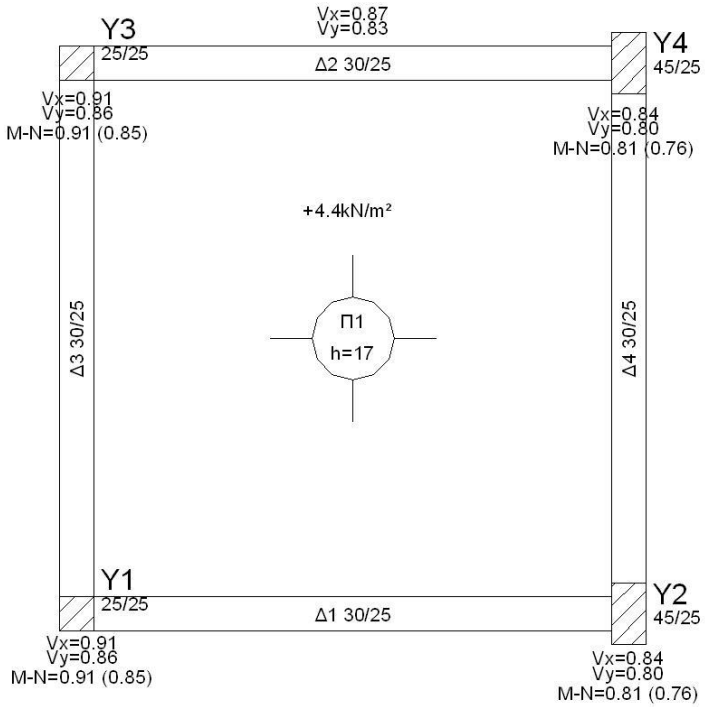


Figure 3: Structure 2

Structure 3, in Figure 4, is similar to structure 2 but with an eccentricity of 42% of the respective length of the structure. The basic modal period in x direction is 0,20sec and in y direction is 0,17sec, for the fixed-base structure. An increment of 16% of base shear force in the y-direction, compared to the fixed-base structure, appears when SSI is considered. This was expected since the basic modal period of the fixed-base structure is less than 0,20 sec. In the x-direction a further reduction of base shear appears. In both directions the variations in base

shear are not distributed uniformly, as the stiffer columns are more relieved than the less stiff ones. The increase of base shear by 16% in y-direction results in an increase of the respective shear force by 24% in less stiff columns, and by only 11% in stiffer columns. The reduction by 22% of base shear force in x direction causes a 30% reduction to stiffer columns and only 3% reduction to less stiffer elements. All columns are acceptable according to the M-N criterion.

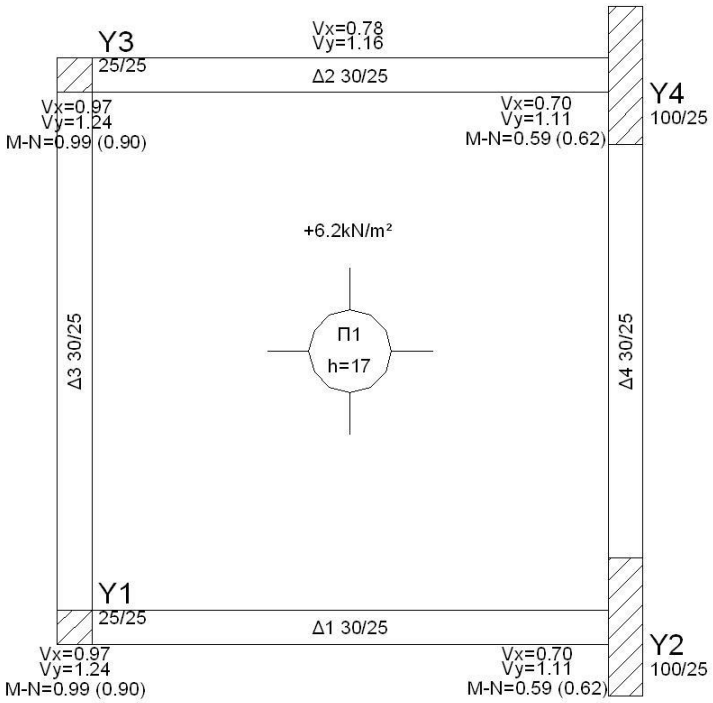


Figure 4: Structure 3

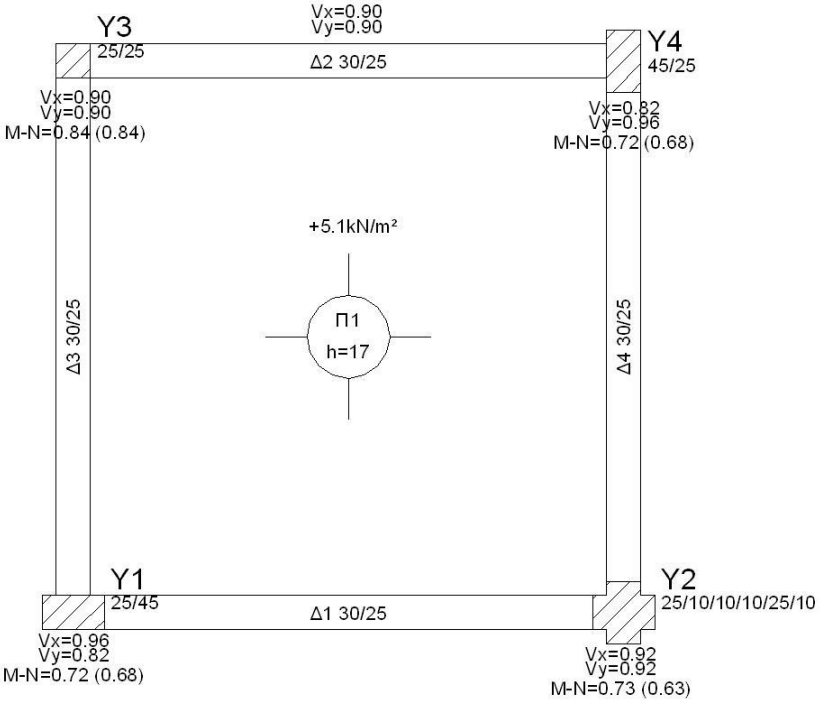


Figure 5: Structure 4

Structure 4, in Figure 5, has eccentricity of 22% of the respective length of the structure, in both axes. The basic modal period of fixed structure in both directions is 0,17sec. A reduction of base shear force in both directions appears when SSI is considered, as compared to the fixed-base condition, but again it's distribution is not uniform. Still all vertical elements are sufficient according to the M-N criterion.

In structure 5, in Figure 6, a larger eccentricity, equal to 40%, in both directions, is applied and as result the total base shear increases at 42%, compared to the fixed-base condition. This is mainly due to the increased overall stiffness of the structure, which is indicated by the lower basic modal period of 0,11sec. However, the distribution of the base shear changes in a non-uniform manner with less stiff elements receiving most of the change (as compared to the fixed base condition) and even becoming insufficient according to the M-N criterion.

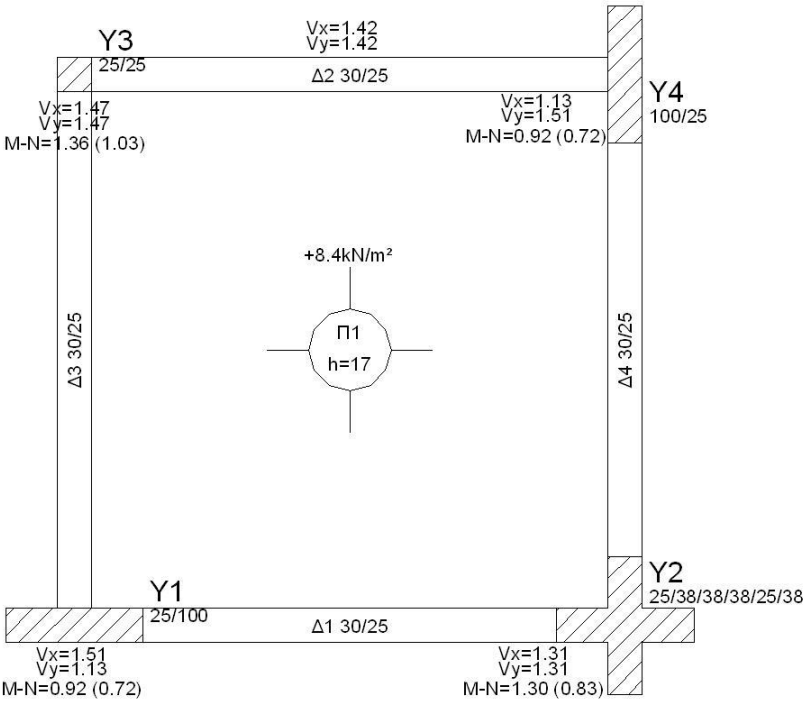


Figure 6: Structure 5

From the analyses of structures 1 to 5 it is not clear if the geometrical irregularity (eccentricity) or the differences in stiffness among the various vertical elements or both is responsible for the redistribution of the internal forces. So the next two structures, i.e. structure 6 in Figure 7, and structure 7 in Figure 8, have the same eccentricity in one direction (17%) and the same basic modal periods (0,17sec in x and 0,20sec in y), but in structure 6 this is achieved with three stiffer columns in one side while in structure 7 with one stiffer column.

In structure 6 a small reduction of base shear forces appears (5% in x and 1% in y), but in structure 7 an increase appears especially in the strong direction (12% in x and 5% in y). In both structures the phenomenon of the stiffer elements being relieved, when SSI is present, is apparent, while at the same time the weaker elements are further stressed. However, this is more intense in structure 7 where the shear force relief of the strong element is 11% and at the same time its neighboring elements experience substantial increases of up to 79%. Thus, it seems that the determining factor for the redistribution of shear force is the differences in stiffness between vertical elements. The stiffer elements are relieved while the highest in-

creases appear in the elements connected to them. In addition, column Y5, directly connected to the strong column Y2 of structure 7, became insufficient in view of the M-N criterion.

Structure 8, shown in Figure 9, is designed with a single stiffer element at its center which receives 30% of the total base shear force, under the assumption of a fixed base. Similarly structure 9, in Figure 10, has an even stiffer element at the same location which receives 50% of the total base shear force. In both cases the total base shear force presents a minor change when SSI is considered. However, due to the redistribution of shear forces the stiffer central columns of structures 8 and 9 are relieved by 13% and 32%, respectively while the largest increases occur at the columns directly connected to the stiffer central column which undertake 25% and 43%, respectively, more shear force under SSI conditions than that under a fixed-base assumption. All these phenomena are, of course, more intense in structure 9, in which the difference in stiffness between the vertical elements is more pronounced. Furthermore, all the columns in the periphery of structure 9 connected to the central column become insufficient for combined biaxial bending and axial force (M-N criterion).

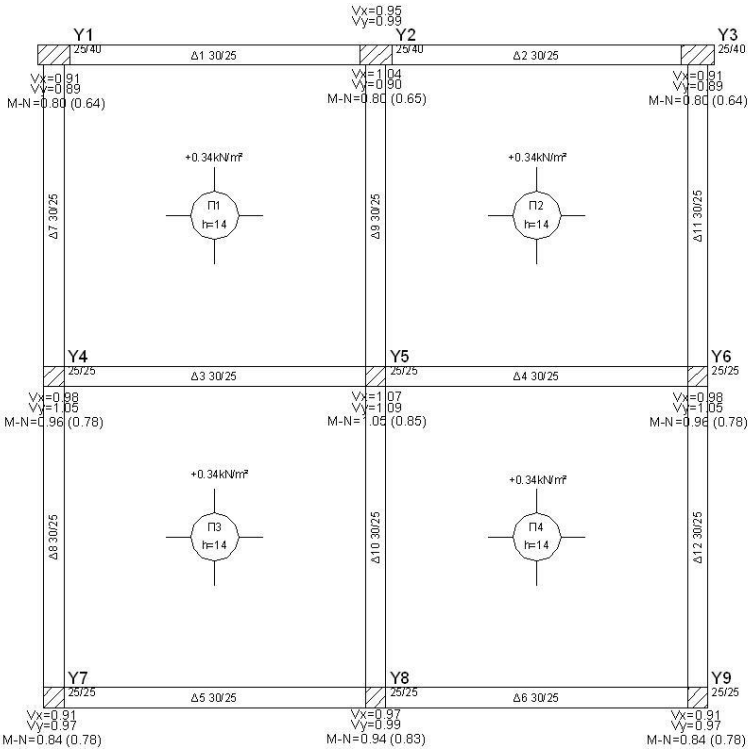


Figure 7: Structure 6

In contrast to structures 8 and 9, structures 10 in Figure 11, and structure 11 in Figure 12, are designed with the stiffer vertical elements in their perimeter, following the usual code suggestions. Under the fixed-base assumption these stronger elements undertake 30% and 50%, respectively, of the total base shear force. In both cases the total base shear force remains virtually unchanged under any boundary condition assumption at the base of the structures.

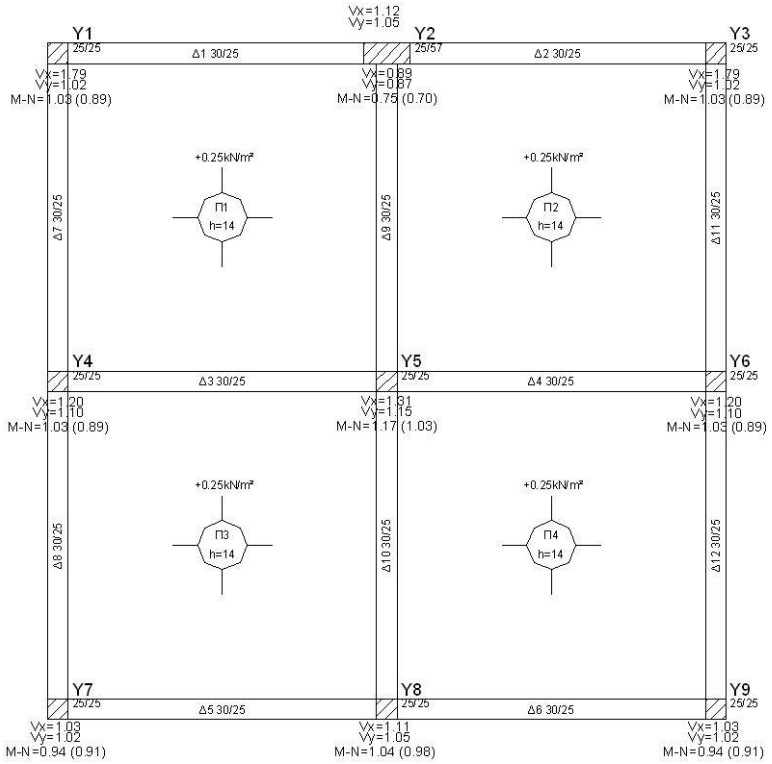


Figure 8: Structure 7

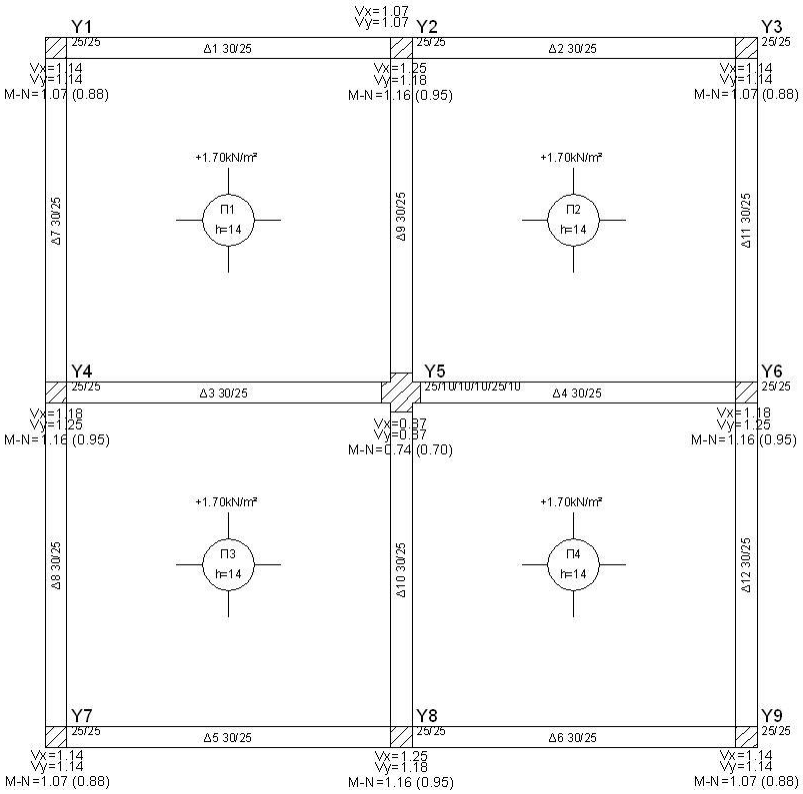


Figure 9: Structure 8

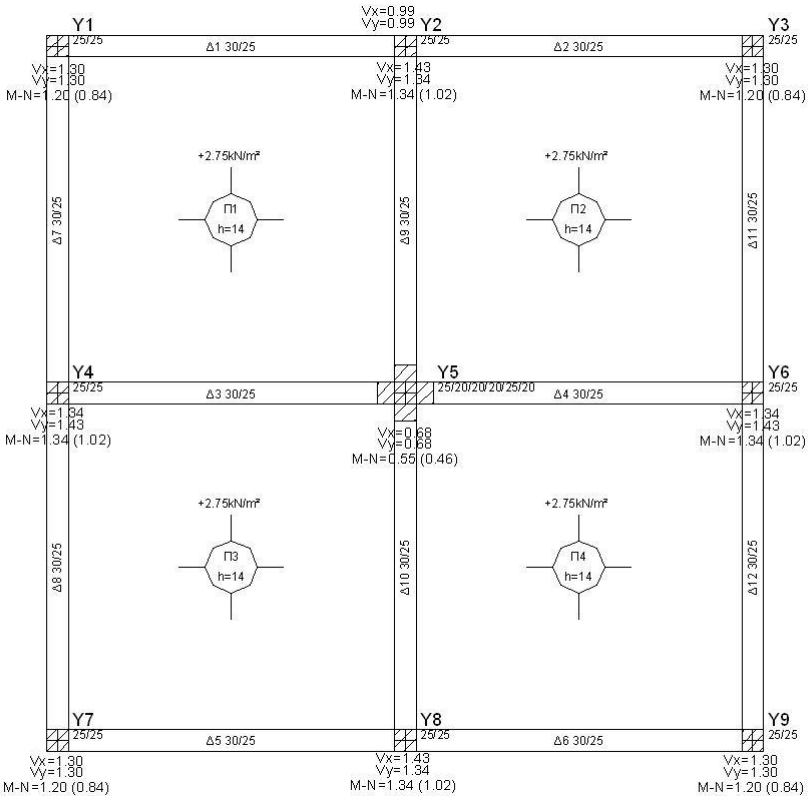


Figure 10: Structure 9

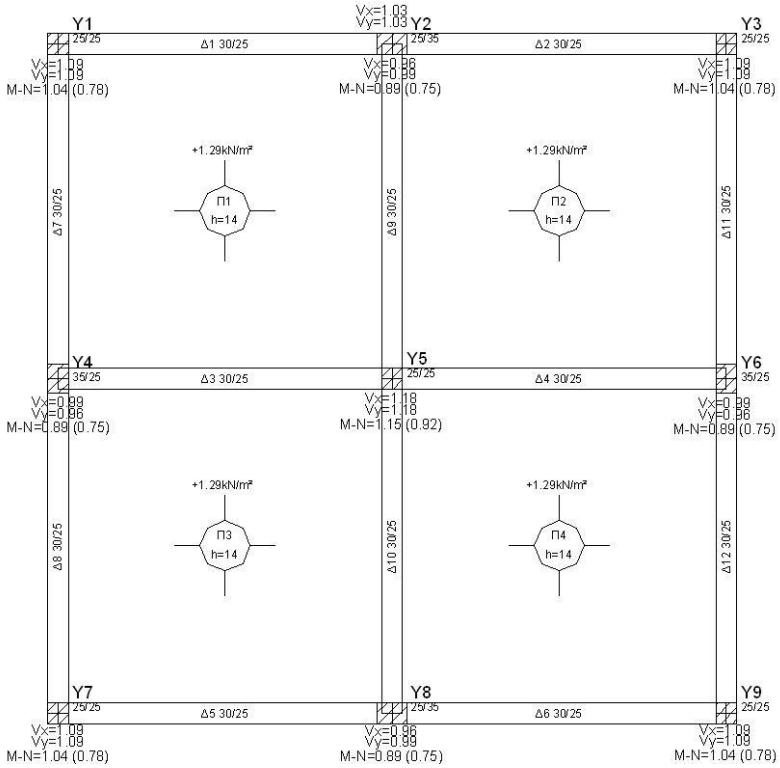


Figure 11: Structure 10

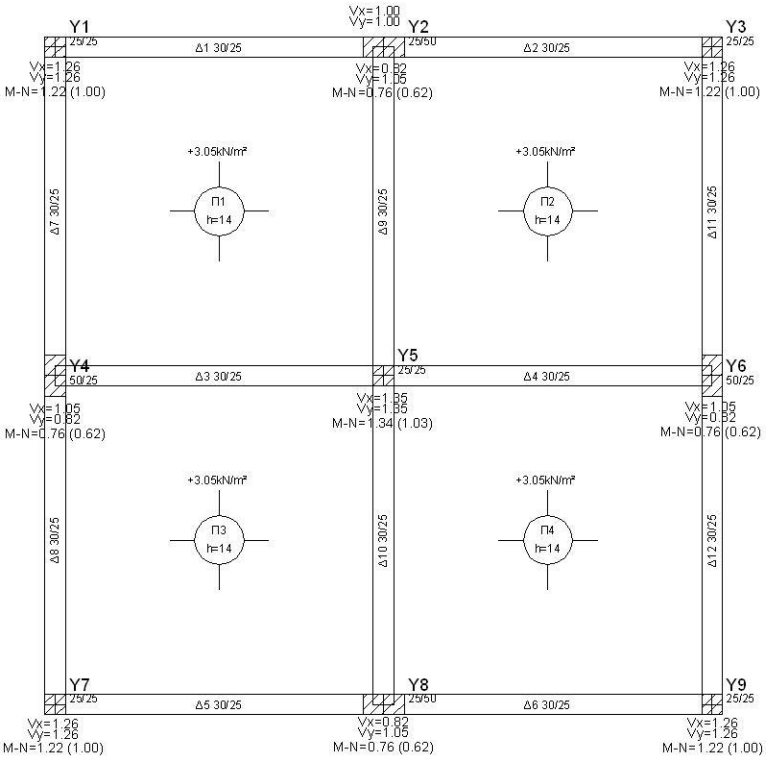


Figure 12: Structure 11

However, the redistribution of shear forces presents the same characteristics as for the structures 8 and 9 but it is less intense. A reduction by 4% and 18%, respectively, to stiffer elements and an increase by 18% and 35% to the less stiff elements is observed. This is another indication that the main role in the redistribution of shear forces belongs to the difference in stiffness between vertical elements while the position of the stronger and weaker elements is secondary but not insignificant. In structure 11 the central column, mainly, and the corner columns become insufficient in view of the M-N criterion.

Structure 12, in Figure 13, has two stiffer columns only in the x direction to which, under the fixed base assumption, corresponds 55% of the total base shear force. As a result its basic modal period is different in the two main axes (0,18sec in x direction and 0,23sec in y direction). This column arrangement causes, under SSI conditions, an 11% increase of total base shear force in the x direction, while in the y direction remains virtually unchanged. The redistribution of shear force, when SSI is considered, presents the same features as in the previous structures, but more intense. Specifically, the stiffer elements experience a reduction 11%, while the less stiff elements are called to withstand up to 51% more shear force.

Structure 13, in Figure 14, and structure 14, in Figure 15, follow a similar arrangement of vertical elements as in structure 11, with the stiffer columns in the perimeter, in both directions, which resist 50% of the total base shear force under fixed-base conditions. However, the spans between columns are not equal in both directions. The results of the analysis show that the redistribution of shear forces, when SSI is considered, is reaching up to 45%, at the weak central column which is connected to stiffer columns in both directions. The corner columns, connected to stiffer columns in one direction, are also strongly affected. Similarly, the central column of structure 13 and one corner column of structure 14 are strongly adversely affected as far as the M-N criterion is concerned, when SSI is considered. Thus, the proximity to stiffer elements seems to be another decisive factor to the redistribution of shear forces.

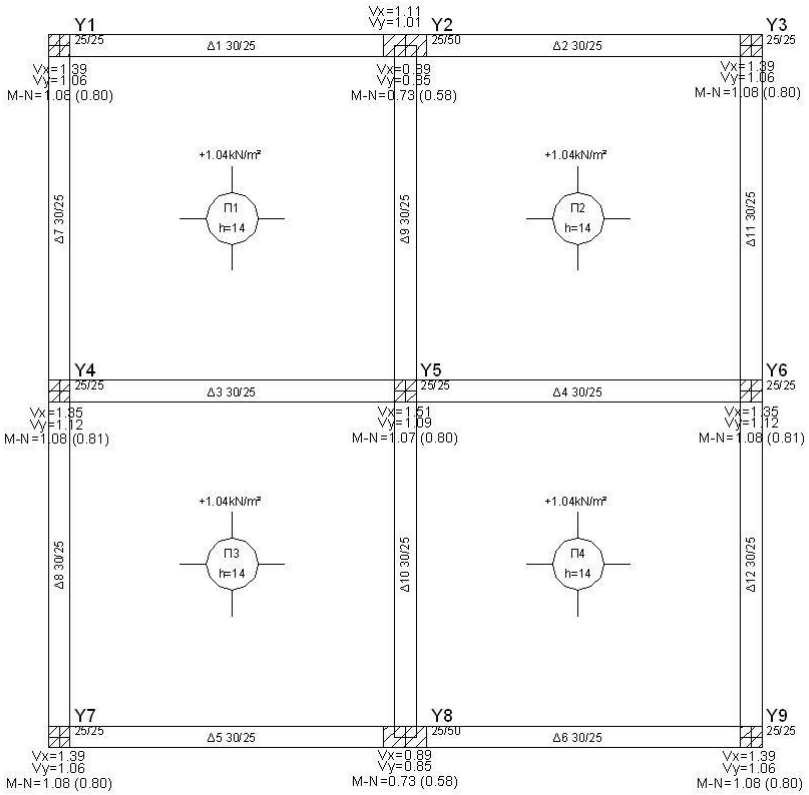


Figure 13: Structure 12

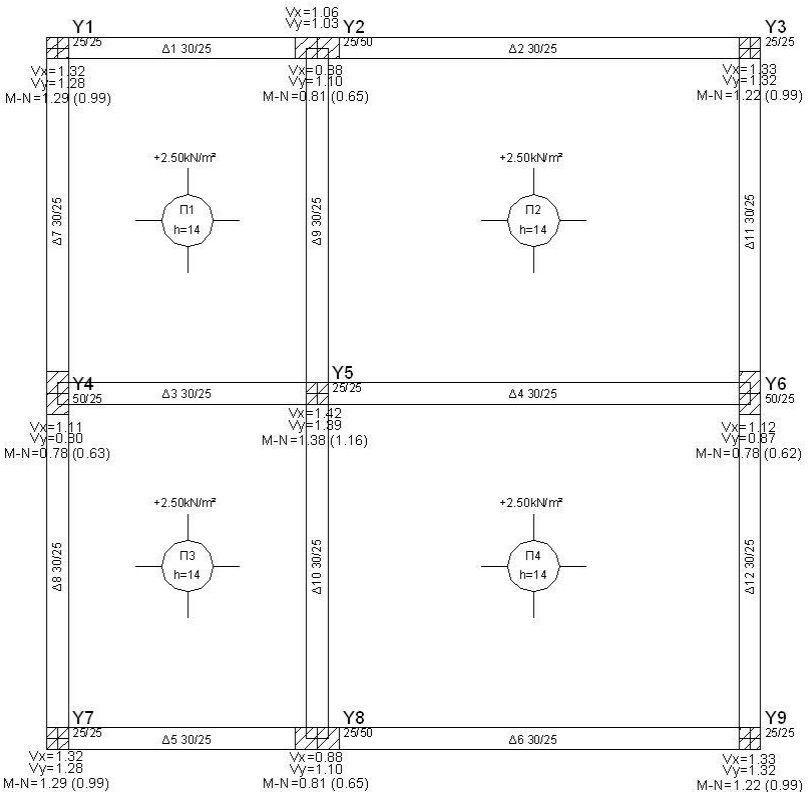


Figure 14: Structure 13

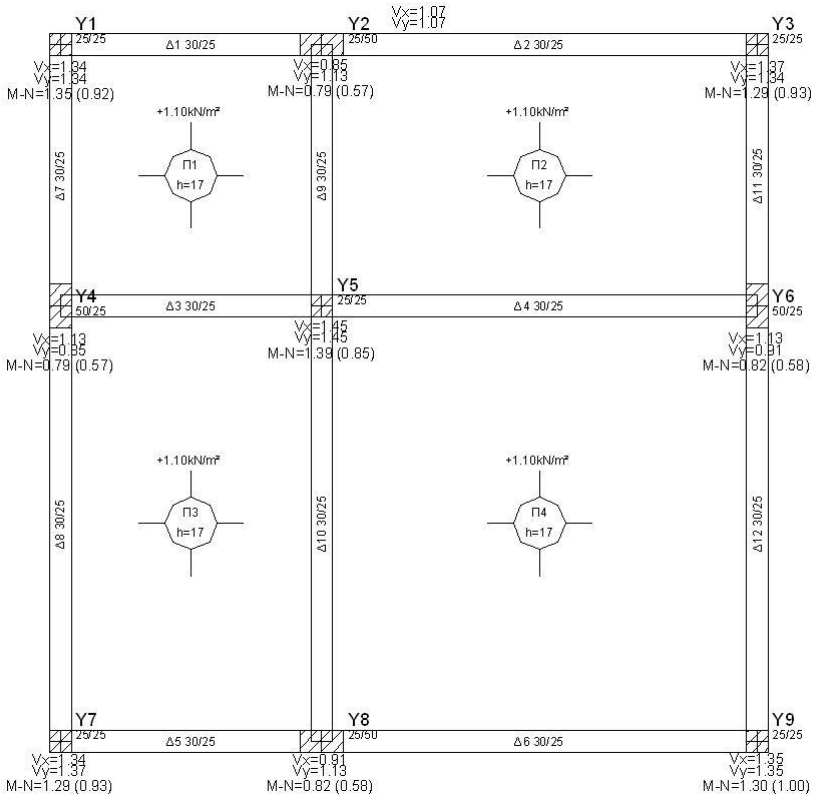


Figure 15: Structure 14

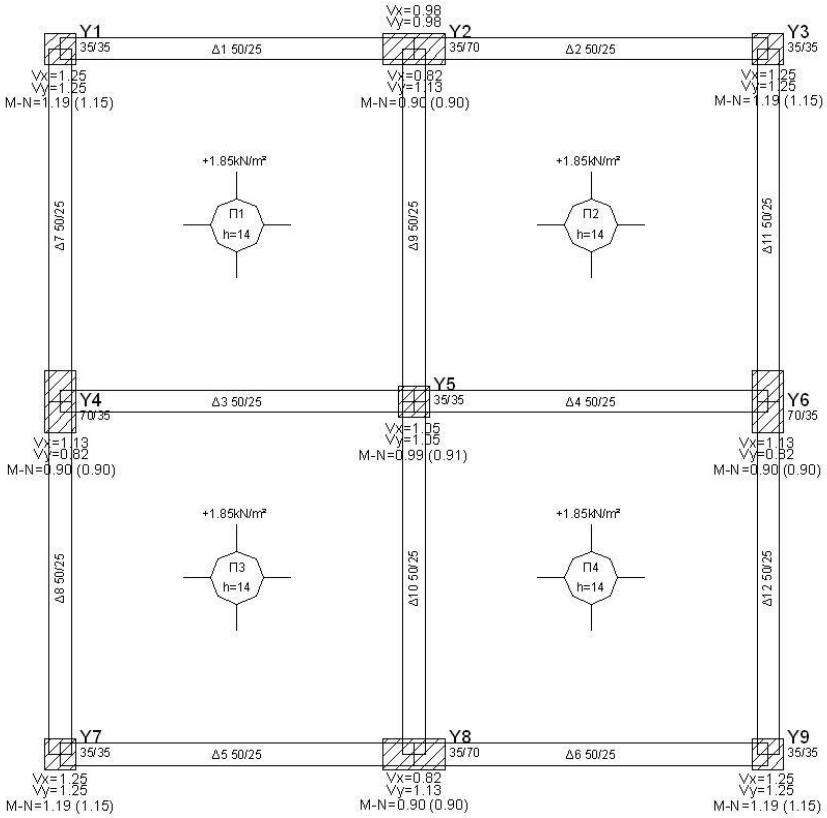


Figure 16: Structure 15

Finally, the layout of the ground flour of a three-storey structure 15 is shown in Figure 16. Like in structures 11, 13 and 14 the stiffer columns are located in the perimeter, in both directions, and they resist 55% of the total base shear force under fixed-base conditions. Under SSI conditions the total base shear force remains almost the same as that recorded with the fixed-base assumption (reduction by 2%). However, when SSI is considered, the stiffer columns are relieved by 18% in their strong direction while overloaded by 10% in their weak one. Now, under SSI conditions, the weak corner columns are overloaded by 25% increase in shear force, while, in contrast to previous examples, the central column experiences a smaller increase by only 5%. Curiously enough, this trend is reversed at the first floor where the central column becames more stressed and the ones at the corners are relieved. In any case all weak vertical elements at the corners are insufficient according to the M-N criterion.

A more detailed discussion on these matters and more such analyses can be found in Mantzaras [5].

4 CONCLUSIONS

The aim of this investigation is to quantify the role of soil-structure interaction, as compared to the usual code-specified fixed-base assumption, in the distribution of shear forces among the vertical elements of 3-D framed structures. To this end, simple concrete structures are designed according to pertinent code provisions and subjected to seismic excitations, consistent with design spectra. The soil-structure interaction is materialized through a set frequency independent springs, dashpots and lumped masses at the soil-foundation interface. The basic conclusions drawn from these analyses are as follows:

1. A substantial redistribution of shear forces among the various columns of a structure occurs when SSI is considered, in reference to the code specified fixed-base condition.
2. The basic factor affecting the redistribution of shear forces is the difference of stiffness among columns.
3. In general, when SSI is considered the stiffer vertical elements are relieved from the load they are called to carry under the assumption of fixed-base conditions. The opposite is true for the less stiff elements which, when SSI is considered, experience substantially higher shear loads. The numerical studies presented in this work have recorded increases under SSI conditions at levels above 50% to those calculated with the fixed base assumption.
4. The most affected of the less stiff elements are those directly connected to substantially stiffer elements or at least are in close proximity to them.

It should be noted that all the analyses presented in this work are linear elastic for the entire soil-foundation-structure system. They also pertain to structures that are supported on an elastic foundation system consisting of distinct footings interconnected via tie beams.

REFERENCES

[1] *Greek Design Code of Reinforced Concrete Structures*, 2000.
[2] *Greek Earthquake Design Code,* 2000.
[3] *Eurocode 8: Design of Structures for Earthquake Resistance,* 2004.
[4] J.S. Mulliken & D.L. Karabalis, Discrete model for dynamic through the soil coupling of 3D foundations and structures, *Earthquake Engng. Struct. Dyn.,* **27**, 687-710, 1998.
[5] G. Mantzaras, *The influence of soil-structure interaction in the redistribution of internal forces in the vertical elements of framed structures,* M.Sc. Thesis, School of Science and Technology, Hellenic Open University, Patras, Greece, 2014.

COMPDYN 2015
5th ECCOMAS Thematic Conference on
Computational Methods in Structural Dynamics and Earthquake Engineering
M. Papadrakakis, V. Papadopoulos, V. Plevris (eds.)
Crete Island, Greece, 25–27 May 2015

SOIL-PILE-STRUCTURE-INTERACTION: EXPERIMENTAL RESULTS AND NUMERICAL SIMULATIONS

Maria Giovanna Durante[1], Luigi Di Sarno[1], Colin A. Taylor[2], George Mylonakis[2], Armando L. Simonelli[1]

[1] Department of Engineering, University of Sannio, Italy,
mgdurante@unisannio.it, ldisarno@unisannio.it, alsimone@unisannio.it
[2]Department of Civil Engineering, University of Bristol, U.K.,
colin.taylor@bristol.ac.uk, G.Mylonakis@bristol.ac.uk

Keywords: Soil-pile-structure interaction, shaking table tests, advanced numerical simulations.

Abstract. *The complex seismic soil-pile-structure interaction phenomenon is related to the interaction between foundation and structure under seismic and dynamic excitations. An effective way to assess such phenomenon is to analyse the response of scaled physical model in 1-g or n-g devices. In this study some results selected from a comprehensive 1-g shaking table tests are reported and discussed. The extensive experimental campaign was carried out on the 3mx3m shaking table of the Bristol Laboratory for Advanced Dynamics Engineering (BLADE) at the University of Bristol (UK), within the framework of the Seismic Engineering Research Infrastructures for European Synergies (SERIES). The physical model comprises a pile group embedded in a by-layer soil deposit with different pile configurations. This paper focuses on the pile group response generated by the presence of a cantilever system (a single-degree-of-freedom, SDOF) connected at the top of the central pile considering no connection among the other pile heads. The selected input motions consist of a set of sinedwell excitations for SDOFs with different structural masses. The experimental data are used to validate an advanced 2D difference element model using the FLAC2D code. The comparisons between the experimental and the numerical results are presented in terms of both envelope and time histories for the free-field and piles responses. The SDOF response is also assessed in terms of displacement time histories. Comparisons between the numerical and experimental test results appear satisfactory; hence numerical approach can be used for further simulations of the soil-pile-structure interaction phenomena.*

1 INTRODUCTION

Pile foundations are usually adopted when shallow soils are not able to carry the vertical loads imposed by the superstructure and it is necessary to reach stiffer soil layers. When such foundations are utilized, the dynamic response of the system may lead to soil-pile-structure interaction (SPSI). This complex phenomenon can be resumed as the combination of two different mechanisms [1-10]: (i) kinematic interaction (Figure 1a) due to the different response of the pile-soil system from the free-field response; (ii) inertial interaction (Figure 1b) due to the additional loads given to the pile by the superstructure inertial actions.

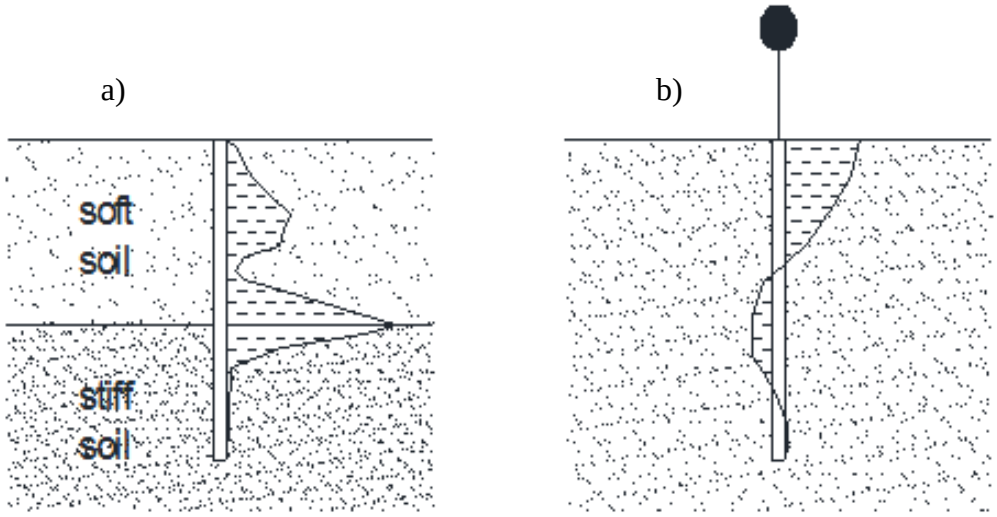


Figure 1. Kinematic (a) and inertial (b) interaction in piled foundations (modified from Simonelli et al., 2013)

The effects of kinematic interaction increase as the stiffness contrast between the crossed layers increases. The maximum bending moment is located in the neighbor of the layer interface.

An effective approach to reliably investigate the SPSI is the testing of physical models and in particular the analysis of the scaled model response through 1-g or n-g devices.

Experimental tests can be targeted to: (i) identify the main aspects that may influence the system response, using different dynamic inputs (i.e. sinusoidal waves, white-noise and earthquakes input); (ii) validate the models utilized in the numerical analyses.

The scope of the present work is to examine the soil-pile-structure interaction referring to a selected set of data coming from high-quality shaking table tests and use these data to validate an advanced difference element numerical model implemented in the computer platform FLAC2D [11]. A cantilever system (a single-degree-of-freedom system, SDOF) connected at the top of the central pile, with no connection among the other pile heads has been considered for the numerical simulations presented herein.

2 SHAKING TABLE TESTS

The experimental campaign was carried out on the 3mx3m 1-g shaking table of the Bristol Laboratory for Advanced Dynamics Engineering (BLADE) at the University of Bristol (UK). The 6-degree-of-freedom earthquake simulator of BLADE and the equivalent shear beam (ESB) laminar container were utilized to this end [12]. The experimental procedure includes the use of: (i) white-noise excitation, a random noise signal of bandwidth 0-100 Hz for the evaluation of the fundamental frequency; (ii) harmonic excitation, sinusoidal wave. Further

details on the equipment and the experimental procedure can be found in some of the Authors previous works [13-16].

2.1 Physical model, and instrumentations

The physical model was formed by a group of 5 pile embedded in a bi-layer deposit (Figure 2). The two-layer soil deposit (obtained by means of pluviation) is made of by Leighton Buzzard sand (LB) fraction E for the top layer and by a mix of LB fractions B and E (85% and 15%, respectively) for the bottom layer. The LB sand characteristics has been extensively utilised in previous experimental studies [17-24]. The main details of the two soil layers are listed in Table 1.

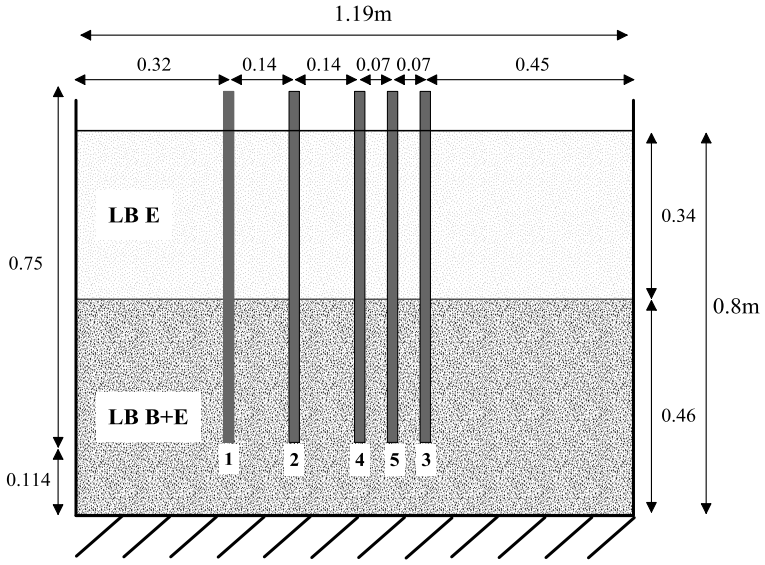


Figure 2. Model details (after Durante et al., 2015)

Soil layers	Thickness H (mm)	Relative density Dr (%)	Dry unit weight γ_d (kN/m^3)
Top LB(E)	340	28	13.63
Bottom LB(E+B)	460	41	17.46

Table 1. Soil layer details

Piles are formed by an alloy aluminium tube (commercial model 6063-T6) with thickness t = 0.71 mm, outer diameter D = 22.23 mm and length L = 750 mm. Pile 3, 4 and 5 are closer to each other with a relative spacing s=70 mm (s/D ≈ 3); pile 1 and 2 are placed at higher distance, equal to 140 mm. The oscillator is formed by an aluminium column (3x12 mm cross section, 100mm high) with extra masses added to its top to achieve different dynamic response; in the set of tests considered in this work the oscillator is connected through a "foundation" directly to the central pile head (pile 5) and there is no connection among the other piles head; more details about masses are listed in Table 2.

Total added mass [g]	Fixed base frequency (f_{fix}) [Hz]	Damping [%]
75	38.0	0.7
125	30.5	1.2
175	26.5	0.9
275	20.5	1.4
475	15.0	1.2
975	10.4	1.5

Table 2. Fixed base frequency for oscillator considered

Accelerometers were employed to monitor the shaking table, the shear stack, the soil along a vertical array (free-field response), the pile head and the superstructure. Linear Variable Displacement Transformer (LVDT) were adopted to assess the pile head and shear stack displacements. For evaluating bending moment a set of 8 pairs of strain gauges were employed for each sample pile to be monitored (i.e. pile 4 and 5). More details of the instrumentation used in the experimental campaign can be found in Durante et al. [25].

2.2 Shear wave velocity profile

An inhomogeneous shear wave velocity profile is adopted for the bi-layer deposit according to the equations:

(1)

where $V_{s1\text{-}2,B}$ are the values of the shear wave at the bottom of the deposit; z is the depth starting from the surface and b is an inhomogeneity coefficient.
$V_{s1,B}$ and $V_{s2,B}$ are obtained employing the procedure proposed in Durante et al. [26], considering the inhomogeneity coefficient (b) equal to *0.5*. Towards this end, the white-noise test results are employed to evaluate the fundamental frequencies of the top layer and of the overall deposit. The initial shear wave profile of the deposit is characterized by to $V_{s1,B}$*=81.7m/s* and $V_{s2,B}$*=100.6m/s* , as pictorially depicted in Figure 3.

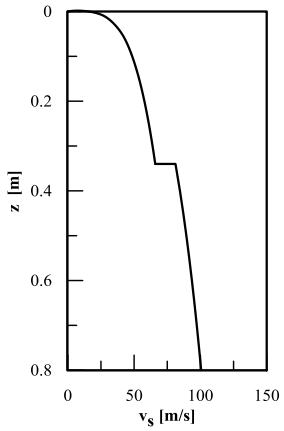


Figure 3. Initial shear wave profile

3 NUMERICAL ANALYSIS

Numerical analyses are carried out at the model scale by means of the advanced difference element code FLAC2D [11]. Soil deposit is modeled considering the hysteretic Ramberg-Osgood constitutive model [27]; the structural elements are modeled by means of pile (for the foundation) and beam elements (for all the SDOF components) implemented in FLAC2D.

3.1 Modeling of soil deposit

The shear wave velocity profile shown in Figure 3 was used. In order to simulate the hysteretic soil behaviour, a multiaxial formulation of the Ramberg-Osgood stress-strain relationship was employed [27], implemented into FLAC as a user-defined constitutive model [28]. The calibration of the two model parameters requires fitting of the Ramberg-Osgood predicted soil behaviour against the experimental *G(γ)* and *D(γ)* curves: in this work the Vucetic and Dobry curves for zero plasticity index were employed [29]. The values used in the modelling can be derived from the curves shown in Figure 4. To compensate for the damping response of the model and the ESB effect at small strain levels, an additional 5% Rayleigh damping is added.

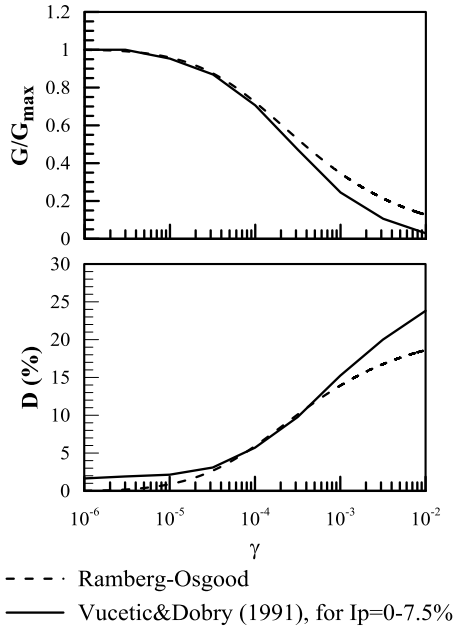


Figure 4. Shear modulus reduction and damping ratio curves adopted (after Durante et al., 2015)

The friction angles of the two layers were obtained based on the well known Bolton [30] and Cavallaro et al. [31] formulations, due to the absence of ad-hoc laboratory tests. Friction angles equal to *35°* and *38°* are adopted for the LB fraction E (upper layer) and fraction B+E (bottom layer), respectively.

For the equilibrium analysis the model was fixed in both the directions at the bottom and only in the horizontal direction at its lateral borders. In the dynamic analyses the lateral restrains were imposed in a simplified way, with the aim of reproducing the boundary conditions imposed by the ESB.

3.2 Modeling of pile and oscillator

Piles were modeled by means of pile elements as implemented in the computer program FLAC [11]. Pile elements interact with the 2D plane strain grid via normal and shear coupling

springs that represent nonlinear connectors able to transfer force and motion between pile elements and the grid in correspondence of the nodes. The calibration of the normal springs is obtained by the force per unit length – relative displacement (p-y) response of the piles based on the analytical method by Georgiadis et al. [32]; the values for piles in cohesionless soils have been used for modelling the sample piles. The values of *k* increases proportionally with depth by means of a subgrade modulus (n_h), which depends on the sand density. In the present work, values of n_h equal to *1500* and *2000 kN/m*^{3} for the top and bottom layers respectively, according to Table 3 [33], are employed. The ultimate soil resistance p_u depends on the unit weight of the soil, the friction angle of sand, the earth pressure at rest and the active earth pressure coefficients and the pile diameter. The shear coupling springs were obtained starting from the soils characteristics, as suggested in Itasca [11].

Relative Density	Loose	Medium	Dense
n_h [kN/m^3]	1100 - 3300	3300 - 11000	11000 - 23400

Table 3. Coefficient of initial subgrade modulus n_h (derived from Terzaghi, 1955)

The foundation, the oscillator column and the mass were realized as beam elements; the different masses were modelled considering different density. The damping ratio for the oscillator is considered assuming the in-built *combined* damping, a variation on *local* damping available in FLAC; in fact the *combined* one is more efficient than the latter, for the significant uniform motion like the sinusoidal waves adopted in these analyses. Local damping is a non-viscous damping, in which the damping force on a node is proportional to the magnitude of the unbalanced force. The values assumed for the damping ratio were obtained from the experimental data with the logarithmic decrement method. A 4.6% value is assumed for the damping in the analyses carried out for the sample models.
The numerical model adopted for the dynamic simulations is shown in Figure 5.

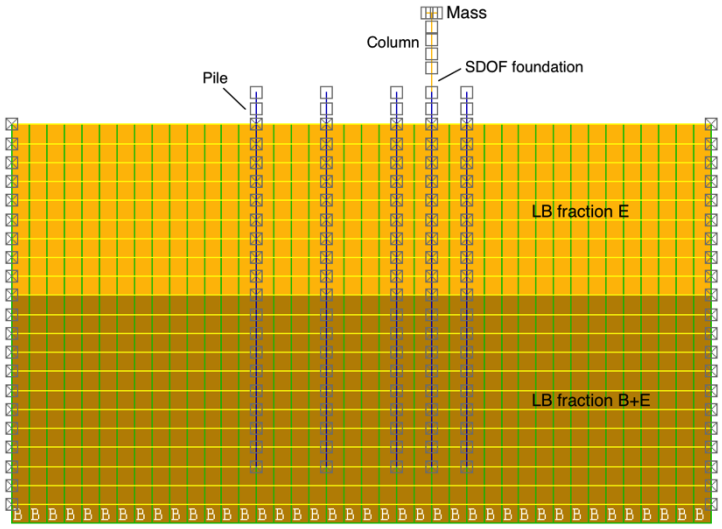


Figure 5. FLAC2D model

4 ANALYSIS RESULTS

The set of data considered in this work refer to the same harmonic input, i.e. a *20 Hz* sinusoidal wave with amplitude equal to *0.1g*.

Figure 6a shows the maximum soil accelerations in the free-field conditions. The results demonstrate that soil response is independent from the mass attached at the oscillator, ensuring that the distance from the piles is large enough to prevent interaction effects to occur.

The bending moment envelope along instrumented piles (pile 4 and pile 5) are reported in Figure 6b and 6c, respectively. The inertial effects are significant at the pile head up to a depth depending on mass value: considering the dynamic response of the system, the increasing of the maximum bending moment at the pile head is related to the resonant condition between the input and the elongated period of the oscillator.

It is found that the oscillator with the maximum SSI effect is the SDOF with a *175g* mass. Utilizing the transfer function between the accelerometer at the top of the oscillator and the accelerometer on the shaking table, a *42%* of period elongation ($T_{SSI}/T_{fix} = 1.42$) was computed, due to the soil-pile-structure interaction ($f_{SSI} = 18.6$ *Hz*); the measured elongation is higher than the ones computed with typical literature formulas [34-37], as reported in Table 4.

	Jennings&Bielak [34] Veletsos&Nair [35]	Wolf [36]	Kumar&Prakash [37]
T_{SSI} / T_{fix}	≈1.00	≈1.00	≈1.15

Table 4. Period elongation computed with literature formulas

Figure 6b shows that pile 4 is influenced by the oscillator even if it is not connected to it; such response depends, indeed, on the short distance between piles 4 and 5 ($s/D \approx 3$). Additionally, the maximum value of the bending moment is not located close to the interface ($z=460$ *mm*); furthermore, it depends on the mass oscillator. This behavior may probably stems from the fact that the oscillator on the central pile (and its resonance condition) tends to influence the pure kinematic interaction of the close pile.

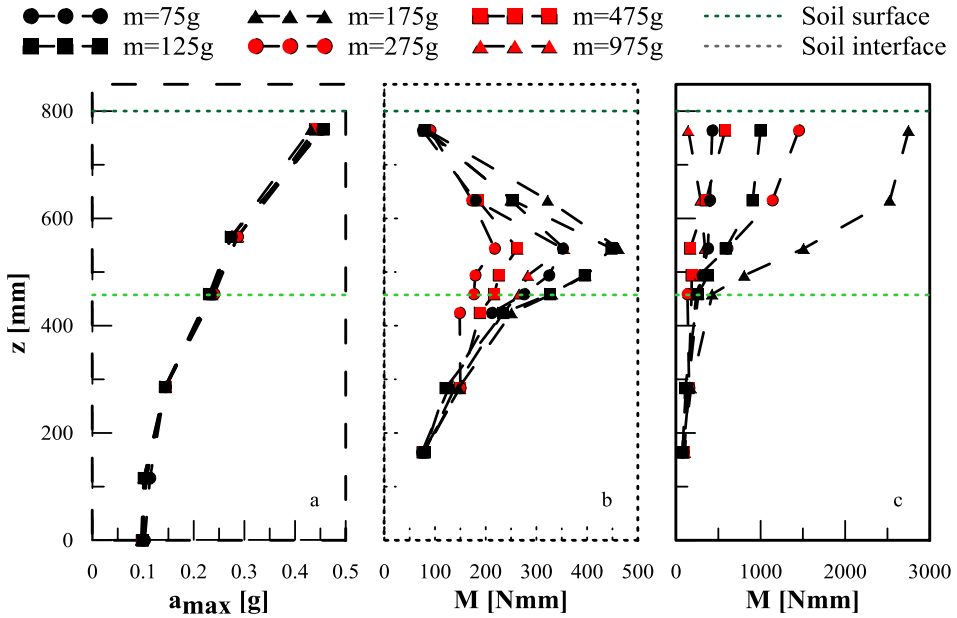


Figure 6. Experimental results: maximum soil acceleration vs. depth (a), maximum bending moment vs. depth for pile 4 (b) and pile 5(c)

Numerical simulations of the above experimental tests were performed by means of FLAC2D code [11]. For brevity, only two typical results are reported in the present paper, namely the tests with oscillator masses equal to 175g and 975g, i.e. the cases corresponding to the lower and upper bound responses.

Figure 7 shows the comparison between the numerical and the experimental data for the free-field (Figure 7a), pile 4 (Figure 7b) and pile 5 (Figure 7c) responses. Figure 7a ensures that soil is adequately simulated in the numerical analyses. The resonance effects are also reliably modeled for pile 5. It is evident, from Figure 7c, that the numerical maximum bending moments at the pile head and at the interface provide close matches with outcomes of the experimental data. Conversely, Figure 7b shows that, for pile 4, the numerical model is able to simulate the maximum bending moment due to the kinematic interaction, nevertheless it cannot reproduce the resonance effect due to the oscillator on the other pile. The latter response is still under investigation by the Authors.

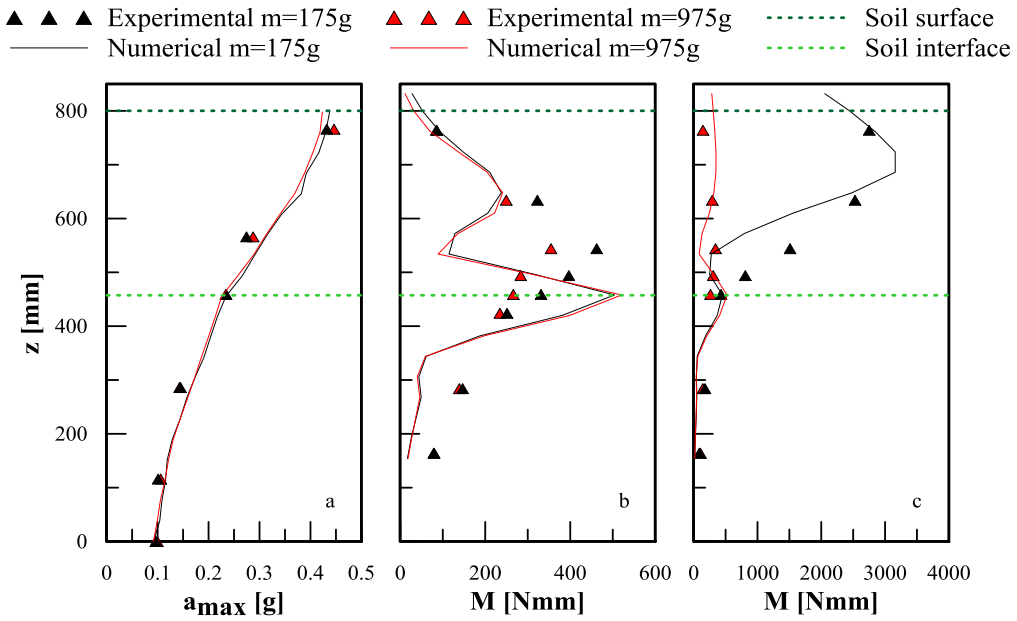


Figure 7. Experimental vs. numerical results: maximum soil acceleration vs. depth (a), maximum bending moment vs. depth for pile 4 (b) and pile 5(c)

Figure 8 shows the comparison in terms of time histories for the test with the mass oscillator equal to 175g. On the left hand side, the comparison for the free-field vertical array at three different elevations (bottom, interface and surface) is provided. It is noticed that there is a full match between computed values and test results. It is worth mentioning that the input was applied to the sample model in terms of accelerations, simulated through an artificial sinusoidal wave (generated directly with a FLAC routine). On the right hand side of Figure 8, the responses close to the pile head (bending moment) and at the top of the oscillator (displacement) are reported. The results confirm that numerical model implemented in FLAC may simulate accurately the experimental data of the shaking table tests. Figure 8 shows a small mismatch of the numerical time histories for the structural elements, that appears after several cycles.

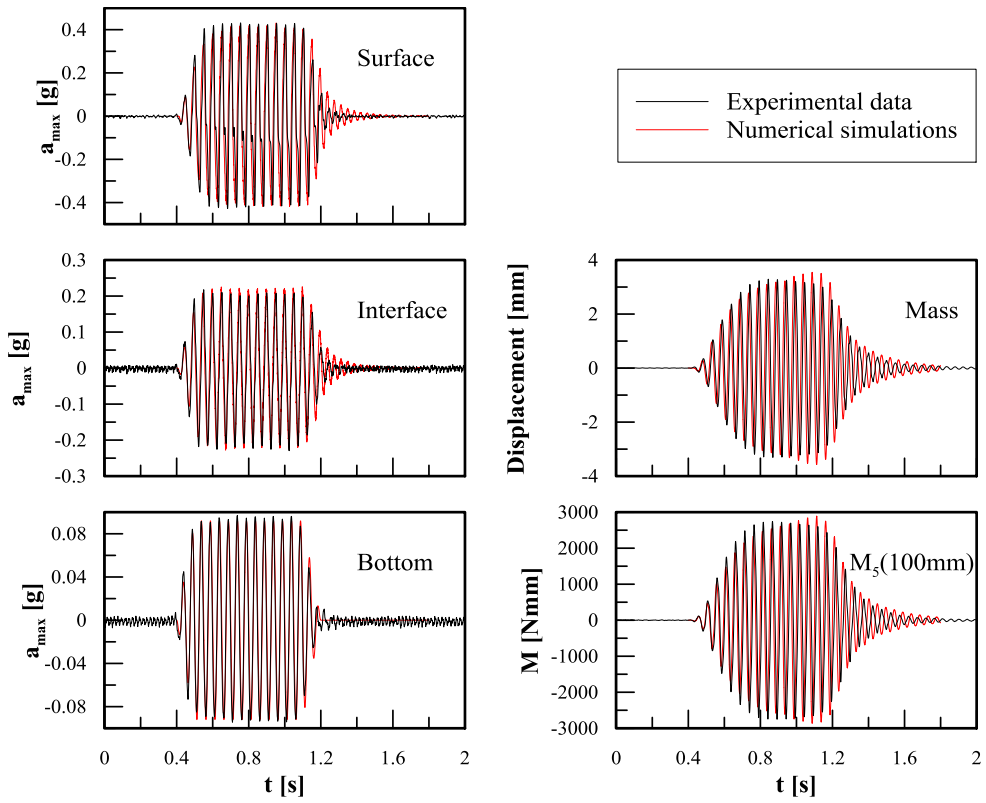


Figure 8. Time histories comparison for the SDOF with mass of 175g

5 CONCLUSIONS

Numerical calibrations were performed by means of an advanced two-dimensional model in FLAC. The numerical model reproduced a scaled model tested on the shaking table of the BLADE laboratory at the University of Bristol. The physical model is formed by a group of five pile embedded in a bi-layer deposit with and oscillator with different masses connected at the top of the central pile. The model accounts for a hysteretic constitutive model for the soil; pile elements for the foundation and beam elements for all the oscillator components were adopted. The interface between piles and soil was simulated by elasto-plastic springs in both shear and normal direction. The preliminary analysis results presented herein have indicated that:

- the numerical model is able to adequately reproduce the free-field response;
- the resonance effects and the bending moment can be reproduced fairly accurately with the numerical model for the pile connected to the oscillator, both in terms of envelope and time history response;
- the soil-pile-structure interaction gives a measured period elongation of 42%: this elongation, which is usually underestimated by the simplified literature formulas is well reproduced by the numerical analysis;
- the numerical model is able to catch effectively the bending moment values due to kinematic interaction; while the maximum bending location is slightly different probably because the influence of the SDOF is not well accounted for.

ACKNOWLEDGEMENTS

The research leading to these results has received funding from the European Union Seventh Framework Programme (FP7/2007-2013) under grant agreement n° 227887, SERIES. The financial support provided by the project ReLUIS (Task MT2) funded by the Italian Civil Protection is also appreciated. The authors would like to acknowledge also all the contributors to the SERIES project.

REFERENCES

[1] Novak, M. *Piles under dynamic loads: State of the art*. Proc. of 2nd International Conference on Recent Advances in Geotechnical Earthquake Engineering and Soil Dynamics, St. Louis, 1991, 3, 2433-2456

[2] Pender, M. *Seismic pile foundation design analysis*. Bulletin of the New Zealand National Society for Earthquake Engineering, 1993, 26(1), 49-160

[3] Gazetas, G. and Mylonakis, G. *Seismic Soil-Structure Interaction: New Evidence and Emerging Issues*. Geot. Earthq. Engng & Soil Dynamics III, Geo-Institute ASCE Conference, Seattle, P. Dakoulas, M.K. Yegian, & R.D. Holtz (eds), 1998, Vol. II, 1119-1174

[4] Mylonakis G. *Simplified model for seismic pile bending at soil layer interfaces*. Soils and Foundations, 2001, 41, 47-58.

[5] Nikolaou S., Mylonakis G., Gazetas G., Tazoh T. *Kinematic pile bending during earthquakes: analysis and field measurements*. Géotechnique, 2001; 51 (5):425-440

[6] Saitoh M. *Fixed-head pile bending by kinematic interaction and criteria for its minimization at optimal pile radius*. Journal of Geotechnical and Geoenvironmental Engineering, 2001, 131 (10): 1243-1251

[7] Cairo R., Dente G. *Kinematic interaction analysis of piles in layered soils*. In 14th European Conference on Soil Mechanics and Geotechnical Engineering, ISSMGE-ERTC 12 Workshop Geotechnical Aspects of EC8, 2007, Madrid (Spain), Pàtron Editore, Bologna, cd-rom, paper n. 13

[8] Sica, S., Mylonakis, G., Simonelli, A. L. *Kinematic bending of piles: analysis vs. code provisions*. Proc. of the 4th International Conference on Earthquake Geotechnical Engineering, 2007, Thessaloniki, Greece

[9] Sica S., Mylonakis G., Simonelli A.L. *Transient kinematic pile bending in two-layer soil*. Soil Dynamics and Earthquake Engineering, 2011, 31, No. 7, 891-905

[10] Di Laora R, Mylonakis G and Mandolini A. Pile-head kinematic bending in layered soil. Earthquake Engineering & Structural Dynamics, 2013, 42(3): 319-337

[11] Itasca. *FLAC – Fast Lagrangian Analysis of Continua* – Version 5.0. Itasca Consulting Group, Inc., Minneapolis, USA; 2005

[12] Crewe A.J., Lings, M.L., Taylor, C.A., Yeung, A.K. & Andrighetto. (1995). *Development of a large flexible shear stack for testing dry sand and simple direct foundations on a shaking table*. European seismic design practice, Elnashai (ed), Balkema, Rotterdam

[13] Simonelli A.L., Di Sarno L., Durante M.G., Sica S., Bhattacharya S., Dietz M., Dihoru L., Taylor C.A., Cairo R., Chidichimo A., Dente G., Anoyatis G., Mylonakis G., Modaressi A., TodoBom L.A. and Kaynia A.M. *Performance of soil-pile-structure systems under seismic waves*. Proceeding of the II Int. Conf. on Performance-Based Design in Earthquake Geotechnical Engineering, Taormina 2012, I

[14] Simonelli A.L., Di Sarno L., Durante M.G., Sica S., Bhattacharya S., Dietz M., Dihoru L., Taylor C.A., Cairo R., Chidichimo A., Dente G., Anoyatis G., Mylonakis G., Modaressi A., TodoBom L.A. and Kaynia A.M. *Experimental investigation of soil-pile-structure seismic interaction*. Proceeding of the 15th World Conference on Earthquake Engineering, Lisbon 2012

[15] Durante M.G., Di Sarno L., Sica S., Mylonakis G., Taylor C., Simonelli A.L. *Seismic Pile-Soil Interaction: Experimental results vs. numerical simulations*. Proceeding of the 4th Intern. Conf. on Computational Methods in Structural Dynamics and Earthquake Engineering. M. Papadrakakis, V. Papadopoulos, V. Plevris (eds.), Kos Island, Greece, 2013

[16] Simonelli AL, Di Sarno L, Durante MG, Sica S, Bhattacharya S, Dietz M, Dihoru L, Taylor CA, Cairo R, Chidichimo A, Dente G, Modaressi A, TodoBom LA, Kaynia AM, Anoyatis G, Mylonakis G. *Chapter 27: Experimental Assessment of Seismic Pile-Soil Interaction*. Seismic Evaluation and Rehabilitation of Structures, Geotechnical, Geological and Earthquake Engineering 2014; Volume 26:455-475

[17] Seed B. H., Idriss I. M. *Soil moduli and damping factors for dynamic response analyses*. Earthquake engineering research center, report no. EERC 70-10, December 1970

[18] Stroud M A. *The behaviour of sand at low stress levels in the simple shear apparatus*. PhD thesis, University of Cambridge, UK; 1971

[19] Tan FSC. *Centrifuge and theoretical modelling of conical footings on sand*. PhD Thesis, University of Cambridge, UK; 1990

[20] Cavallaro A, Maugeri M, Mazzarella R. *Static and dynamic properties of Leighton Buzzard sand from laboratory tests*. 4th International Conference on Recent Advances in Geotechnical Earthquake Engineering and Soil Dynamics 2001, San Diego, CA, Paper 1.13

[21] Lings ML, Dietz MS. *An improved direct shear apparatus for sand*. Geotechnique 2004; 54: 4, 245–256

[22] Moccia F. *Seismic soil pile interaction: experimental evidence*. PhD Thesis, Universita' degli Studi di Napoli Federico II, Napoli; 2009

[23] Visone C, Santucci de Magistris F. *Mechanical behaviour of the Leighton Buzzard Sand 100/170 under monotonic, cyclic and dynamic loading conditions*. Proceeding of the XIII conference: L'ingegneria Sismica in Italia, ANIDIS, Bologna, Italy, 2009

[24] Bui M, *Influence of some particle characteristics on the small strain response of granular materials*. PhD Thesis, University of Southampton, 2009

[25] Durante M. G., Di Sarno L., Sica S., Mylonakis G., Taylor C. A., Simonelli A. L. *Experimental measurements of geotechnical system in 1-g tests*. In: 20th IMEKO TC4 Symposium on Measurements of Electrical Quantities: Research on Electrical and Electronic Measurement for the Economic Upturn,. ISBN: 9789299007327, Benevento, 15-17 September

[26] Durante M. G., Karamitros D., Di Sarno L., Sica S., Taylor C. A., Mylonakis G., Simonelli A. L., *Characterisation of shear wave velocity profiles of non-uniform bi-layer soil deposits: analytical evaluation and experimental validation*. Submitted on Soil Dynamics and Earthquake Engineering, 2015

[27] Ramberg W., Osgood W. R. *Description of stress-strain curve by three parameters*. Technical Note 902, National Advisory Committee for Aeronautics, Washington D. C.

[28] Andrianopoulos K. *Numerical Simulation of Static and Dynamic Loading of Elasto-plastic Soils*. Ph.D. Dissertation, Geotechnical Division, National Technical University of Athens (Greek), 2006

[29] Vucetic M, Dobry R. *Effect of soil plasticity on cyclic response*. Journal of Geotechnical Engineering, ASCE 1991; Vol. 117 (1), pp. 89-107

[30] Bolton M. *The strength and dilatancy of sands*. Geotechnique 1986, 36(1), 65–78

[31] Cavallaro A, Maugeri M, Mazzarella R. *Static and dynamic properties of Leighton Buzzard sand from laboratory tests*. Proc. of 4th Int. Conf. on Recent adv. in Geotech. Earthquake engrg. and soil dyn. and symposium in honour of Prof. WD Liam Finn, San Diego, California, March 26–31, 2001

[32] Georgiadis, M., Anagnostopoulos, C., Saflekou, S. *Centrifugal Testing of laterally loaded piles in sand*. Canadian Geotechnical Journal 1992, 29, pp. 208-216

[33] Terzaghi, K. V. *Evaluation of Coefficient of Subgrade Reaction*. Geotechnique, 1955, 5(4): 297-326

[34] Jennings PC, Bielak J. *Dynamics of building–soil interaction*. Bull SeismolSoc Am 1973;63(1):9–48

[35] Veletsos AS, Nair VVD. *Seismic interaction of structures on hysteretic foundations*. J StructDiv 1975; 101(1): 109–29

[36] Wolf J P. Soil–structure interaction. New Jersey, USA: Prentice Hall; 1985

[37] Kumar S, Prakash S. *Estimation of fundamental period for structures supported on pile foundations*. Geotech Geol Eng 2004; 22: 375–89

COMPDYN 2015
5th ECCOMAS Thematic Conference on
Computational Methods in Structural Dynamics and Earthquake Engineering
M. Papadrakakis, V. Papadopoulos, V. Plevris (eds.)
Crete Island, Greece, 25–27 May 2015

A NEW SEISMIC DESIGN METHOD FOR DEEPLY EMBEDDED FOUNDATIONS ACCOUNTING FOR SSI EFFECTS

Nikos Gerolymos[1], and Athanasios Zafeirakos[2]

[1] National Technical University of Athens, Greece
9, Heroon Polytechniou Str., Polytechnic Campus, Zografos P.C 15780
e-mail: gerolymos@gmail.com

[2] National Technical University of Athens, Greece
9, Heroon Polytechniou Str., Polytechnic Campus, Zografos P.C 15780
e-mail: azafeirakos@gmail.com

Keywords: Deeply embedded foundations, seismic design, Soil structure interaction, Bearing strength surface, Material and geometrical nonlinearities.

Abstract. *A Seismic capacity design method for deeply embedded (or caisson) foundations is proposed based on 3D finite element analysis results. Emphasis is given on the influence of: (a) the kinematic constraints imposed by the superstructure, and (b) the nonlinear behaviour (due to both material and interface nonlinearities) of the foundation on the response of the SSI system. The method involves an analytical formulation of the load path at the caisson head level until complete failure. Interestingly, all load-paths display a particular "over-strength" in bearing capacity that is mobilized by the foundation, identified as the "inverted" pendulum failure mode, irrespective of the stiffness properties of the superstructure and constraints imposed at the foundation level. By exploiting this observation, the paper aims at presenting a flexible design methodology that allows the engineer to orient the seismic performance of the soil-foundation-superstructure system toward a predefined cost-effective failure mode, choosing between failure of the foundation, or failure of the above-ground structure, or a combination of both of them.*

1 INTRODUCTION

The cost-effective earthquake design of structures, requires the role of the nonlinear *soil–foundation–structure interaction* (*SFSI*) on the final performance to be explicitly considered. Thus, for the realistic estimation of maximum and residual displacements of foundation-superstructure systems, which in essence constitutes the core of performance-based design philosophy, all sources of nonlinearities should be taken into account; namely nonlinearities developed above and below ground level. In fact, there is a growing awareness among the geotechnical and structural engineering communities towards incorporating the effects of soil compliance into advanced static and dynamic response analysis techniques (e.g. [1]-[6]). Perhaps surprisingly, the field of seismic design of caisson foundations has received little attention (e.g. [7]-[14]).

Simplistic approaches, usually employed in practice, and refer to (a) the separation between structural and geotechnical design, and (b) the modeling of foundation elements, cannot reproduce many essential features of the actual foundation behaviour. It is to this end that the present paper is directed. By means of a series of numerical analyses in 3-D, the response of deeply embedded foundations supporting a single-degree-of-freedom system, which can be representative of a broad range of superstructures (e.g. bridges, wind turbines, etc), is investigated, with due consideration to nonlinearities developed below (soil, caisson-soil interface) and above ground (superstructure). From the analysis, a closed-form expression for the "actual" monotonic load path in *M-Q* space is developed, and a methodology for the preliminary seismic response evaluation, in capacity terms, of deeply embedded (caisson) foundations is proposed.

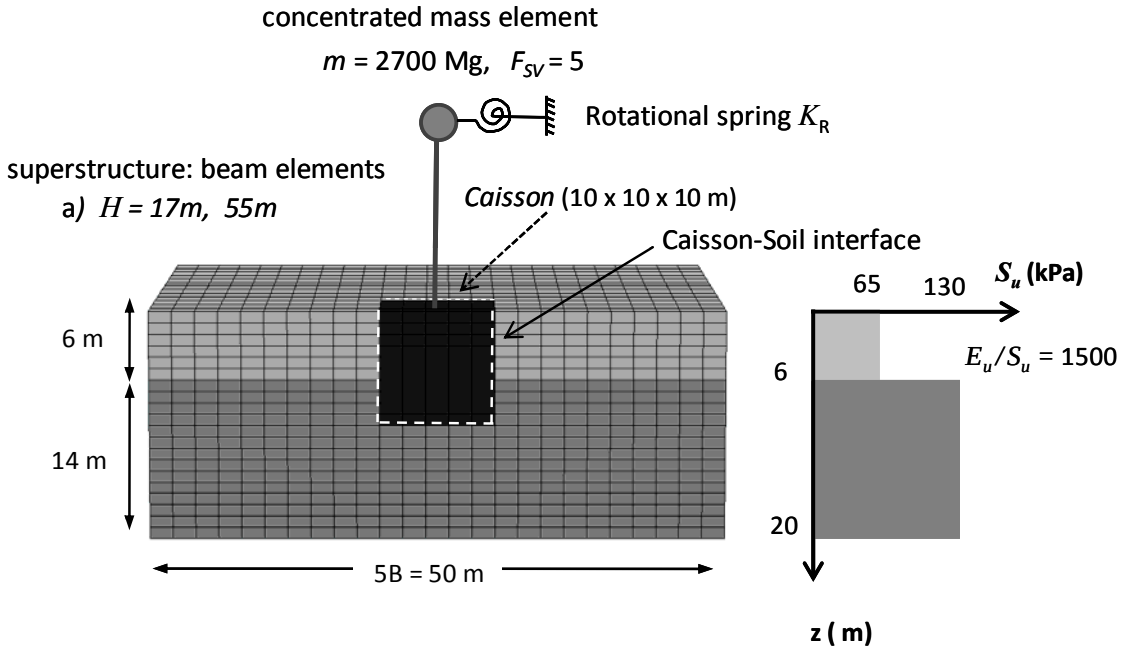


Figure 1. The finite element model

2 PROBLEM DEFINITION

The studied problem is portrayed in Fig. 1. It involves a SDOF system supported by a cubic caisson of side D = 10 m in a 20 m thick 2-layer cohesive soil stratum. The caisson is modeled as a rigid body, with loads and displacements relating to a single load reference point

(LRP), as shown in Fig 2. Two different heights of the superstructure are considered, to represent two different loading conditions with respect to moment loading on the foundation, are used; namely H = 17 m and 55 m. The mass of the system, m, is given the value of 2700 Mg, corresponding to a static factor of safety of FS_V = 5 [11]. The kinematic constraints imposed by the superstructure are simulated by a rotational spring attached at the mass level.

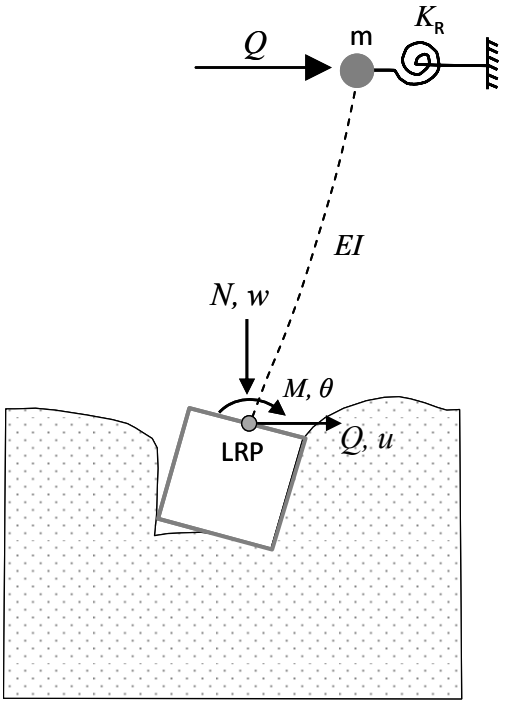


Figure 2. Sketch of the studied problem: A deeply embedded rigid foundation supporting an SDOF superstructure. The kinematic constraints imposed by the superstructure are simulated by a rotational spring attached at the mass level

2.1 Numerical Modeling

The problem is analyzed with use of the finite element code ABAQUS. Both caisson and soil are modeled with 3D 8-noded brick elements, assuming elastic behavior for the former and elasto-plastic for the latter. Fig. 1 shows a half caisson cut through one of the orthogonal planes of symmetry. The size of the finite element mesh is 5B x 5B x 2B carefully weighing the effect of boundaries on the caisson's response and the computational time. Zero-displacement boundary conditions prevent the out of-plane deformation at the vertical sides of the model, while the base is fixed in all three coordinate directions. The caisson is connected to the soil with special contact surfaces, allowing for realistic simulation of the possible detachment and sliding at the soil–caisson interfaces.

The caisson material is modeled as isotropic linear elastic, with a unit weight of γ = 25 kN/m^3, a Young's modulus of E_c = 3 x 10^8 kPa and a Poisson's ratio of v_c = 0.15. However, to ensure rigid body motion appropriate kinematic constraints have been applied between the top central node and all the peripheral nodes of the caisson. The pier columns are modeled with 3-D Timoshenko beam elements, with elasticity modulus E_c = 3 x 10^8 kPa and v_c = 0.15. The stiffness of the rotational spring, K_R, was appropriately modified so that the stiffness ratio:

$$K_{ratio} = \frac{K_R}{\left(\frac{4EI_c}{H}\right)} \tag{1}$$

where ($4EI_c/H$) is the flexural stiffness of the column, yields the following values: $K_{ratio} = 0.1$, 0.25, 0.5, 1.0, for every case examined, covering a wide range of superstructure conditions. Moreover, the case of $K_{ratio} = 0$ (inactive rotational spring) is also provided, for reference.

2.2 Constitutive Models

Soil behavior is described by an elasto-plastic constitutive model [15], which is a reformulation of that originally developed by Armstrong and Frederick [16]. The model is available in the material library of ABAQUS. It uses the Von Mises failure criterion along with a nonlinear combined kinematic—isotropic hardening law and an associated plastic flow rule. The clayey soils are saturated responding in undrained fashion with shear strength S_u = 65 kPa at the upper 6 m, S_u = 130 kPa at the lower 14 m and a constant stiffness to strength ratio E_u / S_u = 1500. The unit weight of the soil materials is taken γ = 20 kN/m^3. To approximate the constant volume response under undrained conditions, a Poisson's ratio of $\nu \approx 0.5$ (= 0.475 to avoid numerical instabilities) was assumed.

Nonlinear response is introduced for the superstructure by means of a bi-linear moment-rotation law (Fig 3) for the rotational spring and a bi-linear moment-curvature law for the pier (beam), The values of the bi-linear laws are deliberately pre-defined, so that structural failure precedes bearing capacity failure of the foundation.

2.3 Failure Envelope

At first, a series of finite element (FE) static pushover-type of analyses are carried out to derive the bearing strength surface of the caisson–soil system in *M*-*Q* space [10], [17], [18]. Firstly, the soil undergoes geostatic loading and then a part of the soil is replaced by the foundation, on which a vertical load is applied till the specified value of the factor of safety (FS_V = 5) is reached. Afterwards, the vertical load is kept constant and a combination of horizontal force *Q* and overturning moment *M* is applied at the head of the caisson until failure. By a series of force-controlled analyses the strength surface is ultimately determined. The surface is presented normalized with respect to the pure moment capacity M_u (with no horizontal loading) and the pure horizontal capacity Q_u (no moment loading) of the foundation (Q_u = 44 MN, and M_u = 430 MNm for the studied cases).

It has been shown in [10], [18], that an ellipsoid of the general form:

$$f = \left(\frac{Q}{Q_u}\right)^{n_1} + \left(\frac{M}{M_u}\right)^{n_2} + n_3\left(\frac{Q}{Q_u}\right)\left(\frac{M}{M_u}\right) - 1 = 0 \tag{2}$$

can adequately fit the numerical results in the normalized *M*-*Q* space at a particular vertical load level (*N*). The coefficients n_1, n_2 affect the skewness with respect to the axis of symmetry, while n_3 controls the size (expansion-contraction) of the surface. They are functions of the embedment ratio D/B, vertical load and interface conditions [19]. For fully bonded interface conditions $n_1 = n_2 = 2$ (zero skewness), while n_3, for any practical reason, depends only on the embedment ratio ([10], [18]):

$$n_3 = 1.84 - 0.21\left(\frac{D}{B}\right)^{-1.98} \tag{3}$$

Apparently, for nonlinear interface conditions (gapping and slippage) the coefficients are described by more complex functions, as suggested in [19].

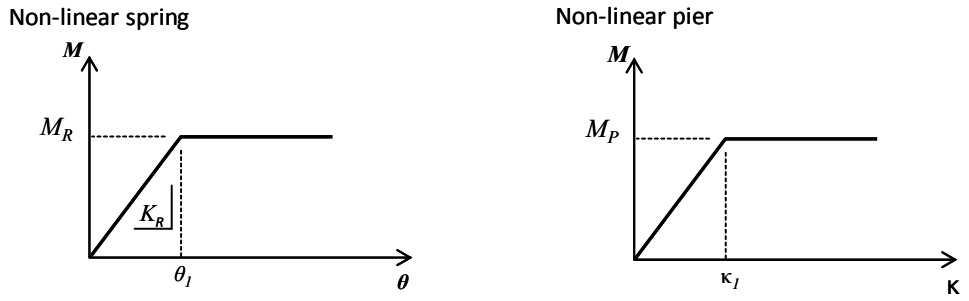


Figure 3. Bi-linear moment-rotation and moment-curvature laws used to model the spring and the pier, respectively.

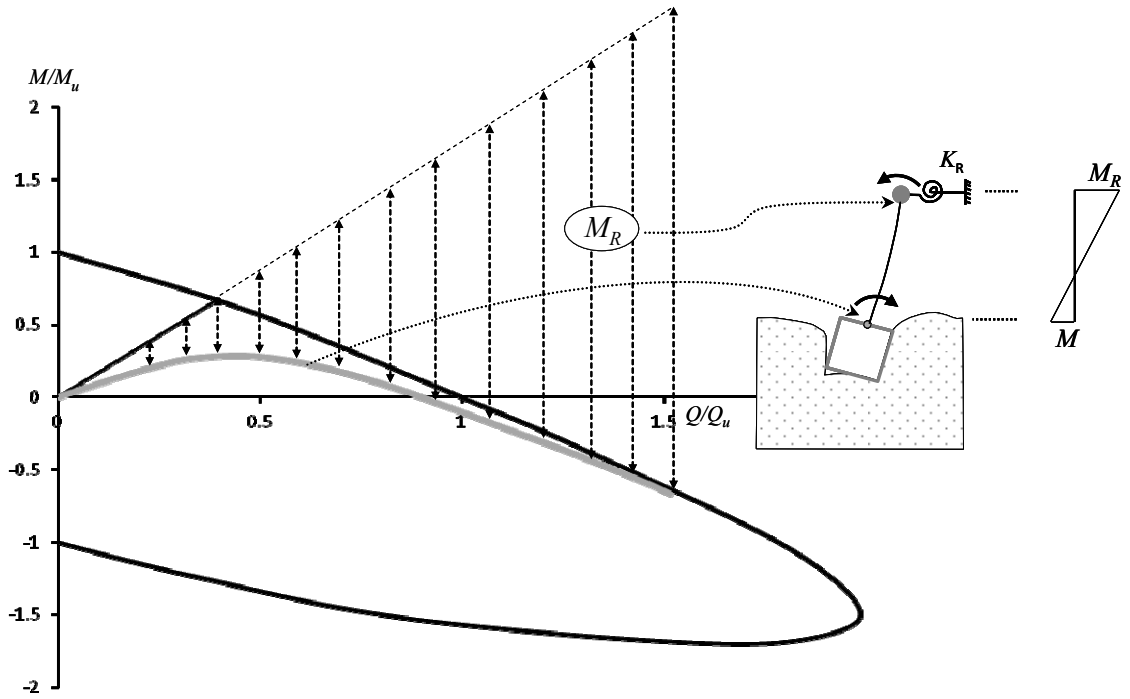


Figure 4. Geometric representation of the moment developed at the head of the caisson (grey solid line) and the rotational spring, M_R , assuming linear response.

3 ANALYSIS RESULTS

Having determined the bearing strength surface of the caisson, the whole soil-foundation-superstructure system is then subjected to lateral loading at the mass level, monotonically increasing until system failure. The analysis terminates either due to bearing capacity failure of the foundation or due to failure of the superstructure. Throughout the analysis, the load path on the foundation is being constantly tracked in *M*-*Q* space.

The presentation of the methodology and the results precedes a graphical illustration (Fig 4) that serves to elucidate the contribution of each of the load-carrying mechanisms within the foundation-superstructure system. Yet, the emphasis is given to the response of the foundation.

The caisson and the pier base are subjected to moment loading that is represented by the load path. The moment that develops at the rotational spring (M_R), however, is given by the

vertical distance between the load path and the (extended) line corresponding to the respective (for that specific pier height) cantilever beam (K_R = 0). It should be noted that Fig. 4 portrays an ideal case, in which the beam and the rotational spring respond elastically, and they are therefore capable of carrying substantial loading.

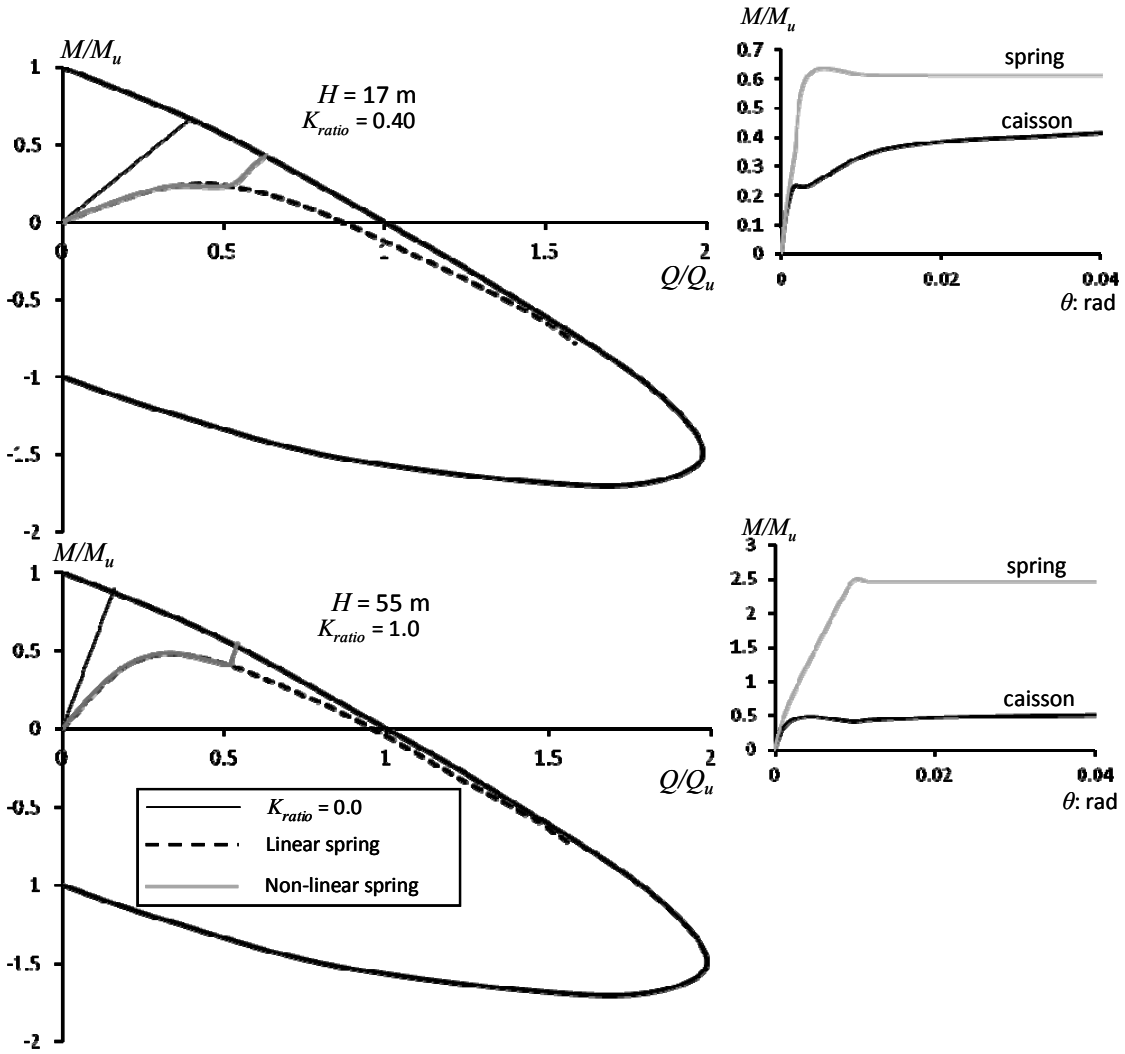


Figure 5. FE results for the load path at the caisson foundation, assuming a linear elastic pier and a nonlinear or linear rotational spring. The corresponding evolution of the moment developed at the top of the caisson (solid black line) and at the rotational spring (solid grey line) with respect to the caisson's rotation, are plotted alongside.

To begin with, we consider a nonlinear rotational spring attached to the top of an elastic pier column. Three characteristic cases are examined, the properties of which, along with the predefined values of the bilinear moment-rotation model for the spring, are given in Table 1.

H : m	M_R : MNm	K_{ratio}	θ_1 : rad
17	276	0.40	0.0023
55	1070	1.0	0.0035

Table 1. Predefined bilinear moment-rotation values for the rotational spring

The results are shown in Fig 5. For reference, each characteristic response is accompanied with the respective ones considering (a) cantilever beam (K_R = 0), and (b) a linear rotational spring. Moreover, the evolution of the normalized moment loading on the foundation (solid black line) and of the rotational spring (solid grey line) with respect to the caisson rotation, are given alongside. For clarity reasons, the negative (in sign) moment developed at the rotational spring is plotted in absolute values.

The computed response can be interpreted as follows: as long as the spring is loaded within its elastic regime, the loading on the foundation follows the respective nonlinear path (dashed line). However, when the moment capacity of the spring (M_R) is reached, denoting the formation of a plastic hinge, the spring cannot sustain any further increase in moment loading. The additional moment is now imposed onto the foundation as positive (in sign) loading, and the system exhibits the response of a caisson carrying a cantilever beam; the load path is tracked parallel to the respective one of a cantilever with height H, and continues until bearing capacity failure of the foundation occurs.

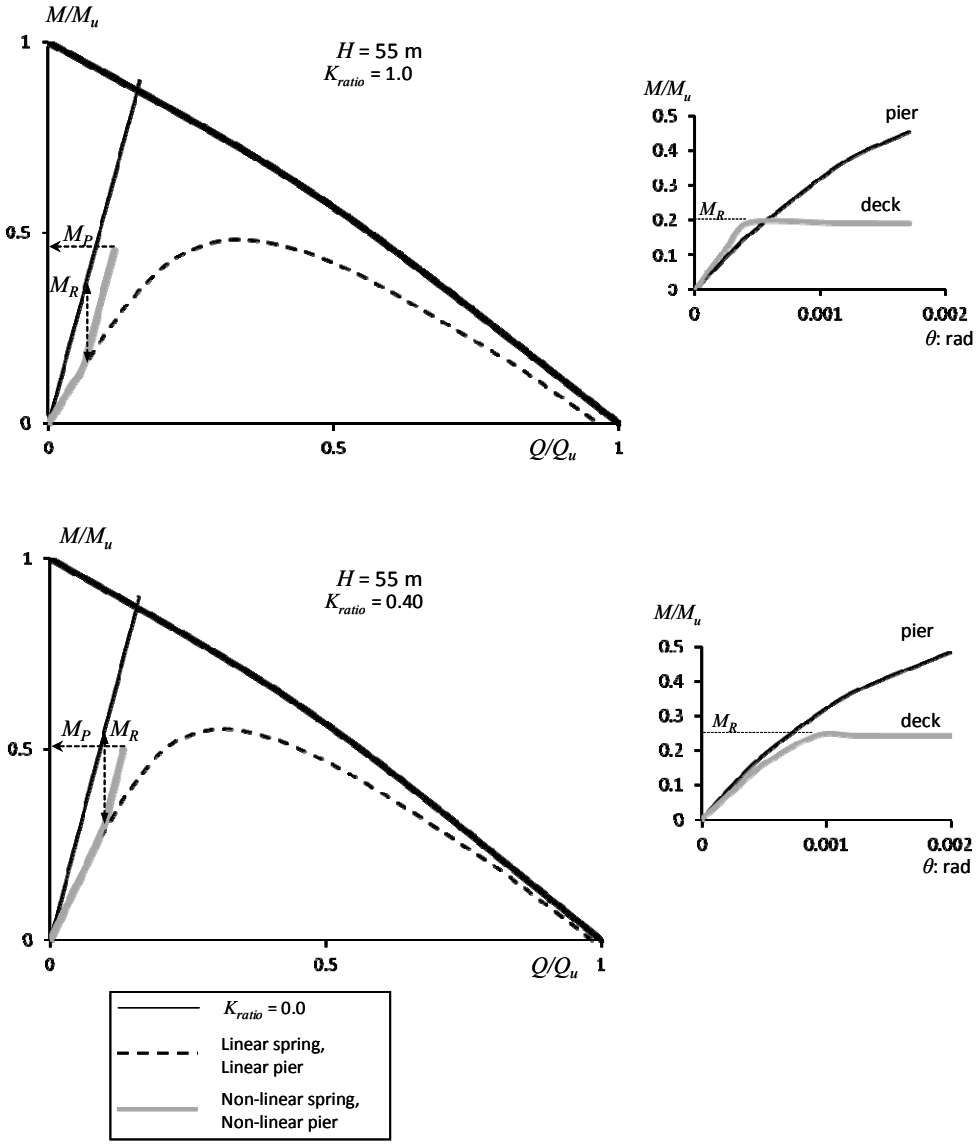


Figure 6. FE results for the load path at the caisson foundation, assuming (a) linear, and (b) nonlinear rotational spring and pier. The corresponding evolution of the moment developed at the top of the caisson (solid black line) and at the rotational spring (solid grey line) with respect to the caisson's rotation, are plotted alongside.

The response is now examined accounting for nonlinear behaviour of both the pier and the rotational spring. Two characteristic cases are considered: a pier height of H = 55 m, kinematically restrained at the mass level by a rotational spring that yields a stiffness ratio of (a) K_{ratio} = 0.40, and (b) K_{ratio} = 1.0. The values for the bi-linear models (as schematically shown in Fig 5) are given in Table 2. Given that the determination of shear strength, and especially of shear deformation characteristics of (e.g. reinforced concrete) structures are still controversial issues [20], the interplay between shear and flexure in the inelastic regime is not taken into account and the controlled mode of failure of the piers is assumed to be flexure-dominated.

H : m	M_P:MNm	κ_1 : rad/m	κ_2 : rad/m	M_R:MNm	K_{ratio}	θ_1 : rad
55	215	0.0000544	0.000055	107	0.4	0.00089
55	195	0.0000493	0.000051	85	1.0	0.00028

Table 2. Predefined bilinear moment-curvature and moment-rotation values for the pier column and rotational spring, respectively

The results, provided in Fig 6, highlight that contrary to the "ductile" progressive failure of the superstructure-foundation system observed following the yielding of the rotational spring, column yielding leads in an abrupt system failure. This "brittle-type" system response is further illustrated from the graphs of the normalized moment loading at the pier base (solid black line) and the rotational spring (solid grey line) with respect to the caisson rotation, which are plotted alongside the load paths.

In summary of the above, Fig 7 schematically represents the nonlinear SFSI effects, and identifies the possible failure modes of the system; point 1 signifies pier column failure; point 2 corresponds to yielding of the rotational spring, followed by a ductile foundation response; point 3 indicates bearing capacity failure of the foundation.

4 DESIGN METHODOLOGY

Based on the analysis presented in the preceding section, an analytical representation of the load path in M-Q space is attempted. Hence, a generalized expression of the following form is considered:

$$\frac{M}{M_u} = \gamma \left[(1+\alpha) \left(1 - e^{-\beta \frac{Q}{Q_u}} \right) - \alpha \frac{Q}{Q_u} \right] \tag{4}$$

where the coefficients α, β and γ control the shape of the load path, and depend on: the properties of the beam (H, I_c), the rotational stiffness of the spring (K_R), and the pure uniaxial capacities of the foundation (Q_u, M_u), which incorporate the effects of soil conditions and foundation's geometry. The determination of the three unknown coefficients requires the consideration of appropriate conditions. These conditions are identified from Fig 8, where the collection of the load paths for all examined cases is plotted, and detailed in the same figure. More specifically:

1. Point ***C***, is the point on the failure envelope associated with the "inverted" pendulum failure mechanism, on which the load paths terminate. Point ***C*** can be considered as an attractor of the caisson response at failure, irrespective of the stiffness properties and constraints at the superstructure system. Its coordinates can be derived from the following conditions:

Point ***C*** lies on the failure envelope. Therefore, satisfaction of the respective equation ($f = 0$) for caisson foundations [10], [18], [19] requires that:

$$f = \left(\frac{Q}{Q_u}\bigg|_C \right)^{n_1} + \left(\frac{M}{M_u}\bigg|_C \right)^{n_2} + n_3 \left(\frac{Q}{Q_u}\bigg|_C \right)\left(\frac{M}{M_u}\bigg|_C \right) - 1 = 0 \tag{5}$$

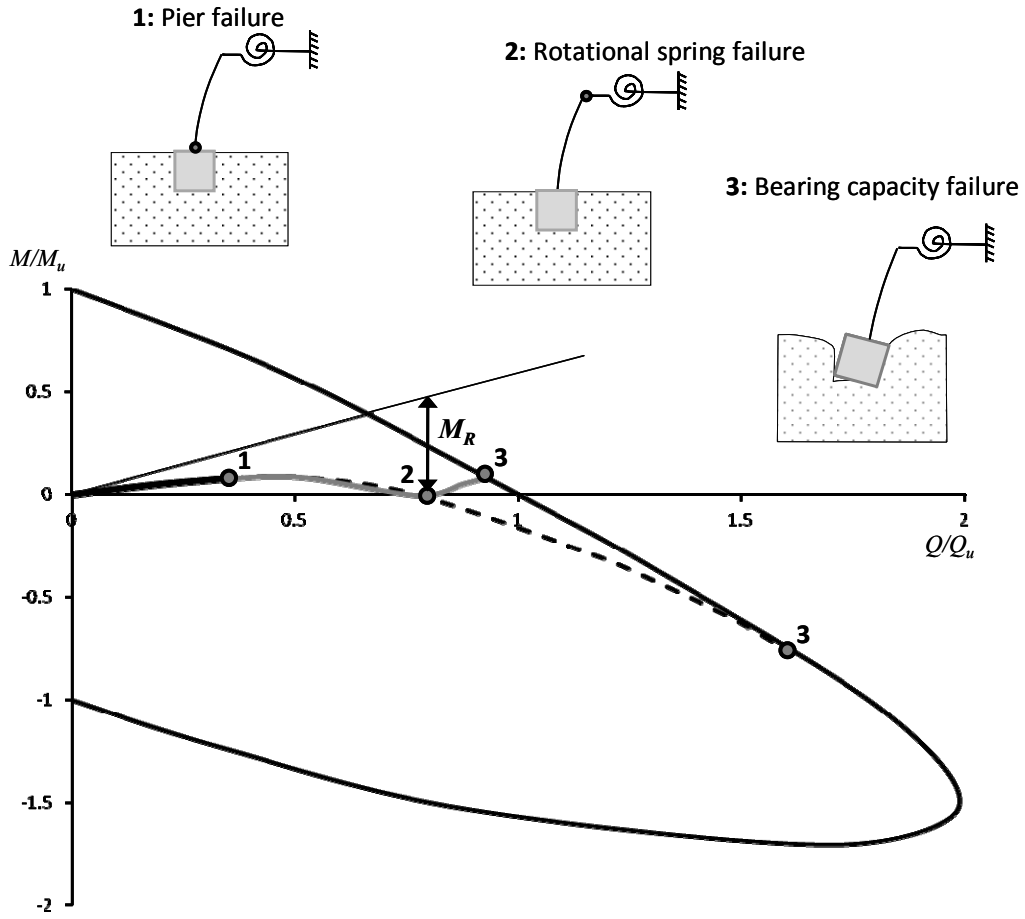


Figure 7. Schematic illustration of all possible failure modes of a caisson supported superstructure accounting for nonlinearities above and below ground level.

Invoking normality conditions for the incremental plastic deformation of the caisson (with respect to its head) at failure, as has been conjectured by several researchers (e.g. [10], for deeply embedded foundations, D/B > 1 and [21], [22] for shallow embedded foundations, D/B < 1), the ratio of the plastic displacement increments can be obtained by differentiating Eq 5 with respect to Q and M, respectively. However, the incremental plastic displacement to rotation ratio for rigid caisson foundations at failure is by definition equal to the depth of the rotation pole, z_p , which in turn is equal to the embedment depth of the caisson ($z_p = D$) when the "inverted" pendulum failure mechanism is manifested. This results in an additional equation that must be satisfied by the coordinates of point ***C***:

$$\frac{\delta u_p}{\delta \vartheta_p} = \frac{\dfrac{\partial f}{\partial Q}}{\dfrac{\partial f}{\partial M}} = \frac{\dfrac{M\, n_3}{M_u\, Q_u} + \dfrac{n_1\, \mathrm{sign} Q \left(\dfrac{|Q|}{|Q_u|}\right)^{n_1-1}}{|Q_u|}}{\dfrac{Q\, n_3}{M_u\, Q_u} + \dfrac{n_2\, \mathrm{sign} M \left(\dfrac{|M|}{|M_u|}\right)^{n_2-1}}{|M_u|}} = D \tag{6}$$

in which δu_p and $\delta \vartheta_p$ are the incremental plastic displacement and rotation at failure, respectively, with respect to the caisson head. Eqs 5 and 6 form a nonlinear algebraic system, from which the coordinates of point ***C*** can be derived.

Substituting the solution of the aforementioned system ($\left.\frac{Q}{Q_u}\right|_C$, $\left.\frac{M}{M_u}\right|_C$) into Eq 4, gives the equation for the first condition:

$$\left.\frac{Q}{Q_u}\right|_C = \gamma \left[(1+\alpha)\left(1 - e^{-\beta\frac{\pi}{2}}\right) - \alpha \left.\frac{M}{M_u}\right|_C \right] \tag{7}$$

2. Point ***A***, that corresponds to the slope of the tangent to the load path at the initial stages of loading. The tangent represents the load path when considering a cantilever beam of initial effective height H_{eff}. Given that $M = H_{eff}\, Q$, the equation of the tangent in the normalized $M/M_u - Q/Q_u$ space can be rewritten as:

$$\frac{M}{M_u} = \left(H_{eff} \frac{Q_u}{M_u} \right) \frac{Q}{Q_u} \tag{8}$$

where $H_{eff} \dfrac{Q_u}{M_u}$ is the respective slope. By differentiating Eq.7 with respect to Q/Q_u, one obtains:

$$\frac{\partial\left(\dfrac{M}{M_u}\right)}{\partial\left(\dfrac{Q}{Q_u}\right)} = \gamma \left[(1+\alpha)\left(1 + \beta e^{-\beta\frac{Q}{Q_u}}\right) - \alpha \right] \tag{9}$$

At the region of initial lateral loading, where $Q/Q_u \to 0$, the slope of the tangent can be substituted into Eq 9, resulting in the following condition:

$$H_{eff} \frac{Q_u}{M_u} = \gamma \left[(1+\alpha)(1+\beta) - \alpha \right] \tag{10}$$

The effective height can be estimated by the following analytical expression:

$$H_{eff} = \frac{2EI_c K_R K_{HM} - 2EI_c K_{HM}^2 H - K_R K_{HM}^2 H^2 + K_R K_H K_M H^2 + 2EI_c K_H K_M H}{2\left(EI_c K_R K_H - K_R K_{HM}^2 H - EI_c K_{HM}^2 + EI_c K_H K_M + K_R K_H K_M H\right)} \tag{11}$$

in which K_H, K_M , K_{HM} and K_{MH} are the swaying, rocking and cross-swaying-rocking initial (elastic) stiffnesses, respectively, of the caisson.

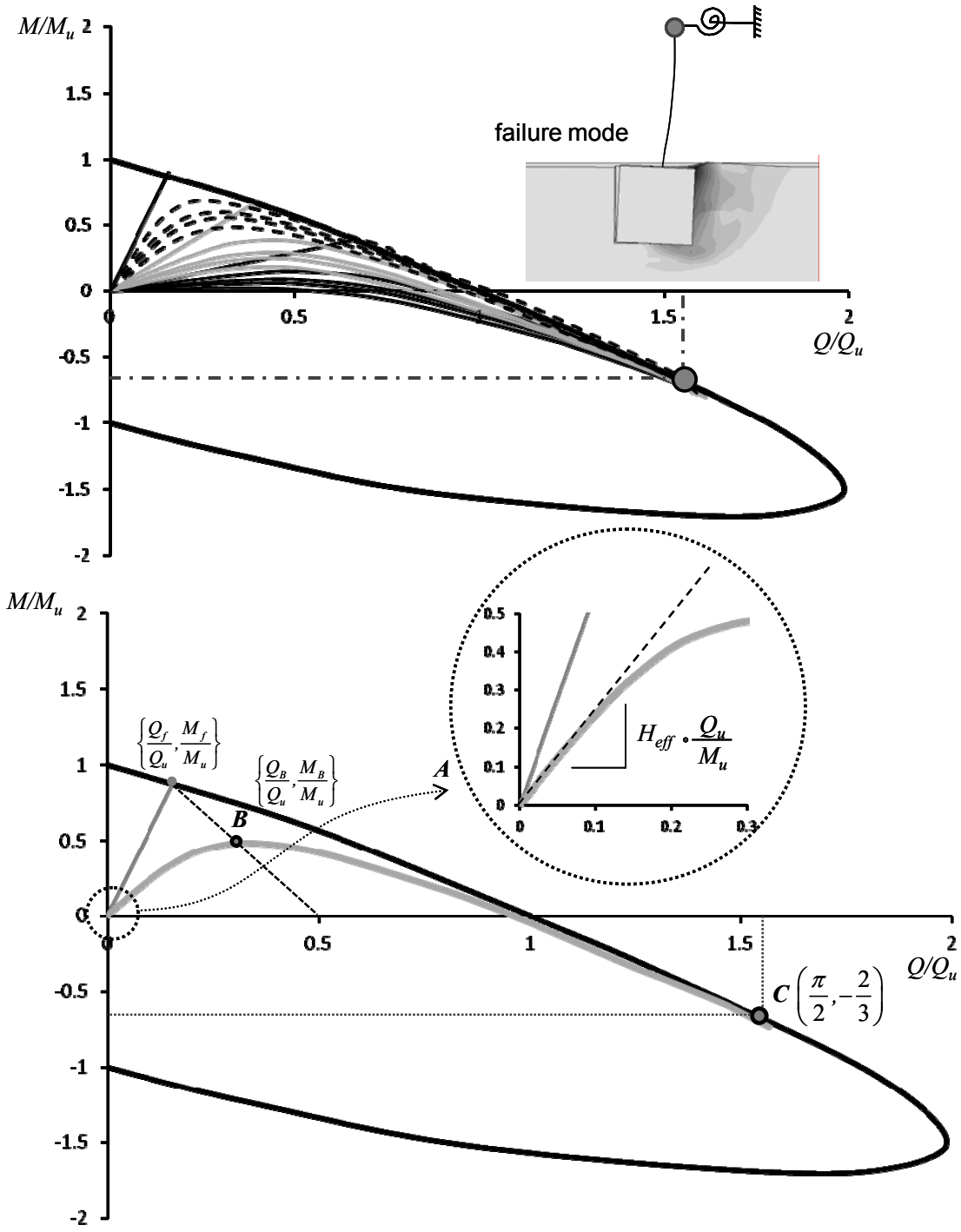


Figure 8. (top) Calculated load paths for all cases examined in this study assuming linear superstructure. All paths are associated with a failure mechanism of the inverted pendulum type (as shown by the corresponding snapshot at failure of the deformed FE mesh. (Bottom) Graphical representation of the three conditions applied for the extraction of a closed-form expression for the load path. The particular coordinates at point ***C*** belong to the failure envelope of caisson foundations with D/B = 1.

3. Point ***B***, which marks the maximum positive (in sign) value of M/M_u, with coordinates $\left\{\frac{Q_B}{Q_u},\frac{M_B}{M_u}\right\}$. Furthermore, point ***B*** is also the point of intersection between (a) the nonlinear load path, and (b) the (dashed) line that connects the point where the linear load path of the respective cantilever (K_R = 0) meets the failure envelope $\left\{\frac{Q_f}{Q_u},\frac{M_f}{M_u}\right\}$, and the abscissa at $\{0.5,\ 0\}$. Hence, and after some algebra, the following expression for the third condition is derived:

$$\frac{1}{\beta}ln\left(\frac{\beta(1+\alpha)}{\alpha}\right)\left(\frac{-2HQ_u}{HQ_u-M_u}-\alpha\gamma\right)-(\gamma+\alpha\gamma)\left(\frac{\alpha}{\beta(1+\alpha)}+1\right)=\frac{HQ_u}{HQ_u-M_u} \tag{12}$$

Eqs 7, 10 and 12 constitute a system of nonlinear algebraic equations, the solution of which yields the parameters α, β and γ, and thus the equation of the load path from the beginning of loading until complete failure of the caisson.

With the load path known, or alternatively, with known the moment and shear force at the head of the caisson (or at the base of the pier), the moment of the rotational spring is calculated by subtracting the response with respect to the caisson head from the hypothetic one of the respective cantilever:

$$M_R = HQ - M \tag{13}$$

Based on the aforementioned methodology, the dimensions of the caisson (width B and depth D), can be effectively estimated targeting either to bearing capacity (foundation) failure, or to structural (pier) failure.

5 CONCLUSION

3D finite element analyses were carried out for the lateral response of deeply embedded (caisson) foundations supporting kinematically constrained single-degree-of-freedom systems, via a rotational spring attached to the mass. The results are used for developing a versatile design methodology allowing for the seismic performance of the soil-foundation-superstructure system to be directed toward a predefined cost-effective failure mode, choosing between failure of the foundation, or failure of the above-ground structure or a combination of both of them.

ACKNOWLEDGEMENTS

Nikos Gerolymos acknowledges the financial support from the European Union (European Social Fund-ESF) and Greek national funds through the Operational Program "Education and Lifelong Learning" of the National Strategic Reference Framework (NRSF)-Research Funding Program: THALES. Investing in Knowledge society through the European Social Fund.

REFERENCES

[1] Bienen B, Cassidy MJ. Advances in the three-dimensional fluid-structure-soil interaction analysis of offshore jack-up structures. *Marine Structures*, 19 (2-3), 110-140, 2006.

[2] Cassidy MJ, Eatock TR, Houlsby GT. Analysis of jack-up units using a Constrained New Wave methodology. *Applied Ocean Research*, 23, 221-234, 2001.

[3] Cassidy MJ, Taylor PH, Eatock TR, Houlsby GT. Evaluation of long-term extreme response statistics of jack-up platforms. *Ocean Engineering*, 29(13), 1603-1631, 2002.

[4] Cassidy MJ, Byrne BW, Randolph MF. A comparison of the combined load behaviour of spudcan and caisson foundations on soft normally consolidated clay. *Géotechnique*, 54(2), 91-106, 2004.

[5] Martin CM, Houlsby GT. Jackup units on clay: structural analysis with realistic modelling of spudcan behaviour. In: *Proc. 31st Offshore Technology Conf.*, Houston, 1999, OTC 10996.

[6] Vlahos G, Cassidy M.J, Martin CM. Numerical simulation of pushover tests on a model jack-up platform on clay. *Géotechnique*, 61 (11), 947-960, 2011.

[7] Williams MS, Thompson RSG, Houlsby GT. Non-linear dynamic analysis of offshore jack-up units. *Computers and Structures*, 69(2), 171-180, 1998.

[8] Hutchinson TC, Chai YH, Boulanger RW, Idriss IM. Inelastic Seismic Response of Extended Pile-Shaft-Supported Bridge Structures. EERI *Earthquake Spectra*, 20(4), 1057-1080, 2004.

[9] Silva PF, Manzari MT. Nonlinear Pushover Analysis of Bridge Columns Supported on Full-Moment Connection CISS Piles on Clays. EERI *Earthquake Spectra*, 24(3), 751-774, 2008.

[10] Gerolymos N, Zafeirakos A, Souliotis C. Insight to Failure Mechanisms of Caisson Foundations Under Combined Loading: a Macro-Element Approach. In: *Proceedings of the 2nd International Conference on Performance-Based Design in Earthquake Geotechnical Engineering*, 28-30 May, Taormina, Italy, Paper No: 11.10, 2012.

[11] Zafeirakos A, Gerolymos N. On the seismic response of *under*-designed caisson foundations. *Bulletin of Earthquake Engineering*, 11(5), 1337–72, 2013.

[12] Zafeirakos A, Gerolymos N, Drosos V. Incremental dynamic analysis of caisson-pier interaction. *Soil Dynamics and Earthquake Engineering*, 48, 71–88, 2013.

[13] Varun, Assimaki D, Gazetas G. A simplified model for lateral response of large diameter caisson foundations-Linear elastic formulation. *Soil Dynamics and Earthquake Engineering*, 29(2), 268-291, 2009.

[14] Tsigginos C, Gerolymos N, Assimaki D, Gazetas G. Seismic response of bridge pier on rigid caisson foundation in soil stratum. *Earthquake Engineering & Engineering Vibration*, 7(1), 33-44, 2008.

[15] Gerolymos N, Gazetas G. Static and dynamic response of massive caisson foundations with soil and interface nonlinearities–validation and results. Soil Dynamics and Earthquake Engineering, 26(5), 377–94, 2006.

[16] Armstrong PJ, Frederick CO. A mathematical representation of the multiaxial Bauschinger effect. Technical Report RD/B/N 731, Central Electricity Generating Board,

Berkeley, UK, 1966 [Reprint in: Armstrong PJ, Frederick CO. A mathematical representation of the multiaxial Bauschinger effect. *Materials at High Temperatures*, 24(1), 1–26, 2007.

[17] Gourvenec S. Bearing capacity under combined loading - a study of the effect of shear strength heterogeneity. In: *Proceedings of the 9th Australian and New Zealand Conference on Geomechanics*, Auckland, New Zealand, 527-533, 2004.

[18] Karapiperis K, Gerolymos N. Combined loading of caisson foundations in cohesive soil: Finite element versus Winkler modeling. *Computers and Geotechnics*, 56, 100–120, 2014.

[19] Karapiperis K. Insight to the numerical modeling of the lateral response of caisson foundation to static and cyclic loading, *Diploma thesis*, NTUA, 2013.

[20] Mergos PE, Kappos AJ. Seismic damage analysis including inelastic shear–flexure interaction. *Bulletin of Earthquake Engineering*, 8, 27–46, 2010.

[21] Cassidy MJ, Randolph MF, Byrne BW. A plasticity model describing caisson behaviour in clay. *Applied Ocean Research*, 28, 345–358, 2006.

[22] Martin CM, Houlsby GT. Combined loading of spudcan foundations on clay: Numerical modelling. *Géotechnique* , 51(8), 687-699, 2001.

COMPDYN 2015
5th ECCOMAS Thematic Conference on
Computational Methods in Structural Dynamics and Earthquake Engineering
M. Papadrakakis, V. Papadopoulos, V. Plevris (eds.)
Crete Island, Greece, 25–27 May 2015

DISPERSION ANALYSIS OF ACOUSTIC WAVES IN FLUID MEDIA DISCRETIZED BY ENERGY-ORTHOGONAL FINITE ELEMENTS

Francisco José Brito Castro

Departamento de Ingeniería Industrial, Universidad de La Laguna,
Calle Méndez Núñez 67-2C, Santa Cruz de Tenerife 38001, Spain
fjbrito@ull.es

Keywords: energy-orthogonal stiffness, numerical dispersion, acoustic waves.

Abstract. *This paper studies the dispersion of acoustic waves in fluid media discretized by the finite element method. The element stiffness matrix is split into basic and higher order components which are respectively related to the mean and deviatoric components of the gradient of acoustic pressure. This decomposition is applied to the kinetic energy. The dispersion analysis yields a correlation between the higher order kinetic energy and the kinetic energy error. The use of this correlation as a reference to apply the higher order energy as an error indicator for the acoustic cavity modes computed by the finite element method is explored.*

1 INTRODUCTION

It is well known that analytical solutions to the governing equation of motion for any mechanical wave exist for just the simplest cases and only approximate solutions are feasible for the others. One method for obtaining approximate solutions is to use numerical procedures which often introduce phenomena, such as the numerical dispersion, that are not present in the physical system [1, 2].

The dispersion of acoustic waves in fluid media discretized by the finite element method is the principal topic of research in this paper. The fluid is assumed to be inviscid, compressible and homogeneous; moreover, the fluid particles oscillate in the absence of gravity and no ambient flow with small magnitude movements. The pressure and density of the fluid also undergo small perturbations respect to the ambient quantities. The resulting waves are termed linear acoustic waves. A short review of the basic theory of linear acoustic waves and the proper finite element formulation is a prerequisite in order to facilitate the subsequent developments.

1.1 Basic theory of linear acoustic waves

We consider linear acoustic waves in a fluid domain Ω with a complementary solid domain Ωs and the surface Γ representing the closed boundary of Ω and Ωs. The propagation of linear acoustic waves is described by the equation obtained by the linearization of the continuum mechanics equations of the ideal fluid [3],

$$\Delta p(\mathbf{r},t) - \frac{1}{c(\mathbf{r})^2}\frac{\partial^2 p(\mathbf{r},t)}{\partial t^2} - \nabla \ln \rho(\mathbf{r}) \cdot \nabla p(\mathbf{r},t) = 0, \quad \mathbf{r} \in \Omega \subset \mathrm{R}^3 \tag{1}$$

where: p, small perturbation of pressure or acoustic pressure; ρ, density of the fluid in the absence of acoustic wave; c, adiabatic sound velocity; t, time coordinate.

In a homogeneous medium the last term in Eq. (1) vanishes and Eq. (1) reduces to the wave equation

$$\Delta p(\mathbf{r},t) - \frac{1}{c^2}\frac{\partial^2 p(\mathbf{r},t)}{\partial t^2} = 0, \quad \mathbf{r} \in \Omega \subset \mathrm{R}^3 \tag{2}$$

For time-harmonic acoustic waves, time may be removed from the problem by writing

$$p(\mathbf{r},t) = \tilde{p}(\mathbf{r}) \exp(-i\omega t), \quad \mathbf{r} \in \Omega \subset \mathrm{R}^3 \tag{3}$$

where: $\tilde{p}(\mathbf{r})$, complex amplitude of acoustic pressure; $\omega = 2\pi / T$, circular frequency; T, period of wave.

Applying the time-harmonic dependence Eq. (3) to the wave equation Eq. (2) leads to the Helmholtz equation for the acoustic pressure

$$\Delta \tilde{p}(\mathbf{r}) + \frac{\omega^2}{c^2}\tilde{p}(\mathbf{r}) = 0, \quad \mathbf{r} \in \Omega \subset \mathrm{R}^3 \tag{4}$$

To complete a solution, the differential equation Eq. (4) requires specifying boundary conditions. Neumann boundary conditions can be assumed [4],

$$\frac{\partial \tilde{p}(\mathbf{r})}{\partial n} = \rho\omega^2 \tilde{u}_n(\mathbf{r}), \quad \mathbf{r} \in \Gamma \tag{5}$$

where: $u_n = \mathbf{u}^S \cdot \mathbf{n}$, normal component of the prescribed displacement of the boundary, $\mathbf{u}^S(\mathbf{r},t) = \tilde{\mathbf{u}}^S(\mathbf{r})\exp(-i\omega t)$; **n**, normal unit vector pointing outwards of Ω.

Dirichlet boundary conditions $\tilde{p}(\mathbf{r}) = \tilde{p}_0(\mathbf{r})$ also can be assumed.

In addition to fulfill the Helmholtz equation and the boundary conditions, solutions to scattering and radiation problems in unbounded media require that both the diffracted and radiated waves fulfill the decay condition at infinity, or Sommerfeld radiation condition [5]. In a finite computational domain different artificial boundary conditions have been proposed in order to fulfill this condition [6].

The linear acoustic waves in a homogeneous medium can be alternatively characterized by the acoustic displacement potential [3], determined by the expression

$$\mathbf{u}(\mathbf{r},t) = \nabla\psi(\mathbf{r},t), \quad \mathbf{r} \in \Omega \subset \mathrm{R}^3 \tag{6}$$

where: **u**, small displacement of the fluid particles; ψ, potential of displacement.

The relation between displacement potential and acoustic pressure will be

$$p(\mathbf{r},t) = -\rho\frac{\partial^2\psi(\mathbf{r},t)}{\partial t^2}, \quad \mathbf{r} \in \Omega \subset \mathrm{R}^3 \tag{7}$$

From Eq. (7), for time-harmonic acoustic waves, the relation between the complex amplitudes of acoustic pressure and displacement potential will be

$$\tilde{p}(\mathbf{r}) = \rho\omega^2\tilde{\psi}(\mathbf{r}), \quad \mathbf{r} \in \Omega \subset \mathrm{R}^3 \tag{8}$$

1.2 Finite element formulation

The boundary value problem Eq. (4) and (5) is posed in variational form [4]

$$\int_\Omega (\nabla p \cdot \nabla\delta p - \frac{\omega^2}{c^2}\, p\delta p)dV = \rho\omega^2\int_\Gamma (u_n\delta p)dS \tag{9}$$

The variational form Eq. (9) is discretized by the finite element method yielding the following matrix expression

$$(\mathbf{K} - \omega^2\mathbf{M})\mathbf{p} = \rho\omega^2\mathbf{\Theta}\mathbf{u}_N \tag{10}$$

where: **K**, global stiffness matrix; **M**, global mass matrix; **p,** column matrix containing the nodal values of acoustic pressure; **Θ**, boundary mass matrix; $\mathbf{u}_N$, column matrix containing the nodal values of the prescribed normal displacement of the boundary.

Defining at element level the matrix $\mathbf{B}^e$ relating the gradient of acoustic pressure to the nodal values of acoustic pressure,

$$\nabla p^e = \mathbf{B}^e\mathbf{p}^e \tag{11}$$

the element stiffness matrix is then written $\mathbf{K}^e = \int_{\Omega e}(\mathbf{B}^e)^T\mathbf{B}^e dV$.

The acoustic kinetic energy of the fluid occupying the bounded domain Ω will be

$$E_{ko} = \frac{1}{2\rho\omega^2}\int_\Omega \mathrm{Re}[i\nabla p]\cdot\mathrm{Re}[i\nabla p]dV \tag{12}$$

For the discretized domain, inserting Eq. (11) into Eq. (12) at element level, the element acoustic kinetic energy is yielded. The kinetic energy of the finite element assemblage will be the sum of the element energies. Then,

$$E_k = \frac{1}{2\rho\omega^2} \mathrm{Re}[i(\mathbf{p})^T]\mathbf{K}\,\mathrm{Re}[i\mathbf{p}] \tag{13}$$

1.2.1 Energy-orthogonal decomposition

The matrix relating the gradient of acoustic pressure to the nodal values of acoustic pressure at element level Eq. (11) is partitioned into mean and deviatoric components, $\mathbf{B}^e = \overline{\mathbf{B}}^e + \mathbf{B}_d^e$, where $\overline{\mathbf{B}}^e V^e = \int_{\Omega e} \mathbf{B}^e dV$ and $\mathbf{B}_d^e = \mathbf{B}^e - \overline{\mathbf{B}}^e$.

The element stiffness matrix is then written

$$\mathbf{K}^e = \mathbf{K}_b^e + \mathbf{K}_h^e \tag{14}$$

where: $\mathbf{K}_b^e = \int_{\Omega e} (\overline{\mathbf{B}}^e)^T \overline{\mathbf{B}}^e dV$, basic stiffness matrix; $\mathbf{K}_h^e = \int_{\Omega e} (\mathbf{B}_d^e)^T \mathbf{B}_d^e dV$, higher order stiffness matrix.

In this case it is said that the element stiffness matrix is decomposed in energy-orthogonal form [7]. The concept of energy-orthogonal stiffness matrix regarded in this paper was explicitly introduced in the context of the linear elasticity by Bergan and Nygärd within the framework of the Free Formulation [8], and by Felippa within the framework of the Parametrized Variational Principles [9].

The decomposition in Eq. (14) holds for the complete model whenever $\mathbf{K}_b^e$ and $\mathbf{K}_h^e$ are independently assembled,

$$\mathbf{K} = \mathbf{K}_b + \mathbf{K}_h \tag{15}$$

Inserting Eq. (15) into Eq. (13), we obtain the basic and higher order acoustic kinetic energies of the finite element assemblage.

1.2.2 Stationary waves

For a stationary wave, the amplitude of the acoustic pressure is a real-valued function. Then, from Eq. (13), the period-averaged acoustic kinetic energy of the fluid for the discretized domain will be

$$\overline{E}_k = \frac{1}{2\rho\omega^2} \tilde{\mathbf{p}}^T \mathbf{K} \tilde{\mathbf{p}} \int_0^1 \sin^2(2\pi\tau) d\tau$$

$$\overline{E}_k = \frac{1}{4\rho\omega^2} \tilde{\mathbf{p}}^T \mathbf{K} \tilde{\mathbf{p}} \tag{16}$$

where: $\tau = t/T$, $0 \le \tau \le 1$, dimensionless time; $\tilde{\mathbf{p}}$, column matrix containing the real nodal amplitudes of the acoustic pressure.

1.3 Scope of research

In this paper the dispersion properties and the density of period-averaged kinetic energy are computed for plane harmonic waves in unbounded media discretized by regular meshes of energy-orthogonal finite elements. Given the mesh, in the limit of

long wavelength, although the kinetic energy density does not vanish, its higher order component does vanish. Similarly, given the wavelength, as the solution converges on account of mesh refinement, the kinetic energy density is increasingly dominated by its basic component. The above heuristic argument motivates to research the relationship between the higher order kinetic energy and the discretization error in order to explore the behaviour of this energy component as an error indicator. To be precise, by the dispersion analysis, a correlation between the percentage of higher order kinetic energy and the kinetic energy error will be yielded. The use of this correlation as a reference to apply the higher order kinetic energy as an error indicator for the acoustic modes computed by the finite element method will be explored. A similar correlation has been proposed for linear gravity waves in fluid media [10]. Arguments to support the higher order energy as an error indicator have been established in the context of the linear elasticity [9].

2 DISPERSION ANALYSIS

2.1 Characteristic equations

The unbounded fluid domain is discretized by a regular mesh of finite elements. Three different isoparametric finite elements are considered: the hexahedron with twenty nodes and brick geometry HE20, Fig. 1, the pentahedron with fifteen nodes and right prismatic isosceles geometry PE15, Fig. 2, and the tetrahedron with ten nodes TE10. The mesh with TE10 elements is formed by dividing the unbounded domain in bricks with twenty seven nodes and then dividing each brick into six tetrahedrons [11], Fig. 3. The nodal lattice formed by the finite element assemblage has four, five and eight nodes per unit cell, respectively. Different meshes with the same element volume are yielded by selecting the aspect ratio parameter, where $0 < \gamma \leq 1$; additionally, for the HE20 and TE10 meshes, the skew angle also can be selected, where $0 \leq \beta < 90º$. The finite element analysis will be performed by using the rectangular coordinate system XYZ.

For an uniform plane harmonic wave propagating in the unbounded fluid domain,

$$\widetilde{p}(\mathbf{r}) = A\exp(i\kappa\mathbf{n}\cdot\mathbf{r}) \tag{17}$$

where: A, wave amplitude; $\mathbf{n}$, wave normal, unit vector indicating the direction of wave propagation; $\kappa = \omega/c = 2\pi/\lambda$, wave number; λ, wavelength.

The wave normal has the components, Fig. 4,

$$\mathbf{n} = (\cos\phi\sin\theta, \sin\phi\sin\theta, \cos\theta) \tag{18}$$

where: ϕ, $0 \leq \phi \leq 180º$, azimuthal angle; θ, $0 \leq \theta \leq 180º$, polar angle.

For the plane acoustic wave Eq. (17) the density of period-averaged kinetic energy can be computed by the equation [12]

$$\overline{E}_{ko} = \frac{A^2}{4\rho c^2} \tag{19}$$

The characteristic equations can be found assuming harmonic waves Eq. (17) with different amplitudes in each node of the unit cell,

$$\widetilde{p} = A_j \exp(i\kappa\mathbf{n}\cdot\mathbf{r}), \quad j = 1,\ldots,N \tag{20}$$

where: N, number of nodes per unit cell.

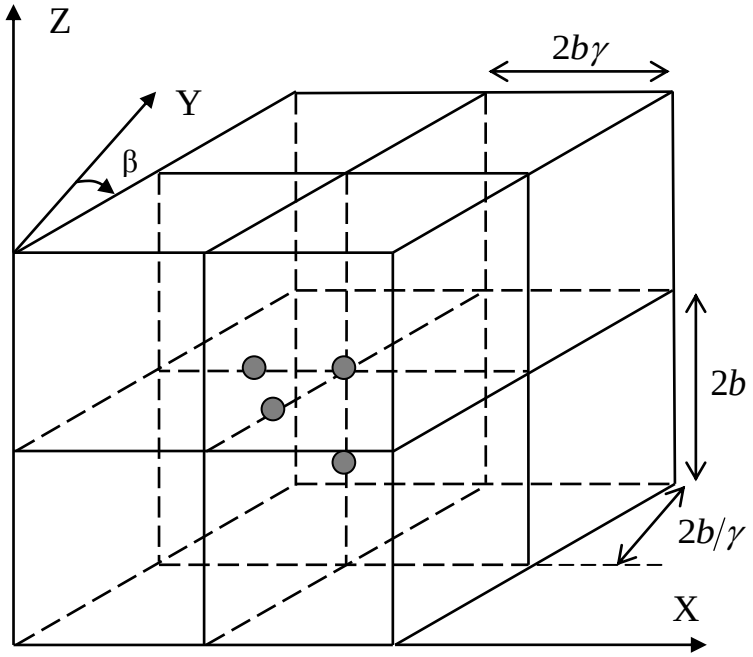


Figure 1: Regular mesh of twenty-nodes hexahedral elements and unit cell.

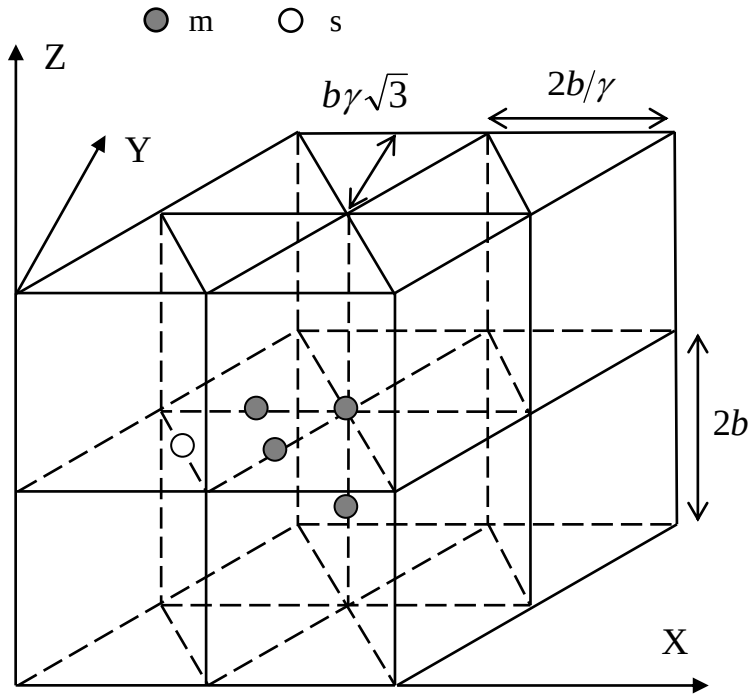


Figure 2: Regular mesh of fifteen-nodes pentahedral elements and unit cell.

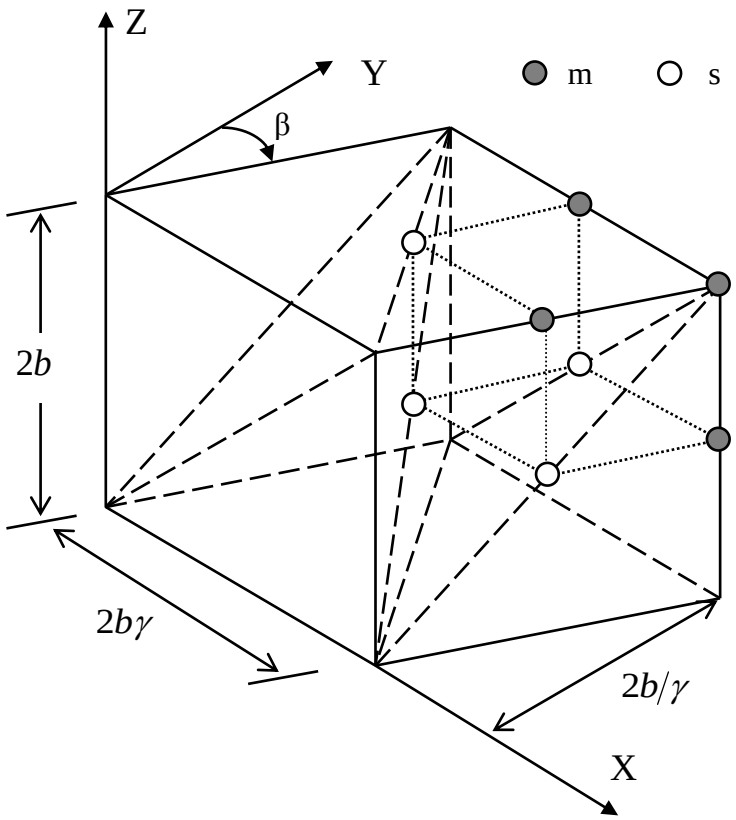


Figure 3: Regular mesh of ten-nodes tetrahedral elements and unit cell.

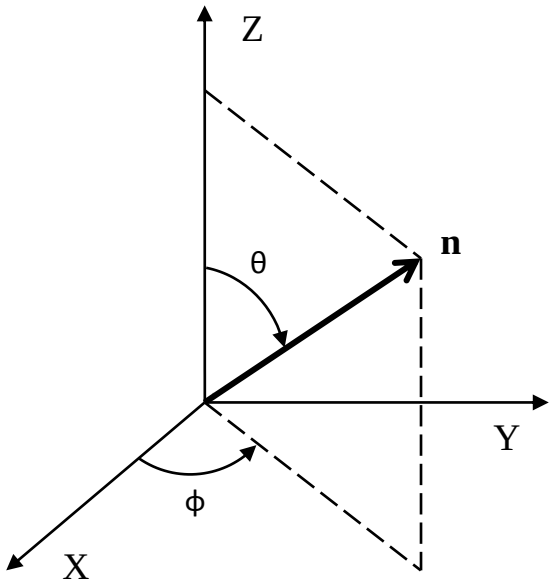


Figure 4: Unit vector indicating the direction of wave propagation.

Inserting the solutions Eq. (20) into the homogeneous part of Eq. (10), the characteristic equation for each node of the unit cell is yielded by equilibrium of generalized nodal forces [13]. A homogeneous system of N algebraic equations is formed,

$$\begin{gathered}\mathbf{ZA}=\mathbf{0}\\ z_{ij}A_j=0,\quad i,j=1,\ldots,N\end{gathered} \tag{21}$$

$$z_{ij}=a_{ij}(m,\phi,\theta,\boldsymbol{\varepsilon})+\varpi^2 b_{ij}(m,\phi,\theta,\boldsymbol{\varepsilon}) \tag{22}$$

$$m=\frac{b\kappa}{\pi}=\frac{2b}{\lambda},\quad \varpi=\frac{2b}{c}\omega \tag{23}$$

where: m, dimensionless wave number, $0 < m < 1$; b, half of the element size; ϖ, dimensionless frequency of the discretized fluid domain; $\boldsymbol{\varepsilon}=(\gamma,\beta)$ form parameters for HE20 and TE10 meshes, or $\boldsymbol{\varepsilon}=(\gamma)$ form parameter for PE15 mesh.

2.2 Dispersion equations

The system of homogeneous algebraic equations given in Eq. (21) has a non-trivial solution only if the matrix $\mathbf{Z}$ is singular; that is,

$$\det\left[\mathbf{Z}(m,\phi,\theta,\boldsymbol{\varepsilon},\varpi)\right]=0 \tag{24}$$

From Eq. (24) the following polynomial equation is yielded

$$\sum_{r=0}^{N} c_r q^r=0,\quad c_N=1 \tag{25}$$

where: $q=\varpi^2$; $c_r(m,\phi,\theta,\boldsymbol{\varepsilon})$, coefficients obtained from a_{ij} and b_{ij}, Eq. (22).

Either of Eq. (24) and (25) is called a characteristic frequency equation for the plane wave propagation.

It is an important fact that the N zeroes of a polynomial of degree $N \geq 1$ with complex coefficients depend continuously upon the coefficients [14]. Thus, sufficiently small changes in the coefficients of a polynomial can lead only to small changes in any zero. However, if the zeros are numerically computed, there is no simple way to define a function which takes the N coefficients (all but the leading 1) of a monic polynomial of degree N to the N zeroes of the polynomial, since there is no natural way to define an ordering among the N zeroes. In the case of the HE20 mesh, for which the polynomial Eq. (25) is quartic, the above difficulty has been overcome by computing the zeroes in closed form as functions of its coefficients. Then, the components

$$q_k=q_k(c_0,\ldots,c_3),\ k=1,\ldots,4 \tag{26}$$

or, alternatively,

$$\varpi_k=\varpi_k(m,\phi,\theta,\boldsymbol{\varepsilon}),\quad k=1,\ldots,4 \tag{27}$$

will be continuous functions precisely defined. They are called dispersion equations. Obviously, we suppose that the coefficients $c_r(m,\phi,\theta,\boldsymbol{\varepsilon})$ are also continuous functions.

Substituting Eq. (27) into Eq. (21), the wave amplitudes corresponding to the nodes of the unit cell for the HE20 mesh are yielded for each dispersion equation. In this work,

each set of linear algebraic equations is numerically solved by using the singular value decomposition method SVD [15].

To find the zeros of a polynomial equation as functions of its coefficients beyond the quartic equation is a very difficult mathematical problem [16]. Then, for the meshes PE15 and TE10 which have five and eight nodes per unit cell, respectively, if the zeros of Eq. (25) are numerically computed, the above mentioned ordering difficulty could be a problem. In this case, by considering the initial condition,

$$\lim_{m\to 0} \varpi_1(\phi, \theta, \boldsymbol{\varepsilon}) = 0 \tag{28}$$

we propose to compute the first dispersion equation by a reduced unit cell obtained by a procedure of exact dynamic condensation [17].

Assume that the total nodes at the unit cell are categorized as master nodes (m) and slave nodes (s), where the number of master nodes is four, and the number of slave nodes is one and four for P15 and TE10 meshes, respectively, see Fig. 2 and 3. With this arrangement, the system of characteristic equations Eq. (21) may be partitioned as

$$\begin{pmatrix} \mathbf{Z}_{mm} & \mathbf{Z}_{ms} \\ \mathbf{Z}_{sm} & \mathbf{Z}_{ss} \end{pmatrix} \begin{pmatrix} \mathbf{A}_m \\ \mathbf{A}_s \end{pmatrix} = \begin{pmatrix} \mathbf{0} \\ \mathbf{0} \end{pmatrix} \tag{29}$$

where:

$$\begin{aligned} \mathbf{Z}_{mm} &= \mathbf{a}_{mm} + q\mathbf{b}_{mm}, \quad \mathbf{Z}_{ms} = \mathbf{a}_{ms} + q\mathbf{b}_{ms} \\ \mathbf{Z}_{sm} &= \mathbf{a}_{sm} + q\mathbf{b}_{sm}, \quad \mathbf{Z}_{ss} = \mathbf{a}_{ss} + q\mathbf{b}_{ss} \end{aligned} \tag{30}$$

The relation of wave amplitudes between the master and slave nodes may be obtained from Eq. (29) as

$$\mathbf{A}_s = -\mathbf{Z}_{ss}^{-1}(q)\mathbf{Z}_{sm}(q)\mathbf{A}_m \tag{31}$$

Then, by back-substituting, the system of characteristic equations of the reduced unit cell is obtained as

$$\begin{aligned} \mathbf{Z}_R(q)\mathbf{A}_m &= \mathbf{0} \\ (\mathbf{K}_R(q) + q\mathbf{M}_R(q))\mathbf{A}_m &= \mathbf{0} \end{aligned} \tag{32}$$

where:

$$\begin{aligned} \mathbf{K}_R(q) &= \mathbf{a}_{mm} - \mathbf{Z}_{ms}\mathbf{Z}_{ss}^{-1}\mathbf{a}_{sm} + \mathbf{Z}_{ms}\mathbf{Z}_{ss}^{-1}\mathbf{a}_{ss}\mathbf{Z}_{ss}^{-1}\mathbf{Z}_{sm} - \mathbf{a}_{ms}\mathbf{Z}_{ss}^{-1}\mathbf{Z}_{sm} \\ \mathbf{M}_R(q) &= \mathbf{b}_{mm} - \mathbf{Z}_{ms}\mathbf{Z}_{ss}^{-1}\mathbf{b}_{sm} + \mathbf{Z}_{ms}\mathbf{Z}_{ss}^{-1}\mathbf{b}_{ss}\mathbf{Z}_{ss}^{-1}\mathbf{Z}_{sm} - \mathbf{b}_{ms}\mathbf{Z}_{ss}^{-1}\mathbf{Z}_{sm} \end{aligned} \tag{33}$$

Then, from Eq. (32), the reduced form of the characteristic frequency equation is obtained

$$\begin{aligned} q^4 + c_{3R}q^3 + c_{2R}q^2 + c_{1R}q + c_{0R} &= 0 \\ c_{rR}(m, \phi, \theta, \boldsymbol{\varepsilon}, q), \quad r &= 0, \ldots, 3 \end{aligned} \tag{34}$$

The first dispersion equation is computed by the following iterative procedure:
Set by Eq. (28) the initial value $q_{i1} = 0$.

Do for $0 < m < 1$, step Δm

1. Compute the coefficients $c_{rR}(m, \phi, \theta, \boldsymbol{\varepsilon}, q_{i1})$ of Eq. (34).

2. Compute the zero q_1 of the quartic polynomial Eq. (34).

Do while ($\left|\frac{q_1 - q_{i1}}{q_1}\right| \geq \delta$)

1. Refresh initial value $q_{i1} = q_1$.
2. Compute the coefficients $c_{rR}(m, \phi, \theta, \boldsymbol{\varepsilon}, q_{i1})$ of Eq. (34).
3. Compute the zero q_1 of the quartic polynomial Eq. (34).

End do

3. Substituting q_1 into Eq. (32) to compute the wave amplitudes at the master nodes.
4. Substituting q_1 into Eq. (31) to compute the wave amplitudes at the slave nodes.
5. Refresh initial value $q_{i1} = q_1$ for the next step.

End do

The range of dimensionless wave number values where each dispersion equation represents the propagation of acoustic waves in the discretized medium will be called the acoustical branch of the dispersion equation. In order to determine the acoustical branches, a preliminary constraint condition over the dimension of the null space of **Z** for the H20 mesh, or $\mathbf{Z}_R$ for PE15 and TE10 meshes, must be imposed,

$$\dim[\mathbf{N}(\mathbf{Z})] = 1 \quad or \quad \dim[\mathbf{N}(\mathbf{Z}_R)] = 1 \tag{35}$$

The constraint condition Eq. (35) implies that the subspace of solutions to Eq. (21) or Eq. (32) must be one-dimensional. In this case the vector of wave amplitudes **A** or $\mathbf{A}_{\mathrm{m}}$ is arbitrary to the extent that a scalar multiple of it is also a solution. Then the following constraint conditions are imposed,

$$A_1 = 1, \quad \begin{cases} A_2(m, \phi, \theta, \boldsymbol{\varepsilon}) > 0 \\ A_3(m, \phi, \theta, \boldsymbol{\varepsilon}) > 0 \\ A_4(m, \phi, \theta, \boldsymbol{\varepsilon}) > 0 \end{cases} \tag{36}$$

$$\left(\frac{\partial \varpi}{\partial m}\right)_{\phi, \theta, \boldsymbol{\varepsilon}} > 0 \tag{37}$$

In molecular physics, condition Eq. (36) is called the restriction of the lattice spectrum to the acoustical branch [18]. Obviously, if the constraint condition Eq. (35) is not imposed, the constraint condition Eq. (36) is meaningless.

From Eq. (23) we obtain both the phase velocity and group velocity of the discretized medium,

$$c_d = \frac{c}{2\pi} \frac{\varpi}{m} \tag{38}$$

$$c_{g,d} = \frac{\partial \omega}{\partial \kappa} = \frac{c_g}{2\pi} \frac{\partial \varpi}{\partial m} \tag{39}$$

where: c, phase velocity of the continuum (adiabatic sound velocity) ; c_g , group velocity of the continuum.

From Eq. (39), the constraint condition Eq. (37) is equivalent to

$$c_{g,d} > 0 \tag{40}$$

It can be proven that for general periodic motion the energy propagates with the group velocity [19]; therefore, the constraint condition Eq. (40) imposes that the energy propagates into the wave direction. From this point, for each dispersion equation only the acoustical branch will be considered. This one represents the physically admissible solution for mechanical wave propagation.

It must be recall that the group velocity of the continuum will be equal to the phase velocity because the waves propagate non-dispersively. Nevertheless, for the dispersive discretized medium the group velocity will be different from the phase velocity; therefore, the velocity of energy transport will be different from the phase velocity. As a consequence, when we consider the numerical dispersion associated with the finite element spatial discretization, not only the effect over the phase velocity must be analyzed but also the effect over the group velocity or velocity of energy transport.

2.3 Kinetic energy at the unit cell

For a fluid domain discretized by a regular mesh of finite elements, the stiffness matrix can be expressed in the suitable form $\mathbf{K} = (2b)\mathbf{K}^0$. Then, from Eq. (13) and (23), the kinetic energy at the unit cell over a period will be

$$E_k = \frac{1}{2\rho c^2 \varpi^2}(2b)^3 \,\mathrm{Re}[i(\tilde{\mathbf{p}})^T \exp(-i2\pi\tau)]\,\mathrm{Re}[i\tilde{\mathbf{G}}^0 \exp(-i2\pi\tau)] \tag{41}$$

where: $\mathbf{G}^0 = \tilde{\mathbf{G}}^0 \exp(-i2\pi\tau)$, column matrix of generalized forces at the nodes of the unit cell, obtained from the stiffness matrix $\mathbf{K}^0$.

From Eq. (41), the density of period-averaged kinetic energy is computed,

$$\overline{E}_k = \frac{C}{2\rho c^2 \varpi^2}\int_0^1 \mathrm{Re}[i(\tilde{\mathbf{p}})^T \exp(-i2\pi\tau)]\,\mathrm{Re}[i\tilde{\mathbf{G}}^0 \exp(-i2\pi\tau)]d\tau \tag{42}$$

where: $C = 1$, for HE20 and TE10 meshes; $C = 2/\sqrt{3}$, for PE15 mesh.

From the decomposition in Eq. (15), $\mathbf{K}^0 = \mathbf{K}_b^0 + \mathbf{K}_h^0$, the density of period-averaged kinetic energy Eq. (42) can be partitioned as addition of basic and higher order components. The latter component will be

$$\overline{E}_{kh} = \frac{C}{2\rho c^2 \varpi^2}\int_0^1 \mathrm{Re}[i(\tilde{\mathbf{p}})^T \exp(-i2\pi\tau)]\,\mathrm{Re}[i\tilde{\mathbf{G}}_h^0 \exp(-i2\pi\tau)]d\tau \tag{43}$$

where: $\mathbf{G}_h^0 = \tilde{\mathbf{G}}_h^0 \exp(-i2\pi\tau)$, column matrix of higher order generalized forces at the nodes of the unit cell, obtained from the higher order stiffness matrix $\mathbf{K}_h^0$.

From Eq. (43) and (42), the percentage of period-averaged higher order kinetic energy can be defined as

$$e_h = \frac{\overline{E}_{kh}}{\overline{E}_k}, \quad e_h = e_h(m, \phi, \theta, \boldsymbol{\varepsilon}) \tag{44}$$

2.4 Indicators of discretization error

By considering Eq. (38) and (39), the indicators of the dispersion associated with spatial discretization that is introduced by the finite element model are defined as

$$e_d = \frac{c_d}{c} = \frac{\varpi}{2m\pi}, \quad e_d = e_d(m, \phi, \theta, \boldsymbol{\varepsilon}) \tag{45}$$

$$e_{g,d} = \frac{c_{g,d}}{c_g} = \frac{1}{2\pi}\frac{\partial \varpi}{\partial m}, \quad e_{g,d} = e_{g,d}(m, \phi, \theta, \boldsymbol{\varepsilon}) \tag{46}$$

These indicators consider the effect of the spatial discretization over the wave velocity and the velocity of energy transport, respectively.

From Eq. (42) and (19), the indicator of kinetic energy error associated with spatial discretization that is introduced by the finite element model is defined as

$$e_k = \frac{\overline{E}_k}{\overline{E}_{ko}}, \quad e_k = e_k(m, \phi, \theta, \boldsymbol{\varepsilon}) \tag{47}$$

Alternatively, the percentage of kinetic energy error can be defined as

$$\varepsilon_k = e_k - 1, \quad \varepsilon_k = \varepsilon_k(m, \phi, \theta, \boldsymbol{\varepsilon}) \tag{48}$$

2.5 Numerical research

Three different meshes having the same element volume will be considered for each of the analyzed elements. Specifically, for HE20 and TE10 elements, Fig. 1 and 3:

Q1; square section, $\gamma = 1, \quad \beta = 0$

Q2; rectangular section with aspect ratio 1:2, $\gamma = \frac{1}{\sqrt{2}}, \quad \beta = 0$

Q3; skewed section, $\gamma = 1, \quad \beta = 45^{\circ}$

and, for PE15 element, Fig. 2:

Q1; triangular section of equilateral geometry, $\gamma = 1$

Q2; triangular section of right geometry, $\gamma^2 = \frac{1}{\sqrt{3}}$

Q3; triangular section with angle of 30º opposite to the base, $\gamma^2 = \frac{\tan 75^{\circ}}{\sqrt{3}}$

The indicators Eq. (44) to (48) are computed versus dimensionless wave number for different directions of wave propagation.

For the mesh HE20-Q3, the indicator of dispersion Eq. (45) is plotted in Fig. 5. Given the azimuthal angle ϕ, three values of the polar angle θ are considered in order to represent the anisotropy induced by the spatial discretization. The numerical dispersion is clearly displayed as the dimensionless wave number increases. A discontinuity in phase velocity is observed around $m = 1/2$ for $\theta = 0^{\circ}$. In this case the discretized fluid domain acts like a band-pass filter [13]. This discontinuity was already described by Brillouin [18] for lattices consisting of different particles.

For the mesh Q1 and a selected direction of wave propagation the indicators Eq. (47) and Eq. (44) are plotted versus dimensionless wave number for each of the considered elements, Fig. 6 and 7. It is observed that the kinetic energy error vanishes both as the mesh is refined and in the limit of long wavelength, as it is expected. Similarly, the density of higher order kinetic energy also vanishes both as the mesh is refined and in the limit of long wavelength. This latter behaviour also is expected because the acoustic

pressure field inside each element becomes uniform. As a conclusion, the dispersion analysis reveals that the higher order kinetic energy behaves as an error indicator.

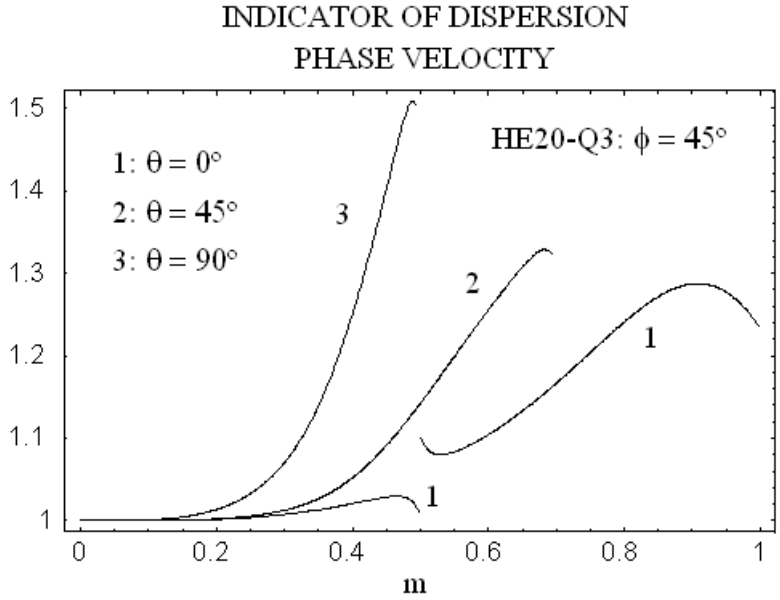


Figure 5: Indicator of dispersion associated with the phase velocity versus dimensionless wave number.

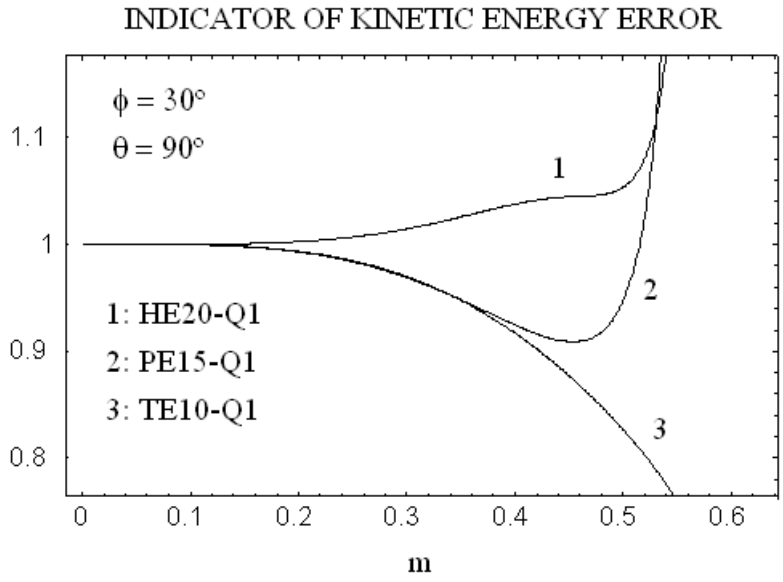


Figure 6: Indicator of kinetic energy error versus dimensionless wave number.

In order to explore the behaviour of the higher order kinetic energy as an error indicator, a correlation between the percentage of higher order kinetic energy and the kinetic energy error is pursued. As a first step, from Eq. (44) and (48), a mapping that associates a value of percentage of kinetic energy error to each value of percentage of higher order kinetic energy is defined,

$$\varepsilon_k = \varepsilon_k(e_h, \phi, \theta, \boldsymbol{\varepsilon}) \tag{49}$$

For the mesh Q1 and a selected direction of wave propagation the mapping Eq. (49) is plotted in Fig. 8 for each of the considered elements. It is observed that in each case, and for moderate values of percentage of higher order kinetic energy, this mapping could be approximated by the following cubic correlation,

$$\varepsilon_k = (A * e_h + B) * e_h^2 \tag{50}$$

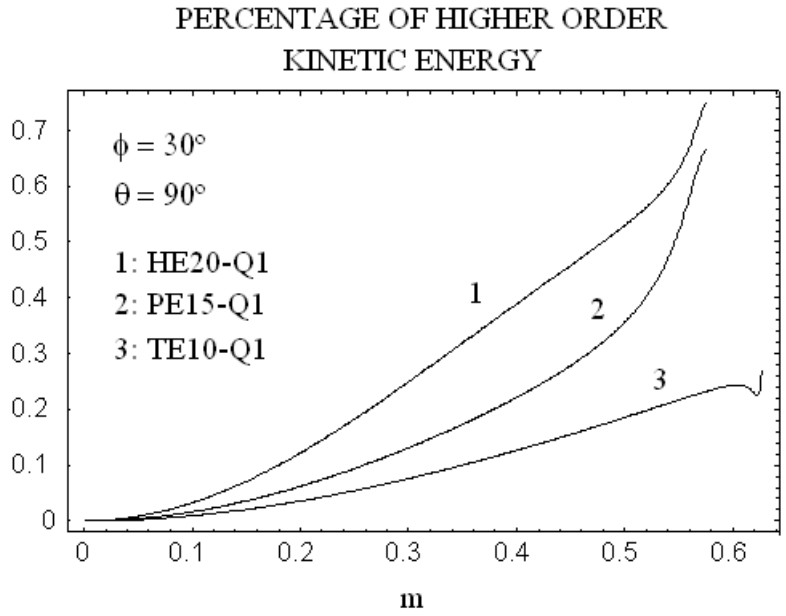


Figure 7: Percentage of higher order kinetic energy versus dimensionless wave number.

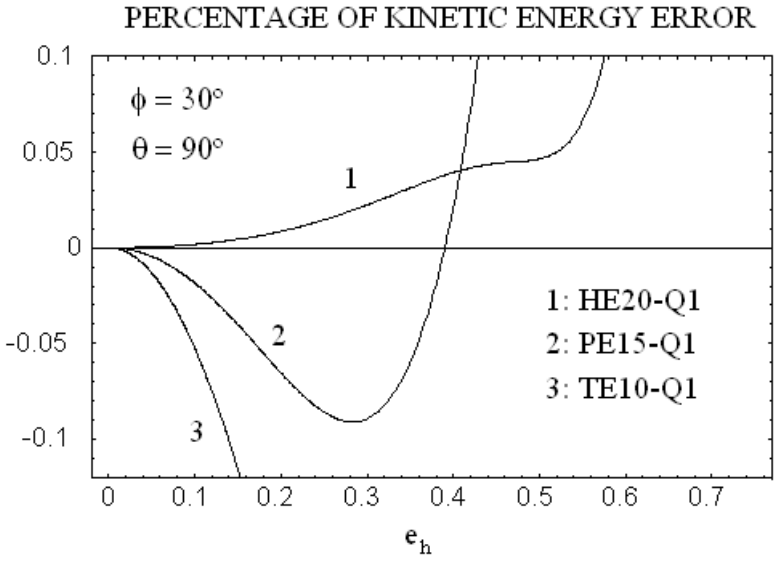


Figure 8: Percentage of kinetic energy error versus percentage of higher order kinetic energy.

As a second step, for each of the considered elements, two values of percentage of higher order kinetic energy Eq. (44) are selected as reference ones,

$$HE20: \quad e_{h1} = 0.10 \quad e_{h2} = 0.20 \tag{51}$$

$$PE15: \quad e_{h1} = 0.075 \quad e_{h2} = 0.15 \tag{52}$$

$$TE10: \quad e_{h1} = 0.03 \quad e_{h2} = 0.06 \tag{53}$$

From Eq. (44) and Eq. (51) to (53), the first and the second reference dimensionless wave number are defined for each of the considered elements,

$$m_1 = f_{m1}(\phi, \theta, \boldsymbol{\varepsilon}) \tag{54}$$

$$m_2 = f_{m2}(\phi, \theta, \boldsymbol{\varepsilon}) \tag{55}$$

As a third step, from Eq. (48) and (54), and from Eq. (48) and (55), the first and the second reference values of percentage of kinetic energy error are defined,

$$\varepsilon_{k1} = f_{k1}(\phi, \theta, \boldsymbol{\varepsilon}) \tag{56}$$

$$\varepsilon_{k2} = f_{k2}(\phi, \theta, \boldsymbol{\varepsilon}) \tag{57}$$

Similar reference values can be defined for the indicator of dispersion associated with the group velocity,

$$e_{g1} = f_{g1}(\phi, \theta, \boldsymbol{\varepsilon}) \tag{58}$$

$$e_{g2} = f_{g2}(\phi, \theta, \boldsymbol{\varepsilon}) \tag{59}$$

For the element TE10 and the mesh Q3, Eq. (55), (57) and (59) are displayed versus polar angle θ for selected values of azimuthal angle ϕ, Fig. 9 to 11.

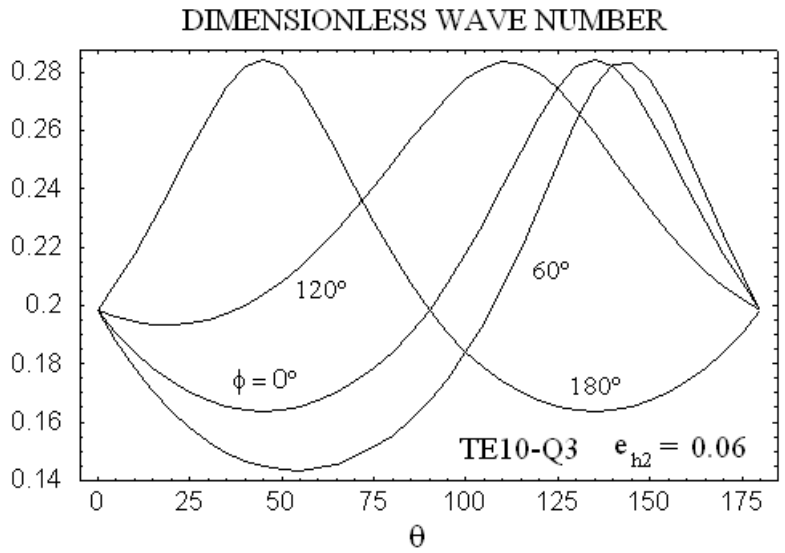


Figure 9: Second reference value of dimensionless wave number versus the polar angle.

As a fourth step, for each of the considered elements, the root-mean-square value and the maximum absolute value of Eq. (56) and (57) are computed over the range of azimuthal and polar angles. The results are shown in Tables 1 to 3. Also, the mean values of Eq. (54) and (55), and the mean values of Eq. (58) and (59), are computed.

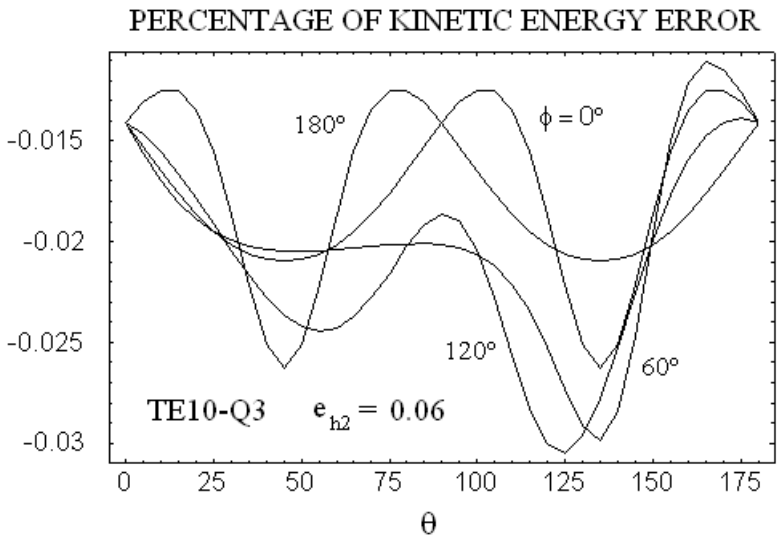


Figure 10: Second reference value of percentage of kinetic energy error versus the polar angle.

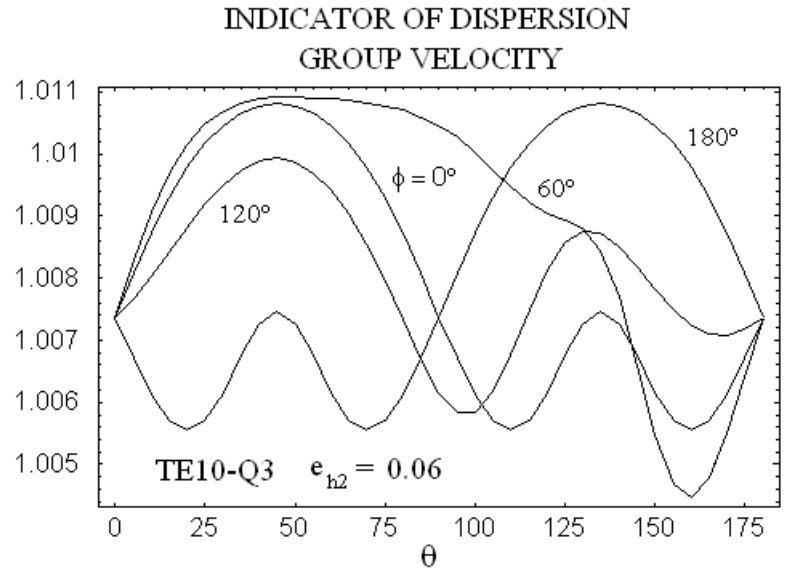


Figure 11: Second reference value of indicator of dispersion associated with the group velocity versus the polar angle.

As a last step, for each of the considered elements, we propose to apply the cubic correlation Eq. (50) to define a mapping that associates a standard value of percentage of kinetic energy error to each value of percentage of higher order kinetic energy. The coefficients *A* and *B* are solved using the averaging of root-mean-square values computed for Eq. (56) and (57), Tables 1 to 3. Specifically,

$$\varepsilon_k^{HE20} = (0.416000 * e_h + 0.273100) * e_h^2, \quad 0 < e_h \leq 0.20 \tag{60}$$

$$\varepsilon_k^{PE15} = (0.337185 * e_h + 0.828222) * e_h^2, \quad 0 < e_h \leq 0.15 \tag{61}$$

$$\varepsilon_k^{TE10} = (2.722222 * e_h + 5.856111) * e_h^2, \quad 0 < e_h \leq 0.06 \tag{62}$$

In Fig. 12 the standard correlations Eq. (60) to (62) are displayed. In each case the interval of application can be moderately extended beyond the upper limit of percentage of higher order kinetic energy used to compute the coefficients *A* and *B*. It is observed that the correlation between standard percentage of kinetic energy error and percentage of higher order kinetic energy is highly dependent of the considered element. The correlation for PE15 element is between the ones for TE10 and HE20 elements, as it could be expected.

HE20				
$e_{h1} = 0.10$	ε_{k1}^{RMS}	ε_{k1}^{MAX}	$\overline{m}_1$	$\overline{e}_{g1}$
MESH Q1	0.003279	0.006283	0.1797	1.002710
MESH Q2	0.003126	0.006151	0.1752	1.002680
MESH Q3	0.003035	0.008281	0.1711	1.003330
Averaged value	0.003147	0.006905	0.1753	1.002907
$e_{h2} = 0.20$	ε_{k2}^{RMS}	ε_{k2}^{MAX}	$\overline{m}_2$	$\overline{e}_{g2}$
MESH Q1	0.014991	0.030342	0.2627	1.011810
MESH Q2	0.013883	0.029227	0.2561	1.011680
MESH Q3	0.013882	0.041620	0.2500	1.014770
Averaged value	0.014252	0.033730	0.2563	1.012753

Table 1: Characteristic reference values for HE20 element over the range of azimuthal and polar angles.

PE15				
$e_{h1} = 0.075$	ε_{k1}^{RMS}	ε_{k1}^{MAX}	$\overline{m}_1$	$\overline{e}_{g1}$
MESH Q1	0.004139	0.010875	0.1833	1.002700
MESH Q2	0.004900	0.017457	0.1805	1.002990
MESH Q3	0.005365	0.020527	0.1779	1.002900
Averaged value	0.004801	0.016286	0.1806	1.002863
$e_{h2} = 0.15$	ε_{k2}^{RMS}	ε_{k2}^{MAX}	$\overline{m}_2$	$\overline{e}_{g2}$
MESH Q1	0.016810	0.045641	0.2667	1.011470
MESH Q2	0.020345	0.076963	0.2627	1.012680
MESH Q3	0.022165	0.084933	0.2589	1.012340
Averaged value	0.019773	0.069179	0.2628	1.012163

Table 2: Characteristic reference values for PE15 element over the range of azimuthal and polar angles.

Also, for each of the considered elements, we propose to apply a quadratic correlation to define a mapping that associates a mean value of dimensionless wave number to each value of percentage of higher order kinetic energy,

$$\overline{m} = (A * e_h + B) * e_h, \quad 0 < e_h \leq e_{h2} \tag{63}$$

The coefficients *A* and *B* are solved using the averaging of mean dimensionless wave number computed for Eq. (54) and (55), Tables 1 to 3. The correlation Eq. (63) is

displayed in Fig. 13. For a particular mesh and direction of wave propagation, in Fig. 7 the quadratic dependence between dimensionless wave number and percentage of higher order kinetic energy can be observed is approximately fulfilled for each of the considered elements in the interested range of percentage of higher order kinetic energy.

TE10				
$e_{h1} = 0.03$	ε_{k1}^{RMS}	ε_{k1}^{MAX}	$\overline{m}_1$	$\overline{e}_{g1}$
MESH Q1	0.005607	0.009749	0.1454	1.002380
MESH Q2	0.005479	0.010164	0.1423	1.002160
MESH Q3	0.004946	0.007412	0.1471	1.002060
Averaged value	0.005344	0.009108	0.1449	1.002200
$e_{h2} = 0.06$	ε_{k2}^{RMS}	ε_{k2}^{MAX}	$\overline{m}_2$	$\overline{e}_{g2}$
MESH Q1	0.022668	0.041343	0.2100	1.009610
MESH Q2	0.022113	0.040651	0.2056	1.008740
MESH Q3	0.020229	0.030939	0.2125	1.008370
Averaged value	0.021670	0.037644	0.2094	1.008907

Table 3: Characteristic reference values for TE10 element over the range of azimuthal and polar angles.

2.6 Remark

It is clear that the harmonic acoustic waves cannot be exactly captured by a regular mesh of finite elements HE20, PE15 or TE10. This fact is a consequence of the element interpolation which is quadratic. A substitute wave field [20] or alias field [21] has been obtained in the discretized unbounded medium by performing a dispersion analysis. The alias field is yielded by collocating Eq. (20) in each node of the unit cell. The assumption of different amplitudes is introduced because the equation of equilibrium is different for each node. The analysis yields the relative wave amplitudes and the dispersion relation under which the alias field may propagate. In each element the alias field will be

$$\tilde{p}^a = \sum N_{S,i} \tilde{p}_i \tag{64}$$

where: $\tilde{p}_i$, the values of Eq. (20) at the nodes; $N_{S,i}$, the element shape functions.

Finally we must remark that the dispersion analysis can be alternatively performed characterizing the plane harmonic wave by the displacement potential. Obviously, in that case, we obtain the same results.

3 ACOUSTIC CAVITY MODES

3.1 Introduction

It is well known that the reflection of waves from boundaries or from other discontinuities creates an interference field that, if composed solely of waves of frequency equal to a natural frequency of the system, takes the form of a stationary wave field which is a natural mode of the continuum system [22]; therefore, if a finite volume of compressible fluid is bounded by the motionless and reflecting walls of a cavity it can oscillate according to stationary waves called acoustic modes. In this

section we approach the subject of the acoustic modes in three-dimensional cavities which have no analytical solution and will be solved by the finite element method.

In order to conveniently pose an algebraic eigenvalue problem, the acoustic field will be characterized by the displacement potential. Then, inserting Eq. (8) into Eq. (10), the governing equation of the discretized fluid medium will be

$$(\mathbf{K} - \omega^2 \mathbf{M})\boldsymbol{\psi} = \boldsymbol{\Theta}\mathbf{u}_N \tag{65}$$

where: $\boldsymbol{\psi}$, column matrix containing the nodal values of displacement potential.

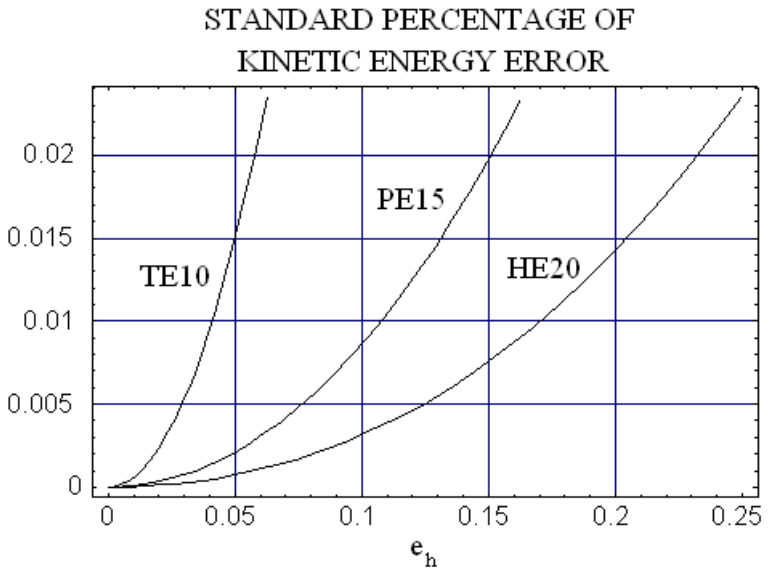


Figure 12: Standard percentage of kinetic energy error versus percentage of higher order kinetic energy.

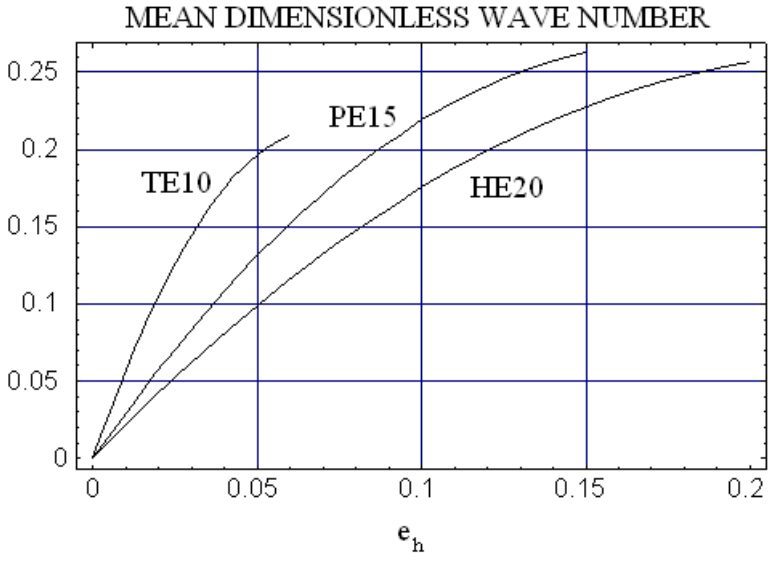


Figure 13: Mean dimensionless wave number versus percentage of higher order kinetic energy.

By considering the homogeneous part of Eq. (65) and assuming stationary waves, it is produced the so called generalized eigenproblem [23],

$$\mathbf{K}\tilde{\boldsymbol{\psi}}_j = \lambda_j \mathbf{M}\tilde{\boldsymbol{\psi}}_j \tag{66}$$

where: $\lambda_j = \omega_j^2$, the *j*-eigenvalue; $\tilde{\boldsymbol{\psi}}_j$, the *j*-eigenvector.

It is well known that the eigenvalue can be physically interpreted as the square of the natural frequency of the discretized fluid medium. The eigenvector and the element interpolation functions shape the finite element mode. Obviously, as the finite element mesh is refined and discretization error decreases, both the finite element eigenvalues and the finite element modes must converge to the eigenvalues and the eigenfunctions associated with the differential governing equation and its boundary conditions [24].

The kernel of the global stiffness matrix **K** is of dimension 1; therefore, this matrix is positive semidefinite. The generalized eigenproblem Eq. (66) has been solved by the subspace iteration method [23]. The algorithm requires that **K** be nonsingular. This restriction can be met by using an eigenvalue shift [25].

An important relation fulfilled by the eigenvectors is that of **M**-orthonormality,

$$\tilde{\boldsymbol{\psi}}_i^T \mathbf{M}\tilde{\boldsymbol{\psi}}_j = \delta_{ij} \tag{67}$$

where δ_{ij} is the Kronecker delta.

Premultiplying Eq. (66) by $\tilde{\boldsymbol{\psi}}_i^T$ and using Eq. (67), it is produced

$$\tilde{\boldsymbol{\psi}}_i^T \mathbf{K}\tilde{\boldsymbol{\psi}}_j = \delta_{ij}\omega_j^2 \tag{68}$$

If the acoustic field is characterized by the displacement potential, by Eq. (8) and (16) the modal kinetic energy of the discretized fluid medium will be

$$\overline{E}_k = \frac{1}{4}\rho\omega^2 \tilde{\boldsymbol{\psi}}^T \mathbf{K}\tilde{\boldsymbol{\psi}} \tag{69}$$

By introducing the decomposition in Eq. (15) into Eq. (69) we obtain both the basic and higher order modal kinetic energy. The latter component will be

$$\overline{E}_{kh} = \frac{1}{4}\rho\omega^2 \tilde{\boldsymbol{\psi}}^T \mathbf{K}_h \tilde{\boldsymbol{\psi}} \tag{70}$$

Finally, by introducing Eq. (68) into Eq. (69), the following expression for the modal kinetic energy it is produced

$$\overline{E}_k = \frac{1}{4}\rho\omega^4 \tag{71}$$

3.2 Numerical research

In this section it is investigated the application of the percentage of higher order kinetic energy as an error indicator for the acoustic modes computed by the finite element method. This percentage will be evaluated by Eq. (69) and (70),

$$PHE = \frac{\overline{E}_{kh}}{\overline{E}_k} \tag{72}$$

An estimation of the error for the natural frequencies and modal displacement potentials obtained with the discretized fluid domain will be presented. The reference model will be obtained by dividing each element of the actual mesh into eight elements.

The modal displacement potentials obtained with the actual model and the ones obtained with the reference model will be compared by the modal kinetic energy error

$$KEE = \frac{\overline{E}_k - \overline{E}_k^{REF}}{\overline{E}_k^{REF}} \tag{73}$$

where $\overline{E}_k$ and $\overline{E}_k^{REF}$ are defined by Eq. (69).

By considering Eq. (71), the modal kinetic energy error Eq. (73) can be evaluated as

$$KEE = \left(\frac{\omega}{\omega^{REF}} \right)^4 - 1 \tag{74}$$

Obviously, from Eq. (74) the natural frequency error is inferred.

In order to investigate the behaviour of the percentage of higher order kinetic energy as a modal error indicator, the application of the standard correlation, yielded by the numerical dispersion analysis, between the percentage of higher order kinetic energy and the kinetic energy error, Eq. (60) to (62), is explored. The kinetic energy error computed by the above correlation from the percentage of higher order modal kinetic energy associated with the actual model will be called the standard modal kinetic energy error, SKEE. This standard error will be compared with the one computed by Eq. (74). Two acoustic cavities will be analyzed: a tapered cavity discretized by HE20 element, Fig. 14; and a half of pyramidal cavity discretized by TE10 element, Fig. 15. The results are shown in Tables 4 and 5, respectively.

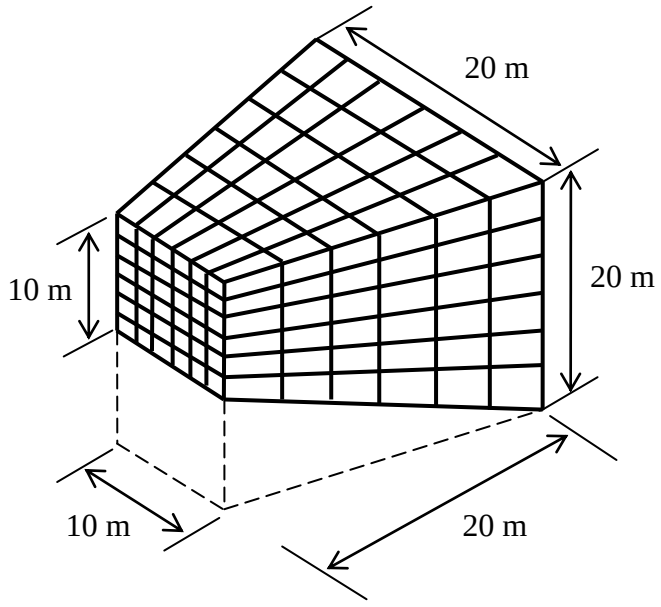


Figure 14: Tapered cavity. Sound velocity, c = 346 m/s.

From Tables 4 and 5, it is observed that both the percentage of higher order kinetic energy Eq. (72) and the kinetic energy error Eq. (74) increase with the modal order. The percentage of higher order kinetic energy decreases as the mesh is refined. Clearly, the numerical research reveals that the percentage of higher order kinetic energy behaves as

a modal error indicator. This result is consistent with the one obtained by the numerical dispersion analysis carried out for harmonic waves.

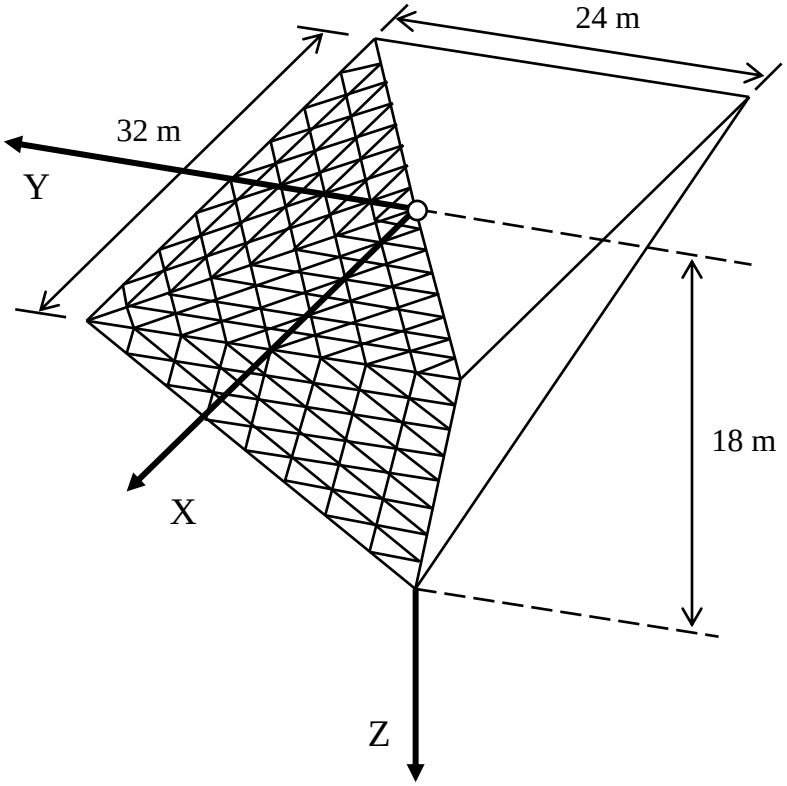


Figure 15: Half of pyramidal cavity. Sound velocity, c = 346 m/s.

From Tables 4 and 5, and Fig. 16 and 17, it is observed that the standard error SKEE generally overestimates the modal kinetic energy error KEE, Eq. (74), at least in the interested range of error. Typically it is considered that a kinetic energy error around one per cent is an optimum upper bound to properly capture the acoustic modes, at least from the engineering point of view. In this case, the natural frequency error would be negligible. It can be observed that by the standard error SKEE the corresponding cutoff modal order can be properly captured. As a final remark, a one per cent of kinetic energy error roughly corresponds to six elements per wavelength for TE10 element, and between four and five elements per wavelength for HE20 element, Fig. 12 and 13. In this case, from Tables 1 and 3, it can be inferred that the effect of the spatial discretization over the group velocity and therefore over the wave velocity is negligible.

4 CONCLUSIONS

This paper studies the propagation of time-harmonic acoustic waves in fluid media discretized by energy-orthogonal finite elements. In this formulation the element stiffness matrix is split into basic and higher order components which are related to the mean and deviatoric components of the gradient of acoustic pressure, respectively. This decomposition is applied both to the stiffness matrix and to the kinetic energy of the finite element assemblage. The research is focused on the properties of the higher order kinetic energy as an error indicator. The noteworthy conclusions of this paper are:

- By numerical dispersion analysis of plane harmonic waves a standard correlation between percentage of higher order kinetic energy and kinetic energy error is yielded. The above correlation is highly dependent of the considered element.
- The standard correlation is used as a reference to apply the percentage of higher order kinetic energy as an error indicator for the acoustic cavity modes computed by the finite element method. Typically it is considered that a kinetic energy error around one per cent is an optimum upper bound to properly capture the acoustic modes. The numerical research reveals that by the standard correlation the modal kinetic energy error is generally overestimated in the interested error range, and a cutoff modal order can be properly selected.

The application of the proposed procedure to more complex waves and media is subject of research.

MODE	FR REF Hz	PEH REF	PEH	KEE	SKEE
1	8.367348	0.005253	0.020643	0.000213	0.000120
2	10.254183	0.005863	0.023076	0.000181	0.000150
3	10.723037	0.006894	0.027061	0.000270	0.000208
4	13.900437	0.012186	0.047503	0.000244	0.000661
5	15.248240	0.014688	0.056427	0.001358	0.000944
6	16.185534	0.013126	0.050982	0.000460	0.000765
7	17.653668	0.021225	0.081510	0.002510	0.002040
8	19.383300	0.025091	0.094649	0.003049	0.002799
9	19.625853	0.023625	0.089744	0.001444	0.002500
10	19.661165	0.024308	0.092719	0.002912	0.002679
11	21.216222	0.028169	0.106661	0.002819	0.003612
12	21.777377	0.029530	0.111531	0.002592	0.003974
13	21.955504	0.030879	0.116365	0.003246	0.004353
14	22.166654	0.027799	0.104825	0.001992	0.003480
15	24.842269	0.036216	0.134124	0.004083	0.005917
16	25.251863	0.046891	0.171357	0.010896	0.010112
17	25.989087	0.045434	0.164372	0.010063	0.009226
18	26.399584	0.043411	0.160458	0.004899	0.008750
19	27.144879	0.042850	0.156726	0.005206	0.008310
20	27.919302	0.051046	0.183629	0.009410	0.011785
21	28.007702	0.046622	0.170426	0.008902	0.009991
22	28.312110	0.052364	0.189307	0.011058	0.012609
23	29.157168	0.056376	0.205599	0.013495	0.015160
24	29.295293	0.048908	0.171845	0.006822	0.010176
25	29.454904	0.051953	0.192371	0.012197	0.013068
26	29.963084	0.055955	0.202152	0.011436	0.014597
27	30.800392	0.053507	0.193305	0.008889	0.013210
28	31.240025	0.063252	0.226136	0.014250	0.018776
29	31.575416	0.050851	0.179857	0.007838	0.011255
30	32.278370	0.063521	0.214050	0.016066	0.016592

Table 4: Estimation of the modal discretization error for a tapered cavity.

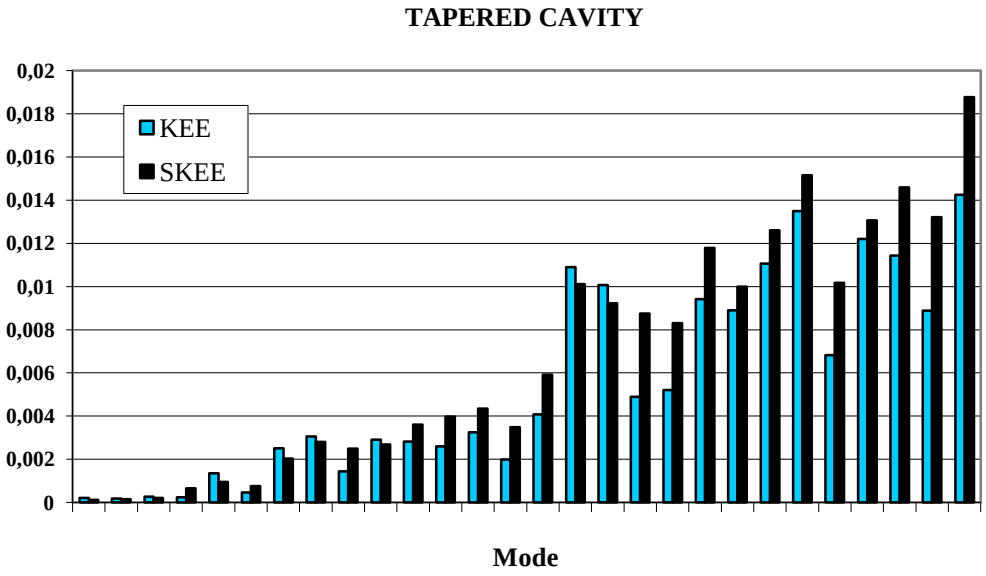


Figure 16: Standard modal kinetic energy error SKEE versus modal kinetic energy error KEE for a tapered cavity.

MODE	FR REF Hz	PEH REF	PEH	KEE	SKEE
1	7.742879	0.001256	0.004498	0.000328	0.000119
2	10.924825	0.003408	0.012184	0.000586	0.000874
3	11.245958	0.003474	0.012425	0.000520	0.000909
4	14.935495	0.006377	0.022751	0.002579	0.003063
5	16.378355	0.008045	0.028249	0.005197	0.004735
6	18.695083	0.009152	0.031975	0.006154	0.006076
7	20.527646	0.011413	0.039084	0.008533	0.009108
8	20.816339	0.012021	0.041525	0.007681	0.010293
9	21.655237	0.011962	0.041286	0.006978	0.010173
10	22.553624	0.014465	0.049086	0.012879	0.014432
11	23.969180	0.017444	0.059538	0.015512	0.021333
12	25.862455	0.019508	0.064886	0.020359	0.025399
13	26.730454	0.017795	0.060549	0.014438	0.022074
14	26.918635	0.021915	0.074262	0.023056	0.033410
15	28.492760	0.023006	0.078155	0.023469	0.037070
16	29.274352	0.024027	0.079723	0.028826	0.038599
17	30.061341	0.026414	0.085174	0.033624	0.044166
18	31.121104	0.026708	0.088292	0.029118	0.047525
19	31.339265	0.026567	0.086435	0.032736	0.045509
20	31.604209	0.027741	0.090491	0.032800	0.049971

Table 5: Estimation of the modal discretization error for a half of pyramidal cavity.

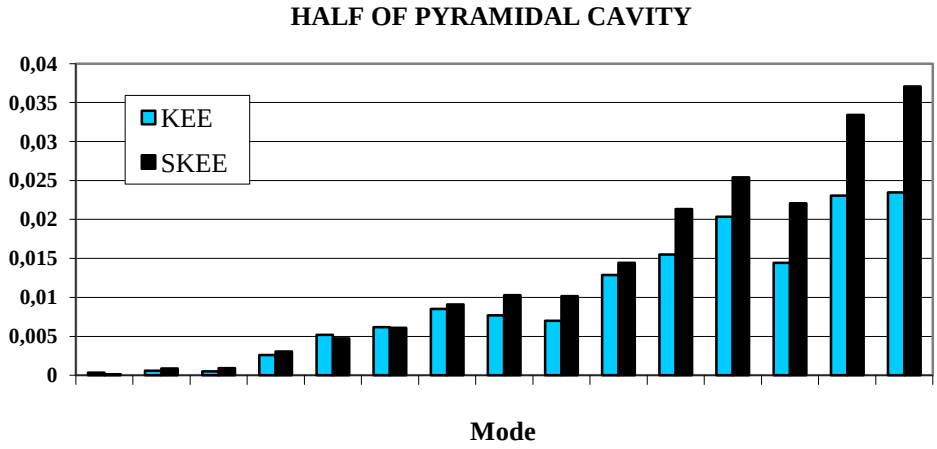


Figure 17: Standard modal kinetic energy error SKEE versus modal kinetic energy error KEE for a half of pyramidal cavity.

REFERENCES

[1] H.L. Schreyer, Dispersion of semidiscretized and fully discretized systems. T. Belytschko, T.J.R. Hughes eds. *Computational methods for transient analysis*. Elsevier Science, 1983.

[2] I. Harari, Dispersion, pollution and resolution. S. Marburg, B. Nolte eds. *Computational acoustics of noise propagation in fluids*. Springer, 2008.

[3] L.M. Brekhovskikh, Yu.P. Lysanov, *Fundamentals of ocean acoustics*. Springer, 2003.

[4] S. Marburg, B. Nolte, A unified approach to finite and boundary element discretization in linear time-harmonic acoustic. S. Marburg, B. Nolte eds. *Computational acoustics of noise propagation in fluids*. Springer, 2008.

[5] F. Ihlenburg, *Finite element analysis of acoustic scattering*. Springer, 1998.

[6] D. Givoli, Computational absorbing boundaries. S. Marburg, B. Nolte eds. *Computational acoustics of noise propagation in fluids*. Springer, 2008.

[7] C.A. Felippa, B. Haugen, C. Militello, From the individual element test to finite element templates: evolution of the Patch Test. *International Journal for Numerical Methods in Engineering*, **38**, 199-229, 1995.

[8] P.G. Bergan, M.K. Nygärd, Finite elements with increased freedom in choosing shape functions. *International Journal for Numerical Methods in Engineering*, **20**, 643-664, 1984.

[9] C.A. Felippa, A survey of parametrized variational principles and applications to computational mechanics. *Computer Methods in Applied Mechanics and Engineering*, **113**, 109-139, 1994.

[10] F.J. Brito Castro, Dispersion analysis of gravity waves in fluid media discretized by energy-orthogonal finite elements. *International Journal for Computational Methods in Engineering Science and Mechanics*, **15**, 499-511, 2014.

[11] O.C. Zienkiewicz, R.L. Taylor, *The finite element method, Vol. 1*. Butterworth-Heinemann, 2000.

[12] D. Royer and E. Dieulesaint, *Elastic waves in solids, Vol. 1*. Springer, 2000.

[13] M. Okrouhlík, C. Höschl, A contribution to the study of dispersive properties of one-dimensional lagrangian and hermitian elements. *Computers and Structures*, **49**, 779-795, 1993.

[14] R.A. Horn and C.R. Johnson, *Matrix analysis*. Cambridge University Press, 1992.

[15] W.H. Press, S.A. Teukolsky, W.T. Vetterling and B.P. Flannery, *Numerical recipes in fortran*. Cambridge University Press, 1992.

[16] R.B. King, *Beyond the quartic equation*. Birkhäuser, 1996.

[17] Z-Q. Qu, *Model order reduction techniques: with applications in finite element analysis*. Springer, 2004.

[18] L. Brillouin, *Wave propagation in periodic structures*. Dover Publications, 2003.

[19] J.D. Achenbach, *Wave propagation in elastic solids*. Elsevier, 1975.

[20] J. Barlow, More on optimal stress points-reduced integration, element distortions, and error estimation. *International Journal for Numerical Methods in Engineering*, **28**, 1487-1504, 1989.

[21] R.H. MacNeal, *Finite elements: their design and performance*. Marcel Dekker, 1994.

[22] F.J. Fahy, *Sound and structural vibration: radiation, transmission and response*. Academic Press, 1985.

[23] K.J. Bathe, *Finite element procedures*. Prentice Hall, 1996.

[24] J.N. Reddy, *Applied functional analysis and variational methods in engineering*. Krieger Publishing Company, 1986.

[25] R.D. Cook, D.S. Malkus, and M.E. Plesha, *Concepts and applications of finite element analysis*. John Wiley, 1989.

COMPDYN 2015
5th ECCOMAS Thematic Conference on
Computational Methods in Structural Dynamics and Earthquake Engineering
M. Papadrakakis, V. Papadopoulos, V. Plevris (eds.)
Crete Island, Greece, 25–27 May 2015

WAVE BASED DESIGN OPTIMISATION OF COMPOSITE STRUCTURES OPERATING IN DYNAMIC ENVIRONMENTS

D. Chronopoulos[1], M. Collet[2], M. Ichchou[3], and I. Antoniadis[4]

[1]Division of Materials, Mechanics and Structures
University Park, The University of Nottingham, NG7 2RD, UK
e-mail: dimitrios.chronopoulos@nottingham.ac.uk

[2]LTDS, UMR-CNRS 5513
36 Avenue Guy de Collongue, 69130 Ecully, France
e-mail: manuel.collet@ec-lyon.fr

[3]Ecole Centrale de Lyon
36 Avenue Guy de Collongue, 69130 Ecully, France
e-mail: mohamed.ichchou@ec-lyon.fr

[4] Machine Design and Control Systems Section
School of Mechanical Engineering, National Technical University of Athens, Greece
e-mail: antogian@central.ntua.gr

Keywords: Structural design optimisation, Vibroacoustic response, Composite structures, Wave propagation

Abstract. *The optimal mechanical and geometric characteristics for layered composite structures subject to vibroacoustic excitations are derived. A Finite Element description coupled to Periodic Structure Theory is employed for the considered layered panel. Structures of arbitrary anisotropy as well as geometric complexity can thus be modelled by the presented approach. Initially, a numerical continuum-discrete approach for computing the sensitivity of the acoustic wave characteristics propagating within the modelled periodic composite structure is exhibited. The first and second order sensitivities of the acoustic transmission coefficient expressed within a Statistical Energy Analysis context are subsequently derived as a function of the computed acoustic wave characteristics. Having formulated the gradient vector as well as the Hessian matrix, the optimal mechanical and geometric characteristics satisfying the considered mass, stiffness and vibroacoustic performance criteria are sought by employing Newton's optimisation method.*

1 INTRODUCTION

Layered and complex structures are nowadays widely used within the aerospace, automotive, construction and energy sectors with a general increase tendency, mainly because of their high stiffness-to-mass ratio and the fact that their mechanical characteristics can be designed to suit the particular purposes. Unluckily however, this high stiffness-to-mass ratio being responsible for the increased mechanical efficiency, at the same time induces high acoustic transmission through the structure. The need for simultaneously optimising an industrial structure of minimum mass and maximum static stiffness, while attaining satisfactory dynamic response performance levels is a challenging task for the modern engineer; especially when considering acoustic transmission through a layered structure which depends on the mechanical and geometric characteristics of each individual layer, resulting in a great number of design parameters to be optimised.

The numerical analysis of wave propagation within periodic structures was firstly considered in [1], while the work was extended to two dimensional media in [2, 3]. The so called Wave Finite Element (WFE) method was introduced in [4, 5] in order to facilitate the post-processing of the eigenproblem solutions and further improve the computational efficiency of the method. The interest in predicting the vibroacoustic response of a structure in a wave context is far from being new with the pioneering works of the authors in [6, 7, 8, 9] being probably the earliest ones. A layer-wise model for the prediction of acoustic wave propagation within continuous layered structures was presented in [10]. More recently, the prediction of the acoustic wave characteristics based on FE formulations allowed for more complex structures to be included in the dynamic response computations [11, 12, 13, 14, 15, 16, 17].

Structural sensitivity analysis is of great importance for understanding the overall impact of a design parameter variation to the structural performance which is to be optimised. Accurate sensitivity models are an important tool for design optimization, system identification as well as for statistical mechanics analysis. Many authors [18, 19, 20, 21] have been focusing on the eigenvalue derivative analysis of a structural system. With regard to the variability analysis of the waves travelling within a structural medium the conducted work has been mainly focused on deriving expressions [22, 23] of the stochastic wave parameters from analytical models. In [24] the authors conduct a design sensitivity analysis by a wave based approach. Considering numerical approaches the authors in [25] used Bloch's theorem in conjunction with the FE method in order to calculate the sensitivity of the acoustic waves within an auxetic honeycomb, while with regard to the computation of the variability of the propagating waves the authors in [26, 27] have presented a stochastic WFE method approach for computing the stochastic wave propagation in one dimensional media. With regard to optimising the design characteristics of a layered structure the developed approaches have generally focused on genetic algorithms or particle swarm type techniques [28, 29, 30]. When it comes to optimising the structural design vis-a-vis the dynamic response performance of a structure, wave based optimisation techniques have been developed [31, 32, 33, 34] by adopting Periodic Structure Theory (PST) assumptions.

In this work an established wave based SEA approach is employed in order to predict the vibroacoustic performance of a composite layered panel. The novelty of the work focuses on the derivation of the first and second order sensitivity of the acoustic transmission coefficient expressed through SEA with respect to the structural design characteristics of the modelled structure. The considered design parameters include the entirety of the mechanical characteristics, the density as well as the thickness of each individual structural layer. Non conservative structural systems are also modelled by the exhibited approach. Employing a three dimensional

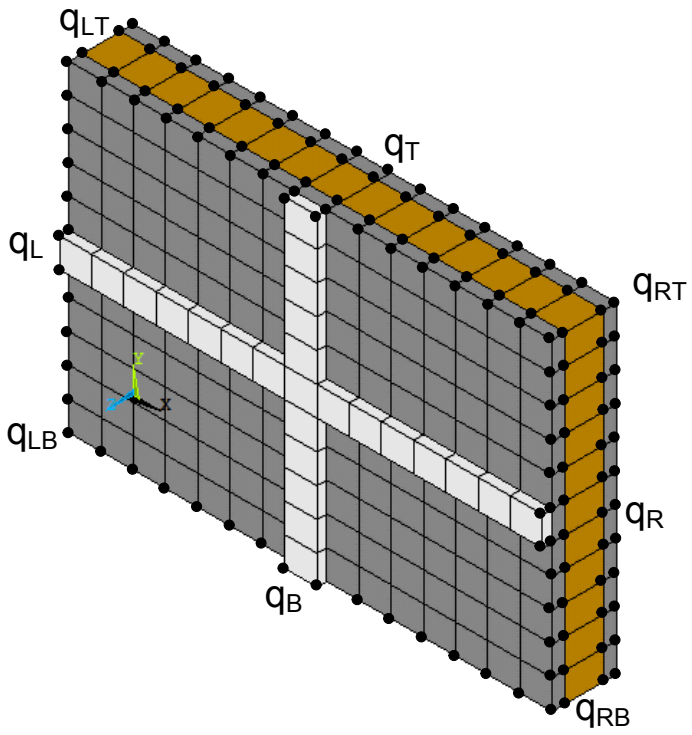


Figure 1: Caption of a FE modelled composite layered panel

FE description of the modelled structure allows for capturing the entirety of the sound transmitting propagating structural waves, while employing a PST formulation allows for drastically reducing the computational cost related to calculating the SEA parameters and the Hessian matrix for each configuration. Although not discussed in this work, the method is straightforward to apply to curved structures by expressing the FE structural matrices and wave propagation properties in polar coordinates.

2 ACOUSTIC WAVE SENSITIVITY

2.1 Formulation of the PST for an arbitrary structural segment

A periodic segment of a panel having arbitrary layering is hereby considered (see Fig.1) with L_x, L_y its dimensions in the x and y directions respectively. The segment is modelled using a conventional FE software. The mass, damping and stiffness matrices of the segment $\mathbb{M}$, $\mathbb{C}$ and $\mathbb{K}$ are extracted and the DoF set $\mathbf{q}$ is reordered according to a predefined sequence such as:

$$\mathbf{q} = \{\mathbf{q_I}\ \mathbf{q_B}\ \mathbf{q_T}\ \mathbf{q_L}\ \mathbf{q_R}\ \mathbf{q_{LB}}\ \mathbf{q_{RB}}\ \mathbf{q_{LT}}\ \mathbf{q_{RT}}\}^\top \tag{1}$$

corresponding to the internal, the interface edge and the interface corner DoF (see Fig.1). The free harmonic vibration equation of motion for the modelled segment is written as:

$$[\mathbb{K} + \mathrm{i}\omega\mathbb{C} - \omega^2\mathbb{M}]\mathbf{q} = \mathbf{0} \tag{2}$$

The analysis then follows as in [3] with the following relations being assumed for the displacement DoF under the passage of a time-harmonic wave:

$$\begin{aligned} \mathbf{q_R} &= \mathrm{e}^{-i\varepsilon_x}\mathbf{q_L},\ \ \mathbf{q_T} = \mathrm{e}^{-i\varepsilon_y}\mathbf{q_B} \\ \mathbf{q_{RB}} &= \mathrm{e}^{-i\varepsilon_x}\mathbf{q_{LB}},\ \ \mathbf{q_{LT}} = \mathrm{e}^{-i\varepsilon_y}\mathbf{q_{LB}},\ \ \mathbf{q_{RT}} = \mathrm{e}^{-i\varepsilon_x - i\varepsilon_y}\mathbf{q_{LB}} \end{aligned} \tag{3}$$

with ε_x and ε_y the propagation constants in the x and y directions related to the phase difference between the sets of DoF. The wavenumbers k_x, k_y are directly related to the propagation constants through the relation:

$$\varepsilon_x = k_x L_x, \;\; \varepsilon_y = k_y L_y \tag{4}$$

Considering Eq.3 in tensorial form gives:

$$\mathbf{q} = \begin{bmatrix} \mathbf{I} & \mathbf{0} & \mathbf{0} & \mathbf{0} \\ \mathbf{0} & \mathbf{I} & \mathbf{0} & \mathbf{0} \\ \mathbf{0} & \mathbf{I}e^{-i\varepsilon_y} & \mathbf{0} & \mathbf{0} \\ \mathbf{0} & \mathbf{0} & \mathbf{I} & \mathbf{0} \\ \mathbf{0} & \mathbf{0} & \mathbf{I}e^{-i\varepsilon_x} & \mathbf{0} \\ \mathbf{0} & \mathbf{0} & \mathbf{0} & \mathbf{I} \\ \mathbf{0} & \mathbf{0} & \mathbf{0} & \mathbf{I}e^{-i\varepsilon_x} \\ \mathbf{0} & \mathbf{0} & \mathbf{0} & \mathbf{I}e^{-i\varepsilon_y} \\ \mathbf{0} & \mathbf{0} & \mathbf{0} & \mathbf{I}e^{-i\varepsilon_x - i\varepsilon_y} \end{bmatrix} \mathbf{x} = \mathbf{R}\mathbf{x} \tag{5}$$

with $\mathbf{x}$ the reduced set of DoF: $\mathbf{x} = \{\mathbf{q_I} \;\; \mathbf{q_B} \;\; \mathbf{q_L} \;\; \mathbf{q_{LB}}\}^\top$. The equation of free harmonic vibration of the modelled segment can now be written as:

$$[\mathbf{R}^* \mathbb{K} \mathbf{R} + \mathrm{i}\omega \mathbf{R}^* \mathbb{C} \mathbf{R} - \omega^2 \mathbf{R}^* \mathbb{M} \mathbf{R}]\mathbf{x} = \mathbf{0} \tag{6}$$

with * denoting the Hermitian transpose. The most practical procedure for extracting the wave propagation characteristics of the segment from Eq.6 is injecting a set of assumed propagation constants ε_x, ε_y. The set of these constants can be chosen in relation to the direction of propagation towards which the wavenumbers are to be sought and according to the desired resolution of the wavenumber curves. Eq.6 is then transformed into a standard eigenvalue problem and can be solved for the eigenvector $\mathbf{x}$ which describe the deformation of the segment under the passage of each wave type at an angular frequency equal to the square root of the corresponding eigenvalue $\lambda = \omega^2$. It is noted that the computed angular frequency quantities $\omega = \omega_r + \mathrm{i}\omega_i$ will have $\mid \omega_i \mid > 0$ implying complex values for the wavenumbers of the propagating wave types, otherwise interpreted as spatially decaying motion and from which the loss factor of each computed wave type w can directly be determined.

A complete description of each passing wave including its x and y directional wavenumbers and its wave shape for a certain frequency is therefore acquired. It is noted that the periodicity condition is defined modulo 2π, therefore solving Eq.6 with a set of ε_x, ε_y varying from 0 to 2π will suffice for capturing the entirety of the structural waves. Further considerations on reducing the computational expense of the problem are discussed in [3]. It should be noted that only propagating waves will be considered in the subsequent analysis.

2.2 Parametric sensitivity

For an undamped structural segment the sensitivity of the real eigenvalues λ_p can be written as

$$\frac{\partial \lambda_p}{\partial \beta_i} = \mathbf{x}_p^\top \left(\frac{\partial \mathbf{K}}{\partial \beta_i} - \lambda_p \frac{\partial \mathbf{M}}{\partial \beta_i} \right) \mathbf{x}_p \tag{7a}$$

$$\begin{aligned} \frac{\partial^2 \lambda_p}{\partial \beta_j \partial \beta_i} =& \mathbf{x}_p^\top \left(\frac{\partial^2 \mathbf{K}}{\partial \beta_j \partial \beta_i} - \lambda_p \frac{\partial^2 \mathbf{M}}{\partial \beta_j \partial \beta_i} - \frac{\partial \lambda_p}{\partial \beta_j} \frac{\partial \mathbf{M}}{\partial \beta_i} - \frac{\partial \lambda_p}{\partial \beta_i} \frac{\partial \mathbf{M}}{\partial \beta_j} \right) \mathbf{x}_p \\ &+ \mathbf{x}_p^\top \left(\frac{\partial}{\partial \beta_j} \left[\mathbf{K} - \lambda_p \mathbf{M} \right] \right) \frac{\partial \mathbf{x}_p}{\partial \beta_i} + \mathbf{x}_p^\top \left(\frac{\partial}{\partial \beta_i} \left[\mathbf{K} - \lambda_p \mathbf{M} \right] \right) \frac{\partial \mathbf{x}_p}{\partial \beta_j} \end{aligned} \tag{7b}$$

with the sensitivity of the real mode shapes $\dfrac{\partial \mathbf{x}_p}{\partial \beta_j}$ to be calculated by the approach exhibited in [18]. The global mass and stiffness matrices $\mathbb{M}, \mathbb{K}$ of the structural segment are formed by adding the local mass and stiffness matrices of individual FEs. Eq.7 can be written as

$$\frac{\partial \lambda_p}{\partial \beta_i} = \mathbf{x}_p^\top \left(\mathbf{R}^* \frac{\partial \mathbb{K}}{\partial \beta_i} \mathbf{R} - \lambda_p \mathbf{R}^* \frac{\partial \mathbb{M}}{\partial \beta_i} \mathbf{R} \right) \mathbf{x}_p \tag{8a}$$

$$\begin{aligned} \frac{\partial^2 \lambda_p}{\partial \beta_j \partial \beta_i} =& \mathbf{x}_p^\top \left(\mathbf{R}^* \frac{\partial^2 \mathbb{K}}{\partial \beta_j \partial \beta_i} \mathbf{R} - \lambda_p \mathbf{R}^* \frac{\partial^2 \mathbb{M}}{\partial \beta_j \partial \beta_i} \mathbf{R} - \mathbf{R}^* \frac{\partial \lambda_p}{\partial \beta_j} \frac{\partial \mathbb{M}}{\partial \beta_i} \mathbf{R} - \mathbf{R}^* \frac{\partial \lambda_p}{\partial \beta_i} \frac{\partial \mathbb{M}}{\partial \beta_j} \mathbf{R} \right) \mathbf{x}_p + \\ & \mathbf{x}_p^\top \left(\frac{\partial}{\partial \beta_j} \left[\mathbf{R}^* \mathbb{K} \mathbf{R} - \lambda_p \mathbf{R}^* \mathbb{M} \mathbf{R} \right] \right) \frac{\partial \mathbf{x}_p}{\partial \beta_i} + \mathbf{x}_p^\top \left(\frac{\partial}{\partial \beta_i} \left[\mathbf{R}^* \mathbb{K} \mathbf{R} - \lambda_p \mathbf{R}^* \mathbb{M} \mathbf{R} \right] \right) \frac{\partial \mathbf{x}_p}{\partial \beta_j} \end{aligned} \tag{8b}$$

For the conservative system it is known however that $\dfrac{\partial \lambda_p}{\partial \beta_i} = \dfrac{\partial (\omega_p^2)}{\partial \beta_i}$, therefore

$$\frac{\partial \lambda_p}{\partial \beta_i} = \frac{\dfrac{\partial (\omega_p^2)}{\partial \omega_p}}{\dfrac{\partial \beta_i}{\partial \omega_p}} = 2\omega_p \frac{\partial \omega_p}{\partial \beta_i} \Leftrightarrow \frac{\partial \omega_p}{\partial \beta_i} = \frac{1}{2\omega_p} \frac{\partial \lambda_p}{\partial \beta_i} \tag{9a}$$

$$\frac{\partial^2 \lambda_p}{\partial \beta_j \partial \beta_i} = 2 \frac{\partial \omega_p}{\partial \beta_j} \frac{\partial \omega_p}{\partial \beta_i} + 2\omega_p \frac{\partial^2 \omega_p}{\partial \beta_j \partial \beta_i} \Leftrightarrow \frac{\partial^2 \omega_p}{\partial \beta_j \partial \beta_i} = \frac{1}{2\omega_p} \left(\frac{\partial^2 \lambda_p}{\partial \beta_j \partial \beta_i} - 2 \frac{\partial \omega_p}{\partial \beta_j} \frac{\partial \omega_p}{\partial \beta_i} \right) \tag{9b}$$

with ω_p the angular frequency at which the set of ε_x, ε_y is true for the p wave type described by the $\mathbf{x}_p$ deformation. For the wavenumber sensitivity $\dfrac{\partial k_p}{\partial \beta_i}$ the following is true

$$\frac{\partial k_p}{\partial \beta_i} = -\frac{\partial k_p}{\partial \omega_p} \frac{\partial \omega_p}{\partial \beta_i} = -\frac{1}{c_{g,p}} \frac{\partial \omega_p}{\partial \beta_i} \tag{10a}$$

$$\frac{\partial^2 k_p}{\partial \beta_j \partial \beta_i} = \frac{1}{c_{g,p}^3} \frac{\partial c_{g,p}}{\partial k_p} \frac{\partial \omega_p}{\partial \beta_j} \frac{\partial \omega_p}{\partial \beta_i} - \frac{1}{c_{g,p}} \frac{\partial^2 \omega_p}{\partial \beta_j \partial \beta_i} \tag{10b}$$

with $c_{g,p} = \dfrac{\partial \omega_p}{\partial k_p}$ the group velocity associated with the wave type p at frequency ω_p and the quantities $c_{g,p}$, $\dfrac{\partial c_{g,p}}{\partial \omega_p}$ to be evaluated by the solution of the baseline structural design.

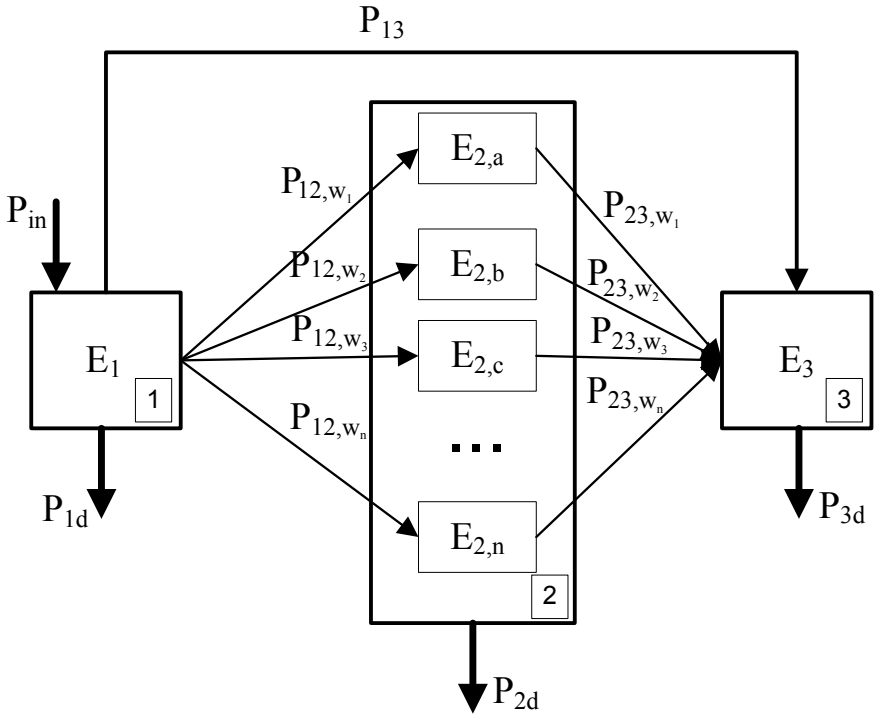


Figure 2: A schematic representation of the SEA power exchanges and energies for the modelled system.

3 SEA SENSITIVITY ANALYSIS

3.1 The employed SEA model

The impact of the parametric alterations on the vibroacoustic performance of the structure under investigation is exhibited in this section by deriving expressions for the sensitivity of the SEA results with respect to the propagating acoustic waves.

The total acoustic transmission coefficient τ is one of the most important indices of the vibroacoustic performance of a structure. The system to be modelled comprises one acoustically excited chamber (subsystem 1) and one acoustically receiving chamber (subsystem 3) separated by the modelled composite panel (subsystem 2). It is considered that each wave type is excited and transmits acoustic energy independently from the rest, therefore each considered wave type $w = w_1, w_2 ... w_n$ propagating within the composite panel is considered as a separate SEA subsystem. No flanking transmission is considered in the SEA model. The energy balance between the subsystems as it is considered within an SEA approach (see [8]) is illustrated in Fig.2, in which E_1, E_3 stand for the acoustic energy of the source room and the receiving room respectively and E_2 for the vibrational energy of the composite panel. Moreover P_{in} is the injected power in the source room, P_{1d}, P_{2d} and P_{3d} stand for the power dissipated by each subsystem and P_{13} is the non-resonant transmitted power between the rooms.

The derivation of an expression for the total acoustic transmission coefficient τ of the composite structure by merely accounting for its structural dynamic behaviour is exhibited in [11] and reads

$$\tau = \sum_{w=w_1}^{w_n} \tau_w + \frac{P_{13}}{P_{inc}} \tag{11}$$

with τ_w being the transmission coefficient of the wave type w given as

$$\tau_w = \frac{8\rho^2 c^4 \pi \sigma_{rad,w}^2 n_w}{\rho_s \omega^2 A(\rho_s \omega \eta_w + 2\rho c \sigma_{rad,w})} \tag{12}$$

The non resonant transmission coefficient $\tau_{nr} = P_{13}/P_{inc}$ for a diffused acoustic field can be written as in [10]:

$$\tau_{nr}(\omega) = \frac{1}{\pi(\cos^2\theta_{min} - \cos^2\theta_{max})} \int_0^{2\pi} \int_0^{\theta_{max}} \frac{4Z_0^2}{\mid \mathrm{i}\omega\rho_s + 2Z_0 \mid^2} \sigma(\theta, \phi, \omega) \cos^2\theta \sin\theta \mathrm{d}\theta \mathrm{d}\phi \tag{13}$$

in which θ and ϕ are the incidence angle and the direction angle of the acoustic wave respectively and $Z_0 = \rho c / \cos\theta$ is the acoustic impedance of the medium. The term θ_{max} stands for the maximum incidence angle, accounting for the diffuseness of the incident field. It is hereby considered that $\theta_{max} = \pi/2$ for all the results presented in the current work. The term $\sigma(\theta, \phi, \omega)$ is the corrected radiation efficiency term. It is used in order to account for the finite dimensions of the panel and it is calculated using a spatial windowing correction technique presented in [35].

Eventually the STL of the panel can be expressed as

$$\mathrm{STL} = 10 \log_{10}\left(\frac{1}{\tau}\right) \tag{14}$$

by definition.

3.2 Parametric sensitivity of the total acoustic transmission

In order to formulate the expression of the Hessian matrix describing the variation of the vibroacoustic performance of the structure with respect to its design parameters, the second order derivative of τ with respect to the considered set of parameters should be derived and expressed as

$$\frac{\partial \tau}{\partial \beta_i} = \sum_{w=w_1}^{w_n} \frac{\partial \tau_w}{\partial \beta_i} + \frac{\partial \tau_{nr}}{\partial \beta_i} \tag{15a}$$

$$\frac{\partial^2 \tau}{\partial \beta_j \partial \beta_i} = \sum_{w=w_1}^{w_n} \frac{\partial^2 \tau_w}{\partial \beta_j \partial \beta_i} + \frac{\partial^2 \tau_{nr}}{\partial \beta_j \partial \beta_i} \tag{15b}$$

while the sensitivity of the STL index can directly be expressed with regard to τ as

$$\frac{\partial (STL)}{\partial \beta_i} = \frac{\mathrm{d}(STL)}{\mathrm{d}\tau} \frac{\partial \tau}{\partial \beta_i} = -\frac{10}{\ln(10)\tau} \frac{\partial \tau}{\partial \beta_i} \tag{16a}$$

$$\begin{aligned} \frac{\partial^2 (STL)}{\partial \beta_j \partial \beta_i} &= \frac{\partial^2 (STL)}{\partial \tau^2} \frac{\partial \tau}{\partial \beta_j} \frac{\partial \tau}{\partial \beta_i} + \frac{\partial (STL)}{\partial \tau} \frac{\partial^2 \tau}{\partial \beta_j \partial \beta_i} \\ &= \frac{10}{\ln(10)\tau^2} \frac{\partial \tau}{\partial \beta_j} \frac{\partial \tau}{\partial \beta_i} - \frac{10}{\ln(10)\tau} \frac{\partial^2 \tau}{\partial \beta_j \partial \beta_i} \end{aligned} \tag{16b}$$

In the following sections the evaluation of Eq.15 is discussed.

3.3 Modal density sensitivity

Using Courant's formula [36], the modal density of each wave type w can be written at a propagation angle ϕ as a function of the propagating wavenumber and its corresponding group velocity c_g:

$$n_w(\omega,\phi) = \frac{A k_w(\omega,\phi)}{2\pi^2 |c_{g,w}(\omega,\phi)|} \tag{17}$$

The angularly averaged modal density of the structure is therefore given as

$$n_w(\omega) = \int_0^{\pi} n_w(\omega,\phi)\,\mathrm{d}\phi \tag{18}$$

Thanks to the chain differentiation rule the first and second order derivatives of the modal density for each wave type with respect to design variables β_i, β_j can be expressed as

$$\begin{aligned}\frac{\partial n_w(\omega,\phi)}{\partial\beta_i} &= \frac{\partial n_w(\omega,\phi)}{\partial k_w(\omega,\phi)}\frac{\partial k_w(\omega,\phi)}{\partial\beta_i} + \frac{\partial n_w(\omega,\phi)}{\partial c_{g,w}(\omega,\phi)}\frac{\partial c_{g,w}(\omega,\phi)}{\partial\beta_i} \qquad (19a)\\ &= \frac{A}{2\pi^2|c_{g,w}(\omega,\phi)|}\frac{\partial k_w(\omega,\phi)}{\partial\beta_i} - \frac{A k_w(\omega,\phi)\,\mathrm{sgn}(c_{g,w}(\omega,\phi))}{2\pi^2|c_{g,w}(\omega,\phi)|^2}\frac{\partial c_{g,w}(\omega,\phi)}{\partial k_w(\omega,\phi)}\frac{\partial k_w(\omega,\phi)}{\partial\beta_i}\end{aligned}$$

$$\begin{aligned}\frac{\partial^2 n_w(\omega,\phi)}{\partial\beta_j\partial\beta_i} &= \frac{\partial^2 n_w(\omega,\phi)}{\partial k_w(\omega,\phi)^2}\frac{\partial k_w(\omega,\phi)}{\partial\beta_j}\frac{\partial k_w(\omega,\phi)}{\partial\beta_i} + \frac{\partial n_w(\omega,\phi)}{\partial k_w(\omega,\phi)}\frac{\partial^2 k_w(\omega,\phi)}{\partial\beta_j\partial\beta_i} \qquad (19b)\\ &+ \frac{\partial^2 n_w(\omega,\phi)}{\partial c_{g,w}(\omega,\phi)^2}\frac{\partial c_{g,w}(\omega,\phi)}{\partial\beta_j}\frac{\partial c_{g,w}(\omega,\phi)}{\partial\beta_i} + \frac{\partial n_w(\omega,\phi)}{\partial c_{g,w}(\omega,\phi)}\frac{\partial^2 c_{g,w}(\omega,\phi)}{\partial\beta_j\partial\beta_i}\\ &= \frac{A}{2\pi^2|c_{g,w}(\omega,\phi)|}\frac{\partial^2 k_w(\omega,\phi)}{\partial\beta_j\partial\beta_i} + \frac{A k_w(\omega,\phi)\,\mathrm{sgn}(c_{g,w}(\omega,\phi))}{\pi^2|c_{g,w}(\omega,\phi)|^3}\left(\frac{\partial c_{g,w}(\omega,\phi)}{\partial k_w(\omega,\phi)}\right)^2\frac{\partial k_w(\omega,\phi)}{\partial\beta_j}\frac{\partial k_w(\omega,\phi)}{\partial\beta_i}\\ &- \frac{A k_w(\omega,\phi)\,\mathrm{sgn}(c_{g,w}(\omega,\phi))}{2\pi^2|c_{g,w}(\omega,\phi)|^2}\left(\frac{\partial^2 c_{g,w}(\omega,\phi)}{\partial k_w(\omega,\phi)^2}\frac{\partial k_w(\omega,\phi)}{\partial\beta_j}\frac{\partial k_w(\omega,\phi)}{\partial\beta_i} + \frac{\partial c_{g,w}(\omega,\phi)}{\partial k_w(\omega,\phi)}\frac{\partial^2 k_w(\omega,\phi)}{\partial\beta_j\partial\beta_i}\right)\end{aligned}$$

while for the spatially averaged modal density

$$\frac{\partial n_w(\omega)}{\partial\beta_i} = \int_0^{\pi}\frac{\partial n_w(\omega,\phi)}{\partial\beta_i}\mathrm{d}\phi \tag{20a}$$

$$\frac{\partial^2 n_w(\omega)}{\partial\beta_j\partial\beta_i} = \int_0^{\pi}\frac{\partial^2 n_w(\omega,\phi)}{\partial\beta_j\partial\beta_i}\mathrm{d}\phi \tag{20b}$$

suggesting that the modal density sensitivity can be expressed merely by

- The sensitivity of the characteristics of the waves travelling within the considered structure with respect to the structural design (already determined in Sec.2).
- The sensitivity of the modal density with respect to the characteristics of the waves travelling in it.

A similar approach can be followed for computing all the remaining necessary SEA quantities.

3.4 Radiation efficiency sensitivity

In order to avoid the computationally inefficient frequency and directional averaging of the modal dependent radiation efficiency sensitivity $\frac{\partial \sigma_{rad,w}(\omega,\phi)}{\partial \beta_i}$, it is practical to employ expressions introducing a direct wavenumber dependence of $\sigma_{rad,w}$ such as the ones exhibited in [6, 9, 3]. For a generic periodic structure including discontinuities the assumption of sinusoidal mode shapes is no longer valid, therefore the radiation efficiency should be calculated directly from the PST derived wave mode shapes. The radiation efficiency expression as derived in [3] can therefore be employed. For continuous structures, mode shapes of sinusoidal form can be assumed in order to avoid any FE discretization errors in the solution. The set of asymptotic formulas given in [9] can be used for computing the averaged wavenumber dependent radiation efficiency of the panel as

$$\sigma_{rad,w} = \frac{1}{\sqrt{1-\mu^2}} \qquad \mu < 0.90 \tag{21a}$$

$$\sigma_{rad,w} = \frac{L_x + L_y}{\pi \mu \kappa L_x L_y \sqrt{\mu^2 - 1}} \left(\ln\left(\frac{\mu+1}{\mu-1}\right) + \frac{2\mu}{\mu^2-1} \right) \qquad \mu > 1.05 \tag{21b}$$

$$\sigma_{rad,w} = \left(0.5 - 0.15 \min(L_x, L_y)/\max(L_x, L_y)\right) \sqrt{k \min(L_x, L_y)} \qquad \mu = 1 \tag{21c}$$

with $\mu = \left(\frac{k_x^2 + k_y^2}{\kappa^2} \right)^{1/2}$, where $\kappa = \omega/c$ is the acoustic wavenumber. In the region $0.90 < \mu < 1.05$ a shape preserving Hermite interpolation function is employed assuring the continuity and double differentiability for the entire spectrum of the $\sigma_{rad,w}$ expression. The sensitivity expressions for the radiation efficiency of the panel can therefore be derived as a function of the propagating flexural wavenumbers by Eq.21, while the interpolation function is used for expressing the sensitivity of $\sigma_{rad,w}$ for the remaining spectrum.

3.5 Sensitivity of the resonant acoustic transmission

Taking a look at Eq.12 it can be observed that the sensitivity of the resonant acoustic transmission coefficient with respect to the design parameters of the composite structure can be expressed as

$$\frac{\partial \tau_w}{\partial \beta_i} = \frac{\partial \tau_w}{\partial \sigma_{rad,w}} \frac{\partial \sigma_{rad,w}}{\partial \beta_i} + \frac{\partial \tau_w}{\partial n_w} \frac{\partial n_w}{\partial \beta_i} + \frac{\partial \tau_w}{\partial \rho_s} \frac{\partial \rho_s}{\partial \beta_i} \tag{22a}$$

$$\begin{aligned} \frac{\partial^2 \tau_w}{\partial \beta_j \partial \beta_i} = {} & \frac{\partial^2 \tau_w}{\partial \sigma_{rad,w}^2} \frac{\partial \sigma_{rad,w}}{\partial \beta_j} \frac{\partial \sigma_{rad,w}}{\partial \beta_i} + \frac{\partial \tau_w}{\partial \sigma_{rad,w}} \frac{\partial^2 \sigma_{rad,w}}{\partial \beta_j \partial \beta_i} \\ & + \frac{\partial^2 \tau_w}{\partial n_w^2} \frac{\partial n_w}{\partial \beta_j} \frac{\partial n_w}{\partial \beta_i} + \frac{\partial \tau_w}{\partial n_w} \frac{\partial^2 n_w}{\partial \beta_j \partial \beta_i} \\ & + \frac{\partial^2 \tau_w}{\partial \rho_s^2} \frac{\partial \rho_s}{\partial \beta_j} \frac{\partial \rho_s}{\partial \beta_i} + \frac{\partial \tau_w}{\partial \rho_s} \frac{\partial^2 \rho_s}{\partial \beta_j \partial \beta_i} \end{aligned} \tag{22b}$$

with the transmission coefficient related sensitivity terms being expressed as

$$\frac{\partial \tau_w}{\partial \sigma_{rad,w}} = \frac{16\pi c^4 n_w \rho^2 \sigma_{rad,w}}{A\omega^2 \rho_s (\eta_w \omega \rho_s + 2c\rho\sigma_{rad,w})} - \frac{16\pi c^5 n_w \rho^3 \sigma_{rad,w}^2}{A\omega^2 \rho_s (\eta_w \omega \rho_s + 2c\rho\sigma_{rad,w})^2} \tag{23a}$$

$$\frac{\partial^2 \tau_w}{\partial \sigma_{rad,w}^2} = \frac{16\pi c^4 n_w \rho^2}{A\omega^2 \rho_s (\eta_w \omega \rho_s + 2c\rho\sigma_{rad,w})} - \frac{64\pi c^5 n_w \rho^3 \sigma_{rad,w}}{A\omega^2 \rho_s (\eta_w \omega \rho_s + 2c\rho\sigma_{rad,w})^2} + \frac{64\pi c^6 n_w \rho^4 \sigma_{rad,w}^2}{A\omega^2 \rho_s (\eta_w \omega \rho_s + 2c\rho\sigma_{rad,w})^3} \tag{23b}$$

$$\frac{\partial \tau_w}{\partial n_w} = \frac{8\pi c^4 \rho^2 \sigma_{rad,w}^2}{A\omega^2 \rho_s (\eta_w \omega \rho_s + 2c\rho\sigma_{rad,w})} \tag{23c}$$

$$\frac{\partial^2 \tau_w}{\partial n_w^2} = 0 \tag{23d}$$

$$\frac{\partial \tau_w}{\partial \rho_s} = -\frac{8\pi c^4 n_w \rho^2 \sigma_{rad,w}^2}{A\omega^2 \rho_s^2 (\eta_w \omega \rho_s + 2c\rho\sigma_{rad,w})} - \frac{8\pi c^4 \eta_w n_w \rho^2 \sigma_{rad,w}^2}{A\omega \rho_s (\eta_w \omega \rho_s + 2c\rho\sigma_{rad,w})^2} \tag{23e}$$

$$\frac{\partial^2 \tau_w}{\partial \rho_s^2} = \frac{16\pi c^4 \eta_w^2 n_w \rho^2 \sigma_{rad,w}^2}{A\rho_s (\eta_w \omega \rho_s + 2c\rho\sigma_{rad,w})^3} + \frac{16\pi c^4 n_w \rho^2 \sigma_{rad,w}^2}{A\omega^2 \rho_s^3 (\eta_w \omega \rho_s + 2c\rho\sigma_{rad,w})} + \frac{16\pi c^4 \eta_w n_w \rho^2 \sigma_{rad,w}^2}{A\omega \rho_s^2 (\eta_w \omega \rho_s + 2c\rho\sigma_{rad,w})^2} \tag{23f}$$

All the necessary quantities have by now been computed from the considerations introduced above and the resonant acoustic transmission sensitivity can thus be evaluated in Eq.22. Given that $\rho_s = \sum_{l=l_1}^{l_{max}} \rho_{m,l} h_l$ with $\rho_{m,l}$ the mass density of layer l and h_l its thickness, it is straightforward to derive the quantities $\frac{\partial \rho_s}{\partial \beta_i}\frac{\partial \rho_s}{\partial \beta_j}$ and $\frac{\partial^2 \rho_s}{\partial \beta_i \partial \beta_j}$ for the composite panel.

4 THE OPTIMISATION PROBLEM

The Newton's method will be hereby employed (ensuring quadratic convergence towards the solution) in order to optimise the considered set of parameters, which in the general orthotropic multilayer case can be expressed as

$$\mathbf{p} = \left\{ \; E_{x,1} E_{y,1} E_{z,1} v_{xy,1} v_{xz,1} v_{yz,1} G_{xy,1} G_{xz,1} G_{yz,1} h_1 \rho_{m,1} \cdots \rho_{m,l_{max}} \; \right\}^\top \tag{24}$$

with l_{max} the maximum number of layers. It is interesting to note that including η in an optimisation procedure will not provide any helpful information, as $\delta\eta$ will not directly affect neither the mass, nor the stiffness of the panel. On the other hand it will always be beneficial for the reduction of τ_w, which suggests that a maximum η will always be the result of the optimisation process. Some of the parameters may be considered to be constrained (e.g. $\beta_i \in [\beta_{i,min}, \beta_{i,max}]$). The objective function $\mathcal{F}(\mathbf{p})$ to be minimised is eventually to be decided. It is evident that the cost of added mass, as well as the one of static stiffness loss should be included in $\mathcal{F}(\mathbf{p})$ (if not maximising the mass of the panel would be the evident solution for minimising the acoustic transmission). There is a number of cost criteria that can be applied to the stress-strain matrix coefficients [37] of a laminate in order to account for its axial, shear and flexural stiffness. Dependence between the mass, stiffness and damping coefficient of each employed material can also be introduced.

The cost function can eventually be expressed as

$$\mathcal{F}(\mathbf{p}) = \xi_3\tau^3(\mathbf{p})+\xi_2\tau^2(\mathbf{p})+\xi_1\tau(\mathbf{p})+\xi_0+\delta_3\rho_s^3(\mathbf{p})+\delta_2\rho_s^2(\mathbf{p})+\delta_1\rho_s(\mathbf{p})+\delta_0+\zeta_3 d_s^3(\mathbf{p})+\zeta_2 d_s^2(\mathbf{p})+\zeta_1 d_s(\mathbf{p})+\zeta_0 \tag{25}$$

with ξ_i, δ_i, ζ_i coefficients that allow the designer to apply a simple polynomial curve fitting to the available cost data, thus facilitating the differentiability of $\mathcal{F}(\mathbf{p})$. Higher order polynomial or exponential fitting functions may be applied without loss of accuracy.

5 NUMERICAL CASE STUDIES

In order to validate the exhibited optimisation approach, an asymmetric sandwich panel comprising two facesheets and a core is modelled in this section. The lower facesheet has a thickness h_1=1mm and is made of a material having $\rho_{m,1}$=3000e^{-9}kg/mm^3, $E_1 = 70$GPa and a Poisson's ration v_1=0.1. The upper facesheet has a thickness equal to h_3=2mm and is made of the same material as the lower facesheet. The core has a thickness h_2=10mm and is made of a material with $\rho_{m,2}$=50e^{-9}kg/mm^3, $E_2 = 0.07$GPa and v_2=0.4. Three FEs are used in the sense of thickness in order to model the structure. All computations were conducted using the R2013a version of MATLAB®.

5.1 Results on the wave sensitivity analysis of a layered structure

In this section the sensitivity of the wave characteristics with respect to the mechanical and geometric characteristics of the sandwich panel are sought as discussed in Sec.2. The results are compared to a FD approach throughout this section. In order to implement the FD approach a perturbation of 0.1% was considered for each structural parameter. The resulting FD sensitivity can be computed by

$$\frac{\partial k}{\partial \beta} = \frac{k_p - k_0}{\beta_p - \beta_0} \tag{26}$$

with k_p the perturbed wavenumber value for β_p and ω_0 the corresponding wavenumber for the unperturbed parameter β_0.

The sensitivity of k with respect to the thickness of the sandwich core layer is presented in Fig.3. A very interesting effect is that the influence of δh_2 on the flexural wavenumber becomes maximum for a certain frequency (approximately 2000 Hz), where the stiffening effect of δh_2 becomes maximum. An intense nonlinearity is observed in the relation of $\delta\omega$ to δk. A constant decrease of this influence is observed beyond that point. The stiffening effect is probably due to the greater separation of the two facesheets with δh_2. It is very probable however that for higher wavenumber values δh_c will have a softening effect on the flexural wavenumber with the depicted curve passing to positive values ok δk.

In Fig.4, the sensitivity of k with respect to the mass density of the sandwich facesheet layers is presented. As expected, both $\delta\rho_{m,1}$ and $\delta\rho_{m,3}$ will shift the wavenumber curve to higher values, suggesting a softening phenomenon. This effect will be greater for the thicker upper facesheet at low k values. A highly nonlinear behaviour is again observed and it is interesting to see that there is a critical frequency value at which the effect of $\delta\rho_{m,1}$ and $\delta\rho_{m,3}$ will be the same. Beyond this critical wavenumber the softening effect will paradoxically be more intense for $\delta\rho_{m,1}$.

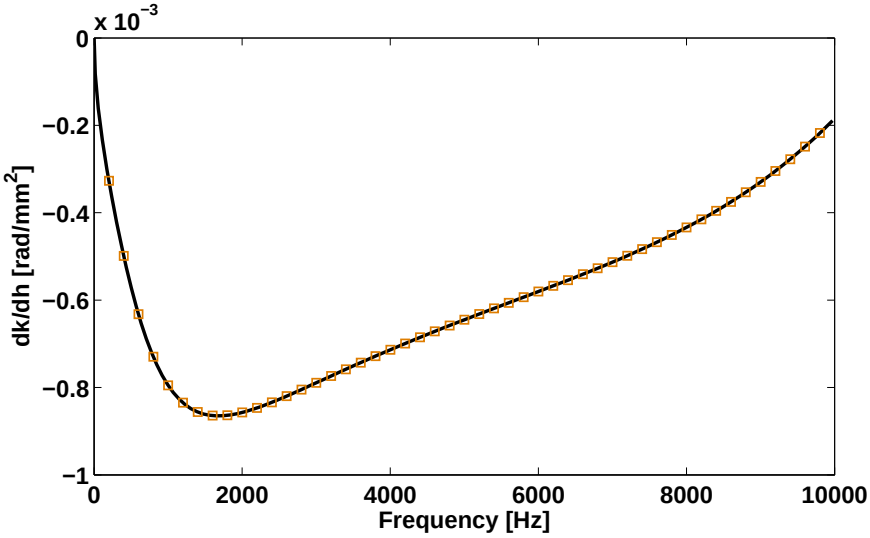


Figure 3: Sensitivity of the propagating wavenumber k under a perturbation of h_2 for the first flexural wave type of the layered structure: Presented approach ($-$), FD computation ($\square$)

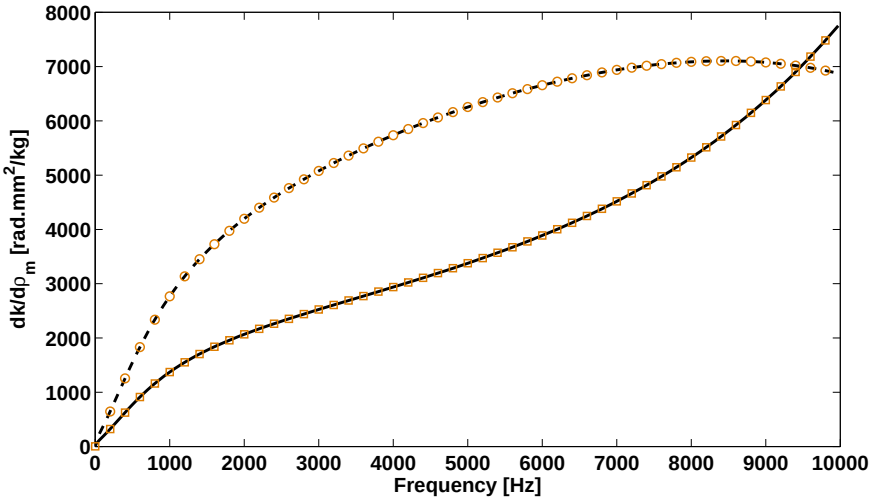


Figure 4: Sensitivity of the propagating wavenumber k under a perturbation of the mass density of the sandwich facesheets for the first flexural wave type: Presented approach for $\rho_{m,1}$ ($-$), FD computation for $\rho_{m,1}$ ($\square$), Presented approach for $\rho_{m,3}$ ($--$), FD computation for $\rho_{m,3}$ ($\circ$)

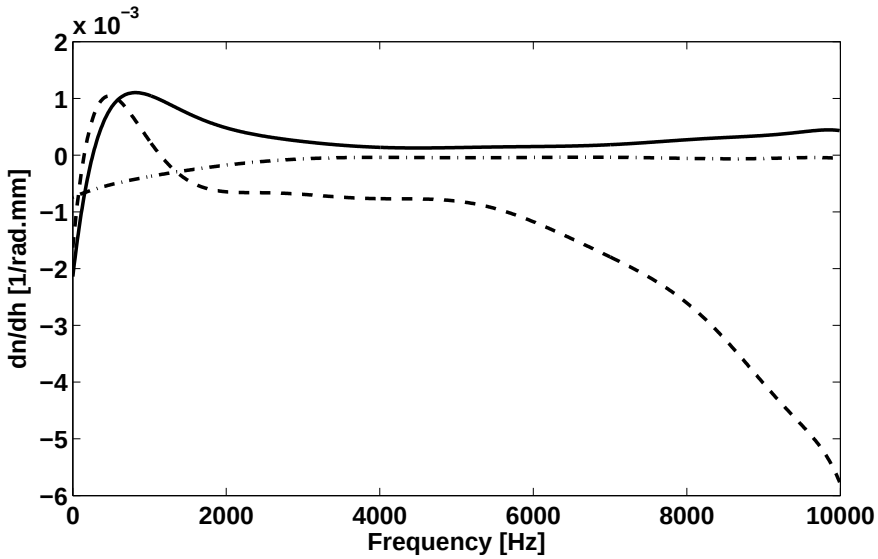


Figure 5: Sensitivity of the modal density n of the first flexural propagating wave with respect to the layer thicknesses: with respect to the thickness of the lower facesheet h_1 $(-)$, with respect to the thickness of the upper facesheet h_3 $(--)$, with respect to the thickness of the core h_2 $(- \cdot -)$

5.2 Results on the SEA sensitivity analysis of a layered structure

In this section the sensitivity of the SEA quantities, namely the modal density, the radiation efficiency and the damping loss factor are computed as discussed in Sec.3 and evaluated.

The first order sensitivity of the modal density of the composite panel with regard to the layer thicknesses are exhibited in Figs.5. It can be observed that the stiffening effect induced by δh_3 in the high frequency range, also induces a high reduction of the modal density, while a maximum softening effect is observed for both δh_1, δh_3 in the low frequency range (approximately 1000 Hz).

The sensitivity of the acoustic radiation efficiency for the composite panel with regard to the layer thicknesses is presented in Fig.6. In order to use a clearer logarithmic scale the quantity $\delta 10\log(\sigma)/\delta h$ is plotted. It is generally observed that altering the thickness of the thicker facesheet h_3 will have a maximum effect on the radiation efficiency, while the opposite is true for altering the thickness of the core layer. The maximum impact on σ is as expected observed around the acoustic coincidence frequency (approximately 5800 Hz in this case study). It is interesting to note that the effect of δh_1 will have an opposite effect on σ compared to δh_3.

The impact of the structural parameters on the acoustic transmission coefficient and the sound TL of the composite structure is eventually computed. In Fig.7 the sensitivity of the structure's TL with regard to the layer thicknesses is presented. It is evident that altering the thickness of the upper thicker layer will induce the maximum effect on TL, especially close to the acoustic coincidence region. On the other hand, altering the core thickness will have an insignificant effect on the TL index.

5.3 Structural design optimisation of the layered structure

As discussed in Sec.4, the criteria to be considered within the optimisation process of the mechanical and geometric characteristics of the panel are its mass, stiffness and vibroacoustic performance. The surface mass of the panel ρ_s is chosen as a representative mass index, the total acoustic transmission coefficient τ is selected as the vibroacoustic performance index,

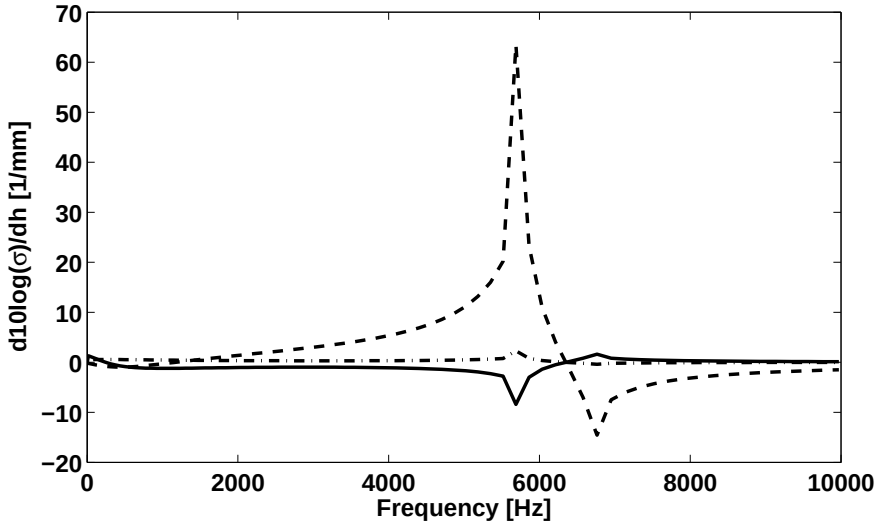


Figure 6: Sensitivity of the logarithmic acoustic radiation efficiency ($10\log(\sigma)$) of the first flexural propagating wave with respect to the layer thicknesses: with respect to the thickness of the lower facesheet h_1 ($-$), with respect to the thickness of the upper facesheet h_3 ($--$), with respect to the thickness of the core h_2 ($- \cdot -$)

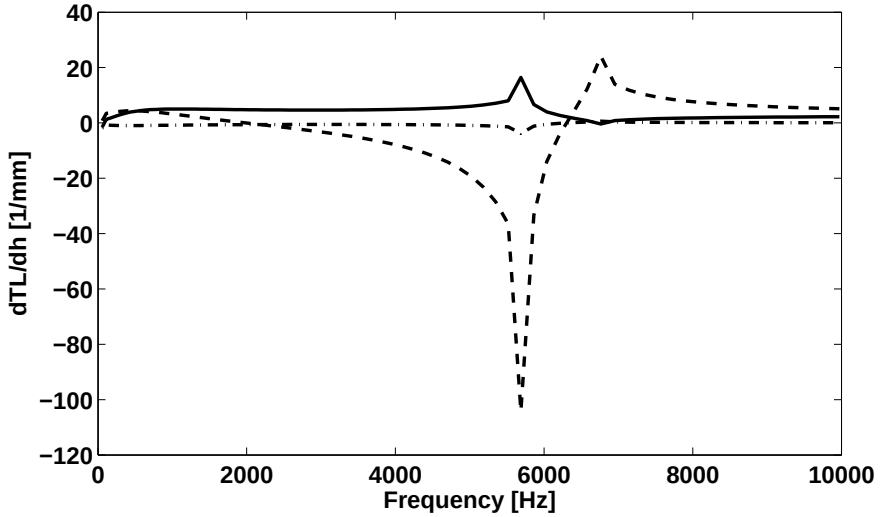


Figure 7: Sensitivity of the sound TL with respect to the layer thicknesses: with respect to the thickness of the lower facesheet h_1 ($-$), with respect to the thickness of the upper facesheet h_3 ($--$), with respect to the thickness of the core h_2 ($- \cdot -$)

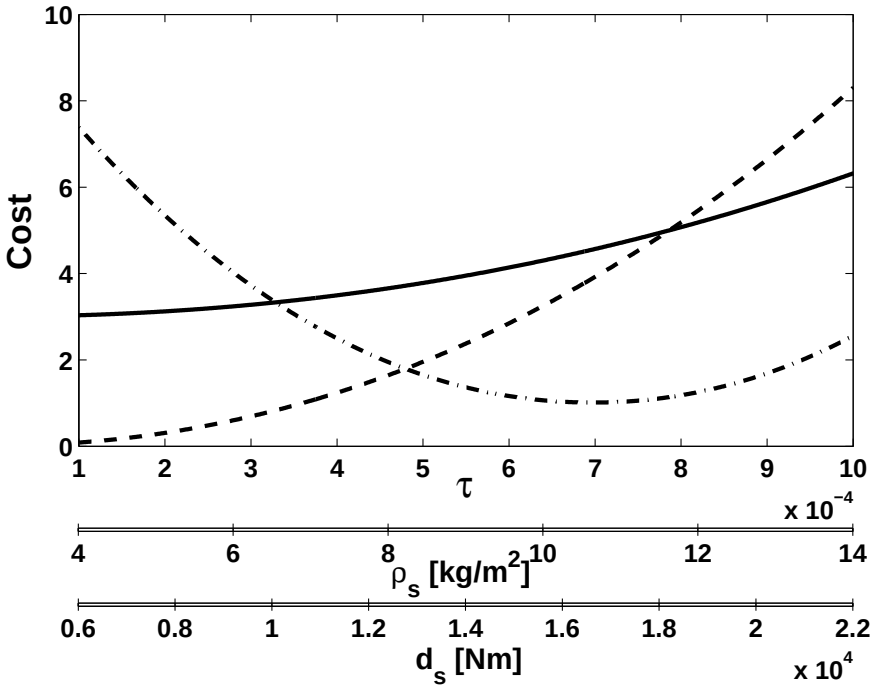


Figure 8: Representation of the cost functions employed within the current optimisation process. Cost function corresponding to: The acoustic transmission coefficient τ $(-)$, The surface mass density ρ_s $(--)$, The flexural stiffness d_s of the panel $(- \cdot -)$

while with regard to the structural stiffness and for the sake of simplicity we will hereby assume that we are solely interested in the sum of the static flexural stiffnesses of the panel D_{xx}, D_{yy} expressed as

$$d_s = D_{xx} + D_{yy} = \frac{1}{3}\sum_{l=l_1}^{l_{max}} \left((Q_{xx,l} + Q_{yy,l})(z_l^3 - z_{l-1}^3)\right) \tag{27a}$$

$$Q_{xx,l} = E_{x,l}\frac{1 - v_{yz,l}^2}{\Delta_l} \tag{27b}$$

$$Q_{yy,l} = E_{y,l}\frac{1 - v_{xz,l}^2}{\Delta_l} \tag{27c}$$

$$\Delta_l = 1 - v_{xy,l}^2 - v_{yz,l}^2 - v_{zx,l}^2 - 2v_{xy,l}v_{yz,l}v_{zx,l} \tag{27d}$$

which in the case of an isotropic composite panel gives

$$d_s = \frac{2}{3}\sum_{l=l_1}^{l_{max}} \left(Q_l(z_l^3 - z_{l-1}^3)\right) \tag{28}$$

with z_l the coordinate of the upper surface of layer l in the thickness direction. The design cost functions, employed in order to decide the relation between ρ_s, τ and d_s and the corresponding induced design cost are exhibited in Fig.8.

Additional constraints (e.g. minimum axial and/or flexural stiffness, maximum surface mass e.t.c) can be considered. The constrained optimization problem is solved using Newton's method.

5.4 Optimal parameters and discussion on the computational efficiency

The optimisation problem is solved for $k = 0.13$rad/mm, and the optimal material and geometric parameters that minimise the sum of the costs as presented in Fig.8 are computed as follows

$$E_1 = 80.9\text{GPa},\ v_1 = 0.12,\ h_1 = 1.19\text{mm},\ \rho_{m,1} = 1647\text{kg/m}^3$$
$$E_2 = 110\text{MPa},\ v_2 = 0.37,\ h_2 = 10.53\text{mm},\ \rho_{m,2} = 14.6\text{kg/m}^3$$
$$E_3 = 58.3\text{GPa},\ v_3 = 0.19,\ h_3 = 1.74\text{mm},\ \rho_{m,3} = 1500\text{kg/m}^3$$

It is noted that the only quantities laying on the limits of the predefined constraints which could potentially further improve the overall structural performance are the Young's modulus of the core layer E_2 as well as the mass density of the upper layer $\rho_{m,3}$. Optimising the structure in a broadband frequency range can be done by averaging the optimal parameters over the frequency range of interest or by introducing a weighting average for the frequency bands that are considered more important (e.g. frequency of the external acoustic excitation). The optimisation process was completed in 8 iterations each of which lasted approximately 78 seconds, resulting in a total computation time of 630s. This suggests that a broadband structural optimisation is feasible within a few hours, even with a conventional computing equipment.

6 Conclusions

In this work, the optimal mechanical and geometric characteristics for layered composite structures subject to vibroacoustic excitations were derived in a wave SEA context. The main conclusions of the paper are summarised as:

(i) An intense frequency dependent variation of the sensitivity of the propagating wave characteristics has been observed as a function of the design of the composite structure. This also implies frequency dependence of the optimal design parameters.

(ii) Expressions for the first and second order sensitivities of the SEA quantities, namely the modal density and the radiation efficiency of the composite panel were derived. The design parametric sensitivity for each of the SEA quantities, as well as of the acoustic transmission coefficient were found to be highly frequency dependent. The impact of the design alteration on the vibroacoustic response was maximised in the vicinity of the acoustic coincidence range for most parameters.

(iii) The suggested optimisation process is computationally efficient, allowing for a broadband structural optimisation of a layered structure in a rational period of time, even with the use of a conventional computing equipment.

REFERENCES

[1] D. J. Mead, "A general theory of harmonic wave propagation in linear periodic systems with multiple coupling," *Journal of Sound and Vibration*, vol. 27, no. 2, pp. 235–260, 1973.

[2] R. Langley, "A note on the force boundary conditions for two-dimensional periodic structures with corner freedoms," *Journal of Sound and Vibration*, vol. 167, no. 2, pp. 377–381, 1993.

[3] V. Cotoni, R. S. Langley, and P. J. Shorter, "A statistical energy analysis subsystem formulation using finite element and periodic structure theory," *Journal of Sound and Vibration*, vol. 318, no. 4-5, pp. 1077–1108, 2008.

[4] B. R. Mace, D. Duhamel, M. J. Brennan, and L. Hinke, "Finite element prediction of wave motion in structural waveguides," *The Journal of the Acoustical Society of America*, vol. 117, no. 5, pp. 2835–2843, 2005.

[5] J.-M. Mencik and M. Ichchou, "Multi-mode propagation and diffusion in structures through finite elements," *European Journal of Mechanics-A/Solids*, vol. 24, no. 5, pp. 877–898, 2005.

[6] G. Maidanik, "Response of ribbed panels to reverberant acoustic fields," *the Journal of the Acoustical Society of America*, vol. 34, no. 6, pp. 809–826, 1962.

[7] C. Wallace, "Radiation resistance of a rectangular panel," *The Journal of the Acoustical Society of America*, vol. 51, no. 3B, pp. 946–952, 1972.

[8] R. Lyon, *Statistical energy analysis of dynamical systems: theory and applications*. MIT press Cambridge, 1975.

[9] F. G. Leppington, E. G. Broadbent, and K. H. Heron, "Acoustic radiation efficiency of rectangular panels," in *Proceedings of The Royal Society of London, Series A: Mathematical and Physical Sciences*, vol. 382, pp. 245–271, 1982.

[10] S. Ghinet, N. Atalla, and H. Osman, "The transmission loss of curved laminates and sandwich composite panels," *The Journal of the Acoustical Society of America*, vol. 118, no. 2, pp. 774–790, 2005.

[11] D. Chronopoulos, M. Ichchou, B. Troclet, and O. Bareille, "Computing the broadband vibroacoustic response of arbitrarily thick layered panels by a wave finite element approach," *Applied Acoustics*, vol. 77, pp. 89–98, 2014.

[12] D. Chronopoulos, B. Troclet, M. Ichchou, and J. Lainé, "A unified approach for the broadband vibroacoustic response of composite shells," *Composites Part B: Engineering*, vol. 43, no. 4, pp. 1837–1846, 2012.

[13] D. Chronopoulos, B. Troclet, O. Bareille, and M. Ichchou, "Modeling the response of composite panels by a dynamic stiffness approach," *Composite Structures*, vol. 96, pp. 111–120, 2013.

[14] D. Chronopoulos, M. Ichchou, B. Troclet, and O. Bareille, "Efficient prediction of the response of layered shells by a dynamic stiffness approach," *Composite Structures*, vol. 97, pp. 401–404, 2013.

[15] D. Chronopoulos, M. Ichchou, B. Troclet, and O. Bareille, "Predicting the broadband vibroacoustic response of systems subject to aeroacoustic loads by a krylov subspace reduction," *Applied Acoustics*, vol. 74, no. 12, pp. 1394–1405, 2013.

[16] D. Chronopoulos, M. Ichchou, B. Troclet, and O. Bareille, "Thermal effects on the sound transmission through aerospace composite structures," *Aerospace Science and Technology*, vol. 30, no. 1, pp. 192–199, 2013.

[17] D. Chronopoulos, M. Ichchou, B. Troclet, and O. Bareille, "Predicting the broadband response of a layered cone-cylinder-cone shell," *Composite Structures*, vol. 107, pp. 149–159, 2014.

[18] R. B. Nelson, "Simplified calculation of eigenvector derivatives," *AIAA journal*, vol. 14, no. 9, pp. 1201–1205, 1976.

[19] R. T. Haftka and H. M. Adelman, "Recent developments in structural sensitivity analysis," *Structural optimization*, vol. 1, no. 3, pp. 137–151, 1989.

[20] S. Adhikari and M. I. Friswell, "Eigenderivative analysis of asymmetric non-conservative systems," *International Journal for Numerical Methods in Engineering*, vol. 51, no. 6, pp. 709–733, 2001.

[21] K. K. Choi and N.-H. Kim, *Structural sensitivity analysis and optimization 1: linear systems*, vol. 1. Springer, 2006.

[22] K. Sobczyk, *Stochastic wave propagation*. Elsevier, 1985.

[23] A. Belyaev, "Comparative study of various approaches to stochastic elastic wave propagation," *Acta mechanica*, vol. 125, no. 1-4, pp. 3–16, 1997.

[24] K. Koo, B. Pluymers, W. Desmet, and S. Wang, "Vibro-acoustic design sensitivity analysis using the wave-based method," *Journal of Sound and Vibration*, vol. 330, no. 17, pp. 4340–4351, 2011.

[25] M. Ruzzene and F. Scarpa, "Directional and band-gap behavior of periodic auxetic lattices," *physica status solidi (b)*, vol. 242, no. 3, pp. 665–680, 2005.

[26] M. Ichchou, F. Bouchoucha, M. Ben Souf, O. Dessombz, and M. Haddar, "Stochastic wave finite element for random periodic media through first-order perturbation," *Computer Methods in Applied Mechanics and Engineering*, vol. 200, no. 41, pp. 2805–2813, 2011.

[27] B. Souf, O. Bareille, M. Ichchou, F. Bouchoucha, and M. Haddar, "Waves and energy in random elastic guided media through the stochastic wave finite element method," *Physics Letters A*, vol. 377, no. 37, pp. 2255–2264, 2013.

[28] R. Le Riche and R. T. Haftka, "Optimization of laminate stacking sequence for buckling load maximization by genetic algorithm," *AIAA journal*, vol. 31, no. 5, pp. 951–956, 1993.

[29] M. Walker and R. E. Smith, "A technique for the multiobjective optimisation of laminated composite structures using genetic algorithms and finite element analysis," *Composite Structures*, vol. 62, no. 1, pp. 123–128, 2003.

[30] S. Omkar, D. Mudigere, G. N. Naik, and S. Gopalakrishnan, "Vector evaluated particle swarm optimization (vepso) for multi-objective design optimization of composite structures," *Computers & structures*, vol. 86, no. 1, pp. 1–14, 2008.

[31] R. Langley, N. Bardell, and P. Loasby, "The optimal design of near-periodic structures to minimize vibration transmission and stress levels," *Journal of Sound and Vibration*, vol. 207, no. 5, pp. 627–646, 1997.

[32] M. I. Hussein, G. M. Hulbert, and R. A. Scott, "Dispersive elastodynamics of 1d banded materials and structures: analysis," *Journal of sound and vibration*, vol. 289, no. 4, pp. 779–806, 2006.

[33] M. I. Hussein, K. Hamza, G. M. Hulbert, R. A. Scott, and K. Saitou, "Multiobjective evolutionary optimization of periodic layered materials for desired wave dispersion characteristics," *Structural and Multidisciplinary Optimization*, vol. 31, no. 1, pp. 60–75, 2006.

[34] M. Collet, K. A. Cunefare, and M. N. Ichchou, "Wave motion optimization in periodically distributed shunted piezocomposite beam structures," *Journal of Intelligent Material Systems and Structures*, 2008.

[35] J. Allard and N. Atalla, *Propagation of Sound in Porous Media: Modelling Sound Absorbing Materials 2e*. John Wiley & Sons, 2009.

[36] R. Courant and D. Hilbert, *Methoden der mathematischen Physik, vol. 1*, vol. 2. Berlin, 1931.

[37] R. M. Jones, *Mechanics of composite materials*. CRC Press, 1998.

COMPDYN 2015
5th ECCOMAS Thematic Conference on
Computational Methods in Structural Dynamics and Earthquake Engineering
M. Papadrakakis, V. Papadopoulos, V. Plevris (eds.)
Crete Island, Greece, 25–27 May 2015

NEW REDUCED ORDER FINITE ELEMENT FORMULATIONS FOR VIBRATION ATTENUATION USING PIEZOELECTRIC SHUNT DAMPING

W. Larbi, L. P. da Silva and J.-F. Deü

Structural Mechanics and Coupled Systems Laboratory,
Conservatoire National des Arts et Métiers,
292 rue Saint-Martin, 75141 Paris Cedex 03, France
e-mail: walid.larbi@cnam.fr

Keywords: Vibration reduction, Piezoelectric patches, Shunt damping, Modal superposition, Reduced order model.

Abstract. *In this work, various reduced order finite element models for the prediction of passive reduction of structural vibration by means of shunted piezoelectric system are presented. The problem consists of an elastic structure with surface-mounted piezoelectric patches. The piezoelectric elements are connected with resonant shunt circuits in order to damp specific resonant frequencies of the structure. An efficient electromechanical finite element formulation for the dynamic analysis of the problem is first recalled. Different strategies to solve the problem using a modal reduction approach are then proposed. These strategies are based of the use of two original projection bases: (i) the combined basis formed by both the short-circuited and open-circuited modes, and (ii) the coupled basis formed by the electromechanical modes that take into account the effect of the inductances of the electrical shunts circuit. Various results are presented in order to validate and illustrate the efficiency of the proposed new finite element reduced order formulations.*

1 INTRODUCTION

Piezoelectric materials are widely used in vibration damping and noise reduction. These materials, which enable the transformation of mechanical energy into electrical energy (direct piezoelectric effect) and vice-versa (inverse piezoelectric effect), allow direct connection with an input/output electrical signal and make them well adapted to distributed sensing and actuation. This work is focused on passive control strategies using piezoelectric elements for vibration damping. As compared to the active control techniques, passive techniques have the advantage of being simple to implement, always stable and do not require digital signal processors and bulky power amplifiers. Examples of active control systems can be found for example in [1, 2].

In this paper, the specific application of passive vibration reduction by means of shunted piezoelectric patches is addressed. In this technology, the elastic structure is equipped with piezoelectric patches that are connected to a passive electrical circuit, called a shunt. The piezoelectric patches transform mechanical energy of the vibrating structure into electrical energy, which is then dissipated into the form of Joule heat to provide electrical damping to the structure by the shunt circuits. Several shunt circuits can be considered: the classical R- and RL-shunts, proposed by Hagood and Von Flotow [3], improvements of those techniques, by the use of several piezoelectric elements [4, 5, 6], active fiber composites [7] or adaptive shunts [8], and recently semi-passive techniques, commonly known as switch techniques [9, 10, 11]. Since those techniques are passive (or semi-passive if some electronic components have to be powered), a critical issue is that their performances, in terms of damping efficiency, directly depend on the electromechanical coupling between the host structure and the piezoelectric elements, which has to be maximized.

The present work concerns the numerical modeling of vibration reduction of elastic structures in the low frequency range by using shunted piezoelectric elements. The aim is to propose efficient reduced order finite element models able to predict the shunt damping. An electromechanical finite element formulation for the dynamic analysis of smart structures with piezoelectric elements is first proposed. In this formulation, the electrical state is fully described by very few global discrete unknowns [12]: (i) the electric charge contained in the electrodes and (ii) the voltage between the electrodes. This formulation is well adapted to practical applications since realistic electrical boundary conditions, such that equipotentiality on the electrodes and prescribed global electric charges, naturally appear. The charge/voltage global variables are also intrinsically adapted to include any external electrical circuit into the electromechanical problem and to simulate the effect of shunt damping techniques. We present then different strategies to solve the problem using a modal reduction approach. In this technique, the electromechanical coupled system is solved by projecting the mechanical displacement unknown on a truncated basis composed by the first structural normal modes while the few initial electrical unknowns are kept in the reduced system. The projection bases widely used in the literature are obtained using the short-circuited or open-circuited eigenvalue problems [13, 14]. We propose in this work two new modal projection bases: (i) the combined basis formed by both the short-circuited and open-circuited modes, and (ii) the coupled basis formed by the electromechanical modes that take into account the effect of the inductances of the electrical shunts circuit. Numerical examples are finally presented in order to evaluate the effectiveness of the proposed new strategies of modal projection compared to the classic ones in terms of prediction of the vibration attenuation using piezoelectric shunt systems.

2 FINITE ELEMENT FORMULATION

We briefly recall in this section the finite element formulation of an elastic structure with surface mounted shunted piezoelectric patches.

An elastic structure occupying the domain Ω_E is equipped with P piezoelectric patches (figure 1). Each piezoelectric patch is covered on its upper and lower surfaces with a very thin electrode. The pth patch, $p \in \{1, \cdots, P\}$, occupies a domain $\Omega^{(p)}$ such that $(\Omega_E, \Omega^{(1)}, \cdots, \Omega^{(P)})$ is a partition of the all structure domain Ω_S. In order to reduce the vibration amplitudes of the problem, a resonant shunt circuit made up of a resistance $R^{(p)}$ and an inductance $L^{(p)}$ in series is connected to each patch [3, 11].

Moreover, the structure is clamped on a part Γ_u and subjected to a given surface force density F_i^d on the complementary part Γ_σ of its external boundary.

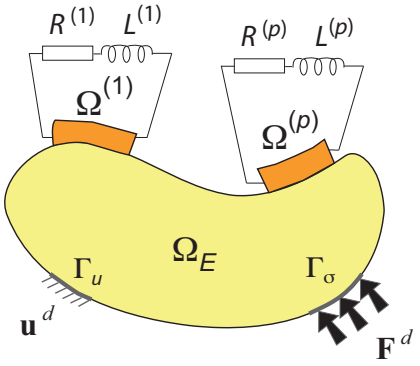


Figure 1: Vibrating structure connected to RL shunt circuits.

For each piezoelectric patch, a set of hypotheses, which can be applied to a wide spectrum of practical applications, are formulated:

- The piezoelectric patches are thin, with a constant thickness, denoted $h^{(p)}$ for the pth patch;
- The thickness of the electrodes is much smaller than $h^{(p)}$ and is thus neglected;
- The piezoelectric patches are polarized in their transverse direction (i.e. the direction normal to the electrodes).

Under those assumptions, the electric field vector, of components $E_k^{(p)}$, can be considered normal to the electrodes and uniform in the piezoelectric patch [12], so that for all $p \in \{1, \cdots, P\}$:

$$E_k^{(p)} = -\frac{V^{(p)}}{h^{(p)}} n_k \quad \text{in} \quad \Omega^{(p)} \tag{1}$$

where E_i is the electric field, $V^{(p)}$ is the potential difference between the upper and the lower electrode surfaces of the pth patch which is constant over $\Omega^{(p)}$ and n_k is the kth component of the normal unit vector to the surface of the electrodes.

After variational formulation and finite element discretization, we obtain the following matrix system in frequency domain:

$$\begin{bmatrix} \mathbf{K}_u & \mathbf{C}_{uV} \\ -\mathbf{C}_{uV} & \mathbf{K}_V \end{bmatrix} \begin{bmatrix} \mathbf{U} \\ \mathbf{Q} \end{bmatrix} - \omega^2 \begin{bmatrix} \mathbf{M}_u & \mathbf{0} \\ \mathbf{0} & \mathbf{0} \end{bmatrix} \begin{bmatrix} \mathbf{U} \\ \mathbf{V} \end{bmatrix} = \begin{bmatrix} \mathbf{F} \\ \mathbf{Q} \end{bmatrix} \tag{2}$$

where $\mathbf{U}$ is the column vector of nodal values of mechanical displacement of length N_s (N_s is the number of mechanical degrees of freedom); $\mathbf{M}_u$ and $\mathbf{K}_u$ are the mass and stiffness matrices of the structure (elastic structure and piezoelectric patches) of size $N_s \times N_s$ and $\mathbf{F}$ is the applied mechanical force vector of length N_s. Moreover, $\mathbf{Q} = (Q^{(1)}\, Q^{(2)} \cdots Q^{(P)})^T$ and $\mathbf{V} = (V^{(1)}\, V^{(2)} \cdots V^{(P)})^T$ are the column vectors of electric charges and potential differences; $\mathbf{C}_{uV}$ is the electric mechanical coupled stiffness matrix of size $N_s \times P$; $\mathbf{K}_V = \text{diag}\left(C^{(1)}\, C^{(2)} \cdots C^{(P)}\right)$ is a diagonal matrix filled with the P capacitances of the piezoelectric patches where $C^{(p)} = \epsilon_{33} S^{(p)}/h^{(p)}$, ϵ_{33} being the piezoelectric permittivity in the direction normal to the electrodes and $S^{(p)}$ the area of the patch electrodes surfaces.

The above discretized formulation equation is adapted to any elastic structure with surface-mounted piezoelectric patches. Its originality lies in the fact that the system electrical state is fully described by very few global discrete unknowns: only a couple of variables per piezoelectric patch, namely (1) the electric charge contained in the electrodes and (2) the voltage between the electrodes. Once the electrical part of the problem is fully discretized at the weak formulation step, by introducing the above cited voltage/charge variables, without any restriction on the mechanical part of the problem, any standard FE formulation can be easily modified to include the piezoelectric patches and thus the effect of an external electrical action. A second advantage of this formulation is that since global electrical variables are used, realistic electrical boundary conditions are naturally introduced. First, the equipotentiality in any of the patches electrodes is exactly satisfied when introducing the potential difference variable. Second, the use of the global charge contained in the electrodes, as the second electrical variable, is realistic since plugging an external electrical circuit to the electrodes of the patches imposes only the global charge contained in the electrodes and not a local charge surface density. Another advantage of using the global charge voltage variables is that they are intrinsically adapted to include any external electrical circuit into the electromechanical problem and to simulate the effect of shunt damping techniques. In this case, neither $\mathbf{V}$ nor $\mathbf{Q}$ is prescribed by the electrical network but the latter imposes only a relation between them [3]. For the case of a resonant shunt composed of a resistor R and an inductor L in series, connected to the pth patch, the relation writes

$$-\omega^2 L^{(p)} Q^{(p)} + i\omega R^{(p)} Q^{(p)} + V^{(p)} = 0 \tag{3}$$

Combining equations (2) and (3), we finally obtain the general FE formulation of the electromechanical spectral problem when the piezoelectric patches are shunted

$$-\omega^2 \begin{bmatrix} \mathbf{M}_u & \mathbf{0} \\ \mathbf{0} & \mathbf{L} \end{bmatrix} \begin{bmatrix} \mathbf{U} \\ \mathbf{Q} \end{bmatrix} + i\omega \begin{bmatrix} \mathbf{0} & \mathbf{0} \\ \mathbf{0} & \mathbf{R} \end{bmatrix} \begin{bmatrix} \mathbf{U} \\ \mathbf{Q} \end{bmatrix} + \begin{bmatrix} \mathbf{K}_u + \mathbf{C}_{uV}\mathbf{K}_V^{-1}\mathbf{C}_{uV}^T & \mathbf{C}_{uV}\mathbf{K}_V^{-1} \\ \mathbf{K}_V^{-1}\mathbf{C}_{uV}^T & \mathbf{K}_V^{-1} \end{bmatrix} \begin{bmatrix} \mathbf{U} \\ \mathbf{Q} \end{bmatrix} = \begin{bmatrix} \mathbf{F} \\ \mathbf{0} \end{bmatrix} \tag{4}$$

where $\mathbf{R} = \text{diag}\left(R^{(1)}\, R^{(2)} \cdots R^{(P)}\right)$ and $\mathbf{L} = \text{diag}\left(L^{(1)}\, L^{(2)} \cdots L^{(P)}\right)$ are the diagonal matrices filled with the electrical resistances and the electrical inductances of the shunt circuits. Note that since $\mathbf{K}_V$ is diagonal, the evaluation of $\mathbf{K}_V^{-1}$ is straightforward.

3 REDUCED ORDER MODELS

In order to evaluate the electrical and mechanical frequency response functions of an elastic structure with shunted piezoelectric patches and subjected to a considered harmonic mechanical excitation, the full finite element model of Eq. (4) is applicable only to a small model and low

frequency band. To overcome these limitations, a model reduction approach based on a normal mode expansion and truncation of high-frequency modes is proposed in this section. We present first a review of the existing reduced order models. These models, widely used in the literature, are obtained using the short-circuited or open-circuited basis. In this paper, two original reduced order models are proposed to solve the problem at lower cost: (i) the combined basis formed by both the short-circuited and open-circuited modes, and (ii) the coupled basis formed by the electromechanical modes taking into account the effect of the inductances of the electrical shunt circuits. A comparative study of the effectiveness of these reduced order models in terms of prediction of the vibration attenuation using piezoelectric shunt systems is proposed in next section.

3.1 Projection on the short-circuited basis

The first M_s eigenmodes of the elastic structure with all patches short-circuited are obtained from the following equation:

$$\left[\mathbf{K}_u - \omega_i^2 \mathbf{M}_u\right] \mathbf{\Phi}_i = \mathbf{0} \quad \text{for } i \in \{1, \cdots, M_s\} \tag{5}$$

where $(\omega_i, \mathbf{\Phi}_i)$ are the natural frequency and eigenvector for the ith structural mode. These modes verify the following orthogonality properties

$$\mathbf{\Phi}_i^T \mathbf{M}_u \mathbf{\Phi}_j = \delta_{ij} \quad \text{and} \quad \mathbf{\Phi}_i^T \mathbf{K}_u \mathbf{\Phi}_j = \omega_i^2 \delta_{ij} \tag{6}$$

where δ_{ij} is the Kronecker symbol and $\mathbf{\Phi}_i$ have been normalized with respect to the structure mass matrix. Note that the structure is fixed on Γ_u, which eliminates any rigid body motion.

By introducing the matrix $\mathbf{\Phi} = [\mathbf{\Phi}_1 \ \cdots \ \mathbf{\Phi}_{M_s}]$ of size $(N_s \times M_s)$ corresponding to the basis previously defined (N_s is the total number of degrees of freedom in the finite elements model associated to the structure), the displacement $\mathbf{U}$ is sought as

$$\mathbf{U} = \mathbf{\Phi}\mathbf{q}(t) \tag{7}$$

where the vector $\mathbf{q} = [q_1 \ \cdots \ q_{M_s}]^T$ is the unknown modal amplitudes.

By applying the Ritz-Galerkin projection method, which consists of substituting Eq. (7) into Eq. (4) and premultiplying the first row by $\mathbf{\Phi}^T$, we obtain the reduced matrix system

$$-\omega^2 \begin{bmatrix} \mathbf{\Phi}^T \mathbf{M}_u \mathbf{\Phi} & \mathbf{0} \\ \mathbf{0} & \mathbf{L} \end{bmatrix} \begin{bmatrix} \mathbf{q} \\ \mathbf{Q} \end{bmatrix} + i\omega \begin{bmatrix} \mathbf{0} & \mathbf{0} \\ \mathbf{0} & \mathbf{R} \end{bmatrix} \begin{bmatrix} \mathbf{q} \\ \mathbf{Q} \end{bmatrix} + \begin{bmatrix} \mathbf{\Phi}^T \left(\mathbf{K}_u + \mathbf{C}_{uV} \mathbf{K}_V^{-1} \mathbf{C}_{uV}^T\right) \mathbf{\Phi} & \mathbf{\Phi}^T \mathbf{C}_{uV} \mathbf{K}_V^{-1} \\ \mathbf{K}_V^{-1} \mathbf{C}_{uV}^T \mathbf{\Phi} & \mathbf{K}_V^{-1} \end{bmatrix} \begin{bmatrix} \mathbf{q} \\ \mathbf{Q} \end{bmatrix} = \begin{bmatrix} \mathbf{\Phi}_s^T \mathbf{F} \\ \mathbf{0} \end{bmatrix} \tag{8}$$

This matrix equation represents the reduced-order model using the short-circuited basis of the vibration reduction problem with piezoelectric shunt-damping treatments. If only few modes are kept for the projection, the size of this reduced-order model $(Ms + P)$ is much smaller than the initial one $(Ns+P)$. Eq. (8) can be also written in the following form of coupled differential equations:

- M_s mechanical oscillators

$$-\omega^2 q_i + 2i\omega\xi_i\omega_i q_i + \omega_i^2 q_i + \sum_{p=1}^{P} \sum_{k=1}^{N_s} \frac{\gamma_i^{(p)} \gamma_k^{(p)}}{C^{(p)}} q_i + \sum_{p=1}^{P} \frac{\gamma_i^{(p)}}{C^{(p)}} Q^{(p)} = F_i \tag{9}$$

- P electrical equations

$$-\omega^2 L^{(p)} Q^{(p)} + i\omega R^{(p)} Q^{(p)} + \frac{Q^{(p)}}{C^{(p)}} + \sum_{i=1}^{N_s} \frac{\gamma_i}{C^{(p)}} q_{si} = 0 \tag{10}$$

where $F_i = \mathbf{\Phi}_i^T \mathbf{F}$ is the mechanical excitation of the ith mode and $\gamma_i = \mathbf{\Phi}_i^T \mathbf{C}_{uV}$ is the electromechanical coupling factors.
Note that the modal damping coefficients ξ_i have been added in Eq. (9) in order to take into account the structural damping, which can be measured experimentally. This is mandatory in order to quantify the attenuation due to the shunt at the resonance (of course, without damping, the amplitude of the response at the resonance is theoretically infinite).

The major interest of choosing the short-circuit eigenmodes as the expansion basis is that its can be computed with a classical elastic mechanical problem. This operation can thus be done by any standard finite elements code.

3.2 Projection on the open-circuited basis

The first M_s natural frequencies $\widehat{\omega}_i$ and eigenvectors $\widehat{\mathbf{\Phi}}_i$ of the elastic structure with all patches open-circuited are obtained from the following equation:

$$\left[(\mathbf{K}_u + \mathbf{C}_{uV}\mathbf{K}_V^{-1}\mathbf{C}_{uV}^T) - \widehat{\omega}_i^2 \mathbf{M}_u\right] \widehat{\mathbf{\Phi}}_i = \mathbf{0} \quad \text{for } i \in \{1, \cdots, M_s\} \tag{11}$$

These modes verify the following orthogonality properties

$$\widehat{\mathbf{\Phi}}_i^T \mathbf{M}_u \widehat{\mathbf{\Phi}}_j = \delta_{ij} \quad \text{and} \quad \widehat{\mathbf{\Phi}}_i^T (\mathbf{K}_u + \mathbf{C}_{uV}\mathbf{K}_V^{-1}\mathbf{C}_{uV}^T) \widehat{\mathbf{\Phi}}_j = \widehat{\omega}_i^2 \delta_{ij} \tag{12}$$

Thus, the displacement $\mathbf{U}$ is sought as

$$\mathbf{U} = \widehat{\mathbf{\Phi}} \widehat{\mathbf{q}}(t) \tag{13}$$

where the matrix $\widehat{\mathbf{\Phi}} = \left[\widehat{\mathbf{\Phi}}_1 \cdots \widehat{\mathbf{\Phi}}_{M_s}\right]$ of size $(N_s \times M_s)$ corresponds to the projection basis constituted by the first M_s eigenmodes of the structure with all patches open-circuited and where the vector $\widehat{\mathbf{q}} = [\widehat{q}_1 \cdots \widehat{q}_{M_s}]^T$ is the unknown modal amplitudes.

By applying the Ritz-Galerkin projection method using the procedure described in section 3.1, we obtain the following coupled differential equations:

- M_s mechanical oscillators

$$-\omega^2 \widehat{q}_i + 2i\omega\xi_i\widehat{\omega}_i\widehat{q}_i + \widehat{\omega}_i{}^2 \widehat{q}_i + \sum_{p=1}^{P} \frac{\widehat{\gamma}_i^{(p)}}{C^{(p)}} Q^{(p)} = \widehat{F}_i \tag{14}$$

- P electrical equations

$$-\omega^2 L^{(p)} Q^{(p)} + i\omega R^{(p)} Q^{(p)} + \frac{Q^{(p)}}{C^{(p)}} + \sum_{i=1}^{N_s} \frac{\widehat{\gamma}_i}{C^{(p)}} \widehat{q}_i = 0 \tag{15}$$

where $\widehat{F}_i = \widehat{\mathbf{\Phi}}_i^T \mathbf{F}$ and $\widehat{\gamma}_i = \widehat{\mathbf{\Phi}}_i^T \mathbf{C}_{uV}$ are the mechanical excitation and the electromechanical coupling factor of the ith mode respectively.

3.3 Projection on the combined basis

This method consists in building a projection basis formed by both the short-circuited and open-circuited modes:

$$\boldsymbol{\Phi}_c = \left[\boldsymbol{\Phi}\ \widehat{\boldsymbol{\Phi}}\right] = \left[\boldsymbol{\Phi}_1 \cdots \boldsymbol{\Phi}_{M_s}\ \widehat{\boldsymbol{\Phi}}_1 \cdots \widehat{\boldsymbol{\Phi}}_{M_s}\right] \tag{16}$$

Thus, the displacement $\mathbf{U}$ is sought as

$$\mathbf{U} = \boldsymbol{\Phi}_c \mathbf{q}_c(t) = \boldsymbol{\Phi}\mathbf{q}(t) + \widehat{\boldsymbol{\Phi}}\widehat{\mathbf{q}}(t) \tag{17}$$

By applying the Ritz-Galerkin projection method, which consists of substituting Eq. (17) into Eq. (4) and premultiplying the first row by $\boldsymbol{\Phi}_c^T$, we obtain the reduced matrix system,

$$\begin{aligned} -\omega^2 \begin{bmatrix} \boldsymbol{\Phi}_c^T \mathbf{M}_u \boldsymbol{\Phi}_c & \mathbf{0} \\ \mathbf{0} & \mathbf{L} \end{bmatrix} \begin{bmatrix} \mathbf{q}_c \\ \mathbf{Q} \end{bmatrix} + i\omega \begin{bmatrix} \mathbf{0} & \mathbf{0} \\ \mathbf{0} & \mathbf{R} \end{bmatrix} \begin{bmatrix} \mathbf{q}_c \\ \mathbf{Q} \end{bmatrix} + \\ \begin{bmatrix} \boldsymbol{\Phi}_c^T \left(\mathbf{K}_u + \mathbf{C}_{uV}\mathbf{K}_V^{-1}\mathbf{C}_{uV}^T\right)\boldsymbol{\Phi}_c & \boldsymbol{\Phi}_c^T \mathbf{C}_{uV}\mathbf{K}_V^{-1} \\ \mathbf{K}_V^{-1}\mathbf{C}_{uV}^T\boldsymbol{\Phi}_c & \mathbf{K}_V^{-1} \end{bmatrix} \begin{bmatrix} \mathbf{q}_c \\ \mathbf{Q} \end{bmatrix} = \begin{bmatrix} \boldsymbol{\Phi}_c^T \mathbf{F} \\ \mathbf{0} \end{bmatrix} \end{aligned} \tag{18}$$

For this technique, two drawbacks exist: (i) two modal analysis are required and (ii) the short-circuited and open-circuited eigenvectors are not mutually orthogonal with respect to the mass and stiffness matrices of the problem. Thus, a Gram-Schmidt algorithm is applied in this work to orthogonalize these eigenvectors and build well-conditioned matrices.

3.4 Projection on the coupled basis

In the case of a resonant shunt, this technique consists in computing the eigenmodes of the real conservative system associated to Eq. (4). Thus, the inductances of the shunt circuits are taken into account in the mass matrix, whereas the effect of the resistances and mechanical damping is not considered. The eigenmode $(\tilde{\omega}_i, \tilde{\boldsymbol{\Phi}}_i)$ of this problem is solution of the following equation:

$$\left(-\tilde{\omega}_i^2 \begin{bmatrix} \mathbf{M}_u & \mathbf{0} \\ \mathbf{0} & \mathbf{L} \end{bmatrix} + \begin{bmatrix} \mathbf{K}_u + \mathbf{C}_{uV}\mathbf{K}_V^{-1}\mathbf{C}_{uV}^T & \mathbf{C}_{uV}\mathbf{K}_V^{-1} \\ \mathbf{K}_V^{-1}\mathbf{C}_{uV}^T & \mathbf{K}_V^{-1} \end{bmatrix}\right) \tilde{\boldsymbol{\Phi}}_i = \begin{bmatrix} \mathbf{0} \\ \mathbf{0} \end{bmatrix} \tag{19}$$

where the eigenvector $\tilde{\boldsymbol{\Phi}}_i^T = \begin{bmatrix} \tilde{\boldsymbol{\Phi}}_{si}^T & \tilde{\boldsymbol{\Phi}}_{qi}^T \end{bmatrix}$ consists of the mechanical degrees-of-freedom $\tilde{\boldsymbol{\Phi}}_{si}$ of size N_s followed by the electric degrees-of-freedom $\tilde{\boldsymbol{\Phi}}_{qi}$ of size P.

By introducing the modal basis $\tilde{\boldsymbol{\Phi}} = \left[\tilde{\boldsymbol{\Phi}}_{s1} \cdots \tilde{\boldsymbol{\Phi}}_{sM_s}\right]$ of size $(N_s \times M_s)$, the displacement $\mathbf{U}$ is sought as

$$\mathbf{U} = \tilde{\boldsymbol{\Phi}}\tilde{\mathbf{q}}(t) \tag{20}$$

By applying the Ritz-Galerkin projection method, which consists of substituting Eq. (20) into Eq. (4) and premultiplying the first row by $\tilde{\boldsymbol{\Phi}}^T$, we obtain the reduced matrix system,

$$\begin{aligned} -\omega^2 \begin{bmatrix} \tilde{\boldsymbol{\Phi}}^T \mathbf{M}_u \tilde{\boldsymbol{\Phi}} & \mathbf{0} \\ \mathbf{0} & \mathbf{L} \end{bmatrix} \begin{bmatrix} \tilde{\mathbf{q}} \\ \mathbf{Q} \end{bmatrix} + i\omega \begin{bmatrix} \mathbf{0} & \mathbf{0} \\ \mathbf{0} & \mathbf{R} \end{bmatrix} \begin{bmatrix} \tilde{\mathbf{q}} \\ \mathbf{Q} \end{bmatrix} + \\ \begin{bmatrix} \tilde{\boldsymbol{\Phi}}^T \left(\mathbf{K}_u + \mathbf{C}_{uV}\mathbf{K}_V^{-1}\mathbf{C}_{uV}^T\right)\tilde{\boldsymbol{\Phi}} & \tilde{\boldsymbol{\Phi}}^T \mathbf{C}_{uV}\mathbf{K}_V^{-1} \\ \mathbf{K}_V^{-1}\mathbf{C}_{uV}^T\tilde{\boldsymbol{\Phi}} & \mathbf{K}_V^{-1} \end{bmatrix} \begin{bmatrix} \tilde{\mathbf{q}} \\ \mathbf{Q} \end{bmatrix} = \begin{bmatrix} \tilde{\boldsymbol{\Phi}}^T \mathbf{F} \\ \mathbf{0} \end{bmatrix} \end{aligned} \tag{21}$$

Remarks:

- This method requires the knowledge of the optimal values of the electric inductances before the computation of the eigenmodes.

- The projection for the various methods concerns concerns only the mechanical variables $\mathbf{U}$. The electrical unknown field $\mathbf{Q}$ is not concerned by the reduction because the dimension of this vector corresponds to the number of piezo-patches and therefore is very small compared to the mechanical finite element degrees-of-freedom (displacement in the host structure and the piezo-patches).

- Substituting $\tilde{\mathbf{\Phi}}_{qi}$ in terms of $\tilde{\mathbf{\Phi}}_{si}$ from the second line of Eq. (19), the modal problem amounts to solve:

$$\Big(-\tilde{\omega}_i^2\mathbf{M}_u + \Big[\mathbf{K}_u + \mathbf{C}_{uV}\mathbf{K}_V^{-1}\mathbf{C}_{uV}^T - \mathbf{C}_{uV}\mathbf{K}_V^{-1}\left(\mathbf{K}_V^{-1} - \tilde{\omega}_i^2\mathbf{L}\right)^{-1}\mathbf{K}_V^{-1}\mathbf{C}_{uV}^T\Big]\Big)\tilde{\mathbf{\Phi}}_{si} = \mathbf{0} \quad (22)$$

Two cases can be distinguished, depending on the value of the inductance:

– short-circuit case (inductances $L^{(i)} = \mathbf{0}$)

$$\left[\mathbf{K}_u - \tilde{\omega}_i^2\mathbf{M}_u\right]\tilde{\mathbf{\Phi}}_{si} = \mathbf{0} \quad (23)$$

– open-circuit case (inductances $L^{(i)} = \infty$)

$$\left[\left(\mathbf{K}_u + \mathbf{C}_{uV}\mathbf{K}_V^{-1}\mathbf{C}_{uV}^T\right) - \tilde{\omega}_i^2\mathbf{M}_u\right]\tilde{\mathbf{\Phi}}_{si} = \mathbf{0} \quad (24)$$

4 NUMERICAL EXAMPLES

4.1 Cantilever beam with shunted piezoelectric patch

In this first example, we propose to compare the proposed modal reduction techniques in terms of prediction of vibration attenuation with piezoelectric shunt on a simple system. The system under study consists of a cantilever beam with one piezoelectric device, as sketched in Figure 2. The beam is made of aluminum (E = 74 GPa, ν = 0.33, and ρ = 2700 kg/m^3) with

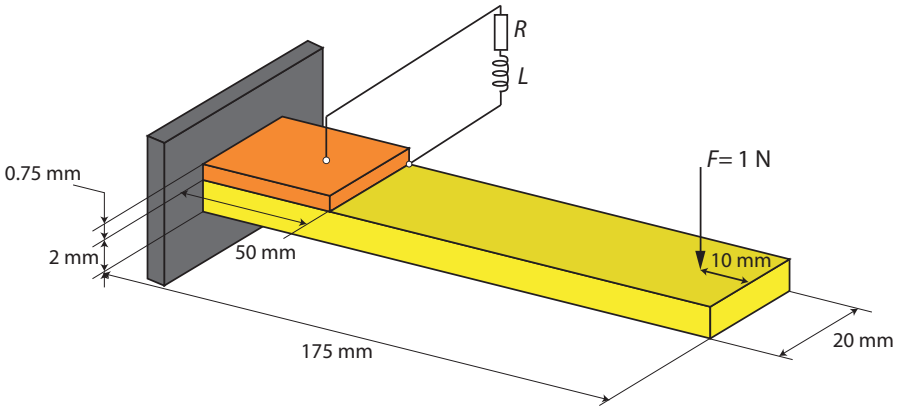


Figure 2: Cantilever beam partially covered with collocated piezoelectric element: geometrical data.

L_b=175 mm (length), w_b=10 mm (width), and h_b=2 mm (thickness). The piezoelectric element

in PIC-151 is assumed to be perfectly bounded to the beam and has the same width. For the mechanical and electrical characteristics of the piezoelectric material PIC-151, the reader can be referred to [15]. Concerning the finite element discretization, the beam is modelled in 2D using 672 four nodes plate elements (QUAD4). The portion of the plate covered by the piezoelectric patch and the patch itself is modeled according to laminated theory [16].

Table 1 presents the first five eigenfrequencies of the beam (with short-circuit or open-circuit patches) and the corresponding effective electromechanical modal coupling factor (EEMCF), characterizing the energy exchanges between the mechanical structure and the piezoelectric patches and defined by:

$$k_{eff,i}^2 = \frac{\hat{\omega}_{si}^2 - \omega_{si}^2}{\omega_{si}^2} \tag{25}$$

The first, second and fourth frequencies are associated with the first three bending modes lower than 1100 Hz, while the third one corresponds to the first bending mode in the plane and the fifth frequency to the first torsional vibration mode. This classification is found from the mode shapes which are not shown here for the sake of brevity. Moreover, as expected for bending modes, the natural frequencies of the open-circuit modes are higher than those obtained in the short-circuited case due to the electrical effect of the patch. The bending mode in the plane and the torsional mode do not present any electromechanical coupling due to the transverse polarization of the patch.

Type	Short circuit frequencies	Open circuit frequencies	k_{eff}
F	71.89	73.48	21.15
F	379.49	383.97	15.42
F_p	587.02	587.02	0
F	969.11	970.05	4.41
T	1048.71	1048.71	0

F: Bending mode, F_p Bending mode in the plane, T: Torsional mode

Table 1: Computed frequencies (Hz) of the beam and the electromechanical coupling coefficient.

The beam is now excited by a harmonic transverse load (see Figure 2). In addition, no mechanical damping was introduced in this example. The vibration output is detected at the excitation point. Figure 3 presents the frequency response of the system in terms of the transverse displacement computed with a direct method in which the displacement and the charge vectors are calculated at each frequency step.

In order to achieve maximum vibration dissipation of the first mode, the patch is tuned to an RL shunt circuit. The resistance R and the inductance L can be adjusted and properly chosen to maximize the damping effect of a particular mode. The optimal resistance and inductance of the ith mode for a series resonant shunt are given by [3]:

$$R^{\text{opt}} = \frac{\sqrt{2k_{\text{eff},i}^2}}{C\omega_i(1+k_{\text{eff},i}^2)} \tag{26a}$$

$$L^{\text{opt}} = \frac{1}{C\omega_i^2(1+k_{\text{eff},i}^2)} \tag{26b}$$

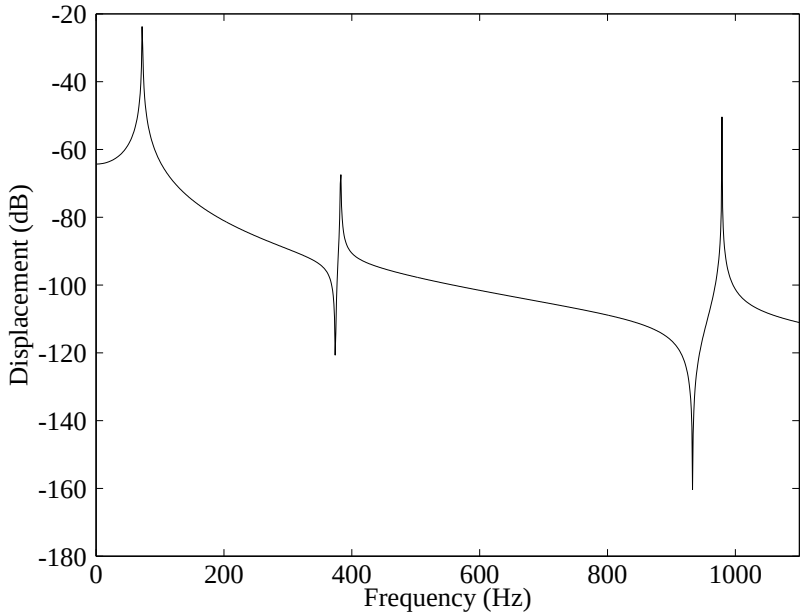


Figure 3: Frequency response function of the cantilever beam with short circuited patch and subjected to a harmonic transverse load.

where ω_i is the short circuit natural frequency of the ith mode, C is the capacitance of the piezoelectric patch and $k_{\text{eff},i}$ is the effective electromechanical coupling coefficient given in Eq. (25).

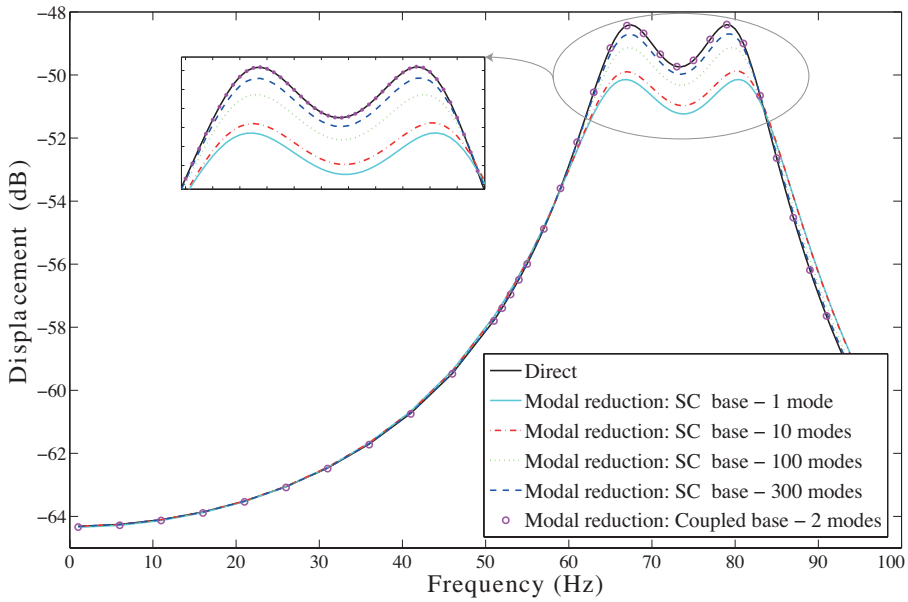


Figure 4: Frequency responses of the cantilever beam with shunted piezoelectric patch: comparison between (i) the direct approach, (ii) modal reduction using short-circuited basis and (iii) modal reduction using coupled basis.

Figures 4 and 5 show a comparison between the frequency responses of the cantilever beam when the shunt circuit is tuned to damp the first vibration mode. We compare all the proposed reduction techniques to the direct approach. The following observations can be made:

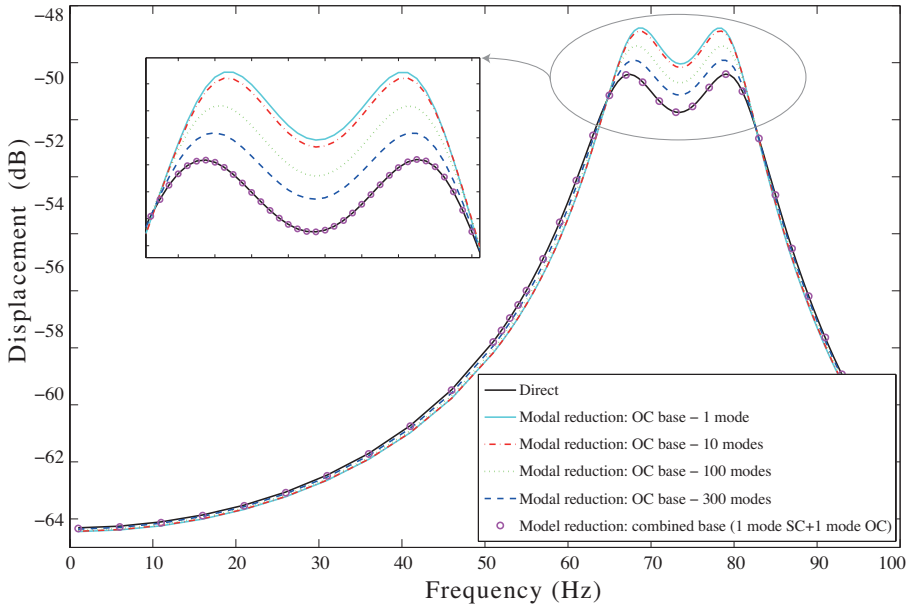


Figure 5: Frequency responses of the cantilever beam with shunted piezoelectric patch: comparison between (i) the direct approach, (ii) modal reduction using open-circuited basis and (iii) modal reduction using combined basis.

- The reduced order models built from the short-circuit or the open circuit basis converge with a large number of eigenvectors. With a small number of eigenvectors, the short-circuit basis overestimates the attenuation while the open-circuit basis underestimates it.

- The reduced order model computed from the combined basis gives an excellent results with only one short-circuited mode and one open-circuited mode. This efficiency is related to the introduction of additional electromechanical coupling terms in the reduced system which allows better modeling of the effects of the piezo-patches and the shunt-circuit on the response of the system.

- The reduced order model built from the coupled basis is extremely effective. The model response converges when projecting the unknown mechanical displacements only on the first two eigenvectors. The attenuation of a resonance mode with the shunt technique is characterized by a decrease of the amplitudes of the peaks around the targeted frequency. In this example, these two peaks correspond to the first two modes of the coupled basis with mode shapes very close. This leads us to conclude that this basis formed by the real modes of the coupled system (elastic structure with shunted piezoelectric patches), is very effective in the prediction of vibration attenuation.

4.2 Multimode shunt control of a vibrating plate

In this last example, a clamped rectangular plate with two rectangular piezoelectric patches perfectly bonded on its surface is considered. The plate of 2-mm-thick is made in aluminum and the patches of 0.5-mm-thick are in PIC 151 (we used the same properties as the previous example). The geometrical data of the problem are given in Figure 6. Concerning the finite element discretization, the plate is modelled with 672 QUAD4. The portion of the plate covered by the piezoelectric patches and the patch itself are modeled according to laminated theory. The plate is excited by a normal unit sinusoidal force as sketched in Figure 6. The vibration output is detected at the excitation point, where the displacement reaches a maximum. Figure 7 presents

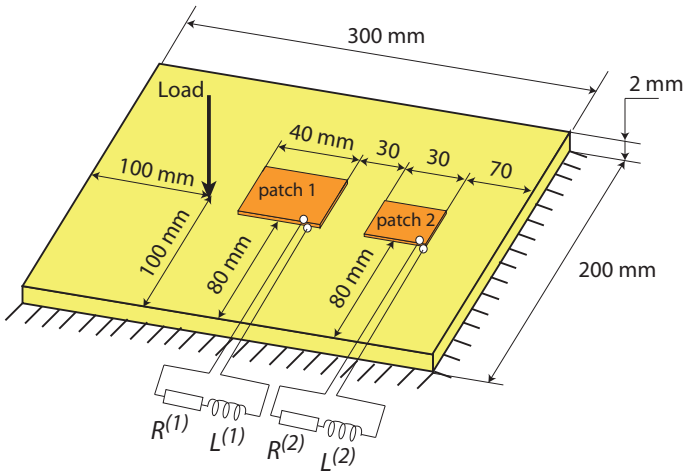


Figure 6: Clamped plate partially covered with two collocated piezoelectric elements: geometrical data.

the frequency response of the system in terms of the transverse displacement computed with direct nodal method.

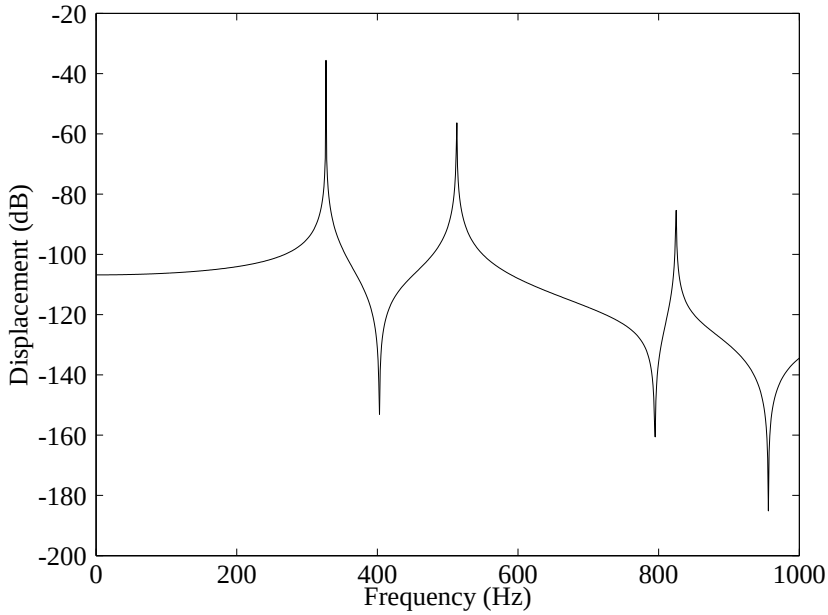


Figure 7: Frequency response function of the plate with short circuited patches and subjected to a harmonic load.

Table 2 presents the first ten eigenfrequencies of (i) the clamped plate with all patches short-circuited, (ii) the clamped plate with all patches open-circuited and (iii) the coupled problem given by Eq. (18). For the third case, the two patches are tuned to the two first vibration modes respectively and the used optimal inductances are computed from Eqs. 26b. For each frequency of the open-circuit case, except for modes without electromechanical coupling, corresponds two frequencies in the coupled case (one lower and the other higher to this frequency). The mode shapes associated to these frequencies are very similar to the mode of the original one. These modes are not shown here for the sake of brevity.

Figures 8 and 9 show a comparison between the frequency responses of the clamped plate

Short circuit frequencies	Open circuit frenquencies	Coupled frenquencies
326.98	327.85	306.68
512.76	516.10	348.79
824.66	827.05	486.10
829.68	829.68	544.23
1005.77	1005.77	829.68
1265.51	1265.61	836.79
1291.48	1291.48	1005.77
1600.37	1604.25	1265.63
1727.30	1727.30	1291.48
1751.45	1763.06	1617.75

Table 2: Computed frequencies (Hz) of the plate with piezoelectric patches in: (i) short-circuit case, (ii) open-circuited case and (iii) coupled case.

when the shunt circuits are tuned to damp the first two vibration modes. We compare all the proposed reduction techniques to the direct approach. The results confirm the findings obtained with the previous example:

- The reduced order models built from the short-circuited or open-circuited bases does not fully converge with a reduced number of eigenvectors.
- Using the combined bases, excellent results are obtained in the resonance zones when the unknown mechanical displacements are projected on the basis formed by the first two short-circuited modes and the first two open-circuited. Using the first 38 short-circuited (respectively open-circuited) modes and the first two open-circuited (respectively short-circuited) modes, the response of the model converges in areas of resonance and also outside these areas.
- The reduced order model built from the coupled basis gives excellent results compared to the results of the direct method. This convergence is achieved by using the first 40 modes. We note that with only four modes (modes resulting from the resonant shunt technique), the convergence is limited to resonant frequencies and is not assured in the other areas.

These Figures show also that the modal resonant magnitude for each considered mode have been significantly reduced simultaneously. Indeed, the strain energy present in the piezoelectric material is converted into electrical energy and hence dissipated into heat using the RL shunt device.

From these two examples, we can confirm the good performances of the combined and coupled projection bases compared to the results of the direct method with a reduced number of modes. However, the reduced order model using the coupled modes may be applied only in the case of a resonant shunt and requires knowledge of the optimal values of inductors before projection. For the combined basis, two drawbacks remain: (i) the need to carry two modal calculations (short-circuit and open-circuit) and (ii) the loss of orthogonality after projection of the mass and stiffness matrices.

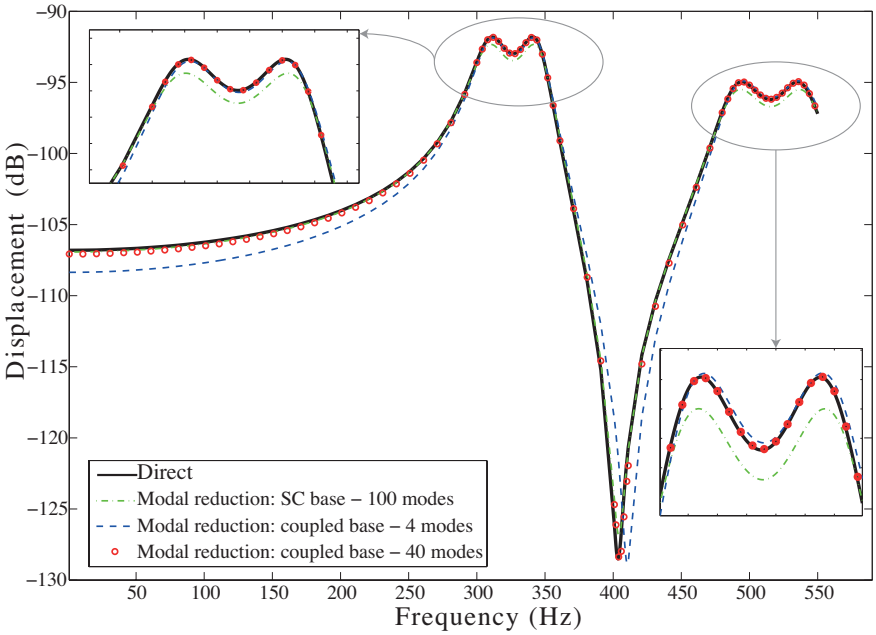


Figure 8: Frequency responses of the plate with shunted piezoelectric patches: comparison between (i) the direct approach, (ii) modal reduction using short-circuited basis and (iii) modal reduction using coupled basis.

5 CONCLUSIONS

In this paper, reduced order finite element formulations for passive reduction of structural vibration by means of shunted piezoelectric system are presented. Two new reduced-order models, based on a normal mode expansion, are then developed: (i) the combined basis, and (ii) the coupled basis. Despite their reduced size, these model are proved to be very efficient with a reduced number of modes compared to classical bases for simulations of vibration attenuation of selected frequency resonances. However, some drawbacks remain and concerns the necessity of two modal calculations for the combined basis and the knowledge of the optimal values of inductors before projection for the coupled basis. Despite these disadvantages, these new techniques can be recommanded for the resolution of electromechanical problems with shunt devices.

REFERENCES

[1] M.A Trindade, A. Benjeddou, R. Ohayon, Finite element modeling of hybrid active-passive vibration damping of multilayer piezoelectric sandwich beams. Part 1: formulation, *International Journal for Numerical Methods in Engineering*, **51(7)**, 835–854, 2001.

[2] B. Kim, G.N. Washington, H.-S. Yoon, Active Vibration Suppression of a 1D Piezoelectric Bimorph Structure Using Model Predictive Sliding Mode Control, *Smart Structures and*

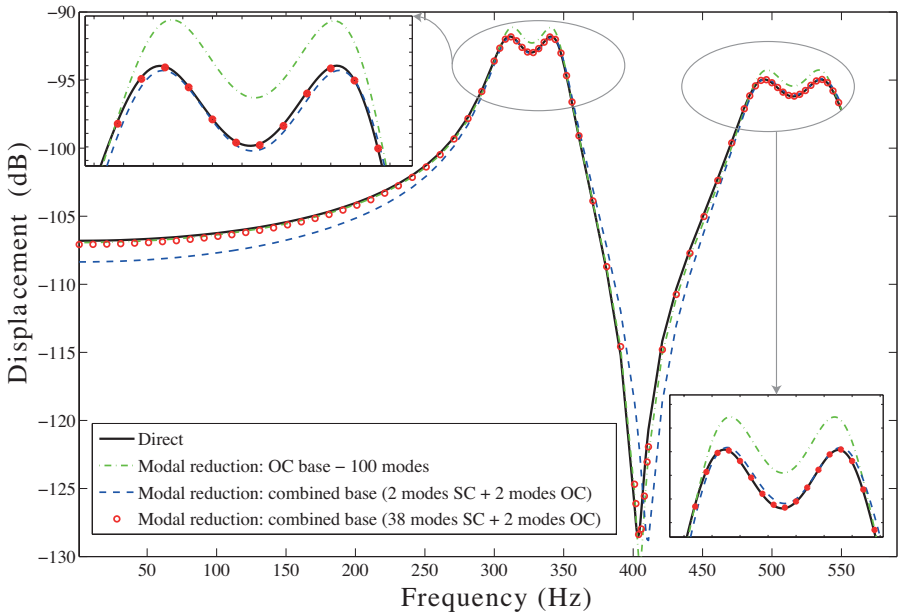


Figure 9: Frequency responses of the plate with shunted piezoelectric patches: comparison between (i) the direct approach, (ii) modal reduction using open-circuited basis and (iii) modal reduction using combined basis.

Systems, **11(6)**, 623–635, 2013.

[3] N.W. Hagood, A.V. Flotow, Damping of structural vibrations with piezoelectric materials and passive electrical networks, *Journal of Sound and Vibration*, **146(2)**, 243–268, 1991.

[4] F. dellIsola, C. Maurini, M.A. Porfiri, Passive damping of beam vibrations through distributed electric networks and piezoelectric transducers: prototype design and experimental validation, *Smart Materials and Structure*, **13(2)**, 299-308, 2004.

[5] M. Collet, K.A. Cunefare, M.N. Ichchou, Wave motion optimization in periodically distributed shunted piezocomposite beam structures, *Journal of Intelligent Material Systems and Structures*, **20(7)**, 787–808, 2009.

[6] F. Casadei, M. Ruzzene,L. Dozio, K.A. Cunefare, Broad band vibration control through periodic arrays of resonant shunts: experimental investigation on plates, *Smart Materials and Structures*, **19(1)**, 015002, 2010.

[7] A. Belloli, D. Niedereberger, S. Pietrzko, M. Morari, P. Ermanni, Structural vibration control via rl-shunted active fiber composites, *Journal of Intelligent Material Systems and Structures*, **18(3)**, 275–287, 2007.

[8] D. Niederberger, A. Fleming, S.O.R. Moheimani, M. Morari, Adaptive multi-mode resonant piezoelectric shunt damping, *Smart Materials and Structures*, **13(5)**, 1025–1035, 2004.

[9] D. Guyomar, A. Faiz, L. Petit, C. Richard, Wave reflection and transmission reduction using piezoelectric semipassive nonlinear technique, *The Journal of the Acoustical Society of America*, **119(1)**, 285–298, 2006.

[10] J. Ducarne, O. Thomas, J.-F. Deü, Structural vibration reduction by switch shunting of piezoelectric elements: modeling and optimization, *Journal of Intelligent Materials Systems and Structures*, **21(8)**, 797–816, 2010.

[11] W. Larbi, J.-F. Deü, M. Ciminello, R. Ohayon, Structural-acoustic vibration reduction using switched shunt piezoelectric patches: a finite element analysis, *Journal of Vibration and Acoustics*, **132(5)**, 051006, 2010.

[12] O. Thomas, J.-F. Deü, J. Ducarne, Vibrations of an elastic structure with shunted piezoelectric patches: efficient finite elements formulation and electromechanical couplings coefficients. *International Journal for Numerical Methods in Engineering* **80(2)**, 235–268, 2009.

[13] J.-F. Deü, W. Larbi, R. Ohayon, R. Sampaio, Piezoelectric shunt vibration damping of structural-acoustic systems: Finite element formulation and Reduced-Order Model, *Journal of Vibration and Acoustics*, **136(3)**, 031007, 2014.

[14] W. Larbi, J.-F. Deü, R. Ohayon, R. Sampaio, Coupled FEM/BEM for control of noise radiation and sound transmission using piezoelectric shunt damping, *Applied Acoustics*, **86**, 146–153, 2014.

[15] L. Pereira da Silva, W. Larbi, J.-F. Deü, Topology optimization of shunted piezoelectric elements for structural vibration reduction, *Journal of Intelligent Material Systems and Structures*, **in press**, 2015.

[16] J. Reddy, *Mechanics of Laminated Composite Plates and Shells: Theory and Analysis*, CRC, Boca Raton, FL, 2004.

COMPDYN 2015
5th ECCOMAS Thematic Conference on
Computational Methods in Structural Dynamics and Earthquake Engineering
M. Papadrakakis, V. Papadopoulos, V. Plevris (eds.)
Crete Island, Greece, 25–27 May 2015

SYSTEM IDENTIFICATION AND ACTIVE MODAL CONTROL OF A FLEXIBLE TRUSS STRUCTURE

C. F. Joventino[1], **G. L. C. M. Abreu**[1], **V. Lopes Jr.**[1]

[1] Univ Estadual Paulista, Department Mechanical Engineering
Av. Brasil, 56, Centro, Ilha Solteira-SP, Brazil
e-mail: jcarlosfernando@gmail.com, gustavo@dem.feis.unesp.br, vicente@dem.feis.unesp.br

Keywords: Flexible Structures, Active Control, System Identification.

Abstract: *The aim of this paper is to illustrate the active control of vibration of a flexible truss structure using a model-based digital controller. The state-space model of the system is derived using a system identification technique known as the Observer/Kalman Filter Identification (OKID) method together with Eigensystem Realization Algorithm (ERA). Based on the measured response of the structure to a chirp input, an explicit state-space model of the equivalent linear system is determined. To reduce the vibrations caused by an impulse force, two active strut members are installed along a vertical of the base bay of the truss. The active strut element consists of a piezoelectric ceramic stack actuator, a force transducer and mechanical interfaces. An integral controller is designed to suppress vibration of the truss. The controller, formulated with the root locus approach, is designed to maximize modal damping of a constructed truss structure. Experimental results illustrate that the active piezoceramic strut actuators and the integral controller can effectively reduce vibration of the truss.*

1 INTRODUCTION

Smart structures, which use actuators, sensors and a controller, can be used to suppress vibration in situations where passive measures are undesirable because of weight or space constraints. Frequently, piezoelectric actuators and sensors are used as they are light, cheap and convenient to bond to structures ([1], [2]). Lead zirconate titanate (PZT) is often used as an actuator because it is relatively stiff and couples well to a structure.

A truss structure is one of the most commonly used structures in aerospace and civil engineering [3]. Because it is desirable to use the minimum amount of material for construction, the trusses are becoming lighter and more flexible which means they are more susceptible to vibration. A convenient way of controlling a truss structure is to incorporate a piezoelectric stack actuator into one of the truss members [4]. Research on the damping of truss structures began in the late 80's. Fanson et al. [5], Chen et al. [6] and Anderson et al. [7] designed active members made of piezoelectric transducers. Preumont et al. [8] used a local control strategy to suppress the low frequency vibrations of a truss structure using piezoelectric actuators. Their strategy involved the application of integrated force feedback using two force gauges each collocated with the piezoelectric actuators, which were fitted into different beam elements in the structure. Carvalhal et al. [9] used an efficient modal control strategy for the active vibration control of a truss structure. In that approach, a feedback force is applied to each mode to be controlled according to a weighting factor that is determined by assessing how much that mode is excited by the primary source. To test the effectiveness of the control strategy it was compared with an alternative approach and the numerical results showed that with the proposed strategy it is possible to significantly reduce the control effort required, with a minimal reduction in control performance. Abreu et al. [10] used a standard H_∞ robust controller design framework to suppress undesirable structural vibrations in a truss structure containing piezoelectric actuators and collocated force transducers. Li and Huang [11] developed a linear-quadratic-Gaussian (LQG) model for vibration control for an adaptive truss. Numerical examples and the vibration control experiments were used to validate the efficiency of the proposed method. Abreu et al. [2] verified experimentally the application of a self-organizing fuzzy controller (SOFC) to suppress the vibrations of a truss structure using a pair of piezoceramic stack actuators. In that study, a decentralized active damping with local SOFCs connecting each actuator to its collocated force transducer were used. Experimental tests were performed, which illustrated the effectiveness of the controller in reducing the vibrations of a truss structure. The experimental results have shown that piezoceramic stack actuators control efficiently the vibrations of the truss structure.

Active damping of truss structures with integral control was introduced at the beginning of the 90's [8] and has since been thoroughly studied both theoretically and experimentally [12]. This paper investigates numerically an integral force feedback controller for suppressing the undesired structural vibrations in a truss structure containing piezoelectric stack actuators and collocated force sensors forming a so-called smart/intelligent truss structure. It is shown that the control system consists of independent SISO loops, i.e. a decentralized active damping with local controllers connecting each actuator to its collocated force sensor. It is also demonstrated that this control problem can be formulated with the root locus approach.

Although actuators and sensors are crucial elements in the design of a smart structure, they are not the focus of this paper. The focus is on the design of the integral controller. The model based controller can be further subdivided into two types; one type uses a numerical model of the structure derived theoretically, using finite element models ([13], [14]), for example. The second type involves the determination of a model of the structure using measured input and output data [15]. This paper concentrates on this approach, and demonstrates the procedure to design such a

controller. The main objective is to investigate the combination of a system identification method and the integral control technique to actively control vibration in a truss structure.

Ljung [16] provides an excellent introduction to the subject of system identification, and describes the various methodologies that have been developed. Among the time domain methods, the Observer/Kalman Filter Identification (OKID) algorithm has shown to be efficient and robust ([17], [18]), and has been applied to space structures, such as the Shuttle Remote Manipulator System [19]. It has several advantages for the active vibration control application discussed here. First, it assumes that the system is a discrete linear time-invariant (LTI) state-space system. Second, it requires only input and output data to formulate the model (no priori knowledge of the plant is needed). Third, a pseudo-Kalman state estimator is produced, and lastly, any residual truncation errors will be small. Together with the OKID algorithm, the Eigensystem Realization Algorithm (ERA) ([18], [20]) generates a low order state-space model of the system to be controlled.

The paper is organized as follows. In section 2, the OKID and ERA approaches are summarized. Section 3 describes the experimental work in which the model and the controller of the truss structure, fitted with piezoelectric actuators and force sensors, is determined. Following this, real time control is implemented to demonstrate the efficacy of the integral control approach. Section 4 concludes the paper with some concluding remarks.

2 IDENTIFICATION OF THE DYNAMIC MODEL

In this section an overview is given of system identification technique used to determine a model of the system to be controlled. It consists of two parts: the OKID method to determine the system's Markov parameters, and the ERA to translate these parameters into a state-space model of the system.

2.1 Description of the Okid technique

The OKID method was developed to compute the Markov parameters of a linear system, which are the same as the sampled impulse response of the system. It is a time domain method which can work with general response data such as random vibration, impulsive signals or chirps. First, the observer Markov parameters are calculated, then the system Markov parameters are determined recursively from the Markov parameters of the observer system. The process of system identification using this method is described in ([17], [18]). In this section a brief overview of the process is given.

Consider first a general linear system expressed in discrete-time state-space form as

$$\mathbf{x}(k+1) = \mathbf{A}\mathbf{x}(k) + \mathbf{B}\mathbf{u}(k)$$
$$\mathbf{y}(k) = \mathbf{C}\mathbf{x}(k) + \mathbf{D}\mathbf{u}(k) \qquad (1a,b)$$

where $\mathbf{x}$ is an $n \times 1$ state vector, $\mathbf{u}$ an $m \times 1$ input or control vector and $\mathbf{y}$ a $q \times 1$ output vector. Matrices $\mathbf{A}$, $\mathbf{B}$, $\mathbf{C}$ and $\mathbf{D}$ are the state, input, output, and direct influence matrix, respectively. The integer k represents sampled time.

The input–output description of the system with zero initial conditions can be obtained from Eq. (1) recursively as

$$\mathbf{y}(k) = \sum_{i=0}^{k-1} \mathbf{Y}_i \, \mathbf{u}(k-i-1) + \mathbf{D}\mathbf{u}(k) \tag{2}$$

where $\mathbf{Y}_i = \mathbf{C}\mathbf{A}^i\mathbf{B}$ and $\mathbf{D}$ are the Markov parameters of the system. They are also samples of the system impulse response. For a lightly damped system, many Markov parameters are needed because the impulse response takes a long time to decay away. To reduce this number, an observer is introduced to artificially add damping and hence reduce the length of the impulse response of the combined system. If $(\mathbf{A}, \mathbf{C})$ is an observable pair, then there exists an observer of the form

$$\begin{aligned} \hat{\mathbf{x}}(k+1) &= \mathbf{A}\hat{\mathbf{x}}(k) + \mathbf{B}\mathbf{u}(k) - \mathbf{M}[\mathbf{y}(k) - \hat{\mathbf{y}}(k)] \\ &= (\mathbf{A} + \mathbf{M}\mathbf{C})\hat{\mathbf{x}}(k) + (\mathbf{B} + \mathbf{M}\mathbf{D})\mathbf{u}(k) - \mathbf{M}\mathbf{y}(k) \end{aligned} \tag{3a,b}$$

$$\hat{\mathbf{y}}(k) = \mathbf{C}\hat{\mathbf{x}}(k) + \mathbf{D}\mathbf{u}(k)$$

Matrix $\mathbf{M}$ can be interpreted as an observer gain matrix. Consider the special case where all eigenvalues of $\mathbf{A} + \mathbf{M}\mathbf{C}$ are zero. Thus, the estimated state $\hat{\mathbf{x}}$ converges to the true state $\mathbf{x}(k)$ after at most n steps where n is the order of the system. Equation (3) then becomes

$$\begin{aligned} \mathbf{x}(k+1) &= (\mathbf{A} + \mathbf{M}\mathbf{C})\mathbf{x}(k) + (\mathbf{B} + \mathbf{M}\mathbf{D})\mathbf{u}(k) - \mathbf{M}\mathbf{y}(k) \\ \mathbf{y}(k) &= \mathbf{C}\mathbf{x}(k) + \mathbf{D}\mathbf{u}(k) \end{aligned} \tag{4a,b}$$

The input–output description of the system described by Eq. (4) is given by (for $k \geq n$)

$$\mathbf{y}(k) = \sum_{i=0}^{n-1} \overline{\mathbf{Y}}_i \, [\mathbf{u}(k-i-1) \quad \mathbf{y}(k-i-1)]^T + \mathbf{D}\mathbf{u}(k) \tag{5}$$

where

$$\overline{\mathbf{Y}}_i = \left[\mathbf{C}(\mathbf{A} + \mathbf{M}\mathbf{C})^i(\mathbf{B} + \mathbf{M}\mathbf{D}) \quad -\mathbf{C}(\mathbf{A} + \mathbf{M}\mathbf{C})^i\mathbf{M}\right] = \left[\overline{\mathbf{Y}}_i^{(1)} \quad \overline{\mathbf{Y}}_i^{(2)}\right],$$

in which $\overline{\mathbf{Y}}_i$ and $\mathbf{D}$ are the Markov parameters of the observer system.

A particular feature of this type of observer is that the Markov parameters $\overline{\mathbf{Y}}_i$ will become identically zero after a finite number of time steps. A standard recursive least-squares technique is used to solve Eq. (5) and then the observer Markov parameters are computed. Once the Markov parameters of the observer system are identified, the actual system Markov parameters can be calculated. The relationship between the Markov parameters of the observer system and those of the actual system is given by

$$\mathbf{Y}_i = \mathbf{C}\mathbf{A}^i\mathbf{B} = \overline{\mathbf{Y}}_i^{(1)} + \sum_{k=0}^{i-1} \overline{\mathbf{Y}}_k^{(2)} \, \mathbf{Y}_{i-k-1} + \overline{\mathbf{Y}}_i^{(2)}\mathbf{D} \tag{6}$$

Once the system Markov parameters have been determined, a state-space model of the system can then be derived using the ERA, which is described in the following section.

2.2 Minimum realization of the system model using the ERA

The estimated state-space model $(\widehat{\mathbf{A}}, \widehat{\mathbf{B}}, \widehat{\mathbf{C}}, \widehat{\mathbf{D}})$ of a system is determined from the system Markov parameters $\mathbf{Y}_i$ obtained by OKID using the ERA. Details of this approach can be found in ([18],

[20]), so only a brief overview is given here. The algorithm begins by forming the $l \times l$ block Hankel matrix $\mathbf{H}(l, i)$ given by

$$\mathbf{H}(l,i) = \begin{bmatrix} \mathbf{Y}_i & \mathbf{Y}_{i+1} & \cdots & \mathbf{Y}_{i+l-1} \\ \mathbf{Y}_{i+1} & \mathbf{Y}_{i+2} & \cdots & \mathbf{Y}_{i+l} \\ \vdots & \vdots & & \vdots \\ \mathbf{Y}_{i+l-1} & \mathbf{Y}_{i+l} & \cdots & \mathbf{Y}_{i+2l-2} \end{bmatrix} \tag{7}$$

The order of the system is determined from the singular value decomposition of $\mathbf{H}(l, 0)$ which is given by

$$\mathbf{H}(l,0) = \mathbf{U}\boldsymbol{\Sigma}\mathbf{V}^T \tag{8}$$

where the matrix $\mathbf{U}$ and $\mathbf{V}$ are unitary matrices, $\boldsymbol{\Sigma}$ is an $n \times n$ diagonal matrix of positive singular values, and n is the order of the system. Defining a $q \times lq$ matrix $\mathbf{E}_q^T$ and an $m \times lm$ matrix $\mathbf{E}_m^T$ made up of identity and null matrices of the form

$$\begin{aligned} \mathbf{E}_q^T &= [\mathbf{I}_q \quad \mathbf{0}_{q\times(l-1)q}] \\ \mathbf{E}_m^T &= [\mathbf{I}_m \quad \mathbf{0}_{m\times(l-1)m}], \end{aligned} \tag{9a,b}$$

a discrete-time minimal order realization of the system can be written as

$$\widehat{\mathbf{A}} = \boldsymbol{\Sigma}^{-1/2}\mathbf{U}^T\mathbf{H}(l,1)\mathbf{V}\boldsymbol{\Sigma}^{-1/2} \tag{10}$$

$$\widehat{\mathbf{B}} = \boldsymbol{\Sigma}^{1/2}\mathbf{V}^T\mathbf{E}_m \tag{11}$$

$$\widehat{\mathbf{C}} = \mathbf{E}_q^T\mathbf{U}\boldsymbol{\Sigma}^{1/2} \tag{12}$$

and the direct influence matrix $\widehat{\mathbf{D}}$ can be identified by solving Eq. (5).

Obviously, the $\widehat{\mathbf{A}}$, $\widehat{\mathbf{B}}$, $\widehat{\mathbf{C}}$, $\widehat{\mathbf{D}}$ matrices describe the state space model, which are functions of the singular values of the collected data. Note that now the state space variables allow one to give a clear physical meaning to the identified state-space system.

3 EXPERIMENTAL WORK

The system identification procedure and the subsequent controller design methodology were carried out in a truss structure with a multiple-input multiple-output system. Figure 1 shows the experimental setup.

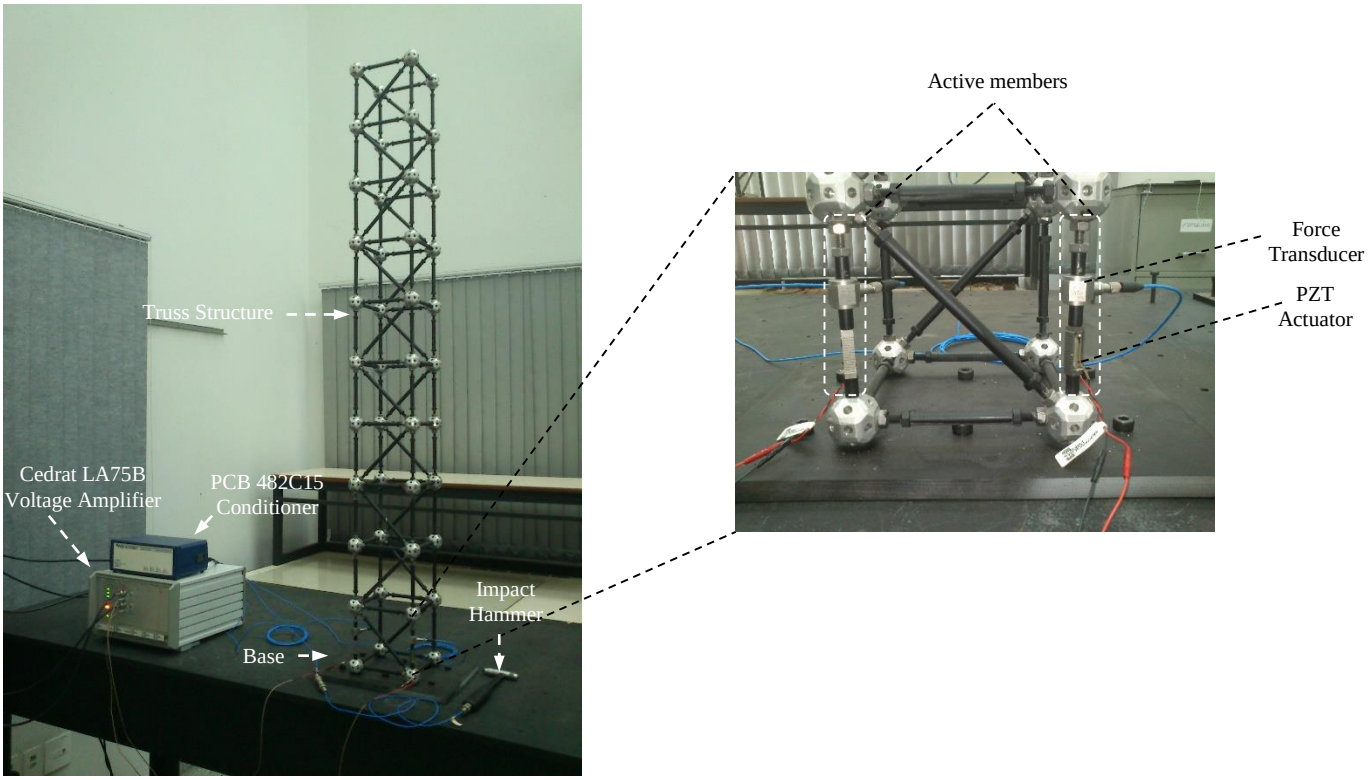


Figure 1. Truss structure used in the experimental tests. The detail shows the active member, with force transducer and the PZT stack actuator (Cedrat model PPA20M)

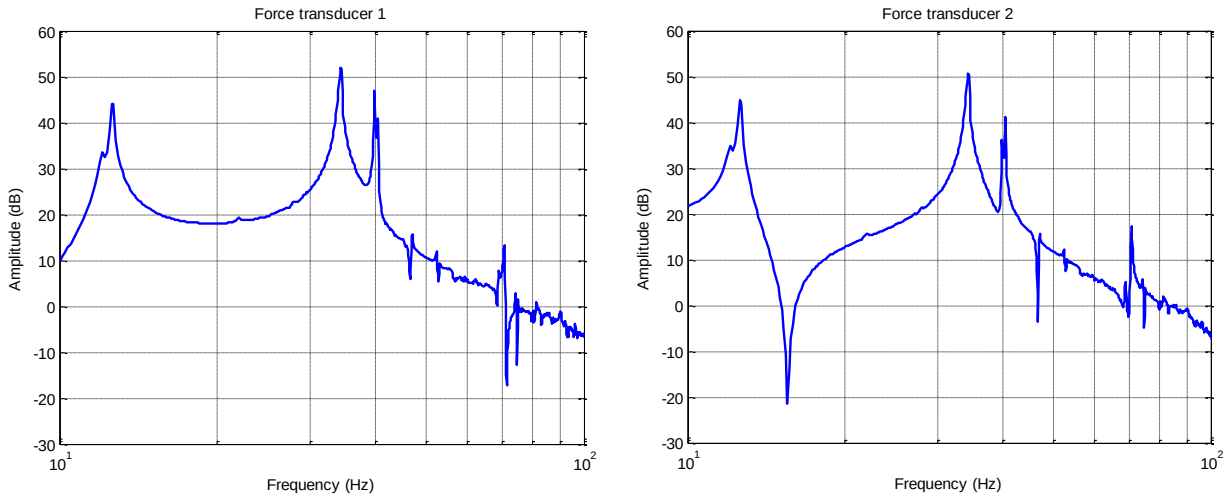
The truss structure (Fig. 1) is composed of 10 cubic bays assembled from a combination of 104 elements that begin and terminate in an aluminum node ball. There are a total of 44 node balls constituting the truss and the nodes at the bottom are clamped. The passive members are made of steel with a diameter of 8 mm. The structure is approximately 135 mm in length, 135 mm wide and 1.3 m tall (from the base plate).

To excite the vibration of the truss, an impact hammer (model PCB 086C04) was used. To achieve the maximum excitation effect, the truss was excited at its free end by the impact hammer. To achieve active suppression of the vibration of the truss, a pair of active members (Fig. 1) which consists of a force transducer (model PCB 208C03) and a PZT stack actuator were installed as vertical active members in the bay next to the base. Each active member replaces a regular strut member. A more detailed description of the truss and its finite element model and the positions of PZT actuator/force sensor can be found in reference [21].

In this experiment, the PZT stack actuator (model PPA20M) manufactured by Cedrat was used. This preloaded PZT actuator is a high resolution linear translator for static and dynamic applications. It provides sub millisecond response and sub nanometric resolution. The translators are equipped with high reliability multilayer PZT ceramic stacks protected by an internally spring-preloaded non-magnetic stainless steel case. The actuator provides a displacement up to 20 µm, a push force and a pulling force up to 800 N and 400 N, respectively, and an operating voltage range of -20 to 150 V. The voltage amplifier (model Cedrat LA75B) and the charge amplifier (model PCB 482C15 with gain of 20 V/V) shown in Fig. 1 were used to power the PZT stack actuator and to condition the signal from the force transducers, respectively. The truss response was measured by the force sensors collocated with the PZT stack actuators. The dSPACE system along with Matlab/Simulink® was used for digital data acquisition and real-time control.

3.1 Frequency response identification

Prior to designing the active controller, it was necessary to identify the frequency response of the truss system [2], whose input was the force of the impact hammer that excited at free end of the truss and whose output is each force sensor. The frequency response functions of the impact hammer-sensor systems were obtained using the Matlab/Simulink® software together with a PC and the dSPACE 1103 board. The frequency responses (calculated from 20 averages) of the system (in terms of the impact force applied by the hammer and the voltage measured from the force transducer) from 0 to 100 Hz are displayed in Fig. 2.



(a) (b)

Figure 2. Frequency response of the force transducers: (a) 1 and (b) 2.

By examining the frequency response plots, the frequency of the dominant mode below 20 Hz is determined to be at 12.57 and 34.42 Hz. The strategy is to control simultaneously the first two modes ($\omega_1 = 78.98$ rad/s and $\omega_2 = 216.27$ rad/s) by using two active members (PZT struts) positioned in the elements shown in Fig. 1, and two decentralized integral controllers connecting each actuator to its collocated force transducer.

3.2 Identification of a model for the truss structure

To identify a model of the system, the experimental setup shown in Fig. 3 was used. A dSPACE 1103 board together with the Matlab/Simulink® software were used to generate and process the signals. The truss was driven with chirp signal (with frequency of 0 up to 100 Hz in 41 seconds) through the PZT actuators and the truss responses were measured using the force sensors. A sampling frequency of 1 kHz was used.

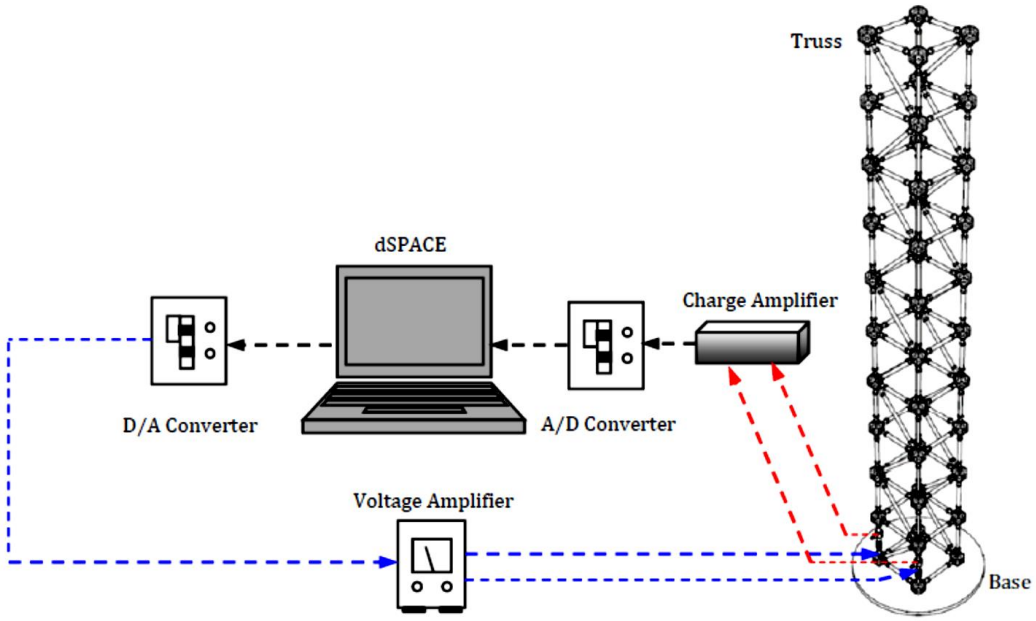
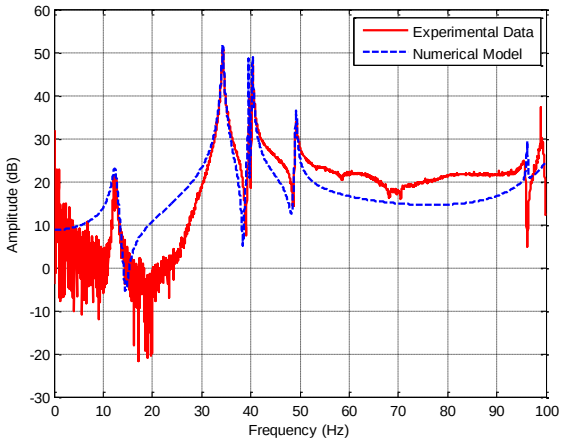


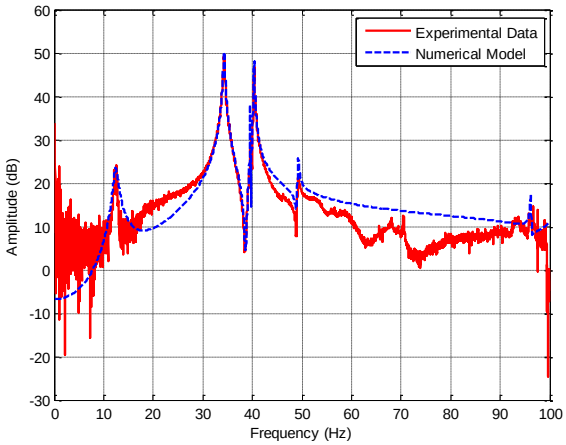
Figure 3. Experimental setup for model identification of the system.

Using the method described previously, the Markov parameters of the observer and the system were calculated, and consequently a state-space model of the truss structure was determined by using 45 states. As it was intended to control the first two modes of the system only, it was necessary to reduce the state space model. The Hankel norm model reduction technique [22] was used generate a fourteenth order model of the system.

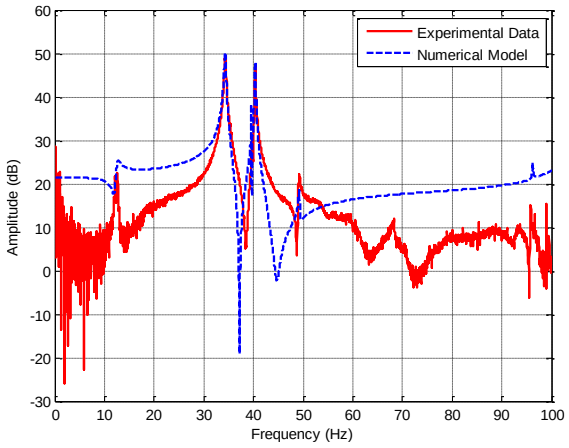
The measured frequency response functions (calculated from 20 averages) of the system (in terms of the voltage applied to the PZT actuators and the force signals measured from the force sensors) together with the reconstructed frequency response functions from the model are shown in Fig. 4. It can be seen that the frequency responses of the identified model are a reasonable match to the frequency responses of the actual system for the first two modes.



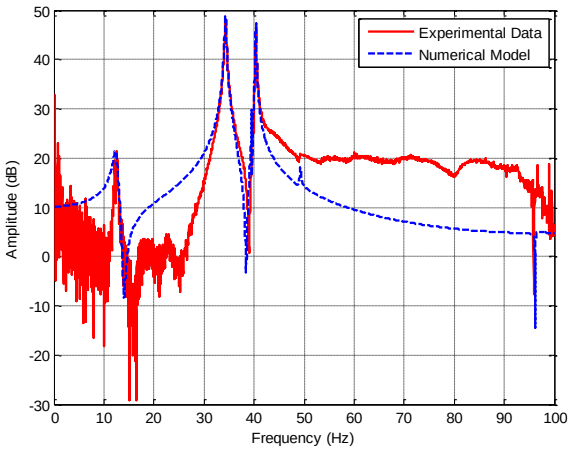
(a)



(b)



(c)



(d)

Figure 4. Frequency response functions: (a) actuator 1 to force sensor 1; (b) actuator 1 to force sensor 2; (c) actuator 2 to force sensor 1 and (d) actuator 2 to force sensor 2.

3.3 Controller design

According to the integral control technique [12], the collocated i-th force sensor (y_i) is integrated and fed back to the i-th control input voltage (u_i):

$$u_i(s) = -\frac{k_i}{s+\varepsilon} y_i(s) \tag{13}$$

where k_i is the gain of the i-th controller and the constant ε is a forgetting factor that can be introduced by slightly moving the pole of the compensator from the origin to the negative real axis. In this paper, ε is assumed be equal to $\varepsilon = \frac{\omega_1}{2} = 39.49$ rad/s. The integral term $1/s$ introduces a 90º phase shift in the feedback path and thus damping in the system. It also introduces a -20 dB/dec slope in the open-loop frequency response, and thus reduces the risks of spillover instability [6].

The control law described by (13) can be implemented in a decentralized manner, with each actuator interacting only with the collocated sensor. In this case, the control system consists of independent SISO loops, whose stability can be readily established from the root locus of [12]:

$$k_i C_i(s) G_i(s) \tag{14}$$

where $G_i(s)$ is the structure transfer function between the actuator and the collocated sensor (Figs. 4a and 4d), and $C_i(s)$ is the active compensator given by $C_i(s) = \frac{1}{s+\varepsilon}$.

Figure 5 shows the root locus of the closed-loop system when the controller is tuned on mode 1 (5a and 5b) and mode 2 (5c and 5d), respectively, i.e., it shows the evolution of the closed-loop poles when k_1 and k_2 increase from 0 to $+\infty$.

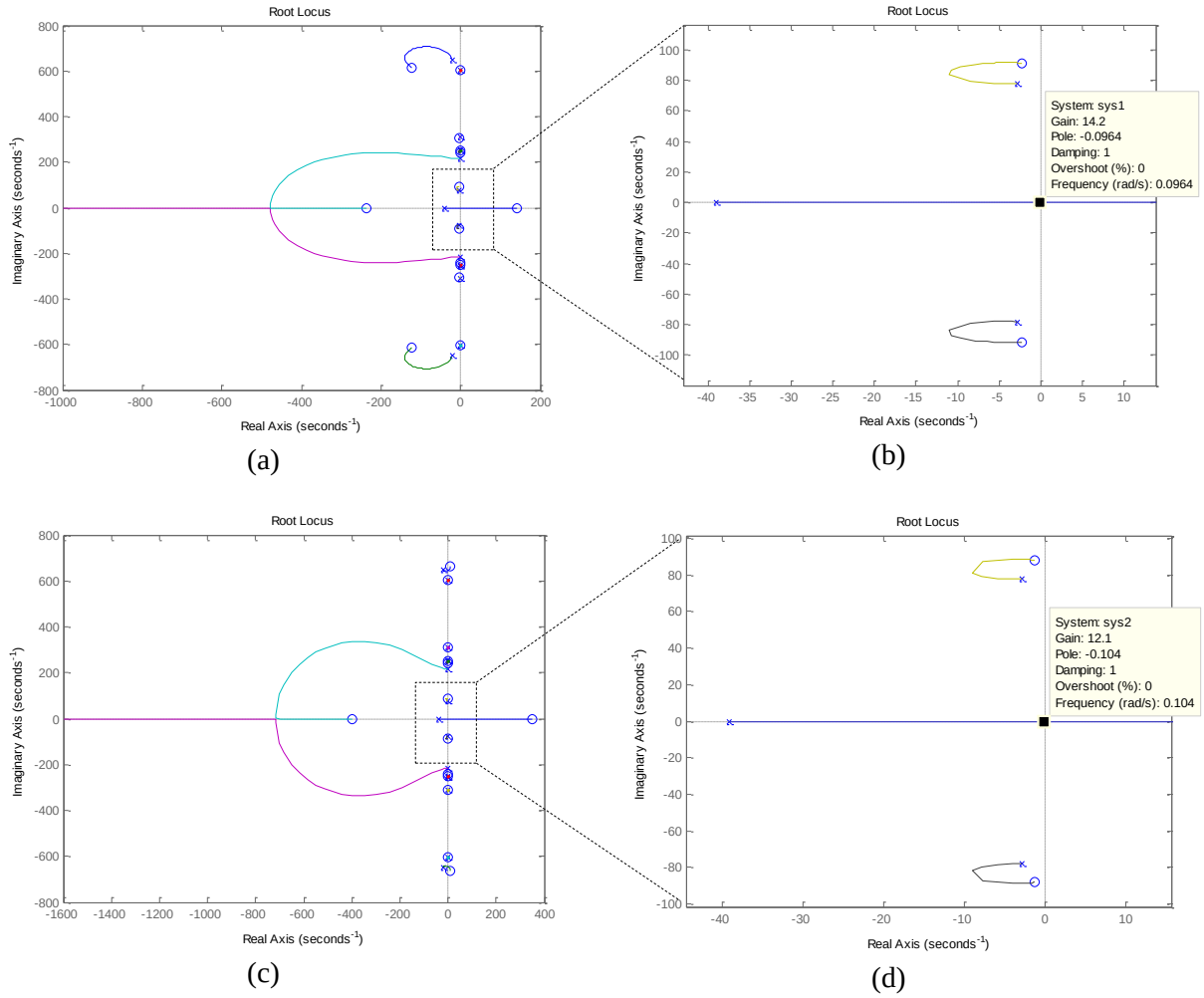


Figure 5. Root locus of the closed-loop system when the controller is tuned on (a), (b) mode 1 and (c), (d) mode 2.

Examining the Fig. 5, it is readily established from the root locus that the system is conditionally stable for a specific value of the gain k_i. Thus, as shown in Figs. 5b and 5d, there are stability limits which are reached when the closed-loop gains are equal to 14.2 for k_1, and 12.1 for k_2, respectively. A slightly upper value of the gain k_1 or k_2 would make the closed-loop system unstable. Therefore, the gains k_1 and k_2 can be chosen in such a way to avoid that condition. In this work, the gains k_i were chosen equal to 10 for both integral controllers.

3.4 Experimental results

As the controller was designed using the procedure discussed previously, some preliminary experiments were carried out with some initial control parameters set arbitrarily. The experiment was set up as shown in Fig. 3 but now the computer was set in control mode instead of system identification mode. The controller was implemented using Matlab/Simulink® software together with a PC and the dSPACE 1103 board. Figure 6 shows a Simulink® block diagram of the controller.

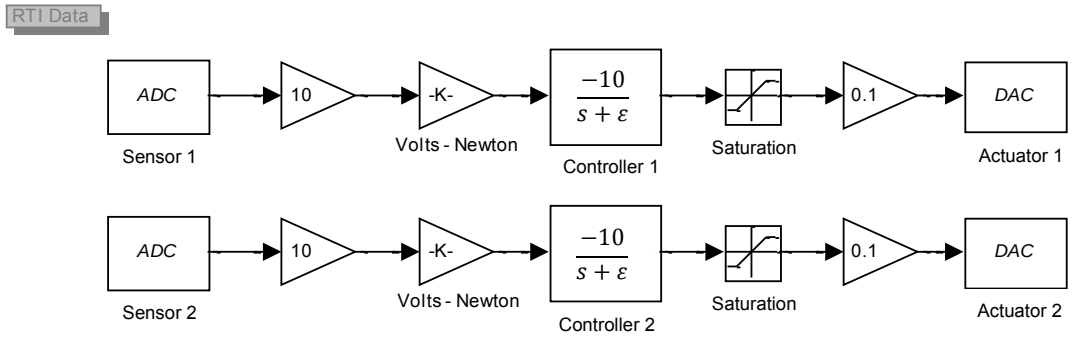


Figure 6. Simulink® block diagram of the controller.

The truss was excited at its free end by using the impact hammer (model PCB 086C04) shown in Fig. 1. The responses of the truss were measured by the sensor forces, with and without control. The time-domain results of the control experiment are given in Fig. 7.

Figures 7a and 7b show the open and closed-loop responses of the force sensors, and Figs. 7c and 7d show the corresponding control voltages. It is thus clear that the main effect of the control was to add more damping to the system.

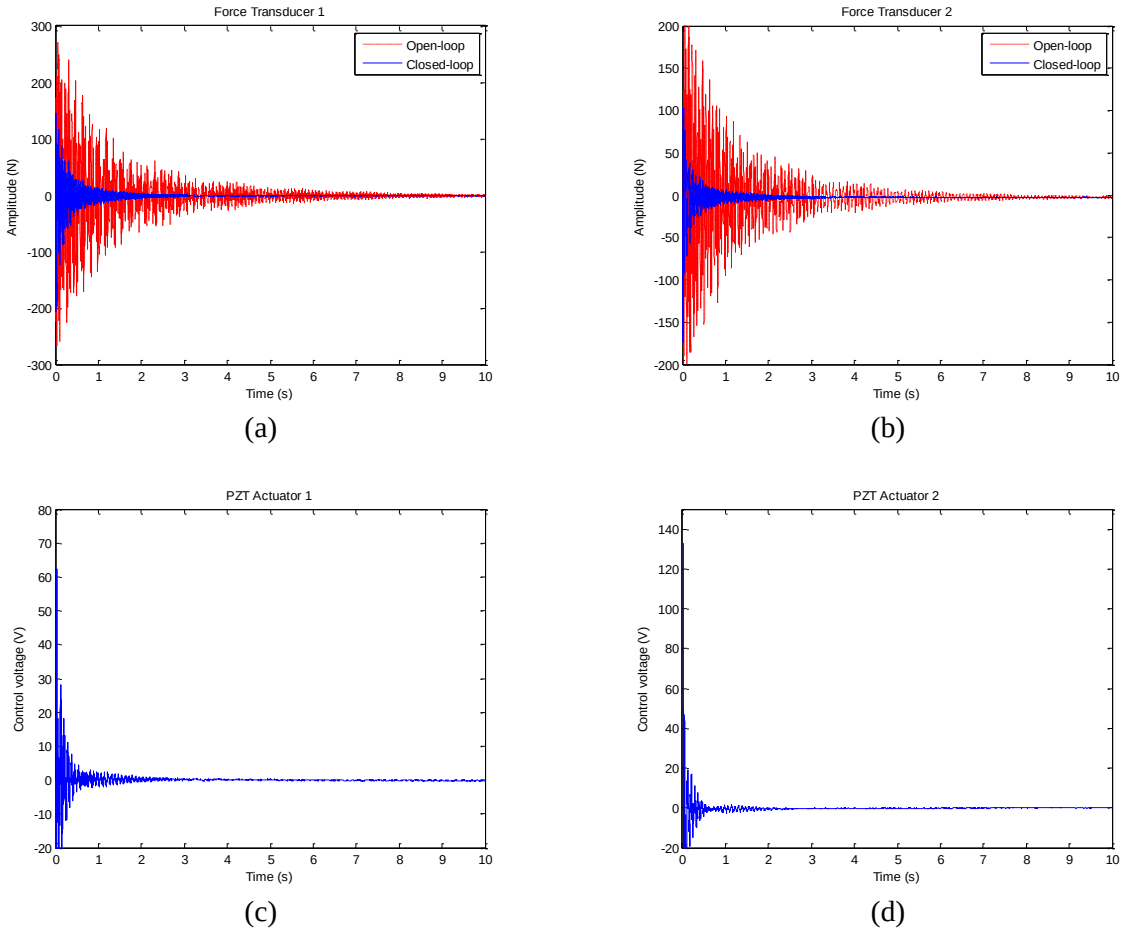
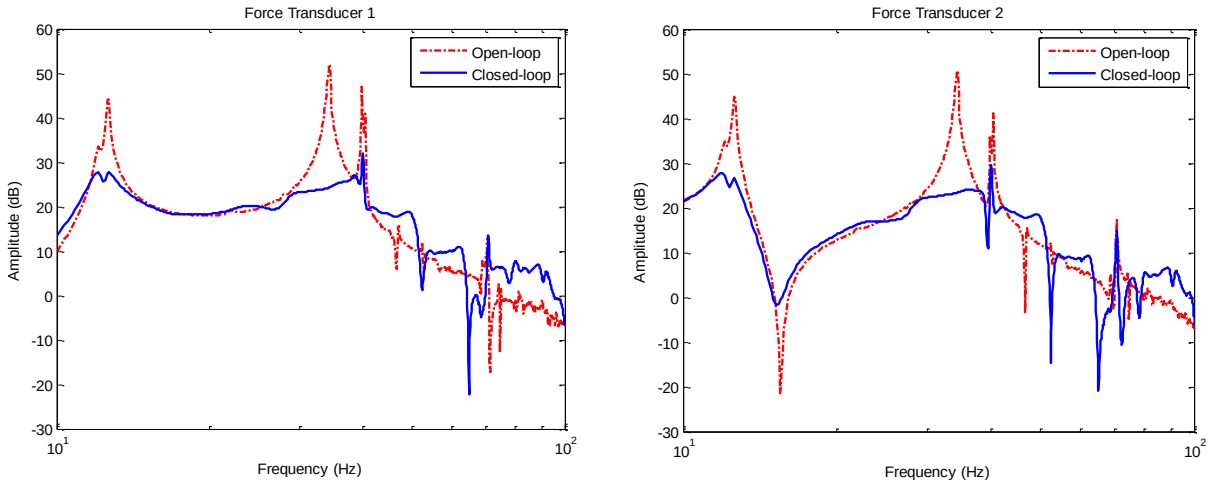


Figure 7. Time histories from the control experiments in which an impulsive force was applied to the free-end of the truss using a hammer, (a) and (b) force transducers 1 and 2 (c) and (d) control voltages applied to the PZT actuators 1 and 2.

Figure 8 shows the experimental open-loop and closed-loop frequency response functions determined from the time histories shown in Figs. 7a and 7b, and the time history of the force applied to the truss using the instrumented hammer. It can be noted that the control system reduced the vibrations in the frequency range containing the first two modes. From the results shown bellow, it can be observed that the frequency responses are reduced greatly, approximately 20 dB for first mode and 30 dB for second mode.



(a) (b)

Figure 8. Open and closed-loop transfer functions of the truss in which an impulsive force was applied to the free-end of the structure using a hammer (a) force sensor 1, (b) force sensor 2.

4 CONCLUSIONS

This paper has described the system identification, controller design, and subsequent implementation to control the vibration of a truss structure. An integral controller was designed and experimentally implemented on a truss structure containing a pair of piezoelectric linear actuators collinear with force transducers. It was demonstrated that this control problem can be formulated with the root locus approach by using a model obtained through OKID/ERA system identification technique, using inputs and outputs vibration data from the truss. Two modes of the truss were controlled. From the experimental results, it was observed that satisfactory performance of vibration attenuation was achieved.

ACKNOWLEDGEMENTS

The authors acknowledge the financial support of CNPq Brazilian Research Agency and FAPEMIG through INCT-EIE.

REFERENCES

[1] G. L. C. M. Abreu, S. M. Conceição, V. Lopes Jr., M. J. Brennan, M. T. S. Alves, *System Identification and Active Vibration Control of a Flexible Structure*, Journal of the Brazilian Society of Mechanical Sciences and Engineering, Vol. 34, pp. 386-392 (2012).

[2] G. L. C. M. Abreu, G. P. Melo, V. Lopes Jr., M. J. Brennan, *Active Modal Damping Control of a Smart Truss Structure using a Self-Organizing Fuzzy Controller*, Journal of the Brazilian Society of Mechanical Sciences and Engineering, Vol. 1, pp. 1-10 (2014).

[3] Y. J. Yan, L. H. Yam, *A synthetic analysis of optimum control for an optimized intelligent structure*, Journal of Sound and Vibration, Vol. 249, pp. 775-784, (2002).

[4] D. K. Anthony, S. J. Elliot, *On reducing vibration transmission in a two-dimensional cantilever truss structure using geometric optimization and active vibration control techniques*, Journal of the Acoustical Society of America, Vol. 110, pp. 1191-1194 (2005).

[5] J. L. Fanson, G. H. Blackwood, C. C. Chu, *Active Member Control of Precision Structures*, SDM Conference, pp. 1480-1494 (1989).

[6] G. S. Chen, B. J. Lurie, B. K. Wada, *Experimental Studies of Adaptive Structures for Precision Performance*, SDM Conference, pp. 1462-1472 (1989).

[7] E. H. Anderson, D. M. Moore, J. L. Fanson, *Development of an Active Truss Element for Control of Precision Structures*, Optical Engineering, Vol. 29, Nº 11, pp. 1333-1341 (1990).

[8] A. Preumont, J. P. Dufour, C. Malekian, *Active damping by a local force feedback with piezoelectric actuators*, Journal of Guidance, Control and Dynamics, Vol. 15, pp. 390-395 (1992).

[9] R. Carvalhal, V. Lopes Jr., M. J. Brennan, *An efficient modal control strategy for the active vibration control of a truss structure*, Shock and Vibration, Vol. 14, pp. 393-406 (2007).

[10] G. L. C. M. Abreu, V. Lopes Jr., M. J. Brennan, *Robust Control of an Intelligent Truss Structure*, 10th International Conference on Recent Advances in Structural Dynamics, Southampton University, United Kingdom-UK (2010).

[11] W. P. Li, H. Huang, *Integrated Optimization of Actuator Placement and Vibration Control for Piezoelectric Adaptive Trusses*, Journal of Sound and Vibration, Vol. 332, pp. 17-32 (2013).

[12] A. Preumont, *Vibration Control of Active Structures: An Introduction*, Kluwer (2002).

[13] H. Allik, T. J. R. Hughes, *Finite Method for Piezoelectric Vibration*, International Journal for Numerical Methods in Engineering, No. 2, pp. 151-157 (1970).

[14] H. S. Tzou, C. I. Tseng, *Distributed Piezoelectric Sensor/Actuator Design for Dynamic Measurement/Control of Distributed Parameter Systems: A Piezoelectric Finite Element Approach*, Journal of Sound and Vibration, Vol. 138, No. 1, pp. 17-34 (1990).

[15] Z. Wang, S. Chen, W. Han, *Integrated Structural and Control Optimization of Intelligent Structures*, Engineering Structures, Vol. 21, pp. 183-191 (1999).

[16] L. Ljung, *System Identification: Theory for the User*, Englewood Cliffs, 2nd Ed., NJ: Prentice-Hall (1999).

[17] J. N. Juang, M. Phan, L. G. Horta, *Identification of Observer/Kalman Filter Markov Parameters: Theory and Experiments*, Journal of Guidance, Control and Dynamics, Vol. 16, No. 2, pp. 320-329 (1993).

[18] J. N. Juang, M. Phan, *Identification and Control of Mechanical Systems*, Cambridge University Press, New York (2001).

[19] M. Scott, M. Gilbert, M. Demeo, *Active Vibration Damping of the Space Shuttle Remote Manipulator System*, Journal of Guidance, Control and Dynamics, Vol. 16, No. 2, pp. 275-280 (1993).

[20] J. N. Juang, R. S. Pappa, *An Eigensystem Realization Algorithm for Modal Parameter Identification and Model Reduction*, Journal of Guidance, Control and Dynamics, Vol. 8, No. 5, pp. 620-627 (1985).

[21] G. L. C. M. Abreu, V. Lopes Jr., M. J. Brennan, *A Self-Organizing Fuzzy Controller for the Active Vibration Control of a Smart Truss Structure*, Vibration Control, Mickail Lallart (Ed.), ISBN: 978-953-307-117-6, Sciyo, pp. 215-234 (2010).

[22] W. K. Gawronski, *Advanced Structural Dynamics and Active Control of Structures*, Institute of Technology of P Institute of Technology of Pasadena, California, USA (1998).

COMPDYN 2015
5th ECCOMAS Thematic Conference on
Computational Methods in Structural Dynamics and Earthquake Engineering
M. Papadrakakis, V. Papadopoulos, V. Plevris (eds.)
Crete Island, Greece, 25–27 May 2015

A 2D WAVE FINITE ELEMENT-BASED SUPERELEMENT FORMULATION FOR ACOUSTIC ANALYSIS OF CAVITIES OF ARBITRARY SHAPES

J.-M. Mencik[1], D. Duhamel[2], and M.-L. Gobert[1]

[1]INSA Centre Val de Loire, Université François Rabelais de Tours, LMR EA 2640
Campus de Blois, 3 Rue de la Chocolaterie, CS 23410, 41034 Blois Cedex, France
e-mail: {jean-mathieu.mencik,marie-laure.gobert}@insa-cvl.fr

[2] Université Paris-Est, Laboratoire Navier, ENPC/IFSTTAR/CNRS
6 et 8 Avenue Blaise Pascal, Cité Descartes, Champs-sur-Marne, 77455 Marne La Vallée Cedex 2, France
e-mail: denis.duhamel@enpc.fr

Keywords: Wave Finite Element Method, Acoustic Superelements, Substructuring, Mid-Frequencies.

Abstract. *A substructuring technique is proposed which enables fast computation of the acoustic response of arbitrary-shaped 2D cavities subject to different kinds of excitations. It combines rectangular superelements which are modeled by means of the wave finite element (WFE) method, and arbitrary-shaped superelements modeled using component mode synthesis (CMS). Within the WFE framework, the so-called receptance matrices of rectangular superelements — which link the pressure vectors to the acoustic force vectors over the boundaries — can be derived in an efficient way in terms of wave modes, without the need of explicitly condensing the internal degrees of freedom of the systems. A model reduction strategy is proposed which aims at expressing the receptance matrices with a few wave modes only. The proposed strategy involves enclosing each rectangular superelement in a finite element (FE) layer with a small width. In this way, smoothed pressure fields are likely to occur over the WFE superelements, hence enabling these superelements to be described with a few wave modes only. By considering those WFE-based rectangular superelements surrounded by FE layers, this yields the so-called hybrid WFE/FE superelements whose dynamic stiffness matrices can be computed in a very fast way. Modeling a whole arbitrary-shaped acoustic cavity follows from conventional assembly procedure between hybrid WFE/FE superelements, CMS superelements and other FE components. Numerical experiments are carried out to highlight the relevance of the proposed substructuring technique.*

1 INTRODUCTION

Developing fast and accurate numerical tools for assessing the acoustic behavior of arbitrary-shaped cavities over wide frequency ranges appears to be an open industrial challenge, leading the way of proposing efficient solutions to noise reduction. Popular examples of such cavities are passenger compartments in cars, and aircraft cabins. The finite element (FE) and boundary element (BE) methods are popular techniques for computing internal acoustic problems, but have however to face several severe issues as soon as the number of degrees of freedom (DOFs) involved reaches excessive values. The issue lies in the computation of large-sized matrix systems (FE framework), or the consideration of dense matrices which require high memory storage (BE framework), at many discrete frequencies. This means numerical techniques which are either time consuming or inaccurate.

Reduction methods like FE-based substructuring or wave-based analytical techniques seem to constitute efficient alternatives to the conventional FE and BE methods. Among the FE-based substructuring techniques, one can mention the Craig-Bampton method [1] which focuses on partitioning a whole system into several components and modeling these components by means of static modes and fixed interface modes. The tough issue when dealing with the CB method concerns the determination of the fixed interface modes which would need to be retained for assessing the acoustic behavior of cavities with accurate precision. This explains why, in practice, many fixed interface modes are usually retained to ensure the convergence of the CB solutions, hence impacting the CPU times required for modeling the CB components. On the other hand, Trefftz techniques like the wave based method (WBM) [2] aim a using a few analytical wave functions to describe the acoustic behavior of 2D cavities, even in the short wavelength domain. In this sense, they appear to be efficient in terms of CPU times. Their disadvantage, however, is that they invoke dense matrices in the same way as the BE method.

A new FE-based substructuring technique is proposed here which overcomes the aforementioned issues. It makes use of the wave finite element (WFE) method which aims at assessing numerical wave modes traveling along periodic systems [3, 4, 5]. Within this framework, a so-called hybrid WFE/FE superelement is formulated which consists in a rectangular acoustic domain, with a periodic FE mesh, surrounded by an arbitrary-meshed FE layer with a small width. The interesting feature of this superelement is that the receptance matrix of the rectangular domain — i.e., which links the vector of nodal pressures to that of the nodal forces over the boundary — can be expressed by means of a small number of wave modes. The fact that a few wave modes are only used is explained because the pressure field is expected to be smooth over the rectangular domain, it being understood that local singularities near excitations and boundary conditions are managed by the FE layer. In doing so, the proposed superelement can be modeled using a dynamic stiffness matrix of small size whose computation doesn't require excessive CPU times. Modeling a whole acoustic cavity follows from conventional FE procedure by assembling several hybrid WFE/FE superelements, as well as CMS-based superelements and other FE components together.

The rest of the paper is organized as follows. In Section 2, the basics of the WFE method are recalled which concern the description of wave modes traveling along a rectangular acoustic domain with a periodic FE mesh. Also, the strategy for computing the forced response of periodic systems is presented. In Section 3, the WFE-based procedure for expressing the receptance matrix of a rectangular domain is proposed. Also, the formulation of the WFE/FE hybrid superelement is proposed. Finally, numerical experiments are carried out in Section 4 to highlight the computational efficiency of the proposed approach in comparison with the conventional CB

method.

2 WFE METHOD

2.1 Wave mode computation

The basics of the WFE method, which concern the description of wave modes traveling along a one-dimensional periodic system, are recalled hereafter. Within the present scope, emphasis will be placed on the study of rectangular acoustic domains with a FE mesh which is periodic along one straight direction, i.e., composed of identical substructures connected to each other, as shown in Figure 1. Such a rectangular acoustic domain is supposed to be excited by harmonic excitations (the angular frequency being denoted as ω) which are confined to the left and right edges only, and modeled in terms of two vectors of acoustic forces $\mathbf{F}_0$ and $\mathbf{F}_0^\star$ (see Figure 1).

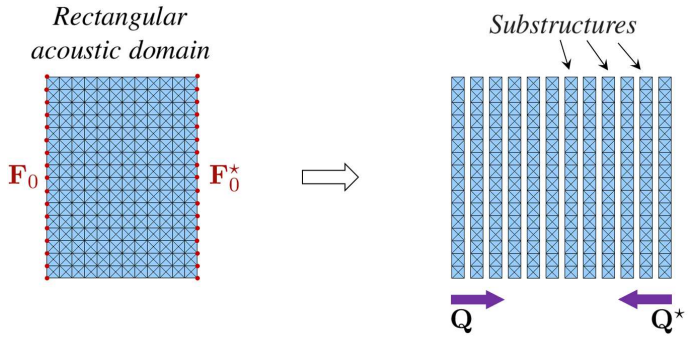


Figure 1: Rectangular acoustic domain with a periodic FE mesh, and related WFE modeling.

For the purpose of wave mode description, the WFE method requires one to know the acoustic mass matrix $\mathbf{M}$ and acoustic stiffness matrix $\mathbf{K}$ of a substructure, and ultimately the condensed dynamic stiffness matrix $\mathbf{D}^* = \mathbf{D}_{\mathtt{BB}} - \mathbf{D}_{\mathtt{BI}}\mathbf{D}_{\mathtt{II}}^{-1}\mathbf{D}_{\mathtt{IB}}$, where $\mathbf{D} = -\omega^2\mathbf{M} + \mathbf{K}$ is the dynamic stiffness matrix of the substructure Here, the subscript $\mathtt{B}$ refers to the degrees of freedom (DOFs) on the left and right edges of the substructure, while the subscript $\mathtt{I}$ refers to the internal DOFs (i.e., which do not belong to the left and right edges). Denote as n the number of DOFs on the left (or right) edge of the substructure. Following the WFE framework [4, 3], the wave modes are sought as the solutions of an eigenproblem of the form $\mathbf{S}\boldsymbol{\phi}_j = \mu_j\boldsymbol{\phi}_j$ in which $\mathbf{S}$ is a $2n \times 2n$ symplectic matrix expressed by

$$\mathbf{S} = \left[\begin{array}{c|c} -\mathbf{D}_{\mathtt{LR}}^{*-1}\mathbf{D}_{\mathtt{LL}}^* & -\mathbf{D}_{\mathtt{LR}}^{*-1} \\ \hline \mathbf{D}_{\mathtt{RL}}^* - \mathbf{D}_{\mathtt{RR}}^*\mathbf{D}_{\mathtt{LR}}^{*-1}\mathbf{D}_{\mathtt{LL}}^* & -\mathbf{D}_{\mathtt{RR}}^*\mathbf{D}_{\mathtt{LR}}^{*-1} \end{array}\right], \tag{1}$$

where the subscripts $\mathtt{L}$ and $\mathtt{R}$ refer to the left and right edges of the substructure, respectively. The eigenvectors of $\mathbf{S}$ — namely, $\{\boldsymbol{\phi}_j\}_j$ — are the so-called wave shapes which are partitioned into pressure and force components as $\boldsymbol{\phi}_j = [(\boldsymbol{\phi}_j)_{\mathtt{P}}^T(\boldsymbol{\phi}_j)_{\mathtt{F}}^T]^T$. Also, since the matrix $\mathbf{S}$ is symplectic, its eigenvalues come in pairs as $(\mu_j, 1/\mu_j)$.

From the numerical point of view, a so-called $\mathbf{S} + \mathbf{S}^{-1}$ transformation of the eigenproblem (1) can be considered [6, 7] for accurately computing the eigensolutions $\{\mu_j\}_j$ and $\{\boldsymbol{\phi}_j\}_j$. The interesting feature of the $\mathbf{S} + \mathbf{S}^{-1}$ transformation lies in the use of skew-symmetric matrices $(\mathbf{N}'\mathbf{J}\mathbf{L}'^T + \mathbf{L}'\mathbf{J}\mathbf{N}'^T)$ and $\mathbf{L}'\mathbf{J}\mathbf{L}'^T$, leading to the following eigenproblem whose eigenvalues are of the form $\lambda_j = \mu_j + 1/\mu_j$:

$$\left((\mathbf{N}'\mathbf{J}\mathbf{L}'^T + \mathbf{L}'\mathbf{J}\mathbf{N}'^T) - \lambda_j\mathbf{L}'\mathbf{J}\mathbf{L}'^T\right)\mathbf{z}_j = \mathbf{0}, \tag{2}$$

where

$$\mathbf{L}' = \begin{bmatrix} \mathbf{0} & \mathbf{I}_n \\ \mathbf{D}^*_{\mathtt{LR}} & \mathbf{0} \end{bmatrix} \quad , \quad \mathbf{N}' = \begin{bmatrix} \mathbf{D}^*_{\mathtt{RL}} & \mathbf{0} \\ -(\mathbf{D}^*_{\mathtt{LL}} + \mathbf{D}^*_{\mathtt{RR}}) & -\mathbf{I}_n \end{bmatrix} \quad , \quad \mathbf{J} = \begin{bmatrix} \mathbf{0} & \mathbf{I}_n \\ -\mathbf{I}_n & \mathbf{0} \end{bmatrix}. \tag{3}$$

Once the eigenvalues $\{\lambda_j\}_j$ in Eq. (2) are found, the original eigenvalues $\{\mu_j\}_j$ are found analytically by solving a quadratic equation of the form

$$x^2 - \lambda_j x + 1 = 0. \tag{4}$$

Also, once the eigenvectors $\{\mathbf{z}_j\}_j$ in Eq. (2) are found, the original eigenvectors $\{\boldsymbol{\phi}_j\}_j$ are found analytically as follows [7]:

$$\boldsymbol{\phi}_j = \begin{bmatrix} \mathbf{I}_n & \mathbf{0} \\ \mathbf{D}^*_{\mathtt{RR}} & \mathbf{I}_n \end{bmatrix} \mathbf{w}'_j \qquad \text{where} \qquad \mathbf{w}'_j = \mathbf{J} \left(\mathbf{L}'^T - \frac{1}{\mu_j} \mathbf{N}'^T \right) \mathbf{z}_j. \tag{5}$$

2.2 Conventions and matrix notations

As was mentioned in Section 2.1, the eigenvalues of the matrix $\mathbf{S}$ are pairs $(\mu_j, 1/\mu_j)$. This leads to the consideration of n right-going wave modes for which $|\mu_j| \leq 1$, and n left-going wave modes for which $|\mu_j| \geq 1$. Regarding the case $|\mu_j| = 1$, the right-going (resp. left-going) wave modes are defined so that $(\mathtt{i}\omega/4)\boldsymbol{\phi}_j^H \mathbf{J} \boldsymbol{\phi}_j > 1$ (resp. $(\mathtt{i}\omega/4)\boldsymbol{\phi}_j^H \mathbf{J} \boldsymbol{\phi}_j < 1$), which means that the related energy flows [8] are conveyed towards the right (resp. left) direction of the system.

For the sake of clarity, the sets of right- and left- going wave modes will be denoted as $\{(\mu_j, \boldsymbol{\phi}_j)\}_{j=1,\ldots,n}$ and $\{(\mu_j^\star, \boldsymbol{\phi}_j^\star)\}_{j=1,\ldots,n}$, where it is understood that $\mu_j^\star = 1/\mu_j \, \forall j \in \{1, \ldots, n\}$. Also, by considering Eq. (5), the wave shapes $\boldsymbol{\phi}_j$ and $\boldsymbol{\phi}_j^\star$ are expressed as

$$\boldsymbol{\phi}_j = \begin{bmatrix} \mathbf{I}_n & \mathbf{0} \\ \mathbf{D}^*_{\mathtt{RR}} & \mathbf{I}_n \end{bmatrix} \mathbf{J} \left(\mathbf{L}'^T - \mu_j^\star \mathbf{N}'^T \right) \mathbf{z}_j \quad , \quad \boldsymbol{\phi}_j^\star = \begin{bmatrix} \mathbf{I}_n & \mathbf{0} \\ \mathbf{D}^*_{\mathtt{RR}} & \mathbf{I}_n \end{bmatrix} \mathbf{J} \left(\mathbf{L}'^T - \mu_j \mathbf{N}'^T \right) \mathbf{z}_j, \tag{6}$$

where $\mathbf{z}_j$ is an eigenvector of Eq. (2) corresponding to the eigenvalue λ_j. In matrix form, the wave modes can thus be written as

$$\boldsymbol{\mu} = \mathtt{diag}\{\mu_j\}_{j=1,\ldots,n} \quad , \quad \boldsymbol{\mu}^\star = \boldsymbol{\mu}^{-1} \quad , \quad \boldsymbol{\Phi} = [\boldsymbol{\phi}_1 \ldots \boldsymbol{\phi}_n] \quad , \quad \boldsymbol{\Phi}^\star = [\boldsymbol{\phi}_1^\star \ldots \boldsymbol{\phi}_n^\star], \tag{7}$$

with the property that $||\boldsymbol{\mu}||_2 \leq 1$ ($||.||_2$ being the $2-$norm). Also, the matrices $\boldsymbol{\Phi}$ and $\boldsymbol{\Phi}^\star$ are to be partitioned into pressure and force components, as follows:

$$\boldsymbol{\Phi} = \begin{bmatrix} \boldsymbol{\Phi}_{\mathtt{P}} \\ \boldsymbol{\Phi}_{\mathtt{F}} \end{bmatrix} \quad , \quad \boldsymbol{\Phi}^\star = \begin{bmatrix} \boldsymbol{\Phi}^\star_{\mathtt{P}} \\ \boldsymbol{\Phi}^\star_{\mathtt{F}} \end{bmatrix}, \tag{8}$$

where $\boldsymbol{\Phi}_{\mathtt{P}}$, $\boldsymbol{\Phi}_{\mathtt{F}}$, $\boldsymbol{\Phi}^\star_{\mathtt{P}}$ and $\boldsymbol{\Phi}^\star_{\mathtt{F}}$ are $n \times n$ matrices which are full rank [9].

2.3 Forced response computation

Within the framework of the WFE method, the vectors of pressures and acoustic forces of an assembly of N substructures like the one displayed in Figure 1 are expressed in terms of wave shapes, as follows [10]:

$$\mathbf{p}^{(k)} = \boldsymbol{\Phi}_{\mathrm{p}}\boldsymbol{\mu}^{k-1}\mathbf{Q}+\boldsymbol{\Phi}_{\mathrm{p}}^{\star}\boldsymbol{\mu}^{N-k+1}\mathbf{Q}^{\star} \quad , \quad \pm\mathbf{F}^{(k)} = \boldsymbol{\Phi}_{\mathrm{F}}\boldsymbol{\mu}^{k-1}\mathbf{Q}+\boldsymbol{\Phi}_{\mathrm{F}}^{\star}\boldsymbol{\mu}^{N-k+1}\mathbf{Q}^{\star} \qquad k=1,\ldots,N+1. \tag{9}$$

where the subscript (k) designates any substructure boundary, i.e., either a coupling interface/edge between two consecutive substructures $k-1$ and k, or the left/right edge of the whole domain; also, $\mathbf{Q}$ and $\mathbf{Q}^{\star}$ are vectors of wave amplitudes which are respectively defined at the left and right edges of the whole domain, i.e., at the substructure boundaries (1) and $(N+1)$. In Eq. (9), the sign ahead of $\mathbf{F}^{(k)}$ should be negative in case when a left boundary is considered, and positive for a right boundary.

The problem behind the computation of the forced response of the acoustic domain can be stated as to find the vectors of wave amplitudes $\mathbf{Q}$ and $\mathbf{Q}^{\star}$. This is achieved by considering the boundary conditions (BCs) on the left and right edges, the other substructure boundaries being assumed to be free from excitations sources (see Figure 1). Those BCs may involve prescribed pressures or acoustic forces. In view of the subsequent developments made in this paper, we will restrict the present analysis to the study of two vectors of prescribed forces $\mathbf{F}_0$ and $\mathbf{F}_0^{\star}$ that apply over the substructure boundaries (1) and $(N+1)$, respectively, as shown in Figure 1. The related wave expansion, Eq. (9), yields

$$-\mathbf{F}_0 = \boldsymbol{\Phi}_{\mathrm{F}}\mathbf{Q} + \boldsymbol{\Phi}_{\mathrm{F}}^{\star}\boldsymbol{\mu}^{N}\mathbf{Q}^{\star} \quad , \quad \mathbf{F}_0^{\star} = \boldsymbol{\Phi}_{\mathrm{F}}\mathbf{Q}\boldsymbol{\mu}^{N} + \boldsymbol{\Phi}_{\mathrm{F}}^{\star}\mathbf{Q}^{\star}. \tag{10}$$

As a result, a wave-based matrix system can be derived whose resolution provides the vectors of wave amplitudes $\mathbf{Q}$ and $\mathbf{Q}^{\star}$. According to Eq. (10), it is expressed as follows:

$$\mathbf{A}\left[\begin{array}{c}\mathbf{Q}\\ \mathbf{Q}^{\star}\end{array}\right] = \mathbf{B}\left[\begin{array}{c}\mathbf{F}_0\\ \mathbf{F}_0^{\star}\end{array}\right], \tag{11}$$

where $\mathbf{A}$ and $\mathbf{B}$ are $2n\times 2n$ matrices defined as

$$\mathbf{A} = \left[\begin{array}{cc}\mathbf{I} & \boldsymbol{\Phi}_{\mathrm{F}}^{-1}\boldsymbol{\Phi}_{\mathrm{F}}^{\star}\boldsymbol{\mu}^{N}\\ \boldsymbol{\Phi}_{\mathrm{F}}^{\star-1}\boldsymbol{\Phi}_{\mathrm{F}}\boldsymbol{\mu}^{N} & \mathbf{I}\end{array}\right] \quad , \quad \mathbf{B} = \left[\begin{array}{cc}-\boldsymbol{\Phi}_{\mathrm{F}}^{-1} & \mathbf{0}\\ \mathbf{0} & \boldsymbol{\Phi}_{\mathrm{F}}^{\star-1}\end{array}\right]. \tag{12}$$

To derive the matrices $\mathbf{A}$ and $\mathbf{B}$, it has been assumed that the matrices $\boldsymbol{\Phi}_{\mathrm{F}}$ and $\boldsymbol{\Phi}_{\mathrm{F}}^{\star}$ are invertible (a proof of this statement is brought in ref. [9]). The motivation behind the use of the matrix inverses $\boldsymbol{\Phi}_{\mathrm{F}}^{-1}$ and $\boldsymbol{\Phi}_{\mathrm{F}}^{\star-1}$ is to make the matrix $\mathbf{A}$ well-conditioned [9]. The determination of the vectors of wave amplitudes $\mathbf{Q}$ and $\mathbf{Q}^{\star}$ hence follows from Eq. (11):

$$\left[\begin{array}{c}\mathbf{Q}\\ \mathbf{Q}^{\star}\end{array}\right] = \mathbf{A}^{-1}\mathbf{B}\left[\begin{array}{c}\mathbf{F}_0\\ \mathbf{F}_0^{\star}\end{array}\right]. \tag{13}$$

3 SUPERELEMENT MODELING

3.1 Introduction

Consider now a rectangular acoustic domain which undergoes acoustic forces over its left/right and bottom/top edges, as depicted in Figure 2. The motivation behind the proposed study is to

express a so-called receptance matrix $\mathbf{H}$ which links the vector of pressures of the boundary nodes $\mathbf{p}_{\mathtt{B}}$ to that of the vector of acoustic forces $\mathbf{F}_{\mathtt{B}}$, where the subscript $\mathtt{B}$ refers to the nodes belonging to the left/right and bottom/top edges. This relation is expressed by $\mathbf{p}_{\mathtt{B}} = \mathbf{H}\mathbf{F}_{\mathtt{B}}$. The key idea here is to express the receptance matrix $\mathbf{H}$ in terms of wave modes (Section 2) traveling along both horizontal and vertical directions, as shown in Figure 2. This yields a superelement modeling whose derivation follows from the well-known superposition principle (see Section 3.2).

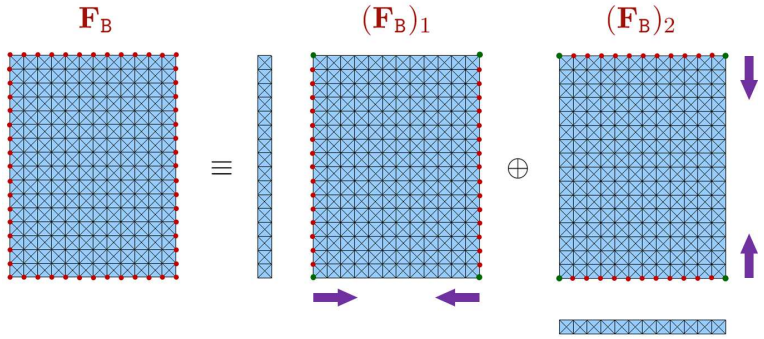


Figure 2: Illustration of the superposition principle involving a vector of acoustic force decomposed into two ones acting respectively along the left/right and bottom/top edges.

3.2 Receptance matrix

The key idea behind the present approach is to decompose the vector of acoustic forces $\mathbf{F}_{\mathtt{B}}$ into two states of excitation $(\mathbf{F}_{\mathtt{B}})_1$ and $(\mathbf{F}_{\mathtt{B}})_2$ that operate, respectively, on the vertical and horizontal edges (see Figure 2). This means two WFE modelings (namely, 1 and 2), and related substructures, for assessing the wave propagation along the horizontal and vertical directions. For each WFE modeling i ($i = 1, 2$), the number of right/left- (or top/bottom-) going wave modes involved is n_i — n_1 and n_2 being the number of DOFs contained over the left/right edge and bottom/top edge, respectively — while the number of substructures is N_i — N_1 and N_2 being the number of substructures involved along the horizontal and vertical directions, respectively. For the sake of simplicity, it is assumed that the boundary nodes of the "vertical" substructures (WFE modeling 1) are only confined to their left and right edges, while those of the "horizontal" substructures (WFE modeling 2) are only confined to their bottom and top edges (see Figure 2). By considering the superposition principle, this yields

$$\mathbf{F}_{\mathtt{B}} = (\mathbf{F}_{\mathtt{B}})_1 + (\mathbf{F}_{\mathtt{B}})_2 \quad \Rightarrow \quad \mathbf{p}_{\mathtt{B}} = (\mathbf{p}_{\mathtt{B}})_1 + (\mathbf{p}_{\mathtt{B}})_2. \tag{14}$$

This means that the vector of pressures $\mathbf{p}_{\mathtt{B}}$ produced by the vector of acoustic forces $\mathbf{F}_{\mathtt{B}}$ is expressed as the sum of two vectors $(\mathbf{p}_{\mathtt{B}})_1$ and $(\mathbf{p}_{\mathtt{B}})_2$ which are respectively induced by the vectors of acoustic forces $(\mathbf{F}_{\mathtt{B}})_1$ and $(\mathbf{F}_{\mathtt{B}})_2$ as acting independently on the acoustic domain. It should be noticed that the vectors $\mathbf{F}_{\mathtt{B}}$, $(\mathbf{F}_{\mathtt{B}})_1$, $(\mathbf{F}_{\mathtt{B}})_2$, $\mathbf{p}_{\mathtt{B}}$, $(\mathbf{p}_{\mathtt{B}})_1$ and $(\mathbf{p}_{\mathtt{B}})_2$ have the same size, i.e., $n_{\mathtt{B}} \times 1$, where $n_{\mathtt{B}} = 2(n_1 - 1) + 2(n_2 - 1)$ represents the number of boundary DOFs of the rectangular domain. Also, it should be pointed out that the vectors $(\mathbf{F}_{\mathtt{B}})_1$ and $(\mathbf{F}_{\mathtt{B}})_2$ contain, respectively, $2(n_2 - 1)$ and $2(n_1 - 1)$ zero-components. Those vectors are expressed as

$$(\mathbf{F}_{\mathtt{B}})_1 = \mathcal{P}_1 \mathbf{F}_{\mathtt{B}} \quad , \quad (\mathbf{F}_{\mathtt{B}})_2 = \mathcal{P}_2 \mathbf{F}_{\mathtt{B}}, \tag{15}$$

where $\mathcal{P}_1$ and $\mathcal{P}_2$ are two $n_{\mathtt{B}} \times n_{\mathtt{B}}$ matrices which relate the partitioning depicted in Figure 2 and which are defined so that

$$\mathcal{P}_1 + \mathcal{P}_2 = \mathbf{I}_{n_{\mathtt{B}}}. \tag{16}$$

In fact, the matrices $\mathcal{P}_1$ and $\mathcal{P}_2$ are diagonal and mostly composed of 1 and 0 components to enforce the fact that certain nodes are excited, while other are free. Other components equal to $1/2$ should also be considered which specifically address the acoustic forces at the corners of the domain (Figure 2), it being understood they are to be equally partitioned between the states of excitation $(\mathbf{F}_{\mathtt{B}})_1$ and $(\mathbf{F}_{\mathtt{B}})_2$.

The acoustic behavior of the rectangular domain, as subjected either to $(\mathbf{F}_{\mathtt{B}})_1$ or $(\mathbf{F}_{\mathtt{B}})_2$, can be assessed using the strategy depicted in Section 2.3. For each state i, the strategy consists in considering $n_i \times 1$ vectors of acoustic forces $(\mathbf{F}_0)_i$ and $(\mathbf{F}_0^\star)_i$ acting over the left/right or bottom/top edges. These vectors are linked to the full vector of acoustic forces $(\mathbf{F}_{\mathtt{B}})_i$ as follows:

$$\left[\begin{array}{c} (\mathbf{F}_0)_i \\ (\mathbf{F}_0^\star)_i \end{array} \right] = (\mathcal{B}_{\mathtt{F}})_i (\mathbf{F}_{\mathtt{B}})_i \qquad i = 1, 2, \tag{17}$$

where $(\mathcal{B}_{\mathtt{F}})_i$ is a $2n_i \times n_{\mathtt{B}}$ Boolean matrix. According to Eqs. (13), (15) and (17), the vectors of wave amplitudes are expressed as

$$\left[\begin{array}{c} \mathbf{Q}_i \\ \mathbf{Q}_i^\star \end{array} \right] = \mathbf{A}_i^{-1} \mathbf{B}_i (\mathcal{B}_{\mathtt{F}})_i \mathcal{P}_i \mathbf{F}_{\mathtt{B}} \qquad i = 1, 2, \tag{18}$$

where

$$\mathbf{A}_i = \left[\begin{array}{cc} \mathbf{I}_{n_i} & (\mathbf{\Phi}_{\mathtt{F}})_i^{-1} (\mathbf{\Phi}_{\mathtt{F}}^\star)_i \boldsymbol{\mu}_i^{N_i} \\ (\mathbf{\Phi}_{\mathtt{F}}^\star)_i^{-1} (\mathbf{\Phi}_{\mathtt{F}})_i \boldsymbol{\mu}_i^{N_i} & \mathbf{I}_{n_i} \end{array} \right] \quad , \quad \mathbf{B}_i = \left[\begin{array}{cc} -(\mathbf{\Phi}_{\mathtt{F}})_i^{-1} & \mathbf{0}_{n_i \times n_i} \\ \mathbf{0}_{n_i \times n_i} & (\mathbf{\Phi}_{\mathtt{F}}^\star)_i^{-1} \end{array} \right] \qquad i = 1, 2. \tag{19}$$

In a similar way as Eq. (17), there exists a relation which links the vector of nodal pressures $\mathbf{p}_i^{(k_i)}$ on a given substructure boundary (k_i) ($k_i = 1, \ldots, N_i + 1$) with the vector of nodal pressures $(\mathbf{p}_{\mathtt{B}})_i$ on the edges of the rectangular domain. This yields

$$\left[\begin{array}{c} \mathbf{p}_i^{(1)} \\ \mathcal{L}_i^{(2)} \mathbf{p}_i^{(2)} \\ \vdots \\ \mathcal{L}_i^{(N_i)} \mathbf{p}_i^{(N_i)} \\ \mathbf{p}_i^{(N_i+1)} \end{array} \right] = (\mathcal{B}_{\mathtt{p}})_i (\mathbf{p}_{\mathtt{B}})_i \qquad i = 1, 2, \tag{20}$$

where $\mathcal{L}^{(k_i)}$ ($k_i = 2, \ldots, N_i$) is a $2 \times n_i$ Boolean matrix which localizes among the DOFs of the substructure boundary (k_i), those belonging to the edges of the domain. The way the matrix $\mathcal{L}^{(k_i)}$ works is highlighted in Figure 3. Notice that both $\mathbf{p}_i^{(1)}$ and $\mathbf{p}_i^{(N_i+1)}$ are considered in the left-hand side of Eq. (20) since all their components relate nodal pressures on the edges of the domain (see Figure 3). Finally, in Eq. (20), $(\mathcal{B}_{\mathtt{p}})_i$ is a $n_{\mathtt{B}} \times n_{\mathtt{B}}$ orthogonal Boolean matrix whose purpose is to renumber the rows and columns of the matrix occurring in the left-hand side so as to match the node numbering scheme of the vectors $\mathbf{p}_{\mathtt{B}}$ and $\mathbf{F}_{\mathtt{B}}$, Eq. (14), which may be arbitrary a priori.

Invoking the wave expansion (9) into Eq. (20) while using the fact that the matrix $(\mathcal{B}_{\mathtt{p}})_i$ is orthogonal — i.e., $(\mathcal{B}_{\mathtt{p}})_i^{-1} = (\mathcal{B}_{\mathtt{p}})_i^T$ —, this yields

$$(\mathbf{p}_{\mathtt{B}})_i = (\mathcal{B}_{\mathtt{p}})_i^T (\mathbf{\Psi}_{\mathtt{p}})_i \left[\begin{array}{c} \mathbf{Q}_i \\ \mathbf{Q}_i^\star \end{array} \right] \qquad i = 1, 2, \tag{21}$$

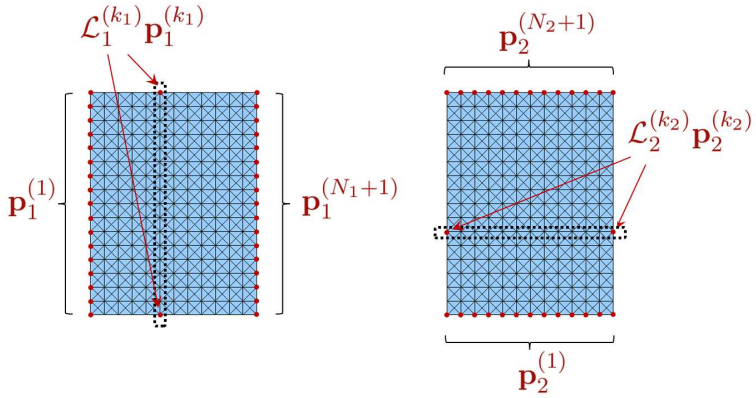


Figure 3: Illustration of the vectors $\mathcal{L}_1^{(k_1)}\mathbf{p}_1^{(k_1)}$ and $\mathcal{L}_2^{(k_2)}\mathbf{p}_2^{(k_2)}$.

where $(\boldsymbol{\Psi}_{\mathtt{p}})_i$ is a $n_{\mathtt{B}} \times 2n_i$ matrix defined by

$$(\boldsymbol{\Psi}_{\mathtt{p}})_i = \left[\begin{array}{c|c} (\boldsymbol{\Phi}_{\mathtt{p}})_i & (\boldsymbol{\Phi}^\star_{\mathtt{p}})_i \boldsymbol{\mu}_i^{N_i} \\ \mathcal{L}_i^{(2)}(\boldsymbol{\Phi}_{\mathtt{p}})_i \boldsymbol{\mu}_i & \mathcal{L}_i^{(2)}(\boldsymbol{\Phi}^\star_{\mathtt{p}})_i \boldsymbol{\mu}_i^{N_i-1} \\ \vdots & \vdots \\ \mathcal{L}_i^{(N_i)}(\boldsymbol{\Phi}_{\mathtt{p}})_i \boldsymbol{\mu}_i^{N_i-1} & \mathcal{L}_i^{(N_i)}(\boldsymbol{\Phi}^\star_{\mathtt{p}})_i \boldsymbol{\mu}_i \\ (\boldsymbol{\Phi}_{\mathtt{p}})_i \boldsymbol{\mu}_i^{N_i} & (\boldsymbol{\Phi}^\star_{\mathtt{p}})_i \end{array}\right] \qquad i = 1, 2. \tag{22}$$

By considering Eqs. (21) and (18), a relation linking the vector of pressures $(\mathbf{p}_{\mathtt{B}})_i$ and acoustic forces $\mathbf{F}_{\mathtt{B}}$ can be derived as follows:

$$(\mathbf{p}_{\mathtt{B}})_i = (\mathcal{B}_{\mathtt{p}})_i^T (\boldsymbol{\Psi}_{\mathtt{p}})_i \mathbf{A}_i^{-1} \mathbf{B}_i (\mathcal{B}_{\mathtt{F}})_i \mathcal{P}_i \mathbf{F}_{\mathtt{B}} \qquad i = 1, 2. \tag{23}$$

The derivation of the receptance matrix $\mathbf{H}$ — defined as $\mathbf{p}_{\mathtt{B}} = \mathbf{H}\mathbf{F}_{\mathtt{B}}$ where $\mathbf{p}_{\mathtt{B}} = (\mathbf{p}_{\mathtt{B}})_1 + (\mathbf{p}_{\mathtt{B}})_2$ — finally follows as

$$\mathbf{H} = (\mathcal{B}_{\mathtt{p}})_1^T (\boldsymbol{\Psi}_{\mathtt{p}})_1 \mathbf{A}_1^{-1} \mathbf{B}_1 (\mathcal{B}_{\mathtt{F}})_1 \mathcal{P}_1 + (\mathcal{B}_{\mathtt{p}})_2^T (\boldsymbol{\Psi}_{\mathtt{p}})_2 \mathbf{A}_2^{-1} \mathbf{B}_2 (\mathcal{B}_{\mathtt{F}})_2 \mathcal{P}_2. \tag{24}$$

3.3 Model reduction

3.3.1 Introduction

One way to speed up the computation of the receptance matrix $\mathbf{H}$ is to make use of reduced wave mode bases. In this framework, the vectors of pressures and acoustic forces are assessed by means of reduced sets of wave shapes $\{(\widetilde{\boldsymbol{\phi}}_{\mathtt{p}j})_i\}_{j=1,\ldots,m_i} \cup \{(\widetilde{\boldsymbol{\phi}}^\star_{\mathtt{p}j})_i\}_{j=1,\ldots,m_i}$ and $\{(\widetilde{\boldsymbol{\phi}}_{\mathtt{F}j})_i\}_{j=1,\ldots,m_i} \cup \{(\widetilde{\boldsymbol{\phi}}^\star_{\mathtt{F}j})_i\}_{j=1,\ldots,m_i}$ extracted from the full sets $\{(\boldsymbol{\phi}_{\mathtt{p}j})_i\}_{j=1,\ldots,n_i} \cup \{(\boldsymbol{\phi}^\star_{\mathtt{p}j})_i\}_{j=1,\ldots,n_i}$ and $\{(\boldsymbol{\phi}_{\mathtt{F}j})_i\}_{j=1,\ldots,n_i} \cup \{(\boldsymbol{\phi}^\star_{\mathtt{F}j})_i\}_{j=1,\ldots,n_i}$, where $m_i \leq n_i$. This yields a small sized $m_i \times m_i$ matrix $\widetilde{\boldsymbol{\mu}}_i = \mathtt{diag}\{(\widetilde{\mu}_j)_i\}_{j=1,\ldots,m_i}$, and small sized $n_i \times m_i$ matrices $(\widetilde{\boldsymbol{\Phi}}_{\mathtt{p}})_i = [(\widetilde{\boldsymbol{\phi}}_{\mathtt{p}1})_i \ldots (\widetilde{\boldsymbol{\phi}}_{\mathtt{p}m_i})_i]$, $(\widetilde{\boldsymbol{\Phi}}^\star_{\mathtt{p}})_i = [(\widetilde{\boldsymbol{\phi}}^\star_{\mathtt{p}1})_i \ldots (\widetilde{\boldsymbol{\phi}}^\star_{\mathtt{p}m_i})_i]$, $(\widetilde{\boldsymbol{\Phi}}_{\mathtt{F}})_i = [(\widetilde{\boldsymbol{\phi}}_{\mathtt{F}1})_i \ldots (\widetilde{\boldsymbol{\phi}}_{\mathtt{F}m_i})_i]$ and $(\widetilde{\boldsymbol{\Phi}}^\star_{\mathtt{F}})_i = [(\widetilde{\boldsymbol{\phi}}^\star_{\mathtt{F}1})_i \ldots (\widetilde{\boldsymbol{\phi}}^\star_{\mathtt{F}m_i})_i]$. As a result, the receptance matrix can be approximated as $\mathbf{H} \approx \widetilde{\mathbf{H}}$, where (cf. Eq. (24)):

$$\widetilde{\mathbf{H}} = (\mathcal{B}_{\mathtt{p}})_1^T (\widetilde{\boldsymbol{\Psi}}_{\mathtt{p}})_1 \widetilde{\mathbf{A}}_1^{-1} \widetilde{\mathbf{B}}_1 (\mathcal{B}_{\mathtt{F}})_1 \mathcal{P}_1 + (\mathcal{B}_{\mathtt{p}})_2^T (\widetilde{\boldsymbol{\Psi}}_{\mathtt{p}})_2 \widetilde{\mathbf{A}}_2^{-1} \widetilde{\mathbf{B}}_2 (\mathcal{B}_{\mathtt{F}})_2 \mathcal{P}_2. \tag{25}$$

Here, the matrices $\widetilde{\mathbf{A}}_i$ and $\widetilde{\mathbf{B}}_i$ are to be expressed as follows (cf. Eq. (19)):

$$\widetilde{\mathbf{A}}_i = \begin{bmatrix} \mathbf{I}_{m_i} & (\widetilde{\mathbf{\Phi}}_{\mathtt{F}})_i^+ (\widetilde{\mathbf{\Phi}}_{\mathtt{F}}^\star)_i \widetilde{\boldsymbol{\mu}}_i^{N_i} \\ (\widetilde{\mathbf{\Phi}}_{\mathtt{F}}^\star)_i^+ (\widetilde{\mathbf{\Phi}}_{\mathtt{F}})_i \widetilde{\boldsymbol{\mu}}_i^{N_i} & \mathbf{I}_{m_i} \end{bmatrix} \quad , \quad \widetilde{\mathbf{B}}_i = \begin{bmatrix} -(\widetilde{\mathbf{\Phi}}_{\mathtt{F}})_i^+ & \mathbf{0}_{m_i \times n_i} \\ \mathbf{0}_{m_i \times n_i} & (\widetilde{\mathbf{\Phi}}_{\mathtt{F}}^\star)_i^+ \end{bmatrix} \qquad i = 1, 2, \tag{26}$$

where $(\widetilde{\mathbf{\Phi}}_{\mathtt{F}})_i^+$ and $(\widetilde{\mathbf{\Phi}}_{\mathtt{F}}^\star)_i^+$ are the left pseudo-inverse of the matrices $(\widetilde{\mathbf{\Phi}}_{\mathtt{F}})_i$ and $(\widetilde{\mathbf{\Phi}}_{\mathtt{F}}^\star)_i$. Also, in Eq. (25), the matrices $(\widetilde{\mathbf{\Psi}}_{\mathtt{p}})_1$ and $(\widetilde{\mathbf{\Psi}}_{\mathtt{p}})_2$ are expressed by (cf. Eq. (22)):

$$(\widetilde{\mathbf{\Psi}}_{\mathtt{p}})_i = \left[\begin{array}{c|c} \mathcal{L}_i^{(1)}(\widetilde{\mathbf{\Phi}}_{\mathtt{p}})_i & \mathcal{L}_i^{(1)}(\widetilde{\mathbf{\Phi}}_{\mathtt{p}}^\star)_i \widetilde{\boldsymbol{\mu}}_i^{N_i} \\ \mathcal{L}_i^{(2)}(\widetilde{\mathbf{\Phi}}_{\mathtt{p}})_i \widetilde{\boldsymbol{\mu}}_i & \mathcal{L}_i^{(2)}(\widetilde{\mathbf{\Phi}}_{\mathtt{p}}^\star)_i \widetilde{\boldsymbol{\mu}}_i^{N_i-1} \\ \vdots & \vdots \\ \mathcal{L}_i^{(N_i+1)}(\widetilde{\mathbf{\Phi}}_{\mathtt{p}})_i \widetilde{\boldsymbol{\mu}}_i^{N_i} & \mathcal{L}_i^{(N_i+1)}(\widetilde{\mathbf{\Phi}}_{\mathtt{p}}^\star)_i \end{array}\right] \qquad i = 1, 2. \tag{27}$$

3.3.2 Hybrid WFE/FE superelement modeling

Although interesting, the use of reduced sets of wave shapes $\{(\widetilde{\phi}_{\mathtt{p}j})_i\}_{j=1,\ldots,m_i} \cup \{(\widetilde{\phi}_{\mathtt{p}j}^\star)_i\}_{j=1,\ldots,m_i}$ and $\{(\widetilde{\phi}_{\mathtt{F}j})_i\}_{j=1,\ldots,m_i} \cup \{(\widetilde{\phi}_{\mathtt{F}j}^\star)_i\}_{j=1,\ldots,m_i}$ may be subject to strong issues, e.g., in case when excitation sources are applied on the edges of the rectangular superelements. In this case, the pressure field is likely to be strongly heterogeneous in the vicinity of the excitation sources, meaning that almost the full sets of wave shapes are required to describe the acoustic behavior of the system with accurate precision. To solve this issue, it is proposed to surround any WFE-based rectangular superelement by means of a thin FE layer whose thickness is not necessarily uniform, as shown in Figure 4.

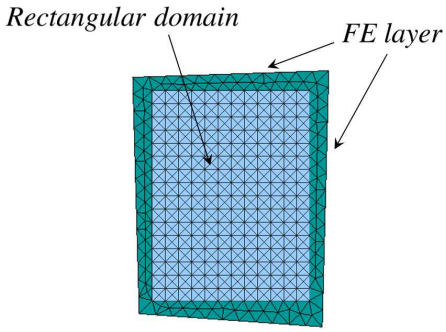


Figure 4: Illustration of a WFE superelement surrounded by a thin FE layer with a non-uniform thickness.

While the rectangular domain exhibits a periodic FE mesh, the layer can be discretized in arbitrary ways. By coupling a WFE-based rectangular element whose dimensions can be large, with a small FE layer, this yields the consideration of a so-called hybrid WFE/FE superelement which is well-suited for model reduction purpose. The modeling of this superelement is achieved as follows.

In matrix form, the dynamic equilibrium equation of the FE layer is expressed as

$$\begin{bmatrix} \mathbb{D}_{\mathtt{BB}} & \mathbb{D}_{\mathtt{BR}} \\ \mathbb{D}_{\mathtt{RB}} & \mathbb{D}_{\mathtt{RR}} \end{bmatrix} \begin{bmatrix} \widetilde{\mathbf{p}}_{\mathtt{B}} \\ \widetilde{\mathbf{p}}_{\mathtt{R}} \end{bmatrix} = \begin{bmatrix} -\widetilde{\mathbf{F}}_{\mathtt{B}} \\ \widetilde{\mathbf{F}}_{\mathtt{R}} \end{bmatrix}, \tag{28}$$

where the subscript $\mathtt{B}$ refers to the interface DOFs — i.e., where coupling with the WFE-based rectangular superelement occurs — while the subscript $\mathtt{R}$ refers to the remaining DOFs. Also, the tilde sign indicates that vector terms result from the reduced modeling of the WFE-based rectangular superelement, with the assumption that $\widetilde{\mathbf{H}}\widetilde{\mathbf{F}}_{\mathtt{B}} = \widetilde{\mathbf{p}}_{\mathtt{B}}$ (see after Eq. (23)). Note that the term $-\widetilde{\mathbf{F}}_{\mathtt{B}}$ in the right hand side of Eq. (28) reflects the opposite of the vector of nodal acoustic forces acting on the edges of the rectangular superelement, and results from the action-reaction law. Also, the term $\widetilde{\mathbf{F}}_{\mathtt{R}}$ refers to the vector of nodal acoustic forces acting on the remaining nodes of the FE layer. In left-multiplying the first row block of the matrix system in Eq. (28) by $\mathbb{D}_{\mathtt{BB}}\widetilde{\mathbf{H}}$, where $\widetilde{\mathbf{H}}$ is the receptance matrix of the rectangular domain, this yields

$$\begin{bmatrix} \mathbb{D}_{\mathtt{BB}}\widetilde{\mathbf{H}}\mathbb{D}_{\mathtt{BB}} & \mathbb{D}_{\mathtt{BB}}\widetilde{\mathbf{H}}\mathbb{D}_{\mathtt{BR}} \\ \mathbb{D}_{\mathtt{RB}} & \mathbb{D}_{\mathtt{RR}} \end{bmatrix} \begin{bmatrix} \widetilde{\mathbf{p}}_{\mathtt{B}} \\ \widetilde{\mathbf{p}}_{\mathtt{R}} \end{bmatrix} = \begin{bmatrix} -\mathbb{D}_{\mathtt{BB}}\widetilde{\mathbf{H}}\widetilde{\mathbf{F}}_{\mathtt{B}} \\ \widetilde{\mathbf{F}}_{\mathtt{R}} \end{bmatrix}. \tag{29}$$

By using the fact that $\widetilde{\mathbf{H}}\widetilde{\mathbf{F}}_{\mathtt{B}} = \widetilde{\mathbf{p}}_{\mathtt{B}}$, thus it turns out from Eq. (29) that the dynamic equilibrium equation of the hybrid WFE/FE superelement can be expressed as follows:

$$\begin{bmatrix} \mathbb{D}_{\mathtt{BB}} + \mathbb{D}_{\mathtt{BB}}\widetilde{\mathbf{H}}\mathbb{D}_{\mathtt{BB}} & \mathbb{D}_{\mathtt{BB}}\widetilde{\mathbf{H}}\mathbb{D}_{\mathtt{BR}} \\ \mathbb{D}_{\mathtt{RB}} & \mathbb{D}_{\mathtt{RR}} \end{bmatrix} \begin{bmatrix} \widetilde{\mathbf{p}}_{\mathtt{B}} \\ \widetilde{\mathbf{p}}_{\mathtt{R}} \end{bmatrix} = \begin{bmatrix} \mathbf{0} \\ \widetilde{\mathbf{F}}_{\mathtt{R}} \end{bmatrix}. \tag{30}$$

3.3.3 Superelement assembly

Modeling a whole arbitrary-shaped acoustic cavity involves assembling several hybrid WFE/FE superelements with conventional FE components and CMS superelements, as shown in Figure 5. Within the CMS framework, the condensed dynamic stiffness matrices of superelements may be assessed by considering the Craig-Bampton (CB) method [1], i.e., by means of static modes and fixed interface modes. In matrix form, the dynamic equilibrium equations of these FE components and CB-based superelements may be translated as follows, respectively:

$$\mathbf{D}^{\mathtt{FE}}\widetilde{\mathbf{p}} = \widetilde{\mathbf{F}}, \quad , \quad \widetilde{\mathbf{D}}^{\mathtt{CB}}\widetilde{\mathbf{p}}_{\mathtt{B}} = \widetilde{\mathbf{F}}_{\mathtt{B}}, \tag{31}$$

where $\mathbf{D}^{\mathtt{FE}}$ is the classic dynamic stiffness matrix of a FE component ($\widetilde{\mathbf{p}}$ and $\widetilde{\mathbf{F}}$ being the vectors of nodal pressures and nodal forces of the component), while $\widetilde{\mathbf{D}}^{\mathtt{CB}}$ is the condensed dynamic stiffness matrix of a superelement, whose expression can be found in [11]; also, the subscript $\mathtt{B}$ refers to the boundary DOFs, while the tilde sign of $\widetilde{\mathbf{D}}^{\mathtt{CB}}$ indicates that a reduced number of fixed interface modes are used to derive the matrix. On the other hand, the dynamic equilibrium equation of a hybrid WFE/FE superelement is expressed as follows (Eq. (30)):

$$\widetilde{\mathbf{D}}^{\mathtt{SE}}\widetilde{\mathbf{p}}_{\mathtt{Lay}} = \widetilde{\mathbf{F}}_{\mathtt{Lay}}, \tag{32}$$

where

$$\widetilde{\mathbf{D}}^{\mathtt{SE}} = \begin{bmatrix} \mathbb{D}_{\mathtt{BB}} + \mathbb{D}_{\mathtt{BB}}\widetilde{\mathbf{H}}\mathbb{D}_{\mathtt{BB}} & \mathbb{D}_{\mathtt{BB}}\widetilde{\mathbf{H}}\mathbb{D}_{\mathtt{BR}} \\ \mathbb{D}_{\mathtt{RB}} & \mathbb{D}_{\mathtt{RR}} \end{bmatrix}. \tag{33}$$

In Eq. (30), $\widetilde{\mathbf{p}}_{\mathtt{Lay}}$ and $\widetilde{\mathbf{F}}_{\mathtt{Lay}}$ are the vectors of nodal pressures and nodal forces of the layer, expressed by

$$\widetilde{\mathbf{p}}_{\mathtt{Lay}} = \begin{bmatrix} \widetilde{\mathbf{p}}_{\mathtt{B}} \\ \widetilde{\mathbf{p}}_{\mathtt{R}} \end{bmatrix} \quad , \quad \widetilde{\mathbf{F}}_{\mathtt{Lay}} = \begin{bmatrix} \mathbf{0} \\ \widetilde{\mathbf{F}}_{\mathtt{R}} \end{bmatrix}. \tag{34}$$

The numerical model of a whole cavity composed of several WFE/FE superelements, FE components and CB superelements hence follows from conventional FE procedure, by assembling several dynamic stiffness matrices $\widetilde{\mathbf{D}}_r^{\mathtt{SE}}$, $\mathbf{D}_s^{\mathtt{FE}}$ and $\widetilde{\mathbf{D}}_t^{\mathtt{CB}}$ $(r,s,t=1,2,\ldots)$. This yields the following dynamic equilibrium equation

$$\widetilde{\mathbf{D}}^{\mathtt{Cav}}\widetilde{\mathbf{p}} = \widetilde{\mathbf{F}}, \tag{35}$$

where $\widetilde{\mathbf{p}}$ and $\widetilde{\mathbf{F}}$ are to be understood as the full vectors of nodal pressures and forces of the cavity, respectively. Also, the matrix $\widetilde{\mathbf{D}}^{\mathtt{Cav}}$ is expressed by

$$\widetilde{\mathbf{D}}^{\mathtt{Cav}} = \sum_r (\mathbf{L}_r^{\mathtt{SE}})^T \widetilde{\mathbf{D}}_r^{\mathtt{SE}} \mathbf{L}_r^{\mathtt{SE}} + \sum_s (\mathbf{L}_s^{\mathtt{FE}})^T \mathbf{D}_s^{\mathtt{FE}} \mathbf{L}_s^{\mathtt{FE}} + \sum_t (\mathbf{L}_t^{\mathtt{CB}})^T \widetilde{\mathbf{D}}_t^{\mathtt{CB}} \mathbf{L}_t^{\mathtt{CB}}. \tag{36}$$

where $\mathbf{L}_r^{\mathtt{SE}}$, $\mathbf{L}_s^{\mathtt{FE}}$ and $\mathbf{L}_t^{\mathtt{CB}}$ are conventional Boolean localization matrices.

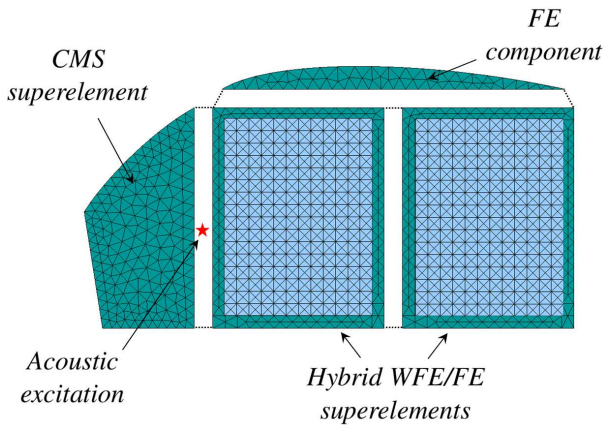


Figure 5: Illustration of an assembly involving two hybrid WFE/FE superelements, one FE component and one CMS superelement.

4 NUMERICAL RESULTS

4.1 Hybrid WFE/FE superelement

The concept of hybrid WFE/FE superelement is first investigated in the case of a two-dimensional rectangular cavity filled with air. Following the strategy depicted in Section 3, this acoustic domain is composed of a WFE-based superelement of dimensions 3 m $\times 2$ m surrounded by a uniform FE layer of thickness 0.02 m (Figure 6(a)). Both WFE domain and FE layer are meshed by means of square linear acoustic elements owning 1 DOF per node, of size 0.01 m $\times\, 0.01$ m (Figure 6(b)). The FE layer therefore contains 2 elements in its thickness, involving a total number of $3,024$ DOFs. The mesh of the WFE-based internal domain consists of $N_1 = 300$ elements in the horizontal $x-$direction and $N_2 = 200$ elements in the vertical $y-$direction. Each left/right and bottom/top edge contains respectively $n_1 = 201$ and $n_2 = 301$ DOFs, the total number of DOFs on the interface between the WFE domain and the FE layer being $n_{\mathtt{B}} = 1,000$.

The hybrid WFE/FE superelement modeling is used to investigate the frequency behavior of the cavity which is subject to two acoustic point sources on the external boundary of the FE layer, as shown in Figure 6(a). These acoustic point forces have equal frequency-dependent

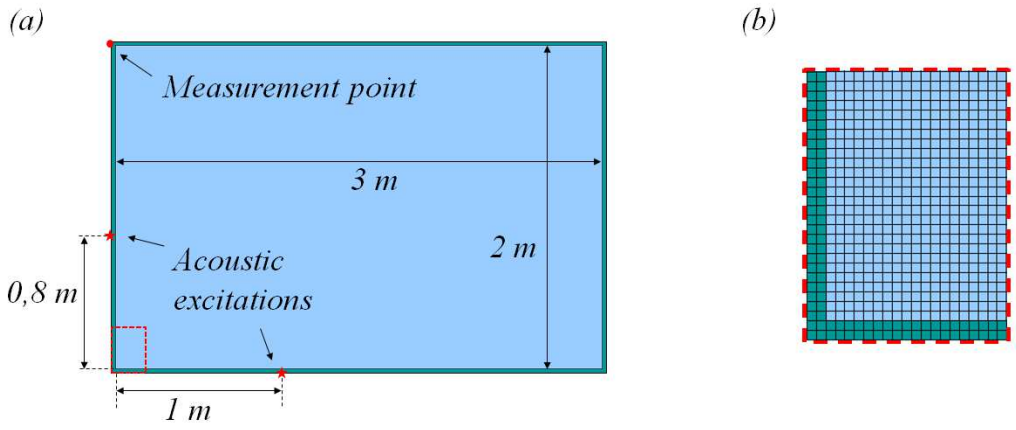


Figure 6: Hybrid WFE/FE superelement: (a) dimensions and test configuration; (b) detailed view of the mesh.

magnitudes of $F_0 = 2\sqrt{\frac{\omega P}{\rho_0}}$ where $P = 10^{-6}$ W.m^{-1}. The fluid, considered as compressible and barotropic, is characterized by its mean density $\rho_0 = 1.25$ kg.m^{-3} and sound velocity $c_0 = 343$ m.s^{-1}. Also, a fluid viscosity is taken into account through the Stokes' law of sound attenuation, i.e., the Helmholtz equation that governs the acoustic pressure in the cavity is modified by an attenuation coefficient α:

$$\Delta p + \left(\frac{\omega}{c_0} - i\,\alpha\right)^2 p = 0. \tag{37}$$

The damping is here frequency-dependent and given by $\alpha = \frac{2\,\eta\,\omega^2}{3\,\rho_0\,c_0^3}$, where $\eta = 18.27\,10^{-6}$ Pa.s is the dynamic viscosity of air.

The pressure FRF is assessed at the node located at the top left corner of the FE layer (Figure 6(a)), for 246 discrete frequencies uniformly spaced over the range $[10$ Hz, 500 Hz$]$ with a frequency step of 2 Hz. The mesh is supposed to be fine enough to accurately capture the dynamic behavior of the system throughout the whole frequency range, i.e., by considering the usual criterion that the acoustic wavelengths should be discretized by a minimum of 8 elements. As was explained in Section 3, the computation of the FRF of the hybrid WFE/FE superelement involves several steps which includes the calculation of matrices of reduced wave bases $(\widetilde{\mathbf{\Phi}}_{\mathtt{p}})_i$, $(\widetilde{\mathbf{\Phi}}^{\star}_{\mathtt{p}})_i$, $(\widetilde{\mathbf{\Phi}}_{\mathtt{F}})_i$, $(\widetilde{\mathbf{\Phi}}^{\star}_{\mathtt{F}})_i$ for each direction $i = 1, 2$. These are used to form the $n_{\mathtt{B}} \times n_{\mathtt{B}}$ receptance matrix $\widetilde{\mathbf{H}}$, see Eq. (25). The receptance matrix is finally combined to the dynamic stiffness matrix $\mathbb{D}$ of the FE layer to form the matrix $\widetilde{\mathbf{D}}^{\mathtt{SE}}$ (Eqs. (30), (33)) of the hybrid WFE/FE superelement, with a view to solving the matrix system (35) at each frequency of interest.

The motivation behind the use of the FE layer, around the WFE domain, is to highly reduce the sizes of the wave bases without significantly altering the accuracy of the solution. In the present case, the pressure FRF has been computed by only retaining $m_1 = 20$ right/left- and $m_2 = 20$ top/bottom-going wave modes among the $n_1 = 201$ and $n_2 = 301$ modes of the full wave bases. The resulting dB pressure levels, i.e., $20\,\mathtt{log}_{10}(\frac{|p|}{p_{\mathtt{ref}}})$ where $p_{\mathtt{ref}} = 20\times10^{-6}\,Pa$, are shown in Figure 7 (dotted pink line). For validation purpose, a reference FE solution issued from the commercial FE software Comsol Multiphysics® is also displayed in Figure 7 (black solid line). It can be seen that the reference levels are correctly retrieved by the hybrid superelement approach over the whole frequency band, despite a few slight differences regarding some low-frequency anti-resonance peaks and the resonance peak at $f = 378$ Hz.

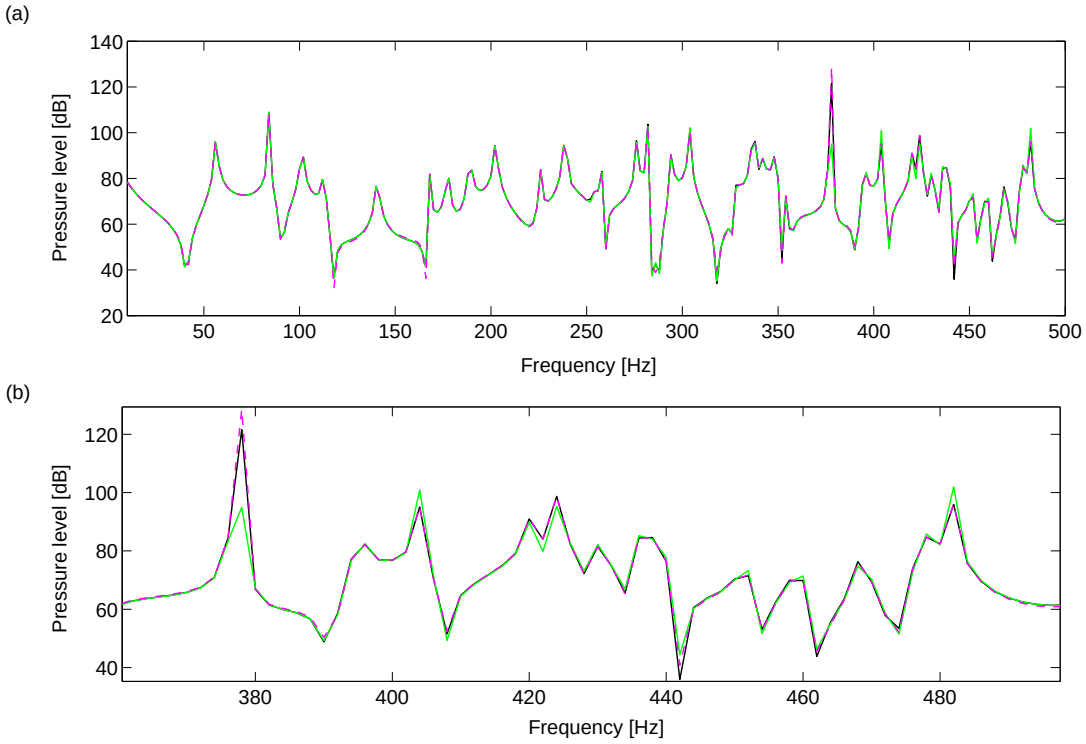


Figure 7: Pressure FRFs of the rectangular hybrid WFE/FE cavity: (—) FE reference solution; (– –) WFE/FE solution; (—) CB solution with $1,000$ elastic modes; (a) full frequency range; (b) focus in the range $[360$ Hz, 500 Hz$]$.

Regarding CPU times, it takes as a whole $852\,s$ to achieve the computation of the pressure FRF (including the computations of wave modes) with MATLAB® and using an Intel® Core(TM) i7-3720QM @2.6 GHz processor. By considering full wave bases instead of reduced wave bases, it would have taken $1,888$ s to compute the FRF. Thus the use of reduced wave bases yields a reduction of 54.9% of the computational cost, hence giving credit to the proposed model reduction strategy.

Also, the efficiency of the method is assessed when compared to the Craig-Bampton (CB) method [1]. In this framework, the condensed dynamic stiffness matrix $\widetilde{\mathbf{D}}^{\mathtt{CB}}$ of the cavity is modeled by means of $1,016$ static modes and $1,000$ fixed interface modes. The related FRF is displayed in Figure 7 in green solid line. As it can be seen in Figure 7(b), the CB solution fails to accurately describe the resonance peaks of the reference FE solution above 300 Hz, as opposed to the hybrid WFE/FE-based approach. Besides, the CPU time involved in the CB approach is 966 s, which exceeds that of the hybrid WFE/FE-based approach. To summarize, it appears from the analysis of this first test case that the hybrid WFE/FE-based approach constitutes an efficient alternative to the CB method.

4.2 Superelement assembly

In the following, the above rectangular cavity is embedded in an arbitrary-shaped assembly depicted in Figure 8. The latter is composed of a hybrid WFE/FE superelement which is connected to a CMS superelement, modeled by means of the CB method. The system is excited by means of an acoustic point source located inside the CMS superelement. In the present case,

the hybrid WFE/FE superelement is made up of a WFE-based rectangular domain which is connected to a non-uniform FE layer over two of its edges only. In doing so, large reduction of the sizes of the WFE wave bases is expected over a reasonable frequency range — which is chosen to be $[10 \text{ Hz}, 300 \text{ Hz}]$ — without significantly penalizing the accuracy of the proposed approach.

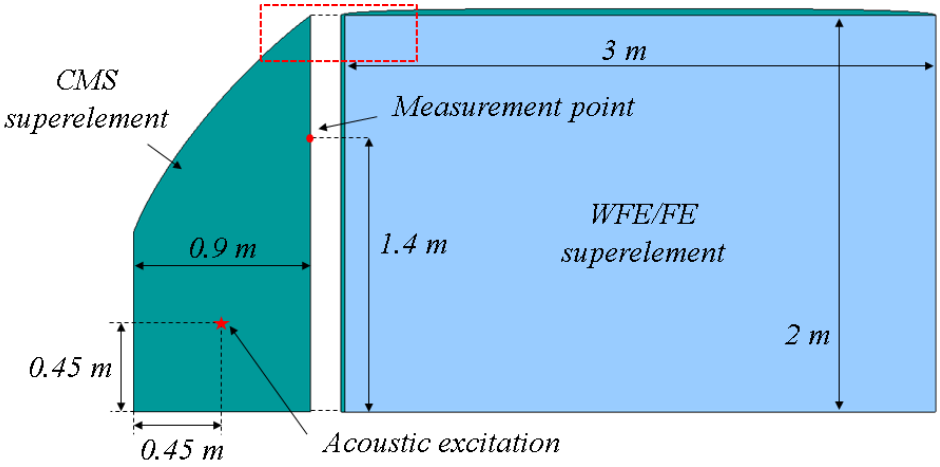


Figure 8: Assembly of a hybrid WFE/FE superelement and a CMS superelement: dimensions and test configuration.

The WFE-based rectangular domain is meshed as in the previous case, i.e., using square linear elements of size 0.01 m $\times 0.01$ m. Regarding the FE layer, square linear elements are used in the vertical portion of the layer, as well as triangular linear elements in the curved portion at the top of the WFE domain (Figure 9). The mesh of the FE layer hence contains $1,698$ DOFs, including 501 DOFs on the interface with the WFE domain. Finally, the mesh of the CMS superelement is composed of triangular and rectangular linear elements, which involves a total of $12,047$ DOFs including 530 DOFs uniformly spread on the superelement boundary. Within the framework of the present approach, two dynamic stiffness matrices $\widetilde{\mathbf{D}}^{\text{SE}}$ and $\widetilde{\mathbf{D}}^{\text{CB}}$ are thus involved which are of respective sizes 875×875 and 530×530, while the full assembly contains $73,540$ DOFs.

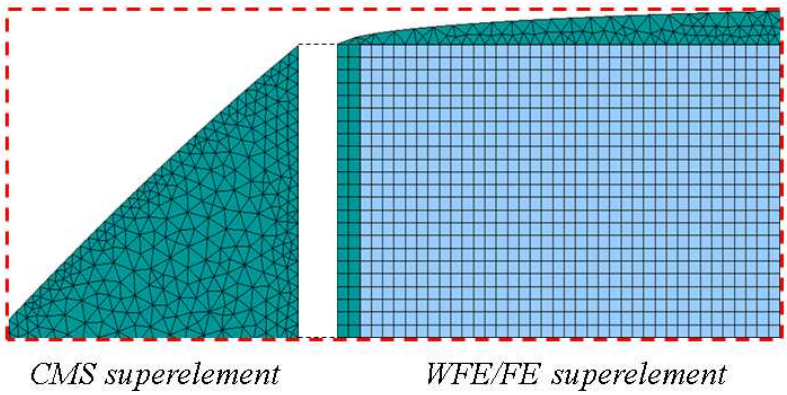


Figure 9: Detailed view of the assembly meshes.

The pressure FRF is computed at a node located on the interface between the CMS and

hybrid WFE/FE superlements, as shown in Figure 8. The resulting pressure levels are plotted in Figure 10. Again, $m_1 = 20$ right/left- and $m_2 = 20$ top/bottom-going wave modes are retained for modeling the hybrid WFE/FE superelement, while 500 fixed interface modes are considered for modeling the CMS/CB superelement. Again, the WFE-based solution correctly matches the FE reference solution over the whole frequency range, despite some very slight differences above 200 Hz which appear to be less than 3dB, however.

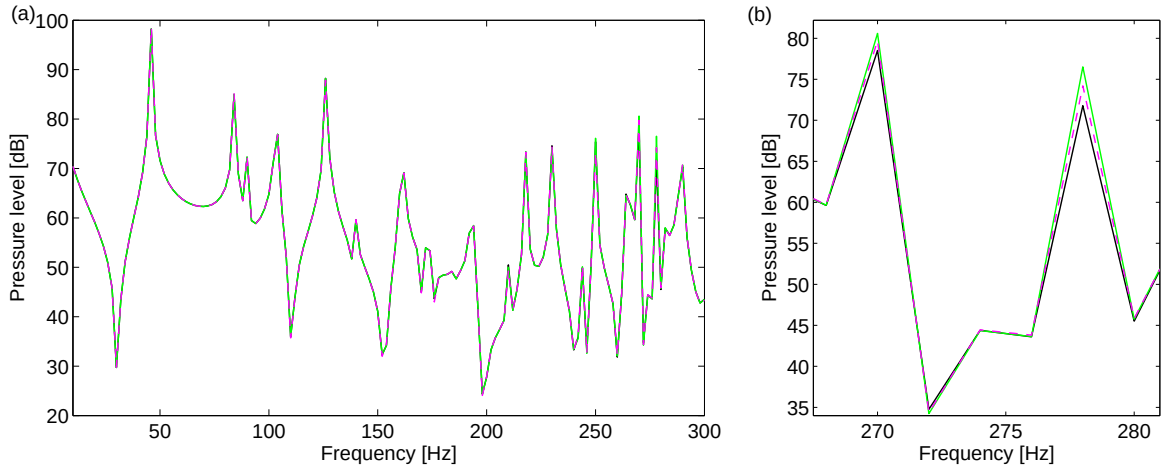


Figure 10: Pressure FRFs of the assembly: (—) FE reference solution; (– –) solution obtained with the hybrid WFE/FE superelement and a CB superelement with 500 fixed interface modes; (—) solution obtained using two CB superelements with 500 and 1000 fixed interface modes; (a) full frequency range; (b) focus in the range $[267$ Hz, 281 Hz$]$.

The efficiency of the method is assessed in comparison with the conventional CB method. For this purpose, two CMS/CB superelements are considered which concern the one depicted in Figure 8 and the previous WFE/FE superelement. Here, 500 and $1,000$ fixed interface modes are respectively used for modeling these superelements. The CB-based pressure FRF is displayed in Figure 10, which appears to be a little bit less accurate than the WFE-based solution, as shown Figure 10(b). The interesting feature of the proposed hybrid WFE/FE modeling lies in the reduction of the CPU times. It actually takes 433 s for computing the pressure FRF with the hybrid WFE/FE-based approach, compared to 905 s with the conventional CB method. This means 52.2% of time reduction, which fully gives credit to the proposed approach.

5 CONCLUSIONS

A new substructuring technique has been proposed for the prediction of the acoustic behavior of arbitrary-shaped 2D cavities. It involves WFE/FE hybrid superelements, consisting in a rectangular domain, with a periodic FE mesh and modeled by means of the WFE method, surrounded by a FE layer with a small width. The interesting feature behind this modeling is that a few wave modes are only required to describe the dynamic stiffness matrices of those WFE/FE hybrid superelements, meaning that they can be computed in a very fast way. Modeling a whole arbitrary-shaped acoustic cavity follows from conventional FE assembly procedure, i.e., by coupling several WFE/FE hybrid superelements together as well as with other CMS superelements and classical FE components. Numerical experiments have been carried out which highlight the relevance of the proposed substructuring technique, in terms of accuracy and computational

saving, in comparison with the conventional CMS technique.

REFERENCES

[1] R. R. Craig, M. C. C. Bampton, Coupling of substructures for dynamic analyses, AIAA Journal 6 (7) (1968) 1313–1319.

[2] B. V. Genechten, B. Pluymers, D. Vandepitte, W. Desmet, A hybrid wave based - modally reduced finite element method for the efficient analysis of low- and mid-frequency car cavity acoustics, SAE International Journal of Passenger cars - Mechanical systems 2 (1) (2009) 1494–1504.

[3] W. X. Zhong, F. W. Williams, On the direct solution of wave propagation for repetitive structures, Journal of Sound and Vibration 181 (3) (1995) 485–501.

[4] J.-M. Mencik, M. N. Ichchou, Multi-mode propagation and diffusion in structures through finite elements, European Journal of Mechanics - A/Solids 24 (5) (2005) 877–898.

[5] D. Duhamel, B. Mace, M. J. Brennan, Finite element analysis of the vibrations of waveguides and periodic structures, Journal of Sound and Vibration 294 (1-2) (2006) 205–220.

[6] R. Patel, On computing the eigenvalues of a symplectic pencil, Linear Algebra and its Applications 188-189 (1993) 591–611.

[7] J.-M. Mencik, D. Duhamel, A wave-based model reduction technique for the description of the dynamic behavior of periodic structures involving arbitrary-shaped substructures and large-sized finite element models, Finite Elements in Analysis and Design (accepted).

[8] R. S. Langley, Wave evolution, reflection, and transmission along inhomogeneous waveguides, Journal of Sound and Vibration 227 (1) (1999) 131–158.

[9] J.-M. Mencik, On the low- and mid-frequency forced response of elastic systems using wave finite elements with one-dimensional propagation, Computers and Structures 88 (11-12) (2010) 674–689.

[10] J.-M. Mencik, New advances in the forced response computation of periodic structures using the wave finite element (WFE) method, Computational Mechanics 54 (3) (2014) 789–801.

[11] J.-M. Mencik, Model reduction and perturbation analysis of wave finite element formulations for computing the forced response of coupled elastic systems involving junctions with uncertain eigenfrequencies, Computer Methods in Applied Mechanics and Engineering 200 (45-46) (2011) 3051–3065.

COMPDYN 2015
5th ECCOMAS Thematic Conference on
Computational Methods in Structural Dynamics and Earthquake Engineering
M. Papadrakakis, V. Papadopoulos, V. Plevris (eds.)
Crete Island, Greece, 25–27 May 2015

ON THE IMPLEMENTATION OF BOUNDARY CONDITIONS IN RBF-PS METHOD APPLIED TO VIBRATION ANALYSIS OF KIRCHHOFF PLATES

Artur Krowiak

Institute of Computing Science, Cracow University of Technology
Al. Jana Pawla II 37, 31-864 Krakow
e-mail: krowiak@mech.pk.edu.pl

Keywords: Meshless methods, Radial Basis Functions, Pseudospectral techniques, Multiple boundary conditions, Hermite type interpolation.

Abstract. *The paper deals with the implementation of multiple boundary conditions in the radial basis function-based pseudospectral method. This numerical technique belongs to the wide range of meshless discretization methods, combining the flexibility of the meshless discretization with efficiency and simplicity of the pseudospectral techniques. The method can be directly applied to lower order equation, where the number of boundary conditions at a boundary node corresponds to the number of degrees of freedom at this node. For higher order equations the problem arises during collocation procedure due to multiple boundary conditions. In the present paper two approaches to overcome this inconvenience are shown. One is based on the Hermite interpolation idea while the other is a slight modification of the direct approach. The convergence and accuracy of both approaches are examined in the problem of free vibration analysis of plates. Square plates as well as irregular shaped plates with various types of boundary conditions are taken under consideration. Uniform as well as scattered node distributions are applied. The results confirm that both approaches can be useful in the application to plate vibration analysis.*

1 INTRODUCTION

In recent years a significant effort has been made to develop meshless numerical techniques [1, 2]. The main feature of these methods is the use of scattered nodes to discretize the domain of the problem under consideration. Due to this feature, they can easily discretize irregular shapes and problems defined in more than two dimensions. This type of discretization is also very effective in association with adaptation techniques.

Several formulations of meshless methods have been developed till now. Some of them are derived from the weak formulation, while the others are used to discretize directly differential equation. The method investigated in the present paper, called the radial basis function-based pseudospectral method (RBF-PS) falls into the second category. It uses radial basis functions (RBFs) to approximate derivatives in a governing equation in the view of the pseudospectral mode. Using this approximation and applying the collocation procedure, the governing equation is transformed into the set of algebraic equations. The method has been used to solve problems from various disciplines of science. A collection of papers by Fasshauer [3] and Ferreira and Fasshauer [4, 5] devoted to the method and its application to engineering problems deserves a particular attention. It is also known a slight modification of this method called the radial basis function-based differential quadrature (RBF-DQ) [6]. Some applications of the latter can be found in papers by Shu [6, 7] and others [8].

Since the method uses collocation procedure, one discrete equation can be associated with one degree of freedom at a node. Therefore, a problem arises for differential equations possessing multiple boundary conditions. In this case the number of boundary conditions usually exceeds the number of degrees of freedom at boundary node. This problem has been undertaken in [9], where the Hermite interpolation with RBFs has been proposed to approximate the sought solution of a problem. It has introduced additional degrees of freedom at boundary nodes and therefore has allowed the multiple boundary conditions to be conveniently implemented. The numerical tests carried out till now [9, 10] indicate that the method is effective in eigenvalue problems, although the problem of ill-conditioned interpolation matrix following from the RBF interpolation is particularly important in this approach due to larger sized matrices.

In the present paper another approach that allows the multiple boundary conditions to be easily implemented is proposed. In this approach none of additional degrees of freedom are introduced, therefore, the size of the interpolation matrix is appropriately decreased. The proposed approach is compared with the above-mentioned one in the problem of free vibration analysis of thin plates. The layout of the paper is as follows: In section 2 the RBF-PS method as well as its extension based on the Hermite interpolation are briefly described and then the proposed approach is explained. In section 3 the method is applied to free vibration analysis of square plates as well as irregular shaped plates. Convergence and accuracy of these two approaches are compared as a result of numerical tests. On this base some conclusions are drawn in section 4.

2 RADIAL BASIS FUNCTION-BASED PSEUDOSPECTRAL METHOD

In the RBF-PS method the sought solution of a differential equation is approximated by a global interpolation function of the form

$$u(\mathbf{x}) = \sum_{j=1}^{N} \alpha_j \varphi\left(\left\|\mathbf{x} - \boldsymbol{\xi}_j\right\|\right) \tag{1}$$

In Eq. (1) α_j are the interpolation coefficients, $\varphi_j(\mathbf{x}) = \varphi\left(\left\|\mathbf{x} - \xi_j\right\|\right)$ are the RBFs, where ξ_j denote the special points called the centers. These special points coincide with the nodes imposed $\mathbf{x}_i$, $i = 1, \ldots, N$.

Using interpolation conditions

$$\sum_{j=1}^{N} \alpha_j \varphi\left(\left\|\mathbf{x}_i - \mathbf{x}_j\right\|\right) = u_i, \quad i = 1, ..., N \tag{2}$$

the interpolation coefficients can be expressed in terms of sought function values u_i at the nodes, what can be put in the matrix notation as

$$\boldsymbol{\alpha} = \boldsymbol{\Phi}^{-1}\mathbf{u} \tag{3}$$

where $\boldsymbol{\alpha} = \begin{bmatrix}\alpha_1 & \cdots & \alpha_N\end{bmatrix}^T$, $\mathbf{u} = \begin{bmatrix}u_1 & \cdots & u_N\end{bmatrix}^T$ and $\boldsymbol{\Phi}_{ij} = \varphi(\left\|\mathbf{x}_i - \mathbf{x}_j\right\|)$, $i, j = 1, ..., N$.

To obtain the approximation for derivatives contained in the governing equation, appropriate differential operator L has to be imposed on the interpolant (1) and obtained expression has to be evaluated at each interior node $\mathbf{x}_i^I, i = 1, ..., N^I$, what yields

$$\mathbf{u}_L = \boldsymbol{\Phi}_L \boldsymbol{\alpha} \tag{4}$$

where $\left(\mathbf{u}_L\right)_i = \left[Lu(\mathbf{x})\right]_{\mathbf{x}=\mathbf{x}_i^I}$, $i = 1, ..., N^I$, $\left(\boldsymbol{\Phi}_L\right)_{ij} = \left[L\varphi\left(\left\|\mathbf{x} - \boldsymbol{\xi}\right\|\right)\right]_{\substack{\xi=\mathbf{x}_j \\ \mathbf{x}=\mathbf{x}_i^I}}$, $i = 1, ..., N^I$, $j = 1, ..., N$.

In Eq. (4) L acts on the radial function treated as a function of $\mathbf{x}$ variable. Introducing Eq. (3) into Eq. (4) one can express derivative $\mathbf{u}_L$ in terms of the sought function values from all over domain as

$$\mathbf{u}_L = \boldsymbol{\Phi}_L \boldsymbol{\Phi}^{-1}\mathbf{u} \tag{5}$$

where $\boldsymbol{\Phi}_L \boldsymbol{\Phi}^{-1}$ is so-called the differentiation matrix.

Taking advantage of this approximation and using collocation procedure the governing equation can be discretized at each interior node. To impose boundary conditions, boundary equations should be collocated at boundary nodes $\mathbf{x}_i^B, i = 1, ..., N^B$ and possible derivatives contained in these equations are approximated similarly as in steps (4)-(5).

Since there is one degree of freedom at each node (the sought function value u_i) only one boundary condition can be easily imposed at each boundary node according to collocation technique. This fact makes it difficult to solved higher order equations that are characterized by multiple boundary conditions.

2.1 Hermite interpolation in RBF-PS

To extend the possibilities of the application of the RBF-PS method to higher order equations, one can modify the interpolant (1) introducing additional degrees of freedom at boundary nodes. This idea, known in the interpolation theory as Hermite interpolation, has been applied for the RBF-PS approach in [9]. For coherence of the present paper the main features of this approach are briefly presented below. Now, the global interpolation function has the form

$$u(\mathbf{x}) = \sum_{j=1}^{N^I} \alpha_j \varphi\left(\left\|\mathbf{x} - \boldsymbol{\xi}\right\|\right)\Big|_{\xi=\mathbf{x}_j^I} + \sum_{j=1}^{N^B} \beta_j \left[B_1^{\xi}\varphi\left(\left\|\mathbf{x} - \boldsymbol{\xi}\right\|\right)\right]_{\xi=\mathbf{x}_j^B} + \sum_{j=1}^{N^B} \gamma_j \left[B_2^{\xi}\varphi\left(\left\|\mathbf{x} - \boldsymbol{\xi}\right\|\right)\right]_{\xi=\mathbf{x}_j^B} \tag{6}$$

In Eq. (6), it is assumed that at each boundary node two degrees of freedom, represented by differential operators $B_1^{\boldsymbol{\xi}}$ and $B_2^{\boldsymbol{\xi}}$, are introduced. These differential operators correspond to those contained in boundary conditions and act on the radial function treated as a function of $\boldsymbol{\xi}$ variable. Remaining symbols used in Eq. (6) denote: N^I and N^B – numbers of interior nodes $\mathbf{x}^I$ and boundary nodes $\mathbf{x}^B$, respectively and α, β, γ – interpolation coefficients.

Enforcing interpolation conditions in the following form

$$\sum_{j=1}^{N^I}\alpha_j\varphi\left(\left\|\mathbf{x}_i^I-\boldsymbol{\xi}\right\|\right)\Big|_{\boldsymbol{\xi}=\mathbf{x}_j^I}+\sum_{j=1}^{N^B}\beta_j\left[B_1^{\boldsymbol{\xi}}\varphi\left(\left\|\mathbf{x}_i^I-\boldsymbol{\xi}\right\|\right)\right]_{\boldsymbol{\xi}=\mathbf{x}_j^B}+\sum_{j=1}^{N^B}\gamma_j\left[B_2^{\boldsymbol{\xi}}\varphi\left(\left\|\mathbf{x}_i^I-\boldsymbol{\xi}\right\|\right)\right]_{\boldsymbol{\xi}=\mathbf{x}_j^B}=u(\mathbf{x}_i^I),\quad i=1,\ldots,N^I \tag{7}$$

$$\sum_{j=1}^{N^I}\alpha_j\left[B_1^{\mathbf{x}}\varphi\left(\left\|\mathbf{x}-\boldsymbol{\xi}\right\|\right)\right]_{\substack{\boldsymbol{\xi}=\mathbf{x}_j^I\\ \mathbf{x}=\mathbf{x}_i^B}}+\sum_{j=1}^{N^B}\beta_j\left[B_1^{\mathbf{x}}\left[B_1^{\boldsymbol{\xi}}\varphi\left(\left\|\mathbf{x}-\boldsymbol{\xi}\right\|\right)\right]_{\boldsymbol{\xi}=\mathbf{x}_j^B}\right]_{\mathbf{x}=\mathbf{x}_i^B}+\sum_{j=1}^{N^B}\gamma_j\left[B_1^{\mathbf{x}}\left[B_2^{\boldsymbol{\xi}}\varphi\left(\left\|\mathbf{x}-\boldsymbol{\xi}\right\|\right)\right]_{\boldsymbol{\xi}=\mathbf{x}_j^B}\right]_{\mathbf{x}=\mathbf{x}_i^B}=\left[B_1^{\mathbf{x}}u(\mathbf{x})\right]_{\mathbf{x}=\mathbf{x}_i^B},\quad i=1,\ldots,N^B \tag{8}$$

$$\sum_{j=1}^{N^I}\alpha_j\left[B_2^{\mathbf{x}}\varphi\left(\left\|\mathbf{x}-\boldsymbol{\xi}\right\|\right)\right]_{\substack{\boldsymbol{\xi}=\mathbf{x}_j^I\\ \mathbf{x}=\mathbf{x}_i^B}}+\sum_{j=1}^{N^B}\beta_j\left[B_2^{\mathbf{x}}\left[B_1^{\boldsymbol{\xi}}\varphi\left(\left\|\mathbf{x}-\boldsymbol{\xi}\right\|\right)\right]_{\boldsymbol{\xi}=\mathbf{x}_j^B}\right]_{\mathbf{x}=\mathbf{x}_i^B}+\sum_{j=1}^{N^B}\gamma_j\left[B_2^{\mathbf{x}}\left[B_2^{\boldsymbol{\xi}}\varphi\left(\left\|\mathbf{x}-\boldsymbol{\xi}\right\|\right)\right]_{\boldsymbol{\xi}=\mathbf{x}_j^B}\right]_{\mathbf{x}=\mathbf{x}_i^B}=\left[B_2^{\mathbf{x}}u(\mathbf{x})\right]_{\mathbf{x}=\mathbf{x}_i^B},\quad i=1,\ldots,N^B \tag{9}$$

it is possible to express the interpolation coefficients in terms of the sought function values at interior nodes and differential operators evaluated at boundaries. In Eq. (8)-(9) $B_1^{\mathbf{x}}$ and $B_2^{\mathbf{x}}$ denote the same differential operators as $B_1^{\boldsymbol{\xi}}$ and $B_2^{\boldsymbol{\xi}}$, but acting on the radial function viewed as a function of $\mathbf{x}$ variable. It makes the coefficient matrix of the system (7)-(9) be a symmetric one.

Then, the differential operator from the governing equation is imposed on interpolant (6) and evaluated at each interior node, what yields

$$\left[L^{\mathbf{x}}u(\mathbf{x})\right]_{\mathbf{x}=\mathbf{x}_i^I}=\sum_{j=1}^{N^I}\alpha_j\left[L^{\mathbf{x}}\varphi\left(\left\|\mathbf{x}-\boldsymbol{\xi}\right\|\right)\right]_{\substack{\boldsymbol{\xi}=\mathbf{x}_j^I\\ \mathbf{x}=\mathbf{x}_i^I}}+\sum_{j=1}^{N^B}\beta_j\left[L^{\mathbf{x}}\left[B_1^{\boldsymbol{\xi}}\varphi\left(\left\|\mathbf{x}-\boldsymbol{\xi}\right\|\right)\right]_{\boldsymbol{\xi}=\mathbf{x}_j^B}\right]_{\mathbf{x}=\mathbf{x}_i^I}+\sum_{j=1}^{N^B}\gamma_j\left[L^{\mathbf{x}}\left[B_2^{\boldsymbol{\xi}}\varphi\left(\left\|\mathbf{x}-\boldsymbol{\xi}\right\|\right)\right]_{\boldsymbol{\xi}=\mathbf{x}_j^B}\right]_{\mathbf{x}=\mathbf{x}_i^I},\quad i=1,\ldots,N^I \tag{10}$$

Introducing the interpolation coefficients determined from Eqs. (7)-(9) into Eq. (10), one can express the derivatives contained in the governing equation $\left[L^{\mathbf{x}}u(\mathbf{x})\right]_{\mathbf{x}=\mathbf{x}_i^I}$ in terms of the sought function values at interior nodes as well as in terms of the derivatives contained in boundary conditions, evaluated at boundary nodes $\left[B_1^{\mathbf{x}}u(\mathbf{x})\right]_{\mathbf{x}=\mathbf{x}_i^B}$, $\left[B_2^{\mathbf{x}}u(\mathbf{x})\right]_{\mathbf{x}=\mathbf{x}_i^B}$. It can be put in matrix notation as

$$\mathbf{u}_{L^{\mathbf{x}}}=\bar{\boldsymbol{\Phi}}_L\cdot\bar{\boldsymbol{\Phi}}^{-1}\cdot\bar{\mathbf{u}} \tag{11}$$

In Eq. (11) $\bar{\mathbf{\Phi}}_L \cdot \bar{\mathbf{\Phi}}^{-1}$ can be found as a generalization of the differentiation matrix, where

$$\bar{\mathbf{\Phi}}_L = \begin{bmatrix} \mathbf{\Phi}_{L^{\mathbf{x}}} & \mathbf{\Phi}_{L^{\mathbf{x}}B_1^{\xi}} & \mathbf{\Phi}_{L^{\mathbf{x}}B_2^{\xi}} \end{bmatrix}, \quad \bar{\mathbf{\Phi}} = \begin{bmatrix} \mathbf{\Phi} & \mathbf{\Phi}_{B_1^{\xi}} & \mathbf{\Phi}_{B_2^{\xi}} \\ & \mathbf{\Phi}_{B_1^{\mathbf{x}}B_1^{\xi}} & \mathbf{\Phi}_{B_1^{\mathbf{x}}B_2^{\xi}} \\ sym & & \mathbf{\Phi}_{B_2^{\mathbf{x}}B_2^{\xi}} \end{bmatrix} \text{ and } \bar{\mathbf{u}} = \begin{bmatrix} \mathbf{u} \\ \mathbf{u}_{B_1^{\mathbf{x}}} \\ \mathbf{u}_{B_2^{\mathbf{x}}} \end{bmatrix}$$

In the above expressions the block matrices have following forms

$$\left(\mathbf{\Phi}_{L^{\mathbf{x}}}\right)_{ij} = \left[L^{\mathbf{x}}\varphi\left(\left\|\mathbf{x}-\boldsymbol{\xi}\right\|\right)\right]_{\substack{\boldsymbol{\xi}=\mathbf{x}_j^I \\ \mathbf{x}=\mathbf{x}_j^I}}, \quad i,j=1,...,N^I$$

$$\left(\mathbf{\Phi}_{L^{\mathbf{x}}B_1^{\xi}}\right)_{ij} = \left[L^{\mathbf{x}}\left[B_1^{\xi}\varphi\left(\left\|\mathbf{x}-\boldsymbol{\xi}\right\|\right)\right]_{\boldsymbol{\xi}=\mathbf{x}_j^B}\right]_{\mathbf{x}=\mathbf{x}_i^I}, \quad i=1,...,N^I, j=1,...,N^B$$

$$\left(\mathbf{\Phi}_{L^{\mathbf{x}}B_2^{\xi}}\right)_{ij} = \left[L^{\mathbf{x}}\left[B_2^{\xi}\varphi\left(\left\|\mathbf{x}-\boldsymbol{\xi}\right\|\right)\right]_{\boldsymbol{\xi}=\mathbf{x}_j^B}\right]_{\mathbf{x}=\mathbf{x}_i^I}, \quad i=1,...,N^I, j=1,...,N^B$$

$$\mathbf{\Phi}_{ij} = \varphi\left(\left\|\mathbf{x}_i^I-\boldsymbol{\xi}\right\|\right)\Big|_{\boldsymbol{\xi}=\mathbf{x}_j^I}, \quad i,j=1,...,N^I$$

$$\left(\mathbf{\Phi}_{B_1^{\xi}}\right)_{ij} = \left[B_1^{\xi}\varphi\left(\left\|\mathbf{x}_i^I-\boldsymbol{\xi}\right\|\right)\right]_{\boldsymbol{\xi}=\mathbf{x}_j^B}, \quad i=1,...,N^I, j=1,...,N^B$$

$$\left(\mathbf{\Phi}_{B_2^{\xi}}\right)_{ij} = \left[B_2^{\xi}\varphi\left(\left\|\mathbf{x}_i^I-\boldsymbol{\xi}\right\|\right)\right]_{\boldsymbol{\xi}=\mathbf{x}_j^B}, \quad i=1,...,N^I, j=1,...,N^B$$

$$\left(\mathbf{\Phi}_{B_1^{\mathbf{x}}B_1^{\xi}}\right)_{ij} = \left[B_1^{\mathbf{x}}\left[B_1^{\xi}\varphi\left(\left\|\mathbf{x}-\boldsymbol{\xi}\right\|\right)\right]_{\boldsymbol{\xi}=\mathbf{x}_j^B}\right]_{\mathbf{x}=\mathbf{x}_i^B}, \quad i,j=1,...,N^B$$

$$\left(\mathbf{\Phi}_{B_1^{\mathbf{x}}B_2^{\xi}}\right)_{ij} = \left[B_1^{\mathbf{x}}\left[B_2^{\xi}\varphi\left(\left\|\mathbf{x}-\boldsymbol{\xi}\right\|\right)\right]_{\boldsymbol{\xi}=\mathbf{x}_j^B}\right]_{\mathbf{x}=\mathbf{x}_i^B}, \quad i,j=1,...,N^B$$

$$\left(\mathbf{\Phi}_{B_2^{\mathbf{x}}B_2^{\xi}}\right)_{ij} = \left[B_2^{\mathbf{x}}\left[B_2^{\xi}\varphi\left(\left\|\mathbf{x}-\boldsymbol{\xi}\right\|\right)\right]_{\boldsymbol{\xi}=\mathbf{x}_j^B}\right]_{\mathbf{x}=\mathbf{x}_i^B}, \quad i,j=1,...,N^B$$

$$\mathbf{u} = u(\mathbf{x}_i^I), \ \left(\mathbf{u}_{B_1^{\mathbf{x}}}\right)_i = \left[B_1^{\mathbf{x}}u(\mathbf{x})\right]_{\mathbf{x}=\mathbf{x}_i^B}, \ \left(\mathbf{u}_{B_2^{\mathbf{x}}}\right)_i = \left[B_2^{\mathbf{x}}u(\mathbf{x})\right]_{\mathbf{x}=\mathbf{x}_i^B}, i=1,...N^B$$

In the similar manner any number of boundary conditions can be involved during discretization of a differential operator from a governing equation. The boundary conditions are not discretized separately, what is another advantage of the approach.

2.2 Simplified implementation of boundary conditions in RBF-PS

The approach presented in section 2.1 introduces additional degrees of freedom at the boundary. The size of the interpolation matrix $\bar{\mathbf{\Phi}}$ from Eq. (11) is then increased comparing to matrix $\mathbf{\Phi}$ from direct approach (Eq. (3)). It is well-known that the size of the interpolation matrix is one of factors that influence conditioning of the problem in the case of the RBF interpolation. To maintain the same number of degrees of freedom as in the conventional RBF-PS method and its simplicity, in the present section another approach is proposed.

In this approach, the boundary nodes are split into appropriate number of groups. This number corresponds to the number of boundary conditions. The nodes are chosen by turns to

appropriate group. Each boundary condition is implemented at nodes from another group, what is shown in Fig. 1 in the case of two boundary conditions.

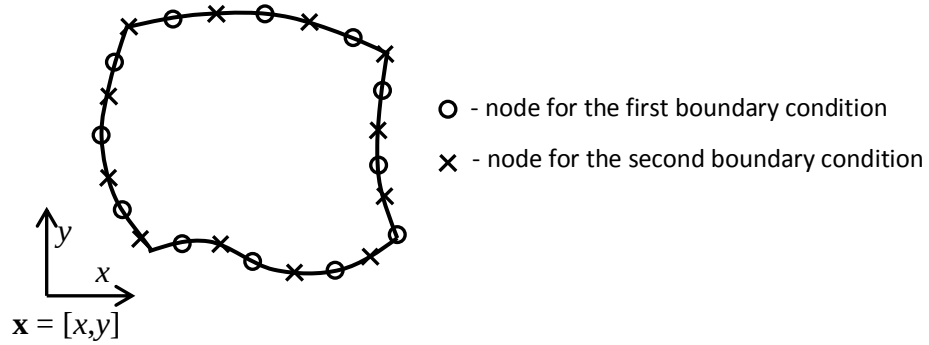


Figure 1: Implementation of boundary conditions.

To derive the differentiation matrix one can modify interpolant (6) in the following way

$$u(\mathbf{x}) = \sum_{j=1}^{N^I} \alpha_j \varphi\left(\left\|\mathbf{x}-\boldsymbol{\xi}\right\|\right)\Big|_{\xi=\mathbf{x}_j^I} + \sum_{j=1}^{N^{B_1}} \beta_j \left[B_1^{\xi}\varphi\left(\left\|\mathbf{x}-\boldsymbol{\xi}\right\|\right)\right]_{\xi=\mathbf{x}_j^{B_1}} + \sum_{j=1}^{N^{B_2}} \gamma_j \left[B_2^{\xi}\varphi\left(\left\|\mathbf{x}-\boldsymbol{\xi}\right\|\right)\right]_{\xi=\mathbf{x}_j^{B_2}} \qquad (12)$$

where N^{B_1} and N^{B_2} denote the numbers of boundary nodes for the groups of nodes $\mathbf{x}^{B_1}$ and $\mathbf{x}^{B_2}$ associated with the first and the second boundary condition, respectively. Note, that $N^{B_1} + N^{B_2} = N^B$ is the number of all nodes imposed on boundaries of the domain.
Then, one should enforce interpolation conditions for interpolant (12), similarly as in Eqs. (7)-(9), but using appropriate group of boundary nodes to evaluate boundary conditions. Finally, differential operator from governing equation has to be imposed on the interpolation function as in Eq. (10) and the differentiation matrix, as in Eq. (11), can be derived. Now, this matrix has similar structure as in section 2.1 but the block matrices connected with boundary conditions are evaluated using different nodes. All of the block matrices, used in the present approach, have the form

$$\left(\boldsymbol{\Phi}_{L^{\mathbf{x}}}\right)_{ij} = \left[L^{\mathbf{x}}\varphi\left(\left\|\mathbf{x}-\boldsymbol{\xi}\right\|\right)\right]_{\substack{\xi=\mathbf{x}_j^I \\ \mathbf{x}=\mathbf{x}_j^I}}, \quad i,j=1,\ldots,N^I$$

$$\left(\boldsymbol{\Phi}_{L^{\mathbf{x}}B_1^{\xi}}\right)_{ij} = \left[L^{\mathbf{x}}\left[B_1^{\xi}\varphi\left(\left\|\mathbf{x}-\boldsymbol{\xi}\right\|\right)\right]_{\xi=\mathbf{x}_j^{B_1}}\right]_{\mathbf{x}=\mathbf{x}_i^I}, \quad i=1,\ldots,N^I,\ j=1,\ldots,N^{B_1}$$

$$\left(\boldsymbol{\Phi}_{L^{\mathbf{x}}B_2^{\xi}}\right)_{ij} = \left[L^{\mathbf{x}}\left[B_2^{\xi}\varphi\left(\left\|\mathbf{x}-\boldsymbol{\xi}\right\|\right)\right]_{\xi=\mathbf{x}_j^{B_2}}\right]_{\mathbf{x}=\mathbf{x}_i^I}, \quad i=1,\ldots,N^I,\ j=1,\ldots,N^{B_2}$$

$$\boldsymbol{\Phi}_{ij} = \varphi\left(\left\|\mathbf{x}_i^I-\boldsymbol{\xi}\right\|\right)\Big|_{\xi=\mathbf{x}_j^I}, \quad i,j=1,\ldots,N^I$$

$$\left(\boldsymbol{\Phi}_{B_1^{\xi}}\right)_{ij} = \left[B_1^{\xi}\varphi\left(\left\|\mathbf{x}_i^I-\boldsymbol{\xi}\right\|\right)\right]_{\xi=\mathbf{x}_j^{B_1}}, \quad i=1,\ldots,N^I,\ j=1,\ldots,N^{B_1}$$

$$\left(\boldsymbol{\Phi}_{B_2^{\xi}}\right)_{ij} = \left[B_2^{\xi}\varphi\left(\left\|\mathbf{x}_i^I-\boldsymbol{\xi}\right\|\right)\right]_{\xi=\mathbf{x}_j^{B_2}}, \quad i=1,\ldots,N^I,\ j=1,\ldots,N^{B_2}$$

$$\left(\boldsymbol{\Phi}_{B_1^{\mathbf{x}}B_1^{\xi}}\right)_{ij} = \left[B_1^{\mathbf{x}}\left[B_1^{\xi}\varphi\left(\left\|\mathbf{x}-\boldsymbol{\xi}\right\|\right)\right]_{\xi=\mathbf{x}_j^{B_1}}\right]_{\mathbf{x}=\mathbf{x}_i^{B_1}}, \quad i,j=1,\ldots,N^{B_1}$$

$$\left(\boldsymbol{\Phi}_{B_1^{\mathbf{x}}B_2^{\xi}}\right)_{ij} = \left[B_1^{\mathbf{x}}\left[B_2^{\xi}\varphi\left(\left\|\mathbf{x}-\boldsymbol{\xi}\right\|\right)\right]_{\xi=\mathbf{x}_j^{B_2}}\right]_{\mathbf{x}=\mathbf{x}_i^{B_1}}, \quad i=1,\ldots,N^{B_1},\ j=1,\ldots,N^{B_2}$$

$$\left(\mathbf{\Phi}_{B_2^{\mathbf{x}}B_2^{\xi}}\right)_{ij} = \left[B_2^{\mathbf{x}}\left[B_2^{\xi}\varphi\left(\left\|\mathbf{x}-\xi\right\|\right)\right]_{\xi=\mathbf{x}_j^{B_2}}\right]_{\mathbf{x}=\mathbf{x}_i^{B_2}}, \quad i,j=1,...,N^{B_2}$$

$$\mathbf{u} = u(\mathbf{x}_i^I),\ \left(\mathbf{u}_{B_1^{\mathbf{x}}}\right)_i = \left[B_1^{\mathbf{x}}u(\mathbf{x})\right]_{\mathbf{x}=\mathbf{x}_i^{B_1}}, i=1,...N^{B_1},\ \left(\mathbf{u}_{B_2^{\mathbf{x}}}\right)_i = \left[B_2^{\mathbf{x}}u(\mathbf{x})\right]_{\mathbf{x}=\mathbf{x}_i^{B_2}}, i=1,...N^{B_2}$$

By splitting boundary nodes into appropriate number of groups it is possible to implement any number of boundary conditions using presented approach.

3 APPLICATION OF RBF-PS TO VIBRATION ANALYSIS OF PLATES

To assess the usefulness of presented approaches for a dynamic problem described by higher order equation, they have been applied to free vibration analysis of quadrilateral, thin, isotropic plates of various shapes. The governing equation for this problem is as follows

$$\frac{\partial^4 w}{\partial x^4} + 2\frac{\partial^4 w}{\partial x^2\,\partial y^2} + \frac{\partial^4 w}{\partial y^4} = \Omega^2 w \tag{13}$$

where w denotes the mode of vibration and Ω is the free vibration parameter related to free vibration frequency ω by the formula: $\Omega = \omega a^2\sqrt{\rho h/D}$ (ρ – density of the plate material, D – plate stiffness, h – plate thickness, a – characteristic plate dimension).

Taking into account the quadrilateral plate, where two boundary conditions are applied at kth edge of this plate, the interpolant for displacement function w, in the view of the Hermite RBF-PS method (section 2.1), should be written as

$$w(\mathbf{x}) = \sum_{j=1}^{N^I}\alpha_j\varphi\left(\left\|\mathbf{x}-\xi\right\|\right)_{|\xi=\mathbf{x}_j^I} + \sum_{k=1}^{4}\left[\sum_{j=1}^{N_k^B}\beta_{kj}\left[B_{k1}^{\xi}\varphi\left(\left\|\mathbf{x}-\xi\right\|\right)\right]_{\xi=\mathbf{x}_j^{Bk}} + \sum_{j=1}^{N_k^B}\gamma_{kj}\left[B_{k2}^{\xi}\varphi\left(\left\|\mathbf{x}-\xi\right\|\right)\right]_{\xi=\mathbf{x}_j^{Bk}}\right] \tag{14}$$

By slight modification of Eq. (14) one can obtain the interpolant used in the approach described in section 2.2

$$w(\mathbf{x}) = \sum_{j=1}^{N^I}\alpha_j\varphi\left(\left\|\mathbf{x}-\xi\right\|\right)_{|\xi=\mathbf{x}_j^I} + \sum_{k=1}^{4}\left[\sum_{j=1}^{N_k^{B_1}}\beta_{kj}\left[B_{k1}^{\xi}\varphi\left(\left\|\mathbf{x}-\xi\right\|\right)\right]_{\xi=\mathbf{x}_j^{Bk1}} + \sum_{j=1}^{N_k^{B_2}}\gamma_{kj}\left[B_{k2}^{\xi}\varphi\left(\left\|\mathbf{x}-\xi\right\|\right)\right]_{\xi=\mathbf{x}_j^{Bk2}}\right] \tag{15}$$

In the present paper, the plates with combination of simply supported, clamped and free boundary conditions are considered. The general description of these boundary conditions for the kth edge in terms of differential operators contained in Eq. (14) and (15) can be written as

$$B_{k1}^{\mathbf{x}}w = 0,\ B_{k2}^{\mathbf{x}}w = 0 \tag{16}$$

where

$$\begin{aligned} B_{k1}^{\mathbf{x}} &= 1 \\ B_{k2}^{\mathbf{x}} &= \left(\cos^2(\theta)+\nu\sin^2(\theta)\right)\frac{\partial^2}{\partial x^2} + \left(\sin^2(\theta)+\nu\cos^2(\theta)\right)\frac{\partial^2}{\partial y^2} + 2(1-\nu)\cos(\theta)\sin(\theta)\frac{\partial^2}{\partial x\,\partial y} \end{aligned} \tag{17}$$

for the simply supported edge (S)

$$B_{k1}^{\mathbf{x}} = 1$$
$$B_{k2}^{\mathbf{x}} = \cos(\theta)\frac{\partial}{\partial x} + \sin(\theta)\frac{\partial}{\partial y} \tag{18}$$

for the clamped edge (C) and

$$B_{k1}^{\mathbf{x}} = \left(\cos^2(\theta) + \nu\sin^2(\theta)\right)\frac{\partial^2}{\partial x^2} + \left(\sin^2(\theta) + \nu\cos^2(\theta)\right)\frac{\partial^2}{\partial y^2} + 2(1-\nu)\cos(\theta)\sin(\theta)\frac{\partial^2}{\partial x\,\partial y}$$
$$B_{k2}^{\mathbf{x}} = \sin(\theta)(1-\cos^2(\theta)(\nu-1))\frac{\partial^3}{\partial y^3} + \cos(\theta)(-2\cos^2(\theta)(\nu-1) + \sin^2(\theta)(\nu-1) + \nu)\frac{\partial^3}{\partial y^2\partial x} \tag{19}$$
$$+ \sin(\theta)(\cos^2(\nu-1) - 2\sin^2(\theta)(\nu-1) + \nu)\frac{\partial^3}{\partial x^2\partial y} + \cos(\theta)\left(1-\sin^2(\theta)(\nu-1)\right)\frac{\partial^3}{\partial x^3}$$

for the free edge (F).

In Eqs. (17)-(19) θ is the angle between the normal to the plate boundary and the *x*-axis, ν is the Poisson's ratio.

With interpolants (14) and (15), appropriate differentiation matrices for biharmonic operator contained in Eq. (13) have been determined. Then, Eq. (13) has been transformed into the algebraic eigenvalue problem of the form

$$\mathbf{A}\mathbf{w} = \Omega^2\mathbf{w} \tag{20}$$

where **A** is the differentiation matrix modified by deleting the columns associated with degrees of freedom at boundary nodes and **w** denotes the vector containing function values at interior nodes.

3.1 Numerical results

As a benchmark problem, the square plate has been considered. Uniform grid node distribution as well as irregular one has been assumed. The obtained results, in the form of convergence tests for non-dimensional free vibration frequency Ω and number of nodes used *N*, are presented in Figs. 2-5.

The results from Figs. 2-5 indicate that the approaches preserve a proper convergence trend. Increasing the number of nodes makes the results more accurate, regardless of the assumed node distribution (uniform or irregular). In the view of these results one can conclude that the method based on the Hermite interpolation (section 2.1) gives faster convergence than the RBF-PS approach from section 2.2, in the case of irregular node distribution. In the case of the uniform node distribution the results are comparable. Note that the use of the Hermite interpolation increases the number of degrees of freedom, while the number of nodes *N* remains the same, what can explain faster convergence.

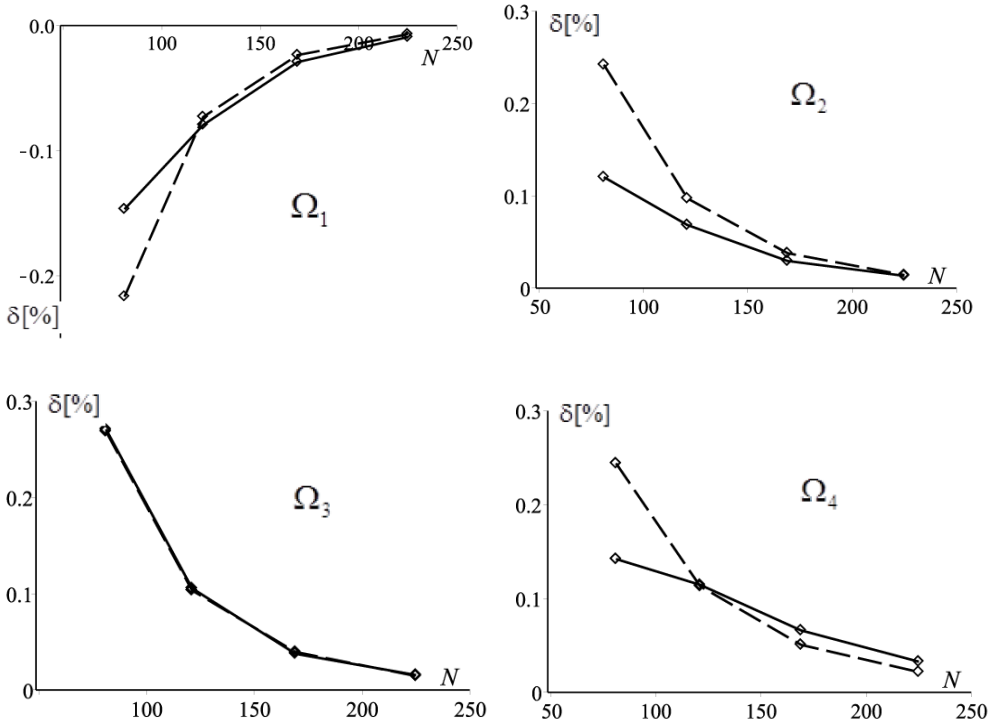


Figure 2: Results for the square SSSS plate obtained with uniform grid. Dash line – the method from section 2.1, solid line - the method from section 2.2.

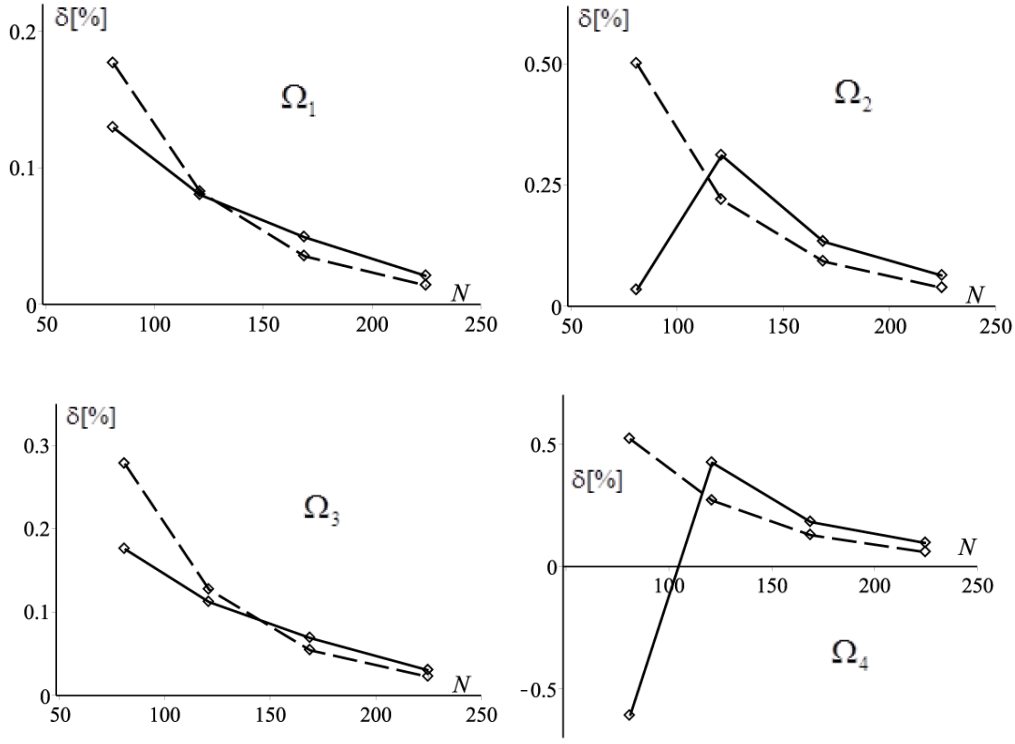


Figure 3: Results for the square SCSC plate obtained with uniform grid. Dash line – the method from section 2.1, solid line - the method from section 2.2.

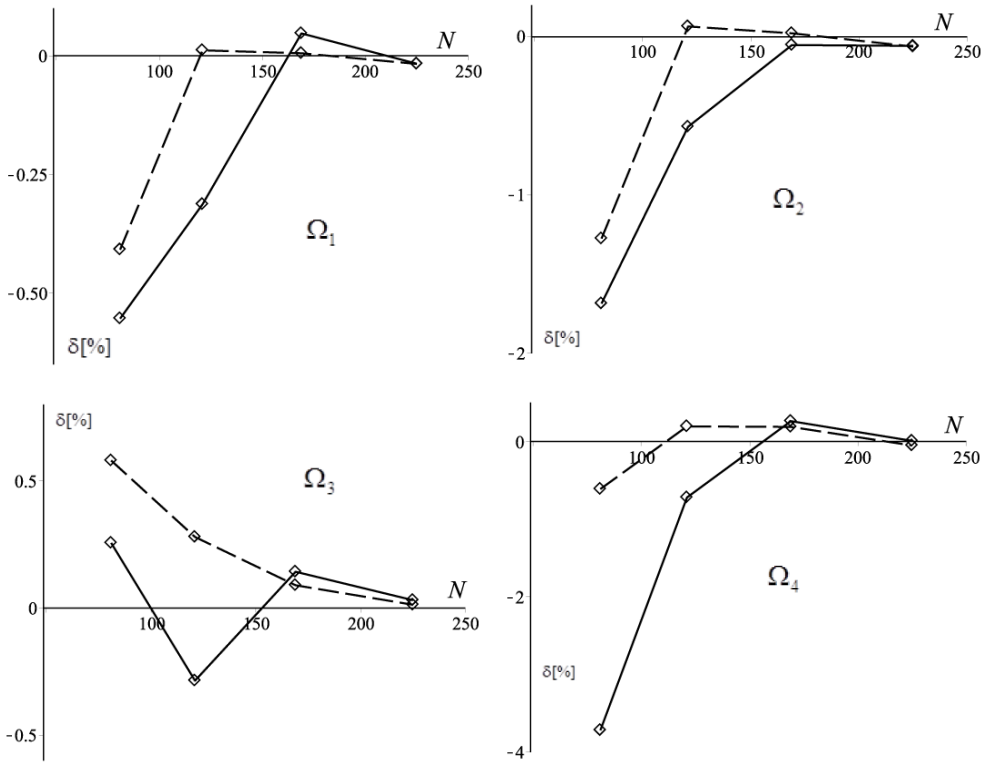


Figure 4: Results for the square CCCC plate obtained with irregular grid. Dash line – the method from section 2.1, solid line - the method from section 2.2.

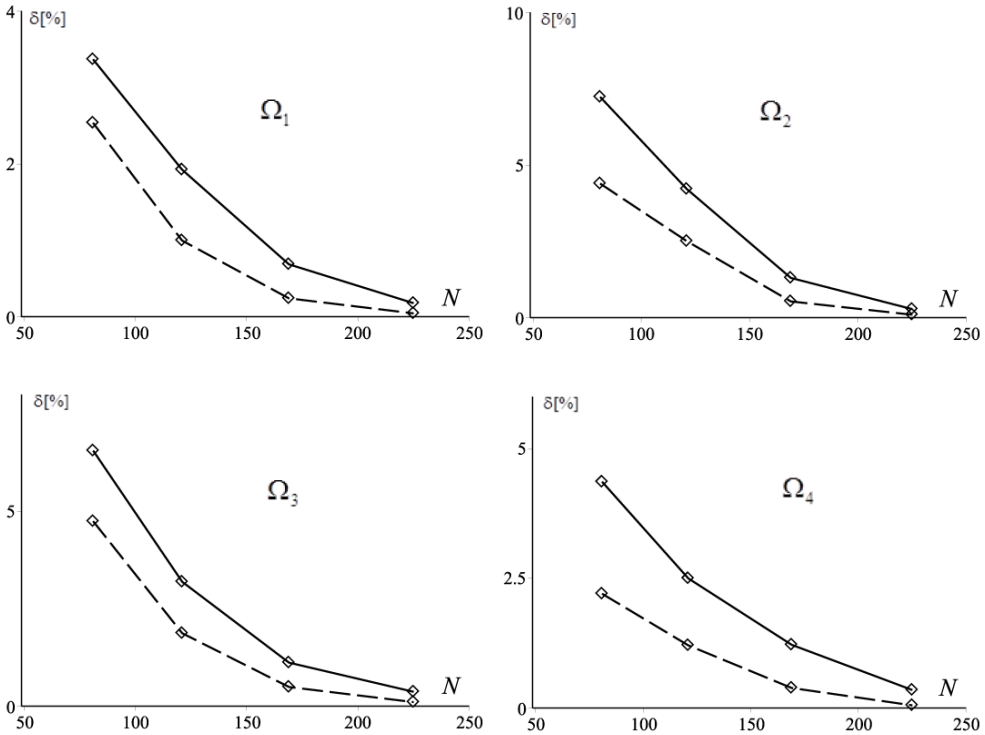


Figure 5: Results for the square SFSF plate obtained with irregular grid. Dash line – the method from section 2.1, solid line - the method from section 2.2.

Similar computation has been carried out for the irregular shaped plate presented in Fig. 6. The obtained results are shown in Tab. 1 and Tab. 2.

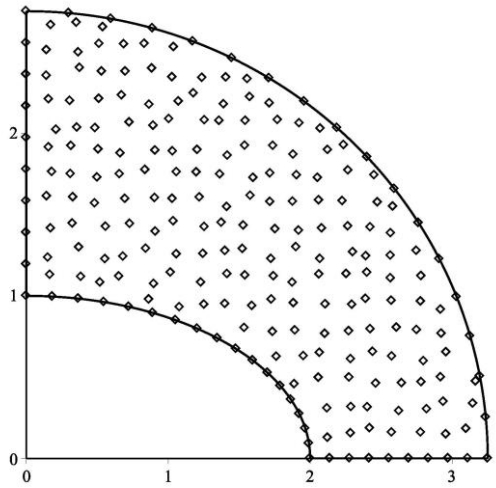


Figure 6: Quarter section of the elliptical plate with an example of the node distribution.

It should be noted that in this computation, besides the different numbers of interior nodes, two types of boundary grid patterns have been assumed. The latter differ from each other by the density of nodes imposed on boundaries.

It has been found that the method based on the Hermite interpolation provides accurate results regardless of the density of boundary nodes, while the RBF-PS approach from section 2.2 gives accurate results with the pattern possessing dense enough boundary node distribution (Tab. 2).

	Ω_1	Ω_2	Ω_3	Ω_4	Ω_5
SSSS					
N =233, N^I = 181	4.800	7.520	11.424	16.032	16.614
N =374, N^I = 322	4.832	7.586	11.500	16.020	16.701
Reference results	4.894	7.598	11.436	16.086	16.635
CCCC					
N =233, N^I = 181	9.286	12.746	16.709	21.206	23.890
N =374, N^I = 322	9.617	12.833	17.194	22.604	24.099
Reference results	9.595	12.717	16.743	22.275	24.068
SCSC					
N =233, N^I = 181	9.138	12.068	15.158	19.675	23.490
N =374, N^I = 322	9.134	11.958	15.428	19.767	23.303
Reference results	9.142	12.003	15.321	19.920	23.493

Table 1: Results for the quarter section of the elliptical plate obtained by the Hermite RBF-PS approach.

	Ω_1	Ω_2	Ω_3	Ω_4	Ω_5
SSSS					
N =245, N^I = 181	4.815	7.559	11.359	15.987	16.618
N =386, N^I = 322	4.815	7.519	11.471	16.014	16.679
Reference results	4.894	7.598	11.436	16.086	16.635
CCCC					
N =245, N^I = 181	9.654	12.210	16.729	20.426	24.023
N =386, N^I = 322	9.601	12.718	16.715	22.098	23.928
Reference results	9.595	12.717	16.743	22.275	24.068
SCSC					
N =245, N^I = 181	9.238	11.608	15.294	18.372	23.549
N =386, N^I = 322	9.134	12.062	15.468	19.831	23.432
Reference results	9.142	12.003	15.321	19.920	23.493

Table 2: Results for the quarter section of the elliptical plate obtained by the RBF-PS approach from section 2.2.

In all computations, the multiquadric RBFs have been used with the so-called shape parameter assumed as 0.7. The reference results contained in Tab. 1 and 2 have been obtained with the use of differential quadrature method with domain transformation. The details of this method can be found in [11].

4 CONCLUSION

In the paper two approaches for the implementation of multiple boundary conditions in the RBF-PS method have been presented and examined on the example of the free vibration analysis of plates. The main advantage of this method is its meshless character that allows easily to apply it for problems with irregular domains. The presented approaches can be successfully used for various types of boundary conditions encountered in plate analysis. The method based on the Hermite interpolation seems to be more versatile and works correctly regardless of the boundary node distribution, while the RBF-PS approach described in section 2.2 needs to have dense enough boundary grid to provide acceptable results.

REFERENCES

[1] T. Belytschko, Y. Krongauz, D. Organ, M. Flrming, P. Krysl, Meshless methods: an overview and recent developments. *Computer Methods in Applied Mechanics and Engineering*, **139**, 3-47, 1996.

[2] G.R. Liu, *Meshlees Methods – Moving beyond the Finite Element Method*. CRC Press, 2003.

[3] G.E. Fasshauer, *Meshfree Approximation Methods with Matlab*. World Scientific Publishing, 2007.

[4] A.J.M Ferreira, G.E. Fasshauer, Computation of natural frequencies of shear deformable beams and plates by an RBF-pseudospectral method. *Computer Methods in Applied Mechanics and Engineering*, **196**, 134-146, 2006.

[5] A.J.M Ferreira, G.E. Fasshauer, Analysis of natural frequencies of composite plates by an RBF-pseudospectral method. *Composite Structures*, **79**, 202-210, 2007.

[6] C. Shu, H. Ding, K.S. Yeo, Solution of partial differential equations by a global radial basis function-based differential quadrature method. *Engineering Analysis with Boundary Elements*, **28**, 1217-1226, 2004.

[7] C. Shu, H. Ding, K.S. Yeo, Local radial basis function-based differential quadrature method and its application to solve two-dimensional incompressible Navier-Stokes equations, *Computer Methods in Applied Mechanics and Engineering*. **192**, 941-954, 2003.

[8] M.R. Hashemi, F. Hatam, Unsteady seepage analysis using local radial basis function-based differential quadrature method. *Applied Mathematical Modelling*, **35**, 4934-4950, 2011.

[9] A. Krowiak, Hermite type radial basis function-based differential quadrature method for higher order equations. *Applied Mathematical Modelling*, submitted for publication.

[10] A. Krowiak, Free vibration of structures by radial basis function – Pseudospectral method. *Vibrations in Physical Systems*, **26**, 113-120, 2014.

[11] A. Krowiak, Vibration analysis of irregularly shaped plates by the spline-based differential quadrature method. *Vibrations in Physical Systems*, **25**, 241-246, 2012.

COMPDYN 2015
5th ECCOMAS Thematic Conference on
Computational Methods in Structural Dynamics and Earthquake Engineering
M. Papadrakakis, V. Papadopoulos, V. Plevris (eds.)
Crete Island, Greece, 25–27 May 2015

MODELLING OF THE VIBRO-ACOUSTIC TRANSMISSION ON MULTI-PLATE PERFORATED PANELS USING TWO-SCALE HOMOGENIZATION

Eduard Rohan[1] **and Vladimír Lukeš**[2]

[1]Department of Mechanics, Faculty of Applied Sciences,
University of West Bohemia,
Univerzitní 22, 30614 Plzeň, Czech Republic
e-mail: rohan@kme.zcu.cz

[2]European Centre of Excellence, NTIS New Technologies for Information Society, Faculty of Applied Sciences,
University of West Bohemia,
Univerzitní 22, 30614 Plzeň, Czech Republic
e-mail: vlukes@kme.zcu.cz

Keywords: Acoustic Transmission, Multi-plate Panel, Reissner-Mindlin Plate, Homogenization

Abstract. *We consider problems of the acoustic wave propagation through panels consisting of several vibrating periodically perforated Reissner-Mindlin plates. The proposed model of the wave transmission through a layer involving the acoustic fluid and the panel is derived using the homogenization method. This provides homogenized transmission conditions which are prescribed on a flat interface representing the panel, so that the computational complexity of the vibroacoustic problem is reduced, although the geometrical arrangement of pores in the panel is respected in a detail. For a suitable mutual arrangement of holes in two, or more parallel plates there is a coupling between transverse and surface acoustic waves propagating along the panel.*

1 INTRODUCTION

The paper deals with modelling the acoustic wave propagation through vibrating perforated panels composed of several plates. Usually the models of acoustic impedance are based on semi-empirical formulae which are tuned by experiments, see e.g. [11]. Therefore, it is desirable to develop a computationally tractable model which takes into account the perforation geometry in a rigorous way. In this work we present a reduced model of the vibroacoustic transmission which is based on the two-scale homogenization [2]. For this we extend the approach developed in [6], where homogenization of rigid plates was pursued to derive effective nonlocal transmission conditions. A model of the single-plate perforated compliant panel was considered in [10] in the context the optimal perforation design problem. Using a slightly different modelling ansatz related to the plate thickness scaling, we derive a homogenized model of the acoustic transmission through a layer in which two periodically perforated elastic plates of the Reissner-Mindlin type are situated. This construction of the panel with different perforations of the two plates admits special acoustic transmission effects due to coupling the transverse and surface acoustic waves propagating along the panel.

The paper is organized, as follows. In Section 1.1 the global problem is defined which governs the wave propagation in the fluid part and in the solid part. The final form of the reduced global problem is announced in Section 1.2. In Section 2 we introduce the transmission layer containing the perforated plates and define the problem which is subject of the asymptotic analysis with respect to the layer thickness and size of the perforation. The homogenized transmission conditions are reported in Section 3. In Section 4 we illustrate the influence of some geometrical parameters of the coefficients involved in the transmission conditions.

1.1 The global problem – acoustics in perforated domain

We consider open bounded domain Ω^G which contains the compliant periodically perforated panel represented by domain Σ_ε. By ε we denote a small parameter which corresponds to the thickness of the panel and to the characteristic period of the perforation. Therefore, the labelling by superscript $^\varepsilon$ is used to indicate the dependence on size of the perforations. The problem of the acoustic harmonic wave propagation is imposed in domain Ω^G involving the solid part Σ_ε and the acoustic fluid occupying domain $\Omega^{*\varepsilon} = \Omega^G \setminus \Sigma_\varepsilon$, whereby the vibroacoustic transmission is prescribed on interface $\Gamma^\varepsilon = \partial\Sigma_\varepsilon \cap \partial\Omega^{*\varepsilon}$. The acoustic potential p^ε and the displacement field $\boldsymbol{u}^\varepsilon$ satisfy

$$
\begin{aligned}
c^2\nabla^2 p^\varepsilon + \omega^2 p^\varepsilon &= 0 \quad \text{in } \Omega^{*\varepsilon}\ , \\
\nabla\cdot\boldsymbol{\sigma}^\varepsilon(\boldsymbol{u}^\varepsilon) &= 0 \quad \text{in } \Sigma^\varepsilon\ , \\
\left.\begin{aligned}
\boldsymbol{n}\cdot\boldsymbol{\sigma}^\varepsilon(\boldsymbol{u}^\varepsilon) &= \mathrm{i}\omega\rho_0 p^\varepsilon \boldsymbol{n}\ , \\
\boldsymbol{n}\cdot\nabla p^\varepsilon &= -\mathrm{i}\omega \boldsymbol{n}\cdot\boldsymbol{u}^\varepsilon\ ,
\end{aligned}\right\} &\quad \text{on } \Gamma^\varepsilon\ , \\
\boldsymbol{u} &= 0 \quad \text{on } \partial\Sigma^\varepsilon \setminus \Gamma^\varepsilon\ , \\
\text{boundary conditions} &\quad \text{on } \partial\Omega^G\ ,
\end{aligned}
\tag{1}
$$

where ω is the wave frequency, c is the speed of sound propagation, $\boldsymbol{\sigma}(\boldsymbol{u}) = \mathbb{D}\nabla^S\boldsymbol{u}$ is the stress tensor related to the strain $\nabla^S\boldsymbol{u}$ by the (3D) elasticity tensor $\mathbb{D}$, and $\boldsymbol{n}$ is the normal vector.

The solid elastic body Σ^ε is constituted by elastic plates Σ^ε_K, thus $\Sigma^\varepsilon = \bigcup_K \Sigma^\varepsilon_K$. Behaviour of each elastic plate Σ^ε_K is described using the Reissner-Mindlin (R-M) plate model whereby the generalized loads are derived by taking into account the specific perforation geometry and the loading by the acoustic field; to derive them, the R-M plate kinematic constraints of deformation

are considered.

For each plate $K = I, II$ represented by the perforated mid-plane, i.e. by the domain $\Gamma_K^\varepsilon \subset \Gamma_K$, specified by its thickness $h_K^\varepsilon = \varepsilon \bar{h}_K$, and by the elastic coefficients $\mathbb{C}, \gamma$, the following equations in Γ_K^ε govern the plate displacements $(\boldsymbol{u}^{\varepsilon,K}, w^{\varepsilon,K})$ and rotations $\boldsymbol{\theta}^{\varepsilon,K}$ (below in equation (2) the suffix K is omitted for brevity)

$$\left\{\begin{array}{rcl} -\omega^2 h^\varepsilon \rho \boldsymbol{u}^\varepsilon - h^\varepsilon \overline{\nabla} \cdot [\mathbb{C} \overline{\nabla}^S(\boldsymbol{u}^\varepsilon)] &=& \boldsymbol{t}^\varepsilon \ , \\ -\omega^2 h^\varepsilon \rho w^\varepsilon - h^\varepsilon \overline{\nabla} \cdot [\gamma(\overline{\nabla} w^\varepsilon - \boldsymbol{\theta}^\varepsilon)] &=& f^\varepsilon \ , \\ -\omega^2 \frac{(h^\varepsilon)^3}{12} \rho \boldsymbol{\theta}^\varepsilon - \frac{(h^\varepsilon)^3}{12} \mathrm{div}[\mathbb{C} \overline{\nabla}^S(\boldsymbol{\theta}^\varepsilon)] & & \\ -h^\varepsilon \gamma(\overline{\nabla} w^\varepsilon - \boldsymbol{\theta}^\varepsilon) &=& \overline{\boldsymbol{m}}^\varepsilon \ , \end{array}\right. \tag{2}$$

where $\overline{\nabla} = (\partial_\alpha)$, $\alpha = 1, 2$ is the "in-plane" gradient, $\boldsymbol{t}^\varepsilon = (\bar{b}_\alpha)$, $f^\varepsilon = \bar{b}_3$ are derived from the boundary traction forces $\boldsymbol{b}^\varepsilon = \mathrm{i}\omega\rho_0 \boldsymbol{n} p^\varepsilon$ acting on the 3D representation of the plate and involving the acoustic potential p^ε. The plates are clamped on $\partial\Gamma_K$ and the Neumann conditions corresponding to the traction forces being expressed in terms of p^ε, are prescribed on the holes $\partial\Gamma_K^\varepsilon \setminus \partial\Gamma_K$.

1.2 Limit global problem

The aim of the work reported in this paper was to derive a limit problem describing the wave propagation in a homogenized layer containing the panel, so that transmission conditions can be obtained which allow for reformulation of problem (1) in domain $\Omega^G = \Omega^+ \cup \Omega^- \cup \Gamma_0$, where Ω^+ and Ω^- are non-overlapping parts and the planar surface Γ_0 represents the panel. The main result is formulation of the following "reduced" problem of the vibro-acoustic wave propagation: Find p such that

$$\begin{array}{rl} c^2 \nabla^2 p + \omega^2 p = 0 & \text{in } \Omega^+ \cup \Omega^- \ , \\ \dfrac{\partial p}{\partial n} = \pm \mathrm{i}\omega g^0 & \text{on } \Gamma^\pm \ , \\ \text{boundary conditions} & \text{on } \partial\Omega^G \ , \\ \mathcal{G}([p]_-^+, g^0) = 0 & \text{on } \Gamma_0 \end{array} \tag{3}$$

where $\Gamma^\pm = \partial\Omega^\pm \cap \Gamma_0$, $[p]_-^+ = p|_{\Gamma^+} - p|_{\Gamma^-}$ and $\mathcal{G}(\cdot,\cdot)$ is an implicit form of the transmission conditions on interface Γ_0 which describe the behaviour of the perforated multi-plate panel; it is constituted by the homogenized model given in Section 3.3, equations (42). In fact, $\mathcal{G}$ represents the Dirichlet-to-Neumann operator.

2 Problem in the transmission layer

In this section we describe the model of the vibroacoustic transmission which was subject of the homogenization procedure leading to the limit problem reported in Section 3. By $\Gamma_0 \subset \mathbb{R}^2$ we designate the mid-plane of the layer $\Omega_\delta \subset \mathbb{R}^3$ bounded by surfaces Γ_δ^+ and Γ_δ^- equidistant to Γ_0 with the distance $\delta/2$, so that $\Omega_\delta = \Gamma_0 \times]-\delta/2, \delta/2[\subset \mathbb{R}^3$. Recall that ε is the characteristic size of the perforation of all the plates, whereby $\delta = \varkappa\varepsilon$ for a given $\varkappa > 0$, see Fig. 1.

The microstructure of the perforation is periodic, being generated by the representative periodic cell $Y = \Xi \times \varkappa]-1/2, +1/2]$, where $\Xi =]0, b_1[\times]0, b_2[$. Further we define the solid part $S \subset Y$ such that

$$S = \bigcup_K \Xi_K^S \times \left(\bar{h}\right] - 1/2, +1/2] + \hat{z}_K\right) \ , \tag{4}$$

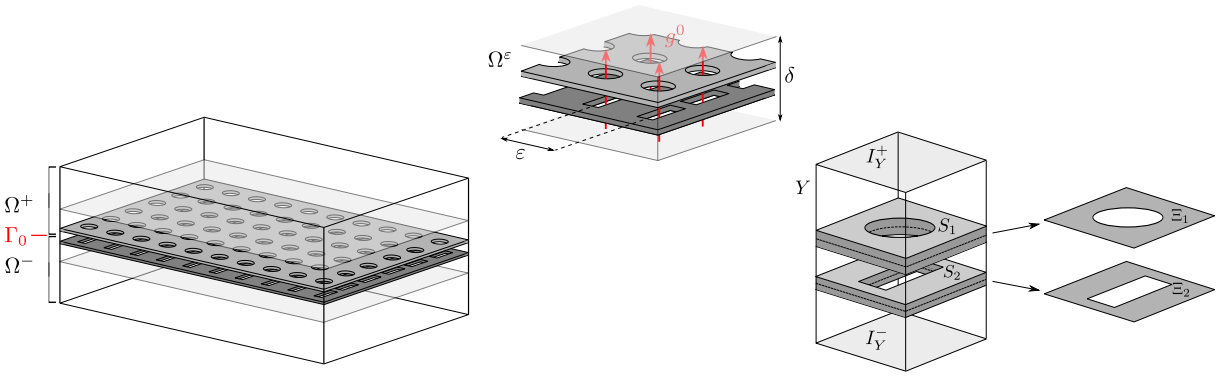


Figure 1: Scheme of the transmission layer with 2 plates. The layer thickness $\delta = \varkappa\varepsilon$, the plate thickness $h_K^\varepsilon = \varepsilon\bar{h}_K$

where $\Xi_K^S \subset \Xi$ represents the K-th plate perforated mid-plane and $\hat{z}_K$ is the "vertical" dilated position of the plate mid-plane. Using $Y^* = Y \setminus \overline{S}$ we define

$$\Omega^\varepsilon = \bigcup_{k\in\mathbb{Z}^2} \varepsilon(Y^* + \sum_{i=1,2} k_i b_i \vec{e_i}) \cap \Omega_\delta \ , \tag{5}$$

where $\Omega^\varepsilon = \Omega_\delta \setminus \Sigma^\varepsilon$ is the domain occupied by the fluid. We introduce the solid part of the layer $\Sigma^\varepsilon = \Omega_\delta \setminus \Omega^\varepsilon$. By $\hat{x}_3^K$ we denote the (non-dilated) transverse position of the K-th plate mid-plane, $\bar{x}_3^{\pm K}$ is the (non-dilated) transverse position of the K-th plate upper(+) and lower(-) surfaces.The solid panel is formed by individual plates Σ_K^ε, so that

$$\begin{aligned} \Sigma^\varepsilon &= \bigcup_{K=I,II} \Sigma_K^\varepsilon \ , \quad \Sigma_K^\varepsilon = \Gamma_K^\varepsilon \times h_K^\varepsilon] - 1/2, 1/2[\ , \\ \Gamma_K^\varepsilon &= \bigcup_{k\in\mathbb{Z}^2} \left(\hat{x}_3^K + \varepsilon \left(\Xi_K + \sum_{i=1,2} k_i b_i \vec{e_i} \right) \cap \Gamma_0 \right) \ . \end{aligned} \tag{6}$$

Thus, Γ_K^ε is the "2D" representation of the K-th plate which has its thickness $h_K^\varepsilon = \varepsilon\bar{h}_K$.

Through the paper we use the following decomposition of coordinates: for $x \in \Omega^G$, the position can be written as $x = (x', x_3)$ where $x' \in \Gamma_0$; for $y \in Y$, we have $y = (y', z)$ where $y' \in \Xi$.

2.1 Acoustic problem in the layer

To derive the acoustic transmission conditions, we consider the vibro-acoustic problem in the layer. The total acoustic potential, p^ε satisfies the Helmholtz equation in Ω^ε and Neumann conditions on $\partial\Omega^\varepsilon$

$$\begin{aligned} c^2\nabla^2 p^\varepsilon + \omega^2 p^\varepsilon &= 0 \quad \text{in } \Omega^{\varepsilon\delta} \ , \\ \text{velocity of "external" fluid} \quad \frac{\partial p^\varepsilon}{\partial n} &= -\mathrm{i}\omega g^{\varepsilon\pm} \quad \text{on } \Gamma^{\pm\delta} \ , \\ \text{velocity of solid structure} \quad \frac{\partial p^\varepsilon}{\partial n} &= -\mathrm{i}\omega \boldsymbol{n}\cdot\boldsymbol{u}^\varepsilon \quad \text{on } \partial\Sigma^\varepsilon \ , \\ \frac{\partial p^\varepsilon}{\partial n} &= 0 \quad \text{on } \partial\Omega^{\delta\infty} \ , \end{aligned} \tag{7}$$

where $g^{\varepsilon\pm}$ is the given data representing the transverse acoustic velocity which couples the problem (7) with the global problem (3). The surface $\partial\Omega^\varepsilon$ splits into disjoint parts, $\partial\Omega^\varepsilon =$

$\partial\Sigma^\varepsilon \cup \Gamma_\delta^+ \cup \Gamma_\delta^- \cup \partial\Omega^{\delta\infty}$, where $\partial\Omega^{\delta\infty}$ represents the fixed wall of a duct in which the panel is fitted.

The response of the solid panel is governed by the plate equations (2) adapted for each plate (note that this set of equations describes one plate) where the r.h.s. terms are expressed in terms of the acoustic potential p^ε.

2.2 Weak formulation of the coupled vibroacoustic problem

We write the system of equations describing the fluid and the structure response to the transverse acoustic velocity $\mathrm{i}\omega g^{\varepsilon\pm}$. It consists of three parts:

1. Acoustic fluid response p^ε in the transmission layer responds to the excitation by the transverse acoustic velocity $\mathrm{i}\omega g^{\varepsilon\pm}$ on the upper and lower boundary and by the vibrating structure. In the dilated configuration, where the layer has the thickness $\varkappa$, the acoustic potential $p^\varepsilon(x', z)$ satisfies

$$\begin{aligned} c^2\int_{\Omega^\varepsilon}\hat\nabla p^\varepsilon\cdot\hat\nabla q^\varepsilon-\omega^2\int_{\Omega^\varepsilon}p^\varepsilon q^\varepsilon=-\frac{\mathrm{i}\omega c^2}{\varepsilon}\int_{\Gamma^\pm}\hat g^{\varepsilon\pm}q^\varepsilon-\frac{\mathrm{i}\omega c^2}{\varepsilon}\sum_{K=I,II}\int_{\Gamma_K^\varepsilon}w^{\varepsilon,K}\langle q^\varepsilon\rangle_{K-}^{K+}\\ -\frac{\mathrm{i}\omega c^2}{\varepsilon}\sum_{K=I,II}\int_{\partial\Gamma_K^\varepsilon}\varepsilon\bar h_K\int_{-1/2}^{1/2}\bar{\boldsymbol{n}}\cdot(\boldsymbol{u}^{\varepsilon,K}-\varepsilon\bar h_K\zeta\boldsymbol{\theta}^{\varepsilon,K})q^\varepsilon(\cdot,\hat x_3^K+\varepsilon\bar h_K\zeta)\mathrm{d}\zeta\ , \end{aligned} \tag{8}$$

for all q^ε where $\hat\nabla=(\overline\nabla,\frac{1}{\varepsilon}\partial_z)$, recalling $\overline\nabla=(\partial_\alpha)$, $\alpha=1,2$ is the "in-plane" gradient, $\bar{\boldsymbol{n}}=(n_\alpha)$ is the in-plane normal vector, and $\langle p^1\rangle_{K-}^{K+}=v(\cdot,\bar x_3^{+K})-v(\cdot,\bar x_3^{-K})$.

2. For each plate K, the deflection – rotation modes $(w^{\varepsilon,K},\boldsymbol{\theta}^{\varepsilon,K})$ response to the loading by the acoustic pressure p^ε is governed by the following equation, where $(v_3^\varepsilon,\boldsymbol{\vartheta}^\varepsilon)$ are test functions:

$$\begin{aligned} -\omega^2\int_{\Gamma_K^\varepsilon}\rho_S\left[\varepsilon\bar h_K w^\varepsilon v_3^\varepsilon+\varepsilon^3\frac{\bar h_K^3}{12}\boldsymbol{\theta}^\varepsilon\cdot\boldsymbol{\vartheta}^\varepsilon\right]\\ +\varepsilon^3\frac{\bar h_K^3}{12}\int_{\Gamma_K^\varepsilon}\mathbb{C}_K^\varepsilon\overline\nabla^S\boldsymbol{\theta}^\varepsilon:\overline\nabla^S\boldsymbol{\vartheta}^\varepsilon+\varepsilon\bar h_K\int_{\Gamma_K^\varepsilon}\gamma_K(\overline\nabla w^\varepsilon-\boldsymbol{\theta}^\varepsilon)\cdot(\overline\nabla v_3^\varepsilon-\boldsymbol{\vartheta}^\varepsilon)\\ =\mathrm{i}\omega\rho_0\left[\int_{\Gamma_K^\varepsilon}v_3^\varepsilon\langle p^\varepsilon\rangle_{K-}^{K+}+(\varepsilon\bar h_K)^2\int_{\partial\Gamma_K^\varepsilon}\int_{-1/2}^{1/2}p^\varepsilon(\cdot,\hat x_3^K+\varepsilon\bar h_K\zeta)\bar{\boldsymbol{n}}\cdot(-\zeta\boldsymbol{\vartheta}^\varepsilon)\mathrm{d}\zeta\right]\ , \end{aligned} \tag{9}$$

where $\overline\nabla^S=\frac12(\overline\nabla^T+\overline\nabla)$.

3. For each plate K, the in-plane deformation described by displacements $\boldsymbol{u}^{\varepsilon,K}$ is the response to the loading by the acoustic pressure p^ε, where $\boldsymbol{v}^\varepsilon$ is the test function:

$$\begin{aligned} -\omega^2\varepsilon\bar h_K\int_{\Gamma_K^\varepsilon}\rho_S\boldsymbol{u}^\varepsilon\cdot\boldsymbol{v}^\varepsilon+\varepsilon\bar h_K\int_{\Gamma_K^\varepsilon}\mathbb{C}_K^\varepsilon\overline\nabla^S\boldsymbol{u}^\varepsilon:\overline\nabla^S\boldsymbol{v}^\varepsilon\\ =\mathrm{i}\omega\rho_0\varepsilon\bar h_K\int_{\partial\Gamma_K^\varepsilon}\bar{\boldsymbol{n}}\cdot\boldsymbol{v}^\varepsilon\int_{-1/2}^{1/2}p^\varepsilon(\cdot,\hat x_3^K+\varepsilon\bar h_K\zeta)\mathrm{d}\zeta \end{aligned} \tag{10}$$

Weak formulation. For given external transverse velocities $g^{\varepsilon\pm}$ defined on $\Gamma^\pm$, find $(\boldsymbol{u}^{\varepsilon,K},w^{\varepsilon,K},\boldsymbol{\theta}^{\varepsilon,K})$ for $K=I,II$ and p^ε such that equations (9),(10) and (8) hold for all test functions $(q^\varepsilon,\boldsymbol{v}^\varepsilon,v_3^\varepsilon,\boldsymbol{\vartheta}^\varepsilon)$.

2.3 Coupling of the layer with external acoustic fields

The following coupling identity is considered, which expresses the jump of the exterior field $p_{\rm ext}$ across the layer with finite $\delta > 0$,

$$\int_{\Gamma_\delta^+} \ p_{\rm ext}^{\delta+} - \int_{\Gamma_\delta^-} \ p_{\rm ext}^{\delta-} = \int_{\Gamma_0} \ \int_{-\delta/2}^{\delta/2} \partial_{x_3} \tilde{p}^\varepsilon \quad \forall \psi \in L^2(\Gamma_0) \ , \tag{11}$$

where we assume $\psi = \psi(x')$, $x' \in \Gamma_0$, and by $\tilde{}$ we denote an extension of p^ε to the whole Ω_δ. We may apply the dilation formula at the r.h.s. of (11) to get

$$\left(\int_{\Gamma_\delta^+} \ p_{\rm ext}^{\delta+} - \int_{\Gamma_\delta^-} \ p_{\rm ext}^{\delta-} \right) \approx \int_{\Gamma_0} \ (p_{\rm ext}^{\delta_0+} - p_{\rm ext}^{\delta_0-}) = \varepsilon \int_{\Gamma_0} \ \int_{-\varkappa/2}^{\varkappa/2} \frac{1}{\varepsilon} \partial_z \tilde{p}^\varepsilon \quad \forall \psi \in L^2(\Gamma_0) \ . \tag{12}$$

Further we consider a finite layer thickness $\delta_0 = \varkappa\varepsilon_0 > 0$ in the l.h.s. expression of (12), whereas we pass to the limit on its r.h.s. , so that we obtain the following approximation of the discontinuity of $p_{\rm ext}$ along Γ_0:

$$\begin{aligned} \frac{1}{\varepsilon_0} \int_{\Gamma_0} \ (p_{\rm ext}^{\delta_0+} - p_{\rm ext}^{\delta_0-}) &\approx \lim_{\varepsilon\to 0} \int_{\Gamma_0} \ \int_{-\varkappa/2}^{\varkappa/2} \frac{1}{\varepsilon} \fint_\Xi \partial_z \mathcal{T}_\varepsilon(\tilde{p}^\varepsilon) \\ &= \int_{\Gamma_0} \ \int_{-\varkappa/2}^{\varkappa/2} \fint_\Xi \partial_z \tilde{p}^1 = \int_{\Gamma_0} \psi [\tilde{p}^1]_-^+ \\ &= \int_{\Gamma_0} \ \left(\fint_{I_y^+} p^1 - \fint_{I_y^-} p^1 \right) \quad \forall \psi \in L^2(\Gamma_0) \ . \end{aligned} \tag{13}$$

3 Homogenized transmission layer

The asymptotic analysis of problem (9),(10), and (8) yields the recovery sequences $\boldsymbol{Q}^{R\varepsilon} = (p^{0,\varepsilon}, p^{1,\varepsilon}, \boldsymbol{u}^{0,K\varepsilon}, \boldsymbol{u}^{1,K\varepsilon}, w^{0,K\varepsilon}, w^{1,K\varepsilon}, \boldsymbol{\theta}^{K\varepsilon})$ which allow us to obtain the limit homogenized two-scale model of the wave propagation in the transmission layer; the following truncated expansions hold, where $x' \in \Gamma^0$ and

$$\begin{aligned} p^\varepsilon(x) &\approx p^{0,\varepsilon}(x') + \varepsilon p^{1,\varepsilon}(x', y', z) \ , \quad y' \in \Xi \ , \quad z \in [-1/2, +1/2] \ , \\ \boldsymbol{u}^{K,\varepsilon}(x') &\approx \boldsymbol{u}^{0,K\varepsilon}(x') + \varepsilon \boldsymbol{u}^{1,K\varepsilon}(x', y') \ , \quad y' \in \Xi_K \ , \\ w^{K,\varepsilon}(x') &\approx w^{0,K\varepsilon}(x') + \varepsilon w^{1,K\varepsilon}(x', y') \ , \quad y' \in \Xi_K \ , \\ \boldsymbol{\theta}^\varepsilon(x') &\approx \boldsymbol{\theta}^{K\varepsilon}(x', y') \ , \quad y' \in \Xi_K \ , \end{aligned} \tag{14}$$

where $x' \in \Gamma^0$. The functions $\boldsymbol{Q}^{R\varepsilon}$ converge in the unfolded space to the limit functions $\boldsymbol{Q}$, where $\boldsymbol{Q} = (p^0, p^1, \boldsymbol{u}^{0,K}, \boldsymbol{u}^{1,K}, w^{0,K}, w^{1,K}, \boldsymbol{\theta}^K)$ which are the solutions of the homogenized problem arising from (8),(9), and (10) for $\varepsilon \to 0$. Note that all functions in $\boldsymbol{Q}$ are Ξ-periodic in the y' variable; we use the space $H^1_{\underline{\#}}(Y) \subset H^1(Y)$ containing only Ξ-periodic functions.

3.1 Local problems and scale decoupling

From the limit of equation (8), the following identity can be obtained which holds for a.a. $x' \in \Gamma_0$,

$$\begin{aligned}&\fint_{Y^*} (\overline{\nabla}_x p^0 + \overline{\nabla}_y p^1)\cdot\overline{\nabla}_y q^1 + \fint_{Y^*} \partial_z p^1 \partial_z q^1 = -\mathrm{i}\omega g^0 \left(\fint_{I_y^+} q^1 - \fint_{I_y^-} q^1\right)\\ &-\mathrm{i}\omega\left[\sum_{K=I,II}\left(w^{0,K}\fint_{\Xi_K}\langle q^1\rangle_{K-}^{K+} + \bar{h}_K \boldsymbol{u}^0\cdot\fint_{\Gamma_\Xi^K}\bar{\boldsymbol{n}}\int_{-1/2}^{1/2} q^1(x',y',\hat{z}_K+\bar{h}_K\zeta)\mathrm{d}\zeta\right)\right],\end{aligned} \tag{15}$$

for all $q^1 \in H^1_{\underline{\#}}(Y^*)$. Due to linearity, the following split can be introduced:

$$p^1 = \pi^\beta \partial^x_\beta p^0 + \mathrm{i}\omega\left[\xi g^0 + \sum_{K=I,II}\left(\eta_K w^{0,K} + \mu^\alpha_K u^{0,K}_\alpha\right)\right], \tag{16}$$

where the corrector basis functions $\pi^\beta, \xi, \eta_K, \mu^\alpha_K$ which are Ξ-periodic are solutions of the local problems: Find $\pi^\beta, \xi, \eta_K, \mu^\alpha_K \in H^1_{\underline{\#}}(Y^*)/\mathbb{R}$ such that

$$\begin{aligned}&\fint_{Y^*}\nabla_y\pi^\beta\cdot\nabla_y\psi = -\fint_{Y^*}\partial^y_\beta\psi\,,\\ &\fint_{Y^*}\nabla_y\xi\cdot\nabla_y\psi = -\left(\fint_{I_y^+}\psi - \fint_{I_y^-}\right),\\ &\fint_{Y^*}\nabla_y\eta_K\cdot\nabla_y\psi = -\fint_{\Xi_K}\left(\psi(\cdot,\bar{z}^{K+}) - \psi(\cdot,\bar{z}^{K-})\right) = -\fint_{\Xi_K}\langle\psi\rangle_{K-}^{K+}\,,\\ &\fint_{Y^*}\nabla_y\mu^\beta_K\cdot\nabla_y\psi = -\bar{h}_K\fint_{\Gamma_\Xi^K} n_\beta\int_{-1/2}^{1/2}\psi(\cdot,\hat{z}^K+\zeta)\mathrm{d}\zeta\,,\end{aligned} \tag{17}$$

for all $\psi \in H^1_{\underline{\#}}(Y^*)$, where $\bar{z}^{K\pm} = \hat{z}^K \pm \frac{\bar{h}_K}{2}$ and recalling $\nabla_y = (\partial^y_\alpha, \partial_z)$.

Next we consider the limit form of the plate deflection-rotation arising from (9); for a.a. $x' \in \Gamma_0$, we obtain

$$\frac{\bar{h}_K^3}{12}\fint_{\Xi_K}\mathbb{C}\overline{\nabla}^S_y\boldsymbol{\theta} : \overline{\nabla}^S_y\boldsymbol{\vartheta} + \bar{h}_K\int_{\Xi_K}\gamma\big(\overline{\nabla}_x w^0 + \overline{\nabla}_y w^1 - \boldsymbol{\theta}\big)\cdot\big(\overline{\nabla}_y v^1 - \boldsymbol{\vartheta}\big) = 0\,, \tag{18}$$

for all $v^1 \in H^1_\#(\Xi_K), \boldsymbol{\vartheta} \in [H^1_\#(\Xi_K)]^2$. Using the corrector basis functions $\chi^\alpha_K \in H^1_\#(\Xi_K)/\mathbb{R}$ and $\boldsymbol{\varphi}^\alpha_K \in [H^1_\#(\Xi_K)]^2$ we introduce the split

$$w^{1,K} = \chi^\alpha_K\partial^x_\alpha w^{0,K}\,,\quad \boldsymbol{\theta}^K = \boldsymbol{\varphi}^\alpha_K\partial^x_\alpha w^{0,K}\,, \tag{19}$$

where the couple $(\boldsymbol{\varphi}^\alpha_K, \chi^\alpha_K)$ satisfies

$$\begin{aligned}&\frac{\bar{h}_K^2}{12}\fint_{\Xi_K}\mathbb{C}\overline{\nabla}^S_y\boldsymbol{\varphi}^\alpha_K : \overline{\nabla}^S_y\boldsymbol{\psi} + \fint_{\Xi_K}\gamma(\overline{\nabla}_y\chi^\alpha_K - \boldsymbol{\varphi}^\alpha_K)\cdot(\overline{\nabla}_y v - \boldsymbol{\psi}) = -\fint_{\Xi_K}\gamma(\partial^y_\alpha v - \psi_\alpha)\\ &\qquad\qquad \forall v \in H^1_\#(\Xi_K),\ \boldsymbol{\psi}\in[H^1_\#(\Xi_K)]^2\,.\end{aligned} \tag{20}$$

Finally we consider the limit of (10) describing the "in-plane" deformation of the plate. This yields, for a.a. $x' \in \Gamma_0$,

$$\bar{h}_K \fint_{\Xi_K} \mathbb{C}(\overline{\nabla}^S_x \boldsymbol{u}^{0,K} + \overline{\nabla}^S_y \boldsymbol{u}^{1,K}) : \overline{\nabla}^S_y \boldsymbol{v}^1 = \mathrm{i}\omega\rho_0 \bar{h}_K p^0 \fint_{\Gamma^K_\Xi} \boldsymbol{n} \cdot \boldsymbol{v}^1 \ , \tag{21}$$

for all $\boldsymbol{v}^1 \in [H^1_\#(\Xi_K)]^2$. Using the corrector basis functions $\boldsymbol{\chi}^{\alpha\beta}_K, \boldsymbol{\chi}^P_K \in [H^1_\#(\Xi_K)]^2$ we define the split

$$\boldsymbol{u}^{1,K} = \boldsymbol{\chi}^{\alpha\beta}_K \partial_\beta u^{0,K}_\alpha + \mathrm{i}\omega\rho_0 \boldsymbol{\chi}^P_K p^0 \ , \tag{22}$$

where the following two local corrector problem must be solved:

$$\begin{aligned} \fint_{\Xi_K} \mathbb{C}\overline{\nabla}^S_y(\boldsymbol{\chi}^{\alpha\beta}_K + \boldsymbol{\Pi}^{\alpha\beta}) : \overline{\nabla}^S_y \boldsymbol{v} = 0 \quad \forall \boldsymbol{v} \in [H^1_\#(\Xi_K)]^2 \ , \\ \fint_{\Xi_K} \mathbb{C}\overline{\nabla}^S_y \boldsymbol{\chi}^P_K : \overline{\nabla}^S_y \boldsymbol{v} = \fint_{\Gamma^K_\Xi} \boldsymbol{n} \cdot \boldsymbol{v} \quad \forall \boldsymbol{v} \in [H^1_\#(\Xi_K)]^2 \ . \end{aligned} \tag{23}$$

3.2 Macroscopic equations and Homogenized coefficients

In this section we introduce the homogenized coefficients involved in the limit transmission problem. From the limit form of equation (8), we obtain the following identity related to the acoustic fluid response:

$$\begin{aligned} & c^2 \int_{\Gamma_0} \fint_{Y^*} (\overline{\nabla}_x p^0 + \overline{\nabla}_y p^1) \cdot \overline{\nabla}_x q^0 - \omega^2 \int_{\Gamma_0} \fint_{Y^*} p^0 q^0 \\ & = -\mathrm{i}\omega c^2 \int_{\Gamma_0} q^0 \left[\left(\fint_{I^+_y} g^{1+} - \fint_{I^-_y} g^{1-} \right) + \bar{h}_K \sum_{K=I,II} \left(\fint_{\Gamma^K_\Xi} \bar{\boldsymbol{n}} \cdot \boldsymbol{u}^1 - \bar{h}_K \fint_{\Gamma^K_\Xi} \bar{\boldsymbol{n}} \cdot \boldsymbol{\theta}^K \int_{-1/2}^{1/2} \zeta \right) \right] \ . \end{aligned} \tag{24}$$

Using the split formulae (16), (19) and (22), the homogenized coefficients are computed:

$$\begin{aligned} A_{\alpha\beta} &= \fint_{Y^*} \nabla_y(\pi^\beta + y_\beta) \cdot (\pi^\alpha + y_\alpha) \ , \\ B_\alpha &= \fint_{Y^*} \partial^y_\alpha \xi \ , \\ P^K_\alpha &= \fint_{Y^*} \partial^y_\alpha \eta_K \ , \\ R^K_{\alpha\beta} &= \fint_{Y^*} \partial^y_\alpha \mu^\beta_K \ , \\ S^K_{\alpha\beta} &= \bar{h}_K \fint_{\Gamma^K_\Xi} \boldsymbol{n} \cdot \boldsymbol{\chi}^{\alpha\beta}_K \ , \\ T^K &= \fint_{\Gamma^K_\Xi} \boldsymbol{n} \cdot \boldsymbol{\chi}^P_K \ , \end{aligned} \tag{25}$$

Further, we substitute the split form of p^1 (16) in (13) which yields the following coefficients:

$$
\begin{aligned}
F &= -\fint_{I_y^+}\xi + \fint_{I_y^-}\xi = \int_{Y^*}\nabla_y\xi\cdot\nabla_y\xi\ ,\\
C_\alpha &= \fint_{I_y^+}\pi^\alpha - \fint_{I_y^-}\pi^\alpha = -\int_{Y^*}\nabla_y\xi\cdot\nabla_y\pi^\alpha = B_\alpha\ ,\\
W^K &= \fint_{I_y^+}\eta_K - \fint_{I_y^-}\eta_K = -\int_{Y^*}\nabla_y\xi\cdot\nabla_y\eta_K = -N^K\ ,\\
X^K_\alpha &= \fint_{I_y^+}\mu^\alpha_K - \fint_{I_y^-}\mu^\alpha_K = -\int_{Y^*}\nabla_y\xi\cdot\nabla_y\mu^\alpha_K = -N^K_\alpha\ .
\end{aligned}
\tag{26}
$$

From (9), we obtain the following identity related to the K-th plate deflection response:

$$
-\omega^2\bar{h}_K\int_{\Gamma_K}\big(\fint_{\Xi_K}\rho_S\big)w^0v^0 + \bar{h}_K\int_{\Gamma_K}\gamma\big(\overline{\nabla}_x w^0 + \overline{\nabla}_y w^1 - \boldsymbol{\theta}\big)\cdot\overline{\nabla}_x v^0 = \mathrm{i}\omega\rho_0\int_{\Gamma_K}v^0\fint_{\Xi_K}\langle p^1\rangle^{K+}_{K-}\ .
\tag{27}
$$

Using the split formulae (16), (19) and (22), the following homogenized coefficients are identified:

$$
\begin{aligned}
G^K_{\alpha\beta} &= \fint_{\Xi_K}\gamma\left[\overline{\nabla}_y(y_\alpha+\chi^\alpha_K) - \boldsymbol{\varphi}^\alpha_K\right]\cdot\overline{\nabla}_y y_\beta\\
&= \fint_{\Xi_K}\left[\gamma\delta_{\alpha\beta} - \frac{\bar{h}_K^2}{12}\mathbb{C}\overline{\nabla}^S_y\boldsymbol{\varphi}^\alpha : \overline{\nabla}^S_y\boldsymbol{\varphi}^\beta + \gamma\overline{\nabla}_y(\chi^\alpha_K - \boldsymbol{\varphi}^\alpha)\cdot(\chi^\beta_K - \boldsymbol{\varphi}^\beta)\right]\ ,\\
D^K_\beta &= \fint_{\Xi_K}\langle\pi^\beta\rangle^{K+}_{K-} = P^K_\beta\ ,\\
M^{KL}_{33} &= -\fint_{\Xi_K}\langle\eta_L\rangle^{K+}_{K-}\ ,\\
M^{KL}_{3\alpha} &= -\fint_{\Xi_K}\langle\mu^\alpha_L\rangle^{K+}_{K-} = M^{LK}_{\alpha 3}\ ,\\
N^K &= -\fint_{\Xi_K}\langle\xi\rangle^{K+}_{K-} = \int_{Y^*}\nabla_y\eta_K\cdot\nabla_y\xi\ .
\end{aligned}
\tag{28}
$$

In analogy, from (10), we obtain the identity related to the K-th plate in-plane deformation response:

$$
\begin{aligned}
-\omega^2\bar{h}_K\int_{\Gamma_K}\big(\fint_{\Xi_K}\rho_S\big)\boldsymbol{u}^0\cdot\boldsymbol{v}^0 + \bar{h}_K\int_{\Gamma_K}\fint_{\Xi_K}\mathbb{C}(\overline{\nabla}^S_x\boldsymbol{u}^0 + \overline{\nabla}^S_y\boldsymbol{u}^1) : \overline{\nabla}^S_x\boldsymbol{v}^0&\\
= \mathrm{i}\omega\rho_0\bar{h}_K\int_{\Gamma_K}\boldsymbol{v}^0\cdot\fint_{\Gamma^K_\Xi}\boldsymbol{n}\int_{-1/2}^{1/2}p^1(\cdot,\hat{z}^K+\zeta)\mathrm{d}\zeta\ .&
\end{aligned}
\tag{29}
$$

Upon substituting there the split formulae (16), (19) and (22), the following homogenized coefficients and their alternative expressions are obtained, where $\boldsymbol{\Pi}^{ij} = (\Pi^{ij}_k)$, with $\Pi^{ij}_k = y_j\delta_{ik}$

with $i,j,k,l=1,2$,

$$
\begin{aligned}
C^K_{ijkl} &= \bar{h}_K \fint_{\Xi_K} \mathbb{C}\overline{\nabla}^S_y(\boldsymbol{\chi}^{kl}+\boldsymbol{\Pi}^{kl}) : \overline{\nabla}^S_y(\boldsymbol{\chi}^{ij}+\boldsymbol{\Pi}^{ij}) \,, \\
Q^K_{\alpha\beta} &= \bar{h}_K \fint_{\Xi_K} \mathbb{C}\overline{\nabla}^S_y \boldsymbol{\chi}^P_K : \overline{\nabla}^S_y \boldsymbol{\Pi}^{\alpha\beta} = -S^K_{\alpha\beta} \,, \\
Z^K_{\alpha\beta} &= \bar{h}_K \fint_{\Gamma^K_\Xi} n_\alpha \int_{-1/2}^{1/2} \pi^\beta(\cdot,\hat{z}^K+\zeta)\mathrm{d}\zeta = \fint_{Y^*} \nabla_y \mu^\alpha_K \cdot \nabla_y \pi^\beta = -R^K_{\beta\alpha} \,, \\
M^{KL}_{\alpha\beta} &= -\bar{h}_K \fint_{\Gamma^K_\Xi} n_\alpha \int_{-1/2}^{1/2} \eta_L(\cdot,\hat{z}^K+\zeta)\mathrm{d}\zeta = \fint_{Y^*} \nabla_y \mu^\alpha_K \cdot \nabla_y \mu^\beta_L \,, \\
M'^{KL}_{\alpha 3} &= -\bar{h}_K \fint_{\Gamma^K_\Xi} n_\alpha \int_{-1/2}^{1/2} \mu^\beta_L(\cdot,\hat{z}^K+\zeta)\mathrm{d}\zeta = \fint_{Y^*} \nabla_y \mu^\alpha_K \cdot \nabla_y \eta_L = M^{LK}_{3\alpha} \,, \\
N^K_\alpha &= -\bar{h}_K \fint_{\Gamma^K_\Xi} n_\alpha \int_{-1/2}^{1/2} \xi(\cdot,\hat{z}^K+\zeta)\mathrm{d}\zeta = \fint_{Y^*} \nabla_y \mu^\alpha_K \cdot \nabla_y \xi \,.
\end{aligned}
\tag{30}
$$

3.3 Homogenized vibroacoustic problem

Using the homogenized coefficients defined above, the macroscopic model of the vibroacoustic response in the layer can be derived from equations (24), (27), (29), and (13). For brevity, we present the problem defined on Γ_0 using differential equations (31)-(34), whereby the clamped plate boundary conditions and the rigid wall condition for p^0 at $\partial\Gamma_0$ are considered.

$$
\begin{aligned}
&-\omega^2 \left[\frac{\overline{\rho_S}^K}{\rho_0} \bar{h}_K \boldsymbol{u}^{0,K} + \sum_{L=I,II} \left(M^{KL}_{\alpha\beta} u^{0,L}_\beta + M^{,KL}_{\alpha 3} w^{0,L} \right) + N^K_\alpha g^0 \right] \\
&\quad -\overline{\nabla}^S_x \cdot \rho_0^{-1} (\mathbb{C}^K \overline{\nabla}^S_x \boldsymbol{u}^{0,K}) - \mathrm{i}\omega \overline{\nabla}^S_x \cdot (\boldsymbol{Q}^K p^0) - \mathrm{i}\omega \boldsymbol{Z}^K \overline{\nabla}_x p^0 = 0 \,,
\end{aligned}
\tag{31}
$$

$$
\begin{aligned}
&-\omega^2 \left[\frac{\overline{\rho_S}^K}{\rho_0} \bar{h}_K w^{0,K} + \sum_{L=I,II} \left(M^{KL}_{3\alpha} u^{0,L}_\beta + M^{,KL}_{33} w^{0,L} \right) + N^K g^0 \right] \\
&\quad -\rho_0^{-1} \overline{\nabla}_x \cdot (\boldsymbol{G}^K \overline{\nabla}_x w^{0,K}) - \mathrm{i}\omega \boldsymbol{D}^K \cdot \overline{\nabla}_x p^0 = 0 \,,
\end{aligned}
\tag{32}
$$

$$
\begin{aligned}
&-\frac{\omega^2}{c^2} p^0 + \overline{\nabla}_x \cdot \boldsymbol{A} \overline{\nabla}_x p^0 - \mathrm{i}\omega \overline{\nabla}_x \cdot (\boldsymbol{B} g^0) - \mathrm{i}\omega \sum_{K=I,II} \overline{\nabla}_x \cdot \left(\boldsymbol{R}^K \boldsymbol{u}^{0,K} + \boldsymbol{P}^K w^{0,K} \right) \\
&\quad + \sum_{K=I,II} \left(\omega^2 \rho_0 T^K p^0 - \mathrm{i}\omega \boldsymbol{S}^K : \overline{\nabla}^S_x \boldsymbol{u}^{0,K} \right) = -\left(\fint_{I^+_y} g^{1+} - \fint_{I^-_y} g^{1-} \right) \,,
\end{aligned}
\tag{33}
$$

$$
\mathrm{i}\omega \boldsymbol{C} \cdot \overline{\nabla}_x p^0 + \omega^2 F g^0 - \omega^2 \sum_{K=I,II} \left(N^K w^{0,K} + \boldsymbol{N}^K \cdot \boldsymbol{u}^{0,K} \right) = \frac{\mathrm{i}\omega}{\varepsilon_0} [p_{\mathrm{ext}}]^+_- \,. \tag{34}
$$

The following symmetries and relationship between the homogenized coefficients can be proved:

$$
\begin{aligned}
&\boldsymbol{X}^K = -\boldsymbol{N}^K \,, \quad W^K = -N^K \,, \quad \boldsymbol{D}^K = \boldsymbol{P}^K \,, \quad \boldsymbol{Z}^K = -(\boldsymbol{R}^K)^T \,, \\
&(\boldsymbol{Q}^K)^T = \boldsymbol{Q}^K = -\boldsymbol{S}^K \,, \quad \boldsymbol{C} = \boldsymbol{B} \,.
\end{aligned}
\tag{35}
$$

After respecting these symmetry relationships in (31)-(34) and denoting

$$\Delta g^1 = \left(\fint_{I_y^+} g^{1+} - \fint_{I_y^-} g^{1-} \right) , \tag{36}$$

we can rewrite (31)-(34), as follows:

$$\begin{aligned} -\omega^2 \left[\frac{\overline{\rho_S}^K}{\rho_0} \bar{h}_K \boldsymbol{u}^{0,K} + \sum_{L=I,II} \left(M^{KL}_{\alpha\beta} u^{0,L}_\beta + M^{,KL}_{\alpha 3} w^{0,L} \right) + N^K_\alpha g^0 \right] \\ -\overline{\nabla}^S_x \cdot \rho_0^{-1} (\mathbb{C}^K \overline{\nabla}^S_x \boldsymbol{u}^{0,K}) + \mathrm{i}\omega \overline{\nabla}^S_x \cdot (\boldsymbol{S}^K p^0) + \mathrm{i}\omega \boldsymbol{R}^K \overline{\nabla}_x p^0 = 0 , \end{aligned} \tag{37}$$

$$\begin{aligned} -\omega^2 \left[\frac{\overline{\rho_S}^K}{\rho_0} \bar{h}_K w^{0,K} + \sum_{L=I,II} \left(M^{KL}_{3\alpha} u^{0,L}_\beta + M^{,KL}_{33} w^{0,L} \right) + N^K g^0 \right] \\ -\rho_0^{-1} \overline{\nabla}_x \cdot (\boldsymbol{G}^K \overline{\nabla}_x w^{0,K}) - \mathrm{i}\omega \boldsymbol{P}^K \cdot \overline{\nabla}_x p^0 = 0 , \end{aligned} \tag{38}$$

$$\begin{aligned} -\frac{\omega^2}{c^2} p^0 + \overline{\nabla}_x \cdot \boldsymbol{A} \overline{\nabla}_x p^0 - \mathrm{i}\omega \overline{\nabla}_x \cdot (\boldsymbol{B} g^0) - \mathrm{i}\omega \sum_{K=I,II} \overline{\nabla}_x \cdot \left(\boldsymbol{R}^K \boldsymbol{u}^{0,K} + \boldsymbol{P}^K w^{0,K} \right) \\ + \sum_{K=I,II} \left(\omega^2 \rho_0 T^K p^0 - \mathrm{i}\omega \boldsymbol{S}^K : \overline{\nabla}^S_x \boldsymbol{u}^{0,K} \right) = -\Delta g^1 , \end{aligned} \tag{39}$$

$$\mathrm{i}\omega \boldsymbol{B} \cdot \overline{\nabla}_x p^0 + \omega^2 F g^0 - \omega^2 \sum_{K=I,II} \left(N^K w^{0,K} + \boldsymbol{N}^K \cdot \boldsymbol{u}^{0,K} \right) = \frac{\mathrm{i}\omega}{\varepsilon_0} [p_{\mathrm{ext}}]^+_- . \tag{40}$$

To observe the symmetric structure of the problem, it advantageous to introduce the following matrices:

$$\begin{aligned} \mathbb{M}^{KL} = \begin{bmatrix} M^{KL}_{\alpha\beta} & M^{KL}_{\alpha 3} \\ M^{LK}_{3\beta} & M^{KL}_{33} \end{bmatrix} , \quad \mathbb{N} = \begin{bmatrix} N^K_\alpha \\ N^K \end{bmatrix} , \quad \mathbb{P} = \begin{bmatrix} S^K_{\alpha\beta} + R^K_{\alpha\beta} \\ P^K_\beta \end{bmatrix} . \\ \mathbb{D}^K = \rho_0^{-1} \begin{bmatrix} \mathbb{C}^K & 0 \\ 0 & \boldsymbol{G}^K \end{bmatrix} , \qquad \overline{\nabla} \mathbf{u}^K = \begin{bmatrix} \overline{\nabla}^S \boldsymbol{u}^{0,K} \\ \overline{\nabla} w^{0,K} \end{bmatrix} , \end{aligned} \tag{41}$$

The mass matrix $\mathbb{M}^{KL}$ is symmetric and represents the "added mass". The coupling effects are represented by matrices $\mathbb{N}^K$, $\mathbb{P}^K$ and by coefficients $\boldsymbol{B}$. The plate stiffness is represented by $\mathbb{D}^K$ including the bending effects. The anisotropic propagation of the acoustic wave in the fluid is described in terms of the tensor $\boldsymbol{A}$, whereas the transverse impedance of the panel is given by F. The vibroacoustic response is described by the fields $\mathbf{u}^K = (\boldsymbol{u}^{0,K}, w^{0,K})$ satisfying the

following differential equations imposed on Γ_0:

$$
\begin{aligned}
-\omega^2\left(m^K\boldsymbol{I}+\sum_{L=I,II}\mathbb{M}^{KL}\right)\mathbf{u}^L-\overline{\nabla}\cdot\mathbb{D}^K\overline{\nabla}\mathbf{u}^K+\mathrm{i}\omega\mathbb{P}^K\overline{\nabla}p^0-\omega^2\mathbb{N}^Kg^0=\boldsymbol{0}\ , \quad \text{for } K=I,II\ ,\\
\mathrm{i}\omega\sum_{L=I,II}\mathbb{P}^L\overline{\nabla}\mathbf{u}^L-\omega^2\frac{1}{c^2}p^0+\overline{\nabla}\cdot\boldsymbol{A}\overline{\nabla}p^0-\mathrm{i}\omega\boldsymbol{B}\cdot\overline{\nabla}g^0=-\Delta g^1\ ,\\
-\omega^2\sum_{L=I,II}\mathbb{N}^L\cdot\mathbf{u}^L+\mathrm{i}\omega\boldsymbol{B}\cdot\overline{\nabla}p^0+\omega^2Fg^0=\frac{\mathrm{i}\omega}{\varepsilon_0}[p]^+_-\ ,\\
\left.\begin{aligned}\bar{\boldsymbol{n}}\cdot\overline{\nabla}p^0&=0\ ,\\ \boldsymbol{u}^K&=0\ ,\ K=I,II\ ,\end{aligned}\right\}\quad\text{on }\partial\Gamma_0\ ,
\end{aligned}
\tag{42}
$$

where $[p]^+_- = p^+ - p^-$ is the jump of the "external field" p across Γ_0 and $m^K = \bar{h}^K\rho_S/\rho_0$.

The Global Acoustic Problem. To conclude this section, we reformulate the global problem imposed in domain Ω^G. The acoustic potential p defined in Ω^G is discontinuous on Γ_0, satisfies the equations (3) with the implicit transmission condition $\mathcal{G}([p]^+_-, g^0) = 0$ is given by (42), where $\boldsymbol{u}^K$ and p^0 serve as the internal variables.

Note that $\overline{\nabla}g^0$ is not needed in the weak formulation of (42). The "unknown" coupling function Δg^1, see (36) can be released to simplify the problem. Another option is to use an iterative algorithm which, in this context, defines Δg^1 using the "old approximation" of the outer acoustic field p. This will be issued in our further papers.

4 Examples

In this section we illustrate the sensitivity of the homogenized coefficients to the geometrical arrangement of the perforated panels. We assume two periodically perforated plates, the first one with the rectangular perforation, the second one with the circular perforation. The local corrector problems are solved using the representative volume elements, one (3D) for the fluid domain Y^* and two (2D) for the compliant plates Ξ_K , see Fig. 2. The geometrical parameters of the perforation (defined with respect to the unit cel Y) are: $a = 1$, $b = 0.6$, $c = 0.3$, $d = 0.5$. The thickness of both the perforated plates is $\bar{h} = 0.08$ and their distance $h_{12} = 0.26$.

We consider the change in the relative "in-plane" position of the holes associated with the two plates, described by the parameter d_c. Fig. 3, illustrates the sensitivity of the homogenized coefficients to the geometrical arrangement.

Figure 4 shows the dependence of the selected homogenized coefficients ($\boldsymbol{B}$, F, $\boldsymbol{P}^1$, $\boldsymbol{P}^2$, $\boldsymbol{R}^1$, $\boldsymbol{R}^2$) on the mutual shift of the perforations (defined by d_c). In particular, $\boldsymbol{B}$, $\boldsymbol{P}^1$, $\boldsymbol{P}^2$ are the most sensitive coefficients responsible for the coupling effects between transverse and surface acoustic waves. These coefficients vanish for $d_c \longrightarrow 0$, so that the 2nd equation in (42) governs the distribution of the acoustic fluid potential p^0 independently of g^0 and plate vibrations $\{\mathbf{u}^K\}$.

5 Conclusion

In this paper the homogenized model of the vibroacoustic interaction on perforated double-plates was presented. The detailed derivation of the model will be considered in a separate paper. Some symmetries of the model due relationship between the homogenized coefficients

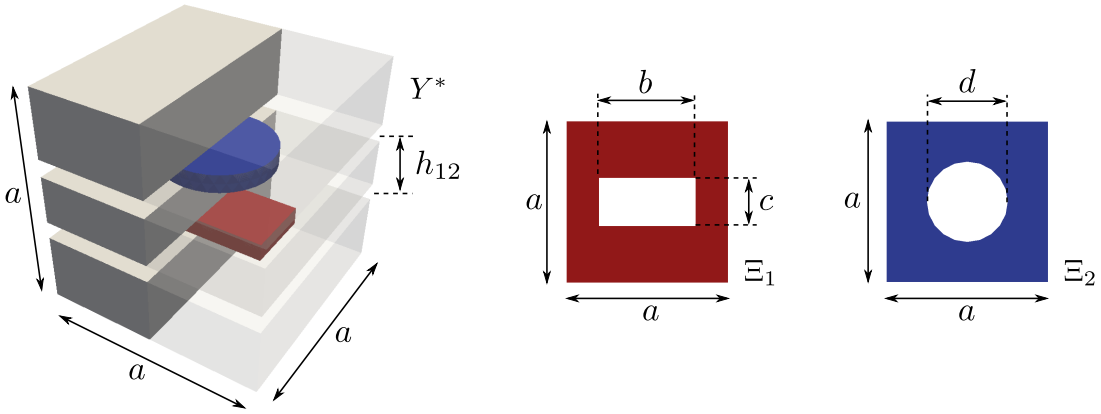


Figure 2: The representative volume elements corresponding to Y^* (3D), Ξ_1 and Ξ_2 (2D) domains.

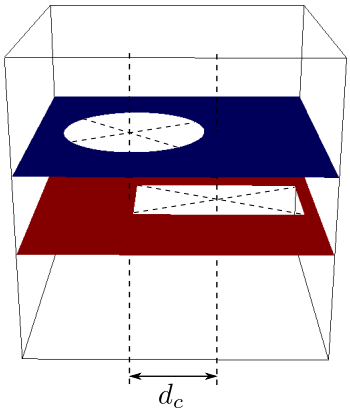


Figure 3: The change in the mutual positions of the holes (perforations) described by the parameter d_c.

were observed. It is worth noting that the plate rotations are not involved explicitly in the homogenized equations, however, the bending stiffness is respected by the homogenized elasticity coefficients. The obtained model represents implicit transmission conditions. As the main advantage, this model enables to reduce quite significantly the computational complexity of solving the acoustic wave propagation in the neighbourhood of the plate panel. Although the model was derived rigorously using the homogenization method, its verification and study of the modelling approximation properties is the further step to be done.

Acknowledgments The research of was supported by the European Regional Development Fund (ERDF), project "NTIS – New Technologies for Information Society", European Centre of Excellence, CZ.1.05/1.1.00/02.0090, in part by the Czech Scientific Foundation projects GACR P101/12/2315.

REFERENCES

[1] R. Cimrman, SfePy - Write Your Own FE Application, in: Proceedings of the 6th European Conference on Python in Science (EuroSciPy 2013), 2014, pp. 65–70, http://arxiv.org/abs/1404.6391.

[2] D. Cioranescu, A. Damlamian, G. Griso, The periodic unfolding method in homogenization, SIAM Journal on Mathematical Analysis 40 (4) (2008) 1585–1620.

[3] A. Cioranescu, D. Damlamian, G. Griso, D. Onofrei, The periodic unfolding method for perforated domains and Neumann sieve models, Journal de Mathématiques Pures et Appliquées 89 (3) (2008) 248–277.

[4] A. Bonnet-Bendhia, D. Drissi, N. Gmati, Mathematical analysis of the acoustic diffraction by a muffler containing perforated ducts, Math. Models and Methods in Appl. Sci. 15 (7) (2005) 1059–1090.

[5] S. e. Jung, Sound absorption of micro-perforated panel, Journal of the Korean Physical Society 50 (2007) 1044–1051.

[6] E. Rohan, V. Lukeš, Homogenization of the acoustic transmission through perforated layer, J. of Comput. and Appl. Math. 234 (2010) 1876–1885.

[7] E. Rohan, B. Miara, Band gaps and vibration of strongly heterogeneous Reissner-Mindlin elastic plates, Comptes Rendus Mathematique 349 (2011) 777–781.

[8] E. Rohan, V. Lukeš, Homogenized perforated interface in acoustic wave propagation – modeling and optimization, in: J. e. Náprstek (Ed.), Proc. of the 10th International Conference on Vibration Problems, ICOVP 2011, Vol. 139 of Springer Proceedings in Physics, Springer, 2011, pp. 321–327.

[9] E. Rohan, V. Lukeš, Sensitivity analysis for optimal design of perforated plates in vobroacoustics: homogenization approach, in: Proceedings of ISMA 2012 – USD 2012, KU Leuven, 2012, pp. 4201–4214.

[10] E. Rohan, V. Lukeš, Homogenized perforated interface in acoustic wave propagation – modeling and optimization, in: Z. D. et.al. (Ed.), Proc. of the 11th International Conference on Vibration Problems, ICOVP 2013, Lisbon, Portugal, 2013, pp. 1–10, (paper 501). http://www.icovp.com.

[11] K. Sakagami, K. Matsutani, M. Morimoto, Sound absorption of a double-leaf micro-perforated panel with an air-back cavity and a rigid-back wall: Detailed analysis with a Helmholtz-Kirchhoff integral formulation, Applied Acoustics 71 (2010) 411–417.

[12] E. Sanchez-Palencia, Non-homogeneous media and vibration theory, no. 127 in Lecture Notes in Physics, Springer, Berlin, 1980.

[13] F.-A. Stremtan, I. Lupea, Assessing the sound absorption of micro-perforated panels by using the transfer function and the impedance tube, RJAV IX (2) (2012) 94–99, ISSN 1584-7284.

[14] J. Zhou, A. Bhaskar, X. Zhang, Sound transmission through a double-panel construction lined with poroelastic material in the presence of mean flow, Journal of Sound and Vibration 332 (2013) 3724–3734.

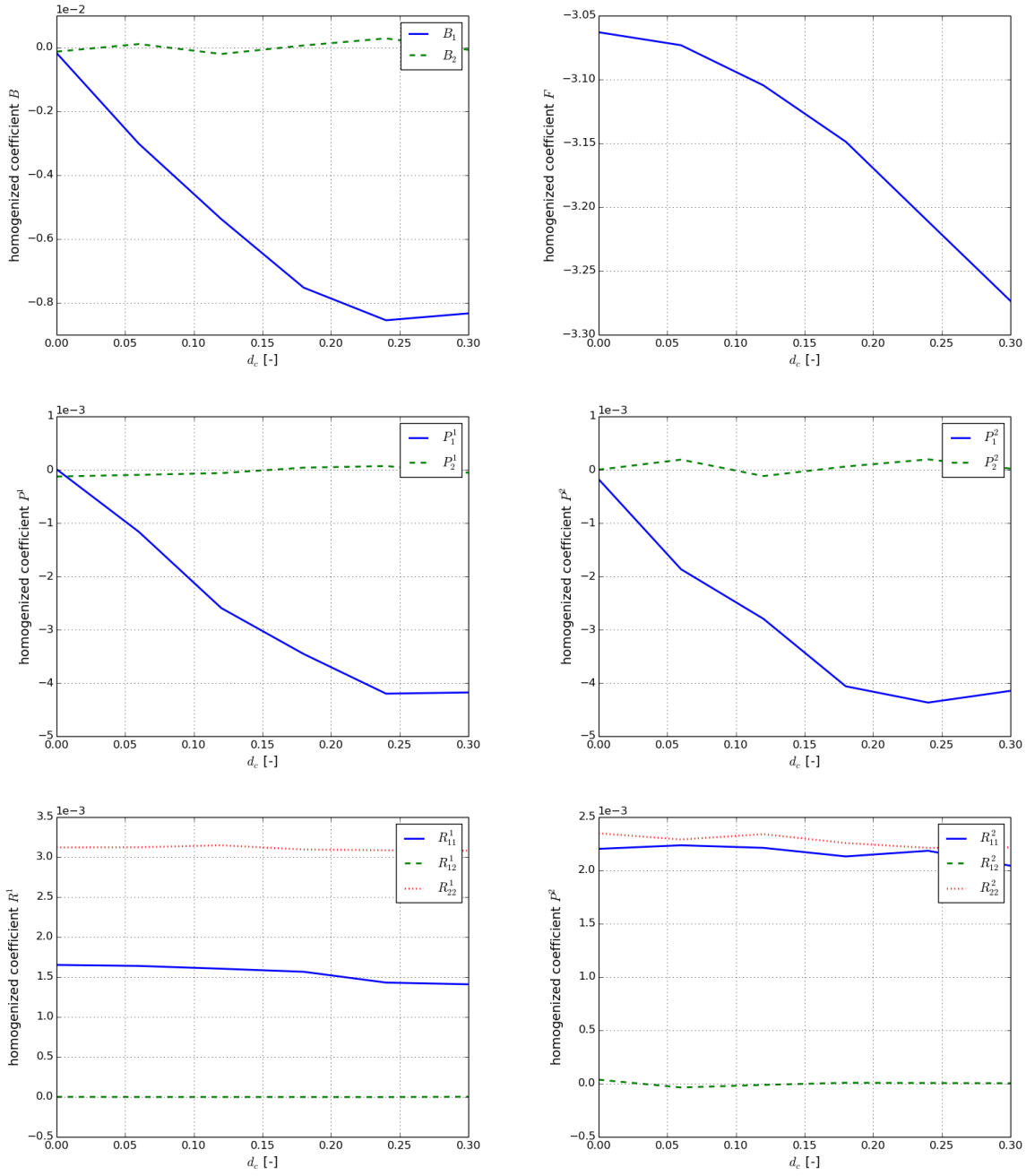


Figure 4: The sensitivity of the homogenized coefficients $\boldsymbol{B}$, F, $\boldsymbol{P}^1$, $\boldsymbol{P}^2$, $\boldsymbol{R}^1$, $\boldsymbol{R}^2$ to the geometrical parameter d_c.

COMPDYN 2015
5th ECCOMAS Thematic Conference on
Computational Methods in Structural Dynamics and Earthquake Engineering
M. Papadrakakis, V. Papadopoulos, V. Plevris (eds.)
Crete Island, Greece, 25–27 May 2015

DRY FRICTION INFLUENCE ON STRUCTURE DYNAMICS

Marco C. De Simone[1], **Domenico Guida**[1]

[1]Dept Industrial Engineering - University of Salerno
Via Giovanni Paolo II, 132 - 84084 - Fisciano (SA) - Italy
e-mail: {mdesimone,guida}@unisa.it

Keywords: Dry Friction, Friction Pendulum System, Frequency Response, Base Isolation, Vibration Mitigation

Abstract. *In this paper we have analysed the influence of dry friction on the response of a two story building model. We have assumed that this structure is mounted on two FPSs (Friction Pendulum Systems) and have modelled these devices by a spring and a dry friction force.*
We have shown how dry friction influences the response of the system and determined numerically the dynamical response under periodic ground excitation.

1 INTRODUCTION

FPSs are devices by which we can mitigate the effects of seismic excitations on buildings or structures. These devices allow us to make more safe structures in a very easy way provided that we have machines for installing them. These devices are very simple mechanical systems. They are made of two bodies which can slide one on other along a path with assigned form and able to dissipate energy by a friction mechanism [1, 2]. By the dynamical viewpoint these devices can be modelled by a linear spring and dry friction devices. The spring acts as filter of vibrations while friction device acts as a damper.
This devices can be divided into active and passive devices and according to the material they are made of. For example, Rubber Bearings, used extensively in bridge structures and prestressed and precast concrete buildings are made of EPDM, SBR and Natural Rubber, Neoprene Rubber, etc. Such devices allow vibration dampening, prevent sound transfer, reduce the destructive action of the vibrations in the structures by allowing displacements caused by normal expansion costranction and materials [3, 4]. In this work we have investigated the use of a particular passive system for the mitigation of vibrations in structures, the Friction Pendulum System (FPS). This device uses friction to ensure flexibility to the structural system and to add damping to the isolated structure. This device represents the simplest sliding system that works without the aid of active restoring forces. The radius of curvature of the dishes of FPS influences in a decisive manner relative displacements between the upper plate connected to the structure and the lower one connected to ground so that fundamental period of the base-isolated structure can be shifted further away from the predominant period of near-fault ground motions [5]. We therefore decided to use such a device, to investigate possible forms of instability that may arise due to the presence of dry friction between the moving parts of FPS [6, 7].
We organized the paper as follows. On The Response Of A Mass-Spring-Dry Friction section we studied the influence of discontinuous and continuous friction model on describing the dynamical behaviour of the system. In Mathematical Model section we discussed the dimensionless equation used to describe the motion of the structure considered in presence of dry friction. In Numerical Simulations we have reported some details about the values used to describe different configurations of the device in different scenarios with the simplifying assumptions made. In Final section we presented the conclusions.

2 ON THE RESPONSE OF A MASS-SPRING-DRY FRICTION

Let us consider the system indicated in figure 1. The equation of motion can be written in the following dimensionless form:

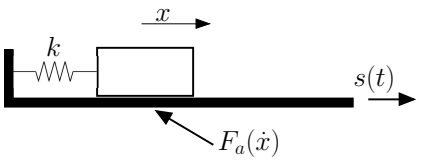


Figure 1: One Degree of Freedom System

$$\ddot{z} + f(\dot{z} + 1) + z = 0 \tag{1}$$

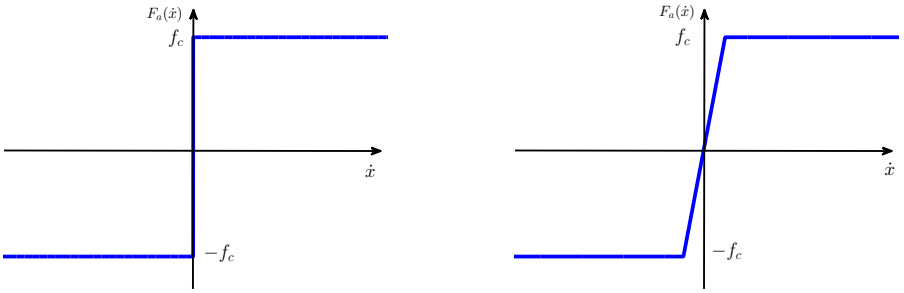
having put

$$\overline{z} = x - s; \qquad \tau = \omega_n t; \qquad z = \frac{\overline{z}}{\frac{\dot{s}}{\omega_n}};$$

$$\omega_n^2 = \frac{k}{m}; \qquad \frac{F(\dot{z}+1)}{m\omega_n \dot{s}} = f(\dot{z}+1).$$

By assuming the friction force between the slide and ground described by a Coulomb friction model (see figure 2(a)) we have calculated the response and indicated it in figure 3 without ground excitation.

We can observe that every point which belongs to the set $-f_c$, f_c is an equilibrium point of the



(a) (b)

Figure 2: Dry Friction Coulomb Model

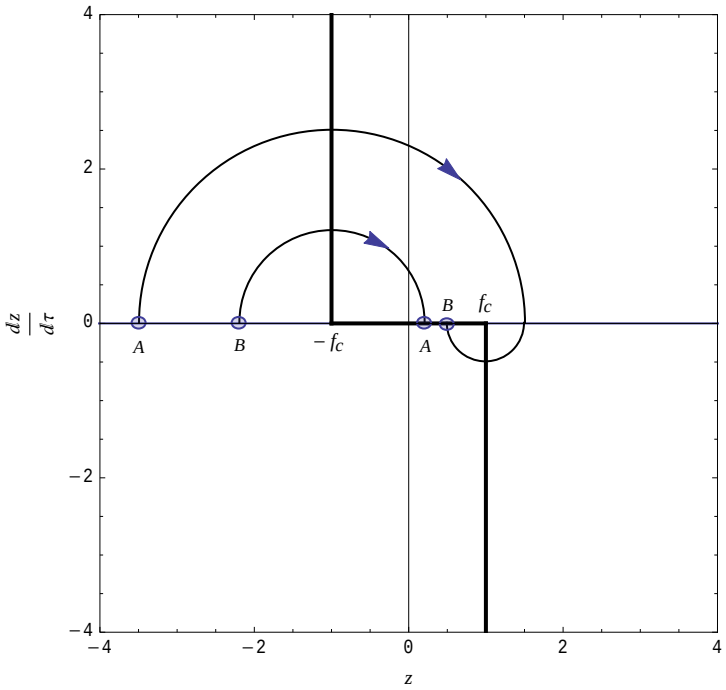


Figure 3: Dynamical Response with Discontinuous Friction Characteristic

system.

On the other hand, if we make continuous the friction characteristic, so as indicated in figure 2(b), the response of the system will be that of the figure 4.

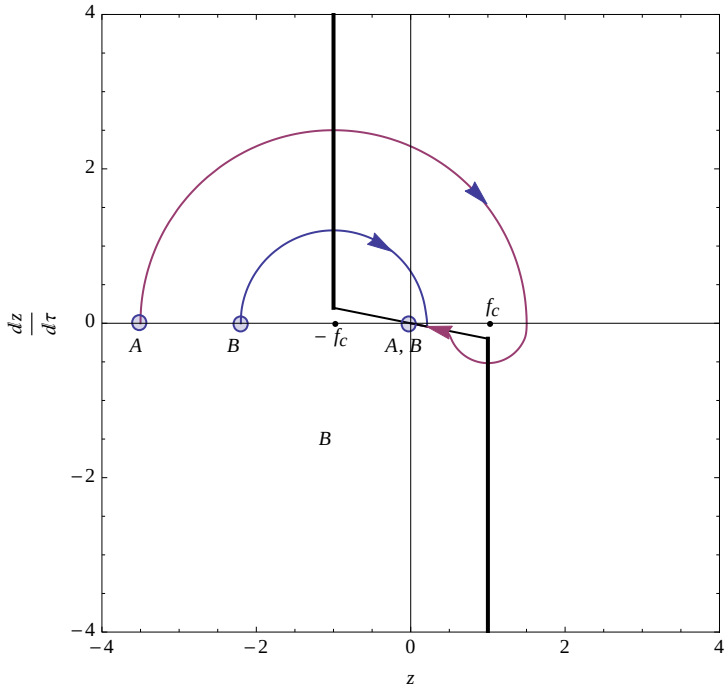


Figure 4: Dynamical Response with Continuous Friction Characteristic

By comparing figures 3 and 4 we can conclude that by making continuous the Coulomb friction in that way is a bad approximation about describing the dynamical behaviour of the system 1. If we consider the system excited by a ground motion, the system has not equilibrium point and, except singular solutions, the body is never undergone to stopping conditions (stick phase). On the basis of these last consideration we can assume that when the system is excited by external force we can make continuous the friction characteristic without drawbacks on the numerical simulations.

3 RESPONSE OF A TWO STORY BUILDING ON FPSs

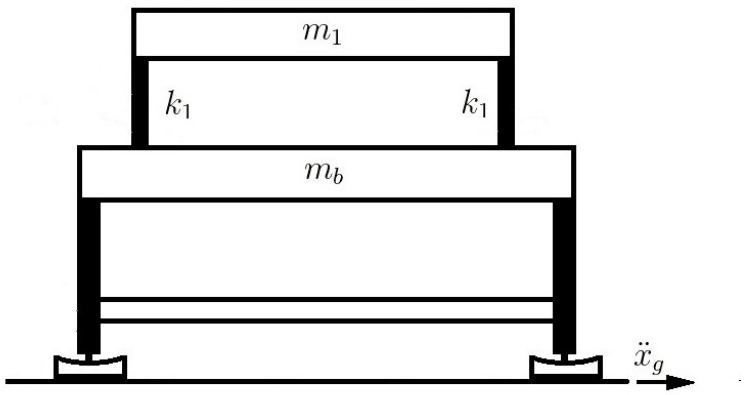


Figure 5: Mechanical System

In figure 5 is reported the mechanical model of the two degrees of freedom system used to

study the dynamic behaviour in presence of dry friction. The equation of motion is reported by equations 2:

$$\begin{aligned} &m_b\ddot{\tilde{x}}_b(t) + k_b(\tilde{x}(t) - \tilde{x}(t)) + f_{a,b}(\dot{\tilde{x}}_b(t) - \dot{\tilde{x}}_g(t)) + k_1(\tilde{x}(t) - \tilde{x}_1(t)) = 0; \\ &m_1\ddot{\tilde{x}}_1(t) + k_1(\tilde{x}_1(t) - \tilde{x}(t)) = 0. \end{aligned} \tag{2}$$

If we choose to measure displacement, velocity and acceleration of each mass compared to the ground, $\tilde{x}, \dot{\tilde{x}}_g, \ddot{\tilde{x}}_g$ respectively, we introduce relative measurements as showed below. We can now write a new set of equation in matrix notation as reported in 3

$$\begin{cases} \tilde{x} = x_b + \tilde{x}_g \\ \tilde{x}_1 = x_1 + \tilde{x}_g \end{cases}$$

$$\mathbf{M}\ddot{\mathbf{x}}(t) + \mathbf{K}\mathbf{x}(t) + \mathbf{F_a}(\dot{\mathbf{x}}_b) = -\mathbf{M}\ddot{\tilde{\mathbf{x}}}_g(t); \tag{3}$$

where $\mathbf{x}(t)$,$\dot{\mathbf{x}}(t)$ and $\ddot{\mathbf{x}}(t)$ are vectors of relative displacement, velocity and acceleration and $\ddot{\tilde{x}}_g$ represents the ground acceleration. With $\mathbf{M}$ and $\mathbf{K}$ are reported respectively the mass and stiffness matrix and with $\mathbf{F_a}$ the dry friction terms.

$$\mathbf{M} = \begin{bmatrix} m_b & 0 \\ 0 & m_1 \end{bmatrix} \tag{4}$$

$$\mathbf{K} = \begin{bmatrix} k_b + k_1 & -k_1 \\ -k_1 & k_1 \end{bmatrix} \tag{5}$$

$$\mathbf{F_a} = \begin{Bmatrix} f_{a,b}(\dot{x}_b) \\ 0 \end{Bmatrix} \tag{6}$$

For the discontinuous function used to describe dry friction we have chosen the function reported in figure 2(a) having the following characteristic:

$$f_a(\dot{x}_b) = \begin{cases} \mu_b(m_b + m_1)g & \dot{x}_b > 0 \\ -\mu_b(m_b + m_1)g < f_{a,b} < \mu_b(m_b + m_1)g & \dot{x}_b = 0 \\ -\mu_b(m_b + m_1)g & \dot{x}_b < 0 \end{cases}$$

The equation that describes the dynamic motion of the base mass becomes the following:

$$m_b\ddot{x}_b + (k_b + k_1)x_b - k_1x_1 + f_{a,b}(\dot{x}_b) = -m_b\ddot{\tilde{x}}_g \tag{7}$$

while the equation that describes the motion of the other mass is the following:

$$m_1\ddot{x}_1 + k_1x_1 - k_1x_b = -m_1\ddot{\tilde{x}}_g \tag{8}$$

making explicit the friction term, equation 7 becomes:

$$m_b\ddot{x}_b + (k_b + k_1)x_b - k_1x_1 + \mu(m_b + m)g\frac{\dot{x}_b}{|\dot{x}_b|} = -m_b\ddot{\tilde{x}}_g \tag{9}$$

Dividing equation 9 by m_b and equation 8 by m_1 we obtain:

$$\ddot{x}_b + \frac{k_b + k_1}{m_b}x_b - \frac{k_1}{m_b}x_1 + \mu\frac{m_b + m_1}{m_b}g\frac{\dot{x}_b}{|\dot{x}_b|} = -\ddot{\tilde{x}}_g \tag{10}$$

$$\ddot{x}_1 + \frac{k_1}{m_1}x_1 - \frac{k_1}{m_1}x_b = -\ddot{\tilde{x}}_g \tag{11}$$

By performing the following positions:

$$\omega^2{}_b = \frac{k_b + k_1}{m_b}; \qquad \omega^2{}_1 = \frac{k_1}{m_1}; \qquad \tau = \omega_1 t;$$

$$(') = \frac{d}{d\tau}; \qquad \Omega = \frac{\omega}{\omega_1}; \qquad y_i = \frac{x_i}{|\tilde{x}_g''|};$$

dividing equations 10 and 11 by $\omega^2{}_1$, assuming for the external forcing a cosinosuidale law and introducing the following parameters:

$$\beta_1 = \frac{k_b}{k_1}; \qquad \beta_2 = \frac{m_1}{m_b}; \qquad \beta_3 = \frac{m_1 g}{k_1};$$

$$\alpha_1 = (1 + \beta_1)\beta_2; \qquad \alpha_2 = \mu_b \beta_3; \qquad \alpha_3 = (1 + \beta_2)\alpha_2.$$

the equations can be rewritten in dimensionless form as follows:

$$\begin{aligned} &y''{}_b + \alpha_1 y_b - \beta_2 y_1 + \alpha_3 \frac{y'{}_b}{|y'{}_b|} = cos(\Omega\tau); \\ &y''{}_1 + y_1 - y_b = cos(\Omega\tau). \end{aligned} \tag{12}$$

4 NUMERICAL ANALISYS

We have developed a numerical procedure to investigate the influence of dry friction on the dynamic behaviour of a structure. The parameters considered to carry out this investigation are stiffness ratio β_1 between k_b and k_1, the mass ratio β_2 between m_1 and m_b and the friction coefficient μ_b between upper body and the base. For β_1 we have considered values $[0.1, 0.01]$ assuming that the equivalent stiffness of the friction pendulum system should be at least one order of magnitude lower compared to the stiffness of the pillars and for β_2 we have considered the following values in brackets $[1, 0.1]$ and are reported in Tab. 1. Further for the friction coefficient, we considered four scenarios with μ_b equal to values reported in brackets $[0.1, 0.3, 0.5, 0.7]$, using values frequently encountered in most cases. The assumptions made in this paper are the following:

$\beta_2 \setminus \beta_1$	0.1	0.01
1	$k_b = 0.1k_1$	$k_b = 0.01k_1$
	$m_b = m_1$	$m_b = m_1$
0.1	$k_b = 0.1k_1$	$k_b = 0.01k_1$
	$m_b = 0.1m_1$	$m_b = 0.1m_1$

Table 1: Several Configurations of the Two Degrees of Freedom System Considered

- Linear law for elastic constants;
- Friction force remains constant with respect to sliding velocity;
- Sinusoidal law for ground acceleration;
- Order of magnitude of the upper structure mass m_1 is one order of magnitude lower than the elastic constant k_1.

The simulations for the cases considered, have been carried out by the use of calculation software Matlab, in Simulink environment. Of the four simulations carried out, the three most significant graphs of the coefficient of amplification have been reported for the first and second mass respectively in fig 6 and 7.

5 CONCLUSIONS

In this paper the presence of eventual forms of instability due to the presence of dry friction in the dynamics of a mechanical system were investigated . Through appropriate positions and appropriate hypothesis the system under consideration has been brought back to a two degrees of freedom system that can represent a single-storey building isolated by fps, friction pendulum system. The reported results, clearly demonstrate how the dynamic behaviour of a mechanical systems subject to dry friction for low values of the friction coefficient is not affected if not in a partial way of the presence of friction while, for high values of the friction coefficient, the response of the system is significantly different.

REFERENCES

[1] V. A. Zayas, S. S. Low, S. A. Mahin *A simple pendulum technique for achieving seismic isolation*. Earthquake spectra 6(2) (1990): 317-333.

[2] A. Mokha, M. C. Constantinou, A. M. Reinhorn *Experimental study of friction-pendulum isolation system*. Journal of Structural Engineering, ASCE (1991): 117:120117.

[3] R. Y. Tan, M. C. Huang *System identification of a bridge with lead-rubber bearings*. Computers & Structures 74.3 (2000): 267-280.

[4] R. S. Jangid, *Optimum lead-rubber isolation bearings for near-fault motions*. Engineering Structures 29.10 (2007): 2503-2513.

[5] R. S. Jangid, *Optimum friction pendulum system for near-fault motions*. Engineering Structures 27.3 (2005): 349-359.

[6] D. Guida, F. Nilvetti, C. M. Pappalardo. *Dry Friction Infuence on Cart Pendulum Dynamics*. International Journal of Mechanics, 3(2), 2009.

[7] R. S. Jangid, Y. B. Londhe. *Effectiveness of elliptical rolling rods for base-isolation*. Journal of Structural Engineering, ASCE (1998) 124: 46972.

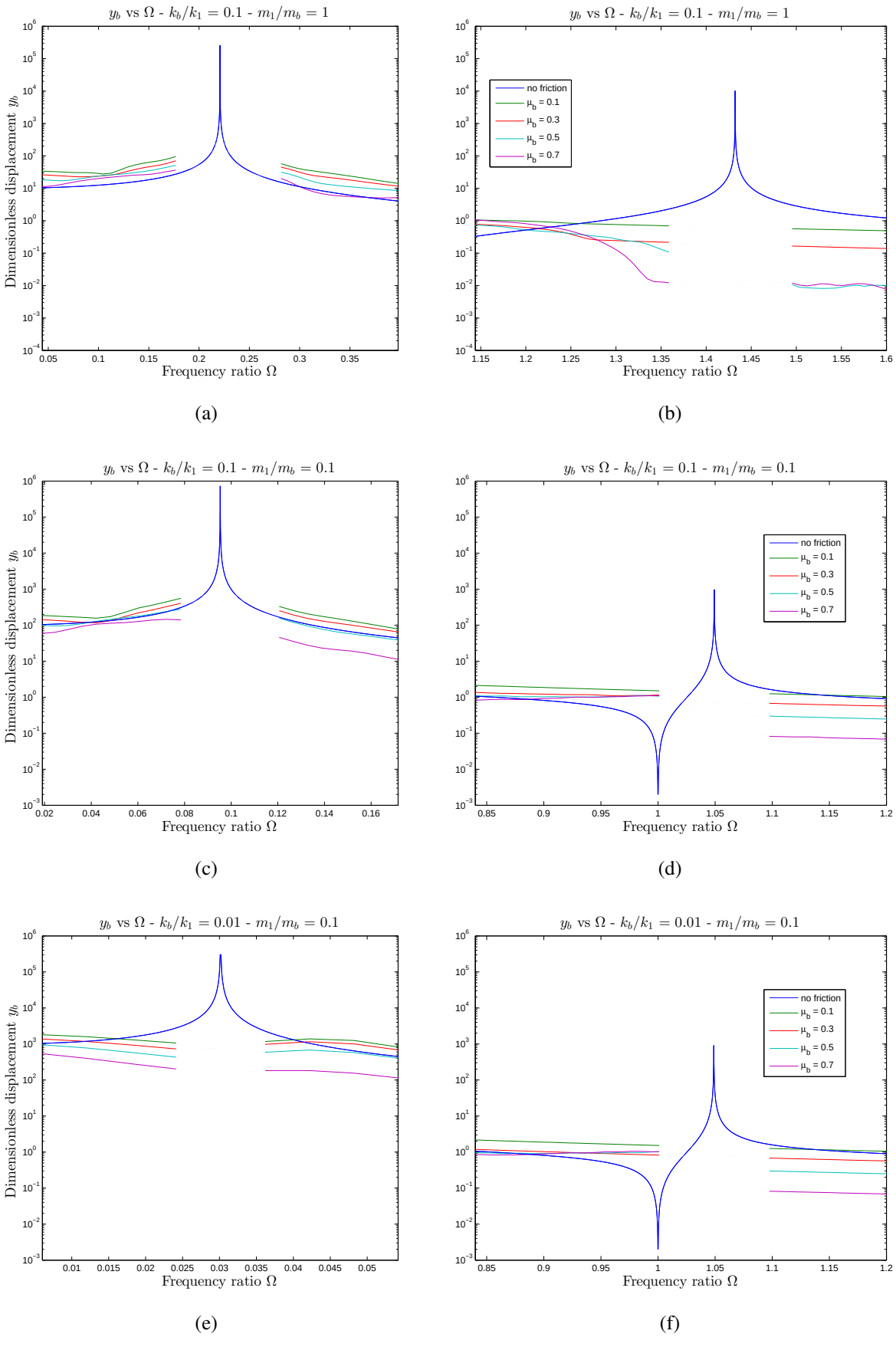


Figure 6: Response of the Base Floor of the Reduced System

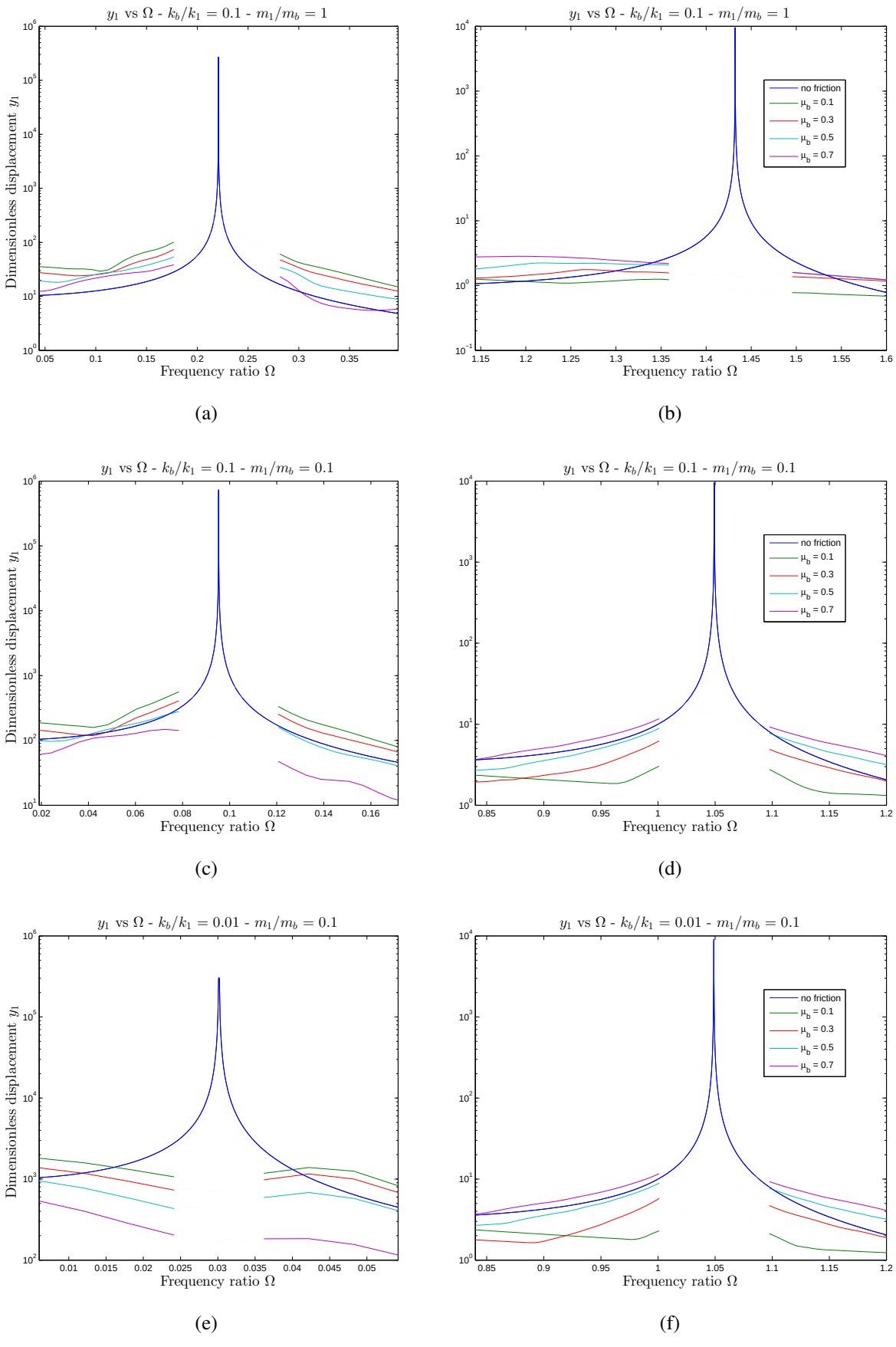


Figure 7: Response of the First Floor of the Reduced System

COMPDYN 2015
5th ECCOMAS Thematic Conference on
Computational Methods in Structural Dynamics and Earthquake Engineering
M. Papadrakakis, V. Papadopoulos, V. Plevris (eds.)
Crete Island, Greece, 25–27 May 2015

ANALYSIS OF VIBRO-ACOUSTIC PROPAGATION IN A MOBILE SCREW COMPRESSOR FOR THE DETERMINATION OF EMITTED ACOUSTIC POWER RADIATED OUTSIDE ITS HOUSING

Jan Dupal[1], Jan Vimmr[1], Vítězslav Adámek[1], and Ondřej Bublík[1]

[1]European Centre of Excellence NTIS - New Technologies for the Information Society,
Faculty of Applied Sciences, University of West Bohemia
Univerzitní 8, Pilsen, CZ-306 14, Czech Republic
e-mail: {dupal,jvimmr,vadamek,obublik}@kme.zcu.cz

Keywords: Screw Compressor, Vibro-Acoustics, Helmholtz Equation, Finite Element Method.

Abstract. *The method for a numerical solution of the vibro-acoustic problem in a mobile screw compressor is proposed and in-house 3D finite element (FE) solver is developed. In order to reduce the complexity of the problem, attention is paid to the numerical solution of the acoustic pressure field in the compressor cavity interacting with the linear elastic compressor housing. Propagation of acoustic pressure in the cavity is mathematically described by the Helmholtz equation in the amplitude form and is induced by periodically varying surface velocity of the engine and compressor assembly. In accordance with prescribed boundary conditions, numerical solution of the Helmholtz equation for the distribution of acoustic pressure amplitudes within the cavity is performed using the finite element method on tetrahedral meshes. For the FE discretisation of the elastic compressor housing, a new 6-noded thin flat shell triangular finite element with 21 DOF based on the Kirchhoff plate theory was developed and implemented. The resulting strong coupled system of linear algebraic equations describing the vibro-acoustic problem, i.e., the problem of interaction between the air inside the cavity and the screw compressor housing, is solved numerically by well-known algorithms implemented in MATLAB. By considering two different benchmark test cases, the developed 3D FE solver is successfully verified against the numerical results provided by the professional computational FE system Radioss. Finally, the vibro-acoustic problem is solved in a simplified model of a real mobile screw compressor by prescribing experimentally measured acoustic velocity on the surface of the engine and compressor assembly. The numerical solution is carried out only with the professional computational FE system Radioss as our developed solver is still unable to process large-sized problems without encountering memory limits. Thus, for the assessment of results computed by Radioss, we use results acquired during experimental measurements on a real mobile screw compressor under operating conditions.*

1 INTRODUCTION

Considering customer requirements and the necessity to satisfy hygienic standards, the producers of mobile screw compressors are compelled to minimise the emitted acoustic power and the related noise. The ongoing research is focused on a proposal of suitable and efficient method and its implementation within a 3D finite element (FE) solver for the numerical solution of the acoustic power radiation from screw compressors.

This paper is primarily focused on numerical solution of the vibro-acoustic problem in a simplified model of real mobile screw compressor. Main attention is paid to the acoustic pressure distribution in the compressor cavity interacting with the linear elastic housing of the screw compressor. It is assumed that the propagation of the acoustic pressure in the cavity is induced by periodically varying surface velocity of the engine and compressor assembly, which is known a priori. Since the periodic function can be expressed in the form of a Fourier series, the problem can be solved for a single excitation frequency value and with regards to linearity of the problem the global solution can be derived using a superposition of the harmonic solutions.

The main contribution of the present study, which follows and extends our previous study [1], is the verification of our developed 3D FE solver against the professional computational FE system Radioss and the numerical solution of vibro-acoustic problem in a simplified model of the real mobile screw compressor PDP70, the geometry of which is prepared according to technical drawings provided by the compressor producer ATMOS Chrást, Ltd. Note that due to memory limitations encountered by our solver, the vibro-acoustic problem in the simplified compressor model is numerically solved only by Radioss. In this case, the obtained numerical results are compared with experimental data measured on a real mobile screw compressor under operating conditions.

2 PROBLEM FORMULATION

For the solution of the vibro-acoustic problem in mobile screw compressors, the computational domain is divided into two subdomains: the compressor cavity $\Omega \subset \mathbf{R}^3$ and the elastic compressor housing $\tilde{\Omega} \subset \mathbf{R}^3$, as displayed in Figure 1. The cavity subdomain Ω is bounded by the boundary $\partial\Omega = \Gamma_{in} \cup \Gamma_{out} \cup \Gamma_w \cup \Gamma_t$, where Γ_{in}, Γ_{out} and Γ_w denote the inlet, the outlet and the rigid walls of the computational domain, respectively. The elastic housing $\tilde{\Omega}$ is bounded by boundary $\partial\tilde{\Omega} = \Gamma_f \cup \Gamma_u \cup \Gamma_t$ where Γ_f denotes the boundary with prescribed force loads and Γ_u denotes the boundary with prescribed displacement field. The interface between the two interacting subdomains, i.e., between the cavity Ω and the housing $\tilde{\Omega}$, is denoted as Γ_t.

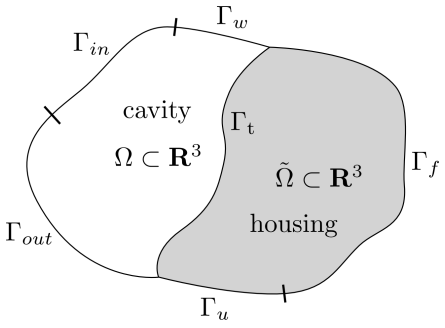


Figure 1: Computational domain $(\Omega \cup \tilde{\Omega}) \subset \mathbf{R}^3$.

Because of the assumption that the excitation is a periodic process, this excitation can be expressed in the form of a Fourier series. Then, with regards to the linearity of the vibro-acoustic problem, its solution, i.e., the distribution of acoustic pressure within the cavity and the distribution of acoustic velocity at the housing surface, can be sought for a single excitation frequency value. Based on this assumption, the acoustic pressure $p'(\boldsymbol{x}, t)$ and the acoustic velocity $\mathbf{v}'(\boldsymbol{x}, t)$ can be expressed in the complex harmonic form $p'(\boldsymbol{x}, t) = p(\boldsymbol{x})e^{i\omega t}$ and $\mathbf{v}'(\boldsymbol{x}, t) = \mathbf{v}(\boldsymbol{x})e^{i\omega t}$, respectively, where ω is the angular frequency of compressor engine movement.

Taking into consideration the harmonic character of the solution, we can write the Helmholtz equation, which describes the distribution of acoustic pressure $p(\boldsymbol{x})$ in the cavity subdomain Ω, in its amplitude form [2]

$$k^2 p + \Delta p = 0, \tag{1}$$

where $k = \frac{\omega}{c}$ is the wave number and c is the speed of sound. In the rest of this paper, all time-dependent variables will be represented by their complex amplitudes. The weak solution of the Helmholtz equation (1) is given as

$$\int_\Omega k^2 \varphi\, p \,\mathrm{d}\Omega - \int_\Omega \nabla\varphi \nabla p \,\mathrm{d}\Omega + \int_{\partial\Omega} \varphi \,\frac{\partial p}{\partial n}\,\mathrm{d}S = 0, \tag{2}$$

where $\varphi(\boldsymbol{x})$ is a well chosen test function and $\boldsymbol{n}$ is the outer unit vector normal to the boundary $\partial\Omega$. The momentum conservation law for the inviscid fluid yields [3]

$$\frac{\partial p}{\partial n} = -i\omega\varrho_a v_n, \tag{3}$$

where i is the imaginary unit, ϱ_a is the air density and $v_n = \boldsymbol{v}\cdot\boldsymbol{n}$ is the normal acoustic velocity. The third integral in Eq. (2) can be expressed for each boundary part as follows:

- the rigid wall boundary Γ_w – the boundary condition $v_n = 0$ is prescribed, which yields $\int_{\Gamma_w} \varphi \,\frac{\partial p}{\partial n}\,\mathrm{d}S = -\int_{\Gamma_w} \varphi\, i\,\omega\varrho_a v_n \,\mathrm{d}S = 0$;
- the anechoic outlet Γ_{out} – the normal velocity v_n is given as [2]

$$v_n = \frac{p}{\varrho_a c}, \tag{4}$$

  which yields $\int_{\Gamma_{out}} \varphi \,\frac{\partial p}{\partial n}\,\mathrm{d}S = -\int_{\Gamma_{out}} \varphi\, i\,\frac{\omega}{c}\, p \,\mathrm{d}S$;
- the inlet boundary Γ_{in} – the surface acoustic velocity v_n is prescribed;
- the interface Γ_t between the cavity and the elastic housing – we apply the following expression $\int_{\Gamma_t} \varphi \,\frac{\partial p}{\partial n}\,\mathrm{d}S = -\int_{\Gamma_t} \varphi\, i\,\omega\varrho_a v_n \,\mathrm{d}S$, where the normal acoustic velocity v_n is an unknown velocity resulting from the interaction between the acoustic environment in the cavity and the elastic housing of the screw compressor.

By including the integrals mentioned above into Eq. (2), we obtain the following equation

$$\int_\Omega k^2 \varphi\, p \,\mathrm{d}\Omega - \int_\Omega \nabla\varphi \nabla p \,\mathrm{d}\Omega - i\,\frac{\omega}{c}\int_{\Gamma_{out}} \varphi\, p \,\mathrm{d}S - i\omega\varrho_a \int_{\Gamma_{in}} \varphi\, v_n \,\mathrm{d}S - i\omega\varrho_a \int_{\Gamma_t} \varphi\, v_n \,\mathrm{d}S = 0. \tag{5}$$

Note that the normal velocity v_n in the fourth integral is given, whereas in the fifth integral it is unknown.

The solution in the housing subdomain $\tilde{\Omega}$ is based on the principle of virtual work (PVW) in the following form

$$\int_{\tilde{\Omega}} \delta\boldsymbol{\varepsilon}^T \boldsymbol{\sigma} \,\mathrm{d}\tilde{\Omega} = -\int_{\tilde{\Omega}} \varrho_h \delta\boldsymbol{u}^T \ddot{\boldsymbol{u}} \,\mathrm{d}\tilde{\Omega} + \int_{\Gamma_t} p\, \delta\boldsymbol{u}^T \boldsymbol{n} \,\mathrm{d}S, \tag{6}$$

where $\boldsymbol{\varepsilon} = [\varepsilon_x, \varepsilon_y, \varepsilon_z, \gamma_{yz}, \gamma_{xz}, \gamma_{xy}]^T$ is the strain vector, $\boldsymbol{\sigma} = [\sigma_x, \sigma_y, \sigma_z, \tau_{yz}, \tau_{xz}, \tau_{xy}]^T$ is the stress vector, $\boldsymbol{u} = [u, v, w]^T$ is the displacement vector and ϱ_h is the material density of the housing. The surface integrals over the boundary Γ_u with prescribed zero displacements and Γ_f with prescribed zero loads are equal to zero and are therefore omitted from Eq. (6).

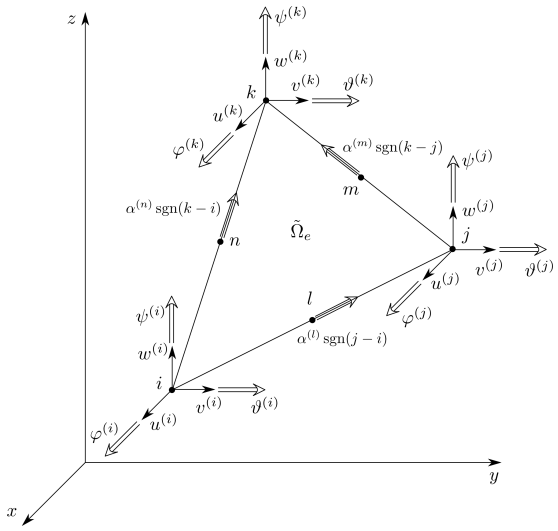


Figure 2: Six-noded thin flat shell triangular finite element $\tilde{\Omega}_e$ after transformation.

3 FINITE ELEMENT DISCRETISATION

If we consider the Helmholtz equation for the cavity in the weak form (5) and the equation of motion (6) for the housing in the amplitude form for the given excitation frequency, then the solution of both aforementioned equations will take the form of complex pressure amplitudes within the cavity and velocity amplitudes at the housing surface.

The FE discretisation of the Helmholtz equation, describing the distribution of acoustic pressure amplitudes within the cavity subdomain $\Omega \subset \mathbf{R}^3$, was carried out using a tetrahedral 3D finite element described in [1]. For the FE discretisation of the housing subdomain $\tilde{\Omega} \subset \mathbf{R}^3$, a new 6-noded thin flat shell triangular finite element $\tilde{\Omega}_e$ with 21 degrees of freedom (DOF) was developed. The proposed thin flat shell element is based on the Kirchhoff plate theory [4]. After transformation, each corner node i, j and k contains three displacements u, v, w and three rotations φ, ϑ and ψ. The midside nodes l, m and n store the information about the rotation angle around the element edge, where the sense of rotation is determined by the sign of difference of numbers of the corresponding edge corner nodes, see Figure 2. For more details, see [1].

The FE discretisation of both the cavity and the housing subdomains yields the following equation describing their interaction in the vibro-acoustic problem solved in this paper

$$\begin{bmatrix} i\omega\mathbf{H} + \mathbf{G} + \frac{1}{i\omega}\mathbf{F} & \mathbf{Z} \\ \mathbf{Z}^T & i\omega\mathbf{M} + \mathbf{B} + \frac{1}{i\omega}\mathbf{K} \end{bmatrix} \begin{bmatrix} \mathbf{p} \\ \dot{\mathbf{q}} \end{bmatrix} = \begin{bmatrix} \mathbf{A}_f\mathbf{v}^{in} \\ \mathbf{f} \end{bmatrix}, \tag{7}$$

where $\mathbf{M}$, $\mathbf{B}$ and $\mathbf{K}$ are the matrices of mass, damping and stiffness, respectively. In the case of the cavity subdomain (the upper part of Eq. (7)), the coupling matrix $\mathbf{Z}$ represents the boundary condition of normal velocity shared by the cavity boundary and the housing subdomain (the fifth term in Eq. (5)). In the case of the housing subdomain, it corresponds to the pressure exerted by the cavity on the housing. The matrices $\mathbf{H}$ and $\mathbf{F}$ are the result of FE discretisation of the first two terms in Eq. (5), which describe the distribution of acoustic pressure amplitudes within the cavity without the influence of boundary conditions. The application of the anechoic outlet boundary condition yields the matrix $\mathbf{G}$, which corresponds to the third term in Eq. (5) and expresses the fact that the acoustic wave is reflection-free. The prescription of given velocity amplitudes at the inlet leads to $\mathbf{A}_f\mathbf{v}^{in}$, which corresponds to the fourth term in Eq. (5). The

vector $\mathbf{f}$ is the complex amplitude vector of external forces exerted on the housing subdomain. Note that the derivation of the matrices appearing in Eq. (7) was demonstrated in the paper [1] for one finite element. The global matrices are assembled using a standard FEM procedure.

The resulting emitted acoustic power can be computed from normal acoustic velocities and amplitudes of acoustic pressure defined in points located at the housing surface. The amplitudes of acoustic pressure can be determined from the condition of anechoic outlet (4) applied to the outer surface of the housing subdomain Γ_t. Then, for the emitted acoustic power, it holds

$$P_{acoustic} = \int_{\Gamma_t} \boldsymbol{v} \cdot \boldsymbol{n}\, p \,\mathrm{d}S = \int_{\Gamma_t} v_n\, p \,\mathrm{d}S \overset{\text{Eq.(4)}}{=} \int_{\Gamma_t} v_n^2\, \varrho_a\, c \,\mathrm{d}S. \tag{8}$$

4 NUMERICAL RESULTS

The proposed methodology for the numerical solution of vibro-acoustic problems in mobile screw compressors was implemented in our in-house 3D FE solver developed in MATLAB. The computational ability of this solver was tested on two examples – test cases No.1 a No.2 described in Sections 4.1 and 4.2.

4.1 Test case No.1

The numerical solution of the vibro-acoustic problem was first carried out for a test computational domain, the geometry of which was that of a $1 \times 0.7 \times 0.5\,\mathrm{m}$ block shown in Figure 3. The bottom of the computational domain was assumed to be perfectly rigid and corresponding to the cavity subdomain boundary Γ_w. The remaining walls of the computational domain formed the interface Γ_t between the cavity and the elastic structure (housing), which was made of a thin metal sheet with thickness of $1\,\mathrm{mm}$, density $\varrho_h = 7\,800\,\mathrm{kg/m^3}$, Young's modulus $E = 2.1 \times 10^{11}\,\mathrm{Pa}$ and Poisson ratio $\mu = 0.3$. Within the cuboidal cavity, there was another smaller perfectly rigid block $(0.1 \times 0.2 \times 0.2\,\mathrm{m})$, Figure 3, situated $0.1\,\mathrm{m}$ above the bottom of the computational domain. At the upper and lower walls (domain boundary Γ_{in}) of the smaller block, we prescribed a normal velocity $v_n \equiv v_y$ with amplitude $0.05\,\mathrm{m/s}$ and excitation frequency $f = 100\,\mathrm{Hz}$. At the side walls, zero normal velocity v_n was given. The density of air within the cavity was set equal to $\varrho_a = 1.2\,\mathrm{kg/m^3}$ and the speed of sound was assumed to be $c = 340\,\mathrm{m/s}$. In this test case, the system without damping was considered. The space discretisation of the cavity for the developed 3D FE solver as well as the professional computational FE system Radioss was carried out for an unstructured tetrahedral mesh consisting of around 15 000 elements with edge lengths around $5\,\mathrm{cm}$, Figure 7 (right). Moreover, the solution in Radioss also required the elastic structure (housing) to be discretised with around 2 700 thin shell elements, the size of which was approximately the same as in the case of the cavity mesh.

Figure 4 shows the distribution of acoustic pressure amplitudes in the axial longitudinal section of the cavity subdomain computed by the developed 3D FE solver. This acoustic pressure distribution was compared with the results provided by the professional computational FE system Radioss using the modal approach for the solution of the considered vibro-acoustic problem. The computations in the system Radioss were carried out for different numbers of eigenfrequencies and eigenmodes of the cavity and the elastic structure considered by the computation of the system response. As expected, the obtained numerical results showed that both the distribution of the acoustic pressure in the cavity and the distribution of the acoustic velocity at the structure surface are dependent on the number of considered eigenmodes. Taking into consideration the computed maximum values of acoustic pressure, this dependency is well

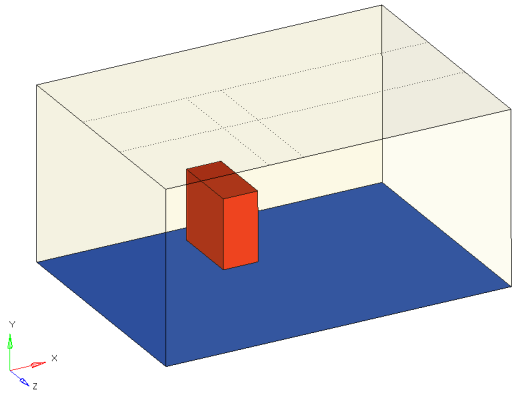


Figure 3: Geometry of the computational domain considered in the test case No.1.

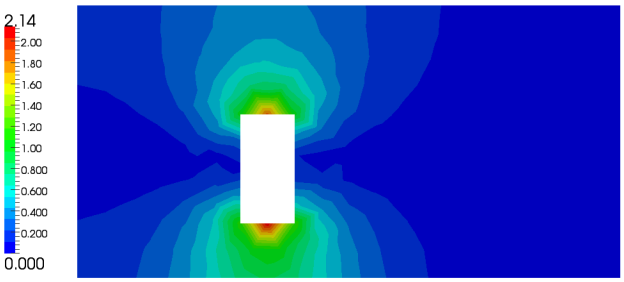


Figure 4: Acoustic pressure amplitudes in the axial longitudinal section of the cavity computed by the developed 3D FE solver.

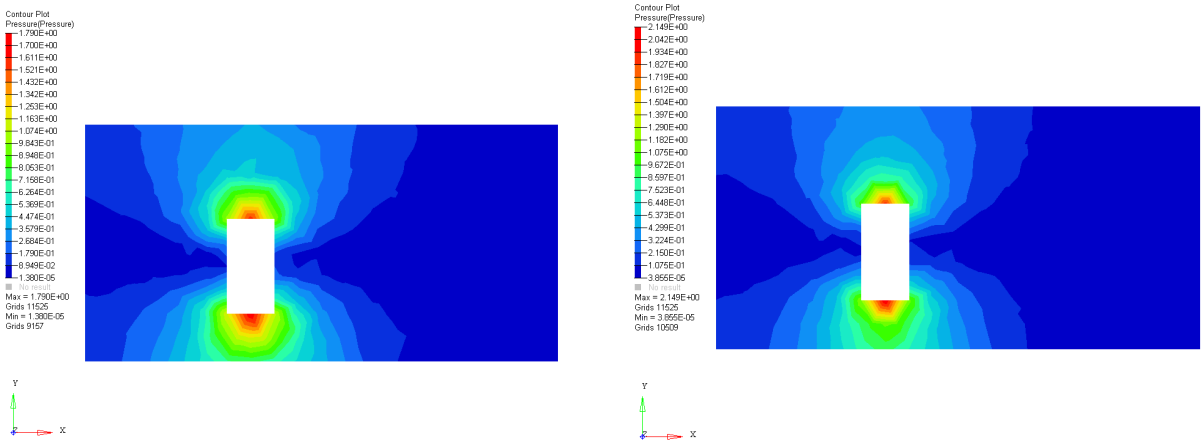


Figure 5: Acoustic pressure amplitudes in the axial longitudinal section of the cavity computed by the professional FE system Radioss for 1 000 and 50 (*left*) and 2 000 and 100 (*right*) cavity and structure eigenmodes.

No. of eigenmodes		
cavity	structure	p_{max} [Pa]
200	200	1.126
500	200	1.433
1 000	200	1.790
1 000	500	1.791
2 000	500	2.149
1 000	100	1.790
1 000	50	1.790
3 000	50	2.118
2 000	100	2.149

Table 1: Number of cavity and structure eigenmodes with corresponding maximum pressure amplitudes p_{max}.

apparent from Table 1. With the help of the developed direct 3D FE solver, the maximum acoustic pressure was determined as 2.14 Pa, see Figure 4. From Table 1, it can be also noted that in order to achieve an acoustic pressure amplitude comparable with the one provided by the developed direct 3D FE solver, it is necessary to consider at least 2 000 eigenmodes of the

cavity and 100 eigenmodes of the structure. The eigenfrequencies corresponding to the 2 000th eigenmode of the cavity and the 100th eigenmode of the structure are 2.67 kHz and 180 Hz. Figure 5 shows the distribution of acoustic pressure amplitudes in the axial longitudinal section of the cavity computed by the professional computational FE system Radioss for the combination of 1 000 and 50 or 2 000 and 100 cavity and structure eigenmodes. By comparing Figure 4 and Figure 5 (right), it is possible to observe that the results computed by the developed 3D FE solver and the professional computational FE system Radioss are in relatively good agreement when the combination of 2 000 and 100 eigenmodes is taken into consideration. A similarly good agreement between both solvers could be achieved for the computation of acoustic velocity amplitudes at the surface of the elastic structure, as apparent from Figures 6 and 7. The maximum velocity amplitude computed by the developed 3D FE solver was $2.25 \times 10^{-4}\,\mathrm{m/s}$, Figure 6, while the professional FE solver Radioss provided a value of $2.03 \times 10^{-4}\,\mathrm{m/s}$, see Figure 7 (right).

In accordance with Eq. (8), the emitted acoustic power was computed as $2.1663 \times 10^{-6}\,\mathrm{W}$.

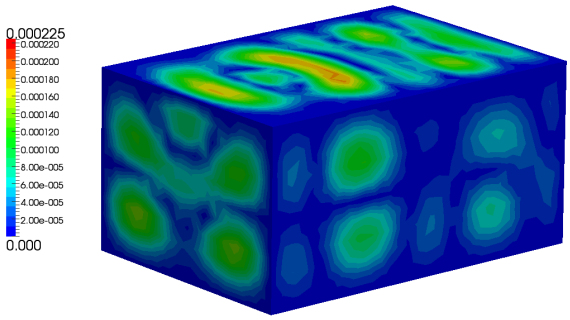


Figure 6: Velocity amplitudes at the surface of the elastic structure computed by the developed 3D FE solver.

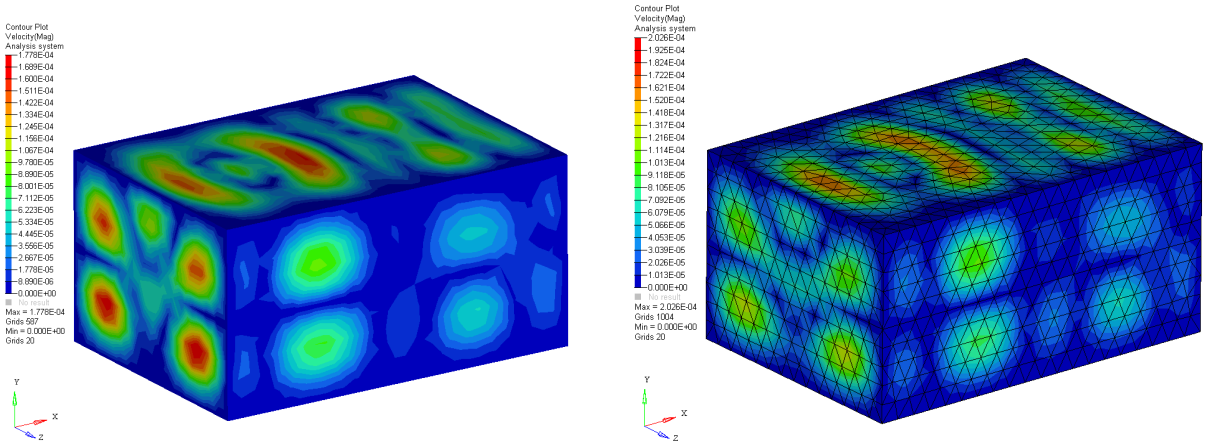


Figure 7: Velocity amplitudes at the surface of the elastic structure computed by the professional FE system Radioss for 1 000 and 50 (*left*) and 2 000 and 100 (*right*) cavity and structure eigenmodes.

4.2 Test case No.2

Following the previous test case, the vibro-acoustic problem was numerically solved in a $2.6 \times 1.3 \times 1.1$ m test computational domain, the geometry of which corresponded to the housing of a real mobile screw compressor, Figure 8. The numerical solution was carried out under

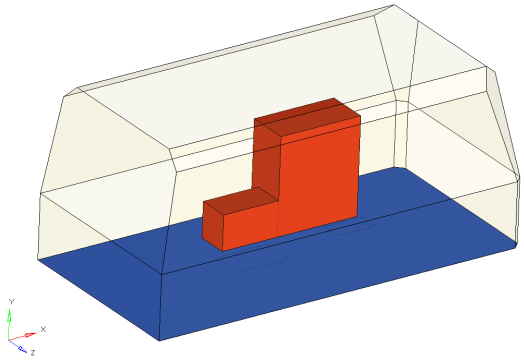


Figure 8: Geometry of the computational domain considered in the test case No.2.

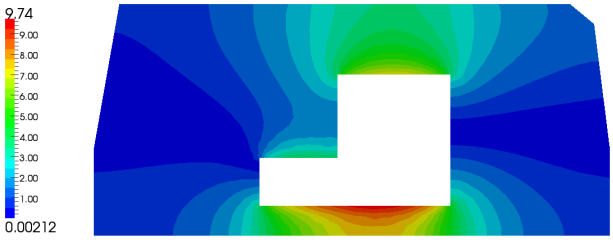


Figure 9: Acoustic pressure amplitudes in the central longitudinal section of the cavity computed by the developed 3D FE solver.

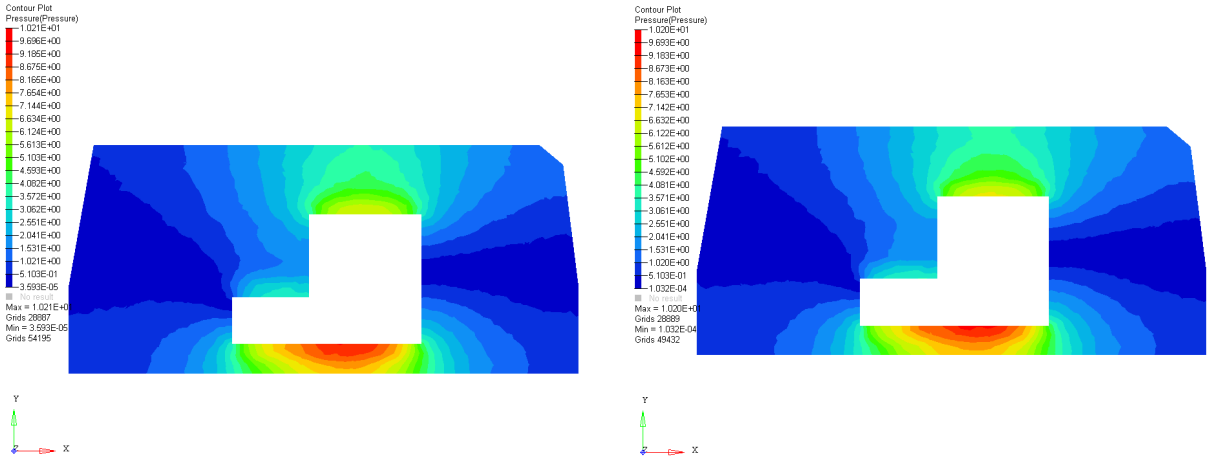


Figure 10: Acoustic pressure amplitudes in the axial longitudinal section of the cavity computed by the professional FE system Radioss for 2 000 and 100 (*left*) and 5 000 and 400 (*right*) cavity and structure eigenmodes.

the same conditions and assumptions as in the previous test case, with the only exception that the size and position of the excitation source now better reflected the size and position of the real engine and compressor assembly within the cavity. Once again the normal velocity $v_n \equiv v_y$ was prescribed at the upper and lower walls of the assembly, while the amplitude and frequency were chosen to be the same as in the previous test case. The space discretisation of the cavity for the developed 3D FE solver as well as the professional computational FE system Radioss was carried out for an unstructured tetrahedral mesh consisting of approximately 151 000 tetrahedral elements with edge lengths around 5 cm, see Figure 12 (right). The solution in Radioss additionally required the elastic structure (housing) to be discretised with around 13 500 thin shell elements, the size of which was approximately the same as in the case of the cavity mesh.

Figure 9 shows the distribution of acoustic pressure amplitudes in the axial longitudinal section of the cavity computed by the developed direct FE solver. Similarly to the previous test case, this distribution was compared with the one provided by the professional FE system Radioss, see Figure 10. The left picture in Figure 10 shows the distribution of acoustic pressure amplitudes computed for considered 2 000 cavity and 100 structure eigenmodes. Note that the eigenfrequencies of the system corresponding to the 2000th cavity and the 100th structure eigenmodes were 1.54 kHz and 52 Hz, respectively. The combination of 5 000 cavity and 400 structure eigenmodes is shown in Figure 10 (right). Here, the corresponding eigenfrequencies

were stated to be 1.94 kHz a 158 Hz. As can be noted from Figure 10, the distribution of acoustic pressure amplitudes is almost identical in both eigenmode combinations, especially when they yielded the same maximum acoustic pressure of 10.2 Pa. The results are in very good agreement with the ones computed by the developed direct FE solver, Figure 9, which provided maximum acoustic pressure of 9.74 Pa. A good result agreement between the developed FE solver and the professional FE system Radioss could be also achieved by the computation of acoustic velocity amplitudes at the housing surface, as seen when comparing Figures 11 and 12 (right). The maximum velocity amplitude computed by the developed FE solver was $2.43 \times 10^{-3}\,\mathrm{m/s}$, Figure 11, while the professional FE system Radioss provided a value of $2.31 \times 10^{-3}\,\mathrm{m/s}$ when the combination of 5 000 cavity and 400 structure eigenmodes was taken into consideration, Figure 12 (right). From Figure 12 (left), it is well apparent that the combination of 2 000 cavity and 100 structure eigenmodes (this modal reduction) is not suitable for the computation of acoustic velocities, even though it is able to provide a distribution of acoustic pressure amplitudes that is comparable with that computed by the developed direct FE solver.

In accordance with Eq. (8), the emitted acoustic power was computed as 4.044×10^{-4} W.

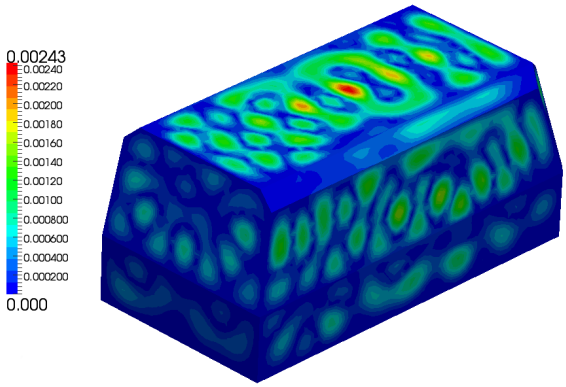


Figure 11: Velocity amplitudes at the housing surface computed by the developed 3D FE solver.

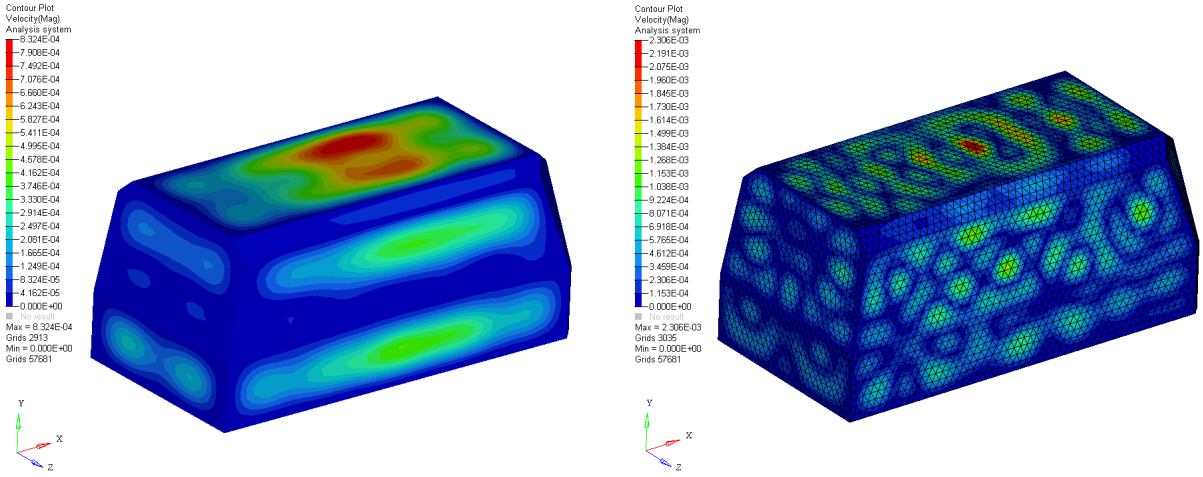


Figure 12: Velocity amplitudes at the housing surface computed by the professional FE system Radioss for 2 000 and 100 (*left*) and 5 000 and 400 (*right*) cavity and structure eigenmodes.

4.3 Vibro-acoustic problem in a simplified model of real mobile screw compressor

By using the professional computational FE system Radioss, the numerical solution of the vibro-acoustic problem is carried out in a computational domain that represents a simplified model of the real mobile screw compressor PDP70, Figure 13 (left), the geometry of which was prepared according to the technical drawings provided by the compressor producer ATMOS Chrást, Ltd. The bottom of the computational domain was assumed to be perfectly rigid and corresponding to the cavity subdomain boundary Γ_w. The cavity contained the most significant compressor components such as the pressure vessel of the oil separator, the fuel tank, the battery and the fan cover, Figure 13 (right), which were all connected to the cavity bottom. The cavity subdomain was surrounded by an elastic wall made of a thin metal sheet with thickness of 1.5 mm and enforced by stiffening ribs with thickness between 1.5 and 3 mm (the housing of the compressor). The presence of the stiffening ribs is well apparent in Figure 13. In this vibro-acoustic problem, the source of excitation was the engine and compressor assembly, which was once again assumed to be rigid. The surface of this assembly corresponded to the domain boundary Γ_{in} with prescribed acoustic velocity. Experimental measurements of velocity were performed at this surface at three points denoted as M1, M6 and M20, see Figure 13 (right). The Fourier spectrum of velocity components measured at the aforementioned points is shown in Figure 14 for the excitation frequency range between 20 Hz to 2 kHz. With regard to the fact that a rigid body has 6 DOF, the number of prescribed velocity components at each of the three points was chosen as follows: v_x, v_y, v_z at M1, v_y, v_z at M6 and v_z at M20. The material parameters used for the numerical solution of this vibro-acoustic problem were taken the same as in the previous two test cases. However, compared to the two test cases, the current problem considered a damped system. The space discretisation of the cavity was carried out by using an unstructured mesh consisting of around 1 800 000 tetrahedral elements, while the housing was discretised with almost 120 000 thin shell elements, the size of which was approximately 2 cm.

Using the modal approach in the professional computational FE system Radioss, the numerical solution of the vibro-acoustic problem was carried out up to the eigenfrequency of 2 kHz for both the cavity and the compressor housing. This eigenfrequency threshold corresponds to the 3164th and the 4708th considered eigenmodes of the cavity and the elastic structure (housing), respectively. The results of the numerical solution consisted of the complex amplitudes of acoustic pressure within the cavity and the complex amplitudes of acoustic velocity at the hous-

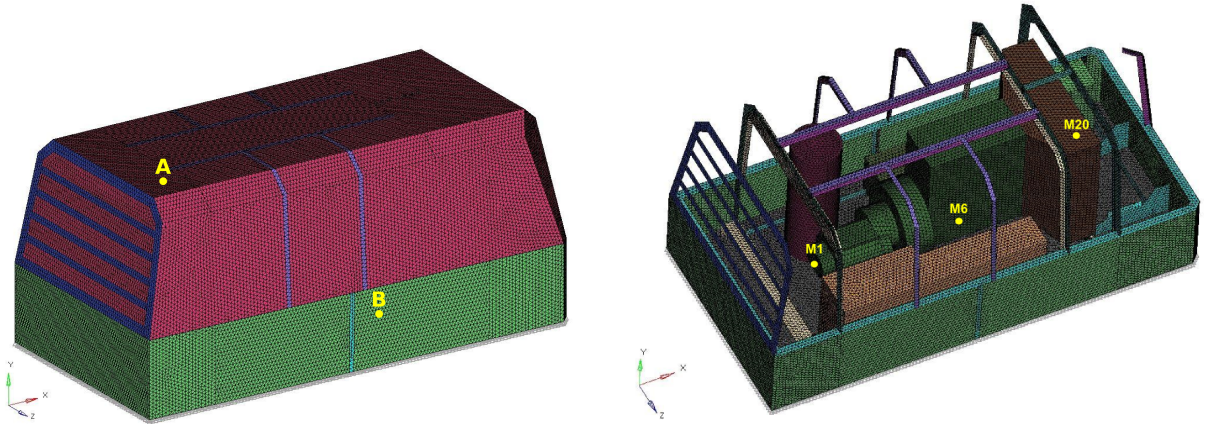


Figure 13: Simplified model of a real mobile screw compressor – housing (*left*) and cavity with the most significant components (*right*).

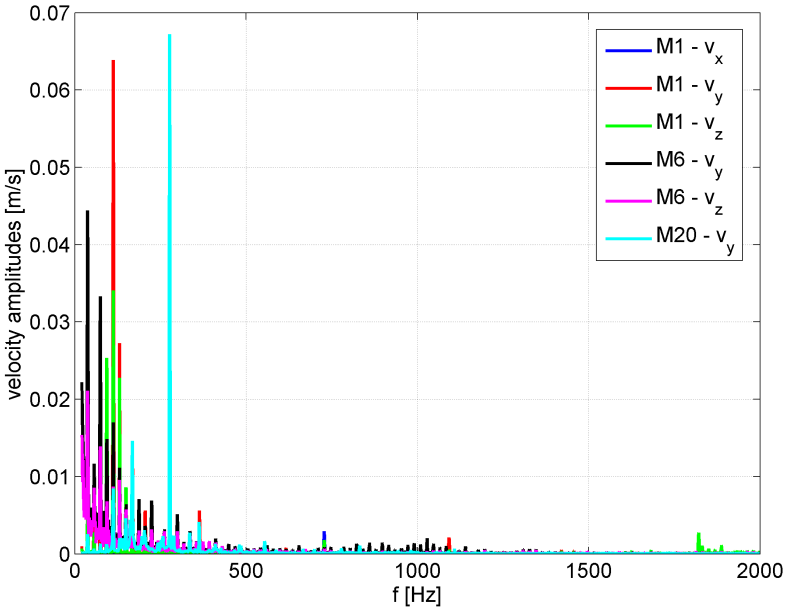


Figure 14: Fourier spectrum of velocity components measured at the points shown in Figure 13 (right).

ing surface, computed for each excitation frequency. Figure 15 shows the obtained distributions of acoustic pressure amplitudes in selected sections of the cavity for the excitation frequencies 1 kHz and 2 kHz. The final distribution of acoustic pressure amplitudes after the superposition over all excitation frequencies, which were taken in accordance with the frequency range considered during the experimental measurements (Figure 14), is shown in Figure 16.

In the same context as in the case of acoustic pressure amplitudes, Figures 17 and 18 show the distributions of amplitudes of the acoustic velocity components v_y and v_z, respectively, at the housing surface for the excitation frequencies 1 kHz and 2 kHz. The resulting amplitude distribution of both aforementioned acoustic velocity components after the superposition over all excitation frequencies, which were taken in accordance with the frequency range considered during the experimental measurements (Figure 14), is visualised in Figure 18.

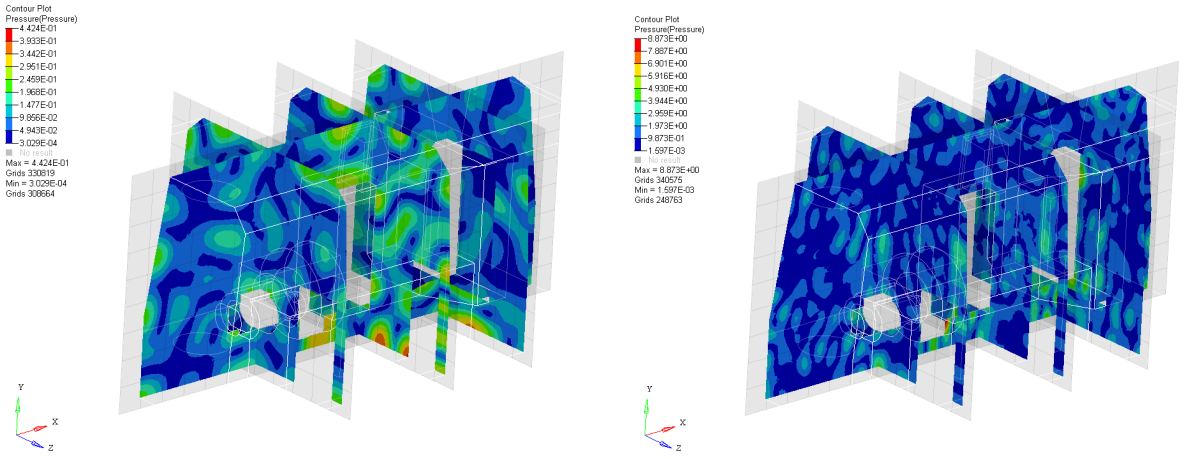


Figure 15: Acoustic pressure amplitudes in selected sections of the cavity computed by the professional FE system Radioss for the excitation frequencies 1 kHz (*left*) and 2 kHz (*right*).

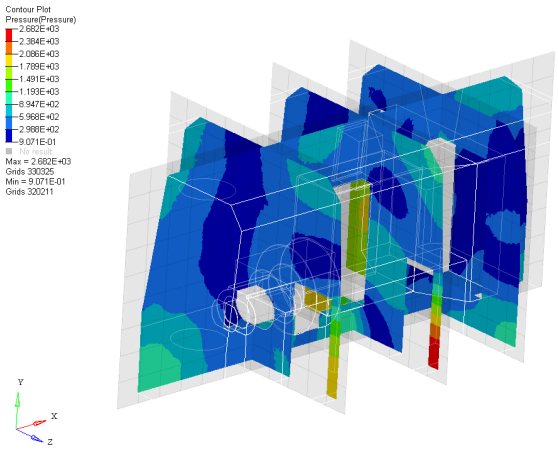


Figure 16: Acoustic pressure amplitudes in selected sections of the cavity after the superposition over all excitation frequencies.

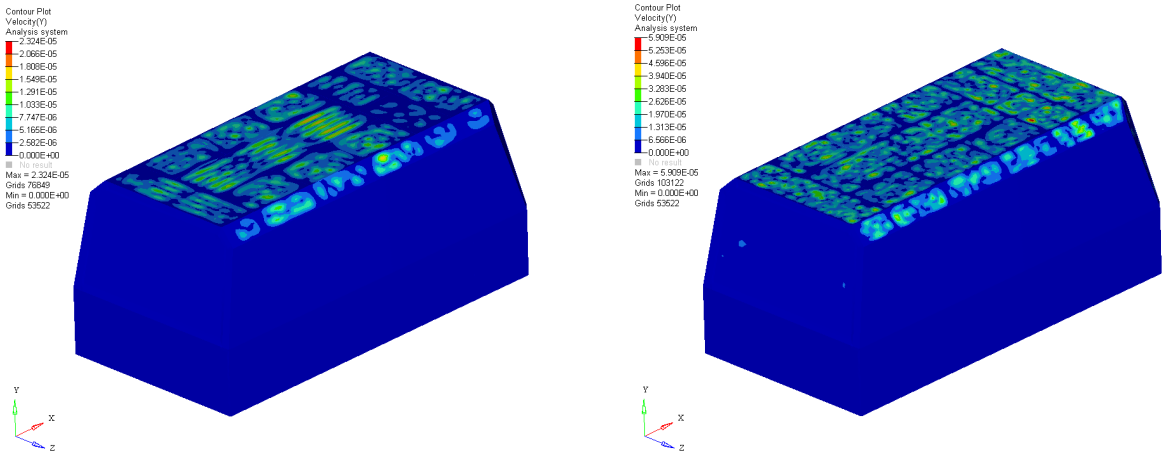


Figure 17: Amplitudes of the acoustic velocity component v_y at the housing surface computed by the professional FE system Radioss for the excitation frequencies 1 kHz (*left*) and 2 kHz (*right*).

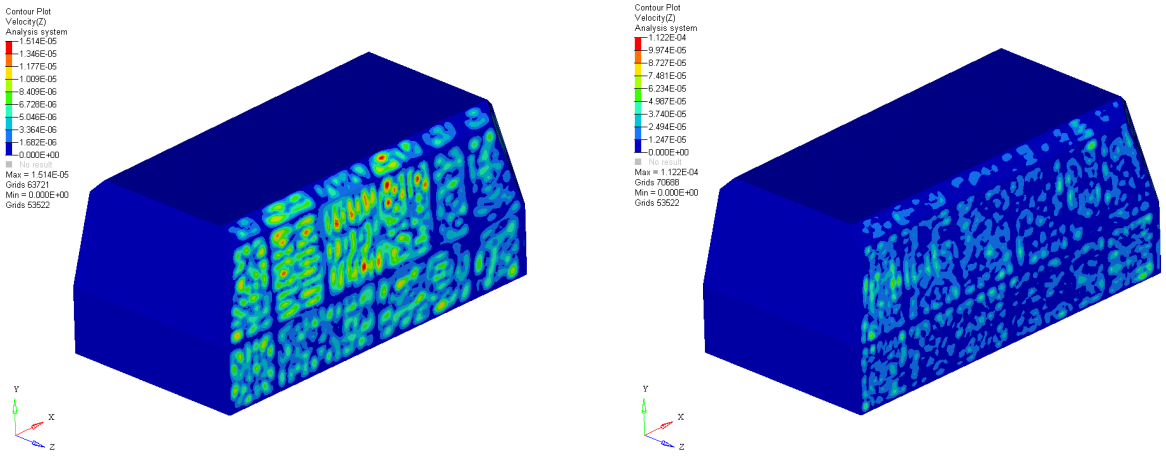


Figure 18: Amplitudes of the acoustic velocity component v_z at the housing surface computed by the professional FE system Radioss for the excitation frequencies 1 kHz (*left*) and 2 kHz (*right*).

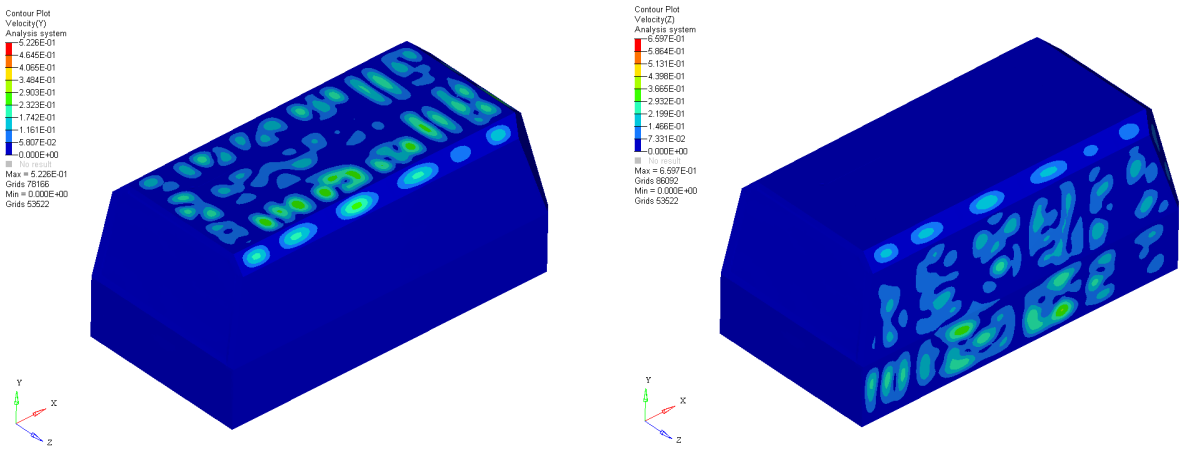


Figure 19: Amplitudes of the acoustic velocity components v_y (*left*) and v_z (*right*) after the superposition over all excitation frequencies.

A comparison of computed and measured acoustic velocity components v_y in the frequency domain was carried out for one selected point located on the housing roof (denoted by A in Figure 13 (left)) with the result shown in Figure 20. Analogously, Figure 21 provides the comparison of computed and measured acoustic velocity components v_z in the frequency domain for one selected point located on the housing side (denoted by B in Figure 13 (left)). On the basis of both comparisons, it can be noted that a good agreement between the computed and measured values was not reached. By taking into consideration the fact that the experimental measurements were carried out on a real mobile screw compressor under operating conditions, it is possible to deduce several factors that may have caused the observed differences. The first one is related to the simplified geometry of the cavity space, which did not include all of the components found in the real screw compressor, such as pressure hoses and cables. A certain influence on the computed results can be also attributed to the applied geometry of the engine and compressor assembly, which was simplified to the maximum possible extent. Although the

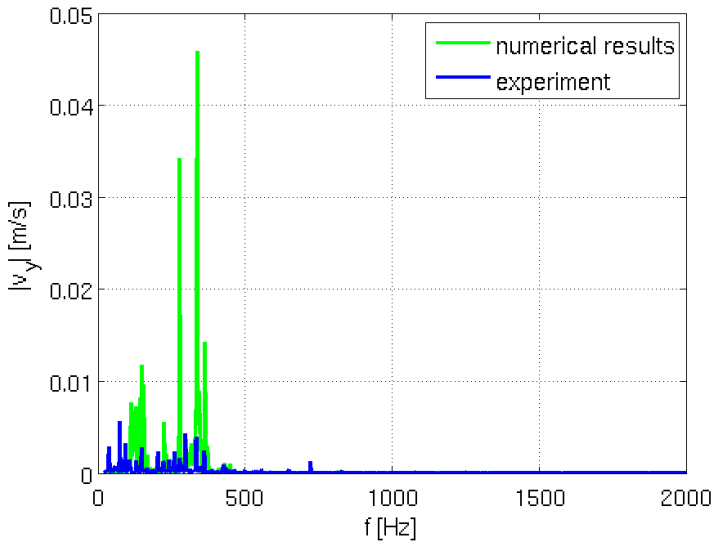


Figure 20: Comparison of computed and measured acoustic velocity components v_y in the frequency domain for the point A denoted in Figure 13 (left).

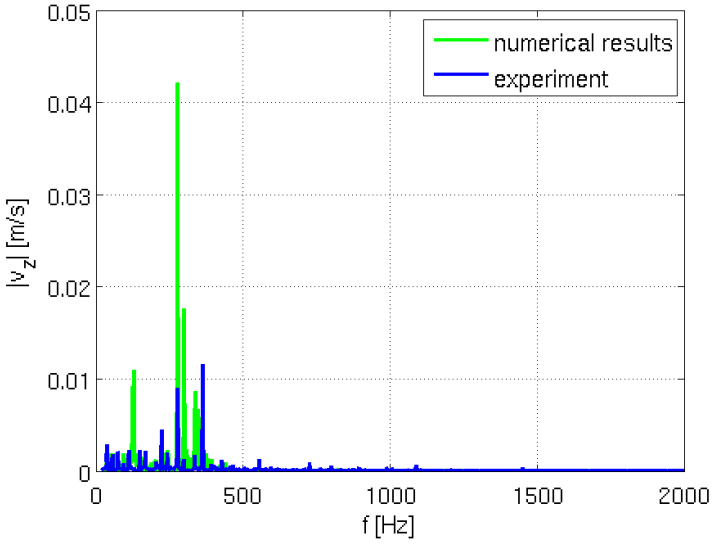


Figure 21: Comparison of computed and measured acoustic velocity components v_z in the frequency domain for the point B denoted in Figure 13 (left).

aforementioned simplifications certainly played a role in the disagreement between the computed and measured values, they were probably not the main cause. The reason why there are differences between the numerical and experimental data is most likely due to the computation of acoustic pressure within the cavity and housing vibrations, which were taken as a result of acoustic wave propagation from the engine and compressor assembly to the housing via the cavity. In reality, the housing vibrations are strongly influenced by the direct transmission of vibrations from the assembly to the housing through their joints. Compared to the performed experiments, the transmitted vibration was not considered in the present numerical study. Another cause of dissimilarities between the computed and measured results was the assumption that the engine and compressor assembly, including other cavity components, were modelled as rigid, even though in reality they are compliant to a certain extent.

5 CONCLUSIONS

For the FE discretisation of the compressor housing subdomain carried out in this study, a new 6-noded thin flat shell triangular finite element with 21 DOF (6 DOF in corner nodes and 1 DOF in each element midside) was developed and implemented in the developed 3D FE solver for the numerical solution of vibro-acoustic problems in mobile screw compressors. The correctness of the developed flat shell finite element, the proposed methodology and the developed FE solver were verified for two test cases described in this study. The verification was carried out by comparing amplitudes of acoustic pressure within the cavity and amplitudes of acoustic velocity at the surface of the elastic structure (housing) computed by the developed direct FE solver with those provided by the modal approach of the professional FE system Radioss. A very good agreement between both FE solvers was achieved in both test cases. The development of our in-house FE solver is motivated by our effort to acquire a code open for future changes and modifications that would enable a consequent parameter optimisation aimed at the elimination or minimisation of the emitted acoustic power. In this case, the optimisation process could include a sensitivity analysis to determine how changes in the geometry and material parameters can affect the emitted noise. The considered test cases also revealed that

the developed direct FE solver was almost three times faster than the professional one when run on the same computer.

Unfortunately, due to high memory demands, the direct FE solver developed in MATLAB is not capable to solve large vibro-acoustic problems discretised to contain more than 1 500 000 finite elements. It is, therefore, understandable that our future efforts regarding the solver improvement will be oriented towards memory usage optimisation. The aforementioned high memory demands are the main reason why the numerical solution of the vibro-acoustic problem involving the simplified model of real mobile screw compressor, was carried out only by the professional FE system Radioss. To assess the numerical results, we compared them with the experimental data provided by measurements carried out under operating conditions on the real mobile screw compressor PDP70 produced by the company ATMOS Chrást, Ltd. As already discussed in Section 4.3, the observed differences in results were mainly caused by the following factors, which can be seen as the limitations of the study:

- The experimental data included vibrations caused by energy transmission between the engine and compressor assembly and the housing via their joints. Compared to this, our study respected the vibration transmission between the aforementioned components only through the acoustic component, i.e., the observed vibrations were the result of acoustic wave propagation from the assembly surface to the surrounding housing via the compressor cavity.
- Compared to the reality, the present study also adopted the simplification that the engine and compressor assembly, including other components situated within the cavity, were assumed to be rigid. Moreover, the experimental data only contained information on the measured amplitude spectra of velocity components and did not provide the corresponding phase.
- In this study, the real geometry of the cavity subdomain was considerably simplified by omitting components such as pressure hoses and electrical cables. The shape of the engine and compressor assembly was simplified, as well.

ACKNOWLEDGEMENTS

This study was supported by the European Regional Development Fund (ERDF), project NTIS – New Technologies for the Information Society, European Centre of Excellence, CZ.1.05/1.1.00/02.0090. The authors of this study would like to thank the company ATMOS Chrást, Ltd., which as a compressor producer provided the necessary technical drawings. The experimental data used for the purpose of this study were acquired by Ing. Oldřich Tureček, Ph.D. and Ing. Martin Sýkora, Ph.D. from the Faculty of Electrical Engineering, University of West Bohemia, whose help is thereby gratefully acknowledged. The assistance of Ing. Alena Jonášová, Ph.D. during the preparation of the manuscript is acknowledged, as well.

REFERENCES

[1] J. Dupal, J. Vimmr, O. Bublík, M. Hajžman, Modelling of acoustic power radiation from mobile screw compressors. Z. Dimitrovová et al. eds. *11th International Conference on Vibration Problems*, Lisbon, Portugal, September 9-12, 2013.

[2] L.E. Kinsler, A.R. Frey, A.B. Coppens, J.V. Sanders, *Fundamentals of acoustics, 4th Edition*. John Wiley & Sons, Inc., 2000.

[3] S. Temkin, *Elements of acoustics*. Acoustical Society of America, 2001.

[4] E. Oñate, *Structural analysis with the finite element method. Linear statics. Volume 2 – Beams, plates and shells*. Lecture Notes on Numerical Methods in Engineering and Sciences, CIMNE, 2013.

COMPDYN 2015
5th ECCOMAS Thematic Conference on
Computational Methods in Structural Dynamics and Earthquake Engineering
M. Papadrakakis, V. Papadopoulos, V. Plevris (eds.)
Crete Island, Greece, 25–27 May 2015

INTERNAL PARAMETRIC RESONANCE AND AEROELASTIC EFFECTS FOR LONG-SPAN SUSPENSION BRIDGES

Raffaele Ardito[1], Antonio Capsoni[2], and Andrea Guerrieri[1,2]

[1] Dept. of Civil and Environmental Engineering, Politecnico di Milano
Piazza Leonardo da Vinci 32, Milan, Italy
raffaele.ardito@polimi.it

[2] Dept. of Architecture, Built Environment and Construction Engineering, Politecnico di Milano
Piazza Leonardo da Vinci 32, Milan, Italy
antonio.capsoni@polimi.it, andrea.guerrieri@mail.polimi.it

Keywords: Suspension Bridges, Non-linear Dynamics, Aeroelasticity, Stability, Parametric Resonance, Floquet Theory.

Abstract. *The potential occurrence of internal parametric resonance phenomena has been recently indicated as a possible cause of failure for long-span suspension bridges. At the same time, suspension bridges, in view of their flexibility, are prone to aeroelasticity driven response, such as vortex shedding, torsional divergence and flutter. In this paper, a non-linear dynamic model of a suspension bridge is devised, with the purpose of providing a unified framework for the study of aeroelastic and internal resonance instabilities. Inspired by the pioneering work of Herrmann and Hauger, the analyses have been based on a linearized formulation that is able to represent the main structural non-linear effects and the coupling given by aerodynamic forces. The results confirm that the interaction between aeroelastic effects and non-linear internal resonance leads to unstable phenomena for wind speeds which are by far lower than the critical threshold for standard aeroelasticity.*

1 INTRODUCTION

The emergence of new materials and advanced structural engineering technology makes suspension bridges a spontaneous answer for demands of larger spans, light weight, high strength, ease of construction, and aesthetic appearance. On one hand, the flexibility caused by the cable system and its long span makes the suspension bridges sensitive to dynamic loads; on the other hand, the relatively simple geometry of cable structures makes continuum approaches still very attractive, since can be based on a minimal number of non-dimensional parameters.
Early attempts on static equilibrium of suspension bridge were made by Moisseiff, who extended the elastic theory to the well-established Deflection Theory [1,2] by enforcing equilibrium in the deformed position, and accounting for the stiffening effect in the main cables. Earliest continuum models for the linear vertical vibrations of suspension bridges reproduced the effects of the stiffening truss girder by means of an Euler–Bernoulli beam supported by the main cables through inextensible and distributed vertical hangers. In this regard, the classic continuum model for the linear vertical vibration of suspension bridges, based on the so called linearized deflection theory, was first proposed by Bleich et al. [3], and Steinman [4], which derived some formulas for computing natural frequencies and mode shapes, and recently reviewed by Luco and Turmo [5]. The last authors showed that the linear vibration of the considered suspension bridge model is completely governed by two non-dimensional parameters: the classic Irvine parameter of suspended cables, first introduced by Irvine [6] and a second parameter accounting for the relative stiffness of the girder with respect to the main cable system. Abdel-Ghaffar in the late 1970's [7-9] developed the methodology of free vertical, torsional and lateral vibration analysis of suspension bridges by means of a variational principle and a finite element approach. Then, the same author [10-12] extended the continuum formulation to include coupling between vertical–torsional vibrations, nonlinear effects occurring in the case of large vibrations and the effects of distortional deformation of the girder cross-section.
Nowadays, in the design of suspension bridges a comprehensive set of wind related responses are taken into consideration, such as static divergence, vortex-shedding, buffeting and flutter. Hence, the risk of developing aeroelastic instabilities is always the matter while designing any lightweight long-span structures, characterized by high flexibility due to a low bending/torsional stiffness and a high width-to-depth ratio. Although the phenomenon was already well known in aviation, the research on flutter in civil engineering field started as the collapse of the Tacoma Narrows Bridge (USA) in 1940, when the catastrophe was seen mainly as a direct consequence of flutter [13] that developed on the bridge deck at wind speed much lower than the design one. Flutter is generally studied within linearized aeroelastic models, which can provide the range of wind speeds where Hopf bifurcation occurs. To consider the effects due to the unsteadiness of the relative motion between the section and the air flow, indicial Theodorsen type [14,15] formulations can be adopted to predict more accurately the critical wind speed at the onset of the flutter instability [16] with respect to the quasi-steady formulation. The equations of motion for suspension bridges were employed for aeroelastic investigations in [17], where analysis are centered on experimentally determined flutter derivatives, and a full three-dimensional modal analysis of the structure.
It's well known from non-linear dynamics that, between coupled oscillators, energy transfer [18] can occur as far as the energetic levels reaches critical well established thresholds. Classically this behaviour is referred to as the *internal resonance* phenomenon. Many authors applied this principles to study the vibrations response of suspension bridges. The authors of [19,20] used the continuous model proposed by Abdel-Ghaffar [11], and solve the system of

equations by means of the multiple scale perturbative technique [21]. Recently, Airoli and Gazzola [22], trying to explain why did torsional oscillations suddenly appears before the Tacoma Narrows collapse, found out that also in isolated systems as vertical oscillations become large enough they may switch to torsional ones. The problem was already tackled by other authors [23-27] but no one was able to identify the actual causes of that sudden large torsional oscillations. Hence, they paved the way for future works concerning the interaction between internal resonance and aeroelastic phenomena, as the present paper wants to do.
The article intends to study the stability of a suspension bridge model using the continuum formulation proposed by Abdel-Ghaffar in [11] enriched by the terms coming from Theodorsen [15] indicial formulation for the wind-structure interaction. The stability will be checked in Lyapunov asymptotic sense exploiting the well-known Floquet theory [28]. The varational system of equations is obtained following the procedure proposed by Herrman [29] assuming small but finite flexural perturbations coming from vortex-shedding excitation. The possibility of parametric internal resonances such as harmonic, sub-harmonic and super-harmonic, or additive combinational and anti-resonances will be checked by means of suitable stability maps.
Section 2 starts with a brief review of the parametric modal analysis for the continuum suspension bridge model [11] focusing on the so called cross over frequencies already proposed in [5] for the only flexural oscillations, and here extended to the torsional component. In Section 3, the aerodynamic additional mass, stiffness and damping are introduce in the original model by means of the analytical formulation [30] for the so called Flutter derivatives. Section 3 is devoted to the linearized variational system of equations projected in the modal space. The analysis of stability maps confirm the possibility of parametric resonance of 2:1 type between flexural and torsional motion already verified by other authors [11,19,20] by means of analytical procedure but on the complete non-linear original system of equations. The importance of bridge's deck sectional shape factor will be stressed out in order to explain Parametric resonance phenomenon by means of Strohual linear law for vortex-shedding excitation. Conclusions will be delegate to Section 4.

2 STRUCTURAL PROBLEM FORMULATION

A continuum model of single span, linearly elastic, suspension bridge is considered (Fig. 1). The bridge, having a span length *l*, is composed by two main cables that support the stiffening girder (bridge deck) through uniformly distributed, massless and inextensible vertical hangers. The main cables are hinged at fixed anchors placed at the same vertical elevation and are modeled as mono-dimensional continua with negligible flexural, torsional and shear rigidities. The stiffening girder is modeled as an equivalent, uniform, Euler-Bernoulli beam, with flexural hinges and torsional forks at its ends. The distortional deformation of the cross-section is neglected. The cross-section of the girder has double symmetry with respect to vertical and horizontal local axes, y and z respectively (Fig. 1). The contribution of the stiffening girder in carrying dead loads is disregarded: dead loads are entirely carried by the main cables and are assumed to be uniformly distributed along the longitudinal axis.

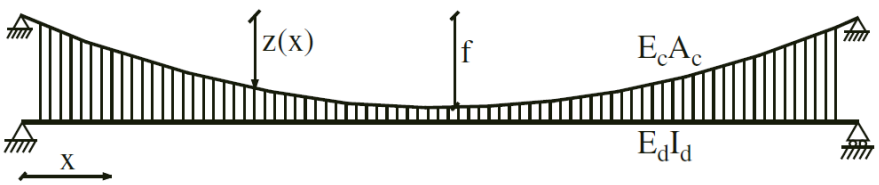


Figure 1: Single span suspension bridge model

2.1 Nonlinear coupled equations of motion

The motion of the bridge is described by means of three generalized displacement functions (Fig. 2): vertical deflection $w_d(x,t)$, twist rotation $\theta_d(x,t)$ about the longitudinal centerline of the deck-cables system and warping displacement $u_d(x,t)$ of the cross-section, t denoting time. The equations of motion are derived by means of Hamilton's principle $\delta\left\{\int_{t_1}^{t_2}(T-V+W)dt\right\}=0$, where $\delta\{\cdot\}$ is the variational operator, T and V are the total kinetic and potential energies of the system, respectively, W is the work done by external forces and t_1 and t_2 are arbitrary time instants.

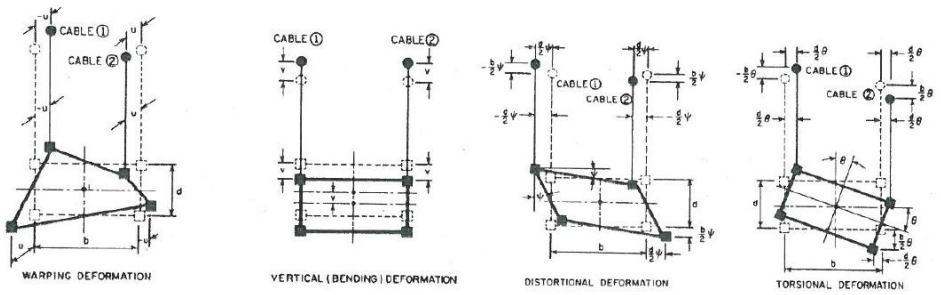


Figure 2: Four principal different kinds of displacements

The development of Hamilton's equation yields the non-linear coupled equations of motion of the suspension bridge with the associated boundary conditions. Detailed calculations are omitted for the sake of brevity. After some manipulations, the following dimensionless equations are obtained. Notice that the equations are written separating the linear from the quadratic and cubic parts on different rows.

$$\frac{d^2\tilde{w}_d}{d\tau^2}+\mu^2\cdot\tilde{w}_d{}^{\prime v}-\tilde{w}_d{}^{\prime\prime}+\lambda_L{}^2\tilde{h}_w+$$

$$flexural\ :\quad -\lambda_Q{}^2\cdot\left[\tilde{h}_w\cdot\tilde{w}_d{}^{\prime\prime}+\tilde{h}_\vartheta\cdot\tilde{\vartheta}_d{}^{\prime\prime}-\frac{1}{2}\left(\tilde{h}_{w'w'}+\tilde{h}_{\vartheta'\vartheta'}\right)\right]+\quad=\tilde{q}(\xi,\tau)\qquad(1)$$

$$\left\lfloor\quad -\lambda_C{}^2\cdot\left[\frac{1}{2}\left(\tilde{h}_{w'w'}+\tilde{h}_{\vartheta'\vartheta'}\right)\cdot\tilde{w}_d{}^{\prime\prime}+\tilde{h}_{w'\vartheta'}\cdot\tilde{\vartheta}_d{}^{\prime\prime}\right]\quad\right\rfloor$$

$$\tilde{J}_t\cdot\frac{d^2\tilde{\vartheta}_d}{dt^2}+\frac{\beta^2}{\chi^2}\cdot\tilde{\vartheta}_d{}^{\prime v}-(1+\beta^2)\cdot\tilde{\vartheta}_d{}^{\prime\prime}+\lambda_L{}^2\tilde{h}_\vartheta+$$

$$\text{torsional}\ :\qquad -\lambda_Q{}^2\cdot\left[\tilde{h}_\vartheta\cdot\tilde{w}_d{}^{\prime\prime}+\tilde{h}_w\cdot\tilde{\vartheta}_d{}^{\prime\prime}-\tilde{h}_{w'\vartheta'}\right]+\qquad=\tilde{m}(\xi,\tau)\qquad(2)$$

$$\left\lfloor-\lambda_C{}^2\cdot\left[\tilde{h}_{w'\vartheta'}\cdot\tilde{w}_d{}^{\prime\prime}+\frac{1}{2}\left(\tilde{h}_{w'w'}+\tilde{h}_{\vartheta'\vartheta'}\right)\cdot\tilde{\vartheta}_d{}^{\prime\prime}\right]\right\rfloor$$

The following non-dimensional parameters have been introduced.

$$\begin{array}{lll} \xi = \frac{x}{l} & {\lambda_L}^2 = \frac{E_c A_c}{H}\frac{l}{L_c}(y''l)^2 = & \widetilde{J_t} = \frac{(J_t + 2m_c b^2)}{(m_d + 2m_c)\cdot b^2} \\ & = 8{\lambda_Q}^2 = 64{\lambda_C}^2 & \\ \tau = t \cdot \frac{1}{l}\sqrt{\frac{2H}{(m_d+2m_c)}} & \mu^2 = \frac{E_d I_d}{2Hl^2} & \tilde{h}_{ij} = \int_0^1 i \cdot j \, d\xi \\ \widetilde{w}_d(\xi,\tau) = \frac{w_d(x,t)}{f} & \chi^2 = \frac{G_d J_d l^2}{E_d \Gamma_d} & \tilde{q}(\xi,\tau) = \frac{l^2}{2Hf} q(\xi,\tau) \\ \begin{cases} \tilde{\vartheta}_d(\xi,\tau) = \frac{\vartheta_d(x,t)\cdot b}{f} \end{cases} & \begin{cases} \beta^2 = \frac{G_d J_d}{2Hb^2} \end{cases} & \begin{cases} \widetilde{m}(\xi,\tau) = \frac{l^2}{2Hfb} m(\xi,\tau) \end{cases} \end{array} \tag{3}$$

where x is the bridge axis coordinate, l the main span length, t the time variable, H the initial cables tension, m_d and m_c respectively the deck and single cable mass per unit length, $w_d(x,t)$ and $\vartheta_d(x,t)$ respectively the flexural and torsional motion of the of the deck axis, f the initial cables sag, and b the half width of the deck section.

The Irvine parameter ${\lambda_L}^2$ of the main cables [6], which is crucial in determining the eigen-properties of the bridge, depends also upon the axial stiffness of the cables system $E_c A_c$, the cables initial length L_c and the initial cables curvature assumed by the parabolic shape $y'' = 8f/l^2$. Notice that the assumption of initial parabolic shape of the main cables allows us to define in a simple form the quadratic and cubic Irvine terms.

Other relevant non-dimensional parameters are μ^2 (Steinman's stiffness factor [2]) and β^2, that reflect the relative flexural and torsional rigidities of the girder, respectively. They depends upon the deck flexural $E_d I_d$ and the primary (St. Venant) torsional $G_d J_d$ stiffness. Moreover, in order to account for the warping deformability of the section we need to introduce the so called warping coefficient reflecting the ratio between the primary and secondary $E_d \Gamma_d$ (Vlasov-Wagner) torsional stiffness.

We can define a dimensionless equivalent torsional inertia per unit length dependent both on the cables and deck contribution J_t. The so called stiffening operator $\tilde{h}_{ij}$ synthetize in different terms the stiffness contribution coming from the main cables tension increment (stiffening behavior). Finally we need to introduce some dimensionless external forces normalizing the generalized vertical force $q(\xi,\tau)$ and torsional couple $m(\xi,\tau)$ acting on the bridge deck axis.

2.2 Linear free vibrations

A solution of the equations of motion is sought with the following general modal expansion form.

$$\widetilde{w}_d(\xi,\tau) = \sum_{n=1}^{\infty} W_n(\xi) \cdot \left\{ Z_n \cdot \exp\left(i \cdot \widetilde{\omega}_{w,n} \cdot \tau\right) + c.c. \right\} \quad with \;\; n \in \aleph \backslash \{0\} \tag{4}$$

$$\tilde{\vartheta}_d(\xi,\tau) = \sum_{m=1}^{\infty} \Theta_m(\xi) \cdot \left\{ \Gamma_m \cdot exp\left(i \cdot \widetilde{\omega}_{\vartheta,m} \cdot \tau\right) + c.c. \right\} \quad with \;\; m \in \aleph \backslash \{0\} \tag{5}$$

Being the general dimensionless circular frequency defined as :

$$\widetilde{\omega}_{(\cdot)} = \omega_{(\cdot)} \cdot l \sqrt{\frac{(m_d + 2m_c)}{2H}} \tag{6}$$

By enforcing the suitable boundary conditions for the flexural hinges $\{\widetilde{w}_d(0,\tau) = \widetilde{w}_d(1,\tau) = 0 \; ; \; \widetilde{w}_d{}''(0,\tau) = \widetilde{w}_d{}''(1,\tau) = 0\}$ and for the torsional forks $\{\tilde{\vartheta}_d(0,\tau) = \tilde{\vartheta}_d(1,\tau) = 0 \; ; \; \tilde{\vartheta}_d{}''(0,\tau) = \tilde{\vartheta}_d{}''(1,\tau) = 0\}$, one obtains the natural frequencies and the symmetric and anti-symmetric modes. get the following symmetric modal shape expressions. It is worth noting

that the former include trigonometric and hyperbolic functions, conversely the latter are represented by simple sinusoidal shapes.

The influence of the main parameters ${\lambda_L}^2$, χ^2, μ^2, and β^2 has been investigated through a parametric analysis, based on the available data collected from literature [5,12,31-40]. Besides realistic values also extreme situations are considered such as ${\lambda_L}^2 = 0$ (flat cables), ${\lambda_L}^2 = \infty$ (inextensible cables), $\mu^2 = 0$ (flexible deck), $\chi^2 = 0$ (rigid warping), $\chi^2 = \infty$ (free warping), $\beta^2 = 0$ (flexible deck).

For the sake of brevity, we will report just the results obtained for the second mode of vibrations, that shows more interesting features than the first one. Figure 3 shows the flexural eigenfrequency, as a function of the dimensionless deck bending stiffness, for different values of the Irvine parameter. Figure 4 is referred to torsional eigenfrequency, in the case of free warping.

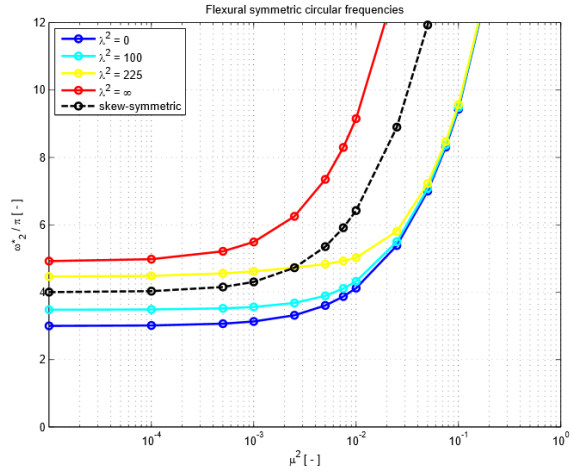


Figure 3: Circular eigen-frequencies of flexural symmetric mode 2.

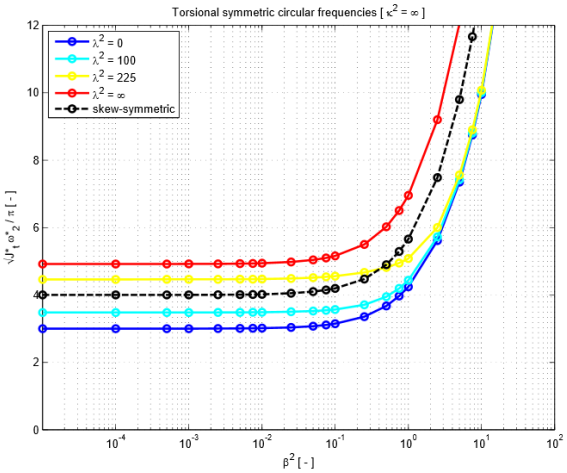


Figure 4: Circular eigen-frequencies of torsional symmetric mode 2 for $\chi^2 = \infty$.

The modal shapes associated to previously analyzed frequencies are very similar for flexural and torsional vibrations (Figures 5 and 6). The upward (negative) displacement increases as the Irvine parameter ${\lambda_L}^2$ does, since as cables become more and more inextensible, their initial parabolic shape turns out to be much more influent on deck deformation. As ${\lambda_L}^2 = \infty$, the modal shapes coalesce approximately to a single sinusoidal curve for any value of μ^2 and β^2. Similarly, if higher modes are considered ($n > 4$), one gets modal shapes closer to sinusoidal ones since the hyperbolic cosine contribution becomes negligible, meaning that deck stiffness is less influent on bridge vibration. Notice that increasing the relative deck stiffness (flexural and torsional) the positive antinodal points move away from the midspan. Concerning torsional modes only, passing from $\chi^2 = \infty$ to $\chi^2 = 0$ we noticed that the deck relative stiffness becomes much more relevant in the latter case.

2.3 Cross over frequencies and modes

As previously mentioned frequencies and modal shapes associate to higher order modes features interesting behavior. First, we want to focus the attention on the so-called [5] Cross Over Frequency (COF), that is the frequency common to symmetric and skew-symmetric modes. As this particular condition occurs, symmetric modal shapes will vibrate according to frequencies proper of skew-symmetric ones. In order to reach the COF threshold condition the structural parameters of the suspension bridge has to be properly tuned (as shown in Figures 3 and 4).

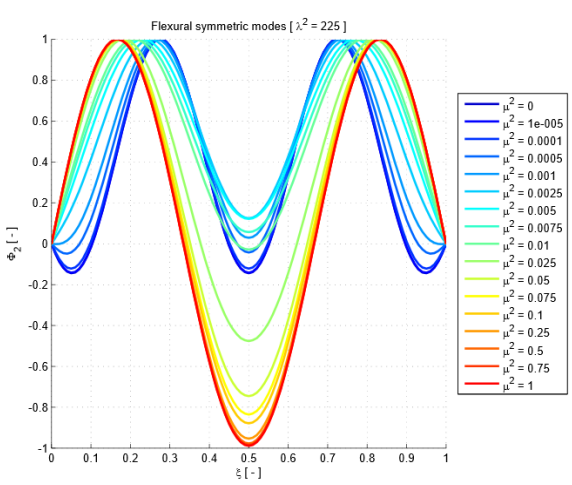


Figure 5: Modal shape of flexural mode 2 for ${\lambda_L}^2 = 225$.

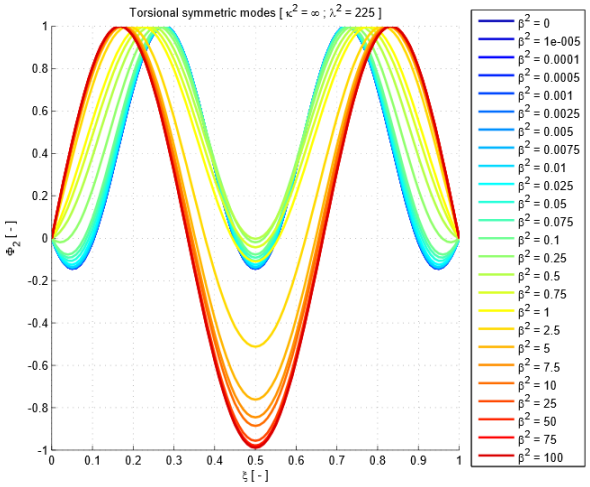


Figure 6: Modal shape of torsional mode 2 for ${\lambda_L}^2 = 225$ and $\chi^2 = \infty$.

As can be seen from Figures 5-6, the modal shapes are strongly influenced by the structural parameters of the suspension bridges. In the design process, it can be useful to tune some parameters in order to improve the bridge performance, such as in regard of edge slope and peak upward motion. Enforcing the vanishing of the latter two parameters, we get critical conditions for the modal shapes, that, by analogy with the previous treatment, we can be referred to as Cross Over Modes (COM). Concerning the COM conditions we can state that only the first symmetric modes has a unique critical curve: in fact, as the edge slopes vanish the peak upward displacement does the same.

3 AEROELASTIC ANALYSIS

For sake of simplicity, the wind-structure interaction has been modelled by means of Theodorsen Theory that consider a thin airfoil immersed in a uniform and constant potential air stream. The main advantage is that the formulation will be independent from the actual sectional shape of the bridge's deck. Though we are implicitly modelling the deck by means of a thin plate, the inaccuracy introduced by the modelling could be comparable to numerical approximations typical of finite elements discretization.

3.1 Theodorsen formulation

Let's write the aerodynamic lift and couple acting on the axis of the bridge's deck.

$$L(t) = \pi b^2 \rho_a \cdot \ddot{w}_d + 2\pi b \rho_a U \cdot \left\{ C_w \cdot \dot{w}_d + \frac{b}{2}(1 + C_\theta) \cdot \dot{\theta}_d \right\} + 2\pi b \rho_a U^2 C_\theta \cdot \theta_d \qquad (7)$$

$$M(t) = -\frac{\pi}{8} b^4 \rho_a \cdot \ddot{\vartheta}_d + \pi b^2 \rho_a U \cdot \left\{ C_w \cdot \dot{w}_d + \frac{b}{2}(1 - C_\theta) \cdot \dot{\theta}_d \right\} + \pi b^2 \rho_a U^2 C_\theta \cdot \theta_d \qquad (8)$$

Where we have used the air density $\rho_a \cong 1.18\, kg/m^3$, the mean wind speed U and the so-called Theodorsen complex functions, that notice, being dependent on the actual reduced frequency $\tilde{k}_{(\cdot)}$, are different for the flexural C_w and the torsional motion C_θ.

$$C_{(\cdot)} = C\left(\tilde{k}_{(\cdot)}\right) = F\left(\tilde{k}_{(\cdot)}\right) + i \cdot G\left(\tilde{k}_{(\cdot)}\right) \qquad (9)$$

$$\tilde{k}_{(\cdot)} = \omega_{(\cdot)} \frac{b}{U} \qquad (10)$$

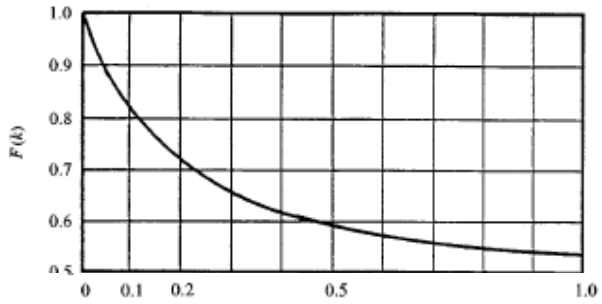


Figure 7: Real part of Theodorsen complex function.

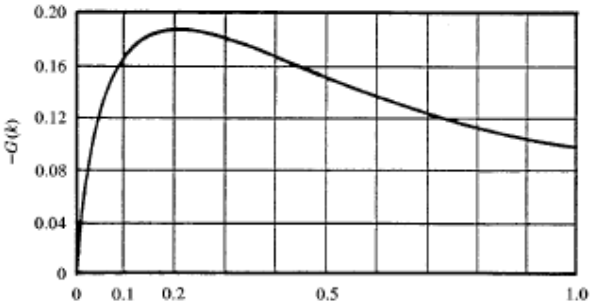


Figure 8: Imaginary part of Theodorsen complex function.

3.2 Linear coupled equations on motion

Before proceeding, we stress the fact that aeroelastic forces introduces additional linear terms only. Hence, also the linear equations of motion becomes coupled and the system loses its symmetries in stiffness and damping, thus becoming susceptible of static divergence and flutter dynamic instability. The dimensionless linear coupled equations of motion reads:

$$\frac{d^2\tilde{w}_d}{d\tau^2} + \tilde{c}_{ww} \cdot \frac{d\tilde{w}_d}{d\tau} + \tilde{c}_{w\vartheta} \cdot \frac{d\tilde{\vartheta}_d}{d\tau} + \mu^2 \cdot \tilde{w}_d{}'^{v} - \tilde{w}_d{}'' + \lambda_L{}^2 \tilde{h}_w + 2\tilde{k}_{\vartheta\vartheta} \cdot \theta_d = 0 \qquad (11)$$

$$\widetilde{J_t} \cdot \frac{d^2\tilde{\vartheta}_d}{d\tau^2} + \tilde{c}_{\vartheta\vartheta} \cdot \frac{d\tilde{\vartheta}_d}{d\tau} + \tilde{c}_{\vartheta w} \cdot \frac{d\tilde{w}_d}{d\tau} + \frac{\beta^2}{\chi^2} \cdot \tilde{\vartheta}_d{}'^{v} - (1+\beta^2) \cdot \tilde{\vartheta}_d{}'' - \tilde{k}_{\vartheta\vartheta} \cdot \theta_d + \lambda_L{}^2 \tilde{h}_\vartheta = 0 \qquad (12)$$

In the above equations, we have neglected the additional mass $\widetilde{m}_a$ and torsional inertia $\widetilde{J_a}$ coming from the participating air mass. In fact from the available data [5,12,31-40] it turns out that they are always negligible contributions with respect to structural ones.
The following definitions hold.

$$\begin{aligned}
\tilde{c}_{ww} &= 2\left(\xi_w \cdot \tilde{\omega}_w + \sqrt{\widetilde{J_t} \cdot \widetilde{m}_a} \cdot \tilde{\Omega}_\vartheta \cdot \tilde{u} \cdot C_w\right) \\
\tilde{c}_{w\vartheta} &= \sqrt{\widetilde{J_t} \cdot \widetilde{m}_a} \cdot \tilde{\Omega}_\vartheta \cdot \tilde{u} \cdot (1 + C_\theta) \\
\tilde{c}_{\vartheta\vartheta} &= 2\sqrt{\widetilde{J_t}} \cdot \left\{\xi_\vartheta \cdot \sqrt{\widetilde{J_t}} \cdot \tilde{\omega}_\vartheta + \frac{1}{4} \cdot \sqrt{\widetilde{m}_a} \cdot \tilde{\Omega}_\vartheta \cdot \tilde{u} \cdot (1 - C_\theta)\right\} \\
\tilde{c}_{\vartheta w} &= -\sqrt{\widetilde{J_t} \cdot \widetilde{m}_a} \cdot \tilde{\Omega}_\vartheta \cdot \tilde{u} \cdot C_w \\
\tilde{k}_{\vartheta\vartheta} &= \widetilde{J_t} \cdot \tilde{\Omega}_\vartheta{}^2 \cdot \tilde{u}^2 \cdot C_\theta
\end{aligned} \qquad (13)$$

where $\xi_{(\cdot)}$ is the structural equivalent viscous damping ratio, assumed for simplicity constant and equal to 0.5%, whilst $\tilde{u}$ represent the mean wind speed U normalized with respect to the static divergence one U_D in correspondence of the same structural parameters.

$$U_D = \sqrt{\widetilde{J_t} \cdot \tilde{\Omega}_\vartheta{}^2} \cdot \sqrt{\frac{2H}{\pi \rho_a l^2}} \qquad (14)$$

Notice the difference between $\tilde{\Omega}_{(\cdot)}$ and $\tilde{\omega}_{(\cdot)}$, which represent, respectively, the circular frequency obtained from the undamped structural model and the one coming from the complete aeroelastic analysis. Consequently, the first will be constant and the second will vary as the mean wind speed does.
Lastly, the generic dimensionless reduced frequencies can be defined as follows.

$$\tilde{k}_{(\cdot)} = \left(\tilde{\omega}_{(\cdot)} - i\tilde{\alpha}_{(\cdot)}\right) \cdot \sqrt{\tilde{m}_a} / \left(\sqrt{\tilde{J}_t} \cdot \tilde{\Omega}_\vartheta \cdot \tilde{u}\right) \tag{15}$$

The linearized equation, considered in this Section, is of basic importance in order to obtain the wind speed which corresponds to flutter onset. In fact, having obtained a modal projection of the governing equations, one can enforce the flutter conditions by considering a null value for torsional or flexural damping. Figure 9 shows an example of computation: for the specific structural parameters, torsional flutter happens in correspondence of the wind speed marked by a red circle.

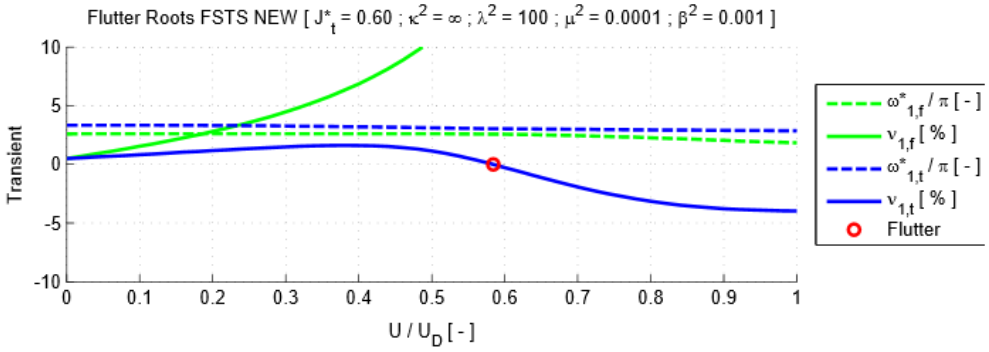


Figure 9 Variation of flexural and torsional frequencies and damping ratios with wind speed level.

4 INTERNAL PARAMETRIC RESONANCE

The recent work by Airoli and Gazzola [22] and previous works by different authors [19,20] contain the numerical and analytical proof, respectively, that suspension bridges can suffer of internal parametric resonance. This kind of phenomenon strongly differs from the well-known ordinary resonance characteristic of linear vibrating systems. The main differences lie in the fact that, regarding the parametric resonance, no external sources of energy are a priori needed since energy is just transferred from one mode to another.

4.1 Modal projection of nonlinear aeroelastic equations

In order to catch the internal resonance phenomenon, it is necessary to consider the fully nonlinear equation of motion, supplemented by the aeroelastic terms considered in Section 3. By applying a modal projection of the governing equations, based on generic (rather than exponential) time-varying functions, one finds:

$$\begin{aligned} &M_{w,n} \cdot \ddot{z}_n + C_{w,n} \cdot \dot{z}_n + C_{w\vartheta,nm} \cdot \dot{\gamma}_m + K_{w,n}^{(L)} \cdot z_n + K_{w\vartheta,nm}^{(L)} \cdot \gamma_m + \\ &+K_{w,n}^{(Q)} \cdot {z_n}^2 + K_{w\vartheta,nm}^{(Q)} \cdot {\gamma_m}^2 + \\ &\left(+K_{w,n}^{(C)} \cdot {z_n}^3 + K_{w\vartheta,nm}^{(C)} \cdot z_n \cdot {\gamma_m}^2 \right) \end{aligned} = \Gamma_{w,n} \tag{16}$$

$$\begin{aligned} &J_{\vartheta,m} \cdot \ddot{\gamma}_m + C_{\vartheta,m} \cdot \dot{\gamma}_m + C_{\vartheta w,mn} \cdot \dot{z}_n + K_{\vartheta,m}^{(L)} \cdot \gamma_m + \\ &+K_{\vartheta w,mn}^{(Q)} \cdot \gamma_m \cdot z_n + \\ &\left(+K_{\vartheta,m}^{(C)} \cdot {\gamma_m}^3 + K_{\vartheta w,mn}^{(C)} \cdot \gamma_m \cdot {z_n}^2 \right) \end{aligned} = \Gamma_{\vartheta,m}(\xi,\tau) \tag{17}$$

The following equivalent masses, damping, stiffness and forcing terms have been introduced.

$$M_{w,n} = \int_0^1 {W_n}^2(\xi)d\xi; \quad C_{w,n} = \tilde{c}_{ww} \cdot M_{w,n}; \quad C_{w\vartheta,nm} = \tilde{c}_{w\vartheta} \cdot \tilde{h}_{W_n,\Theta_m} \tag{18}$$

$$K_{w,n}^{(L)} = \int_0^1 W_n(\xi) \cdot [\mu^2 \cdot {W_n}^{IV}(\xi) - {W_n}''(\xi)]d\xi + {\lambda_L}^2 \cdot \tilde{h}_{{W_n}^2}; \quad K_{w\vartheta,nm}^{(L)} = 2\tilde{k}_{\vartheta\vartheta} \cdot \tilde{h}_{W_n,\Theta_m} \tag{19}$$

$$K_{w,n}^{(Q)} = \frac{3}{2} \cdot {\lambda_Q}^2 \cdot \tilde{h}_{W_n} \cdot \tilde{h}_{W_n'^2}; \quad K_{w\vartheta,nm}^{(Q)} = {\lambda_Q}^2 \cdot \left\{\tilde{h}_{\Theta_m} \cdot \tilde{h}_{W_n',\Theta_m'} + \frac{1}{2} \cdot \tilde{h}_{W_n} \cdot \tilde{h}_{\Theta_m'^2}\right\} \tag{20}$$

$$K_{w,n}^{(C)} = \frac{1}{2} \cdot {\lambda_C}^2 \cdot \left(\tilde{h}_{W_n'^2}\right)^2; \quad K_{w\vartheta,nm}^{(C)} = {\lambda_C}^2 \cdot \left\{\frac{1}{2} \cdot \tilde{h}_{\Theta_m'^2} \cdot \tilde{h}_{W_n'^2} + \left(\tilde{h}_{W_n',\Theta_m'}\right)^2\right\} \tag{21}$$

$$M_{\vartheta,m} = \int_0^1 {\Theta_m}^2(\xi)d\xi \Rightarrow J_{\vartheta,m} = \widetilde{J_t} \cdot M_{\vartheta,m} \tag{22}$$

$$C_{\vartheta,m} = \tilde{c}_{\vartheta\vartheta} \cdot M_{\vartheta,m}; \quad C_{\vartheta w,mn} = \tilde{c}_{\vartheta w} \cdot \tilde{h}_{W_n,\Theta_m} \tag{23}$$

$$K_{\vartheta,m}^{(L)} = \int_0^1 \Theta_m(\xi) \cdot \left[\frac{\beta^2}{\chi^2} \cdot {\Theta_m}^{IV}(\xi) - (1+\beta^2) \cdot {\Theta_m}''(\xi)\right] d\xi + {\lambda_L}^2 \cdot \tilde{h}_{{\Theta_m}^2} - \tilde{k}_{\vartheta\vartheta} \cdot M_{\vartheta,m} \tag{24}$$

$$K_{\vartheta w,mn}^{(Q)} = {\lambda_Q}^2 \cdot \begin{Bmatrix} 2 \cdot \tilde{h}_{\Theta_m} \cdot \tilde{h}_{W_n',\Theta_m'} + \\ \\ +\tilde{h}_{W_n} \cdot \tilde{h}_{\Theta_m'^2} \end{Bmatrix} \tag{25}$$

$$K_{\vartheta,m}^{(C)} = {\lambda_C}^2 \cdot \left(\tilde{h}_{\Theta_m'^2}\right)^2; \quad K_{\vartheta w,mn}^{(C)} = {\lambda_C}^2 \cdot \left\{\left(\tilde{h}_{W_n',\Theta_m'}\right)^2 + \frac{1}{2} \cdot \tilde{h}_{W_n'^2} \cdot \tilde{h}_{\Theta_m'^2}\right\} \tag{26}$$

$$\Gamma_{\vartheta,m} = \int_0^1 \Theta_m(\xi) \cdot \tilde{m}(\xi,\tau)d\xi \tag{27}$$

It is important to notice that in the torsional equation of motion it is not possible to define a second order term independently from the flexural component. This is because the rotations of the deck introduces an asymmetric response of the two main cables, which strongly depend on the flexural amplitude of vibration affecting the stiffness of the cables system. This property of the system will be fundamental in the following in order to study the stability of vibrations.

4.2 Vortex-shedding modelling

In many real-life systems, mainly in the electrical field, the parameters which govern the equations of motion may vary periodically in time [41]. When dealing with suspension bridges, this is not the case since structural parameters are fixed and can vary only in a very long period. Nevertheless, in view of the peculiar non-linear coupling of the governing equations and accounting for the presence of aeroelastic phenomena, one can easily realize that parametric resonance may occur in suspension bridge in the presence of a periodic external action. This may happen even if the wind velocity remains constant, because of the vortex-shedding phenomenon. It is well known that, under certain conditions, vortex detaches from the immersed body in a regular and periodic variation in time and space. This condition is the so-called Von Kármán vortex street phenomenon, that has been verified experimentally to occur in circular cylinders in a range of Reynolds number of about $250 < Re < 2 \cdot 10^5$.
In the case of bridges, vortex-shedding effect can be represented by means of a sinusoidal transverse force:

$$F_L = \frac{1}{2} \cdot \rho_a \cdot B \cdot U^2 \cdot C_L \cdot \sin(\omega_{VS} \cdot t) \tag{28}$$

where ω_{VS} is the frequency of vortex shedding and C_L is the lift coefficient, which basically depends on the cross section shape, on the Reynolds number and on the surface roughness. The equivalent modal lift force has the following dimensionless format.

$$\Gamma_{w,n} = \Gamma_0 \cdot \tilde{h}_{W_n} \cdot \sin(\tilde{\omega}_{VS} \cdot \tau) \tag{29}$$

$$\Gamma_0 = \tilde{B} \cdot \tilde{c}_L \cdot \tilde{J}_t \cdot \tilde{\Omega}_{\vartheta,m}{}^2 \cdot \tilde{u}^2 \tag{30}$$

where we have introduced the non-dimensional counterpart for the deck's width and the normalized lift coefficient with respect to the analytical one characterizing thin airfoils.

$$\tilde{B} = B/f = 0.17 \div 0.51 \cong 0.32 \tag{31}$$

$$\tilde{c}_L = C_L(\theta_d)/2\pi \tag{32}$$

It is worth noting that the stability analyses will be carried out by considering the forcing frequency as an independent variable. When examining the results, it will be necessary to account for the well-known Strouhal relationship, which connects the vortex shedding frequency to the mean wind speed:

$$\omega_{VS} = 2\pi \cdot f = 2\pi \cdot St \cdot U/D \tag{33}$$

Moreover, the presence of the lock-in region will be accounted for, by considering an interval of wind velocity in which there is a synchronism between structural and vortex shedding frequency. The dimensionless format of Strouhal relationship reads:

$$\tilde{\omega}_{St} = \pi \cdot St \cdot \left(\tilde{\alpha}/\sqrt{\tilde{m}_a}\right) \cdot \sqrt{\tilde{J}_t} \cdot \tilde{\Omega}_{\vartheta,m} \cdot \tilde{u} \tag{34}$$

where $\tilde{\alpha} = B/D$ is the aspect ratio of the cross section: from avalable bridges data [5,12,31-40] $\tilde{\alpha} = 3 \div 12$. Concerning the Strouhal number St, we will make reference to numerical investigations of [43]: it seems reasonable to consider $St \cong 0.1$.
Finally, we must remember that vortex-shedding is a self-limited phenomenon due to the additional viscous aerodynamic damping. By experimental investigations, it is known that oscillations of circular cylinders never overcome the 20% of the cross flow dimension of the body. Consequently an empirical upper bound for dimensionless vertical vibrations should be taken about equal to 0.01.

4.3 Formulation of perturbed system of equations

In order to study the stability of the suspension bridge vibrations as long as dominant flexural motion occurs, we will make reference to the work of Hermann and Hauger [29].
First, we need to assume small flexural vibrations and negligible torsional ones, allowing us to study the linear equation of motion of a SDOF damped and periodically forced oscillator:

$$z_n(t) < \varepsilon \Rightarrow z_n{}^2(t)\ ;\ z_n{}^3(t)\ \cong 0 \tag{35}$$

$$\gamma_m(t) \cong 0 \Rightarrow \tilde{c}_L = C_L(\theta_d = 0)/2\pi \tag{36}$$

The governing equation reads:

$$M_{w,n} \cdot \ddot{z}_n + C_{w,n} \cdot \dot{z}_n + K_{w,n}^{(L)} \cdot z_n = \Gamma_0 \cdot \tilde{h}_{W_n} \cdot sin(\tilde{\omega}_{St} \cdot \tau) \tag{37}$$

The solution will be given by the superposition of a homogenous solution and a particular steady integral. Since we are looking for unstable solutions, the transient conditions are not of interest. Hence the steady state solution will be driven as usual by the so called complex dynamic amplification factor.

$$z_{n,SS}(t) = z_{n,0} \cdot sin(\tilde{\omega}_{St} \cdot \tau - \varphi) \tag{38}$$

$$z_{n,0} = \Gamma_0 \cdot \tilde{h}_{W_n} \cdot |H(\delta)|/M_{w,n} \tag{39}$$

$$|H(\delta)| = \left\{ \tilde{\Omega}_{w,n}{}^2 \cdot \sqrt{\left(1 - \delta^2 - \left(\tilde{c}_{ww}{}^I / \tilde{\Omega}_{w,n}\right) \cdot \delta\right)^2 + \left(\left(\tilde{c}_{ww}{}^R / \tilde{\Omega}_{w,n}\right) \cdot \delta\right)^2} \right\}^{-1} \tag{40}$$

$$tg(\varphi) = \left(\tilde{c}_{ww}{}^R / \tilde{\Omega}_{w,n}\right) \cdot \delta / \left(1 - \delta^2 - \left(\tilde{c}_{ww}{}^I / \tilde{\Omega}_{w,n}\right) \cdot \delta\right) \tag{41}$$

$$\delta = \tilde{\omega}_{St} / \tilde{\Omega}_{w,n} \tag{42}$$

The second step requires to introduce a small perturbation to the actual forced system, in terms of both flexural and torsional DOF:

$$z_n(t) = z_{n,0} \cdot \sin(\tilde{\omega}_{St} \cdot \tau - \varphi) + z_{P,n}(t) \quad with \quad z_{P,n}(t) < \varepsilon \tag{43}$$

$$\gamma_m(t) = \gamma_{P,m}(t) \quad with \quad \gamma_{P,m}(t) < \varepsilon \tag{44}$$

Then, by substituting the above definitions in the complete modal aeroelastic system of equations and by suitable linearization, one gets the so-called Perturbed system.

$$M_{w,n}\ddot{z}_{P,n} + C_{w,n}\dot{z}_{P,n} + C_{w\vartheta,nm}\dot{\gamma}_{P,m} + K_{w,n}^{(L)} z_{P,n} + K_{w\vartheta,nm}^{(L)} \gamma_{P,m} = 0 \tag{45}$$

$$J_{\vartheta,m}\ddot{\gamma}_{P,m} + C_{\vartheta,m}\dot{\gamma}_{P,m} + C_{\vartheta w,mn}\dot{z}_{P,n} + \left\{K_{\vartheta,m}^{(L)} + K_{\vartheta w,mn}^{(Q)} z_{n,0} \sin(\tilde{\omega}_{St}\tau - \varphi)\right\}\gamma_{P,m} = 0 \tag{46}$$

As previously mentioned, the second order term of torsional motion is dependent simultaneously and linearly on both motions while the flexural one depends quadratically on the two independent contributions. This makes possible that a small but not vanishing vertical perturbation influences the torsional response, even in a linearized formulation. This kind of phenomenon can be classified as a Parametric excitation problem. In fact, in the perturbed system there is no forcing term but just a periodically varying structural parameter. The fact that it depends on the actual vortex-shedding excitation is hidden inside the terms $z_{n,0}$ and φ.
We have stressed many times the fact that being a self-limiting phenomenon; vortex shedding is able to induce just small flexural perturbations. However, because their effects on torsional vibrations is amplified by the quadratic coupled modal stiffness $K_{\vartheta w,mn}^{(Q)}$, it will be of basic importance to understand its influence on the system response. Consequently, we can say that in the design process will be useful whether is possible to tune the geometrical and mechanical properties of the suspension bridge in order to minimize that cross stiffness.

4.4 Floquet stability conditions

In the previous section, we ended up with the definition of the perturbation system, that is a system of two ordinary differential equation of second order and with periodic coefficients. The stability of such a system can be easily analyzed by exploiting the well-known Floquet Theorem. It has been proved [28] that solutions of those kind of systems can be written as the product between a periodic function $P(t)$ and an exponential one $M(t)$. Consequently, we get asymptotically stable solutions in Lyapunov sense if the periodic function does not diverge.
To check this, we need first to reduce the perturbed system (45-46) of Hill's equation to an equivalent system of the first order.

$$\dot{\boldsymbol{x}} = \boldsymbol{J} \cdot \boldsymbol{x} \tag{47}$$

The procedure requires a simple change of variables that leads to the following definition of Jacobian matrix J.

$$\boldsymbol{x} = \{z_{P,n} \quad \gamma_{P,m} \quad \dot{z}_{P,n} \quad \dot{\gamma}_{P,m}\}^T \tag{48}$$

$$\boldsymbol{J} = \begin{Bmatrix} 0 & \boldsymbol{I} \\ -\boldsymbol{M}^{-1} \cdot \boldsymbol{K} & -\boldsymbol{M}^{-1} \cdot \boldsymbol{D} \end{Bmatrix} \tag{49}$$

$$\boldsymbol{M} = \begin{Bmatrix} M_{w,n} & 0 \\ 0 & J_{\vartheta,m} \end{Bmatrix} \tag{50}$$

$$\boldsymbol{D} = \begin{Bmatrix} C_{w,n} & C_{w\vartheta,nm} \\ C_{\vartheta w,mn} & C_{\vartheta,m} \end{Bmatrix} \tag{51}$$

$$\boldsymbol{K} = \begin{Bmatrix} K_{w,n}^{(L)} & K_{w\vartheta,nm}^{(L)} \\ 0 & K_{\vartheta,m}^{(L)} + K_{\vartheta w,mn}^{(Q)} \cdot z_{n,0} \cdot \sin(\widetilde{\omega}_{St} \cdot \tau - \varphi) \end{Bmatrix} \tag{52}$$

The so-called monodromy matrix gives us the variation of the solution vector after a period. Hence, in order to compute such a matrix, it is simply necessary to perform a numerical integration of the equivalent first order system over the reference period $T = 2\pi$ assuming a number of initial conditions equal to the number of unknowns. The initial values has to be chosen in such a way that the fundamental matrix of solutions is unitary on the main diagonal at the initial instant. This allows us to define the monodromy matrix as follows.

$$\boldsymbol{C} = \{[\boldsymbol{x}(T)]_{z(0)=1} \quad [\boldsymbol{x}(T)]_{\gamma(0)=1} \quad [\boldsymbol{x}(T)]_{\dot{z}(0)=1} \quad [\boldsymbol{x}(T)]_{\dot{\gamma}(0)=1}\} \tag{53}$$

Finally, in order to check the stability of the system it is necessary that any of the eigenvalues of the Monodromy matrix exceeds the unity, in absolute value.

4.5 Stability maps analysis

In the following, we will comment the numerical results obtained from a parametric analysis of the stability of the perturbed system. Results will be collected inside stability maps that are able to synthetize the main information necessary to distinguish between stable and unstable regions. Each of them, in fact, will be characterized by the circular frequency of vortex shedding Ω_{VS} and by a mean wind speed level U.

Two model will be analyzed. The first, called Structural, accounts for geometrical and mechanical properties of the suspension bridge only. This preliminary analysis is useful in order to check if the non-linearities of the dynamic system are strong enough to find out resonance conditions different from the primary linear one. Hence, in this model the term playing a fundamental role is $K_{\vartheta w,mn}^{(Q)}$ since it's the only one able to couple the equations of motion. In fact all damping and stiffening terms coming from aeroelastic effects will not be taken in account.

In the second, Aeroelastic, model both structural and aerodynamic parameters will be considered. The task of this model is to find out if and under which conditions wind effect on suspension bridges, coupled with parametric resonance, is able to lead the structure to unstable conditions. Results will be of relevance only if the structure reaches those critical conditions in correspondence of a wind speed lower than the flutter one.

In both models we will analyze different resonance conditions besides the linear primary one, such as harmonic, subharmonic and superharmonic of order two for both the flexural and the torsional vibrations, and further additive combinational and anti-resonance type.

$$harmonic \;:\; \Omega_{VS} = \omega_i \tag{54}$$

$$subharmonic \;:\; \Omega_{VS} = 2 \cdot \omega_i \tag{55}$$

$$superharmonic \;:\; \Omega_{VS} = \omega_i / 2 \tag{56}$$

$$combinational\ \ sum \;:\; \Omega_{VS} = \omega_w + \omega_\vartheta \tag{57}$$

$$anti - resonance \;:\; \Omega_{VS} = |\omega_w - \omega_\vartheta| \tag{58}$$

We choose to consider just the second order type of internal resonance since we want to catch just the critical conditions near the classical primary linear resonance.
Let's analyze some numerical results starting from the Structural model.
As we can see, Figure 10, the Structural model is able to catch the main resonance of the system. In fact, besides the primary linear flexural one the system undergoes resonance also as the forcing frequency is near the torsional one. Since the excitation frequency is associated to flexural motion, this kind of phenomenon can be associated to an internal resonance of kind 1:1. Further, the model is able to catch also the so-called 2:1 internal resonance as the flexural motion is characterized by a frequency that doubles the torsional one. On the other hand, the effect of other kind of resonances is less evident.
It is worth noting that the presence of internal resonances reduces drastically the critical wind speed level, that in the case of the simple structural model is represented by the torsional divergence speed. However, it's evident that in this case the vortex-shedding phenomenon does not seem to be able to explain any of the previous unstable conditions. In fact, the linear model proposed by Strouhal never reaches the critical conditions in terms of frequencies and amplitudes (wind speed) that lead the system response to diverge in time.

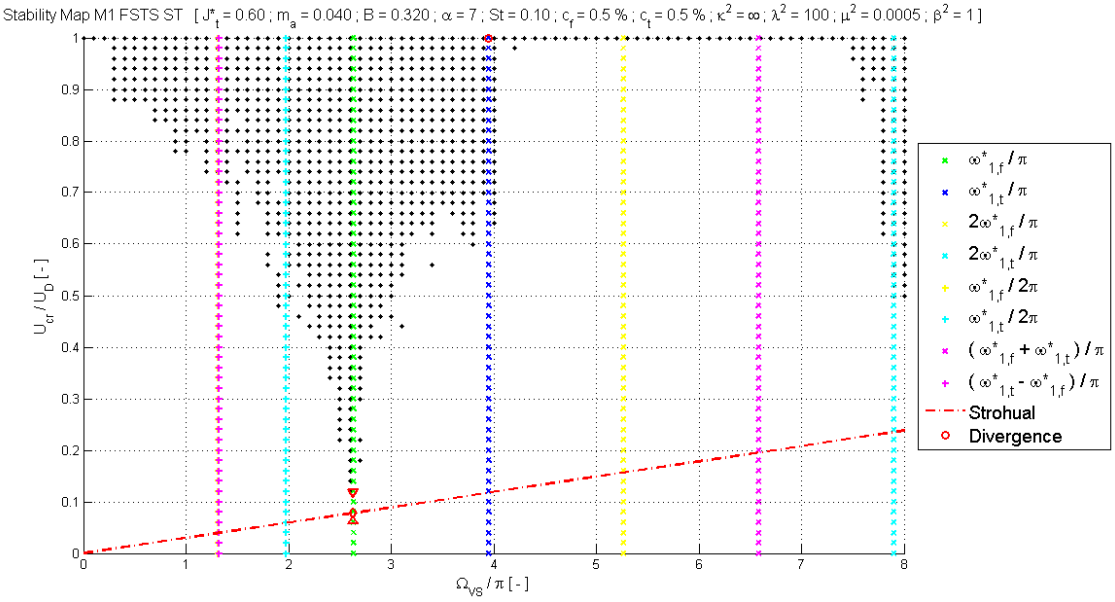


Figure 10: Stability map of the Structural model for slender deck section. The lock-in interval is denoted by a couple of red triangular marks around the critical vortex shedding frequency (red diamond mark).

As already mentioned, in the definition of the dimensionless Strohual circular frequency, a relevant role is played by the deck sectional aspect ratio. In fact, it strongly modifies the slope of the Strohual curve, which consequently can enter the unstable regions. This means that in the design process is fundamental to take in consideration this fact, since the choice of the sectional dimensions of the deck will be of fundamental importance for the dynamic stability of the overall structure.
As we can see in Figure 11, by reducing the aspect ratio down to $\tilde{\alpha} = 3$ the vortex shedding phenomenon is able to explain the main resonant unstable conditions that are the flexural primary linear and the second order subharmonic internal torsional ones.

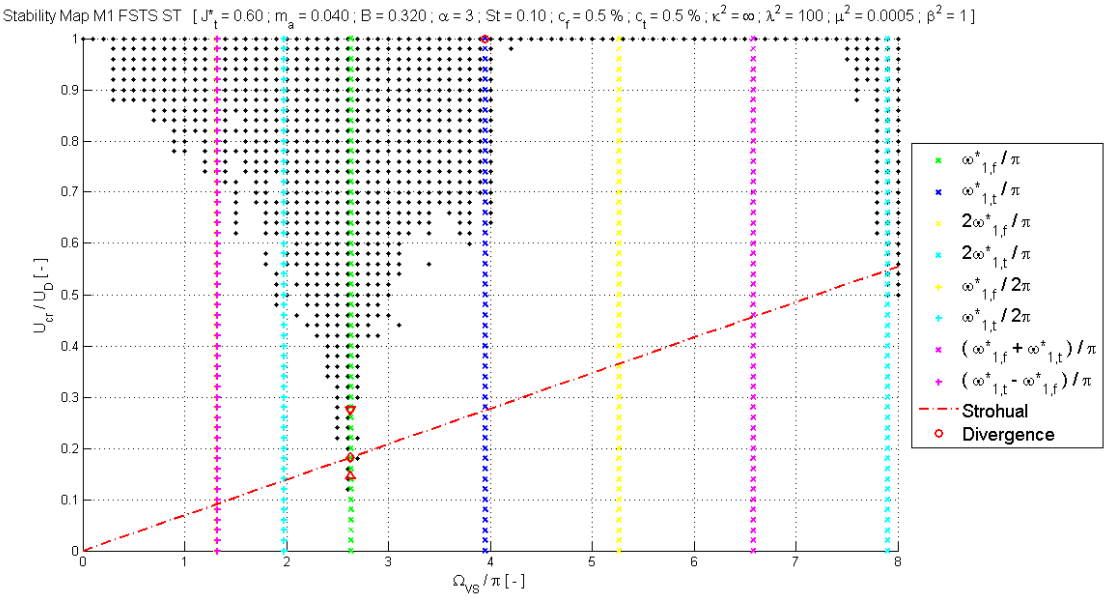


Figure 11: Stability map of the Structural model for bluff deck section.

Hence, we can conclude that very bluff deck sections can be useful to increase torsional and mainly flexural stiffness of the suspension bridge, but they lead the structure to be more susceptible to parametric instabilities due to vortex shedding.

Let's now analyze the Aeroelastic model accounting for the fluid-structure interaction effects on the dynamic stability if the system, Figure 12. As already mentioned in the flutter analysis, the fluid-structure interaction makes the frequencies being dependent on the actual wind speed level, consequently we see curved lines representing the main internal or external resonance conditions. Moreover, the wind-structure interaction enlarges the unstable regions. This is valid also for wind speed which is by far lower than the one required to reach the critical flutter condition. Hence, the interaction between Aeroelasticity and Parametric resonance can lead to unexpected unstable conditions.

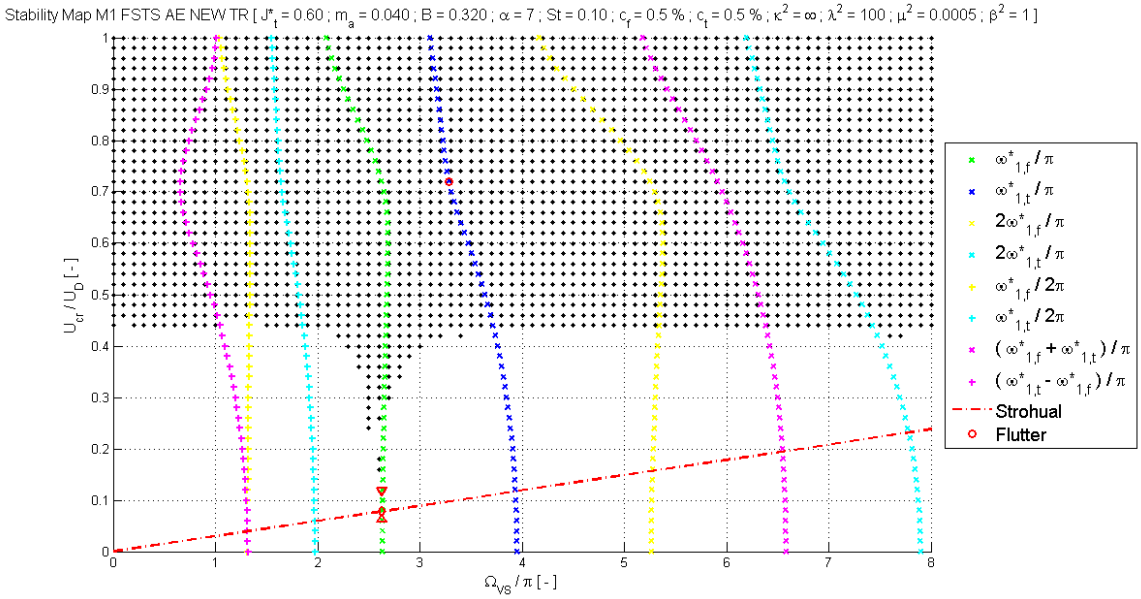


Figure 12: Stability map of the Aeroelastic model for slender deck section.

Even though the unstable region is more merged than in the pure structural model, we still recognize the main resonances, that are the linear primary and the 2:1 internal ones. The presence of wind not only obscures the stability maps but it also reduces (increases) the critical wind speed required to reach the torsional 2:1 internal (the flexural 1:1 external) resonances. In fact, as we can see the flutter instability is of torsional type.
An interesting feature is that near the curve of anti-resonance we get always a larger stable region. In fact, as reported also in different papers [41], the so called anti-parametric resonance with respect to the parametric and additive parametric ones has a stabilizing effect on the dynamic response of the system. This is due primary to the fact that this phenomenon is able to increase significantly the damping of the system. This particular property can be exploited trying to find the optimal geometrical and mechanical parameters able to maximize this intrinsic damping effect. The physical explanation of this feature hides behind the fact that as parametric excitation occur there is energy transfer between the two main interacting modes. Consequently, since higher order modes are characterized by higher damping ratios, then the system is able to dissipate faster that energy with respect to the system without Parametric excitation. Notice that we are dealing with an energetic exchange; hence, being the energy transfer not unidirectional, we should observe modulated vibrations time histories.
As we can see, as long as the deck is slender enough vortex sheeding is not sufficient to bring the structure to unstable conditions, while as the deck sectional aspect ratio reduces, Figure 13, the dynamic response diverges as the wind speed reaches levels that are much lower than those expected by the only flutter analysis.

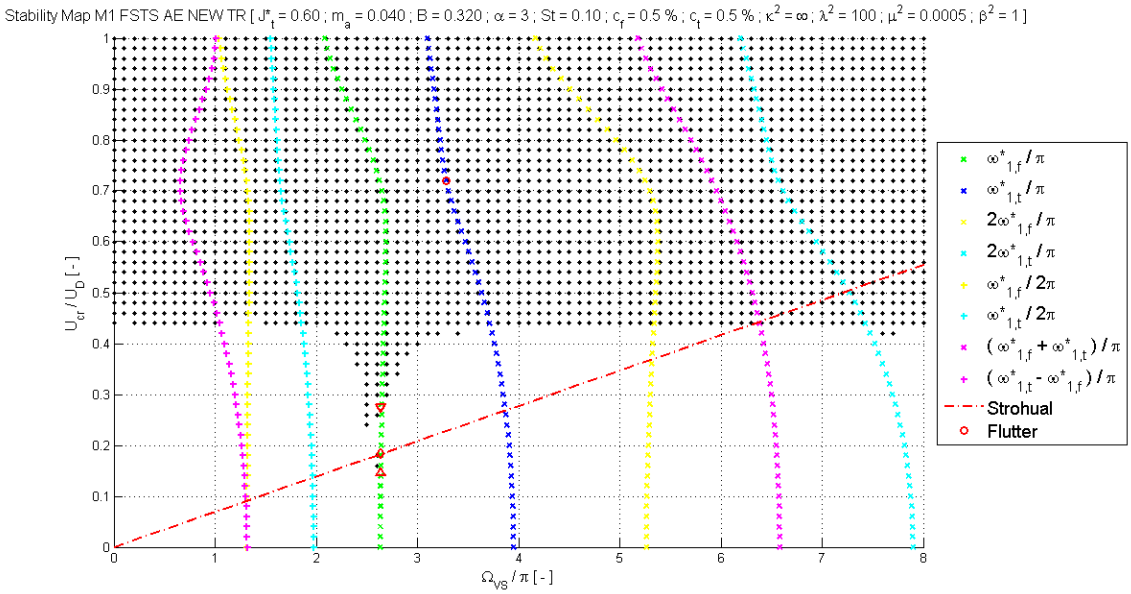


Figure 13: Stability map of the Aeroelastic model for bluff deck section.

Now we are able to comment the previous information in terms of flexural antinodal displacements by means the singles degree of freedom oscillator formulation. In fact, once we define the wind speed and the shedding frequency we know respectively the forcing term Γ_0 and the complex dynamic amplification factor $H(\delta)$. Considering Figure 14, we recognize immediately the usual shape characterizing every SDOF forced oscillator. We must remind that the equivalent oscillator is much more damped in the Aeroelastic model. Nevertheless, the total damping is never high enough to limit flexural oscillations to be lower than the cable's initial sag.

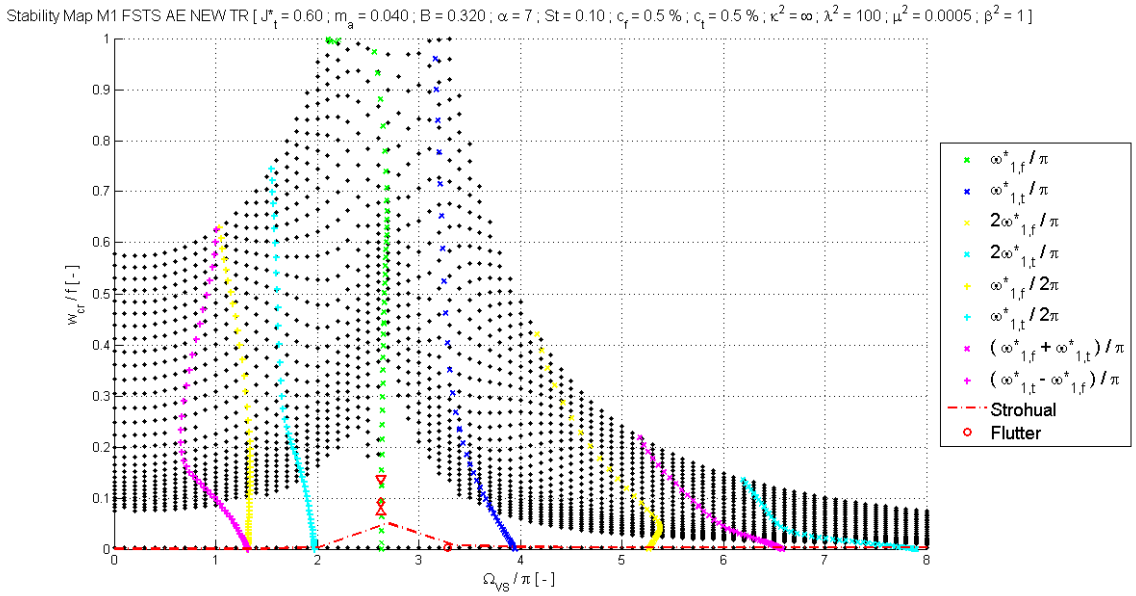


Figure 14 Unstable antinodal displacements of the Aeroelastic model for slender deck section.

Concerning the results related to bluff decks' section, for which unstable conditions are feasible, it is better to focus the attention on amplitudes that ranges up to $0.1 \cdot f$ (Figure 15).
First, it is worth noting that we have a lower bound representing the flexural motion in correspondence of torsional flutter instability for the Aeroelastic model. Second, it is important to underline that, according to Strouhal linear law, only in correspondence of 2:1 internal resonances the unstable conditions are feasible: in fact, all the other situations require too much high antinodal displacements that are difficult to observe in real life situations. Notice that the critical amplitudes so obtained are small enough to fulfil approximately the empirical limit threshold $z_{max} = 0.2 \cdot D/f \cong 0.009$ reminding us that vortex-shedding is a self-limiting phenomenon.

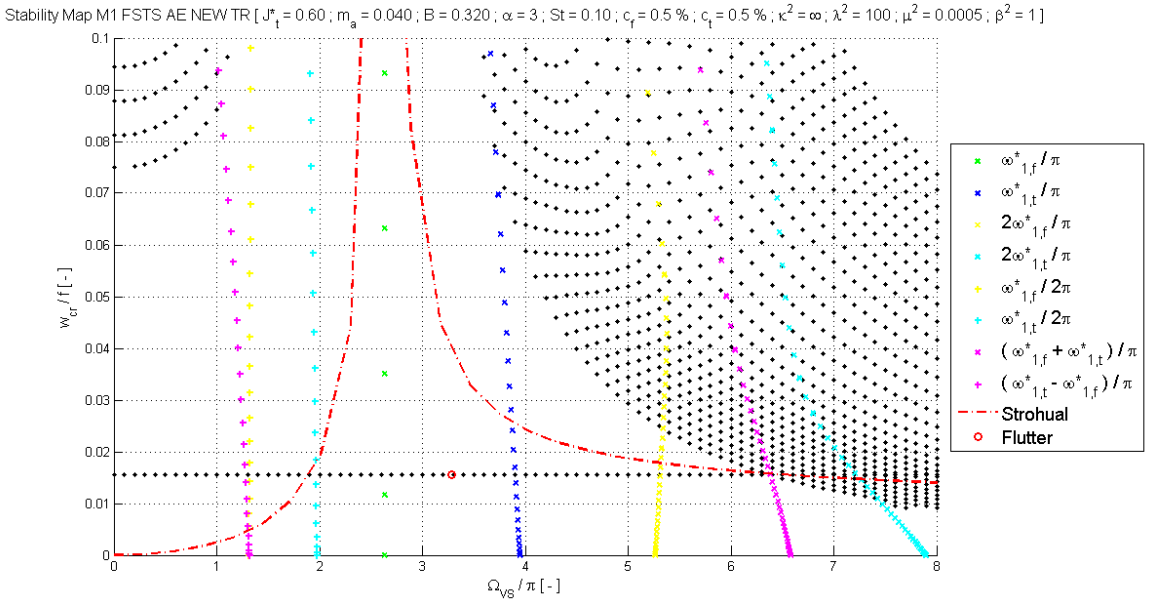


Figure 15 Unstable antinodal displacements of the Aeroelastic model for bluff deck section.

5 CONCLUSIONS

In this paper, a non-linear dynamic model of a suspension bridge is devised, with the purpose of providing a unified framework for the study of aeroelastic and internal parametric resonance instabilities.
Following the classical Deflection Theory, it has been possible to write the nonlinear static flexural response of a suspension bridge. The next step has consisted in the generalization of the displacement field in order to account for the torsional response of the deck-cables system.
A deep insight in analytical aerodynamic field paves the way for the study of aeroelastic effects. Wind forces introduce additional mass, damping and stiffness that not only couples the linear equations of motion but also led the system to be no more self-adjoint. In fact, it loses its symmetries both in damping and stiffness matrices, making the structure susceptible respectively to flutter instabilities and static divergence problems.
The non-linear system has been treated in the framework of Floquet stability theory, thus achieving the stability maps in terms of wind speed and frequency of vortex shedding. After a thorough examination of the achieved results, we can conclude saying that parametric resonance is a critical phenomenon that can be activated by vortex-shedding as far as the sectional shape factor is low enough. This should warn very much engineers, since a phenomenon like vortex-shedding is usually taken in consideration just concerning serviceability limit states. On the contrary, we have just found that under certain conditions such a phenomenon may lead to very strong and critical unstable conditions in correspondence of wind speed that can be considered safe with respect to classical static divergence or dynamic flutter instabilities.
The present study can be improved by considering the possible slackening of vertical hangers, which may introduce an additional non-linearity to the system. In fact, the structural model considered herein is based on perfectly bilateral behavior of hangers, so that the deck displacement parameters are univocally connected to the cable displacements. In the presence of large upward displacement, slackening may occur, thus leading to a loss of stiffness for the whole system. In spite of this limitation, the model still provides valid results: in fact, view that the first modes are considered only, the unstable behavior corresponds to small displacements, see Figure 15. In the future development of this work, when dealing with higher modes, it will be unavoidable to introduce the loss of stiffness due to slackening.

REFERENCES

[1] A. Pugsley, *The theory of suspension bridges*. 2nd ed. Edward Arnold, 1968.

[2] D.B. Steinman, *A practical treatise on suspension bridges*. Wiley, 1953.

[3] F. Bleich, C. Mccullogh, R. Rosecrans, G. Vincent, *The mathematical theory of vibration in suspension bridges*, U.S. Government Printing Office, 1950.

[4] D. B. Steinman, A generalized deflection theory for suspension bridges, *Transaction of ASCE*, **100**, 1133-1234, 1935.

[5] J. Luco, J. Turmo, Linear vertical vibrations of suspension bridges: A review of continuum models and some new results, *Soil Dynamics and Earthquake Engineering*, **30**, 769–781, 2010.

[6] H. Irvine, *Cable structures*, MITpress, 1981.

[7] A. M. Abdel-Ghaffar, Vertical vibration analysis of suspension bridges, *ASCE Journal of Structural Division*, 106, 2053-2075, 1980.

[8] A. M. Abdel-Ghaffar, Free torsional vibrations of suspension bridges, *ASCE Journal of Structural Division*, 105, 767–788, 1979.

[9] A. M. Abdel-Ghaffar, Free lateral vibrations of suspension bridges, *ASCE Journal of Structural Division*, 104, 503-525, 1978.

[10] A. M. Abdel-Ghaffar, Suspension bridge vibration: continuum formulation, *ASCE Journal of the Engineering Mechanics Division*, 108, 1215–1232, 1982.

[11] A.M. Abdel-Ghaffar, L. Rubin, Nonlinear free vibrations of suspension bridges: Theory, *Journal of Engineering Mechanics*, 109, 313–329, 1983.

[12] A.M. Abdel-Ghaffar, L. Rubin, Nonlinear free vibrations of suspension bridges: Application, *Journal of Engineering Mechanics*, 109, 330–345, 1983.

[13] O.H. Ammann, T. Von Kármán, G.B. Woodruff, The failure of the Tacoma Narrows Bridge : a report to the honorable John M. Carmody, Federal Works Agency, 1941.

[14] R. L. Bisplinghoff, H. Ashley, R. L. Halfman, *Aeroelasticity*, Addison-Wesley, 1955.

[15] T. Theodorsen, General theory of aerodynamic instability and the mechanism of flutter, NACA Report n. 496, 1979.

[16] L. Salvatori, C. Borri, Frequency- and time-domain methods for the numerical modeling of full-bridge aeroelasticity, *Computers and Structures*, 85, 675-687, 2007.

[17] A. Arena, W. Lacarbonara, Nonlinear parametric modeling of suspension bridges under aeroelastic forces: torsional divergence and flutter, *Nonlinear Dynamics*, **70**, 2487-2510, 2012.

[18] D. Sado, Energy transfer in two-degree-of-freedom vibrating system : a survey, *Journal of Theoretical and Applied Mechanics*, 31, 151-173, 1993.

[19] Y. A. Rossikhin, M. V. Shitikova, Analysis of nonlinear free vibrations of suspension bridges, *Journal of Sound and Vibration*, 186, 369-393, 1995.

[20] M. Cevik, M. Pakdemirli, Non linear vibrations of suspension bridges with external excitation, *International Journal of Nonlinear Mechanics*, 40, 901-923, 2005.

[21] A. H. Nayfeh, Introduction to perturbation techniques, Wiley, 1993.

[22] G. Airoli, F. Gazzola, A new mathematical explanation of what triggered the catastrophic torsional mode of the Tacoma Narrows Bridge, *Applied Mathematical Modelling*, 39, 901-912, 2015.

[23] K. S. Moore, Large torsional oscillations in a suspension bridge: Multiple periodic solutions to a nonlinear wave equation, *SIAM Journal on Mathematical Analysis*, 33, 1411-1429, 2002.

[24] P.J. McKenna, Large torsional oscillations in suspension bridges revised: Fixing an old approximation, *American Mathematics Monthly*, 106, 1-18, 1999.

[25] D. Jacover, P. J. McKenna, Nonlinear torsional flexing in a periodically forced suspended beam, *Journal of Computational and Applied Mathematics*, 52, 241-265, 1994.

[26] R.H. Plaut, Snap loads and torsional oscillations of the original Tacoma Narrows Bridge, *Journal of Sound and Vibration*, 309, 613–636, 2008.

[27] R.H. Plaut, F.M. Davis, Sudden lateral asymmetry and torsional oscillations of section models of suspension bridges, *Journal of Sound and Vibration* 307, 2007, 894–905, 2007

[28] L. Cesari, Asymptotic behaviour and stability problems in ordinary differential equations, Springer, 1971.

[29] G. Herrmann, W. Hauger, On the interrelation of divergence, flutter and auto-parametric resonance, *Ingeneur-Archiv*, 42, 81-88, 1973.

[30] E. Simiu, R.H. Scanlan, *Wind effects on structures*, Wiley, 1996.

[31] J. M. W. Brownjohn, F. Magalhaes, E. Caetano, A. Cunha, Ambient vibration re-testing and operational modal analysis of the Humber Bridge, *Engineering Structures*, 32, 2003-2018, 2010.

[32] F. Nieto, S. Hernandez, J. A. Jurado, A. Mosquera, Analytical approach to sensitivity analysis of flutter speed in bridges considering deck mass, *Advances in Engineering Software*, 42, 117-129, 2011.

[33] S. Adnur, M. Gunaydin, A. C. Altunisik, B. Sevim, Construction stage analysis of Humber suspension bridge, *Applied Mathematical Modelling*, 36, 5492-5505, 2012.

[34] K. Kaptan, S. Tezacn, S. Altin, S. Cherry, Dynamic analysis of suspension bridges and full scale testing, *Procedia Engineering*, 14, 1065-1070, 2011.

[35] N. M. Apaydin, Earthquake performance assessment and retrofit investigations of two suspension bridges in Instanbul, *Soil Dynamics and Earthquake Engineering*, 30, 702-710, 2010.

[36] F. Ubertini, Effects of cables damage on vertical and torsional eigenproperties of suspension bridges, *Journal of Sound and Vibrations*, 333, 2404-2421, 2014.

[37] H. Wang, T. Tao, R. Zhou, X. Hua, A. Kareem, Parameter sensitivity study on flutter stability of long-span triple-tower suspension bridge, *Journal of Wind Engineering and Industrial Aerodynamics*, 128, 12-21, 2014.

[38] D. Cobo del Arco, A. C. Aparicio, Preliminary static analysis of suspension bridges, *Engineering Structures*, 23, 1096-1103, 2001.

[39] R. Karoumi, Some modelling aspects in the nonlinear finite element analysis of cable supported bridges, *Computer and Structures*, 71, 397-412, 1999.

[40] J. Malik, Sudden lateral asymmetric and torsional oscillations in the original Tacoma suspension bridge, *Journal of Sound and Vibration*, 332, 3772-3789, 2013.

[41] J. Welte, T. Kniffka, H. Ecker, Parametric excitation in a two degree of freedom MEMS system, *Shock and Vibrations*, 20, 1113-1124, 2013.

[42] S. Deniz, T. Staubli, Oscillating rectangular and octagonal profiles: interaction of leading- and trailing-edge vortex formation, *Journal of Fluids and Structures*, 11, 3–31, 1997.

[43] A. Larsen, J. H. Walther, Discrete vortex simulation of flow around five generic bridge deck sections, *Journal of Wind Engineering and Industrial Aerodynamics*, 77-78, 591-602, 1998.

COMPDYN 2015
5th ECCOMAS Thematic Conference on
Computational Methods in Structural Dynamics and Earthquake Engineering
M. Papadrakakis, V. Papadopoulos, V. Plevris (eds.)
Crete Island, Greece, 25–27 May 2015

FEM SIMULATION OF THE EXPERIMENTAL RESPONSE OF AAC MASONRY INFILLS IN RC FRAMES

Riccardo R. Milanesi[1], Paolo Morandi[2], Guido Magenes[2], and Baris Binici[3]

[1] IUSS Pavia
Via Ferrata 1, Pavia, Italy
riccardo.milanesi@umeschool.it

[2] Dep. of Civil Engineering and Architecture of University of Pavia
Via Ferrata 1/3, Pavia, Italy
paolo.morandi@unipv.it , guido.magenes@unipv.it

[3] Dep. of Civil Engineering of Middle East Technical University
Structural and Earthquake Engineering Laboratory, K2, Ankara, Turkey
binici@metu.edu.tr

Keywords: AAC masonry; masonry infill; FEM modeling; infill- structure interaction.

Abstract. *Unreinforced masonry non-structural infills in RC structures are widely used in many countries. However, they are often designed with simplified methods which do not consider accurately their interaction with the structure. The limitation of their damage induced by earthquakes is of major interest for the prevention of extensive economic losses and possible threats to human lives. During the last decades several researches have been accomplished all around the world, and many different aspects have been investigated. The increasing interest on masonry infill is due to both the observation of unsatisfactory behaviour of infilled frame structures after real earthquakes and the difficulty to reach a widely scientifically recognized solution. Even if measures for the prevention of infill damage are to some extent included in modern seismic design code, an effective design procedure has not yet been achieved. The object of this study is to perform a numerical Finite Element Model simulation of a reinforced concrete frame specimen infilled with unreinforced Autoclaved Aerated Concrete masonry infill, in order to be able to study accurately the influence and the interaction of the non-structural wall to the reinforced concrete frame. A meso-modelling approach has been followed and the calibration has been performed according to the results of in-plane cyclic tests on single bay – single storey bare and infilled frames which have been carried out at the Department of Civil Engineering and Architecture of the University of Pavia [1, 3]. In order to obtain the parameters of the infill material, the numerical simulation has been performed, in first instance, with reference to tests of mechanical characterization and to in-plane cyclic tests on load-bearing AAC masonry, similar to the one used for the infill [2, 3]. The model has been validated via non-linear static analyses. Moreover, the change in moment and shear demands on the RC members of the frame due to the influence of the presence of the infill as respect to the bare frame condition has also been investigated.*

1 INTRODUCTION

Unreinforced masonry is nowadays widely used in European countries as non-structural infill in reinforced concrete frame structures. Infills are commonly used as interior partitions, exterior enclosures and façade veneers to appropriately fulfill architectural needs. The current code provisions recognize the high seismic vulnerability of inherently brittle masonry infills; however, they often provide few recommendations for non-structural elements, being often insufficient, incomplete or not clearly defined for the specific prevention of infill damage. Field observations after major seismic events repeatedly point towards the high seismic vulnerability of masonry infills, not exclusively in older buildings but also in more recently designed RC frame structures [4, 5, 6, 7, 8]. In the last decades several earthquakes have occurred on the Italian territory and problems related to the performance of masonry infill countries, prone to seismic activity, have been identified (Figure 1).



Figure 1: Masonry infill damage after Emilia earthquake in 2012 (Magenes, et al.) [6].

Furthermore, infills are usually considered only in terms of mass and dead loads; their stiffness and resistance contributes are often neglected. The limitation of the infill damage induced by earthquake is of major interest for the prevention of extensive economic losses and possible threats to human lives. During the last decades several researches have been accomplished worldwide, and many different aspects have been investigated through experimental [9, 10, 11, 12, 13, 14] and/or numerical [15, 16, 17, 18, 19] studies.

The poor seismic behaviour of non-structural infills may not only be due to the inherent weakness of traditional unreinforced masonry but, in some cases, also caused by deficiencies in the design approach. On the other hand, a wide range of masonry types is available on the market and research is increasingly focused on possible improvements of the performance in seismic conditions through the introduction of new products and innovative construction techniques.

The use of Autoclaved aerated concrete (AAC) blocks for both structural and non-structural purposed is increasing. Its main advantages are the lightness, the excellent thermal insulation and fire resistance. However, research of AAC masonry infill is not widespread yet, therefore some experimental campaigns combined with adequate numerical research are necessary.

The object of this study is to perform a numerical Finite Element Model simulation of a RC frame specimen infilled with unreinforced AAC masonry infill in order to be able to study accurately the influence and the interaction of the non-structural wall to the RC frame.

2 CURRENT EUROPEAN SEISMIC CODE PROVISIONS

According to Eurocode 8 [20], structures in seismic regions have to be designed and constructed such that fundamental performance requirements associated with adequate degrees of reliability related to life safety and damage limitation are satisfied. Consequently, ultimate limit states (ULS), associated with no-collapse or life safety requirements, have to be verified at a reference design seismic action for which a reference return period of T_{ULS} is defined in the National Annex of each country. Eurocode 8 [20] states that the structures shall be designed and constructed to withstand the ULS seismic action without local or global collapse, thus retaining its structural integrity and a residual load bearing capacity after the seismic event. The verification of damage limit state (DLS) is required for the corresponding seismic action with a return period T_{DLS}, having a larger probability of occurrence than the design seismic action. Structures shall be designed and constructed to withstand the DLS seismic action without the occurrence of damage and the associated limitations of use. The design procedure to be followed according to Eurocode 8 [20] provisions for the seismic design of RC structures is illustrated in Figure 2.

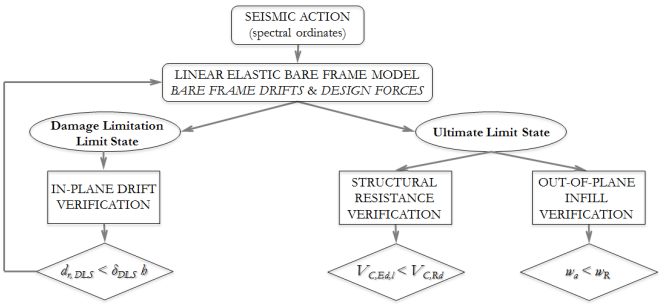


Figure 2: Current design procedure for masonry infilled RC structures according to Eurocode 8 [20].

The damage limitation requirements, according to Eurocode 8 [20], are considered satisfied if the inter-storey drift $d_{r,DLS,j}/h_j$ ($d_{r,DLS,j}$ representing the inter-storey displacement for storey j induced by the damage limitation seismic action and h_j the storey height) do not exceed the inter-storey drift limitation δ_{DLS} (Equation 4) equal to 0.50%, for buildings with brittle non-structural elements fixed such that they do not interfere with structural deformations, and equal to 1.0% in case of structures without non-structural elements.
No further specifications are provided referring to the definition of brittle and ductile non-structural elements. Probably in most cases masonry infills will intuitively be classified as brittle.

At the ULS, the safety verification has to be accomplished in terms of resistance to seismic action effects for both structural and non-structural elements. In particular, for non-structural elements that might, in case of failure, cause risk for human life or affect the main structure of the building or services of critical facilities, the verification of resistance for the design seismic action is foreseen and a simplified procedure is proposed for the evaluation of the seismic force acting on the non-structural element. Thus, the effects of the seismic action may be determined applying a horizontal force F_a, acting at the centre of mass of the non-structural element in the most unfavourable direction, Structural inter-storey drift limitation.

For the local effects, the Eurocode 8 [20] prescribes to assume the critical length equal to the total height for columns at the ground floor or in case the infill is in full column with the column only on one side (Figure 3).

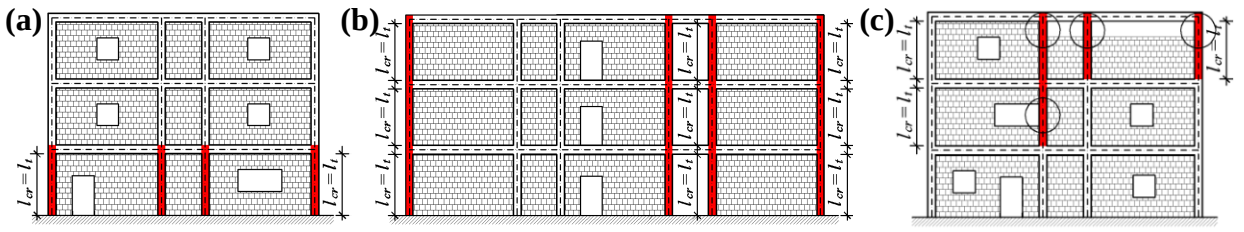


Figure 3: Critical length of the columns (a) in the ground floor, (b) in full contact with the infill on one side, and (c) in partial contact with the infill [31].

The contact length l_c of the column, over which the equivalent diagonal strut force of the infill acts on the column causing a local pressure f_t and introducing a concentration of forces (Figure 4a), should be verified in shear for the demand $V_{C,Ed,l}$ evaluated as the smaller of the following two shear forces (Equation 1):

- the shear demand $V_{C,Ed,w}$ equal to the horizontal component $F_{w,hor}$ of the infill, that can be assumed equal to the strength of the panel (Equation 2);
- the shear demand $V_{C,Ed,M}$ determined following the capacity design principle (Equation 3), assuming that the flexural column capacity develops at the ends of the contact length l_c, as shown in Figure 3b.

$$V_{C,Ed,l} = \min\left(V_{C,Ed,w}; V_{C,Ed,M}\right) \tag{1}$$

$$V_{C,Ed,w} = min\left(f_{v0} t_w l_w; \frac{f_t t_w l_w}{b}\right) \tag{2}$$

$$V_{C,Ed,M} = \gamma_{Rd} \frac{2M_{C,Rd}}{l_c} \tag{3}$$

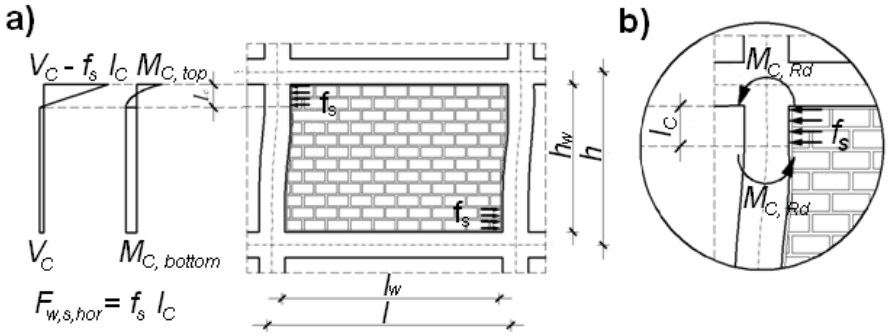


Figure 4: Local effects on an infill adjacent column [31].

3 DESCRIPTION OF THE EXPERIMENTAL CAMPAIGN

In the late '90s, some experimental tests on different weak clay masonry infills in reinforced concrete frames have been executed in an extensive experimental research performed by Calvi and Bolognini [1]. Full-scale, single-storey, single-bay frame specimens were designed according to modern seismic code provisions and subjected to in-plane and out-of-plane tests. The experiments consisted in a cyclic pseudo-static in-plane test up to 3.6% drift for the bare frame, also vertical constant load of 400 kN was applied at the top of each column. Figure 3 illustrates the dimensions and the reinforcement of the frame (5a), the point of application of the loads during the tests (5b) and the Force-Displacement curve of the bare frame obtained from the in-plane test (5c).

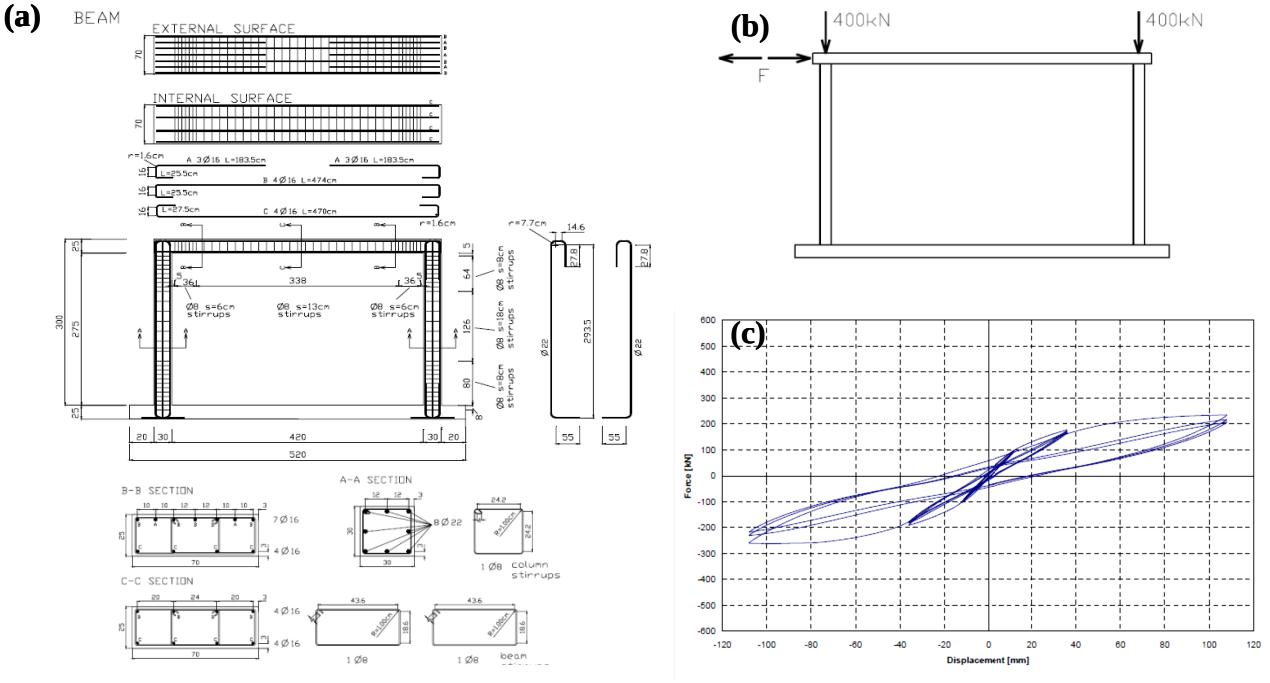


Figure 5: (a) Dimensions and reinforcement of the RC frame; (b) Application points of the loads during the test; (c) Force-Displacement curve of the bare frame obtained from in-plane cyclic pseudo-static test.

In 2006 several tests on AAC masonry infills have been conducted by Penna and Calvi [3], using the same RC frames of the research by Calvi and Bolognini [1]. Different AAC infills were tested: unreinforced, reinforced with a RC mid-height beam, reinforced with steel bars in the bed joints and with and without opening.

For the aim of this study, only in-plane tests on the bare frame and the unreinforced AAC infill have been considered. In Figure 6 the cracking pattern at the end of the selected AAC infill (6a) and the corresponding Force-Displacement curve (6b) are reported; the specimen has been tested up to a drift of 1.2%.

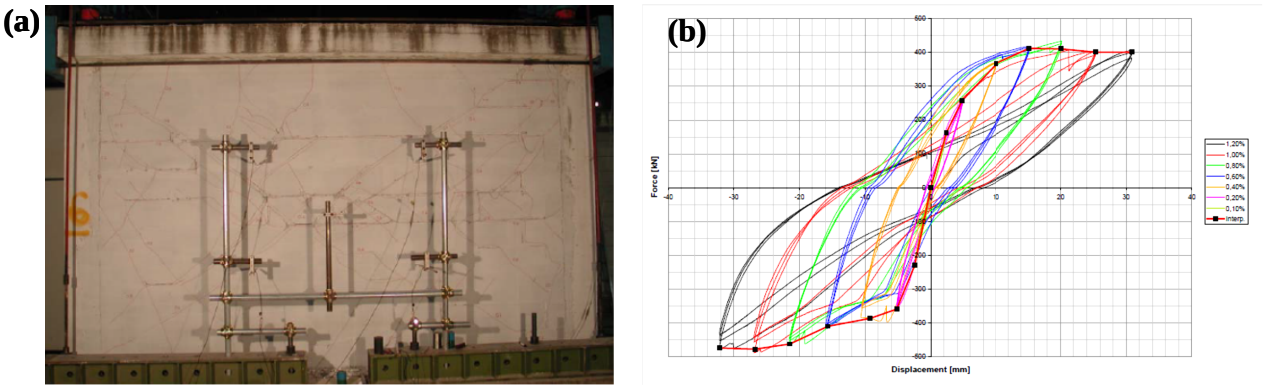


Figure 6: Unreinforced AAC infill. Crack pattern (a) and Force-Displacement curve (b) [3].

Penna and Calvi [3] have additionally carried out experiments of mechanical characterization on AAC units, hardened mortar and masonry wallets; some of them, in particular the vertical and the horizontal compression tests and diagonal compression tests (Figure 7a) on the masonry specimens, have been used in the present work to calibrate the numerical model.

A type of AAC masonry similar to the one tested as infill has also been investigated by Costa et al. [2], where in-plane cyclic tests, with cantilever boundary conditions, on load bearing masonry piers were performed at the University of Pavia on 4 panels with different dimensions and diverse applied vertical loads (Figure 7b). All the specimens were 2.75 m height and 0.30 m thick, however, the first 2 specimens had the same length (1.5 m) but they differed for the vertical load applied which was 200 kN and 300 kN, respectively. In the last 2 experiments the same vertical load of 300 kN was applied, however the panels had different width (3.0 m and 4.5 m). The in-plane response of some of the first two experiments have also been used to better calibrate the finite element model.

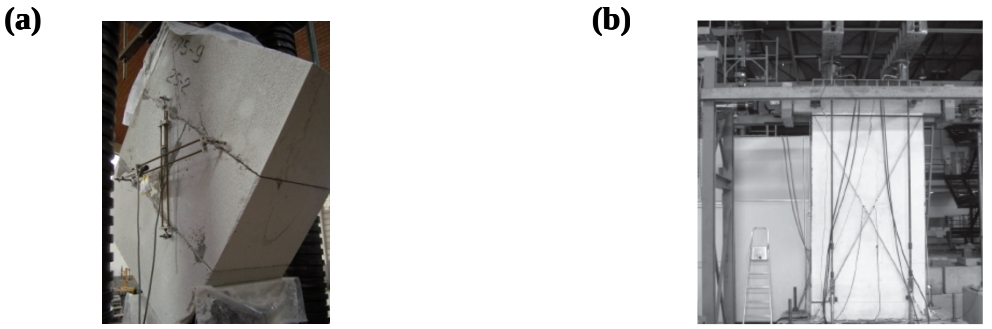


Figure 7: (a) Diagonal compression test on AAC masonry [3]; (b) Setup of the test conducted on the load bearing AAC wall [2].

4 DESCRIPTION OF THE FINITE ELEMENT MODEL

Several different modeling approaches have been developed by the passing of the decades. Crisafulli et al. [21] classified the model used for RC infilled structured into two groups: micro-model, also called local models, where the structure is divided into numerous elements to take into account the local effects in details; and the macro-models, also called simplified models, they are based on a physical understanding of the behaviour of the infill panel. However, the classification proposed by Crisafulli might not be enough detailed; Lourenço [22] proposed to classify the micro model depending on the level of refinement. The masonry can be represented as an homogenous material, sometimes, these models are defined as "meso-models". It is also possible to model the masonry as composed by masonry unit continuous elements and interface elements as mortar joints. A third approach consists in modeling the masonry as two-phase materials; masonry units and mortar joints are modeled as two different continuous elements and their mechanical behaviour of is specified separately.
For the present study a meso-model has been used with the aim on TNO Diana software [23].

4.1 Crack models

Finite element approaches for the modeling of a masonry infill in a reinforced concrete frame may usually refer to two well known crack models: discrete and smeared (Roots [24]). The discrete crack criterion appears to be able to reach more detailed results, however, it suffers from two major drawbacks: it necessitates a continuous change in nodal connectivity, which unfits the nature of the finite element displacement method and force the crack to follow a predefined path along the element edges, which baffles the accuracy of the approach. In the smeared crack criterion the materials are instead idealized to be a homogeneous continuum. The smeared crack criterion can be categorized into a fixed and rotating smeared crack approach.

In the present work, the total strain crack model has been used, originally proposed by Vecchio and Collins [25]. The strain vector $\boldsymbol{\varepsilon_{xyz}}$ in the element coordinate system *"xyz"* is updated at each step using the strain increment $\boldsymbol{\Delta\varepsilon_{xyz}}$ according to Equation 4.

$$^{t+\Delta t_{i+1}}\varepsilon_{xyz} = {}^{t}\varepsilon_{xyz} + {}^{t+\Delta t_{i+1}}\Delta\varepsilon_{xyz} \tag{4}$$

The strain vector in the element coordinates *"xyz"* is transformed to strain vector in the crack directions *"nst"* with the strain transformation matrix **T**.

$$^{t+\Delta t_{i+1}}\varepsilon_{nst} = T\,{}^{t+\Delta t_{i+1}}\varepsilon_{xyz} \tag{5}$$

The strain transformation matrix **T** is fixed upon cracking in the fixed approach, whereas it depends on the current strain vector in the coaxial rotating crack approach:

$$T = T\left({}^{t+\Delta t_{i+1}}\varepsilon_{xyz}\right) \tag{6}$$

Both in the fixed and in the rotating approach, the compressive stress is evaluated in the rotated coordinate system. However, in the fixed approach case, the behaviour in compression is evaluated in the fixed coordinate system which defines the direction of cracks. The constitutive model is formulated in the cracked coordinate system that is given by Equation 7.

$$^{t+\Delta t_{i+1}}\sigma_{nst} = \sigma\left({}^{t+\Delta t_{i+1}}\varepsilon_{nst}\right) \tag{7}$$

Updated stress vector in the element coordinate system is finally given by Equation 8.

$$^{t+\Delta t_{i+1}}\sigma_{xyz} = T\,{}^{t}T\,{}^{t+\Delta t_{i+1}}\sigma_{nst} \tag{8}$$

Moreover, in the fixed crack model it is necessary to model the degradation of the shear behaviour along the crack whereas, in the rotating crack model, the direction of the principal stress is assumed to coincide with the direction of the principal strains; in fact, no shear strain occurs perpendicular to the cracking and only two normal stress components may be calculated using stress-strain models.

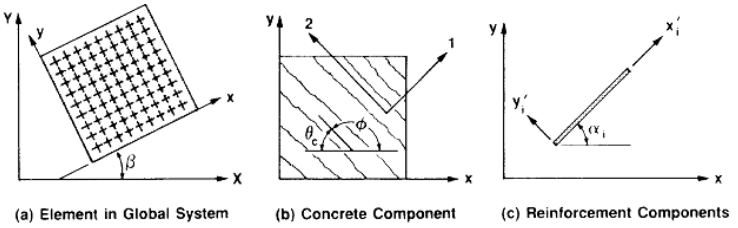


Figure 8: Reference coordinate system for elements [22].

In the present work both the concrete and the AAC masonry infill have been modeled using the smeared total strain rotating crack model.

4.2 Elements used in the FEM

Both the frame and the masonry infill have been modeled with an eight-node quadrilateral isoparametric plane stress element (Figure 9a) based on quadratic interpolation and Gauss integration. The frame-infill interface were modeled using six-node interface elements (Figure 9b).

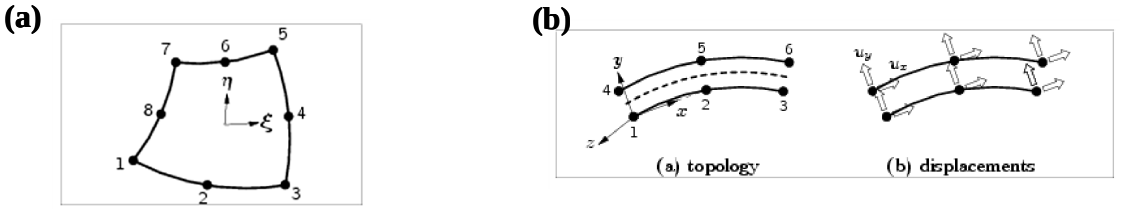


Figure 9: (a) 8-node quadrilateral isoparametric plane stress element; (b) Frame-infill 6-node interface element.

4.3 Material constitutive models

The same constitutive model has been used for the concrete of the frame and for the AAC masonry infill. A parabolic behaviour under compression has been assumed for the concrete and the AAC masonry (Figure 10a) and the compressive strength, along with the compressive fracture energy, has been defined. The "crack bandwidth" *(h)* which is contingent on the element size and the type of element used has been computed automatically by Diana, and it avoids the "size effect". The reduction of the compressive strength due to lateral cracking has been considered according to the relationship proposed by Vecchio and Collins [25] (Figure 10b). In addition, the increase of the compressive strength due to lateral confinement has been taken into account, using the model proposed by Selby and Vecchio [26].

The tensile behaviour has been idealized according to the model developed by Hordijk [27] (Figure 10c). The tensile strength f_{ctm} has been computed according to Eurocode 2 [28], and the Mode-I fracture energy has been considered according to CEB-FIP Model Code 2010 [29] (Equation 9).

$$G_F^I = 0.70 \cdot 73 f_{cm}^{0.18} \div 1.30 \cdot 73 f_{cm}^{0.18} \tag{9}$$

where f_{cm} is the mean value of concrete cylinder compressive strength. The minimum value of the interval of the Mode-I fracture energy has been assumed. As an alternative, an elastic-brittle tensile constitutive model has also been used.

For the reinforcing steel, the Von Mises yield criterion was adopted, with a bilinear stress-strain curve in uniaxial tension. The reinforcement steel bars have been considered as "embedded reinforcement" which do not have degrees of freedom on their own but add stiffness to the finite element model. In this modeling technique, reinforcing bars are assumed not to occupy any space or mass in the finite element model and the addition of embedded bars do not provide any weight to the mother element. The strains of the reinforcement are computed from the displacement field of the mother elements assuming perfect bond with the surrounding material.

The frame-infill interface elements employ a Coulomb Friction criterion (Figure 10d). The linear normal and tangential stiffness of the interface elements were assumed to be equal. The cohesion *c* and the friction coefficient *tanΦ* were computed from initial shear tests according to EN 1052-3 [30]. This model assumes that a gap forms if the tensile strength is exceeded.

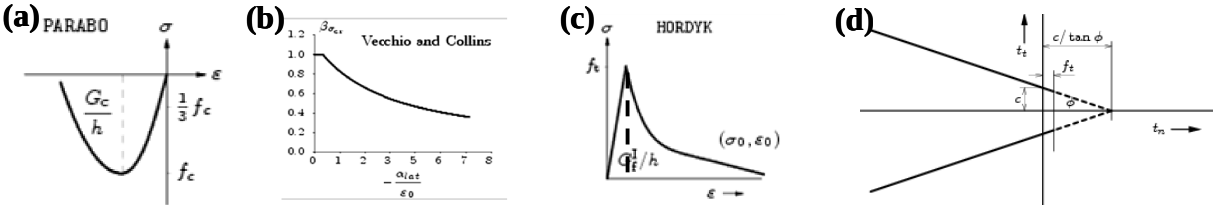


Figure 10: (a) Parabolic compressive behaviour which can be used in rotating crack model; (b) Vecchio and Collins relationship for reduction factor due to lateral cracking; (c) Hordijk tensile constitutive law which can be used in rotating crack model, brittle tensile constitutive law in dashed line; (d) Coulomb friction criterion with tensile strength limit.

5 CALIBRATION OF THE AAC MASONRY ON THE TESTS OF CHARACTERIZATION AND ON THE IN-PLANE CYCLIC TESTS OF LOAD-BEARING PIERS

In order to evaluate the mechanical characteristics of the AAC masonry, different type of tests on small specimens were performed in the study on the AAC infills by Penna and Calvi [3]; for the sake of this work, the results of the vertical, the horizontal and the diagonal compressive strength tests have been taken into consideration. In addition, in order to investigate the seismic response of load-bearing masonry piers, different in-plane cyclic tests have been executed in the framework of the research conducted by Costa et al. [2].

Some of the most relevant results of the monotonic push-over analyses obtained by the FEM modeling calibrated on the results of the tests of characterization and of the in-plane cyclic tests on masonry piers are hereafter presented.

The masonry studied was composed by 30 cm thick AAC unit and both horizontal and vertical thin layers of mortar.

5.1 Calibration of the AAC masonry on the vertical and horizontal compression tests

The Figure 11 illustrates some phases of the vertical and the horizontal compression tests on masonry wallets . A mean value of about 2.0 MPa was found for the compressive strength of the wallets and the values of deformations were measured through linear potentiometers.

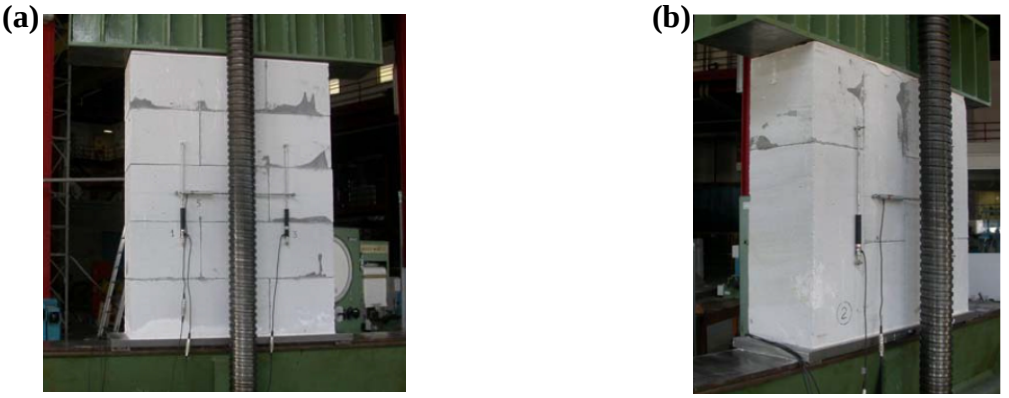


Figure 11: Tests on AAC masonry carried out at the University of Pavia [3]: (a) vertical compression test; (b) horizontal compression test.

The masonry has been modeled as an isotropic homogenous material. The elastic-brittle and the Hordijk constitutive models for the tensile behaviour of the masonry have been used. Figure 12 reports the comparison between the experimental tests and the FEM analyses in terms of stress-strain relationship (Figure 12a for the vertical and Figure 12b for the horizontal compression). For both vertical and lateral compression three cyclic tests have been performed, in Figure 12 their stress-strain curves are also reported. The results appear to be in good agreement, although the peak stress is not perfectly attained in both the cases (vertical and horizontal compression). Moreover, the two laws used for modeling the tensile behaviour of the material have provided similar results in the case of the vertical compression tests but a different deformation capacity for the case of the horizontal compression tests, being the Hordijk model more conservative.

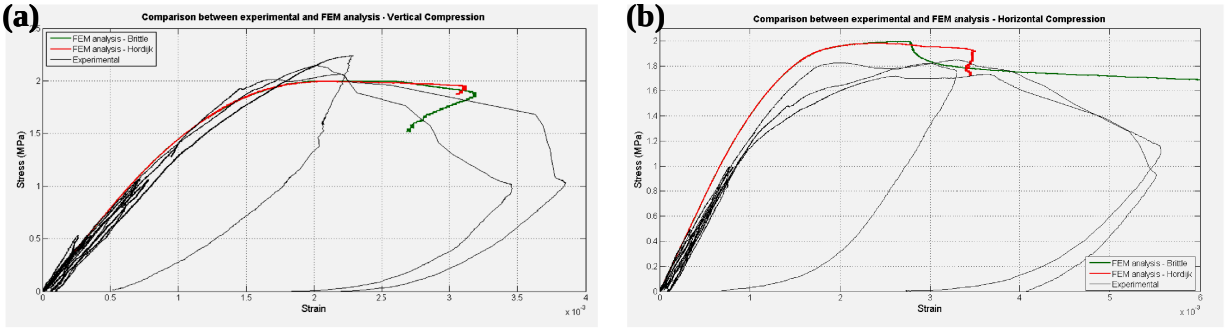


Figure 12: Comparison between experimental and FEM analysis: (a) vertical compression; (b) horizontal compression.

5.2 Calibration of AAC masonry on the diagonal compression tests

Seven monotonic diagonal compression tests on masonry wallets were carried out (Figure 13a). The average tension strength obtained was of about 0.28 MPa.

A comparison between experimental, Hordijk and elastic-brittle tensile behaviour is shown in Figure 13b. The parameters of these analyses are the same used for the comparison with the results of the vertical/diagonal compression tests. The Hordijk tensile behaviour presents a better accuracy in the descending branch, whereas the brittle model appears to predict slightly better the peak and its location in the load-displacement coordinates. In both the cases the stiffness and the obtained ultimate displacement have found to be accurate. The Hordijk tensile behaviour has been preferred to the elastic-brittle one. Table 1 summarizes the obtained maximum load. Figure 14 displays the principal stresses in the specimen at different steps, with the results in good agreement with the cracking pattern of the masonry wallet.

	Max Load	Horizontal displacement at peak
Experimental average	115.1 kN	0.281 mm
Elastic-brittle constitutive law in tension	116.4 kN	0.311 mm
Hordijk constitutive law in tension	118.0 kN	0.315 mm

Table 1: Comparison of the peak values between experimental results and the one obtained from the FEM analysis with the two tensile constitutive models.

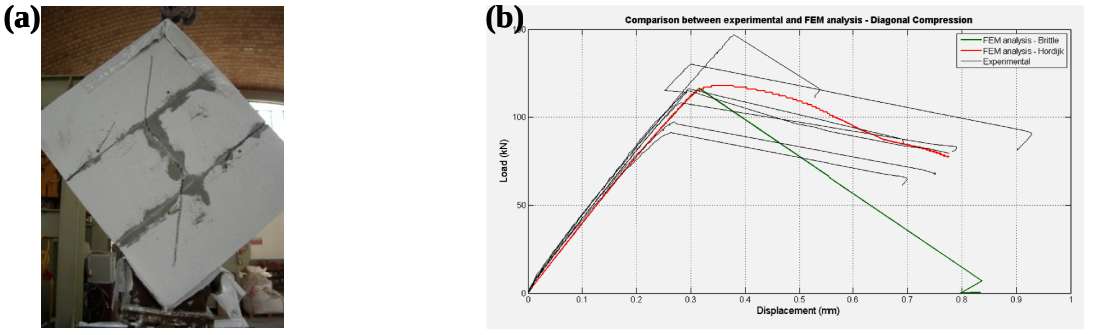


Figure 13: Comparison between experimental and FEM analysis:(a) vertical compression; (b) horizontal compression.

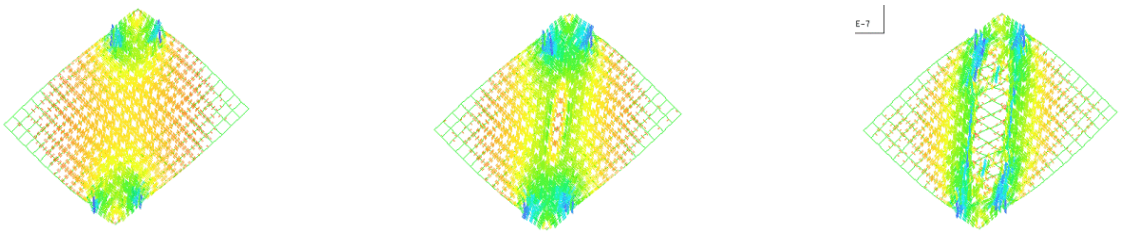


Figure 14: Principal stresses at different steps.

5.3 Calibration of AAC masonry on the in-plane cyclic tests of load-bearing piers

Two of the cyclic tests conducted in the study performed by Costa [2] have been here considered. The analysis conducted on pier 1, the one with a vertical load of 200 kN, presented a rocking failure with a horizontal crack at the bottom part of the masonry wall; such a failure is very similar to the one observed during the tests. Figure 15 displays the cracking paths of specimen 1 at different steps.

The masonry has been modeled using the tensile constitutive law proposed by Hordijk and the parameters are the ones calibrated through the FEM analyses conducted on the vertical, the horizontal and the diagonal compression tests.

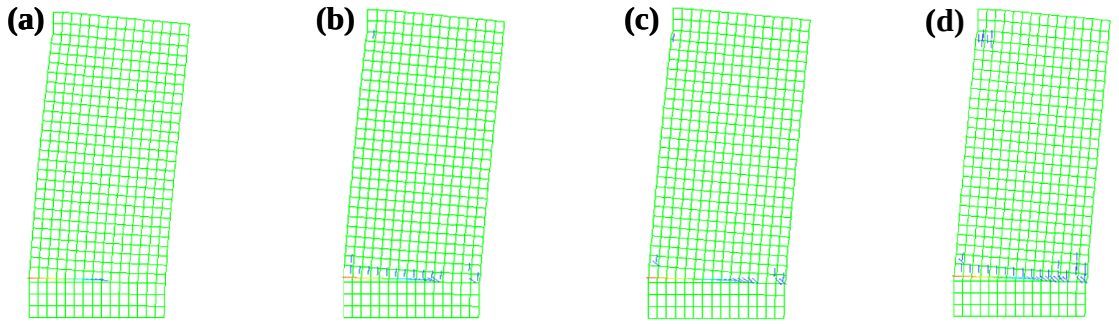


Figure 15: Crack path of specimen 1 at 0.3% drift (a), 0.45% drift (b), 0.6% drift (c) and 0.73% drift (d).

A comparison between experimental and analysis data highlights a similar overall behaviour; in fact, the stiffness obtained from finite element analysis is very similar to the real one. The maximum force attained is approximately 10% higher than the experimental one: 54 kN in the FEM analysis and 48.8 kN in the test.

The analysis conducted on wall 2, the one with a vertical load of 300 kN, shows a rocking failure with a horizontal crack at the bottom part of the masonry wall and a vertical cracking with a shape similar to a hourglass; also in this case the failure is very similar to the one observed during the tests. Figure 16 presents the cracking path of specimen 2 at different steps.

The results acquired from pushover analysis are capable to predict with enough precision the stiffness, the peak lateral force and the overall behaviour.

The numerical results presented at Figure 17 appear to match accurately the envelope of the experimental ones.

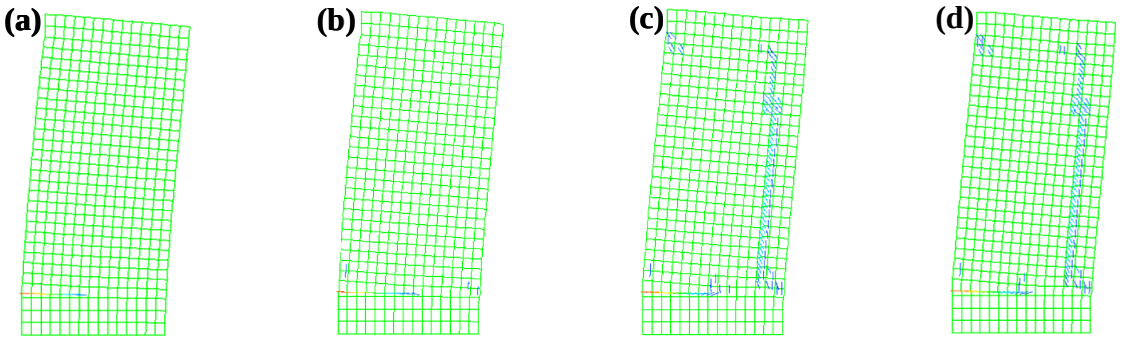


Figure 16: Crack path of specimen 2 at 0.3% drift (a), 0.45% drift (b), 0.6% drift (c) and 0.73% drift (d).

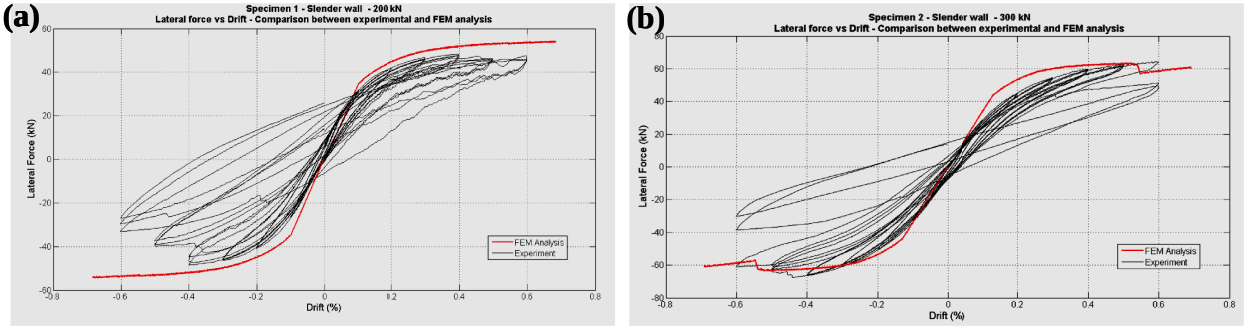


Figure 17: Comparison between the experimental and the pushover analysis results. (a) Specimen 1; (b) Specimen 2.

6 NUMERICAL SIMULATION OF THE CYCLIC RESPONSE OF A R.C. FRAME WITH AAC MASONRY INFILL

Nonlinear static FEM analyses of a single bay-single storey r.c. frame without infill and of a fully infilled frame with AAC masonry have been performed, using the parameters of the materials described in *Sections 4* and *5*.

6.1 R.c. bare frame

The test on the single bay-single storey r.c. frame without infill (bare frame) was conducted within the experimental research conducted by Calvi and Bolognini [1] at University of Pavia and described in *Section 3*.

The in-plane cyclic response of the bare frame has been simulated firstly in order to obtain a reliable finite element model of the RC frame, and, at a later stage, to study the influence of the masonry AAC infill (see *Section 6.2)*. In fact, it is extremely important to interpret the behaviour of the bare RC frame to better understand the influence of the infill on the structure.

A phased analysis has been performed; firstly the vertical loads were applied, secondly an incremental imposed displacement was imposed (pushover analysis). Four materials have been used according to the characterization material tests: the concrete of the beam, the concrete of the column, the steel of the longitudinal reinforcement and the steel of the transversal reinforcement. According to the reinforcement details, a clear cover of the concrete elements equal to 27 mm has been used. Only few experimental data on the mechanical characteristics of the concrete were available and, therefore, some values have been assumed making reference to the Eurocode 2 [25] and the CEB FIP 2010 Model Code [26]. The properties of the concrete and of the reinforcement steel used in the FEM model are reported in Table 2.

	Experi-mental	FEM analysis	Standards formulae	
COLUMN CONCRETE				
Young Modulus [MPa]	---	24303	$0.8\ E_{cm}=0.8\ 22[(f_{cm})/10]^{0.3}$	E_{cm} *from Table 3.1 EC2*
Poisson ratio	---	0.2	0.2	*3.1.3(4) EC2*
Density [kg/m^3]	---	2500	---	---
Tension Strength [MPa]	---	2.307	$f_{ctm}=0.30\ f_{ck}^{(2/3)}$	*Table 3.1 EC2*
Tension Fracture Energy [Nmm/mm^2]	---	0.0939	$0.7\ 73\ f_{cm}^{0.18} \le G_F^I \le 1.3\ 73\ f_{cm}^{0.18}$	*CEB FIP 2010*
Compression Strength [MPa]	29.32	29.32	---	---
BEAM CONCRETE				
Young Modulus [MPa]	---	25532	$0.8\ E_{cm}=0.8\ 22[(f_{cm})/10]^{0.3}$	E_{cm} *from Table 3.1 EC2*
Poisson ratio	---	0.2	0.2	*3.1.3(4) EC2*
Density [kg/m^3]	---	2500	---	---
Tension Strength [MPa]	---	2.671	$f_{ctm}=0.30\ f_{ck}^{(2/3)}$	*Table 3.1 EC2*
Tension Fracture Energy [Nmm/mm^2]	---	0.0967	$0.7\ 73\ f_{cm}^{0.18} \le G_F^I \le 1.3\ 73\ f_{cm}^{0.18}$	*CEB FIP 2010*
Compression Strength [MPa]	34.56	34.56	---	---
LONGITUDINAL REINFORCEMENT STEEL				
Young Modulus [MPa]	---	200000	*200000*	*3.2.7(4) EC2*
Poisson ratio	---	0.3	0.3	*3.2.5(1) EC3*
Yield Strength [MPa]	558	558	---	---
Ultimate Strength [MPa]	649	649	---	---
Ultimate Strain	---	0.023	---	*3.3.6(7) EC2*
TRANSVERSAL REINFORCEMENT STEEL				
Young Modulus [MPa]	---	200000	*200000*	*3.2.7(4) EC2*
Poisson ratio	---	0.3	0.3	*3.2.5(1) EC3*
Yield Strength [MPa]	557	557	---	---
Ultimate Strength [MPa]	630	630	---	---
Ultimate Strain	---	0.023	---	*3.3.6(7) EC2*

Table 2: Material properties values used for concrete and reinforcement steel.

Calvi and Bolognini [1] estimated the initial stiffness of the r.c. bare frame equal to 12087 kN/m. The maximum horizontal force reached in the test, according to the envelope curves, was 227.7 kN. As reported in Figure 18a, the pushover analysis conducted on the FEM numerical model has been able to accurately predict the overall response of the bare frame, especially the peak strength (equal to 225.5 kN) and the post-yielding behaviour. In order to match the results in terms of initial stiffness (in the FEM model equal to 14316 kN/m), a value for the Young elastic modulus E equal to 80% of the average elastic modulus (E_{cm}) evaluated according to the expressions in the EC2, was used; this approximation is however in line with the common dispersion of the values of this parameter. In Figure 18b, the deformed shape at the last drift (3.6% drift) has been reported.

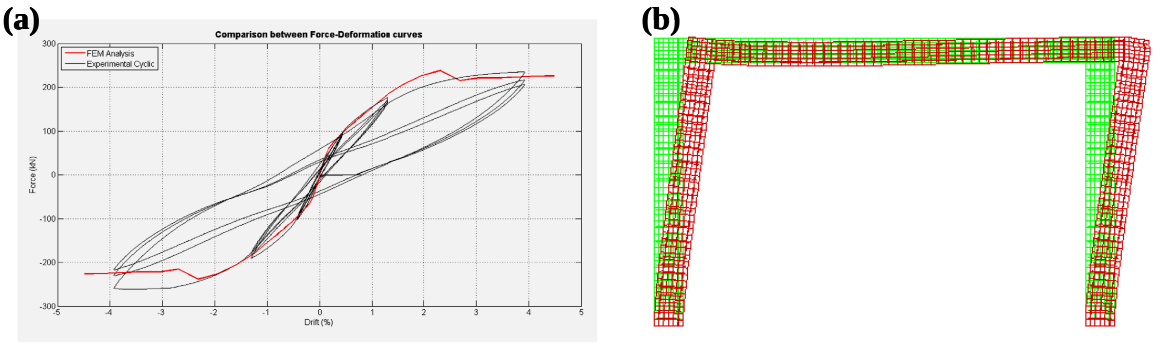


Figure 18: (a) Comparison Force-Deformation curves. Pushover FEM analysis results versus experimental cyclic results. (b) Deformed shape at 4.3% drift.

6.2 AAC masonry infilled frame

The experimental test conducted at the University of Pavia by Penna and Calvi [3] had demonstrated that the masonry infilled frame performed a very different lateral response as respect to the bare frame. A lower maximum drift was reached and the infilled RC frame presented a stiffer behaviour and reached an higher maximum force peak.

The same phased FEM analysis conducted for the model described in *Section 6.1* has been here carried out. The material properties of the concrete and of the steel rebars assumed for the bare frame have also been used for this model; in addition, the properties of the interface mortar and of the AAC masonry, calibrated with the simple models described in *Section 5*, have been considered and reported in Table 3.

	Experimental	FEM analysis	
AAC MASONRY			
Young Modulus [MPa]	1498	1498	*From tests of characterization*
Density [kg/m^3]	484	484	*From tests of characterization*
Tension Strength [MPa]	---	0.279	*From tests of characterization*
Tension Fracture Energy [Nmm/mm^2]	---	0.0567	*Calibrated on the cyclic test*
Compression Strength [MPa]	2.0	2.0	*From tests of characterization*
INTERFACE MORTAR			
Cohesion [MPa]	---	1.15	*Calibrated on the cyclic test*
Friction Angle	---	0.31	*Calibrated on the cyclic test*
Tensile Strength [MPa]	---	0.10	*Calibrated on the cyclic test*

Table 3: Material properties values used for masonry and interface mortar..

The experimental secant stiffness calculated at 40% of the maximum force was 80972 kN/m, whereas the one obtained from the numerical analysis is 75369 kN/m, whereas the initial stiffness, measured at 10% of the maximum strength, is 81340 kN/m and 86551 kN/m for experimental and FEM analysis, respectively. The maximum strength reached during the test, according to the average envelope, was 439 kN and the horizontal load peak for the finite element analysis is 388 kN. However, Figure 19a shows that the results of the FEM analysis are able to accurately predict the overall behaviour of the structure. Figure 19b shows how the results of the FEM analysis predicts better the third cycle than the first one, meaning that the assumptions made on the material properties represent appropriate conservative choices.

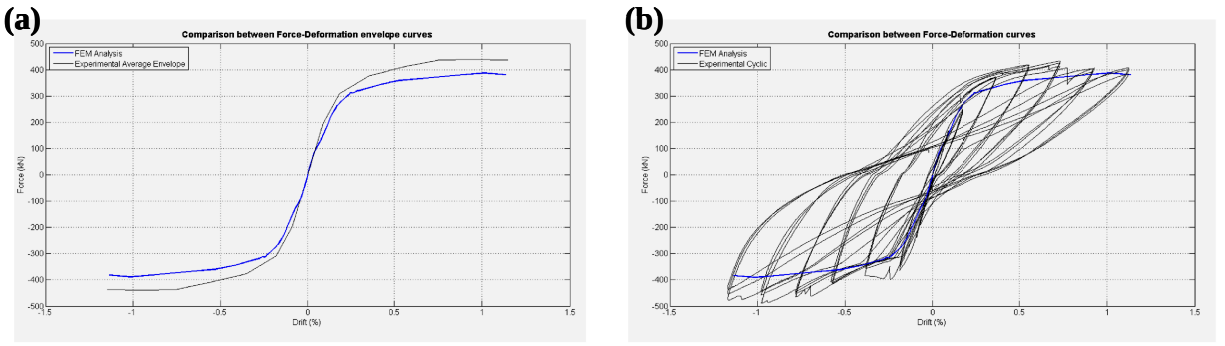


Figure 19: (a) Comparison Force-Deformation: (a) envelope curves; (b) cyclic curve.

Figure 20a, 20b and 20c show the crack pattern at 0.40%, 0.75% and 1.10% drift, respectively.

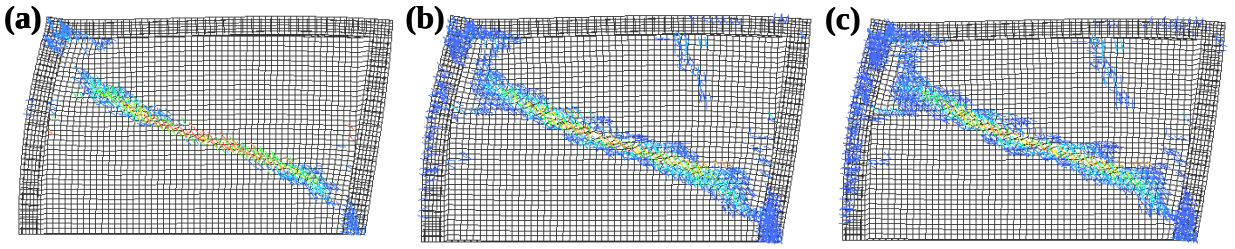


Figure 20: Crack pattern at 0.40% drift (a); 0.75% drift (b); 1.10% drift (c).

Moreover, the numerical simulation has allowed to compare the results in terms of cracking pattern. The results of the analysis appear to be in line to those of the cyclic tests, as reported in Figure 21a in the case of 0.40% drift. Figure 21b shows a comparison between the experimental and analytical crack patterns considering the experimental cracks due to the load applied in the same direction of the pushover analysis. In Figure 21b is clearly visible that the results of the FEM analysis is able to capture the main diagonal crack, although it cannot predict in a precise way some of the minor cracks.

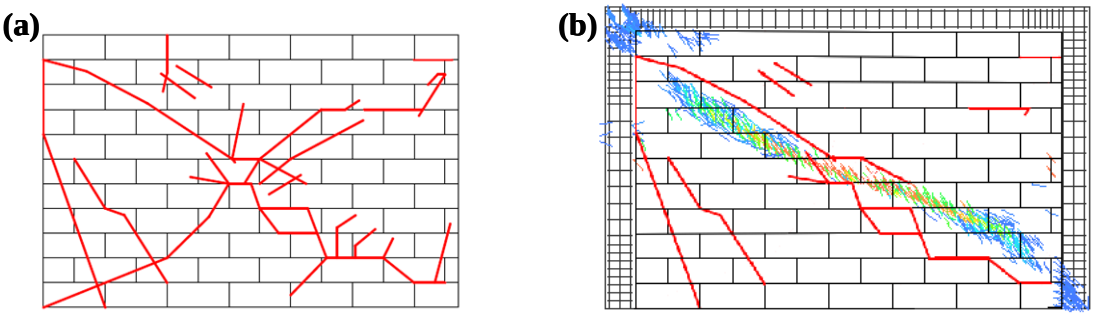


Figure 21: (a) Experimental crack pattern at 0.40% drift [3]. (b) Comparison between experimental and analytical crack patterns at 0.40% drift.

6.3 Effect of the infills on the response of the r.c. frame

It has been clearly demonstrated, both experimentally and numerically how the global behaviour of the infill can be modified due to the presence of the infill. Figure 23 illustrates the numerical average positive envelope of the Force-Drift curves of the bare and the infilled frame; moreover, the difference between the infilled and the bare frame response has been evaluated and it is reported with the red curve and it represents a simplified way to estimate the infill contribution of the lateral response. The infill contribution $F_{w,hor}$ at the correspond-

ing displacement d_m' to the overall capacity F_{max} at the displacement d_{max} has been evaluated subtracting the average force displacement curve of the bare frame from that of the infilled one. Figure 22 sketches the procedure. F_{max} is the maximum strength reached by the infilled frame, corresponding to a displacement d_{max}, while $F_{w,hor}$ is the peak horizontal masonry infill strength achieved at d_m'.

It is therefore clearly noticeable the influence of the AAC masonry infill on the overall response of the infilled frame. The peak force of the infill contribution is reached at 0.53% drift, which corresponds to a complete activation of the strength of the infill.

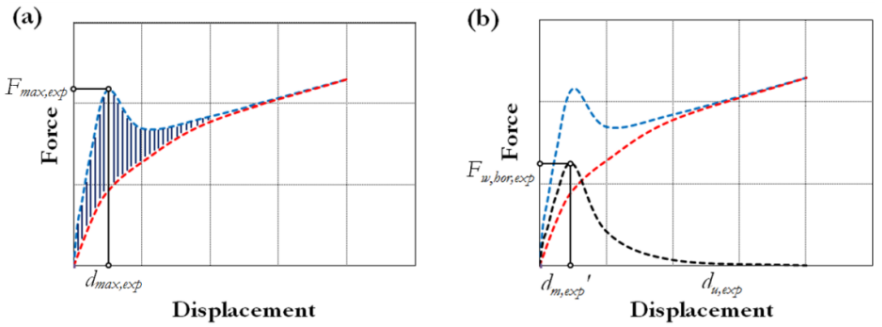


Figure 22: (a) Average capacity curves for bare and infilled frames; (b) Average force contribution of the masonry infill [30].

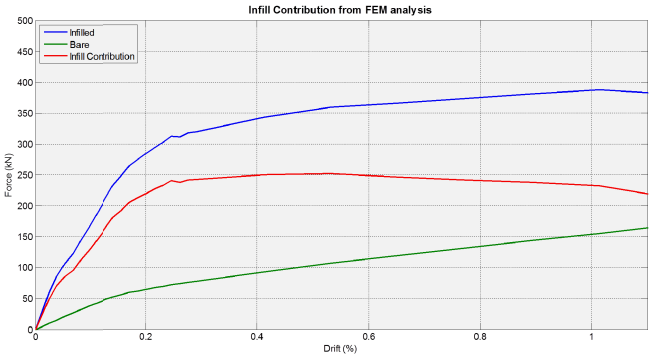


Figure 23: Infill contribution from numerical results.

6.4 Local effects on the r.c. columns due to the infill

As reported by Hak et al. [31], the possible occurrence of local effects on structural elements of infilled RC frames with masonry infills is widely recognized and also supported by field evidence from recent earthquakes events. In particular, local damage and eventually brittle failure can commonly be caused on columns which are in partial contact with masonry infill, causing a reduction of the clear height of the column and, hence, inducing locally increased shear and displacement demands. However, detrimental effects on columns of RC frames structures can be caused by the interaction with masonry infills also in the case of full contact along the height of the column, in particular when masonry infill typologies of high strength and stiffness properties are used in construction, and/or when the infill is located only on one side of the column. Specifically, additional concentrated shear demands may be imposed on the column at its ends in the region of contact with the masonry infill due to the activation of compressive diagonal strut forces, possibly causing local column damage or shear failure. Assuming that additional shear is imposed on the columns of the frame due to the activation of a diagonal strut force in the masonry panel, it has to be pointed out that the full

strut action is achieved only after a certain inter-storey demand has been reached. In *Section 6.3* it has been observed that the complete strut activation occurred at 0.53% drift. Therefore a comparison between bare and infilled frame at 0.53% drift has been studied. More specifically, Figure 24a and Figure 24b illustrate how the distribution of the bending moment and of the shear of the infilled frame assume different shapes along the height of the column adjacent to the infill as respect to the r.c. column of the bare frame.

(a) **(b)**

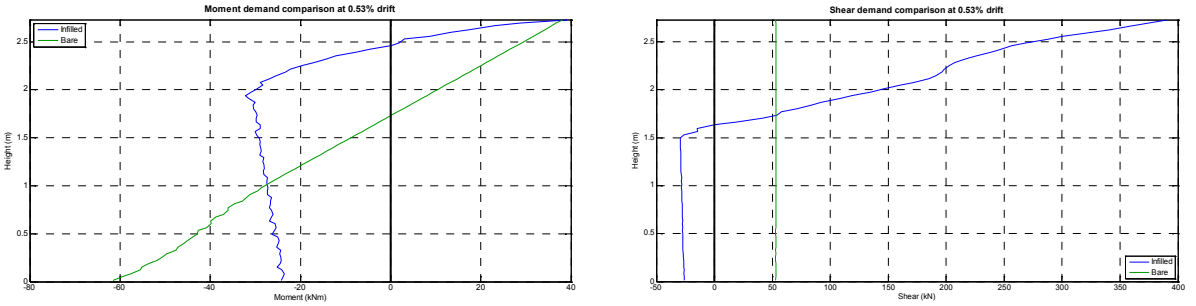


Figure 24: Comparison between bare and infilled r.c frame at 0.53% drift: (a) moment and (b) shear distribution on the r.c. column.

The contact length corresponds at 1.25 m (45% of total height of the column) and it has been computed from the change of the gradient in Figure 24b.

7 CONCLUSIONS

In the present work a study about the meso-modeling of an AAC masonry infill has been developed. A numerical calibration according to the tests conducted at the University of Pavia [1, 3] has been performed.

Different models based on smeared crack approach, total strain rotating crack model have been carried out. Both masonry and concrete have been modeled using eight-node quadrilateral isoparametric plane stress elements. An isotropic behaviour and, finally, a Hordijk tensile constitutive law have been assumed.

The model developed have been calibrated replicating the characterization tests (vertical, horizontal and diagonal compression of AAC masonry wallets) performed at the University of Pavia. Furthermore, two AAC load-bearing piers have been modeled to refine the calibration conducted on the characterization tests. Different tensile behaviours (Hordijk and elastic-brittle), have been compared and the former is the most suitable for the aim of this work. The modeling of AAC load-bearing masonry walls was able to predict the envelope of the experimental cyclic behaviour, the stiffness, the peak lateral force and the overall behaviour with a good accuracy. Moreover, the obtained numerical failure mode matched the experimental.

The pseudo-static experiments conducted at University of Pavia by Calvi and Bolognini [1] and by Penna and Calvi [3] have been modeled and numerically replicated through some pushover analyses. A good matching of the behaviours of the bare and infilled frames have been observed. A comparison between the experimental and the finite element crack paths has been fulfilled, and also the effects of the infills on the response of the RC frame and the local effects have been taken into account. Thus, the moment, the shear demands and the contact length on the adjacent RC column in case of bare and infilled frame have been evaluated.

One of the main finding of the study is that, using a meso-model for AAC masonry infills and calibrating it according to few characterization tests on masonry wallets and infill-frame interface, it is possible to simulate a full scale in plane cyclic test on a RC frame with AAC infill. This model can also predict the actual moment and shear distribution on the adjacent

columns which strongly differ from the ones of the bare frame. Thus, also the contact length can be computed starting from the actual shear distribution on the column. Finally, it is noticeable both experimentally and numerically that the masonry infill interacts with the structure and it modifies the behaviour of the frame; therefore different results in term of displacements, stiffness and internal force distribution have been observed.

ACKNOWLEDGEMENTS

The research upon which this work is carried out at the University of Pavia, EUCENTRE Pavia and Middle East Technical University, and it is sponsored by the Erasmus Mundus Programme. The financial support of this is gratefully acknowledged.

REFERENCES

[1] G.M. Calvi, D. Bolognini, Seismic response of reinforced concrete frames infilled with weakly reinforced masonry panels, *Journal of Earthquake Engineering*, **5**, 153-185, 1999.

[2] A. Costa, A. Penna, G. Magenes, Seismic Performance of Autoclaved Aerated Concrete (AAC) Masonry: From Experimental Testing of In-Plane Capacity of Walls to Building Response, *Journal of Earthquake Engineering*, **15**, 1-31, 2011.

[3] A. Penna, G.M. Calvi, Campagna sperimentale su telai in c.a. con tamponamenti in Gasbeton (AAC) con diverse soluzioni di rinforzo [in Italian], *Experimental Report, University of Pavia*, Italy, 2006.

[4] F. Braga, V. Manfredi, A. Masi, A. Salvatori, M. Vona, Performance of nonstructural elements in RC buildings during the L'Aquila 2009 earthquake, *Bulletin of Earthquake Engineering*, **9**, 307-324, 2011.

[5] P. Ricci, V. Manfredi, F. De Luca, G.M. Verderame, 6th April 2009 L'Aquila earthquake, Italy: reinforced concrete building performance, *Bulletin of Earthquake Engineering*, **9**, 285-305, 2011.

[6] G. Magenes, S. Bracchi, F. Graziotti, M. Mandirola, C.F. Manzini, P. Morandi, M. Palmieri, A. Penna, A. Rosti, M. Rota, M. Tondelli, Preliminary damage survey to masonry structures after the May 2012 Emilia earthquakes, **v.1**, *http://eqclearinghouse.org/2012-05-20-italy-it*, 2012.

[7] C.F. Manzini, P. Morandi, Rapporto preliminare sulle prestazioni ed i danneggiamenti agli edifici in muratura portante moderni a seguito degli eventi sismici emilani del 2012 [in Italian], **v.1**, Eucentre, *http://eqclearinghouse.org/2012-05-20-italy/*, 2012.

[8] L.D. Decanini, D. Liberatore, L. Liberatore, L. Sorrentino, Preliminary Report on the 2012, May 20, Emilia Earthquake, **v.1**, *http://eqclearinghouse.org/2012-05-20-italy-it/*, 2012.

[9] A.B. Mehrabi, Behavior of masonry-infilled reinforced concrete frames subjected to lateral loading, *PhD Thesis*, University of Colorado, USA, 1994.

[10] F.J. Crisafulli, Seismic behaviour of reinforced concrete structures with masonry infills, *PhD Thesis*, University of Canterbuty - Christchurch, New Zealand, 1997.

[11] G.M. Calvi, D. Bolognini, Seismic response of R.C. frames infilled with weakly reinforced hollow masonry panels, University of Pavia, Italy, 1999.

[12] F. Da Porto, G. Guidi, M. Dalla Benetta, N. Verlato, Sistemi costruttivi e risultati sperimentali Reluis Research Report [in Italian], *Experimental Report*, University of Padova, Italy, 2012.

[13] S. Hak, P. Morandi, G. Magenes, Experimental tests on masonry infilled frames, Pavia, Italy, 2013.

[14] K.M.A. Mosalam, Experimental and Computational Strategies for the Seismic Behavior Evaluation of Frames with Infill Walls, *PhD Thesis*, Cornell University, USA, 1996.

[15] J.M. Leuchars, J.C. Scrivener, Masonry Infill Panels Subjected to Cyclic In-Plane Loading, *Bulletin of Nwe Zealand National Society for Earthquake Engineering*, **9**, 122-131, 1976.

[16] P. Lourenço, An Orthotropic Continuum Model for the Analysis of Masonry Structures, Delft University of Technology, Netherland, 1995.

[17] A. Stavridis, Analytical and Experimental Study of Seismic Performance of Reinforced Concrete Frames Infilled with Masonry Walls, *PhD Thesis*, University of California, USA, 2009.

[18] J.R. van Noort, Computational Modeling of Masonry Structures, *PhD Thesis*, Delft University of Technology, Netherland, 2012.

[19] L. Decanini, F. Mollaioli, A. Mura, R. Saragoni, Seismic performance of masonry infilled RC frames, *Proc. of the 13th World Conference on Earthquake Engineering*, Vancouver, Canada, 2004.

[20] CEN, Eurocode 8 - Design of structures for earthquake resistance, Brussels, Belgium, *European Committee for Standardisation*, Part 1: General rules, seismic actions and rules for building, 2004.

[21] F.J. Crisafulli, A.J. Carr, R. Park, Analytical Modeling of Infilled Frame Structures - A General Review, *Bulletin of the New Zealand Society for Earthquake Engineering*, **33**, 2000.

[22] P.B. Lourenço, *An Orthotropic Continuum Model for the Analysis f Masonry Structures*, Delft, University of Technology, Netherland, 1995.

[23] TNO-Diana, *User's Manual - Version 9.4.3*, Delft, Netherland, 2010.

[24] J.G. Roots, Computational modeling of concrete fracture, *PhD Thesis*, Delft, University of Technology, Netherland, 1988.

[25] F.J. Vecchio, M.P. Collins, The Modified Compression-Field Theory for Reinforced Concrete Elements Subjected to Shear, *ACI Structural Journal*, **83**, 219-231, 1986.

[26] R.G. Selby, F.J. Vecchio, Three-dimensional Constitutive Relations for Reinforced Concrete, *Technical Report 93-02*, University of Toronto, Toronto, Canada, 1993.

[27] D.A. Hordijk, Local Approach to Fatigue of Concrete, *PhD Thesis*, Delft, University of Technology, Netherland, 1991.

[28] CEN, Eurocode 2 - Design of concrete structures, Brussels, Belgium, *European Committee for Standardisation*, Part 1.1: General rules and rules for building, 2004.

[29] CEB/FIP, Model Code 2010, 2010.

[30] CEN, UNI EN 1052-3 - Methods of test for masonry, Brussels, Belgium, *European Committee for Standardisation,* Part 3: Determination of initial shear strength, 2007.

[31] S. Hak, P. Morandi, G. Magenes, Evaluation of infill strut properties based on in-plane cyclic tests, *Gravedinar*, **65**, 411-422, 2013.

[32] S. Hak, P. Morandi, G. Magenes, Local effects in the seismic design of rc frame structures with masonry infills, *4th ECCOMAS Thematic Conference on Computational Methods in Structural Dynamics and Earthquake Engineering, 2013.*

COMPDYN 2015
5th ECCOMAS Thematic Conference on
Computational Methods in Structural Dynamics and Earthquake Engineering
M. Papadrakakis, V. Papadopoulos, V. Plevris (eds.)
Crete Island, Greece, 25–27 May 2015

DOUBLE-LAYER PLATFORM OF HIGH PERFORMANCE COMPUTING FOR DAMAGE PREDICTION OF RC BUILDINGS SUBJECT TO EARTHQUAKE AND SUBSEQUENT TSUNAMI IN A TARGET AREA

P. Latcharote[1] and Y. Kai[2]

[1] Department of Infrastructure Systems Engineering, Kochi University of Technology, Japan
e-mail: panoname@hotmail.com

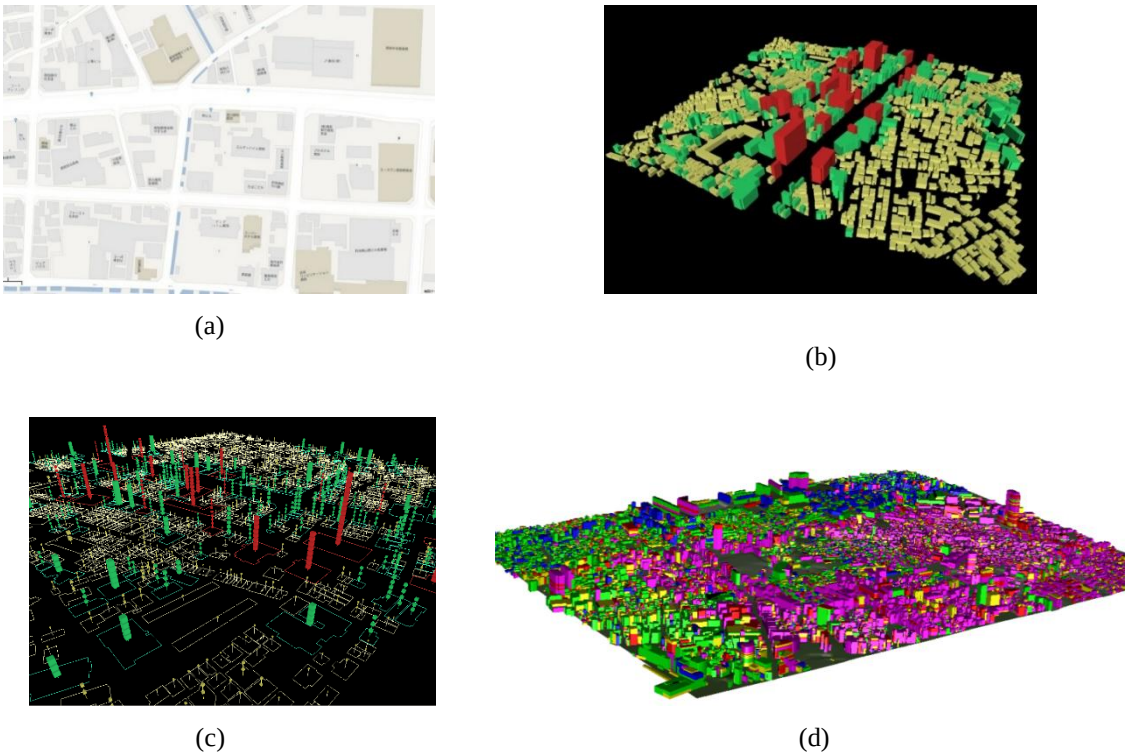
[2] Department of Infrastructure Systems Engineering, Kochi University of Technology, Japan
e-mail: kai.yoshiro@kochi-tech.ac.jp

Keywords: Damage Prediction, Earthquake and Subsequent Tsunami, Sequential Earthquake and Tsunami Simulation, Double-Layer Platform, CUDA.

Abstract. *For tsunami scenarios, evaluation of tsunami load acting each building depends on surrounding circumstance. Therefore, modeling of all buildings in a target area is important for damage prediction from earthquake and subsequent tsunami. In this study, sequential earthquake and tsunami simulation was developed to predict structural damage from earthquake and subsequent tsunami by means of the application in Integrated Earthquake Simulation (IES). Since IES can simulate only earthquake scenarios with bean-column frame models, IES was modified for input tsunami load acting on a proposed wall-frame model in order to simulate tsunami scenarios using predicted data of tsunami inundation depth. A target area in Kochi city was selected to simulate an earthquake and tsunami scenario because this area has many public buildings and is important for economic activities. A double-layer platform of high performance computing was proposed to simulate this earthquake and tsunami scenario with parallel processing on CPUs and GPUs. The results of sequential earthquake and tsunami simulation show that three-story RC buildings had a significant risk that maximum drift ratio could occur during sequential tsunami response. However, maximum drift ratio from sequential tsunami response was still less than 0.3% in which structural damage didn't occur obviously. For the worst case scenario that tsunami inundation depth was double, structural damage from sequential tsunami response was much more serious than that of the normal-case scenario in which maximum drift ratio was less than 5% for a four-story RC building. In addition, it was found that low-rise buildings (three- to seven-story) had a significant risk that maximum drift ratio was higher than 1% during sequential tsunami response. The results of sequential earthquake and tsunami simulation can be used to construct further prevention measures.*

1 INTRODUCTION

Based on past experience in the Great East Japan earthquake and tsunami, many buildings in Tohoku area were seriously damaged by earthquake and subsequent tsunami. In the future, severe damage as serious as the previous earthquake and tsunami may occur in other area of Japan, such as Tokai, Tonankai, Nankai area. In order to reduce the loss of human life in future earthquake and tsunami, damage prediction is a key role for constructing prevention measure and raising awareness of people. For damage prediction in a target area, computer technology has been applied to simulate earthquake scenarios, such as Integrated Earthquake Simulation (IES) [1-7]. Integrated Earthquake Simulation (IES) is an earthquake simulation tool for predicting and illustrating structural damage of all buildings in the target area simultaneously in selected earthquake scenarios. Based on Geographic Information System (GIS) data in Figure 1(a), thousands of buildings in the target area are modeled to polygon shapes in Figure 1(b) from building shape and height. Based on building design code, Common Modeling Data (CMD) is a modeling approach to convert a polygon shape in Figure 2(a) as a structural model in Figure 2(b), consisting of beam and column elements including section and material properties of each element. In Figure 1(c), nonlinear structural analysis of all buildings in the target area is performed to predict structural damage and then illustrate structural damage of all buildings simultaneously as shown in Figure 1(d).

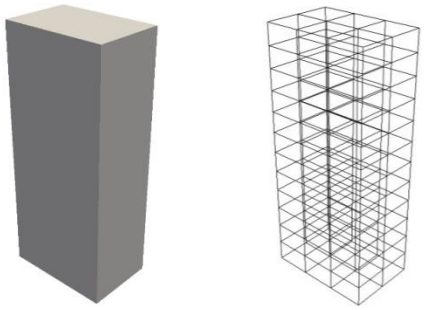


(a) (b) (c) (d)

Figure 1: Integrated Earthquake Simulation [4]

For a target area, structural damage of each building is predicted from the results of nonlinear structural analysis. Object-Based Structural Analysis (OBASAN), a structural analysis program, which has been developed by our laboratory, is proposed to perform nonlinear structural analysis in IES. Therefore, there are two main parts in this study: the first part is IES for building modeling and the second part is OBASAN for nonlinear structural analysis. For thousands of buildings in the target area, IES can visualize structural damage to raise awareness of disaster prevention among people in that area. Since high performance computing

(HPC) is a key role to carry out a large number of buildings in the target area, OpenMPI application has been applied to IES in order to enable parallel processing on the Central Processing Units (CPUs).



(a) (b)

Figure 2: Common Modeling Data (CMD) [10]

2 DOUBLE-LAYER PLATFORM OF HIGH PERFORMANCE COMPUTING

For damage prediction in a target area, thousands of buildings are modeled to perform nonlinear structural analysis. Since high performance computing (HPC) is a key role to carry out a large number of buildings in the target area, OpenMPI application has been applied to IES in order to enable parallel processing on the Central Processing Units (CPUs) for building modeling of all buildings [1-7]. In this study, a double-layer platform of HPC was proposed to simulate earthquake and tsunami scenarios in a reasonably short time. Since OBASAN has been developed by C++ programing language, CUDA application was applied to OBASAN in order to enable parallel processing on the Graphic Processing Units (GPUs) for nonlinear structural analysis of a building. Therefore, HPC was achieved by a double layer of parallel processing on CPUs and GPUs as shown in Figure 3.

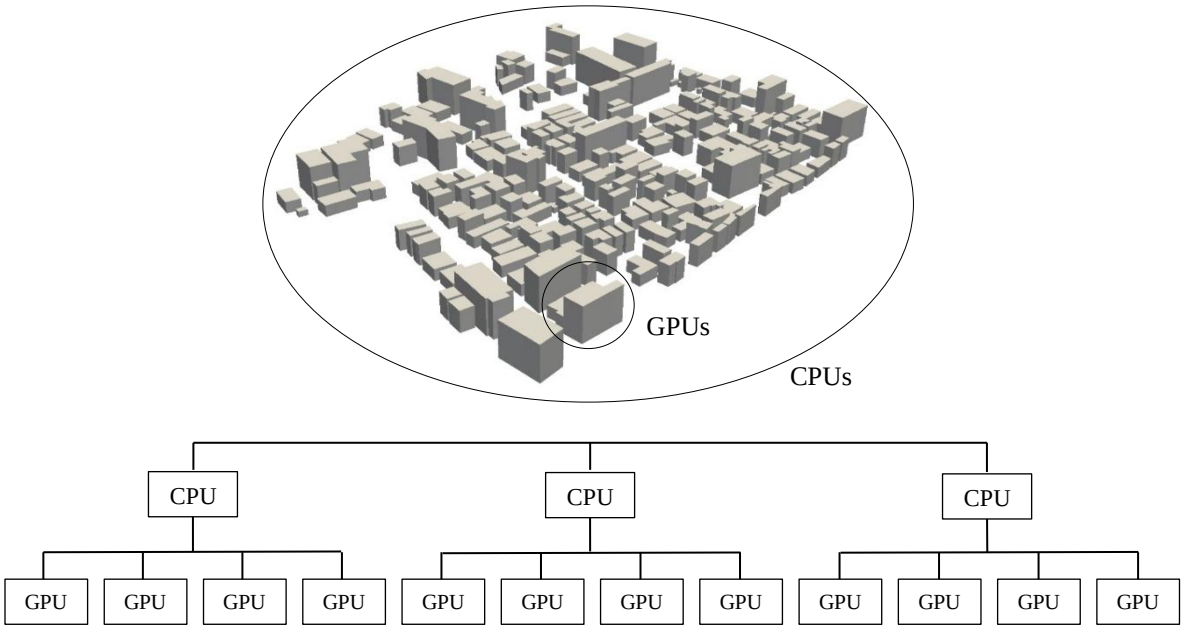


Figure 3: A proposed double layer of parallel processing on CPUs and GPUs

CUDA application is one of General-Purpose computing on Graphic Processing Units (GPGPUs) which has high capability to carry out a large amount of data and a large number

of simple calculation [11-12]. For nonlinear structural analysis in OBASAN, it was found that most of execution time was occupied by matrix operation Ax = b, so CUDA application was used to solve this matrix operation at every analysis steps on GPUs using CUBLAS and CUSPARSE library.

3 DAMAGE PREDICTION FROM EARTHQUAKE AND TSUNAMI

In this study, damage prediction of all RC buildings in a target area from earthquake and subsequent tsunami was proposed by means of the application in IES. Since IES can simulate only earthquake scenarios, IES was modified to input tsunami load acting on each building in order to simulate tsunami scenarios using data of tsunami inundation depth provided by Japan Cabinet Office (JCO). In IES, evaluation of tsunami load was included for all RC buildings as the same approach as earthquake scenarios and new building modeling was proposed to perform nonlinear structural analysis of each RC building subject to tsunami load.

3.1 Evaluation of tsunami load

For earthquake scenarios, the wave data of strong ground motion was input to all RC buildings as same as previous in IES. For tsunami scenarios, the predicted data of tsunami inundation depth was input to all RC buildings in order to evaluate tsunami load, which also depends on surrounding circumstance in the target area. However, in this study, tsunami load was calculated by means of triangle distribution of hydrostatic pressure recommend by JCO shown in Figure 4. Due to considering effect of impact force, tsunami load in Eq. (1) was magnified by a factor, which can vary from 1.0 to 3.0 depending on surrounding circumstance.

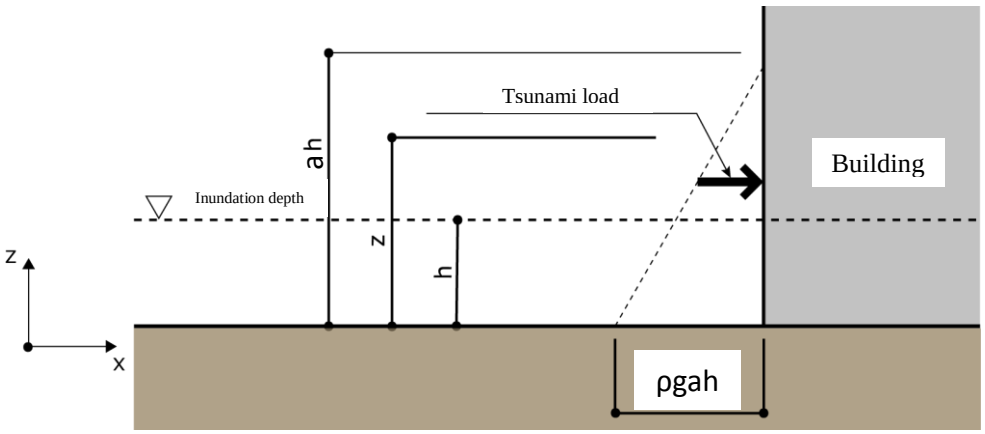


Figure 4: Triangle distribution of hydrostatic pressure (JCO)

$$q_z = \rho_s g(ah - z) \tag{1}$$

in which q_z: hydrodynamic force, ρ_s: density of salt water = 1128 kg/m3, g: gravitational acceleration = 9.81 m/s^2, h: inundation depth, z: height from ground level ($0 \le z \le h$), a: impact factor ($1.0 \le a \le 3.0$)

Figure 5 shows the location of RC buildings (grey colour) and wooden houses (green colour) in a target area. Unless tsunami inundation depth and flow velocity, tsunami load acting on each building also depended on tsunami direction to this area, building location from coastal line, and building arrangement in this area. Focusing on one RC building in Figure 5, tsunami load can be reduced by surrounding buildings and environment, whereas tsunami

load can be increased by wooden debris from collapsed houses. As can be seen in Figure 5, it shows that surrounding circumstance had a significant effect on evaluation of tsunami load for all RC buildings in the target area.



Figure 5: Location of RC buildings and wooden houses in a target area

In Table 1, the a factor was investigated to evaluate tsunami load in Eq. (1) based on damage observation after the 2011 Great East Japan earthquake [13]. As shown in Table 1, the investigation of the a factor was separated to only two cases: area with structures to reduce tsunami load and area without structures to reduce tsunami load.

Coefficient	Area with structures to reduce tsunami load	Area without structures to reduce tsunami load
a	1.0	≥ 1.7

Table 1: The a factor based on damage observation after the 2011 Great East Japan earthquake [13]

The direction of tsunami load acting on each RC building in this study was assumed in both x- and y- directions as shown in Figure 6.

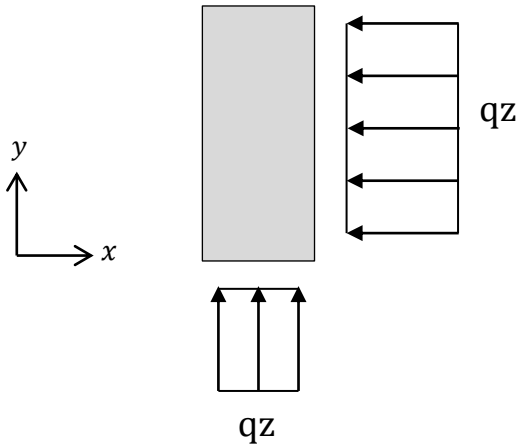
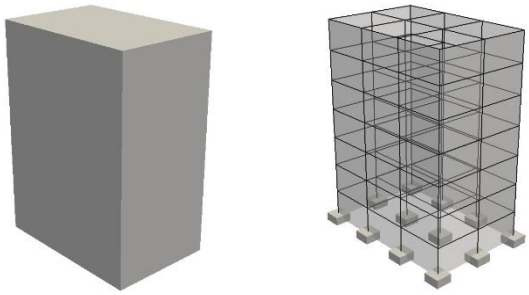


Figure 6: The direction of tsunami load acting on each RC building in a target area

3.2 Proposed building modeling

In IES, Common Modeling Data (CMD) is a modeling approach to convert a polygon shape as a structural model, consisting of beam and column elements, based on building design code. As the first part of the simulation in this study, building modeling in CMD was modified to include wall elements to a structural model in order to perform nonlinear structural analysis of RC buildings subject to tsunami load. As shown in Figure 7, a polygon shape in Figure 7(a) was converted to a structural model in Figure 7(b), consisting of beam, column, wall elements.



(a) (b)

Figure 7: Proposed building modeling

Since tsunami load was a distributed pressure acting on outside of RC buildings as shown in Figure 4 and Figure 6, wall elements were arranged to outside frames for resisting a distributed pressure of tsunami load. In order to apply this proposed building modeling of wall elements as the concept of CMD, wall elements were arranged to all outside frames of RC buildings covering building surface as wall cladding shown in Figure 8. For this proposed building modeling, macro plate model was applied to represent wall elements in the structural model.

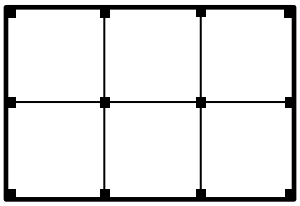


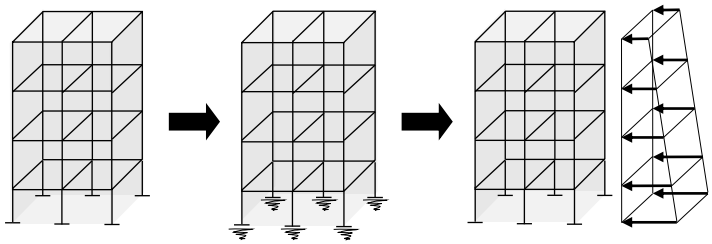
Figure 8: Common Modeling Data for wall elements

In conclusion, all RC buildings in a target area were represented as a structural model, consisting of beam, column and wall elements, in order to perform nonlinear structural analysis of each RC building subject to earthquake and subsequent tsunami.

4 SEQUENTIAL ANALYSIS FROM EARTHQUAKE AND TSUNAMI

Object-Based Structural Analysis (OBASAN), a structural analysis program, which has been developed by our laboratory, was proposed to perform nonlinear structural analysis as the second part of the simulation. For earthquake and tsunami scenarios, strong ground motion shakes all buildings and causes some structural damage to all buildings in a target area. Subsequently, a tsunami reaches the target area and tsunami load causes more structural damage to buildings. In OBASAN, RC buildings were analyzed by inputting a sequential load of earthquake and tsunami as shown in Figure 9. In the case of earthquake in Figure 9(b), dy-

namic structural response analysis was performed to predict structural damage of each building, which was subject to strong ground motion. Sequentially, static pushover analysis was performed to predict more structural damage to each building, which was subject to tsunami load in Figure 9(c).



(a) (b) (c)

Figure 9: Sequential analysis of earthquake and tsunami

In order to simulate sequential behavior of earthquake and tsunami response, nonlinear structural analysis was performed by means of the same hysteresis model shown in Figure 10. The red line represents nonlinear structural analysis in earthquake scenario and the blue line represents nonlinear structural analysis in tsunami scenario. During an earthquake, nonlinear structural analysis starts from point A and moves along the red line of hysteresis loop. Then, nonlinear structural analysis stops at point B and some structural damage occurred from earthquake scenario. During tsunami scenario, nonlinear structural analysis starts from point B and moves along the blue line. Then nonlinear structural analysis stops at point C and more structural damage might occur from tsunami scenario.

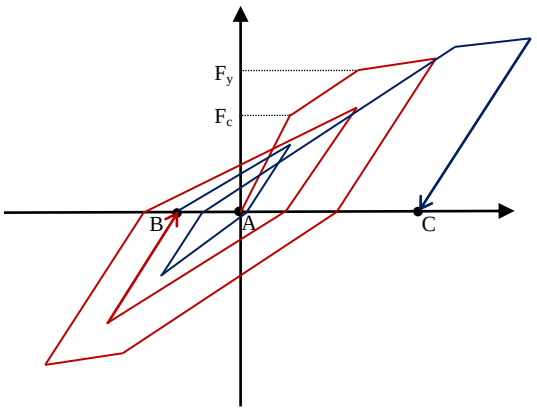


Figure 10: Hysteretic loop for earthquake and subsequent tsunami

5 EARTHQUAKE AND TSUNAMI SCENARIO IN KOCHI CITY

In this study, a target area in Kochi city was selected to simulate an earthquake and tsunami scenario as shown in Figure 11. This selected target area is in the center of Kochi city which has many public buildings and is important for economic activities. For damage prediction in this target area, an earthquake and tsunami scenario was simulated from input data, such as GIS data for building modeling, wave data of strong ground motion, and predicted data of tsunami inundation depth.

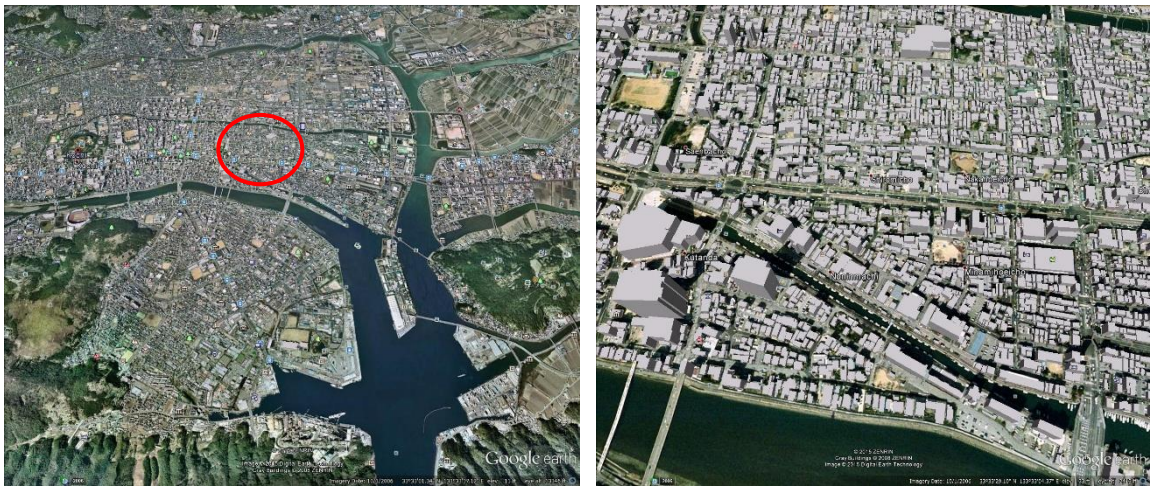


Figure 11: A selected target area in Kochi city

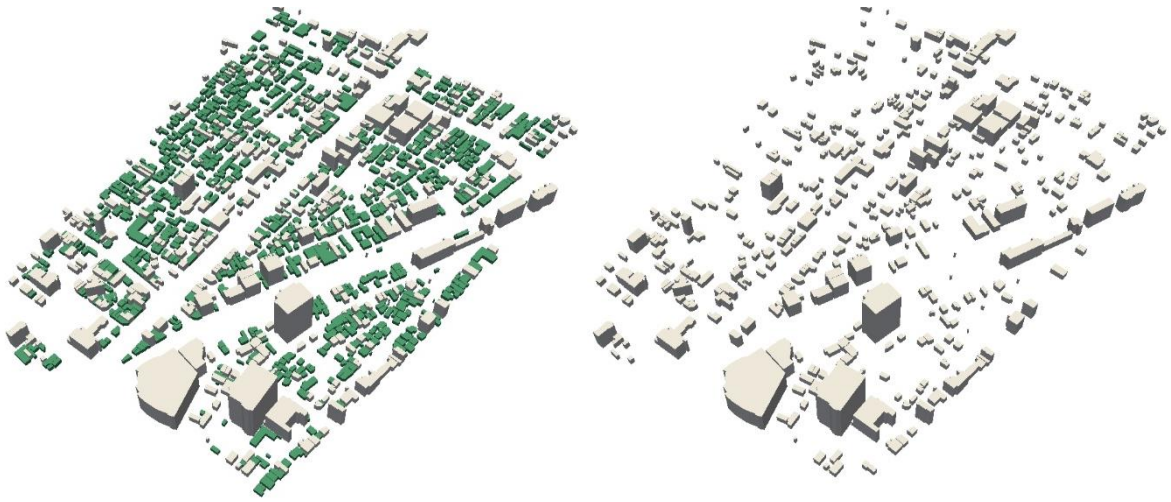
5.1 GIS data for building modeling

Figure 12 shows GIS data of this selected target area. In GIS data, building dimensions and number of floors were used to generate building shapes of all buildings as shown in Figure 13(a) in which each building can be classified to RC buildings, steel buildings, and wooden houses.



Figure 12: GIS data of this target area

In Figure 13(a), this selected target area had 480 RC buildings (grey color) and 1311 wooden houses (green color). Since damage prediction of all RC buildings in a target area from earthquake and subsequent tsunami was proposed in this study, 480 RC buildings in Figure 13(b) were applied to simulate an earthquake and tsunami scenario.



(a) (b)

Figure 13: Building shapes from GIS data

5.2 Wave data of strong ground motion

The wave data of Kochi city has been developed by a study group of the Great Nankai earthquake model from Japan Cabinet Office (JCO) in 2012. This selected target area was separated to north zone and south zone according to two source data of earthquake model as shown in Figure 14.

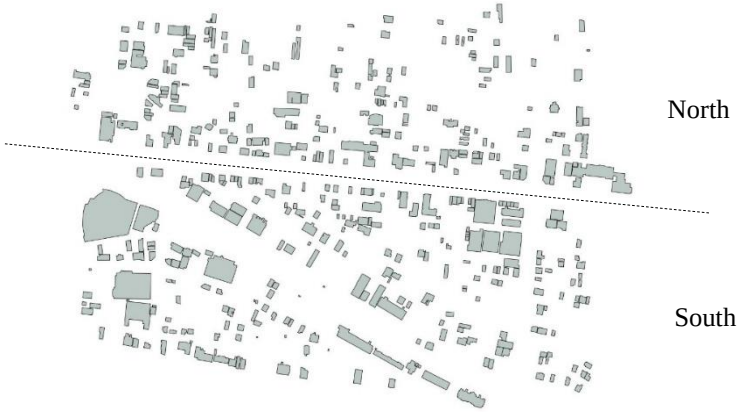
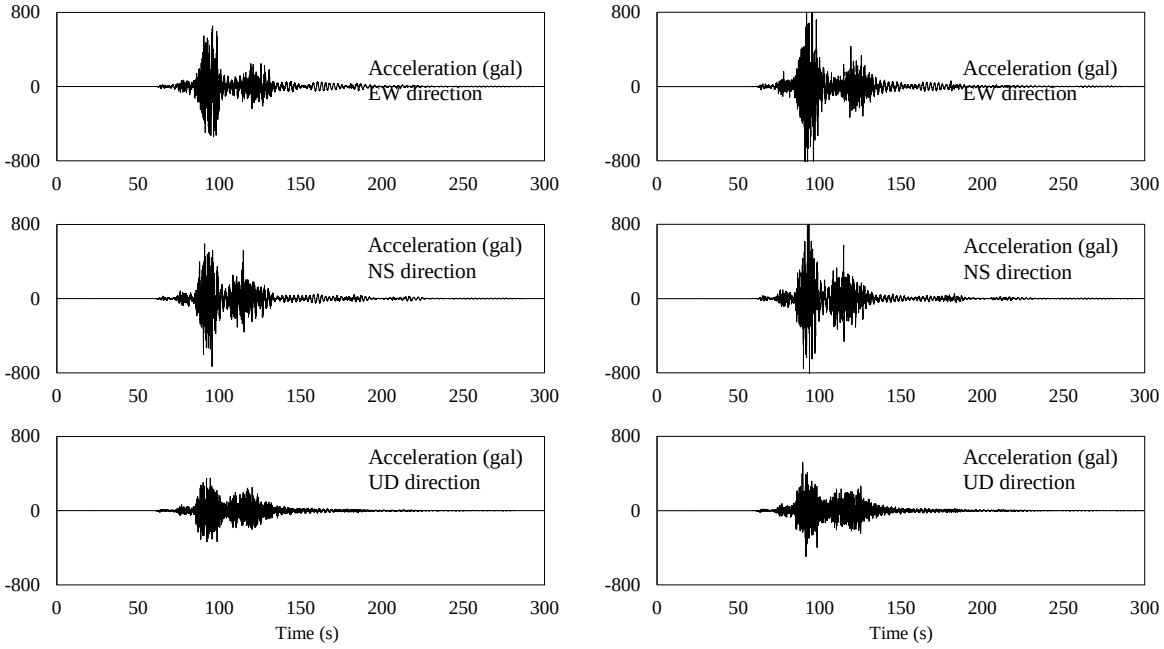


Figure 14: Two separated zone for two source data of earthquake model

Figure 15 shows the wave data of strong ground motion for this selected target area. The wave data in Figure 15(a) was applied to all RC buildings in south zone and the wave data in Figure 15(b) was applied to all RC buildings in north zone. As can be seen in Figure 15(a) and 15(b), three motion components in the east-west, north-south, and up-down direction (EW, NS, and UD respectively) have been developed in a wave form of ground acceleration in which shear wave velocity (Vs) is equal to 300 m/s. The peak ground acceleration of north zone in all EW, NS, and UD directions is higher than that of south zone.



(a) (b)

Figure 15: The wave data of strong ground motion (JCO, 2012)

5.3 Predicted data of tsunami inundation depth

Japan Cabinet Office (JCO) has studied and predicted tsunami inundation depth in future earthquake and tsunami for all risk area in Japan. Based on tsunami hazard map provided by JCO, this selected target area was divided to seven area shown in Figure 16 consist of three area (N1, N2, and N3) in north zone and four area (S1, S2, S3, and S4) in south zone for tsunami inundation data in time history. In this target area, the maximum inundation depth was varied from 2.0 m to 3.5 m.

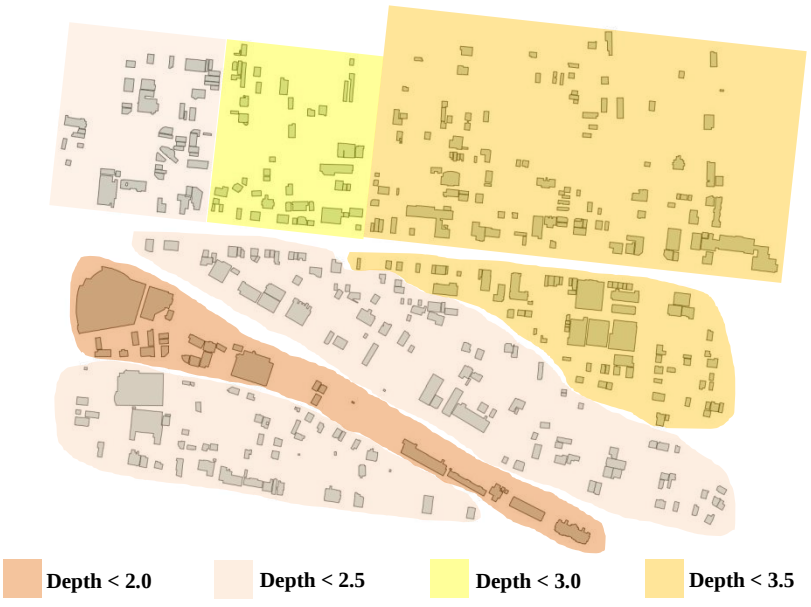


Figure 16: Seven divided area for tsunami inundation data

Figure 17 shows the predicted data of tsunami inundation depth for this selected target area. The inundation data in Figure 17(a) was used to evaluate tsunami load for all RC buildings in south zone and the inundation data in Figure 17(b) was used to evaluate tsunami load for all RC buildings in north zone.

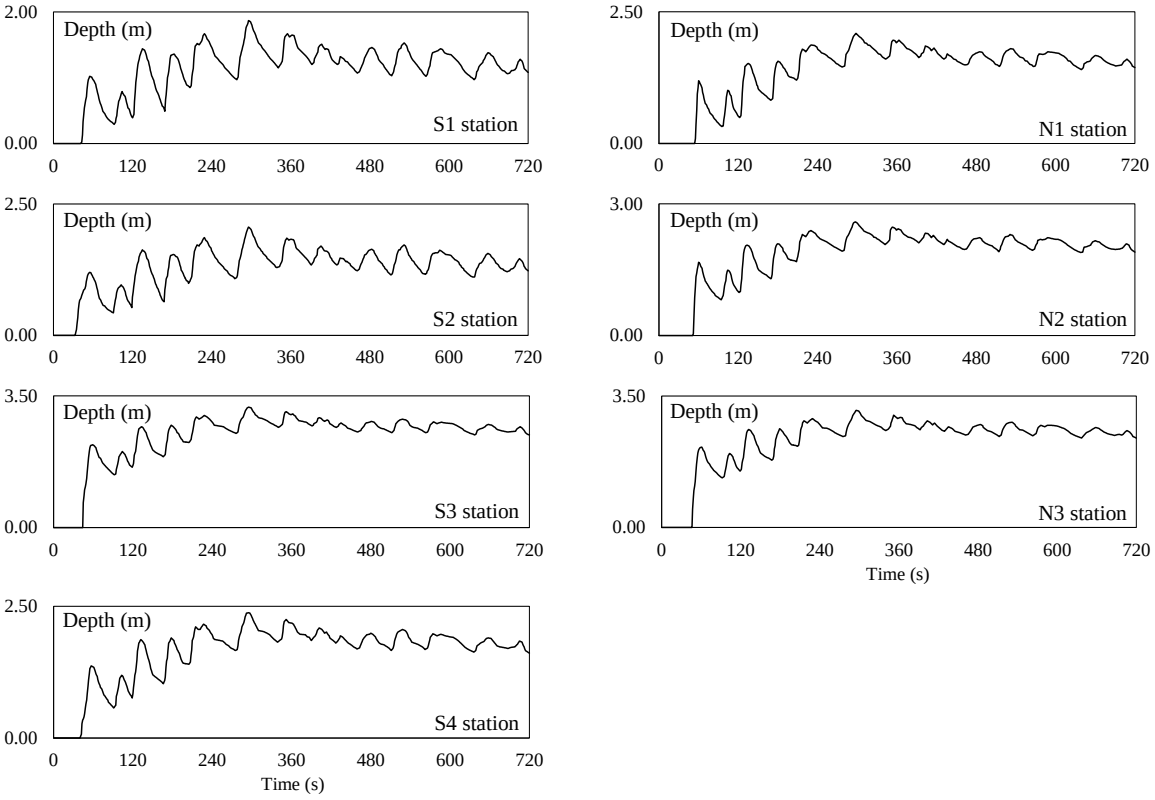


Figure 17: Predicted inundation depth at each station (Kochi Prefecture Office)

6 RESULTS OF SEQUENTIAL EARTHQUAKE AND TSUNAMI SIMULATION

The results of sequential earthquake and tsunami simulation can be visualized as shown in Figure 18. For each RC building, structural damage can be predicted by means of maximum story drift ratio.

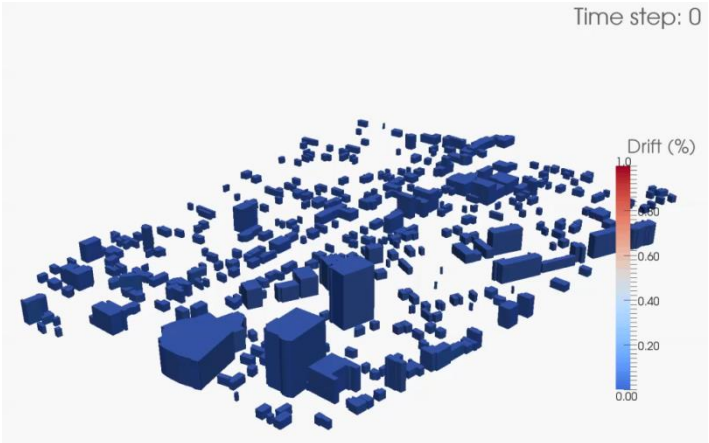


Figure 18: Visualization of damage prediction

For each RC building, the results of story displacement at 1st floor in x- and y- directions can be obtained as shown in Figure 19. Figure 19(a) shows the results of a three-story RC building and Figure 19(b) shows the results of an eight-story RC building. As can be seen in Figure 19, sequential tsunami response in y-direction had a significant effect on a three-story RC building. In addition, residual displacement occurred from earthquake response in x-direction. Therefore, the effect of sequential tsunami response depended on building height and also the direction of tsunami load.

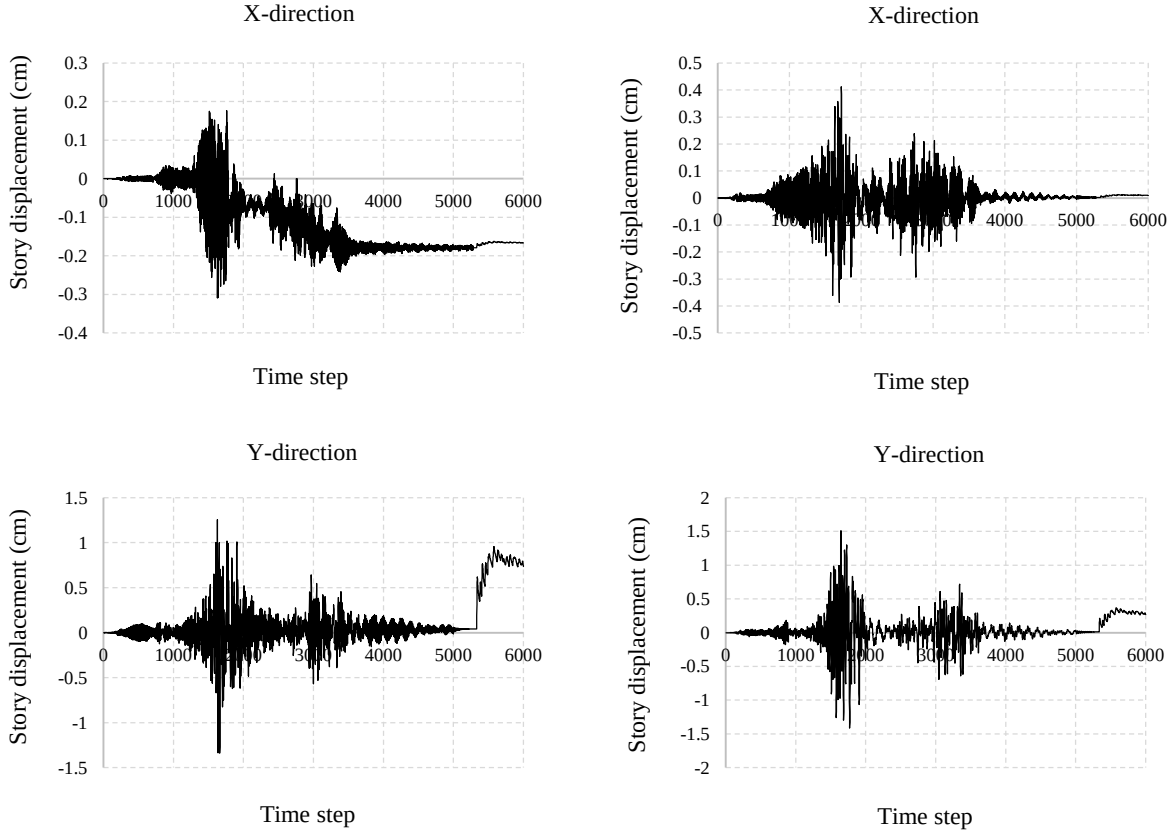


Figure 19: Story displacement at 1st floor

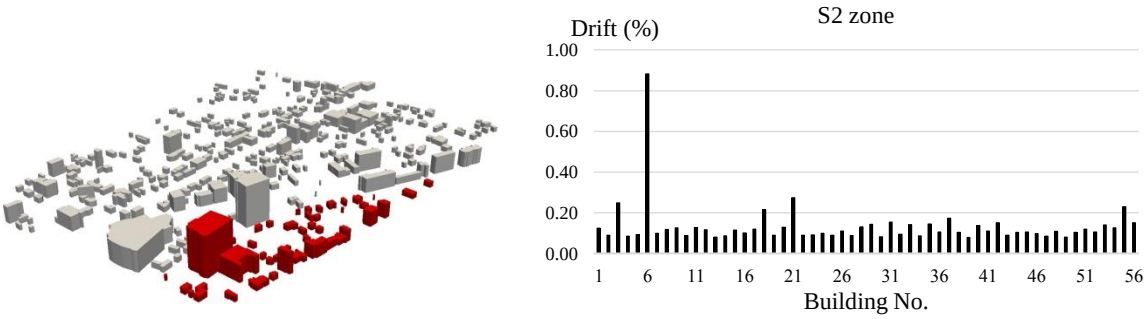


Figure 20: Maximum story drift ratio for zone S2

Figure 20 shows the results of maximum story drift ratio for each RC building in zone S2. For each RC building in Figure 20, number of floors, maximum story drift ratio, occurrence during earthquake response or sequential tsunami response, and location of maximum story drift can be seen in Appendix I.

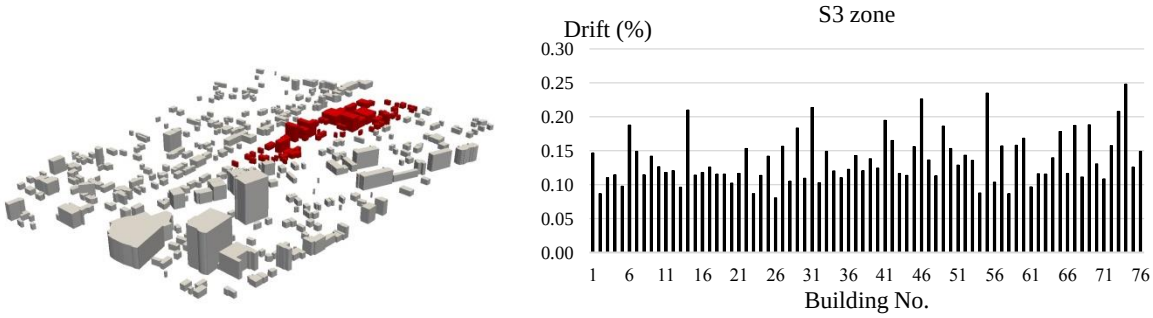


Figure 21: Maximum story drift ratio for zone S3

Figure 21 shows the results of maximum story drift ratio for each RC building in zone S3. For each RC building in Figure 21, number of floors, maximum story drift ratio, occurrence during earthquake response or sequential tsunami response, and location of maximum story drift can be seen in Appendix II.

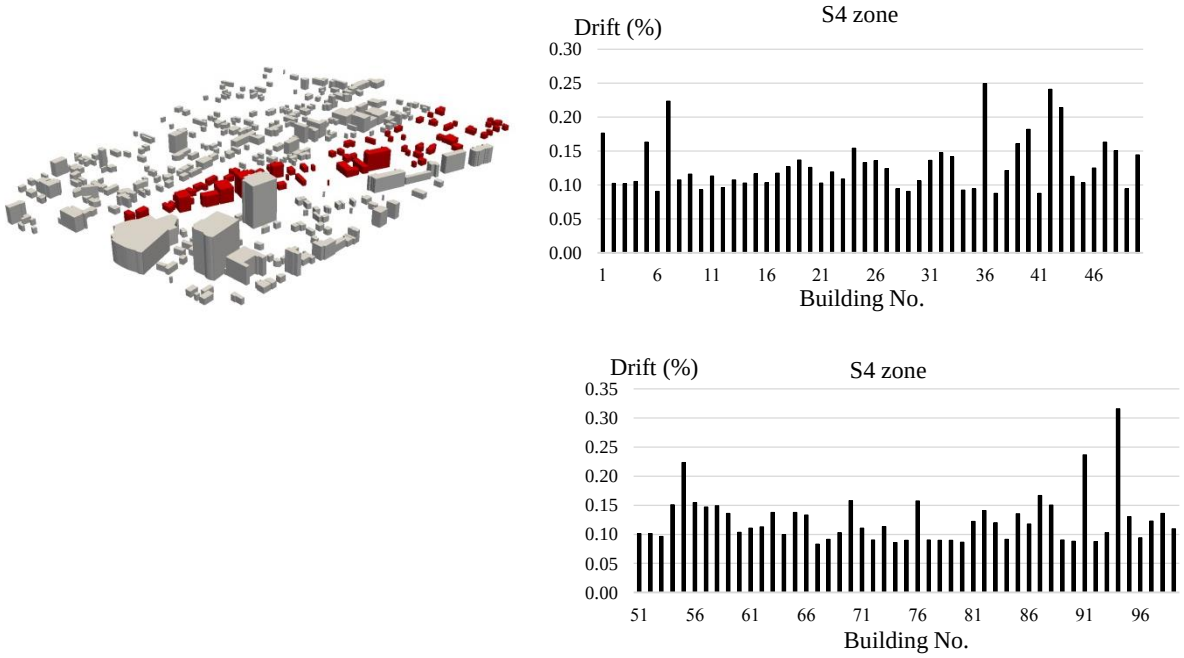


Figure 22: Maximum story drift ratio for zone S4

Figure 22 shows the results of maximum story drift ratio for each RC building in zone S4. For each RC building in Figure 22, number of floors, maximum story drift ratio, occurrence during earthquake response or sequential tsunami response, and location of maximum story drift can be seen in Appendix III.

Table 2 shows number of RC buildings in which maximum story drift ratio occurred during earthquake response and sequential tsunami response.

Zone	Number of RC buildings	Max drift during earthquake	Max drift during tsunami
N1	50	50	0
N2	51	50	1
N3	114	111	3
S1	31	24	7
S2	56	40	16
S3	76	45	31
S4	99	71	28
Total	477	391 (81.97%)	86 (18.03%)

Table 2: Number of RC buildings for maximum story drift ratio

7 THE WORSE-CASE SCENARIO

Figure 23 shows sequential earthquake and tsunami simulation assuming the worst-case scenario by increasing double of tsunami inundation depth. From the visualization of results in Figure 23, maximum story drift ratio can occur less than 5% in which that of maximum story drift ratio in Figure 18 can occur less than 1%.

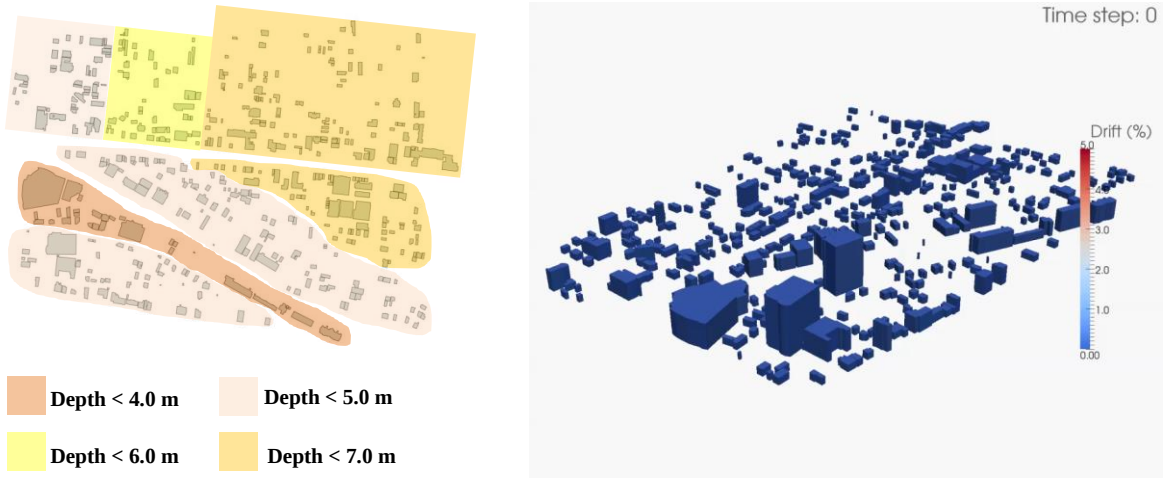


Figure 23: The worst-case scenario by increasing double of tsunami inundation depth

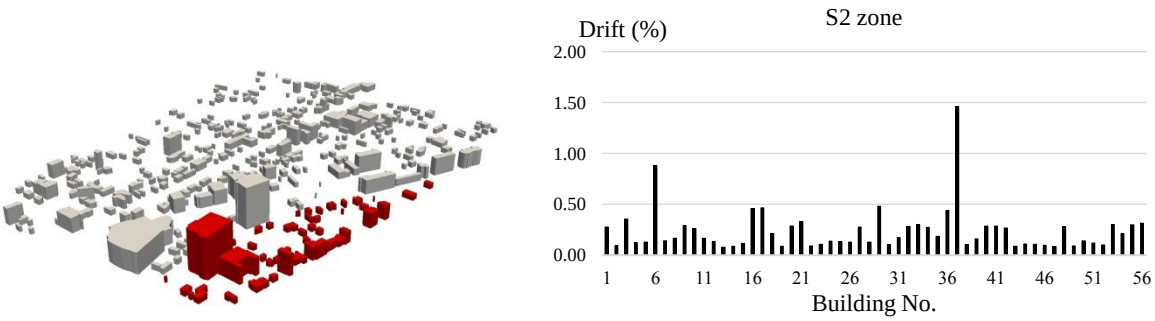


Figure: 24 Maximum story drift ratio for zone S2 (worst case)

Figure 24 shows the results of the worst-case scenario for each RC building in zone S2. For each RC building in Figure 24, number of floors, maximum story drift ratio, occurrence

during earthquake response or sequential tsunami response, and location of maximum story drift can be seen in Appendix IV.

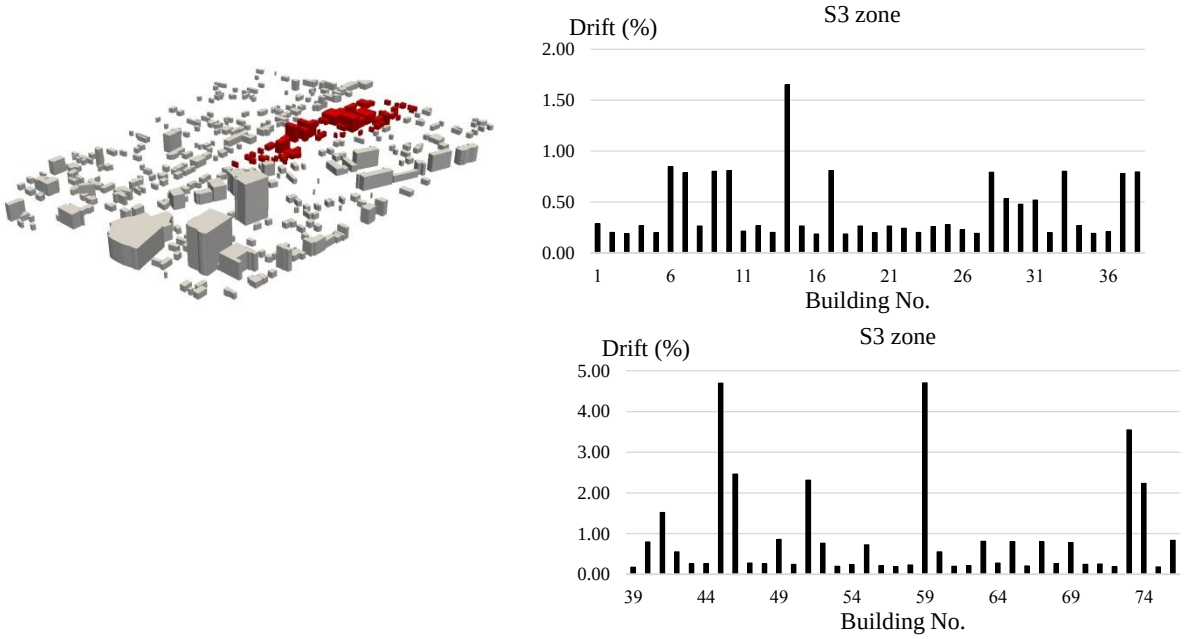


Figure 25: Maximum story drift ratio for zone S3 (worst case)

Figure 25 shows the results of the worst-case scenario for each RC building in zone S3. For each RC building in Figure 25, number of floors, maximum story drift ratio, occurrence during earthquake response or sequential tsunami response, and location of maximum story drift can be seen in Appendix V.

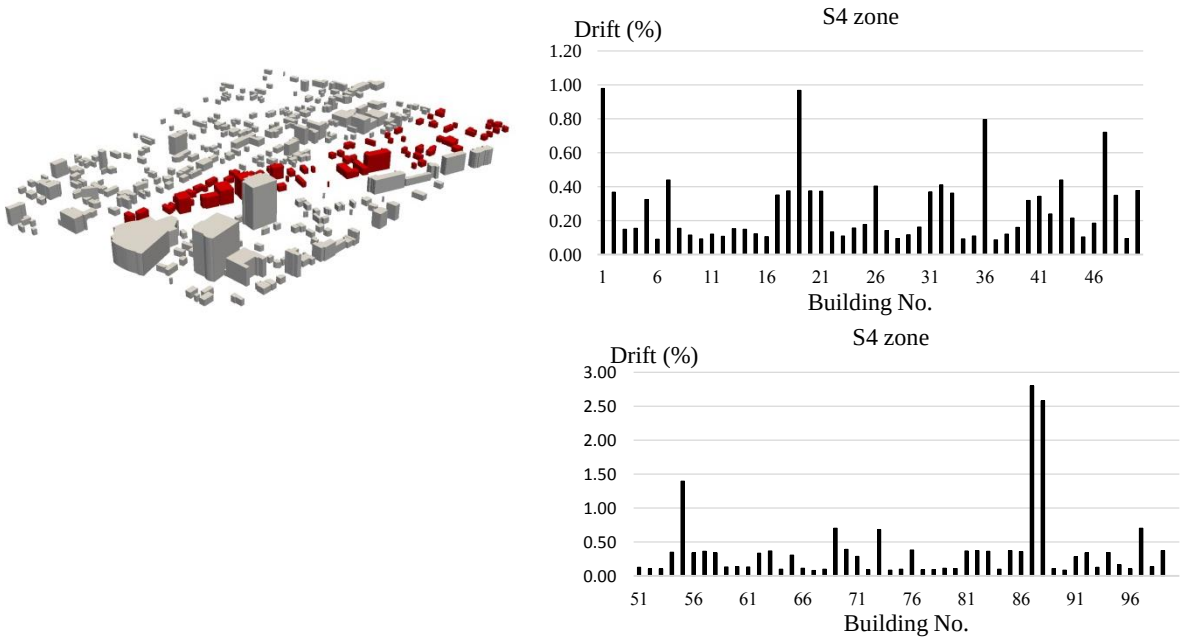


Figure 26: Maximum story drift ratio for zone S4 (worst case)

Figure 26 shows the results of the worst-case scenario for each RC building in zone S4. For each RC building in Figure 26, number of floors, maximum story drift ratio, occurrence during earthquake response or sequential tsunami response, and location of maximum story drift can be seen in Appendix VI.

Table 3 shows number of RC buildings for the worse-case scenario in which maximum story drift ratio occurred during earthquake response and sequential tsunami response. Comparing Table 3 with Table 2 for most of RC buildings, maximum story drift ratio could occur during sequential tsunami response.

Zone	Number of RC buildings	Max drift during earthquake	Max drift during tsunami
N1	50	14	36
N2	51	3	48
N3	114	27	87
S1	31	13	18
S2	56	14	42
S3	76	0	76
S4	99	21	78
Total	477	92 (19.29%)	385 (80.71%)

Table 3 Number of RC buildings for maximum story drift ratio (worst case)

8 CONCLUSIONS

For sequential earthquake and tsunami simulation in the target area of Kochi city, most of RC buildings had maximum drift ratio during earthquake response in which maximum drift ratio was 0.88% for a twenty-one story building in zone S2. In zone S3, many RC buildings had maximum drift ratio during sequential tsunami response in which tsunami inundation depth was a little higher than other zones. For all RC buildings, maximum drift ratio during sequential tsunami response was 0.22% occurred with a three-story building in zone S4 in which structural damage didn't occur obviously. For all zones, three-story buildings had a significant risk that maximum drift ratio could occur during tsunami response analysis.

For the worst-case scenario, most of RC buildings had maximum drift ratio during sequential tsunami response in which maximum drift ratio was 4.71% for a four-story building in zone S3. For all zone, low-rise buildings (three-story to seven-story) had a significant risk that maximum drift ratio was higher than 1% during sequential tsunami response. For the worst-case scenario, structural damage from sequential tsunami response was much more serious than that of the normal-case scenario in which tsunami inundation depth was double.

The results of earthquake and tsunami simulation can be used to designate tsunami evacuation buildings, which must be secured for people living in a surrounding area. These results can indicate a weak point of a city area and focus on this weak point. In addition, these results can be used to construct prevention measures in order control overall damage of a city area from earthquake and subsequent tsunami.

9 APPENDIX

Appendix I The results of damage prediction for zone S2

No.	Floors	Max drift (%)	During	Location
1	1	0.12	T	3
2	1	0.09	E	3
3	2	0.25	E	7
4	1	0.09	E	3
5	1	0.09	T	3
6	1	0.88	E	21
7	1	0.10	T	3
8	1	0.12	T	3
9	1	0.13	T	3
10	1	0.09	E	3
11	1	0.13	E	3
12	1	0.12	E	3
13	1	0.08	E	3
14	1	0.09	E	3
15	1	0.12	E	3
16	1	0.10	E	3
17	1	0.12	E	3
18	2	0.22	E	11
19	1	0.09	E	3
20	1	0.13	T	3
21	1	0.27	E	9
22	1	0.09	E	3
23	1	0.09	E	3
24	1	0.10	T	3
25	1	0.09	T	3
26	1	0.11	E	3
27	1	0.09	T	3
28	2	0.13	E	3
29	1	0.14	T	3
30	1	0.08	E	3
31	2	0.15	E	6
32	2	0.09	E	3
33	1	0.14	T	3
34	1	0.09	E	3
35	1	0.14	E	3
36	2	0.11	E	3
37	2	0.17	E	4
38	1	0.10	E	3
39	1	0.08	E	3
40	1	0.14	T	3
41	1	0.11	T	3
42	1	0.15	E	3
43	1	0.09	E	3
44	1	0.10	E	3
45	1	0.11	E	3
46	1	0.10	E	3
47	1	0.09	E	3
48	1	0.11	T	3
49	1	0.08	E	3
50	1	0.10	E	3
51	1	0.12	E	3
52	1	0.11	E	3
53	1	0.14	T	3
54	2	0.13	E	8
55	1	0.23	E	8
56	1	0.15	T	3

Appendix II The results of damage prediction for zone S3

No.	Floors	Max drift (%)	During	Location
1	3	0.15	T	1
2	3	0.09	E	1
3	3	0.11	E	1
4	3	0.11	T	1
5	3	0.10	E	1
6	3	0.19	T	1
7	3	0.15	T	1
8	3	0.11	T	1
9	3	0.14	T	1
10	3	0.13	T	1
11	3	0.12	E	1
12	3	0.12	T	1
13	3	0.10	E	1
14	3	0.21	T	1
15	3	0.11	T	1
16	3	0.12	E	1
17	3	0.13	T	1
18	3	0.12	E	1
19	3	0.12	T	1
20	3	0.10	E	1
21	3	0.12	T	1
22	3	0.15	E	1
23	3	0.09	E	1
24	3	0.11	E	1
25	3	0.14	T	1
26	3	0.08	E	1
27	3	0.16	E	1
28	3	0.11	T	1
29	9	0.18	E	2
30	3	0.11	E	1
31	10	0.21	E	2
32	3	0.10	E	1
33	3	0.15	E	1
34	3	0.12	T	1
35	3	0.11	E	1
36	3	0.12	E	1
37	3	0.14	E	1
38	3	0.12	T	1

No.	Floors	Max drift (%)	During	Location
39	3	0.14	E	1
40	3	0.12	T	1
41	7	0.20	E	2
42	7	0.17	E	2
43	3	0.12	T	1
44	3	0.11	T	1
45	4	0.16	T	1
46	6	0.23	E	2
47	3	0.14	T	1
48	3	0.11	T	1
49	8	0.19	E	2
50	3	0.15	E	1
51	4	0.13	E	2
52	3	0.14	E	1
53	3	0.14	E	1
54	3	0.09	E	1
55	9	0.24	E	1
56	3	0.10	E	1
57	3	0.16	E	1
58	3	0.09	E	1
59	4	0.16	T	1
60	7	0.17	E	2
61	3	0.10	E	1
62	3	0.12	E	1
63	3	0.12	E	1
64	3	0.14	T	1
65	3	0.18	T	1
66	3	0.12	E	1
67	3	0.19	T	1
68	3	0.11	T	1
69	3	0.19	T	1
70	3	0.13	E	2
71	3	0.11	E	1
72	3	0.16	E	1
73	5	0.21	E	2
74	6	0.25	E	2
75	3	0.13	E	1
76	3	0.15	T	1

Appendix III The results of damage prediction for zone S4

No.	Floors	Max drift (%)	During	Location
1	5	0.18	E	2
2	3	0.10	T	1
3	3	0.10	T	1
4	3	0.11	T	1
5	7	0.16	E	2
6	3	0.09	E	1
7	8	0.22	E	2
8	3	0.11	T	1
9	3	0.12	E	1
10	3	0.09	E	1
11	3	0.11	E	1
12	3	0.10	E	1
13	3	0.11	T	1
14	3	0.10	T	1
15	3	0.12	E	1
16	3	0.10	E	1
17	3	0.12	E	1
18	3	0.13	T	1
19	3	0.14	E	2
20	3	0.13	T	1
21	3	0.10	E	1
22	3	0.12	E	1
23	3	0.11	E	1
24	3	0.15	E	1
25	3	0.13	E	1
26	3	0.14	T	1
27	3	0.12	T	1
28	3	0.09	E	1
29	3	0.09	E	1
30	3	0.11	T	1
31	3	0.14	T	1
32	3	0.15	T	1
33	3	0.14	T	1
34	3	0.09	E	1
35	3	0.09	E	1
36	6	0.25	E	2
37	3	0.09	E	1
38	3	0.12	E	1
39	3	0.16	E	1
40	7	0.18	E	2
41	3	0.09	E	1
42	8	0.24	E	2
43	8	0.21	E	2
44	3	0.11	E	1
45	3	0.10	E	1
46	3	0.13	T	1
47	3	0.16	T	1
48	3	0.15	E	1
49	3	0.09	E	1
50	3	0.14	T	1

No.	Floors	Max drift (%)	During	Location
51	3	0.10	E	1
52	3	0.10	E	1
53	3	0.10	E	1
54	3	0.15	E	1
55	3	0.22	T	1
56	3	0.15	E	1
57	3	0.15	T	1
58	3	0.15	E	1
59	3	0.14	E	1
60	3	0.10	E	1
61	3	0.11	E	1
62	3	0.11	E	1
63	3	0.14	E	1
64	3	0.10	E	1
65	3	0.14	E	1
66	3	0.13	T	1
67	3	0.08	E	1
68	3	0.09	E	1
69	3	0.10	E	1
70	3	0.16	T	1
71	3	0.11	E	1
72	3	0.09	E	1
73	3	0.11	T	1
74	3	0.09	E	1
75	3	0.09	E	1
76	3	0.16	T	1
77	3	0.09	E	1
78	3	0.09	E	1
79	3	0.09	E	1
80	3	0.09	E	1
81	3	0.12	T	1
82	3	0.14	E	1
83	3	0.12	E	1
84	3	0.09	E	1
85	3	0.14	T	1
86	3	0.12	T	1
87	4	0.17	E	2
88	4	0.15	E	2
89	3	0.09	E	1
90	3	0.09	E	1
91	11	0.24	E	2
92	3	0.09	E	1
93	3	0.10	E	2
94	10	0.32	E	1
95	3	0.13	E	1
96	3	0.09	E	1
97	3	0.12	T	1
98	3	0.14	E	1
99	3	0.11	T	1

Appendix IV The results of damage prediction for zone S2 (worst case)

No.	Floors	Max drift (%)	During	Location
1	3	0.28	T	1
2	3	0.10	T	1
3	7	0.36	T	1
4	3	0.12	T	1
5	3	0.13	T	1
6	21	0.88	E	1
7	3	0.14	T	1
8	3	0.17	T	1
9	3	0.29	T	1
10	3	0.26	T	1
11	3	0.17	T	1
12	3	0.14	E	1
13	3	0.08	E	1
14	3	0.09	T	1
15	3	0.12	E	1
16	3	0.46	T	1
17	3	0.47	T	1
18	11	0.22	T	1
19	3	0.09	E	1
20	3	0.29	T	1
21	9	0.33	T	1
22	3	0.09	E	1
23	3	0.11	T	1
24	3	0.14	T	1
25	3	0.13	T	1
26	3	0.13	T	1
27	3	0.28	T	1
28	3	0.13	E	2

No.	Floors	Max drift (%)	During	Location
29	3	0.48	T	1
30	3	0.11	T	1
31	6	0.17	T	1
32	3	0.28	T	1
33	3	0.30	T	1
34	3	0.27	T	1
35	3	0.19	T	1
36	3	0.44	T	1
37	4	1.46	T	1
38	3	0.10	E	1
39	3	0.16	T	1
40	3	0.29	T	1
41	3	0.29	T	1
42	3	0.27	T	1
43	3	0.09	E	1
44	3	0.11	T	1
45	3	0.11	E	1
46	3	0.10	E	1
47	3	0.09	E	1
48	3	0.28	T	1
49	3	0.09	T	1
50	3	0.14	T	1
51	3	0.12	E	1
52	3	0.10	E	1
53	3	0.30	T	1
54	8	0.21	T	1
55	8	0.30	T	1
56	3	0.32	T	1

Appendix V The results of damage prediction for zone S3 (worst case)

No.	Floors	Max drift (%)	During	Location
1	3	0.29	T	1
2	3	0.20	T	1
3	3	0.19	T	1
4	3	0.27	T	1
5	3	0.20	T	1
6	3	0.85	T	1
7	3	0.79	T	1
8	3	0.26	T	1
9	3	0.80	T	1
10	3	0.81	T	1
11	3	0.21	T	1
12	3	0.27	T	1
13	3	0.20	T	1
14	3	1.65	T	1
15	3	0.27	T	1
16	3	0.19	T	1
17	3	0.81	T	1
18	3	0.19	T	1
19	3	0.27	T	1
20	3	0.20	T	1
21	3	0.26	T	1
22	3	0.24	T	1
23	3	0.20	T	1
24	3	0.26	T	1
25	3	0.28	T	1
26	3	0.23	T	1
27	3	0.19	T	1
28	3	0.79	T	1
29	9	0.53	T	1
30	3	0.48	T	1
31	10	0.52	T	1
32	3	0.20	T	1
33	3	0.80	T	1
34	3	0.27	T	1
35	3	0.19	T	1
36	3	0.21	T	1
37	3	0.78	T	1
38	3	0.80	T	1
39	3	0.17	T	1
40	3	0.79	T	1
41	7	1.52	T	1
42	7	0.55	T	1
43	3	0.26	T	1
44	3	0.27	T	1
45	4	4.70	T	1
46	6	2.46	T	1
47	3	0.28	T	1
48	3	0.27	T	1
49	8	0.86	T	1
50	3	0.24	T	1
51	4	2.32	T	1
52	3	0.77	T	1
53	3	0.20	T	1
54	3	0.24	T	1
55	9	0.73	T	1
56	3	0.21	T	1
57	3	0.19	T	1
58	3	0.23	T	1
59	4	4.71	T	1
60	7	0.55	T	1
61	3	0.20	T	1
62	3	0.22	T	1
63	3	0.82	T	1
64	3	0.28	T	1
65	3	0.81	T	1
66	3	0.21	T	1
67	3	0.81	T	1
68	3	0.26	T	1
69	3	0.78	T	1
70	3	0.24	T	1
71	3	0.26	T	1
72	3	0.19	T	1
73	5	3.55	T	1
74	6	2.23	T	1
75	3	0.18	T	1
76	3	0.83	T	1

Appendix VI The results of damage prediction for zone S4 (worst case)

No.	Floors	Max drift (%)	During	Location
1	5	0.98	T	1
2	3	0.37	T	1
3	3	0.15	T	1
4	3	0.15	T	1
5	7	0.33	T	1
6	3	0.09	E	1
7	8	0.44	T	1
8	3	0.16	T	1
9	3	0.12	E	1
10	3	0.09	E	1
11	3	0.12	T	1
12	3	0.11	T	1
13	3	0.15	T	1
14	3	0.15	T	1
15	3	0.12	T	1
16	3	0.11	T	1
17	3	0.35	T	1
18	3	0.38	T	1
19	3	0.97	T	1
20	3	0.38	T	1
21	3	0.37	T	1
22	3	0.13	T	1
23	3	0.11	E	1
24	3	0.16	T	1
25	3	0.18	T	1
26	3	0.40	T	1
27	3	0.14	T	1
28	3	0.09	E	1
29	3	0.12	T	1
30	3	0.16	T	1
31	3	0.37	T	1
32	3	0.41	T	1
33	3	0.36	T	1
34	3	0.09	E	1
35	3	0.11	T	1
36	6	0.80	T	1
37	3	0.09	E	1
38	3	0.12	E	1
39	3	0.16	E	1
40	7	0.32	T	1
41	3	0.34	T	1
42	8	0.24	E	2
43	8	0.44	T	1
44	3	0.22	T	1
45	3	0.10	T	1
46	3	0.18	T	1
47	3	0.72	T	1
48	3	0.35	T	1
49	3	0.09	E	1
50	3	0.38	T	1

No.	Floors	Max drift (%)	During	Location
51	3	0.10	T	1
52	3	0.10	T	1
53	3	0.10	T	1
54	3	0.15	T	1
55	3	0.22	T	1
56	3	0.15	T	1
57	3	0.15	T	1
58	3	0.15	T	1
59	3	0.14	E	1
60	3	0.10	T	1
61	3	0.11	T	1
62	3	0.11	T	1
63	3	0.14	T	1
64	3	0.10	E	1
65	3	0.14	T	1
66	3	0.13	E	1
67	3	0.08	E	1
68	3	0.09	T	1
69	3	0.10	T	1
70	3	0.16	T	1
71	3	0.11	T	1
72	3	0.09	E	1
73	3	0.11	T	1
74	3	0.09	E	1
75	3	0.09	T	1
76	3	0.16	T	1
77	3	0.09	E	1
78	3	0.09	T	1
79	3	0.09	T	1
80	3	0.09	T	1
81	3	0.12	T	1
82	3	0.14	T	1
83	3	0.12	T	1
84	3	0.09	T	1
85	3	0.14	T	1
86	3	0.12	T	1
87	4	0.17	T	2
88	4	0.15	T	2
89	3	0.09	T	1
90	3	0.09	E	1
91	11	0.24	T	2
92	3	0.09	T	1
93	3	0.10	E	2
94	10	0.32	T	1
95	3	0.13	T	1
96	3	0.09	T	1
97	3	0.12	T	1
98	3	0.14	E	1
99	3	0.11	T	1

REFERENCES

[1] M. Hori, S. Tanaka, T. Ichimura, M. Lalith, T. Miyamura, M. Ogino, and S. Okazawa, Application of HPC to earthquake engineering - seismic structure response analysis and urban area earthquake simulation. *4th ECCOMAS Thematic Conference on Computational Methods in Structural Dynamics and Earthquake Engineering*, 1728, 2013

[2] M. Hori, *Introduction to computational earthquake engineering*. 2nd Edition, Imperial College Press, London, 2011.

[3] M. Hori and T. Ichimura, Current state of integrated earthquake simulation for earthquake hazard and disaster. *Journal of Seismology*, Spriger science, 12, 307-321, 2008.

[4] M. Hori, T. Ichimura and K. Oguni, Development of integrated earthquake simulation for estimation of strong ground motion, structural responses and human action in urban areas. *Asian Journal of Civil Engineering (Building and Housing)*, 7, 4, 381-392, 2006.

[5] T. Ichimura, M. Hori, K. Terada and T. Yamakawa, On integrated earthquake simulator prototype: combination of numerical simulation and geographical information system. *Structural Eng./Earthquake Eng.*, JSCE, 22, 2, 233s-243s, 2005.

[6] T. Ichimura and M. Hori, Development of prototype of integrated earthquake disaster simulator using digital city and strong ground motion simulator with high-resolution. *13th World Conference on Earthquake Engineering*, 1418, 2004.

[7] G. Sobhaninejad, M. Hori, and T. Kabeyasawa, Enhancing integrated earthquake simulation with high performance computing. Elsevier, *Advances in Engineering Software*, 42, 286-292, 2011.

[8] M.L.L. Wijerathne, M. Hori, T. Kabeyasawa, and T. Ichimura, Strengthening of parallel computation performance of integrated earthquake simulation. ASCE, *Journal of Computing in Civil Engineering*, 2012.

[9] T. Ichimura, T. Samo, M. Hori, and H. Itami, Integrated earthquake simulator to generate advanced earthquake disaster information. *Internet Journal for Society for Social Management Systems (SSMS)*,2009.

[10] L. Maddegedara and M. Hori, Application of high performance computation for the prediction of urban area earthquake disaster. *Internet Journal for Society for Social Management Systems (SSMS)*, 2011.

[11] D. B. Kirk and W. W. Hwu, *Programming Massively Parallel Processors.* 2nd Edition, Elsevier, Morgan Kaufmann, 2013.

[12] NVIDIA Corporation, *NVIDIA Developer Zone.* 2014

[13] T. Asai, Y. Nakano, T. Tateno, H. Fukuyama, K. Fujima, Y. Haga, T. Sugano, and T. Okada, Tsunami load evaluation based on damage observation after the 2011 Great East Japan earthquake. *Proceedings of the International Symposium on Engineering Lessons Learned from the 2011 Great East Japan Earthquake*, Tokyo, Japan, 2012.

COMPDYN 2015
5th ECCOMAS Thematic Conference on
Computational Methods in Structural Dynamics and Earthquake Engineering
M. Papadrakakis, V. Papadopoulos, V. Plevris (eds.)
Crete Island, Greece, 25–27 May 2015

DETERMINATION OF THE PERIODS OF COUPLED SHEAR WALLS BY RECURSIVE DIFFERENTIATION METHOD

Duygu Ozturk[1], **Kanat Burak Bozdogan**[2]

[1] Ege University
Engineering Faculty, Civil Engineering Department, İzmir, Turkey
duygu.ozturk.ege@gmail.com

[2] Kirklareli University
Engineering Faculty, Civil Engineering Department, Kırklareli, Turkey
kbbozdogan@klu.edu.tr

Keywords: Shear Wall, Recursive Differentiation Method, Free Vibration.

Abstract. *Coupled shear walls are commonly used in the constructions to meet the architectural requirements and to improve the lateral resistance of the structure. Evaluation of the behavior of the structures with coupled shear walls under earthquake loads is carried out by dynamic analysis. For the dynamic analysis, identification of the dynamic properties of the coupled shear walls is important. The period of the structure is an important design parameter used in the dynamic analysis. There are various methods used for the determination of the periods. In this study, the periods of the coupled shear walls are determined by using Recursive Differentiation Method. At the end of study, good results are received by the example that is solved to investigate the presented method.*

1 INTRODUCTION

There are several studies with regard to the analysis of coupled shear walls [1] – [11]. In this study, Recursive Differentiation Method is proposed for the determination of the periods of coupled shear walls.

The assumptions made in the study are: the material is linearly elastic and the displacements are small, P-Δ effects are neglected, the influence of shear deformation of the shear walls is neglected, material and geometrical properties of the shear walls are same throughout the height of the structure.

2 METHOD

In this part of the study, Recursive Differentiation Method that is detailed in the literature [12] is applied to the determination of the periods of coupled shear walls and the method is explained. Equations of the coupled shear walls can be written as in Equation (1) and (2).

$$EI\frac{d^4y}{dx^4} - K\left(\frac{d^2y}{dx^2} - \frac{d^2y_b}{dx^2}\right) + m\omega^2 y = 0 \tag{1}$$

$$D\frac{d^3y}{dx^3} = -K\left(\frac{dy}{dx} - \frac{dy_b}{dx}\right) \tag{2}$$

Here, y is the total displacement, y_b is the displacement due to bending and x is the vertical axis. Boundary conditions are

$$y(0) = 0 \tag{3}$$

$$\frac{dy}{dx}_{x=0} = 0 \tag{4}$$

$$\frac{dy_b}{dx}_{x=0} = 0 \tag{5}$$

$$EI\frac{d^2y}{dx^2}_{x=H} = 0 \tag{6}$$

$$D\frac{d^2y_b}{dx^2}_{x=H} = 0 \tag{7}$$

$$EI\frac{d^3y}{dx^3}_{x=H} - K\frac{dy}{dx}_{x=H} + K\frac{dy_b}{dx}_{x=H} = 0 \tag{8}$$

EI is the total flexural rigidity of the coupled shear wall represented in Figure (1) and calculated by Equation (9).

$$EI = \sum_{i=1}^{n}(EI)_i \tag{9}$$

K is the shear rigidity and D is the global flexural rigidity.

$$K = K_b\frac{K_c}{K_c + K_b} \tag{10}$$

$$K_c = \sum_{i=1}^{n-1}\frac{12EI_{c,i}}{h^2} \tag{11}$$

$$K_b = \sum_{i=1}^{n}\frac{6EI_{b,i}\left[(l+s_1)^2+(l+s_2)^2\right]}{l^3h\left(1+\frac{12kEI_b}{l^2GA_b}\right)} \tag{12}$$

$$D = E\sum_{j=1}^{n}A_{c,j}\,t_j^2 \tag{13}$$

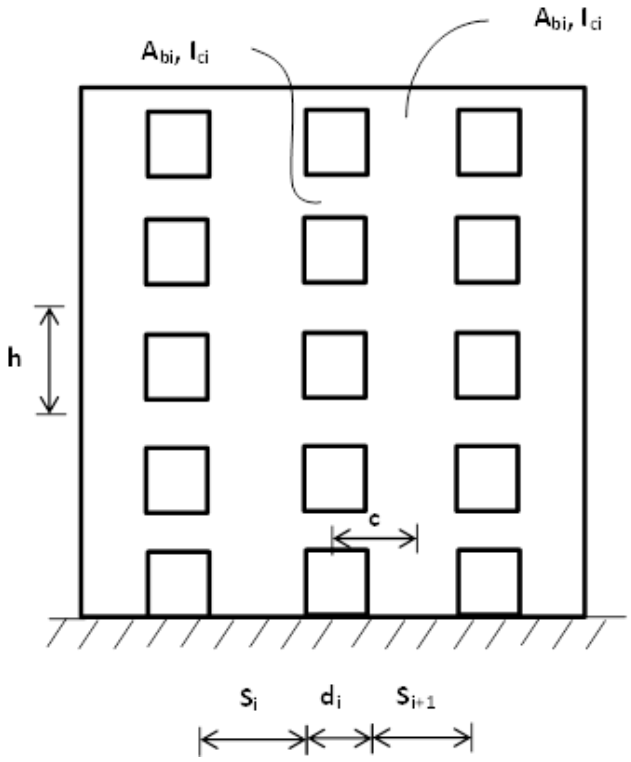


Figure 1: Coupled shear wall.

To get the non-dimensional forms of Equation (1) and (2), Ɛ=x/H transform is applied and Equation (14) and (15) are obtained.

$$\frac{d^4y}{d\varepsilon^4} - a\left(\frac{d^2y}{d\varepsilon^2} - \frac{d^2y_b}{d\varepsilon^2}\right) + py = 0 \tag{14}$$

$$\frac{d^3y}{dx^3} = -b\left(\frac{dy}{dx} - \frac{dy_b}{dx}\right) \tag{15}$$

a, b and p parameters are found according to Equations (16), (17) and (18)

$$a = H^2\frac{K}{(EI)} \tag{16}$$

$$b = H^2\frac{K}{D} \tag{17}$$

$$p = \frac{H^4\omega^2 m}{EI} \tag{18}$$

With the purpose of the reduction of the order of the differential equation, $\frac{dy_b}{dx}$ rotation is named as θ_b

$$\frac{dy_b}{dx} = \theta_b \tag{19}$$

Thus, the differential equations return into the equations below:

$$\frac{d^4y}{d\varepsilon^4} - a\left(\frac{d^2y}{d\varepsilon^2} - \frac{d\theta_b}{dx}\right) + py = 0 \tag{20}$$

$$\frac{d^2\theta_b}{dx^2} = -b\left(\frac{dy}{dx} - \theta_b\right) \tag{21}$$

To put the equation into final form, boundary conditions are as below:

$$y(0) = 0 \tag{22}$$

$$\frac{dy}{d\varepsilon_{x=0}} = 0 \tag{23}$$

$$\theta_b(0) = 0 \tag{24}$$

$$\frac{d^2y}{d\varepsilon^2{}_{\varepsilon=1}} = 0 \tag{25}$$

$$\frac{d\theta_b}{d\varepsilon}_{\varepsilon=1} = 0 \tag{26}$$

$$\frac{d^3y}{d\varepsilon^3{}_{\varepsilon=1}} - a\frac{dy}{d\varepsilon_{\varepsilon=1}} + \theta_{b\,\varepsilon=1} = 0 \tag{27}$$

In the Recursive Differentiation Method, expressions of the derivatives taken can be written recursively by the Equations (20) and (21)

$$\frac{d^{(i+4)}y}{d\varepsilon^{(i+4)}{}_1} = a\left(\frac{d^{(i+2)}y}{d\varepsilon^{(i+2)}} - \frac{d^{(i+1)}\theta_b}{d\varepsilon^{(i+1)}}\right) - p\frac{d^iy}{d\varepsilon^i} \tag{28}$$

$$\frac{d^{(i+2)}\theta_b}{d\varepsilon^{(i+2)}} = -b\left(\frac{d^{(i+1)}y}{d\varepsilon^{(i+1)}} - \frac{d^i\theta_b}{d\varepsilon^i}\right) \tag{29}$$

Displacement and flexural rotation of the top of the coupled shear wall are written as in the equations below:

$$y(1) = y(0) + \frac{y^{\prime}(0)}{1} + \frac{y^{\prime\prime}(0)}{2!} + \cdots + \frac{y^k(0)}{k!} + \cdots .. \tag{30}$$

$$\theta_b(1) = \theta_b(0) + \frac{{\theta_b}^{\prime}(0)}{1} + \frac{{\theta_b}^{\prime\prime}(0)}{2!} + \cdots + \frac{{\theta_b}^k(0)}{k!} + \cdots .. \tag{31}$$

As the boundary conditions are written by means of these two equations, Equations (32) - (34) are obtained.

$$y''(1) = y''(0) + \frac{y^{\prime\prime\prime}(0)}{1} + \frac{y^{IV}(0)}{2!} + \cdots + \frac{y^k(0)}{(k-2)!} + \cdots .. = 0 \tag{32}$$

$${\theta_b}'(1) = {\theta_b}'(0) + \frac{{\theta_b}^{\prime\prime}(0)}{1} + \frac{{\theta_b}^{III}(0)}{2!} + \cdots + \frac{{\theta_b}^k(0)}{(k-1)!} + \cdots .. = 0 \tag{33}$$

$$y'''(1) - ay'(1) + a\theta_b(1) = \left(y'''(0) + \frac{y^{IV}(0)}{1} + \frac{y^V(0)}{2!} + \cdots + \frac{y^k(0)}{(k-3)!} + \cdots ..\right) - a\left(y'(0) + \frac{y''(0)}{1} + \frac{y^{III}(0)}{2!} + \cdots + \frac{y^k(0)}{(k-1)!}\right) + a\left(\theta_b(0) + \frac{{\theta_b}^{\prime}(0)}{1} + \frac{{\theta_b}^{\prime\prime}(0)}{2!} + \cdots + \frac{{\theta_b}^k(0)}{k!} + \cdots\right) = 0 \tag{34}$$

In this equation system derivatives are written in terms of y"(0), y'"(0), θ_b'(0) and with the help of Equations (28) and (29), matrix equation below is obtained.

$$[A] * \begin{Bmatrix} y''(0) \\ y'''(0) \\ {\theta_b}'(0) \end{Bmatrix} = \begin{Bmatrix} 0 \\ 0 \\ 0 \end{Bmatrix} \tag{35}$$

In this matrix equation, the determinant of A should be zero for non-trivial solution.

Angular frequencies are obtained by Equation (36).

$$\omega_i = \frac{1}{H^2}\sqrt{\frac{p_iEI}{m}} \tag{36}$$

3 EXAMPLE

The coupled shear wall for the example is given in Figure 2. The properties of the coupled shear wall system are given in Table1.

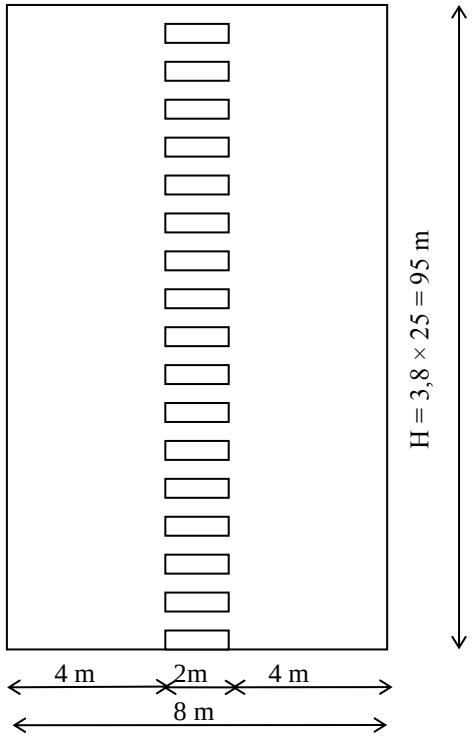


Figure 2: Coupled shear wall.

Title 1	Title 2
EI	2,9808*10^8 kNm^2
K	4550446*10^5 kN
D	1,58976 *10^9 kNm^2
m	831,6 t
a	13,7774
b	5,5833

Table 1: Properites of the coupled shear wall system in the example.

Mod No	Proposed Method **1**	Kuang **2**	Ratio **1 / 2**
1	0,660	0,667	0,990
2	2,897	2,925	0,990
3	7,104	7,159	0,992
4	13,20	13,28	0,994
5	21,33	21,44	0,995
6	31,48	31,61	0,996
7	43,67	43,82	0,997
8	57,88	58,04	0,997
9	74,12	74,30	0,998
10	92,41	92,57	0,998

Table 2: Natural frequencies of the example

With the solution of the example, good results are received and the differences between the results of the method and the literature [10] are given in Table 2.

4 CONCLUSIONS

In this study, Recursive Differentiation Method is proposed for the determination of the periods of coupled shear walls. The method for the solution of the periods according to the Recursive Differentiation Method is explained in detail. In consequence of the comparison of the presented method and the literature by the example at the end of the study, good results are received.

REFERENCES

[1] O. Aksoğan, H.M. Arslan, B.S. Choo, Forced Vibration Analysis of Stiffened Coupled Shear Walls Using Continuous Connection Method. *Engineering Structures*, **25,** 499-506, 2003.

[2] A. Basu, A. K. Nagpal, R.S Bajaj, A. Guliani, Dynamic Characteristics of Coupled Shear walls, *Journal of Structural Engineering-ASCE*, **105**, 1637-1651, 1979.

[3] K.B. Bozdogan, D.Ozturk, A. Nuhoglu, An Approximate Method for Static and Dynamic Analyses of Multi-Bay Coupled Shear Walls, *The Structural Design of Tall and Special Buildings*, **18**, 1-12, 2009.

[4] Y.H. Chai, Y. Chen, Reexamination of the Vibrational Period of Coupled Shear Walls by Differential Transformation, *Journal of Structural Engineering-ASCE*, **135(11),** 1330-1339, 2009.

[5] Q. Wang, L.Y Wang, Estimating Periods of Vibration of Buildings with Coupled Shear Wall, *Journal of Structural Engineering-ASCE*, **131(12)**, 1931-1935, 2005.

[6] G. Potzta, L.P. Kollar, Analysis of Building Structures by Replacement Sandwich Beams, *International Journal of Solids and Structures*, **40**, 535-553, 2003.

[7] G.Q. Li and B.S. Choo, A Continuous-discrete Approach to the Free Vibration Analysis of Stiffened Pierced Walls on Flexible Foundations, *International Journal of Solids and Structures*, **33(2)**, 249-263, 1996.

[8] H.S. Kim, D.G. Lee, Analysis of Shear Wall with Openings Using Super Elements, *Engineering Structures*, **25**, 981-991, 2003

[9] J.S. Kuang,. C.K.Chau, Free Vibration of Stiffened Coupled Shear Walls, *The Structural Design of Tall and Special Buildings*, **7**, 135-145, 1998.

[10] O. Chaallal, D. Gauthier, P. Malenfant, Classification Methodology for Coupled Shear Walls, *Journal of Structural Engineering-ASCE*, **122(12)**, 1453-1458, 1996.

[11] J. Wdowicki, E., Wdowicka, Analysis of non-planar shear wall structures with stiffening beams, *CMM-2011 – Computer Methods*, 2011.

[12] M. Taha, Recursive Differentiation Method for Boundary Value Problems Application to Analysis of a Beam Column On An Elastic Foundation, *Journal of Theoretical and Applied Mechanics*, **44(2)**, 57-70, 2014.

COMPDYN 2015
5th ECCOMAS Thematic Conference on
Computational Methods in Structural Dynamics and Earthquake Engineering
M. Papadrakakis, V. Papadopoulos, V. Plevris (eds.)
Crete Island, Greece, 25–27 May 2015

SEISMIC BEHAVIOUR OF BRIDGE STRUCTURES MADE OF NATURAL FIBRE REINFORCED POLYMER-CONCRETE COMPOSITE

Jiaxin Chen[1] **and Nawawi Chouw**[1]

[1] The University of Auckland
Private Bag 92019, Victoria Street West, Auckland 1142, New Zealand
e-mail: jche872@aucklanduni.ac.nz and n.chouw@auckland.ac.nz

Keywords: Bridge Pier, Seismic Response, Natural Fibre, Polymer-Concrete Composite, Shake Table experiments

Abstract. *In contrast to current conventional construction materials, i.e. steel or steel reinforced concrete, natural fibre reinforced polymer-concrete composite is environmentally friendly. In addition to the reduction of structural mass and thus the inertia forces activated in the structure during an earthquake loading, the most significant advantage is the avoidance of the long-term effect of corrosion on the integrity of the structures. In this paper a preliminary result of a simple bridge pier, made of flax fibre reinforced polymer and coconut fibre reinforced concrete, under earthquake loadings is discussed. The ground motions are simulated stochastically based on Japanese design spectrum for a hard soil condition. Shake table experiments are performed. The consequence of double tube confinement of the coconut fibre reinforced concrete core for the responses of the structure is presented.*

1 INTRODUCTION

Bridge structures made of conventional construction materials, steel and concrete with steel reinforcement, especially in coastal regions deteriorate with the time due to corrosion of steel. The usage of non-corrosive materials, e.g. glass or carbon fibre reinforced polymer (G/CFRP), in civil infrastructure is very limited because of the high initial cost. The other factors that impede the usage of G/CFRP are the unknown long-term performance, risk of fire and non-yielding behaviour of the materials. The reinforcement can take many forms, e.g. of glass fibre reinforced polymer rods [1]. Even though these materials have the potential to replace steel as reinforcing material due to their significant properties, e.g. high strength, its usage is mainly for retrofitting earthquake prone structures [2].

To overcome the high cost natural materials can be utilized without compromising the strength of the composite material and thus can lead to construction materials for structures in the future [3]. Raftery and Kelly [4] proposed the usage of basalt fibre reinforced polymer for strengthening timber structures. Cheah [5] investigated the usage of flax fibre in traditional earth houses. Ali et al. [6-8] proposed the usage of coconut fibre reinforced concrete for low-cost earthquake-resistant low-damage structures, especially in earthquake regions in developing countries. The low-damage structures are achieved by letting each structural member to move relative to each other. Hence, each structural member performs rigid body movements whenever the earthquake loading exceeds a threshold. To ensure the re-centering the structural members have interlocking keys. In addition to re-centering after an uplift movement the keys have the function to transfer eventual shear forces.

The natural materials considered in this study are flax and coconut fibres. The pre-fabricated flax fibre reinforced polymer (FFRP) tubes serve as lightweight permanent formworks for fresh coconut fibre reinforced concrete (CFRC) core. The pre-fabrication of the tubes accelerate the construction process [9]. Under axial loading the tubes provide confinement and thus enhance the compressive strength of the FFRP-CFRC composite. As flexural structural members, in addition to the standard function of an internal resistance in the compressive zone the concrete core provides an internal support of the outer FFRP tube and enhances the buckling resistance of the whole composite. The randomly distributed coconut fibres enable a distribution of small cracks over a large region and thus contribute to the ductility of the FFRP-CFRC composite and enhance the material damping [10-14]. As anticipated the behaviour of this environmentally-friendly FFRP-CFRC composite is strongly determined by the bond between FFRP and CFRC [15].

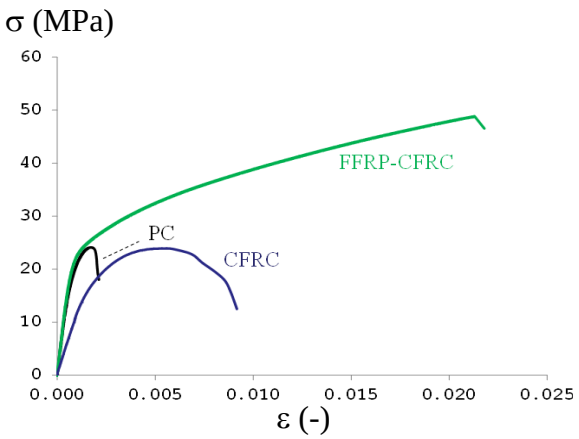


Figure 1. Effect of natural fibre on the stress-strain relationship of the composite

In contrast to current conventional seismic design of steel reinforced concrete structures the use of natural fibre reinforced polymer instead of steel reinforcement will reduce the total structural mass and also avoid the long-term corrosion effect of steel. Because of the smaller mass and the corrosion-free materials the new composite structures can withstand more loads and require less running maintenance cost. The research focuses on engineering design of new composite structural members and assembled structures. FFRP and CFRC will be used to carry the activated tensile and compressive stresses, respectively.

Figure 1 shows the relationship between compressive stress σ and the axial strain ε. In the case considered the compressive strength of the concrete core is about 22 MPa. The inclusion of coconut fibre does not increase the compressive strength. However, the ductility of the coir-concrete composite does increase significantly. A confinement of the coir reinforced concrete core due to the outer FFRP tube leads to an increase of the compressive strength to more than double of that of plain concrete (PC). It also enhances the ductility of the FFRP-CRFC composite significantly [11]. The ductility of the composites is strongly determined by the bond strength between natural fibres and surrounding matrix and the bond strength at the interface between FFRP and CRFC [7, 15].

In this paper a simple bridge pier is investigated. The earthquake loading is simulated by a shake table. The impact of the earthquake loading can be further reduced by having even less mass. Instead of a solid CFRC core double FFRP tubes can be used. The inner FFRP tube serves as inner permanent formwork. The consequence of the earthquake magnitude and the additional inner tube for the seismic behaviour of the FFRP-CFRC bridge pier is presented.

2 FFRP-CFRC BRIDGE PIER UNDER AN EARTHQUAKE LOADING

Figure 2 shows a scale model of the bridge pier with a CFRC core diameter of 10 cm. The inner and outer FFRP tubes have the thickness of 3.05 mm and 5.3 mm, respectively. The inner diameter of the inner tube is 2.5 cm.

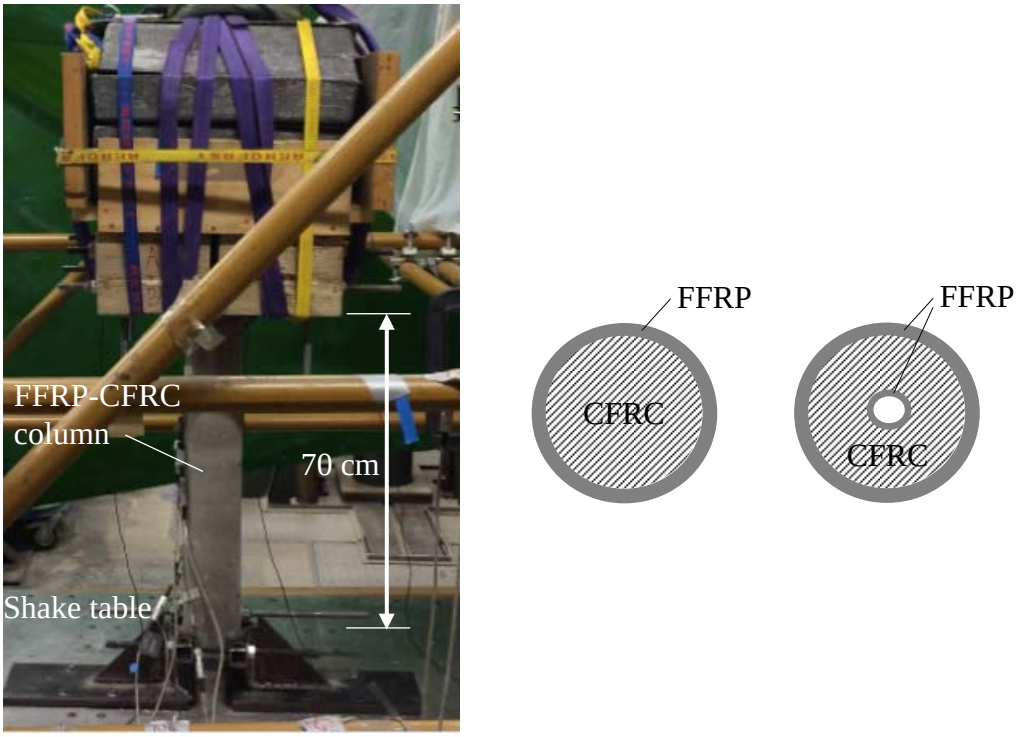


Figure 2. Single and double FFRP tubes confined CFRC composite bridge pier

The bridge girder is simplified as a single degree of freedom. Two different pier systems, i.e. CFRC core confined by single FFRP tube and by double FFRP tubes. The top mass is selected so that the fixed base fundamental frequency of both systems is about 2.929 Hz. The system period is then 0.34 s. Figure 3 shows the response spectrum of the two stochastically simulated ground motions based on Japanese design spectrum for a hard soil condition (bold dashed line) [16]. It can be anticipated from the spectra that the bridge pier structure will experience the strongest excitation. The simulated ground motions have a peak ground displacement (PGD) of 30.82 cm.

In order not to damage the structure immediately, the experiments were performed with gradually increasing PGD. With increasing PGD it can be expected that the fundamental frequency of the structure will reduced, i.e. with increasing fundamental period the structure will experience roughly the same excitation as can be estimated from the response spectra in Figure 3. The first experiment was performed with the ground motion of PGD = 20 mm, i.e. only 6.5% of the original excitation. The subsequent experiments on the same structure were performed with an increasing PGD up to 90 mm, i.e. 29.2% of the original excitation. Following each subsequent experiment the fundamental frequency is determined from the free vibration of a snap-back test. Following the 90 mm PGD experiment the system has a fundamental frequency of 2.44 Hz or a fundamental period of 0.41 s.

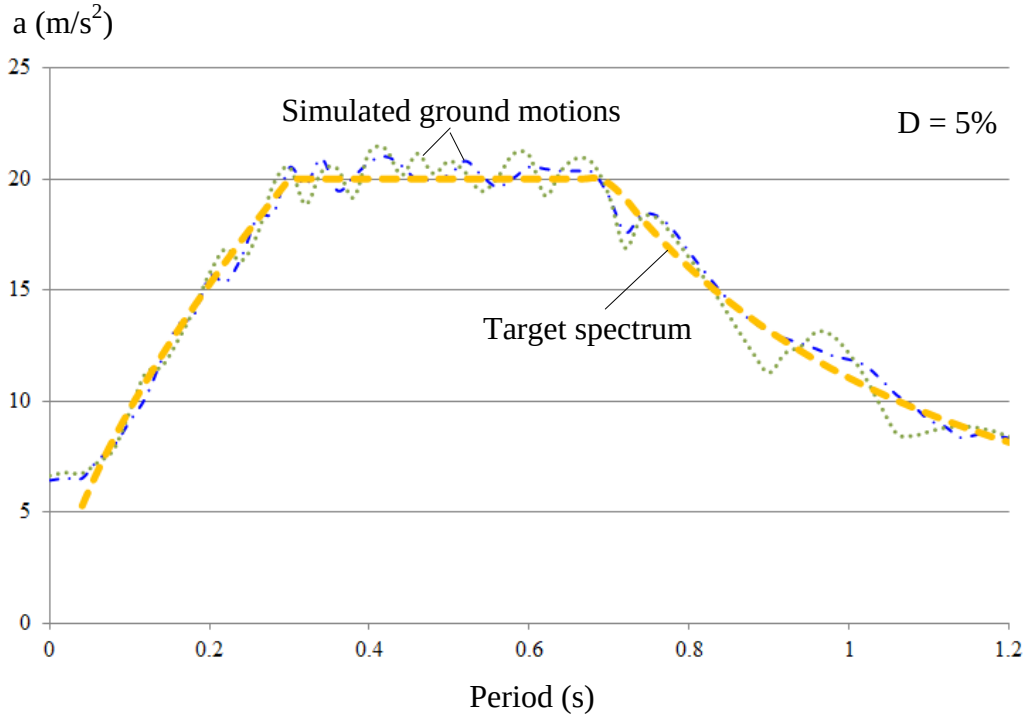


Figure 3: Simulated ground excitation and Japanese design target spectrum for a hard soil condition.

Figure 4 shows a comparison between the displacements at the top of the same bridge pier due to the same ground motion with an assumption of undamaged (linear behaviour) and damaged bridge pier. The bridge pier has only one FFRP tube confinement. The linear response is obtained from the experiment with a very small PGD of 20 mm while the nonlinear response is achieved with PGD of 90 mm. In order to compare the two results, the linear response is multiplied by a factor of 4.5. The response of the stiffer linear system can be clearly seen in a shorter period (solid line) in comparison with the nonlinear response (dashed line). In the case considered the stiffer linear system responded with smaller amplitudes. The dam-

age to the bridge pier could take place at the interface between FFRP tube and CFRC core. Previous preliminary study with much stronger ground excitation resulted in no damage to the FFRP tube [17]. In the case considered, also no damage to the FFRP tube was observed.

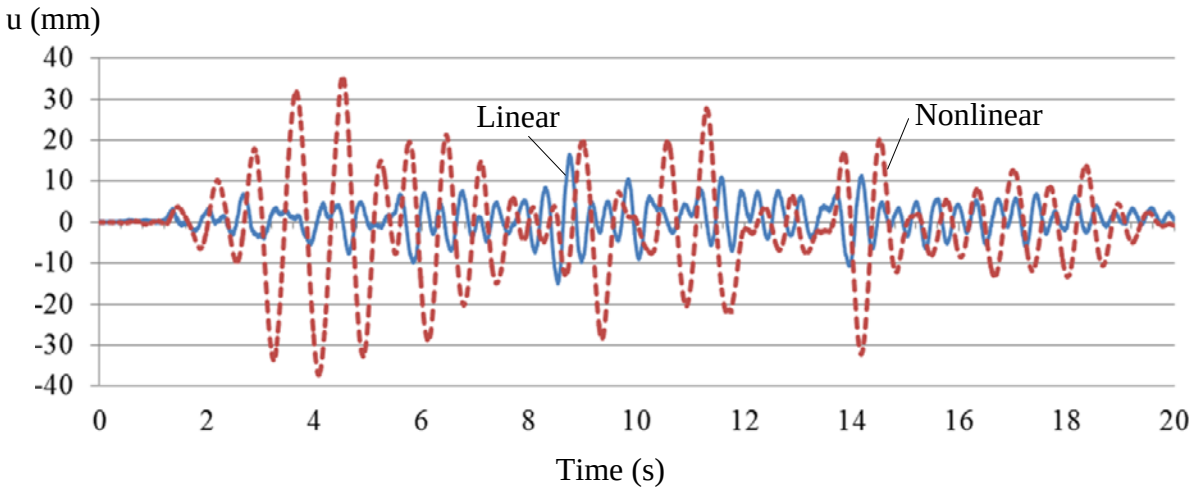


Figure 4. Displacement at the pier top

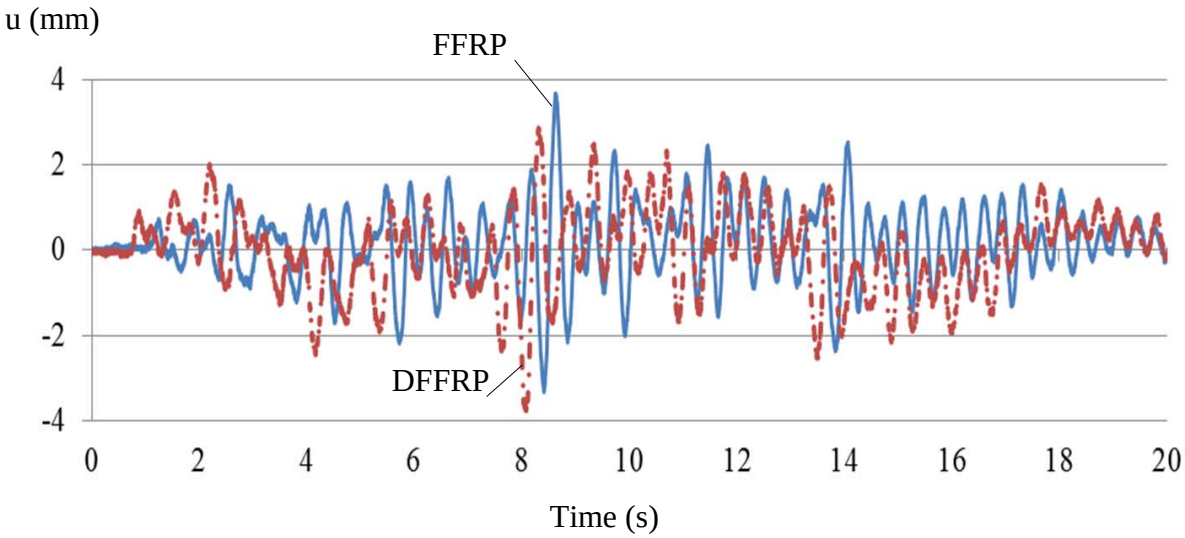


Figure 5. Influence of double shells on the top pier displacement

Figure 5 shows the influence of double FFRP tubes on the linear response of the top displacement of the bridge pier. The ground motion considered has the PGD of 20 mm. The maximum response of the bridge pier with one and double FFRP tubes is 3.68 mm and 3.77 mm, respectively. Despite less materials are used in the case of double FFRP tube pier, both maximum displacements are almost the same.

3 CONCLUSIONS

New construction materials consist of flax fibre reinforced polymer (FFRP) and coconut fibre reinforced concrete (CFRC) composite is investigated for possible usage in earthquake-resistant structures. A simple bridge pier is constructed. Single and double FFRP tubes were

used as permanent formworks for CFRC core. The ground motions are simulated based on Japanese design spectrum for a hard soil condition.

The results show:

- The bond at the interface between FFRP tube and CFRC core is critical for the seismic performance of the bridge pier.
- The usage of double tubes can have significant advantage, since less mass is considered.
- Linear bridge piers with single and double FFRP tubes perform in similar manner.

Further investigations are necessary to fully understand the seismic performance of structures using these new construction materials.

ACKNOWLEDGEMENTS

The author would like to thank the Ministry of Business, Innovation and Employment for the support through the National Hazards Research Platform under the Awards 3701868.

REFERENCES

[1] G.M. Raftery, C. Whelan, Low-grade glued laminated timber beams reinforced using improved arrangements of bonded-in GFRP rods. *Construction and Building Materials*, **52**, 209-220, 2014.

[2] L. Hollaway, Key issues in the use of fibre reinforced polymer (FRP) composites in the rehabilitation and retrofitting of concrete structure. In: V.M. Karbhari and L.S. Lee (Eds.) *Service life estimation and extension of civil engineering structures*, Cambridge: Woodead Publishing Limited, 23-25, 2011.

[3] L. Yan, N. Chouw, Behaviour and analytical modeling of natural flax fibre reinforced polymer tube confined plain concrete and coir fibre reinforced concrete. *Composite Material* **47** (17), 2133-2148, 2012.

[4] G.M. Raftery, F. Kelly, Basalt FRP rods for reinforcement and repair of timber. *Composites Part B: Engineering*, **70** (11), 9 – 19, 2015.

[5] J.S. J. Cheah, *Development of a flax-fibre reinforced, cement-stabilized rammed earth housing solution (Uku) for rural Maori communities*. The University of Auckland, PhD thesis, 334 pages, 2014.

[6] M. Ali, R. Briet, N. Chouw, Dynamic response of mortar-free interlocking structures. *Construction and Building Materials*, **42**, 168-189, 2013.

[7] M. Ali, X. Li, N. Chouw, Experimental investigations on bond strength between coconut fibre and concrete. *Materials and Design*, **44**, 596-605, 2013.

[8] M. Ali, A. Liu, S. Hao, N. Chouw, N, Mechanical and dynamic properties of coconut fibre reinforced concrete. *Construction and Building Materials*, **30**, 814-825, 2012.

[9] T. Ozbakkaloglu, Compressive behaviour of concrete-filled FRP tube columns: Assessment of critical column parameters. Engineering Structures, **51**, 188-199, 2013.

[10] L. Yan, N. Chouw, Natural FRP tube confined fibre reinforced concrete under pure axial compression: A comparison with glass/carbon FRP, *Thin-Walled Structures* (in print).

[11] L. Yan, N. Chouw, Dynamic and static properties of flax fibre reinforced polymer tube confined coir fibre reinforced concrete. *Composite Materials* (in print).

[12] L. Yan, N. Chouw, K. Jayaraman, Effect of column parameters on flax FRP confined coir fibre reinforced concrete, *Construction and Building Materials*, **55**, 299-312, 2014.

[13] L. Yan, N. Chouw, A comparative study of steel reinforced concrete and flax fibre reinforced polymer tube confined coconut fibre reinforced concrete beams. *Reinforced Plastics and Composites*, **32** (16), 1155-1164, 2013.

[14] L. Yan, N. Chouw, K. Jayaraman, Flax fibre and its composites - A review. *Composites Part B: Engineering*, **56**, 296-317, 2014.

[15] L. Yan, A. Duchez, N. Chouw, Effect of bond on compressive behaviour of flax FRP tube confined coir fibre reinforced concrete. *Journal of Reinforced Plastics and Composites*, **32** (4), 273-285, 2013.

[16] Japan Society of Civil Engineers (JSCE), *Earthquake resistant design codes in Japan*, Maruzen, Tokyo, 2000.

[17] L. Yan, F. Dong, N. Chouw, N., K. Jayaraman, Seismic performance of flax FRP encased coconut fibre reinforced concrete column. *Proceedings of the 2013 Australian Earthquake Engineering Society Conference*, Hobart, Tasmania, Australia. 15 - 17 November 2013.

COMPDYN 2015
5th ECCOMAS Thematic Conference on
Computational Methods in Structural Dynamics and Earthquake Engineering
M. Papadrakakis, V. Papadopoulos, V. Plevris (eds.)
Crete Island, Greece, 25–27 May 2015

FINITE ELEMENT ELASTIC ANALYSIS OF 3-D FLEXIBLE PAVEMENTS UNDER MOVING LOADS

Niki D. Beskou[1], Stefanos V. Tsinopoulos[2], and Dimitrios D. Theodorakopoulos[1]

[1] Department of Civil Engineering
University of Patras, GR-26504, Greece
e-mail: nikidiane@gmail.com, d.d.theod@upatras.gr

[2] Department of Mechanical Engineering
Technological Educational Institute of Western Greece, Patras, GR-26334, Greece
e-mail: stsinop@gmail.com

Keywords: Flexible Pavements, Moving Loads, Elastodynamics, Finite Elements, Uniform and Layered Half-space.

Abstract. *The dynamic response of flexible road pavements to moving vehicles is numerically obtained by the time domain finite element method under 3-dimensional conditions with the aid of the commercial program ANSYS. Both the uniform and layered elastic half-space are considered. The moving with constant speed loads (wheels) of the vehicle are simulated by assigning time dependent load values at all the surface nodes along the vehicle path, which are activated at the time it takes for every wheel to travel the distance from the origin to every node's location. Simple supports on rollers and viscous absorbing boundaries of the pavement domain are both considered. Comparisons with analytical exact solutions for the half-space model under moving loads and analytical approximate solutions for the layered half-space model under static loads are made for validation and comparison reasons, respectively. The cases of static versus dynamic loads, of single load versus a series of loads and of low versus high vehicle's velocity are also compared and discussed from the viewpoint of how they affect the response of the pavement.*

1 INTRODUCTION

During the last 25 years or so, a lot of research on the analysis and design of flexible and rigid pavements under moving vehicles and realistic geometries with the aid of numerical methods, such as the finite element method (FEM), has been successfully conducted [1,2]. The vehicle models can be either concentrated or distributed loads moving with constant speeds, or more complicated ones involving spring-mass-damping systems with variable speed. The pavement models can be simple beams or plates on Winkler elastic foundations or layered half-spaces under conditions of plane strain or full three-dimensionality [2].

Eventhough some works dealing with nonlinear pavement behavior have appeared recently, most of the works on pavement dynamics are associated with linear elastic material behavior including viscoelasticity and poroelasticity [2]. Due to the complexity of vehicle and pavement modeling even when elastic material behavior is assumed, use of numerical methods, such as the FEM, is imperative.

Flexible pavements, modeled as elastic layered half-spaces under stationary or moving loads, have been analysed by various numerical methods such as the FEM, the boundary element method (BEM) or the layered system theory in matrix form [3-8].

In this work, the FEM is employed for the numerical determination of the response of flexible pavements composed of three layers on deformable soil to constant speed moving vehicles consisting of multiple axles under three-dimensional conditions. The material behavior of the layers and the supporting soil is assumed to be linear elastic. The FEM is employed and used in the time domain with the aid of the commercial computer program ANSYS [9].

Three- dimensional solid finite elements are used for the discretization of the space domain. Nonreflecting viscous boundaries at the four vertical faces and the bottom horizontal face of the pavement domain as well as nodal springs at the bottom face are introduced in ANSYS on the basis of the theories described in [10] and [11]. The moving with constant speed loads (wheels) of the vehicle are simulated by assigning time dependent load values at all the surface nodes along the vehicle path, which are activated at the time it takes for every wheel to travel the distance from the origin to every node's location. This process is provided to ANSYS through an attached to it computer program.

The above mentioned FEM is validated by comparing it with the analytical solutions involving the elastic half-space under a single, vertical, concentrated or equivalent distributed moving or stationary load [12, 13] and the elastic layered half-space under a distributed vertical static load [14]. Further numerical studies are also made to investigate the cases of static versus dynamic loading, of a single load versus a series of loads and of low versus high velocity of vehicles in order to determine their effects on the pavement response.

2 FINITE ELEMENT MODELING OF PAVEMENT STRUCTURE

Half of a typical three layer flexible road pavement structure in a three-dimensional (3-D) space is shown in Fig.1 with the plane zx to be the plane of symmetry. This structure has dimensions 29.45 m along the vertical z direction, 15.00 m along the lateral (transverse) y direction and 30.00m along the longitudinal x direction and is supported by a deformable soil. It consists of three elastic layers fully bonded to each other and to the supporting soil with the top one being the surface asphaltic layer of thickness 0.15 m, the intermediate one, the granular base layer, of thickness 0.30 m and the bottom one, the subgrade layer, of thickness 6.00 m. The material properties of the layers are E_1 = 1000 MPa, v_1 = 0.35, ρ_1 = 2500 kg/m^3 for the top layer, E_2 = 400 MPa, v_2 = 0.35, ρ_2 = 2100 kg/m^3 for the intermediate layer and E_3 = 80 MPa, v_3 = 0.40, ρ_3 = 2000 kg/m^3 for the bottom layer, where E, v and ρ denote modulus of elasticity, Poisson's ratio and mass density, respectively.

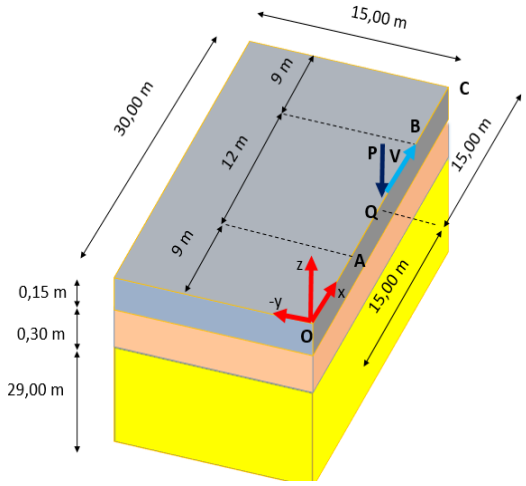


Figure 1: The three layered road pavement structure.

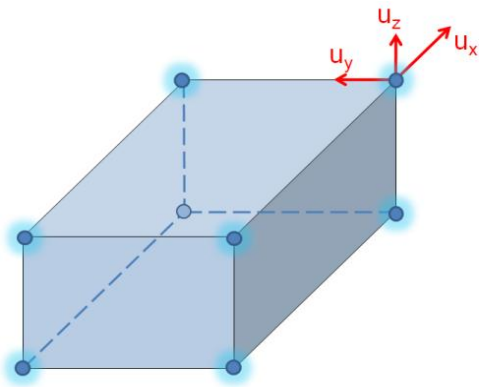


Figure 2: The 8-node 3-D finite element (SOLID185, with 24 d.o.f.)

The above pavement structure is discretized into a finite number of 8-noded 3-D solid elements (bricks) as shown in Fig.2 symbolized as SOLID185 in the commercial computer program ANSYS [9] and having in total 24 degrees of freedom (d.o.f.). The thickness of these elements increases as one goes from top to bottom of the structure. After some trials one can finally end up with an optimum discretization consisting of 145920 elements or 155961 nodes (3*155961 = 467883 d.o.f.).

Because the three vertical faces (the fourth one is the zx plane of symmetry) and the bottom horizontal face of the pavement structure are artificial boundaries, waves generated by the motion of the vehicle along the surface of the pavement propagate inside the pavement domain are reflected at those artificial boundaries and pollute the wave propagation inside the domain. For this reason, one usually introduces absorbing or non-reflecting devices at those boundaries. The most widely used absorbing boundaries because of their simplicity, are the standard viscous boundaries of Lysmer and Kuhlemeyer [15]. This type of absorbing boundaries, as described for the 3-D case in Hatzigeorgiou and Beskos [10], is used in this work.

The artificial vertical boundaries in this work are discretized by rectangular vertical elements, which are actually the vertical faces of the 3-D solid elements (bricks) used to descretize the domain. The dimensions of those elements/faces are a*b as shown in Fig.3. To every nodal point one assigns two vertical and one horizontal (perpendicular to the vertical element/face) dashpots with values

$$c_s = (ab)\rho V_s, \quad c_n = (ab)\rho V_p \tag{1}$$

as shown in Fig.3, where ρ is the mass density and V_s and V_p are the shear wave and dilatational wave velocities, respectively, defined by

$$V_s = \sqrt{\frac{\quad}{\quad}}, \qquad V_p = \sqrt{\frac{\quad}{\quad}} \tag{2}$$

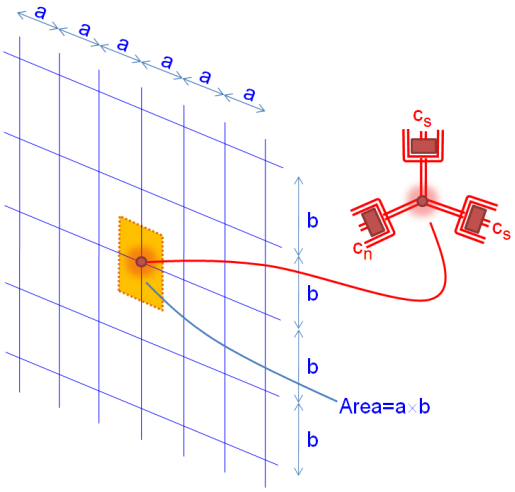


Figure 3: Vertical artificial boundary (external face of brick finite elements) and viscous dashpots

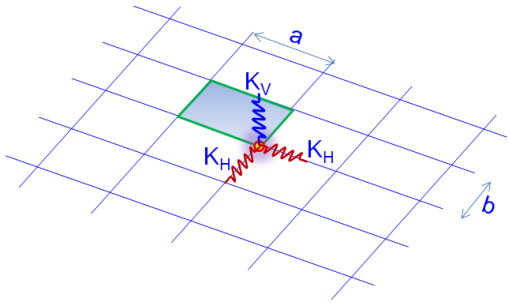


Figure 4: Bottom artificial boundary with nodal soil springs

Viscous dashpots are assigned to all the nodal points of the bottom face of the pavement domain in a similar way. At this bottom face one has also to introduce elastic springs at every node to simulate the supporting soil medium. The two horizontal spring constants K_H and the vertical spring constant K_V at every bottom node, as shown in Fig.4, are provided by the Mulliken and Karabalis [11] expressions

$$K_H = \text{————}, \quad K_V = \text{———} \tag{3}$$

where D is the half-length of the side of an equivalent square to the rectangular a*b of Fig.4, which is given by

$$D = \overline{\quad}/2 \tag{4}$$

The aforementioned dashpots and springs are appropriately introduced into the main ANSYS [9] program. For comparison purposes, in this work, rollers are also used at the three vertical faces and the bottom one.

3 MODELING OF MOVING VEHICLE LOADS

Consider a typical heavy vehicle (DAF truck model FAD CF75) of Fig.5 with four axles of concentrated loads $P_A = P_B = P_C = 16$ kN and $P_D = 32$ kN and axle distances $L_{AB} = 1.40$ m, $L_{BC} = 2.95$ m and $L_{CD} = 2.05$ m. Thus, the total axle length L = 6.40 m and the total weight of the vehicle is 80 kN = 18 kips, the standard weight used in US codes [1].

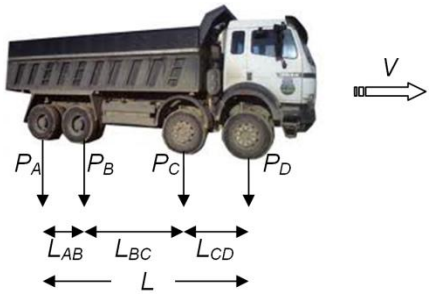


Figure 5: Typical heavy vehicle (truck) with four axles and total weight of 80 kN

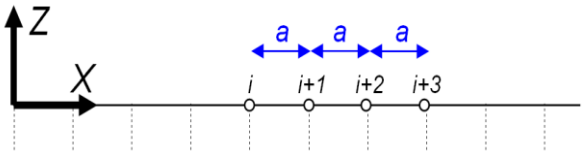


Figure 6: Top of discretized plane y=0 of the pavement system of Fig.1 with four successive nodes along the x axis

Consider next the top of the discretized plane y=0 of the pavement system of Fig.1 with four successive surface nodes along the direction of the vehicle's motion as shown in Fig.6. It is assumed that the distance a between two successive nodes is less than or equal to 1.0m so that $a<L_{AB}$. It is assumed that at time t=0 wheel D is on node i. At that instant one has $P_i=P_D$, $P_{i+1}=P_{i+2}=P_{i+3}=0$. For the vehicle to move a distance a the required time is $t_a=a/V$, where V is the constant speed of the vehicle. Hence wheel D will be on nodes i+1,i+2 and i+3 at times t_a, $2t_a$ and $3t_a$, respectively. In that case one has

$$P_{i+1}=P_D \text{ at } t=t_a, \quad P_{i+2}=P_D \text{ at } t=2t_a, \quad P_{i+3}=P_D \text{ at } t=3t_a \tag{5}$$

Without loss of generality, the subsequent analysis concentrates on node i+1. At time t=0 node i+1 is unloaded. After that, node i+1 starts being loaded since load P_D leaves node i and moves towards node i+1. Using isoparametric finite element concepts, load P_D is distributed to nodes i and i+1 in a linear manner during the time interval $0\le t\le t_a$ and the same happens for nodes i+1 and i+2 for the time interval $t_a\le t\le 2t_a$, as shown in Fig.7. The full unloading of node i+1 occurs after load P_D has reached node i+2. Taking into account that the vehicle considered has four axles, the total loading will be the result of the superposition of loads P_A, P_B, P_C and P_D, as shown in Fig.8. The loading configuration of Fig.8 for node i+1 is repeated for every other node of the pavement surface with the only difference being from node to node the commencement time of the above quadruple loading. Following this idea, one can model the 3-D distributed moving load as a sequence of many point loads along the x and y direction moving with a constant speed along the x direction.

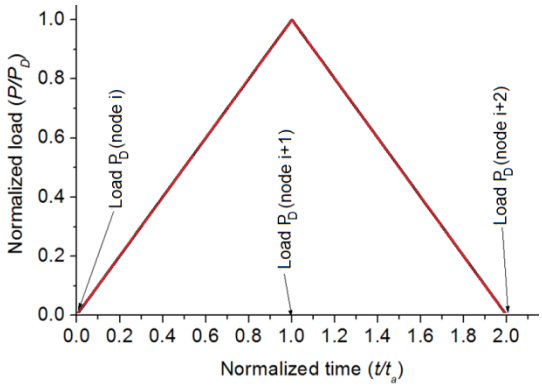


Figure 7: Loading of node *i*+1 by load P_D

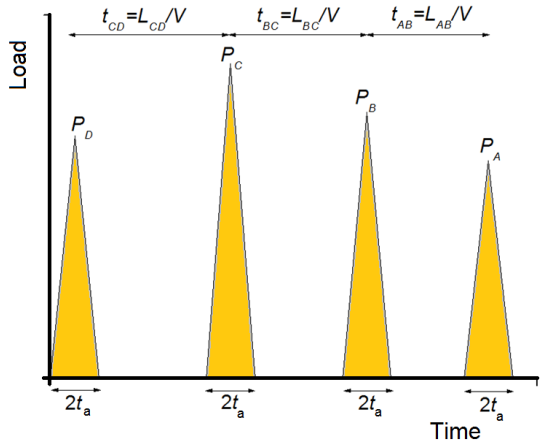


Figure 8: Total loading of node *i*+1 by the whole vehicle

The aforementioned procedure of load application in the time domain has been programmed and that program has been appropriately interfaced with the main ANSYS [9] program.

4 FINITE ELEMENT SOLUTION IN THE TIME DOMAIN

On the basis of the spatial modeling of the pavement structure of section 2, ANSYS [9] forms the mass matrix **M** and stiffness matrix **K** as well as the matrix equation of motion of that structure, which reads as

$$M\ddot{u} + Ku = F \tag{6}$$

where **u** is the vector of nodal displacements and **F** is the vector of nodal external forces on the surface z=0 coming from the moving wheel loads of the vehicle. The moving load starts at point A under zero initial conditions and terminates at point B, as shown in Fig.1. Structural damping is assumed to be zero.

Equation (6) is solved in the time domain to accommodate the in time evolution of the moving vehicle loads. The step-by-step time integration algorithm of Newmark [16] of the constant average acceleration type under zero initial conditions is employed in this work. This algorithm is unconditionally stable and provides highly accurate results provided an appropriate time step Δt has been selected.

The selection of an appropriate Δt is done on the basis of the guidelines in [16]. Thus if L_{el} is the maximum finite element length and V_p the dilatational wave velocity one has

$$\Delta t \leq L_{el}/V_p \tag{7}$$

An empirical relation provides Δt directly as [16]

$$\Delta t \leq 1/20f \tag{8}$$

where f is the highest loading frequency in Hz. Thus, on the assumption that for a truck the highest loading frequency f = 20 Hz, one obtains from (8) that $\Delta t \leq 0.0025$ sec. On the other hand, for L_{el}=0.15m (along the x axis) and V_p=500m/s, one has from (7) that $\Delta t \leq 0.3*10^{-3}$ sec. Thus, computations can commence with $\Delta t=0.6*10^{-3}$secs and contin-

ue with smaller values of Δt until convergence of the response results is established or an acceptable error is reached at convergence in case the exact value of the response is available.

5 NUMERICAL RESPONSE STUDIES

In this section validation studies of the proposed modeling are first presented. These have to do with comparisons on the basis of a uniform half-space under moving loads between numerical and analytical solutions. Comparisons on the basis of a layered half-space between numerical solutions for the cases of moving and stationary loads are also made. Numerically obtained responses for a single and a series of loads moving on a half-space medium are also compared.

5.1 Uniform half-space elastic medium under moving loads

Consider the road pavement structure of Fig.1 with identical properties in all three layers and the supporting soil, i.e., with $E = 50*10^6$ N/m^2, $v = 0.25$ and $\rho = 2000$ kg/m^3. The resulting domain becomes an elastic half-space with wave velocities of propagation $V_p = 173.2$ m/s and $V_s = 100$ m/s as obtained with the aid of Eqs (2). For this elastic half-space adopted from Eason [12], the Rayleigh wave velocity $V_R = 92$ m/s is the resonance wave velocity for a moving concentrated load. In road pavements, realistic velocities of moving vehicles do not exceed V = 50 m/s (180 km/h) and hence one deals with the subsonic case ($V<V_s$) and does not worry about resonance.

Table 1 lists the maximum values of the vertical displacement u_z at a depth of z = -1.0 m below the point Q (15, 0, 0) in the middle of the total length OC of the road (Fig.1) as obtained by ANSYS [9] for the velocity V=20m/s of the single concentrated moving load P = 80 kN, three types of boundary conditions and three time steps Δt together with the corresponding analytical values from Eason [12]. The case of the single concentrated load P is realized by assigning the values of $P_D = P = 16+16+16+32 = 80$ kN and $P_A = P_B = P_C = 0$ in the general four wheel vehicle case of Fig.5. Table 1 also shows the relative per cent error of the present numerical approximation as compared to the 'exact' analytic values of Eason [12]. It is observed that convergence of the numerical results is obtained for $\Delta t = 0.3*10^{-3}$sec for all cases of boundary conditions. However, only the error of the case of absorbing boundaries (about 2-3%) is considered acceptable for displacements, because naturally one expects the error to be higher for stresses and strains but no more than 10%, which is usually the limit for design purposes.

	Δt (secs)	Rollers at bottom	Rollers everywhere	Absorbing boundaries
Eason [12] u_z= $0.81608*10^{-3}$m	$0.6*10^{-3}$	u_z= $0.85186*10^{-3}$m e=4.38%	u_z= $0.826032*10^{-3}$m e=1.22%	u_z= $0.816635*10^{-3}$m e=0.08%
	$0.3*10^{-3}$	u_z= $0.878057*10^{-3}$m e=7.59%	u_z= $0.85980*10^{-3}$m e=5.36%	u_z= $0.836078*10^{-3}$m e=2.45%
	$0.15*10^{-3}$	u_z= $0.879081*10^{-3}$m e=7.72%	u_z= $0.857455*10^{-3}$m e=5.07%	u_z= $0.843428*10^{-3}$m e=3.35%

Table 1: Maximum vertical displacement u_z at depth z=-1.0m below Q due to a vertical point load P=80kN moving with a speed V=20m/s on the surface of half-space for three types of boundary conditions and three values of Δt.

Consider now the case of a moving distributed load on the surface of the half-space. The area in the full domain on which the load P=80 kN acts, on the basis of the adopted discretization as well as Huang [1], is A=0.45*0.30 m^2 yielding a pressure p=0.5926 MPa. Table 2 provides the maximum values of the vertical displacement u_z at a depth z=-1.0 m below Q due to the above pressure p moving at a speed V=20 m/s on the surface of the half-space for three types of boundary conditions and three values of Δt. Approximate analytical results from Eason [12] are also given in Table 2. It is seen from that table that convergence of the numerical results with acceptable error (about 2%) is obtained for $\Delta t=0.3*10^{-3}$secs for either the 'rollers everywhere' or the absorbing boundaries. It is also observed from Table 2 that the response to the distributed load is less than that to the point load, as expected.

Another comparison study on the basis of the elastic half-space model involved the maximum values of the displacement u_z as computed by using a single total load P = 80 kN and a series of four concentrated loads $P_A = P_B = P_C = 16$ kN and $P_D = 32$ kN, as shown in Fig.5. It was found that for the case of V = 20 m/s and Δt = 0.0003 secs, the maximum displacement u_z, as obtained for the case of the series of moving loads, is $0.352775*10^{-3}$ m, i.e., smaller than the corresponding one $0.836078*10^{-3}$ m for the case of the single moving load, as expected.

	Δt (secs)	Rollers at bottom	Rollers everywhere	Absorbing boundaries
Modified Eason[12] u_z= $0.800765*10^{-3}$m	$0.6*10^{-3}$	u_z= $0.785836*10^{-3}$m e=-1.86%	u_z= $0.752302*10^{-3}$m e=-6.05%	u_z= $0.748779*10^{-3}$m e=-6.49%
	$0.3*10^{-3}$	u_z= $0.819808*10^{-3}$m e=1.90%	u_z= $0.785013*10^{-3}$m e=-1.96%	u_z= $0.780815*10^{-3}$m e=-2.49%
	$0.15*10^{-3}$	u_z= $0.820634*10^{-3}$m e=2.48%	u_z= $0.786049*10^{-3}$m e=-1.84%	u_z= $0.782750*10^{-3}$m e=-2.25%

Table 2: Maximum vertical displacement u_z at depth z=-1.0 m below Q due to a vertical distributed load p=0.5926 MPa moving at speed V=20 m/s on surface of half-space for three types of boundary conditions and three values of Δt.

Since in pavement design, static analytic solutions for the uniform or the layered half space under distributed load are widely used [1], a comparison between analytical due to Boussinesq [13] and numerical results obtained here for the half-space under static distributed load is shown in Table 3. It is observed in that table that the error for the displacement is almost the same with that of the dynamic case (Table 2), while the error for stresses is higher, as expected. Furthermore, it is observed that for the numerical results $\sigma_x \neq \sigma_y$, as expected because of lack of axisymmetry in the numerical model.

	Analytic	Numerical	error%
u_z	$-0.781237*10^{-3}$m	$-0.762646*10^{-3}$m	-2.38
σ_z	$-36.2610*10^{-3}$MPa	$-34.9024*10^{-3}$MPa	-3.75
σ_x	$2.70265*10^{-3}$MPa	$2.60308*10^{-3}$MPa	-3.68
σ_y	$2.70265*10^{-3}$MPa	$2.79802*10^{-3}$MPa	-3.53

Table 3: Vertical deflection and stresses at z=-1.00 m below Q due to a vertical distributed static load p=0.5926 MPa acting on the surface of the uniform half-space.

5.2 Layered half-space elastic medium under moving loads

Consider the layered half-space model of Fig.1 with elastic material properties as described in section 2 under the moving with speed V=20 m/s distributed load p=0.5926 MPa. Using absorbing boundary conditions and $\Delta t=0.3*10^{-3}$ secs, Table 4 provides maximum vertical displacements, stresses and strains for the above pavement structure at z=-0.15m and -0.45m, usually needed for design purposes. The vertical deflection u_z at the surface of the top layer was found to be $-0.89667*10^{-3}$ m.

z(m)	u_z(m)	σ_z (MPa)	σ_x (MPa)	σ_y (MPa)	ε_z ($*10^{-3}$)	ε_x ($*10^{-3}$)	ε_y ($*10^{-3}$)
-0.15	$-0.849042*10^{-3}$	-0.692631	-0.244614	-0.207232	-0.551984	0.109700	0.211367
-0.45	$-0.668003*10^{-3}$	-0.111987	0.106403	0.108179	-0.465643	0.268868	0.278996

Table 4: Maximum vertical displacements, stresses and strains in elastic layered pavement structure under a moving distributed load with V=20 m/s.

Consider now the previous pavement structure under the same load, which is applied statically. Table 5 provides values for the same response quantities as Table 4 but for the static case. Values in parentheses indicate approximate analytical values obtained by the method of Odemark [14]. The static vertical deflection u_z at the surface of the pavement was found to be $-0.85730*10^{-3}$m numerically and $-0.91830*10^{-3}$m analytically. It is observed from Table 5 that while the numerical results for displacements are rather close to the approximate analytical ones, this is not always the case for stresses and strains. Finally, a comparison between the dynamic results of Table 4 and the static ones of Table 5 reveals that the former are always larger than the latter ones for displacements and in almost all the cases for stresses and strains.

z(m)	u_z(m)	σ_z (MPa)	σ_x (MPa)	σ_y (MPa)	ε_z ($*10^{-3}$)	ε_x ($*10^{-3}$)	ε_y ($*10^{-3}$)
-0.15	-0.813351 $*10^{-3}$ (-0.86250 $*10^{-3}$)	-0.4464 (-0.3890)	-0.09653 (-0.04512)	-0.06617 (-0.04512)	-0.4895 (-0.88217)	-0.0592 (0.26272)	0.1180 (0.26272)
-0.45	-0.632773 $*10^{-3}$ (-0.69230 $*10^{-3}$)	-0.08217 (-0.0742)	0.05167 (0.00092)	0.05439 (0.00092)	-0.46299 (0.93669)	0.26063 (-0.37789)	0.276045 (-0.37789)

Table 5: Displacements, stresses and strains in elastic layered pavement structure under static distributed load (approximate analytic values are in parentheses).

6 CONCLUSIONS

- An effort has been made to construct in the framework of the ANSYS computer program a general 3-D model for the simulation in the time domain of the dynamic response of a flexible road pavement to the motion of a vehicle under linear elastic material behavior.

- This modeling required the construction of a special moving loads program, which makes possible the loading of the road pavement structure as the vehicle moves at a constant speed and is connected with the main ANSYS program as well as special viscous absorbing boundaries at the vertical faces and bottom face of the domain to avoid wave reflections at its boundaries and special springs at its bottom face to simulate the supporting soil.

- The above model was used to study the dynamic and static responses of the pavement to moving or stationary loads for the cases of the homogeneous half-space and the layered half-space and compare them against those from analytical methods.

- Comparison and convergence studies led to the optimum domain model and its discretization and an approximate time step for obtaining solutions of acceptable accuracy at a reasonable computational cost.

- It was found that dynamic response is always higher than the corresponding static one and that increasing values of vehicle speed increase the pavement response. Furthermore, it was also found that a series of moving loads or a distributed moving load result in a lower response than a single moving load of intensity equal to the sum of intensities of the series of loads or to the resultant force of the distributed load.

- More work is required in order to complete this study that includes the effect of viscous damping on the response and consideration of linear viscoelastic material behavior for the top (asphalt) layer as well as comparisons with experimental results.

ACKNOWLEDGEMENT

The first author (Niki D.Beskou) acknowledges with thanks the support provided to her by the 'IKY fellowships of excellence for postgraduate studies in Greece-Siemens program'.

REFERENCES

[1] Y.H. Huang, *Pavement analysis and design*, Pearson Prentice-Hall, Upper Saddle River, N.Jersey, U.S.A., 2004.

[2] N.D. Beskou and D.D. Theodorakopoulos, Dynamic effects of moving loads on road pavements: A review, *Soil Dynamics and Earthquake Engineering*, **31**, 547-567, 2011.

[3] Y.H. Cho, B.F. McCulough, J. Weissmann, Considarations on finite element method application in pavement structural analysis, *Transportation Research Record*, **1539**, 96-101, 1996.

[4] H. Grundmann, M. Lieb, E. Trommer, The response of a layered half-space to traffic loads moving along its surface, *Archive of Applied Mechanics*, **69**, 55-67, 1999.

[5] S.H. Ju, Finite element investigation of traffic induced vibrations, *Journal of Sound and Vibration*, **321**, 837-853, 2009.

[6] S. Hirose, Boundary element modeling and analysis of moving loads in time and frequency domain, N.Chouw, G.Schmid eds., *Wave 2000*, A.A.Balkema, Rotterdam, 2000, 71-82.

[7] Y.B. Yang, H.H. Hung, A 2.5D finite/infinite element approach for modeling visco-elastic bodies subjected to moving loads, *International Journal for Numerical Methods in Engineering*, **51**, 1317-1336, 2001.

[8] J.H. Lee, J.K. Kim, J.L. Tassoulas, Dynamic analysis of a layered half-space subjected to moving line loads, *Soil Dynamics and Earthquake Engineering*, **47**, 16-31, 2013.

[9] ANSYS, ANSYS LS-DYNA User's Guide, Release 13, ANSYS Inc. Southpointe, Canonsburg, PA, USA, 2010.

[10] G.D. Hatzigeorgiou, D.E. Beskos, Soil-structure interaction effects on seismic inelastic analysis of 3-D tunnels, *Soil Dynamics and Earthquake Engineering*, **30**, 851-861, 2010.

[11] J.S. Mulliken, D.L. Karabalis, Discrete model for dynamic through-the-soil coupling of 3-D foundations and structures, *Earthquake Engineering and Structural Dynamics*, **27**, 687-710, 1998.

[12] G. Eason, The stresses produced in a semi-infinite solid by a moving surface force, *International Journal of Engineering Science*, **2**, 581-609, 1965.

[13] J.V. Boussinesq, *Applications des Potentiels a L'Etude de l'Equilibre et du Movement des Solides Elastiques*, Gauthier Villars, Paris, 1885.

[14] N. Odemark, *Investigations as to the elastic properties of soils and design of pavements according to the theory of elasticity,* Meddelanden 77 fran Statens Vaginstitut, Stockholm, Sweden, 1949.

[15] J. Lysmer, R.L. Kuhlemeyer, Finite dynamic model for infinite media, *Journal of the Engineering Mechanics Division of ASCE,* **95(4)**, 859-877, 1969.

[16] K.J. Bathe, *Finite element procedures*, Prentice Hall, Englewood Cliffs, New Jersey, USA, 1996.

COMPDYN 2015
5th ECCOMAS Thematic Conference on
Computational Methods in Structural Dynamics and Earthquake Engineering
M. Papadrakakis, V. Papadopoulos, V. Plevris (eds.)
Crete Island, Greece, 25–27 May 2015

NUMERICAL ANALYSIS OF THE PLANE WAVES SCATTERING BY SEMI-SPHERICAL ALLUVIAL VALLEY

S L.Chen[1], X J. Zhu[2]

[1] Department of Civil Engineering, Nanjing University of Aeronautics and Astronautics
Nanjing, 210016, China
e-mail: iemcsl@nuaa.edu.cn

[2] Department of Civil Engineering, Nanjing University of Aeronautics and Astronautics
Nanjing, 210016, China
zhuxj@nuaa.edu.cn

Keywords: Wave Scattering, Transfer Matrix Method, Transmitting Boundary Condition, Finite Element Method, Semi-Spherical Alluvial Valley.

Abstract. *One of the major concerns of engineering seismology is to understand and explain vibration properties of the soil excited by near earthquakes. Alluvial deposits, often very irregular geometrically, may affect significantly the amplitudes of incident seismic waves. A numerical method is presented for scattering and diffraction of plane waves(SH,P and SV) of arbitrary angle of incidence from three-dimensional complicated topography in this study. The wave input is realized through the free field wave motion obtained by Thomson-Haskell transfer matrix method. The wave motions are calculated by the method of lumped-mass explicit finite element and local transmitting artificial boundary condition. The method is applied to the analytically solved case of semi-spherical alluvial valley on homogenous elastic half space to verify its accuracy.*

1 INTRODUCTION

Topographical and geological irregularities can induce large amplifications and variations in ground motion during earthquakes. The focusing and scattering of the energy carried by seismic waves seem to be the causes of such effects. Large differences of motion between nearby places may be significant in the response of important facilities, like bridges, dams, and life-line systems. Many authors have studied the problem of two-dimensional irregularities for various incident wave fields[3,6-10].Three-dimensional problems have received less attension duo to the increased difficulties which arise in solving this class of problems[1-2,4-5,12-13]. The response of a 3D topography, either a mountain or a canyon, is very sensitive to the azimuth, angle and type of incident wave. To study the half-space problem using the domain discretization technique, such as finite element method and finite difference method, we should introduce a fictitious boundary to make the computation region finite and impose a condition on this boundary to account for the effect of the unbounded medium. The difficulty of wave scattering and diffraction problem solved using numerical method is to deal with the input and the artificial boundary condition. In this paper, a numerical method is presented to solve wave scattering and diffraction problem conveniently.

2 METHOD OF ANALYSIS

The three-dimensional model to be analyzed is shown in Fig.1. It consists of a semi-spherical valley of radius r. The soil is assumed to be elastic, isotropic and homogeneous, and the contact between the valley and the half-space is assumed to be welded. The material properties are given by mass density ρ ,the velocity of the shear waves β and Poisson ratio ν. The subscript R designates these constant in the valley and E in half space. We assume that the half-space is subjected to the incident plane wave traveling upward and to the right along a ray which makes an angle θ with the z axis . The solution of this problem has been obtained by F.J.Sanchez-Sesma(1983,1989).

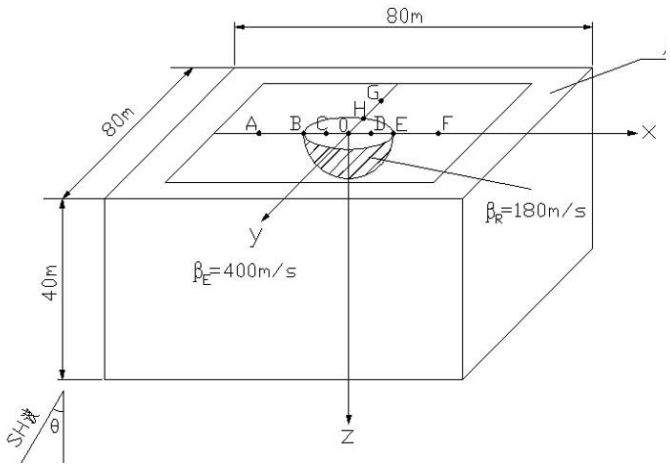


Figure.1 semi-spherical valley and the surrounding half-space

2.1 Input of the Scattering Problem

The incident waves come from the domain exterior to the computation region. Far from the valley the incident waves are reflected from the free surface and incident and reflected waves interfere to give the resulting free-field motion u_f. Close to the valley, the total motion u

comprises of the free-field motion u_f and the waves u_s, reflected and diffracted by the material discontinuity. That is

$$u = u_f + u_s \tag{1}$$

For the interior node, the total displacement can be obtained through finite element method. For the artificial boundary node, the diffraction displacements u_s can be calculated through artificial boundary condition and the total displacements can be obtained by superposition of $(u_s + u_f)$. The free-field motion can be obtained through Thomson-Haskell transfer matrix method[11]. The governing equations of the interior nodes and the boundary nodes may be formulated as follows.

2.2 Governing Equations of the Interior Nodes

The governing equations of the interior nodes may be set up using the standard finite element technique. What should be noted is that the lumped-mass formulation is suggested for the spatial discretization in this study. This is because not only the lumped-mass formulation is much more practical than the consistent-mass for large-scale computations, but also it is the simplest manner to reflect the local feature of wave motion. The governing equations of the interior nodes are written in the following form (Z.P.Liao,2002)

$$m_i \ddot{\boldsymbol{u}}_i + \boldsymbol{F}_i - \boldsymbol{P}_i = 0 \tag{2}$$

where,

$$\left.\begin{aligned} m_i &= \sum_{e}\sum_{j} M_{ij}^{e} \\ M_{ij}^{e} &= \int_{V_e} N_i \rho N_j \mathrm{d}V_e \end{aligned}\right\} \qquad \left.\begin{aligned} \boldsymbol{F}_i &= \sum_{e} \boldsymbol{f}_i^{e} \\ \boldsymbol{f}_i^{e} &= \int_{V_e} (\mathbf{L}\mathbf{N}_i)^T \boldsymbol{\tau} dV_e \end{aligned}\right\} \tag{3}$$

$$\boldsymbol{P}_i = \sum_{e}\left[\int_{V_e} N_i \boldsymbol{g} dV_e + \int_{S_e} N_i \boldsymbol{\tau}_b dS_e\right] \tag{4}$$

$$L = \begin{bmatrix} \partial/\partial_{x_1} & 0 & 0 \\ 0 & \partial/\partial_{x_2} & 0 \\ 0 & 0 & \partial/\partial x_3 \\ \partial/\partial_{x_2} & \partial/\partial_{x_1} & 0 \\ 0 & \partial/\partial_{x_3} & \partial/\partial_{x_3} \\ \partial/\partial_{x_3} & 0 & \partial/\partial_{x_1} \end{bmatrix} \tag{5}$$

m_i is the lumped mass on node i. $\boldsymbol{N}_i$ is shape function matrix for node i. $\boldsymbol{F}_i$ is the constitutive force vector exerted on node i. $\boldsymbol{P}_i$ is a given external force vector exerted on node i, $\boldsymbol{g}$ is the body force,

$\boldsymbol{\tau}_b$ is the stress vector prescribed on boundary.

Assuming the linear viscoelastic constitutive relationship and using central difference integral scheme, Eqn.(2) can be re-written as

$$\boldsymbol{u}_i^{p+1} = 2\boldsymbol{u}_i^p - \boldsymbol{u}_i^{p-1} - \frac{\Delta t^2}{m_i}\left[\sum_e \sum_k K_{l(i)k}^e \boldsymbol{u}_{j(k)}^p + \sum_e \sum_j C_{l(i)k}^e (\boldsymbol{u}_{j(k)}^p - \boldsymbol{u}_{j(k)}^{p-1}) + \boldsymbol{P}_i^p\right] \tag{6}$$

where, $u_i^p = u(p\Delta t, i\Delta x)$, Δt is time step and Δx is spatial step. $K_{l(i)k}^e$ and $C_{l(i)k}^e$ are the element stiffness matrix and element damping matrix, respectively. The subscript $l(i)$ means that the global node index i corresponds to the element local node index l .The subscript $j(k)$ in $\boldsymbol{u}_{j(k)}^p$ means that the global node index j corresponds to the element local node index k . The $\sum_e$ means summation of all elements which includes the global node index i .

2.3 Governing Equations of the Boundary Nodes

The local ABC called as Muti-Transmitting Formula (MTF) is adopted here, which is written as (Z.P.Liao,1996)

$$\overline{u}_{s,0}^{p+1} = \sum_{j=1}^{N} (-1)^{j+1} C_j^N \overline{u}_{s,j}^{p+1-j} \tag{7}$$

where， C_j^N are binomial coefficients.

$$C_j^N = \frac{N!}{(N-j)!\ j!} \tag{8}$$

$$\overline{u}_{s,j}^p = u_s\left(p\Delta t, -jc_a\Delta t\right) \tag{9}$$

N is the approximation order of MTF, c_a is artificial speed. The coordinates $x = -jc_a\Delta t$ indicate the sampling points on the x-axis, which is perpendicular to the artificial boundary at a boundary point under consideration. Since the point $x = -jc_a\Delta t$ do not generally coincide with the discrete nodes $x = -n\Delta x$, in order to implement Eqn.(7), an interpolation scheme is required to express $u_s(t, -jc_a\Delta t)$ in terms of $u_s(t, -n\Delta x)$. After a quadratic interpolation, the second-order ($N = 2$) MTF can be expressed as

$$u_{s,0}^{p+1} = 2\overline{u}_{s,1}^p - \overline{u}_{s,2}^{p-1} = 2\times\sum_{k=1}^{3} t_{1,k} u_{s,k-1}^p - \sum_{k=1}^{5} t_{2,k} u_{s,k-1}^{p-1} \tag{10}$$

$$t_{1,1} = (2-S)(1-S)/2, t_{1,2} = S(2-S), t_{1,3} = S(S-1)/2 \tag{11}$$

$$\left.\begin{aligned} &t_{2,1} = t_{1,1}^2, t_{2,2} = 2t_{1,1}t_{1,2}, t_{2,3} = 2t_{1,1}t_{1,3} + t_{1,2}^2 \\ &t_{2,4} = 2t_{1,2}t_{1,3}, t_{2,5} = t_{1,3}^2 \end{aligned}\right\} \tag{12}$$

where, $S = c_a \Delta t / \Delta x$, $u_{s,j}^{p} = u_s\left(p\Delta t, -j\Delta x\right)$.

Assuming that the responses of the system are known before time $(p+1)\Delta t$, the responses at time $(p+1)\Delta t$ can be calculated as follows

(1) Calculate the free-field displacements using the transfer matrix method[11], and the diffraction displacements at time $p\Delta t$ and $(p-1)\Delta t$ can be obtained through Eqn.(1).

(2) The displacements of interior node at time $(p+1)\Delta t$ can be calculated using Eqn.(6)

(3) Calculate the diffraction displacements of artificial boundary points at time $(p+1)\Delta t$ using Eqn.(10), and the total displacements of artificial boundary points can be obtained by Eqn.(1).

(4) Repeating the steps above, the response of the system can be obtained at successive time.

3 NUMERICAL EXAMPLES

The dimension of the calculation region is $80\times80\times40m^3$ and $r=10m$, as shown in Fig.1. The material properties of the valley are: shear wave velocity $\beta_R = 180m/s$,mass density $\rho_R = 3000kg/m^3$,modulus of elasticity $E_R = 1.248\times10^9 Pa$,Poisson ratio $v_R = 0.3$ and damping ratio $\xi_R = 0.02$. The material properties of the half space are: $\beta_E = 400m/s$, $\rho_E = 3000kg/m^3$, $E_E = 1.248\times10^9 Pa$, $v_E = 0.25$, $\xi_E = 0.02$. Eight-node hexahedron elements are employed and the dimension of the element is about $1m\times1m\times1m$. The time step is 0.0005s, and the total time steps is 8192.

The incident wave is shown in Fig.2, which is impulse displacement, and the corresponding spectrum is shown in Fig.3. The incident angle θ is selected as 0^o, 30^o, 60^o and 90^o, respectively.

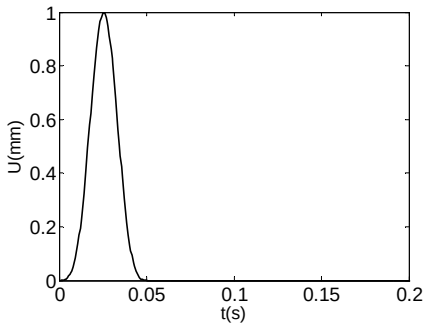


Figure 2. Incident wave

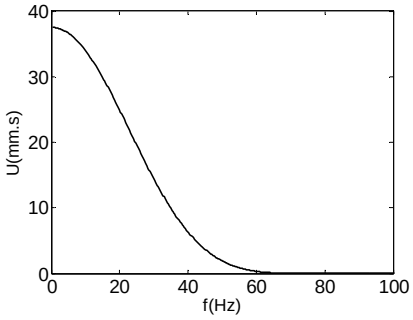
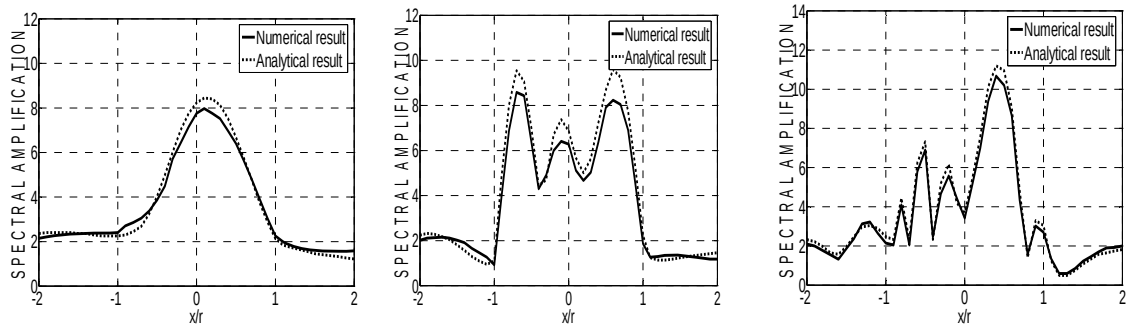


Figure 3. The spectrum of incident wave

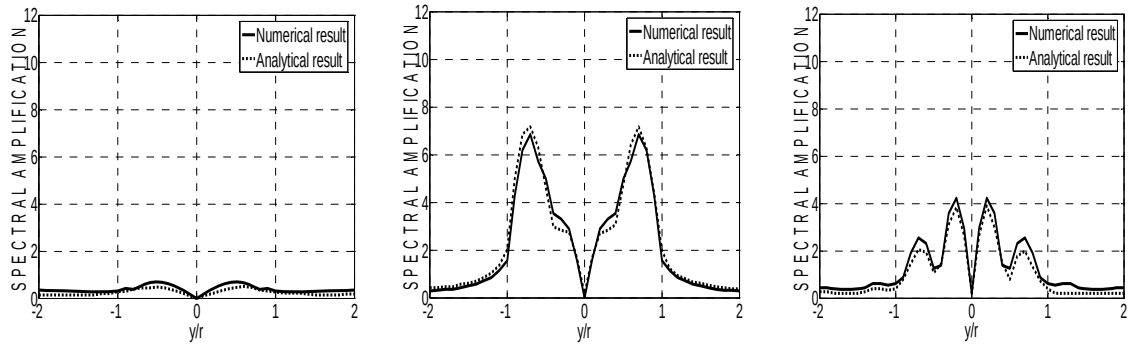
3.1 SH wave case

For SH incident wave, this problem was studied by F.J.Sanchez-Sesma(1983,1989). The results are demonstrated as spectral amplification $\left|\frac{U(\omega)}{U_I(\omega)}\right|$ versus dimensionless frequency $\eta = \frac{\omega r}{\pi\beta_E} = \frac{2\pi fr}{\pi\beta_E} = \frac{2r}{\lambda}$, λ is the wavelength. For incident angle 30^o, the displacement spectral amplification along x and y axis, are given in Fig.4-Fig.7.



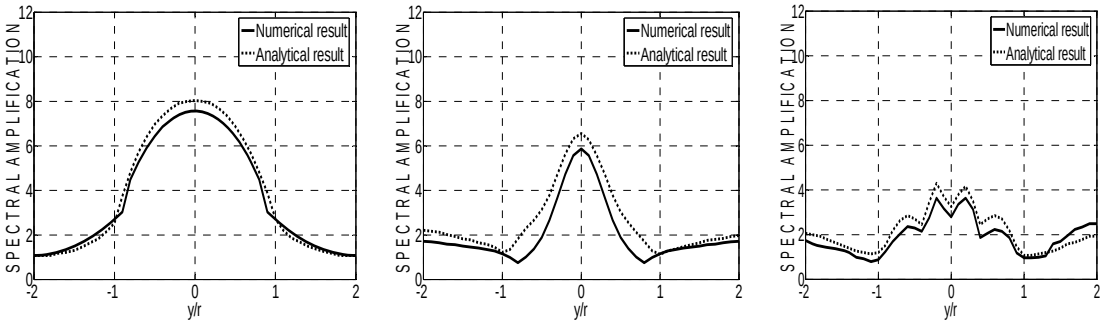
（a） $\eta = 0.5$ （b） $\eta = 1.0$ (c) $\eta = 2.0$

Figure 4 surface spectral amplification of horizontal y-component displacement



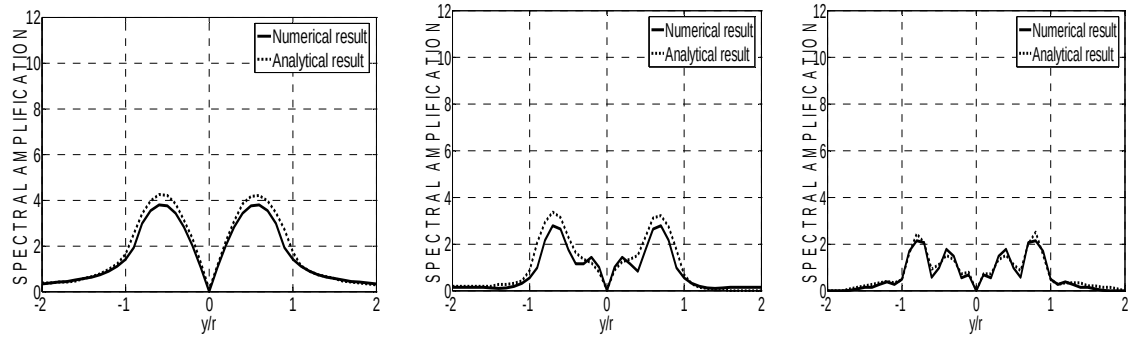
（a） $\eta = 0.5$ （b） $\eta = 1.0$ (c) $\eta = 2.0$

Figure 5 surface spectral amplification of horizontal x-component displacement



（a） $\eta = 0.5$ （b） $\eta = 1.0$ (c) $\eta = 2.0$

Figure 6 surface spectral amplification of horizontal y-component displacement



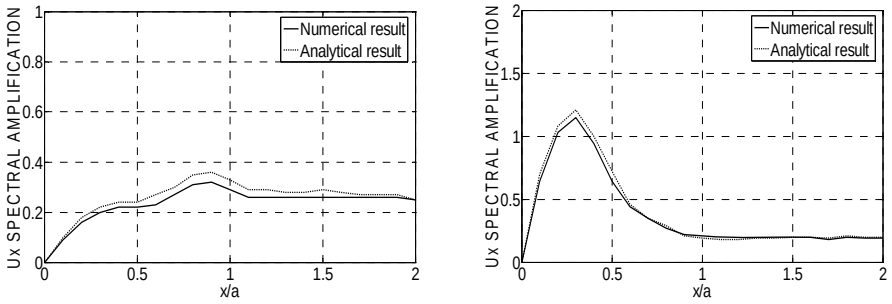
（a） $\eta = 0.5$ （b） $\eta = 1.0$ (c) $\eta = 2.0$

Figure 7 surface spectral amplification of vertical z-component displacement

Fig.4-Fig.7 compares the amplifications obtained by the presented method along the valley with those obtained by J.Sanchez-Sesma(1983,1989), the solid line denotes the numerical results from the proposed method in this study, and the dash line represents the analytical results obtained by J.Sanchez-Sesma(1983,1989). The agreement is very good for both horizontal and vertical component, which tests the accuracy and efficiency of the proposed method.

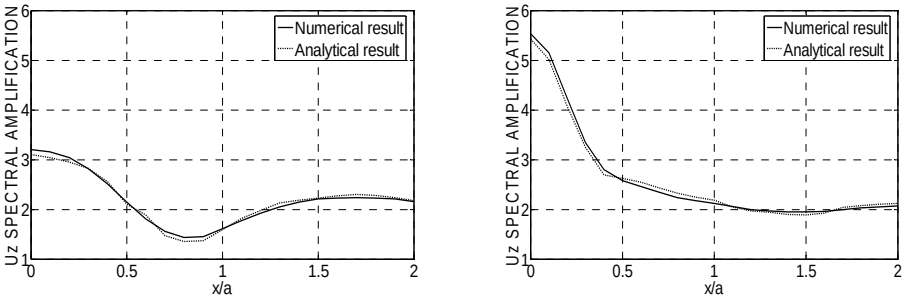
3.2 P wave case

For comparison with the solution obtained by F.J.Sanchez-Sesma(1983,1989) for incident angle 0^o, the displacement spectral amplification are given in Fig.8-Fig.9. The agreement is also very good for both horizontal and vertical component, which further tests the accuracy and efficiency of the proposed method.



（a） $\eta = 0.5$ （b） $\eta = 1.0$

Figure 8 surface spectral amplification of horizontal x-component displacement



（a） $\eta = 0.5$ （b） $\eta = 1.0$

Figure 9 surface spectral amplification of vertical z-component displacement

4 CONCLUSIONS

A numerical method has been applied to solve the scattering and diffraction of elastic waves by three-dimensional surface irregularities. The method consists of lumped-mass explicit FEM, Multi-transmitting boundary condition and Thomson-Haskell transfer matrix method. The scattering and diffraction of Plane SH and P waves by a semi-spherical valley are analyzed, and the accuracy of this method is validated through comparison with the results of F.J.Sanchez-Sesma(1983,1989). For the fixed geometrical and physical properties of the valley and its surrounding medium, the degree of complexity of the spectral amplification

pattern increase with the increase of frequency of the incident waves. The method in this study can be used to arbitrarily irregular topography.

ACKNOWLEDGEMENT

The authors gratefully acknowledge the financial support of this work by the National Natural Science Foundation of China (No.50978135, No.51178222)

REFERENCES

[1] Abdollah Sohrabi-Bidar, Mohsen Kamalian, Effects of three-dimensionality on seismic response of Gaussian-shaped hills for simple incident pulses, *Soil Dynamics and Earthquake Engineering.* **52**,1-12,2013.

[2] E.Reinoso, L.C.Wrobel, Three-dimensional scattering of seismic waves from topographical structures. *Soil Dynamics and Earthquake Engineering.*,**16**,41-61, 1997.

[3] F.J.Sanchez-Sesma, E.Rosenblueth, Ground motion at canyons of arbitrary shape under incident SH waves, *Int.J.Earthquake Eng.Struct.Dyn.*.**7,**441-450,1979.

[4] F.J.Sanchez-Sesma, Diffraction of elastic waves by three-dimensional surface irregularities. *Bull.Seism.Soc.Am.***73,**1621-1636,1983.

[5] F.J.Sanchez-Sesma, Diffraction of elastic waves by three-dimensional surface irregularities Part II. *Bull.Seism.Soc.Am.***79,**101-112,1989.

[6] H.L.Wong, M.D.Trifunac, Scattering of plane SH waves by a semi-elliptical canyon. *Earthquake engineering and structural dynamics,* **3,**157-169,1974.

[7] H.L.Wong, M.D.Trifunac, Surface motion of a semi-elliptical alluvial valley for incident plane SH-waves. *Bull.Seism.Soc.Am.,* **64,**1389-1408,1974.

[8] H.L.Wong, P.C.Jennigs, Effect of canyon topographies or strong ground motion. *Bull.Seism.Soc.Am.***65,**1239-1257,1975

[9] M.D.Trifunc, Surface motion of a semi-cylindrical alluvial valley for incident plane SH-waves. *Bull.Seism.Soc.Am.* **61,**1755-1770,1971.

[10] M.D.Trifunc, Scattering of plane SH waves by a semi-cylindrical canyon. *Earthquake engineering and structural dynamics,* **1**,267-281,1973.

[11] N.Haskell, The dispersion of surface waves in multilayered media, *Bull.Seism.Soc.Am.***43,**17-34,1953.

[12] V.W.Lee, Three-dimensional diffraction of plane P,SV&SH waves by a hemispherical alluvial valley, *Soil Dynamics and Earthquake Engineering.* **3**,133-144,1984.

[13] V.W.Lee， G.Y.Zhu, A note on three-dimensional scattering and diffraction by a hemispherical canyon:Vertically incident plane P-wave. *Soil Dynamics and Earthquake Engineering.* **61**,197-211,2014.

[14] Z.P.Liao, *Introduction to wave motion theories in engineering, 2nd Edition*. Science Press, Beijin, 2002.

[15] Z.P.Liao, Extrapolation non-reflecting boundary conditions,*Wave motion,***24,**117-138,1996.

COMPDYN 2015
5th ECCOMAS Thematic Conference on
Computational Methods in Structural Dynamics and Earthquake Engineering
M. Papadrakakis, V. Papadopoulos, V. Plevris (eds.)
Crete Island, Greece, 25–27 May 2015

PLANE WAVE AT THE INTERFACE BETWEEN WATER AND A GASSY POROELASTIC LAYER WITH UNDERLYING ELASTIC SEABED

Weiyun Chen[1], **Guoxing Chen**[1]

[1] Institute of Geotechnical Engineering, Nanjing Tech University, Nanjing 210009, China;

e-mail: vic_chen@126.com

Keywords: Plane wave, Reflection coefficient, Gassy marine sediments, Ocean floor;

Abstract. *Based on the multiphase poroelasticity theory, the reflection characteristics of an obliquely incident plane wave upon a plane interface between overlying water and a gassy marine sediment layer with underlying elastic solid seabed are investigated. The sandwiched gassy layer is modeled as a porous material with finite thickness, which is saturated by two compressible and viscous fluids (liquid and gas). The closed-form expression for the amplitude ratio of the reflected wave, i.e., reflection coefficient, is derived according to the boundary conditions at the upper and lower interfaces in the proposed model. Using numerical calculation, the influences of incident angle, wave frequency, layer thickness and liquid saturation of sandwiched porous layer on the reflection coefficient are analyzed, respectively. It is revealed that the reflection coefficient is closely associated with incident angle and sandwiched layer thickness. Moreover, in different frequency ranges, the dependence of the wave reflection characteristics on moisture (or gas) variations in the intermediate marine sediment layer is distinguishing.*

1 INTRODUCTION

Wave reflection coefficient is an important parameter representing the quantitative characterization of the geoacoustic properties of the seabed sediment and its subbottom structure. During the past several decades, the subject of plane reflection from the ocean floor is important in the applications such as geophysics, seismology, underwater acoustics, petroleum engineering, and hydrogeology [1-6]. The fundamental theory of the elastic plane wave propagation in fluid-saturated porous media was initially introduced by Biot who predicted the existence of three types of bulk waves propagating in the fluid-filled porous material: P1 wave, P2 wave and S wave [7]. The P2 wave was observed firstly in sintered glass beads [8] and then in natural air-filled sand-stone [9]. Based on Biot theory and its extension to unsaturated media, the transmission and reflection of bulk waves at the boundary between water and fluid-saturated porous sediment were discussed [2,10,11,12] Stoll & Kan investigated the reflection and transmission of seismic waves at interface between water and a material which is believed to be a realistic model of marine sediment [2]. Albert compared two different interfaces, the air/air-filled porous medium and the water/water-saturated porous medium [13]. Denneman et al. studied the wave properties at a fluid/porous-medium interface through simple closed-form expressions for the reflection and transmission coefficients [14]. From the Biot - Gassmann theory for fluid-saturated porous rocks, Russell et al. first derived a general formula for fluid-property discrimination and combined it with an AVO inversion to show its geophysical applications in the extraction of information about the fluid properties of the reservoir. Considering volume scattering, Ohkawa et al. studied the reflection and transmission coefficients at the surface of sandy seabed [16] and then Ohkawa [12] confirmed the efficiency of Biot theory to describe wave problems in water-saturated granular marine sediment. Dai & Kuang obtained the reflection and transmission coefficients at the interface between water and double porosity solid half-space [17].

In these aforementioned studies, the seabed model was regarded as a isotropic and homogeneous porous half-space. More often, though, ocean floor is covered by the marine sediment layer with finite thickness, which can be considered as multi-phase porous medium consisting of solid skeleton and two compressible and viscous fluids (i.e., liquid and gas). Thus some other researches were also carried out by modeling the ocean floor as layered sediments with an underlying substrate. Kuo used an plane wave scattering model for three homogeneous layers consisting of a thin solid sediment layer sandwiched by semi-infinite water and solid basalt media [18]. Ainslie derived the simple expressions of wave reflection and transmission coefficients for a layered fluid sediment layer sandwiched between a uniform fluid above and a uniform solid substrate below[19]. Wang et al. [20] and Lyu et al. [21] investigated plane wave propagation at the interface between water and porous sediment with an underlying solid substrate and double porosity substrate, respectively.

However, it has been extensively accepted that some natural sedimentary materials are not fully saturated by liquid. The above-mentioned literatures modeling the ocean floor as layered seabed sediments with an underlying half-space seldom took the moisture (or gas) variations of marine sediment layer into account. The model of Boyle & Chotiros [22] found that very small amounts of gas were sufficient to dominate other wave scattering mechanisms from the ocean floor. In fact, Biot theory did not involve the case when two different immiscible phase fluids coexist in the interstice of porous sedment. Due to the appearance of gas phase, besides two longitudinal waves (P1 wave and P2 wave) and one transverse wave (S wave) in Biot theory, which appear in the fully liquid-saturated porous medium, an additional longitudinal wave (P3 wave) emerges [23-27]. Based on the three-phase porous theory, reflection and

transmission phenomenon of incident waves at the plane surface of semi-infinite porous material were discussed [28,29].

Until now, to the best of our knowledge, no investigation have been launched to study the reflection and transmission of plane waves at the plane interface between water and ocean floor comprising an upper gassy poroelastic layer and underlying elastic seabed. The purpose of the present paper is to discuss this issue. This problem is meaningful and essential for exploring oil, gas, or water contained in the fissured rocks of the ocean floor. Our procedure is formulated within the framework of the continuum theory of mixtures. The closed-form expressions for the amplitude ratios of reflected and transmitted plane waves are derived based on the linear viscoporoelastic model [27, 29]. In a systematic manner, these coefficients are then used to analyze the influences of incident angle, wave frequency, layer thickness and liquid saturation of sandwiched porous layer on the wave reflection characteristics upon the gassy poroelastic layer, respectively.

2 BASIC WAVE THEORY

The following analytical process is carried out basing on the standard elastic wave analysis. Fig. 1 shows the coordinate system for the problem of plane wave incidence, reflection and transmission. This system comprises the overlying water, the poroeastic sediment layer containing free gas, and the underlying solid seabed. The overlying water is assumed as ideal compressible fluid. The sandwiched sediment layer is modeled as linear three-phase porous medium with finite thickness H. The underlying substrate is considered as linear elastic solid half-space. Here, z axis is directed vertically upwards and the x axis is assumed along horizontal direction as shown in Fig. 1. $z = 0$ and $z = -H$ represent two plane interfaces separating the overlying water, the gassy poroelastic layer and the underlying solid half-space, respectively. The interface along $z = -H$ is in perfect contact in such a way that the fluid cannot flow from porous medium to the solid substrates.

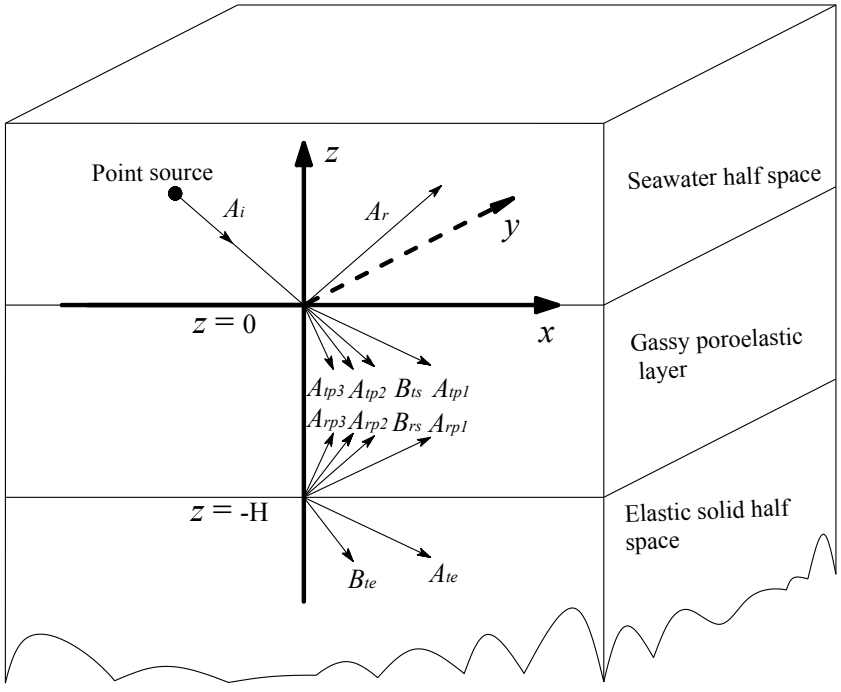


Figure 1. Coordinate system for the incident, reflected and transmitted waves

2.1. Sandwiched gassy poroelastic layer

In this paper, the sandwiched gassy poroelastic medium is considered as a mixture consisting of a deformable solid frame, a liquid phase and a gas phase, designated by the superscripts "*S*", "*L*", and "*G*", respectively. The character α is used to denote an individual phase, i.e., $\alpha = S, L, G$. In the framework of the multiphase continuum theory [23, 25, 30], the motion equations for the gassy poroelastic medium, which can degenerate to the form of Biot model in fully liquid-saturated state, are given [27,29]:

$$\begin{pmatrix} n_S\rho_S & 0 & 0 \\ 0 & n_L\rho_L & 0 \\ 0 & 0 & n_G\rho_G \end{pmatrix}\begin{pmatrix} \ddot{\mathbf{u}}^S \\ \ddot{\mathbf{u}}^L \\ \ddot{\mathbf{u}}^G \end{pmatrix}+\begin{pmatrix} \xi_L+\xi_G & -\xi_L & -\xi_G \\ -\xi_L & \xi_L & 0 \\ -\xi_G & 0 & \xi_G \end{pmatrix}\begin{pmatrix} \dot{\mathbf{u}}^S \\ \dot{\mathbf{u}}^L \\ \dot{\mathbf{u}}^G \end{pmatrix}$$

$$=\begin{pmatrix} (r_{SS}+n_S\lambda_S+n_S\mu_S)\nabla(\nabla\cdot\mathbf{u}^S)+n_S\mu_S\nabla^2\mathbf{u}^S+r_{SL}\nabla(\nabla\cdot\mathbf{u}^L)+r_{SG}\nabla(\nabla\cdot\mathbf{u}^G) \\ r_{SL}\nabla(\nabla\cdot\mathbf{u}^S)+r_{LL}\nabla(\nabla\cdot\mathbf{u}^L)+r_{LG}\nabla(\nabla\cdot\mathbf{u}^G) \\ r_{SG}\nabla(\nabla\cdot\mathbf{u}^S)+r_{LG}\nabla(\nabla\cdot\mathbf{u}^L)+r_{GG}\nabla(\nabla\cdot\mathbf{u}^G) \end{pmatrix}, \tag{1}$$

where ∇ and ∇^2 are the gradient operator and Laplace operator in the Cartesian coordinate, respectively. $\mathbf{u}^\alpha$ ($\alpha = S, L, G$) represents the displacement vector of α phase; $\dot{}$ and $\ddot{}$ denote the velocities and accelerations of individual component, respectively. ρ_α is the material density of α phase; λ_S and μ_S are the classical Lamé's constants of the empty porous solid; n_α denotes the fraction of the volume occupied by α phase; ξ_L and ξ_G are the drag force parameters representing the viscous dissipation between the fluids (liquid and gas) and the solid skeleton, respectively, the detailed expressions of which can be found in the references [25, 31, 32]. r_{SS}, r_{LL}, r_{GG}, r_{SL}, r_{SG} and r_{LG} are the coefficients pertinent to the coupling between different phases and can be determined from the relationships between them and the measurable parameters, which was detailed discussed in the porosity theory [27].

With the aid of the usual Helmholtz resolution of a vector, the three displacement vectors can be conveniently written in the following forms:

$$\mathbf{u}^\alpha = \nabla\psi_\alpha + \nabla\times\mathbf{H}_\alpha, \quad \nabla\cdot\mathbf{H}_\alpha = 0, \tag{2}$$

where ψ_α and $\mathbf{H}_\alpha$ ($\alpha = S, L, G$) are the scalar and vector potential functions for the solid, liquid and gas phases, respectively.

Substituting Eq. (2) into Eq. (1) and then applying divergence and curl operators to both sides of Eq. (1) respectively, we obtain

$$\begin{pmatrix} n_S\rho_S & 0 & 0 \\ 0 & n_L\rho_L & 0 \\ 0 & 0 & n_G\rho_G \end{pmatrix}\begin{pmatrix} \ddot{\psi}_S \\ \ddot{\psi}_L \\ \ddot{\psi}_G \end{pmatrix}+\begin{pmatrix} \xi_L+\xi_G & -\xi_L & -\xi_G \\ -\xi_L & \xi_L & 0 \\ -\xi_G & 0 & \xi_G \end{pmatrix}\begin{pmatrix} \dot{\psi}_S \\ \dot{\psi}_L \\ \dot{\psi}_G \end{pmatrix}=\nabla^2\begin{pmatrix} r_{SS}+n_S\lambda_S+2n_S\mu_S & r_{SL} & r_{SG} \\ r_{SL} & r_{LL} & r_{LG} \\ r_{SG} & r_{LG} & r_{GG} \end{pmatrix}\times\begin{pmatrix} \psi_S \\ \psi_L \\ \psi_G \end{pmatrix} \tag{3}$$

and

$$\begin{pmatrix} n_S\rho_S & 0 & 0 \\ 0 & n_L\rho_L & 0 \\ 0 & 0 & n_G\rho_G \end{pmatrix}\begin{pmatrix} \ddot{\mathbf{H}}_S \\ \ddot{\mathbf{H}}_L \\ \ddot{\mathbf{H}}_G \end{pmatrix}+\begin{pmatrix} \xi_L+\xi_G & -\xi_L & -\xi_G \\ -\xi_L & \xi_L & 0 \\ -\xi_G & 0 & \xi_G \end{pmatrix}\begin{pmatrix} \dot{\mathbf{H}}_S \\ \dot{\mathbf{H}}_L \\ \dot{\mathbf{H}}_G \end{pmatrix}=\nabla^2\begin{pmatrix} n_S\lambda_S & 0 & 0 \\ 0 & 0 & 0 \\ 0 & 0 & 0 \end{pmatrix}\begin{pmatrix} \mathbf{H}_S \\ \mathbf{H}_L \\ \mathbf{H}_G \end{pmatrix}. \tag{4}$$

Eqs. (3) and (4) describe the propagation of the P wave and S wave in three-phase porosity media, respectively. The general solutions of Eqs. (3) and (4) are of the forms:

$$\psi_\alpha = A_\alpha \exp[\mathrm{i}k_p(lx+nz-c_pt)], \tag{5}$$

$$\mathbf{H}_{\alpha} = \mathbf{B}_{\alpha} \exp[\mathrm{i}k_s(lx + nz - c_s t)], \tag{6}$$

where $\mathrm{i} = \sqrt{-1}$; k_p and k_s are the wave numbers of P wave and S wave respectively; l and n are the values of direction vectors; c_p and c_s are the phase velocities of the P wave and S wave respectively.

Substituting Eq. (5) into Eq. (3), we get the following characteristic equation for P wave:

$$\det[A] = 0, \tag{7}$$

where $[A]$ is a symmetric matrix of order 3×3 with its elements given by

$$a_{11} = \mathrm{i}\omega(\xi_L + \xi_G) + \omega^2\rho_S - k_p{}^2(r_{SS} + n_S\lambda_S + 2n_S\mu_S),\ a_{22} = \mathrm{i}\omega\xi_L + \omega^2\rho_L - k_p{}^2 r_{LL},$$

$$a_{33} = \mathrm{i}\omega\xi_G + \omega^2\rho_G - k_p{}^2 r_{GG},\ a_{12} = a_{21} = -\mathrm{i}\omega\xi_L - k_p{}^2 r_{SL},$$

$$a_{13} = a_{31} = -\mathrm{i}\omega\xi_G - k_p{}^2 r_{SG},\ a_{23} = a_{32} = -k_p{}^2 r_{LG}.$$

In a similar manner, substituting Eq. (6) into Eq. (4), the following characteristic equation for S wave is derived:

$$\det[B] = 0, \tag{8}$$

where $[B]$ is also a symmetric matrix of order 3×3, its entries are given by

$$b_{11} = \mathrm{i}\omega(\xi_L + \xi_G) + \omega^2\rho_S - n_S\mu_S k_s{}^2,\ b_{22} = \mathrm{i}\omega\xi_L + \omega^2\rho_L,\ b_{33} = \mathrm{i}\omega\xi_G + \omega^2\rho_G,$$

$$b_{12} = b_{21} = -\mathrm{i}\omega\xi_L,\ b_{13} = b_{31} = -\mathrm{i}\omega\xi_G,\ b_{23} = b_{32} = 0.$$

Eqs. (7) and (8) indicate in a physical sense that there exist one type of S wave and three types of P wave in the sandiwiched elastic porous layer containing two immiscible fluids, typically denoted as P1 wave, P2 wave and P3 wave in descending order of phase speed [23, 25,26,27].

In an isotropic three-phase porous medium, the constitutive expressions representing the stress-strain relationships take the following forms [27]:

$$\boldsymbol{\sigma}^S = [(r_{SS} + n_S\lambda_S)\nabla^2\psi_S + r_{SL}\nabla^2\psi_L + r_{SG}\nabla^2\psi_G]I + 2n_S\mu_S\varepsilon_S, \tag{9}$$

$$-p^L = (r_{SL}\nabla^2\psi_S + r_{LL}\nabla^2\psi_L + r_{LG}\nabla^2\psi_G)I, \tag{10}$$

$$-p^G = (r_{SG}\nabla^2\psi_S + r_{LG}\nabla^2\psi_L + r_{GG}\nabla^2\psi_G)I, \tag{11}$$

where $\boldsymbol{\sigma}^S$ is the stress in porous solid; p^L and p^G are the pressures of liquid and gas respectively; I is unit tensor matrix. ε_S denotes the strain tensor of the solid skeleton, i.e., $\varepsilon_S = \frac{1}{2}[\nabla\mathbf{u}^S + (\nabla\mathbf{u}^S)^T]$, the superscript T represents the transpose.

2.2. Overlying seawater half-space

The motion equation of overlying water has the following form:

$$\rho_W \ddot{\quad} \quad {}_{,'}\nabla\nabla\cdot\mathbf{u}^W, \tag{12}$$

where K_W is the bulk modulus of the water, ρ_W is the water density and $\mathbf{u}^W$ is its displacement vector.

The fluid pressure in the upper water is

$$p_W = -K_W\nabla\cdot\mathbf{u}^W. \tag{13}$$

2.3. Underlying elastic half-space

The underlying elastic half-space represents the bedrock under the shallow poroelastic sediment layer and has the governing equation as:

$$(\lambda_E + \mu_E)\nabla\nabla\cdot\mathbf{u}^E + \mu_E\nabla^2\mathbf{u}^E = \rho_E\ddot{} \quad , \tag{14}$$

where λ_E and μ_E are Lame's constants, ρ_E is the solid density, and $\mathbf{u}^E$ is the displacement vector with the following form:

$$\mathbf{u}^E = \nabla\psi_E + \nabla\times\mathbf{H}_E\,, \tag{15}$$

where ψ_E and $\mathbf{H}_E$ are the scalar and vector displacement potentials, respectively.

3 BOUNDARY CONDIIONS

As depicted in Fig. 1, a plane P wave (plane wave) propagates through the upper water half-space and then impinges upon the interface (z = 0) with an angular frequency ω and an angle of incidence θ_i. In this circumstance, one reflected P wave (plane wave) is generated in the overlying water (z > 0). Furthermore, according to Eqs. (7) and (8), four transmitted bulk waves from the upper interface and four reflected bulk waves from the lower interface are predicted to be excited in the sandwiched gassy poroelastic layer (-H < z < 0) and two transmitted waves exist in the elastic substrate (z < -H). Accordingly, the displacement potential functions of the incident, reflected and transmitted waves can be expressed as:
(i) In the overlying water (z > 0):

$$\psi_W = A_i\exp[\mathrm{i}k_{ip}(l_{ip}x - n_{ip}z - c_{ip}t)] + A_r\exp[\mathrm{i}k_{rp}(l_{rp}x + n_{rp}z - c_{rp}t)]\,, \tag{16a}$$

(ii) In the gassy poroelastic layer (-H < z < 0):

$$\psi_S = \sum_{n=1}^{3}A_{tpn}^S\exp[\mathrm{i}k_{tpn}(l_{tpn}x - n_{tpn}z - c_{tpn}t)] + \sum_{n=1}^{3}A_{rpn}^S\exp[\mathrm{i}k_{rpn}(l_{rpn}x + n_{rpn}z - c_{rpn}t)]\,, \tag{16b}$$

$$\psi_L = \sum_{n=1}^{3}A_{tpn}^L\exp[\mathrm{i}k_{tpn}(l_{tpn}x - n_{tpn}z - c_{tpn}t)] + \sum_{n=1}^{3}A_{rpn}^L\exp[\mathrm{i}k_{rpn}(l_{rpn}x + n_{rpn}z - c_{rpn}t)]\,, \tag{16c}$$

$$\psi_G = \sum_{n=1}^{3}A_{tpn}^G\exp[\mathrm{i}k_{tpn}(l_{tpn}x - n_{tpn}z - c_{tpn}t)] + \sum_{n=1}^{3}A_{rpn}^G\exp[\mathrm{i}k_{rpn}(l_{rpn}x + n_{rpn}z - c_{rpn}t)]\,, \tag{16d}$$

$$H_S = B_{ts}^S\exp[\mathrm{i}k_{ts}(l_{ts}x - n_{ts}z - c_{ts}t)] + B_{rs}^S\exp[\mathrm{i}k_{rs}(l_{rs}x + n_{rs}z - c_{rs}t)]\,, \tag{16e}$$

$$H_L = B_{ts}^L\exp[\mathrm{i}k_{ts}(l_{ts}x - n_{ts}z - c_{ts}t)] + B_{rs}^L\exp[\mathrm{i}k_{rs}(l_{rs}x + n_{rs}z - c_{rs}t)]\,, \tag{16f}$$

$$H_G = B_{ts}^G\exp[\mathrm{i}k_{ts}(l_{ts}x - n_{ts}z - c_{ts}t)] + B_{rs}^G\exp[\mathrm{i}k_{rs}(l_{rs}x + n_{rs}z - c_{rs}t)]\,, \tag{16g}$$

(iii) In the elastic substrate (z < -H)

$$\psi_E = A_{pe}\exp[\mathrm{i}k_{pe}(l_{pe}x - n_{pe}z - c_{pe}t)]\,, \tag{16h}$$

$$H_E = B_{se}\exp[\mathrm{i}k_{se}(l_{se}x - n_{se}z - c_{se}t)]\,. \tag{16i}$$

where the subscripts i, r and t refer to the quantities corresponding to the incidence, reflection and transmission, respectively.

Substituting Eqs. (16b) – (16g) into Eqs. (7) and (8), we obtain the following relations between the various values of the amplitudes of reflected and transmitted waves:

$$\delta_{Ln} = \frac{A^L_{rpn}}{A^S_{rpn}} = \frac{A^L_{tpn}}{A^S_{tpn}} = \frac{a^{(n)}_{13}a^{(n)}_{22} - a^{(n)}_{23}a^{(n)}_{12}}{a^{(n)}_{23}a^{(n)}_{11} - a^{(n)}_{13}a^{(n)}_{21}}, \ (n = 1, 2, 3) \tag{17a}$$

$$\delta_{Gn} = \frac{A^G_{rpn}}{A^S_{rpn}} = \frac{A^G_{tpn}}{A^S_{tpn}} = \frac{a^{(n)}_{32}a^{(n)}_{21} - a^{(n)}_{22}a^{(n)}_{31}}{a^{(n)}_{22}a^{(n)}_{33} - a^{(n)}_{23}a^{(n)}_{32}}, \ (n = 1, 2, 3) \tag{17b}$$

$$\delta_{LS} = \frac{B^L_{rs}}{B^S_{rs}} = \frac{B^L_{ts}}{B^S_{ts}} = -\frac{b_{22}}{b_{21}}, \tag{17c}$$

$$\delta_{GS} = \frac{B^G_{rs}}{B^S_{rs}} = \frac{B^G_{ts}}{B^S_{ts}} = \frac{b_{21}b_{12} - b_{11}b_{22}}{b_{13}b_{22}}. \tag{17d}$$

When Eqs. (17a) – (17d) are combined with Eqs. (16a) – (16i), there remain unknown complex amplitudes which could be determined by considering the boundary conditions. These boundary conditions concerning stress and displacement components need to insure the continuity across the upper and lower plane interfaces at $z = 0$ and $z = -H$. Due to the difficulty to determine the fluid flow impedance across the interface between overlying water and gassy poroelastic layer [3], sealed-pore boundary condition is employed here for simplicity.

The interface between the overlying water and gassy poroelastic layer ($z = 0$) yields

continuity of normal stress: $\boldsymbol{\sigma}^S_{zz} = -p_W$; (18a)

continuity of normal displacement: $\mathbf{u}^S_z = \mathbf{u}^W_z$; (18b)

disappearance of relative displacements: $\mathbf{u}^L_z - \mathbf{u}^S_z = 0$, $\mathbf{u}^G_z - \mathbf{u}^S_z = 0$; (18c,d)

disappearance of tangential stress: $\boldsymbol{\sigma}^S_{xz} = 0$; (18e)

The interface between the gassy poroelastic layer and underlying solid half-space (z = -H) yields

continuity of normal displacement: $\mathbf{u}^S_z = \mathbf{u}^E_z$; (18f)

continuity of tangential displacement: $\mathbf{u}^S_x = \mathbf{u}^E_x$; (18g)

continuity of tangential stress: $\boldsymbol{\sigma}^S_{xz} = \boldsymbol{\sigma}^E_{xz}$; (18h)

continuity of normal stress: $\boldsymbol{\sigma}^S_{zz} = \boldsymbol{\sigma}^E_{zz}$; (18i)

disappearance of relative displacements: $\mathbf{u}^L_z - \mathbf{u}^S_z = 0$, $\mathbf{u}^G_z - \mathbf{u}^S_z = 0$; (18j,k)

Combining the potential functions (16a) – (16i) and the boundary conditions (18a) – (18k) and then considering Snell's law at the interface, we get the following set of equations:

$$[M][A_r, A^S_{tp1}, A^S_{tp2}, A^S_{tp3}, A^S_{rp1}, A^S_{rp2}, A^S_{rp3}, B^S_{ts}, B^S_{rs}, A_{te}, B_{te}]^T = A_i[Q], \tag{19}$$

where the corresponding elements in the matrixes $[M]$ and $[Q]$ are given in Appendix.

4 NUMERICAL RESULTS AND DISCUSSION

In order to investigate the dependence of the amplitude coefficient of the reflected waves (i.e., A_r / A_i) on the incident angle, frequency, liquid saturation of the porous layer, and the layer thickness, a numerical study is carried out by Matlab. In fact, the energy of the incident and reflected wave in the seawater is proportional to the amplitude. So the amplitude reflec-

tion coefficient in this paper could also express the fraction of the energy of the reflected wave. And this methodology has the potential to be used on real data through AVO analysis. Based on the method of Fatti et al [33], Russell, et al. [34] estimated the P and S-wave impedances using a standard inversion technique. The material parameters needed in the numerical simulation are summarized in Table. 1. The reflection coefficient is calculated with respect to the various model parameters from the formulas derived in the previous section.

It is worth noting that, when the excitation frequency ω exceeds a certain transition frequency ω_c, the viscous coupling coefficient becomes frequency-dependent and the frequency correction should be introduced. The transition frequency for the porous medium saturated by two immiscible fluids is defined as $\omega_c = \tau^{-1}$ [36], where τ is considered as the sum of two "damping time scales" for liquid and gas in the pore as:

$$\tau = \tau_L + \tau_G = k(\rho_L k_r^L / \eta_L + \rho_G k_r^G / \eta_G). \tag{20}$$

where k is the intrinsic permeability of the porous medium; η^F ($F = L,G$) is the fluid viscosity; k_r^F is the relative permeability simplified to be a function of saturation. So the transition frequency ω_c can be viewed as a function of water saturation. Based on the material parameters given in table 1, the transition frequency corresponding to the various water saturations (from 0 to 1) is calculated to be: $\omega_c \geq 3.3\times10^6$ rad/s. In the following calculations, the wave excitation frequency is restricted to be: $f \leq$ 1000Hz, which is much smaller than the minimum value of transition frequency ω_c. As discussed above, in this "low frequency range", the effect of the frequency correction factor can be negligible.

Table 1 Material properties of the model

Overlying water
$\rho_W = 1000\text{kg/m}^3$, $K_W = 2.2\text{GPa}$,
Elastic solid half-space
$\mu_E = 5\text{GPa}$, $\lambda_E = 12\text{GPa}$, $\rho_E = 2460\,\text{kg/m}^3$,
Sandwiched poroelastic medium
$n = 0.3$, $\rho_S = 2650\,\text{kg/m}^3$, $\rho_L = 1000\ \text{kg/m}^3$, $\rho_G = 1.2\,\text{kg/m}^3$, $K_S = 36\,\text{GPa}$,
$K_L = 2.2\,\text{GPa}$, $K_G = 0.1\,\text{MPa}$, $k = 3.0\times10^{-13}\ \text{m}^2$, $\eta^G = 1.8\times10^{-5}\ \text{Pa}\cdot\text{s}$, $\eta^L = 0.001\ \text{Pa}\cdot\text{s}$.
$\lambda_S = 9.0\,\text{GPa}$, $\mu_S = 4.0\,\text{GPa}$, $m_{vg} = 0.5$, $\alpha_{vg} = 0.0001\,\text{Pa}^{-1}$, $k = 3\times10^{-13}\,\text{m}^2$.

4.1 Bulk waves in the gassy poroelastic layer

From the characteristic equations (7) and (8), the propagation speed and attenuation of the four bulk waves, typically characterized as P1, P2, P3 and S waves, can be analyzed. In the limiting case for a complete saturation, the motion equation (1) can be reduced to a simpler form of classic Biot model, which was discussed by Chen et al. [22]. Among these four bulk waves, P1 wave travels fastest with lowest attenuation, which is similar to the fast P wave in the Biot theory. In the context of the Biot-Gassmann theory, Russell et al. [34] only considered the fast P wave when calculated P-wave velocity in the saturated porous medium. Similarly, since the P1 wave are analogous to the regular P wave in elastic solid, the other P2 and P3 waves are negligible when this methodological investigation is developed in geophysical applications. The phase velocities of P1 and S waves are several orders magnitude lager than those of P2 and P3 waves, while their attenuation coefficients are several orders magnitude smaller than those of P2 and P3 waves [27]. Thus, the P1 wave and S wave occupy the vast majority of the transmitted wave energy across the interface at $z = 0$. Base on the physical pa-

rameters listed in Table 1, Fig. 2 shows the frequency-dependent and saturation-dependent behavior of P1 and S waves in the gassy poroelastic layer. The attenuation coefficient is denoted by the imaginary part of the corresponding complex wave number. The liquid saturation considered here is from 20% to 99.99% and the frequency is taken to be 1 Hz, 10 Hz, 100 Hz and 1000Hz, respectively. As depicted in Figs. 2 (a), the speed of P1 wave is independent of frequency and decreases almost linearly during the change of saturation in the unsaturated case and then increases abruptly when it is close to the fully saturated case. The attenuation of P1 wave almost bears the opposite trend compared with its propagation speed. In Fig. 2 (b), the S wave speed decreases linearly with liquid saturation degree. The attenuation of both P1 and S waves increases with increasing frequency. Like P1 wave, the wave speed of S wave is frequency-independent and its attenuation increases with increasing saturation.

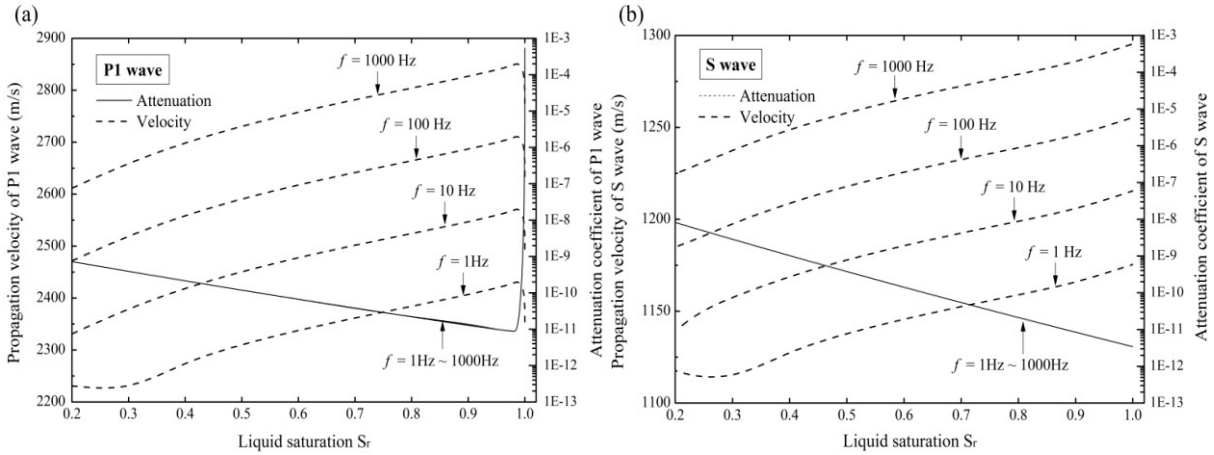


Figure 2. Variation of acoustic velocity (refer to left axes) and attenuation coefficient (refer to right axes) with liquid saturation of the gassy poroelastic layer for: (a) P1 wave, (b) S wave.

4.2 Variation of reflection coefficient with the incident angle

Fig. 3 shows the variation of the magnitude of the reflection coefficient A_r / A_i with incident angle θ_i using Eq. (19). The frequency f is set to be 100Hz and the liquid saturation of the porous layer Sr is 90%. Four different layer thicknesses: H = 0m, 5m, 50m and 500m are discussed, respectively. For the physical parameters listed in Table 1, the speed of the incident wave in the overlying water v_i is 1483.2 m/s, the speeds of P and S wave in the underlying elastic half-space are 2990.5 and 1425.7m/s, respectively. The speeds of P1 and S waves in the intermediate gassy porous layer are 2366.8 and 1147.9m/s, respectively. We note in passing that, for the traditional wave reflection and transmission problem at the interface between two semi-infinite half-spaces, the angles of incidence and emergence are related by Snell's law. When one of the angles corresponding to a reflected or transmitted wave increases to 90°, a critical angle of incidence is defined as θ_{cr} for the generating wave. The critical angle for the incident P wave (plane wave) discussed in our paper can be determined from: $\theta_{cr} = \sin^{-1}(v_i / v_t)$, where v_i and v_t are the speeds of the incident and transmitted waves, respectively. When the incident angle θ_i equals to critical angle θ_{cr}, the transmitted wave becomes evanescent and the normal to the wavefront becomes theoretically horizontal. In this paper, when the gassy porous sediment is absent (H = 0), the considered layered model reduces to the wave problem at the interface between upper water and underlying elastic solid half-space. In this case, one critical incident angle exists for the incident wave as θ_{cr1} = 29.7°. In the other limiting case,

when the thickness of porous layer H approaches infinity, our model corresponds to the wave reflection and transmission at the water/porous-medium interface. And the corresponding value of the critical incident angle θ_{cr2} =38.8°. As shown in Fig. 3, with regard to the thickness of the porous layer H equals to 0m, the reflection coefficient has a maximum value at $\theta_i = \theta_{cr1}$. When the gassy porous layer becomes more thick, such as H = 50m and 500m, it achieves a maximum value around $\theta_i = \theta_{cr2}$. It is probably because that, with the thickness of the interface layer increasing, the calculation results appear to be more close to the aforementioned model, i.e., water/gassy porous-medium interface model with a fixed critical angle θ_{cr2}.

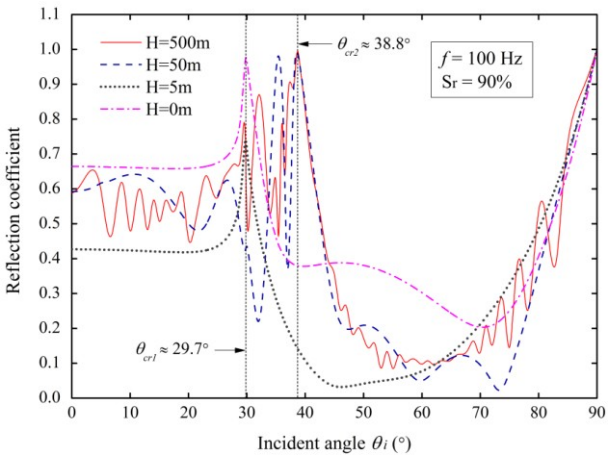


Figure 3. Reflection coefficient (A_r / A_i) as a function of incident angle θ_i for four different layer thicknesses: H = 0m, 5m, 50m and 500m.

Fig. 4 depicts the variation of reflection coefficient with the incident angle at three different liquid saturations of the gassy porous layer: Sr =80%, 90% and 99.99%. The thickness of the porous layer is set as 50m and the frequency f is 100Hz. When the interstices of the porous medium is almost filled with water, i.e., Sr =99.99%, the calculated result differs greatly from those of the other two cases. It is shown that, when the intermediate porous layer approaches totally liquid saturated, the reflection coefficient attains its maximal value near θ_{cr1} = 29.7°.

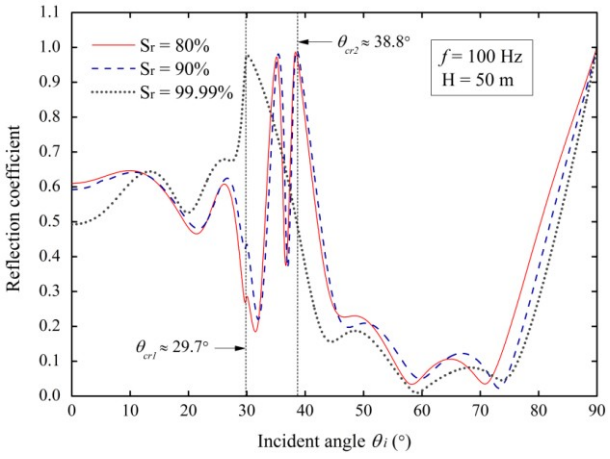


Figure 4. Reflection coefficient (A_r / A_i) as a function of incident angle θ_i for three different liquid saturations: Sr =80%, 90% and 99.99%.

4.3 Variation of reflection coefficient with the layer thickness

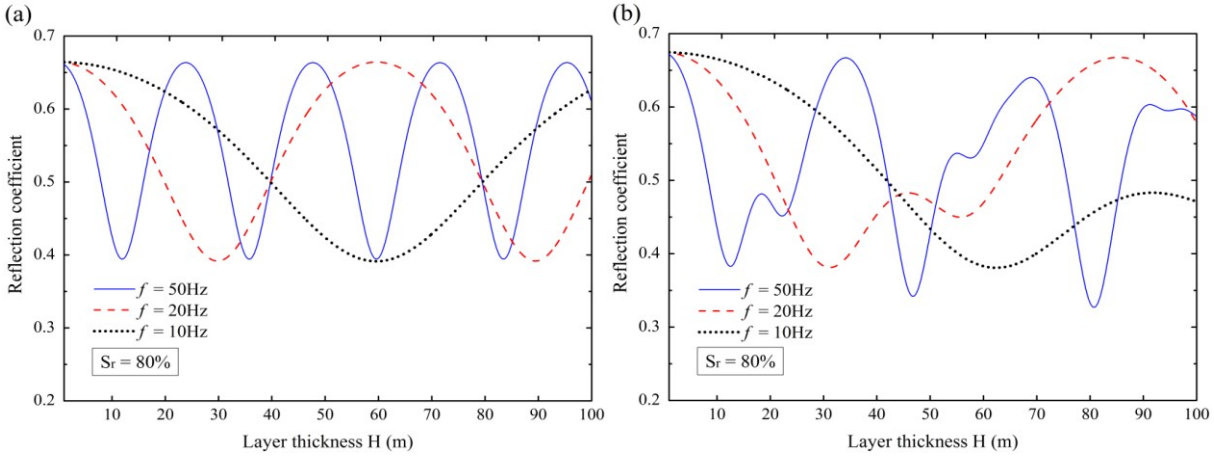


Figure 5. Reflection coefficient (A_r / A_i) as a function of layer thickness H for three different frequencies: f = 10Hz, 20Hz and 50Hz. (a) incident angle θ_i = 0° and (b) incident angle θ_i = 25°.

To analyze the effect of interlayer thickness on the reflection coefficient clearly, Figs. 5(a) and (b) show A_r / A_i in the overlying water as a function of layer thickness H (0m ≤ H ≤ 100m) at 10Hz, 20Hz and 50Hz, respectively. The liquid of the porous layer Sr is postulated to be 80%. In the case of θ_i = 0° (see Fig. 5(a)), the reflection coefficient fluctuates periodically with layer thickness. The oscillation of reflection coefficient results from the resonant response of the P waves in the porous layer. This is because when the incident wave strikes at the interface (z = 0) vertically from the overlying water, only three types of P waves (i.e., P1wave P2 wave and P3 wave) are generated in the lower gassy porous layer. Moreover, due to the high damping of the P2 and P3 waves, the P1wave could be viewed as the major factor affecting the reflection coefficient. In this low frequency range, the phase speed of P1 wave in porous layer is found to be frequency-independent and equals to 2384m/s. Therefore, the wavelengths of the P1 wave corresponding to 20Hz and 50Hz are nearly 119m and 48m, respectively. Meanwhile, it is shown in Fig. 5(a) that, the change circle of reflection coefficient in 20Hz and 50Hz approximate to 60m and 24m, respectively. This indicates that, at the normal incidence (i.e., θ_i = 0°), the change circle of reflection coefficient with respect to the thickness of the gassy poroelastic layer is equal to half of the wavelength of the P1 wave. However, when the incident wave is no longer perpendicular to the interface, there is a transmitted S wave other than the three types of transmitted P wave exist in the lower gassy porous layer. In this case, the reflection of the waves at the interface is simultaneously influenced by both P wave and S wave in the subjacent porous layer and hence the reflection coefficient becomes more indeterminate. For instance, when incident angle θ_i = 25° as demonstrated in Fig. 5(b), the reflection coefficient fluctuates with the increase of thickness irregularly. The effect of frequency on the reflection coefficient can also be revealed from both Figs. 5(a) and 5(b). The wave reflection upon the interface has a close correlation with wavelengths of the waves in the lower layer. With the increasing of frequency (i.e., decreasing of wavelength), the fluctuation of the reflection coefficient with layer thickness becomes more frequent.

4.4 Variation of reflection coefficient with the liquid saturation of the layer

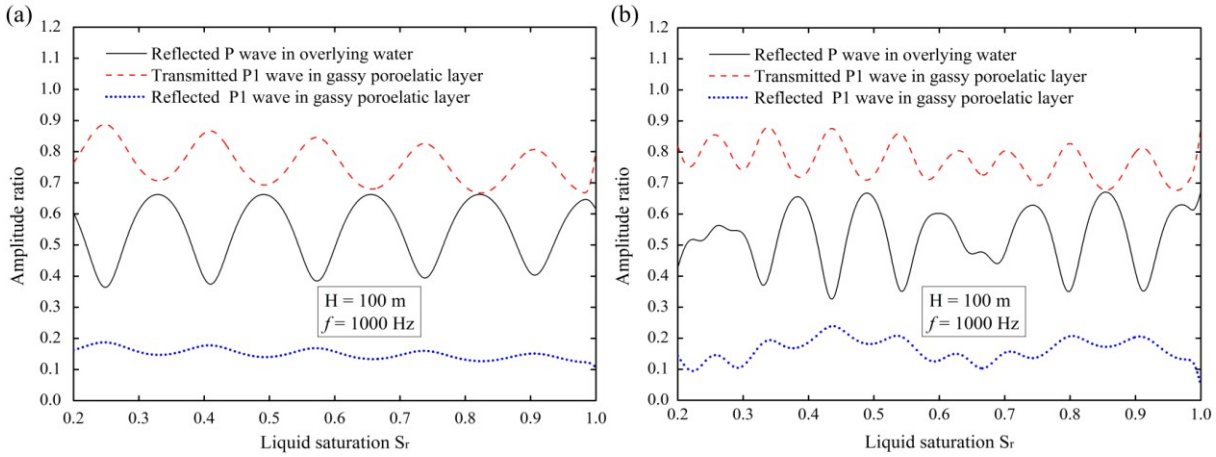


Figure 6. Amplitude ratios of the reflected wave (A_r / A_i), transmitted P1 wave (A_{tp1}^S / A_i) and reflected P1 wave (A_{rp1}^S / A_i) as a function of liquid saturation Sr. (a) incident angle $\theta_i = 0°$ and (b) incident angle $\theta_i = 25°$.

Figs. 6 (a) and (b) show the effect of the liquid saturation of the intermediate gassy porous layer on the amplitude ratios of the reflected P wave (i.e., reflection coefficient), transmitted P1 wave and reflected P1 wave, respectively. The liquid saturation degree Sr ranges from 20% to 99.99%. The thickness H is assumed to be 100m and the wave frequency f is taken to be 1000Hz. Similarly, the numerical results of the incident angle θ_i = 0° and 25° are given in Figs. 6 (a) and (b), respectively. When the incident wave spreads at the interface perpendicularly, all the amplitude ratios of the reflected P wave, transmitted P1 wave and reflected P1 wave almost fluctuate with liquid saturation periodically. While in the case of θ_i = 25°, the phenomenon of the fluctuation is observed to be relatively irregular.

Furthermore, it is worth noting that, in both of these two cases of different incident angles, the trend of reflected P wave in the upper water almost bear the opposite trend comparing with those of transmitted and reflected P1 waves in the lower porous layer. This phenomenon is due the energy conservation among the incident wave, reflected waves and transmitted waves.

Figs. 7(a) and (b) show the reflection coefficient as a function of liquid saturation at $\theta_i = 0°$ and 25°, respectively. The numerical results considering four different frequencies, i.e., f = 1Hz, 10Hz, 100Hz and 1000Hz, are presented. The layer thickness is 100m. As the same shown in Figs. 5(a) and (b), the influence of wave frequency on the reflection coefficient is remarkable. When the frequency is in low range, e.g., f = 1Hz, the effect of saturation change on the reflection coefficient is insignificant and the relationship between the reflection coefficient and change of saturation is almost linearly dependent. In other words, when the wavelength of the waves in lower layer is long enough, the effect of saturation change could be negligible. With the increasing of frequency, the fluctuation of the reflection coefficient with liquid saturation becomes more notable. It is also noteworthy that, in Fig. 7(b), when the saturation approaches fully saturated state, the calculation results for different frequencies tend to converge at $A_r / A_i \approx 0.67$.

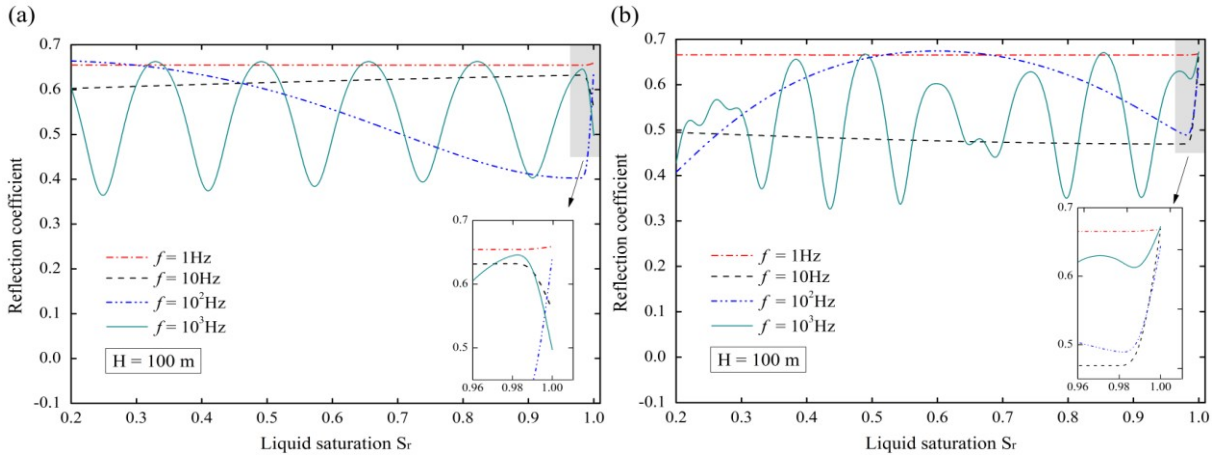


Figure 7. Reflection coefficient (A_r / A_i) as a function of liquid saturation Sr for four different frequencies: f = 1Hz, 10Hz, 100Hz and 1000Hz. (a) incident angle θ_i = 0° and (b) incident angle θ_i = 25°.

5 CONCLUSIONS

- In the sandwiched gassy poroelastic layer, one transverse wave and three longitudinal waves coexist at oblique incidence. In these various mode waves, P1 and S wave propagate faster and attenuate relatively slowly, and thus influence the wave reflection characteristics at the surface of the porous layer significantly.
- The numerical results indicate that the incident angle renders a significant influence on the amplitude ratio of the reflected wave, i.e., reflection coefficient. It is also shown that, the reflection coefficient attains its maximum value at θi = θcr1 ~ θcr2, where θcr1 and θcr2 denote the critical incident angles for the two limiting cases (H = 0 and H ≈ ∞).
- When the incident wave strikes upon the interface perpendicularly, the reflection coefficient seems to fluctuate periodically with the layer thickness. However, if the plane wave is not normally incident, a transmitted S wave is generated, and the reflection coefficient fluctuates with the increase of the thickness irregularly. With the increasing of frequency, the fluctuation of the reflection coefficient with layer thickness becomes more frequent.
- It is found that, in the low frequency range, the effect of saturation change on the reflection coefficient is not obvious. With the increasing of frequency, the fluctuation of the reflection coefficient with liquid saturation becomes more significant.Papers must be translated to Portable Document Format (PDF) before submission through the Conference website.

Appendix：

The explicit expressions of the elements of $[M]$ are given as follows:

$$m_{1,1} = -K_W k_{rp}^{\ 2},\ m_{1,2} = (r_{SS} + n_S\lambda_S + r_{SL}\delta_{L1} + r_{SG}\delta_{G1} + 2n_S\mu_S n_{tp1}^{\ 2})k_{tp1}^{\ 2},$$

$$m_{1,3} = (r_{SS} + n_S\lambda_S + r_{SL}\delta_{L2} + r_{SG}\delta_{G2} + 2n_S\mu_S n_{tp2}^{\ 2})k_{tp2}^{\ 2},\ m_{1,4} = (r_{SS} + n_S\lambda_S + r_{SL}\delta_{L3} + r_{SG}\delta_{G3} + 2n_S\mu_S n_{tp3}^{\ 2})k_{tp3}^{\ 2},$$

$$m_{1,5} = (r_{SS} + n_S\lambda_S + r_{SL}\delta_{L1} + r_{SG}\delta_{G1} + 2n_S\mu_S n_{rp1}^{\ 2})k_{rp1}^{\ 2},\ m_{1,6} = (r_{SS} + n_S\lambda_S + r_{SL}\delta_{L2} + r_{SG}\delta_{G2} + 2n_S\mu_S n_{rp2}^{\ 2})k_{rp2}^{\ 2},$$

$$m_{1,7} = (r_{SS} + n_S\lambda_S + r_{SL}\delta_{L3} + r_{SG}\delta_{G3} + 2n_S\mu_S n_{rp3}^{\ 2})k_{rp3}^{\ 2},\ m_{1,8} = -2n_S\mu_S l_{ts} n_{ts} k_{ts}^{\ 2},\ m_{1,9} = 2n_S\mu_S l_{rs} n_{rs} k_{rs}^{\ 2},$$

$$m_{1,10} = 0,\ m_{1,11} = 0;\ m_{2,1} = -n_{rp}k_{rp},\ m_{2,2} = -n_{tp1}k_{tp1},\ m_{2,3} = -n_{tp2}k_{tp2},\ m_{2,4} = -n_{tp3}k_{tp3},\ m_{2,5} = n_{rp1}k_{rp1},$$

$$m_{2,6} = n_{rp2}k_{rp2},\ m_{2,7} = n_{rp3}k_{rp3},\ m_{2,8} = l_{ts}k_{ts},\ m_{2,9} = l_{rs}k_{rs},\ m_{2,10} = 0,\ m_{2,11} = 0;\ m_{3,1} = 0,$$

$$m_{3,2} = (\delta_{L1} - 1)n_{tp1}k_{tp1},\ m_{3,3} = (\delta_{L2} - 1)n_{tp2}k_{tp2},\ m_{3,4} = (\delta_{L3} - 1)n_{tp3}k_{tp3},\ m_{3,5} = (1 - \delta_{L1})n_{rp1}k_{rp1},$$

$m_{3,6}=(1-\delta_{L2})n_{rp2}k_{rp2}$, $m_{3,7}=(1-\delta_{L3})n_{rp3}k_{rp3}$, $m_{3,8}=l_{ts}k_{ts}(1-\delta_{LS})$, $m_{3,9}=l_{rs}k_{rs}(1-\delta_{LS})$, $m_{3,10}=0$,
$m_{3,11}=0$; $m_{4,1}=0$, $m_{4,2}=(\delta_{G1}-1)n_{tp1}k_{tp1}$, $m_{4,3}=(\delta_{G2}-1)n_{tp2}k_{tp2}$, $m_{4,4}=(\delta_{G3}-1)n_{tp3}k_{tp3}$,
$m_{4,5}=(1-\delta_{G1})n_{rp1}k_{rp1}$, $m_{4,6}=(1-\delta_{G2})n_{rp2}k_{rp2}$, $m_{4,7}=(1-\delta_{G3})n_{rp3}k_{rp3}$, $m_{4,8}=l_{ts}k_{ts}(1-\delta_{GS})$,
$m_{4,9}=l_{rs}k_{rs}(1-\delta_{GS})$, $m_{4,10}=0$, $m_{4,11}=0$; $m_{5,1}=0$, $m_{5,2}=2n_{tp1}l_{tp1}k_{tp1}{}^2$, $m_{5,3}=2n_{tp2}l_{tp2}k_{tp2}{}^2$,
$m_{5,4}=2n_{tp3}l_{tp3}k_{tp3}{}^2$, $m_{5,5}=-2n_{rp1}l_{rp1}k_{rp1}{}^2$, $m_{5,6}=-2n_{rp2}l_{rp2}k_{rp2}{}^2$, $m_{5,7}=-2n_{rp3}l_{rp3}k_{rp3}{}^2$, $m_{5,8}=(n_{ts}{}^2-l_{ts}{}^2)k_{ts}{}^2$,
$m_{5,9}=(n_{rs}{}^2-l_{rs}{}^2)k_{rs}{}^2$, $m_{5,10}=0$, $m_{5,11}=0$; $m_{6,1}=0$, $m_{6,2}=-n_{tp1}k_{tp1}\exp(\mathrm{i}n_{tp1}k_{tp1}\mathrm{H})$,
$m_{6,3}=-n_{tp2}k_{tp2}\exp(\mathrm{i}n_{tp2}k_{tp2}\mathrm{H})$, $m_{6,4}=-n_{tp3}k_{tp3}\exp(\mathrm{i}n_{tp3}k_{tp3}\mathrm{H})$, $m_{6,5}=n_{rp1}k_{rp1}\exp(-\mathrm{i}n_{rp1}k_{rp1}\mathrm{H})$,
$m_{6,6}=n_{rp2}k_{rp2}\exp(-\mathrm{i}n_{rp2}k_{rp2}\mathrm{H})$, $m_{6,7}=n_{rp3}k_{rp3}\exp(-\mathrm{i}n_{rp3}k_{rp3}\mathrm{H})$, $m_{6,8}=l_{ts}k_{ts}\exp(\mathrm{i}n_{ts}k_{ts}\mathrm{H})$,
$m_{6,9}=l_{rs}k_{rs}\exp(-\mathrm{i}n_{rs}k_{rs}\mathrm{H})$, $m_{6,10}=n_{pe}k_{pe}\exp(\mathrm{i}n_{pe}k_{pe}\mathrm{H})$, $m_{6,11}=-l_{se}k_{se}\exp(\mathrm{i}n_{se}k_{se}\mathrm{H})$; $m_{7,1}=0$,
$m_{7,2}=l_{tp1}k_{tp1}\exp(\mathrm{i}n_{tp1}k_{tp1}\mathrm{H})$, $m_{7,3}=l_{tp2}k_{tp2}\exp(\mathrm{i}n_{tp2}k_{tp2}\mathrm{H})$, $m_{7,4}=l_{tp3}k_{tp3}\exp(\mathrm{i}n_{tp3}k_{tp3}\mathrm{H})$,
$m_{7,5}=l_{rp1}k_{rp1}\exp(-\mathrm{i}n_{rp1}k_{rp1}\mathrm{H})$, $m_{7,6}=l_{rp2}k_{rp2}\exp(-\mathrm{i}n_{rp2}k_{rp2}\mathrm{H})$, $m_{7,7}=l_{rp3}k_{rp3}\exp(-\mathrm{i}n_{rp3}k_{rp3}\mathrm{H})$,
$m_{7,8}=n_{ts}k_{ts}\exp(\mathrm{i}n_{ts}k_{ts}\mathrm{H})$, $m_{7,9}=-n_{rs}k_{rs}\exp(-\mathrm{i}n_{rs}k_{rs}\mathrm{H})$, $m_{7,10}=-l_{pe}k_{pe}\exp(\mathrm{i}n_{pe}k_{pe}\mathrm{H})$,
$m_{7,11}=-n_{se}k_{se}\exp(\mathrm{i}n_{se}k_{se}\mathrm{H})$;

$m_{8,1}=0$, $m_{8,2}=-2n_S\mu_S n_{tp1}l_{tp1}k_{tp1}{}^2\exp(\mathrm{i}n_{tp1}k_{tp1}\mathrm{H})$, $m_{8,3}=-2n_S\mu_S n_{tp2}l_{tp2}k_{tp2}{}^2\exp(\mathrm{i}n_{tp2}k_{tp2}\mathrm{H})$,
$m_{8,4}=-2n_S\mu_S n_{tp3}l_{tp3}k_{tp3}{}^2\exp(\mathrm{i}n_{tp3}k_{tp3}\mathrm{H})$, $m_{8,5}=2n_S\mu_S n_{rp1}l_{rp1}k_{rp1}{}^2\exp(-\mathrm{i}n_{rp1}k_{rp1}\mathrm{H})$,
$m_{8,6}=2n_S\mu_S n_{rp2}l_{rp2}k_{rp2}{}^2\exp(-\mathrm{i}n_{rp2}k_{rp2}\mathrm{H})$, $m_{8,7}=2n_S\mu_S n_{rp3}l_{rp3}k_{rp3}{}^2\exp(-\mathrm{i}n_{rp3}k_{rp3}\mathrm{H})$,
$m_{8,8}=(l_{ts}{}^2-n_{ts}{}^2)n_S\mu_S k_{ts}{}^2\exp(\mathrm{i}n_{ts}k_{ts}\mathrm{H})$, $m_{8,9}=(l_{rs}{}^2-n_{rs}{}^2)n_S\mu_S k_{rs}{}^2\exp(-\mathrm{i}n_{rs}k_{rs}\mathrm{H})$,
$m_{8,10}=2\mu_E n_{pe}l_{pe}k_{pe}{}^2\exp(\mathrm{i}n_{pe}k_{pe}\mathrm{H})$, $m_{8,11}=(n_{se}{}^2-l_{se}{}^2)\mu_E k_{se}{}^2\exp(\mathrm{i}n_{se}k_{se}\mathrm{H})$; $m_{9,1}=0$,
$m_{9,2}=-(r_{SS}+n_S\lambda_S+r_{SL}\delta_{L1}+r_{SG}\delta_{G1}+2n_S\mu_S n_{tp1}{}^2)k_{tp1}{}^2\exp(\mathrm{i}n_{tp1}k_{tp1}\mathrm{H})$,
$m_{9,3}=-(r_{SS}+n_S\lambda_S+r_{SL}\delta_{L2}+r_{SG}\delta_{G2}+2n_S\mu_S n_{tp2}{}^2)k_{tp2}{}^2\exp(\mathrm{i}n_{tp2}k_{tp2}\mathrm{H})$,

$m_{9,4}=-(r_{SS}+n_S\lambda_S+r_{SL}\delta_{L3}+r_{SG}\delta_{G3}+2n_S\mu_S n_{tp3}{}^2)k_{tp3}{}^2\exp(\mathrm{i}n_{tp3}k_{tp3}\mathrm{H})$,

$m_{9,5}=-(r_{SS}+n_S\lambda_S+r_{SL}\delta_{L1}+r_{SG}\delta_{G1}+2n_S\mu_S n_{rp1}{}^2)k_{rp1}{}^2\exp(-\mathrm{i}n_{rp1}k_{rp1}\mathrm{H})$,
$m_{9,6}=-(r_{SS}+n_S\lambda_S+r_{SL}\delta_{L2}+r_{SG}\delta_{G2}+2n_S\mu_S n_{rp2}{}^2)k_{rp2}{}^2\exp(-\mathrm{i}n_{rp2}k_{rp2}\mathrm{H})$,
$m_{9,7}=-(r_{SS}+n_S\lambda_S+r_{SL}\delta_{L3}+r_{SG}\delta_{G3}+2n_S\mu_S n_{rp3}{}^2)k_{rp3}{}^2\exp(-\mathrm{i}n_{rp3}k_{rp3}\mathrm{H})$, $m_{9,8}=2n_S\mu_S l_{ts}n_{ts}k_{ts}{}^2\exp(\mathrm{i}n_{ts}k_{ts}\mathrm{H})$,
$m_{9,9}=-2n_S\mu_S l_{rs}n_{rs}k_{rs}{}^2\exp(-\mathrm{i}n_{rs}k_{rs}\mathrm{H})$, $m_{9,10}=(\lambda_E+2\mu_E n_{pe}{}^2)k_{pe}{}^2\exp(\mathrm{i}n_{pe}k_{pe}\mathrm{H})$,
$m_{9,11}=-2\mu_E n_{se}l_{se}k_{se}{}^2\exp(\mathrm{i}n_{se}k_{se}\mathrm{H})$; $m_{10,1}=0$, $m_{10,2}=(\delta_{L1}-1)n_{tp1}k_{tp1}\exp(\mathrm{i}n_{tp1}k_{tp1}\mathrm{H})$,
$m_{10,3}=(\delta_{L2}-1)n_{tp2}k_{tp2}\exp(\mathrm{i}n_{tp2}k_{tp2}\mathrm{H})$, $m_{10,4}=(\delta_{L3}-1)n_{tp3}k_{tp3}\exp(\mathrm{i}n_{tp3}k_{tp3}\mathrm{H})$,
$m_{10,,5}=(1-\delta_{L1})n_{rp1}k_{rp1}\exp(-\mathrm{i}n_{rp1}k_{rp1}\mathrm{H})$, $m_{10,6}=(1-\delta_{L2})n_{rp2}k_{rp2}\exp(-\mathrm{i}n_{rp2}k_{rp2}\mathrm{H})$,
$m_{10,7}=(1-\delta_{L3})n_{rp3}k_{rp3}\exp(-\mathrm{i}n_{rp3}k_{rp3}\mathrm{H})$, $m_{10,8}=l_{ts}k_{ts}(1-\delta_{LS})\exp(\mathrm{i}n_{ts}k_{ts}\mathrm{H})$,
$m_{10,9}=l_{rs}k_{rs}(1-\delta_{LS})\exp(-\mathrm{i}n_{rs}k_{rs}\mathrm{H})$, $m_{10,10}=0$, $m_{10,11}=0$; $m_{11,1}=0$, $m_{11,2}=(\delta_{G1}-1)n_{tp1}k_{tp1}\exp(\mathrm{i}n_{tp1}k_{tp1}\mathrm{H})$,
$m_{11,3}=(\delta_{L2}-1)n_{tp2}k_{tp2}\exp(\mathrm{i}n_{tp2}k_{tp2}\mathrm{H})$, $m_{11,4}=(\delta_{L3}-1)n_{tp3}k_{tp3}\exp(\mathrm{i}n_{tp3}k_{tp3}\mathrm{H})$,
$m_{11,5}=(1-\delta_{G1})n_{rp1}k_{rp1}\exp(-\mathrm{i}n_{rp1}k_{rp1}\mathrm{H})$, $m_{11,6}=(1-\delta_{G2})n_{rp2}k_{rp2}\exp(-\mathrm{i}n_{rp2}k_{rp2}\mathrm{H})$,
$m_{11,7}=(1-\delta_{G3})n_{rp3}k_{rp3}\exp(-\mathrm{i}n_{rp3}k_{rp3}\mathrm{H})$, $m_{11,8}=l_{ts}k_{ts}(1-\delta_{GS})\exp(\mathrm{i}n_{ts}k_{ts}\mathrm{H})$,
$m_{11,9}=l_{rs}k_{rs}(1-\delta_{GS})\exp(-\mathrm{i}n_{rs}k_{rs}\mathrm{H})$, $m_{11,10}=0$, $m_{11,11}=0$;

The explicit expressions of the elements of $[Q]$ are as follows:

$q_1 = K_W k_{ip}^{\ 2}$, $q_2 = -n_{ip} k_{ip}$, $q_3 = 0$, $q_4 = 0$, $q_5 = 0$, $q_6 = 0$, $q_7 = 0$, $q_8 = 0$, $q_9 = 0$, $q_{10} = 0$, $q_{10} = 0$, $q_{11} = 0$.

REFERENCES

[1] J. Geertsma, D.C. Smit, Some aspects of elastic wave propagation in fluid-saturated porous solids, *Geophysics,* **26**, 169–181, 1961.

[2] R.D. Stoll, T.K. Kan, Reflection of acoustic wave at a water-sediment interface, *J. acoust. Soc. Am.*, **70**, 149–156, 1981.

[3] K. Wu, Q. Xue, L. Adler, Reflection and transmission of elastic waves from a fluid saturated porous solid boundary, *J. acoust. Soc. Am.*, **87**, 2349–2358, 1990.

[4] J.E. Santos, J.M. Corbero, C.L. Ravazzoli, J.L. Hensley, Reflection transmission coefficients in fluid–saturated porous media, *J. acoust. Soc. Am.*, **91**, 1911–1923, 1992.

[5] A. Madeo, S. Gavrilyuk, Propagation of acoustic waves in porous media and their reflection and transmission at a pure-fluid/porous-medium permeable interface, *Eur. J. Mech. A-Solid.*, **29**, 897–910, 2010.

[6] M.D. Sharma, M. Kumar, Reflection of attenuated wave s at the surface of a porous solid saturated with two immiscible viscous fluids, *Geophys. J. I nt.* **184**, 371–384, 2011.

[7] M.A. Biot, Theory of propagation of elastic waves in a fluid-saturated porous solid. I. Low-frequency range, *J. acoust. Soc. Am.*, **28**,168–178, 1956.

[8] T.J. Plona, Observation of a second bulk compressional wave in a porous medium at ultrasonic frequencies, *Appl. Phys. Lett.* 36, 259–261, 1980.

[9] P. Nagy, L. Adler, B. Bonner, Slow wave propagation in air-filled porous materials and natural rocks, *Appl. Phys. Lett.* **56**, 2504–2506, 1990.

[10] K.L. Williams, An effective fluid model for acoustic propagation in sediments derived from Biot theory, *J. acoust. Soc. Am.*, **110**, 2276–2281, 2001.

[11] N.P. Chotiros, M.J. Isakson, A broadband model of sandy ocean sediments: Biot-Stoll with contact squirt flow and shear drag, *J. acoust. Soc. Am.*, **116**, 2011-2022, 2004.

[12] K. Ohkawa, Confirmation of the Biot theory for water-saturated sands at high frequencies and effects of scattering on the attenuation of sound waves, *J. acoust. Soc. Am.*, **119**, 709–711, 2006.

[13] D.G. Albert, A comparison between wave propagation in water-saturated and air-saturated porous materials, *Appl. Phys. Lett.*, **73**, 28–36, 1993.

[14] A.I.M. Denneman, G.G. Drijkoningen, D.M.J. Smeulders, K. Wapenaar, Reflection and transmission of waves at a fluid/porous-medium interface, *Geophysics,* **67**, 282–291, 2002.

[15] B.H. Russell, K. Hedlin, F.J. Hilterman, L. R. Lines, Fluid-property discrimination with AVO: A Biot-Gassmann perspective, *Geophysics*, 68, 29-39, 2003.

[16] K. Ohkawa, H. Yamaoka, T. Yamamoto, Acoustic backscattering from a sandy seabed, *IEEE. J. Oceanic. Eng.,* **30**, 700–708, 2005.

[17] Z.J. Dai, Z.B. Kuang, Reflection and transmission of elastic waves at the interface between water and a double porosity solid, *Transport. Porous. Med.*, **72**, 369–392, 2008.

[18] E.Y.T. Kuo, Acoustic wave scattering from two solid boundaries at the ocean bottom: Reflection loss, *IEEE. J. Oceanic. Eng.,* **17**, 159–170, 1992.

[19] M.A. Ainslie, Reflection transmission coefficients for a layered fluid sediment overlying a uniform solid substrate, *J. acoust. Soc. Am.*, **99**, 893–902, 1996.

[20] J.T. Wang, F. Jin, C.H. Zhang, Reflection and transmission of plane waves at an interface of water/porous sediment with underlying solid substrate, *Ocean. Eng.,* **63**, 8–16, 2013.

[21] D.D. Lyu, J.T. Wang, F. Jin, C.H. Zhang, Reflection and transmission of plane waves at a water–porous sediment interface with a double porosity substrate, *Transport. Porous. Med.,* **103**, 25–45, 2014.

[22] F.A. Boyle, N.P. Chotiros, A model for high frequency backscatter from gas bubbles in sandy sediments, *J. acoust. Soc. Am.*, **98**, 531–541, 1995.

[23] C. Wei, K.K. Muraleetharan, A continuum theory of porous media saturated by multiple immiscible fluids: I. Linear poroelasticity, *Int. J.Eng. Sci.*, **40**, 1807–1833, 2002.

[24] W.C. Lo, E. Majer, G. Sposito, Wave propagation through elastic porous media containing two immiscible fluids, *Water. Resour. Res.,* **41**, 1–20, 2005.

[25] J.F. Lu, A. Hanyga, Linear dynamic model for porous media saturated by two immiscible fluids, *Int. J. Solids. Struct.,* **42**, 2689–2709, 2005.

[26] B. Albers, Analysis of the propagation of sound waves in partially saturated soils by means of a macroscopic linear poroelastic model, *Transport. Porous. Med.,***80**, 173–192, 2009.

[27] W.Y. Chen, T.D. Xia, W.T. Hu, A mixture theory analysis for the surface-wave propagation in an unsaturated porous medium, *Int. J. Solids. Struct.,* **48**, 2402–2412, 2011.

[28] C.L. Yeh, W.C. Lo, C.D. Jan, C.C. Yang, Reflection and refraction of obliquely incident elastic waves upon the interface between two porous elastic half-spaces saturated by different fluid mixtures, *J Hydrol.* **395**, 91–102, 2010.

[29] W.Y. Chen, T.D. Xia, M.M. Sun, C.J. Zhai, Transverse wave at a plane interface between isotropic elastic and unsaturated porous elastic solid half-spaces, *Transport. Porous. Med.,***94**, 417–436, 2012.

[30] K.K. Muraleetharan, C. Wei, Dynamic behaviour of unsaturated porous media: Governing equations using the theory of mixtures with interfaces (TMI). *Int. J. Numer. Anal. Methods. Geomech.* **23**, 1579–1608, 1999.

[31] S.K. Garg, A.H. Nayfeh, Compressional wave propagation in liquid and or gas saturated elastic porous media. *J. Appl. Phys.*, **60**, 3045–3055, 1986.

[32] J.G. Berryman, L. Thigpen, R.C.Y. Chin, Bulk elastic wave propagation in partially saturated porous solids, *J. acoust. Soc. Am.*, **84**, 360–373, 1988.

[33] J. Fatti, G. Smith, P. Vail, P. Strauss, P. Levitt, Detection of gas in sandstone reservoirs using AVO analysis: a 3D Seismic Case History Using the Geostack Technique, *Geophysics*, **59**, 1362-1376, 1994.

[34] Russell, B.H., Hedlin, K., Hilterman, F.J. Lines, L. R., 2003. Fluid-property discrimination with AVO: A Biot-Gassmann perspective, *Geophysics*, **68**, 29-39.

[35] W.C. Lo, G. Sposito, E. Majer, Low-frequency dilatational wave propagation through unsaturated porous media containing two immiscible fluids. *Transp*. *Porous*. *Med.*, **68**, 91–105, 2007.

COMPDYN 2015
5th ECCOMAS Thematic Conference on
Computational Methods in Structural Dynamics and Earthquake Engineering
M. Papadrakakis, V. Papadopoulos, V. Plevris (eds.)
Crete Island, Greece, 25–27 May 2015

A WAVE-BASED REDUCTION TECHNIQUE FOR THE DYNAMIC BEHAVIOR OF PERIODIC STRUCTURES

Denis Duhamel [1] **and Jean-Mathieu Mencik** [2]

[1] Université Paris-Est, Laboratoire Navier, ENPC/IFSTTAR/CNRS, 6 et 8 Avenue Blaise Pascal, Cité Descartes, Champs-sur-Marne, 77455 Marne La Vallée Cedex 2, France
e-mail: denis.duhamel@enpc.fr
[2] INSA Centre Val de Loire, Université François Rabelais de Tours, LMR EA 2640, Campus de Blois, 3 Rue de la Chocolaterie, CS 23410, 41034 Blois Cedex, France
e-mail: jean-mathieu.mencik@insa-cvl.fr

Keywords: Wave Finite Element Method, Periodic Structures, Model Reduction, Structural Dynamics.

Abstract. *The wave finite element (WFE) method is investigated to describe the dynamic behavior of periodic structures like those composed of arbitrary-shaped substructures along a certain straight direction. A generalized eigenproblem based on the so-called* $\mathbf{S}+\mathbf{S}^{-1}$ *transformation is proposed for accurately computing the wave modes which travel in right and left directions along those periodic structures. Besides, a model reduction technique is proposed which involves partitioning a whole periodic structure into one central structure surrounded by two extra substructures. In doing so, a few wave modes are only required for modeling the central periodic structure. A comprehensive validation of the technique is performed on a 2D periodic structure. Also, its efficiency in terms of CPU time savings is highlighted regarding a 3D periodic structure that exhibits substructures with large-sized FE models.*

1 Introduction

Predicting the dynamic behavior of complex periodic structures like those encountered in engineering applications, by means of accurate and fast numerical tools, constitutes an open industrial challenge. In many cases, these systems are made up of arbitrary-shaped substructures which are identical to each other and are assembled along one straight direction. The need to reduce the CPU times involved by the computation of the forced response of this kind of periodic structures relates the motivation of the present paper. This issue is addressed here by means of the wave finite element (WFE) combined with an original model reduction technique.

Originally, the WFE method has been initiated to describe the wave propagation along one-dimensional periodic elastic systems [1, 2]. The computation of the forced response of bounded elastic waveguides — i.e., periodic structures which are made up of straight substructures — subject to Neumann and Dirichlet boundary conditions (BCs) has been addressed in several ways using the WFE method [3, 4, 5, 6]. The procedure consists in assessing the kinematic and mechanical fields of a structure by means of numerical wave modes traveling in right and left directions. Their computation follows by considering a generalized eigenproblem that is expressed from the mass and stiffness matrices of a particular substructure. Actually, there exist two main WFE-based strategies to compute the forced response of periodic structures. These are labeled as dynamic stiffness matrix (DSM) approach and wave amplitudes (WA) approach, and respectively involve expressing the condensed dynamic stiffness matrix of a periodic structure in terms of wave modes [3], or the vectors of wave amplitudes of the right-going and left-going modes [4, 7, 8]. The feature of the WFE method is that it makes use of the FE model of one single substructure only, rather than considering the full FE model of a whole periodic structure. This makes the WFE method quite fast for describing the dynamic behavior of periodic structures when compared to the conventional FE method and FE-based CMS methods like the Craig-Bampton method [9].

Two features are addressed in this work. One feature is the use of a generalized eigenproblem based on the so-called $\mathbf{S} + \mathbf{S}^{-1}$ transformation to compute the wave modes with accurate precision. In this context, exact analytic relations can be considered so as to ensure the coherence between the right-going and left-going wave modes. Besides, the Lanczos method [10] is used to speed up the computation of the WFE eigenproblem with a view to calculating a reduced number of wave modes only. To achieve this task, an error indicator already proposed in [11] is considered to select in an a priori process the number of wave modes that need to be computed. As a second feature of this work, an efficient model reduction technique is proposed which consists in partitioning a whole periodic structure into one central structure surrounded by two extra substructures. In doing so, a few wave modes are only required for modeling the central periodic structure, hence enabling the computation of those wave modes to be achieved in a very fast way by means of the Lanczos method.

The rest of the paper is organized as follows. In Section 2, the basics of the WFE method for describing the wave propagation along a one-dimensional periodic structure are recalled. The strategy to compute the wave modes by means of a generalized eigenproblem based on the $\mathbf{S} + \mathbf{S}^{-1}$ transformation is proposed. In Section 3, the WFE-based model reduction technique, which consists in partitioning a whole periodic structure into one central structure surrounded by two extra substructures, is fully developed. Numerical experiments are finally brought in Section 4 that concern a 2D structure as well as a 3D stiffened shell with a periodic distribution of longitudinal and circumferential stiffeners.

2 WFE method

2.1 Basic framework

The basics of the WFE method for describing waves which travel in right and left directions along a one-dimensional periodic structure (see Figure 1) are recalled hereafter.

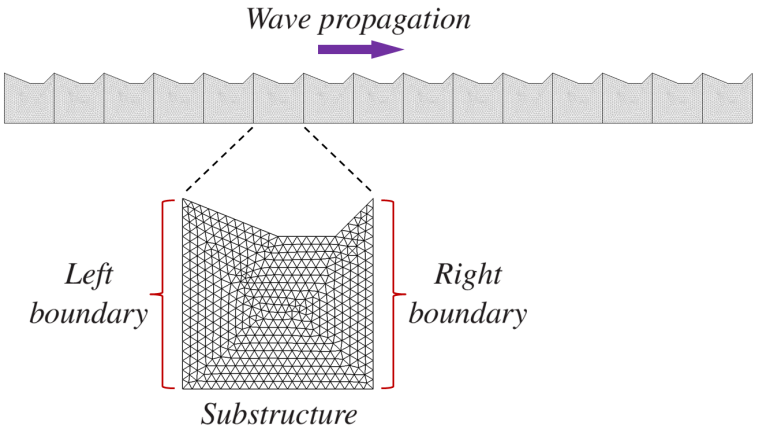


Figure 1: FE mesh of a periodic structure and related substructure.

Within the present framework, the structures are assumed to be linear, elastic and damped by means of a constant loss factor η. Also, they involve excitation sources which are assumed to be harmonic time-dependent, i.e., of the form $g(\omega)\texttt{exp}(\texttt{i}\omega t)$ where ω denotes the pulsation. Besides, the substructures are modeled by means of the same FE mesh with a same number (say, n) of DOFs over their left and right boundaries. In matrix form, the dynamic equilibrium equation of a given substructure is expressed in the frequency domain as

$$\mathbf{D}\mathbf{q} = \mathbf{F}, \tag{1}$$

where $\mathbf{D}$ is the dynamic stiffness matrix of the substructure. It is expressed as $\mathbf{D} = -\omega^2\mathbf{M} + (1 + \texttt{i}\eta)\mathbf{K}$ where $\mathbf{M}$ and $\mathbf{K}$ refer to the mass and stiffness matrices, respectively. Also in Eq. (1), $\mathbf{q}$ and $\mathbf{F}$ are, respectively, the vectors of nodal displacements/rotations and nodal forces/moments of the substructure. The key idea behind the WFE method is to express a relation which links the kinematic/mechanical quantities on the right boundary of the substructure to those on its left boundary. From Eq. (1), it is expressed as [12]:

$$\mathbf{u}_{\texttt{R}} = \mathbf{S}\mathbf{u}_{\texttt{L}}, \tag{2}$$

where $\mathbf{u}_{\texttt{R}}$ and $\mathbf{u}_{\texttt{L}}$ are $2n \times 1$ state vectors, expressed as

$$\mathbf{u}_{\texttt{R}} = \begin{bmatrix} \mathbf{q}_{\texttt{R}} \\ \mathbf{F}_{\texttt{R}} \end{bmatrix} \quad , \quad \mathbf{u}_{\texttt{L}} = \begin{bmatrix} \mathbf{q}_{\texttt{L}} \\ -\mathbf{F}_{\texttt{L}} \end{bmatrix}. \tag{3}$$

In Eq. (3), the subscripts $\texttt{L}$ and $\texttt{R}$ denote the DOFs which belong to the left and right boundaries of the substructure, respectively. Also, $\mathbf{S}$ is a $2n \times 2n$ matrix expressed as

$$\mathbf{S} = \left[\begin{array}{c|c} -\mathbf{D}_{\texttt{LR}}^{*-1}\mathbf{D}_{\texttt{LL}}^{*} & -\mathbf{D}_{\texttt{LR}}^{*-1} \\ \hline \mathbf{D}_{\texttt{RL}}^{*} - \mathbf{D}_{\texttt{RR}}^{*}\mathbf{D}_{\texttt{LR}}^{*-1}\mathbf{D}_{\texttt{LL}}^{*} & -\mathbf{D}_{\texttt{RR}}^{*}\mathbf{D}_{\texttt{LR}}^{*-1} \end{array} \right], \tag{4}$$

where $\mathbf{D}^*$ refers to the dynamic stiffness matrix of the substructure condensed on its left and right boundaries.

We are looking for wavemodes $\{(\mu_j, \boldsymbol{\phi}_j)\}_j$ which are the eigenvalues and the eigenvectors of the matrix $\mathbf{S}$ such that

$$\mathbf{S}\boldsymbol{\phi}_j = \mu_j \boldsymbol{\phi}_j \tag{5}$$

Due to the symplectic nature of the matrix $\mathbf{S}$, its eigenvalues come in pairs as $(\mu_j, 1/\mu_j)$. So the set $\{(\mu_j, \boldsymbol{\phi}_j)\}_j$ can be partitioned into n right-going wave modes $\{(\mu_j, \boldsymbol{\phi}_j)\}_{j=1,\ldots,n}$ for which $|\mu_j| < 1$, and n left-going wave modes $\{(\mu_j^\star, \boldsymbol{\phi}_j^\star)\}_{j=1,\ldots,n}$ for which $\mu_j^\star = 1/\mu_j$, with $|\mu_j^\star| > 1$.

2.2 Wave mode computation

To find the eigenvectors and eigenvalues of $\mathbf{S}$, the so-called $\mathbf{S} + \mathbf{S}^{-1}$ transformation of the eigenproblem is considered [13], which yields an eigenproblem whose eigenvalues are of the form $\lambda_j = \mu_j + 1/\mu_j$, i.e.

$$\left((\mathbf{N}'\mathbf{J}\mathbf{L}'^T + \mathbf{L}'\mathbf{J}\mathbf{N}'^T) - \lambda_j \mathbf{L}'\mathbf{J}\mathbf{L}'^T \right) \mathbf{z}_j = \mathbf{0}, \tag{6}$$

where

$$\mathbf{L}' = \begin{bmatrix} \mathbf{0} & \mathbf{I}_n \\ \mathbf{D}^*_{\mathtt{LR}} & \mathbf{0} \end{bmatrix} \quad , \quad \mathbf{N}' = \begin{bmatrix} \mathbf{D}^*_{\mathtt{RL}} & \mathbf{0} \\ -(\mathbf{D}^*_{\mathtt{LL}} + \mathbf{D}^*_{\mathtt{RR}}) & -\mathbf{I}_n \end{bmatrix} \quad , \quad \mathbf{J} = \begin{bmatrix} \mathbf{0} & \mathbf{I}_n \\ -\mathbf{I}_n & \mathbf{0} \end{bmatrix}. \tag{7}$$

$$\mathbf{N}'\mathbf{J}\mathbf{L}'^T + \mathbf{L}'\mathbf{J}\mathbf{N}'^T = \begin{bmatrix} \mathbf{D}^*_{\mathtt{RL}} - \mathbf{D}^*_{\mathtt{LR}} & (\mathbf{D}^*_{\mathtt{LL}} + \mathbf{D}^*_{\mathtt{RR}}) \\ -(\mathbf{D}^*_{\mathtt{LL}} + \mathbf{D}^*_{\mathtt{RR}}) & \mathbf{D}^*_{\mathtt{RL}} - \mathbf{D}^*_{\mathtt{LR}} \end{bmatrix}, \tag{8}$$

and

$$\mathbf{L}'\mathbf{J}\mathbf{L}'^T = \mathbf{N}'\mathbf{J}\mathbf{N}'^T = \begin{bmatrix} \mathbf{0} & -\mathbf{D}^*_{\mathtt{RL}} \\ \mathbf{D}^*_{\mathtt{LR}} & \mathbf{0} \end{bmatrix}. \tag{9}$$

One feature of the eigenproblem (6) is that it involves skew-symmetric matrices which are useful for speeding up the computation of the eigensolutions. Also, the eigenvectors $\{\mathbf{z}_j\}_j$ are expressed in terms of displacement/rotation components only. It is worth recalling that the eigenvalues of the eigenproblem come in pairs as $(\mu_j, \mu_j^\star = 1/\mu_j)$, meaning that the eigenvalues of the eigenproblem (6) are double, i.e., $(\lambda_j, \lambda_j^\star = \lambda_j)$. By considering the fact that $\lambda_j = \mu_j + 1/\mu_j$, each pair of eigenvalues $(\mu_j, \mu_j^\star)$ can be found analytically by solving a quadratic equation of the form

$$x^2 - \lambda_j x + 1 = 0, \tag{10}$$

where it is understood that the relation $\mu_j^\star = 1/\mu_j$ can be verified with accurate precision. Also, there exist closed-form expressions linking the eigenvectors of the eigenproblem (6) to those of $\mathbf{S}$ (see [14]):

$$\mathbf{w}'_j = \mathbf{J}(\mathbf{L}'^T - \mu_j^\star \mathbf{N}'^T)\mathbf{z}_j \quad , \quad \mathbf{w}'^\star_j = \mathbf{J}(\mathbf{L}'^T - \mu_j \mathbf{N}'^T)\mathbf{z}_j. \tag{11}$$

$$\boldsymbol{\phi}_j = \begin{bmatrix} \mathbf{I}_n & \mathbf{0} \\ \mathbf{D}^*_{\mathtt{RR}} & \mathbf{I}_n \end{bmatrix} \mathbf{w}'_j \quad , \quad \boldsymbol{\phi}_j^\star = \begin{bmatrix} \mathbf{I}_n & \mathbf{0} \\ \mathbf{D}^*_{\mathtt{RR}} & \mathbf{I}_n \end{bmatrix} \mathbf{w}'^\star_j, \tag{12}$$

where $\{\mathbf{w}'^\star_j\}_j$ denote the eigenvectors associated to the eigenvalues $\{\mu_j^\star\}_j$ which are such that $|\mu_j^\star| > 1$ and the wave shapes $\{\boldsymbol{\phi}_j\}_j$ and $\{\boldsymbol{\phi}_j^\star\}_j$ are the eigenvectors of $\mathbf{S}$. The state vector $\mathbf{u}^{(k)}_{\mathtt{L}}$ in section k can be expanded as $\mathbf{u}^{(k)}_{\mathtt{L}} = \sum_j \mathtt{exp}(-\mathtt{i}\beta_j d) Q_j^{(k-1)} \boldsymbol{\phi}_j$. Also, the eigenvalues of $\mathbf{S}$ are expressed as $\mu_j = \mathtt{exp}(-\mathtt{i}\beta_j d)$, where $\{\beta_j\}_j$ have the meaning of wavenumbers.

2.3 Forced response computation

We consider here the structure shown in figure 2 which is made of a periodic part connected to two elastic subsystems. The focus is on a better modeling of the periodic part. In fact, there exist two main strategies for computing the forced response of a periodic structure, as shown in Figure 2, namely the dynamic stiffness matrix (DSM) approach and the wave amplitude (WA) approach. The DSM approach focuses on expressing a matrix relation to link the vector of forces/moments to that of displacements/rotations on the left and right ends of the structure. On the other hand, the WA approach focuses on assessing the wave reflection/transmission coefficients at the BCs while considering the spatial variation of the wave amplitudes along the structure.

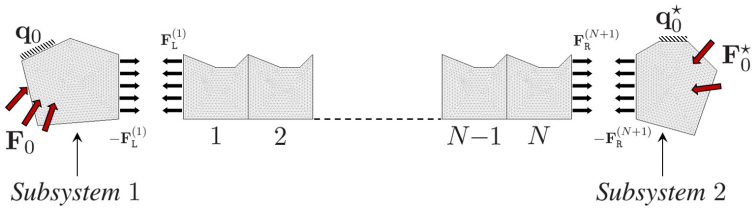


Figure 2: Periodic structure connected to two elastic subsystems.

2.3.1 DSM approach

The framework of the DSM approach is to consider the following matrix equation, which links the DOFs on the left and right ends of a periodic structure made up of N substructures:

$$\begin{bmatrix} \mathbf{F}_{\mathtt{L}}^{(1)} \\ \mathbf{F}_{\mathtt{R}}^{(N+1)} \end{bmatrix} = \mathbf{D}_s \begin{bmatrix} \mathbf{q}_{\mathtt{L}}^{(1)} \\ \mathbf{q}_{\mathtt{R}}^{(N+1)} \end{bmatrix}, \tag{13}$$

where the superscripts (1) and $(N+1)$ denote the left and right ends of the structure, respectively. Also, $\mathbf{D}_s$ is the dynamic stiffness matrix of the structure which is condensed on its left and right ends. It is expressed as (see [3])

$$\begin{aligned} \mathbf{D}_s \;=\; & \begin{bmatrix} \mathbf{D}_{\mathtt{LL}}^* & \mathbf{0} \\ \mathbf{0} & \mathbf{D}_{\mathtt{RR}}^* \end{bmatrix} + \begin{bmatrix} \mathbf{D}_{\mathtt{LR}}^* & \mathbf{0} \\ \mathbf{0} & \mathbf{D}_{\mathtt{RL}}^* \end{bmatrix} \begin{bmatrix} \boldsymbol{\Phi}_{\mathtt{q}}^\star \boldsymbol{\mu}^{N-1} \boldsymbol{\Phi}_{\mathtt{q}}^{\star -1} & \boldsymbol{\Phi}_{\mathtt{q}} \boldsymbol{\mu} \boldsymbol{\Phi}_{\mathtt{q}}^{-1} \\ \boldsymbol{\Phi}_{\mathtt{q}}^\star \boldsymbol{\mu} \boldsymbol{\Phi}_{\mathtt{q}}^{\star -1} & \boldsymbol{\Phi}_{\mathtt{q}} \boldsymbol{\mu}^{N-1} \boldsymbol{\Phi}_{\mathtt{q}}^{-1} \end{bmatrix} \\ & \times \begin{bmatrix} \boldsymbol{\Phi}_{\mathtt{q}}^\star \boldsymbol{\mu}^{N} \boldsymbol{\Phi}_{\mathtt{q}}^{\star -1} & \mathbf{I}_n \\ \mathbf{I}_n & \boldsymbol{\Phi}_{\mathtt{q}} \boldsymbol{\mu}^{N} \boldsymbol{\Phi}_{\mathtt{q}}^{-1} \end{bmatrix}^{-1}, \end{aligned} \tag{14}$$

where $\boldsymbol{\Phi}_{\mathtt{q}}$ and $\boldsymbol{\Phi}_{\mathtt{q}}^\star$ are square $n \times n$ matrices defined as $\boldsymbol{\Phi}_{\mathtt{q}} = [\boldsymbol{\phi}_{\mathtt{q}1} \cdots \boldsymbol{\phi}_{\mathtt{q}n}]$ and $\boldsymbol{\Phi}_{\mathtt{q}}^\star = [\boldsymbol{\phi}_{\mathtt{q}1}^\star \cdots \boldsymbol{\phi}_{\mathtt{q}n}^\star]$. Also, $\boldsymbol{\mu}$ is a $n \times n$ diagonal matrix whose components relate the eigenvalues for the right-going wave modes (see Section 2.1), i.e., $\boldsymbol{\mu} = \mathtt{diag}\{\mu_j\}_{j=1,\ldots,n}$. Notice that the $2-$norm [10] of the matrix $\boldsymbol{\mu}$ is less than one, i.e., $\|\boldsymbol{\mu}\|_2 < 1$, which is explained because $\|\boldsymbol{\mu}\|_2 = \mathtt{max}|\mu_j| < 1$ by convention. The dynamic stiffness matrix $\mathbf{D}_s$ of the periodic structure can be readily assembled with the dynamic stiffness matrices of other elastic subsystems as this is usually done in the FE method, with a view to expressing a global dynamic stiffness matrix.

2.3.2 WA approach

Within the WFE framework, the vectors of displacements/rotations and forces/moments on the substructure boundary (k) are estimated by means of a wave expansion, as follows [8]:

$$\mathbf{q}^{(k)} = \mathbf{\Phi}_{\mathtt{q}}\boldsymbol{\mu}^{k-1}\mathbf{Q} + \mathbf{\Phi}^{\star}_{\mathtt{q}}\boldsymbol{\mu}^{N+1-k}\mathbf{Q}^{\star} \quad , \quad \pm\mathbf{F}^{(k)} = \mathbf{\Phi}_{\mathtt{F}}\boldsymbol{\mu}^{k-1}\mathbf{Q} + \mathbf{\Phi}^{\star}_{\mathtt{F}}\boldsymbol{\mu}^{N+1-k}\mathbf{Q}^{\star}, \tag{15}$$

where $\mathbf{\Phi}_{\mathtt{F}} = [\boldsymbol{\phi}_{\mathtt{F}1} \cdots \boldsymbol{\phi}_{\mathtt{F}n}]$ and $\mathbf{\Phi}^{\star}_{\mathtt{F}} = [\boldsymbol{\phi}^{\star}_{\mathtt{F}1} \cdots \boldsymbol{\phi}^{\star}_{\mathtt{F}n}]$. Also, in Eq. (15), $\mathbf{Q}$ and $\mathbf{Q}^{\star}$ are vectors of wave amplitudes at the left and right ends of the whole periodic structure, respectively. Finally, the sign ahead of $\mathbf{F}$ results from the choice of description considered, i.e., it is negative when the left boundary of a substructure is of concern, and positive for the right boundary.

The determination of the vectors of wave amplitudes $\mathbf{Q}$ and $\mathbf{Q}^{\star}$ involves considering the BCs on the left and right ends of the whole periodic structure. For instance, regarding the case shown in Figure 2 when the left and right ends of the periodic structure are connected to extra elastic subsystems, the BCs are expressed as:

$$-\mathbf{F}^{(1)}_{\mathtt{L}} = \mathbb{D}\mathbf{q}^{(1)}_{\mathtt{L}} + \mathbb{D}_{\mathtt{q}}\mathbf{q}_0 + \mathbb{D}_{\mathtt{F}}\mathbf{F}_0 \quad , \quad -\mathbf{F}^{(N+1)}_{\mathtt{R}} = \mathbb{D}^{\star}\mathbf{q}^{(N+1)}_{\mathtt{R}} + \mathbb{D}^{\star}_{\mathtt{q}}\mathbf{q}^{\star}_0 + \mathbb{D}^{\star}_{\mathtt{F}}\mathbf{F}^{\star}_0, \tag{16}$$

where $\mathbb{D}$ and $\mathbb{D}^{\star}$ denote the dynamic stiffness matrices of the subsystems which are condensed on the interface DOFs. Also, $\mathbb{D}_{\mathtt{q}}$ and $\mathbb{D}^{\star}_{\mathtt{q}}$ (resp. $\mathbb{D}_{\mathtt{F}}$ and $\mathbb{D}^{\star}_{\mathtt{F}}$) are matrices which reflect the effects of prescribed vectors of displacements/rotations ($\mathbf{q}_0$,$\mathbf{q}^{\star}_0$) (resp. prescribed vectors of forces/moments ($\mathbf{F}_0$,$\mathbf{F}^{\star}_0$)) that may be applied to the subsystems.

By considering the wave expansion (15), the BCs can be expressed in wave-based form, as follows:

$$\mathbf{Q} = \mathbb{C}\boldsymbol{\mu}^{N}\mathbf{Q}^{\star} + \mathbb{F} \quad , \quad \mathbf{Q}^{\star} = \mathbb{C}^{\star}\boldsymbol{\mu}^{N}\mathbf{Q} + \mathbb{F}^{\star}, \tag{17}$$

where $\mathbb{C}$ and $\mathbb{C}^{\star}$ are $n \times n$ scattering matrices whose components relate the reflection coefficients for the wave modes incident to the boundaries, while $\mathbb{F}$ and $\mathbb{F}^{\star}$ are $n \times 1$ vectors which relate the effects of the excitation sources. Expressions for $\mathbb{C}$, $\mathbb{C}^{\star}$, $\mathbb{F}$ and $\mathbb{F}^{\star}$ follow from the aforementioned BCs, i.e:

$$\begin{aligned} \mathbb{C} &= -[\mathbb{D}\mathbf{\Phi}_{\mathtt{q}} - \mathbf{\Phi}_{\mathtt{F}}]^{-1}[\mathbb{D}\mathbf{\Phi}^{\star}_{\mathtt{q}} - \mathbf{\Phi}^{\star}_{\mathtt{F}}] \quad , \quad \mathbb{C}^{\star} = -[\mathbb{D}^{\star}\mathbf{\Phi}^{\star}_{\mathtt{q}} + \mathbf{\Phi}^{\star}_{\mathtt{F}}]^{-1}[\mathbb{D}^{\star}\mathbf{\Phi}_{\mathtt{q}} + \mathbf{\Phi}_{\mathtt{F}}], \\ \mathbb{F} &= -[\mathbb{D}\mathbf{\Phi}_{\mathtt{q}} - \mathbf{\Phi}_{\mathtt{F}}]^{-1}[\mathbb{D}_{\mathtt{q}}\mathbf{q}_0 + \mathbb{D}_{\mathtt{F}}\mathbf{F}_0] \quad , \quad \mathbb{F}^{\star} = -[\mathbb{D}^{\star}\mathbf{\Phi}_{\mathtt{q}} + \mathbf{\Phi}_{\mathtt{F}}]^{-1}[\mathbb{D}^{\star}_{\mathtt{q}}\mathbf{q}^{\star}_0 + \mathbb{D}^{\star}_{\mathtt{F}}\mathbf{F}^{\star}_0]. \end{aligned} \tag{18}$$

By considering the wave-based BCs, Eq. (17), a whole matrix equation is established as follows:

$$\mathcal{A}\mathcal{Q} = \mathcal{F}, \tag{19}$$

where

$$\mathcal{A} = \begin{bmatrix} \mathbf{I}_n & -\mathbb{C}\boldsymbol{\mu}^{N} \\ -\mathbb{C}^{\star}\boldsymbol{\mu}^{N} & \mathbf{I}_n \end{bmatrix} \quad , \quad \mathcal{Q} = \begin{bmatrix} \mathbf{Q} \\ \mathbf{Q}^{\star} \end{bmatrix} \quad , \quad \mathcal{F} = \begin{bmatrix} \mathbb{F} \\ \mathbb{F}^{\star} \end{bmatrix}. \tag{20}$$

Solving the matrix equation (19) yields the vectors of wave amplitudes as $\mathcal{Q} = \mathcal{A}^{-1}\mathcal{F}$.

3 Model reduction

3.1 Motivation and framework

As it is well known, waves traveling along a structure like the one shown in Figure 1 can be classified into weakly evanescent, which would be propagative if there were no damping, and strongly evanescent, i.e., which decay exponentially from the excitation sources. So, one may assume that far from the sources these evanescent waves are weakly contributing to the

structure dynamics. Here, a central periodic structure consisting of $N-2$ substructures is considered which is surrounded by two extra substructures. Such a central periodic structure is analyzed by means of the WFE method (Section 2.3), while the extra substructures are modeled by means of the FE method and are treated as BCs like those involved by Eq. (18).

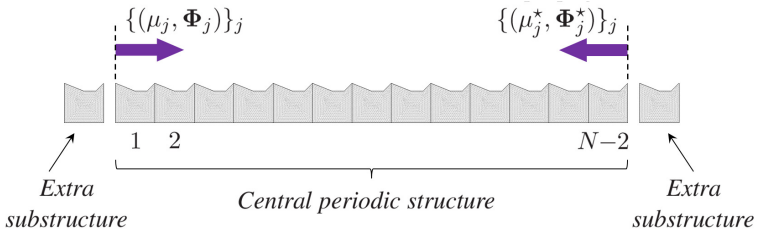


Figure 3: Central periodic structure surrounded by two extra substructures.

Prior to any rigorous derivation, a simple qualitative analysis is proposed here to quantify the error made when some strong evanescent wave modes are neglected in the WFE-based formulations. Consider the central periodic structure as shown in Figure 3, which is enclosed between the substructure boundary (1) and the substructure boundary $(N-1)$. Assume that the excitation sources occur on the left boundary of the left extra substructure, and the right boundary of the right extra substructure, only. Denote as $\mathbf{Q}$ the vector of wave amplitudes at the left end of the left extra substructure, and $\mathbf{Q}^\star$ the vector of wave amplitudes at the right end of the right extra substructure. By considering the wave expansion (15), the vectors of displacements/rotations and forces/moments along the central periodic structure are expressed as

$$\mathbf{q}^{(k)} = \sum_{j=1}^{n} \left(\mu_j^k \mathbf{q}_j + \mu_j^{N-k} \mathbf{q}_j^\star \right) = \sum_{j=1}^{n} \mu_j \left(\mu_j^{k-1} \mathbf{q}_j + \mu_j^{N-1-k} \mathbf{q}_j^\star \right), \tag{21}$$

$$\pm \mathbf{F}^{(k)} = \sum_{j=1}^{n} \left(\mu_j^k \mathbf{F}_j + \mu_j^{N-k} \mathbf{F}_j^\star \right) = \sum_{j=1}^{n} \mu_j \left(\mu_j^{k-1} \mathbf{F}_j + \mu_j^{N-1-k} \mathbf{F}_j^\star \right), \tag{22}$$

where $\mathbf{q}_j = Q_j \mathbf{\Phi}_{\mathbf{q}j}$, $\mathbf{q}_j^\star = Q_j^\star \mathbf{\Phi}_{\mathbf{q}j}$, $\mathbf{F}_j = Q_j \mathbf{\Phi}_{\mathbf{F}j}$ and $\mathbf{F}_j^\star = Q_j^\star \mathbf{\Phi}_{\mathbf{F}j}^\star$. Since the integer k is such that $1 \leq k \leq N-1$, one has $k-1 \geq 0$ and $N-1-k \geq 0$, and then $|\mu_j|^{k-1} \leq 1$ and $|\mu_j|^{N-1-k} \leq 1$. This is explained because $|\mu_j| < 1$ by convention. Let us denote as $\bar{\mathbf{q}}^{(k)}$ and $\bar{\mathbf{F}}^{(k)}$ the parts of the vectors of displacements/rotations and forces/moments which are induced by strongly evanescent wave modes, only. Denote as $\{(\bar{\mu}_j, \bar{\boldsymbol{\phi}}_j)\}_{j=1,\ldots,n-m}$ and $\{(\bar{\mu}_j^\star, \bar{\boldsymbol{\phi}}_j^\star)\}_{j=1,\ldots,n-m}$ those evanescent wave modes which are such that $\{(\bar{\mu}_j, \bar{\boldsymbol{\phi}}_j)\}_{j=1,\ldots,n-m} \subset \{(\mu_j, \boldsymbol{\phi}_j)\}_{j=1,\ldots,n}$ and $\{(\bar{\mu}_j^\star, \bar{\boldsymbol{\phi}}_j^\star)\}_{j=1,\ldots,n-m} \subset \{(\mu_j^\star, \boldsymbol{\phi}_j^\star)\}_{j=1,\ldots,n}$ where $m > 1$. From Eqs. (21) and (22), $\bar{\mathbf{q}}^{(k)}$ and $\bar{\mathbf{F}}^{(k)}$ are expressed as

$$\|\bar{\mathbf{q}}^{(k)}\| = \| \sum_{j=1}^{n-m} \bar{\mu}_j \left(\bar{\mu}_j^{k-1} \bar{\mathbf{q}}_j + \bar{\mu}_j^{N-1-k} \bar{\mathbf{q}}_j^\star \right) \| \leq \sum_{j=1}^{n-m} |\bar{\mu}_j| \left(\|\bar{\mathbf{q}}_j\| + \|\bar{\mathbf{q}}_j^\star\| \right), \tag{23}$$

$$\|\bar{\mathbf{F}}^{(k)}\| = \| \sum_{j=1}^{n-m} \bar{\mu}_j \left(\bar{\mu}_j^{k-1} \bar{\mathbf{F}}_j + \bar{\mu}_j^{N-1-k} \bar{\mathbf{F}}_j^\star \right) \| \leq \sum_{j=1}^{n-m} |\bar{\mu}_j| \left(\|\bar{\mathbf{F}}_j\| + \|\bar{\mathbf{F}}_j^\star\| \right), \tag{24}$$

where $\|.\|$ denotes the $2-$norm. Since highly evanescent wave modes are of concern, one expects $|\bar{\mu}_j| \ll 1$. To summarize, it seems logical to neglect these wave modes.

3.2 Reduced modelings

3.2.1 DSM approach

By expanding the vectors of displacements/rotations and forces/moments of the structure onto the reduced wave basis $\{\tilde{\boldsymbol{\phi}}_j\}_{j=1,\ldots,m} \cup \{\tilde{\boldsymbol{\phi}}_j^\star\}_{j=1,\ldots,m}$, the dynamic stiffness matrix of the central periodic structure — namely, $\mathbf{D}_s^r$ — can be approximated as $\mathbf{D}_s^r \approx \tilde{\mathbf{D}}_s^r$, where $\tilde{\mathbf{D}}_s^r$ is defined so that

$$\begin{bmatrix} \tilde{\mathbf{F}}_{\mathtt{L}}^{(1)} \\ \tilde{\mathbf{F}}_{\mathtt{R}}^{(N-1)} \end{bmatrix} = \tilde{\mathbf{D}}_s^r \begin{bmatrix} \tilde{\mathbf{q}}_{\mathtt{L}}^{(1)} \\ \tilde{\mathbf{q}}_{\mathtt{R}}^{(N-1)} \end{bmatrix}. \tag{25}$$

Here, $\tilde{\mathbf{q}}_{\mathtt{L}}^{(1)}$ and $\tilde{\mathbf{F}}_{\mathtt{L}}^{(1)}$ (resp. $\tilde{\mathbf{q}}_{\mathtt{R}}^{(N-1)}$ and $\tilde{\mathbf{F}}_{\mathtt{R}}^{(N-1)}$) refer to the approximated vectors of displacements/rotations and forces/vectors, respectively, on the left (resp. right) end of the central structure. The derivation of the dynamic stiffness matrix $\tilde{\mathbf{D}}_s^r$ follows from that of $\mathbf{D}_s$, i.e.

$$\begin{aligned} \tilde{\mathbf{D}}_s^r \;=\; & \begin{bmatrix} \mathbf{D}_{\mathtt{LL}}^* & \mathbf{0} \\ \mathbf{0} & \mathbf{D}_{\mathtt{RR}}^* \end{bmatrix} + \begin{bmatrix} \mathbf{D}_{\mathtt{LR}}^* & \mathbf{0} \\ \mathbf{0} & \mathbf{D}_{\mathtt{RL}}^* \end{bmatrix} \begin{bmatrix} \tilde{\boldsymbol{\Phi}}_{\mathtt{q}}^\star \tilde{\boldsymbol{\mu}}^{N-3} \tilde{\boldsymbol{\Phi}}_{\mathtt{q}}^{\star +} & \tilde{\boldsymbol{\Phi}}_{\mathtt{q}} \tilde{\boldsymbol{\mu}} \tilde{\boldsymbol{\Phi}}_{\mathtt{q}}^{+} \\ \tilde{\boldsymbol{\Phi}}_{\mathtt{q}}^\star \tilde{\boldsymbol{\mu}} \tilde{\boldsymbol{\Phi}}_{\mathtt{q}}^{\star +} & \tilde{\boldsymbol{\Phi}}_{\mathtt{q}} \tilde{\boldsymbol{\mu}}^{N-3} \tilde{\boldsymbol{\Phi}}_{\mathtt{q}}^{+} \end{bmatrix} \\ & \times \begin{bmatrix} \tilde{\boldsymbol{\Phi}}_{\mathtt{q}}^\star \tilde{\boldsymbol{\mu}}^{N-2} \tilde{\boldsymbol{\Phi}}_{\mathtt{q}}^{\star +} & \mathbf{I}_m \\ \mathbf{I}_m & \tilde{\boldsymbol{\Phi}}_{\mathtt{q}} \tilde{\boldsymbol{\mu}}^{N-2} \tilde{\boldsymbol{\Phi}}_{\mathtt{q}}^{+} \end{bmatrix}^{-1} \end{aligned} \tag{26}$$

where $\tilde{\boldsymbol{\Phi}}_{\mathtt{q}}$ and $\tilde{\boldsymbol{\Phi}}_{\mathtt{q}}^\star$ are $n \times m$ rectangular matrices defined so that $\tilde{\boldsymbol{\Phi}}_{\mathtt{q}} = [\tilde{\boldsymbol{\phi}}_{\mathtt{q}1} \cdots \tilde{\boldsymbol{\phi}}_{\mathtt{q}m}]$ and $\tilde{\boldsymbol{\Phi}}_{\mathtt{q}}^\star = [\tilde{\boldsymbol{\phi}}_{\mathtt{q}1}^\star \cdots \tilde{\boldsymbol{\phi}}_{\mathtt{q}m}^\star]$; also $\tilde{\boldsymbol{\mu}}$ is a $m \times m$ diagonal matrix defined as $\tilde{\boldsymbol{\mu}} = \mathtt{diag}\{\tilde{\mu}_j\}_{j=1,\ldots,m}$; finally, $\tilde{\boldsymbol{\Phi}}_{\mathtt{q}}^+$ and $\tilde{\boldsymbol{\Phi}}_{\mathtt{q}}^{\star +}$ are the left pseudo-inverses of $\tilde{\boldsymbol{\Phi}}_{\mathtt{q}}$ and $\tilde{\boldsymbol{\Phi}}_{\mathtt{q}}^\star$, which are defined so that $\tilde{\boldsymbol{\Phi}}_{\mathtt{q}}^+ = [\tilde{\boldsymbol{\Phi}}_{\mathtt{q}}^H \tilde{\boldsymbol{\Phi}}_{\mathtt{q}}]^{-1} \tilde{\boldsymbol{\Phi}}_{\mathtt{q}}^H$ and $\tilde{\boldsymbol{\Phi}}_{\mathtt{q}}^{\star +} = [\tilde{\boldsymbol{\Phi}}_{\mathtt{q}}^{\star H} \tilde{\boldsymbol{\Phi}}_{\mathtt{q}}^\star]^{-1} \tilde{\boldsymbol{\Phi}}_{\mathtt{q}}^{\star H}$, where the superscript H is the conjugate transpose. The dynamic stiffness matrix $\tilde{\mathbf{D}}_s^r$ is to be assembled with the dynamic stiffness matrices of the left and right extra substructures (Figure 3) to express the dynamic stiffness matrix $\tilde{\mathbf{D}}_s$ of the whole periodic structure, i.e., the one composed of N substructures.

3.2.2 WA approach

From Eq. (15), the approximated vectors of nodal displacements/rotations and forces/moments on a substructure boundary (k) $(1 \leq k \leq N-1)$ along the central periodic structure are expressed as

$$\tilde{\mathbf{q}}^{(k)} = \tilde{\boldsymbol{\Phi}}_{\mathtt{q}} \tilde{\boldsymbol{\mu}}^{k-1} \tilde{\mathbf{Q}} + \tilde{\boldsymbol{\Phi}}_{\mathtt{q}}^\star \tilde{\boldsymbol{\mu}}^{N-1-k} \tilde{\mathbf{Q}}^\star \quad , \quad \pm \tilde{\mathbf{F}}^{(k)} = \tilde{\boldsymbol{\Phi}}_{\mathtt{F}} \tilde{\boldsymbol{\mu}}^{k-1} \tilde{\mathbf{Q}} + \tilde{\boldsymbol{\Phi}}_{\mathtt{F}}^\star \tilde{\boldsymbol{\mu}}^{N-1-k} \tilde{\mathbf{Q}}^\star, \tag{27}$$

where $\tilde{\boldsymbol{\Phi}}_{\mathtt{q}} = [\tilde{\boldsymbol{\phi}}_{\mathtt{q}1} \cdots \tilde{\boldsymbol{\phi}}_{\mathtt{q}m}]$, $\tilde{\boldsymbol{\Phi}}_{\mathtt{q}}^\star = [\tilde{\boldsymbol{\phi}}_{\mathtt{q}1}^\star \cdots \tilde{\boldsymbol{\phi}}_{\mathtt{q}m}^\star]$, $\tilde{\boldsymbol{\Phi}}_{\mathtt{F}} = [\tilde{\boldsymbol{\phi}}_{\mathtt{F}1} \cdots \tilde{\boldsymbol{\phi}}_{\mathtt{F}m}]$ and $\tilde{\boldsymbol{\Phi}}_{\mathtt{F}}^\star = [\tilde{\boldsymbol{\phi}}_{\mathtt{F}1}^\star \cdots \tilde{\boldsymbol{\phi}}_{\mathtt{F}m}^\star]$. The computation of $\tilde{\mathbf{Q}}$ and $\tilde{\mathbf{Q}}^\star$ follows from the following reduced matrix equation (cf. Eq. (19)):

$$\tilde{\mathcal{A}} \tilde{\mathcal{Q}} = \tilde{\mathcal{F}}, \tag{28}$$

where

$$\tilde{\mathcal{A}} = \begin{bmatrix} \mathbf{I}_m & -\tilde{\mathbb{C}} \tilde{\boldsymbol{\mu}}^{N-2} \\ -\tilde{\mathbb{C}}^\star \tilde{\boldsymbol{\mu}}^{N-2} & \mathbf{I}_m \end{bmatrix} \quad , \quad \tilde{\mathcal{Q}} = \begin{bmatrix} \tilde{\mathbf{Q}} \\ \tilde{\mathbf{Q}}^\star \end{bmatrix} \quad , \quad \tilde{\mathcal{F}} = \begin{bmatrix} \tilde{\mathbb{F}} \\ \tilde{\mathbb{F}}^\star \end{bmatrix}. \tag{29}$$

$$\tilde{\mathbb{C}} = -[\mathbb{D} \tilde{\boldsymbol{\Phi}}_{\mathtt{q}} - \tilde{\boldsymbol{\Phi}}_{\mathtt{F}}]^+ [\mathbb{D} \tilde{\boldsymbol{\Phi}}_{\mathtt{q}}^\star - \tilde{\boldsymbol{\Phi}}_{\mathtt{F}}^\star] \quad , \quad \tilde{\mathbb{C}}^\star = -[\mathbb{D}^\star \tilde{\boldsymbol{\Phi}}_{\mathtt{q}}^\star + \tilde{\boldsymbol{\Phi}}_{\mathtt{F}}^\star]^+ [\mathbb{D}^\star \tilde{\boldsymbol{\Phi}}_{\mathtt{q}} + \tilde{\boldsymbol{\Phi}}_{\mathtt{F}}], \tag{30}$$

$$\tilde{\mathbb{F}} = -[\mathbb{D} \tilde{\boldsymbol{\Phi}}_{\mathtt{q}} - \tilde{\boldsymbol{\Phi}}_{\mathtt{F}}]^+ [\mathbb{D}_{\mathtt{q}} \mathbf{q}_0 + \mathbb{D}_{\mathtt{F}} \mathbf{F}_0] \quad , \quad \tilde{\mathbb{F}}^\star = -[\mathbb{D}^\star \tilde{\boldsymbol{\Phi}}_{\mathtt{q}} + \tilde{\boldsymbol{\Phi}}_{\mathtt{F}}]^+ [\mathbb{D}_{\mathtt{q}}^\star \mathbf{q}_0^\star + \mathbb{D}_{\mathtt{F}}^\star \mathbf{F}_0^\star], \tag{31}$$

where the superscript $+$ denotes the left pseudo-inverse.

3.3 Error indicator

The selection of the number m of right-going and left-going wave modes in the central periodic structure that need to be computed from the Lanczos method is addressed here using the strategy proposed in [11]. In this work, it is suggested to bound the relative errors, for the vectors of nodal displacements/rotations and forces/moments, as follows:

$$\frac{\|\widetilde{\mathbf{q}}^{(k)}-\mathbf{q}^{(k)}\|}{\|\mathbf{q}^{(k)}\|}\leq\mathcal{E}_s \quad , \quad \frac{\|\widetilde{\mathbf{F}}^{(k)}-\mathbf{F}^{(k)}\|}{\|\mathbf{F}^{(k)}\|}\leq\mathcal{E}_s \qquad \forall k, \tag{32}$$

where

$$\begin{aligned}\mathcal{E}_s \;=\; \mathtt{max}\Bigg\{&\left[(\epsilon_1^{\mathbf{E}}+\epsilon_2^{\mathbf{E}})+\frac{\|\mathbf{A}^s\|}{1-\|\mathbf{A}^s\|}(\epsilon_1^{\mathbf{A}}+\epsilon_2^{\mathbf{A}})\right]\frac{1+\|\mathbf{A}^s\|}{1-\|\mathbf{A}^s\|} \quad , \\ &\left[(\epsilon_1^{\mathbf{E}^\star}+\epsilon_2^{\mathbf{E}^\star})+\frac{\|\mathbf{A}^{\star s}\|}{1-\|\mathbf{A}^{\star s}\|}(\epsilon_1^{\mathbf{A}^\star}+\epsilon_2^{\mathbf{A}^\star})\right]\frac{1+\|\mathbf{A}^{\star s}\|}{1-\|\mathbf{A}^{\star s}\|}\Bigg\}.\end{aligned} \tag{33}$$

Within the present framework, those matrix/vector terms are expressed as:

$$\mathbf{A}=\mathbb{C}\boldsymbol{\mu}^{N-2}\mathbb{C}^\star\boldsymbol{\mu}^{N-2} \quad , \quad \mathbf{A}^\star=\mathbb{C}^\star\boldsymbol{\mu}^{N-2}\mathbb{C}\boldsymbol{\mu}^{N-2}, \quad , \quad \mathbf{B}=\mathbb{C}\boldsymbol{\mu}^{N-2}\mathbb{F}^\star+\mathbb{F}$$

$$\mathbf{B}^\star=\mathbb{C}^\star\boldsymbol{\mu}^{N-2}\mathbb{F}+\mathbb{F}^\star, \quad , \quad \mathbf{E}_s=\left(\sum_{p=0}^{s-1}\mathbf{A}^p\right)\mathbf{B} \quad , \quad \mathbf{E}_s^\star=\left(\sum_{p=0}^{s-1}\mathbf{A}^{\star p}\right)\mathbf{B}^\star, \tag{34}$$

where ($\mathbb{C}$, $\mathbb{F}$) and ($\mathbb{F}^\star$, $\mathbb{C}^\star$) are scattering matrices and vectors of excitation sources that relate the coupling conditions between the central structure and the extra substructures, see Eqs. (18). Also, in Eq. (34), s is an integer defined so that

$$s=\mathtt{max}\left\{u:||\mathbf{A}^u||\geq 0.1 \text{ and } ||\mathbf{A}^{\star u}||\geq 0.1\right\}. \tag{35}$$

Besides, in Eq. (33), $\epsilon_1^{\mathbf{E}}$, $\epsilon_2^{\mathbf{E}}$, $\epsilon_1^{\mathbf{E}^\star}$ and $\epsilon_2^{\mathbf{E}^\star}$ are error parameters expressed as

$$\epsilon_1^{\mathbf{E}}=\frac{\|\widetilde{\mathbf{E}}_s-\widetilde{\mathcal{L}}\mathbf{E}_s\|}{\|\mathbf{E}_s\|}, \;\; \epsilon_2^{\mathbf{E}}=\frac{\|\mathcal{L}_{\mathtt{r}}\mathbf{E}_s\|}{\|\mathbf{E}_s\|}, \;\; \epsilon_1^{\mathbf{E}^\star}=\frac{\|\widetilde{\mathbf{E}}_s^\star-\widetilde{\mathcal{L}}\mathbf{E}_s^\star\|}{\|\mathbf{E}_s^\star\|}, \;\; \epsilon_2^{\mathbf{E}^\star}=\frac{\|\mathcal{L}_{\mathtt{r}}\mathbf{E}_s^\star\|}{\|\mathbf{E}_s^\star\|}, \tag{36}$$

$$\epsilon_1^{\mathbf{A}}=\frac{\|\widetilde{\mathbf{A}}^s\widetilde{\mathcal{L}}-\widetilde{\mathcal{L}}\mathbf{A}^s\|}{\|\mathbf{A}^s\|}, \;\; \epsilon_2^{\mathbf{A}}=\frac{\|\mathcal{L}_{\mathtt{r}}\mathbf{A}^s\widetilde{\mathcal{L}}^T\|}{\|\mathbf{A}^s\|}, \;\; \epsilon_1^{\mathbf{A}^\star}=\frac{\|\widetilde{\mathbf{A}}^{\star s}\widetilde{\mathcal{L}}-\widetilde{\mathcal{L}}\mathbf{A}^{\star s}\|}{\|\mathbf{A}^{\star s}\|}, \;\; \epsilon_2^{\mathbf{A}^\star}=\frac{\|\mathcal{L}_{\mathtt{r}}\mathbf{A}^{\star s}\widetilde{\mathcal{L}}^T\|}{\|\mathbf{A}^{\star s}\|}, \tag{37}$$

where $\mathcal{L}_{\mathtt{r}}$ and $\widetilde{\mathcal{L}}$ are Boolean incidence matrices that localize, respectively, the rejected and retained wave modes. One of the features of the proposed error analysis is that the error bound $\mathcal{E}_s$ is to be computed at the maximum discrete frequency considered within the frequency band of interest, only, as explained in [11].

4 Numerical experiments

To highlight the efficiency of the proposed reduction method (Section 3), two test cases are investigated that concern: (i) a 2D periodic structure undergoing plane stresses (see Figure 1); (ii) a 3D cylindrical shell with a periodic distribution of longitudinal and circumferential stiffeners (see Figure 7). Both structures exhibit substructures which are not symmetric. Within the framework of the DSM and WA approaches, the FRFs of the structures are computed using MATLAB®. These are compared with reference results issued from the conventional FE method when the FRFs are computed using a commercial FE software.

4.1 2D periodic structure

As a first example, the frequency forced response of a 2D periodic structure, undergoing plane stresses, is investigated (see Figure 1). The whole periodic structure is made up of $N = 15$ identical substructures whose dimensions are shown in Figure 4. Each substructure is meshed by means of 2D linear triangular elements whose nodes exhibit horizontal and vertical displacement DOFs. Also, the structure exhibits the following material characteristics: Young's modulus of $210GPa$, density of $7800kg/m^3$, Poisson's ratio of 0.3 and a loss factor of 0.001. Also, its thickness is $0.001m$. The structure is excited by a unit point force acting along the horizontal $x-$direction at the bottom corner of the left end; also, it is clamped over its right end.

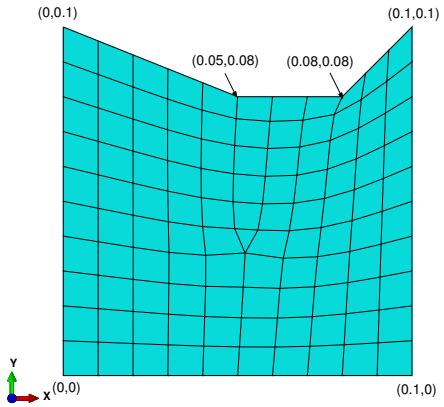


Figure 4: Geometry and mesh of a substructure composing the 2D periodic structure displayed in Figure 1 (dimensions are provided in meters).

The DSM approach proposed in Section 3.2.1 is used to compute the FRF of the structure — i.e., the frequency evolution of the modulus of the displacement at the location of the input force — over a frequency band $[1Hz\,,\ 2000Hz]$. For this purpose, the reduction method proposed in Section 3 is investigated. It consists in dividing the whole periodic structure into one central structure having $N - 2 = 13$ substructures, which is surrounded by two extra-substructures (Figure 3). The FRF of the whole structure is computed by considering different numbers m of right-going and left-going wave modes. The related results are displayed in Figure 5 along with the reference FE solution, i.e., which is issued from a commercial FE software. Here, a moderately dense mesh is used, leading to $n = 22$ DOFs over the left/right boundary of each substructure. As it can be seen, considering $m = 2$ right/left-going wave modes of the central structure is clearly not enough. However, considering three or more wave modes (i.e., $m \geq 3$) yields the expected results with accurate precision. This might be explained by investigating the first four propagation constants (see Table 1) — namely, μ_1, μ_2, μ_3 and μ_4 — at $2000Hz$, among all the 22 propagation constants whose moduli are less than one. Here, it appears that two waves are slowly damped, one is moderately decreasing while the last one is strongly decreasing, i.e., the amplitude $|\mu_4|$ is very small. This means that the third wave mode should be kept, while the subsequent modes may be ignored.

Consider the case when the whole structure is partitioned into a left periodic structure made up of $N - 1 = 14$ substructures, and a right extra substructure. Assume that the periodic structure is modeled by means of a reduced number m of right/left-going wave modes, while the right extra substructure is modeled by means of the conventional FE method. The related FRF is displayed in Figure 6, when different number m of wave modes are dealt with. As

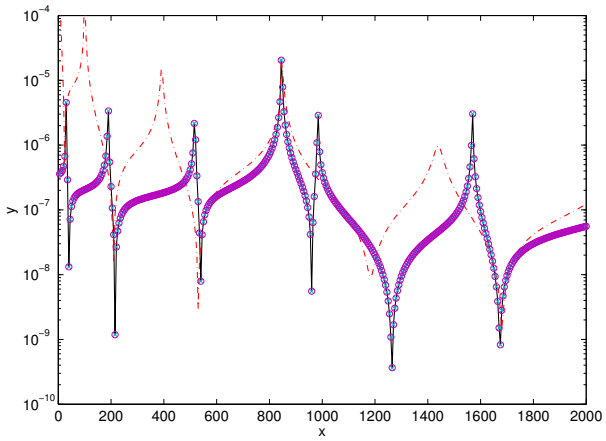


Figure 5: FRF of the 2D periodic structure, as composed of a central periodic structure (13 substructures) surrounded by two extra-substructures: FE solution (———), WFE solution when the central periodic structure is modeled by means of $m = 2$ wave modes (– · –), $m = 3$ wave modes (× × ×) and $m = 4$ wave modes (○ ○ ○).

$\lvert\mu_1\rvert$	$\lvert\mu_2\rvert$	$\lvert\mu_3\rvert$	$\lvert\mu_4\rvert$
0.999876	0.999704	0.387754	0.007128

Table 1: Modulus of the first propagation constants, at $2000Hz$.

shown in Figure 6, the WFE solution doesn't match the reference FE curve even though half the wave modes are kept (i.e., $m = 11$). Convergence is reached when all the wave modes are kept, only. This highlights the fact that near the excitation source, almost the full wave mode basis is needed to recover the dynamic behavior of the system.

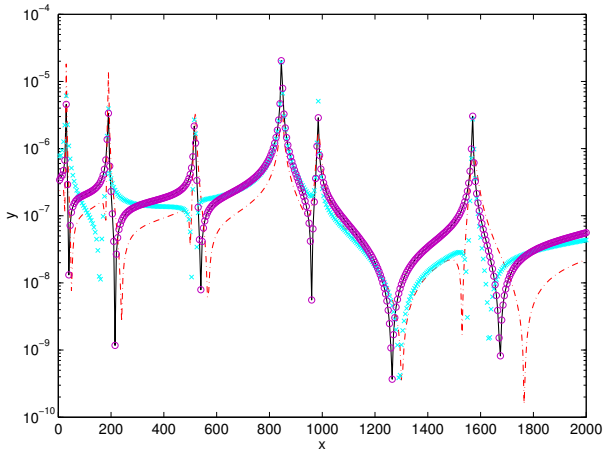


Figure 6: FRF of the 2D periodic structure, as composed of a left periodic structure (14 substructures) coupled with a right extra substructure: FE solution (———), WFE solution when the left periodic structure is modeled by means of $m = 3$ wave modes (– · –), $m = 11$ wave modes (× × ×) and $m = n = 22$ wave modes (○ ○ ○).

4.2 3D periodic structure

As a second example, the harmonic behavior of a complex 3D periodic structure is analyzed by means of the WA approach (Section 3.2.2). The structure under concern consists in a stiffened cylindrical shell, as shown in Figure 7. It is composed of $N = 20$ identical substructures, each of these being made up of eighteen longitudinal flat stiffeners and one circumferential L-shaped stiffener. The cylindrical shell and the stiffeners share the following characteristics:

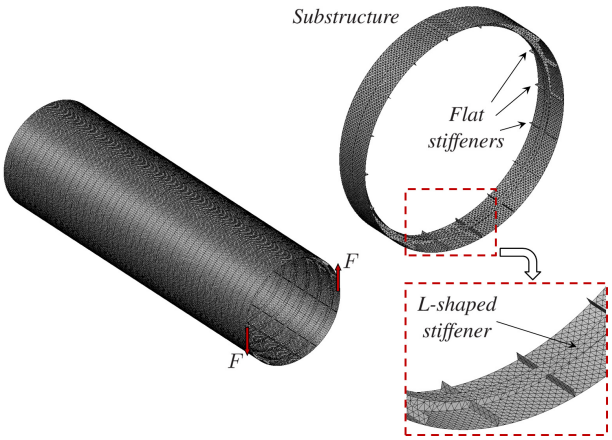


Figure 7: FE model of a stiffened cylindrical shell composed of 20 substructures.

Young's modulus of $70GPa$, density of $2700kg/m^3$, Poisson's ratio of 0.3, loss factor of 0.005, thickness of $0.002m$. The length and the external diameter of the whole structure are $10m$ and $3m$, respectively. Also, the longitudinal stiffeners have a height of $0.05m$, while the circumferential L-shaped stiffener has a height and a width of $0.1m$. The substructures are meshed in a same manner, i.e., by means of 2D triangular shell elements with three nodes and six DOFs per node that incorporate 3D displacements/rotations. As a whole, each substructure is meshed using $32,616$ DOFs, which are partitioned into $n = 1188$ DOFs on each left/right cross-section, and $30,240$ internal DOFs. Also, the total number of DOFs used to model the whole periodic structure is $629,748$, which appears to be large.

Besides, the periodic structure is subject on its left end to vertical point forces of magnitude $F = 1000N$ acting in opposite directions on the cross-section DOFs of two diametrically opposed longitudinal stiffeners (Figure 7). Regarding the right end of the periodic structure, the cross-section DOFs of the longitudinal stiffeners are translationally fixed and rotationally free, while the cross-section DOFs of the cylindrical shell are free. The FRF of the periodic structure is estimated using 300 discrete frequencies which are equally spaced over the frequency band $[0.5Hz\,,\,150Hz]$. Prior to the computation of the wave modes, the condensed dynamic stiffness matrix $\mathbf{D}^*$ of a substructure needs to be assessed at each discrete frequency involved within the frequency band of concern. This is achieved using the CB method (cf. Section 3.1), by considering 1000 fixed interface modes of the substructure. The computation of the wave modes follows by considering the eigenproblem (6). The Lanczos method enables one to compute a reduced set of wave modes, only. For this purpose, the WA method proposed in Section 3.2.2 is considered along with the wave mode selection process proposed in Section 3.3. Here, the number of retained wave modes is determined when the value of the error bound $\mathcal{E}_s$ shrinks under a tolerance threshold of 10%. This provides $m = 125$ right/left-going wave modes to be retained, which represents almost 10% of the total number $n = 1188$ of wave modes involved when the eigenproblem (6) is solved directly.

The FRF of the periodic structure is displayed in Figure 8. Here, the magnitude of the radial displacement is assessed at a measurement point located $1.5m$ far from the excitation sources, along the longitudinal direction. The solution issued from the WA approach (Section 3.2.2) is computed using MATLAB® and compared to the solution issued from a conventional FE software. As it can be seen, the WFE and FE solutions (black and violet curves) perfectly match to each other, hence giving credit to the proposed approach. In terms of CPU times, it takes around $5826s$ with the WFE method to compute the FRF of the structure using MATLAB® and an Intel® Core™ i7-3720QM processor, against $13,618s$ with a commercial FE software and the same processor. This means 57% time savings in benefit of the WFE method.

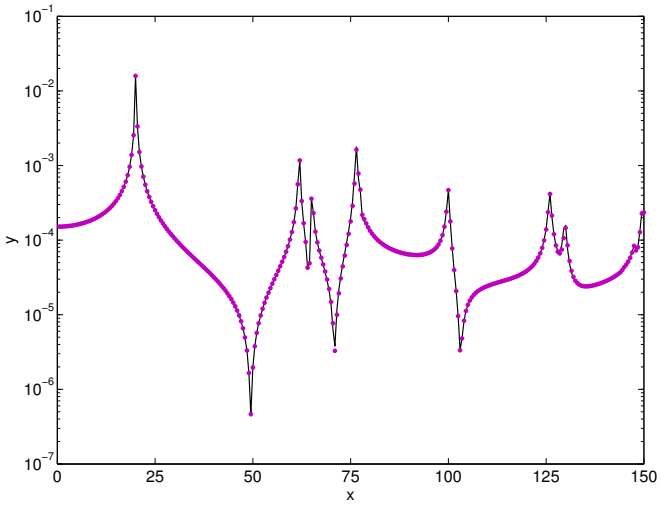


Figure 8: FRF of the stiffened cylindrical shell: FE solution (——) and WFE solution when the central periodic structure is modeled by means of $m = 125$ wave modes (• • •).

5 Concluding remarks

A model reduction technique has been developed within the framework of the WFE method for the description of the dynamic behavior of structures with one-dimensional periodicity. An efficient generalized eigenproblem based on the so-called $\mathbf{S} + \mathbf{S}^{-1}$ transformation has been proposed for computing the wave modes traveling in right and left directions along a periodic structure composed of arbitrary-shaped substructures. An error indicator has been proposed for selecting in an a priori process those wave modes which mostly contribute to the structure dynamics. It has been shown that the efficiency of the procedure can be greatly improved by partitioning the whole periodic structure into one central structure surrounded by two extra substructures. The feature of this technique lies in the use of a few wave modes for modeling the central structure, hence enabling the CPU times associated to the computation of the WFE eigenproblem to be largely decreased. The relevance of this reduction technique has been clearly validated regarding a 2D periodic structure. Also, it has been successfully applied to model a 3D periodic stiffened shell that contains several substructures with large-sized FE models.

REFERENCES

[1] D. Mead, A general theory of harmonic wave propagation in linear periodic systems with multiple coupling, Journal of Sound and Vibration 27 (2) (1973) 235–260.

[2] W. X. Zhong, F. W. Williams, On the direct solution of wave propagation for repetitive structures, Journal of Sound and Vibration 181 (3) (1995) 485–501.

[3] D. Duhamel, B. Mace, M. J. Brennan, Finite element analysis of the vibrations of waveguides and periodic structures, Journal of Sound and Vibration 294 (1-2) (2006) 205–220.

[4] J.-M. Mencik, On the low- and mid-frequency forced response of elastic systems using wave finite elements with one-dimensional propagation, Computers and Structures 88 (11-12) (2010) 674–689.

[5] J. Renno, B. Mace, On the forced response of waveguides using the wave and finite element method, Journal of Sound and Vibration 329 (26) (2010) 5474–5488.

[6] Y. Waki, B. Mace, M. Brennan, Numerical issues concerning the wave and finite element method for free and forced vibrations of waveguides, Journal of Sound and Vibration 327 (1-2) (2009) 92–108.

[7] J.-M. Mencik, A wave finite element-based formulation for computing the forced response of structures involving rectangular flat shells, International Journal for Numerical Methods in Engineering 95 (2) (2013) 91–120.

[8] J.-M. Mencik, New advances in the forced response computation of periodic structures using the wave finite element (WFE) method, Computational Mechanics 54 (3) (2014) 789–801.

[9] R. R. Craig, M. C. C. Bampton, Coupling of substructures for dynamic analyses, AIAA Journal 6 (7) (1968) 1313–1319.

[10] G. J. Golub, C. F. V. Loan, Matrix Computations, The Johns Hopkins University Press, Baltimore and London, 1996.

[11] J.-M. Mencik, A model reduction strategy for computing the forced response of elastic waveguides using the wave finite element method, Computer Methods in Applied Mechanics and Engineering 229-232 (2012) 68–86.

[12] J.-M. Mencik, M. N. Ichchou, Multi-mode propagation and diffusion in structures through finite elements, European Journal of Mechanics - A/Solids 24 (5) (2005) 877–898.

[13] R. Patel, On computing the eigenvalues of a symplectic pencil, Linear Algebra and its Applications 188-189 (1993) 591–611.

[14] W.-W. L. T.-M. Huang, J. Qian, Structure-preserving algorithms for palindromic quadratic eigenvalue problems arising from vibration of fast trains, SIAM Journal on Matrix Analysis and Applications 30 (4) (2009) 1566–1592.

5th ECCOMAS Thematic Conference on
Computational Methods in Structural Dynamics and Earthquake Engineering
M. Papadrakakis, V. Papadopoulos, V. Plevris (eds.)
Crete Island, Greece, 25–27 May 2015

ANALYSIS OF GROUND MOTION ALONG A TOPOGRAPHIC RELIEF: THE CERRETO DI SPOLETO CASE-HISTORY (CENTRAL ITALY).

Dario Rinaldis[1], Salomon Hailemikael[2] , Antonella Paciello[2] and Guido Martini[3]

[1] ENEA, CR Casaccia, Roma Italy
e-mail: dario.rinaldis@enea.it

[2] ENEA, CR Casaccia, Roma Italy
{salomon.hailemikael,antonella.paciello}@enea.it

[3] ENEA, CR Frascati, Roma Italy
e-mail: guido.martini@enea.it

Keywords: temporary seismometric network, permanent accelerometric network, topographic amplification, horizontal-to-vertical spectral ratio method.

Abstract. *With the aim of evaluating the seismic hazard and vulnerability of villages with valuable historical monuments in Central Italy, since the late 80's ENEA operated an accelerometric network at the Cerreto di Spoleto village in the area of Central Apennines. The area is characterized by high level instrumental seismicity and seismic hazard. The accelerometric network, consisting of one station located at a rock site close to the hill base and of two accelerometers located inside a building at the relief top, recorded the Umbria-Marche aftershocks of 1997 as well as more recent earthquake sequences. In 2001 a temporary seismometric network was deployed at Cerreto di Spoleto village in order to better characterize the ground motion spatial variability along the ridge. The accelerometric network, consisting of one station located at a rock site close to the hill base and of two accelerometers located inside a building at the relief top, recorded the Umbria-Marche aftershocks of 1997 as well as more recent earthquake sequences. Analysis of the accelerometric records pointed out broadband seismic amplification above 1 Hz at the relief top. In 2001 a temporary seismometric network was deployed at Cerreto di Spoleto village in order to better characterize the ground motion spatial variability along the ridge. The seismic station were deployed at the ridge base and along the crest. To this aim we analyzed waveform in the frequency domain through the Horizontal-to-vertical spectral ratio method. Except for the trapped waves effect, the results showed no clear evidence of ground motion amplification for the stations located on the crest. This evidence suggests that the seismic amplification observed on the accelerometric records is not related to topographic amplification.*

1 INTRODUCTION

In reports of destructive earthquakes is often described more severe damage in relief areas with respect to foothills [1] and amplifications of ground motion on top of topographic features have been widely highlighted in the scientific literature [5,6].

In general the experimental observations obtained by either time domain or spectral methods demonstrated that: (i) the seismic motion amplification occurs at mountain tops and it is larger in the horizontal component normal to the ridge trending axis; (ii) amplification is usually moderate, reaching maximum values of about 10 fold in few particular case studies [10]; (iii) the frequency at which amplification occurs is related to the fundamental mode of vibration of the topographic feature and corresponds to wavelengths comparable to ridge half width.

The present work is devoted to the analysis of occurrence of topographic amplification at the Cerreto di Spoleto hill which is an elongated ridge located in an area of the Italian territory characterized by moderate seismicity and selected in 2001 as a test site for site effects evaluation.

2 GENERAL SETTINGS

The Cerreto di Spoleto ridge is located in the Central Apennines, which is a mountain range crossing almost the entire Italian peninsula from N to S and is characterized by a thrust belt structure [2]. The study area is in the Umbria-Marche section of the Apennines, close to the Nera river valley (Valnerina) (Fig. 1a).

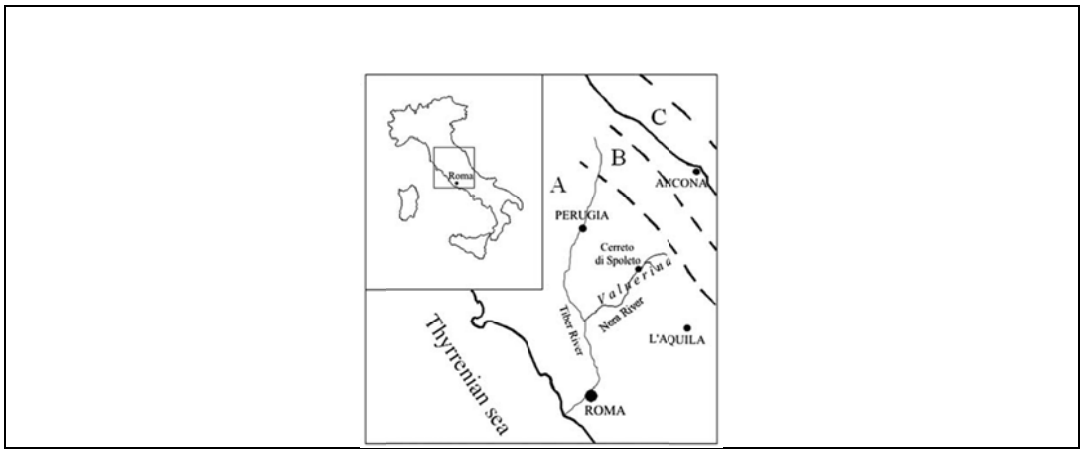


Figure 1a. Study area location, after [9].

The region is characterized by an important seismic activity both instrumental and historical. In fact, the Valnerina area was struck by several earthquake swarms during the centuries, such as the 1703 (estimated epicentral intensity XI MCS) sequence and the recent 1997 sequence (average intensity, VIII MCS). The Cerreto di Spoleto hill is a NW-SE trending ridge with height ranging between 200 to 250 m with respect to the adjacent Nera river valley and steep flanks. The hill is mainly made of limestone rock. The ridge is characterized by the presence of several faults belonging to two major systems: one trending about NS and one with strike about N30°W (Fig. 1b).

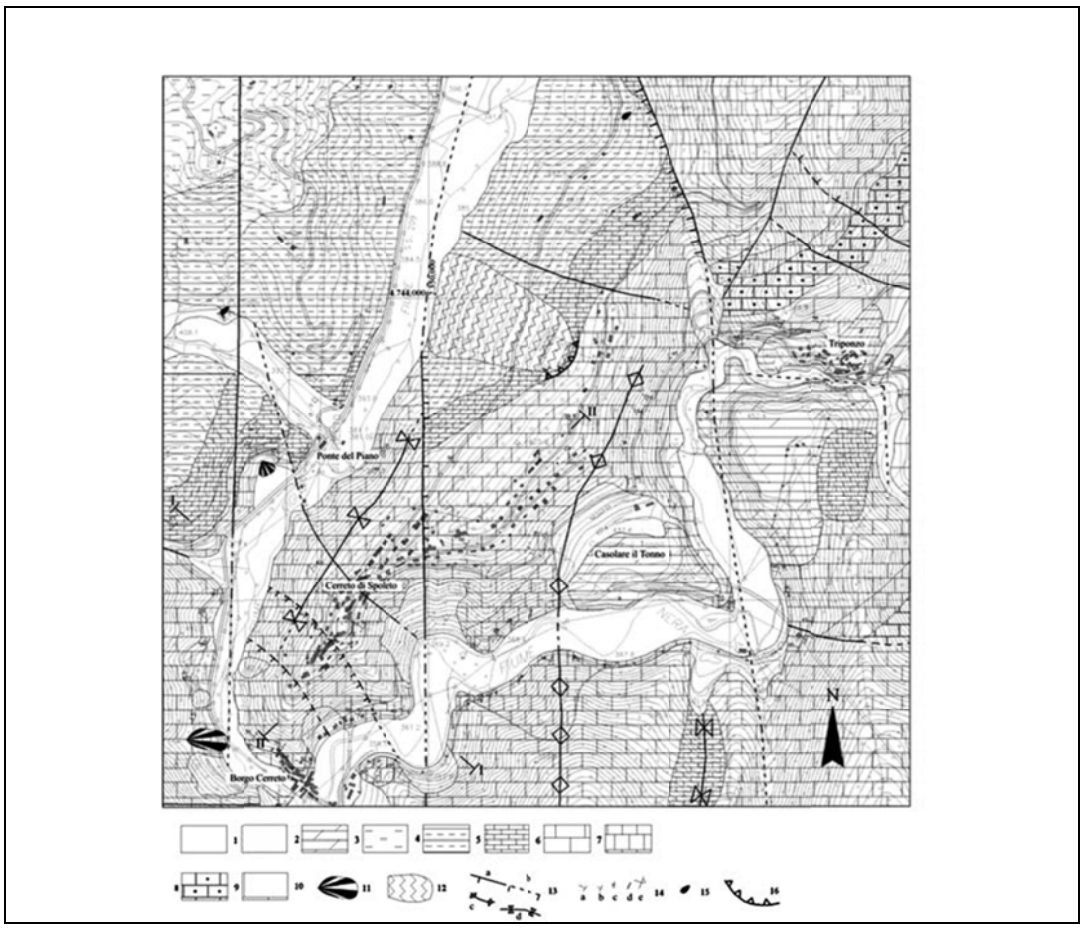


Figure 1b. Geologic map of the Cerreto di Spoleto area. (1) alluvial deposits; (2) slope debris; (3) travertine deposits; (4) Bisciaro Formation (lower Miocene–middle Miocene); (5) Scaglia Cinerea Formation (upper Eocene–lower Miocene); (6) Scaglia Variegata Formation (middle–upper Eocene); (7) Scaglia Rossa Formation (upper Cretaceous–middle Eocene); (8) Scaglia Bianca Formation (lower Cretaceous–middle Cretaceous); (9) Marne a Fucoidi Formation (lower Cretaceous); (10) Maiolica Formation (upper Jurassic); (11) alluvial fan; (12) landslide debris; (13) certain fault (a), uncertain fault (b), anticlinal axis (c), synclinal axis (d); (14) attitude of beds: <30 (a), 30-50 (b), >50 (c), vertical (d), reverse (e); (15) spring; (16) landslide scarp, after [9].

3 SEISMOMETRIC DATA ANALYSIS

In order to evaluate the occurrence of topographic effects at the top of the Cerreto di Spoleto hill, we performed spectral analysis of a previously acquired waveform dataset. The weak motion data were recorded during a seismic monitoring experiment performed in 2001 and aimed at site effect estimation along the Nera river valley and across the Cerreto di Spoleto hill. The temporary network was made by 7 stations, deployed as depicted in Figure 2, equipped with K2 Kinemetrics acquisition system coupled with 3-1 component Ranger SS1-1Hz seismometers aligned with the NS, EW and Vertical directions. The stations were equipped with GPS for absolute timing and the sampling frequency was set to 200 Hz. The network recorded about 20 small magnitude local events which were analyzed by means of standard spectral ratio (SSR) [3, 4] as well as Horizontal-to-vertical spectral ratio (H/V) [7, 8] techniques in a previous paper [9]

was observed site amplification at one of the stations located at ridge top as a consequence of trapped wave propagation inside a fault zone, i.e. a very local effect not related with topography.

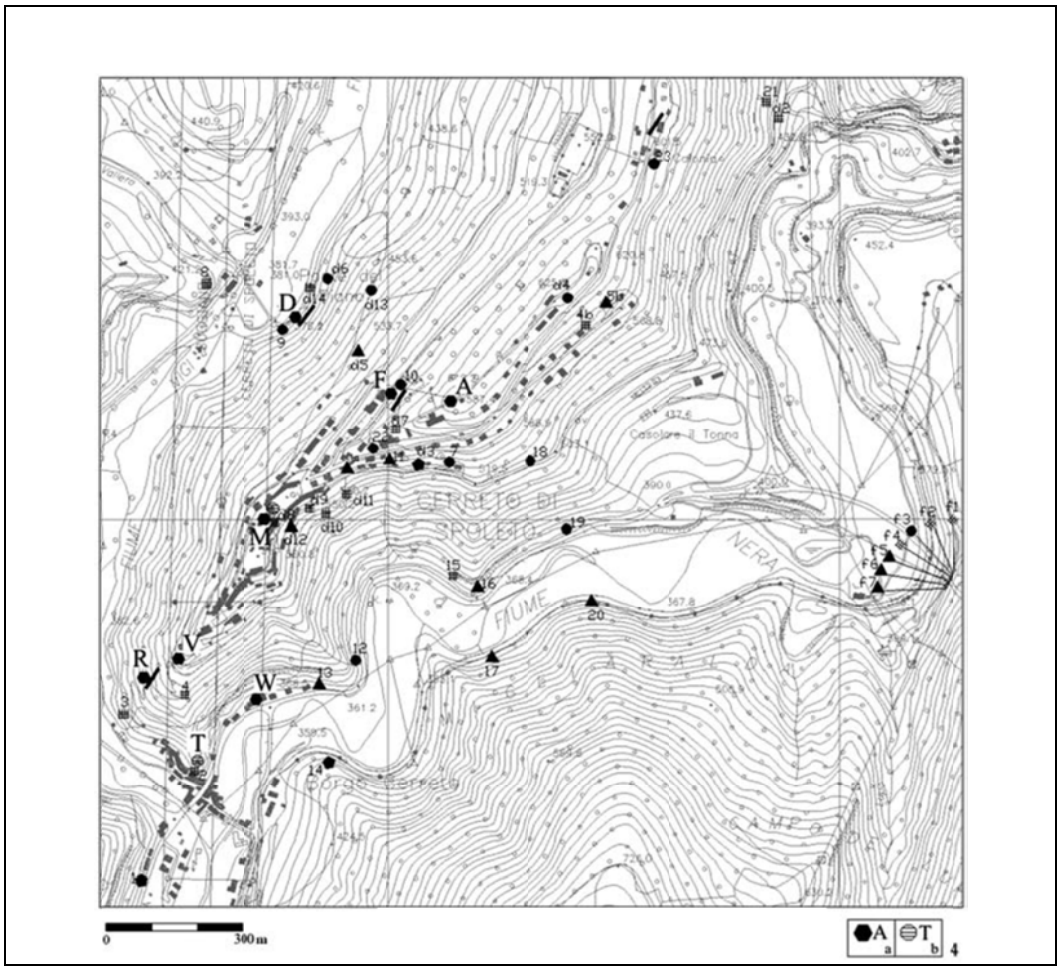


Figure 2. Velocimetric (a) and accelerometric (b) station locations, after [9].

With respect to previous analysis we decided to analyze this dataset with the same techniques, but windowing the waveform around the S phase. In particular, we selected 6 events with SNR>3 among the dataset and decided to use signals recorded only at stations M, F and A located along the ridge crest and at station R considered as reference. After correcting for the instrument response, the records of each event and component were windowed around the S phase. To window the data we used a 5% cosine-taper window which started about 1 second prior the S phase onset and ended 10 s later. The resulting signals were de-trended and converted to the frequency domain. The calculated spectra were smoothed using a 0.35-Hz running frequency window. Finally we used the smoothed spectra of the north-south (NS), west-east (WE) and vertical (V) components to calculate the SSR and the NS/V and WE/V spectral ratios. We derived the H/V curve, for each event and station, as the geometric average of the NS/V and WE/V ratios and the SSR curve as the geometric average of the NS and WE smoothed

spectra divided by the geometric average of the same components recorded at the reference station. The results are depicted in Figure 3a and Figure 3b, in terms of average SSR and H/V functions respectively, in the frequency band 0.5-10 Hz.

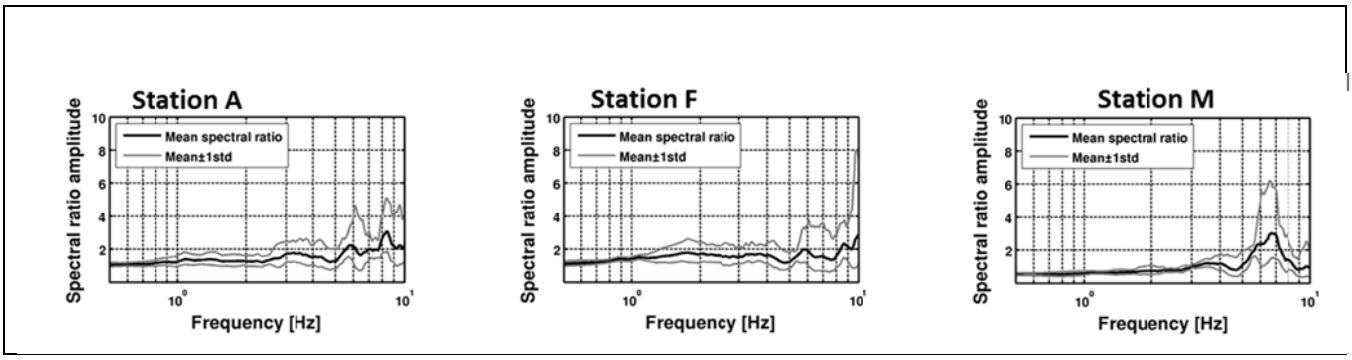


Figure 3a. SSR functions calculated at the considered stations

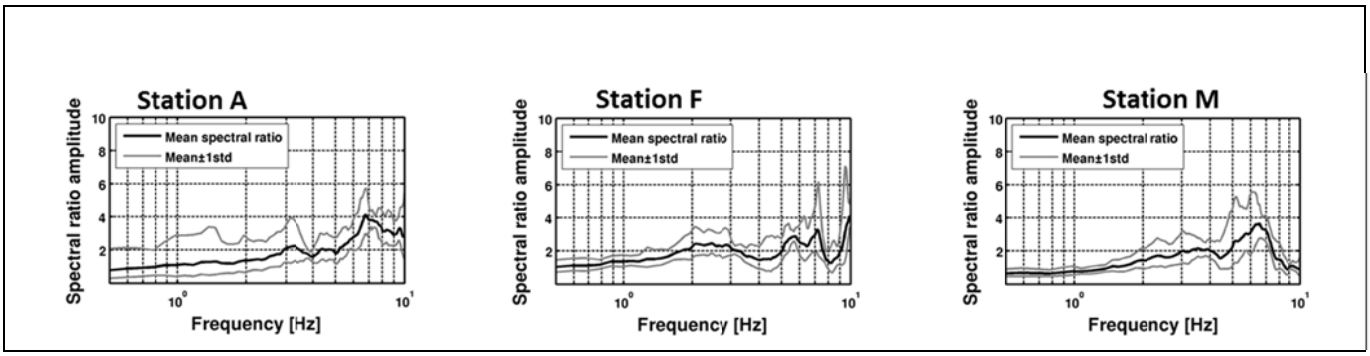


Figure 3b. H/V functions calculated at the considered stations

The results confirmed the occurrence of ground motion amplification both in terms of SSR and H/V functions at the M station. The average amplification level is between 3 and 4 in the narrow frequency band between 6-7 Hz. At station F, the average SSR function shows flat shape with amplitude value between 1 and 2, while the H/V function shows amplitude just above level 2 in the frequency band 2-3 Hz and 5-7 Hz and about 10 Hz. At station A, the average amplitude of SSR function is about 1 almost in the whole considered frequency band, while the H/V function shows maximum amplitude level between 6 and 8 Hz. While the results obtained at station M are in agreement with those obtained by [9] and related with trapped wave propagation, the results obtained at the F and A station suggest to exclude the occurrence of topographic site effects. In fact, given the high frequency range of the SSR and H/V maxima at the two stations, as the dimension of the hill is in the order of hundreds of meters, the slight amplification is likely related to the presence of a weathered rock layer below the stations, rather than to the hill fundamental mode.

4 ACCELEROMETRIC RECORDS

The accelerometric array of Cerreto di Spoleto [11], since the deployment, recorded several seismic events. Here records obtained during the period 2005-2010 at all the accelerometric stations are analyzed. Frequency domain analysis, by means of acceleration Fourier Amplitude Spectrum (FAS) of records, were performed. In figure 2 the position of the stations of the accelerometric array is shown. In particular, on the ridge, M is the station of Municipio (the building where the City Hall is located), where two digital accelerometers were deployed (the first one at the basement of the building, CMC station; the other at roof, CMS station). Then T is the station near a bell-tower named BCT. Events recorded at all stations (BCT, CMC and CMS) are listed in Table 1 with date, time origin, epicentral coordinates and magnitude. The maximum PGA between the two horizontal components of the analyzed records are also listed. As shown, event magnitudes were small, and ground-motion PGA was ranging between few gals to 0.1 g (at CMS station). The first 5 records listed in table 1 were originated in Val Topino (see figure 4a) when the others were originated in Val Nerina (see figure 4b). Figure 5a and 5b shows the FAS of acceleration (NS and WE components) for the records obtained at the BCT station and figures 5c and 5d the same for the CMC station.

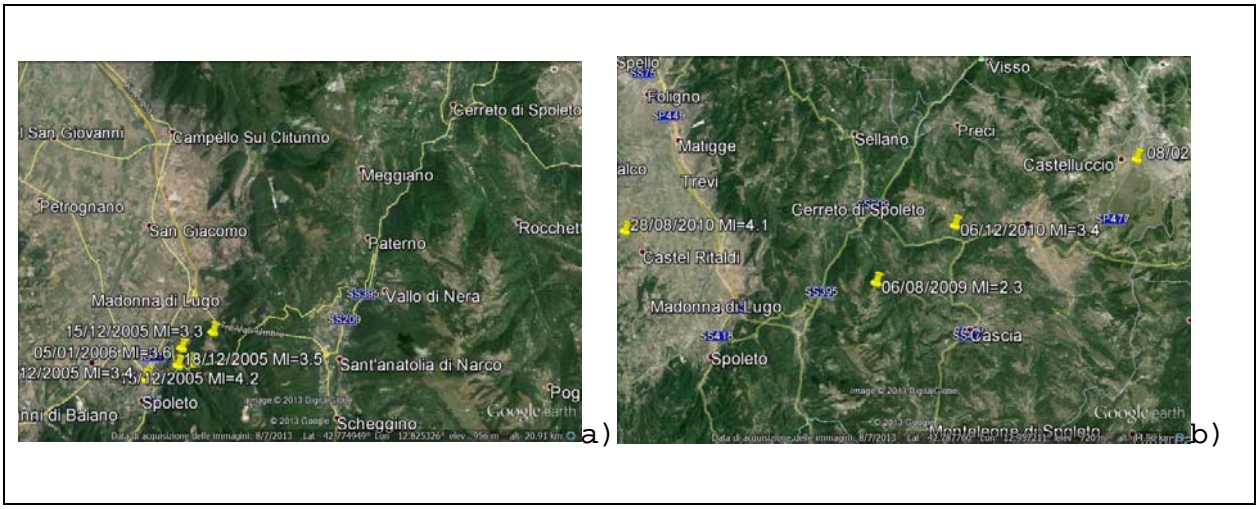


Figure 4. a) Recorded Events in Val Topino; b) Recorded events in Val Nerina.

EVENT DATA				RECORD DATA		
Date	Time	Epic. Coord.	Magnitude	PGA CMC (cm/s^2)	PGA CMS (cm/s^2)	PGA BCT (cm/s^2)
15.12.2005	06:00:30	42.748 12.773	Ml=3.3	8.40	31.40	11.75
15.12.2005	13:28:37	42.738 12.760	Ml=4.2	27.95	71.03	27.81
16.12.2005	20:12:36	42.735 12.735	Ml=3.4	7.64	29.77	10.76
18.12.2005	08:06:46	42.738 12.753	Ml=3.5	8.82	20.82	12.87
05.01.2006	17:30:39	42.744 12.756	Ml=3.6	11.86	35.70	20.18
08.02.2007	01:32:55	42.820 13.217	Ml=3.8	19.25	43.68	11.47
06:08.2009	10:23:41	42.793 13.176	Ml=2.3	8.02	27.07	8.60
10.01.2010	08:33:38	43.119 13.445	Ml=4.0	6.77	20.63	6.86
12.01.2010	08:25:14	43.119 13.451	Ml=4.1	7.81	21.58	8.83
12.01.2010	13:35:48	43.135 13.433	Ml=4.2	5.92	14.23	6.74
28.08.2010	07:07:56	42.834 12.654	Ml=4.1	6.54	17.01	6.58
06.12.2010	10:32:04	42.793 13.011	Ml=3.4	19.24	96.10	27.29

Table 1. Records from Cerreto di Spoleto strong-motion array (ETNA).

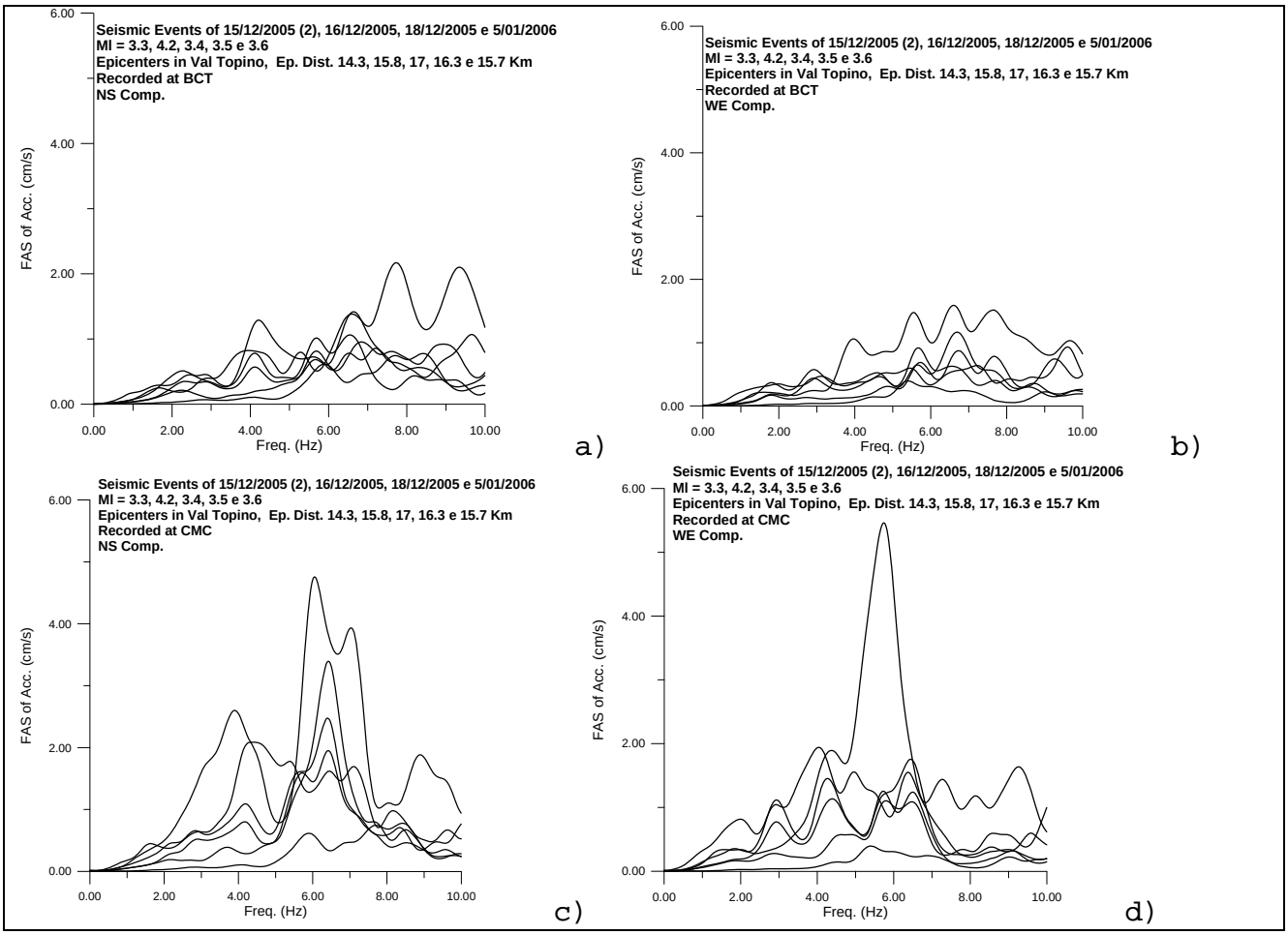


Figure 5. FAS of acceleration (NS and WE components) for the records obtained at the BCT (a and b) and CMC (c and d) stations.

In previous papers [11, 12] was stated, as preliminary result, that for all the analyzed events the FAS of acceleration at the CMC station is larger than the one obtained at BCT station in the frequency interval between 2-8 Hz.

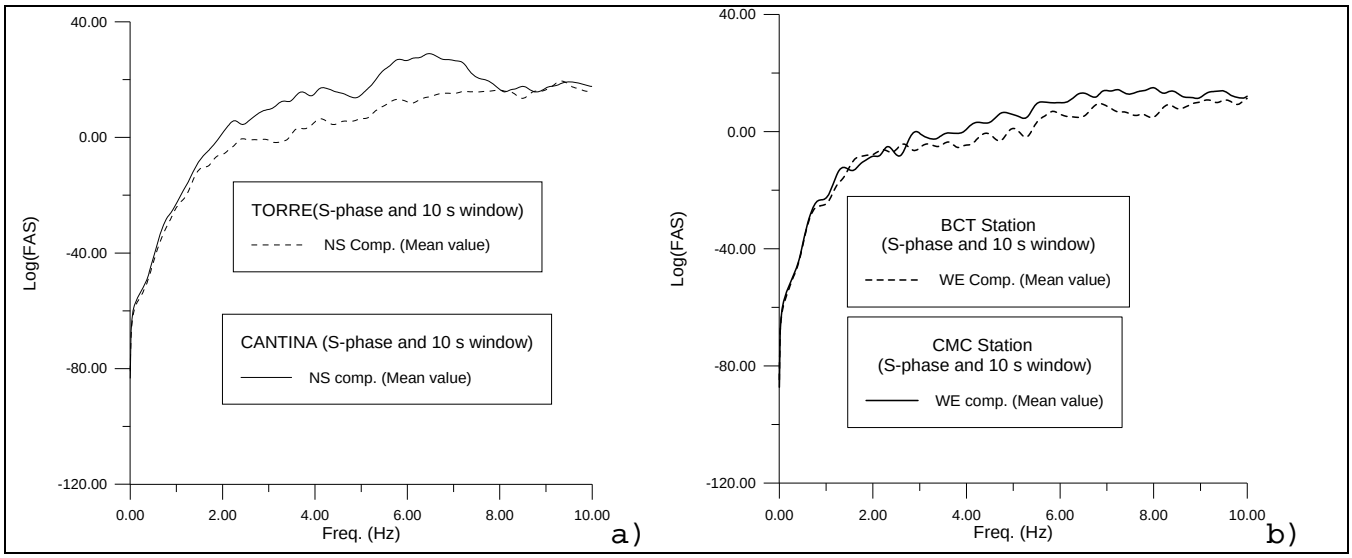


Figure 6. Cerreto di Spoleto accelerometric array: mean values of FAS of recorded accelerations at BCT and CMC stations (a) NS component; (b) WE component.

To confirm this behaviour a mean of the spectra was computed at both BCT and CMC stations. Figure 6a shows the averaged spectra for the NS components and figure 6b the WE ones: the FAS of acceleration in the frequency interval of 2-8 Hz is larger at the CMC.
Then a spectral ratio between the two horizontal component of acceleration, recorded at CMC and BCT, was computed to have a better evidence of the spectral amplification. Figure 7a and 7b show a clear amplification in the interval of interest. The averaged records were from the last six events listed in table 1. The results should be interpreted carefully since the standard deviation is large.

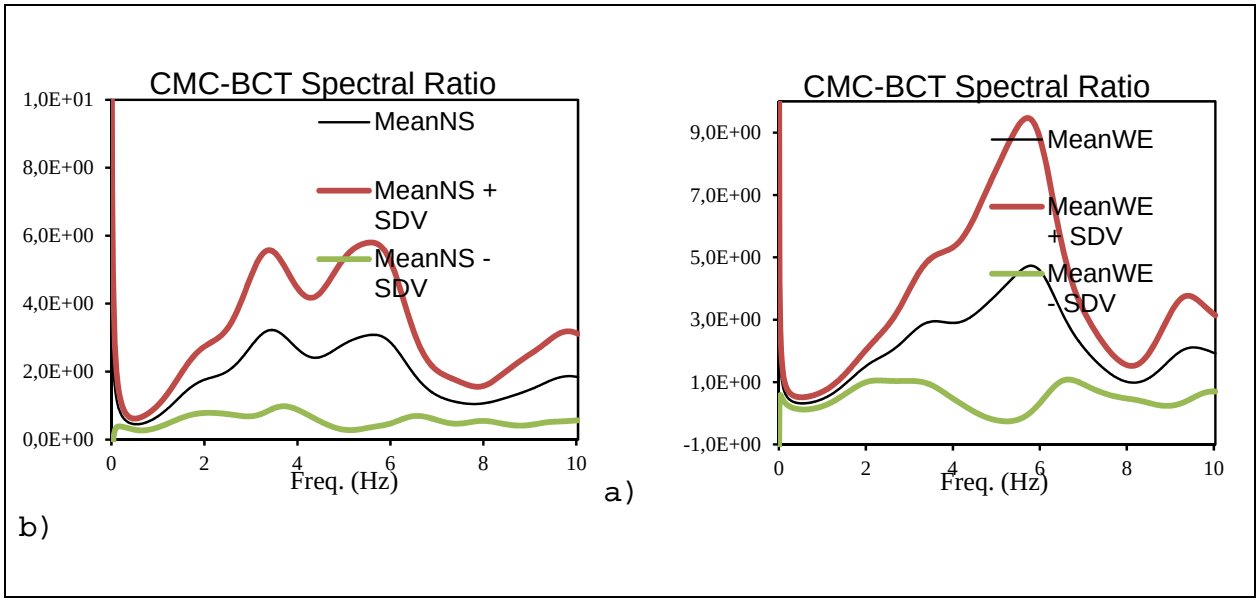


Figure 1. Mean Ratio between the FAS of acceleration of six events recorded at the BCT and CMC stations of the Cerreto di Spoleto accelerometric array: NS component (a), WE component (b).

5 CONCLUSIONS

As already highlighted by [9], the analysis of waveform recorded at the Cerreto di Spoleto hill, showed the occurrence of ground motion amplification in the frequency band 6-7 Hz at the ridge top in a specific location and related to trapped wave propagation. At other two stations located at the ridge top, we did not observed the occurrence of ground motion amplification at frequencies consistent with the hill dimension. We observed slight amplification at one station in terms of H/V function, above 6 Hz, likely related to the presence of a shallow weathered rock layer. The analysis of accelerometric waveforms recorded at the ridge top and base, showed ground motion amplification in a broad frequency band between 2 and 8 Hz. While the amplification above 6 Hz at ridge top is consistent with that obtained by the analysis of velocimetric records, the 2- 6 Hz amplification was not observed by the 2001 seismic experiment. These results, seems to indicate a particular behavior of the Cerreto Torre accelerometric station, which may de-amplify the seismic ground motion in the 2-6 Hz frequency band.

REFERENCES

[1] Celebi M., Topographical and geological amplifications determined from strong-motion and aftershock records of the 3 march chile earthquake. *Bull. Soc. Seism. Am.*, 77(4):1147–1167, 1987.

[2] Ciarapica, G. and Passeri, L., Evoluzione paleogeografica degli Appennni, *Atti Ticinensi di Scienze della Terra* 40, 233–290 (in italian)., 1998.

[3] Borcherdt, R. D., Effects of local geology on ground motion near San Francisco Bay, *Bull. Soc. Seism. Am.*, 60, 29–61, 1970.

[4] Borcherdt, R. D, Estimates of site-dependent response spectra for design (methodology and justification), *Earthquake Spectra* 10, 617–653, 1994.

[5] Chavez-Garcia, F. J., Sanchez, L. R., and Hatzfeld, D., Topographic site effects and HVSR. A comparison between observation and theory, *Bull. Soc. Seism. Am.* 86, 1559–1573, 1996.

[6] Chavez-Garcia, F. J., Rodriguez, M., Field, E. H., and Hatzfeld, D., Topographic site effects. A comparison of two nonreference methods, *Bull. Soc. Seism. Am.* 87, 1667–1673, 1997.

[7] Field, E. H. and Jacob, K., A comparison and test of various site response estimation techniques, including three that are non-reference-site dependent, *Bull. Soc. Seism. Am.* 85, 1127–1143, 1995.

[8] Langstom, C. A., Structure under Mount Ranger, Washington, inferred from teleseismic body waves, *J. Geophys. Res.* 84, 4749–4762, 1979.

[9] Martino S., Minutolo A., Paciello A., Rovelli A., Scarascia Mugnozza G., and V. Verrubbi. Evidence of amplification effects in fault zone related to mass jointing. *Natural Hazards*, 39:419–449, 2006. doi: 10.1007/s11069-006-0001-2.

[10] Paolucci R., Faccioli E., and F. Maggio. 3d response analysis of an instrumented hill at matsuzaki, japan, by a spectral method. *Journal of Seismology*, 3:191–209, 1999.

[11] Rinaldis D., Verrubbi V. and Martini G., Cerreto di Spoleto (Umbria-Italy): Topographic amplification at the ENEA local array stations. *Proceedings of 15th WCEE*, Lisbon, 2012;

[12] Rinaldis D. The Umbria-Marche sequence: digital recordings at ENEA stations. *IACMAG 12th International Conference*, 2008,1-6 October, Goa, India.

COMPDYN 2015
5th ECCOMAS Thematic Conference on
Computational Methods in Structural Dynamics and Earthquake Engineering
M. Papadrakakis, V. Papadopoulos, V. Plevris (eds.)
Crete Island, Greece, 25–27 May 2015

A PERFECTLY MATCHED LAYER FOR SEISMIC WAVE PROPAGATION IN UNBOUNDED DOMAIN BY USING HETEROGENEOUS MULTI-TIME STEP SUBDOMAIN METHODS

Zafati E.[1], Brun M.[1], and Djeran-Maigre I.[1]

[1]INSA de Lyon
Batiment Coulomb 20, Avenue A. Einstein 69621 Villeurbanne cedex (France)
e-mail: eliass.zafati@insa-lyon.fr

Keywords: wave propagation, perfectly matched layers, multi−step coupling algorithms.

Abstract. *In the framework of the Finite Element Method, Perfectly Matched Layer (or PML) is recognized as a very effective tool for reproducing unbounded domains (Basu et al. [13]). Nonetheless, the computation time required by the PML may be large, especially when an explicit time integration scheme is adopted for dealing with the wave propagation problem both in the domain of interest and in the PML medium (Basu et al. [13]). The paper proposed to investigate subdomain strategies enabling to choose the appropriate time integration scheme in the PML with its own time step, independently on the choice of the explicit time scheme in the domain of interest associated with a fine time step satisfying the stability criterion (CFL condition). The investigated subdomain strategy, proposed by Gravouil and Combescure [14], is based on the Schur dual approach, characterized by the introduction of Lagrange multipliers at the interface between subdomains for ensuring the velocity continuity.*

1 Introduction

The simulation of wave motion in unbounded media often compels a numerical solution using artificial boundaries surrounding the finite computational domain. Several techniques have been developped to repoduce unbounded domain: the infinite elements (Bettess [1]), the absorbing boundaries methods (Enquist $et\ al.$ [2]) and the absorbing layers methods such as the Rayleigh damping layers (Semblat $et\ al.$ [3], Rajagopal $et\ al.$ [4] et Zafati $et\ al.$ [5]) and the perfectly matched layers (PML) (Chew $et\ al.$ [6]).

The perfectly matched layers (PML) is an absorbing layer method which surrounds the computational domain with an uniform thickness layer. The PMLs are characterized by their capabilities of providing the same attenuation for all frequencies without, from the analytical point of view, reflections at the interface for all angles of incidence and frequencies.

In the beginning, the PMLs have been developed for the Maxwell's equations by Bérenger $et\ al.$ [7] using a field-splitting formulation and have became one of the most widely used methods in the simulation of wave propagation problems in unbounded media. The technique was then adapted to the elastodynamics equations. Hastings $et\ al.$ [8] extended the PML from electromagnetics to elastodynamics using a formulation in terms of displacement potentials implemented in the finite difference framework. Using also the finite difference method, Chew $et\ al.$ [6] introduced a new split-field formulation, velocity$-$stress, applied to the isotropic medium and also implemented using the finite difference method. Later on, Collino $et\ al.$ [9] proposed a finite difference split$-$field formulation similar to Chew $et\ al.$ [6], applied to anisotropic media. In [10], Wang *et al.* developed a new PML formulation, called C$-$PML, using the convolution features adapted to the finite difference method. Matzen [11] extended the C-PML approach to the finite element method. In this work, we are interested in an unsplit$-$field formulation developed for the finite element method in [12] and [13] by Basu $et\ al.$ for applications involving 2D media.

When addressing the numerical implementation, it is often interesting, for several applications, to use an implicit time integration scheme (the average acceleration method) for the absorbing layer such as the PML, while the physical domain is integrated in time by an explicit scheme (central difference method). The subdomain method proposed by Gravouil and Combescure [14] provides the suitable properties for coupling an explicit integrator for the subdomain of interest with an implicit one for the absorbing layers. The method follows a dual Schur approach by ensuring the velocity continuity at the interface through Lagrange multipliers. The method is proved to be stable for any Newmark integrators [15] using the so-called energy method (Hughes, [16]). It leads to the first order of accuracy when coupling second order accurate time integration schemes due to a slight spurious dissipation at the interface as soon as different time steps are adopted. When adopting the same time step, second order of accuracy is achieved [17].

In this paper, the technique of the absorbing layers using the PMLs is adopted. First, we propose to present the multi$-$time step coupling algorithm between the PML, formulated by Basu $et\ al.$ in [13], and the physical domain assumed to be linear isotropic medium. Then, we report numerical results using 2D applications and demonstrating the efficiency of the coupling method.

2 Perfectly matched layer

2.1 Strong form of the PML in frequency domain

The PML model used in this work has been developed by Basu *et al* ([13] and [18]). It is built using the classical elastodynamic equations by introducing the complex transform functions λ_i. The main idea is to replace the real coordinates x_i with the complex ones $x_i \rightarrow \tilde{x}_i : \mathbb{R} \rightarrow \mathbb{C}$. The complex coordinates are defined as:

$$\frac{\partial \tilde{x}_i}{\partial x_i} = \lambda_i(x_i) = 1 + f_i^e(x_i) - i\frac{f_i^p(x_i)}{k_s} \tag{1}$$

where $k_s = \frac{\omega}{c_s}$ (c_s being the S-wave velocity) and f_i^e, f_i^p are positive functions that vanish at the interfaces between the PML and the physical domain. The function f_i^p is introduced to attenuate the propagative waves in the x_i direction, whereas the function f_i^e attenuates the evanescent wave. The dependence on the angular frequency of the complex term in Eq. (1), in the equation (1), makes the imaginary part of the wave number independent of the frequency. In other words, all frequencies are damped in the same way.

The PML formulation is obtained by modifying the governing equations defined in the frequency domain. The equations are re-written by substituting x_i by $\tilde{x}_i$ as follows:

$$\begin{aligned} \Sigma_j \frac{1}{\lambda_j(x_j)} \frac{\partial \sigma_{ij}}{\partial x_j} &= -\omega^2 \rho u_j \\ \sigma_{ij} &= \Sigma_{k,l} C_{ijkl} \varepsilon_{ij} \\ \varepsilon_{ij} &= \frac{1}{2}\left[\frac{1}{\lambda_j(x_j)}\frac{\partial u_i}{\partial x_j} + \frac{1}{\lambda_i(x_i)}\frac{\partial u_j}{\partial x_i}\right] \end{aligned} \tag{2}$$

2.2 Strong form of the PML in time domain

Applying the inverse Fourier transform to the system given above, the time strong form is written as:

$$\begin{aligned} \nabla.(\underline{\underline{\sigma}}\tilde{F}^e + \underline{\underline{\Sigma}}\tilde{F}^p) &= \rho f_m \ddot{\underline{u}} + \rho c_s f_c \dot{\underline{u}} + \mu f_k \underline{u} \\ \underline{\underline{\sigma}} &= C : \underline{\underline{\varepsilon}} \\ F^{eT}\dot{\underline{\underline{\epsilon}}}F^e + F^{pT}\underline{\underline{\varepsilon}}F^e + F^{eT}\underline{\underline{\varepsilon}}F^p + F^{pT}\underline{\underline{E}}F^p &= \frac{1}{2}(\nabla\dot{\underline{u}}^T F^e + F^{eT}\nabla\dot{\underline{u}}) + \frac{1}{2}(\nabla\underline{u}^T F^p + F^{pT}\nabla\underline{u}) \end{aligned} \tag{3}$$

with:

$$\begin{aligned} F^e &= \begin{bmatrix} 1+f_1^e(x_1) & 0 \\ 0 & 1+f_2^e(x_2) \end{bmatrix}, \quad F^p = \begin{bmatrix} c_s f_1^p(x_1) & 0 \\ 0 & c_s f_2^p(x_2) \end{bmatrix} \\ \tilde{F}^e &= \begin{bmatrix} 1+f_2^e(x_2) & 0 \\ 0 & 1+f_1^e(x_1) \end{bmatrix}, \quad \tilde{F}^p = \begin{bmatrix} c_s f_2^p(x_2) & 0 \\ 0 & c_s f_1^p(x_1) \end{bmatrix} \end{aligned} \tag{4}$$

and:

$$\begin{aligned} f_m : &= (1+f_1^e(x_1))\,(1+f_2^e(x_2)) \\ f_c : &= (1+f_1^e(x_1))\,f_2^p(x_2) + (1+f_2^e(x_2))\,f_1^p(x_1) \\ f_k : &= f_1^p(x_1)\,f_2^p(x_2) \end{aligned} \tag{5}$$

The tensors $\underline{\underline{\Sigma}}$ and $\underline{\underline{E}}$ are related to $\underline{\underline{\sigma}}$ and $\underline{\underline{\varepsilon}}$ by :

$$\underline{\underline{\Sigma}} = \int_{t=0}^{t} \underline{\underline{\sigma}}\, dt \qquad \underline{\underline{E}} = \int_{0}^{t} \underline{\underline{\varepsilon}}\, dt \tag{6}$$

In this work the damping function f_i^e, f_i^p will be linear as follow:

$$f_i^\alpha = a_\alpha \left(\frac{x_i - x_0}{d} \right)^n \qquad \alpha = e, p \qquad x_0 \leq x_i \leq x_0 + d \tag{7}$$

where a_α a positive integer.

Assuming a normal incidence and using the damping functions defined in Eq. (7), a_α can be expressed as a function of the reflection coefficient R by [13]:

$$a_\alpha = \frac{\frac{c_p}{c_s}(n+1)}{2d} \ln(\frac{1}{R}) \tag{8}$$

where c_p is the P wave velocity and c_s is the shear wave velocity.

2.3 Displacement based weak form of the PML

In this section, the discretization process proposed by Basu *et al* in [13] is presented. The space discretization is obtained using the finite element method while the time discretization is obtained using the classical Newmark schemes [15]. Let $\underline{v}$ be the test function belonging to an appropriate space, the weak formulation is obtained by integrating over the computational domain Ω:

$$\int_\Omega \rho f_m\, \underline{v}.\ddot{\underline{u}}\, d\Omega + \int_\Omega \rho\, c_s f_c \underline{v}.\dot{\underline{u}}\, d\Omega + \int_\Omega \mu\, f_k \underline{v}.\underline{u}\, d\Omega + \int_\Omega \underline{\underline{\tilde{\varepsilon}}}^e : \underline{\underline{\sigma}}\, d\Omega + \int_\Omega \underline{\underline{\tilde{\varepsilon}}}^p : \underline{\underline{\Sigma}}\, d\Omega = \int_\Gamma \underline{\omega}.(\underline{\underline{\sigma}}\tilde{F}^e + \underline{\underline{\Sigma}}\tilde{F}^p).\underline{n}\, d\Gamma \tag{9}$$

with $\Gamma = \partial\Omega$ the boundary of Ω, and $\underline{n}$ the normal vector to the Γ. $\underline{\underline{\tilde{\varepsilon}}}^e$ et $\underline{\underline{\tilde{\varepsilon}}}^p$ are given by:

$$\underline{\underline{\tilde{\varepsilon}}}^e = \frac{1}{2}(grad\underline{v}\, \tilde{F}^e + \tilde{F}^{eT}\, (grad\underline{v})^T) \qquad \underline{\underline{\tilde{\varepsilon}}}^p = \frac{1}{2}(grad\underline{v}\, \tilde{F}^p + \tilde{F}^{pT}\, (grad\underline{v})^T) \tag{10}$$

The mass, the damping and the stiffness matrices are given by:

$$m_{IJ} = \int_\Omega \rho f_m N_I N_J d\Omega\, I_d \quad c_{IJ} = \int_\Omega \rho f_c c_s N_I N_J d\Omega\, I_d \quad k_{IJ} = \int_\Omega \mu f_k N_I N_J d\Omega\, I_d \tag{11}$$

where N_I is the shape function of the node I. Taking into account the Eq. (9), the internal force term p_{n+1}^e is defined by:

$$p_{n+1}^e = \int_{\Omega_e} \tilde{B}^{eT} \hat{\sigma}_{n+1} + \int_{\Omega_e} \tilde{B}^{pT} \hat{\Sigma}_{n+1} \tag{12}$$

with $\tilde{B}^e$ and $\tilde{B}^p$ matrices depend on the shape functions and the damping functions given in terms of their nodal submatrices by:

$$\tilde{B}_I^e = \begin{bmatrix} \tilde{N}_{I1}^e & 0 \\ 0 & \tilde{N}_{I2}^e \\ \tilde{N}_{I2}^e & \tilde{N}_{I1}^e \end{bmatrix} \qquad \tilde{B}_I^p = \begin{bmatrix} \tilde{N}_{I1}^p & 0 \\ 0 & \tilde{N}_{I2}^p \\ \tilde{N}_{I2}^p & \tilde{N}_{I1}^p \end{bmatrix} \tag{13}$$

with:

$$\tilde{N}_{Ii}^e = \tilde{F}_{ji}^e N_{I,j} \quad et \quad \tilde{N}_{Ii}^p = \tilde{F}_{ji}^p N_{I,j} \tag{14}$$

The Voigt notation is adopted for the field $\hat{\sigma} = \begin{bmatrix} \sigma_{11} \\ \sigma_{22} \\ \sigma_{12} \end{bmatrix}$ and $\hat{\Sigma} = \begin{bmatrix} \Sigma_{11} \\ \Sigma_{22} \\ \Sigma_{12} \end{bmatrix}$ assumed to be linked according to the relationship:

$$\hat{\Sigma}_{n+1} = \hat{\Sigma}_n + dt\, \hat{\sigma}_{n+1} \tag{15}$$

It follows:

$$p_{n+1}^e = \int_{\Omega_e} \tilde{B}^T \hat{\sigma}_{n+1} + \int_{\Omega_e} \tilde{B}^{pT} \hat{\Sigma}_n \tag{16}$$

where:

$$\tilde{B}^T = \tilde{B}^{eT} + dt\, \tilde{B}^{pT} \tag{17}$$

The knowledge of $\hat{\sigma}_{n+1}$ depends on $\hat{\varepsilon}_{n+1}$ obtained by discretizing the 3^{rd} equation of the system (3) and assuming $\dot{\varepsilon}(t_{n+1}) = \frac{\varepsilon_{n+1} - \varepsilon_n}{dt}$ and $E(t_{n+1}) = E_n + dt\, \varepsilon_n$:

$$\hat{\varepsilon}_{n+1} = \frac{1}{dt} \left[B^{\varepsilon} \dot{U}_{n+1} + B^Q U_{n+1} + \frac{1}{dt} \hat{F}^{\varepsilon} \hat{\varepsilon}_n - \hat{F}^Q \hat{E}_n \right] \tag{18}$$

where B^{ε}, B^Q, $\hat{F}^{\varepsilon}$ and $\hat{F}^Q$ are matrices depending on the shape functions and the damping functions (see appendix A). The element interal force p_{n+1}^e can now be written in terms of the vectors v_{n+1} et u_{n+1} and the quantities at the time $t_n = ndt$. Finally, the weak form at the time t_{n+1} can be expressed as:

$$M\ddot{U}_{n+1} + (C + \widetilde{C})\dot{U}_{n+1} + (K + \widetilde{K})U_{n+1} + P(\varepsilon_n, E_n, \Sigma_n) = F_{ext} \tag{19}$$

P being an operator depending on the quatities at t_n.The global matrices $\widetilde{C}$, $\widetilde{K}$ are built using the following element submatrices:

$$\widetilde{c}^e = \frac{1}{dt} \int_{\Omega_e} \tilde{B}^T D B^{\varepsilon} \qquad \widetilde{k}^e = \frac{1}{dt} \int_{\Omega_e} \tilde{B}^T D B^Q \tag{20}$$

where D is given by:

$$D = \begin{bmatrix} \kappa + \frac{4}{3}\mu & \kappa - \frac{2}{3}\mu & 0 \\ \kappa - \frac{2}{3}\mu & \kappa + \frac{4}{3}\mu & . \\ 0 & 0 & \mu \end{bmatrix} \tag{21}$$

where μ is the shear modulus and κ is the bulk modulus. The last step involves the use of the Newmark schemes [15] and solves the problem in terms of displacement, velocity or acceleration.

3 Coupling algorithme physical domain and PML

Let Ω a bounded domain from $\mathbb{R}^2$ with a regular boundary. We assume that the domain Ω is divided into two parts Ω_1 and Ω_2 as illustrated in Figure 1 such as: $\Omega_1 \cap \Omega_2 = \oslash$ and $\partial\Omega_1 \cap \partial\Omega_2 = \Gamma^{12}$. Γ^{12} represents the interface between the two subdomains. The subdomain Ω_1 related to a non dissipative linear elastic behavior and the subdomain Ω_2 is related to a dissipative behavior characterized by the PML weak form given in Eq. (19).

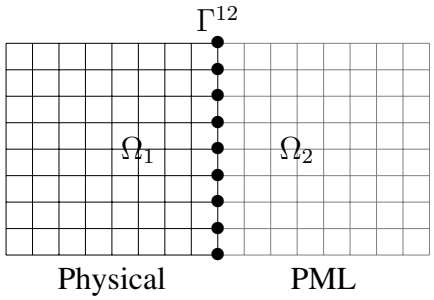


Figure 1: Domaine Ω partitionn en deux sous domaines Ω_1 et Ω_2

Subdomain Ω_1:

It is assumed that the medium Ω_1 is linear elastic characterized by the mass matrix M_1 and the stiffness matrix K_1. The semi-discrete in space equation of motion is given by:

$$M_1\ddot{U}_1 + K_1U_1 = F_{ext,1} - L_1^T\hat{\lambda} \tag{22}$$

where $\hat{\lambda}$ being the Lagrange multiplier vector corresponding to the nodal forces at the interface.

Subdomain Ω_2:

We assume that the subdomain 2 is governed by the discretized equation of motion in PML (19):

$$M_2\ddot{U}_2 + (C_2 + \widetilde{C}_2)\dot{U}_2 + (K_2 + \widetilde{K}_2)U_2 + P_2(\varepsilon_n, E_n, \Sigma_n) = -L_2^T\hat{\lambda} \tag{23}$$

L_1 and L_2 defined in Eq. (22) and Eq. (19) are boolean matrices, operating on nodal vectors associated with the two subdomains 1 and 2, and picks out the degrees of freedom lying on the interface Γ^{12} in order to ensure the velocity continuity at the interface, we write the following kinematic relationship:

$$L_1\dot{U}_1 + L_2\dot{U}_2 = 0 \tag{24}$$

In the following, the GC method [14] is employed to solve the previous problem. It is based on a dual Schur approach by introducing Lagrange multipliers $\hat{\lambda}$ to ensure the kinematic continuity at the interface. When discretizing in time the equation of motions for both subdomains, we have to choose the quantity (displacement, velocity or acceleration) whose continuity is imposed at the interface. Following the GC method, it has been proven by the authors that any Newmark time integrators can be coupled (for example, explicit central difference scheme

with implicit average acceleration scheme) when the continuity of velocities at the interface is prescribed. Thus, the constraint defined on velocities was adopted as written in Eq. (24).

Next the subdomain Ω_1 is integrated in time with an explicit time integration scheme (central difference scheme), characterized by the parameters $\gamma_1 = 0.5$ and $\beta_1 = 0$, whereas the subdomain Ω_2 is handled with an implicit time integration scheme (constant acceleration scheme), characterized by the parameters $\gamma_2 = 0.5$ and $\beta_2 = 0.25$. Note that main advantages of the coupling GC method is to provide heterogeneous time integration and multi-time step capabilities. The multi-time step capability is of great interest for minimizing the computation time required in the absorbing layer while keeping a target accuracy in the subdomain of interest. We focus on heterogeneous time integration of the coupled problem by using different time steps in the two subdomains. For this purpose, we define the fine time scale Δt_1 for the explicit domain and the coarse time scale Δt_2 for the implicit domain with $\Delta t_2 = m\Delta t_1$. The equation of motion is written for the subdomain 1 is prescribed at the time $t_m = \Delta t_2$ while the equation of motion of the subdomain 2 is prescribed at the time $t_j = j\Delta t_1$ $(j = 1, 2, ...m)$ as follows:

- Subdomain 1:

$$M_1\ddot{U}_1^j + K_1U_1^j = F_1^{ext,j} - L_1^T\hat{\lambda}^j \tag{25}$$

- Subdomain 2:

$$M_2\ddot{U}_2^m + (C_2 + \widetilde{C}_2)\dot{U}_2^m + (K_2 + \widetilde{K}_2)U_2^m + P_2(\varepsilon_0, E_0, \Sigma_0) = -L_2^T\hat{\lambda}^m \tag{26}$$

At the interface, the continuity of velocities is imposed at time t_j as:

$$L_1\dot{U}_1^j + L_2\dot{U}_2^j = 0 \tag{27}$$

From Newmark formula, we introduce the predictor quantities $U_1^{n-1,p}$ and $\dot{U}_1^{n-1,p}$ related to a time range $[t_n\,, t_{n+1}]$. They are determined from the quantities known at the beginning of time step as:

$$U_k^{n-1,p} = U_k^{n-1} + \Delta t\,\dot{U}_k^{n-1} + \Delta t^2\,(\frac{1}{2} - \beta_k)\,\ddot{U}_k^{n-1} \tag{28}$$

$$\dot{U}_k^{n-1,p} = \dot{U}_k^{n-1} + \Delta t\,(1 - \gamma_k)\,\ddot{U}_k^{n-1} \tag{29}$$

Using the expressions of the kinematic quantities in Eqs. (28) and (29), both equations of motion can be written in the form:

$$\widetilde{M_1}\ddot{U}_1^j = F_1^{ext,j} - K_1U_1^{j-1,p} - L_1^T\hat{\lambda}^j \tag{30}$$

$$\widetilde{M_2}\ddot{U}_2^m = -P_2(\varepsilon_0, E_0, \Sigma_0) - (C_2 + \widetilde{C}_2)\dot{U}_2^{0,p} - (K_2 + \widetilde{K}_2)U_2^{0,p} - L_2^T\hat{\lambda}^m \tag{31}$$

with the effective stiffness matrices defined for both subdomains by:

$$\widetilde{M_1} = M_1 + \beta_1\Delta t_1^2K_1 \tag{32}$$

$$\widetilde{M_2} = M_2 + \beta_2\Delta t_2^2(K_2 + \widetilde{K}_2) + \gamma_2\Delta t(C_2 + \widetilde{C}_2) \tag{33}$$

The procedure proposed by Gravouil and Combescure is based on splitting the kinematic quantities into two parts: the free and the linked quantities. The free quantities are obtained by only considering the internal and external forces, whereas the linked quantities are obtained by taking into account only the interface loads defined by the Lagrange multiplier vector $\hat{\lambda}$. For example, if we consider the subdomain Ω_2, the discrete equation of motion is split into two parts as follows:

$$\begin{cases} \widetilde{M}_2 \ddot{U}_2^{free,m} = -P_2(\varepsilon_0, E_0, \Sigma_0) - (C_2 + \widetilde{C}_2)\dot{U}_2^{0,p} - (K_2 + \widetilde{K}_2)U_2^{0,p} \\ \widetilde{M}_2 \ddot{U}_2^{link,m} = -L_2^T \hat{\lambda}^m \end{cases} \tag{34}$$

The complete accelerations are obtained by summing the two parts as: $\ddot{U}_2^m = \ddot{U}_2^{free,m} + \ddot{U}_2^{link,m}$.

The same procedure is applied to the subdomain Ω_1 at each time t_j. Furthermore, the kinematic quantities of the subdomain 2 at t_j are interpolated as well as the Lagrange multiplier :

$$\begin{cases} \hat{\lambda}^j = (1 - \frac{j}{m})\hat{\lambda}^0 + \frac{j}{m}\hat{\lambda}^m \\ W_2^j = (1 - \frac{j}{m})W_2^0 + \frac{j}{m}W_2^m \end{cases} \tag{35}$$

Where W_2^j denote the free or the linked velocities of the subdomain 2 at t_j. Using the kinematic condition at the interface in Eq. (27) at each time t_j, we obtain:

$$L_1 \dot{U}_1^{link,j} + L_2 \dot{U}_2^{link,j} = -L_1 \dot{U}_1^{free,j} - L_2 \dot{U}_2^{free,j} \tag{36}$$

Then, by using Eq. (35) and the expression of the velocities as a function of accelerations, the following interface problem can be derived:

$$H\hat{\lambda}^j = b_j \tag{37}$$

with the interface operator and the second side member vector defined by:

$$\begin{cases} H = \gamma_1 \Delta t L_1 \widetilde{M}_1^{-1} L_1^T + \gamma_2 \Delta t L_2 \widetilde{M}_2^{-1} L_2^T \\ b_j = L_1 \dot{U}_1^{free,j} + L_2 \dot{U}_2^{free,j} \end{cases} \tag{38}$$

Finally, once we get the values of the Lagrange multiplier vector at the end time of the time step, linked accelerations are obtained and thus complete accelerations as well as displacements and velocities from Newmark formula in Eqs. (28) and (29).

4 Numerical examples

In the following numerical applications, non harmonic waves will be investigated by considering a Ricker incident wave Ric defined by:

$$Ric\,(t,\, t_p,\, t_s) = A\,(2\,\pi^2\,\frac{(t-t_s)^2}{t_p^2} -\, 1)\,\exp(-\pi^2 \frac{(t-t_s)^2}{t_p^2}) \tag{39}$$

The Ricker wave is characterized by three parameters: the fundamental period t_p, the time shift t_s and the amplitude A. The chosen values are: $t_p = 3s$, $t_s = 3s$ and $A = 0.1$, as illustrated in Figure 2.

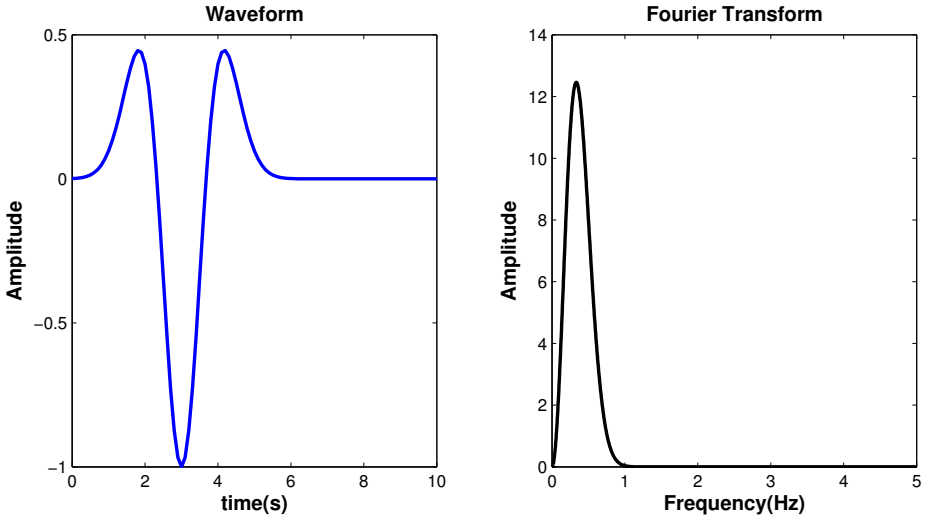


Figure 2: Waveform and Fourier transform of the Ricker wavelet

4.1 Lamb Test

Lamb's test consists in applying a concentrated load, characterized by the Ricker form in our study, to the surface of a ground assumed to be infinite in both directions. A sensor is located at a distance d from the load point in order to record the vertical and the horizontal displacements at this point. In 1904 Lamb [19] analytically calculated the displacements at a given point of the surface by assuming an isotropic linear elastic behavior for the soil. The derived theoretical solution exhibits the complexity of the problem since there are many types of waves traveling through the soil (P and S-waves, Rayleigh waves, etc).

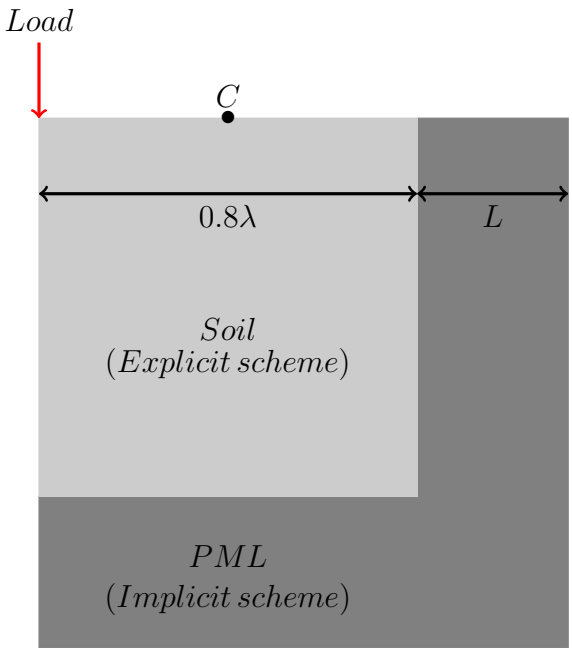


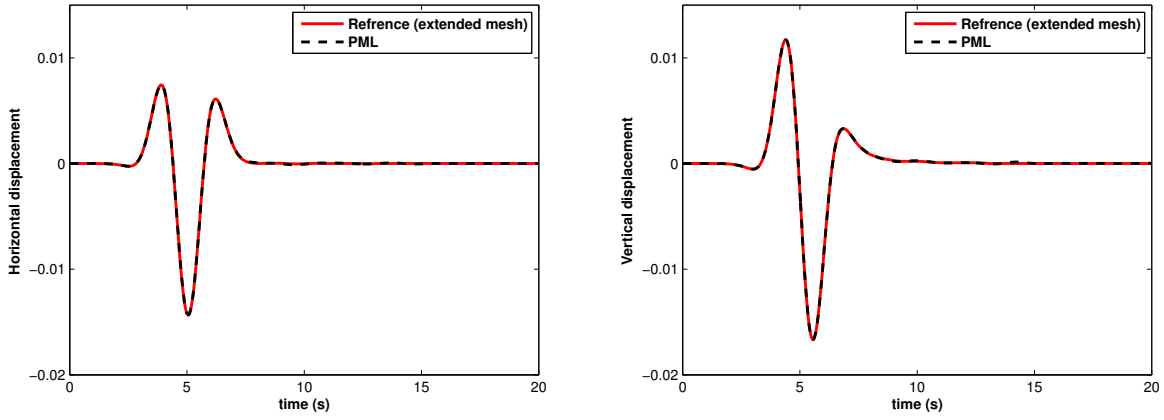
Figure 3: Modeling Lamb test using PMLs. The soil is integrated using explicit time scheme while the PML is integrated using implicit time scheme.

The Lamb test is modeled using the bounded-domain-PML as illustrated in Figure 3, com-

posed of a bounded soil (subdomain 1) with a size of 0.8λ and a PML (subdomain 2) characterized by a thickness L, The bounded problem is descritized using the four-node bilinear isoparametric elements. The soil is supposed to be linear elastic with ρ_1, $E_1 = 1$ and $\nu_1 = 0.24$. The attenuation functions are chosen as $f_i^e = 0$ and $f_i^p = a_p \left(\frac{x_i - x_0}{L}\right)$ with $a_p = 10$ and $x_0 = 4$. The length $L = 2$ is calculated using the following value of the reflection coefficient $R = 0.001$ and the relationship in Eq. (8). Finally, a point C located at the distance of 2 from the load point is chosen in order to record the vertical and the horizontal displacements.

In this part, the numerical solution is computed using the multi time step GC method. Two computations are distinguished: the first called Explicit/Explicit computation deals with the case where the both subdomains are intergrated with the explicit scheme and the second called Explicit/Implicit computation deals with the case where the subdomain 1 is integrated with the explicit scheme and the subdomain 2 is integrated with the implicit scheme. Next, the purpose is to analyze the effect of varying the ratio m on the accuracy of the results given in terms of displacements at the point C and energies in the physical domain (soil).

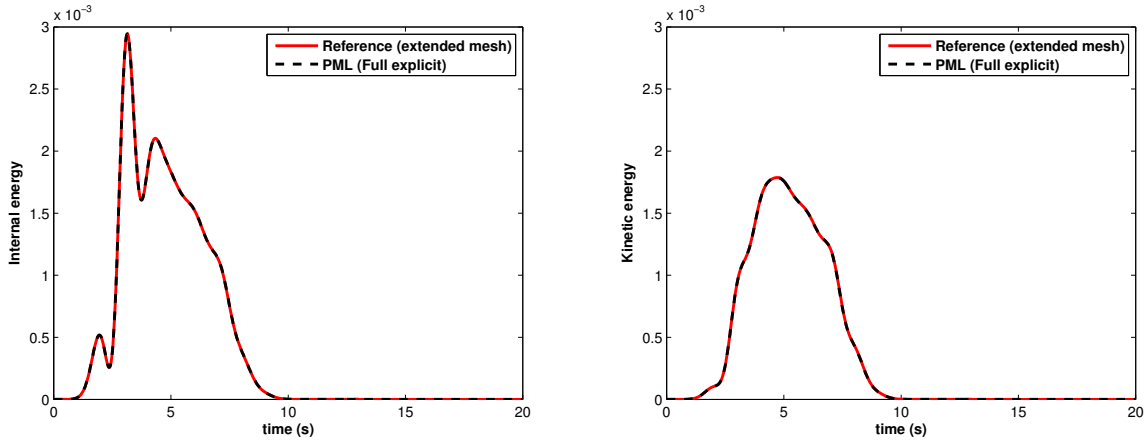
Before going further, we start by estimating the error introduced by the PML model with respect to the initial problem with an unbounded domain. For this purpose, we define the relative error due to the PML model and related to the quantity E over the time range $[0, T]$ by $err = \frac{\|E_{PML} - E_{ref}\|_{L^2([0,T])}}{\|E_{ref}\|_{L^2([0,T])}}$, where E_{PML} is the value of E obtained using the PML and E_{ref} is the value of E obtained using an extended mesh. In both cases, the computation is dealt with an explicit scheme. Figures 4 and 5 compare the displacements and energies obtained using the PML model with results obtained using an extended mesh. Note the excellent agreement between the results since the error, defined above, does not exceed 1% for the displacements and 0.1% for the energies.



(a) Horizontal displacement

(b) Vertical displacement

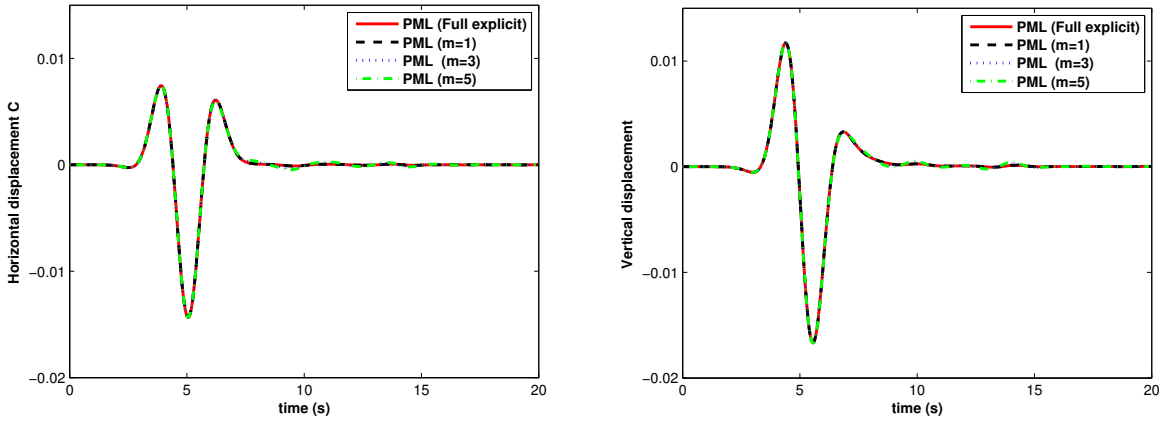
Figure 4: Vertical and horizontal displacements plotted at point C using time homogeneous explicit PMLs compared to the reference results using an extended mesh.



(a) Energie potentielle (b) Energie cintique

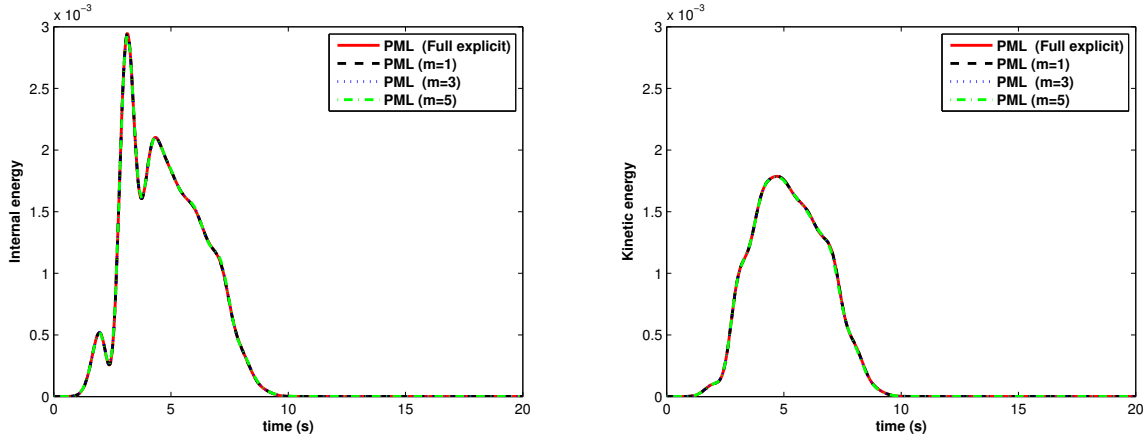
Figure 5: Kinetic and internal energies computed using time homogeneous explicit PMLs compared to the reference results using an extended mesh.

The error due to the coupling strategy Explicit/Implicit over the time range $[0, T]$ is defined by $err = \frac{\|E_{I/E}^{(m)} - E_{ref}\|_{L^2([0,T])}}{\|E_{ref}\|_{L^2([0,T])}}$, where $E_{I/E}^{(m)}$ is the value of E obtained using the GC method with the ratio m and E_{ref} is the value of E obtained using a full explicit computation. Figures 6 and 7 compare the results obtained using the Explicit/Implicit computation with different values of m with the results obtained using the Explicit/Explicit computation. One can remark that the different quantities (displacements and energies) are in a good agreement even if small fluctuations can be observed in the case of $m = 5$. Table 1 summarizes the errors computed for each quantity by varying the ratio m from 1 to 5. It can be observed that the errors are globally small and does not exceed 3.6% for the displacements and 0.7% for the energies.



(a) Horizontal displacement (b) Vertical displacement

Figure 6: Vertical and horizontal displacements plotted at point C using time heterogeneous implicit PMLs for different values of the tiem step ratio m compared to the reference results using a full explicit integration.



(a) Energie potentielle

(b) Energie cintique

Figure 7: Kinetic and internal energies computed using time heterogeneous implicit PMLs for different values of time step ratio m compared to the reference results using a full explicit integration.

	Kinetic energy	Internal energy	Horizontal displacement	Vertical displacement
$m = 1$	0.0002%	0.003%	0.001%	0.001%
$m = 3$	0.3%	0.1%	1.8%	1.3%
$m = 5$	0.7%	0.3%	3.6%	2.6%

Table 1: Relative errors related to the kinetic and internal energies computed for PMLs for different time step ratios m.

4.2 Rigid strip on a homogeneous isotropic elastic half-plane

In Figure 8, the classical problem of the rigid strip-footing (strip Young's modulus very important with respect to the soil Young's modulus) on a half plane is considered. The study is very similar to the previous one except that the strip will play the role of the third subdomain integrated with the implicit scheme. Using the GC method, the system composed of the PML and the strip will be integrated with the same time step computed from the soil properties instead of the strip properties which will be very small due to the stiffness of the strip.

We keep the same properties of the soil and the PML given in the previous Lamb test. The cross section is characterized by a half width 0.5 and a Young's modulus 100 times that of the soil. The load is varying as a Ricker wave with the parameters defined before and is applied uniformly to the strip as it is shown in Figure 8. The comparison will be in terms of displacements computed at the point C and energies by considering the system composed of the strip and the soil.

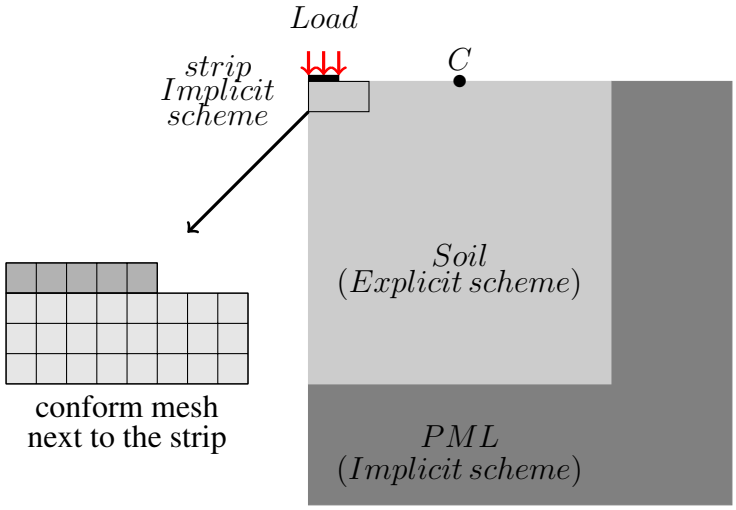
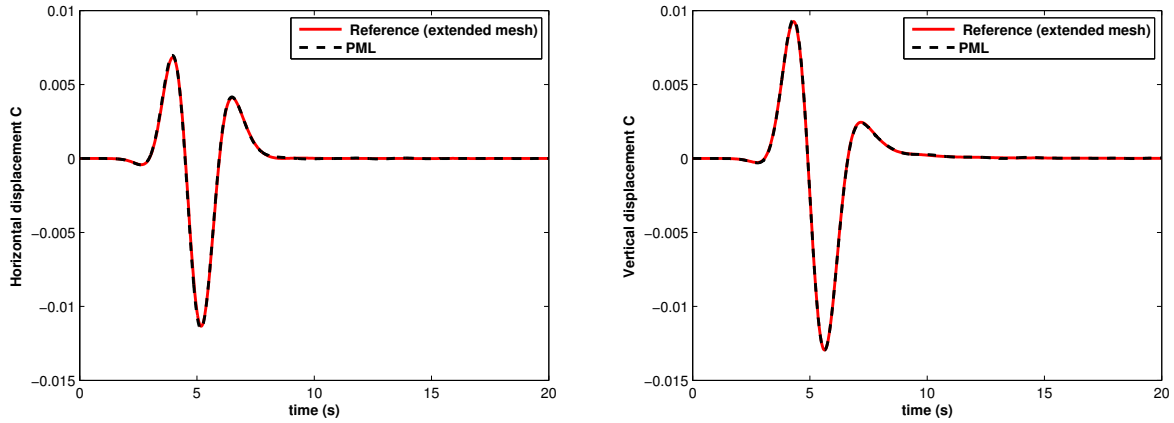


Figure 8: Rigid strip on a homogeneous soil. The soil and the strip are integrated using explicit time scheme while the PML is integrated using implicit time scheme.

Figure 9 compares the displacements at C obtained using the PML model and the extended mesh (reference results). It can be observed that the results closely match the reference results with an error, estimated using the definition in the previous example, less than 2%.

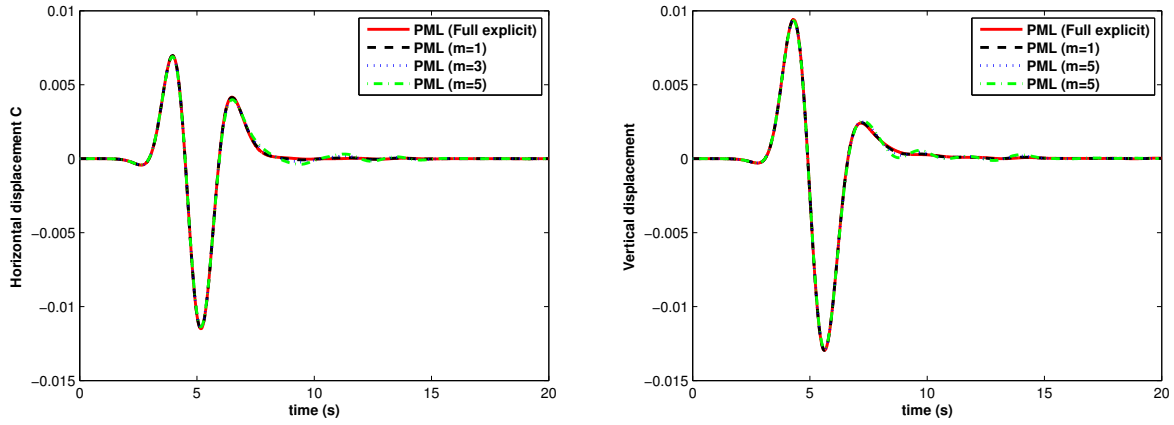


(a) Horizontal displacement

(b) Vertical displacement

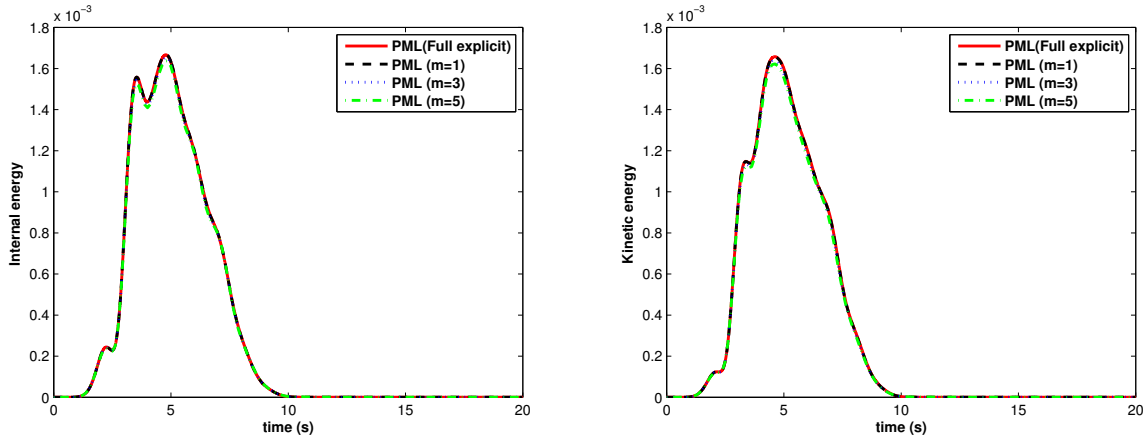
Figure 9: Vertical and horizontal displacements plotted at point C using the PMLs compared to the reference results using an extended mesh.

Considering the subdomain decomposition described before, Figures 10 and 11 compare the displacements and the energies obtained using the Explicit/Implicit strategy by varying the time ratio m with the results obtained using a full explicit integration. It can be noted that the different curves are quite close with an error less than 5% for the displacements and 2.4% for the energies (Table 2). Furthermore, an important reduction in time computation has been observed which is on the order of 6,16 and 21 times less than the full explicit computation for $m = 1$, $m = 3$ and $m = 5$ respectively.



(a) Horizontal displacement (b) Vertical displacement

Figure 10: Vertical and horizontal displacements plotted at point C using time heterogeneous implicit PMLs for different values of time step ratios m compared the reference results using a full explicit integration.



(a) Energie potentielle (b) Energie cintique

Figure 11: Kinetic and internal energies computed using time heterogeneous implicit PMLs for different values of time step ratios m compared to the reference results using a full explicit integration.

	Kinetic energy	Internal energy	Horizontal displacement	Vertical displacement
$m = 1$	0.2%	0.1%	0.8%	0.6%
$m = 3$	1.3%	0.9%	3%	2%
$m = 5$	2.4%	1.8%	5%	3.7%

Table 2: Relative errors related to the kinetic and internal energies computed for the system composed of the strip and the soil by varying the time step ratios m from 1 to 5.

5 Conclusion

In this paper, we presented the multi−time step coupling algorithm, based on GC method, between the PML developed by Basu *et al* in [13] and a physical domain assumed to be linear isotropic. The resulting algorithm was tested numerically through the computation of displacements and energies for two 2D applications. These tests indicate that the proposed coupling strategy offers interesting results in terms of accuracy and CPU time. However, a sensitivity to a relatively small values of the time ratio m was observed for both tests, maybe due the numerical dissipation introduced by the GC method. The extension of this method to other coupling strategies (Brun *et al* [20] for example) is in progress.

Anppendix A

The matrices B^{ϵ},B^{Q}, $\hat{F}^{\epsilon}$ and $\hat{F}^{Q}$ in equation 18 are defined by:
First, we give the following definitions:

$$F^{l} = \left[F^{p} + \frac{F^{e}}{dt}\right]^{-1} \qquad F^{\epsilon} = F^{e}F^{l} \quad F^{Q} = F^{p}F^{l} \tag{40}$$

The matrix B^{ϵ} is given in term of the submatrix for the node I by:

$$B^{\epsilon}_{I} = \begin{bmatrix} F^{\epsilon}_{11}N^{l}_{I1} & F^{\epsilon}_{21}N^{l}_{I1} \\ F^{\epsilon}_{12}N^{l}_{I2} & F^{\epsilon}_{22}N^{l}_{I2} \\ F^{\epsilon}_{11}N^{l}_{I2} + F^{\epsilon}_{12}N^{l}_{I1} & F^{\epsilon}_{21}N^{l}_{I12} + F^{\epsilon}_{22}N^{l}_{I1} \end{bmatrix} \tag{41}$$

with:

$$N^{l}_{Ii} = F^{l}_{ij}N_{I,j} \tag{42}$$

The matrix B^{Q} is defined, similarly, by replacing F^{ϵ} with F^{Q}. Finally, the matrix $\hat{F}^{\epsilon}$ is given by:

$$\hat{F}^{\epsilon} = \begin{bmatrix} (F^{\epsilon}_{11})^{2} & (F^{\epsilon}_{21})^{2} & F^{\epsilon}_{11}F^{\epsilon}_{21} \\ (F^{\epsilon}_{12})^{2} & (F^{\epsilon}_{22})^{2} & F^{\epsilon}_{12}F^{\epsilon}_{22} \\ 2F^{\epsilon}_{11}F^{\epsilon}_{12} & 2F^{\epsilon}_{21}F^{\epsilon}_{22} & F^{\epsilon}_{11}F^{\epsilon}_{22} + F^{\epsilon}_{12}F^{\epsilon}_{21} \end{bmatrix} \tag{43}$$

likewise, the matrix $\hat{F}^{Q}$ is obtained by replacing F^{ϵ} with F^{Q}.

References

[1] P. Bettess. Infinite elements. *International Journal for Numerical Methods in Engineering*, 11:53–64, 1977.

[2] B. Enquist and A. Majda. Absorbing boundary conditions for the numerical simulation of waves. *Mathematics of Computation*, 31:629–65, 1977.

[3] J. F. Semblat, L. Lenti, and A. Gandomzadeh. A simple multi-directional absorbing layer method to simulate elastic wave propagation in unbounded domains. *International Journal for Numerical Methods in Engineering*, 85:1543–1563, 2011.

[4] P. Rajagopal, M. Drozdz, E. A. Skelton, M.J. S. Lowe, and R. V. Craster. On the use of the absorbing layers to simulate the propagation of elastic waves in unbounded isotropic media using commercially available finite element packages. *NDT&E International*, 51:30–40, 2012.

[5] E. Zafati, M. Brun, I. Djeran-Maigre, and F. Prunier. Multi-directional and multi-time step absorbing layer for unbounded domain. *Comptes Rendus Mecanique*, 342:539–557, 2014.

[6] W.C. Chew and Q.H. Liu. Perfectly matched layers for elastodynamics: a new absorbing boundary condition. *Journal of Computational Acoustics*, 4:341–359, 1996.

[7] J. Bérenger. A perfectly matched layer for the absorption of electromagnetic waves. *Journal of Computational Physics*, 114:185–200, 1994.

[8] F. Hastings, J.B. Schneider, and S.L. Broschat. Application of the perfectly matched layer (pml) absorbing boundary condition to elastic wave propagation. *The Journal of the Acoustical Society of America*, 100:3061–3069, 1996.

[9] F. Collino and C. Tsoga. Application of the perfectly matched layer model to the linear elastodynamic problem in anisotropic heterogeneous media. *Geophysics*, 66:294–307, 2001.

[10] T. Wang and X. Tang. Finite-difference modeling of elastic wave propagation: a nonsplitting perfectly matched approach. *Geophysics*, 68:1749–1755, 2003.

[11] R. Matzen. An efficient finite element time-domain formulation for the elastic second-order wave equation: A non split complex frequency shifted convolutional pml. *International Journal for Numerical Methods in Engineering*, 88:951–973, 2011.

[12] U. Basu and A.K. Chopra. Perfectly matched layers for time-harmonic elastodynamics of unbounded domains: theory and finite-element implementation. *International Journal for Numerical Methods in Engineering*, 192:1337–1375, 2003.

[13] U. Basu and A.K. Chopra. Perfectly matched layers for transient elastodynamics of unbouded domains. *International Journal for Numerical Methods in Engineering*, 59:1039–1074, 2004.

[14] A. Combescure and A. Gravouil. A numerical scheme to couple subdomains with different time-steps for predominantly linear transient analysis. *Computer Methods in Applied Mechanics and Engineering*, 191:1129–1157, 2002.

[15] N.M. Newmark. A method of computation for structural dynamics. *Journal of the Engineering Mechanics Division (ASCE)*, 85:67–94, 1959.

[16] T.J.R. Hughes. *The Finite Element Method: Linear Static and Dynamic Finite Element Analysis*. Prentice-Hall, Englewood Cliffs, NJ, 1987.

[17] N. Mahjoubi, A. Gravouil, and A. Combescure. Coupling subdomains with heterogeneous time integrators and incompatible time steps. *Computational Mechanics*, pages DOI 10.1007/s00466–009–0413–4, 2009.

[18] U. Basu. Explicit finite element perfectly matched layer for transient three-dimensional elastic waves. *International Journal for Numerical Methods in Engineering*, 77:151–176, 2009.

[19] H. Lamb. On the propagation of tremors over the surface of an elastic solid. *Proceeedings of the Royal Society of London*, 72:128–130, 1903.

[20] M. Brun, A. Gravouil, A. Combescure, and A. Limam. Two FETI-besed heterogeneous time step coupling methods for Newmark and α-schemes derived from the energy method. *Computer methods in applied mechanics and engineering*, 283:130–176, 2015.

COMPDYN 2015
5th ECCOMAS Thematic Conference on
Computational Methods in Structural Dynamics and Earthquake Engineering
M. Papadrakakis, V. Papadopoulos, V. Plevris (eds.)
Crete Island, Greece, 25–27 May 2015

LONGITUDINAL SEISMIC VIBRATIONS OF A SEGMENTED PIPELINE CONSIDERED AS THE PERIODICALLY INHOMOGENEOUS ROD

Mukhady Sh. Israilov[1]

[1] Research Institute on Mathematical Physics and Seismodynamics. Grozny,

Chechen Republic, Russia

israiler@hotmail.com

Keywords: seismic vibrations, underground pipeline, periodically inhomogeneous rod, flexible joints.

Abstract. *Underground segmented pipeline with flexible joints is considered as a periodically piecewise homogeneous rod. Longitudinal vibrations of the rod are investigated by utilizing E.A. Ilyushina's method which reduces this problem to vibration study of separation boundaries between homogeneous parts of the rod. In this way, the averaged differential equations of motion and the average wave velocities are obtained for inhomogeneous rod when its cell of periodicity contains two, three, and more elastic components. It is shown that the average velocities are the same as the ones calculated through effective static moduli of the composite rod.*

The iron/steel pipelines with rubber and lead rings at joints are considered as examples. In these examples the average wave velocities in segmented pipeline (calculated by the method mentioned above) are significantly less than the wave velocity in the iron/steel pipe itself. The last result justifies the necessity of supersonic case study (the case in which wave velocity in the pipe less than seismic wave velocity in the soil) when earthquake response of buried pipelines is investigated. Usually this case is ignored assuming that the wave velocity in the pipe exceeds the wave velocity in the soil. The results of this paper clearly demonstrate that for segmented pipeline this assumption may not be true.

1 LONGITUDINAL VIBRATIONS OF PIECEWISE INHOMOGENEOUS PIPELINE: STUDY METHOD

Let us consider longitudinal displacements $u(z,t)$ of an elastic pipeline $z_1 \le z \le z_{N+1}$ consisting of N different homogeneous segments with interfaces at $z = z_r$ $(r = 2, \dots, N)$. As boundary conditions stresses $\sigma_{11}(t)$ or displacements $u(t)$ can be defined at the ends of the pipeline at $z = z_1$ and $z = z_{N+1}$. We will consider stationary vibrations of the pipeline assuming that the boundary conditions are harmonic functions of time. Hence displacements of r-th segment $u_r(z,t) = U_r(z)\exp(-i\omega t)$ will obey the following equation:

$$U_r''(z) + \omega_{1r}^2 U_r(z) = 0 \tag{1}$$

where the prime denotes the derivative with respect to the argument and $\omega_{1r} = \omega/c_r$ ($c_r = \sqrt{E_r/\rho_r}$ is a velocity of wave propagation in r-th segment with Young modulus E_r and density ρ_r).

The general solution of equation (1) has the form

$$U_r(z) = A_1^r \cos\omega_{1r} z + A_2^r \sin\omega_{1r} z \tag{2}$$

Following the method of H.A Ilyushina [1] developed for oscillation study of an inhomogeneous structure, we find the relation between the displacement U and stress Σ_{11} ($\sigma_{11}(z, t) = \Sigma_{11}(z)\exp(-i\omega t)$) on the left side of the r-th segment ($z = z_r$) with that on its right side ($z = z_{r+1}$).

We introduce a two-dimensional vector $\boldsymbol{Y}^r$ in the following way:

$$Y_1^r = U_r(z), \qquad Y_2^r = \frac{1}{E_0\omega_{10}}\Sigma_{11}^r = \frac{E_r}{E_0\omega_{10}}U_r', \tag{3}$$

where E_0, c_0- normalization constants and $\omega_{10} \equiv \omega/c_0$.

From the common solution of equations (2) and (3) it follows that

$$A_1^r = Y_1^r \cos\omega_{1r} z - P_r Y_2^r \sin\omega_{1r} z,$$
$$A_2^r = Y_1^r \sin\omega_{1r} z + P_r Y_2^r \cos\omega_{1r} z,$$
$$P_r \equiv \frac{E_0\omega_{10}}{E_r\omega_{1r}}$$

or in matrix form:

$$\boldsymbol{A}^r = C^r\boldsymbol{Y}^r;\ C^r \equiv \begin{Vmatrix} \cos\omega_{1r} z & -P_r \sin\omega_{1r} z \\ \sin\omega_{1r} z & P_r \cos\omega_{1r} z \end{Vmatrix} \tag{4}$$

Writing the relation (4) for the r-th and r+1-th segments and using the condition of continuity of U and Σ_{11} on the interface between these segments, we obtain (where $h_r \equiv z_{r+1} - z_r$ is length of r-th segment):

$$Y_1^{r+1}(z_{r+1}) = Y_1^r(z_{r+1}) = A_1^r \cos\omega_{1r}(z_r + h_r) + A_2^r \sin\omega_{1r}(z_r + h_r)$$
$$= Y_1^r(z_r)\cos\omega_{1r} h_r + P_r Y_2^r(z_r)\sin\omega_{1r} h_r,$$
$$Y_2^{r+1}(z_{r+1}) = Y_2^r(z_{r+1}) = [-A_1^r \sin\omega_{1r}(z_r + h_r) + A_2^r \cos\omega_{1r}(z_r + h_r)]/P_r =$$
$$= -(Y_1^r(z_r)\sin\omega_{1r} h_r)/P_r + Y_2^r(z_r)\cos\omega_{1r} h_r$$

or in matrix form:

$$\boldsymbol{Y}^{r+1}(z_{r+1}) = D^r \boldsymbol{Y}^r(z_r)\,,\ D^r \equiv \left\| \begin{matrix} cos\,\omega_{1r}h_r & P_r\,sin\,\omega_{1r}h_r \\ -\frac{1}{P_r} sin\,\omega_{1r}h_r & cos\,\omega_{1r}h_r \end{matrix} \right\| \tag{5}$$

Recurrence equations (5) give the relation between the values of the vector $\boldsymbol{Y}^r$ of r-th segment at $z = z_r$ and values $\boldsymbol{Y}^{r+1}$ r+1-th section at $z = z_{r+1}$ and allow us to find the values of U and Σ_{11} on any internal interface of the pipeline, if the values on one of its ends are defined.

2 VIBRATIONS OF TWO-COMPONENT AND MULTICOMPONENT PERIODIC PIPELINES

Let us consider the case of an infinite two-component (two-segment) pipeline which consists of repetitive homogeneous sections of two types (Figure 1) with the constants: r-th interval - E_1, ω_{11}, h_1; r+1-th interval - E_2, ω_{12}, h_2. This case is very important for practical applications. Writing the relation (5) for two adjacent segments, we find

$$\boldsymbol{Y}^{r+2} = D\,\boldsymbol{Y}^r,\ D = D^2D^1, \tag{6}$$

where

$$D = \left\| \begin{matrix} d_{11} & d_{12} \\ d_{21} & d_{22} \end{matrix} \right\|, \tag{7}$$

$$\begin{aligned}
d_{11} &= \cos\omega_{11}h_1\ \cos\omega_{12}h_2\ -\ \frac{P_2}{P_1}\sin\omega_{11}h_1\ \sin\omega_{12}h_2\,,\\
d_{12} &= P_1\ \sin\omega_{11}h_1\ \cos\omega_{12}h_2 + P_2\cos\omega_{11}h_1\sin\omega_{12}h_2\,,\\
d_{21} &= -\ \frac{1}{P_2}\cos\omega_{11}h_1\ \sin\omega_{12}h_2\ -\ \frac{1}{P_1}\sin\omega_{11}h_1\cos\omega_{12}h_2\,,\\
d_{22} &= -\ \frac{P_1}{P_2}\ \sin\omega_{11}h_1\ \sin\omega_{12}h_2\ +\ \cos\omega_{11}h_1\cos\omega_{12}h_2
\end{aligned}$$

The whole set of interfaces of infinite periodic two-component pipeline is divided into two classes. The first class consists of the interfaces for which the segments of the material 1are located on the right side and the segments of the material 2 – on the left side (the interfaces of this class are marked in Fig. 1 by bold dots); and the second class consists the interfaces for which, on the contrary, the segments of the material 2 are located to the right and the segments of the material 1 - to the left (in Fig. 1 they are marked by crosses).

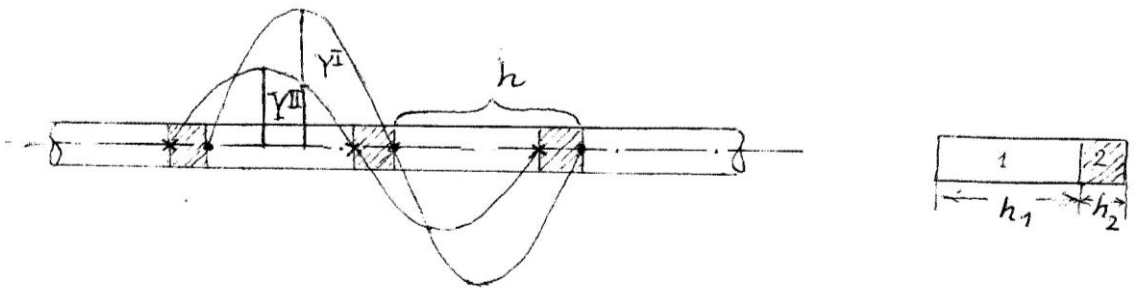


Figure 1: Two-component periodic pipeline geometry

For such periodic structure is natural to assume that the interfaces of the first and second classes vibrate in similar way, i.e. with the same frequency, but with different amplitudes, as shown in (Fig. 1). Below, in Sec. 3, it was investigated when this assumption is satisfied and have place a phenomenon of the transmission of frequency by the periodic structure, and when it fails, and there is aperiodic motion of the structure (the phenomenon of locking or filtering out frequencies). In this assumption vector $\boldsymbol{Y}^r$ can be represented as ($h \equiv h_1 + h_2$)

$$\boldsymbol{Y}^r = \begin{cases} Y^I e^{ikrh/2}, & r = \pm 2, \pm 4, \pm 6, \ldots; \\ Y^{II} e^{ik[\frac{(r+1)h}{2} - h_2]}, & r = \pm 1, \pm 3, \pm 5, \ldots \end{cases} \tag{8}$$

Then after substituting (8) into equation (6) we obtain the following characteristic equation

$$\begin{vmatrix} d_{11} - e^{ikh} & d_{12} \\ d_{21} & d_{22} - e^{ikh} \end{vmatrix} = 0 \tag{9}$$

Using in (9) expressions for d_{ij} from (7), we obtain the spectral equation of two-component segmented pipeline

$$\cos kh = \cos(\omega_{11} h_1 + \omega_{12} h_2) - \gamma \sin \omega_{11} h_1 \sin \omega_{12} h_2, \tag{10}$$

$$\gamma \equiv \frac{1}{2}\left(\frac{P_1}{P_2} + \frac{P_2}{P_1}\right) - 1 > 0$$

Since length of seismic wave $\Lambda = 2\pi/k$ (many tens to hundreds of meters) is much longer than length of an pipeline's cell of periodicity h (in practice up to ten meters), for the spectral equation (10) is a good approximation, the so-called, long-wave approximation, when in it for small k and ω, and hence small $\omega_{11} = \omega/c_1$ and $\omega_{12} = \omega/c_2$, in the Taylor series of incoming functions we keep members up to the second order. Then equation (10) proceeds to the next:

$$k^2 h^2 = \omega^2 \left[\frac{h_1^2}{c_1^2} + \frac{h_2^2}{c_2^2} + 2(1+\gamma)\frac{h_1}{c_1}\frac{h_2}{c_2}\right]$$

This shows that the average or "averaged" velocity of propagation of longitudinal perturbations in two-component pipeline for small k and ω is

$$c_L \equiv \langle c \rangle = \frac{h}{\sqrt{\left(\frac{h_1}{c_1}\right)^2 + \left(\frac{h_2}{c_2}\right)^2 + \left(\frac{P_1}{P_2} + \frac{P_2}{P_1}\right)\frac{h_1}{c_1}\frac{h_2}{c_2}}} \tag{11}$$

Thus, when the length of the seismic wave substantially larger than the characteristic size of inhomogeneity (the length of the periodicity cell) of the segmented pipeline, it may be considered as a homogeneous rod which has averaged, or as they say, effective mechanical properties. In this case, averaged equation of longitudinal vibrations of such homogeneous pipeline has the form

$$U''(z) + \frac{\omega^2}{\langle c \rangle^2} U(z) = 0$$

For average velocity can be easily obtained the following important theorems.

Theorem 1. The average velosity of propagation of longitudinal waves in the segmented pipeline can be calculated on the basis of its effective static characteristics, considering the pipeline as a composite [2], *namely,*

$$c_L \equiv \langle c \rangle = \sqrt{\langle E \rangle / \langle \rho \rangle}\,, \tag{12}$$

where

$$\langle \rho \rangle = \frac{h_1\rho_1 + h_2\rho_2}{h} \quad , \quad \langle E \rangle = \frac{h}{h_1/E_1 + h_2/E_2} \tag{13}$$

are the average density and the effective Young's modulus of bi-component rod, respectively.

The expression for the average density in (13) is obvious, and for the effective Young's modulus obtained by introducing the concept of the average strain of the periodicity cell by the formula (σ - longitudinal stress)

$$\langle \varepsilon \rangle h \equiv \frac{\sigma}{\langle E \rangle} h = \varepsilon_1 h_1 + \varepsilon_2 h_2 = \frac{\sigma}{E_1} h_1 + \frac{\sigma}{E_2} h_2.$$

To prove statement of the theorem we transform the right-hand side of (12) using (13). That leads to

$$\sqrt{\frac{\langle E \rangle}{\langle \rho \rangle}} = \sqrt{\frac{h}{h_1/E_1 + h_2/E_2} \cdot \frac{h}{h_1\rho_1 + h_2\rho_2}} = h \Big/ \sqrt{\left(\frac{h_1}{c_1}\right)^2 + \left(\frac{h_2}{c_2}\right)^2 + h_1 h_2 \left(\frac{\rho_1}{E_2} + \frac{\rho_2}{E_1}\right)}$$

From which we obtain the desired result if we note that

$$\frac{\rho_1}{E_2} + \frac{\rho_2}{E_1} = \frac{1}{c_1 c_2}\left(\frac{P_1}{P_2} + \frac{P_2}{P_1}\right)$$

Theorem 2. Without loss of generality, assume that $c_1 > c_2$. Then $c_L \equiv \langle c \rangle < c_1$, that is, the average velocity is less than the greater of the wave velocities in the internal parts of the two-component cell of the pipeline.

To prove the theorem let us use elementary transformation:

$$\langle c \rangle = \frac{h}{\sqrt{\left(\frac{h_1}{c_1}\right)^2 + \left(\frac{h_2}{c_2}\right)^2 + \left(\frac{P_1}{P_2} + \frac{P_2}{P_1}\right)\frac{h_1}{c_1}\frac{h_2}{c_2}}} = \frac{h}{\sqrt{\left(\frac{h_1}{c_1} + \frac{h_2}{c_2}\right)^2 + \left(\frac{P_1}{P_2} + \frac{P_2}{P_1} - 2\right)\frac{h_1}{c_1}\frac{h_2}{c_2}}}$$

The second term under the radical in the last expression is positive (because of the inequality $x + \frac{1}{x} > 2$ for $x > 0$ and $x \neq 1$ (for $x = P_1/P_2$)), therefore

$$\langle c\rangle < \frac{h}{\frac{h_1}{c_1}+\frac{h_2}{c_2}} \equiv c_*$$

But

$$c_* = \frac{c_1 c_2}{\frac{h_1}{h}c_2+\frac{h_2}{h}c_1} = c_1\frac{1}{\frac{h_1}{h}+\frac{h_2}{h}\frac{c_1}{c_2}} = c_1\frac{1}{1+\frac{h_2}{h}\left(\frac{c_1}{c_2}-1\right)} < c_1$$

since by assumption $c_1 > c_2$. Thus, it is found that $\langle c\rangle < c_* < c_1$.

It should be noted that the average velocity can be less than the smallest velocity of wave propagation in the segments of the pipeline (which is equal to c_2 by assumption).This is easily seen if we transform expression (11) or (12) to the form

$$\langle c\rangle = \frac{c_2}{\sqrt{1+\left(\frac{h_1}{h}\right)^2\left[\left(\frac{c_2}{c_1}\right)^2-1\right]+\frac{h_1 h_2}{h\,h}\left[\frac{\rho_1}{\rho_2}+\frac{\rho_2}{\rho_1}\left(\frac{c_2}{c_1}\right)^2-2\right]}}$$

From this formula, it is also clear that the average velocity $\langle c\rangle$ is less than c_2 in the case of $c_2 = c_1$ (but with segments of different materials).

Thus, from the prof provided above, we can conclude that the use of damping material on the joints reduces the velocity of wave propagation in the pipeline and that runs the risk of transition to supersonic regime when resonance may occur [3].

Outlined procedure can be applied to the calculation of the average wave propagation velocity in the three and $N-$ component periodic pipeline. Although this involves considerable analytical calculations but the result can be obtained. In these cases, the matrix *D* in the formulas, analogous to (6), is a product of three or more (generally *N*) matrices of type (5) and, therefore, it does not work to write the characteristic equations as for the two-component periodic rod (equations like (10)). However, one can easily write down the asymptotic analogs of these characteristic equations for small k and ω with retention of members to the second order (a situation that is just implemented during strong earthquakes), of which have been set to the average velocity. We write out the results obtained in this way. In the case of the three-component periodic pipeline the averaged velocity is

$$\langle c\rangle = \frac{h}{\sqrt{\left(\frac{h_1}{c_1}\right)^2+\left(\frac{h_2}{c_2}\right)^2+\left(\frac{h_3}{c_3}\right)^2+\left(\frac{P_1}{P_2}+\frac{P_2}{P_1}\right)\frac{h_1}{c_1}\frac{h_2}{c_2}+\left(\frac{P_1}{P_3}+\frac{P_3}{P_1}\right)\frac{h_1}{c_1}\frac{h_3}{c_3}+\left(\frac{P_2}{P_3}+\frac{P_3}{P_2}\right)\frac{h_2}{c_2}\frac{h_3}{c_3}}},$$

and for pipeline with N components in the periodicity cell we obtain

$$\langle c\rangle = \frac{h}{\sqrt{\sum_{k=1}^{N}\left(\frac{h_k}{c_k}\right)^2+\sum_{k,l=1;l>k}^{N}\left(\frac{P_k}{P_l}+\frac{P_l}{P_k}\right)\frac{h_k}{c_k}\frac{h_l}{c_l}}}$$

3 EXAMPLES: THE EXISTENCE OF PERIODIC SOLUTIONS AND THE NUMERICAL VALUES FOR AVERAGE VELOCITY IN TWO-COMPONENT PIPELINE

To quantify the effect of flexible joints consider two examples: a) pipeline consisting of iron pipes (large diameter) length of 5.97 m, connected in complex joints with rubber gaskets width of 3 cm and b) a pipeline consisting of iron pipe length 5.90 m, in complex junctions connected with lead strips of 10 cm width. In both cases, the length of the periodicity cell h = 6 m. Necessary for calculating the average velocity by the formula (11) mechanical properties of the pipeline material (iron, lead and rubber) are taken from Kaye and Laby [4] and are given in SI by values:

a) $c_1 = 4{,}3 \cdot 10^3$ m/s, $c_2 = 0{,}7 \cdot 10^2$ m/s, $E_1 = 13{,}0 \cdot 10^{10}$ N/m^2, $E_2 = 0{,}4 \cdot 10^7$ N/m^2;

b) $c_1 = 4{,}3 \cdot 10^3$ m/s, $c_2 = 1{,}2 \cdot 10^3$ m/s, $E_1 = 13{,}0 \cdot 10^{10}$ N/m^2, $E_2 = 1{,}62 \cdot 10^{10}$ N/m^2.

For our two-component periodic pipeline has been assumed the existence of periodic solutions of the form (8) with a real k, meaning that both types of interface oscillate with the same frequency. We define in the examples the regions of small ω, in which this assumption holds, or otherwise, the intervals in which the right-hand side of the characteristic equation (10) is less than one in modulus. The latter is valid in intervals where the graph of the function $y_1 = \cos X$, $X \equiv (\lambda_1 + \lambda_2)\omega$ is located between curves $y_2 = \alpha \cos \varkappa X + \beta$ and $y_3 = \alpha \cos \varkappa X - \beta$, where $\lambda_1 \equiv h_1/c_1$, $\lambda_2 \equiv h_2/c_2$, $\varkappa \equiv (\lambda_2 - \lambda_1)/(\lambda_2 + \lambda_1)$, $\alpha \equiv \gamma/(2+\gamma)$, $\beta \equiv 2/(2+\gamma)$.

Fig. 2 and 3 present graphs of these functions for small ω for examples *a* and *b*, respectively. As can be seen, there is a periodic solution for positive $X \lesssim 0.2$ (which corresponds to the frequency $\omega/2\pi \equiv f \lesssim$ 17 Hz) in Example *a* and for $X \lesssim 2.9$ (which corresponds $f \lesssim 325$ Hz) in Example *b*. Thus, in the case of rubber gaskets in complex junctions, since moderate earthquakes of intensity 2 - 3 on the Richter scale (the predominant frequency of seismic vibrations ~ 10 Hz [5]), there are periodic oscillations of the pipeline. And only in the case of weak shocks it is possible aperiodic motion. With lead seals periodic oscillations occur except in narrow regions near the points of change X in vicinity of X = -3, and X = 3 (Fig. 3), which is explained not as big a difference in velocity of wave propagation in the elements of the periodicity cell of the pipeline in this case.

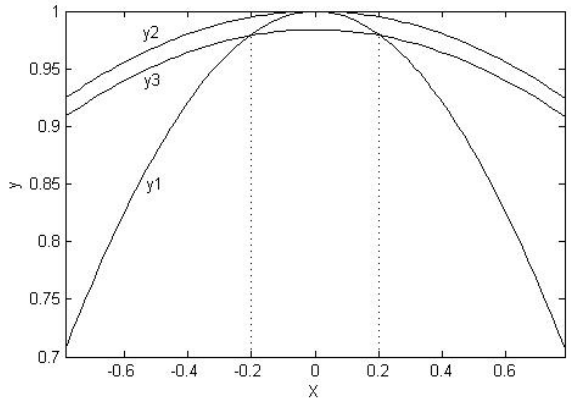


Figure 2: Region of periodic oscillations for iron pipeline with rubber gaskets

The average velocities of wave propagation, calculated by the formula (11), take in examples under consideration the values: *a)* $\langle c \rangle \approx 350$ m/s and *b)* $\langle c \rangle \approx 4.05 \cdot 10^3$ m/s. In the first example (with rubber gaskets), the average velocity of an order of magnitude smaller than the velocity of waves in the iron segment of the composite pipe and less than the velocity of propagation of longitudinal waves in typical soils (~ 500 ÷ 1500 m/s), which may have a significant impact and influence to earthquake safety of buried pipelines because of the nature of the solutions in the supersonic region [3].

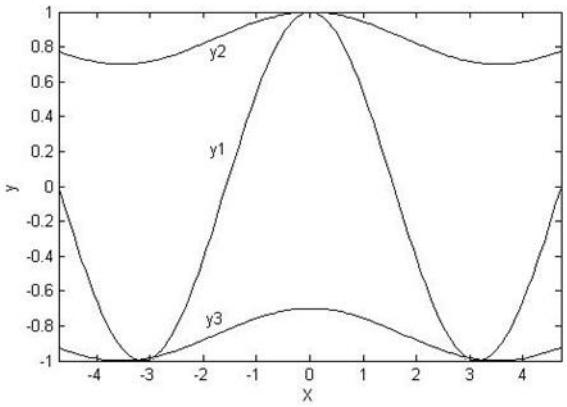


Figure 3. Region of periodic oscillations for iron pipeline with lead strips at junctions

4 CONCLUSION

The main conclusions derived from this study are summarized as follows:

1). A new method developed for study of longitudinal vibrations of multi-component periodically inhomogeneous pipeline (segmented pipeline with flexible joints) subjected to seismic waves. This method reduces the problem to vibration problem for corresponding homogeneous rod (or pipe) with average mechanical properties. It is shown that the reduction is a valid approximation when the length of seismic wave is much longer than the length of the of pipeline's periodicity cell.

2). Analytical expressions for average wave velocities are found for two, three, and N-component pipelines. It is proved that the average velocity is less than the greatest velocities of all pipeline components and can even be less than the smallest of them.

3). Theoretical results of this study are applied to the periodic steel pipeline with flexible joints consisting of rubber or lead gaskets. In examples of common practical interest numerical values for average velocities, which were calculated on the base of the developed theory, are significantly less than the wave velocity in the steel segment of the pipeline. And in the example with rubber gaskets the average velocity (~ estimates as 350 m/s) is less than the velocity of propagation of longitudinal waves in typical soils. Thus, this, so-called, supersonic regime cannot be ignored (as is usually done) in earthquake response analysis of segmented underground pipelines.

4). Here during investigation of the segmented pipeline as a periodic piecewise homogeneous structure it was assumed that all interfaces vibrate with the same frequency. The frequency intervals, in which this assumption is satisfied, are discussed and illustrated by the plots (Figures 2 and 3) in the examples.

REFERENCES

[1] Ilyushina H. A. Variant of elasticity theory with couple-stresses for one-dimensional continuous medium of inhomogeneous periodic texture. // Prikladnaja matematika i mekhanika. 1972. Vol. 36, № 6. P. 1086-1093 (*in Russian*).

[2] Christensen R. M. Theory of viscoelasticity. An introduction. 1971. N.-Y.: Academic press. 246 p.

[3] Israilov M. Sh. Seismodynamics of an underground pipeline. // Problems of Mechanics Journal. Uzbekistan Academy of sciences. 2012, issue 3. P. 18-24 (*in Russian*).

[4] Kaye G. W. C. & T. H. Laby. Tables of physical and chemical constants. 9-th edition. 1941. London: Longmans. 250 p.

[5] Kanai K. Engineering seismology. 1983. Tokyo: Univ. of Tokyo press. 252 p.

COMPDYN 2015
5th ECCOMAS Thematic Conference on
Computational Methods in Structural Dynamics and Earthquake Engineering
M. Papadrakakis, V. Papadopoulos, V. Plevris (eds.)
Crete Island, Greece, 25–27 May 2015

EXAMINING THE INITIATION MECHANISMS OF STATIC AND DYNAMIC LIQUEFACTION USING THREE DIMENSIONAL DEM SIMULATIONS

Zitao Zhang[1] **and Yu-Hsing Wang**[2]

[1] Department of Civil and Environmental Engineering, The Hong Kong University of Science and Technology, HKSAR, China
e-mail: zzhangaf@ust.hk

[2] Department of Civil and Environmental Engineering, The Hong Kong University of Science and Technology, HKSAR, China
ceyhwang@ust.hk

Keywords: Static Liquefaction, Cyclic Loading, Contact Force Distribution, Discrete Element Method.

Abstract. *Static and dynamic liquefaction may produce different levels of damages on the infrastructures and various numbers of casualties. Understanding the associated initiation mechanisms therefore is very important for geotechnical engineers to predict and manage the relevant hazards. In this study, a series of DEM simulations of undrained triaxial compression tests and a cyclic undrained triaxial test are carried out to examine the initiation mechanisms from a micromechanical perspective. The simulation results demonstrate a continuous decrease in the mean of contact normal forces and a continuous increase in the associated COV as the shear strain increases during undrained compression of a loose sample. Such kind of evolution trend found in the contact force distribution was not observed in the simulations of undrained compression tests on medium dense to dense sand samples. However, the same behavior can be detected in the cyclic undrained triaxial tests on a dense sample, i.e., a continuous decrease in the mean of contact normal forces and a continuous increase in the associated COV. Hence, such an evolution tendency of contact force distributions can serve as a basis to explain the initiation mechanisms of the static and dynamic liquefaction from a micromechanical point of view.*

1 INTRODUCTION

Liquefaction describes a condition where the effective stress of the soil reaches a very low value (i.e., close to zero) due to the buildup of pore pressures. Liquefaction may be induced by monotonic or static loading, which is commonly referred to as static liquefaction. Static liquefaction may lead to different types of hazards, e.g., failures of the submarine slopes, dams and tailings structures, and most of these case histories occurred in very loose to loose saturated sand [1]. Even though static liquefaction can hardly occur in medium dense to dese sand, a cyclic loading, e.g., earthquake shaking, may induce the decrease in the effectives stress, and the liquefaction state might be reached after a certain number of loading cycles. Once the liquefaction state is reached, large strains might be developed in the subsequent loading cycles to cause casualties [2]. For example, as summarized by [3], bridge collapses due to liquefaction have been observed during the 1964 Niigata (Japan) and Alaska earthquakes, 1975 Haicheng (China) earthquake, 1976 Tanshang (China) earthquake, 2008 Wenchuan (China) earthquake and 2010 Maule (Chile) earthquake. Hence, understanding the initiation mechanisms of static and dynamic liquefaction (induced by cyclic loading) is very important for geotechnical engineers to predict and manage these associated hazards.

The undrained triaxial compression tests, triaxial extension tests and simple shear tests have been frequently conducted to examine the undrained soil behavior under a static loading (e.g., [1, 4-9]). Fig. 1 presents typical responses during the undrained triaxial compression tests carried out by [10]. For a loose sample with a void ratio of 0.93, the deviatoric stress $q = \sigma_v' - \sigma_r'$ initially increases with increasing shear strain (γ) until the soil reaches the peak state (as shown by the solid triangle in Fig. 1a), and the mean effective stress $p' = (\sigma_v' + 2\sigma_r')/3$ decreases with increasing γ. Note that σ_v' and σ_r' are the vertical and radial effective stresses, respectively. The shear strain γ is described by $\gamma = \varepsilon_a - \varepsilon_r$, where ε_a and ε_r are the vertical and radial strains, respectively. After the peak state, both the values of p' and q decrease with increasing γ until liquefaction ($p' = q = 0$). For the dense sample with a void ratio of 0.861, the deviatoric stress q continuously increases with increasing γ, and p' initially decreases and then increases with increaseing γ. In addition, for the medium dense sand with a void ratio of 0.868, q initially increases and then decreases with increasing γ, which is similar to the response in the early stage of undrained compression for a loose sample. Afterwards, the sample reaches a quasi-steady state (as shown by the solid circle in Fig. 1a), and then both the values of p' and

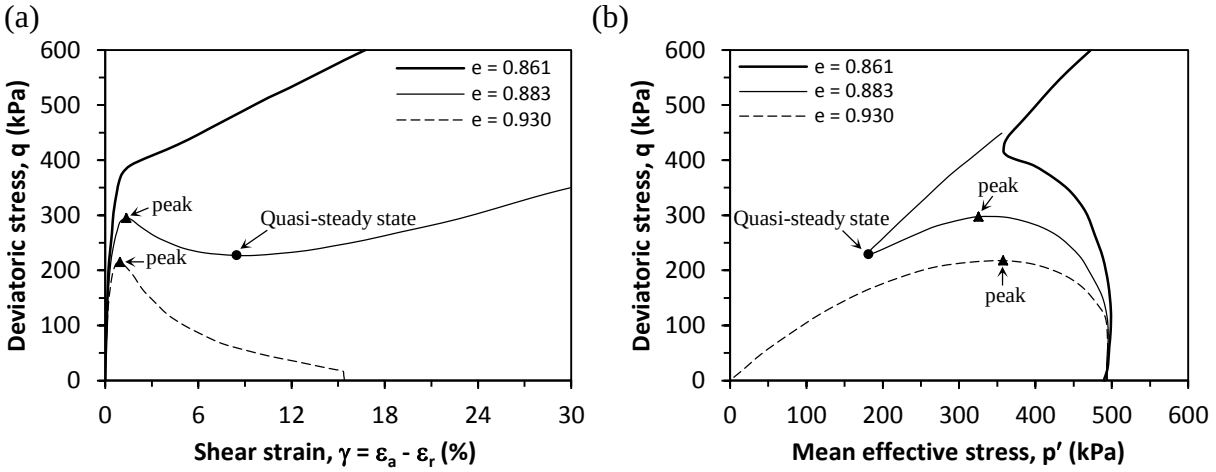


Figure 1: Typical responses during the undrained static compression tests: (a) stress-strain responses and (b) stress paths (after [10]).

q increase with increasing γ, which is similar to the response in the latter stage of a dense sample. Hence, the liquefaction state cannot be reached for the medium dense to dense samples. This explains why most of the case histories of static liquefaction occur in very loose to loose sand but not in medium dense to dense sand. However, the micromechanical basis of static liquefaction cannot be obtained based on these experimental observations.

To understand the undrained soil behavior under a cyclic loading, cyclic undrained simple shear tests and cyclic undrained triaxial tests have been carried out (e.g., [11-17]). Fig. 2 presents typical responses of a dense sample during a cyclic undrained triaxial test conducted by [18]. After isotropic consolidation, the sample was subjected to a cyclic loading under a stress-controlled undrained condition. The initial liquefaction seems to be reached at the 9th cycle, and the butterfly shaped loops have been reached afterwards (as shown in Fig. 2b). As noted, the values of the double amplitude axial strain (DA) for the cycles after initial liquefaction are much larger than those before initial liquefaction. Those experimental responses explain why liquefaction can occur in medium dense to dense sand during earthquakes. However, once again, the associated initiation mechanisms from a micromechanical perspective cannot be provided by these experiments.

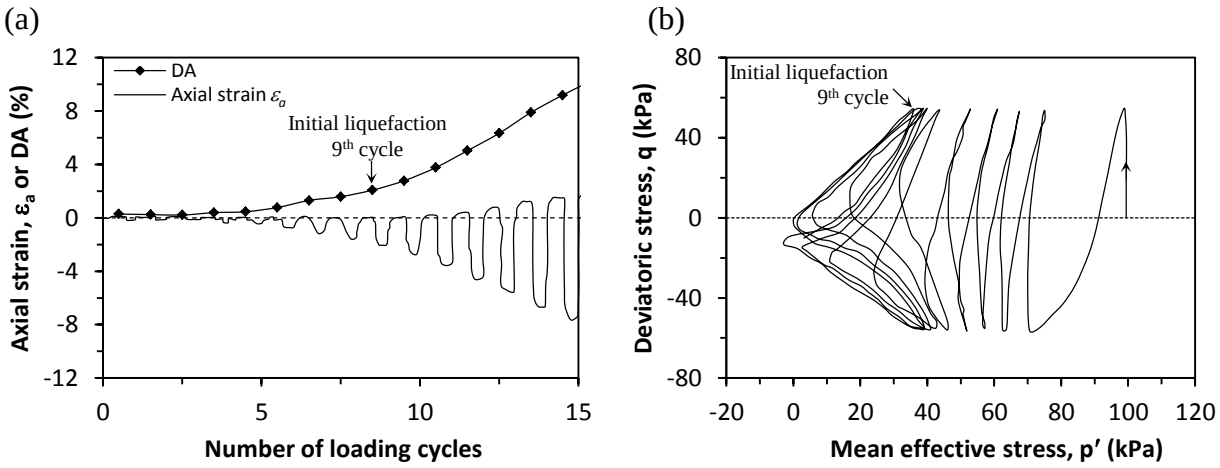


Figure 2: Typical responses during a cyclic undrained triaxial test (after [18]): (a) variations of the axial strain ε_a and double amplitude axial strain (DA) with the number of cycles and (b) stress paths. Note that only the stress paths for the initial nine loading cycles are shown in Fig. 2b. The stress paths for the following cycles are similar to the stress path for the 9th cycle.

Numerical simulations using the discrete element method (DEM) have been used to simulate the undrained soil responses for further analyses and examinations (e.g, [19-27]). Using DEM simulations can obtain not only the macroscopic stress and strain responses but also the information at the particle and contact scales, e.g., contact forces. Hence, DEM simulations can be used to effectively elucidate the involved micromechanical. Soroush & Ferdowsi [21] carried out DEM simulations of strain-controlled cyclic loading tests and qualitatively analyzed the variations of the contact force distribution with increasing number of loading cycles. However, quantitative and statistical analyses for the cyclic loading processes, especially for the stress-controlled cyclic loading, remain insufficient.

The objective of this study is to examine the initiation mechanisms of static liquefaction and dynamic liquefaction (induced by cyclic loading) from the micromechanical perspective. A series of DEM simulations of undrained triaxial compression tests and a cyclic undrained triaxial test are carried out. The simulations first aim to reproduce experimental findings (as

shown in Figs. 1 and 2). Then, variations of the contact force distributions are examined to explore the initiation mechanisms of liquefaction.

2 DETAILS OF THE DEM SIMULATIONS

The DEM software, Particle Flow Code in 3 Dimensions (PFC3D version 4.0, Itasca Company, USA) was used in this study. The Hertz-Mindlin contact model was used to regulate the force-displacement relationships in the normal and tangential directions. In addition, a rolling resistance model was adopted to account for the contact moments including the interlocking effects between real soil particles. Details of these contact models and the calibration of the parameters can be found in [28]. Table 1 summarizes the values of the parameters used in the DEM simulations.

Sample properties and parameters	Value
Contact model parameters	
Shear modulus G	1.0 GPa
Poisson's ratio ν	0.2
Inter-particle friction coefficient μ	0.32
Rolling stiffness coefficient J_n	2
Maximum rolling resistance coefficient μ_r	12
Particle size	
Largest particle diameter	0.212 mm
Smallest particle diameter	0.150 mm
Mean particle diameter d_{50}	0.172 mm
Properties of the samples	
Particle number	13528
Void ratio of the samples for UC1 and UC1-cyclic	0.745
Void ratio of the sample for UC2	0.783
Void ratio of the sample for UC3	0.792
Local damping used to dissipate kinetic energy	0.7

Table 1: Sample properties and parameters used in the DEM simulations of this study

Three DEM simulations of undrained triaxial compression tests were conducted. These simulations are denoted by UC1, UC2 and UC3 in the following discussion. The radius expansion method was used to prepare the samples. Particles were firstly generated with radii smaller than the assigned values and randomly positioned in the sample container, and then these radii were expanded to achieve the assigned values by multiplying a factor. After that, particles were rearranged under a friction-free condition where the inter-particle friction coefficient μ is set to be 0. When the sample reached equilibrium, the values of μ were set as 0.12, 0.18 and 0.20 for the samples of UC1, UC2 and UC3, respectively. The samples were then compressed under a confining pressure of 20 kPa. After this stage, the value of μ was increased to the assigned value, i.e., 0.32, for each sample, followed by an isotropic compression until the stress reached 100 kPa. As illustrated in Table 1, the void ratios were 0.745, 0.783 and 0.792 for the samples of UC1, UC2 and UC3, respectively before shearing. The samples were subjected to a strain-controlled undrained compression for shearing. Note that the undrained condition was simulated by applying boundary movements on the sample to make the sample volume maintain constant, which follows the same as the general practice.

In addition to those simulations of undrained compression tests, a simulation of a cyclic undrained triaxial test was conducted. The sample was identical to that used in UC1 after isotropic consolidation under a confining pressure of 100 kPa, and then the sample was subjected to a stress-controlled cyclic loading with the maximum deviatoric stress of 60 kPa. Note that both the values of the confining pressure after isotropic compression and the maximum deviatoric stress during cyclic loading were the same as those used in the experiment shown in Fig. 2. This test is denoted as UC1-cyclic in the following discussion.

3 SIMULATION RESULTS

3.1 Undrained compression tests

Fig. 3 presents the simulation results of the undrained compression tests, UC1, UC2 and UC3. Similar responses like the experimental findings (as shown in Fig. 1) are reproduced by the DEM simulations. To obtain the associated mechanisms from a micromechanical perspective, variations of the contact force distribution in terms of the mean and the coefficient of variation (COV) are examined in the following discussion.

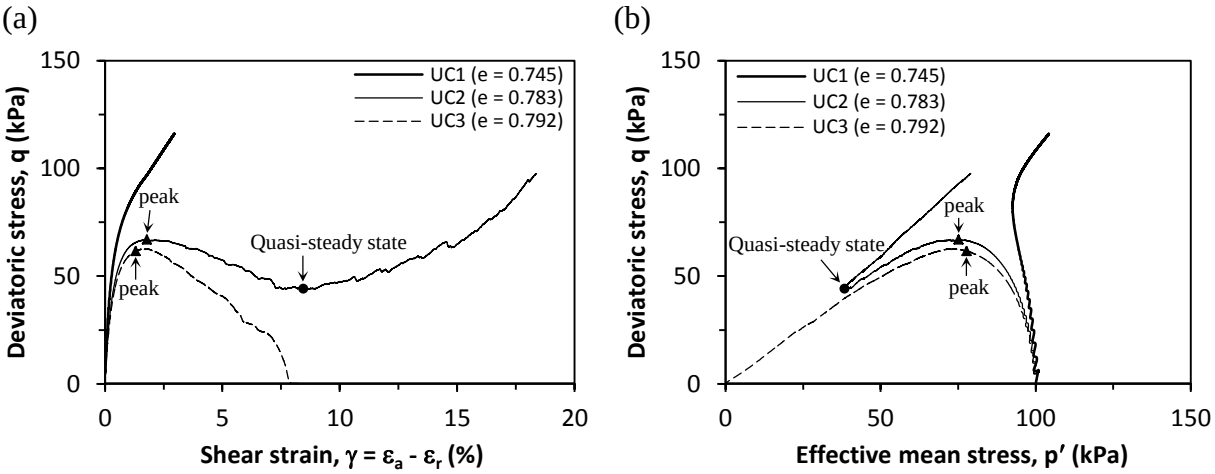


Figure 3: Simulation results of the undrained compression tests UC1, UC2 and UC3: (a) stress-strain responses and (b) stress paths.

Figs. 4a and 4b present variations of the mean and the COV of contact normal forces during the undrained compression tests, respectively. Fig. 7 presents the evolution of the mean value versus COV. Note that Fig. 7 summarizes the results from all the simulation cases and show that there are different trends of the mean versus COV for the samples with different void ratios. For loose sample UC3, the mean of contact forces decreases with increasing shear strain γ, while the associated COV increases with increasing γ. An interesting point is that these trends occur during both stages, i.e., before and after the peak state. This suggests that these trends, i.e., a decrease in the mean and an increase in the COV, are not influenced by the change of the deviatoric stress q with increasing γ.

For the medium dense sample UC2, the variations of the mean value and COV before the quasi-steady state are similar to those for UC1. Those trends of decreasing the mean value and increasing COV are also observed before the peak state and from the peak state to the quasi-steady state. However, after the steady state, the mean of contact normal forces increases with increasing γ, while COV decreases with increasing γ. This demonstrates that the contact nor-

mal forces become more and more uniform after the quasi-steady state. For the dense sample UC1, the initial responses are also showing a decrease in the mean and an increase in COV. However, the evolution trend of contact force distributions is different in the subsequent compression stage, which is found increasing in both the mean and the COV. Hence, the evolution type of the contact force distributions might be considered as the micromechanical basis for static liquefaction in loose sand.

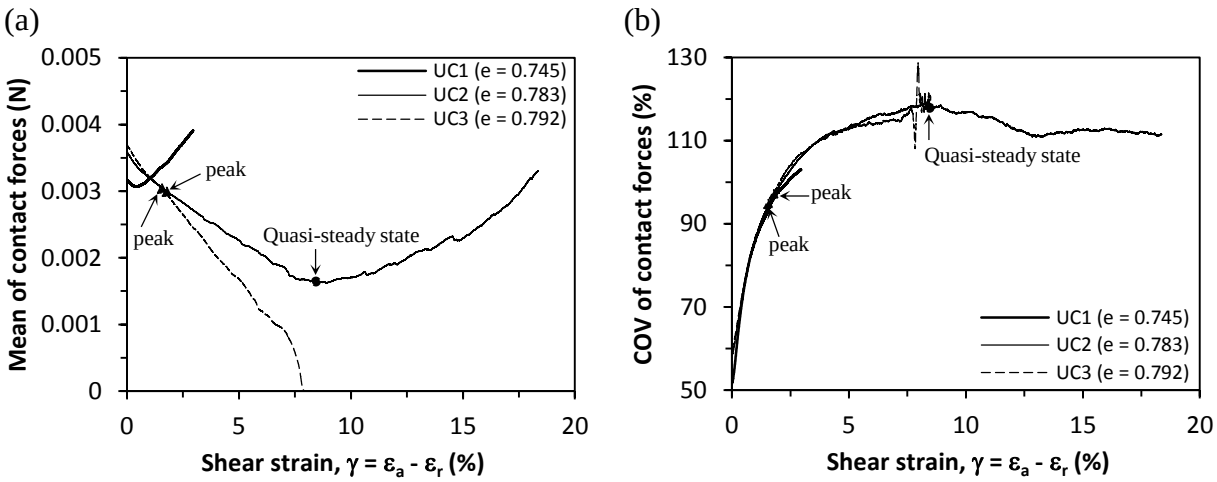


Figure 4: Variations of (a) the mean of contact normal forces and (b) the COV of contact normal forces during the undrained compression tests.

3.2 Cyclic undrained triaxial test

Fig. 5 presents the simulation results of the cyclic undrained triaxial test, UC1-cyclic. Once again, similar responses like the experimental findings (as shown in Fig. 2) are reproduced by the DEM simulations. Fig. 5b demonstrates that the soil reached the initial liquefaction state ($p' = q = 0$) at the 9th cycle. As shown in Fig. 5a, the values of the double amplitude axial strain (DA) for the cycles after the initial liquefaction, i.e., the 9th and 10th cycles, are much larger than the values of DA for the cycles before the initial liquefaction, i.e., from the 1st to

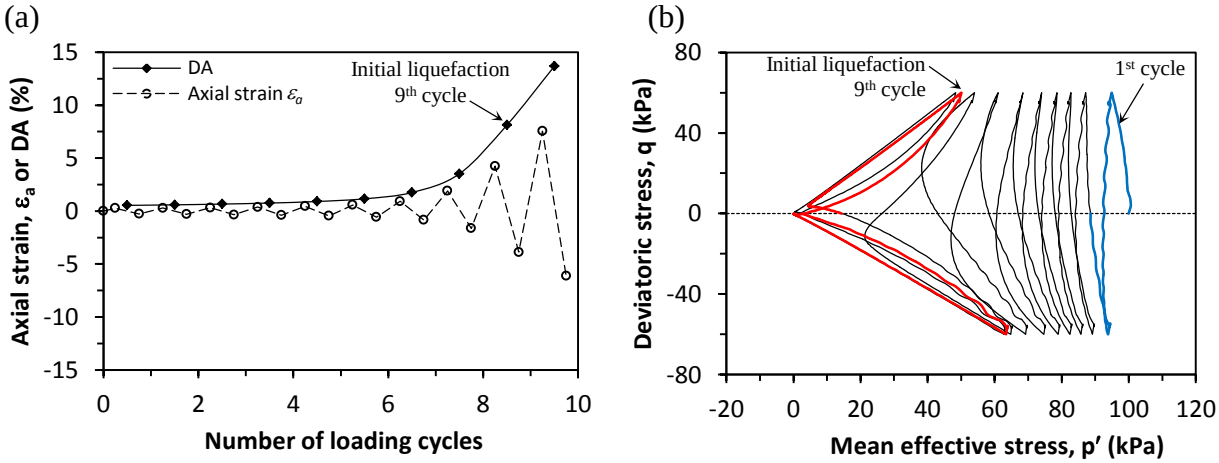


Figure 5: Simulation results of the cyclic undrained triaxial test UC1-cyclic: (a) variations of the axial strain ε_a and the double amplitude axial strain (DA) with the number of loading cycles and (b) stress paths. Note that only the minimum and maximum axial strains in a cycle are presented in Fig. 5a.

8th cycle. In the following discussion, variations of the mean and COV of all the contact normal forces are examined.

Figs. 6a and 6b present the variations of the mean and the COV of contact normal forces during the cyclic undrained triaxial test UC1-cyclic, respectively. For those loading cycles before initial liquefaction, there is a net decrease in the mean of contact normal forces and a net increase in the COV in each cycle, e.g., the 1st cycle. Hence, the overall trend for both the mean and the COV values at a given deviatoric stress q, e.g., q = 60 kPa, decreases in the mean and increases in the COV of contact normal forces. To facilitate the comparison between these results with those of the undrained compression tests, the mean versus the COV response of the test UC1-cyclic is also included in Fig. 7. As shown in Fig. 7, the mean versus COV response during the initial loading stage in the 1st cycle is identical to that during UC1. However, the mean versus COV response in the subsequent unloading process in UC1-cyclic does not follow the original trend as in the loading process. The overall trend of the mean versus COV response is characterized by a decreased mean and increased COV of contact normal forces, which is similar to the behavior of undrained compression for a loose sample, i.e., UC3. This suggests that this evolution type of contact force distribution can also be used to explain the initiation mechanisms of the liquefaction induced by cyclic loading from a micromechanical perspective.

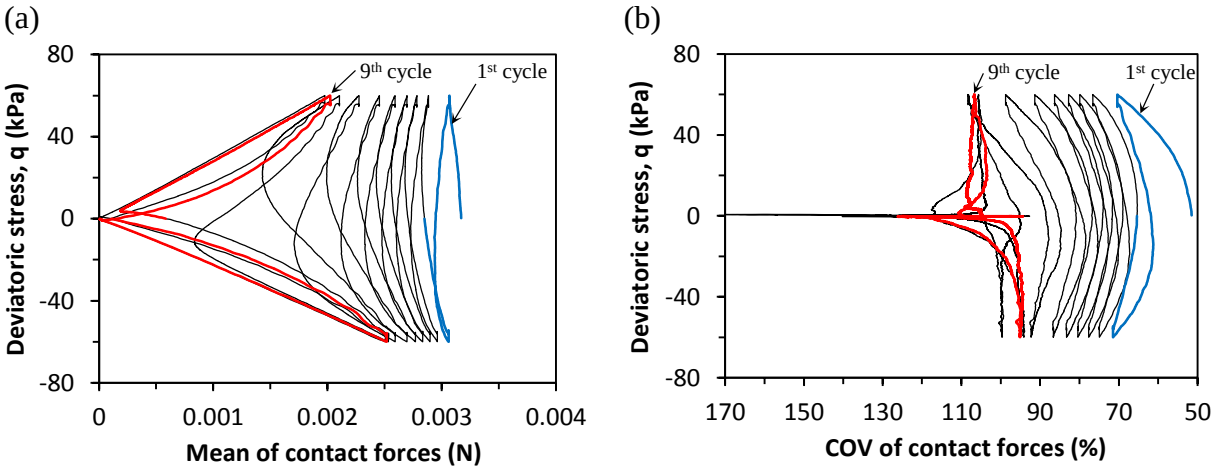


Figure 6: Variations of (a) the mean of contact normal forces and (b) the COV of contact normal forces during the cyclic undrained triaxial test.

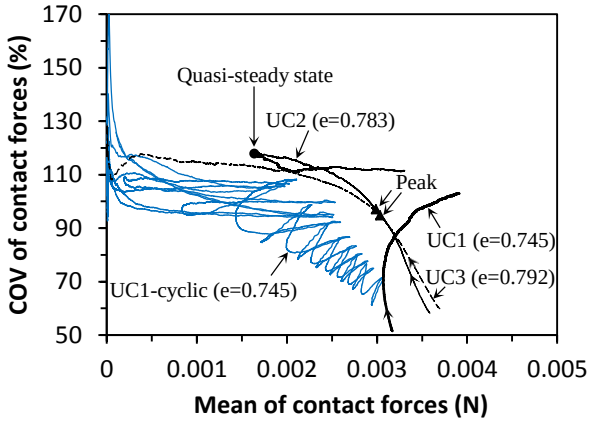


Figure 7: The mean versus the COV of contact forces responses for the undrained compression tests, i.e., UC1, UC2 and UC3, and the cyclic undrained triaxial test UC1-cyclic.

4 CONCLUSIONS

To examine the initiation mechanisms of static liquefaction and dynamic liquefaction induced by cyclic loading, a series of DEM simulations of undrained triaxial compression tests and a cyclic undrained triaxial test were carried out. The DEM simulation results can reproduce similar responses like the experimental findings, e.g., stress-strain responses and stress paths. Changes in the contact force distribution were examined in terms of mean and COV of contact normal forces. The salient findings are summarized as follows.

The mean versus COV response during undrained compression tests is influenced by the sample void ratio. For the loose sample, the evolution type is characterized by a continuous decrease in the mean value and a continuous increase in the COV as the shear strain increases. For the medium dense sample, the response before the quasi-steady state is similar to that observed in the loose sample, whereas the response after the quasi-steady state demonstrates an increase in the mean and a decrease in the COV. In addition, for the dense sample, the mean value initially decreases and then increases with increasing shear strain while the COV continuously increases with increasing shear strain. Hence, the evolution type characterized by a continuous decrease in the mean value and a continuous increase in the COV might be considered as the micromechanical basis for static liquefaction in loose sand. In fact, such an evolution type of mean versus COV can also be found in the DEM simulation of cyclic undrained triaxial test on a dense sample. That is, this evolution type of contact force distribution, i.e., a decrease in mean and an increase in COV, can serve as a basis to explain the initiation mechanisms of static and dynamic liquefaction from a micromechanical perspective.

ACKNOWLEDGEMENT

This research was supported by the Hong Kong Research Grants Council (HKUST9/CRF/09 and HKUST6/CRF/12R). The authors are grateful to the reviewers for their valuable comments.

REFERENCES

[1] J.A. Yamamuro, P.V. Lade, Static liquefaction of very loose sands. *Canadian Geotechnical Journal*, **34**, No. 6, 905-917, 1997.

[2] H.B. Seed, Soil liquefaction and cyclic mobility evaluation for level ground during earthquakes. *Journal of the Geotechnical Engineering Division*, **105**, No. 2, 201-255, 1979.

[3] S. Bhattacharya, A. Kappos, On the collapse of bridge foundations in liquefiable soils during earthquakes. In *2ed European Conference on Earthquake Engineering and Seismology*, Istanbul, August 25-29, 2014.

[4] K. Ishihara, Liquefaction and flow failure during earthquakes. *Géotechnique*, **43**, No. 3, 351-451, 1993.

[5] P.V. Lade, Creep effects on static and cyclic instability of granular soils. *Journal of Geotechnical Engineering*, **120**, No. 2, 404-419, 1994.

[6] T. Doanh, E. Ibraim, R. Matiotti, Undrained instability of very loose Hostun sand in triaxial compression and extension. Part 1: experimental observations. *Mechanics of Cohesive‐frictional Materials*, **2**, No. 1, 47-70, 1997.

[7] M. Yoshimine, K. Ishihara, Flow potential of sand during liquefaction. *Soils and Foundations*, **38**, No. 3, 189-198, 1998.

[8] M. Yoshimine, P.K. Robertson, C.E. Wride, Undrained shear strength of clean sands to trigger flow liquefaction. *Canadian Geotechnical Journal*, **36**, No. 5, 891-906, 1999.

[9] E. Ibraim, H. Di Benedetto, T. Doanh, Time-dependent behaviour and static liquefaction phenomenon of sand. *Geotechnical and Geological Engineering*, **27**, No. 1, 181-191, 2009.

[10] R. Verdugo, Characterization of sandy soil behavior under large deformation. Ph.D. thesis, University of Tokyo, 1992.

[11] K. Ishihara, H. Takatsu, Effects of overconsolidation and K_0 conditions on the liquefaction characteristics of sands. *Soils and Foundations*, **19**, No. 4, 59-68, 1979.

[12] Y. Yoshimi, K. Tokimatsu, Y. Hosaka, Evaluation of liquefaction resistance of clean sands based on high-quality undisturbed samples. *Soils and Foundations*, **29**, No. 1, 93-104, 1989.

[13] M.D. Evans, S. Zhou, Liquefaction behavior of sand-gravel composites. *Journal of Geotechnical Engineering*, **121**, No. 3, 287-298, 1995.

[14] D. Erten, M.H. Maher, Cyclic undrained behavior of silty sand. *Soil Dynamics and Earthquake Engineering*, **14**, No. 2, 115-123, 1995.

[15] T. Kokusho, T., Hara, R. Hiraoka, Undrained shear strength of granular soils with different particle gradations. *Journal of Geotechnical and Geoenvironmental Engineering*, **130**, No. 6, 621-629, 2004.

[16] V.N. Ghionna, D. Porcino, Liquefaction resistance of undisturbed and reconstituted samples of a natural coarse sand from undrained cyclic triaxial tests. *Journal of geotechnical and geoenvironmental engineering*, **132**, No. 2, 194-202, 2006.

[17] M.L. Taylor, M. Cubrinovski, B.A. Bradley, Cyclic strength of Christchurch sands with undisturbed samples. *New Zealand Society for Earthquake Engineering Annual Conference (NZSEE2013)*, Wellington, New Zealand, April 26-28, 2013.

[18] H.Y. Sze, J. Yang, Failure modes of sand in undrained cyclic loading: impact of sample preparation. *Journal of Geotechnical and Geoenvironmental Engineering*, **140**, No. 1, 152-169, 2013.

[19] T.T. Ng, R. Dobry, Numerical simulations of monotonic and cyclic loading of granular soil. *Journal of Geotechnical Engineering*, **120**, No. 2, 388-403, 1994.

[20] X. Li, Micro-scale investigation on the quasi-static behavior of granular material. 2006. Ph.D. thesis, Hong Kong University of Science and Technology.

[21] A. Soroush, B. Ferdowsi, Three dimensional discrete element modeling of granular media under cyclic constant volume loading: a micromechanical perspective. *Powder Technology*, **212**, No. 1, 1-16, 2011.

[22] G. Gong, P. Lin, Y. Qin, J. Wei, DEM simulation of liquefaction for granular media under undrained axisymmetric compression and plane strain conditions. *Acta Mechanica Solida Sinica*, **25**, No. 6, 562-570, 2012.

[23] G. Gong, X. Zha, C. Wan, A microscopic definition of liquefaction for sand. *Procedia Earth and Planetary Science*, **5**, 140-145. 2012.

[24] A. Dabeet, D. Wijewickreme, P. Byrne, Simulation of cyclic direct simple shear loading response of soils using discrete element modeling. In *15th World Conf. Earthquakes Eng.* Lisboa, 2012.

[25] M.R. Kuhn, H.E. Renken, A.D. Mixsell, S.L. Kramer, Investigation of Cyclic Liquefaction with Discrete Element Simulations. *Journal of Geotechnical and Geoenvironmental Engineering*, **140**, No. 12, 2014.

[26] A. Dabeet, D. Wijewickreme, P. Byrne, Application of discrete element modeling for simulation of cyclic direct simple shear response of granular materials. In *National Conference on Earthquake Engineering*, Anchorage, Alaska, July 21-25, 2014.

[27] J. Wei, G. Wang, Cyclic mobility and post-liquefaction behaviors of granular soils under cyclic loading: micromechanical perspectives. In *10th U.S. National Conference on Earthquake Engineering*, Anchorage, Alaska, July 21-25, 2014.

[28] Z. Zhang, Y.H. Wang, Three-dimensional DEM simulations on monotonic jacking in sand. Submitted to *Granular Matter*, 2015.

COMPDYN 2015
5th ECCOMAS Thematic Conference on
Computational Methods in Structural Dynamics and Earthquake Engineering
M. Papadrakakis, V. Papadopoulos, V. Plevris (eds.)
Crete Island, Greece, 25–27 May 2015

DAMAGE CHARACTERIZATION IN WAVEGUIDES WITH ULTRASONIC SHEAR WAVES

Dimitra V. Achillopoulou[1], Annamaria Pau[2], and Fabrizio Vestroni[3]

[1] Dipartimento di Ingegneria Strutturale e Geotecnica,
Universita' di Roma La Sapienza, via Eudossiana 18, 00185 Roma, Italia
e-mail: dimitra.achillopoulou@uniroma1.it

[2] Dipartimento di Ingegneria Strutturale e Geotecnica,
Universita' di Roma La Sapienza, via Gramsci 53, 00197 Roma, Italia
annamaria.pau@ uniroma1.it

[3] Dipartimento di Ingegneria Strutturale e Geotecnica
Universita' di Roma La Sapienza, via Eudossiana 18, 00185 Roma, Italia
vestroni@ uniroma1.it

Keywords: wave propagation, frp laminate, damage characterization, acoustic waveguides

Abstract. *Damage can be viewed as a continuum discontinuity. In order to identify and quantify damage, the present study investigates the dependence of reflection and transmission coefficients from a discontinuity in a waveguide using a finite element model. A parametric study of a fiber reinforced polymer laminate beam is presented with five different ratios of reduced cross-section with two different kinds of geometry: symmetric and asymmetric, in three discontinuity lengths. What is more, finite element results are compared with the corresponding results of a semi- analytical model based on the principle of reciprocity in elastodynamics. The analysis shows that: a) depending on the kind of discontinuity, the diagnostic potential of the used guided wave depends on the mode existence and on the magnitude of its wavelength in relation to the discontinuity extension, b) reflection and transmission coefficients can be used to identify and characterize damage both in symmetrical and asymmetrical damaged cross sections.*

1 INTRODUCTION

Guided wave propagation plays an important role in non-destructive tests and health monitoring of structures. Several applications to analyse different conditions, such as corrosion, state of prestress, defects, cracks, can be found in literature [1-3]. Such monitoring techniques are based on the fact that, in the presence of discontinuities, waves interact with cracks and voids [5-6]. The amplitude and shape of the resulting scattered field is related to the characteristics of the defect and may be used in an inverse problem to detect and characterize discontinuities themselves.

The current study deals with the characterization of the response of a waveguide with a discontinuity consisting in a double change of cross-section. Such a discontinuity conventionally represents a notch. A finite element simulation of the propagation of shear waves in a plate has been performed. Two different geometries for the discontinuity are considered, that is symmetric and asymmetric (one-sided). The asymmetric damage is the most common damage that exists in practice, therefore it is of high interest to investigate on the response of waveguides in this case. Three different damage lengths and five different percentages of cross section reduction are investigated. The results for the symmetric case have been compared to the analytical results of a semi-analytical model based on the principle of reciprocity in elastodynamics [7].

2 DESCRIPTION OF THE FE MODEL

The simulation was performed using a proper finite element software (Ansys) [8]. The specimens were chosen in order to simulate an FRP laminate (Table 1) used to rehabilitate long concrete bridge spans.

E modulus of Elasticity [MPa]	Density ρ [kg/m^3]	Poisson ratio v	Shear Wave Velocity c_s [m/s]
165000	1600	0.2	6555.5

Table 1: FRP mechanical properties

The laminate was modeled as a 3D solid using SOLID185 element which is defined by eight nodes having three degrees of freedom at each node. The solid used is a parallelepiped with height h=0.10 m, thickness s=0.003 m and length L=12 m with all the displacements restrained at one end. It is meshed allowing prism and tetrahedral degenerations of elements in irregular regions. A mesh of appropriate density was chosen in order to properly describe wave propagation. The symmetric and asymmetric discontinuities consist in a double change of cross section as shown in Figure 1, whose geometry is described through the parameters length (l_d) and height of reduced cross section (s_r).

The structure is excited with a force whose time-history is a high-frequency sine burst with frequency f=12000 Hz, applied at the free-end and acting along direction y. All the nodes are constrained according to directions x and z since pure shear waves are generated.

The investigated damage geometry (l_d, s_r) is described using the non-dimensional ratio λ/l_d, where λ is the wavelength of the shear wave propagating in the plate ($\lambda=c_p/f$), and $r = 1-s_r/s$ is a measure of notch magnitude ($r=0$ corresponds to no damage, r=1 to a fully cracked cross section). The ranges of values of λ and r used in the analysis are collected in Tables 2 and 3.

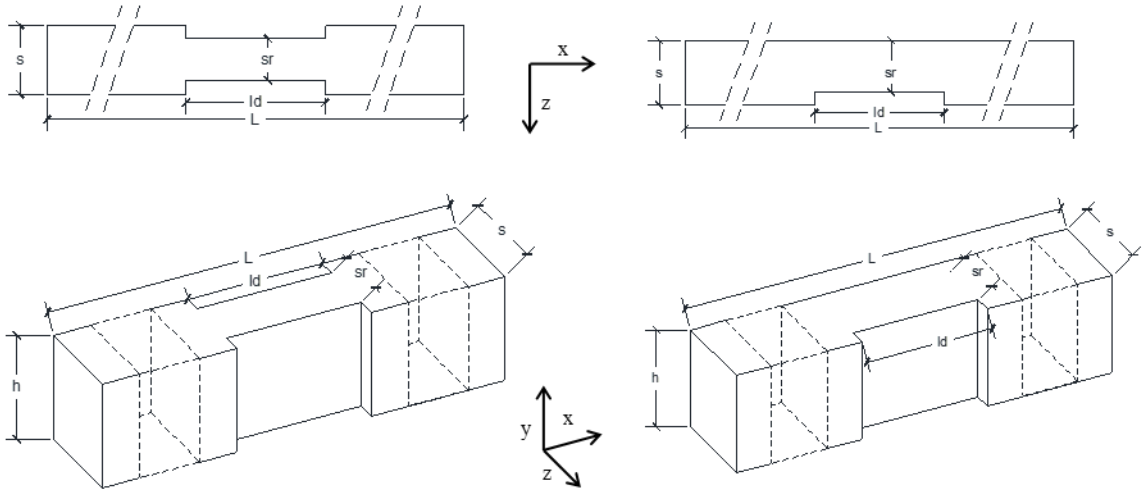


Figure 1: Discontinuities on FRP laminate specimens (m).

l_d [m]	1.09	0.55	0.27
λ/l_d	0.5	1	2

Table 2: Discontinuity length

s_r [m]	0.00249	0.00201	0.00150	0.00099	0.00051
r (%)	17	33	50	67	83

Table 3: Discontinuity thickness

3 RESULTS

The forcing function is applied at the free end of the laminate and acts in *y* direction. It generates an incident wave travelling along the waveguide and interacting with the cross-section reduction. At every geometric change, part of the wave is reflected and part is transmitted in a way which depends on the characteristics of the discontinuity.

The current study focuses on the investigation of transmissions and reflections as a function of damage geometry. The amplitude of the scattered field is extracted from the amplitude of the response of nodes located close to the discontinuity (1m before and after the starting/ending abscissa of the damaged area). Figure 2 sketches the way amplitudes were extracted. A describes the maximum amplitude of the incident wave, while A_t and A_r are the maximum amplitudes of the transmitted and reflected wave, respectively.

3.1 Reflections and Transmissions

The amplitude of the scattered fields is shown in Figures 3 and 4 for the symmetric and asymmetric case. The reported amplitudes of both transmitted and reflected wave are normalized to the value of the amplitude of the incident wave.

Figures 3 and 4 respectively show the amplitude of the transmitted and reflected fields, which varies as a function of r and of the ratio λ/l_d. In cases of deep damage (r close to 1) the transmitted amplitude (A_t/A) is reduced while the reflected (A_r/A) rises, meaning that in heavily damaged cross sections (r>83%) the wave cannot be fully transmitted and tends to be reflected. On the contrary, when r is small, the travelling wave is nearly entirely transmitted.

Speaking about the dependence of these coefficients from the ratio λ/l_d, as the wavelength λ of the incident wave becomes of the same order of magnitude of the damaged length or larger (Figure 3a, b, c and Figure 4a, b, c: λ/l_d=0.5, 1 or 2) the response tends to be more sensitive to the presence of the notch because the curves are less sharp than for higher values of λ/l_d [6]. This is due to the fact that the waves are reflected from the first and second change in cross-section and can interact in different ways, constructively or destructively. As shown in [6], to detect small damage, small wavelength are to be used. If the wavelength is large, the destructive interference hides the presence of discontinuities.

As far as the differences noted from the symmetric and asymmetric specimens are concerned, in cases of small λ/l_d ratio (0.5), meaning an extensive damage, the results coincide. The results tend to differentiate when the ratio λ/l_d increases, that is when the wavelength is large in relation to the damaged length. The maximum discrepency observed (12%) is for the transmission coefficient and λ/l_d= 2 (Figure 3c). Reflection coefficients do not present appreciable difference between the symmetric and asymmetric case.

The frequency used (12kHz) is actually too low to detect differences in response of the symmetric and asymmetric damaged cross-section. The difficulty in observing mode conversion due to the asymmetry of the cross-section strongly depends on the existence of shear modes at the frequency under investigation. As is shown in Figure 5, which reports the group velocity (c_G) as a function of frequency, at 12000 Hz only the first symmetric mode exists. In this way, differences between the symmetric and asummetric case are small.

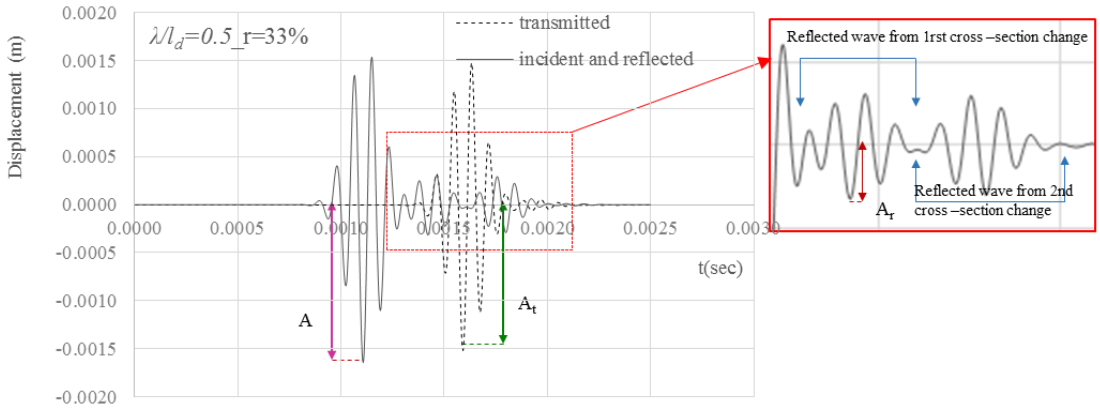


Figure 2: Sample time history

3.2 Comparison of SAFE and FEA

The results obtained from the FE model were compared with a semi-analytical finite element model (SAFE, [4]), where the scattered fields are studied exploiting the principle of reciprocity in elastodynamics (see ref. [7] for all details):

$$\int_{s_i}\left(\sigma_{ij}^{B}u_j^{A}-\sigma_{ij}^{A}u_j^{B}\right)n_i dS+\int_{s_0}\left(\sigma_{ij}^{B}u_j^{A}-\sigma_{ij}^{A}u_j^{B}\right)n_i dS=0 \tag{3}$$

where the superscript A refers to the response of a waveguide in the presence of a discontinuity and B to the waveguide response to a virtual wave propagating in the absence of the discontinuity. The reflected and transmitted fields in case A are expressed as a linear superposition of reflected and transmitted waves whose coefficients for the p-th wave A_r/A and A_t/A depend on

the *q*-th incident wave. The linear superposition is a series which theoretically should extend to all the modes existing at the given frequency, however, for the frequency chosen and the width of the specimens investigated it only the first symmetric shear wave mode exists. This is shown in Figure 5, therefore, only this mode is taken into account in the semi-analytical model.

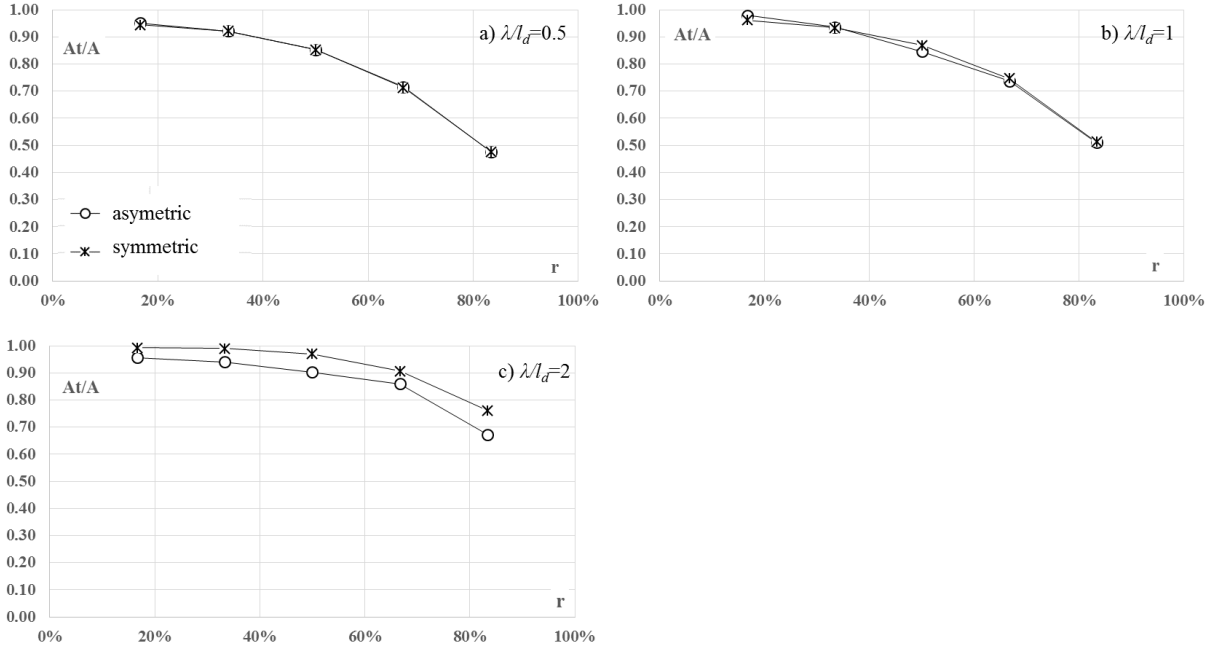


Figure 3: Transmission coefficients as a function of different ratios of cross section reduction for different damage lengths (FEA): a) λ/l_d=0.5, b) λ/l_d=1, c) λ/l_d=2

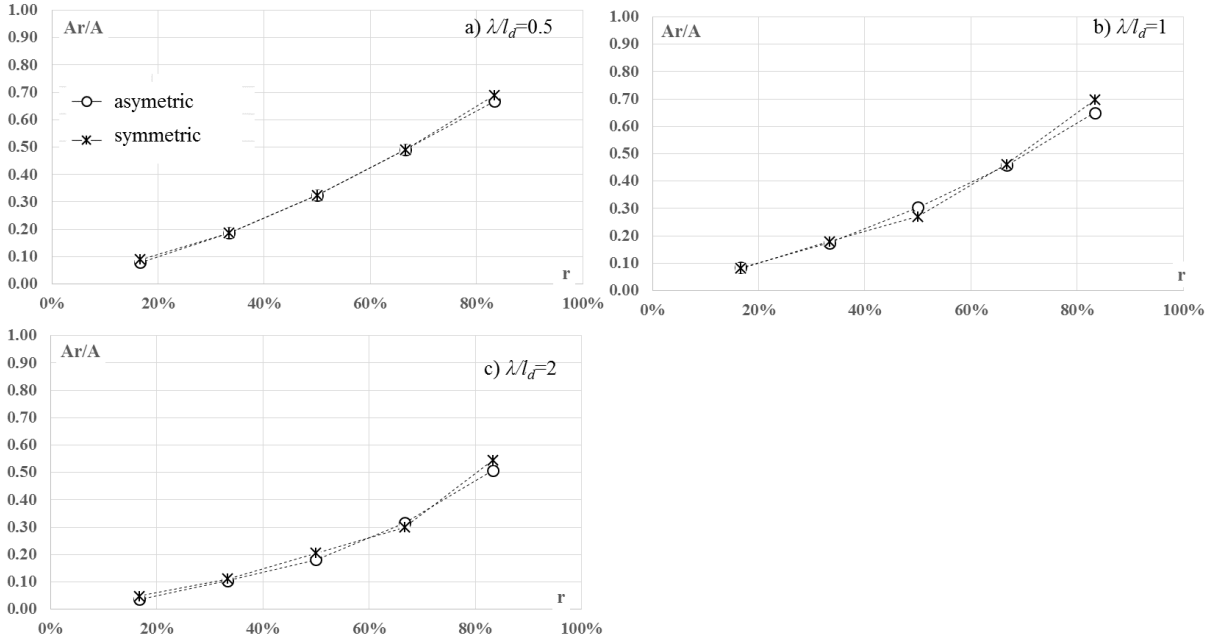


Figure 4: Reflection coefficients as a function of different ratios of cross section reduction for different damage lengths (FEA): a) λ/l_d=0.5, b) λ/l_d=1, c) λ/l_d=2

A comparison between the scattering coefficients obtained from the principle of reciprocity and from the FE analysis is reported in Figure 6 for the symmetric case only. The difference between the values varies as a function of cross section reduction (r) and in general is greater for the transmitted coefficient than for the reflected.

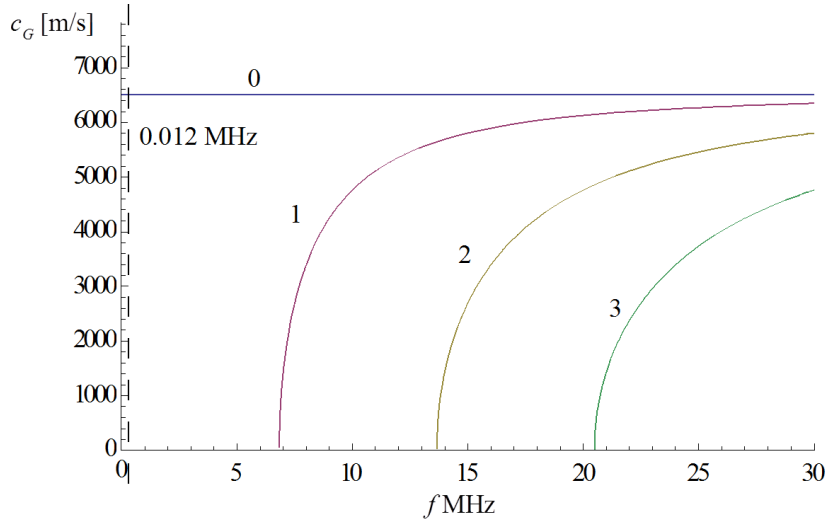


Figure 5: Phase velocity c_G as a function of frequency f.

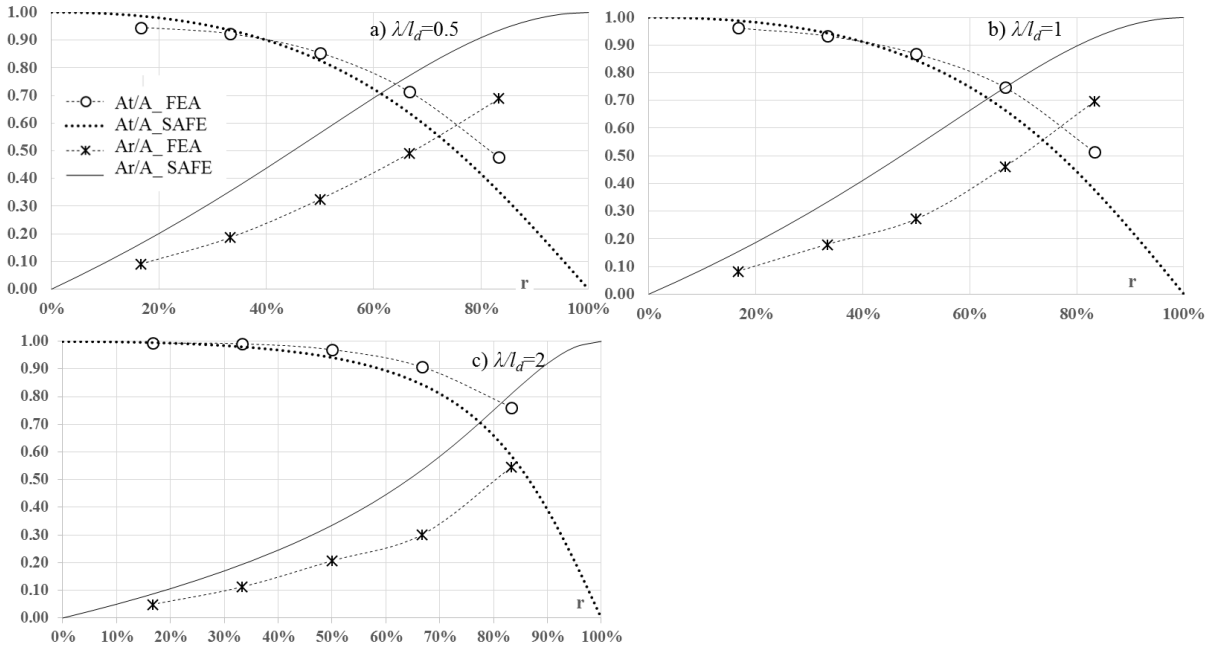


Figure 6: Comparison of reflection and transmission coefficients in SAFE and FEA model.

These differences are due to the fact that part of the energy in the FEA is lost due to numerical damping. This is shown in Figure 7 which reports the quantity $\left((A_r/A)^2+(A_t/A)^2\right)^{1/2}$ which is a measure of the conservation of energy. Data are reported for all the cases under study both for FEA and SAFE results. While SAFE model always provides a unit value, for FEA the values are always smaller. In order to investigate the loss of energy, an undamaged FE model

was considered. The ratio between kinetic energies of the response measured at the points 1 and 2, where A_r (l_d-1) and A_t (l_d+1) were extracted, was calculated as

$$\int_0^T v_2^2 dt / \int_0^T v_1^2 dt$$

for the ratio λ/l_d =1 only, providing 0.95. This value confirms that in the FE model a certain amount of energy loss occurs.

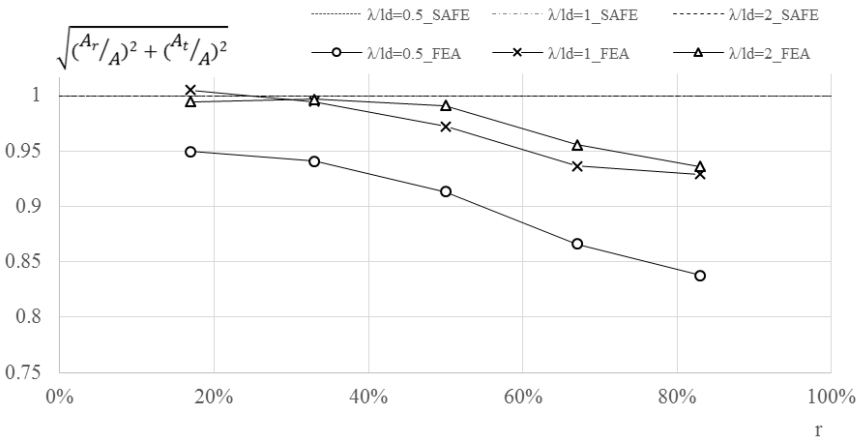


Figure 7: Energy conservation curves.

4 CONCLUSIONS

The current study focuses on the characterization of the scattered field from discontinuities in plates by observing the shear wave response. Two different kinds of discontinuities are examined, that is symmetrical and asymmetrical change of cross-section. The results of a FE model were compared with those of a semi-analytical model. For five different cross section reductions and three damage lengths (l_d), the amplitude of transmitted and reflected waves was observed. It is noted that the scattered field depends on the severity of damage which makes it a suitable quantity do be used in an inverse problem, provided that waves with wavelength of the same order of magnitude in respect to the extension of damage are used. The differences reported in both scenarios of symmetric and asymmetric damaged cross sections are small especially in cases with extended damage. The use of high frequencies is suggested in cases of asymmetric damage, as higher wave modes enable to more precisely detect the presence of asymmetries in the cross-section. The SAFE results are in acceptable agreement with the FEA results of the symmetric scenario, making such method appropriate to be applied even in more complex cases. It is also observed that the FE model exhibits lacks in conservation of energy due to numerical damping that varies as a function of the reduction of the cross- section.

REFERENCES

[1] Schoefs F., Abraham O., Popovics J.S., Quantitative evaluation of contactless impact echo for non-destructive assessment of void detection within tendon ducts, *Construction and Building Materials* (2012), 37, pp. 885-892.

[2] Rose J.L., Pilarski A., Ditri J.J. Approach to guided wave mode selection for inspection of laminated plate, *Journal of Reinforced Plastics and Composites* (1993), 12 (5), pp. 536-544.

[3] Park S., Ahmad S., Yun C.-B., Roh, Y., Multiple crack detection of concrete structures using impedance-based structural health monitoring techniques, *Experimental Mechanics* (2006), 46 (5), pp. 609-618.

[4] Marzani A., Viola E., Bartoli I., Lanza di Scalea F., Rizzo P., A semi-analytical finite element formulation for modeling stress wave propagation in axisymmetric damped waveguides, *Journal of Sound and Vibration* (2008), 318 (3), pp. 488-505.

[5] Rose J.L., *Ultrasonic Guided Waves in Solid Media*, Cambridge University Press, (2014).

[6] Pau A., Vestroni F., Wave propagation in one-dimensional axial waveguides for damage characterization, *Journal of Intelligent Material Systems and Structures* (2011), 22 (16), pp. 1869-1877.

[7] Pau A., Capecchi D., Vestroni F., Reciprocity principle for scattered fields from discontinuities in waveguides, *Ultrasonics* (2015), 55, pp. 85-91.

[8] Ansys Tutorials, 2014

COMPDYN 2015
5th ECCOMAS Thematic Conference on
Computational Methods in Structural Dynamics and Earthquake Engineering
M. Papadrakakis, V. Papadopoulos, V. Plevris (eds.)
Crete Island, Greece, 25–27 May 2015

APPLICATION OF NEW DAMAGE INDICATOR-BASED SEQUENTIAL LAW TO ESTIMATE FATIGUE LIFE OF OFFSHORE JACKET STRUCTURES

Redion Kajolli[1], Sudath C.Siriwardane[2], and Ove T. Gudmestad[3]

[1] Wood Group Kenny Norge AS, Løkkeveien 99, 4008 Stavanger, Norway
Redion.Kajolli@woodgroupkenny.com

[2] Department of Structural, Mechanical Engineering and Material Science, University of Stavanger, Norway.

[3] Department of Structural, Mechanical Engineering and Material Science, University of Stavanger, Norway.

Keywords: Fatigue life, Wave-structure interaction, Time-history dynamic analysis, Offshore jacket structure.

Abstract. *The most of current fatigue life estimation methods of offshore jacket structures are based on Miner's rule. Miner's rule has always been acknowledged as a simplification that is easy to use in design where detailed loading history is unknown. However, under random amplitude loading, Miner´s rule might provide incorrect results because of its omission of the loading sequence effect. Recently, a new damage indicator- based sequential law has been proposed to capture the loading sequence effect more precisely than the Miner's rule. As offshore steel structures are subjected to variable amplitude loading and the state of the art methodology available allows us to measure or predict the detailed loading history, it is advisable to utilize the new damage indicator- based sequential law for offshore steel structures. Therefore, the objective of this study is to propose a sequential law employed new approach to estimate fatigue life of offshore steel jacket structures. The proposed approach consists mainly of the predicted stress histories, the recently developed sequential law and a technique for transferring the partially known S-N curve to a full range curve. Then the proposed approach is applied to predict fatigue life of an offshore jacket structure as a case study. The case study consists of 3D-modeling of a jacket platform, wave-structure interaction modeling, FEM-employed dynamic time history analysis, hot spot stress analysis, a technique for obtaining the full range S-N curve and fatigue life estimation based on the newly proposed sequential law. Finally, the proposed and the conventional approach´s predicted fatigue lives are compared to confirm the significance of the new approach.*

1 INTRODUCTION

The demand for exploration and production of oil and gas has grown ever since the early offshore activities began in the North Sea in the 1960's. The first steel structures to operate in the North Sea were transferred from the Gulf of Mexico, where exploration and production activities had been on going since the 1930's. Shortly after, it became clear that these structures were not adequate when operating in more severe weather conditions such as in the North Sea [1]. Early examples of fatigue damage are found in the "Sedco 135" triangular semi-submersible drilling rigs operating in the North Sea, as well as the jack-up drilling rig "Ranger 1" and the infamous "Alexander L. Kielland" platform – capsizing in March of 1980, leading to the loss of 212 personnel. Though the detail and quality of the fatigue design have improved since 1975, a significant amount of effort has been directed towards the development of structural health monitoring and non-destructive assessment methods of offshore steel structures in order to keep up with the gradual deterioration of strength due to crack growth, with the goal of applying design, inspection, maintenance and repair measures – thus ensuring adequate safety, as well as profitability with respect to using the same structures for further exploiting of the oil fields [2,3]. Therefore, it is essential highlighting the importance of understanding the deficiencies of currently available approaches, in order to progress and propose precise models to prevent similar kinds of future failures and even take measures for life extension.

The approach for fatigue design and fatigue assessment currently available is based on a combination of response data found by using the specific loading case (i.e. stress analysis and stress spectrum), material data describing the fatigue strength based on code provided S-N curves and a failure criteria which is based on the assumption of a cumulative damage commonly expressed by the Palmgren-Miner hypothesis (Miner`s rule). Further, if a crack is detected or the previous loading history is not known, fatigue strength is commonly based on fracture mechanics analysis (FMA). It is thus safe to say that the Palmgren-Miner rule has and still is accepted as the damage criteria for fatigue life estimation of offshore steel structures, and is acknowledged as an approved approximation that is easy to use in fatigue design where the detailed loading history (loading sequence) is unknown. However, research shows that under random amplitude loading, Miner´s rule might provide incorrect results because of its inability to precisely capture the loading sequence effect. Similarly, offshore steel structures are subjected to variable amplitude loading and the state of the art methodology available allows us to measure the detailed loading history to some extent. Recently, a new damage indicator- based sequential law has been proposed to capture the loading sequence more precisely [4]. The application of this model has not been studied for offshore steel structures. This is the question of concern in this paper.

Therefore, the objective of this study is to propose a sequential law employed new approach to estimate fatigue life of offshore steel structures. The proposed approach consists mainly of the predicted stress histories, the recently developed sequential law and a technique for transferring the partially known S-N curve to a full range S-N curve. Further, verification of the proposed approach is conducted by comparing the sequential law predicted damage behavior and corresponding fatigue life against the experimentally measured fatigue life and damage behavior of some materials respectively.

First, the paper presents the proposed approach for fatigue life estimation. Then verification of the proposed approach is presented by comparing experimental fatigue lives against theoretical predictions. Further, the proposed approach is applied to estimate the fatigue life of an offshore steel jacket structure and obtained fatigue life estimations are compared with

the estimations obtained by the conventional theory of the Palmgren-Miner hypothesis. Finally the significance and applicability of the proposed approach is discussed.

2 PROPOSED APPROACH

This section presents the new proposed approach for fatigue life estimation of offshore steel structures. First, the general structural appraisal is presented before introducing the technique for obtaining the full range S-N curve, and the newly proposed damage indicator sequential law.

2.1 Wave-structure interaction and stress history evaluation

The following section presents the method for estimating the wave loads acting on the jacket legs, through the application of linear wave theory – where the final goal is determination of hot spot stress history of tubular joints.

Hydrodynamic loads are obtained on the basis of hydrostatics, hydrodynamics and linear wave theory, which is the core theory of ocean surface waves used in ocean and coastal engineering. This is the simplest wave theory, where wave height is considered to be much smaller than both the wave length and the water depth, and takes advantage of the linearized boundary conditions, where waves are considered as regular waves with sinusoidal shape, propagating with a permanent form. Linear wave theory is approved when assessing long period waves generated from distant storms (swell sea) [5]. Each wave has a distinct wavelength **λ**, wave period **T**, and wave height **H**. Application of linear wave theory requires that the following conditions be fulfilled:

- Continuity of mass – the net mass flow into an element equals the mass increase of the element.
- Based on the constant density of the fluid, the fluid is labeled incompressible.
- Another physical principle when assessing hydrodynamics is considering the water to be an ideal fluid where no shear forces occur between the particles (in other terms, consider the fluid to have a frictionless flow). Based on the assumption of non-rotational flow, the rotation of a water particle around its COG should be equal to zero.

Given that these conditions are present, a potential function **φ** exist such that the partial derivatives of this function with respect to the directions (x, y and z), give the velocities in each direction. If such a function exists, it is referred to as the velocity potential. Applying a set of boundary conditions set from physical principles (i.e. bottom condition, wall condition, kinematic surface condition and dynamical boundary condition), we are able to define the velocity potential as expressed in Eq. 1.

$$\varphi(x,z,t) = \frac{\xi_0 g \cosh k(z+d)}{\omega \quad \cosh(kd)} \cos(\omega t - kx) \tag{1}$$

Further, all types of offshore structures other than large floating bodies consist of slender cylinders – where a slender cylinder is defined as a cylinder of such geometry, which allows the diameter to be small in comparison with the wavelength (i.e. legs and braces of an offshore structure, subsea pipelines, umbilical cables etc.) Wave and current induced loads on slender members can be obtained from the Morrison`s load formula – consisting of an inertia force proportional to acceleration and a drag force proportional to the square of velocity [5]. The total force acting on the entire cylinder is as given as:

$$F(t) = F_1(t) + F_D(t) = \int_{-d}^{\xi} f_I(z,t)dz + \int_{-d}^{\xi} f_D(z,t)dz \tag{2}$$

where

$$f_I = \rho.(1 + C_A).A.\dot{u}$$

$$f_D = \frac{1}{2}.\rho.C_D.A.u.|u|$$

where C_A and C_D are the mass- and drag coefficients respectively. These hydrodynamic coefficients are based on experimental data and the relation between these coefficients and the governing parameters are as follows:

$$C_A = C_A(R_{e,}K_c, \Delta)$$

$$C_D = C_D(R_{e,}K_c, \Delta)$$

The drag term obtained from the Morrison´s load formula is quadratic and 90° out of phase with respect to the inertia term. One tries to avoid using the complete Morrison equation unless it is absolutely necessary. A simple way of doing this is by studying the Keulegan-Carpenter (K_c), which is a very important parameter for determining the relative importance of drag versus inertia forces for the case under consideration. Based on this one can determine whether the drag or inertia force is negligible, whether the drag force can be linearized, or whether one must use the full Morrison`s equation with its nonlinear drag.

In general, given the linear wave theory extrapolation and its corresponding assumptions, it is further assumed that the wave-induced motions are of the harmonic nature as well, and can be expressed by a sinusoidal function as in Eq. 3.

$$u(t) = u_o \sin(\omega t) \tag{3}$$

In general, it follows that the dynamic equilibrium equation for a fixed structural member can be written as:

$$\begin{gathered} m\ddot{r} + c\dot{r} + kr = F(t) \\ m\ddot{r} + c\dot{r} + kr = F_I(t) + \frac{1}{2}.\rho.C_D.D.\Delta I.u_0^2.sin\omega t.|sin\omega t| \end{gathered} \tag{4}$$

Notice that the drag term is neither proportional to the wave amplitude, nor harmonic. Linearization is required given a situation where the drag term can`t be neglected. Previous research shows that linearization can be given by a constant $\frac{8}{3\pi}$ times an unknown parameter A [6,7]:

$$\begin{gathered} u_w(t) = u_a cos\omega t \\ A = \sqrt{(u_a - \omega.r_2)^2 + \omega^2.r_1^2} \end{gathered} \tag{5}$$

Where u_a is the amplitude of a regular wave`s velocity function, and r_1 and r_2 are the sine and cosine response components, respectively. It follows that for a system with small response amplitudes, the damping term from the drag forces can be neglected ($r_1 = r_1 = 0$ and $= u_a$. This gives the following linearized dynamic equilibrium equation:

$$m\ddot{r} + c\dot{r} + kr = F_I(t) + \frac{1}{2}.\rho.C_D.D.\Delta I.\frac{8}{3\pi}.u_a^2.cos\omega t \tag{6}$$

Should the structural response amplitude become significant, one shall take account for the relative velocity between the structural member and the water.

A finite element employed time history analysis is conducted with the goal of obtaining the nominal stress histories of the most critical members. Wave loads described by time history functions are utilized as input load time history. Fatigue analysis based on S-N data is typically related to a nominal- or hot spot stress approach. When assessing other types of structural details (i.e. welding details), the nominal stress range should be modified in order to take account for the local conditions affecting the stresses at a specific location. The local stress at this location is expressed by a stress concentration factor multiplied with the nominal stress (Eq. 7). It is most common that the stress concentration factor results into an amplification of

the nominal stress. However, there are cases where a stress concentration factor less than 1 can validly exist.

$$\sigma_{local} = SCF.\sigma_{nominal} \tag{7}$$

Stress concentration factors for different frame elements and the different loading conditions are to be calculated in reference with recommended practice [8], where a huge variety of equations are presented – defining stress concentration factors for different types of joints under different loading conditions.

Further, nominal stress history output is used for calculating and identifying the hot spot stress at the crown and saddle points. Furthermore, the hot spot of each structural component is to be calculated around the circumference of the intersection (Fig. 2), where the highest value obtained defines the hot spot. Further analysis and fatigue life estimation of the structural component is based on the corresponding hot spot. Fatigue life estimations of the tubular members, which are to be presented in Section 4 are based on T-curves with cathodic protection.

The hot spot of the chord member is to be assessed at three different locations (i.e. brace-chord intersections with the left hand side brace, middle brace and the right hand side brace – as sketched in Fig. 1). This means that when assessing the chord, one ends up with having to evaluate the stresses at eight different points (as shown in Fig. 2), for each of the three intersection locations (Fig. 1) – where the highest value obtained identifies the hot spot for the chord. Else, when assessing each brace, one only looks at the specific brace-chord intersection place of the corresponding brace. Note that each "stress point" represents its unique stress-history function.

2.2 Fully known S-N curve

S-N curves are in general obtained from fatigue tests of specimen mainly subjected to axial and bending loads. The basic design S-N curve can hence be expressed as follows.

$$\log N = log\bar{a} - mlog\Delta\sigma \tag{8}$$

However, the regular S-N curve only describes the stress ranges corresponding only to tens of thousands of failure cycles (i.e. only describes the high cycle fatigue region), hence they are often labeled as partially known S-N curves [9]. Extending the partially known S-N curve to a full range curve is therefore of the essence when assessing fatigue based on the damage-indicator based sequential law. The method for this transformation is mainly based on Kohout and Vechet Wöhler curve modeling technique [10]. A schematic overview of this technique is presented in Fig. 3.

Where the horizontal line 1 along the ultimate tensile strength is the asymptote $s = s_u$ for the low cycle fatigue region. The horizontal line 2 represents the stress range for the high cycle fatigue region (where $s = s_{¥}$), while line 3 represents the tangent for the region of finite life described by equation (or curve) of the partially known S-N curve provided by the design code. Location B and C show the intersection points of the tangent line 3 with the horizontal lines 1 and 2. The full range curve is at any given point expressed by the following expression [9, 10].

$$\sigma = \sigma_{\infty}\left(\frac{N+B}{N+C}\right)^{b} \tag{9}$$

where *b* is the slope of the tangent.

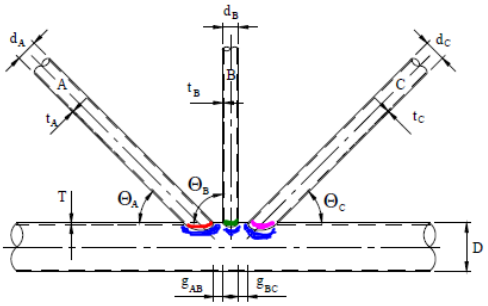


Fig. 1:Arbitrary KT-joint [8]

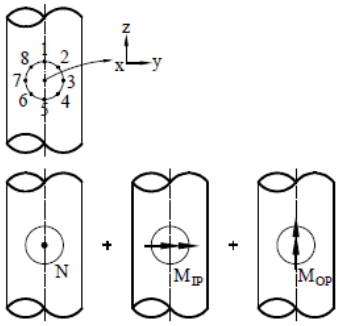


Fig. 2: Hot spot around the circumference of the intersection [8]

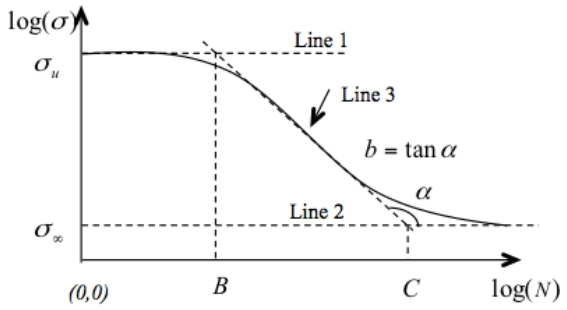


Fig. 3: Schematic presentation of the full range S-N curve modeling technique

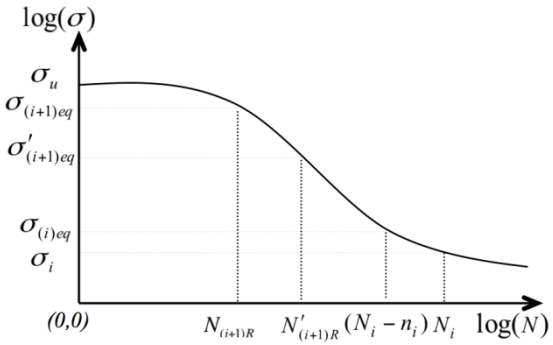


Fig. 5: Schematic representation of the sequential law parameters versus the S-N curve

2.3 Damage indicator based-sequential law

The modern day technology allows us to measure the loading history on most of the existing civil structures, whether they are onshore or at sea. The sequential law provides an algorithm for properly assessing the fatigue cumulative model – especially under variable loading conditions, and was developed for the purpose of capturing the loading sequence effect more precisely [4,10].

A new damage indicator based sequential law is used to obtain more realistic fatigue life estimation of offshore steel structures. The sequential law provides an algorithm for properly assessing the fatigue cumulative model – especially under variable loading conditions [4]. The supposition of this fatigue criterion is that if the physical state of damage is the same – then fatigue life depend on the loading condition only..

A detailed description of the damage stress model and the definition of damage indicator, D_i, is described in the corresponding paper [9], [10]. Here within, only the concept is summarized with an algorithm for comprehension (see flow chart presentation in Fig. 4). Suppose a structural component is subjected to an arbitrary stress amplitude or stress range s_i for n_i number of cycles at load level i, where N_i denotes the fatigue life corresponding to s_i. The residual fatigue life at load level i is obtained from N_i - n_i. The equivalent stress amplitude or stress range corresponding to the residual fatigue life is denoted $s_{(i)eq}$, and is equal to s_i for the first cycle.

Further, the new damage indicator, D_i, is then expressed by Eq. 10. It also follows that the damage indicator is equal to zero at the first cycle given the fact that $s_{(i)eq} = s_i$ at the first cycle.

$$D_i = \frac{\sigma_{(i)eq} - \sigma_i}{\sigma_u - \sigma_i} \tag{10}$$

Where s_u is defined by the intercept of the S-N curve with the ordinate at one-quarter of the first fatigue cycle [9,10]. Furthermore, s_u is also commonly known as the ultimate tensile

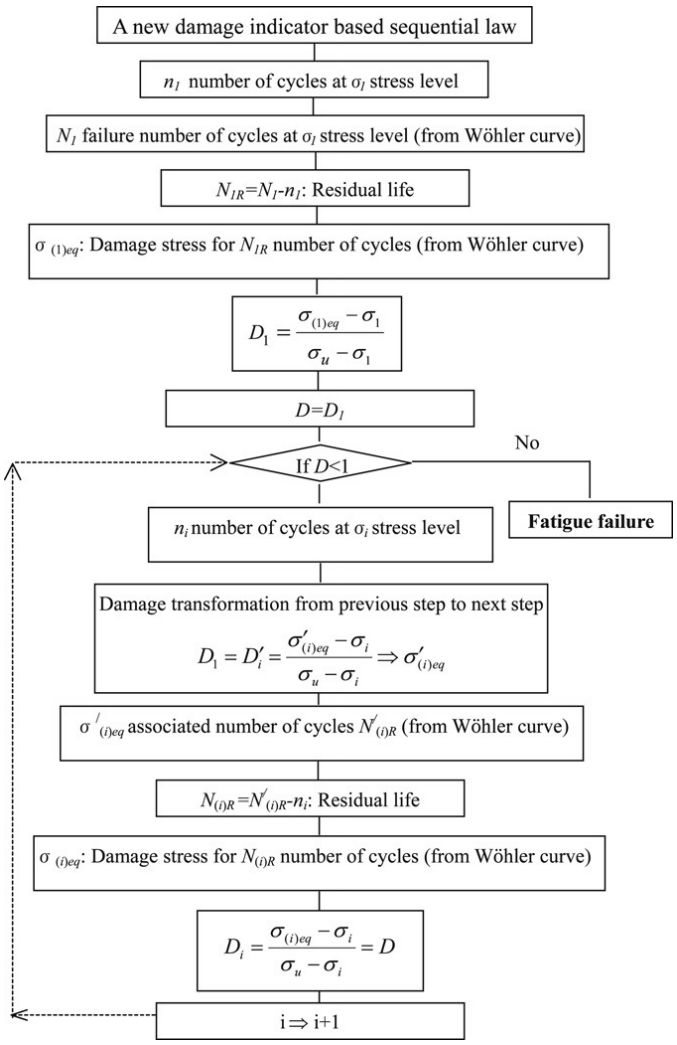


Fig. 4: Flow chart for the damage indicator based sequential law

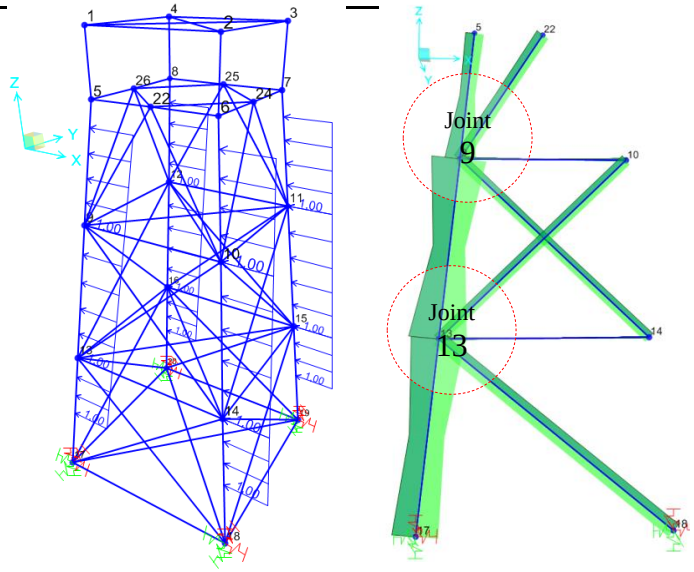


Fig. 6: Unidirectional wave loading and envelope stresses

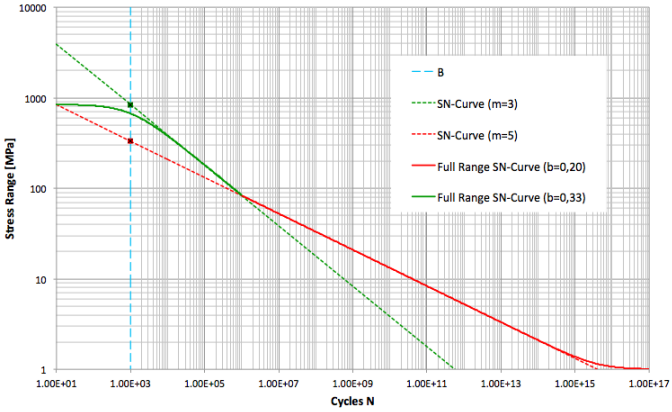


Fig. 7: Full range T-curve

strength amplitude or range for rotating bending test-based S-N curves, and it is the ultimate shear strength amplitude or range for torsional fatigue test-based S-N curves.

The same damage indicator D_i is further transformed to the next level, $i+1$, and the damage equivalent stress at the very same level is derived from the mathematical relation in Eq. 11.

$$D_i=\frac{\sigma_{(i)eq}-\sigma_i}{\sigma_u-\sigma_i}=\frac{\sigma'_{(i+1)eq}-\sigma_{i+1}}{\sigma_u-\sigma_{i+1}} \tag{11}$$

Further simplifications gives,

$$\sigma'_{(i+1)eq}=D_i(\sigma_u-\sigma_{i+1})+\sigma_{i+1} \tag{12}$$

Where $s'_{(i+1)eq}$ is the damage equivalent stress at load level $i+1$ and the corresponding number of cycles to failure is denoted $N'_{(i+1)R}$. Applying an arbitrary stress amplitude or stress range $s_{(i+1)}$ at the level $i+1$ for $n_{(i+1)}$ number of cycles, gives a corresponding residual life as follows.

$$N_{(i+1)R}=N'_{(i+1)R}-n_{(i+1)} \tag{13}$$

The damage stress amplitude or stress range $s_{(i+1)eq}$ corresponding to $N_{(i+1)R}$ at load level $i+1$, is then obtained from the schematic presentation of the S-N curve in Fig. 3. Furthermore, the cumulative damage at the very same load level is defined as,

$$D_{(i+1)} = \frac{\sigma_{(i+1)eq} - \sigma_{i+1}}{\sigma_u - \sigma_{i+1}} \tag{14}$$

Similarly, the same procedure is followed until D_i is equal to one, where at this point $s_{(i)eq}$ becomes equal to the ultimate tensile strength stress amplitude s_u.

3 CASE STUDY

3.1 Considered jacket structure

A previous report on stochastic fatigue analysis of jacket type offshore structures is the case under consideration [11]. All structural elements of the jacket platform are modeled as tubular beam elements of steel grade S355. The main dimensions of the steel jacket are 27m x 27m x 62.5m in the global x-, y-, and z-direction respectively. The cross-sectional diameters and thicknesses are as defined in Table 1. The total mass of the deck is assumed to be 4.8·106 kg [11] and is distributed to the deck plane connections as point loads. The foundation plane is consisting of four connections modeled as flexible springs of the linear elastic nature. Spring properties are presented in Table 2. Further, the principles of the design of the steel jacket are in reference with NORSOK-N004.

3.2 Wave load modeling

The idea is to simulate different waves, obtain the corresponding hydrodynamic loads based on the theory presented in section 2.1.1 and assign these loads to the jacket model. The wave simulation is based on a scatter diagram for the Northern North Sea (1973-2001)[12], which gives a description of the sea state, the probability of the occurrence usually expressed in the number of observations during a period of time and the expected energy corresponding to each sea state [6]. Three different wave heights are chose in reference with the previously mentioned scatter diagram (Table 3), and are assumed to be consecutively generating during the course of one day. Further, for short-term wave conditions, the sea state is in general assumed to be stationary for an interval of 20 minutes up to 3- or 6- hours [5, 6]. Hence, each sea state is in this case assumed to be stationary for 3 hours and the wave loads acting on the platform legs are to be calculated from the maximum wave height . Having obtained the wave loads for each sea state, we are able to extrapolate and plot time-history functions. The time-history functions are extrapolated for a 24-hour period, making these functions valid for one single day. Further, it is assumed that the structure will have this loading history throughout its service life. Meaning that we now have a simplified simulation of three waves of different wave heights, being generated consecutively after one another during the course of one single day.

3.3 Finite element analysis

A comprehensive, state-of-the art FEM software for the design and analysis of civil structures (SAP2000) is used for static design- and dynamic time history analysis of the structure. In order to ensure adequate static design, several verification steps are taken, amongst them:

- A design-check of the structure is performed in order to ensure that no member exceeds the capacity given by the design code.
- Verification that all steel frames pass the stress-capacity ratio.

Table 3: Cross-sectional data of the frame elements [11]

Members	Diameter [m]	Thickness [mm]
Deck legs	2.0	50.0
Jacket legs	1.2	16.0
Braces in the vertical plane	1.2	16.0
Braces in the horizontal plane		
Elevation: +5m	0.8	8.0
-10m	1.2	14.0
-30m	1.2	14.0
-30m (diagonals)	1.2	16.0
-50m	1.2	14.0

Table 2: Spring properties [11]

Horizontal stiffness	$1.2 \cdot 10^5\ kN/m$
Vertical stiffness	$1.0 \cdot 10^6\ kN/m$
Rotational stiffness	$1.2 \cdot 10^6\ kNm/rad$

Table 3: Most observed wave heights and the corresponding peak periods [12]

H_s [m]	t_p [s]
1.5	9
2.0	9
2.5	9

Furthermore, a dynamic time-history analysis gives the stress distribution of each frame element, allowing us to identify the two most critical connections, which are singled in Fig. 13, and are used as reference points. Nominal stresses due to axial load, in-plane and out-of-plane bending moment for each frame element are plotted as time-history functions. These functions are used as reference points when determining the stress concentration factors for each structural component in each connection, and are reference points for hot spot stress history evaluation.

4 FATIGUE LIFE ESTIMATION

4.1 Fatigue life estimation based on the conventional approach

The failure criteria when estimating fatigue life on the basis of the conventional theory of a linear cumulative damage is commonly expressed by the Palmgren-Miner hypothesis and a fatigue design factor [8].

$$D = \sum_{i=1}^{k} \frac{n_i}{N_i} = \frac{1}{a} \sum_{i=1}^{k_b} n_i \,.\, (\Delta\sigma_i)^m \leq \frac{1}{FDF} \tag{15}$$

where

k_b – number of stress blocks

FDF – fatigue design factor

Classification of the fatigue design factor is depending on the significance of the structural component, with emphasis being put on structural integrity and availability for inspection (or repair). First and foremost, one has to determine whether failure of the structural component will lead to danger of loss of human lives, environmental pollution and whether there are financial consequences. Both NORSOK and Det Norske Veritas provide clear guidelines for assessing this matter.

Fatigue assessment is based on the deterministic method, which is often considered to be a simplification of the spectral method. The deterministic approach is applicable when there is a linear relation between wave loads and the structural response due to these loads. Results of the fatigue life estimation until crack initiation are presented in the following tables.

Results show that the chord governs the fatigue life of each joint. Hence, the chord in joint 9 will govern the fatigue life of the whole jacket platform – with a fatigue life of 17 years. Fatigue life estimations are based on fatigue design factors of 1 and 3. The "real" fatigue of the chord will be somewhere between these two parameters. Note that the there is a linear relation between the results obtained from the Palmgren-Miner theory.

Table 7: Fatigue life estimation of joint 9

			Fatigue Life in Years	
	Element No.	Member	FDF=1	FDF=3
Joint 9	32	Chord	50	17
	63	Brace A	∞	∞
	13	Brace B	∞	∞
	56	Brace C	∞	315
			Where members labeled ∞, are not subjected to fatigue.	

Table 7: Fatigue life estimation of joint 13

			Fatigue Life in Years	
	Element No.	Member	FDF=1	FDF=3
Joint 13	32	Chord	90	30
	55	Brace A	∞	∞
	19	Brace B	∞	∞
	48	Brace C	∞	369
			Where members labeled ∞, are not subjected to fatigue.	

Table 7: Fatigue life estimation of joint 9 based on the damage indicator sequential law

			Fatigue Life in Years	
	Element No.	Member	FDF=1	FDF=3
Joint 9	32	Chord	41	13
	63	Brace A	NA	NA
	13	Brace B	NA	NA
	56	Brace C	NA	261

Table 7: Fatigue life estimation of joint 13 based on the damage indicator sequential law

			Fatigue Life in Years	
	Element No.	Member	FDF=1	FDF=3
Joint 13	32	Chord	74	24
	55	Brace A	NA	NA
	19	Brace B	NA	NA
	48	Brace C	NA	306

4.2 Full range T-curve in sea water with cathodic protection

A technique for defining the full range S-N curve was presented in the previous section. However, fatigue assessment of tubular members is to be based on T-curves. The design code T-curve provided by DNV-RP-C203 consists of two different curve slopes. A point in question is how to obtain the full range T-curve. A proposed approach is presented in section 3. First and foremost, the design code given T-curve stretches along the green dotted line all the way to the intersection with the red curve. It then stretches along the red curve all the way to interception point $s_{¥}=1$. The intersection between the green and red curve represents change in the negative inverse slope of the T-curve. The red curve represents the full range of a T-curve with tangent slope $b=0.20$. The green curve represents the full range of a T-curve with tangent slope $b=0.33$. Both full range curves are obtained from Eq. 9.

A proposed approach is to base the fatigue assessment on the red colour curve. This is because stress history evaluation shows that the stress ranges for each structural component are in the high cycle region. Further, the stress ranges for each structural component are in the region where $m=5$ ($Ds \leq \approx 83MPa$). However, the fatigue testing data of the specimen and the application of the full range technique would allow us to plot a more accurate full range curve.

The full range T-curve presented in section 3 is the basis for the sequential law fatigue life estimations.

4.3 Fatigue life estimation based on the proposed approach

The proposed fatigue approach for uniaxial fatigue is utilized to predict the fatigue life until crack initiation. Fatigue life estimations in this section consist of huge numerical iterations of the sequential law (2.3), and the associated full range S-N curve. The structural components that were proven to not be subjected to fatigue in Section 4.1 are not attended in this section. Results obtained are presented in Table 6 and 7.

Results show that the chord in joint 9, with a fatigue life of 13 years (for a FDF of 3) remains the governing member both from a local, and global point of view. Further, it is observed that there no longer is a linear relation between the fatigue life where FDF is equal to 1 versus the fatigue life for the case consisting of a FDF of 3. Furthermore, it is observed that for the case where the FDF is three, results show a reduction of ca. 24% from the Miner`s prediction (consisting of the same FDF).

Results presented in Table 7 show that the chord remains the governing member with respect to local assessment of joint 13. However, joint 9 governs the fatigue life of the jacket structure. Outputs from the damage indicator based sequential law and the associated full range S-N curve show a reduction of each structural member somewhere in the range of 17-24% (depending from one member to another). Even though results show significant deviation, one should point out that verification results presented in Fig. 12 show cases where the deviations are of significantly higher amounts.

5 CONCLUSIONS

A new damage indicator based sequential law employed new approach was proposed to estimate fatigue life of offshore steel structures. A verification of the new damage model was conducted by comparing the theoretically predicted damage and fatigue life with experimentally observed damage and fatigue life respectively. The proposed approach was further utilized to estimate the fatigue life of offshore jacket structure as a case study.

The experimental verification reveals that the proposed approach, which consists of a new damage indicator and a fully known S-N curve modeling technique, provides a more realistic fatigue life than the Miner's employed conventional approach. Wave-structure interaction was reasonably modeled based on linear wave theory and the Morrison's load formula. Definition of the sea state was based on a scatter diagram valid for the North Sea. The FEM- employed time history analysis was conducted to obtain the nominal stress histories of all legs/chords and braces. Then hot spot stress histories of critical tubular joints were obtained by SCF's given in DNV-RP-C203. The DNV-RP-C203 code provided S-N curve of tubular joint was transferred to a full range S-N curve by applying the proposed technique. Then new damage indicator based sequential law was applied to estimate the fatigue lives of the identified critical joints. The fatigue lives were also estimated by employing Miner's conventional approach. Comparisons of these fatigue lives show a ≈17-24% deviation. This deviation of the remaining fatigue lives highlights the necessity of a proper fatigue theory, which describes the loading sequence effect precisely, and the importance of a reasonably accurate approach to predict the stress histories. Designing for 20 years of lifetime, a difference of ~25% in fatigue life estimation in either direction (~25% less or more), results in a significant amount of years.

Finally, these observations tend to conclude that the application of the damage indicator-based sequential law is advisable for the evaluation of fatigue lives of offshore jacket structures. Further verification and comparison between different case studies is recommended for

future studies in order to ensure the precision of the proposed approach. Future case studies will be based on more realistic wave measurements and their corresponding sequence.

REFERENCES

[1] Almar-Næss, A., 1985, "Fatigue Handbook – Offshore Steel Structures"

[2] Vårdal, O.T., Moan, T., Hellevig, N.C., 1999, "Comparison Between Observed and Predicted Characteristics of Fatigue Cracks in North Sea Jackets", Offshore Technology Conference

[3] Moan, T., 2007, "Fatigue Reliability of Marine Structures, from the Alexander Kielland Accident to Life Cycle Assessment", International Journal of Offshore and Polar Engineering, Vol. 17, pp.1-21

[4] Mesmacque, G., Garcia, S., Amrouche, A., Rubio-Gonzalez. C., 2005, "Sequential Law in Multiaxial Fatigue, A New Damage Indicator", International Journal of Fatigue, 27(4), pp-461-467

[5] Det Norske Veritas, 2010, "DNV-RP-C205: Environmental Conditions and Environmental Loads"

[6] Larsen, C.M., 2005, "Notes for Special Topics: Dynamic Analysis of Marine Structures", Norwegian University of Science and Technology

[7] Gudmestad, O.T., Connor, J.J., 1983, "Linearization Methods and the Influence of Current on the Nonlinear Hydrodynamic Force", Applied Ocean Research Vol. 5 No. 4

[8] Det Norske Veritas, 2012, "DNV-RP-C203: Fatigue design of Offshore Steen Structures"

[9] Siriwardane, S.A.S.C., Ohga, M., Dissanayake, P.B.R., Kaita, T., 2010, "Structural Appraisal-Based Different Approach to Estimate the Remaining Fatigue Life of Railway Bridges", Structural Health Monitoring: an International Journal, 9(4), 323-339.

[10] Siriwardane, S.A.S.C., Ohga, M., Dissanayake, P.B.R., Kaita, T., 2009, "Remaining Fatigue Life Estimation of Existing Railway Bridges", Railway Transportation: Policies, Technology and Perspectives, (Book Chapter), pp.181-216.

[11] Sigurdsson, G., 1988, "Stochastic Fatigue Analysis of Jacket Type Offshore Structures", ISSN 0902-7513 R8828

[12] Chakrabarti, S.K., 2005, "Handbook of Offshore Engineering Volume 1".

COMPDYN 2015

Proceedings of the
5th International Conference on
Computational Methods in Structural Dynamics and Earthquake Engineering

M. Papadrakakis, V. Papadopoulos, V. Plevris (Eds)

First Edition, September 2015

ISBN: 978-960-99994-7-2



Institute of Structural Analysis and Antiseismic Research
National Technical University of Athens, Greece